

# Free radicals formed by H(Mu) addition to fluoranthene

Jean-Claude Brodovitch, Brenda Addison-Jones, Khashayar Ghandi, Iain McKenzie, Paul W. Percival, and Joachim Schüth

**Abstract:** Muonium has been used as an H atom analogue to investigate the free radicals formed by H addition to the polyaromatic hydrocarbon fluoranthene. There are nine unique carbons in the molecule, but only five radicals were detected. Muon and proton hyperfine constants were determined by transverse field  $\mu$ SR and  $\mu$ LCR, respectively, and compared with calculated values. All signals were assigned to radicals formed by Mu addition to C-H sites. There is no evidence for addition to the tertiary carbons at ring junctions.

**Key words:** muonium, fluoranthene, free radical, hyperfine constants.

**Résumé :** Les radicaux libres formés par addition de l'atome d'hydrogène à la molécule aromatique du fluoranthène ont été étudiés en utilisant le muonium comme analogue de l'atome d'hydrogène. Il y a neuf carbones non-équivalents présents dans la molécule, toutefois, seulement cinq radicaux libres ont été détectés. Les constantes hyperfines du muon et de certains des protons ont pu être déterminées par spectroscopies  $\mu$ SR et  $\mu$ LCR et les valeurs obtenues ont été comparées à des valeurs calculées. Tous les signaux observés ont pu être attribués aux radicaux libres formés par l'addition de Mu aux carbones portant le groupe C-H; l'addition de Mu aux carbones tertiaires qui joignent les cycles aromatiques ne se fait pas.

**Mots clés :** muonium, fluoranthène, radicaux libres, constantes hyperfines.

## Introduction

One of the interesting questions raised in the past decade of research on fullerenes is how reactivity to radical attack is influenced by curvature of a carbon skeleton (1–3). Consider the addition of a single H atom or other small radical to  $C_{60}$  and to  $C_{70}$ . In the former case there is only one possible radical product, since all carbons are identical. In contrast, the ellipsoidal  $C_{70}$  has five chemically inequivalent sets of carbon atoms, and therefore five distinct radicals could be formed. Of these, the least reactive is the carbon at the “equator” where the curvature is least. Since high reactivity is associated with release of strain energy at a site of high curvature (1), it follows that planar carbon sites would be least reactive.

To test the reactivity of “flat” polyaromatic hydrocarbons (PAHs) we investigated Mu or H atom addition to pyrene, whose carbon skeleton can be considered a fragment of  $C_{70}$  (4). Three radicals were identified, but all are formed by Mu addition to secondary carbons at the edge of the molecule, in the same way that cyclohexadienyl is formed by H or Mu

addition to benzene. No evidence was found for addition at the tertiary carbon sites that most resemble those of a fullerene.

The present study is an extension of our investigation to fluoranthene (Fig. 1). Although the PAH itself is planar, its carbon skeleton is a common fragment of fullerenes where isolated five-membered rings are surrounded by 6-rings. Since this feature introduces curvature to a fullerene, its presence might promote radical addition at ring junctions in PAHs.

As far as we know there is no literature data on mono-hydrofluoranthene radicals.

## Muon spin rotation and muon level-crossing resonance experiments

Experiments were performed at the M20 muon beam line of the TRIUMF cyclotron facility in Vancouver, BC. The sample was pure fluoranthene sealed oxygen-free in a stainless steel vessel fitted with a thin steel foil window. Its temperature was maintained at  $\approx 117^\circ\text{C}$  (above the melting point of fluoranthene) by passing fluid from a constant temperature bath (set at  $120^\circ\text{C}$ ) through the sample mount, which was surrounded by vacuum. A liquid sample was needed to ensure sharp spectral features by averaging anisotropic hyperfine parameters. The alternative to a neat liquid is to use a solution, as in the previous study (4), but this generally leads to less intense radical signals, as a fraction of the incident muons end up in the solvent.

Transverse field muon spin rotation ( $\mu$ SR) and muon (avoided) level-crossing resonance (LCR) spectra were accumulated over a period of several days. Apart from the higher

Received 18 October 2002. Published on the NRC Research Press Web site at <http://canjchem.nrc.ca> on 14 January 2003.

J.-C. Brodovitch, B. Addison-Jones, K. Ghandi, I. McKenzie, P.W. Percival,<sup>1</sup> and J. Schüth.<sup>2</sup> Department of Chemistry and TRIUMF, Simon Fraser University, Burnaby, BC V5A 1S6, Canada.

<sup>1</sup>Corresponding author (e-mail: [percival@sfu.ca](mailto:percival@sfu.ca)).

<sup>2</sup>Present address: debis Systemhaus Information Security Services GmbH, Rabinstrasse 8, 53111 Bonn, Germany.



**Fig. 1.** The fluoranthene molecule and the IUPAC numbering system used in this paper.

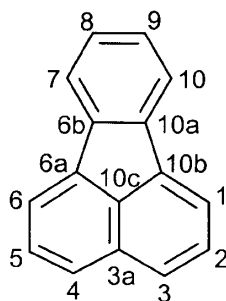
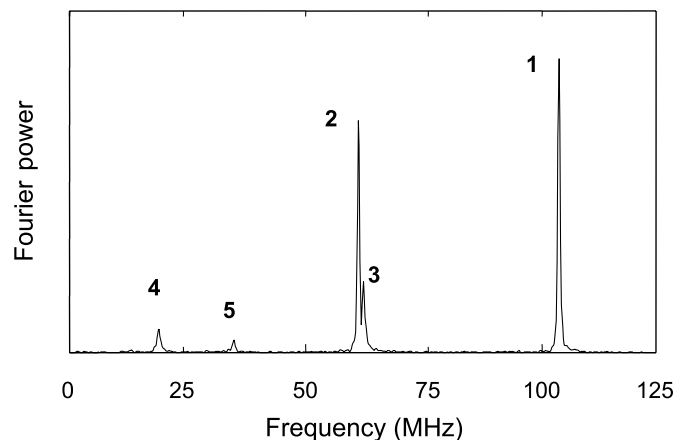


**Fig. 2.** Part of the Fourier power  $\mu$ SR spectrum from liquid fluoranthene at 118°C in an applied magnetic field of 17.34 kG. The peaks labeled 1–5 are due to free radicals formed by Mu addition to different sites in the fluoranthene molecule.



temperature, the apparatus and measurement procedures were as described previously (4). Spin-polarized positive muons (4 MeV) were extracted from the beam line and stopped in the sample, which was mounted in the HELIOS  $\mu$ SR spectrometer whose magnetic field was aligned along the beam direction. Transverse muon polarization was used for the  $\mu$ SR measurements and longitudinal polarization for LCR, with the positron counters arranged accordingly (4). Figure 2 shows an example of a  $\mu$ SR spectrum at a fixed magnetic field, 17.34 kG. The LCR spectrum displayed in Fig. 3 is a composite of many individual runs over different field ranges. Repeated runs were needed to achieve acceptable signal-to-noise for the weakest signals.

The signals of five radicals are evident in the transverse field  $\mu$ SR spectra; two of them are almost degenerate (close to 60 MHz in Fig. 2). Although each radical gives rise to a pair of muon precession frequencies ( $\nu_{R1}$  and  $\nu_{R2}$ ; see eq. [1] below), only the lower frequency signals are visible in the range displayed in Fig. 2. (Their higher frequency partners are less intense, mainly because of the limited time resolution of the apparatus.) Measurements at different magnetic fields confirmed the assignment of the signals to muoniated radicals. Their muon hyperfine constants ( $A_\mu$ ) were calculated from theoretical expressions for the precession frequencies (4, 5)

**Fig. 3.** Muon level-crossing resonance spectrum from liquid fluoranthene at 117°C.

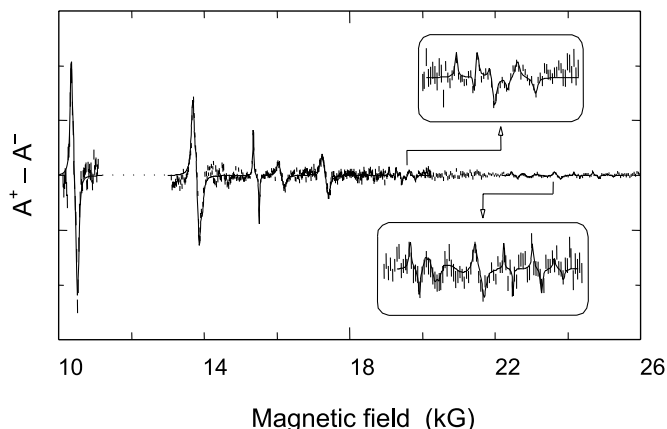


**Table 1.** Measured muon hyperfine constants for the five observed Mu-fluoranthenyl radicals and their relative abundance derived from  $\mu$ SR signal amplitudes.<sup>a</sup>

Radical	$A_\mu$ (MHz)	Abundance (%)
1	263.87(1)	35.8(7)
2	348.95(2)	26.8(7)
3	347.35(3)	14.2(7)
4	434.86(5)	13.7(6)
5	402.25(6)	9.5(1.1)

<sup>a</sup>Statistical uncertainties are shown in parentheses.

$$[1] \quad \nu_{R1} = \nu_{\text{mid}} - \frac{1}{2} A_\mu \quad \text{and} \quad \nu_{R2} = \nu_{\text{mid}} + \frac{1}{2} A_\mu$$

where

$$[2] \quad \nu_{\text{mid}} = \frac{1}{2} \left[ \sqrt{A_\mu^2 + (\nu_e + \nu_\mu)^2} - \nu_e + \nu_\mu \right]$$

and  $\nu_e$  and  $\nu_\mu$  are the electron and muon Larmor frequencies.

The results are summarized in Table 1, which also lists the relative abundances of the five radicals as determined from the signal amplitudes. In principle, nine different radicals could be formed by Mu addition to fluoranthene, since there are nine unique carbons (1, 2, 3, 7, 8, 10a, 10b, 10c, and 3a; all but the last two are doubly degenerate; see Fig. 1). Assignment of the  $\mu$ SR signals to specific radical structures is not possible without further information, so at this stage they are simply labeled 1–5 in decreasing order of intensity.

Interpretation of the LCR spectrum (Fig. 3) is more complicated. Each of the five radicals detected by  $\mu$ SR will also have hyperfine interactions between the unpaired electron and the protons in the molecule. Since fluoranthene has ten protons, each muoniated radical could potentially give rise to ten LCR resonances, with the signals from different radicals distributed in overlapping field regions. In practice only the largest proton couplings are likely to give detectable signals, and the LCR signals will also be scaled by the radical abundances (Table 1). Up to 17 resonances can be distinguished in Fig. 3. Their differential-like shape is a result of square-wave modulation of a small component of the ap-



**Table 2.** Fitted parameters of muon level-crossing resonances detected for Mu-fluoranthenyl radicals.

Field (kG)	Width (G)	Relative amplitude
10.434(1)	38(2)	1.00
13.771(1)	53(2)	0.60(2)
13.867(3)	42(5)	0.18(2)
15.4272(5)	15.4(7)	0.38(1)
16.120(4)	57(7)	0.11(8)
17.325(5)	70(14)	0.18(2)
19.161(2)	13(3)	0.067(8)
19.349(2)	20(4)	0.077(8)
19.466(4)	17(8)	0.033(8)
19.721(4)	24(6)	0.042(6)
22.819(34)	45(19)	0.013(7)
23.717(7)	46(14)	0.03(4)
24.246(6)	11(8)	0.03(2)
24.771(7)	24(11)	0.026(8)

plied magnetic field, which is used to suppress some of the baseline fluctuations (4). The resonances were fitted with a Lorentzian line shape; the fit parameters for the strongest 14 are gathered in Table 2. The few extra features that could not be fitted with physically meaningful parameters are barely above the noise and were ignored in the final analysis.

For protons, the resonance field is given by (4,5)

$$[3] \quad B_{\text{LCR}} \approx \frac{1}{2} \left[ \frac{A_{\mu} - A_{\text{p}}}{\gamma_{\mu} - \gamma_{\text{p}}} - \frac{A_{\mu} + A_{\text{p}}}{\gamma_{\text{e}}} \right]$$

where  $A_{\text{p}}$  is the proton hyperfine constant (hfc) and  $\gamma_{\mu}$ ,  $\gamma_{\text{p}}$ , and  $\gamma_{\text{e}}$  are the magnetogyric ratio of the muon, proton, and electron, respectively. In addition, the width and the amplitude of a resonance are given by

$$[4] \quad \text{Width} = \frac{1}{2} \frac{\sqrt{\omega_{\text{LCR}}^2 + \lambda_{\text{eff}}^2}}{\pi(\gamma_{\mu} - \gamma_{\text{p}})}$$

$$[5] \quad \text{Amplitude} \propto \frac{\omega_{\text{LCR}}^2}{\omega_{\text{LCR}}^2 + \lambda_{\text{eff}}^2}$$

where  $\omega_{\text{LCR}}$  is the frequency at resonance and  $\lambda_{\text{eff}}$  the effective relaxation rate (muon decay rate plus any additional relaxation contribution),

$$[6] \quad \omega_{\text{LCR}} = \frac{\sqrt{c\pi A_{\mu} A_{\text{p}}}}{\gamma_{\text{e}} B_{\text{LCR}}}$$

and  $c$  is the number of magnetically equivalent protons at resonance.

Clearly, to calculate the hyperfine constant of a particular proton from its resonance field position ( $B_{\text{LCR}}$ ) it is necessary to know the value of the muon hfc ( $A_{\mu}$ ) for that particular radical. Thus, the first step in assigning the LCR resonances is to deduce which resonances correspond to which  $A_{\mu}$  values. Our experience interpreting the LCR spectrum of muoniated pyrenyl isomers was beneficial, and following the procedure described in ref. (4) we identified five resonances due to the  $-\text{CHMu}-$  group. As indicated in

**Table 3.** Assignment of muon level-crossing resonances due to methylene ( $-\text{CHMu}-$ ) groups in Mu-fluoranthenyl radicals.

Field (kG)	Assignment	$A_{\mu}$ (MHz)	$A_{\text{p}}$ (MHz)	$(A_{\mu}/A_{\text{p}})/3.183$
10.434(1)	<b>1</b>	263.87(1)	68.81(2)	1.20
13.771(1)	<b>2</b>	348.95(2)	91.50(3)	1.20
13.867(3)	<b>3</b>	347.35(3)	88.13(6)	1.24
16.120(4)	<b>5</b>	434.86(5)	111.01(10)	1.23
17.325(5)	<b>4</b>	402.25(6)	100.93(9)	1.25

**Table 4.** Relative energies of formation and muon hfcs calculated for the nine possible fluoranthenyl radicals, compared with the experimental muon hfcs and the radical assignment.

Mu site	$\Delta E$ (kJ mol <sup>-1</sup> ) <sup>a</sup>	$A_{\mu}$ (calcd.) (MHz) <sup>a,b</sup>	$A_{\mu}$ (exptl.) (MHz)	Radical
C-3	0	278	264	<b>1</b>
C-1	17	346	347	<b>3</b>
C-8	35	355	349	<b>2</b>
C-2	42	394	402	<b>5</b>
C-7	43	430	435	<b>4</b>
C-6a	58	441	—	—
C-6b	72	498	—	—
C-10c	107	732	—	—
C-3a	139	893	—	—

<sup>a</sup>Single point UB3LYP/6-31G\*\* on UB3LYP/STO-3G optimized geometry.

<sup>b</sup>Includes a factor of 1.20 to account for the primary isotope effect.

Table 3, the ratio of muon and proton hfcs is in the range 1.20–1.25 after correction for the different magnetic moments (correction factor = 3.183). This muon–proton isotope effect is typical for cyclohexadienyl type radicals and is consistent with zero-point vibrational effects in anharmonic vibrational modes (5, 6).

The remaining resonances from Table 2 are narrower than those assigned to the methylene groups and can be attributed to  $\alpha$  protons (protons attached to a carbon that carries significant unpaired spin density). Beyond that one must turn to theoretical prediction to help in the assignment.

## Computation and discussion

Model calculations were performed on the nine isomeric H atom adducts of fluoranthene using density functional theory (DFT) as implemented in the Gaussian suite of programs (7). The structures were optimized at the UB3LYP/STO-3G level, and then single-point computations were performed at the UB3LYP/6-31G\*\* level to calculate the hyperfine constants and Hartree–Fock energies.

The molecular geometry for each H adduct radical should also be valid for the muoniated species, within the Born–Oppenheimer approximation. Similarly, electron distributions should be identical for isotopomers. However, zero-point vibrational effects are larger for normal modes involving Mu, and this can result in considerable isotope effects on vibrationally averaged hyperfine interactions. In particular, such effects have been investigated for cyclohexadienyl (6) and HC<sub>60</sub> (8). In view of the preliminary assignments and hfc ratios indicated in Table 3 we scaled computed proton hfcs by a factor of 1.20 to predict the muon hfc (a factor of



**Table 5.** Comparison between calculated<sup>a</sup> and experimental muon and proton hfcs (in MHz) for the five assigned Mu-fluoranthenyl radicals (Mu-FA). The experimental proton hfcs were determined from eq. [3] and are listed in order of the corresponding level-crossing resonances.

Nucleus	Site	1 (3-Mu-FA)		2 (8-Mu-FA)		3 (1-Mu-FA)		4 (7-Mu-FA)		5 (2-Mu-FA)	
		Calcd.	Exptl.	Calcd.	Exptl.	Calcd.	Exptl.	Calcd.	Exptl.	Calcd.	Exptl.
Mu	...	278 <sup>b</sup>	263.87	355 <sup>b</sup>	348.95	346 <sup>b</sup>	347.35	430 <sup>b</sup>	434.86	394 <sup>b</sup>	402.25
H	C3	68.8 <sup>c</sup>	68.81(2)	...	...	...	...	...	...	...	...
H	C8	...	...	87.4 <sup>c</sup>	91.50(3)	...	...	...	...	...	...
H	C1	...	...	...	...	85.4 <sup>c</sup>	88.13(6)	...	...	...	...
H	C2	-31.2	-23.70(1)	...	...	...	...	...	...	...	...
H	C2	...	...	...	...	...	...	...	...	97.1 <sup>c</sup>	100.93(9)
H	C7	...	...	...	...	...	...	105.9 <sup>c</sup>	111.01(10)	...	...
H	C2	...	...	...	...	-9.3	-9.93(5) <sup>d</sup>	...	...	...	...
H	C8	...	...	...	...	-10.8	...	...	...	...	...
H	C5	...	...	...	...	-14	...	...	...	...	...
H	C10	...	...	...	...	-11.1	-13.43(4) <sup>d</sup>	...	...	...	...
H	C7	...	...	-19.9	-14.00(8)	...	...	...	...	...	...
H	C9	...	...	-27.7	-18.74(7)	...	...	...	...	...	...
H	C6	...	...	...	...	...	...	...	...	-18.8	-23.2(6) <sup>d</sup>
H	C4	...	...	...	...	...	...	...	...	-17.0	...
H	C3	...	...	...	...	...	...	...	...	-47.9	-39.8(1)
H	C8	...	...	...	...	...	...	-22.8	-17.22(12)	...	...
H	C10	...	...	...	...	...	...	-31.6	-26.94(14)	...	...

<sup>a</sup>Single point UB3LYP/6-31G\*\* on UB3LYP/STO-3G optimized geometry.

<sup>b</sup>Includes a factor of 1.20 to account for primary isotope effect.

<sup>c</sup>Includes a factor of 0.94 to account for secondary isotope effect.

<sup>d</sup>Accidentally doubly degenerate (see text).

3.183 is also required to account for the magnetic moment). Similarly, taking account of prior experience (4), we used a factor of 0.94 for the corresponding H in a -CHMu- group.

The relative Hartree-Fock energies of the nine H adduct radical isomers are listed in Table 4 together with the corresponding predicted muon hfcs. The hfcs of the first five entries (lowest energies) are well matched to the experimental data, although one cannot exclude the H adduct to carbon 6a on this ground alone. The radicals were thus assigned as in the last column of Table 4. It is significant that, as in the case of pyrene (4), only products of attack at H-bearing carbons are experimentally detected. Otherwise, we would have found a muon hfc without a corresponding -CHMu- proton; Table 3 shows that this was not the case.

The calculations also provide the hfc of each proton for each radical species. Using eqs. [3-6], the LCR field, width, and amplitude (weighted with the radical abundance) of the corresponding signals may be predicted. It is then possible to test if the calculated hfc values are found to be a reasonably close match with experimental data obtained after making an a priori assumption of the muon hfc to use for each level-crossing resonance. The results of our analysis are displayed in Table 5.

In this fashion most of the observed LCR signals were assigned, although ambiguity and inconsistency remain for some of the weaker features observed. For example, in the case of the Mu-1-fluoranthenyl radical (radical 3), calculations predict four negative hfcs for protons in positions 2 (-9.3 MHz), 8 (-10.8 MHz), 5 (-14.1 MHz), and 10 (-11.1 MHz). Experimentally, in the expected field region only two LCR resonances are observed (at 19.35 kG and 19.47 kG), from which one derives proton hfcs of -9.93 MHz and -13.43 MHz. A

good fit is obtained if it is assumed that each of these resonances is actually accidentally doubly degenerate, which suggests that protons in positions 2, 8 and 5, 10 have, pairwise, very close hfcs not quite reproduced by the calculations.

## Conclusions

Five muoniated radicals (out of the possible nine) are formed by the addition of muonium to fluoranthene. Using DFT calculations as guides for the assignment of the various experimental spectral features, the hyperfine constants of the muon and selected protons in the various radicals could be obtained. The results are summarized in Fig. 4, in which all the assigned hfcs are shown on the structure diagrams for the radicals detected. Unlike the situation for C<sub>60</sub> or C<sub>70</sub>, there is no evidence of a radical being formed by Mu attack on one of the trigonal carbon sites (positions 3a, 6a/10b, 6b/10a, 10c), although calculations suggest that an attack at position 6a/10b might be possible.

From the hyperfine constants of the  $\alpha$ -protons obtained experimentally, it is also possible to deduce the distribution of unpaired  $\pi$ -spin density  $\rho_\alpha$  on the corresponding carbon using McConnell's relation (9)

$$[7] \quad A_H = Q_\alpha \rho_\alpha, \text{ where } Q_\alpha \approx -75 \text{ MHz}$$

The results are displayed in schematic form in Fig. 5. For clarity, only positive spin densities are displayed. Since the experimental data reported here give no *direct* information on carbon atoms not bearing a hydrogen (such information could be obtained from experiments on <sup>13</sup>C enriched fluoranthene), the corresponding unpaired spin density displayed



**Fig. 4.** Assigned hyperfine constants (in MHz) for the five fluoranthenyl radicals. Alternative assignments or degenerate values for radicals **3** and **5** are shown by question marks.

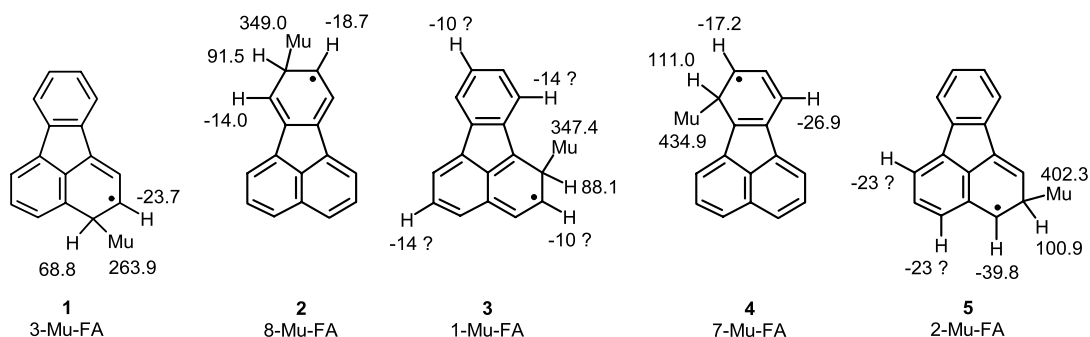
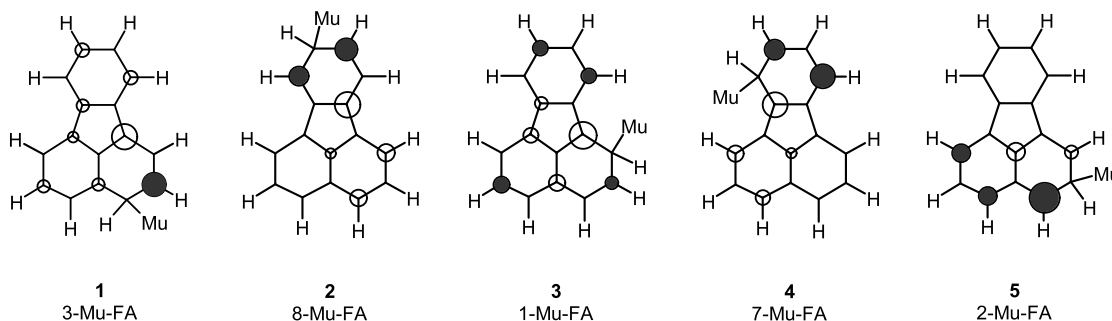


**Fig. 5.** Principal sites of positive unpaired  $\pi$ -spin density in the five muoniated fluoranthenyl radicals detected. The circled areas are proportional to the spin density as determined from calculations and confirmed from experimentally determined proton hyperfine constants (shaded areas).



in Fig. 5 was taken from the calculations. It is apparent that most of the protons adjacent to significant unpaired spin density have been detected in the present experiment. However, the calculations seem to indicate that there is significant unpaired spin density on carbons 1 and 3 of radical **2** and carbons 4 and 6 of radical **4**, and that the corresponding proton hfc's may be measurable. In addition, there are a few cases where negative spin density may be sufficient to give rise to measurable *positive*  $\alpha$ -proton hfc's.

It is evident from Fig. 5 that radical **1**, the lowest energy isomer, is also the one with the greatest spread of unpaired  $\pi$ -spin density, consistent with a general notion of resonance stabilization. However, it would be dangerous to infer much from the apparent correlation between  $A_\mu$  and radical energy (Table 4), since other factors contribute to both the relative energies of the radicals and to the muon hfc. In particular, the hfc depends on geometric factors (the dihedral angle between the C—Mu bond and the  $z$ -axis of the  $\pi$ -spin system) and the unpaired spin density on the adjacent carbon atoms (10, 11).

Similarly, the fact that the lower energy radicals were detected and not those corresponding to Mu(H) addition at trigonal carbon sites is related to the energy required to distort the carbon skeletons of the latter. However, it is important to realize that the relative abundance of the radical isomers depends on *kinetic* competition for the various sites, and that this reactivity is determined by the *activation* energy for Mu(H) addition, which is only indirectly linked to the radical (product) energy.

The findings reported in this paper and the preceding study of Mu addition to pyrene (**4**) show that planar PAHs

are not good models to investigate the reactivity of fullerene fragments. Therefore, as the next stage in our exploration of this topic we have undertaken a study of Mu addition to a pyrenophane, a PAH with a curved carbon skeleton (12).

## Acknowledgments

We thank the staff of the TRIUMF  $\mu$ SR Facility for technical support. This research was financially supported by the Natural Sciences and Engineering Research Council of Canada (NSERC) and, through TRIUMF, by the National Research Council Canada (NRC). J. Schüth was the recipient of a NATO postdoctoral fellowship administered by DAAD (Deutscher Akademischer Austauschdienst).

## References

1. R.C. Haddon. *Science* (Washington, D.C.), **261**, 1545 (1993).
2. F. Diederich and C. Thilgen. *Science* (Washington, D.C.), **271**, 317 (1996).
3. A. Hirsch. *In Fullerenes and related structures: Topics in current chemistry*. Vol. 199. *Edited by A. Hirsch*. Springer-Verlag, Berlin. 1999. pp. 1–65.
4. P.W. Percival, B. Addison-Jones, J.C. Brodovitch, K. Ghandi, and J. Schüth. *Can. J. Chem.*, **77**, 326 (1999).
5. E. Roduner. *The positive muon as a probe in free radical chemistry: Lecture notes in chemistry*. No. 49. Springer-Verlag, Berlin. 1988.
6. D. Yu, P.W. Percival, J.C. Brodovitch, S.K. Leung, R.F. Kiefl, K. Venkateswaran, and S.F.J. Cox. *Chem. Phys.* **142**, 229 (1990).



7. M.J. Frisch, G.W. Trucks, H.B. Schlegel, G.E. Scuseria, M.A. Robb, J.R. Cheeseman, V.G. Zakrzewski, J.A. Montgomery, R.E. Stratmann, J.C. Burant, S. Dapprich, J.M. Millam, A.D. Daniels, K.N. Kudin, M.C. Strain, O. Farkas, J. Tomasi, V. Barone, M. Cossi, R. Cammi, B. Mennucci, C. Pomelli, C. Adamo, S. Clifford, J. Ochterski, G.A. Petersson, P.Y. Ayala, Q. Cui, K. Morokuma, D.K. Malick, A.D. Rabuck, K. Raghavachari, J.B. Foresman, J. Cioslowski, J.V. Ortiz, B.B. Stefanov, G. Liu, A. Liashenko, P. Piskorz, I. Komaromi, R. Gomperts, R.L. Martin, D.J. Fox, T. Keith, M.A. Al-Laham, C.Y. Peng, A. Nanayakkara, C. Gonzalez, M. Challacombe, P.M.W. Gill, B.G. Johnson, W. Chen, M.W. Wong, J.L. Andres, M. Head-Gordon, E.S. Replogle, and J.A. Pople. 1998. Gaussian 98 [computer program]. Revision A.1. Gaussian, Inc., Pittsburgh, PA.
8. J.R. Morton, F. Negri, and K.F. Preston. *Phys. Rev. B.* **49**, 12446 (1994).
9. H.M. McConnell. *J. Chem. Phys.* **24**, 764 (1956).
10. D. Whiffen. *Mol. Phys.* **6**, 223 (1963).
11. P.W. Percival and S. Wlodek. *Chem. Phys. Lett.* **196**, 317 (1992).
12. G.J. Bodwell, J.N. Bridson, T.J. Houghton, J.W.J. Kennedy, and M.R. Mannion. *Angew. Chem. Int. Ed. Engl.* **35**, 1320 (1996).



# Formation of the charge-transfer exciton in 1,3,5-triphenyl-2-pyrazoline nanocrystals

Hongbing Fu, Debao Xiao, Ruimin Xie, Xuehai Ji, and Jian-Nian Yao

**Abstract:** A series of 1,3,5-triphenyl-2-pyrazoline (TPP) nanocrystals were prepared by the reprecipitation method. The electronic transitions of TPP nanocrystals have been studied using both absorption and fluorescence spectra. An absorption feature at about 400 nm gradually appeared with increasing nanocrystal size. This feature resulted from the formation of the charge-transfer (CT) exciton in nanocrystals. It was also supported by the longer decay time of the nanocrystal emission from CT compared with that of the solution emission from  $S_1$  at 298 K. On the other hand, the different behavior of the molecular  $\pi-\pi^*$  and  $n-\pi^*$  transitions originates from the different overlapping modes of the pyrazoline  $\pi$  orbital and n-electron orbital, according to the molecular model calculations. The nanocrystal emission from both the  $S_1$  and CT states was found at 77 K; moreover, the emission intensity redistributed from  $S_1$  to CT with increasing nanocrystal size. In contrast, at 298 K, only the emission from the CT states was observed, since the thermal fluctuation easily relaxes the excited electrons into CT states through vibration.

**Key words:** reprecipitation method, organic nanocrystals, charge-transfer exciton, size-dependent property.

**Résumé:** Utilisant la méthode de réprécipitation, on a préparé une série de nanocristaux de 1,3,5-triphényl-2-pyrazoline (TPP). On a étudié les spectres d'absorption et de fluorescence ainsi que les transitions électroniques des nanocristaux de TPP à l'échelle nanocristalline. Une caractéristique d'absorption aux environs de 400 nm apparaît graduellement avec une augmentation de la taille nanocristalline qui conduit à la formation de l'exciton de transfert de charge (TC) dans les nanocristaux; ceci est supporté par le fait que, à 298 K, le temps de décroissance de l'émission nanocristalline à partir de l'état TC est plus long que celui de l'émission en solution à partir de  $S_1$ . Par ailleurs, il semble sur la base de calculs de modèles moléculaires, que le comportement différent des transitions  $\pi-\pi^*$  et  $n-\pi^*$  moléculaires trouve son origine dans un mode de recouvrement différent de l'orbitale  $\pi$  de la pyrazoline et de l'orbitale de l'électron n. À 77 K, on a observé une émission nanocristalline tant à partir de l'état  $S_1$  que de l'état TC; toutefois, avec une augmentation de la taille nanocristalline, on observe que l'intensité de l'émission se redistribue de  $S_1$  à TC. Toutefois, à 298 K, on n'observe que l'émission provenant des états de TC puisque la fluctuation thermique permet de faire facilement passer les électrons excités vers les états de TC par le biais de vibrations.

**Mots clés :** méthode de réprécipitation, nanocristaux organiques, exciton de transfert de charge, propriété qui varie avec la taille.

[Traduit par la Rédaction]

## Introduction

In the past decades, the synthesis of semiconductor nanocrystals with controlled size (1–2), shape (3), and composition (4) have paved the way for numerous spectroscopic studies, which assigned the quantum dot electronic states and mapped their evolution as a function of size. One of the most interesting findings is the strong effect of confinement on electron-hole pairs in semiconductor quantum dots, which leads to their size-tunable optical properties (5). This type of confinement is not expected in organic crystals because of the small radius of the Frenkel exciton, which is the

reason for the scarcity of reports on the preparation of nanocrystals from general organic molecules (6–11). However, by alternating multiple quantum-well structures grown by organic molecular beam deposition, Forrest and co-workers (12, 13) were able to report the confinement effect on the charge-transfer exciton in 3,4,9,10-perylenetetracarboxylic dianhydride (PTCDA) and 3,4,7,8-naphthalenetetracarboxylic dianhydride (NTCDA). Because of the great diversity of organic molecules compared with inorganic compounds, there is a challenge to extend the research on nanocrystals from metals and semiconductors to the organic field. The electronic and optical properties of organic semiconductors are fundamentally different from those of inorganic metals and semiconductors owing to the weakness of the van der Waals type intermolecular interaction forces (14, 15). To understand how these properties develop as a function of size is of fundamental (16) and technological interest (17).

Pyrazoline derivatives have been widely used as optical brightening agents for textiles and paper because of strong fluorescence (18, 19) and as a hole-conducting medium in

Received 11 September 2001. Published on the NRC Research Press Web site at <http://canjchem.nrc.ca> on 20 January 2003.

H. Fu, D. Xiao, R. Xie, X. Ji, and J.-N. Yao.<sup>1</sup> Center for Molecular Science, Institute of Chemistry, CAS, Beijing 100080, P. R. China.

<sup>1</sup>Corresponding author (e-mail: [jnyao@infoc3.icas.ac.cn](mailto:jnyao@infoc3.icas.ac.cn)).



photoconductive materials (20, 21) and electro-luminescence (EL) devices (22). 2-Pyrazolines containing electron donors and acceptors at their 1- and 3-positions have intrinsically large molecular hyperpolarizabilities and are considered to be important organic heterocyclic semiconductors (23). In our previous work, the optical size dependence of nanoparticles of 1-phenyl-3-((dimethylamino)styryl)-5-((dimethylamino)phenyl)-2-pyrazoline (PDDP) was identified and found to originate from the formation of the charge-transfer (CT) exciton. The optical size dependence was found to correspond to increasing nanoparticle size (24). The research outlined in this article is an extension of the above research. For this paper 1,3,5-triphenyl-2-pyrazoline (TPP) nanocrystals of different sizes have been prepared; further, their optical properties have been found to present as a function of crystal size owing to the formation of the charge-transfer exciton. The optical size effects presented by pyrazoline nanocrystals are likely to be important, considering future luminescence applications of organic materials.

## Experimental section

### Materials

The compound 1,3,5-triphenyl-2-pyrazoline (TPP) was synthesized according to ref. 18 and confirmed by NMR and MS. TPP nanocrystals were prepared as follows: quantities of TPP-ethanol solution ( $1.0 \times 10^{-3} \text{ mol}\cdot\text{L}^{-1}$ ) were injected, with vigorous stirring, into 10 mL of water using a 100  $\mu\text{L}$  microsyringe. The TPP molecules began to aggregate at once and nanocrystals dispersed in water were obtained. By controlling both the quantity of TPP-ethanol solution injected into water and the temperature, the size of the nanocrystals could also be controlled. For example, when 40 and 100  $\mu\text{L}$  of the TPP-ethanol solution was injected, the final nanocrystal sizes were 60 and 125 nm at 25°C or 90 and 170 nm at 50°C, respectively.

### Methods

The UV-vis absorption spectra of the nanocrystals in water dispersion were measured using a SHIMADZU UV-1601 PC double beam spectrophotometer. The steady-state fluorescence excitation and emission spectra were recorded with a Hitachi F-4500 spectrometer. The measurements of fluorescence lifetimes with excitation at 360 nm were performed, with monitoring at 445 nm for the solution and at 465 nm for the nanocrystals, on a Horiba NAES 1100 nanosecond fluorometer. The sizes and shapes of the nanocrystals were observed by means of the field emission scanning electron microscope (JSM-6301F). The mean size and the size distribution of nanocrystals dispersed in water were also evaluated by the dynamic light-scattering (DLS) technique using a Zetaplus BI-9000 (Brookhaven Instruments Corporation, U.S.A.). The same instrument was also used to measure the surface electric  $\xi$ -potential of the nanocrystals.

Molecular modeling calculations were carried out using CHEM3D Pro 4.0, which was developed by CambridgeSoft Corporation (Mass., U.S.A.). Molecular modeling was done on a Pentium 266 using an MM2 force field. The structures of two neighboring TPP molecules in the nanocrystals were drawn and the minimum energy of configuration was obtained by energy minimization in vacuum conditions. The

modeling was also done using the PM3 semiempirical quantum mechanical method for a TPP molecule pair in the nanocrystal. The minimization procedure involved systematically altering the coordinates of the atoms and estimating the conformation until a minimum energy configuration was reached.

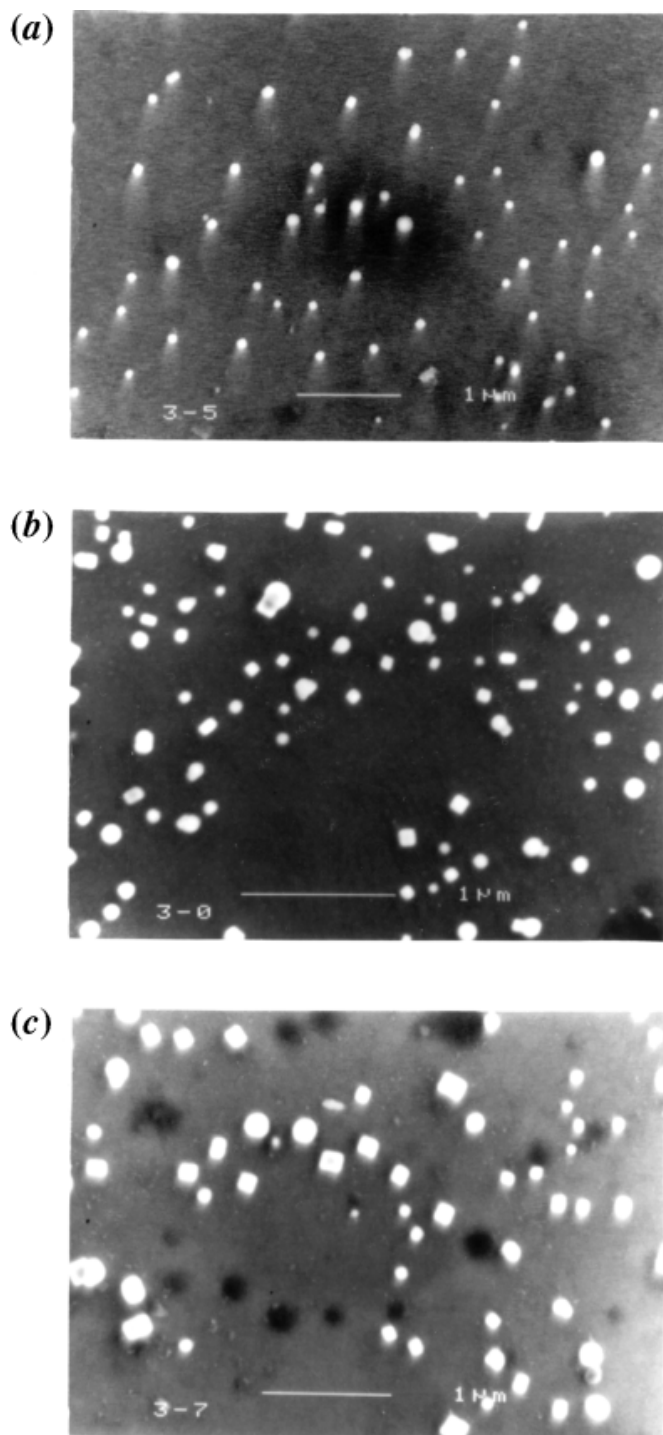
## Results and discussion

We successfully prepared a series of TPP nanocrystals ranging in size from tens to hundreds of nanometers, labelled NC1, NC2, NC3, NC4, and NC5 — corresponding to the average nanocrystal sizes 30, 60, 90, 125, and 170 nm, respectively. The nanocrystal dispersions in water appeared turbid white because of the light scattering property of nanocrystals; moreover, the color deepened as the nanocrystal size increased. Some of the field emission scanning electron microscopy (FESEM) photographs are shown in Fig. 1, in which the average crystal sizes are 60, 125, and 170 nm. These values agree roughly with those determined by the dynamic light scattering (DLS) technique. It can be seen from Fig. 1 that the shape of the TPP nanocrystals is cubic, which suggests that the crystallization of the TPP nanocrystals is good. In the process of observation, the original sharp margins of the cubic nanocrystals was blurred over time by the bombardment of electrons, as a result of the surface effect, which caused a reduction in the melting point (16). The measurements of the surface electric  $\xi$ -potential of the nanocrystals shows that they are negatively charged.

Figure 2 displays the UV-vis absorption spectra of different sizes of TPP nanocrystals dispersed in water. For comparison, the spectrum of a dilute TPP-ethanol solution ( $1.0 \times 10^{-5} \text{ mol}\cdot\text{L}^{-1}$ ), which has three peaks at 240, 305, and 357 nm, is also displayed (Fig. 2(m)). It has been reported that the UV band at 240 nm arises from the phenyl ring ( $P_{\text{phenyl}}$ ), and the other two peaks at 305 and 357 nm are due to the pyrazoline ring  $n-\pi^*$  ( $P_{n-\pi^*}$ ) and  $\pi-\pi^*$  ( $P_{\pi-\pi^*}$ ) transitions, respectively (25–27). No spectral changes were observed when the concentration changed from  $1.0 \times 10^{-5}$  to  $1.0 \times 10^{-3} \text{ mol}\cdot\text{L}^{-1}$ . As the nanocrystal size increases from NC1 to NC5, the  $P_{\text{phenyl}}$  of the TPP nanocrystal is observed to shift to longer wavelengths, while the  $P_{n-\pi^*}$  remains at almost the same position. Moreover, the peak in the region of 350–425 nm broadens and its shape changes from symmetric to asymmetric. The asymmetric peak located at approximately 350–425 nm actually consists of two peaks, especially for NC4 or NC5. The one at shorter wavelengths originates from the  $\pi-\pi^*$  transition of TPP molecules. The other at longer wavelengths is strongly affected by the nanocrystal size, becoming vanishingly small for crystal sizes  $\leq 30$  nm. This behavior is expected for an aggregate state arising from the  $\pi-\pi$  orbital overlap of closely stacked TPP molecules in nanocrystals; it is similar to previous observations of absorption by aggregate states in other organic molecular crystals such as  $\alpha$ -perylene (28),  $C_{60}$  (29), and 3,4,9,10-perylenetetracarboxylic dianhydride (30). In addition, the absorption spectrum of the solution has no detectable peak in the region of 400–420 nm, in contrast to the absorption spectrum of NC1, although the solution concentration of TPP molecules in the system is greater than that of the NC1–water dispersion, which was prepared by injecting



**Fig. 1.** The FESEM photographs of TPP nanocrystals: (a) 60, (b) 125, and (c) 170 nm.



40  $\mu\text{L}$  of a  $1.0 \times 10^{-3} \text{ mol}\cdot\text{L}^{-1}$  TPP-ethanol solution into 10 mL of water at  $0^\circ\text{C}$ . From this, we infer that the peak at longer wavelengths is associated only with aggregate formation; we have labelled it  $P_{\text{CT}}$ .

To accurately determine the detailed behavior of absorption transitions based on nanocrystal sizes, each spectrum in Fig. 2 was fitted to four Gaussian peaks using the parameters provided in Table 1. The inset in Fig. 2 is a sample fit for the spectrum of NC4. The most interesting phenomenon

**Fig. 2.** The UV-vis absorption spectra of different sizes of TPP nanocrystal dispersed in water. The spectrum of a  $1.0 \times 10^{-5} \text{ mol}\cdot\text{L}^{-1}$  TPP-ethanol solution (m). Inset: the sample numerical fit to the absorption spectrum of NC4.

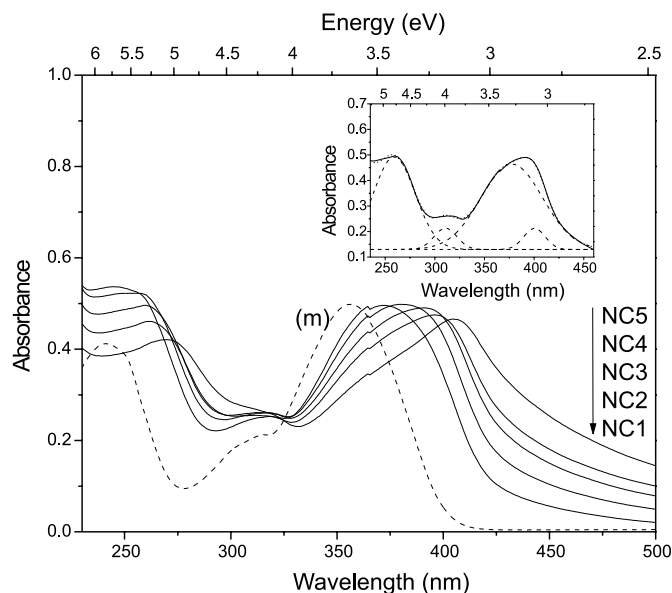
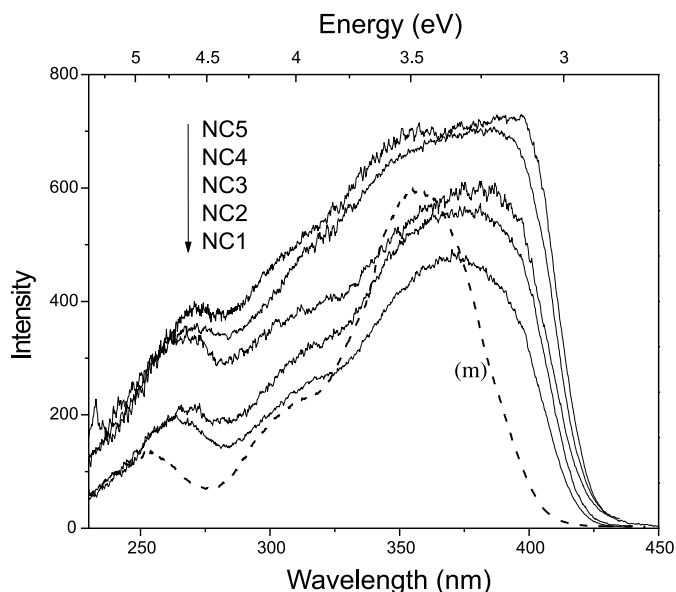


**Fig. 3.** The fluorescence excitation spectra of different sizes of TPP nanocrystals dispersed in water, measured at room temperature. The spectrum of a  $1.0 \times 10^{-5} \text{ mol}\cdot\text{L}^{-1}$  TPP-ethanol solution (m).



is that the relative oscillator strength of the  $\pi-\pi^*$  transition,  $F_{\pi-\pi^*}$ , which was determined from the peak area percentage of  $\pi-\pi^*$  absorption for the whole absorption of the pyrazoline ring, basically keeps the same value (about 83.5%) for different nanocrystal sizes. On the other hand,  $F_{n-\pi^*}$  decreases from 14.2 to 4.9%; this decrease is accompanied by an increase of  $F_{\text{CT}}$  from 3.8 to 10.7% with increasing nanocrystal size (from 30 to 170 nm).

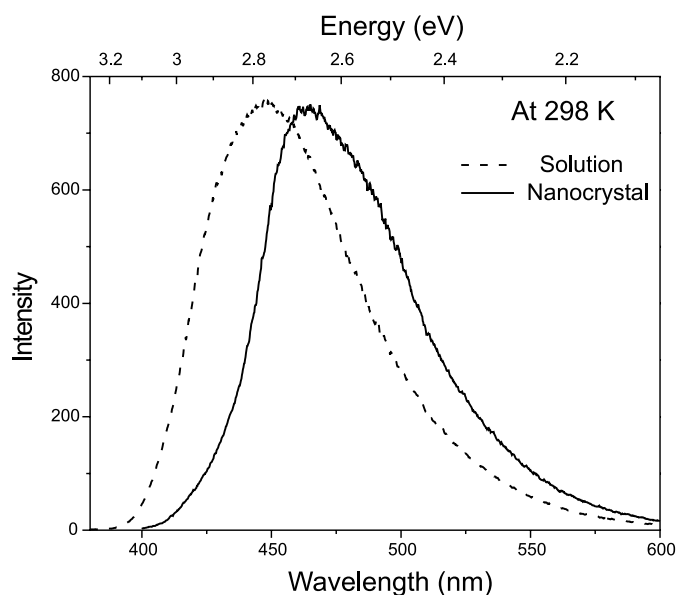
The fluorescence excitation spectra of TPP nanocrystals in Fig. 3 show similar changes to those found in the absorption



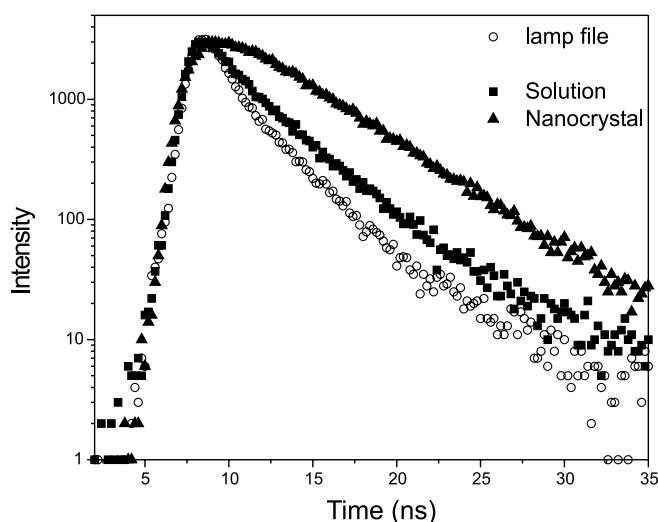
**Table 1.** The results of a numerical fit to the absorption spectra of a dilute solution of TPP (m) and different sizes of nanocrystals (NC1 to NC5).

Sample	$P_{\text{phenyl}}$	$P_{n-\pi^*}$	$F_{n-\pi^*}^a$ (%)	$P_{\pi-\pi^*}$	$F_{\pi-\pi^*}^a$ (%)	$P_{\text{CT}}$	$F_{\text{CT}}^a$ (%)
	Position (nm)	Position (nm)		Position (nm)		Position (nm)	
m	240	304	17.0	357	83.0	—	—
NC1	253	308	14.2	368	82.0	398	3.8
NC2	255	310	9.7	372	83.5	400	6.8
NC3	259	311	7.5	378	84.0	402	8.5
NC4	262	311	6.8	382	83.8	405	9.4
NC5	270	310	4.9	390	84.4	408	10.7

<sup>a</sup> $F_i$  were determined from the area percentage of peak  $i$  for the whole absorption of the pyrazoline ring;  $i$  denotes  $P_{n-\pi^*}$ ,  $P_{\pi-\pi^*}$ , and  $P_{\text{CT}}$ , respectively.

**Fig. 4.** The fluorescence emission spectra of NC4 and the dilute solution ( $1.0 \times 10^{-5} \text{ mol}\cdot\text{L}^{-1}$ ) measured at room temperature. The spectrum of a  $1.0 \times 10^{-5} \text{ mol}\cdot\text{L}^{-1}$  TPP-ethanol solution (m). The excitation wavelength is 360 nm.

spectra. The dashed line in Fig. 4 is the emission spectrum for a  $1.0 \times 10^{-5} \text{ mol}\cdot\text{L}^{-1}$  TPP-ethanol solution, with an asymmetric peak centered at 445 nm. The emission spectrum of NC4, with a peak at 465 nm, presents as a typical example of nanocrystal emission, since the nanocrystal size hardly influences its shape and peak energy. Note that the shape of the nanocrystal emission is similar to that of the solution emission; only the peak energy is red-shifted by 0.12 eV from the value for the dilute solution. Moreover, no significant changes in the emission shape were observed as the pump energy changed from  $E = 4.96$  to 3.1 eV for both the solution and nanocrystal. To further clarify their assignment, fluorescence decays were measured for the solution (monitored at 445 nm) and for the nanocrystal (monitored at 465 nm) with the same excitation wavelength at 360 nm. All decay curves shown in Fig. 5 are well described using a single-exponential function with high accuracy. The fluorescence lifetimes of the solution and the nanocrystal were determined to be  $\tau_s = 1.43 \pm 0.12 \text{ ns}$  and  $\tau_n = 3.86 \pm 0.44 \text{ ns}$ , respectively. Since monomers are the dominant species in the dilute solution, and since the solution emission spectrum does not change with concentration, the solution emission

**Fig. 5.** Fluorescence decay curves for the dilute solution (monitored at 445 nm) and for NC4 (monitored at 465 nm) with excitation at 360 nm, at 298 K.

spectrum is assigned to the direct monomer transition from  $S_1$  to  $S_0$ . In general, the emission from the intermolecular charge-transfer (CT) state exhibits a longer decay time than that from the initially excited state (31). As stated above,  $\tau_n$  is about  $2.5 \times \tau_s$ . Therefore, it is likely that the increased fluorescence lifetime of  $\tau_n$  results from the emission from CT to the ground state. Returning to Fig. 2, the gradually appearing absorption feature by aggregates at about 400 nm ( $P_{\text{CT}}$ ) reasonably corresponds to the absorption from  $S_0$  to CT.

To interpret the data of Figs. 2–5, we have indicated schematically the various transitions between the lowest energy states found for TPP nanocrystals (Fig. 6). Here, the lower energy of CT, as compared with  $S_1$ , is also consistent with this picture, where CT states are found generally at energies lower than the corresponding maxima of the monomer spectrum (14, 15). The difference between the solution and nanocrystals is that the latter presents the transitions involving CT states; the former rarely does. However, the fine structure shown in Fig. 6 cannot be observed at room temperature because of thermal fluctuation. Therefore, we have also measured the emission spectra, with excitation at 360 nm, in liquid nitrogen (temperature 77 K), as shown in Fig. 7.

In Fig. 7(m), the solution emission spectrum measured at 77 K, four peaks are observed at 405, 428, 454, and 482 nm, respectively. The equal spacing between them indicates that



**Fig. 6.** Proposed transitions for TPP molecules in nanocrystals. The wavy lines indicate the vibrational relaxation process. The dashed arrows indicate those transitions occurring only at 77 K.

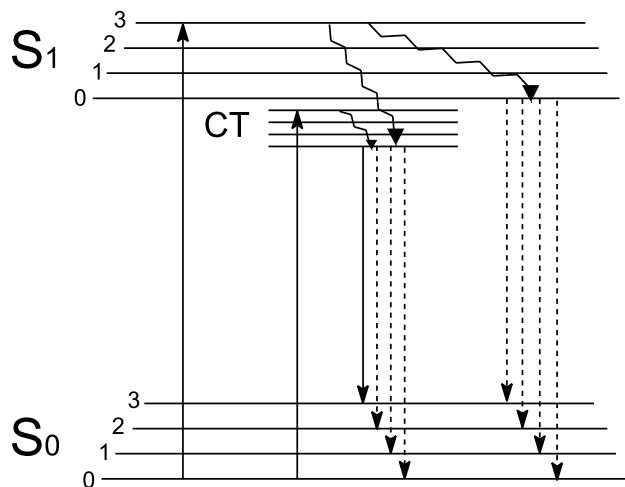
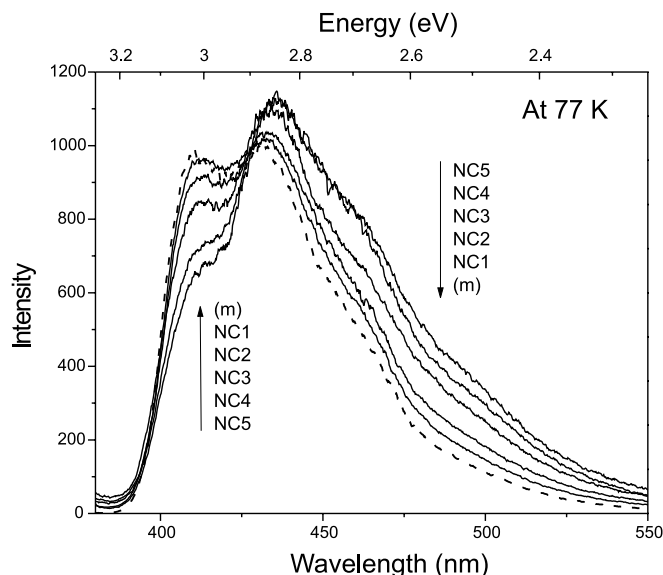
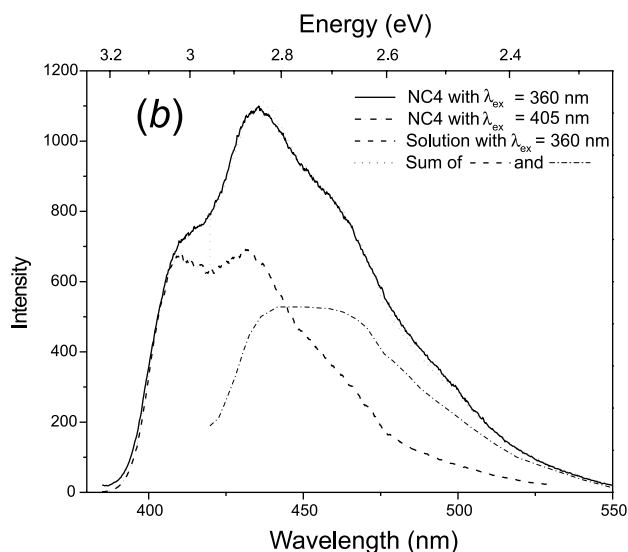
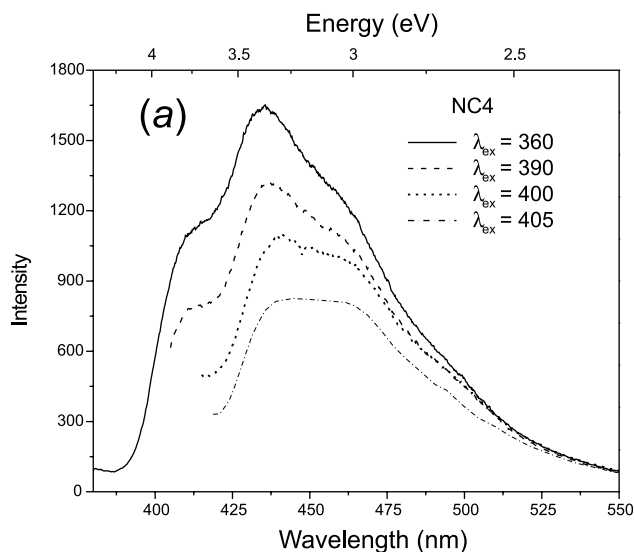


**Fig. 7.** The emission spectra of different sizes of TPP nanocrystals dispersed in water measured at 77 K. The spectrum of a  $1.0 \times 10^{-5} \text{ mol}\cdot\text{L}^{-1}$  TPP-ethanol solution (m). The excitation wavelength is 360 nm.



they originate from different vibrational states ( $v_n = 0, 1, 2, 3$ ) in  $S_0$ . As for nanocrystals, the intensity of the peak at 405 nm,  $I_{405}$ , gradually decreases with increasing nanocrystal size; moreover, the low energy tail extends to longer wavelengths simultaneously. The nanocrystal emission at 77 K is different from that at room temperature, as it is influenced not only by nanocrystal size but also by the excitation wavelength  $\lambda_{\text{ex}}$ . An example is shown in Fig. 8(a), where the emission spectra of NC4 with different  $\lambda_{\text{ex}}$  display this tendency. When  $\lambda_{\text{ex}}$  is less than 400 nm, corresponding to excitation directly into  $S_1$ ,<sup>2</sup> the two low-energy peaks (<450 nm) gradually rise as  $\lambda_{\text{ex}}$  increases. When  $\lambda_{\text{ex}}$  is bigger than

**Fig. 8.** The emission spectra of NC4 measured at 77 K using different excitation wavelengths.

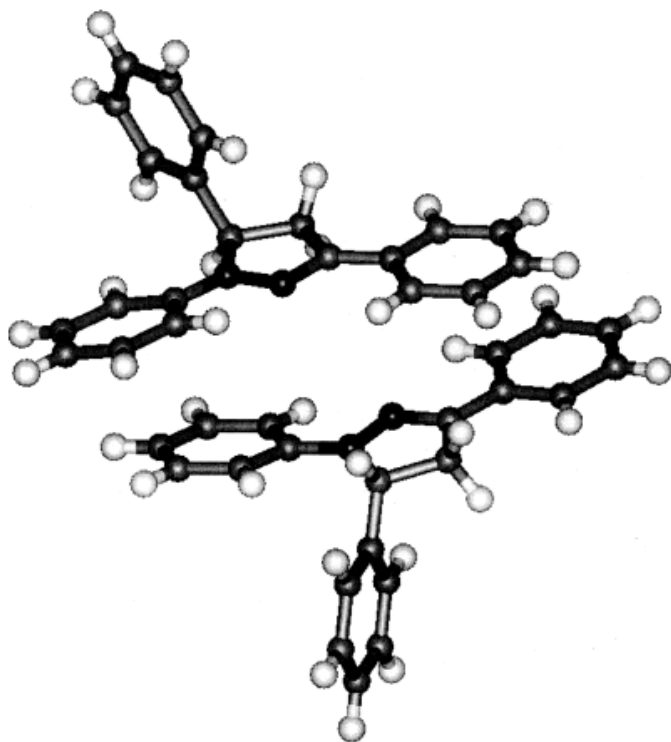


400 nm with excitation into CT states,<sup>2</sup> the nanocrystal emission is similar to that of the solution and may come directly from the CT states. In Fig. 8(b), we have added the solution emission spectrum (dashed line) — of which the intensity at 405 nm has been adjusted to be equal to  $I_{405}$  of NC4 excited at 360 nm — to the emission spectrum of NC4 excited at 405 nm (alternating dashed and dotted line). It is interesting that the sum (dotted line) is superposed with the emission spectrum of NC4 excited at 360 nm (solid line). This indicates that the nanocrystal emission originates from both  $S_1$  and CT at 77 K when excitation energy is above  $S_1$  (cf. Fig. 6). Further, the intensity is redistributed from  $S_1$  to CT with increasing nanocrystal size. The coexistence of emission transitions [ $S_1 \rightarrow S_0$ ] and [ $\text{CT} \rightarrow S_0$ ] indicates that the  $S_1$  and CT states are in equilibrium in the nanocrystals at

<sup>2</sup> According to the absorption spectra of TPP nanocrystals with parameters listed in Table 1, the wavelength 400 nm (3.1 eV) is just the dividing line between the  $S_1$  and CT states.



**Fig. 9.** The optimized structure of two neighboring molecules in nanocrystals.



77 K. At room temperature, the  $S_1$  states are efficiently deactivated nonradiatively via the exciton band by thermal activation and energy hopping, and thus only the [CT- $S_0$ ] emission can be observed.

Figure 9, the optimized structure of two neighboring TPP molecules in the nanocrystals, provides a clue to help our understanding of how the intermolecular charge transfer occurs in TPP nanocrystals. It can be seen from Fig. 9 that the phenyl and pyrazoline rings of two neighboring molecules overlap to some extent, resulting in their absorption shifting to the lower energy side. Because of the inverse orbital orientation of  $n$  electrons the orbital overlap between them is small, leading to the small differences in  $n-\pi^*$  absorption with differing nanocrystal sizes. In 2-pyrazolines, the charge distribution of N-1 (N at the 1-position) changes from negative in the ground state to positive in the excited state because of the conjugated charge-transfer from N-1 to C-3 (23). We infer that the intermolecular charge-transfer may occur from N-1 of one molecule to its neighbors. This should lead to a decrement in the probability of optical transitions that involve the  $n$  electrons of nitrogen and is further supported by the simultaneous occurrence of the decrement of  $F_{n-\pi^*}$  and the increment of  $F_{CT}$  with increasing nanocrystal size, as mentioned above. The increment of  $F_{CT}$  reflects the formation process of the CT exciton in TPP nanocrystals.

## Summary

In summary, the size-dependent optical properties of TPP nanocrystals were studied using absorption and fluorescence spectra on nanocrystals of different sizes. Their absorption

and emission transitions, as compared with those of a dilute solution, have been investigated, as a function of nanocrystal size, at both 298 and 77 K. We found that the optical properties of TPP nanocrystals possess a special size-dependence because of the formation of the charge-transfer exciton and the various interactions between different molecular orbitals according to the molecular model calculations. The present study adds to our understanding of excitons in organic semiconductors.

## Acknowledgments

This paper was sponsored by the National Natural Foundation of China. The support of this research by the National Research Fund for Fundamental Key Projects No. 973 (G19 990 330) and the Chinese Academy of Sciences is also gratefully acknowledged.

## References

1. C.B. Murry, D.J. Norris, and M.G. Bawendi. *J. Am. Chem. Soc.* **115**, 8706 (1993).
2. A.A. Guzelian, J.E.B. Katari, A.V. Kadavanich, U. Banin, K. Hamad, E. Juban, and A.P. Alivizatos. *J. Phys. Chem.* **100**, 7212 (1996).
3. X.G. Peng, L. Manna, W.D. Yang, J. Wickham, E. Scher, A. Kadavanich, and A.P. Alivizatos. *Nature (London)*, **404**, 59 (2000).
4. B.O. Dabbousi, J. Rodriguez-Viejo, F.V. Mikulec, J.R. Heine, H. Mattoussi, R. Ober, K.F. Jensen, and M.G. Bawendi. *J. Phys. Chem.* **101**, 9463 (1997).
5. A.P. Alivizatos. *Science (Washington, D.C.)*, **271**, 933 (1996).
6. H. Kasai, H. Kamatani, S. Okada, H. Oikawa, H. Matsuda, and H. Nakanishi. *Jpn. J. Appl. Phys.* **35**, L221 (1996).
7. H. Nakanishi and H. Katagi. *Supramol. Sci.* **5**, 289 (1998).
8. A. Ibanez, S. Maximov, A. Guiu, C. Chaillout, P.L. Baldeck. *Adv. Mater.* **10**, 1540 (1998).
9. Y.Z. Shen, D. Jakubczyk, F.M. Xu, J. Swiatkiewicz, P.N. Prasad, and B.A. Reinhardt. *Appl. Phys. Lett.* **76**, 1 (2000).
10. I.A. Akimov, I.Y. Denisjuk, and A.M. Meshkov. *Opt. Spectrosc. (Transl. of Opt. Spektrosk.)* **77**, 858 (1994).
11. F. Debuigne, L. Jeuniau, M. Wiame, and J.B. Nagy. *Langmuir*, **16**, 7605 (2000).
12. Z.L. Shen and S.R. Forrest. *Phys. Rev. B*, **55**, 10578 (1997).
13. S.R. Forrest. *Chem. Rev.* **97**, 1793 (1997).
14. E.A. Silinsh. *Organic molecular crystals: Their electronic states*. Springer-Verlag, Berlin. 1980.
15. M. Pope and C.E. Swenberg. *Electronic processes in organic crystals*. Oxford University Press, Oxford. 1982.
16. Q. Jiang, H.X. Shi, and M. Zhao. *J. Chem. Phys.* **111**, 2176 (1999).
17. F. Spano and S. Mukamel. *Phys. Rev. A*, **15**, 5783 (1989).
18. S.R. Sandler and K.C. Tsou. *J. Chem. Phys.* **39**, 1062 (1963).
19. J. Barbera, K. Clays, R. Gimenez, S. Houbrechts, A. Persoons, and J.L. Serrano. *J. Mater. Chem.* **8**, 1725 (1998).
20. P.M. Borsenberger and L.B. Schein. *J. Phys. Chem.* **98**, 233 (1994).
21. P.J. Melz, R.B. Champ, L.S. Chang, C. Chiou, G.S. Keller, L.C. Licican, R.R. Neiman, M.D. Schattuck, W.J. Weiche. *Photo. Sci. Eng.* **21**, 73 (1977).
22. X.H. Zhang, W.Y. Lai, and S.K. Wu. *Chem. Phys. Lett.* **320**, 77 (2000).



23. J.O. Morley, V.J. Docherty, and D. Pugh. *J. Mol. Electron.* **5**, 117 (1989).
24. H.B. Fu and J.N. Yao. *J. Am. Chem. Soc.* **123**, 1434 (2001).
25. M. Mukai, T. Miura, M. Nanbu, and T.Y. Shindo. *Can. J. Chem.* **57**, 360 (1979).
26. R.N. Nurmukhametov and V.G. Tishchenko. *Opt. Spectrosc.* (Transl. of *Opt. Spektrosk.*), **23**, 83 (1967).
27. F. Wilkinson, G.P. Kelly, and C. Michael. *J. Photochem. Photobiol. A*, **52**, 309 (1990).
28. J. Tanaka. *Bull. Chem. Soc. Jpn*, **36**, 1237 (1963).
29. M.K. Kelly, P. Etchegoin, D. Fuchs, W. Kratschmer, and K. Fostiropoulos. *Phys. Rev. B*, **46**, 4963 (1992).
30. V.P. Bulovic, E. Burrows, S.R. Forrest, J.A. Cronin, and M.E. Thompson. *Chem. Phys.* **210**, 1 (1996).
31. S.G. Schulman. *Fluorescence and phosphorescence spectroscopy: Physicochemical principles and practice*. Oxford, New York, 1977.



# An ab initio study of conformations and IR spectra of 5-substituted 1,3-cyclopentadienes

Cory C. Pye, James D. Xidos, D. Jean Burnell, and Raymond A. Poirier

**Abstract:** A computational study of 5-substituted cyclopentadienes is presented. The substituents considered are the group 14–17 elements of the second through fifth periods, saturated by hydrogens as needed to fulfill normal valence requirements. The conformational characteristics are examined and rationalized using bond–antibond interactions and steric arguments. Trends in vibrational frequencies are discussed and compared with experiment where possible.

**Key words:** cyclopentadiene, ab initio, spectra.

**Résumé:** On présente les résultats d'une étude théorique de cyclopentadiènes portant des substituants en position 5. Les substituants considérés sont les éléments des groupes 14 à 17, de la deuxième à la cinquième période, saturés par des atomes d'hydrogène pour satisfaire les valences normales requises. On a examiné les caractéristiques conformationnelles et on les a rationalisées en faisant appel à des arguments stériques et d'autres basés sur des interactions liantes et antiliantes. On discute des tendances dans les fréquences de vibration et on les compare avec des valeurs expérimentales lorsque celles-ci sont disponibles.

**Mots clés:** cyclopentadiène, ab initio, spectres.

[Traduit par la Rédaction]

## Introduction

During the course of our investigations of facial selectivity in the Diels–Alder reaction, we found that 5-substituted cyclopentadienes could give a range of facial selectivities from 100% *syn* to 100% *anti* selectivity, simply by varying the substituent (1,2). Although a variety of explanations have been proposed (3–6), our own investigations have suggested that a simple modification of the concept of steric bulk is sufficient to explain this phenomena (7,8).

The synthesis of 5-substituted cyclopentadienes and their subsequent reaction with dienophiles is useful for validating or refuting theories of facial selectivity, but the existence of these compounds is sometimes fleeting. The identification of these species, once created, needs to be proven. In this paper, various spectroscopic data are calculated and compared to known experimental literature data where available. It is hoped that the following analysis will eventually aid in the experimental detection of other as yet unknown species. In particular, we will give information on the structure and harmonic vibrational frequencies to facilitate comparison with experimental diffraction, microwave measurements, and IR and Raman spectra, respectively. In addition, a full examination of substituent conformation is presented and rationalized.

## Method

Calculations were performed using MUNGAUSS (9), Gaussian 92 (10), or Gaussian 98 (11), utilizing the STO-3G (12), 3-21G (13), 6-31G\* (14), and 6-31+G\* (15) basis sets. Huzinaga's basis sets for Ge–Br (4333/433/4) and Sn–I (43333/4333/44), decontracted in the *sp*-valence region (21/21) and polarization functions added, were used in conjunction with the 6-31G\* basis set (16). Cartesian (six) *d*-functions were used throughout except for STO-3G. Diffuse functions were determined in an even-tempered fashion separately for the *s* and *p* shells and then geometrically averaged to give the exponent of an *sp* diffuse shell. These augmented the Huzinaga basis sets for use in conjunction with the 6-31+G\* calculations, as in reference (17). The resulting diffuse-*sp* exponents are 0.015 (Ge), 0.019 (As), 0.036 (Se), 0.042 (Br), 0.021 (Sn), 0.026 (Sb), 0.030 (Te), and 0.034 (I). For brevity, the results and discussion using the STO-3G and 3-21G basis sets are presented in the supplementary material<sup>2</sup> (18).

The MP2 calculations utilize the frozen core approximation. Default optimization specifications were normally used. For the 6-31G\* and higher basis sets, a frequency calculation was performed at the same level and the resulting Hessian was used in the following optimization. Z-matrix coordinates constrained to the appropriate symmetry were used as required to speed up the optimizations. If symmetry constraints led to a transition state instead of a minimum, this would show up as the presence of one or more imaginary frequencies not belonging to the totally symmetric irreducible representation. The Hessian was evaluated at the first geometry for the first level in a series in order

Received 16 August 2002. Published on the NRC Research Press Web site at <http://canjchem.nrc.ca/> on 28 January 2003.

**C.C. Pye.**<sup>1</sup> Department of Chemistry, Saint Mary's University, Halifax, NS B3H 3C3, Canada.

**J.D. Xidos.** Computer Aided Molecular Design Laboratory, Mayo Clinic, 200 First St. SW, Rochester, MN 55905, U.S.A.

**D.J. Burnell and R.A. Poirier.** Department of Chemistry, Memorial University, St. John's, NL A1B 3X7, Canada.

<sup>1</sup>Corresponding author (e-mail: [cory.pye@stmarys.ca](mailto:cory.pye@stmarys.ca)).

<sup>2</sup>Supplementary data may be purchased from the Depository of Unpublished Data, Document Delivery, CISTI, National Research Council Canada, Ottawa, ON K1A 0S2, Canada ([http://www.nrc.ca/cisti/irm/unpub\\_e.shtml](http://www.nrc.ca/cisti/irm/unpub_e.shtml) for information on ordering electronically).



to aid geometry convergence.

In all tables, bond lengths are given in Ångströms and angles in degrees. A general trend that was noticed is that *d*-polarization functions added to heteroatoms of the first and second row tend to shorten bonds to adjacent atoms, whereas when they are added to heteroatoms to the third and fourth row they tend to leave unchanged or to increase bond lengths to adjacent atoms. Of course, for first and second row atoms the *d*-functions are genuine polarization functions in the sense that they augment the basis set with functions of higher symmetry. For third and fourth row atoms, however, these functions may serve partly to describe the more diffuse region of the occupied *d*-shells in addition to polarizing the atom in the molecular environment.

## Results and discussion

### Geometry and conformation

#### 1,3-Cyclopentadiene

The structure of cyclopentadiene is presented in Fig. 1. The total electronic energies, selected geometrical data, lower-level conformational energies, predicted IR spectra of synclinal structures, and a short discussion of the lower-level results are found in the supplementary material. Within Hartree–Fock levels the structure varied little with basis set, and the largest structural changes were about 0.015 Å in the C—C bond lengths, 0.012 Å in the C—H bond lengths, and about 1° in the angles (see Table 1 and Supplementary Table S5). At the MP2 level the angles are relatively unchanged; however, the bond lengths are changed. The C—C single bond length decreases by up to 0.01 Å, whereas the C=C double bond increases by 0.025 Å. The C—H bond length increases by about 0.01 Å. The 6-31G\*\* structure differed from the 6-31G\* structure only in the last reported significant figure and is not listed, whereas the 6-31+G\* differed a little more. The geometry is reasonably close to previous ab initio calculations (19,20) and to the experimental temperature-independent microwave structures (21–24), but somewhat further from the temperature-dependent X-ray (25), electron diffraction (26) (see Table 2), and NMR (27) structures. The errors at the MP2/6-31+G\* level are within 0.01 D (1 D =  $3.335641 \times 10^{-30}$  C m) (dipole moment; expt = 0.420 ± 0.003 (24)) and 0.01 Å (structure).

In the C<sub>5</sub>-substituted cyclopentadienes similar basis set changes occur in the cyclopentadienyl unit. The largest geometry changes upon substitution should occur in the bond lengths and angles adjacent to the substituent.

#### 5-Halocyclopentadienes

The structures of 5-halocyclopentadienes are given in Fig. 1. The picture of 5-fluorocyclopentadiene in particular shows how this diene would react *syn*, as the C—F bond is angled away from the  $\pi$ -system; therefore, it would not have to distort as much for *syn* addition as for *anti* addition (7,8). Accurate geometries for 5-halocyclopentadienes have not yet been determined experimentally, though all have been prepared (28–30). The X—C—H and X—C—C angles decrease down the group at the 6-31G\* level, whereas the H—C—C angle increases (Table 3).

The addition of diffuse functions and of adding correlation has very little effect on the bond angles listed. The effect of adding diffuse functions is to shorten the carbon—halogen bond

**Table 1.** Selected geometric parameters of 1,3-cyclopentadiene.

Parameter	Hartree–Fock		Møller–Plesset	
	6-31G*	6-31+G*	6-31G*	6-31+G*
C <sub>2</sub> —C <sub>3</sub>	1.4764	1.4770	1.4647	1.4661
C <sub>2</sub> —C <sub>1</sub>	1.3285	1.3294	1.3540	1.3550
C <sub>1</sub> —C <sub>5</sub>	1.5064	1.5070	1.5009	1.5020
C <sub>2</sub> —H <sub>2</sub>	1.0742	1.0735	1.0855	1.0853
C <sub>1</sub> —H <sub>1</sub>	1.0735	1.0730	1.0846	1.0846
C <sub>5</sub> —H <sub>5</sub>	1.0890	1.0884	1.0993	1.0994
C <sub>3</sub> —C <sub>2</sub> —C <sub>1</sub>	109.17	109.13	109.20	109.17
C <sub>5</sub> —C <sub>1</sub> —C <sub>2</sub>	109.59	109.11	109.11	109.59
C <sub>4</sub> —C <sub>5</sub> —C <sub>1</sub>	102.47	103.37	103.37	102.52
H <sub>2</sub> —C <sub>2</sub> —C <sub>3</sub>	124.39	124.38	124.67	124.67
H <sub>1</sub> —C <sub>1</sub> —C <sub>2</sub>	126.70	126.64	126.76	126.67
H <sub>5</sub> —C <sub>5</sub> —H <sub>5</sub>	106.72	106.96	106.35	106.58
H <sub>5</sub> —C <sub>5</sub> —C <sub>1</sub>	111.94	111.81	111.81	111.90
$\mu$ (D)	0.3049	0.3324	0.3982	0.4286

length by about 0.005 Å, except for fluorine, for which it increases it by a similar amount. The effect of adding correlation is to decrease the carbon—halogen bond length by up to 0.01 Å, except for fluorine, where the bond length increases by 0.03 Å. These results demonstrate the extreme importance of basis set and correlation effects for fluorine-containing systems.

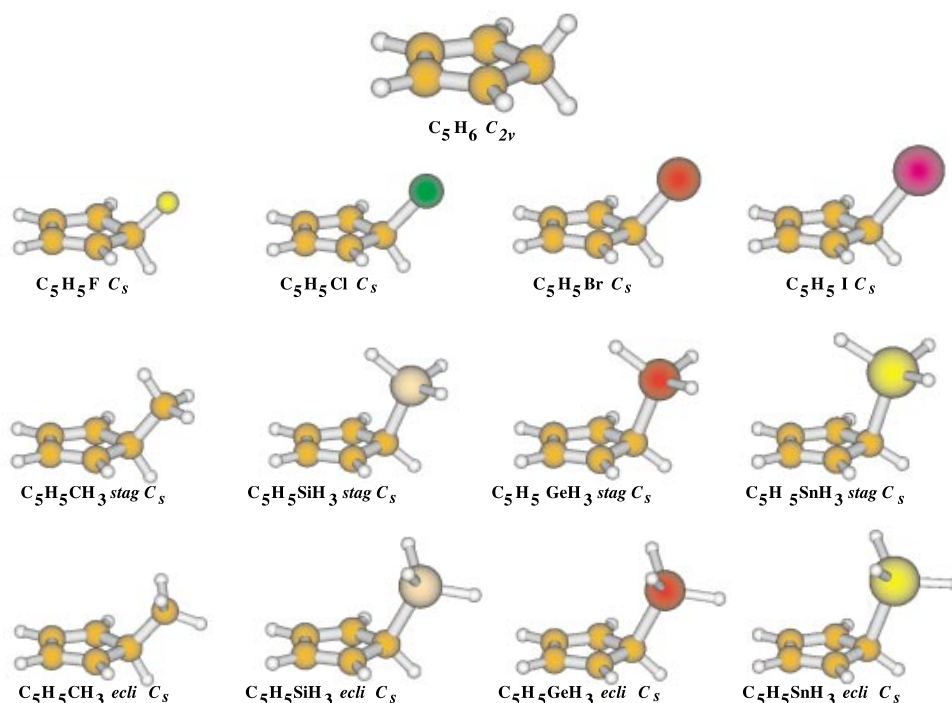
#### 5-Chalcocyclopentadienes and conformation

No unsubstituted 5-chalcocyclopentadienes have been isolated, presumably because of a rapid [1,5]-sigmatropic rearrangement (i.e., 1,2-hydrogen shift) to give an enol analogue followed by rapid conversion via a 1,3-hydrogen shift to the corresponding ketone analogue (see Fig. 2). 5-Chalcocyclopentadienes have been implicated in the decomposition of substituted dicyclopentadienes (Cp<sub>2</sub>OX, X = H, COCH<sub>3</sub>) (31,32) via a retro-Diels–Alder reaction. The MNDO method estimates that 2,4-cyclopentadien-1-ol is about 30 kJ mol<sup>−1</sup> less stable than its isomeric enol forms (33), as suggested by the acetate derivative ratios (34). Some examples of substituted derivatives that have been prepared include the pentamethyl-2,4-cyclopentadiene-1-ol and its methyl ether, the analogous thiol and S-oxidized forms (35,36), and 1-(methylthio)cyclopenta-2,4-diene (37).

Figure 3 gives the structures of all four conformations for all four compounds. Tables S7, S8, S9, and S10 show that the C—C bond is lengthened relative to cyclopentadiene, but this difference decreases quickly down the series. The O—C—C, S—C—C, Se—C—C, and Te—C—C angles are all larger than the corresponding H—C—C angle of cyclopentadiene, as was noted previously for CpF, but this difference also decreases down the series. The H—C—C angle is smaller in both CpOH and CpSH than in CpH, but the other two members of the series show little difference.

Adding correlation increases the C—O and the O—H bond lengths by 0.02–0.03 Å. With the exception of H—O—C, the bond angles seem insensitive to level. The S—C bond length hardly changes when correlation is included, but the S—H bond length increases by about 0.015 Å. Correlation effects on the geometry of CpSeH and CpTeH are similar to that of CpSH. It should be noted that there are relatively few ab initio calculations for organic selenium and tellurium compounds (38–40).



**Fig. 1.** Structures of 1,3-cyclopentadiene and with halo and group-14 derivatives**Table 2.** Literature parameters of 1,3-cyclopentadiene.

Parameter	ED (26)	MW (22)	MW (23)	MW (24)	XR (25)	STO-3G (19)	DZ (20)
C <sub>2</sub> —C <sub>3</sub>	1.46	1.469		1.4682	1.44	1.490	1.480
C <sub>2</sub> —C <sub>1</sub>	1.35	1.342		1.3445	1.32	1.319	1.329
C <sub>1</sub> —C <sub>5</sub>	1.53	1.509		1.5063	1.495	1.522	1.516
C <sub>2</sub> —H <sub>2</sub>			1.08	1.0797		1.081	1.067
C <sub>1</sub> —H <sub>1</sub>			1.08	1.0782		1.080	1.067
C <sub>5</sub> —H <sub>5</sub>			1.09	1.0993		1.091	1.084
C <sub>3</sub> -C <sub>2</sub> -C <sub>1</sub>	109	109.3		109.29	109.5		109.3
C <sub>5</sub> -C <sub>1</sub> -C <sub>2</sub>	110	109.3		109.24	109		109.7
C <sub>4</sub> -C <sub>5</sub> -C <sub>1</sub>	101	102.7		102.93	102		102.1
H <sub>2</sub> -C <sub>2</sub> -C <sub>3</sub>			125	124.67			124.4
H <sub>1</sub> -C <sub>1</sub> -C <sub>2</sub>			131	127.13			126.7
H <sub>5</sub> -C <sub>5</sub> -H <sub>5'</sub>			110	106.33		107.4	107.4

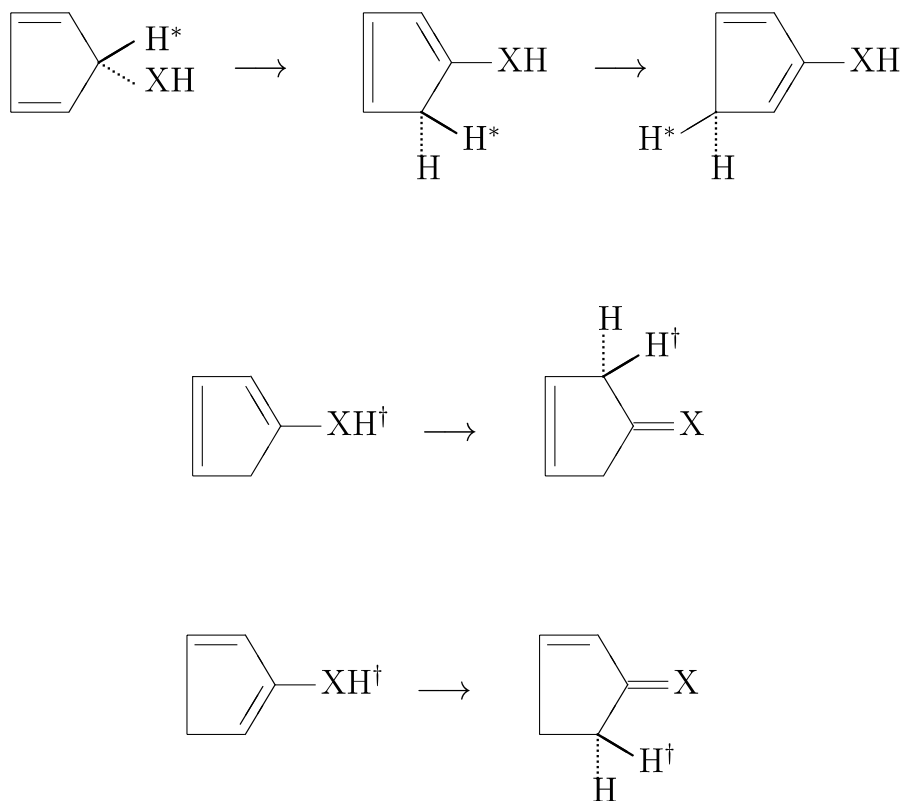
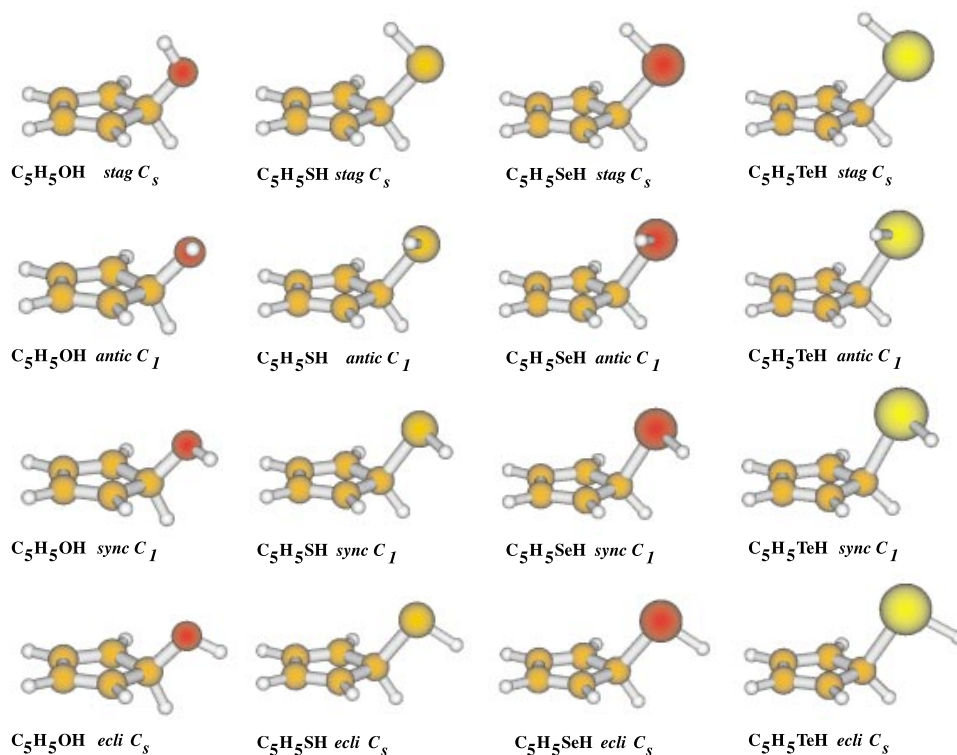
An alternate conformational view of chalcogenocyclopentadienes is shown in Fig. 4. The conformational changes resemble in many respects those presented in reference (41). In general, when there is an eclipsing interaction between the X—H bond and either a C—C or C—H bond the X—H bond shortens (by up to 0.006 Å) and the connecting X—C bond lengthens (by up to 0.017 Å). In general, the H—X—C bond angle increases by at most 1.6° upon eclipsing, but as one goes down a group this increase becomes smaller, especially when comparing the two asymmetric structures. The X—C—H bond angle is anomalously small in the *anti*-periplanar conformers (by up to 5°), but this becomes less pronounced as one progresses down the group. The H—C—C angle changes by at most 2°, but in no obvious pattern. The X—C—C angle undergoes large changes of up to 5°, with the smallest angle consistently being for the synclinal conformer in which the C—C bond is *trans* to the X—H bond. For CpOH,

the largest X—C—C angle is found for the anticlinal conformer in which the C—C bond is *cis* to the X—H bond, whereas for the others the *anti*-periplanar conformer gives the largest angle. For the larger atoms, the relation between torsion and X—C—C is fairly flat near the maximum X—C—C angle.

### 5-Pnictocyclopentadienes

Very recently, the first report of the preparation of unsubstituted 2,4-cyclopentadienylphosphine and arsine appeared (42). The amine and stibine are unknown. Several substituted derivatives are known, such as the cyclopentadienyl difluorophosphine (46–48) and the pentamethylcyclopentadienyl amine (35, 36, 43), phosphine (44), and dichlorostibine (45). In addition, an MNDO study of the [1,5]-sigmatropic rearrangement involving the motion of the phosphorus group has been carried out (49, 50).

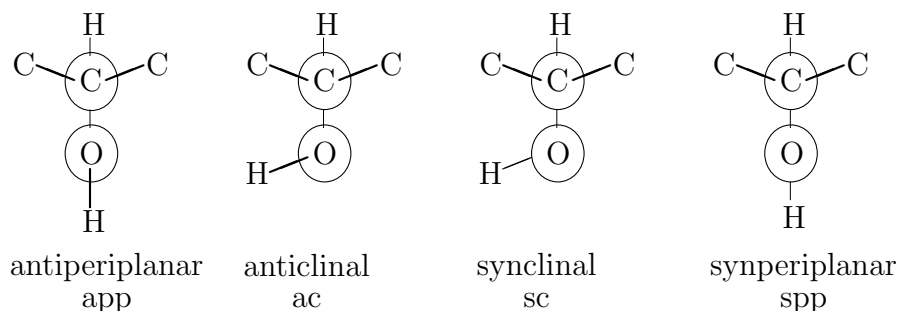
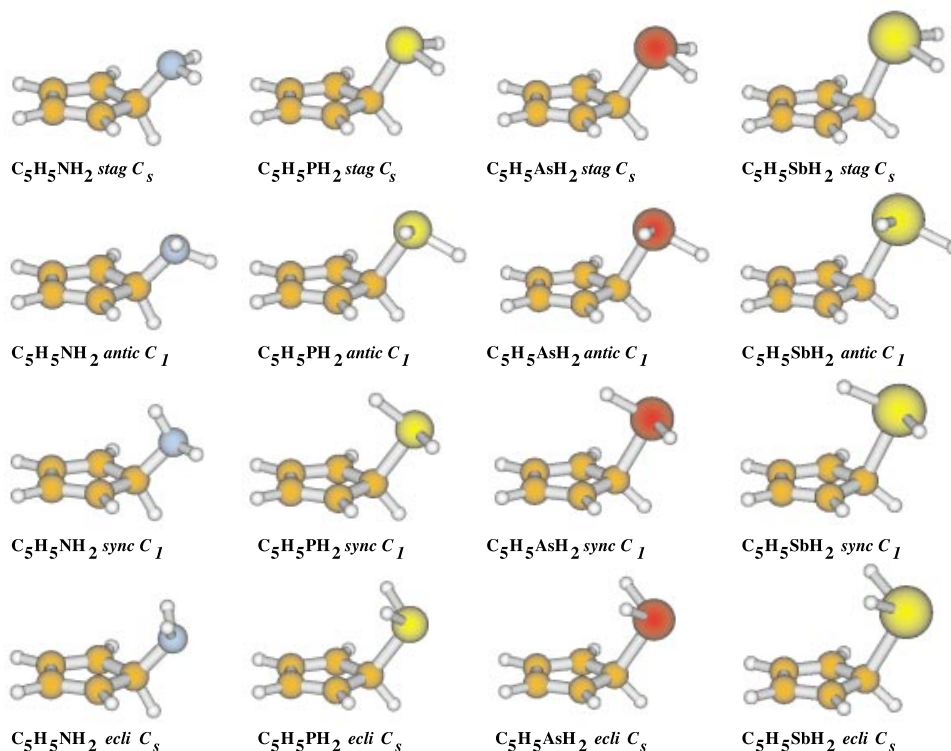


**Fig. 2.** Possible decomposition routes for 2,4-cyclopentadien-1-ol analogues.**Fig. 3.** Structures of 2,4-cyclopentadiene-1-ol analogues.

The structures are given in Fig. 5. In general, the adjacent C—C bond shortens, the X-C-C and X-C-H angles become

smaller, and the H-C-C angle becomes larger as one goes down this group. The trend is the same as that for the chalcosubstituted



**Fig. 4.** Conformation of 2,4-cyclopentadien-1-ol.**Fig. 5.** Structures of 2,4-cyclopentadienylamine analogues.

cyclopentadienes, but unlike these, the angular parameters are not disposed predominantly to one side of those of CpH, which is most likely a result of the electronegativity changes relative to hydrogen. The parameters of CpPH<sub>2</sub> most closely resemble CpH. Diffuse functions have little effect on the geometry, whereas adding correlation effects increases the N—C bond length by about 0.01 Å and the X—H bond length by about 0.015 Å.

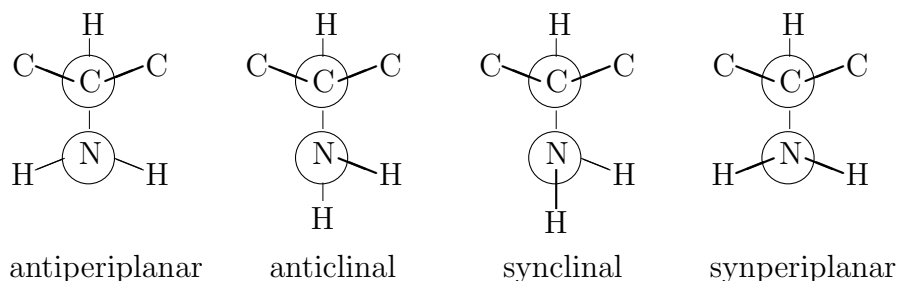
An alternate view of conformation of pnictocyclopentadienes is shown in Fig. 6, in which the conformational designation refers to the pnictogen lone pair. If there exists an eclipsing interaction with an X—H bond, then the X—C bond lengthens by up to 0.02 Å, and the X—H bond shortens by as much as 0.008 Å in some cases. An eclipsing interaction can also increase the H—X—C angle by up to 2°. The X—C—H angle is anomalously *larger* in the *anti*-periplanar conformation by up to 5°. The largest X—C—C angle always occurs in the synclinal structure,

in which the nitrogen lone pair is *trans* to the C—C bond in question. The smallest X—C—C angle usually occurs in the *anti*-periplanar structure.

#### Group 14 cyclopentadienes

The group 14 cyclopentadienes have been the most extensively studied of our series. 5-Methylcyclopentadiene was first separated from its more stable isomers by Csicsery (51) using vapor-phase chromatography, and it constituted about 3% of the total equilibrium mixture. It can also be prepared by the methylation of CpMgBr at 263 K, but this isomerizes to the 1-isomer at 298 K in about 3 h. Further isomerization to an equilibrium mixture of the 1- and 2-isomers occurs within a couple of days (52). The isomerization was shown to proceed by a 1,2-hydrogen shift with an activation barrier of  $83.3 \pm 1.3$  kJ mol<sup>-1</sup> as determined by NMR (53, 54). Evidence for methyl migration was also seen in trimethylcyclopentadienes with a barrier of about 185 kJ mol<sup>-1</sup> (55), which agreed well



**Fig. 6.** Conformation of 2,4-cyclopentadienylamine.

with the MINDO/3 result of  $194.3 \text{ kJ mol}^{-1}$  for CpMe (56).

Silylcyclopentadiene was first prepared by the reaction of potassium cyclopentadienide with silyl bromide at 77 K (57). The structure was determined by electron diffraction soon after (58). CpSiH<sub>3</sub> undergoes a rapid 1,2-silyl migration (248 K) and a slower 1,2-hydrogen shift (339 K) (59). A joint photoelectron and ab initio study suggested that the fluxional behavior of CpSiH<sub>3</sub> may be related to the delocalization of the Si—C bonding orbital with the  $\pi$ -system (60). The activation barrier for silyl migration was determined both from proton ( $59.4 \pm 1.0 \text{ kJ mol}^{-1}$ ) and <sup>13</sup>C NMR lineshape analysis ( $57.7 \pm 0.1 \text{ kJ mol}^{-1}$ ) (61). An MNDO study overestimates this barrier ( $99.1 \text{ kJ mol}^{-1}$ ) (62).

Germylcyclopentadiene was prepared in a similar fashion to silylcyclopentadiene and the NMR behavior suggested a fluxional molecule (63). The X-ray and electron diffraction structure of this compound has been published (64). The trimethyl derivative undergoes a 1,2-shift with a barrier of  $38.5 \pm 4.2 \text{ kJ mol}^{-1}$ , and the corresponding stannane,  $32.6 \pm 4.2 \text{ kJ mol}^{-1}$  (65).

Tables S15, S16, S17, and S18 show that, upon substitution, the C—C bond length becomes slightly longer in the case of CpCH<sub>3</sub>, but becomes shorter for the higher analogues. The X—C—C and X—C—H angles decrease upon going down a group, with only the CpCH<sub>3</sub> angle being larger than cyclopentadiene, whereas the H—C—C angle increases. The effect of correlation is to slightly lengthen the X—H bond lengths.

The existence of only two conformational possibilities simplifies our analysis considerably. The X—C and C—C bonds in the *syn*-periplanar conformer are longer than in the staggered conformer by as much as 0.015 Å and 0.005 Å, respectively, whereas no clear trend exists for the H—X bond length. The X—C—C and H—C—C angles increase and decrease by as much as 2.7° and 1.8°, respectively, upon eclipsing. The X—C—H angle always decreases (except for CpCH<sub>3</sub>) by up to 1.4°. No persistent trend for the angles surrounding the substituent emerges.

A comparison between the experimental and our best theoretical structures is given in Table 4. The X—C and X—H distance is overestimated here, whereas no obvious trend is seen for the C—C distance. It is understandable that the hydrogen positions are given with poor accuracy by these diffraction techniques. The calculated results are outside the error bars of experiment because they provide the  $r_e$  structure (0 K, bottom of PES), whereas the experiment measures the time-averaged structure at a finite temperature, resulting in a sampling of several vibrational states. It is also possible that the agreement may improve with an extension of the basis set. A microwave-determined structure for these compounds would prove useful in this case,

as with cyclopentadiene itself. In addition, the barrier to rotation could possibly be determined in this way (66).

### Conformation energies

#### Chalcocyclopentadienes

The barriers to rotation are shown in Table 5. The barriers  $E_{sc \rightarrow spp}$  are compared to the corresponding results for CH<sub>3</sub>XH at 6-31G\* (67) (See Table S20. The ‘\*’ represents our calculated value). In general, the methanol analogue barriers are larger for O and S, similar for Se, and smaller for Te. Generally speaking, adding diffuse functions or correlation effects changes the relative potential energies usually by less than 1 kJ mol<sup>-1</sup>.

#### Pnictocyclopentadienes

The barriers to internal rotation in 5-pnictocyclopentadienes are shown in Table 6. The preference for an *anti*-periplanar conformer increases as one goes down a period, even though CpNH<sub>2</sub> itself assumes the synclinal conformer at 6-31G\*. In general the barriers in substituted cyclopentadienes are larger than the corresponding pnictomethanes, as seen from Table S20. The effect of adding diffuse functions or correlation effects is still small, but larger than the effect for the chalcogen-containing systems. Correlation is the more important of the two effects.

#### Group 14 Cyclopentadienes

From Table 7, the barriers are seen to be relatively insensitive to basis set with the values agreeing quite well at the split-valence level. The barriers are larger than in the corresponding methyl derivatives (see Table S20). Diffuse functions have little effect, but correlation energy seems to be very important here for the silyl-, germyl-, and stannyl-substituted cyclopentadienes. This follows the trend of the increasing importance of correlation energy as the number of attached hydrogens increases.

### Discussion of conformation

There are numerous ways of explaining the conformational preferences about a  $\sigma$ -bond, but the approach used in this work will be that taken by Brunck, Reed, and Weinhold (68, 69), which states that the predominant conformational preferences can be explained by bond–antibond interactions. Other studies (70) have used Fourier analysis, but are strictly applicable only to molecules possessing a rough three-fold symmetry axis and thus cannot be applied meaningfully to molecules involving the higher pnictogen series in which the H—X—H angles are closer



**Table 3.** Selected geometric parameters of 5-halocyclopentadienes (CpX).

X	Parameter	Hartree-Fock		Møller-Plesset	
		6-31G*	6-31+G*	6-31G*	6-31+G*
F	F—C	1.3694	1.3731	1.3983	1.4073
	C—C	1.5093	1.5104	1.5061	1.5065
	H—C	1.0865	1.0845	1.1014	1.0990
	F-C-C	113.42	113.55	113.55	113.12
	H-C-C	110.06	109.36	109.36	110.51
	F-C-H	106.85	107.07	107.07	106.49
Cl	Cl—C	1.8027	1.8000	1.7947	1.7938
	C—C	1.5062	1.5072	1.5019	1.5030
	H—C	1.0822	1.0817	1.0967	1.0968
	Cl-C-C	112.78	112.69	113.34	112.93
	H-C-C	111.57	110.85	110.17	111.38
	Cl-C-H	105.18	105.92	105.94	105.23
Br	Br—C	1.9755	1.9695	1.9732	1.9687
	C—C	1.5022	1.5035	1.4976	1.4989
	H—C	1.0797	1.0795	1.0943	1.0944
	Br-C-C	111.81	110.96	111.38	111.73
	H-C-C	113.07	113.12	112.72	112.98
	Br-C-H	103.84	104.44	104.46	104.26
I	I—C	2.2004	2.1956	2.1965	2.1929
	C—C	1.4992	1.5003	1.4939	1.4950
	H—C	1.0794	1.0791	1.0938	1.0940
	I-C-C	111.36	110.15	110.29	111.35
	H-C-C	113.96	114.24	114.11	113.88
	I-C-H	102.83	103.53	103.53	103.03

**Table 4.** Comparison between calculated MP2/6-31+G\* and experimental structures of 2,4-cyclopentadienyl-1-silane and germane.

Parameter	Silane		Germane		
	ED (47)	Calcd	ED (64)	XR (64)	Calcd
X—C	1.881	1.910	1.969	1.965	1.986
X—H		1.483		1.4	1.545
C—C	1.500	1.490	1.478	1.474	1.486
X-C-C	106.6	106.6	106.3	107.7	106.0
X-C-H		107.9		104	106.7
H-X-C		109.1		109	108.6

to 90° than 109.5°. The justification for our chosen approach will lie in the ease of explanation of the major geometric and energetic conformational trends.

If we consider the *anti*-periplanar form of CpOH, then we can count four *trans* vicinal localized orbital interactions, giving an interaction energy

$$[1] \quad E_{\text{antiperiplanar}} = 2E_{n,\sigma_{\text{CC}}^*} + E_{\sigma_{\text{OH}},\sigma_{\text{CH}}^*} + E_{\sigma_{\text{CH}},\sigma_{\text{OH}}^*}$$

Similarly, the synclinal form of CpOH gives

$$[2] \quad E_{\text{synclinal}} = E_{n,\sigma_{\text{CC}}^*} + E_{n,\sigma_{\text{CH}}^*} + E_{\sigma_{\text{OH}},\sigma_{\text{CC}}^*} + E_{\sigma_{\text{CC}},\sigma_{\text{OH}}^*}$$

The strongest interactions are normally those involving lone pairs donating into vicinal antibonds polarized toward the rotation axis, i.e., corresponding to vicinal bonds (such as C—F)

polarized away from the axis, since in this case the overlap is greatest. The C—H bond is slightly polarized toward the carbon atom — which has the higher electronegativity — and thus its ‘antibond’ would be slightly polarized toward the hydrogen. This results in poorer overlap with the ‘lone pair’ than that seen in a C—C antibond. In this case the *anti*-periplanar conformer will be favored. Because the overlap depends on the distance between the axis atoms, the difference in energy between these conformers should decrease as oxygen is successively replaced by sulfur, selenium, and tellurium, which it does. In fact, the two conformers of CpTeH are essentially degenerate on the potential energy surface.

If we consider the *anti*-periplanar form of CpNH<sub>2</sub>, then we can count five *trans* interactions, giving an interaction energy

$$[3] \quad E_{\text{antiperiplanar}} = E_{n,\sigma_{\text{CH}}^*} + 2E_{\sigma_{\text{NH}},\sigma_{\text{CC}}^*} + 2E_{\sigma_{\text{CC}},\sigma_{\text{NH}}^*}$$



**Table 5.** Conformational energies of chalcocyclopentadienes (kJ mol<sup>-1</sup>).

System	Energy	HF		MP2	
		6-31G*	6-31+G*	6-31G*	6-31+G*
CpOH	$E_{\text{app} \rightarrow \text{ac}}$	13.36	12.13	13.28	11.48
	$E_{\text{app} \rightarrow \text{sc}}$	9.96	8.91	9.79	8.52
	$E_{\text{app} \rightarrow \text{spp}}$	13.91	12.29	14.91	12.55
	$E_{\text{sc} \rightarrow \text{ac}}$	3.40	3.23	3.49	2.96
	$E_{\text{sc} \rightarrow \text{spp}}$	3.95	3.38	5.12	4.03
CpSH	$E_{\text{app} \rightarrow \text{ac}}$	13.14	13.04	12.40	12.59
	$E_{\text{app} \rightarrow \text{sc}}$	5.05	5.28	4.64	5.21
	$E_{\text{app} \rightarrow \text{spp}}$	10.32	10.20	11.39	11.03
	$E_{\text{sc} \rightarrow \text{ac}}$	8.09	7.76	7.75	7.38
	$E_{\text{sc} \rightarrow \text{spp}}$	5.27	4.92	6.74	5.82
CpSeH	$E_{\text{app} \rightarrow \text{ac}}$	10.65	9.42	9.37	8.57
	$E_{\text{app} \rightarrow \text{sc}}$	2.86	2.16	2.02	1.67
	$E_{\text{app} \rightarrow \text{spp}}$	7.46	6.76	8.95	8.27
	$E_{\text{sc} \rightarrow \text{ac}}$	7.79	7.26	7.34	6.90
	$E_{\text{sc} \rightarrow \text{spp}}$	4.60	4.60	6.92	6.60
CpTeH	$E_{\text{app} \rightarrow \text{ac}}$	7.27	7.37	6.08	6.54
	$E_{\text{app} \rightarrow \text{sc}}$	-0.09	-0.10	-1.34	-1.12
	$E_{\text{app} \rightarrow \text{spp}}$	3.87	3.71	5.70	5.41
	$E_{\text{sc} \rightarrow \text{ac}}$	7.36	7.46	7.41	7.67
	$E_{\text{sc} \rightarrow \text{spp}}$	3.96	3.81	7.04	6.53

**Table 6.** Conformational energies of pnictocyclopentadienes (kJ mol<sup>-1</sup>).

System	Energy	HF		MP2	
		6-31G*	6-31+G*	6-31G*	6-31+G*
CpNH <sub>2</sub>	$E_{\text{app} \rightarrow \text{ac}}$	5.52	4.80	6.91	5.75
	$E_{\text{app} \rightarrow \text{sc}}$	-10.79	-9.86	-10.56	-9.17
	$E_{\text{app} \rightarrow \text{spp}}$	5.67	5.73	5.09	5.12
	$E_{\text{sc} \rightarrow \text{ac}}$	16.31	14.66	17.46	14.92
	$E_{\text{sc} \rightarrow \text{spp}}$	16.46	15.59	15.64	14.29
CpPH <sub>2</sub>	$E_{\text{app} \rightarrow \text{ac}}$	12.67	11.95	16.09	14.58
	$E_{\text{app} \rightarrow \text{sc}}$	-1.01	-1.63	-0.07	-1.41
	$E_{\text{app} \rightarrow \text{spp}}$	13.96	13.48	14.94	14.29
	$E_{\text{sc} \rightarrow \text{ac}}$	13.68	13.58	16.15	15.99
	$E_{\text{sc} \rightarrow \text{spp}}$	14.97	15.10	15.01	15.70
CpAsH <sub>2</sub>	$E_{\text{app} \rightarrow \text{ac}}$	11.80	11.31	15.20	14.49
	$E_{\text{app} \rightarrow \text{sc}}$	1.01	0.96	2.05	1.69
	$E_{\text{app} \rightarrow \text{spp}}$	13.90	13.81	14.70	14.55
	$E_{\text{sc} \rightarrow \text{ac}}$	10.79	10.35	13.15	12.81
	$E_{\text{sc} \rightarrow \text{spp}}$	12.89	12.85	12.65	12.86
CpSbH <sub>2</sub>	$E_{\text{app} \rightarrow \text{ac}}$	10.80	10.35	12.15	12.81
	$E_{\text{app} \rightarrow \text{sc}}$	3.91	3.70	5.88	5.32
	$E_{\text{app} \rightarrow \text{spp}}$	14.52	15.00	16.97	17.50
	$E_{\text{sc} \rightarrow \text{ac}}$	6.89	7.16	9.60	10.03
	$E_{\text{sc} \rightarrow \text{spp}}$	10.61	11.30	11.09	12.17

Similarly, the synclinal form of CpNH<sub>2</sub> gives

$$[4] \quad E_{\text{synclinal}} = E_{n, \sigma_{\text{CC}}^*} + E_{\sigma_{\text{NH}}, \sigma_{\text{CC}}^*} + E_{\sigma_{\text{NH}}, \sigma_{\text{CH}}^*} \\ + E_{\sigma_{\text{CC}}, \sigma_{\text{NH}}^*} + E_{\sigma_{\text{CH}}, \sigma_{\text{NH}}^*}$$

For similar reasons, the synclinal form of CpNH<sub>2</sub> will be favored in this case. Because of the quicker drop in electronegativity and longer bond lengths in this case the preference does not

persist down the group and other terms start playing an important role, but the difference is still very slight, being less than 4.0 kJ mol<sup>-1</sup>. Steric interactions between the *anti*-periplanar hydrogen and the two vicinal C—C bonds in the larger substituents may favor the *anti*-periplanar arrangement because of the closer match in the lengths of these bonds.

The geometry changes also agree with the idea of bond–antibond interactions. The shorter X—H bond in the *syn*-peri-



**Table 7.** Conformational barrier of group IV cyclopentadienes (kJ mol<sup>-1</sup>).

System	HF		MP2	
	6-31G*	6-31+G*	6-31G*	6-31+G*
CpCH <sub>3</sub>	17.62	17.47	18.37	18.24
CpSiH <sub>3</sub>	13.71	13.46	18.59	17.33
CpGeH <sub>3</sub>	11.11	11.73	15.09	15.67
CpSnH <sub>3</sub>	8.05	8.95	12.42	13.11

planar forms is a result of the *cis*-interaction being weaker than the *trans*-interaction, and thus the antibond contribution is lower. The longer X—C bond may simply be explained by stronger steric interactions in the Lewis structure. In the Group IV series, hardly any trend is noticed, because the X—H antibond, being polarized predominantly toward the hydrogen, is a poor acceptor.

For CpOH, the widening of H—O—C in a *syn*-periplanar arrangement is consistent with a simple steric effect, especially with the C—H bond. As one goes down the group, the steric interaction with the C—C bonds become greater leading to the largest angles in the synclinal form. The ‘anomalous’ smallness of the X—C—H angle in the *anti*-periplanar conformer can be explained simply as the absence of any strong lone pair donation into the C—H antibond, whereas all of the other conformers have either a *cis* or *trans* donation to C—H. For the same reason the smallest X—C—C angle will be that containing no lone pair donation, i.e., *trans* to the X—H bond.

For CpNH<sub>2</sub>, the ‘anomalous’ largeness of the X—C—H angle in the *anti*-periplanar conformer is consistent with a strong interaction of the nitrogen lone pair with the C—H antibond. Similarly, the largest X—C—C angle occurs for the synclinal structure, in which the nitrogen lone pair is *trans* to the C—C bond in question.

### Vibrational frequencies

The vibrational frequencies of cyclopentadiene itself are given in Table 8. Adding diffuse functions hardly affects the frequency (usually within 10 cm<sup>-1</sup>). Adding correlation effects has a large influence on the frequency, generally decreasing it, although some modes are affected much more than others. The correlated frequency could be predicted from the Hartree–Fock frequency by using a mode-specific multiplicative factor (for example, 0.97 for C(sp<sup>3</sup>)—C (or H), 0.962 for C(sp<sup>2</sup>)—H, 0.906 for C=C, 0.94 for CH bends, 0.83–0.90 for out-of-plane (oop) H bends, 0.87–0.95 for ring deformations, and 0.92 for CH<sub>2</sub> rock, twist, and wags).

The IR spectra of cyclopentadiene and 5-methylcyclopentadiene (51) (% transmittance vs. wavelength) were converted to absorbance vs. wavenumber and compared with the theoretical spectra (MP2/6-31+G\*) in Fig. 7. Errors in the experimental estimation of frequencies range from 2–40 cm<sup>-1</sup>. Because of the lack of an internal standard, the intensity scales will be different. The assignment of modes is fairly straightforward here. The most intense modes observed in liquid cyclopentadiene correlate well with the predicted gas phase results. There appears to be an enhancement of the (predicted) very weak C=C stretching motion (1590, 1640), which appears to be in Fermi

**Table 8.** Vibrational frequencies of cyclopentadiene.

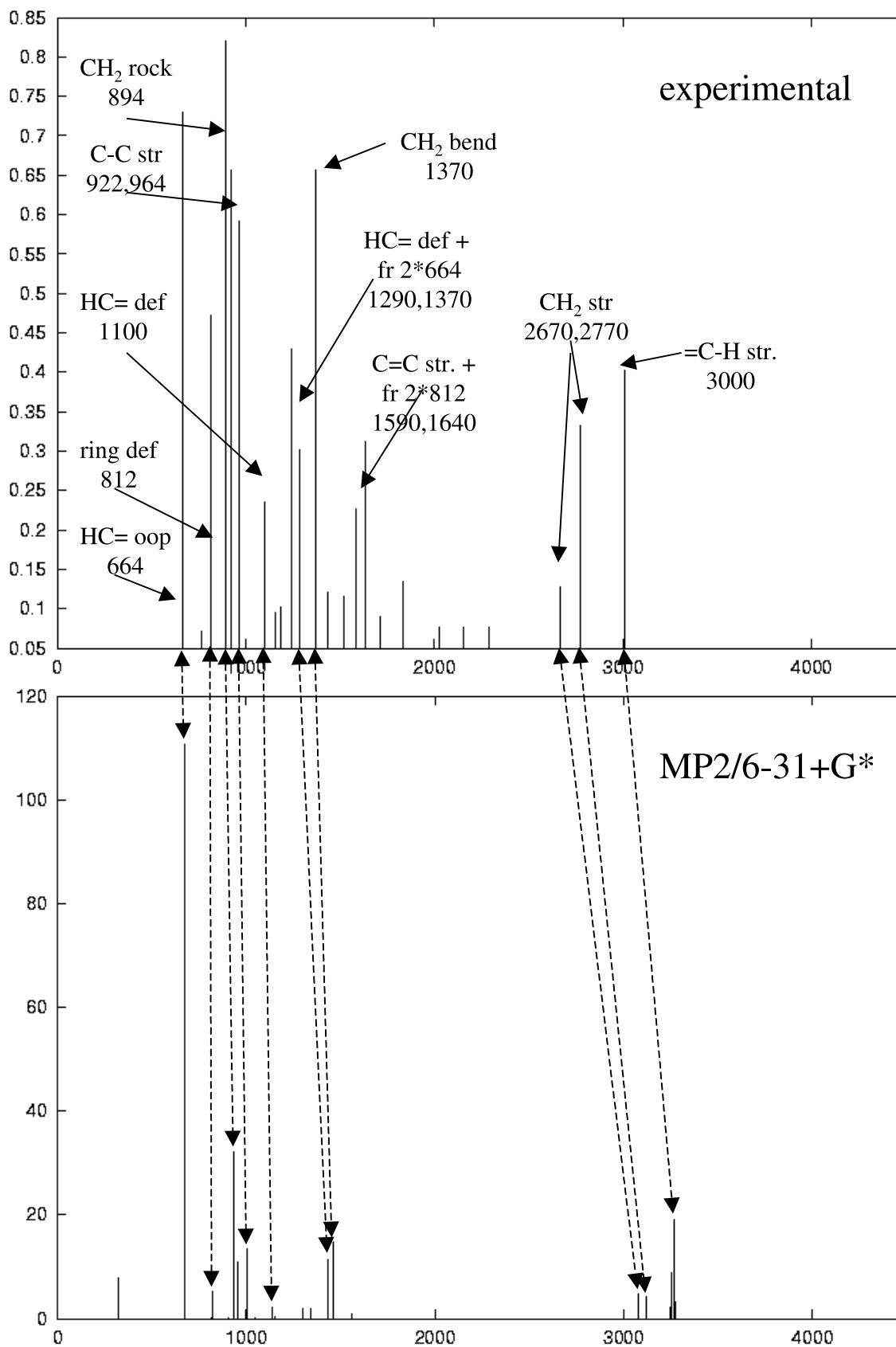
Symmetry	Assignment	HF		MP2	
		6-31G*	6-31+G*	6-31G*	6-31+G*
B <sub>1</sub>	ring def	380	377	334	324
A <sub>2</sub>	ring def	559	556	502	490
B <sub>1</sub>	CH oop	752	746	683	671
A <sub>2</sub>	CH oop	809	806	699	684
A <sub>1</sub>	ring def	866	865	818	816
B <sub>2</sub>	ring def	867	867	820	819
A <sub>1</sub>	CH <sub>2</sub> —C str	985	983	961	956
B <sub>1</sub>	CH <sub>2</sub> rock	1035	1028	947	936
B <sub>2</sub>	CH <sub>2</sub> —C str	1040	1038	1009	1005
A <sub>1</sub>	C—C str	1069	1067	1051	1047
A <sub>2</sub>	CH oop	1074	1069	888	866
B <sub>1</sub>	CH oop	1081	1080	918	907
B <sub>2</sub>	CH def	1217	1213	1141	1135
A <sub>1</sub>	CH def	1233	1229	1157	1151
A <sub>2</sub>	CH <sub>2</sub> twist	1254	1252	1147	1121
B <sub>2</sub>	CH <sub>2</sub> wag	1413	1411	1304	1300
B <sub>2</sub>	CH def	1454	1452	1349	1342
A <sub>1</sub>	CH def	1534	1530	1442	1433
A <sub>1</sub>	CH <sub>2</sub> def	1584	1576	1479	1462
A <sub>1</sub>	C=C str	1741	1721	1578	1560
B <sub>2</sub>	C=C str	1818	1797	1652	1633
A <sub>1</sub>	CH <sub>2</sub> str	3194	3193	3087	3077
B <sub>1</sub>	CH <sub>2</sub> str	3221	3219	3131	3119
B <sub>2</sub>	CH str	3381	3382	3253	3244
A <sub>1</sub>	CH str	3391	3391	3262	3253
B <sub>2</sub>	CH str	3409	3409	3279	3270
A <sub>1</sub>	CH str	3417	3417	3285	3276

resonance with the first overtone of a ring deformation at 812. The H—C= deformation also appears to be in Fermi resonance (1240, 1290) with the first overtone of the H—C out-of-plane deformation at 664. Of course, we cannot rule out environmental effects or impurities.

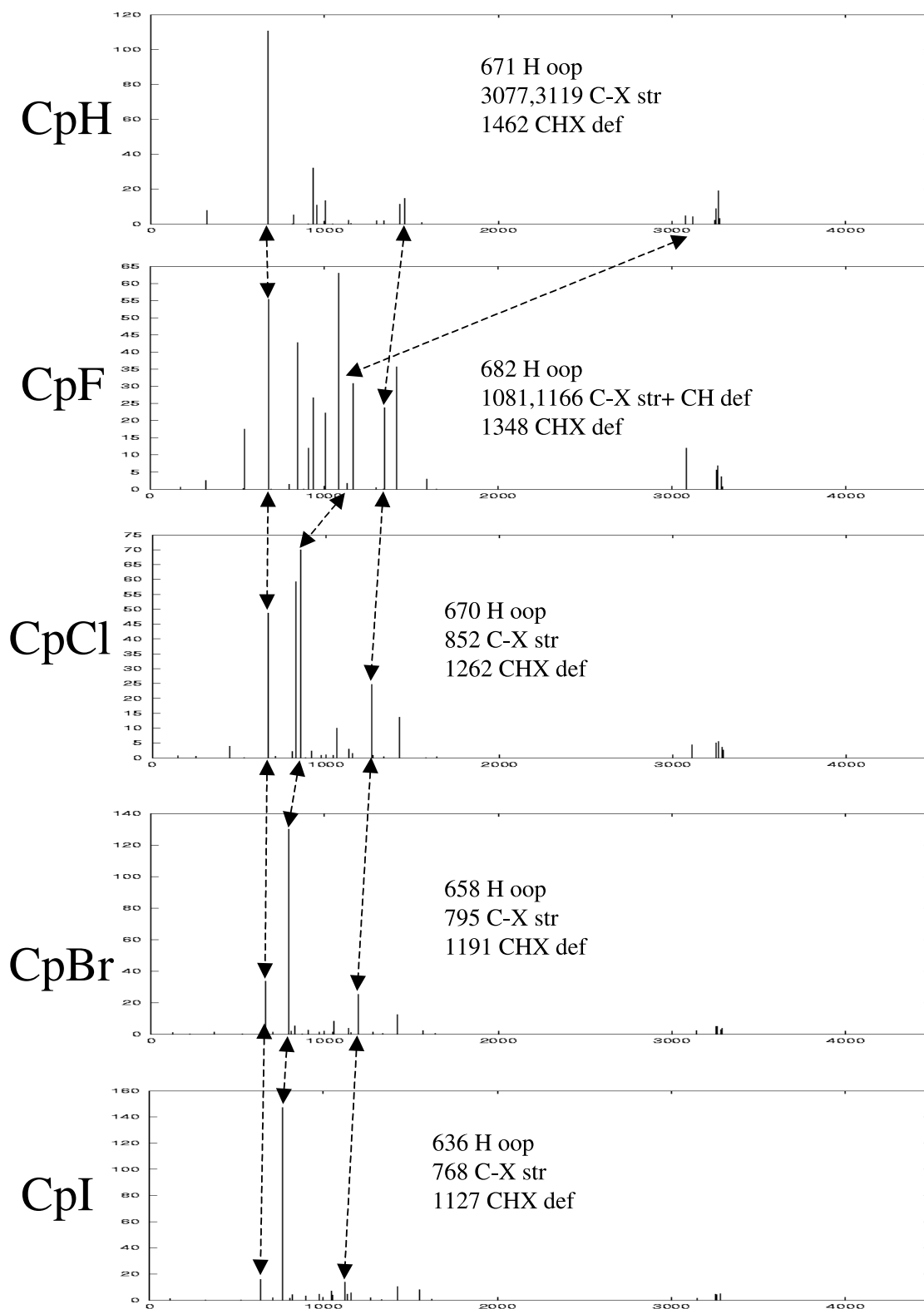
The theoretical spectra of the halosubstituted cyclopentadienes are given in Fig. 8. The intense hydrogen out-of-plane deformation, the carbon-halogen stretching motion, and the HCX hydrogen bending motion increases in frequency on progressing from iodine to fluorine. In the fluoro derivative, many bands are predicted to be more intense in the IR spectra compared with the other halogens. This is probably due to the difference in electronegativity between carbon and fluorine, which gives a large bond dipole. Any normal mode that has a significant C—F stretching component would be increased in intensity.

The theoretical spectra of the *anti*-periplanar and synclinal chalcosubstituted cyclopentadienes are given in Figs. 9 and S1. For the *anti*-periplanar series it is the OH and TeH that give the largest number of intense modes. In these cases, the electronegativity of the substituent is sufficiently different from carbon to give rise to a greater number of intense modes. Some trends when comparing the two conformers are the lower C<sub>5</sub>—H stretching frequency (OH) and HCX deformation frequencies (all) in the synclinal conformers. These indicate that the C—H bond is weaker, which is consistent with strong donation of the chalcogen lone pair into the C—H antibond. If the alcohol is ever observed our predictions suggest that it will predomi-



**Fig. 7.** Experimental and theoretical vibrational frequencies of 1,3-cyclopentadiene.



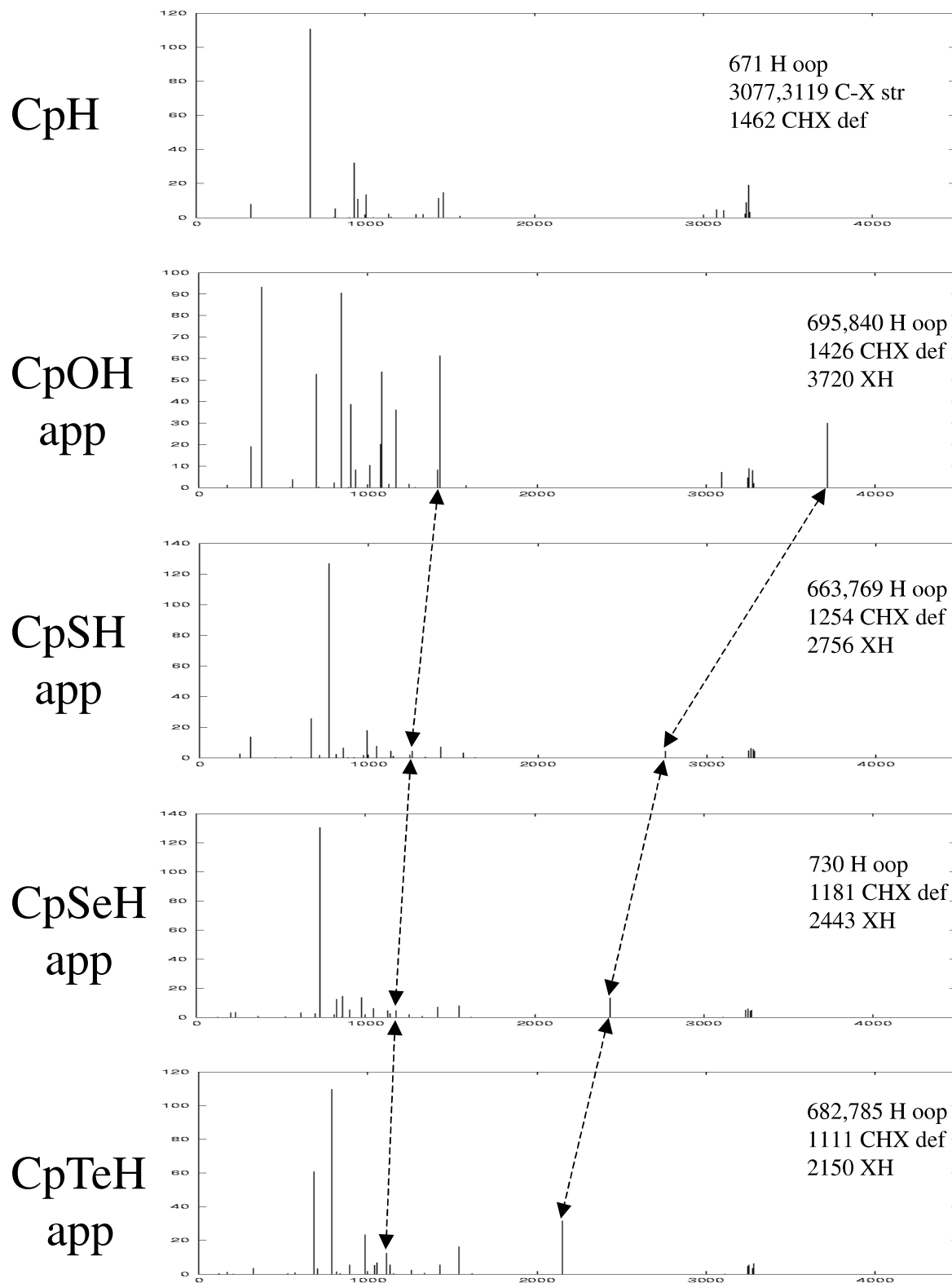
**Fig. 8.** MP2/6-31+G\* frequencies of 5-halo-1,3-cyclopentadiene.

nantly be in the *app* conformer, whereas the higher analogues will have significant contribution from the *sc* conformer, and thus the bands will be averaged out.

The theoretical spectra of the *anti*-periplanar and synclinal

pictosubstituted cyclopentadienes are given in Figs. 10 and S2. Except for the amine, the spectra of the *app* conformer is similar to the *sc* conformer, as contrasted with the chalcogen cases. Except for the amine, the two X-H stretching modes are



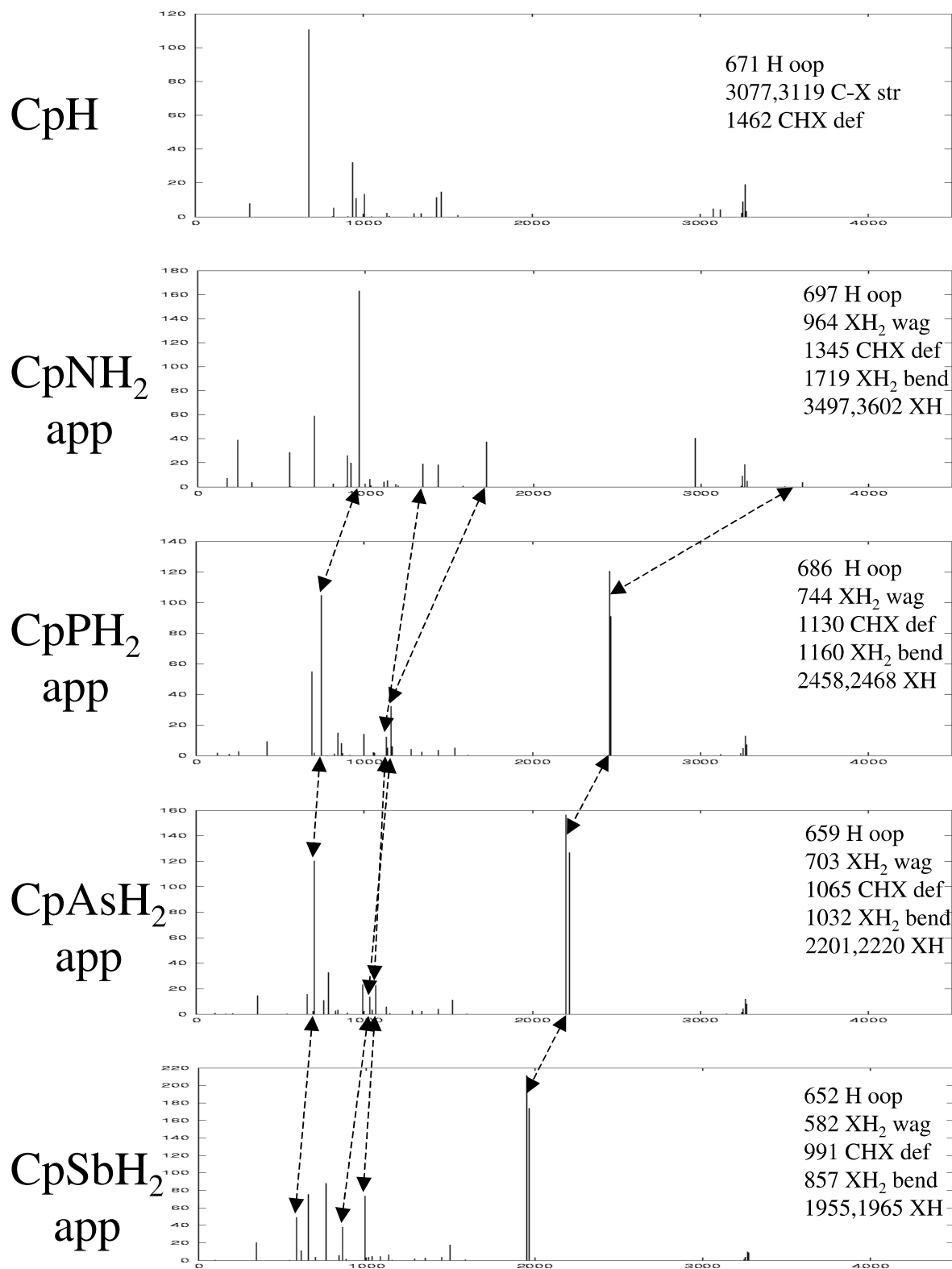
**Fig. 9.** MP2/6-31+G\* frequencies of 5-chalco-1,3-cyclopentadiene.

very intense. The wagging motion of the substituent is also prominent, whereas the bending motion is less intense. The C<sub>5</sub>-H stretching frequency (NH<sub>2</sub>) and the HCX deformation frequencies (all) are lower in the *anti*-periplanar conformer,

which is consistent with interaction of the pnictogen lone pair into the C—H antibond.

The theoretical spectra of the group 14 substituted cyclopentadienes are given in Fig. 11. The H-stretching modes of the

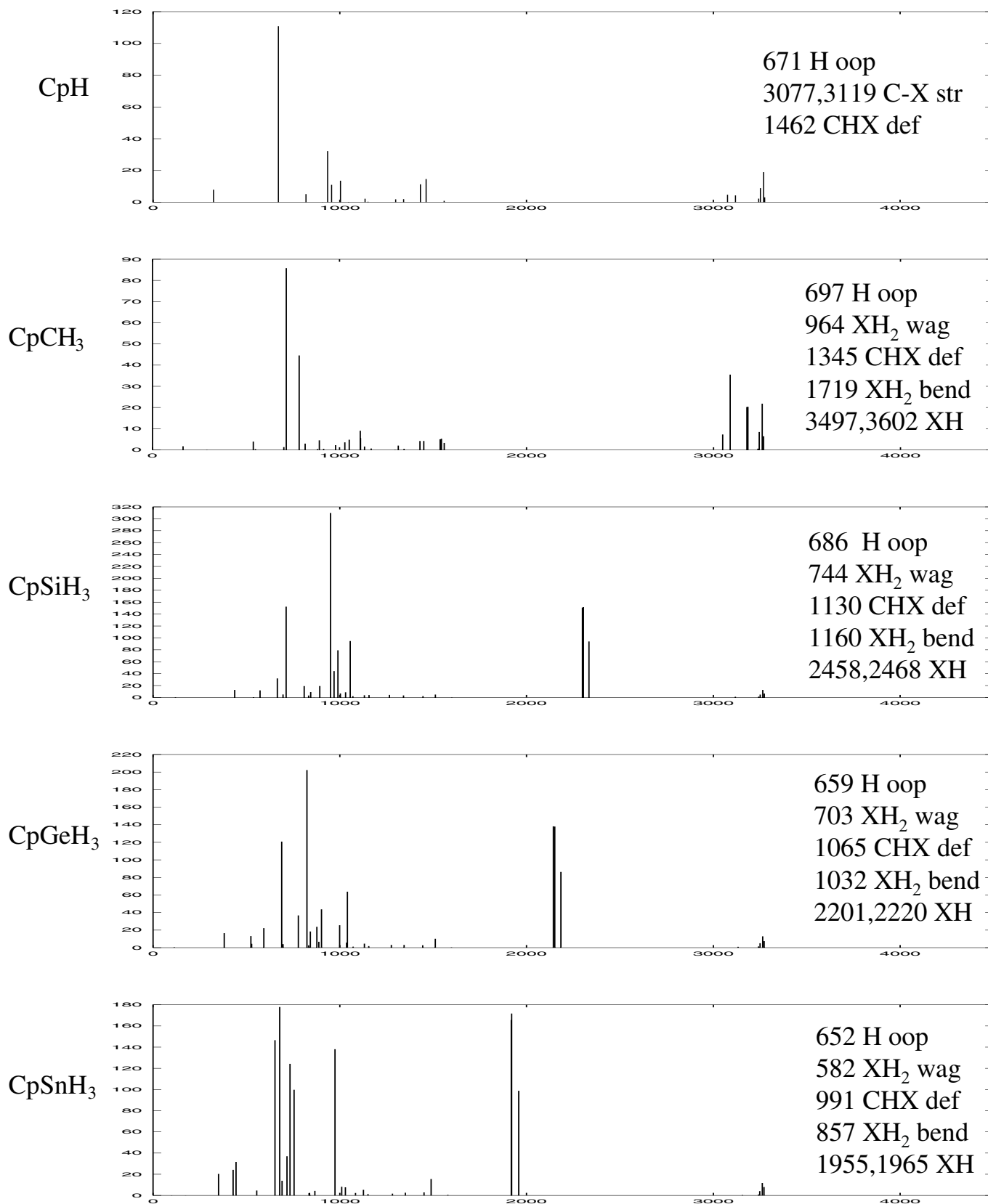


**Fig. 10.** MP2/6-31+G\* frequencies of 5-pnicto-1,3-cyclopentadiene.

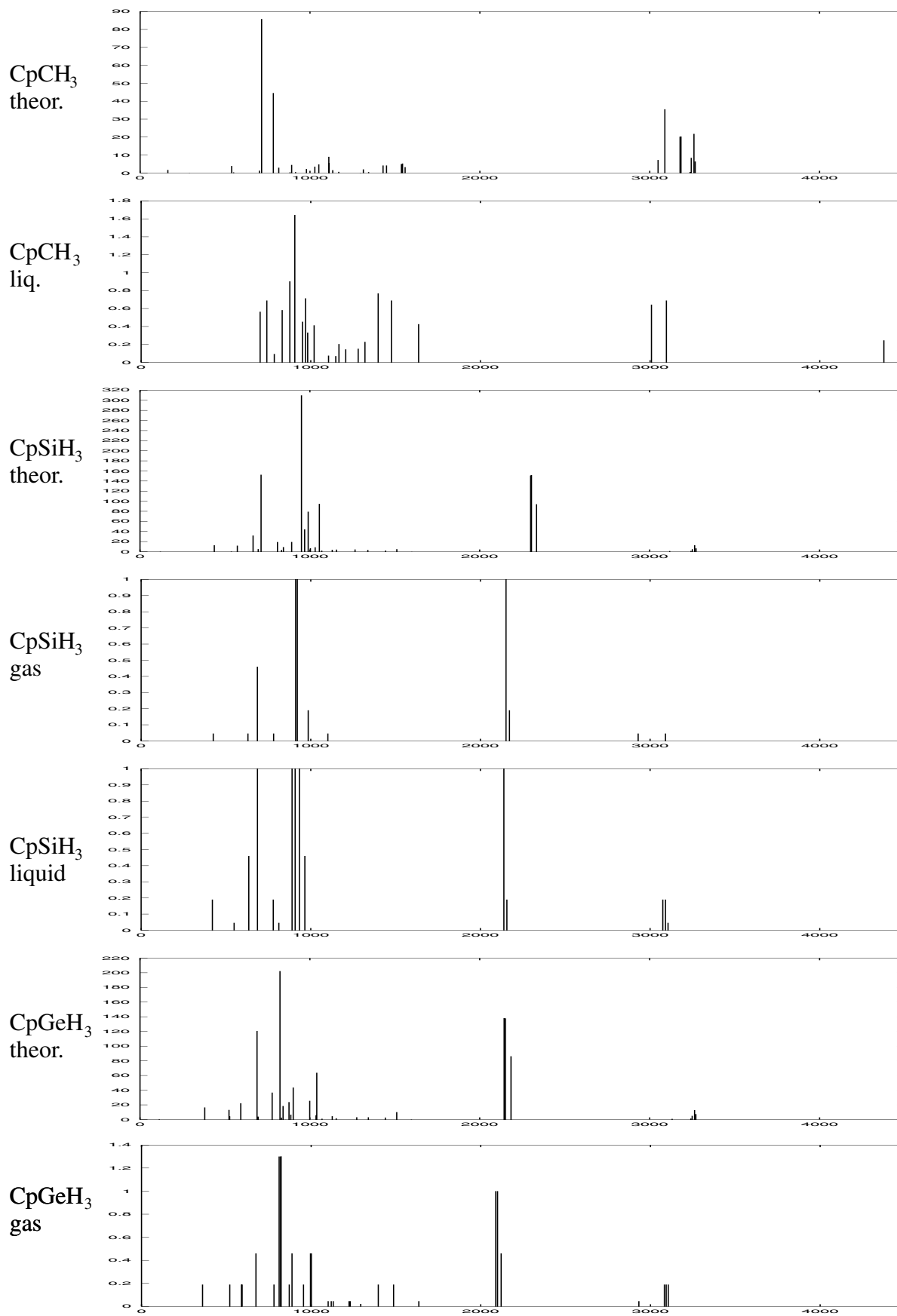
substituent are very prominent in the IR spectra. There is also significant mode delocalization and spreading out of intensity in the case of the stannane. More significant is the compari-

son with the known experimental spectra of the methyl (51), silyl (59), and germyl (63) derivatives in Fig. 12. For the latter two, the intensities were converted from qualitative to quan-



**Fig. 11.** MP2/6-31+G\* frequencies of 5-methyl-1,3-cyclopentadiene, and 2,4-cyclopentadienylsilane, germane and stannane



**Fig. 12.** Experimental and MP2/6-31+G\* frequencies of group 14-substituted cyclopentadienes.



tative designators (vw 95% T, w 90% T, m 65%, s 35%, vs 10% T, vvs 5% T) and then to absorbance. The agreement in both the intensity and frequency axes is very good if one takes into account the standard errors associated with anharmonicity, especially for the modes involving hydrogen stretches.

## Conclusions

The structures of 5-substituted cyclopentadienes agree well with most of the available experimental results. A pronounced basis set dependence of the structures is noted in some cases. The conformational trends in geometry and energy can be explained on the basis of bond–antibond interaction, especially where formal lone pairs are involved. Our calculated structures and vibrational spectra agree with available experimental data.

## Acknowledgements

We would like to thank the Memorial University of Newfoundland Computing and Communications Department (MUN-CC), Newfoundland and Labrador Computer Services (NLCS), and the Saint Mary's University Astronomy and Physics Department (SMU-AP) for computer time. In particular, we would like to thank DEC for providing an Alpha server 4100 (MUN - *tempus*) and Sun Microsystems, the Canada Foundation for Innovation, the Atlantic Canada Opportunities Agency, and SMU for providing a 10-processor Sun Enterprise 450 (SMU - *cygnus*). The continuing support of the Natural Sciences and Engineering Research Council of Canada (NSERC) is acknowledged by CP, RP, and JB. The assistance of Madelaine Tomney in preparing the geometry tables is gratefully acknowledged.

## References

1. M.A. Wellman, L.C. Burry, J.E. Letourneau, J.N. Bridson, D.O. Miller, and D.J. Burnell. *J. Org. Chem.* **62**, 939 (1997).
2. J.E. Letourneau, M.A. Wellman, and D.J. Burnell. *J. Org. Chem.* **62**, 7272 (1997).
3. J.J. Dannenberg. *Chem. Rev.* **99**, 1225 (1999).
4. T. Ohwada. *Chem. Rev.* **99**, 1337 (1999).
5. M. Kaselj, W.-S. Chung, and W.J. le Noble. *Chem. Rev.* **99**, 1387 (1999).
6. A.S. Cieplak. *Chem. Rev.* **99**, 1265 (1999).
7. R.A. Poirier, C.C. Pye, J.D. Xidos, and D.J. Burnell. *J. Org. Chem.* **60**, 2328 (1995).
8. J. D. Xidos, R. A. Poirier, C. C. Pye, and D. J. Burnell. *J. Org. Chem.* **63**, 105 (1998).
9. R.A. Poirier, M.R. Peterson, and A. Yadav. 1990. MUNGAUSS [computer program]. Chemistry Department, Memorial University of Newfoundland, St. John's, NF, Canada.
10. M.J. Frisch, G.W. Trucks, H.B. Schlegel, P.M.W. Gill, B.G. Johnson, M.W. Wong, J.B. Foresman, M.A. Robb, M. Head-Gordon, E.S. Replogle, R. Gomperts, J.L. Andres, K. Raghavachari, J.S. Binkley, C. Gonzalez, R.L. Martin, D.J. Fox, D.J. Defrees, J. Baker, J.J.P. Stewart, and J.A. Pople. 1993. Gaussian 92/DFT [computer program]. Revision F.4. Gaussian, Inc., Pittsburgh PA.
11. M.J. Frisch, G.W. Trucks, H.B. Schlegel, G.E. Scuseria, M.A. Robb, J.R. Cheeseman, V.G. Zakrzewski, J.A. Montgomery, Jr., R.E. Stratmann, J.C. Burant, S. Dapprich, J.M. Millam, A.D. Daniels, K.N. Kudin, M.C. Strain, O. Farkas, J. Tomasi, V. Barone, M. Cossi, R. Cammi, B. Mennucci, C. Pomelli, C. Adamo, S. Clifford, J. Ochterski, G.A. Petersson, P.Y. Ayala, Q. Cui, K. Morokuma, D.K. Malick, A.D. Rabuck, K. Raghavachari, J.B. Foresman, J. Cioslowski, J.V. Ortiz, A.G. Baboul, B.B. Stefanov, G. Liu, A. Liashenko, P. Piskorz, I. Komaromi, R. Gomperts, R.L. Martin, D.J. Fox, T. Keith, M.A. Al-Laham, C.Y. Peng, A. Nanayakkara, M. Challacombe, P.M.W. Gill, B. Johnson, W. Chen, M.W. Wong, J.L. Andres, C. Gonzalez, M. Head-Gordon, E.S. Replogle, and J.A. Pople. 1998. Gaussian 98 [computer program]. Revision A.9. Gaussian, Inc., Pittsburgh, PA.
12. H. Li-F: W.J. Hehre, R.F. Stewart, and J.A. Pople. *J. Chem. Phys.* **51**, 2657 (1969).; He,Ne,Na-Ar: W.J. Hehre, R. Ditchfield, R.F. Stewart, and J.A. Pople. *J. Chem. Phys.* **52**, 2769 (1970).; K, Ca, Ga-Kr: W.J. Pietro, B.A. Levi, W.J. Hehre, and R.F. Stewart. *Inorg. Chem.* **19**, 2225 (1980).; Rb, Se, In-Xe: W.J. Pietro, E.S. Blurock, R.F. Hout, W.J. Hehre, D.J. Defrees, and R.F. Stewart. *Inorg. Chem.* **20**, 3650 (1981).
13. H-Ne: J.S. Binkley, J.A. Pople, and W.J. Hehre. *J. Am. Chem. Soc.* **102**, 939 (1980).; Na-Ar: M.S. Gordon, J.S. Binkley, J.A. Pople, W.J. Pietro, and W.J. Hehre. *J. Am. Chem. Soc.* **104**, 2797 (1982). K,Ca: Ga-Kr,Rb,Sr,In-Xe: K.D. Dobbs and W.J. Hehre. *J. Comput. Chem.* **7**, 359 (1986).
14. C-F 6-31G: W.J. Hehre, R. Ditchfield, and J.A. Pople. *J. Chem. Phys.* **56**, 2257 (1972).; H, C-F polarization functions: P.C. Hariharan and J.A. Pople. *Theor. Chim. Acta (Berlin)*, **28**, 213 (1973).; Na-Ar: M.M. Francl, W.J. Pietro, W.J. Hehre, J.S. Binkley, M.S. Gordon, D.J. Defrees, and J.A. Pople. *J. Chem. Phys.* **77**, 3654 (1982).
15. H, Li-F diffuse: T. Clark, J. Chandrasekhar, G.W. Spitznagel, and P.v.R. Schleyer. *J. Comput. Chem.* **4**, 294 (1983).
16. S. Huzinaga, J. Andzelm, M. Klobutowski, E. Radio-Andzelm, Y. Sakei, and H. Tatewaki. Gaussian basis sets for molecular calculations. Elsevier Science Publishers, Amsterdam, 1984.
17. C.C. Pye. *Int. J. Quant. Chem.* **76**, 62 (2000).
18. C.C. Pye. Ph.D. Thesis. Memorial University, St. John's, NF (1997). Chapter 3, section 1 (pp 44–78) of this thesis contains a discussion of the STO-3G, 3-21G, and 6-31G\* Hartree-Fock calculations.
19. J. Kao and L. Radom. *J. Am. Chem. Soc.* **100**, 379 (1978).
20. S. Saebø, F.R. Cordell, and J.E. Boggs. *J. Mol. Struct. (Theochem)*, **104**, 221 (1983).
21. V.W. Laurie. *J. Chem. Phys.* **24**, 635 (1956).
22. L.H. Scharpen and V.W. Laurie. *J. Chem. Phys.* **43**, 2765 (1965).
23. R.C. Benson and W.H. Flygare. *J. Am. Chem. Soc.* **92**, 7523 (1970).
24. D. Damiani, L. Ferretti, and E. Gallinella. *Chem. Phys. Lett.* **37**, 265 (1976).
25. G. Liebling and R. E. Marsh. *Acta Cryst.* **19**, 202 (1965).
26. V. Schomaker and L. Pauling. *J. Am. Chem. Soc.* **61**, 1769 (1939).
27. C.A. Veracini, M. Guidi, M. Longeri, and A.M. Serra. *Chem. Phys. Lett.* **24**, 99 (1974).
28. R. Breslow and J.M. Hoffman, Jr. *J. Am. Chem. Soc.* **94**, 2110 (1972).
29. M. Saunders, R. Berger, A. Jaffe, J.M. McBride, J. O'Neill, R. Breslow, J.M. Hoffmann, Jr., C. Perchonock, W. Wasserman, R.S. Hutton, and V.J. Kuck. *J. Am. Chem. Soc.* **95**, 3017 (1973).
30. M.A. McClinton and V. Sik. *J. Chem. Soc., Perkin Trans. 1*, 1891 (1992).



31. S. Winstein, M. Shatavsky, C. Norton, and R.B. Woodward. *J. Am. Chem. Soc.* **77**, 4183 (1955).
32. M. Rosenblum. *J. Am. Chem. Soc.* **79**, 3179 (1957).
33. F. Tureček and Z. Havlas. *J. Org. Chem.* **51**, 4066 (1986).
34. V.A. Mironov, M.E. Dolgaya, V.T. Luk'yanov, and S.A. Yankovskii. *J. Org. Chem. USSR*, **12**, 1422 (1976) (*Zh. Org. Khim.* 1436).
35. J.B. Macaulay and A.G. Fallis. *J. Am. Chem. Soc.* **110**, 4074 (1988).
36. J.B. Macaulay and A.G. Fallis. *J. Am. Chem. Soc.* **112**, 1136 (1990).
37. S.B. King and B. Ganem. *J. Am. Chem. Soc.* **113**, 5089 (1991).
38. R.A. Poirier, I.G. Csizmadia. In *The chemistry of organic selenium and tellurium compounds*. Vol 1. Edited by S. Patai and Z. Rappoport. Wiley, New York. 1986. pp. 21–62.
39. S.D. Kahn, J. Korppi-Tommola, R.Y.N. Leung, and B.M. Pinto. *J. Mol. Struct. (Theochem.)*, **303**, 163 (1994).
40. U. Salzner and P.v.R. Schleyer. *J. Am. Chem. Soc.* **115**, 10231 (1993).
41. V.K. Yadav, A. Yadav, and R.A. Poirier. *J. Mol. Struct. (Theochem.)*, **186**, 101 (1989).
42. S. El Chaouch, J.-C. Guillemin, T. Karpai, and T. Veszpremi. *Organometallics*, **20**, 5405 (2001).
43. G. Boche, M. Bernheim, and W. Schrott. *Tetrahedron Lett.* **23**, 5399 (1982).
44. P. Jutzi and H. Saleske. *Chem. Ber.* **117**, 222 (1984).
45. R.A. Bartlett, A. Cowley, P. Jutzi, M.M. Olmstead, and H.-G. Stammer. *Organometallics*, **11**, 2837 (1992).
46. S. Cradock and D.H.W. Rankin. *J. Chem. Soc., Faraday Trans. 2*, 940 (1972).
47. J.E. Bentham, E.A.V. Ebsworth, H. Moretto, and D.W.H. Rankin. *Angew. Chem. Int. Ed. Engl.* **11**, 640 (1972).
48. S. Cradock, E.A.V. Ebsworth, H. Moretto, and D.W.H. Rankin. *J. Chem. Soc., Dalton Trans.* 390 (1975).
49. W.W. Schoeller. *Z. Naturforsch.* **38b**, 1635 (1983).
50. W.W. Schoeller. *Z. Naturforsch.* **39b**, 1767 (1984).
51. S.M. Csicsery. *J. Org. Chem.* **25**, 518 (1960).
52. V.A. Mironov, E.V. Sobolev, and A.N. Elizarova. *Tetrahedron*, **19**, 1939 (1963).
53. S. McLean and P. Haynes. *Tetrahedron Lett.* 2385 (1964).
54. S. McLean, C.J. Webster, and R.J.D. Rutherford. *Can. J. Chem.* **47**, 1555 (1969).
55. J.W. De Haan and H. Kloosterziel. *Rec. Trav. Chim. Pays-Bas*, **87**, 298 (1968).
56. M.J.S. Dewar. *Chem. Brit.* **11**, 97 (1975).
57. A.P. Hagen and P.J. Russo. *Inorg. Nucl. Chem. Lett.* **6**, 507 (1970); *Inorg. Synth.* **7**, 172 (1977).
58. J.E. Bentham and D.W.H. Rankin. *J. Organometal. Chem.* **30**, C54 (1971).
59. A.P. Hagen and P.J. Russo. *J. Organometal. Chem.* **51**, 125 (1973).
60. S. Cradock, R.H. Findlay, and M.H. Palmer. *J. Chem. Soc., Dalton Trans.* 1650 (1974).
61. A. Bonny and S.R. Stobart. *J. Chem. Soc., Dalton Trans.* 224 (1980).
62. A.F. Cuthbertson and C. Glidewell. *J. Organometal. Chem.* **221**, 19 (1981).
63. S.R. Stobart. *J. Organometal. Chem.* **33**, C11 (1971); P. C. Angus and S. R. Stobart. *J. Chem. Soc., Dalton Trans.* 2374 (1973).
64. M.J. Barrow, E.A.V. Ebsworth, M.M. Harding, and D.W.H. Rankin. *J. Chem. Soc., Dalton Trans.* 603 (1980).
65. A.V. Kisin, V.A. Korenevsky, N.M. Sergeyev, and Yu. A. Ustynyuk. *J. Organometal. Chem.* **34**, 93 (1972).
66. C.H. Townes and A.L. Schawlow. *Microwave spectroscopy*. Dover, New York. 1975. Chap 12.
67. W.J. Hehre, L. Radom, P.v.R. Schleyer, and J.A. Pople. *Ab initio molecular orbital theory*. Wiley, New York, 1986.
68. T.K. Brunck and F. Weinhold. *J. Am. Chem. Soc.* **101**, 1700 (1979).
69. A.E. Reed and F. Weinhold. *Israel J. Chem.* **31**, 277 (1991).
70. L. Radom, W.J. Hehre, and J.A. Pople. *J. Am. Chem. Soc.* **94**, 2371 (1972).



# Simultaneous determination of copper, lead, cadmium, zinc, and selenium in cow liver by differential pulse polarography

Güler Somer, Gülbeniz Guliyeva, Güler Ekmekci, and Olcay Sendil

**Abstract:** A fast and simple method was established for the determination of trace elements in liver. DP polarograms of wet digested liver samples were taken in acetate buffer, pH about 4, for lead, cadmium, and zinc determinations. For copper, addition of EDTA at pH 4 was needed for a better separation from the iron peak. Selenite ion was determined using the hydrogen catalytic peak after the addition of Mo(VI) to the same solution. Trace element levels were different for two separate sections of liver. For the first section ( $S_1$ ) the quantities were found to be  $8.12 \pm 0.21 \text{ mg g}^{-1}$  Cu,  $1.16 \pm 0.12 \text{ mg g}^{-1}$  Zn,  $1.09 \pm 0.11 \text{ mg g}^{-1}$  Cd,  $0.59 \pm 0.07 \text{ mg g}^{-1}$  Pb, and  $2.05 \pm 0.22 \text{ mg g}^{-1}$  Se, in dry liver. For the second section ( $S_2$ ) the results were the same for selenium, but Cd was too small to be detected. The other trace element quantities were  $0.48 \text{ mg g}^{-1}$  Cu,  $0.22 \text{ mg g}^{-1}$  Pb, and  $0.29 \text{ mg g}^{-1}$  zinc. The validity of the method was demonstrated with a synthetic sample resembling liver composition. This method enabled the simultaneous determination of heavy trace elements such as copper, lead, cadmium, molybdenum, selenium, and zinc by using an inexpensive instrument and without any separation or pre-concentration procedures.

**Key words:** cow liver, determination, differential pulse polarography, trace elements.

**Résumé :** On a développé une méthode simple et rapide pour déterminer les éléments à l'état de trace dans le foie. Afin d'évaluer les concentrations de plomb, de cadmium et de zinc, on a mesuré les polarogrammes à pulsation différentielle d'échantillons frais de foie dans un tampon d'acétate, à un pH d'environ 4. Pour le cuivre, à un pH de 4, il est nécessaire d'ajouter de l'EDTA afin d'obtenir une meilleure séparation du pic du fer. On a déterminé l'ion sélénite en faisant appel au pic catalytique de l'hydrogène après addition de Mo(VI) à la solution. Les concentrations des éléments à l'état de trace sont différentes pour deux sections différentes du foie. Dans la première section ( $S_1$ ) de foie sec, on a trouvé les quantités suivantes:  $8,21 \pm 0,21 \text{ mg g}^{-1}$  de Cu,  $1,16 \pm 0,12 \text{ mg g}^{-1}$  de Zn,  $1,09 \pm 0,11 \text{ mg g}^{-1}$  de Cd,  $0,59 \pm 0,07 \text{ mg g}^{-1}$  de Pb et  $2,05 \pm 0,22 \text{ mg g}^{-1}$  de Se. Dans la deuxième section ( $S_2$ ) les résultats sont les mêmes pour le sélénium, mais les quantités de Cd sont trop faibles pour être détecter. Les quantités des autres éléments présents à l'état de trace sont de  $0,48 \text{ mg g}^{-1}$  de Cu,  $0,22 \text{ mg g}^{-1}$  de Pb et  $0,29 \text{ mg g}^{-1}$  de zinc. On a démontré la validité de la méthode à l'aide d'un échantillon synthétique dont la composition ressemble à celle du foie. Cette méthode permet de déterminer de façon simultanée des traces d'éléments de métaux lourds, tels le cuivre, le plomb, le cadmium, le molybdène, le sélénium et le zinc en faisant appel à des instruments peu coûteux et sans nécessité de procéder à des séparations ou à des préconcentrations.

**Mots clés:** foie de vache, polarographie à pulsation différentielle, éléments à l'état de trace.

[Traduit par la Rédaction]

## Introduction

The total trace element levels have become of prime importance to aid both the clinician in the diagnosis and treatment of a variety of diseases and the life science researcher in the investigation of the role of trace elements in health and disease. Considering biological research, the role of some trace and ultra-trace elements in the body is very rich

and varied. Some of them are essential to life while others are toxic even at very low concentrations (1–3). Since these elements are taken in mostly by human diet, the determination of their concentration in food is very important. Liver is known to deposit many trace elements; thus, cow liver is a potent source of heavy elements. Unfortunately, very few investigations have been attempted relating to the determination of the concentration of heavy elements. Most of the work has been concentrated on their effect on liver and physiologic body functions (4–6). The effect of ingestion of heliotrope (homeopathic medicine) and copper on the concentration of zinc, selenium, and molybdenum in the liver of the sheep has been studied (4); the ingestion of heliotrope was found to reduce liver concentrations of zinc and molybdenum. The concentration of selenium in the liver was found to increase only when heliotrope was given with copper. The depletion of glutathion in selenium-deficient liver and kid-

Received 15 March 2002. Published on the NRC Research Press Web site at <http://canjchem.nrc.ca> on 24 January 2003.

**G. Somer,<sup>1</sup> G. Guliyeva, and O. Sendil.** Gazi Universitesi, Fen-Edebiyat Fakültesi, Kimya Bölümü, 06500 Ankara, Türkiye.

**G. Ekmekci.** Gazi Üniversitesi, Gazi Eğitim Fakültesi. Kimya Bölümü 06500 Ankara, Türkiye.

<sup>1</sup>Corresponding author (e-mail: [gsomer@gazi.edu.tr](mailto:gsomer@gazi.edu.tr)).



ney of rats lead to necrosis in these organs, which is associated with evidence of lipid peroxidation (7). Some elements such as Co, Se, Mo, and Cu in liver have been analyzed by flame and electrothermal AAS after extraction of their complexes with APDC into chloroform (8). These analyses have shown the analytical details and instrument parameters for the determination of these four elements in National Institute of Standards and Technology standard reference material (NIST SRM) bovine liver. In another study, it was found that the quantitative distribution of trace elements (P, Fe, Zn, Cu, Mn, Mo, Co) in the liver lobes of cattle and of pigs was not uniform, as a result of different metabolism in different parts of the organ (9).

Since many elements important in the biological life of the body deposit in the liver, their concentrations have to be determined very accurately. Determination of trace elements in biological samples is usually difficult because of long and tedious digestion procedures and risks of interference problems. The interfering ions have to be separated by pre-concentration techniques such as solvent extraction, ion exchange, or hydride generation. These are all time-consuming procedures, and losses of elements are also possible. It is therefore very important to accomplish the determination with minimum interference problems. With electrochemical methods, the interference problems can be solved by changing only either the supporting electrolyte or the pH (10, 11). These methods require relatively inexpensive instrumentation, are capable of determining elements accurately at trace and ultra-trace levels, and have demonstrated the ability for multi-element determination.

This paper describes a simple polarographic method for the determination of trace elements in liver. In this proposed method there is no need for sophisticated instruments or tedious separation procedures.

## Experimental

### Materials

A polarographic analyzer (PAR 174 A) equipped with a PAR mercury drop timer was used. The drop time of the electrode was in the range 2 to 3 s ( $2.37 \text{ mg s}^{-1}$ ). A Kalusek electrolytic cell with a reference saturated calomel electrode (SCE), separated by a liquid junction, was used in the three-electrode configuration. The counter electrode was platinum wire. The polarograms were recorded with a Linseis (LY 1600) X-Y recorder under the conditions of a drop life of 1 s, a scan rate of  $5 \text{ mVs}^{-1}$ , and a pulse amplitude of 50 mV.

### Reagents

All reagents used were of analytical reagent grade (pro-analysis). Triply-distilled water was used in the preparation of all solutions and at all stages of analysis. The mercury used in the dropping mercury electrode was obtained from Merck (Darmstadt, Germany). Contaminated mercury was cleaned by passing it successively through dilute  $\text{HNO}_3$  and water columns, in the form of fine droplets, using a platinum wire gauze. The collected mercury was dried between sheets of filter paper. A polarogram of this mercury was taken before use to ensure the absence of impurities.

Stock standard solutions (0.1 M) of Pb, Cu, Cd, and Zn were prepared with triply distilled water from their nitrate

and sulphate salts. Selenite stock solution was prepared from  $\text{SeO}_2$  by dissolving it in hot water. The stock solution of molybdenum was prepared from  $(\text{NH}_4)_2\text{Mo}_7\text{O}_{24} \cdot 4\text{H}_2\text{O}$ . Dilute solutions were prepared before every use to avoid solution degradation.

A 1.0 M acetic acid buffer, pH 4, was prepared as follows: a 1.0 M NaOH solution was added to 1.0 M acetic acid until the chosen pH was reached, according to a pH meter.

## Methods

### Digestion of the liver sample

According to former studies (9), the deposition of trace elements vary in different sections of the liver. Thus two different sections ( $S_1$  and  $S_2$ ) were taken as two separate samples from one cow liver. They were dried for 48 h in an oven at  $120^\circ\text{C}$  to remove the water content and to obtain a constant weight. The water content was found to be 72.2%. Samples of dried liver (3.02 g ( $S_1$ ) and 2.90g ( $S_2$ )) were transferred into a 100 ml long-necked glass flask. For the digestion of the sample, a concentrated acid mixture of 0.5 ml  $\text{H}_2\text{SO}_4$ , 5 ml  $\text{HClO}_4$ , and 5 ml  $\text{HNO}_3$  was added and left to stand overnight. A glass funnel was inserted into the digestion flask to prevent rapid evaporation. The solution was kept in an oil bath at  $50^\circ\text{C}$  until the foaming stopped. Then the temperature was increased to  $150^\circ\text{C}$  and heating was continued until the evolution of brown fumes of nitrogen oxides ceased. When the digestive sample turned yellowish to deep dark brown, there was a danger of explosion, so 5 ml of nitric acid had to be added; the flask was cooled for about 2 min before addition. Heating was continued until nitrogen oxide fumes were no longer given off. The digestion was completed, with the appearance of white fumes of perchloric acid, when approximately 1.0 ml solution remained. Finally, 2.0 ml of hydrochloric acid was added and heated for at least 20 min to convert all selenium to selenium(IV). The final solution was evaporated to approximately 1.0 mL and cooled to room temperature. The funnel was rinsed with water into the flask and the contents transferred into a 10.0 ml teflon flask, which was made up to the mark with triply-distilled water. Depending on the concentration of each element in the liver, the digests had to be diluted 10, 100, or 500 times before use.

To check the recovery of the elements during digestion, the same digestion procedure was applied to a synthetic sample containing the same elements. The recovery efficiencies were found to be between 95 and 97%.

### Voltammetric determination

For the determination of lead, cadmium, and zinc in liver, 10.0 mL of a 1.0 M acetic acid – acetate buffer (about pH 4) in a polarographic cell was deoxygenated by a stream of high-purity nitrogen for 5 min. The DP polarogram was recorded by scanning the potential in the negative direction from 0.0 V to  $-1.5 \text{ V}$  at a scan rate of  $5 \text{ mV s}^{-1}$ . Then, according to the need, 0.05–0.1 mL digested sample of liver was added, and once more the DP polarogram was recorded. Standard additions were made according to the corresponding element. For the determination of copper, EDTA solution was added so that the final concentration was 0.02 M. The selenium content, on the other hand, was determined using the catalytic hydrogen wave. For this purpose, Mo(VI) had



to be added in 50–100 times larger amounts than the concentration of selenite present.

## Results and discussion

### Preliminary experiments

Various supporting electrolytes including KCl, HCl, HAc–NaOAc, and HAc buffer with and without EDTA were used over a wide range of pH. The peak potential values of elements that may be present in liver such as Fe, Cu, Pb, Cd, Zn, Ti, Mo, and Se were determined in these supporting electrolytes. Acetate buffer was found to be the most suitable electrolyte because of its ability to function at various pH values and thus enable the separability of the peaks.

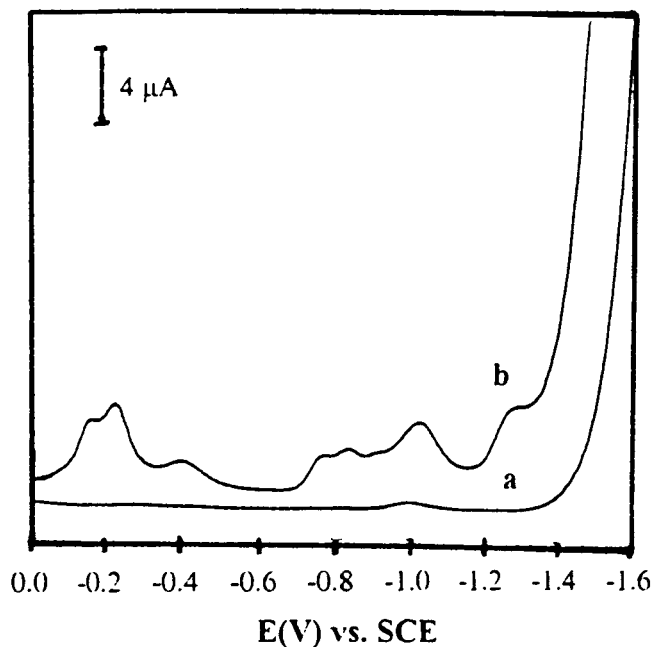
### Determination of trace elements in liver

The DP polarograms of digested liver samples in acetate buffer at pH 4.2 have peaks at  $-0.23$  V,  $-0.40$  V,  $-0.60$  V, and  $-0.98$  V. Figure 1 is given as an example where copper, lead, selenium, and zinc peaks are observable. The polarogram of the  $S_1$  sample had similar peaks, but the copper peak was off the scale because of its high concentration. By the additions of Pb, Cd, and Zn standard solutions, the peaks at  $-0.40$  V,  $-0.60$  V, and  $-0.98$  V increased, respectively, indicating the presence of these ions, as expected. For the determination of these elements a 10-times dilution was sufficient, but for the determination of copper in the  $S_1$  sample, because of its high concentration (the peak was too large to observe), either a 100-times dilution or a change in current density was required. On the other hand, the solution either had to be diluted or the current range had to be adjusted accordingly for selenium, since the very sensitive method of catalytic polarography had been used in that case.

### Determination of selenium

In our earlier polarographic work (12) we observed a hydrogen catalytic peak when Se(IV) and Mo(VI) were present together in a solution. These kinds of catalytic currents are obtained with many organic compounds including amines, proteins, thiols, and phosphines. They are also observed with some inorganic substances, for example, complexes of tungsten (VI) with certain carboxylic acids (13). The catalytic peak obtained with Mo(VI) and Se(IV) has been used for the determination of very low concentrations of both ions in blood (14). The detection limit (signal to noise ratio,  $S/N = 3$ ) of the method for Mo(VI) and for Se(IV) was  $1.5 \times 10^{-9}$  M. For the determination of one of these ions, the second ion concentration had to be about  $10^2$ – $10^3$  times higher than the other ion that was being investigated. However, at concentrations higher than  $10^{-6}$  M, this ratio may be 1:1. Although it is not possible to see a peak for selenite at a concentration lower than  $10^{-6}$  M with DPP, by the addition of Mo(VI) a peak at  $-1.1$  V becomes observable, and by standard additions of selenite the amount of it can be determined. The DP polarogram of a 500-times diluted liver sample in acetate buffer, pH 4, is given in Fig. 2(a). The sample had to be diluted 500 times since at lower dilution the catalytic peak was off the scale. As can be seen in Fig. 2 there was no peak for selenium, but by the addition of Mo(VI) a hydrogen catalytic peak at about  $-1.1$  V appeared. At first with further additions of molybdenum it increased, but then it became

**Fig. 1.** DP polarogram of liver sample  $S_2$ : 10.0 mL of a 1.0 M HAc–Ac buffer (pH = 4.2) and 0.1 mL liver sample (10 times diluted).



constant. At that point standard additions of selenite were made for the determination of selenium (Fig. 2(b)). Because of overlapping peaks, zinc usually interferes with the hydrogen catalytic peak; thus, EDTA addition is needed. However, although zinc was present in this sample, because of the 500-times dilution for selenite determination no peak corresponding to zinc was visible. The Se(IV) content for six different samples were determined with the above method, and the following concentrations were found:  $2.05 \pm 0.22$  mg g $^{-1}$  Se in the  $S_1$  sample and  $2.08 \pm 0.21$  mg g $^{-1}$  Se in the  $S_2$  sample.

### Determination of copper

According to our preliminary experiments, copper and iron peaks may overlap in acetate buffer with pH about 4. Addition of EDTA, however, enabled their separation: the copper peak was found at  $-0.23$  V and the iron peak at  $-0.13$  V. In the liver sample that was diluted only ten times, the polarogram had a very large copper peak at  $-0.23$  V; thus, the sample solution had to be diluted 100 times. The polarogram for this liver sample,  $S_1$ , is given in Fig. 3. As can be seen from the figure, the iron peak, which may appear at  $-0.13$  V, was not observable because of low sensitivity in this medium. According to our previous studies, the current obtained for iron in this medium was ten times smaller than the one that was observed for copper for the same concentration. The copper content was determined with standard additions and was found to be  $8.12 \pm 0.21$  mg g $^{-1}$  in the  $S_1$  sample and  $0.48 \pm 0.02$  mg g $^{-1}$  in the  $S_2$  sample.

### Determination of zinc, cadmium, and lead

As mentioned earlier, the polarogram (Fig. 2) of the liver sample had peaks belonging to lead, cadmium, and zinc. Standard addition was used for the determination of their concentrations. The polarograms are given in Figs. 4, 5, and



**Fig. 2.** Determination of selenium in liver. Panel (a): Formation of the hydrogen catalytic peak: (a) 10.0 mL of a 1.0 M HAc–Ac buffer, pH = 4.3, (b) a + 0.1 mL  $S_1$  sample (500 times diluted), (c) b + 0.2 mL of a  $10^{-3}$  M solution of Mo(VI), (d) c + 0.1 mL of a  $10^{-3}$  M solution of Mo(VI), (e) d + 0.05 mL of a  $10^{-3}$  M solution of Mo(VI); Panel (b): Standard additions of Se (IV): (f) e, taken once more, (g) f + 0.1 mL of a  $10^{-4}$  M solution of Se(IV), (h) g + 0.05 mL of a  $10^{-4}$  M solution of Se(IV), and (i) h + 0.05 mL of a  $10^{-4}$  M solution of Se(IV).

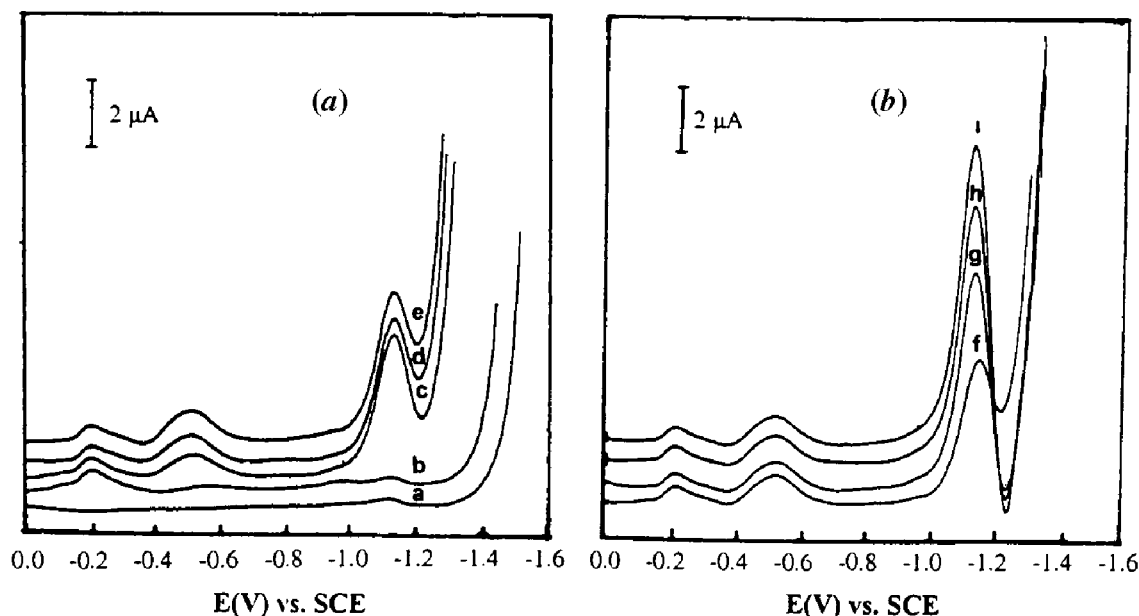


**Fig. 3.** Determination of copper in liver: (a) 2.0 mL of a 1.0 M solution of HAc–Ac buffer + 5.0 mL of a 0.1 M solution of EDTA + 3.0 mL water, pH = 4.3; (b) a + 0.1 mL of the  $S_1$  sample (100 times diluted); (c) b + 0.3 mL of a  $10^{-3}$  M solution of  $\text{Cu}^{2+}$ ; (d) c + 0.3 mL of a  $10^{-3}$  M solution of  $\text{Cu}^{2+}$ ; and (e) d + 0.3 mL of a  $10^{-3}$  M solution of  $\text{Cu}^{2+}$ .

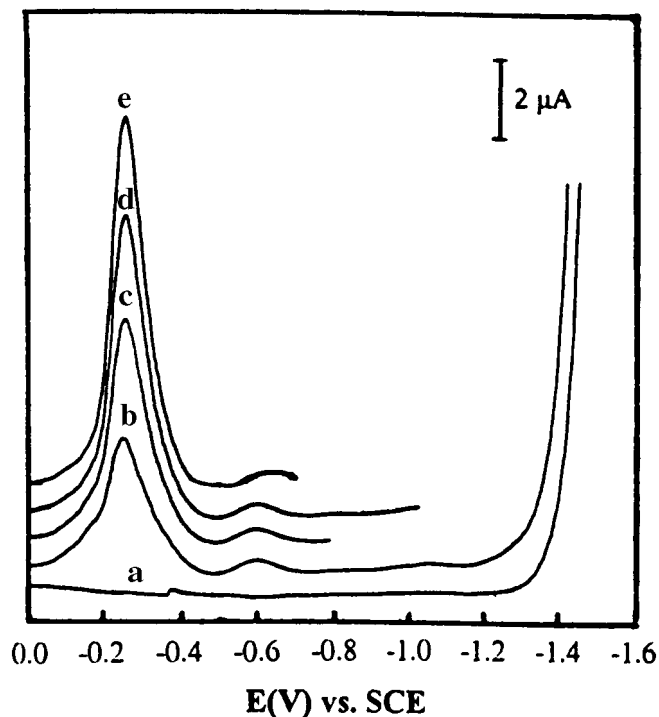
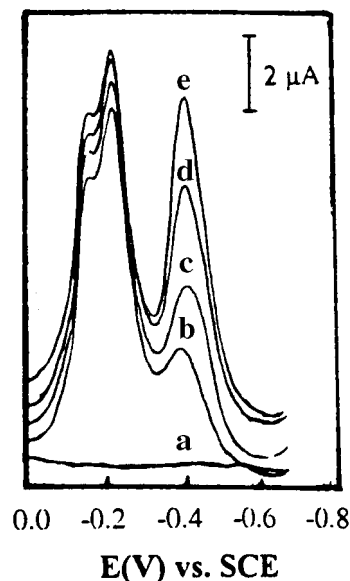


**Fig. 4.** Determination of lead in liver: (a) 10 mL of a 1.0 M HAc–Ac buffer, pH = 4.3; (b) a + 0.1 mL of the  $S_2$  sample (10 times diluted); (c) b + 0.05 mL of a  $10^{-3}$  M solution of  $\text{Pb}^{2+}$ ; (d) c + 0.05 mL of a  $10^{-3}$  M solution of  $\text{Pb}^{2+}$ ; and (e) d + 0.05 mL of a  $10^{-3}$  M solution of  $\text{Pb}^{2+}$ .



and  $1.16 \pm 0.12 \text{ mg g}^{-1}$ , respectively. The  $S_1$  sample was also analyzed by flame AAS for zinc content, and it was found to be  $1.01 \pm 0.24 \text{ mg g}^{-1}$ , which was consistent with the result obtained with polarography. In the  $S_2$  sample, however, while no detectable amount of cadmium was observed, lead content was found to be  $0.22 \pm 0.03 \text{ mg g}^{-1}$ , and zinc content was found to be  $0.29 \pm 0.03 \text{ mg g}^{-1}$ . These results are summarized in Table 1. The trace element quanti-

6. In the  $S_1$  sample, lead, cadmium, and zinc concentrations were found to be  $0.59 \pm 0.04 \text{ mg g}^{-1}$ ,  $1.09 \pm 0.11 \text{ mg g}^{-1}$ ,



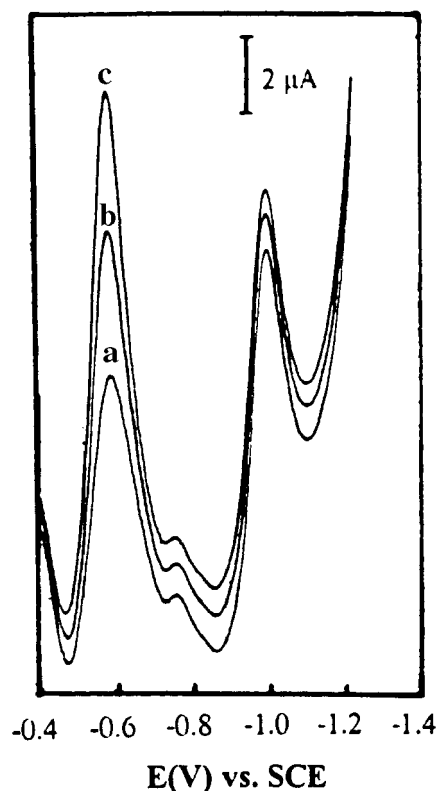
**Table 1.** Trace elements in dry liver, mg g<sup>-1</sup> ( $\bar{x} \pm (txs)/\sqrt{N}$ ).

Sample	Cu(II)	Pb(II)	Cd(II)	Zn(II)	Se (IV)
S <sub>1</sub>	8.12 ± 0.21	0.59 ± 0.14	1.09 ± 0.11	1.16 ± 0.12	2.05 ± 0.22
S <sub>2</sub>	0.48 ± 0.21	0.22 ± 0.03	—	0.29 ± 0.03	2.08 ± 0.21

Note:  $t$  = confidence interval (90%); ( $N$  = 6).

**Table 2.** Determination of trace elements in a synthetic sample.

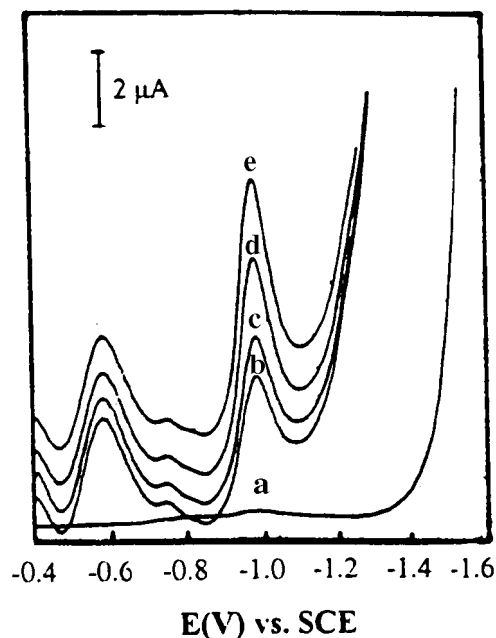
Elements	Cu ( $M \times 10^{-6}$ )	Pb ( $M \times 10^{-7}$ )	Cd ( $M \times 10^{-7}$ )	Zn ( $M \times 10^{-7}$ )	Se ( $M \times 10^{-7}$ )
Present	1.00	1.00	1.00	1.00	1.00
Found	1.07 ± 0.09	1.00 ± 0.11	0.57 ± 0.12	1.21 ± 0.11	1.05 ± 0.09

**Fig. 5.** Determination of cadmium in liver: (a) 10.0 mL of a 1 M HAc–Ac buffer, pH 4.3 + 0.1 mL of the S<sub>1</sub> sample (10 times diluted); (b) a + 0.1 mL of a 10<sup>-3</sup> M solution of Cd<sup>2+</sup>; and (c) b + 0.1 mL of a 10<sup>-3</sup> M solution of Cd<sup>2+</sup>.

ties found in different sections of liver proves that their distribution is not uniform, as mentioned (9) earlier for cattle and pigs.

#### Proposed procedure

About 1–2 g of dried liver was digested and then diluted to 10 or 100 mL. An aliquot (0.1 mL) was added to an acetate buffer (pH 4) solution, and the DP polarogram was taken. Lead, cadmium, and zinc were determined by standard additions. Then EDTA solution was added, so that its final concentration was 0.05 M, and copper content was determined. For selenite, Mo (VI) was added to obtain the hydrogen catalytic peak, and the selenite content was determined by standard additions of selenite.

**Fig. 6.** Determination of zinc in liver: (a) 10.0 mL HAc–Ac, pH = 4.3; (b) a + 0.1 mL of the S<sub>1</sub> sample; (c) b + 0.1 mL of a 10<sup>-3</sup> M solution of Zn<sup>2+</sup>; (d) c + 0.2 mL of a 10<sup>-3</sup> M solution of Zn<sup>2+</sup>; and (e) d + 0.2 mL of a 10<sup>-3</sup> M solution of Zn<sup>2+</sup>.

#### Synthetic sample

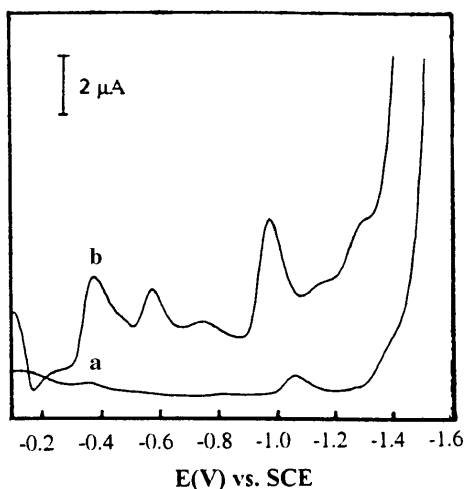
To check the validity of the suggested method, a synthetic sample containing similar amounts of metal ions present in liver was used. The polarogram of the metal ions in acetate buffer at pH 4 is shown in Fig. 7. The elements present were determined with the proposed method. The results are given in Table 2 with their standard deviations. As can be seen, a good consistency was observed for most of the ions, except cadmium. Only 55% of the quantity of cadmium could be determined. This can be explained by the interference of selenium with cadmium (15), which was further investigated by us.

#### Conclusions

The present DP polarographic method, which was used for the first time for the determination of heavy elements in liver, enabled the direct determination of their concentration without any separation or pre-concentration techniques.



**Fig. 7.** DP polarogram of a synthetic sample: (a) 9.5 mL of a 1.0 M HAc–Ac buffer; (b) 0.1 mL of a  $10^{-2}$  M solution of  $\text{Cu}^{2+}$ ; 0.1 mL of a  $10^{-3}$  M solution of  $\text{Pb}^{2+}$ ; 0.1 mL of a  $10^{-3}$  M solution of  $\text{Cd}^{2+}$ ; 0.1 mL of a  $10^{-3}$  M solution of  $\text{Se(IV)}$ ; 0.1 mL of a  $10^{-2}$  M solution of  $\text{Zn}^{2+}$ .



Electroanalytical methods are quite simple, their sensitivity and selectivity are high, and the instruments used are inexpensive. By digestion of about 1–2 g of sample, dilution to 10–100 mL, and by using 0.1 mL aliquots it is possible to determine the concentration of at least five to six elements si-

multaneously. This method can be applied to other biological samples containing complex mixtures of metal ions.

## References

1. R.F. Burk. Trace elements in human health. Vol. 2. New York, Academic Press. 1977. p. 105
2. S.J. Lippard and J.M. Berg. Principles of bioinorganic chemistry. University Science Books, Mill Valley, CA. 1994.
3. W. Mertz. Trace elements in human and animal nutrition. Vol. 1 and Vol. 2. 5th ed. Academic Press, San Diego, California. 1987.
4. H.S. Deol, J.McC. Howell, and P.R. Dorling. J. Comp. Pathol. **110**, 303 (1994).
5. G.F. Combs and S.B. Combs. Annu. Rev. Nutr. **4**, 257 (1984).
6. S. Vadhanavikit and H.E. Ganther. J. Nutr. Biochem. **124**, 882 (1994).
7. R.F. Burk, K.E. Hill, J.A. Awad, J.D. Merrow, and P.R. Lyons. Lab. Invest. **72**, 723 (1995).
8. D.H. Parsley. J. Anal. At. Spectrom. **6**, 289 (1991).
9. E. Taucins and A. Svilane. Akad. Nauk Latv. SSR. Inst. Biol. **3**, 159 (1962).
10. R. Inam and G. Somer. Food Chem. **69**, 345 (2000).
11. G. Ekmekci, R. Inam, and G. Somer. Anal. Sci. **16**, 1151 (2000).
12. R. Inam and G. Somer. Talanta, **50**, 609 (1999).
13. S.G. Mairanovskii. J. Electroanal. Chem. **6**, 77 (1963).
14. R. Inam, G. Ekmekci, and G. Somer. Talanta, **51**, 825 (2000).
15. R. Inam and G. Somer. Anal. Sci. **14**, 609 (1998).



# The differing mechanisms of photo-formation of 7-cyanobenzocyclooctatetraene from 7- and 6-cyano-2,3-benzobicyclo[4.2.0]octa-2,4,7-triene

Christopher Owen Bender, Douglas Dolman, Jeremy Christian Foesier, Sherry Lee Lawson, and Kathryn Elvia Preuss

**Abstract:** It is known that 7-cyanobenzocyclooctatetraene (COT **2**) is a product of the thermolysis and direct photolysis of 7- and 6-cyano-2,3-benzobicyclo[4.2.0]octa-2,4,7-triene (**1** and **5**), though the mechanisms of these rearrangements have not been reported. In the present study experiments have been carried out using the deuterium-labelled trienes **1a** (93%- $d_1$  at C-6) and **5a** (93%- $d_1$  at C-8), which were formed from  $2\pi + 2\pi$  photo-closure (direct irradiation) of COT **2a** labelled at C-8. The results reveal that whereas the thermolysis of **1a** and **5a** and the direct irradiation of **5a** reform COT **2a**, probably via cleavage of the strained cyclobutene C-1—C-6 bond, the direct irradiation of triene **1a** gives a differently labelled COT product, containing the deuterium exclusively at C-9. The mechanism proposed for the latter phototransformation is a modification of the Zimmerman di- $\pi$ -methane rearrangement.

**Key words:** mechanisms, rearrangements, photochemistry, di- $\pi$ -methane rearrangement.

**Résumé :** Il est connu que le cyano-7 benzocyclooctatétrène (COT **2**) est un produit soit lorsqu'on chauffe des solutions des composés cyano-7 et -6 benzo-2,3 bicyclo[4.2.0]octatriènes-2,4,7 (**1** et **5**) ou lorsqu'on les photolyse directement, mais les mécanismes pour les transpositions n'étaient pas données. Ces transpositions ont été réétudiées avec des triènes marqués au deutérium: le triène **1a** contient 93 %- $d_1$  à C-6, tandis que le triène **5a** contient 93 %- $d_1$  à C-8. Des triènes **1a** et **5a** sont issus de l'irradiation directe du COT **2a** marqué au deutérium à C-8 (93 %). Des études de marquages démontrent que le COT **2a** se formant thermiquement du **1a** et du **5a**, et photochimiquement du **5a**, dérive vraisemblablement d'une ouverture de la liaison C-1—C-6 des triènes. Par contre, l'irradiation directe du triène **1a** conduit à COT **2b** marqué au deutérium uniquement à C-9 (93 %). Un mécanisme modifié de Zimmerman est suggéré pour cette dernière transposition, **1a**  $\rightarrow$  **2b**.

**Mots clés :** mécanismes, transpositions, photochimie, di- $\pi$ -méthane.

## Introduction

Routes to cyclooctanoids continue to be of interest because of their wide occurrence in natural products, many of which exhibit potent biological activity, with the anti-cancer drug paclitaxel being a notable example (1). Some time ago (2) we reported that 7-cyanobenzocyclooctatetraene (i.e., 7-cyano-COT, **2**) is the unique product from the thermolysis of 7- and 6-cyano-2,3-benzobicyclo[4.2.0]octa-2,4,7-triene (**1** and **5**; note Scheme 1), and the major product from the direct irradiation of **1** are 7-cyanobenzosemibullvalene (**3**), 4-cyano-7,8-benzotetracyclo[3.3.0.0<sup>2,4</sup>.0<sup>3,6</sup>]oct-7-ene (**4**), and naphthalene. The COT **2** is also formed from the direct photolysis of triene **5**, though only in meager amounts; the main products are 1-cyanobenzosemibullvalene (**6**) and 2-cyanonaphthalene (note Scheme 1). Triplet-sensitized irradiations of either

triene **1** or **5** yield semibullvalenes and naphthalenes but do not generate COT products (**2**). We now report results from the study of deuterium-labelled derivatives of the trienes (viz. **1a** and **5a**, Scheme 2) which show that the skeletal reorganization that occurs in the photoformation of COT **2** from triene **5**, and the thermolyses of **1** and **5**, is different to that observed in the **1**  $\rightarrow$  **2** photoisomerization.

## Results

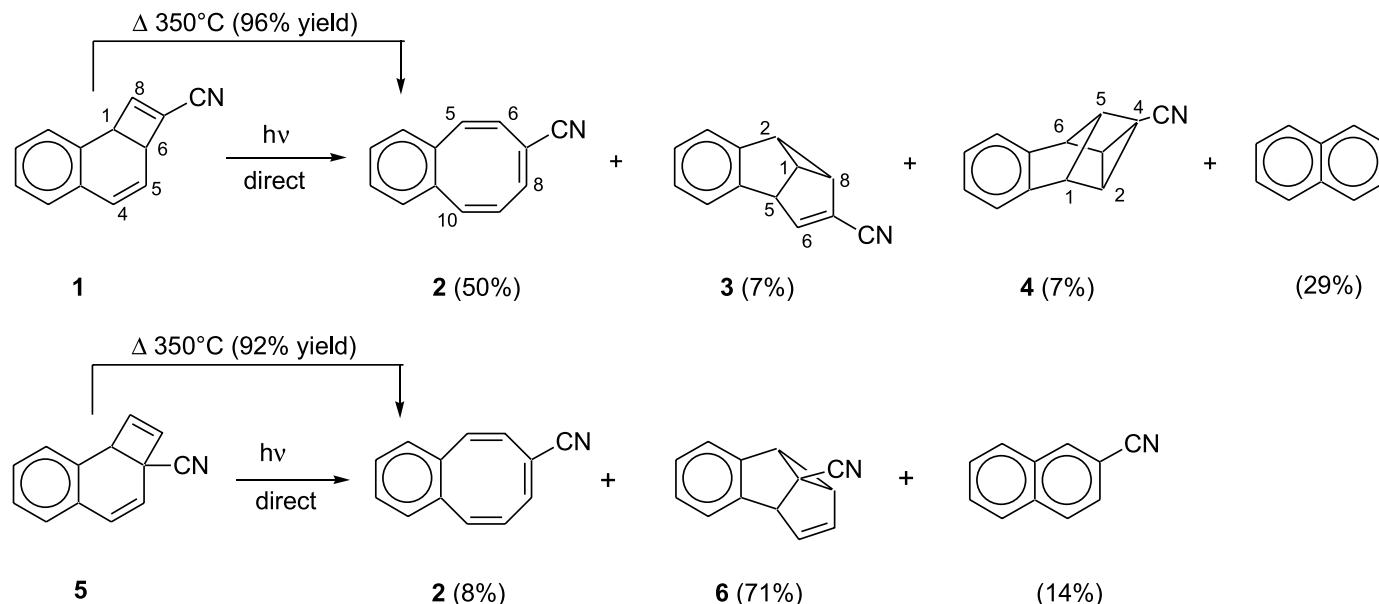
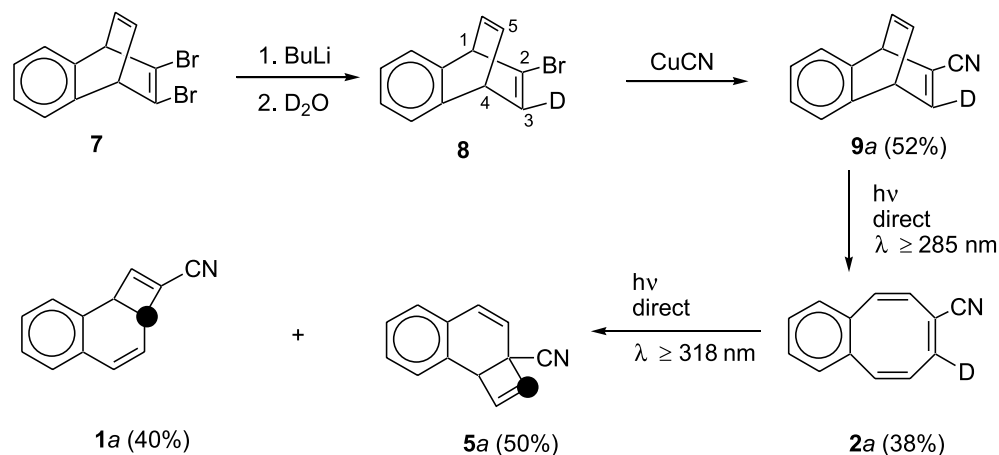
The deuterium-labelled trienes **1a** and **5a** (93%- $d_1$  at C-6 and C-7, respectively) were obtained as outlined in Scheme 2 (yields given in the Schemes are based on amounts of starting materials consumed) from a multistep procedure starting with the readily available 3,4-dibromobenzobarrelene **7** (**3**). All compounds in the synthetic sequence are either known or are deuterium-labelled derivatives of known compounds. Incorporation of deuterium at C-3 of barrelene **8** was achieved by treating dibromide **7** with 1 equiv of butyllithium, followed by quenching the resulting mono-anion with deuterium oxide. Crude **8** was then converted to the cyanolated derivative **9a** (52% overall yield from **7**) using cuprous cyanide according to established methodology (4). The final two synthetic steps are known photorearrangements.

Received 19 August 2002. Published on the NRC Research Press Web site at <http://canjchem.nrc.ca> on 27 January 2003.

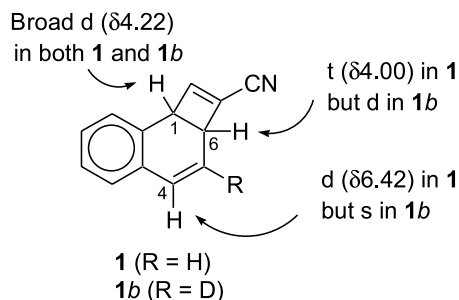
C.O. Bender,<sup>1</sup> D. Dolman, J.C. Foesier, S.L. Lawson, and K.E. Preuss. Department of Chemistry and Biochemistry, University of Lethbridge, Lethbridge, AB T1K 3M4 Canada.

<sup>1</sup>Corresponding author: (e-mail: [bender@uleth.ca](mailto:bender@uleth.ca)).



**Scheme 1.** Thermolysis and direct photolysis products from trienes **1** and **5**.**Scheme 2.** Preparation of deuterium-labelled trienes **1a** and **5a**.

Where  $\bullet$  = ca. 93%-d<sub>1</sub>



The first involves the direct irradiation (Corex filter) of barrelene **9a** to give the labelled COT **2a** as the major product (4). In the second step, the COT was photocyclized (direct irradiation at  $\lambda \geq 318$  nm, conditions under which the photolabile products absorb no light) to the desired triene **1a**, along with the alternate closure isomer **5a** (2).

The assignment of the deuterium attachment at C-6 of **1a** follows from the reduction in integration signal of the lower-

field bridgehead signal in the proton NMR spectrum. Differentiation between the two bridgehead hydrogens (i.e., H-1 at  $\delta$  4.22 and H-6 at  $\delta$  4.00) was previously established (2) from spin decoupling results and the observation that the triplet H-6 signal in nonlabelled triene **1** collapses to a doublet in the spectrum of the deuterium-labelled compound **1b**. As expected, the signal due to H-1 (broad doublet) is essentially unchanged upon replacement of H-5 with deuterium.



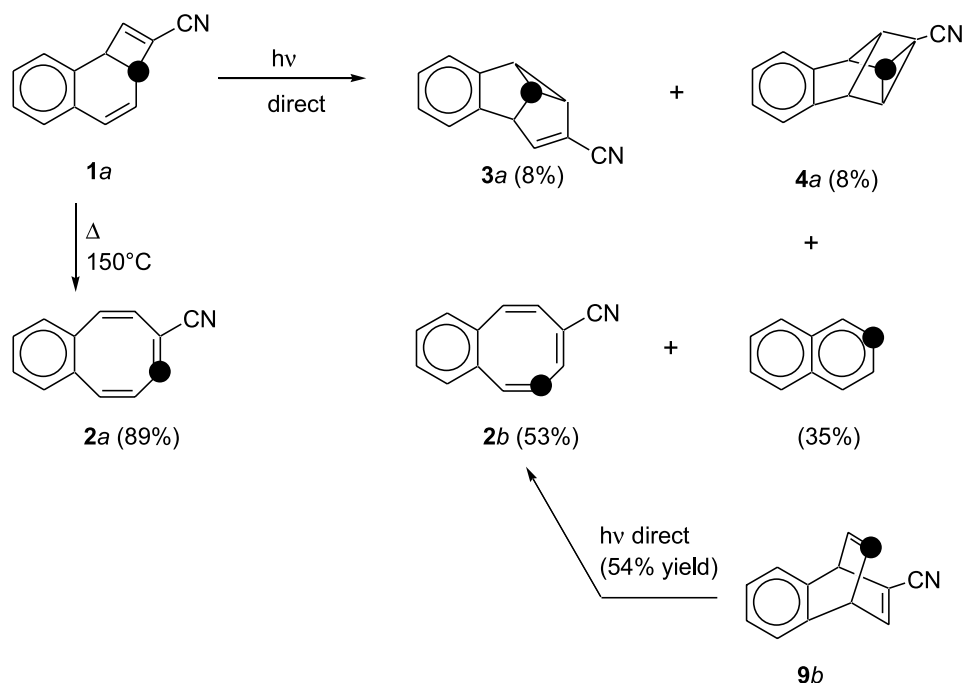
**Table 1.** Hydrogen atom distributions of the nonaromatic positions in deuterium-labelled 7-cyanobenzocyclooctatetraene.

Entry no.	Origin of 7-cyano-COT	Hydrogen atom distributions at: <sup>a</sup>			
		C-5 and C-10 $\delta$ 6.75 and $\delta$ 6.73	C-6 $\delta$ 5.95	C-8 $\delta$ 6.66	C-9 $\delta$ 6.07
1	Observed for direct hv of barrelene <b>9a</b> <sup>b</sup>	2.04H	0.99H	0.07H	0.98H
2	Observed for thermolysis of triene <b>1a</b> <sup>c</sup>	1.98H	0.97H	0.08H	0.95H
3	Observed for direct hv of triene <b>1a</b> <sup>b</sup>	1.98H	1.02H	0.98H	0.10H
4	Calcd. for direct hv of triene <b>1a</b> via route A	2.00H	1.00H	0.07H	1.00H
5	Calcd. for direct hv of triene <b>1a</b> via routes B or C	2.00H	1.00H	0.54H	0.54H
6	Calcd. for direct hv of triene <b>1a</b> via route D	2.00H	1.00H	1.00H	0.07H
7	Observed for thermolysis of triene <b>5a</b> <sup>c</sup>	2.00H	0.99H	0.08H	0.99H
8	Observed for direct hv of triene <b>5a</b> <sup>c</sup>	1.98H	0.98H	0.11H	0.95H

<sup>a</sup>In each case the aromatic multiplet at  $\delta$ 6.95–7.06 was set as the normalized integration standard of 2.00H; the other aromatic multiplet at  $\delta$ 7.22–7.31 gave variable integration values due to the presence of residual  $\text{CHCl}_3$ .

<sup>b</sup>See the experimental section for complete NMR details.

<sup>c</sup>The signal multiplicities were identical to those reported for 8-deuterio-COT (**2a**).

**Scheme 3.** Observed label locations in products from triene **1a** thermolysis and direct photolysis.

The NMR details are given at the triene structures **1/1b**, in Scheme 2. In the case of triene **5a**, the assignment of the deuterium attachment at C-7 is based on the signal designations previously given to nonlabelled **5** (2).

As indicated above, trienes **1** and **5** are known to revert to COT **2** upon heating (2). In the present study, the NMR spectra of the COT material isolated from the thermolyses (in *n*-nonane at 150°C) of the labelled trienes **1a** and **5a** revealed the same label distributions as were found in COT **2a** originally prepared from barrelene **9a** (i.e., deuterium exclusively at C-8; note the observed  $^1\text{H}$  NMR integration values given in Table 1, entries 1, 2, and 7). These findings are consistent with the operation of a mechanism involving cleavage of the strained C-1—C-6 bridging bond of the trienes (see Schemes 3 and 4), and is a ground-state reaction common to other benzobicyclo[4.2.0]octa-2,4,7-trienes (5).

In contrast to the thermal results, NMR analysis of the COT product isolated as the major component from the direct irradiation of labelled triene **1a** shows the deuterium to

be uniquely located at C-9 (Scheme 3; note Table 1, entry 3), i.e., the observed COT product is identical to the known  $\beta$ -labelled compound **2b** previously obtained (4) as the major product from the direct irradiation of the C-5 labelled barrelene **9b** (note Scheme 3). Thus mechanistically, the photoformation of COT **2** from triene **1** is not a simple reversal of the  $2\pi + 2\pi$  photoclosure process proposed in the generation of triene **1** from COT **2**. The other isomeric products (semibullvalene **3a** and tetracycle **4a**) isolated from the direct irradiation of triene **1a** contain deuterium distributions that are unexceptional and fully compatible with those anticipated by previously described mechanistic routes (2), viz. via a Zimmerman di- $\pi$ -methane (DPM) rearrangement (6) in the case of **3a**, and a  $2\pi_s + 2\pi_s$  cycloaddition in the case of **4a** (4).

Interestingly, the photochemical (direct irradiation) behaviour of triene isomer **5a** differs from that of **1a** in giving COT product (Scheme 4) in which the deuterium distribution corresponds to **2a**, within experimental uncertainty (note



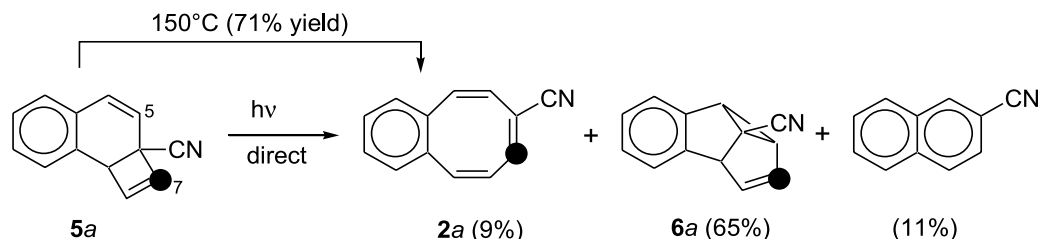
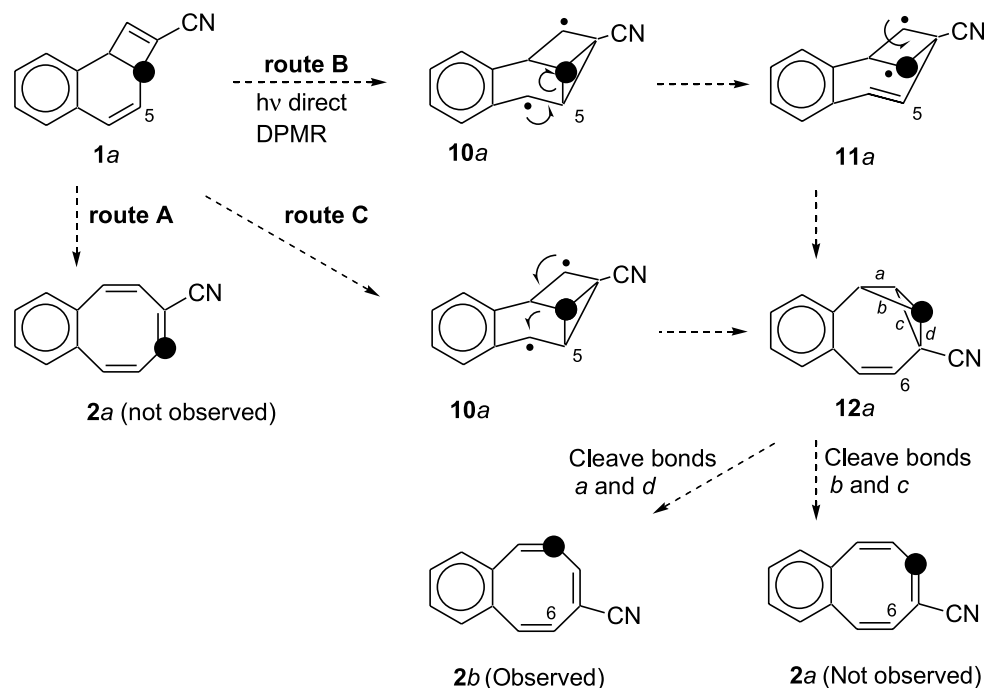
**Scheme 4.** Observed label locations in products from triene **5a** thermolysis and direct photolysis.**Scheme 5.** Mechanisms that do not account for photoformation of COT from triene **1a**.

Table 1, entry 8). The major product from the direct irradiation of **5a** is semibullvalene **6a** labelled at C-7, which is considered to form from a Zimmerman DPM rearrangement (6) involving initial bridging between C-5 and C-7, as proposed in the earlier investigation of triene **5** (2).

## Discussion

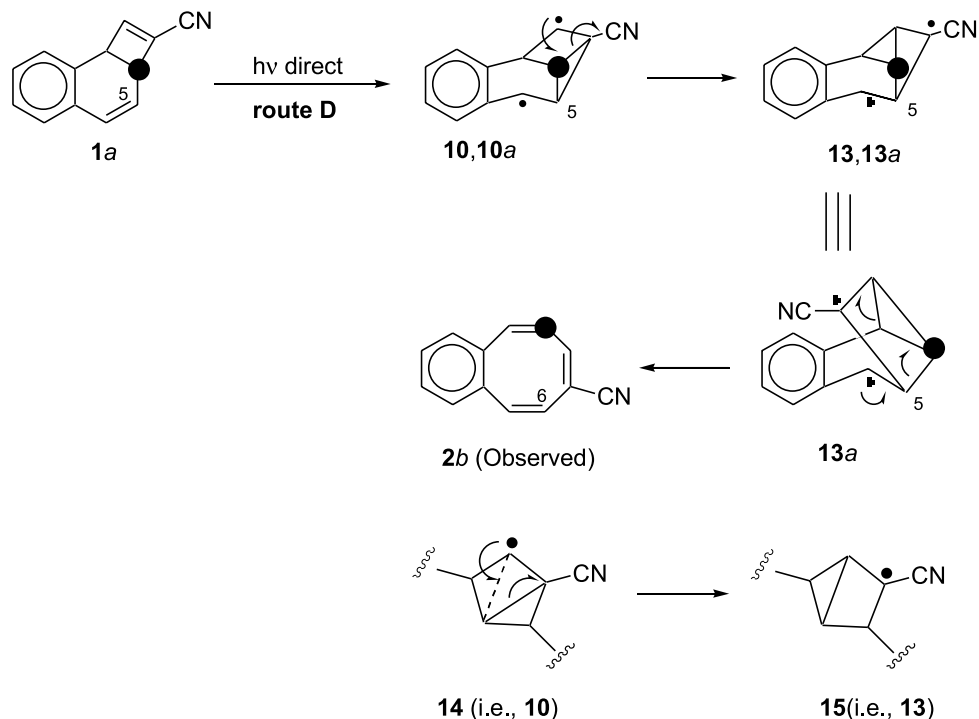
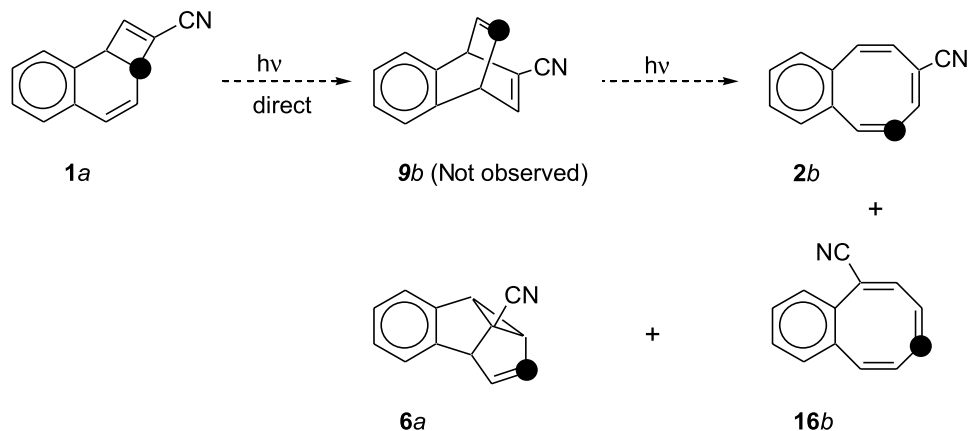
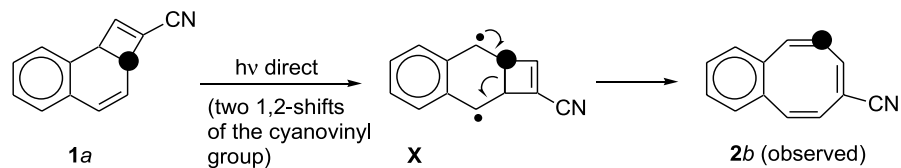
Previous studies of deuterium-labelled 2,3-benzobicyclo[4.2.0]octa-2,4,7-trienes have led to the postulation of at least three mechanistic pathways which may operate in the photogeneration of COTs (7–12). However, none of these pathways (depicted as routes A, B, and C in Scheme 5) can account for the labelling pattern observed in the photoconversion of **1a** to **2b**. Thus, operation of a route A-type mechanism (7–9), which is formally equivalent to a  $2\sigma_s + 2\pi_s$  electrocyclic opening (13), would lead to **2a** (not observed). Operation of a route B-type (10–12) or a route C-type mechanism (11), both of which involve the initial formation of a Zimmerman DPM rearrangement diradical **10a**, should give approximately equal amounts of **2a** (not observed) and **2b** (observed) from the thermal reorganization of the proposed

octavalene intermediate **12a**, assuming minor deuterium isotope effects (14, 15).

To rationalize the photoconversion of **1a** → **2b**, we propose a novel mechanism (route D, Scheme 6) which is a modification of the Zimmerman DPM pathway identified as route B in Scheme 5. The modification allows for the rearrangement of the initially formed diradical **10a** to the more stabilized species **13a** (Scheme 6). The transformation of **10a** to **13a** can be viewed as an interconversion between two housane-type species, i.e., **14** → **15**. Interestingly, the diradical **13**, in which favorable stabilization is afforded the radical centres by the cyano and benzo groups, was invoked previously by us (4) to explain the formation of COT **2b** from the direct irradiation of barrelene **9b** (note Scheme 7)<sup>2</sup>. However, lest it be thought that barrelene **9b** is involved in the present case through a two-step process (viz., **1a** → **9b** → **2b**), the primary step would be an excited-state allowed 1,3-shift), we point out that the subsequent photolysis of **9b** would have led not only to COT **2b** but also to the co-formation of semibullvalene **6a** and COT **16b** (note Scheme 7) (2). Since neither the barrelene **9b** nor **6a** nor **16b** are observed in photolysates of triene **1a**, at any conversion

<sup>2</sup>Following the suggestion of a referee, we note that the same overall skeletal organization of COT **2b** would result from two 1,2-shifts of the cyanovinyl group of triene **1a** via the mechanism given in Fig. 1.



**Scheme 6.** Suggested mechanism for photoformation of COT **2b** from triene **1a**.**Scheme 7.** Pathway not observed from triene **1a** to COT **2b**.**Fig. 1.** Alternative mechanism for photoformation of COT **2b** from triene **1a**.

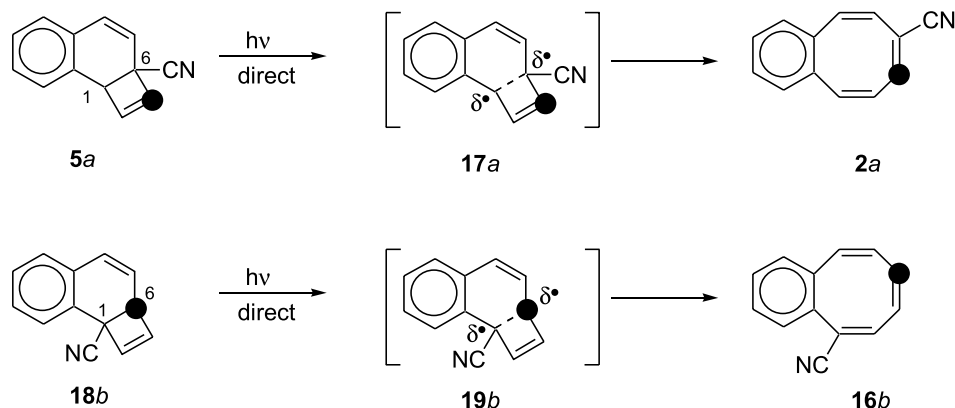
level (GC and NMR monitoring), it follows that **9b** does not feature in the production of COT **2** from triene **1**.

For triene **5a**, the deuterium results are most readily interpreted in terms of a route A-type mechanism, wherein cleavage of the strained C-1—C-6 bond would be particularly favorable due to the extensive stabilization of the “diradical-like” centres in the proposed transition state, approximated by structure **17a** (Scheme 8). A similar explanation was

given to account for the facile photoformation of COT **16b** in the case of triene **18b**, which also contains a cyano group at a bridgehead location (C-1) (8).

A last point of interest is that the deuterium-labelled triene **1b** (i.e., deuterium attached to C-5; note structure **1b** in Scheme 2), which was initially prepared in 1986 to delineate the mechanistic details of the photoformations of semi-bullvalene **3** and **6** from trienes **1** and **5**, respectively (2), is



**Scheme 8.** Possible mechanism for photoformation of COT **2a** from triene **5a**.

not appropriately labelled to distinguish between operation of the route B- (or C-) type mechanisms (Scheme 5) and the novel pathway proposed here (route D, Scheme 6). Thus, according to either route B (or C) in Scheme 5, or the modified mechanism (route D) shown in Scheme 6, a label at C-5 of the triene becomes a label at C-6 in the COT product.<sup>3</sup>

## Experimental

### Instrumentation and general procedures

The NMR spectra were recorded on a Bruker 250-MHz instrument in  $\text{CDCl}_3$  solvent with TMS as the internal standard; the chemical shifts are in  $\delta$  units and the coupling constants ( $J$ ) in Hz. The abbreviations br, s, d, t, q, and m refer to broad, singlet, doublet, triplet, quartet, and multiplet, respectively. The photolysis apparatus consisted of a 450-W Hanovia medium-pressure mercury arc surrounded by a water-cooled quartz immersion well. Unless otherwise stated, the light was filtered through either a cylindrical sleeve of Pyrex or Corex glass, or an aqueous lead nitrate solution (1 g of  $\text{Pb}(\text{NO}_3)_2$  and 100 g of NaBr in 1 L of water; transmittance was 0% below 318 nm) contained in a concentric filter jacket (10 mm path length). Three types of sample cell (A, B, or C) were used. Cell A (250 mL sample volume) consisted of a cylindrical vessel (Pyrex) which surrounded the immersion well. Cell B (200 mL sample volume) consisted of a cylindrical collar (Pyrex) which surrounded the aqueous filter jacket. Both Cells A and B were fitted with gas inlet and outlet ports, and sample solutions were deoxygenated by flushing with argon, before and during irradiations. Cell C (40 mL sample volume) was a test tube-like vessel (quartz), and sample solutions were deoxygenated by flushing with argon and sealed under a positive pressure; the solutions were magnetically stirred throughout the course of the irradiations. Column chromatography was carried out on Lobar (Merck; size B, LiChroprep Si 60) or on Silica Gel 60/ $\text{AgNO}_3$  columns (10:1 by weight). All compounds described in this study are either known or are deuterium-labelled derivatives of known compounds; their purities were estimated to be  $\geq 98\%$  by a combination of NMR and GC analyses.

### 3-Deuteriocyanobarrelene (**9a**) from 2,3-dibromo-1,4-dihydro-1,4-ethenonaphthalene (**7**)

To a magnetically stirred solution of 3.62 g (12 mmol) of 2,3-dibromobenzobarrelene **7** (3) in 90 mL of dry, freshly distilled THF at  $-70^\circ\text{C}$  was added dropwise 8.90 mL (14 mmol) of 1.6 M butyllithium in hexane over a 15 min period under a nitrogen atmosphere. Stirring was continued for an additional 25 min followed by the dropwise addition of 1.8 mL (99 mmol) of deuterium oxide during 5 min at  $-70^\circ\text{C}$ . After stirring for 10 min, the cooling was removed and the reaction mixture allowed to warm to room temperature. The mixture was concentrated on the rotovap and distilled water (200 mL) and hexane (200 mL) were added. The aqueous layer was removed and extracted with hexane (100 mL). The combined organic layers were washed with distilled water ( $2 \times 100$  mL) and dried ( $\text{MgSO}_4$ ). The solvent was removed via the rotovap and the crude 3-deuterio-bromobenzobarrelene **8** was converted without purification to 3-deuterio-2-cyano-1,4-dihydro-1,4-ethenonaphthalene (**9a**) using 2.10 g (23 mmol) of cuprous cyanide, according to the method previously described (4) for the conversion of unlabelled 2-bromo-1,4-dihydro-1,4-ethenonaphthalene to 2-cyano-1,4-dihydro-1,4-ethenonaphthalene. Crystallization of the crude product from 95% ethanol yielded 1.09 g (52%) of **9a**, mp  $65\text{--}67^\circ\text{C}$  (lit. (4) value  $66$  to  $67^\circ\text{C}$  for the non-deuterated parent).  $^1\text{H}$  NMR: 7.61 (dd, 0.06H, residual H-3,  $J_{3,4} = 6$ ,  $J_{1,3} = 2$ ), 7.19–7.3 (m, 2.21H, 2 aromatics and residual  $\text{CHCl}_3$ ), 6.86–7.01 (m, 4.04H, 2 aromatics, H-5 and H-6), 5.00–5.10 (m, 2.00H, H-1 and H-4), corresponding to 94%- $d_1$  at C-3; uncertainties from NMR signal integrations are within  $\pm 0.05\text{H}$  for **9a** and for all subsequent integrations of deuterated compounds.

### 8-Deuterio-7-CN-COT (**2a**) from 3-deuteriocyanobarrelene (**9a**)

A solution containing 1.039 g (5.77 mmol) of labelled cyanobarrelene (**9a**) in 1 L of cyclohexane was irradiated in four equal aliquots in Cell A (Corex filter) for 40 min each. The photolysates were combined and chromatographed as described previously (4) for the preparation of COT **2** from unlabelled cyanobarrelene, to give 395.1 mg (38%) of 8-deuterio-COT (**2a**) as the major product, mp  $99\text{--}101^\circ\text{C}$  (lit.

<sup>3</sup> Triene **1b** does in fact give 7-cyanobenzocyclooctatetraene exclusively labelled with deuterium at C-6 upon direct photolysis (C.O. Bender, P.D. England, and K.E. Preuss. Unpublished results).



(4) value 102 to 103° C for non-deuterated **2**) after recrystallization from 95% ethanol. <sup>1</sup>H NMR: 7.22–7.31 (m, 2.67H, 2 aromatics + residual CHCl<sub>3</sub>), 6.95–7.06 (m, 2.00H, 2 aromatics), 6.75 and 6.73 (d and d, 2.04H, H-5 and H-10,  $J_{5,6} = J_{9,10} = 11.5$ ), 6.66 (d, 0.07H, residual H-8,  $J_{8,9} = 4.5$ ), 6.07 (d, 0.98H, H-9,  $J_{9,10} = 11.5$ ), and 5.95 (d, 0.99H, H-6,  $J_{6,5} = 11.5$ ). Also note <sup>1</sup>H NMR data given in entry number 1 in Table 1.

#### Direct irradiation of 8-deuterio-COT (**2a**)

A solution containing 366.5 mg (2.04 mmol) of **2a** in 200 mL of cyclohexane was irradiated directly in Cell B (Pb(NO<sub>3</sub>)<sub>2</sub> filter) for 96 h. The photolysate was concentrated to 8 mL and chromatographed (in four 2 mL aliquots) on a Lobar column with 1% ethyl acetate – hexane solvent; the eluant was monitored by UV spectroscopy at  $\lambda = 300$  nm. The last band from the column contained 116.6 mg (32%) of labelled 6-cyano-2,3-benzobicyclo[4.2.0]octa-2,4,7-triene (**5a**). <sup>1</sup>H NMR: 7.10–7.30 (m, 4.28H, 4 aromatics + residual CHCl<sub>3</sub>), 6.46 (d, 1.00H, H-4,  $J_{4,5} = 10$ ), 6.19 (dd, 0.06H, residual H-7,  $J_{7,8} = 2.8$ ,  $J_{7,1} = 1$ ), 6.07 (d, 0.95H, H-8,  $J_{8,1} = 1$ ), 5.85 (d, 0.98H, H-5,  $J_{5,4} = 10$ ), and 4.46 (br s, 0.97H, H-1). The first band from the column contained COT **2a** and triene **1a**, and was rechromatographed in three equal aliquots on a Silica Gel 60/AgNO<sub>3</sub> column (0.9 cm × 11 cm; 0.5% ethyl acetate – hexane). The first band gave 93.8 mg (26%) of triene **1a**. <sup>1</sup>H NMR: 7.16–7.22 (m, 2.05H, 2 aromatics), 7.06–7.13 (m, 2.07H, 2 aromatics), 6.71 (d, 1.00H, H-8,  $J_{8,1} = 1$ ), 6.42 (d, 1.00H, H-4,  $J_{4,5} = 10$ ), 5.93 (d, 0.98H, H-5,  $J_{5,4} = 10$ ), 4.22 (br s, 0.99H, H-1), and 4.00 (t, 0.07H, residual H-6,  $J_{6,1} = J_{6,5} = 4.5$ ). The second band gave 133.8 mg (37%) of recovered COT starting material (**2a**). <sup>1</sup>H NMR: 7.22–7.31 (m, 2.08H, 2 aromatics + residual CHCl<sub>3</sub>), 6.95–7.06 (m, 2.00H, 2 aromatics), 6.75 and 6.73 (d and d, 1.95H, H-5 and H-10,  $J_{5,6} = J_{9,10} = 11.5$ ), 6.66 (d, 0.08H, residual H-8,  $J_{8,9} = 4.5$ ), 6.07 (d, 0.94H, H-9,  $J_{9,10} = 11.5$ ), and 5.95 (d, 0.96H, H-6,  $J_{6,5} = 11.5$ ).

#### Thermolysis of triene **1a**

A solution of 8.0 mg (0.044 mmol) of **1a** in 4 mL of *n*-nonane was refluxed (ca. 150°C) under a nitrogen atmosphere for 8 h. The thermolysis product was chromatographed on Silica Gel 60 (0.9 cm × 10 cm) with 3% ethyl acetate – hexane to give 7.1 mg (89%) of 8-deuterio-COT (**2a**) (the <sup>1</sup>H NMR data are given in entry 2, Table 1).

#### Direct irradiation of triene **1a**

A solution containing 42.3 mg (0.24 mmol) of **1a** in 40 mL of cyclohexane was irradiated directly in Cell C (Pyrex filter) for 3.2 h. The photolysate was concentrated and chromatographed on Silica Gel 60 (0.9 cm × 7 cm) with 4% ethyl acetate – hexane to remove polymeric materials, and then rechromatographed on a Lobar column with 2% ethyl acetate – hexane solvent; the eluant was monitored by UV spectroscopy at  $\lambda = 265$  nm. The first band off the column gave 3.3 mg (11%) of naphthalene-*d*<sub>1</sub>. The second band contained a mixture of the triene starting material and COT product. The third band contained ca. 1 mg (2%) of semibullvalene **3a**. <sup>1</sup>H NMR: 7.22–7.31 (m, 1.00H, 1 aromatic), 7.03–7.26 (m, 5.14H, 3 aromatics + residual CHCl<sub>3</sub>), 6.30 (d, 1.03H, H-6,  $J_{6,5} = 2.5$ ), 4.04 (d, 1.02H, H-5,  $J_{5,6} = 2.5$ ),

3.38 (q, 0.09H, residual H-1,  $J_{1,2} = J_{1,5} = J_{1,8} = 6.5$ ), 3.19 (d, 1.03H, H-2,  $J_{2,8} = 6.5$ ), and 2.94 (d, 1.01H, H-8,  $J_{2,8} = 6.5$ ). The last band gave ca. 1 mg (2%) of tetracycle **4a**. <sup>1</sup>H NMR: 7.16–7.28 (m, 4.38H, 4 aromatics and residual CHCl<sub>3</sub>), 4.32–4.36 (m, 2.00H, H-1 and H-6), 3.28 (q, 1.01H, H-5,  $J_{5,1} = J_{5,2} = J_{5,6} = 4.5$ ), and 2.91–2.98 (m, 1.00H, H-2 and residual H-3).

The second band containing the triene starting material and COT product was rechromatographed on a Silica Gel 60/AgNO<sub>3</sub> column (0.9 cm × 11 cm; 0.25% ethyl acetate – hexane), monitored by UV spectroscopy at  $\lambda = 300$  nm. The first band gave 29.0 mg (69%) of recovered triene starting material **1a**. <sup>1</sup>H NMR: 7.16–7.22 (m, 1.99H, 2 aromatics), 7.06–7.13 (m, 2.03H, 2 aromatics), 6.71 (d, 1.00H, H-8,  $J_{8,1} = 1$ ), 6.42 (d, 1.00H, H-4,  $J_{4,5} = 10$ ), 5.93 (d, 0.97H, H-5,  $J_{5,4} = 10$ ), 4.22 (br s, 0.99H, H-1), and 4.00 (t, 0.07H, residual H-6,  $J_{6,1} = J_{6,5} = 4.5$ ). The second band gave 7.0 mg (17%) of COT product **2b**. <sup>1</sup>H NMR: 7.22–7.31 (m, 2.07H, 2 aromatics + residual CHCl<sub>3</sub>), 6.95–7.06 (m, 2.00H, 2 aromatics), 6.75 and 6.73 (d and br s, 1.98H, H-5 and H-10,  $J_{5,6} = 11.5$ ), 6.66 (br s, 0.98H, H-8), 6.07 (dd, 0.10H, residual H-9,  $J_{9,8} = 4.5$ ,  $J_{9,10} = 11.5$ ), and 5.95 (d, 1.02H, H-6,  $J_{6,5} = 11.5$ ); also note the <sup>1</sup>H NMR data given in entry number 3, Table 1.

#### Thermolysis of triene **5a**

A solution of 8.5 mg (0.047 mmol) of **5a** in 5 mL of *n*-nonane was refluxed (ca. 150°C) under a nitrogen atmosphere for 5.2 h. The thermolysis product was chromatographed on Silica Gel 60 (0.9 cm × 10 cm) with 3% ethyl acetate – hexane to give 6.0 mg (71%) of 8-deuterio-COT (**2a**); for <sup>1</sup>H NMR details note entry 7, Table 1.

#### Direct irradiation of 7-deuterio-6-cyano-triene (i.e., triene **5a**)

A solution containing 20.2 mg (0.09 mmol) of **5a** in 40 mL of cyclohexane was irradiated directly in Cell C (Pyrex filter) for 1.5 h. The photolysate was worked up as in the case of the direct irradiation of unlabelled triene **5** (**2**) to give ca. 1 mg (5%) of 2-cyanonaphthalene and ca. 1 mg (5%) of 8-deuterio-COT (**2a**); for the <sup>1</sup>H NMR details note entry number 8, Table 1; 8.5 mg (42%) of recovered triene **5a** (<sup>1</sup>H NMR: 7.10–7.30 (m, 4.50H, 4 aromatics + residual CHCl<sub>3</sub>), 6.46 (d, 1.00H, H-4,  $J_{4,5} = 10$ ), 6.19 (dd, 0.06H, residual H-7,  $J_{7,8} = 2.8$ ,  $J_{7,1} = 1$ ), 6.07 (d, 0.98H, H-8,  $J_{8,1} = 1$ ), 5.85 (d, 1.00H, H-5,  $J_{5,4} = 10$ ), and 4.46 (br s, 1.00H, H-1)); and 7.5 mg (37%) of semibullvalene **6a** (<sup>1</sup>H NMR: 7.32–7.40 (m, 1.00H, 1 aromatic), 7.06–7.25 (m, 3.10H, 3 aromatics + residual CHCl<sub>3</sub>), 5.70 (d, 0.95H, H-6,  $J_{6,5} = 2.5$ ), 5.20 (dd, 0.06H, residual H-7,  $J_{7,6} = 5.0$ ,  $J_{7,8} = 2.5$ ), 4.22 (d, 1.01H, H-5,  $J_{5,6} = 2.5$ ), 3.68 (d, 1.01H, H-2,  $J_{2,8} = 7.0$ ), and 3.35 (d, 1.02H, H-8,  $J_{8,2} = 7$ )).

#### Acknowledgements

The authors thank Paul Bradley England for technical assistance and gratefully acknowledge financial support from the Natural Sciences and Engineering Research Council of Canada (NSERC).



## References

1. G. Mehta and V. Singh. *Chem. Rev.* **99**, 881 (1999).
2. C.O. Bender, D.L. Bengtson, D. Dolman, and S.F. O'Shea. *Can. J. Chem.* **64**, 237 (1986).
3. O. Cakmak and M. Balci. *J. Org. Chem.* **54**, 181 (1989).
4. C.O. Bender, D.W. Brooks, W. Cheng, D. Dolman, S.F. O'Shea, and S.S. Shugarman. *Can. J. Chem.* **56**, 3027 (1978).
5. (a) P.J. Collin and W.H.F. Sasse. *Tetrahedron Lett.* **14**, 1689 (1968); (b) J.A. Elix, M.V. Sargent, and F. Sondheimer. *J. Am. Chem. Soc.* **89**, 5081 (1967); (c) W.H.F. Sasse. *Aust. J. Chem.* **22**, 1257 (1969); (d) P.J. Collin and W.H.F. Sasse. *Aust. J. Chem.* **24**, 2325 (1971).
6. (a) H.E. Zimmerman. *In* Rearrangements in ground and excited states. Vol. 3. *Edited by* P. de Mayo. Academic Press, New York. 1980. Essay 16. pp. 131–166; (b) S.S. Hixon, P.S. Mariano, and H.E. Zimmerman. *Chem. Rev.* **73**, 531 (1973).
7. C.O. Bender and D. Dolman. *Can. J. Chem.* **67**, 82 (1989).
8. C.O. Bender, D.S. Clyne, and D. Dolman. *Can. J. Chem.* **69**, 70 (1991).
9. C.O. Bender, D. Dolman, and N. Tu. *J. Org. Chem.* **56**, 5015 (1991).
10. C.O. Bender, D. Dolman, and G.K. Murphy. *Can. J. Chem.* **66**, 1656 (1988).
11. C.O. Bender, D.L. Bengtson, D. Dolman, and R.T. McKay. *Can. J. Chem.* **72**, 1556 (1994).
12. C.O. Bender. *Can. J. Chem.* **74**, 32 (1996).
13. R.B. Woodward and R. Hoffmann. *In* The conservation of orbital symmetry. Verlag Chemie, Weinheim, and Academic Press, New York. 1970. p. 63.
14. M. Christl and R. Lang. *J. Am. Chem. Soc.* **104**, 4494 (1982).
15. M. Christl and R. Lang. *Tetrahedron*, **42**, 1585 (1986).



# The use of $\beta$ -cyclodextrins to enhance the aqueous solubility of trichloroethylene and perchloroethylene and their removal from soil organic matter: Effect of substituents

Salma Shirin, Erwin Buncel, and Gary W. vanLoon

**Abstract:** This paper describes a systematic study for the evaluation of different substituted  $\beta$ -cyclodextrins ( $\beta$ -CDs), as agents for the enhancement of the aqueous solubility of two major organic pollutants, trichloroethylene (TCE) and perchloroethylene (PCE). The aqueous solubility enhancement occurs through the formation of host-guest inclusion complexes between the CD molecule (host) and the polychloroethylene (guest) and is driven primarily by hydrophobic forces. The CDs evaluated are: methyl- $\beta$ -CD (M $\beta$ -CD), hydroxypropyl- $\beta$ -CD (HP $\beta$ -CD), carboxymethyl- $\beta$ -CD (CM $\beta$ -CD1, CM $\beta$ -CD2), and sulfated- $\beta$ -CD (S $\beta$ -CD1, S $\beta$ -CD2); the degree of substitution was also varied. Using a 5% (w/v) aqueous CD solution, solubility enhancement factors ( $S/S_0$ ) up to 5.5 and 14 were determined for TCE and PCE, respectively. Binding constants ( $K_{11}$ ) for TCE with the substituted CDs were evaluated using an  $^1\text{H}$  NMR technique; these were found to range from 3 to 120  $\text{M}^{-1}$ . It was shown that solubility enhancement, as well as the binding constant, is dependent on the type and degree of substitution of the  $\beta$ -CD molecule; the determining factors are discussed. The CDs are also capable of effective removal of PCE and TCE retained by soil organic matter. Thus, a suitably substituted  $\beta$ -CD may be a valuable additive in pump-and-treat protocols for site remediation of polychlorinated organics.

**Key words:** cyclodextrin, trichloroethylene, perchloroethylene, solubility enhancement, binding constant, soil and water remediation.

**Résumé :** Dans ce travail, on décrit une étude systématique réalisée pour évaluer l'utilité de diverses  $\beta$ -cyclodextrines substituées ( $\beta$ -CD) comme agents d'augmentation de la solubilité aqueuse de deux agents polluants importants, le trichloroéthylène (TCE) et le perchloroéthylène (PCE). L'augmentation de la solubilité aqueuse résulte de la formation de complexes d'inclusion hôte-invité entre une molécule de CD (hôte) et le polychloroéthylène (invité) et elle résulte principalement de forces hydrophobes. On a évalué les CD suivantes en faisant aussi varier le degré de substitution: méthyl- $\beta$ -CD (M-CD), hydroxypropyl- $\beta$ -CD (HP $\beta$ -CD), carboxyméthyl- $\beta$ -CD (CM $\beta$ -CD1; CM $\beta$ -CD2) et de  $\beta$ -CD sulfatées (S $\beta$ -CD1; S $\beta$ -CD2). Utilisant des solutions aqueuses à 5% (m/v) de CD, on a observé des facteurs d'augmentation de la solubilité ( $S/S_0$ ) de 5,5 et 14 respectivement pour TCE et PCE. Faisant appel à une technique de RMN, on a évalué que les constantes de fixation ( $K_{11}$ ) du TCE avec les CD substituées varient de 3 à 120  $\text{M}^{-1}$ . On a montré que le degré d'augmentation de solubilité ainsi que la constante de fixation dépendent du type et du degré de substitution sur la molécule de  $\beta$ -CD; on discute des facteurs déterminants. Les CD sont aussi capables d'extraire de façon efficace les PCE et TCE qui sont retenus dans les portions organiques du sol. Une  $\beta$ -CD substituée de façon appropriée peut être un additif utile dans les protocoles d'extraction de composés organiques polychlorés réalisés pour remédier à des déversements.

**Mots clés :** cyclodextrine, trichloroéthylène, perchloroéthylène, augmentation de la solubilité, constante de fixation, remédier à des contaminations de sol ou d'eau.

[Traduit par la Rédaction]

## Introduction

Trichloroethylene (TCE) and perchloroethylene (PCE) are among a number of chlorinated organic compounds that have

been listed as major organic contaminants in soil and water systems throughout the industrialized areas of North America (1, 2). These two compounds are released into the environment from a variety of industrial sources and are frequently found in aquifers as dense, non-aqueous phase liquids (DNAPLs). The hydrophobic liquids accumulate in relatively large bodies known as pools or as residuals in the form of disconnected blobs and ganglia (2). Because the aqueous solubilities of TCE and PCE are small (200 ppm and 1100 ppm, respectively (2)), only a limited concentration of the DNAPL dissolves in the associated groundwater. In addition, both compounds are resistant to biotic and

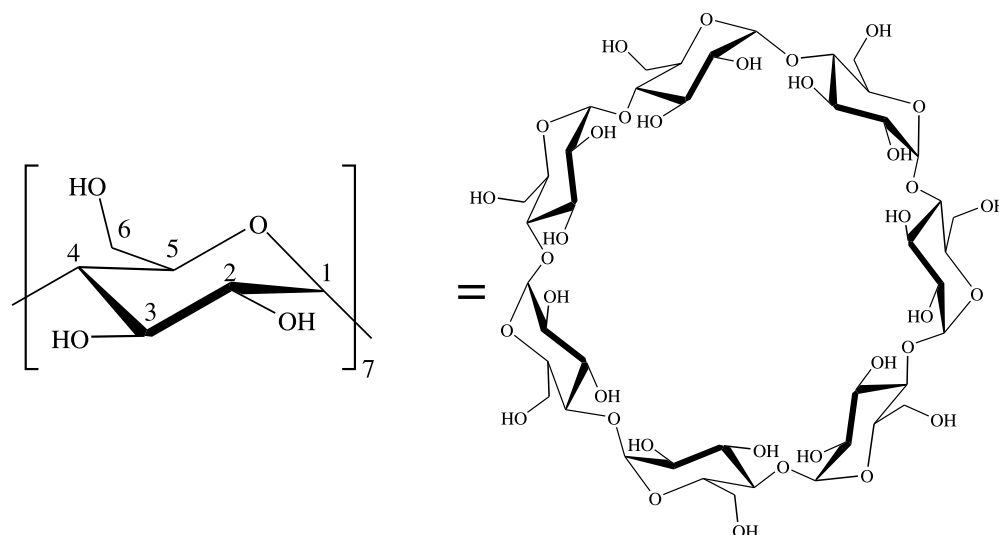
Received 3 October 2002. Published on the NRC Research Press Web site at <http://canjchem.nrc.ca> on 31 January 2003.

S. Shirin, E. Buncel, and G.W. vanLoon.<sup>1</sup> Department of Chemistry, Queen's University, Kingston, ON K7L 3N6, Canada.

<sup>1</sup>Corresponding author (e-mail: [vanloon@chem.queensu.ca](mailto:vanloon@chem.queensu.ca)).



**Fig. 1.** Illustration of the 7 glucose units in  $\beta$ -CD. Substitution can occur at the C-2, C-3, and C-6 hydroxyl functionalities in each unit.



abiotic degradation under most natural environmental conditions. Therefore, the DNAPL is not rapidly removed by either dissolution or degradation and its lifespan in the soil and (or) groundwater system may be on the order of several decades, even centuries. Both TCE and PCE, along with vinyl chloride, one of their daughter products, are considered to be potential carcinogens and mutagens (1, 3). As a result of their environmental persistence and mutagenicity, removal from the subsurface has become a priority, and numerous studies have focused on the environmental remediation of PCE and TCE. The traditional method for remediation of these two and other DNAPL compounds involves pump-and-treat technology where ground water is pumped from the soil, treated chemically or photochemically to destroy the contaminant, and then returned; however, their low aqueous solubility limits the effectiveness of this method (4, 5). In this regard, chemically enhanced dissolution of such organic compounds using surfactants or alcohols is usually considered (6, 7). However, a major problem associated with the use of surfactants and alcohols is that both of them tend to lower the DNAPL–water interfacial tension (8, 9). Lowering of interfacial tension could result in remobilization of DNAPLs in the vertical plane, making the remediation process more difficult. In addition, surfactants tend to be retained in the soil by sorption onto various types of soil particles. To overcome these problems, a new enhanced solubilization strategy involving the use of cyclodextrins may be attractive.

Cyclodextrins (CDs) are cyclic glucose oligosaccharides formed by the action of *Bacillus macerans* on starch (10). Depending on the number of glucose units in the ring, cyclodextrins are classified as  $\alpha$ ,  $\beta$ , or  $\gamma$ , corresponding to 6, 7, or 8 glucose units, respectively. The donut-shaped molecule has one rim lined with primary -OH groups and another rim lined with secondary -OH groups. The -OH groups are directed outward, providing a hydrophilic exterior, while the interior is substantially hydrophobic, a result of the hydrocarbon portion of the glucose skeleton. The combination of these properties enables cyclodextrins to act as “host” in

forming complexes with other “guest” molecules that are either non-polar or of low polarity and that have a size and shape that is complementary to the cavity dimensions of the CD. Several intermolecular interactions have been proposed to account for the formation of CD–inclusion complexes in aqueous solution. They include van der Waals forces between the guest and host molecules, hydrophobic interaction, release of high-energy  $\text{H}_2\text{O}$  molecules from the CD cavity, and relief of conformational strain in a CD–water adduct upon substrate inclusion. (11).

The ability of CDs to form water-soluble inclusion complexes with a wide range of organic compounds makes them suitable for application in a variety of situations (12) including in the pharmaceutical industry (time-release drugs) and in the manufacture of household items (odour reducing spray). Importantly, cyclodextrins are non-toxic, non-carcinogenic, and environmentally benign. Thus far,  $\beta$ -CDs have been used more frequently than other CDs because of the appropriate cavity size with respect to a wide range of organic compounds. However, underivatized  $\beta$ -CD has the lowest aqueous solubility (1.8 g per 100 mL) compared with  $\alpha$ - and  $\gamma$ -CD (14.5 and 23.2 g per 100 mL, respectively) (11). To increase solubility, modification of the -OH groups in the CD molecule can be carried out (11, 13, 14). In principle, any or all of the three -OH groups in each glucose unit of the CD molecule can be functionalized (Fig. 1). Hence, there can be from 0 to 21 degrees of substitution (DS) in each  $\beta$ -CD molecule (three -OH groups per glucose unit and 7 glucose units in each molecule).

The possibility of using derivatized CDs for effecting the remediation of nonpolar and low-polarity organic pollutants in soil and (or) water systems has been investigated in a number of studies (15–23). These reports describe laboratory and field experiments that demonstrate the application of substituted CDs in environmental remediation strategies. In laboratory-based studies, it was found that an increase in aqueous solubility of a range of nonpolar and low-polarity organic compounds, including TCE and PCE, could be achieved using various types of substituted  $\beta$ -CDs such as



**Table 1.** Substituted CDs used in this work: molar mass and degree of substitution.

Compound	Substituent group <i>R</i>	Degree of substitution (average)	Average molar mass (g mol <sup>-1</sup> )
Hydroxypropyl (HP $\beta$ -CD)	-CH <sub>2</sub> CH(OH)CH <sub>3</sub>	3–8 (5.5)	1500
Methyl (M $\beta$ -CD)	-CH <sub>3</sub>	10–16 (12)	1303
Carboxymethyl (CM $\beta$ -CD1)	-CH <sub>2</sub> COO <sup>-</sup>	3	1375
Carboxymethyl <sup>a</sup> (CM $\beta$ -CD2)	-CH <sub>2</sub> COO <sup>-</sup>	1–11 (7)	1671
Sulfated (S $\beta$ -CD1)	-SO <sub>3</sub> <sup>-</sup>	3–16 (4)	1543
Sulfated (S $\beta$ -CD2)	-SO <sub>3</sub> <sup>-</sup>	3–16 (14)	2563

<sup>a</sup>Molar mass was determined from the major peak obtained using FAB-MS. For all other CDs, average values provided by the supplier were used.

hydroxypropyl- $\beta$ -CD (HP $\beta$ -CD), methylated- $\beta$ -CD (M $\beta$ -CD), and carboxymethyl- $\beta$ -CD (CM $\beta$ -CD). For example, aqueous solubility enhancement using 5% HP- $\beta$ CD ranges from ca. 3 (for TCE) to 147 (for anthracene) depending on the size and other properties of the guest molecule (15).

To evaluate the performance of CDs in the field, HP $\beta$ -CD was applied in a waste disposal site (Hill air force base, Utah, U.S.A.) that had been contaminated with TCE as well as with other polar and nonpolar organic compounds (17). Flushing the contaminated aquifer with 10% (w/v) HP $\beta$ -CD resulted in significant reduction of the concentration of organic pollutants in the contaminated zone.

The overall goal of the present research is to develop a rational basis for selecting modified CDs that would be most appropriate for maximizing solubilization of PCE and TCE. To this end, we have examined the following: methyl- $\beta$ -CD (M $\beta$ -CD), hydroxypropyl- $\beta$ -CD (HP $\beta$ -CD), carboxymethyl- $\beta$ -CD (CM $\beta$ -CD1, CM $\beta$ -CD2), and sulfated- $\beta$ -CD (S $\beta$ -CD1, S $\beta$ -CD2); the degree of substitution was also varied. Since an increase of the aqueous solubility of different organic compounds in the presence of CD is believed to be due to guest–host complexation, determination of binding constants (*K*) is informative in assessing the utility of the CD (24, 25).

Finally, the interaction of hydrophobic organic compounds with organic matter present in soil is of importance in the remediation of contaminated sites. TCE and PCE are known to be retained by soil organic matter, and this is reflected in the relatively large log *K*<sub>OW</sub> (octanol–water partition coefficient) values, which are 2.88 and 2.61 for PCE and TCE, respectively (26). The ability of CDs to extract the hydrophobic compounds that are retained by soil into an aqueous medium is an important issue in remediation strategy. To evaluate this, the solubilization of PCE and TCE retained by peat was monitored using solutions of the derivatized CDs. It is shown that a suitably substituted  $\beta$ -CD may be a valuable additive in pump-and-treat technology for site remediation of polychlorinated organics.

## Experimental

The following substituted  $\beta$ -cyclodextrins were used as received: hydroxypropyl-(HP $\beta$ -CD) (Aldrich), sulfated-(S $\beta$ -CD1), sulfated-(S $\beta$ -CD2), methyl-(M $\beta$ -CD), and carboxymethyl-(CM $\beta$ -CD1) (Cerestar). In addition, we used car-

boxymethyl-(CM $\beta$ -CD2), which had been synthesized in the laboratory of Professor G. R. Thatcher at Queen's University (see below for synthetic procedure). The aqueous solubility of each of the substituted CDs was found to be >50% (w/v). Table 1 lists the properties of the CDs, including the type of substituent group, average molar mass, and degree of substitution. The CDs were used as received. Analytical grade TCE and PCE, with reported purities of 99.5+% and 99+%, respectively, were obtained from Aldrich. HPLC-grade acetonitrile was purchased from Fisher. The D<sub>2</sub>O (purity 99.9%) used in the NMR experiments was obtained from Cambridge Isotopic Laboratories. International Humic Substance Society (IHSS) Peat had the following elemental composition (%) (27): C 57.1, H 4.49, O 33.9, N 3.60, S 0.65. The organic matter content of this material was reported to be 100%.

## Synthesis of CM $\beta$ -CD2

To a solution of 4.2 g of NaOH in 98 mL H<sub>2</sub>O at 70°C was added slowly 57.5 g of  $\beta$ -CD, and the mixture was kept at that temperature for 2 h. A Na-chloroacetate solution, made of 101 g of chloroacetic acid in 100 mL H<sub>2</sub>O and neutralized with 42 g NaOH, was added drop-by-drop to the  $\beta$ -CD – Na salt solution; after standing for 5 h at 70°C the reaction mixture was poured into 2.5 L CH<sub>3</sub>OH for precipitation. The solid mass was filtered, washed twice with 150 mL H<sub>2</sub>O, then redissolved in 100 mL H<sub>2</sub>O and reprecipitated in 1.5 L CH<sub>3</sub>OH, followed by washing with 2 × 100 mL water and 2 × 100 mL acetone. Finally, the product was dried under vacuum. The solubility of the compound was >70% (w/v) and the pH of a 1% solution was 7.93. The compound was characterized by <sup>13</sup>C NMR and mass spectroscopy.

<sup>13</sup>C NMR (75.5 MHz, D<sub>2</sub>O)  $\delta$ : 178.3 (COOH), 99.4 (CH-anomeric), 81.2 (CH), 72.0 (CH), 70.5 (CH<sub>2</sub>), 61.7 (CH<sub>2</sub>), 49.4 (CH), and 30.9 (CH). FAB-MS (using glycerol as the matrix) *m/z*: 1430.1, 1510.5, 1590.2, 1670.5 (major), 1750.8, 1830.5, and 1911.3.

## HPLC conditions

HPLC analysis was performed using a Varian 9002 series solvent delivery system fitted with a Varian 9050 variable wavelength UV–vis detector and Varian Star Chromatographic Workstation Version 4.5 for peak integration. For separation, a C<sub>18</sub> APEX ODS 5  $\mu$  particle size column



(Chromatographic Specialties, 4.6 mm × 250 mm) protected by a guard column was employed. The mobile phase was a 70:30 acetonitrile–water solution that had been filtered through a Millipore system. For both PCE and TCE, the detector was set to a wavelength of 210 nm and the flow rate was 1.0 mL min<sup>-1</sup>. Under these conditions, the TCE peak appeared at a retention time of ca. 6.5 min while PCE was detected at ca. 9.5 min. A large, irregular peak ascribed to CD also appeared between ca. 2 to 3 min; therefore, elution of the CDs did not interfere with the peak of interest. The method detection limits, measured as 3 times the standard deviation of the blank signal, were 0.12 ppm for TCE and 0.14 ppm for PCE.

### Solubility enhancement

The experimental procedure for solubility enhancement of PCE and TCE was adapted from ref. 15. To distilled deionized water (25 mL) containing 1% to 5% concentrations of CD in a 100-mL volumetric flask was added a large excess (above the solubility limit) of TCE or PCE. A control flask that contained only water and the substrate was also prepared. TCE or PCE aqueous mixtures containing CD were then equilibrated by shaking on a wrist action shaker for 48 h at room temperature. Samples were transferred into capped, glass centrifuge tubes and centrifuged at 3500 rpm for 20 min. A 100 or 500 µL portion of the aqueous supernatant was withdrawn using a micropipette and diluted with water in a 10-mL volumetric flask. Samples of the diluted solution were then injected into the HPLC, and both peak height and area of the substrate peak were recorded.

### Binding constant

The binding constant ( $K_{11}$ ) was determined using an <sup>1</sup>H NMR titration method (28). For the titration experiments, a 2 × 10<sup>-3</sup> M TCE solution in D<sub>2</sub>O and ca. 0.4 M CD stock solutions in D<sub>2</sub>O were prepared. A 2.00 mL portion of the TCE solution was placed in an NMR tube and the <sup>1</sup>H spectrum was recorded using a Bruker AM-400 spectrophotometer operating at 400.1 MHz. Different amounts of CD stock solution were then added successively into the NMR tube containing TCE solution, using a graduated gas-tight Hamilton syringe. After each addition, the solution was thoroughly mixed before the spectrum was acquired. The chemical shift of the <sup>1</sup>H peak of TCE was monitored after each addition of CD solution, using the residual solvent proton signal HDO peak (at 4.6 ppm relative to internal tetramethylsilane) as the reference. The final ratio of CD to TCE was such that the CD concentration was present in a 10:1 to 20:1 excess compared with the TCE concentration, depending on the CD being used.

### Uptake and release in soil organic matter

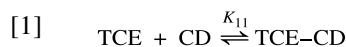
A 50 to 100 mg portion of peat was placed in an 8-mL vial, and the aqueous PCE (165 ppm) or TCE (200 ppm) solution was added without leaving any headspace. Each sample vial was prepared in duplicate along with one control omitting the peat, and these were allowed to equilibrate on the shaker for periods of either 1 or 7 days. After equilibration, the sample vials were centrifuged and the supernatant was withdrawn for HPLC analysis without any further dilution. A 5% CD (w/v) solution was then added to the sample

vials, which were again equilibrated for 18 h overnight before analysis. The sample vials were centrifuged and supernatant was withdrawn for analysis by HPLC.

## Results

### Solubility enhancement

Data obtained for the solubility of TCE and PCE in the presence of varying amounts of different CDs were used to calculate solubility enhancement factors. Under equilibrium conditions and assuming the formation of a 1:1 complex between TCE and CD, eqs. [1] and [2] apply.



$$[2] \quad K_{11} = \frac{[\text{TCE-CD}]}{[\text{TCE}][\text{CD}]}$$

where  $K_{11}$  is the 1:1 binding constant.

When excess TCE is added to an aqueous CD solution, both free TCE,  $[\text{TCE}]_0$ , and complexed TCE ( $[\text{TCE-CD}]$ ) will exist in the solution.  $[\text{TCE}]_0$  represents the aqueous solubility of the uncomplexed material and remains constant upon addition of increasing amounts of CD. In that situation, the total aqueous solubility of TCE at any CD concentration,  $[\text{TCE}]_t$ , can be expressed as:

$$[3] \quad [\text{TCE}]_t = [\text{TCE-CD}] + [\text{TCE}]_0$$

Combining eqs. [2] and [3],  $[\text{TCE}]_t = [\text{TCE}]_0(K_{11}[\text{CD}] + 1)$ . This relation is generally valid for non-polar and low-polarity organic compounds, and can be expressed in general as  $[\text{S}]_t = [\text{S}]_0(K_{11}[\text{CD}] + 1)$ . Therefore,

$$[4] \quad [\text{S}]_t/[\text{S}]_0 = K_{11}[\text{CD}] + 1$$

where  $[\text{S}]_t$  = aqueous concentration of substrate in the presence of CD and  $[\text{S}]_0$  = aqueous solubility, i.e., aqueous concentration of substrate in the absence of CD. The ratio of  $[\text{S}]_t/[\text{S}]_0$  represents the “aqueous solubility enhancement” of the compound for a given concentration of CD.

It was found that upon addition of increasing amounts of CD the solubility of PCE or TCE increased in a linear fashion. In each experiment the intercept of the linear regression line was found to be unity, within experimental error, in accordance with eq. [4]. The  $[\text{S}]_t/[\text{S}]_0$  values, calculated at 5% CD concentration, are listed in Table 2. The 1:1 binding constants ( $K_{11}$ ) obtained from the slope of plots of eq. [4] are reported in Table 3.

### Binding constants ( $K_{11}$ ) obtained by <sup>1</sup>H NMR

In the NMR experiments, as the concentration of CD was increased, the <sup>1</sup>H peak for TCE shifted downfield. The observed chemical shift ( $\delta$ ) is the average of the chemical shifts of the nuclei in TCE and the TCE–CD complex, weighted by the fractional occupancy of these states, i.e.

$$[5] \quad \delta = f_{10}\delta_{\text{TCE}} + f_{11}\delta_{\text{TCE-CD}}$$

where  $f_{10}$  = fraction of free TCE and  $f_{11}$  = fraction of complexed TCE.

The chemical shift difference ( $\Delta$ ) between free and complexed TCE can be expressed as:

$$[6] \quad \Delta = \delta - \delta_{\text{TCE}}$$



**Table 2.** Solubility enhancement factors (standard errors)<sup>a</sup> for PCE and TCE in the presence of 5% substituted CDs.

Compound	HP $\beta$ -CD	M $\beta$ -CD	CM $\beta$ -CD1	CM $\beta$ -CD2	Sb-CD1	S $\beta$ -CD2
PCE	14 $\pm$ 0.4 (8.1) <sup>b</sup>	14 $\pm$ 0.4 (16.1) <sup>b</sup>	10.9 $\pm$ 0.5	2.7 $\pm$ 0.6	9.6 $\pm$ 0.9	1.1 $\pm$ 0.1
TCE	3.1 $\pm$ 0.2 (3.4) <sup>b</sup> (2.6) <sup>c</sup>	5.5 $\pm$ 0.4 (4.6) <sup>b</sup>	2.2 $\pm$ 0.2	1.9 $\pm$ 0.1	2.8 $\pm$ 0.3	1.1 $\pm$ 0.2

<sup>a</sup>Associated error is the standard error of the slope at the 95% confidence level.<sup>b</sup>Values from ref 18.<sup>c</sup>Value from ref. 15.**Table 4.** Retention of PCE and TCE by soil organic matter.

	Amount of peat (mg per 8 mL of solution)	Amount sorbed <sup>a</sup> after 1 day equilibration ( $\mu\text{g g}^{-1}$ peat)	Distribution coefficient <sup>a</sup> $K_d$ (mL g <sup>-1</sup> )	Amount sorbed <sup>a</sup> after 7 days equilibration ( $\mu\text{g g}^{-1}$ peat)
PCE <sup>b</sup>	50	6600 $\pm$ 800	48 $\pm$ 3	6700 $\pm$ 600
PCE	100	5400 $\pm$ 700	48 $\pm$ 4	—
TCE <sup>c</sup>	50	2200 $\pm$ 900	14 $\pm$ 3	3800 $\pm$ 500
TCE	100	3000 $\pm$ 300	16 $\pm$ 2	—

<sup>a</sup>Average value from multiple measurements  $\pm$  SD.<sup>b</sup>Initial [PCE] = 165 ppm.<sup>c</sup>Initial [TCE] = 200 ppm.

At saturation, the maximum change in chemical shift ( $\Delta_{11}$ ) can be described as (28)

$$[7] \quad \Delta_{11} = \delta_{\text{TCE-CD}} - \delta_{\text{TCE}}$$

Combining eqs. [5], [6], and [7]

$$[8] \quad \Delta = f_{11}\Delta_{11}$$

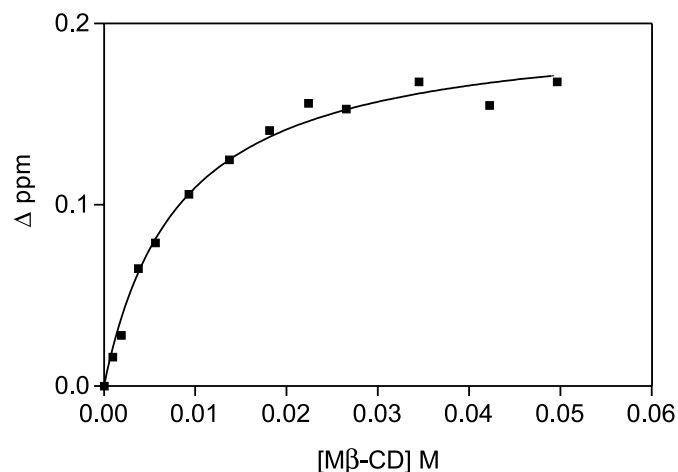
Combining eqs. [8] and [2] and rearranging gives

$$[9] \quad \Delta = \frac{\Delta_{11}K_{11}[\text{CD}]}{1 + K_{11}[\text{CD}]}$$

Equation [9] is valid for a 1:1 binding isotherm. For each CD, the plot of chemical shift difference ( $\Delta$  in ppm) of TCE versus the CD concentration gave a hyperbolic curve that reached a plateau at higher CD concentration.  $K_{11}$  was obtained using non-linear regression analysis of the data set in the Graph Pad Prism program by minimizing the sums of the squares of the residuals. Values of the individual analysis of each of the CDs are listed in Table 3. A representative plot for the TCE–M $\beta$ -CD system is shown in Fig. 2.

### Retention of PCE and TCE by soil organic matter and extraction by CDs

The retention of TCE or PCE by soil organic matter was calculated by comparing the aqueous concentration obtained from samples containing a given amount of peat and known concentrations of added TCE or PCE with that from controls containing the same concentration of added TCE or PCE only. This allowed for the calculation of distribution coefficients ( $K_d$  = concentration of TCE or PCE in peat ( $\mu\text{g g}^{-1}$ ) / concentration in water ( $\mu\text{g mL}^{-1}$ )). Table 4 gives the percent retention of these two compounds under different conditions along with  $K_d$  values. After 5% CD was added, new retention values were determined (Table 5).

**Fig. 2.** Plot showing a change in the chemical shift of TCE upon addition of M $\beta$ -CD. The curve has been fitted to the data using Graph Pad Prism.

## Discussion

### Solubility enhancement

The observed increase in solubility of TCE and PCE upon addition of substituted CDs can be attributed to complexation of the low polarity species within the hydrophobic CD cavity. Solubility enhancement depends on several factors, including size, structure, polarity, and hydrophobicity of the guest molecule (15), as well as size of the CD cavity. As PCE differs from TCE by only one additional Cl atom, size and structure may not be the major factor in this case. However, PCE is less polar and more hydrophobic than TCE, which would favour inclusion for the former. The overall solubility enhancement values for PCE were found to be higher than for TCE (Table 2). Similarly, Boving et al. (18) showed that the enhancement was greater for PCE than TCE



**Table 5.** Effect of added 5% CD on retention of PCE and TCE by soil peat material.

	Residual amount sorbed <sup>a</sup> ( $\mu\text{g g}^{-1}$ peat)	% of sorbed PCE or TCE removed by CDs <sup>b</sup>
PCE + 5% HP $\beta$ -CD	640 $\pm$ 130	90
PCE + 5% S $\beta$ -CD1	140 $\pm$ 40	98
PCE + 5% M $\beta$ -CD	480 $\pm$ 50	93
TCE + 5% HP $\beta$ -CD	600 $\pm$ 150	73
TCE + 5% S $\beta$ -CD1	480 $\pm$ 160	78
TCE + 5% M $\beta$ -CD	150 $\pm$ 60	93

<sup>a</sup>50 mg peat per 8 mL solution and 1 day equilibration.<sup>b</sup>Values obtained comparing the amount of sorbed PCE or TCE on peat (Table 4) with that present after extraction with CD solutions.

for both 5% and 10% HP $\beta$ -CD and M $\beta$ -CD, respectively. Where overlapping data were obtained, most results from their work were in reasonable agreement with the present enhancement factors (Table 2).

Other than the factors noted above, the variation in solubility enhancement values with different CDs can be explained by the presence and nature of the substituent groups on the  $\beta$ -CD molecule. Among the CDs used, S $\beta$ -CD1, S $\beta$ -CD2, CM $\beta$ -CD1, and CM $\beta$ -CD2 are modified by negatively charged substituent groups. In these cases there would be a repulsive interaction between the negatively charged groups and the  $\pi$ -electron cloud density of the C=C double bond in polychloroethylenes. The repulsive interaction would act as a barrier for an electron-rich guest molecule, disallowing its entry into the cavity; it may also destabilize the inclusion complex. In this situation, formation of the inclusion complex will be both kinetically and thermodynamically unfavorable, which is reflected in the lower magnitude of the solubility enhancement found for these CDs in comparison to the CDs with neutral substituents.

Another factor that may affect the extent of enhancement is the degree of substitution (DS) in the CD molecule. A higher DS could cause steric inhibition for an incoming guest molecule. CM $\beta$ -CD2, which showed lower aqueous solubility enhancement for both compounds, has a higher degree of substitution than CM $\beta$ -CD1. Moreover, addition of the highly substituted S $\beta$ -CD2 also contributed to the very low enhancement.

Substitution of the CD by neutral substituent groups increases the hydrophobicity of the molecule as a whole, which leads to increased interaction with a hydrophobic guest molecule (29). With TCE, the enhancement factor was found to be largest for methylated- $\beta$ -CD. The hydroxypropyl group is also neutral but is larger in size compared to the methyl group, so steric interference may again be of importance here (30). In accordance with this argument, TCE showed higher enhancement with M $\beta$ -CD compared to HP $\beta$ -CD. Interestingly, however, PCE showed similar enhancement factors with both HP $\beta$ -CD and M $\beta$ -CD.

### Binding constant

In the CD molecule, the H-3 and H-5 protons of the glucose subunits are projected inwards towards the cavity, and it is these protons that experience a change in chemical shift upon inclusion of a guest molecule, while protons on the outer face are unaffected (31). The observed shifts are a result of the altered magnetic environment due to the presence

of the guest molecule. Furthermore, in the inclusion process, protons of the guest molecule also experience changes in their magnetic environment, thus affecting their chemical shift values (24, 25). The magnitude of chemical shift changes for both guest and host depend on various factors, especially the anisotropic effect, altered solvation, and the conformation of the guest molecule inside the cavity. The maximum chemical shift changes for the  $^1\text{H}$  TCE observed in the experiments conducted here were found to be ca. 0.2 ppm.

Inhomogeneity in the substitution of the CDs used in the present work complicates their observed NMR spectra, causing broadening of some peaks and rendering it difficult to make assignments for individual protons. On the other hand, the guest TCE methine proton gave a sharp peak at 6.6 ppm, and it was possible to follow the change in the chemical shift upon addition of CD. An illustrative figure showing the NMR spectra of both CD and TCE with increasing amounts of CD is provided as Supplementary material.<sup>2</sup> Upon complexation with CD, one sharp downfield-shifted methane peak was observed, indicating that the magnetic environment experienced by the TCE proton is averaged over the environment of the free and bound states. The presence of a singlet can be attributed to a fast equilibrium between the free and bound guest molecules, as is applicable to loosely bound complexes (28).

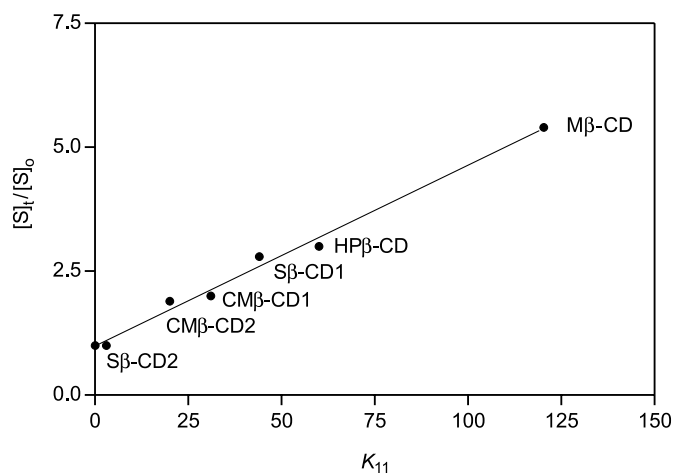
Since TCE is a considerably smaller molecule (0.155 nm<sup>3</sup>) when compared with the size of the CD cavity (0.262 nm<sup>3</sup>), the possibility of there being two guest molecules in each host CD (i.e., a 2:1 complex) must be considered. In treating the NMR results, such a possibility was tested by attempting to fit the experimental data to equations for both 1:1 and 2:1 complexation (28). Using the Graph Pad Prism program, converging fits could be obtained for both cases, but the 2:1 situation gave values with extremely large uncertainties, and in some cases  $K_{21}$  results were negative. On the other hand, when using eq. [9], which is based on a 1:1 model (28), the same data sets converged to consistent values for  $K_{11}$  with relatively small uncertainties (Table 3). The predicted 1:1 binding is supported in the hyperbolic curves generated, with correlation coefficients ranging from 0.98 to 0.99.

A similar situation was encountered in an investigation (32) of the binding of both  $\alpha$ - and  $\beta$ -CDs with a large range of small aliphatic and aromatic molecules. Attempts to fit the data sets into a 2:1 model using both calorimetric and  $^1\text{H}$  NMR measurements were unsuccessful, as the generated parameters were associated with very large errors. The possi-

<sup>2</sup>Supplementary data may be purchased from the Depository of Unpublished Data, Document Delivery, CISTI, National Research Council Canada, Ottawa, ON K1A 0S2, Canada ([http://www.nrc.ca/cisti/irm/unpub\\_e.shtml](http://www.nrc.ca/cisti/irm/unpub_e.shtml) for information on ordering electronically).



**Fig. 3.** Plot of the aqueous solubility enhancement of TCE with different CDs (at 5% concentration) versus respective  $K_{11}$  obtained from  $^1\text{H}$  NMR experiment.  $r^2 = 0.9913$ ; y intercept = 1.05.



bility of 2:1 binding was excluded based on the poor curve fitting.

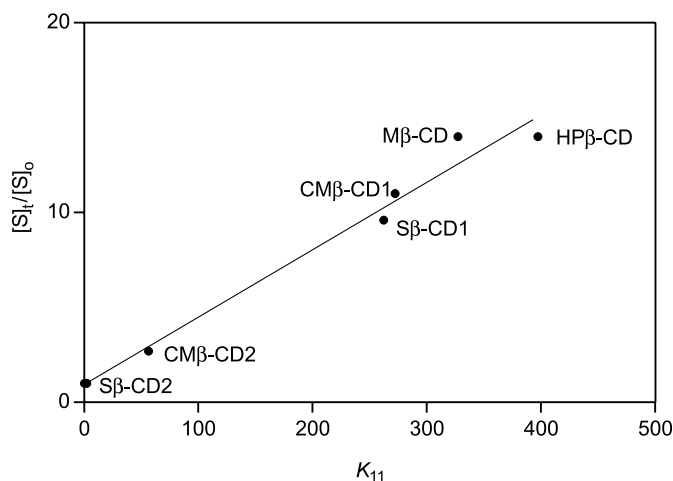
Because of the relatively small size of TCE compared to the host molecules, positioning of the TCE inside the cavity may not be specific and loose binding is expected. Notably, the magnitudes of the binding constant values found in this work (Table 3) are small compared to systems where a complementary fit between guest and host was postulated (10, 11, 14, 25).

As noted above for TCE, plots of  $[S]_t/[S]_o$  against  $[CD]$  according to eq. [4] were linear with intercepts near unity and slopes with values of  $K_{11}$ . An alternative method of treating eq. [4] is to plot  $[S]_t$  against  $[CD]$ . For such plots it has been shown (28) that the slope ( $= K_{11}S_o$ ) is always less than or equal to 1 if only 1:1 complexation occurs. In the present situation, slopes range from 0.2 to 1.0 depending on the CD, again consistent with a 1:1 binding model.

In most cases, for TCE binding with various CDs, we found good agreement (Table 3) between the  $K_{11}$  values obtained from solubility and the NMR experimental results. For PCE, however, the NMR method could not be used because of the lack of a proton as a probe for binding. Theoretically,  $K_{11}$  could be measured using  $^{13}\text{C}$  NMR, but the low aqueous solubility of PCE precluded such experiments. As well, having two tertiary carbons in the PCE molecule contributes to very low sensitivity with respect to  $^{13}\text{C}$  NMR. However, the good agreement (Fig. 3) between the  $K_{11}$  values for TCE using the two methods gives some confidence regarding the corresponding values obtained for PCE by the single applicable procedure. The plot of  $[S]_t/[S]_o$  for PCE against  $K_{11}$  according to eq. [4] was linear with a correlation coefficient of 0.981 (Fig. 4) and an intercept close to unity.

Overall, it is concluded that aqueous solubility enhancement occurs because of the formation of a host-guest complex between CD and TCE or PCE, and it is driven primarily by hydrophobic forces. A high degree of substitution results in steric congestion for cavity opening and, consequently, leads to diminished inclusion of the polychloroethylenes examined. Nonpolar substituents in the CD host enhance binding by creating a more hydrophobic cavity. The interplay of these opposing influences gives rise to the magnitude of

**Fig. 4.** Plot of aqueous solubility enhancement of PCE with different CDs (at 5% concentration) versus respective  $K_{11}$  obtained from eq. [4].  $r^2 = 0.9814$ ; y intercept = 0.962.



binding constants ( $K_{11}$ ) and solubility enhancements ( $[S]_t/[S]_o$ ) found in the present work.

#### Extraction of retained PCE and TCE from soil organic matter by CDs

The ability of CDs to solubilize TCE and other hydrophobic compounds that are bound to soils has been previously observed (16). In soil column experiments, enhanced transport of a range of organic compounds has been achieved in this way. Humic acid, a primary component of peat and soil organic matter in general, is a polydisperse polymeric material composed of a three-dimensional aromatic and alkyl chain framework modified by a variety of mostly oxygen-containing functional groups. The substantially hydrophobic nature of this material contributes to the ability of peat to sorb nonpolar and low-polarity organic compounds (33). Table 4 shows the % retention and  $K_d$  values for TCE and PCE when equilibrated with IHSS peat in an aqueous medium. It is not surprising, then, that of the two compounds investigated here the more hydrophobic PCE showed greater tendency to be retained by peat than did TCE. As expected, the calculated  $K_d$  values were found to be constant, independent of the amount of peat.

In the extraction process, it was found that addition of 5% CD (HPβ-CD or Sβ-CD1 or Mβ-CD) enabled the fairly efficient desorption of PCE or TCE (Table 5); between 2% and 27% of the original material remained after a single extraction. As is predicted from the established  $K_{11}$  values, PCE was more efficiently extracted than TCE. Thus, a suitably substituted β-CD may be a valuable additive for extracting and solubilizing polychlorinated organics during site remediation using pump-and-treat methods.

#### Acknowledgments

The authors thank Adina Dumitrascu, a Post Doctoral Fellow in Dr. Greg Thatcher's laboratory (Queen's University, Canada) for synthesis of the CMβ-CD2. We also thank Cerestar Co. Ltd. for gifts of the other CDs. Financial assistance for this project was provided by the Environmental Science and Technology Alliance Canada (ESTAC).



## References

1. Canadian Environmental Protection Act. Priority Substances List Assessment Report. Environment Canada. 1993.
2. J.F. Pankow and J.A. Cherry. Dense chlorinated solvent and other DNAPLs in groundwater. Waterloo Press, Portland, Oreg. 1996.
3. C.P. Gerba. In *Pollution science. Edited by I.L. Pepper, C.P. Gerba, and M.L. Brusseau*. Academic Press, San Diego, U.S.A. 1996. pp. 117–187 (1996).
4. D.M. Macky and J.A. Cherry. *Environ. Sci. Technol.* **23**, 630 (1989).
5. National Academy of Sciences. Alternatives for ground water cleanup. Report of the National Academy of Science Committee of Groundwater cleanup alternatives. National Academy Press, Washington, D.C. 1994.
6. C.C. West and J.H. Harwell. *Environ. Sci. Technol.* **12**, 2324 (1992).
7. D. Brandes and K.J. Farley. *Water Environ. Res.* **65**, 869 (1993).
8. A.T. Kan and M.B. Thomson. *Environ. Toxicol. Chem.* **9**, 253 (1990).
9. P.T. Imhoff, S.N. Gleyzer, J.F. McBride, L.A. Vancho, I. Okuda, and C.T. Miller. *Environ. Sci. Technol.* **29**, 1966 (1995).
10. M.L. Bender and M. Komiyama. *Cyclodextrin chemistry*. Springer-Verlag, New York. 1978.
11. J. Szejtli. In *Comprehensive supramolecular chemistry*. Vol. 3. Edited by J. Szejtli and T. Osa. Pergamon Elsevier, Oxford. 1996. Chap 5.
12. A.R. Hedges. *Chem. Rev.* **98**, 2035 (1998).
13. In *New trends in cyclodextrins and derivatives*. Edited by D. Duchene. Editions de Sante, Paris. 1991.
14. J. Szejtli. *Cyclodextrins and their inclusion complexes*. Akademiai Kiado, Budapest, Hungary. 1982.
15. X. Wang and M.L. Brusseau. *Environ. Sci. Technol.* **27**, 2821 (1993).
16. M.L. Brusseau, X. Wang, and Q. Hu. *Environ. Sci. Technol.* **28**, 952 (1994).
17. J.E. McCray and M.L. Brusseau. *Environ. Sci. Technol.* **32**, 1285 (1998).
18. T.H. Boving, X. Wang, and M.L. Brusseau. *Environ. Sci. Technol.* **33**, 764 (1999).
19. K.D. Pennel, L.M. Abriola, and G.A. Pope. *J. Contam. Hydrol.* **16**, 35 (1994).
20. J.C. Fountain, A. Klimek, M.G. Beirkirch, and T.M. Middleton. *J. Hazard. Mater.* **28**, 295 (1991).
21. X. Wang and M.L. Brusseau. *Environ. Sci. Technol.* **29**, 2632 (1995).
22. M.L. Brusseau, X. Wang, and W. Wang. *Environ. Sci. Technol.* **31**, 1087 (1997).
23. S. Ko, M.A. Schlautman, and E.R. Carraway. *Environ. Sci. Technol.* **32**, 2765 (1999).
24. H. Schneider, F. Hacket, and F. Rudiegr. *Chem. Rev.* **98**, 1755 (1998).
25. R.J. Bergeron. In *Inclusion compounds*. Vol 3. Edited by J.L. Atwood, J.E. Davis, and D.D. MacNicol. Academic Press, London. 1984. pp. 391–443 and refs. cited therein.
26. R.P. Schwarzenbach, P.M. Gschwend, and D.M. Imboden. *Environmental organic chemistry*. John Wiley & Sons, New York. 1993.
27. W. Rutherford, C.T. Chiou, and D.E. Kile. *Environ. Sci. Technol.* **26**, 336 (1992).
28. K.A. Connors. *Binding constants: The measurement of molecular complex stability*. John Wiley & Sons, New York. 1987.
29. M. Suzuki, H. Takai, K. Tanaka, K. Narita, F. Fujiwara, and H. Ohmori. *Carbohydr. Res.* **75**, 288 (1996).
30. L.D. Wilson and R.E. Verral. *Can. J. Chem.* **76**, 25 (1998).
31. P.V. Demarco and A.L. Thakker. *Chem. Commun.* **2** (1970).
32. M.V. Rekharsky, M.P. Mayhew, R.N. Goldberg, P.D. Ross, Y. Yamashoji, and Y. Inoue. *J. Phys. Chem. B*, **101**, 87 (1997).
33. C.T. Chiou. In *Reactions and movement of organic chemicals in soil*. Special Publication No. 22. Soil Science Society of America and American Society of Agronomy. 1989. pp. 1–29.



# Alkali metal ion catalysis in nucleophilic displacement by ethoxide ion on *p*-nitrophenyl phenylphosphonate: Evidence for multiple metal ion catalysis<sup>1</sup>

Erwin Buncel, Ruby Nagelkerke, and Gregory R.J. Thatcher

**Abstract:** In continuation of our studies of alkali metal ion catalysis and inhibition at carbon, phosphorus, and sulfur centers, the role of alkali metal ions in nucleophilic displacement reactions of *p*-nitrophenyl phenylphosphonate (PNPP) has been examined. All alkali metal ions studied acted as catalysts. Alkali metal ions added as inert salts increased the rate while decreased rate resulted on M<sup>+</sup> complexation with 18-crown-6 ether. Kinetic analysis indicated the interaction of possibly three potassium ions, four sodium ions, and five lithium ions in the transition state of the reactions of ethoxide with PNPP. Pre-association of the anionic substrate with two metals ions in the ground state gave the best fit to the experimental data of the sodium system. Thus, the study gives evidence of the role of several metal ions in nucleophilic displacement reactions of ethoxide with anionic PNPP, both in the ground state and in the transition state. Molecular modeling of the anionic transition state implies that the size of the monovalent cation and the steric requirement of the pentacoordinate transition state are the primary limitations on the number of cations that can be brought to bear to stabilize the transition state and catalyze nucleophilic substitution at phosphorus. The bearing of the present work on metal ion catalysis in enzyme systems is discussed, in particular enzymes that catalyze phosphoryl transfer, which often employ multiple metal ions. Our results, both kinetic and modeling, reveal the importance of electrostatic stabilization of the transition state for phosphoryl transfer that may be effected by multiple cations, either monovalent metal ions or amino acid residues. The more such cations can be brought into contact with the anionic transition state, the greater the catalysis observed.

**Key words:** alkali metal ion catalysis, nucleophilic displacement at phosphorus, multiple metal ion catalysis, phosphoryl transfer.

**Résumé:** Dans le cadre de nos études sur la catalyse par les ions de métaux alcalins et sur l'inhibition au niveau des centres carbonés, phosphorés et sulfurés, on a examiné le rôle des métaux alcalins sur les réactions de substitutions nucléophiles du phénylphosphonate de *p*-nitrophényle (« PNPP »). Tous les ions de métaux alcalins étudiés agissent comme catalyseurs. Les ions de métaux alcalins ajoutés sous la forme de sels inertes augmentent la vitesse alors que l'on observe des diminutions de vitesse lorsque les ions M<sup>+</sup> sont complexés par l'éther 18-couronne-6. L'analyse cinétique indique qu'il pourrait exister une interaction de trois ions potassium, quatre ions sodium et cinq ions lithium dans l'état de transition des réactions de l'éthanolate avec le « PNPP ». Une préassociation du substrat anionique avec deux ions métalliques dans l'état fondamental permet de réaliser le meilleur ajustement des données expérimentales du système du sodium. Cette étude permet donc de mettre en évidence le rôle de plusieurs ions métalliques dans les réactions de substitutions nucléophiles de l'éthanolate avec le « PNPP » anionique, tant dans l'état fondamental que dans l'état de transition. Des calculs de modélisation moléculaire de l'état de transition anionique impliquent que la taille du cation monovalent et les nécessités stériques de l'état de transition pentacoordiné sont les limitations primaires du nombre de cations qui peuvent être amenés à stabiliser l'état de transition et à catalyser la substitution nucléophile au niveau du phosphore. On discute des implications du présent travail sur la catalyse par des ions métalliques sur les systèmes enzymatiques, particulièrement ceux qui catalysent le transfert de groupes phosphoryles qui font souvent appel à de multiples ions métalliques. Nos résultats, tant cinétiques que théoriques, révèlent l'importance de la stabilisation électrostatique de l'état de transition pour le transfert de phosphoryle qui peut être affecté par de plusieurs cations, ions métalliques monovalents ou résidus d'acides aminés; plus on peut amener de tels cations en contact avec l'état de transition anionique meilleure est la catalyse observée.

Received 25 September 2002. Published on the NRC Research Press Web site at <http://canjchem.nrc.ca> on 29 January 2003.

E. Buncel,<sup>2</sup> R. Nagelkerke,<sup>3</sup> and R.J. Thatcher. Department of Chemistry, Queen's University, Kingston, ON K7L 3N6, Canada.

<sup>1</sup>Part 10 in a series on Metal ion catalysis and inhibition in nucleophilic displacement reactions at carbon, phosphorous, and sulfur centers. Part 9: ref. (1).

<sup>2</sup>Corresponding author (e-mail: [buncel@chem.queensu.ca](mailto:buncel@chem.queensu.ca)).

<sup>3</sup>Present address: Department of Chemistry, Centralia College, Centralia, WA 98531, U.S.A.



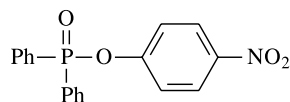
*Mots clés* : catalyse par des ions métalliques alcalins, substitution nucléophile au niveau du phosphore, catalyse par des ions métalliques multiples, transfert de phosphoryle.

[Traduit par la Rédaction]

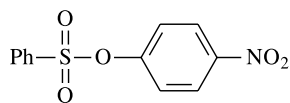
## Introduction

The role of metal ions in the mechanism of phosphoryl transfer reactions (2, 3) has been under extensive investigation owing to the importance of these processes in biological systems (4, 5). The ubiquitous presence of alkali metal ions in biological systems calls for intensive investigation of catalysis by these monovalent ions, but such studies have only rarely been undertaken. The majority of studies have been directed towards the catalytic effects of divalent ions such as  $\text{Mg}^{2+}$ ,  $\text{Ca}^{2+}$ ,  $\text{Mn}^{2+}$ ,  $\text{Fe}^{2+}$ ,  $\text{Cu}^{2+}$ , and  $\text{Zn}^{2+}$  in the hydrolysis of phosphate esters (6–8).

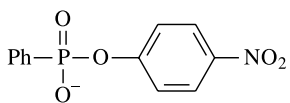
We have initiated systematic studies of the influence of alkali metal ions in nucleophilic displacement reactions at carbon, phosphorus, and sulfur centers (9–20). Our previous reports have shown that in the reaction of alkali metal ethoxides and phenoxides with *p*-nitrophenyl diphenylphosphinate **1** (PNPDP), all the alkali metals functioned as catalysts, with the MOEt reactivity order  $\text{LiOEt} > \text{NaOEt} > \text{KOEt} > \text{CsOEt} > \text{EtO}^-$  (13, 14). However, with *p*-nitrophenyl benzenesulfonate **2** (PNPBS), both catalysis and inhibition was observed, the reactivity order now being  $\text{KOEt} > \text{CsOEt} > \text{NaOEt} > \text{EtO}^- > \text{LiOEt}$  (15, 16).



PNPDP (1)



PNPBS (2)



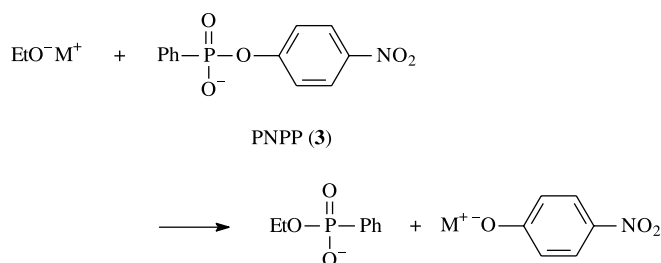
PNPP (3)

In the present work we have extended our investigations to *p*-nitrophenyl phenylphosphonate **3** (PNPP), as the first monoanionic phosphorus ester in this series, noting the importance of charged phosphate esters in biological systems. In the reaction of **3** with alkali metal ethoxides in ethanol the order of catalytic effectiveness was determined to be  $\text{LiOEt} > \text{NaOEt} > \text{KOEt} > \text{CsOEt} > \text{EtO}^-$ , i.e., qualitatively similar to the situation with PNPDP (**1**). However, in-depth analysis shows that the kinds of treatment that we

have applied in the previous cases (i.e., simple ion pair and dissociated ion reaction pathways) are no longer applicable here, but that multiple ion association has to be invoked. Both ground state and transition state interactions are discussed.

## Results

The reaction under investigation is shown below with the assumption that the substrate is fully ionized in basic ethanol.



The rate of the reaction in anhydrous ethanol at 25°C was followed spectrophotometrically by monitoring the formation of *p*-nitrophenoxide ion under pseudo-first-order conditions with the alkoxide in at least 20-fold excess. Excellent first-order kinetics were observed up to 90% reaction and rate constants were obtained from linear  $\log(A_\infty - A_t)$  vs. time plots. Slower reactions were conducted for only one half-life or less, and rate constants were obtained by an initial rate method. Results are presented in Tables 1–3 and displayed in Fig. 1.

The effect of added complexing agent has been examined; Fig. 2 and Table 4 show the effect of added 18-crown-6 on the rate of reaction of PNPP with KOEt at a constant base concentration. The rate decreased until 1 equiv of complexing agent had been added, after which point increasing the crown concentration had no effect on the reaction rate. The constant rate observed after 1 equiv of complexing agent had been added corresponds to the reaction of free ethoxide with the phosphonate ester on the assumption that cations are fully complexed by the added 18-crown-6 and are unreactive. The average rate constant for the free ethoxide so obtained is  $5 \pm 2 \times 10^{-7} \text{ s}^{-1} \text{ M}^{-1}$ .

The role of the metal ion in the reaction mechanism was further investigated by adding metal ions in the form of unreactive salts to reactions of alkali metal ethoxides with **3**. The effect of added LiCl and LiNO<sub>3</sub> on the LiOEt reaction is shown in Table 5. To achieve a substantial [salt]:[base] ratio, a low concentration of base was used for these experiments. The reactions were so slow that plots of absorbance vs. time did not show the curvature expected for first-order reactions. Instead, the absorbance varied linearly with time and zero-order rates were observed. The reported rate constants were determined in the same manner as for initial rates,



**Table 1.** Kinetic data for the reaction of PNPP with LiOEt in EtOH at 25.0°C.

[MOEt] (M)	$k_{\text{obs}}$ ( $\text{s}^{-1}$ )
0.100	$5.18 \times 10^{-6}$
0.106	$3.93 \times 10^{-6}$
0.140	$6.67 \times 10^{-6}$
0.140	$1.25 \times 10^{-5}$
0.200	$1.65 \times 10^{-5}$
0.240	$2.32 \times 10^{-5}$
0.300	$3.95 \times 10^{-5}$
0.320	$4.12 \times 10^{-5}$
0.400	$7.49 \times 10^{-5}$
0.400	$7.31 \times 10^{-5}$
0.400	$6.46 \times 10^{-5}$
0.500	$1.39 \times 10^{-4}$
0.560	$1.83 \times 10^{-4}$
0.600	$2.34 \times 10^{-4}$
0.700	$3.76 \times 10^{-4}$
0.800	$6.34 \times 10^{-4}$

**Table 2.** Kinetic data for the reaction of PNPP with NaOEt in EtOH at 25.0°C.

[MOEt] (M)	$k_{\text{obs}}$ ( $\text{s}^{-1}$ )
0.170	$6.64 \times 10^{-6}$
0.239	$1.32 \times 10^{-5}$
0.242	$1.28 \times 10^{-5}$
0.298	$2.05 \times 10^{-5}$
0.401	$3.82 \times 10^{-5}$
0.501	$6.73 \times 10^{-5}$
0.601	$1.09 \times 10^{-4}$
0.700	$1.70 \times 10^{-4}$
0.800	$2.61 \times 10^{-4}$

converting the change in absorbance per run time,  $\Delta A/\Delta t$ , to a zero-order rate constant and dividing the rate constant by the substrate concentration to get  $k_{\text{obs}}$ .

## Discussion

### Catalytic role of alkali metal ions

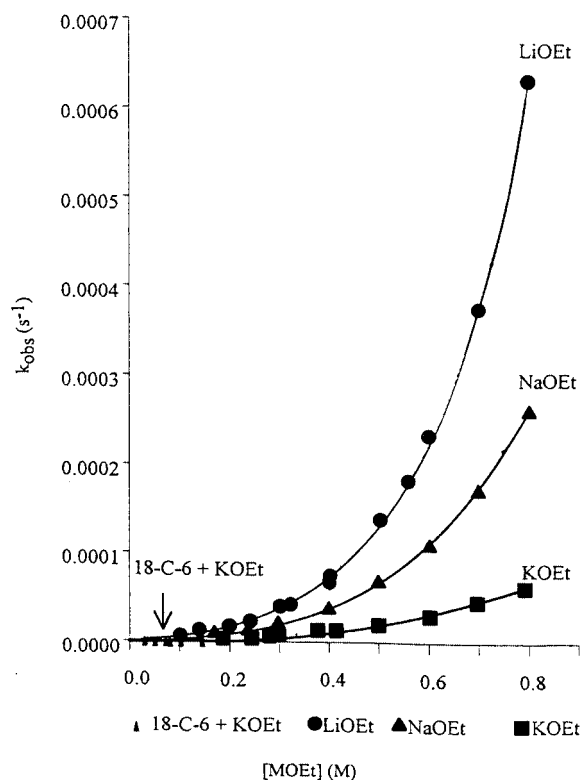
The order of reactivity exhibited (Fig. 1) in the present work with PNPP is  $\text{LiOEt} > \text{NaOEt} > \text{KOEt} \gg \text{EtO}^-$ , which is qualitatively similar to that observed in our previous work with PNPDP (**1**), but the rates of reaction are much smaller in the present work:  $k_{\text{EtO}^-}(\text{PNPP})/k_{\text{EtO}^-}(\text{PNPDP})$  is ca.  $10^{-6}$ . This is in accord with nucleophilic attack occurring in the present case on an anionic substrate. The increase in rate on addition of the unreactive salts LiCl and LiNO<sub>3</sub> to the LiOEt reaction, while moderate (Table 5), is in accord with a catalytic effect of Li<sup>+</sup> (see also ref. 1).

### Catalysis by alkali metal ethoxide ion pairs

In our previous studies with *p*-nitrophenyl diphenylphosphinate (**1**) as well as with *p*-nitrophenyl benzenesulfonate (**2**) results were analyzed in terms of reactivity by dissociated EtO<sup>−</sup> (or PhO<sup>−</sup>) ions and by the associated EtO<sup>−</sup>M<sup>+</sup> (or PhO<sup>−</sup>M<sup>+</sup>) ion pairs (13–17). Since the association constants

**Table 3.** Kinetic data for the reaction of PNPP with KOEt in EtOH at 25.0°C.

[MOEt] (M)	$k_{\text{obs}}$ ( $\text{s}^{-1}$ )
0.189	$3.52 \times 10^{-6}$
0.245	$3.86 \times 10^{-6}$
0.283	$7.47 \times 10^{-6}$
0.300	$6.56 \times 10^{-6}$
0.377	$1.32 \times 10^{-5}$
0.415	$1.28 \times 10^{-5}$
0.500	$1.94 \times 10^{-5}$
0.604	$2.97 \times 10^{-5}$
0.698	$4.57 \times 10^{-5}$
0.792	$6.15 \times 10^{-5}$

**Fig. 1.** Kinetic data for the reaction of PNPP with LiOEt, KOEt, and NaOEt, and with KOEt in the presence of excess 18-crown-6 in EtOH at 25°C.

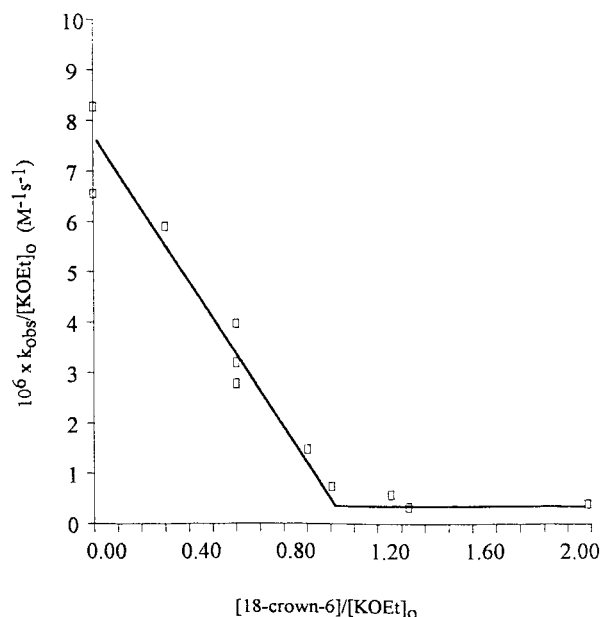
of alkali – metal ethoxides in ethanol are known (21), one could calculate the contribution of each species to the two separate reaction pathways (for the case of PhO<sup>−</sup>M<sup>+</sup> the respective contributions could be evaluated by a mathematical treatment) (14). For the phosphinate **1** it was found that for all the alkali metal ethoxides and phenoxides, associated RO<sup>−</sup>M<sup>+</sup> ion pairs were more reactive than free RO<sup>−</sup> ions. This could be rationalized in terms of a more effective stabilization of the transition state by M<sup>+</sup> than of the ground state. Stabilization energies of the transition state and of the ground state could be evaluated by a method developed originally by Kurz (22) and applied by Mandolini and coworkers (23), Tee (24), and others (25–28). For the sulfonate (**2**) – ethoxide reaction the higher alkali metal ions acted as



**Table 4.** Kinetic data for the reaction of PNPP with KOEt in the presence of 18-crown-6 in EtOH at 25.0°C.

[KOEt] (M)	[18C6] (M)	$k_{\text{obs}}$ ( $\text{s}^{-1}$ )	$k_2$ ( $\text{s}^{-1}\text{M}^{-1}$ )	[18C6]/[KOEt]
0.1008	0	$6.61 \times 10^{-7}$	$6.55 \times 10^{-6}$	0
0.1008	0	$8.35 \times 10^{-7}$	$8.28 \times 10^{-6}$	0
0.1008	0.030	$5.96 \times 10^{-7}$	$5.91 \times 10^{-6}$	0.301
0.1008	0.061	$2.81 \times 10^{-7}$	$2.79 \times 10^{-6}$	0.602
0.1008	0.061	$3.22 \times 10^{-7}$	$3.20 \times 10^{-6}$	0.602
0.1008	0.061	$4.01 \times 10^{-7}$	$3.97 \times 10^{-6}$	0.602
0.1008	0.091	$1.49 \times 10^{-7}$	$1.48 \times 10^{-6}$	0.903
0.1008	0.101	$7.49 \times 10^{-8}$	$7.43 \times 10^{-7}$	1.01
0.1008	0.127	$5.82 \times 10^{-8}$	$5.77 \times 10^{-7}$	1.26
0.1008	0.134	$3.27 \times 10^{-8}$	$3.24 \times 10^{-7}$	1.33
0.1008	0.210	$3.98 \times 10^{-8}$	$3.95 \times 10^{-7}$	2.08

**Note:** Average  $k_{\text{EtO}^-}$  value for  $k_{\text{EtO}^-}$  ([18C6]/[KOEt] > 1.0) =  $5 \pm 2 \times 10^{-7} \text{ s}^{-1}\text{M}^{-1}$ .

**Fig. 2.** Kinetic data for the reaction of PNPP with KOEt in the presence of 18-crown-6 in EtOH at 25°C.

catalysts but  $\text{Li}^+$  acted as inhibitor, which is indicative of greater stabilization of the ground state than of the transition state (17–19).

Applying the free ethoxide – metal ethoxide ion pair model to the present system, with reaction pathways for both species (Scheme 1), leads to the rate eqs. [1] and [2] where  $\text{S}^-$  refers to the substrate

$$[1] \quad \text{rate} = k_{\text{EtO}^-}[\text{EtO}^-][\text{S}^-] + k_{\text{MOEt}}[\text{MOEt}][\text{S}^-]$$

$$[2] \quad k_{\text{obs}}/[\text{EtO}^-] = k_{\text{EtO}^-} + k_{\text{MOEt}}K_a[\text{EtO}^-]$$

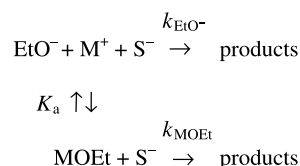
According to eq. [2], plots of  $k_{\text{obs}}/[\text{EtO}^-]$  vs.  $[\text{EtO}^-]$  calculated (see Tables S1–S3)<sup>4</sup> using the known (21) values of  $K_a$  should be linear. However, it may be seen from the curved nature of the plot in Fig. 3 for LiOEt and the very similar plots for NaOEt and KOEt (not shown) that the ion pair mechanism does not adequately describe the reaction of

**Table 5.** (a) Kinetic data for the reaction of PNPP with LiOEt in the presence of LiCl in EtOH at 25.0°C; and (b) kinetic data for the reaction of PNPP with LiOEt in the presence of  $\text{LiNO}_3$  in EtOH at 25.0°C.

(a) Ratio LiCl/LiOEt	$k_{\text{obs}}$ ( $\text{s}^{-1}$ )
0	0 <sup>a</sup>
9.47	$6.2 \times 10^{-7}$
23.7	$6.7 \times 10^{-7}$
37.7	$7.0 \times 10^{-7}$
52.1	$7.8 \times 10^{-7}$
66.3	$8.0 \times 10^{-7}$
(b) Ratio $\text{LiNO}_3/\text{LiOEt}$	$k_{\text{obs}}$ ( $\text{s}^{-1}$ )
0	0 <sup>a</sup>
9.26	$6.4 \times 10^{-7}$
23.2	$7.5 \times 10^{-7}$
37.1	$7.8 \times 10^{-7}$
51.0	$8.4 \times 10^{-7}$
64.9	$9.0 \times 10^{-7}$

**Note:** [LiOEt] = 0.00398 M.

<sup>a</sup>No reaction was observed without added salt.

**Scheme 1.** Metal ethoxide ion pair catalysis.

PNPP with metal ethoxides. The upward curvature in Fig. 3 suggests that higher involvement in  $\text{M}^+$  should be considered.

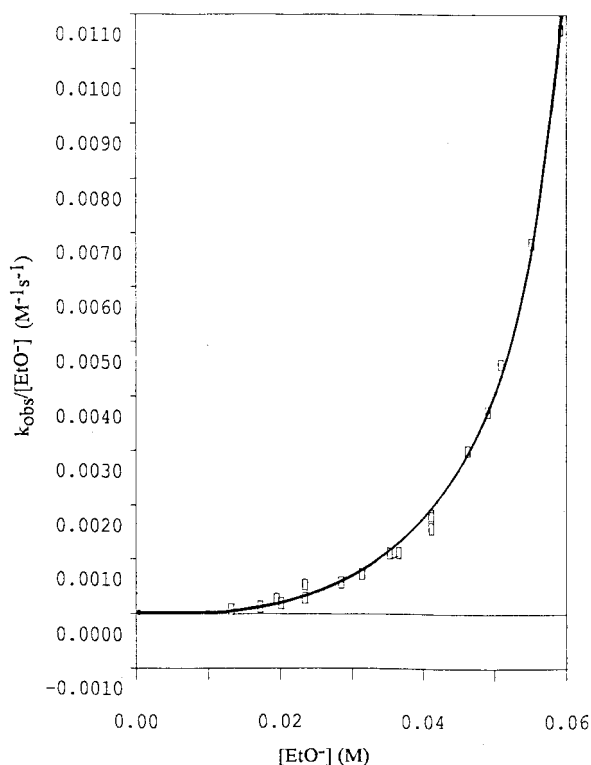
### Catalysis by pre-association mechanism

One can consider a pre-association pathway in which one metal ion associates with the substrate and the consequent reaction of ethoxide with  $\text{S}^- \text{M}^+$ , along with the parallel reactions of  $\text{S}^-$  with  $\text{EtO}^-$  and  $\text{S}^-$  with  $\text{MOEt}$ , as shown in Scheme 2.

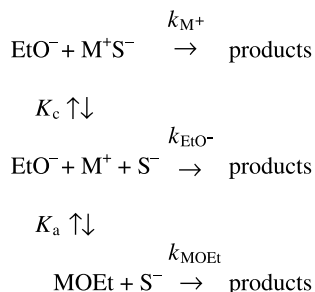
<sup>4</sup>Supplementary data may be purchased from the Depository of Unpublished Data, Document Delivery, CISTI, National Research Council Canada, Ottawa, ON K1A 0S2, Canada ([http://www.nrc.ca/cisti/irm/unpub\\_e.shtml](http://www.nrc.ca/cisti/irm/unpub_e.shtml) for information on ordering electronically).



**Fig. 3.** Ion pairing treatment of the data for the reaction of PNPP with LiOEt in EtOH at 25°C.



**Scheme 2.** Pre-association catalysis.



The rate equation corresponding to Scheme 2 is given in eq. [3] from which eq. [4] follows, which is of the same form as eq. [2].

$$\begin{aligned}
 \text{[3]} \quad \text{rate} &= k_{\text{EtO}^-}[\text{EtO}^-][\text{S}^-] + k_{\text{M}^+}[\text{EtO}^-][\text{M}^+\text{S}^-] \\
 &\quad + k_{\text{MOEt}}[\text{MOEt}][\text{S}^-]
 \end{aligned}$$

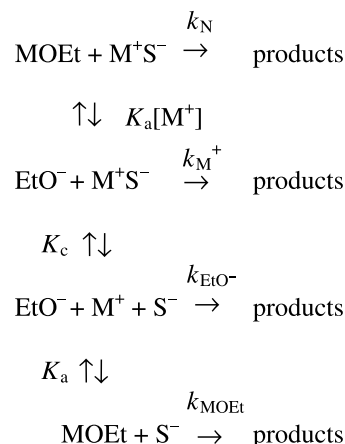
$$\text{[4]} \quad k_{\text{obs}}/[\text{EtO}^-] = k_{\text{EtO}^-} + (k_{\text{M}^+}K_{\text{c}} + k_{\text{MOEt}}K_{\text{a}})[\text{EtO}^-]$$

As before, it follows from eq. [4] that plots of  $k_{\text{obs}}/[\text{EtO}^-]$  vs.  $[\text{EtO}^-]$  should be linear, but as has already been noted these plots (e.g., Fig. 3) are curved upward thus ruling out the pre-associative mechanism of Scheme 2.

### Catalysis by both pre-associative and ion pair mechanism

To explore a pathway involving two metal ions, we consider the possibility of attack on  $\text{S}^-\text{M}^+$  by MOEt in parallel with the pathways shown in Scheme 2. This mechanism,

**Scheme 3.** Ion pair and pre-association catalysis.



given in Scheme 3, leads to the rate law in eq. [5] from which eq. [6] can be derived where  $k_{\text{N}}$  refers to the “new” rate constant for attack of an ion pair on a metal-complexed substrate.

$$\begin{aligned}
 \text{[5]} \quad \text{rate} &= k_{\text{EtO}^-}[\text{EtO}^-][\text{S}^-] + k_{\text{M}^+}[\text{EtO}^-][\text{M}^+\text{S}^-] \\
 &\quad + k_{\text{MOEt}}[\text{MOEt}][\text{S}^-] + k_{\text{N}}[\text{MOEt}][\text{M}^+\text{S}^-]
 \end{aligned}$$

$$\begin{aligned}
 \text{[6]} \quad k_{\text{obs}} &= k_{\text{EtO}^-}[\text{EtO}^-] + (k_{\text{M}^+}K_{\text{c}} + k_{\text{MOEt}}K_{\text{a}})[\text{EtO}^-]^2 \\
 &\quad + k_{\text{N}}K_{\text{c}}K_{\text{a}}[\text{EtO}^-]^3
 \end{aligned}$$

The relationship given in eq. [6] is more complex, having  $[\text{EtO}^-]$ ,  $[\text{EtO}^-]^2$ , and  $[\text{EtO}^-]^3$  terms, and the previously used plot of  $k_{\text{obs}}$  vs. an independent variable (for the PNPP system) is not possible for this relationship. In an attempt to try to fit the experimental data using the relationship presented in eq. [6], a spreadsheet (Lotus 123 (Release 2.01)) was used. Arbitrary values were input for the unknown constants ( $k_{\text{N}}$ ,  $k_{\text{M}^+}$ , and  $K_{\text{c}}$ ) and these values were optimized iteratively until a best fit to the experimental data was observed. Once a relationship was determined, the fit of the calculated values of  $k_{\text{obs}}$  to the experimental value of  $k_{\text{obs}}$  was measured using standard linear regression methods present in the Lotus program.

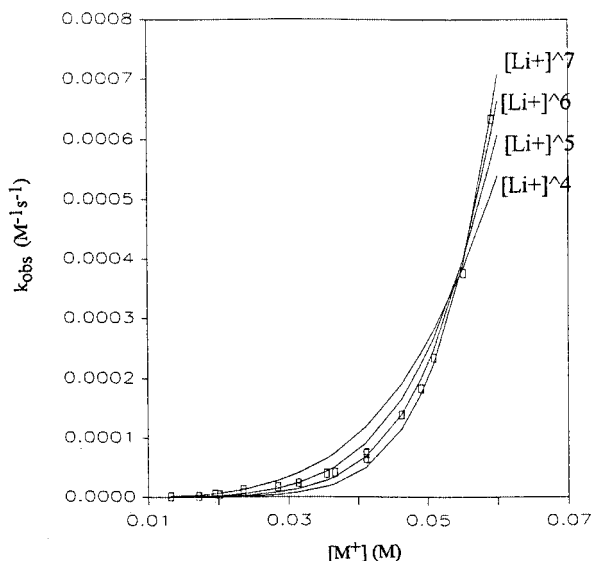
However, no combination of values for the unknown constants could be found for eq. [6] that would satisfactorily fit all the  $k_{\text{obs}}$  experimental data, especially the data for the higher base concentrations (0.06–0.09 M). Equation [6] contains first-, second-, and third-order terms in  $[\text{EtO}^-]$ . However, it will be shown in the following section that a plot of  $k_{\text{obs}}$  vs.  $[\text{EtO}^-]$  has curvature that is adequately fit by a *fifth*-order  $[\text{EtO}^-]$  term and this curvature cannot be fit by second- and third-order terms. This result is taken to indicate that the proposed mechanism in Scheme 3, involving just two metal ions, is not adequate to describe the reaction of metal ethoxides with PNPP.

### Multiple ion catalysis

From attempts to fit the kinetic data to third-order terms in  $[\text{EtO}^-]$  it became apparent that higher order terms in  $[\text{EtO}^-]$  were needed to fit  $k_{\text{obs}}$  over the entire  $[\text{EtO}^-]$  range studied (0–0.1 M). Given that  $[\text{EtO}^-]$  is equal to  $[\text{M}^+]$ ,

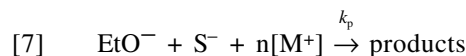


**Fig. 4.** Curve fitting of the data for the reaction of PNPP with LiOEt in EtOH at 25°C with  $[\text{Li}^+]^n$ ,  $n = 4, 5, 6$ , and 7 (see Table 6).



attempts were made to fit the observed kinetic data to  $[\text{M}^+]^n$ . The relationship being examined is shown in eq. [7], where  $k_p$  refers to the rate constant for reaction of free ethoxide with the substrate as mediated by  $n$  metal ions. The results are shown in Figs. 4, 5, and 6. Table 6 gives the coefficients and the goodness of the fits (as measured by  $r^2$ ) for the best fit lines shown in these figures.

The rate increase from reaction of the mono-anion at relatively high concentrations (0.05–0.1 M) of alkali metal ion is consistent with rate constants that are approximately fourth-order in  $\text{K}^+$ , fifth-order in  $\text{Na}^+$ , and sixth-order in  $\text{Li}^+$ , or their kinetic equivalents, as shown below.



$$[8] \quad \text{rate} = k_{\text{obs}}[\text{S}^-]$$

$$[9] \quad k_{\text{obs}} = k_p[\text{M}^+]^n$$

$$[10] \quad k_{\text{obs}} = 1.42 \times 10^4 [\text{Li}^+]^6 = 1.42 \times 10^4 [\text{Li}^+]^5 [\text{EtO}^-]$$

$$[11] \quad k_{\text{obs}} = 60.8 [\text{Na}^+]^5 = 60.8 [\text{Na}^+]^4 [\text{EtO}^-]$$

$$[12] \quad k_{\text{obs}} = 0.963 [\text{K}^+]^4 = 0.963 [\text{K}^+]^3 [\text{EtO}^-]$$

The results are interpreted as approximately three  $\text{K}^+$ , four  $\text{Na}^+$ , and five  $\text{Li}^+$  ions being involved in the transition states of the respective reactions, assuming there is no pre-association with the ground state. Consideration of metal ion association with the substrate will not affect the calculation of the number of metal ions present in the transition state, as shown below. The number of metal ions appears to be related to the size of the ions, which suggests that size limits the number of ions that may participate with the transition state.

The role of the metal ions is not discernible from the above treatment, which only gives an estimate of the number of metal ions that associate with the transition state. It should be noted that the use of eq. [9] (based on eq. [7]) as-

**Fig. 5.** Curve fitting of the data for the reaction of PNPP with NaOEt in EtOH at 25°C with  $[\text{Na}^+]^n$ ,  $n = 4, 5$ , and 6 (see Table 6).

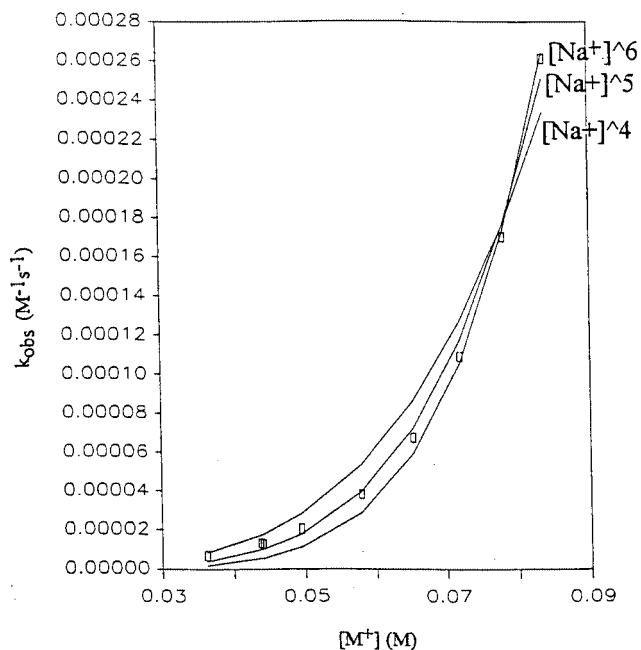
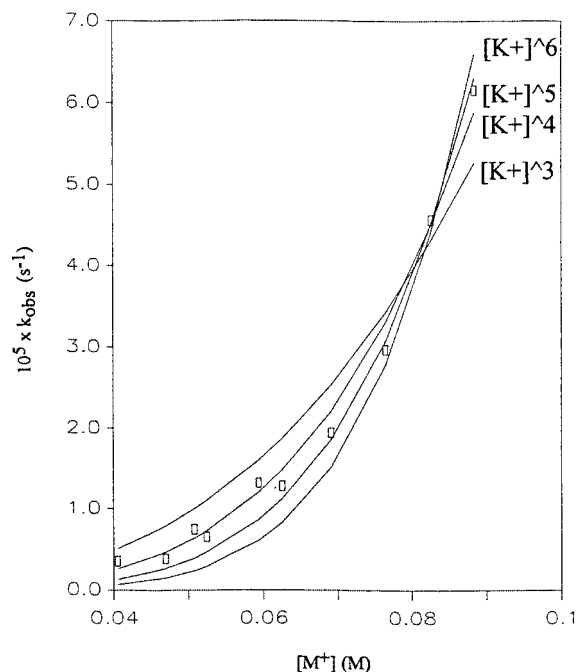


**Fig. 6.** Curve fitting of the data for the reaction of PNPP with KOEt in EtOH at 25°C with  $[\text{K}^+]^n$ ,  $n = 3, 4, 5$ , and 6 (see Table 6).



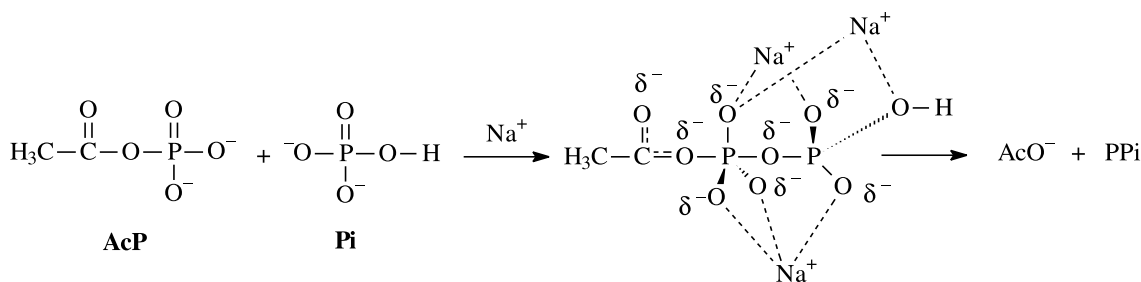
sumes a “one-step”, or elementary, reaction, which would preclude pre-association of these metal ions with the anionic substrate followed by subsequent attack of ethoxide, a two-step reaction. Pre-association of the substrate with metal ions would increase the number of metal ions present in the transition state.



**Table 6.** Table of the coefficients used to fit  $[M^+]^n$  terms to the experimental values of  $k_{\text{obs}}$  for the reaction of MOEt on PNPP in ethanol at 25°C.

Metal ethoxide system	Coefficient ( $r^2$ )				
	$[M^+]^3$	$[M^+]^4$	$[M^+]^5$	$[M^+]^6$	$[M^+]^7$
LiOEt		41.7 (0.928)	783 (0.978)	<b><math>1.42 \times 10^4</math></b> ( <b>0.995</b> )	$2.53 \times 10^5$ (0.991)
NaOEt		4.73 (0.970)	<b>60.8</b> ( <b>0.996</b> )	762 (0.993)	
KOEt	$7.63 \times 10^{-2}$ (0.934)	<b>0.963</b> ( <b>0.990</b> )	11.7 (0.986)	138 (0.951)	

**Note:** Equation to be fit:  $k_{\text{obs}} = (\text{coefficient})[M^+]^n$ . See Figs. 4, 5, and 6. The correlation coefficients ( $r^2$ ) are shown and the terms with the best fit are in bold type. The data for  $k_{\text{obs}}$  are given in supplementary tables S1, S2, and S3.

**Scheme 4.**  $\text{Na}^+$  catalyzed reaction of AcP with Pi.

To further analyze the kinetic data, a detailed reaction mechanism needs to be proposed, which requires assumptions about how many ions interact with the ground state. The data for sodium, for example, could be accounted for by association of one metal ion with the ethoxide and one with the anionic substrate, or, alternatively, by the kinetically equivalent free ethoxide attack on the substrate pre-associated by two metal ions in the ground state, both with possibly four additional ions in the transition state. There are several kinetically equivalent possibilities, which will be discussed below.

#### Pre-association and multiple ion catalysis — Possible rate laws

An example of the complexity of the analysis of multiple ion catalytic participation is given by Herschlag and Jencks who studied the  $\text{Na}^+$  catalyzed reaction of the anions acetyl phosphate (AcP) and orthophosphate (Pi) to yield acetate and pyrophosphate (PPi) anions (7). In their analysis they noted that the data was well fit by a fourth-order term in  $\text{Na}^+$  concentration. When they considered a mechanism that included pre-association of the dianionic substrate they were able to re-analyze their data in terms of the associated rate laws. They interpreted their data in terms of two  $\text{Na}^+$  ions that bind in the ground state and five additional ions that bind in the transition state. They noted, however, that the data could be interpreted by the kinetically equivalent association of two  $\text{Na}^+$  ions with AcP dianion, two  $\text{Na}^+$  ions with Pi dianion, or one  $\text{Na}^+$  ion with each dianion, all in the ground state. On the basis of the kinetic dependence alone, Herschlag and Jencks have speculated on a possible transition state structure for reaction of the dianions of acetyl phosphate and orthophosphate, with three bridging  $\text{Na}^+$  ions and with four additional bound  $\text{Na}^+$  ions not shown (Scheme 4) (7). The transition state for this reaction has a

charge of  $-4$  delocalized over seven monovalent and two divalent oxygens. There is thus ample scope for the four additional bound  $\text{Na}^+$  ions, not shown, to coordinate with several of these oxygens in the transition state.

In an attempt to investigate the possible role of the metal ions in the ground state of the present system, the association of one and two metal ions with mono-anionic PNPP in the ground state was considered. In support for the pre-association of two metal ions in the present system, theoretical ab initio studies of the anion  $\text{PO}_2\text{H}_2^-$  by Streitwieser et al. (29) indicate that the best simple representation of the disodium complex of  $\text{PO}_2\text{H}_2^-$  in the gas phase is the structure  $\text{Na-O-PH}_2^+-\text{O-Na}$ , tetrahedral at phosphorus and containing co-linear  $\text{P-O-Na}$  bonds.

If one metal ion is presumed to associate with the anionic substrate with free ethoxide as the nucleophile, then the following mechanism and associated rate laws may be proposed (Scheme 5).  $K_a$  refers to the association of the substrate with either one or two metal ions,  $k_c$  refers to the rate constant for the attack of free ethoxide on an uncomplexed substrate, and  $k'_c$  refers to the rate constant for the attack of free ethoxide on a metal-complexed substrate.

$$[13] \quad \text{rate} = k_{\text{obs}}[\text{S}]_{\text{total}}$$

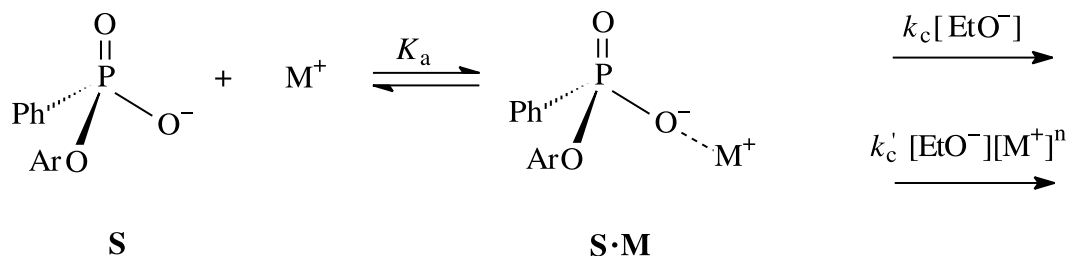
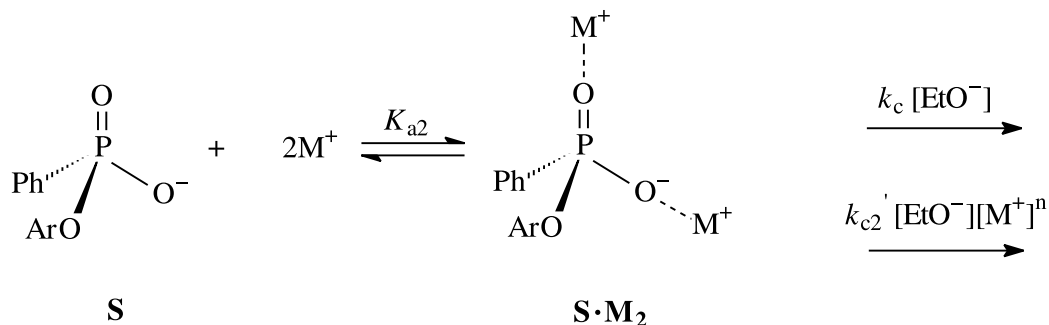
$$[14] \quad \text{rate} = k_{\text{obs}}[\text{S} + \text{S} \cdot \text{M}] = k_c[\text{S} \cdot \text{M}] + k'_c [\text{M}]^n[\text{S} \cdot \text{M}]$$

$$[15] \quad K_a = [\text{S} \cdot \text{M}]/[\text{S}^-][\text{M}^+]$$

$$[16] \quad k_{\text{obs}} = (k_c[\text{S} \cdot \text{M}] + k'_c[\text{M}]^n[\text{S} \cdot \text{M}]) / ([\text{S} + \text{S} \cdot \text{M}])$$

$$[17] \quad k_{\text{obs}} = (k_c K_a [\text{M}^+]) / (1 + K_a [\text{M}^+]) + k'_c [\text{M}^+]^n (K_a [\text{M}^+]) / (1 + K_a [\text{M}^+])$$



**Scheme 5.** Pre-association with one Na<sup>+</sup>.**Scheme 6.** Pre-association with two Na<sup>+</sup>.

If two metal ions are presumed to associate with the anionic substrate and free ethoxide is the nucleophile, then the following mechanism and associated rate laws may be proposed (Scheme 6).

$$[18] \quad \text{rate} = k_{\text{obs}}[\text{S}]_{\text{total}}$$

$$[19] \quad \text{rate} = k_{\text{obs}}[\text{S} + \text{S} \cdot \text{M}_2] = k_{c2} [\text{S} \cdot \text{M}_2] + k'_{c2} [\text{M}]^n [\text{S} \cdot \text{M}_2]$$

$$[20] \quad k_{a2} = [\text{S} \cdot \text{M}_2]/[\text{S}^-][\text{M}^+]^2; [\text{S} \cdot \text{M}_2] = K_{a2}[\text{S}^-][\text{M}^+]^2$$

$$[21] \quad k_{\text{obs}} = (k_{c2}[\text{S} \cdot \text{M}_2] + k'_{c2} [\text{M}]^n [\text{S} \cdot \text{M}_2]) / (\text{S} + \text{S} \cdot \text{M}_2)$$

$$[22] \quad k_{\text{obs}} = (k_{c2}K_{a2}[\text{M}^+]^2)/(1 + K_{a2}[\text{M}^+]^2) + k'_{c2} [\text{M}]^n (K_{a2}[\text{M}^+]^2)/(1 + K_{a2}[\text{M}^+]^2)$$

It was possible to fit the experimental data to the relationships presented in eqs. [17] and [22] using a spreadsheet program. The data for the Na<sup>+</sup> system was arbitrarily used to fit to the models presented above. There are several unknown parameters to be placed in the relationships, namely  $k_{c2}$ ,  $k'_{c2}$ ,  $K_{a2}$ , and  $n$ , the number of metal ions associated with the transition state. By putting in arbitrary values for these constants and optimizing them iteratively, it was possible to find several sets of values that fit the experimental values of  $k_{\text{obs}}$  well, as measured by a linear regression correlation coefficient ( $r^2$ ). In the previous section a good fit to the experimental data for the Na<sup>+</sup> system was given by  $n = 5$ , so this was the value used for this parameter.

The best fit to the experimental data was found via eq. [22] with  $n = 5$  and values from set 8 in Table 7 for the mechanism that had *two* metal ions pre-associated with the substrate in the ground state (Fig. 7,  $r^2 = 0.9994$ ). It is interesting to compare Fig. 7, in which a pre-association term is included in the data treatment, with Fig. 5, in which only the

**Table 7.** Parameters used in curve fitting (Figs. 7–9).

	Set 1	Set 2	Set 3	Set 4
$k_c(\text{M}^{-1}\text{s}^{-1})$	$1.65 \times 10^{-5}$	$5.0 \times 10^{-6}$	$3.9 \times 10^{-6}$	$3.8 \times 10^{-6}$
$k'_c(\text{M}^{-6}\text{s}^{-1})$	136	70	64	67
$K_a(\text{M}^{-2})$	10	60	120	140
Fit ( $r^2$ )	0.9987	0.9964	0.9957	0.9957
	Set 5	Set 6	Set 7	Set 8
$k_{c2}(\text{M}^{-1}\text{s}^{-1})$	$4.5 \times 10^{-4}$	$8.0 \times 10^{-5}$	$4.8 \times 10^{-5}$	$3.5 \times 10^{-5}$
$k'_{c2}(\text{M}^{-6}\text{s}^{-1})$	850	190	142	110
$K_{a2}(\text{M}^{-2})$	10	60	100	160
Fit ( $r^2$ )	0.9982	0.9993	0.9993	0.9994

$[\text{Na}^+]^5$  term was used to fit the kinetic data. It may be seen that inclusion of a term for the pre-association of the substrate with two metal ions in the rate law gives a better fit over the low range of sodium ion concentration (0.03–0.06 M).

In the curve fitting, the values assigned to the parameters  $k_{c2}$ ,  $k'_{c2}$ , and  $K_{a2}$  were arbitrary. Sets 1–4 and 5–8 are just a few of the many possible values that could be used to fit the data. However, it is important to note that the magnitude of  $k_{c(2)}$ , the rate constant for the unassociated ethoxide for both sets of parameters ( $\approx 10^{-6} - 10^{-4}$ ) is much smaller in magnitude than that for the corresponding values of  $k'_{c2}$  ( $\approx 10^1 - 10^2$ ), the rate constant for the associated ethoxide. This is interpreted as further evidence for multiple ion catalysis.

Proceeding to Li<sup>+</sup> and K<sup>+</sup> catalysis, Figs. 8 and 9 show sample fits for the plots of  $k_{\text{obs}}$  vs.  $[\text{M}^+]$ , which were calculated based on the rate laws associated with the pre-association of two metal ions with the substrate using the stoichiometry from eq. [22] and  $n = 4$  (K<sup>+</sup>) and 6 (Li<sup>+</sup>). The arbitrary values for the parameters used are given in the



**Fig. 7.** Multi-ion catalysis treatment, including pre-association of the substrate with two sodium ions, of the data for the reaction of PNPP with NaOEt in EtOH at 25°C. (Data for  $k_{\text{obs}}$  in supplementary table S2 and parameters from set 8). Note the goodness of the fit for the entire range of data.

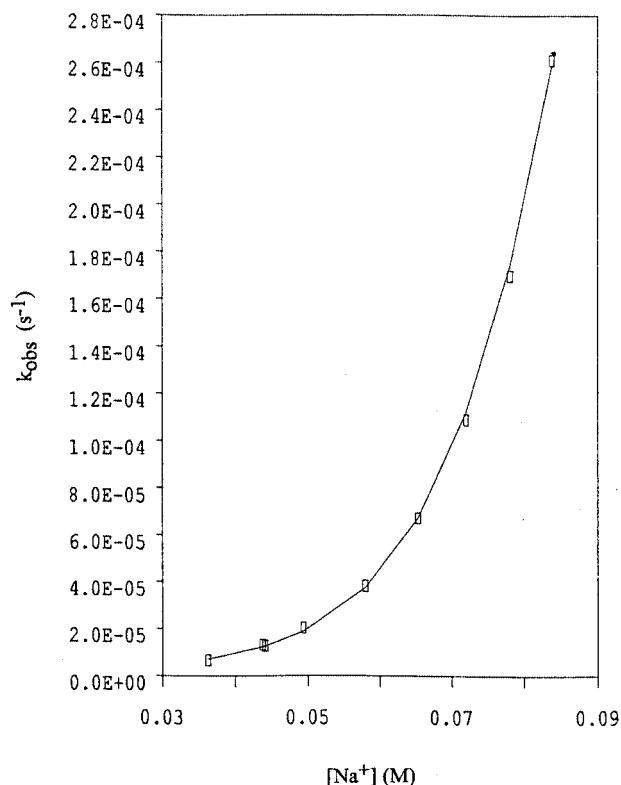


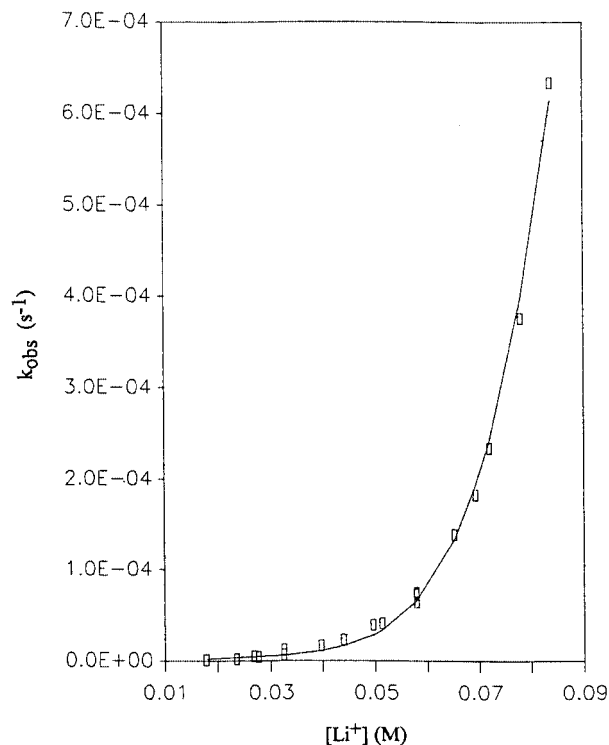
figure captions, as well as the correlation coefficients. Good fits ( $r^2 > 0.99$ ) were obtained for both systems.

#### Pre-association and multiple ion catalysis – Possible mechanisms

It has been shown that alkali metal catalysis of the reaction of ethoxide with PNPP cannot be attributed simply to catalysis by one metal ion, by either ion pair catalysis or a pre-associative mechanism. Even catalysis by two metal ions, as described by a combination of the two modes — namely ion pair catalysis on a single metal-complexed substrate — was not supported by the data treatment. The results of curve fitting the experimental rate data are consistent with the participation of possibly 3–5 metal ions in the transition state, in addition to possible pre-association of metal ions with the ground state. The largest ion ( $\text{K}^+$ ) has probably three and the smallest ion ( $\text{Li}^+$ ) has probably five ions in the transition state, while  $\text{Na}^+$  is intermediate, having probably four. The high sensitivity of the observed reaction rates to the concentration of the metal ion suggests that the metal ions lower charge repulsion between the anionic ethoxide nucleophile and the PNPP substrate. Direct binding of metal ions to the reactants by pre-association or ion pairing could lower charge repulsion between the reactants (7).

The data treatment suggests that pre-association of anionic PNPP with probably two metal ions in the ground state, in addition to multiple cations binding in the transition state, may account for the multiple alkali metal ion catalysis

**Fig. 8.** Multi-ion catalysis treatment, including pre-association of the substrate with two  $\text{Li}^+$  ions, of the data for the reaction of PNPP with LiOEt in EtOH at 25°C ( $r^2 = 0.997$ ). (Data for  $k_{\text{obs}}$  in supplementary table S1 and values for the parameters used are  $k_{c2} = 1 \times 10^{-5} \text{ M}^{-1}\text{s}^{-1}$ ,  $k'_{c2} = 2000 \text{ M}^{-7}\text{s}^{-1}$ , and  $K_{c2} = 1000 \text{ M}^{-2}$ ).



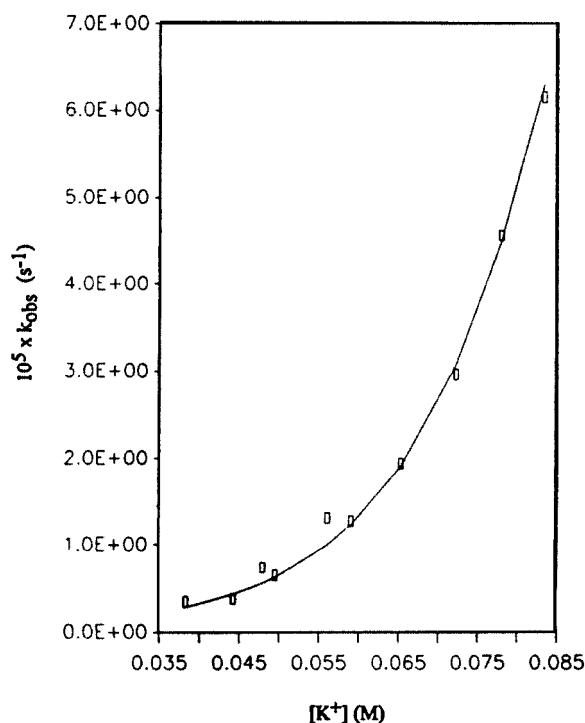
observed for this reaction. A full kinetic analysis was undertaken for sodium based on this multiple ion mechanism, and good fits to the experimental data for all three systems studied were possible with arbitrary values used for the unknown parameters. The unknown parameters were the rate constants for the uncomplexed and complexed ground states and the association constant for the ground state with either one or two metal ions, as well as the number of metal ions added in the transition state.

The mechanism proposed on the basis of the kinetic analysis is just one of several that are possible, but the good agreement with the experimental data is evidence for multiple metal ion catalysis of nucleophilic substitution at phosphorus and suggests possible roles for metal ions in both the ground states and transition states of the reaction.

It is interesting to speculate on the location of the four  $\text{Na}^+$  ions stabilizing the probable trigonal bipyramidal (TBP) transition state structure for PNPP ethanolysis. This transition state bears a charge of  $-2$  and possesses relatively bulky ligands at one equatorial and both apical positions. In contrast, the TBP transition state structure postulated by Herschlag and Jencks (7) for pyrophosphate formation from acetyl phosphate bears a charge of  $-4$ , is stabilized by seven  $\text{Na}^+$  ions, and possesses no equatorial ligands and no bulky hydrocarbon ligands (Scheme 4). The apical-equatorial metal ion coordination proposed for the TBP intermediate in alkaline phosphatase catalysis and in other metalloenzyme-catalyzed phosphoryl transfer reactions would support the transition state structure shown in Fig. 10a. However,



**Fig. 9.** Multi-ion catalysis treatment, including pre-association of the substrate with two  $K^+$  ions, of the data for the reaction of PNPP with KOEt in EtOH at 25°C ( $r^2 = 0.996$ ). (Data for  $k_{\text{obs}}$  in supplementary table S3 and values for the parameters used are  $k_{c2} = 1 \times 10^{-4} \text{ M}^{-1}\text{s}$ ).



molecular orbital calculations on a putative TBP intermediate for PNPP ethanolysis stabilized by four  $Na^+$  ions show that the steric requirement of the aryl, aryloxy, and alkoxy ligands prevents such an ideal geometry (Fig. 10a). In this crowded pentacoordinate TBP transition state, only a smaller number of the larger metal ions can be brought into contact with the anionic oxygens surrounding phosphorus. Our molecular modeling thus provides support for the stoichiometry of the transition states for catalysis by  $Li^+$ ,  $Na^+$ , and  $K^+$  obtained from the kinetic analysis.

## Experimental section

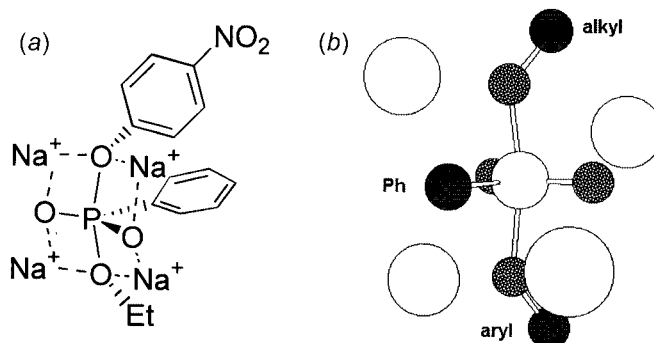
### Materials

The general procedure of Williams and coworkers (30) was followed for the synthesis of the phosphonate PNPP (**1**). The crude product was recrystallized from ethanol to a constant melting point (116–118°C, lit. (31) value mp 117–119°C). 18-Crown-6 (Aldrich) was recrystallized from acetonitrile, then dried over  $P_2O_5$  in vacuo. LiCl (Aldrich, Gold Label) and  $LiNO_3$  (Merck Suprapur) were dried over  $P_2O_5$  in vacuo.

### Kinetic method

The reaction of *p*-nitrophenyl phenylphosphonate (PNPP) with alkali metal ethoxides was studied in anhydrous ethanol at 25°C. The rates of the reactions were determined by monitoring of the formation of *p*-nitrophenoxide spectrophotometrically using either a Varian Cary3 or a Hewlett-Packard 8452A Diode Array spectrophotometer. An at least 20-fold

**Fig. 10.** Possible transition state structures for  $Na^+$  catalyzed ethanolysis of PNPP (net charge +2): (a) idealized geometry, with structure (b) obtained by semi-empirical calculations with alkyl and aryl groups removed for ease of visualization.



excess of base was used (relative to the phosphonate ester concentration) to ensure pseudo-first-order conditions for all reactions. Rate constants were calculated from at least 30 absorbance readings. Rate constants for reactions involving added metal ions were calculated as the slope of a plot of  $\ln(A_\infty - A_t)$  vs. time. Rate constants for reactions involving complexing agents were calculated using initial rate methods (zero-order kinetics) and the data spanned less than one half-life. Plots of absorbance vs. time were linear; therefore, the reported rate constants were determined by converting the observed change in absorbance to a change in concentration of the product and dividing through by the initial concentration of the substrate ( $k_{\text{zero}} = k_1 [\text{substrate}]$ ).

### Molecular modeling

An equilibrium geometry was obtained from geometry optimization at the PM3 level of a putative TBP intermediate ( $[p\text{-NO}_2\text{PhOPPh}(\text{O})_2\text{OEt}]^{2-}$ ). After addition of four sodium atoms and constraint of the four atoms consisting of phosphorus, apical oxygens, and equatorial carbon, an equilibrium geometry was obtained by iterative relaxation of molecular fragments, followed by relaxation of all atoms but the four constrained atoms (Fig. 10b).

## Conclusions

Metal ion catalysis is important in many enzyme systems including those that catalyze phosphoryl transfer (4, 31). In the catalysis of reactions at phosphorus, enzymes often employ multiple metal ions; for example, phospholipase C and nuclease P1 employ two or three catalytic  $Zn^{2+}$  ions at the active site (4). Whilst divalent metal ions and in particular  $Zn^{2+}$  are the most important biological Lewis acid catalysts, catalytic roles for monovalent cations have been suggested in enzymic phosphoryl transfer. The location of two alkali metal ions ( $Na^+$  or  $K^+$ ) in addition to  $Mg^{2+}$  at the ATP binding site of Hsc70 has been explained in terms of a catalytic role in the ATPase activity of Hsc70 involving stabilization of the pentacoordinate transition state (32). Interestingly, the relative size of  $Na^+$  versus  $K^+$  is reflected in quite different coordination in the protein crystal structures and presumably different catalytic effects. Similarly, the active site of fructose-1,6-bisphosphatase contains three metal ion binding sites, one of which is a monovalent cation binding site at



which  $K^+$  is postulated to exert Lewis acid catalysis of nucleophilic substitution at phosphorus (whereas the smaller size of  $Li^+$  results in inhibition rather than activation) (33). In some proteins, cationic amino acid residues replace monovalent metal ions, suggesting that monovalent cations mimic the properties of cationic amino acids in stabilizing anionic transition states.

Enzyme models have been reported that demonstrate bifunctional catalysis by two metal ions (34). However, the best metal-containing systems for acceleration of phosphoryl transfer employ lanthanides (35), exchange-inert  $Co^{3+}$  systems, and ligand-coordinated  $Cu^{2+}$  (36).

The simple system reported herein reveals multiple metal ion catalysis of nucleophilic substitution at phosphorus in a phosphonate monoester monoanion by the monovalent cations  $Na^+$ ,  $K^+$ , and  $Li^+$ . More unexpectedly, the detailed kinetic treatment of the data requires possibly three, four, or five cations in the transition state, even though the putative pentacoordinate transition state is only dianionic. The primary limitation to the number of cations involved in the transition state appears to be the size of the cation and steric limitations on the number of cations that can access the oxygen ligands. Our results, both kinetic and modeling, reveal the importance of electrostatic stabilization of the transition state for phosphoryl transfer that may be effected by multiple cations, either monovalent metal ions or amino acid residues. The more such cations can be brought into contact with the anionic transition state, the greater the catalysis observed.

## Acknowledgment

This research was supported by the Natural Sciences and Engineering Research Council of Canada (NSERC). The award to R.N. of a Postgraduate Scholarship by NSERC is gratefully acknowledged.

## References

1. R. Nagelkerke, G.R.J. Thatcher, and E. Buncel. *Org. Biomol. Chem.* **1**, 163 (2003).
2. G.R.J. Thatcher and R. Kluger. *Adv. Phys. Org. Chem.* **25**, 99 (1989).
3. F.H. Westheimer. *Chem. Rev.* **81**, 313 (1981).
4. W.N. Lipscomb and N. Slater. *Chem. Rev.* **96**, 2375 (1996).
5. W.P. Jencks. *Catalysis in chemistry and enzymology*. Wiley, New York, 1969.
6. R. Breslow. *Adv. Enzymol.* **58**, 1 (1986).
7. D. Herschlag and W.P. Jencks. *J. Am. Chem. Soc.* **109**, 4665 (1987).
8. R.A. Kenley, R.H. Fleming, R.M. Lane, D.S. Tse, and J.S. Winterle. *Inorg. Chem.* **23**, 1870 (1984).
9. M.J. Pregel, E.J. Dunn, and E. Buncel. *Atual. Fis. Quim. Org. Conf. Latinoam. Fis. Quim. Org.* 1st, 110 (1991).
10. R. Nagelkerke, M.J. Pregel, E.J. Dunn, G.R.J. Thatcher, and E. Buncel. *Org. React. Tartu*, **102**, 11 (1995).
11. E. Buncel, E.J. Dunn, R.A.B. Bannard, and J.G. Purdon. *J. Chem. Soc., Chem. Commun.* 162 (1984).
12. E. Buncel and M.J. Pregel. *J. Chem. Soc., Chem. Commun.* 1566 (1989).
13. E.J. Dunn and E. Buncel. *Can. J. Chem.* **67**, 1440 (1989).
14. E.J. Dunn, R.Y. Moir, and E. Buncel. *Can. J. Chem.* **69**, 1837 (1990).
15. M.J. Pregel, E.J. Dunn, and E. Buncel. *Can. J. Chem.* **68**, 1846 (1990).
16. M.J. Pregel, E.J. Dunn, and E. Buncel. *J. Am. Chem. Soc.* **113**, 3545 (1991).
17. M.J. Pregel and E. Buncel. *J. Am. Chem. Soc.* **115**, 10 (1993).
18. M.J. Pregel and E. Buncel. *J. Org. Chem.* **56**, 5583 (1991).
19. M.J. Pregel, E.J. Dunn, R. Nagelkerke, G.R.J. Thatcher, and E. Buncel. *Chem. Soc. Rev.* **24**, 445 (1995).
20. E. J. Dunn and E. Buncel. *In Metal ions in biology and medicine. Edited by Ph. Collery, L.A. Poirier, N.A. Littlefield and J.C. Etienne*. John Libbey Eurotext, Paris, 1994.
21. (a) J.R. Jones. *Prog. React. Kinet.* **7**, 1 (1973); (b) A. Papoutsis, G. Papanastasiou, J. Jannakoudakis, and C. Georgulis. *J. Chim. Phys.* **82**, 913 (1985).
22. J.L. Kurz. *J. Am. Chem. Soc.* **85**, 987 (1963).
23. R. Cacciapaglia and L. Mandolini. *Chem. Soc. Revs.* **22**, 221 (1993).
24. O.S. Tee. *Adv. Phys. Org. Chem.* (1994).
25. R. Wolfenden. *Acc. Chem. Res.* **5**, 10 (1972).
26. E. Buncel and H. Wilson. *Acc. Chem. Res.* **12**, 42 (1979).
27. R.L. Schowen. *In Transition states of biochemical processes. Edited by R.D. Gandour and R.L. Schowen*. Plenum, New York, 1978.
28. A. Fersht. *Enzyme structure and mechanism*. 2nd. ed. W.H. Freeman and Company, New York, 1985.
29. (a) A. Streitwieser, A. Rajca, R.S. McDowell, and R. Glaser. *J. Am. Chem. Soc.* **109**, 4184 (1987); (b) A. Rajca, J.E. Rice, A. Streitwieser, and H.F. Schaeffer. *J. Am. Chem. Soc.* **109**, 4189 (1987).
30. J.S. Loran, R.A. Naylor, and A. Williams. *J. Chem. Soc. Perkin Trans.* **2**, 418 (1977).
31. D.E. Wilcox. *Chem. Rev.* **96**, 2375 (1996).
32. S.M. Wilbanks and D.B. McKay. *J. Biol. Chem.* **270**, 2251 (1995).
33. R. Zhang, V. Villeret, W.N. Lipscomb, and H.J. Fromm. *Biochemistry*, **35**, 3038 (1996).
34. (a) S. Liu and A.D. Hamilton. *Bioorg. & Med. Chem. Lett.* **7**, 1779 (1997); (b) R. Breslow and B. Zhang. *J. Am. Chem. Soc.* **116**, 7893 (1994).
35. (a) W.W. Butcher and F.H. Westheimer. *J. Am. Chem. Soc.* **77**, 2420 (1955); (b) A.A. Neverov and R.S. Brown. *Inorg. Chem.* **40**, 3588 (2001); A.A. Neverov and R.S. Brown. *J. Chem. Soc. Perkin Trans.* **2**, 1039 (2002).
36. (a) M. Wall, R.C. Hynes, and J. Chin. *Angew. Chem.* **105**, 1696 (1993); (b) D. Wahnou, A.-M. Lebuais, and J. Chin. *Angew. Chem., Int. Ed.* **34**, 2412 (1995).



# Taxanes in rooted cuttings vs. mature Japanese yew

Qing-Wen Shi, Tracy L. Petzke, Françoise Sauriol, Orval Mamer, and Lolita O. Zamir

**Abstract:** Two novel taxanes were identified from rooted cuttings of the Japanese yew, *Taxus cuspidata* Sieb. et Zucc. Their structures were characterized as taxa-4(20),11-dien-2 $\alpha$ ,5 $\alpha$ -diacetate-14 $\beta$ -(2'*S*,3'*R*)-3'-hydroxy-2'-methylbutyrate-10 $\beta$ -glucoside (**1**) and 2 $\alpha$ ,5 $\alpha$ ,9 $\alpha$ ,10 $\beta$ -tetraacetox-13 $\alpha$ -(*Z*)-cinnamoyloxy-taxa-4(20),11-diene (**2**). In addition, metabolites **3–43** were also characterized in the same cuttings. Taxanes **3–16** as well as three non-taxane metabolites (**17–19**) have not previously been reported in the needles, stems, seeds, or bark of the mature *T. cuspidata* plant, although they have been found in other yews. The known taxanes **20–43** were also detected for the first time in the rooted cuttings of the Japanese yew.

**Key words:** *Taxus cuspidata*, Taxaceae, taxanes, rooted cuttings, metabolites.

**Résumé :** Deux nouveaux taxanes ont été identifiés pour la première fois dans des boutures de l'if Japonais, *Taxus cuspidata* Sieb. et Zucc. Leurs structures ont été caractérisées : taxa-4(20),11-dien-2 $\alpha$ ,5 $\alpha$ -diacetate-14 $\beta$ -(2'*S*, 3'*R*)- 3'-hydroxy-2'-methylbutyrate-10 $\beta$ -glucoside (**1**) et 2 $\alpha$ ,5 $\alpha$ ,9 $\alpha$ ,10 $\beta$ -tetraacetox-13 $\alpha$ -(*Z*)-cinnamoyloxy-taxa-4(20),11-diene (**2**). De plus, les métabolites **3–43** ont été caractérisés dans les boutures de l'if Japonais. Les taxanes **3–16** ainsi que trois métabolites non-taxanes (**17–19**) isolés dans d'autres ifs n'ont jamais été identifiés dans les tiges, graines ou écorce de la plante mature *T. cuspidata*. Les taxanes connus **20–43** ont aussi été détectés pour la première fois dans les boutures de l'if Japonais.

**Mots clés :** *Taxus cuspidata*, Taxaceae, taxanes, boutures, métabolites.

## Introduction

The Japanese yew *Taxus cuspidata* Sieb. et Zucc. has been investigated since 1963 and more than 90 taxanes have been found in its needles, bark, stem, or seeds (1–6). Rooted cuttings are used for the production of ornamental yews. The required hormones and environmental conditions for their production are kept confidential by competitive garden centres. We were interested to compare the composition of taxanes in rooted cuttings vs. needles of mature plants. Indeed, we thought it could give us some insights about the biosynthetic pathways of taxanes in yews. Taxinine derivatives lacking constituents on C-7 and C-9 have been isolated from the Chinese yew and *T. baccata*, and are sometimes found in higher yield than paclitaxel (7, 8). Taxanes with a substituent on C-14 are very rare in nature (7–9), but are easily obtained from biotransformation reactions (10). In addition, the only taxanes with a sugar substitution found in nature have been 7-xylosylbaccatin III derivatives (7).

In this study, two novel taxinine derivatives are reported from the rooted cuttings of the Japanese yew (*T. cuspidata*

Sieb. et Zucc.). Taxane **1** has a C-10-*O*-glucosyl-group (the first taxane reported with a sugar moiety on ring B) and a C-14 $\beta$ -2'-butyrate. Taxane **2** has a C-13-*cis*-cinnamoyloxy-side chain (Fig. 1). In addition, we characterized 14 taxanes (**3–16**) and three non-taxanes (**17–19**) in the rooted cuttings of the Japanese yew previously isolated in other yews, but found for the first time in *T. cuspidata*. In addition, taxanes **20–43** were found both in rooted cuttings, needles, and stems of *T. cuspidata*, as well as in needles, bark, or roots of other yews (7, 8).

## Results and discussion

### Characterization of the structures of the novel taxanes 1 and 2

Taxane (**1**) was obtained as a colorless amorphous solid in a very low yield from dried rooted cuttings of the Japanese yew. The molecular composition of **1** (C<sub>35</sub>H<sub>54</sub>O<sub>13</sub>) was established from the combined analysis of HR-FAB-MS and 2D-<sup>13</sup>C NMR spectra. The <sup>1</sup>H NMR spectrum of **1** (shown in Table 1) exhibited three-proton signals due to the four

Received 20 August 2002. Published on the NRC Research Press Web site at <http://canjchem.nrc.ca> on 29 January 2003.

Q.-W. Shi, T.L. Petzke, and L.O. Zamir.<sup>1</sup> Université du Québec, INRS-Institut Armand-Frappier-Santé Humaine, 531 Boulevard des Prairies, Laval, QC H7V 1B7, Canada.

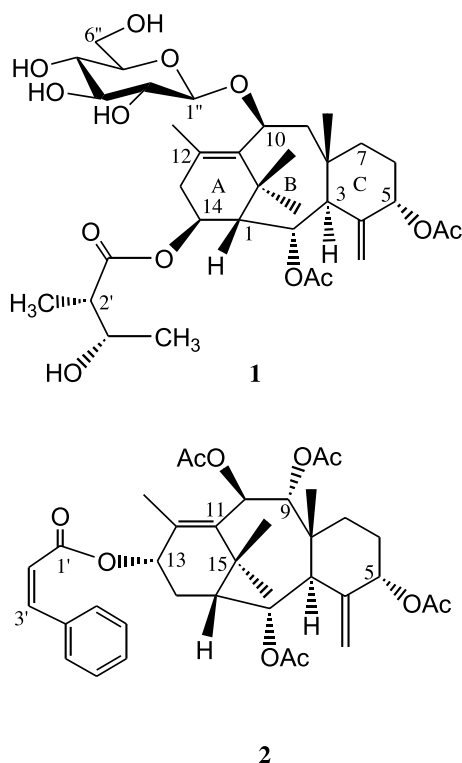
F. Sauriol. Department of Chemistry, Queen's University, Kingston, ON K7L 3N6, Canada.

O. Mamer. Biomedical Mass Spectrometry Unit, McGill University, 1130 Pine Avenue West, Montreal, QC H3A 1A3, Canada.

<sup>1</sup>Corresponding author (e-mail: Lolita.Zamir@inrs-iaf.quebec.ca).

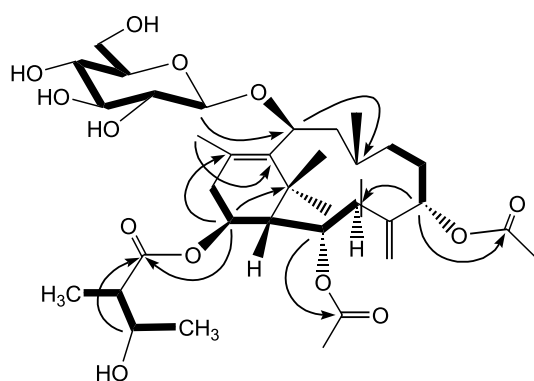


**Fig. 1.** New taxanes from rooted cuttings of *T. cuspidata* Sieb. et Zucc.



methyl groups at  $\delta$ 1.66, 1.16, 1.97, and 0.85 ppm, and two acetyl groups at relatively lower fields ( $\delta$ 2.01 and 2.16 ppm). The  $^{13}\text{C}$  NMR signals at  $\delta$ 21.9, 169.7 and  $\delta$ 21.3, 170.0 ppm confirmed this assignment, suggesting **1** had a taxane-type core skeleton. Indeed, the HMBC correlations of  $\text{H}_3$ -18 to C-11, C-12, and C-13 and  $\text{H}_3$ -16 and  $\text{H}_3$ -17 to C-1, C-11, and C-15 revealed that Me-18 was attached to C-12 whereas Me-16 and Me-17 to C-15, implying that **1** has a regular 6–8–6 ring system. The connectivities of the protons on the skeleton of **1** were determined by analysis of the  $^1\text{H}$ - $^1\text{H}$  COSY spectrum. Interpretation of  $^1\text{H}$  NMR,  $^{13}\text{C}$  NMR, and HMBC spectra permitted the positional assignment of all the functional groups. The  $^1\text{H}$  NMR signals at  $\delta$ 5.26 (1H, *br.s*), 4.81 ppm (1H, *br.s*) together with the signals at  $\delta$ 142.2 and 116.7 ppm in the  $^{13}\text{C}$  NMR spectrum and  $\delta$ 2.86 ppm (1H, *d*,  $J = 7.0$  Hz) in the  $^1\text{H}$  NMR spectrum are characteristic of an exocyclic methylene with C-3 ring junction proton in a taxa-4(20),11-diene (11). Using H-3 as a starting point, the connectivities from C-3 to C-2 to C-1 to C-14 to C-13 were deduced from the  $^1\text{H}$ - $^1\text{H}$  COSY spectrum. The signal at  $\delta$ 5.28 ppm (1H, *br.s*), which correlated with C-3 in the HMBC spectrum, was assigned to H-5. Similarly, using H-5 as a starting point, the spin system derived from C-5 to C-7 was readily interpreted from the analysis of the  $^1\text{H}$ - $^1\text{H}$  COSY spectrum. Detailed analysis of the  $^1\text{H}$ - $^1\text{H}$  COSY spectrum revealed an  $\alpha$ -methyl- $\beta$ -hydroxybutyrate group. This moiety has been found in several natural taxane analogues (7, 8). The  $\alpha$ -methyl- $\beta$ -hydroxybutyrate group was connected to C-14 as deduced from the HMBC correlations. The similarity of the NMR data of the  $\alpha$ -methyl- $\beta$ -hydroxybutyrate moiety with known taxanes reveals the configuration to be (2*S*,3*R*) (12). Taxanes with a C-2, C-5,

**Fig. 2.** Taxane **1**: Arrows show the key HMBC correlations ( $\text{H} \rightarrow \text{C}$ ) of **1**. Bold lines indicate the  $^1\text{H}$ - $^1\text{H}$  COSY correlations.



C-10, and C-14 oxygenation pattern have an unusual chemical shift of  $\delta$ 59.2 ppm for C-1 in the  $^{13}\text{C}$  NMR spectrum (13, 14), a rather unusual chemical shift value for a non-oxygenated methine. Carbon-1 usually resonates at about  $\delta$ 50 ppm (11) when it is a non-oxygenated methine lacking oxygen substitution at C-14. The downfield shifts of H-2 and H-5 signals suggested the position of two acetate groups, and were confirmed by HMBC correlations. An anomeric carbon signal at  $\delta$ 98.2 ppm as well as six hydrogen signals between  $\delta$ 3.35 and 4.42 ppm in the  $^1\text{H}$  NMR spectrum indicated the existence of one sugar moiety in taxane **1**, and it was assigned as a glucopyranosyl unit from the chemical shift, multiplicity, and coupling constant values. Analysis of the 2D NMR data (COSY, HMBC) as well as the MS fragment of  $[\text{M}-\text{OH}-181]^+$  confirmed the presence of the glucopyranosyl group. The coupling constant  $J = 7.7$  Hz for the anomeric proton H-1'' indicated that this moiety is connected to the aglycon via a  $\beta$ -linkage ( $J \sim 6\text{--}8$  Hz). The anomeric proton H-1'' ( $\delta$ 4.35 ppm,  $J = 7.7$  Hz) showed a long-range correlation with C-10 in the HMBC experiment, suggesting the attachment of the glucose at C-10. The chemical shift of H-10 ( $\delta$ 5.23 ppm, 1H) supports this assignment, since the H-10 proton resonates at about  $\delta$ 6.0 ppm (11) when acetoxyated and at about  $\delta$ 5.0 ppm when it is hydroxylated (11). The orientations of the substituents on the taxane skeleton were confirmed by the coupling constants in the proton NMR and the NOESY spectra (Table 1A). We noticed that when the sample was solubilized in  $\text{CHCl}_3$  it solidified as a gel giving broad signals in the NMR spectrum (Table 1A) which initially suggested we did not have a pure compound and had two isomers instead. Indeed, the  $^1\text{H}$  NMR showed two doublets at  $\delta$ 4.35 ppm (major peaks) and at  $\delta$ 4.42 ppm (minor peak) for the anomeric proton. The acetone spectrum, however, (Table 1B) gave sharp signals, only one peak for H-1'' confirming the purity of **1**. The strong NOE correlation of H-14 and H-1 and the small coupling constant between H-1 and H-14 suggested that their dihedral angle was about  $90^\circ$ ; the C-14 side chain is therefore  $\beta$  and H-14 is  $\alpha$ . The chemical structure of **1** was therefore established as taxa-4(20),11-dien-2 $\alpha$ ,5 $\alpha$ -diacetate-14 $\beta$ -(2'*S*,3'*R*)-3'-hydroxy-2'-methylbutyrate-10- $\beta$ -glucoside (**1**). Taxane **1** is the first reported example of a taxane with a glucose substitution on ring B. This is the second report of a C-2-, C-5-, C-10-, and C-14-oxygenated taxane from the Japanese yew, the first one being isolated from the hardwood of this species (9).



**Table 1.**  $^1\text{H}$  and  $^{13}\text{C}$  NMR spectral data of **1** (500 MHz for  $^1\text{H}$  NMR, 125 MHz for  $^{13}\text{C}$  NMR).

Position	$\delta$ ( $^1\text{H}$ ) Multiplicity <sup>a</sup>	$J$ (Hz)	$\delta$ ( $^{13}\text{C}$ ) <sup>b</sup>	HMBC	NOESY <sup>c</sup>
<b>(A) <math>\text{CDCl}_3</math></b>					
1''	4.35 (d) maj 4.42 (d) min	7.7 7.6	98.2 98.9	72.3(10)	3'' <sup>m</sup> , 5'' <sup>s</sup> , 10 <sup>m</sup> , 17 <sup>m</sup>
2''	3.44 (br.t)	~8.2	73.8	1''	
3''	3.55 (t)	8.8	76.5	2'', 4''	
4''	3.64 (t)	9.2	70.6	3'', 5'', 6''	
5''	3.35 (dt)	9.2, 4.2	75.2	1'', 3'', 4''	
6''a/b	3.86 (o.m)		62.5	4'', 5''	
1	1.90 (o.m)	~2.0	59.2		2 <sup>s</sup> , 14 <sup>s</sup> , 3/13a <sup>m</sup> , 16 <sup>s</sup> , 17 <sup>s</sup>
2	5.35 (dd)	7.0, 2.0	70.2	170.0	1 <sup>s</sup> , 3/13a <sup>w</sup> , 9a/13b <sup>m</sup> , 16 <sup>s</sup> , 19 <sup>m</sup>
3	2.86 (d)	7.0	42.4	2, 8	
4	—		142.2		6 <sup>s</sup> , partly overlap 20a
5	5.28 (br.s)		78.2	3, 169.7	
6	1.80 (o.m)		28.0		
7a	1.86 (o.m)		33.9		
7b	1.23 (o.m)				
8	—		39.5		
9a	2.41 (o.m)		44.4		2 <sup>s</sup> , 9b <sup>s</sup>
9b	1.70 (o.m)			10, 8, 11	9a <sup>s</sup> , 1 <sup>s</sup> , 2 <sup>s</sup> , 17 <sup>s</sup> , 19 <sup>m</sup>
10	5.23 (o.m)		72.3	8, 9, 15	1'' <sup>m</sup> , 3/13a <sup>w</sup> , 18 <sup>s</sup>
11	—		135.5		
12	—		137.1		
13a	2.87 (o.m)		39.7	1, 11, 12, 18	13b <sup>s</sup>
13b	2.40 (o.m)				13a <sup>s</sup> , 14 <sup>s</sup>
14	5.02 (dd)	8.7, 4.5	70.5	1, 2, 12, 15, 1'	3/13a <sup>s</sup> , 1 <sup>s</sup>
15	—		37.1		
Me16	1.66 (o.s)		24.9	1, 11, 15, Me	
Me17	1.16 (s)		31.5	1, 11, 15, Me	
Me18	1.97 (br.s)		20.9	11, 12, 13	3/13a <sup>s</sup> , Ac(2.16) <sup>s</sup> , 10 <sup>s</sup>
	1.96 (br.s)		20.9	11, 12, 13	
Me19	0.85 (s)		22.5	3, 7, 8, 9,	
20a	5.26 (br.s)		116.7	3, 4	20bs
20b	4.81 (br.s)			3, 4, 5	20a <sup>s</sup> , Ac (2.01) <sup>m</sup> , 19 <sup>m</sup>
OAc	2.16 (s)		21.9	169.7	18 <sup>m</sup> , 3/13a <sup>m</sup>
OAc	2.01 (s)		21.3	170.0	2 <sup>w</sup> , 20b <sup>m</sup>
1'	—		174.9		
2'	2.40 (o.m)		47.0	1', 3', 5'	
3'	3.86 (o.m)		69.4	1'	2'/9a/13b <sup>m</sup> , 4' <sup>s</sup> , 5' <sup>w</sup>
4'	1.20 (d)	6.5	20.9	2', 3'	
5'	1.16 (o.d)	~7.0	14.1	1', 2', 3'	
<b>(B) <math>\text{CD}_3\text{COCD}_3</math></b>					
1	1.85 (d)	2.0	59.4	2, 11	2 <sup>s</sup> , 14 <sup>s</sup> , 16 <sup>m</sup> , 17 <sup>m</sup>
2	5.37 (dd)	6.5, 2.0	70.0	8, 14, 168.9	1 <sup>s</sup> , 3 <sup>w</sup> , 9a <sup>s</sup> , 17 <sup>s</sup> , 19 <sup>s</sup> , 20b <sup>w</sup>
3	2.98 (d)	6.5	42.1	1, 2, 8, 19, 20	7a <sup>s</sup> , 14 <sup>s</sup>
4	—		143.0		
5	5.24 (o)		77.7	168.7	6 <sup>s</sup>
6ab	1.77 (m)		28.6		
7a	1.97 (o.m)		33.7		3 <sup>s</sup> , 5 <sup>s</sup> , 6 <sup>w</sup> , 7b <sup>s</sup>
7b	1.19 (o.m)				
8	—		39.2		
9a	2.37 (dd)	14.9, 12.2	44.7		2 <sup>s</sup> , 9b <sup>s</sup> , 17 <sup>s</sup> , 19 <sup>s</sup>
9b	1.61 (dd)	14.9, 5.3		3, 7, 8, 10, 11	7b <sup>m</sup> , 9a <sup>s</sup> , 10 <sup>s</sup> , 19 <sup>w</sup>
10	5.31 (dd)	12.2, 5.3	70.9	9, 12, 15, G <sub>1</sub>	7a <sup>s</sup> , 9a <sup>w</sup> , 9b <sup>s</sup> , 18 <sup>s</sup> , G <sub>1</sub> <sup>m</sup>
11	—		135.5		
12	—		136.2		
13a	2.86 (dd)	19.1, 9.4	39.6	1, 11/12, 14, 18	13b <sup>s</sup> , 14 <sup>s</sup>
13b	2.46 (dd)	19.1, 4.7		12	13a <sup>s</sup> , 16 <sup>s</sup>



**Table 1.** (concluded)

Position	$\delta$ ( $^1\text{H}$ ) Multiplicity <sup>a</sup>	$J$ (Hz)	$\delta$ ( $^{13}\text{C}$ ) <sup>b</sup>	HMBC	NOESY <sup>c</sup>
14	4.99 (dd)	9.4, 4.7	69.8	1, 2, 13, 173.4	1 <sup>m</sup> , 3 <sup>s</sup> , 13a <sup>s</sup>
15	—		36.9		
16	1.17 (s)		31.0	1, 11, 15, Me	
17	1.68 (s)		24.3	1, 11, 15, Me	1 <sup>s</sup> , 2 <sup>s</sup> , 9a <sup>s</sup> , 16 <sup>s</sup>
18	2.04 (o.s)		20.2	11, 12, 13	3 <sup>w</sup> , 10s, 13as
19	0.84 (s)		21.9	3, 7, 8, 9, 10 (weak)	2 <sup>s</sup> , 6 <sup>s</sup> , 7b <sup>w</sup> , 9a <sup>s</sup> , 9b <sup>s</sup> , 20b <sup>m</sup>
20a	5.24 (s)		116.0	3, 4	
20b	4.83 (s)			3, 4, 5	
OAc	2.14 (s)		21.0	168.7	
	1.95 (s)		20.4	168.9	
1'	—		173.5		
2'	2.40 (quint)	7.1	47.4	4', 2	
3'	3.88 (quint)	7.1	68.5	2', 3'	
4' (Me)	1.12 (d)	7.0	19.7	2', 3'	
2' (Me)	1.06 (d)	7.2	12.4	2', 3', 173.5	
G <sub>1</sub>	4.32 (d)	7.8	98.5	G <sub>3</sub> , 10	
G <sub>2</sub>	3.25 (t)	8.0	73.7	G <sub>3</sub>	
G <sub>3</sub>	3.35 (o.m)		77.4	G <sub>4</sub>	
G <sub>4</sub>	3.35 (o.m)		70.8	G <sub>3</sub>	
G <sub>5</sub>	3.21 (m)		76.5		
G <sub>6a</sub>	3.84 (dd)	11.7, 2.7	61.9		
G <sub>6b</sub>	3.66 (dd)	11.7, 5.7		G <sub>5</sub>	

<sup>a</sup>Multiplicity: singlet (s), doublet (d), doublet of doublets (dd), doublets of doublets of doublets (ddd), multiplet (m), overlapped (o).

<sup>b</sup>The  $^{13}\text{C}$  NMR chemical shifts were extracted from the HMQC experiment ( $\pm 0.2$  ppm). The numbers in italics represent quaternary carbons whose chemical shifts were obtained from the HMBC experiment ( $\pm 0.2$  ppm).

<sup>c</sup>NOESY intensities are marked as strong (s), medium (m), or weak (w).

Compound **2** was isolated as a stable colorless gummy substance. HR-FAB-MS analysis revealed its molecular formula to be  $\text{C}_{36}\text{H}_{40}\text{O}_{10}$ . Its  $^1\text{H}$  NMR spectrum (listed in Table 2) showed the characteristic signals of taxanes, including four tertiary methyl groups and four acetyls. The chemical shifts of the characteristic proton resonances due to an exomethylene moiety were observed at  $\delta 5.35$  and  $\delta 4.81$  ppm (each 1H, s). The HMBC correlations of H<sub>3</sub>-18 to C-11, C-12, and C-13 and of H<sub>3</sub>-16 and H<sub>3</sub>-17 to C-1, C-11, and C-15 revealed that Me-18 was attached to C-12 and Me-16 and Me-17 attached to C-15. Taxane **2** therefore has a regular 6–8–6 ring system. The connectivities of the protons on the taxane skeleton of **2** were determined by analysis of the  $^1\text{H}$ - $^1\text{H}$  COSY spectrum.

The presence of a cinnamoyloxy-moiety in **2** was revealed by signals at  $\delta 6.26$  (1H, d,  $J = 12.7$  Hz),  $\delta 6.96$  (1H, d,  $J = 12.7$  Hz),  $\delta 7.47$  (2H, dd,  $J = 8.0, 2.1$  Hz), and  $\delta 7.32$ – $7.4$  ppm (3H, m) in the  $^1\text{H}$  NMR spectrum. The fragment ions at  $m/z$  131 [ $\text{C}_9\text{H}_7\text{O}$ ]<sup>+</sup> and [M-cinn]<sup>+</sup> corresponding to the fission of a cinnamoyl group in the HR-FAB-MS spectrum confirmed this assignment. The unusual appearance of H-2' and H-3' as an AX spin system with a coupling constant of  $J = 12.7$  Hz instead of the normal  $J = 16.0$  to  $17.0$  Hz indicated that the double bond in the cinnamoyl group was in the unusual (Z)-geometry (15). The chemical shifts of H-2 $\beta$ , 5 $\beta$ , 9 $\beta$ , and H-10 $\alpha$  suggested that four acetoxyl groups were attached at C-2, C-5, C-9, and C-10 or C-13, and one remaining cinnamoyl group at C-10 or C-13. We observed NOE between H-2' and H<sub>3</sub>-18 in the NOESY spectrum. This would fit if the side chain is at C-10 or C-13. Taxanes with a C-10-cinnamoyl group are not known. Taxanes such as taxinine E

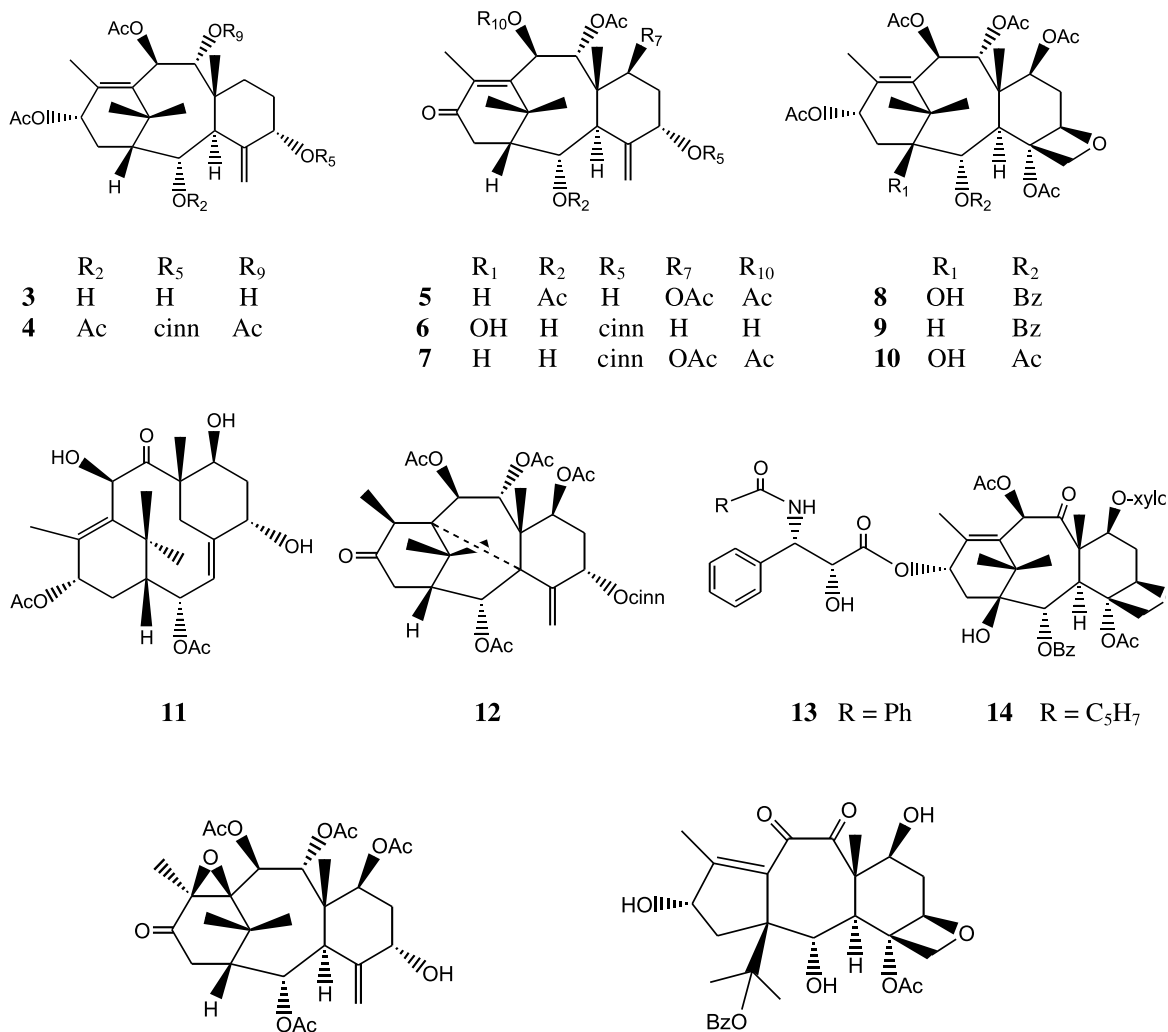
(16) and its analogues (11) have a C-5-cinnamoyl, their NMR spectra is however very different from that of **2**. The three-bond H–C correlation between H-13 $\beta$  and C-1' was not observed, but the other NMR data supports the assignment of taxane **2** as 2 $\alpha,5\alpha,9\alpha,10\beta$ -tetraacetoxy-13 $\alpha$ -(Z)-cinnamoyloxy-taxa-4(20),11-diene. The relative stereochemistry of **2** (Table 2) was shown by NOESY correlations to be the same as its analogs (7, 11).

Taxane **1** is the first reported example of a taxane with a glucose substitution on ring-B and the second taxane with a glucose substitution (7, 17). Taxane **2** is the second taxane with a *cis*-cinnamoyloxy side chain; the first taxane with a *cis*-cinnamoyloxy side chain was isolated recently from the needles of the Canadian yew (*Taxus canadensis*) (18). A new non-taxane derivative with a *cis*-cinnamoyloxy side chain was isolated previously from the Chinese yew, *Taxus mairei* (15). Taxane **2** is only the fourth example of a taxane with a cinnamoyloxy side chain at C-13 (18–20).

### Characterization of taxanes 3–16

Taxanes **3–16** were isolated from *T. cuspidata* Sieb. et Zucc. rooted cuttings and have also been found in the needles, bark, or stems of other yew species, but they have not been previously reported from the Japanese yew. They were identified by comparing their NMR data with those reported in the literature as 2 $\alpha,5\alpha,9\alpha$ -trihydroxy-10 $\beta,13\alpha$ -diacetyltaxa-4(20),11-diene (**3**) (21), taxinine E (**4**) (7), taxinine A (**5**) (2) 5-cinnamoyltaxicin I (**6**) (22), 2-deacetoxytaxinine B (**7**) (23), baccatin VI (**8**) (24), 1 $\beta$ -dehydroxybaccatin VI (**9**) (7), baccatin IV (**10**) (24), deaminoacyltaxine A (**11**) (25), 7-acetoxy-taxuspine C (**12**) (26), 7-( $\beta$ -xylosyl)-10-deacetyl-



**Fig. 3.** The structures of taxanes **3–16** isolated from the rooted cuttings of *T. cuspidata* Sieb. et Zucc.

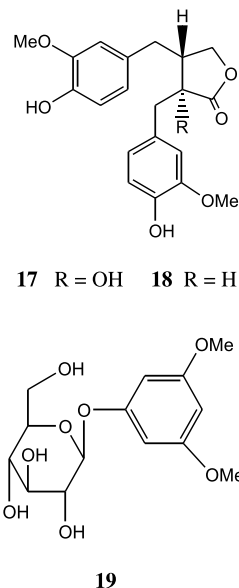
taxol (**13**) (27), 7-( $\beta$ -xylosyl)-10-deacetyltaxol C (**14**) (27), decinnamoyltaxinine B 11,12-oxide (**15**) (28), and 15-benzoyl-10-deacetyl-2-debenzoyl-10-dehydro-1(15 $\rightarrow$ 11)-abeobaccatin III (**16**) (29). The previously recorded spectral data of 7 $\beta$ -xylosyl-10-deacetyltaxol (**13**) and 7 $\beta$ -xylosyl-10-deacetyltaxol C (**14**) were obtained in a mixture of CDCl<sub>3</sub> and DMSO, and their <sup>13</sup>C NMR data were not published (27). In this work, we report their <sup>1</sup>H and <sup>13</sup>C NMR data in acetone-*d*<sub>6</sub> for **13** and in CDCl<sub>3</sub> for **14**.

#### Identification of non-taxane metabolites 17–19

The non-taxane metabolites **17–19** were found previously in the yews *T. baccata* (30), *T. media* (31), and *T. canadensis* (32). They were identified as (–)-2-epinortrachelogenin (**17**) (30), (–)-matairesinol (**18**) (31), and taxicatin (**19**) (32) on the basis of spectroscopic methods and these assignments were confirmed by comparing their spectroscopic data with those found in the literature. These compounds are reported for the first time from the Japanese yew.

#### Identification of known taxanes 20–43

The spectroscopic properties of compounds **20–43** were identical to the literature values. They were characterized as 2-deacetyltaxinine J (**20**) (7), decinnamoyl-taxinine J (**21**)

**Fig. 4.** The structures of non-taxane metabolites **17–19** isolated from the rooted cuttings of *T. cuspidata* Sieb. et Zucc.



**Table 2.**  $^1\text{H}$  and  $^{13}\text{C}$  NMR spectral data of **2** (500 MHz for  $^1\text{H}$ , 125 MHz for  $^{13}\text{C}$ ,  $\text{CDCl}_3$ ).

Position	$\delta$ (H) Multiplicity <sup>a</sup>	$J$ (Hz)	$\delta$ (C) <sup>b</sup>	HMBC	NOESY <sup>c</sup>
1	1.94 (br.d)	9.1	47.8		2 <sup>m</sup> , 14a <sup>s</sup> , 16 <sup>m</sup> , 17 <sup>m</sup>
2	5.48 (dd)	6.9, 2.2	71.2		1 <sup>m</sup> , 3 <sup>m</sup> , 9 <sup>s</sup> , 17 <sup>s</sup> , 19 <sup>m</sup>
3	3.32 (d)	6.9	43.3		14b <sup>m</sup>
4	—				
5	5.34 (o.m)		77.6		See 20a
6	1.89, 1.70		28.5		
7	1.80, 1.71		27.3		
8	—		44.1		
9	5.93 (d)	10.5	75.9	170.2	2 <sup>s</sup> , 10 <sup>w</sup> , 17 <sup>s</sup> , 19 <sup>w</sup>
10	6.02 (d)	10.5	71.6	12	9 <sup>w</sup> , 18 <sup>s</sup>
11	—		133.3		
12	—		137.4		
13	5.89 (br.t)		69.5		14a <sup>w</sup> , 16 <sup>s</sup>
14a	2.60 (dt)		*		1 <sup>s</sup> , 13 <sup>m</sup> , 14b <sup>s</sup>
14b	1.54 (o.m)				3 <sup>s</sup> , 14a <sup>s</sup>
15	—		37.5		
16	1.13 (s)		30.7	1, 11, 15, Me	1 <sup>m</sup> , 13 <sup>s</sup> , 17 <sup>s</sup>
17	1.76 (s)		26.2	1, 11, 15, Me	1 <sup>m</sup> , 2 <sup>s</sup> , 9 <sup>s</sup> , 16 <sup>s</sup> , 19 <sup>m</sup>
18	2.17 (br.s)		14.5	11, 12, 13	3 <sup>m</sup> , 10 <sup>s</sup> , 2 <sup>m</sup>
19	0.89 (s)		17.3	3, 8, 7, 9	9 <sup>w</sup> , 6/7 <sup>w</sup>
20a	5.35 (o.s)		117.4		20b <sup>s</sup>
20b	4.81 (s)				20a <sup>s</sup>
OAc	2.18 (s)		20.8	170.5	
	2.04 (s)		20.1	170.0	
	2.02 (s)		20.7	169.6	
	2.00 (s)		20.3	170.0	
1'	—		*		
2'	6.26 (d)	12.7	119.0		3' <sup>m</sup> , 18 <sup>m</sup>
3'	6.96 (d)	12.7	143.9		2' <sup>m</sup>
Ph'					
<i>o</i>	7.47 (dd)	8.0, 2.1	129.5		
<i>m, p</i>	7.4–7.32 (m)		127.4		
			128.8		

<sup>a</sup>Multiplicity: singlet (s), doublet (d), doublet of doublets (dd), doublets of doublets of doublets (ddd), multiplet (m), overlapped (o).<sup>b</sup>The  $^{13}\text{C}$  NMR chemical shifts were extracted from the HMQC experiment ( $\pm 0.2$  ppm). The numbers in italics represent quaternary carbons whose chemical shifts were obtained from the HMBC experiment ( $\pm 0.2$  ppm).<sup>c</sup>NOESY intensities are marked as strong (s), medium (m), or weak (w).

\*The signals were not detected.

(33), taxezopidine G (**22**) (34), 2 $\alpha$ ,5 $\alpha$ -dihydroxy-7 $\beta$ ,9 $\alpha$ ,10 $\beta$ ,13 $\alpha$ -tetraacetyl-taxa-4(20),11-diene (**23**) (35), 5 $\alpha$ -decinnamoyloxy-9 $\alpha$ ,10 $\beta$ ,13 $\alpha$ -triacetoxytaxa-4(20),11-diene (**24**) (34), 2-deacetyldecinnamoyltaxinine E (**25**) (36), 9-deacetyltaxinine (**26**) (37), 10-deacetyltaxinine B (**27**) (7), 1-hydroxytaxinine A (**28**) (36), 1-hydroxytaxinine (**29**) (7), taxinine (**30**) (2), 5-cinnamoyl-10-acetyltaxacin I (**31**) (38), taxinine M (**32**) (39), 5 $\alpha$ -decinnamoyltaxagifine (**33**) (40), 19-debenzoyl-19-acetyltaxinine M (**34**) (41), taxuspine B (**35**) (42), taxuspine L (**36**) (43), 5 $\alpha$ -cinnamoyl-9 $\alpha$ -acetylphototaxacin I (**37**) (44), baccatin III (**38**) (27), taxayunnansin A (**39**) (45), 10-deacetyltaxol (**40**) (46), 10-deacetylcephalomannine (**41**) (46), taxuyunnansine (**42**) (7), and taxol (**43**) (47).

### Rooted cuttings composition of taxanes vs. mature plants: Insights on biosynthesis of taxanes in yews?

Initially, we started these studies thinking that it will reveal some information about the biosynthesis of taxanes in yews. Taxanes with sugar moieties were not detected in the

needles, stems, or bark of the Japanese yew. However, it could be that the polar fractions containing sugar moieties were not investigated in mature plants. Furthermore, it is quite possible that different parts of the plants have the capability of doing very different chemical reactions. Therefore, we cannot derive simple biosynthetic explanations for these reactions, which might be dependent on many factors. On the other hand, enzymatic extracts from plants of different ages could be useful for biotransformation reactions, which are difficult to perform chemically.

## Experimental

### General experimental procedures (18, 26)

#### Plant material

Rooted cuttings of *T. cuspidata* Sieb. et Zucc. were obtained from Cramer and Cramer Nurseries in April 2001.



**Table 3.**  $^1\text{H}$  and  $^{13}\text{C}$  NMR spectral data of 7-( $\beta$ -xylosy)-10-deacetyltaxol (**13**) (500 MHz for  $^1\text{H}$ , 125 MHz for  $^{13}\text{C}$ , acetone- $d_6$ ).

Position	$\delta$ (H) Multiplicity <sup>a</sup>	<i>J</i> (Hz)	$\delta$ (C) <sup>b</sup>	HMBC	NOESY <sup>c</sup>
1	—		77.6		
OH-1	3.78 (o.s)			1, 14, 15	
2	5.65 (d)	7.1	74.7	1, 3, 8, 14, 165.6	17 <sup>s</sup> , 19 <sup>s</sup> , OH-1 <sup>w</sup>
3	3.93 (d)	7.1	46.6	1, 2, 8, 19	14a <sup>m</sup> , 7 <sup>s</sup> , 10 <sup>w</sup>
4	—		80.1		
5	4.93 (dd)	9.7, 1.6	83.8		6a <sup>m</sup>
6a	2.68 (ddd)	14.9, 9.6, 6.8	35.6		
6b	1.88 (o.m)				
7	4.20 (dd)	10.8, 6.8	81.4	1''	3 <sup>s</sup> , 6a <sup>s</sup> , 10 <sup>s</sup>
8	—		56.3		
9	—		209.7		
10	5.35 (br.s)		74.6	9, 11, 12, 15	3 <sup>w</sup> , 7 <sup>s</sup> , 18 <sup>s</sup> , 1' <sup>m</sup>
11	—		136.0		
12	—		137.3		
13	6.18 (br.t)	8.9	70.9		14b <sup>s</sup> , 16 <sup>s</sup>
14a	2.34 (br.dd)	15.4, 9.7	36.0	1, 2, 15	3 <sup>s</sup> , 14b <sup>s</sup>
14b	2.15 (dd)	15.4, 9.0			13 <sup>s</sup> , 14a <sup>s</sup> , OH-1 <sup>s</sup>
15	—		42.9		
16	1.16 (s)		26.1	1, 11, 15, Me	13 <sup>s</sup>
17	1.13 (s)		20.3	1, 11, 15, Me	2 <sup>s</sup> , 19 <sup>w</sup> , OH-1 <sup>m</sup>
18	1.89 (br.s)		13.6	11, 12, 13	
19	1.45 (s)		10.1	3, 7, 8, 9	2 <sup>s</sup> , 17 <sup>w</sup> , 1''/20 <sup>s</sup>
20ab	4.15 (o.m)		75.7	4	
OAc	2.41 (s)		22.1	170.1	
OBz-2			165.6		
C1					
o	8.10	~8.5	129.9	165.6	
m	7.56 (o.t)		128.5		
p	7.65 (t)	~7.5	133.0		
1'	—		172.7		
2'	4.82 (o.d)	4.9	73.8	3', 172.7	
3'	5.74 (dd)	8.8, 4.9	56.0	2', 139.2, Ph-o, 166.5	2' <sup>w</sup> , 4' <sup>w</sup> , Ph3'-o <sup>m</sup> , Ac <sup>m</sup>
4' NH	8.14 (d)	~8.5	—		
5' CO	—		166.5		
Ph 6'					
o	7.92 (d)	7.5	127.1	166.5	
m	7.43 (o.t)		128.2		
p	7.51 (t)	7.3	131.0		
Ph3'			139.2		
o	7.57 (o.d)		127.2	3'	
m, p	7.40 (o.t)		128.3		
	7.28 (t)	7.5	127.2		
Sugar 1''	4.18 (o.d)	~7.1	105.1	7	5b'' <sup>s</sup> , 10 <sup>s</sup>
2''	3.03 (br.t)	~8.2	73.3		
3''	3.28 (br.t)	~8.3	76.2		
4''	3.42 (m)		69.4		
5a''	3.78 (o.m)		65.4		
5b''	3.21 (dd)	9.9, 11.5			

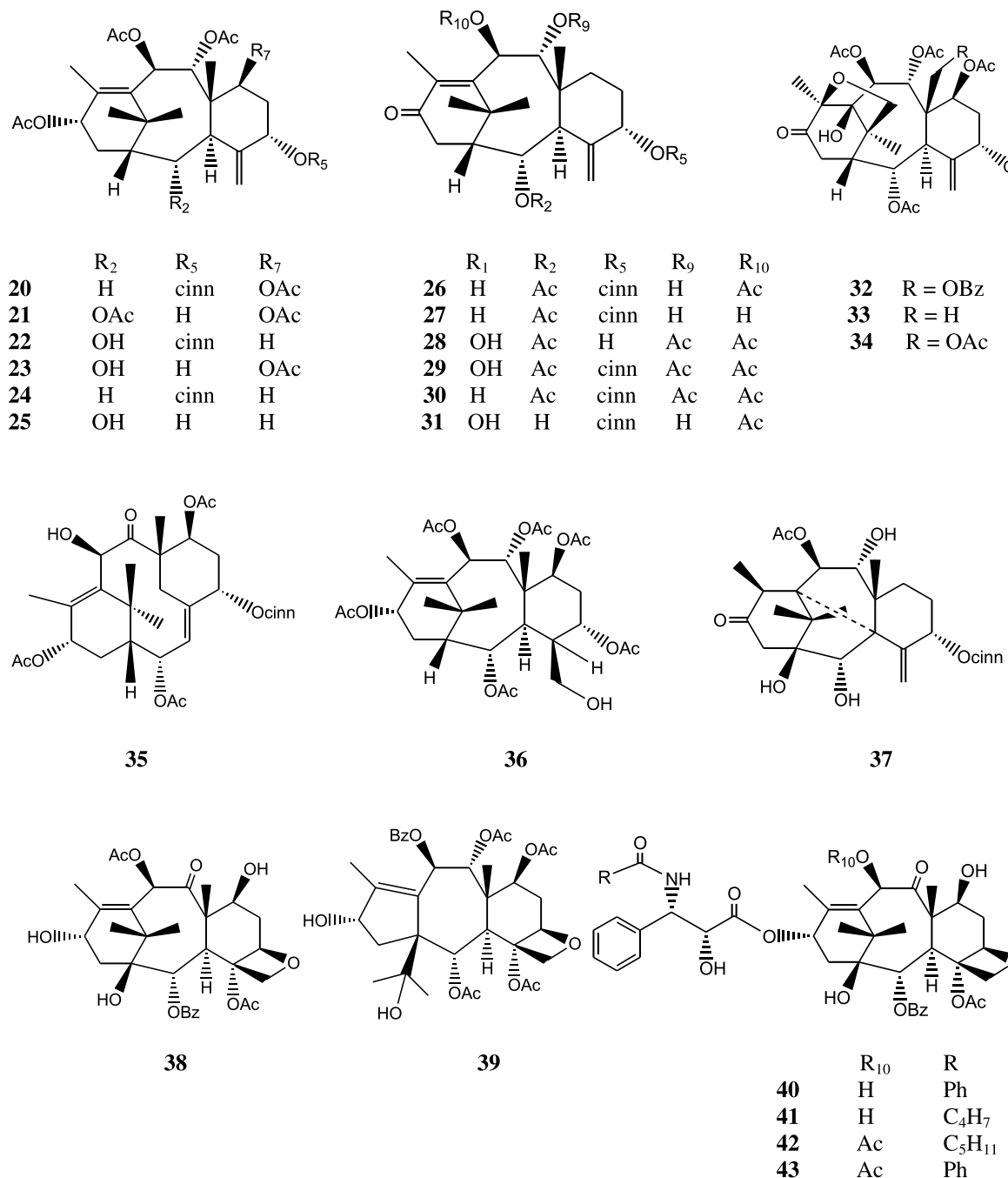
<sup>a</sup>Multiplicity: singlet (s), doublet (d), doublet of doublets (dd), doublets of doublets of doublets (ddd), multiplet (m), overlapped (o).<sup>b</sup>The  $^{13}\text{C}$  NMR chemical shifts were extracted from the HMQC experiment ( $\pm 0.2$  ppm). The numbers in italics represent quaternary carbons whose chemical shifts were obtained from the HMBC experiment ( $\pm 0.2$  ppm).<sup>c</sup>NOESY intensities are marked as strong (s), medium (m), or weak (w).

### Extraction and isolation

Ground air-dried whole rooted cuttings of the Japanese yew (*Taxus cuspidata* Sieb. et Zucc.) (148.8 g) were extracted with 900 mL of MeOH by shaking in the dark for 1 day at room temperature. The ground plants were filtered

and extracted with fresh solvent every day for a week, twice with 900 mL of MeOH, and four times with a mixture of MeOH:CH<sub>2</sub>Cl<sub>2</sub> (1:1). The combined organic extracts were evaporated under reduced pressure. Water was added to the crude extract and lipids were extracted with hexane. The



**Fig. 5.** The structures of known taxanes **20–43** from the rooted cuttings of *T. cuspidata* Sieb. et Zucc.

aqueous phase was then saturated with NaCl and extracted four times with CH<sub>2</sub>Cl<sub>2</sub> (each 750 mL). The combined CH<sub>2</sub>Cl<sub>2</sub> extracts were dried over anhydrous sodium sulphate, filtered, and evaporated using a rotary evaporator to yield about 1 g of a dark brown extract.

The CH<sub>2</sub>Cl<sub>2</sub> extract was dissolved in a minimum volume of acetone and absorbed onto 1.5 g of silica gel. It was then subjected to normal phase column chromatography on silica gel (silica gel 60, 60–200 mesh, 75 g, bed size 3.3 × 20 cm) and eluted successively with a mixture of hexane and acetone (1:1, 1:2, and 100% acetone). Twenty-seven fractions were obtained: Fr<sub>1–7</sub> (hexane:acetone, 1:1), Fr<sub>8–15</sub> (hexane:acetone, 1:2), and Fr<sub>16–27</sub> (100% acetone).

Fr<sub>1</sub> (32 mg) was applied to reversed-phase HPLC, eluted with a linear gradient of CH<sub>3</sub>CN in water from 25 to 100% for 50 min at a flow rate of 18 mL min<sup>-1</sup> and detected at 215 nm. The material eluted at *R*<sub>t</sub> = 50.37 min (a mixture of **20** and **30**, further separated by preparative TLC in hexane:EtOAc (1:1), **20** (0.8 mg, *R*<sub>f</sub> = 0.70), **30** (0.7 mg, *R*<sub>f</sub> = 0.78)) and 53.90 min (**24** (0.4 mg)) was collected and concentrated. Fr<sub>2</sub> (120 mg) was applied to preparative TLC (six plates (each 20 × 20 cm), hexane:EtOAc (50:60, v/v)) and yielded 12 subfractions (Fr<sub>2-1</sub> to Fr<sub>2-12</sub>). The fraction Fr<sub>2-2</sub> (10 mg) was subjected to semipreparative HPLC, and eluted with a linear gradient of CH<sub>3</sub>CN in water (25–100% in 50 min at a flow rate of 3 mL min<sup>-1</sup> detected at 210 nm) to



**Table 4.**  $^1\text{H}$  and  $^{13}\text{C}$  NMR spectral data of 7- $\beta$ -xylosyl-10-deacetyltaxol C (**14**) (500 MHz for  $^1\text{H}$ , 125 MHz for  $^{13}\text{C}$ ,  $\text{CDCl}_3$ ).

Position	$\delta$ ( $^1\text{H}$ )	Multiplicity <sup>a</sup>	$J$ (Hz)	$\delta$ ( $^{13}\text{C}$ ) <sup>b</sup>	HMBC	ROESY <sup>c</sup>
1	—			78.6		
2	5.65 (d)		7.2	74.5		17 <sup>s</sup> , 19 <sup>s</sup>
3	3.89 (d)		7.2	46.2		7 <sup>s</sup> , 18 <sup>w</sup> , 14 <sup>s</sup>
4	—					
5	4.89 (d)		9.9	83.8		6a <sup>m</sup>
6a	2.73 (m)					5 <sup>s</sup> , 6b <sup>s</sup> , 7 <sup>m</sup>
6b	2.02 (m)					6a <sup>s</sup> , 19 <sup>s</sup>
7	4.06 (o.m)			81.5		3 <sup>s</sup> , 6a <sup>m</sup> , 10 <sup>s</sup> , 3'' <sup>w</sup> , 2'' <sup>m</sup> (overlap H-1'')
8	—			57.0		
9	—			211.7		
10	5.16 (s)			74.7	9, 11, 12, 15	3 <sup>w</sup> , 7 <sup>s</sup> , 18 <sup>s</sup>
11	—			135.7		
12	—			138.1		
13	6.18 (br.t)		~9.0	72.3		14 <sup>s</sup> , 16 <sup>s</sup>
14	2.27 (d)		9.3	35.8	12	
15	—			42.9		
16	1.23 (s)			26.4	1, 11, 15, Me	13 <sup>s</sup>
17	1.10 (s)			20.7	1, 11, 15, Me	2 <sup>s</sup>
18	1.83 (br.s)			14.3	11, 12, 13	3 <sup>m</sup> , 10 <sup>s</sup>
19	1.81 (s)			10.8	3, 7, 8, 9	2 <sup>s</sup> , 6b <sup>s</sup> , 20b <sup>s</sup>
20a	4.29 (d)		9.0	76.4		20b <sup>s</sup> , Bz- <i>o</i> <sup>m</sup>
20b	4.19 (d)		9.0			20a <sup>s</sup> , 19 <sup>s</sup> , 2 <sup>w</sup>
OAc	2.35 (s)			22.5	170.5	
1'	—					
2'	4.66 (br.s)			73.1		3' <sup>s</sup> , Ac-4 <sup>m</sup> , Ph-3' <sup>m</sup>
3'	5.57 (dd)		9.5, 1.8	54.4		2' <sup>s</sup> , Ph-3' <sup>s</sup> , Ac-4 <sup>s</sup>
Ph-3'				128.8		
<i>o</i> / <i>m</i>	7.39			126.7	128.8, 137.9	3' <sup>w</sup> , 2' <sup>w</sup>
<i>p</i>	7.34			128.1		
4' NH	6.24 (d)		9.2	—		6' <sup>s</sup> , Ph-3' <sup>s</sup>
5' (CO)	—					
6'	2.20 (t)		7.7	36.6		
7'	1.55 (o.m)			25.3		
8'	1.25 (o.m)			31.3		
9'	1.25 (o.m)			22.2		
10' Me	0.83 (br.t)			13.7	22.2, 31.3	
Sugar 1''	4.06 (o.m)			105.2		See 7
2''	3.24 (o.m)			72.9		1''/7 <sup>s</sup> , 4'' <sup>w</sup> , 3'' <sup>w</sup> , 5''a <sup>s</sup> (overlap with 5''b)
3''	3.48 (o.t)		~8	75.2		2''/5''b <sup>w</sup> , 1'' <sup>w</sup>
4''	3.68 (m)					5''b <sup>w</sup>
5a''	3.96 (dd)		11.7, 4.8	64.9		4'' <sup>w</sup> , 5''b <sup>s</sup>
5b''	3.25 (dd)		11.7, 9.8			5''a <sup>s</sup>
Bz-2						
<i>o</i>	8.09 (d)		8.1	130.0	166.6	
<i>m</i>	7.50 (t)		7.7	128.6		
<i>p</i>	7.61 (t)		7.2	133.5		

<sup>a</sup>Multiplicity: singlet (s), doublet (d), doublet of doublets (dd), doublets of doublets of doublets (ddd), multiplet (m), overlapped (o).<sup>b</sup>The  $^{13}\text{C}$  NMR chemical shifts were extracted from the HMQC experiment ( $\pm 0.2$  ppm). The numbers in italics represent quaternary carbons whose chemical shifts were obtained from the HMBC experiment ( $\pm 0.2$  ppm).<sup>c</sup>NOESY intensities are marked as strong (s), medium (m), or weak (w).

give **21** (3 mg,  $R_t$  = 33.99 min) and **24** (2.0 mg,  $R_t$  = 53.37 min). The subfraction Fr<sub>2-3</sub> (12 mg) was purified by semipreparative HPLC to give **3** (0.7 mg,  $R_t$  = 26.93 min), **21** (1.6 mg,  $R_t$  = 34.02 min), and **41** (3.0 mg,  $R_t$  = 42.22 min). The subfraction Fr<sub>2-4</sub> (9 mg) was separated by a semipreparative HPLC to give **5** (2.0 mg,  $R_t$  = 31.71 min), **15** (1.2 mg,  $R_t$  = 34.58 min), and an impure taxane at  $R_t$  =

42.49 min, which was further purified by preparative TLC to give **8** (2.0 mg, solvent hexane:acetone (3:2),  $R_f$  = 0.58). The subfraction Fr<sub>2-5</sub> (9 mg) was separated by semipreparative HPLC to give **28** (0.5 mg,  $R_t$  = 28.46 min), **26**, **27** (2 mg,  $R_t$  = 39.34 min), and **9** (1.0 mg,  $R_t$  = 45.39 min). The subfraction Fr<sub>2-6</sub> (11 mg) was submitted to HPLC ( $R_t$  = 41.40 min) and further purified by preparative TLC



(hexane:EtOAc, 5:6) to give **31** (1.0 mg,  $R_f$  = 0.49) and **6** (1.5 mg,  $R_f$  = 0.65). The subfraction Fr<sub>2-10</sub> (11 mg) was separated by semipreparative HPLC and afforded **12** (1.0 mg,  $R_f$  = 47.06 min) and **4** (2.0 mg,  $R_f$  = 51.35 min). The subfraction Fr<sub>2-11</sub> (9 mg) was separated by a semipreparative HPLC to give **35** (1.0 mg,  $R_f$  = 44.69 min) and **7** (1.0 mg,  $R_f$  = 48.43 min). The subfraction Fr<sub>2-12</sub> (6 mg) was separated by semipreparative HPLC to give **2** (1 mg,  $R_f$  = 49.87 min). The fraction Fr<sub>3</sub> (110 mg) was applied to preparative TLC (four plates (20 × 20 cm), CH<sub>2</sub>Cl<sub>2</sub>:CNCH<sub>3</sub> (85:25)) to give 14 subfractions (Fr<sub>3-1</sub> to Fr<sub>3-14</sub>). The subfraction Fr<sub>3-2</sub> (10 mg) was subjected to semipreparative HPLC and yielded **11** (3.0 mg,  $R_t$  = 21.18 min), **33** (1.3 mg,  $R_t$  = 24.58 min), and **23** (2.0 mg,  $R_t$  = 26.53 min). The subfraction Fr<sub>3-3</sub> (9 mg) was applied to semipreparative HPLC and afforded **32** (2.2 mg,  $R_t$  = 31.37 min) and **41** (1.2 mg,  $R_t$  = 34.71 min). The subfraction Fr<sub>3-4</sub> (14.7 mg) was separated by HPLC to give **40** (3.2 mg,  $R_t$  = 35.61 min) and **41** (1.0 mg,  $R_t$  = 34.65 min). The subfraction Fr<sub>3-5</sub> (8.0 mg) was subjected to semipreparative HPLC and yielded **38** (1.5 mg,  $R_t$  = 26.73 min), **36** (1.0 mg,  $R_t$  = 30.42 min), and **40** (1 mg,  $R_t$  = 35.62 min). The subfraction Fr<sub>3-7</sub> (7 mg) was applied to semipreparative HPLC to give **10** (1 mg,  $R_t$  = 29.71 min) and **39** (1.5 mg,  $R_t$  = 38.88 min). The subfraction Fr<sub>3-9</sub> (4 mg) was applied to semipreparative HPLC to give **40** (2 mg,  $R_t$  = 21.24 min). The subfraction Fr<sub>3-10</sub> (3 mg) was applied to HPLC and yielded **18** (1 mg,  $R_t$  = 24.76 min). The subfraction Fr<sub>3-12</sub> (6 mg) was applied to semi-preparative HPLC and afforded **22** (2 mg) and **29** (1 mg,  $R_t$  = 46.30 min). The fractions Fr<sub>4</sub> (92 mg) and Fr<sub>5</sub> (46 mg) were combined and applied to preparative TLC (four plates (20 × 20 cm), CH<sub>2</sub>Cl<sub>2</sub>:CNCH<sub>3</sub> (85:30)) and yielded 14 subfractions (Fr<sub>4-1</sub> to Fr<sub>4-14</sub>). The subfraction Fr<sub>4-2</sub> (7 mg) was subjected to semipreparative HPLC to give **34** (1 mg,  $R_t$  = 28.75 min), **11** (1 mg), **37** (1 mg,  $R_t$  = 28.75 min), and **16** (1.0 mg,  $R_t$  = 25.15 min). The subfraction Fr<sub>4-3</sub> (13 mg) was subjected to HPLC and yielded **8** (1 mg), **5** (1 mg,  $R_t$  = 24.58 min), and **32** (1.0 mg,  $R_t$  = 31.37 min). The subfractions Fr<sub>13</sub> (18 mg) and Fr<sub>14</sub> (20 mg) were applied to HPLC to give **43** (2 mg,  $R_t$  = 35.61 min), **13** (2 mg,  $R_t$  = 27.51 min), **14** (4 mg,  $R_t$  = 27.27 min), **1** (1 mg,  $R_t$  = 20.39 min), and **19** (2 mg,  $R_t$  = 9.23 min).

*Taxa-4(20),11-dien-2 $\alpha$ ,5 $\alpha$ -diacetate-14 $\beta$ -(2'S,3'R)-3'-hydroxy-2'-methyl-butyrates-10 $\beta$ -glucoside (1):*

Amorphous gum;  $[\alpha]_D^{22} +15^\circ$  (c 0.05, CHCl<sub>3</sub>). The <sup>1</sup>H and <sup>13</sup>C NMR data are shown in Table 1. HR-FAB-MS  $m/z$ : 721.3205 [M + K]<sup>+</sup> (calcd. for C<sub>35</sub>H<sub>54</sub>O<sub>13</sub>K (721.3202)).

*3 $\alpha$ ,5 $\alpha$ ,9 $\alpha$ ,10 $\beta$ -Tetraacetoxy-13 $\alpha$ -(Z)-cinnamoyloxy-taxa-4(20),11-diene (2):*

Amorphous gum;  $[\alpha]_D^{22} +150^\circ$  (c 0.01, CHCl<sub>3</sub>). The <sup>1</sup>H and <sup>13</sup>C NMR data are shown in Table 2. HR-FAB-MS  $m/z$ : 689.2726 [M + K]<sup>+</sup> (calcd. for C<sub>37</sub>H<sub>46</sub>O<sub>10</sub>K (689.2728)).

## Acknowledgements

We thank the Natural Sciences and Engineering Research Council of Canada (NSERC) and the Canadian Breast Cancer Research Initiative for support via operating grants to L.

O. Z. The Foundation Armand-Frappier is acknowledged for a post-doctoral fellowship to Q.-W. Shi.

## References

1. M. Kurono, Y. Nakadaira, S. Onuma, K. Sasaki, and K. Nakanishi. *Tetrahedron Lett.* 2153 (1963).
2. H.C. Chiang, M.C. Woods, Y. Nakadaira, and K. Nakanishi. *J. Chem. Soc. Chem. Commun.* 1201 (1967).
3. Kobayashi and H. Shigemori. *Med. Res. Rev.* **22**, 305 (2002).
4. H. Morita, A. Gonda, L. Wei, K. Takeya, and H. Itokawa. *Bioorg. Med. Chem. Lett.* **7**, 2387 (1997).
5. H. Morita, A. Gonda, L. Wei, Y. Yamamura, H. Wakabayashi, K. Takeya, and H. Itokawa. *Planta Med.* **64**, 183 (1998).
6. M. Ando, J. Sakai, S. Zhang, Y. Watanabe, K. Kosugi, T. Suzuki, and H. Hagiwara. *J. Nat. Prod.* **60**, 499 (1997).
7. E. Baloglu and D.G.I. Kingston. *J. Nat. Prod.* **62**, 1448 (1999).
8. V.S. Parmar, A. Jha, K.S. Bish, P. Taneja, S.K. Sight, A. Kumar, J.R. Poonam, and C.E. Olsen. *Phytochemistry*, **50**, 1267 (1999).
9. T. Sukiyama, T. Oritani, and T. Oritani. *Biosci. Biotech. Biochem.* **58**, 1923 (1994).
10. D. Sun, F. Sauriol, O. Mamer, and L.O. Zamir. *Can. J. Chem.* **79**, 1381 (2001).
11. G. Appendino. *In The chemistry and pharmacology of taxol and its derivatives. Edited by V. Farina. Elsevier, Amsterdam. 1995. Chap. 22, pp. 55–102.*
12. W. Chen, P. Chang, B. Wu, and Q. Zheng. *Acta Pharm. Sin.* **26**, 747 (1991).
13. W. Ma, R.W. Stahlhut, T.L. Adams, G.L. Park, W.A. Evans, S.G. Blumenthal, G.A. Gomez, M.H. Nieder, and P.J. Hylands. *J. Nat. Prod.* **57**, 1320 (1994).
14. H.J. Zhang, H.D. Sun, and Y. Takeda. *J. Nat. Prod.* **58**, 1153 (1995).
15. Y. Shen, C. Chen, and M. Chung. *Chem. Pharm. Bull.* **48**, 1344 (2000).
16. M.C. Woods, H.C. Chiang, Y. Nakadaira, and K. Nakanishi. *J. Am. Chem. Soc.* **90**, 522 (1968).
17. X.J. Tong, W.S. Fang, J.Y. Zhou, C.H. He, W.M. Chen, and Q.C. Fang. *J. Nat. Prod.* **58**, 233 (1995).
18. Q.W. Shi, F. Sauriol, O. Mamer, and L.O. Zamir. *Bioorg. Med. Chem.* **11**, 293 (2003).
19. K. Tanaka, K. Fuji, T. Yokoyi, T. Shingu, B. Li, and H.D. Sun. *Chem. Pharm. Bull.* **42**, 1539 (1994).
20. H. Morita, A. Gonda, L. Wei, Y. Yamamura, H. Wakabayashi, K. Takeya, and H. Itokawa. *Phytochemistry*, **48**, 857 (1998).
21. Z.P. Zhang, H. Wiedenfeld, and E. Roder. *Phytochemistry*, **38**, 667 (1995).
22. J.N. Baxter, B. Lythgoe, B. Scales, R.M. Scowston, and S. Trippett. *J. Chem. Soc.* 2964 (1962).
23. T.B. Shrestha, S.K.K. Chetri, A.H. Banskota, M.D. Manandehar, and W.C. Taylor. *J. Nat. Prod.* **60**, 820 (1997).
24. D.P. Della Casa de Marcano and T.G. Halsall. *J. Chem. Soc. Chem. Commun.* 365 (1975).
25. G. Appendino, G. Cravotto, R. Enriu, P. Gariboldi, L. Barboni, E. Torregiani, B. Gabetta, G. Zini, and E. Bombardelli. *Phytochemistry*, **36**, 407 (1994).
26. L.O. Zamir, J.Z. Zhang, J.H. Wu, F. Sauriol, and O. Mamer. *Tetrahedron*, **55**, 14 323 (1999).
27. V. Senilh, S. Blechert, M. Colin, D. Guenard, F. Picot, P. Potier, and P. Varenne. *J. Nat. Prod.* **47**, 131 (1984).
28. Q. Yue, Q.C. Fang, and X.T. Liang. *Phytochemistry*, **43**, 639 (1996).



29. J. Zhang, F. Sauriol, O. Mamer, and L.O. Zamir. *Phytochemistry*, **54**, 221 (2000).
30. G. Appendino, G. Cravotto, R. Enriu, P. Gariboldi, L. Barboni, A. Pisetta, B. Gabetta, and E. Bombardelli. *J. Nat. Prod.* **57**, 604 (1994).
31. B. Das, S.P. Rao, K.V.N.S. Srinivas, and J.S. Yadav. *Fitoterapia*, **66**, 475 (1995).
32. C.E. Olsen, R. Singh, S. Gupta, K.S. Bisht, S. Malhotra, R. Jain, S.C. Jain, and V.S. Parmar. *Indian J. Chem. Sect. B: Org. Chem.* **37B**, 828 (1998).
33. D.G.I. Kingston, D.R. Hawkins, and L. Ovington. *J. Nat. Prod.* **45**, 466 (1982).
34. X.X. Wang, H. Shigemori, and J. Kobayashi. *J. Nat. Prod.* **61**, 474 (1998).
35. L. Ettouati, A. Ahond, O. Convert, D. Laurent, C. Poupat, and P. Potier. *Bull. Soc. Chem. Fr.* 749 (1988).
36. L. Barboni, P. Gariboldi, G. Appendino, R. Enriu, B. Gabetta, and E. Bombardelli. *Liebigs Ann.* 345 (1995).
37. J. Sakai, H. Sasaki, K. Kosugi, S. Zhang, N. Hirata, K. Hirose, A. Tomida, T. Tsuruo, and M. Ando. *Heterocycles*, **54**, 999 (2001).
38. G. Appendino, P. Gariboldi, A. Pisetta, E. Bombardelli, and B. Gabetta. *Phytochemistry*, **31**, 4253 (1992).
39. J.A. Butler, G.M. Chmurny, S.A. Look, and K.M. Witherup. *J. Nat. Prod.* **54**, 893 (1991).
40. Z. Zhang, Z. Jia, Z. Zhu, Y. Cui, J. Cheng, and Q. Wang. *Planta Med.* **56**, 293 (1990).
41. L. Barboni, P. Gariboldi, E. Torregiani, G. Appendino, M. Varese, B. Gabetta, and E. Bombardelli. *J. Nat. Prod.* **58**, 934 (1995).
42. J. Kobayashi, A. Ogiwara, H. Hosoyama, H. Shigemori, N. Yoshida, T. Sasaki, Y. Li, S. Iwasaki, M. Naito, and T. Tsuruo. *Tetrahedron*, **50**, 7401 (1994).
43. X.X. Wang, H. Shigemori, and J. Kobayashi. *Tetrahedron*, **52**, 2337 (1996).
44. G. Appendino, H.C. Ozen, P. Gariboldi, B. Gabetta, and E. Bombardelli. *Fitoterapia*, **64**, 47 (1992).
45. H. Zhang, Y. Tadede, and H. Sun. *Phytochemistry*, **39**, 1147 (1995).
46. J.L. McLaughlin, R.W. Miller, R.G. Powell, Jr., and C.R. Smith. *J. Nat. Prod.* **44**, 312 (1981).
47. M.C. Wani, H.L. Taylor, M.E. Wall, P. Coggon, and A.T. McPhail. *J. Am. Chem. Soc.* **93**, 2325 (1971).
48. L.O. Zamir, Z. H.Zhou, G. Caron, M.E. Nedeia, F. Sauriol, and O. Mamer. *J. Chem. Soc. Chem. Commun.* 529 (1995).
49. L.O. Zamir, J. Zhang, K. Kutterer, F. Sauriol, and O. Mamer. *Tetrahedron*, **54**, 15 845 (1998).



# The oxidation of sulfides by chromium(V)

Carmela R. Jackson Lepage, Lynn Mihichuk, and Donald G. Lee

**Abstract:** The mechanism for the oxidation of sulfides by  $[(\text{me}_4\text{-salen})\text{Cr}^{\text{V}}(\text{O})(\text{pyO})]\text{CF}_3\text{SO}_3$ , where  $\text{me}_4\text{-salen}$  is 8,8,8',8'-tetramethylsalen and  $\text{pyO}$  is pyridine *N*-oxide, has been investigated. Results from Hammett correlations on the rates of oxidation of substituted thioanisoles, frontier molecular orbital calculations, and product studies are consistent with a mechanism that is initiated by a single electron transfer to give a radical cation intermediate.

**Key words:** oxidation, chromium(V), sulfides, radical cation, oxygen transfer.

**Résumé :** On a étudié le mécanisme d'oxydation des sulfures par le  $[(\text{me}_4\text{-salen})\text{Cr}^{\text{V}}(\text{O})(\text{pyO})]\text{CF}_3\text{SO}_3$  dans lequel  $\text{me}_4\text{-salen}$  correspond à 8,8,8',8'-tétraméthylsalène et  $\text{pyO}$  est un *N*-oxyde de pyridine. Les résultats de corrélations de Hammett avec les vitesses d'oxydation de thioanisoles substitués, de calculs d'orbitales moléculaires frontières et d'études de produits sont en accord avec un mécanisme qui serait initié par un seul transfert d'oxygène conduisant à la formation d'un intermédiaire cation radical.

**Mots clés :** oxydation, chrome(V), sulfures, cation radical, transfert d'oxygène.

[Traduit par la Rédaction]

## Introduction

The reaction between high valent chromium oxo complexes and sulfides is known to result in the formation of sulfoxides (1). However, the mechanism by which an oxygen atom is transferred from chromium to sulfur in these reactions has not been well defined. By comparison with other similar reactions, there appears to be two primary reaction pathways that should be considered. In one mechanism the reaction would be initiated, as depicted in Scheme 1, by an electron transfer from sulfur to the oxidant, followed by oxygen rebound and solvolysis steps. In this process it is apparent that an intermediate radical cation, **1**, is formed by loss of an electron from sulfur in the initial step.

Alternatively, the reaction could proceed by a concerted oxygen transfer mechanism that does not involve the formation of discrete intermediates, as illustrated in Scheme 2. Although nucleophilic attack on an oxygen atom, as proposed in this scheme, may seem improbable, it should be noted that the process results in a concurrent reduction of the chromium and, therefore, could be regarded as a remote nucleophilic attack on the metal. This process does not involve the formation of intermediate sulfur radicals or cations.

The objective of this work has been to distinguish between these two possible mechanisms for the oxidation of sulfides by a well-characterized chromium(V) complex,  $[(\text{me}_4\text{-salen})\text{Cr}^{\text{V}}(\text{O})(\text{pyO})](\text{CF}_3\text{SO}_3)$ , where  $\text{me}_4\text{-salen}$  is 8,8,8',8'-tetramethylsalen and  $\text{pyO}$  is pyridine *N*-oxide. The approach that has been taken is to test for the presence of radical cations by a Hammett analysis applied to the rates of oxidation of substituted thioanisoles, by the use of frontier

molecular orbital calculations, and by a study of the products obtained from the oxidation of sulfides, which would produce radical cations that can react to form aldehydes and disulfides in addition to sulfoxides.

## Experimental

The preparation and purification of the sulfides and sulfoxides used in this study have been reported previously (2–4).

### Preparation of $[(\text{me}_4\text{-salen})\text{Cr}^{\text{V}}(\text{O})(\text{pyO})]\text{CF}_3\text{SO}_3$

Chromium(II) triflate hexahydrate was prepared from the reaction of chromium metal with triflic acid as follows (5): Trifluoromethanesulfonic acid (9.235 g, 61.54 mmol), obtained from Aldrich, was diluted to 10 mL with distilled and degassed water in a Schlenk tube. Electrolytic Cr chips, size  $\leq 6$  mm, purity 99.997% (1.692 g, 32.54 mmol), obtained from AESAR, were added to the Schlenk tube. One of the chips was dipped in perchloric acid and rinsed with water before addition to provide a fresh, clean surface on which the reaction could start. The Schlenk tube was evacuated and back-filled with argon. This mixture was heated to 40°C and left to stir for 7 days. The royal blue solution produced was divided into two portions using cannula techniques and placed in argon-filled Schlenk tubes. Some unreacted Cr chips (0.148 g) were recovered. Water and triflic acid were evaporated in vacuo with the aid of a heat gun, leaving a pale blue solid. The yield, calculated from the amount of unreacted Cr, was 91.2%. A quartz cell with a side arm Schlenk was used to obtain the UV spectrum of this compound in water. A  $\lambda_{\text{max}}$  observed at 714 nm, corresponds

Received 16 September 2002. Published on the NRC Research Press Web site at <http://canjchem.nrc.ca> on 29 January 2003.

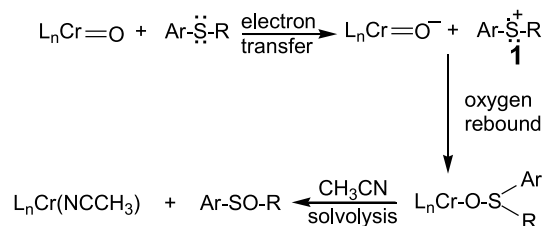
**C.R. Jackson Lepage,<sup>1</sup> L. Mihichuk, and D.G. Lee.<sup>2</sup>** Department of Chemistry, University of Regina, Regina, SK S4S 0A2, Canada.

<sup>1</sup>Present address: Defence R&D Canada – Suffield, P.O. Box 4000, Station Main, Medicine Hat AB T1A 8K6, Canada.

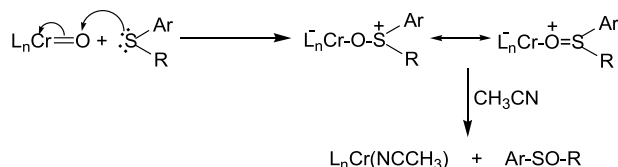
<sup>2</sup>Corresponding author (e-mail: [dglee@uregina.ca](mailto:dglee@uregina.ca)).



Scheme 1.



Scheme 2.



well with that previously reported for chromium(II) compounds (5). There was no maximum at 580 nm corresponding to chromium(III). Since this compound is extremely air-sensitive, it was stored and transferred under argon.

Chromium(II) hexahydrate was ligated with dihydro 8,8,8',8'-tetramethylsalen (6, 7) and oxidized to the corresponding chromium(III) complex as follows: (me<sub>4</sub>-salen)H<sub>2</sub> (3.570 g, 11.00 mmol) was placed in a 100 mL round-bottom flask fitted with a stopcock. The flask was evacuated and back-filled with argon. Methanol (45 mL), freshly distilled under an argon atmosphere, was added to the flask, and [Cr<sup>II</sup>(H<sub>2</sub>O)<sub>6</sub>](CF<sub>3</sub>SO<sub>3</sub>)<sub>2</sub> (3.23 g, 7.05 mmol) in an argon-filled Schlenk tube was dissolved in methanol (5 mL) and added dropwise to the round-bottom flask through a cannula. The mixture, initially blue, turned brown. Stirring was continued for 5 h at room temperature. The flask was opened to the atmosphere and heated to reflux for 1 h. The mixture was cooled and the solvent removed on a rotoevaporator. Distilled water (80 mL) was added and the mixture stirred for 2 h. The rusty-orange solid that formed was collected in a Buchner funnel and placed in a 70°C oven to dry overnight. This solid was recrystallized from water giving 2.59 g (4.63 mmol, 65.6%) purified product. The UV and IR spectra compared satisfactorily with literature spectra for [(me<sub>4</sub>-salen)Cr<sup>III</sup>(H<sub>2</sub>O)<sub>2</sub>](CF<sub>3</sub>SO<sub>3</sub>)<sub>2</sub> (6, 8). UV-vis (CH<sub>3</sub>CN) (nm) (ε (L mol<sup>-1</sup> cm<sup>-1</sup>)): 418 (3049), 320 (8376), 286 (15 000), 230 (36 000), 202 (25 000). IR (Nujol) (cm<sup>-1</sup>): 3389–3553 (b), 2954 (s), 2923 (s), 2854 (s), 1618 (s), 1602 (m), 1551 (m), 1465 (s), 1443 (s), 1401 (w), 1379 (m), 1338 (w), 1284 (m), 1238 (s), 1224 (m), 1173 (m), 1146 (m), 1128 (m), 1027 (m), 958 (w), 907 (w), 880 (w), 843 (w), 797 (w), 752 (m), 639 (m).

This chromium(III) complex was oxidized to the corresponding chromium(V) complex by iodosobenzene as follows: [(me<sub>4</sub>-salen)Cr<sup>III</sup>(H<sub>2</sub>O)<sub>2</sub>](CF<sub>3</sub>SO<sub>3</sub>)<sub>2</sub> (1.21 g, 0.37 mmol) was placed in a 100 mL round-bottom flask, and 80 mL of HPLC-grade acetonitrile (CH<sub>3</sub>CN), obtained from Fisher Scientific, was added along with iodosobenzene (0.60 g, 2.7 mmol), prepared as described in the literature (9). The flask was sealed and the solution stirred. The orange solution that formed initially when the [(me<sub>4</sub>-

Table 1. Electrospray mass spectral data for [(me<sub>4</sub>-salen)Cr<sup>V</sup>(O)]<sup>+</sup>.

Mass	Relative abundance (%)	
	Theoretical	Experimental
388.11	5.18	5.41
389.11	1.21	2.13
390.10	100.00	100.00
391.11	34.73	35.03
392.11	8.69	9.02

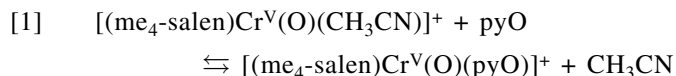
salen)Cr<sup>III</sup>(H<sub>2</sub>O)<sub>2</sub>](CF<sub>3</sub>SO<sub>3</sub>)<sub>2</sub> dissolved became greenish-black, indicative of [(me<sub>4</sub>-salen)Cr<sup>V</sup>(O)]<sup>+</sup>. Prior to rate measurements, any unreacted iodosobenzene was removed by filtration, and pyridine *N*-oxide in acetonitrile was added to produce [(me<sub>4</sub>-salen)Cr<sup>V</sup>(O)(pyO)]<sup>+</sup>. UV-vis spectroscopic analysis indicated that this was the same complex that had been previously characterized (6).

In addition to UV-vis spectroscopy, the [(me<sub>4</sub>-salen)Cr<sup>V</sup>(O)]<sup>+</sup> solution was analyzed using electrospray mass spectrometry (ESI-MS) (10). When the expanded experimental spectrum of the M<sup>+</sup> region (*m/z* 390) was compared with the theoretical spectrum for C<sub>20</sub>H<sub>22</sub>N<sub>2</sub>O<sub>3</sub>Cr<sup>+</sup>, the isotopic distribution and relative intensities in Table 1 were obtained.

The only mass with a relative abundance that is not within 5% of the predicted value is that of *m/z* 389.11. That the resulting abundance, 2.13%, is much greater than the theoretical value of 1.21% is not entirely surprising, since the area of a small peak on the shoulder of a very large peak can be substantially altered by isobaric interferences (11). Overlapping peaks with the same nominal mass can result in a large deviation from the expected value for a small peak. The other isotopic distribution peaks, all within 5% of the expected values, along with a good comparison between the UV-vis spectrum of this complex with that reported for the complex previously characterized (6) provide convincing evidence for its structure.

### Kinetic methods

The visible spectrum of a solution of [(me<sub>4</sub>-salen)Cr<sup>V</sup>(O)]CF<sub>3</sub>SO<sub>3</sub> in acetonitrile decreases in intensity uniformly from 350 to 800 nm. However, when pyridine *N*-oxide (pyO) is added to the solution, a broad band centered at 628 nm appears (in accordance with work previously described in the literature (6)). Data summarized in Fig. 1 indicate that the intensity of this band increases as the concentration of pyO is increased. The most reasonable explanation for this observation is reversible ligation with formation of a new complex, [(me<sub>4</sub>-salen)Cr<sup>V</sup>(O)(pyO)]<sup>+</sup>, when pyridine *N*-oxide is present. Since the absorbance plateaus when the concentration of pyO is 0.1 M or greater, it can be assumed that the equilibrium expressed in eq. [1] lies substantially to the right under such conditions.

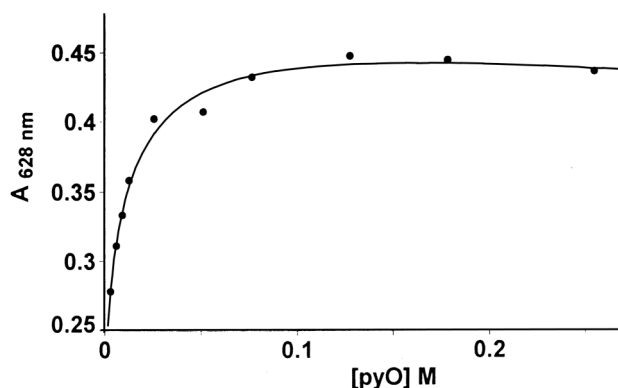
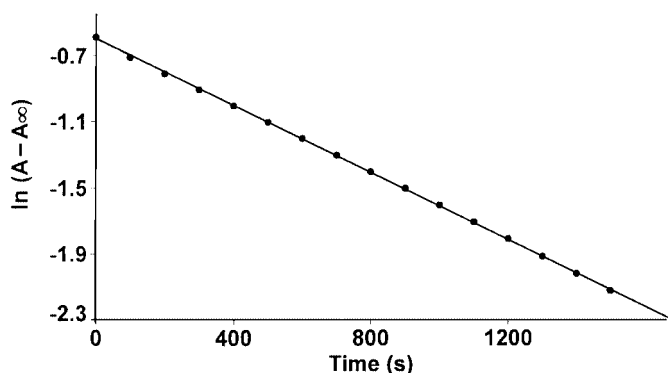


When a reductant is added to these solutions, the band at 628 nm diminishes with time, thus providing a convenient physical change that can be used to monitor reaction rates.

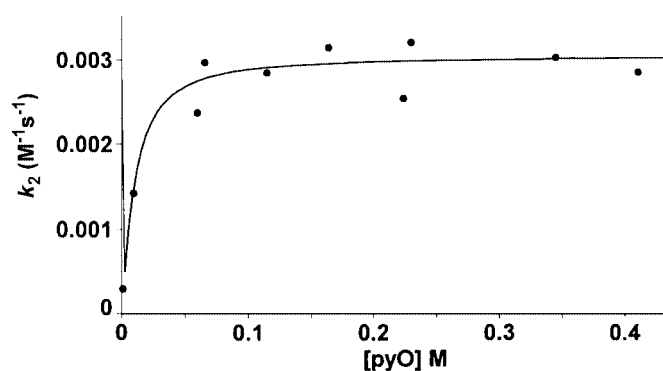


**Table 2.** Rate constants for the oxidation of methyl *p*-tolyl sulfide.<sup>a</sup>

[Sulfide] (M)	$k_{\text{obs}} \times 10^4$ (s <sup>-1</sup> )	$k_b \times 10^5$ (s <sup>-1</sup> )	$k_1 \times 10^4$ (s <sup>-1</sup> )	$k_2 \times 10^3$ (s <sup>-1</sup> M <sup>-1</sup> )
0.02977	3.009	3.191	2.690	9.04
0.02977	3.080	3.100	2.770	9.30
0.08932	7.877	3.694	7.507	8.40
0.08932	8.146	3.834	7.763	8.69
0.1191	10.76	4.648	10.30	8.65
0.1191	11.54	4.495	11.09	9.31
0.1488	14.22	4.611	13.76	9.25
0.1488	13.68	4.002	13.28	8.92
0.1488	14.00	3.312	13.67	9.19
0.1488	13.60	2.759	13.32	8.95

<sup>a</sup>Temperature = 25°C.**Fig. 1.** Dependence of absorbance at 628 nm on pyridine *N*-oxide concentration.  $[(\text{me}_4\text{-salen})\text{Cr}^{\text{V}}(\text{O})]^+ = 2.58 \times 10^{-4}$  M.**Fig. 2.** Pseudo-first-order rate plot for the oxidation of thioanisole. [Thioanisole] = 0.341 M.  $[(\text{me}_4\text{-salen})\text{Cr}^{\text{V}}(\text{O})(\text{pyO})]^+ = 3.69 \times 10^{-4}$  M. Slope =  $-1.01 \times 10^{-3}$  s<sup>-1</sup>.  $r^2 = 0.999$ .

For example, when an excess of thioanisole is added to a solution of  $[(\text{me}_4\text{-salen})\text{Cr}^{\text{V}}(\text{O})(\text{pyO})]^+$ , good pseudo-first-order rate plots are obtained (see Fig. 2). The final product exhibits a spectrum identical to that obtained by adding pyridine *N*-oxide to  $[(\text{me}_4\text{-salen})\text{Cr}^{\text{III}}(\text{H}_2\text{O})_2]^+$ . It is necessary to correct the observed pseudo-first-order rate constants,  $k_{\text{obs}}$ , obtained from the slope of such plots for a slow reduction of the oxidant that occurs in the absence of added reductant. The corrected pseudo-first-order rate constants,  $k_1$ , are obtained by subtraction of the rate constant for the corresponding blank reactions,  $k_b$ , from the observed rate constant ( $k_1 = k_{\text{obs}} - k_b$ ). The observation that the magnitude of  $k_1$  is di-

**Fig. 3.** Dependence of second-order rate constants on pyridine *N*-oxide concentration. [Thioanisole] = 0.328 M.**Table 3.** Effect of added water on rate constants.<sup>a</sup>

[H <sub>2</sub> O] (M)	$k_2 \times 10^3$ (s <sup>-1</sup> M <sup>-1</sup> )
0	2.69 <sup>b</sup>
0.19	2.64 <sup>b</sup>
1.85	2.92 <sup>c</sup>

<sup>a</sup>[Methyl phenyl sulfide] = 0.341 M;  $[(\text{me}_4\text{-salen})\text{Cr}^{\text{V}}(\text{O})(\text{pyO})](\text{CF}_3\text{SO}_3) = 2.40 \times 10^{-4}$  M.<sup>b</sup>[pyO] = 0.115 M.<sup>c</sup>[pyO] = 1.58 M.

rectly proportional to the concentration of added reductant (Table 2) indicates that the reaction is second order overall — first order in oxidant and first order in reductant.

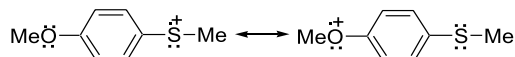
The effect of pyridine *N*-oxide on the reaction kinetics was determined by measuring the rate constants for solutions containing variable concentrations of pyO. As can be seen from Fig. 3, rates are increased by the addition of pyridine *N*-oxide; however, the effect plateaus at about 0.1 M pyO and above. This result is consistent with the absorbance data in Fig. 1 and the previous suggestion that the equilibrium in eq. [1] must be shifted to the right above 0.1 M pyO. To ensure that the effect of pyridine *N*-oxide would be constant throughout this study, its concentration was maintained above 0.1 M in all experiments, the usual working concentration being about 0.3 M.

In a series of similar experiments it was found that addition of water to the solvent had a negligible effect on the magnitudes of the observed rate constants (see Table 3). It is apparent, therefore, that small amounts of moisture would



**Table 4.** Rate constants and activation parameters for the oxidation of X-substituted thioanisoles by [(me<sub>4</sub>-salen)Cr<sup>V</sup>(O)(pyO)]CF<sub>3</sub>SO<sub>3</sub>.

X	$k_2 \times 10^3 \text{ (M}^{-1} \text{ s}^{-1})^a$	$\Delta H^\ddagger \text{ (kJ mol}^{-1})$	$\Delta S^\ddagger \text{ (J mol}^{-1} \text{ K}^{-1})$	$\Delta G^\ddagger \text{ (kJ mol}^{-1})^a$
4-MeO	$47.0 \pm 1.8$	$38.0 \pm 1.7$	$-142.9 \pm 6.0$	$80.6 \pm 2.5$
4-Me	$9.88 \pm 0.21$	$49.6 \pm 1.0$	$-117.6 \pm 3.2$	$84.7 \pm 1.4$
H	$3.27 \pm 0.31$	$49.6 \pm 1.4$	$-127.5 \pm 4.8$	$87.6 \pm 2.0$
4-F	$2.23 \pm 0.03$	$51.3 \pm 1.5$	$-123.8 \pm 4.8$	$88.2 \pm 2.1$
4-Cl	$1.49 \pm 0.08$	$64.3 \pm 2.7$	$-83.3 \pm 9.3$	$89.1 \pm 3.9$
3-Cl	$0.607 \pm 0.023$	$53.0 \pm 1.7$	$-128.8 \pm 5.7$	$91.4 \pm 2.4$

<sup>a</sup>Temperature = 25.0°C.**Scheme 3.**

not have an impact on the accuracy of the measured rate constants.

In a typical kinetic experiment, 2.0 mL aliquots of 0.3 M pyO in acetonitrile were added to two 10-mm cuvettes. One cuvette was fitted with a Teflon septa-seal top. Additional solvent (0.1 mL) was added to the other cuvette to compensate for the volume difference that would occur when reductant was added through the septa-seal. An aliquot of freshly prepared oxidant (0.30 mL) was added to each of the cuvettes. They were then flushed with argon for 3 min and sealed. Both cuvettes were placed in the thermostated cell compartment of an HP8452 Diode Array UV-vis spectrophotometer and held at a constant temperature for 29 min. A solution of thermostated and degassed reductant (0.10 mL) was injected through the septa-seal using a microlitre syringe. This cuvette was inverted several times to ensure good mixing and replaced in the thermostated cell compartment. The reaction rates were then monitored at 628 nm. Observed pseudo-first-order rate constants,  $k_{\text{obs}}$ , were obtained from the data collected from the cuvette containing reductant, and the blank rate constants,  $k_{\text{b}}$ , were simultaneously obtained using data collected for the solution in the other cuvette.

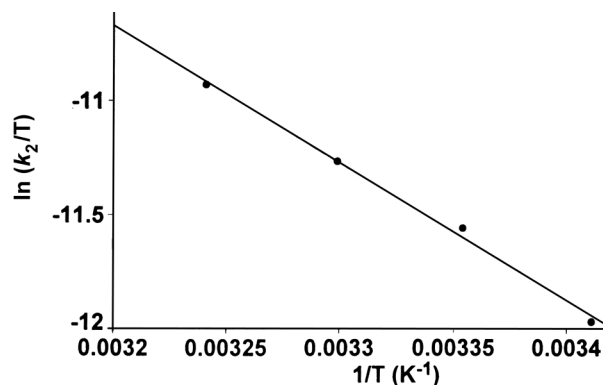
### Activation parameters

Activation parameters, as defined by application of the Eyring Equation (eq. [2]), were determined by measuring the rate constants at several temperatures and preparing plots of  $\ln k_2/T$  vs.  $1/T$  (12). A typical plot has been reproduced in Fig. 4 and the results are summarized in Table 4. Since both of the proposed mechanisms predict second-order kinetics, the large negative entropies of activation observed are consistent with either Scheme 1 or Scheme 2.

$$[2] \quad \ln k_2/T = -\Delta H^\ddagger/RT + \Delta S^\ddagger/R + \ln k_B/h$$

### Results and discussion

If a radical cation (see Scheme 1) is formed during the oxidation of substituted thioanisoles, it would be stabilized by substituents that could enter into a direct resonance interaction with it, as depicted in Scheme 3. Since resonance of this type requires interaction of the 3p orbitals of sulfur with the carbon 2p orbitals of the aromatic ring, it may not make a large contribution to the stability of the radical cation; however, it should be sufficient to cause the rates of oxidation of

**Fig. 4.** Eyring plot for the oxidation of thioanisole. Slope =  $-6.04 \times 10^3 \text{ K}$ . Intercept = 8.68.  $r^2 = 0.996$ .

substituted thioanisoles to correlate somewhat better with Hammett  $\sigma^+$  substituent constants, as compared with the corresponding  $\sigma$  constants. From a comparison of the plots in Figs. 5 and 6, it can be seen that this is, in fact, the case. The correlation is obviously better when  $\sigma^+$  substituent constants are used.

A similar direct resonance effect for the intermediate proposed in Scheme 2 would require overlap between a sulfur 3d orbital and the 2p orbitals of the aromatic ring. Therefore, its contribution to the stability of the transition state would be insignificant, and a better correlation would be expected with  $\sigma$  substituent constants, as observed for the oxidation of sulfides by high valent manganese and ruthenium oxides, both of which exhibit better correlations with  $\sigma$  substituent constants (3, 13, 14). This result, therefore, suggests that the oxidation of sulfides by [(me<sub>4</sub>-salen)Cr<sup>V</sup>(O)(pyO)]<sup>+</sup> likely involves the formation of intermediate radical cations as in Scheme 1.

The observation that sulfoxides are not oxidized by [(me<sub>4</sub>-salen)Cr<sup>V</sup>(O)(pyO)]<sup>+</sup> is also consistent with an electron transfer mechanism. Since the electron density at the sulfoxide sulfur would be decreased by polarization of the S=O bond, as in Scheme 4, the activation energy for electron transfer would be greatly increased. Other oxidants such as permanganate and ruthenium tetroxide, which are believed to proceed by a mechanism similar to the one depicted in Scheme 2, oxidize sulfoxides more readily than sulfides (3, 4).

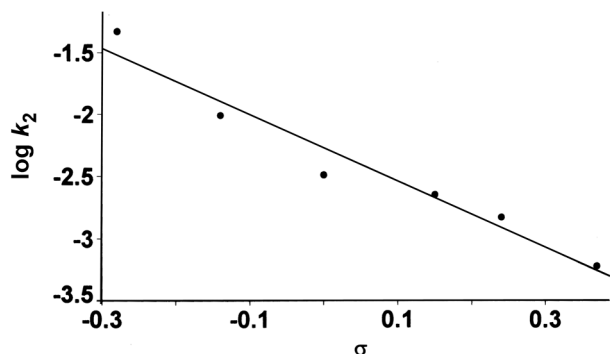
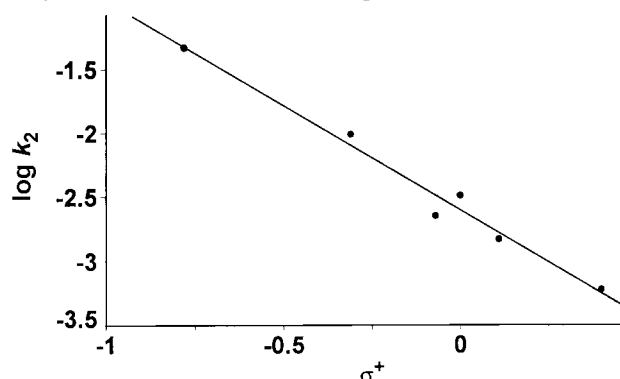
Also consistent with this conclusion is the observation that the rate of oxidation of 4-nitrothioanisole is too slow to measure under these conditions. In this compound the electron density at sulfur is decreased by resonance, as depicted in Scheme 4. Frontier molecular orbital theory predicts that there should be a direct correlation between the energies of



**Table 5.** Product distributions for the oxidation of substituted benzyl phenyl sulfides by  $[(\text{me}_4\text{-salen})\text{Cr}^{\text{V}}(\text{O})(\text{pyO})]\text{CF}_3\text{SO}_3$ .

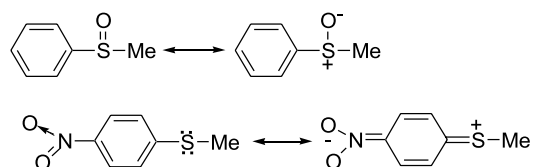
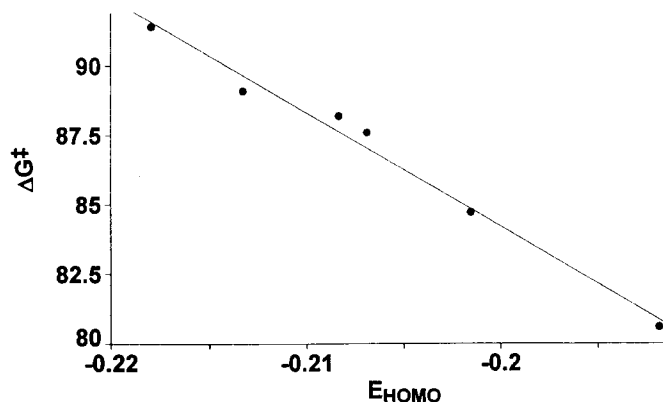
Sulfide	Product Ratios <sup>a</sup>		
	Sulfoxide	Aldehyde	Starting material
Benzyl phenyl sulfide	0.47	—	0.53
4-Methoxybenzyl phenyl sulfide	0.31	0.031	0.66
3,4,5-Trimethoxybenzyl phenyl sulfide	0.16	0.088	0.75

<sup>a</sup>Product ratios were determined, as previously described (2), from the integrals of  $^1\text{H}$  NMR spectra.

**Fig. 5.** Hammett correlation with  $\sigma$ -substituent constants. From left to right the substituents are 4-methoxy, 4-methyl, hydrogen, 4-fluoro, 4-chloro, and 3-chloro. Slope =  $-2.65$ .  $r^2 = 0.95$ .**Fig. 6.** Hammett correlation with  $\sigma^+$ -substituent constants. From left to right the substituents are 4-methoxy, 4-methyl, 4-fluoro, hydrogen, 4-chloro, and 3-chloro. Slope =  $-1.64$ .  $r^2 = 0.98$ .

the sulfide HOMOs and the rates of reactions initiated by single electron transfers. Assuming that the LUMO of the oxidant is at a higher energy than the HOMOs of the sulfides, increasing the energy of the HOMO should result in a faster reaction (15). When the energies of the HOMOs of the substituted thioanisoles were calculated at the B3LYP/6-31G\* level, a good correlation with activation energies was observed (16) (see Fig. 7). This result is most consistent with the mechanism in Scheme 1 where the reaction is initiated by a single electron transfer.

It is also possible to test for the formation of intermediate radical cations by studying the products formed when methoxy-substituted benzyl phenyl sulfides are oxidized. The radical cations formed from these compounds can react to give aldehydes in competition with the formation of sulfoxides in the oxygen rebound step depicted in Scheme 1 (17–19). For example, reaction of 3,4,5-trimethoxybenzyl phenyl sulfide gives only 3,4,5-trimethoxybenzaldehyde and

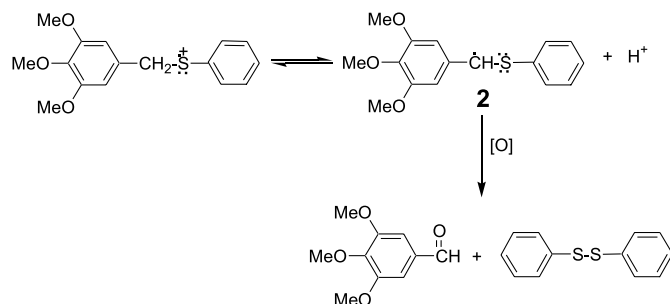
**Scheme 4.****Fig. 7.** Correlation of second-order rate constants with HOMO energies. From left to right the substituents are 3-chloro, 4-chloro, 4-fluoro, hydrogen, 4-methyl, and 4-methoxy. Slope =  $-410$ .  $r^2 = 0.985$ .

diphenyl disulfide when oxidized by cerium(IV) ammonium nitrate, a known one-electron transfer oxidant (2). Previous work has indicated that the formation of aldehydes and disulfides is initiated by loss of a proton from the radical cation to give a free radical, **2**, which is known to be readily oxidized to the corresponding aldehyde, as in Scheme 5. Introduction of the methoxy substituents increases the acidity of the radical cation, promoting proton loss and subsequent aldehyde formation.

When the products obtained from the oxidation of benzyl phenyl sulfide, 4-methoxybenzyl phenyl sulfide, and 3,4,5-trimethoxybenzyl phenyl sulfide were compared, the results summarized in Table 5 were obtained. The product ratios were determined using  $^1\text{H}$  NMR integrals as previously described (2). These data, which show that the ratio of aldehyde to sulfoxide increases from 0 for unsubstituted benzyl phenyl sulfide to 0.10 and 0.55 for 4-methoxybenzyl phenyl sulfide and 3,4,5-trimethoxybenzyl phenyl sulfide, respectively, are most consistent with the reaction mechanism presented in Scheme 1. Oxidations by high valent manganese and ruthenium oxides, which have been proposed to react by a concerted oxygen transfer, as in Scheme 2, give only sulfoxides and sulfones with these same sulfides (2).



Scheme 5.



Although any one of these tests individually do not provide compelling evidence for the electron transfer mechanism, the combined impact of the three tests (i.e., the Hammett analysis, the frontier molecular orbital calculations, and the product studies) is convincing, and it appears that the reaction between sulfides and  $[(me_4\text{-salen})Cr^V(O)(pyO)]^+$  is most likely initiated by a single electron transfer.

It is of interest to note that the oxidation of sulfides by chromium(V) and most other high valent transition metals appears to proceed by different mechanisms. Because the oxidation of proteins and lipids in free radical processes has been associated with the onset of several diseases (20–22), the observed tendency of chromium(V) to react by a one-electron transfer is consistent with the belief that the carcinogenic properties of oxochromium compounds are associated with their tendency to react by free radical oxidation mechanisms. The oxides of manganese, ruthenium, molybdenum, and iron are not carcinogenic, presumably because they react with sulfides by concerted mechanisms that do not involve the formation of intermediate radicals (2, 23).

## Acknowledgments

The authors are pleased to acknowledge financial assistance from the Natural Sciences and Engineering Research Council of Canada (NSERC).

## References

1. M. Hudlicky. *Oxidation in organic chemistry*. ACS monograph 186. American Chemical Society, Washington. 1990. p. 253 and refs. therein.
2. S. Lai, C. Jackson Lepage, and D.G. Lee. *Inorg. Chem.* **41**, 1954 (2002).
3. N. Xie, R.A. Binstead, E. Block, W.D. Chandler, D.G. Lee, T.J. Meyer, and M. Thiruvazhi. *J. Org. Chem.* **65**, 1008 (2000).
4. B.L. May, H. Yee, and D.G. Lee. *Can. J. Chem.* **72**, 2249 (1994).
5. W.H. Tambllyn, E.A. Volger, and J.K. Kochi. *J. Org. Chem.* **45**, 3912 (1980).
6. K. Srinivasan and J.K. Kochi. *Inorg. Chem.* **24**, 4671 (1985).
7. R. Sayre. *J. Am. Chem. Soc.* **77**, 6689 (1955) and refs. therein.
8. E.G. Samsel, K. Srinivasan, and J.K. Kochi. *J. Am. Chem. Soc.* **107**, 7606 (1985).
9. H. Saltzman and J.G. Sharefkin. *Organic synthesis*. Collected volume V. Wiley, New York. 1973. p. 658.
10. W. Agam, S. Hajra, M. Herderich, and C.R. Saha-Moller. *Org. Lett.* **2**, 2773 (2000).
11. R. Willoughby, E. Shechan, and S.A. Mitrovich. *A global view of LC/MS: How to solve your most challenging analytical problems*. Global View Publications, Pittsburgh. 1998. p. 105.
12. S.R. Logan. *Fundamentals of chemical kinetics*. Longman, Burnt Mill. 1996. p. 86.
13. D.G. Lee and T. Chen. *J. Org. Chem.* **56**, 5341 (1991).
14. D.G. Lee and H. Gai. *Can. J. Chem.* **73**, 49 (1995).
15. I. Fleming. *Frontier orbitals and organic chemical reactions*. Wiley, Chichester. 1976. p. 25–27.
16. Details of the theoretical calculations can be found in: C.R. Jackson Lepage, Ph.D. thesis, University of Regina, 2001, available through University Microfilms International or The Library, University of Regina, Regina, SK S4S 0A2, Canada.
17. E. Baciocchi, O. Lanzalunga, and S. Malandrucchio. *J. Am. Chem. Soc.* **118**, 8973 (1996).
18. E. Baciocchi, O. Lanzalunga, and B. Pirozzi. *Tetrahedron*, **53**, 12287 (1997).
19. E. Baciocchi, O. Lanzalunga, and F. Marconi. *Tetrahedron Lett.* **35**, 9771 (1994).
20. A. Rauk. *Can. Chem. News*, **53(5)**, 20 (2001).
21. A. Rauk, D.A. Armstrong, and D.P. Fairlie. *J. Am. Chem. Soc.* **122**, 9761 (2000).
22. L.J. Marnett. *Carcinogenesis*, **21**, 361 (2000).
23. C.A. Bunton and N.D. Gillitt. *J. Phys. Org. Chem.* **15**, 29 (2002).



# A diene-transmissive approach to the quassinoid skeleton

Claude Spino, Bryan Hill, Pascal Dubé, and Stéphane Gingras

**Abstract:** Several tetracyclic molecules were prepared by diene-transmissive Diels–Alder cycloadditions. Control over the stereochemical outcome of the cycloaddition was achieved and the structural features of the precursors affecting the stereochemistry is discussed. Useful information was gathered concerning the factors governing this stereocontrol, which will be indispensable for the future of this strategy.

**Key words:** quassinoid, anticancer agent, diene-transmissive Diels–Alder cycloaddition, oxadiene, hetero Diels–Alder.

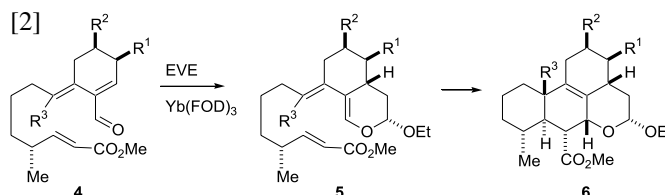
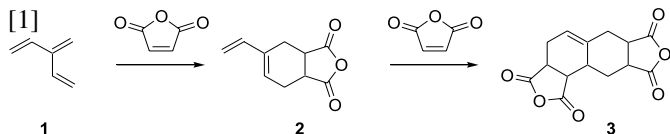
**Résumé :** On a préparé plusieurs molécules tétracycliques en faisant appel à des réactions de cycloaddition de Diels–Alder à diènes-transmissibles. On a pu contrôler le résultat stéréochimique des cycloadditions et on discute des caractéristiques des structures des précurseurs qui affectent la stéréochimie. Des informations utiles ont été accumulées concernant les facteurs qui gouvernent ce contrôle stéréochimique et celles-ci seront indispensables pour le futur de cette stratégie.

**Mots clés :** quassinolide, agent antinéoplasique, cycloaddition de Diels–Alder à diènes-transmissibles, oxadiène, hétéro-Diels–Alder.

[Traduit par la Rédaction]

## Introduction

Blomquist and Bailey and co-workers (1) reported the first diene-transmissive Diels–Alder cycloaddition in 1955. They coupled the unstable cross-conjugated triene 3-methylene-1,4-pentadiene **1** with excess maleic anhydride and obtained tetracyclic adduct **3** in moderate yield (eq. [1]) (1). Later, Tsuge and co-workers and others (2–4) investigated a series of intermolecular diene-transmissive [4 + 2]-cycloadditions on simple substituted cross-conjugated trienes. For several reasons that are explained in previous publications, this strategy stayed without a useful application until our report of a diene-transmissive Diels–Alder approach to the synthesis of anticancer quassinoids (eq. [2]) (5). In this synthetic route to quassinoids, a cross-conjugated oxadiene **4** was transformed into tetracycle **6** via an intermolecular hetero Diels–Alder reaction followed by an intramolecular normal [4 + 2]-cycloaddition. In 1999, Fallis and co-workers (6) reported the use of diene-transmissive Diels–Alder reactions for the construction of advanced intermediates toward the synthesis of other terpenoids.



Quassinoids are formidable synthetic targets. The extent of the oxygenation of their carbon skeleton contributes to the synthetic difficulties (7). Subtropical shrubs of the plant family *Simaroubaceae* constitute the most common source for these degraded triterpenoid natural products (8). They possess a large spectrum of biological activities, including antiviral, antimalarial, antineoplastic, and insect antifeedant properties (8). Recently reported biological activities have increased the interest in the synthesis of this family of terpenes (9). The vast majority of quassinoids possess a C-20 picrasane skeleton, of which quassin **7**, glaucarubolone **8**, and bruceantin **9** are typical examples (Fig. 1) (8). We report herein a comprehensive investigation of the diene-transmissive double Diels–Alder approach to quassinoids. The quassinoid numbering and lettering shown in Fig. 1, will be used throughout this manuscript on all structures for ease of reference to the potential target molecules.

Several stereochemical issues arise from the key cycloaddition reactions. The substituents on the cyclohexene ring in **4** direct the incoming ethylvinyl ether to the  $\alpha$  face of the diene but they may also affect the stereochemical outcome of the intramolecular Diels–Alder reaction (eq. [2]) (10). The appendages on the exocyclic chain serve to differentiate the energies of the two *endo* transition states (TS) accessible to the intermediate **5** (Fig. 2). They must be brought in with

Received 13 July 2002. Published on the NRC Research Press Web site at <http://canjchem.nrc.ca> on 29 January 2003.

C. Spino,<sup>1</sup> B. Hill, P. Dubé, and S. Gingras. Université de Sherbrooke, Département de Chimie, 2500, boulevard Université, Sherbrooke, QC J1K 2R1, Canada.

<sup>1</sup>Corresponding author (e-mail: [claudio.spino@USherbrooke.ca](mailto:claudio.spino@USherbrooke.ca)).



Scheme 1.

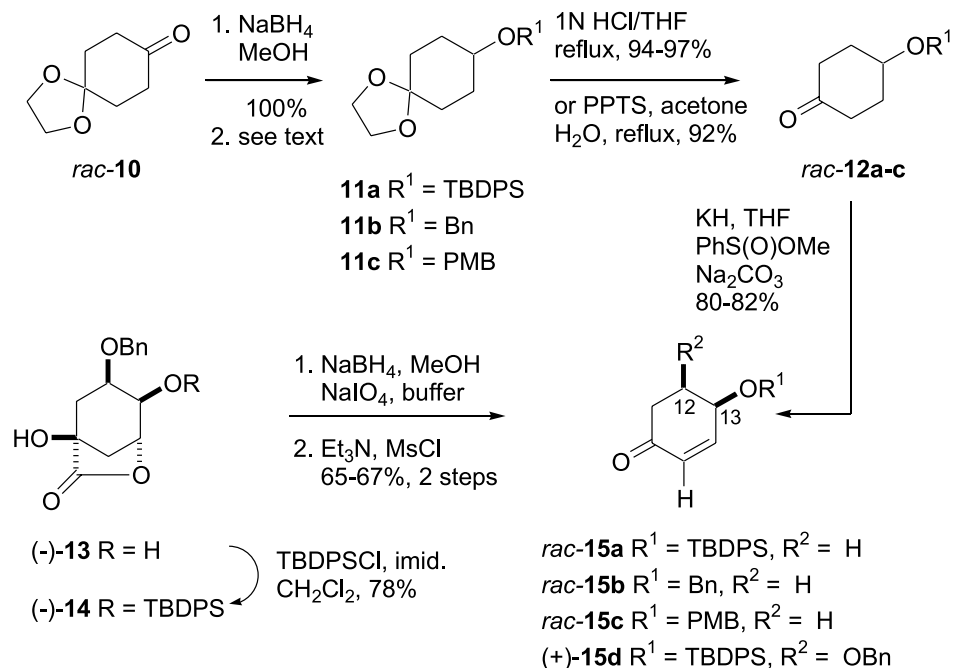


Fig. 1. Three examples of quassinoids.

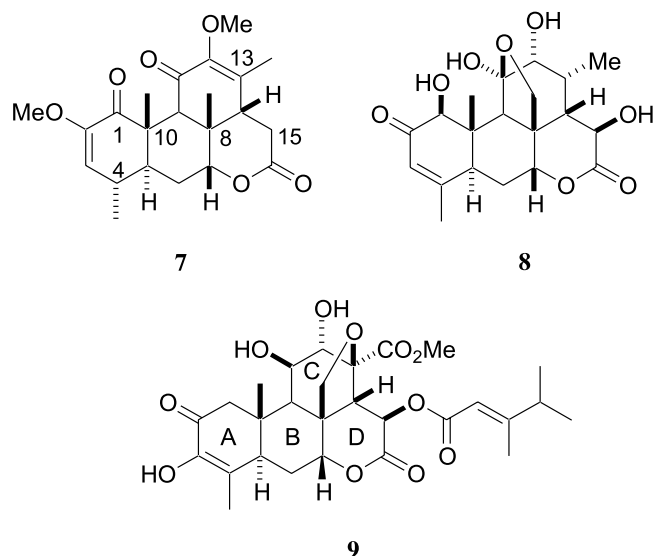
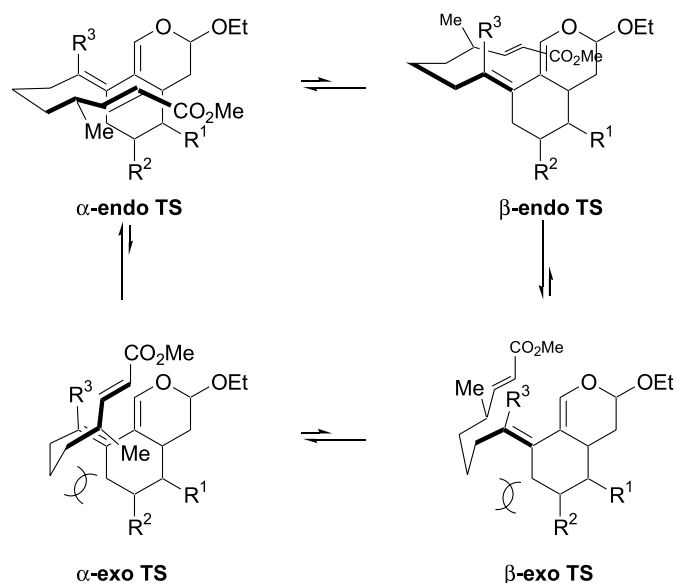


Fig. 2. The four chair-like transition states of 5.



the exact stereochemistry shown for all-equatorial  $\alpha$ -endo TS that will lead to the tetracyclic nucleus **6** having the correct stereochemistry for quassinoids.

### Synthesis of the precursor oxadienes

Besides the introduction of the ring and chain substituents in **4** with the correct stereochemistry, the formation of the exocyclic double bond with the correct geometry represents a fierce challenge (eq. [2]) (11). Compounding the problem is the fact that the exocyclic double bond in **4** and **5** should preferably be a tetra-substituted double bond ( $R^3 = \text{Me}$ ), otherwise the C-10 methyl group (cf. Fig. 1) would have to be introduced at a later stage of the synthesis, a more difficult (though possible) task than introducing the methyl group as

part of the Diels–Alder strategy. Several ways to construct the exocyclic double bonds were envisioned. It was initially thought that starting with an appropriately substituted cyclohexenone would be most expeditious. In that respect, the known compound **13** (12), derived from (–)-quinic acid, presented itself as an attractive starting material (Scheme 1). Protection of the C-13 alcohol as a TBDPS ether was achieved, and reduction of the lactone in **14** followed by in situ oxidative cleavage of the resulting diol afforded a  $\beta$ -hydroxycyclohexanone, which was dehydrated to the desired substituted cyclohexenone **15d**. For simpler model compounds, 1,4-cyclohexadione monoketal **10** was an adequate starting material. It was reduced with  $\text{NaBH}_4$  and then protected as its silyl ether **11a** (TBDPSCI, imid., DMF, quant.),



$\text{H}_2\text{C=CHLi, THF}$   
 $\text{CeCl}_3, 74\text{-}80\%$

$\text{Ac}_2\text{O}$   
 $\text{DMAP}$   
 $\text{CH}_2\text{Cl}_2$   
 $\text{quant.}$

**15a-d** X = H  
**16a-d** X = Br

**17a-d** R = H  
**18a-d** R = Ac

**a**  $\text{R}^1 = \text{TBDPS}, \text{R}^2 = \text{H};$  **b**  $\text{R}^1 = \text{Bn}, \text{R}^2 = \text{H}$   
**c**  $\text{R}^1 = \text{PMB}, \text{R}^2 = \text{H};$  **d**  $\text{R}^1 = \text{TBDPS}, \text{R}^2 = \text{OBn}$

*rac-18a-c*

$\text{RCuCN}$   
 $\text{THF/Et}_2\text{O}$   
 $89\text{-}96\%$

**19a** R =  $-(\text{CH}_2)_3\text{CH=CH}_2, \text{R}^1 = \text{OTBDPS}$   
**19b** R =  $-(\text{CH}_2)_3\text{CH=CH}_2, \text{R}^1 = \text{OBn}$   
**19c** R =  $\text{---CH}_2\text{CH}_2\text{CH}_2\text{CH}_2\text{CH}_2\text{CH}_2\text{OTBS}, \text{R}^1 = \text{OPMB}$

$(\text{CN})\text{Cu}$   $\text{---CH}_2\text{CH}_2\text{CH}_2\text{CH}_2\text{CH}_2\text{OTBS}$   
 $\text{Me}$

**(+)-18d**

$\text{THF/Et}_2\text{O}, 96\%$

**(+)-19d**

Bromination and dehydrobromination of each cyclohexenone **15** gave the corresponding vinylbromide **16** in 80–94% yield (Scheme 2). Subsequent addition of vinyl lithium to **16a–d** in the presence of anhydrous  $\text{CeCl}_3$  afforded **17a–d**, which were converted to the corresponding acetates **18a–d** under standard conditions. Compounds **19a–g**, possessing a tri-substituted exocyclic double bond of *E* configuration, were prepared in one of three ways. Cuprate displacements of allylic acetates **18a–d** with alkylcyanocuprates gave the corresponding products **19a–d** in 89–96% yield (Scheme 2).<sup>2</sup> Alternatively, the palladium-catalyzed substitution of **18a** with malonate furnished **19e** in 81% yield as a single stereoisomer (Scheme 3). Aldehyde **19f** or ester **19g** could be accessed directly from a Claisen rearrangement of **17a**.

**18a**

MeO<sub>2</sub>CCH<sub>2</sub>CO<sub>2</sub>Me  
NaH, Pd(PPh<sub>3</sub>)<sub>4</sub>  
THF, 81%

**19e**

MeO<sub>2</sub>C  
CO<sub>2</sub>Me  
Br  
OTBDPS

**17a**

Hg(O<sub>2</sub>CCF<sub>3</sub>)  
EVE, NEt<sub>3</sub>, 88%  
or HC(OEt)<sub>3</sub>  
EtCO<sub>2</sub>H, PhMe  
reflux, 21%

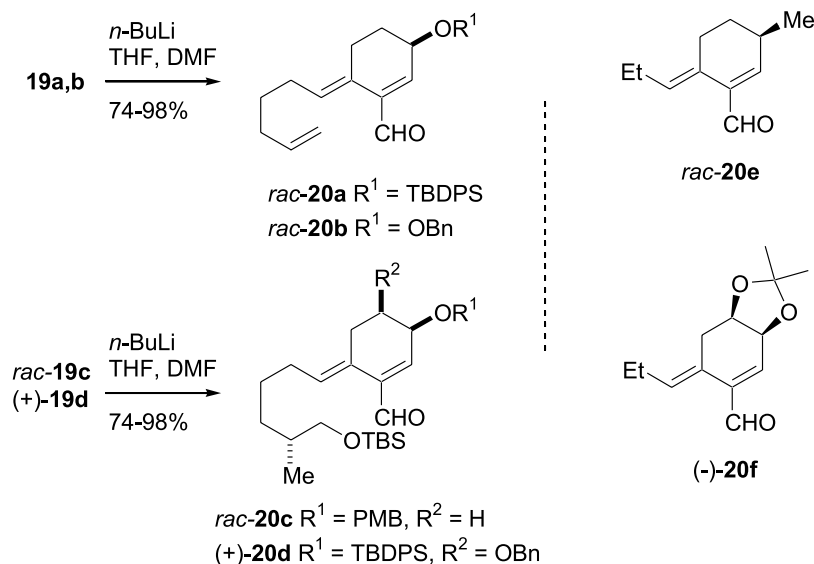
**19f** E = CHO  
**19g** E = CO<sub>2</sub>Et

OTBDPS  
Br  
E

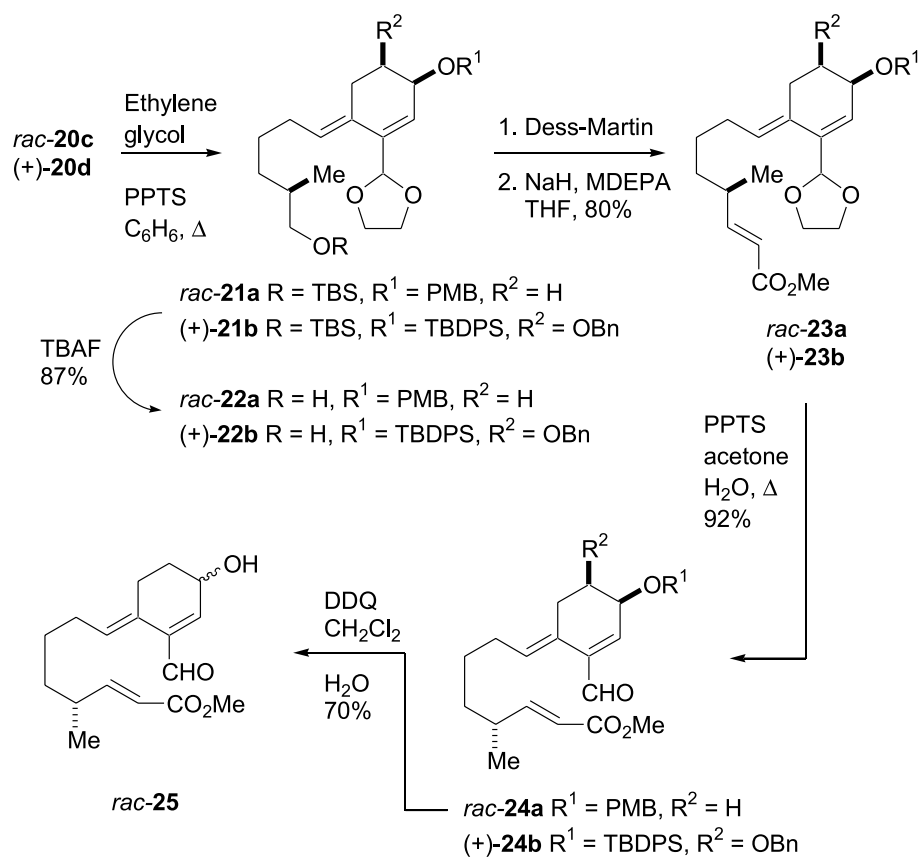
© 2003 NRC Canada



Scheme 4.



Scheme 5.



respectively, and **24a** was deprotected under oxidizing conditions to give **25** (Scheme 5).

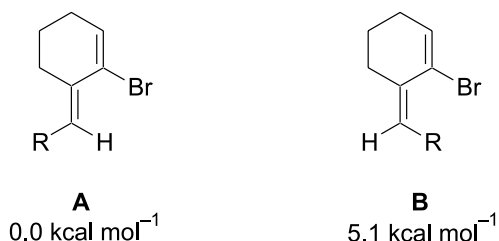
All synthesized alkenes **19a–g** had exclusively the *E*-geometry. This selectivity is attributable to the flatness of the structural system **19** that brings the vinylic hydrogen and the bromine atom in a rigid *syn*-pentane-like relationship (Fig. 3). Any group larger than hydrogen is likely to raise the energy of the system considerably. Basic MM2 calcula-

tions placed the *Z*-isomer **B** 5.1 kcal mol<sup>-1</sup> above the *E*-isomer **A** for  $R = \text{Me}$ .

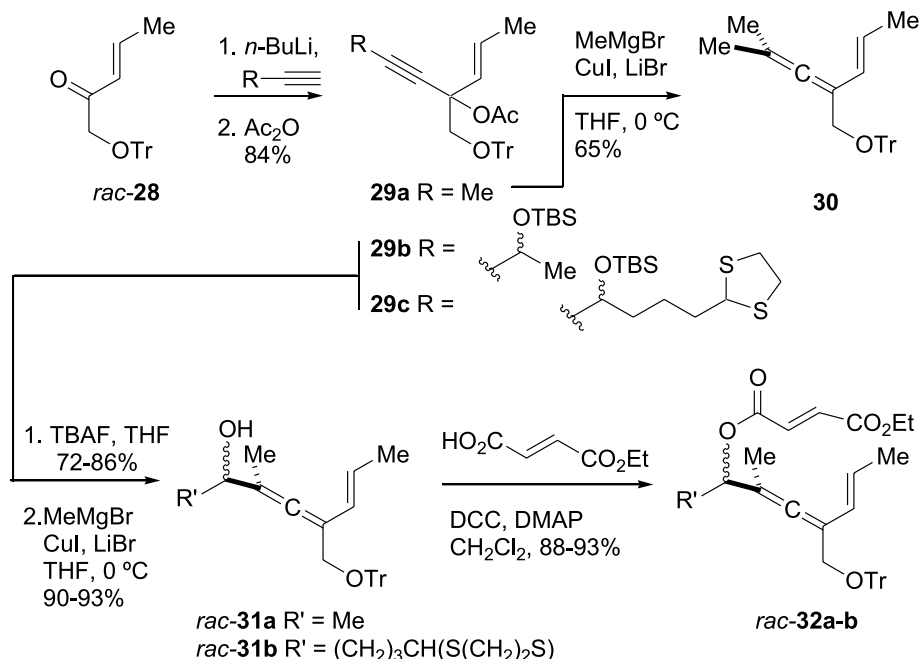
This finding was corroborated by the fact that not a trace of product **27** was formed starting from compound **26a** or **26b** using any of the reactions described in Schemes 2 and 3 under many different reaction conditions (Scheme 6). Most reactions with **26a** and **26b** gave the starting material back or decomposition products under forcing conditions.



**Fig. 3.** Relative energies of the *E* and *Z* geometries in a structural system like **19**.



**Scheme 7.**

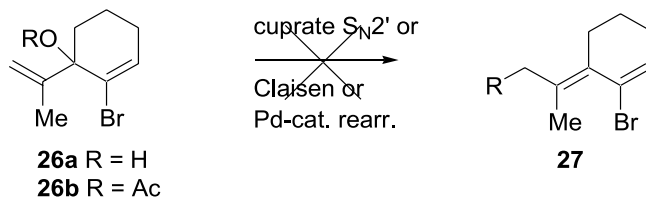


McMurry coupling between **16** and 2-butanone also failed to give any usable yields of an exocyclic alkene (**13**). The prospect of achieving the stereocontrolled synthesis of this tetra-substituted double bond appeared bleak. A reaction was needed that would simultaneously generate the required cyclohexene and the tetra-substituted, exocyclic double bond.

A solution to the problem of the exocyclic, tetra-substituted double bond was found in the [4 + 2]-cycloaddition of vinylallene **30** and **32a** and **32b**. The syntheses of **30** and **32a** and **32b** starting from  $\alpha,\beta$ -unsaturated ketone **28** are shown in Scheme 7. The addition of methylcuprate to acetate **29a** yielded **30** accompanied with 27% of a product resulting from the addition on the alkene. This side product was difficult to separate at this stage, but it was innocuous because it is an enyne incapable of undergoing a Diels–Alder reaction. Compounds **29b** and **29c** were first treated with fluoride and the resulting alcohols underwent methylcuprate addition to give high yields of vinylallene **31a** and **31b**, respectively, as 1:1 mixtures of two diastereomers. This time, less than 10% of alkene-addition products were formed in each case.

Vinylallene **30** reacted with methyl fumarate at the refluxing temperature of benzene to give a single cycloadduct **33** (Scheme 8). The structure of **33** was secured by a single crystal X-ray diffraction analysis of a later derivative

**Scheme 6.**

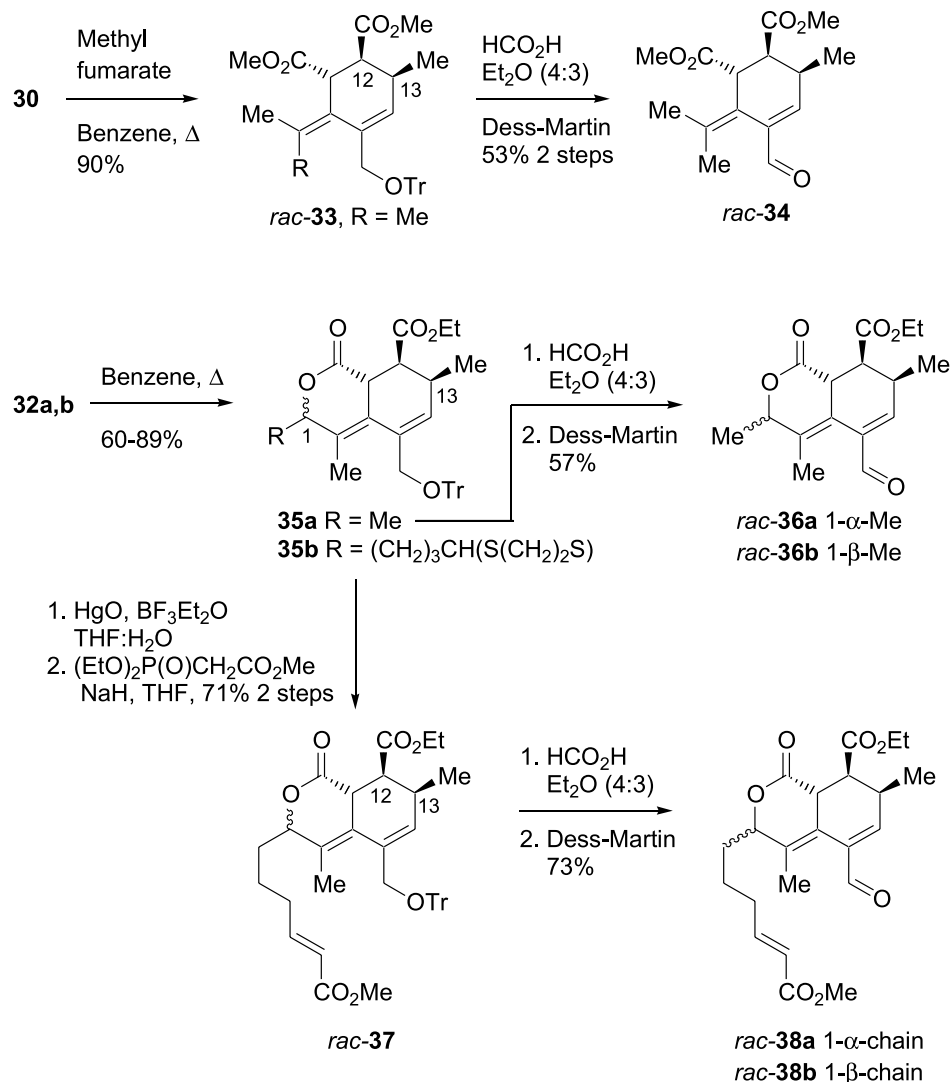


**41** (vide infra). The temperature at which this Diels–Alder reaction occurs is remarkable considering the steric interactions in the final product. In fact, we have reported the synthesis of a series of cycloadducts like **33**, with much larger substituents around the exocyclic double bond and in some cycloadducts, the exocyclic double bond was twisted by more than 20° (14). It can be argued that the Diels–Alder reaction has an early transition state, the structure of which resembles the starting vinylallene where the severe steric interactions of the cycloadduct **33** are not present.

The dienophile always comes from the least-hindered face of the vinylallene in an intermolecular Diels–Alder cycloaddition (12, 15). This would give a cycloadduct with the wrong geometry of the double bond for quassinoid synthesis (as if R were larger than Me in **33**). It was necessary to attach the dienophile to the tether to accomplish the desired synthesis as shown by the conversion of **32a** and **32b** to **35a** and **35b**, respectively. The yields of cycloadducts **35a** and **35b** were good to excellent and the stereochemistry was completely controlled. The stereochemistry of **35a** was deduced by 2D-NOESY spectroscopy and by analogy with the NMR spectra with that of **33**. Note that the enyne side product formed along with **30** and **31a** and **31b** (cf. Scheme 7) are easily removed at this stage. Deprotection of the trityl group in **33** and **35a** and oxidation of the resulting alcohols



Scheme 8.



afforded the required aldehydes **34** and **36** respectively (Scheme 8). The tether in cycloadduct **35b**, was elaborated to enoate-aldehyde **38**, in preparation for the intramolecular Diels–Alder reaction. The deprotection of **35a** and **37** yielded separable diastereomeric alcohols. The subsequent reactions were performed on each isomer separately.

### Hetero Diels–Alder cycloaddition

With the problem of the exocyclic double bond solved, efforts were directed at the investigation of the hetero Diels–Alder reaction for the construction of bicyclic adducts. A series of cycloadditions was performed on model compounds **20** and **24**, bearing oxygen or carbon substituents at C-12 and (or) C-13 (Scheme 9). Most quassinoids possess a carbon at C-13 (either methyl or carboxy ester) and an oxygen atom at C-12. The C-13 position is also often linked to an oxygen atom (cf. Fig. 1). Contrary to oxadienes **20a–f**, oxadienes **24a** and **24b** and **25** (cf. Scheme 4) bear a tethered dienophile capable of undergoing an intramolecular Diels–Alder immediately after the hetero Diels–Alder. In these cases, the intermediates **40a–c** are in fact not isolated

(except for **13 $\beta$** , **14 $\beta$** –**40c**) and their stereochemistry were therefore deduced from the stereochemistry of the corresponding final tetracycle adducts **48–52** (vide infra). The tether in racemic oxadienes **24a** and **25** contains a chiral center that creates up to four possible diastereomers for each of **40a** and **40c**, respectively. Oxadiene **24b** is homochiral, however, and there are only two possible diastereomers for **40b** (Scheme 9). Table 1 displays the results of the intermolecular hetero Diels–Alder cycloadditions of ethylvinyl ether with **20a**, **20b**, **20e**, **20f**, and **24a** and **24b**, and **25** catalyzed by  $\text{Yb}(\text{FOD})_3$ . Only the ratios of **14 $\beta$** - to **14 $\alpha$** -diastereomers are important to the discussion at this stage.

From earlier studies, we knew that a single carbon substituent  $\text{R}^1$  was enough to differentiate between the two faces of the oxadiene (Table 1, entry 3) (**5a**). However, an alcohol or a protected hydroxyl offers little bias for the incoming dienophile, giving nearly equal mixtures of **14 $\beta$**  and **14 $\alpha$**  adducts (entries 2, 5–7). A bulky protecting group is  $\beta$ -face selective (entry 1), presumably because of a preferred conformation **20-A** where the protecting group is eclipsed with the carbinol hydrogen at C-13, placing the bulky phenyl rings underneath the oxadiene as drawn in Fig. 4. It seems



Scheme 9.

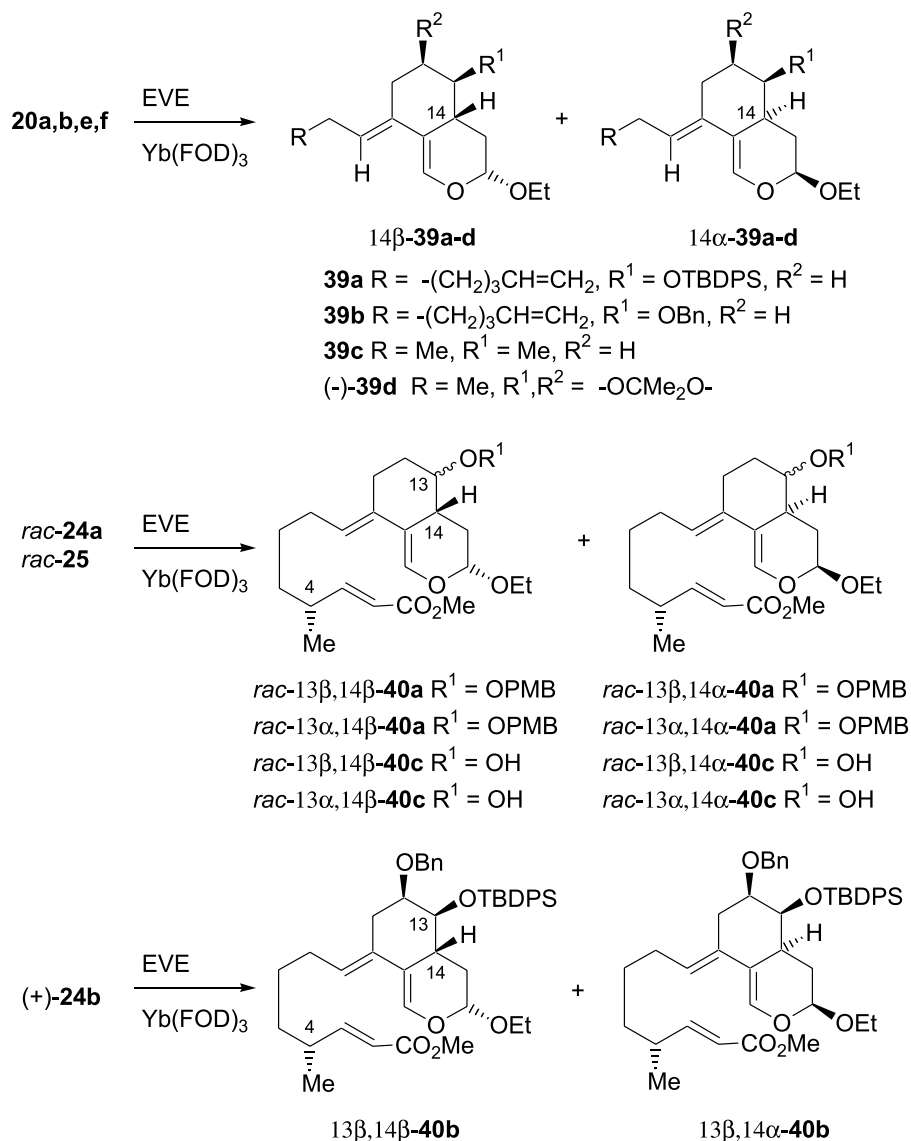


**Table 1.** 14α/14β-Ratio of adducts **39a–d** and **40a–c** from the hetero Diels–Alder reaction (cf. Scheme 9).

Entry	Enal	Product	14β:14α <sup>a</sup>	Yield (%)
1	<b>20a</b>	<b>39a</b>	1:4	96
2	<b>20b</b>	<b>39b</b>	1:1.6	82
3	<b>20e</b>	<b>39c</b>	4:1	96
4	<b>20f</b>	<b>39d</b>	11:1	95
5	<b>24a</b>	<b>40a</b>	1:1	92
6	<b>24b</b>	<b>40b</b>	1:3	82
7	<b>25</b>	<b>40c</b>	1:1	83

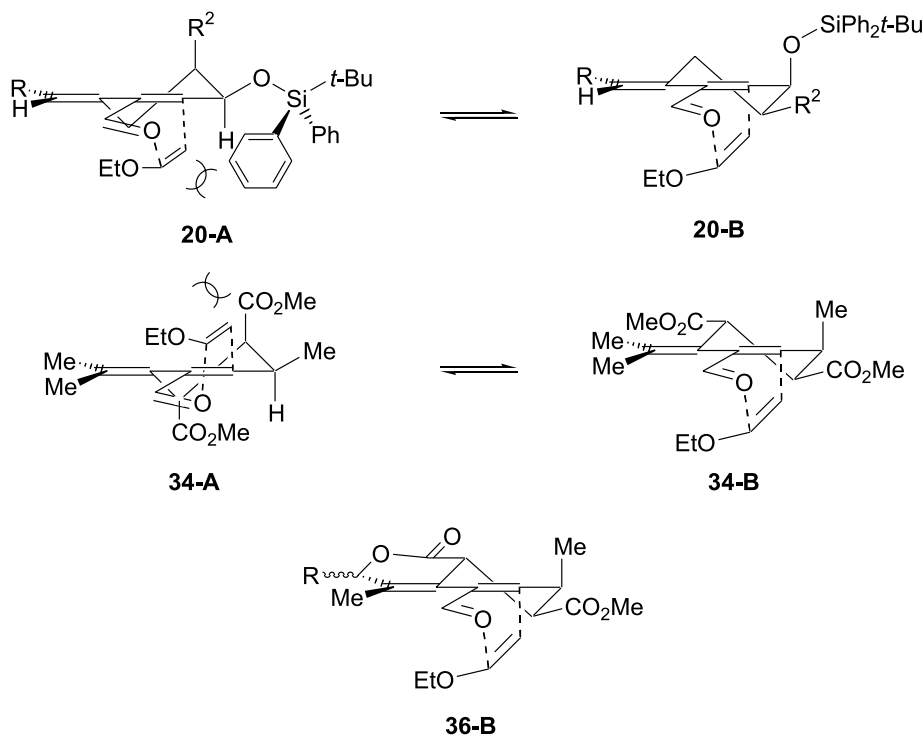
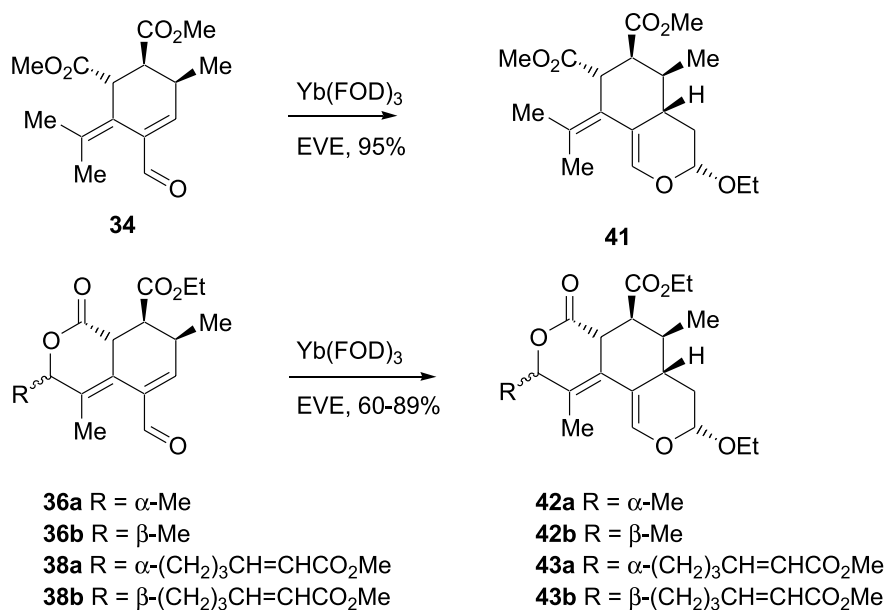
<sup>a</sup>Determined by <sup>1</sup>H NMR.

obvious that if conformation **20-B** were preferred, it would effectively shield the β-face of the oxadiene. To obtain better results, the oxadiene must be induced to adopt the conformation **20-B** or force the C-13 substituent to orient its atoms away from the α-face. The latter case is exemplified by the isopropylidene-protected C-12/C-13 diol **20f** that was able to

hinder sufficiently the β-face of the oxadiene (entry 4) (**5a**). In contrast, protected diol **24b** gave a 3:1 ratio favoring the undesired 13β,14α-**40b** diastereomer (entry 6). Again, the *tert*-butyldiphenylsilyl group is likely responsible for this result, shielding the α-face through a preferred conformation **20-A** (R<sup>2</sup> = OBn, Fig. 4).

In contrast to the results obtained in the hetero Diels–Alder cycloadditions of oxadienes **20a**, **20b**, **20e**, **20f**, **24a** and **24b**, and **25**, results obtained with compounds **34**, **36a** and **36b**, and **38a** and **38b** are particularly helpful (Scheme 10). The cycloadditions of **34**, **36a**, **36b**, **38a**, and **38b** gave only one detectable isomer **41**, **42a**, **42b**, **43a**, and **43b**, respectively. The stereochemistry of **41** was secured from a single crystal X-ray diffraction analysis. Compounds **42a** and **42b** and **43a** and **43b** were characterized by 2D-NMR experiments and their NMR spectra compared well with that of **41**. Most likely, the oxadienes take on conformations **34-B** or **36-B**, forcing the methyl group into a pseudo-axial orientation (Fig. 4).



**Fig. 4.** Possible transition states for the intermolecular hetero Diels–Alder reaction of **20a**, **34**, **36**, and **38**.**Scheme 10.**

### Intramolecular Diels–Alder cycloaddition

The substituents on ring C and D and the substituents on the tether are able to affect the stereochemical outcome of the intramolecular Diels–Alder cycloaddition. This concern had to be addressed first and two things were known from earlier studies (**5a**): (a) in absence of substituent on the tether and on the ring (**44**), the  $\beta$ -*endo* TS (cf. Fig. 1) is favored by a factor of six leading to the formation of **45b** as the major product (Scheme 11); (b) two tether substituents in **46** are able to completely reverse this selectivity in favor of

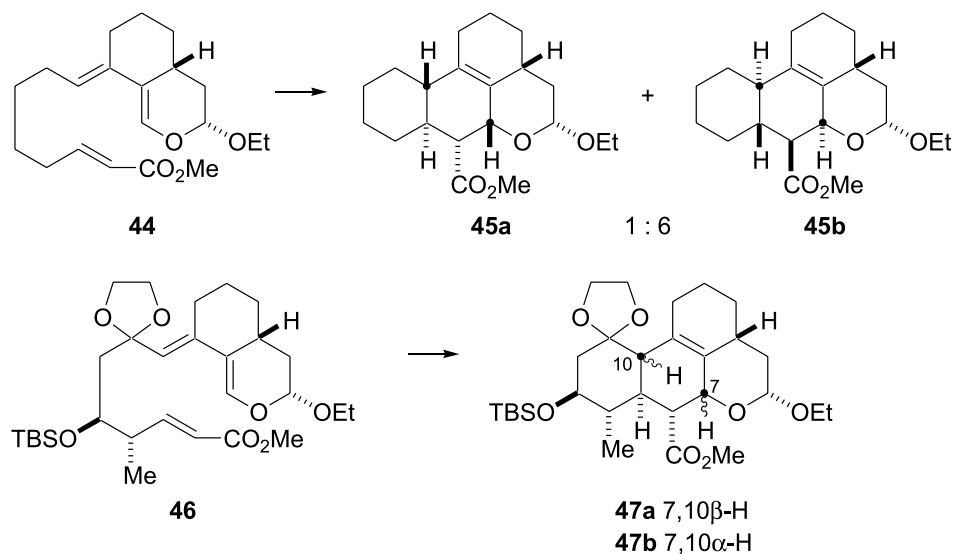
the desired  $\alpha$ -*endo* TS (**47a**, Scheme 11). However, it was also evident that an  $\alpha$ -C-3 substituent (the  $\alpha$ -oxygen of the dioxolane in **47a**) should be avoided as it increases the energy of both  $\alpha$ - and  $\beta$ -*endo* TS to the advantage of the  $\alpha$ -*exo* TS leading to the formation of **47b**.

### Intramolecular Diels–Alder cycloaddition: Results

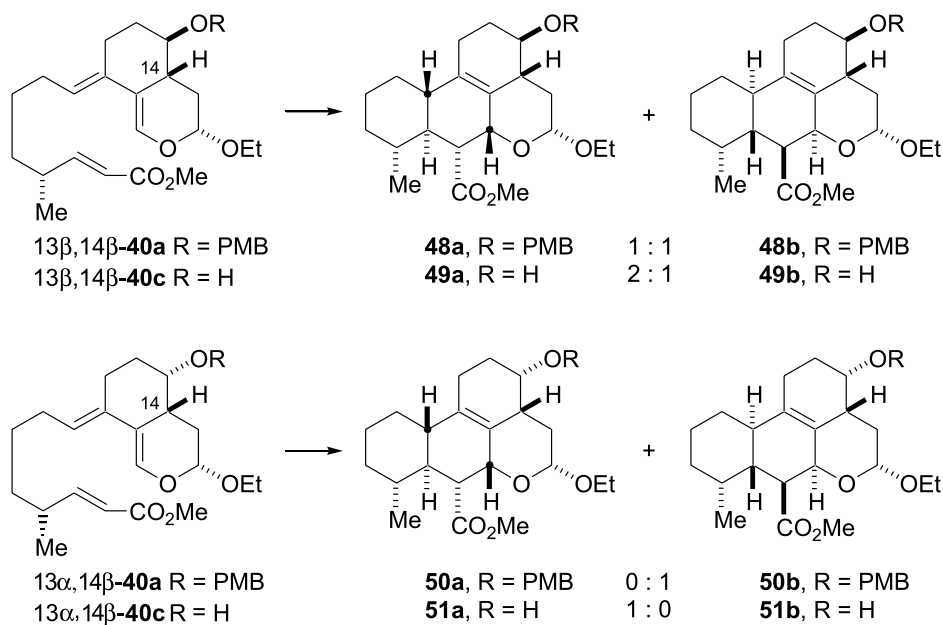
Since intermediates 13 $\beta$ ,14 $\beta$ –**40a**, **40b**, **40c** and 13 $\alpha$ ,14 $\beta$ –**40a**, **40c** were not isolated, their structures were deduced



Scheme 11.



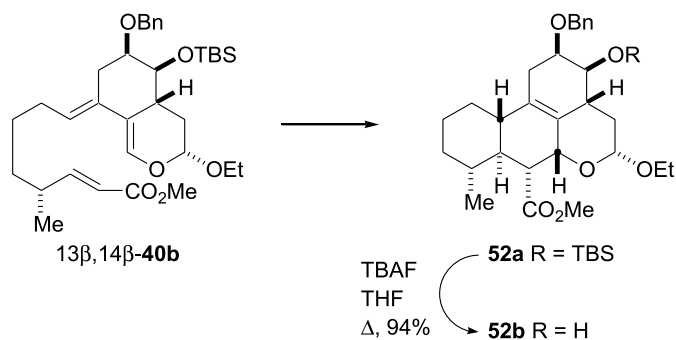
Scheme 12.



from those of the corresponding tetracycles **48–52** (Schemes 12 and 13). Note that intermediates **13β,14α-40a**, **40b**, **40c** and **13α,14α-40a**, **40c** (cf. Scheme 9) are of no interest for quassinoids because they possess the wrong 14-α stereochemistry. Although their corresponding tetracycles were isolated and fully characterized, they will not be discussed further.

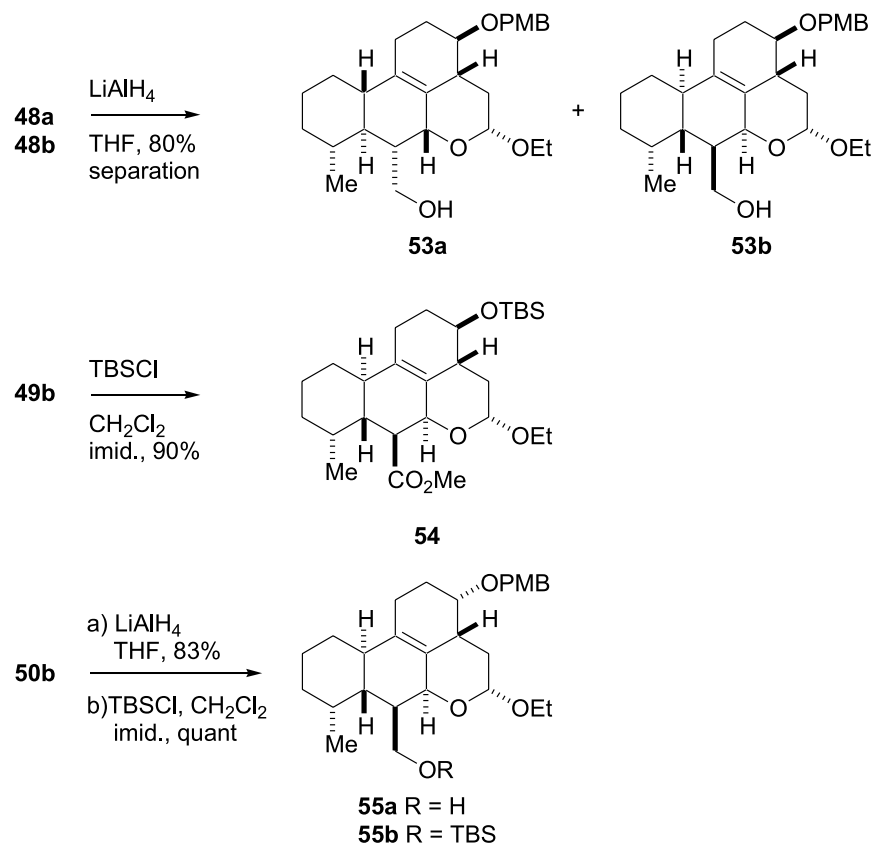
Aldehyde **24a** (racemic mixture of diastereomers) gave a mixture of cycloadducts, of which **48a**, **48b**, and **50b** could be obtained partially pure (Scheme 12). Each cycloadduct was treated with LiAlH<sub>4</sub> and separation of the resulting alcohols yielded pure **53a**, **53b**, and **55a**, respectively, (Scheme 14). The structure of **53a** was deduced from a single crystal X-ray diffraction analysis, which secured the structure of **48a**. The structure of **48b** was correlated with

Scheme 13.





Scheme 14.



that of **49b** (vide infra) because the structure of **53b** could not be determined unambiguously. The primary alcohol in compound **55a** was silylated under standard conditions to give **55b**, for which an X-ray analysis was obtained, confirming the structure for **50b**. With the structures secured, we were able to determine the ratios of tetracycles in the crude mixture of **48** and **50**. Tetracycles **48a** and **48b** were found in a 1:1 ratio while compound **50b** was the sole tetracycle to emanate from intermediate **13 $\alpha$ ,14 $\beta$ -40a**. All of **48a**, **48b**, and **50b** possess the desired 14 $\beta$ -stereochemistry. However, **48b** and **50b** have the wrong configuration at C-5, C-7, and C-10. As explained later, the OPMB group is responsible for the formation of these two diastereomers.

Aldehyde **24b** (diastereo- and enantiomerically pure) gave two tetracycles that were desilylated to separate them more easily. Compound **52a** was the sole product having the 14 $\beta$ -stereochemistry and thus to arise from intermediate **13 $\beta$ ,14 $\beta$ -40b** (Scheme 13). The other tetracycle had the 14 $\alpha$ -stereochemistry and must have come from intermediate **13 $\beta$ ,14 $\alpha$ -40b**. The stereochemistry of **52b** was determined from careful NMR and 2D-NMR analysis of both tetracycles.

Lastly, aldehyde **25** led to a mixture of cycloadducts, of which **49a**, **49b**, and **51a** were separated and isolated in a pure state (Scheme 12). The stereochemistry of **51a** was deduced from a single crystal X-ray diffraction analysis. Cycloadduct **49b** was silylated to afford **54** that was crystalline and amenable to X-ray diffraction analysis (Scheme 14). Conversion of **49b** to **48b** confirmed the structure of the latter. The now known product **48a** was converted to **49a** using DDQ, which proved the structure of **49a**. With the structure

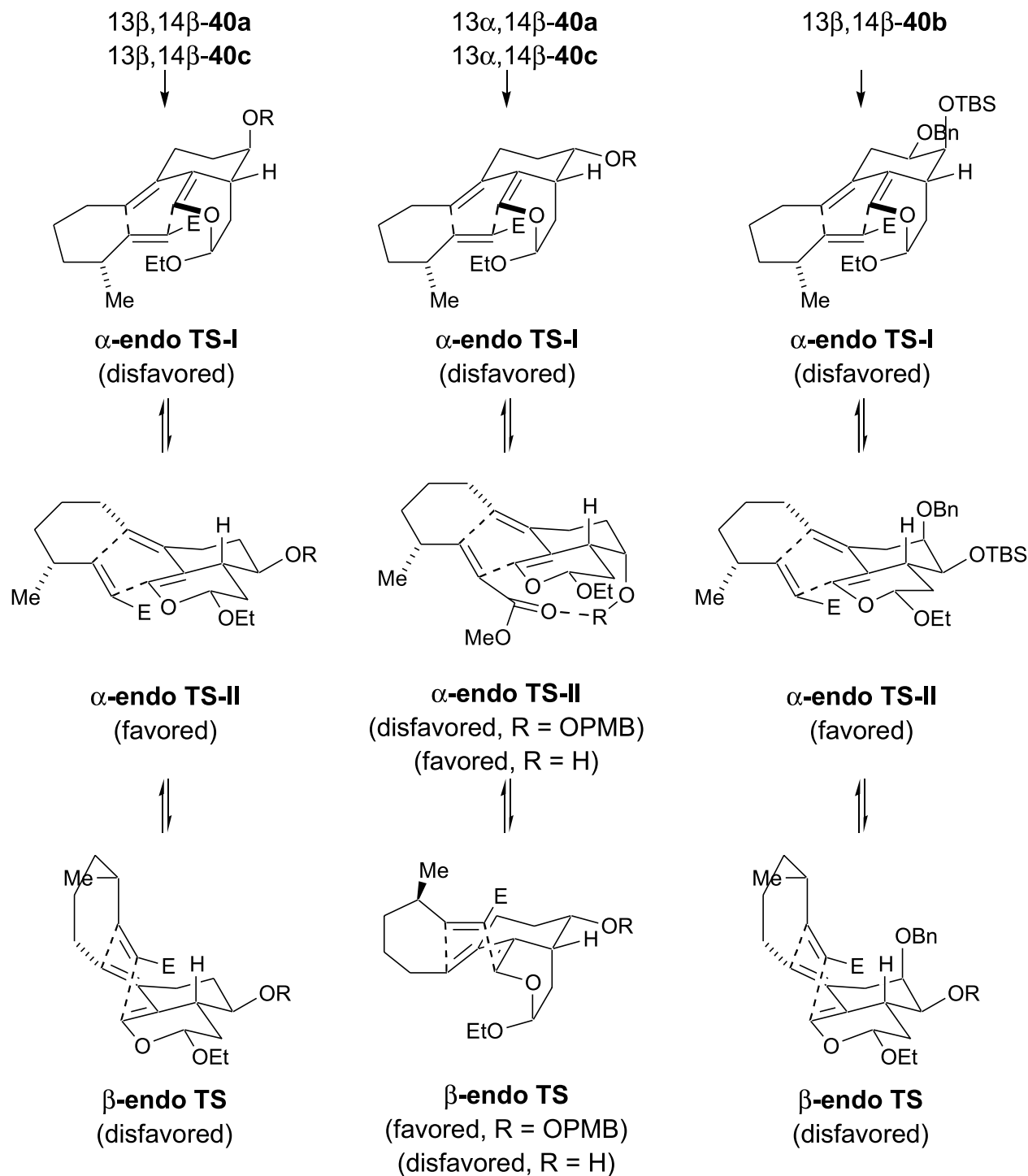
of each cycloadduct secured, it was established that **49a** and **49b** were formed in a 2:1 ratio and arose from the intramolecular Diels–Alder reaction of intermediate **13 $\beta$ ,14 $\beta$ -40c** (Scheme 12). Cycloadduct **51a** was the sole tetracycle to emanate from intermediate **13 $\alpha$ ,14 $\beta$ -40c**. All three diastereomers **49a**, **49b**, and **51a** have the desired 14 $\beta$ -stereochemistry and only **49b**, the minor isomer from **13 $\beta$ ,14 $\beta$ -40c**, has the wrong stereochemistry at C-5, C-7, and C-10. Therefore, removing the PMB group on the C-13 alcohol proved beneficial.

### Intramolecular Diels–Alder cycloaddition: Analysis

It was clear, from the cycloaddition of **44**, that a 14 $\beta$ -stereochemistry favors a  $\beta$ -face attack of the dienophile (**5a**). Fortunately, this trend was partly overcome by the presence of a single methyl group on the tether at C-4 as shown in the conversion of **13 $\beta$ ,14 $\beta$ -40c** into a 2:1 mixture of **49a** and **49b** (Scheme 12). With a protected alcohol (**13 $\beta$ ,14 $\beta$ -40a**) the ratio **48a**:**48b** was 1:1. It was particularly informative to observe the cycloaddition results with alcohol **13 $\alpha$ ,14 $\beta$ -40c** and PMB-protected alcohol **13 $\alpha$ ,14 $\beta$ -40a**. The free alcohol **13 $\alpha$ ,14 $\beta$ -40c** gave a single isomer **51a** arising from an  $\alpha$ -endo transition state (Scheme 12). By contrast, the protected alcohol **13 $\alpha$ ,14 $\beta$ -40a** underwent the IMDAC to give a single adduct **50b** that emerged from a preferred  $\beta$ -endo transition state having the methyl axial.

These results are explained as follows (Fig. 5): two  $\alpha$ -endo TS can be considered, namely  $\alpha$ -endo TS-I and  $\alpha$ -endo



**Fig. 5.** Possible transition states for the intramolecular DAC of **40a-c**.

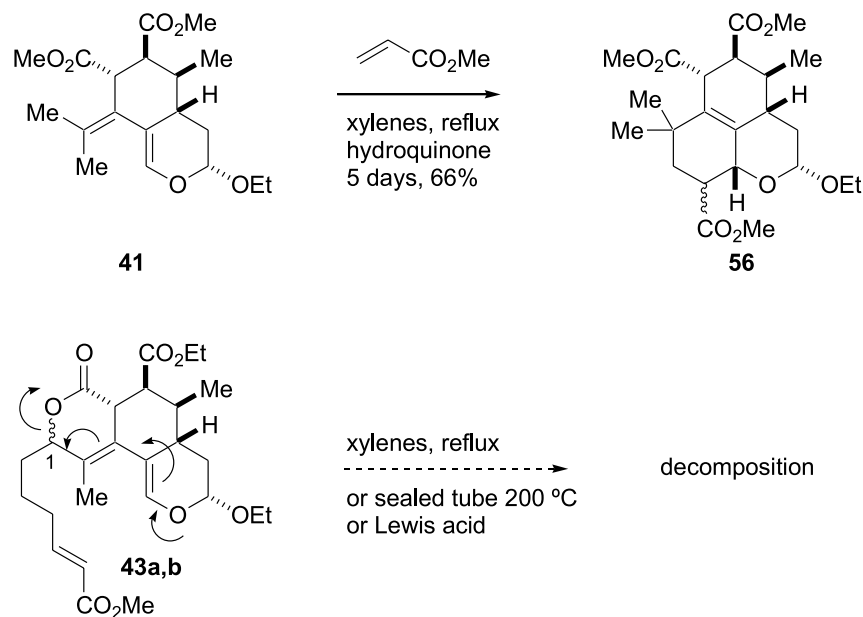
TS-II. All  $\alpha$ -endo TS-Is have the ethoxy group and the dienophile in close proximity resulting in a steric interaction. It is doubtful that any  $\alpha$ -attack would take place via  $\alpha$ -endo TS-I. This is corroborated by MM2 calculations. Therefore, only the  $\alpha$ -endo TS-IIs will be considered in our analysis and their energies will be compared with that of the  $\beta$ -endo TSs.

In the absence of substituents on the ring or on the chain,  $\beta$ -endo TS is favored over  $\alpha$ -endo TS-II by approximately

2 kcal mol<sup>-1</sup> (cf. **44**  $\rightarrow$  **45b**, Scheme 11). An  $\alpha$ -C-4 methyl group will be axial on a  $\beta$ -endo TS and should destabilize it by roughly 2 kcal mol<sup>-1</sup>, approximately counterbalancing the advantage  $\beta$ -endo TS enjoys when there are no substituents. This is what was observed, 13β,14β-**40a** and 13β,14β-**40c** giving nearly equal mixtures of adducts regardless of the C-13  $\beta$ -substituent. The slight difference between the ratios of 13β,14β-**40a** and 13β,14β-**40c** may be attributable to small conformational perturbations. However, an  $\alpha$ -protected



Scheme 15.



alcohol at C-13 (13 $\alpha$ ,14 $\beta$ -**40a**) dramatically raises the energy of the corresponding  $\alpha$ -endo TS-II (or alternatively, it could force a high-energy conformation like  $\alpha$ -endo TS-I). This explains why compound 13 $\alpha$ ,14 $\beta$ -**40a** gave a single tetracycle **50b** via a  $\beta$ -endo TS. The fact that 13 $\alpha$ ,14 $\beta$ -**40c** gave only **51a** can only be explained by a hydrogen bond in  $\alpha$ -endo TS-II. As a matter of fact, the cycloaddition of alcohol 13 $\beta$ ,14 $\beta$ -**40c** was slower than that of alcohol 13 $\alpha$ ,14 $\beta$ -**40c**, the former requiring benzene at reflux to go to completion while the latter occurs rapidly at room temperature. This is consistent with a hydrogen bond activating the ester in  $\beta$ -endo TS for 13 $\alpha$ ,14 $\beta$ -**40c**.

If our analysis is correct, two  $\beta$ -substituents at C-12 and C-13 (as in 13 $\beta$ ,14 $\beta$ -**40b**) should come together to lead to a single tetracycle resulting from  $\alpha$ -endo TS-II. Indeed, regardless of the conformation of the C-ring, one of the substituents at C-12 or C-13 has to be pseudoaxial, thereby significantly raising the energy of the  $\beta$ -endo TS due to steric interaction with the incoming dienophile (Fig. 5, right). Comparatively, the energy of the  $\alpha$ -endo TS-II should not be raised as much. We were pleased to find that diene 13 $\beta$ ,14 $\beta$ -**40b** gave a single tetracycle **52a**, thereby confirming our hypothesis (Scheme 13).

There is now a good indication that a single stereo-defined substituent on the tether and two  $\beta$ -substituents at C-12 and C-13 will force the intramolecular Diels-Alder to take place through an  $\alpha$ -endo TS. Adding a methyl group on the exocyclic double bond should not change anything. However, it became clear in preliminary studies that such a methyl substituent considerably slows down the rate of cycloaddition. For example, compound **41** underwent a clean Diels-Alder cycloaddition reaction at the refluxing temperature of xylenes for 5 days to give **56** as a mixture of two stereoisomers (Scheme 15, ratios and stereochemistry of **56** not determined). While this result indicated that the Diels-Alder is definitely possible, trials with **43a** or **43b** always gave decomposition products because it could not withstand

such harsh conditions. The use of Lewis acids also led to decomposition products only. We have established that the main reason for the decomposition of **43a** and **43b** is the lability of the C-1 oxygen functionality as shown in Scheme 15. We are working to build different models in the hopes of overcoming this obstacle. Those results will be reported in due course.

## Experimental section

All reactions were carried out under an argon atmosphere. Ethyl ether, toluene, and benzene were dried over metallic sodium using benzophenone as an indicator, while tetrahydrofuran was dried over both sodium and potassium using the same indicator. Dichloromethane, dimethyl formamide, carbon tetrachloride, 1,2-dichloroethane, triethylamine, pyridine, acetonitrile, and diisopropylamine were distilled over calcium hydride. Hexanes were purchased in anhydrous form from Aldrich. Ethyl vinyl ether was distilled prior to use. Cerium trichloride was purchased in hydrated form and dried at 200 $^\circ$ C under high vacuum overnight. Thin layer chromatography was performed using 0.25 mm Silica Gel 60 F254 (EM Science-Merck) and flash chromatography using silica gel Kieselgel 60 (230–400 mesh ASTM).

All NMR spectra were taken in deuterated chloroform on a Bruker AC-300 ( $^1\text{H}$  (300 MHz),  $^{13}\text{C}$  (75 MHz)). Chemical shifts are reported in ppm ( $\delta$ ) downfield from tetramethylsilane. The splitting patterns are designated as singlet (s), doublet (d), triplet (t), quartet (q), multiplet (m), and AB quartet (ABq). The IR spectra were determined on a Perkin-Elmer 1600 FT spectrometer. The IR spectra were determined neat, unless otherwise stated. The melting points were performed on a Mettler Toledo model 62. High- and low-resolution mass spectra (HR-MS and LR-MS) were obtained with a micromass spectrometer ZAB-1F model VG.



**tert-Butyldiphenylsilyl ether 11a**

To a cooled 0°C solution of cyclohexanedione, monoethylene ketal (22.1 g, 141 mmol) and methanol was added, in portions, sodium borohydride (5.35 g, 141 mmol). The reaction was stirred for 3 h before being brought to pH 7 by the addition of 1 N HCl. The mixture was partitioned between dichloromethane and brine, and the aqueous phase extracted with CH<sub>2</sub>Cl<sub>2</sub>. The aqueous layer was concentrated until a precipitate began to form and this layer was extracted again with CH<sub>2</sub>Cl<sub>2</sub>. The combined organic layers were dried over MgSO<sub>4</sub>, filtered, and concentrated. The crude alcohol (22.69 g, 100%) was coevaporated with benzene and used without further purification. <sup>1</sup>H NMR (CDCl<sub>3</sub>) δ: 3.85 (s, 4H), 3.67–3.66 (m, 1H), 2.67 (bs, 1H), 1.80–1.68 (m, 4H), 1.61–1.43 (m, 4H). <sup>13</sup>C NMR (CDCl<sub>3</sub>) δ: 108.2 (s), 67.7 (d), 64.0 (t), 31.7 (t), 31.4 (t). LR-MS (*m/z* (relative intensity)): 158 ([M]<sup>+</sup>, 10), 99 (100). HR-MS calcd. for C<sub>8</sub>H<sub>14</sub>O<sub>3</sub>: 158.0943; found: 158.0937. To a solution of this alcohol (5.00 g, 31.6 mmol), imidazole (5.38 g, 79.0 mmol) in DMF (20 mL) was added TBDPSCl (9.86 mL, 37.9 mmol) at room temperature. The mixture was stirred at room temperature for 4 h before being poured into hexane (30 mL). The layers were separated and the DMF layer washed with hexanes (2 × 30 mL) and ethyl ether (30 mL). The combined hexanes – ethyl ether layer was washed with brine, dried over MgSO<sub>4</sub>, filtered, and concentrated. The crude residue was purified by flash chromatography eluted with hexanes:EtOAc (9:1) to give 12.5 g (100%) of ketal **11a** as a colourless oil. IR (cm<sup>-1</sup>): 3446, 3070, 1589, 1472, 1427. <sup>1</sup>H NMR (CDCl<sub>3</sub>) δ: 7.73–7.65 (m, 4H), 7.45–7.34 (m, 6H), 3.98–3.85 (m, 5H), 1.97–1.88 (m, 2H), 1.71–1.63 (m, 4H), 1.51–1.43 (m, 2H), 1.06 (s, 9H). <sup>13</sup>C NMR (CDCl<sub>3</sub>) δ: 135.7 (d), 134.8 (d), 134.5 (s), 129.5 (d), 127.6 (d), 127.4 (d), 108.6 (s), 68.4 (d), 64.1 (t), 31.7 (t), 30.8 (t), 26.9 (q), 19.2 (s). LR-MS (*m/z* (relative intensity)): 339 ([M]<sup>+</sup> – C<sub>4</sub>H<sub>9</sub>), 10), 199 (100), 200 (25). HR-MS calcd. for C<sub>20</sub>H<sub>23</sub>O<sub>3</sub>Si: 339.1416; found: 339.1412. Anal. calcd. for C<sub>24</sub>H<sub>32</sub>O<sub>3</sub>Si: C 72.68, H 8.13, O 12.10, Si 7.08; found: C 72.53, H 8.18, O 11.98.

**Benzyl ether 11b**

To an oil-free suspension of KH (10.19 g, 254 mmol) in THF (400 mL) was added a solution of the same alcohol used to make **11a** (16.4 g, 102 mmol) in THF (50 mL) via cannula at 0°C. After hydrogen evolution had ceased, the mixture was warmed to room temperature and the reaction stirred for 3 h. Benzyl bromide (18.1 mL, 152 mmol) was added neat and the reaction stirred overnight. The reaction was quenched with satd. aq. NH<sub>4</sub>Cl, and the product extracted with CH<sub>2</sub>Cl<sub>2</sub>. The combined organic layers were washed with brine, dried over MgSO<sub>4</sub>, filtered, and concentrated. Purification by flash chromatography (hexanes:EtOAc (9:1 to 3:1)) yielded 20.8 g (83%) of ketal **11b** as a colourless oil. IR (cm<sup>-1</sup>): 3030, 2949, 1370. <sup>1</sup>H NMR (CDCl<sub>3</sub>) δ: 7.34–7.26 (m, 5H), 4.53 (s, 2H), 3.94–3.92 (m, 4H), 3.56–3.50 (m, 1H), 1.89–1.79 (m, 6H), 1.58–1.53 (m, 2H). <sup>13</sup>C NMR (CDCl<sub>3</sub>) δ: 139.0 (s), 128.2 (d), 127.3 (d), 108.4 (s), 74.0 (d), 69.8 (t), 64.2 (t), 31.2 (t), 28.5 (t). LR-MS (*m/z* (relative intensity)): 248 ([M]<sup>+</sup>, 5), 99 (100), 86 (98). HR-MS calcd. for C<sub>15</sub>H<sub>20</sub>O<sub>3</sub>: 248.1412; found:

248.1408. Anal. calcd. for C<sub>15</sub>H<sub>20</sub>O<sub>3</sub>: C 72.55, H 8.12, O 19.33; found: C 72.51, H 8.23.

**PMB ether 11c**

To an oil-free suspension of KH (3.04 g, 75.8 mmol) in THF (200 mL) was added a solution of the same alcohol used to make **11a** (10.0 g, 63.2 mmol) in THF (70 mL) via cannula at 0°C. After hydrogen evolution had ceased (1 h), a solution of PMBCl (10.4 g, 66.4 mmol) and THF (30 mL) was added via cannula. The ice bath was removed and the reaction stirred overnight. The reaction was quenched with satd. aq. NH<sub>4</sub>Cl, and the product extracted with ether (3 × 80 mL). The combined organic layers were washed with brine, dried over MgSO<sub>4</sub>, filtered, and concentrated. Purification by flash chromatography (hexanes:EtOAc (3:1 to 1:1)) yielded 16.9 g (96%) of ketal **11c** as a clear oil. IR (cm<sup>-1</sup>): 2943, 1611, 1513. <sup>1</sup>H NMR (CDCl<sub>3</sub>) δ: 7.26 (d, 2H, *J* = 8.6 Hz), 6.86 (d, 2H, *J* = 8.6 Hz), 4.45 (s, 2H), 3.92 (s, 4H), 3.78 (s, 3H), 3.52–3.47 (m, 1H), 1.86–1.75 (m, 6H), 1.56–1.53 (m, 2H). <sup>13</sup>C NMR (CDCl<sub>3</sub>) δ: 158.9 (s), 131.0 (s), 128.8 (d), 113.6 (d), 108.4 (s), 73.7 (d), 69.4 (t), 64.2 (t), 55.1 (q), 31.2 (t), 28.5 (t). LR-MS (*m/z* (relative intensity)): 278 ([M]<sup>+</sup>, 10), 86 (100), 121 (90), 99 (90), 142 (65). HR-MS calcd. for C<sub>16</sub>H<sub>22</sub>O<sub>4</sub>: 278.1518; found: 278.1515. Anal. calcd. for C<sub>16</sub>H<sub>22</sub>O<sub>4</sub>: C 69.04, H 7.97, O 22.99; found: C 69.05, H 7.95.

**Ketone 12a**

A mixture of ketal **11a** (12.5 g, 31.6 mmol), THF (226 mL), and 1 N HCl (75 mL) was heated to reflux for 3 h. The mixture was cooled, neutralized by the addition of satd. aq. NaHCO<sub>3</sub> and extracted with CH<sub>2</sub>Cl<sub>2</sub>. The combined organic layers were washed with brine, dried over MgSO<sub>4</sub>, filtered, and concentrated. The product was crystallized by the addition of petroleum ether. Three crystallizations yielded 10.8 g (97%) of ketone **12a** as a white solid; mp: 106.0°C. IR (cm<sup>-1</sup>): 3069, 1716, 1427. <sup>1</sup>H NMR (CDCl<sub>3</sub>) δ: 7.69–7.67 (m, 4H), 7.45–7.36 (m, 6H), 4.16–4.13 (m, 1H, *J* = 2.6 Hz), 2.79–2.69 (m, 2H), 2.25–2.17 (dt, 2H, *J* = 14.4, 5.3 Hz), 1.99–1.93 (m, 2H), 1.83–1.78 (m, 2H), 1.09 (s, 9H). <sup>13</sup>C NMR (CDCl<sub>3</sub>) δ: 211.5 (s), 135.6 (d), 133.8 (s), 129.7 (d), 127.6 (d), 66.9 (d), 36.9 (t), 33.7 (t), 26.9 (q), 19.2 (s). LR-MS (*m/z* (relative intensity)): 295 ([M]<sup>+</sup> – C<sub>4</sub>H<sub>9</sub>), 92), 199 (100). HR-MS calcd. for C<sub>18</sub>H<sub>19</sub>O<sub>2</sub>Si: 295.1154; found: 295.1151. Anal. calcd. for C<sub>22</sub>H<sub>28</sub>O<sub>2</sub>Si: C 74.95, H 8.01, O 9.08, Si 7.97; found: C 74.86, H 8.02, O 8.99.

**Ketone 12b**

Followed the same procedure as per **12a**, starting with ketal **11b** yielding 7.70 g (94%) of ketone **12b** as a colourless oil. IR (cm<sup>-1</sup>): 3031, 2941, 1716, 1103. <sup>1</sup>H NMR (CDCl<sub>3</sub>) δ: 7.37–7.28 (m, 5H), 4.59 (s, 2H), 3.83–3.79 (m, 1H), 2.67–2.56 (m, 2H), 2.30–2.22 (m, 2H), 2.19–2.09 (m, 2H), 2.00–1.89 (m, 2H). <sup>13</sup>C NMR (CDCl<sub>3</sub>) δ: 211.0 (s), 138.4 (s), 128.3 (d), 127.4 (d), 127.3 (d), 72.1 (d), 70.1 (t), 37.1 (t), 30.3 (t). LR-MS (*m/z* (relative intensity)): 204 ([M]<sup>+</sup>, 7), 91 (100). HR-MS calcd. for C<sub>13</sub>H<sub>16</sub>O<sub>2</sub>: 204.1150; found: 204.1152. Anal. calcd. for C<sub>13</sub>H<sub>16</sub>O<sub>2</sub>: C 76.44, H 7.90, O 15.67; found: C 76.44, H 7.95.



### Ketone 12c

A solution of ketal **11c** (15.28 g, 54.9 mmol) and PPTS (4.1 g, 16.5 mmol) in wet acetone (550 mL) was heated to reflux for 5.5 h. The mixture was cooled and the solvent removed in vacuo. The residue was taken up in ethyl ether and washed with satd. aq NaHCO<sub>3</sub>, and brine, dried over MgSO<sub>4</sub>. Flash chromatography using a mixture of hexanes:EtOAc (3:1 to 1:1) procured 11.89 g (92%) of ketone **12c** as a white solid; mp: 34.9°C. IR (CHCl<sub>3</sub>, cm<sup>-1</sup>): 3011, 1708, 1612, 1513. <sup>1</sup>H NMR (CDCl<sub>3</sub>) δ: 7.29 (d, 2H, *J* = 8.6 Hz), 6.90 (d, 2H, *J* = 8.6 Hz), 4.53 (s, 2H), 3.81 (s, 3H), 3.82–3.78 (m, 1H), 2.67–2.56 (m, 2H), 2.31–2.22 (m, 2H), 2.17–2.10 (m, 2H), 2.00–1.91 (m, 2H). <sup>13</sup>C NMR (CDCl<sub>3</sub>) δ: 211.2 (s), 159.0 (s), 130.4 (s), 128.9 (d), 113.7 (d), 71.8 (d), 69.8 (t), 55.1 (q), 37.1 (t), 30.4 (t). LR-MS (*m/z* (relative intensity)): 234 ([M]<sup>+</sup>, 35), 121 (100). HR-MS calcd. for C<sub>14</sub>H<sub>18</sub>O<sub>3</sub>: 234.1256; found: 234.1259. Anal. calcd. for C<sub>14</sub>H<sub>18</sub>O<sub>3</sub>: C 71.77, H 7.74, O 20.49; found: C 71.82, H 7.88.

### Lactone 14

To a stirred solution of known diol **13** (8.05 g, 30.4 mmol), imidazole (10.3 g, 152.0 mmol), DMAP (750 mg, 6.08 mmol), and dichloromethane (300 mL) was added TBDPSCl (7.9 mL, 30.4 mmol) at room temperature. The reaction was stirred for 7 days before being partitioned between water and dichloromethane. The aqueous layer was extracted with dichloromethane, washed with brine, dried over MgSO<sub>4</sub>, filtered, and concentrated. Purification by flash chromatography eluted with hexanes:EtOAc (9:1 to 6:1 to 1:1) yielded 12.0 g (78%) of silyl ether **14** and 1.82 g (22%) of starting diol **13**, resulting in a corrected overall yield of 100%. [α]<sub>D</sub>: -48.4° (*c* 1.59, CHCl<sub>3</sub>). IR (cm<sup>-1</sup>): 3439, 3069, 1794, 1427. <sup>1</sup>H NMR (CDCl<sub>3</sub>) δ: 7.73–7.59 (m, 4H), 7.44–7.23 (m, 9H), 7.07–7.04 (m, 2H), 4.40 (t, 1H, *J* = 5.4 Hz), 4.27–4.21 (m, 3H), 3.48–3.41 (m, 1H), 2.84 (d, 1H, *J* = 11.3 Hz), 2.66 (s, 1H), 2.31–2.13 (m, 3H), 1.08 (s, 9H). <sup>13</sup>C NMR (CDCl<sub>3</sub>) δ: 177.8 (s), 137.5 (s), 136.0 (d), 135.6 (d), 133.2 (s), 132.4 (s), 129.9 (d), 129.6 (d), 128.0 (d), 127.6 (d), 127.3 (d), 76.1 (d), 73.3 (d), 72.3 (s), 70.7 (t), 65.8 (d), 36.8 (t), 36.5 (t), 26.8 (q), 19.2 (s). LR-MS (*m/z* (relative intensity)): 445 ([M]<sup>+</sup> - C<sub>4</sub>H<sub>9</sub>), 20, 353 (65), 91 (90), 277 (100). HR-MS calcd. for C<sub>26</sub>H<sub>25</sub>O<sub>5</sub>Si: 445.1471; found: 445.1465. Anal. calcd. for C<sub>30</sub>H<sub>34</sub>O<sub>5</sub>Si: C 71.68, H 6.82, O 15.91, Si 5.59; found: C 71.64, H 6.84, O 16.01.

### Enone 15a

To a solution of ketone **12a** (10.59 g, 30.0 mmol) and PhSO<sub>2</sub>Me (4.70 g, 30.0 mmol) in THF (70 mL) was added an oil-free suspension of KH (3.01 g, 75.2 mmol) in THF (60 mL) via cannula at room temperature. The mixture was stirred at room temperature for 30 min before being concentrated to dryness. The residue was partitioned between dichloromethane (100 mL) and 0.5 M aq H<sub>3</sub>PO<sub>4</sub> (50 mL). The layers were separated and the aqueous layer extracted with dichloromethane (2 × 70 mL). The combined organic layers were dried over MgSO<sub>4</sub>, filtered, and concentrated. The crude residue was taken up in toluene (300 mL) and Na<sub>2</sub>CO<sub>3</sub> (15.9 g, 150 mmol) was added. The suspension was heated to reflux for 30 min, cooled, filtered through Celite, and concentrated. Purification by flash chromatography using

hexanes:EtOAc (20:1 to 9:1) gave 9.80 g (93%) of enone **15a** as a clear liquid. IR (cm<sup>-1</sup>): 3056, 1824, 1684, 1472. <sup>1</sup>H NMR (CDCl<sub>3</sub>) δ: 7.72–7.67 (m, 4H), 7.48–7.38 (m, 6H), 6.78 (dd, 1H, *J* = 10.2, 2.5 Hz), 5.86 (d, 1H, *J* = 10.2 Hz), 4.52–4.47 (m, 1H), 2.52 (dt, 1H, *J* = 16.4, 4.5 Hz), 2.25–2.17 (m, 1H), 2.15–2.03 (m, 2H), 1.08 (s, 9H). <sup>13</sup>C NMR (CDCl<sub>3</sub>) δ: 198.8 (s), 153.1 (d), 135.7 (d), 133.3 (s), 129.9 (d), 129.5 (d), 128.7 (d), 127.7 (d), 67.5 (d), 35.2 (t), 32.5 (t), 26.8 (q), 19.0 (s). LR-MS (*m/z* (relative intensity)): 293 ([M]<sup>+</sup> - C<sub>4</sub>H<sub>9</sub>), 65, 199 (100). HR-MS calcd. for C<sub>18</sub>H<sub>17</sub>O<sub>2</sub>Si: 293.0998; found: 293.0996. Anal. calcd. for C<sub>22</sub>H<sub>26</sub>O<sub>2</sub>Si: C 75.38, H 7.48, O 9.13, Si 8.01; found: C 75.44, H 7.40, O 9.11.

### Enone 15b

Following the procedure outlined for enone **15a**, enone **15b** was prepared starting from ketone **12b**. The yield of enone **15b** was 3.18 g (70%) isolated as a colourless oil. IR (cm<sup>-1</sup>): 3031, 2954, 2870, 1693, 1454, 1201, 1093. <sup>1</sup>H NMR (CDCl<sub>3</sub>) δ: 7.38 (m, 5H), 7.00–6.96 (m, 1H, *J* = 10.4 Hz), 5.99 (dt, 1H, *J* = 10.6, 1.2 Hz), 4.29–4.23 (m, 1H), 2.65–2.56 (m, 1H), 2.39–2.27 (m, 2H), 2.11–1.98 (m, 1H). <sup>13</sup>C NMR (CDCl<sub>3</sub>) δ: 198.6 (s), 150.4 (d), 137.7 (s), 129.6 (d), 128.4 (d), 127.8 (d), 127.6 (d), 127.3 (d), 72.4 (d), 70.9 (t), 35.2 (t), 29.1 (t). LR-MS (*m/z* (relative intensity)): 203 ([M + 1], 48), 220 ([M + NH<sub>4</sub>], 38), 91 (100). HR-MS calcd. for C<sub>13</sub>H<sub>15</sub>O<sub>2</sub>: 203.1072; found: 203.1077. Anal. calcd. for C<sub>13</sub>H<sub>14</sub>O<sub>2</sub>: C 77.20, H 6.98, O 15.82; found: C 77.12, H 7.05.

### Enone 15c

Followed the same procedure as per **15a** yielding 7.80 g (82%) of enone **15c** as a colourless oil. IR (cm<sup>-1</sup>): 2999, 2955, 2836, 1681, 1613, 1514, 1249, 1087. <sup>1</sup>H NMR (CDCl<sub>3</sub>) δ: 7.29 (d, 2H, *J* = 8.6 Hz), 6.96 (d, 1H, *J* = 10.3 Hz), 6.90 (d, 2H, *J* = 8.6 Hz), 5.98 (d, 1H, *J* = 10.3 Hz), 4.58 (AB quartet, 2H, *J* = 11.4, 5.9 Hz), 4.27–4.21 (m, 1H), 3.81 (s, 3H), 2.64–2.56 (m, 1H), 2.39–2.29 (m, 2H), 2.09–1.98 (m, 1H). <sup>13</sup>C NMR (CDCl<sub>3</sub>) δ: 198.5 (s), 159.2 (s), 150.6 (d), 129.5 (s), 129.3 (d), 129.2 (d), 113.8 (d), 71.9 (d), 70.4 (t), 55.1 (q), 35.1 (t), 28.9 (t). LR-MS (*m/z* (relative intensity)): 232 ([M]<sup>+</sup>, 40), 122 (60), 121 (100). HR-MS calcd. for C<sub>14</sub>H<sub>16</sub>O<sub>3</sub>: 232.1099; found: 232.1094. Anal. calcd. for C<sub>14</sub>H<sub>16</sub>O<sub>3</sub>: C 72.39, H 6.94, O 20.66; found: C 72.40, H 6.90.

### Enone 15d

NaBH<sub>4</sub> (499 mg, 13.2 mmol) was added to a 0°C solution of lactone **14b** (6.66 g, 13.2 mmol) and ethyl alcohol (45 mL). The reaction mixture was stirred at 0°C for a total of 2 h before being quenched by the slow addition of aq NH<sub>4</sub>Cl. The ice bath was removed and phosphate buffer and water were added, followed by sodium periodate (3.67 g, 17.1 mmol). The reaction mixture was stirred overnight and the resulting suspension filtered through Celite. The alcohol was extracted with dichloromethane, washed with brine, dried over MgSO<sub>4</sub>, filtered, and concentrated. Purification by flash chromatography (hexanes:EtOAc, 3:1) yielded 4.67 g (75%) of a keto alcohol as a colourless oil. [α]<sub>D</sub>: -22.6° (*c* 3.16, CHCl<sub>3</sub>). IR (cm<sup>-1</sup>): 3433, 3061, 2930, 2854, 1714, 1471, 1427, 1136, 1112. <sup>1</sup>H NMR (CDCl<sub>3</sub>) δ: 7.76–7.67 (m,



4H), 7.45–7.18 (m, 11H), 4.42 (d, 1H,  $J = 11.7$  Hz), 4.32 (d, 1H,  $J = 11.7$  Hz), 4.17–4.15 (m, 1H), 4.08 (dd, 1H,  $J = 6.4$ , 2.3 Hz), 3.84–3.79 (m, 1H), 2.91–2.81 (m, 2H), 2.48 (dd, 1H,  $J = 14.2$ , 3.9 Hz), 2.31–2.24 (m, 1H), 1.77 (d, 1H,  $J = 3.1$  Hz), 1.10 (s, 9H).  $^{13}\text{C}$  NMR ( $\text{CDCl}_3$ )  $\delta$ : 207.5 (s), 138.0 (s), 136.1 (d), 135.8 (d), 133.6 (s), 132.9 (s), 130.0 (d), 129.8 (d), 128.2 (d), 127.8 (d), 127.5 (d), 127.3 (d), 75.5 (d), 73.5 (d), 70.9 (t), 69.5 (d), 44.8 (t), 43.4 (t), 27.0 (q), 19.3 (s). LR-MS ( $m/z$  (relative intensity)): 417 ( $[\text{M}^+ - \text{C}_4\text{H}_9]$ , 8), 249 (95), 91 (100). HR-MS calcd. for  $\text{C}_{25}\text{H}_{25}\text{O}_4\text{Si}$ : 417.1522; found: 417.1533. Anal. calcd. for  $\text{C}_{29}\text{H}_{34}\text{O}_4\text{Si}$ : C 73.38, H 7.22, O 13.48, Si 5.92; found: C 73.41, H 7.35, O 13.32.

To a cooled  $0^\circ\text{C}$  solution of the keto alcohol (4.51 g, 9.49 mmol), methanesulfonyl chloride (880  $\mu\text{L}$ , 11.4 mmol), and dichloromethane (32 mL) was added triethylamine (4 mL, 28.5 mmol). After 15 min at  $0^\circ\text{C}$ , the reaction was quenched with water. After extraction with dichloromethane, the organic layers were washed with satd. aq.  $\text{NaHCO}_3$ , and brine, dried over  $\text{MgSO}_4$ . Filtration, concentration, and purification by flash chromatography (hexanes:ethyl acetate, 3:1) yielded 4.03 g (93%) of enone **15d** as an oil.  $[\alpha]_D^{25} +78.1^\circ$  ( $c$  3.61,  $\text{CHCl}_3$ ). IR ( $\text{cm}^{-1}$ ): 3069, 1682, 1427.  $^1\text{H}$  NMR ( $\text{CDCl}_3$ )  $\delta$ : 7.73–7.65 (m, 4H), 7.47–7.24 (m, 11H), 6.60 (dd, 1H,  $J = 10.3$ , 3.2 Hz), 5.93 (d, 1H,  $J = 10.5$  Hz), 4.62 (d, 1H,  $J = 12.2$  Hz), 4.60–4.57 (m, 1H), 4.54 (d, 1H,  $J = 12.2$  Hz), 3.84–3.80 (m, 1H), 2.89 (dd, 1H,  $J = 16.5$ , 7.1 Hz), 2.43 (dd, 1H,  $J = 16.5$ , 3.2 Hz), 1.10 (s, 9H).  $^{13}\text{C}$  NMR ( $\text{CDCl}_3$ )  $\delta$ : 197.1 (s), 148.5 (d), 138.0 (s), 135.8 (d), 133.3 (s), 132.9 (s), 129.9 (d), 129.6 (d), 128.2 (d), 127.7 (d), 127.4 (d), 76.6 (d), 71.3 (t), 68.4 (d), 40.9 (t), 26.8 (q), 19.2 (s). LR-MS ( $m/z$  (relative intensity)): 399 ( $[\text{M}^+ - \text{C}_4\text{H}_9]$ , 8), 231 (38), 91 (100). HR-MS calcd. for  $\text{C}_{25}\text{H}_{23}\text{O}_3\text{Si}$ : 399.1416; found: 399.1422. Anal. calcd. for  $\text{C}_{29}\text{H}_{32}\text{O}_3\text{Si}$ : C 76.28, H 7.06, O 10.51, Si 6.15; found: C 76.29, H 7.09, O 10.54.

### Bromoenone 16a

To a solution of enone **15a** (19.0 g, 54.3 mmol) in  $\text{CCl}_4$  (500 mL) was added over 1 h a solution of bromine (8.25 g, 51.6 mmol) in  $\text{CCl}_4$  (100 mL) at  $0^\circ\text{C}$ . Once complete the mixture was stirred for 45 min at  $0^\circ\text{C}$  before a solution of triethylamine (9.89 g, 97.8 mmol) in carbon tetrachloride (100 mL) was added over a 20 min period. The reaction mixture was stirred for 20 min and filtered. The filtrate was washed with 1 N HCl and satd. aq.  $\text{NaHCO}_3$ . The aqueous layers were extracted with ether and combined organic layers dried over  $\text{MgSO}_4$ , filtered, and concentrated. Purification by flash chromatography using a mixture of hexanes:EtOAc (20:1 to 8:1) gave 21.0 g (90%) of bromoenone **16a** as a white solid and trace amounts of a dibromoketone; mp:  $78.2^\circ\text{C}$ . IR ( $\text{cm}^{-1}$ ): 3060, 2955, 1699.  $^1\text{H}$  NMR ( $\text{CDCl}_3$ )  $\delta$ : 7.68–7.65 (m, 4H), 7.48–7.38 (m, 6H), 7.20 (d, 1H,  $J = 3.1$  Hz), 4.48 (dt, 1H,  $J = 6.4$ , 3.1 Hz), 2.76 (dt, 1H,  $J = 16.7$ , 5.0 Hz), 2.33 (dt, 1H,  $J = 16.4$ , 8.2 Hz), 2.13–2.06 (m, 2H), 1.08 (s, 9H).  $^{13}\text{C}$  NMR ( $\text{CDCl}_3$ )  $\delta$ : 190.6 (s), 153.1 (d), 135.7 (d), 132.9 (s), 130.2 (d), 127.9 (d), 124.1 (s), 68.8 (d), 34.7 (t), 32.4 (t), 26.8 (q), 19.1 (s). LR-MS ( $m/z$  (relative intensity)): 373 ( $[\text{M}^+ - \text{C}_4\text{H}_9]$ , 50), 371 ( $[\text{M}^+ - \text{C}_4\text{H}_9]$ , 48), 199 (100). HR-MS calcd. for  $\text{C}_{18}\text{H}_{16}\text{BrO}_2\text{Si}$ : 371.0103; found: 371.0098.

### Bromoenone 16b

Followed the same procedure as per **16a**. Purification by flash chromatography using a mixture of hexanes:EtOAc (6:1) gave 7.23 g (78%) of bromoketone **16b** as a thick oil. IR ( $\text{cm}^{-1}$ ): 3066, 2959, 2871, 1703, 1454, 1317, 1096.  $^1\text{H}$  NMR ( $\text{CDCl}_3$ )  $\delta$ : 7.45 (dd, 1H,  $J = 13.0$ , 1.2 Hz), 7.39–7.32 (m, 5H), 4.64 (s, 2H), 4.29–4.24 (m, 1H), 2.84 (ddd, 1H,  $J = 16.8$ , 5.6, 4.5 Hz), 2.53–2.32 (m, 2H), 2.18–2.08 (m, 1H).  $^{13}\text{C}$  NMR ( $\text{CDCl}_3$ )  $\delta$ : 190.4 (s), 150.5 (d), 137.2 (s), 128.5 (d), 128.0 (d), 127.7 (d), 125.0 (s), 73.6 (d), 71.1 (t), 34.7 (t), 29.0 (t). LR-MS ( $m/z$  (relative intensity)): 280 ( $[\text{M}]^+$ , 5), 282 ( $[\text{M}]^+$ , 5), 201 ( $[\text{M}^+ - \text{Br}]$ , 40), 175 (100). HR-MS calcd. for  $\text{C}_{13}\text{H}_{13}\text{BrO}_2$ : 280.0099; found: 280.0107.

### Bromoenone 16c

Same procedure as per **16a**. Purification by flash chromatography eluting with a mixture of hexanes:EtOAc (3:1 to 1:1) gave 9.58 g (92%) of **16c** as a white solid; mp:  $62.7^\circ\text{C}$ . IR ( $\text{cm}^{-1}$ ): 2955, 1697, 1611, 1513, 1463, 1318, 1249, 1174, 1032, 1000, 817.  $^1\text{H}$  NMR ( $\text{CDCl}_3$ )  $\delta$ : 7.42 (d, 1H,  $J = 3.5$  Hz), 7.28 (d, 2H,  $J = 8.6$  Hz), 6.90 (d, 2H,  $J = 8.6$  Hz), 4.57 (s, 2H), 4.27–4.22 (m, 1H), 3.81 (s, 3H), 2.83 (dm, 1H,  $J = 16.8$ , 10.7 Hz), 2.47 (m, 1H,  $J = 16.8$ , 11.7 Hz), 2.37–2.28 (m, 1H), 2.16–2.04 (m, 1H).  $^{13}\text{C}$  NMR ( $\text{CDCl}_3$ )  $\delta$ : 190.4 (s), 159.3 (s), 150.7 (d), 132.0 (s), 129.3 (d), 124.8 (s), 113.9 (d), 73.2 (d), 70.7 (t), 55.2 (q), 34.6 (t), 29.0 (t). LR-MS ( $m/z$  (relative intensity)): 310 ( $[\text{M}]^+$ , 8), 136 (27), 121 (100). HR-MS calcd. for  $\text{C}_{14}\text{H}_{15}\text{O}_3\text{Br}$ : 310.0204; found: 310.0195.

### Bromoenone 16d

Followed the same procedure as per **16a**. Flash chromatography eluting with a mixture of hexanes:EtOAc (6:1) gave 9.27 g (94%) of **16d** as a thick oil.  $[\alpha]_D^{25} +81.9^\circ$  ( $c$  1.81,  $\text{CHCl}_3$ ). IR ( $\text{cm}^{-1}$ ): 3069, 2957, 1700, 1427, 1113, 1066, 741, 702.  $^1\text{H}$  NMR ( $\text{CDCl}_3$ )  $\delta$ : 7.73–7.63 (m, 4H), 7.48–7.22 (m, 11H), 6.99 (d, 1H,  $J = 4.2$  Hz), 4.58 (d, 1H,  $J = 12.3$  Hz), 4.56–4.52 (m, 1H), 4.50 (d, 1H,  $J = 12.2$  Hz), 3.80 (dt, 1H,  $J = 7.1$ , 3.2 Hz), 3.10 (dd, 1H,  $J = 16.4$ , 7.7 Hz), 2.60 (dd, 1H,  $J = 16.4$ , 3.2 Hz), 1.10 (s, 9H).  $^{13}\text{C}$  NMR ( $\text{CDCl}_3$ )  $\delta$ : 189.1 (s), 148.7 (d), 137.6 (s), 135.8 (d), 132.9 (s), 132.6 (s), 130.1 (d), 128.3 (d), 127.9 (d), 127.5 (d), 125.1 (s), 75.9 (d), 71.3 (t), 69.7 (d), 40.3 (t), 26.8 (q), 19.3 (s). LR-MS ( $m/z$  (relative intensity)): 477 ( $[\text{M}^+ - \text{C}_4\text{H}_9]$ , 5), 479 ( $[\text{M}^+ - \text{C}_4\text{H}_9]$ , 5), 311 (30), 309 (30), 91 (100). HR-MS calcd. for  $\text{C}_{25}\text{H}_{22}\text{O}_3\text{SiBr}$ : 477.0521; found: 477.0511.

### Alcohol 17a

To a  $0^\circ\text{C}$  solution of tetravinyl tin (320 mg, 1.41 mmol) in THF (20 mL) was added 1.08 M *n*-butyl lithium (4.73 mL, 5.11 mmol). After 30 min at  $0^\circ\text{C}$  the ice bath was removed and the mixture stirred for 1 h. This solution was added via cannula to a cooled  $-78^\circ\text{C}$  suspension of  $\text{CeCl}_3$  (2.86 g, 7.67 mmol) and ketone **16a** (1.10 g, 2.55 mmol) in THF (40 mL). The reaction mixture was stirred for 4 h at  $-78^\circ\text{C}$  before being quenched with satd. aq.  $\text{NH}_4\text{Cl}$ . The layers were separated (a portion of 1 N HCl was added for clarification) and the aqueous layer extracted with ethyl ether. The organic layers were washed (brine), dried over  $\text{MgSO}_4$ , filtered, and concentrated. Flash chromatography eluting with a mixture of hexanes:EtOAc (9:1) gave 447 mg and 646 mg of two



diastereomeric alcohols (93%) as thick oils. Less polar isomer:  $^1\text{H}$  NMR ( $\text{CDCl}_3$ )  $\delta$ : 7.73–7.65 (m, 4H), 7.46–7.35 (m, 6H), 6.12 (d, 1H,  $J = 3.6$  Hz), 5.72 (dd, 1H,  $J = 17.1$ , 10.6 Hz), 5.26 (d, 1H,  $J = 17.1$  Hz), 5.17 (d, 1H,  $J = 10.6$  Hz), 4.15 (q, 1H), 2.18–2.10 (m, 1H), 1.83–1.67 (m, 2H), 1.06 (s, 9H).  $^{13}\text{C}$  NMR ( $\text{CDCl}_3$ )  $\delta$ : 141.2 (d), 135.7 (d), 135.4 (d), 133.7 (s), 131.1 (s), 129.7 (d), 127.6 (d), 114.9 (t), 74.1 (s), 68.3 (d), 33.0 (t), 28.2 (t), 26.9 (q), 19.1 (s). More polar isomer: IR ( $\text{cm}^{-1}$ ): 3548, 3435, 3066, 2953, 2861, 1630, 1589, 1471, 1425, 1364, 1323, 1076.  $^1\text{H}$  NMR ( $\text{CDCl}_3$ )  $\delta$ : 7.72–7.64 (m, 4H), 7.47–7.35 (m, 6H), 6.10 (d, 1H,  $J = 3.1$  Hz), 5.88 (dd, 1H,  $J = 17.3$ , 10.6 Hz), 5.35 (d, 1H,  $J = 17.2$  Hz), 5.27 (d, 1H,  $J = 10.6$  Hz), 4.29–4.23 (m, 1H), 2.07–2.01 (m, 1H), 1.87–1.80 (m, 1H), 1.77–1.70 (m, 2H), 1.06 (s, 9H).  $^{13}\text{C}$  NMR ( $\text{CDCl}_3$ )  $\delta$ : 141.0 (d), 135.9 (d), 135.7 (d), 133.7 (s), 129.8 (d), 127.6 (d), 115.3 (t), 74.4 (s), 69.1 (d), 34.1 (t), 29.0 (t), 26.8 (q), 19.1 (s). LR-MS ( $m/z$  (relative intensity)): 399 ( $[\text{M}^+ - \text{C}_4\text{H}_9]$ , 5), 199 (100), 200 (41). HR-MS calcd. for  $\text{C}_{20}\text{H}_{20}\text{BrO}_2\text{Si}$ : 399.0416; found: 399.0424. Anal. calcd. for  $\text{C}_{24}\text{H}_{29}\text{BrO}_2\text{Si}$ : C 63.01, H 6.39, Br 17.47, O 6.99, Si 6.14; found: C 62.97, H 6.40, O 6.95.

#### Acetate 18a

To a  $0^\circ\text{C}$  solution of tetravinyl tin (464  $\mu\text{L}$ , 2.55 mmol) in THF (30 mL) was added 1.0 M *n*-butyl lithium (9.30 mL, 9.30 mmol). After 2.5 h at  $0^\circ\text{C}$  this solution was added via cannula to a cooled  $-78^\circ\text{C}$  suspension of  $\text{CeCl}_3$  (5.19 g, 13.9 mmol) and ketone **16a** (1.99 g, 4.64 mmol) in THF (70 mL). The reaction mixture was stirred for 5 h at  $-78^\circ\text{C}$  before being quenched with acetic anhydride (10 mL) and warmed to room temperature. After 30 min, satd. aq  $\text{NH}_4\text{Cl}$  was added and the layers were separated. The aqueous layer extracted with ethyl ether, and the organic layers washed with brine, dried over  $\text{MgSO}_4$ , filtered, and concentrated. Flash chromatography eluting with a mixture of hexanes:EtOAc (15:1) gave 786 mg and 1.05 g (79%) of acetate **18a**. Less polar acetate:  $^1\text{H}$  NMR ( $\text{CDCl}_3$ )  $\delta$ : 7.72–7.65 (m, 4H), 7.46–7.35 (m, 6H), 6.10 (d, 1H,  $J = 4.5$  Hz), 5.87 (dd, 1H,  $J = 10.8$ , 17.4 Hz), 5.23 (d, 1H,  $J = 10.8$  Hz), 5.17 (d, 1H,  $J = 17.4$  Hz), 4.10 (q, 1H,  $J = 4.3$  Hz), 3.00 (dt, 1H,  $J = 11.7$ , 3.2 Hz), 2.12 (s, 3H), 1.97–1.89 (m, 1H), 1.82–1.62 (m, 2H), 1.07 (s, 9H).  $^{13}\text{C}$  NMR ( $\text{CDCl}_3$ )  $\delta$ : 168.9 (s), 136.4 (d), 135.8 (d), 135.7 (d), 135.2 (d), 133.7 (s), 129.7 (d), 127.6 (d), 116.3 (t), 82.3 (s), 66.7 (d), 28.2 (t), 28.0 (t), 26.8 (q), 22.0 (q), 19.1 (s). More polar acetate: IR ( $\text{cm}^{-1}$ ): 3056, 1743, 1635, 1471.  $^1\text{H}$  NMR ( $\text{CDCl}_3$ )  $\delta$ : 7.69–7.63 (m, 4H), 7.45–7.34 (m, 6H), 6.25 (d, 1H,  $J = 2.5$  Hz), 5.88 (dd, 1H,  $J = 17.3$ , 10.7 Hz), 5.37 (d, 1H,  $J = 16.8$  Hz), 5.33 (d, 1H,  $J = 10.4$  Hz), 4.42–4.38 (m, 1H), 2.43 (dt, 1H,  $J = 13.2$ , 3.8 Hz), 2.03 (s, 3H), 2.00–1.92 (m, 1H), 1.81–1.69 (m, 2H), 1.05 (s, 9H).  $^{13}\text{C}$  NMR ( $\text{CDCl}_3$ )  $\delta$ : 169.1 (s), 137.9 (d), 136.7 (d), 135.7 (d), 133.4 (s), 129.8 (d), 127.7 (d), 127.6 (d), 124.4 (s), 116.6 (t), 82.4 (s), 69.5 (d), 30.6 (t), 29.8 (t), 26.8 (q), 21.9 (q), 19.1 (s). LR-MS ( $m/z$  (relative intensity)): 441 ( $[\text{M}^+ - \text{C}_4\text{H}_9]$ , 18), 443 ( $[\text{M}^+ - \text{C}_4\text{H}_9]$ , 16), 241 (100), 199 (70). HR-MS calcd. for  $\text{C}_{22}\text{H}_{22}\text{O}_3\text{BrSi}$ : 441.0521; found: 441.0529. Anal. calcd. for  $\text{C}_{26}\text{H}_{31}\text{BrO}_3\text{Si}$ : C 62.52, H 6.26, Br 16.00, O 9.61, Si 5.62; found: C 62.66, H 6.19, O 9.44.

#### Acetate 18b

Followed the same procedure as per **18a**, starting from **17b**. Flash chromatography using a hexanes:EtOAc (8:1 to 4:1) mixture yielded 2.29 g (83%) of a mixture of acetates **18b** as a colourless oil. Less polar isomer:  $^1\text{H}$  NMR ( $\text{CDCl}_3$ )  $\delta$ : 7.36–7.28 (m, 5H), 6.45 (d, 1H,  $J = 4.5$  Hz), 5.95 (dd, 1H,  $J = 10.8$ , 17.3 Hz), 5.30 (d, 1H,  $J = 10.8$  Hz), 5.28 (d, 1H,  $J = 17.5$  Hz), 4.59 (s, 2H), 3.88 (q, 1H,  $J = 4.3$  Hz), 2.93–2.83 (m, 1H), 2.09 (s, 3H), 2.07–1.81 (m, 3H).  $^{13}\text{C}$  NMR ( $\text{CDCl}_3$ )  $\delta$ : 169.1 (s), 138.3 (s), 136.3 (d), 132.9 (d), 128.4 (d), 127.7 (d), 116.4 (t), 82.4 (s), 71.4 (d), 70.4 (t), 28.5 (t), 24.9 (t), 22.0 (q). More polar isomer: IR ( $\text{cm}^{-1}$ ): 3030, 1745.  $^1\text{H}$  NMR ( $\text{CDCl}_3$ )  $\delta$ : 7.36–7.30 (m, 5H), 6.45 (dd, 1H,  $J = 3.5$ , 2.3 Hz), 5.90 (dd, 1H,  $J = 17.3$ , 10.7 Hz), 5.38 (d, 1H,  $J = 17.2$  Hz), 5.33 (d, 1H,  $J = 10.7$  Hz), 4.58 (ABq, 2H,  $J = 22.1$  Hz), 4.17 (ddd, 1H,  $J = 2.3$ , 5.4, 9.8 Hz), 2.63 (m, 1H,  $J = 3.2$ , 12.9 Hz), 2.14–2.03 (m, 2H), 2.09 (s, 3H), 1.80–1.68 (m, 1H).  $^{13}\text{C}$  NMR ( $\text{CDCl}_3$ )  $\delta$ : 168.9 (s), 137.8 (s), 136.6 (d), 135.0 (d), 128.3 (d), 127.5 (d), 116.7 (t), 82.2 (s), 74.5 (d), 70.3 (t), 30.5 (t), 26.5 (t), 21.9 (q). LR-MS ( $m/z$  (relative intensity)): 368 ( $[\text{M} + \text{NH}_4]$ , 25), 308 ( $[\text{M} + \text{NH}_4 - \text{AcOH}]$ , 25), 291 ( $[\text{M}^+ - \text{AcOH}]$ , 25), 211 (100). HR-MS calcd. for  $\text{C}_{17}\text{H}_{23}\text{NO}_3\text{Br}$ : 368.0861; found: 368.0857. Anal. calcd. for  $\text{C}_{17}\text{H}_{19}\text{BrO}_3$ : C 58.13, H 5.45, Br 22.75, O 13.67; found: C 58.22, H 5.35, O 13.74.

#### Acetate 18c

Followed the same procedure as per acetate **18a**, starting from **17c**. Purification by flash chromatography eluting with hexanes:EtOAc (6:1) yielded 10.01 g (82%) of **20d** as a mixture of two diastereomers. First isomer:  $^1\text{H}$  NMR ( $\text{CDCl}_3$ )  $\delta$ : 7.25 (d, 2H,  $J = 8.6$  Hz), 6.88 (d, 2H,  $J = 8.6$  Hz), 6.42 (d, 1H,  $J = 1.1$  Hz), 5.89 (dd, 1H,  $J = 17.3$ , 10.7), 5.37 (d, 1H,  $J = 18.8$  Hz), 5.32 (d, 1H,  $J = 10.9$  Hz), 4.50 (ABq, 2H,  $J = 13.5$  Hz), 4.17–4.10 (m, 1H), 3.80 (s, 3H), 2.68–2.58 (m, 1H), 2.22–2.20 (m, 2H), 2.08 (s, 3H), 1.77–1.65 (m, 1H).  $^{13}\text{C}$  NMR ( $\text{CDCl}_3$ )  $\delta$ : 169.1 (s), 159.1 (s), 136.5 (d), 135.1 (d), 129.8 (s), 129.2 (d), 125.2 (s), 116.7 (t), 113.7 (d), 82.5 (s), 74.2 (d), 70.1 (t), 55.1 (q), 30.4 (t), 26.5 (t), 21.8 (q). Second isomer: IR ( $\text{cm}^{-1}$ ): 3035, 1744, 1612, 1513.  $^1\text{H}$  NMR ( $\text{CDCl}_3$ )  $\delta$ : 7.28 (d, 2H,  $J = 8.6$  Hz), 6.88 (d, 2H,  $J = 8.6$  Hz), 6.43 (d, 1H,  $J = 4.5$  Hz), 5.94 (dd, 1H,  $J = 17.3$ , 10.9 Hz), 5.29 (d, 1H,  $J = 10.3$  Hz), 5.25 (d, 1H,  $J = 17.0$  Hz), 4.51 (s, 2H), 3.86 (q, 1H,  $J = 4.4$  Hz), 3.80 (s, 3H), 2.86 (dt, 1H,  $J = 11.8$ , 3.4), 2.09 (s, 3H), 2.06–1.99 (m, 1H), 1.92–1.89 (m, 1H), 1.85–1.79 (m, 1H).  $^{13}\text{C}$  NMR ( $\text{CDCl}_3$ )  $\delta$ : 168.9 (s), 159.0 (s), 136.2 (d), 132.9 (d), 130.2 (s), 129.1 (d), 128.9 (s), 116.2 (t), 113.6 (d), 82.2 (s), 70.9 (d), 69.9 (t), 55.1 (q), 28.3 (t), 24.7 (t), 21.8 (q). LR-MS ( $m/z$  (relative intensity)): 323 ( $[\text{M}^+ - \text{OAc}]$ , 10), 321 ( $[\text{M}^+ - \text{OAc}]$ , 10), 184 (40), 121 (100). HR-MS calcd. for  $\text{C}_{16}\text{H}_{18}\text{BrO}_2$ : 321.0490; found: 321.0485. Anal. calcd. for  $\text{C}_{18}\text{H}_{21}\text{BrO}_4$ : C 56.70, H 5.55, Br 20.96, O 16.79; found: C 56.85, H 5.71, O 16.90.

#### Acetate 18d

Followed the same procedure as per **18a**, starting from **17d**. Flash chromatography using hexanes:EtOAc (9:1) as the eluent gave 8.77 g (83%) of a single acetate **18d** as a clear oil.  $[\alpha]_D^{25}$ : +126.5° (c 4.443,  $\text{CHCl}_3$ ). IR ( $\text{cm}^{-1}$ ): 3068,



1749, 1472.  $^1\text{H}$  NMR ( $\text{CDCl}_3$ )  $\delta$ : 7.78–7.74 (m, 4H), 7.44–7.28 (m, 9H), 7.18–7.15 (m, 2H), 5.98 (d, 1H,  $J = 6.0$  Hz), 5.84 (dd, 1H,  $J = 17.3, 10.7$  Hz), 5.20 (d, 1H,  $J = 10.7$  Hz), 5.16 (d, 1H,  $J = 17.3$  Hz), 4.39 (d, 1H,  $J = 12.0$  Hz), 4.30 (d, 1H,  $J = 12.0$  Hz), 4.14–4.12 (m, 1H), 3.38 (dt, 1H,  $J = 12.2, 3.0$  Hz), 3.24 (dd, 1H,  $J = 12.0, 11.7$  Hz), 2.33–2.29 (m, 1H), 2.12 (s, 3H), 1.09 (s, 9H).  $^{13}\text{C}$  NMR ( $\text{CDCl}_3$ )  $\delta$ : 168.4 (s), 138.0 (s), 136.1 (d), 134.1 (s), 133.3 (s), 132.5 (d), 129.6 (d), 129.0 (s), 128.1 (d), 127.4 (d), 116.6 (t), 82.4 (s), 73.1 (d), 69.8 (t), 66.2 (d), 32.7 (t), 26.7 (q), 21.8 (q), 19.3 (s). LR-MS ( $m/z$  (relative intensity)): 547 ( $[\text{M}^+ - \text{C}_4\text{H}_9]$ , 1), 399 (100). HR-MS calcd. for  $\text{C}_{29}\text{H}_{28}\text{BrO}_4\text{Si}$ : 547.0940; found: 547.0947. Anal. calcd. for  $\text{C}_{33}\text{H}_{37}\text{BrO}_4\text{Si}$ : C 65.44, H 6.16, Br 13.19, O 10.57, Si 4.64; found: C 65.41, H 6.22, O 10.50.

### Diene 19a

To a suspension of Mg turnings (336 mg, 13.8 mmol) in ethyl ether (28 mL) was added 1-bromo-5-propene (2.07 g, 13.9 mmol) drop wise, resulting in a refluxing mixture. The reaction was kept at reflux for 3 h, until all the magnesium was consumed. The Grignard was cooled and added via cannula to a suspension of copper(I) iodide (968 mg, 5.08 mmol) in ethyl ether (24 mL) at  $0^\circ\text{C}$ . After 25 min at  $0^\circ\text{C}$  a solution of acetate **18a** (1.269 g, 2.54 mmol) in  $\text{Et}_2\text{O}$  (8 mL) was added via cannula. The resulting mixture was stirred for 1 h at  $0^\circ\text{C}$  then quenched by the addition of satd. aq  $\text{NH}_4\text{Cl}$ . The product was extracted with  $\text{Et}_2\text{O}$ , dried over  $\text{MgSO}_4$ , filtered, and concentrated. The crude residue was purified by flash chromatography (100% hexanes to 25:1 hexanes:  $\text{EtOAc}$ ) to provide 1.24 g (96%) of **19a** as a slightly yellow-coloured liquid. IR ( $\text{cm}^{-1}$ ): 3070, 2930, 2856, 1427, 1105.  $^1\text{H}$  NMR ( $\text{CDCl}_3$ )  $\delta$ : 7.69–7.65 (m, 4H), 7.46–7.35 (m, 6H), 6.09 (d, 1H,  $J = 3.7$  Hz), 5.92 (t, 1H,  $J = 7.4$  Hz), 5.79 (ddt, 1H,  $J = 17.0, 10.2, 6.7$  Hz), 5.03–4.92 (m, 2H), 4.33–4.28 (m, 1H), 2.61 (dt, 1H,  $J = 14.9, 5.9$  Hz), 2.23–2.01 (m, 4H), 1.76–1.69 (m, 2H), 1.45–1.37 (m, 4H), 1.06 (s, 9H).  $^{13}\text{C}$  NMR ( $\text{CDCl}_3$ )  $\delta$ : 138.8 (d), 135.8 (d), 134.0 (s), 133.9 (s), 133.7 (d), 132.6 (d), 131.7 (s), 129.7 (d), 127.7 (d), 126.1 (s), 114.4 (t), 69.0 (d), 33.6 (t), 31.5 (t), 28.7 (t), 28.6 (t), 27.9 (t), 26.9 (q), 23.0 (t), 19.2 (s). LR-MS ( $m/z$  (relative intensity)): 453 ( $[\text{M}^+ - \text{C}_4\text{H}_9]$ , 6), 451 ( $[\text{M}^+ - \text{C}_4\text{H}_9]$ , 6), 199 (100), 200 (23). HR-MS calcd. for  $\text{C}_{29}\text{H}_{37}\text{OBrSi}$ : 508.1797; found: 508.1793

### Diene 19b

Followed the same procedure as per **19a**, starting from **18b**. The crude residue was purified by flash chromatography (hexanes: $\text{EtOAc}$ , 9:1) to provide 737 mg (89%) of **19b** as a colourless liquid.  $^1\text{H}$  NMR ( $\text{CDCl}_3$ )  $\delta$ : 7.36–7.27 (m, 5H), 6.32 (d, 1H,  $J = 3.8$  Hz), 5.98 (t, 1H,  $J = 7.5$  Hz), 5.80 (ddt, 1H,  $J = 17.0, 10.2, 6.7$  Hz), 5.04–4.92 (m, 2H), 4.59 (s, 2H), 4.10–4.06 (m, 1H), 2.65–2.60 (m, 1H), 2.37–2.28 (m, 1H), 2.19–1.91 (m, 5H), 1.87–1.77 (m, 1H), 1.47–1.38 (m, 4H).  $^{13}\text{C}$  NMR ( $\text{CDCl}_3$ )  $\delta$ : 138.7 (d), 138.3 (s), 133.2 (d), 131.5 (s), 130.6 (d), 128.3 (d), 127.6 (d), 114.4 (t), 73.9 (d), 70.2 (t), 33.5 (t), 28.6 (t), 28.0 (t), 27.8 (t), 23.0 (t).

### Diene 19c

To a cooled  $-78^\circ\text{C}$  solution of 4-(*tert*-butyldimethylsilyloxy)-3-methylbutyl iodide (4.51 g, 13.7 mmol) in  $\text{Et}_2\text{O}$

(126 mL) was added a 1.31 M solution of *tert*-butyl lithium (20.9 mL, 27.4 mmol). After 5 min this solution was warmed to  $0^\circ\text{C}$  and stirred for 30 min before being cooled to  $-78^\circ\text{C}$ . This cooled solution was added via cannula to a stirred suspension of  $\text{CuCN}$  (1.22 g, 13.7 mmol) in THF (103 mL) at  $-68^\circ\text{C}$ . This suspension was stirred for 1 h further before a solution of acetate **18c** (3.48 g, 9.13 mmol) in THF (70 mL) was added via cannula at  $-50^\circ\text{C}$ . The reaction mixture was gradually warmed to  $0^\circ\text{C}$  over 1 h, and stirred 2 h at  $0^\circ\text{C}$  before being quenched with a solution of satd. aq  $\text{NH}_4\text{Cl}$ :conc.  $\text{NH}_4\text{OH}$  (9:1). The mixture was extracted with ethyl ether, washed with brine, dried over  $\text{MgSO}_4$ , filtered, and concentrated. The crude product was purified by flash chromatography using hexanes: $\text{EtOAc}$  (15:1) to give 4.43 g (92%) of **19c** as a colourless oil. IR ( $\text{cm}^{-1}$ ): 2952, 2855, 1612, 1513, 1462, 1248, 1089, 1038, 835.  $^1\text{H}$  NMR ( $\text{CDCl}_3$ )  $\delta$ : 7.27 (d, 2H,  $J = 8.6$  Hz), 6.88 (d, 2H,  $J = 8.6$  Hz), 6.31 (d, 1H,  $J = 3.7$  Hz), 5.97 (t, 1H,  $J = 7.4$  Hz), 4.51 (s, 2H), 4.08–4.03 (m, 1H), 3.80 (s, 3H), 3.39 (ddd, 2H,  $J = 9.8, 6.5, 6.0$  Hz), 2.66–2.59 (m, 1H), 2.36–2.31 (m, 1H), 2.16–2.09 (m, 2H), 1.98–1.89 (m, 1H), 1.84–1.77 (m, 1H), 1.61–1.52 (m, 1H), 1.46–1.37 (m, 3H), 1.09–1.02 (m, 1H), 0.89 (s, 9H), 0.86 (d, 3H,  $J = 6.7$  Hz), 0.03 (s, 6H).  $^{13}\text{C}$  NMR ( $\text{CDCl}_3$ )  $\delta$ : 159.1 (s), 133.2 (d), 131.4 (s), 130.7 (d), 130.3 (s), 129.2 (d), 127.3 (s), 113.7 (d), 73.6 (d), 69.9 (t), 68.2 (t), 51.2 (q), 35.6 (d), 32.8 (t), 28.3 (t), 28.0 (t), 26.6 (t), 25.8 (q), 23.0 (t), 18.2 (s), 16.6 (q),  $-5.4$  (q). LR-MS ( $m/z$  (relative intensity)): 465 ( $[\text{M}^+ - \text{C}_4\text{H}_9]$ , 5), 467 ( $[\text{M}^+ - \text{C}_4\text{H}_9]$ , 5), 122 (50), 74 (50), 121 (100). HR-MS calcd. for  $\text{C}_{23}\text{H}_{34}\text{BrO}_3\text{Si}$ : 465.1460; found: 465.1470. Anal. calcd. for  $\text{C}_{27}\text{H}_{43}\text{BrO}_3\text{Si}$ : C 61.93, H 8.28, Br 15.26, O 9.17, Si 5.36; found: C 61.99, H 8.35, O 9.34.

### Diene 19d

Followed the same procedure as per **19c**, starting from **18d**. Purified by flash chromatography using hexanes: $\text{EtOAc}$  (25:1) to give 3.79 g (96%) of **19d** as a colourless oil.  $[\alpha]_D^{25}$ :  $+94.6$  (c 1.80,  $\text{CHCl}_3$ ). IR ( $\text{cm}^{-1}$ ): 2929, 2856, 1471, 1427, 1361, 1250, 1111, 836, 700.  $^1\text{H}$  NMR ( $\text{CDCl}_3$ )  $\delta$ : 7.76–7.64 (m, 5H), 7.44–7.22 (m, 10H), 6.02 (t, 1H,  $J = 7.3$  Hz), 5.90 (d, 1H,  $J = 5.5$  Hz), 4.51 (d, 1H,  $J = 12.1$  Hz), 4.37 (d, 1H,  $J = 12.1$  Hz), 4.33–4.30 (m, 1H), 3.49–3.34 (m, 3H), 2.84–2.81 (m, 1H), 2.62–2.56 (m, 1H), 2.18–2.11 (m, 2H), 1.60–1.37 (m, 5H), 1.08 (s, 9H), 0.89 (s, 9H), 0.87 (d, 3H,  $J = 6.6$  Hz), 0.03 (s, 6H).  $^{13}\text{C}$  NMR ( $\text{CDCl}_3$ )  $\delta$ : 138.4 (s), 136.0 (d), 134.9 (d), 134.1 (s), 133.6 (s), 130.5 (s), 130.1 (d), 129.7 (d), 128.2 (d), 127.8 (s), 127.6 (d), 75.4 (d), 70.4 (t), 68.2 (t), 67.8 (d), 35.7 (d), 33.0 (t), 28.5 (t), 27.9 (t), 26.9 (q), 26.6 (t), 25.9 (q), 19.4 (s), 18.3 (s), 16.7 (q),  $-5.3$  (q). LR-MS ( $m/z$  (relative intensity)): 691 ( $[\text{M}^+ - \text{C}_4\text{H}_9]$ , 18), 689 ( $[\text{M}^+ - \text{C}_4\text{H}_9]$ , 16), 91 (100), 74 (65), 199 (58), 135 (52). HR-MS calcd. for  $\text{C}_{38}\text{H}_{50}\text{BrO}_3\text{Si}_2$ : 689.2482; found: 689.2489. Anal. calcd. for  $\text{C}_{42}\text{H}_{59}\text{BrO}_3\text{Si}$ : C 67.44, H 7.95, Br 10.68, O 6.42, Si 7.51; found: C 67.65, H 7.90, O 6.38.

### Diene 19e

Oil-free  $\text{NaH}$  (45 mg, 1.129 mmol) was suspended in THF (8 mL) and dimethyl malonate (117  $\mu\text{L}$ , 1.03 mmol) was slowly added at  $25^\circ\text{C}$ . The reaction was stirred until gas evolution ceased. Then, this solution was transferred via can-



nula to a solution of acetate **18a** (256 mg, 0.513 mmol) and Pd(PPh)<sub>4</sub> (29 mg, 0.026 mmol). The reaction was stirred at room temperature for 1 h before the THF was evaporated. The residue taken up in Et<sub>2</sub>O and the organic phase washed with brine, dried over MgSO<sub>4</sub>, filtered, and concentrated under reduced pressure. The crude product was purified by flash chromatography using hexanes:EtOAc (15:1) to give 217 mg (74%) of diester **19e** as a colourless oil. <sup>1</sup>H NMR (CDCl<sub>3</sub>) δ: 7.68–7.63 (m, 4H), 7.46–7.33 (m, 6H), 6.13 (d, 1H, *J* = 3.5 Hz), 5.83 (t, 1H, *J* = 7.2 Hz), 4.28 (m, 1H), 3.74 (s, 3H), 3.72 (s, 3H), 3.45 (t, 1H, *J* = 7.6 Hz), 2.73 (t, 2H, *J* = 7.6 Hz), 2.7–2.6 (m, 1H), 2.25–2.17 (m, 1H), 1.8–1.65 (m, 2H), 1.06 (s, 9H).

#### Diene 19f

To a stirred solution of alcohol **17a** (1.74 g, 3.80 mmol), ethylvinyl ether (50 mL), and triethylamine (1 mL) was added mercury(II) trifluoroacetate (1.62 g, 3.80 mmol) at room temperature. The mixture was stirred a total of 3 days before the solvent was removed in vacuo. The residue was taken up in ethyl ether, washed with 10% aq KOH and satd. aq NaHCO<sub>3</sub>, dried over MgSO<sub>4</sub>, filtered, and concentrated. Purification by flash chromatography using a mixture of hexanes:EtOAc (15:1 to 9:1) yielded 1.61 g (88%) of aldehyde **19f**. <sup>1</sup>H NMR (CDCl<sub>3</sub>) δ: 9.79 (s, 1H), 7.72–7.68 (m, 4H), 7.48–7.38 (m, 6H), 6.16 (d, 1H, *J* = 3.7 Hz), 5.87 (t, 1H, *J* = 7.2 Hz), 4.37–4.31 (m, 1H), 2.70–2.63 (m, 1H), 2.60–2.56 (m, 2H), 2.49–2.42 (m, 2H), 2.26–2.21 (m, 1H), 1.80–1.74 (m, 2H), 1.09 (s, 9H). <sup>13</sup>C NMR (CDCl<sub>3</sub>) δ: 201.2 (d), 135.7 (d), 134.6 (d), 133.8 (s), 132.9 (s), 129.7 (d), 129.6 (d), 127.6 (d), 125.4 (s), 68.8 (d), 43.2 (t), 31.5 (t), 26.8 (q), 22.9 (t), 20.6 (t), 19.1 (s). LR-MS (*m/z* (relative intensity)): 425 ([M<sup>+</sup> – C<sub>4</sub>H<sub>9</sub>], 25), 199 (100). HR-MS calcd. for C<sub>22</sub>H<sub>22</sub>O<sub>2</sub>BrSi: 425.0572; found: 425.0575.

#### Diene 19g

Alcohol **17a** was dissolved in toluene (2 mL) along with propionic acid (2 drops) and ethyl orthoacetate (575 μL, 3.14 mmol). The mixture was refluxed overnight and the solvent was removed in vacuo. Purification by flash chromatography using a mixture of hexanes:EtOAc (25:1 to 9:1) yielded 38.9 mg (21%) of ester **19g** and 113 mg of starting alcohol (92% corrected yield). <sup>1</sup>H NMR (CDCl<sub>3</sub>) δ: 7.70–7.65 (m, 4H), 7.46–7.36 (m, 6H), 6.12 (d, 1H, *J* = 3.7 Hz), 5.88 (t, 1H, *J* = 7.2 Hz), 4.31 (m, 1H), 4.13 (q, 2H, *J* = 6.9 Hz), 2.70–2.63 (m, 1H), 2.48–2.38 (m, 4H), 2.29–2.15 (m, 1H), 1.80–1.70 (m, 2H), 1.25 (t, 3H, *J* = 6.9 Hz), 1.06 (s, 9H).

#### Aldehyde 20a

To a cooled –78°C solution of vinyl bromide **19a** (1.10 g, 2.17 mmol) in THF (28 mL) was added 2.0 M *n*-butyl lithium (2.17 mL, 4.34 mmol). After 20 min DMF (1.26 mL, 16.3 mmol) was added at –78°C and the reaction stirred for 1 h further before being quenched with satd. aq NH<sub>4</sub>Cl. The layers were separated and the product extracted with ethyl ether. The combined organic layers were dried over MgSO<sub>4</sub>, filtered, and concentrated. The crude aldehyde was purified by flash chromatography (100% hexanes to hexanes:EtOAc (15:1)) to provide 977 mg (98%) of aldehyde **20a** as a

faintly yellow-coloured oil. IR (cm<sup>–1</sup>): 3069, 2932, 2857, 1696, 1427, 1107. <sup>1</sup>H NMR (CDCl<sub>3</sub>) δ: 9.42 (s, 1H), 7.71–7.67 (m, 4H), 7.47–7.37 (m, 6H), 6.64 (t, 1H, *J* = 7.3 Hz), 6.32 (d, 1H, *J* = 2.9 Hz), 5.78 (ddt, 1H, *J* = 16.9, 10.2, 6.7 Hz), 5.01–4.91 (m, 2H), 4.54–4.48 (m, 1H), 2.55 (dt, 1H, *J* = 15.5, 4.9 Hz), 2.13–1.99 (m, 4H), 1.85–1.77 (m, 1H), 1.73–1.61 (m, 1H), 1.43–1.36 (m, 4H), 1.08 (s, 9H). <sup>13</sup>C NMR (CDCl<sub>3</sub>) δ: 193.9 (d), 151.8 (d), 138.8 (d), 137.1 (s), 135.7 (d), 133.7 (s), 131.3 (d), 129.9 (d), 127.7 (d), 114.3 (t), 68.4 (d), 33.6 (t), 31.2 (t), 28.6 (t), 27.9 (t), 26.8 (q), 22.9 (t), 19.1 (s). LR-MS (*m/z* (relative intensity)): 458 ([M]<sup>+</sup>, 8), 401 ([M<sup>+</sup> – C<sub>4</sub>H<sub>9</sub>], 25), 199 (100), 241 (95), 86 (49). HR-MS calcd. for C<sub>30</sub>H<sub>38</sub>O<sub>2</sub>Si: 458.2641; found: 458.2650.

#### Aldehyde 20b

Followed the same procedure as per aldehyde **20a**, starting with **19b**. The crude aldehyde was purified by flash chromatography (hexanes:EtOAc, 15:1) to provide 320 mg of aldehyde **20b** (74%) as a colourless oil. <sup>1</sup>H NMR (CDCl<sub>3</sub>) δ: 9.56 (s, 1H), 7.38–7.30 (m, 5H), 6.69 (t, 1H, *J* = 7.5 Hz), 6.55 (d, 1H, *J* = 2.9 Hz), 5.80 (ddt, 1H, *J* = 17.0, 10.2, 6.7 Hz), 5.02–4.92 (m, 2H), 4.67 (ABq, 2H, *J* = 18.4 Hz), 4.28–4.26 (m, 1H), 2.62 (m, 1H), 2.19–2.04 (m, 6H), 1.75–1.68 (m, 1H), 1.45–1.39 (m, 4H). <sup>13</sup>C NMR (CDCl<sub>3</sub>) δ: 193.7 (d), 148.6 (d), 138.7 (d), 137.9 (s), 131.7 (d), 128.4 (d), 127.7 (s), 127.6 (d), 114.2 (t), 73.3 (d), 70.6 (t), 33.5 (t), 28.5 (t), 27.9 (t), 27.7 (t), 22.8 (t).

#### Aldehyde 20c

Followed the same procedure as per aldehyde **20a**, starting with **19c**. The residue was purified by flash chromatography using hexane:EtOAc (9:1) as the eluent, providing 2.73 g (90%) of aldehyde **20c** as a clear colourless oil. IR (cm<sup>–1</sup>): 2953, 2855, 1698, 1612, 1513, 1248, 1090, 836. <sup>1</sup>H NMR (CDCl<sub>3</sub>) δ: 9.55 (s, 1H), 7.29 (d, 2H, *J* = 8.6 Hz), 6.89 (d, 2H, *J* = 8.6 Hz), 6.68 (t, 1H, *J* = 7.4 Hz), 6.52 (d, 1H, *J* = 2.8 Hz), 4.60 (ABq, 2H, *J* = 18.2 Hz), 4.28–4.23 (m, 1H), 3.80 (s, 3H), 3.43 (dd, 1H, *J* = 9.8, 5.9 Hz), 3.35 (dd, 1H, *J* = 9.8, 6.5 Hz), 2.63 (dt, 1H, *J* = 15.3, 4.8 Hz), 2.22–2.05 (m, 4H), 1.73–1.54 (m, 2H), 1.48–1.34 (m, 3H), 1.12–1.02 (m, 1H), 0.89 (s, 9H), 0.86 (d, 3H, *J* = 6.7 Hz), 0.03 (s, 6H). <sup>13</sup>C NMR (CDCl<sub>3</sub>) δ: 193.8 (d), 159.3 (s), 148.8 (d), 138.0 (s), 131.8 (d), 130.1 (s), 129.3 (d), 127.8 (s), 113.8 (d), 73.0 (d), 70.4 (t), 68.2 (t), 55.2 (q), 35.6 (d), 32.9 (t), 28.5 (t), 27.8 (t), 26.6 (t), 25.9 (q), 22.9 (t), 18.3 (s), 16.6 (q), –5.3 (q). LR-MS (*m/z* (relative intensity)): 415 ([M<sup>+</sup> – C<sub>4</sub>H<sub>9</sub>], 3), 122 (50), 74 (54), 121 (100). HR-MS calcd. for C<sub>24</sub>H<sub>35</sub>O<sub>4</sub>Si: 415.2304; found: 415.2313.

#### Aldehyde 20d

Followed the same procedure as per **20c**, starting with **19d**. Purification by flash chromatography using hexane:EtOAc (25:1) as the eluent, provided 2.81 g (80%) of aldehyde **20d** as a clear colourless oil. [α]<sub>D</sub>: +47.3° (*c* 1.10, CHCl<sub>3</sub>). IR (cm<sup>–1</sup>): 3070, 2954, 2856, 1700, 1471, 1427, 1255, 1112, 836, 702. <sup>1</sup>H NMR (CDCl<sub>3</sub>) δ: 9.38 (s, 1H), 7.74–7.65 (m, 4H), 7.46–7.28 (m, 11H), 6.78 (t, 1H, *J* = 7.4 Hz), 6.15 (d, 1H, *J* = 3.5 Hz), 4.61–4.58 (m, 1H), 4.56 (ABq, 2H, *J* = 19.4 Hz), 3.59–3.54 (m, 1H), 3.42 (dd, 1H,



$J = 9.7, 5.8$  Hz), 3.32 (dd, 1H,  $J = 9.7, 5.8$  Hz), 2.79 (dd, 1H,  $J = 15.6, 7.2$  Hz), 2.24–2.19 (m, 1H), 2.07 (q, 2H,  $J = 7.2$  Hz), 1.57–1.26 (m, 5H), 1.11 (s, 9H), 0.87 (s, 9H), 0.85 (d, 3H,  $J = 6.6$  Hz), 0.02 (s, 6H).  $^{13}\text{C}$  NMR ( $\text{CDCl}_3$ )  $\delta$ : 193.4 (d), 148.6 (d), 138.5 (s), 137.5 (s), 135.9 (d), 133.7 (d), 133.3 (s), 129.9 (d), 128.2 (d), 127.7 (d), 127.4 (d), 125.8 (s), 75.2 (d), 71.1 (t), 69.3 (d), 68.2 (t), 35.6 (d), 33.0 (t), 28.6 (t), 28.1 (t), 26.9 (q), 26.6 (t), 25.9 (q), 19.3 (s), 18.3 (s), 16.6 (q), –5.4 (q). LR-MS ( $m/z$  (relative intensity)): 696 ( $[\text{M}]^+$ , 20), 639 ( $[\text{M}^+ - \text{C}_4\text{H}_9]$ , 68), 91 (100), 74 (99), 199 (99), 135 (88), 531 (70), 197 (68). HR-MS calcd. for  $\text{C}_{43}\text{H}_{60}\text{O}_4\text{Si}_2$ : 696.4030; found: 696.4037.

### Acetal 21a

A solution of aldehyde **20c** (5.15 g, 10.9 mmol), PPTS (547 mg, 2.18 mmol), and ethylene glycol (6.07 mL, 109 mmol) in benzene (140 mL) was heated to reflux for 6 h. The solvent was removed in vacuo and the residue taken up in  $\text{Et}_2\text{O}$ . The ether layer was washed with satd. aq  $\text{NaHCO}_3$ , and brine. The combined aqueous layers were extracted once with ethyl ether. The organic layers were dried over  $\text{MgSO}_4$ , filtered, and concentrated to give 5.71 g (100%) of acetal **21a** as an oil. The crude acetal was used in the next step without further purification. IR ( $\text{cm}^{-1}$ ): 3030, 1612.  $^1\text{H}$  NMR ( $\text{CDCl}_3$ )  $\delta$ : 7.28 (d, 2H,  $J = 8.6$  Hz), 6.86 (d, 2H,  $J = 8.6$  Hz), 6.21 (d, 1H,  $J = 2.9$  Hz), 5.69 (t, 1H,  $J = 7.2$  Hz), 5.55 (s, 1H), 4.54 (s, 2H), 4.12–4.07 (m, 1H), 4.04–3.99 (m, 2H), 3.97–3.92 (m, 2H), 3.80 (s, 3H), 3.43 (dd, 1H,  $J = 9.7, 5.8$  Hz), 3.33 (dd, 1H,  $J = 9.7, 6.6$  Hz), 2.56 (dt, 1H,  $J = 15.4, 5.5$  Hz), 2.22–2.07 (m, 3H), 2.04–1.94 (m, 1H), 1.74–1.66 (m, 1H), 1.62–1.54 (m, 1H), 1.46–1.32 (m, 3H), 1.08–1.02 (m, 1H), 0.88 (s, 9H), 0.86 (d, 3H,  $J = 6.7$  Hz), 0.03 (s, 6H).  $^{13}\text{C}$  NMR ( $\text{CDCl}_3$ )  $\delta$ : 158.9 (s), 135.2 (s), 131.4 (s), 130.7 (s), 129.0 (d), 126.9 (d), 126.4 (d), 113.6 (d), 101.2 (d), 72.5 (d), 69.6 (t), 68.1 (t), 64.7 (t), 55.0 (q), 35.5 (d), 32.8 (t), 28.2 (t), 26.8 (t), 25.8 (t and q), 22.8 (t), 18.2 (s), 16.6 (q), –5.4 (q). LR-MS ( $m/z$  (relative intensity)): 516 ( $[\text{M}]^+$ , 2), 459 ( $[\text{M} - \text{C}_4\text{H}_9]$ , 8), 186 (70), 74 (75), 121 (100). HR-MS calcd. for  $\text{C}_{26}\text{H}_{39}\text{O}_5\text{Si}$ : 459.2567; found: 459.2574.

### Acetal 21b

Followed the same procedure as per **21a**, starting with **20d**. Purification by flash chromatography eluting with a hexanes:EtOAc (15:1 to 6:1) mixture provided 2.46 g (95%) of acetal **21b** as a colourless oil.  $[\alpha]_D^{25}$ : +105.3° ( $c$  0.74,  $\text{CHCl}_3$ ). IR ( $\text{cm}^{-1}$ ): 3070, 2954, 1471.  $^1\text{H}$  NMR ( $\text{CDCl}_3$ )  $\delta$ : 7.77–7.66 (m, 4H), 7.43–7.22 (m, 1H), 5.82 (d, 1H,  $J = 5.1$  Hz), 5.75 (t, 1H,  $J = 7.1$  Hz), 5.54 (s, 1H), 4.52 (d, 1H,  $J = 12.2$  Hz), 4.41–4.37 (m, 2H), 3.91–3.81 (m, 4H), 3.47–3.41 (m, 2H), 3.34 (dd, 1H,  $J = 9.7, 6.6$  Hz), 2.80–2.72 (m, 1H), 2.54–2.47 (m, 1H), 2.17–2.12 (m, 2H), 1.59–1.33 (m, 5H), 1.07 (s, 9H), 0.89 (s, 9H), 0.86 (d, 3H,  $J = 6.7$  Hz), 0.03 (s, 6H).  $^{13}\text{C}$  NMR ( $\text{CDCl}_3$ )  $\delta$ : 138.8 (s), 136.1 (d), 135.7 (s), 134.5 (s), 134.0 (s), 130.7 (s), 129.5 (d), 128.6 (d), 128.1 (d), 127.4 (d), 127.2 (d), 125.3 (d), 101.2 (d), 76.0 (d), 70.2 (t), 68.3 (t), 66.2 (d), 64.7 (t), 35.7 (d), 33.0 (t), 28.5 (t), 27.2 (t), 27.0 (q), 26.9 (q), 25.9 (d), 19.3 (s), 18.3 (s), 16.7 (q), –5.3 (q). LR-MS ( $m/z$  (relative intensity)): 683

( $[\text{M}^+ - \text{C}_4\text{H}_9]$ , 30), 91 (100). HR-MS calcd. for  $\text{C}_{41}\text{H}_{55}\text{O}_5\text{Si}_2$ : 683.3588; found: 683.3593.

### Alcohol 22a

TBAF (12.6 mL, 12.6 mmol) was added to a solution of acetal **21a** (5.45 g, 10.5 mmol) in THF (105 mL) at room temperature. After 6 h, a solution of EtOAc:ethyl ether (1:1) was added to the mixture. The resulting mixture was washed with satd. aq  $\text{NH}_4\text{Cl}$ , and the aqueous layer extracted once with EtOAc:ethyl ether (1:1). The combined organic layers were dried over  $\text{MgSO}_4$ , filtered, and concentrated. The crude residue was purified by flash chromatography using a mixture of hexanes:EtOAc (3:1 to 1:1) as the eluent to give 3.66 g (87% for two steps) of alcohol **22a** as a colourless oil. IR ( $\text{cm}^{-1}$ ): 3441, 2931, 1613, 1513, 1463, 1247, 1172, 1048, 821.  $^1\text{H}$  NMR ( $\text{CDCl}_3$ )  $\delta$ : 7.28 (d, 2H,  $J = 8.6$  Hz), 6.86 (d, 2H,  $J = 8.6$  Hz), 6.21 (d, 1H,  $J = 2.9$  Hz), 5.68 (t, 1H,  $J = 7.2$  Hz), 5.55 (s, 1H), 4.54 (s, 2H), 4.12–4.07 (m, 1H), 4.04–3.99 (m, 2H), 3.97 (m, 2H), 3.80 (s, 3H), 3.49 (dd, 1H,  $J = 9.5, 5.8$  Hz), 3.41 (dd, 1H,  $J = 9.5, 6.4$  Hz), 2.58 (dt, 1H,  $J = 15.3, 5.3$  Hz), 2.23–2.09 (m, 3H), 2.01–1.94 (m, 1H), 1.74–1.59 (m, 2H), 1.49–1.35 (m, 3H), 1.17–1.08 (m, 1H), 0.91 (d, 3H,  $J = 6.7$  Hz).  $^{13}\text{C}$  NMR ( $\text{CDCl}_3$ )  $\delta$ : 158.9 (s), 135.2 (s), 131.4 (s), 130.6 (s), 129.1 (d), 126.7 (d), 126.5 (d), 113.6 (d), 101.2 (d), 72.4 (d), 69.6 (t), 67.9 (t), 64.7 (t), 55.1 (q), 35.5 (d), 32.7 (t), 28.1 (t), 26.7 (t), 22.8 (t), 16.4 (q). LR-MS ( $m/z$  (relative intensity)): 402 ( $[\text{M}]^+$ , 1), 264 (45), 136 (50), 91 (55), 131 (60), 77 (60), 122 (90), 121 (100). HR-MS calcd. for  $\text{C}_{24}\text{H}_{34}\text{O}_5$ : 402.2406; found: 402.2397. Anal. calcd. for  $\text{C}_{24}\text{H}_{34}\text{O}_5$ : C 71.61, H 8.51, O 19.87; found: C 71.61, H 8.60.

### Alcohol 22b

Followed the same procedure as per **22a**, starting with **21b**. Flash chromatography (6:1 to 3:1 to 1:1 hexanes:ethyl acetate, followed by 100% EtOAc) gave 2.10 g (58%) of alcohol **22b** as a clear colourless oil and 908 mg of diol as a by-product.  $[\alpha]_D^{25}$ : +70.6° ( $c$  1.33,  $\text{CHCl}_3$ ). IR ( $\text{cm}^{-1}$ ): 3439, 3069, 1471.  $^1\text{H}$  NMR ( $\text{CDCl}_3$ )  $\delta$ : 7.81–7.70 (m, 4H), 7.46–7.27 (m, 1H), 5.88 (d, 1H,  $J = 6.0$  Hz), 5.80 (t, 1H,  $J = 7.2$  Hz), 5.59 (s, 1H), 4.57 (d, 1H,  $J = 12.3$  Hz), 4.44 (d, 1H,  $J = 12.3$  Hz), 4.46–4.42 (m, 1H), 3.93–3.83 (m, 4H), 3.52–3.47 (m, 2H), 3.41 (dd, 1H,  $J = 10.5, 6.4$  Hz), 2.86–2.78 (m, 1H), 2.58–2.52 (m, 1H), 2.22–2.15 (m, 2H), 1.73 (s, 1H), 1.65–1.61 (m, 1H), 1.56–1.40 (m, 3H), 1.22–1.15 (m, 1H), 1.12 (s, 9H), 0.94 (d, 3H,  $J = 6.7$  Hz).  $^{13}\text{C}$  NMR ( $\text{CDCl}_3$ )  $\delta$ : 138.7 (s), 136.0 (d), 135.6 (s), 134.4 (s), 133.9 (s), 130.6 (s), 129.4 (d), 128.4 (d), 128.0 (d), 127.4 (d), 127.1 (d), 125.4 (d), 101.1 (d), 75.9 (d), 70.2 (t), 68.0 (t), 66.2 (d), 64.7 (t), 35.5 (d), 32.8 (t), 28.2 (t), 27.3 (t), 26.9 (q), 26.7 (d), 19.3 (s), 16.5 (q). LR-MS ( $m/z$  (relative intensity)): 626 ( $[\text{M}]^+$ , 1), 569 ( $[\text{M}^+ - \text{C}_4\text{H}_9]$ , 20), 91 (100), 83 (80), 199 (65). HR-MS calcd. for  $\text{C}_{30}\text{H}_{50}\text{O}_5\text{Si}$ : 626.3427; found: 626.3417. Anal. calcd. for  $\text{C}_{30}\text{H}_{50}\text{O}_5\text{Si}$ : C 74.72, H 8.04, O 12.76, Si 4.48; found: C 74.61, H 8.01, O 12.79.

### Enoate 23a

To a stirred solution of alcohol **22a** (3.02 g, 7.49 mmol) in dichloromethane (61 mL) at room temperature was added Dess–Martin periodinane (4.76 g, 11.2 mmol). After 1.5 h,



ethyl ether (100 mL) was added to the reaction mixture, followed by a solution (100 mL) of  $\text{Na}_2\text{S}_2\text{O}_3$  (25 g) in satd. aq  $\text{NaHCO}_3$ . The mixture was stirred for 5 min until all the solids had entered solution. The layers were separated and the aqueous extracted with ethyl ether. The etheric layer was washed with satd. aq  $\text{NaHCO}_3$ , water, dried over  $\text{MgSO}_4$ , filtered, and concentrated, yielding 2.98 g (99%) of an aldehyde as a clear colourless oil that was used in the next step without further purification. IR ( $\text{cm}^{-1}$ ): 2934, 2861, 1722, 1613, 1513, 1462, 1247, 1058, 945, 821.  $^1\text{H}$  NMR ( $\text{CDCl}_3$ )  $\delta$ : 9.61 (d, 1H,  $J = 1.9$  Hz), 7.28 (d, 2H,  $J = 8.6$  Hz), 6.87 (d, 2H,  $J = 8.6$  Hz), 6.23 (d, 1H,  $J = 3.0$  Hz), 5.66 (t, 1H,  $J = 7.2$  Hz), 5.53 (s, 1H), 4.54 (s, 2H), 4.13–4.07 (m, 1H), 4.04–3.99 (m, 2H), 3.97–3.92 (m, 2H), 3.80 (s, 3H), 2.62–2.53 (m, 1H), 2.37–2.31 (m, 1H), 2.22–2.12 (m, 3H), 2.01–1.93 (m, 1H), 1.76–1.62 (m, 2H), 1.50–1.34 (m, 3H), 1.09 (d, 3H,  $J = 7.0$  Hz).  $^{13}\text{C}$  NMR ( $\text{CDCl}_3$ )  $\delta$ : 205.0 (d), 158.9 (s), 135.0 (s), 131.9 (s), 130.6 (s), 129.0 (d), 126.8 (d), 126.0 (d), 113.6 (d), 101.2 (d), 72.4 (d), 69.7 (t), 64.7 (t), 55.1 (q), 46.0 (d), 30.0 (t), 28.1 (t), 27.8 (t), 26.6 (t), 22.8 (t), 13.1 (q). LR-MS ( $m/z$  (relative intensity)): 400 ( $[\text{M}]^+$ , 1), 264 (35), 77 (58), 91 (61), 122 (63), 132 (70), 121 (100). HR-MS calcd. for  $\text{C}_{24}\text{H}_{32}\text{O}_5$ : 400.2250; found: 400.2253.

To a  $0^\circ\text{C}$  suspension of NaH (389 mg, 9.74 mmol) in THF (40.5 mL) was added MDEPA (1.78 mL, 9.74 mmol). After 1.25 h at  $0^\circ\text{C}$  this clear colourless solution was added via cannula to a solution of the crude aldehyde (2.98 g, 7.49 mmol) in THF (37.5 mL) at  $0^\circ\text{C}$ . After 30 min at  $0^\circ\text{C}$  the reaction was quenched with satd. aq  $\text{NH}_4\text{Cl}$  and the layers separated. The mixture was extracted with ethyl ether and the combined organic layers dried over  $\text{MgSO}_4$ , filtered, and concentrated. The crude residue was purified by flash chromatography eluting with a mixture of hexanes:EtOAc (3:1) yielding 2.72 g (80% for two steps) of **23a** as a single isomer. IR ( $\text{cm}^{-1}$ ): 3035, 1712, 1655, 1612, 1513.  $^1\text{H}$  NMR ( $\text{CDCl}_3$ )  $\delta$ : 7.27 (d, 2H,  $J = 8.6$  Hz), 6.89–6.81 (m, 3H), 6.21 (d, 1H,  $J = 3.0$  Hz), 5.77 (d, 1H,  $J = 15.7$  Hz), 5.65 (t, 1H,  $J = 7.1$  Hz), 5.53 (s, 1H), 4.54 (s, 2H), 4.12–4.06 (m, 1H), 4.04–3.99 (m, 2H), 3.97–3.92 (m, 2H), 3.80 (s, 3H), 3.72 (s, 3H), 2.59–2.52 (m, 1H), 2.32–2.27 (m, 1H), 2.22–2.10 (m, 3H), 2.00–1.94 (m, 1H), 1.74–1.66 (m, 1H), 1.39–1.36 (m, 4H), 1.03 (d, 3H,  $J = 6.7$  Hz).  $^{13}\text{C}$  NMR ( $\text{CDCl}_3$ )  $\delta$ : 167.1 (s), 158.9 (s), 154.5 (d), 135.1 (s), 131.6 (s), 130.6 (s), 129.0 (d), 126.6 (d), 126.3 (d), 119.2 (d), 113.6 (d), 101.2 (d), 72.4 (d), 69.6 (t), 64.7 (t), 55.0 (q), 51.2 (q), 36.3 (d), 35.6 (t), 28.1 (t), 27.8 (t), 26.9 (t), 22.8 (t), 19.2 (q). LR-MS ( $m/z$  (relative intensity)): 456 ( $[\text{M}]^+$ , 15), 320 (30), 77 (55), 91 (60), 122 (80), 121 (100). HR-MS calcd. for  $\text{C}_{27}\text{H}_{36}\text{O}_6$ : 456.2512; found: 456.2509. Anal. calcd. for  $\text{C}_{27}\text{H}_{36}\text{O}_6$ : C 71.03, H 7.95, O 21.03; found: C 71.00, H 7.92.

### Enoate 23b

Followed the same procedure as per **23a**, starting with **22b**. The aldehyde (clear colourless oil) was used in the next step without further purification. IR ( $\text{cm}^{-1}$ ): 3069, 2930, 2856, 1724, 1427, 1116.  $^1\text{H}$  NMR ( $\text{CDCl}_3$ )  $\delta$ : 9.60 (d, 1H,  $J = 1.9$  Hz), 7.76–7.65 (m, 4H), 7.44–7.22 (m, 11H), 5.84 (d, 1H,  $J = 5.1$  Hz), 5.73 (t, 1H,  $J = 7.2$  Hz), 5.52 (s, 1H), 4.52 (d, 1H,  $J = 12.3$  Hz), 4.41–4.37 (m, 2H), 3.91–3.81 (m, 4H), 3.49–3.42 (m, 1H), 2.80–2.72 (m, 1H), 2.51–2.45 (m,

1H), 2.20–2.10 (m, 2H), 1.74–1.69 (m, 1H), 1.51–1.37 (m, 3H), 1.23–1.18 (m, 1H), 1.08 (d, 3H,  $J = 6.9$  Hz), 1.06 (s, 9H). LR-MS ( $m/z$  (relative intensity)): 624 ( $[\text{M}]^+$ , 1), 567 ( $[\text{M}^+ - \text{C}_4\text{H}_9]$ , 25), 199 (100), 91 (92), 135 (60). HR-MS calcd. for  $\text{C}_{39}\text{H}_{48}\text{O}_5\text{Si}$ : 624.3271; found: 624.3261.

The crude enoate from the following step was purified by flash chromatography eluting with a mixture of hexanes:EtOAc (6:1) yielding 1.34 g (66% for two steps) of **23b** as clear colourless oil.  $[\alpha]_D^{25}$ : +19.5° ( $c$  1.32,  $\text{CHCl}_3$ ). IR ( $\text{cm}^{-1}$ ): 3046, 2929, 2856, 1722, 1427, 1272, 1111, 983.  $^1\text{H}$  NMR ( $\text{CDCl}_3$ )  $\delta$ : 7.78–7.67 (m, 4H), 7.44–7.23 (m, 11H), 6.87 (dd, 1H,  $J = 15.7$ , 8.0 Hz), 5.85 (d, 1H,  $J = 5.1$  Hz), 5.79 (d, 1H,  $J = 15.9$  Hz), 5.74 (t, 1H,  $J = 7.1$  Hz), 5.54 (s, 1H), 4.53 (d, 1H,  $J = 12.3$  Hz), 4.42–4.40 (m, 1H), 4.40 (d, 1H,  $J = 12.3$  Hz), 3.92–3.82 (m, 4H), 3.72 (s, 3H), 3.45 (dt, 1H,  $J = 10.0$ , 3.5 Hz), 2.81–2.73 (m, 1H), 2.53–2.47 (m, 1H), 2.34–2.29 (m, 1H), 2.15–2.13 (m, 2H), 1.42–1.39 (m, 4H), 1.08 (s, 9H), 1.05 (d, 3H,  $J = 6.7$  Hz).  $^{13}\text{C}$  NMR ( $\text{CDCl}_3$ )  $\delta$ : 167.2 (s), 154.7 (d), 138.8 (s), 136.1 (d), 135.7 (s), 134.5 (s), 134.0 (s), 131.0 (s), 129.5 (d), 128.1 (d), 127.4 (d), 127.3 (d), 125.6 (d), 119.3 (d), 101.2 (d), 76.0 (d), 70.3 (t), 66.2 (d), 64.8 (t), 51.4 (q), 36.5 (d), 35.8 (t), 28.1 (t), 27.3 (t), 27.0 (q), 19.4 (q). LR-MS ( $m/z$  (relative intensity)): 680 ( $[\text{M}]^+$ , 2), 623 ( $[\text{M}^+ - \text{C}_4\text{H}_9]$ , 35), 91 (100). HR-MS calcd. for  $\text{C}_{42}\text{H}_{52}\text{O}_6\text{Si}$ : 680.3533; found: 680.3526. Anal. calcd. for  $\text{C}_{42}\text{H}_{52}\text{O}_6\text{Si}$ : C 74.08, H 7.70, O 14.10, Si 4.12; found: C 73.97, H 7.77, O 14.12.

### Aldehyde 24a

A solution of enoate **23a** (2.67 g, 5.84 mmol), PPTS (440 mg, 1.75 mmol), and wet acetone (117 mL) was heated to reflux for 3 h. The solvent was removed in vacuo and the residue taken up in ethyl ether (200 mL) and washed with saturated aq  $\text{NaHCO}_3$  (60 mL) and brine (60 mL). The combined aqueous layers were back-extracted once with ether. The combined organic layers were dried over  $\text{MgSO}_4$ , filtered, and concentrated. Purification by flash chromatography (hexanes:EtOAc, 3:1) yielded 2.23 g (92%) of aldehyde **24a** as a colourless oil. IR ( $\text{cm}^{-1}$ ): 2932, 2857, 1722, 1694, 1656, 1612, 1513, 1435, 1248, 1072, 822.  $^1\text{H}$  NMR ( $\text{CDCl}_3$ )  $\delta$ : 9.53 (s, 1H), 7.29 (d, 2H,  $J = 8.6$  Hz), 6.89 (d, 2H,  $J = 8.6$  Hz), 6.84 (dd, 1H,  $J = 15.7$ , 8.0 Hz), 6.66 (t, 1H,  $J = 7.3$  Hz), 6.53 (d, 1H,  $J = 2.8$  Hz), 5.77 (d, 1H,  $J = 15.6$  Hz), 4.59 (ABq, 2H,  $J = 18.4$  Hz), 4.28–4.22 (m, 1H), 3.80 (s, 3H), 3.71 (s, 3H), 2.65–2.57 (m, 1H), 2.31–2.26 (m, 1H), 2.20–2.02 (m, 4H), 1.72–1.60 (m, 1H), 1.44–1.37 (m, 4H), 1.03 (d, 3H,  $J = 6.7$  Hz).  $^{13}\text{C}$  NMR ( $\text{CDCl}_3$ )  $\delta$ : 193.7 (d), 167.1 (s), 159.2 (s), 154.5 (d), 149.2 (d), 137.7 (s), 131.1 (d), 129.9 (s), 129.2 (d), 127.9 (s), 119.2 (d), 113.7 (d), 72.8 (d), 70.3 (t), 55.1 (q), 51.2 (q), 36.3 (d), 35.5 (t), 28.0 (t), 27.7 (t), 26.7 (t), 22.8 (t), 19.2 (q). LR-MS ( $m/z$  (relative intensity)): 412 ( $[\text{M}]^+$ , 3), 122 (100), 121 (75). HR-MS calcd. for  $\text{C}_{25}\text{H}_{32}\text{O}_5$ : 412.2250; found: 412.2247.

### Aldehyde 24b

Followed the same procedure **24a**, starting from **23b**. After purification by flash chromatography (hexanes:ethyl acetate, 6:1) 467 mg (92%) of aldehyde **24b** were collected as a clear colourless oil.  $[\alpha]_D^{25}$ : +16.4° ( $c$  0.63,  $\text{CHCl}_3$ ). IR ( $\text{cm}^{-1}$ ): 3069, 2930, 2857, 1722, 1698, 1428, 1272, 1112.  $^1\text{H}$  NMR



(CDCl<sub>3</sub>)  $\delta$ : 9.39 (s, 1H), 7.76–7.68 (m, 4H), 7.48–7.24 (m, 11H), 6.86 (dd, 1H,  $J$  = 15.7, 8.0 Hz), 6.80 (t, 1H,  $J$  = 7.4 Hz), 6.20 (d, 1H,  $J$  = 3.5 Hz), 5.78 (d, 1H,  $J$  = 15.6 Hz), 4.64–4.62 (m, 1H), 4.59 (ABq, 2H,  $J$  = 21.0 Hz), 3.71 (s, 3H), 3.62–3.58 (m, 1H), 2.81 (dd, 1H,  $J$  = 15.6, 7.0 Hz), 2.32–2.20 (m, 2H), 2.14–2.05 (m, 2H), 1.46–1.34 (m, 4H), 1.13 (s, 9H), 1.04 (d, 3H,  $J$  = 6.8 Hz). <sup>13</sup>C NMR (CDCl<sub>3</sub>)  $\delta$ : 193.3 (d), 167.1 (s), 154.5 (d), 149.0 (d), 138.4 (s), 137.3 (s), 135.8 (d), 133.5 (s), 133.2 (s), 133.0 (d), 129.8 (d), 127.6 (d), 127.4 (d), 127.3 (d), 125.9 (s), 119.2 (d), 75.1 (d), 71.1 (t), 69.2 (d), 51.2 (q), 36.4 (d), 35.6 (t), 28.1 (t), 26.8 (q), 19.3 (q). LR-MS ( $m/z$  (relative intensity)): 636 ([M]<sup>+</sup>, 10), 579 ([M<sup>+</sup> – C<sub>4</sub>H<sub>9</sub>], 25), 471 (100), 91 (48). HR-MS calcd. for C<sub>40</sub>H<sub>48</sub>O<sub>5</sub>Si: 636.3271; found: 636.3277.

### Alcohol 25

To a cooled 0°C biphasic mixture of aldehyde **24a** (744 mg, 1.80 mmol), dichloromethane (15 mL), and water (830  $\mu$ L) was added DDQ (532 mg, 2.34 mmol) resulting in a deep green coloured mixture. The mixture was stirred for 2.5 h at which time the colour had become orange and TLC indicated reaction completion. The mixture was poured into a separatory funnel containing dichloromethane and satd aq NaHCO<sub>3</sub>. The mixture was vigorously shaken and the layers separated. After extraction with dichloromethane, a brine wash, drying over MgSO<sub>4</sub>, filtration, and concentration in vacuo, the crude product was purified by flash chromatography (hexanes:EtOAc, 3:1 to 1:1) yielded 367 mg (70%) of aldehyde **25** as a colourless oil. IR (cm<sup>-1</sup>): 3426, 2930, 2858, 1719, 1694, 1436, 1274, 1199, 1035, 870. <sup>1</sup>H NMR (CDCl<sub>3</sub>)  $\delta$ : 9.53 (s, 1H), 6.83 (dd, 1H,  $J$  = 15.7, 8.0 Hz), 6.65 (t, 1H,  $J$  = 7.3 Hz), 6.48 (d, 1H,  $J$  = 2.9 Hz), 5.75 (d, 1H,  $J$  = 15.7 Hz), 4.57–4.51 (m, 1H), 3.70 (s, 3H), 2.56 (dt, 1H,  $J$  = 15.4, 4.9 Hz), 2.32–2.02 (m, 6H), 1.58 (dt, 1H,  $J$  = 12.3, 4.4 Hz), 1.43–1.33 (m, 4H), 1.02 (d, 3H,  $J$  = 6.7 Hz). <sup>13</sup>C NMR (CDCl<sub>3</sub>)  $\delta$ : 193.9 (d), 167.3 (s), 154.7 (d), 150.8 (d), 137.5 (s), 131.4 (d), 127.7 (s), 119.2 (d), 66.9 (d), 51.4 (q), 36.5 (d), 35.6 (t), 31.2 (t), 28.1 (t), 26.7 (t), 22.9 (t), 19.3 (q). LR-MS ( $m/z$  (relative intensity)): 292 ([M]<sup>+</sup>, 1), 261 ([M<sup>+</sup> – MeO], 10), 133 (100), 77 (60), 95 (60). HR-MS calcd. for C<sub>17</sub>H<sub>24</sub>O<sub>4</sub>: 292.1674; found: 292.1664. Anal. calcd. for C<sub>27</sub>H<sub>36</sub>O<sub>6</sub>: C 71.03, H 7.95, O 21.03; found: C 71.00, H 7.92.

### Acetate 29a

Propyne (1.65 mL, 29.3 mmol) was condensed at –78°C in a 100 mL round-bottomed flask. THF (15 mL) was added followed by a solution of *n*-BuLi (4.66 mL, 1.88 M in pentane, 8.76 mmol). The resulting white suspension was stirred for 1 h at –78°C. Then, (*E*)-1-triphenylmethoxy-3-penten-2-one **28** (1.96 g, 5.72 mmol) in THF (7 mL) was added to the white suspension. The reaction mixture was warmed to –20°C and stirred for 2 h. Acetic anhydride (1.42 mL, 15.0 mmol) was added and the reaction mixture warmed to 0°C. The reaction was quenched with saturated ammonium chloride and the two phases were separated. The aqueous phase was extracted with Et<sub>2</sub>O, the combined organic fractions were washed with satd. aq NaHCO<sub>3</sub>, water and brine, dried over MgSO<sub>4</sub>, filtered, and evaporated under reduced pressure to give 2.64 g of **29a** as a yellow oil. Flash

chromatography on silica gel eluting with EtOAc and hexanes (20:80) yielded a white solid (2.04 g, 84%). IR (neat, cm<sup>-1</sup>): 3058, 1747. <sup>1</sup>H NMR (C<sub>6</sub>D<sub>6</sub>)  $\delta$ : 7.67–7.62 (m, 6H), 7.15–6.99 (m, 9H), 6.27 (dq, 1H,  $J$  = 15.3, 6.6 Hz), 5.92 (dd, 1H,  $J$  = 15.3, 1.6 Hz), 3.88 (d, 1H,  $J$  = 9.0 Hz), 3.66 (d, 1H,  $J$  = 9.0 Hz), 1.71 (s, 3H), 1.54 (dd, 3H,  $J$  = 6.6, 1.6 Hz), 1.47 (s, 3H). LR-MS ( $m/z$  (relative intensity)): 424 ([M]<sup>+</sup>, 2), 243 (100), 165 (55). HR-MS calcd. for C<sub>29</sub>H<sub>28</sub>O<sub>3</sub>: 424.2038; found: 424.2047.

### Acetate 29b

Followed the same procedure as per acetate **29a**. Flash chromatography on silica gel eluting with EtOAc and hexanes (10:90) gave **29b** as a colourless oil (4.63 g, 90%). IR (neat, cm<sup>-1</sup>): 3060, 2930, 1749, 1229, 1100, 837, 704. <sup>1</sup>H NMR (C<sub>6</sub>D<sub>6</sub>)  $\delta$ : 7.49–7.45 (m, 6H), 7.36–7.14 (m, 9H), 6.10–5.97 (m, 1H), 5.63 (dm, 1H,  $J$  = 15.4 Hz), 4.59 (qd, 1H,  $J$  = 6.5, 2.2 Hz), 3.41–3.28 (m, 2H), 2.02 (s, 3H), 1.72 (dd, 3H,  $J$  = 6.6, 1.0 Hz), 1.41 (dd, 3H,  $J$  = 6.5, 1.8 Hz), 0.86 (s, 9H), 0.07–0.05 (m, 6H). LR-MS ( $m/z$  (relative intensity)): 568 ([M]<sup>+</sup>, 1), 243 (100), 165 (50). HR-MS calcd. for C<sub>36</sub>H<sub>44</sub>O<sub>4</sub>Si: 568.3009; found: 568.3000.

### Acetate 29c

Followed the same procedure as per acetate **29a**. Flash chromatography on silica gel eluting with EtOAc and hexanes (5:95) gave a colourless oil (5.36 g, 85%). IR (neat, cm<sup>-1</sup>): 3059, 2928, 1748. <sup>1</sup>H NMR (CDCl<sub>3</sub>)  $\delta$ : 7.48–7.44 (m, 6H), 7.33–7.21 (m, 9H), 6.10–5.96 (m, 1H), 5.63 (dm, 1H,  $J$  = 14.7 Hz), 4.42–4.36 (m, 2H), 3.39 (d, 1H,  $J$  = 9.0 Hz), 3.29 (d, 1H,  $J$  = 9.0 Hz), 3.23–3.11 (m, 4H), 2.03 (s, 3H), 1.85–1.49 (m, 6H), 1.72 (d, 3H,  $J$  = 6.5 Hz), 0.86 (s, 9H), 0.06–0.04 (m, 6H). LR-MS ( $m/z$  (relative intensity)): 700 ([M]<sup>+</sup>, 5), 640 ([M<sup>+</sup> – AcOH], 20), 243 (100), 165 (100). HR-MS calcd. for C<sub>41</sub>H<sub>52</sub>O<sub>4</sub>S<sub>2</sub>Si: 700.3076; found: 700.3085.

### Allene 30

Copper iodide (2.70 g, 14.2 mmol) and lithium bromide (1.23 g, 14.2 mmol) were suspended in THF (30 mL) and the suspension was cooled to 0°C. A suspension of magnesium bromide (4.73 mL, 3.0 M in Et<sub>2</sub>O, 14.2 mmol) was added and the resulting yellow suspension was stirred for 0.5 h. Acetate **29a** (1.00 g, 2.36 mmol) in THF (10 mL) was added drop wise and the reaction mixture was stirred for an additional 0.5 h at 0°C. Then, Et<sub>2</sub>O was added (40 mL) and the mixture was poured into a saturated aqueous NH<sub>4</sub>Cl–NH<sub>4</sub>OH (9:1) solution and vigorously stirred in an atmosphere of air for 1 h. The phases were separated, the aqueous phase was extracted with Et<sub>2</sub>O, the combined organic fractions were washed with water and brine, dried over MgSO<sub>4</sub>, filtered, and evaporated under reduced pressure to give 1.1 g of a yellow oil. Flash chromatography on silica gel eluting with EtOAc and hexanes (5:95) yielded a colourless oil (837 mg, 93%). IR (neat, cm<sup>-1</sup>): 3058, 1955, 1491. <sup>1</sup>H NMR (C<sub>6</sub>D<sub>6</sub>)  $\delta$ : 7.66–7.61 (m, 6H), 7.15–6.99 (m, 9H), 6.08 (dd, 1H,  $J$  = 15.8, 1.6 Hz), 5.54 (dq, 1H,  $J$  = 15.8, 6.6 Hz), 3.96 (s, 2H), 1.74 (s, 6H), 1.54 (dd, 3H,  $J$  = 6.6, 1.6 Hz). LR-MS ( $m/z$  (relative intensity)): 380 ([M]<sup>+</sup>, 1), 243 (100). HR-MS calcd. for C<sub>28</sub>H<sub>28</sub>O: 380.2140; found: 380.2147.



**Allene 31a**

Acetate **29b** (4.60 g, 8.09 mmol) was dissolved in THF (20 mL). Tetrabutylammonium fluoride (16.17 mL, 1.0 M in THF, 16.17 mmol) was added and the orange solution was stirred for 12 h. Then, the mixture was poured into sat.  $\text{NH}_4\text{Cl}$ , the phases were separated, and the aqueous phase was extracted with  $\text{Et}_2\text{O}$ . The combined organic fractions were washed with water and brine, dried over  $\text{MgSO}_4$ , filtered, and evaporated under reduced pressure to give 3.70 g of an orange oil. Flash chromatography on silica gel eluting with EtOAc and hexanes (20:80) gave a fluffy white powder (2.80 g, 76%). IR (neat,  $\text{cm}^{-1}$ ): 3467, 3023, 1738, 1449.  $^1\text{H}$  NMR ( $\text{C}_6\text{D}_6$ )  $\delta$ : 7.49–7.44 (m, 6H), 7.33–7.22 (m, 9H), 6.10–5.96 (m, 1H), 5.61 (dd, 1H,  $J = 15.4$ , 1.6 Hz), 4.63–4.56 (m, 1H), 3.39–3.30 (m, 2H), 2.04 (s, 3H), 1.73 (dd, 3H,  $J = 6.6$ , 1.6 Hz), 1.46 (d, 3H,  $J = 6.6$  Hz). LR-MS ( $m/z$  (relative intensity)): 454 ( $[\text{M}]^+$ , 1), 243 (100), 165 (75). HR-MS calcd. for  $\text{C}_{30}\text{H}_{30}\text{O}_4$ : 454.2144; found: 454.2151.

The cuprate addition on this compound was performed as per allene **30**. Flash chromatography on silica gel eluting with EtOAc and hexanes (20:80) gave **31a** as a white powder (2.54 g, 100%) as a mixture of two inseparable isomers. IR (neat,  $\text{cm}^{-1}$ ): 3588–3146, 3058, 1950, 1448.  $^1\text{H}$  NMR ( $\text{C}_6\text{D}_6$ )  $\delta$ : 7.50–7.42 (m, 6H), 7.32–7.21 (m, 9H), 5.85 (dm, 1H,  $J = 15.7$  Hz), 5.49–5.36 (m, 1H), 4.34–4.25 (m, 1H), 3.75–3.65 (m, 2H), 1.86 (d, 3H,  $J = 1.8$  Hz), 1.69 (dd, 3H,  $J = 6.6$ , 1.6 Hz), 1.36 (dd, 3H,  $J = 6.4$ , 1.8 Hz). LR-MS ( $m/z$  (relative intensity)): 409 ( $[\text{M} - 1]$ , 10), 259 (50), 243 (100). HR-MS calcd. for  $\text{C}_{29}\text{H}_{29}\text{O}_2$ : 409.2167; found: 409.2149.

**Allene 31b**

Followed the same procedure as per allene **31a**, starting from **29c**. Flash chromatography of the intermediate alcohol on silica gel eluting with EtOAc and hexanes (30:70) gave a white powder (5.09 g, 89%). IR (neat,  $\text{cm}^{-1}$ ): 3407, 3022, 1738.  $^1\text{H}$  NMR ( $\text{CDCl}_3$ )  $\delta$ : 7.48–7.44 (m, 6H), 7.34–7.22 (m, 9H), 6.03 (dq, 1H,  $J = 15.4$ , 6.6 Hz), 5.62 (dd, 1H,  $J = 15.4$ , 1.7 Hz), 4.44 (q, 1H,  $J = 5.7$  Hz), 4.38 (td, 1H,  $J = 7.0$ , 1.8 Hz), 3.39–3.30 (m, 2H), 3.26–3.12 (m, 4H), 2.05 (s, 3H), 1.85–1.70 (m, 4H), 1.74 (dd, 3H,  $J = 6.6$ , 1.7 Hz), 1.64–1.52 (m, 2H), 1.56 (s, 1H). LR-MS ( $m/z$  (relative intensity)): 568 ( $[\text{M}^+ - \text{H}_2\text{O}]$ , 3), 508 (5), 243 (100), 105 (100). HR-MS calcd. for  $\text{C}_{35}\text{H}_{36}\text{O}_3\text{S}_2$ : 568.2106; found: 568.2114.

The alcohol was submitted to the cuprate reaction as per the alcohol precursor of **31a**. Flash chromatography on silica gel eluting with EtOAc and hexanes (20:80) gave **31b** as a white powder (4.31 g, 93%) containing an inseparable mixture of two isomers. IR ( $\text{cm}^{-1}$ ): 3559, 3431, 3021, 1952, 1597.  $^1\text{H}$  NMR ( $\text{CDCl}_3$ )  $\delta$ : 7.49–7.42 (m, 12H), 7.32–7.21 (m, 18H), 5.86 (dd, 2H,  $J = 16.0$ , 1.6 Hz), 5.44 (dm, 2H,  $J = 16.0$  Hz), 4.41 (q, 2H,  $J = 7.1$  Hz), 4.16–4.06 (m, 2H), 3.75–3.65 (m, 4H), 3.27–3.13 (m, 8H), 1.89–1.72 (m, 4H), 1.83 (s, 6H), 1.71–1.48 (m, 8H), 1.70 (dd, 6H,  $J = 6.6$ , 1.6 Hz), 1.55 (s, 2H). LR-MS ( $m/z$  (relative intensity)): 542 ( $[\text{M}]^+$ , 1), 513 ( $[\text{M}^+ - \text{C}_2\text{H}_5]$ , 3), 299 (10), 243 (100). HR-MS calcd. for  $\text{C}_{34}\text{H}_{38}\text{O}_2\text{S}_2$ : 542.2313; found: 542.2309.

**Diester 32a**

Allene **31a** (1.84 g, 4.49 mmol), fumaric acid, monoethyl ester (775 mg, 5.38 mmol), and DMAP (110 mg, 0.90 mmol) were dissolved in  $\text{CH}_2\text{Cl}_2$  (40 mL). The solution

was cooled to  $0^\circ\text{C}$  and stirred for 0.5 h. DCC (1.11 g, 5.38 mmol) was added in small portions and the reaction mixture stirred for 2.5 h during which time a white precipitate formed. The solvent was evaporated and the product purified by flash chromatography on silica gel eluting with EtOAc and hexanes (15:85) giving **32a** as a colourless oil (2.24 g, 93%) containing a 1:1 mixture of inseparable diastereomers. IR (neat,  $\text{cm}^{-1}$ ): 3039, 1957, 1722, 1449.  $^1\text{H}$  NMR ( $\text{C}_6\text{D}_6$ )  $\delta$ : 7.64–7.57 (m, 6H), 7.16–7.09 (m, 9H), 7.06–7.00 (m, 2H), 5.93 (dm, 1H,  $J = 15.8$  Hz), 5.74–5.59 (m, 1H), 5.51–5.39 (m, 1H), 3.94–3.92 (m, 2H), 3.90–3.78 (m, 2H), 1.77 (d, 3H,  $J = 7.8$  Hz), 1.45 (dd, 3H,  $J = 6.6$ , 1.6 Hz), 1.36 (t, 3H,  $J = 6.1$  Hz), 0.84–0.80 (m, 3H). LR-MS ( $m/z$  (relative intensity)): 537 ( $[\text{M} + 1]$ , 2), 243 (95), 167 (90), 105 (100). HR-MS calcd. for  $\text{C}_{35}\text{H}_{37}\text{O}_5$ : 537.2641; found: 537.2622.

**Diester 32b**

Followed the same procedure as per diester **32a**, starting from **31b**. Flash chromatography on silica gel eluting with EtOAc and hexanes (15:85) gave a colourless oil (1.83 g, 88%) containing a mixture of two isomers. IR (neat,  $\text{cm}^{-1}$ ): 3026, 1958, 1723, 1646.  $^1\text{H}$  NMR ( $\text{CDCl}_3$ , integrated for two isomers)  $\delta$ : 7.48–7.42 (m, 12H), 7.32–7.20 (m, 18H), 6.85–6.80 (m, 4H), 5.88–5.73 (m, 2H), 5.47–5.37 (m, 4H), 4.42–4.19 (m, 6H), 3.67 (s, 4H), 3.27–3.10 (m, 8H), 1.95–1.74 (m, 14H), 1.71–1.64 (m, 6H), 1.55–1.41 (m, 4H), 1.30 (t, 3H,  $J = 7.1$  Hz), 1.29 (t, 3H,  $J = 7.1$  Hz). LR-MS ( $m/z$  (relative intensity)): 623 ( $[\text{M}^+ - \text{OEt}]$ , 5), 381 (20), 243 (100). HR-MS calcd. for  $\text{C}_{38}\text{H}_{39}\text{O}_4\text{S}_2$ : 623.2290; found: 623.2303.

**Cycloadduct 33**

Allene **30** (837 mg, 2.2 mmol) and methyl fumarate (634 mg, 4.4 mmol) were dissolved in benzene (10 mL) and refluxed for 12 h. Benzene was evaporated to yield 1.6 g of a yellow oil. Flash chromatography on silica gel eluting with EtOAc and hexanes (5:95) afforded 1.04 g of a colourless oil (90%). IR (neat,  $\text{cm}^{-1}$ ): 3059, 1732, 1448.  $^1\text{H}$  NMR ( $\text{CHCl}_3$ )  $\delta$ : 7.46–7.42 (m, 6H), 7.32–7.19 (m, 9H), 5.92 (d, 1H,  $J = 2.7$  Hz), 4.04 (d, 1H,  $J = 5.1$  Hz), 3.75–3.62 (m, 2H), 3.71 (s, 3H), 3.51 (s, 3H), 2.89 (dd, 1H,  $J = 7.9$ , 5.1 Hz), 2.43–2.33 (m, 1H), 1.76 (s, 3H), 1.43 (s, 3H), 1.20 (d, 3H,  $J = 7.2$  Hz). LR-MS ( $m/z$  (relative intensity)): 524 ( $[\text{M}]^+$ , 0.5), 443 (1), 243 (100), 165 (5). HR-MS calcd. for  $\text{C}_{34}\text{H}_{36}\text{O}_5$ : 524.2563; found: 524.2569.

**Aldehyde 34**

Cycloadduct **33** (369 mg, 0.75 mmol) was dissolved in  $\text{Et}_2\text{O}$  (2 mL). An 88% aqueous solution of formic acid (23 mL) in  $\text{Et}_2\text{O}$  (17 mL) was added and the mixture was stirred for 20 min. It was poured into EtOAc (100 mL). The phases were separated, the organic phase was washed with water, satd.  $\text{NaHCO}_3$  and brine, dried over  $\text{MgSO}_4$ , filtered, and evaporated under reduced pressure to give 215 mg of a yellow oil. Flash chromatography on silica gel eluting with EtOAc and hexanes (30:70) yielded a colourless oil (156 mg, 73%). IR (neat,  $\text{cm}^{-1}$ ): 3454, 1732, 1435.  $^1\text{H}$  NMR ( $\text{CHCl}_3$ )  $\delta$ : 5.69 (d, 1H,  $J = 3.1$  Hz), 4.48 (dd, 1H,  $J = 12.3$ , 5.5 Hz), 4.13 (dd, 1H,  $J = 12.3$ , 5.5 Hz), 4.08 (d, 1H,  $J = 4.9$  Hz), 3.72 (s, 3H), 3.67 (s, 3H), 2.73 (dd, 1H,  $J = 7.0$ ,



4.9 Hz), 2.51–2.39 (m, 1H), 2.28 (t, 1H,  $J = 5.5$  Hz), 1.82 (s, 3H), 1.79 (s, 3H), 1.10 (d, 3H,  $J = 7.3$  Hz). LR-MS ( $m/z$  (relative intensity)): 282 ( $[M]^+$ , 1), 264 ( $[M^+ - H_2O]$ , 5), 232 (20), 204 (100), 173 (85), 145 (60), 91 (30). HR-MS calcd. for  $C_{15}H_{22}O_5$ : 282.1467; found: 282.1471.

This alcohol (146 mg, 0.52 mmol) was dissolved in  $CH_2Cl_2$  (5 mL). Dess–Martin periodinane (288 mg, 0.68 mmol) was added and the mixture was stirred for 0.5 h.  $Et_2O$  (10 mL) was added provoking the formation of a white precipitate. The suspension was neutralized with satd.  $NaHCO_3$  (20 mL) containing 5 g of sodium thiosulfate. The resulting bilayered mixture was vigorously stirred for 0.5 h. The phases were separated, the aqueous phase was extracted with  $Et_2O$ , the combined organic fractions were washed with water and brine, dried over  $MgSO_4$ , filtered, and evaporated under reduced pressure to give 146 mg of **34** as a colourless oil (146 mg, 100%). IR (neat,  $cm^{-1}$ ): 2954, 2713, 1732, 1694.  $^1H$  NMR ( $C_6D_6$ )  $\delta$ : 9.30 (s, 1H), 6.10 (d, 1H,  $J = 3.0$  Hz), 4.24 (d, 1H,  $J = 4.2$  Hz), 3.26 (s, 3H), 3.20 (s, 3H), 3.05 (dd, 1H,  $J = 6.3$ , 4.2 Hz), 2.69 (quint, 1H,  $J = 7.1$ , 3.0 Hz), 1.71 (s, 3H), 1.61 (s, 3H), 1.02 (d, 3H,  $J = 7.3$  Hz). LR-MS ( $m/z$  (relative intensity)): 280 ( $[M]^+$ , 50), 221 (65), 161 (100). HR-MS calcd. for  $C_{15}H_{20}O_5$ : 280.1311; found: 280.1306.

### Cycloadducts 35a

Allene **32a** (2.32 g, 4.32 mmol) was dissolved in benzene (100 mL). The solution was refluxed for 15 h. The solvent was evaporated and the crude product (2.75 g) was purified by flash chromatography on silica gel eluting with EtOAc and hexanes (30:70) giving a white powder (1.59 g, 69%) containing an inseparable mixture of two diastereomers. IR (neat,  $cm^{-1}$ ): 3022, 2978, 1732, 1449.  $^1H$  NMR ( $C_6D_6$ , integrated for two isomers)  $\delta$ : 7.57–7.52 (m, 12H), 7.15–7.01 (m, 18H), 6.38 (d, 1H,  $J = 7.5$  Hz), 6.36 (d, 1H,  $J = 7.5$  Hz), 4.17–4.00 (m, 6H), 3.96–3.70 (m, 6H), 3.32 (dd, 1H,  $J = 11.2$ , 4.8 Hz), 3.23 (dd, 1H,  $J = 11.7$ , 5.0 Hz), 2.77–2.61 (m, 2H), 1.25–1.02 (m, 12H), 0.99 (d, 6H,  $J = 7.0$  Hz), 0.93 (d, 6H,  $J = 7.0$  Hz). LR-MS ( $m/z$  (relative intensity)): 536 ( $[M]^+$ , 1), 491 ( $[M^+ - C_2H_5O]$ , 5), 243 (100). HR-MS calcd. for  $C_{33}H_{31}O_4$ : 491.2222; found: 491.2230.

### Cycloadducts 35b

Followed the same procedure as per **35a**, starting from **32b**. Flash chromatography on silica gel eluting with EtOAc and hexanes (20:80) gave a colourless oil (1.41 g, 69%) containing an inseparable mixture of two isomers. IR (neat,  $cm^{-1}$ ): 3023, 1732, 1597.  $^1H$  NMR ( $CDCl_3$ , integrated for two isomers)  $\delta$ : 7.48–7.38 (m, 12H), 7.33–7.22 (m, 18H), 6.43 (d, 1H,  $J = 7.3$  Hz), 6.38 (d, 1H,  $J = 7.0$  Hz), 4.82 (dm, 1H,  $J = 8.4$  Hz), 4.49–4.40 (m, 3H), 4.24 (q, 2H,  $J = 7.1$  Hz), 4.23 (q, 2H,  $J = 7.1$  Hz), 3.87–3.73 (m, 4H), 3.68 (dm, 1H,  $J = 11.6$  Hz), 3.59 (dt, 1H,  $J = 11.3$ , 2.4 Hz), 3.26–3.12 (m, 8H), 3.04 (dd, 1H,  $J = 11.3$ , 4.8 Hz), 2.97 (dd, 1H,  $J = 11.6$ , 5.0 Hz), 2.89–2.74 (m, 2H), 1.97–1.52 (m, 12 H), 1.60 (s, 3H), 1.57 (s, 3H), 1.32 (t, 3H,  $J = 7.1$  Hz), 1.31 (t, 3H,  $J = 7.1$  Hz), 0.95 (d, 3H,  $J = 7.0$  Hz), 0.93 (d, 3H,  $J = 7.0$  Hz). LR-MS ( $m/z$  (relative intensity)): 668 ( $[M]^+$ , 3), 381 (20), 243 (100). HR-MS calcd. for  $C_{40}H_{44}O_5S_2$ : 668.2630; found: 668.2643.

### Aldehydes 36a and 36b

Followed the same procedure as for the deprotection of **33** and the Dess–Martin oxidation to **34**. Flash chromatography on silica gel eluting with EtOAc and hexanes (40:60) gave two diastereomeric alcohols as a colourless oils (each 256 mg for a total of 512 mg, 82%). Less polar isomer:  $^1H$  NMR ( $CDCl_3$ )  $\delta$ : 6.27 (d, 1H,  $J = 7.0$  Hz), 5.08 (q, 1H, 6.8 Hz), 4.42–4.31 (m, 2H), 4.21 (q, 1H,  $J = 7.2$  Hz), 4.21 (q, 1H,  $J = 7.2$  Hz), 3.63 (dt, 1H,  $J = 10.9$ , 2.5 Hz), 3.04 (dd, 1H,  $J = 10.9$ , 4.8 Hz), 2.86–2.74 (m, 1H), 2.03–2.00 (m, 3H), 1.57 (d, 3H,  $J = 6.8$  Hz), 1.48–1.42 (m, 1H), 1.29 (t, 3H,  $J = 7.2$  Hz), 0.94 (d, 3H,  $J = 7.1$  Hz). More polar isomer: IR (neat,  $cm^{-1}$ ): 3453, 1732, 1454.  $^1H$  NMR ( $CDCl_3$ )  $\delta$ : 6.20 (d, 1H,  $J = 6.9$  Hz), 4.74 (q, 1H,  $J = 6.9$  Hz), 4.41 (dd, 1H,  $J = 12.6$ , 5.2 Hz), 4.32 (dd, 1H,  $J = 12.6$ , 6.2 Hz), 4.23 (q, 2H,  $J = 7.1$  Hz), 3.71 (dt, 1H,  $J = 11.6$ , 1.8 Hz), 2.94 (dd, 1H,  $J = 11.6$ , 5.1 Hz), 2.80–2.69 (m, 1H), 2.04 (d, 3H,  $J = 2.4$  Hz), 1.56 (d, 3H,  $J = 6.9$  Hz), 1.41 (t, 1H,  $J = 5.8$  Hz), 1.30 (t, 3H,  $J = 7.1$  Hz), 0.95 (d, 3H,  $J = 7.1$  Hz). LR-MS ( $m/z$  (relative intensity)): 294 ( $[M]^+$ , 45), 203 (75), 175 (55), 159 (100). HR-MS calcd. for  $C_{16}H_{22}O_5$ : 294.1467; found: 294.1473.

Each of the isomeric alcohols were oxidized separately and each crude product obtained was purified by flash chromatography on silica gel eluting with EtOAc and hexanes (30:70) to give a colourless oil. Aldehyde **36a** having the  $\alpha$ -methyl group (44 mg, 76%). IR (neat,  $cm^{-1}$ ): 2981, 2730, 1732, 1699.  $^1H$  NMR ( $CDCl_3$ )  $\delta$ : 9.55 (s, 1H), 7.04 (d, 1H,  $J = 6.3$  Hz), 5.11 (q, 1H,  $J = 6.7$  Hz), 4.18 (q, 2H,  $J = 7.1$  Hz), 3.62 (dt, 1H,  $J = 8.5$ , 2.6 Hz), 3.16 (dd, 1H,  $J = 8.5$ , 4.5 Hz), 2.98–2.86 (m, 1H), 1.81 (s, 3H), 1.59 (d, 3H,  $J = 6.7$  Hz), 1.27 (t, 3H,  $J = 7.1$  Hz), 1.17 (d, 3H,  $J = 7.2$  Hz). LR-MS ( $m/z$  (relative intensity)): 292 ( $[M]^+$ , 20), 247 (25), 86 (90), 78 (100). HR-MS calcd. for  $C_{16}H_{20}O_5$ : 292.1311; found: 292.1315. Aldehyde **36b** having the  $\beta$ -methyl group (42 mg, 70% yield):  $^1H$  NMR ( $CDCl_3$ )  $\delta$ : 9.57 (s, 1H), 6.97 (d, 1H,  $J = 6.1$  Hz), 4.84 (qd, 1H,  $J = 7.1$ , 0.9 Hz), 4.19 (q, 2H,  $J = 7.1$  Hz), 3.69 (dt, 1H,  $J = 8.4$ , 2.1 Hz), 3.19 (dd, 1H,  $J = 8.4$ , 4.6 Hz), 2.88–2.77 (m, 1H), 1.80 (d, 3H,  $J = 2.5$  Hz), 1.59 (d, 3H,  $J = 7.1$  Hz), 1.28 (t, 3H,  $J = 7.1$  Hz), 1.19 (d, 3H,  $J = 7.2$  Hz).

### Enoates 37

Mercuric oxide red (520 mg, 2.4 mmol) was dissolved in THF:water (85:15) (8.2 mL) and  $BF_3 \cdot OEt_2$  (0.30 mL, 2.4 mmol) was added drop wise. Cycloadduct **35b** (800 mg, 1.2 mmol) in THF (2 mL) was slowly added to the orange mixture, which was stirred for 0.5 h.  $Et_2O$  (30 mL) was added and the resulting precipitate was filtered through a cintered glass. The organic phase was washed with satd.  $NaHCO_3$  and brine, dried over  $MgSO_4$ , filtered, and evaporated under reduced pressure to give a white powder (711 mg, 100%) containing an inseparable mixture of two diastereomers. IR (neat,  $cm^{-1}$ ): 3060, 2724, 1730, 1709, 1598.  $^1H$  NMR ( $CDCl_3$ )  $\delta$ : 9.77 (s, 2H), 7.48–7.39 (m, 12H), 7.33–7.20 (m, 18H), 6.42 (d, 1H,  $J = 7.3$  Hz), 6.38 (d, 1H,  $J = 7.0$  Hz), 4.84 (dm, 1H,  $J = 7.4$  Hz), 4.43 (dm, 1H,  $J = 10.1$  Hz), 4.24 (q, 2H,  $J = 7.1$  Hz), 4.23 (q, 2H,  $J = 7.1$  Hz), 3.86–3.73 (m, 4H), 3.65 (dm, 1H,  $J = 11.7$  Hz), 3.60 (dt, 1H,  $J = 11.5$ , 2.4 Hz), 3.03 (dd, 1H,  $J = 11.5$ , 4.8 Hz), 2.97 (dd, 1H,  $J = 11.7$ , 5.0 Hz), 2.90–2.75 (m, 2H), 2.52 (t, 4H,  $J =$



5.9 Hz), 2.00–1.65 (m, 8 H), 1.60 (s, 3H), 1.57 (s, 3H), 1.32 (t, 3H,  $J = 7.1$  Hz), 1.31 (t, 3H,  $J = 7.1$  Hz), 0.95 (d, 3H,  $J = 6.6$  Hz), 0.92 (d, 3H,  $J = 6.6$  Hz). LR-MS ( $m/z$  (relative intensity)): 610 ( $[M + NH_4]^+$ , 5), 566 (5), 243 (100). HR-MS calcd. for  $C_{38}H_{44}NO_6$ : 610.3168; found: 610.3154.

Sodium hydride (58 mg, 60% in oil, 1.44 mmol) was suspended in THF (7 mL) at 0°C. Methyl diethoxyphosphonoacetate (0.27 mL, 1.44 mmol) was added slowly and the mixture was stirred for 0.5 h. The anion was added via cannula to a solution of the above aldehyde (711 mg, 1.2 mmol) in THF (7 mL) at 0°C. After 1 h, the reaction was poured into a saturated solution of  $NH_4Cl$ , the phases were separated and the aqueous phase was extracted with EtOAc. The combined organic fractions were washed with water and brine, dried over  $MgSO_4$ , filtered, and evaporated under reduced pressure to give 800 mg of a yellow powder. Flash chromatography on silica gel eluting with EtOAc and hexanes (20:80) gave **37** as a white powder (544 mg, 70%) containing an inseparable mixture of two isomers. IR (neat,  $cm^{-1}$ ): 3058, 1729, 1657.  $^1H$  NMR ( $C_6D_6$ , integrated for two isomers)  $\delta$ : 7.45–7.40 (m, 12H), 7.33–7.22 (m, 18H), 6.95 (dt, 1H,  $J = 15.7$ , 6.7 Hz), 6.93 (dt, 1H,  $J = 15.7$ , 6.8 Hz), 6.42 (d, 1H,  $J = 7.3$  Hz), 6.38 (d, 1H,  $J = 7.0$  Hz), 5.84 (dd, 2H,  $J = 15.7$ , 2.1 Hz), 4.82 (dm, 1H,  $J = 8.3$  Hz), 4.42 (dm, 1H,  $J = 10.6$  Hz), 4.24 (q, 2H,  $J = 7.1$  Hz), 4.23 (q, 2H,  $J = 7.1$  Hz), 3.86–3.72 (m, 4H), 3.74 (s, 3H), 3.73 (s, 3H), 3.66 (dm, 1H,  $J = 11.7$  Hz), 3.59 (dt, 1H,  $J = 11.3$ , 2.4 Hz), 3.04 (dd, 1H,  $J = 11.3$ , 4.8 Hz), 2.97 (dd, 1H,  $J = 11.7$ , 5.0 Hz), 2.88–2.73 (m, 2H), 2.31–2.19 (m, 4H), 1.93–1.50 (m, 14 H), 1.31 (t, 3H,  $J = 7.1$  Hz), 1.30 (t, 3H,  $J = 7.1$  Hz), 0.95 (d, 3H,  $J = 7.3$  Hz), 0.93 (d, 3H,  $J = 7.3$  Hz). LR-MS ( $m/z$  (relative intensity)): 666 ( $[M + NH_4]^+$ , 2), 407 (15), 243 (100), 165 (20). HR-MS calcd. for  $C_{41}H_{48}NO_7$ : 666.3431; found: 666.3420.

### Aldehydes **38a** and **38b**

Followed the same procedure as per the deprotection of **33** and oxidation to give **34**. Flash chromatography on silica gel eluting with EtOAc and hexanes (30:70) gave two separable alcohols as colourless oils (153 mg, 46% and 153 mg, 46%). Less polar isomer:  $^1H$  NMR ( $CDCl_3$ )  $\delta$ : 6.97 (dt, 1H,  $J = 15.7$ , 6.9 Hz), 6.28 (d, 1H,  $J = 7.0$  Hz), 5.86 (d, 1H,  $J = 15.7$  Hz), 4.89 (dm, 1H,  $J = 8.9$  Hz), 4.40–4.30 (m, 2H), 4.21 (q, 2H,  $J = 7.1$  Hz), 3.73 (s, 3H), 3.61 (dt, 1H,  $J = 10.8$ , 2.5 Hz), 3.03 (dd, 1H,  $J = 10.8$ , 4.8 Hz), 2.84–2.74 (m, 1H), 2.30 (q, 2H,  $J = 6.9$  Hz), 2.00 (s, 3H), 1.99–1.78 (m, 3H), 1.72–1.60 (m, 1H), 1.57 (s, 1H), 1.29 (t, 3H,  $J = 7.1$  Hz), 0.93 (d, 3H,  $J = 7.1$  Hz). More polar isomer: IR (neat,  $cm^{-1}$ ): 3480, 1732, 1658.  $^1H$  NMR ( $CDCl_3$ )  $\delta$ : 6.95 (dt, 1H,  $J = 15.7$ , 7.0 Hz), 6.19 (d, 1H,  $J = 6.8$  Hz), 5.86 (d, 1H,  $J = 15.7$  Hz), 4.54 (dm, 1H,  $J = 10.2$  Hz), 4.42–4.29 (m, 2H), 4.22 (q, 2H,  $J = 7.1$  Hz), 3.73 (s, 3H), 3.67 (dm, 1H,  $J = 11.4$  Hz), 2.95 (dd, 1H,  $J = 11.4$ , 5.1 Hz), 2.79–2.69 (m, 1H), 2.34–2.23 (m, 2H), 2.04 (d, 3H,  $J = 2.5$  Hz), 2.00–1.55 (m, 4H), 1.30 (t, 3H,  $J = 7.1$  Hz), 0.94 (d, 3H,  $J = 7.1$  Hz). LR-MS ( $m/z$  (relative intensity)): 406 ( $[M]^+$ , 15), 297 (50), 175 (100). HR-MS calcd. for  $C_{22}H_{30}O_7$ : 406.1991; found: 406.1999.

Each alcohol was then oxidized separately. Flash chromatography on silica gel eluting with EtOAc and hexanes (30:70) gave a colourless oil. Aldehyde **38a** with the  $\alpha$ -chain

(180 mg, 87%): IR (neat,  $cm^{-1}$ ): 2728, 1738, 1714, 1694.  $^1H$  NMR ( $CDCl_3$ )  $\delta$ : 9.53 (s, 1H), 7.04 (d, 1H,  $J = 6.3$  Hz), 6.97 (dt, 1H,  $J = 15.7$ , 7.0 Hz), 5.87 (d, 1H,  $J = 15.7$  Hz), 4.94 (dm, 1H,  $J = 8.7$  Hz), 4.19 (q, 2H,  $J = 7.1$  Hz), 3.74 (s, 3H), 3.61 (dt, 1H,  $J = 8.5$ , 2.6 Hz), 3.15 (dd, 1H,  $J = 8.5$ , 4.5 Hz), 2.97–2.86 (m, 1H), 2.31 (q, 2H,  $J = 7.0$  Hz), 2.00–1.82 (m, 3H), 1.79 (s, 3H), 1.78–1.60 (m, 1H), 1.27 (t, 3H,  $J = 7.1$  Hz), 1.16 (d, 3H,  $J = 7.2$  Hz). LR-MS ( $m/z$  (relative intensity)): 422 ( $[M + NH_4]^+$ , 15), 405 ( $[M + H]^+$ , 100). HR-MS calcd. for  $C_{22}H_{29}O_7$ : 405.1913; found: 405.1911. Aldehyde **38b** with the  $\beta$ -chain (52 mg, 100%):  $^1H$  NMR ( $CDCl_3$ )  $\delta$ : 9.55 (s, 1H), 6.96 (d, 1H,  $J = 5.6$  Hz), 6.95 (dt, 1H,  $J = 15.6$ , 7.0 Hz), 5.86 (d, 1H,  $J = 15.6$  Hz), 4.66 (dm, 1H,  $J = 9.7$  Hz), 4.18 (q, 2H,  $J = 7.1$  Hz), 3.73 (s, 3H), 3.63 (dt, 1H,  $J = 7.4$ , 2.2 Hz), 3.27 (dd, 1H,  $J = 7.4$ , 4.8 Hz), 2.82–2.72 (m, 1H), 2.34–2.25 (m, 2H), 1.96–1.75 (m, 3H), 1.79 (d, 3H,  $J = 2.2$ ), 1.72–1.60 (m, 1H), 1.27 (t, 3H,  $J = 7.1$  Hz), 1.22 (d, 3H,  $J = 7.2$  Hz).

### Cycloadducts **14 $\beta$ -39a** and **14 $\alpha$ -39a**

Followed the same procedure as per the preparation of cycloadduct **39b**. The crude mixture was purified by flash chromatography (mixture of hexanes:EtOAc, 15:1) to provide 145 mg (84%) of cycloadducts as an approximate 4:1 mixture of two separable diastereomers. **14 $\alpha$ -39a**:  $^1H$  NMR ( $CDCl_3$ )  $\delta$ : 7.7–7.3 (m, 10H), 6.51 (d, 1H,  $J = 0.5$  Hz), 5.80 (ddt, 1H,  $J = 17.0$ , 10.3, 6.6 Hz), 5.28 (t, 1H,  $J = 6.8$  Hz), 4.97 (dt, 1H,  $J = 17.0$ , 1.0 Hz), 4.90 (dt, 1H,  $J = 10.3$ , 1.0 Hz), 4.78 (dd, 1H,  $J = 7.8$ , 0.5 Hz), 4.09 (m, 1H), 3.88 (dq, 1H,  $J = 9.5$ , 7.0 Hz), 3.55 (dq, 1H,  $J = 9.5$ , 7.0 Hz), 2.40–2.33 (m, 1H), 2.21–2.17 (m, 3H), 2.06–1.87 (m, 3H), 1.85–1.77 (m, 2H), 1.48–1.37 (m, 1H), 1.36–1.28 (m, 3H), 1.23–1.07 (m, 2H), 1.21 (t, 3H,  $J = 7.0$  Hz), 1.09 (s, 9H). **14 $\beta$ -39a**:  $^1H$  NMR ( $CDCl_3$ )  $\delta$ : 7.7–7.3 (m, 10H), 6.60 (d, 1H,  $J = 0.5$  Hz), 5.81 (ddt, 1H,  $J = 17.0$ , 10.3, 6.6 Hz), 5.08–4.90 (m, 3H), 4.94 (dd, 1H,  $J = 7.8$ , 0.5 Hz), 4.03 (m, 1H), 3.96 (dq, 1H,  $J = 9.5$ , 7.0 Hz), 3.11 (dq, 1H,  $J = 9.5$ , 7.0 Hz), 2.55–2.41 (m, 1H), 2.25–2.00 (m, 4H), 1.85–1.79 (m, 1H), 1.77–1.20 (m, 9H), 1.27 (t, 3H,  $J = 7.0$  Hz), 1.05 (s, 9H).

### Cycloadducts **14 $\beta$ -39b** and **14 $\alpha$ -39b**

To a stirred solution of aldehyde **20b** (307 mg, 0.990 mmol) and ethyl vinyl ether (4.6 mL) was added  $Yb(FOD)_3$  (127 mg, 0.120 mmol) at room temperature. The reaction mixture was stirred for 1 day before a solution of brine was added. This mixture was stirred for about 1 h then separated and the product extracted with ethyl ether, dried over  $MgSO_4$ , filtered, and concentrated. The crude mixture was purified by flash chromatography (mixture of hexanes:EtOAc, 15:1) to provide 308 mg (81%) of cycloadducts as an approximate 1:1 mixture of inseparable diastereomers. IR (neat,  $cm^{-1}$ ): 3076, 1640.  $^1H$  NMR ( $CDCl_3$ )  $\delta$ : 7.35–7.24 (m, 5H), 1 isomer 6.44 (d, 1H,  $J = 2.1$  Hz), one isomer 6.39 (d, 1H,  $J = 1.9$  Hz), 5.80 (ddt, 1H,  $J = 17.0$ , 10.3, 6.6 Hz), 5.34–5.26 (m, 1H), 5.03–4.91 (m, 2H), 4.85–4.81 (m, 1H), one isomer 4.67 (d, 1H,  $J = 11.4$  Hz), one isomer 4.64 (d, 1H,  $J = 12.1$  Hz), one isomer 4.47 (d, 1H,  $J = 11.4$  Hz), one isomer 4.42 (d, 1H,  $J = 12.2$  Hz), 4.01–3.91 (m, 1H), one isomer 3.64–3.61 (m, 1H), 3.61–3.53 (m, 1H), one isomer 3.20–3.12 (m, 1H), one isomer 2.64 (dt, 1H,  $J = 14.3$ ,



3.5 Hz), 2.54–1.94 (m, 7H), 1.83–1.74 (m, 1H), 1.63–1.52 (m, 1H), 1.44–1.29 (m, 5H), 1.26 (t, 3H,  $J = 7.1$  Hz).  $^{13}\text{C}$  NMR ( $\text{CDCl}_3$ )  $\delta$ : 138.9 (d), 138.6 (s), 136.7 (d), 136.4 (d), 134.3 (s), 133.9 (s), 128.4 (d), 128.2 (d), 127.8 (d), 127.6 (d), 127.3 (d), 122.3 (d), 121.5 (d), 116.8 (s), 116.2 (s), 114.2 (t), 100.1 (d), 99.9 (d), 82.5 (d), 74.1 (d), 73.7 (d), 71.0 (t), 70.5 (t), 64.5 (t), 64.4 (t), 39.9 (d), 38.8 (d), 33.7 (t), 33.5 (t), 30.9 (t), 30.1 (t), 29.4 (t), 28.5 (t), 27.7 (t), 27.6 (t), 27.4 (t), 25.4 (t), 21.3 (t), 15.2 (q). LR-MS ( $m/z$  (relative intensity)): 382 ( $[\text{M}]^+$ , 40), 91 (100). HR-MS calcd. for  $\text{C}_{25}\text{H}_{34}\text{O}_3$ : 382.2520; found: 382.2553.

### Cycloadducts 40a–c

These cycloadducts were not isolated because they spontaneously underwent the subsequent intramolecular cycloaddition. Their stereochemistries were therefore deduced from the isolation of tetracycles **48–51**.

### Cycloadduct 41

Aldehyde **34** (140 mg, 0.50 mmol) was dissolved in ethyl vinyl ether (5 mL) and  $\text{Yb}(\text{FOD})_3$  (79 mg, 0.075 mmol) was added. After 12 h, the solvent was evaporated and a colourless oil was obtained (260 mg). Flash chromatography on silica gel eluting with EtOAc and hexanes (10:90) yielded **41** as a white crystalline compound (167 mg, 95%). IR (neat,  $\text{cm}^{-1}$ ): 2975, 1733, 1640, 1164, 1132.  $^1\text{H}$  NMR ( $\text{C}_6\text{D}_6$ )  $\delta$ : 6.47 (d, 1H,  $J = 2.3$  Hz), 4.83 (dd, 1H,  $J = 9.3$ , 2.9 Hz), 4.21 (d, 1H,  $J = 3.1$  Hz), 3.90 (dq, 1H,  $J = 9.5$ , 7.1 Hz), 3.38–3.27 (m, 2H), 3.32 (s, 3H), 3.32 (s, 3H), 2.36–2.24 (tm, 1H,  $J = 11.6$  Hz), 1.97 (ddd, 1H,  $J = 12.7$ , 4.5, 3.1 Hz), 1.80 (s, 3H), 1.76 (s, 3H), 1.75–1.65 (m, 1H), 1.57–1.46 (m, 1H), 1.10 (t, 3H,  $J = 7.1$  Hz), 0.91 (d, 3H,  $J = 6.5$  Hz).  $^{13}\text{C}$  NMR ( $\text{C}_6\text{D}_6$ )  $\delta$ : 175.2 (s), 174.8 (s), 141.6 (d), 129.1 (s), 124.6 (s), 114.2 (s), 100.6 (d), 64.5 (t), 52.1 (q), 51.5 (q), 51.1 (d), 47.1 (d), 36.6 (d), 35.5 (d), 33.4 (t), 23.8 (q), 21.7 (q), 17.7 (q), 15.7 (q). LR-MS ( $m/z$  (relative intensity)): 352 ( $[\text{M}]^+$ , 60), 221 (80), 189 (50), 161 (100), 129 (40), 91 (40). HR-MS calcd. for  $\text{C}_{28}\text{H}_{28}\text{O}$ : 352.1886; found: 352.1875.

### Cycloadducts 42a and 42b

Each aldehyde **36a** and **36b** were separately submitted to the same protocol as per cycloadduct **41**. Each crude product was purified by flash chromatography on silica gel eluting with EtOAc and hexanes (30:70) to give a white powder. Cycloadduct **42a**: IR (neat,  $\text{cm}^{-1}$ ): 2977, 1735, 1626.  $^1\text{H}$  NMR ( $\text{C}_6\text{D}_6$ )  $\delta$ : 6.02 (d, 1H,  $J = 2.3$  Hz), 4.74 (dd, 1H,  $J = 7.5$ , 3.0 Hz), 4.24 (qd, 1H,  $J = 7.7$ , 1.9 Hz), 4.20–4.01 (m, 2H), 3.80 (qd, 1H,  $J = 9.4$ , 7.1 Hz), 3.52 (dt, 1H,  $J = 11.9$ , 2.5 Hz), 3.31 (qd, 1H,  $J = 9.4$ , 7.1 Hz), 3.09 (dd, 1H,  $J = 11.9$ , 4.8 Hz), 2.16–2.07 (m, 1H), 1.90–1.82 (m, 1H), 1.74–1.58 (m, 2H), 1.41 (d, 3H,  $J = 1.9$  Hz), 1.11 (t, 3H,  $J = 7.1$  Hz), 1.07–1.02 (m, 6H), 0.90 (d, 3H,  $J = 7.2$  Hz). LR-MS ( $m/z$  (relative intensity)): 364 ( $[\text{M}]^+$ , 10), 318 (90), 78 (100). HR-MS calcd. for  $\text{C}_{20}\text{H}_{28}\text{O}_6$ : 364.1886; found: 364.1888. Cycloadduct **42b**:  $^1\text{H}$  NMR ( $\text{C}_6\text{D}_6$ )  $\delta$ : 6.12 (d, 1H,  $J = 2.2$  Hz), 4.73 (dd, 1H,  $J = 7.4$ , 2.6 Hz), 4.28 (qd, 1H,  $J = 6.8$ , 1.2 Hz), 4.25–4.02 (m, 2H), 3.79 (qd, 1H,  $J = 9.4$ , 7.1 Hz), 3.72 (dt, 1H,  $J = 11.6$ , 1.9 Hz), 3.31 (qd, 1H,  $J = 9.4$ , 7.1 Hz), 3.07 (dd, 1H,  $J = 11.6$ , 6.0 Hz), 2.12–2.01 (m, 1H), 1.93–1.85 (m, 1H), 1.73 (ddd, 1H,  $J = 13.1$ , 5.9, 2.6 Hz), 1.62–1.52 (m, 1H), 1.30 (d, 3H,  $J = 2.4$  Hz), 1.10

(t, 3H,  $J = 7.0$  Hz), 1.06 (t, 3H,  $J = 7.1$  Hz), 1.01 (d, 3H,  $J = 6.8$  Hz), 0.89 (d, 3H,  $J = 7.1$  Hz).

### Cycloadducts 43a and 43b

Followed the same procedure as per **42a** and **42b**. Isomers **38a** and **38b** were reacted separately. Flash chromatography on silica gel eluting with EtOAc and hexanes (30:70) gave a white powder. Cycloadduct **43a** having the  $\alpha$ -chain (41 mg, 72%):  $^1\text{H}$  NMR ( $\text{C}_6\text{D}_6$ )  $\delta$ : 6.89 (dt, 1H,  $J = 15.7$ , 6.9 Hz), 6.18 (d, 1H,  $J = 1.6$  Hz), 5.80 (d, 1H,  $J = 15.7$  Hz), 4.74 (dd, 1H,  $J = 7.4$ , 2.6 Hz), 4.19 (dm, 1H,  $J = 10.8$  Hz), 4.16 (q, 1H,  $J = 7.1$  Hz), 4.07 (q, 1H,  $J = 7.1$  Hz), 3.81 (dq, 1H,  $J = 9.4$ , 7.1 Hz), 3.74 (dt, 1H,  $J = 11.3$ , 2.3 Hz), 3.45 (s, 3H), 3.32 (dq, 1H,  $J = 9.4$ , 7.0 Hz), 3.05 (dd, 1H,  $J = 11.3$ , 5.7 Hz), 2.07–1.94 (m, 2H), 1.79–1.71 (m, 1H), 1.70–1.52 (m, 3H), 1.48–1.20 (m, 4H), 1.36 (d, 3H,  $J = 2.3$  Hz), 1.11 (t, 3H,  $J = 7.0$  Hz), 1.06 (t, 3H,  $J = 7.1$  Hz), 0.89 (d, 3H,  $J = 6.7$  Hz).  $^{13}\text{C}$  NMR ( $\text{C}_6\text{D}_6$ )  $\delta$ : 173.4 (s), 171.1 (s), 166.6 (s), 148.6 (d), 142.1 (d), 128.8 (s), 126.0 (s), 125.1 (s), 121.8 (d), 99.0 (d), 82.9 (d), 64.2 (t), 60.7 (t), 51.0 (q), 45.0 (d), 39.5 (d), 35.6 (d), 34.5 (d), 33.6 (t), 31.5 (t), 30.9 (t), 24.3 (t), 17.0 (q), 16.6 (q), 15.3 (q), 14.3 (q). Cycloadduct **43b** having the  $\beta$ -chain (40 mg, 71%): IR (neat,  $\text{cm}^{-1}$ ): 2955, 1729, 1630.  $^1\text{H}$  NMR ( $\text{C}_6\text{D}_6$ )  $\delta$ : 6.97 (dt, 1H,  $J = 15.7$ , 6.9 Hz), 6.09 (d, 1H,  $J = 2.2$  Hz), 5.85 (d, 1H,  $J = 15.7$  Hz), 4.76 (dd, 1H,  $J = 7.8$ , 2.7 Hz), 4.21 (dm, 1H,  $J = 7.2$  Hz), 4.15 (q, 1H,  $J = 7.1$  Hz), 4.08 (q, 1H,  $J = 7.1$  Hz), 3.82 (dq, 1H,  $J = 9.4$ , 7.1 Hz), 3.60 (dt, 1H,  $J = 11.7$ , 2.2 Hz), 3.45 (s, 3H), 3.33 (dq, 1H,  $J = 9.4$ , 7.1 Hz), 3.11 (dd, 1H,  $J = 11.7$ , 5.0 Hz), 2.17–2.07 (m, 1H), 1.98–1.90 (m, 1H), 1.77–1.59 (m, 4H), 1.54–1.40 (m, 1H), 1.42 (d, 3H,  $J = 2.2$  Hz), 1.39–1.15 (m, 3H), 1.12 (t, 3H,  $J = 7.1$  Hz), 1.05 (t, 3H,  $J = 7.1$  Hz), 0.93 (d, 3H,  $J = 7.2$  Hz).  $^{13}\text{C}$  NMR ( $\text{C}_6\text{D}_6$ )  $\delta$ : 173.4 (s), 171.9 (s), 166.7 (s), 148.9 (d), 142.5 (d), 129.2 (s), 129.2 (s), 127.8 (s), 121.7 (d), 99.3 (d), 79.3 (d), 64.1 (t), 60.7 (t), 51.0 (q), 43.2 (d), 41.6 (d), 36.6 (d), 34.7 (d), 34.1 (t), 31.8 (t), 31.1 (t), 24.1 (t), 17.0 (q), 15.3 (q), 14.7 (q), 14.2 (q). LR-MS ( $m/z$  (relative intensity)): 476 ( $[\text{M}]^+$ , 1), 432 (65), 305 (100). HR-MS calcd. for  $\text{C}_{26}\text{H}_{37}\text{O}_8$ : 477.2488; found: 477.2477.

### Tetracycles 53a and 53b

Aldehyde **24a** underwent the same procedure as per the formation of cycloadduct **41**. The crude tetracycles **48** (186 mg, 0.384 mmol) were isolated in 92% combined yield but only two could be obtained pure and characterized. Therefore, the crude mixture was mixed with  $\text{LiAlH}_4$  (32 mg, 0.844 mmol) in THF (4 mL). The yield of the combined reduced tetracycles was 80% and the yield of pure tetracycle **53** was 45 mg (21% for two steps) and the yield of **53b** was 30 mg (14% for two steps). Tetracycle **53a**: mp 131.4°C. IR ( $\text{CHCl}_3$ ,  $\text{cm}^{-1}$ ): 3506, 3008, 2927, 2857, 1612, 1513, 1380, 1249, 1066, 1035.  $^1\text{H}$  NMR ( $\text{C}_6\text{D}_6$ )  $\delta$ : 7.24 (d, 2H,  $J = 8.6$  Hz), 6.78 (d, 2H,  $J = 8.6$  Hz), 4.52 (d, 1H,  $J = 11.4$  Hz), 4.44 (dd, 1H,  $J = 9.6$ , 2.1 Hz), 4.23 (d, 1H,  $J = 11.4$  Hz), 4.07–4.02 (m, 1H), 3.90 (dd, 1H,  $J = 9.4$ , 3.0 Hz), 3.87 (dq, 1H,  $J = 9.3$ , 7.0 Hz), 3.67–3.66 (m, 1H), 3.32 (dq, 1H,  $J = 9.3$ , 7.0 Hz), 3.28 (s, 3H), 3.01 (ddd, 1H,  $J = 11.5$ , 8.3, 3.2 Hz), 2.95 (bs, 1H), 2.63 (ddd, 1H,  $J = 12.6$ , 4.8, 2.1 Hz), 2.36 (m, 1H), 2.00–1.93 (m, 1H), 1.83–1.78 (m, 3H), 1.66–1.61 (m, 2H), 1.59–1.26 (m, 5H), 1.25 (s, 3H),



1.24–1.00 (m, 3H), 1.06 (t, 3H,  $J = 7.0$  Hz), 0.79–0.70 (m, 1H).  $^{13}\text{C}$  NMR (acetone  $d_6$ )  $\delta$ : 160.6 (s), 135.2 (s), 132.8 (s), 130.6 (d), 129.2 (s), 114.9 (d), 103.1 (d), 82.0 (d), 74.1 (d), 71.4 (t), 64.9 (t), 63.6 (t), 56.0 (q), 49.7 (d), 47.9 (d), 45.8 (d), 43.1 (d), 40.4 (t), 38.5 (t), 35.2 (d), 30.1 (t), 28.3 (t), 27.9 (t), 27.0 (t), 24.4 (q), 16.2 (q). LR-MS ( $m/z$  (relative intensity)): 456 ( $[\text{M}]^+$ , 5), 121 (100), 122 (89). HR-MS calcd. for  $\text{C}_{28}\text{H}_{40}\text{O}_5$ : 456.2876; found: 456.2868. X-ray data can be found in the supplementary material.<sup>3</sup> Tetracycle **53b**:  $^1\text{H}$  NMR ( $\text{C}_6\text{D}_6$ )  $\delta$ : 7.25 (d, 2H,  $J = 8.6$  Hz), 6.86 (d, 2H,  $J = 8.6$  Hz), 5.00 (t, 1H,  $J = 7.3$  Hz), 4.60 (d, 1H,  $J = 11.2$  Hz), 4.37–4.33 (m, 2H), 3.84–3.74 (m, 1H), 3.79 (s, 3H), 3.68–3.61 (m, 1H), 3.49 (dq, 1H,  $J = 9.8$ , 7.0 Hz), 3.24 (dd, 1H,  $J = 11.2$ , 2.6 Hz), 3.08 (ddd, 1H,  $J = 11.6$ , 8.5, 3.1 Hz), 2.59 (ddd, 1H,  $J = 13.5$ , 7.0, 4.0 Hz), 2.35–2.10 (m, 4H), 2.07–1.96 (m, 2H), 1.90–1.81 (m, 2H), 1.57–1.40 (m, 5H), 1.21 (t, 3H,  $J = 7.1$  Hz), 1.17–0.99 (m, 3H), 0.96 (d, 3H,  $J = 7.0$  Hz), 0.73–0.66 (m, 1H).

### Tetracycles 49a and 49b

Aldehyde **25** underwent the same treatment as per the formation of cycloadduct **41**. A mixture of tetracycles **49a** and **49b** was isolated and purified by flash chromatography on silica gel eluting with EtOAc and hexanes (1:3) in 84% combined yield. Of this mixture, **49a** and **49b** could be isolated in pure form in 12 and 7%, respectively (the reported ratio was determined by GC from the crude mixture after characterization of the pure compounds). In this particular case, some of the precursor 13 $\beta$ ,14 $\beta$ -**40c** (starting material) could be isolated pure. When 13 $\beta$ ,14 $\beta$ -**40c** was refluxed in benzene overnight, it gave 97% of pure tetracycle **49a** and **49b** (same 2:1 ratio). Tetracycle **49a**: mp 159.4°C. IR ( $\text{cm}^{-1}$ ): 3499, 1738, 1434.  $^1\text{H}$  NMR ( $\text{CDCl}_3$ )  $\delta$ : 4.50 (dd, 1H,  $J = 9.7$ , 1.8 Hz), 3.84–3.77 (m, 2H), 3.65 (s, 3H), 3.47–3.39 (m, 2H), 2.67 (dd, 1H,  $J = 11.9$ , 7.2 Hz), 2.36–2.29 (m, 1H), 2.15–2.00 (m, 4H), 1.96–1.76 (m, 3H), 1.67–1.58 (m, 3H), 1.50–1.21 (m, 4H), 1.17 (t, 3H,  $J = 7.1$  Hz), 1.02–0.89 (m, 1H), 0.83 (d, 3H,  $J = 6.1$  Hz).  $^{13}\text{C}$  NMR ( $\text{CDCl}_3$ )  $\delta$ : 173.4 (s), 132.8 (s), 124.6 (s), 101.5 (d), 73.3 (d), 69.4 (d), 63.7 (t), 50.9 (q), 49.0 (d), 44.3 (d), 43.0 (d), 41.9 (d), 39.9 (d), 37.6 (t), 36.5 (t), 31.2 (t), 29.2 (t), 26.7 (t), 20.6 (q), 15.0 (q). LR-MS ( $m/z$  (relative intensity)): 363 ( $[\text{M}^+ - \text{H}]$ , 5), 318 (70), 301 (100). HR-MS calcd. for  $\text{C}_{21}\text{H}_{31}\text{O}_5$ : 363.2171; found: 363.2180. Anal. calcd. for  $\text{C}_{21}\text{H}_{32}\text{O}_5$ : C 69.20, H 8.85, O 21.95; found: C 69.25, H 8.80. Tetracycle **49b**:  $^1\text{H}$  NMR ( $\text{CDCl}_3$ )  $\delta$ : 4.95 (t, 1H,  $J = 7.2$  Hz), 4.28–4.25 (m, 1H), 3.75 (dq, 1H,  $J = 9.8$ , 7.1 Hz), 3.66 (s, 3H), 3.46 (dq, 1H,  $J = 9.8$ , 7.1 Hz), 3.45–3.36 (m, 1H), 2.91 (t, 1H,  $J = 8.4$  Hz), 2.49 (ddd, 1H,  $J = 13.6$ , 6.8, 4.2 Hz), 2.37–2.30 (m, 1H), 2.16–2.05 (m, 2H), 2.02–1.77 (m, 4H), 1.69–1.58 (m, 4H), 1.56–1.42 (m, 4H), 1.28–1.23 (m, 1H), 1.19 (t, 3H,  $J = 7.1$  Hz), 0.92 (d, 3H,  $J = 7.1$  Hz).

### Tetracycle 51a

Followed the same procedure as per cycloadduct **41**, starting with aldehyde **25**. IR ( $\text{cm}^{-1}$ ): 3499, 1738, 1434.  $^1\text{H}$  NMR

( $\text{CDCl}_3$ )  $\delta$ : 4.61 (dd, 1H,  $J = 8.2$ , 2.3 Hz), 4.03–4.01 (m, 1H), 3.88–3.86 (m, 1H), 3.84 (dq, 1H,  $J = 9.5$ , 7.1 Hz), 3.66 (s, 3H), 3.44 (dq, 1H,  $J = 9.5$ , 7.0 Hz), 2.73 (dd, 1H,  $J = 11.5$ , 7.1 Hz), 2.50–2.47 (m, 1H), 2.28–2.20 (m, 2H), 2.15–2.07 (m, 1H), 1.99–1.69 (m, 5H), 1.65–1.44 (m, 4H), 1.38–1.20 (m, 2H), 1.17 (t, 3H,  $J = 7.1$  Hz), 1.12–1.02 (m, 1H), 0.85 (d, 3H,  $J = 6.5$  Hz).  $^{13}\text{C}$  NMR ( $\text{CDCl}_3$ )  $\delta$ : 174.3 (s), 133.0 (s), 123.3 (s), 100.2 (d), 69.8 (d), 66.6 (d), 63.1 (t), 51.1 (q), 49.6 (d), 43.5 (d), 39.6 (d), 38.8 (d), 36.3 (t), 32.3 (t), 29.0 (t), 26.4 (t), 21.5 (t), 20.6 (q), 15.0 (q). LR-MS ( $m/z$  (relative intensity)): 363 ( $[\text{M}^+ - \text{H}]$ , 5), 318 (70), 301 (100). HR-MS calcd. for  $\text{C}_{21}\text{H}_{31}\text{O}_5$ : 363.2171; found: 363.2180. Anal. calcd. for  $\text{C}_{21}\text{H}_{32}\text{O}_5$ : C 69.20, H 8.85, O 21.95; found: C 69.16, H 8.81. X-ray data can be found in the supplementary material.<sup>3</sup>

### Tetracycle 52b

Followed the same procedure as per cycloadduct **41**, starting with aldehyde **24b**. Flash chromatography yielded 414 mg (82%) of **52** as a mixture of two tetracycles of which only the one with the 14 $\alpha$ -stereochemistry could be isolated pure. Therefore, the crude mixture (440 mg, 0.62 mmol) was treated with a 1.0 M solution of TBAF (2.5 mL, 2.5 mmol) in THF (1 mL). The mixture was refluxed for 4 h before being cooled and concentrated to dryness. The crude residue was purified by flash chromatography (hexanes:EtOAc, 3–1:1) to give 69 mg (24%) of the TBS-hydrolysis product **52b** and 205 mg (70%) of its stereoisomers as amorphous solids for a combined yield of 94%. Tetracycle **52b**: IR (film,  $\text{cm}^{-1}$ ): 3482, 2925, 1736.  $^1\text{H}$  NMR ( $\text{C}_6\text{D}_6$ )  $\delta$ : 7.25–7.07 (m, 5H), 4.43 (dd, 1H,  $J = 9.4$ , 1.9 Hz), 4.38 (s, 2H), 3.91 (dq, 1H,  $J = 9.5$ , 7.1 Hz), 3.80–3.78 (m, 1H), 3.55–3.52 (m, 1H), 3.48 (s, 3H), 3.39 (dq, 1H,  $J = 9.5$ , 7.1 Hz), 3.26 (dd, 1H,  $J = 8.0$ , 2.3 Hz), 2.59 (dd, 1H,  $J = 12.0$ , 7.7 Hz), 2.44–2.37 (m, 3H), 2.05–1.99 (m, 1H), 1.91–1.51 (m, 5H), 1.49–1.19 (m, 5H), 1.14 (t, 3H,  $J = 7.1$  Hz), 0.99 (s, 3H), 0.87–0.76 (m, 1H).  $^{13}\text{C}$  NMR ( $\text{C}_6\text{D}_6$ )  $\delta$ : 172.7 (s), 139.5 (s), 130.6 (s), 128.6 (d), 128.3 (d), 127.7 (d), 126.2 (s), 101.9 (d), 76.7 (d), 74.1 (d), 71.6 (t), 69.4 (d), 63.7 (t), 50.6 (q), 49.3 (d), 43.7 (d), 42.8 (d), 40.5 (d), 39.2 (d), 37.6 (t), 36.9 (t), 30.8 (t), 29.8 (t), 26.9 (t), 21.1 (q), 15.5 (q). LR-MS ( $m/z$  (relative intensity)): 424 ( $[\text{M}^+ - \text{EtOH}]$ , 35), 91 (100), 315 (72). HR-MS calcd. for  $\text{C}_{26}\text{H}_{32}\text{O}_5$ : 424.2250; found: 424.2248.

### Tetracycle 54

Tetracycle **49b** (42 mg, 0.116 mmol) was mixed with imidazole (20 mg, 0.29 mmol), TBSCl (23 mg, 0.151 mmol) in  $\text{CH}_2\text{Cl}_2$  (0.5 mL). The mixture was stirred overnight and quenched with water. The aqueous layer was extracted with  $\text{CH}_2\text{Cl}_2$  and the combined organic fractions were washed with brine, dried over  $\text{MgSO}_4$ , filtered, and concentrated under reduced pressure. Flash chromatography on silica gel (hexanes:EtOAc, 6:1) of the crude product gave **54** (50 mg, 90%).  $^1\text{H}$  NMR ( $\text{CDCl}_3$ )  $\delta$ : 4.93 (t, 1H,  $J = 7.2$  Hz), 4.28–4.25 (m, 1H), 3.76 (dq, 1H,  $J = 9.7$ , 7.1 Hz), 3.66 (s, 3H),

<sup>3</sup>Supplementary data (DUD no. 3454) may be purchased from the Depository of Unpublished Data, Document Delivery, CISTI, National Research Council Canada, Ottawa, ON K1A 0S2, Canada ([http://www.nrc.ca/cisti/irm/unpub\\_e.shtml](http://www.nrc.ca/cisti/irm/unpub_e.shtml) for information on ordering electronically). CCDC 199040, 199041, 199042, and 199044 contain the supplementary data for this paper. These data can be obtained, free of charge, via [www.ccdc.cam.ac.uk/conts/retrieving.html](http://www.ccdc.cam.ac.uk/conts/retrieving.html) (or from the Cambridge Crystallographic Data Centre, 12 Union Road, Cambridge, U.K.; fax +44 1223 336033; or [deposit@ccdc.cam.ac.uk](mailto:deposit@ccdc.cam.ac.uk)).



3.45 (dq, 1H,  $J = 9.7, 7.1$  Hz), 3.44–3.34 (m, 1H), 2.89 (t, 1H,  $J = 8.6$  Hz), 2.43–2.27 (m, 2H), 2.18–2.07 (m, 1H), 2.05–1.82 (m, 6H), 1.70–1.55 (m, 3H), 1.51–1.44 (m, 3H), 1.20 (t, 3H,  $J = 7.1$  Hz), 1.14–1.08 (m, 1H), 0.91 (d, 3H,  $J = 7.1$  Hz), 0.88 (s, 9H), 0.04 (s, 3H), 0.03 (s, 3H). X-ray data can be found in the supplementary material.<sup>3</sup>

### Tetracycles 55a and 55b

Tetracycle **50b** was reduced following the procedure for the reduction of **48a**. The alcohol **55a** was isolated in 80% yield (51 mg). <sup>1</sup>H NMR (CDCl<sub>3</sub>)  $\delta$ : 7.24 (d, 2H,  $J = 8.6$  Hz), 6.86 (d, 2H,  $J = 8.6$  Hz), 5.02 (t, 1H,  $J = 7.3$  Hz), 4.55 (d, 1H,  $J = 11.9$  Hz), 4.43–4.42 (m, 1H), 4.35 (d, 1H,  $J = 11.9$  Hz), 3.84–3.74 (m, 1H), 3.79 (s, 3H), 3.68–3.60 (m, 2H), 3.48 (dq, 1H,  $J = 9.8, 7.0$  Hz), 3.29 (dd, 1H,  $J = 11.1, 2.6$  Hz), 2.36–2.31 (m, 1H), 2.17–1.89 (m, 9H), 1.76 (d, 1H,  $J = 13.8, 7.8$  Hz), 1.57–1.39 (m, 5H), 1.21 (t, 3H,  $J = 7.0$  Hz), 1.09–0.98 (m, 1H), 0.95 (d, 3H,  $J = 7.1$  Hz), 0.78–0.72 (m, 1H). Alcohol **55a** was protected, as per the protection of tetracycle **49b**, which gave **55b** (186 mg, 100%); mp 221.8°C. IR (cm<sup>-1</sup>): 3007, 2929, 2856, 1612, 1513, 1249, 1059, 1036. <sup>1</sup>H NMR (CDCl<sub>3</sub>)  $\delta$ : 7.24 (d, 2H,  $J = 8.6$  Hz), 6.85 (d, 2H,  $J = 8.6$  Hz), 4.97 (t, 1H,  $J = 7.2$  Hz), 4.54 (d, 1H,  $J = 11.9$  Hz), 4.36 (d, 1H,  $J = 11.9$  Hz), 4.21–4.19 (m, 1H), 3.87 (dd, 1H,  $J = 9.5, 4.4$  Hz), 3.79 (s, 3H), 3.76 (dq, 1H,  $J = 9.9, 7.1$  Hz), 3.58–3.56 (m, 1H), 3.48 (dq, 1H,  $J = 9.9, 7.1$  Hz), 3.23 (t, 1H,  $J = 9.5$  Hz), 2.25–2.20 (m, 1H), 2.12–1.88 (m, 9H), 1.66 (dt, 1H,  $J = 13.7, 7.3$  Hz), 1.51 (bs, 3H), 1.47–1.33 (m, 2H), 1.19 (t, 3H,  $J = 7.1$  Hz), 1.15–1.07 (m, 1H), 0.92 (d, 3H,  $J = 7.1$  Hz), 0.87 (s, 9H), 0.01 (d, 6H,  $J = 2.2$  Hz). <sup>13</sup>C NMR (CDCl<sub>3</sub>)  $\delta$ : 158.9 (s), 131.1 (s), 129.5 (s), 129.3 (d), 113.6 (d), 98.1 (d), 72.3 (d), 69.9 (t), 66.8 (d), 64.3 (t), 62.5 (t), 55.3 (q), 43.6 (d), 43.4 (d), 34.2 (d), 33.8 (d), 33.2 (t), 33.1 (d), 30.9 (t), 30.2 (t), 25.9 (q), 25.5 (t), 20.9 (t), 20.2 (t), 18.2 (s), 15.4 (q), 13.4 (q), -5.2 (q). LR-MS ( $m/z$  (relative intensity)): 524 ([M<sup>+</sup> - C<sub>2</sub>H<sub>6</sub>O], 15), 74 (100), 403 (93). HR-MS calcd. for C<sub>32</sub>H<sub>48</sub>O<sub>4</sub>Si: 524.3322; found: 524.3318. X-ray data can be found in the supplementary material.<sup>3</sup>

### Tetracycles 56

Cycloadduct **41** (97 mg, 0.28 mmol), hydroquinone (1.5 mg, 0.014 mmol), and methyl acrylate (0.25 mL, 2.8 mmol) were dissolved in *m*-xylene (10 mL). The solution was heated to reflux for 5 days. Methyl acrylate (0.25 mL, 2.8 mmol) was added and reflux was continued for 2 days. Methyl acrylate (0.25 mL, 2.8 mmol) was added one last time and reflux was continued 1 more day and the reaction was monitored by TLC. The solvent was evaporated to give a yellow oil (150 mg). Flash chromatography on silica gel eluting with EtOAc and hexanes (20:80) gave **56** as a colourless oil (82 mg, 66%) containing two separable diastereomers. First isomer: <sup>1</sup>H NMR (C<sub>6</sub>D<sub>6</sub>)  $\delta$ : 4.82–4.71 (m, 2H), 4.00–3.87 (m, 1H), 3.81–3.75 (m, 1H), 3.44 (s, 3H), 3.43–3.33 (m, 1H), 3.30 (s, 3H), 3.27 (s, 3H), 3.01–2.90 (m, 2H), 2.02–1.87 (m, 2H), 1.75–1.34 (m, 3H), 1.24 (t, 3H,  $J = 7.0$  Hz), 1.20–0.98 (m, 1H), 0.95 (s, 3H), 0.94 (s, 3H), 0.83 (d, 3H,  $J = 6.6$  Hz). Second isomer: IR (neat, cm<sup>-1</sup>): 2954, 1738, 1435. <sup>1</sup>H NMR (C<sub>6</sub>D<sub>6</sub>)  $\delta$ : 4.71 (m, 1H,  $J = 8.7, 5.4$  Hz), 4.49 (dm, 1H,  $J = 7.3$  Hz), 3.92–3.85 (m, 1H), 3.84–3.72 (m, 1H), 3.50 (s, 3H), 3.33–3.23 (m, 1H), 3.27 (s,

6H), 3.03–2.96 (m, 2H), 2.09–1.90 (m, 3H), 1.87–1.75 (m, 1H), 1.57–1.45 (m, 2H), 1.15 (t, 3H,  $J = 7.1$  Hz), 1.00 (s, 3H), 0.93 (d, 3H,  $J = 6.7$  Hz), 0.80 (s, 3H). <sup>13</sup>C NMR (C<sub>6</sub>D<sub>6</sub>)  $\delta$ : 174.4 (s), 173.3 (s), 172.1 (s), 135.7 (s), 134.2 (s), 98.4 (d), 63.2 (d), 62.4 (t), 51.7 (q), 51.5 (q), 51.2 (q), 50.9 (d), 44.5 (d), 41.0 (d), 33.0 (t), 36.8 (d), 36.1 (d), 34.4 (t), 32.3 (s), 27.2 (q), 26.8 (q), 19.4 (q), 15.4 (q). LR-MS ( $m/z$  (relative intensity)): 456 ([M + NH<sub>4</sub>], 5), 437 ([M - 1], 30), 393 (100), 361 (70). HR-MS calcd. for C<sub>23</sub>H<sub>33</sub>O<sub>8</sub>: 437.2175; found: 437.2159.

## Conclusion

We have successfully completed an in-depth study of the stereochemical aspect of the cycloadditions involved in the diene-transmissive Diels–Alder strategy. The results clearly show that the stereochemistry of both cycloadditions can be controlled by proper positioning of substituents in the precursors. The study also procured useful information about what structural features should be avoided in the cycloaddition precursors that lead to lower selectivity. Importantly, we were able to construct vinyl allene precursors possessing the C-10 methyl group and showed that those precursors underwent two highly stereoselective Diels–Alder cycloadditions. We were not yet able, however, to effect the third and last Diels–Alder reaction in those systems. Current investigations are aimed at solving this difficulty.

## Acknowledgements

We thank the Natural Sciences and Engineering Council of Canada (NSERC) and the Université de Sherbrooke for financial support.

## References

- (a) A.T. Blomquist and J.A. Verdol. *J. Am. Chem. Soc.* **77**, 81 (1955); (b) W.J. Bailey and J. Economy. *J. Am. Chem. Soc.* **77**, 1133 (1955); (c) W.J. Bailey, C.H. Cunov, and L. Nicholas. *J. Am. Chem. Soc.* **77**, 2787 (1955).
- (a) O. Tsuge, E. Wada, and S. Kanemasa. *Chem. Lett.* 239 (1983); (b) O. Tsuge, E. Wada, S. Kanemasa, and H. Sakoh. *Bull. Chem. Soc. Jpn.* **57**, 3221 (1984); (c) O. Tsuge, S. Kanemasa, H. Sakoh, and E. Wada. *Bull. Chem. Soc. Jpn.* **57**, 3234 (1984); (d) E. Wada, S. Kanemasa, and O. Tsuge. *Bull. Chem. Soc. Jpn.* **62**, 1198 (1989); (e) O. Tsuge, T. Hatta, K. Yakata, and H. Maeda. *Chem. Lett.* 1833 (1994); (f) O. Tsuge, T. Hatta, H. Yoshitomi, K. Kurosaka, T. Fujiwara, H. Maeda, and A. Kakehi. *Heterocycles*, **41**, 225 (1995); (g) O. Tsuge, T. Hatta, T. Fujiwara, T. Yokohari, and A. Tsuge. *Heterocycles*, **50**, 661 (1999).
- See also: (a) W. Adam, T. Deufel, R. Finzel, A.G. Griesbeck, and J. Hirt. *J. Org. Chem.* **57**, 3991 (1992); (b) S. Motoki, Y. Matsuo, and Y. Terauchi. *Bull. Chem. Soc. Jpn.* **63**, 284 (1990); (c) T. Saito, H. Kimura, K. Sakamaki, T. Karakasa, and S. Moriyama. *Chem. Commun.* 811 (1996); (d) T. Saito, H. Kimura, T. Chonan, T. Soda, and T. Karakasa. *Chem. Commun.* 1013 (1997).
- See other examples in O. Tsuge, S. Kanemasa, E. Wada, and H. Sakoh. *Yuki Gosei Kagaku Kyokaishi*, **44**, 756 (1986), and refs. cited therein.



5. (a) C. Spino, G. Liu, N. Tu, and S. Girard. *J. Org. Chem.* **59**, 5596 (1994); (b) C. Spino and G. Liu. *J. Org. Chem.* **58**, 817 (1993).
6. (a) A.G. Fallis, S. Parra, S. Legoupy, and S. Woo. *Org. Lett.* **1**, 1013 (1999); (b) A.G. Fallis, N. Squire, and S. Woo. *Org. Lett.* **1**, 573 (1999).
7. For a review on the synthetic aspect of quassinoids, see: K. Kawada, M. Kim, and D.S. Watt. *Org. Prep. Proceed. Int.* **21**, 521 (1989). Recent syntheses include: (a) D.P. Walker and P.A. Grieco. *J. Am. Chem. Soc.* **121**, 9891 (1999); (b) P.A. Grieco, J.L. Collins, and J.C. Huffman. *J. Org. Chem.* **63**, 9576 (1998); (c) T.K.M. Shing and Q. Jiang. *J. Org. Chem.* **65**, 7059 (2000).
8. For reviews on the isolation and biological activities of quassinoids, see: (a) J. Polonsky. *Fortschr. Chem. Org. Naturst.* **30**, 101 (1973); (b) J. Polonsky. *Fortschr. Chem. Org. Naturst.* **47**, 221 (1985).
9. For selected reports see: (a) S. Tamura, N. Fukamiya, X.Y. Mou, T. Mukainaka, H. Tokuda, H. Nishino, K. Tagahara, K. Koike, and K.H. Lee. *Chem. Pharm. Bulletin*, **48**, 876 (2000); (b) I. Watanabe, K. Koike, T. Satou, and T. Nikaido. *Biol. Pharm. Bull.* **23**, 723 (2000); (c) G. Francois, C. Diakanamwa, G. Timperman, G. Bringmann, T. Steenackers, G. Atassi, M. Vanlooveren, J. Holenz, J.P. Tassin, and L.A. Assi. *Int. J. Parasitology*, **28**, 635 (1998); (d) S. Rahman, S.N. Fukamiya, M. Okano, K. Tagahara, and K.H. Lee. *Chem. Pharm. Bull.* **45**, 1527 (1997).
10. For a recent review on the intramolecular Diels–Alder reaction, see: (a) W.R. Roush. *Adv. Cycloaddit.* **2**, 91 (1990). See also: (b) M.E. Jung. *Synlett*, **4**, 186 (1990); (c) D. Craig. *Chem. Soc. Rev.* **16**, 187 (1987); (d) C. Engelbert. *Org. React.* **32**, 1 (1984); (e) A.G. Fallis. *Can. J. Chem.* **62**, 183 (1984).
11. For exocyclic double bonds, see: K. Nakatani, T. Izawa, and S. Isoe. *J. Org. Chem.* **59**, 5961 (1994), and refs. cited therein.
12. S. Hanessian, J. Pan, A. Carnell, H. Bouchard, and L. Lesage. *J. Org. Chem.* **62**, 465 (1997).
13. J.E. McMurry. *Chem. Rev.* **89**, 1513 (1989), and refs. cited therein.
14. C. Spino, C. Thibault, and S. Gingras. *J. Org. Chem.* **63**, 5283 (1998).
15. (a) H.J. Reich, E.K. Eisenhart, W.L. Whipple, and M.J. Kelly. *J. Am. Chem. Soc.* **110**, 6432 (1988); (b) H.J. Reich and E.K. Eisenhart. *J. Org. Chem.* **49**, 5282 (1984).



# From T-antigen to plasmalogen-derived aldehydes: The identification of a marker of colorectal cancer in human rectal mucous

**Jiri J. Krepinsky, Gabor P. Kandel, Ka Sing Yeung, Jacek Chociej, Min Chen, Gideon Cohen, Stephen P. Douglas, Rudolf Furrer, Vishal Kukreti, Niculina Lupescu, Enocha Richens, and Keith L. Tanner**

**Abstract:** Recently, a simple noninvasive screening test for colorectal cancer was proposed, based on a hypothesis involving galactose-containing carbohydrate moieties such as the Thomsen–Friedenreich antigen. According to the hypothesis, such carbohydrate moieties, present in the human rectal mucous of patients with colorectal cancer, can be specifically oxidized with galactose oxidase to form substances that, upon reaction with Schiff reagent, yield purple (magenta) coloured compounds. While evaluating this proposed test, we discovered that the colour formation is not due to the proposed reaction between oxidized galactose moieties present in rectal mucous and Schiff reagent. We found instead that the mucous from colorectal cancer patients contains compounds that form purple (magenta) adducts with the Schiff reagent directly, i.e., they do not require oxidation by galactose oxidase. We have identified these compounds as long-chain aliphatic aldehydes, mainly palmitic aldehyde  $C_{15}H_{31}CH=O$  and stearic aldehyde  $C_{17}H_{35}CH=O$ . We have further found that the aldehydes originate from plasmalogens present in the phospholipid fraction of the mucous obtained from colorectal cancer patients. The aldehydes, present in plasmalogens as enol ethers, are released by the acidity of the Schiff reagent and in turn react with the Schiff reagent to form the coloured adducts. Correct identification of these markers could lead to the development of a more accurate colorectal cancer screening tool and to a deeper understanding of colorectal carcinogenesis.

**Key words:** T-antigen, plasmalogen-derived aldehydes, colorectal cancer marker.

**Résumé :** Récemment une nouvelle méthode simple et non invasive de dépistage du cancer colorectal a été proposée; elle est fondée sur une hypothèse impliquant des portions de sucre contenant du galactose, tel l'antigène de Thomsen–Friedenreich. Selon cette hypothèse, de telles portions de sucre présentes dans les muqueuses rectales de patients humains atteints d'un cancer colorectal peuvent être spécifiquement oxydées par l'oxydase du galactose pour former des substances qui réagissent avec le réactif de Schiff et qui produisent des composés colorés en violet magenta. En évaluant la méthode proposée, on a découvert que la formation de la couleur n'est pas due à la réaction suggérée du réactif de Schiff et des portions de galactose oxydé présentes dans la muqueuse rectale. On a plutôt trouvé que la muqueuse de patients atteints de cancer colorectal contiennent des composés qui, avec le réactif de Schiff, forment directement des adduits colorés en violet magenta, c'est-à-dire qu'il n'est pas nécessaire de procéder par l'oxydation à l'aide d'oxydase du galactose. On a identifié ces composés comme étant des aldéhydes aliphatiques à longues chaînes carbonées, principalement l'aldéhyde palmitique,  $C_{15}H_{31}CH=O$ , et l'aldéhyde stéarique,  $C_{17}H_{35}CH=O$ . On a de plus trouvé que ces aldéhydes trouvent leur origine dans les plasmalogènes présents dans la fraction phospholipide de la muqueuse des patients atteints de cancer colorectal. Ces aldéhydes sont présents dans le plasmalogène sous la forme d'éthers énoles, ils sont libérés par l'acidité du réactif de Schiff et ils réagissent alors avec le réactif de Schiff pour former les adduits colorés. L'identification correcte de ces marqueurs pourrait conduire au développement d'un outil de dépistage plus précis du cancer colorectal et à une meilleure compréhension du développement de ce type de cancer.

**Mots clés :** antigène T, aldéhydes dérivés du plasmalogène, marqueur du cancer colorectal.

[Traduit par la Rédaction]

Received 8 November 2001. Published on the NRC Research Press Web site at <http://canjchem.nrc.ca> on 30 January 2003.

*Dedicated to the memory of Professor Raymond U. Lemieux.*

**J.J. Krepinsky,<sup>1</sup> J. Chociej, M. Chen, G. Cohen, S.P. Douglas, R. Furrer, V. Kukreti, N. Lupescu, E. Richens, and K.L. Tanner.** Department of Medical Genetics and Microbiology, University of Toronto, Toronto, ON M5S 1A8, Canada.

**G.P. Kandel.** St. Michael's Hospital, 30 Bond Street, Toronto, ON M5B 1W8, Canada, and Department of Medicine, University of Toronto, Toronto, ON M5S 1A8, Canada.

**K.S. Yeung.** Department of Public Health Sciences, University of Toronto, Toronto, ON M5S 1A8, Canada.

<sup>1</sup>Corresponding author (e-mail: [george.krepinsky@utoronto.ca](mailto:george.krepinsky@utoronto.ca)).



## Introduction

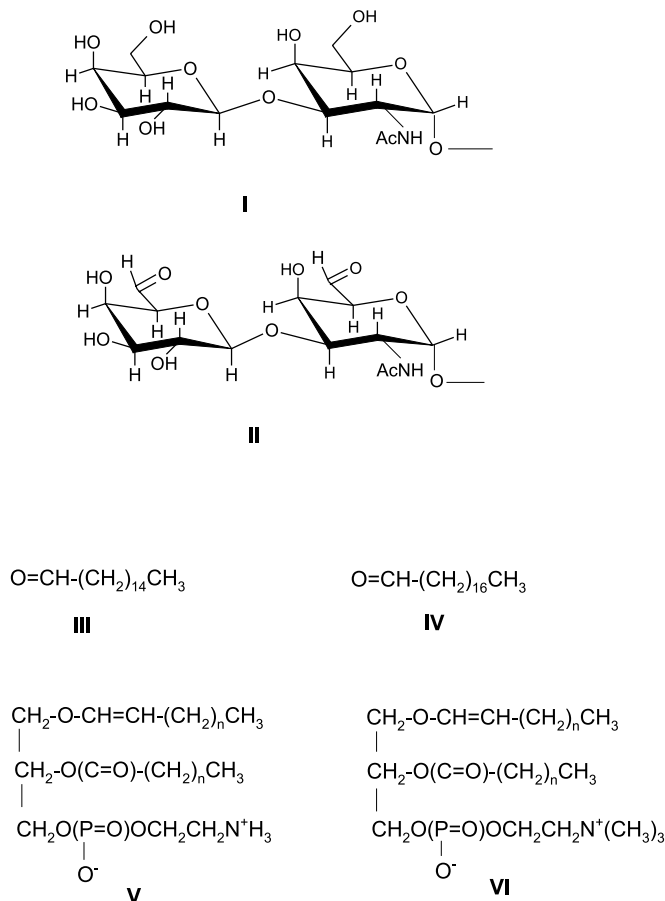
Colorectal carcinoma is the second most frequent cause of cancer mortality in men and women in industrialized countries (1, 2). Primary prevention (i.e., averting the development of the tumour by altering risk factors) is not yet feasible, since the etiology of the disease is not adequately understood. Therefore, there has recently been a great deal of interest in secondary preventive measures (i.e., detection at an asymptomatic, curable stage).

Recently, a promising screening test was proposed. It is based on the observation that most colorectal neoplasms express a disaccharide D-Galp(β1-3)-D-GalpNAcα1 (also called Thomsen–Friedenreich antigen or T-antigen) — bound as an *O*-glycoside to (-)-Ser or (-)-Thr (**I**; Scheme 1) — among the carbohydrate components of colonic mucin. This antigen is usually detected by applying fluorescently labeled peanut agglutinin (PNA) (3, 4) to histological specimens obtained from the tumour. Obviously, obtaining biopsy specimens from neoplasms inside the colon for screening purposes is not possible. Therefore, a technique (5) was proposed whereby this carbohydrate marker could be detected in colorectal mucous collected during digital rectal examination. The technique further assumes that the two galactose moieties in T-antigen are oxidizable by galactose oxidase to C-6 aldehydes in dialdehyde **II**. These two C-6 aldehydes, on subsequent reaction with Schiff reagent (6, 7), would yield an adduct detectable by its purple (magenta) colour (5, 8). Other galactose-containing oligosaccharides were subsequently added to T-antigen as carbohydrate markers of colorectal cancer (9). In addition to being simple and noninvasive, this technique has the advantage that it samples mucous from the whole colorectum because mucous from the total length of the colon flows towards the rectum. (5)

Because of the potential advantage of such a screening test, we initiated its clinical and laboratory evaluation in 1989. In 1991 we discovered unexpectedly that colorectal mucous from individuals with colorectal neoplasia developed a purple (magenta) colour after *direct* addition of Schiff reagent to the mucous specimens, without the treatment with galactose oxidase (10). The oxidation step was somewhat puzzling, since the galactose oxidase treatment could be shortened to 10 min (8) without any effect on the test results, although the oxidation of a terminal galactose to the C-6 aldehyde usually requires 15–30 min at 37°C, while nonterminal galactose units are much less efficient substrates (10). Seeking an explanation to why colorectal mucus from patients with colorectal cancer developed a magenta colour directly upon addition of Schiff reagent, we first found that the component(s) of the mucous responsible for the colour development (referred to as a marker in this article) were soluble in lipophilic solvents. This suggested that the marker could not be a carbohydrate, which should be hydrophilic. We also found that asialofetuin (a suitable model glycoprotein because it contains T-antigen) does not undergo a change in colour when reacted with Schiff reagent, whether treated with galactose oxidase or not.

Since the marker reacted with Schiff reagent *directly*, we speculated that such a marker could become the basis of a simpler and more economical screening test (11) than the test involving galactose oxidase. The elimination of the oxidation step would reduce the costs of chemicals, equipment,

**Scheme 1.** Chemical formulae of T-antigen before (**I**) and after (hypothesized **II**) oxidation with galactose oxidase, palmitic (**III**) and stearic (**IV**) aldehydes, and plasmalogens of ethanolamine (**V**) and choline (**VI**) types.



and technician time. The first step toward this practical goal was to identify the chemical structure(s) of the marker(s). In this article we describe both the isolation and the identification of the chemical structure of the markers. Although the objective of this investigation has been the identification of the chemical structure of the markers, patient data gathered while collecting colorectal mucous in the process of the identification of the markers are presented (cf. Fig. 1 for examples). These data suggest that further epidemiologic investigations of the usefulness of the markers in a screening test for colorectal cancer are warranted.

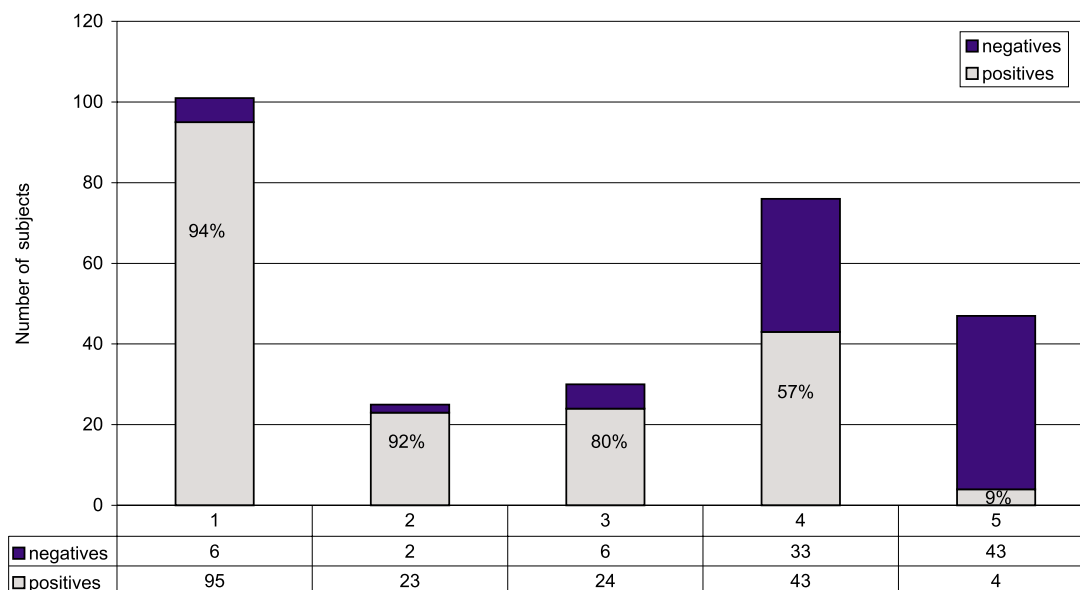
## Materials and methods

### Materials and general procedures

Thin layer chromatography (TLC) was performed on silica gel 60 plates (thickness 0.25 mm) or preparative plates (thickness 1 mm). Analytical plates were visualized by spraying with 50% aq  $\text{H}_2\text{SO}_4$  and heating to 200°C. Silica gel (200–400 mesh, Toronto Research Chemicals) was used for column chromatography. PE (brain extract) and PC (heart extract) plasmalogens were purchased from Doosan Serdary Research Laboratories (Toronto, Canada). Schiff reagent was prepared from *p*-rosaniline chloride (#1528, also basic fuchsin or magenta from Sigma Chemical Co.,



**Fig. 1.** Proportion of positives on five groups of subjects. Mucus examples were (1) from colectomy specimens from colorectal cancer patients obtained in several Toronto hospitals; (2) from individuals scheduled for colonoscopy at the Endoscopy suite, Wellesley Hospital, Toronto, subsequently diagnosed with cancer (mucus specimens were collected immediately before colonoscopy); (3) from individuals scheduled for colonoscopy at the Endoscopy suite, Wellesley Hospital, Toronto, subsequently diagnosed with large (larger than 1 cm in diameter) polyps (mucus specimens were collected immediately before colonoscopy); (4) from individuals scheduled for colonoscopy at the Endoscopy suite, Wellesley Hospital, Toronto, subsequently diagnosed with small (1 cm or smaller in diameter) polyps (mucus specimens were collected immediately before colonoscopy); (5) symptoms-free young adults (without any lavage performed before mucus collection). Note that colorectal cancer often, but not always, develops in polyps.



St. Louis, Mo.) or from basic fuchsin (ICN, Aurora, Ohio). Asialofetuin (A1908 and A4781) and galactose oxidase were purchased from Sigma. HPLC was performed on a variety of silica gel columns (5  $\mu$ m, e.g., Hypersil) using a Beckman System Gold with a Beckman UV 166P detector or a Varex Evaporative Light Scattering Detector IIA.  $^1\text{H}$  NMR spectra were recorded at 500 MHz with a Varian Unity spectrometer in the NMR spectroscopy laboratory of the Molecular Medicine Research Centre, University of Toronto. Spectra were obtained in  $\text{CDCl}_3$ , mixtures of  $\text{CDCl}_3$ – $\text{CD}_3\text{OD}$  containing a trace of TMS ( $\delta = 0$  ppm) as the internal standard, or  $\text{D}_2\text{O}$  and are reported using a  $\delta$  (ppm) scale. Mass spectra were recorded with VG Analytical ZAB-SE, SCIEX API III, or Voyager-Elite MALDI (Perseptive Biosystems) mass spectrometers in the mass spectrometry laboratory, Molecular Medicine Research Centre, University of Toronto. *O*-(2,3,4,5,6-Pentafluorobenzyl)oximes of aldehydes were analyzed by GC–CI(–)–MS (reagent gas: ammonia) using a VG-Trio 2A quadrupole mass spectrometer interfaced to a Hewlett-Packard 5890 Series II gas chromatograph at the Hospital for Sick Children, Toronto. Visible spectra were recorded with a Beckman DU 600 or a Varian CARY 300 Bio UV–Vis spectrometer (in solution or on the plates in transmittance mode). Reflectance scans were executed directly on the plates with a Varian CARY 50 spectrometer with remote reflectance probe.

#### Isolation of markers from surgical (colectomy) specimens

##### Mucous collection

Mucous was obtained from colectomy specimens from surgeries performed in operating theatres of several hospitals

in Toronto, Ont., Canada. The colectomy specimens were washed with water to remove blood and fecal matter 15–20 min after surgery. Mucous was collected by gently scraping the surface with a small spatula. The scraped mucous was placed into small plastic vials and frozen. One colectomy specimen typically yielded 0.5–1.0 g of mucous; some specimens, however, were much larger. To determine whether the collected mucous gave a colour reaction with Schiff reagent, the frozen vials were allowed to thaw at room temperature for 60 min, and a small amount of mucous on the tip of a spatula was smeared on the support and tested as described in the following section.

##### Separation of mucous components

Mucous collected as above was pooled (66 g) and lyophilized for 24 h to give a semi-solid residue (6.0 g). This residue was consecutively extracted with hexane, ethylacetate, chloroform–methanol (2:1), modified Folch extraction (12), and water; the final residue after extractions was a gel-like solid (colonic mucin). Ethylacetate extract gave a weak colour reaction with Schiff reagent, while the chloroform–methanol extract gave a very strong colour reaction with Schiff reagent. Both extracts giving colour with Schiff reagent (i.e., positive) were combined and subjected to chromatography on a column of silica gel using solvents of increasing polarity: hexane, ethylacetate, chloroform, chloroform–methanol (with increasing contents of methanol), and methanol. Chloroform–methanol (7:2.5) afforded positively reacting fractions, which were combined and evaporated to dryness to give an amorphous residue containing phospholipids (36.6 mg), which reacted strongly positive with Schiff reagent (using conditions described in the



preceding paragraphs). This fraction was repeatedly chromatographed on a series of silica gel columns using chloroform with a gradient of methanol to give two highly positively reacting fractions, PL-1 and PL-2, which were further analyzed by  $^1\text{H}$  NMR spectroscopy.

### Testing mucous obtained in digital rectal examination

#### *Mucous collection*

Mucous samples were collected from individual human subjects by a physician during routine digital rectal examination using a gloved finger lubricated with MUKO or a similar lubricant that would not react with the Schiff reagent under the testing conditions. Informed consent of the tested individuals was obtained as per the protocol approved by the Ethics Committee, University of Toronto. Mucous collected on the gloved finger was smeared onto a support (e.g., glass fibre (Whatman GF) or polyester (polymacron, Dupont, Wilmington, Del.) fabric), showing through an aperture of 1.0–1.3 cm in diameter and fastened between two glass plates (7.5 × 7.5 cm) or sealed between two plastic plates (of microscope slide size). The plates with smeared mucous samples were sent to a laboratory for processing. If processed at the place of collection, the work-up should have started no earlier than 90 min after depositing the sample to obtain sufficient specimen adherence to the fabric. The plates carrying specimens could be stored for short periods of time at room temperature (several days) or stored frozen for prolonged periods of time (several months).

#### *Treatment of mucous specimens with Schiff reagent*

Plates carrying mucous specimens were placed in the holder part of a Wheaton glass staining dish (capacity 10 plates), immersed in phosphate buffer (0.1 M, pH 7.0), and washed by gentle agitation for 10 min. The holder was then transferred into a dish containing distilled water and gently agitated for 3 min. The aqueous wash was repeated; any excess water was allowed to drip for 10–15 min to render the plates and the holder visibly dry. The holder was then immersed into a dish containing Schiff reagent for 2 min under gentle agitation followed by three washes with distilled water (3 min each). The plates were removed from the holder and air dried. The pink-red-magenta colour (positive reaction) appeared almost immediately in some cases (or within a few minutes (20–25 min at the most)) after removal from the Schiff reagent.

#### *Preparation of suitable Schiff reagent*

Many variations of the reagent are described (6). The Schiff reagent used in this study was prepared as follows: *p*-rosaniline (0.4 g; also basic fuchsin, magenta) was added to distilled water (220 mL) at approximately 95–97°C. The mixture was stirred well, brought to boil for 5 min, cooled to 50°C, and filtered through doubly folded paper filter. Aqueous HCl (1 N, 34 mL) was added to the filtrate with stirring and was allowed to cool to room temperature. Sodium bisulfite (2.34 g) was added and the solution was stirred well — the flask was sealed with parafilm — and stored in the dark at room temperature for 4 days. To the resulting straw-coloured solution was added charcoal (NORIT; 300 mg); the mixture was vigorously stirred for 1.5 min, and the charcoal

was removed by filtration. The resulting colourless solution was stored in a dark-glass bottle at 3–5°C.

### Identification of compounds giving colour reaction with Schiff reagent

#### *2,4-Dinitrophenylhydrazones of aldehydes from mucous*

Mucous (4.27 g) obtained from a colectomy as described above and giving a colour reaction with Schiff reagent was spread with a spatula on five sheets (10 × 4 cm) of polyester fabric (polymacron) and allowed to dry for 1 h. The sheets were soaked in phosphate buffer (pH 7) for 20 min, then lifted from the buffer, washed with water until all the dark coloured material was removed and the sheets were slightly yellow, and air-dried. The sheets were then cut into smaller pieces (1 × 2 cm) and immersed into a solution of 2,4-dinitrophenylhydrazine hydrochloride (30 mL; prepared by dissolving 2,4-dinitrophenylhydrazine hydrochloride (0.25 g) in 6 N HCl (100 mL)) at room temperature for 30 min. The polyester cuttings were then removed from the reagent solution and washed with water until the eluant remained colourless; the deep-yellow 2,4-dinitrophenyl hydrazones were extracted from the cuttings by acetonitrile. Acetonitrile was removed on a rotary evaporator; ethylacetate (10 mL) was added and evaporated (to remove traces of water) to yield a dry yellow residue. The residue was dissolved in dry acetonitrile (1.5 mL) and applied on a silica gel 60 plate (20 × 20 cm; thickness 1 mm) in a single line; the plate was developed with a hexane – ethyl acetate solution (4:1). The yellow band at  $R_f$  0.37 containing 2,4-dinitrophenylhydrazones was cut out and extracted with 10% MeOH in  $\text{CH}_2\text{Cl}_2$ ; the solvents were evaporated to give a deeply yellow solid, which was subsequently analyzed by MS. Two major ions were  $[\text{M}+\text{H}]^+$  ( $m/z = 421$ ) and  $[\text{M}+\text{H}]^+$  ( $m/z = 449$ ).  $^1\text{H}$  NMR ( $\text{CDCl}_3$ ) confirmed the presence of 2,4-dinitrophenyl derivatives of long chain aldehydes: 0.88 (t, 3H,  $\text{CH}_3$ ,  $J = 6.84$  and 7.08 Hz), 1.25–1.42 (m,  $\text{CH}_2$ ), 6.96 (t,  $\text{CH}=\text{N}$ ), 7.53 (t,  $\text{CH}=\text{N}$ ), 7.93 (d, H-6 (arom),  $J = 9.52$  Hz), 7.96 (d, H-6 (arom),  $J = 9.52$  Hz), 8.29 (dd, H-5 (arom),  $J = 3.18$  and 9.76 Hz), 8.33 (dd, H-5 (arom),  $J = 3.17$  and 9.52 Hz), 9.12 (d, H-3 (arom),  $J = 2.45$  Hz), 9.14 (d, H-3 (arom),  $J = 2.45$  Hz), 11.00 (s, NH), 11.18 (s, NH).

Two controls were applied: (1) the above procedure up to the chromatography was repeated with blank polyester sheets (no mucous deposited) — no reaction with 2,4-dinitrophenylhydrazine was detectable; and (2) the above procedure was repeated using mucus from colectomies that did not give a colour reaction with Schiff reagent — no reaction with 2,4-dinitrophenylhydrazine was detectable.

#### *2,4-Dinitrophenylhydrazone of palmitic aldehyde from a plasmalogen*

A mixture of PE plasmalogen (from brain extract; 10 mg in 2 mL  $\text{CHCl}_3$ ), a solution of 2,4-dinitrophenylhydrazine hydrochloride (25 mL, prepared as above), and isooctane (20 mL) was stirred for 1 h at room temperature. The aqueous phase was separated and washed with isooctane; organic phases were combined and evaporated to dryness. The yellow residue was dissolved in dry acetonitrile (0.4 mL) and applied on a silica gel 60 plate (20 × 20 cm; thickness 0.2 mm) in a single line, and the plate was developed with



hexane – ethyl acetate (4:1). The yellow band containing 2,4-dinitrophenylhydrazone was cut out and extracted with 10% MeOH in  $\text{CH}_2\text{Cl}_2$ . Solvents were removed from the extract by evaporation to give a yellow amorphous solid, which was examined by MS. The major ion was  $[\text{M}+\text{H}]^+$  ( $m/z = 421$ ).  $^1\text{H}$  NMR ( $\text{CDCl}_3$ ; major isomer is *E* (*syn*); minor isomer is *Z* (*anti*)): 0.88 (t, 3H,  $\text{CH}_3$ ,  $J = 6.84$  and 7.08 Hz), 1.25–1.42 (m, 24H,  $\text{CH}_2$ ), 1.61 (q, 2H,  $\text{CH}_2 \beta$  to CH,  $J = 7.33$  Hz and  $J = 14.65$  Hz, *E* isomer), 1.67 (q, 2H,  $\text{CH}_2 \beta$  to CH,  $J = 7.06$  Hz and  $J = 15.38$  Hz, *Z* isomer), 2.38 (ddd, 2H,  $\text{CH}_2 \alpha$  to CH,  $J = 5.44$ , 7.33, and 12.94 Hz, *Z* isomer), 2.43 (ddd, 2H,  $\text{CH}_2 \alpha$  to CH,  $J = 5.70$ , 7.57 Hz and  $J = 12.94$  Hz, *E* isomer), 6.96 (t, 1H,  $\text{CH}=\text{N}$ ,  $J = 5.37$  and 5.62 Hz, *Z* isomer), 7.53 (t, 1H,  $\text{CH}=\text{N}$ ,  $J = 5.37$  and 5.13 Hz, *E* isomer), 7.93 (d, 1H, H-6 (arom),  $J = 9.52$  Hz, *E* isomer), 7.96 (d, 1H, H-6 (arom),  $J = 9.52$  Hz, *Z* isomer), 8.29 (dd, 1H, H-5 (arom),  $J = 3.18$  and 9.76 Hz, *E* isomer), 8.33 (dd, 1H, H-5 (arom),  $J = 3.17$  and 9.52 Hz, *Z* isomer), 9.12 (d, 1H, H-3 (arom),  $J = 2.45$  Hz, *E* isomer), 9.14 (d, 1H, H-3 (arom),  $J = 2.46$  Hz, *Z* isomer), 11.00 (s, 1H, NH, *E* isomer), 11.18 (s, 1H, NH, *Z* isomer).

#### Preparation of palmitic aldehyde (13)

A solution of diisobutylaluminum hydride (DIBAL-H) in toluene (1 M, 2.95 mL, 2 eq) was added dropwise over 5 min to a solution of methyl palmitate (0.4 g, 1.48 eq) in dry toluene (10 mL) cooled to  $-70^\circ\text{C}$ . The reaction mixture was stirred for an additional 15 min, and excess reagent was decomposed by 2 N HCl (10 mL); the mixture was allowed to warm up to  $0^\circ\text{C}$ , and the aqueous layer was separated and extracted with ethyl acetate ( $2 \times 10$  mL). The combined organic extracts were washed with water ( $3 \times 5$  mL), dried over  $\text{Na}_2\text{SO}_4$ , and evaporated to dryness to give an amorphous solid containing both the aldehyde (60%) and starting ester (40%).  $^1\text{H}$  NMR ( $\text{CDCl}_3$ ) (aldehyde): 9.77 (d,  $J_{1,2} = 1.95$  Hz,  $\text{CH}_2\text{CH}=\text{O}$ ), 2.42 (m,  $J_{1,2} = 1.95$  Hz,  $\text{CH}_2\text{CH}=\text{O}$ ); (unreacted ester): 3.7 (s,  $\text{CH}_3\text{OC}[\text{=O}]$ -).

#### Preparation of 2,4-dinitrophenylhydrazone of palmitic aldehyde

The crude aldehyde (50 mg) dissolved in isooctane (25 mL) and a solution of 2,4-dinitrophenylhydrazine hydrochloride (25 mL, prepared as above) was stirred at room temperature for 1 h. After work-up (analogous to the work-up described for 2,4-dinitrophenylhydrazones of aldehydes from plasmalogens) and ensuing chromatography, a yellow amorphous solid was obtained. MS:  $[\text{M}+\text{H}]^+$   $m/z = 421$ . The chemical shifts in the  $^1\text{H}$  NMR spectrum were identical with the shifts in the  $^1\text{H}$  NMR spectrum of 2,4-dinitrophenylhydrazone of stearic aldehyde (cf. below).

#### Preparation of stearic aldehyde

A 1 M solution of diisobutylaluminum hydride (DIBAL-H) in toluene (2.95 mL, 2 eq) was added dropwise over 5 min to a solution of methyl stearate (0.44 g, 1.48 eq) in dry toluene (10 mL) cooled to  $-70^\circ\text{C}$ . The reaction mixture was stirred for an additional 15 min, and excess reagent was decomposed by 2 N HCl (10 mL); the mixture was allowed to warm up to  $0^\circ\text{C}$ , and the aqueous layer was separated and extracted with ethyl acetate ( $2 \times 10$  mL). The combined organic extracts were washed with water ( $3 \times 5$  mL), dried

over  $\text{Na}_2\text{SO}_4$ , and evaporated to dryness to give an amorphous solid containing both the aldehyde (30%) and starting ester (70%).  $^1\text{H}$  NMR ( $\text{CDCl}_3$ ) (aldehyde): 9.77 (d,  $J_{1,2} = 1.95$  Hz,  $\text{CH}_2\text{CH}=\text{O}$ ); 2.42 (m,  $J_{1,2} = 1.95$  Hz,  $\text{CH}_2\text{CH}=\text{O}$ ); (unreacted ester): 3.7 (s,  $\text{CH}_3\text{OC}[\text{=O}]$ -).

#### Preparation of 2,4-dinitrophenylhydrazone of stearic aldehyde

A solution of the crude aldehyde (50 mg) in  $\text{CH}_2\text{Cl}_2$  (4 mL) with added solution of 2,4-dinitrophenylhydrazine hydrochloride (26 mL, prepared as above) was stirred at room temperature overnight. After work-up (analogous to the work-up described for 2,4-dinitrophenylhydrazone of palmitic aldehyde) and following thin layer chromatography on silica gel, a yellow amorphous solid was obtained. MS: 449 ( $[\text{M}+\text{H}]^+$ ).  $^1\text{H}$  NMR ( $\text{CDCl}_3$ , major isomer: *E*, minor isomer: *Z*): 0.88 (t, 3H,  $\text{CH}_3$ ,  $J = 6.84$  and 7.08 Hz), 1.25–1.43 (m, 28H,  $\text{CH}_2$ ), 1.61 (q, 2H,  $\text{CH}_2 \beta$  to CH,  $J = 7.31$  Hz and  $J = 14.89$  Hz, *E* isomer), 1.67 (q, 2H,  $\text{CH}_2 \beta$  to CH,  $J = 7.08$  Hz and  $J = 15.65$  Hz, *Z* isomer), 2.38 (ddd, 2H,  $\text{CH}_2 \alpha$  to CH,  $J = 5.44$ , 7.33, and 12.94 Hz, *Z*-isomer), 2.43 (ddd, 2H,  $\text{CH}_2 \alpha$  to CH,  $J = 5.68$ , 7.57 Hz and  $J = 12.94$  Hz, *E* isomer), 6.96 (t, 1H,  $\text{CH}=\text{N}$ ,  $J = 5.38$  and 5.37 Hz, *Z* isomer), 7.53 (t, 1H,  $\text{CH}=\text{N}$ ,  $J = 5.61$  and 5.13 Hz, *E* isomer), 7.93 (d, 1H, H-6 (arom),  $J = 9.52$  Hz, *E* isomer), 7.96 (d, 1H, H-6 (arom),  $J = 9.52$  Hz, *Z* isomer), 8.29 (dd, 1H, H-5 (arom),  $J = 3.17$  and 9.52 Hz, *E* isomer), 8.33 (dd, 1H, H-5 (arom),  $J = 3.17$  and 9.52 Hz, *Z* isomer), 9.12 (d, 1H, H-3 (arom),  $J = 2.44$  Hz, *E* isomer), 9.14 (d, 1H, H-3 (arom),  $J = 2.45$  Hz, *Z* isomer), 11.00 (s, 1H, NH, *E* isomer), 11.18 (s, 1H, NH, *Z* isomer).

#### O-(2,3,4,5,6-Pentafluorobenzyl) oximes of aldehydes (14)

The above compounds were prepared from O-(2,3,4,5,6-pentafluorobenzyl)hydroxylamine (250  $\mu\text{L}$  of a 0.05 M solution in sodium acetate buffer, pH 5), added, in separate experiments, to the phospholipid mixtures PL-1 and PL-2 (cf. section "Separation of mucous components") as well as to authentic specimens of palmitic and stearic aldehydes (1 mg in 100  $\mu\text{L}$  of water), vortexed for 1 min, and allowed to react for 30 min. Then 1 N HCl (10  $\mu\text{L}$ ) was added, and the reaction mixture was extracted three times with hexane (1 mL). The combined hexane extracts were dried over sodium sulfate and evaporated to dryness under a stream of nitrogen; the residue was redissolved in hexane (50  $\mu\text{L}$ ). This solution (1  $\mu\text{L}$  injections) was used for GLC–MS identification of the aldehydes. Negative ion CI-MS (reagent gas: ammonia) was executed on a quadrupole mass spectrometer VG-Trio 2A interfaced with a Hewlett-Packard 6890 Series II GC using a DB-5 capillary column (length: 30 m, diameter: 0.25  $\mu\text{m}$ ), employing helium as the carrier gas at a flow rate of 1 mL  $\text{min}^{-1}$ , and with the temperature increasing from 60 to  $310^\circ\text{C}$  while maintaining the injection port temperature at  $250^\circ\text{C}$  (15).

## Results

### Aldehyde identification

Analytical chemists have been using Schiff reagent for decades to demonstrate that the aldehydic group is present in the examined samples. However, although the reagent is



very sensitive, it is extremely difficult to isolate the products of its reaction with aldehydes (6, 7). 2,4-Dinitrophenylhydrazine in a strongly acid solution, on the other hand, produces chemically stable 2,4-dinitrophenylhydrazones, which can be isolated and purified; often they can be obtained in a crystalline form. Employing modern spectroscopic methods, the chemical structure of such pure compounds can be determined with relative ease. As no aldehydic hydrogen  $H-C=O$  could be identified in the NMR spectra of the extracts from which 2,4-dinitrophenylhydrazones were prepared, the aldehydes had to be released from precursors during the treatment with Schiff reagent. Since both Schiff reagent and 2,4-dinitrophenylhydrazine operate in strongly acidic environments, it is reasonable to presume that the acidity of the reagents allowed for the release of the aldehydes from their precursors. Therefore, 2,4-dinitrophenylhydrazones (2,4-DNPH) are valuable derivatives for the identification of the structure of markers. Indeed, palmitic and stearic aldehydes were identified via their 2,4-dinitrophenylhydrazones as the aldehydes originating in colorectal mucous from cancer patients by the combination of MS and  $^1H$  NMR spectroscopy. First, strong molecular ions were found in FAB-MS, which corresponded to the 2,4-dinitrophenylhydrazones of palmitic ( $[M+H]^+$ :  $m/z = 421$ ) and stearic ( $[M+H]^+$ :  $m/z = 449$ ) aldehydes. This finding was confirmed by  $^1H$  NMR spectroscopy, by comparison of the NMR spectra of the 2,4-DNPH of aldehydes obtained from mucous fractions with synthetic authentic specimens, and by a further comparison with the previously published  $^1H$  NMR data. As expected, two geometric isomers were present in all specimens of 2,4-DNPH of aldehydes and assigned as described in reference 16. The  $^1H$  NMR chemical shifts of the 2,4-dinitrophenylhydrazones of palmitic and stearic aldehydes were found to be practically identical. These results indicated that the above aldehydes are the markers detected by Schiff reagent in colorectal mucous. The next question to be answered was: From what precursors were the aldehydes released?

During the chromatography of colorectal mucous, we observed that the fractions containing phospholipids produced the strongest colour with Schiff reagent. Since the only phospholipids that could release the long chain aliphatic aldehydes by treatment with acids are the plasmalogens, we therefore attempted to detect plasmalogens in the phospholipid fraction. To purify the plasmalogens, the phospholipid fraction was further rechromatographed on silica gel columns. Two well-separated groups of phospholipids (PL-1 and PL-2) were obtained. The first group contained ethanolamine and the other contained choline classes of phospholipids; both groups gave strong colouration on treatment with Schiff reagent. As these groups could not be further fractionated, we employed  $^1H$  NMR spectroscopy to confirm the presence of the plasmalogens in these fractions (and consequently, to confirm the hypothesis that the aldehydes were released from the plasmalogens).

### Plasmalogen identification

$^1H$  NMR analysis (17) showed that both fractions were phospholipids with long fatty chain acids (*sn*-glycero-3-phosphoryl derivatives) based on  $^1H$  resonances characteristic for glycerol and  $CH_2$ -groups of polar head groups and for

aliphatic chains of fatty acid ester groups. The less polar fraction consisted of a mixture of phospholipids containing ethanolamine (PL-1), while the more polar fraction contained a mixture of phospholipids with choline (PL-2); neither of the two fractions was further separable by chromatography on silica gel. In the fraction PL-1, hydroxyls in the 2-position and partially in the 1-position of *sn*-glycerol were esterified with fatty acids. The ethanolamine ( $-OCH_2CH_2NH_2$ ) moiety was identified by  $^1H$  resonances at  $\delta = 3.13$  ppm (triplet) and at  $\delta = 4.03$  ppm (overlapping with H-3 of *sn*-glycerol). The presence of a signal of an  $\alpha,\beta$ -unsaturated ether was confirmed through a doublet ( $J_{1,2} = 6.1$  Hz) at  $\delta = 5.90$  ppm, which was assigned to the vinylic proton  $O-CH=CH-$ . This proton was further coupled to a quartet at  $\delta = 4.38$  ppm and a multiplet at  $\delta = 2.02$  ppm in a COSY spectrum confirming the presence of the  $O-CH=CH-CH_2$  moiety in the molecule. Other allylic  $CH_2$  groups giving rise to signals at  $\delta = 2.82-2.88$  ppm were probably present in the olefinic chains of aliphatic acids. Two  $^1H$  multiplets assigned to H-2 of the glycerol moiety centered at  $\delta = 5.18$  ppm and  $\delta = 5.25$  ppm suggested that this fraction contained two derivatives of ethanolamine-containing phospholipids. The integrations of the vinylic signal and the H-2 glycerol signal at  $\delta = 5.18$  ppm were of the same intensity (1:1). The estimate of the ratio (7:3) between the 1-alk-1'-enyl-2-acyl-*sn*-glycerophospholipids (= plasmalogens) and 1,2-diacyl-*sn*-glycerophospholipids was made on the basis of a comparison of the integration of signals for CH-2 of the glycerol moiety (cf. above).

In the more polar fraction PL-2, OH-2 and, partially, OH-1 in *sn*-glycerol were again esterified with fatty acids. The signals at  $\delta = 3.24$  ppm and  $\delta = 3.40$  ppm were identified as belonging to two different phospholipids containing a choline moiety ( $CH_2CH_2-N(CH_3)_3$ ). As in the PL-1 fraction, this fraction contained an  $\alpha,\beta$ -unsaturated ether, which was confirmed through a doublet at  $\delta = 5.90$  ppm assigned to the vinylic proton  $O-CH=CH-$ . Two proton multiplets, centered at  $\delta = 5.16$  ppm and  $\delta = 5.25$  ppm and assigned to H-2 of the glycerol moiety, suggested that this fraction contained two derivatives of choline-containing phospholipids. The integration of the vinylic signal and the H-2 *sn*-glycerol signal at  $\delta = 5.16$  were again of the same intensity (1:1). The ratio between the 1-alk-1'-enyl-2-acyl-*sn*-glycerophospholipids (= plasmalogens) and 1,2-diacyl-*sn*-glycerophospholipids in PL-2 was estimated to be 4:1 by comparison of the integration of signals for CH-2 of the glycerol moiety (cf. above).

Stereochemistry of the glycerol moiety was not determined, although it was assumed that it does not differ from stereochemistry commonly found in natural phospholipids based on comparisons of the  $^1H$  NMR spectra. Similarly, the geometry of the vinylic ether double bond in plasmalogens isolated from the colorectal mucus of cancer patients and plasmalogens from other natural sources was found to be identical (based on the identity of the coupling constant of the vinylic signal for  $^1H$  at  $\delta = 5.90$  ppm).

The aldehydes released by hydrolysis of PL-1 and PL-2 were identified as stearaldehyde and palmitaldehyde by comparison with authentic specimens of *O*-(2,3,4,5,6-pentafluorobenzyl oxime)s of the aldehydes using MS combined with GLC. These derivatives exhibited positive ions at  $m/z$



435 ([M – H]), 415 ([M – 20]), and 350 ([M – 50]) — with [M – 20] predominating owing to the loss of HF (palmitaldehyde) — and at  $m/z$  463 ([M – H]), 443 ([M – 20]), and 413 ([M – 50]), again with [M – 20] predominating, for stearaldehyde.

### Structure of the marker

Thus, we have identified the markers as a mixture of long chain aliphatic aldehydes released from plasmalogens, predominantly palmitic (**III**) and stearic (**IV**) aldehydes (cf. Scheme 1). Plasmalogens are phospholipids of both the ethanolamine **V** and the choline **VI** types (cf. Scheme 1) in which the aldehydes are cryptic in the form of unsaturated ethers (18). A minor contribution from other aldehydes cannot be excluded; similarly, acetal phospholipids in which the aldehydes are bound as acetals to the C1–C2 of glycerol may be minor precursors. Because of the acid lability of unsaturated ether bonds, the aldehydes are released from plasmalogens under very mild acid conditions (19); therefore, it is not surprising that the aldehydes are released upon exposure to the strongly acidic Schiff reagent. The free aldehydes, on reaction with the *leuko* (colorless) form of the dye in Schiff reagent, provide shades of magenta colour considered characteristic of aldehydes (7, 8).

The lack of colour of the Schiff reagent depends critically on the presence, in sufficient concentration, of SO<sub>2</sub> and HCl in the reagent. Should this concentration decrease, the Schiff reagent may be partially restored to the original red colour of *p*-rosaniline. Therefore, depending on the aldehyde concentration, the shade of colour on the solid support may be observed as a mixture of red (20) and magenta (purple). The adduct of *p*-rosaniline–aldehyde (resulting from the reaction of an aldehyde with Schiff reagent) has a typical absorption >560 nm; therefore, the presence of such an absorption band in a reflectance spectrum should resolve the occasional colour identification problems (21). Schiff reagent further reverts to the original colour of *p*-rosaniline on treatment with an excess of basic substances, for instance, basic amino acids such as lysine, histidine, and arginine; nucleosides such as cytidine; or simple bases such as sodium carbonate. Thorough washing with water and a buffer solution ensures that all such result-altering components of mucus are removed from the specimens before treatment with the Schiff reagent.

### Potential of the detection of marker aldehydes in a screening test for colorectal cancer

In the course of the marker identification studies it was necessary to use mucus from individuals whose disease status was known (usually determined by colonoscopy). It was also necessary to determine whether the treatment of the collected mucus with Schiff reagent resulted in colour formation (positive reaction). Therefore, rectal mucus was obtained from patients with colorectal cancer, from patients with various other pathological findings, and from individuals who had no complaints and thus were presumed to be disease free. It was also necessary to establish suitable conditions (as described in the Material and methods section) of the treatment of specimens, such as length of time for the reaction with the Schiff reagent, washings with buffers and water, different supports on which the treatment was per-

formed, and the choice of a variant of Schiff reagent. Through these investigations we could confirm that nearly all mucus specimens from patients with colorectal cancer were positive. For instance, the aldehydes were detected in close to 94% of the mucus samples removed from colectomy specimens obtained in several Toronto hospitals from 101 patients diagnosed with colorectal cancer by colonoscopy (cf. Fig. 1). In rectal mucous specimens collected from colorectal cancer patients attending the Endoscopy suite of the Wellesley Hospital (after the lavage of the colon but before the colonoscopy) and in the rectal mucous of patients with polyps a high proportion of positive results was obtained (cf. Fig. 1). Similar results were obtained with mucus from patients before the lavage (data not shown). In symptom-free individuals (47 students of medicine, ages 20–29), the aldehydes were not detectable in mucus from 43 individuals. Mucous specimens were treated with Schiff reagent as described in the Materials and methods section.

### Discussion

A number of clinical (8) and population studies on the mucus test employing the sequence galactose oxidase – Schiff reagent have shown (22) that the test has the potential (23) to become an alternative to the fecal occult blood test (FOBT) (24) as an efficacious, simple, and economical screening tool for colorectal cancer (25). Some of the shortcomings of the galactose oxidase – Schiff reagent test appear to be due to the targeting of the incorrect carbohydrate marker, one which required repeated, extensive washings and treatments with enzymes (galactose oxidase and catalase), leading to the loss of the marker from test plates. Our finding — that the marker of the mucus test for colorectal cancer screening is of a lipid rather than of a carbohydrate character (including the disaccharide T-antigen) — makes it possible to correlate more accurately the presence of the marker with the disease and to develop a more reliable screening test for the disease. Significantly increased quantities of the plasmalogens in neoplasms of the large bowel (26, 27) and some other tissues (28, 29) were independently found by <sup>31</sup>P NMR spectroscopy. Since the amounts of both the ethanolamine and choline families of plasmalogens in neoplastic tissues appear to be significantly increased compared with disease-free tissues, it appears likely that it is a biochemical pathway leading to the unsaturated ether formation that has a connection with the neoplastic transformation.

Plasmalogens are a class of ubiquitous membrane phospholipids. Although the highest levels are normally found in tissues such as brain and heart, small concentrations have been reported in most other normal tissues, and small increases in plasmalogen levels in cancer cells have been previously observed (30, 31). Increased concentrations in the colon were ascribed to a combination of an increased level of the synthetic enzyme CTP – phosphocholine cytidyltransferase and a decreased concentration of hydrolytic enzymes, phospholipases C and D (32). However, biosynthesis of the “aldehydic moiety” of plasmalogens is varied (33, 34).

Presently, a connection between colorectal cancer and plasmalogens can only be hypothesized. For instance, plasmalogens, because of their effect on membrane fluidity, may



facilitate the cellular uptake of carcinogenic substances (35), e.g., of dietary (36) or microbial origin (37, 38). It is of interest to note that the majority of strict anaerobes contain detectable plasmalogens, while aerobic and facultative anaerobic bacteria lack plasmalogens (39). However, plasmalogen-like fecal mutagens (fecapentaenes, produced in the human colon by several anaerobes) seem to play no role in the etiology of human colon cancer (19).

An aldehyde-based test for colorectal cancer screening would be expected to have an advantage over fecal occult blood test (FOBT) and colonoscopy (for screening purposes only!). It could, potentially, uncover earlier stages of the neoplastic progression than both FOBT and colonoscopy because the latter two techniques target more developed cancer. Therefore, *the aldehyde test could detect cases not sufficiently developed to be detected by colonoscopy*. For instance, we have found several patients with strongly positive aldehyde mucus tests who were given a clean bill of health by colonoscopy (therefore they were rated as "false" positives). The same patients returned to the clinic within no later than 1–2 years with frank cancer. Given the lengthy progression of colon carcinogenesis, it is not unlikely that these individuals already harbored the disease at the time of the first aldehyde test. Since it is believed that the progression from early neoplastic changes to frank cancer may span decades (40), an earlier detection of the disease may lead to the realization of the hope that drugs could control and perhaps reverse the disease progression. Early results with non-steroid antiinflammatory drugs (e.g., aspirin) (41), inhibitors of cyclooxygenase-2 (COX-2) (42), and identification of molecular targets of these drugs (43) suggest that such hopes are not unrealistic. Equally encouraging is the prospect that the early neoplastic changes could be reverted, for example, through dietary or other lifestyle measures.

In summary, we believe that the identification of aldehydes from plasmalogens — rather than galactose-containing oligosaccharides — as the substances in colonic mucous that seem to correlate with colorectal cancer and that react with Schiff reagent, will make it possible to design meaningful epidemiologic studies that will confirm whether the aldehydes are indeed markers of colorectal cancer suitable for population screening.

## Acknowledgments

We are grateful to our clinical collaborators without whom the study would not be possible: Claude Burul and Thomas Harmantas (St. Joseph's Health Centre, Toronto, Ont., Canada); Jean Couture, Robin S. McLeod, Carol J. Swallow, Helen M. McRae, Zane Cohen, R. Warren, J. Hartwick, Alan Wolff, and Joanne Boone (Mt. Sinai Hospital, Toronto, Ont., Canada); Gregory Haber, Paul Kortan, Joseph Mamazza, and Norman E. Marcon (St. Michael's Hospital, Toronto, Ont., Canada); and Michael A. P. Smith (Rudd Clinic, Toronto, Ont., Canada). We thank the staff of the Molecular Medicine Research Centre, University of Toronto, for NMR and MS analyses and Dr. D.C. Lehotay, Hospital for Sick Children, Toronto, for GC-MS analyses of *O*-(2,3,4,5,6-pentafluorobenzyl) oximes of aldehydes. The financial support of this research program from the National

Cancer Institute of Canada (NCIC), the Natural Sciences and Engineering Research Council of Canada (NSERC), and ProcyonBiopharma, Inc. (Montréal, Que., Canada) is gratefully appreciated.

## References

1. H.E. Mulcahy, M.J.G. Farthing, and D.P. O'Donoghue. *Br. Med. J.* **314**, 285 (1997).
2. R.F. Thoeni. *In* Neoplasms of the digestive tract: imaging, staging, and management. *Edited by* M.A. Meyers. Lippincott-Raven Publishers, Philadelphia, PA. 1998. p. 237.
3. S.H. Itzkowitz, M. Yuan, C.A. Montgomery, T. Kjeldsen, H.K. Takahashi, W.L. Bigbee, and Y.S. Kim. *Cancer Res.* **49**, 197 (1989).
4. G.D. MacLean and B.M. Longenecker. *Semin. Cancer Biol.* **2**, 433 (1991).
5. H. Xu, K. Sakamoto, and A.M. Shamsuddin. *Arch. Pathol. Lab. Med.* **116**, 1234 (1992).
6. F.H. Kasten. *Int. Rev. Cytol.* **10**, 1 (1960).
7. (a) J.H. Robins, G.D. Abrams, and J.A. Pincock. *Can. J. Chem.* **58**, 339 (1980); (b) G.S. Nettleton and A.-M. Carpenter. *Stain Technol.* **52**, 63 (1977).
8. A.M. Shamsuddin. *Anticancer Res.* **16**, 2193 (1996).
9. A.M. Shamsuddin. U.S. Patent 5 348 860, September 20, 1994.
10. C.G. Hamberg and M. Tolvanen. *In* Guide to techniques in glycobiology. *Methods in Enzymology*. Vol. 230. *Edited by* W.J. Lennarz and G.W. Hart. Academic Press, San Diego, CA. 1994. p. 32.
11. K.S. Yeung, J. Chociej, G.P. Kandel, and J.J. Krepinsky. *Proc. Annu. Meet. Am. Assoc. Cancer Res.* **36**, A1251 (1995).
12. J. Folch, M. Lees, and G.H. Sloan-Stanley. *J. Biol. Chem.* **226**, 497 (1957).
13. E. Winterfeldt. *Synthesis*, 617 (1975).
14. F.J.G.M. van Kuijk, D.W. Thomas, R.J. Stephens, and E.A. Dratz. *Biochem. Biophys. Res. Commun.* **139**, 144 (1986).
15. X.P. Luo, M. Yazdanpanah, N. Bhooi, and D.C. Lehotay. *Anal. Biochem.* **228**, 294 (1995).
16. S.F. Tayyari, J.L. Speakman, M.B. Arnold, W. Cai, and M.A. Behforouz. *J. Chem. Soc. Perkin Trans.* **2**, 2195 (1998).
17. M.L. Sparling, R. Zidovetzki, L. Muller, and S.I. Chan. *Anal. Biochem.* **178**, 67 (1989).
18. F. Paltauf. *Chem. Phys. Lipids*, **74**, 101 (1994).
19. J.J. Krepinsky. *Prog. Biochem. Pharmacol.* **22**, 35 (1988).
20. H. Zollinger. *Colour chemistry. Syntheses, properties and applications of organic dyes and pigments*. 2nd ed. VCH Publishers, Weinheim. 1981. p. 398.
21. J.J. Krepinsky, R. Furrer, M. Chen, S.P. Douglas, and J. Campbell. *J. Chem. Soc. Chem. Commun.* 2003. In preparation.
22. D.Y. Zhou, F.C. Fang, Y.L. Zhang, Z.S. Lai, W.D. Zhang, L.B. Li, G.L. Xu, T.M. Wan, D.S. Pan, D. Zhou, Y.C. Zhang, and S.B. Li. *Chin. Med. J.* **106**, 739 (1993).
23. M.A. Shamsuddin, G.T. Tyner, and G.Y. Yang. *Cancer Res.* **55**, 149 (1995).
24. S. Otto and S. Eckhardt. *J. Surg. Oncol.* **75**, 220 (2000).
25. I.T. Said, A.M. Shamsuddin, M.A. Sherief, S.G. Taleb, W.F. Aref, and D. Kumar. *Histol. Histopathol.* **14**, 351 (1999).
26. T.E. Merchant, J.N. Kasimos, P.W. de Graaf, B.D. Minsky, L.W. Glerke, and T. Glonek. *Int. J. Colorectal Dis.* **6**, 121 (1991).



27. T.E. Merchant, P.M. Diamantis, G.Y. Lauwers, T. Haida, J.N. Kasimos, J. Guillem, T. Glonek, and B.D. Minsky. *Cancer*, **76**, 1715 (1995).
28. T.E. Merchant, P. Meneses, L.W. Gierke, W. Den Otter, and T. Glonek. *Br. J. Cancer*, **63**, 693 (1991).
29. T.E. Merchant, B.D. Minsky, G.Y. Lauwers, P.M. Diamantis, T. Haida, and T. Glonek. *NMR Biomed.* **12**, 184 (1999).
30. F. Snyder and R. Wood. *Cancer Res.* **28**, 972 (1968).
31. F. Snyder and C. Snyder. *Prog. Biochem. Pharmacol.* **10**, 1 (1975).
32. D.-A. Dueck, M. Chan, K. Tran, J.T. Wong, F.T. Jay, C. Littman, R. Stimpson, and C.P. Choy. *Mol. Cell. Biochem.* **162**, 97 (1996).
33. F. Paltauf. *In* *Ether lipids. Edited by* H.K. Mangold and F. Paltauf. Academic Press, New York, N.Y. 1983. p. 107.
34. H. Hayashi and M. Hara. *J. Biochem.* **121**, 978 (1997).
35. S. Christen, T.M. Hagen, M.K. Shigenaga, and B.N. Ames. *In* *Microbes and malignancy (Infection as a cause of human cancer). Edited by* J. Parsonnet. Oxford University Press, London. 1999. p. 35.
36. B.N. Ames and L.S. Gold. *Biotherapy*, **11**, 205 (1998).
37. J.B. Brooks, W.B. Cherry, L. Thacker, and C.C. Alley. *J. Infect. Dis.* **126**, 143 (1972).
38. K. Kanazawa, F. Konishi, T. Mitsuoka, A. Terada, K. Itoh, S. Narushima, M. Kumemura, and H. Kimura. *Cancer*, **77** (Suppl. 8), 1701 (1996).
39. H. Goldfine and P.-O. Hagen. *In* *Ether lipids. Edited by* F. Snyder. Academic Press, New York, NY. 1972. p. 329.
40. J.-L. Tsao, Y. Yatabe, R. Salovaara, H.J. Järvinen, J.-P. Mecklin, L.A. Aaltonen, S. Tavaré, and D. Shibata. *Proc. Natl. Acad. Sci. U.S.A.* **97**, 1236 (2000).
41. E. Giovannucci, K.M. Egan, D.J. Hunter, M.J. Stampfer, G.A. Colditz, W.C. Willett, and F.E. Speizer. *N. Engl. J. Med.* **333**, 609 (1995).
42. M. Tsuji, S. Kawano, and R.N. DuBois. *Proc. Natl. Acad. Sci. U.S.A.* **94**, 3336 (1997).
43. I. Shureiqui, D. Chen, J.J. Lee, P. Yang, R.A. Newman, D.E. Brenner, R. Lotan, S.M. Fischer, and S.M. Lippman. *J. Natl. Cancer Inst.* **92**, 1135 (2000).



# A new phenolic metabolite, involutone, isolated from the mushroom *Paxillus involutus*

Róża Antkowiak, Wiesław Z. Antkowiak, Izabela Banczyk, Lucyna Mikolajczyk

**Abstract:** A new optically active metabolite, involutone, was found in methanol, ethanol, or *n*-butanol extracts of freshly collected *Paxillus involutus*. The structure of this compound was proved to be 5-(3,4-dihydroxyphenyl)-2-(4-hydroxyphenyl)-2-hydroxy-4-cyclopenten-1,3-dione on the basis of the spectral and chemical properties of involutone and its tetraacetyl derivative. In addition, a number of compounds of known structures such as linoleic and crotonic acids, mannitol, ergosterol, involutin, as well as methyl, ethyl, or *n*-butyl- $\beta$ -D-glucopyranosides, and methyl, ethyl, or *n*-butyl linoleates, depending in both cases on the alcohol used in the extraction, were also isolated in a pure state from the mushroom.

**Key words:** *Paxillus involutus*, Brown Roll-rim, metabolite isolation, structure study, quaternary hydroxycyclopentanedione, NMR of mushroom pigments, glucosides and linoleates, enzymic glucosylation and esterification.

**Résumé :** L'extraction de *Paxillus involutus* par du méthanol, de l'éthanol ou du butanol a permis d'isoler un nouveau métabolite optiquement actif, l'involutone. Sur la base des propriétés spectrales et chimiques de l'involutone et de son dérivé tétraacétylé, on a déterminé sa structure, la 5-(3,4-dihydroxyphényl)-2-(4-hydroxyphényl)-2-hydroxycyclopent-4-ène-1,3-dione. De plus, les extractions du champignon ont permis d'isoler à l'état pur un certain nombre de composés de structures connues, dont les acides linoléique et crotonique, du mannitol, de l'ergostérol, de l'involutine ainsi que des  $\beta$ -D-glucopyranosides de méthyle, d'éthyle ou de butyle et des linoléates de méthyle, éthyle ou butyle suivant, dans chaque cas, la nature de l'alcool utilisé pour les extractions.

**Mots clés :** *Paxillus involutus*, chanterelle brune, isolement d'un métabolite, étude de structure, hydroxycyclopentanedione quaternaire, RMN des pigments, glucosides et linoléates du champignon, glucosylation et estérification enzymatique.

[Traduit par la Rédaction]

## Introduction

The usefulness of *Paxillus involutus* (Brown Roll-rim) as an edible mushroom has been a matter of controversy for a long time, which is evident both in the literature and especially when comparing the opinions of amateur mushroom gatherers with those of most research reports, and the problem was the subject of a few review articles (1, 2). The hemolytic symptoms caused by *P. involutus* consumption, which are most often reported as being very serious, were found in the cases of both laboratory animals (3–5) and of human beings (6–11), yet the chemical compound responsible for the mortal toxicity is still unknown.

Research on the chemical composition of the mushroom carried out at the end of the 1960s and in the early 1970s of the previous century showed, mainly on the basis of paper chromatography, electrophoresis and TLC pattern, the presence of such metabolites as fatty acids, carbohydrates, and

nitrogen-containing compounds (including traces of muscarine and  $\beta$ -acetylcholine) known from their occurrence in other fungi species (12, 13). In another laboratory, involutin, an unknown pigment at that time, was isolated and its structure determined on the grounds of spectral data and chemical properties (14, 15). In subsequent years, the supposed presence in *P. involutus* of two additional compounds, chamonixin (16) and anhydroinvolutin (17), both with closely related structures to involutin, was suggested. More recently, studies on the absolute configuration of involutin and chamonixin were reported (18). Additionally, the content and metabolism of polyamines occurring in *P. involutus* has been of interest in recent years (19).

## Results and discussion

Research carried out recently in our laboratory confirmed the occurrence of involutin<sup>2</sup> in *P. involutus*. Moreover, for

Received 23 April 2002. Published on the NRC Research Press Web site at <http://canjchem.nrc.ca> on 31 January 2003.

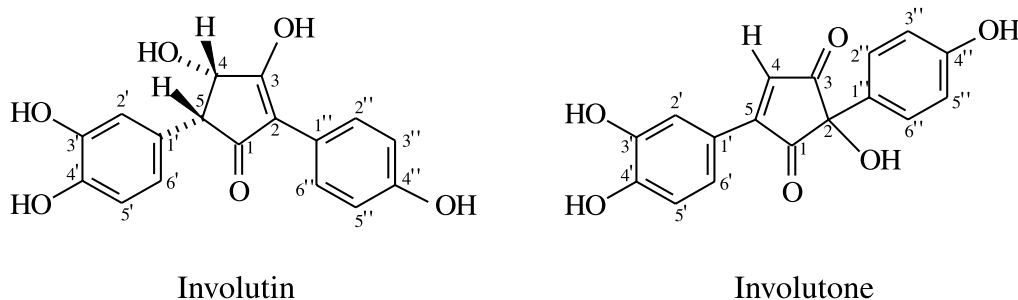
This paper is dedicated to Dr. O.E. Edwards (NRC) in recognition of his outstanding contribution to the chemistry of natural products.

R. Antkowiak, W.Z. Antkowiak,<sup>1</sup> I. Banczyk, and L. Mikolajczyk. Faculty of Chemistry, A. Mickiewicz University, Grunwaldzka 6, 60-780 Poznań, Poland.

<sup>1</sup>Corresponding author (e-mail address: [wzantk@amu.edu.pl](mailto:wzantk@amu.edu.pl)).

<sup>2</sup>The structure of involutin reported in the literature was confirmed by our HMBC experiments, the results of which are quoted in the experimental part of this paper.



**Scheme 1.** The structural relationship between involutin and involutone.

the first time ever, we have isolated from this mushroom several metabolites in an homogeneous form, namely D-mannitol, crotonic acid, (–)-ergosterol, and β-methyl, -ethyl, or -n-butyl-D-glucopyranosides,<sup>3</sup> depending on the alcohol (MeOH, EtOH, or n-BuOH) used for the extraction at room temperature. Additionally, the presence in the mushroom of some fatty acids with linoleic acid as the main component was proved, but most of the acid was isolated in the form of methyl, ethyl, or n-butyl linoleate, depending on the alcohol (MeOH, EtOH, or n-BuOH) used for the extraction, respectively; according to GC–MS, the presence of a small amount of palmitic acid and oleic acid was also identified.

The formation of both glucosides and linoleate esters from the original metabolites<sup>4</sup> suggests enzymatically catalyzed reactions and, consequently, the presence of the suitable, active enzymes (glucosidase or glucosyltransferase and lipase, respectively) as the constituents of *P. involutus*.

A number of mushrooms are able to produce metabolites as a response to a mechanical injury of the fruit bodies, but, as a rule, this involves an enzymatically induced oxidation process (20). The syntheses of glycosides and fatty acid esters can also be catalyzed by enzymes of fungal origin but mostly derived from lower fungi (21–23).

The ability of *P. involutus* to produce some artefacts in the isolation procedure and, thereby, changing its original chemical composition (especially if transglucosylation and (or) transesterification takes place), could be responsible for the hitherto difficulties in finding the right metabolite which causes the toxic properties of the mushroom.

Additionally to the compounds of known structure, we found and isolated with a high degree of purity an optically active metabolite of an unknown structure, which melted at 181 to 182°C and showed a specific rotation ( $[\alpha]_D +96.3^\circ$ ), and was yellow or, when hydrated, orange in colour. The molecular formula of this metabolite was determined to be  $C_{17}H_{12}O_6$  on the basis of HR-MS. The trivial name involutone was given to that compound, referring both to the mushroom species as well as to the elemental compositions only differing from that of involutin by two hydrogens (Scheme 1).

In spite of the small difference in elemental composition, the structural analysis showed that the new compound is not

the product of a simple oxidation of the secondary alcohol (involutin) to a corresponding ketone (didehydroinvolutin). Such a transformation would leave the asymmetric benzylic carbon, to which one hydrogen is attached, as the only chiral center. According to the literature data (14, 15, 24), the NMR absorption of a benzylic proton of similar systems was recorded as being somewhere in the range of 3.98–4.32 ppm. In the case of involutone, the absence of an absorption in that region eliminated such a chiral center in the molecule.

Other spectroscopic data recorded for involutone showed the absence of protons attached to  $sp^3$  hybridized carbons ( $^1H$  NMR, Distortionless enhancement by polarization transfer (DEPT) and the presence in the molecule of two substituted benzene rings, 4-hydroxyphenyl and 3,4-dihydroxyphenyl (the aromatic ring protons gave the AA'XX' and AMX systems, respectively, in the range 7.59–6.79 ppm). The region of aromatic carbons (158–115 ppm) contained, apart from the 10 signals originating from the 12 carbons composing the two benzene rings, two additional peaks of vinyl carbons. One of these carbon atoms, absorbing at 139.57 ppm (C-4), is bonded to a proton of chemical shift 7.51 ppm (Heteronuclear correlation spectroscopy (HETCOR) experiment), while the other one (C-5) of the vinyl system gave a resonance absorption, together with the signals of the carbon atoms of the  $sp^2$  hybridization bearing the OH groups, in the range of 158.19–145.78 ppm.

The presence of the three phenolic groups and one additional hydroxyl in the molecule was demonstrated by a broad and intense IR absorption with the maximum at  $3350\text{ cm}^{-1}$ , and the strong band at  $1250\text{ cm}^{-1}$ . Especially important in this respect was, however, the  $^1H$  NMR spectrum run in  $DMSO-d_6$  solution, which consisted of three signals of phenolic OH in the region 9.4–10.0 ppm and of one singlet at 6.60 ppm of the fourth hydroxyl proton separated from those of aromatic OH by about 3 ppm. Further evidence, which confirmed the presence of four hydroxyl groups in the molecule, followed from the observations that four protons are easily exchangeable for deuterium ( $^1H$  NMR) and that the metabolite can be easily transformed into its tetraacetyl derivative.

Besides the carbons of the aromatic rings and the vinyl system, the molecule of involutone contains three additional

<sup>3</sup> In the cases of ethyl and n-butyl β-glucosides, the chemical shifts of the diastereotopic protons of the aglycone methylene group attached to the anomeric carbon through oxygen differ by 0.33 ppm ( $J_{gem} = 9.6\text{ Hz}$ ), due to the long range influence of the D-glucose molecule's chirality.

<sup>4</sup> The transformations proceeded in a corresponding alcohol, being diluted with a great deal of water occurring naturally in the mushroom.



carbons, from which two (absorbing at 202.86 and 200.63 ppm) are components of the two carbonyl groups, giving both a weak and a strong absorption at 1740 and 1692  $\text{cm}^{-1}$  for C=O and C=C-C=O, respectively. The non-aromatic structural elements, together with the final remaining carbon, which shows a weak resonance signal at 78.30 ppm, compose a cyclopentenone skeleton, to which the two substituted phenyl rings and a hydroxyl group are attached. This, consequently, gave a system in which the only  $sp^3$  hybridized carbon constitutes a chiral center, binding either both the differently substituted phenyl rings (while the nonphenolic hydroxyl is involved in an enol system) or one of the phenolic rings and the OH group. This problem was solved by an examination of the intramolecular proton interactions through the space and the heteronuclear long-range connectivity through bonds.

First, to avoid autooxidation when treated with acetic anhydride in the presence of pyridine, involutone was transformed quantitatively into a tetraacetyl derivative, the chromatography of which gave bright yellow crystals of mp 68–70°C and  $[\alpha]_D +44.2^\circ$ .

A routine analysis of the  $^1\text{H}$  and  $^{13}\text{C}$  NMR spectra of the obtained product<sup>5</sup> showed, as in the case of nonacetylated involutone, the presence in the molecule of tri- (1, 3, 4) and di- (1, 4) substituted phenyl rings, a vinyl system, as well as two keto carbonyls and, additionally, four acetoxy groups.

On the basis of the HMQC and HMBC experiments carried out for the  $\text{CD}_3\text{CN}$  solutions of the tetraacetyl involutone, the assignments of all carbons in the molecule were possible. The presence of a five-membered ring was proved by the observed correlation of the vinyl hydrogen H-4, that absorbed at 7.70 ppm then and at 7.51 ppm before acetylation, with the two carbonyl carbons (C-3 and C-1) absorbing at 197.36 and 196.03 ppm, respectively. The differentiation of these carbonyl carbons was based on the different intensities of the cross-peaks from H-4 to C-1 and from H-4 to C-3, the smaller for the former being coupled through three bonds in comparison with the latter, which was more intense because of the coupling through two bonds only. An additional correlation of proton H-4 was found with both the vinyl carbons C-4 (141.12 ppm) and C-5 (153.55 ppm) by HETCOR and HMBC, respectively, and with the  $sp^3$  hybridized carbon (C-2) absorbing at 81.70 ppm.

Apart from the two signals of the ketone function carbons, the  $^{13}\text{C}$  NMR spectrum showed the presence of four ester carbonyl carbons. The protons of one of the four acetoxy groups (2.18 ppm) were found to be correlated ( $^4J_{\text{C-H}}$ ) with C-2 (81.70 ppm) being the only  $sp^3$  hybridized element of the five-membered ring. The remaining three (169.90, 169.03, and 168.80 ppm) were recognized as the elements of acetoxy substituents attached to phenyl rings on the basis of their carbonyl carbons' coupling with the suitable aromatic ring protons<sup>6</sup> through four bonds, which gave cross-peaks (of weak intensities, but easily recognizable) in the HMBC

spectrum. Already knowing the chemical shifts of aromatic ring protons at that time, we were able to find the position of attachment to the phenyl ring of each of the acetoxy groups. The two-proton signal of H-3' and H-5' (7.16 ppm) gave a correlation point with carbonyl carbon absorption at 169.90 ppm, showing on a coupling through C-4'', to which that acetoxy group has to be bound. Similarly, the coupling of H-2' (7.92 ppm) with the carbonyl carbon giving a signal at 169.03 ppm made it possible to locate the acetoxy group at C-3', while the correlation of the chemical shift of H-5' (7.40 ppm) with that at 168.80 ppm showed the position C-4' as the attachment point for the acetoxy group responsible for that absorption. The assignment of the chemical shift of 146.16 ppm to C-4' was proved by its correlation with both H-2' (7.92 ppm) and H-6' (7.95 ppm) of the trisubstituted phenyl ring, while of the value 152.55 ppm to C-4'', due to its correlation ( $^3J_{\text{CH}}$ ) with H-2'' and H-6'' (7.46 ppm). The assignment of the third aromatic ring carbon bearing the acetoxy group resulted from the coupling of H-2' (7.92 ppm) and H-5' (7.40 ppm) with C-3' absorbing at 143.50 ppm through two and three bonds, respectively.

The assignment of the chemical shifts 127.72 and 129.91 ppm to the aromatic ring carbons C-1' and C-1'', respectively, was based on the observation that the 127.72 ppm value is correlated with the chemical shift of H-5' and H-4 ( $^3J_{\text{CH}}$ ), which proved the C-1' position for that carbon, while H-3' and H-5'' is coupled ( $^3J_{\text{CH}}$ ) with the carbon absorbing at 129.91 ppm, which has to be C-1''. The other pair of protons of that ring (H-2'' and H-6'' (7.46 ppm)) gave a cross-peak with C-2 (81.70 ppm), which, as an element of the five-membered ring, binds the 4-acetoxyphenyl group.

The protons (H-2' and H-6') mentioned above in connection with the phenyl carbon – proton relationship elucidation, are additionally correlated with a  $sp^2$ -hybridized carbon of a chemical shift 153.55 ppm, which, in turn, gave a strong cross-peak ( $^2J_{\text{C-H}}$ ) with vinyl proton H-4. This observation led us to the conclusion that the carbon of 153.55 ppm is C-5 of the vinyl system and constitutes the position of the attachment of the 3,4-diacetoxyphenyl group to the five-membered ring.

The conclusions concerning the location of both the phenolic substituents and the hydroxyl group in the molecule were confirmed by a NOE difference experiment, which indicated that a significant interproton contact through the space of the vinyl hydrogen (H-4) only exists with H-2' and H-6' of the 3,4-diacetoxyphenyl ring (a diagnostic enhancement of signals at  $\delta$  7.92 and 7.95 ppm), while the corresponding protons (H-2'' and H-6'') of the monoacetoxyphenyl ring revealed inertness when the vinyl proton was irradiated. These observations indicated the presence of a  $(\text{AcO})_2\text{C}_6\text{H}_3\text{-C}=\text{C-H}$  fragment in the molecule, thus, ruling out the previously considered possibility of the immediate, geminal vicinity of both phenolic substituents.

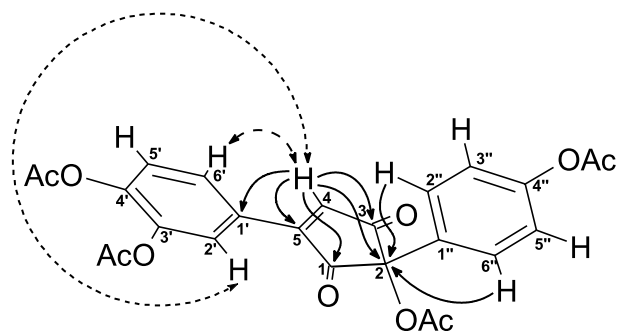
Based on the presented arguments, the structure of 5-(3,4-dihydroxyphenyl)-2-(4-hydroxyphenyl)-2-hydroxy-4-

<sup>5</sup>The acetylation of involutone to its tetraacetyl derivative caused the chemical shift of the chiral carbinol carbon to be move downfield from 78.30 to 81.85 ppm, and of the four aromatic carbons (C-2', C-5', C-3'', and C-5'') being *ortho* to OAc positions to be deshielded by about 8 ppm.

<sup>6</sup>Besides, there is an evident coupling ( $^2J_{\text{C-H}}$ ) with the methyl protons, which, however, appeared to be difficult to analyse, due to the small differences between the chemical shifts of the methyl protons.



**Scheme 2.** Selected HMBC ( $\longleftrightarrow$ ) and NOE ( $\dashrightarrow$ ) correlations in the structure of tetraacetylinvolutone.



cyclopenten-1,3-dione for the new pigment involutone was assigned.<sup>7</sup> The most significant observations for structure elucidation concerning the scalar coupling (HMBC) and through-space interactions (1D NOE) are shown in Scheme 2.

## Experimental

Melting points were determined on a Büchi 535 capillary apparatus and are uncorrected. Optical rotations were determined with a PerkinElmer 243B digital polarimeter. UV spectra were taken with a JASCO V-550 spectrophotometer in an acetonitrile solution. IR spectra were measured on a FT IR Bruker IFS 113v instrument for KBr discs.  $^1\text{H}$  and  $^{13}\text{C}$  NMR spectra were recorded on Varian Mercury-300 and Bruker DRX-600 spectrometers. A Bruker DRX-600 spectrometer, operating at 600.055 MHz ( $^1\text{H}$ ) and 150.898 MHz ( $^{13}\text{C}$ ), was used for 2D spectra. All spectra were acquired with a Bruker 5 mm inverse triple resonance gradient probe (TBI), using standard Bruker pulse sequences for the respective experiments. Proton and carbon assignments were based on COSY, NOE, HETCOR, HMQC, and HMBC experiments. MS spectral data were obtained on an AMD 402 mass spectrometer.

TLC analyses were carried out using Uniplat<sup>TM</sup> silica gel plates GHLF 250  $\mu$  (Analtech, Inc.) and PhH- $\text{CHCl}_3$ -MeOH (3:6:1) as a developing system. Column chromatography was carried out using Merck Kieselgel 60 (230–400 mesh) and a 2:1 mixture of Whatman cellulose-silica gel (MN-Kieselgel 60, 100–200 mesh) as the stationary phase, while hexane, benzene, AcOEt,  $\text{CH}_2\text{Cl}_2$ ,  $\text{CHCl}_3$ , and 5% MeOH in  $\text{CHCl}_3$  were successively applied as the eluting solvents.

The fruit bodies of the mushroom *P. involutus* (growing near birch trees) were collected in Rybojedzko, a southern district of Poznan, Poland, every September in recent successive years.

## General procedure of the metabolite isolation

Freshly collected fruit bodies of *P. involutus* were, first rinsed with water to remove sand and pieces of grass and leaves, then, either cut into small pieces or ground and, next treated with methanol, ethanol, or *n*-butanol (1.5 mL of the alcohol per 1 g of the mushroom) at room temperature for a few weeks or months.<sup>8</sup> When MeOH or EtOH were used, some foam appeared on the surface in the first hours of digestion. The resulting dark brown alcohol solution, after separation from the insoluble, semi-solid material by decantation and filtration, was concentrated under diminished pressure until all the alcohol was removed. The remaining aqueous residue, containing the naturally occurring mushroom components, including water (or a solid residue in the case of the *n*-butanol extract), was digested successively with *n*-hexane (A), benzene (B), ethyl acetate (C), and a mixture of PhH, AcOEt, and MeCN (1:2:4) (D). When kept for a week, the aqueous residue separated a light-brown solid (E) of a carbohydrate character.

Following this procedure in an experiment taken by way of example, the extraction of 900 g of fresh fruit bodies gave the individual fractions as follows: 0.84 g (A), 0.52 g (B), 0.53 g (C), 1.39 g (D), and 1.75 g (E). In the case of the extracts A–D, the soluble material was recovered by drying the particular solution over  $\text{Na}_2\text{SO}_4$ , followed by concentrating it under diminished pressure, and, finally, as a rule, subjecting the residue to chromatographic separation on silica gel. The products of the known structure isolated in a homogeneous state, namely methyl, ethyl, or *n*-butyl linoleate (A), linoleic acid, ergosterol (B), methyl, ethyl, or *n*-butyl- $\beta$ -D-glucoside, involutin (C), crotonic acid, mannitol (D), were identified on the basis of their physical properties, including the comparisons of their EI-MS and NMR spectra with those reported in the literature (the source of consistent data was shown in a reference following the spectral method).

### Linoleic acid ((Z,Z)-9,12-octadecadienoic acid)

The pure acid was obtained from extract B by an elution of the silica gel column with PhH-*n*-hexane (1:1) solution. References: EI-MS (25),  $^1\text{H}$  NMR (25),  $^{13}\text{C}$  NMR (26).

### Linoleic acid esters

The A and B extracts, during the chromatography on silica gel, gave a methyl, ethyl, or *n*-butyl ester as a colourless oil when *n*-hexane, benzene, and 10% AcOEt-*n*-hexane were used as the eluents.

### Methyl linoleate

References: EI-MS (27),  $^1\text{H}$  NMR (28),  $^{13}\text{C}$  NMR (29).

### Ethyl linoleate

References: EI-MS (25),  $^1\text{H}$  NMR (25),  $^{13}\text{C}$  NMR (25).

<sup>7</sup>A possible synthetic relationship between involutin and involutone can consist of a process in which the former is subjected both to a water molecule elimination and the benzylic position oxidation, as suggested by the reviewer, to whom we are very grateful. To preserve the optical activity in such a biotransformation, when not assisted by an enzyme, the benzylic oxidation should precede the elimination.

<sup>8</sup>The treatment of the freshly collected mushrooms (being under nitrogen) with ethyl acetate at room temperature led to the formation of acetic acid, most likely due to enzymic hydrolysis of the solvent.



***n*-Butyl linoleate**

<sup>1</sup>H NMR (600 MHz, CDCl<sub>3</sub>): δ 5.40–5.31 (4H, *m*, H-9, H-10, H-12 and H-13), 4.07 (2H, *t*, *J* = 6.7 Hz, H-1'), 2.77 (2H, *t*, *J* = 6.8 Hz, H-11), 2.29 (2H, *t*, *J* = 7.5 Hz, H-2), 2.07–2.01 (4H, *m*, H-8 and H-14), 1.63–1.53 (4H, *m*, H-3 and H-2'), 1.42–1.25 (16H, *m*, H-4, H-5, H-6, H-7, H-15, H-16, H-17 and H-3'), 0.93 (3H, *t*, *J* = 7.1 Hz, H-4'), 0.92 (3H, *t*, *J* = 7.1 Hz, H-18). <sup>13</sup>C NMR of the alcohol moiety (see ref. (30)). EI-MS *m/z* (%): 336 ([M]<sup>+</sup>), 279, 263, 220, 209, 196, 185, 164, 150, 137, 129, 123, 109, 79, 67 (100), 57, 41.

**Ergosterol**

The continuing chromatography of fraction B, after removing linoleic acid and its methyl, ethyl, or *n*-butyl ester, led to obtaining, by elution with benzene, a colourless solid, the rechromatography of which, carried out twice, gave crystals of mp 168 to 169°C and [α]<sub>D</sub> –135° (*c* = 1, CHCl<sub>3</sub>). The spectral data of the product were consistent with those for ergosterol reported elsewhere (EI-MS (31), IR (32*a*), <sup>1</sup>H NMR and <sup>13</sup>C NMR (33*a*, 34)).

**Alkyl-β-D-glucopyranosides**

A suitable (methyl, ethyl, or *n*-butyl) β-glucoside was obtained when fraction C was chromatographed on silica gel and the column was washed with CHCl<sub>3</sub>. With the exception of the OH proton absorptions, the <sup>1</sup>H and <sup>13</sup>C NMR data obtained for these glucosides dissolved in DMSO-*d*<sub>6</sub> were close to the corresponding values reported for D<sub>2</sub>O solutions (35). Each of the glucosides was additionally characterized by the properties of its tetraacetyl derivative obtained when a solution of the corresponding alkyl-β-glucoside in Ac<sub>2</sub>O (supplied with a catalytic amount of pyridine) was kept at room temperature for 10 h, followed by an ice addition. After 30 min, the product was taken up into AcOEt.

**Methyl-β-D-glucopyranoside**

A recrystallization from MeOH gave colourless needles of mp 110 to 111°C and [α]<sub>D</sub> –33° (*c* = 1, MeOH). References for: EI-MS (36), <sup>1</sup>H NMR (35, 37), <sup>13</sup>C NMR (35, 37).

**2,3,4,6-Tetra-*O*-acetyl-1-methyl-β-D-glucopyranoside**

A colourless solid of mp 108 to 109°C and [α]<sub>D</sub> –18.89° (*c* = 0.5, MeOH). References for: EI-MS (38), <sup>1</sup>H NMR (38, 37), <sup>13</sup>C NMR (37).

**Ethyl-β-D-glucopyranoside**

A colourless semi-solid of [α]<sub>D</sub> –35.2° (*c* = 0.565, MeOH). <sup>1</sup>H NMR: see refs. (35, 39). <sup>13</sup>C NMR: see ref. (35). EI-MS *m/z* (%): 207 ([M – 1]<sup>+</sup>), 177, 159, 144, 131, 118, 98, 88, 75, 74, 73, 71, 61, 60 (100), 59, 57, 47, 43, 31.

**2,3,4,6-Tetra-*O*-acetyl-1-ethyl-β-D-glucopyranoside**

A colourless solid of mp 102.5 to 103.5°C and [α]<sub>D</sub> –30.6° (*c* = 0.20, MeOH). <sup>1</sup>H NMR: see ref. (39). <sup>13</sup>C NMR (75 MHz, CDCl<sub>3</sub>): δ: 170.61 (COCH<sub>3</sub>), 170.23 (COCH<sub>3</sub>), 169.31 (COCH<sub>3</sub>), 169.25 (COCH<sub>3</sub>), 100.54 (C-1), 72.89 (C-3), 71.75 (C-5), 71.34 (C-2), 68.45 (C-4), 65.66 (C-1'),

62.00 (C-6), 20.79 (COCH<sub>3</sub>), 20.71 (COCH<sub>3</sub>), 20.67 (COCH<sub>3</sub>), 20.65 (COCH<sub>3</sub>), 15.08 (C-2'). EI-MS *m/z* (%): 375 ([M – 1]<sup>+</sup>), 331, 303, 256, 243, 214, 200, 183, 169, 157, 145, 141, 127, 115, 112, 102, 98, 81, 70, 69, 43 (100).

***n*-Butyl-β-D-glucopyranoside**

A colourless solid of mp 52–54°C, [α]<sub>D</sub> –25.6° (*c* = 0.55, MeOH). <sup>1</sup>H NMR: see ref. (35). <sup>13</sup>C NMR: see ref. (35). EI-MS *m/z* (%): 237 ([M + 1]<sup>+</sup>), 205, 187, 163, 145, 144, 116, 103, 98, 97, 87, 85, 74, 73, 60 (100), 57 (95), 44, 42.

**2,3,4,6-Tetra-*O*-acetyl-1-*n*-butyl-β-D-glucopyranoside**

A colourless solid of mp 54.5 to 55.5°C, [α]<sub>D</sub> –9.36° (*c* = 0.435, MeOH). IR (KBr, cm<sup>–1</sup>): 2967, 2904, 2871, 1759, 1743, 1433, 1378, 1226, 1169, 1099, 1069, 1040, 958, 603.<sup>1</sup> <sup>1</sup>H NMR (600 MHz, CDCl<sub>3</sub>): δ: 5.21 (1H, *t*, *J* = 9.6 Hz, H-3), 5.09 (1H, *dd*, *J* = 9.8 Hz, *J* = 9.6 Hz, H-4), 4.99 (1H, *dd*, *J* = 9.6 Hz, *J* = 8.0 Hz, H-2), 4.49 (1H, *d*, *J* = 8.0 Hz, H-1), 4.27 (1H, *dd*, *J*<sub>gem</sub> = 12.3 Hz, *J* = 4.8 Hz, H<sub>A</sub>-6), 4.14 (1H, *dd*, *J*<sub>gem</sub> = 12.3 Hz, *J* = 1.9 Hz, H<sub>B</sub>-6), 3.88 (1H, *dq*, *J*<sub>gem</sub> = 9.6 Hz, *J* = 7.1 Hz, H<sub>A</sub>-1'), 3.69 (1H, *ddd*, *J* = 9.8 Hz, *J* = 4.8 Hz, *J* = 1.9 Hz, H-5), 3.48 (1H, *dq*, *J*<sub>gem</sub> = 9.6 Hz, *J* = 7.1 Hz, H<sub>B</sub>-1'), 2.09 (3H, *s*, COCH<sub>3</sub>), 2.04 (3H, *s*, COCH<sub>3</sub>), 2.03 (3H, *s*, COCH<sub>3</sub>), 2.01 (3H, *s*, COCH<sub>3</sub>), 1.54 (2H, *quintet*, *J* = 7.0 Hz, H-2'), 1.35 (2H, *sextet*, *J* = 7.1 Hz, H-3'), 0.90 (3H, *t*, *J* = 7.1 Hz, H-4'). <sup>13</sup>C NMR (150 MHz, CDCl<sub>3</sub>): δ: 170.55 (COCH<sub>3</sub>), 170.17 (COCH<sub>3</sub>), 169.24 (COCH<sub>3</sub>), 169.14 (COCH<sub>3</sub>), 100.79 (C-1), 72.84 (C-3), 71.70 (C-5), 71.33 (C-2), 69.93 (C-1'), 68.46 (C-4), 62.00 (C-6), 31.44 (C-2'), 20.84 (COCH<sub>3</sub>), 20.73 (2 × COCH<sub>3</sub>), 20.70 (COCH<sub>3</sub>), 19.03 (C-3'), 13.82 (C-4'). EI-MS *m/z* (%): 403 ([M – 1]<sup>+</sup>), 345, 331, 284, 243, 211, 200, 157, 115, 81, 43 (100).

**Involutin****(5-(3,4-dihydroxyphenyl)-3,4-dihydroxy-2-(4-hydroxyphenyl)-2-cyclopenten-1-one)**

After the elution of glucosides from fraction C, the silica gel column was washed with a 3% solution of MeOH in CHCl<sub>3</sub>, which gave a cream-coloured solid of mp 173–175°C (with decomp.) and [α]<sub>D</sub> –24.7° (*c* = 0.4, AcOEt). An addition of 10% aq NaOH to a methanol solution of the product changed its colour to deep purple. IR: see ref. (18). <sup>1</sup>H NMR (300 MHz, CD<sub>3</sub>CN): δ:<sup>9</sup> 7.68 (2H, *d* of AA'XX', *J* = 9.0 Hz, H-2'' and H-6''), 6.83 (2H, *d* of AA'XX', *J* = 9.0 Hz, H-3'' and H-5''), 6.75 (1H, *d*, *J* = 8.0 Hz, H-5'), 6.59 (1H, *d*, *J* = 2.2 Hz, H-2'), 6.52 (1H, *dd*, *J* = 8.0 Hz, *J* = 2.2 Hz, H-6'), 4.69 (1H, *d*, *J* = 6.9 Hz, H-4), 3.95 (1H, *d*, *J* = 6.9 Hz, H-5). <sup>13</sup>C NMR (150 MHz, CD<sub>3</sub>CN): δ: 190.50 (C-1), 174.63 (C-3), 156.91 (C-4''), 145.25 (C-3'), 144.77 (C-4'), 130.48 (C-2'',6''), 128.95 (C-1'), 123.53 (C-1''), 123.02 (C-6'), 117.60 (C-2'), 116.75 (C-2), 116.21 (C-5'), 115.76 (C-3'',5''), 71.88 (C-4), 55.14 (C-5). HMBC (600 MHz, CD<sub>3</sub>CN): H-2'' (<sup>3</sup>*J*<sub>CH</sub>) ⇒ C-4''; H-3'' (<sup>2</sup>*J*<sub>CH</sub>) and H-5'' (<sup>2</sup>*J*<sub>CH</sub>) ⇒ C-4''; H-5' (<sup>3</sup>*J*<sub>CH</sub>) ⇒ C-3'; H-2' (<sup>3</sup>*J*<sub>CH</sub>) and H-6' (<sup>3</sup>*J*<sub>CH</sub>) ⇒ C-4'; H-5 (<sup>2</sup>*J*<sub>CH</sub>) and H-5' (<sup>3</sup>*J*<sub>CH</sub>) ⇒ C-1'; H-3'' (<sup>3</sup>*J*<sub>CH</sub>) and H-5'' (<sup>3</sup>*J*<sub>CH</sub>) ⇒ C-1''; H-2''

<sup>9</sup>The <sup>1</sup>H and <sup>13</sup>C NMR data recorded by us for CD<sub>3</sub>CN and CD<sub>3</sub>OD solutions were very similar to each other, but differed to some extent from those reported in ref. (18). The use of CD<sub>3</sub>CN as a solvent made it possible to observe the C-1, C-2, and C-3 signals.



( $^3J_{\text{CH}}$ ) and H-6'' ( $^3J_{\text{CH}}$ )  $\Rightarrow$  C-2; H-2' ( $^3J_{\text{CH}}$ ) and H-6' ( $^3J_{\text{CH}}$ )  $\Rightarrow$  C-5. EI-MS: see ref. (18).

### D-Mannitol

The crude residue obtained after a concentration of the PhH–AcOEt–MeCN extract (fraction D) was dissolved in hot MeOH and the solution allowed to cool. The separated colourless crystals of mannitol, when recrystallized from MeOH, melted at 168 to 168.5°C and showed  $[\alpha]_{\text{D}} \pm 0^\circ$  ( $c = 1$ , H<sub>2</sub>O). The spectral data (EI-MS, IR,  $^1\text{H}$  NMR, and  $^{13}\text{C}$  NMR) were consistent with those reported elsewhere (40, 32b, 33b).

### Hexaacetyl-D-mannitol

Mannitol obtained in the above way, when treated with Ac<sub>2</sub>O in the presence of pyridine, gave hexaacetylmannitol in a yield of above 80%. A recrystallization from AcOEt furnished colourless needles of mp 124 to 125°C and  $[\alpha]_{\text{D}} +24.83^\circ$  ( $c = 1$ , CHCl<sub>3</sub>).  $^1\text{H}$  NMR (300 MHz, CDCl<sub>3</sub>)  $\delta$ : 5.45 (2H, d,  $J = 8.8$ , H-3 and H-4), 5.08 (2H, ddd,  $J = 8.8$ ,  $J = 5.1$ ,  $J = 2.7$ , H-2 and H-5), 4.22 (2H, dd,  $J_{\text{gem}} = 12.5$ ,  $J = 2.7$ , H<sub>A</sub>-1 and H<sub>A</sub>-6), 4.07 (2H, dd,  $J_{\text{gem}} = 12.5$ ,  $J = 5.1$ , H<sub>B</sub>-1 and H<sub>B</sub>-6), 2.10 (6H, s, COCH<sub>3</sub>), 2.08 (6H, s, COCH<sub>3</sub>), 2.06 (6H, s, COCH<sub>3</sub>).  $^{13}\text{C}$  NMR (75 MHz, CDCl<sub>3</sub>)  $\delta$ : 170.37 (2  $\times$  COCH<sub>3</sub>), 169.70 (2  $\times$  COCH<sub>3</sub>), 169.49 (2  $\times$  COCH<sub>3</sub>), 71.47 (C-2 and C-5), 67.38 (C-3 and C-4), 61.84 (C-1 and C-6), 20.94 (2  $\times$  COCH<sub>3</sub>), 20.76 (2  $\times$  COCH<sub>3</sub>), 20.68 (2  $\times$  COCH<sub>3</sub>). EI-MS: see ref. (41).

### Involutone

#### (5-(3,4-dihydroxyphenyl)-2-(4-hydroxyphenyl)-2-hydroxy-4-cyclopenten-1,3-dione)

The soluble in MeOH material of fraction D, after mannitol separation by crystallization, contained crotonic acid in an amount of about 50%, which was sublimed off at 40°C and 0.06 mmHg (1 mmHg = 133.322 Pa); (mp 64 to 65°C.  $^1\text{H}$  NMR (300 MHz, CDCl<sub>3</sub>)  $\delta$ : 12.20 (1H, s, COOH), 7.10 (1H, dq,  $J = 15.5$ ,  $J = 6.9$ , H-3), 5.86 (1H, dq,  $J = 15.5$ ,  $J = 1.7$ , H-2), 1.92 (1H, dd,  $J = 6.9$ ,  $J = 1.7$ , H-4). A nonvolatile deep orange residue was subjected to column chromatography on silica gel, which allowed, first, the removal from it of the remaining crotonic acid by using hexane–benzene (1:1), and, next, the isolation of a product, the rechromatography of which, when 10% AcOEt in PhH was used as an eluant, afforded a bright yellow, hygroscopic solid ( $R_f$  0.23) melting sharply at 181 to 182°C and showing  $[\alpha]_{\text{D}} +96.3^\circ$  ( $c = 0.3$ , MeOH). Treated with 10% aq NaOH, the compound changed colour to purple-violet.<sup>10</sup> IR (KBr, cm<sup>-1</sup>): 3350, 1740, 1692, 1609, 1565, 1512, 1443, 1301, 1250, 1177, 1120, 1060, 875, 833.  $^1\text{H}$  NMR (300 MHz, CD<sub>3</sub>CN)  $\delta$ : 7.59 (1H, d,  $J = 2.2$  Hz, H-2'), 7.56 (1H, dd,  $J = 8.2$  Hz,  $J = 2.2$  Hz, H-6'), 7.51 (1H, s, H-4), 7.22 (2H, d of AA'XX',  $J = 8.8$  Hz, H-2'' and H-6''), 6.95 (1H, d,  $J = 8.2$  Hz, H-5'), 6.79 (2H, d of AA'XX',  $J = 8.8$  Hz, H-3'' and H-5'').  $^1\text{H}$  NMR (300 MHz, DMSO-*d*<sub>6</sub>)  $\delta$ : 10.02 (1H, s, OH), 9.59 (1H, s, OH), 9.43 (1H, s, OH), 7.73

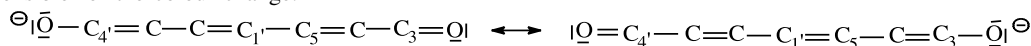
(1H, s, H-4), 7.59 (1H, d,  $J = 2.2$  Hz, H-2'), 7.53 (1H, dd,  $J = 8.2$  Hz,  $J = 2.2$  Hz, H-6'), 7.11 (2H, d of AA'XX',  $J = 8.8$  Hz, H-2'' and H-6''), 6.89 (1H, d,  $J = 8.2$  Hz, H-5'), 6.72 (2H, d of AA'XX',  $J = 8.8$  Hz, H-3'' and H-5''), 6.60 (1H, s, OH).  $^{13}\text{C}$  NMR (75 MHz, CD<sub>3</sub>CN)  $\delta$ : 202.86 (C=O), 200.63 (C=O), 158.19, 156.87, 149.91, 145.78 (C-5, C-3', C-4', C-4''), 139.57 (C-4), 129.27 (C-1' or C-1''), 128.36 (C-2'' and C-6''), 124.09 (C-6'), 122.13 (C-1' or C-1''), 117.00 (C-2'), 116.69 (C-5'), 115.52 (C-3'' and C-5''), 78.26 (C-2).  $^{13}\text{C}$  NMR (75 MHz, DMSO-*d*<sub>6</sub>)  $\delta$ : 203.57 (C=O), 201.32 (C=O), 157.61, 155.55, 150.27, 145.92 (C-5, C-3', C-4', C-4''), 138.39 (C-4), 128.05 (C-1' or C-1''), 127.58 (C-2'' and C-6''), 122.96 (C-6'), 120.52 (C-1' or C-1''), 116.36 (C-2'), 116.11 (C-5'), 77.39 (C-2). EI-MS  $m/z$  (%): 312 ([M]<sup>+</sup>), 296, 284, 239, 189, 181, 163, 134, 121 (100), 93, 91, 77, 65. HR-MS calcd. for C<sub>17</sub>H<sub>12</sub>O<sub>6</sub>: 312.06339; found: 312.06170.

### Tetraacetyl involutone

#### (5-(3,4-diacetoxyphenyl)-2-(4-acetoxyphenyl)-2-acetoxy-4-cyclopenten-1,3-dione)

A solution of involutone ( $[\alpha]_{\text{D}} +96.3^\circ$ , 6.5 mg) in 1 mL of Ac<sub>2</sub>O was supplied with one drop of anhydrous pyridine and stirred at room temperature for 60 h. The reaction mixture was worked up in a usual way and the product taken up into AcOEt. The solution, when washed with aq Na<sub>2</sub>CO<sub>3</sub>, dried over Na<sub>2</sub>SO<sub>4</sub>, and concentrated, gave 9.9 mg (99% yield) of a yellow crude tetraacetate. The pure product was eluted from silica gel column by 2% AcOEt in PhH and the resulting solution, when concentrated, afforded an oil (solidifying eventually) of  $R_f$  0.76, mp 68–70°C and  $[\alpha]_{\text{D}} +44.2^\circ$  ( $c = 0.275$ , CHCl<sub>3</sub>). UV (CH<sub>3</sub>CN)  $\lambda_{\text{max}}$  ( $\epsilon$ ): 231 (18 480), 312 (11 720). IR (KBr, cm<sup>-1</sup>): 3076 (w), 2935 (w), 2853 (w), 1770 (s), 1743 (s), 1714 (s), 1609 (m), 1574 (m), 1505 (s), 1429 (m), 1372 (s), 1265–1165 (s, b with max at 1202), 1118 (m), 1051 (m), 1013 (m), 904 (m), 846 (m).  $^1\text{H}$  NMR (600 MHz, CD<sub>3</sub>CN)  $\delta$ : 7.95 (1H, dd,  $J = 8.4$  Hz,  $J = 2.2$  Hz, H-6'), 7.92 (1H, d,  $J = 2.2$  Hz, H-2'), 7.70 (1H, s, H-4), 7.46 (2H, d of AA'XX',  $J = 8.8$  Hz, H-2'' and H-6''), 7.40 (1H, d,  $J = 8.4$  Hz, H-5'), 7.16 (2H, d of AA'XX',  $J = 8.8$  Hz, H-3'' and H-5''), 2.29 (3H, s, COCH<sub>3</sub>), 2.28 (3H, s, COCH<sub>3</sub>), 2.23 (3H, s, COCH<sub>3</sub>), 2.18 (3H, s, 2-OCOCH<sub>3</sub>).  $^1\text{H}$  NMR (300 MHz, CDCl<sub>3</sub>)  $\delta$ : 7.92–7.88 (2H, m, H-2' and H-6'), 7.46 (2H, d of AA'XX',  $J = 9.0$  Hz, H-3'' and H-5''), 7.43 (s, H-5), 7.35 (1H, d,  $J = 8.2$  Hz, H-5'), 7.11 (2H, d of AA'XX',  $J = 9.0$  Hz, H-2'' and H-6''), 2.33 (COCH<sub>3</sub>), 2.32 (COCH<sub>3</sub>), 2.29 (COCH<sub>3</sub>), 2.19 (COCH<sub>3</sub>).  $^{13}\text{C}$  NMR (150 MHz, CD<sub>3</sub>CN)  $\delta$ : 197.36 (C-3), 196.03 (C-1), 170.79 (2-OCOCH<sub>3</sub>), 169.90 (4'-OCOCH<sub>3</sub>), 169.03 (3'-OCOCH<sub>3</sub>), 168.80 (4'-OCOCH<sub>3</sub>), 153.55 (C-5), 152.55 (C-4''), 146.14 (C-4'), 143.50 (C-3'), 141.12 (C-4), 129.91 (C-1''), 128.65 (C-2'' and C-6''), 128.47 (C-6'), 127.72 (C-1'), 125.25 (C-2'), 125.22 (C-5'), 123.44 (C-3'' and C-5''), 81.70 (C-2), 21.09 (OCOCH<sub>3</sub>), 20.73 (OCOCH<sub>3</sub>), 20.65 (OCOCH<sub>3</sub>), 19.97 (C<sub>2</sub>-OCOCH<sub>3</sub>). HMBC–NMR (600 MHz, CD<sub>3</sub>CN): see Scheme 2.  $^{13}\text{C}$  NMR (75 MHz, CDCl<sub>3</sub>)  $\delta$ : 196.33 and

<sup>10</sup>The phenoxide ion, formed as a result of the C(4')-OH proton abstraction, constitutes a conjugated system, made by 10  $\pi$  and  $n$  electrons and can be responsible for the colour change.





195.15 (C-1 and C-3), 169.82 (OCOCH<sub>3</sub>), 168.97 (OCOCH<sub>3</sub>), 167.93 (OCOCH<sub>3</sub>), 167.64 (OCOCH<sub>3</sub>), 152.70, 151.73, 145.22, and 142.55 (C-5, C-4'', C-4', and C-3'), 138.68 (C-4), 128.49 (C-2'' and C-6''), 127.61 (C-6'), 124.47 (C-2'), 124.29 (C-5'), 122.32 (C-3'' and C-5''), 128.49 (C-1' or C-1''), 122.29 (C-1' or C-1''), 80.82 (C-2), 21.08 (OCOCH<sub>3</sub>), 20.66 (OCOCH<sub>3</sub>), 20.55 (OCOCH<sub>3</sub>), and 19.91 (OCOCH<sub>3</sub>). EI-MS *m/z* (%): 480 ([M]<sup>+</sup>), 452, 438, 410, 396, 380, 368, 354, 312, 296, 284, 239, 163, 134, 121, 105, 93, 69, 43 (100). HR-MS calcd. for C<sub>25</sub>H<sub>20</sub>O<sub>10</sub>: 480.10565; found: 480.10534.

## Acknowledgments

W. Z. Antkowiak wishes to thank his students, A. Galek, A. Klimecka, B. Koziarska, and K. Walenczak, for their profitable technical assistance in the isolation studies. Special thanks are addressed to Martin Court for watching over our English.

## References

1. S. Grzymala. *Rocz. Panstw. Zakl. Hig.* **9**, 277 (1958).
2. W.Z. Antkowiak. The chemistry and toxicology of mushroom alkaloids. In *Chemistry and toxicology of diverse classes of alkaloids*. Edited by M.S. Blum. Alaken, Inc., Fort Collins. 1996. Chap. 4.
3. W. Lasota and W. Fortak. *Acta Pol. Pharm.* **23**, 81 (1966).
4. W. Lasota, G. Rybarkiewicz, and H. Mlodecki. *Acta Pol. Pharm.* **24**, 75 (1967).
5. M.H. Malone, V.E. Tyler, Jr. and L.R. Brady. *Lloydia*, **30**, 250 (1967).
6. F. Bschor, J. Kohlmeyer, and H.J. Mallach. *Z. Pilzkd.* **29**, 1 (1963).
7. F. Bschor and H.J. Mallach. *Arch. Toxikol.* **20**, 82 (1963).
8. J. Schmidt, W. Hartmann, A. Würstlin, and H. Deicher. *Dtsch. Med. Wochenschr.* **96**, 1188 (1971).
9. H. Deicher and W. Stangel. *Verh. Dtsch. Ges. Inn. Med.* **83**, 1606 (1977).
10. M. Winkelmann, F. Borchard, W. Stangel, and B. Grabensee. *Dtsch. Med. Wochenschr.* **107**, 1190 (1982).
11. M. Winkelmann, W. Stangel, I. Schedel, and B. Grabensee. *Klin. Wochenschr.* **64**, 935 (1986).
12. W. Lasota. *Farm. Pol.* **4**, 317 (1970).
13. W. Lasota. *Zeszyty Naukowe Bromatologii i Chemii Toksykologicznej*, **3**, 9 (1970).
14. R.L. Edwards, G.C. Elsworth, and N. Kale. *J. Chem. Soc. (C)*, 405 (1967).
15. R.L. Edwards and M.Gill. *J. Chem. Soc. Perkin Trans. 1*, 1529 (1973).
16. W. Steglich, A. Thilmann, H. Besl, and A. Bresinsky. *Z. Naturforsch. C: J. Biosci.* **32C**, 46 (1977).
17. M. Gill and W. Steglich. *Pigments of fungi (Macromycetes)*. In *Prog. Chem. Org. Nat. Prod.* Vol. 51. Edited by W. Herz, H. Grisebach, G.W. Kirby and Ch. Tamm. Springer-Verlag, Wien, New York. 1987. pp. 64 and 67.
18. R. Feling, K. Polborn, W. Steglich, J. Mühlbacher, and G. Bringmann. *Tetrahedron*, **57**, 7857 (2001); corrigendum *Tetrahedron*, **57**, 10 231 (2001).
19. (a) J. Zarb and D.R. Walters. *Lett. Appl. Microbiol.* **18**, 5 (1994); (b) S. Fornale, T. Sarjala, and N. Bagni. *New Phytol.* **143**, 581 (1999).
20. M. Stadler and O. Sterner. *Phytochemistry*, **49**, 1013 (1998).
21. (a) N. Mitsuo, H. Takeichi, and T. Satoh. *Chem. Pharm. Bull.* **32**, 1183 (1984); (b) S.L. Flitsch and G.M. Watt. *Enzymes in carbohydrate chemistry: formation of glycosidic linkages*. In *Biotechnology*. 2nd ed. Vol. 8b. Edited by H.-J. Rehm and G. Reed. Wiley-VCH, Weinheim, New York. 2000. pp. 243–274.
22. C.-A. Chen and C.J. Sih. *J. Org. Chem.* **63**, 9620 (1998).
23. T. Matsumoto, W. Trueb, R. Gwinner, and C.H. Eugster. *Helv. Chim. Acta*, **52**, 716 (1969).
24. H. Besl, A. Bresinsky, W. Steglich, and K. Zipfel. *Chem. Ber.* **106**, 3223 (1973).
25. M.-H. Chang, G.-J. Wang, Y.-H. Kuo, and C.-K. Lee. *J. Chin. Chem. Soc.* **47**, 1131 (2000).
26. R. Radeaglia, H. Poleschner, and M. Heydenrich. *Magn. Reson. Chem.* **29**, 1028 (1991).
27. L.C.D. Stasi, J.C. Gomes, and W. Vilegas. *Chem. Pharm. Bull.* **47**, 890 (1999).
28. S. Murata. *Bull. Chem. Soc. Jpn.* **57**, 3597 (1984).
29. L. Crombie and A.D. Heavers. *J. Chem. Soc. Perkin Trans. 1*, 1929 (1992).
30. G. Knothe and T.C. Nelsen. *J. Chem. Soc. Perkin Trans. 2*, 2019 (1998).
31. J.A. Elix and K.L. Gaul. *Aust. J. Chem.* **39**, 613 (1986).
32. (a) The Aldrich library of FT-IR spectra. 2nd ed. **3**, 4222 B (1997); (b) The Aldrich library of FT-IR spectra. **1**, 270A (1997).
33. (a) C.J. Pouchert and J. Behnke. *The Aldrich library of <sup>13</sup>C and <sup>1</sup>H FT NMR spectra*. 1st ed. **3**, 570 B (1993); (b) *The Aldrich library of <sup>13</sup>C and <sup>1</sup>H FT NMR spectra*. 1st ed. **1**, 289C (1993).
34. W. Zhou and W.D. Nes. *Tetrahedron Lett.* **41**, 2791 (2000).
35. B.W. Sigurskjold, I. Haunstrup, and K. Bock. *Acta Chem. Scand.* **46**, 451 (1992).
36. P.A. Finan, R.I. Reed, W. Snedden, and J.M. Wilson. *J. Chem. Soc.* 5945 (1963).
37. M. Budesinsky, M. Cerny, I. Cerny, S. Samek, and T. Trnka. *Collect. Czech. Chem. Commun.* **60**, 311 (1995).
38. M. Curini, F. Epifano, M.C. Marcotullio, O. Rosati, and M. Rossi. *Synth. Commun.* **30**, 1319 (2000).
39. H. Prawat, C. Mahidol, S. Ruchirawat, U. Prawat, P. Tuntiwachwuttikul, U. Tooptakong, W.C. Taylor, C. Pakawatchai, B.W. Skelton, and A.H. White. *Phytochemistry*, **40**, 1167 (1995).
40. A.B. Pomilio, M.D. Gonzalez, and C.C. Eceizabarrena. *Phytochemistry*, **41**, 1393 (1996).
41. M.K. Higgins, R.S. Bly, and S.L. Morgan. *Anal. Chem.* **66**, 2656 (1994).



# Semiclassical and quantum-mechanical study of the reaction mechanism for the $N_2 + N_2^+$ electron transfer system

Yu-Mei Xing, Lan Chen, Chong Zhang, Zun-Sheng Cai, and Xue-Zhuang Zhao

**Abstract:** Density functional theory (DFT) calculations, including electron correlation, were carried out on the  $N_2 + N_2^+$  electron transfer system. Six geometries of the precursor complex were assumed and their stabilities were calculated and compared. The activation energy, the electronic transmission factor, and the electronic coupling matrix element in the electron transfer process were also calculated. The electronic transmission factor for this system was far less than unity (ca. 0.006–0.09); thus, the electron transfer reaction was considered to be diabatic in nature. Therefore, the electron transfer rate for the selected structures was calculated using semiclassical and quantum-mechanical theories. The calculated values were compared with each other and were in good agreement with the experimental value.

**Key words:**  $N_2 + N_2^+$  electron transfer reaction, semiclassical and quantum-mechanical theories, electronic transmission factor, electronic coupling matrix element, B3LYP.

**Résumé :** On a effectué des calculs selon la théorie de la densité fonctionnelle (TDF), y compris une corrélation électronique, du système de transfert d'électron  $N_2 + N_2^+$ . On pris pour acquis les six géométries du complexe précurseur et on a calculé et comparé leurs stabilités. On a aussi calculé l'énergie d'activation, le facteur de transmission électronique et l'élément de matrice du couplage électronique du processus de transfert d'électron. Le facteur de transmission électronique pour ce système est de beaucoup inférieur à l'unité (environ de 0,006 à 0,09); on en a déduit que la réaction de transfert d'électron est de nature diabatique. On a donc calculé la vitesse de transfert d'électron en faisant appel à des calculs selon les théories de mécanique quantique et semiclassique pour des structures choisies. Les valeurs calculées ont été comparées entre elles et elles sont en bon accord avec la valeur expérimentale.

**Mots clés :** réaction de transfert d'électron  $N_2 + N_2^+$ , théories de mécanique quantique et semiclassique, facteur de transmission électronique, élément de matrice du couplage électronique, B3LYP.

[Traduit par la Rédaction]

## Introduction

In the last two decades, the simple electron transfer (ET) theory provided by Marcus (1), Hush (2), Sutin (3), and Newton and coworkers (4, 5) has been very actively pursued, both theoretically and experimentally (6–16). This interest is not surprising, considering the ubiquity of the electron transfer process in chemistry, physics, and biology. ET reactions are commonly thought to be embodied by two potential surfaces, one for the reactants and the other for the products, and are well understood within two distinct limits (see Fig. 1) (17–19). First, for a very weak electronic coupling between the two potential surfaces (the so-called “diabatic limit”), the theoretical developments include semiclassical extensions of the classical formalisms, as well as quantum-mechanical treatments in which the ET is treated with a perturbation theory (7, 20), and its lowest order perturbation in

the electronic coupling leads to the Fermi golden rule expression of the ET rate constant. For the opposite limit (the “adiabatic limit”), in which the electronic coupling is large and the ET reaction is actually limited on one potential surface, the rate is well described by classical transition rate theory (7).

In the two diabatic theories, two important quantities — the electronic coupling interaction and the FC factor — depend strongly on the potential energy surfaces of the reactant and product and on the structural properties of the precursor complex. A considerable effort has been focused on understanding how the structural properties, such as the distance and orientation between donors and acceptors, affects the electron transfer rate (12, 13, 16, 21, 22).

$N_2 + N_2^+$  is a gas-phase ion–molecule ET reaction that plays an important role in stratospheric chemistry. Although the  $N_4^+$  dimer cation, which may be identified as the precursor complex of the above ET reaction, has received much attention from both the experimental and theoretical standpoints (23, 24), the kinetics of this ET reaction has not been explicitly investigated. This reaction would involve a collision between the ion and the molecule, followed by the ET step, and detection. The encounter complex must be formed for the collision process to occur. Three methods were adopted to investigate the mechanism and calculate the

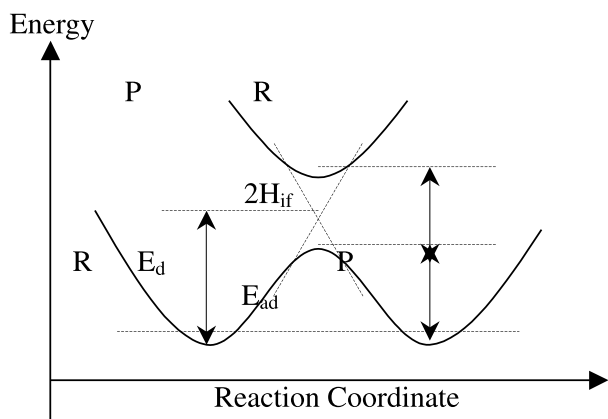
Received 6 August 2002. Published on the NRC Research Press Web site at <http://canjchem.nrc.ca> on 7 February 2003.

Y.-M. Xing, L. Chen, C. Zhang, Z.-S. Cai,<sup>1</sup> and X.-Z. Zhao. Department of Chemistry, Nankai University, Tianjin 300071, People's Republic of China.

<sup>1</sup>Corresponding author (e-mail: [caizunsh@nankai.edu.cn](mailto:caizunsh@nankai.edu.cn)).



**Fig. 1.** Parabolic energy profiles of two diabatic states along the reaction coordinate.

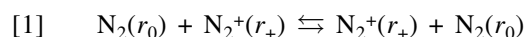


rate of the ET process. The main purposes of this investigation are: (i) to obtain a more complete understanding of the nature of the interaction between the donor ( $N_2$ ) and the acceptor ( $N_2^+$ ) at the DFT level; (ii) to compare the electronic structural properties and the relative stability of various possible precursor complexes; (iii) to obtain relevant ET kinetic parameters and to compare their contributions to the ET rate from various precursor structures; and (iv) to compare the applicability of the semiclassical expressions, the quantum-mechanical method, and the golden rule simplification in studying the nonadiabatic ET problem of the  $N_2 + N_2^+$  self-exchange system.

## Theoretical model and computational details

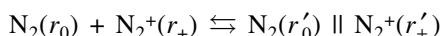
### Simple description of theoretical model

For the following thermal electron transfer process (eq. [1]),

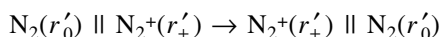


according to the framework of the outer-sphere self-exchange ET model (1, 2, 6, 8), the electron transfer between the acceptor,  $N_2^+(X^2\Sigma_g^+)$ , and the donor,  $N_2(X^1\Sigma_g^+)$ , can be separated into the following three distinct steps:

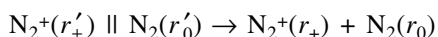
1. Formation of the precursor complex or the encounter complex



2. Activation of the precursor complex, electron transferring, and then relaxation into the successor complex



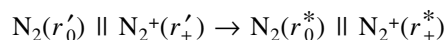
3. Dissociation of the successor complex into products



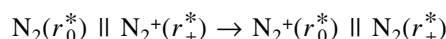
In step 2, it is assumed that there is an energy barrier for the precursor complex to surpass. This process conforms to the Marcus model: an electron is transferred between the donor and the acceptor with very little coupling resonance interaction and with an energy barrier largely originating from

Franck–Condon restrictions, i.e., the electron transfer occurs on a time scale in which the positions of all atomic nuclei are frozen. For ease of discussion we may separate step 2 into three detailed steps:

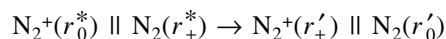
(i) Reorganization of the precursor complex



(ii) Elementary electron transfer step (according to the Franck–Condon principle)



(iii) Relaxation into the successor complex



Obviously, step 1 is the collision process between the ion and the molecule. Its energy change corresponds to the stabilization energy ( $E_s$ ), which is the sum of the electrostatic work required to bring the reactants closer with an optimized constant distance of  $R$  and the energy associated with the change of geometry from  $r$  to  $r'$ . The product in step 1 is the precursor complex and may exist in various structural forms.

Using the steady state approximation, assuming the reaction is not diffusion limited, and assuming that dissociation in step 3 is fast, the overall rate ( $k_{\text{ovr}}$ ), which is usually observed, is determined as the product of the equilibrium constant for the formation of the precursor complex ( $K_{\text{pre}}$ ) and the rate of electron transfer ( $k_{\text{et}}$ ), i.e., the overall rate includes the collision and ET processes.

$$[2] \quad k_{\text{ovr}} = K_{\text{pre}} k_{\text{et}},$$

where the unimolecular rate constant for the ET ( $k_{\text{et}}$ ) may be determined by either the semiclassical or the quantum-mechanical method.

### Semiclassical method

Taking quantum effects into account, the rate of the ET reaction,  $k_{\text{et}}$ , can be expressed as (4, 5, 9–11, 25, 26)

$$[3] \quad k_{\text{et}} = v_n \Gamma_n \kappa_{\text{el}} \exp(-\Delta G^*/RT),$$

where  $v_n$  is the nuclear frequency factor ( $\text{s}^{-1}$ ),  $\Gamma_n$  is the nuclear tunneling factor,  $\kappa_{\text{el}}$  is the electronic transmission coefficient, and  $\Delta G^*$  is the activated free energy of the reaction. If the entropy effects are not taken into account, the activated free energy can be substituted by the activated energy  $E_{\text{ad}}$  (see below for definition). At room temperature, nuclear tunneling does not typically contribute significantly to the electron transfer rate, so  $\Gamma_n$  is assumed to be equal to unity throughout this study (27, 28).

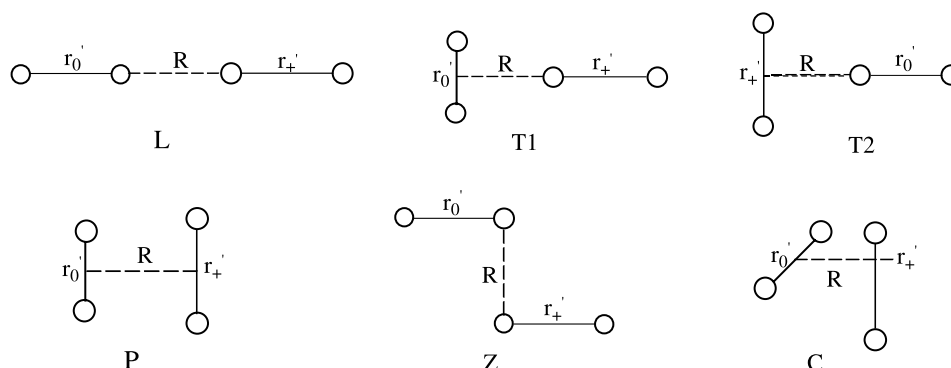
The electronic transmission factor denotes the diabaticity of the ET reaction and must be treated explicitly. For the weak coupling electron transfer system, as in the outer-sphere mechanism, the Landau–Zener (LZ) model (29, 30) is available. In terms of the LZ model, the electronic transmission coefficient can be expressed as

$$[4] \quad \kappa_{\text{el}} = 2P_0/(1 + P_0),$$

where the probability ( $P_0$ ) of hopping from the initial state potential energy surface ( $i$ ) to the final state potential energy



**Fig. 2.** Geometrical structure of the precursor complex ( $r'_0$  and  $r'_+$  denote the N—N bond distance of  $N_2$  and  $N_2^+$  in the precursor complex;  $R$  is the contact distance)



surface (f) on a single passage of the system through the crossing region is given by

$$[5] \quad P_0 = 1 - \exp(-4\pi^2 H_{if}^2 / (h v_s |S_2 - S_1|)),$$

where  $h$  is the Planck constant and  $v_s$  is the velocity (assumed constant) of the reacting system passing through the crossing region along the reaction coordinate.  $|S_2 - S_1|$  is the net force exerted on the system, tending to return it to the original and the final state;  $S_1$  and  $S_2$  are the negative slopes of the potential energy surfaces, at the transition state, of the reactant and product, respectively.  $H_{if}$  is the electronic coupling matrix element between the initial state and the final state.

Obviously, the main factors influencing the electron transfer rate are the activated energy, the coupling matrix element, and the slopes of the potential energy surfaces, and these quantities depend strongly on the potential energy surface of the reacting system (31). In the following section, some valid schemes are introduced to determine these quantities on the basis of the potential energy surfaces obtained from ab initio calculations, including electron correlation.

### Quantum-mechanical method

Instead of using the LZ expression for the electronic transmission coefficient, the quantum-mechanical expression for the ET rate is given as (9, 14, 32–35)

$$[6] \quad k_{et} = (4\pi^2/h) Z^{-1} \sum_v \sum_w \exp(-\beta E_{rv}) \times |\langle \chi_{rv} | \langle \phi_r | H | \phi_p \rangle | \chi_{pw} \rangle|^2 \delta(E_{rv} - E_{pw}) \\ = (4\pi^2/h) H_{if}^2 Z^{-1} \sum_v \sum_w \exp(-\beta E_{rv}) \times |\langle \chi_{rv} | \chi_{pw} \rangle|^2 \delta(E_{rv} - E_{pw}) \\ = (4\pi^2/h) H_{if}^2 \quad (\text{DWFC}),$$

where  $Z$  denotes the vibrational partition function. This expression gives the probability per unit time that a system in an initial vibration state  $\phi_r(r, Q) \chi_{rv}(Q, t)$  will pass to a set of final vibration states  $\phi_p(r, Q) \chi_{pw}(Q, t)$ . DWFC is the density weighted Franck–Condon factor. This formulation is correct for the case of diabatic ET within the Franck–Condon approximation; for adiabatic ET, the ET is processed on one potential energy surface and can be treated using transition state theory. For the  $N_2 + N_2^+$  reacting system, we focus on

the treatment of diabatic ET; thus, the application of eq. [6] leads to (7, 10, 11, 32–34)

$$[7] \quad k_{et} = (4\pi^2/h) H_{if}^2 \quad (\text{FC}),$$

where  $\lambda$  is the reorganization energy. In the classical limit, and when frequency changes in individual vibrational modes are neglected, the FC factor given in eq. [7] reduces to (18, 25)

$$[8] \quad \text{FC} = (4\pi\lambda RT)^{-1/2} \exp(-(\Delta G^\circ + \lambda)^2 / (4\lambda RT)),$$

where  $(4\pi\lambda RT)^{-1/2}$  is the classical density of states and  $\Delta G^\circ$  is the standard Gibbs free energy of the reaction and equal to zero for the self-exchange ET reaction.

One can also use other approximations to represent the DWFC factor in eq. [6]. According to the golden rule (9, 10, 14), we can rewrite eq. [6] into the formula of the Fermi golden rule (36)

$$[9] \quad k_{et} = (4\pi^2/h) H_{if}^2 \rho(E_f),$$

where  $\rho(E_f)$  denotes the density of the final (product) state (see below).

### Computational details

Standard ab initio molecular orbital calculations were performed with the GAUSSIAN 94 program package, Revision E.3 (37). The B3LYP procedure was employed in the density functional theory (DFT) (38) calculations, which cover electron correlation in the self-consistent Kohn–Sham procedure through the functions of electron density. It also gives good descriptions for systems that require sophisticated treatments of electron correlation in the conventional ab initio approach. A large basis set of 6–311+G\* (39) was used at the B3LYP level. For the precursor complex, six structural forms, i.e., collinear (L), two T-type ( $T_1$  and  $T_2$ ), parallel (P), Z-type (Z), and crossing (C) (see Fig. 2), were assumed and optimized under the symmetry constraint and by optimizing in turn the contact distance ( $R$ ) and the N—N distances ( $r_0$  in the  $N_2$  fragments and  $r_+$  in the  $N_2^+$  fragments of the precursor complex). The first five forms were assumed to be coplanar to keep the largest overlap of the orbitals, while the crossing one was assumed to be nonplanar, owing to the rotation of one of the two molecular fragments by  $90^\circ$  about the  $C_2$  principal axis in the P structure.

The stabilization energy ( $E_s$ ) of the corresponding precursor complex was defined as the difference between the



**Table 1.** Calculated structural and spectroscopic properties for  $N_2(X^1\Sigma_g^+)$  and  $N_2^+(X^2\Sigma_g^+)$ .

		$r_e$ (Å)	$\omega_e$ (cm <sup>-1</sup> )	$f^a$ (10 $\mu$ N Å <sup>-1</sup> )	$g^a$ (10 $\mu$ N Å <sup>-2</sup> )	$\alpha^a$ (Å <sup>-1</sup> )	$D_e$ (kJ mol <sup>-1</sup> )
$N_2$	Expt. (40)	1.0977	2358.57	22.95	186.48	2.709	941.581
	HF/6-311+G*	1.0706	2734.48	30.85	414.61	4.480	462.884
	B3LYP/6-311+G*	1.0956	2444.34	24.65	207.90	2.809	940.577
	MP2(full)/6-311+G*	1.1195	2181.33	19.63	149.76	2.543	914.149
$N_2^+$	Expt. (40)	1.1164	2207.00	20.09	161.72	2.683	840.563
	HF/6-311+G*	1.0871	2548.50	26.79	427.53	5.318	285.351
	B3LYP/6-311+G*	1.1087	2332.66	22.45	192.59	2.860	826.221
	MP2(full)/6-311+G*	1.1384	2089.00	18.00	135.77	2.514	857.800

<sup>a</sup>From the Dunham expression of the Morse function,  $f = 4\pi^2 c^2 \omega_e^2 \mu / N_A$ ,  $\alpha = (f/2D_e)^{1/2}$ , and  $g = 3f^{3/2}/(2D_e)^{1/2}$ ;  $\mu$  is the reduced mass.

corresponding precursor complex and the isolated species,  $N_2(X^1\Sigma_g^+)$  and  $N_2^+(X^2\Sigma_g^+)$ , in step 1. The diabatic transition state — which by no means corresponds to a real structure that exists physically — was defined as the “structure” along the seam of crossing between the two diabatic potential energy surfaces, corresponding to the initial and the final states of the ET. On the other hand, the adiabatic transition state was defined at the saddle point on one potential surface, which can be found by transition state theory.

## Results and discussion

### Optimized structure and properties of the isolated species

Before we start the discussion on the structure of the precursor complex for the ET system, it is useful to test the applicability of ab initio calculation levels to this system. The calculations on the isolated species,  $N_2(X^1\Sigma_g^+)$  and  $N_2^+(X^2\Sigma_g^+)$ , were performed at the Hartree–Fock (HF), B3LYP, and MP2 (full) levels with the 6-311+G\* basis set. The optimized structures, energies, and relevant spectroscopic properties are summarized in Table 1.

By comparing the calculated and experimental values for the structure and the force constants, some trends regarding the dependence of the quality of the results on the level of theory can be identified. It can be noted that, even if a larger basis set such as 6-311+G\* is used, the calculated equilibrium N—N bond lengths for both species,  $N_2(X^1\Sigma_g^+)$  and  $N_2^+(X^2\Sigma_g^+)$ , possess larger errors at the HF level (about 0.03 Å shorter than the experimental values); even the vibrational frequencies are higher, at about 340–375 cm<sup>-1</sup> (70–85 cm<sup>-1</sup> if the scale factor of 0.8929 is considered), than the experimental values. At the MP2 level, full electron correlation correction may decrease the errors, but the calculation still deviates from experimental values. However, the B3LYP calculations are in good agreement with the experimental values. For the bond length, the largest deviation is 0.0077 Å, and 35 cm<sup>-1</sup> (considering the scale factor of 0.9613) is the largest deviation for the vibrational frequency. Especially for the dissociation energy ( $D_e$ ) and the force constants ( $f$  and  $g$ ), the result is indeed improved effectively at the electron correlation level. Of course, the deviation trend of the force constants ( $f$  and  $g$ ) from experimental values is the same as that for vibrational frequency. Comparison of the experimental  $r_e$ ,  $D_e$ , and force constants values with HF, B3LYP, and MP2 (full) results indicates that signif-

icant accuracy is achieved at the B3LYP/6-311+G\* level for  $N_2$  and  $N_2^+$  systems.

### The geometry of the complexes in precursor state

The geometrical configuration of the precursor complex directly influences not only the activated energy of the reaction but also the electron transfer coupling matrix element and, thus, the ET rate. Therefore, it is very important to find all possible geometrical configurations for the precursor complex. For the ET reaction between  $N_2$  and  $N_2^+$ , six possible precursor-state structures have been assumed (Fig. 2). The geometrical parameters and relevant energies are displayed in Table 2. However, the Z-type and C-type geometries did not converged at the B3LYP/6-311+G\* level, which may be due to the limitation of the method employed or to the extreme instability of these two configurations. So, in the following discussions, only the four remaining geometries are considered. From Table 2, it can be seen that the N—N bond lengths of the fragments have minor changes compared with the isolated  $N_2(X^1\Sigma_g^+)$  molecule and  $N_2^+(X^2\Sigma_g^+)$  ion. From the viewpoint of energy, the larger is the  $E_s$ , the more stable the complex. So, the most stable precursor complex is L (172.52 kJ mol<sup>-1</sup>), and the order of stabilization energy is L > T2 > T1 > P.

### Transition state of the reaction and the activated energies

According to Marcus' outer-sphere or diabatic ET theory, the interaction between the donor and the acceptor in this case should be very weak and can thus be neglected in some calculations (8, 41–43). Thus, the energy of every point on the potential energy curve of the reactant or the product may be estimated as the sum of energies of the donor and the acceptor. We can write  $E(q) = E_{N_2}(q) + E_{N_2^+}(q)$  in general terms, where  $q$  specifies the location on the potential curves. According to part (ii) of step 2, and as presented by Bu et al. (44), the energy of the activated complex  $N_2(r_0^*)||N_2^+(r_+^*)$  before ( $E_i$ ) and after ( $E_f$ ) ET can be expressed as

$$[10] \quad E_i = E_{N_2}(r_0^*) + E_{N_2^+}(r_+^*)$$

and

$$[11] \quad E_f = E_{N_2^+}(r_0^*) + E_{N_2}(r_+^*),$$

respectively, and we have the energy conservation principle,  $E_f = E_i$ . Therefore,



**Table 2.** The geometrical parameters, relevant energies, coupling matrix elements, and rate constants calculated at the B3LYP/6–311+G\* level for the reacting system in the precursor complex and the transition state.

	L	T <sub>1</sub>	T <sub>2</sub>	P
Coupling state	<sup>2</sup> Σ <sub>g</sub>	<sup>2</sup> A <sub>1</sub>	<sup>2</sup> A <sub>1</sub>	<sup>2</sup> A <sub>1</sub>
precursor complex				
<i>R</i> (Å)	2.1736	2.4791	2.4339	2.6293
<i>r</i> <sub>0</sub> ' (Å)	1.10085	1.110	1.101	1.1054
<i>r</i> <sub>+</sub> ' (Å)	1.1009	1.1011	1.112	1.1068
<i>E</i> <sub>s</sub> (kJ mol <sup>−1</sup> )	172.52	132.38	132.51	102.47
Transition state				
<i>E</i> <sub>d</sub> (kJ mol <sup>−1</sup> )	0.45			
<i>r</i> <sub>0</sub> * = <i>r</i> <sub>+</sub> * (Å)	1.10088	1.1056	1.1065	1.1061
<i>E</i> <sub>ad</sub> (kJ mol <sup>−1</sup> )	0.12	0.26	0.33	0.0097
<i>H</i> <sub>if</sub> (kJ mol <sup>−1</sup> )	0.33	0.19	0.12	0.44
<i>S</i> <sub>2</sub> − <i>S</i> <sub>1</sub>   (kJ mol <sup>−1</sup> Å <sup>−1</sup> )	53.828	47.244	44.242	44.294
κ <sub>el</sub>	0.0404	0.0158	0.00673	0.0833
10 <sup>−17</sup> ρ ( <i>E</i> <sub>F</sub> ) (J <sup>−1</sup> )	2.941	3.825	3.687	4.303
<i>k</i> <sub>ovr</sub> (L mol <sup>−1</sup> s <sup>−1</sup> ) <sup>a</sup>	3.85 × 10 <sup>9</sup> ~10 <sup>10</sup>	1.41 × 10 <sup>9</sup> ~10 <sup>10</sup>	5.89 × 10 <sup>8</sup> ~10 <sup>9</sup>	6.98 × 10 <sup>10</sup> ~10 <sup>11</sup>
<i>k</i> <sub>ovr</sub> (L mol <sup>−1</sup> s <sup>−1</sup> ) <sup>b</sup>	1.94 × 10 <sup>12</sup>	6.42 × 10 <sup>11</sup>	2.56 × 10 <sup>11</sup>	3.447 × 10 <sup>12</sup>
<i>k</i> <sub>ovr</sub> (L mol <sup>−1</sup> s <sup>−1</sup> ) <sup>c</sup>	5.25 × 10 <sup>12</sup>	2.27 × 10 <sup>12</sup>	8.71 × 10 <sup>10</sup>	1.37 × 10 <sup>13</sup>

<sup>a</sup>The results of the semiclassical method according to eq. [3].<sup>b</sup>The results of the quantum-mechanical method according to eq. [7].<sup>c</sup>The results of Fermi golden rule according to eq. [9].

$$[12] \quad E_{N_2}(r_0^*) + E_{N_2^+}(r_+^*) = E_{N_2^+}(r_0^*) + E_{N_2}(r_+^*)$$

Or it may simply be written as

$$[13] \quad E(r^*) = E_{N_2}(r^*) + E_{N_2^+}(r^*),$$

where *r*\* is *r* in the activated state, i.e., *r*<sub>0</sub>\* = *r*<sub>+</sub>\* = *r*\*. Evidently, eq. [13] represents the energy curve constructed at the crossing point between the two diabatic potential energy surfaces, and the lowest *E*(*r*), with varying *r*, is the energy of the activated complex (*E*(*r*\*)) at the crossing point with geometry *r*\*.

However, to ensure the ET reaction occurs, the two diabatic potential energy curves must be coupled to a certain extent so that the crossing point of the two curves is avoided and a 2*H*<sub>if</sub> separation between the lower and upper potential curves arises (see Fig. 1). Indeed, *H*<sub>if</sub> = 0 means no ET happens, which can be indicated by equations of *k*<sub>et</sub>. That is, the interaction of the donor and the acceptor should be taken into account when we refer to the activated state of the ET reaction. The activation energy is then defined by subtracting the energy of the precursor complex from the corresponding energy at the activated state; namely,

$$[14] \quad E_{ad} = E_{N_2 \parallel N_2^+}(r^*, r^*) - E_{N_2 \parallel N_2^+}(r'_0, r'_+),$$

where the energies on the right hand side are the single point energies calculated at B3LYP of DFT at the same contact distance *R*, but with the relevant internal coordinates being optimized as before.

The definition of the diabatic activated energy *E*<sub>d</sub> we have adopted here is found in eq. [15] (44)

$$[15] \quad E_d = E_{N_2}(r^*) + E_{N_2^+}(r^*) - E_{N_2}(r_0) - E_{N_2^+}(r_+)$$

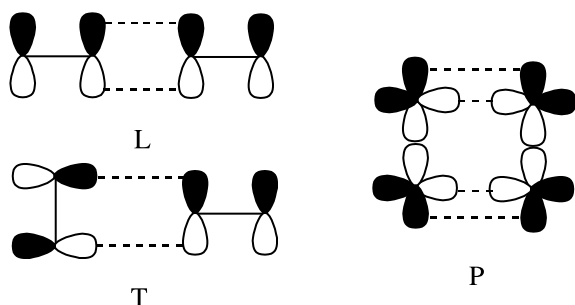
The interaction between acceptor and donor can be quantitatively described by the coupling matrix element (*H*<sub>if</sub>). Accurate theoretical calculations on *H*<sub>if</sub> have been made by Newton (45), German (46), and German and Kuznetsov (47). The magnitude of *H*<sub>if</sub> is a direct parameter, determining the degree of diabatic character in the electron exchange reaction. If the interaction is strong, the values of the electronic transmission factors are high (κ<sub>el</sub> tend to 1) and the system can remain in the lower potential surface; that is, the reaction is adiabatic and the reaction process can be treated by classical transition state theory. As shown in Fig. 1, because *E*<sub>ad</sub> and *E*<sub>d</sub> denote the adiabatic and diabatic activation energy, respectively, the magnitude of the coupling matrix element *H*<sub>if</sub> at the crossing point is approximated by (6, 48)

$$[16] \quad H_{if} = E_d - E_{ad} \\ = E_{N_2}(r^*) + E_{N_2^+}(r^*) - E_{N_2}(r_0) - E_{N_2^+}(r_+) \\ - E_{N_2 \parallel N_2^+}(r^*, r^*) + E_{N_2 \parallel N_2^+}(r'_0, r'_+)$$

For the precursor complex N<sub>2</sub>(*r*'<sub>0</sub>) || N<sub>2</sub><sup>+</sup>(*r*'<sub>+</sub>), of the four different geometries, the activated energies (calculated at the B3LYP/6–311+G\* level) are 0.33 (T2), 0.26 (T1), 0.12 (L), and 0.0097 (P) kJ mol<sup>−1</sup>, respectively, and the coupling matrix elements are 0.33 (L), 0.19 (T1), 0.12 (T2), and 0.44 (P) kJ mol<sup>−1</sup>, respectively. The P-type transition state with C<sub>2v</sub> symmetry has the largest coupling matrix element and the T2-type transition state with C<sub>2v</sub> symmetry has the smallest. This phenomenon may be explained in terms of the orbital overlap interaction between the donor and the acceptor (see Fig. 3). Although the contact distance is larger than the other structures, the P-type structure is favorable with both π<sub>−</sub> and π<sub>1</sub> maximum overlaps and the largest coupling matrix element. For the L-type structure, the smallest contact distance is favorable for the orbital overlap. T1-type and T2-type



**Fig. 3.** The diagram of the orbital couplings between the donor and the acceptor.



structures have similar geometries that may be presented by a T-type orbital coupling diagram. Due to the symmetry restriction on the orbital overlap, its coupling interaction should be small.

According to the Franck–Condon principle, the definition of the reorganization energy is the energy that is required to reorganize the molecular structure of the reactants and the surrounding solvent to be compatible with ET. In this gas-phase ET reaction, it may be defined by (49, 50)

$$[17] \quad \lambda = E_{N_2^+}(r_+) - E_{N_2}(r_+) + E_{N_2^+}(r_0) - E_{N_2}(r_0)$$

The reorganization energy calculated according to eq. [17] is 2.43 kJ mol<sup>-1</sup>, which is consistent with the previous study (2.20 kJ mol<sup>-1</sup>) (50).

### The slopes of the potential energy surfaces and the final-state density

For a given potential energy surface,  $E(q)$ , the value of its slope,  $S_j$ , can be obtained from the relationship

$$[18] \quad S_j = -\partial E_j(q)/\partial q,$$

where  $j = 1$  corresponds to the reactant and  $j = 2$  corresponds to the product. Considering that  $E(q)$  can be expressed as the sum of  $E_r$  and  $E_o$ , where the subscripts  $r$  and  $o$  stand for the reduced and oxidized fragment of the reaction system at the crossing point, eq. [18] may be further written as

$$[19] \quad S_1 = -\partial E_i(q_r)/\partial q_r = -\partial E_r(q_r)/\partial q_r + \partial E_o(x - q_r)/\partial(x - q_r) = S_r - S_o$$

$$[20] \quad S_2 = -\partial E_i(q_o)/\partial q_o = -\partial E_r(x - q_o)/\partial(x - q_o) + \partial E_o(q_o)/\partial q_o = -S_r + S_o,$$

where it is assumed that  $q_r + q_o = x$ . Thus, the difference in slope between the reactant state and the product state may be further expressed as

$$[21] \quad |S_2 - S_1| = 2|S_r - S_o|,$$

where  $S_r$  and  $S_o$  denote the slopes of the diabatic potential energy surfaces of the reduced and the oxidized fragments, respectively, at the crossing point of the two diabatic potential surfaces.

Moreover, the slopes of one dimensional potential curves can be calculated in terms of the Morse potential function

( $E(q) = D_e(1 - \exp(-\alpha q))^2$ ). Thus, the calculation formula is expressed as

$$[22] \quad S_j = -2D_e\alpha(1 - \exp(-\alpha q_l))\exp(-\alpha q_t),$$

where  $j$  ( $= r, o$ ) denotes the reduced and the oxidized species, respectively, and  $q_t$  denotes the geometry at the crossing point. The calculated results of the slopes are displayed in Table 2 and they are similar to each other.

To define the final-state density,  $\rho(E_f)$ , one may note that under perturbation there must be three product states, which all come from the same initial state of  $E_i$ . These final states have energy  $E_i + \Delta E$ ,  $E_i$ , and  $E_i - \Delta E$ , so that there are three final states per  $2\Delta E$  (51, 52). Hence, the maximum value of the final state density is

$$[23] \quad \rho(E_f) = dN/dE = 3/(2\Delta E),$$

where  $\Delta E$  is the difference between the initial- and the final-state energies and can be taken as the perturbation or uncertainty in the electron energy,  $\Delta E = (\Delta p)^2/(2m_e)$ . Then, according to the uncertainty principle,

$$[24] \quad \rho(E_f) = 3m_e/(\Delta p)^2 = 3m_e(\Delta x)^2/h^2,$$

where  $\Delta x$  is the uncertainty in the position of an electron at the crossing point and may be approximately equal to the contact distance. This indicates that the longer the distance, the larger the final-state density. The final results of  $\rho(E_f)$  are also displayed in Table 2.

### Electron transfer rate

The electronic transmission coefficients were calculated in terms of eqs. [4] and [5]. The results were also listed in Table 2. The values were far less than unity (0.006–0.09); thus, the electron transfer reaction was indeed diabatic in nature. Moreover, it shows the validity of using quantum-mechanical theory to calculate this ET rate.

Once the electronic transmission coefficient, the coupling matrix element, and the relevant energies are obtained, the rate of the ET reaction can be found in terms of eqs. [3], [7], and [9], according to the different methods. At the semiclassical theoretical level, considering the role of the collision between the  $N_2$  molecule and  $N_2^+$  ion, the effective collision frequency  $Z_{\text{eff}}$  (the combination of  $K_{\text{pre}} \cdot v_n \cdot \Gamma_n$ ) lies between  $10^{11}$ – $10^{12}$  L mol<sup>-1</sup> s<sup>-1</sup> (53). All the calculated results are shown in Table 2. It can be seen that the P-type mechanism has the largest rate constant, then the L-type, and the T-type has the smallest at all the calculated levels. The mean values of the overall ET rates are  $3.21 \times 10^9$ – $10^{10}$ ,  $1.57 \times 10^{12}$ , and  $5.32 \times 10^{12}$  L mol<sup>-1</sup> s<sup>-1</sup> at the semiclassical (eq. [3]), quantum-mechanical (eq. [7]), and golden rule (eq. [9]) levels, respectively. The experimental value for the ET rate of the  $N_2 + N_2^+$  system in the gaseous phase was found to be about  $3.97 \times 10^{11}$  L mol<sup>-1</sup> s<sup>-1</sup> (54, 55). Our calculated values showed a good agreement with the experimental values, considering the many approximations employed. On comparing the results of the rate constant it can be seen that the values obtained from the quantum-mechanical theory are higher than those from the semiclassical theory, and the rate constant derived from the final-state density also provides a valid treatment for the diabatic ET reaction.



## Conclusions

The structures, properties, and electron-transfer reactivity of the  $N_2 + N_2^+$  system in the gas phase have been studied using semiclassical and quantum-mechanical methods based on the single point energies calculated at the B3LYP/6-311+G\* level. Six possible precursor structures were assumed and the order of their stability was  $L > T2 > T1 > P$ . For these precursor complexes, the larger the contact distance, the weaker is the interaction between the donor and the acceptor, and the floppier is the structure. So, neglecting the interaction between the donor and the acceptor is reasonable in the  $N_2 + N_2^+$  ET reaction. The electronic transmission factor for this system is generally substantially less than unity (ca. 0.006–0.09), thus this ET reaction is diabatic in nature. The coupling matrix elements were calculated and were found to be a crucial factor in determining ET occurrence and an important factor in determining ET rate. The rate constant was found to be strongly dependent on the slopes of the potential energy surface at the crossing point. The results of ET rates from the semiclassical and quantum-mechanical theories were in good agreement with the experimental values, which indicates that it is reasonable to neglect the entropy effects of the reaction in the semiclassical calculation and take into account the vibrational ground state contribution only on the FC term in the quantum-mechanical calculation. Moreover, it can be concluded that if the interaction is so weak that it can be represented by a perturbation, this reacting system can be treated using the Fermi golden rule (i.e., first-order perturbation theory). Most importantly, it was demonstrated that both theories are successful in interpreting the diabatic electron transfer reaction.

Since the  $N_2 + N_2^+$  system is a simple and typical diabatic ET reaction system, demonstrating its reaction mechanism is useful for a forthcoming investigation — the pattern and rule of diabatic character for self-exchange ET in the periodic table.

## References

1. R.A. Marcus. *J. Chem. Phys.* **24**, 966 (1956); *Annu. Rev. Phys. Chem.* **15**, 155 (1964); *J. Chem. Phys.* **43**, 679 (1965); **43**, 3477 (1965); *Faraday Discuss. Chem. Soc.* **74**, 7 (1982).
2. N.S. Hush. *Trans. Faraday Soc.* **57**, 557 (1961); *Electrochim. Acta*, **13**, 1005 (1968).
3. N. Sutin. *Annu. Rev. Nucl. Sci.* **12**, 285 (1962).
4. M.D. Newton. *Int. J. Quantum Chem. Quantum Chem. Symp.* **14**, 363 (1980).
5. M.D. Newton and N. Sutin. *Annu. Rev. Phys. Chem.* **35**, 437 (1984).
6. R.D. Connon. *Electron transfer reactions*. Butterworths, London. 1980.
7. R.A. Marcus and N. Sutin. *Biochim. Biophys. Acta*, **811**, 265 (1985).
8. L. Eberson. *Electron transfer reaction in organic chemistry*. Springer-Verlag, Heidelberg. 1987.
9. K.V. Mikkelsen and M.A. Ratner. *Chem. Rev.* **87**, 113 (1987).
10. M.D. Newton. *Chem. Rev.* **91**, 767 (1991).
11. M.R. Wasielewski. *Chem. Rev.* **92**, 435 (1992).
12. C.C. Moser, J.M. Keske, K. Warncke, R.S. Farid, and P.L. Dutton. *Nature (London)*, **355**, 796 (1996).
13. H.B. Gray and J.R. Winkler. *Annu. Rev. Biochem.* **65**, 537 (1996), and refs. therein.
14. P.F. Barbara, T.J. Meyer and M.A. Ratner. *J. Phys. Chem.* **100**, 13148 (1996).
15. H. Tributsch and L. Pohlmann. *Science (Washington, D.C.)*, **279**, 1891 (1998).
16. L.K. Skov, T. Pascher, J.R. Winkler, and H.B. Gray. *J. Am. Chem. Soc.* **120**, 1102 (1998).
17. N.R. Kestner, J. Logan, and J. Jortner. *J. Phys. Chem.* **78**, 2148 (1974).
18. J. Ulstrup and J. Jortner. *J. Chem. Phys.* **63**, 4358 (1975).
19. J. Jortner. *J. Chem. Phys.* **64**, 4860 (1976).
20. R.C. Dougherty. *J. Chem. Phys.* **106**, 2621 (1997).
21. L.B. Knight, Jr., K.D. Johannessen, D.C. Cobranchi, E.A. Earl, D. Feller, and E.R. Davidson. *J. Chem. Phys.* **87**, 885 (1987).
22. C.C. Han, J.L. Wilbur, and J.I. Brauman. *J. Am. Chem. Soc.* **114**, 887 (1992).
23. C. Leonard, P. Rosmus, S. Carter, and N.C. Handy. *J. Phys. Chem. A*, **103**, 1846 (1999).
24. P.J.F. de Rege, S.A. Williams, and M.J. Therien. *Science (Washington, D.C.)*, **269**, 1409 (1995).
25. R.A. Marcus. *Int. J. Chem. Kinet.* **13**, 865 (1981).
26. J.T. Hupp and M.J. Weaver. *J. Electroanal. Chem.* **152**, 1 (1983).
27. N. Sutin. *Inorganic reaction and methods*. Vol. 15. *Edited by J.J. Zuckerman*. VCH Publishers, Deerfield Beach. 1986. p 30.
28. B.S. Brunschwig, J. Logan, M.D. Newton, and N. Sutin. *J. Am. Chem. Soc.* **102**, 5798 (1980).
29. L. Landau. *Phys. Z. Sowjetunion*, **2**, 6 (1932).
30. C. Zener. *Proc. R. Soc. London Ser. A*, **137**, 696 (1932); **140**, 660 (1933).
31. Y. Bu and C. Deng. *J. Phys. Chem.* **100**, 18093 (1996).
32. C. Creutz, M.D. Newton, and N. Sutin. *J. Photochem. Photobiol. A*, **82**, 47 (1994).
33. A. Yoshimura, K. Norzaki, N. Ikeda, and T. Ohno. *J. Am. Chem. Soc.* **115**, 7521 (1993).
34. P. Siddarth and R. A. Marcus. *J. Phys. Chem.* **97**, 2400 (1993).
35. S.H. Pullen, M.D. Edington, S.L. Studer-Martinez, and J.D. Simon. *J. Phys. Chem. A*, **103**, 2740 (1997).
36. W. Pauli. *Pauli lectures on physics*. *Edited by C.P. Enz*. MIT Press, Cambridge, Massachusetts and London, England. 1973. pp. 150–151.
37. M.J. Frisch, G.W. Trucks, H.B. Schlegel, P.M.W. Gill, B.G. Johnson, M.A. Robb, J.R. Cheeseman, T. Keith, G.A. Petersson, J.A. Montgomery, K. Raghavachari, M.A. Al-Laham, V.G. Zakrzewski, J.V. Ortiz, J.B. Foresman, J. Cioslowski, B.B. Stefanov, A. Nanayakkara, M. Challacombe, C.Y. Peng, P.Y. Ayala, W. Chen, M.W. Wong, J.L. Andres, E.S. Replogle, R. Gomperts, R.L. Martin, D.J. Fox, J.S. Binkley, D.J. Defrees, J. Baker, J.P. Stewart, M. Head-Gordon, C. Gonzalez, and J.A. Pople. 1995. *Gaussian 94* [computer program]. Revision E.3. Gaussian Inc., Pittsburgh, PA.
38. W. Kohn and L.J. Sham. *Phys. Rev. Sect. A*, **140**, 1133 (1965).
39. W.J. Hehre, L. Radom, P.V.R. Schleyer, and J.A. Pople. *Ab initio molecular orbital theory*. Wiley, New York. 1986.
40. K.P. Huber and G. Herzberg. *Molecular spectra and molecular structure IV. Constants of diatomic molecules*. Van Nostrand, New York. 1979.
41. Y.F. Zhai, H.L. Jiang, W.L. Zhu, J.D. Gu, J.Z. Chen, K.X. Chen, and R.Y. Ji. *Sci. China Ser. B Chem. Life Sci. Earth Sci.* **29**, 201 (1999).
42. R.A. Marcus. *Annu. Rev. Phys. Chem.* **15**, 155 (1964).
43. N. Agmon. *Int. J. Chem. Kinet.* **13**, 333 (1981).
44. Y. Bu, Y. Wang, H. Sun, and C. Deng. *THEOCHEM*, **429**, 143 (1998).



45. M.D. Newton. J. Phys. Chem. **90**, 3734 (1986); **92**, 3049 (1988).
46. E.D. German. Rev. Inorg. Chem. **5**, 123 (1984).
47. E.D. German and A.M. Kuznetsov. J. Chem. Soc. Faraday Trans. 1, **81**, 1153 (1985).
48. Y. Bu and C. Deng. J. Phys. Chem. **100**, 18093 (1996).
49. Y. Bu, X. Song, and C. Deng. Chem. Phys. Lett. **250**, 455 (1996).
50. Y. Bu and X. Song. J. Phys. Chem. **98**, 5049 (1994).
51. Y. Bu, D. Zhou, Q. Zhou, and C. Deng. THEOCHEM, **459**, 177 (1999).
52. H. Ai and Y. Bu. Acta. Phys. Chim. Sin. **17**, 210 (2001).
53. R.P. Wayne. Comprehensive chemical kinetics. Vol. 2. *Edited by* C.H. Bamford and C.F. H. Tipper. Elsevier Scientific Publishing Company, Netherlands. 1969. p. 30.
54. Y. Ikezoe, S. Matsuoka, M. Takebe, and A. Viggiano. Gas phase ion-molecule reaction rate constants through 1986. Maruzen, Tokyo. 1987. p. 103.
55. T.B. McMahon, P.G. Miasek, and J.L. Beauchamp. Int. J. Mass. Spectrom. Ion Phys. **21**, 63 (1976).



# The influence of competing factors on the endothermic nature of bile salt binding by cationic adsorbent

Celia K. Williams, William C. Galley, and G. Ronald Brown

**Abstract:** The binding of sodium chenodeoxycholate, a hydrophobic bile salt, by a polyacrylamide resin with *N,N,N*-trimethylammonium dodecyl chloride (QPDA12) pendant groups was studied in the presence of elevated concentrations of competing anions. The equilibrium bile salt concentration was determined from HPLC data for a range of initial bile salt concentrations. Binding constants extracted from the fit of the isotherms to the Langmuir equation were obtained for data for temperatures from 24 to 60°C. A reduction in chenodeoxycholate binding affinity was observed in comparison with that reported previously at lower overall anion concentrations. A van't Hoff analysis of the data revealed that a decrease in the favourable entropy of binding was responsible for this reduced affinity. Decomposition of the binding constants into specific contributions for the competing buffer anions and the chenodeoxycholate anion returned positive values of  $\Delta H^\circ$  and  $\Delta S^\circ$  for the binding of both the competing ions and bile salt. These findings reveal that the weakening of the bile salt binding that occurs with added salt is not due to Debye screening of an attraction between ions of opposite charge. A binding mechanism consistent with the thermodynamics observed was proposed in which the dominant role of hydration changes that occur on binding provides the principal driving force for the process.

**Key words:** bile salts, endothermic binding, polymer sorbents, solvent randomization.

**Résumé :** La liaison d'un sel biliaire hydrophobique, le chénodeoxycholate de sodium, par une résine de polyacrylamide comportant des substituants chlorure de *N,N,N*-triméthylododecylammonium a été étudiée en présence d'une forte concentration d'ions compétiteurs. Les concentrations en sel biliaire libre à l'équilibre, pour différentes concentrations initiales, ont été obtenues à partir de mesures HPLC. Les constantes de liaison ont été extraites des isothermes ajustés à l'équation de Langmuir pour des températures de 24°C à 60°C. Une analyse van't Hoff des données a révélé qu'une diminution de l'entropie favorable à la liaison était responsable de l'affinité réduite. Des valeurs positives de  $\Delta H^\circ$  et  $\Delta S^\circ$  pour la liaison des ions compétiteurs ainsi que pour le sel biliaire ont été obtenues par la décomposition des constantes de liaison. Ces résultats révèlent que l'affaiblissement de la liaison du sel biliaire n'est pas seulement due à l'effet d'écran de Debye sur l'attraction d'ions de charges opposées. Un mécanisme de liaison incluant les changements d'hydratation a été proposé pour expliquer les caractéristiques du processus de liaison.

**Mots clés :** sels biliaires, liaison endothermique, sorbents polymères, désorganisation de la cage d'hydratation.

## Introduction

The ingestion of insoluble polymeric resins serves to sequester bile acids in the intestines, resulting in their elimination through the gastrointestinal tract. Prevention of their reabsorption stimulates the breakdown of cholesterol to bile acids, which in turn leads to a reduction in plasma cholesterol levels. The resins currently in wide clinical use, cholestyramine (Questran), a styrene-divinylbenzene copolymer developed in 1959 (1), and colestipol (Colestid), a copolymer of tetraethylene-pentamine and epichlorohydrin (2),

are cationic in nature, as are many of the other resins investigated for this purpose. Although the use of these polymeric sequestrants for the removal of bile acids from the gastrointestinal tract is an accepted means of lowering plasma cholesterol levels, little work has been done to elucidate the nature of the binding interactions.

The binding of bile salts with the cationic resins has been considered to be dominated by the attraction between the oppositely charged ions (3–5). Comparisons of the binding affinities of cationic polymeric resins with uncharged resins have been taken as evidence for the contribution of coulombic interactions in the binding process (3–8). In addition, the significant impact of added salt (6, 7, 9) and phosphate buffer in reducing the binding through Debye screening of an ionic interaction has been taken as support (4, 5, 8) for a model in which ion-pair formation provides the driving force for the process. As a consequence, it has been implicitly assumed that the binding of the participating ions is an exothermic process.

However, recent temperature-dependent studies of the binding of bile salts to a quaternized polyacrylamide resin

Received 26 March 2002. Published on the NRC Research Press Web site at <http://canjchem.nrc.ca> on 19 February 2003.

**C.K. Williams and W.C. Galley.**<sup>1</sup> Department of Chemistry, McGill University, 801 Sherbrooke Street West, Montreal, QC H3A 2K6, Canada.

**G.R. Brown.**<sup>2</sup> Faculty of Arts and Science, Brock University, St. Catharines, ON L2S 3A1, Canada.

<sup>1</sup>Corresponding author (e-mail: [william.galley@mcgill.ca](mailto:william.galley@mcgill.ca)).

<sup>2</sup>Deceased.



conjugated with *N,N,N*-trimethylammonium dodecyl chloride (QPDA12) (Fig. 1) demonstrated that the binding affinity was enhanced with increasing temperature (10). This indicated that an increase in entropy was responsible for the binding and that a considerable enthalpic barrier had to be surmounted in the process. The observed endothermic nature of the process is inconsistent with an association dominated by favourable coulombic interactions between the participating bile salt and resin. Calorimetric binding studies of bile salts with human serum albumin and bovine serum albumin have been observed in previous work to be endothermic. This was taken as evidence for a major hydrophobic involvement in the association of bile salts with these plasma proteins (11).

Alternate molecular descriptions to those that involve a simple electrostatic attraction between bile salts and macromolecular assemblies are required to account, at least qualitatively, for the thermodynamic parameters that are associated with binding. These models, however, must also encompass the earlier evidence that supports the role of ionic interactions in the binding process (3–8).

To provide additional data that might assist in reconciling the endothermic nature of the binding with the known dependence on added salt, binding studies were carried out as a function of temperature and electrolyte composition. The adsorption of sodium chenodeoxycholate with QPDA12 was examined in the presence of an elevated buffer ion concentration and with added salt. A van't Hoff analysis was used to obtain a measure of the  $\Delta H^\circ$  and  $\Delta S^\circ$  associated with the binding. The manner in which the bile salt binding thermodynamics are influenced by the ionic composition of the medium are interpreted in terms of binding of competing anions in the system and of the role of solvation in the overall process.

## Experimental

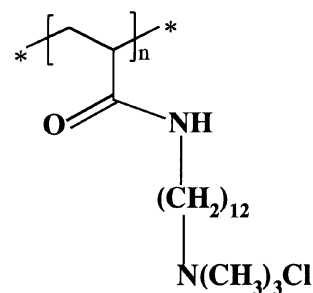
### Materials

Sodium chenodeoxycholate (NaCDC) was purchased from Sigma and was used as received. Sodium cacodylate ( $(\text{CH}_3)_2\text{AsO}_2\text{Na}$ ) was from Baker. The QPDA12 resin with chloride as counter ions was a previously synthesized and quaternized sample (12). The functionality (*f*) was determined to be  $2.00 \pm 0.07$  mmol of trimethylammonium pendant groups per gram of dry resin, performed by gravimetric analysis. The chloride counter-ions were precipitated in the form of silver chloride by the addition of 1:1 of 16 M nitric acid and 0.103 M silver nitrate. The precipitate was filtered, washed, dried, and weighed to constant weight.

### Adsorption studies

The procedures used for the sorption studies were as described previously (13). The bile salt solutions were prepared in aqueous 50 mM sodium cacodylate buffer, a mixture of 5 mM sodium cacodylate and 41 mM sodium chloride, and a mixture of 5 mM and 8 M urea all at a pH of 7.2. A stock bile salt solution (7 mM) was normally diluted with buffer to generate concentrations as low as 0.23 mM. The polymer resin (10 mg) was added to 20 mL of buffer solution containing varying bile salt concentrations. These mixtures were agitated with a mechanical shaker in a con-

**Fig. 1.** The chemical structure of (*N,N,N*)-trimethylammonium dodecyl chloride (QPDA12) resin.



stant temperature bath at 120 oscillations per minute for more than 18 h at the desired temperature (24–60°C). The density change of the bile salt solutions over this temperature range was less than 1%; therefore the concentrations of the bile salt solutions were not corrected for increase in temperature. Reverse-phased high-performance liquid chromatography (HPLC) was used to follow the binding according to procedures described previously (13). The bile salt concentrations in the solutions at equilibrium ( $C_{eq}$ ) and the amount of bile salt bound per gram of resin  $Q$  (mmol  $\text{g}^{-1}$ ) were calculated, and the binding isotherms were plotted from these results. The isotherms were then analyzed in terms of the Langmuir equation, eq. [14],

$$[1] \quad Q = \frac{Q_m K C_{eq}}{1 + K C_{eq}}$$

with the use of SigmaPlot Software Version 5.00, which yielded the “best-fit” values for  $K$  and  $Q_m$ , the equilibrium site binding constant and maximum  $Q$  or binding capacity, respectively.

From the thermodynamic relation

$$[2] \quad \Delta G_T^\circ = -RT \ln K$$

the standard Gibb's free energy change for a process can be related to  $K$ , which is unitless in that the concentrations of the species involved are expressed relative to that of the standard state that is chosen. With an experimental binding constant expressed in terms of molarity, the standard state is the state in which the ligand, or binding species, is at a concentration of 1.0 M, assuming ideal behaviour.

## Results

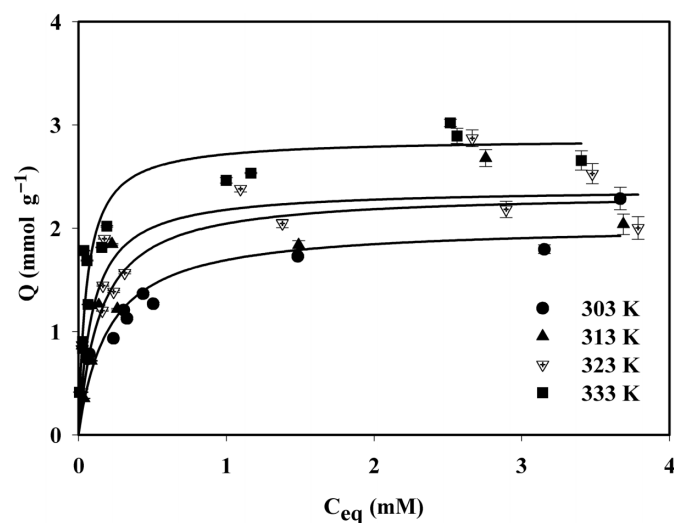
The binding isotherms for chenodeoxycholate to QPDA12 in 50 mM cacodylate buffer appear in Fig. 2. The equilibrium bile salt concentration required to produce half saturation of the binding sites can be seen to decrease with rising temperature, reflecting an increasing binding affinity. This enhanced affinity with temperature is accompanied by an increase in concentration of the bile salt required to saturate the resin. The shape of the isotherms within experimental error remains unaltered. The increase with temperature in both the affinity and the available binding sites for the bile salt reflects the pattern of behaviour observed previously at a 10-fold lower cacodylate buffer concentration (10). These observed changes in binding with temperature cannot be



Table 1.

Temperature (K)	Buffer	$K \times 10^{-3} \text{ (M}^{-1}\text{)}$	$\Delta G^\circ = -RT \ln K \text{ (kJ mol}^{-1}\text{)}$	$n = Q_m/f$
297	5 mM cacodylate	$8 \pm 3$	$-22.1 \pm 0.9$	0.6
	41 mM sodium chloride	$6 \pm 3$	$-22 \pm 1$	0.5
303	5 mM cacodylate	$12 \pm 3$	$-23.7 \pm 0.7$	0.8
	50 mM sodium cacodylate	$5 \pm 1$	$-21.5 \pm 0.7$	1.0
	41 mM sodium chloride	$8 \pm 3$	$-23 \pm 1$	0.7
313	5 mM cacodylate	$28 \pm 5$	$-26.6 \pm 0.5$	1.0
	50 mM sodium cacodylate	$7 \pm 3$	$-23 \pm 1$	1.2
	41 mM sodium chloride	$10 \pm 2$	$-23.9 \pm 0.5$	1.0
323	5 mM cacodylate	$25 \pm 16$	$-27 \pm 2$	1.5
	50 mM sodium cacodylate	$11 \pm 3$	$-24.9 \pm 0.8$	1.2
	41 mM sodium chloride	$11 \pm 3$	$-25.1 \pm 0.6$	1.2
333	5 mM cacodylate	$103 \pm 19$	$-32.0 \pm 0.5$	1.2
	50 mM sodium cacodylate	$18 \pm 4$	$-27.2 \pm 0.6$	1.4

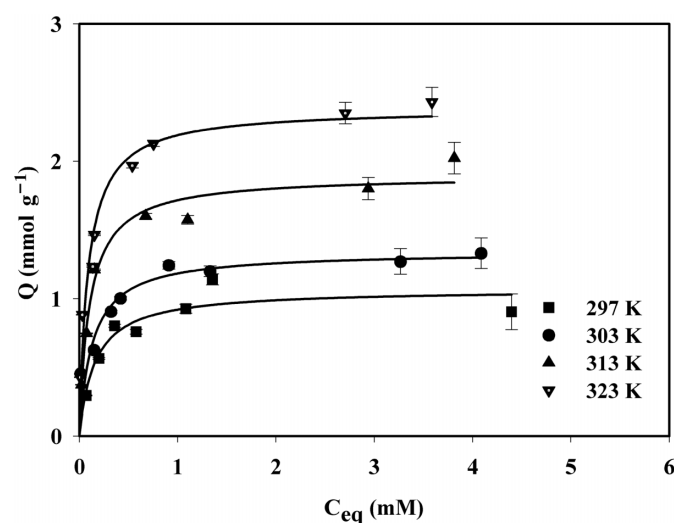
Fig. 2. Binding isotherms of sodium chenodeoxycholate by QPDA12 in 50 mM sodium cacodylate buffer.



accounted for by a change in pH. In the temperature range studied (24–60°C) only a 0.1 decrease in pH was observed.

The binding isotherms illustrated in Fig. 2 were fitted to the Langmuir equation, eq. [14], with the values of  $K$ , the equilibrium site binding constant, the corresponding  $\Delta G^\circ$ , and the number of available binding sites  $n$  being listed in Table 1. The increase in  $K$  with rising temperature, characteristic of an endothermic process, is apparent in Table 1. Binding constants for chenodeoxycholate with QPDA12 at 5 mM cacodylate buffer concentration plus 41 mM sodium chloride<sup>3</sup> are also included in Table 1. The particular sodium chloride concentration was chosen to achieve the ionic strength as the 50 mM cacodylate buffer system. The values of  $K$  in the presence of added sodium chloride were derived from the isotherms appearing in Fig. 3. The magnitude of the  $K$  values is also seen to increase with temperature. The values of  $K$  under both conditions are smaller than those obtained with the lower buffer concentration (10), as shown in Table 1 from earlier data (10). This result is in agreement with weakening of the binding observed in the presence of

Fig. 3. Binding isotherms of sodium chenodeoxycholate by QPDA12 in 5 mM sodium cacodylate and 41 mM sodium chloride buffer.



increased buffer and salt concentrations that has been demonstrated previously with other systems of this type (6, 7, 9).

The van't Hoff plot in Fig. 4 was generated from site binding constants from the isotherms obtained in the presence of 50 mM cacodylate buffer and the buffer mixture of 5 mM cacodylate and 41 mM sodium chloride. The negative slope under both conditions reflects the increase in binding constant  $K$  with temperature or the endothermic nature of the process. A linear analysis on the binding data in the 50 mM buffer yielded values of  $\Delta H^\circ$  and  $\Delta S^\circ$  of  $36 \pm 4 \text{ kJ mol}^{-1}$  and  $190 \pm 12 \text{ J mol}^{-1} \text{ K}^{-1}$  from the slope and intercept, respectively.

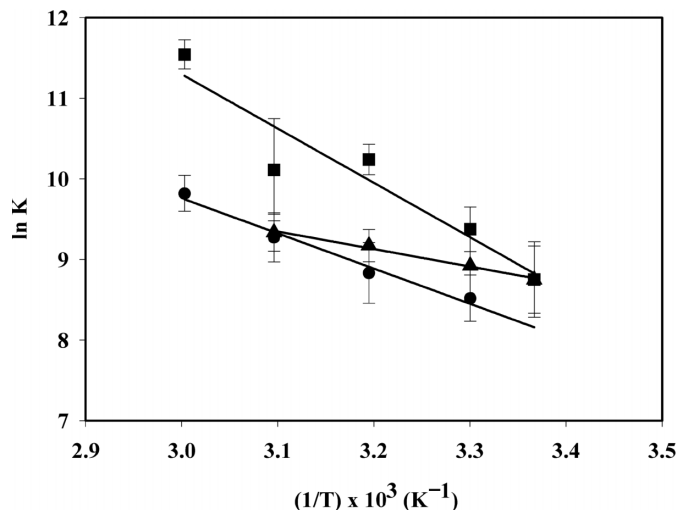
The  $\Delta H^\circ$  and  $\Delta S^\circ$  for the system with the buffer mixture of 5 mM cacodylate and 41 mM sodium chloride are  $18 \pm 1 \text{ kJ mol}^{-1}$  and  $134 \pm 4 \text{ J mol}^{-1} \text{ K}^{-1}$ . Comparison of data obtained at the lower 5 mM buffer concentration yielded a  $\Delta H^\circ$  of  $53 \pm 11 \text{ kJ mol}^{-1}$  and  $\Delta S^\circ$  of  $253 \pm 34 \text{ J mol}^{-1} \text{ K}^{-1}$  (10). The steeper van't Hoff plot for the binding at the low buffer concentration is included for comparison with the data ob-

<sup>3</sup>Refers to an increased chloride concentration greater than the 1 mM of chloride already present from the chloride counter-ion of the resin. This value was calculated by dividing the functionality of the resin by the 20 mL of the bile salt solution used in the binding experiments.



**Table 2.** The thermodynamic parameters associated with bile salt binding by QPDA12 under three different buffer conditions, 5 mM sodium cacodylate, 50 mM sodium cacodylate buffer and a buffer mixture of 5 mM sodium cacodylate and 41 mM sodium chloride.

Buffer	$\Delta H^\circ$ (kJ mol <sup>-1</sup> )	$\Delta S^\circ$ (J mol <sup>-1</sup> K <sup>-1</sup> )	$\Delta G^\circ_{313} = \Delta H^\circ - T\Delta S^\circ$ (kJ mol <sup>-1</sup> )
5 mM sodium cacodylate	53 ± 11	253 ± 34	-26.2
50 mM sodium cacodylate	36 ± 4	190 ± 12	-23.5
5 mM sodium cacodylate + 41 mM sodium chloride	18 ± 1	134 ± 4	-23.9

**Fig. 4.** The van't Hoff Plot for the binding of sodium chenodeoxycholate by QPDA12 in 5 mM (■) and 50 mM (●) sodium cacodylate and 5 mM sodium cacodylate with 41 mM sodium chloride buffer (▲).

tained in the present study. The values of  $\Delta H^\circ$ ,  $\Delta S^\circ$ , and  $\Delta G^\circ$  at 313 K under all three conditions appear in Table 2.

The thermodynamic parameters in Table 2 illustrate the fact that despite the lower unfavourable  $\Delta H^\circ$ , or enthalpy barrier, observed with the higher buffer or salt concentrations, binding is weaker than at low salt concentrations. The weaker binding reflected in the more positive  $\Delta G^\circ_{313}$  values at high salt concentrations derives from the lower  $\Delta S^\circ$  values that represent the driving force for the binding under all conditions. The influence of the changes that occurred in the enthalpic and entropic contributions becomes more evident at a specific temperature. Using data from the temperature of 313 K as an example, the increase in buffer concentration from 5 to 50 mM results in a reduction of 17 kJ mol<sup>-1</sup> in the enthalpic barrier and is offset by a corresponding larger decrease of 19.7 kJ mol<sup>-1</sup> in  $T\Delta S^\circ$ . In agreement with the initial observations (10), binding of chenodeoxycholate with the resin does not occur as a consequence of a favourable energetic interaction. It derives rather from an overall randomization that occurs within the system.

## Discussion

The van't Hoff enthalpies ( $\Delta H_{vH}$ ) in this work were calculated from a simple equilibrium involving binding of the bile salt to a resin-binding site. In recent years, with the widespread use of isothermal calorimetry discrepancies have been found between van't Hoff binding enthalpies and directly determined calorimetric enthalpies,  $\Delta H_{cal}$  (15). It has

been suggested that  $\Delta H_{vH}$  to a first approximation represented values for the intrinsic binding, while  $\Delta H_{cal}$  included concomitant reactions involving, for example, hydration or conformation changes that do not directly affect the binding (16, 17). However, an analysis of the errors on a recent study of a binding reaction involving protein conformational isomerization (18) revealed that the  $\Delta H_{vH}$  and  $\Delta H_{cal}$  within experimental errors were the same. Concomitant processes involving solvent rearrangements such as hydrophobic interactions, which do not appear explicitly in the binding equilibrium, directly influence  $K$  and its temperature dependence, and their influence will contribute to the van't Hoff enthalpy.

The thermodynamic parameters associated with the binding of the bile salt with the polymeric resin and the changes in those parameters observed in the presence of higher buffer and added salt concentrations can be accounted for in terms of a binding model. The model emphasizes competition for the binding of the bile salt anion with the buffer or other anions in the system. Changes in hydration on binding, particularly within the resin, feature as a dominant factor in accounting for the sign and magnitude of the thermodynamic parameters that are observed.

## Consideration of binding models: A model for the binding of chenodeoxycholate with the hydrophobic cationic resin

### Competitive binding

Binding equilibria involving a common binding site are assumed, and an equation for an isotherm for the binding of bile salt in the presence of added competing ions is derived. The Langmuir equation from eq. [1] was rewritten in the form of eq. [3] (19).

$$[3] \quad Q = \frac{Q_m K_{eff} C_{eq}}{1 + K_{eff} C_{eq}}$$

where

$$K_{eff} = \frac{K_B}{1 + K_S[S]}$$

in which  $[S]$  is the equilibrium concentration of the competing anion involved and  $K_B$  and  $K_S$  are the specific binding constants for the bile salt and competing anion, respectively. With the use of binding isotherms at more than one concentration of competing anion, the experimental values of  $K_{eff}$  were decomposed into specific binding constants for the bile salt and competing anion. Decomposition of this kind at several temperatures provided a measure of the temperature dependence of the specific binding constants and, as a result, within the assumptions of the analysis, a measure of the  $\Delta H^\circ$  and  $\Delta S^\circ$  associated with each process.



**Table 3.** The resulting standard enthalpy, entropy changes and Gibbs free energy changes (313 K) associated with sodium chenodeoxycholate and cacodylate ion obtained from binding data of sodium chenodeoxycholate by QPDA12 in 50 mM sodium cacodylate buffer.

	$\Delta H^\circ$ (kJ mol <sup>-1</sup> )	$\Delta S^\circ$ (J mol <sup>-1</sup> K <sup>-1</sup> )	$\Delta G^\circ$ at 313 K (kJ mol <sup>-1</sup> )
Sodium chenodeoxycholate	62	282	-26.8
Cacodylate ion	34	142	-10.9

The values of the bile salt ( $K_B$ ) and cacodylate ion ( $K_S$ ) at a given temperature were obtained by solving eq. [3] simultaneously for  $K_{\text{eff}}$  at two different salt [ $S$ ] concentrations of 4.5 and 45 mM basic cacodylate anion. The concentrations of the cacodylate anion were obtained from substituting the 5 and 50 mM total buffer concentrations into the Henderson–Hasselbach equation at a pH of 7.2. The resulting values of the specific binding constants for  $K_B$  and  $K_S$  appear in the form of a van't Hoff plot in Fig. 5. The line was obtained from the linear regression on the data.

The negative slopes in these plots reveal that the cacodylate binding and the bile salt binding for the cationic resin are both endothermic. It is this endothermic nature of the competing anion binding that produces the observed reduction in the magnitude of the slope for the van't Hoff plot for the apparent chenodeoxycholate binding. The decrease arises from the increase in the buffer anion concentration. With increasing temperature, the increasing  $K_B$  is in competition with a concomitant increase in the  $K_S$  for the cacodylate anion. The  $\Delta H^\circ$ ,  $\Delta S^\circ$ , and  $\Delta G^\circ_{313}$  values for both  $K_B$  and  $K_S$  appear in Table 3. The  $\Delta H^\circ$  values associated with the bile salt and the cacodylate binding are 62 and 34 kJ mol<sup>-1</sup>, respectively, and the  $\Delta S^\circ$  values are 282 and 142 J mol<sup>-1</sup> K<sup>-1</sup>. It is clear from the value for  $\Delta G^\circ_{313}$  that cacodylate anion binding is considerably weaker than that of the bile salt. Weaker binding for the cacodylate anion relative to that of the bile salt is seen to be due to a significant decrease in the favourable binding entropy and, despite a 45% reduction in the positive, or unfavourable,  $\Delta H^\circ$  of binding.

The decomposition of  $K_{\text{eff}}$  at the two chloride ion concentrations into specific site binding constants for the bile salt ( $K_B$ ) and chloride ion ( $K_S$ ) with QPDA12 was performed in the same manner as with the cacodylate buffer. The equilibrium concentrations of chloride were not determined by HPLC analysis, but under weak binding conditions it was assumed that the initial and final concentration of chloride was the same and the initial concentration of chloride was employed. The result of the extraction of  $K_B$  and  $K_S$  appear in Fig. 6 in the form of a van't Hoff plot.

As with the cacodylate perturbation, the specific binding constant for the added chloride ion is much weaker than that for the bile salt, and the numbers are still within the same range as of the cacodylate anion. The analysis of the temperature dependence of the specific bile salt and chloride binding constants yielded the same pattern of behavior that was observed with the cacodylate ion, which is that  $\Delta H^\circ$  and  $\Delta S^\circ$  are both positive, as seen in Table 4. The  $\Delta H^\circ$  of 115 kJ mol<sup>-1</sup> and  $\Delta S^\circ$  of 403 J mol<sup>-1</sup> K<sup>-1</sup> derived for  $K_S$  are actually more positive than the corresponding  $\Delta H^\circ$  of 88 kJ mol<sup>-1</sup> and  $\Delta S^\circ$  of 368 J mol<sup>-1</sup> K<sup>-1</sup> associated with the specific bile salt binding ( $K_B$ ). This implies that while the binding of the competing chloride ion is also weaker than that of

**Fig. 5.** Computed van't Hoff plots for competitive binding of sodium chenodeoxycholate and cacodylate anions.

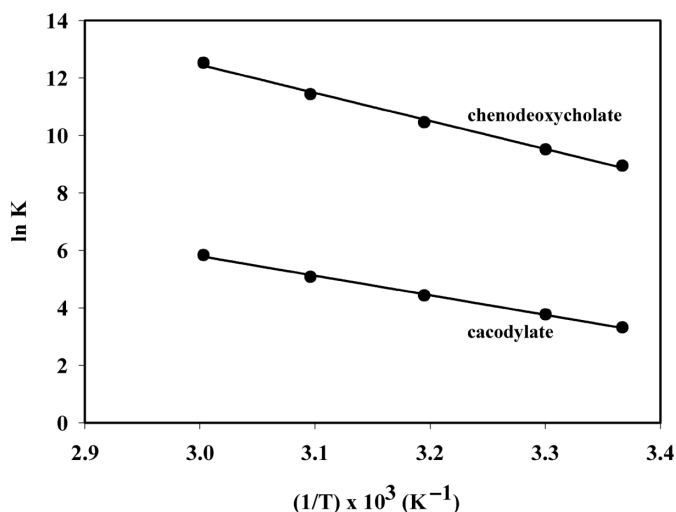
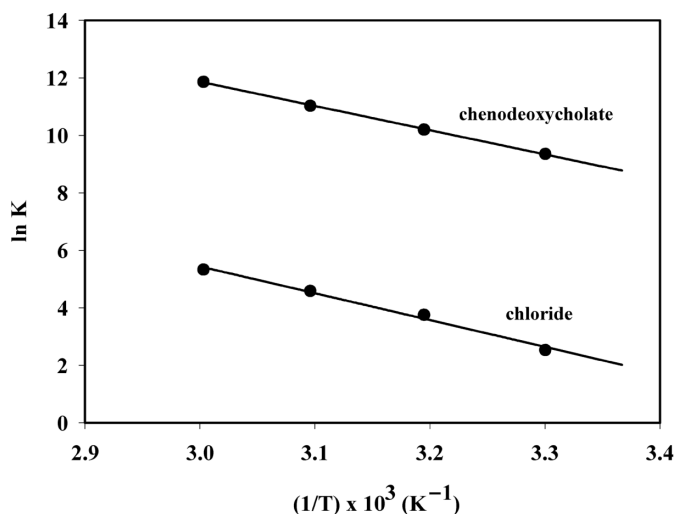


**Fig. 6.** Computed van't Hoff plots for competitive binding of sodium chenodeoxycholate and chloride anions.



the bile salt, in this case it is due to a relatively higher enthalpic barrier rather than a lower  $\Delta S^\circ$ .

Competition for binding by the resin between bile salt and other anionic counterions or co-ions in the system can account for the endothermic nature of the bile salt binding as well as the impact of higher concentrations of the competing ions. However, as revealed by the decomposition of the observed salt binding isotherms into  $K_B$  and  $K_S$ , binding of the competing ions must also be endothermic and entropy-driven. It is the endothermic nature of the competitive ion binding that accounts for the large decreases observed in the



**Table 4.** The resulting standard enthalpy, entropy changes and Gibbs free energy changes (313 K) associated with sodium chenodeoxycholate and chloride ion obtained from binding data of sodium chenodeoxycholate by QPDA12 in 5 mM sodium cacodylate and 41 mM NaCl buffer.

	$\Delta H^\circ$ (kJ mol <sup>-1</sup> )	$\Delta S^\circ$ (J mol <sup>-1</sup> K <sup>-1</sup> )	$\Delta G^\circ$ at 313 K (kJ mol <sup>-1</sup> )
Sodium chenodeoxycholate	88	368	-27.0
Chloride ion	115	403	-11.0

**Table 5.** Summary of the signs of the thermodynamic parameters involved in step I (state I  $\rightarrow$  II), step 2 (state II  $\rightarrow$  III) and for the overall process (state I  $\rightarrow$  III) for the binding of aqueous bile salt by QPDA12 resin.

	State I $\rightarrow$ II	State II $\rightarrow$ III	State I $\rightarrow$ III
$\Delta H^\circ$	+	-	+
$\Delta S^\circ$	+	0	+
$\Delta G^\circ$	+	-	-

slope of the van't Hoff plots for bile salt sequestering at the higher salt concentrations. The enhancement in sodium chenodeoxycholate binding observed with increasing temperature becomes significantly reduced in the presence of high salt because there is also an enhancement in the competing process as the temperature rises. The presence of a competing endothermic process appears as a definitive requirement in accounting for the data irrespective of the precision of the site-binding model.

#### Molecular model involving changes in hydration

An overall molecular description of chenodeoxycholate sequestering by the cationic QPDA12 resin must, within the context of the competitive binding model, account for the endothermic and entropy-driven nature of the binding of the competing ions as well as that of the bile salt. Changes in hydration on binding are proposed as a major feature of the bile salt binding or ion-exchange process.

The molecular model is centered on the existence of an equilibrium between two putative solvated states of an unoccupied pendant-binding site<sup>4</sup> as depicted in Fig. 7. In the process of binding the bile salt or competing anions with state II of the system to form the bound state III, the equilibrium is shifted from state I to the otherwise less favoured state II. The proposed state I to state II transition is accompanied by large positive  $\Delta H^\circ_{I \rightarrow II}$  and  $\Delta S^\circ_{I \rightarrow II}$  values that compensate, resulting in smaller positive  $\Delta G^\circ_{I \rightarrow II}$  values.

The direct associations (state II  $\rightarrow$  III, in Fig. 7) of the chenodeoxycholate or competing anions with the resin are considered to be enthalpically favoured ( $\Delta H^\circ_{II \rightarrow III} = (-)$ ). The  $\Delta S^\circ_{II \rightarrow III}$  associated with the direct binding to state II of the resin is purported to involve a balance between a positive contribution due to solvent liberation from the ions and a negative contribution from loss in the degrees of freedom possessed by the free ions themselves. The resulting  $\Delta G^\circ_{II \rightarrow III}$  values for these transitions are negative and sufficiently favourable to shift the equilibrium in the resin in the direction of overall binding.

The large  $\Delta H^\circ_{I \rightarrow II}$  and  $\Delta S^\circ_{I \rightarrow II}$  values associated specifically with the state I  $\rightarrow$  II transition within the resin are proposed to involve the hydrophobic pendant groups. The positive  $\Delta H^\circ_{I \rightarrow II}$  during contraction of the binding area arises from an increased electrostatic repulsion between quaternary ammonium-terminated pendant groups and the disruption of the hydrophobic hydration of the methylene chains.

This relaxation of the extended pendant chains (elastomer contribution) and the liberation of the ordered hydrophobic solvation form the basis of the accompanying positive  $\Delta S^\circ_{I \rightarrow II}$ . The compensating enthalpy and entropy contributions result in a relatively smaller positive  $\Delta G^\circ$  that, in the absence of anions, favours the expanded state I.

It is only the addition of state II  $\rightarrow$  III transitions in the presence of anions that shifts the equilibrium resulting in an overall favourable  $\Delta G^\circ$  for binding that nonetheless displays large positive  $\Delta H^\circ$  and  $\Delta S^\circ$  values that in large part reflect the contraction of the resin binding area. It should be noted that these significant positive contributions would appear irrespective of whether the chenodeoxycholate or other competing anions are involved. The thermodynamic parameters for the separate stages in the model and the predicted overall transition are summarized in Table 5.

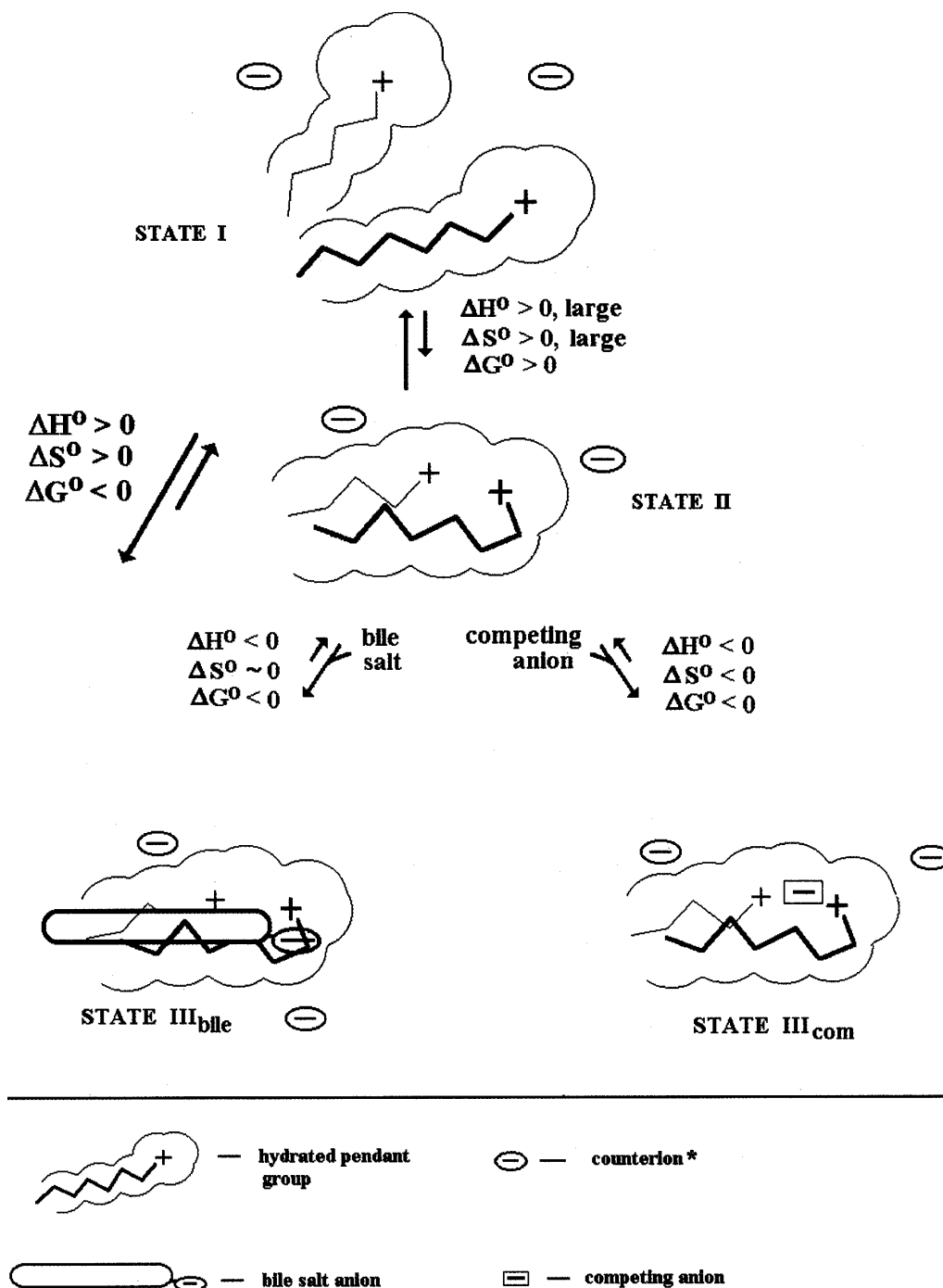
The changes observed in the enthalpy and entropy of bile salt binding in the presence of higher buffer and sodium chloride concentrations that can be accounted for with the present model cannot be reconciled with other common mechanisms. Debye screening of the attraction between the opposing charges or an ionic strength effect has often been assumed to be responsible for the general weakening of bile salt binding with added salt (4–8). However, such an effect would be manifested as a decrease in the attraction between bile salt and resin or an increase in binding enthalpy, which is clearly inconsistent with the data.

The general endothermic and entropy-driven nature of the bile salt sequestering process could be accounted for in terms of a direct interaction between the bile salt and resin

<sup>4</sup>The pendant binding areas of the resin are viewed as fluctuating among the many members within the assembly of states that exist at a given temperature. These states are arbitrarily divided here into two classes: the more extended members (state I) and the more contracted members (state II) that favour binding. A model involving pre-existing states in equilibrium is employed as compared with one in which the final state of the pendant binding area is induced by binding.



**Figure 7.** Molecular model for bile salt and competitive anion binding consistent with the observed thermodynamic parameters.



\* The counterion and competing ion could be the same species.

that was largely hydrophobic in character. However, such a model does not readily account for the nature of the perturbations introduced at higher buffer or sodium chloride concentrations. An essential element of the proposed model involves the local contraction of the binding area of the resin (state I  $\rightarrow$  II). It should be noted that this step, in association with large positive enthalpy and entropy contributions, occurs with both sodium chloride and buffer ion binding and with the anion of the bile salt. This feature accounts for the

endothermic binding of the competing inorganic anions with the hydrophobic cationic resin that would not be accounted for in a more direct hydrophobic bile salt – resin interaction.

The significance of hydration changes in the process follows not only from the recurring enthalpy–entropy compensation observed in this work. A major perturbation to the temperature dependence of the bile salt binding was observed when 8 M urea, a known solvent structure breaker, was added to 5 mM sodium cacodylate buffer solution. The



large positive entropy and enthalpy contributions that were observed without urea disappeared, and the process appears exothermic with a  $\Delta H^\circ$  of  $-3.4 \text{ kJ mol}^{-1}$  and a  $\Delta S^\circ$  of  $56.4 \text{ J mol}^{-1} \text{ K}^{-1}$ . This dramatic change in the thermodynamic parameters supports the model in which solvent plays a key role in the binding.

## Conclusions

The enhancement in the binding of sodium chenodeoxycholate by QPDA12 observed with increasing temperature was significantly reduced in the presence of elevated competing ion concentration. This was entirely due to the positive entropy manifested in the decrease in the slope of the van't Hoff plot. A competing model was used to describe the binding process and the decomposition of the observed binding constants produced positive values for  $\Delta H^\circ$  and  $\Delta S^\circ$  for binding both the competing ions ( $K_s$ ) and the bile salt ( $K_B$ ).

The dominant feature of the model involves equilibrium between an expanded (low energy, low entropy) state of the binding site in the resin and a more contracted (high energy, high entropy) state. In this picture the expanded, more hydrated state is favoured in the absence of bile salt or other anions. These anions, however, preferentially stabilize the contracted state, shifting the equilibrium. The loss of hydration accompanying this transition is primarily responsible for the endothermic and entropy-driven nature of the overall process.

## Acknowledgements

Financial support from the Natural Sciences and Engineering Research Council of Canada (NSERC) is gratefully acknowledged. Dr. G. Ronald Brown passed away during the

preparation of this manuscript. It is with many fond memories that we dedicate this article to him.

## References

1. S.S. Bergen, T.B. VanItallie, D.M. Tennen, and W.H. Sebrell. *Proc. Soc. Exp. Biol. Med.* **102**, 676 (1959).
2. N.A. Nelson and G.E. Vanderberg. U.S. Patent 3 692 895 (1972).
3. G. Wu, G.R. Brown, and L.E. St-Pierre. *Langmuir*, **12**, 466 (1996).
4. X.X. Zhu, G.R. Brown, and L.E. St-Pierre. *J. Pharm. Sci.* **81**, 65 (1992).
5. W.E. Baille, W.Q. Huang, M. Nichifor, and X.X. Zhu. *J. Macromol. Sci. Pure Appl. Chem.* **A37**, 677 (2000).
6. W.H. Johns and T.R. Bates. *J. Pharm. Sci.* **59**, 329 (1970).
7. S. Lindenbaum and T. Higuchi. *J. Pharm. Sci.* **64**, 1887 (1975).
8. X.X. Zhu, G.R. Brown, and L.E. St-Pierre. *J. Macromol. Sci. Pure Appl. Chem.* **A29**, 711 (1992).
9. W.H. Johns and T.R. Bates. *Pharm. Sci.* **58**, 179 (1969).
10. C.K. Williams, W.C. Galley, and G.R. Brown. *Can. J. Chem.* **80**, 89 (2002).
11. F. Scagnolari, A. Roda, A. Fini, and B. Grigolo. *Biochim. Biophys. Acta*, **791**, 274 (1984).
12. G. Wu and G.R. Brown. *React. Polym.* **14**, 49 (1991).
13. X.X. Zhu and G.R. Brown. *Anal. Lett.* **23**, 2011 (1990).
14. I. Langmuir. *J. Am. Chem. Soc.* **40**, 1361 (1918).
15. H. Naghibi, A. Tamura, and J.M. Sturdevant. *Proc. Natl. Acad. Sci. U.S.A.* **92**, 5597 (1995).
16. B.W. Sigurskjold and D.R. Bundle. *J. Biol. Chem.* **267**, 8371 (1992).
17. N.J. Faergeman, B.W. Sigurskjold, B.B. Kragelund, K.V. Andersen, and J. Knudsen. *Biochemistry*, **35**, 14 118 (1996).
18. J.R. Horn, D. Russell, E.A. Lewis, and K.P. Murphy. *Biochemistry*, **40**, 1774 (2001).
19. R.H. Fowler and E.A. Guggenheim. *Statistical thermodynamics*. Cambridge University Press, Cambridge, U.K. 1952.



# Chemical potential and concentration fluctuation in some aqueous alkane-mono-ols at 25°C

Jianhua Hu, Charles A. Haynes, Amy H.Y. Wu, Candy M.W. Cheung, Mark M. Chen, Eric G.M. Yee, Takehiko Ichioka, Keiko Nishikawa, Peter Westh, and Yoshikata Koga

**Abstract:** Vapour pressures of binary aqueous solutions of methanol, ethanol, 1-propanol, 2-propanol, 1-butanol, and 1-hexanol were measured at 25.00°C in small compositional increments over the entire compositional range. Without resorting to any fitting function, the partial pressures were calculated numerically by methods based on the Gibbs–Duhem relation. When the system had an azeotrope, near which the numerical methods caused large errors, a graphical readjustment was applied such that the concentration fluctuation,  $S_{XX}(0) = RT(1 - x_{AL})/(\partial\mu_{AL}^E/\partial x_{AL})$ , connected smoothly across the azeotrope. Values of  $S_{XX}(0)$  from scattering experiments were also used as a guide for the readjustment procedure. Hence, we report here chemical potential data free from any model or any fitting function.

**Key Words:** aqueous mono-ols, partial pressures by the Boissonnas method, concentration fluctuations.

**Résumé :** Opérant à 25.00°C sur toute la plage de compositions en procédant à de faibles incréments de composition, on a mesuré les tensions de vapeur de mélanges binaires aqueux de méthanol, d'éthanol, de propan-1-ol, de propan-2-ol, de butan-1-ol et d'hexan-1-ol. Sans faire appel à aucune fonction d'ajustement, on a pu calculer d'une façon numérique les tensions de vapeur partielles à l'aide de méthodes basées sur la relation de Gibbs–Duhem. Quand le système comporte un azéotrope près duquel les méthodes numériques peuvent provoquer de graves erreurs, on a appliqué un ajustement graphique de façon à ce que la fluctuation de la concentration  $S_{XX}(0) = RT(1 - x_{AL})/\partial\mu_{AL}^E/\partial x_{AL}$  puisse être arrimée pour tout l'azéotrope. Comme guide pour la méthode de réajustement, on a aussi utilisé des valeurs de  $S_{XX}(0)$  obtenues à partir d'expériences de diffusion. On rapporte donc ici des données de potentiel chimique qui ne sont pas liées à un modèle ou à une fonction d'ajustement.

**Mots clés :** monoalcools aqueux, tensions de vapeur partielles par la méthode de Boissonnas, fluctuations de concentration.

[Traduit par la Rédaction]

## Introduction

For the last decade or so, we have been studying aqueous solutions of alkane-mono-ols (abbreviated as AL hereinafter) by determining the following partial molar quantities: the excess chemical potential ( $\mu_{AL}^E$ ), the excess partial molar enthalpy ( $H_{AL}^E$ ), and the entropy ( $S_{AL}^E$ ) of alcohols. They were all determined accurately and in small increments, so that we were able to graphically take the derivatives with respect to the mole fraction without resorting to any fitting function. The resulting higher-order derivative quantities provided a model-free, experimentally accessible measure for intermolecular interactions. With the aid of these higher-

order derivative quantities, we have successfully advanced our understanding of the mixing schemes, or “structures”, of aqueous solutions (1–3).

Briefly, there are three distinct compositional regions; in each of these regions, the mixing scheme is qualitatively different from those in other regions. In the most water-rich region, “mixing scheme I” is operative, in which alcohol molecules enhance the hydrogen-bond network of H<sub>2</sub>O in their immediate vicinities — the so called “iceberg formation”. At the same time, the hydrogen bond probability of bulk H<sub>2</sub>O away from solute molecules is reduced. “Mixing scheme II”, operative in the intermediate region, is understood to consist of two kinds of clusters, each rich in H<sub>2</sub>O

Received 11 February 2002. Accepted 13 January 2003. Published on the NRC Research Press Web site at <http://canjchem.nrc.ca> on 20 February 2003.

**J. Hu and C.A. Haynes.** Biotechnology Laboratory, The University of British Columbia, 6174 University Boulevard, Vancouver, B.C. V6T 1Z3, Canada.

**A.H.Y. Wu, C.M.W. Cheung, M.M. Chen, E.G.M. Yee, and Y. Koga.**<sup>1</sup> Department of Chemistry, The University of British Columbia, 2036 Main Mall, Vancouver, B.C. V6T 1Z1, Canada.

**T. Ichioka, K. Nishikawa and Y. Koga.** Division of Diversity Science, Graduate School of Science and Technology, Chiba University, 1–33 Yayoi, Inage-ku, Chiba 263–8522, Japan.

**P. Westh.** Department of Chemistry, Roskilde University, Roskilde DK-4000, Denmark.

<sup>1</sup>Corresponding author (e-mail: [koga@chem.ubc.ca](mailto:koga@chem.ubc.ca)).



and in AL, respectively. In “mixing scheme III”, in the solute-rich region, the solute molecules cluster together and H<sub>2</sub>O interacts with the solute cluster as single H<sub>2</sub>O molecules, at least for aqueous 2-butoxyethanol (BE) (4, 5) and DMSO (6, 7).

For small alcohols (3), however, mixing scheme III may deviate from what is described for BE–H<sub>2</sub>O (5) and DMSO–H<sub>2</sub>O (6), above. The excess partial molar enthalpies of AL are not strictly zero, though very small in the AL-rich region (3). For BE–H<sub>2</sub>O (5) and DMSO–H<sub>2</sub>O (6), they are equal to zero and constant, which signifies a strictly constant value of the excess partial molar enthalpy of H<sub>2</sub>O,  $H_W^E$ , in the AL-rich region.

In continuation of our effort to advance the understanding of mixing schemes by determining model-free, higher-order derivative quantities, we wish to study the mixing schemes in the AL-rich region in detail for a series of aqueous monols. This compositional region is far less studied than water-rich systems, and its properties may have a bearing on water-stressed biopolymers and the effect of H<sub>2</sub>O molecules inside membranes (8) and protein conformations. This work is the first step, in which we determine the excess chemical potentials.

Table 1 lists the references for the excess partial molar quantity data (at 25°C) that we have determined so far. We use the following abbreviations: methanol (ME), ethanol (ET), 1-propanol (1P), 2-propanol (2P), 1-butanol (1B), 1-hexanol (1H), *tert*-butanol (TBA), and 2-*n*-butoxyethanol (BE). In this work we have determined the excess chemical potentials in aqueous ME, ET, 1P, 2P, 1B, and 1H over the entire concentration range.

### Data analysis

In a binary system consisting of AL and W (water), the chemical potentials are conveniently determined by measurement of the vapour pressure,  $p$ , in small increments of the mole fraction of AL,  $x_{AL}$ . From the  $(x_{AL}, p)$  data set, the partial pressures  $p_{AL}$  and  $p_W$  are calculated basically by two techniques. The commonly used method, which originated with Barker (17), is to assume a fitting function for the Gibbs energy,  $G$ , and curve-fit to the observed vapour pressure data. The second technique is to analyze the data purely numerically by using the Gibbs–Duhem relation, as per Boissonnas (18), or using the equivalent method by Lam and Benoit (19). With the resulting  $p_{AL}$  and  $p_W$  data, the excess chemical potential is then calculated as

$$[1] \quad \mu_i^E = RT \ln \{p_i / (p_i^* x_i)\},$$

where the subscript  $i = AL$  or  $W$ ,  $p_i^*$  is the vapour pressure of pure  $i$  at the same temperature, and  $x_i$  is the mole fraction of  $i$ . Strictly, eq. [1] should also contain the virial correction term owing to nonideality in the gas phase. However, for TBA–H<sub>2</sub>O (10) and BE–H<sub>2</sub>O (4), the value of the first term on the right of eq. [1] is orders of magnitude larger than the correction term on the left, and thus it was ignored. We assumed that the same situation prevails in other aqueous solutions, and ignored the virial correction.  $\mu_i^E$  reflects the degree of nonideality in solution, comprising both enthalpy and entropy effects. In aqueous solutions, however, the entropy–enthalpy compensation is prevalent, and the resulting

**Table 1.** Literature references for the partial molar quantities.

AL	$\mu_{AL}^E$	$\mu_W^E$	$H_{AL}^E$	$H_W^E$	$S_{AL}^E$	$S_W^E$
ME			3			
ET			3			
1P	14 <sup>a</sup>	14 <sup>a</sup>	3		14 <sup>a</sup>	
2P	15 <sup>b</sup>	15 <sup>b</sup>	3		15 <sup>b</sup>	
1B	9 <sup>c</sup>	9 <sup>c</sup>	9 <sup>c</sup>		9 <sup>c</sup>	
TBA	10	10	11, 12	13	10	10
1H	16 <sup>d</sup>					
BE	4	4	5	5	4	4

<sup>a</sup>In the water-rich region only,  $x_{1P} < 0.3$ .

<sup>b</sup> $x_{2P} < 0.2$ .

<sup>c</sup>Up to the two phase boundary,  $x_{1B} < 0.0018$ .

<sup>d</sup>Up to the two phase boundary,  $x_{1H} < 0.001$ .

value of excess chemical potential becomes rather small in comparison (20). Thus, in discussing molecular processes in solution, the excess partial molar enthalpy and entropy are together more useful than the resulting excess chemical potential alone, though the net effect is shown in the latter. A more sensitive indication of nonideality than excess chemical potential may be the osmotic coefficient,  $\phi$ , calculated as

$$[2] \quad \phi = 1 + (\mu_W^E / RT) / \ln(x_W).$$

Barker’s method (17) or its various modifications start off by assuming that an analytic function can be fitted to the excess Gibbs function over the entire compositional range. Since we did not wish to resort to any fitting function, we instead used the second numerical methods, as we have been doing for all the vapour pressure measurements (4, 9, 10, 14, 15). Briefly, the Boissonnas method makes use of the differential form of the Gibbs–Duhem or the Duhem–Margules relations, which are rearranged as

$$[3] \quad \Delta p_{AL} = k_{AL} \Delta p,$$

$$[4] \quad k_{AL} = 1 / \{1 - (p_W / p_{AL})(x_{AL} / x_W)\}$$

Thus, if the  $(x_{AL}, p_{AL}, p_W)$  data are known at a point, then the measured total pressure increment to the next point,  $\Delta p$ , may be converted to  $\Delta p_{AL}$  through eqs. [3] and [4]. To start the procedure, however, the first data point in the H<sub>2</sub>O-rich region was assumed to be in the Henry’s law region, and the vapour pressure of the major component,  $p_W$ , was calculated using Raoult’s law. The subsequent data points were then solved successively by eqs. [3] and [4].

This Boissonnas procedure could be initiated from the AL-rich end by interchanging the subscripts in eq. [3] and [4]. Both treatments are identical mathematically, but in practice it is preferential to start from the end that brings the absolute values of  $k_i$  ( $i = AL$  or  $W$ ) closer to unity.

The method by Lam and Benoit (19) uses the integral form of the Gibbs–Duhem relation,

$$[5] \quad \ln p_W = \ln p_W^0 - \int_{x_{AL}^0}^{x_{AL}} (x_{AL} / x_W) d(\ln p_{AL}),$$

where the superscript 0 stands for the data for the first, most dilute, solution, which is also assumed to be in the Henry’s law region. Equation [5] was used to improve the values of



$p_{\text{AL}}$  and  $p_{\text{W}}$ , which were initially estimated. The iteration was repeated until the resulting data converged.

As will become evident below, 1P–H<sub>2</sub>O and 2P–H<sub>2</sub>O systems possess a maximum in the  $p$  vs.  $x_{\text{AL}}$  plots, similarly to TBA–H<sub>2</sub>O (5), i.e.,  $\Delta p = 0$ . This is the azeotrope at which the gas phase composition is identical to that of the liquid phase. Hence, the absolute values of  $k_{\text{AL}}$  and  $k_{\text{W}}$  are infinite, and eq. [3] becomes indefinite. The integration method, eq. [5], also results in chaotic behaviour at this point. These problems can be resolved by applying the Boissonnas procedure from both ends, starting separately at the W-rich and the AL-rich sides, respectively, and working towards the azeotrope. This was done for TBA–H<sub>2</sub>O (10). The azeotrope occurred at  $x_{\text{TBA}} = 0.6$  at 25°C, and at data points close to the azeotrope the values of  $k_{\text{W}}$  and  $k_{\text{TBA}}$  were not infinity but were large:  $k_{\text{TBA}} = 4$  at  $x_{\text{TBA}} = 0.52$  and  $k_{\text{W}} = -6$  at  $x_{\text{TBA}} = 0.66$  (10). Barker's method was then used, in the range  $0.39 < x_{\text{TBA}} < 1$ , with only marginal success (10). In this work, to keep our principle of not resorting to any fitting function and to circumvent the difficulty associated with the azeotrope, we used data for the concentration fluctuation,

$$[6] \quad S_{\text{XX}}(0) = RT(1 - x_{\text{AL}})/(\partial\mu_{\text{AL}}/\partial x_{\text{AL}}),$$

determined by a scattering technique, to more correctly evaluate partial pressures near the azeotrope.

The determination of the concentration fluctuation in the liquid mixtures and the long-wavelength limit of the structure factor,  $S_{\text{XX}}(0)$  — and its relationship with the “structure” of aqueous solution — started with pioneering work by T. Fujiyama and co-workers (21–23). A more direct method of obtaining  $S_{\text{XX}}(0)$  is small angle X-ray scattering (SAXS), as has been used in previous studies of aqueous alcohols (24–29). The forward SAXS intensity is the sum of two terms, proportional to the  $S_{\text{XX}}(0)$  that we are interested in and the density fluctuation that can be calculated in a standard manner using isothermal compressibility data, respectively (24–29). Thus, as long as the latter data are available,  $S_{\text{XX}}(0)$  can be evaluated from the forward SAXS intensity. Usually, where the value of  $S_{\text{XX}}(0)$  is relatively large, its uncertainty is approximately equal to a few %, while the same data calculated as the right hand side of eq. [6] above could have a large uncertainty, since the slope of  $\mu_{\text{AL}}$  is small. Thus,  $S_{\text{XX}}(0)$  data from the SAXS measurement provides a rigorous test for  $\mu_{\text{AL}}^{\text{E}}$  data from vapour pressure measurements.

## Experimental

H<sub>2</sub>O was distilled three times (twice in a Pyrex glass immediately before use). Methanol (Aldrich, 99.9+% GLC), ethanol (Aldrich, H<sub>2</sub>O < 0.005%), 1-propanol (Aldrich, 99.5% HPLC), 2-propanol (Sigma–Aldrich, 99.5% by HPLC), 1-butanol (Sigma, ACS Reagent, 99.9%), and 1-hexanol (Aldrich, 98%) were handled in a dry nitrogen atmosphere.

Vapour pressures were determined by a static method. Details have been described elsewhere (4, 10). The total vapour

**Table 2.** Degree of nonideality in AL–H<sub>2</sub>O and the hydrophobic moiety of AL.

	$\mu_{\text{AL}}^{\text{E}}$ at $x_{\text{AL}} = 0$ (kJ mol <sup>−1</sup> )	$\mu_{\text{W}}^{\text{E}}$ at $x_{\text{AL}} = 1$ (kJ mol <sup>−1</sup> )	$\phi$ min.	$S_{\text{XX}}(0)$ max.
ME	1.2	1.2	0.72	0.37
ET	3.2	2.1	0.45	0.8
1P	6.4	3.4	0.20	3.2
2P	4.8	2.7	0.26	1.5
1B	10 <sup>a</sup>	4.2		
1H		4.0		
TBA	6.7 <sup>b</sup>	3.0 <sup>b</sup>		
BE	9.2 <sup>c</sup>	0.2 <sup>c</sup>		

**Note:** Order in AL: column I, ME < ET < 2P < 1P ≤ TBA < BE < 1B; column II, BE < ME < ET < 2P < TBA < 1P < 1H ≤ 1B; column III, ME < ET < 2P < 1P; column IV, ME < ET < 2P < 1P.

<sup>a</sup>Reference 9.

<sup>b</sup>Reference 10.

<sup>c</sup>Reference 4.

pressures were corrected for a temperature of 25.00°C by the Gibbs–Konovalov method (4, 10). The excess partial molar enthalpy data,  $H_{\text{AL}}^{\text{E}}$  and  $H_{\text{W}}^{\text{E}}$ , necessary for the correction, were taken either from references listed in Table 1 or from our unpublished data. The precision of the vapour pressures is estimated to be ±0.01 Torr (1 Torr = 101 325/760 Pa) or better. SAXS measurements for aqueous methanol were made at 25 ± 1°C using a Kratky camera. Details have been described elsewhere (24). The SAXS intensity curve was detected by a position sensitive proportional counter (PSPC), also described elsewhere (25).

## Results and discussion

Table II (ME), III (ET), IV (1P), V (2P), VI (1B), and VII (1H) have been deposited as supplemental material<sup>2</sup> and contain the total vapour pressure,  $p$ , of the six AL–H<sub>2</sub>O systems at 25.00°C. Figure 1 shows the plots of  $p$  against  $x_{\text{AL}}$ . Where available, the previously reported data, though not exhaustive, have also been plotted for comparison (see Fig. 1).

### Methanol(ME) – H<sub>2</sub>O and ethanol (ET) – H<sub>2</sub>O systems

The Boissonnas method was first applied from the H<sub>2</sub>O-rich end, for both the ME–H<sub>2</sub>O and ET–H<sub>2</sub>O data. The values of  $k_{\text{AL}}$  for both start at an ideal value of about 1.1. However,  $k_{\text{ME}}$  increases to about 1.5 at the ME-rich end for ME–H<sub>2</sub>O. For ET–H<sub>2</sub>O, on the other hand,  $k_{\text{ET}}$  increases gradually to 1.3 at  $x_{\text{ET}} = 0.28$  and rapidly to about 8 at  $x_{\text{ET}} = 0.8$ . Thereupon,  $k_{\text{ET}}$  values fluctuate wildly. This is due to the flatness of the  $p$  vs.  $x_{\text{ET}}$  curve in this range. We therefore used the integral form of the Gibbs–Duhem relation, eq. [6], for data analysis for both ET–H<sub>2</sub>O and ME–H<sub>2</sub>O. The resulting partial pressures are listed in Table II. The uncertainty in the resulting partial pressure is estimated to be ±0.03 Torr (1 Torr = 101 325/760 Pa) or better. The chemical potentials are calculated using eq. [1] and are listed in Table II and plotted in Figs. 2 and 3. The uncertainty is estimated to be

<sup>2</sup>Tables II, III, IV, V, VI, and VII have been deposited. Copies of the material on deposit may be purchased from the Depository of Unpublished Data, Document Delivery, CISTI, National Research Council Canada, Ottawa, ON, Canada K1A 0S2 ([http://nrc.ca/cisti/irm/unpub\\_e.shtml](http://nrc.ca/cisti/irm/unpub_e.shtml) for information on ordering electronically).



**Fig. 1.** (a) Vapour pressures of aqueous alcohols at 25°C over the entire compositional range. Filled symbols, this work. Hollow symbols, literature values; (b) vapour pressures of ME-H<sub>2</sub>O at 25°C in the dilute region; (c) vapour pressures of ET-H<sub>2</sub>O at 25°C in the dilute region; (d) vapour pressures of 2P-H<sub>2</sub>O at 25°C in the dilute region.

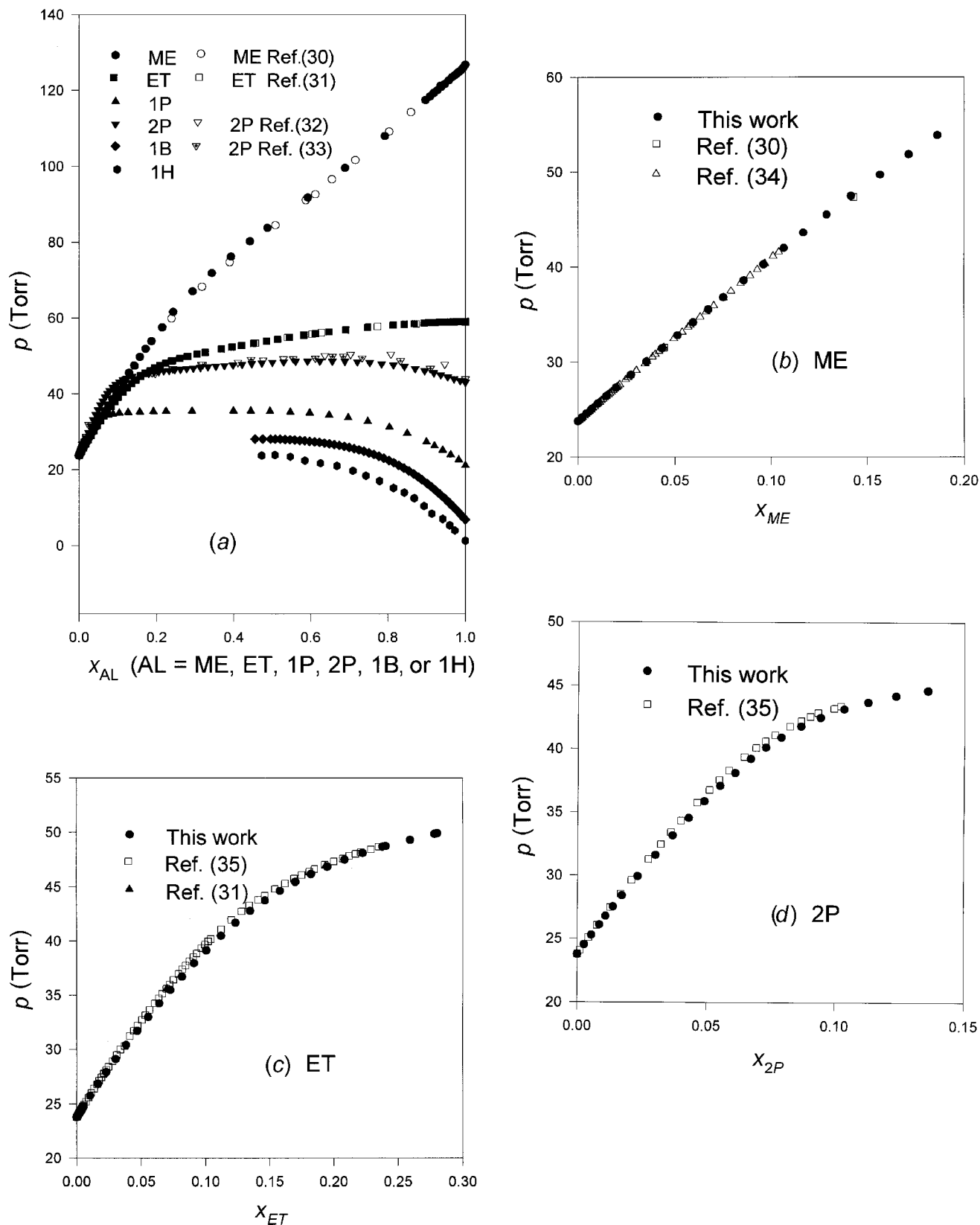
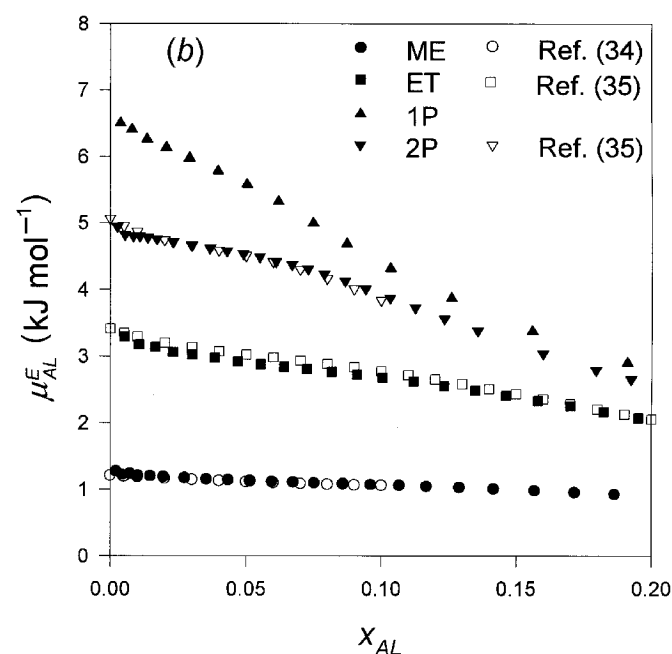
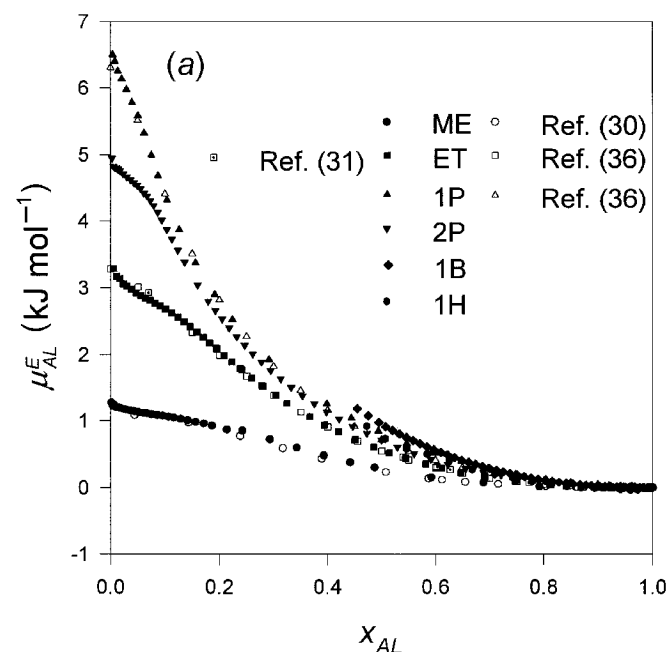


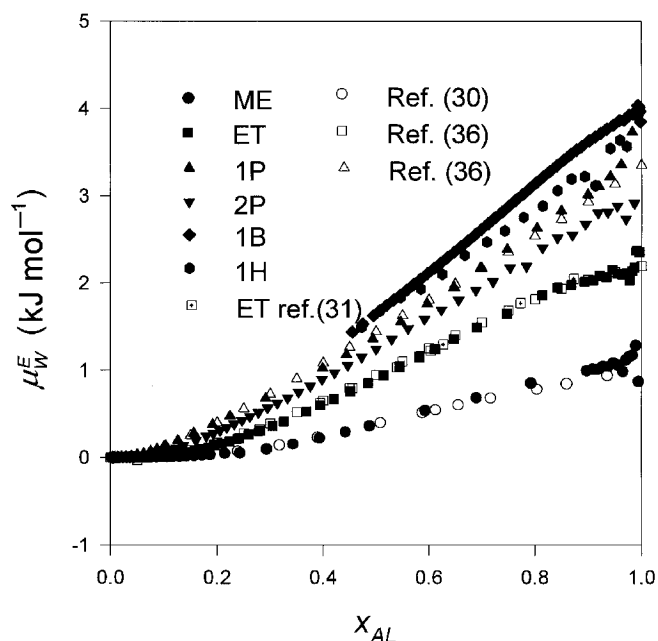


**Fig. 2.** (a) Excess chemical potentials of alcohols in aqueous solution at 25°C over the entire compositional range. Filled symbols, this work, without using a fitting function. Hollow symbols, literature data by curve fitting; (b) excess chemical potentials of alcohols in aqueous solutions at 25°C in the dilute region.



$\pm 0.05 \text{ kJ mol}^{-1}$ . The osmotic coefficients calculated using eq. [2] are plotted in Fig. 4. Figure 5 shows the concentration fluctuation, calculated using eq. [4], and  $S_{XX}(0)$ , as determined by SAXS. Since the scattering intensity for ME-H<sub>2</sub>O is low, the uncertainty in  $S_{XX}(0)$  is substantial, as shown in Fig. 5a. The literature vapour pressure data (30, 31, 34, 35) were analyzed using Barker's method. The following polynomial was assumed to represent the excess molar Gibbs energy,  $G_m^E$ , as,

**Fig. 3.** Excess chemical potentials of H<sub>2</sub>O in aqueous alcohols at 25°C.



$$[7] \quad G_m^E = x_{AL}(1 - x_{AL}) \sum g_n (1 - x_{AL})^n,$$

where  $g_n$  are the adjustable parameters. For ME-H<sub>2</sub>O in the limited H<sub>2</sub>O-rich region (34), the first three terms were used. For the entire compositional range, Fenby and co-workers used four terms for ME-H<sub>2</sub>O (30) and five for ET-H<sub>2</sub>O (31). The resulting data are also plotted in Figs. 2, 3, and 4a. As is evident from Figs. 1, 2, 3, 4a, and 4b, an almost negligible deviation in the  $p$ -data (Fig. 1) leads to a small but still negligible difference from our numerical results for the chemical potentials (Figs. 2 and 3). Some curve-fitting imperfections, however, appear more conspicuous in  $\phi$  (Fig. 4a). In particular, the  $x_{ME}$ -dependence of  $\phi$  with a three-term polynomial, as discussed by Christian et al. (34), shows an upwards trend of concavity, towards the upper data limit of the mole fraction. This may be a result of the cut-off effect of the fitted polynomial. Indeed, the authors themselves later cautioned against blindly curve fitting using polynomials (37). Figure 4a shows a small but systematic deviation in  $\phi$  between our numerical analysis and a four-term curve fitting (31). This may suggest that the number of terms should be increased.

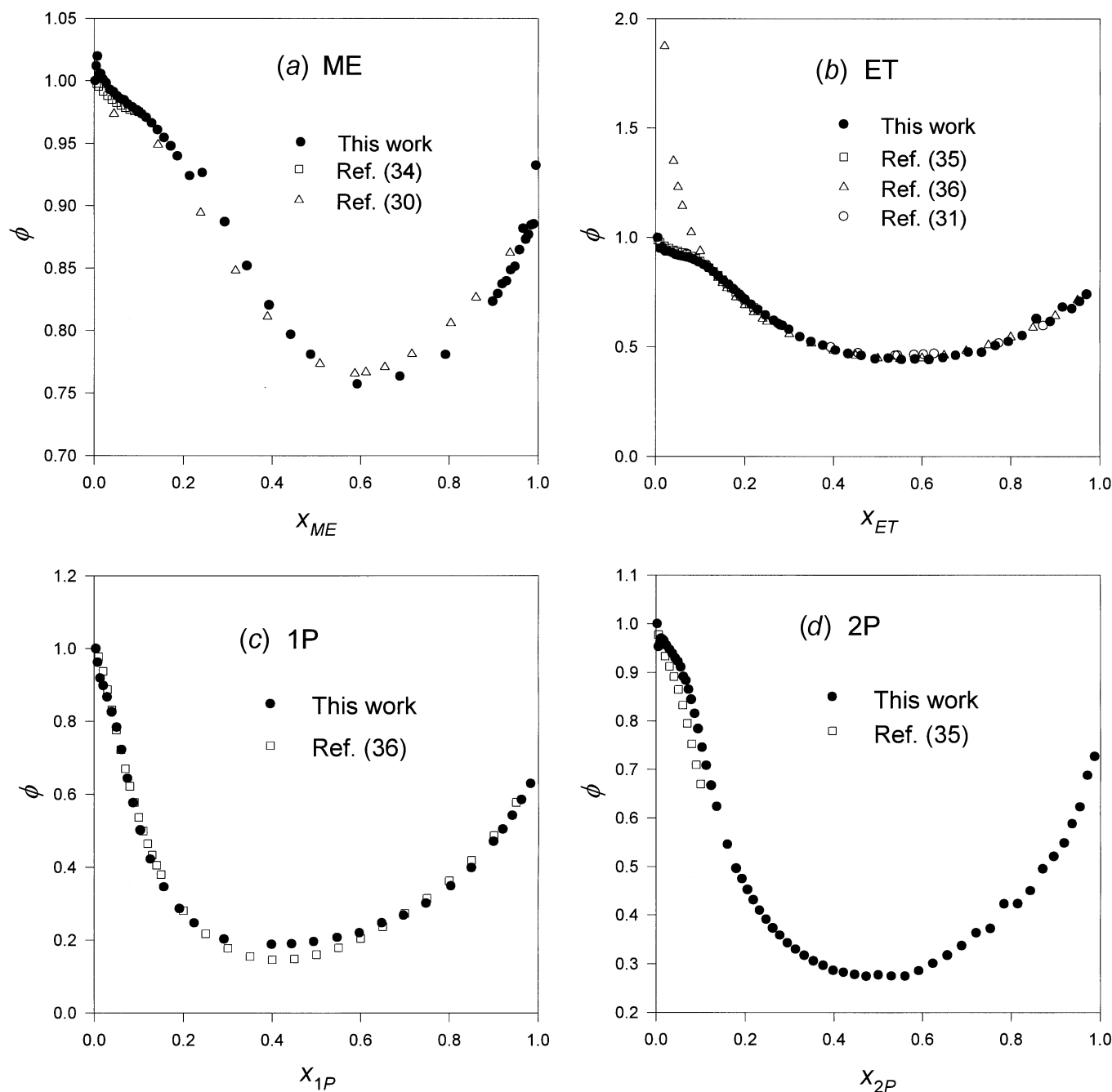
Hansen and Miller (36) determined the gas phase compositions for about 10 data points by analysis and, hence, determined the partial pressures directly for ET-H<sub>2</sub>O and 1P-H<sub>2</sub>O, at 25°C, over the entire compositional range. Unfortunately, these partial pressure data were not published. However, they fitted the following function relating to the excess chemical potential of ET,  $\mu_{ET}^E/RT$ ,

$$[8] \quad \mu_{ET}^E/RT = (1 - x_{ET})^2 \{A + Bx_{ET} + C \exp(-Dx_{ET})\}$$

and the consistent equation for  $\mu_W^E/RT$ . The resulting plots are shown in Figs. 2a, 3, and 4b. It is evident that eq. [8] is not satisfactory in the range  $x_{ET} < 0.2$  in terms of  $\phi$  (see Fig. 4b), while such an imperfection is not conspicuous in



**Fig. 4.** (a) Osmotic coefficient of ME-H<sub>2</sub>O at 25°C. Filled symbols, this work, numerically calculated. Hollow symbols, literature data by curve fitting; (b) osmotic coefficient of ET-H<sub>2</sub>O at 25°C; (c) osmotic coefficient of 1P-H<sub>2</sub>O at 25°C; (d) osmotic coefficient of 2P-H<sub>2</sub>O at 25°C.



$\mu_{ET}^E$  or  $\mu_W^E$  (see Figs. 2a and 3). The six-term polynomial, eq. [7], used by Nord et al. (35) and the five-term polynomial used by Phutela et al. (31) appear to be reasonable even for  $\phi$  (see Fig. 4b). The general smoothness of  $S_{XX}(0)$  calculated from our chemical potential data suggests that the raw data and the subsequent data analysis are reasonable.

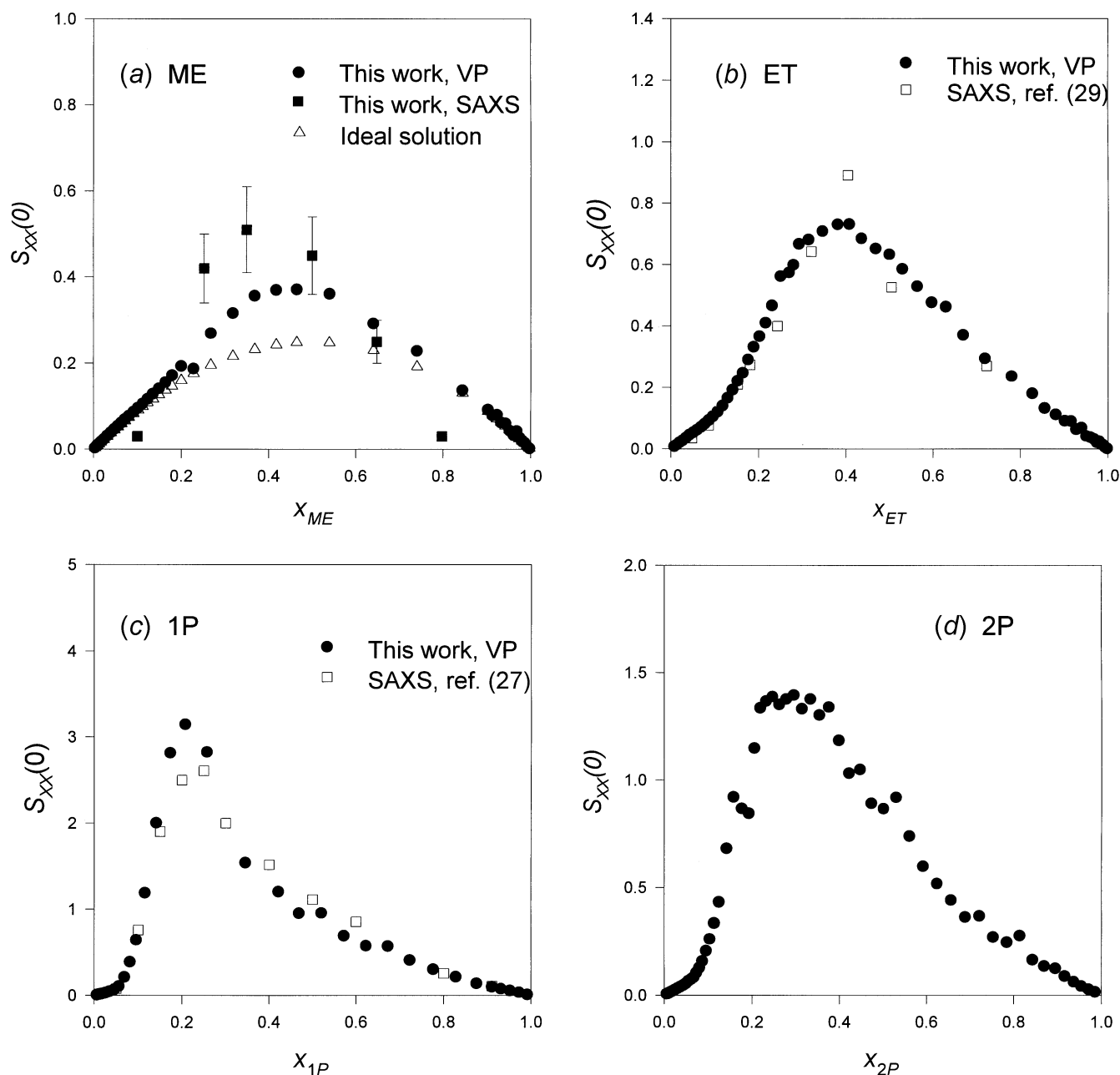
#### 1-Propanol (1P) – H<sub>2</sub>O system

The  $p$  vs.  $x_{1P}$  curve, Fig. 1, shows a rather flat plateau, and the position of the azeotrope is not immediately obvious. In

a review of azeotropic data (38), the azeotropic composition at 25°C is quoted as  $x_{1P} = 0.3770$ . The original data (39) consist of partial pressures determined by the transpiration method at the following compositions: 0.01, 0.02, 0.05, 0.1, 0.2, 0.4, 0.6, 0.8, 0.9, 0.95, and 1. Thus, the azeotropic data quoted above is not measured but is estimated using these rather widely-spaced data points. Here we present closely-spaced data points (Table IV), which indicate that the maximum in  $p$  appears to be at about  $x_{1P} = 0.3987$ . We determined the actual value to be 0.390 as described below. The



**Fig. 5.** (a) Concentration fluctuation in ME-H<sub>2</sub>O at 25°C, calculated using vapour pressure (VP) and SAXS data; (b) concentration fluctuation in ET-H<sub>2</sub>O at 25°C, calculated using vapour pressure (VP) and SAXS data; (c) concentration fluctuation in 1P-H<sub>2</sub>O at 25°C, calculated using vapour pressure (VP) and SAXS data; (d) concentration fluctuation in 2P-H<sub>2</sub>O at 25°C, calculated using vapour pressure (VP) data.

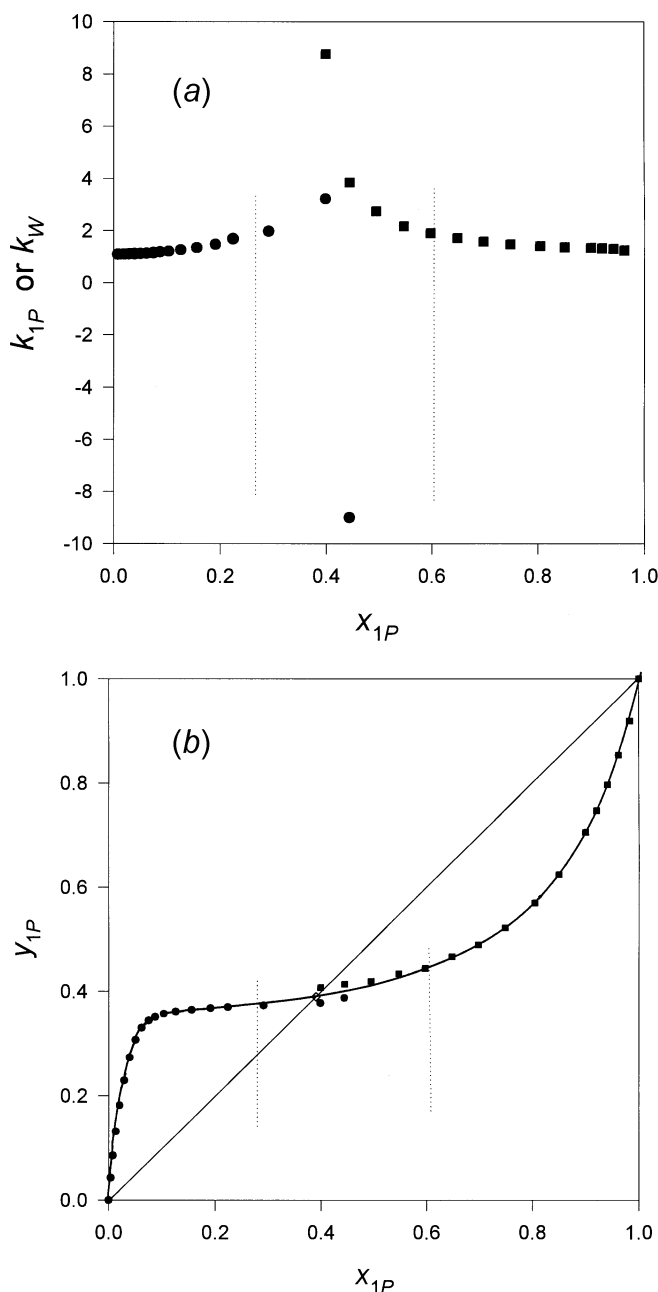


Boissonnas method was applied from both ends. The values of  $k_{1P}$  and  $k_W$  are plotted in Fig. 6a. In the range  $0.3 < x_{1P} < 0.6$ , near the azeotrope,  $k_{1P}$  and  $k_W$  are significantly larger than unity, and the resulting partial pressures would have some systematic errors. Figure 6b shows the plots of the gas-phase mole fraction,  $y_{1P} = p_{1P}/p$ , against  $x_{1P}$ . The data points in Fig. 6b are reliable except for the above region near the azeotrope. By the aid of a flexible ruler, the reliable

portion of the data points were connected smoothly, as shown in the figure. The values of  $y_{1P}$  were read off the smooth, drawn curve and the values of  $p_{1P}$  were recalculated accordingly. The resulting data are listed in Table IV and plotted in Figs. 2, 3, 4c, and 5c. Comparison with  $S_{XX}(0)$  data from the SAXS measurement (27) indicates that our re-adjusted  $y_{1P}$  data are acceptable. The uncertainty in this re-adjusted region is estimated to be, at most, twice that of the



**Fig. 6.** (a) Boissonnas coefficients,  $k_{1P}$  and  $k_W$ , for 1P–H<sub>2</sub>O. See eq. [4] and text; (b) graphical method of solving partial pressure near azeotrope. See text.



normal uncertainty. From the point of intersection of the smooth curve drawn with the line of  $y_{1P} = x_{1P}$  in Fig. 6b, we conclude that the azeotrope of 1P–H<sub>2</sub>O at 25°C is at  $x_{1P} = 0.390 \pm 0.005$ . It is evident that the fitting function devised by Hansen and Miller (36),

$$[9] \quad \mu_{1P}^E/RT = (1 - x_{1P})^2 \{Ax_{1P} + B \exp(-Cx_{1P}) + Dx_{1P} \exp(-Ex_{1P})\},$$

seems reasonable even for  $\phi$  (Fig. 4c).

## 2-Propanol (2P) – H<sub>2</sub>O system

For 2P–H<sub>2</sub>O, the analysis was identical to that for 1P–H<sub>2</sub>O above. The azeotrope was found to be at  $x_{2P} = 0.640 \pm 0.005$ . An azeotropic data collection (38) gave  $x_{2P} = 0.6650$ , and 0.6700 for the azeotropic mole fraction. Both were estimated using data obtained by a dynamic method (33, 40). A dynamic method, while the partial pressures are determined directly, may be less advantageous for locating an azeotrope than the static method we have used here. Furthermore, we have two to three times more data points. The graphical re-adjustment was made in the region  $0.58 < x_{2P} < 0.69$ . Figure 5d shows the plots of  $S_{XX}(0)$ , and we conclude the connection around the azeotrope,  $x_{2P} = 0.640$ , is acceptably smooth. It is unfortunate that there are no compressibility data for 2P–H<sub>2</sub>O in the literature and, hence,  $S_{XX}(0)$  data cannot be calculated, although the zero-angle SAXS data are available (27). Small discrepancies (Fig. 1d) between Nord et al.'s  $p$ -data (35) and ours are not conspicuous in the chemical potentials (see Figs. 2b and 3), while the  $\phi$  data show clear differences (see Fig. 4d).

Both 1B–H<sub>2</sub>O and 1H–H<sub>2</sub>O systems were analyzed from the AL-rich end to the respective phase separation boundary,  $x_{1B} = 0.50$  and  $x_{1H} = 0.54$ . For both cases, the values of  $k_W$  were found to be from 1.0 to 1.3. The resulting data can be found in the respective tables and plotted in Figs. 2 and 3.

Thus, we have devised a way of circumventing the difficulty associated with the azeotrope when obtaining partial pressures by numerical methods, and we present here the model-free partial pressures data, obtained without resorting to any fitting function for aqueous mono-ols. We point out that various curve fitting attempts in the literature have had mixed success, as shown above, and there is no guarantee that a chosen function can account for the data over the entire compositional range. Instead, we have used a purely numerical method, circumventing the difficulties associated with azeotropes. These partial pressure data, except for the first few points at the dilute end, are correct and model-free. Thus, we now have various indications of nonideality of AL–H<sub>2</sub>O systems in terms of chemical potentials (first derivatives of  $G$ ), osmotic coefficients (calculated using  $\mu_W^E$ ), and concentration fluctuations (second derivative of  $G$ ). The fact that  $\mu_{AL}^E$  and  $\mu_W^E$  stay positive and, hence,  $\phi$  is less than 1 indicates that AL–H<sub>2</sub>O is an unfavorable mixture and tends to separate. Indeed, the fact that the concentration fluctuation,  $S_{XX}(0)$ , is positive and shows a maximum is a reflection of this tendency. In the event that  $S_{XX}(0)$  becomes infinity, phase separation occurs. The positive values of  $\mu_{AL}^E$  or  $\mu_W^E$  seem generally to increase in the order of increasing size of the hydrophobic moiety (Figs. 2 and 3). This suggests that the predominant effect of AL on solution properties arises from its hydrophobicity, at least for the alcohols studied here. Table 2 summarizes this evidence. With the additional data relating to TBA (10) and BE (4) in Table 2, the order of the effect of AL on H<sub>2</sub>O (and particularly the effect of H<sub>2</sub>O on AL) cannot be rationalized simply with respect to the hydrophobicity of AL (see column ranking in Table 2). As mentioned in the discussion of the data analysis, although the chemical potentials show the net effect, the detailed molecular mechanism is not very apparent in their behaviour, owing to entropy–enthalpy compensation, prevalent particularly in aqueous solutions (20). Thus, an elucidation of these



details requires further data of partial molar enthalpies and entropies and perhaps even higher order derivatives of  $G$ .

In a subsequent paper, we will calculate the excess partial molar entropy of AL,  $S_{AL}^E$ , using the present  $\mu_{AL}^E$  data and previously-determined  $H_{AL}^E$  data (3). By the aid of  $S_{AL}^E$  data, we will make an attempt at confirming or adding to the mixing schemes mentioned above in the Introduction section, particularly for the W-rich region. In the W-rich region, the absolute values of  $H_{AL}^E$  and  $S_{AL}^E$  are much larger and their changes are much sharper than in the AL-rich region, where they are small, almost zero. Hence, to study the mixing schemes operating in the AL-rich region in more detail, it is advantageous to determine  $H_W^E$  and  $S_W^E$  data and learn from their compositional dependence. We have just started determining the excess partial molar enthalpies of  $H_2O$ ,  $H_W^E$ , in the AL-rich regions of aqueous mono-ols. In the event of the completion of these determinations, we can then calculate the excess partial molar entropies of  $H_2O$ ,  $S_W^E$ . These, together with other second derivative quantities, excess partial molar volumes, heat capacities, compressibilities, and thermal expansivities, we plan to study the details of for mixing schemes in the AL-rich region.

## Acknowledgments

This work was supported by the Natural Sciences and Engineering Research Council of Canada (NSERC) and the Ministry of Education, Science, and Culture of Japan. The guest professorship awarded to YK at Chiba University was supported by the project, "Strategic Foundation of Centers of Excellence in Education and Research" at the Ministry of Education and Science. YK thanks Professor Nishikawa and her group members for their hospitality during his stay at Chiba University.

## References

1. Y. Koga. *J. Phys. Chem.* **100**, 5172 (1996).
2. Y. Koga. *J. Crystallogr. Soc. Jpn.* **37**, 172 (1995).
3. S.H. Tanaka, H.I. Yoshihara, A.W.-C. Ho, F.W. Lau, P. Westh, and Y. Koga. *Can. J. Chem.* **74**, 713 (1996).
4. Y. Koga. *J. Phys. Chem.* **95**, 4119 (1991).
5. W. Siu and Y. Koga. *Can. J. Chem.* **67**, 671 (1989).
6. J.T.W. Lai, F.W. Lau, D. Robb, P. Westh, G. Nielsen, C. Trandum, A. Hvidt, and Y. Koga. *J. Solution Chem.* **24**, 89 (1995).
7. Y. Koga, Y. Kasahara, K. Yoshino, and K. Nishikawa. *J. Solution Chem.* **30**, 885 (2001).
8. H. Binder, B. Kohlstrunk, and H.H. Heerklotz. *Chem. Phys. Lett.* **304**, 329 (1999).
9. K. Tamura, J. Hu, Ch. Trandum, P. Westh, C.A. Haynes, and Y. Koga. *Phys. Chem. Chem. Phys.* **2**, 355 (2000).
10. Y. Koga, W.W.Y. Siu, and T.Y.H. Wong. *J. Phys. Chem.* **94**, 7700 (1990).
11. Y. Koga. *Can. J. Chem.* **64**, 204 (1986).
12. Y. Koga. *Can. J. Chem.* **66**, 1187 (1988).
13. Y. Koga. *Can. J. Chem.* **66**, 3171 (1988).
14. E.C.H. To, J. Hu, C.A. Haynes, and Y. Koga. *J. Phys. Chem.* **B102**, 10 958 (1998).
15. J. Hu, W.M.-D. Chiang, P. Westh, D.H.C. Chen, C.A. Haynes, and Y. Koga. *Bull. Chem. Soc. Jpn.* **74**, 809 (2001).
16. P. Westh, C. Trandum, and Y. Koga. *Biophys. Chem.* **89**, 53 (2001).
17. J.A. Barker. *Aust. J. Chem.* **6**, 207 (1953).
18. C.G. Boissonnas. *Helv. Chim. Acta*, **22**, 541 (1939).
19. S.Y. Lam and R.L. Benoit. *Can. J. Chem.* **52**, 718 (1974).
20. R. Lumry and S. Rajender. *Biopolymers*, **9**, 1125 (1970).
21. K. Iwasaki, Y. Katayanagi, and T. Fujiyama. *Bull. Chem. Soc. Jpn.* **49**, 2988 (1976).
22. T. Kato and T. Fujiyama. *J. Phys. Chem.* **80**, 2771 (1976).
23. K. Iwasaki and T. Fujiyama. *J. Phys. Chem.* **81**, 1908 (1977).
24. Y. Koga. *Chem. Phys. Lett.* **111**, 176 (1984).
25. K. Nishikawa, Y. Kodera, and T. Iijima. *J. Phys. Chem.* **91**, 3694 (1987).
26. K. Nishikawa, H. Hayashi, and T. Iijima. *J. Phys. Chem.* **93**, 6559 (1989).
27. H. Hayashi, K. Nishikawa, and T. Iijima. *J. Phys. Chem.* **94**, 8334 (1990).
28. H. Hayashi and Y. Udagawa. *Bull. Chem. Soc. Jpn.* **65**, 155 (1992).
29. K. Nishikawa and T. Iijima. *J. Phys. Chem.* **97**, 10 824 (1993).
30. Z.S. Kover, R.C. Phutela, and D.V. Fenby. *Aust. J. Chem.* **33**, 9 (1980).
31. R.C. Phutela, Z.S. Kooner, and D.V. Fenby. *Aust. J. Chem.* **32**, 2353 (1979).
32. H.D. Crockford, W. Bailey and J.E. Land. *J. Ala. Acad. Sci.* **21**, 12 (1952).
33. V.P. Sazonov. *Zh. Prikl. Khim.* **59**, 1451 (1986).
34. S.D. Christian, E.H. Lane, and E.E. Tucker. *J. Solution Chem.* **10**, 181 (1981).
35. L. Nord, E.E. Tucker, and S.D. Christian. *J. Solution Chem.* **13**, 849 (1984).
36. R.S. Hansen and F. A. Miller. *J. Phys. Chem.* **58**, 193 (1954).
37. S.D. Christian, E.E. Tucker and L. Nord. *J. Solution Chem.* **13**, 869 (1984).
38. J. Gmehling, J. Menke, K. Fischer, and J. Krafczyk. *Azeotropic data*. VCH, Weinheim. 1994.
39. J.A.V. Butler, D.W. Thomson, and W.H. MacLennan. *J. Chem. Soc.* 674 (1933).
40. J.E. Schumacher and H. Hunt. *Ind. Eng. Chem.* **34**, 201 (1942).



# Excess partial molar entropy of alkane-mono-ols in aqueous solutions at 25°C

Yoshikata Koga, Peter Westh, and Keiko Nishikawa

**Abstract:** In the preceding paper, we reported the values of model-free chemical potentials for aqueous methanol, ethanol, 1-propanol, 2-propanol, 1-butanol, and 1-hexanol at 25°C over the entire compositional region. Using alcohol excess partial molar enthalpies,  $H_{AL}^E$ , determined earlier in this laboratory (Can. J. Chem. **74**, 713 (1996)), we have calculated excess partial molar entropies for the alcohols,  $S_{AL}^E$ , where AL stands for an alcohol. We then calculated, numerically, the entropic interaction,  $S_{AL-AL}^E = N(\partial S_{AL}^E / \partial n_{AL})_{p,T,n_W}$ , where  $n_{AL}$  is the amount of AL,  $n_W$  is the amount of H<sub>2</sub>O, and  $N$  is the total amount of solution.  $S_{AL-AL}^E$  signifies the effect of addition of AL upon the entropic situation of existing AL in solution. Using these quantities, the mixing schemes in aqueous alcohols have been studied. The earlier conclusions, which used  $H_{AL}^E$  and  $H_{AL-AL}^E$  alone, are confirmed. Furthermore, the order of the relative hydrophobic nature of alcohols is established from the behaviour of  $S_{AL-AL}^E$  and of  $H_{AL-AL}^E$  as methanol < ethanol < 2-propanol < 1-propanol.

**Key Words:** aqueous alcohols, excess partial molar entropies, entropic interaction mixing schemes, hydrophobicity ranking.

**Résumé :** Dans le travail précédent, on a rapporté des valeurs de potentiels chimiques qui ne dépendent d'aucun modèle pour des mélanges binaires aqueux de méthanol, d'éthanol, de propan-1-ol, de propan-2-ol, de butan-1-ol et d'hexan-1-ol, à 25°C, sur l'ensemble des plages de composition. Utilisant les enthalpies molaires partielles en excès de l'alcool,  $H_{AL}^E$ , déterminées antérieurement (Can. J. Chem. **74**, 713 (1996)) dans ce laboratoire, on a calculé les entropies molaires partielles en excès des alcools,  $S_{AL}^E$ , où AL représente un alcool. On a par la suite calculé d'une façon numérique l'interaction entropique  $S_{AL-AL}^E = N(\partial S_{AL}^E / \partial n_{AL})_{p,T,n_W}$  où  $n_{AL}$  = quantité d'alcool,  $n_W$  = quantité d'eau et  $N$  = quantité totale de solution. La valeur de  $S_{AL-AL}^E$  définie plus haut correspond à l'effet d'une addition d'alcool sur la situation entropique réelle d'alcool existant en solution. Utilisant ces quantités, on a étudié les schémas de mélange dans alcools en solutions aqueuses. Les conclusions auxquelles on était arrivé antérieurement en se basant uniquement sur des valeurs de  $H_{AL}^E$  et  $H_{AL-AL}^E$  sont confirmées. De plus, sur la base des valeurs de  $S_{AL-AL}^E$  et de  $H_{AL-AL}^E$ , on a établi que l'ordre de l'hydrophobicité relative des alcools est méthanol < éthanol < propan-2-ol < propan-1-ol.

**Mots clés :** alcools en solutions aqueuses, entropies molaires partielles en excès, entropie d'interaction, schémas de mélange, valeurs relatives d'hydrophobicité.

[Traduit par la Rédaction]

## Introduction

In the preceding paper (1), called paper I hereinafter, we have reported the excess chemical potentials of alcohols (abbreviated as AL),  $\mu_{AL}^E$ , and those of water,  $\mu_W^E$ , for aqueous solutions at 25°C. They were calculated from total vapour pressure data without resorting to any fitting function. In another earlier paper (2), called paper II, we directly deter-

mined alcohol excess partial molar enthalpies,  $H_{AL}^E$ , at 25°C. Thus, we can now calculate model-free alcohol excess partial molar entropies,  $S_{AL}^E$ , purely experimentally.  $H_{AL}^E$  and  $S_{AL}^E$  are the second derivatives of  $G$ .  $S_{AL}^E$ , for example, is

$$[1] \quad S_{AL}^E = (\partial S^E / \partial n_{AL}) = -\{\partial^2 G / (\partial T \partial n_{AL})\},$$

where  $n_{AL}$  is the number of moles of AL in the aqueous solution. In this paper, partial differentiation is understood as being performed by keeping other variables constant. Equation [1] implies that  $S_{AL}^E$  is the response of the entire system in terms of excess entropy when  $n_{AL}$  alone is perturbed. Hence, it signifies the actual contribution of alcohol towards  $S^E$  of the system or the actual entropic situation of AL in the solution. If we have accurate  $S_{AL}^E$  data in small increments in composition, as is the present case, then the following derivative can be calculated to within an uncertainty of several %:

$$[2] \quad S_{AL-AL}^E \equiv N(\partial S_{AL}^E / \partial n_{AL}) \\ = (1 - x_{AL}) (\partial S_{AL}^E / \partial x_{AL}),$$

Received 11 July 2002. Accepted 13 January 2003. Published on the NRC Research Press Web site at <http://canjchem.nrc.ca> on 20 February 2003.

**Y. Koga.**<sup>1</sup> Department of Chemistry, The University of British Columbia, 2036 Main Mall, Vancouver, BC V6T 1Z1, Canada.

**P. Westh.** Department of Chemistry, Roskilde University, Roskilde DK-4000, Denmark.

**K. Nishikawa.** Division of Diversity Sciences, Graduate School of Science and Technology, Chiba University, 1-33 Yayoi, Inage-ku, Chiba 263-8522, Japan.

<sup>1</sup>Corresponding author (e-mail: [koga@chem.ubc.ca](mailto:koga@chem.ubc.ca))



where  $x_{\text{AL}}$  is the mole fraction of AL and  $N$  is the total number of moles of the solution. The last derivative of eq. [2] is, in practice, calculated as  $(\delta S_{\text{AL}}^{\text{E}}/\delta x_{\text{AL}})$ , where  $\delta$  represents the difference in the values of two data points taken from the smooth curve drawn through all the data points by the aid of a flexible ruler. The issue of an appropriate size of  $\delta x_{\text{AL}}$  was dealt with earlier in detail (3) and led us to choose  $\delta x_{\text{AL}} = 0.01$  for this paper. The physical meaning of  $S_{\text{AL-AL}}^{\text{E}}$ , eq. [2], is the effect of the addition of an infinitesimal amount of AL on the actual entropic situation of alcohol in the solution. Thus, we define  $S_{\text{AL-AL}}^{\text{E}}$  as the entropic interaction between AL molecules in the system (4, 5). In paper II (2), the enthalpy analogs of eqs. [1] and [2],  $H_{\text{AL}}^{\text{E}}$  and  $H_{\text{AL-AL}}^{\text{E}}$ , were used to study the mixing schemes in aqueous alcohol solutions, and some findings were briefly summarized in the Introduction of paper I (1). In this paper, we add information provided by the  $x_{\text{AL}}$ -dependences of  $S_{\text{AL}}^{\text{E}}$  and  $S_{\text{AL-AL}}^{\text{E}}$  and examine if any additional or clearer pictures emerge from them. We direct our attention mainly to methanol (ME), ethanol (ET), 1-propanol (1P), and 2-propanol (2P).

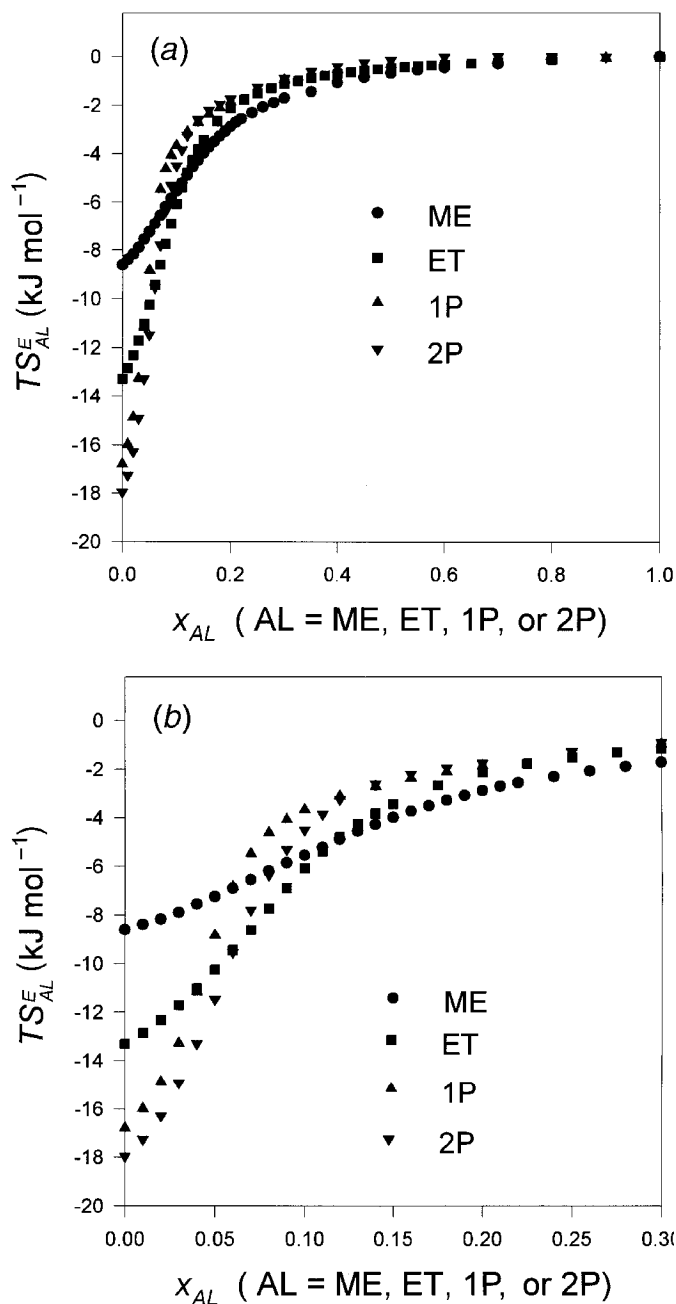
## Results and discussion

Table I, deposited at CISTI,<sup>2</sup> lists smoothed values of  $\mu_{\text{AL}}^{\text{E}}$  from paper I (1) and  $H_{\text{AL}}^{\text{E}}$  values from paper II (2) for AL = ME, ET, 1P, or 2P, from which  $TS_{\text{AL}}^{\text{E}}$  were calculated and also listed in Table I. Figure 1 shows the plots of  $TS_{\text{AL}}^{\text{E}}$  thus calculated. As for  $H_{\text{AL}}^{\text{E}}$ , the plots of  $TS_{\text{AL}}^{\text{E}}$  exhibit a sharp  $x_{\text{AL}}$ -dependence in the H<sub>2</sub>O-rich region. In the AL-rich region, on the other hand,  $TS_{\text{AL}}^{\text{E}}$  is almost zero and almost independent of composition. This immediately suggests that there are at least two compositional regions, in each of which the thermodynamic behaviour and, hence, the mixing scheme are different. Whether there is an intermediate region, as for 2-butoxyethanol (BE)–H<sub>2</sub>O (4–8), is not so obvious from  $H_{\text{AL}}^{\text{E}}$  and  $S_{\text{AL}}^{\text{E}}$  data alone. The existence of the intermediate region for other AL–H<sub>2</sub>O systems becomes evident when we calculate  $S_{\text{AL-AL}}^{\text{E}}$  data, as shown below.

In the alcohol-rich region, the fact that the values of  $S_{\text{AL}}^{\text{E}}$  and  $H_{\text{AL}}^{\text{E}}$  (2) are almost zero suggests that the thermodynamic situation of the alcohol in solution is very close to that of the pure alcohol. It is likely that alcohol molecules cluster together in almost the same manner as in the pure state. This is consistent with structural studies conducted using neutron scattering (9–11). Dixit et al. (9) claim that cluster formation occurs over the entire compositional range and, hence, cast doubt on the classical picture of “iceberg formation”. Their detailed neutron-scattering study was performed at the ME-rich region, at  $x_{\text{ME}} = 0.7$ . As shown below, this composition falls in the region of mixing scheme III. We stress that Fig. 1 and the  $H_{\text{AL}}^{\text{E}}$  data in paper II (2) indicate that the mixing scheme operating in the H<sub>2</sub>O-rich region, mixing scheme I, must be qualitatively different from that of the alcohol-rich region.

Table 1 lists the values of  $TS_{\text{AL}}^{\text{E}}$  at infinite dilution together with the values of  $H_{\text{AL}}^{\text{E}}$  from paper II (2). Thus, an alcohol molecule breaks away from its pure state and is dissolved into pure H<sub>2</sub>O with a large enthalpy gain (–7 to

**Fig. 1.** Excess partial molar entropy of the alcohol multiplied by the temperature at 25°C ( $TS_{\text{AL}}^{\text{E}}$ ).



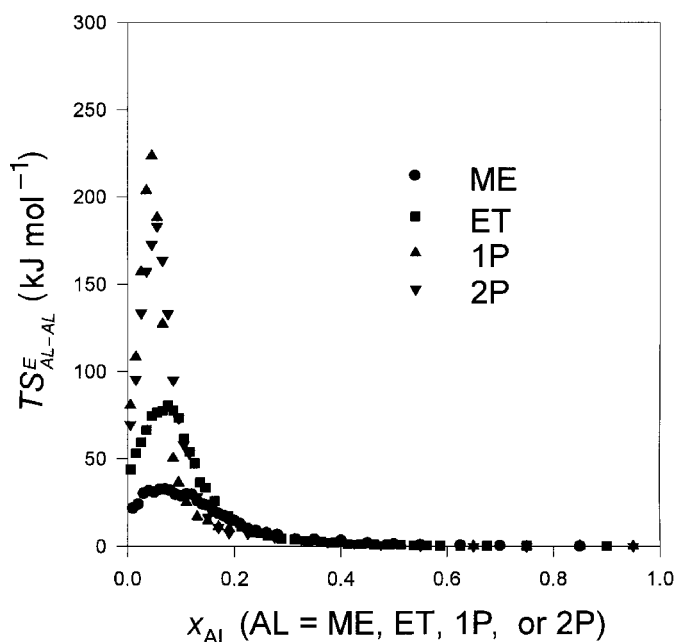
–17 kJ mol<sup>–1</sup>) and a larger entropy loss (–9 to –26 kJ mol<sup>–1</sup>). This is consistent with the enhancement of the hydrogen bond network of H<sub>2</sub>O in the vicinity of solute molecules, i.e., “iceberg formation”. Figure 1 also indicates that in the H<sub>2</sub>O-rich region, the sharpness of the  $x_{\text{AL}}$ -dependence seems to increase roughly with the increasing order of the alkyl group size. This hints that the predominant cause of thermodynamic behaviour in this range is the effect of the hydrophobic alkyl group. The sharpness of the  $x_{\text{AL}}$ -dependence is much more accurately represented in the interaction  $S_{\text{AL-AL}}^{\text{E}}$ .

<sup>2</sup>Supplementary data may be purchased from the Depository of Unpublished Data, Document Delivery, CISTI, National Research Council Canada, Ottawa, ON K1A 0S2, Canada ([http://www.nrc.ca/cisti/irm/unpub\\_e.shtml](http://www.nrc.ca/cisti/irm/unpub_e.shtml) for information on ordering electronically).

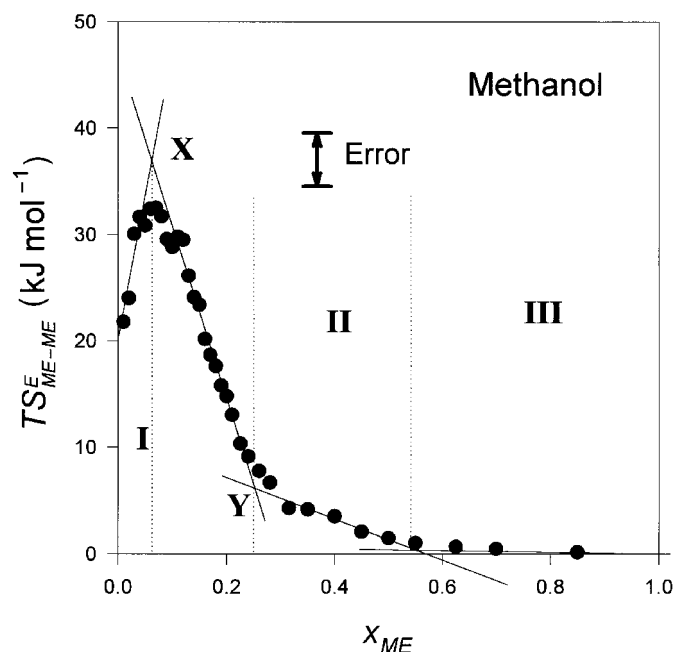


**Table 1.** The values of  $TS_{AL}^E$  and  $H_{AL}^E$  at infinite dilution.

Alcohol	Abbreviation	$H_{AL}^E$ at $x_{AL} = 0$ (kJ mol <sup>-1</sup> )	$TS_{AL}^E$ at $x_{AL} = 0$ (kJ mol <sup>-1</sup> )
Methanol	ME	-7.4 <sup>a</sup>	-8.6
Ethanol	ET	-10.2 <sup>a</sup>	-13.3
1-Propanol	1P	-10.4 <sup>a</sup>	-16.8
2-Propanol	2P	-13.1 <sup>a</sup>	-18.0
<i>tert</i> -Butanol	TBA	-17.0 <sup>b</sup>	-23.6 <sup>c</sup>
2-Butoxyethanol	BE	-17.0 <sup>d</sup>	-26.2 <sup>e</sup>

<sup>a</sup>Reference (2).<sup>b</sup>Reference (12).<sup>c</sup>Reference (13).<sup>d</sup>Reference (6).<sup>e</sup>Reference (8).**Fig. 2.** AL–AL entropic interaction multiplied by the temperature at 25°C ( $TS_{AL-AL}^E$ ).

Using the smoothed data in Table I, we have calculated the entropic interaction,  $TS_{AL-AL}^E$  (eq. [2]), with  $\delta x_{AL} = 0.01$ . The results are plotted in Figs. 2–6. It is striking that the  $x_{AL}$ -dependences are all similar to each other among the different alcohols, except for the varying scales. This suggests, again, that all the alcohol–water systems studied here share the same thermodynamic behaviour. Furthermore, the  $x_{AL}$ -dependences of  $TS_{AL-AL}^E$  are also similar to those of  $H_{AL-AL}^E$  shown in paper II (2). This is a direct consequence of entropy–enthalpy compensation (14). Following the same argument as in paper II (2), we recognize the regions of mixing schemes I, II, and III, as indicated in the figures. The transition from mixing scheme I to II starts at point X and ends at Y. Table 2 summarizes the loci of these points observed from the behaviour of  $TS_{AL-AL}^E$ . In Table 3, corresponding points observed by  $H_{AL-AL}^E$  from paper II (2) are shown. The sharpness of the  $x_{AL}$ -dependence in the H<sub>2</sub>O-rich region is reflected in the maximum value of  $TS_{AL-AL}^E$  and the loci of points X and Y. The sharper the dependence, the larger the maximum value and the smaller the loci of X

**Fig. 3.** ME–ME entropic interaction multiplied by the temperature at 25°C ( $TS_{ME-ME}^E$ ).**Table 2.** The maximum values of  $TS_{AL-AL}^E$  and the loci of mixing scheme boundaries.

AL	Max. $TS_{AL-AL}^E$ (kJ mol <sup>-1</sup> )	X	Y	II–III
ME	34±3	0.065	0.25	0.54
ET	81±5	0.05	0.19	0.38
1P	225±10	0.05	0.09	0.30
2P	1851±0	0.05	0.11	0.19
TBA <sup>a</sup>	360±20	0.045	0.065	0.38
BE <sup>b</sup>	1150±50	0.017	0.021	0.43

and Y. In terms of these quantities given in Tables 2 and 3, the strength of the effect of alcohol on H<sub>2</sub>O is in the order of ME < ET < 2P < 1P < TBA < BE. We suggest that this provides a measure of the hydrophobicity of the mono-ols. It is puzzling, however, that the values of  $TS_{AL}^E$  and  $H_{AL}^E$  at infinite



**Fig. 4.** ET–ET entropic interaction multiplied by the temperature at 25°C ( $TS_{ET-ET}^E$ ).

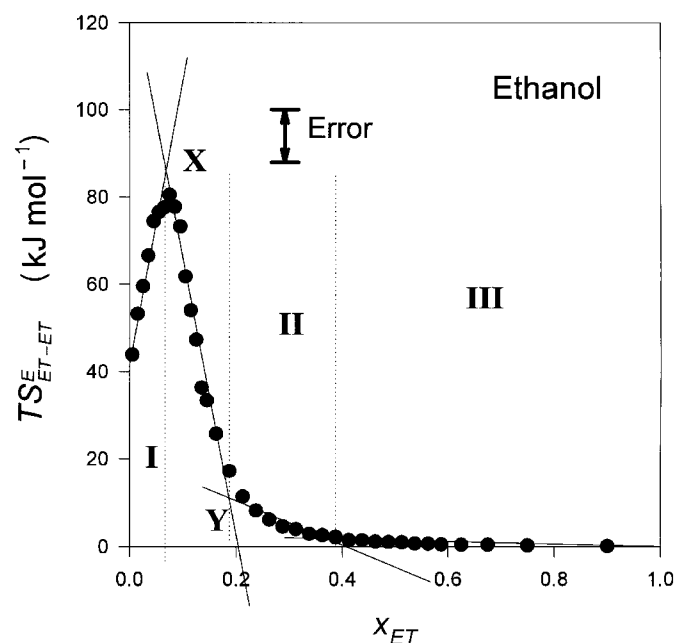
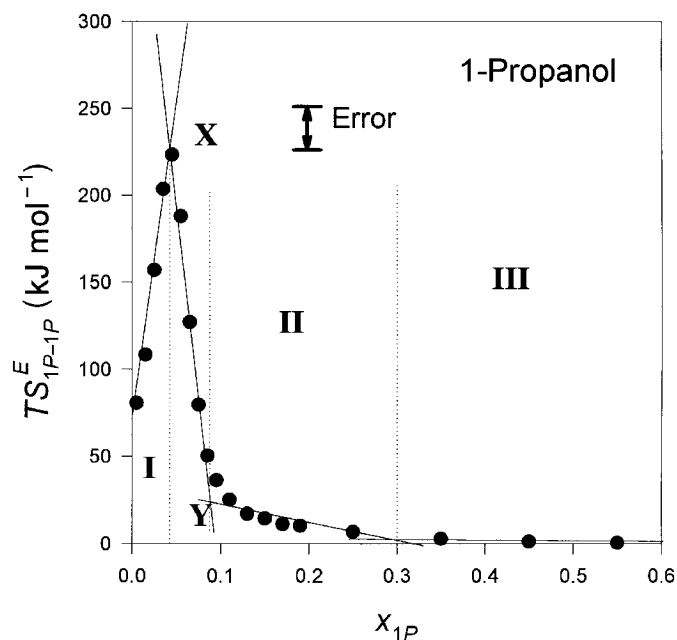


**Fig. 5.** 1P–1P entropic interaction multiplied by the temperature at 25°C ( $TS_{1P-1P}^E$ ).



dilution (see Table 1) do not follow the same order. In particular, the order of 1-propanol and 2-propanol is reversed, in terms of information given in Table 1. The values of  $T S_{AL}^E$  and  $H_{AL}^E$  at infinite dilution is associated with the process of an alcohol molecule (or an appropriate cluster thereof) breaking away from its pure environment and mixing into bulk  $H_2O$ . The latter process may be broken down into: (a) creating a cavity of the size of the alcohol molecule in bulk  $H_2O$  and (b) allowing the surrounding  $H_2O$  molecules to relax into its final form of “iceberg structure” with a

**Fig. 6.** 2P–2P entropic interaction times the temperature at 25°C ( $TS_{2P-2P}^E$ ).

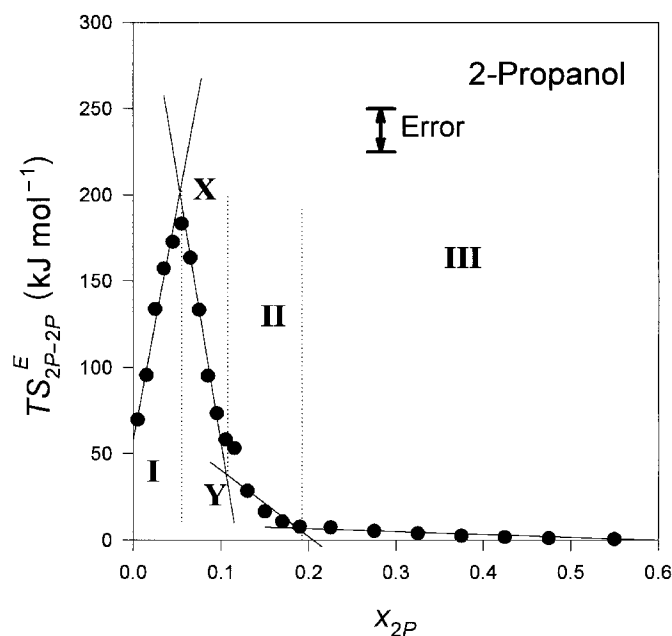


**Table 3.** Maximum values of  $H_{AL-AL}^E$  and the loci of mixing scheme boundaries.

AL	Max. $H_{AL-AL}^E$ (kJ mol <sup>-1</sup> )	X	Y	II–III
ME	32 ± 3	0.07	0.25	0.45
ET	73 ± 5	0.06	0.19	0.35
1P	210 ± 10	0.05	0.09	0.27
2P	180 ± 10	0.05	0.11	0.16
TBA <sup>a</sup>	350 ± 20	0.045	0.065	0.38
BE <sup>b</sup>	1100 ± 50	0.017	0.021	0.42

**Note:** Data mostly taken from paper II (2), unless otherwise indicated.

<sup>a</sup>Reference (12).

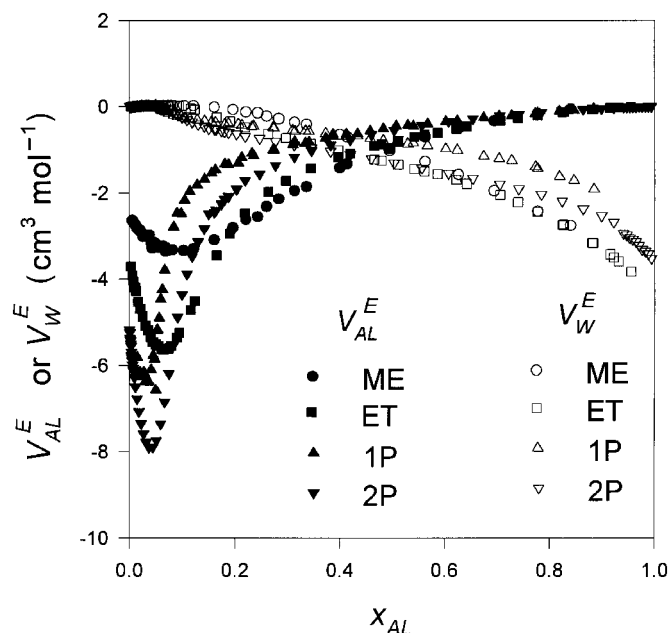
<sup>b</sup>Reference (6).

concomitant reduction of the hydrogen-bond probability of bulk  $H_2O$  away from the solute. Both processes (a) and (b) are associated with an order-of-magnitude larger absolute value of entropy and enthalpy changes with opposite signs, resulting in the net values of  $TS_{AL}^E$  and  $H_{AL}^E$  of the order of  $-7$  to  $-30$  kJ mol<sup>-1</sup>. A subtle alcohol-specific difference in either process could bring about a few kJ mol<sup>-1</sup> difference in the resulting values of  $TS_{AL}^E$  and (or)  $H_{AL}^E$ , which is sufficient to change the order of apparent hydrophobicity. Furthermore, we generally note that the thermodynamic information contained in the higher-order derivative of  $G$  is more detailed (4, 5). Thus, at this point, the most reliable ranking of the effect of alcohol on  $H_2O$ , derived here from  $TS_{AL-AL}^E$  and  $H_{AL-AL}^E$ , is ME < ET < 2P < 1P < TBA < BE. This seems reasonable considering the amount of nonpolar surface area for these six alcohols.

As mentioned above,  $S_{AL}^E$  is the second derivative and  $S_{AL-AL}^E$  is the third derivative of  $G$ . Another second derivative of  $G$  is the excess partial molar volume,  $V_{AL}^E$ :



**Fig. 7.** Excess partial molar volumes of AL and H<sub>2</sub>O ( $V_{AL}^E$  and  $V_W^E$ , respectively) at 25°C, calculated using the density data from refs. (19) and (20).



$$[3] \quad V_{AL}^E = (\partial V^E / \partial n_{AL}) = \{\partial^2 G / (\partial p \partial n_{AL})\}$$

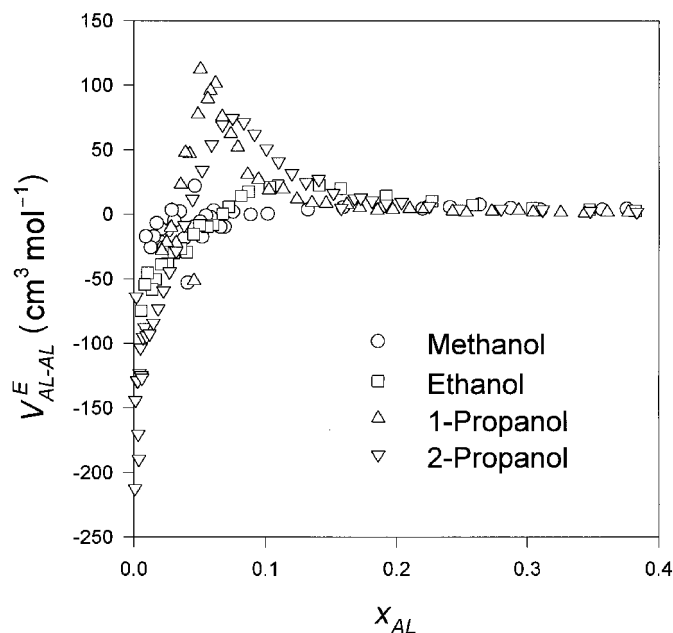
In analogy with eq. [2], we define (4, 5) the volumetric interaction,  $V_{AL-AL}^E$ , as

$$[4] \quad V_{AL-AL}^E \equiv N(\partial V_{AL}^E / \partial n_{AL}) = (1 - x_{AL}) (\partial V_{AL}^E / \partial x_{AL}).$$

Figure 7 shows  $V_{AL}^E$  values calculated graphically using literature density data at 25°C (15, 16). The initial decrease in  $V_{AL}^E$ , as  $x_{AL}$  increases from infinite dilution, was earlier attributed to being one of the signatures of mixing scheme I (4, 5). Equivalently, the excess partial molar volume of H<sub>2</sub>O,  $V_W^E$ , initially increases, owing to the Gibbs–Duhem relation, as is evident in Fig. 7. This is a reflection of “iceberg formation”. Moreover,  $V_{AL}^E$  at infinite dilution is determined by the size difference between the alcohol and water molecules (sand-and-pebble analogy) and the characteristic bulkiness of liquid H<sub>2</sub>O due to the hydrogen-bond network. The size-difference effect alone gives a negative value of  $V_{AL}^E$ , while the latter effect has a positive contribution, resulting in the net value of  $V_{AL}^E$  at infinite dilution. As  $x_{AL}$  increases, the latter contribution decreases because of the reduction of the hydrogen-bond probability of bulk H<sub>2</sub>O away from an “iceberg”-clad solute, while the former is basically independent of  $x_{AL}$ . As a result, the value of  $V_{AL}^E$  decreases; or, rather, the fact that  $V_{AL}^E$  shows the characteristic initial decrease was used as evidence for the reduction of the hydrogen-bond probability of bulk H<sub>2</sub>O away from solute. We point out that this initial decrease is also clearly evident for ME–H<sub>2</sub>O. Thus, there must be a hydrophobic effect operating in this system that is different from the mixing scheme operating in the AL-rich region.

Figure 8 shows the third derivative quantity,  $V_{AL-AL}^E$  (see eqs. [3] and [4]). These quantities also show anomalous be-

**Fig. 8.** AL–AL volumetric interaction ( $V_{AL-AL}^E$ ) at 25°C, calculated using the data from refs. (19) and (20).



haviour near the mixing scheme boundary between I and II. To obtain  $V_{AL-AL}^E$ , two consecutive graphical differentiations of the raw density data were required. Hence, the precision of  $V_{AL-AL}^E$  data is poorer than that for the  $S_{AL-AL}^E$  and  $H_{AL-AL}^E$  data. Thus, we did not attempt to locate points X and Y. Nevertheless, Fig. 8 shows that the maximum value of  $V_{AL-AL}^E$  evidently increases in the order ME < ET < 2P < 1P, consistent with the order observed for  $H_{AL-AL}^E$  and  $S_{AL-AL}^E$ . Our earlier measurements of the density of 2-butoxyethanol (BE) – H<sub>2</sub>O was performed for the purpose of evaluating  $V_{AL-AL}^E$  by two successive graphical differentiations. We therefore determined about 200 densities in the range  $0 < x_{BE} < 0.04$ .  $V_{BE-BE}^E$  thus obtained showed anomalous behaviour at exactly the same locus as  $H_{AL-AL}^E$ ,  $S_{AL-AL}^E$ , and other third derivative quantities (4–8, 17–20). This fact was used as supporting evidence for the existence of the transition between mixing schemes I and II in BE–H<sub>2</sub>O mixtures.

Kozak et al. (21) have suggested the same ranking for the first four alcohols, ME < ET < 2P < 1P, using the virial coefficients,  $B$ , in the expansion of the logarithm of the activity coefficient of the solvent W,  $\gamma_W$  (see eq. [5]). However, TBA does not follow this trend, even though TBA is more hydrophobic than 1P (See Table 1 in ref. (21)). The logarithm of  $\gamma_W$  is written as

$$[5] \quad \ln \gamma_W \equiv \mu_W^E / RT = Bx_{AL}^2 + Cx_{AL}^3 + \dots$$

It follows from the Gibbs–Duhem relation that

$$[6] \quad (\partial \mu_W^E / \partial n_{AL}) = -2RTB(1 - x_{AL})^2 + \dots$$

Thus, the use of  $B$  is equivalent to using  $(\partial \mu_W^E / \partial n_{AL})$  at infinite dilution rather than the entropic interaction  $S_{AL-AL}^E$  (eq. [2]). Due to the entropy–enthalpy compensation (14), sharp changes in the entropic and the enthalpic interactions,  $S_{AL-AL}^E$  and  $H_{AL-AL}^E$ , are compensated by each other, and as



a result the changes in  $(\partial\mu_W^E/\partial n_{AL})$  usually becomes less conspicuous. Thus, it is more advantageous to use  $S_{AL-AL}^E$  and  $H_{AL-AL}^E$  than  $(\partial\mu_W^E/\partial n_{AL})$  or its equivalent  $B$  in contrasting the propensities of the hydrophobic moieties.

Determination of the boundary between mixing schemes II and III using  $H_{AL-AL}^E$  and  $S_{AL-AL}^E$  data is problematic, as is evident in Table 2 and 3 and Figs. 3–6. This is due to shallow intersections between two curves of  $TS_{AL-AL}^E$  (and  $H_{AL-AL}^E$ ) against  $x_{AL}$ . Furthermore, the values of  $H_{AL}^E$  and  $S_{AL}^E$  themselves are small, and subtle changes in curvature are not very conspicuous. To locate the boundary between mixing schemes II and III and, further, to study subtle differences in mixing scheme III among individual alcohols, data are needed for the excess partial molar enthalpy and entropy of  $H_2O$ ,  $H_W^E$ , and  $S_W^E$  in the alcohol-rich region. In this region the absolute values of  $H_W^E$  and  $S_W^E$  are expected to be larger than those of  $H_{AL}^E$  and  $S_{AL}^E$  and, hence, their  $x_{AL}$ -dependences should be more conspicuous.

## Acknowledgments

This work was supported by Natural Sciences and Engineering Research Council of Canada (NSERC), the Danish National Research Council, and the Ministry of Education and Science of Japan.

## References

1. J. Hu, C.A. Haynes, A.H.Y. Wu, C.M.W. Cheung, M.M. Chen, E.G.M. Yee, T. Ichioka, K. Nishikawa, and Y. Koga. *Can. J. Chem.* **81**, 141 (2003).
2. S.H. Tanaka, H.I. Yoshihara, A.W.-C. Ho, F.W. Lau, P. Westh, and Y. Koga. *Can. J. Chem.* **74**, 713 (1996).
3. M.T. Parsons, P. Westh, J.V. Davies, C. Trandum, E.C.H. To, W.M. Chiang, E.G.M. Yee, and Y. Koga. *J. Solution Chem.* **30**, 1007 (2001).
4. Y. Koga. *J. Phys. Chem.* **100**, 5172 (1996).
5. Y. Koga. *J. Crystallogr. Soc. Jpn.* **37**, 172 (1995).
6. W. Siu and Y. Koga. *Can. J. Chem.* **67**, 671 (1989).
7. Y. Koga, W.W.Y. Siu, and T.Y.H. Wong. *J. Phys. Chem.* **94**, 3879 (1990).
8. Y. Koga. *J. Phys. Chem.* **95**, 4119 (1991).
9. S. Dixit, J. Crain, W.C.K. Poon, J.L. Finney, and A.K. Soper. *Nature*, **416**, 829 (2002).
10. A.K. Soper and J.L. Finney. *Phys. Rev. Lett.* **71**, 4346 (1993).
11. D.T. Bowron, A.K. Soper, and J.L. Finney. *J. Chem. Phys.* **114**, 6203 (2001).
12. Y. Koga. *Can. J. Chem.* **66**, 1187 (1988).
13. Y. Koga, W.W.Y. Siu, and T.Y.H. Wong. *J. Phys. Chem.* **94**, 7700 (1990).
14. R. Lumry and S. Rajender. *Biopolymers*, **9**, 1125 (1970).
15. G.C. Benson and O. Kiyohara. *J. Solution Chem.* **9**, 791 (1980).
16. M. Sakurai. *J. Solution Chem.* **17**, 267 (1988).
17. P. Westh, A. Hvidt, and Y. Koga. *Chem. Phys. Lett.* **217**, 245 (1994).
18. J.V. Davies, F.W. Lau, L.T.N. Le, J.T.W. Lai, and Y. Koga. *Can. J. Chem.* **70**, 2659 (1992).
19. Y. Koga. *J. Phys. Chem.* **96**, 10 446 (1992).
20. Y. Koga, J. Kristiansen, and Aa. Hvidt. *J. Chem. Thermodyn.* **25**, 51 (1993).
21. J.J. Kozak, W.S. Knight, and W. Kauzmann. *J. Chem. Phys.* **48**, 675 (1968).



# A new method for the preparation of peroxymonophosphoric acid

Tian Zhu, Hou-min Chang, and John F. Kadla

**Abstract:** A new method for the preparation of peroxymonophosphoric acid ( $\text{H}_3\text{PO}_5$ ) has been developed. It utilizes a biphasic solution to moderate the vigorous reaction between phosphorous pentoxide ( $\text{P}_2\text{O}_5$ ) and hydrogen peroxide ( $\text{H}_2\text{O}_2$ ).  $\text{P}_2\text{O}_5$  is suspended in carbon tetrachloride ( $\text{CCl}_4$ ), and concentrated  $\text{H}_2\text{O}_2$  is slowly added while being vigorously stirred at low temperature. Careful control of the reaction temperature through the slow addition of  $\text{H}_2\text{O}_2$  is critical. Using typical preparation conditions ( $\text{P}_2\text{O}_5:\text{H}_2\text{O}_2 = 0.5:1$ ,  $\text{H}_2\text{O}_2$  70 wt %,  $2^\circ\text{C}$ , 120–180 min), ~70% of the  $\text{H}_2\text{O}_2$  is effectively converted to  $\text{H}_3\text{PO}_5$ . Increasing the concentration of  $\text{H}_2\text{O}_2$ , as well as the mole ratio of  $\text{P}_2\text{O}_5:\text{H}_2\text{O}_2$ , leads to an even higher % conversion of  $\text{H}_2\text{O}_2$  to  $\text{H}_3\text{PO}_5$ . The addition of glacial acetic acid to the  $\text{P}_2\text{O}_5:\text{H}_2\text{O}_2$  suspension at the end of the 120–180 min reaction ( $\text{P}_2\text{O}_5:\text{H}_2\text{O}_2:\text{CH}_3\text{COOH} = 0.5:1:0.3$ ) leads to the formation of peracetic acid in addition to  $\text{H}_3\text{PO}_5$ , and to an overall increase in the conversion ratio of total peroxy acids based on  $\text{H}_2\text{O}_2$  (>95%).

**Key words:** peroxymonophosphoric acid, synthesis, stability, conversion ratio.

**Résumé :** On a mis au point une nouvelle méthode de préparation de l'acide peroxymonophosphorique ( $\text{H}_3\text{PO}_5$ ). Elle fait appel à une solution biphasique pour modérer la réaction vigoureuse du pentoxyde de phosphore ( $\text{P}_2\text{O}_5$ ) et du peroxyde d'hydrogène ( $\text{H}_2\text{O}_2$ ). Le  $\text{P}_2\text{O}_5$  est mis en suspension dans le tétrachlorure de carbone ( $\text{CCl}_4$ ) et le  $\text{H}_2\text{O}_2$  est ajouté lentement à basse température sous agitation vigoureuse. Il est critique de bien contrôler la température de la réaction par une addition lente du  $\text{H}_2\text{O}_2$ . Utilisant des conditions de préparation typiques ( $\text{P}_2\text{O}_5:\text{H}_2\text{O}_2 = 0,5:1$ ;  $\text{H}_2\text{O}_2$  à 70% en poids; à  $2^\circ\text{C}$ ; 120–180 min), environ 70% du  $\text{H}_2\text{O}_2$  est effectivement converti en  $\text{H}_3\text{PO}_5$ . Une augmentation de la concentration du  $\text{H}_2\text{O}_2$  ainsi qu'une augmentation du rapport molaire  $\text{P}_2\text{O}_5:\text{H}_2\text{O}_2$  conduit à des pourcentages encore plus élevés de conversion du  $\text{H}_2\text{O}_2$  en  $\text{H}_3\text{PO}_5$ . L'addition d'acide acétique glacial à la suspension de  $\text{P}_2\text{O}_5:\text{H}_2\text{O}_2$  à la fin de la réaction de 120 à 180 min ( $\text{P}_2\text{O}_5:\text{H}_2\text{O}_2:\text{CH}_3\text{COOH} = 0,5:1:0,3$ ) conduit à la formation d'acide peracétique en plus du  $\text{H}_3\text{PO}_5$  et à une augmentation globale du rapport de conversion globale en peroxyacides par rapport à la quantité de  $\text{H}_2\text{O}_2$  utilisée (>95%).

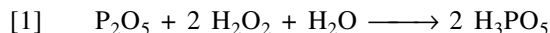
**Mots clés :** acide peroxymonophosphorique, synthèse, stabilité, rapport de conversion.

[Traduit par la Rédaction]

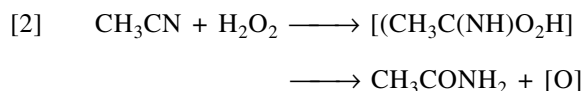
## Introduction

Peroxy acids are widely used, versatile oxidizing agents. The mechanisms of reactions involving peroxy acids have been extensively studied by a variety of techniques and have provided a fundamental understanding of autoxidation and other reactions involving peroxygen compounds (1,2). In spite of their importance as oxidants, the number of peroxy acids available for organic synthesis and oxidation chemistry is rather limited: peroxy formic acid and peroxy trifluoroacetic acid are formed readily in situ from hydrogen peroxide and the corresponding acid, whereas peracetic acid, *m*-chloro-peroxy benzoic acid (MCPBA), and the potassium salt of peroxymonosulfuric acid (OXONE®) are commercially available products.

In addition to peroxymonosulfuric acid, several other inorganic peroxy acids have been utilized in oxidation reactions, e.g., pernitric acid (3) and peroxymonophosphoric acid (4–8). Peroxymonophosphoric acid was first prepared in 1910 by Schmidlin and Massini according to the following reaction (eq. [1]) (9):



However, the reaction was extremely vigorous, generating a large amount of heat, which rapidly decomposed the peroxy acid. As a result, only a small amount of peroxy acid could be obtained by this method. Subsequently, in 1937, Toennies tried to moderate the vigorous reaction by introducing acetonitrile as an "inert diluent", and claimed to obtain relatively stable solutions containing 51% peroxy acid at  $-11^\circ\text{C}$  (10). However, problems concerning reproducibility exist, as hydrogen peroxide and peroxy acids are known to hydrolyze acetonitrile (eq. [2]) (11, 12).



As a result, the most widely used method for preparing  $\text{H}_3\text{PO}_5$  is the hydrolysis of potassium or lithium

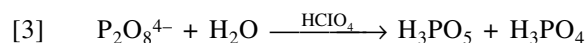
Received 28 September 2002. Published on the NRC Research Press Web site at <http://canjchem.nrc.ca> on 27 February 2003.

T. Zhu, H.-m. Chang, and J.F. Kadla,<sup>1</sup> College of Natural Resources, North Carolina State University, Raleigh, NC 27695–8005, U.S.A.

<sup>1</sup>Corresponding author (e-mail: [jfkadla@ncsu.edu](mailto:jfkadla@ncsu.edu)).



peroxodiphosphate in a strong acid solution such as  $\text{HClO}_4$  (eq. [3]) (13).



Unfortunately, the extreme reagents, combined with the high costs and the low peroxy acid yields have hindered its utilization in large-scale commercial applications. Several other methods for preparing  $\text{H}_3\text{PO}_5$  have been utilized and include electrolysis of solutions of phosphates (14), as well as the reaction of  $\text{H}_4\text{P}_2\text{O}_7$  with hydrogen peroxide (15). However, none of these methods gave reasonable yields of  $\text{H}_3\text{PO}_5$ . In this study we report a novel method for the preparation of  $\text{H}_3\text{PO}_5$  in high yields.

## Experimental

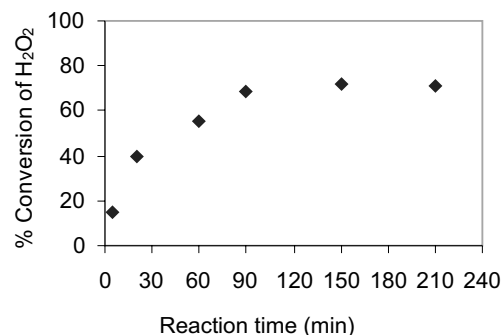
### Materials

Phosphorous pentoxide (ACS reagent grade), carbon tetrachloride (ACS reagent grade), ceric sulfate (0.25 N), sodium thiosulfate (0.1 N), potassium iodide (1.0 N), Ferroin (1,10-phenanthroline ferrous sulfate), sulfuric acid (ACS reagent grade), and glacial acetic acid were purchased from Aldrich Chemicals and used as received. Hydrogen peroxide (70% and 90%) was obtained from FMC Corporation (Tonamanda, N.Y.). DTPA (diethylenetriaminepentaacetic acid) and DTMPA (diethylenetriaminepentamethylene phosphonic acid) were gifts from Buchman Chemicals Inc. All solutions were prepared in deionized water.

### $\text{H}_3\text{PO}_5$ synthesis

In the preparation of  $\text{H}_3\text{PO}_5$ ,  $\text{P}_2\text{O}_5$  (17.0 g, 0.061 mole) was suspended in  $\text{CCl}_4$  (10 mL), and the suspension was cooled in an ice bath to a temperature of  $\sim 2^\circ\text{C}$  while being vigorously stirred. Aqueous hydrogen peroxide (0.121 mole, 5 mL of 70 wt %) was then added dropwise to the suspension, while the reaction temperature was carefully monitored. CAUTION: the addition rate of  $\text{H}_2\text{O}_2$  must be carefully controlled to maintain the reaction temperature below  $5^\circ\text{C}$ . If the addition of  $\text{H}_2\text{O}_2$  is too fast, the reaction is too vigorous and a violent exotherm can occur. However, if the addition of  $\text{H}_2\text{O}_2$  is too slow, the  $\text{P}_2\text{O}_5$  powder will tend to form larger aggregate particles, which are slow to react with the  $\text{H}_2\text{O}_2$  and result in the accumulation of  $\text{H}_2\text{O}_2$ , and a potentially violent reaction can occur. Therefore, careful monitoring of the temperature while adding  $\text{H}_2\text{O}_2$  at a sufficient rate to minimize  $\text{P}_2\text{O}_5$  aggregation is required. Upon complete addition of  $\text{H}_2\text{O}_2$  the biphasic reaction system was further stirred, for up to 3 h, to maximize peroxy acid yield (Fig. 1); prolonged mixing can lead to decreased  $\text{H}_3\text{PO}_5$  yields. The aqueous phase was separated and the  $\text{CCl}_4$  layer was extracted 2–3 times with deionized water (5 mL) to extract the  $\text{H}_3\text{PO}_5$  along with phosphoric acid and hydrogen peroxide. The aqueous solutions were combined and the concentration of  $\text{H}_3\text{PO}_5$  and  $\text{H}_2\text{O}_2$  were determined by chemical methods. Accordingly, a sample of the reaction mixture (0.2 mL) was acidified with  $\text{H}_2\text{SO}_4$  (200 mL, 1 N  $\text{H}_2\text{SO}_4$ ) and cooled in an ice bath to permit titration within a temperature range of  $0$ – $10^\circ\text{C}$ . Three drops of Ferroin solution was added, and the mixture was titrated with 0.1 N ceric sulfate until the disappearance of the salmon color. KI (5 mL, 1.0 N KI) was added, and the iodine liberated was ti-

**Fig. 1.** The effect of reaction time on % conversion of  $\text{H}_2\text{O}_2$  to  $\text{H}_3\text{PO}_5$  ( $\text{P}_2\text{O}_5\text{:H}_2\text{O}_2 = 0.5\text{:}1$ , 70 wt %  $\text{H}_2\text{O}_2$ ,  $2^\circ\text{C}$ ).



trated with sodium thiosulfate (0.1 N) to a starch end point. The amount (%) of peroxy acid and hydrogen peroxide was calculated according to eqs. [4] and [5], respectively.

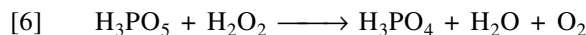
$$[4] \quad \% \text{ peroxy acid} = \frac{\text{mL Na}_2\text{S}_2\text{O}_3 \times 0.1\text{N} \times 0.038 \times 100}{\text{sample weight}}$$

$$[5] \quad \% \text{ hydrogen peroxide} = \frac{\text{mL Ce(SO}_4)_2 \times 0.1\text{N} \times 0.017 \times 100}{\text{sample weight}}$$

## Results and discussion

Analogous to the work of Toennies (10), we have focused on moderating the reaction between  $\text{H}_2\text{O}_2$  and  $\text{P}_2\text{O}_5$  (eq. [1]). To avoid some of the problems associated with acetonitrile, we have chosen an inert solvent,  $\text{CCl}_4$ , which unlike acetonitrile is inert to most oxidants, and neither  $\text{P}_2\text{O}_5$  nor  $\text{H}_2\text{O}_2$  are soluble in it.

In a typical preparation, the reaction mixture was mixed for no longer than 3 h to maximize peroxy acid yield (Fig. 1). Careful control of the reaction system is required, as longer reaction times result in lower yields of  $\text{H}_3\text{PO}_5$  because of the slow reaction between  $\text{H}_3\text{PO}_5$  and  $\text{H}_2\text{O}_2$  (eq. [6]).



By controlling the volume of  $\text{CCl}_4$ , the stirring speed, and the rate of the addition of hydrogen peroxide, approximately 70% of  $\text{H}_2\text{O}_2$  was converted to  $\text{H}_3\text{PO}_5$  at a mole ratio  $\text{P}_2\text{O}_5\text{:H}_2\text{O}_2 = 0.5\text{:}1$ . To the best of our knowledge such a high conversion ratio has never been reported.

### Effect of $\text{P}_2\text{O}_5\text{:H}_2\text{O}_2$ on the preparation of $\text{H}_3\text{PO}_5$

The conversion ratio of  $\text{H}_3\text{PO}_5$  based on  $\text{H}_2\text{O}_2$  can be increased by increasing the mole ratio of  $\text{P}_2\text{O}_5\text{:H}_2\text{O}_2$  (Fig. 2). When the mole ratio of  $\text{P}_2\text{O}_5\text{:H}_2\text{O}_2$  is greater than 0.9, 100% conversion was achieved.

### Effect of $\text{H}_2\text{O}_2$ concentration

The effect of  $\text{H}_2\text{O}_2$  concentration on the preparation of  $\text{H}_3\text{PO}_5$  is shown in Fig. 3. As expected, the concentration of  $\text{H}_2\text{O}_2$  had a dramatic influence on the generation of  $\text{H}_3\text{PO}_5$ . Increasing the peroxide concentration decreases the amount



**Fig. 2.** Effect of increasing  $P_2O_5:H_2O_2$  on the conversion of  $H_2O_2$  to  $H_3PO_5$  (70 wt %  $H_2O_2$ , 2°C, 120 min).

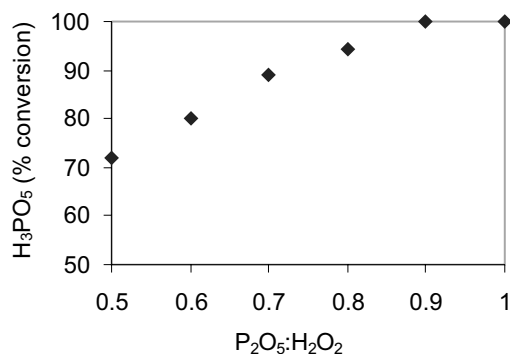
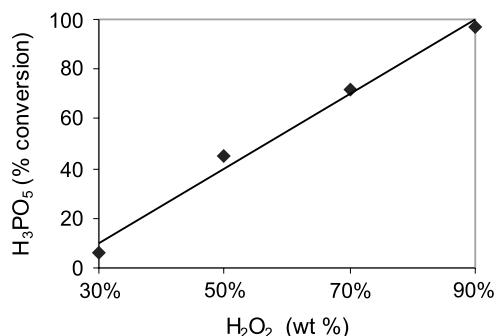


**Fig. 3.** Effect of  $H_2O_2$  concentration on the conversion of  $H_2O_2$  to  $H_3PO_5$  ( $P_2O_5:H_2O_2 = 0.5:1$ , 2°C, 120 min).



of water available for the hydrolysis of  $P_2O_5$  (eq. [7]). As a result, a higher percent of the  $H_2O_2$  is converted into  $H_3PO_5$ . As can be seen from Fig. 3, 90 wt %  $H_2O_2$  gave quantitative conversion. However, concerns exist regarding the safe handling of such highly concentrated  $H_2O_2$  solutions. Therefore, the 70 wt %  $H_2O_2$ , which gave satisfactory results (>70% conversion), is a good compromise between  $H_2O_2$  conversion and safe handling.

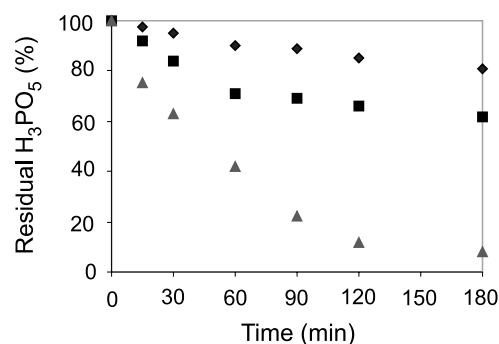


### $H_3PO_5$ stability

To further characterize the peroxy acid synthesis, the stability of the respective peroxides was determined during the reaction process. Five reactions were conducted ( $P_2O_5:H_2O_2$  (0.5:1), 2°C, 180 min), and the total peroxide species present was determined. Analysis of the aqueous solution, which contained  $H_3PO_5$ ,  $H_2O_2$ , and  $H_3PO_4$ , showed a total peroxide concentration of  $98.2 \pm 0.5\%$ . In fact, after 30 days of refrigeration ( $\sim 5^\circ\text{C}$ ), more than 95% of the  $H_3PO_5$  remained. Thus, any decomposition of the peroxide species during the preparation protocol or storage at low temperature is negligible. This remarkable stability provides the possibility that  $H_3PO_5$  may not need to be generated on site when it is utilized in commercial processes.

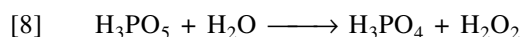
The thermal stability at higher temperatures was also investigated. Figure 4 shows the effect of increasing temperature on  $H_3PO_5$  stability. As expected, increasing the temperature from 50 to  $90^\circ\text{C}$  resulted in a dramatic decrease

**Fig. 4.** Effect of temperature on  $H_3PO_5$  stability:  $\blacklozenge$   $50^\circ\text{C}$ ,  $\blacksquare$   $70^\circ\text{C}$ ,  $\blacktriangle$   $90^\circ\text{C}$ . Initial  $[H_3PO_5] = 0.100\text{ M}$ ,  $[H_2O_2] = 0.0\text{ M}$ , pH = 1.02.



in  $H_3PO_5$  stability. At  $90^\circ\text{C}$  more than 90% of the peroxy acid was decomposed within 120 min.

The decrease in  $H_3PO_5$  concentration may be attributed to several factors, e.g., thermal- and (or) metal-catalyzed decomposition or aqueous hydrolysis. It is known that under acidic conditions in the presence of water peroxy acid hydrolysis takes place according to the equilibrium reaction present in eq. [8] (2).



The hydrolysis of  $H_3PO_5$  would result in the corresponding liberation of  $H_2O_2$  and  $H_3PO_4$ . During the thermal treatments we monitored the concentration of  $H_3PO_5$  and  $H_2O_2$ . Figure 5 shows the results obtained at  $90^\circ\text{C}$ .

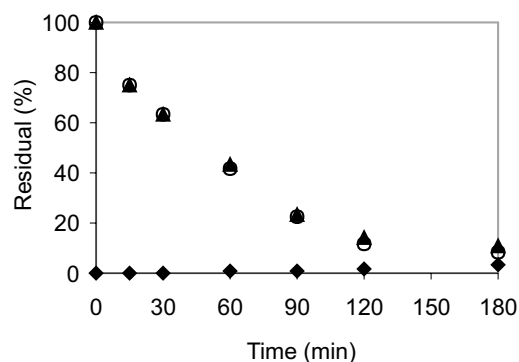
It can be seen that very little  $H_2O_2$  is generated during the 180 min of thermal treatment. However, this may be because of the thermal decomposition of the generated  $H_2O_2$ . To eliminate this possibility,  $H_2O_2$  was thermally treated under the same reaction conditions (pH 1,  $90^\circ\text{C}$ ), and no decomposition was observed. These results indicate that the rate of  $H_3PO_5$  hydrolysis is extremely slow, and not responsible for the observed decrease in  $H_3PO_5$  concentration under the conditions used. These results are in agreement with those of Battaglia and Edwards who reported that the hydrolysis of  $H_3PO_5$  is negligible unless the pH is much less than 0 (16).

It is well established that peroxides undergo facile decomposition in the presence of transition metal ions. A kinetic chain reaction can be catalyzed by traces (10–20 ppm) of transition metal ions, particularly iron, cobalt, manganese, and copper, and is often referred to as Fenton's chemistry (2, 17). Under such conditions the peroxide acts as both a reducing and an oxidizing reagent with the transition metal ions in the higher and lower valence states, respectively (Scheme 1).

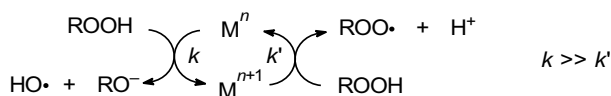
To minimize the effect of transition-metal-induced decomposition reactions, many techniques have been employed, which include the addition of sequestering agents and (or) inorganic salts to remove the majority of these metal ion contaminants (2, 18). To avoid the influence of trace amount of metal ions, which may be introduced during the preparation of  $H_3PO_5$ , the effect of DTPA on the reaction system was studied. Increasing concentrations of DTPA were used, and the effect on  $H_3PO_5$  stability measured. There was no observable difference among any of the DTPA-included



**Fig. 5.** Decomposition of  $\text{H}_3\text{PO}_5$  at  $90^\circ\text{C}$ :  $\blacklozenge$   $\text{H}_2\text{O}_2$ ,  $\circ$   $\text{H}_3\text{PO}_5$ ,  $\blacktriangle$   $\text{H}_2\text{O}_2 + \text{H}_3\text{PO}_5$ . Initial  $[\text{H}_3\text{PO}_5] = 0.10 \text{ M}$ ,  $[\text{H}_2\text{O}_2] = 0.0 \text{ M}$ ,  $\text{pH} = 1.02$ .

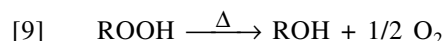


**Scheme 1.**



reactions, and this indicates that metal-induced decomposition is not prevalent in our system.

Thermodynamically, peroxides, particularly peroxy acids, are potentially unstable, decomposing exothermically according to eq. [9].



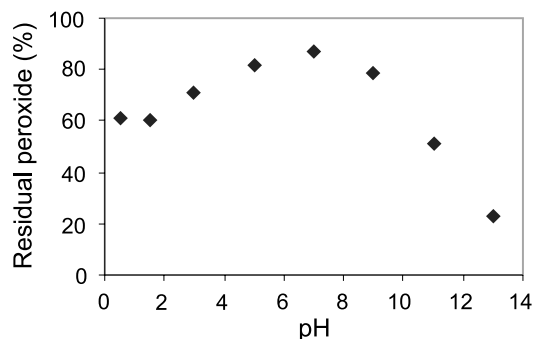
The facile decomposition is a result of the weak O—O bonds,  $\sim 31 \text{ kcal mol}^{-1}$  for  $\text{CH}_3\text{C}(\text{O})\text{O—OH}$  vs.  $51 \text{ kcal mol}^{-1}$  for  $\text{HO—OH}$ , which are easily cleaved by light and heat (2). In both peroxy acids and hydroperoxides, heating above a critical temperature (peracetic acid:  $\sim 80^\circ\text{C}$ ,  $\text{H}_2\text{O}_2$ :  $\sim 120^\circ\text{C}$  (19)) initiates homolysis of the O—O bond, leading to the formation of radical species. What ensues is the kinetic decomposition of the peroxide to a variety of radical intermediates (2). Although we did not calculate the critical temperature for  $\text{H}_3\text{PO}_5$ , we are of the opinion that the decreased stability is mainly due to the thermal decomposition of  $\text{H}_3\text{PO}_5$ .

Finally, the effect of pH on the stability of  $\text{H}_3\text{PO}_5$  (0.10 M) was studied at  $70^\circ\text{C}$  (Fig. 6). To avoid the influence of trace amounts of metal ions at high pH conditions where DTPA is not effective, DTMPA (0.1%) was added (20). The reaction was maintained at constant pH and temperature for 120 min, at which time the residual  $\text{H}_3\text{PO}_5$  was determined. The results are shown in Fig. 6 and reveal that at approximately pH 7,  $\text{H}_3\text{PO}_5$  has the maximum stability, which rapidly decreases with increasing pH.

#### Peracetic acid – peroxyphosphoric acid preparation

To further increase the peroxy acid concentration of the reaction system, we investigated the effect of acetic acid addition. In previous studies, we found that the addition of acetic acid during peroxymonosulfuric acid synthesis results in an increase in peroxy acid concentration through the production of peracetic acid (21). In this system, the unreacted  $\text{H}_2\text{O}_2$  reacts with the acetic acid to form peracetic acid,  $\text{CH}_3\text{CO}_3\text{H}$ , and the conversion ratio of the total peroxy acids

**Fig. 6.** Effect of pH on the stability of  $\text{H}_3\text{PO}_5$  at  $70^\circ\text{C}$  and 120 min (initial  $[\text{H}_3\text{PO}_5] = 0.10 \text{ M}$ ).



based on  $\text{H}_2\text{O}_2$  is increased. Therefore, glacial acetic acid was added to the  $\text{P}_2\text{O}_5$ – $\text{H}_2\text{O}_2$  reaction system prior to working up the reaction system (after approximately 2–3 h of reaction). The system was mixed for a further 30 to 45 min to promote  $\text{CH}_3\text{CO}_3\text{H}$  formation (21). The peroxy acids were then extracted from the  $\text{CCl}_4$  layer and the concentration of peroxy acids and remaining hydrogen peroxide were determined by chemical methods. In a typical preparation, at a mole ratio of  $\text{P}_2\text{O}_5:\text{H}_2\text{O}_2:\text{CH}_3\text{COOH} = 0.5:1:0.3$ , using 70 wt %  $\text{H}_2\text{O}_2$ , the overall conversion ratio of  $\text{H}_2\text{O}_2$  to peroxy acids was  $>95\%$ .

Normally, the generation of peracetic acid from acetic acid and hydrogen peroxide requires a strong acid catalyst such as  $\text{H}_2\text{SO}_4$ . The advantage of this method is that no additional strong acid catalyst is needed, as  $\text{H}_3\text{PO}_4$  and  $\text{H}_3\text{PO}_5$  are both medium to strong acids. Although both acetic acid and peracetic acid are soluble in the  $\text{CCl}_4$ , they can be easily extracted by water at the end of the reaction. In fact, after 2–3 extractions (30 mL) with water, there was no acetic acid or peroxy acids left in the  $\text{CCl}_4$ . Thus, this system enables the  $\text{CCl}_4$  to be reused, addressing some of the concerns surrounding its use.

## Conclusions

In this paper we describe a new method for the preparation of peroxyphosphoric acid ( $\text{H}_3\text{PO}_5$ ). It utilizes a biphasic solution to moderate the vigorous reaction between phosphorous pentoxide ( $\text{P}_2\text{O}_5$ ) and hydrogen peroxide ( $\text{H}_2\text{O}_2$ ). Through careful control of the reaction temperature by the slow dropwise addition of  $\text{H}_2\text{O}_2$ ,  $\text{H}_2\text{O}_2$  can be converted to  $\text{H}_3\text{PO}_5$  with high conversion ratios. Typical preparation conditions involve suspending the  $\text{P}_2\text{O}_5$  in  $\text{CCl}_4$ , cooling the reaction system to  $2^\circ\text{C}$ , then slowly adding the 70 wt %  $\text{H}_2\text{O}_2$  ( $\text{P}_2\text{O}_5:\text{H}_2\text{O}_2 = 0.5:1$ ) while vigorously mixing the solution. The preparation is then left mixing at  $2^\circ\text{C}$  for between 120–180 min. Increasing the concentration of  $\text{H}_2\text{O}_2$  as well as the mole ratio of  $\text{P}_2\text{O}_5:\text{H}_2\text{O}_2$  leads to a higher % conversion of  $\text{H}_2\text{O}_2$  to  $\text{H}_3\text{PO}_5$ . The addition of glacial acetic acid to the  $\text{P}_2\text{O}_5:\text{H}_2\text{O}_2$  suspension at the end of the 120–180 min reaction ( $\text{P}_2\text{O}_5:\text{H}_2\text{O}_2:\text{CH}_3\text{COOH} = 0.5:1:0.3$ ) leads to the formation of peracetic acid in addition to  $\text{H}_3\text{PO}_5$  and an overall increase in the conversion ratio of total peroxy acids based on  $\text{H}_2\text{O}_2$  ( $>95\%$ ).

The  $\text{H}_3\text{PO}_5$  solution can be stored for more than 30 days under refrigeration with only minimal loss in  $\text{H}_3\text{PO}_5$  concen-



tration. Temperature and pH have dramatic effects on the  $\text{H}_3\text{PO}_5$  stability. At high temperature ( $70^\circ\text{C}$ ), the maximum  $\text{H}_3\text{PO}_5$  stability was observed at a pH  $\sim 7$ , with both increasing and decreasing pH resulting in a decrease in residual  $\text{H}_3\text{PO}_5$  after 120 min. Increasing the temperature to  $90^\circ\text{C}$  lead to the rapid reduction in  $\text{H}_3\text{PO}_5$  concentration. Experimental results indicate that aqueous mediated hydrolysis and transition-metal-catalyzed decomposition are not prevalent. The observed decrease in  $\text{H}_3\text{PO}_5$  can be attributed to the thermal homolysis of the peroxygen bond.

## References

1. D. Swern. Organic peroxides. R.E. Krieger Pub. Co., Malabar, Fla. 1981.
2. S. Patai. The chemistry of peroxides. Wiley, New York. 1983.
3. E.L. Springer. Tappi J. **77**, 103 (1994).
4. Y. Ogata, K. Tomizawa, and T. Morikawa. J. Org. Chem. **44**, 352 (1979).
5. Y. Ogata, Y. Sawaki, K. Tomizawa, and T. Ohno. Tetrahedron, **37**, 1485 (1981).
6. P. Keswani, A.K. Gupta, and Y.K. Gupta. J. Indian Chem. Soc. **62**, 878 (1985).
7. M. Vijayasree, K. Srinivas, and P.V.S. Rao. Indian J. Chem. Sect. A Inorg. Phys. Theor. Anal. **22**, 241 (1983).
8. J.F. Kadla, T. Zhu, H.-m. Chang, and H. Jameel. Holzforschung, **57**, 44 (2003).
9. J. Schmidlin and P. Massini. Ber. **43**, 1162 (1910).
10. G. Toennies. J. Am. Chem. Soc. **59**, 555 (1937).
11. G. Laus. J. Chem. Soc. Perkin Trans. 2, 864 (2001).
12. Y. Ogata and Y. Sawaki. Bull. Chem. Soc. Jpn. **38**, 194 (1965).
13. D.H. Fortnum, C.J. Battaglia, S.R. Cohen, and J.O. Edwards. J. Am. Chem. Soc. **82**, 778 (1960).
14. N.E. Khomutov, O.B. Khachaturyan, and T.P. Kotova. S.U. Patent 247 258. 1969; *Chem. Abstr.* 71:131 123.
15. S.M. Afzal. Pak. J. Sci. **32**, 201 (1980).
16. C.J. Battaglia and J.O. Edwards. Inorg. Chem. **4**, 552 (1965).
17. J.F. Kadla and H.-m. Chang. In Oxidative delignification chemistry: fundamentals and catalysis. Edited by D.S. Argyropoulos. ACS Symposium Series 785. Oxford University Press. 2001. p. 108.
18. E. Koubek, J.O. Edwards, C.J. Battaglia, M.L. Haggett, K.M. Ibnerasa, and H.V. Pyun. J. Am. Chem. Soc. **85**, 2263 (1963).
19. D.R. Lide. CRC handbook of chemistry and physics. 71st ed. CRC Press, Cleveland, Ohio. 1990. p. 9.
20. J.F. Kadla, H.M. Chang, and H. Jameel. Holzforschung, **51**, 428 (1997).
21. S. Wang. Ph.D. Thesis, North Carolina State University, Raleigh, North Carolina, 1995.



# Electrocatalytic oxidation and flow amperometric detection of hydrazine on a dinuclear ruthenium phthalocyanine-modified electrode

Mehrdad Ebadi

**Abstract:** Electrocatalytic oxidation of hydrazine on a dinuclear ruthenium phthalocyanine ((RuPc)<sub>2</sub>) modified electrode was studied using cyclic voltammetry (CV) and rotating disc electrode (RDE) techniques. At pH = 13, a four-electron oxidation of hydrazine to N<sub>2</sub> was observed. A suitable mechanism was proposed by analyzing the rate equation and the Tafel slope. The flow injection analysis was performed to characterize the (RuPc)<sub>2</sub>-modified electrode as an amperometric sensor for the detection of hydrazine. The electrode displays an excellent accuracy and precision in phosphate solution at pH 12 and 13. The linearity range was from 30 nM to 1 mM with a correlation coefficient of 0.9998.

**Key words:** ruthenium phthalocyanine, electrocatalysis, surface-modified electrode, hydrazine, amperometric sensor.

**Résumé :** On a étudié l'oxydation électrocatalytique de l'hydrazine sur une électrode modifiée de phthalocyanine de ruthénium dinucléaire (RuPc)<sub>2</sub> en faisant appel aux techniques de voltampérométrie cyclique (VC) et d'électrode à disque tournant (EDT). À un pH = 13, on observe une oxydation à quatre électrons de l'hydrazine en N<sub>2</sub>. On propose un mécanisme approprié en faisant une analyse de l'équation de vitesse et de la pente de Tafel. On a réalisé une analyse de l'écoulement de l'injection pour caractériser l'électrode modifiée de (RuPc)<sub>2</sub> comme détecteur ampérométrique pour la détection de l'hydrazine. L'électrode est à la fois exacte et précise dans une solution de phosphate à des pH de 12 et 13. La plage de linéarité va de 30 nM à 1 mM avec un coefficient de corrélation de 0,9998.

**Mots clés :** phthalocyanine de ruthénium, électrocatalyse, électrode à surface modifiée, détecteur ampérométrique.

[Traduit par la Rédaction]

## Introduction

Recently (1) we reported the electrochemical properties of the dinuclear ruthenium phthalocyanine (RuPc)<sub>2</sub> species and the electroreduction of O<sub>2</sub> and H<sub>2</sub>O<sub>2</sub> catalyzed by (RuPc)<sub>2</sub>-modified graphite electrodes. The solution and surface cyclic voltammetry of (RuPc)<sub>2</sub> displays a series of metal-localized processes. Previous studies of ruthenium phthalocyanine complexes have focused on their synthesis and chemical and physical properties (2–9). The exploration of ruthenium phthalocyanine as a catalyst has not been adequately investigated. Most of the work reported in the literature on catalysis by metallophthalocyanine species (MPcs) has been directed toward the study of cobalt and iron phthalocyanine. However, our work indicates that ruthenium phthalocyanine is as versatile a catalyst as CoPc and FePc (10). The modified (RuPc)<sub>2</sub> electrode exhibits catalytic activity towards a wide variety of molecules, including hydrazine.

There have been many published reports on the mechanism and kinetics of hydrazine oxidation. Oxidation of hydrazine catalyzed by platinum (11, 12), palladium (13, 14), nickel (15), gold (16), mercury (17), silver (18), vanadium (19), manganese (20, 21), iridium (22), rhodium (23), iron (24), cobalt (25–27), ruthenium (28), and graphite electrodes modified by metallophthalocyanines of VO, Fe, Zn, Co, Cu, Ni, and Mn (29, 30) have been reported. In aqueous

solutions, four-electron oxidation of hydrazine to N<sub>2</sub> was reported, while a two-electron oxidation to N<sub>2</sub>H<sub>2</sub> was observed in organic solvents (12, 31).

The electrode materials and solvents have a profound influence on the oxidation mechanism. Fukumoto et al. studied the catalytic activity of metal electrodes in the anodic oxidation of hydrazine by means of the palladium membrane method (32). The experimental results revealed that the initial step in the mechanism occurred either through deprotonation of hydrazine followed by four-electron oxidation to N<sub>2</sub> (mechanism I) or via formation of the N<sub>2</sub>H<sub>3</sub> radical followed by three-electron oxidation to N<sub>2</sub> (mechanism II). The oxidation of hydrazine on Pt, Ir, and Co proceeds via mechanism I, whereas on metals such as Pd, Au, and Ni oxidation occurs via mechanism II.

Zagal and co-workers have reported the oxidation of hydrazine catalyzed by MPc, MTSPc, and MP compounds (M = Cu, Cr, Ni, Fe, Co, VO, Zn, or Mn; TSPc = tetrasulphophthalocyanine; P = porphyrin) adsorbed on graphite electrodes (25). They proposed that the initial step in the mechanism involves oxidation of the metal center, followed by catalytic oxidation of coordinated hydrazine.

Many reports have become available on the detection of hydrazine using techniques such as amperometry (33–40), chemiluminescence (41–43), and spectrophotometry (44–48). In the spectrophotometry and chemiluminescence methods,

Received 19 September 2002. Published on the NRC Research Press Web site at <http://canjchem.nrc.ca> on 28 February 2003.

E. Mehrdad. Chemistry Department, York University, Toronto, ON M3J 1P3, Canada. (e-mail: Mehrdad.ebadi@penw.com).



hydrazine is analyzed through its ability to inhibit or promote a chemical reaction. An example is the kinetic-spectrophotometric determination of hydrazine via inhibition of the reaction between bromate and hydrochloric acid (46).

In the amperometric method, hydrazine is detected by oxidation on a working electrode. The oxidation potential of 1.0 V vs. AgCl/Ag is reported (37). To reduce the applied potential and increase the electrode sensitivity, many groups have reported the use of chemically modified electrodes (CME). The choice of the surface modifier is based on its catalytic activity and stability towards hydrazine.

In this article, the catalytic activity of the (RuPc)<sub>2</sub>-modified electrodes toward the oxidation of hydrazine is described. The main products of the redox reaction are determined using electrochemical methods such as cyclic voltammetry (CV) and rotating disc electrode (RDE). A suitable mechanism is proposed by analyzing the Tafel slopes and the rate equations. The performance of an (RuPc)<sub>2</sub>-modified electrode for the detection of hydrazine in a flow-through system is reported.

## Experimental

### Material

Hydrazine sulfate (NH<sub>2</sub>NH<sub>2</sub>·H<sub>2</sub>SO<sub>4</sub>) (Analar), potassium hydrogen phosphate monobasic (KH<sub>2</sub>PO<sub>4</sub>) (Analar), and sodium hydroxide (NaOH) (Analar) were used without further purification. THF was distilled over sodium wire.

The buffer solutions were prepared using 0.1 M KH<sub>2</sub>PO<sub>4</sub>. The desired pH was obtained by the addition of a 0.1 M phosphoric acid or a 0.1 M NaOH solution. Nitrogen gas was used to remove dissolved oxygen in the solutions prior to the cyclic voltammetric experiment (CV).

The following parameters were used in all calculations:  $D_{N_2H_4} = 1.4 \times 10^{-5} \text{ cm}^2 \text{ s}^{-1}$ , and  $0.01 \text{ cm}^2 \text{ s}^{-1}$  for the kinematic viscosity of water (49).

### Apparatus and electrode preparation

Electrochemical measurements were performed with an RDE3 Pine potentiostat and an X-Y recorder. A pyrolytic graphite disc, sealed to a copper shaft with polyolefin heat-shrinkable tubing, was used as a working electrode in the surface CV experiments. The graphite electrode was mounted on the shaft with the basal plane of the graphite exposed (BPG). The surface of the electrode was polished with 0.05  $\mu\text{m}$  alumina powder, sonicated in doubly distilled water, and rinsed with acetone and water before each experiment. A saturated calomel electrode was used as a reference electrode.

The chromatograms were obtained using an HPLC system consisting of a Waters 590 isocratic pump, a Waters 715 auto sampler, and an HP G1049 electrochemical cell. An AgCl/Ag electrode was used as a reference electrode and glassy carbon (GC) was used as a working electrode. The GC electrode was modified as described below.

Exposing polished GC and BPG electrodes to the THF solution of (RuPc)<sub>2</sub> (0.1 mM) modified the graphite electrodes. After 1 min of soaking, the electrode was removed, rinsed with doubly distilled water, and transferred to an electrochemical cell. The (RuPc)<sub>2</sub> that was deposited on the electrode was determined to be between 3 to 5 layers thick,

assuming that (RuPc)<sub>2</sub> adsorbed flat onto the surface of BPG (1, 10).

## Results and discussion

### Solution and surface CV of (RuPc)<sub>2</sub>

In our previous paper (1) we have reported the solution and surface CV of (RuPc)<sub>2</sub> in organic and inorganic media. The solution CV of (RuPc)<sub>2</sub> in THF displays four reversible redox waves at 0.98 V (wave I), 0.48 V (wave II), -0.13 V (wave III), and -0.55 V (wave IV) vs. SCE and an irreversible wave at -1.38 V (wave V) vs. SCE. The reversible waves are assigned to one-electron redox couples centered at metal centers, and the irreversible wave is assigned to a two-electron redox process centered at the Pc rings (1, 10).

- [1] Wave I:  $[(\text{Ru(III)Pc}(-2))_2]^{2+} + e^- \rightleftharpoons [(\text{Ru(II, III)Pc}(-2))_2]^+$
- [2] Wave II:  $[(\text{Ru(II, III)Pc}(-2))_2]^+ + e^- \rightleftharpoons (\text{Ru(II)Pc}(-2))_2$
- [3] Wave III:  $(\text{Ru(II)Pc}(-2))_2 + e^- \rightleftharpoons [(\text{Ru(I, II)Pc}(-2))_2]^-$
- [4] Wave IV:  $[(\text{Ru(I, II)Pc}(-2))_2]^- + e^- \rightleftharpoons [(\text{Ru(I)Pc}(-2))_2]^{2-}$
- [5] Wave V:  $[(\text{Ru(I)Pc}(-2))_2]^{2-} + 2e^- \rightleftharpoons [(\text{Ru(I)Pc}(-3))_2]^{4-}$

The surface CV of (RuPc)<sub>2</sub> in methylene dichloride displays four quasi-reversible surface waves at 0.85 V (wave A), 0.31 V (wave B), -0.45 V (wave C), and -0.94 V (wave D) vs. AgCl/Ag. They are assigned to the metal localized processes corresponding in assignment to those described above as I, II, III, and IV (1, 10). The surface CV of (RuPc)<sub>2</sub> in aqueous medium displays pH-dependent surface waves (Fig. 1). At low pH, two reversible surface waves (waves C and D) are observed, while at high pH two additional waves (waves A and B), positive of wave C, are detected. Wave A is only observed at very high pH values (not shown) (1, 10).

- [6] Wave D:  $[(\text{Ru(I, II)Pc}(-2))_2]\text{H} + e^- + \text{H}^+ \rightleftharpoons [(\text{Ru(I)Pc}(-2))_2]2\text{H}$
- [7] Wave C:  $[(\text{Ru(II)Pc}(-2))_2] + e^- + \text{H}^+ \rightleftharpoons [(\text{Ru(I, II)Pc}(-2))_2]\text{H}$
- [8] Wave B:  $[\text{OH}(\text{Ru(II, III)Pc}(-2))_2] + e^- \rightleftharpoons [(\text{Ru(II)Pc}(-2))_2] + \text{OH}^-$
- [9] Wave A:  $[(\text{OHRu(III)Pc}(-2))_2] + e^- \rightleftharpoons [\text{OH}(\text{Ru(II, III)Pc}(-2))_2] + \text{OH}^-$

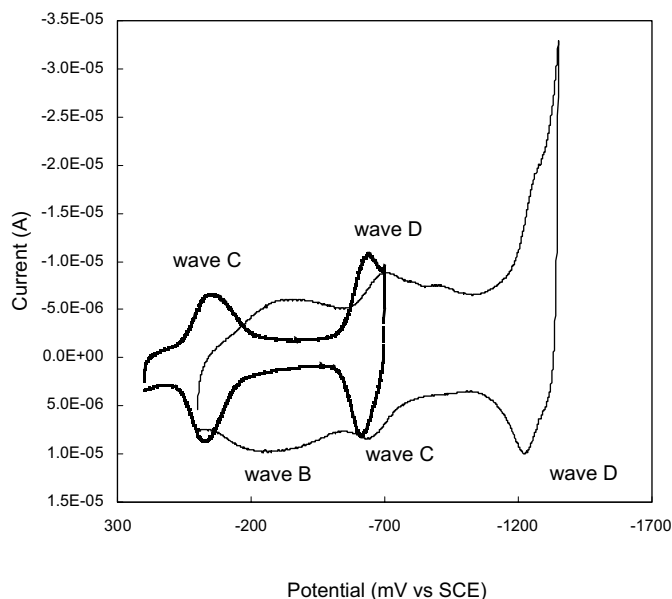
A Pourbaix diagram of waves B, C, and D along with the hydrazine oxidation wave are shown in Fig. 2.

### Hydrazine electrocatalytic oxidation

An (RuPc)<sub>2</sub>-modified electrode shows strong catalytic activity towards the oxidation of hydrazine at pH = 13, while a



**Fig. 1.** Cyclic voltammetry of surface bound (RuPc)<sub>2</sub> on a BPG electrode in phosphate buffer solution; pH = 11.3 (—) and pH = 2.4 (---).



bare BPG electrode shows no activity toward the oxidation of hydrazine (Fig. 3). A plot of the hydrazine oxidation current as a function of the square root of the scan rate yields a straight line ( $R = 0.999$ ,  $n = 8$ ), characteristic of a diffusion-controlled process.

The oxidation current shows a strong dependence on pH (Fig. 2). As the pH decreases, the oxidation peak potential shifts toward a more positive potential and at the same time the oxidation current decreases. At pH values lower than 9, the (RuPc)<sub>2</sub>-modified electrode loses its activity toward the oxidation of hydrazine. Similar behavior has been reported for hydrazine oxidation catalyzed by polymeric iron tetraaminophthalocyanine (50). The oxidation current is at its highest intensity at pH = 13. As the pH is lowered, the current intensity gradually decreases until pH = 8, where the catalyst loses its activity (50).

To calculate the number of electrons involved in the oxidation at pH = 13, a series of rotating disc electrode CVs was conducted at different spin velocities. In these experiments, the catalytic activity of the (RuPc)<sub>2</sub>-modified electrode was reduced by 10% after each cycle. The decrease in activity was due to gradual loss of (RuPc)<sub>2</sub> from the surface of the electrode. By increasing the number of adsorbed (RuPc)<sub>2</sub> layers, the loss of activity was significantly reduced. To eliminate the surface variation and the loss of electrode activity a new surface was used for each spin velocity.

For a rotating-disc electrode, the mass transfer limiting current is described by (51)

$$[10] \quad I_d = 0.201zFAD^{2/3}\nu^{-1/6}\omega^{1/2}C_o,$$

where  $A$  (cm<sup>2</sup>) is the area of the electrode,  $\nu$  (cm<sup>2</sup> s<sup>-1</sup>) is the kinematic viscosity,  $\omega$  (rpm) is the spin rate,  $C_o$  (mole cm<sup>-3</sup>) is the bulk concentration of the redox active species, and  $z$  is the number of electrons involved in the redox reaction.

For a first order reaction, the plot of  $1/I_{RD}$  vs.  $1/\omega^{1/2}$ , known as the Koutecky-Levich plot, yields a straight line ( $R = 0.99$ ,  $n = 6$ ). The slopes of the plots obtained in the mass transfer region at pH = 13 (slope =  $8.5 \times 10^3$ ) correspond well with a theoretical value for  $z = 4$  (slope =  $8.3 \times 10^3$ ). The linearity of the plot also indicates that hydrazine oxidation is first order with respect to dissolved N<sub>2</sub>H<sub>4</sub>.

In a confirmatory experiment, the oxidation of N<sub>2</sub>H<sub>4</sub> at pH = 13 was examined during CV at an (RuPc)<sub>2</sub>-modified electrode. For a totally irreversible redox reaction, the peak current in cyclic voltammetry is expressed as (51):

$$[11] \quad I_p = 2.99 \times 10^5 z(\alpha n_\alpha)^{1/2} AC_o D^{1/2} \nu^{1/2}$$

where  $\nu$  (V s<sup>-1</sup>) is the scan rate and  $\alpha n_\alpha$  is a parameter reflecting the irreversibility of the reaction. When  $A$ ,  $C_o$ ,  $D$ , and  $\alpha n_\alpha$  are known, the value of  $z$  can be calculated from the slope of  $I_p$  vs.  $\nu^{1/2}$ .

To determine the value of  $\alpha n_\alpha$ , one can use the relation for the peak potential.

$$[12] \quad E_p = k - (0.03/\alpha n_\alpha) \log(\nu)$$

The value of  $\alpha n_\alpha$  can then be calculated from the slope of  $E_p$  vs.  $\log(\nu)$ . The slope of the line at high over-potential yields a value of  $\alpha n_\alpha = 0.22$  ( $R = 0.999$ ,  $n = 8$ ). By substituting this value into eq. [11] along with known values for the other parameters the number of electrons involved in the oxidation of hydrazine is calculated to be  $z = 4.2$ .

The calculated number of electrons at pH = 13 (i.e.,  $z = 4$ ) indicates that the net oxidation of hydrazine occurs as follows (11–32)



Using the procedure described above, a value of  $z = 1$  at pH = 9 was observed. A value of  $z = 0.7$  has been reported for hydrazine oxidation in organic solvents (12, 31). The experimental data show that the formation in the solution of N<sub>2</sub>H<sub>5</sub><sup>+</sup>, which is not easily oxidizable, resulted in the small  $z$  value. Based on the above argument we propose that at pH values lower than 9, the formation of N<sub>2</sub>H<sub>5</sub><sup>+</sup> in solution and (or) the incapability of the solution to deprotonate the coordinated N<sub>2</sub>H<sub>4</sub> prevents the oxidation of hydrazine to nitrogen.

### Kinetics of N<sub>2</sub>H<sub>4</sub> oxidation at pH = 13

The rate of hydrazine oxidation can be defined as

$$[14] \quad I = zFAk [\text{N}_2\text{H}_4]^p [\text{OH}^-]^q,$$

where  $k$  is the heterogeneous rate constant,  $z$  is the total number of electrons involved in the oxidation reaction, and  $p$  and  $q$  are the reaction orders of hydrazine and hydroxide ion, respectively. The reaction order of hydrazine is determined from a plot of the logarithm of the kinetic current vs.  $\log [\text{N}_2\text{H}_4]$ . The slope of the line is close to unity (slope = 0.9,  $R = 0.99$ ,  $n = 5$ ), indicating first-order dependence.

The reaction order of OH<sup>-</sup> is determined from a plot of the hydrazine oxidation peak potential as a function of pOH. The slope of the line (slope = 100 mV per pH) is close to the theoretical value of  $59 q \alpha n_\alpha^{-1}$  for  $q = 1$  and  $\alpha n_\alpha = 0.5$ , indicating that one OH<sup>-</sup> is involved in the rate-determining step of hydrazine oxidation (10, 51, 52). Substituting these values



**Fig. 2.** A Pourbaix diagram indicating the pH dependence of waves B, C, and D and the hydrazine oxidation peak potential.

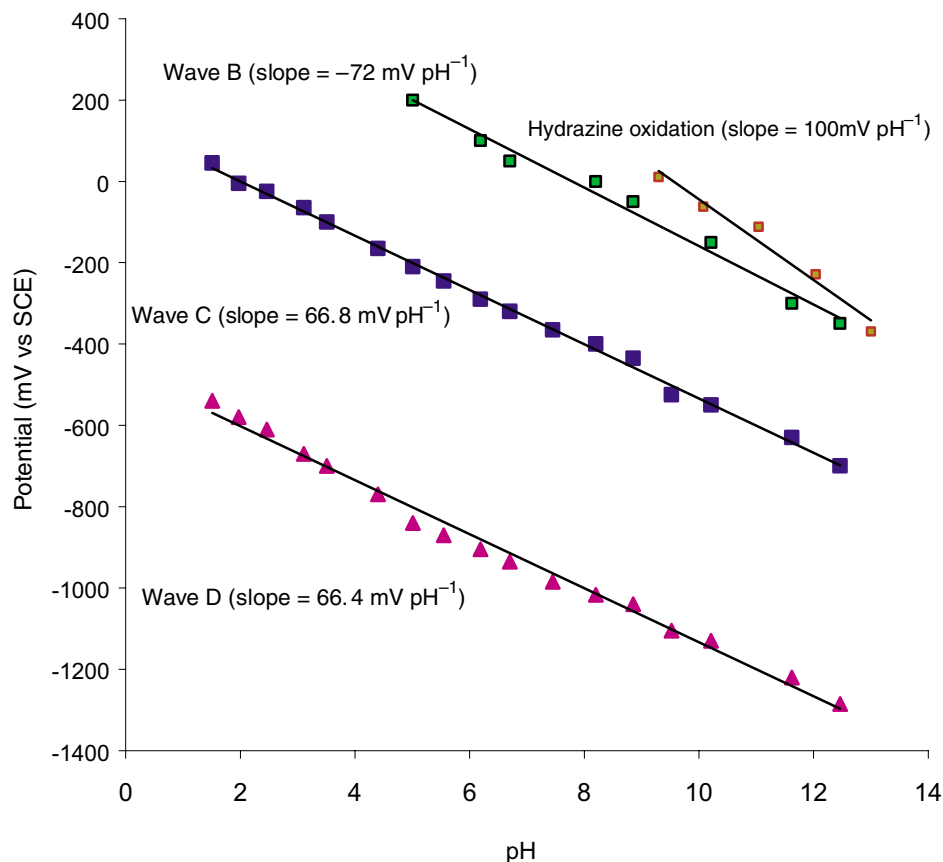
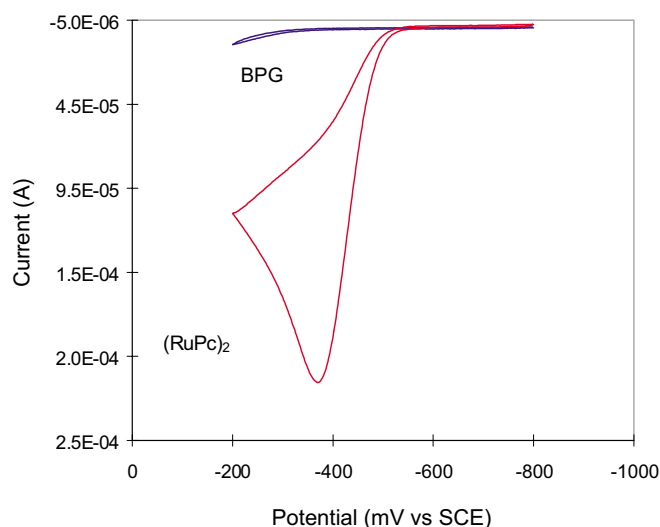


**Fig. 3.** Cyclic voltammetry of  $\text{N}_2\text{H}_4$  oxidation ( $2.0 \times 10^{-3} \text{ M}$ ) on an  $(\text{RuPc})_2$ -modified and bare BPG electrode in  $0.1 \text{ M NaOH}$  ( $\text{pH} = 13$ ); scan rate =  $25 \text{ mV s}^{-1}$ .



into eq. [14], one then derives  $k = 1.19 \times 10^{-10} \text{ cm}^4 \text{ mole s}^{-1}$  at  $E = -0.4 \text{ vs. SCE}$ . We would not attempt to compare the observed  $k$  value to published data since the experimental conditions, such as cell design, applied potential, and concentration of electrolytes, will have a profound influence on the value of the rate constant. A quantitative comparison

will require that the studies be performed under similar conditions.

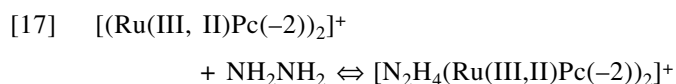
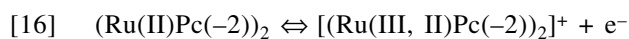
According to these results, the kinetic current of hydrazine oxidation can be written as:

$$[15] \quad I = zFAk [\text{N}_2\text{H}_4][\text{OH}^-]$$

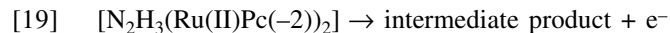
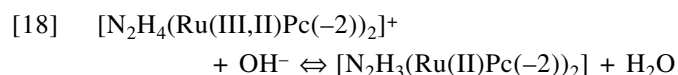
### Mechanism of $\text{N}_2\text{H}_4$ oxidation at $\text{pH} = 13$

Oxidation of hydrazine at  $\text{pH} = 13$  occurs in the positive waves C and D (Fig. 2). The CVs of  $(\text{RuPc})_2$  obtained in the presence and the absence of  $\text{N}_2\text{H}_4$  show that hydrazine oxidation occurs at the potential where wave B is observed, indicating that the active catalyst on the surface is  $[(\text{Ru(III, II)Pc}(-2))_2]^+$ . By transferring the  $(\text{RuPc})_2$  surface into an  $\text{N}_2\text{H}_4$ -free solution following a hydrazine oxidation experiment, the initial surface CV of  $(\text{RuPc})_2$  is observed, showing that the ruthenium dimer retains its structure during and after the oxidation process.

Based on our CV data, the calculated electron stoichiometries, and previously published reports, we propose the following mechanism for the oxidation of hydrazine on an  $(\text{RuPc})_2$ -modified electrode.







The steps following eq. [19] are very fast and are not rate-determining steps. These steps would lead to the formation of  $\text{N}_2$  as the final oxidation product.

The rate equation for the proposed mechanism for hydrazine oxidation (eq. [16] to [19]) under steady-state conditions is as follows (10, 52):

$$[20] \quad I = \frac{zFAk_2S[\text{NH}_2\text{NH}_2][\text{OH}^-]}{\{((k_2[\text{N}_2\text{H}_4][\text{OH}^-]/k_1^0)\exp(-(1-\alpha_1)f\eta_1) + (k_2[\text{OH}^-][\text{N}_2\text{H}_4]/k_4^0)\exp(-(1-\alpha_4)f\eta_4) + k_2[\text{N}_2\text{H}_4]/k_3 + (k_2[\text{N}_2\text{H}_4]K_3/k_4^0)\exp(-(1-\alpha_4)f\eta_4) + [\text{OH}^-] + k_{-2}/k_3 + (k_{-2}K_3/k_4^0)\exp(-(1-\alpha_4)f\eta_4) + (k_{-2}K_3/k_4^0)\exp(-(1-\alpha_4)f\eta_4)\exp(-f\eta_1) + [\text{OH}^-]\exp(-f\eta_1) + k_{-2}k_3\exp(-f\eta_1))\}}$$

where  $S$  (mole  $\text{cm}^{-2}$ ) =  $(\text{Ru}(\text{II})\text{Pc}(-2))_2 + [(\text{Ru}(\text{III}, \text{II})\text{Pc}(-2))_2]^+ + [\text{N}_2\text{H}_4(\text{Ru}(\text{III}, \text{II})\text{Pc}(-2))_2]^+ + [\text{N}_2\text{H}_3(\text{Ru}(\text{II})\text{Pc}(-2))_2]$ ;  $[\text{NH}_2\text{NH}_2]$  and  $[\text{OH}^-]$  are concentrations with units of mole  $\text{cm}^{-3}$ ;  $\eta_i$  is defined as  $(E_{\text{applied}} - E_i^0)$ ;  $k_1$ ,  $k_{-2}$ ,  $k_{-3}$ ,  $k_{-1}$ , and  $k_4$  have units of  $\text{s}^{-1}$  while  $k_2$  and  $k_3$  have units of  $\text{cm}^3 \text{mole}^{-1} \text{sec}^{-1}$ ; and  $K_3 = k_{-3}/k_3$ .<sup>1</sup>

The analysis of the rate equation — to predict experimentally observed data such as the Tafel slope and the rate dependence — has been used as a diagnostic method, to examine the validity of the proposed mechanism (10, 52). The experimental Tafel slopes are obtained from the plot of  $E_p$  vs.  $\log(v)$ , and the rate dependence of hydrazine oxidation towards  $[\text{N}_2\text{H}_4]$  and  $[\text{OH}^-]$  is described above.

When  $k_3 \ll k_1^0$ ,  $k_4^0$ ,  $K_3$ ,  $k_2$ , and  $k_{-2}$ , eq. [20] simplifies to

$$[21] \quad I = \frac{zFA[\text{NH}_2\text{NH}_2][\text{OH}^-]k_2S}{(k_2[\text{N}_2\text{H}_4]/k_3 + k_{-2}/k_3\exp(-f\eta_1) + k_{-2}/k_3)}$$

Equation [21] predicts first-order dependency on dissolved hydrazine,  $[\text{OH}^-]$ , and a Tafel slope of 60 mV per decade for  $\eta_1 \ll 0$  or infinity for  $\eta_1 \gg 0$ .

When  $k_4^0 \ll k_2[\text{NH}_2\text{NH}_2][\text{OH}^-]$ ,  $k_1^0$ ,  $k_{-2}$ ,  $k_{-3}$ , and  $k_3$ , eq. [20] can be written as

$$[22] \quad I = \frac{zFAk_2S[\text{NH}_2\text{NH}_2][\text{OH}^-]}{(\exp(-(1-\alpha_4)f\eta_4)(k_2[\text{N}_2\text{H}_4][\text{OH}^-]/k_4^0 + k_2[\text{N}_2\text{H}_4]K_3/k_4^0 + k_{-2}K_3/k_4^0)\exp(-f\eta_1))}$$

When  $\eta_1 \gg 0$ , eq. [22] simplifies to

$$[23] \quad I = \frac{zFA[\text{NH}_2\text{NH}_2][\text{OH}^-]k_2S\exp((1-\alpha_4)f\eta_4)}{[k_2[\text{N}_2\text{H}_4][\text{OH}^-]/k_4^0 + k_2[\text{N}_2\text{H}_4]K_3/k_4^0 + k_{-2}K_3/k_4^0]}$$

Equation [23] predicts a Tafel slope of  $60/(1-\alpha_4)$  at high over-potential. The reaction orders in hydrazine and  $\text{OH}^-$  are

$$[24] \quad p = \partial \log i / \partial \log [\text{N}_2\text{H}_4] = 1 - \frac{[k_2[\text{N}_2\text{H}_4][\text{OH}^-] + k_2[\text{N}_2\text{H}_4]K_3]}{[k_2[\text{N}_2\text{H}_4][\text{OH}^-] + k_2[\text{N}_2\text{H}_4]K_3 + k_{-2}K_3]}$$

$$[25] \quad q = \partial \log i / \partial \log [\text{OH}^-] = 1 - \frac{k_2[\text{N}_2\text{H}_4][\text{OH}^-]}{[k_2[\text{N}_2\text{H}_4][\text{OH}^-] + k_2[\text{N}_2\text{H}_4]K_3 + k_{-2}K_3]}$$

In a case where  $k_{-2} \gg K_3$  and  $k_2$ , both eqs. [24] and [25] predict a first-order dependence towards  $[\text{N}_2\text{H}_4]$  and  $[\text{OH}^-]$ .

The experimentally observed Tafel slope of 64 mV ( $R = 0.998$ ,  $n = 6$ ) at low over-potential ( $\eta_1 \ll 0$ ) is consistent with the slope predicted by eq. [21], and the observed slope of 134 mV ( $R = 0.998$ ,  $n = 6$ ) at high over-potential ( $\eta_1 \gg 0$ ) is predicted by eq. [23] using  $\alpha_4 = 0.5$ . Equation [21] also predicts the correct rate dependence toward  $[\text{N}_2\text{H}_4]$  and

$[\text{OH}^-]$ . Equation [23] predicts the correct rate dependence under the condition mentioned above.

#### Detection of hydrazine at $(\text{RuPc})_2$ under flow injection conditions

Figure 4 illustrates the chromatograph of a hydrazine sample (0.1 mM) on an  $(\text{RuPc})_2$ -modified GC and a bare GC electrode. The intense LC signals are observed only on the

<sup>1</sup>  $k_{-1}$  and  $k_1$  have the same magnitude and dimension (i.e.,  $k_{-1}/k_1 = 1$ ) (10, 52).



Table 1.

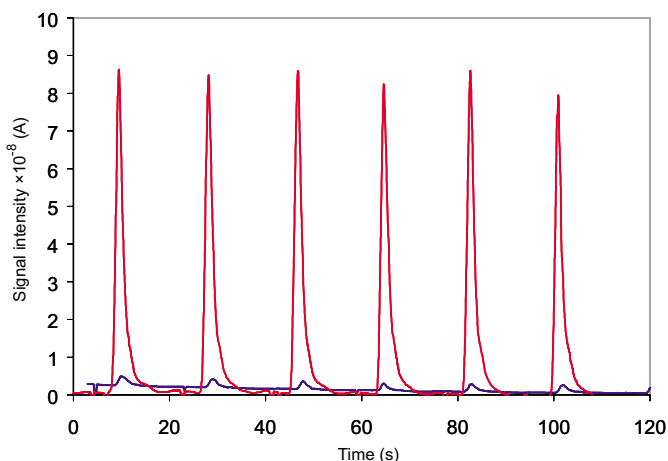
Method	Detection limit (LOD) ( $\mu\text{g L}^{-1}$ )	Range ( $\mu\text{g L}^{-1}$ )	Correlation coefficient	Reference
Amperometric	0.96	0.96–32000	0.9992	This work <sup>a</sup>
Amperometric	0.5	1–800	0.992	33
Amperometric	3 <sup>b</sup>	0.0128–0.128 <sup>c</sup>	0.9963	34
Amperometric	2.56	3.2–320		35
Amperometric	0.1	0.3–500	0.995	36
Amperometric	19.84		0.999	37
Amperometric	3.2	6.4–12 800	0.9998	38
Amperometric	320	3200–19 200	0.998	38
Amperometric	3.2	5.76–19 200	0.998	40
Chemiluminescence	2	5–40 000		41
Chemiluminescence	0.04	0.1–100		42
Chemiluminescence	3	10–10 000		43
Spectrophotometric	0.05	0.12–60		44
Spectrophotometric	99.2	150–992	0.994	45
Spectrophotometric	2.72	9.6–1024	0.999	46
Spectrophotometric	40	50–5000		47
Spectrophotometric	100	150–1000		48

<sup>a</sup>HPLC system; flow rate  $0.5 \text{ mL min}^{-1}$ ; mobile phase NaOH– $\text{KHCO}_3$  buffer (pH = 12.0); injection volume  $5 \mu\text{L}$ ; potential applied =  $0.0 \text{ V vs. AgCl/Ag}$ .

<sup>b</sup>Units are ( $\text{mg L}^{-1}$ ) for this entry only.

<sup>c</sup>Units are ( $\text{g L}^{-1}$ ) for this entry only.

**Fig. 4.** Chromatogram of hydrazine on an  $(\text{RuPc})_2$ -modified GC and bare GC electrodes. HPLC parameters: flow rate =  $0.5 \text{ mL min}^{-1}$ , mobile phase phosphate solution (pH = 12.0), injection volume  $5 \mu\text{L}$ , potential applied =  $0.0 \text{ V vs. AgCl/Ag}$ .



modified electrode, demonstrating that hydrazine can only be detected by an  $(\text{RuPc})_2$  GC electrode at  $0.0 \text{ V vs. AgCl/Ag}$ . The applied potential of  $0.0 \text{ V vs. SCE}$  was selected to eliminate interference arising from the reduction of any  $\text{O}_2$  dissolved in the mobile phase. The precision, accuracy, linearity, and detection limits of the hydrazine detection method, utilizing an  $(\text{RuPc})_2$ -modified GC electrode, are discussed below.

The precision of the hydrazine detection method, using an  $(\text{RuPc})_2$ -modified electrode, was examined by multiple injections of  $0.1 \text{ mM N}_2\text{H}_4$  in a mobile phase consisting of phosphate solution at pH = 12. After twenty successive injections ( $5 \mu\text{L}$  each) of the sample solution, a relative standard deviation of 2.7% (peak height) was observed, which

indicates a good precision and stability of the surface. The precision of the method was further examined using sample solutions containing  $0.1 \text{ mM}$  to  $0.01 \text{ M}$  hydrazine. Only at hydrazine concentrations of not more than  $1 \text{ mM}$  a good precision was observed.

To determine a desirable pH, the response factor of a  $0.1 \text{ mM}$  sample at  $0.0 \text{ V vs. AgCl/Ag}$  was examined at different pH. The best response factor was observed in the pH range of 12–13. At lower pH, the signal intensity would significantly decrease until pH = 9 where the surface would lose its catalytic activity.

To determine the optimum injection volume, multiple injections of from 1 to  $100 \mu\text{L}$  of a  $0.1 \text{ mM N}_2\text{H}_4$  sample were performed, and the signal precision was examined. The best results were obtained for an injection volume of  $5 \mu\text{L}$ .

Based on the above results, the optimum method parameters are an injection volume of  $5 \text{ mL}$ , a hydrazine concentration  $<1 \text{ mM}$ , and a mobile phase pH between 12 and 13.

The accuracy of the method was examined by spiking drinking water with known amounts of hydrazine. 100% hydrazine recovery was observed for the samples containing  $1 \text{ mM}$  hydrazine. The substances present in the drinking water showed no interference with the analysis of hydrazine.

The linearity and detection limits of this method were studied using the parameters selected during the precision study. The detection limits and the linearity data are summarized in Table 1, along with published data for comparison. The linear response for hydrazine is in the range of  $30 \text{ nM}$  to  $1 \text{ mM}$  with a correlation coefficient of 0.9998. In comparison with the published work (Table 1), this method displays an acceptable linearity range with an excellent correlation coefficient.

The detection limit of this method is estimated to be  $30 \text{ nM}$ , based on a signal-to-noise ratio of 3:1 (Fig. 5). The



**Fig. 5.** Chromatogram of hydrazine at 30 nM concentration on an (RuPc)<sub>2</sub>-modified GC. HPLC parameters: flow rate = 0.5 mL min<sup>-1</sup>, mobile phase phosphate solution (pH = 12.0), injection volume 5  $\mu$ L, potential applied = 0.0 V vs. AgCl/Ag.

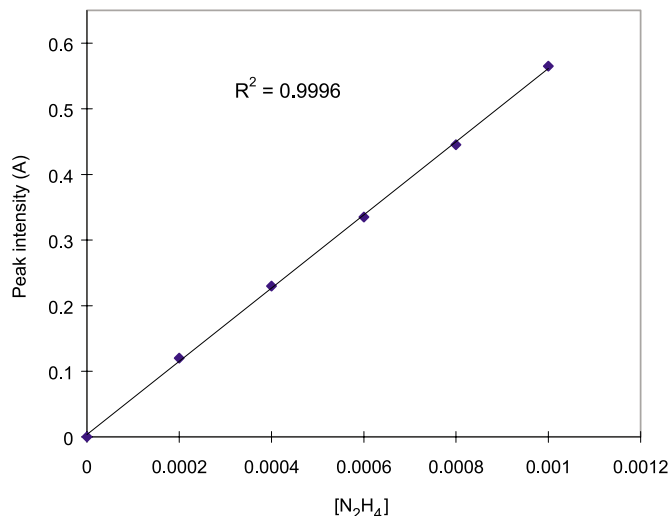
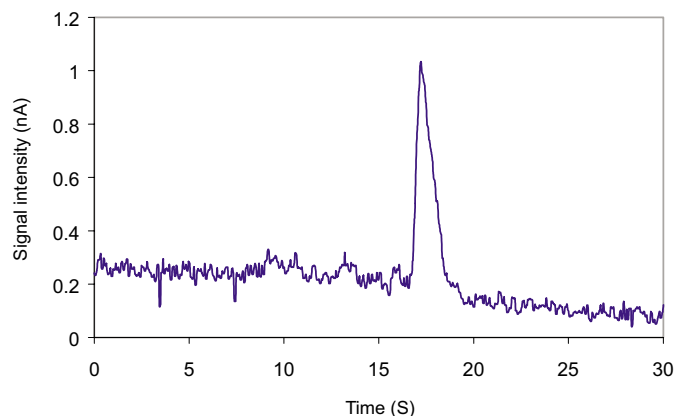


**Fig. 6.**



modified surface has a good detection limit in comparison to published work (Table 1).

In the interference tests, the presence of species such as F<sup>-</sup>, Cl<sup>-</sup>, Br<sup>-</sup>, I<sup>-</sup>, [SO<sub>4</sub>]<sup>2-</sup>, [CH<sub>3</sub>COO]<sup>-</sup>, [NO<sub>3</sub>]<sup>-</sup>, [CO<sub>3</sub>]<sup>2-</sup>, and [HCO<sub>3</sub>]<sup>-</sup> in the sample solution did not produce any significant interference.

The results presented here illustrate that an (RuPc)<sub>2</sub>-modified GC is a very sensitive electrode for the detection of hydrazine, and it can accurately and precisely measure hydrazine concentration in water samples. It also has an excellent linearity range.

## Conclusion

An (RuPc)<sub>2</sub>-modified electrode is catalytically active toward the oxidation of hydrazine. Based on the experimentally observed Tafel plot, the analysis of the rate equations, and the calculated electron stoichiometries, a suitable mechanism has been proposed. The pH-dependence experiment shows that the active catalyst on the surface is [(Ru(III, II)Pc(-2))<sub>2</sub>]<sup>+</sup>. The initial step is the oxidation of [(Ru(II)Pc(-2))<sub>2</sub>] to [(Ru(III, II)Pc(-2))<sub>2</sub>]<sup>+</sup>, followed by coordination of

hydrazine to the ruthenium metal center. The hydrazine coordinated with Ru<sup>III</sup> loses first a proton and then an electron in consecutive steps until all the protons are removed and nitrogen is formed on the surface. N<sub>2</sub> will then dissociate from (RuPc)<sub>2</sub>, and the catalytic cycle continues. At low pH values ( $\leq 9$ ), the chemical steps involving the removal of protons from the coordinated hydrazine are hindered, and therefore the complete oxidation to nitrogen does not take place.

The (RuPc)<sub>2</sub>-modified electrode has been shown to be an excellent hydrazine detector with an acceptable linearity range and detection limit.

## Acknowledgments

We would like to thank the Natural Sciences and Engineering Research Council of Canada (NSERC) for financial support, the Johnson Matthey Company for a loan of ruthenium trichloride, and Prof. A.B.P. Lever for valuable discussions.

## References

1. M. Ebadi, C. Alexiou, and A.B.P. Lever. *Can. J. Chem.* **79**, 992 (2001).
2. Y.G. Kang, H. Kim, L.R. Subramania, and M. Hanack. *Synth. Met.* **78**, 11 (1996).
3. J. Pohmer, M. Hanack, and J.O. Borcia. *J. Mater. Chem.* 957 (1996).
4. C. Ercolani, J. Jubb, G. Pennesi, U. Russo, and G. Trigiante. *Inorg. Chem.* 2535 (1995).
5. M. Hanack, A. Lange, and R. Grosshans. *Synth. Met.* **45**, 59 (1991).
6. M.A.T. Gilmartin, R.J. Ewen, and J.P. Hart. *J. Electroanal. Chem.* **401**, 127 (1996).
7. W. Kobel and M. Hanack. *Inorg. Chem.* **25**, 103 (1986).
8. (a) A. Capobianchi, M. Paoletti, G. Pennesi, G. Rossi, R. Caminiti, and C. Ercolani. *Inorg. Chem.* **33**, 4635 (1994); (b) R. Caminiti, M.P. Donzello, C. Ercolani, and C. Sadun. *Inorg. Chem.* **38**, 3027 (1999).
9. (a) L. Alagna, A. Capobianchi, P. Marovino, G. Pennesi, T. Prosperi, and G. Rossi. *J. Phys. IV.* **C2**, 1261 (1997); (b) L. Alagna, A. Capobianchi, P. Marovino, A.M. Paoletti, G. Pennesi, T. Prosperi, and G. Rossi. *Inorg. Chem.* **38**, 3688 (1999).
10. M. Ebadi. Ph.D. Thesis, York University, Toronto, Canada. 2002.
11. N.V. Harrison and Z.A. Khan. *J. Electroanal. Chem.* **26**, 1 (1970).
12. (a) G. Kokkinidis, A.D. Jannakoudakis, *J. Electroanal. Chem.* **130**, 153 (1981); (b) A.D. Jannakoudakis, G. Kokkinidis, *J. Electroanal. Chem.* **133**, 311 (1982).
13. J. Heitbaum and W. Vielstich. *Electrochim. Acta*, **17**, 1529 (1972).
14. T. Li and E. Wang. *Electroanal.* **9**, 1205 (1997).
15. J. Heitbaum and W. Vielstich. *Electrochim. Acta*, **18**, 501 (1973).
16. K. Korinek, J. Koryta, and M. Musilova. *J. Electroanal. Chem.* **21**, 319 (1969).
17. K. Tamura and T. Kahara. *J. Electrochem. Soc.* **123**, 776 (1976).
18. J. Heitbaum and W. Vielstich. *Electrochim. Acta*, **18**, 967 (1973).



19. G. Ramababu, P.V.S. Rao, K. Ramakrishna, P. Syamala, and A. Satyanarayana. *J. Indian Chem. Soc.* **78**, 237 (2001).
20. B. Mondal and R. Banerjee. *Transition Met. Chem.* **26**, 395 (2001).
21. A.B. Mondal, A.K. Bhattacharya, D. Maji, and R. Banerjee. *Polyhedron*, **17**, 1693 (1998).
22. M.S. Uretazanartu and P.B.O.L. Correa. *Soc. Chil. Quim.* **39**, 245 (1994).
23. J. Prasad and J.L. Gland. *Surf. Sci.* **258**, 67 (1991).
24. P. Ardiles, E. Trollund, M. Isaacs, F. Armijo, J.C. Canales, M.J. Aguirre, and M.J. Canales. *J. Mol. Catal. A Chem.* **165**, 169 (2001).
25. M. Isaacs, M.J. Aguirre, A. Toro-Labbe, J. Costamagna, M. Paez, and J.H. Zagal. *Electrochim. Acta*, **43**, 1821 (1998).
26. S.M.I. Golabi and F. Noor-Mohammadi. *J. Solid State*, **2**, 30 (1998).
27. J.J. Zhang, Y.M. Tse, W.J. Pietro, and A.B.P. Lever. *J. Electroanal. Chem.* **406**, 203 (1996).
28. I.G. Casella, M.R. Guascito, A.M. Salvi, and E. Desimoni. *Anal. Chim. Acta*, **354**, 333 (1997).
29. (a) J.H. Zagal. *J. Electroanal. Chem.* **109**, 389 (1990); (b) J.H. Zagal and S. U-Zanartu. *J. Electrochem. Soc.* **129**, 2242 (1982); (c) J.H. Zagal, E. Munoz, and S. U-Zanartu. *Electrochim. Acta*, **27**, 1373 (1982); (d) J.H. Zagal, S. Lira, and S. U-Zanartu. *J. Electroanal. Chem.* **95**, 210 (1986); (e) J.H. Zagal. *Coord. Chem. Rev.* **119**, 89 (1992).
30. K.M. Korfhage, K. Ravichandran, and R.P. Baldwin. *Anal. Chem.* **56**, 1514 (1984).
31. X. Cao, B. Wang, and Q. Su. *J. Electroanal. Chem.* **361**, 211 (1993).
32. Y. Fukumoto, T. Matsunaga, and T. Hayashi. *Electrochim. Acta*, **26**, 631 (1981).
33. M. Yang and H.L. Li. *Mikrochim. Acta*, **138**, 65 (2002).
34. D.R. Shankaran and S.S. Narayanan. *Russ. J. Electrochem.* **37**, 1149 (2001).
35. C. Zhao, J.F. Song, and J.C. Zhang. *Anal. Lett.* **34**, 2111 (2001).
36. M. Yang and H.L. Li. *Talanta*, **55**, 479 (2001).
37. J.M. Pingarron, I.O. Hernandez, A. Gonzalez-Cortes, and P. Yanez-Sedeno. *Anal. Chim. Acta*, **439**, 281 (2001).
38. T.Y. You, L. Niu, J.Y. Gui, S.J. Dong, and E.K. Wang. *J. Pharm. Biomed. Anal.* **19**, 231 (1999).
39. E.F. Perez, G.D. Neto, A.A. Tanaka, and L.T. Kubota. *Electroanal.* **10**, 111 (1998).
40. I.G. Casella, M.R. Guascito, A.M. Salvi, and E. Desimoni. *Anal. Chim. Acta*, **354**, 333 (1997).
41. Z.H. Song, L. Wang, J.L. Lu, and T.Z. Zhao. *Chin. Chem. Lett.* **12**, 799 (2001).
42. Z.H. Song, L. Wang, and T.Z. Zhao. *Anal. Lett.* **34**, 399 (2001).
43. B.X. Li, Z.J. Zhang, X.W. Zheng, and C.L. Xu. *Chemia Analityczna*, **45**, 709 (2000).
44. M.I. Evgenev, I.I. Evgeneva, and R.N. Ismailova. *J. Anal. Chem.* **55**, 933 (2000).
45. S.H. Wang, L.Y. Du, A.M. Zhang, and D.J. Liu. *Mikrochim. Acta*, **134**, 167 (2000).
46. A. Afkhami and A. Afshar-E-Asl. *Anal. Chim. Acta*, **419**, 101 (2000).
47. A.A. Ensafi, M.M. Sadeghie, and F. Emaei. *J. Anal. Chem.* **54**, 1024 (1999).
48. L.Y. Du, S.H. Wang, and A.M. Zhang. *Chin. J. Anal. Chem.* **27**, 927 (1999).
49. M. Dekker. *Encyclopedia of electrochemistry of the elements*. Vol. VIII. *Edited by* W.J. Plieth and A.J. Bard. Wiley, New York. 1973.
50. P. Ardiles, E. Trollund, M. Isaacs, F. Armijo, J.C. Canales, M.J. Agurre, and M.J. Canales. *J. Mol. Catal. A Chem.* **165**, 169 (2001).
51. J. Bard and L.R. Faulkner. *Electrochemical methods: Fundamentals and application*. Wiley, New York. 1980.
52. (a) F. Van Den Brink, W. Visscher, and E. Barendrecht. *J. Electroanal. Chem.* **157**, 305 (1983); (b) F. Van Den Brink, W. Visscher, and E. Barendrecht. *J. Electroanal. Chem.* **172**, 301 (1984).



# The relative stabilities of $\text{PhE}(\text{NH-}t\text{-Bu})_2$ and $\text{PhE}(\mu\text{-N-}t\text{-Bu})_2\text{EPh}$ ( $E = \text{As, Sb, and Bi}$ ): X-ray structures of $\{\text{Li}_2[\text{PhAs}(\text{N-}t\text{-Bu})_2]\}_2$ and $\text{PhE}(\mu\text{-N-}t\text{-Bu})_2\text{EPh}$ ( $E = \text{Sb, Bi}$ )

Glen G. Briand, Tristram Chivers, and Masood Parvez

**Abstract:** The reaction of  $\text{PhECl}_2$  with 2 equiv of  $\text{LiHN-}t\text{-Bu}$  has been studied for the series  $E = \text{As, Sb, and Bi}$  to determine the effect of the phenyl group on subsequent amine condensation processes. For  $\text{PhAsCl}_2$ , the metathesis product  $\text{PhAs}(\text{NH-}t\text{-Bu})_2$  **4** was obtained as a colourless oil. Similar reactions involving  $\text{PhECl}_2$ , where  $E = \text{Sb or Bi}$ , yielded the cyclodipnict(III)azanes  $\text{PhE}(\mu\text{-N-}t\text{-Bu})_2\text{EPh}$  **5** ( $E = \text{Sb}$ ) and **6** ( $E = \text{Bi}$ ), respectively. Treatment of **4** with 2 equiv of  $n\text{-BuLi}$  produced the dilithium salt  $\text{Li}_2[\text{PhAs}(\text{N-}t\text{-Bu})_2]$  **7a**. Products **4**, **5**, **6**, and **7a** were characterized by  $^1\text{H}$ ,  $^7\text{Li}$  (**7a**), and  $^{13}\text{C}$  NMR spectra, while **5**, **6**, and **7a** were also structurally characterized by X-ray crystallography. Compound **7a** is dimeric in the solid state via intermolecular  $\text{Li}\cdots\text{N}$  and  $\eta^6\text{-Li}\cdots\text{Ph}$  interactions. The cyclodipnict(III)azanes **5** and **6** have similar structures, with the exocyclic phenyl groups in *trans* positions relative to the  $\text{E}_2\text{N}_2$  ring. This synthetic approach provides a new route to the four-membered rings  $\text{RE}(\mu\text{-N-}t\text{-Bu})_2\text{ER}$  ( $E = \text{Sb, Bi}$ ) and the first example of a bis(organyl)cyclodibism(III)azane.

**Key words:** arsenic, antimony, bismuth, amides, imides.

**Résumé :** Afin de pouvoir déterminer l'effet du groupe phényle sur les processus subséquents de condensation de l'amine, on a étudié la réaction de  $\text{PhECl}_2$  ( $E = \text{As, Sb et Bi}$ ) avec deux équivalents de  $\text{LiHN-}t\text{-Bu}$ . Dans le cas du  $\text{PhAsCl}_2$ , le produit de dismutation,  $\text{PhAs}(\text{NH-}t\text{-Bu})_2$  (**4**), a été obtenu sous la forme d'huile incolore. Les réactions semblables de  $\text{PhECl}_2$  dans lesquelles  $E = \text{Sb ou Bi}$  conduisent respectivement aux cyclodipnict(III)azanes,  $\text{PhE}(\mu\text{-N-}t\text{-Bu})_2\text{EPh}$  (**5**,  $E = \text{Sb}$ ) et (**6**,  $E = \text{Bi}$ ). Le traitement du composé **4** avec deux équivalents de  $\text{BuLi}$  conduit à la formation du sel dilithié  $\text{Li}_2[\text{PhAs}(\text{N-}t\text{-Bu})_2]$  (**7a**). Les produits **4**, **5**, **6** et **7a** ont été caractérisés par leurs spectres RMN du  $^1\text{H}$  et du  $^7\text{Li}$  (**7a**) et des spectres RMN du  $^{13}\text{C}$  alors que les produits **5**, **6** et **7a** ont aussi été caractérisés par diffraction des rayons X. À l'état solide, le composé **7a** existe à l'état trimère par le biais d'interactions  $\text{Li}\cdots\text{N}$  et  $\eta^6\text{-Li}\cdots\text{Ph}$ . Les cyclodipnict(III)azanes **5** et **6** ont des structures semblables avec des groupes phényles exocycliques en positions *trans* par rapport au cycle  $\text{E}_2\text{N}_2$ . Cette approche fournit une nouvelle voie de synthèse vers les cycles à quatre chaînons  $\text{RE}(\mu\text{-N-}t\text{-Bu})_2\text{ER}$  ( $E = \text{Sb, Bi}$ ) et le premier exemple d'une bis(organyl)cyclodibism(III)azane.

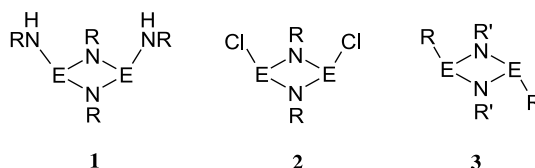
**Mots clés :** arsenic, antimoine, bismuth, amides, imides.

[Traduit par la Rédaction]

## Introduction

Pnicogen(III) compounds of secondary amines have been employed extensively as reagents for the preparation of compounds containing other functional groups (1). Homoleptic species  $\text{E}(\text{NR}_2)_3$  ( $E = \text{P, As, Sb, Bi}$ ) are synthesized via simple metathesis reactions of a pnicogen(III) halide with the appropriate amine or alkali metal amide. Analogous studies involving primary amines, on the other hand, have proven to be less predictable as a result of the remaining acidic amino

proton after initial  $\text{E}-\text{N}$  bond formation. Reactions involving primary amines and  $\text{PCl}_3$  do not afford tris(amino)pnictines  $\text{P}(\text{NHR})_3$ ; rather, further amine elimination occurs to yield [cyclodiphosph(III)azanes] **1**, **2**, cyclic systems  $(\text{CIPNR})_3$ ,  $\text{P}_4(\text{NR})_6$  cages, or other condensation products, depending on the choice of amine substituent and reaction stoichiometry (2, 3). Although there have been fewer such studies involving  $\text{ECl}_3$  ( $E = \text{As, Sb, Bi}$ ), similar condensation reactions are observed (4–12).



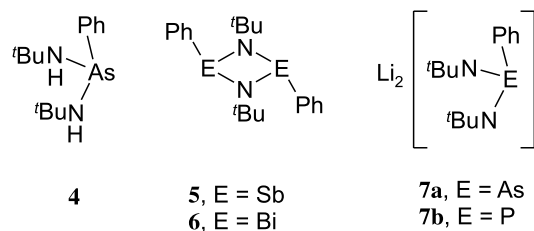
Received 16 October 2002. Published on the NRC Research Press Web site at <http://canjchem.nrc.ca> on 3 March 2003.

G.G. Briand, T. Chivers,<sup>1</sup> and M. Parvez. Department of Chemistry, The University of Calgary, Calgary, AB T2N 1N4, Canada.

<sup>1</sup>Corresponding author (e-mail: [chivers@ucalgary.ca](mailto:chivers@ucalgary.ca)).



In contrast to reactions involving  $\text{PCl}_3$ , metathesis products of  $\text{H}_2\text{N-}t\text{-Bu}$  and  $\text{RPhCl}_2$  ( $\text{R} = \text{Ph, Me, -}t\text{-Bu, C}_5\text{Me}_5$ ) yield  $\text{RP(NH-}t\text{-Bu)}_2$  rather than the condensation products **3** ( $\text{E} = \text{P}$ ) (6c, 13). The intermediates  $\text{RP(NH-}t\text{-Bu)Cl}$  ( $\text{R} = \text{Me, } t\text{-Bu}$ ) are also isolable, given the appropriate reaction stoichiometry (14). Similar observations have been made for reactions of  $\text{H}_2\text{N-}t\text{-Bu}$  and  $\text{RAsCl}_2$ , which yield  $\text{RAs(NH-}t\text{-Bu)}_2$  and  $\text{RAsCl(NH-}t\text{-Bu)}$  with formation of minor amounts of **3** ( $\text{E} = \text{As}$ ;  $\text{R}' = t\text{-Bu}$ ) (15). To our knowledge, related studies involving  $\text{RECl}_2$  ( $\text{E} = \text{Sb, Bi}$ ) have not been reported. They are of interest in determining the effect of the pnictogen organyl substituent on condensation processes in these systems. We now report the results of an investigation of the reaction between  $\text{LiHN-}t\text{-Bu}$  and  $\text{PhECl}_2$  for the series  $\text{E} = \text{As, Sb, and Bi}$ , which gives the metathesis product **4** for arsenic and the condensation products **5** and **6** for antimony and bismuth, respectively. Further, we describe the metallation of **4** to give **7a**, and the solid-state structures of **5**, **6**, and **7a**.



## Experimental section

### Reagents and general procedures

Solvents were dried and distilled over Na/benzophenone prior to use: diethyl ether and *n*-hexane. Phenylarsonic acid, triphenylantimony, and thionyl chloride were used as received from Aldrich. Antimony(III) chloride, triphenylbismuth, and bismuth(III) chloride were used as received from Strem.  $\text{PhAsCl}_2$  (16),  $\text{PhSbCl}_2$  (17),  $[\text{PhBiCl}_2(\text{thf})]$  (18), and  $\text{LiHN-}t\text{-Bu}$  (19) were prepared according to literature procedures (thf = tetrahydrofuran). Compound **4** has been reported previously, but was prepared via a different route and characterized by elemental analysis only (15a).

### Instrumentation

$^1\text{H}$ ,  $^{13}\text{C}$ ,  $^{31}\text{P}$ , and  $^7\text{Li}$  NMR spectra were recorded on a Bruker DRX 400 NMR spectrometer at 298 K. Chemical shifts are reported relative to  $\text{Me}_4\text{Si}$  in  $\text{C}_6\text{D}_6$  ( $^1\text{H}$  and  $^{13}\text{C}$ ), 85%  $\text{H}_3\text{PO}_4$  in  $\text{D}_2\text{O}$  ( $^{31}\text{P}$ ), and 1 M  $\text{LiCl}$  in  $\text{D}_2\text{O}$  ( $^7\text{Li}$ ). Elemental analyses were provided by the Analytical Services Laboratory, Department of Chemistry, University of Calgary.

### Preparation of $\text{PhAs(NH-}t\text{-Bu)}_2$ , **4**

A slurry of  $\text{LiHN-}t\text{-Bu}$  (4.134 g, 52.29 mmol) in diethyl ether (40 mL) was added dropwise to a solution of  $\text{PhAsCl}_2$  (5.828 g, 26.14 mmol) in diethyl ether (15 mL) at  $-90^\circ\text{C}$  to give a cloudy white mixture. The mixture was allowed to warm to  $23^\circ\text{C}$ , and after 18 h, the solvent was removed under vacuum. Hexane (30 mL) was added and the mixture was centrifuged. The supernatant was decanted and the solvent removed under vacuum to give **4** as a yellow oil, which was distilled ( $10^{-3}$  mm,  $\sim 80^\circ\text{C}$ ) to give a colourless oil

(5.140 g, 17.35 mmol, 66%). NMR data (thf- $d_8$ ):  $^1\text{H}$  NMR  $\delta$ : 1.25 (s, 18 H, N-*t*-Bu), 1.85 (s, 2 H, NH), 7.21–7.25 (m, 1 H, AsPh-*p*), 7.28–7.32 (m, 2H, AsPh-*o*), 7.69–7.72 (m, 2 H, AsPh-*m*).  $^{13}\text{C}$  NMR  $\delta$ : 33.7 (NCMe<sub>3</sub>), 52.5 (NCMe<sub>3</sub>), 128.9 (AsPh), 129.0 (AsPh), 131.6 (AsPh), 150.1 (AsPh).

### Preparation of $\text{PhSb}(\mu\text{-N-}t\text{-Bu})_2\text{SbPh}$ , **5**

A slurry of  $\text{LiHN-}t\text{-Bu}$  (2.108 g, 26.67 mmol) in diethyl ether (20 mL) was added dropwise to a solution of  $\text{PhSbCl}_2$  (3.597 g, 13.33 mmol) in diethyl ether (5 mL) at  $0^\circ\text{C}$  to give a cloudy yellow mixture, which was allowed to warm to  $23^\circ\text{C}$ . After 18 h, the solvent was removed under vacuum. Hexane (20 mL) was added, and the mixture was centrifuged. The supernatant was decanted, and the solvent was removed under vacuum to give **5** as a yellow-orange oil (3.071 g, 5.69 mmol, 85%). The oily product crystallized on standing at  $23^\circ\text{C}$  for 1 day. NMR data (thf- $d_8$ ):  $^1\text{H}$  NMR  $\delta$ : 1.26 (s, 18 H, N-*t*-Bu), 7.25–7.31 (m, 6 H, SbPh-*p/o*), 7.54–7.72 (m, 4 H, SbPh-*m*).  $^{13}\text{C}$  NMR  $\delta$ : 35.1 (NCMe<sub>3</sub>), 52.4 (NCMe<sub>3</sub>), 128.9 (SbPh), 129.2 (129.3) (SbPh), 134.1 (135.2) (SbPh). Anal. calcd. for  $\text{C}_{20}\text{H}_{28}\text{N}_2\text{Sb}_2$  (%): C 44.49, H 5.23, N 5.19; found: C 43.95, H 4.81, N 5.42.

### Preparation of $\text{PhBi}(\mu\text{-N-}t\text{-Bu})_2\text{BiPh}$ , **6**

A slurry of  $\text{LiHN-}t\text{-Bu}$  (0.100 g, 1.27 mmol) in diethyl ether (5 mL) was added dropwise to a solution of  $[\text{PhBiCl}_2(\text{thf})]$  (0.272 g, 0.633 mmol) in diethyl ether (5 mL) at  $0^\circ\text{C}$  to give a cloudy orange mixture, which was allowed to warm to  $23^\circ\text{C}$ . After 3 h, the solvent was removed under vacuum. After addition of hexane (5 mL), the mixture was centrifuged, and the supernatant was decanted and concentrated to 1 mL. After 2 days, red crystals of **6** were collected (0.040 g, 0.056 mmol, 18%). NMR data (thf- $d_8$ ):  $^1\text{H}$  NMR  $\delta$ : 0.66 (s, 18 H, N-*t*-Bu), 7.33 (m, 2 H, BiPh-*p*), 7.64 (m, 4 H, BiPh-*o*), 8.78 (m, 4 H, BiPh-*m*).  $^{13}\text{C}$  NMR  $\delta$ : 35.5 (NCMe<sub>3</sub>), 55.1 (NCMe<sub>3</sub>), 128.8 (BiPh), 131.3 (BiPh), 136.7 (BiPh). Anal. calcd. for  $\text{C}_{20}\text{H}_{28}\text{Bi}_2\text{N}_2$  (%): C 33.62, H 3.95, N 3.92; found: C 33.84, H 4.03, N 4.17.

### Preparation of $\text{Li}_2[\text{PhAs(N-}t\text{-Bu)}_2]$ , **7a**

A solution of 2.5 M *n*-BuLi in hexanes (8.10 mL, 20.28 mmol) was added dropwise to a solution of  $\text{PhAs(NH-}t\text{-Bu)}_2$  (3.003 g, 10.14 mmol) in diethyl ether (30 mL) at  $0^\circ\text{C}$  to give a cloudy yellow mixture, which was allowed to warm to  $23^\circ\text{C}$ . After 5 h, the solvent was removed under vacuum. The resulting product was washed with *n*-hexane ( $3 \times 5$  mL) to give **7a** as a white powder (2.002 g, 6.50 mmol, 64%). X-ray quality crystals were grown from diethyl ether – hexane at  $-15^\circ\text{C}$ . NMR data (thf- $d_8$ ):  $^1\text{H}$  NMR  $\delta$ : 1.04 (s, 18 H, N-*t*-Bu), 6.95 (t, 1 H, AsPh-*p*), 7.06 (t, 2 H, AsPh-*o*), 7.60 (d, 2 H, AsPh-*m*).  $^{13}\text{C}$  NMR  $\delta$ : 38.2 (NCMe<sub>3</sub>), 53.5 (NCMe<sub>3</sub>), 126.0, (AsPh), 127.5 (AsPh), 131.1 (AsPh).  $^7\text{Li}$  NMR  $\delta$ : 1.92, 2.41. Anal. calcd. for  $\text{C}_{14}\text{H}_{23}\text{AsLi}_2\text{N}_2$  (%): C 54.57, H 7.52, N 9.09; found: C 55.83, H 7.44, N 8.98.

### X-ray structural analyses

Crystals of **5**, **6**, and **7a** were coated with oil (Paratone 8277, Exxon) and mounted on glass fibres. Measurements were made on a Nonius KappaCCD diffractometer using



**Table 1.** Crystallographic data for **5**, **6**, and **7a**.

	<b>5</b>	<b>6</b>	<b>7a</b>
Empirical formula	C <sub>20</sub> H <sub>28</sub> N <sub>2</sub> Sb <sub>2</sub>	C <sub>20</sub> H <sub>28</sub> Bi <sub>2</sub> N <sub>2</sub>	C <sub>14</sub> H <sub>23</sub> AsLi <sub>2</sub> N <sub>2</sub>
Formula mass	539.94	714.40	308.14
Space group	<i>P</i> 2 <sub>1</sub> / <i>c</i>	<i>P</i> 2 <sub>1</sub> / <i>c</i>	<i>P</i> $\bar{1}$
<i>a</i> (Å)	6.6067(2)	9.0544(3)	9.0354(1)
<i>b</i> (Å)	20.1293(6)	9.3725(2)	10.1088(2)
<i>c</i> (Å)	8.4739(3)	12.6567(5)	10.6036(3)
$\alpha$ (°)	90	90	87.9151(9)
$\beta$ (°)	106.475(2)	92.641(1)	67.968(1)
$\gamma$ (°)	90	90	64.324(1)
<i>V</i> (Å <sup>3</sup> )	1080.66(6)	1072.94(6)	799.86(3)
<i>Z</i>	2	2	2
<i>F</i> (000)	528	656	320
<i>D</i> <sub>calcd</sub> (g cm <sup>-3</sup> )	1.659	2.211	1.279
$\mu$ (mm <sup>-1</sup> )	2.50	16.4	2.11
<i>T</i> (K)	170(2)	170(2)	170(2)
$\lambda$ (Å)	0.71069	0.71073	0.71073
<i>R</i> <sub>1</sub> <sup>a</sup>	0.048	0.024	0.027
<i>wR</i> <sub>2</sub> <sup>a</sup>	0.111	0.059	0.066

$$^a R_1 = (\Sigma |F_o| - |F_c|) / (\Sigma |F_o|) \text{ for } (F_o^2 > 2\sigma(F_o^2)), [I > 2\sigma(I)]; wR_2 = \{[\Sigma w(F_o^2 - F_c^2)^2] / [\Sigma w(F_o^2)^2]\}^{1/2} \text{ (all data)}.$$

monochromated Mo K $\alpha$  radiation. Crystallographic data are summarized in Table 1.<sup>2</sup>

Data were measured using  $\omega$  and  $\phi$  scans. The crystals showed no sign of decay during data collection, and no decay correction was employed. Cell constants were obtained from the refinement (20) of 2330 (**5**), 2208 (**6**), or 3484 (**7a**) reflections in the range  $1 < \phi < 27.5^\circ$ . The space groups for **5** and **6** were uniquely determined from the systematic absences. The data were corrected for Lorentz and polarization effects and for absorption using the multiscan method (20). The structures were solved using direct methods (21) and expanded using Fourier techniques (22) (SHELXL97) (23). The nonhydrogen atoms were refined anisotropically. Hydrogen atoms were included at geometrically idealized positions and were not refined.

The Sb atom in **5** was disordered over two sites, Sb1 and Sb2, with occupancy factors 0.574(1) and 0.426(1), respectively. The *t*-Bu group exhibited rotational disorder wherein the methyl C atoms were located over two sites each with site occupancy factors 0.83(1) and 0.17(1). The disorder in the phenyl ring was also apparent from the large thermal displacement parameters of its carbon atoms.

## Results and discussion

### Synthetic and NMR studies

The treatment of PhAsCl<sub>2</sub> with 2 equiv of LiHN-*t*-Bu in diethyl ether yields PhAs(NH-*t*-Bu)<sub>2</sub> **4** in ca. 65% yield, as a colourless oil, after vacuum distillation. <sup>1</sup>H and <sup>13</sup>C NMR spectra of the unpurified material show that primarily one product is formed in this reaction with very minor amounts

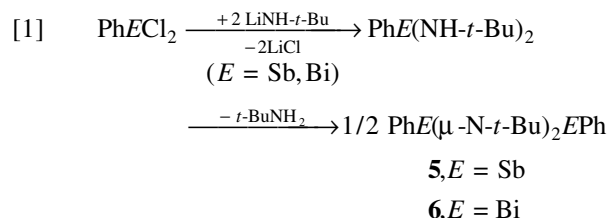
of impurities. The absence of the condensation product **3** (*E* = As, *R* = *R'* = *t*-Bu) represents an improvement on the existing synthesis of **4** (15a). The identity of **4** was established by <sup>1</sup>H and <sup>13</sup>C NMR spectra and by metallation with 2 equiv of *n*-butyllithium to yield the dilithium salt Li<sub>2</sub>[PhAs(N-*t*-Bu)<sub>2</sub>] **7a** (*R* = Ph), cf., the formation of Li<sub>2</sub>[PhP(N-*t*-Bu)<sub>2</sub>] **7b** from PhP(NH-*t*-Bu)<sub>2</sub> (13a). The resulting colourless crystals were of sufficient quality to allow a definitive characterization via X-ray crystallographic analysis (vide infra). Wright and co-workers have recently described extensive studies of the formation of the [As(N-*t*-Bu)<sub>3</sub>]<sup>3-</sup> trianion by the reaction of As(NMe<sub>2</sub>)<sub>3</sub> (1 equiv) with a mixture of *t*-BuNH<sub>2</sub> and *t*-BuNHLi (3:3 equiv) (24). Although the formation of As(NH-*t*-Bu)<sub>3</sub> is implied in this synthesis, this intermediate was not isolated. The authors propose a facile condensation to produce the cyclo-diars(III)azane, *t*-BuN(H)As(μ-N-*t*-Bu)<sub>2</sub>AsN(H)-*t*-Bu (**3**, *E* = As, *R* = *R'* = *t*-Bu) to explain this observation (24).

The reaction of PhSbCl<sub>2</sub> with 2 equiv of LiHN-*t*-Bu yields a yellow-orange oil after removal of the solvent. The oil crystallizes after 1 day at 23°C, and it was identified by CHN analyses and NMR spectra as the condensation product PhSb(μ-N-*t*-Bu)<sub>2</sub>SbPh **5**. Compound **5** was obtained in 85% yield and the <sup>1</sup>H and <sup>13</sup>C NMR spectra of the unpurified material indicated a single product. For PhBiCl<sub>2</sub>, the corresponding reaction proceeds in a similar manner but, in this case, the crude product was isolated as a solid. Crystals were obtained from *n*-hexane and characterized as PhBi(μ-N-*t*-Bu)<sub>2</sub>BiPh **6**. The <sup>1</sup>H NMR spectrum of the reaction mixture exhibits three N-*t*-Bu resonances at  $\delta$  0.66, 1.01, and 1.07, with approximate relative intensities 1:2:1, in addition to a

<sup>2</sup>Supplementary data may be purchased from the Depository of Unpublished Data, Document Delivery, CISTI, National Research Council Canada, Ottawa, ON K1A 0S2, Canada ([http://www.nrc.ca/cisti/irm/unpub\\_e.shtml](http://www.nrc.ca/cisti/irm/unpub_e.shtml) for information on ordering electronically). CCDC 188507(**7a**), 188508(**5**), and 188509(**6**) contain the supplementary data for this paper. These data can be obtained, free of charge, via [www.ccdc.cam.ac.uk/conts/retrieving.html](http://www.ccdc.cam.ac.uk/conts/retrieving.html) (or from the Cambridge Crystallographic Data Centre, 12 Union Road, Cambridge, U.K.; fax +44 1223 336033; or [deposit@ccdc.cam.ac.uk](mailto:deposit@ccdc.cam.ac.uk)).



complex set of overlapping Ph resonances. The *trans*-isomer of **6** was isolated in ca. 20% yield and shown to be attributable to the resonance at  $\delta$  0.66. It is tentatively proposed that one of the other products is the *cis*-isomer of **6**, but attempts to isolate this component by fractional crystallization were unsuccessful. A candidate for the second unidentified product is the monosubstituted derivative  $\text{PhBi}(\text{Cl})(\text{NH-}t\text{-Bu})$ . However, when the reaction was carried out in a 1:1 stoichiometry, no resonances were observed at  $\delta$  0.66, 1.01, or 1.07 in the  $^1\text{H}$  NMR spectrum. Resonances attributable to the *N-t*-Bu groups of an unidentified product appeared at  $\delta$  1.70 and 1.88.



For both **5** and **6**, the  $^1\text{H}$  NMR spectra of the pure products show resonances for *N-t*-Bu and Ph groups in the ratio 1:1, suggesting that a condensation reaction has occurred (eq. [1]). Previous routes to bis(organyl)cyclodistib(III)azanes **3** ( $E = \text{Sb}$ ;  $R = \text{Me}$ , *t*-Bu) involve metathesis reactions between the organolithium reagents and  $\text{ClSb}(\mu\text{-N-}t\text{-Bu})_2\text{SbCl}$  (**2**,  $E = \text{Sb}$ ,  $R = t\text{-Bu}$ ), which is prepared from  $\text{SbCl}_3$  and  $\text{Li}(\text{Me}_3\text{Si})\text{N-}t\text{-Bu}$  (**24a**, **24b**). Bismuth analogues of **3** ( $E = \text{Bi}$ ) have not been reported, nor have the dichloro derivatives **2** ( $E = \text{Bi}$ ). The reaction of organyldihalopnictines and lithiated primary amides thus represents a novel synthetic route to these cyclodipnict(III)azanes.

### X-ray structural analyses

ORTEP diagrams of **5** and **6** are shown in Figs. 1 and 2, respectively. The X-ray structure analyses of **5** and **6** confirm the formation of condensation products. In both structures, the exocyclic Ph groups are in a *trans* arrangement with respect to the  $\text{E}_2\text{N}_2$  ring. In the case of **5**, there is a static disorder in the Sb atom over two positions, giving two unique molecules (Fig. 1). In one molecule, Sb(1) is bound to C(5) of the phenyl ring and N(1) of the *N-t*-Bu group, giving a *trans*- $\text{PhSb}(\mu\text{-N-}t\text{-Bu})_2\text{SbPh}$  structure, as a result of inversion symmetry. The second molecule shows Sb(2) bound to C(6) of the phenyl ring, as well as N(1) of the *N-t*-Bu group, giving an  $\text{Sb}_2\text{N}_2$  ring that also has a *trans*- $\text{PhSb}(\mu\text{-N-}t\text{-Bu})_2\text{SbPh}$  structure. The Sb—N and Sb—N\* interactions are quite different in one molecule, but not in the other (Sb(1)—N(1) = 1.988(4) Å, Sb(1)—N(1\*) = 2.063(4) Å; Sb(2)—N(1) = 2.019(4) Å, Sb(2)—N(1\*) = 2.034(4) Å). However, the average Sb—N bond distances are similar for the two molecules (|Sb(1)—N| = 2.02(4) Å; |Sb(2)—N| = 2.027(8) Å), while the Sb—C<sub>phenyl</sub> bond distances are significantly different (Sb(1)—C(5) = 2.169(5) Å; Sb(2)—C(6) = 2.234(7) Å). The structural parameters for **5** and **6** are compared in Table 2. As expected, bond lengths to the bismuth centre in **6** are longer than those to the antimony centres (Bi—C = 2.285(4) Å vs. Sb—C = 2.169(5) and 2.234(7) Å; Bi—N = 2.163(3) and 2.167(3) Å vs. Sb—N = 1.988(4)–2.063(4) Å), and the bond angles at the bismuth centre are

**Fig. 1.** ORTEP diagram of **5** showing the two disordered molecules (30% probability ellipsoids). Symmetry transformations used to generate equivalent atoms:  $-x + 1$ ,  $-y$ ,  $-z + 1$ .

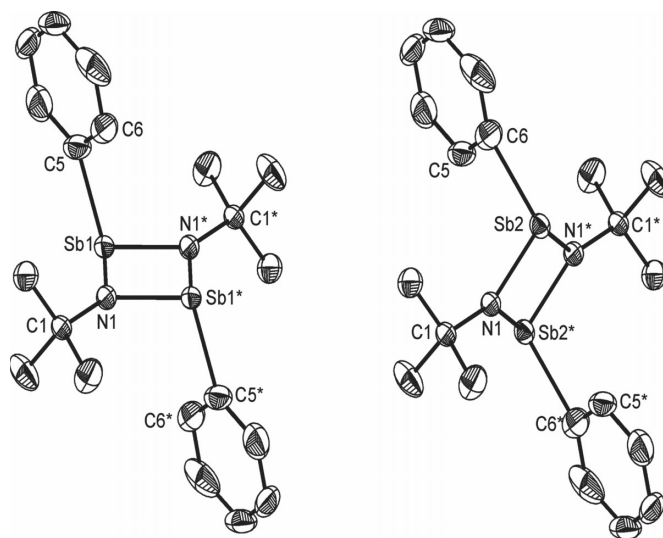
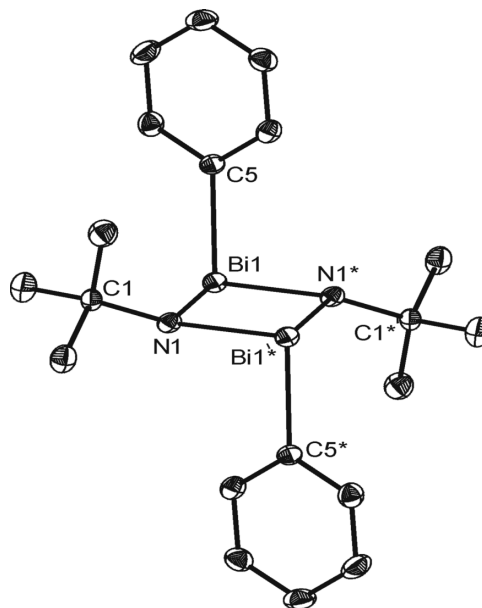


**Fig. 2.** ORTEP diagram of **6** (30% probability ellipsoids). Symmetry transformations used to generate equivalent atoms:  $-x$ ,  $-y$ ,  $-z + 1$ .



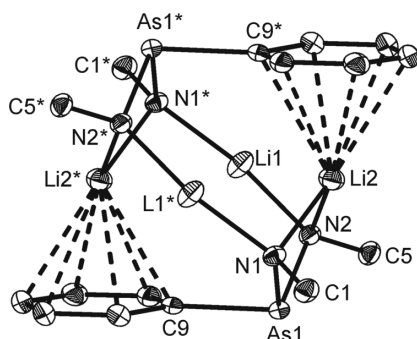
considerably smaller than those at antimony. These observations can be attributed to the larger covalent radius of Bi(III) vs. Sb(III).

Only one example of a bis(organyl)cyclodistib(III)azane has been structurally characterized, i.e., *trans-t*-BuSb( $\mu\text{-N-}t\text{-Bu}$ )<sub>2</sub>Sb-*t*-Bu **8** (25). Comparison of the bond angles and Sb—N<sub>ring</sub> bond distances in **5** and **8** show all values to be in the same range. The Sb—C bond distances in **5** are shorter than those of **8** (2.252(6) Å), presumably as a result of  $sp^2$  rather than  $sp^3$  hybridization of carbon. Comparison with other analogues shows that the bond angles at antimony in **5** are greater than those in  $[(\text{RHN})\text{Sb}(\mu\text{-NR})_2(\text{NHR})]$  ( $R = 2,6\text{-Me}_2\text{C}_6\text{H}_3$ ) **9** (8), while the Sb—N<sub>ring</sub> bond distances are in



**Table 2.** Selected bond lengths (Å) and bond angles (°) for **5** and **6**.

	<b>5</b>	<b>6</b>
<b>Bond lengths (Å)</b>		
<i>E</i> (1)—C(5)	2.169(5)	2.285(4)
<i>E</i> (1)—N(1)	1.988(4)	2.167(3)
<i>E</i> (1)—N(1*)	2.063(4)	2.163(3)
<i>E</i> (2)—C(6)	2.234(7)	
<i>E</i> (2)—N(1)	2.019(4)	
<i>E</i> (2)—N(1*)	2.034(4)	
<b>Bond angles (°)</b>		
C(5)— <i>E</i> (1)—N(1)	103.7(2)	93.4(1)
C(5)— <i>E</i> (1)—N(1*)	103.3(2)	102.2(1)
N(1)— <i>E</i> (1)—N(1*)	77.7(2)	78.7(1)
<i>E</i> (1)—N(1)— <i>E</i> (1*)	102.3(2)	101.3(1)
C(6)— <i>E</i> (2)—N(1)	104.9(3)	
C(6)— <i>E</i> (2)—N(1*)	104.3(2)	
N(1)— <i>E</i> (2)—N(1*)	77.7(2)	
<i>E</i> (1)—N(1)— <i>E</i> (1*)	102.3(2)	

**Fig. 3.** ORTEP diagram of **7a** (*R* = Ph; methyl carbon atoms of *t*-Bu groups are removed for clarity; 30% probability ellipsoids). Symmetry transformations used to generate equivalent atoms:  $-x + 1, -y, -z + 2$ .

same range. As **6** is the first structurally characterized example of a bis(organyl)cyclodibism(III)azane,  $R\text{Bi}(\mu\text{-NR}')_2\text{BiR}$ , no direct structural comparisons can be made. However, comparison with  $[(\text{RHN})\text{Bi}(\mu\text{-NR}')_2(\text{NHR})]$  (*R* = 2,6-*i*-Pr<sub>2</sub>C<sub>6</sub>H<sub>3</sub>) **10**, the only reported analogue (9), shows the bond angles in **6** to be larger, while the Bi—N<sub>ring</sub> bond distances are similar. The larger bond angles for **5** and **6** are counterintuitive given the steric bulk of the substituted phenyl substituents in **9** and **10**, respectively.

An ORTEP diagram of **7a** is depicted in Fig. 3. The complex **7a** is isostructural with **7b**, reported previously (13a), and the metrical parameters are compared in Table 3. The structure shows the pnictogen atom bound to a phenyl carbon atom and two *tert*-butylamido nitrogen atoms in a pyramidal arrangement. One of the lithium atoms (Li(2)) is symmetrically chelated by the ligand in an *N,N'* manner (Li(2)—N(1) = 2.015(4) Å; Li(2)—N(1) = 2.011(4) Å), while the second lithium atom (Li(1)) is bound to one nitrogen atom (N(1)) only (1.916(4) Å). The resulting moiety dimerizes via a short Li(1)—N(2\*) interaction (1.920(4) Å) and an η<sup>6</sup>-Li···Ph\* interaction (Li(2)—C<sup>phenyl</sup>\* = 2.624(4)–2.752(4) Å) to the second molecule. The most significant differences in

**Table 3.** Selected bond lengths (Å) and bond angles (°) for **7a** (*E* = As) and **7b** (*E* = P).

	<b>7a</b>	<b>7b<sup>a</sup></b>
<b>Bond lengths (Å)</b>		
<i>E</i> (1)—C(9)	2.004(2)	1.867(3)
<i>E</i> (1)—N(1)	1.853(2)	1.693(2)
<i>E</i> (1)—N(2)	1.850(2)	1.686(3)
Li(1)—N(1)	1.916(4)	1.918(5)
Li(1)—N(2*)	1.920(4)	1.928(6)
Li(2)—N(1)	2.015(4)	2.027(6)
Li(2)—N(2)	2.011(4)	2.017(5)
Li(2)—C <sup>phenyl</sup> *	2.624(4)–2.752(4)	2.618(6)–2.750(6)
<b>Bond angles (°)</b>		
C(9)— <i>E</i> (1)—N(1)	97.21(7)	99.8(1)
C(9)— <i>E</i> (1)—N(2)	97.32(7)	100.8(1)
N(1)— <i>E</i> (1)—N(2)	97.15(7)	102.8(1)

<sup>a</sup>Values for one of two unique molecules (13a).

the structures of **7a** and **7b** involve the longer *E*—C and (or) *E*—N bond distances and the smaller bond angles at the pnictogen center in **7a** (see Table 3), both of which are a result of the larger covalent radius of As(III) vs. P(III). For comparison with the unsolvated structure of **7a**, crystallization of **7a** from THF produces the trisolvated monomer  $\{(\text{THF})_3\text{Li}_2[\text{PhAs}(\text{N-}t\text{-Bu})_3]\}$  in which the  $[\text{PhAs}(\text{N-}t\text{-Bu})_2]^{2-}$  ligand is *N,N'* chelated to both Li<sup>+</sup> ions. Each Li<sup>+</sup> ion is further coordinated by one terminal and one bridging THF molecule (26).

## Conclusions

The reaction of  $\text{PhECl}_2$  with 2 equiv of  $\text{LiHN-}t\text{-Bu}$  has been studied for comparison with previous work on the analogous phosphorus systems, which yield bis(amido)organylphosphines. These reactions result in the formation of  $\text{PhAs}(\text{NH-}t\text{-Bu})_2$  in the case of arsenic, while a subsequent condensation reaction to afford the *trans*-cyclodipnict(III)azanes  $\text{PhE}(\mu\text{-N-}t\text{-Bu})_2\text{EPh}$  is observed for both the antimony and bismuth systems. This synthetic route represents a novel pathway to  $\text{RE}(\mu\text{-NR}')_2\text{ER}$  (*E* = Sb, Bi) species, including the first example of a bismuth analogue. The metallation of  $\text{PhAs}(\text{NH-}t\text{-Bu})_2$  with  $\text{Li-}n\text{-Bu}$  produces a dimeric dilithiated derivative that is isostructural with the phosphorus analogue.

## Acknowledgments

We thank Dr. Gabriele Schatte, Dorothy Fox, Qiao Wu, and Dr. Raghav Yamdagni for assistance in collecting NMR data and the Natural Sciences and Engineering Research Council of Canada (NSERC) for funding.

## References

- For a review see: M.A. Beswick, D.S. Wright. *Coord. Chem. Rev.* **176**, 373 (1998), and refs. therein.
- (a) T.G. Hill, R.C. Haltiwanger, M.L. Thompson, S.A. Katz, and A.D. Norman. *Inorg. Chem.* **33**, 1770 (1994); (b) N.D. Reddy, A.J. Elias, and A. Vij. *J. Chem. Soc. Dalton Trans.* 2167 (1997); (c) I. Schranz, L. Stahl, and R.J. Staples. *Inorg. Chem.* **37**, 1493 (1998); (d) N. Burford, T.S. Cameron, K.D.



- Conroy, B. Ellis, C.L.B. MacDonald, R. Ovans, A.D. Phillips, P.J. Ragogna, and D. Walsh. *Can. J. Chem.* **80**, 1404 (2002).
3. (a) V.D. Romanenko, A.B. Drapailo, A.N. Chernega, and L.N. Markovskii. *Zh. Obshch. Khim.* **61**, 2434 (1991); (b) R. Murugavel, S.S. Krishnamurthy, J. Chandrasekhar, and M. Nethaji. *Inorg. Chem.* **32**, 5447 (1993); (c) R.R. Holmes. *J. Am. Chem. Soc.* **83**, 1334 (1961); (d) F.A. Cotton, J.G. Riess, C.E. Rice, and B.R. Stults. *Inorg. Chem.* **17**, 3521 (1978); (e) M.L. Thompson, R.C. Haltiwanger, and A.D. Norman. *J. Chem. Soc. Chem. Comm.* 647 (1979); (f) M.L. Thompson, A. Tarassoli, R.C. Haltiwanger, and A.D. Norman. *J. Am. Chem. Soc.* **103**, 6770 (1981); (g) M.L. Thompson, A. Tarassoli, R.C. Haltiwanger, and A.D. Norman. *Inorg. Chem.* **26**, 684 (1987).
4. (a) H.J. Vetter, H. Strametz, and H. Nöth. *Angew. Chem.* **75**, 417 (1963); (b) U. Wirringa, H.W. Roesky, M. Noltemeyer, and H.G. Schmidt. *Angew. Chem. Int. Ed. Engl.* **32**, 1628 (1993).
5. (a) H.J. Vetter, H. Nöth, and W. Jahn. *Z. Anorg. Allg. Chem.* **328**, 144 (1964); (b) J. Weiss and W. Eisenhuth. *Z. Anorg. Allg. Chem.* **350**, 9 (1967).
6. (a) G.A. Olah and A.A. Oswald. *Can. J. Chem.* **38**, 1428 (1960); (b) R. Bohra, H.W. Roesky, M. Noltemeyer, and G.M. Sheldrick. *Acta Crystallogr.* **C40**, 1150 (1984); (c) J.T. Ahlemann, H.W. Roesky, R. Murugavel, E. Parisini, M. Noltemeyer, H.G. Schmidt, O. Müller, R. Herbst-Irmer, L.N. Markovskii, and Y.G. Shermolovich. *Chem. Ber.* **130**, 1113 (1997).
7. D.C. Haagenson, L. Stahl, and R.J. Staples. *Inorg. Chem.* **40**, 4491 (2001).
8. R. Bryant, S.C. James, J.C. Jeffrey, N.C. Norman, A.G. Orpen, and U. Weckmann. *J. Chem. Soc. Dalton Trans.* 4007 (2000).
9. U. Wirringa, H.W. Roesky, M. Noltemeyer, and H.-G. Schmidt. *Inorg. Chem.* **33**, 4607 (1994).
10. S.C. James, N.C. Norman, A.G. Orpen, M.J. Quayle, and U. Weckmann. *J. Chem. Soc. Dalton Trans.* 4159 (1996).
11. N. Burford, C.L.B. MacDonald, K.N. Robertson, and T.S. Cameron. *Inorg. Chem.* **35**, 4013 (1996).
12. P.B. Hitchcock, M.F. Lappert, A.K. Rai, and H. Williams. *J. Chem. Soc. Chem. Commun.* 1633 (1986).
13. (a) B. Eichhorn, H. Nöth, and T. Seifert. *Eur. J. Inorg. Chem.* 2355 (1999); (b) T. Bauer, S. Schulz, and M. Nieger. *Z. Anorg. Allg. Chem.* **627**, 266 (2001); (c) A.P. Lane, D.A. Morton-Blake, and D. Payne. *J. Chem. Soc. A*, 1492 (1967); (d) P.B. Hitchcock, H.A. Jasim, M.F. Lappert, and H.D. Williams. *J. Chem. Soc. Chem. Comm.* 1634 (1986).
14. O.J. Scherer and P. Klusmann. *Angew. Chem. Int. Ed. Engl.* **8**, 752 (1969).
15. (a) G.I. Kokorev, R.Z. Musin, S.K. Badrutdinov, F.G. Khlitov, A.B. Platonov, and F.D. Yambushev. *Zh. Obshch. Khim.* **59**, 1551 (1989); (b) E.V. Avtomonov, K. Megges, X. Li, J. Lorberth, S. Wocadlo, W. Massa, K. Harms, A.V. Churakov, and J.A.K. Howard. *J. Organomet. Chem.* **544**, 79 (1997).
16. W. Steinkopf and S. Schmidt. *Ber. Dtsch. Chem. Ges.* **61**, 675 (1928).
17. M. Nunn, B. Sowerby, and D.M. Wesolek. *J. Organomet. Chem.* **51**, C45 (1983).
18. W. Clegg, R.J. Errington, G.A. Fisher, R.J. Flynn, and N.C. Norman. *J. Chem. Soc. Dalton Trans.* 637 (1993).
19. N.D.R. Barnett, W. Clegg, L. Horsburgh, D.M. Lindsay, Q-Y. Liu, F.M. MacKenzie, R.E. Mulvey, and P.G. Williard. *Chem. Commun.* 2321 (1996).
20. DENZO-SMN: Z. Otwinowski and W. Minor. *Methods Enzymol.* **276**, 307 (1997).
21. SIR92: A. Altomare, M. Cascarano, C. Giacovazzo, and A. Guagliardi. *J. Appl. Crystallogr.* **26**, 343 (1993).
22. DIRDIF94: P.T. Beurskens, G. Admiraal, G. Beurskens, W.P. Bosman, R. de Gelder, R. Israel, and J.M.M. Smits. *The DIRDIF-94 program system. Technical Report of the Crystallographic Laboratory, University of Nijmegen, The Netherlands*, 1994.
23. G.M. Sheldrick. 1997. SHELXL97: Program for the Solution of Crystal Structures [computer program]. Version 2. University of Göttingen, Göttingen, Germany.
24. A. Bashall, A.D. Bond, A.D. Hopkins, S.J. Kidd, M. McPartlin, A. Steiner, R. Wolf, A.D. Woods, and D.S. Wright. *J. Chem. Soc. Dalton Trans.* 343 (2002).
25. (a) B. Ross, J. Belz, and M. Nieger. *Chem. Ber.* **123**, 975 (1990); (b) N. Kuhn and O.J. Scherer. *Z. Naturforsch.* **34b**, 888 (1979).
26. G.G. Briand, T. Chivers, and M. Parvez. *J. Chem. Soc. Dalton Trans.* 3785 (2002).



# Solvent-dependent rate constants of muonium atom reactions

Stefan Karolczak, Hugh A. Gillis, Gerald B. Porter, and David C. Walker

**Abstract:** The rates of reaction of muonium atoms with solutes, ionic and organic, were studied in solvents of widely differing polarities (water, methanol, and hexane) and their rate constants were compared, where possible. In these reactions — which are those of a highly reactive atom, an isotope of hydrogen — it transpires that the reaction rates are higher in solvents in which the solute is more soluble and muonium diffuses faster. This study leads to various kinetic-solvent-effect ratios and to the observation of the reaction of muonium with free radicals being among the fastest reactions recorded so far between two neutral species in solution.

**Key words:** muonium atoms, kinetic isotope effects, solvent-dependent rates, non-aqueous solvents, muon spin rotation technique.

**Résumé :** Opérant dans des solvants de polarités extrêmement différentes (eau, méthanol et hexane), on a déterminé les vitesses de réaction des atomes de muonium avec des solutés ioniques et organiques et, dans les cas où cela était possible, on a comparé leurs constantes de vitesse. Dans ces réactions — qui sont celles d'un atome très réactif, un isotope de l'hydrogène il est normal que les vitesses de réaction soient plus élevées dans les solvants dans lesquels le soluté est le plus soluble et le muonium diffuse le plus rapidement. Cette étude conduit à divers rapports « d'effet cinétique du solvant » et à l'observation que les vitesses de réactions des muonium avec des radicaux libres sont les plus élevées qui aient pu être mesurées pour des réactions entre des espèces neutres en solution.

**Mots clés :** atomes de muonium effets isotopiques cinétiques, vitesses de réaction qui varient avec le solvant, solvants non aqueux, technique de la rotation de spin du muon.

[Traduit par la Rédaction]

## Introduction

Reactions in solution are expected to have rates that are somewhat influenced by the physicochemical properties of the solvent and its interactions with the reacting solutes. In this paper we explore the potential of using the muonium atom ( $\text{Mu}$ ,  $\mu^+e^-$ ) to study solvent-dependent kinetics and its possible value in determining cross-solvent kinetic isotope effects. Water and *n*-hexane were taken as a pair of solvents at opposite extremes in terms of polarity and solvating power, with methanol squarely in between. Muonium is readily formed in all three solvents and is sufficiently long-lived ( $>1 \mu\text{s}$ ) in each to allow for the evaluation of muonium-reaction rate constants,  $k_M$ . In these experiments  $k_M$  is evaluated by directly observing the rate-of-disappearance of Mu due to the presence of solutes at known concentrations.

Whereas there is a wealth of data on the reaction of H-atoms with solutes dissolved in water (1), for comparison with Mu (2), there is a dearth of comparable information in organic solvents.

## Experimental

These were transverse-field muon spin rotation experiments (TF- $\mu\text{SR}$ ). They involved placing deoxygenated solutions in 50 mL round-bottomed glass flasks in the SFUMU cart in the “backward” muon beam of the M9B beamline at TRIUMF. The results are now archived as experiments 15 045 – 15 109 in the  $\mu\text{SR}$  Facility. The observed count rates were subjected to on-line analysis; and then computer-fitted to the usual TF- $\mu\text{SR}$  equation, eq. [1] (3).

$$[1] \quad N_t = N_0 \exp(-t/\tau) [1 + A_M \exp(-\lambda t) \cos(\omega_M t + \phi_M) + A_D \cos(\omega_D t + \phi_D)] + N_0 B_g$$

In this equation,  $N$  (at times  $t$  and 0) is the observed count rate,  $\tau$  is the mean muon lifetime of  $2.2 \mu\text{s}$ ,  $B_g$  a background factor,  $A_M$ ,  $\omega_M$ , and  $\phi_M$  are, respectively, the asymmetry, precession frequency, and initial phase of the Mu signal, with  $A_D$ ,  $\omega_D$ , and  $\phi_D$  the corresponding values for all diamagnetic muon states collectively designated as D. For these experi-

Received 7 November 2002. Published on the NRC Research Press Web site at <http://canjchem.nrc.ca> on 28 February 2003.

**S. Karolczak.** Instytut Techniki Radiacyjnej, Politechnika, 93–590 Lodz, Wroblewskiego 15, Poland.

**H.A. Gillis.** St Francis Xavier University, Antigonish, NS B2G 2W5, Canada.

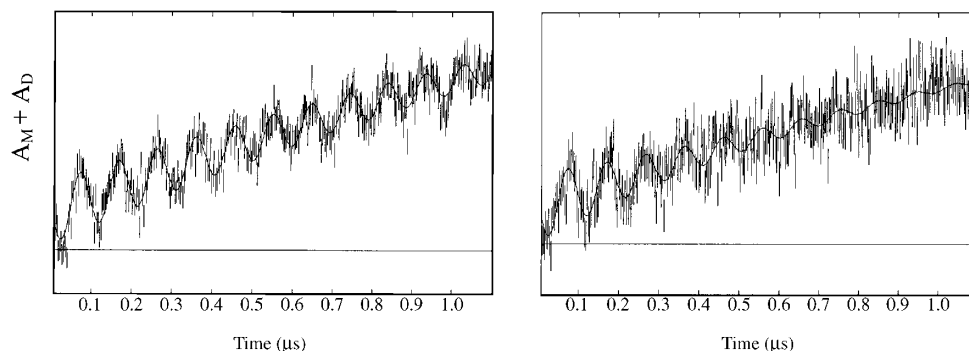
**G.B. Porter.** Chemistry Department, The University of British Columbia, Vancouver, BC V6T 1Z1, Canada.

**D.C. Walker**<sup>1</sup>. Chemistry Department and TRIUMF, The University of British Columbia, Vancouver, BC V6T 1Z1, Canada.

<sup>1</sup>Corresponding author (e-mail: [walker@triumf.ca](mailto:walker@triumf.ca)).



**Fig. 1.** (a) Plot of the TF- $\mu$ SR asymmetry ( $A_M + A_D$ ) over the first  $\mu$ s in neat  $n$ -hexane at room temperature with an applied transverse magnetic field of 7.5 G. (The 0.1  $\mu$ s (10.5 MHz) oscillation corresponds to  $A_M$ , which is superposed on the  $A_D$  oscillation at 0.1 MHz — where the latter happens to appear as the overall gradual rise because its initial phase is caught in an upward arch in these plots from the UP counter of SFUMU.) (b) Analogous plot to that in (a), except the hexane contains nitrobenzene at a concentration of 0.15 mM. (The “relaxation” (decay) of the 10.5 MHz Mu signal in (b) compared with (a) corresponds to  $\lambda$  for the reaction of nitrobenzene with Mu.)



ments the important parameter is  $\lambda$ , a pseudo first-order rate constant representing the decay of Mu by chemical reactions (and by any other Mu-loss processes beyond the spontaneous muon decay accounted for in the  $\exp(t/\tau)$  term). On-line computer analysis based on eq. [1] gives “best-fit” values for  $\lambda$ .

A typical plot of “asymmetry” ( $A_M + A_D$ ) versus time is shown in Fig. 1a for neat hexane and Fig. 1b for a solution of nitrobenzene. Here the computer has plotted asymmetry alone by dividing by the  $\exp(t/\tau)$  term, so that the only relaxation of the signal is represented by  $\lambda$ . (It also renormalizes  $N$  by subtracting the background factor.) In all the experiments reported here a transverse magnetic field of 7.5 G was applied, so  $\omega_M$  is about 10.5 MHz (corresponding to the wiggles seen in the asymmetry plot), whereas  $\omega_D$  is merely 0.1 MHz, and its time variation is seen only as the general upward curvature corresponding to one tenth of one cycle over the first microsecond. The effect of a solute that reacts with Mu appears as a relaxation of the Mu asymmetry signal as can be seen in Fig. 1 by comparing 1b with 1a. This represents a “direct” method of observing Mu as it reacts with a solute in an analogous manner to many pulse radiolysis studies.

The organic solvents used were the best commercially available to us and were not purified further because they had acceptable Mu background decay constants ( $\lambda_0$ ), which arise from a combination of inherent impurities and reaction with the solvent. The hexane was from ACROS Organics and gave  $\lambda_0 \sim 0.7 \mu\text{s}^{-1}$ , the methanol from Aldrich gave  $\lambda_0 \sim 0.5 \mu\text{s}^{-1}$ , and the water purified locally had  $\lambda_0 < 0.2 \mu\text{s}^{-1}$ . These  $\lambda_0$  values contributed to the overall errors in the values of  $k_M$  reported, because  $\lambda = \lambda_0 + k_M[S]$ , and  $k_M$  is evaluated from the slope of plots of  $\lambda$  versus solute concentration  $[S]$ . In fact the realistic error-bars on  $k_M$  were usually in the  $\pm 15$ –25% range because of different sensitivities of one counter compared with another in the  $\mu$ SR measurement itself due to variations in positioning and thickness of cell walls, etc. For all solutions the “up” and “down” counters on the SFUMU cart were treated as separate detectors to give a pair of readings at each concentration of solute. A typical  $\lambda$  versus  $[S]$  plot involved six or eight points covering three or four con-

**Table 1.** Rate constants ( $k_M$  ( $10^9 \text{ M}^{-1} \text{ s}^{-1}$ )) for Mu reactions in three solvents at  $\sim 295 \text{ K}$ .

Solute	$k_M$ (water)	$k_M$ (methanol)	$k_M$ (hexane)
$\text{NO}_2^-$	8.0 ( $\pm 1.5$ )	5.3 ( $\pm 1.5$ )	—
$\text{NO}_3^-$	1.5 ( $\pm 0.2$ ) <sup>a</sup>	1.1 ( $\pm 0.3$ )	—
TEMPO	16 ( $\pm 3$ )	48 ( $\pm 7$ )	80 ( $\pm 20$ )
TEMPO-OH	14 ( $\pm 3$ )	50 ( $\pm 10$ )	60 ( $\pm 20$ )
Nitrobenzene	11 ( $\pm 3$ ) <sup>b</sup>	—	13 ( $\pm 1.5$ )
$\text{CCl}_4$	—	0.3 ( $\pm 0.2$ )	<0.5 ( $\pm 0.2$ )

<sup>a</sup>Reference (4) (and confirmed in ref. (10)).

<sup>b</sup>Reference (5).

centrations. When using the TF- $\mu$ SR technique it is necessary to keep changing the concentration of the solute until the chemical lifetime of Mu falls into the narrow observation window of about 0.3 to 1.5  $\mu$ s. This can be tedious when  $k_M$  is completely unknown.

## Results

The values obtained for muonium rate constants ( $k_M$ ) in water, methanol, and hexane towards six solutes are given in Table 1 (where solubility and reactivity allowed). Of the six solutes studied, two were a related pair of ionic solutes (nitrate and nitrite), two were a related pair of organic free-radicals (“TEMPO”, 2,2,6,6-tetramethyl-1-piperidine-*N*-oxyl, and “TEMPO-OH”, 4-hydroxy-TEMPO), and two were powerful electron scavengers (nitrobenzene and  $\text{CCl}_4$ ). The two values in water referenced in Table 1 (nitrate and nitrobenzene) are data already published.

Various ratios of these values of  $k_M$  are collected in Table 2 from the data in Table 1. These include (i) the Mu-to-H kinetic isotope effect (KIE,  $k_M/k_H$ ) in water using published data for  $k_H(\text{water})$  and (ii) the ratio of  $k_M$  in methanol and hexane compared with water, where possible. Unfortunately, KIEs in non-aqueous solvents cannot be determined at present because of the scarcity of H-atom data in solvents other than water.



**Table 2.** Various ratios of  $k_M$  values and kinetic isotope effects (KIE) relative to published data for  $k_H$  (water) where available.

Solute	$k_H$ (water) <sup>a</sup>	KIE (water) ( $k_M/k_H$ )	$k_M$ (methanol)/ $k_M$ (water)	$k_M$ (hexane)/ $k_M$ (water)
NO <sub>2</sub> <sup>−</sup>	1.62 (±0.05)	5 (±1)	0.66 (±0.2)	—
NO <sub>3</sub> <sup>−</sup>	0.005 (±0.001)	270 (±50)	0.73 (±0.2)	—
TEMPO	4.9	3.7 (±1)	3.0 (±0.5)	5.0 (±1.7)
TEMPO-OH	—	—	3.5 (±0.5)	4.3 (±1.5)
Nitrobenzene	1.6 (±0.6)	7 (±3)	—	1.2 (±0.4)

<sup>a</sup>Reference (1), with  $k_H$  in units of  $10^9 \text{ M}^{-1}\text{s}^{-1}$ .

## Discussion

Several interesting points emerge from the information reported in Tables 1 and 2.

(1) The water-soluble ions evidently react with Mu marginally faster in water than in methanol, while the TEMPO solutes react faster in hexane than in methanol and faster in methanol than in water. Nitrobenzene, on the other hand, reacts at virtually the same rate in water and hexane. Several solvent-dependent factors must be involved to account for this variety of  $k_M$  data.

These factors will undoubtedly include the following: (i) the degree-of-solvation of Mu (and solute) in the different solvents; (ii) the relative mobility of Mu in the different solvents, including the ratio of inverse-viscosities of the solvents for those values of  $k_M$  that are approaching the diffusion-controlled limit; and (iii) the relative tunneling probability for Mu in the different solvents, especially for the reactions with the free radicals TEMPO and TEMPO-OH that could alternatively interact by spin-exchange. All these factors have been discussed in various forms previously (see, for example refs. (6), (7), and (8)).

(2) The KIEs for NO<sub>2</sub><sup>−</sup> and NO<sub>3</sub><sup>−</sup> make an interesting contrast, the first being in the commonly found range of 1 to 5, while the latter is exceptionally large at ~270 (8). This massive KIE shown by NO<sub>3</sub><sup>−</sup> ions was noted 25 years ago when Mu was first observed in water and when the first basic reactions of Mu were studied (4). This leads to the idea that  $k_M$  might be exceptionally large because of the possibility of a depolarizing spin-exchange involving a particularly long-lived, pre-equilibrium, paramagnetic transition state of Mu–NO<sub>3</sub><sup>−</sup>. This would register as a “chemical reaction” in the case of Mu, but not of H.

Here the KIE of NO<sub>2</sub><sup>−</sup> is seen to be ~5, and all  $k_M$  values with NO<sub>2</sub><sup>−</sup> and NO<sub>3</sub><sup>−</sup> in methanol are in the same range as in water; therefore a spin-exchange explanation for  $k_M$  is an unlikely explanation for KIE being 270 for NO<sub>3</sub><sup>−</sup> in water. In fact these results indicate that it is the H+NO<sub>3</sub><sup>−</sup> reaction that is the “exception”. This H-atom reaction has already been reported (9) to have an unusually high Arrhenius pre-exponential A-factor ( $2 \times 10^{15} \text{ M}^{-1} \text{ s}^{-1}$ ) and a very high activation barrier (49 kJ mol<sup>−1</sup>) for such a simple interaction. This is in sharp contrast with the Mu + NO<sub>3</sub><sup>−</sup> reaction, where particularly small values of both A ( $2 \times 10^{10} \text{ M}^{-1} \text{ s}^{-1}$ ) and  $E_a$  (6 kJ mol<sup>−1</sup>) were obtained (10), together with a shallow convex-upward Arrhenius plot indicative of a dominant tunneling mechanism.

(3) Other implications of the data include the following: (i) All these KIEs show Mu to be more reactive than H towards the solutes (by factors of 3.7 to 7). In general it has been found that KIEs are >1 in water for all reaction types

except those with high activation barriers (such as “abstraction” reactions) where the zero-point energy effect favours H (8). This suggests that the reaction of Mu with NO<sub>2</sub><sup>−</sup> has a “combination” rate-determining step, with subsequent dissociation to OMu<sup>−</sup>, rather than direct “abstraction” of O<sup>−</sup>. (ii) The similarity of the ratio of values of  $k_M$  of TEMPO and TEMPO-OH in the different solvents indicates that the extra –OH group does not affect the relative rates regardless of the polarity of the solvent. Their absolute rates change by factors of about 1 to 3 to 5 with solvent and are probably close to their diffusion-controlled limits. This suggests the reaction rate may be governed by the mobility of Mu in water versus methanol versus hexane. But the ratios of inverse viscosities are only 1 to 1.6 to 3.0, so other factors, such as tunneling propensity in the different solvents, might be involved. (iii) The highest absolute rate constant for a Mu reaction seen here is with TEMPO in hexane, which at  $8 \times 10^{10} \text{ M}^{-1} \text{ s}^{-1}$ , makes it one of the fastest reactions reported so far between a pair of neutral species in the liquid phase, in any solvent.

## Acknowledgements

We are most grateful to Dr. Arthur Salmon for his help and advice in planning these experiments, and to Ben Clifford for providing the pure water with  $\lambda_0^{-1} \sim 5 \mu\text{s}$ . We also gratefully acknowledge very important practical help from Drs. Donald Arseneau and Khashayar Ghandi, and technical support provided by Dr. Bassam Hitti and the  $\mu\text{SR}$  Facility at TRIUMF. The Natural Sciences and Engineering Research Council (NSERC) of Canada is also gratefully acknowledged for providing an ongoing research grant to DCW.

## References

1. K.P. Madden. 1996. NDRL Radiation Chemistry Data Center (H-atoms) [online]. Available from [www.rcdc.nd.edu/compilations/HAtom/H.HTM](http://www.rcdc.nd.edu/compilations/HAtom/H.HTM) [updated 2003; cited Feb. 2003].
2. S. Karolczak and D. Walker. 2002. Muonium Data Base [online]. Available from [www.mbaza.mm.com.pl](http://www.mbaza.mm.com.pl) [cited Feb. 2003].
3. D.G. Fleming, D.M. Garner, L.C. Vaz, D.C. Walker, J.H. Brewer, and K.M. Crowe. Adv. Chem. Ser. **175**, 279 (1979).
4. (a) P.W. Percival, H. Fischer, M. Camani, F.N. Gygax, W. Rugg, A. Schenck, H. Schilling, and H. Graf. Chem. Phys. Lett. **39**, 333 (1976). (b) P.W. Percival, E. Roduner, H. Fischer, M. Camani, F.N. Gygax, and A. Schenck. Chem. Phys. Lett. **47**, 11 (1977).
5. J.M. Stadlbauer, B.W. Ng, R. Ganti, and D.C. Walker. J. Amer. Chem. Soc. **106**, 3151 (1984).



6. A.M. Lossack, E. Roduner, and D.M. Bartels. *Phys. Chem. Chem. Phys.* **3**, 2031 (2001)
7. J.M. Stadlbauer, K. Venkateswaran, G.B. Porter, and D.C. Walker. *Hyperfine Interact.* **87**, 942 (1994), and refs. therein.
8. D.C. Walker *J. Chem. Soc., Faraday Trans.* **94**, 1 (1998)
9. S.P. Mezyk, and D.M. Bartels. *J. Phys. Chem. A*, **101**, 6233 (1997)
10. B.W. Ng, Y.C. Jean, Y. Ito, T. Suzuki, J.H. Brewer, D.G. Fleming, and D.C. Walker. *J. Phys. Chem.* **85**, 454 (1981).



# Aqueous nonelectrolyte solutions. Part XIX. Congruent dissociation melting point and the formula of structure II methane hydrate

David N. Glew

**Abstract:** Twenty-four equilibrium pressures,  $P(h_2I_1g)$ , of structure II methane hydrate  $h_2$  with water  $I_1$  between 27.0 and 46.9°C are well represented by a four-parameter equation, which indicates a standard error (SE) of 1.95% on a single pressure measurement. Forty equilibrium constants  $K_p(h_2 \rightarrow I_1g)$  for dissociation of structure II methane hydrate into water and methane between 27.0 and 47.7°C and at pressures up to 784 MPa at 45.0°C are best represented by a three-parameter thermodynamic equation, which indicates an SE 1.25% on a single  $K_p(h_2 \rightarrow I_1g)$  determination. The congruent dissociation melting point  $C(h_2I_1gx_m)$  of structure II methane hydrate is at 47.71°C with SE 0.03°C and at pressure 533 MPa with SE 5 MPa. The congruent  $K_p(h_2 \rightarrow I_1g)$  is 102.9 with SE 0.3 MPa,  $\Delta H^\circ(h_2 \rightarrow I_1g)$  is 61 531 with SE 244 J mol<sup>-1</sup>, and the congruent formula is CH<sub>4</sub>·5.670H<sub>2</sub>O with SE 0.061H<sub>2</sub>O. At congruent point  $\Delta V(h_2 \rightarrow I_1g) = 0$  and its estimate is 1.0 with SE 1.6 cm<sup>3</sup> mol<sup>-1</sup>. Stability range of structure II methane hydrate with water extends from quadruple point  $Q(h_1h_2I_1g)$  at 26.7°C and 55.5 MPa up to quadruple point  $Q(h_2h_3I_1g)$  at 47.3°C and 620 MPa. The metastability range of structure I methane hydrate with water is discussed.

**Key words:** methane hydrate, clathrate structure II, stability range, dissociation equilibrium constant, formula, congruent melting point, metastability of structure I hydrate.

**Résumé :** Vingt-quatre pressions d'équilibre,  $P(h_2I_1g)$ , de la structure II de l'hydrate de méthane,  $h_2$ , avec de l'eau,  $I_1$ , entre 27,0 et 46,9°C sont bien représentées par une équation à quatre paramètres qui indique que l'erreur standard (ES) est de 1,95% pour chaque mesure individuelle de pression. Quarante constantes d'équilibre,  $K_p(h_2 \rightarrow I_1g)$  pour la dissociation de la structure II de l'hydrate de méthane en eau et en méthane, entre 27,0 et 47,7°C et à des pressions allant jusqu'à 784 MPa, à 45°C, sont bien représentées par une équation thermodynamique à trois paramètres qui indique que l'erreur standard (ES) est de 1,25% pour chaque détermination individuelle de  $K_p(h_2 \rightarrow I_1g)$ . Le point de fusion dissociation congruent,  $C(h_2I_1gx_m)$ , de la structure II de l'hydrate de méthane se situe à 47,71°C, avec une ES de 0,03°C, et à une pression de 533 MPa, avec une ES de 5 MPa. La valeur congruente de  $K_p(h_2 \rightarrow I_1g)$  est de 102,9 MPa avec une ES de 0,3 MPa, celle de  $\Delta H^\circ(h_2 \rightarrow I_1g)$  est de 61 531 avec une ES de 244 J mol<sup>-1</sup> et la formule congruente est CH<sub>4</sub>·5,670H<sub>2</sub>O avec une ES de 0,061H<sub>2</sub>O. Au point congruent  $\Delta V(h_2 \rightarrow I_1g) = 0$  et elle est évaluée à 1,0 avec une ES de 1,6 cm<sup>3</sup> mol<sup>-1</sup>. La plage de stabilité de la structure II de l'hydrate de méthane avec l'eau s'étend du point quadruple,  $Q(h_1h_2I_1g)$ , à 26,7°C et une pression de 55,5 MPa jusqu'au point quadruple,  $Q(h_2h_3I_1g)$ , à 47,3°C et une pression de 620 MPa. On discute de la plage de métastabilité de la structure I de l'hydrate de méthane avec l'eau.

**Mots clés :** hydrate de méthane, clathrate de structure II, plage de stabilité, constante d'équilibre de dissociation, formule, point de fusion congruent, métastabilité de la structure I de l'hydrate.

[Traduit par la Rédaction]

## Introduction

The natural abundance of methane hydrate in the permafrost and oceanic regions of the world is enormous (1, 2) and is conservatively estimated within an order of magnitude as  $3 \times 10^{15}$  m<sup>3</sup>, making it greater than that estimated for all conventional natural gas reserves. Naturally occurring methane hydrate deposits are formed over millions of years, so that these deposits exist in their thermodynamically stable forms, in temperature, pressure, and composition equilibrium with their environment. The formulae and the stability

ranges of the methane hydrates are clearly important to more accurately assess the methane content stored in the naturally occurring methane hydrate deposits.

Recent work (3) gives formula estimates for two methane hydrates and shows that structure I methane hydrate, phase  $h_1$ , is the stable phase in equilibrium with water between the quadruple points  $Q(h_1s_1I_1g)$  at -0.29°C and 2.53 MPa and  $Q(h_1h_2I_1g)$  at 26.7°C and 55.5 MPa. Structure II methane hydrate, phase  $h_2$ , is the stable phase in equilibrium with water from quadruple point  $Q(h_1h_2I_1g)$  up to 46.87°C and 397 MPa.

In the present work we evaluate additional measurements at higher pressure for the three-phase ( $h_2I_1g$ ) equilibrium of structure II methane hydrate with water, from 27.0°C at 56.9 MPa up to 47.7°C at 572 MPa and down to 43.7°C at 816 MPa. The 13 methane hydrate pressure measurements of

Received 24 October 2002. Published on the NRC Research Press Web site at <http://canjchem.nrc.ca> on 3 March 2003.

D.N. Glew, 536 Highbury Park, Sarnia, ON N7V 2J9, Canada (telephone: (519) 337-3136).



data set MSK64 by Marshall et al. (4) serve as the base set with which we compare 27 measurements from Dyadin and Aladko (5): 11 measurements of data set D&A96 lie within the temperature and pressure range of data set MSK64 (4), and 16 measurements are at higher pressure. The level of agreement between these two data sets (4, 5) is good, considering the totally different methods of measurement.

The earlier study MSK64 (4) achieves hydrate equilibrium in a rocked 95 cm<sup>3</sup> stainless steel cell, and the methane pressure change is recorded with a slow variation of the temperature of the hydrate cell. Methane pressures are accurate to 0.1%, and temperatures are accurate to 0.004°C (4). In data set D&A96 (5) the equilibrium hydrate decomposition temperature is measured by thermocouple using a high-pressure DTA method on a small sample of compressed methane gas plus water and methane hydrate. Methane pressures are accurate to 1.0% (5), and hydrate temperatures are accurate to 0.1°C.

The present study of methane hydrate extends our earlier work (3) to higher pressure and uses the same numerical methods and thermodynamic equations.

A third data set, NMO99, of 16 hydrate pressures between 31.93 and 47.39°C by Ohgaki et al. (6) deviates systematically with higher pressures than the earlier work (4, 5) because of persistence of the meta-stable structure I methane hydrate.

In the temperature range from quadruple point  $Q(h_1h_2l_1g)$  at 26.7°C up to the congruent dissociation melting point  $C(h_2l_1gx_m)$  at 47.7°C we reconfirm that, in equilibrium with water and gaseous methane, the stable methane hydrate is phase  $h_2$  (3), the clathrate structure II methane hydrate (7–10) first observed and characterized by Chou et al. (9, 10).

### Equilibrium pressure $P(h_2l_1g)$ of structure II methane hydrate with water between 27.0 and 46.9°C

In the temperature range from 27.0 to 46.9°C the equilibrium total pressure  $P(h_2l_1g)$  of methane hydrate  $h_2$  with liquid water  $l_1$  is well represented by the unbiased thermodynamic equation,

$$[1a] \quad \ln P(h_2l_1g) = b_0 + b_1u_1 + b_2u_2 + b_3u_3.$$

This equation is mathematically equivalent (11) to the numerically ill-conditioned unbiased thermodynamic equation,

$$[1b] \quad \ln P(h_2l_1g) = A + B/T + C \ln T + DT.$$

Temperature variables  $u_1$  to  $u_3$  in [1a] are described briefly in Appendix A and in greater detail in ref. (11).

Table 1 presents 24 estimates of  $P(h_2l_1g)$  between 27.0 and 46.9°C, using the 13 measurements of data set MSK64 (4) and 11 measurements from data set D&A96 (5). The arrangement and range of Table 1 is the same as for Table 7 in ref. (3).

The least-squares estimates of the four parameters and their standard errors (SE)s in eq. [1a] are  $b_0 = 3.7425$  (0.0269),  $b_1 = 43.975$  (3.02),  $b_2 = -818.02$  (171), and  $b_3 = 10\,386$  (2070). These parameters give an SE estimate of 0.0193 on  $\ln P$ , or of 1.95% on a single methane hydrate pressure determination with 20 degrees of freedom. The coefficient of determination  $R^2$  is 0.9992. The 13 measure-

**Table 1.** Equilibrium pressure for structure II methane hydrate with water.

Data set	$t$ (°C)	$w^{1/2}$	$P(h_2l_1g)$ (MPa)		Diff (%)	SE (%)
			Obsd	Calcd		
$Q(h_1h_2l_1g)$	26.7	—	—	55.5	—	9.08
MSK64	26.98	1	56.9	55.5	2.56	0.94
MSK64	28.37	1	65.4	65.9	-0.68	0.62
MSK64	28.43	1	65.4	66.3	-1.33	0.61
MSK64	33.54	1	110.8	112.3	-1.35	0.68
MSK64	37.15	1	152.7	154.6	-1.22	0.48
MSK64	39.54	1	187.3	190.2	-1.51	0.47
MSK64	40.48	1	206.3	206.8	-0.20	0.49
MSK64	41.04	1	223.9	217.4	3.01	0.50
MSK64	41.87	1	237.5	234.6	1.20	0.51
MSK64	43.65	1	271.7	278.3	-2.38	0.48
MSK64	45.15	1	319.7	324.6	-1.52	0.47
MSK64	46.42	1	367.8	373.4	-1.52	0.63
MSK64	46.87	1	397.0	393.0	1.03	0.74
D&A96	27.6	1	59	60.0	-1.65	0.75
D&A96	30.4	1	84	82.6	1.72	0.65
D&A96	34.0	1	117	117.2	-0.17	0.65
D&A96	35.5	1	133	134.0	-0.73	0.56
D&A96	37.5	1	162	159.4	1.65	0.47
D&A96	37.8	1	166	163.6	1.50	0.46
D&A96	40.7	1	216	210.9	2.43	0.50
D&A96	42.4	1	242	246.6	-1.87	0.51
D&A96	45.2	1	317	326.5	-2.91	0.47
D&A96	45.9	1	358	352.2	1.64	0.53
D&A96	46.9	1	405	394.5	2.67	0.75

ments of data set MSK64 give a root mean squared (rms) deviation of 0.0167 on  $\ln P$  or of 1.68% on  $P$ . The 11 measurements of data set D&A96 give a larger rms deviation of 0.0188 on  $\ln P$  or of 1.89% on  $P$  and a mean methane hydrate pressure estimate 0.69% larger than data set MSK64.

### Equilibrium constant for dissociation of structure II methane hydrate between 27.0 and 47.7°C

The equilibrium constant for dissociation of 1 g molar mass of structure II methane hydrate of formula  $CH_4 \cdot nH_2O$  phase  $h_2$  into  $n$  mol of pure water  $l_1$  plus 1 mol of gaseous methane is written  $K_p(h_2 \rightarrow l_1g)$  and is defined by eq. [2],

$$[2] \quad \ln K_p(h_2 \rightarrow l_1g) = \ln f_2(h_2l_1g) + n \ln x_1^{l_1} + n(1/RT) \int_{0.1 \text{ MPa}}^{P(h_2l_1g)} (V_1^{l_1} - V_1^{h_2}) dP.$$

In eq. [2]  $V_1^{l_1}$  is the molar volume of water and  $V_1^{h_2}$  is the molar volume of structure II lattice water at pressure  $P(h_2l_1g)$  and temperature  $T$ . Equilibrium values of  $P(h_2l_1g)$  are given in Tables 1 and 3. Equilibrium values of methane fugacity  $f_2(h_2l_1g)$  are evaluated from  $P(h_2l_1g)$  using the IUPAC fugacity eq. [12] and are given in Table 3. Equilibrium volumes of compressed water are interpolated from tables by Haar et al. (13). Equilibrium values of  $x_1^{l_1} = (1 - x_2^{l_1})$  are from  $x_2^{l_1}$  values, which are listed in Table 2 and



evaluated using the equation of Rettich et al. (14). Estimates for  $V_1^{h_2}$  cm<sup>3</sup> mol<sup>-1</sup> and its SE at temperature  $t$  and at pressure  $P$  are  $22.63 \pm 0.24$  at 26.98°C and 56.92 MPa,  $22.37 \pm 0.24$  at 37.15°C and 152.7 MPa,  $21.89 \pm 0.23$  at 45.2°C and 317 MPa,  $21.28 \pm 0.23$  at 47.71°C and 533 MPa, and  $20.57 \pm 0.22$  at 45.0°C and 784 MPa.

The 40 equilibrium constants between 27.0 and 47.7°C from data sets MSK64 and D&A96 are converged as described in ref. (3) and are best (11) represented by the unbiased thermodynamic equation

$$[3] \quad \ln K_p(h_2 \rightarrow l_1g) = d_0 + d_1 u_1 + d_2 u_2.$$

Temperature variables  $u_1$  and  $u_2$  and thermodynamic parameters  $d_0$  to  $d_2$  are defined at reference temperature  $\Theta = 298.15$  K (25°C) and are described in Appendix A. The uncertainty of parameter  $d_2$  is such that we are unable to converge and solve the three-parameter equation, eq. [3], directly. Thus the dependent variable is modified to  $(\ln K_p(h_2 \rightarrow l_1g) - d_2 u_2)$  with a pre-defined  $d_2$  and the complementary two-parameter thermodynamic eq. [4],

$$[4] \quad (\ln K_p(h_2 \rightarrow l_1g) - d_2 u_2) = d_0 + d_1 u_1,$$

is converged and solved by least-squares for parameters  $d_0$  and  $d_1$ .

The parameters of the best converged eq. [4] with their (SE)s are  $d_0 = 2.9279$  (0.0056) and  $d_1 = 23.421$  (0.099) with the pre-defined  $d_2 = 18.4$  and SE estimate of 10.6. The SE estimate on a single determination of unit weight of  $\ln K_p(h_2 \rightarrow l_1g)$  is 0.0124 or 1.25% for  $K_p(h_2 \rightarrow l_1g)$  with 37 degrees of freedom. The number of degrees of freedom is counted from the 40 data minus the two undetermined parameters minus the one weighted datum leaving 37. The coefficient of determination  $R^2$  is 0.9998.

Because we assign unit weight to the 26 measurements of data set D&A96 (5) equal to the unit weight assigned to the less extensive but more accurate 13 measurements of data set MSK64 (4), the best equation for  $\ln K_p(h_2 \rightarrow l_1g)$  in this work is slightly different numerically from that given earlier (3). The present equation is preferred because it represents a greater number and wider range of equilibrium measurements.

The rms of the 13  $K_p(h_2 \rightarrow l_1g)$  residuals for data set MSK64 is 1.02%, the same as earlier (3). The rms of the 27 residuals, one weighted, for data set D&A96 is 1.31%. The equilibrium constants from data set D&A96 are an average of 0.38% larger than those from data set MSK64.

Table 2 has the same arrangement as Table 8 in ref. (3) and extends the measurements of MSK64 (4) to higher pressure with the measurements of D&A96 (5).

Table 2 shows the 40 converged best estimates of the equilibrium constant  $K_p(h_2 \rightarrow l_1g)$  for dissociation of structure II methane hydrate to liquid water and methane gas with  $n = r$ . Standard thermodynamic function changes refer to dissociation of 1 g mol of  $CH_4 \cdot rH_2O$   $h_2$  at 0.10 MPa to form  $r$  g mol of pure water  $l_1$  at 0.10 MPa and 1 g mol of methane gas at 1.0 MPa fugacity. Parameter  $r$  is used to indicate the best estimate of  $n$ , as described in ref. (3).

The estimates of  $K_p(h_2 \rightarrow l_1g)$  observed in Table 2 are seen to increase monotonously from 22.0 MPa at 26.98°C to 84.7 MPa at 45.2°C, increase more slowly to a maximum between 102.7 and 104.3 MPa at 47.7°C, and then decrease

to 84.4 MPa at 45.0°C. It is noted that the  $K_p(h_2 \rightarrow l_1g)$  observed at 45.2°C and 317 MPa pressure is substantially the same as that observed at 45.0°C and 784 MPa pressure.

The calculated  $K_p(h_2 \rightarrow l_1g)$  estimates in Table 2 properly represent these changes with an SE of 1.25% on a single determination of unit weight. The maximum of  $K_p(h_2 \rightarrow l_1g)$  near 47.7°C and at pressure between 527 and 572 MPa defines the invariant congruent dissociation melting point of  $h_2$  methane hydrate, to be discussed fully and located more accurately later.

The measurement at 43.7°C and 816 MPa is an outlier and is assigned weight  $w^{1/2} = 0.001$  because its deviation from the best converged eq. [4] is 76 times its estimated standard error.

### Standard enthalpy change $\Delta H^{ot}(h_2 \rightarrow l_1g)$ and formula number estimate $r$ for structure II methane hydrate with water

The first four columns in Table 3 list the data set, the Celsius temperature (ITS-90), the equilibrium hydrate total pressure  $P(h_2 l_1g)$  MPa, and the equilibrium methane fugacity  $f_2(h_2 l_1g)$  MPa, respectively. Table 3 also presents the converged best estimates of the standard enthalpy change  $\Delta H^{ot}(h_2 \rightarrow l_1g)$  and the approximate formula number  $r$  for standard dissociation of structure II methane hydrate  $CH_4 \cdot rH_2O$  into water and methane gas. The SE on  $\Delta H^{ot}(h_2 \rightarrow l_1g)$  is 244 J mol<sup>-1</sup> and on  $r$  is 0.061 at all temperatures.

The predefined standard heat capacity change  $\Delta C_p^{ot}(h_2 \rightarrow l_1g)$  is 153 with SE 88 J mol<sup>-1</sup> deg<sup>-1</sup>. The SE is evaluated for eq. [3] with three parameters using the SE  $\ln K_p(h_2 \rightarrow l_1g) = 0.0124$ .

At quadruple point  $Q(h_1 h_2 l_1g)$  26.7°C the estimated formula for structure II methane hydrate  $h_2$  is  $CH_4 \cdot 5.766H_2O$  with SE 0.061  $H_2O$ ; this agrees roughly with the earlier estimate  $CH_4 \cdot 5.822H_2O$  with SE 0.064  $H_2O$  given in (3). The new formula estimate for structure II methane hydrate at 26.7°C is nearer to the equilibrium formula found (3) for the structure I methane hydrate  $h_1$   $CH_4 \cdot 5.759H_2O$  with SE 0.077  $H_2O$ . These three formula estimates are insignificantly different from each other.

In Table 3 the value of  $r$  is shown to decrease with increasing temperature and attains its minimum value 5.670 with SE 0.061 at 47.7°C. This gives the limiting formula  $CH_4 \cdot 5.670H_2O$  with SE 0.061  $H_2O$  for the congruent structure II methane hydrate (7–10) estimated from the equilibrium pressures (4, 5) and the volumetric properties of methane (12) and of water (13).

The number of methane guest molecules, defined as  $m$  per unit cell of  $136H_2O$ , increases from 23.59 with SE 0.25 at 26.7°C and 55.5 MPa to 23.95 with SE 0.26 at 45.2°C and 317 MPa to a maximum of 23.99 with SE 0.26 at 47.7°C and 536 MPa, and it decreases to 23.95 with SE 0.26 at 45.0°C and 784 MPa. These values of  $m$  between 26.7 and 47.7°C show the increasing number of the 24 lattice sites that must be occupied by methane guests to stabilize the structure II methane hydrate against thermal collapse due to increasing temperature.

Consistent with the observed equilibrium constants, we note that  $m$  at 45.2°C and 317 MPa has the same value as at



**Table 2.** Equilibrium constant for structure II methane hydrate with water.

Data set	<i>t</i> (°C)	<i>w</i> <sup>1/2</sup>	<i>K<sub>p</sub></i> (h <sub>2</sub> →l <sub>1</sub> g) (MPa)		Diff (%)	SE (%)	1000 <i>x</i> <sub>2</sub> <sup>1</sup>
			Obsd	Calcd			
<i>Q</i> (h <sub>1</sub> h <sub>2</sub> l <sub>1</sub> g)	26.7	—	—	21.3	—	7.31	4.57
MSK64	26.98	1	22.0	21.8	0.84	0.49	4.61
MSK64	28.37	1	24.3	24.3	−0.17	0.45	4.85
MSK64	28.43	1	24.3	24.4	−0.55	0.45	4.85
MSK64	33.54	1	36.1	36.1	−0.17	0.31	5.88
MSK64	37.15	1	46.9	47.4	−1.11	0.24	6.52
MSK64	39.54	1	55.7	56.7	−1.78	0.21	6.88
MSK64	40.48	1	60.3	60.8	−0.80	0.20	7.02
MSK64	41.04	1	64.2	63.3	1.45	0.20	7.14
MSK64	41.87	1	67.5	67.3	0.28	0.20	7.18
MSK64	43.65	1	75.4	76.7	−1.68	0.21	7.24
MSK64	45.15	1	85.0	85.5	−0.56	0.22	7.19
MSK64	46.42	1	93.6	93.8	−0.20	0.24	6.99
MSK64	46.87	1	98.0	96.9	1.18	0.25	6.83
D&A96	27.6	1	22.6	22.9	−1.24	0.47	4.66
D&A96	30.4	1	29.0	28.4	2.10	0.39	5.34
D&A96	34.0	1	37.6	37.4	0.55	0.30	6.00
D&A96	35.5	1	41.8	41.9	−0.27	0.27	6.25
D&A96	37.5	1	49.1	48.7	0.85	0.23	6.65
D&A96	37.8	1	50.1	49.8	0.67	0.23	6.69
D&A96	40.7	1	62.4	61.8	1.04	0.20	7.09
D&A96	42.4	1	68.8	70.0	−1.72	0.20	7.18
D&A96	45.2	1	84.7	85.9	−1.39	0.22	7.19
D&A96	45.9	1	91.7	90.3	1.46	0.23	7.05
D&A96	46.9	1	99.0	97.1	1.98	0.25	6.78
D&A96	47.2	1	98.5	99.2	−0.71	0.25	6.52
D&A96	47.2	1	97.3	99.2	−1.97	0.25	6.46
D&A96	47.6	1	104.8	102.1	2.64	0.26	6.32
D&A96	47.6	1	100.8	102.1	−1.25	0.26	5.99
D&A96	47.7	1	102.7	102.9	−0.17	0.26	5.80
D&A96	47.7	1	102.6	102.9	−0.20	0.26	5.72
D&A96	47.7	1	102.9	102.9	0.03	0.26	5.61
D&A96	47.7	1	104.3	102.9	1.38	0.26	5.38
D&A96	47.6	1	102.4	102.1	0.26	0.26	5.31
D&A96	47.6	1	103.5	102.1	1.32	0.26	5.21
D&A96	47.4	1	99.6	100.7	−1.08	0.26	5.12
D&A96	46.8	1	95.0	96.4	−1.49	0.25	4.59
D&A96	45.9	1	92.1	90.3	1.99	0.23	3.91
D&A96	45.5	1	86.9	87.8	−1.01	0.23	3.78
D&A96	45.0	1	84.4	84.6	−0.22	0.22	3.49
D&A96	43.7	0.001	65.9	77.0	−14.38	0.21	3.25

45.0°C and 784 MPa despite the large difference of methane equilibrium pressure. These externally applied methane pressures remain relatively small, being only 12.4% and 30.7% of the hydrate internal pressure 2551 MPa at 46.87°C (3).

### Congruent dissociation melting point of structure II methane hydrate

Eighteen methane hydrate measurements between 317 MPa and 784 MPa from data set D&A96 (5) show that the equilibrium hydrate temperature can be accurately represented by eq. [5] as an empirical quartic function of the equilibrium hydrate pressure,

$$[5] \quad t \text{ (°C)} = e_0 + e_1\Delta P + e_2(\Delta P)^2 + e_3(\Delta P)^3 + e_4(\Delta P)^4.$$

In eq. [5], *t* (°C) is the equilibrium methane hydrate temperature (ITS-90),  $\Delta P$  is the equilibrium pressure difference (*P*(h<sub>2</sub>l<sub>1</sub>g) − 532.75) MPa, and 532.75 MPa with SE 5.13 MPa is the estimated pressure at maximum hydrate temperature, *t*<sub>max</sub>. The estimated maximum congruent dissociation melting temperature of structure II methane hydrate is *t*<sub>max</sub> = *e*<sub>0</sub> = 47.714°C with SE 0.032°C. Parameter *e*<sub>1</sub> = 2.87 × 10<sup>−12</sup> with SE 4.2 × 10<sup>−4</sup>, parameter *e*<sub>2</sub> = −5.80 × 10<sup>−5</sup> with SE 4.3 × 10<sup>−6</sup>, parameter *e*<sub>3</sub> = 1.94 × 10<sup>−8</sup> with SE 1.1 × 10<sup>−8</sup>, and parameter *e*<sub>4</sub> = 1.63 × 10<sup>−10</sup> with SE 8.3 × 10<sup>−11</sup>. The SE estimate on a single methane hydrate tempera-



**Table 3.** Standard enthalpy change for dissociation and the formula of structure II methane hydrate with water.<sup>a</sup>

Data set	<i>t</i> (°C)	<i>P</i> (h <sub>2</sub> l <sub>1</sub> g) (MPa)	<i>f</i> <sub>2</sub> (h <sub>2</sub> l <sub>1</sub> g) (MPa)	$\Delta H^{\text{ol}}(\text{h}_2 \rightarrow \text{l}_1\text{g})$ (J mol <sup>-1</sup> )	<i>r</i>
<i>Q</i> (h <sub>1</sub> h <sub>2</sub> l <sub>1</sub> g)	26.7	55.5	41.4	58 318	5.766
MSK64	26.98	56.9	42.7	58 362	5.765
MSK64	28.37	65.4	51.8	58 574	5.756
MSK64	28.43	65.4	51.8	58 583	5.756
MSK64	33.54	110.8	127.8	59 365	5.728
MSK64	37.15	152.7	264.5	59 917	5.711
MSK64	39.54	187.3	460.6	60 282	5.700
MSK64	40.48	206.3	617.1	60 427	5.696
MSK64	41.04	223.9	803.0	60 512	5.694
MSK64	41.87	237.5	979.7	60 639	5.691
MSK64	43.65	271.7	1597	60911	5.684
MSK64	45.15	319.7	3089	61 140	5.678
MSK64	46.42	367.8	5834	61 336	5.674
MSK64	46.87	397.0	8513	61 404	5.673
D&A96	27.6	59	44.9	58 456	5.761
D&A96	30.4	84	76.4	58 885	5.745
D&A96	34.0	117	143	59 435	5.726
D&A96	35.5	133	189	59 665	5.718
D&A96	37.5	162	308	59 971	5.709
D&A96	37.8	166	328	60 017	5.708
D&A96	40.7	216	714	60 460	5.695
D&A96	42.4	242	1046	60 720	5.689
D&A96	45.2	317	2978	61 149	5.678
D&A96	45.9	358	5143	61 256	5.676
D&A96	46.9	405	9434	61 409	5.673
D&A96	47.2	443	15 270	61 455	5.672
D&A96	47.2	450	16 670	61 455	5.672
D&A96	47.6	467	20 560	61 516	5.670
D&A96	47.6	506	33 280	61 516	5.670
D&A96	47.7	527	42 950	61 531	5.670
D&A96	47.7	536	47 910	61 531	5.670
D&A96	47.7	548	55 390	61 531	5.670
D&A96	47.7	572	73 880	61 531	5.670
D&A96	47.6	580	81 380	61 516	5.670
D&A96	47.6	590	91 670	61 516	5.670
D&A96	47.4	600	103 500	61 485	5.671
D&A96	46.8	658	206 200	61 393	5.673
D&A96	45.9	734	502 900	61 256	5.676
D&A96	45.5	749	601 000	61 195	5.677
D&A96	45.0	784	902 500	61 118	5.679
D&A96	43.7	816	1 328 000	60 919	5.684

<sup>a</sup>The standard errors of  $\Delta H^{\text{ol}}(\text{h}_2 \rightarrow \text{l}_1\text{g})$  and *r* are 244 J mol<sup>-1</sup> and 0.061, respectively.

ture determination is 0.088°C with 13 degrees of freedom and is in good agreement with the 0.1°C accuracy of temperature measurement indicated by the authors (5). The coefficient of determination *R*<sup>2</sup> is 0.9934.

The estimate of parameter *e*<sub>1</sub> is zero. Estimates of parameters *e*<sub>0</sub> = *t*<sub>max</sub> and *e*<sub>2</sub> are highly significant and could arise by random chance with a probability less than 0.05%. The estimate of parameter *e*<sub>3</sub> could arise by random chance with a probability ~4.9% and the estimate of parameter *e*<sub>4</sub> could arise by chance with a probability ~3.8%. This quartic equation gives a flatter maximum and better representation of the methane hydrate temperatures than the best cubic equation.

At the congruent temperature *t*<sub>max</sub>, (dt/d*P*) = 0; thus, the volume change for the hydrate dissociation melting reaction is  $\Delta V(\text{h}_2 \rightarrow \text{l}_1\text{g}) = (\text{dt/d}P) \Delta H(\text{h}_2 \rightarrow \text{l}_1\text{g})/T = 0$ , with  $\Delta H(\text{h}_2 \rightarrow \text{l}_1\text{g})/T > 0$ .

In the two-component methane–water system, the congruent dissociation melting point of structure II methane hydrate is an invariant three-phase point, denoted *C*(h<sub>2</sub>l<sub>1</sub>g*x*<sub>m</sub>), at which the volume and composition *x*<sub>m</sub> of the equilibrium methane hydrate phase h<sub>2</sub> is equal to the volume and composition of its fused reaction products, water and methane.

At the congruent point *C*(h<sub>2</sub>l<sub>1</sub>g*x*<sub>m</sub>), 47.71°C, and 533 MPa, the thermodynamic model gives a maximum equilibrium



constant  $K_p(h_2 \rightarrow l_1g)$  of 102.9 MPa with SE 0.3 MPa and a maximum  $CH_4:H_2O$  mol ratio for the methane hydrate formula  $CH_4 \cdot 5.670 \pm 0.061H_2O$  with an  $h_2$  formula volume  $120.7 \pm 1.3 \text{ cm}^3 \text{ mol}^{-1} CH_4$  and a cubic hydrate lattice (7–10) spacing  $1.688 \pm 0.006 \text{ nm}$ . The equilibrium volume (12) of methane  $g$  is  $32.3 \pm 0.3 \text{ cm}^3 \text{ mol}^{-1} CH_4$ , and the equilibrium water volume (13) of  $5.670H_2O$   $l_1$  is  $89.3 \pm 1.0 \text{ cm}^3 \text{ mol}^{-1} CH_4$ . At  $C(h_2l_1gx_m)$  the estimated  $\Delta V$  (products – reactants) =  $1.0 \pm 1.6 \text{ cm}^3 \text{ mol}^{-1} CH_4$ . Similarly, for the hydrate with formula  $CH_4 \cdot 5.678 \pm 0.061H_2O$  at  $45.2^\circ\text{C}$  and 317 MPa  $\Delta V = 5.1 \pm 1.7 \text{ cm}^3 \text{ mol}^{-1} CH_4$  and with formula  $CH_4 \cdot 5.679 \pm 0.061H_2O$  at  $45.0^\circ\text{C}$  and 784 MPa  $\Delta V = -1.2 \pm 1.6 \text{ cm}^3 \text{ mol}^{-1} CH_4$ .

Between quadruple point  $Q(h_1h_2l_1g)$  55.5 MPa at  $26.7^\circ\text{C}$  and up to hydrate pressure 533 MPa at  $47.71^\circ\text{C}$ , it is shown that with increasing temperature methane from the gas phase is forced into the equilibrium structure II methane hydrate lattice, enriching its methane content up to its congruent maximum. At methane pressures beyond 533 MPa, increasing up to 816 MPa, the mechanically compressed structure II methane hydrate is forced increasingly to exude guest methane into the gas phase, thereby destabilizing the solid methane hydrate so that it can only exist in equilibrium with water at increasingly lower temperatures.

The quadruple point with a denser hydrate at 620 MPa reported in (5, 15) defines the four measurements between  $46.8^\circ\text{C}$  at 658 MPa and  $45.0^\circ\text{C}$  at 784 MPa to be in a region of meta-stable equilibrium. Nonetheless these measurements are members of the same ( $h_2l_1g$ ) equilibrium set as those measurements at pressures less than 527 MPa. This is proved by the accurate representations of the methane hydrate measurements by eqs. [4] and [5] between 317 and 784 MPa.

It is particularly valuable that the high-pressure experimental DTA decomposition technique developed by Dyadin et al. (5) enables the determination of meta-stable ( $h_2l_1g$ ) equilibria.

There is little doubt that the more stable and denser methane hydrate, indicated by quadruple point  $Q(h_2h_3l_1g)$  at 620 MPa and  $47.3^\circ\text{C}$  and by its smooth ( $h_3l_1g$ ) decomposition curve between  $48.6^\circ\text{C}$  at 642 MPa and  $53.6^\circ\text{C}$  at 1000 MPa (5, 15), is the clathrate structure-H methane hydrate phase  $h_3$  first described and characterized by Chou et al. (10). The growth of single crystals of clathrate structure-H methane hydrate is shown during slow cooling at  $33^\circ\text{C}$  and 910 MPa (10). The hexagonal clathrate structure-H methane hydrate is confirmed by a single crystal synchrotron X-ray structure determination at  $25^\circ\text{C}$  and 600 MPa, together with a Raman spectrum at 880 MPa (10).

The congruent dissociation melting point of structure II methane hydrate is not unique. Dyadin et al. (16) describe an entirely similar behaviour for structure II argon hydrate with a very gentle maximum congruent dissociation melting point  $33.4^\circ\text{C}$  at about 620 MPa going down slightly to  $31.5^\circ\text{C}$  at 720 MPa.

## Metastability of structure I methane hydrate

The present work and earlier studies (3, 9, 10) show that structure I methane hydrate is metastable between  $26.7^\circ\text{C}$  at

55.5 MPa,  $47.7^\circ\text{C}$  at 572 MPa, and  $45.0^\circ\text{C}$  at 784 MPa and that the structure II methane hydrate clathrate is the stable phase, as demonstrated by Chou et al. (9, 10) at  $25^\circ\text{C}$  and at pressures between 100 and 600 MPa.

The initial methane hydrate made at  $7^\circ\text{C}$  by Nakano et al. (6) is structure I. The 16 equilibrium pressures reported (6) between  $31.93$  and  $47.39^\circ\text{C}$  are all higher than the pressures estimated for the structure II methane hydrate (4, 5). The positive pressure deviations increase continuously from 1.5 MPa at  $31.93^\circ\text{C}$  to 34.7 MPa at  $47.39^\circ\text{C}$  and indicate that structure I methane hydrate is meta-stable relative to structure II methane hydrate. The Raman spectrum at 100 MPa pressure (4) confirms the structure I methane hydrate at  $31.93^\circ\text{C}$ , and continuity of the spectral shifts confirms the structure I hydrate between 100 MPa at  $31.93^\circ\text{C}$  and 500 MPa at  $47.39^\circ\text{C}$ . It is remarkable that the single crystal of methane hydrate annealed and aged at  $47.85^\circ\text{C}$  and 493 MPa (6) retained its meta-stable structure I form. Over the short experimental time frame of a few days, the metastability of structure I methane hydrate is demonstrated between  $32^\circ\text{C}$  at 100 MPa and  $47.4^\circ\text{C}$  at 500 MPa (6).

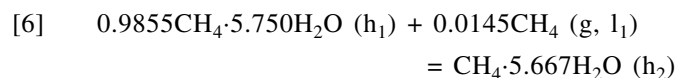
The work of Hirai et al. (17, 18) shows the formation of structure I methane hydrate at room temperature at between 200 and 300 MPa, and with compression up to 700 MPa. The authors provide a powder X-ray diffraction pattern at 400 MPa showing structure I methane hydrate and give unit cell parameters at pressures 260, 300, 380, and 700 MPa, which confirm retention of the structure I hydrate. Structure factor analyses show (17, 18) that within the structure I unit cell both the six tetrakaidcahedral sites and the two pentagonal dodecahedral sites are completely filled by methane at all pressures between 260 and 700 MPa at room temperature. Our estimate of a 99.84% filled structure I methane hydrate at 55.5 MPa and  $26.7^\circ\text{C}$  (3) indicates full site occupancy by methane at higher pressures and temperatures. Over the short experimental time frame of days the metastability of structure I methane hydrate at room temperature between 200 and 700 MPa pressure is demonstrated (17, 18).

Chou et al. (9) point out that in some experiments structure I methane hydrate is found to exist metastably at higher pressures. The Raman spectra of metastable structure I methane hydrate are shown at  $25^\circ\text{C}$  and at pressures of 125, 649, and 880 MPa (9) and are contrasted with the spectrum of the stable structure II methane hydrate at  $25^\circ\text{C}$  and 125 MPa (9, 10). Direct optical observation of single crystals of structure II methane hydrate by Chou et al. (9) shows structure II crystal survival at  $41^\circ\text{C}$  and 223 MPa and structure II crystal growth at temperatures down to  $35^\circ\text{C}$  and 136 MPa in the presence of metastable structure I methane hydrate. Chou et al. (9, 10) confirm the cubic clathrate structure II methane hydrate by a complete single-crystal synchrotron X-ray structure determination at  $25^\circ\text{C}$  and 250 MPa.

The work of Loveday et al. (19) starts with the polycrystalline neutron diffraction pattern of metastable structure I methane D-hydrate at room temperature and 800 MPa pressure and thereby unfortunately misses the entire equilibrium three-phase region for formation of the clathrate structure II methane hydrate (9, 10), from  $26.7^\circ\text{C}$  at 55.5 MPa up to  $47.7^\circ\text{C}$  at 572 MPa and down to  $45.0^\circ\text{C}$  at 784 MPa (3–5).



The metastability of clathrate structure I methane hydrate with water relative to clathrate structure II methane hydrate at room temperature and at pressures between 200 and 880 MPa (6, 9, 17–19) most probably derives from the slow kinetics of reaction [6],



in which additional methane (gaseous or aqueous) is required to drive and balance the reaction at temperatures below  $Q(\text{h}_1\text{h}_2\text{I}_1\text{g})$  at 26.7°C.

We consider the slow kinetics at 25°C to be due to (i) the lack of excess gaseous and aqueous methane in contact with the methane-full structure I hydrate to force the reaction, (ii) the small positive difference of hydrate water molar volume,  $\Delta V_1 = V_1^{\text{h}_2} - V_1^{\text{h}_1} = 0.41 \text{ cm}^3 \text{ mol}^{-1}$ , which increases rather than decreases the lattice water Gibbs' energy difference with increasing pressure, and (iii) the small negative difference of mean molecular volume of about  $-1.0 \text{ \AA}^3$ , which decreases the overall Gibbs' energy of the structure II hydrate relative to the structure I hydrate with increasing pressure. Apparently the increased applied pressures of 900 to 1500 MPa at room temperature (17–19) are sufficient to squeeze methane from the gaseous and aqueous phases into faster reaction with the metastable methane-full structure I hydrate lattice to form the more stable methane-full structure II hydrate lattice. This view is supported by the relatively unhindered growth kinetics of single crystals of clathrate structure II methane hydrate (9, 10) in the presence of clathrate structure I methane hydrate at 35.0°C and at low pressures between 130 and 600 MPa.

## References

1. E.D. Sloan, Jr. Clathrate hydrates of natural gases. 2nd ed. Marcel Dekker, Inc., New York. 1997. pp. 457–537.
2. R. Corfield. Chem. Britain, **38**(5), 22 (2002).
3. D.N. Glew. Can. J. Chem. **80**, 418 (2002).
4. D.R. Marshall, S. Saito, and R. Kobayashi. AIChE J. **10**, 202 (1964).
5. Y.A. Dyadin and E.Y. Aladko. In Proceedings of the 2nd International conference on natural gas hydrates. Edited by J.P. Monfort. Toulouse. 2–6 June, 1996. p. 67.
6. S. Nakano, M. Moritoki, and K. Ohgaki. J. Chem. Eng. Data, **44**, 254 (1999).
7. D.W. Davidson. In Water: A comprehensive treatise. Vol. 2. Edited by F. Franks. Plenum Press, New York. 1973. p. 128.
8. D.W. Davidson, Y.P. Handa, C.I. Ratcliffe, J.S. Tse, and B.M. Powell. Nature (London), **311**, 142 (1984).
9. I.-M. Chou, A. Sharma, R.C. Burruss, R.J. Hemley, A.F. Goncharov, L.A. Stern, and S.H. Kirby. J. Phys. Chem. A, **105**, 4664 (2001).
10. I.-M. Chou, A. Sharma, R.C. Burruss, J. Shu, H.-K. Mao, R.J. Hemley, A.F. Goncharov, L.A. Stern, and S.H. Kirby. PNAS, **97**, 13484 (2000).
11. E.C.W. Clarke and D.N. Glew. Trans. Faraday Soc. **62**, 539 (1966).
12. S. Angus, B. Armstrong, and K.M. de Reuck. International thermodynamic tables of the fluid state — 5 methane. International Union of Pure and Applied Chemistry, Pergamon Press, Oxford. 1978.
13. L. Haar, J.S. Gallagher, and G.S. Kell. NBS/NRC steam tables. Hemisphere Publishing Corporation, New York. 1984.
14. T.R. Rettich, Y.P. Handa, R. Battino, and E. Wilhelm. J. Phys. Chem. **85**, 3230 (1981).
15. Y.A. Dyadin, E.Y. Aladko, and E.G. Larionov. Mendelev Comm. **34** (1997).
16. Y.A. Dyadin, E.G. Larionov, D.S. Mirinski, T.V. Mikina, and L.I. Starostina. Mendelev Comm. **32** (1997).
17. H. Hirai, T. Kondo, M. Hasegawa, T. Yagi, Y. Yamamoto, T. Komai, K. Nagashima, M. Sakashita, H. Fujihisa, and K. Aoki. J. Phys. Chem. **B104**, 1429 (2000).
18. H. Hirai, M. Hasegawa, T. Yagi, Y. Yamamoto, K. Nagashima, M. Sakashita, K. Aoki, and T. Kikegawa. Chem. Phys. Lett. **325**, 490 (2000).
19. J.S. Loveday, R.J. Nemes, M. Guthrie, S.A. Belmonte, D.R. Allan, D.D. Klug, J.S. Tse, and Y.P. Handa. Nature (London), **410**, 661 (2001).

## Appendix A: Definition of thermodynamic parameters at reference $\Theta$ K

When the dependence of equilibrium constant  $K_p$  on temperature  $T$  is properly represented by the unbiased, three-variable, four-parameter, thermodynamic equation, eq. [A1]

$$[A1] \quad \ln K_p = A + B/T + C \ln T + DT,$$

then ref. (11) shows that an identical temperature representation of  $K_p$  can be obtained using the unbiased, three-variable, four-parameter, thermodynamic equation, eq. [A2]

$$[A2] \quad \ln K_p = b_0 + b_1 u_1 + b_2 u_2 + b_3 u_3.$$

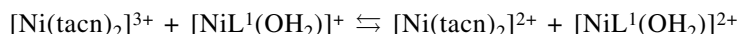
The least-squares fits of  $K_p$  data sets by eqs. [A1] and [A2] are identical when the variables  $u_1$ ,  $u_2$ , and  $u_3$  in [A2] are defined as functions of temperature  $T$  and a predefined reference temperature  $\Theta$ , with  $u_1 = [(T - \Theta)/T]$ ,  $u_2 = [(\Theta - T)/T + \ln(T/\Theta)]$ , and  $u_3 = [(T - \Theta)(T + \Theta)/\Theta T - 2 \ln(T/\Theta)]$ , and then the corresponding thermodynamic parameters  $b_0$  to  $b_3$  are defined at reference  $\Theta$ , with  $b_0 = (\ln K_p)_\Theta = -\Delta G_\Theta^\circ/R\Theta$ ,  $b_1 = \Delta H_\Theta^\circ/R$ ,  $b_2 = \Delta C_p^\circ/R$ , and  $b_3 = \Theta(d\Delta C_p^\circ/dT)_\Theta/2R$ . Reference  $\Theta = 298.15$  is used here and in ref. (3).



# Outer-sphere electron transfer reactions of aqua(5,5,7,12,12,14-hexamethyl-1,4,8,11-tetraazacyclotetradecane-1-acetato)nickel(II) and (III).

Robert I. Haines and Dean R. Hutchings

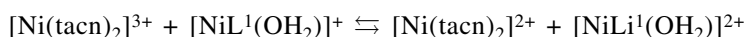
**Abstract:** The outer-sphere oxidation of the nickel(II) complex of the deprotonated pendant-arm macrocycle, 5,5,7,12,12,14-hexamethyl-1,4,8,11-tetraazacyclotetradecane-1-acetate,  $[\text{NiL}^1(\text{OH}_2)]^+$  by bis-(1,4,7-triazacyclononane)nickel(III),  $[\text{Ni}(\text{tacn})_2]^{3+}$  has been studied in aqueous perchlorate media. The reaction displays reversible second-order behaviour and the kinetic study reveals the forward and reverse rate constants for the reaction:



The kinetics show the forward reaction to be acid dependent, a feature that is attributed to protonation of the acetato group of the nickel(II) complex. Using Marcus theory, the self-exchange rate for the  $[\text{NiL}^1(\text{OH}_2)]^{+/2+}$  couple has been calculated. The nickel(II/III) electron transfer is a reversible one electron process with  $E^\circ = 1.04 \text{ V}$  (vs. S.H.E.). The formation of the authentic nickel(III) product has been confirmed by esr spectroscopy. The kinetics of reduction of the  $[\text{NiL}^1(\text{OH}_2)]^{2+}$  species by  $\text{Fe}^{2+}(\text{aq})$  exhibits a second-order rate law, the reaction being independent of acid. Using the calculated self-exchange rate for the nickel complex, its reaction with  $\text{Fe}^{2+}(\text{aq})$  has been examined in terms of an inner- versus outer-sphere mechanism.

**Key words:** nickel(III), pendant-arm macrocycles, hexaaquaion(II), outer sphere, kinetics, Marcus theory.

**Résumé :** Opérant en solution aqueuse de perchlorate, on a étudié l'oxydation dans la sphère extérieure du complexe de nickel du macrocycle à bras pendant déprotoné 5,5,7,12,12,14-hexaméthyl-1,4,8,11-tétraazacyclotétradécane-1-acétate,  $[\text{NiL}^1(\text{OH}_2)]^+$ , par le bis-(1,4,7-triazacyclononane)nickel(III),  $[\text{Ni}(\text{tacn})_2]^{3+}$ . La réaction présente un comportement réversible du deuxième ordre et l'étude cinétique permet de mesurer les constantes de vitesse pour les deux directions de la réaction:



La cinétique montre que la réaction vers la droite dépend de l'acide, une caractéristique qui est attribuée à la protonation du groupe acétate du complexe de nickel(II). Faisant appel à la théorie de Marcus, on a calculé la vitesse d'autoéchange du couple  $[\text{NiL}^1(\text{OH}_2)]^{+/2+}$ . Le transfert d'électron nickel(II/III) et un processus réversible à un électron avec  $E^\circ = 1,04 \text{ V}$  (vs S.H.E.). La formation du produit authentique nickel(III) a été confirmée par spectroscopie RPE. La cinétique de la réduction d'espèces  $[\text{NiL}^1(\text{OH}_2)]^{2+}$  par le  $\text{Fe}^{2+}(\text{aq})$  présente une équation de vitesse du deuxième ordre et la réaction est indépendante de l'acide. Utilisant la vitesse d'autoéchange calculée pour le complexe de nickel, on a examiné sa réaction avec le  $\text{Fe}^{2+}(\text{aq})$  en fonction des mécanismes à l'intérieur ou à l'extérieur de la sphère.

**Mots clés :** macrocycles à bras pendant, hexaaquafer(II), extérieur de la sphère, théorie de Marcus.

[Traduit par la Rédaction]

## Introduction

Pendant-arm macrocyclic complexes, because of their thermodynamic stability and extremely slow acid-dependent dissociation, have important radioimmunotherapeutic value (1, 2). Although many studies examine the properties of amino-, nitro-, and pyridyl-arms, the majority involve car-

boxylato-pendant arms (3). The ability of polyazamacrocycles to stabilize transition metal ions in unusual oxidation states has been well known for many years (4). We are interested in the redox behaviour of transition metal macrocycles that contain pendant carboxylato-arms, since these appendages coordinate to the central metal ion and may provide an inner-sphere pathway for electron transfer to or from other

Received 7 December 2002. Published on the NRC Research Press Web site at <http://canjchem.nrc.ca> on 3 March 2003.

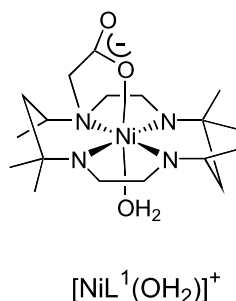
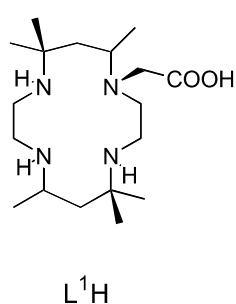
**R.I. Haines<sup>1</sup> and D.R. Hutchings.** Department of Chemistry, University of Prince Edward Island, 550 University Avenue, Charlottetown, PE C1A 4P3, Canada.

<sup>1</sup>Corresponding author (e-mail: [rhaines@upei.ca](mailto:rhaines@upei.ca)).



metal centres. Such behaviour has application, for example, in reductive dissolution of iron(III)-bearing ferrites, which constitute corrosion films found in industrial boilers and nuclear reactors (5). Such complexes also find application as chemical sensors for detection of heavy metals in natural waters (6) and as lanthanide complexing agents for use in magnetic resonance imaging (7). Related work in our laboratory involves the use of platinum(II) and (IV) complexes of these macrocycles as potential anti-tumour agents (8).

This work examines the kinetics of oxidation of the nickel(II) tetraazamacrocyclic complex, 5,5,7,12,12,14-hexamethyl-1,4,8,11-tetraazacyclotetradecane-1-acetate,  $[\text{NiL}^1(\text{OH}_2)]^+$ , which bears one pendant acetato group to the nickel(III) state. The use of the resulting nickel(III) macrocycle as a potential inner-sphere oxidant is also discussed in relation to its reaction with hexaaquairon(II).



## Experimental

### Materials

All reagents were of AnalaR grade and were used as received. Sodium perchlorate (Aldrich) solutions were standardized by passing an aliquot through a Dowex ion exchange resin and titrating the liberated acid. Stock solutions of iron(II) perchlorate were prepared by dissolving iron(II) perchlorate (Aldrich) in perchloric acid under a nitrogen atmosphere. The iron(II) concentration was determined spectrophotometrically as  $[\text{Fe}(\text{phen})_3]^{2+}$  ( $\epsilon_{510} = 11\,200\text{ dm}^3\text{ mol}^{-1}\text{ cm}^{-1}$ ) after addition of an excess of 1,10-phenanthroline to the solution. The presence of iron(III) in the solutions, tested for by addition of sulfite and 1,10-phenanthroline, was found to be negligible. Acid concentration was determined by titration with standard NaOH, using phenolphthalein indicator. All solutions were prepared using deionized, double-distilled water.

Solutions of hexaaquacobalt(III) ( $\epsilon_{605} = 35.3\text{ dm}^3\text{ mol}^{-1}\text{ cm}^{-1}$ ) (9) were prepared by electrochemical oxidation of  $\text{Co}(\text{ClO}_4)_2$  in  $5.0\text{ mol dm}^{-3}\text{ HClO}_4$  under nitrogen at  $5^\circ\text{C}$  in the dark. Stock solutions were stored at  $-12^\circ\text{C}$  and were diluted and standardized freshly each day. Solutions of  $[\text{Ni}(\text{tacn})_2]^{3+}$ , to be used for kinetics studies, were prepared in situ by oxidation of the Ni(II) form with a stoichiometric deficiency of  $\text{Co}^{3+}(\text{aq})$ . The resultant  $\text{Co}^{2+}(\text{aq})$  is inert with respect to interaction with the nickel macrocycles under study, and so  $\text{Co}^{3+}(\text{aq})$  can be used safely to generate Ni(III) without interference from the  $\text{Co}^{2+}(\text{aq})$  formed in situ.

### Synthesis of ligands and complexes

1,4,7-Triazacyclononane (tacn) and its nickel(II) perchlorate complex were synthesized by a modified literature

method (10). The functionalized macrocycle meso-5,5,7,12,12,14-hexamethyl-1,4,8,11-tetraazacyclotetradecane-1-acetic acid ( $\text{L}^1\text{H}$ ) and the nickel(II) complex bromide,  $[\text{NiL}^1(\text{OH}_2)]\text{Br}$ , were prepared according to the literature (11). The nature of the nickel complex was confirmed by X-ray crystallography. Pink needles ( $0.04 \times 0.15 \times 0.80\text{ mm}$ ), grown by the vapour diffusion method, crystallized in the  $P2_1/n$  (#14) space group. Empirical formula is  $\text{C}_{18}\text{H}_{39}\text{BrN}_4\text{NiO}_3$ . Unit cell dimensions were  $a = 9.203(4)\text{ \AA}$ ,  $b = 19.952(3)\text{ \AA}$ ,  $c = 12.538(4)\text{ \AA}$ , and  $\beta = 106.35(3)^\circ$ . Since the crystal structure of this compound has been reported previously (11), the details of the structure, which agree with the literature, will not be repeated here. For kinetic studies, the nickel complex was converted to the perchlorate salt and was recrystallized from water prior to use.

### ESR spectroscopy

The ESR spectrum of  $[\text{NiL}^1(\text{OH}_2)]^{2+}$ , generated in situ by oxidation of the nickel(II) complex by peroxodisulfate, was run on a Varian E360 spectrometer at  $77\text{ K}$  in frozen  $0.10\text{ M HClO}_4$ . An internal standard of diphenylpicrylhydrazine (DPPH) was used.

### Cyclic voltammetry

The cyclic voltammogram for a  $1.00 \times 10^{-3}\text{ mol dm}^{-3}$  solution of  $[\text{NiL}^1(\text{OH}_2)]^+$  was measured in  $0.50\text{ mol dm}^{-3}\text{ HClO}_4$  using a platinum disc working electrode, a platinum wire counter electrode, and an aqueous silver – silver chloride reference electrode. An EG & G model 283 potentiostat-galvanostat was used. Solutions were purged for 15 min with argon and voltammograms were collected with the solutions blanketed by argon at  $25^\circ\text{C}$ .

### Kinetics

Kinetic measurements were made using a Hi Tech SF61-DX2 stopped flow spectrometer, thermostatted to  $\pm 0.05^\circ\text{C}$  with a Lauda model RM6 refrigerated recirculating water bath. A constant ionic strength ( $\text{NaClO}_4/\text{HClO}_4$ ) was maintained for all experiments. The reactions were followed by monitoring the increase in absorbance at  $440\text{ nm}$  due to formation of the nickel(III) complex. Pseudo-first-order rate constants were determined by non-linear least-squares fitting of absorbance-time data, using Hi Tech's "Kinetasyst" software, on a Dell 466 MHz Pentium III computer.

Ionic strength was kept constant at  $0.500\text{ mol dm}^{-3}$  for the oxidation of  $[\text{NiL}^1(\text{OH}_2)]^+$  by  $[\text{Ni}(\text{tacn})_2]^{3+}$ . Pseudo-first-order conditions were maintained using a concentration of  $2.00 \times 10^{-5}\text{ mol dm}^{-3}$  of  $[\text{NiL}^1(\text{OH}_2)]^+$  with an excess of both  $[\text{Ni}(\text{tacn})_2]^{3+}$  (varied between  $1.10 \times 10^{-3}$  and  $2.30 \times 10^{-3}\text{ mol dm}^{-3}$ ) and  $[\text{Ni}(\text{tacn})_2]^{2+}$  (held constant at  $2.01 \times 10^{-4}\text{ mol dm}^{-3}$ ). The presence of both forms (Ni(II) and Ni(III)) of the tacn complex is explained in the Results and Discussion Section below.

In the oxidation of hexaaquairon(II) by  $[\text{NiL}^1(\text{OH}_2)]^{2+}$ , the kinetics were studied under pseudo-first-order conditions using an excess of reductant. The oxidant concentration was kept constant at  $5.0 \times 10^{-5}\text{ mol dm}^{-3}$ . The ionic strength was maintained at  $0.100\text{ mol dm}^{-3}$  using  $\text{NaClO}_4\text{--HClO}_4$ . For the study of the acid dependence on this reaction, the ionic strength was  $1.00\text{ mol dm}^{-3}$  (to allow a wide range of  $[\text{H}^+]$  to be used).



## Results and discussion

### ESR spectroscopy and electrochemistry

Figure 1 shows the ESR spectrum of the  $[\text{NiL}^1(\text{OH}_2)]^{2+}$  cation in frozen  $0.10 \text{ mol dm}^{-3} \text{ HClO}_4$ , at 77 K. The typical spectrum of a low-spin  $d^7$  nickel(III) centre shows distinct  $g_{\parallel}$  and  $g$  features when the single unpaired electron resides in the  $d_{z^2}$  orbital and when the system is tetragonally distorted. In the present case, there appears to be only slight distortion from an octahedral environment, since the ESR signal is almost isotropic. A  $g_{\parallel}$  feature is discernable, and values of  $g_{\parallel}$  and  $g$  were measured at 2.031 and 2.182, respectively. Similarly, slight deviations from octahedral geometry have been seen previously for nickel(III) centres, for the family of tris-bidentate chelate complexes,  $[\text{Ni}(\text{LL})_3]^{3+}$ , where LL is 2,2'-bipy, phen, and their derivatives (12).

The cyclic voltammogram of the  $[\text{NiL}^1(\text{OH}_2)]^{2+}$  couple in  $0.500 \text{ mol dm}^{-3} \text{ HClO}_4$  is shown in Fig. 2. The peak separation is  $75 \pm 10 \text{ mV}$ , (for sweep rates between 25 and  $100 \text{ mV s}^{-1}$ ), corresponding to a reversible one-electron redox process. This is reasonable because the purple aqueous solution of  $[\text{NiL}^1(\text{OH}_2)]^+$  indicates the presence of an octahedrally coordinated high-spin nickel(II) centre that is also present in the solid state (from crystallography). The ESR spectrum also indicated an octahedrally coordinated nickel(III) centre for the complex in its oxidized form. Hence there is expected to be little structural change on electron transfer. The electrode potential for the nickel(II/III) couple was measured at 1.04 V (vs. S.H.E.). The stabilization of tervalent nickel by polyazamacrocycles has been well known for more than 30 years (4). The presence of an acetato pendant arm coordinated to the nickel centre lends further stabilization, resulting in a lower electrode potential for the nickel(II/III) couple. This is seen by comparing the electrode potential for the mono-acetato-complex in the present study (1.04 V) with those of the analogues nickel macrocycles with no ( $\text{L}^2$ ) or two ( $\text{L}^3$ ) acetato arms (1.24 and 0.72 V, respectively) (13, 14). Indeed, there is an almost linear relationship among the electrode potentials of these three nickel macrocycles and the number of pendant acetato arms (incremental drop in  $E^\circ = 0.26 \pm 0.06 \text{ V}$ ). Busch et al. (13) have shown that there is an additive relationship between electrode potentials of nickel macrocycles and structural features for which a drop of 0.43 V per charge was found for systems with delocalized charges in the macrocyclic ring. Axial anionic ligands such as sulfate are also well known to stabilize nickel(III) macrocycles (4). While the  $[\text{Ni}(\text{tacn})_2]^{3+}$  cation is not a strong enough oxidant to oxidize  $[\text{NiL}^2]^{2+}$ , it easily oxidizes  $[\text{NiL}^3]^{2+}$  (14). The electrode potential of  $[\text{NiL}^1(\text{OH}_2)]^+$  is close to that of  $[\text{Ni}(\text{tacn})_2]^{3+}$ , allowing for an equilibrium redox reaction to occur. One advantage of such a situation is that the equilibrium constant for the cross reaction may be obtained kinetically and may be used in a Marcus theory analysis of the electron transfer mechanism.

### Kinetics

#### Oxidation of $[\text{NiL}^1(\text{OH}_2)]^+$ by $[\text{Ni}(\text{tacn})_2]^{3+}$

The  $[\text{Ni}(\text{tacn})_2]^{3+}$  cation is a well-known outer-sphere oxidant that is not susceptible to protonation or deprotonation reactions in solution (15). Thus, it provides a useful probe

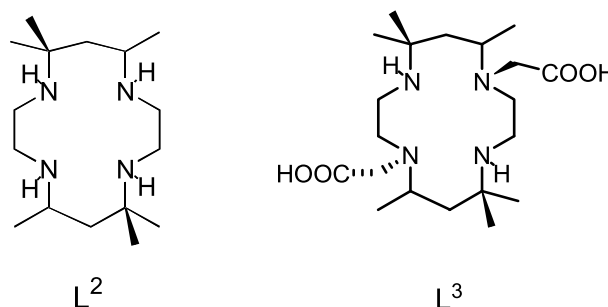
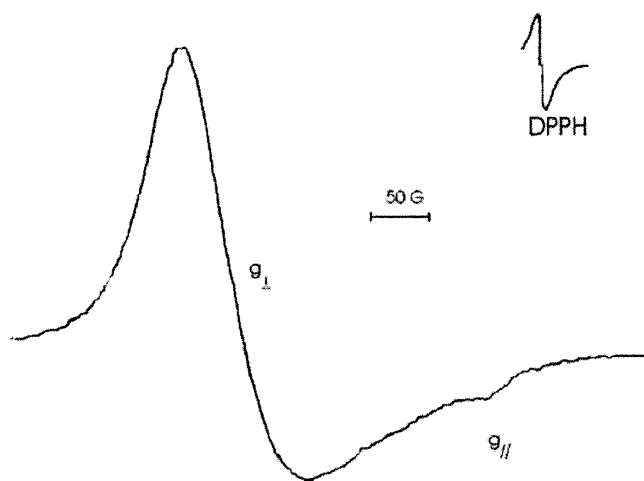
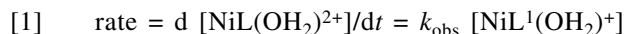


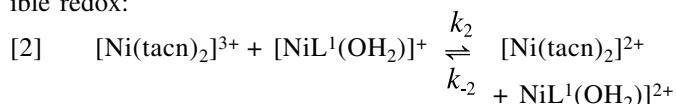
Fig. 1. ESR spectrum of the  $[\text{NiL}^1(\text{OH}_2)]^{2+}$  cation in frozen  $0.10 \text{ mol dm}^{-3} \text{ HClO}_4$ , at 77 K.



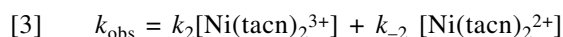
for the elucidation of the mechanisms of electron transfer reactions of oxidizable substrates. In the present study oxidation of  $[\text{NiL}^1(\text{OH}_2)]^+$  occurred smoothly under conditions of excess  $[\text{Ni}(\text{tacn})_2]^{3+}$ , the reaction being first-order in nickel(II) complex, according to the expression:



Preliminary studies using varying concentrations of oxidant at a constant  $[\text{H}^+]$  showed a linear dependence of rate on oxidant concentration with persistent intercepts in the plots of  $k_{\text{obs}}$  versus  $[\text{Ni}(\text{tacn})_2]^{3+}$  concentration. Hence the observed pseudo-first-order rate constant has the form  $k_{\text{obs}} = a + b[\text{Ni}(\text{tacn})_2]^{3+}$ . Reaction of  $[\text{NiL}^1(\text{OH}_2)]^{2+}$  with  $[\text{Ni}(\text{tacn})_2]^{2+}$  using excess oxidant also resulted in an electron transfer reaction producing  $[\text{NiL}^1(\text{OH}_2)]^+$  and  $[\text{Ni}(\text{tacn})_2]^{3+}$ . This is the reverse of reaction [1], and so the overall reaction may be described as a second-order reversible redox:



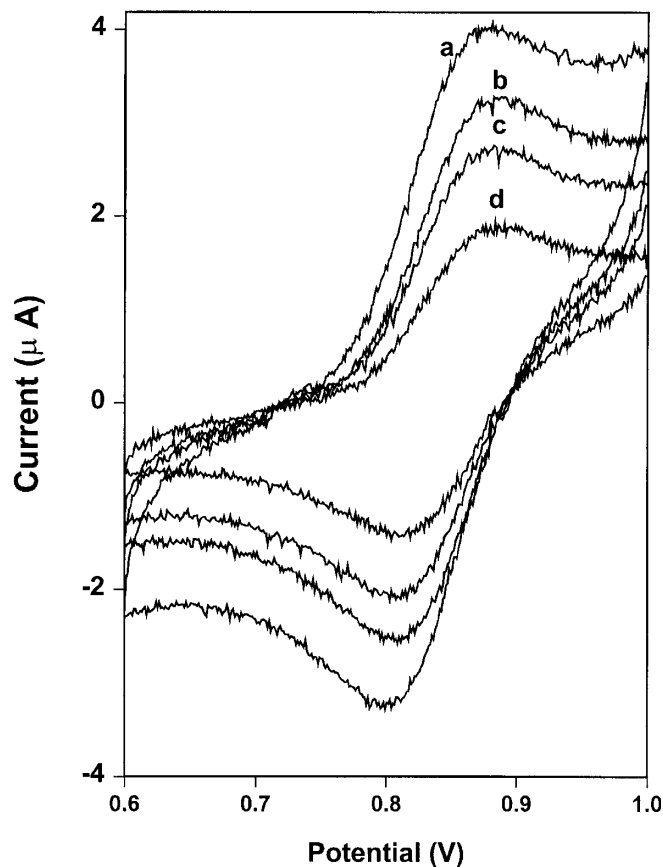
Subsequent kinetics measurements were performed under conditions of excesses of both  $[\text{Ni}(\text{tacn})_2]^{3+}$  and  $[\text{Ni}(\text{tacn})_2]^{2+}$ , according to the method of Pellizzetti and Mentasti (16). This procedure avoids the need to use complex integrated rate laws (17) and yields a pseudo-first-order expression identical to eq. [1], where





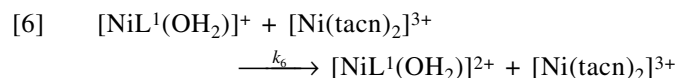
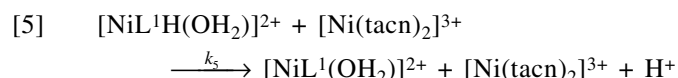
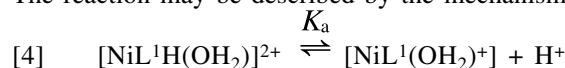
**Table 1.** Observed first-order rate constants,  $k_{\text{obs}}$  ( $\text{s}^{-1}$ ), for the oxidation of  $[\text{NiL}^1(\text{OH}_2)]^+$  by  $[\text{Ni}(\text{tacn})_2]^{3+}$  as a function of acid concentration and temperature.

$[\text{H}^+]$ ( $\text{mol dm}^{-3}$ )	$k_{\text{obs}}$ ( $\text{s}^{-1}$ )				
Temperature (K)	285.3	294.1	301.0	306.7	312.0
0.250	0.86(3)	1.76(6)		2.67(4)	3.68(6)
0.300	0.84(1)	1.57(4)	2.27(7)	2.88(6)	3.44(4)
0.350	0.78(2)				3.29(9)
0.400	0.79(2)	1.33(7)	2.17(4)	2.52(4)	3.08(9)
0.500	0.70(1)	1.22(4)	1.78(7)	2.22(10)	2.93(5)
0.600	0.65(1)	1.11(1)	1.53(4)	1.73(3)	2.53(4)
0.700	0.62(1)	0.950(3)	1.39(6)	1.76(3)	2.16(6)
0.800		0.950(3)	1.18(4)	1.56(4)	
0.850	0.62(2)				1.92(3)
0.900			1.14(5)	1.41(1)	
1.00	0.57(1)	0.89(2)	1.08(4)	1.36(3)	1.76(2)

**Fig. 2.** Cyclic voltammogram of the  $[\text{NiL}^1(\text{OH}_2)]^+$  cation in  $0.500 \text{ mol dm}^{-3} \text{ HClO}_4$ , at  $25^\circ\text{C}$ . Scan rates: (a)  $25 \text{ mV s}^{-1}$ , (b)  $50 \text{ mV s}^{-1}$ , (c)  $75 \text{ mV s}^{-1}$ , and (d)  $100 \text{ mV s}^{-1}$ .

The reaction was found to be dependent on  $[\text{H}^+]$ , with the reaction rate decreasing with increasing  $[\text{H}^+]$ . Table 1 gives the raw data for the acid dependence of the oxidation of  $[\text{NiL}^1(\text{OH}_2)]^{2+}$  by  $[\text{Ni}(\text{tacn})_2]^{3+}$  at an ionic strength of  $1.00 \text{ mol dm}^{-3}$  for a range of temperatures. There is a small but real and reproducible dependence of rate on acid concentration. Values for  $k_2$  and  $k_{-2}$  reported in Table 2 were derived from  $k_{\text{obs}}$  vs.  $[\text{Ni}(\text{tacn})_2^{3+}]$  at constant  $[\text{Ni}(\text{tacn})_2^{2+}]$ , according to eq. [3]. Separate kinetic studies on the oxidation of

iron(II) by  $[\text{NiL}^1(\text{OH}_2)]^{2+}$ , reported later in this paper, were independent of acid. This suggested that, since the  $[\text{Ni}(\text{tacn})_2]^{2/3+}$  system is known to be unaffected by acid (15), the source of the  $[\text{H}^+]$  dependence must be from a protonation equilibrium involving the  $[\text{NiL}^1(\text{OH}_2)]^+$  species. The reaction may be described by the mechanism:



Using the law of mass balance,  $k_2 = (k_5 + k_6 K_a [\text{H}^+]) / (1 + K_a [\text{H}^+])$ , whence the expression for the pseudo-first-order rate constant becomes:

$$[7] \quad k_{\text{obs}} = \left[ \frac{k_5 + k_6 K_a [\text{H}^+]}{1 + K_a [\text{H}^+]} \right] [\text{Ni}(\text{tacn})_2^{3+}] + k_{-2} [\text{Ni}(\text{tacn})_2^{2+}]$$

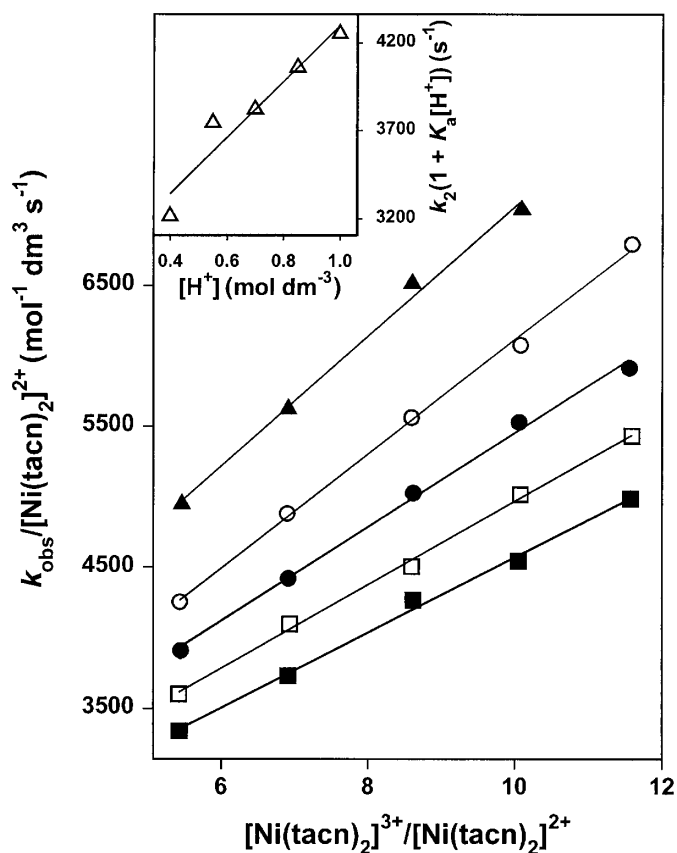
Hence a plot of  $k_{\text{obs}}/[\text{Ni}(\text{tacn})_2^{2+}]$  versus  $[\text{Ni}(\text{tacn})_2^{3+}]/[\text{Ni}(\text{tacn})_2^{2+}]$  is linear, with a slope of  $(k_5 + k_6 K_a [\text{H}^+]) / (1 + K_a [\text{H}^+])$  and an intercept of  $k_{-2}$  (Fig. 3). A consequent plot of  $k_2(1 + K_a [\text{H}^+])$  versus  $[\text{H}^+]$  (Fig. 3 inset) yields  $k_6$  as slope/ $K_a$  and  $k_5$  as the intercept. Thus, at  $25^\circ\text{C}$ ,  $k_5$  and  $k_6$  have values of  $110$  and  $2700 \text{ mol}^{-1} \text{ dm}^3 \text{ s}^{-1}$ , respectively. A non-linear least-squares curve fit of the  $k_{\text{obs}}$  versus  $[\text{H}^+]$  gave a value for the protonation constant,  $K_a$  for  $[\text{NiL}^1(\text{OH}_2)]^+$  of  $15 \pm 4 \text{ mol}^{-1} \text{ dm}^3$ . Although the value of  $K_a$  was estimated at several temperatures, it was found to vary little with temperature. We have not determined activation parameters for pathways  $k_5$  and  $k_6$  because the estimated values of  $k_5$  and  $k_6$  at the various temperatures have large uncertainties due to the limited range of acid concentrations possible. From the  $k_{-2}$  data,  $\Delta H^\ddagger$  and  $\Delta S^\ddagger$  were estimated for the reverse of reaction [2] to be  $30 \pm 2 \text{ kJ mol}^{-1}$  and  $-60 \pm 5 \text{ J K}^{-1} \text{ mol}^{-1}$ , respectively. Such values for activation parameters are typical of outer sphere electron transfer reactions.



**Table 2.** Observed first-order rate constants,  $k_{\text{obs}}$  ( $\text{s}^{-1}$ ) and derived second-order rate constants,  $k_2$ ,  $k_{-2}$  ( $\text{mol}^{-1} \text{dm}^3 \text{s}^{-1}$ ) for the oxidation of  $[\text{NiL}^1(\text{OH}_2)]^+$  by  $[\text{Ni}(\text{tacn})_2]^{3+}$ ; ionic strength maintained at  $0.500 \text{ mol dm}^{-3}$  ( $\text{HClO}_4$ );  $[\text{Ni}(\text{tacn})_2^{2+}] = 2.01 \times 10^{-4} \text{ mol dm}^{-3}$ .

$[\text{Ni}(\text{tacn})_2^{3+}] (\times 10^3) (\text{mol dm}^{-3})$	$k_{\text{obs}} (\text{s}^{-1})$				
Temperature (K)	288.2	293.1	299.3	305.6	312.5
1.10	1.69(6)	2.00(5)	2.70(5)	3.48(3)	4.71(9)
1.40	1.83(2)	2.27(4)	3.09(5)	4.06(6)	5.36(8)
1.70	2.01(4)	2.50(5)	3.48(9)	4.53(8)	5.93(8)
2.00	2.25(2)	2.77(5)	3.83(4)	4.93(9)	6.60(9)
2.30	2.46(2)	3.06(2)	4.14(4)	5.44(8)	7.22(9)
$k_2$	$740 \pm 40$	$940 \pm 40$	$1190 \pm 30$	$1520 \pm 60$	$2100 \pm 100$
$k_{-2}$	$3900 \pm 100$	$4600 \pm 200$	$7300 \pm 100$	$9700 \pm 200$	$11\,900 \pm 300$

**Fig. 3.** Plot of  $k_{\text{obs}}/[\text{Ni}(\text{tacn})_2^{2+}]$  versus  $[\text{Ni}(\text{tacn})_2^{3+}]/[\text{Ni}(\text{tacn})_2^{2+}]$  at  $25.0^\circ\text{C}$  and ionic strength  $1.00 \text{ mol dm}^{-3}$ .  $[\text{H}^+]$ : (▲)  $0.40 \text{ mol}^{-1} \text{dm}^{-3}$ , (○)  $0.55 \text{ mol}^{-1} \text{dm}^{-3}$ , (●)  $0.70 \text{ mol}^{-1} \text{dm}^{-3}$ , (□)  $0.85 \text{ mol}^{-1} \text{dm}^{-3}$ , (■)  $1.00 \text{ mol}^{-1} \text{dm}^{-3}$ . Inset Fig. shows acid dependence of  $k_2$  (see text).



The rate of oxidation of the deprotonated nickel macrocycle is approximately 25 times faster than the protonated form. This difference is in keeping with the discussion above and may be attributed to a lower electrode potential of the deprotonated form since the negatively charged acetato group will tend to stabilize the tervalent nickel centre. This is not unusual; for example, in redox reactions involving  $\text{Co}^{3+}(\text{aq})$ , the inverse acid dependence in the rates of its redox reactions is due to the reactivity of the hydrolysed form,  $\text{CoOH}^{2+}(\text{aq})$  (9). Similarly, ascorbate is several orders of magnitude more reactive than ascorbic acid (18).

Owing to the equilibrium nature of this reaction, we may estimate the cross-reaction equilibrium constant for reduction of the deprotonated nickel(III) macrocycle by  $[\text{Ni}(\text{tacn})_2]^{2+}$  as  $k_{-2}/k_6$ . At  $25^\circ\text{C}$ , this has a value of 0.77. Since the self-exchange rate for the  $[\text{Ni}(\text{tacn})_2]^{2+/3+}$  couple is known (19), Marcus theory may be used to determine the self-exchange rates for the  $[\text{NiL}^1(\text{OH}_2)]^{+/2+}$  couple.

According to Marcus theory (20), for an outer-sphere electron transfer mechanism, the rate constant for the cross-reaction ( $k_{12}$ ) is related to the rate constants for the self-exchange rates of the components,  $k_{11}$  and  $k_{22}$ , and the cross reaction equilibrium constant ( $K_{12}$ ) by the expression:

$$[8] \quad k_{12} = (k_{11} k_{22} K_{12} f_{12})^{1/2} W_{12}$$

where

$$\ln f_{12} = \frac{[\ln K_{12} + (w_{12} - w_{21})/RT]^2}{4[\ln(k_{11}k_{22}/Z^2) + (w_{11} + w_{22})/RT]}$$

and

$$W_{12} = \exp[-(w_{12} + w_{21} - w_{11} - w_{22})/2RT]$$

where  $w_{ij} = 4.225 \times 10^3 Z_i Z_j / \sigma_{ij} (1 + 0.329 \sigma_{ij} (\mu^{1/2}))$ . The term  $w_{ij}$  is the work required to bring the ions  $i$  and  $j$  (with charges  $Z_i$  and  $Z_j$ , respectively) to the separation distance  $\sigma_{ij}$ . This distance is assumed to be equal to the sum of the radii of the ions  $i$  and  $j$ ; and  $\mu$  is the ionic strength.

The self-exchange rate,  $k_{11}$ , for the  $[\text{NiL}^1(\text{OH}_2)]^{+/2+}$  system is calculated from eq. [8] as  $870 \text{ mol}^{-1} \text{dm}^3 \text{s}^{-1}$ , where  $K_{12}$  has a value of 0.77 (above) and  $k_{12}$  ( $= k_{-2}$  in our mechanistic scheme) was measured as  $2.00 \times 10^3 \text{ mol}^{-1} \text{dm}^3 \text{s}^{-1}$ . The estimate of  $k_{11}$  is in close agreement with self-exchange rates of other nickel(II/III) macrocyclic systems (21). It is interesting to note that the self-exchange rate for the diacetato complex  $[\text{NiL}^3]^{0/+}$  has been estimated (14) at  $55 \text{ mol}^{-1} \text{dm}^3 \text{s}^{-1}$ , whereas those for nickel complexes of planar tetraazamacrocycles of the type  $\text{L}^2$  have self-exchange rates in the region of  $1500 \text{ mol}^{-1} \text{dm}^3 \text{s}^{-1}$ . This trend may be explained by an increase in internal reorganizational energies with increasing stricture of the metal ion within the macrocycle. The nickel ion is quite confined in the octahedral complex of  $\text{L}^2$ . For planar tetraazamacrocyclic complexes, the nickel(III) form, being in a tetragonally distorted octahedral geometry, has axial ligands that are not tethered to the macrocycle and so can "breathe". This lack of tethering allows for bond length changes on electron transfer. A similar situation pertains to the case of



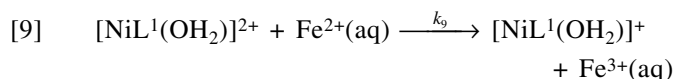
**Table 3.** Observed first-order rate constants,  $k_{\text{obs}}$  ( $\text{s}^{-1}$ ), together with the derived second-order rate constants,  $k_9$  ( $\text{mol}^{-1} \text{dm}^3 \text{s}^{-1}$ ), for the oxidation of  $\text{Fe}^{2+}(\text{aq})$  by  $[\text{Ni}^{\text{III}}\text{L}(\text{OH}_2)]^{2+}$  in  $1.00 \text{ mol dm}^{-3} \text{HClO}_4$ , for a series of temperatures.

$[\text{Fe}^{2+}] (\times 10^4) (\text{mol dm}^{-3})$	$k_{\text{obs}} (\text{s}^{-1})$				
Temperature (K)	287.9	291.2	294.6	298.1	303
4.58	15.6(1)	18.0(1)	20.7(2)	25.0(2)	30.8(1)
9.16	31.3(3)	36.0(2)	41.8(3)	49.5(2)	61.0(3)
18.3	63.4(5)	73.2(7)	84.0(2)	99.6(8)	122(1)
27.5	96.8(9)	111(1)	128(1)	150(2)	184(2)
36.6	130(3)	149(2)	173(2)	203(2)	248(3)
$k_9 (\text{mol}^{-1} \text{dm}^3 \text{s}^{-1})$	$35\,100 \pm 100$	$40\,500 \pm 300$	$47\,100 \pm 400$	$55\,800 \pm 400$	$68\,300 \pm 500$

$[\text{Ni}(\text{tacn})_2]^{2+/3+}$ , in which, even though the complex is octahedral, the macrocyclic ligands cap the metal ion and can move in or out with changes in metal-ligand bond length upon change in the metal ion oxidation state. The mono-acetato-macrocyclic in the present study is intermediate in that one axial position of the metal ion is confined by the co-ordinated pendant-arm group but the other axial position, co-ordinated to an aqua ligand, can “breathe”. Hence it seems reasonable that the self-exchange rate for the last case is intermediate between the previous two.

#### Oxidation of $\text{Fe}^{2+}(\text{aq})$ by $[\text{NiL}^1(\text{OH}_2)]^{2+}$

The pendant-arm macrocyclic complex  $[\text{NiL}^1(\text{OH}_2)]^{2+}$  was originally chosen for study because it provides the possibility of an acetato bridging ligand, which might provide a conduit for an inner-sphere electron transfer, from iron(II) to the nickel(III) centre. The reaction was followed by monitoring the disappearance of the strong absorption at  $440 \text{ nm}$  ( $\epsilon = 8000 \text{ mol}^{-1} \text{dm}^3 \text{cm}^{-1}$ ), typical of UV–visible spectra of nickel(III) macrocycles (4). Spectrophotometric titration showed the reaction to have a 1:1 stoichiometry, within experimental error. The reaction is clearly first order with respect to the oxidant, and the dependence of the rate on  $[\text{Fe}^{2+}]$  also exhibits excellent first-order behaviour (Table 3). Owing to the high reaction rate, the range of iron(II) concentrations was limited to between  $4.7 \times 10^{-4}$  and  $1.3 \times 10^{-3} \text{ mol dm}^{-3}$ . The lower limit ensured a sufficient excess of reductant for pseudo-first-order conditions ( $[\text{NiL}^1(\text{OH}_2)]^{2+} = 4.0 \times 10^{-5} \text{ mol dm}^{-3}$  for all experiments). The reaction was studied at various acid concentrations between 0.10 and 1.00 M  $\text{HClO}_4$  (at constant ionic strength) at  $14^\circ\text{C}$  for a constant iron(II) concentration of  $9.98 \times 10^{-4} \text{ mol dm}^{-3}$ . The rate was found to be independent of  $[\text{H}^+]$ , with a mean value of  $k_{\text{obs}}$  of  $37.0 \pm 0.5 \text{ s}^{-1}$  at  $14^\circ\text{C}$ . The lack of dependence of the rate on  $[\text{H}^+]$  suggests that there is negligible hydrolysis of either reactant under the experimental conditions. This is not unexpected, since a similar lack of dependence on acid concentration has been observed previously for oxidation of iron(II) by  $[\text{Ni}(\text{oxime})]^{2+}$  (22) and  $[\text{Ni}(\text{bipy})_3]^{3+}$  (23). While hydrolysis of diaquanickel(III) macrocycles is common, the aquanickel(III) complex in the present study contains a deprotonated pendant acetato group coordinated to the metal centre, resulting in an overall 2+ charge on the complex. Thus, hydrolysis of this species is expected to be minimal. Addition of  $[\text{NiL}^1(\text{OH}_2)]^+$  to the system had no effect on rate, indicating that equilibrium conditions do not obtain in this reaction. Hence the reaction equation is



and it obeys a simple second-order overall rate law:

$$[10] \quad \text{rate} = -d[\text{NiL}^1(\text{OH}_2)]^{2+}/dt = k_9[\text{NiL}^1(\text{OH}_2)]^{2+}[\text{Fe}^{2+}]$$

The activation enthalpy and entropy were calculated, from the data in Table 3, to be  $29.9 \pm 0.5 \text{ kJ mol}^{-1}$  and  $-54 \pm 2 \text{ J K}^{-1} \text{mol}^{-1}$ , respectively. The magnitudes of the activation parameters are similar to those for oxidation of iron(II) by other nickel(III) macrocycles (24) and by metal complexes (25, 26). In these systems, an outer-sphere mechanism has been invoked. Since we have evaluated the self-exchange rate for the  $[\text{NiL}^1(\text{OH}_2)]^{2+/3+}$  couple (vide supra), we can compare the experimental value of the cross-reaction rate constant ( $k_9$ ) with that calculated from Marcus theory.

The self-exchange rate of the  $\text{Fe}^{2+/3+}$  couple ( $k_{22}$ ) has been reported as  $1.1 \text{ mol}^{-1} \text{dm}^3 \text{s}^{-1}$  by Sutin and co-workers (27) and by Swaddle and co-workers (28), whereas Jordan (29) suggests that the true rate of self-exchange is  $4.2 \text{ mol}^{-1} \text{dm}^3 \text{s}^{-1}$ , after compensation for an inner-sphere pathway via a hydroxo-bridged species. We have used Jordan's value in our calculations. The equilibrium constant,  $K_{12}$ , was estimated at  $4.0 \times 10^4$  from the difference in electrode potentials between the reactants. Using eq. [8], the theoretical cross-reaction rate constant for eq. [9] is calculated to be  $1.2 \times 10^4 \text{ mol}^{-1} \text{dm}^3 \text{s}^{-1}$  (using  $k_{11} = 870 \text{ mol}^{-1} \text{dm}^3 \text{s}^{-1}$ ). There is good agreement with the experimentally measured value for  $k_9$  of  $5.57 \times 10^4 \text{ mol}^{-1} \text{dm}^3 \text{s}^{-1}$ , lending support to the conclusion that the oxidation of iron(II) by the acetato pendant-arm macrocyclic nickel(III) complex is outer-sphere.

The hexaaquairon(II) species is labile with a solvent exchange rate (30) of  $4.4 \times 10^6 \text{ M}^{-1} \text{s}^{-1}$  at  $25^\circ\text{C}$ . Since the cross-reaction rate is significantly slower than this, it is conceivable that an inner-sphere pathway for electron transfer is possible. In this case, rapid dissociation of an aqua-ligand from the iron(II) centre, followed by coordination of the bridging acetato pendant arm to the iron(II) centre is required. Rapid electron transfer from iron(II) to the nickel(III) centre would result in a bridged  $\text{Ni}(\text{II})\text{-OCO-Fe}(\text{III})$  species. Since the acetato group is coordinated to the nickel(II) centre, both in the solid state and in solution, and iron(III) is a hard Lewis acid, it is conceivable that the bridged intermediate may be isolated or, at least, be kinetically observable. We were unable to isolate or kinetically detect such an intermediate. Conversely, since



iron(II) is a soft Lewis acid, it will not have a high affinity for the oxygen donor atom of the acetato group and so the inner-sphere pathway will be less favoured. Additionally, the magnitude and sign of the activation parameters obtained for this reaction are in keeping with those for outer-sphere oxidations of iron(II) (26–28). Thus, while the system has the requisite conditions for an inner-sphere mechanism, viz. a bridging ligand, a labile reductant, and a cross-reaction rate that is slower than the solvent-exchange rate of the reductant, the experimental rate constant is in very good agreement with that calculated for an outer-sphere mechanism from Marcus theory.

## Acknowledgements

We are grateful to the Natural Science and Engineering Research Council (NSERC) of Canada for financial support. Thanks too go to the University of Prince Edward Island Senate Committee on Research for a research grant. Funding for the stopped-flow spectrometer and electrochemical equipment was obtained from the Canadian Foundation for Innovation (CFI), the Atlantic Canada Opportunities Agency (ACOA), and the Levesque Foundation. The X-ray crystallography was performed by Dr. S. Cameron, Dalhousie University.

## References

1. J.P.L. Cox, K.J. Jankowski, R. Katak, D. Parker, N.R.A. Beeley, B.A. Boyce, M.A.W. Eaton, K. Miller, A.T. Millian, A. Harrison, and C. Walker. *J. Chem. Soc., Chem. Commun.* 797 (1989).
2. J.R. Morphy, D. Parker, R. Katak, A. Harrison, M.A.W. Eaton, A. Millian, A. Phipps, and C. Walker. *J. Chem. Soc., Chem. Commun.* 792 (1989).
3. A.D. Sherry, R.D. Brown, C. Gerald, S.H. Koenig, K.T. Kuan, and M. Spiller. *Inorg. Chem.* **28**, 620 (1989).
4. R.I. Haines and A. McAuley. *Coord. Chem. Rev.* **39**, 77 (1981).
5. R.A. Speranzini, P.A. Burchart, and K.A. Kanhai. *Mater. Perform.* **28**, 67 (1989); E. Tachikawa, M. Hoshi, and C. Sagawa. *Nucl. Technol.* **65**, 138 (1984).
6. E. Kimura, T. Koike, and M. Takahashi. *J. Chem. Soc., Chem. Commun.* 385 (1985).
7. S. Aime, M. Botta, D. Parker, and J.A.G. Williams. *J. Chem. Soc., Dalton Trans.* 2259 (1995); S. Aime, M. Botta, M. Fasano, S.G. Crich, and E. Terreno. *Coord. Chem. Rev.* **186**, 321 (1999).
8. R.I. Haines, D.R. Hutchings, and T. McCormack. *J. Inorg. Biochem.* **85**, 1 (2001).
9. J.C. Brodovitch and A. McAuley. *Inorg. Chem.* **20**, 1667 (1981).
10. G.H. Searle and R.J. Geue. *Aust. J. Chem.* **37**, 959 (1984).
11. J.-D. Xu and S.-S. Ni. *Inorg. Chim. Acta*, **111**, 61 (1986).
12. J.C. Brodovitch, R.I. Haines, and A. McAuley. *Can. J. Chem.* **59**, 1610 (1981).
13. F.V. Lovecchio, E.S. Gore, and D.H. Busch. *J. Am. Chem. Soc.* **96**, 3109 (1974).
14. R.I. Haines, D.R. Hutchings, R.J. Lucas, and D. Miller. *Can. J. Chem.* **79**, 54 (2001).
15. M.G. Fairbank, A. McAuley, P.R. Norman, and O.A. Olubuyide. *Can. J. Chem.* **63**, 2983 (1985).
16. E. Pelizzetti and E. Mentasti. *Inorg. Chem.* **18**, 583 (1979).
17. E.L. King. *Int. J. Chem. Kin.* **14**, 1285 (1982).
18. K. Lemma, A.M. Sargeson, and L.I. Elding. *J. Chem. Soc., Dalton Trans.* 1167 (2000).
19. A. McAuley, P.R. Norman, and O. Olubuyide. *Inorg. Chem.* **23**, 1938 (1984).
20. R.A. Marcus. *Ann. Rev. Phys. Chem.* **15**, 155 (1964); N.S. Hush. *Trans. Faraday Soc.* **57**, 557 (1961); N. Sutin. *Acc. Chem. Res.* **15**, 275 (1982); R.A. Marcus and N. Sutin. *Biochim. Biophys. Acta*, **811**, 265 (1985); R.B. Jordan. *Reaction mechanisms of inorganic and organometallic systems*, 2nd ed. Oxford University Press, New York, 1991, Chapt. 6, p. 203.
21. A. McAuley, D.H. Macartney, and T. Oswald. *J. Chem. Soc., Chem. Commun.* 274 (1982); A. McAuley, O. Olubuyide, L. Spencer, and P.R. West. *Inorg. Chem.* **23**, 2594 (1984).
22. A.G. Lappin and M.C.M. Laranjeira. *J. Chem. Soc., Dalton Trans.* 1861 (1982).
23. D.H. Macartney and N. Sutin. *Inorg. Chem.* **22**, 3530 (1983).
24. D.H. Macartney, A. McAuley, and O.A. Olubuyide. *Inorg. Chem.* **24**, 307 (1985).
25. M. Chou, C. Creutz, and N. Sutin. *J. Am. Chem. Soc.* **99**, 5615 (1977).
26. M.J. Weaver and E.L. Yee. *Inorg. Chem.* **19**, 1936 (1980).
27. B.S. Brunschwig, C. Creutz, D.H. Macartney, T.-K. Sham, and N. Sutin. *Disc. Faraday Soc.* **74**, 113 (1982).
28. W.H. Jolley, D.R. Stranks, and T.W. Swaddle. *Inorg. Chem.* **29**, 1948 (1990).
29. R.B. Jordan. *Reaction mechanisms of inorganic and organometallic systems*, 2nd ed., Oxford University Press, New York, 1998, Chaps. 3 and 4.
30. Y. Ducommun, K.E. Newman, and A.E. Merbach. *Inorg. Chem.* **18**, 3696 (1980).



# XANES of chromium in sludges used as soil ameliorants

R.R. Martin, S.J. Naftel, T.K. Sham, B. Hart, and M.A. Powell

**Abstract:** Samples of sewage sludges proposed for use as soil ameliorants in an Indo-Canadian project were tested for chromium content. Standard aqua regia extractions found one sludge to have excessive amounts of Cr. X-ray absorption near-edge structure (XANES) spectroscopy, however, indicated that the Cr was present in the relatively benign Cr(III) oxidation state in all the sludge samples.

*Key words:* soil, chromium, synchrotron, XANES.

**Résumé :** On a déterminé la teneur en chrome d'échantillons de boues d'égouts dont l'utilisation a été proposée pour l'amélioration de sols dans un projet indo-canadien. Des extractions standards à l'eau régale ont permis de montrer qu'une de ces boues contient des quantités excessives de chrome. Toutefois, la spectroscopie d'absorption des rayons X (XANES) indique que, dans toutes les échantillons de boues, le chrome est présent à l'état d'oxydation relativement bénin de Cr(III).

*Mots clés :* sol, chrome, synchrotron, XANES.

[Traduit par la Rédaction]

## Introduction

Various solid organic wastes can be added to soil, both as an effective means of disposal and for soil amelioration. The practice of adding wastes to soils can improve the soil fertility and the physical and chemical properties of the soil such as organic content and pH. There is some concern, however, that adding wastes to soil may also introduce toxic heavy metals into the soil environment and subsequently into the food chain. Analysis by standard extraction techniques may exaggerate the risk, as metals may be present but may not be bioavailable or may be in a relatively benign form.

Chromium is one of the more abundant trace elements in the lithosphere, ranging in concentration from <1 to 1000s of mg kg<sup>-1</sup> in soils, with an average near 100 mg kg<sup>-1</sup> (1, 2), and is most abundant in soils developed on ultramafic-basaltic igneous rocks, which may host Cr at concentrations >10 000 mg kg<sup>-1</sup>. Anthropogenic sources of Cr are varied and may contribute significantly to soil Cr (3, 4). Both fly ash and sewage sludge have been identified as major sources of soil Cr when used as agricultural amendments (4–8).

Soil Cr has received considerable attention in the literature; much of the interest is related to the potential of the soil as a starting point for Cr in the food chain and, second-

arily, as a reservoir that can release Cr into groundwater under certain conditions. While the abundance of Cr in a soil is closely related to parent material, the addition of soil amendments such as sewage sludge and fly ash (from coal burning power plants) can account for the majority of soil Cr (3, 5, 6, 9).

The role of chromium in plant and animal nutrition is not well understood (6, 9–11). It is, however, well known that Cr can be toxic to both plants and animals (4). The relative toxic, mutagenic, and (or) carcinogenic affects of Cr are a function of the oxidation state present (1, 12). Cr(VI) is acutely toxic to plants and animals at small concentrations and is highly soluble and, hence, mobile. The much more abundant Cr(III), typically found in soil environments, is comparatively harmless and relatively insoluble.

Because Cr is a transition group metal, much of its behaviour in the near-surface environment (soils and groundwater) is controlled by the redox chemistry of chromium and the local pH (12–14), which in turn are affected by the occurrence and form of organic matter (15, 16) in the soils and groundwater. Hence, the factors that control the transition from Cr(VI) to Cr(III) are the most important in determining toxicity and mobility. Cr(VI) is easily reduced by a variety of reductants that are common in soils, including Fe(II) (either aqueous or crystalline), humic and (or) fulvic acids, and sulfides (1, 17). Once Cr has been reduced in a soil, the transition back to the oxidized state is very difficult and requires the presence of dissolved oxygen or compounds such as MnO<sub>2</sub> under most soil conditions.

The data presented here are derived from samples collected as part of a large Indo-Canadian project designed to test the viability of using municipal sludge mixed with fly ash (from thermal power generation) to regenerate degraded soils in India. The main focus of this paper is to highlight the oxidation state (from X-ray absorption near-edge

Received 16 September 2002. Published on the NRC Research Press Web site at <http://canjchem.nrc.ca> on 3 March 2003.

**R.R. Martin,<sup>1</sup> S.J. Naftel, and T.K. Sham.** Department of Chemistry, University of Western Ontario, London, ON N6A 5B7, Canada.

**B. Hart and M.A. Powell.** Department of Earth Sciences, University of Western Ontario, London, ON N6A 5B7, Canada.

<sup>1</sup>Corresponding author (e-mail: [rrhm@uwo.ca](mailto:rrhm@uwo.ca)).



structure (XANES) analysis) of Cr in some of the sludges in order to address the potential for Cr toxicity in the amended soil. The selected sludges are from Kanpur, Uttar Pradesh and Jaipur, Rajasthan, India.

### Sample locations

Two sample sites were chosen for this study because of their potential for Cr contamination. At the Kanpur, Uttar Pradesh site, samples were collected from domestic sludge drying beds. The distinction of "domestic" is made because this sludge was not supposed to receive any effluent from the extensive tannery operations in the area. However, field observations indicated that there is a partial contribution to this sludge from the tannery industries, a major source of Cr contamination. The Jaipur, Rajasthan site sludge samples were collected from a municipal sludge treatment facility that receives both domestic and industrial effluents. The major sources of Cr in the Jaipur sludge are metal plating and dyeing industries.

### Extraction analysis of chromium in the sludges

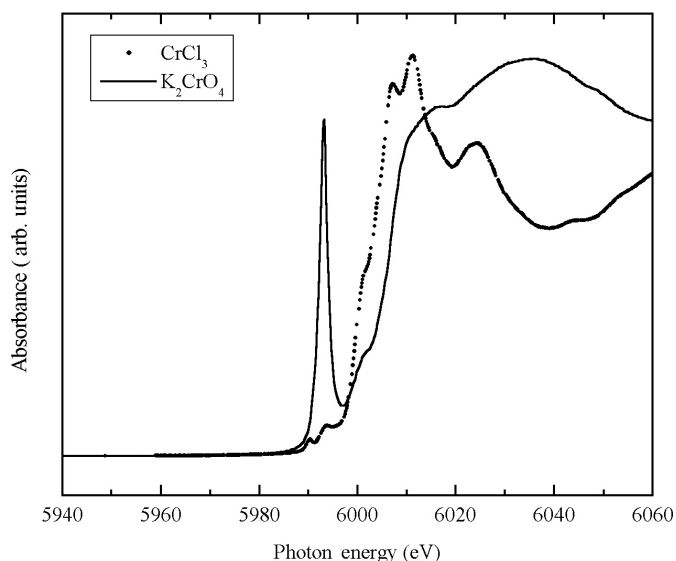
Metal speciation studies are typically preceded by the determination of the background concentration of the metal in the material of interest. Data presented here represent the two sludges of interest and the soils receiving them, since Cr concentrations in both must be considered when biosolids are used in agriculture. The concentration of Cr in air-dried sludges worldwide varies significantly, from a few  $\text{mg kg}^{-1}$  to approximately 10% (3, 4, 18, 19). All samples were air dried, desegregated, passed through a 2 mm sieve, and ground to <150 microns prior to aqua regia extraction and analysis by inductively coupled plasma - optical emission spectroscopy (ICP-OES) according to standard analytical techniques.

The average concentration of Cr in the Kanpur sludge is  $6200 \text{ mg kg}^{-1}$ . This sludge was planned for application to alkaline-sodic soils around Hardoi, Uttar Pradesh, which contain  $32 \text{ mg kg}^{-1}$  Cr ( $n = 71$ , std. deviation =  $8 \text{ mg kg}^{-1}$ ). The Kanpur sludge was rejected for use based on this high Cr content.

Sludge from Jaipur, Rajasthan contains an average of  $126 \text{ mg kg}^{-1}$  Cr. The Jaipur sludge was planned for application to a stony soil near Bundi, Rajasthan, where both pit soils and reservoir tank sediments are mixed with the sludge. Unlike the Hardoi soil, both the pit soils and tank sediments at Bundi were highly variable in Cr content, ranging from  $37\text{--}788 \text{ mg kg}^{-1}$  for the tank sediments and  $31\text{--}2416 \text{ mg kg}^{-1}$  for the pit soils. Thus, the soils and sediments at Bundi could be the major source of Cr, rather than the sewage sludge.

In this work, samples of the two sewage sludges were analysed using XANES spectroscopy to determine the oxidation state of Cr. The soil materials were not analysed as part of this study, although this would be important for the Bundi soils. As noted above, the oxidation state of the Cr is essential in assessing the bioavailability of Cr and, hence, the potential risk in using the sludges as ameliorants.

**Fig 1.** Cr K-edge XANES spectra of  $\text{CrCl}_3$  [ $\text{Cr}^{3+}$ ] and  $\text{K}_2\text{CrO}_4$  [ $\text{Cr}^{6+}$ ].



### Methods

Two representative sludge samples were selected for XANES analysis: a Kanpur high-chromium sludge (~5000 ppm) and a relatively low-chromium sludge from Jaipur (~120 ppm). The dried sludge material was spread thinly on clear tape to make the XANES measurements. The Cr K-edge XANES were taken at the PNC-CAT, 20-BM-B beamline at the Advanced photon source (APS) Argonne national laboratory.

The XANES of the sludges were measured in fluorescence yield mode using an Oxford instruments NaI scintillation detector placed at right angles to the incident beam. The Cr standard materials ( $\text{CrCl}_3 \cdot 6\text{H}_2\text{O}$  and  $\text{K}_2\text{CrO}_4$ ), used to establish the oxidation state(s) of chromium in the sludge material, were obtained from Fisher Scientific Co. and used as received. Standards were spread thinly on tape and the XANES measured in transmission mode.

The spectra shown all represent the average of at least 3 scans and have had a linear pre-edge background removed. The energy scales shown have not been calibrated to a Cr metal standard.

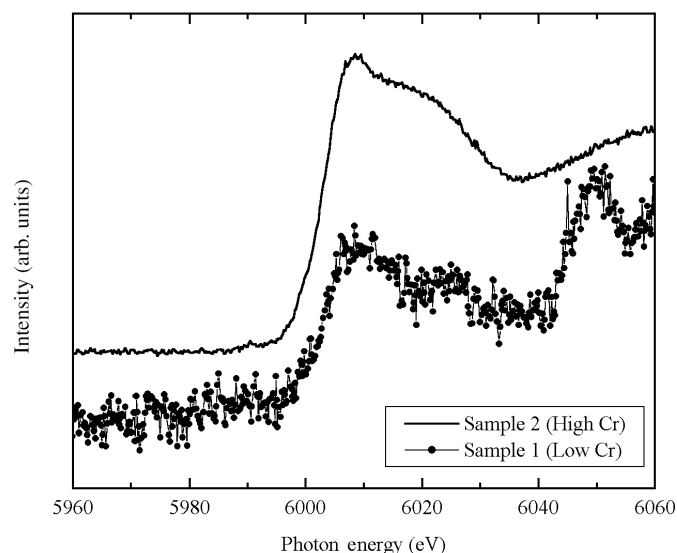
### Results and discussion

Synchrotron radiation techniques are becoming important analytical techniques for studying metals in soil (20, 21) and other environmentally important matrices, where the analysis of small volumes containing low concentrations of analyte is required. Naturally the ability of XANES to provide chemical information makes this technique especially attractive.

As the oxidation state of an atom increases, the core electronic states become more tightly bound, producing a measurable shift in the XANES spectra to higher photon energies. The local geometry around the absorbing atom also affects the XANES spectra. The spectra of four-coordinate transition metal ions (such as those of Cr (VI)) exhibit an



**Fig 2.** Cr K-edge XANES spectra of the Kanpur and Jaipur sludge samples. The spectra have been shifted vertically for clarity.



intense pre-edge peak due to  $3d-4p$  mixing (22–25). The XANES spectra of Cr (III) compounds do not have this sharp feature; thus, the differences between the two oxidation states of Cr can be clearly seen, as shown in Fig. 1.

The XANES of the two sludge samples are shown in Fig. 2. The spectra have been scaled for clarity. Neither the high-Cr (Kanpur) sludge nor the low-Cr (Jaipur) sludge spectra exhibit a pre-edge peak indicative of the presence of Cr(VI), indicating that only Cr(III) was present in the sludges within the detection limits. A conservative estimate of the detection limits in the present analyses can be obtained by multiplying the concentration of chromium in the sample by the percentage noise level relative to the edge jump. This gives 19 ppm and 50 ppm for the low-Cr sludge and the high-Cr sludge, respectively.

While the XANES data shown here provides an unambiguous identification of the oxidation state of the chromium present in the sludge, the chemical speciation of chromium cannot be identified from the XANES spectrum without matching standards. The spectra may be consistent with organic chromium species and (or) adsorbed chromium. The spectra do suggest that the high chromium levels do not represent a significant environmental hazard in the form in which the samples have been received.

## Conclusions

Virtually all the chromium in the sludges studied was present as the relatively benign Cr(III), and, as a result, these sludges might be used as agricultural amendments at proper application rates; however, additional measurements should be carried out to ensure that these results are representative of all the sludge materials. The result has been obtained from both high- and low-chromium samples, providing evidence that XANES is an effective technique for studying the oxidation states of metals in low concentration in real, environmentally relevant samples. It also provides important in-

formation for the regulation of metal concentrations in sensitive soil systems.

This result is consistent with measurements of chromium bioavailability in other contaminated soils (26).

## Acknowledgments

Research at UWO is supported by The Natural Sciences and Engineering Research Council of Canada (NSERC), which also supplied a Major Facilities Access Grant. Work done at PNC-CAT at APS is supported through by the U.S. Department of Energy, Basic Energy Sciences, Office of Science under Contract #W-31-109-Eng-38. Work at PNC-CAT is also supported by the U.S. DOE under contract #DE-FG03-97ER45628.

## References

1. C.D. Palmer and R.W. Puls. *In* EPA environmental assessment sourcebook. Edited by J.R. Boulding. An Arbor Press, Chelsea, Michigan. 1996.
2. D.C. Adriano. Trace elements in the terrestrial environment. Springer-Verlag, New York. 1986.
3. J.O. Nriagu and J.M. Pacyna. *Nature* (London), **333**, 134 (1988).
4. A. Kabata-Pendias and H. Pendias. Trace elements in soils and plants. 2nd ed. CRC Press, Boca Raton, Florida. 1994.
5. J.E. Rechcigl (*Editor*). Soil amendments and environmental quality. CRC Press, Boca Raton, Florida. 1995.
6. A. Kabata-Pendias and H. Pendias. Trace elements in soils and plants. CRC Press, Boca Raton, Florida. 1984.
7. D.C. Adriano, A.L. Page, A.A. Elseewi, A.C. Chang, and I. Straughan. *J. Environ. Qual.* **9**, 333 (1980).
8. R.L. Cheney. *BioCycle*, **31**, 54 (1990).
9. B.J. Alloway (*Editor*). Heavy metals in soils. John Wiley & Sons, Inc., New York. 1990.
10. I. Pais and J.B. Jones. The handbook of trace elements. St. Lucie Press, Boca Raton, Florida. 1997.
11. E. Frieden (*Editor*). Biochemistry of the essential ultratrace elements. Plenum Press, New York. 1981.
12. M.D. Szulczewski, P.A. Helmke, and W.F. Bleam. *Environ. Sci. Technol.* **31**, 2954 (1997).
13. D. Rai, B.M. Sass, and D.A. Moore. *Inorg. Chem.* **26**, 345 (1987).
14. D. Rai, J.M. Zachara, L.E. Eary, C.C. Ainsworth, J.E. Amonette, C.E. Cowan, R.W. Szelmeczka, C.T. Resch, R. L. Schmidt, S.C. Smith, and D.C. Girvin. Chromium reactions in geologic materials, EPRI EA-5741. Electric Power Research Institute, Palo Alto, California. 1988.
15. F.J. Stevenson. *In* Micronutrients in agriculture, SSSA book series #4. Edited by J.J. Mortwedt. Soil Science Society of America, Madison, Wisconsin. 1991.
16. G. Sposito. The chemistry of soils. Oxford University Press, New York. 1989.
17. J.E. McLean and B.E. Bledsoe. *In* EPA environmental assessment sourcebook. Edited by J.R. Boulding. An Arbor Press, Chelsea, Michigan. 1996.
18. T.J. Logan and R.L. Chaney. *In* Utilization of wastewaters and sludge on land. Edited by A.L. Page. University of California, Riverside. 1983.
19. J.E. Hall (*Editor*). Alternative uses for sewage sludge. Pergamon Press, New York. 1991.
20. G.E. Brown, A.L. Foster, and J.D. Ostergren. *Proc. Natl. Acad. Sci. U.S.A.* **96**, 3388 (1999).



21. M. Zaw, R. Szymczak, and J. Twining. Nucl. Instrum. Methods Phys. Res. Sect. B, **190**, 856 (2002).
22. S. Bajt, S.B. Clark, S.R. Sutton, M.L. Rivers, and J.V. Smith. Anal. Chem. **65**, 1800–1804 (1993).
23. S.R. Sutton, K.W. Jones, B. Gordon, M.L. Rivers, S. Bajt, and J.V. Smith. Geochim. Cosmochim. Acta, **57**, 461–468 (1993).
24. F.W. Lytle and R.B. Gregor. Phys. Rev. B, **37**, 1550–1562 (1988).
25. M.L. Peterson, G.E. Brown, Jr., G.A. Parks, and C.L. Stein. Geochim. Cosmochim. Acta, **61**, 3399 (1997).
26. B. Lottermoser. Environ. Geochem. Health, **24**, 183 (2002).



# Nitroarene reduction using Raney nickel alloy with ammonium chloride in water

Kankan Bhaumik and K.G. Akamanchi

**Abstract:** Aromatic nitroarenes are reduced in high yields using a user-friendly combination of Raney nickel alloy and ammonium chloride in water at 80–90°C.

**Key words:** Raney nickel alloy, nitroarenes reduction, ammonium chloride, water.

**Résumé :** Les nitroarènes aromatiques sont réduits avec des rendements élevés à l'aide d'une combinaison d'un mélange facile à utiliser pour l'utilisateur d'un alliage de nickel de Raney et de chlorure d'ammonium, dans l'eau, à des températures allant de 80 à 90°C.

**Mots clés :** alliage de nickel de Raney, réductions de nitroarènes, chlorure d'ammonium, eau.

[Traduit par la Rédaction]

## Introduction

Nitroarene reduction is one of the fundamental organic transformations and varieties of methods are available (1). The most commonly used reagents (2) are zinc, tin, or iron in the presence of an acid, catalytic hydrogenation (3) with catalysts such as Ni, Pd/C, or PtO<sub>2</sub>, and many more. Other reagents include sulfides (4) (sodium sulfhydrylate, ammonium sulfide, or polysulfides and others), metal-reducing agents such as Sm (5), In (6), etc., metal-hydride complexes, such as NaBH<sub>4</sub>-NiCl<sub>2</sub> (7). It can also be reduced electrochemically (8) and enzymatically (9). Reduction of nitroarene compounds often generates a mixture of nitroso- and hydroxylamine (10) products, which then couple to form azoxy (11), azo (12), hydrazo, and hydrazine (13) compounds. Raney nickel alloy in alkali (14) solution appears to be a very good reagent for convenient quantitative general reduction of nitroarenes and cleavage of -N—N- and -N—O- bonds and hence practically no formation of by-products. However, a strong basic condition, a vigorous reaction with exothermicity, and a large evolution of hydrogen gas make this system less attractive. To overcome these problems we have developed a new system using Raney nickel alloy and ammonium chloride in water instead of drastic Raney nickel alloy and alkali for the reduction of nitroarenes to aminoarenes. The new system was studied using different substrates and the results are presented in Table 1.

## Experimental

All compounds used were purified before use. Solvents were obtained commercially and used without further drying or purification. Each reaction was performed in an efficient

fume hood. All reactions were magnetically stirred and monitored by thin layer chromatography (TLC).

### Typical procedure for the reduction of 4-nitrocumene to 4-cumidine

4-Nitrocumene (0.5 g, 3.03 mmol) was added to a 100 mL round-bottomed flask and a solution of NH<sub>4</sub>Cl (0.40 g, 7.48 mmol) in distilled water (60 mL) was added to it. Then Raney nickel alloy (0.60 g, 1.5 times by wt. of NH<sub>4</sub>Cl) was added with a lot of stirring and the reaction mixture was heated to 80–90°C for 1.5 h. Progress of the reaction was monitored by TLC. The reaction mixture was cooled to room temperature (rt) and ethyl acetate (50 mL) was added and the mixture was stirred for 30 min. The solids (solids contain generated active Raney nickel (to be disposed of carefully)) were then filtered off and the organic layer separated; the aqueous phase was extracted with ethyl acetate (2 × 30 mL). The combined organic layer was concentrated under reduced pressure. The residue obtained was purified by extracting with 15 mL of concd HCl, followed by charcoaling and reextraction with ethyl acetate (2 × 50 mL) after basification. The organic layer was dried over sodium sulphate and concentrated under reduced pressure to yield (0.385 g, 96%) 4-cumidine as a liquid. It was characterized by comparing with a known sample.

## Results and discussion

In this work, we investigated the aqueous medium reduction of nitroarenes using Raney nickel (Ni–Al (1:1)) alloy in combination with NH<sub>4</sub>Cl. To the best of our knowledge this system is still not reported. The system is good enough for the reduction of nitroarenes (Table 1, entries 1–10). All reac-

Received 22 July 2002. Published on the NRC Research Press Web site at <http://canjchem.nrc.ca> on 11 March 2003.

K. Bhaumik and K.G. Akamanchi.<sup>1</sup> Department of Pharmaceutical Sciences and Technology, UICT, Matunga, Mumbai 400 019, India.

<sup>1</sup>Corresponding author (e-mail: [kgap@rediffmail.com](mailto:kgap@rediffmail.com)).



**Table 1.** Reduction of nitroarenes with Raney nickel alloy with  $\text{NH}_4\text{Cl}$  in water.

Entry	Substrate	Time (h)	Products	Isolated yield (%) <sup>a</sup>
1	$\text{PhNO}_2$	2.1	$\text{PhNH}_2$	92
2	$2\text{-CH}_3\text{-C}_6\text{H}_4\text{-NO}_2$	1.5	$2\text{-CH}_3\text{-C}_6\text{H}_4\text{-NH}_2$	95
3	$4\text{-CH}_3\text{-C}_6\text{H}_4\text{-NO}_2$	1.5	$4\text{-CH}_3\text{-C}_6\text{H}_4\text{-NH}_2$	96
4	$4\text{-Isopropyl-C}_6\text{H}_4\text{-NO}_2$	1.5	$4\text{-Isopropyl-C}_6\text{H}_4\text{-NH}_2$	96
5	$4\text{-Isobutyl-C}_6\text{H}_4\text{-NO}_2$	1.5	$4\text{-Isobutyl-C}_6\text{H}_4\text{-NH}_2$	90
6	$3\text{-NH}_2\text{-C}_6\text{H}_4\text{-NO}_2$	2	$3\text{-NH}_2\text{-C}_6\text{H}_4\text{-NH}_2$	92
7	$2\text{-CH}_3\text{-4-NH}_2\text{-C}_6\text{H}_3\text{-NO}_2$	2.1	$2\text{-CH}_3\text{-4-NH}_2\text{-C}_6\text{H}_3\text{-NH}_2$	86
8	$2\text{-CH}_3\text{CONH-C}_6\text{H}_4\text{-NO}_2$	2.1	$2\text{-CH}_3\text{CONH-C}_6\text{H}_4\text{-NH}_2$	91
9	$2\text{-OH-C}_6\text{H}_4\text{-NO}_2$	2	$2\text{-OH-C}_6\text{H}_4\text{-NH}_2$	91
10	$4\text{-OH-C}_6\text{H}_4\text{-NO}_2$	2	$4\text{-OH-C}_6\text{H}_4\text{-NH}_2$	90
11	$2\text{-Cl-C}_6\text{H}_4\text{-NO}_2$	2	$2\text{-Cl-C}_6\text{H}_4\text{-NH}_2$	80 (20) <sup>b</sup>
12	$2\text{-CH}_3\text{-4-Cl-C}_6\text{H}_3\text{-NO}_2$	2.1	$2\text{-CH}_3\text{-4-Cl-C}_6\text{H}_3\text{-NH}_2$	80
13	$3\text{-EtO}_2\text{C-C}_6\text{H}_4\text{-NO}_2$	3	$3\text{-EtO}_2\text{C-C}_6\text{H}_4\text{-NH}_2$	60
14	$3\text{-CHO-C}_6\text{H}_4\text{-NO}_2$	3	$3\text{-CHO-C}_6\text{H}_4\text{-NH}_2$	66
15	$3\text{-NH}_2\text{CO-C}_6\text{H}_4\text{-NO}_2$	3	$3\text{-NH}_2\text{CO-C}_6\text{H}_4\text{-NH}_2$	57

<sup>a</sup>All product anilines are known compounds and characterized by comparing with the authentic sample.

<sup>b</sup>Dehalogenated product (20%) was formed.

tions were carried out by refluxing a mixture of substrate, Raney nickel alloy, and ammonium chloride in water. There was no vigorous reaction, nor foaming, and also no vigorous evolution of hydrogen gas and the pH of the medium was neutral. The method is very simple to adopt in the laboratory. However, it has low chemoselectivity towards aldehydes, esters, amides, and halogenated nitroarenes (Table 1, entries 11–15). This lack of chemoselectivity is very similar to that of Raney nickel alloy in an alkali system.

In conclusion, we have demonstrated a mild user-friendly method for reduction of nitroarenes to aminoarenes that can be used for laboratory synthesis. The method is valuable because of its simplicity.

## Acknowledgments

KB thanks the University Grants Commission of India (UGC) for the Senior Research Fellowship.

## References

- (a) R.C. Larock. *Comprehensive organic transformations: a guide to functional group preparations*. 2nd ed. VCH, New York. 1999. pp. 821–828; (b) G.W. Kabalka and R.S. Varma. *Comprehensive organic synthesis*. Vol. 8. Edited by B.M. Trost and I. Fleming. Pergamon Press, Oxford. 1991. pp. 363–379; (c) J. March and M.B. Smith. *March's advanced organic chemistry*. 5th ed. Wiley, New York. 2001. pp. 1552–1559.
- (a) G.H. Coleman, S.M. McClosely, and F.A. Stuart. *Org. Synth. Coll.* **III**, 668 (1955); (b) W.W. Hartman, J.B. Dickey, and J.G. Stampfli. *Org. Synth. Coll.* **II**, 175 (1943); (c) C.A. Merlic, S. Motamed, and B.J. Quinn. *J. Org. Chem.* **60**, 3365 (1995); (d) K.M. Doozee, M. Feigel, K.D. Stewart, J.W. Canary, C.B. Knobler, and D.J. Cram. *J. Am. Chem. Soc.* **109**, 3098 (1987).
- (a) A.M. Tafesh and J. Weiguny. *Chem. Rev.* **96**, 2035 (1996); (b) G.V. Smith and F. Nohteisz. *Heterogeneous catalysis in organic chemistry*. Academic Press, New York. 1999. pp. 71–79.
- H.K. Porter. *Org. React. (N.Y.)*, **20**, 455 (1973).
- (a) C. Yu, B. Liu, and L. Hu. *J. Org. Chem.* **66**, 919 (2001); (b) B.K. Banik, C. Mukhopadhyay, M.S. Venkatraman, and F.F. Becker. *Tetrahedron Lett.* **39**, 7243 (1998); (c) L. Wang, L. Zhon, and Y. Zhang. *Synlett*, 1065 (1999).
- C.J. Moody and M.R. Pitts. *Synlett*, 1028 (1998).
- A. Nose and T. Kudo. *Chem. Pharm. Bull.* **29**, 1159 (1981).
- J.M. Chapuzet, R. Labrecque, and M.J. LaVoie. *J. Chim. Phys. Phys. Chim. Biol.* **93**, 601 (1996).
- T.I. Davidenko and G.L. Bondarenko. *Appl. Biochem. Microbiol. (Transl. of Prikl. Biokhim. Mikrobiol.)*, **36**, 63 (2000).
- (a) C.S. Rondstvedt and T.A. Johnson. *Synthesis*, 850 (1977); (b) I.D. Entwistle, T. Gilkerson, R.A.W. Johnstone, and R.P. Telford. *Tetrahedron*, **34**, 213 (1978); (c) P.W. Oxley, B.M. Adger, M.J. Sasse, and M.A. Forth. *Org. Synth.* **67**, 187 (1989); (d) K. Yanada, H. Yamaguchi, H. Meguri, and S. Uchida. *J. Chem. Soc., Chem. Commun.* 1655 (1986); (e) H. Feuer, R.S. Bartlett, B.F. Vincent, and R.S. Anderson. *J. Org. Chem.* **30**, 2880 (1965).
- R.O. Hutchins, D.W. Lamson, L. Rua, C. Milewski, and B. Maryanoff. *J. Org. Chem.* **36**, 803 (1971).
- (a) K.J. Ohe, S. Uemura, N. Sugita, H. Masuda, and T. Taga. *J. Org. Chem.* **54**, 4169 (1989); (b) Y. Ogata and J. Mibae. *J. Org. Chem.* **27**, 2048 (1962).
- (a) A. Furst and R.E. Moore. *J. Am. Chem. Soc.* **79**, 5492 (1957); (b) G.A. Olah. *J. Am. Chem. Soc.* **81**, 3165 (1959); (c) B.M. Adger and R.G. Young. *Tetrahedron Lett.* **25**, 5219 (1984); (d) F. Yuste, M. Saldana, and F. Walls. *Tetrahedron Lett.* **23**, 147 (1982).
- (a) E. Schwenk, D. Papa, B. Whiteman, and H. Ginsberg. *J. Org. Chem.* **9**, 1 (1944); (b) G. Lunn and E.B. Sansone. *Synthesis*, 1104 (1985); (c) P. Sarmah and N.C. Barua. *Tetrahedron Lett.* **31**, 4065 (1990); (d) L.K. Keefer and G. Lunn. *Chem. Rev.* **89**, 459 (1989).



# Hot model of muonium formation in liquids

David C. Walker, Stefan Karolczak, Hugh A. Gillis, and Gerald B. Porter

**Abstract:** The mechanism of formation of muonium atoms from positive muons was studied here through measurements of the yield of diamagnetic muon states in dipolar aprotic solvents and for scavenger solutions in hexane and methanol. The results are compared with published data on common solvents covering a full range of the physico-chemical properties of liquids that affect an ionic formation mechanism, namely their static dielectric constants, electron mobilities, and radiolysis yields of electrons. It is concluded that muonium is not formed by a thermal charge-neutralization reaction in these chemically-active media, though that mechanism does contribute to muonium formation in inert media like liquefied noble gases. It is clear that muonium materializes on a much shorter timescale than the recently proposed “delayed” mechanism (microseconds) and the earlier “spur” model (nanoseconds). In contrast, the data referring to all these liquids are consistent with the intra-track “hot” model. This is the only Mu-formation model proposed so far in which the immediate precursors of Mu ( $\text{Mu}_{(\text{hot})}$ ) are neither scavengable nor ionic.

**Key words:** muonium atoms, formation mechanism, hot model, spur model, delayed-muonium-formation model, diamagnetic yields.

**Résumé :** On a étudié le mécanisme de formation des atomes de muonium à partir de muons positifs en faisant appel à des mesures de rendement d'états muons diamagnétiques dans des solvants aprotiques dipolaires et pour des solutions de pièges dans l'hexane et le méthanol. On compare les résultats obtenus avec les données publiées pour divers solvants communs couvrant l'ensemble des propriétés physicochimiques des liquides qui affectent un mécanisme de formation ionique, soit les constantes diélectriques statiques, les mobilités électroniques et les rendements en électrons lors de la radiolyse. On en conclut que, dans ces milieux chimiquement actifs, le muonium ne se forme pas par une réaction de neutralisation de charge même si ce mécanisme contribue à la formation du muonium dans des milieux inertes comme les gaz rares liquéfiés. Il est clair que le muonium se forme à une vitesse beaucoup plus rapide que celle proposée récemment sur la base d'un mécanisme « à retardement » (microsecondes) ou du modèle des « spur » (nanosecondes). Par ailleurs, les données se référant à tous ces liquides sont en accord avec le modèle « intra-track chaud ». Ce modèle de formation du Mu est le seul jusqu'à maintenant dans lequel les précurseurs intermédiaires du Mu ( $\text{Mu}_{(\text{chaud})}$ ) ne sont ni piègeables ni ioniques.

**Mots clés :** atomes de muonium, mécanisme de formation, modèle chaud, modèle des « spur », modèle de formation du muonium à retardement, rendements diamagnétiques.

[Traduit par la Rédaction]

## Introduction

Whereas the muonium atom ( $\text{Mu}$ ,  $\mu^+e^-$ ) has already yielded about 150 rate constants for kinetic-isotope-effect comparisons with the hydrogen atom (1) and has provided many new free radical structures (2), its formation mechanism (3–5) is still (6–8) in dispute after 25 years. The issue of how Mu is actually formed at the end of the track of a high-energy positive muon remains to be resolved.

When high-energy positive muons ( $\mu^+$ ) reach thermal-energy after impinging on a material they are observed by the muon-spin-rotation technique ( $\mu\text{SR}$ ) (3) to exist in one of three chemical states — as free muonium atoms ( $\text{Mu}$ ), as muoniated free radicals in which Mu typically has added to a double or triple bond ( $\text{R}$ ), or as “diamagnetic” muon states

(D). The latter includes free  $\mu^+$  ions and diamagnetic molecules with Mu substituting for H. All such diamagnetic muon states are recorded collectively as “D” because one cannot distinguish among them with current  $\mu\text{SR}$  techniques.

The “yields” of these different muon states are presented as  $P$ -values or “fractions” of the total number of incident muons (see Experimental section). Thus  $P_{\text{M}}$ ,  $P_{\text{R}}$ , and  $P_{\text{D}}$  represent the fractions of incident muons that are observed as Mu atoms, Mu-radicals, and D, respectively. When  $P_{\text{M}}$ ,  $P_{\text{R}}$ , and  $P_{\text{D}}$  sum to less than 1.0, the remainder is known as the missing (lost) fraction,  $P_{\text{L}}$ . For liquids with no unsaturated bonds,  $P_{\text{R}} = 0$  because free radicals are not formed; for most saturated hydrogenated materials  $P_{\text{L}}$  has been found to be similar in magnitude to  $P_{\text{M}}$ . This arises after thermalization of Mu because evidently about half of the Mu atoms that are

Received 20 September 2002. Published on the NRC Research Press Web site at <http://canjchem.nrc.ca> on 11 March 2003.

**D.C. Walker.**<sup>1</sup> Department of Chemistry and TRIUMF, The University of British Columbia, Vancouver, BC V6T 1Z1, Canada.  
**S. Karolczak.** Instytut Techniki Radiacyjnej, Politechnika, 93-590 Lodz, Wroblewskiego 15, Poland.

**H.A. Gillis.** St Francis Xavier University, Antigonish, NS B2G 2W5, Canada.

**G.B. Porter.** Department of Chemistry, The University of British Columbia, Vancouver, BC V6T 1Z1, Canada.

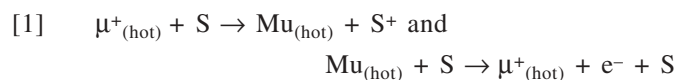
<sup>1</sup>Corresponding author (e-mail: [walker@triumf.ca](mailto:walker@triumf.ca)).



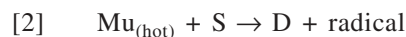
formed initially are depolarized by paramagnetic species such as electrons, radicals, and H-atoms on the timescale of the “expanding track” (9) either by combination or spin-exchange. Longitudinal-field repolarization studies confirm this (10), since all muon spins are recovered in high fields. For common solvents that do not form Mu-radicals one thus has  $P_D = 1 - P_{M(\text{initial})}$  and since  $P_{M(\text{init})} \approx P_{M(\text{obs})} + P_L \approx 2P_M$ , then  $P_D \approx 1 - 2P_M$ . Consequently, no change in  $P_D$  implies no change in Mu formation. In this paper we look for changes in  $P_D$  as a test for changes in the yield of Mu.

There are two fundamentally different models in the literature used to describe the mechanism by which Mu atoms are initially formed at the end of muon tracks:

(1) The “hot” model, in which some of the hot-Mu atoms formed during charge-exchange cycles undergo hot-abstraction or hot-substitution reactions before thermalization to form stable diamagnetic species such as MuH, MuOH, and  $C_nH_{2n+1}Mu$ . Those that do not undergo such a hot-atom reaction may reach thermal energy as free Mu atoms or occasionally as  $\mu^+$  ions. The charge-exchange cycles of  $\mu^+_{(\text{hot})}/Mu_{(\text{hot})}$  interchanges from  $\sim 10^4$  to  $\sim 10$  eV are represented by the reactions in [1], where S is a solvent molecule.

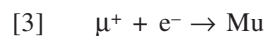


Hot Mu reactions that produce diamagnetic species can be represented by eq. [2], where D may be MuH, MuOH, Mu-R, etc., and the radical does not contain the muon when S has no multiple bonds.



Hot atom reactions are well known in the gas phase (11) but should be somewhat different from those in a liquid, as here, because of third-body effects and the importance of inter-molecular structures for liquids.

(2) The alternative model calls for Mu atoms to be formed as a consequence of the thermal, post-track, neutralization reaction, represented by [3].



The presumption here is that all the muons emerge “unattached” from the charge-exchange cycles as thermalized  $\mu^+$  ions. They may subsequently encounter an electron from the radiolysis track of the muon to produce Mu (with yield  $P_M$ ), otherwise they remain as  $\mu^+$  and constitute the diamagnetic yield ( $P_D$ ).

Reaction [3] represents the “spur” model (4) when geminate-electrons are involved and the “delayed-muonium-formation” model (DMF) (6) when free-electrons are involved. In radiation chemistry terms, “geminate” electrons are those still within the Onsager escape distance ( $e^2/\epsilon k_B T$ ) and doomed to return to geminate cations, whereas “free” electrons are those whose distance exceeds the critical Onsager distance and which first escape from their geminate ion and then from the whole track. Geminate electrons thus have intra-spur lifetimes only on the nanosecond timescale, whereas free electrons can have lifetimes of microseconds or longer. The timescale of the hot model, on the other hand, corresponds to the thermalization time of the charge-

exchange cycles during approximately the last  $10^4$  eV of the track of the muon, which is less than  $10^{-10}$  s (12).

Formation of Mu by the DMF process (reaction [3]) has been shown by external electric field effects to occur on the microsecond timescale in four chemically inert liquids (superfluid He, Ne, Ar, and  $N_2$ ) at very low temperatures (13). A DMF model was also developed from the simulation of hydrocarbon data at room temperature and was interpreted in terms of reaction [3] over the 1–10  $\mu$ s timescale (6). But this microsecond timescale has now been shown to be totally inconsistent with electron scavenger effects at low concentrations in chemically reactive media such as hexane (8).

In this paper we report data obtained for some special liquids at room temperature including the dipolar aprotic solvents that have the distinction of high cation, low anion solvation energies. A fully fluorinated saturated carbon compound was also studied. In addition, we report here results for solutions of *n*-hexane, and one for methanol, containing high concentrations of scavengers for electrons or muons or both. These solutions have high enough scavenging powers ( $k[c]$ ) to completely eliminate one or the other (or both) of the species of a “thermal” reaction such as [3]. However, the solutes are not at sufficiently high concentrations to interfere directly with “hot” reactions as represented by [1] and [2], as already seen in solvent mixtures (14).

## Experimental

The experiments conducted in this work were transverse-field muon spin rotation experiments (TF- $\mu$ SR) and involved placing a sample of deoxygenated liquid (plus additives as indicated) in 50 mL round-bottomed flasks in the SFUMU cart in the “backward” muon beam of the M9B beamline at TRIUMF. The results are now archived as experiments in the range 15000–15109 at the  $\mu$ SR Facility. The observed count rates were subjected to computer-fitting to the familiar TF- $\mu$ SR equation, eq. [4] (3, 15).

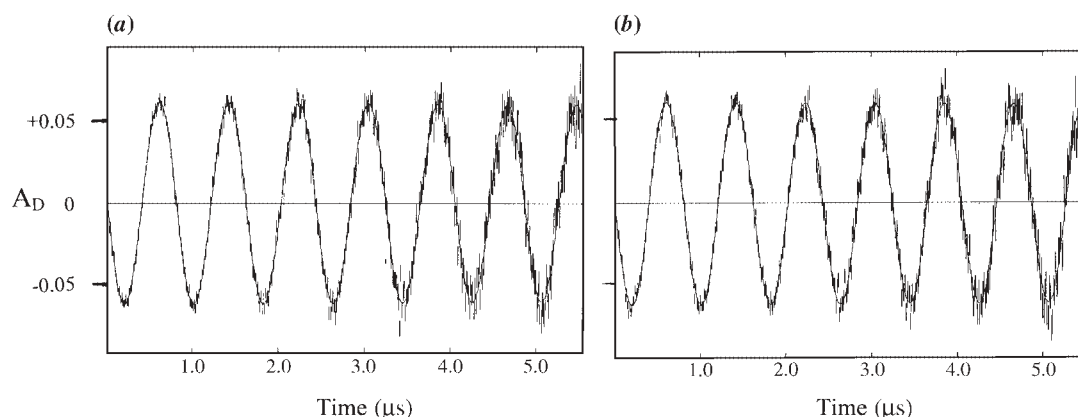
$$[4] \quad N_t = N_0 \exp(-t/\tau) [1 + A_M \exp(-\lambda t) \cos(\omega_M t + \phi_M) + A_D \cos(\omega_D t + \phi_D)] + N_0 B_g$$

In this equation,  $N$  (at times  $t$  and 0) is the observed count rate,  $\tau$  is the mean muon lifetime of 2.2  $\mu$ s,  $\lambda$  is the Mu decay constant,  $B_g$  is a background factor,  $A_M$ ,  $\omega_M$ , and  $\phi_M$  are, respectively, the asymmetry, precession frequency, and initial phase of the Mu signal, with  $A_D$ ,  $\omega_D$ , and  $\phi_D$  being the corresponding values for all diamagnetic muon states collectively designated as D. The  $A_M$  term corresponds to free Mu atoms and  $A_D$  to all muon states that are diamagnetic. In the on-line analysis the computer was made to divide out the natural muon decay factor ( $\exp(-t/\tau)$ ), deduct the background ( $B_g$ ), and display only the asymmetries ( $A$ ). This enables one to distinguish the “decay” of Mu and D as chemical species from the spontaneous decay of the muon itself.

The computer-fitted  $A_D$  values were converted to fractional muon yields,  $P_D$ , using  $P_{D(x)} = (A_{D(x)}/A_{D(\text{water})}) \times 0.62$ , based on the diamagnetic yield in water of 0.62 (3, 4). There is a possible error-bar of  $\pm 5\%$  on all reported  $P_D$  values. This arises because each beam has an inherent polarization, each liquid has a different density, and each cell has a slightly different glass thickness, shape, and position. All these differ-



**Fig. 1.** Plot of  $A_D$  vs. time from the  $\mu$ SR analysis of muons injected into (a) pure hexane and (b) hexane containing 0.2 M nitrobenzene (a powerful electron scavenger). (The initial yields are seen to be the same and there is no decay evident in either.)



ences alter the mean penetration depth of the muons or the effective stopping-power in the path of the decay positrons on their way to the counters. This causes variations of the positrons' mean polarization, which alters the magnitude of all  $A$ -values. They have to be referenced to a sample, cell, and liquid of similar density with a known  $P$ -value. Water was used here.

For these experiments, magnetic fields of 91 G were used (and 500 G merely for confirmation purposes). This made the precession frequencies of Mu too high to observe ( $\omega_M = 123$  and 131 MHz), so the only asymmetry seen corresponded to  $A_D$  ( $\omega_D = 1.23$  MHz). An example of the asymmetry of D is given in Fig. 1 for (a) pure hexane and (b) a solution of hexane containing a powerful electron scavenger, nitrobenzene, at 0.2 M concentration.

The liquids were used as obtained from commercial sources without further purification, except for deoxygenation by bubbling with pure nitrogen. The hexane and methanol were seen in other experiments (8) to be pure enough for Mu to have a chemical lifetime in excess of 1  $\mu$ s. The dipolar aprotic solvents were of "reagent grade" quality whereas the perfluoromethylcyclohexane was only of "technical grade" and known to contain ~5% impurities which were probably mainly in the form of other saturated fluorinated compounds. As the results with hexane and methanol show, purity is not an important factor in most  $P_D$  measurements. In fact for water, hexane, and formamide, for instance, it was found that the same  $P_D$  value was obtained whether the liquid had been deoxygenated or was air-saturated.

## Results

The first 16 entries of Table 1 contain the basic results for the observed values of  $P_D$  in these liquids and solutions. They are then compared with published data on other common solvents, as given in the lower 7 entries of Table 1.<sup>2</sup> Table 1 also provides values of the physicochemical properties that are expected to be directly related to the efficacy of re-

action [3] in these solvents:  $\epsilon$ , the static dielectric constant (relative permittivity);  $\mu_e$ , the mobility of electrons in the liquid ( $\text{cm}^2 \text{V}^{-1} \text{s}^{-1}$ );  $G(\text{fi})$ , the radiolysis yields of free electrons that escape the track; and  $G(\text{gi})$ , the radiolysis yields of geminate electrons that do not escape the coulombic field of geminate cations. (There is a possible error of  $\pm 0.5$  in the values of  $G(\text{gi})$  as these were estimated from an assumed total ionization yield of  $4.5 \pm 0.5$  for all the liquids, based on a mean ion yield of  $W \approx 22 \text{ eV mol}^{-1}$  (16).)

All the  $P_D$  values fall within the small range 0.53 to 0.68, with the majority of saturated H/C/O/N compounds lying within the even narrower range of  $0.60 \pm 0.03$ .  $P_D$  was also measured in methanol and hexane containing high concentrations of electron scavengers, as reported in Table 1. These additives would be powerful scavengers for the solvated electrons (in methanol) or quasi-free/localized electrons (in hexane) in reaction [3]. In fact, nitrobenzene, benzophenone, styrene,  $\text{CCl}_4$ , and oxygen all have rate constants for electron capture in hexane of the order of  $10^{12} \text{ M}^{-1} \text{s}^{-1}$  (17), yet they do not alter the yield of D. This is displayed directly in Fig. 1, where the initial asymmetry of (b) is seen to be essentially the same as (a), despite the lifetime of any electrons in hexane having been reduced to  $< 5 \text{ ps}$  in (b). In addition, one can see that there was no change in  $A_D$  over the 5  $\mu$ s of Figs. 1a and 1b, which would have been evident had reaction [3] occurred on the DMF timescale.

In the cases of  $\text{N}(\text{C}_2\text{H}_5)_3$  and  $\text{CH}_3\text{OH}$  as scavengers, they are expected to capture and hold onto free  $\mu^+$  ions by virtue of being good proton acceptors. As final confirmation, in two experiments (lines 15 and 16 of Table 1), both an electron and a muon scavenger were present. In these experiments there would be a greatly reduced chance of Mu being formed by reaction [3], even if the "adducts" from  $e^-$  and  $\mu^+$  scavenging eventually encountered each other.

## Discussion

Table 1 shows that for all these liquids and solutions,  $P_D$  has no dependence on any of the physicochemical properties

<sup>2</sup>Table 1 (lower part) does not include liquids that are known to have quite different  $P_D$  values for other reasons (9, pp. 66–67; 166–168). Thus, unsaturated compounds that form muoniated free radicals during thermalization were not included (benzene having  $P_D = 0.17$  and  $P_R = 0.83$ , for instance), nor were chlorinated compounds that evidently undergo pre-thermalization reactions to give  $P_D$  values according to the number of halogen atoms (with  $\text{CH}_2\text{Cl}_2 = 0.70$ ,  $\text{CHCl}_3 = 0.85$ , and  $\text{CCl}_4 = 1.0$ , for instance) nor "inert" liquids such as the condensed noble gases.



**Table 1.** The  $P_D$  values obtained in this study; also given are the values, where available, of dielectric constant ( $\epsilon$ ), electron mobility ( $\mu_e$  ( $\text{cm}^2 \text{V}^{-1} \text{s}^{-1}$ )), radiolysis free ion yield ( $G(\text{fi})$ ), and geminate ion yield ( $G(\text{gi})$ ) based on total ion yields of  $4.5 \pm 0.5$ ; comparisons with literature values of  $P_D$  for a range of other saturated, non-chlorinated liquids are also shown (last seven rows).

Liquid	$P_D$	$\epsilon$	$\mu_e^a$	$G(\text{fi})^a$	$G(\text{gi})$
Experimental data (this work)					
HCONH <sub>2</sub>	0.63	109		3.3	1.2
HCON(CH <sub>3</sub> ) <sub>2</sub>	0.55	38.3		2.0	2.5
N(C <sub>2</sub> H <sub>5</sub> ) <sub>3</sub>	0.62	2.4		0.24	4.3
(CH <sub>3</sub> ) <sub>2</sub> SO	0.60	47.2		1.8	2.7
<i>c</i> -C <sub>6</sub> F <sub>13</sub> CF <sub>3</sub>	0.68	1.8		0.028	4.5
Methanol	0.58	33.0	0.00059	2.0	2.5
+ styrene (0.2 M)	0.55				
<i>n</i> -hexane	0.61	1.9	0.076	0.13	4.4
+ nitrobenzene (0.2 M)	0.59				
+ benzophenone (0.1 M)	0.60				
+ CCl <sub>4</sub> (4 mM)	0.6				
+ oxygen (8 mM)	0.60				
+ N(C <sub>2</sub> H <sub>5</sub> ) <sub>3</sub> (0.2 M)	0.60				
+ methanol (0.5 M)	0.61				
+ N(C <sub>2</sub> H <sub>5</sub> ) <sub>3</sub> (0.2 M) + nitrobenzene (0.2 M)	0.60				
+ methanol (0.5 M) + styrene (0.1 M)	0.61				
Previously published data <sup>b</sup>					
H <sub>2</sub> O	0.62	80.1	0.00187	2.7	1.8
D <sub>2</sub> O	0.57	79.8	0.00151	3.0	1.5
Ethanol	0.59	25.3	0.00025	1.7	2.8
2-propanol	0.62	20.2	0.00051	1.2	3.3
<i>c</i> -hexane	0.69	2.0	0.23	0.14	4.4
Neopentane	0.55	1.8	71	1.1	3.4
Si(CH <sub>3</sub> ) <sub>4</sub>	0.53	1.9	100	0.74	3.8

<sup>a</sup>Reference (17).

<sup>b</sup>Reference (9, pp. 166–168).

that should affect the neutralization reaction [3]. Specifically,  $P_D$  changes by <20% (much less in most cases) while: (i)  $\epsilon$  changes by a factor of 60, from 1.8 to 109; (ii)  $\mu_e$  by a factor of 400 000, from 0.00025 to 100  $\text{cm}^2 \text{V}^{-1} \text{s}^{-1}$ ; and (iii)  $G(\text{fi})$  by a factor of 118, from 0.028 to 3.3. Two of these limits arose from the new liquids studied in this paper. In other words, the yield of D (and hence Mu) is not influenced by the coulombic force between reactants, nor by the mobility of electrons in the medium, nor by the number (local concentration) of electrons available for reaction. Therefore, reaction [3] cannot be a significant source of Mu atoms in these systems.

Equally conclusive is the direct evidence provided by the electron and muon scavengers in hexane and methanol (methanol itself being a  $\mu^+$  trap, like water). In those solutions, free electrons and free muons are simply not available to react together in reaction [3]. These electron scavengers react at rate constants of about  $10^{12} \text{M}^{-1}\text{s}^{-1}$  in hexane, so the lifetime of  $e^-$  would be reduced to a few picoseconds in the nitrobenzene, styrene, and benzophenone solutions, thereby almost completely inhibiting reaction [3] on its proposed timescales. Figure 1 shows that the yield of D, and hence Mu, is not affected by capturing electrons by nitrobenzene on the picosecond timescale.  $P_D$  would have increased to almost 1.0 in Fig. 1b if the yields were governed by reaction [3]. Even at the concentrations used for CCl<sub>4</sub> and oxygen the

lifetime of electrons would be <500 ps. In the solutions that contain both electron and muon scavengers, the probability of both of their “adducts” reacting at the same rate as the free species is negligible. Thus it must be concluded that Mu is not formed to any measurable extent in a thermalized ionic reaction in this range of solvents, even on the timescale of intraspur reactions.

The literature already contains considerable evidence that has been interpreted in this way. The most obvious examples are data for solvent mixtures covering the whole composition range: for *c*-hexane, CCl<sub>4</sub>, and CH<sub>3</sub>OH versus benzene, and CHCl<sub>3</sub> versus CH<sub>3</sub>OH, none of which showed the curvature to be expected if scavenging occurred (9, pp. 68–70). In the case of water, there is overwhelming scavenger evidence against reaction [3] in addition to the expectation that  $\mu^+$  would be solvated like H<sup>+</sup> and thus assimilated into the water structure as MuHO within picoseconds (9, p. 79).

All of these factors prove that reaction [3] is not the source of Mu. They are not in conflict with reactions [1] and [2], however, and in fact conform to what one would expect from a hot model in which the precursors (hot Mu) are neither scavengable electrons nor scavengable muons. The hot model wins by default! This conclusion corroborates, using a new range of media, the arguments presented earlier against reaction [3] as the source of Mu atoms in water (9, pp. 77–92).



## Acknowledgments

We are particularly grateful to Dr. Arthur Salmon for his help and advice in planning these experiments in which he was eventually unable to participate. We also acknowledge very important practical help from Drs. Don Arseneau and Khashayar Ghandi and technical support provided by Dr. Bassam Hitti and the  $\mu$ SR Facility. The Natural Sciences and Engineering Research Council (NSERC) of Canada is also gratefully acknowledged for providing an ongoing research grant to DCW.

## References

1. S. Karolczak and D.C. Walker. 2002. Muonium Data Base [online]. Available from <http://mbaza.mm.com.pl> [cited February 2003].
2. E. Roduner. *Chem. Soc. Rev.* **22**, 337, (1993).
3. J.H. Brewer, K.M. Crowe, F.N. Gygax, and A. Schenck. *In* Muon physics. *Edited by* V.W. Hughes and C.S. Wu. 1975. Vol. 3. pp. 3–139.
4. (a) P.W. Percival, E. Roduner, and H. Fischer. *Chem. Phys.* **32**, 353 (1978); (b) P.W. Percival, E. Roduner, and H. Fischer. *Adv. Chem. Ser.* **175**, 335 (1979). (c) O.E. Mogensen and P.W. Percival. *Radiat. Chem. Phys.* **28**, 85 (1986).
5. D.C. Walker, Y.C. Jean, and D.G. Fleming. *J. Chem. Phys.* **70**, 4534 (1979).
6. L.D.A. Siebbeles, S.M. Pimblott, and S.F.J. Cox. *J. Chem. Phys.* **111**, 7493 (1999) (for an example of the DMF model).
7. A.M. Lossack, E. Roduner, and D.M. Bartels. *Phys. Chem. Chem. Phys.* **3**, 2031 (2001) (for a current example of the spur model).
8. D.C. Walker, S. Karolczak, G.B. Porter, and H.A. Gillis., *J. Chem. Phys.* **118**, 3233 (2003) (for a current example of the hot model in liquids).
9. D.C. Walker. *Muon and muonium chemistry*. Cambridge University Press. 1983. pp. 90–91.
10. Y. Miyake, Y. Ito, K. Nishiyama, K. Nagamine, and Y. Tabata. *Radiat. Phys. Chem.* **28**, 99 (1986).
11. (a) D.G. Fleming, M. Senba, D.J. Arseneau, I.D. Reid, and D.M. Garner. *Can. J. Chem.* **64**, 57 (1986); (b) J.R. Kempton, D.J. Arseneau, D.G. Fleming, M. Senba, A.C. Gonzalez, J.J. Pan, A. Templemann, and D.M. Garner. *J. Phys. Chem.* **95**, 7338 (1991).
12. M. Senba. *J. Phys. B*, **31**, 5233 (1998).
13. (a) E. Krasnoperov, E. Meilikov, R. Abela, D. Herlach, E. Morenzoni, F.N. Gygax, A. Schenck, and D. Eschenko. *Phys. Rev. Lett.* **69**, 1560 (1992); (b) V. Storchak, J.H. Brewer, and G.D. Morris. *Phys. Rev. Lett.* **76**, 2969 (1996).
14. Y.C. Jean, B.W. Ng, J.H. Brewer, D.G. Fleming, and D.C. Walker. *J. Phys. Chem.* **85**, 451 (1981).
15. D.G. Fleming, D.M. Garner, L.C. Vaz, D.C. Walker, J.H. Brewer, and K.M. Crowe. *Adv. Chem. Ser.* **175**, 279 (1979).
16. D.E. Lea. *Actions of radiations on living cells*. Cambridge University Press. 1946.
17. (a) Y. Tabata, Y. Ito, and S. Tagawa (*Editors*). *Handbook of radiation chemistry*. CRC Press. 1991. Chaps. VI and VII; (b) K.H. Schmidt, P. Han, and D.M. Bartels. *J. Phys. Chem.* **99**, 10530 (1995).



# Kinetics of oxidation of $\alpha,\beta$ -unsaturated aldehydes by quinolinium dichromate

Girija S. Chaubey, Simi Das, and Mahendra K. Mahanti

**Abstract:** A series of  $\alpha,\beta$ -unsaturated aldehydes (crotonaldehyde, cinnamaldehyde, acrylaldehyde, and methacrylaldehyde) were oxidized by quinolinium dichromate in sulfuric acid to the corresponding acids in 50% (v/v) acetic acid – water medium. The kinetic data have been discussed with reference to the aldehyde hydration equilibria. The kinetic results support a mechanistic pathway proceeding via a rate-determining oxidative decomposition of the chromate ester of the aldehyde hydrate.

**Key words:** kinetics, oxidation, unsaturated aldehydes, quinolinium dichromate.

**Résumé :** Le dichromate de quinolinium dans l'acide sulfurique utilisé en solution d'acide acétique aqueux à 50% (v/v) permet d'oxyder une série d'aldéhydes  $\alpha,\beta$ -insaturés (crotonaldéhyde; cinnamaldéhyde; acrylaldéhyde; méthacrylaldéhyde) en acides correspondants. On discute des données cinétiques en fonction de l'équilibre d'hydratation de l'aldéhyde. Les données cinétiques sont en accord avec un mécanisme réactionnel impliquant une décomposition oxydante de l'ester chromique de l'hydrate d'aldéhyde qui serait cinétiquement limitante.

**Mots clés :** cinétique, oxydation, aldéhydes insaturés, dichromate de quinolinium.

[Traduit par la Rédaction]

## Introduction

In the oxidation of  $\alpha,\beta$ -unsaturated aldehydes, it has been suggested that the reaction could proceed by way of (a) enolization being the rate-determining step (1, 2); (b) hydration of the double bond to form a  $\beta$ -hydroxyaldehyde (3); or (c) oxidation of the aldehyde hydrate (4).

With a view to establishing the mechanistic pathway for this oxidation process, we have carried out a kinetic study of the oxidation of  $\alpha,\beta$ -unsaturated aldehydes (crotonaldehyde, cinnamaldehyde, acrylaldehyde, and methacrylaldehyde) by quinolinium dichromate (QDC,  $(C_9H_7N^+H)_2Cr_2O_7^{2-}$ ) in 50% acetic acid – water medium under a nitrogen atmosphere. This study forms part of our continuing efforts, concerning the quinolinium dichromate oxidation of organic substrates in general (5) and aldehydes in particular (6).

## Experimental

### Materials and methods

Acrylaldehyde and methacrylaldehyde (Aldrich) and crotonaldehyde and cinnamaldehyde (Merck-Schuchardt) were used without further purification. The oxidant, quinolinium dichromate (QDC,  $(C_9H_7N^+H)_2Cr_2O_7^{2-}$ ) was prepared by the reported method (7), and its purity was checked by spectral analysis. The IR spectrum (KBr) exhibited bands at 930, 875, 765, and 730  $cm^{-1}$ , characteristic of

the dichromate ion. Acetic acid (SD, AR grade) was distilled before use. Sulfuric acid (E. Merck) was used after a check of its physical constants. The deuterated compounds were prepared by the reported method (8). The IR spectra were recorded on a Bomem DA-8 FT-IR spectrophotometer.

The method used for the kinetic determinations has been described previously (5). All the reactions were performed under nitrogen. The rate constants have been evaluated from the linear ( $r > 0.995$ ) plots of  $\log[QDC]$  against time, and the values reported are the mean of two or more runs (reproducibility  $\pm 3\%$ ). The solvent was 50% aqueous acetic acid, and the dielectric constant was varied using acetic acid – water mixtures. The reaction mixtures remained homogeneous in the solvent systems used.

### Product analysis

Thirty mL of water was taken and cooled in ice. Concentrated  $H_2SO_4$  (7.9 g, 0.08 M) was added slowly with constant cooling. When the acid solution had cooled to room temperature, quinolinium dichromate (QDC 9.52 g, 0.02 M) was added and the mixture was warmed to 313 K for complete dissolution of the QDC. To this mixture, 0.01 M of substrate (0.71 g of methacrylaldehyde, 0.57 g of acrylaldehyde, 0.71 g of crotonaldehyde, and 1.33 g of cinnamaldehyde) taken up in 25 mL of a 50% acetic acid – water solution was added. The reaction mixture was stirred at 313 K for 48 h under nitrogen. The organic layer was extracted thrice with ether (25 mL each time) and the combined organic extracts were washed with water and dried over anhydrous  $Na_2SO_4$ . The oxidized products (methacrylic acid from methacrylaldehyde, acrylic acid from acrylaldehyde, crotonic acid from crotonaldehyde, and cinnamic acid from cinnamaldehyde) were obtained after the complete removal of ether (boiling and melting points were

Received 22 July 2002. Published on the NRC Research Press Web site at <http://canjchem.nrc.ca> on 12 March 2003.

G.S. Chaubey, S. Das, and M.K. Mahanti.<sup>1</sup> Department of Chemistry, North-Eastern Hill University, Shillong 793 022, India.

<sup>1</sup>Corresponding author (e-mail: [mkmahanti@yahoo.com](mailto:mkmahanti@yahoo.com)).



**Table 1.** Rate data for the oxidation of  $\alpha,\beta$ -unsaturated aldehydes in 50% acetic acid at 313 K.

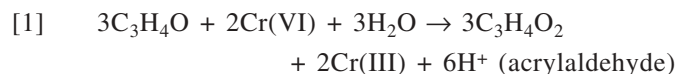
$10^2$ [Substrate] (M)	$10^2$ [QDC] (M)	$[\text{H}_2\text{SO}_4]$ (M)	$10^3 k \text{ (s}^{-1}\text{)}$			
			Methacrylaldehyde	Acrylaldehyde	Crotonaldehyde	Cinnamaldehyde
3.1	0.31	0.51	1.3	1.2	0.51	0.080
10.0	0.30	0.52	4.6	4.0	1.5	0.26
17.0	0.31	0.51	7.6	7.1	2.9	0.41
25.0	0.30	0.51	11	9.9	4.1	0.62
30.0	0.32	0.53	14	12	4.9	0.78
3.0	0.12	0.50	1.3	1.2	0.52	0.081
3.2	0.06	0.52	1.3	1.3	0.51	0.080
3.1	0.04	0.50	1.3	1.2	0.54	0.082
3.0	0.03	0.51	1.3	1.2	0.53	0.083
3.1	0.31	0.75	2.0	1.8	0.81	0.12
3.1	0.32	1.02	2.7	2.4	1.1	0.16
3.0	0.30	1.25	3.4	3.1	1.4	0.21
3.2	0.31	1.50	4.0	3.7	1.6	0.25

in agreement with literature values; yields  $\approx$  85–90%). Each reaction product was characterized by IR analysis.

## Results and discussion

The oxidation of  $\alpha,\beta$ -unsaturated aldehydes (crotonaldehyde, cinnamaldehyde, acrylaldehyde, and methacrylaldehyde) by QDC results in the formation of the corresponding acids. Under the present experimental conditions, there is no further oxidation of the acids.

The stoichiometry of the reaction was determined (5). Stoichiometric ratios,  $\Delta[\text{QDC}]/\Delta[\text{substrate}]$ , in the range 0.66 to 0.69 conform to the following overall equation (representative):



Using pseudo-first-order conditions, individual kinetic runs are first order in QDC. The pseudo-first-order rate constants ( $k$ ) are independent of the initial concentration of the oxidant (Table 1). The order of the reaction with respect to substrate concentration has been obtained by varying the aldehyde concentration and observing the effect on the rate at constant [QDC] and  $[\text{H}^+]$ . The order with respect to the concentration of acid, at constant [aldehyde] and [QDC], is unity. The kinetic results are shown in Table 1. In the range of acid concentrations used, the protonation of the aldehydes would be less significant, though it cannot be ruled out. At present, it may not be possible to decide whether protonation of the aldehyde or protonation of the dichromate results in the observed acid catalysis, since these two processes cannot be distinguished on the basis of the data obtained. Since the acid concentrations used were in the range 0.5 to 1.5 M, it would be justified to suggest that the dichromate ion would be the predominant species in these oxidation reactions.

The oxidation of the substrates by QDC has been studied over the temperature range 303–323 K. The rate data and activation parameters are shown in Table 2. The negative values of  $\Delta S^\ddagger$  provide support for a polar bimolecular reaction.

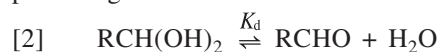
The effect of a change in the solvent composition (water – acetic acid, %, v/v) on the rate of oxidation has been deter-

mined. The dielectric constants ( $D$ ) of water – acetic acid mixtures have been calculated (at 313 K: water = 73.28, acetic acid = 6.29) (9). The data in Table 3 shows that a decrease in  $D$  of the medium results in an increase in the rate of the reaction (Table 3). The magnitude of this effect could be analyzed by suggesting that, for the equilibrium  $2\text{HCrO}_4 \rightleftharpoons \text{Cr}_2\text{O}_7^{2-} + \text{H}_2\text{O}$ , a decrease in  $D$  of the medium (increase in the acetic acid content) favors the dichromate form over the chromate form. If ion pairs are formed in this medium, they would have a higher ion-pair association constant for the dichromate ion, and this would again favor the dichromate ion. Although the range of  $D$  used for these reactions is not large, plots of  $\log k$  versus  $1/D$  are linear, with positive slopes, suggesting an ion–dipole type of interaction (10).

There is no induced polymerization of acrylonitrile (11), which indicates that a one-electron oxidation is quite unlikely. Control experiments, performed in the absence of the substrate, did not show any appreciable change in the concentration of QDC.

Variations in the ionic strength of the medium, using sodium perchlorate ( $\mu = 0.01$ – $0.25$  M), did not influence the rates of these reactions.

Aldehydes are extensively hydrated in aqueous solutions and many oxidation reactions have been reported to proceed via the hydrated form (12–17). Table 4 records the experimental rate constants ( $k$ ) for the oxidation of the aldehydes by QDC. The aldehyde hydrate dissociation constants ( $K_d$ ) pertaining to the reaction:



are also given (12). From  $k$  and  $K_d$ , two sets of rate constants for the oxidation of the aldehyde in only one of the forms present in solution are computed. The values of  $k_{\text{Hy}}$  ( $\text{Hy}$  = hydrated form of the substrate) are obtained by assuming that only the hydrate form appears in the rate law:



Similarly, the values of  $k_{\text{A}}$  ( $\text{A}$  = substrate) are calculated using the concentration of free aldehyde according to the rate law:



**Table 2.** Temperature and activation parameters for the oxidation of  $\alpha,\beta$ -unsaturated aldehydes<sup>a</sup> in 50% acetic acid by QDC.

<i>T</i> (K)	$10^3 k$ (s <sup>-1</sup> )			
	Methacrylaldehyde	Acrylaldehyde	Crotonaldehyde	Cinnamaldehyde
303.0	0.71	0.62	0.25	0.031
308.1	1.0	0.91	0.39	0.062
313.0	1.3	1.2	0.51	0.081
318.0	2.0	1.9	0.77	0.130
323.1	2.7	2.5	1.10	0.16
$\Delta H^\ddagger$ (kJ mol <sup>-1</sup> )	52 ± 1.9	54 ± 2.6	57 ± 2.2	63 ± 2.4
$\Delta S^\ddagger$ (J mol <sup>-1</sup> K <sup>-1</sup> )	-135 ± 6	-129 ± 7	-127 ± 6	-123 ± 8

<sup>a</sup>[Substrate] = 0.03 M; [QDC] = 0.003 M; [H<sub>2</sub>SO<sub>4</sub>] = 0.5 M.**Table 3.** Solvent effect for oxidation of  $\alpha,\beta$ -unsaturated aldehydes<sup>a</sup> by QDC at 313 K.

H <sub>2</sub> O:AcOH (%, v/v)	Dielectric constants <i>D</i>	$10^3 k$ (s <sup>-1</sup> )			
		Methacrylaldehyde	Acrylaldehyde	Crotonaldehyde	Cinnamaldehyde
60:40	46.48	0.79	0.64	0.36	0.053
55:45	43.14	1.1	0.93	0.43	0.065
50:50	39.79	1.3	1.2	0.51	0.080
45:55	36.44	1.7	1.5	0.59	0.10
40:60	33.09	2.1	1.9	0.67	0.13

<sup>a</sup>[Substrate] = 0.03 M; [QDC] = 0.003 M; [H<sub>2</sub>SO<sub>4</sub>] = 0.5 M.**Table 4.** QDC oxidation of  $\alpha,\beta$ -unsaturated aldehydes at 313 K.

Aldehydes	<i>K</i> <sub>d</sub> <sup>a</sup>	$10^3 k$ (s <sup>-1</sup> )	<i>k</i> <sub>Hy</sub> (M <sup>-1</sup> s <sup>-1</sup> )	<i>k</i> <sub>A</sub> (M <sup>-1</sup> s <sup>-1</sup> )
Methacrylaldehyde	2.3	1.3	34 ± 0.23	15 ± 0.30
Acrylaldehyde	1.7	1.2	23 ± 0.24	13 ± 0.23
Crotonaldehyde	1.1	0.51	5.9 ± 0.25	5.4 ± 0.27
Cinnamaldehyde	0.6	0.080	0.51 ± 0.22	0.85 ± 0.24

<sup>a</sup>Reference 12.

$$[4] \quad v = k_A [\text{QDC}] [\text{RCHO}].$$

The values of *k*<sub>Hy</sub> and *k*<sub>A</sub> have been shown in Table 4. Using the  $\sigma$  values as reported by Taft and co-workers (18), a plot of log *k*<sub>Hy</sub> against  $\sigma$  is found to be linear, with a slope of  $\rho = -0.92$  ( $r = 0.993$ ). On the other hand, the correlation of  $\sigma$  with *k*<sub>A</sub> gave a value of  $\rho = -0.56$  ( $r = 0.997$ ). This might suggest the involvement of the aldehyde hydrate in the oxidation process. Hence, a mechanism involving a direct hydrogen transfer reaction between a free aldehyde and QDC is very unlikely. In the chromic acid oxidation of benzaldehyde, it has been shown that the reaction proceeds via the chromic acid ester of hydrated benzaldehyde as the intermediate (19). This similarity provides additional support for the mechanistic pathway suggested in the present investigation: that the rate-determining step involves the oxidative decomposition of the chromate ester of an aldehyde hydrate.

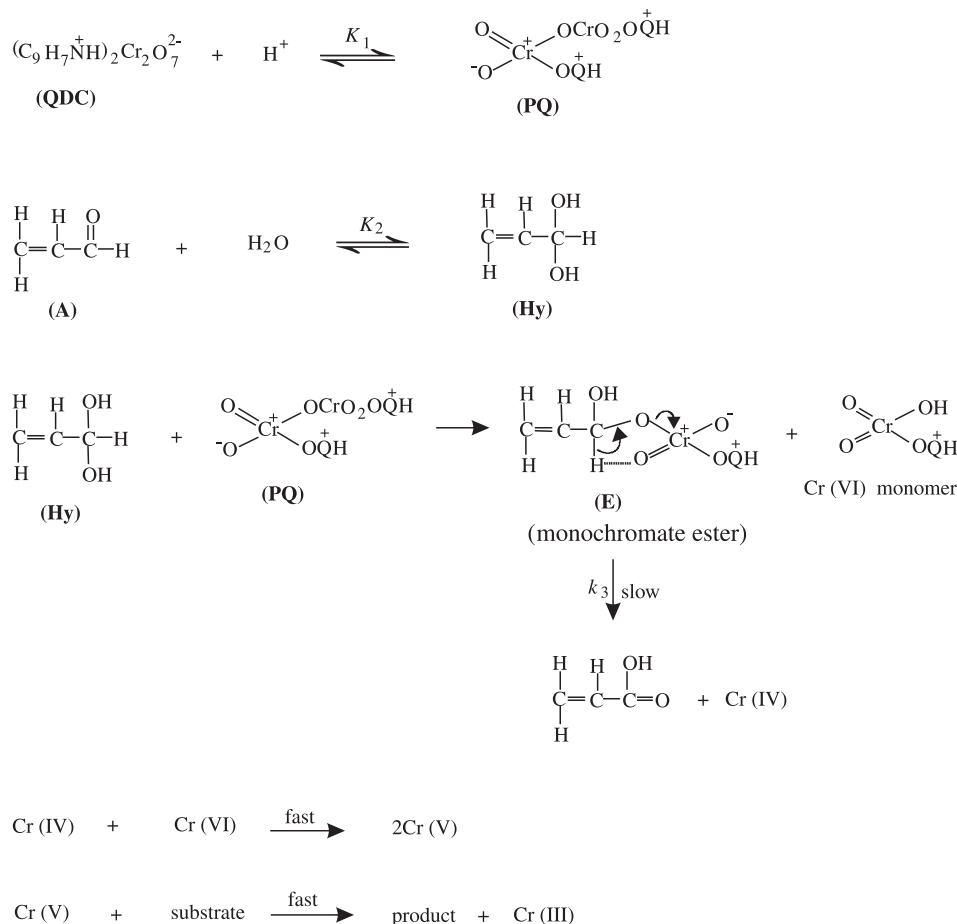
Since aldehyde hydrates very closely resemble alcohols both in structure and in many aspects of oxidation, a similarity in the nature of the two oxidation reactions is expected. In the oxidation of alcohols by chromic acid, the rate-determining step has been shown to be the decomposition of the protonated acid chromate ester (20). By analogy, the oxidation of aldehydes would proceed via the formation of a similar intermediate (an ester of the aldehyde hydrate),

which would undergo decomposition in the rate-determining step (21). The ester of the aldehyde hydrate would be in equilibrium with the free aldehyde and the aldehyde hydrate and could be formed either by a carbonyl addition reaction to the free aldehyde or by the esterification of the hydrate (22). It may be added that the esterification reaction has more utility, since it helps one to understand and predict aldehyde oxidation reactions and their relationship to the closely related oxidation of alcohols.

The rate data shows that both acrylaldehyde and methacrylaldehyde are oxidized at approximately equal rates, with methacrylaldehyde reacting marginally faster than acrylaldehyde (Table 1), which suggests that the  $\alpha$ -CH<sub>3</sub> group has little influence on the rates. It is justified to assume that the oxidation process does not involve an enolization step. The enolization of acrylaldehyde would have yielded hydroxyallene, which would be improbable. Further, the oxidation of methacrylaldehyde is a rapid reaction even though there is no enolizable hydrogen atom. The argument that unsaturated aldehydes could undergo a reaction involving the hydration of the double bond to form a  $\beta$ -hydroxyaldehyde can be ruled out, since no such intermediate could be isolated from the reaction. The order of reactivity is: methacrylaldehyde > acrylaldehyde > crotonaldehyde > cinnamaldehyde (Table 1). The presence of the methyl group (in methacrylaldehyde) accelerates the reaction by increasing the electron availability at the oxygen of the aldehydic carbonyl group. In crotonaldehyde, the methyl group at the  $\beta$ -position is far removed from the site of reaction, suggesting that  $\beta$ -substitution influences the rate of the reaction to a much lesser extent. Hence, the reactivity of crotonaldehyde is much less than that of methacrylaldehyde. The presence of the phenyl group in cinnamaldehyde exerts a deactivating influence on the rate of the reaction and hence its reactivity is the lowest in the series.



Scheme 1.



The mechanistic pathway involves the formation of the ester of the aldehyde hydrate (step 1), followed by the slow oxidative decomposition of this ester (step 2). A cyclic structure for the reaction intermediate would explain all the features of the oxidation reaction. The manner of electron transfer must be established. Electron flow in a cyclic transition state has been considered (23) and can be rationalized by assuming that if the chromium is coordinated through the -OH group (of the aldehyde hydrate), then the process of electron transfer could take place through the carbon—oxygen—chromium bonds, enabling the formation of the chromate ester and enhancing the ease of conversion to the product.

The slow step of the reaction involves the participation of the aldehyde hydrate, protonated QDC, and two electrons in a cyclic system. Removal of the hydrogen (on the carbon) is part of this step, as seen from the kinetic isotope effect for the oxidation of the respective aldehyde- $d_1$  compounds (Table 5), which indicates a cleavage of the carbon—hydrogen bond in the rate-determining step of the reaction.

This step allows one to envisage a reaction via an electrocyclic mechanism involving six electrons; being a Hückel-type system ( $4n+2$ ), this is an allowed process (24). The kinetic isotope effect could be interpreted to indicate that the reaction proceeds via the formation of the chromate ester of the aldehyde hydrate as an intermediate, and that this is converted to the product in the rate-determining step.

Table 5. Kinetic isotope effect at 313 K.<sup>a</sup>

Substrate	$10^3 k_H \text{ (s}^{-1}\text{)}$	$10^3 k_D \text{ (s}^{-1}\text{)}$	$k_H/k_D$
Crotonaldehyde- $d_1$	0.51	0.084	6.25
Cinnamaldehyde- $d_1$	0.080	0.013	6.15

<sup>a</sup>[Substrate] = 0.03 M; [QDC] = 0.003 M; [H<sub>2</sub>SO<sub>4</sub>] = 0.5 M.

The last step would be rate-determining, in accord with the observation of the deuterium kinetic isotope effect. Further, the oxidation rate for the aldehydes is not increased as rapidly by a decrease in the water concentration in acetic acid—water mixtures (Table 3), which suggests that a molecule of water is involved in a kinetically important stage in the oxidation of the aldehydes.

The sequence of reactions for the oxidation of  $\alpha,\beta$ -unsaturated aldehydes by QDC is shown in Scheme 1. In acidic medium, the oxidant QDC is converted to the protonated dimetallic chromium(VI) species (PQ) (in the acid range used for the present investigation, the Cr(VI) in the protonated QDC would exist mainly as Cr<sub>2</sub>O<sub>7</sub><sup>2-</sup>). The substrate (A) is converted to the hydrated form (Hy). The reaction of the hydrated form (Hy) with the protonated QDC (PQ) results in the formation of the monochromate ester (E) and a Cr(VI) monomer. The monochromate ester (E) undergoes decomposition in the rate-determining step to give the product (the corresponding acid), along with the Cr(IV) species. The conversion of Cr(IV) to Cr(III) is a disproportion-



tionation reaction. It has been shown that for the reaction  $\text{Cr(IV)} + \text{Cr(VI)} \rightarrow 2\text{Cr(V)}$ , the standard potential for the  $\text{Cr(VI)}\text{--Cr(V)}$  couple is extremely favourable ( $E^\circ = 0.62\text{ V}$ ) (25), and this reaction proceeds rapidly. The  $\text{Cr(V)}\text{--Cr(III)}$  couple has a potential of 1.75 V, which enables the rapid conversion of  $\text{Cr(V)}$  to  $\text{Cr(III)}$  after the reaction of  $\text{Cr(V)}$  with the substrate (25, 26).

If the mechanism shown in Scheme 1 is correct, then the attack of the protonated QDC (**PQ**) on the aldehyde hydrate (**Hy**) is crucial and would be favored by the formation of the cyclic chromate ester (**E**). The rate law has been derived as follows:

$$[5] \quad -d[\text{QDC}]/dt = k_3[\text{E}] = k_3[\text{Hy}][\text{PQ}],$$

where  $[\text{PQ}] = K_1[\text{QDC}][\text{H}^+]$  and  $[\text{Hy}] = K_2[\text{A}][\text{H}_2\text{O}]$ .

Hence,  $-d[\text{QDC}]/dt = K_1K_2k_3[\text{A}][\text{QDC}][\text{H}^+]$ , which shows a first-order dependence on each of the concentrations (substrate, oxidant, and acid). Hence,  $-2.303d(\log[\text{QDC}])/dt = k = K_1K_2k_3[\text{A}][\text{QDC}][\text{H}^+]$ . This rate law explains all the experimentally observed results.

The data collected demonstrates that the QDC oxidation of  $\alpha,\beta$ -unsaturated aldehydes results in the formation of carboxylic acids, substantiating the mechanism wherein there is an attack of the oxidant on the aldehyde hydrate. There is no cleavage of the carbon—carbon bond, thus ruling out the possibility of any enolization. This study emphasizes the efficiency of QDC reacting with  $\alpha,\beta$ -unsaturated aldehydes, suggesting a regioselective route for the synthesis of carboxylic acids.

## Acknowledgment

Financial support from the University Grants Commission, New Delhi, under the Special Assistance Program, is gratefully acknowledged.

## References

1. H. Land and W.A. Waters. *J. Chem. Soc.* 4312 (1957).
2. W.A. Waters. *Prog. Org. Chem.* **5**, 1 (1963).
3. R.H. Hall and E.S. Stern. *J. Chem. Soc.* 490 (1950).
4. J. Rocek. *The chemistry of carbonyl group. Edited by S. Patai. Vol. 1. Interscience, London. 1966. Chap 10.*
5. (a) B. Kuotsu, E. Tiewsoh, A. Debroy, and M.K. Mahanti. *J. Org. Chem.* **61**, 8875 (1996) and refs. therein; (b) R. Kharmutee, A. Debroy, and M.K. Mahanti. *Oxid. Commun.* **21**, 553 (1998); (c) E. Karim and M.K. Mahanti. *Oxid. Commun.* **21**, 559 (1998); (d) N. Thangkhiew, A. Debroy, and M.K. Mahanti. *Oxid. Commun.* **22**, 136 (1999).
6. (a) M.K. Mahanti. *Oxid. Commun.* **22**, 142 (1999); (b) G.S. Chaubey and M.K. Mahanti. *Oxid. Commun.* **23**, 500 (2000); (c) G.G. Kharnaor, G.S. Chaubey, and M.K. Mahanti. *Oxid. Commun.* **24**, 377 (2001).
7. K. Balasubramanian and V. Prathiba. *Indian J. Chem.* **25B**, 326 (1986).
8. K.B. Wiberg. *J. Am. Chem. Soc.* **76**, 5371 (1954).
9. R.C. Weast (*Editor*). *CRC handbook of chemistry and physics*. CRC Press, Ohio. 1978.
10. E.S. Amis. *Solvent effects on reaction rates and mechanisms*. Academic Press, New York. 1967. p. 42.
11. J.S. Littler and W.A. Waters. *J. Chem. Soc.* 1299 (1959).
12. R.P. Bell. *Adv. Phys. Org. Chem.* **4**, 1 (1964).
13. J. Rocek. *Tetrahedron Lett.* **5**, 1 (1959).
14. K.K. Banerji. *Tetrahedron*, **43**, 5949 (1987).
15. V.K. Sharma, K. Sharma, and N. Mishra. *Oxid. Commun.* **16**, 33 (1993).
16. K.K. Bupathi, P. Saroja, and S. Kandlikar. *Oxid. Commun.* **23**, 532 (2000).
17. K.B. Wiberg and F. Freeman. *J. Org. Chem.* **65**, 573 (2000).
18. C. Hansch, A. Leo, and R.W. Taft. *Chem. Rev.* **91**, 165 (1991).
19. G.T.E. Graham and F.H. Westheimer. *J. Am. Chem. Soc.* **80**, 3022 (1958).
20. J. Rocek, F.H. Westheimer, A. Eschenmoser, L. Moldovanyi, and J. Schreiber. *Helv. Chim. Acta*, **45**, 2554 (1962).
21. J. Rocek and C.S. Ng. *J. Am. Chem. Soc.* **96**, 1522 (1974).
22. (a) U. Klanning. *Acta Chem. Scand.* **11**, 313 (1957); (b) **12**, 576 (1958).
23. C.G. Swain, R.F.W. Bader, R.M. Estene, and R.N. Griffin. *J. Am. Chem. Soc.* **83**, 1951 (1961).
24. J.S. Littler. *Tetrahedron*, **27**, 81 (1971).
25. F.H. Westheimer. *Chem. Rev.* **45**, 419 (1949).
26. J.F. Perez-Benito, C. Arias, and D. Lamrhari. *Chem. Commun.* 472 (1992).



# One-pot synthesis of terpyridines and macrocyclization to C<sub>3</sub>-symmetric cyclohexipyridines

Lucie Masciello and Pierre G. Potvin

**Abstract:** Four examples of 2,6-dicinnamoylpyridines were obtained in 60–65% yields in condensations of commercially available 2,6-diacetylpyridine and benzaldehydes in 1:2 stoichiometry. At 2:1 ratios, four related 6,6''-diacetylated-4'-arylterpyridines were isolated in 70–73% yields in one-pot condensations in the presence of NH<sub>3</sub>. 4,4'-Azobenzaldehyde, prepared from nitrobenzaldehyde in three steps and 40% overall yield was similarly converted to a novel azo-linked bis(terpyridine) in 50% yield in a reaction that assembles seven molecules in one step. The 6,6''-diacetylated-4'-arylterpyridines and the correspondingly substituted 2,6-dicinnamoylpyridines were condensed in 1:1 ratio together with NH<sub>3</sub> to form 4,4'',4<sup>IV</sup>-triarylcyclohexipyridines in 22–26% yields. These were obtained as mixed Na<sup>+</sup> and K<sup>+</sup> complexes and were insoluble amorphous solids, except for one example bearing 4-neopentoxyphenyl substituents. <sup>1</sup>H NMR showed that the 4,4'',4<sup>IV</sup>-tri(4-neopentoxyphenyl)cyclohexipyridine complexes form aggregates in solution and at low concentrations show twofold symmetry arising from a loss of planarity.

**Key words:** terpyridines, 4'-aryl-6,6''-diacetylterpyridines, azo-bisterpyridine, cyclohexipyridines, macrocyclization.

**Résumé :** La condensation de la 2,6-diacétylpyridine avec des benzaldéhydes commercialement disponibles, à une stoechiométrie de 1:2, a permis d'obtenir quatre 2,6-dicinnamoylpyridines avec des rendements de 60 à 65 %. Lors de condensations monotopes, à des rapports de 2:1, en présence d'ammoniac, les quatre 6,6''-diacétyl-4'-arylterpyridines apparentées peuvent être isolées avec des rendements de 70 à 73 %. Le 4,4'-azobenzaldéhyde qui a été préparé en trois étapes et avec un rendement global de 40 % à partir du nitrobenzaldéhyde a été converti, avec un rendement de 50 %, en une nouvelle bis(terpyridine) liée par une fonction azo qui permet d'assembler sept molécules en une seule étape. Les 6,6''-diacétyl-4'-arylterpyridines et les 2,6-dicinnamoylpyridines substituées de la même façon peuvent être condensées l'une à l'autre dans un rapport de 1:1 en présence d'ammoniac, pour former de 4,4'',4<sup>IV</sup>-triarylcyclohexipyridines avec des rendements allant de 22 à 26 %. Celles-ci sont obtenues sous la forme de complexes avec des ions Na<sup>+</sup> et K<sup>+</sup> et il s'agit de solides amorphes insolubles, à l'exception de celle portant des substituants 4-néopentoxyphényles. Les spectres RMN du <sup>1</sup>H montrent que les complexes de 4,4'',4<sup>IV</sup>-tri(4-néopentoxyphényle)cyclohexipyridines forment des agrégats en solution et que, à faibles concentrations, ils présentent une symétrie binaire qui découle d'une perte de planéité.

**Mots clés :** terpyridines, 4'-aryl-6,6''-diacetylterpyridines, azo-bisterpyridine, cyclohexipyridines, macrocyclisation.

[Traduit par la Rédaction]

## Introduction

The parent, C<sub>6</sub>-symmetric cyclohexipyridine **1** (Scheme 1) was first reported by Newkome and Lee in 1983 (1) as the insoluble and uncharacterized product of a seven-step synthesis. Kelly et al. (2) prepared the curious, inverted cyclohexipyridine **2**, a highly insoluble and partly characterized C<sub>3</sub>-symmetric *tris*(bipyridine), after a lengthy synthetic sequence. Bell and Firestone (3) used Friedlander reactions to assemble torand **3**, a C<sub>3</sub>-symmetric hexaazakekulene derivative with rigidifying ethylene bridges and solubilizing butyl side-chains, isolated in 3% yield after 11 steps as a Ca<sup>2+</sup> complex in which the Ca<sup>2+</sup> apparently originated as a minute

impurity in a reagent. Toner (4) reported C<sub>2</sub>-symmetrical cyclohexipyridines (e.g., **4**) prepared from bipyridines as insoluble and only partly characterized Na<sup>+</sup> complexes, in which the Na<sup>+</sup> was apparently abstracted from the glassware.

Macrocyclic polypyridines such as cyclohexipyridine constitute interesting, rigid supramolecular hosts for cations and H-bond donors, and this was the motivation for the earlier work. With competition experiments, Bell et al. showed that the related torands, with stronger imino dipoles and a more rigid architecture than in crown ethers, are extremely strong complexing agents (5). We anticipated that cyclohexipyridines would also be interesting ligands for transition metals in that they would provide a planar, conjugated  $\pi$  system occupying the equatorial plane of the metal, as do the porphyrins and phthalocyanines. However, unlike those ligands, the cyclopolypyridines are neutral and do not form a contiguous aromatic system. The macroligand LUMO would thus remain relatively high energy, as would any MLCT transition and photochemistry therefrom, and the reduction potentials would remain relatively more negative. The binding geome-

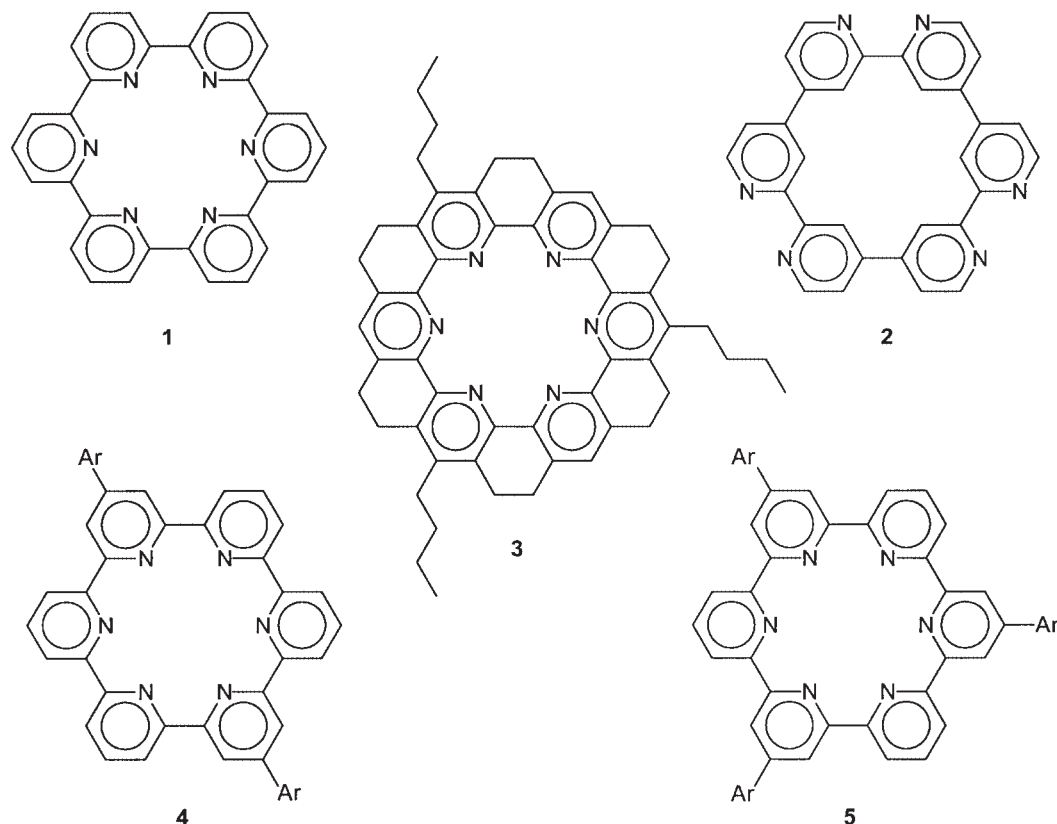
Received 31 July 2002. Published on the NRC Research Press Web site at <http://canjchem.nrc.ca> on 19 March 2003.

**L. Masciello and P.G. Potvin.**<sup>1</sup> Department of Chemistry, York University, 4700 Keele Street, Toronto, ON M3J 1P3, Canada.

<sup>1</sup>Corresponding author (e-mail: [pgpotvin@yorku.ca](mailto:pgpotvin@yorku.ca)).



Scheme 1.



try could be trigonal or (distorted) square planar and the binding may be fluxional.

For studies of cyclohexypyridine coordination, one would need a short, high-yield synthesis of material. In the course of our work with Ru(II) complexes of nonmacrocyclic polypyridines, we developed a one-step route from commercially available materials to symmetrical dipyrzinyldipyrindines (6) and recently applied it to the synthesis of two phenylene-linked *bisterpyridines* (7, 8). This provided an opening to an expedient synthesis of novel  $C_3$ -symmetric cyclohexypyridines (e.g., **5**), which, we reasoned, should be more soluble than Toner's  $C_2$ -symmetric varieties yet much easier to prepare than were the torands. Furthermore, our ability to prepare *bisterpyridines* provides an entry to an unprecedented *bis*(cyclohexypyridine). In this paper, we report the preparation of a number of diacetylated terpyridines and an azo-linked *bisterpyridine* that are of distinct interest and on macrocyclization reactions to form  $C_3$ -symmetric cyclohexypyridines.

## Experimental section

### General

NMR spectra were acquired on a Bruker AMX 400 MHz spectrometer in  $CDCl_3$  unless otherwise indicated. A Kratos Profile mass spectrometer was used for EI-MS acquisitions. MALDI-MS spectra were acquired on a Voyager-DE STR instrument. High resolution mass spectroscopy was performed by the McMaster Regional Centre for Mass Spectrometry in Hamilton, Ont. Mass peaks are presented as mass-to-charge ratios ( $m/z$ ) with, in brackets, peak assign-

ments and % relative intensities. UV-visible spectra were obtained at room temperature on a Hewlett-Packard 8452A diode array spectrophotometer. IR spectra were obtained on a Genesis II FT-IR spectrometer. Elemental analyses were performed by Guelph Chemical Laboratories Ltd. in Guelph, Ont.

DMF and  $CH_2Cl_2$  were made anhydrous by distillation of reagent grade material over  $MgSO_4$  or  $P_2O_5$ , respectively, and stored over 4 Å molecular sieves. All other materials were used as received, except for *p*-tolualdehyde and 4-*tert*-butylbenzaldehyde, which were washed with 5% aq. NaOH, dried ( $MgSO_4$ ), and then stored under Ar. Thin layer chromatography used Macherey–Nagel Alugram silica gel plates. Preparative thin layer chromatography used EM Science silica gel 60F glass plates. The petroleum ether (PE) used had a bp range of 60–80°C.

### 2,6-Di-(3-*p*-tolylpropenoyl)pyridine (7a)

A solution of 2,6-diacetylpyridine (3.08 g, 1.9 mmol) in MeOH (40 mL) was added to a solution of *p*-tolualdehyde (4.99 g, 42 mmol) in a 1:2 mixture of MeOH and 5% aq. KOH (60 mL), and the resulting mixture was stirred vigorously at room temperature for 48 h. The precipitate was isolated by vacuum filtration. A second crop was obtained by adding 30 mL of  $H_2O$  to the filtrate, allowing it to stir for 8 h, and collecting the precipitate by vacuum filtration. The combined crops were dissolved in  $CHCl_3$  and extracted with  $H_2O$  (3 × 25 mL), 5% aq.  $NaHSO_3$  (2 × 25 mL), and brine (2 × 25 mL). The combined organic fractions were dried with  $MgSO_4$ , filtered, and freed of solvent in vacuo. The



resulting yellow residue was recrystallized ( $\text{CHCl}_3$ :MeOH) to afford yellow needles (4.51 g, 65%). mp 198–200°C.  $^1\text{H}$  NMR (ppm)  $\delta$ : 8.43 (d,  $J$  = 16 Hz, 2H, H-3'), 8.39 (d,  $J$  = 7.5 Hz, 2H, H-3), 8.10 (t,  $J$  = 7.9 Hz, 1H, H-4), 8.03 (d,  $J$  = 16 Hz, 2H, H-2'), 7.69 (d,  $J$  = 8.0 Hz, 4H, Ar H-3), 7.29 (d,  $J$  = 7.1 Hz, 4H, Ar H-2), 2.46 (s, 6H,  $\text{CH}_3$ ).  $^{13}\text{C}$  NMR (ppm)  $\delta$ : 188.7, 153.3, 145.1, 141.4, 138.3, 132.5, 129.8, 128.8, 125.8, 119.8, 21.7; EI-MS: 367 ( $[\text{M}^+]$ , 100). Elemental analysis calcd. for  $\text{C}_{25}\text{H}_{21}\text{NO}_2$ : C 81.72, H 5.76, N 3.81; found: C 81.79, H 5.36, N 3.89.

### 2,6-Di-(3-(4-chlorophenyl)propenoyl)pyridine (7b)

A mixture of 2,6-diacetylpyridine (1.28 g, 7.82 mmol) in MeOH (20 mL) and 4-chlorobenzaldehyde (2.39 g, 17.2 mmol) in 1:2 MeOH:15% aq. KOH (60 mL) reacted at room temperature for 2 d and the product mixture was worked up as with **7a** to provide a yellow residue that recrystallized (cold  $\text{CHCl}_3$ ) as a pale yellow powder (1.97 g, 62%). mp 210–212°C.  $^1\text{H}$  NMR (warm  $\text{CDCl}_3$ ) (ppm)  $\delta$ : 8.41 (d,  $J$  = 8.8 Hz, 2H, H-3), 8.38 (d,  $J$  = 16 Hz, 2H, H-3), 8.12 (t,  $J$  = 8.6 Hz, 1H, H-4), 7.99 (d,  $J$  = 16 Hz, 2H, H-2'), 7.69 (d,  $J$  = 9.1 Hz, 4H, Ar H-3), 7.45 (d,  $J$  = 8.9 Hz, 4H, Ar H-2). EI-MS: 407 ( $[\text{M}^+]$ , 100). Elemental analysis calcd. for  $\text{C}_{23}\text{H}_{15}\text{NO}_2\text{Cl}_2$ : C 67.66, H 3.70, N 3.43; found: C 67.37, H 3.62, N 3.44.

### 2,6-Di-(3-(4-*tert*-butylphenyl)propenoyl)pyridine (7c)

By an entirely analogous process, 2,6-diacetylpyridine (1.02 g, 6.25 mmol) in MeOH (25 mL) and 4-*tert*-butylbenzaldehyde (2.51 g, 15.5 mmol) in 1:2 MeOH:5% aq. KOH (75 mL) reacted for 2 d at room temperature, and the product mixture was worked up as with **7a** to provide a yellow residue that was converted to a yellow powder by sonication in MeOH (25 mL) and then recrystallized ( $\text{CHCl}_3$ :MeOH) to afford yellow needles (1.69 g, 60%). mp 169–171°C.  $^1\text{H}$  NMR (ppm)  $\delta$ : 8.4 (d,  $J$  = 16 Hz, 2H, H-3'), 8.40 (d,  $J$  = 7.8 Hz, 2H, H-3), 8.10 (t,  $J$  = 7.7 Hz, 1H, H-4), 8.05 (d,  $J$  = 16 Hz, 2H, H-2'), 7.76 (d,  $J$  = 8.5 Hz, 4H, Ar H-3), 7.52 (d,  $J$  = 8.3 Hz, 4H, Ar H-2), 1.40 (s, 18H).  $^{13}\text{C}$  NMR (ppm)  $\delta$ : 188.5, 154.5, 153.2, 144.9, 138.4, 132.6, 128.6, 126.0, 125.7, 120.2, 35.0, 31.2. EI-MS: 451 ( $[\text{M}^+]$ , 100). Elemental analysis calcd. for  $\text{C}_{31}\text{H}_{33}\text{NO}_2$ : C 82.44, H 7.37, N 3.10; found: C 82.48, H 7.81, N 3.16.

### 4-Neopentoxybenzaldehyde

A suspension of NaH (1.25 g, 52.1 mmol) in anhydrous DMF (15 mL) was vigorously stirred in a three-neck round-bottom flask fitted with a condenser and an Ar inlet. A dropwise solution of 4-hydroxybenzaldehyde (1.05 g, 8.59 mmol) in anhydrous DMF (4 mL) was added to this suspension. After 10 min, a solution of neopentyl tosylate (**9**) (3.93 g, 16.4 mmol) and tetrabutylammonium iodide (0.34 g) in anhydrous DMF (5 mL) was added by syringe pump at a rate of 1 drop per 10 s. The solution was heated to reflux for 2 d, poured into  $\text{H}_2\text{O}$  (100 mL), and extracted with diethyl ether (4  $\times$  100 mL). The combined ether layers were concentrated and then washed with 5% aq. NaOH (2  $\times$  50 mL) and brine (2  $\times$  50 mL). The organic fraction was dried with  $\text{MgSO}_4$ , filtered, and freed of solvent in vacuo. The residue was dissolved in a small amount of  $\text{CHCl}_3$  and separated from contaminants (starting materials, identified

by  $^1\text{H}$  NMR) by preparative TLC (5:95 EtOAc:PE). The major UV-active band was scraped off and extracted by sonicating in 30:70 MeOH: $\text{CH}_2\text{Cl}_2$ . The extract was filtered, reduced in vacuo, and dried to afford a colourless oil (0.70 g, 42%). The  $^1\text{H}$  NMR, EI-MS, IR, and elemental analysis data were in agreement with the literature data (10).

### 2,6-Di-(3-(4-neopentoxyphenyl)propenoyl)pyridine (7d)

By analogy to the preparation of **7a**, a mixture of 2,6-diacetylpyridine (56.2 mg, 0.345 mmol) in MeOH (5 mL) and 4-neopentoxybenzaldehyde (130.5 mg, 0.680 mmol) reacted at room temperature for 48 h. As with **7a**, working up provided a yellow residue that recrystallized (MeOH: $\text{H}_2\text{O}$ ) as a bright yellow powder (111 mg, 63%). mp 143–145°C.  $^1\text{H}$  NMR (ppm)  $\delta$ : 8.39 (d,  $J$  = 7.9 Hz, 2H, H-3), 8.35 (d,  $J$  = 16 Hz, 2H, H-3'), 8.08 (t,  $J$  = 7.9 Hz, 1H, H-4), 7.9 (d,  $J$  = 16 Hz, 2H, H-2'), 7.73 (d,  $J$  = 8.3 Hz, 4H, Ar H-3), 6.70 (d,  $J$  = 8.5 Hz, 4H, Ar H-2), 3.70 (s, 4H,  $\text{CH}_2$ ), 1.09 (s, 18H,  $\text{CH}_3$ ). EI-MS: 511 ( $[\text{M}^+]$ , 100). Elemental analysis calcd. for  $\text{C}_{33}\text{H}_{37}\text{NO}_4$ : C 77.47, H 7.29, N 2.74; found: C 77.21, H 7.52, N 2.73.

### 3-(*p*-Tolyl)-1-(2-(6-acetylpyridyl))-2-propenone (8a)

A solution of 2,6-diacetylpyridine (3.08 g, 18.9 mmol) in MeOH (50 mL) was added to a vigorously stirring solution of *p*-tolualdehyde (2.23 g, 18.6 mmol) in a 1:4 mixture (50 mL) of MeOH and 2.5% aq. KOH with a syringe pump at a rate of one drop per 10 s. The resulting mixture was stirred vigorously at room temperature for 24 h. The precipitate was isolated by vacuum filtration. A second crop was obtained by adding 30 mL of  $\text{H}_2\text{O}$  to the filtrate, allowing it to stir for 8 h, and collecting the precipitate by vacuum filtration. The combined crops were dissolved in  $\text{CHCl}_3$  and extracted with  $\text{H}_2\text{O}$  (3  $\times$  25 mL), 5% aq.  $\text{NaHSO}_3$  (2  $\times$  25 mL), and brine (2  $\times$  25 mL). The organic fraction was dried with  $\text{MgSO}_4$ , filtered, and freed of solvent in vacuo. The residue was sonicated in MeOH to precipitate the contaminating bispropenone **7a** as a yellow powder (0.58 g) from the mixture. The yellow filtrate was freed of solvent in vacuo and the remaining yellow residue recrystallized (MeOH: $\text{H}_2\text{O}$ ) as yellow flakes (3.31 g, 67%). mp 114–116°C.  $^1\text{H}$  NMR (ppm)  $\delta$ : 8.37 (d,  $J$  = 7.7 Hz, 1H, H-3/5), 8.30 (d,  $J$  = 16 Hz, 1H, H-3'), 8.24 (d,  $J$  = 7.8 Hz, 1H, H-5/3), 8.04 (t,  $J$  = 7.8 Hz, 1H, H-4), 7.98 (d,  $J$  = 16 Hz, 1H, H-2'), 7.63 (d,  $J$  = 8.1 Hz, 2H, Ar H-3), 7.28 (d,  $J$  = 8.0 Hz, 2H, Ar H-2), 2.89 (s, 3H,  $\text{COCH}_3$ ), 2.44 (s, 3H, Ar  $\text{CH}_3$ ).  $^{13}\text{C}$  NMR (ppm)  $\delta$ : 199.4, 188.6, 153.7, 152.6, 145.7, 141.4, 137.9, 132.7, 129.3, 128.8, 126.1, 124.5, 119.4, 25.8, 22.2. EI-MS: 265 ( $[\text{M}^+]$ , 100). Elemental analysis calcd. for  $\text{C}_{17}\text{H}_{15}\text{NO}_2$ : C 76.96, H 5.70, N 5.28; found: C 76.55, H 5.51, N 5.27.

Alternatively, the residue containing the two products can be separated by column chromatography (silica, gradient eluent beginning with 3:95 EtOAc:PE and adding 5:95 EtOAc:PE) to afford each as pure yellow products.

### 3-(4-*tert*-Butylphenyl)-1-(2-(6-acetylpyridyl))-2-propenone (8c)

As for **8a**, 2,6-diacetylpyridine (1.25 g, 7.7 mmol) in MeOH (30 mL) and *p*-*tert*-butylbenzaldehyde (1.25 g, 7.7 mmol) in 1:2 MeOH:2.5% aq. KOH (90 mL) reacted for



24 h, and the reaction mixture was worked up as before. The residue was dissolved in a minimal amount of EtOAc and passed down a short column (silica, 10:90 EtOAc:PE). The major yellow fore-fraction was collected, freed of solvent in vacuo, and sonicated in MeOH (25 mL) to precipitate the bispropenone **7c** in pure form (0.18 g). The filtrate was freed of solvent and the yellow residue recrystallized (MeOH:H<sub>2</sub>O) as yellow needles (0.44 g, 19%). mp 83–85°C. <sup>1</sup>H NMR (ppm) δ: 8.39 (d, *J* = 7.8 Hz, 1H, H-3/5), 8.35 (d, *J* = 16 Hz, 1H, H-3'), 8.26 (d, *J* = 7.7 Hz, 1H, H-5/3), 8.05 (t, *J* = 8.0 Hz, 1H, H-4), 8.02 (d, *J* = 16 Hz, 1H, H-2'), 7.70 (d, *J* = 8.4 Hz, 2H, Ar H-3), 7.51 (d, *J* = 8.4 Hz, 2H, Ar H-2), 2.90 (s, 3H, COCH<sub>3</sub>), 1.38 (s, 9H, C(CH<sub>3</sub>)<sub>3</sub>). EI-MS: 307 ([M<sup>+</sup>], 100). Elemental analysis calcd. for C<sub>20</sub>H<sub>21</sub>NO<sub>2</sub>: C 78.15, H 6.88, N 4.55; found: C 78.29, H 7.00, N 4.49.

### 6,6''-Diacetyl-4'-(*p*-tolyl)-2,2':6',2''-terpyridine (**9a**)

#### One-pot method A

A solution of 2,6-diacetylpyridine (1.51 g, 9.27 mmol) in MeOH (35 mL) was quickly added to a vigorously stirring solution of *p*-tolualdehyde (0.56 g, 4.64 mmol) in MeOH (10 mL), 30% aq. KOH (7.5 mL), and concd. NH<sub>4</sub>OH (7.5 mL). An additional 30 mL of NH<sub>4</sub>OH was added and the mixture was allowed to stir at room temperature for 4–5 d. The precipitate was filtered by vacuum filtration, washed with H<sub>2</sub>O, and dissolved in CHCl<sub>3</sub>. The solution was washed sequentially with H<sub>2</sub>O (2 × 25 mL) and brine (2 × 25 mL). The organic fraction was dried with MgSO<sub>4</sub> and freed of solvent in vacuo. The residue was sonicated in MeOH (30 mL) to afford a golden yellow powder that was filtered and recrystallized (CHCl<sub>3</sub>:MeOH) as a brown-yellow powder (0.76 g, 70%). mp 191–193°C (dec.). <sup>1</sup>H NMR (ppm) δ: 8.89 (d, *J* = 7.6 Hz, 2H, H-5), 8.85 (s, 2H, H-3'), 8.14 (d, *J* = 7.7 Hz, 2H, H-3), 8.03 (t, *J* = 7.7 Hz, 2H, H-4), 7.81 (d, *J* = 7.8 Hz, 2H, Ar H-3), 7.43 (d, *J* = 8.0, 2H, Ar H-2), 2.91 (s, 6H, COCH<sub>3</sub>), 2.50 (s, 3H, Ar CH<sub>3</sub>). EI-MS: 407 ([M<sup>+</sup>], 68), 365 ([M<sup>+</sup>-COCH<sub>3</sub>], 45), 43 ([COCH<sub>3</sub>], 100). Elemental analysis calcd. for C<sub>26</sub>H<sub>21</sub>N<sub>3</sub>O<sub>2</sub>: C 76.64, H 5.19, N 10.31; found: C 76.26, H 5.05, N 10.65.

#### Two-step method B

A solution of 2,6-diacetylpyridine (409 mg, 2.51 mmol) in MeOH (20 mL) was quickly added to a vigorously stirring solution of the propenone **8a** (664 mg, 2.51 mmol) in MeOH (62.5 mL) and 15% aq. KOH (22 mL). Concentrated NH<sub>4</sub>OH (60 mL) was added in portions and the mixture was allowed to stir at room temperature for 4–5 d. The precipitate was filtered by vacuum filtration, dissolved in CHCl<sub>3</sub>, and washed sequentially with H<sub>2</sub>O (2 × 25 mL) and brine (2 × 25 mL). The organic fraction was dried with MgSO<sub>4</sub> and freed of solvent in vacuo. The residue was triturated with MeOH (20 mL) to afford a golden yellow powder that was filtered and recrystallized (CHCl<sub>3</sub>:MeOH) as a brown-yellow powder (358 mg, 35%). The mp and <sup>1</sup>H NMR data were identical to those from material obtained by Method A.

### 6,6''-Diacetyl-4'-(4-chlorophenyl)-2,2':6',2''-terpyridine (**9b**)

By analogy to the preparation of **9a** by Method A, 2,6-diacetylpyridine (1.960 g, 12.0 mmol) in MeOH (40 mL) re-

acted with 4-chlorobenzaldehyde (819 mg, 5.85 mmol) in MeOH (20 mL), 15% aq. KOH (7 mL) and concd. NH<sub>4</sub>OH (10 mL) at room temperature for 3 days, and the reaction mixture was worked up as before. The yellow solid crude product was passed down a short column (silica, 20:80 EtOAc:PE) with slow elution of the major yellow band and 10:90 MeOH:CH<sub>2</sub>Cl<sub>2</sub> for elution of the baseline fraction. Both fractions were combined and recrystallized (CHCl<sub>3</sub>:MeOH) to afford a pure brown-yellow powder (1.80 g, 72%). mp 166–168°C. <sup>1</sup>H NMR (ppm) δ: 8.89 (d, *J* = 7.8 Hz, 2H, H-5), 8.82 (s, 2H, H-3'), 8.15 (d, *J* = 7.4 Hz, 2H, H-3), 8.06 (t, *J* = 7.8 Hz, 2H, H-4), 7.83 (d, *J* = 8.5 Hz, 2H, Ar H-3), 7.57 (d, *J* = 8.41 Hz, 2H, Ar H-2), 2.91 (s, 6H, CH<sub>3</sub>). EI-MS: 427 ([M<sup>+</sup>], 100). Elemental analysis calcd. for C<sub>25</sub>H<sub>18</sub>N<sub>3</sub>O<sub>2</sub>Cl: C 70.18, H 4.24, N 9.82; found: C 69.70, H 4.24, N 9.57.

### 6,6''-Diacetyl-4'-(4-*tert*-butylphenyl)-2,2':6',2''-terpyridine (**9c**)

By analogy to the preparation of **9a** by Method A, 2,6-diacetylpyridine (1.503 g, 9.22 mmol) in MeOH (35 mL) reacted with 4-*tert*-butylbenzaldehyde (0.742 g, 4.58 mmol) in MeOH (10 mL), 30% aq. KOH (7.5 mL) and concd. NH<sub>4</sub>OH (7.5 mL) at room temperature for 3–4 days, and the reaction mixture was worked up as before. The yellow solid crude product was dissolved in a small amount of CHCl<sub>3</sub> and separated from contaminants by preparative TLC (silica, 1:9 EtOAc:hexane). The major UV-active band was extracted from the silica with 30:70 MeOH:CH<sub>2</sub>Cl<sub>2</sub>, filtered, and reduced in vacuo to afford a white residue. Sonication in MeOH (30 min, 100 mL) and recrystallization (CHCl<sub>3</sub>:Et<sub>2</sub>O) afforded a white powder (1.51 g, 73%). mp 185–187°C (dec.). <sup>1</sup>H NMR (ppm) δ: 8.88 (d, *J* = 7.8 Hz, 2H, H-5), 8.85 (s, 2H, H-3), 8.12 (d, *J* = 7.6 Hz, 2H, H-3), 8.04 (t, *J* = 7.7 Hz, 2H, H-4), 7.86 (d, *J* = 8.1 Hz, 2H, Ar H-3), 7.64 (d, *J* = 8.2 Hz, 2H, Ar H-2), 2.93 (s, 6H, COCH<sub>3</sub>), 1.74 (s, 9H, C(CH<sub>3</sub>)<sub>3</sub>). EI-MS: 449 ([M<sup>+</sup>], 100). Elemental analysis calcd. for C<sub>29</sub>H<sub>27</sub>N<sub>3</sub>O<sub>2</sub>: C 77.48, H 6.05, N 9.35; found: C 77.82, H 6.34, N 8.89.

### 6,6''-Diacetyl-4'-(4-neopentoxyphenyl)-2,2':6',2''-terpyridine (**9d**)

By analogy to the preparation of **9a** by Method A, 2,6-diacetylpyridine (335 mg, 2.05 mmol) in MeOH (5 mL) reacted with 4-neopentoxybenzaldehyde (191 mg, 0.99 mmol) in MeOH (10 mL), 30% aq. KOH (2.5 mL), and concd. NH<sub>4</sub>OH (2.5 mL) at room temperature for 4 days, and the reaction mixture was worked up as before. Purification of the yellow solid crude product by preparative TLC (1:3 EtOAc:hexane) gave a major yellow band that was extracted from the silica with 30:70 MeOH:CH<sub>2</sub>Cl<sub>2</sub>, filtered, and reduced in vacuo. The yellow solid proved difficult to recrystallize and was isolated as a golden-yellow powder by drying under vacuum (334 mg, 70%). mp 167–170°C. <sup>1</sup>H NMR (ppm) δ: 8.88 (d, *J* = 7.8 Hz, 2H, H-5), 8.83 (s, 2H, H-3'), 8.13 (d, *J* = 7.7 Hz, 2H, H-3), 8.05 (t, *J* = 7.6 Hz, 2H, H-4), 7.85 (d, *J* = 8.2 Hz, 2H, Ar H-3), 7.15 (d, *J* = 8.1 Hz, 2H, Ar H-2), 3.75 (s, 2H, CH<sub>2</sub>), 2.92 (s, 6H, COCH<sub>3</sub>), 1.10 (s, 9H, C(CH<sub>3</sub>)<sub>3</sub>). EI-MS: 479 ([M<sup>+</sup>], 87). Elemental analysis calcd. for C<sub>30</sub>H<sub>29</sub>N<sub>3</sub>O<sub>3</sub>: C 75.16, H 6.10, N 8.79; found: C 74.80, H 6.49, N 8.48.



**4',4'',4<sup>v</sup>-Tri-(*p*-tolyl)-[(2,6)-pyridyl-6-corand-6] (5a)****Method A**

A mixture of **9a** (40.1 mg, 0.098 mmol) and bispropenone **7a** (37.9 mg, 0.103 mmol) were heated at reflux in glacial acetic acid (25 mL) and excess concd.  $\text{NH}_4\text{OAc}$  (1.3 g) for 24 h. The precipitate was filtered hot and washed with  $\text{CHCl}_3$ , MeOH, and  $\text{Et}_2\text{O}$  to give a dark black solid (16.5 mg, 22%). This solid was found to be insoluble in all common organic solvents examined. mp 207–210°C (dec.). MALDI-MS: 755.1 ( $[\text{M}^+ + \text{Na}^+]$ , 100). 771.0 ( $[\text{M}^+ + \text{K}^+]$ , 7). HRMS calcd. for  $\text{C}_{51}\text{H}_{36}\text{N}_6\text{K}$ : 771.264; found: 771.262  $\pm$  0.005.

**Method B**

A mixture of bispropenone **10** (5.0 mg, 8.17  $\mu\text{mol}$ ) and 2,6-di[2-(*N*-pyridyl)-1-oxoethyl]pyridine diiodide **11** (4.6 mg, 8.23  $\mu\text{mol}$ ) were heated to reflux in glacial acetic acid (25 mL) containing  $\text{NH}_4\text{OAc}$  (0.72 g) for 24 h. The precipitate was filtered hot and washed with  $\text{CHCl}_3$ , MeOH, and  $\text{Et}_2\text{O}$  to give a dark black solid (1.23 mg, 20%), identical in all respects to material obtained by Method A.

**4',4'',4<sup>v</sup>-Tri-(4-chlorophenyl)-[(2,6)-pyridyl-6-corand-6] (5b)**

The preparation of **5a** by Method A was followed by using **9b** (43.4 mg, 0.102 mmol) and bispropenone **7b** (38.5 mg, 0.0946 mmol) to obtain a dark brown, insoluble solid (16.7 mg, 22%). mp 198–200°C (dec.). MALDI-MS: 815.2 ( $[\text{M}^+ + \text{Na}^+]$ , 100). 831.2 ( $[\text{M}^+ + \text{K}^+]$ , 7). HRMS calcd. for  $\text{C}_{48}\text{H}_{27}\text{N}_6\text{Cl}_3\text{Na}$ : 815.125; found: 815.126  $\pm$  0.005.

**4',4'',4<sup>v</sup>-Tri-(4-*tert*-butylphenyl)-[(2,6)-pyridyl-6-corand-6] (5c)**

A solution of **9c** (24.3 mg, 0.054 mmol) in 4:1 *n*-butanol:MeOH (25 mL) was added to a stirring solution of bispropenone **7c** (17.0 mg, 0.0377 mmol) in 2:1 *n*-butanol:MeOH (15 mL), 30% aq. KOH (10 mL) and concd.  $\text{NH}_4\text{OH}$  (30 mL). The mixture was heated at reflux for 24 h. The precipitate was filtered hot and washed with  $\text{H}_2\text{O}$ ,  $\text{CHCl}_3$ , and MeOH to give a tan solid (9.0 mg, 26%) that was insoluble in all common organic solvents examined. mp 204–207°C (dec.). MALDI-MS: 881.4 ( $[\text{M}^+ + \text{Na}^+]$ , 25), 897.4 ( $[\text{M}^+ + \text{K}^+]$ , 37). HRMS calcd. for  $\text{C}_{60}\text{H}_{54}\text{N}_6\text{Na}$  and  $\text{C}_{60}\text{H}_{54}\text{N}_6\text{K}$ : 881.431 and 897.405; found: 881.427  $\pm$  0.005 and 897.408  $\pm$  0.005.

**4',4'',4<sup>v</sup>-Tri-(4-neopentoxyphenyl)-[(2,6)-pyridyl-6-corand-6] (5d)**

In analogy to the preparation of **5a** by Method A, **9d** (42.3 mg, 0.0885 mmol) and bispropenone **7d** (45.4 mg, 0.0888 mmol) were used to provide a fine precipitate, which was filtered hot, dissolved in  $\text{CHCl}_3$ , and washed with  $\text{H}_2\text{O}$  (3  $\times$  15 mL). The organic layer was freed of solvent in vacuo and dried under vacuum to give a yellow solid (18.5 mg, 22%). mp 173–175°C (dec.). UV-vis ( $\text{CHCl}_3$ )  $\lambda_{\text{max}}$  (nm) ( $\epsilon$  ( $10^3 \text{ M}^{-1} \text{ cm}^{-1}$ )): 264 (45), 316 (49).  $^1\text{H}$  NMR (ppm) (0.64  $\mu\text{M}$ , refer to Fig. 1 for assignments)  $\delta$ : 9.04 (2H, s, H-3B), 8.95 (2H, d, H-3/5C), 8.83 (2H, s, H-3/5D), 8.83 (1H, t, H-4F), 8.76 (2H, d, H-5/3C), 8.14 (2H, d, H-3F), 8.07 (2H, t, H-4C), 7.97 (2H, d, H-2A or H-2/6E), 7.92 (2H, d, H-2A or H-2/6E), 7.92 (2H, s, H-5/3D), 7.14 (8H, d, H-3A, H-

3/5E, H-2A or H-2/6E), 3.75 (6H, s,  $\text{CH}_2$ ), 2.89 (3H, s, OAc  $\text{CH}_3$ ), 1.13 (27H, s,  $\text{CH}_3$ ). MALDI-MS: 971.2 ( $[\text{M}^+ + \text{Na}^+]$ , 100). 987.4 ( $[\text{M}^+ + \text{K}^+]$ , 37).

**4'-(*p*-Tolyl)-6,6''-di-(3-(*p*-tolyl)propenoyl)-2,2':6',2''-terpyridine (10)**

A solution of **9a** (100.3 mg, 0.25 mmol) in THF (20 mL) was added, dropwise, to a vigorously stirring solution of *p*-tolualdehyde (208.4 mg, 1.74 mmol), MeOH (23 mL), and 15% aq. KOH (25 mL), and the mixture was stirred for 3 d. The precipitate was filtered, dissolved in  $\text{CHCl}_3$ , and washed sequentially with 5% aq.  $\text{NaHSO}_3$  (2  $\times$  15 mL),  $\text{H}_2\text{O}$  (2  $\times$  15 mL), and brine (2  $\times$  15 mL). The product was contaminated with a small quantity of unreacted **9a** that was partially removed by seven cycles of preparative TLC (silica, 10:90 EtOAc:PE). The baseline fraction was removed from the silica (30:70 MeOH: $\text{CH}_2\text{Cl}_2$ ), freed of solvent, and recrystallized ( $\text{CHCl}_3$ :MeOH) to afford a tan powder (30.1 mg, 20%).  $^1\text{H}$  NMR (ppm)  $\delta$ : 8.89 (d,  $J$  = 8.0 Hz, 2H, H-5), 8.85 (s, 2H, H-3'), 8.53 (d,  $J$  = 16 Hz, 2H, H-3), 8.14 (d,  $J$  = 7.2 Hz, 2H, H-3), 8.05 (t,  $J$  = 7.6 Hz, 2H, H-4), 8.04 (d,  $J$  = 16 Hz, 2H, H-2), 7.81 (d,  $J$  = 8.0 Hz, 2H, Ar H-3), 7.70 (d,  $J$  = 7.9 Hz, 2H, Ar H-3), 7.43 (d,  $J$  = 7.9 Hz, 6H, Ar H-2), 2.50 (s, 6H, Ar  $\text{CH}_3$ ), 2.46 (s, 3H, Ar  $\text{CH}_3$ ). MALDI-MS: 611 ( $[\text{M}^+]$ , 87).

**2-(4-Nitrophenyl)-1,3-dioxolane (12)**

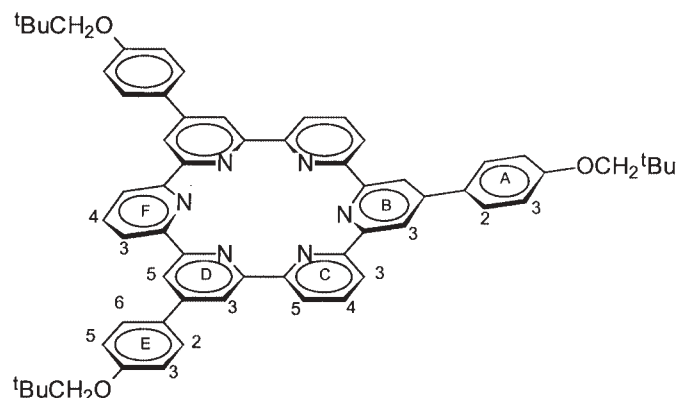
A mixture of 4-nitrobenzaldehyde (1.508 g, 9.9 mmol), ethylene glycol (1.21 mL, 21.7 mmol), and chlorotrimethylsilane (5.61 mL, 44.2 mmol) in anhydrous  $\text{CH}_2\text{Cl}_2$  (55 mL) was stirred at reflux under Ar for 48 h. A 5% aq. solution of  $\text{NaHCO}_3$  (100 mL) was added and the mixture was extracted with  $\text{Et}_2\text{O}$  (4  $\times$  75 mL). The ether layer was extracted with brine (4  $\times$  75 mL), dried with  $\text{MgSO}_4$ , filtered, and reduced in vacuo. The yellow residue was recrystallized ( $\text{CHCl}_3$ ) as cream flakes (1.523 g, 79%).  $^1\text{H}$  NMR, EI-MS, and mp data were in agreement with those reported in the literature (12, 13).

**4,4'-Di-(1,3-dioxolanyl)azobenzene (13)**

A suspension of  $\text{LiAlH}_4$  (1.510 g, 3.98 mmol) in  $\text{Et}_2\text{O}$  (50 mL) was vigorously stirred at  $-78^\circ\text{C}$  in a three-neck round-bottom flask fitted with a mechanical stirrer, dropping funnel, and an Ar inlet. To this suspension, a solution of 2-(4-nitrophenyl)-1,3-dioxolane **12** (0.6954 g, 3.58 mmol) in  $\text{Et}_2\text{O}$  (40 mL) was added, dropwise. The mixture was allowed to slowly warm to room temperature (3 h) and stirred for an additional 30 min. The reaction was quenched slowly and successively with EtOAc, MeOH, and  $\text{H}_2\text{O}$  with vigorous stirring. The addition of a 5% aq.  $\text{H}_2\text{SO}_4$  solution produced two brightly coloured (orange and yellow) layers. The orange layer was extracted into  $\text{Et}_2\text{O}$  (40 mL), and the ether layer was washed with  $\text{H}_2\text{O}$  (1  $\times$  25 mL),  $\text{NaHCO}_3$  (2  $\times$  25 mL), and brine (2  $\times$  25 mL). The ether-borne extract was concentrated and purified by preparative TLC (silica, 1:3 EtOAc:hexane). The major orange band was extracted from the silica with 30:70 MeOH: $\text{CH}_2\text{Cl}_2$ . The extract was filtered, concentrated in vacuo, and recrystallized (cold MeOH) to afford a bright orange powder (0.7236 g, 62%). mp 140–142°C.  $^1\text{H}$  NMR (ppm)  $\delta$ : 7.96 (d,  $J$  = 7.9 Hz, 4H, H-2), 7.66 (d,  $J$  = 8.0 Hz, 4H, H-3), 5.92 (s, 2H, Ar-CH),



**Fig. 1.** Cyclohexipyridine **5d**, showing twisting of rings A and F out of plane. The  $^1\text{H}$  NMR assignments used the position numbers given.



4.20–4.08 (m, 8H,  $\text{CH}_2$ ). EI-MS: 326 ( $[\text{M}^+]$ , 48). 149 ( $[\text{M}^+ - \text{C}_9\text{H}_9\text{O}_2]$ , 100). Elemental analysis calcd. for  $\text{C}_{18}\text{H}_{18}\text{N}_2\text{O}_4$ : C 66.25, H 5.56, N 8.58; found: C 66.77, H 5.69, N 8.31.

#### 4,4'-Azobenzaldehyde (**14**)

A 10% aq.  $\text{H}_2\text{SO}_4$  solution (100 mL) was added to a vigorously stirring solution of 4,4'-di-(1,3-dioxolanyl)azobenzene **13** (0.700 g, 2.15 mmol) in MeOH (60 mL) at room temperature. The mixture was allowed to stir for 20 h, filtered, dissolved in  $\text{CHCl}_3$ , and washed sequentially with 5% aq.  $\text{NaHCO}_3$  (1  $\times$  75 mL),  $\text{H}_2\text{O}$  (1  $\times$  75 mL), and brine (2  $\times$  50 mL). The organic fraction was dried with  $\text{MgSO}_4$ , freed of solvent in vacuo, and recrystallized (MeOH) to afford red leaflets (0.420 g, 82%).  $^1\text{H}$  NMR, EI-MS, and mp data were in agreement with those reported in the literature (14–16). UV-vis ( $\text{CHCl}_3$ )  $\lambda_{\text{max}}$  (nm) ( $\epsilon$  ( $\text{M}^{-1} \text{cm}^{-1}$ )): 336 (53 500), 478 (1 240).

#### 4,4'-Di-(4'-(6,6''-diacetyl-2,2':6',2''-terpyridinyl))azobenzene (**15**)

A solution of 2,6-diacetylpyridine (0.4890 g, 3.0 mmol) in MeOH (10 mL) was added slowly to a vigorously stirring mixture of 4,4'-azobenzaldehyde **14** (0.1017 g, 0.49 mmol), MeOH (90 mL), 15% aq. KOH (2.5 mL), and concd.  $\text{NH}_4\text{OH}$  (23 mL). The mixture was heated to reflux for 20 h. The orange precipitate was filtered and washed with  $\text{H}_2\text{O}$ . Trituration with  $\text{CHCl}_3$  afforded an orange filtrate and an insoluble orange precipitate. The filtrate was washed with  $\text{NaHCO}_3$  (2  $\times$  25 mL), NaOH (1  $\times$  25 mL), and brine (2  $\times$  25 mL), dried with  $\text{MgSO}_4$ , and freed of solvent in vacuo. The residue was purified by preparative TLC (silica, 31:2:1 MeCN: saturated  $\text{KNO}_3:\text{H}_2\text{O}$ ). The baseline fraction was extracted from the silica with 30:70 MeOH: $\text{CH}_2\text{Cl}_2$ . The extract was filtered and concentrated in vacuo. The orange solid recrystallized ( $\text{CHCl}_3:\text{MeOH}$ ) as an orange powder (175.0 mg, 50%). mp 207–209°C. UV-vis ( $\text{CHCl}_3$ )  $\lambda_{\text{max}}$  (nm) ( $\epsilon$  ( $\text{M}^{-1} \text{cm}^{-1}$ )): 356 (12 400), 274 (31 400). IR (neat) ( $\text{cm}^{-1}$ ): 1698 (s, C=O).  $^1\text{H}$  NMR (ppm)  $\delta$ : 8.94 (d,  $J$  = 7.6 Hz, 4H, H-5), 8.91 (s, 4H, H-3'), 8.23 (d,  $J$  = 7.6 Hz, 4H, H-3), 8.15 (d+d,  $J$  = 7.8 Hz, 8H, Ar H-2 & H-3), 8.10 (t,  $J$  = 7.5 Hz, 4H, H-4), 2.94 (s, 12H,  $\text{CH}_3$ ). MALDI-MS: 812 ( $[\text{M}^+]$ , 100). HRMS calcd. for  $\text{C}_{50}\text{H}_{37}\text{N}_8\text{O}_4$ : 813.294. found: 813.295  $\pm$  0.005.

## Results and discussion

As illustrated in Scheme 2, we explored two approaches to the synthesis of  $\text{C}_3$ -symmetrical cyclohexipyridines: (i) coupling a diacetylterpyridine **9** with a bispropenone **7** in the presence of a source of  $\text{NH}_3$  via a dihydropyridine intermediate and (ii) coupling a more elaborate bispropenone **10** with the salt **11** under Kröhnke's conditions (17). Both approaches required diacetylated terpyridines **9** whose synthesis was to make use of our one-pot preparation of dipyrzinyldipyrindines (**6**), essentially a modified Chichibabin synthesis (18). This would start from commercial 2,6-diacetylpyridine **6**, which would be the only source of pre-manufactured pyridine rings and would require a differential reactivity of the two acetyl groups.

The substituents on the macroring, originating from aromatic aldehydes, could presumably be varied at will. In principle, this approach can also lead to less symmetrical products with one macroring substituent different from the other two, but this possibility was not explored here. Our initial goal was to prepare three examples of cyclohexipyridines, one with electron-releasing substituents, another with electron-withdrawing substitution, and the first example of a *bis*(cyclohexipyridine) with an azo linkage. The latter necessitated the preparation of a novel azo-linked *bisterpyridine*.

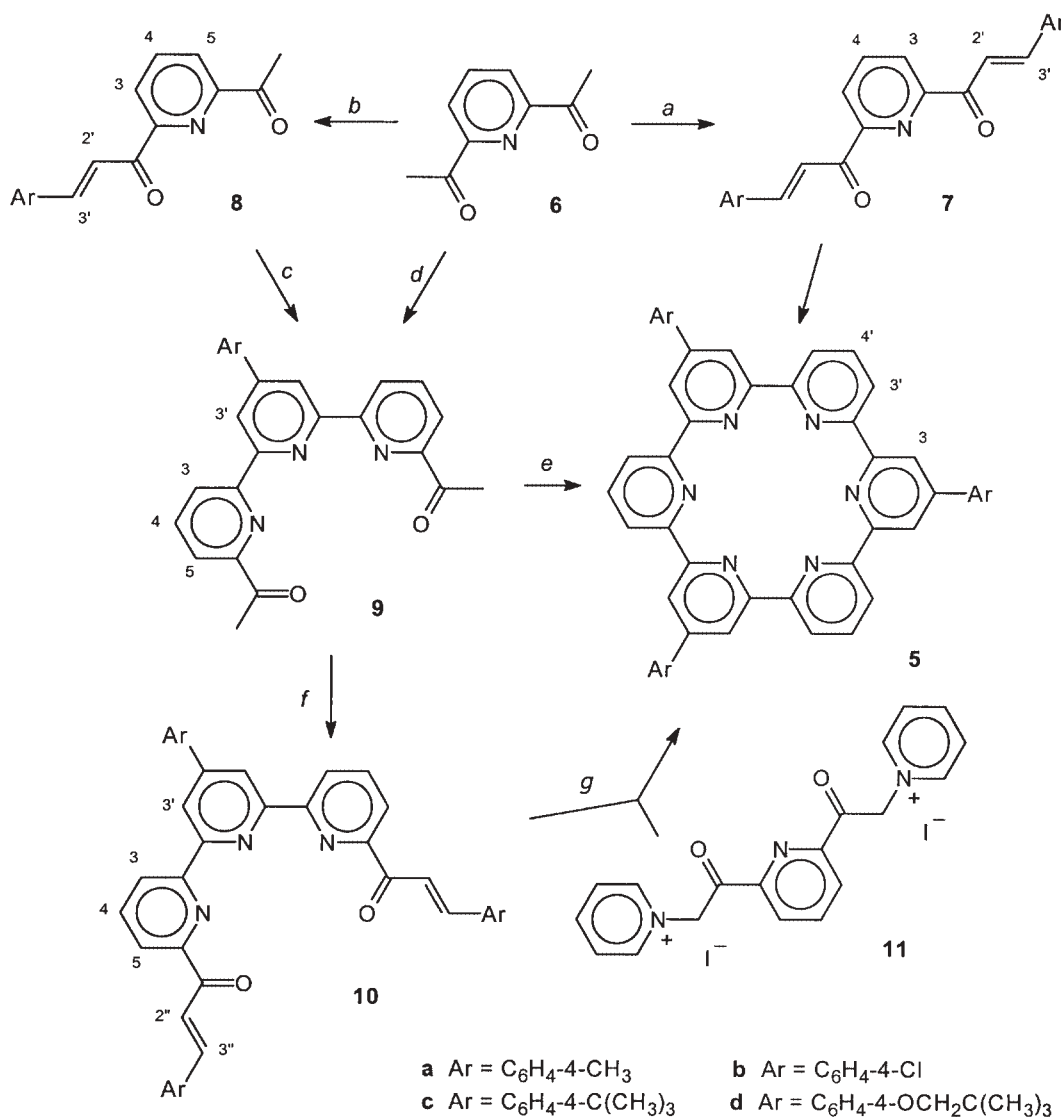
Diacetylpyridine **6** was treated with 2 equiv of *p*-tolualdehyde under basic conditions to afford a 65% isolated yield of recrystallized bispropenone **7a** (Scheme 2). Similarly, 4-chlorobenzaldehyde afforded **7b** in 62% isolated yield. Their NMR and EI-MS spectra and their elemental analyses were consistent with the proposed structures. According to  $^1\text{H}$  NMR, they appeared to be exclusively *trans,trans* isomers. When only 1 equiv of *p*-tolualdehyde and weaker base were used, a 67% isolated yield of monopropenone **8a** was isolated, again as the *trans* isomer according to  $^1\text{H}$  NMR, along with some **7a**. Hence, the two acetyl groups of **6** seem to react fairly independently, and the reaction of one apparently reduces the reactivity of the other, thereby making our approach promising.

When **6** and propenone **8a** were combined in 1:1 ratio under basic conditions in the presence of  $\text{NH}_3$  at room temperature, a precipitate formed over the course of several days. After collection, washing, and recrystallization, a 35% yield of diacetylterpyridine **9a** was obtained. If, instead, *p*-tolualdehyde or 4-chlorobenzaldehyde were combined with 2 equiv of **6** in the presence of  $\text{NH}_3$ , terpyridines **9a** and **9b** precipitated in essentially pure form over a few days at room temperature. These terpyridines were isolated in 70% and 72% yields, respectively, after recrystallization. Given the number of intermediates involved in the assembly of the central pyridine ring, such yields are remarkable. Both of these terpyridines were fully characterized by NMR, EI-MS, and elemental analyses. A distinctive feature of these materials was the appearance of a new aromatic singlet in their  $^1\text{H}$  NMR spectra, signalling the creation of the symmetrical, central pyridine ring.

By an analogous process, 4,4'-azobenzaldehyde (**14**) and 4 equiv of **6** were converted to the novel azo-linked *bis*(terpyridine) **15**, an orange solid, in 50% yield after preparative TLC and recrystallization (Scheme 3). Considering



**Scheme 2.** Conditions: (a)  $\geq 2$  equiv Ar-CHO, 5–15% aq. KOH, MeOH, 2 d; (b) 1 equiv Ar-CHO, 2.5% aq. KOH, MeOH, 24 h; (c) 1 equiv **6**, 15% aq. KOH, concd.  $\text{NH}_4\text{OH}$ , MeOH, 4–5 d; (d) 0.5 equiv **6**, 15–30% aq. KOH, concd.  $\text{NH}_4\text{OH}$ , MeOH, 3–5 d; (e) 1 equiv **7a,b**, or **d**,  $\text{NH}_4\text{OAc}$ , HOAc, reflux, 24 h, or 1 equiv **7c**, 30% aq. KOH, concd.  $\text{NH}_4\text{OH}$ , MeOH:*n*-BuOH, reflux, 24 h; (f) 7 equiv  $\text{CH}_3\text{C}_6\text{H}_4\text{-4-CHO}$ , 15% aq. KOH, MeOH, 3 d; (g) 1 equiv **11**,  $\text{NH}_4\text{OAc}$ , HOAc, reflux, 24 h. The  $^1\text{H}$  NMR assignments used the position numbers given.



that this transformation assembled a total of seven molecules (including  $\text{NH}_3$ ) and eliminated a total of six molecules of  $\text{H}_2\text{O}$  (as well as 2 equiv of  $\text{H}_2$ ), the 50% yield is quite remarkable. For this synthesis, the known dialdehyde **14** (14–16) was prepared from 4-nitrobenzaldehyde involving its TMSCl-catalyzed (19) protection to nitroacetal **12** (12, 13) (79% yield), reductive coupling with cold  $\text{LiAlH}_4$  (20) to the previously unknown azo-acetal intermediate, the bright orange **13** (62% yield), followed by deprotection (82% yield). The nitro-azo transformation caused an upfield migration of the aromatic signals and the structure of **13** was otherwise supported by MS and elemental analysis as well as its transformation to **14**. In the  $^1\text{H}$  NMR spectrum of **15**, the azophenyl doublets (identified by COSY) were overlapping. This had been also observed with the aromatic doublets from **14** where the aldehyde group is conjugated with the azo group but not in **12** or **13** where the aldehyde is masked.

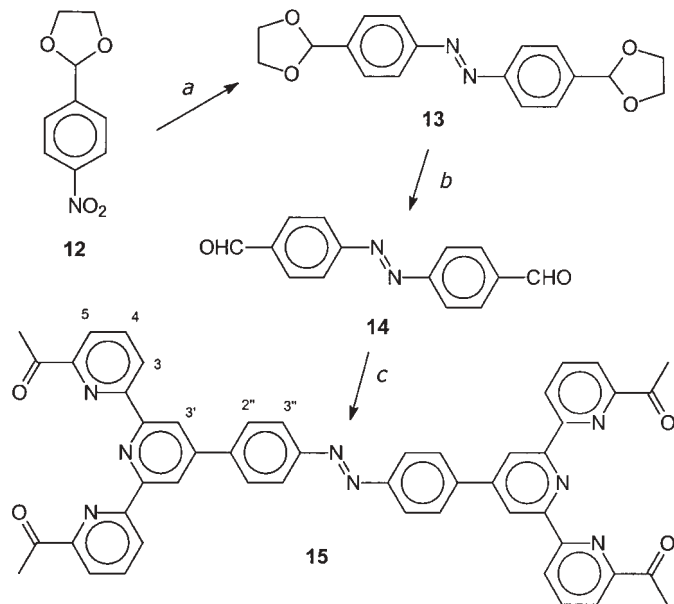
The overlap with **15** is therefore consistent with conjugation of the terpyridine unit with the azo group and hence  $\pi$ -overlap among the terpyridines. The high degree of conjugation present was also evident from the energy of the  $\pi \rightarrow \pi^*$  band for **15** (356 nm), which is at a lower energy than had been found with a phenylene-linked *bis*(terpyridine) (280 nm) (7) or with azobenzene itself (320 nm) (21, 22).

These terpyridine compounds are also of evident interest in transition metal complexation. The synthesis provides for variation of the 4' substituent, and the products may be further elaborated at the acetyl groups, for instance, to prepare macrocyclic Schiff bases with diamines.

To effect macrocyclization, **7a** and **9a** were combined in 1:1 ratio and heated to reflux in acetic acid in the presence of excess  $\text{NH}_4\text{OAc}$ . This produced a black powder in 22% yield that was insoluble in all solvents tested and appeared to decompose on the melting point apparatus. NMR analysis



**Scheme 3.** Conditions: (a)  $\text{LiAlH}_4$ ,  $\text{Et}_2\text{O}$ ,  $-78^\circ\text{C} \rightarrow \text{RT}$ , 30 min; (b) 10% aq.  $\text{H}_2\text{SO}_4$ , MeOH, 20 h; (c) 6 equiv **6**, 15% aq. KOH, concd.  $\text{NH}_4\text{OH}$ , MeOH, reflux, 20 h. The  $^1\text{H}$  NMR assignments used the position numbers given.



of the mother liquor was not informative. MALDI-MS analysis of the insoluble material revealed two principal signals consistent with the presence of both  $\text{Na}^+$  ( $M + 23$ ) and  $\text{K}^+$  ( $M + 39$ ) complexes of cyclohexipyridine **5a**, in roughly 15:1 ratio, with no sign of metal-free macrocycle. This result is consistent with Toner's obtention of his cyclohexipyridine as a  $\text{NaOAc}$  complex. It seems that the presence of a third substituent on our macroring failed to produce a more soluble product. Essentially the same result was obtained by the analogous combination of the chlorophenyl-bearing terpyridine **9b** with chlorophenyl-bispropenone **7b**; a 22% yield of an insoluble black powder analyzing as  $\text{Na}^+$  and  $\text{K}^+$  complexes of macrocycle **5b** in ca. 15:1 ratio.

The condensation reactions forming the last two pyridine rings of the macrocycle actually produce dihydropyridines that require aerial oxidation. In case this might be rate-limiting and contribute to the low yields of macrocycles **5**, an alternative synthesis was performed using Kröhnke methodology (17) such as was applied by Toner (4) and by Kelly et al. (2). This leads to fully formed pyridines without need for aerial oxidation but requires extra steps in substrate preparation. Diacetylterpyridine **9a** was converted to the *trans,trans*-bispropenone **10** by base-catalyzed condensation with excess *p*-tolualdehyde. This gave a disappointing, though unoptimized, yield of 20% of material that was, moreover, contaminated with some unreacted **9a** that proved to be very tedious to remove. Compound **10** was not fully characterized, but its structure was proven by MALDI-MS and  $^1\text{H}$  NMR, which showed the absence of acetyl  $\text{CH}_3$  signals, the appearance of *trans*-alkenyl signals, and the presence of two benzylic  $\text{CH}_2$  signals in 2:1 integration ratio. Bispropenone **10** was subsequently treated with the known dipyridinium salt **11** and excess  $\text{NH}_4\text{OAc}$  in acetic acid at reflux, according to the Kröhnke method (17). This afforded the  $\text{Na}^+$  and  $\text{K}^+$  complexes of **5a** identical in all respects to

material prepared earlier and in a similar yield (20%). There was, therefore, no apparent advantage to applying the Kröhnke method and aerial oxidation was evidently not a limiting factor. We also attempted the direct, one-pot approach that was successful in our terpyridine synthesis using a 1:1 ratio of **6** and *p*-tolualdehyde in the presence of  $\text{NH}_3$ . However, the major product was the monopropanone **8a**. It appears that, once the first acetyl group of **6** has reacted to give **8a**, the reaction of the second is too slow in Michael addition to the propenone moiety of **8a**.

By analogy to other flat, extended  $\pi$ -conjugated systems such as phthalocyanines (23, 24), the insolubility of these cyclohexipyridines was likely due to aggregation. To discourage this, we turned to the commercially available 4-*tert*-butylbenzaldehyde to deliver bulkier substituents. We were able to prepare the *tert*-butylated bispropenone **7c** and terpyridine **9c** in yields very similar to those obtained previously (60 and 73%, respectively), but the monopropanone **8c** was obtained in just 19% yield, in part because of difficulty encountered in separating it from the **7c** that accompanies it, and **8c** was not used further. The macrocyclization was performed this time under basic conditions analogous to those used in our terpyridine synthesis, as opposed to the acidic conditions used earlier for **5a** and **5b**, to control the cation content of the reaction mixture. Thus, terpyridine **9c** and bispropenone **7c** were treated with aqueous KOH and concentrated  $\text{NH}_4\text{OH}$  in a butanol–MeOH mixture to produce a tan deposit in 26% yield that again analyzed as a mix of  $\text{Na}^+$  and  $\text{K}^+$  complexes of cyclohexipyridine **5c**, this time in a K-rich ratio of ca. 2:3  $\text{Na}:\text{K}$ , with  $\text{OH}^-$  as the likely counterion. The  $\text{Na}^+$  probably again originated from the glass reaction vessel, and the failure of the large excess of  $\text{K}^+$  in solution to prevent the incorporation of  $\text{Na}^+$  suggests that the latter forms the stronger complexes. Indeed, Bell et al. measured equilibrium binding constants for torand **2** and found a ca. 2.5-fold preference for  $\text{Na}^+$  over  $\text{K}^+$  (5). This contrasts with the usual preference for  $\text{K}^+$  by crowns (25) and discounts the primacy of cavity size in cation selection, i.e., the “hole-size concept”, by which the cyclohexipyridine cavity size, estimated at 1.3 Å (26), better fits the hexacoordinate ionic radius of  $\text{K}^+$  (1.38 Å) than that of  $\text{Na}^+$  (1.02 Å) and is therefore expected to better bind  $\text{K}^+$ .

In any case, macrocycle **5c** was just as insoluble as the previous two examples. We then turned to neopentox groups to provide solubilizing power, as had been used with success to prepare soluble phthalocyanines (27). There is a two-step published preparation of 4-neopentoxylbenzaldehyde (10), but we prepared it by alkylation of 4-hydroxybenzaldehyde using neopentyl tosylate (9) in 42% isolated yield. Conversions to bispropenone **7d** and terpyridine **9d** proceeded in the same fashion and in similar yields (63% **7d**, 70% **9d**) as for their analogues. Also, the macrocyclization proceeded as well as the previous examples (22% isolated yield) but this time the precipitated product was soluble in a variety of solvents, though not aromatic ones. This material defied all attempts at crystallization. TLC with various eluents showed that it was chromatographically homogeneous and free of impurities. MALDI-MS identified the material as **5d**, again obtained as a mix of  $\text{Na}^+$  and  $\text{K}^+$  complexes in ca. 5:2 ratio.

$^1\text{H}$  NMR showed broad aliphatic singlets for this material, one for  $\text{C}(\text{CH}_3)_3$  and one for  $\text{OCH}_2$  in 9:2 ratio, in accord



with the structure, as well as one attributable to the OAc counterion, but the aromatic region contained broad and overlapping signals, indicating a pronounced tendency to aggregate in spite of being well dissolved. Heating the sample to 62°C failed to affect the spectrum, but dilution caused a sharpening of the signals. Progressively sharper signals were obtained with progressive dilution, confirming that **5d**, as a Na<sup>+</sup>:K<sup>+</sup> complex, was subject to aggregation. Even at its sharpest, at sub-micromolar concentrations, the NMR spectrum was not readily interpretable, and it became evident that the symmetry was lower than threefold. Since COSY could not be performed at such high dilutions, homodecoupling experiments were carried out to help assign the signals, and a total of 11 aromatic signals were thereby located. Their number, multiplicities, and integration values were consistent with twofold symmetry, allowing for some accidental overlap, compared with the five signals expected with the threefold symmetry. Twofold symmetry may result from an out-of-plane twist of any one of the six pyridine rings or of any transannularly opposed pair of rings, as depicted in Fig. 1. Such out-of-plane twisting was indeed present in the crystal structures of the torand alkali metal complexes (26) and was predicted by computation to occur with the Na<sup>+</sup> and Li<sup>+</sup> complexes of the parent cyclohexypyridine (28), but those structures were of D<sub>3</sub>-symmetry, with the pyridine rings twisting “up” then “down” in alternation, a reduction from the sixfold symmetry of the flat ligands. The D<sub>3</sub> conformation probably minimizes lone pair – lone pair repulsions and contacts between pyridine H-3/5. The same conformation with the less symmetrical complexes of **5d** would place all three neopentoxy groups on the same face of the macroring, which may be destabilizing.

Twofold symmetry would give rise to a maximum 14 aromatic signals, 12 with free rotation of the side-chains. Our analysis of the 11 signals observed implies that one of the H-2/6 2H doublets has suffered an *upfield* shift of about 0.8 ppm, consistent with an out-of-plane twist of one phenylene ring such that its H-2 and H-6 are thereby less deshielded by the neighbouring pyridines. This analysis also implies that the two equivalent side-chains (rings E), if not all three, are not freely rotating owing to conjugation and (or) aggregation.

Metal-free torand **3** was isolated after macrocyclization catalyzed by triflic acid (3). We attempted to prepare **5d** in the same manner from **9d** and **7d** using excess NH<sub>4</sub>OAc in glacial acetic acid spiked with 4% triflic acid. However, heating this to reflux for 3 d failed to cause any precipitation, and NMR indicated the presence of only the starting materials. Triflic acid apparently inhibited the macrocyclization, likely because of its stronger acidity and the favourable protonation of the pyridine rings in the starting materials.

Interestingly, sonicating a CDCl<sub>3</sub> solution of **5d** with a solution of potassium picrate in D<sub>2</sub>O for 24 h failed to cause any detectable anion or cation exchange according to NMR and MALDI-MS. Encapsulating hosts also showed slow ion exchanges (5).

Azo-*bis*(terpyridine) **15** was also subjected to our macrocyclization conditions with 2.2 equiv of **7d** for 48 h and a precipitate formed as before. Though four neopentoxy groups were intended to be present, this material proved to

be insoluble in all solvents tested, as was true with **5a–c**. MALDI-MS revealed numerous high-mass species, but none at or near *m/z* 1798, the molecular weight expected for the desired *bis*(cyclohexypyridine). No further cyclization attempts were made.

## Conclusion

We have extended our one-pot synthesis of dipyrazinylpyridines and phenylene-linked *bis*terpyridines to four examples of terpyridines and one example of an azo-linked *bis*terpyridine. The simple terpyridines were converted to novel C<sub>3</sub>-symmetrical triarylated cyclohexypyridines without resorting to the Kröhnke method, but this was only soluble with neopentoxy substitution. Aggregation and demetalation remain issues to be resolved.

## Acknowledgement

The authors thank the Natural Sciences and Engineering Research Council of Canada (NSERC) for funding.

## References

1. G.R. Newkome and H.W. Lee. *J. Am. Chem. Soc.* **105**, 5956 (1983).
2. T.R. Kelly, Y.J. Lee, and R.J. Mears. *J. Org. Chem.* **62**, 2774 (1997).
3. T.W. Bell and A. Firestone. *J. Am. Chem. Soc.* **108**, 8109 (1986).
4. J.L. Toner. *Tetrahedron Lett.* **24**, 2707 (1983).
5. T.W. Bell, A. Firestone, and R. Ludwig. *J. Chem. Soc. Chem. Commun.* 1902 (1989).
6. R. Liegghio, P.G. Potvin, and A.B.P. Lever. *Inorg. Chem.* **40**, 5485 (2001).
7. S. Vaduvescu. M.Sc. thesis, York University, Toronto, Ont. 2002.
8. S. Vaduvescu and P.G. Potvin. *Inorg. Chem.* **41**, 4081 (2002).
9. F.M. Beringer and H.S. Schultz. *J. Am. Chem. Soc.* **77**, 5533 (1955).
10. R.A. Widenhoefer and S.L. Buchwald. *J. Am. Chem. Soc.* **120**, 6504 (1998).
11. L.C. King. *J. Am. Chem. Soc.* **66**, 894 (1944).
12. H.E. Baumgarten, D.L. Pederson, and M.W. Hunt. *J. Am. Chem. Soc.* **80**, 1977 (1958).
13. W.C. Danen, C.T. West, T.T. Kensler, and T.J. Tipton. *J. Am. Chem. Soc.* **94**, 4830 (1972).
14. F.J. Always and W.D. Bonner. *J. Am. Chem. Soc.* **27**, 1107 (1905).
15. P. Freundler. *Comptes Rendus*, **134**, 1360 (1905).
16. J.M. Khurana and A. Ray. *Bull. Chem. Soc. Jpn.* **69**, 407 (1996).
17. F. Kröhnke. *Synthesis*, 1 (1976).
18. A.E. Chichibabin. *J. Russ. Phys. Chem. Soc.* **37**, 1229 (1906).
19. T.H. Chan, M.A. Brook, and T. Chaly. *Synthesis*, 203 (1983).
20. R.F. Nystrom and W.G. Brown. *J. Am. Chem. Soc.* **70**, 3738 (1948).
21. H. Suzuki. *Electronic absorption spectra and geometry of organic molecules*. Academic Press, New York. 1967. Chap 23.
22. P.P. Birnbaum, J.H. Linford, and W.G. Doyle. *Trans. Faraday Soc.* **49**, 735 (1953).
23. M. Hanack and M. Lang. *Adv. Mater.* **6**, 822 (1994).



24. E. Sielcken, M. Van Tilborg, M.F.M. Roks, W. Drenth, and J.M. Nolte. *J. Am. Chem. Soc.* **109**, 4261 (1987).
25. P.G. Potvin and J.M. Lehn. *In* Synthesis of macrocycles: The design of selective complexing agents. *Edited by* R.M. Izatt and J.J. Christensen. John Wiley & Sons, New York. 1987. p. 167.
26. T.W. Bell, P.J. Cragg, M.G. Drew, and A.M. Firestone. *Angew. Chem. Int. Ed.* **31**, 345 (1992).
27. C.C. Leznoff, S.M. Marcuccio, S. Greenberg, A.B.P. Lever, and K.B. Tomer. *Can. J. Chem.* **63**, 623 (1985).
28. S.T. Howard and I.A. Fallis. *J. Chem. Soc., Perkin Trans. 2*, 2501 (1999).



# Photobehavior of aqueous uranyl ion and photo-oxygenation of isobutane using light from the visible region

Trevor M. Bergfeldt, William L. Waltz, Xiangrong Xu, Petr Sedláč, Uwe Dreyer, Hermann Möckel, Jochen Lilie, and John W. Stephenson

**Abstract:** The photochemical and photophysical behavior of the aqueous uranyl ion  $[\text{UO}_2(\text{H}_2\text{O})_5]^{2+}$  has been studied under the influence of visible light and with added perchloric acid over the range of 0.01–4 M. In the presence of 2-methylpropane (isobutane), photo-oxygenation of isobutane occurs to yield, as the major product, 2-methyl-2-propanol (*tert*-butyl alcohol) along with lesser amounts of 2-methyl-2-propene (isobutene) and other C1–C8 products. The quantum yield for formation of *tert*-butyl alcohol is independent of light intensity at the irradiation wavelength of 415 nm and of uranyl concentration, but it increases from  $0.016 \pm 0.001$  at 0.01 M  $\text{HClO}_4$  (pH 2) to  $0.13 \pm 0.01$  at 4 M  $\text{HClO}_4$ . The emission spectrum from the electronically excited uranyl ion and the associated quantum yields have been measured in the presence and absence of isobutane, as a function of added perchloric acid. While in both cases the shape of the spectrum remains invariant, the quantum yields increase with increasing perchloric acid concentration. The strong dependence on added perchloric acid is interpreted within the context of the presence and interconversion of two electronically excited species, an acid form,  $*[\text{UO}_2(\text{H}_2\text{O})_5]^{2+}$ , and a base form,  $*[\text{UO}_2(\text{H}_2\text{O})_n(\text{OH})]^+$ . It is proposed that both forms react with isobutane to give a *tert*-butyl radical, and that oxidation of coordinated aqua ligands occur, the latter generating a hydroxyl radical whose reaction with isobutane rapidly leads also to a *tert*-butyl radical. The reaction of this alkyl radical with ground-state  $[\text{UO}_2(\text{H}_2\text{O})_5]^{2+}$  then gives rise to the stable *tert*-butyl alcohol product and reduced forms of uranyl ion. Based upon the values of the quantum yields and of excited-state lifetime measurements reported in the literature, a comprehensive mechanism has been developed in a quantitative manner to provide calculated values of the rate constants for the individual mechanistic steps. The calculated rate constants provide a basis to calculate the values of quantum yields for emission and chemical reaction, as well as for lifetimes, that agree very satisfactorily with the experimental values over a 400-fold concentration change in added perchloric acid.

**Key words:** photo-oxidation, photo-oxygenation, uranyl ion, isobutane, *tert*-butyl alcohol, lifetime, quantum yield, acid–base dissociation.

**Résumé :** On a étudié les comportements photochimique et photophysique de l'ion uranyle aqueux  $[\text{UO}_2(\text{H}_2\text{O})_5]^{2+}$  sous l'influence de la lumière visible, en présence d'acide perchlorique ajouté à des concentrations allant de 0,01 M à 4 M. En présence de 2-méthylpropane (isobutane), il se produit une photooxygénation de l'isobutane qui conduit à la formation de 2-méthylpropan-2-ol (*tert*-butanol) comme produit principal aux côtés de quantités plus faibles de 2-méthylprop-2-ène (isobutène) ainsi que d'autres produits comportant de un à huit atomes de carbone. À une longueur d'onde d'irradiation de 415 nm, le rendement quantique pour la formation du *tert*-butanol est indépendant de l'intensité de la lumière et de la concentration en uranyle, mais il augmente de  $0,016 \pm 0,001$  à une concentration de  $\text{HClO}_4$  de 0,01 M (pH = 2) jusqu'à  $0,13 \pm 0,01$  à une concentration de  $\text{HClO}_4$  de 4 M. On a mesuré le spectre d'émission de l'ion uranyle électroniquement excité et les rendements quantiques associés, en présence et en l'absence d'isobutane et en fonction de la quantité d'acide perchlorique ajouté. Même si dans les deux cas la forme des spectres ne varie pas, les rendements quantiques augmentent avec une augmentation de la concentration d'acide perchlorique. Cette forte dépendance sur l'acide perchlorique ajouté est interprétée dans le contexte de la présence et de l'interconversion de deux espèces électroniquement excitées, une forme acide  $*[\text{UO}_2(\text{H}_2\text{O})_5]^{2+}$  et une forme basique  $*[\text{UO}_2(\text{H}_2\text{O})_n(\text{OH})]^+$ . Il est

Received 10 October 2002. Published on the NRC Research Press Web site at <http://canjchem.nrc.ca> on 19 March 2003.

Contribution from the Department of Chemistry and Department of Mathematics and Statistics, University of Saskatchewan, 110 Science Place, Saskatoon, SK S7N 5C9, Canada and the Hahn-Meitner-Institut Berlin GmbH, Glienicke Str. 100, D-14109 Berlin, Germany.

**Trevor M. Bergfeldt, William L. Waltz,<sup>1</sup> Xiangrong Xu, Petr Sedláč.** Department of Chemistry, University of Saskatchewan, 110 Science Place, Saskatoon, SK S7N 5C9, Canada.

**Uwe Dreyer, Hermann Möckel, Jochen Lilie.** Hahn-Meitner-Institut Berlin GmbH, Glienicke Str. 100, D-14109 Berlin, Germany.

**John W. Stephenson.** Department of Mathematics and Statistics, University of Saskatchewan, 106 Wiggins, Saskatoon, SK S7N 5E6, Canada.

<sup>1</sup>Corresponding author (e-mail: [bill.waltz@usask.ca](mailto:bill.waltz@usask.ca)).



suggéré que les deux formes réagissent avec l'isobutane pour produire le radical *tert*-butyle et qu'il se produit une oxydation des ligands aqua coordonnés qui génèrent la formation du radical hydroxyle qui, par réaction avec l'isobutane, conduit aussi rapidement à la formation du radical *tert*-butyle. La réaction de ce radical avec du  $[\text{UO}_2(\text{H}_2\text{O})_5]^{2+}$  à l'état fondamental conduit alors à la formation du *tert*-butanol, le produit stable, ainsi qu'aux formes réduites de l'ion uranyle. Sur la base des valeurs des rendements quantiques et des mesures de temps de vie rapportées dans la littérature, on a développé un mécanisme global de manière quantitative qui permet d'obtenir des valeurs calculées pour les constantes de vitesse de chacune des étapes mécanistiques individuelles. Les constantes de vitesse calculées ont permis de calculer des valeurs des rendements quantiques de l'émission et de la réaction chimique ainsi que des temps de vie qui sont en bon accord avec les valeurs expérimentales pour des changements de concentration en acide perchlorique ajouté qui varient par un facteur allant jusqu'à quatre cents.

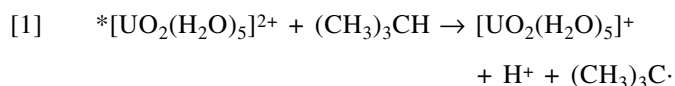
**Mots clés :** photooxydation, photooxygénation, ion uranyle, isobutane, *tert*-butanol, temps de vie, rendement quantique, dissociation acide-base.

[Traduit par la Rédaction]

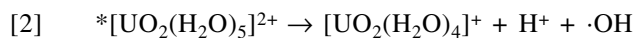
## Introduction

This investigation was undertaken with two complementary objectives in mind: namely, to investigate in a quantitative manner the photochemical and photophysical features of the electronically excited uranyl ion,  $^*[\text{UO}_2(\text{H}_2\text{O})_5]^{2+}$ , and at the same time to study the use of this species as a quantitative means to convert 2-methylpropane (isobutane) into 2-methyl-2-propanol (*tert*-butyl alcohol). Baird and Kemp have recently provided an in-depth review of the many facets of the intriguing yet complicated photobehavior of the uranyl ion and other related forms found in aqueous media (1). Uranyl ion absorbs in the 350–500 nm region to yield a long-lived excited state ( $\mu\text{s}$  timescale); however, its behavior is sensitive to pH, temperature, and the nature and concentration of the counter anion. Under our conditions, where we have used the perchlorate salt and added amounts of perchloric acid (0.01–4 M) to vary the pH, the ground state species is the monomeric form  $[\text{UO}_2(\text{H}_2\text{O})_5]^{2+}$ . At the higher concentrations of added  $\text{HClO}_4$ , ion pairing between  $^*[\text{UO}_2(\text{H}_2\text{O})_5]^{2+}$  and  $\text{ClO}_4^-$  is likely to occur to some extent in the excited-state species (2); however, our results can be satisfactorily interpreted without invoking this facet.

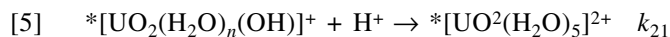
Electronically excited uranyl ion is a powerful oxidant ( $E^\circ \sim 2.6$  V) and is well known to engage in electron-transfer processes and to participate in hydrogen-abstraction reactions with many organic compounds (1, 3–16). Thus one anticipates that in the presence of isobutane, the excited state will abstract a hydrogen atom to generate an alkyl radical and the uranoyl ion,  $[\text{UO}_2]^+$ , leading to subsequent free radical reactions to form the organic products. Mao and Bakac have found with related alkanes and alcohols that the logarithm of the quenching constant for excited uranyl ion increases with decreasing C—H bond energy, which is supportive of hydrogen-abstraction mechanisms (17). The extension of this observation to isobutane implies that hydrogen abstraction will occur preferentially at the tertiary hydrogen rather than at the primary positions, and our findings that the tertiary alcohol is the major product in deaerated media — whereas acetone occurs in the presence of dioxygen — is commensurate with the major occurrence of the *tert*-butyl radical (18).



However, two additional features need to be considered in evaluating our results. There is now substantial evidence that because of the powerful oxidizing nature of  $^*[\text{UO}_2(\text{H}_2\text{O})_5]^{2+}$ , water can be oxidized to form a hydroxyl radical that will readily react with isobutane to form further amounts of *tert*-butyl radical (1, 10, 19–21).



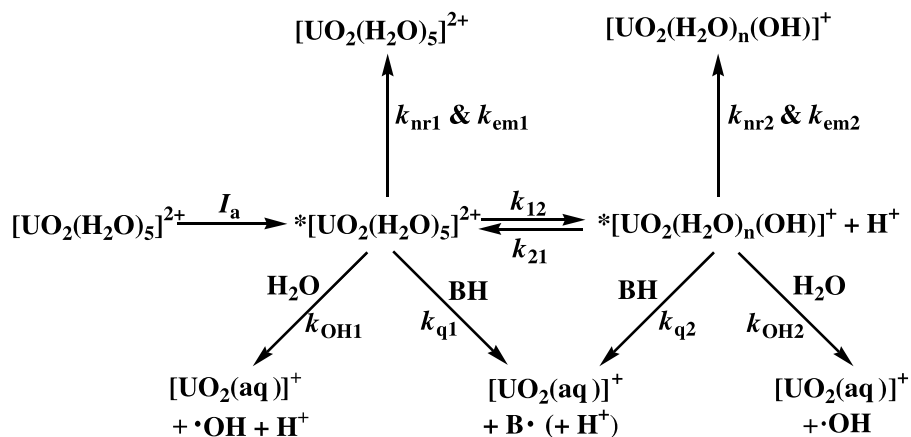
Above, we have portrayed that the oxidation of water is of coordinated water because Xu (21) finds that when the coordinated waters are replaced by a fluoride ion, the oxidation of isobutane is not detectable. The observations by many researchers that the excited-state reactivity and emission lifetime are strongly dependent on the acidity of the media has given rise to different mechanistic interpretations. Marcantonios proposed, at relatively high concentrations of uranyl ion, the additional formation of an exciplex complex,  $^*[\text{U}_2\text{O}_4\text{H}]^{2+}$ , to account for bi-exponential lifetimes, multiple emission spectra, and dependence of such on concentrations of acid and uranyl ion (1, 12). Under our conditions we do not observe bi-exponential behavior or multiple emission, and thus we conclude that exciplex formation is not a significant factor in our study. Burrows and co-workers initially offered a mechanism focusing on the interconversion between two closely spaced excited states of the uranyl ion (1, 22). More recently they have adopted the proposal made by Darmanyan, Khudyakov, and co-workers of an electronically excited acid–base mechanism in competition with other reactivity modes (22, 23); the number of waters of hydration for the base form,  $^*[\text{UO}_2(\text{H}_2\text{O})_n(\text{OH})]^+$ , are unknown.



Our findings are consistent with these acid–base steps, as shown in more detail in the Discussion section (see Fig. 1). In this report, we present a comprehensive mechanism incorporating acid–base behavior, radiative and nonradiative processes, and quenching by water and isobutane; specific values are provided for the rate constants associated with the individual steps of the mechanism. A comprehensive and self-consistent set of values has not been available, to our knowledge, until now. The estimates of the rate constant val-



**Fig. 1.** Schematic diagram of the proposed acid–base model. Note: Processes involving the acid and base forms are distinguished by subscripts 1 and 2, respectively;  $I_a$  is the intensity of absorbed light; and BH and B. are the isobutane and *tert*-butyl radical, respectively.



ues have been achieved by using an integrated package of information obtained from both time-resolved and steady-state experiments. Specifically we have measured the integrated emission intensities that lead to emission quantum yields and chemical quantum yields for *tert*-butyl alcohol as a function of acidity. We have used and analyzed in detail the lifetime measurements reported by Moriyasu et al. after we first confirmed that their findings are appropriate to our conditions (13).

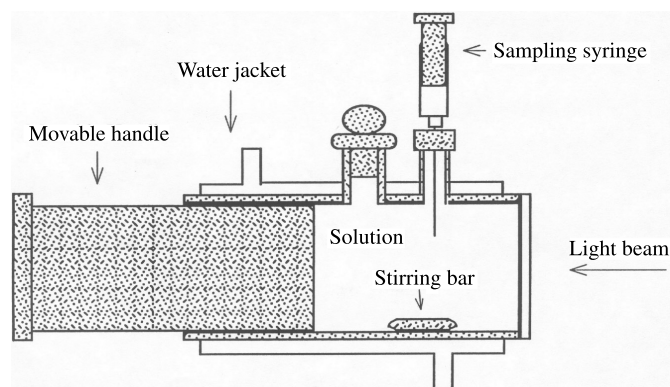
The choice of isobutane used here in the quenching and photo-oxygenation processes warrants comment because it has associated with it several useful and advantageous features. Nizova and Shul'pin appear to have been the first to report on the photo-oxygenation of alkanes (cyclohexane and methane) with uranyl ion, although such was performed in acetic acid and acetonitrile solvents (24). Subsequently Mao and Bakac extended such studies to aqueous 0.1 M  $\text{H}_3\text{PO}_4$  for alkyl aromatic compounds (17). Of concern in such studies is that the products of the reactions are known or expected to be highly reactive in their own right. To minimize such secondary reactions is difficult; however, our observed major product *tert*-butyl alcohol is considerably less reactive as a quenching agent and in its reaction with hydroxyl radical than is isobutane. Even to a much higher conversion (ca. 65%) than normally done here (ca. 10%), we find no evidence for complications arising from the reactivity of the alcohol product. As a further precaution, we have in general carried out the experiments with continuous bubbling of the isobutane gas through the liquid phase before and during photolysis.

## Experimental

### Apparatus

For steady-state measurements of quantum yields and product analysis, a 1000 W Hg–Xe arc lamp (Oriol 6293) was used with the collimated light beam being passed through an 11-cm water cell and a 9.6-cm cell of 0.1 M  $\text{CuSO}_4(\text{aq})$  (310 nm < band pass < 640 nm) to filter out IR and UV light. In addition, either a cut-off filter (Schott Glass Technologies Inc., GG400) or, for quantum-yield determinations, an interference filter (Edmund Scientific Co.,

**Fig. 2.** Variable pathlength cell.



CWL415,  $\lambda_{\text{max}} = 415$  nm, fwhm = 12 nm) was placed in the light beam prior to the reaction cell. Two types of reaction cells (water-cooled,  $25.0 \pm 0.15^\circ\text{C}$ ) were used: one of fixed path length (8.7 cm) and the second of variable path length (ca. 5 cm to 10 cm). The latter was constructed from a 100 mL syringe (J. Young Scientific, GTS/100/GS) with the end of the barrel having — affixed to it by optical adhesive (Norland 61) — a borosilicate window. A schematic diagram of this cell is shown in Fig. 2. A major advantage of this arrangement is that periodic sampling of the liquid solution can be done during the course of irradiation without the development of a separate gas phase. For ease of carrying out the actinometry, both the actinometric solution and the uranyl solutions have been irradiated under optically dense conditions (absorbance = 2–2.5). Because of this procedure and because of the longer light path, a more dilute concentration of the ferrioxalate actinometry solution (3.9 mM) was used than is generally employed (25); however, all such measurements have been carried out using linear calibration plots. Spectroscopic data were obtained using a Cary 2315 or HP 8451A PhotoDiode Array spectrophotometer for UV–vis spectra; Spex Fluorolog-2 for emission spectra; Bio-Rad FTS-40 FT-IR and FT-NMR, Bruker AM-300 MHz ( $^1\text{H}$ ). Mass spectrometry was done with a Fisons GC 8000 (in splitless mode) interfaced with a VG70-VSE mass spectrometer with a Dec Vax 4000 model 60 workstation; authentic



samples and the NIST library were used to identify products. Gamma radiolysis experiments of saturated isobutane without the presence of uranyl ion were performed with a Gammacell  $^{60}\text{Co}$  source (Serial #260, Atomic Energy of Canada Limited (AECL)) using either Millipore or triply distilled water, and acidified with  $\text{HClO}_4$  (Ultrapure, BDH). These radiolysis results allow us to compare the nature of the organic products arising from the reaction of the hydroxyl radical with isobutane to those products formed in the photolysis of the uranyl-isobutane solutions.

### Chromatography

A Hewlett-Packard 5890 GC was employed in conjunction with a PC286 computer with Baseline 810 software. The injection port and FI-detector temperatures were  $200^\circ\text{C}$ . For aqueous solutions, injections were either 1 mL samples taken directly from the photolysis cell, 1 mL tetrahydrofuran (THF) extractions, or an injection of solid phase micro-extraction fibres. THF extractions were prepared as follows: a sample was withdrawn from the photolysis cell with a 5-mL syringe and passed through a Sep-Pak cartridge (Millipore, Sep-Pak Plus, t-C18) using a syringe pump (rate  $1\text{ mL min}^{-1}$ , Sage Instruments 341B). The retained organic material was then eluted at the same rate with 1.2 mL of THF solution containing isopropanol as the GC internal standard followed by 1.5 mL of THF. Extraction using solid phase micro-extraction (SPME) involved the following procedure: a sample was withdrawn from the photolysis cell with a 5 mL syringe and transferred to a 2 dram vial containing 2 g NaCl and a magnetic stirring bar; 0.5 mL 1,4-dioxane was added as the GC internal standard. The SPME fibre (100 mm polydimethyl-siloxane, Supelco) was introduced into the headspace of the sealed vial and the solution magnetically stirred for a period of 10 min in a thermostated water jacket set at  $50^\circ\text{C}$ . The fibre was then introduced into the injection port of the GC and left to desorb for 5 min. There was found to be no difference between results obtained by Sep-Pak and SPME methods ( $\pm 10\%$ ). The use of these two different procedures gives considerable confidence as to the validity of the results in the context of our desire to keep the percent product formation as low as possible (normally  $<10\%$ ). The use of the SPME technique also permitted us to carry out reactions at much higher concentrations of  $\text{HClO}_4$  ( $>0.1\text{ M}$ ) than was possible with the Sep-Pak cartridge approach. To circumvent the degradation of the SPME fibres in the headspace at extreme acid conditions, appropriate amounts of aqueous NaOH were added to bring the pH of the solutions up to approximately one. For gaseous samples, 5–100 mL gas-tight syringes were used to draw samples from the reaction vessel. For hydrocarbon substances of a carbon number less than 5, a GSQ column (J&W Scientific,  $30\text{ m} \times 0.546\text{ mm}$ ) was used, while a DB-210 column (J&W Scientific,  $30\text{ m} \times 0.53\text{ mm}$ ) was employed for all other analyses. Calibration of the GC for isobutane was done by injection of weighted amounts of isobutane dissolved in isopropanol. For our typical irradiated solution (ca. 35 mM aqueous uranyl solution at  $\text{pH} = 1$  ( $\text{HClO}_4$ )), the solubility of isobutane was found to be  $0.91 \pm 0.02\text{ mM}$  at  $22^\circ\text{C}$  and 95.33 kPa partial pressure of isobutane; this compares very favorably with that of 0.94 mM isobutane in pure water at  $25^\circ\text{C}$  and 101.325 kPa (26).

### Materials and solutions

Aqueous solutions were prepared from water purified by a Millipore Super-Q system, and where compared with those of triply distilled water, the results were found to be the same. The chemicals employed were: isobutane (Linde, instruments grade; Aldrich, 99.9%); isobutene (Matheson, 99.0% min); 2,2,3,3-tetramethylbutane (Aldrich, 99%); *tert*-butyl and *iso*-butyl alcohols (BDH, reagent); and tetrahydrofuran (BDH, AnalaR grade). Identifications by GC retention times of  $\text{C}_1$ – $\text{C}_4$  alkanes and alkenes were made using a Matheson standard gas mixture. Uranium solutions were prepared from  $\text{UO}_2(\text{ClO}_4)_2 \cdot 6\text{H}_2\text{O}$  (ROC/RIC, reagent; reclaimed uranium) or more generally from  $\text{UO}_3$  (Cameco, 99.4%, natural abundance). As these two sources gave the same results, the background radioactivity of the uranium was not a detectable factor. Uranyl stock solutions were typically prepared by dissolving 178 g  $\text{UO}_3$  in 102 mL of 70% perchloric acid (BDH, analytical grade) and 150 mL water, heating at  $80^\circ\text{C}$  until dissolution followed by filtering, and allowing the solution to stand for 1 day before use. The concentration of uranyl ion was determined spectrophotometrically using a calibration curve based on dissolved  $\text{UO}_3$  in perchloric acid, and this was verified by using  $\text{U}_3\text{O}_8$  as an alternate source. The latter was prepared from heating, at  $800^\circ\text{C}$  for 4 h, uranyl acetate (Fisher, ACS grade), and the uranium content was measured by laser phosphorescence and delayed neutron counting (Saskatchewan Research Council). The molar absorption coefficients, at 414 nm, of  $[\text{UO}_2(\text{aq})]^{2+}$  in aqueous perchloric acid media were  $7.8 \pm 0.2\text{ M}^{-1}\text{ cm}^{-1}$  (pH 1.1),  $8.0 \pm 0.2\text{ M}^{-1}\text{ cm}^{-1}$  (pH 2.0), and  $8.3 \pm 0.2\text{ M}^{-1}\text{ cm}^{-1}$  (pH 3.0); Bell et al. (27) reported  $7.7\text{ M}^{-1}\text{ cm}^{-1}$  at pH 0.95 ( $\text{HClO}_4$ ).

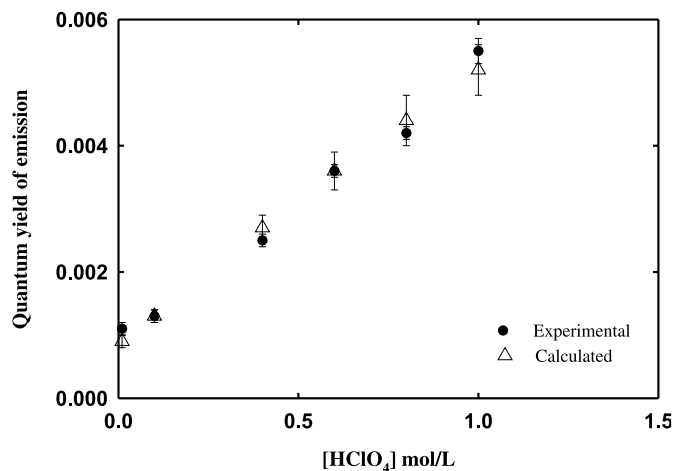
Uranium(V) was measured spectrophotometrically, in the presence of  $[\text{UO}_2(\text{aq})]^{2+}$ , where a complex  $[\text{U}_2\text{O}_4]^{3+}$  occurs with an absorption peak at 740 nm ( $\epsilon = 24.3\text{ M}^{-1}\text{ cm}^{-1}$ ) (28, 29). Uranium(IV) in aqueous perchloric acid media (pH  $\sim 1$ ) was prepared by photoreduction of uranyl ion in the presence of ethanol, and its concentration was determined by using potassium dichromate oxidation – titration (30). From this procedure, the molar absorption coefficient at 652 nm was determined to be  $43.2 \pm 0.9\text{ M}^{-1}\text{ cm}^{-1}$  (pH 1.0,  $22^\circ\text{C}$ ), which agrees with that reported by Betts (31).

### Results

Our most frequently used condition was a pH of 1 and 35 mM  $[\text{UO}_2(\text{aq})]^{2+}$  with the solutions being deaerated and saturated with isobutane by continuously bubbling with isobutane gas during and prior to irradiation (30 min or more at room pressure before irradiation to achieve saturation). For specific cases, the concentration of uranyl ion was varied from 25–148 mM, the light was changed from  $2.1 \times 10^{-7} - 1.2 \times 10^{-6}\text{ ein L}^{-1}\text{ s}^{-1}$  ( $1\text{ ein} = 1\text{ mol of light photons}$ ), and the concentration of  $\text{HClO}_4$  ranged from 0.01–4 M. At pHs of about 2 and higher, polyuranium species occur, leading in part to bi-exponential decay of the electronically excited uranyl ion. To confirm the mono-exponential decay behavior reported by Moriyasu and co-workers (13, 14) for conditions very similar to our perchloric acid media, lifetime measurements were performed using laser excitation at 347 nm with a pH of 1 for both argon-saturated and aerated solutions. We



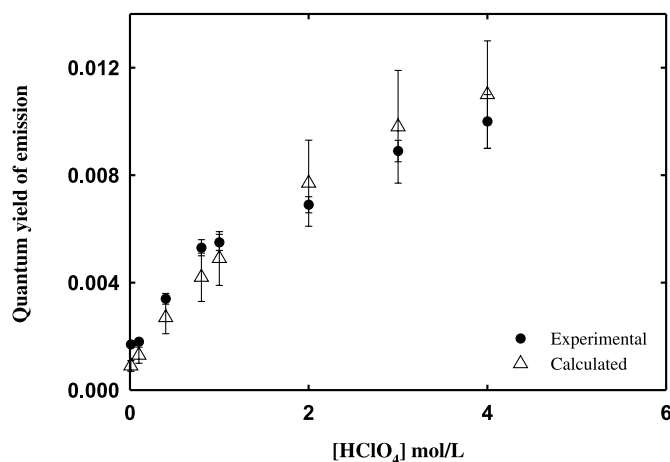
**Fig. 3.** Plot of the experimental (●) and calculated (△) values of the emission quantum yield of the electronically excited uranyl ion  $[\text{UO}_2(\text{aq})]^{2+}$  in the absence of isobutane, as a function of the concentration of  $\text{HClO}_4$  at 34.8 mM  $[\text{UO}_2(\text{aq})]^{2+}$ . Average root-mean-square difference between experimental and calculated values is  $\pm 8\%$ .



find the emission decay (510 nm), as well as the excited-state absorption decay (590 nm), to exhibit a single exponential decay with a lifetime of  $2.2 \pm 0.1 \mu\text{s}$ . This single-decay behavior and the value of the associated lifetime are in agreement with the findings of Moriyasu and co-workers, as well as those of other reports (1, 7, 13–16). Results presented earlier by us indicate that quenching by isobutane is about  $3 \times 10^7 \text{ M}^{-1} \text{ s}^{-1}$  (20). In our modeling studies, as put forward in the Discussion section, this value has proven useful as a guide; however, the value is, from our current findings, indicative of the quenching by isobutane of two excited-state species coupled through acid–base processes (see below).

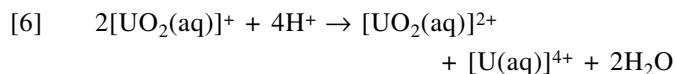
As one would anticipate from the presence of acid–base processes, the emission quantum yields are strongly dependent on the acidity of the medium, as shown in Figs. 3 and 4 (solid circles). These quantum yields and emission spectra were determined as follows. The emission spectrum, centered at the 506 nm peak, is broad and overlaid with a vibrational structure (1, 32); maxima or estimated maxima for shoulders occurred at 470, 484, 506, 530, and 546 nm. The positions of the maxima and their relative intensities did not change whether the solutions were aerated or saturated with either oxygen or argon, and thus, in general the data was obtained for aerated media. The emission spectrum was recorded two to four times at each concentration of perchloric acid (0.01–4 M), and then for each recording the emission intensities from 430–600 nm were integrated with reference to a Rhodamine B quantum counter (Spex Fluorolog-2 Spectrofluorometer) and averaged for each set of perchloric acid concentrations. The reproducibility of the integrated emission values was good, being within several percent. To minimize the possibility of systematic error, the measurements for different acid concentrations were done in a random manner. The emission spectra were recorded for 35 and 10 mM uranyl ion; the latter concentration was used by Moriyasu et al. in their lifetime studies (0.01–10 M  $\text{HClO}_4$ ) (13). While the integrated emission intensities were, for

**Fig. 4.** Plot of the experimental (●) and calculated (△) values of the emission quantum yield of the electronically excited uranyl ion in the presence of isobutane, as a function of the concentration of  $\text{HClO}_4$  at 34.8 mM  $[\text{UO}_2(\text{aq})]^{2+}$ . Average percent difference between experimental and calculated values is  $\pm 21\%$ .



10 mM, lower than for 35 mM uranyl ion, the calculated quantum yields for emission were the same within experimental error. Of particular note is that while the emission intensities increased with perchloric acid concentration, the spectral features for the peak maxima and minima and their relative intensities were invariant. Thus we conclude that under our conditions, the emission is predominantly from one species, and because the emission intensities are greatest at high concentrations of  $\text{HClO}_4$ , the emission can be ascribed to  $^*[\text{UO}_2(\text{H}_2\text{O})_5]^{2+}$ , the acid form. Baird and Kemp in their review (1) have proposed that the absolute emission quantum yield value of 0.0055 for 1.0 M  $\text{HClO}_4$ , found by Katsumura et al. (33), was the most reliable measurement, and we have used this value to convert our integrated emission intensities into the quantum yields shown in Figs. 3 and 4.

Aqueous uranyl solutions saturated with isobutane and kept in the dark are found to be thermally unreactive. Upon exposure to steady-state irradiation at 415 nm radiation, the major products are *tert*-butyl alcohol (*t*-BuOH) and the inorganic products  $[\text{UO}_2(\text{aq})]^+$  and  $[\text{U}(\text{aq})]^{4+}$ , accompanied by minor amounts of isobutene and other organic products. The U(IV) observed is likely due to the disproportionation of uranoyl  $[\text{UO}_2(\text{aq})]^+$  (28, 34):

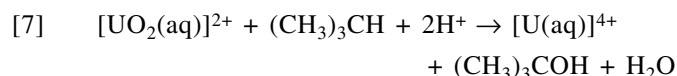


At pH 3, where the disproportionation of uranoyl to U(IV) is slow, the visible spectrum clearly shows the characteristic peaks of  $[\text{U}(\text{aq})]^{4+}$  at 652 nm and of the U(V)–U(VI) complex  $[\text{U}_2\text{O}_4]^{3+}$  at 400 and 740 nm, whereas only  $[\text{U}(\text{aq})]^{4+}$  is seen at pH 1 (28, 34). The results of our mass-balance experiments at pH 1 show the ratios of  $d[\text{U(VI)}]/d[\text{U(IV)}]$  and  $d[\text{isobutane}]/d[\text{U(IV)}]$  to be  $(1.0 \pm 0.1)/1$  and  $(0.9 \pm 0.1)/1$ , respectively.

The organic products are indicative of C–H bond activation. The *tertiary* alcohol accounts for  $85 \pm 5\%$  of the loss of isobutane, along with isobutene (ca. 5%) and, to a lesser amount, other C1–C8 products. Although isobutene can un-



dergo hydrolysis to yield *t*-BuOH, we find that the thermal rate is approximately two to three times slower than the photoproduction of *t*-BuOH. This is in accord with the results of a previous study (35), and therefore, it seems unlikely that the observed *t*-BuOH is the result of the hydrolysis of isobutene. The possible bimolecular self-recombination products arising from *tert*-butyl and (or) *iso*-butyl radicals (i.e., 2,2,3,3-tetramethylbutane, 2,2,4-trimethylpentane, and 2,5-dimethylhexane) are found only in trace amounts. Gamma radiolysis of aqueous solutions at pH 2, saturated with isobutane but without uranyl ion, results in the major products (>80%) being the aforementioned bimolecular self-recombination products, while *t*-BuOH is a minor product (~20%). Additionally, when an aqueous acidic uranyl ion solution containing both oxygen and isobutane is irradiated, the major products are acetone and *tert*-butyl alcohol (18). These results all point to the *tert*-butyl radical as the common reactive intermediate resulting from hydrogen abstraction. The overall major chemical reaction at pH 1 can therefore best be described as

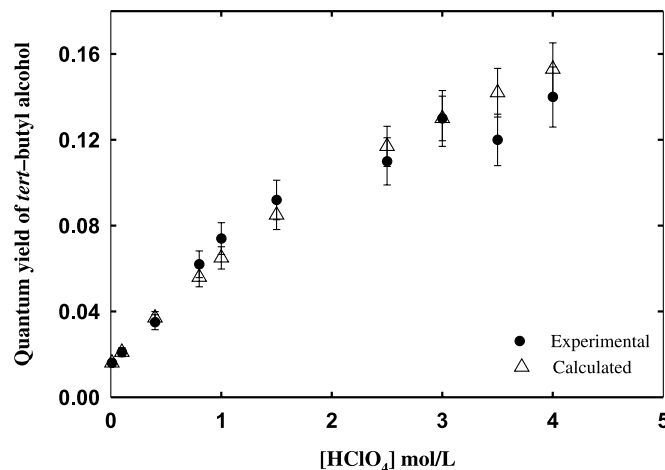


The chemical quantum yield measurements were constrained to *t*-BuOH, owing to the low concentrations of the other products. The quantum yield ( $\Phi$ ) for formation of *t*-BuOH was determined from the slope of plots of the quotient (alcohol concentration)  $\times$  (irradiation volume)/(absorbed light intensity) vs. time. Where the conversion of isobutane was high (upwards of 65%, as in the mass-balance experiments), curvature in the plots occurred. Linear plots were obtained, however, when isobutane was bubbled through the reaction solution during the entire irradiation period. At pH 1, the average observed quantum yield of *t*-BuOH was  $0.022 \pm 0.002$ , as determined from the slopes. In the mass-balance experiments, the curvature was well described by a second order polynomial. The average coefficient for the linear term gave the same average  $\Phi$  value as that previously cited for the continuous bubbling experiments. This comparison indicates that continuous bubbling of isobutane did not give rise to detectable loss of *t*-BuOH from the liquid phase. The chemical quantum yield is independent of light intensity ( $2.1 \times 10^{-7} - 1.2 \times 10^{-6} \text{ ein L}^{-1} \text{ s}^{-1}$ ) and of uranyl concentration (25–148 mM) but is dependent on the concentration of added HClO<sub>4</sub>, as shown in Fig. 5 (solid circles).

## Discussion

Results from numerous studies have established that the electronically excited uranyl ion in aqueous media can abstract a hydrogen atom from the C—H bonds of hydrocarbon materials, and, in some instances, products also arise from C—C bond cleavage (1, 4, 6, 17). Our results are in agreement with these features, as we observe *tert*-butyl alcohol as the major product arising from activation of the weaker tertiary C—H bond ( $85 \pm 5\%$ ). Activation of the primary C—H bonds and C—C bonds also occurs, as evidenced by formation of isobutene (ca. 5%) along with much lesser amounts of methane, propane, and radical recombina-

**Fig. 5.** Plot of the experimental (●) and calculated (△) quantum yields of *t*-BuOH as a function of the concentration of HClO<sub>4</sub> at 34.8 mM [UO<sub>2</sub>(aq)]<sup>2+</sup>. Average root-mean-square difference between experimental and calculated values is  $\pm 8\%$ .



tion products. Our earlier report on the photo-oxidation of water in aqueous uranyl solutions using conductivity detection shows the formation of a hydroxyl radical (eq. [2]). Thus, one recognizes that both hydrogen abstraction (eq. [1]) and hydroxyl radical reaction with isobutane (eq. [3]) lead to generation of the *tert*-butyl radical, designated as B·, and its subsequent conversion to *tert*-butyl alcohol (*t*-BuOH).

The emission and lifetimes of the uranyl ion in aqueous acidic solutions are well documented to be dependent on pH (1, 2, 13, 14, 16, 22, 23, 36–39). Our results for the emission quantum yield and quantum yields for formation of *t*-BuOH show that the yields increase with increasing HClO<sub>4</sub> (Figs. 3–5). The yields of *t*-BuOH range from 0.016 at 0.01 M HClO<sub>4</sub> to 0.13 at 4 M HClO<sub>4</sub> ( $\pm 10\%$ ).

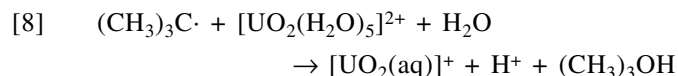
We have interpreted our results in terms of the presence of acid–base processes for two electronically excited species, to account for this strong dependence on acid concentration. The electronically excited “acid” form is denoted as  $^*[\text{UO}_2(\text{H}_2\text{O})_5]^{2+}$ , and it is the nascent species formed upon absorption of visible light by the ground-state species  $[\text{UO}_2(\text{H}_2\text{O})_5]^{2+}$ , according to the Franck–Condon Principle. Subsequent and rapid loss of a proton from one of the coordinated aqua ligands (eq. [4]) can then lead to the formation of the “base” form  $^*[\text{UO}_2(\text{H}_2\text{O})_n(\text{OH})]^+$ ; however, reprotonation of this conjugate base must occur to some extent, to account for the observed dependence on acid concentration. The important roles played by coordinated water both in these acid–base steps and in the nonradiative events is underscored by the fact that the replacement of aqua ligands by fluoride and phosphate anions, which are not easily oxidized, leads to much longer lifetimes (1, 14).

The excited-state portion of our mechanism is given in Fig. 1. We have assumed that both the acid and base forms undergo reactions with isobutane to form the *tert*-butyl radical  $(\text{CH}_3)_3\text{C}\cdot$ , and that both excited-state species can oxidize coordinated water to give rise to a hydroxyl radical; the results of our modeling studies, given below, support this interpretation. The second-order rate constants  $k_{q1}$  and  $k_{q2}$



pertain to the hydrogen-abstraction processes for the quenching by isobutane of the acid and base entities, respectively. Correspondingly, the first-order constants  $k_{\text{OH1}}$  and  $k_{\text{OH2}}$  pertain to the formation of hydroxyl radical, which reacts rapidly under our conditions to yield additional amounts of *tert*-butyl radical, eq. [3]. Consequently, two competitive modes are envisioned in the formation of the *tert*-butyl radical. Nonradiative decays of the excited states are designated by  $k_{\text{nr1}}$  (acid form) and  $k_{\text{nr2}}$  (base form) and those for emission by  $k_{\text{em1}}$  and  $k_{\text{em2}}$ . The invariant shape of the emission spectrum with changes in acid concentration, however, implies that  $k_{\text{em2}}$  is of little consequence under our conditions, and the outcomes of our modeling investigation are supportive of this.

The *tert*-butyl radical formed via the foregoing excited-state events and via eq. [3] is proposed to react primarily — and nearly quantitatively — with ground state  $[\text{UO}_2(\text{H}_2\text{O})_5]^{2+}$  to yield *t*-BuOH and, initially, uranyl ion, which can then undergo disproportionation (eq. [6]).

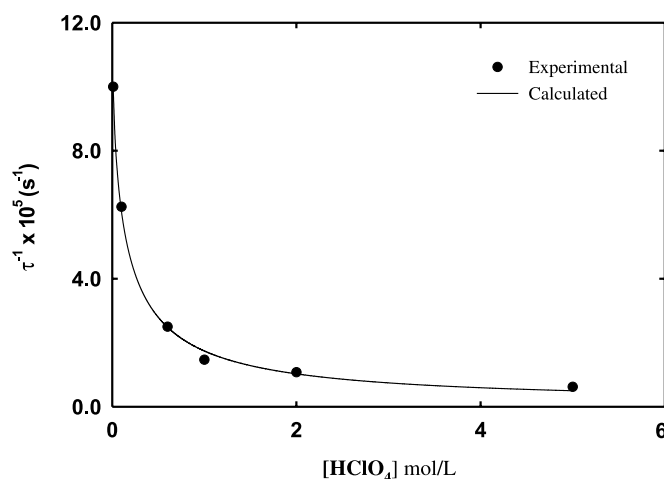


The basis for this proposal rests, in part, on the fact that *t*-BuOH is the major product ( $85 \pm 5\%$ ) and on the mass-balance ratios given in the Results section, although the actual source of oxygen in *t*-BuOH is not known. Furthermore, the products of bimolecular self-reactions of *tert*-butyl and *iso*-butyl radicals such as isobutene (disproportionation), 2,2,3,3-tetramethylbutane, 2,2,4-trimethylpentane, and 2,5-dimethylhexane (recombination), which are major products in steady-state gamma radiolysis in the absence of uranyl ion, are found to be minor products of photolysis in the presence of uranyl ion.

Both the *tert*-butyl radical and the  $\alpha$ -ethyl alcohol radical react readily with the mild oxidant  $[\text{Fe}(\text{CN})_6]^{3-}$  ( $E^\circ = 0.36 \text{ V}$ ), and the latter also reacts with  $[\text{UO}_2(\text{aq})]^{2+}$  ( $E^\circ = 0.16 \text{ V}$ ) (7, 40–42). The electrochemistry of the *tert*-butyl radical in acetonitrile also indicates it is a mild reducing agent (43). These comparisons point towards a reaction of  $[\text{UO}_2(\text{aq})]^{2+}$  with *tert*-butyl radical (eq. [8]). Attempts to measure the rate constant for the reaction of  $[\text{UO}_2(\text{aq})]^{2+}$  with *tert*-butyl radical were undertaken using our pulse-radiolysis conductivity and optical techniques at low dose ( $0.5 \mu\text{M}$  radical concentration, pH 2.7), to try to minimize the self-reaction of the *tert*-butyl radical. This pulse radiolysis approach was only partially successful because even at low dose, the bimolecular self-reactions of the *tert*-butyl radical dominated. An estimate to the upper limit for the rate constant in eq. [8] is  $1 \times 10^6 \text{ M}^{-1} \text{ s}^{-1}$ . In the context of our steady-state photolysis experiments where the radical concentration will be very low ( $\ll 10^{-8} \text{ M}$ ), the situation is likely to be quite different. Even if the rate constant was many powers of ten below  $10^6 \text{ M}^{-1} \text{ s}^{-1}$ , the rate of eq. [8] would prevail over other processes, particularly second-order events such as the self-reaction of *tert*-butyl radical, which has, therefore, not been included in our treatment.

To fit our model and thus obtain values of the rate constants, both time-resolved measurements of lifetimes and quantum yields are required. The mathematical development for the lifetimes is given elsewhere (32, 38), and two time

**Fig. 6.** Comparison of the data of Moriyasu et al. (●) and the fitted values based on our model (△) for the inverse lifetime of the electronically excited uranyl ion as a function of the concentration of  $\text{HClO}_4$ . Average root-mean-square difference between experimental (Moriyasu et al. (13)) and calculated values is  $\pm 6\%$ .



constants (lifetimes) occur where the entry into the excited-state scheme (Fig. 1) takes place by a short pulse of light absorbed by  $[\text{UO}_2(\text{H}_2\text{O})_5]^{2+}$  to give the electronically excited  $^*[\text{UO}_2(\text{H}_2\text{O})_5]^{2+}$ . The values of the rate constants given below indicate that the shorter of the two time constants is less than 100 ns, so it is not observed on the  $\mu\text{s}$  time scale either by us or by Moriyasu et al. (13). The longer time constant gives rise, on the  $\mu\text{s}$  scale, to mono-exponential decay in emission and excited-state absorption under both our and Moriyasu's conditions, and the reciprocal lifetime ( $\tau^{-1}$ ) that equals the observed first-order rate constant in the absence of isobutane is given by

$$[9] \quad \tau^{-1} = 1/2 \{ (k_1 + k_{(2)} + k_{21}[\text{H}^+]) - ((k_1 - k_{(2)} - k_{21}[\text{H}^+])^2 + 4k_{12}k_{21}[\text{H}^+])^{1/2} \}$$

where:

$$[10] \quad k_1 = k_{\text{nr1}} + k_{\text{em1}} + k_{12} + k_{\text{OH1}}$$

$$[11] \quad k_{(2)} = k_{\text{nr2}} + k_{\text{em2}} + k_{\text{OH2}}$$

$$[12] \quad k_2 = k_{(2)} + k_{21}[\text{H}^+]$$

We have used the lifetimes measured by Moriyasu et al. over the range of 0.01–5 M  $\text{HClO}_4$  (13) for 10 mM uranyl perchlorate at 25°C. The software program SigmaPlot for Windows 4.00, SPSS Inc. was then employed to fit the lifetime data, to obtain values of the parameters  $k_1$ ,  $k_{(2)}$ ,  $k_{12}$ , and  $k_{21}$ . The SigmaPlot program employs a convergence routine, and as a confirmation of the SigmaPlot results, an Excel spreadsheet (Microsoft Office 2000) was used to allow for the input of a range of values for the individual rate constants. The two approaches were in agreement. This procedure has been used in the other cases of the fitting of data, as described below. For the lifetimes, the resulting best fit of the experimental points and the calculated curve is shown in Fig. 6. The fit is very “rigid” in the sense that changes as small as  $\pm 10\%$  to the individual rate constants give rise to clearly discernable differences in lifetimes between the cal-



**Table 1.** Summary of values of the rate constants and efficiencies.

Reaction	$k_i$	$k$ value	Efficiency <sup>a</sup> ( $\eta_i$ )
$*[\text{UO}_2(\text{H}_2\text{O})_5]^{2+} \rightarrow [\text{UO}_2(\text{H}_2\text{O})_5]^{2+} + h\nu'$	$k_{\text{em1}}$	$900 \text{ s}^{-1}$	0.00083
$*[\text{UO}_2(\text{H}_2\text{O})_5]^{2+} \rightarrow [\text{UO}_2(\text{H}_2\text{O})_5]^{2+} + \Delta$	$k_{\text{nr1}}$	$1.8 \times 10^4 \text{ s}^{-1}$	0.017
$*[\text{UO}_2(\text{H}_2\text{O})_5]^{2+} \rightarrow *[\text{UO}_2(\text{H}_2\text{O})_n(\text{OH})]^+ + \text{H}^+$	$k_{12}$	$1.1 \times 10^6 \text{ s}^{-1}$	0.97
$*[\text{UO}_2(\text{H}_2\text{O})_n(\text{OH})]^+ + \text{H}^+ \rightarrow *[\text{UO}_2(\text{H}_2\text{O})_5]^{2+}$	$k_{21}$	$2.2 \times 10^7 \text{ M}^{-1} \text{ s}^{-1}$	0.39 <sup>b</sup>
$*[\text{UO}_2(\text{H}_2\text{O})_n(\text{OH})]^+ \rightarrow [\text{UO}_2(\text{H}_2\text{O})_n(\text{OH})]^+ + h\nu''$	$k_{\text{em2}}$	$0 \text{ s}^{-1}$	0
$*[\text{UO}_2(\text{H}_2\text{O})_n(\text{OH})]^+ \rightarrow [\text{UO}_2(\text{H}_2\text{O})_n(\text{OH})]^+ + \Delta$	$k_{\text{nr2}}$	$3.5 \times 10^6 \text{ s}^{-1}$	0.61 <sup>b</sup>
$*[\text{UO}_2(\text{H}_2\text{O})_5]^{2+} + \text{BH} \rightarrow [\text{UO}_2(\text{H}_2\text{O})_5]^+ + \text{B} \cdot + \text{H}^+$	$k_{q1}$	$1.0 \times 10^7 \text{ M}^{-1} \text{ s}^{-1}$	0.0088 <sup>c</sup>
$*[\text{UO}_2(\text{H}_2\text{O})_5]^{2+} + \text{H}_2\text{O} \rightarrow [\text{UO}_2(\text{H}_2\text{O})_5]^+ + \cdot\text{OH} + \text{H}^+$	$k_{\text{OH1}}$	$1500 \text{ s}^{-1}$	0.0014
$*[\text{UO}_2(\text{H}_2\text{O})_n(\text{OH})]^+ + \text{BH} \rightarrow [\text{UO}_2(\text{H}_2\text{O})_5]^+ + \text{B} \cdot$	$k_{q2}$	$2.0 \times 10^7 \text{ M}^{-1} \text{ s}^{-1}$	0.0033 <sup>b,c</sup>
$*[\text{UO}_2(\text{H}_2\text{O})_n(\text{OH})]^+ + \text{H}_2\text{O} \rightarrow [\text{UO}_2(\text{H}_2\text{O})_5]^+ + \cdot\text{OH}$	$k_{\text{OH2}}$	$2500 \text{ s}^{-1}$	0.00044 <sup>c</sup>

<sup>a</sup>Efficiency is defined as  $\eta_{1i} = k_{1i} / \sum k_{1i}$  and  $\eta_{2i} = k_{2i} / \sum k_{2i}$ , where subscripts 1 and 2 refer to acid and base forms, respectively (e.g., the efficiency of the dissociation of the acid form to the base form is given by  $\eta_{12}$ ; the efficiency of the reverse reaction is given by  $\eta_{21}$ ).

<sup>b</sup> $[\text{HClO}_4] = 0.1 \text{ M}$ .

<sup>c</sup> $[\text{isobutane}] = [\text{BH}] = 0.9 \text{ mM}$ .

culated and experimental values. The “best” fit has been determined from the minimization of the value of the root-mean-square difference between the calculated points and experimental ones; the average difference is small ( $\pm 6\%$ ). Furthermore, the differences show no readily apparent systematic trend over the 500-fold change in perchloric acid concentration. Thus the fit is considered to be satisfactory, and the values of the calculated parameters are:  $k_1 = 1.1 \times 10^6 \text{ s}^{-1}$ ,  $k_{(2)} = 3.5 \times 10^6 \text{ s}^{-1}$ ,  $k_{12} = 1.1 \times 10^6 \text{ s}^{-1}$ , and  $k_{21} = 2.2 \times 10^7 \text{ M}^{-1} \text{ s}^{-1}$ . The ratio of  $k_{12}/k_{21}$  leads to a  $\text{p}K_a$  of 1.3. A range of values from 1.7 to  $>3.6$  have been reported by others (1, 32). However, some caution should be exercised in comparing the different  $\text{p}K_a$  values. Different methods have been used to obtain the values and, frequently, for systems having different counter anions, so ion pairing may play a subtle but notable role. From the viewpoint of the dependence of the behaviors of the excited states on the acid concentration, the  $\text{p}K_a$  value is not the critical facet; rather, it is the values of  $k_{12}$  and  $k_{21}$  in relation to the rate constants of the competing processes that determines the course of events. The rate constants given above, in conjunction with the quantum yields for emission and for formation of the *tert*-butyl alcohol, now provide the basis to evaluate the chemical and nonchemical rate constants for the reactions in competition with the acid and base processes.

The expression for the total quantum yield for the production of *t*-BuOH alcohol arising from the hydrogen-abstraction reactions ( $k_{q1}$  and  $k_{q2}$ ) and from generation of the  $\cdot\text{OH}$  radical ( $k_{\text{OH1}}$  and  $k_{\text{OH2}}$ ), followed by eqs. [3] and [8], is

$$[13] \quad \Phi_{\text{Total}} = \{1/(1 - \eta_{12}^{\text{BH}} \eta_{21}^{\text{BH}})\} (k_{\text{RX}}^{\text{A}}/k_1 + k_{\text{RX}}^{\text{B}}/k_2)$$

The derivation is given in Appendix 1, and it is based on the assumption that multiple passes between  $*[\text{UO}_2(\text{H}_2\text{O})_5]^{2+}$  and  $*[\text{UO}_2(\text{H}_2\text{O})_n(\text{OH})]^+$  via eqs. [4] and [5] occur in the decay of these excited-state species. The symbols  $\eta_{12}^{\text{BH}}$  and  $\eta_{21}^{\text{BH}}$  designate the efficiencies of loss of a proton from the acid  $*[\text{UO}_2(\text{H}_2\text{O})_5]^{2+}$  to form the base  $*[\text{UO}_2(\text{H}_2\text{O})_n(\text{OH})]^+$  (eq. [4]) and the re-protonation of the latter (eq. [5]) in the presence of saturated isobutane solutions, respectively. The value,  $k_{\text{RX}}^{\text{A}}$ , represents the sum,  $k_{q1}[\text{BH}] + k_{\text{OH1}}$ , that leads to the formation of *tert*-butyl al-

cohol via the hydrogen abstraction and the formation of  $\cdot\text{OH}$  from the acid excited-state species. Correspondingly,  $k_{\text{RX}}^{\text{B}}$  equals  $k_{q2}[\text{BH}] + k_{\text{OH2}}$  for the base where  $[\text{BH}]$  is the concentration of isobutane (0.91 mM). Thus, the ratios  $k_{\text{RX}}^{\text{A}}/k_1$  and  $k_{\text{RX}}^{\text{B}}/k_2$  pertain to the total efficiencies for the chemical reactions from  $*[\text{UO}_2(\text{H}_2\text{O})_5]^{2+}$  and  $*[\text{UO}_2(\text{H}_2\text{O})_n(\text{OH})]^+$ , respectively.

Values for  $k_{q1}$ ,  $k_{q2}$ ,  $k_{\text{OH1}}$ , and  $k_{\text{OH2}}$  were obtained by “best fitting” the calculated quantum yields to the experimental ones. The fits were judged on the basis of the minimization of root-mean-square differences, and they are very sensitive to changes in the inputted values of the  $k_q$ s and  $k_{\text{OH}}$ s ( $\pm 10\%$ ). The comparison between the calculated and experimental values for the best fit is shown in Fig. 5 with the two sets agreeing very well within experimental error ( $\pm 8\%$  average root-mean-square difference), and the deviations appear to be random. The error bars shown for the experimental points (filled circles) are the estimated standard deviations (1  $\sigma$ ), and the calculated points are shown with a deviation of  $\pm 10\%$ . (The same procedure has been used for the emission results presented in Figs. 3 and 4). The rate constants obtained from the fit in Fig. 5 are  $k_{q1} = 1.0 \times 10^7 \text{ s}^{-1}$ ,  $k_{q2} = 2.0 \times 10^7 \text{ s}^{-1}$ ,  $k_{\text{OH1}} = 1500 \text{ s}^{-1}$ , and  $k_{\text{OH2}} = 2500 \text{ s}^{-1}$ . Gaziev et al. (10) provided an estimate of  $k_{\text{OH}}$  from the photo-stimulated  $^{18}\text{O}$  exchange of  $4.4 \times 10^4 \text{ s}^{-1}$ , and that obtained from time-resolved lifetime measurements by Waltz et al. (20) is  $5.4 \times 10^4 \text{ s}^{-1}$ ; the latter studies also yielded a value of  $3.3 \times 10^7 \text{ M}^{-1} \text{ s}^{-1}$  for quenching by isobutane. Our values of  $k_{\text{OH1}}$  and  $k_{\text{OH2}}$  are lower by a factor of about ten, whereas the values of  $k_{q1}$  and  $k_{q2}$  are of the same magnitude as that report previously (20). The comparison of our present results and those reported previously is perhaps somewhat tenuous because the previous studies were modeled on the presence of only one excited-state species (i.e., the acid form).

In the absence of isobutane, our model gives rise (Appendix 2) to the following expression for the quantum yield of emission, where the efficiencies are,

$$[14] \quad \Phi_{\text{em}}^{\text{Total}} = (\eta_{\text{em1}} + \eta_{\text{em2}} \eta_{12}^{\circ}) \{1/(1 - \eta_{12}^{\circ} \eta_{21}^{\circ})\}$$

as previously, symbolized by  $\eta$ s. The comparison between the experimental results and the calculated ones is shown in



Fig. 3. The average root-mean-square difference for all points is  $\pm 8\%$  with no apparent systematic deviations. Although we initially assumed that both excited-state species could emit, the best fit as shown here was obtained for a  $k_{em1}$  of  $900\text{ s}^{-1}$  and for  $k_{em2}$  being zero, i.e.,  $k_{em2} \ll k_{em1}$ . This situation implies that the emission arises predominantly from  $^*[\text{UO}_2(\text{H}_2\text{O})_5]^{2+}$ , and this is consistent with the emission spectral features remaining stationary as the perchloric acid concentration was varied, as described in the Results section. Using the aforementioned rate constants derived from the model, we extended the fitting procedure to the situation where isobutane was now present. The expression for  $\Phi_{em}^{\text{Total}}$  is given in Appendix 2, and it is analogous to that of eq. [14]. The results are shown in Fig. 4. The average root-mean-square difference between the calculated and experimental yields is somewhat larger, at  $\pm 21\%$ , than that in the absence of isobutane ( $\pm 8\%$ ) with deviations being more apparent at low concentrations of perchloric acid. This less satisfactory situation seems to derive, in part, from the low signal levels for integrated emission encountered at low acid concentrations (coupled perhaps with scattered light) and from the further lowering of emission in the presence of isobutane relative to that in its absence.

The information given in Table 1 summarizes the values of the rate constants calculated from the excited-state model. To provide perspective on the relative influence of the different excited-state processes, the efficiencies ( $\eta_i$ ) of the individual steps are presented based upon calculations for the condition of  $0.1\text{ M HClO}_4$  and  $0.9\text{ mM}$  isobutane. For the acid form  $^*[\text{UO}_2(\text{H}_2\text{O})_5]^{2+}$ , the dominant event for all of our conditions is the deprotonation reaction (eq. [4]) with a  $\eta_{12}$  of ca.  $0.97$ . Furthermore, the efficiency of hydrogen-abstraction reactions is greater for the acid form than for the base species, whereas the reverse prevails in the generation of hydroxyl radical. The efficiency of protonation of  $^*[\text{UO}_2(\text{H}_2\text{O})_n(\text{OH})]^+$  is  $0.39$  at  $0.1\text{ M HClO}_4$ ; however, this value rapidly increases on going to higher acid concentrations. Consequently, the calculated percentage of *tert*-butyl alcohol, which has its origins in the hydrogen-abstraction and  $\cdot\text{OH}$ -formation reactions of the acid form  $^*[\text{UO}_2(\text{H}_2\text{O})_5]^{2+}$ , accounts for greater than  $90\%$  ( $0.8\text{--}4\text{ M HClO}_4$ ) of the product formation. Even at our lowest perchloric acid concentration, the acid form is the dominant reacting species ( $64\%$ ).

The mechanism that is provided here, involving the acid-base processes of the electronically excited uranyl ion, provides a comprehensive framework in which to interpret the experimental results. For over a 400-fold change in perchloric acid concentration ( $0.01\text{--}4\text{ M HClO}_4$ ), this model predicts well the lifetimes of the excited uranyl ion, the quantum yields of emission in both the absence and presence of a quencher (i.e., isobutane), as well as the quantum yields for the production of *tert*-butyl alcohol.

This study clearly brings into focus the fact that organic products can arise from both hydrogen-abstraction processes and the competitive occurrence of the oxidation of coordinated water to generate hydroxyl radical, which is, in general, highly reactive towards a large variety of organic substances (19). The apparent quantum yields for organic products derived from alkanes reported here and elsewhere (17) tend to be low, partly owing to solubility limitations.

For a saturated isobutane solution, the percent quenching is, in total, about  $7\%$ . Because isobutane is a condensable gas at room temperature, it was not feasible to increase the pressure and thus its concentration. However, with less condensable, low molar mass alkanes such as methane, which is known to quench excited uranyl (24), the solubility factor should prove less restrictive through the use of increased pressure and lower temperatures. As a further approach to increasing the apparent quantum yields, the free radicals generated can be used to initiate chain processes. In this context, we report elsewhere (21, 32) that the addition of millimolar amounts of potassium peroxydisulphate gives a 75-fold increase in the apparent quantum yield for *tert*-butyl alcohol formation ( $\Phi_{\text{observed}} \sim 1.5$ ) with the additional advantage that there is no net consumption of  $[\text{UO}_2(\text{aq})]^{2+}$  (i.e., the  $[\text{U}(\text{aq})]^{4+}$  product is oxidized back to  $[\text{UO}_2]^{2+}$  during photolysis). The use of visible light coupled with the broad absorption spectrum of uranyl ion provides a strategy to explore further the conversion of alkanes, in particular ones with low molecular mass where product selectivity is of lesser concern, into useful oxygenated products.

## Acknowledgments

We thank the Natural Sciences and Engineering Research Council of Canada (NSERC) for financial support, Dr. D. Garratt of the Cameco Corporation for uranium trioxide, and Mr. Ken Thoms for GC-MS and helpful suggestions.

## References

1. C.P. Baird and T.J. Kemp. *Prog. React. Kinet.* **22**, 87 (1997).
2. M.D. Marcantonatos, M. Deschaux, F. Celardin, and M. Levental. *Chem. Phys. Lett.* **65**, 316 (1979).
3. V. Balzani, F. Bolletta, M.T. Gandolfi, and M. Maestri. *Top. Curr. Chem.* **75**, 1 (1978).
4. H.D. Burrows and T.J. Kemp. *J. Chem. Soc. Rev.* **3**, 139 (1974).
5. E. Rabinowitch and R.L. Belford. *Spectroscopy and photochemistry of uranyl compounds*. Pergamon Press, Oxford. 1964.
6. D.M. Roundhill. *Photochemistry and photophysics of metal complexes*. Plenum Press, New York. 1994. Chap 8.
7. M.E.D.G. Azenha, H.D. Burrows, S.J. Formosinho, and M. da G.M. Miguel. *J. Chem. Soc. Faraday Trans.* **85**, 2625 (1989).
8. H.D. Burrows and S.J. Formosinho. *J. Chem. Soc. Faraday Trans. 2*, **73**, 201 (1977).
9. M. Deschaux and M.D. Marcantonatos. *Chem. Phys. Lett.* **63**, 283 (1979).
10. S.A. Gaziev, N.G. Gorshkov, L.G. Mashirov, and D.N. Suglov. *Inorg. Chim. Acta*, **139**, 345 (1987).
11. R.J. Hill, T.J. Kemp, D.M. Allen, and A.J. Cox. *J. Chem. Soc. Faraday Trans 1*, **70**, 847 (1974).
12. M.D. Marcantonatos. *J. Chem. Soc. Faraday Trans. 1*, **76**, 1093 (1980).
13. M. Moriyasu, Y. Yokoyama, and S. Ikeda. *J. Inorg. Nucl. Chem.* **39**, 2211 (1977).
14. M. Moriyasu, Y. Yokoyama, and S. Ikeda. *J. Inorg. Nucl. Chem.* **39**, 2199 (1977).
15. Y.-Y. Park and H. Tomiyasu. *J. Photochem. Photobiol. A*, **64**, 25 (1992).
16. Y.-Y. Park, Y. Sakai, R. Abe, T. Ishii, M. Harada, T. Kojima, and H. Tomiyasu. *J. Chem. Soc. Faraday Trans.* **86**, 55 (1990).



17. Y. Mao and A. Bakac. *J. Phys. Chem.* **100**, 4219 (1996).
18. C. Sonntag and H.-P. Schuchmann. *Angew. Chem. Int. Ed. Engl.* **30**, 1229 (1991).
19. G.V. Buxton, C.L. Greenstock, W.P. Helman, and A.B. Ross. *J. Phys. Chem. Ref. Data*, **17**, 513 (1988).
20. W.L. Waltz, J. Lilie, X. Xu, P. Sedláč, and H. Möckel. *Inorg. Chim. Acta*, **285**, 322 (1999).
21. X. Xu. Ph.D. Dissertation. Department of Chemistry, University of Saskatchewan, Saskatoon, Sask., Canada. 1997.
22. M.E.D.G. Azenha, H.D. Burrows, S.J. Formosinho, M. da G.M. Miguel, A.P. Darmanyan, and I.V. Khudyakov. *J. Lumin.* **48/49**, 522 (1991).
23. A.P. Darmanyan and I.V. Khudyakov. *Photochem. Photobiol.* **52**, 293 (1990).
24. G.V. Nizova and G.B. Shul'pin. *Zh. Obshch. Khim.* **60**, 2124 (1990). English Translation: *J. Gen. Chem.* **60**, 1895 (1991).
25. J.G. Calvert and J.N. Pitts. *Photochemistry*. Wiley, New York. 1966. pp. 783–786.
26. D.B. Wetaufr. *J. Am. Chem. Soc.* **86**, 508 (1964).
27. J.T. Bell and R.E. Biggers. *J. Mol. Spectrosc.* **22**, 262 (1967).
28. A. Ekstrom. *Inorg. Chem.* **13**, 2237 (1974).
29. J.T. Bell, H.A. Friedman, and M.R. Billings. *J. Inorg. Nucl. Chem.* **36**, 2563 (1974).
30. Z.F. Zhao and D.A. Liu (*Editors*). *Analytical chemistry*. People's Education, Beijing. 1978. p. 295.
31. J. H. Betts. *Can. J. Chem.* **33**, 1775 (1955).
32. T.M. Bergfeldt. Ph.D. Dissertation. Department of Chemistry, University of Saskatchewan, Saskatoon, Sask., Canada, 2001.
33. Y. Katsumura, H. Abe, T. Yotsuyanagi, and K. Ishingure. *J. Photochem. Photobiol. A*, **50**, 183 (1989).
34. T.W. Newton and F.B. Baker. *Inorg. Chem.* **4**, 1166 (1965).
35. H.J. Lucas and W.F. Eberz. *J. Am. Chem. Soc.* **56**, 460 (1934).
36. M.D. Marcantonatos. *J. Chem. Soc. Faraday Trans. 1*, **75**, 2273 (1979).
37. M.D. Marcantonatos and M.M. Pawlowska. *J. Chem. Soc. Faraday Trans. 1*, **85**, 2481 (1989).
38. S.J. Formosinho and M. da G.M. Miguel. *J. Chem. Soc. Faraday Trans. 1*, **80**, 1717 (1984).
39. M. da G. M. Miguel, S.J. Formosinho, and A.C. Cardoso. *J. Chem. Soc. Faraday Trans. 1*, **80**, 1735 (1984).
40. S. Steenken and P. Neta. *J. Am. Chem. Soc.* **104**, 1244 (1982).
41. E. Hensler and W.J. Lorenz. *In Standard potentials in aqueous solutions*. Edited by A.J. Bard, R. Parsons, and J. Jordan. Marcel Dekker, New York. 1985. Chap 14.
42. L. Martinot and J. Fuger. *In Standard Potentials in Aqueous Solutions*. Edited by A.J. Bard, R. Parsons, and J. Jordan. Marcel Dekker, New York. 1985. Chap 21.
43. D.D.M. Wayner, D.J. McPhee, and D. Griller. *J. Am. Chem. Soc.* **110**, 132 (1988).

## Appendix 1: Derivation of the expression for the total chemical quantum yield by species A (acid form) and B (base form)

The quantum yield for the reaction of the A species is given by

$$[A1] \quad \phi_{Rx}^A = \eta'_{q1} + \eta'_{q1} \eta_{i2}^{BH} \eta_{21}^{BH} + \eta'_{q1} (\eta_{i2}^{BH} \eta_{21}^{BH})^2 + \dots$$

For multiple passes through the excited states via protonation and deprotonation and for  $\eta$ s less than one, this series converges to the limit of

$$[A2] \quad \phi_{Rx}^A = \frac{\eta'_{q1}}{1 - \eta_{i2}^{BH} \eta_{21}^{BH}}$$

where

$$[A3] \quad \eta'_{q1} = \frac{k_{q1}[BH]}{k_1 + k_{q1}[BH]}$$

$$[A4] \quad \eta_{i2}^{BH} = \frac{k_{i2}}{k_1 + k_{q1}[BH]}$$

$$[A5] \quad \eta_{21}^{BH} = \frac{k_{21}}{k_2 + k_{q2}[BH]}$$

Accounting for hydrogen abstraction of isobutane by hydroxyl radical produced by species A

$$[A6] \quad \phi_{OH1} = \frac{\eta_{OH1}}{1 - \eta_{i2}^{BH} \eta_{21}^{BH}}$$

where

$$[A7] \quad \eta_{OH1} = \frac{k_{OH1}}{k_1 - k_{q1}[BH]}$$

Similarly, the quantum yield for the reaction from species B, along with hydrogen abstraction from isobutane by hydroxyl radical produced by species B are given by

$$[A8] \quad \phi_{Rx}^B = \frac{\eta_{i2}^{BH} \eta'_{q2}}{1 - \eta_{i2}^{BH} \eta_{21}^{BH}}$$

$$[A9] \quad \phi_{OH2} = \frac{\eta_{i2}^{BH} \eta_{OH2}}{1 - \eta_{i2}^{BH} \eta_{21}^{BH}}$$

The total quantum yield is

$$[A10] \quad \phi_{Total} = \phi_{Rx}^A + \phi_{OH1} + \phi_{Rx}^B + \phi_{OH2}$$

or

$$[A11] \quad \phi_{Total} = \frac{\eta'_{q1} + \eta_{OH1} + \eta_{i2}^{BH} (\eta'_{q2} + \eta_{OH2})}{1 - \eta_{i2}^{BH} \eta_{21}^{BH}}$$

Using the rate constants from the fitting of Moriyasu et al.'s data (A1),  $\eta_{i2}^{BH} = 0.973$ . Let  $\eta_Q$  represent the total efficiency of quenching of both species by isobutane; then

$$[A12] \quad \eta_Q = \eta'_{q1} + \eta_{i2}^{BH} \eta'_{q2} \equiv \eta'_{q1} + \eta'_{q2}$$

and

$$[A13] \quad \eta_{OH} = \eta_{OH1} + \eta_{i2}^{BH} \eta_{OH2} \equiv \eta_{OH1} + \eta_{OH2}$$

Equation [A1.11] can be written as

$$[A14] \quad \phi_{Total} = \left( \frac{1}{1 - \eta_{i2}^{BH} \eta_{21}^{BH}} \right) \left( \frac{k_{Rx}^A}{k_1} + \frac{k_{Rx}^B}{k_2} \right)$$

where

$$[A15] \quad \frac{k_{Rx}^A}{k_1} = \frac{k'_{q1} + k_{OH1}}{k_1} = \eta'_{q1} + \eta_{OH1}$$



and

$$[A16] \quad \frac{k_{Rx}^B}{k_2} = \frac{k_{q2}' + k_{OH2}}{k_2} = \eta_{q2}' + \eta_{OH2}$$

where

$$[A17] \quad k_1 = k_{nr1} + k_{em1} + k_{12} + k_{OH1}$$

$$[A18] \quad k_2 = k_{nr2} + k_{em2} + k_{OH2} + k_{21}[H^+]$$

## References

A1. M. Moriyasu, Y. Yokoyama, and S. Ikeda. J. Inorg. Nucl. Chem. **39**, 2211 (1977).

## Appendix 2. Derivation of expression for emission quantum yields

The efficiencies of emission by the acid (A) species ( $\eta_{em1}$ ) and the base (B) species ( $\eta_{em2}$ ) can be expressed as:

$$[B1] \quad \eta_{em1} = \frac{k_{em1}}{k_1}$$

$$[B2] \quad \eta_{em2} = \frac{k_{em2}}{k_2}$$

where

$$[B3] \quad k_1 = k_{nr1} + k_{em1} + k_{12} + k_{OH1}$$

$$[B4] \quad k_2 = k_{nr2} + k_{em2} + k_{OH2} + k_{21}[H^+]$$

The quantum yield of emission by the A species in the absence of isobutane can be expressed as

$$[B5] \quad \phi_{em1} = \eta_{em1} + \eta_{12}^o \eta_{21}^o \eta_{em1} + (\eta_{12}^o \eta_{21}^o)^2 \eta_{em1} + \dots$$

where

$$[B6] \quad \eta_{12}^o = \frac{k_{12}}{k_1}$$

$$[B7] \quad \eta_{21}^o = \frac{k_{21}[H^+]}{k_2}$$

For  $\eta_{12}^o \eta_{21}^o < 1$ , eq. [A2.5] converges to

$$[B8] \quad \phi_{em1} = \frac{\eta_{em1}}{1 - \eta_{12}^o \eta_{21}^o}$$

Similarly, the quantum yield of emission of the B species in the absence of isobutane can be shown to be

$$[B9] \quad \phi_{em2} = \frac{\eta_{em2} \eta_{12}^o}{1 - \eta_{12}^o \eta_{21}^o}$$

The total emission quantum yield from both species in the absence of isobutane is

$$[B10] \quad \phi_{em}^{Total} = (\eta_{em1} + \eta_{em2} \eta_{12}^o) \left( \frac{1}{1 - \eta_{12}^o \eta_{21}^o} \right)$$

In the presence of isobutane, the total emission quantum yield from both species is

$$[B11] \quad \phi_{em}^{Total} = (\eta_{em1} + \eta_{em2} \eta_{12}^{BH}) \left( \frac{1}{1 - \eta_{12}^{BH} \eta_{21}^{BH}} \right)$$

where

$$[B12] \quad \eta_{12}^{BH} = \frac{k_{12}}{k_1 + k_{q1}[BH]}$$

$$[B13] \quad \eta_{21}^{BH} = \frac{k_{21}[H^+]}{k_2 + k_{q2}[BH]}$$

and  $k_{q1}$  and  $k_{q2}$  are the quenching constants of the A species and the B species by isobutane, respectively.



# Aqueous–gas phase partitioning and hydrolysis of organic iodides

G.A. Glowa and J.C. Wren

**Abstract:** The volatility and decomposition of organic iodides in a reactor containment building are important parameters to consider when assessing the potential consequences of a nuclear reactor accident. However, there are few experimental data available for the volatilities (often reported as partition coefficients) or few rate constants regarding the decomposition (via hydrolysis) of organic iodides. The partition coefficients and hydrolysis rate constants of eight organic iodides, having a range of molecular structures, have been measured in the current studies. This data, and data accumulated in the literature, have been reviewed and discussed to provide guidelines for appropriate organization of organic iodides for the purpose of modelling iodine behaviour under postulated nuclear reactor accident conditions. After assessment of the partition coefficients and their temperature dependences of many classes of organic compounds, it was found that organic iodides could be divided into two categories based upon their volatility relative to molecular iodine. Similarly, hydrolysis rates and their temperature dependences are assigned to the two categories of organic iodides.

**Key words:** organic iodide, hydrolysis, partition coefficient, iodine behaviour model, nuclear reactor safety.

**Résumé :** La volatilité et la décomposition d'iodures organiques dans un bâtiment contenant un réacteur sont des paramètres importants à considérer lorsqu'on évalue les conséquences potentielles d'un accident à un réacteur nucléaire. Toutefois, il y a peu de données expérimentales relatives aux volatilités (souvent rapportées sous la forme de coefficient de partage) ou de constantes de vitesse concernant la décomposition (par voie d'hydrolyse) des iodures organiques. Dans le présent travail, on a mesuré les coefficients de partage et les constantes d'hydrolyse de huit iodures organiques représentatifs de diverses structures moléculaires. On a fait une revue de ces données et de celles recueillies dans la littérature et on en discute dans le but de fournir des indications claires pour l'organisation appropriée des iodures organiques dans le but d'établir un modèle du comportement de l'iode dans les conditions postulées lors d'un accident dans un réacteur nucléaire. Après une évaluation des coefficients de partage de plusieurs classes de composés organiques et de leurs dépendances sur la température, on a trouvé que les composés organiques peuvent être divisés en deux catégories suivant leur volatilité relative en iode organique. Les vitesses d'hydrolyse et leurs dépendances sur la température ont aussi été divisées de la même manière.

**Mots clés :** iodure organique, hydrolyse, coefficient de partage, modèle de comportement de l'iode, sécurité d'un réacteur nucléaire.

[Traduit par la Rédaction]

## 1. Introduction

The production and decomposition of volatile forms of radioiodine in, and their release from, a reactor containment building are important processes to consider when assessing the potential consequences of a nuclear reactor accident. A considerable number of studies on these processes have been carried out with the objective of developing a model that can predict iodine volatility in containment during the course of an accident (1–6). Recent critical reviews on iodine behaviour in containment (7, 8, and refs. therein) provide a comprehensive technical background on this subject.

Iodine would be released into the containment atmosphere from fuel via the reactor coolant system, mainly as nonvolatile species (e.g., CsI under most accident conditions) (8).

The initial fraction of volatile iodine species (i.e., molecular iodine and organic iodides) in containment would be very small. However, although CsI is water soluble and would initially be dissolved in containment water, a small fraction of the nonvolatile  $I^-$  initially dissolved in water would be continuously oxidized to volatile molecular iodine ( $I_2$ ) in the presence of the high radiation field following an accident. Molecular iodine reacts easily with organic compounds in the presence of radiation to form organic iodides. Therefore, a significant portion of the gaseous iodine in containment would be in the form of organic iodides. Measurements at the TMI (Three Mile Island) 2-reactor following the 1979 accident showed that organic iodides were a major component of the small amount of iodine that became airborne (9). Studies on total iodine volatility under containment accident

Received 12 August 2002. Published on the NRC Research Press Web site at <http://canjchem.nrc.ca> on 14 March 2003.

G.A. Glowa and J.C. Wren.<sup>1</sup> AECL, Chalk River Laboratories, Stn. 86, Containment & Thermalhydraulics Analysis Branch, Chalk River, ON K0J 1J0, Canada.

<sup>1</sup>Corresponding author (email: [wrenc@aecl.ca](mailto:wrenc@aecl.ca)).



conditions in an intermediate-scale facility have also shown that the organic iodide fraction in the gas phase could be as high as 90% in the presence of painted surfaces (7). Organic iodides are thus very important in the assessment of the radiological consequences of a nuclear reactor accident.

Early studies on organic iodide formation and decomposition under potential nuclear reactor accident conditions focused mainly on  $\text{CH}_3\text{I}$  because it is the simplest organic iodide with a high volatility. Recent studies have shown, however, that organic iodides are formed mainly from the reaction of  $\text{I}_2$  with organic impurities in the aqueous phase, which then become airborne, and that a large fraction of the organic iodides formed in the aqueous phase under containment conditions would be less volatile than  $\text{CH}_3\text{I}$  (7, 10, 11). A wide range of organic radicals may be formed by the radiolytic degradation (10) of a wide range of organic impurities dissolved in the containment sump water from containment paints (7, 11). This, in turn, leads to formation of a wide range of organic iodides, whose volatility and decomposition rates differ considerably. The contribution of each of these species to the overall iodine gas-phase concentration will therefore vary considerably from one species to another. Therefore, the partition coefficients and hydrolysis rate constants of eight organic iodides, having a range of molecular structures, have been measured in the current studies.

## 2. Background

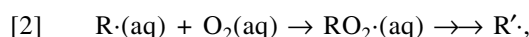
Although the possibility of formation of various organic iodides in containment had been recognized, early studies on organic iodide formation focused mainly on  $\text{CH}_3\text{I}$ . As mentioned above, this was because it is the simplest organic iodide, and it has a high volatility. Radioiodine Test Facility (RTF)<sup>2</sup> experiments performed in painted vessels have found, however, that a large fraction of the organic iodides formed from containment paint impurities are less volatile than  $\text{CH}_3\text{I}$  (7). Formation of low volatility compounds has been further supported by bench-scale studies on the dissolution of organic solvents from painted surfaces into water (11, 12) and on the radiolytic decomposition of organic impurities in water (10, 13–18). Studies on the dissolution of organic solvents from painted surfaces have shown that the molecular structure of compounds released varies (e.g., aromatics, alcohols, and ketones), and that commonly used paint solvents contain from one to 10 carbons (Table 1). Calculations suggest that the amount of organic solvents released from painted surfaces into the sump could result in concentrations of up to  $1 \times 10^{-2} \text{ mol dm}^{-3}$  (11, 12). (Note that this concentration is subject to many parameters that would be accident scenario and reactor specific such as paint thickness, paint age, compound solubility, water volume, and paint area in contact with water, etc.).

Once released into the sump water, these organic solvents would undergo radiolytic decomposition. Studies on methyl ethyl ketone (MEK) in the absence of iodine species (10,13,14) have shown that the radiolytic decomposition of MEK in the aqueous phase under aerated conditions results

**Table 1.** Some commonly used paint solvents.

No. of carbons	Organic solvent constituents
1	Methanol
2	Ethanol
3	Propanol, propanone
4	2-Butanone, butanol
5	Furfuryl alcohol
6	4-Methyl-2-pentanone
7	2-Heptanone, methylbenzene
8	Xylene, ethylbenzene
9	Trimethyl benzene

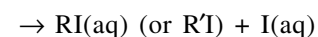
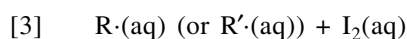
in the sequential formation of smaller and more oxidized organic compounds, and eventually complete conversion to  $\text{CO}_2$ :



alcohols, aldehydes, acids, and  $\text{CO}_2$

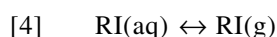
where RH and  $\text{R}\cdot$  (or  $\text{R}'\cdot$ ) represent an organic compound and organic radical, respectively. Among the intermediate decomposition products observed during the radiolysis of MEK were 3-hydroxy-2-butanone, 2,3-butanedione, ethanoic acid, ethanal, and methanal (13).

The dissolution and MEK radiolysis studies imply that the range of organic compounds present in the sump could be considerable, with a large proportion of them being highly soluble oxygen-containing compounds (i.e., alcohols, ketones, and carboxylic acids). Various organic radicals would be formed from these organic compounds and, in the presence of  $\text{I}_2$ , which is known as a very good radical scavenger, a small fraction of the radicals would react with  $\text{I}_2$  to form organic iodides:



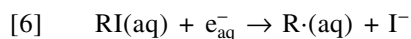
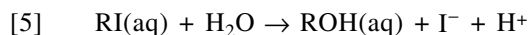
where RI (or  $\text{R'I}$ ) represents an organic iodide. Consequently, the range of organic iodides formed under containment accident conditions could be large and could include alkyl iodides, iodoketones, -alcohols, -phenols, and -acids. With the exception of the alkyl iodides, these species would have low volatility (discussed in Section 5.2), and would be very difficult to detect in the gas phase. Generally, only alkyl iodides are detected during RTF tests, or bench-scale experiments (15) by gas chromatographic methods.

Organic iodides, which can be formed in irradiated solutions of iodide and organic compounds (7, 15, 16), will partition between the aqueous and gas phases (rxn. [4]) according to Henry's Law (see Section 3.2). Meanwhile, organic iodides in the aqueous phase will undergo decomposition via hydrolysis (rxn. [5]) and radiolysis (rxn. [6]).



<sup>2</sup>The Radioiodine Test Facility (RTF) is an intermediate scale facility containing a 345  $\text{dm}^3$  containment vessel that provides a combination of potential reaction media (gas phase, aqueous phase, and a variety of surfaces) and conditions (pH, temperature, radiation, initial concentrations, and speciation of iodine), to simulate a reactor containment building following an accident (7).





Therefore, to determine the overall behaviour of organic iodides, and their contributions to the gaseous iodine concentration under containment accident conditions, the formation and the decomposition of organic iodides must be adequately quantified. The rate of the hydrated electron reaction (rxn. [6]) is diffusion-controlled and is therefore nearly independent of the type of organic iodide. Therefore, the current study focuses on the partitioning and the hydrolysis of organic iodides. The partition coefficients (see Section 3.2 for its definition) and the hydrolysis rate constants of a range of organic iodides have been measured, and compared with the literature data of organic iodides, if available, and also with compounds of similar structure that do not contain iodine. These values were reviewed for the purpose of providing guidelines to appropriately group organic iodides so that modelling of organic iodide behaviour under radiolytic conditions can be more easily managed.

### 3. Experimental

A small set of compounds was chosen to cover the major structural possibilities (methyl, primary, secondary, tertiary, benzyl, aryl) of organic compounds that may be present in reactor containment. For example, a primary alcohol (iodoethanol) and a carboxylic acid (iodoethanoic acid) were chosen to explore the effect of neighbouring oxygen-containing functional groups on hydrolysis rate and partition coefficients. All compounds studied were purchased from Aldrich Chemical Co., except (iodomethyl)benzene, which was from Alfa-Aesar (a Johnson Matthey company), and 2-iodobenzenol, which was from ICN Biomedicals Inc. Compounds were of the highest purity available and were used as received without further purification.

#### 3.1 Measurement of hydrolysis rates

Two methods were used to study the hydrolysis rates of these compounds. The first method used a solid-state ion selective electrode (ISE) designed for iodide measurements (Orion 9553) with a double junction reference electrode (Orion 900200) to measure the concentration of iodide produced by hydrolysis. These probes were connected to a Fisher Accumet 950 pH meter. The electrode was calibrated for each temperature of interest using NaI solutions of known concentration. The plot of mV vs.  $\log_{10} [\text{I}^-]$  was found to be linear over the concentration range studied. This method was successfully used for the hydrolysis of 2-iodobutane. Due to baseline drift however, this method was found to be unsuitable for the time periods required to measure the hydrolysis rates of the other compounds.

For the majority of the studies, the hydrolysis rates were determined from the growth of the absorbance of  $\text{I}^-$  ( $\epsilon = 12\,980 \text{ dm}^3 \text{ mol}^{-1} \text{ cm}^{-1}$  at 225 nm) monitored using a HP 8450A spectrophotometer. In some cases there was minor absorbance at 225 nm attributed to the starting material and (or) the resulting alcohol, in addition to the absorbance by  $\text{I}^-$ . But because the change in concentration of the three components (organic iodide, alcohol, and  $\text{I}^-$ ) occurs at the same rate, the first-order hydrolysis rate constant of the organic

compound can still be obtained from the change in absorbance at 225 nm (see Section 4.1 for the relationship between the absorbance and the first-order rate constant).

In general, the measurements were repeated at least once. The reproducibility of the measurements was better (<5%) when measuring fast hydrolysis rates (i.e., for 2-iodobutane and (iodomethyl)benzene). During the measurement of slow hydrolysis rates (i.e., iodomethane and iodoethane), reproducibility was generally in the 20% range. Measurements lasted between 3–5 half-lives during experiments using the electrode method. For each spectrometer measurement, the absorbance at 225 nm was then monitored until a limiting absorbance was approached (generally > 3 half-lives).

Solutions were prepared by adding the pure compound (as received) to purified (distilled and deionized) water (Millipore Milli-Q Plus) in a temperature-controlled cell. After dissolution of the compound, the electrodes were introduced, and the  $\text{I}^-$  signal was monitored until completion. For the spectrophotometric method, an aliquot of the solution was removed and placed in a temperature-controlled optical cell (10 cm path length). Starting concentrations of all species for these measurements were approximately  $1 \times 10^{-4} \text{ mol dm}^{-3}$ . This concentration is below the saturation level of the compounds studied, but high enough to ensure an adequate increase in absorbance as the reaction progresses. To avoid loss of the compound to the gas phase, the cell was completely filled to eliminate any headspace. The water pH was slightly acidic (~pH 6) at the start of a test, but was not controlled or buffered and generally decreased to ~4 during the hydrolysis.

#### 3.2 Partition coefficient determination

In this report, the partition coefficient ( $^H K$ ) is defined as the ratio of the aqueous phase concentration to the gas phase concentration at equilibrium.

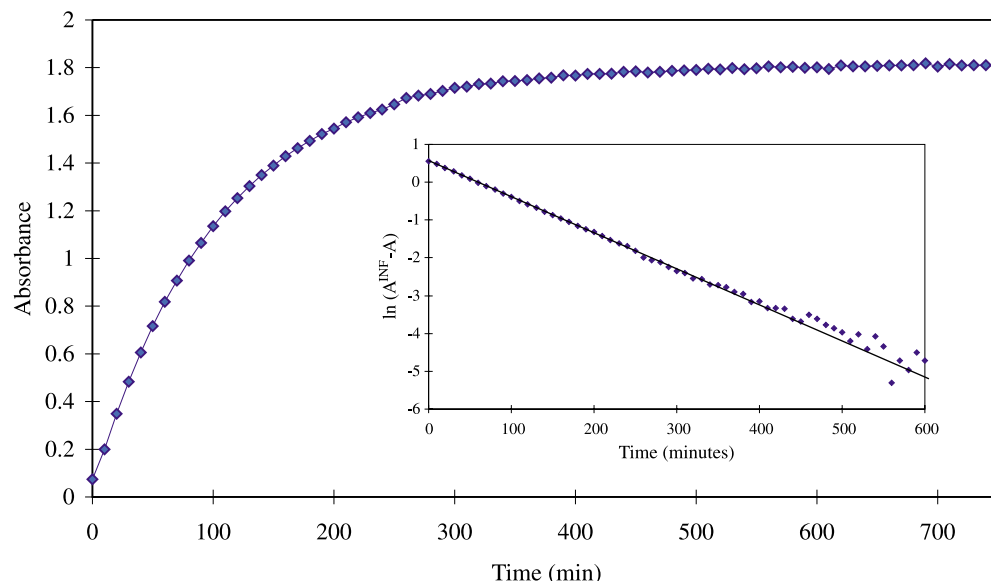
$$[7] \quad {}^H K = \frac{[\text{Compound(aq)}]_{\text{eq}}}{[\text{Compound(g)}]_{\text{eq}}}$$

Partition coefficients were determined in ~400 mL temperature-controlled cells at ambient pressure. Prior to being added to the temperature-controlled cell, 200 mL of purified water was purged with high purity air for 20–30 min. The vessel and water was conditioned at a given temperature for several hours before the pure compound, or an aliquot of a concentrated stock solution, was added to the aqueous phase of the vessel. A concentration of approximately  $1 \times 10^{-4} \text{ mol dm}^{-3}$  was typically used for the partition coefficient measurement. For iodoethanol and iodoethanoic acid, a higher concentration ( $\sim 1 \times 10^{-3} \text{ mol dm}^{-3}$ ), which is still below saturation concentration, was used because of their low volatility.

Aqueous samples (400–1000  $\mu\text{L}$ ) were analyzed using a Waters high performance liquid chromatography system (LC-18 DB column, detection by UV at 254 nm). Gas samples (200–500  $\mu\text{L}$ ) were analyzed by gas chromatography (GC). The volatile species (iodomethane, iodoethane, and 2-iodobutane) were detected using a Varian GC system fitted with a photoionization detector, and an Altec polymethyl siloxane column (30 m, 0.53 mm i.d., 5  $\mu\text{m}$  film thickness). The less volatile species required thinner phase capillary



**Fig. 1.** Growth of absorbance at 225 nm during the hydrolysis of iodoethane at 80°C. Inset shows the log plot of  $A_{225\text{nm}}^{\text{INF}} - A_{225}$ .



columns more suitable for polar compounds (which was on our HP Model 5972 GC-MS system). For iodophenol and iodoethanol, a J&W Scientific DB-1 column (30 m, 0.32 mm i.d., 3.0  $\mu\text{m}$  film thickness) was used, and a HP-5 column (25 m, 0.32 mm i.d., 0.17  $\mu\text{m}$  film thickness) was used for iodoacetic acid. Iodoethanoic acid, the least volatile of the compounds studied, required a solid phase micro extraction (SPME) technique (acrylate fibre) to concentrate material from the gas phase (17). This SPME fibre was calibrated with solutions of known concentration of iodoethanoic acid.

Equilibrium of the organic iodides between the gas and aqueous phase was generally reached within an hour, but sampling continued for several hours (every 30–60 min). Experiments were performed in duplicate.

## 4. Results

### 4.1 Hydrolysis rates

A typical absorbance growth curve at 225 nm observed during the hydrolysis of organic iodides is shown in Fig. 1.

The first-order rate constant for the hydrolysis of an organic compound was obtained from the growth curve of the absorbance at 225 nm as a function of time. The absorbance is related to the rate constant of the hydrolysis of the organic compound as follows.

Assuming that the rate of the hydrolysis reaction (rxn. [5]) has a first-order rate dependence<sup>3</sup> (more discussion in Section 5.1), the following expressions can be written:

$$[8] \quad -\frac{d[\text{RI}(\text{aq})]_t}{dt} = \frac{d[\text{I}^-]_t}{dt} = k \cdot [\text{RI}(\text{aq})]_t$$

$$[9] \quad [\text{RI}(\text{aq})]_t = [\text{RI}(\text{aq})]_0 \cdot e^{-kt}$$

$$[10] \quad [\text{I}^-]_t = [\text{I}^-]_0 + [\text{RI}(\text{aq})]_0(1 - e^{-kt})$$

$$[11] \quad [\text{ROH}(\text{aq})]_t = [\text{ROH}(\text{aq})]_0 + [\text{RI}(\text{aq})]_0(1 - e^{-kt})$$

where  $k$  is the rate constant for the hydrolysis reaction of organic iodide,  $[\text{RI}(\text{aq})]_t$ ,  $[\text{I}^-]_t$ , and  $[\text{ROH}(\text{aq})]_t$  are the concentrations of reactant, organic iodide, and products, iodide and alcohol, at time  $t$ , and  $[\text{RI}(\text{aq})]_0$  and  $[\text{I}^-]_0$  are the initial concentrations of organic iodide and iodide.

The main contributor to the absorbance at 225 nm is  $\text{I}^-$ , but alcohols and organic iodides also absorb at this wavelength:

$$[12] \quad A_{225\text{nm}}(t) = \epsilon_{\text{I}^-}[\text{I}^-]_t + \epsilon_{\text{ROH}}[\text{ROH}(\text{aq})]_t + \epsilon_{\text{RI}}[\text{RI}(\text{aq})]_t$$

where  $A_{225\text{nm}}$  is the observed absorbance at 225 nm, and  $\epsilon_{\text{I}^-}$ ,  $\epsilon_{\text{RI}}$ ,  $\epsilon_{\text{ROH}}$  are the molar absorptivities of iodide, the organic iodide, and the corresponding alcohol, at 225 nm, respectively. Therefore, the observed absorbance as a function of time,  $A_{225\text{nm}}(t)$  has the following relationship:

$$[13a] \quad A_{225\text{nm}}(t) = \epsilon_{\text{I}^-}([\text{I}^-]_0 + [\text{RI}(\text{aq})]_0(1 - e^{-kt})) + \epsilon_{\text{ROH}}([\text{ROH}(\text{aq})]_0 + [\text{RI}(\text{aq})]_0(1 - e^{-kt})) + \epsilon_{\text{RI}}[\text{RI}(\text{aq})]_0 \cdot e^{-kt} = (\epsilon_{\text{I}^-}[\text{I}^-]_0 + \epsilon_{\text{ROH}}[\text{ROH}(\text{aq})]_0 + \epsilon_{\text{RI}}[\text{RI}(\text{aq})]_0) + (\epsilon_{\text{I}^-} + \epsilon_{\text{ROH}} - \epsilon_{\text{RI}})[\text{RI}(\text{aq})]_0(1 - e^{-kt}) = A_{225\text{nm}}(t=0) + (\epsilon_{\text{I}^-} + \epsilon_{\text{ROH}} - \epsilon_{\text{RI}})[\text{RI}(\text{aq})]_0(1 - e^{-kt}) = A_{225\text{nm}}^{\text{INF}} - (\epsilon_{\text{I}^-} + \epsilon_{\text{ROH}} - \epsilon_{\text{RI}})[\text{RI}(\text{aq})]_0 e^{-kt}$$

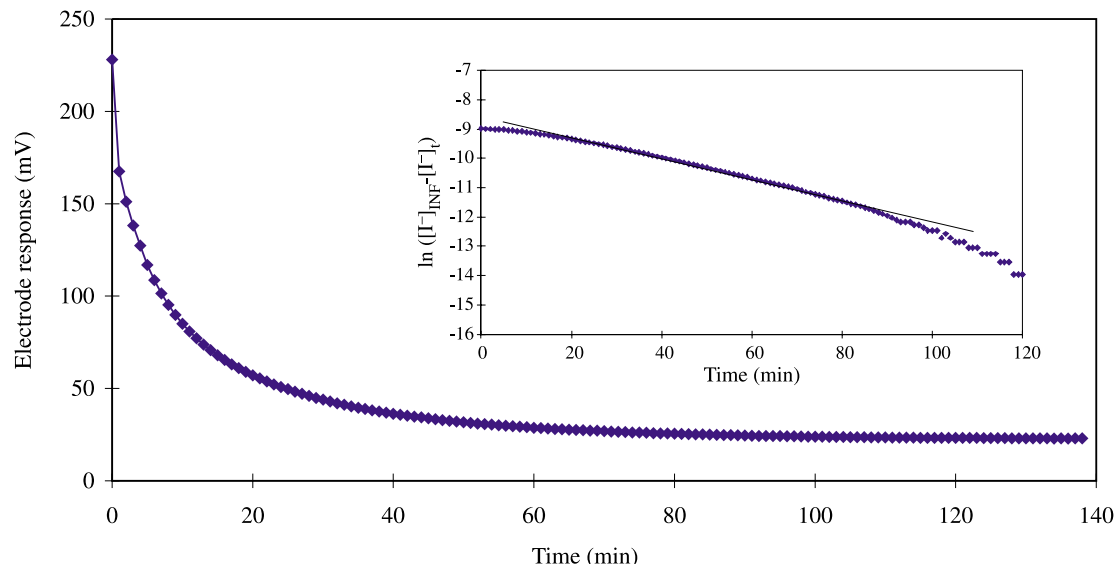
where  $A_{225\text{nm}}(t=0)$  is the absorbance at 225 nm at time zero (see eq. [12]) and  $A_{225\text{nm}}^{\text{INF}}$  is the absorbance at 225 nm at time infinity (i.e., when the reaction is completed);

$$[13b] \quad A_{225\text{nm}}^{\text{INF}} = A_{225\text{nm}}(t=\infty) = A_{225\text{nm}}(t=0) + (\epsilon_{\text{I}^-} + \epsilon_{\text{ROH}} - \epsilon_{\text{RI}})[\text{RI}(\text{aq})]_0$$

<sup>3</sup>The hydrolysis of organic iodides occurs via either an  $\text{S}_{\text{N}}1$  or  $\text{S}_{\text{N}}2$  mechanism (see section 5.1). For a given constant pH, both mechanisms yield a first-order dependent rate equation.



**Fig. 2.** Plot of electrode response during the hydrolysis of 2-iodobutane at 60°C. Inset shows the log plot of  $[I^-]$ .



Equation [13a] can be rewritten as:

$$[13c] \quad \ln A_{225nm}^{INF} (-A_{225nm}(t)) = \ln ((\epsilon_{I^-} + \epsilon_{ROH} - \epsilon_{RI})[RI(aq)]_0) - kt = \text{const} - kt$$

The plot of  $\ln A_{225nm}^{INF} (-A_{225nm}(t))$  vs. time therefore provides the rate constant for hydrolysis of RI. The absorbance growth curve is replotted in the semi-log scale in the inset of Fig. 1 and shows first-order behaviour.

A sample electrode response observed of the hydrolysis of 2-iodobutane is shown in Fig. 2. The signal was first converted into  $I^-$  concentration according to the probe calibration. The  $[I^-]_{\infty} - [I^-]_t$  is plotted on a log scale in the inset of Fig. 2, because the slope yields the rate constant.

$$[14] \quad \ln ([I^-]_{\infty} - [I^-]_t) = \text{const} - kt$$

Because the response is nonlinear, there is greater uncertainty at the beginning of the experiment. The uncertainty becomes larger again later when the electrode response is very small. This was considered when extracting a *pseudo*-first-order rate constant from the log plot, i.e., more weight was given to the data points in the middle of the test. As mentioned in Section 3.1, the iodide electrode method was used only for the hydrolysis of 2-iodobutane.

The hydrolysis of all the organic iodides studied in this work exhibited a first-order dependence on organic iodide concentration. Furthermore, the rate constant ( $k$ ) for the organic iodide hydrolysis was, in general, observed to have a simple Arrhenius temperature dependence (Figs. 3–5), suggesting that the main hydrolysis mechanism did not change over the temperature range studied.

Repeat measurements agreed to within 10%, except for iodomethane and iodoethanoic acid. For these cases, the longer duration required for each measurement made reproducibility more difficult to achieve. The rate constants at 70°C (or at a specified temperature if 70°C data were not obtained) and the activation energies are summarized in Table 2. Also given in the table are the values of the preexponential factors that provide the best fits to the data

over the studied temperature ranges. Individual data are discussed in more detail below.

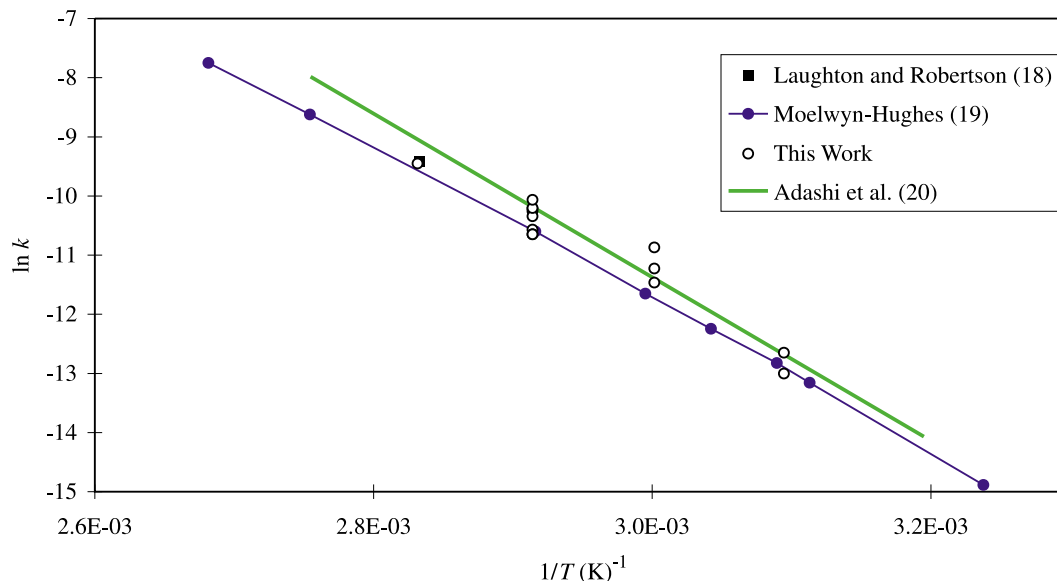
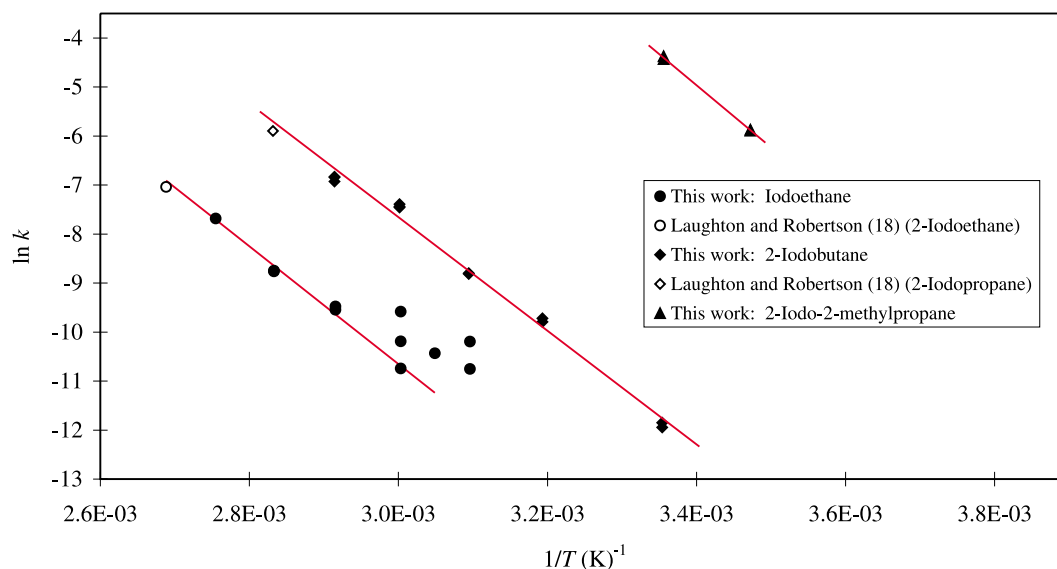
### Iodoalkanes

The hydrolysis rate for alkyl iodides was observed to increase from primary (iodomethane and iodoethane) to secondary (2-iodobutane) to tertiary (2-iodo-2-methylpropane) compounds. Because of the low rate, measurements for iodomethane were made only at higher temperatures. The rate constants obtained at 50 and 60°C have higher uncertainty because only a small portion of the organic iodide had hydrolysed over the test period. The reproducibility improved at 70°C, where the standard error was ~20%, based on the standard deviation of the measurements made at each temperature. The iodomethane data obtained in this work were compared to data available in the literature (Fig. 3), showing reasonable agreement with data taken from Laughton and Robertson (18), Moelwyn-Hughes (19), and Adachi et al. (20). Adachi et al. (20) presented formulas to generate both the  $S_N1$  and the  $S_N2$  rate constants at each temperature. The line in Fig. 3 attributed to Adachi et al. (20) was generated from the formula for the  $S_N1$  rate constant.

The activation energy measured in the current work is  $(104 \pm 10) \text{ kJ mol}^{-1}$  and is slightly lower than the value  $(115 \text{ kJ mol}^{-1})$  reported by Adachi et al. (20). A fit to Moelwyn-Hughes' data provides an activation energy of  $106 \text{ kJ mol}^{-1}$ . The uncertainty quoted for the activation energies measured in the current work is the statistical standard error of the regression analysis.

The hydrolysis rate of iodoethane (a primary alkyl iodide) was only marginally faster than that of iodomethane at a given temperature (Fig. 4). An activation energy of  $(100 \pm 6) \text{ kJ mol}^{-1}$  was determined for the hydrolysis of iodoethane. For the determination of the activation energy, less emphasis was placed on the lower temperature data points due to the uncertainty in the measurements. Also shown in Fig. 4 is the value measured by Laughton and Robertson (18) at 99°C, which falls on the linear extrapolation of the Arrhenius dependence of our 60–90°C data.



**Fig. 3.** Arrhenius plot for the hydrolysis of iodomethane.**Fig. 4.** Arrhenius plot for the hydrolysis of iodoethane, 2-iodobutane, and 2-iodo-2-methylpropane. Laughton and Robertson's (18) values for iodoethane and 2-iodopropane (another secondary iodide) are also included. Note that the "hydrolysis" of 2-iodo-2-methylpropane was performed in a 70% methanol:30% water solution.

The hydrolysis rates of the secondary alkyl iodide (2-iodobutane) were obtained using the iodide specific electrode method. The observed rates are in line with other data in the literature on hydrolysis of secondary iodides (Fig. 4). Extrapolating the 2-iodobutane results to  $80^\circ\text{C}$  yields a hydrolysis rate of about  $3.3 \times 10^{-3} \text{ s}^{-1}$ , which is comparable to Laughton and Robertson's (18) 2-iodopropane value of  $(2.75 \pm 0.004) \times 10^{-3} \text{ s}^{-1}$  at this temperature. An activation energy of  $(97 \pm 5) \text{ kJ mol}^{-1}$  was determined for 2-iodobutane.

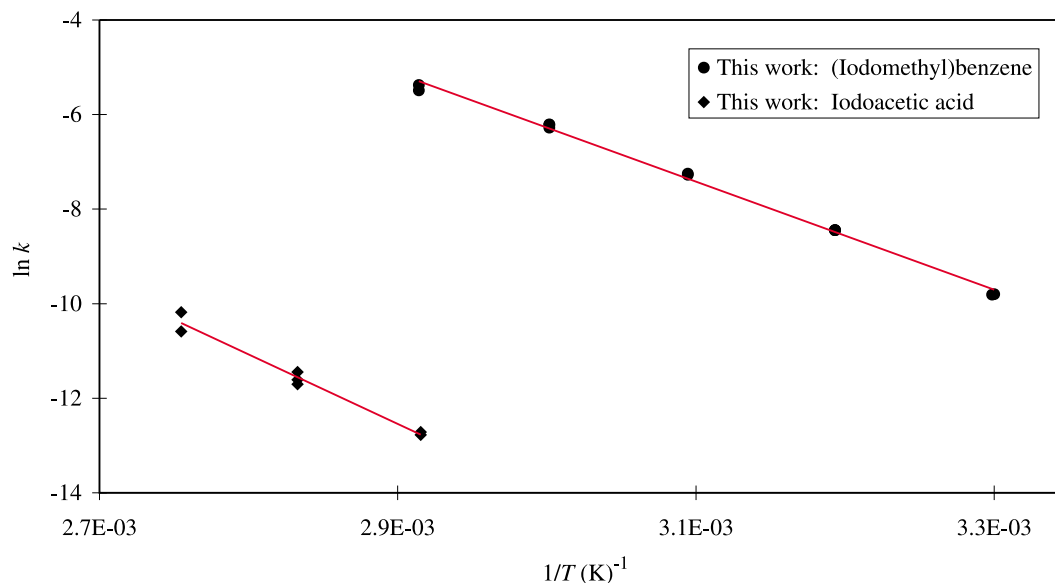
The hydrolysis rate for the tertiary alkyl iodide (2-iodo-2-methylpropane) was very fast, and could not be measured in pure water using the chosen method. Instead, a lower limit for the hydrolysis rate for the compound was determined in a 30% water, 70% methanol solution at only two temperatures (15 and  $25^\circ\text{C}$ ) (Fig. 4). This slowed the reaction down

to the point where it could be measured ( $t_{1/2} \sim 60 \text{ s}$ ), however, there may be a mixture of reactions occurring (i.e., the methanol may be reacting with the 2-iodo-2-methylpropane to form an ether). Therefore, the measurement is considered to be a lower limit for the hydrolysis reaction. An activation energy of  $\sim 106 \text{ kJ mol}^{-1}$  was determined from the data assuming a simple Arrhenius dependence.

#### Organic iodides with functional groups

The hydrolysis rates for (iodomethyl)benzene (benzyl iodide) were measured using the spectrophotometric method. Difficulties encountered due to the low solubility of this compound were circumvented by decanting an aliquot of homogeneous solution from a dissolution vessel to avoid undissolved globules of (iodomethyl)benzene at the bottom of the reaction vessel.



**Fig. 5.** Arrhenius plot for the hydrolysis of (iodomethyl)benzene and iodoacetic acid.**Table 2.** Hydrolysis rates and temperature dependencies.

Compound	Hydrolysis rate at 70°C (s <sup>-1</sup> ) <sup>a</sup>	Temperature dependence ( $Ae^{-E_a/RT}$ )	
		$\ln(A)$ <sup>b</sup>	$E_a$ (kJ mol <sup>-1</sup> ) <sup>b</sup>
Iodomethane	$(3.2 \pm 0.7) \times 10^{-5}$	$26.0 \pm 4.0$	$104 \pm 10$
Iodoethane	$(7.4 \pm 0.3) \times 10^{-5}$	$25.4 \pm 2.0$	$100 \pm 6$
2-Iodobutane	$(1.04 \pm 0.06) \times 10^{-3}$	$27.1 \pm 1.2$	$97 \pm 5$
Iodoethanoic acid	$(2.92 \pm 0.08) \times 10^{-6}$	$33.6 \pm 3.2$	$122 \pm 10$
(Iodomethyl)benzene	$(4.4 \pm 0.3) \times 10^{-3}$	$27.1 \pm 0.8$	$95 \pm 5$
Iodoethanol <sup>c</sup>	$(1.8 \pm 0.1) \times 10^{-5}$ (at 90°C)	Not determined	Not determined
2-Iodobenzenol	$<6 \times 10^{-8}$ (at 80°C) <sup>d</sup>	Not determined	Not determined
2-Iodo-2-methylpropane	$>1.2 \times 10^{-2}$ (at 25°C) <sup>e</sup>	$38.2 \pm 0.9$ <sup>f</sup>	$106 \pm 2$ <sup>f</sup>

<sup>a</sup>Uncertainty given is the statistical standard error in the duplicate measurements at a given temperature. The error given for the rate is the standard deviation among the measured values.

<sup>b</sup>Uncertainty is the statistical standard error of the Arrhenius fit to the data.

<sup>c</sup>Only two measurements were made, both at 90°C.

<sup>d</sup>Estimated upper limit.

<sup>e</sup>Lower limit estimated in a 70% methanol/30% water solution. It is not known if methanol is reacting with the 2-iodo-2-methylpropane as well.

<sup>f</sup>Estimate based on data from a 70% methanol/30% water solution.

The Arrhenius plot (Fig. 5) appears linear over the range of temperatures measured (30–70°C), and extrapolation to the entire aqueous range (0–100°C, at a total pressure of 1 bar) should be acceptable. The rates of this reaction can be compared to those of other benzyl halides measured by Laughton and Robertson (18) ( $2.7 \times 10^{-4} \text{ s}^{-1}$  at 30°C for (bromomethyl)benzene and  $5.8 \times 10^{-4} \text{ s}^{-1}$  at 60°C for (chloromethyl)benzene). The rate of (iodomethyl)benzene hydrolysis seems to fall in between the rates of (bromomethyl)benzene and (chloromethyl)benzene hydrolysis, a trend that has been noted in the past for alkyl halides (18, 19). An activation energy of  $95 \pm 5 \text{ kJ mol}^{-1}$  was extracted from the data.

The hydrolysis rate of iodoethanoic acid was slower than that of iodoethane (and therefore only high temperature measurements were made), even though the basic carbon chain is the same. Iodoethanoic acid has a  $\text{p}K_a$  of 3.12 (21); therefore, most of it would have been dissociated at the start-

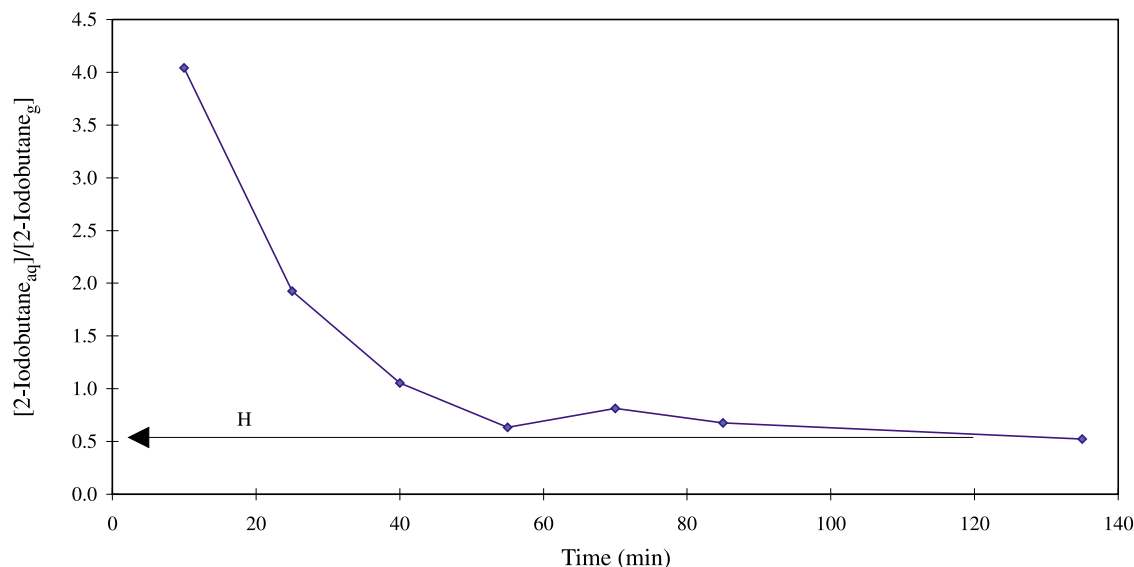
ing pH of the solution (measured at approximately 4.5). One can speculate that perhaps the hydrolysis occurs with primarily the neutral form, the concentration of which, under these conditions, is effectively reduced. The larger field and steric effects of the carboxylic acid group in iodoethanoic acid, compared to the effects of alkyl group in iodoethane, may also contribute to the slower hydrolysis rate (22). An activation energy of  $122 \pm 5 \text{ kJ mol}^{-1}$  was extracted from the Arrhenius plot.

Iodoethanol has a very slow hydrolysis rate. Due to the length of time required for the measurements, the rate constant was measured only at 90°C, and was found to be  $(1.8 \pm 0.1) \times 10^{-5} \text{ s}^{-1}$  (average of two values).

The rate of hydrolysis for 2-iodobenzenol (2-iodophenol) was too slow to measure directly. The rate was estimated to be less than  $6 \times 10^{-8} \text{ s}^{-1}$ , based upon the minor increase in absorbance observed after 85 h at 80°C.



**Fig. 6.** Ratio of the aqueous to gas phase concentration of 2-iodobutane as a function of time after the pure compound is introduced into the aqueous phase of the vessel (60°C).



#### 4.2 Partition coefficients

Henry's Law states that at equilibrium, the solubility of a gas is proportional to the partial pressure of the gas ( $P_{\text{Compound}}$ ) above the liquid phase:<sup>4</sup>

$$[15] \quad \text{Henry's Constant} = \left( \frac{[\text{Compound}(\text{aq})]}{P_{\text{Compound}}} \right)_{\text{eq}}$$

There are many units available to describe this ratio because there are many different units of pressure and concentration (e.g.,  $\text{mol dm}^{-3} \text{ atm}^{-1}$ ). In this document, we use the term "partition coefficient" and the symbol " ${}^{\text{H}}K$ " to signify a unitless form of Henry's Law constants as it is a more commonly adopted definition in the nuclear industry (see eq. [7]).

Henry's Law constants depend upon temperature, and are independent of the volume of gas or volume of liquid phase. The partition coefficients of the organic iodides were observed to follow a simple exponential temperature dependence over the studied temperature range:

$$[16] \quad \ln {}^{\text{H}}K^T = \ln {}^{\text{H}}K^{298} + \left( \frac{-\Delta_r H^\circ}{R} \left( \frac{1}{T} - \frac{1}{298} \right) \right)$$

where  $T$  is absolute temperature,  $R$  is the gas constant,  $\Delta_r H^\circ$  is the enthalpy of reaction (i.e., gas–aqueous phase partitioning) and  ${}^{\text{H}}K^T$  and  ${}^{\text{H}}K^{298}$  are the partition coefficients of a given compound at temperature  $T$  and 25°C (298 K).<sup>5</sup>

In this work, the aqueous and gas samples were analyzed simultaneously as a function of time until the system reached equilibrium between the aqueous and gas phases. The equilibrium was generally reached within an hour, but sampling continued for several hours (every 30–60 min). An example of the ratio of the aqueous phase concentration to the gas phase concentration observed as a function of time is shown in Fig. 6. Shown in the figure are data for 2-iodobutane at 60°C. The limiting value provides the partition coefficient ( ${}^{\text{H}}K$ ).

The results are summarized in Tables 3 and 4 along with the literature values of similar organic iodides. The examples of the scatter in the data for the partition coefficient and its temperature dependence are presented in Figs. 7 and 8 for iodomethane and iodoethanol. Individual data are discussed below.

#### Iodoalkanes

The partition coefficient of iodomethane determined in this study showed an exponential relationship of  $\ln {}^{\text{H}}K = (3430 \pm 60)/T - (9.9 \pm 0.2)$  (Fig. 7). Our results agree with the partition coefficient measured by Hunter-Smith et al.

<sup>4</sup>This law holds for solutions dilute enough that the environment of the solute remains constant. Mackay and Shiu (23) suggest a mol fraction of 0.01 as an upper limit.

<sup>5</sup>The partition coefficient is an equilibrium constant, and has the following relationship at a given temperature:

$$\Delta_r G^\circ = -RT \ln ({}^{\text{H}}K/RT) = \Delta_r H^\circ - T\Delta_r S^\circ$$

$$\text{or } \ln ({}^{\text{H}}K) - \ln (RT) = -(\Delta_r H^\circ/RT) + \Delta_r S^\circ/R$$

where  ${}^{\text{H}}K$  is the Henry's constant as defined in eq. [15]. The use of eq. [16] to determine the exponential temperature dependence of the partition coefficient thus implies that the  $\Delta_r H^\circ$  value reported in this document is the average enthalpy of the gas–liquid partitioning over a temperature range of the aqueous phase. Over the studied temperature range, the enthalpy of the partitioning of the organic iodides appears to be nearly temperature-independent. The use of eq. [16] also implies that the second term of the left hand side of the above thermodynamic relationship ( $\ln (RT)$ ) is ignored in obtaining the slope (the contribution of the term to the slope is very small). Thus, the  $\Delta_r H^\circ$  value reported here is the enthalpy of reaction to a first-order approximation.



**Table 3.** Effect of iodine atoms on partition coefficients.

Compound	$^H K$ (25°C)	Reference	Iodine-substituted compound	$^H K$ (25°C)	Reference	Rel. ratio
Methane	0.04	27	Iodomethane	$4.82 \pm 0.01$	This work	120
			Diiodomethane	56	23	1400
			Triiodomethane	88	28	2200
Ethane	0.05	27	Iodoethane	$2.84 \pm 0.01$	This work	57
Propane	0.04	27	1-Iodopropane	2.6	23	65
			2-Iodopropane	2.2	23	55
Butane	0.03	27	1-Iodobutane	1.5	23	50
			2-Iodobutane	$2.1 \pm 0.3$	This work	70
Benzene	4.5	27	Iodobenzene	19	27	4
Chloromethane	2.6	27	Chloriodomethane	22	23	8
Ethanol	4900	23	Iodoethanol	$73\,000 \pm 3000$	This work	15
Ethanoic acid	127\,000	23	Iodoethanoic acid	$490\,000 \pm 90\,000$	This work	4

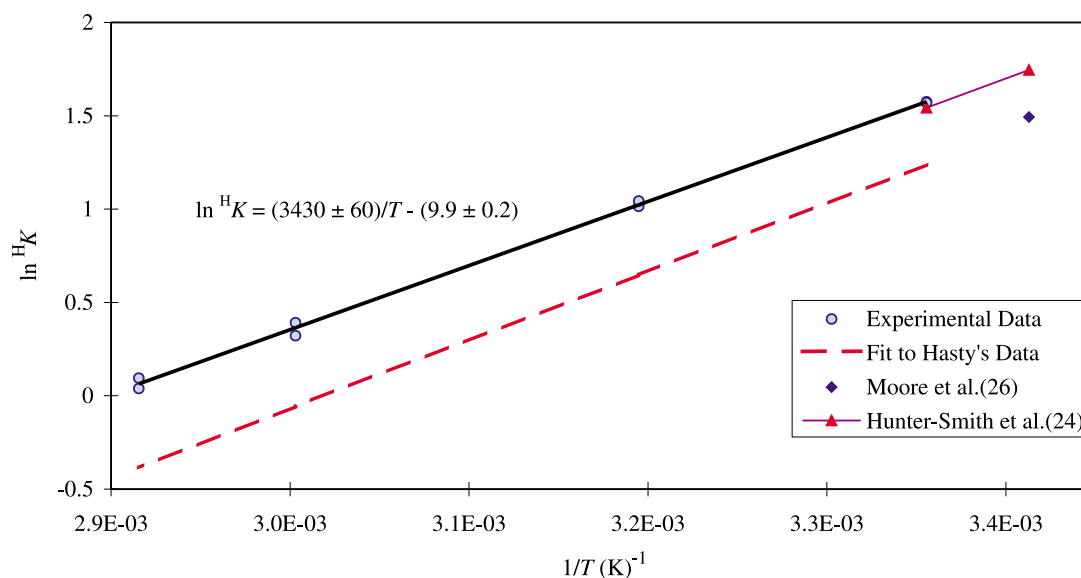
**Note:** The errors listed are the statistical standard error.

**Table 4.** The temperature dependence of partition coefficients of compounds with and without iodine atoms.

Compound	$-\Delta_r H^\circ/R^a$ (K)	Reference	Iodine-substituted compound	$-\Delta_r H^\circ/R^a$ (K)	Reference
Methane	1800	23	Iodomethane	$3430 \pm 60$	This work
			Diiodomethane	5000	26
Chloromethane	3000	26	Chloriodomethane	4300	26
Ethane	2300	23	Iodoethane	$3800 \pm 120$	This work
Butane	3100	23	2-Iodobutane	$3400 \pm 400$	This work
Ethanol	6600	23	Iodoethanol	$7900 \pm 600$	This work
Ethanoic acid	6400	23	Iodoethanoic acid	$11\,500 \pm 800$	This work

**Note:** The errors listed are the statistical standard error.

<sup>a</sup>See footnote 5.

**Fig. 7.** Temperature dependence of the partition coefficient of iodomethane.

(24), and to within 20–60% of those obtained by Hasty (25), and Moore et al. (26). The partition coefficients of Iodoethane and 2-iodobutane and their temperature dependences are very similar to those of iodomethane (Tables 3 and 4).

#### Organic iodides with functional groups

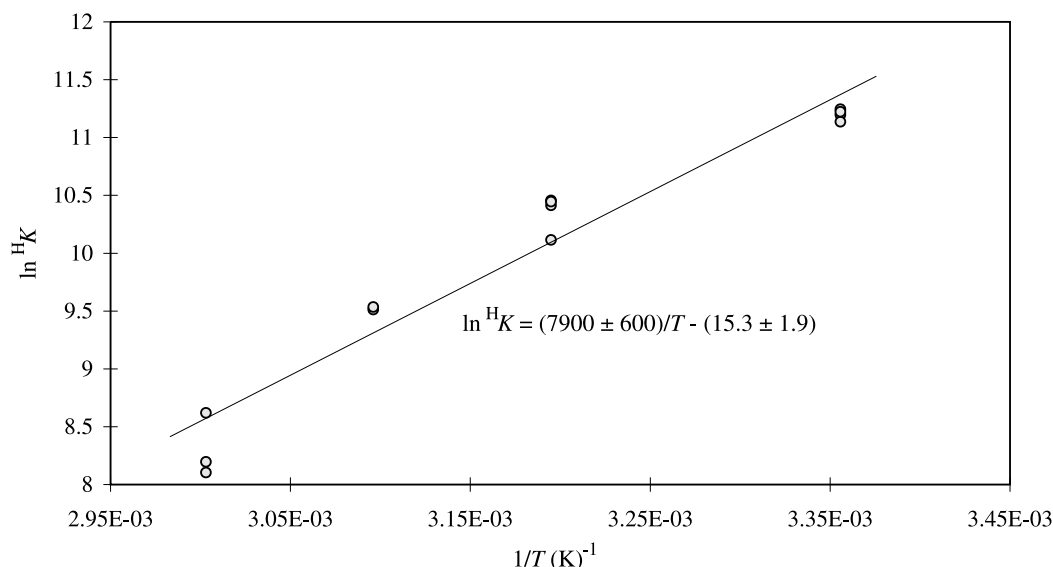
For the remaining compounds, the partition coefficients of only iodoethanol and iodoethanoic acid were obtained.<sup>6</sup> These compounds are highly soluble in water and have very high partition coefficients and steep temperature

<sup>6</sup>The partition coefficients of (iodomethyl)benzene and 2-iodo-2-methylpropane could not be determined because they hydrolysed too quickly to obtain any meaningful results.



**Table 5.** Literature hydrolysis rates.

Compound	Temperature (°C)	Rate constant (s <sup>-1</sup> )	Reference
Iodomethane	60	$8.72 \times 10^{-6}$	19
Iodomethane	60	$2.3 \times 10^{-5}$	20
Iodomethane	70	$2.49 \times 10^{-5}$	19
Iodomethane	80	$2.34 \times 10^{-4}$	20
Iodomethane	80	$8.19 \times 10^{-5}$	18
Iodomethane	90	$1.8 \times 10^{-4}$	19
Iodoethane	99	$8.78 \times 10^{-4}$	18
2-Iodopropane	80	$2.75 \times 10^{-3}$	18
1-Iodopropane	100	$5.49 \times 10^{-4}$	18
1-Iodo-2-methylpropane	100	$3.55 \times 10^{-4}$	18

**Fig. 8.** Temperature dependence of the partition coefficient of iodoethanol.

dependences (Tables 3 and 4, see also Fig. 8). Because of the high partition coefficients, a higher aqueous concentration ( $\sim 1 \times 10^{-3}$  mol dm<sup>-3</sup>) was used for these compounds to ensure a detectable amount in the gas phase. Furthermore, for iodoethanoic acid, a microextraction technique was used for the gas phase detection, in which small amount of iodoethanoic acid was adsorbed and concentrated onto a micro-extraction fibre before injection into the GC.

## 5. Discussion

### 5.1 Hydrolysis rates

Hydrolysis of halogenated aliphatic compounds (rxn. [5]) occurs via well-known nucleophilic substitution mechanisms (S<sub>N</sub>1 and S<sub>N</sub>2). Because the relative contribution of these two mechanisms to the overall hydrolysis of organic iodides impacts on the dependence of its rate on the OH<sup>-</sup> concentration, the nucleophilic substitute mechanisms are reviewed briefly below, prior to the discussion on the hydrolysis rate of organic iodides.

The S<sub>N</sub>2 hydrolysis reaction of iodo-compounds is a second-order process, with a rate dependent upon the concentration of both OH<sup>-</sup> and the organic iodide. Because of the dependence on [OH<sup>-</sup>], the hydrolysis rate of organic iodides would depend strongly on pH. Because the S<sub>N</sub>2 mechanism

involves the hydroxide ion approaching the reactive carbon, steric hindrance affects the rate. Therefore, the relative S<sub>N</sub>2 hydrolysis rate at a given pH and temperature, is as follows (21, 29):

methyl > primary > benzylic > secondary > tertiary

The S<sub>N</sub>1 reaction rate depends only on the concentration of iodo-alkane because the rate-determining step is the unimolecular dissociation of the carbon—halogen bond. Thus, for S<sub>N</sub>1, the hydrolysis rate depends on the stability (and therefore, the structure) of the intermediate carbocation, and the relative S<sub>N</sub>1 rates are (21, 29):

tertiary > secondary, benzylic > primary, methyl

The structure of the iodo-compound and the OH<sup>-</sup> concentration governs which one of the two nucleophilic substitution mechanisms is dominant. The primary alkyl-iodides should be the most sensitive to pH, as they can hydrolyse faster than other iodo-compounds via the S<sub>N</sub>2 reaction, where the nucleophile is OH<sup>-</sup>. Thus, if there were any significant pH dependence of hydrolysis rate, it would be most pronounced for iodomethane. Adachi et al. (20) have measured both the S<sub>N</sub>1 and S<sub>N</sub>2 rates of iodomethane hydrolysis



separately, over a temperature range of 25–65°C. Their measurements show that, at a given temperature, the  $S_N2$  contribution to the overall hydrolysis of iodomethane is negligible at pH 6, and does not become significant until about pH 11. Therefore, the  $S_N2$  portion of the reaction can be ignored for the pH range studied in this work. Furthermore, since methyl iodide represents the structure which undergoes  $S_N2$  hydrolysis the fastest, it follows that the  $S_N2$  portion of the hydrolysis rates of all other iodinated compounds can be ignored as well, for the pH range used in this work, and for the pH range (pH 4–10) expected in containment.

Table 5 lists the hydrolysis rates of various alkyl iodides reported by other groups (18–20). (The hydrolysis rates measured in the current study are summarized in Table 2). A hydrolysis rate of  $(3.2 \pm 0.7) \times 10^{-5} \text{ s}^{-1}$  at 70°C and an activation energy of  $(104 \pm 10) \text{ kJ mol}^{-1}$  obtained for iodomethane in this study are in good agreement with the values observed by Molewyn-Hughes (19): a hydrolysis rate of  $2.49 \times 10^{-5} \text{ s}^{-1}$  at 70°C and an activation energy of  $106 \text{ kJ mol}^{-1}$ . Adachi et al. (20) obtained an activation energy of  $113 \text{ kJ mol}^{-1}$  for the  $S_N1$  portion of the reaction, and also provided an expression for the temperature dependence for the  $S_N2$  contribution.

Since the main mechanism for the hydrolysis of organic iodides under the experimental conditions (and also expected under accident conditions) is  $S_N1$ , the hydrolysis can be expressed as a simple first-order process. The first-order rate constant ( $k$ ) for the hydrolysis of organic iodides (given in Tables 2 and 5) varies widely at a given temperature. The observed trend is in good agreement with the relative rates expected for  $S_N1$  reactions previously discussed: slow for primary alkyl iodides (e.g.,  $(3.2 \pm 0.7) \times 10^{-5} \text{ s}^{-1}$  at 70°C for iodomethane) and aromatic iodides (e.g., less than  $6 \times 10^{-8} \text{ s}^{-1}$  for 2-iodobenzenol) and faster for benzylic and secondary alkyl iodides (e.g.,  $(4.4 \pm 0.3) \times 10^{-3} \text{ s}^{-1}$  for (iodomethyl)benzene and  $(1.04 \pm 0.05) \times 10^{-3} \text{ s}^{-1}$  for 2-iodobutane) and fastest for tertiary alkyl iodides (e.g., very fast even at 25°C for 2-iodo-2-methylpropane). As could be predicted by its nucleophilic substitution mechanism, the most important factor affecting hydrolysis rate is the position of the iodine atom on the carbon structure, rather than the number of carbons in the molecule. For example, 1-iodobutane would be expected to have a hydrolysis rate comparable to that of iodoethane (another primary iodide).

Functional groups adjacent to the iodide atom appear to modify the rates slightly as well (e.g., the hydrolysis rates of iodoethanoic acid and iodoethanol are lower than that of iodoethane). More data would be required to fully assess the effect of functional groups.

The rate constants of the organic iodides studied were observed to have a simple Arrhenius temperature dependence, indicating that for a given compound, the main hydrolysis mechanism (i.e.,  $S_N1$  for all the compounds studied) did not change over the temperature range studied. The observed trend for the activation energy also follows that expected from the  $S_N1$  mechanism, lower for (iodomethyl)benzene and 2-iodobutane than for primary alkyl iodides or iodoethanoic acid.

## 5.2 Partition coefficients

Partition coefficients reported in the literature, along with our data, are listed in Tables 3 and 6. Also shown in these

**Table 6.** Selected partition coefficients (25°C) for various classes of compounds.

Compound class	Examples	$^H K$ (approx.) <sup>a</sup>
Alkanes	Hexane	0.02
Alcohols	Methanol	5300
	Ethanol	4900
	Butanol	2900
	Hexanol	1500
	Phenylmethanol	220 000
Diols	1,2-Ethanediol	$9.8 \times 10^7$
Aldehydes	Formaldehyde	73 000
	Acetaldehyde	370
	Hexanal	120
Ketones	Acetone	730
	Methyl ethyl ketone	500
	Methyl isobutyl ketone	54
Carboxylic acids	Ethanoic acid	122 000
	Phenylmethanolic acid	580 000
	Hexanoic acid	29 000
Aromatic	Benzene	4.5
	Toluene	4.1
	1,4-Dimethylbenzene	3.2
	Ethyl benzene	3.2
	Styrene	9
Phenolic	Benzenol	39 000
	4-Methylbenzenol	15 000
Multifunctional	Phenylmethanol	220 000
	Hydroxyethanol	1 000 000
	Hydroxypropanoic acid	$1.7 \times 10^9$
	Propanonal	780 000

<sup>a</sup>Values taken from refs. 23 and 27.

tables are the partition coefficients of non-iodine substituted organic compounds. Comparison of the partition coefficients of these organic iodides with their non-iodine-substituted counterparts provides a reasonable approach to estimate the partition coefficients of other organic iodides. The partition coefficients of organic compounds at 25°C are reviewed first, followed by their temperature dependencies.

Table 3 compares the partition coefficients at 25°C of the few measured organic iodides to those of their non-iodine-substituted counterpart. An examination of Table 3 shows that substituting an iodine atom into a molecule makes the compound less volatile, but the impact of the change decreases as the partition coefficient increases.

Studies on Henry's Law constants have found relationships between the partition coefficient and structural components of a molecule, such as bonds and functional groups (30–33). In general, hydrophilic components such as halogen, oxygen, nitrogen, and sulphur containing functional groups increase the partition coefficient, whereas hydrophobic components such as long chains of carbon—carbon bonds and carbon—hydrogen bonds, decrease the partition coefficient. Some of these trends are apparent by examining the values listed in Tables 3 and 6. Several methods of estimating partition coefficients by empirically correlating partition coefficients with structural parameters have been devised (30–33). These methods provide ways to predict Henry's Law constants for molecules with different functional groups to within a factor of two or three, based upon



**Table 7.** Range of temperature dependencies of  $^H K$  for various classes of organic compounds.

Compound Class	Range of $-\Delta_r H^\circ/R^a$ (K)	Examples	$-\Delta_r H^\circ/R^a$ (K)
Alkanes	1500–8000	Methane	1800
		Butane	3100
Alcohols	5000–8000	Methanol	5400
		Butanol	7300
		2-Propanol	7500
Aldehydes	4000–9000	Methanal	7000
		Ethanal	5000
		Hexanal	6500
Ketones	4000–10 000	Propanone	5000
		2-Butanone	5500
		3-Pentanone	9200
Carboxylic acids	5700–11 000	Ethanoic acid	6400
		Phenylmethanoic acid	6500
		Hexanoic acid	6300
Aromatic (one ring)	3000–5000	Benzene	4000
		Methylbenzene	4000
		1,4-Dimethylbenzene	5000
Phenolic	7000–8000	Benzenol	7000
		4-Methylbenzenol	7300
Multifunctional	—	Hydroxyethanol	4600
		Propanonal	7500

<sup>a</sup>Ranges and approximate values taken from ref. 27.

sets of compounds for which the constant has been experimentally determined. These structure-based calculation methods predict the trend observed in Table 3 that the substitution of an iodine atom for a hydrogen atom within a molecule generally increases the partition coefficient. This increase ranges from two orders of magnitude for low solubility alkane organic compounds (i.e., methane to butane in Table 3), to a factor of 5–10 for highly soluble organic compounds containing a carbonyl, alcohol, or carboxylic acid group.

Table 6 lists the partition coefficients of non-iodinated compounds, from which the partition coefficients of the counterpart organic iodides can be estimated. In general, the partition coefficient increases with the number of oxygen atoms, and decreases with length of the carbon chain. Not all functional groups containing one oxygen atom are equal though; for example, alcohols have much higher partition coefficients than ketones.

The temperature dependences for the partition coefficients of organic iodides reported in the literature and from this work are compared with the temperature dependence of corresponding non-iodine-substituted (parent) organic compounds in Tables 4 and 7.

The value of  $-\Delta_r H^\circ/R$  of an organic iodide is consistently higher than that of the corresponding non-iodine-substituted organic compound for the small number of comparisons available (Table 4). However, the increase is small enough that the temperature dependencies of the partition coefficient of an organic iodide may be approximated from that of non-iodine-substituted counterpart. Table 7 lists the range of  $-\Delta_r H^\circ/R$  for various classes of organic compounds. The value of  $-\Delta_r H^\circ/R$  ranges from about 500–10 000 K. Organic iodides and corresponding non-iodine-substituted organic compounds that are more volatile than  $I_2$  at 25°C (i.e., alkane and aromatic compounds), have  $-\Delta_r H^\circ/R$ , of the order

of 3400 K, whereas the other more soluble compounds have a  $-\Delta_r H^\circ/R$  of the order of 6500 K. Note that the partition coefficient of  $I_2$  has a temperature dependence ( $-\Delta_r H^\circ/R$ ) of ~4000 K (34–36).

The pH is not likely to affect the partitioning of a compound, unless the solubility of a compound is affected, which is not expected to occur at the pH range expected in containment (pH < 11). However, for the compounds that have pKa values within the pH range being considered, the distribution between the acid and base forms must be considered.

### 5.3 Proposed grouping of organic iodides for reactor safety analysis applications

The wide range of organic iodides expected to be formed in containment following an accident presents several problems for models of iodine behaviour. The precise nature of the important organic iodides to be modelled cannot be predicted because of the number of different sources of organic material within containment, and the variety of organic species that may be derived from these sources. Detailed physical modelling of all of the possible organic species would be computationally intensive and fraught with uncertainty because precise rate information is lacking for many of the potential species. The review of the partition coefficients and hydrolysis rates provides a basis for reasonable and defensible grouping of organic iodide species, and the assignment of common rate constants. This would greatly simplify the challenge facing those who model iodine behaviour. The suggested grouping is presented below.

#### Recommended hydrolysis rates

If the division of organic iodides based on hydrolysis rates is required, it is recommended that the division be done on the basis of molecular structure because the hydrolysis rates



of organic iodides are sensitive to the structure. Based on the hydrolysis rates listed in Tables 2 and 8, it is proposed that organic iodides be divided into two groups, primary alkyl iodides (PRI) and nonprimary organic iodides (NRI). The NRI group would include secondary, tertiary, and benzylic iodides, as well as any other carbon structure that would enhance hydrolysis rate.

The hydrolysis rates of primary alkyl iodides range from  $(2.92 \pm 0.08) \times 10^{-6} \text{ s}^{-1}$  (iodoethanoic acid) to  $(7.4 \pm 0.3) \times 10^{-5} \text{ s}^{-1}$  (iodoethane) at 70°C. Iodomethane appears to adequately represent the average behaviour of the primary alkyl group. After conversion to 25°C (using the activation energy measured in this work), the iodomethane values can be used to represent the primary alkyl iodides:

$$[17] \quad \ln k_{\text{PRI}} = \ln k_{\text{PRI}}^{298} + \frac{\Delta E_a}{8.3145} \cdot \left( \frac{1}{298} - \frac{1}{T} \right)$$

where  $k_{\text{PRI}}^{298} = (1.3 \pm 0.9) \times 10^{-7} \text{ s}^{-1}$  and  $\Delta E_a = 104 \pm 10 \text{ kJ mol}^{-1}$ .

For the second group, the hydrolysis rate constants are larger than  $1 \times 10^{-4} \text{ s}^{-1}$  at 70°C. For this group, 2-iodobutane is recommended to represent the average of the NRI organic iodides (after conversion to 25°C):

$$[18] \quad \ln k_{\text{NRI}} = \ln k_{\text{NRI}}^{298} + \frac{\Delta E_a}{8.3145} \cdot \left( \frac{1}{298} - \frac{1}{T} \right)$$

where  $k_{\text{NRI}}^{298} = (7.7 \pm 0.3) \times 10^{-6} \text{ s}^{-1}$  and  $\Delta E_a = 97 \pm 5 \text{ kJ mol}^{-1}$ .

### Recommended partition coefficients

Examination of Tables 3 to 7 reveals that the range of volatility of organic iodides can be enormous. However, under accident conditions, organic iodides would be formed from the reaction between organic radicals and molecular iodine (rxn. [3]). The fraction of molecular iodine converted to organic iodides is nearly independent of the type of organic impurities present in the containment sump. Hence, the most logical organization of organic iodides for modelling the volatility of organic iodides in containment following an accident is based on their partition coefficient with respect to that of molecular iodine, i.e., whether the compound is more or less volatile than molecular iodine. The partition coefficient of iodine (~79 at 25°C) (27, 34–36) is such that the division essentially corresponds to whether the compound contains oxygen or not. Except in rare cases, the presence of a single oxygen atom within a molecule raises the partition coefficient at a given temperature to above 100, whereas multiple oxygen atoms within a molecule generally raise the partition coefficient to well above 1000. Thus, the proposed strategy for managing the wide range of partition coefficients in containment under accident conditions is to divide organic iodides into two groups, which are based on their volatility relative to the volatility of  $\text{I}_2$ : (i) "high" volatility organic iodides (HVRI) such as alkyl iodides (e.g., methyl-, ethyl-, and butyl-iodides) and aromatic iodides (e.g., iodo-benzene); and (ii) "low" volatility organic iodides (LVRI) containing oxygen such as alcohol and acid (e.g., iodo-ethanol and iodoethanoic acid).

Since iodomethane exhibits the average behaviour of HVRI, the partition coefficient of iodomethane and its tem-

perature dependence are recommended to represent the HVRI compounds:

$$[19] \quad \ln^H K_{\text{HVRI}} = \ln^H K_{\text{HVRI}}^{298} + \left( (3430 \pm 60) \cdot \left( \frac{1}{T} - \frac{1}{298} \right) \right)$$

The LVRI compounds encompass a much broader range of compounds containing oxygen. A partition coefficient of  $(1000 \pm 250)$ , which is a conservatively averaged (i.e., a low value that provides a conservatively large gas phase concentration) value of alcohols, aldehydes, ketones, and acids from Table 6, is recommended to represent the partition coefficient of LVRI at 25°C. The temperature dependence of the partition coefficients of the LVRI compounds is also somewhat steeper than those of the HVRI compounds, with  $-\Delta H/R$  generally ranging from 5000 to 7500 K. An intermediate value of  $(6500 \pm 1000) \text{ K}$  for  $-\Delta H/R$  is therefore recommended to represent the temperature dependence of LVRI:

$$[20] \quad \ln^H K_{\text{LVRI}} = \ln^H K_{\text{LVRI}}^{298} + \left( (6500 \pm 1000) \cdot \left( \frac{1}{T} - \frac{1}{298} \right) \right)$$

where  $K_{\text{LVRI}}^{298} = (1000 \pm 250)$ .

The proposed organization and the assignment of the average partition coefficients should be evaluated with the proposed strategies for handling the other aspects of organic reactions. For example, the overall rate of organic iodide formation (via rxns. [1]–[3]) and the relative ratio of HVRI and LVRI formation are also crucial in determining organic iodide volatility in containment. The organization should be also consistent with the organic iodide decomposition processes, such as hydrolysis and radiolysis.

### Conclusions

Experiments have been performed to obtain the partition coefficients and hydrolysis rates of various organic iodides. These data, and data accumulated in the literature, have been reviewed to provide guidelines for appropriate organization of organic iodides for the purpose of modelling iodine behaviour under postulated nuclear reactor accident conditions.

If the grouping of organic iodides based on hydrolysis rates is required, it could be done on the basis of molecular structure because the hydrolysis rates of organic iodides are sensitive to the structure. Thus, organic iodides could be divided into two groups, primary alkyl iodides (PRI) and nonprimary organic iodides (NRI). The NRI group would include secondary, tertiary, and benzylic iodides, as well as any other carbon structure that would enhance hydrolysis rate.

Based on the partition coefficients, organic iodides could be divided into two groups based upon their volatility relative to molecular iodine: (i) HVRI (high volatility organic iodides), which is comprised of alkyl iodides having a partition coefficient smaller than  $\text{I}_2$ ; and (ii) LVRI (low volatility organic iodides), which is comprised of compounds generally containing at least one oxygen atom, and having a partition coefficient higher than that of  $\text{I}_2$ .



## Acknowledgements

The authors wish to thank Dr. J.M. Ball and Dr. R. Lemire at AECL and Mr. K.R. Weaver at Nuclear Safety Solutions Limited for their helpful discussion and for reviewing the document. This work was funded by the COG (CANDU Owners Group) R&D Safety and Licensing Program, Work Package No. 20601 under the joint participation of AECL, Ontario Power Generation, and Hydro Quebec.

## References

1. J.C. Wren and J.M. Ball. *Radiat. Phys. Chem.* **60**, 577 (2001).
2. S. Dickinson and H.E. Sims. *Nucl. Tech.* **129**, 374 (2000).
3. J. Bardelay. Present status of iodine research at IPSN and its application to reactor safety. *In* Proceedings of the OECD Workshop on the Chemistry of Iodine in Reactor Safety, June 10–12. Wurenlingen, Switzerland, PSI Report 97–02, NEA/CSNI/R(96)6, 41 (1996).
4. J.M. Ball. Computer code comparison exercise based on a radioiodine test facility (RTF) experiment on iodine behaviour in containment under severe accident conditions. *In* Proceedings of OECD Workshop on Iodine Aspects of Severe Accident Management. Vantaa, Finland, May 18–20, 1999, NEA/CSNI/R(99)7, pp. 311–325, Committee on the Safety of Nuclear Installations/Organization for Economic Cooperation and Development (1999).
5. J.C. Wren, G.A. Glowa, and J.M. Ball. A simplified model for containment iodine chemistry and transport: model description and validation using stainless steel RTF test results. OECD Workshop on Aspects of Severe Accident Management, Vantaa, Finland, May 18–20, 1999. NEA/CSNI/R(99)7, 327 (1999).
6. C. Cripps and S. Guntay. Further assessment of the chemical modelling of iodine in IMPAIR3 code using ACE/RTF data. *In* Proceedings of the OECD workshop on the chemistry of iodine in reactor safety, June 10–12, Wurenlingen, Switzerland, PSI Report 97–02, NEA/CSNI/R(96)6, 437 (1996).
7. J.C. Wren, J.M. Ball, and G.A. Glowa. *Nucl. Tech.* **125**, 337 (1999).
8. J.C. Wren, J.M. Ball, and G.A. Glowa. *Nucl. Tech.* **129**, 297 (2000).
9. (a) J.E. Cline, P.G. Voilleque, C.A. Pelletier, and C.D. Thomas. <sup>131</sup>I studies at TMI unit 2. Electric Power Research Institute, EPRI-NP-1389 (1980); (b) A.M. Deane. Organic iodide chemistry relevant to nuclear reactors: a review. U.K. At. Energy Auth., Harwell lab., [Rep.] AERE-R 12 359. 1988.
10. G.A. Glowa, P.A. Driver, and J.C. Wren. *Radiat. Phys. Chem.* **58**, 49 (2000).
11. J.C. Wren, D.J. Jobe, G.G. Sanipelli, and J.M. Ball. *Can. J. Chem.* **78**, 464 (2000).
12. J.M. Ball, J.C. Wren, and J.R. Mitchell. The dissolution of solvents from Amerlock 400 Epoxy paint. *Can J. Chem.* 2003. Submitted.
13. P.A. Driver, G.A. Glowa, and J.C. Wren. *Radiat. Phys. Chem.* **57**, 37 (2000).
14. J.C. Wren and G.A. Glowa. *Radiat. Phys. Chem.* **58**, 341 (2000).
15. F. Taghipour and G.J. Evans. *Environ. Sci. Technol.* **34**, 3012 (2000).
16. S. Dickinson, H.E. Sims, E. Belval-Haltier, D. Jacquemain, C. Poletiko, F. Funke, S. Hellmann, T. Karjunen, and R. Zilliacus. *Nucl. Eng. Des.* **209**, 193 (2001).
17. Z. Znang and J. Pawliszyn. *Anal. Chem.* **65**, 1843 (1993).
18. P.M. Laughton and R.E. Robertson. *Can. J. Chem.* **37**, 1491 (1959).
19. E.A. Molewyn-Hughes. *Proc. Roy. Soc. Ser. A*, **164**, 295 (1938).
20. M. Adachi, W. Eguchi, and T. Haoka. *J. Chem. Eng. Jpn.* **7**, 364 (1974).
21. David R. Lide (*Editor*). *CRC handbook of chemistry and physics*. 71st ed. CRC Press, Ann Arbor. 1990.
22. J. March. *Advanced organic chemistry*. 3rd ed. John Wiley and Sons, Toronto. 1985.
23. D. Mackay and W.Y. Shiu. *J. Phys. Chem. Ref. Data*, **10**, 1175 (1981).
24. R.J. Hunter-Smith, P.W. Balls, and P.S. Liss. *Tellus*, **35B**, 170 (1983).
25. R.A. Hasty. *Can. J. Chem.* **46**, 1643 (1967).
26. R.M. Moore, C.E. Geen, and V.K. Tait. *Chemosphere*, **30**, 6, 1183 (1995).
27. R. Sander. 1999. Compilation of Henry's Law constants for inorganic and organic species of potential importance in environmental chemistry [online]. Version 3. <http://www.mpch-mainz.mpg.de/~sander/res/henry.html> [cited 2 December 1999].
28. J.C. Wren, J. Paquette, D.J. Wren, and G.G. Sanipelli. The formation and volatility of organic iodides. *In* Proceedings of the 1st Committee on the Safety of Nuclear Installations Workshop on Iodine Chemistry in Reactor Safety, Harwell, U.K. September 1985. At. Energy Res. Establ. (G.B.) [Rep.], AERE-R11 974. 1986.
29. K.P.C. Vollhardt. *Organic chemistry*. W.H. Freeman and Company, New York. 1987.
30. J. Hine and P.K. Mookerjee. *J. Org. Chem.* **40**, 292 (1975).
31. T. Suzuki, K. Ohtaguchi, and K. Koide. *Comput. Chem.* **16**, 41 (1992).
32. N. Nirmalakhandan, R.A. Brennan, and R.E. Speece. *Water Res.* **31**, 1471 (1997).
33. C.J. Russel, S.L. Dixon, and P.C. Jurs. *Anal. Chem.* **64**, 1350 (1992).
34. S.M. Ali, R.J. Bawden, A.M. Deane, K. Garbett, and N.R. Large. Chemical data for the calculation of fission product releases in design basis faults in PWRs. AERE [Rep.] 10 494, 1982.
35. R.J. Lemire, J. Paquette, D.F. Torgerson, D.J. Wren, and D.W. Fletcher. Assessment of Iodine Behaviour in Reactor Containment Buildings from a Chemical Perspective. At. Energy Can. Ltd., [Rep.] AECL-6812 (1981).
36. D.D. Wagman, W.H. Evans, V.B. Parker, R.H. Schumm, I. Halow, S.M. Bailey, K.L. Churney, and R.L. Nuttall. *J. Phys. Chem. Ref. Data Suppl.* **11**, 2 (1982).



# Medium-sized cyclophanes. Part 62:<sup>1</sup> Formylation of *anti*-[*n*.2]metacyclophanes — Through-space electronic interactions between two benzene rings

Takehiko Yamato, Tsuyoshi Furukawa, Kan Tanaka, Tsutomu Ishi-i, and Masashi Tashiro

**Abstract:** Formylation of *anti*-[*n*.2]metacyclophanes (**1**) (*n* = 2, 3, 4) with dichloromethyl methyl ether in the presence of TiCl<sub>4</sub> occurred selectively at *para*-position to the internal methyl substituents of *anti*-[*n*.2]metacyclophanes. Similar reaction of *anti*-5,13-di-*tert*-butyl-8,16-dimethyl[2.2]metacyclophane (**6a**) with dichloromethyl methyl ether in the presence of TiCl<sub>4</sub> led to *ipso*-formylation at the *tert*-butyl group to give *anti*-5-*tert*-butyl-13-formyl-8,16-dimethyl[2.2]-metacyclophane (**7a**) as well as the corresponding 2,7-di-*tert*-butyl-*trans*-10b,10c-dimethyl-10b,10c-dihdropyrene (**10**), *anti*-5-*tert*-butyl-8,16-dimethyl-13-(3-methyl-1-butene-2-yl)[2.2]metacyclophane (**8**), and *anti*-5,13-di-*tert*-butyl-*exo*-1-hydroxy-8,16-dimethyl[2.2]metacyclophane (**9**) depending on the reaction conditions. The higher yield of *ipso*-formylated product is obtained in the presence of AlCl<sub>3</sub> MeNO<sub>2</sub> in 80% yield along with *anti*-5-*tert*-butyl-8,16-dimethyl-13-(3-methyl-1-butene-2-yl)[2.2]metacyclophane (**13**). Thus, the yield of *ipso*-formylation at the *tert*-butyl group of **6a** was strongly affected by the activity of the formylation catalyst. Interestingly, in the formylation of *anti*-6,14-di-*tert*-butyl-9,17-dimethyl[3.2]metacyclophane (**6b**) under the same reaction conditions, *syn*-6,14-di-*tert*-butyl-7-formyl-9,17-dimethyl[3.2]metacyclophane (**14b**) was obtained in 40% yield arising from the *anti*-*syn*-ring inversion of the formylation intermediate along with *ipso*-formylation product **7b** in 42% yield. In the formylation of *anti*-[4.2]metacyclophane (**6c**) only the mono-*ipso*-formylated product **7c** was obtained in 92% yield. The formation of a two-fold *ipso*-formation product, i.e., *anti*-5,13-di-formyl-8,16-dimethyl[2.2]metacyclophane (**3a**), was not observed under the reaction conditions used. The mechanism of the *ipso*-formation as well as the formation of the present novel reaction products **8** and **9** is also discussed.

**Key words:** cyclophanes, strained molecules, electrophilic aromatic substitution, *ipso*-formylation,  $\sigma$ -complex intermediates, through-space electronic interactions.

**Résumé :** La formylation des *anti*-[*n*.2]métacyclophanes (**1**) (*n* = 2, 3, 4) à l'aide d'oxyde de méthyle et de dichlorométhyle, en présence de TiCl<sub>4</sub>, se produit d'une façon sélective en position *para* par rapport aux substituants méthyles internes des *anti*-[*n*.2]métacyclophanes. Une réaction semblable de l'*anti*-5,13-di-*tert*-butyl-8,16-diméthyl[2.2]métacyclophane (**6a**) avec de l'oxyde de méthyle et de dichlorométhyle, en présence de TiCl<sub>4</sub>, conduit à une formylation en position *ipso* par rapport au groupe *tert*-butyle et, suivant les conditions réactionnelles à la formation de l'*anti*-5-*tert*-butyl-13-formyl-8,16-diméthyl[2.2]métacyclophane (**7a**) ainsi que du 2,7-di-*tert*-butyl-*trans*-10b,10c-diméthyl-10b,10c-dihdropyrène (**10**), de l'*anti*-5-*tert*-butyl-8,16-diméthyl-13-(3-méthylbut-1-én-2-yl)[2.2]métacyclophane (**8**) et de l'*anti*-5,13-di-*tert*-butyl-*exo*-1-hydroxy-8,16-diméthyl[2.2]métacyclophane (**9**). Le rendement le plus élevé de produit formylé en position *ipso* (80%) est obtenu en présence de AlCl<sub>3</sub>, dans le MeNO<sub>2</sub>; à ses côtés, il se forme aussi de l'*anti*-5-*tert*-butyl-8,16-diméthyl-13-(3-méthylbut-1-én-2-yl)[2.2]métacyclophane (**13**). Le rendement en formylation en position *ipso* par rapport au groupe *tert*-butyle du produit **6a** est donc fortement affecté par l'activité du catalyseur de formylation. Il est intéressant de noter que la formylation de l'*anti*-6,14-di-*tert*-butyl-9,17-diméthyl[3.2]métacyclophane (**6b**) dans les mêmes conditions expérimentales conduit à la formation, avec un rendement de 40%, du *syn*-6,14-di-*tert*-butyl-7-formyl-9,17-diméthyl[3.2]métacyclophane (**14b**) qui résulte d'une inversion de cycle *anti*-*syn* de l'intermédiaire de formylation; ce produit se forme aux côtés du produit de formylation *ipso* (**7b**) obtenu avec un rendement de 42%. Lors

Received 22 November 2002. Published on the NRC Research Press Web site at <http://canjchem.nrc.ca> on 19 March 2003.

**T. Yamato<sup>2</sup> and T. Furukawa.** Department of Applied Chemistry, Faculty of Science and Engineering, Saga University, Honjo-machi 1, Saga-shi, Saga 840-8502, Japan.

**K. Tanaka.** Department of Industrial Chemistry, Faculty of Science and Engineering, Tohwa University, 1-1-1 Chikushigaoka, Minami-ku, Fukuoka-shi, Fukuoka 815-8510, Japan.

**T. Ishi-i and M. Tashiro.** Research Institute of Advanced Material Study, Kyushu University, 6-1, Kasuga-kohen, Kasuga-shi, Fukuoka 816, Japan.

<sup>1</sup>Part 61. See ref. 1.

<sup>2</sup>Corresponding author (e-mail: [yamatot@cc.saga-u.ac.jp](mailto:yamatot@cc.saga-u.ac.jp)).



de la formylation de l'*anti*-[4.2]métacyclophane (**6c**), on n'obtient que le produit de formylation *ipso* (**7c**) avec un rendement de 92%. Dans les conditions réactionnelles utilisées, on n'a pas observé de formation de double formylation *ipso*, l'*anti*-5,13-diformyl-8,16-diméthyl[2.2]métacyclophane (**3a**). On discute du mécanisme de formation des produits de formylation *ipso* ainsi que de la formation des nouveaux produits **8** et **9**.

**Mots clés :** cyclophanes, molécules tendues, substitution aromatique électrophile, formylation *ipso*, complexes- $\sigma$  comme intermédiaires, interactions électroniques à travers l'espace.

[Traduit par la Rédaction]

## Introduction

Because of electronic interaction between two benzene rings, the proximity of 8,16-positions, and the considerable strain energy, [2.2]metacyclophane (MCP = metacyclophane) is prone to giving transannular reaction products under the electrophilic, radical, and photolytic reaction conditions together with other transformation products derived from tetrahydropyrene (2,3). These products have usually been rationalized as involving initial dehydrogenation to 4,5,9,10-tetrahydropyrene.

Maquestiau et al. (4) reported formylation of [2.2]MCP with dichloromethyl *n*-butyl ether in the presence of  $\text{TiCl}_4$  according to the Rieche procedure (5) to give 4-formyl[2.2]MCP, as shown in Scheme 1. This result was different from other electrophilic aromatic substitution of [2.2]MCP; e.g., bromination, iodination, and nitration, which afforded the corresponding 2-substituted 4,5,9,10-tetrahydropyrenes via addition-elimination mechanism (2). The relatively late transition state in the formylation of [2.2]MCP compared with other electrophilic aromatic substitution might be proposed.

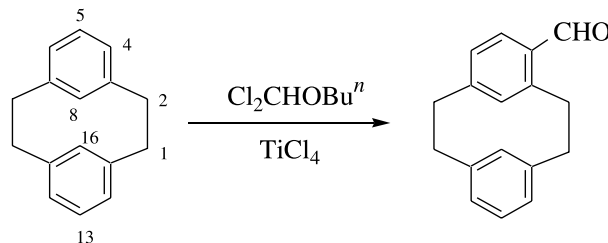
However, there is no report concerning the formylation of internally substituted [2.2]MCPs. We undertook the present work to obtain further information about the chemical behaviour of [2.2]MCPs as well as [3.2]- and [4.2]MCPs, which are less strained than [2.2]MCPs.

## Results and discussion

When formylation of *anti*-8,16-dimethyl[2.2]MCP (**1a**) (6) with dichloromethyl methyl ether in the presence of  $\text{TiCl}_4$  as a catalyst was carried out at 0°C for 1 h, *anti*-5-formyl-8,16-dimethyl[2.2]MCP (**2a**) and *anti*-5,13-diformyl-8,16-dimethyl[2.2]MCP (**3a**) were obtained in 20 and 80% yield, respectively. Treatment of **1a** with dichloromethyl methyl ether at room temperature for 3 h increased the yield of the diformyl compound (**3a**) to 95% (Scheme 2).

Formylation of *anti*-9,17-dimethyl[3.2]- (**1b**) (7) and *anti*-10,18-dimethyl[4.2]MCP (**1c**) (7) at 0°C for 1 h under the same conditions used with **1a**, afforded diformyl derivatives (**3b**) and (**3c**) in 93 and 91% yield, respectively. In the [3.2]- and [4.2]MCP systems the diformylations were both completed within 1 h, which is different from the result that the complete diformylation required at least 3 h in the [2.2]MCP system. The different formylation behaviors of [n.2]MCPs can be explained by the stability of the cationic intermediates, which could arise from the through-space electronic interaction with the benzene ring located on the opposite side. Thus, in the case of the [2.2]MCP system, the second electrophilic substitution with dichloromethyl methyl ether

Scheme 1.



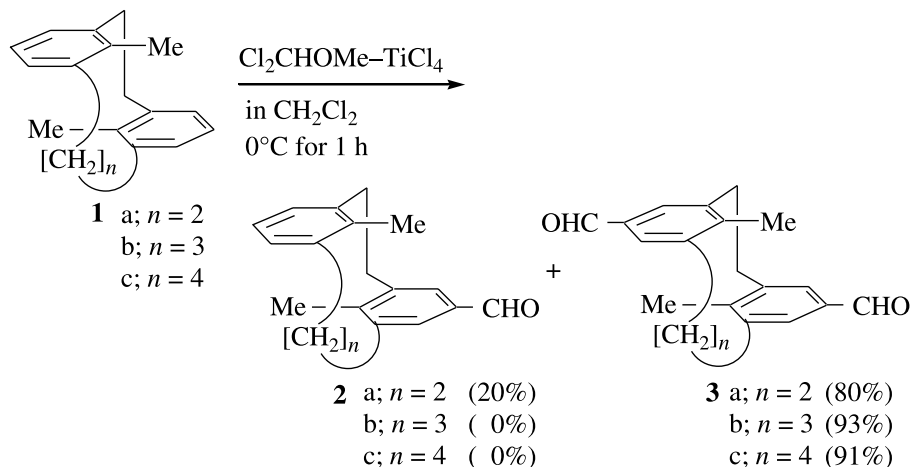
can be more strongly suppressed because of deactivation of the second aromatic ring by  $\text{CH}(\text{OMe})\text{Cl}$  group-like nitration of 8,16-dimethyl[2.2]MCP, which only afforded mononitration product even in the drastic nitration conditions (8).

It should be noted that formyl groups of **2a** and **3a** are introduced at positions 5 and 13 of the MCP ring with formylation occurring selectively *para* to the methyl substituents of [2.2]MCP. Similar orientations are observed in the [3.2]- and [4.2]MCP systems. In contrast, treatment of 1,2,3-trimethylbenzene (**4**) with dichloromethyl methyl ether under the same conditions used with **1** afforded a 90% yield of 2,3,4-trimethylbenzaldehyde (**5**). The above results suggest that the orientation of the formylation of **1** is determined by the internal methyl substituents in place of methylene groups of the bridges and quite different from the orientation that can be expected from the result of formylation of 1,2,3-trimethylbenzene (**4**). The deviation of the benzyl carbon atom of methylene groups from the plane of the benzene ring (9) might decrease the degree of stabilization of the  $\sigma$ -complex intermediate by hyperconjugation compared with that of the internal methyl groups.

Attempted formylation of *anti*-5,13-di-*tert*-butyl-8,16-dimethyl[2.2]MCP (**6a**) (6) with dichloromethyl methyl ether (Table 1) in the presence of  $\text{TiCl}_4$  at room temperature for 0.5 h gave mono-*ipso*-formylated product *anti*-5-formyl-13-*tert*-butyl-8,16-dimethoxy[2.2]MCP (**7a**) in 25% yield as a major product along with *anti*-5,13-di-*tert*-butyl-*exo*-1-hydroxy-8,16-dimethyl[2.2]MCP (**9**), *anti*-5-*tert*-butyl-8,16-dimethyl-13-(3-methyl-1-butene-2-yl)[2.2]MCP (**8**), and the corresponding 2,7-di-*tert*-butyl-*trans*-10b,10c-dimethyl-10b,10c-dihydropyrene (**10**), depending on the reaction conditions. Thus, decreasing the reaction temperature from 25°C to 0°C or to -20°C decreases the yield of *ipso*-formylated product **7a** but increases the yield of **8** and **9**. In contrast, prolonging the reaction time to 3 h or increasing the reaction temperature to 40°C leads to a slight increase of the yield of *ipso*-formylated product **7a**. Therefore, the present *ipso*-formylation at the *tert*-butyl group of **6a** was found to be strongly affected by the reaction time and temperature.



Scheme 2.

**Table 1.** Treatment of [2.2]MCP **6a** with dichloromethyl methyl ether in the presence of titanium tetrachloride.

Run	Temp (°C)	Time (h)	Products (%) <sup>a</sup>			
			<b>6a</b>	<b>7a</b>	<b>8</b>	<b>9</b>
1 <sup>b</sup>	0	0.5	9	15	25	27
2 <sup>b</sup>	-20	0.5	6	13	31	27
3 <sup>b</sup>	25	0.5	4	25	16	20
4	25	3	3	35	6	15
5	40	0.5	<1	30	<1	<1

<sup>a</sup>Isolated yields are shown.<sup>b</sup>Small amount of 2,7-di-*tert*-butyl-*trans*-10b,10c-dimethyl-10b,10c-dihydripyrene (**10**) was obtained.

However, in spite of the prolonged reaction time, di-*ipso*-formylated compound **3a** was not obtained. Furthermore, formation of the corresponding *syn*-8,16-dimethyl[2.2]MCP arising from the *anti-syn*-ring inversion like the nitration of *anti*-5,13-di-*tert*-butyl-8,16-dimethoxy[2.2]MCP was also not observed (**10**).

Formylation of *anti*-6,14-di-*tert*-butyl-9,17-dimethyl[3.2]MCP (**6b**) and *anti*-7,15-di-*tert*-butyl-10,18-dimethyl[4.2]MCP (**6c**), carried out under the same conditions, afforded *anti*-6-formyl-14-*tert*-butyl-9,17-dimethyl[3.2]MCP (**7b**) in 95% yield but the latter MCP (**6c**) afforded only recovered. From this finding, the order of reactivity of *anti*-[*n*.2]MCPs for formylation is estimated to be [2.2]- > [3.2]- > [4.2]MCP. This finding also suggests that the degree of the stability of the cation intermediate, which may be due to a through-space electronic interaction with the opposing benzene ring, decreases as the size of the polymethylene bridge increases.

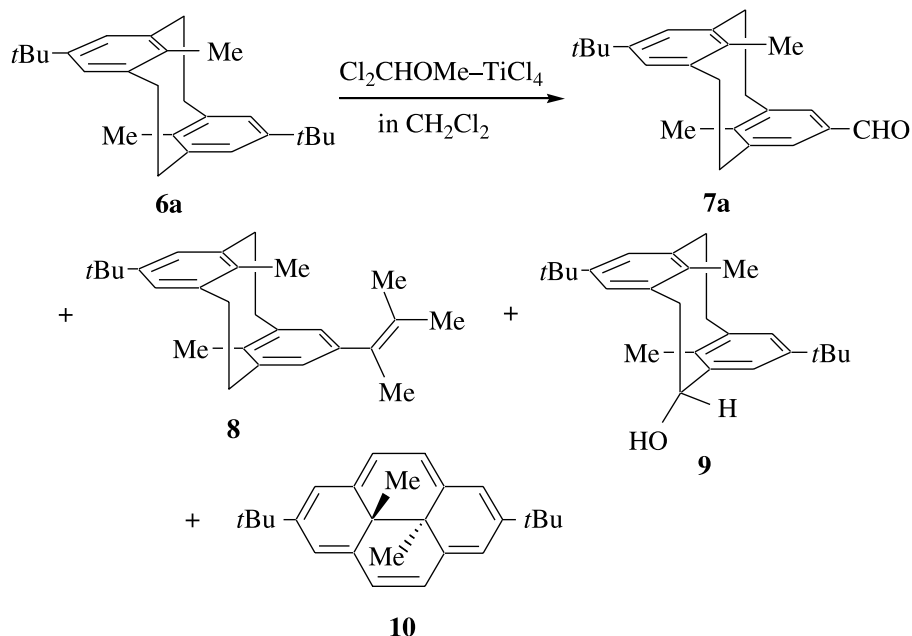
On the other hand, Reinhoudt and co-workers (11) reported the high-yield four-fold *ipso*-nitration of *tert*-butylcalix[4]arenes. To the best of our knowledge, none of the *ipso*-formylation reactions have been reported in the normal aromatic systems (12). In the MCP system, a first  $\sigma$ -complex intermediate would be stabilized by a through-space electronic interaction with the opposing benzene ring, thus accelerating the reaction. However, only one *tert*-butyl group is *ipso*-formylated because of deactivation of the second aromatic ring by the CH(OMe)Cl group.

The structures of products **7a** and **8** were determined on the basis of their elemental analyses and spectral data. The IR (NaCl) spectrum of **7a** shows  $\nu_{\text{C=O}}$  at 1670 cm<sup>-1</sup>, typical of an aromatic aldehyde. The <sup>1</sup>H NMR (CDCl<sub>3</sub>) spectrum of **7a** shows two methyl protons at 0.49 and 0.64 ppm, a *tert*-butyl proton at 1.30 ppm, two aromatic protons at 7.14 and 7.64 ppm, and a formyl proton at 9.84 ppm, respectively. The <sup>1</sup>H NMR spectrum of **8** shows internal methyl protons as singlets at  $\delta$  0.58 and 0.69 and three methyl protons as singlets at  $\delta$  1.65, 1.80, and 1.93 (relative intensity 1:1:1). Two aromatic protons are observed at  $\delta$  6.89 and 7.12 as singlets that are clearly associated with the protons at C-12 and C-14, and C-4 and C-6, respectively. Structure **8** can also be determined by the fact that there are five nonequivalent methyl groups at 14.38, 14.70, 20.70, 20.75, and 22.16 and two olefinic carbons at 126.25 and 129.86 in <sup>13</sup>C NMR spectrum. Furthermore, when **8** was treated with cetyltrimethylpermanganate in methylene dichloride (13), the corresponding oxidation product *anti*-5-acetyl-13-*tert*-butyl-8,16-dimethyl[2.2]MCP (**11**) was obtained in 87% yield (Scheme 4). On the basis of this chemical conversion and spectral data, **8** is assigned the structure *anti*-5-*tert*-butyl-8,16-dimethyl-13-(3-methyl-2-butene-2-yl)[2.2]MCP. It was also found that the formylation of **8** in methylene dichloride under the same reaction conditions did not afford *ipso* substitution product **7a**. Only the recovery of the starting compound **8** resulted. This finding suggests that the intermediate for the formation of **7a** is not **8**.

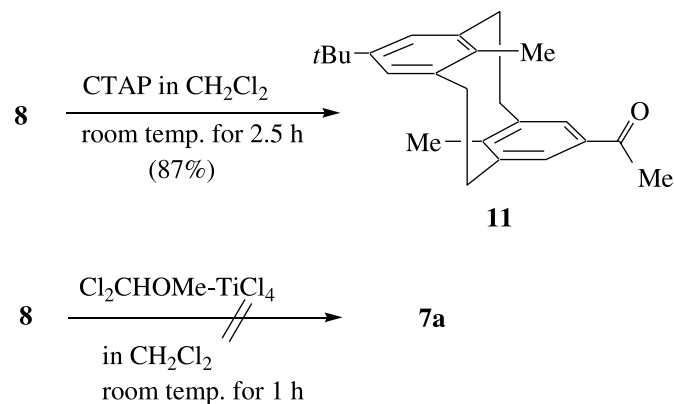
The structures of products **9** and **10** were also determined on the basis of their elemental analyses and spectral data. The assignment of **10** was carried out by the comparison with physical properties and spectral data of the authentic sample (14). We previously assigned (15) the <sup>1</sup>H NMR signals of *anti*-1-*exo*-5,13-trichloro-8,16-dimethyl[2.2]MCP and have assigned the <sup>1</sup>H NMR signals of **9** in a similar fashion. Thus, the <sup>1</sup>H NMR spectrum of **9** shows two internal methyl resonances as singlets at  $\delta$  0.52 and 0.86 and a bridge methine signal as double doublets at  $\delta$  5.34 (*J* = 2.2/4.6 Hz). One of the two methyl protons is in a strongly deshielding region of oxygen atoms of *exo*-OH on the ethylene bridge resulting in a much larger downfield shift ( $\delta$  0.86) than that of the other methyl proton ( $\delta$  0.52). In contrast, the



Scheme 3.



Scheme 4.



aromatic protons were observed as a multiplet around  $\delta$  7.18–7.21 that is almost same as that for the *exo*-Cl arrangement of *anti*-1-*exo*-5,13-trichloro-8,16-dimethyl[2.2]-MCP ( $\delta$  7.0–7.3). A deshielded aromatic proton due to the *endo*-OH oxygen atom on the ethylene bridge was not observed. On the basis of the spectral data, compound **9** is assigned the structure *anti*-5,13-di-*tert*-butyl-*exo*-1-hydroxy-8,16-dimethyl[2.2]MCP.

Although the detailed mechanism of formation of **8** is not clear, a reaction pathway for the formation of **8** from **6a** is tentatively proposed in Scheme 5. The *ipso*-electrophilic attack at the *tert*-butyl group could afford the cation intermediate **A**, which could eliminate the isobutene to afford intermediate **B** following hydrolysis by the quenched with water to give *ipso*-formylation product **7a**. On the other hand, Brüggem et al. (16) reported that isobutene reacts with dichloromethyl methyl ether to afford the addition product **12**. In fact, generated isobutene was trapped by the reaction with toluene in the presence of AlCl<sub>3</sub> under the Ar gas flow condition to afford *tert*-butyltoluene. Thus, the addition product generated in the present system can react with **6a** on

the *ipso*-position at the *tert*-butyl group to afford the intermediate **C** from which the elimination of formaldehyde and HCl form the cyclopropane ring (intermediate **D**) following the ring opening reaction that occurs to afford **8**.

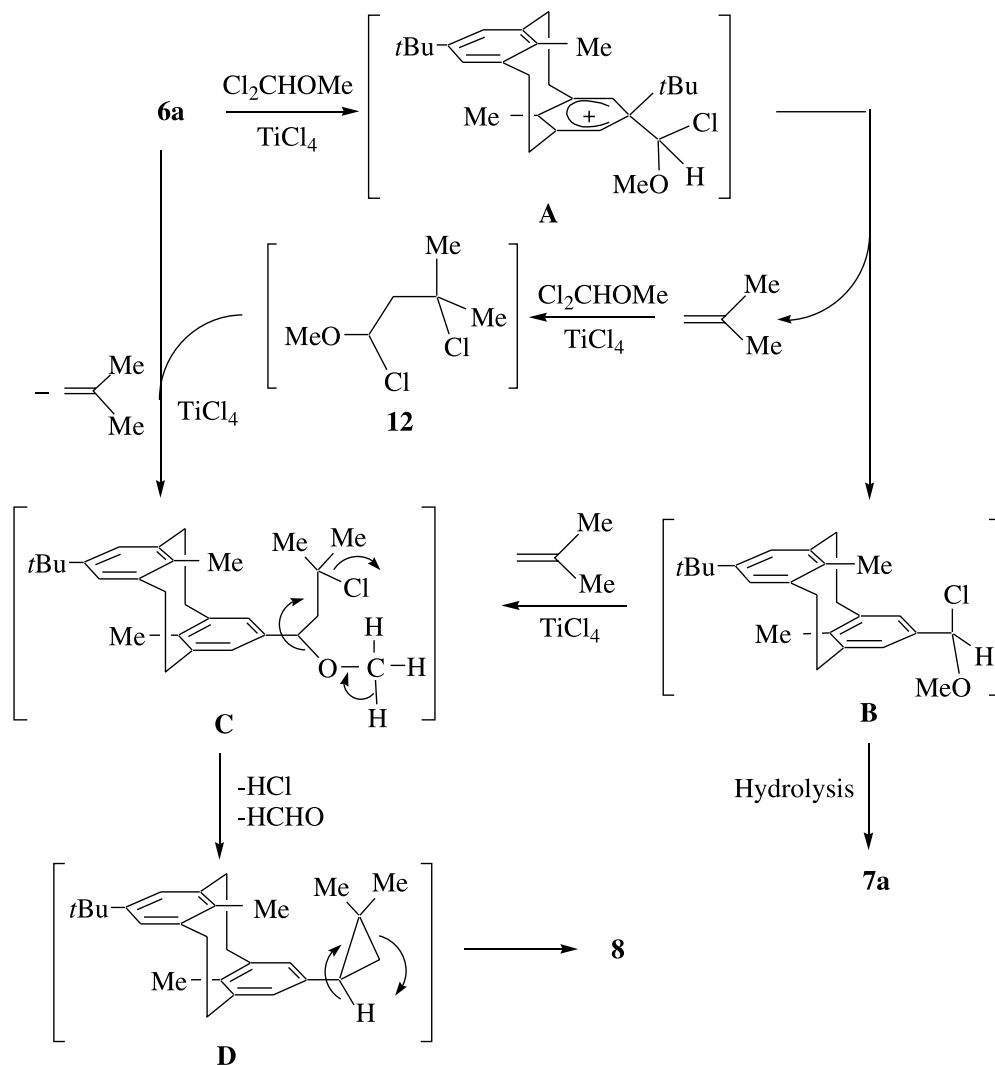
The formation of alcohol **9** during the formylation of **6a** with dichloromethyl methyl ether leads to the first direct introduction of hydroxy group into the methylene group of [2.2]MCP **6a**. However, the detailed mechanism of formation of **9** is not clear in the present stage.

It was also found that dehydration of alcohol **9** with TiCl<sub>4</sub> or concd. HCl in benzene at room temperature for 80 h afforded *trans*-10b,10c-dimethyl-10b,10c-dihydropyrene **10** in 10% and 32% along with recovery of the starting compound. Therefore, the reaction pathway for the formation of *trans*-10b,10c-dimethyl-10b,10c-dihydropyrene **10** in the present formylation reaction via the elimination of H<sub>2</sub>O from the alcohol **9** itself to afford the corresponding [2.2]MCP-1-ene can be proposed. From [2.2]MCP-1-ene, **10** might be produced via intermediate [2.2]MCP-1,9-diene, as expected on the basis of earlier reported observations that [2.2]MCP-1,9-dienes gave the tautomerization product 10b,10c-dihydropyrenes (17).

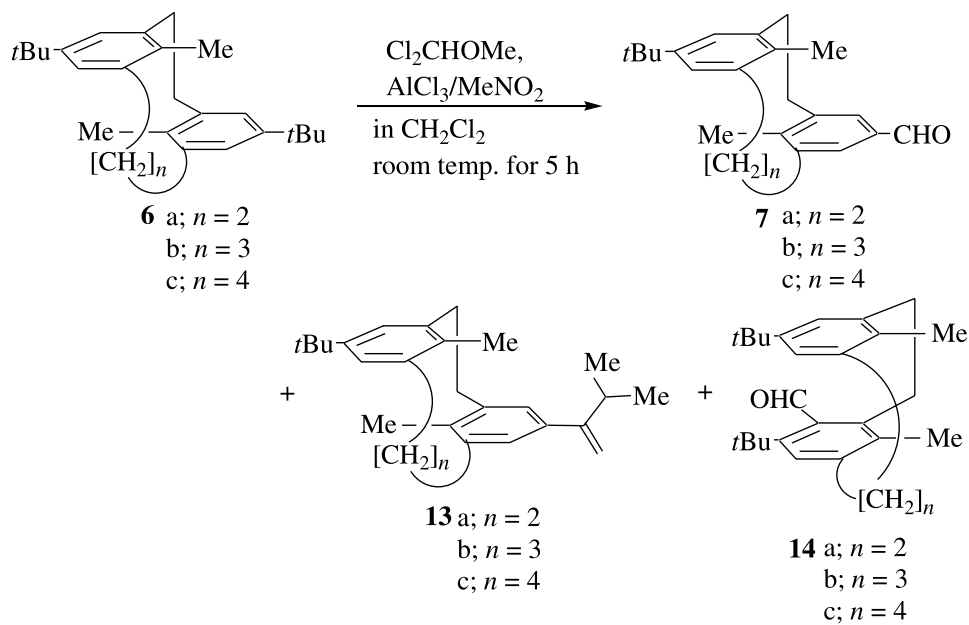
Interestingly, the higher yield of *ipso*-formylated product is obtained in the presence of AlCl<sub>3</sub>-MeNO<sub>2</sub> in 80% yield along with *anti*-5-*tert*-butyl-8,16-dimethyl-13-(3-methyl-1-butene-2-yl)[2.2]MCP (**13a**). Thus, the yield of *ipso*-formylation at the *tert*-butyl group of **6a** was strongly affected by the activity of the formylation catalyst. In contrast, in the formylation of *anti*-6,14-di-*tert*-butyl-9,17-dimethyl-[3.2]MCP (**6b**) under the same reaction conditions, *syn*-6,14-di-*tert*-butyl-7-formyl-9,17-dimethyl[3.2]MCP (**14b**) was obtained in 40% yield arising from the *anti*-*syn*-ring inversion of the formylation intermediate along with *ipso*-formylation product **7b** in 42% yield. In the formylation of *anti*-[4.2]MCP (**6c**) only the mono *ipso*-formylated product **7c** was obtained in 92% yield. The formation of a two-fold *ipso*-formation product, i.e., *anti*-5,13-diformyl-8,16-di-



Scheme 5.



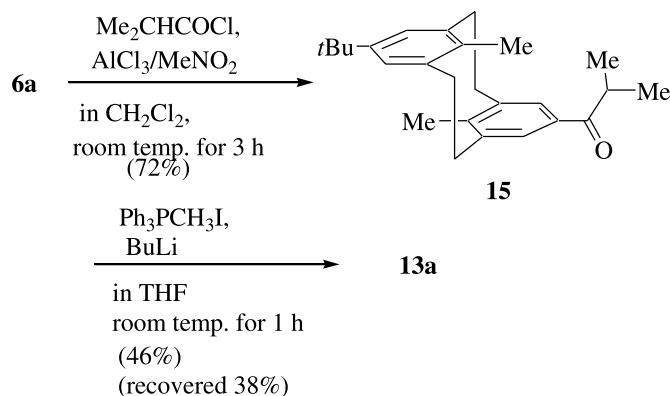
Scheme 6.





**Table 2.** Treatment of [*n*.2]MCPs **6a–c** with dichloromethyl methyl ether in the presence of AlCl<sub>3</sub> MeNO<sub>2</sub>.<sup>a</sup>

Run	Substrate	Number of methylene units ( <i>n</i> )	Products (%) <sup>b,c</sup>		
1	<b>6a</b>	2	<b>7a</b> (80)[60]	<b>13a</b> (20)[15]	<b>14a</b> (0)
2	<b>6b</b>	3	<b>7b</b> (42)[35]	<b>13b</b> (0)	<b>14b</b> (40)[22]
3	<b>6c</b>	4	<b>7c</b> (92)[72]	<b>13c</b> (0)	<b>14c</b> (0)

<sup>a</sup>Conditions: AlCl<sub>3</sub> (5 equiv) Cl<sub>2</sub>CHOMe (14 equiv).<sup>b</sup>Relative yields determined by GLC analysis are shown.<sup>c</sup>Isolated yields are shown in square brackets.**Scheme 7.**

methyl[2.2]MCP (**3a**), was not observed under the reaction conditions used (Scheme 6, Table 2).

Previously we reported (7b) that *anti*-**6b** is thermally stable and does not interconvert at 150°C in DMSO solution or at 400°C in the solid state. Although the detailed mechanistic conclusion to rationalize the present observation of *anti*-to-*syn*-conversion is not clear, one might assume similar behavior to that of the nitration or protic acid induced intramolecular condensation of *anti*-8,16-dimethoxy[2.2]MCP to afford the corresponding 17-oxa[2.2.1](1,3,2)cyclophane via *anti*-to-*syn*-ring inversion (9).

The structures of products **13a** and **14b** were determined on the basis of their elemental analyses and spectral data. The <sup>1</sup>H NMR spectrum of **13a** shows internal methyl protons as singlets at  $\delta$  0.59 and 0.65 and two methyl protons as a doublet at  $\delta$  1.11. Two *exo*-methylenes are observed at  $\delta$  4.92 and 5.08 as doublets ( $J = 1.3$  Hz). Furthermore, **13a** was alternatively prepared by the *ipso*-acylation of **6a** with isobutanoyl chloride in the presence of TiCl<sub>4</sub> followed by Wittig reaction of **15** with methyltriphenylphosphonium iodide in the presence of butyllithium (Scheme 7). On the basis of the spectral data and the comparison of the authentic sample synthesized, **13a** is assigned the structure *anti*-5-*tert*-butyl-8,16-dimethyl-13-(3-methyl-1-butene-2-yl)[2.2]MCP.

The IR (NaCl) spectrum of **14b** shows  $\nu_{\text{C=O}}$  at 1683 cm<sup>-1</sup>, typical of an aromatic aldehyde. Especially, the mass spectral data for **14b** ( $M^+ = 390$ ) strongly support the mono formylated product for **6b**. Interestingly, the <sup>1</sup>H NMR spectra of **14b** showed the methyl protons at  $\delta$  1.73 and 1.96 ppm, respectively, quite a different chemical shift from that of **6a** ( $\delta$  0.68 ppm) because of the ring current of the opposite aromatic ring (2,18). The aromatic protons were observed at  $\delta$  6.71 and 7.12 ppm (relative intensity 2:1). The former protons are observed at much higher field position than that of *anti*-**6a** (7.04 ppm) because of the face-to-face

overlapping between the two benzene rings. These findings strongly support the theory that the structure of **14a** adopts *syn*-conformation. It was also found that one of the ethano-bridge protons has been observed in a deshielded region ( $\delta$  3.45–3.50) owing to the formyl group at position seven (the ortho position for the ethano-bridge). Consequently, **14b** is assigned the structure *syn*-6,14-di-*tert*-butyl-7-formyl-9,17-dimethyl[3.2]MCP.

## Experimental

All melting points (Yanagimoto MP-S1) were uncorrected. Proton nuclear magnetic resonance (<sup>1</sup>H NMR) spectra were recorded on a Nippon Denshi JEOL FT-270 spectrometer. Chemical shifts are reported as  $\delta$  values (ppm) relative to internal Me<sub>4</sub>Si. Mass spectra were obtained on a Nippon Denshi JMS-01SG-2 mass spectrometer at an ionization energy of 70 eV using a direct-inlet system through GLC;  $m/z$  values reported include the parent ion peak. Infrared (IR) spectra were obtained on a Nippon Denshi JIR-AQ2OM spectrophotometer as KBr disks. Elemental analyses were performed by Yanaco MT-5. Gas-liquid chromatograph (GLC) analyses were performed using a Shimadzu gas chromatograph (GC-14A); silicone OV-1, 2 m; programmed temperature rise, 12°C min<sup>-1</sup>; carrier gas nitrogen, 25 mL min<sup>-1</sup>.

## Materials

The preparation of *anti*-5,13-di-*tert*-butyl-8,16-dimethyl[2.2]metacyclophane (**6a**), *anti*-6,14-di-*tert*-butyl-9,17-dimethyl[3.2]MCP (**6b**), and *anti*-7,15-di-*tert*-butyl-10,18-dimethyl[4.2]MCP (**6c**) was carried out as previously reported (6,7).

### Formylation of dimethyl[2.2]MCP (1) with Cl<sub>2</sub>CHOCH<sub>3</sub>. Typical procedure

To a solution of *anti*-8,16-dimethyl[2.2]MCP (**6**) (**1a**) (236 mg, 1.0 mmol) and Cl<sub>2</sub>CHOCH<sub>3</sub> (0.56 mL, 6.2 mmol) in CH<sub>2</sub>Cl<sub>2</sub> (10 mL) was added a solution of TiCl<sub>4</sub> (0.45 mL, 4.1 mmol) in CH<sub>2</sub>Cl<sub>2</sub> (4 mL). After the reaction mixture was stirred at 0°C for 1 h, it was poured into a large amount of ice-water and extracted with CH<sub>2</sub>Cl<sub>2</sub>. The CH<sub>2</sub>Cl<sub>2</sub> extract was washed with water, dried over Na<sub>2</sub>SO<sub>4</sub>, and evaporated in vacuo to leave a residue that was chromatographed on silica gel (CHCl<sub>3</sub> as an eluent) to give **2a** (52.8 mg, 20%) and **3a** (232.4 mg, 80%), respectively.

### *anti*-5-Formyl-8,16-dimethyl[2.2]MCP (**2a**)

Colorless prisms (hexane), mp 182–185°C. IR (KBr)  $\nu_{\text{max}}$ : 3050, 2940, 2860, 2810, 1685 (C=O), 1580, 1375, 1265,



1180, 1110, 780, 745, 720.  $^1\text{H}$  NMR ( $\text{CDCl}_3$ )  $\delta$ : 0.52 (s, 3 H), 0.65 (s, 3H), 2.60–3.20 (m, 8H), 6.84–7.23 (m, 3H), 7.64 (s, 2H), 9.85 (s, 1H). MS  $m/z$ : 264 ( $[\text{M}]^+$ ). Anal. calcd. for  $\text{C}_{19}\text{H}_{20}\text{O}$ : C 86.32, H 7.62; found: C 86.33, H 7.65.

#### **anti-5,13-Diformyl-8,16-dimethyl[2.2]MCP (3a)**

Colorless prisms (hexane), mp 280–282°C. IR (KBr)  $\nu_{\text{max}}$ : 2960, 2825, 2790, 2725, 1670 (C=O), 1585, 1550, 1450, 1375, 1330, 1315, 1260, 1245, 1200, 1190, 1145, 1115, 970, 910, 755, 725, 685.  $^1\text{H}$  NMR ( $\text{CDCl}_3$ )  $\delta$ : 0.58 (s, 6H), 2.60–3.30 (m, 8H), 7.64 (s, 4H), 9.86 (s, 2H). MS  $m/z$ : 292 ( $[\text{M}]^+$ ). Anal. calcd. for  $\text{C}_{20}\text{H}_{20}\text{O}_2$ : C 82.16, H 6.89; found: C 82.20, H 6.93.

Formylation of *anti*-9,17-dimethyl[3.2]MCP (**1b**) (7) and *anti*-10,18-dimethyl[4.2]MCP (**1c**) (7) was carried out as a same procedure as described above to afford (**3b**) and (**3c**) in 93 and 91% yield, respectively.

#### **anti-6,14-Diformyl-9,17-dimethyl[3.2]MCP (3b)**

Colorless prisms (hexane), mp > 300°C. IR (KBr)  $\nu_{\text{max}}$ : 2950, 1680 (C=O), 1590, 1570, 1550, 1445, 1387, 1265, 1255, 1137, 1123, 1111, 1025, 965, 907, 885, 753, 732, 678.  $^1\text{H}$  NMR ( $\text{CDCl}_3$ )  $\delta$ : 0.77 (s, 6H), 1.62 (s, 4H), 2.65–3.20 (m, 6H), 7.60 (s, 4H), 9.91 (s, 2H). MS  $m/z$ : 306 ( $[\text{M}]^+$ ). Anal. calcd. for  $\text{C}_{21}\text{H}_{22}\text{O}_2$ : C 82.31, H 7.23; found: C 82.24, H 7.30.

#### **anti-7,15-Diformyl-10,18-dimethyl[4.2]MCP (3c)**

Colorless prisms (hexane), mp 202–205°C. IR (KBr)  $\nu_{\text{max}}$ : 2950, 2810, 1672 (C=O), 1582, 1560, 1425, 1378, 1258, 1184, 1138, 1103, 1015, 956, 876, 745, 772.  $^1\text{H}$  NMR ( $\text{CDCl}_3$ )  $\delta$ : 0.97 (s, 6H), 1.32 (m, 2H), 1.50–1.70 (m, 4H), 2.30–2.47 (m, 2H), 2.79–3.19 (m, 4H), 7.44 (d,  $J = 1.5$  Hz, 2H), 7.69 (d,  $J = 1.5$  Hz, 2 H), 9.93 (s, 2H). MS  $m/z$ : 320 ( $[\text{M}]^+$ ). Anal. calcd. for  $\text{C}_{22}\text{H}_{24}\text{O}_2$ : C 82.46, H 7.55; found: C 82.62, H 7.71.

#### **Formylation of 1,2,3-trimethylbenzene (4) with $\text{Cl}_2\text{CHOCH}_3$**

To a solution of 1,2,3-trimethylbenzene (**4**) (240 mg, 2.0 mmol) and  $\text{Cl}_2\text{CHOCH}_3$  (0.56 mL, 6.2 mmol) in  $\text{CH}_2\text{Cl}_2$  (10 mL) was added a solution of  $\text{TiCl}_4$  (0.45 mL, 4.1 mmol) in  $\text{CH}_2\text{Cl}_2$  (4 mL). After the reaction mixture was stirred at 0°C for 1 h and at room temperature for 3 h, it was treated as described above to give 2,3,4-trimethylbenzaldehyde (**5**) as a pale yellow oil (266.4 mg, 90%); IR (NaCl)  $\nu_{\text{max}}$ : 1670 (C=O).  $^1\text{H}$  NMR ( $\text{CDCl}_3$ )  $\delta$ : 2.20 (s, 3H), 2.33 (s, 3H), 2.57 (s, 3H), 7.13 (d,  $J = 8.1$  Hz, 1H), 7.53 (d,  $J = 8.1$  Hz, 1H), 9.80 (s, 1H). MS  $m/z$ : 148 ( $[\text{M}]^+$ ). Anal. calcd. for  $\text{C}_{10}\text{H}_{12}\text{O}$ : C 81.04, H 8.16; found: C 81.30, H 8.10.

#### **General procedure for treatment of *anti*-5,13-di-*tert*-butyl-8,16-dimethyl[2.2]MCP (6a) with $\text{Cl}_2\text{CHOCH}_3$ in the presence of $\text{TiCl}_4$**

To a solution of **6a** (348 mg, 1.0 mmol) and  $\text{Cl}_2\text{CHOCH}_3$  (0.54 mL, 6.0 mmol) in  $\text{CH}_2\text{Cl}_2$  (10 mL) was added, dropwise, titanium tetrachloride (0.44 mL, 4.0 mmol) in  $\text{CH}_2\text{Cl}_2$  (4 mL) at 0°C under an argon. After the reaction mixture was stirred under several reaction conditions, it was poured into ice-water and extracted with  $\text{CH}_2\text{Cl}_2$  (30 mL  $\times$  3). The extracts were washed with water, dried over  $\text{Na}_2\text{SO}_4$ ,

and concentrated. The residue was chromatographed over silica gel (Wako, C-300; 100 g) with hexane–ether (1:1) as eluent to give **7a**, **8**, **9**, and **10**. The reaction conditions and product yields are compiled in Table 1.

The isobutene, which was generated in the reaction system, was passed through a mixture of toluene (10 mL) containing aluminium chloride (5 mg, 0.037 mmol) with argon gas at room temperature. The reaction mixture was poured into ice-water and extracted with  $\text{CH}_2\text{Cl}_2$  (10 mL  $\times$  3). The extracts were washed with brine, dried over  $\text{Na}_2\text{SO}_4$ , and evaporated in vacuo (30°C 20 torr $^{-1}$ ) (1 torr = 133.322 Pa). The residue was analyzed by  $^1\text{H}$  NMR spectroscopy and gas chromatography from which the formation of *tert*-butyltoluene was qualitatively confirmed.

#### **anti-5-*tert*-Butyl-13-formyl-8,16 dimethyl[2.2]metacyclophane (7a)**

Pale yellow oil. IR (NaCl)  $\nu_{\text{max}}$ : 1670 (C=O).  $^1\text{H}$  NMR ( $\text{CDCl}_3$ )  $\delta$ : 0.49 (s, 3H), 0.64 (s, 3H), 1.30 (s, 9H), 2.70–3.10 (m, 8H), 7.14 (s, 2H), 7.64 (s, 2H), 9.84 (s, 1H). MS  $m/z$ : 320 ( $[\text{M}]^+$ ). Anal. calcd. for  $\text{C}_{23}\text{H}_{28}\text{O}$  (320.48): C 86.20, H 8.81; found: C 86.45, H 8.65.

#### **2,7-Di-*tert*-butyl-*trans*-10b,10c-dimethyl-10b,10c-dihydro-pyrene (10)**

Colorless prisms (hexane); mp 203–204°C (lit. (14) value mp 203–204°C).

#### **anti-5-*tert*-Butyl-8,16-dimethyl-13-(3-methyl-2-butene-2-yl)[2.2]metacyclophane (8)**

Colorless needles (hexane), mp 141–142°C. IR (KBr)  $\nu_{\text{max}}$ : 2990, 2960, 2890, 1465, 1360, 1290, 1280, 1190, 890, 860, 740, 710.  $^1\text{H}$  NMR ( $\text{CDCl}_3$ )  $\delta$ : 0.58 (s, 3H, Me-8), 0.69 (s, 3H, Me-16), 1.29 (s, 9H, *t*-Bu), 1.65 (s, 3H, Me), 1.80 (s, 3H, Me), 1.93 (s, 3H, Me), 2.57–2.99 (m, 8H,  $\text{CH}_2$ ), 6.89 (s, 2H, ArH-4,6), 7.12 (s, 2H, ArH-12,14).  $^{13}\text{C}$  NMR ( $\text{CDCl}_3$ )  $\delta$ : 14.38 (q,  $\text{CH}_3$ -8), 14.70 (q,  $\text{CH}_3$ -16), 20.70, 20.75, 22.16 (q,  $\text{CH}_3$ ), 31.39 (q,  $\text{C}(\text{CH}_3)_3$ ), 33.93 (s,  $\text{C}(\text{CH}_3)_3$ ), 36.46, 36.60 (t,  $\text{CH}_2$ ), 124.10 (d, ArCH), 126.25 (s,  $\beta$ -olefin), 127.10 (d, ArCH), 129.86 (s,  $\alpha$ -olefin), 136.17, 136.58, 139.48, 140.41, 140.61, 146.77 (s, ArC). MS  $m/z$ : 360 ( $[\text{M}]^+$ ). Anal. calcd. for  $\text{C}_{27}\text{H}_{36}$  (360.59): C 89.94, H 10.06; found: C 89.81, H 10.20.

#### **anti-5,13-Di-*tert*-butyl-*exo*-1-hydroxy-8,16-dimethyl-[2.2]metacyclophane (9)**

Colorless needles (hexane), mp 258–259°C. IR (KBr)  $\nu_{\text{max}}$ : 3580 (OH), 2980, 2880, 1475, 1460, 1360, 1280, 1190, 1020, 880, 770.  $^1\text{H}$  NMR ( $\text{CDCl}_3$ )  $\delta$ : 0.52 (s, 3H, Me), 0.86 (s, 3H, Me), 1.27 (s, 9H, *t*-Bu), 1.30 (s, 9H, *t*-Bu), 2.01 (broad s, 1H, OH, exchange with  $\text{D}_2\text{O}$ ), 2.73–3.13 (m, 6H,  $\text{CH}_2$  and  $\text{CH}_2\text{CH}(\text{OH})$ ), 5.34 (dd, 1H,  $J = 2.2/4.6$  Hz,  $\text{CHOH}$ ), 7.01 (d, 1H,  $J = 2.0$  Hz, ArH), 7.18–7.21 (m, 3H, ArH).  $^{13}\text{C}$  NMR ( $\text{CDCl}_3$ )  $\delta$ : 14.03, 14.34 (q,  $\text{CH}_3$ ), 31.30, 31.34 (q,  $\text{C}(\text{CH}_3)_3$ ), 33.84, 33.89 (s,  $\text{C}(\text{CH}_3)_3$ ), 35.83, 36.34 (t,  $\text{CH}_2\text{CH}_2$ ), 44.56 (t,  $\text{CH}_2\text{CH}(\text{OH})$ ), 80.66 (d,  $\text{CH}(\text{OH})$ ), 122.73, 124.98, 125.21, 125.80 (d, ArCH), 133.65, 135.22, 136.71, 136.94, 139.66, 140.77, 146.23, 146.34 (s, ArC). MS  $m/z$ : 364 ( $[\text{M}]^+$ ). Anal. calcd. for  $\text{C}_{26}\text{H}_{36}\text{O}$  (360.59): C 85.66, H 9.95; found: C 85.35, H 9.78.



**Oxidation of 8 with cetyltrimethylpermanganate affording *anti*-5-acetyl-13-*tert*-butyl-8,16-dimethyl-[2.2]MCP (11)**

To a solution of **8** (36 mg, 0.1 mmol) in CH<sub>2</sub>Cl<sub>2</sub> (1 mL) was added, dropwise, CTAP (40 mg, 0.1 mmol) in CH<sub>2</sub>Cl<sub>2</sub> (1 mL) within 1 min at room temperature. After being stirred for 2.5 h, the reaction mixture was filtered over celite and Na<sub>2</sub>SO<sub>4</sub>. The filtrate was evaporated in vacuo to give **11** (29 mg, 87%) as a colourless solid. Recrystallization from hexane gave the *title compound* **11** as colorless prisms; mp 155–157°C; IR (KBr)  $\nu_{\max}$ : 1665 (C=O). <sup>1</sup>H NMR (CDCl<sub>3</sub>)  $\delta$ : 0.50 (s, 3H), 0.63 (s, 3H), 1.30 (s, 9H), 2.55 (s, 3H), 2.73–3.04 (m, 8H), 7.13 (s, 2H), 7.73 (s, 2H). MS *m/z*: 334 ([M]<sup>+</sup>). Anal. calcd. for C<sub>24</sub>H<sub>30</sub>O: C 86.18, H 9.04; found: C 86.65, H 8.98.

**Conversion of 9 to 10: Typical procedure**

A solution of **9** (182 mg, 0.5 mmol) in CH<sub>2</sub>Cl<sub>2</sub> (5 mL) or benzene (5 mL) was stirred at room temperature for several times. The reaction mixture was evaporated in vacuo. The residue was purified through silica gel column by eluting with hexane–ether (1:1) to give **10**. When titanium tetrachloride (379 mg, 0.22 mL, 2.0 mmol) or concd. HCl (1 drop) was used as an additive the reaction mixture was poured into ice-water and extracted with CH<sub>2</sub>Cl<sub>2</sub>. The extracts were washed with brine, dried over Na<sub>2</sub>SO<sub>4</sub>, and evaporated in vacuo. The residue was purified according to the same manner described above.

**General procedure for treatment of 6 with Cl<sub>2</sub>CHOCH<sub>3</sub> in the presence of AlCl<sub>3</sub> MeNO<sub>2</sub>**

To a solution of **6b** (207 mg, 0.572 mmol) and Cl<sub>2</sub>CHOCH<sub>3</sub> (0.72 mL, 7.9 mmol) in CH<sub>2</sub>Cl<sub>2</sub> (12 mL) was added, dropwise, a solution of AlCl<sub>3</sub> (458 mg, 3.4 mmol) in MeNO<sub>2</sub> (1.0 mL) at 0°C under argon. After the reaction mixture was stirred at 0°C for 1 h and at room temperature for 5 h it was poured into ice-water and extracted with CH<sub>2</sub>Cl<sub>2</sub> (30 mL  $\times$  3). The extracts were washed with water, dried over Na<sub>2</sub>SO<sub>4</sub>, and concentrated to give, as an oil, a mixture of (161 mg, 82%), in the ratio 50:50 (GLC analysis). The residue was chromatographed over silica gel (Wako, C-300; 100 g) with benzene and benzene–CHCl<sub>3</sub> (1:1) as eluent to give **7b** (77 mg, 35%) and **14b** (42 mg, 22%) as an oil, respectively.

**syn-6,14-Di-*tert*-butyl-7-formyl-9,17-dimethyl[3.2]metacyclopheane (14b)**

Pale yellow oil. IR (NaCl)  $\nu_{\max}$ : 1683 (C=O). <sup>1</sup>H NMR (CDCl<sub>3</sub>)  $\delta$ : 1.28 (9 H, s), 1.46 (s, 9H), 1.73 (s, 3H), 1.96 (s, 3H), 2.25–2.35 (m, 2H), 2.15–3.20 (m, 7H), 3.45–3.50 (m, 1H), 6.71 (broad s, 2H), 7.12 (s, 1H), 10.09 (s, 1H). MS *m/z*: 390 ([M]<sup>+</sup>). Anal. calcd. for C<sub>28</sub>H<sub>38</sub>O (390.61): C 86.10, H 9.81; found: C 86.24, H 9.52.

***anti*-14-*tert*-Butyl-6-formyl-9,17-dimethyl[3.2]MCP (7b)**

Pale yellow oil. IR (NaCl)  $\nu_{\max}$ : 1680 (C=O). <sup>1</sup>H NMR (CDCl<sub>3</sub>)  $\delta$ : 0.64 (s, 3H), 0.78 (s, 3H), 1.30 (s, 9H), 2.00–2.20 (m, 2H), 2.50–3.20 (m, 8H), 7.04 (d, 1H, *J* = 2.0 Hz), 7.08 (d, 1H, *J* = 2.0 Hz), 7.56 (s, 2H), 9.87 (s, 1H). MS *m/z*: 334 ([M]<sup>+</sup>). Anal. calcd. for C<sub>24</sub>H<sub>30</sub>O (334.51): C 86.18, H 9.04; found: C 86.40, H 9.25.

Similarly, compounds **7a**, **13a**, and **7c** were prepared in the same manner as described above in 60, 15, and 72% yields, respectively.

***anti*-5-*tert*-Butyl-8,16-dimethyl-13-(3-methyl-1-butene-2-yl)[2.2]metacyclopheane (13a)**

Colorless needles (hexane), mp 154–155°C. IR (KBr)  $\nu_{\max}$ : 2970, 2930, 2860, 1615, 1470, 1455, 1350, 1270, 1180, 890, 880, 850. <sup>1</sup>H NMR (CDCl<sub>3</sub>)  $\delta$ : 0.59 (s, 3H), 0.65 (s, 3H), 1.11 (d, 6H, *J* = 6.6 Hz), 1.29 (s, 9H), 2.70–3.03 (m, 9H, CH<sub>2</sub> and CH), 4.92, 5.08 (d, each 1H, *J* = 1.3 Hz, olefinic proton), 7.12 (s, 4H). MS *m/z*: 360 ([M]<sup>+</sup>, 57), 303 ([M<sup>+</sup> – *t*-Bu]). Anal. calcd. for C<sub>27</sub>H<sub>36</sub> (360.59): C 89.93, H 10.07; found: C 89.65, H 10.01.

***anti*-15-*tert*-Butyl-7-formyl-10,18-dimethyl[4.2]MCP (7c)**

Pale yellow prisms (hexane), mp 86–89°C. IR (KBr)  $\nu_{\max}$ : 1693 (C=O). <sup>1</sup>H NMR (CDCl<sub>3</sub>)  $\delta$ : 0.85 (s, 3H), 0.99 (s, 3H), 1.31 (s, 9H), 1.05–1.20 (m, 4H), 2.16–2.42 (m, 2H), 2.71–3.11 (m, 6H), 6.87 (d, 1H, *J* = 1.8 Hz), 7.15 (d, 1H, *J* = 1.8 Hz), 7.36 (d, 1H, *J* = 1.8 Hz), 7.65 (d, 1H, *J* = 1.8 Hz), 9.91 (s, 1H, CHO). MS *m/z*: 348 ([M]<sup>+</sup>). Anal. calcd. for C<sub>25</sub>H<sub>32</sub>O (348.53): C 86.15, H 9.19; found: C 86.37, H 9.25.

**Acylation of 6a with isobutanoyl chloride in the presence of TiCl<sub>4</sub>**

To a solution of **6a** (299.1 mg, 0.858 mmol) and isobutanoyl chloride (365.3 mg, 3.43 mmol) in CH<sub>2</sub>Cl<sub>2</sub> (6.6 mL) was added, dropwise, a solution of TiCl<sub>4</sub> (1.21 mL, 11.03 mmol) in CH<sub>2</sub>Cl<sub>2</sub> (1.5 mL) at 0°C under an argon. After the reaction mixture was stirred at 0°C for 1 h and at room temperature for 1 h, it was poured into ice-water and extracted with CH<sub>2</sub>Cl<sub>2</sub> (30 mL  $\times$  3). The extracts were washed with water, dried over Na<sub>2</sub>SO<sub>4</sub>, and concentrated. The residue was chromatographed over silica gel (Wako, C-300; 100 g) with CHCl<sub>3</sub> as an eluent to give **15** as prisms. Recrystallization from hexane gave *anti*-13-*tert*-butyl-5-isobutanoyl-8,16-dimethyl[2.2]metacyclopheane (**15**) (223 mg, 71.8%) as colorless prisms (hexane), mp 114–116°C. IR (KBr)  $\nu_{\max}$ : 1672 (C=O). <sup>1</sup>H NMR (CDCl<sub>3</sub>)  $\delta$ : 0.52 (s, 3H), 0.63 (s, 3H), 1.30 (s, 9H), 1.20 (d, 6H, *J* = 6.7 Hz), 2.70–3.10 (m, 8H), 3.50–3.60 (m, 1H), 7.13 (s, 2H), 7.75 (s, 2H). MS *m/z*: 362 ([M]<sup>+</sup>). Anal. calcd. for C<sub>26</sub>H<sub>34</sub>O (360.59): C 86.13, H 9.45; found: C 86.08, H 9.51.

**Wittig reaction of 15 with methyltriphenylphosphonium iodide affording *anti*-5-*tert*-butyl-8,16-dimethyl-13-(3-methyl-1-butene-2-yl)[2.2]MCP (13a)**

To a suspension of methyltriphenylphosphonium iodide (121 mg, 0.3 mmol) in dry THF (10 mL) was added, dropwise, 1.6 N butyllithium hexane solution (0.19 mL, 0.30 mmol) within 1 min at room temperature under an argon. After the reaction mixture was stirred for 0.5 h, a solution of **15** (54 mg, 0.15 mmol) in dry THF (1 mL) was added, dropwise, within 1 min. After being stirred for 1 h, the reaction mixture was poured into ice-water and extracted with ether. The extracts were washed with water, dried over Na<sub>2</sub>SO<sub>4</sub>, and evaporated in vacuo. The residue was purified through silica gel column (Wako, C-300; 100 g) by eluting with hexane to give **13a** (25 mg, 46%) and unchanged **15**



(21 mg, 38%) as colourless solid. Recrystallization from hexane gave **13a** as colorless prisms.

## Conclusions

We conclude that the selective *ipso*-formylation reactions of *anti*-di-*tert*-butyl[*n*.2]MCPs **6** led to the first-reported direct introduction of one formyl group because of a through-space electronic interaction with the opposing benzene ring, similar to the electrophilic aromatic substitution of MCPs. The yield of *ipso*-formylation of **6** was controlled by the activity of the catalyst used. Especially, the present *ipso*-formylation with dichloromethyl methyl ether in the presence of AlCl<sub>3</sub> MeNO<sub>2</sub> provides excellent yields and easy isolation of the products. The presently developed procedure was further applied to the direct removal of a *tert*-butyl group by electrophilic substitution of *anti*-di-*tert*-butyl-8,16-dimethyl[2.2]MCP **6a**, which are prone to give transannular reaction products under the electrophilic reaction conditions. The chemical behaviours of [*n*.2]MCPs for other electrophilic reagents are now under study.

## References

1. Part 61: T. Yamato, T. Furukawa, S. Saito, K. Tanaka, and H. Tsuzuki. *New J. Chem.* **26**, 1035 (2002).
2. (a) P.M. Keehn and S.M. Rosenfield. *Cyclophanes*. Vol. 1. Academic Press, New York. 1983; (b) F. Vögtle. *Cyclophane chemistry*. John Wiley & Sons Ltd., New York. 1993; (c) L. Ernst. *Prog. Nucl. Magn. Reson. Spectrosc.* **37**, 47 (2000).
3. (a) N.L. Allinger, M.A. DaRooge and R.B. Hermann. *J. Am. Chem. Soc.* **83**, 1974 (1961); (b) M. Fujimoto, T. Sato, and K. Hata. *Bull. Chem. Soc. Jpn.* **40**, 600 (1967); (c) T. Sato, S. Akabori, S. Muto, and K. Hata. *Tetrahedron*, **24**, 5567 (1968); (d) N.L. Allinger, B.J. Goldon, S.E. Hu, and R.A. Ford. *J. Org. Chem.* **32**, 2772 (1967); (e) T. Sato, M. Wakabayashi, and Y. Okamura. *Bull. Chem. Soc. Jpn.* **40**, 2363 (1967); (f) T. Sato and T. Takemura. *J. Chem. Soc. Perkin Trans. 2*, 1195 (1976); (g) T. Yamagishi, K. Torizuka, and T. Sato. *Bull. Chem. Soc. Jpn.* **55**, 1140 (1982); (h) V. Boekelheide and J. B. Phillips. *J. Am. Chem. Soc.* **85**, 1545 (1963).
4. A. Maquestiau, Y. V. Haverbeke, R. Flammang, M. Flammang-Barbieux, and N. Clerbois. *Tetrahedron Lett.* 3259 (1973).
5. A. Rieche, H. Gross, and E. Höft. *Chem. Ber.* **93**, 88 (1960).
6. (a) M. Tashiro and T. Yamato. *Synthesis*, 435 (1978); (b) M. Tashiro, T. Yamato. *J. Org. Chem.* **46**, 1543 (1981).
7. (a) T. Yamato, H. Sakamoto, K. Kobayashi, and M. Tashiro. *J. Chem. Res. Synop.* 352 (1986); *J. Chem. Res. Miniprint*, 2866 (1986); (b) T. Yamato, J. Matsumoto, S. Ide, K. Tokuhisa, K. Suehiro, and M. Tashiro. *J. Org. Chem.* **57**, 5243 (1992).
8. M. Tashiro, S. Mataka, Y. Takezaki, M. Takeshita, T. Arimura, A. Tsuge, and T. Yamato. *J. Org. Chem.* **54**, 451 (1989).
9. (a) W.S. Lindsey, P. Stokes, L.G. Humber, and V. Boekelheide. *J. Am. Chem. Soc.* **83**, 943 (1961); (b) R.W. Griffin, Jr. *Chem. Rev.* **63**, 45 (1963); (c) B. H. Smith. *Bridged aromatic compounds*. Academic Press, New York. 1964.
10. T. Yamato, H. Kamimura, and T. Furukawa. *J. Org. Chem.* **62**, 7560 (1997).
11. (a) W. Verboom, A. Durie, R.J.M. Egberink, Z. Asfari, and D.N. Reinhoudt. *J. Org. Chem.* **57**, 1313 (1992); (b) E. Kelderman, L. Derhaeg, G.J.T. Heesink, W. Verboom, J.F.J. Engbersen, N.F. van Hulst, A. Persoons, and D.N. Reinhoudt. *Angew. Chem. Int. Ed. Engl.* **31**, 1075 (1992).
12. G.A. Olah. *Acc. Chem. Res.* **4**, 240 (1971).
13. (a) V. Bhushan, R. Rathore, and S. Chandrasekaran. *Synthesis*, 431 (1984); (b) R. Rathore and S. Chandrasekaran. *J. Chem. Res. (S)* 458 (1986).
14. M. Tashiro and T. Yamato. *J. Am. Chem. Soc.* **104**, 3701 (1982).
15. (a) M. Tashiro, T. Yamato, and K. Kobayashi. *J. Org. Chem.* **49**, 3380 (1984); (b) T. Yamato, J. Matsumoto, T. Ando, K. Tokuhisa, and M. Tashiro. *J. Chem. Res. Synop.* 276 (1991).
16. U. von der Brüggen and H. Mayr. *Chem. Ber.* **121**, 191 (1988).
17. (a) V. Boekelheide and T. Miyasaka. *J. Am. Chem. Soc.* **89**, 1709 (1967); (b) V. Boekelheide and E. Sturm. *J. Am. Chem. Soc.* **91**, 902 (1969).
18. (a) M. Tashiro and T. Yamato. *J. Org. Chem.* **46**, 4556 (1981); (b) M. Tashiro and T. Yamato. *J. Org. Chem.* **48**, 1461 (1983).



# A pentanortriterpenoid with a novel carbon skeleton and a new pregnane from *Trichilia connaroides*

Hua-Ping Zhang, Shao-Hua Wu, Yue-Mao Shen, Yun-Bao Ma, Da-Gang Wu, Shu-Hua Qi, and Xiao-Dong Luo

**Abstract:** A new rearranged pentanortriterpenoid (trijugin C) and a new pregnane (3 $\beta$ ,4 $\alpha$ -dihydroxypregnan-16-one) were isolated from the EtOH extract of *Trichilia connaroides* (Meliaceae). Trijugin C has been shown to be a derivative of methyl angolensate with a novel carbon skeleton. The structures were elucidated on the basis of spectral analysis including  $^1\text{H}$ - $^1\text{H}$  COSY, HMQC, HMBC, and NOESY experiments. The possible biogenetic pathway of trijugin C is discussed.

**Key words:** *Trichilia connaroides*, Meliaceae, pentanortriterpenoid, trijugin C, pregnane.

**Résumé :** On a isolé un nouveau pentanortriterpénoïde réarrangé, la trijucine C, et un nouveau dérivé du prégnane, la 3 $\beta$ ,4 $\alpha$ -dihydroxypregnan-16-one, à partir des solutions éthanoliques d'extraction du *Trichilia connaroides* (Meliaceae). On a montré que la trijucine C est un dérivé de l'angolensate de méthyle à base d'un nouveau squelette carboné. On a élucidé les structures à l'aide d'analyses spectrales, y compris des expériences de « COSY », « HMQC », « HMBC » et « NEOSY »  $^1\text{H}$ - $^1\text{H}$ . On discute des voies de formations biogénétiques possibles de la trijucine C.

**Mots clés :** *Trichilia connaroides*, Meliaceae, pentanortriterpénoïde, trijucine C, prégnane.

[Traduit par la Rédaction]

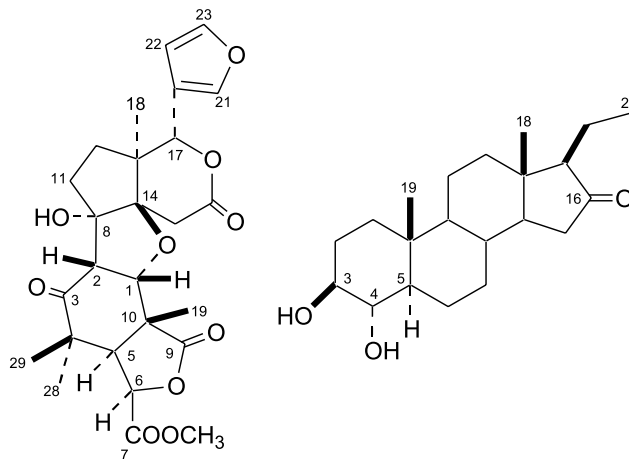
## Introduction

The roots of *Trichilia connaroides* Wight. & Arn. (syn: *Heynea trijuga* Roxb.) (Meliaceae) are used as a Chinese crude drug to treat arthritis, pharyngitis, tonsillitis, and other ailments (1). Four tetranortriterpenoids (trijugin A, trijugin B, trijugin B acetate, and 2-hydroxy-3-*O*-tigloyl-6-*O*-acetylswietenolide) have been isolated from the leaves and pericarps of this plant previously (2–4). Our investigation of the EtOH extract of the roots of *T. connaroides* resulted in the isolation of a rearranged pentanortriterpenoid (trijugin C (1)) with a new carbon skeleton, and a new pregnane (3 $\beta$ ,4 $\alpha$ -dihydroxypregnan-16-one (2)) (Fig. 1).

## Results and discussion

Trijugin C (1) showed a  $[M]^+$  ion at  $m/z$  502.1837 in the HR-EI-MS spectrum, indicating a molecular formula of  $\text{C}_{26}\text{H}_{30}\text{O}_{10}$ . Twenty-six carbon signals were observed in the  $^{13}\text{C}$  NMR spectrum. The multiplicities of the carbons determined by DEPT led to the attribution: 5  $\text{CH}_3$ , 3  $\text{CH}_2$ , 8  $\text{CH}$ , 10  $\text{C}$ , including one ketone ( $\delta$  217.2), three ester carbonyls

Fig. 1. Structures of 1 and 2.



( $\delta$  174.9, 169.9, 168.9), a  $\beta$ -substituted furan ( $\delta$  143.2, 139.9, 121.5, 108.6), one methoxyl group ( $\delta$  52.9), three oxymethines ( $\delta$  80.8, 79.0, 74.1), and two oxyquaternary carbons ( $\delta$  92.3, 87.6). The absorption band at  $3491\text{ cm}^{-1}$  in the IR spectrum showed the presence of the hydroxyl group. Based on the molecular formula and  $^{13}\text{C}$  DEPT spectrum, only one hydroxyl was present in the structure. The  $^1\text{H}$  and  $^{13}\text{C}$  NMR spectra of 1 showed similarities to those of trijugin A (2). The signals of the  $\beta$ -substituted furan ring in the  $^1\text{H}$  NMR spectrum occurred at  $\delta$  7.39 (H-21), 7.37 (H-23), and 6.25 (H-22) and the corresponding carbon signals at  $\delta$  139.9, 143.2 and 108.6, respectively, in the HMQC spectrum. Ring D was oxidized to a C-16 lactone, with H-17 oc-

Received 15 July 2002. Published on the NRC Research Press Web site at <http://canjchem.nrc.ca> on 19 March 2003.

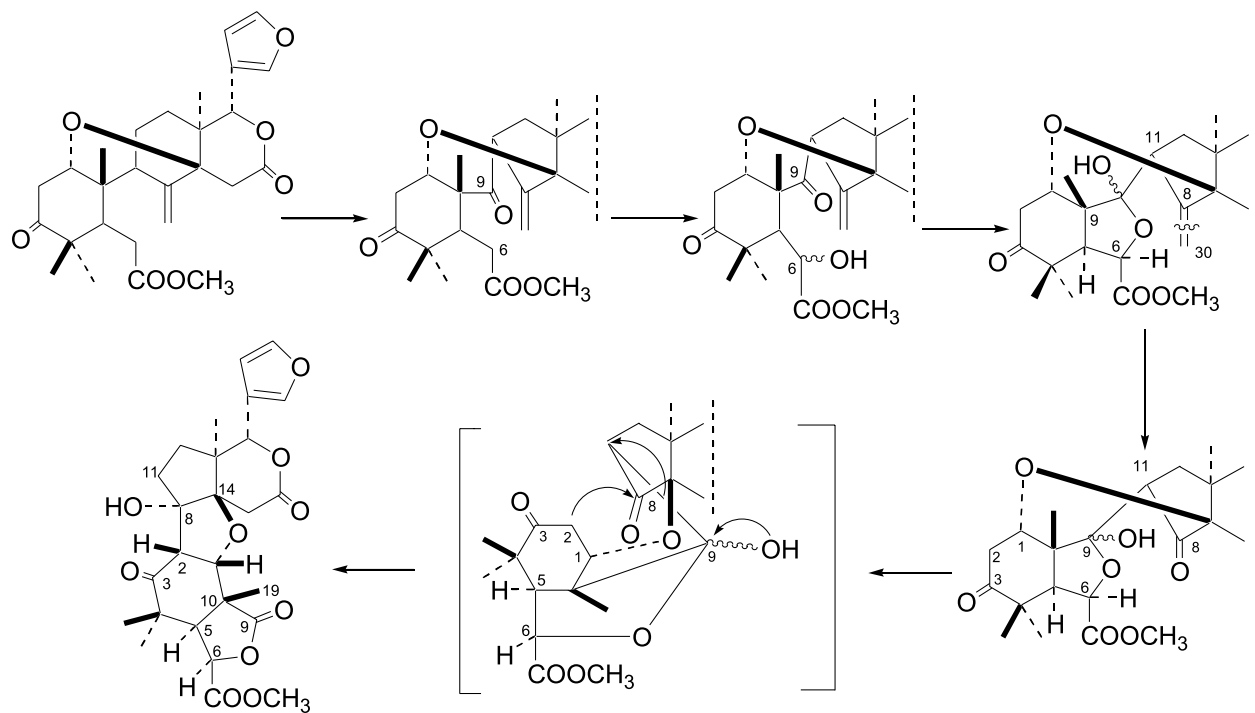
H.-P. Zhang, S.-H. Wu, Y.-M. Shen, Y.-B. Ma, D.-G. Wu, S.-H. Qi, and X.-D. Luo.<sup>1</sup> State Key Laboratory of Phytochemistry and Plant Resources in West China, Kunming Institute of Botany, The Chinese Academy of Sciences, Kunming, Yunnan 650204, P.R. China.

<sup>1</sup>Corresponding author: (e-mail: [xdluo@mail.kib.ac.cn](mailto:xdluo@mail.kib.ac.cn)).

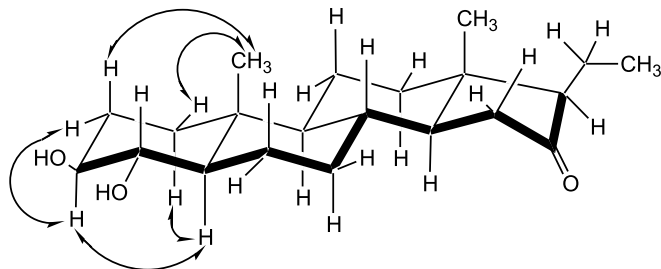


**Table 1.**  $^1\text{H}$ ,  $^{13}\text{C}$ , HMBC, and NOESY spectra data of trijugin C (**1**) (in  $\text{CDCl}_3$ ).<sup>a</sup>

Position	$\delta_{\text{H}}$	$\delta_{\text{C}}$	HMBC correlation (H-C)	NOESY (H-H)
1	4.31 (d, 4.2)	79.0	C-3, 5, 10, 19	H-2, 11 $\beta$ , 12 $\beta$ , 19
2	2.81 (d, 4.2)	52.9	C-3, 8, 11, 14	H-1, 11 $\beta$ , 19, 29, OH
3		217.2		
4		47.9		
5	3.28 (d, 8.6)	45.4	C-1, 3, 4, 6, 9, 10, 19, 28, 29	H-6, 15 $\beta$ , 28
6	5.03 (d, 8.6)	74.1	C-5, 7, 9, 10	H-5, 28
7		169.9		
8		87.6		
9		174.9		
10		43.1		
11 $\alpha$	2.34 (m)	42.4	C-2, 8, 12	H-11 $\beta$ , 12 $\alpha$ , 18
11 $\beta$	2.07 (m)		C-2, 8, 12, 13, 14	H-1, 2, 11 $\alpha$
12 $\alpha$	1.50 (m)	33.0	C-11, 13, 17, 18	H-11 $\alpha$ , 12 $\beta$ , 18
12 $\beta$	1.73 (m)		C-8, 11, 13, 18	H-1, 12 $\alpha$
13		48.2		
14		92.3		
15 $\alpha$	2.88 (d, 17.0)	36.7	C-8, 14, 16	H-15 $\beta$ , 18
15 $\beta$	2.09 (d, 17.0)		C-13, 14, 16	H-5, 15 $\alpha$
16		168.9		
17	5.62 (s)	80.8	C-12, 13, 14, 18, 20, 21, 22	H-12 $\beta$
18	0.97 (s)	15.6	C-12, 13, 14, 17	H-11 $\alpha$ , 12 $\alpha$ , 15 $\alpha$ , 22
19	1.56 (s)	19.1	C-1, 5, 9, 10	H-1, 2, 29
20		121.5		
21	7.39 (s)	139.9	C-22, 23	
22	6.25 (s)	108.6	C-20, 21, 23	
23	7.37 (s)	143.2	C-20, 21	
28	1.41 (s)	25.0	C-3, 4, 5, 29	H-5, 6, 29
29	1.11 (s)	20.9	C-3, 4, 5, 28	H-2, 19
OMe	3.85 (s)	52.9	C-7	
OH	5.87 (s)		C-2, 8, 11	H-2

<sup>a</sup>In ppm relative to the internal TMS run at 500 MHz. Multiplicities and splittings (Hz) are given in brackets.**Scheme 1.** Proposed biogenetic pathway of trijugin C (**1**).



**Fig. 2.** Selected NOESY correlations of **2**.

curing as a singlet at  $\delta$  5.62 and  $H_2$ -15 occurring as a pair of doublets at  $\delta$  2.88 and 2.09 ( $J = 17.0$  Hz). Four shielded methyl singlets at  $\delta$  1.56, 1.41, 1.11, and 0.97 were attributed to  $H_3$ -19,  $H_3$ -28,  $H_3$ -29, and  $H_3$ -18, respectively. The signal at  $\delta$  3.85 (3H, s) showed an HMBC correlation with an ester carbonyl carbon at  $\delta$  169.9 (Table 1), indicating the presence of a carbomethoxy group at C-7.  $H_2$ -11 ( $\delta$  2.34 (1H, m), 2.07 (1H, m)) and  $H_2$ -12 ( $\delta$  1.73 (1H, m), 1.50 (1H, m)) were assigned from their  $^1H$ - $^1H$  COSY correlations as well as an HMBC correlation to C-18. In addition, HMBC correlations were observed for  $H$ -15 $\alpha$  ( $\delta$  2.88) to C-8 ( $\delta$  87.6) and C-14 ( $\delta$  92.3), and for  $H$ -11 $\beta$  ( $\delta$  2.07) to C-8 and C-14, supporting a contracted ring C formed by C-11, 12, 13, 14, 8. This was also confirmed by the absence of other coupling to the  $H_2$ -11 in the  $^1H$ - $^1H$  COSY spectrum.

In the HMBC spectrum, correlations were observed for H-6 ( $\delta$  5.03) to two ester carbonyl carbons C-7 ( $\delta$  169.9) and C-9 ( $\delta$  174.9), and for  $H_3$ -19 ( $\delta$  1.56) and H-5 ( $\delta$  3.28) to C-9. The presence of two C-11 protons and the absence of an HMBC correlation between H-11 and C-9 suggested that the C-9—11 bond had been cleaved. Thus, C-5, C-6, O, C-9, and C-10 formed a five-membered lactone ring.

The exchangeable sharp singlet at  $\delta$  5.87 (1H) in the  $^1H$  NMR spectrum (removed on addition of  $D_2O$ ) was ascribed to the proton of the hydroxyl group attached to C-8 supported by HMBC correlations between the hydroxyl proton and C-2 ( $\delta$  52.9), C-8 ( $\delta$  87.6), and C-11 ( $\delta$  42.4). Cross peaks observed from H-2 ( $\delta$  2.81) to C-3 ( $\delta$  217.2), C-8 ( $\delta$  87.6), C-11 ( $\delta$  42.4), and C-14 ( $\delta$  92.3), and from  $H_2$ -11 ( $\delta$  2.34, 2.07) to C-2, C-8, and C-14 suggested the linkage of ring A and ring C by the C-2—8 bond. Finally, a 1,14-ether linkage (as found in trijugin A) was proposed to satisfy the molecular formula and the deshielded nature of C-1 ( $\delta$  79.0) and C-14 ( $\delta$  92.3).

The relative stereochemistry at the chiral centers is suggested by the NOESY correlations summarized in Table 1. The NOESY plot showed a correlation between  $H_3$ -18 and H-22, suggesting the  $\alpha$ -orientation of the furan ring at C-17, and correlations among H-2 and H-1, H-11 $\beta$ , H-12 $\beta$ ,  $H_3$ -29 and  $H_3$ -19, revealing the  $\beta$ -orientation of H-2 and H-1 further supported by the small coupling constant ( $J = 4.2$  Hz) of H-1 to H-2. Furthermore, the hydroxyl proton showed a correlation with H-2 but no correlation with H-1,  $H_2$ -11, and  $H_2$ -12, thus the hydroxyl group attached to C-8 was in the  $\alpha$  orientation. Based on the above spectral data, the structure of trijugin C was determined to be as shown for **1**.

Usually tetranortriterpenoids with an open ring B have an 8,30 double bond. Trijugin class compounds have a rare contracted ring C and Connolly and co-workers (2) postulated

that the trijugins may be formed by ring C contraction occurring by a pinacol–pinacolone rearrangement of a 9,11-dihydroxy precursor and anticipated more detailed examination of such compounds would be necessary. Up to now, 11 other analogues, E.P.4, E.P.5 (5), capensolactones 1, 2a, 2b, 3a, and 3b (6), voamatin A, B (7), and voamatin C, D (8) have been reported. These 14 compounds have either an 8,30 double bond or an 8,30-epoxide by oxidation, and either an exocyclic carbonyl or a hemi-ketal carbon atom at C-9. In pentanortriterpenoid **1**, C-30 has been removed by further oxidation of the 8,30 double bond. Retro-aldol cleavage of the C-9 (11) bond was followed by an aldol condensation between C-2 and C-8 to form a new ring. The cleavage and the formation of these C—C bonds have not been described before. A suggested biogenesis for **1**, starting with methyl angolensate (9), is given in Scheme 1. The oxidation of C-6 of tetranortriterpenoids with a lactone ring D and an opened ring B had been reported (10, 11).

Compound **2** had a molecular formula of  $C_{21}H_{34}O_3$ , as confirmed by HR-EI-MS ( $m/z$  334.2511  $[M]^+$ , calcd. 334.2508) and the  $^{13}C$  NMR spectrum showing 21 carbon signals (3 C, 7 CH, 8  $CH_2$ , 3  $CH_3$ , including two oxymethines at  $\delta$  76.3, 75.3 and a ketonic carbonyl at  $\delta$  219.6). The absorption bands at 3564, 3271, and 1741  $cm^{-1}$  in the IR spectrum were attributable to two hydroxyl groups and a five-membered ring ketone. The skeleton of **2** was similar to those of 2 $\alpha$ ,3 $\beta$ -dihydroxypregnan-16-one and 2 $\beta$ ,3 $\beta$ -dihydroxypregnan-16-one (12, 13) by comparison of the NMR spectral data, as confirmed by  $^1H$ - $^1H$  COSY, HMQC, and HMBC spectra. The A/B ring junction was deduced as *trans* by the chemical shift value  $\delta$  13.5 of the C-19 methyl carbon (14). The two hydroxyl groups were concluded to be adjacent to each other, since the correlation was observed between the two oxymethine protons at  $\delta$  3.34 (1H, m) and 3.23 (1H, dd,  $J = 8.9, 11.2$  Hz) in the  $^1H$ - $^1H$  COSY spectrum. Moreover, the correlations between the proton at  $\delta$  3.34 with a methylene group and the proton at  $\delta$  3.23 with a methine group indicated the only possibility for the positions of these two hydroxyl groups on the tetracyclic skeleton to be at C-3 and C-4. The large coupling constants (8.9 and 11.2 Hz) of H-4 indicated that H-3, H-4, and H-5 were axial. This result was also substantiated by H-5 and H-3, H-2 $\alpha$  and H-3 showing spatial proximity in the NOESY experiment (Fig. 2). Thus, the structure of compound **2** was determined as 3 $\beta$ ,4 $\alpha$ -dihydroxypregnan-16-one.

## Experimental

### General procedure

The melting point was uncorrected. Instrumentation used for:  $[\alpha]_D$ : Horiba-300; NMR spectra: Bruker DRX-500; IR: Bio-Rab FTS-135; MS: VG Autospec-3000.

### Plant material

The roots of *T. connaroides* were collected at Xishuangbanna, Yunnan Province, the People's Republic of China in August 1997 and identified by Professor Guoda Tao, Xishuangbanna Botany Garden, Chinese Academy of Sciences. A voucher specimen (No. 0620834) was deposited at the Herbarium of the Kunming Institute of Botany, Chinese Academy of Sciences.



**Table 2.**  $^1\text{H}$  NMR,  $^{13}\text{C}$  NMR, and HMBC spectra data of  $3\beta,4\alpha$ -dihydroxypregnan-16-one (**2**) (in  $\text{CDCl}_3$ ).<sup>a</sup>

Position	$\delta_{\text{H}}$	$\delta_{\text{C}}$	HMBC correlation (H-C)
1 $\alpha$	1.67 (m)	35.9	C-2, 3, 5, 9, 10, 19
1 $\beta$	1.04 (m)		C-2, 3, 9, 10, 19
2 $\alpha$	1.85 (m)	28.3	C-1, 3, 4
2 $\beta$	1.49 (m)		C-1, 3, 4
3	3.34 (m)	76.3	C-2, 4
4	3.23 (dd, 8.9, 11.2)	75.3	C-3, 5, 6
5	1.01 (m)	50.6	C-4, 9, 10, 19
6 $\alpha$	1.91 (m)	22.4	C-5, 8, 10
6 $\beta$	1.15 (m)		C-4, 5, 8, 10
7 $\alpha$	1.70 (m)	31.7	C-6, 9
7 $\beta$	0.90 (m)		C-6, 9
8	1.49 (m)	34.0	C-7, 9, 10
9	0.85 (m)	54.4	C-11, 19
10		37.3	
11 $\alpha$	1.57 (m)	20.4	C-8, 9, 12, 13
11 $\beta$	1.32 (m)		C-8, 9, 12, 13
12 $\alpha$	1.31 (m)	38.1	C-9, 11, 13, 18
12 $\beta$	1.86 (m)		C-9, 11, 13, 18
13		42.0	
14	1.36 (m)	50.4	C-8, 9, 13, 15, 18
15	2.18 (dd, 10.8, 7.4)	38.4	C-13, 14, 16
	1.72 (dd, 10.8, 8.0)		C-8, 14, 16
16		219.6	
17	1.62 (m)	65.3	C-12, 13, 16, 18, 21
18	0.65 (s)	13.4	C-12, 13, 14, 17
19	0.85 (s)	13.5	C-1, 5, 9
20	1.60(m), 1.22 (m)	17.6	C-13, 16, 17, 21
21	0.99 (t, 7.4)	13.4	C-17, 20

<sup>a</sup>In ppm relative to the internal TMS run at 500 MHz. Multiplicities and splittings (Hz) are given in brackets.

## Extraction and isolation

Dried and powdered roots (3.5 kg) of *T. connaroides* were extracted with 95% ethanol three times at room temperature. After removal of the solvent by evaporation, the residues (250 g) were suspended in  $\text{H}_2\text{O}$ , and then extracted with  $\text{CHCl}_3$ . The  $\text{CHCl}_3$  extract was evaporated to give a red extract (40 g), which was subjected to a Si gel column, eluting with a  $\text{CHCl}_3$ - $\text{Me}_2\text{CO}$  mixture containing increasing amounts of  $\text{Me}_2\text{CO}$  to afford seven fractions. Fraction 6 was purified further on a Si gel column, eluted with  $\text{CHCl}_3$ - $\text{Me}_2\text{CO}$  (4:1) to yield compound **1** (12 mg). Fraction 5 was rechromatographed on a Si gel column and eluted with  $\text{CHCl}_3$ - $\text{Me}_2\text{CO}$  (10:1) to give compound **2** (32 mg).

Trijugin C (**1**): amorphous, mp 144–146 °C,  $[\alpha]_{\text{D}}^{27} -49.4$  (*c* 0.18,  $\text{CHCl}_3$ ). IR (KBr)  $\nu_{\text{max}}$  ( $\text{cm}^{-1}$ ): 3491, 1743, 1636, 1503, 874.  $^1\text{H}$  and  $^{13}\text{C}$  NMR data, see Table 1. EI-MS  $m/z$  (%): 502 ( $[\text{M}]^+$ , 93) 487, 95 (100). HR-EI-MS  $m/z$ : 502.1837  $[\text{M}]^+$ .

$3\beta,4\alpha$ -Dihydroxypregnan-16-one (**2**): colorless needles (petroleum ether – acetone), mp 152–154 °C,  $[\alpha]_{\text{D}}^{27} -128.3$  (*c* 0.31,  $\text{CHCl}_3$ ). IR (KBr)  $\nu_{\text{max}}$  ( $\text{cm}^{-1}$ ): 3564, 3271, 1741, 1451, 1380, 1055, 1010.  $^1\text{H}$  and  $^{13}\text{C}$  NMR data, see Table 2. EI-MS  $m/z$  (%): 335 ( $[\text{M} + \text{H}]^+$ , 40), 334 ( $[\text{M}]^+$ , 82), 316 ( $[\text{M} - \text{H}_2\text{O}]^+$ , 13), 248 (100). HR-EI-MS  $m/z$ : 334.2511  $[\text{M}]^+$ .

## Acknowledgments

The authors are grateful to the National Natural Science Foundation of China (Project No. C30000213), Yunnan Committee of Science and Technology (Project No. 2000YP23), and The Chinese Academy of Sciences (XiBuZhiGuang Project) for financial support, and members of the analytical group in the Laboratory of Phytochemistry, Kunming Institute of Botany, for the spectral measurements.

## References

1. Chiangsu New Medical College (*Editor*). Dictionary of Chinese crude drugs. Shanghai Scientific Technologic Publisher, Shanghai. 1977. pp. 1925.
2. K.K. Purushothaman, M. Venkatanarasimhan, A. Sarada, J.D. Connolly, and D.S. Rycroft. *Can. J. Chem.* **65**, 35 (1987).
3. M. Venkatanarasimhan and A.B. Kundu. *Ind. J. Chem.* **29B**, 970 (1990).
4. A. Inada, M. Konishi, H. Murata, and T. Nakanishi. *J. Nat. Prod.* **57**, 1446 (1994).
5. A.R.H. Kehrli, D.A.H. Taylor, and M. Niven. *Phytochemistry*, **29**, 153 (1990).
6. D.A. Mulholland and S.E. Iourine. *Phytochemistry*, **47**, 1357 (1998).



7. D.A. Mulholland, S.L. Schwikkard, and M. Randrianarivelogosa. *Phytochemistry*, **52**, 705 (1999).
8. D.A. Mulholland, M. Randrianarivelogosa, C. Lavaud, J. Nuzillard, and S.L. Schwikkard. *Phytochemistry*, **53**, 115 (2000).
9. C.W.L. Bevan, J.W. Powell, D.A.H. Taylor, T.G. Halsall, P. Toft, and M. Welford. *J. Chem. Soc. (C)*, 163 (1967); W.R. Chan, K.E. Magnus, and B.S. Mootoo. *J. Chem. Soc. (C)*, 171 (1967).
10. D.A.H. Taylor. *J. Chem. Soc., Perkin Trans. 1*, 437 (1974).
11. R.G. Powell, K.L. Mikolajczak, B.W. Zilkowski, E.K. Mantus, D. Cherry, and J. Clardy. *J. Nat. Prod.* **54**, 241 (1991).
12. L.L. Rogers, L. Zeng, and J.L. McLaughlin. *J. Org. Chem.* **63**, 3781 (1998).
13. M.T. Pupo, P.C. Vieira, J.B. Fernandes, M.F.G.F. da Silva, and E. Rodrigues Fo. *Phytochemistry*, **45**, 1495 (1997).
14. A. Inada, H. Murata, Y. Inatomi, T. Nakanishi, and D. Darnaedi. *Phytochemistry*, **45**, 1225 (1997).



# Considerations about phenol electrohydrogenation on electrodes made with reticulated vitreous carbon cathode

François Laplante, Louis Brossard, and Hugues Ménard

**Abstract:** The electrocatalytic hydrogenation (ECH) of phenol was carried out in aqueous media with catalytic powders. The catalytic powders were composed of palladium nanoaggregates deposited on various substrates such as  $\text{Al}_2\text{O}_3$ ,  $\text{BaSO}_4$ , and  $\text{BaCO}_3$ . Composite powders are trapped (upon stirring) into a reticulated vitreous carbon (RVC) matrix, allowing a rapid in situ build-up of the electrode and alleviating the use of a binder, since the latter may have a detrimental effect on the ECH. For a given amount of noble metal (5% palladium by weight), it is observed that the ECH of phenol to cyclohexanol increases in the following order:  $\text{Pd/BaCO}_3 < \text{Pd/BaSO}_4 < \text{Pd/Al}_2\text{O}_3$ . It is deduced that the ECH rate is largely dependent on the adsorption of organic molecules on the nonmetallic substrate, and a model is considered to explain such a behavior. The ECH of phenol is also feasible at a reasonable rate with composite  $\text{Pd/Al}_2\text{O}_3$  (0.25% Pd by weight) powders fabricated by physical vapor deposition because the peripheral distribution of Pd nanoaggregates is favorable towards the ECH.

**Key words:** electrocatalytic hydrogenation (ECH) of phenol, reticulated vitreous carbon (RVC), alumina-based catalyst, agglomeration process, adlineation point, adsorption.

**Résumé :** On a effectué l'hydrogénation électrocatalytique (HEC) du phénol, en milieu aqueux, en présence de diverses poudres catalytiques. Ces poudres étaient formées de nanoagrégats de palladium déposés sur divers substrats, tels que  $\text{Al}_2\text{O}_3$ ,  $\text{BaSO}_4$  et  $\text{BaCO}_3$ . Les poudres composites sont piégées (par agitation) sur une matrice de carbone vitreux réticulé (CVR) qui permet d'obtenir une accumulation rapide in situ de l'électrode, ce qui permet d'éviter d'avoir à utiliser un agglomérant puisque ceux-ci peuvent avoir un effet néfaste sur l'HEC. Pour une quantité donnée de métal noble (5 % de palladium en poids), on a observé que l'HEC du phénol en cyclohexanol augmente dans l'ordre suivant:  $\text{Pd/BaCO}_3 < \text{Pd/BaSO}_4 < \text{Pd/Al}_2\text{O}_3$ . On en déduit que la vitesse d'HEC dépend grandement sur l'adsorption des molécules organiques sur le substrat non métallique et on considère un modèle pour expliquer un tel comportement. L'HEC du phénol peut se faire à une vitesse raisonnable avec des poudres composites de  $\text{Pd/Al}_2\text{O}_3$  (0,25 % de Pd en poids) préparées par déposition physique de vapeur parce que la distribution périphérique des nanoagrégats de Pd est favorable à l'HEC.

**Mots clés :** hydrogénation électrocatalytique (HEC) du phénol, carbone vitreux réticulé (CVR), catalyseur à base d'alumine, processus d'agglomération, point d'adlinéation, adsorption.

[Traduit par la Rédaction]

## Introduction

The electrode materials used for the electrocatalytic hydrogenation (ECH) of organic molecules are of paramount importance, since the kinetics of the electrohydrogenation process is quite dependent on the nature of the electrode materials (1). As far as the electrodes made with pressed metallic powder particles are concerned (1–3), their mechanical

strength is generally weak without the use of a binding material (4). The electrohydrogenation process may also be carried out in the presence of composite metallic powder particles by an alternate method: the powder particles are trapped inside the pores of a porous electrode possessing a very high hydrogen (molecular or adsorbed) overpotential. Such electrodes are made by the entrapment of composite powder particles with nano-deposits of a metal at their surface, and thus the use of a binding material is not necessary (2, 5, 6). It is an attractive way to discriminate the ability of new powders for use in the electrohydrogenation process without changing their chemical and (or) physical characteristics.

Reticulated vitreous carbon (RVC) is particularly suitable, since this excellent electronic conductor is generally electrochemically stable and has a well-developed tridimensional network of large pores (7–11) (Fig. 1). The specific RVC surface is  $66 \text{ cm}^2 \text{ per cm}^3$  for a 100 pore-per-inch (1 inch = 25.4 mm) matrix with a void volume of 97% (7). The high

Received 8 November 2002. Published on the NRC Research Press Web site at <http://canjchem.nrc.ca> on 19 March 2003.

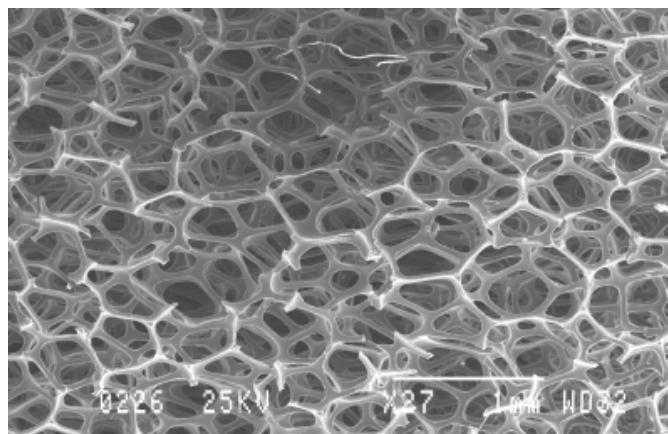
**F. Laplante, L. Brossard,<sup>1,2</sup> and H. Ménard.** Centre de recherche en électrochimie et électrocatalyse, Département de chimie, Université de Sherbrooke, 2500 boul. Université, Sherbrooke, Québec, QC 1K 2R1, Canada.

<sup>1</sup>Corresponding author (e-mail: [brossard.louis@ireq.ca](mailto:brossard.louis@ireq.ca)).

<sup>2</sup>Present address: Institut de recherche d'Hydro-Québec (IREQ), 1800 boul. Lionel-Boulet, Varennes, QC J3X 1S1, Canada.



**Fig. 1.** Electron scanning micrograph of a piece of reticulated vitreous carbon foam of 80 pores per inch (ppi).



porosity of the RVC offers a great number of large pores accessible to the composite powder particles. The electrolyte penetrates through the RVC by forced convection, and the electrocatalytic particles in suspension in the electrolyte are trapped inside the pores. Recently, papers dealing with the use of agglomerated electrodes in the dechlorination of polychlorophenol and the electrocatalytic hydrogenation of lignin showed the successful use of Pd–alumina and Rh–alumina electrocatalysts (2, 5, 6).

The rate of the electrohydrogenation process is largely dependant on several experimental parameters, particularly those connected to the electrode fabrication. The present paper deals with the key parameters for the successful entrapment of the electrocatalytic particles by the RVC, that is: the size of the particles, the applied current density during the agglomeration process, and the appropriate design of the electrochemical cell used for the agglomeration process. The reaction under consideration is phenol electrohydrogenation. In addition, different palladium powders supported on various adsorbents (substrates) were considered, to show that the adsorption of the phenol molecule may be the rate-determining step of the ECH process for a given amount of palladium (5% w/w).

## Experimental

### The electrodes

The electrode was a piece of RVC foam (25 mm × 20 mm × 6 mm, 100 pores per inch (ppi), Electrosynthesis Co.). The electrode was mounted by inserting a glass rod (OD 5–6 mm, ID 3.5 mm) in the horizontal axis of a piece of RVC (20 mm × 40 mm × 6 mm). The excess of RVC was then removed and a copper wire was inserted into the RVC to be further cemented with silver epoxy (Epoxy Technology). Finally, the electrical contact zone on the RVC matrix was glued to the glass rod with epoxy, to isolate the electrical contact from the electro-active part of the electrode. The use of a nickel strip, as a contact with the RVC electrode, should be avoided because the activity of the nickel towards the electrocatalytic hydrogenation of ketone (12) may affect the data.

The physical embodiment of the composite material into the RVC occurred under moderate stirring of the catholyte

(~450 rpm), and the catalyst powder particles were trapped into the RVC matrix pores spontaneously (provided that no sudden perturbation occurred); the RVC electrode was under cathodic polarization during the agglomeration process. The catalytic powder remained in the pores of the RVC electrode (without any apparent loss during polarization); it also remained cathodically polarized ( $J = 100 \text{ mA dm}^{-2}$ ) for the electrohydrogenation process and was in electrical contact with the matrix (Fig. 2). With this type of RVC, the diameter of the particle size should be between 15 and 43  $\mu\text{m}$ . The entrapment process is completed within 2 h, up to a charge of 50 C. The dimensions of the H-cell and those related to the other parts are given in Fig. 3. We observed that the agglomeration process was successful with this specific cell, since the process is closely dependent on the fluid dynamics. The powder characteristics are summarized in Table 1. Note that the average particle size refers to composite Pd – support-particles when Pd is present.

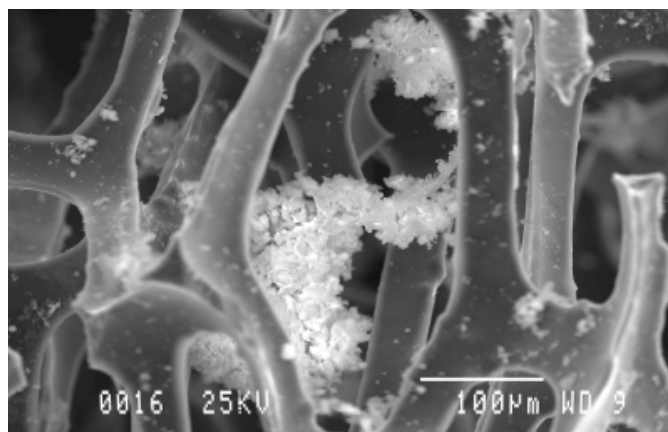
### Electrolysis

The electrolysis was carried out in a two-compartment, jacketed glass H-cell (Fig. 3), having a Nafion-324 (E.I. Dupont de Nemours & Co) membrane as a separator. The cell temperature was fixed at 21°C during the electrohydrogenation process by a circulating thermostated bath (VWR 1160A); to prevent analyte evaporation, a water-cooled condenser was added to the top of the cell. Afterwards, the cathodic compartment was filled with a phosphate buffer (29 mL, 1 M  $\text{KH}_2\text{PO}_4$  + 1 M NaOH) previously adjusted to pH 7, and 200 mg of the composite powder was added to the catholyte. The electrode was built-up in situ, using the previously described technique. The anodic compartment was filled with a 1 M NaOH solution (Fisher); the counter-electrode was a platinum mesh. Prior to the electrohydrogenation process, 1 mL of a phenol solution in water (25 mg  $\text{mL}^{-1}$ ) was added to the catholyte, giving a total volume of 30 mL and a phenol concentration of 8.8  $\text{mMol L}^{-1}$ . Further, the electrocatalytic hydrogenation was performed under galvanostatic control ( $J = 100 \text{ mA dm}^{-2}$ ) using an EG&G PAR model 273. All of the commercial powder particles considered in the present paper (Pd/ $\text{Al}_2\text{O}_3$ , Pd/ $\text{BaCO}_3$ , Pd/ $\text{BaSO}_4$  5 or 10 w/w %) were bought from Aldrich and used as received.

During the electrocatalytic hydrogenation process (ECH), 500  $\mu\text{L}$  aliquots were withdrawn from the catholyte, further saturated with NaCl, acidified to pH 1 with HCl (HCl concn. 10 N), and then extracted with 1 mL ethyl acetate, to be further dried under sodium sulfate. After the completion of ECH, both the RVC electrode and the whole cell were rinsed with pure water. Internal standard (ISTD, 2-cyclohexen-1-one) was added to the cell solution; further, the extraction was carried out twice ( $2 \times 20 \text{ mL}$ ) with distilled ethyl acetate. The organic layer was dried on sodium sulfate and filtered. The filtrate was collected in a 50 mL volumetric flask containing an external standard (ESTD, 3-methylcyclohexanol). The GC analyses were carried out on a Hewlett-Packard 5890 chromatograph equipped with an FID detector on a 30-m-long HP-5 column. The products were then identified by comparison with the retention time of the authentic compound, and the mass balance was obtained from the ISTD:ESTD ratio of the corrected peak surface area.



**Fig. 2.** SEM micrograph of Pd–alumina (5%) entrapped in RVC pores ( $I_{\text{app}} = 5 \text{ mA}$ ,  $T = 25^\circ\text{C}$ , pH 7).



### RVC electrode plated with mercury

Mercury depositions on RVC were achieved in accordance with the method described by Armalis and Kubiliene (13).

### Catalyst synthesis

Noncommercial catalyst synthesis was carried out according to the technique described by Fournier et al. (14).

### Galvanostatic measurements

The potentials were recorded vs. standard calomel electrode (SCE). Reagents (NaOH 99.999% and  $\text{KH}_2\text{PO}_4$  99.99%) used for the galvanostatic measurements were provided by Aldrich, and high purity water from a Milli-Q unit was used for the preparation of solutions. A constant applied current (from 250 to  $0.02 \text{ mA dm}^{-2}$ ) with an applied current time of 10 s was used to record the galvanostatic traces.

## Results and discussion

### Catalyst characterization

Despite the presence of a small amount of metal deposited onto the surface of the powder particles, a disk made with pressed composite powder particles (commercially available) is characterized by a very high electrical resistance. However, those powder particles, when agglomerated inside the RVC pores, show an electrocatalytic activity. The beneficial effect of the composite powder particles entrapped in an RVC electrode on the evolution of hydrogen is illustrated in Fig. 4 (curve A and B). At a current density of  $100 \text{ mA cm}^{-2}$ , the hydrogen overpotential is  $\sim 50 \text{ mV}$  lower when  $\text{Pd/Al}_2\text{O}_3$  is present, as compared with the absence of any catalyst. To show that the current may circulate through the agglomerated composite powder particles — the latter being in electrical contact with the RVC electrode surface — mercury was electrodeposited on a bare RVC electrode. As anticipated, the overpotential for water reduction is very high on an Hg–RVC cathode (Fig. 4, curve C). The picture is completely different with  $\text{Pd/Al}_2\text{O}_3$  particles agglomerated on the Hg–RVC cathode (Fig. 4, curve D): the hydrogen overpotential is considerably lower. From the curves of Fig. 4, it

is deduced that the agglomerated powder particles are in electrical contact with the RVC electrode.

Composite  $\text{Pd/Al}_2\text{O}_3$  powders were fabricated by physical vapor deposition (PVD) of Pd on alumina powder particles according to the method described in ref. 14. Palladium nanoaggregates are randomly distributed over the entire alumina particle surfaces (Fig. 5). In Fig. 6, galvanostatic traces show the influence of both powders (that is, commercially available or obtained through PVD) on the electrocatalytic activity towards the hydrogen evolution reaction. A tremendous beneficial effect is observed for the hydrogen-evolution reaction with the catalyst obtained by PVD ( $\text{Pd/Al}_2\text{O}_3$  0.1% w/w) relative to the commercial catalyst ( $\text{Pd/Al}_2\text{O}_3$  5% w/w). The overpotential shift of  $+410 \text{ mV}$  at  $100 \text{ mA dm}^{-2}$  is related to peripheral distribution of the palladium nanoaggregate (Fig. 5). Palladium deposited onto alumina by PVD favors an efficient electrical contact between the powder particles and the RVC matrix, since the preferential location of nanoaggregates is in the “skin” of the powder particles. Moreover, the electrolyte may easily reach the Pd nanoaggregates. On the other hand, the particles of the commercial  $\text{Pd/Al}_2\text{O}_3$  powder, which are obtained by an impregnation method, are most likely characterized by a large amount of Pd deposited deeply inside the pores of the alumina and in such a way that the contact with the Pd–RVC matrix is hindered.

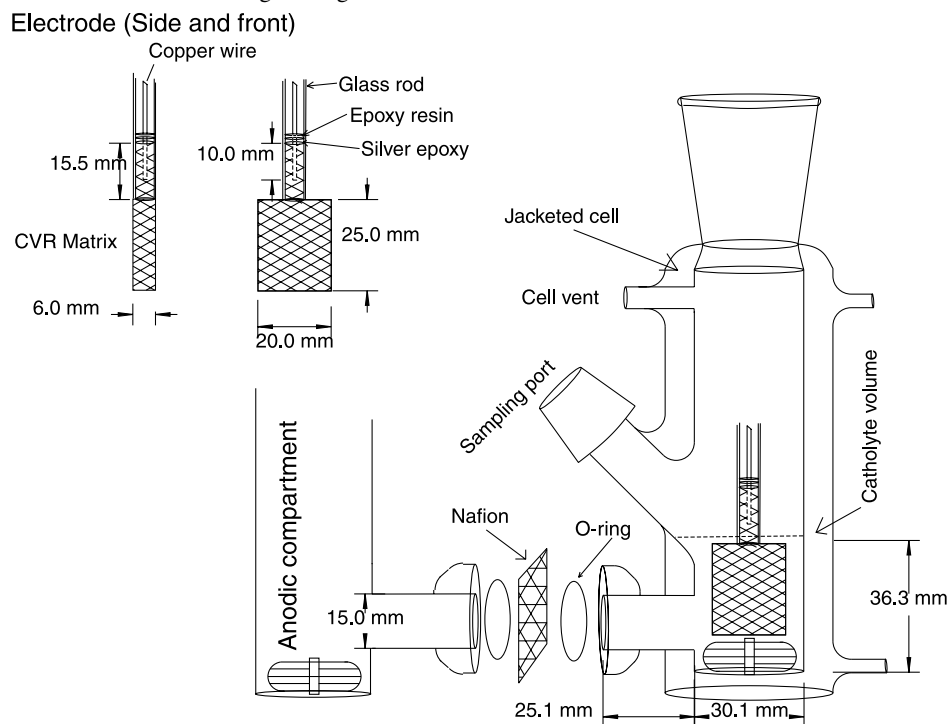
### Kinetics

The ECH process of phenol in the presence of commercially available  $\text{Pd/Al}_2\text{O}_3$  (5% w/w) results in the formation of cyclohexanone and, further, cyclohexanol (Fig. 7). The amount of cyclohexanone is at its maximum for a charge of  $\sim 200 \text{ C}$ , with the phenol being almost completely exhausted. For a charge ( $Q$ ) larger than  $200 \text{ C}$ , the larger the  $Q$ , the larger the amount of cyclohexanol and the lower the amount of cyclohexanone. If the amount of palladium is 10% w/w rather than 5% w/w, the current efficiency of the cyclohexanol production remains practically unchanged (Table 2).

The ECH of phenol, made with the catalytic powder produced by PVD (0.25% of Pd w/w), shows a significant activity despite the low amount of metal present at the surface. However, the rate of ECH is lower compared with that for the commercial powders (Fig. 8). The higher ECH yield observed with the commercial powder is attributed to lower hydrogen flow rate, the hydrogen evolution reaction being in competition with the ECH reaction.

Since alumina is slightly soluble in alkaline solution and  $\text{BaSO}_4$  is not, the effect of pH over a range of 4.1 to 14.0 on the kinetics of phenol ECH was investigated with  $\text{BaSO}_4$  as the adsorbent (Fig. 9). The rate of the reaction is considerably lower at pH 14.0 — by a factor of 25 — in comparison with the rates at pH 7.0 and 4.1. The adsorption ability of the matrix is linked to the nature of the molecules (ionized or not) present in the solution. In a basic media, phenol is in the phenolate form, which has a strong affinity for polar solvents, and the adsorption of phenol is sluggish; hence phenol adsorption becomes the rate-limiting step for the ECH process. The picture is different at pH 7.0 and below since phenol is principally in its molecular form ( $\text{pK}_a$  9.9), and the adsorption is greatly promoted. In addition, the phenolate form most likely induces the enhancement of the resonance, which in return renders the ECH of phenol more difficult.



**Fig. 3.** Electrochemical cell and electrode design. Length: mm.**Table 1.** Powder characteristics.

Entry	Particles <sup>a</sup>	BET surface (m <sup>2</sup> g <sup>-1</sup> )	Average particle size (10 <sup>-3</sup> mm)	Particle entrapment in RVC <sup>b</sup>
1	Alumina	119.0	11.5	None <sup>c</sup>
2	BaSO <sub>4</sub>	4.3	5.0	None
3	BaCO <sub>3</sub>	1.5	10.17	None
4	Pd/Al <sub>2</sub> O <sub>3</sub> (1% Pd)	237.2	68.5	Fair <sup>d</sup>
5	Pd/Al <sub>2</sub> O <sub>3</sub> (5% Pd)	78.3	12.4	Very good <sup>e</sup>
6	Pd/Al <sub>2</sub> O <sub>3</sub> (10% Pd)	85.3	42.6	Very good
7	Pd/BaSO <sub>4</sub> (5% Pd)	4.4	14.9	Very good
8	Pd/BaCO <sub>3</sub> (5% Pd)	4.9	16.8	Very good
9	Pd/Al <sub>2</sub> O <sub>3</sub> <sup>f</sup> (0.25% Pd)	98.0	16.0	Very good
10	RVC	50.0 <sup>g</sup>	—	—

<sup>a</sup>Commercially available from Aldrich.<sup>b</sup>Step under galvanostatic control (5mA).<sup>c</sup>No agglomeration. Those powders were not further used for the ECH process.<sup>d</sup>The agglomeration was not complete in the sense that some particles were remaining in the solution. Those powders were not further used for the ECH process.<sup>e</sup>The particles were completely agglomerated in the electrode, i.e., the solution was becoming very clear.<sup>f</sup>Catalyst synthesized by PVD.<sup>g</sup>Specific surface calculated in cm<sup>2</sup> per cm<sup>3</sup>.

In acidic media, the rate of the phenol ECH is unchanged in comparison with the rate in neutral media. The difference recorded between the production of cyclohexanol and cyclohexanone can be explained by the hydrogen evolution reaction (HER), which is favoured in acidic media. Hence, the cyclohexanol production is retarded because the Heyrovsky and (or) the Tafel steps (eqs. [5] and [6] below) for the hydrogen evolution are easier.

In Table 2, the remaining concentration of phenol during its electrohydrogenation is expressed against Q for different electrode materials. The main features are: (i) in the presence of the bare RVC matrix, the rate of the ECH process is

marginal; (ii) in the presence of an RVC electrode entirely covered with Pd metal, the rate of ECH is very slightly improved; (iii) the activity towards the ECH increases in the following order: Pd/BaCO<sub>3</sub> (5%) < Pd/BaSO<sub>4</sub> (5%) < Pd/Al<sub>2</sub>O<sub>3</sub> (5–10%). Alumina is recognized as an efficient adsorbent for organic molecules; this is ascribed to the presence of aluminum sites (15), which become the Lewis sites. For a given amount of palladium, it is deduced that the adsorption of organic compounds is lower for BaSO<sub>4</sub> and BaCO<sub>3</sub> in comparison with Al<sub>2</sub>O<sub>3</sub>.

It is generally admitted that the noble metals possess the ability to generate hydrogen and to adsorb unsaturated mole-



**Fig. 4.** Galvanostatic traces of agglomerated electrodes without any catalyst (curve A,  $\blacktriangle$  and C,  $\bullet$ ) and with Pd/Al<sub>2</sub>O<sub>3</sub> 5%\* (curve B,  $\blacktriangle$  and D,  $\bullet$ ). Both curve C and D are RVC mercury plated. Solution  $T = 21^\circ\text{C}$ , pH 7, applied current time = 10 s. \*Commercially available.

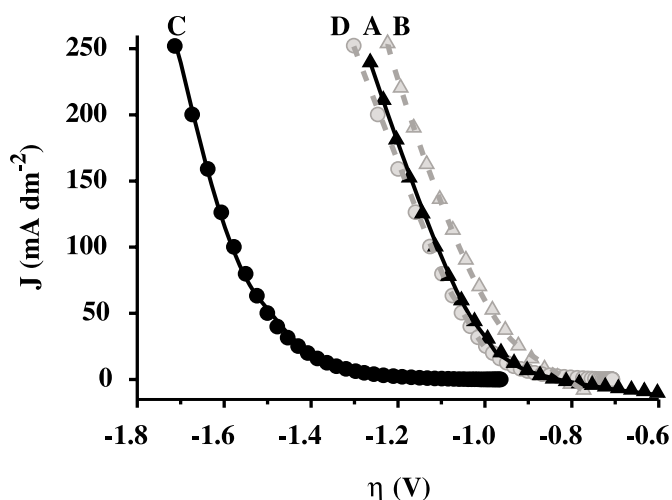
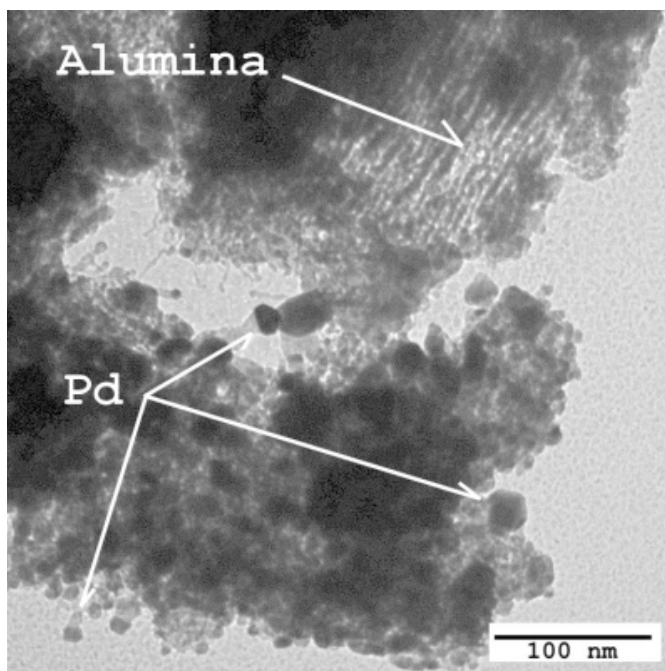


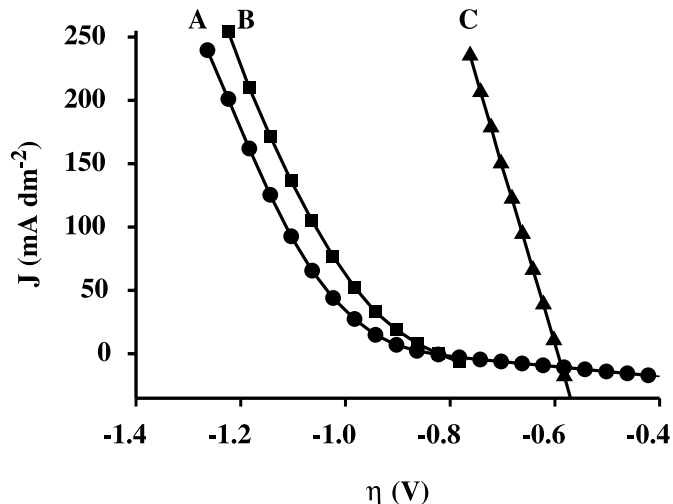
**Fig. 5.** TEM micrograph of Pd on alumina deposited by PVD (0.1% of Pd).



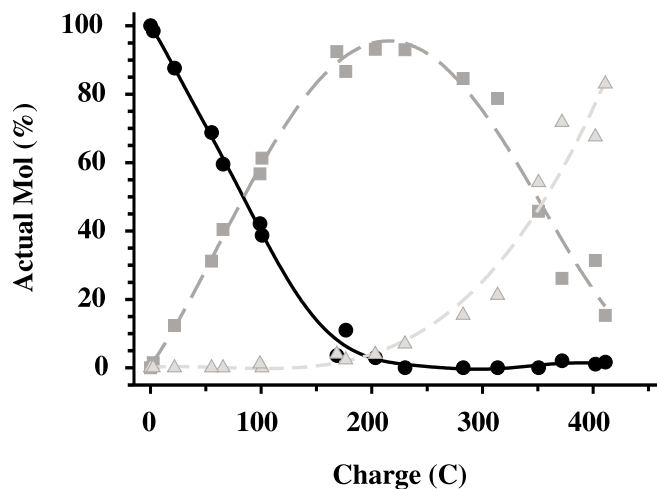
cules (16). Since the phenol electrohydrogenation may not be carried out on a Pd foil, it is tentatively deduced that the adsorption of the unsaturated organic molecule on Pd is marginal.

Assuming that Pd deposited onto the oxide surface possesses marginal specific adsorptive properties, the choice of the adsorbent becomes of prime importance. The existence of such a discrimination between the adsorbent and the metal (adlineation point) in catalytic hydrogenation was previously suggested by Maxted and Ali (17). Later, Chou and Vannice (18) refer to the adlineation point to explain their

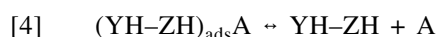
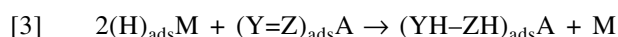
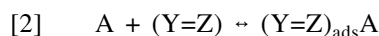
**Fig. 6.** Galvanostatic traces on RVC (80 ppi) electrodes without any catalyst (curve A,  $\bullet$ ), with Pd/Al<sub>2</sub>O<sub>3</sub> 5%\* (curve B,  $\blacksquare$ ), and with Pd/Al<sub>2</sub>O<sub>3</sub> 0.1% obtained by PVD (curve C,  $\blacktriangle$ ). Applied current time = 10 s. \*Commercially available.



**Fig. 7.** ECH of phenol through cyclohexanol with Pd/Al<sub>2</sub>O<sub>3</sub> 5%\*, RVC 80 ppi,  $I_{\text{app}} = 5 \text{ mA}$ ,  $T = 21^\circ\text{C}$ , pH 7. ( $\bullet$ ) Phenol, ( $\blacksquare$ ) cyclohexanone, and ( $\blacktriangle$ ) cyclohexanol. \*Commercially available.



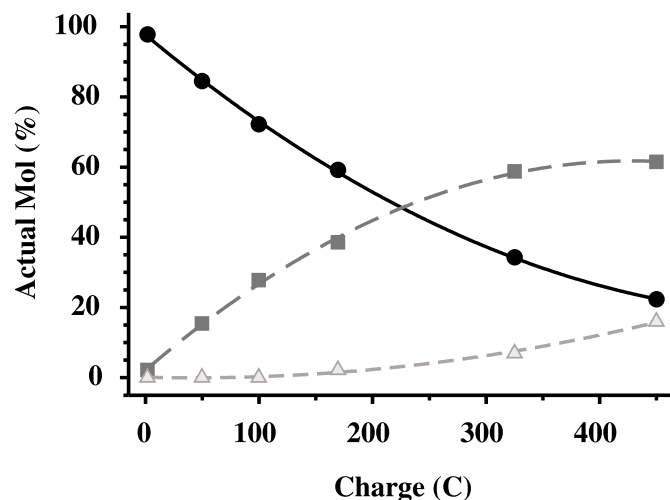
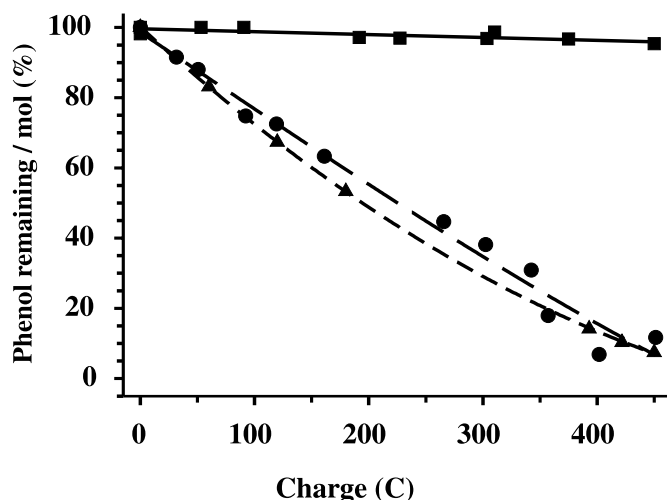
results on the gas-phase hydrogenation of benzene. Similarly, in HEC, a discrimination between the adsorption sites (A) and the metallic sites (M) was proposed to explain the ECH process on composite materials, i.e., a metal deposited onto an oxide. The mechanism proposed for the electrohydrogenation of unsaturated bonds is described by eqs. [1]–[4]. First, electrosorbed hydrogen is formed on the metallic aggregates by reduction of water (eq. [1], where  $(\text{H})_{\text{ads}}\text{M}$  is the electrosorbed hydrogen).



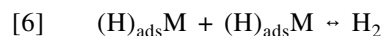
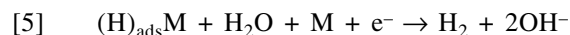


**Table 2.** Percentage of organic compound after the ECH of phenol (charge consumption = 450 C).

Entry	Particles (% of metal)	Relative %			Current efficiency
		Phenol	Cyclohexanone	Cyclohexanol	
1	RVC	100	0	0	0
2	Pd/Al <sub>2</sub> O <sub>3</sub> 5%	2.2	19.7	78.1	26.3
3	Pd/Al <sub>2</sub> O <sub>3</sub> 10%	0.0	26.0	74.0	25.2
4	Pd/BaSO <sub>4</sub> 5% <sup>a</sup>	11.7	33.0	55.3	18.8
5	Pd/BaSO <sub>4</sub> 5% <sup>b</sup>	7.4	77.8	14.8	5.1
6	Pd/BaSO <sub>4</sub> 5% <sup>c</sup>	95.4	3.3	1.3	0.4
7	Pd/BaCO <sub>3</sub> 5%	87.6	12.4	0	0
8	Pd on RVC <sup>d</sup>	94.9	3.4	1.7	0.6
9	Pd foil <sup>e</sup>	95.0	5.0	0	0
10	Pd/Al <sub>2</sub> O <sub>3</sub> <sup>f</sup> 0.25%	22.3	61.5	16	5.5

<sup>a</sup>Neutral media in a phosphate buffer at pH 7.<sup>b</sup>Acid media, pH 4.1, in KH<sub>2</sub>PO<sub>4</sub> 1 M.<sup>c</sup>Basic media (NaOH 1 M).<sup>d</sup>Galvanic deposition of 105 mg of palladium deposited from a PdCl<sub>2</sub> solution.<sup>e</sup>2 × 2.5 cm<sup>2</sup>.<sup>f</sup>Catalyst synthesized by PVD.**Fig. 8.** ECH of phenol through cyclohexanol with Pd/Al<sub>2</sub>O<sub>3</sub> 0.25% obtained by PVD, RVC 80 ppi,  $I_{app} = 5$  mA,  $T = 21^\circ\text{C}$ , pH 7. (●) Phenol, (■) cyclohexanone, and (▲) cyclohexanol.**Fig. 9.** Phenol depletion ( $I_{app} = 5$  mA,  $T = 25^\circ\text{C}$ ) through ECH with Pd/BaSO<sub>4</sub> 5% at different pH: (●) pH 7.0, (▲) pH 4.1, (■) pH 14.0.

Hydrogenation of the C=C bond then proceeds as in catalytic hydrogenation, i.e., by the reaction of the adsorbed substrate with the electrosorbed hydrogen (eq. [3], adsorption step shown in eq. [2]) at the adlineation point followed by the desorption of the product (eq. [4]). The adlineation point can be defined as the junction between the adsorbent and the metal; it is the site of the ECH process. For a given adsorbent, the larger the area related to the adlineation point, the higher the rate of the ECH reaction. It is relevant to point out that the efficiency of the ECH of a given organic compound depends also on the relative rates of the adsorption step, the hydrogenation step (eq. [3]), and the hydrogen desorption (eqs. [5] and [6]).



The hydrogen desorption can be controlled by adjusting the current density at the electrode to optimize the current efficiency.

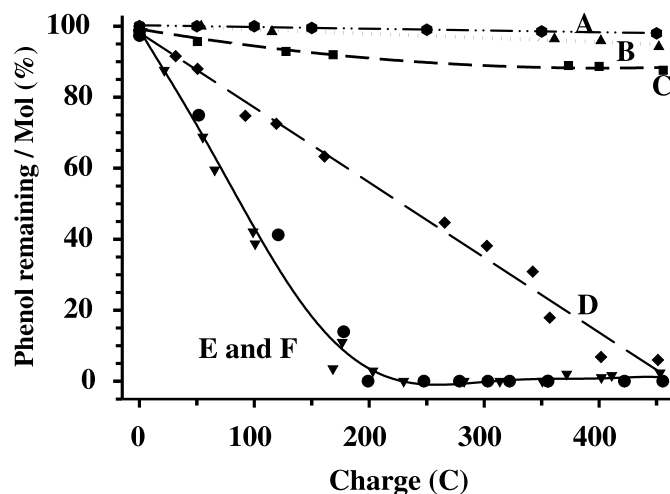
The effect of the adsorption process on the kinetics of the ECH is illustrated in Fig. 10. From the suggested ECH mechanisms, eq. [2], and the curves of Fig. 10, barium carbonate is considered a less efficient support for the adsorption of phenol than is barium sulphate. Both catalysts have the same amount of metal on the surface and have approximately the same specific surface area.

The use of a bare RVC matrix (Table 2, entry 1) shows no catalytic properties. The absence of metallic sites (M) and weak adsorptive properties between the RVC and phenol explain the poor yield of hydrogenation. We suspect that the phenol is practically not adsorbed onto vitreous carbon unless it is modified with an organic functional group (19–21).

By controlling the chemical nature of the adsorption sites and the metallic nanoaggregates, our goal is to tailor a cata-



**Fig. 10.** The effect of the adsorbent on the ECH of phenol ( $I_{app} = 5$  mA,  $T = 25^\circ\text{C}$ , pH 7). (●, A) RVC matrix; (▲, B) RVC + Pd (105.3 mg)–Pd foil; (■, C) Pd/BaCO<sub>3</sub>; (◆, D) Pd/BaSO<sub>4</sub>; (●, E) Pd/Al<sub>2</sub>O<sub>3</sub> (5%); and (▼, F) Pd/Al<sub>2</sub>O<sub>3</sub> (10%), pH 7.



lyst that has some selectivity for targeted molecules. Adsorption sites determine catalyst selectivity and influence the chemical nature of the collected organic products; this is in agreement with the views of Neri et al. (22). Neri uses the idea that the catalytic support plays a predominant role in phenol hydrogenation. Moreover, it was stated that hydrogenation occurs through the phenol adsorption onto the adsorption sites followed by transfer of the chemisorbed hydrogen.

However, the catalyst performance remains highly influenced by the kinetics of hydrogenation, which is highly influenced by the nature of the metal used. In this case, the adsorption is not the limiting step; the rate-determining step is the hydrogen transfer itself from the metal surface to the unsaturated molecule (eq. [6]).

## Conclusion

The key parameters for the agglomeration process of catalytic powders are the catalyst particle size and the applied cathodic current. Composite electrode material powders of Pd nanoaggregates deposited onto oxide particles, which were different in nature, were characterized for the electrocatalytic hydrogenation of phenol. A model is proposed to explain the kinetics of the ECH, in which the sites for the adsorption of generated atomic hydrogen are the metallic sites (M) and the sites for the adsorption of the organic molecules to be hydrogenated are the oxide sites (A).

## Acknowledgments

The authors thank Ghislaine Luc from the civil engineering department of Sherbrooke University for the catalyst particle size measurements. We would like to thank also the Natural Sciences and Engineering Research Council of Canada (NSERC) and le Fonds Québécois de la recherche sur la nature et les technologies (FQRNT) for their financial support.

## References

1. B. Mahdavi, P. Chambrion, J. Binette, E. Martel, and J. Lessard. *Can. J. Chem.* **73**, 846 (1995).
2. A. Cyr, F. Chiltz, P. Jeanson, A. Martel, L. Brossard, and H. Ménard. *Can. J. Chem.* **78**, 307 (2000).
3. A. Martel, B. Mahdavi, J. Lessard, L. Brossard, and H. Ménard. *Can. J. Chem.* **75**, 1862 (1997).
4. J.-M. Lalancette, E. Potvin, and H. Ménard. U.S. Patent 4 886 591. 1989.
5. P. Dabo, A. Cyr, F. Laplante, F. Jean, H. Ménard, and J. Lessard. *Environ. Sci. Technol.* **34**, 1265 (2000).
6. P. Dabo, A. Cyr, J. Lessard, L. Brossard, and H. Ménard. *Can. J. Chem.* **77**, 1225 (1999).
7. J. Wang. *Electrochim. Acta*, **26**, 1721 (1981).
8. A. Alvarez-Gallegos and D. Pletcher. *Electrochim. Acta*, **44**, 853 (1999).
9. A. Alvarez-Gallegos and D. Pletcher. *Electrochim. Acta*, **44**, 2483 (1999).
10. A. Czerwinski and M. Dmochowska. *J. Power Sources*, **77**, 28 (1999).
11. P. Dubé, F. Kerdouss, F. Laplante, P. Proulx, L. Brossard, and H. Ménard. *J. Appl. Electrochem.* In press.
12. S. Armalis and E. Kubiliene. *Anal. Chim. Acta*, **423**, 287 (2000).
13. J. Fournier, H. Ménard, and L. Brossard. *J. Appl. Electrochem.* **25**, 923, (1995).
14. J.T. Richardson. *In Principles of catalyst development, fundamental and applied catalysis*. Plenum Press, New York. 1992.
15. J.M. Chapuzet, A. Lasia, and J. Lessard. *In Electrocatalysis frontiers of electrochemistry series. Edited by J. Lipkowski and P.N. Ross*. VCH Publishers Inc., New York. 1998. pp. 155–196.
16. E.B. Maxted and S. Ali. *J. Am. Chem. Soc.* **83**, 4137 (1961).
17. P. Chou and M.A. Vannice. *J. Catal.* **107**, 129 (1987).
18. N. Peña, M. Romero, F.J.M. de Villena, A.J. Reviejo, and J.M. Pingarrón. *Electroanalysis*, **11**, 85 (1999).
19. X. Tang, B. Xie, P.O. Larsson, B. Danielsson, M. Khayyami, and G. Johansson. *Anal. Chim. Acta*, **374**, 185 (1998).
20. G. Neri, A.M. Visco, A. Donato, C. Milone, M. Malentacchi, and G. Gubitosa. *Appl. Catal. A*, **110**, 49 (1994).



# A novel synthesis of *N*-fluoroalkanesulfonyl-amidines using a three-component reaction

Shizheng Zhu, Yong Xu, and Guifang Jin

**Abstract:** A novel, general, and efficient multicomponent reaction of fluoroalkanesulfonyl azides, secondary amines, and carbonyl compounds for the synthesis of *N*-fluoroalkanesulfonylamidines is presented. This reaction gave a good yield of products under very mild reaction conditions.

**Key words:** multicomponent reactions, synthetic methods, *N*-fluoroalkanesulfonyl azide, *N*-fluoroalkanesulfonylamidine.

**Résumé :** On présente une nouvelle réaction générale, efficace et à plusieurs composants des azotures de fluoroalcane-sulfonyles avec une amine primaire et des composés carbonyles qui permet de faire la synthèse de *N*-fluoroalcane-sulfonylamidines. Cette réaction s'effectue avec de bons rendements, dans des conditions réactionnelles très douces.

**Mots clés :** réactions à plusieurs composants, méthodes synthétiques, azoture de *N*-fluoroalcane-sulfonyles, *N*-fluoroalcane-sulfonylamidine.

[Traduit par la Rédaction]

## Introduction

Multicomponent reactions (MCRs), by virtue of their convergence, productivity, facile execution, and generally high yields of products, have attracted much attention from the vantage point of combinatorial chemistry (1). Of pivotal importance in this area are the isocyanide-based MCRs such as the versatile Ugi reactions (2–3).

In the context of our ongoing studies on the reaction of fluoroalkanesulfonylazide with the electron-rich olefines such as vinyl ether, enamines appeared attractive from the viewpoint of devising a novel MCR (4–5).

Prompted by the recent successful preparation of *N*-fluoroalkanesulfonylamidines from the reaction of fluoroalkanesulfonyl azides **1** with the  $\beta$ -ketoester enamines or 1,2-dihydro-pyridines (6–8) (see Scheme 1), we reasoned that a three-component reaction (3-CR, i.e., the azide, amine, and the carbonyl substrate) would be workable.

It is well known that enamine compounds are formed by treatment of the carbonyl compound with a secondary amine; in this reaction, the equilibrium between the enamine and the carbonyl compound should go forward if the added azide **1** could react fast enough with the enamine.

## Experiment section

### Typical procedure for the preparation of **4** and **6**

#### *N*-Perfluorobutanesulfonyl-*N,N*-cyclo(ethyleneoxyethylene)-cyclopentanamide (**4a**)

To a solution of cyclohexanone **2a** (0.118 g, 1.2 mmol) and morpholine (0.113 g, 1.3 mmol) in absolute Et<sub>2</sub>O (5 ml),

fluoroalkanesulfonyl azide **1a** (0.325 g, 1.0 mmol) was added dropwise with magnetic stirring at room temperature. The reaction was completed after 5 h (monitored by TLC). After removal of solvent, the residue obtained was purified by column chromatography (petroleum ether:EtOAc, 6:1, *R*<sub>f</sub> = 0.42) to give the pure product **4a** (colorless oil) (0.357 g, 77%).

#### **4a**

FT-IR (KBr) ( $\nu$ , cm<sup>-1</sup>): 1540 (C=N), 1478 (SO<sub>2</sub>), 1120–1236 (C-F). <sup>1</sup>H NMR (CDCl<sub>3</sub>)  $\delta$ : 3.85 (m, 2H), 3.73 (m, 4H), 3.60 (m, 2H), 3.55 (m, 1H), 2.12 (m, 2H), 1.87 (m, 4H), 1.70 (m, 2H). <sup>19</sup>F NMR (CDCl<sub>3</sub>)  $\delta$ : -79.9 (s, 3F), -113.0 (m, 2F), -120.8 (m, 2F), -125.8 (m, 2F). MS (70 eV) *m/z* (%): 465 ([M<sup>+</sup> + 1], 17.53), 245 ([M<sup>+</sup> - R<sub>f</sub>], 2.85), 181 ([M<sup>+</sup> - SO<sub>2</sub>R<sub>f</sub>], 3.63), 86 ([C<sub>4</sub>H<sub>8</sub>NO<sup>+</sup>], 100.00). Elemental anal. calcd. for C<sub>14</sub>H<sub>17</sub>F<sub>9</sub>N<sub>2</sub>O<sub>3</sub>S (%): C 36.21, H 3.66, N 6.02; found: C 36.14, H 3.78, N 5.87.

#### **6a**

FT-IR (KBr) ( $\nu$ , cm<sup>-1</sup>): 1542 (C=N), 1487 (SO<sub>2</sub>), 1123–1274 (C-F). <sup>1</sup>H NMR (CDCl<sub>3</sub>)  $\delta$ : 3.82 (m, 2H), 3.76 (m, 6H), 3.48 (m, 1H), 1.82 (m, 1H), 1.70 (m, 1H), 1.38 (d, 3H, *J* = 11.0 Hz), 1.05 (t, 3H, *J* = 7.0 Hz). <sup>19</sup>F NMR (CDCl<sub>3</sub>)  $\delta$ : -80.0 (s, 3F), -113.8 (m, 2F), -120.2 (m, 2F), -125.3 (m, 2F). MS (70 eV) *m/z* (%): 453 ([M<sup>+</sup> + 1], 6.50), 424 ([M<sup>+</sup> - C<sub>2</sub>H<sub>4</sub>], 2.71), 217 ([M<sup>+</sup> - OR<sub>f</sub>], 4.29), 86 ([C<sub>4</sub>H<sub>8</sub>NO<sup>+</sup>], 100.00). Element anal. calcd. for C<sub>13</sub>H<sub>17</sub>F<sub>9</sub>N<sub>2</sub>O<sub>3</sub>S (%): C 34.51, H 3.76, N 6.19; found: C 34.12, H 3.81, N 6.22.

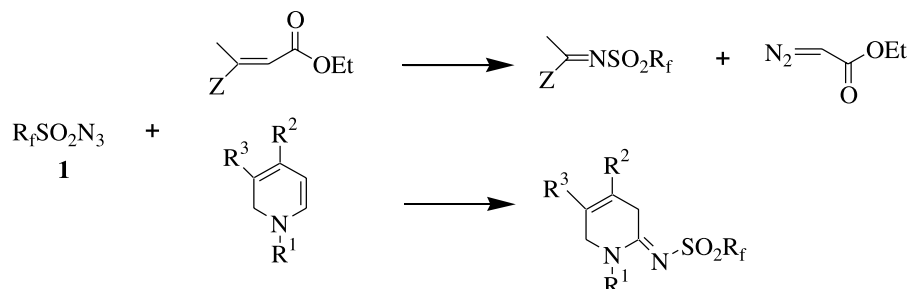
Received 11 November 2002. Published on the NRC Research Press Web site at <http://canjchem.nrc.ca> on 31 March 2003.

Shizheng Zhu,<sup>1</sup> Yong Xu, and Guifang Jin. Shanghai Institute of Organic Chemistry, Chinese Academy of Sciences, 354 Fenglin Lu, Shanghai 200 032, China.

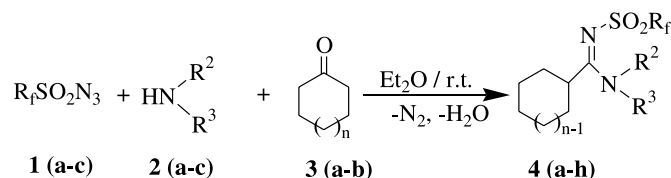
<sup>1</sup>Corresponding author (e-mail: zhuzs@pub.sioc.ac.cn).



Scheme 1.



Scheme 2.

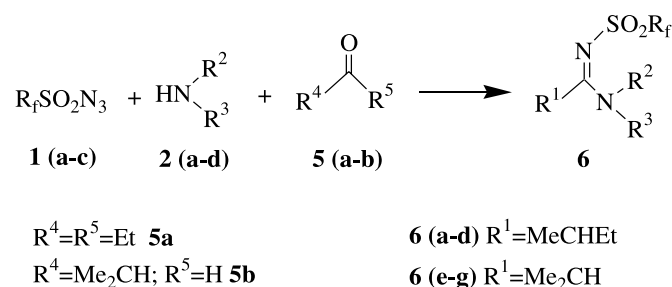


$R_f = C_4F_9$  **1a**;  $I(CF_2)_2O(CF_2)_2$  **1b**;  $p-CH_3C_6H_5$  **1c**

$R^2R^3$ :  $-(CH_2)_2O(CH_2)_2-$  **2a**;  $R^2$ : Me  $R^3$ : Ph **2b**;  $R^2=R^3=Et$  **2c**;  $-(CH_2)_4-$  **2d**

$n=1$  **3a**;  $n=2$  **3b**

Scheme 3.



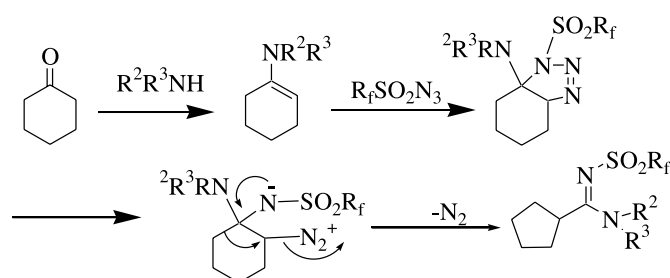
$R^4=R^5=Et$  **5a**

$R^4=Me_2CH$ ;  $R^5=H$  **5b**

**6 (a-d)**  $R^1=MeCHEt$

**6 (e-g)**  $R^1=Me_2CH$

Scheme 4.



## 6e

FT-IR (KBr) ( $\nu$ ,  $cm^{-1}$ ): 2981 (C-H), 1546 (C=N), 1455 ( $SO_2$ ), 1321 (C-F).  $^1H$  NMR ( $CDCl_3$ )  $\delta$ : 3.71–3.64 (m, 4H), 3.22 (m, 1H), 2.09 (m, 2H), 1.95 (m, 2H), 1.28 (d, 6H,  $J = 7.1$  Hz).  $^{19}F$  NMR ( $CDCl_3$ )  $\delta$ : -79.7 (s, 2F), -109.3 (s, 2F), -116.7 (s, 2F), -122.1 (s, 2F). MS (70eV)  $m/z$  (%): 423 ( $[M^+ + 1]$ , 31.08), 203 ( $[M^+ - C_4F_9]$ , 16.40), 70 ( $[C_4H_8N]^+$ , 100.0). Element anal. calcd. for  $C_{12}H_{15}F_9N_2O_2S$  (%): C 34.12, H 3.55, N 6.64; found: C 34.36, H 3.66, N 6.69.

## Results and discussion

The result of our investigations are presented here.

Initially, fluoroalkanesulfonyl azide **1a** was added slowly to a solution of morpholine **2a** and cyclohexanone **3a** in dry toluene at room temperature; TLC analysis showed that the reaction was finished in 5 h. The one-carbon ring contraction condensation product **4a** was obtained in 66% yield (see Scheme 2). Its structure was fully characterized by spectral methods and elemental analysis. Other solvents such as ben-

zene, THF, and ether were also suitable for this reaction, and it was found that the reaction gave the best yield in diethyl ether. For example, when the reaction of **1a** with **2a** and **3a** were carried out in  $Et_2O$ , the yield could be increased to 77%.

The three component reactions were found to be general and efficient. The amine used could be cyclic, such as morpholine and pyrrolidine, or acyclic, such as *N*-methyl aniline or diethylamine, etc. It should be noted that the less reactive tosyl azide **1c** can also react with **2** and **3** to give the corresponding *N*-tosyl-substituted amidine in the presence of activated 4 Å molecular sieves (see Scheme 2).

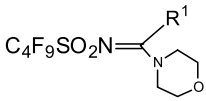
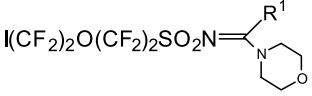
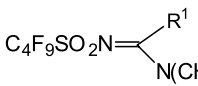
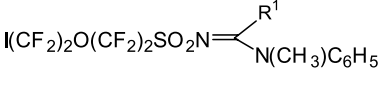
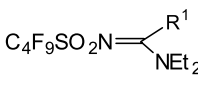
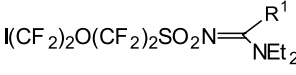
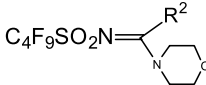
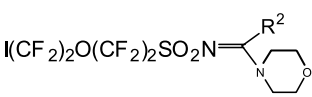
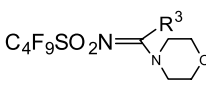
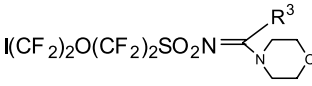
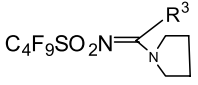
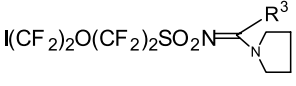
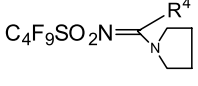
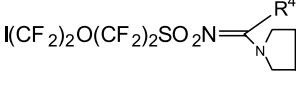
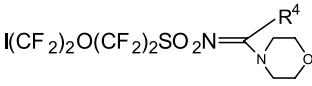
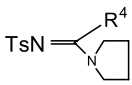
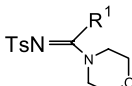
To further explore the scope of this reaction, we have extended it to other carbonyl substrates. We found that the acyclic ketone and aldehydes such as 3-pentanone and isobutyraldehyde were readily present in this reaction; in the case of the aldehyde, the reaction occurred more rapidly: it finished in 1 h (Scheme 3).

A possible reaction pathway is shown in Scheme 4.

All the reaction results are summarized in Table 1.



**Table 1.** Preparation of *N*-fluoroalkanesulfonyl amides using a three-component reaction.

Entry	1	2	3 (or 5)	Product 4 (or 6)	Yield (%) <sup>a</sup>
1	1a	2a	3a		4a 77
2	1b	2a	3a		4b 70
3	1a	2b	3a		4c 81
4	1b	2b	3a		4d 89
5	1a	2c	3a		4e 58 <sup>b</sup>
6	1b	2c	3a		4f 57 <sup>b</sup>
7	1a	2a	3b		4g 53
8	1b	2a	3b		4h 54
9	1a	2a	5a		6a 53
10	1b	2a	5a		6b 48
11	1a	2d	5a		6c 83 <sup>b</sup>
12	1b	2d	5a		6d 74 <sup>b</sup>
13	1a	2d	5b		6e 68
14	1b	2d	5b		6f 75
15	1b	2a	5b		6g 47
16	1c	2d	5b		6h 84
17	1c	2a	3a		6i 76



**Table 1** (*concluded*).

18	<b>1c</b>	<b>2b</b>	<b>3a</b>		<b>6j</b>	57
19	<b>1c</b>	<b>2c</b>	<b>3a</b>		<b>6k</b>	59

Note:

 $R^1$ : ;  $R^2$ : ;  $R^3$ :  $\text{CH}_3\text{CH}_2\text{CHCH}_3$  ;  $R^4$ :  $\text{CH}(\text{CH}_3)_2$ 
<sup>a</sup> Isolated yield<sup>b</sup> 0.4 g of activated 4 Å MS is added for 1 mmol azides **1**.

In conclusion, we uncovered a novel and efficient multi-component reaction of fluoroalkanesulfonyl azides, secondary amines, and carbonyl compounds for the synthesis of *N*-fluoroalkanesulfonylamidines. This reaction also conforms to the principle of green chemistry and atom economics, as the by-products are water and nitrogen gas and, also, the solvent can be reused.

## Acknowledgment

This work was supported by the National Natural Science Foundation of China (NNSFC) (No. 20 072 049 and No. 20 032 010) and the Innovation Foundation of Chinese Academy of Science.

## Reference

1. I. Ugi. Isonitrile chemistry. Academic Press, New York. 1971.
2. I. Ugi, S. Lohberger, and R. Karl. *In* Comprehensive organic synthesis. Edited by B.M. Trost and I. Fleming. Pergamon, Oxford. 1991. Chap. 2, p. 1083.
3. A. Domling and I. Ugi. *Angew. Chem. Int. Ed.* **39**, 3168 (2000).
4. L. Weber, K. Illgen, and M. Almsretter. *Synlett*, **3**, 366 (1999).
5. V. Nair, A.U. Vinod, and C. Rajesh. *J. Org. Chem.* **66**, 4427 (2001).
6. S.Z. Zhu, Y. Xu, and Y.L. Wang. *J. Fluorine Chem.* **104**, 195 (2000).
7. S.Z. Zhu, Y. Xu, Y.L. Wang, and G.Y. Zhu. *J. Fluorine Chem.* **106**, 133 (2000).
8. S.Z. Zhu and Y. Xu. *Tetrahedron*, **57**, 3909 (2001).



# Synthesis and in vitro reactivity of *cis*-dichloro-(pyridin-2-ylcarboxaldimine)platinum(II) complexes with DNA

Liliya G. Nikolcheva, Christopher M. Vogels, R. Alexandra Stefan, Hanni A. Darwish, Stephen J. Duffy, Robert J. Ireland, Andreas Decken, Robert H.E. Hudson, and Stephen A. Westcott

**Abstract:** Five platinum pyridin-2-ylcarboxaldimine complexes of the type *cis*-[PtCl<sub>2</sub>(2-C<sub>5</sub>H<sub>4</sub>NCH=NR)] (R = CH<sub>2</sub>CH<sub>2</sub>OH (1); R = N(CH<sub>2</sub>CH<sub>2</sub>)<sub>2</sub>O (2); R = C<sub>6</sub>H<sub>5</sub> (3); R = 1-C<sub>10</sub>H<sub>7</sub> (4); R = (CH<sub>2</sub>)<sub>8</sub>CH=CH(CH<sub>2</sub>)<sub>7</sub>CH<sub>3</sub> (5)) were prepared and their in vitro reactivity towards a 20-base pair (single- and double-stranded) DNA determined using nuclease digest studies and RP-HPLC. Variation of the imine functionality allowed for the design of compounds with different physical and chemical properties. Complexes 1 and 3 showed binding to both single- and double-stranded DNA comparable to that of cisplatin (*cis*-[PtCl<sub>2</sub>(NH<sub>3</sub>)<sub>2</sub>]). Crystals of 1 were monoclinic, space group *P*2(1)/*n*, *a* = 9.6612 (15), *b* = 12.9678 (19), *c* = 9.7004(13) Å, β = 117.73(3)°, *Z* = 4.

**Key words:** platinum, pyridin-2-ylcarboxaldimines, DNA binding studies.

**Résumé :** On a préparé cinq complexes de pyridin-2-carboxaldimine et de platine du type *cis*-[PtCl<sub>2</sub>(2-C<sub>5</sub>H<sub>4</sub>NCH=NR)] (R = CH<sub>2</sub>CH<sub>2</sub>OH (1); R = N(CH<sub>2</sub>CH<sub>2</sub>)<sub>2</sub>O (2); R = C<sub>6</sub>H<sub>5</sub> (3); R = 1-C<sub>10</sub>H<sub>7</sub> (4); R = (CH<sub>2</sub>)<sub>8</sub>CH=CH(CH<sub>2</sub>)<sub>7</sub>CH<sub>3</sub> (5)) et, faisant appel à des études de « RP-HPLC » et de digestion par une nucléase, on a évalué leur réactivité in vitro une molécule d'ADN à vingt paires de bases (à simple et à double brin). La variation de la fonction imine a permis de mettre au point des composés ayant des propriétés physiques et chimiques différentes. La fixation des complexes 1 et 3 à l'ADN à simple et à double brin semble être comparable à celle du cisplatine, *cis*-[PtCl<sub>2</sub>(NH<sub>3</sub>)<sub>2</sub>]. Les cristaux du composé 1 sont monocliniques, groupe d'espace *P*2(1)/*n*, avec *a* = 9,6612(15), *b* = 12,9678(19) et *c* = 9,7004(13) Å, β = 117,73(3)° et *Z* = 4.

**Mots clés :** platine, pyridin-2-ylcarboxaldimines, études de fixation à l'ADN.

[Traduit par la Rédaction]

## Introduction

Cisplatin (*cis*-[PtCl<sub>2</sub>(NH<sub>3</sub>)<sub>2</sub>]) and a few related platinum-based complexes such as carboplatin and oxaliplatin are currently used as cancer therapeutic agents and exhibit particular effectiveness against testicular and ovarian malignancies (1–15). The mechanism of action of this family of drugs is believed to arise primarily from their interactions with DNA. The platinum center reacts with the N-7 position of purine bases, especially guanine, commonly resulting in the forma-

tion of 1,2-intrastrand adducts. This interaction can severely distort the DNA duplex geometry and it is believed that these structural distortions are responsible for altered DNA – protein interactions, which ultimately cause programmed cell death (13). There are several limitations to cisplatin therapy, however, such as neural and kidney toxicity as well as intrinsic and acquired resistance of tumor cells to the drug (14). These complications have spurred further research in the development of platinum-based complexes that are less toxic than cisplatin and show enhanced specificity towards cancer cells.

Since structural analogues of cisplatin react with DNA in a way similar to the parent drug, a new platinum drug candidate should demonstrate unique biological activity that eliminates multifactorial drug resistance. Therefore, considerable research has focused on designing platinum complexes that do not follow the classical structure–activity relationships for cisplatin analogues. Indeed, recent studies have shown that *cis*-amminedichloro(2-methylpyridine)platinum(II) (AMD473 or ZD0473, Fig. 1) shows considerable cytotoxicity in cisplatin-resistant cell lines (15, 16). Steric crowding from the methyl group is believed to decrease the rates of hydrolysis and substitution reactions of AMD473 thereby permitting high selectivity in binding with DNA (17). Toward this goal, we have begun to develop AMD473

Received 11 December 2002. Published on the NRC Research Press Web site at <http://canjchem.nrc.ca> on 4 April 2003.

**L.G. Nikolcheva, C.M. Vogels, H.A. Darwish, S.J. Duffy, and S.A. Westcott.**<sup>1</sup> Department of Chemistry, Mount Allison University, Sackville, NB E4L 1G8, Canada.

**R.A. Stefan and R.H.E. Hudson.**<sup>2</sup> Department of Chemistry, The University of Western Ontario, London, ON N6A 5B7, Canada.

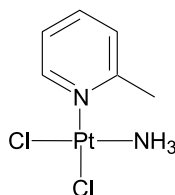
**R.J. Ireland.** Department of Biology and Biochemistry, Mount Allison University, Sackville, NB E4L 1G7 Canada.

**A. Decken.** Department of Chemistry, University of New Brunswick, Fredericton, NB E3B 5A3 Canada.

<sup>1</sup>Corresponding author (e-mail: [swestcott@mta.ca](mailto:swestcott@mta.ca)).

<sup>2</sup>Corresponding author (e-mail: [robert.hudson@uwo.ca](mailto:robert.hudson@uwo.ca)).



**Fig. 1.** AMD473 (ZD0473).

analogues by replacing the  $\text{NH}_3$  group with a pendant imine group. Varying the imine functionality allows us to design compounds with a wide range of physical and chemical properties that may provide steric congestion around the platinum atom (18). As well, the use of didentate ligands prevents trans-labilization and undesired displacement of the ligands by sulfur and nitrogen donors in biomolecules, interactions believed responsible for some of the adverse side effects associated with cisplatin (12). We report herein our initial results on the synthesis and in vitro testing of the DNA-binding properties of five *cis*-dichloro(pyridin-2-ylcarboxaldimine)platinum(II) compounds with various physical properties.

## Experimental

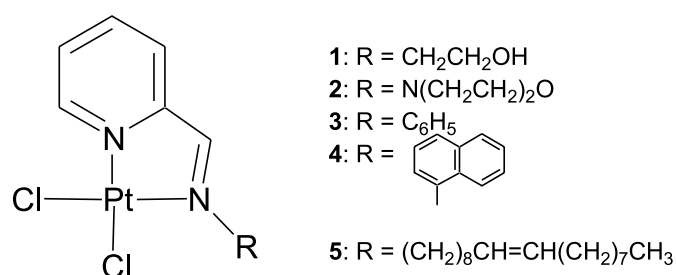
Reagents and solvents used were obtained from Aldrich Chemicals. Platinum salts were obtained from Precious Metals Online Ltd. NMR spectra were recorded on a JEOL JNM-GSX270 FT NMR spectrometer.  $^1\text{H}$  NMR chemical shifts are reported in ppm and referenced to residual protons in deuterated solvent at 270 MHz.  $^{13}\text{C}$  NMR chemical shifts are referenced to solvent carbon resonances as internal standards at 68 MHz. Multiplicities are reported as singlet (s), doublet (d), triplet (t), quartet (q), multiplet (m), broad (br), and overlapping (ov). Infrared spectra were obtained using a Mattson Genesis II FT-IR spectrometer and reported in  $\text{cm}^{-1}$ . Melting points were measured uncorrected with a Mel-Temp apparatus. Microanalyses for C, H, and N were carried out at Desert Analytics (Tucson, AZ). All reactions were carried out in the air and products are stable indefinitely under such conditions.

### General procedure for the preparation of complexes 1–5

The pyridin-2-ylcarboxaldimines were prepared by the addition of equimolar amounts of the primary amine and 2-pyridinecarboxaldehyde in  $\text{CH}_2\text{Cl}_2$  containing 4 Å molecular sieves. Filtration and removal of the solvent under vacuum afforded the desired ligand. The corresponding pyridin-2-ylcarboxaldimine (0.55 mmol) was then dissolved in 5 mL of  $\text{CH}_2\text{Cl}_2$  and added drop-wise to a stirred solution of  $[\text{PtCl}_2(\text{coe})]_2$  (0.25 mmol, *coe* = *cis*-cyclooctene) in 10 mL of  $\text{CH}_2\text{Cl}_2$  at  $0^\circ\text{C}$ . The resulting precipitate was collected by suction filtration and washed with  $\text{CH}_2\text{Cl}_2$  (2 mL), hexane ( $3 \times 5$  mL), and  $\text{Et}_2\text{O}$  ( $3 \times 5$  mL) and dried under vacuum. Complex **3** was prepared as described previously (18). Complex **5** was isolated by removing solvent followed by an  $\text{Et}_2\text{O}$  ( $3 \times 5$  mL) trituration.

### Complex 1

Yield: 68%, mp  $172^\circ\text{C}$  (decomp.). IR (Nujol): 3419, 2931, 2856, 1597, 1460, 1377, 1298, 1240, 1163, 1113, 1049, 928,

**Fig. 2.** Platinum complexes tested in this study.

868, 781, 733, 666, 571, 523.  $^1\text{H}$  NMR ( $\text{DMSO}-d_6$ )  $\delta$ : 9.38 (d,  $J = 5$  Hz,  $J_{\text{H-Pt}} = 37$  Hz, 1H, Ar), 9.03 (s,  $J_{\text{H-Pt}} = 100$  Hz, 1H, C(H) = N), 8.39 (dd,  $J = 5$  Hz, 1H, Ar), 8.21 (d,  $J = 5$  Hz, 1H, Ar), 7.91 (dd,  $J = 5$  Hz, 1H, Ar), 5.07 (br, 1H, OH), 4.03 (t,  $J = 5$  Hz,  $J_{\text{H-Pt}} = 37$  Hz, 2H,  $\text{NCH}_2$ ), 3.78 (br t,  $J = 5$  Hz, 2H,  $\text{NCH}_2\text{CH}_2$ ).  $^{13}\text{C}$  NMR ( $\text{DMSO}-d_6$ )  $\delta$ : 171.8, 157.5, 149.5, 141.3, 129.5, 128.8, 62.4, 59.5. Anal. calcd. for  $\text{C}_8\text{H}_{10}\text{N}_2\text{O}_2\text{Pt}$ : C 23.08, H 2.43, N 6.73; found: C 23.36, H 2.45, N 6.43.

### Complex 2

Yield: 63%, mp  $240^\circ\text{C}$  (decomp.). IR (Nujol): 2937, 2912, 2860, 1606, 1543, 1464, 1377, 1271, 1250, 1144, 1111, 1095, 1068, 1011, 918, 876, 769, 700, 598.  $^1\text{H}$  NMR ( $\text{DMSO}-d_6$ )  $\delta$ : 9.28 (d,  $J = 6$  Hz,  $J_{\text{H-Pt}} = 41$  Hz, 1H, Ar), 8.81 (s,  $J_{\text{H-Pt}} = 69$  Hz, 1H, C(H) = N), 8.32 (dd,  $J = 6$  Hz, 1H, Ar), 8.00 (d,  $J = 6$  Hz, 1H, Ar), 7.75 (dd,  $J = 6$  Hz, 1H, Ar), 3.79 (m, 6H,  $\text{CH}_2$ ), 3.44 (br, 2H,  $\text{CH}_2$ ).  $^{13}\text{C}$  NMR ( $\text{DMSO}-d_6$ )  $\delta$ : 157.8, 153.3, 148.9, 141.1, 127.4, 127.1, 66.0, 55.1. Anal. calcd. for  $\text{C}_{10}\text{Cl}_2\text{H}_{13}\text{N}_3\text{O}_2\text{Pt}$ : C 26.26, H 2.87, N 9.19; found: C 26.00, H 2.82, N 8.84.

### Complex 4

Yield: 68%, mp  $246^\circ\text{C}$  (decomp.). IR (Nujol): 2926, 2856, 1734, 1506, 1462, 1377, 1346, 1300, 1269, 1225, 1157, 939, 816, 783, 760, 737, 669, 586.  $^1\text{H}$  NMR ( $\text{DMSO}-d_6$ )  $\delta$ : 9.52 (d,  $J = 6$  Hz, 1H, Ar), 9.49 (s,  $J_{\text{H-Pt}} = 94$  Hz, 1H, C(H) = N), 8.48 (dd,  $J = 6$  Hz, 1H, Ar), 8.24 (d,  $J = 6$  Hz, 1H, Ar), 8.16 (m, 1H, Ar), 8.05–8.01 (ov m, 3H, Ar), 7.64–7.59 (ov m, 3H, Ar), 7.51 (d,  $J = 6$  Hz, 1H, Ar).  $^{13}\text{C}$  NMR ( $\text{DMSO}-d_6$ )  $\delta$ : 174.0, 156.9, 149.0, 144.0, 140.6, 132.8, 129.8, 129.7, 128.5, 127.7, 127.4, 126.5, 126.4, 124.9, 123.1, 120.3. Anal. calcd. for  $\text{C}_{16}\text{Cl}_2\text{H}_{12}\text{N}_2\text{Pt}$ : C 38.56, H 2.43, N 5.62; found: C 38.77, H 2.31, N 5.57.

### Complex 5

Yield: 56%, mp  $124^\circ\text{C}$  (decomp.). IR (Nujol): 2914, 2858, 1622, 1595, 1464, 1377, 1300, 1238, 1151, 1120, 919, 767, 723, 519.  $^1\text{H}$  NMR ( $\text{CDCl}_3$ )  $\delta$ : 9.49 (d,  $J = 6$  Hz,  $J_{\text{H-Pt}} = 38$  Hz, 1H, Ar), 8.74 (s,  $J_{\text{H-Pt}} = 97$  Hz, 1H, C(H) = N), 8.14 (dd,  $J = 6$  Hz, 1H, Ar), 7.92 (d,  $J = 6$  Hz, 1H, Ar), 7.63 (dd,  $J = 6$  Hz, 1H, Ar), 5.30 (m, 2H,  $\text{CH}=\text{CH}$ ), 4.10 (t,  $J = 6$  Hz,  $J_{\text{H-Pt}} = 45$  Hz, 2H,  $\text{NCH}_2$ ), 1.99–1.90 (ov m, 4H,  $\text{CH}_2\text{CH}=\text{CH}$ ), 1.24 (br, 24H,  $\text{CH}_2$ ), 0.85 (t,  $J = 7$  Hz, 3H,  $\text{CH}_2\text{CH}_3$ ).  $^{13}\text{C}$  NMR ( $\text{CDCl}_3$ )  $\delta$ : 168.0, 157.2, 149.7, 139.7, 130.1, 129.8, 128.2, 127.8, 61.1, 32.0, 31.1, 29.9, 29.8 (2C), 29.7, 29.6, 29.5, 29.4 (2C), 29.3, 27.3, 26.5, 22.5, 14.2. Anal. calcd. for  $\text{C}_{24}\text{Cl}_2\text{H}_{40}\text{N}_2\text{Pt}$ : C 46.29, H 6.49, N 4.50; found: C 46.12, H 6.63, N 4.62.



Complex	1
Formula	C <sub>8</sub> H <sub>10</sub> Cl <sub>2</sub> N <sub>2</sub> OPt
fw	416.17
Crystal system	Monoclinic
Space group	<i>P</i> 2(1)/ <i>n</i>
<i>a</i> (Å)	9.6612(15)
<i>b</i> (Å)	12.9678(19)
<i>c</i> (Å)	9.7004(13)
β (°)	117.734(3)
<i>V</i> (Å <sup>3</sup> )	1075.7(3)
<i>Z</i>	4
ρ <sub>calcd</sub> (mg m <sup>−3</sup> )	2.570
Crystal size (mm <sup>3</sup> )	0.6 × 0.25 × 0.2
Temperature (K)	198(2)
Radiation	MoKα (λ = 0.71073)
μ (mm <sup>−1</sup> )	13.508
Total reflections <sup>a</sup>	7456
Total unique relections	2439
No. of variables	165
<i>R</i> <sub>int</sub>	0.0419
θ range (°)	2.85–27.49
Largest difference peak; hole (e Å <sup>−3</sup> )	1.370; −2.094
<i>S</i> <sup>a</sup> (GoF) on <i>F</i> <sup>2</sup>	1.089
<i>R</i> 1 <sup>b</sup> ( <i>I</i> > 2σ( <i>I</i> ))	0.0218
<i>wR</i> 2 <sup>c</sup> (all data)	0.0497

## X-ray crystallography

**Table 2.** Selected bond lengths (Å) and angles (°) for **1**.

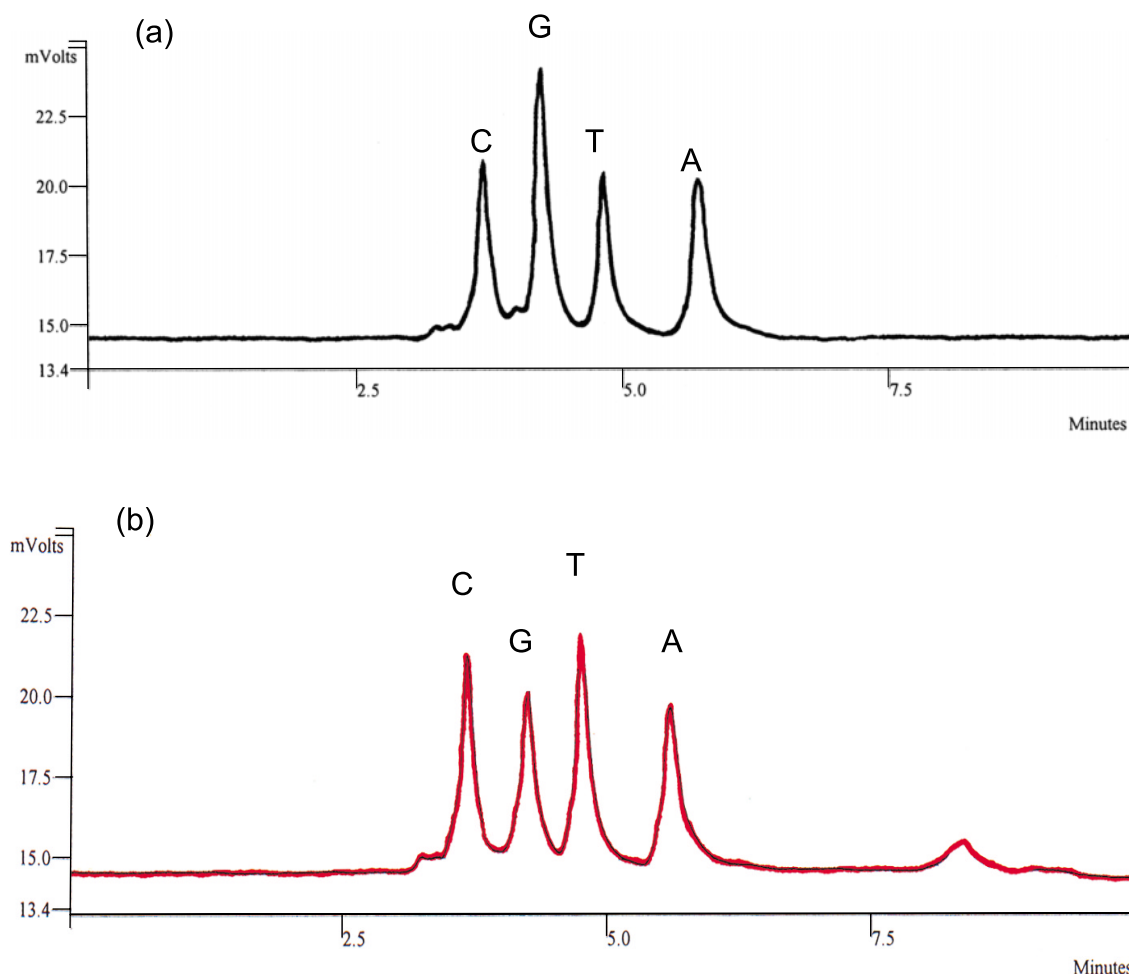
Pt(1)—N(8)	1.985(3)
Pt(1)—N(1)	1.996(3)
Pt(1)—Cl(2)	2.2759(8)
Pt(1)—Cl(1)	2.2914(9)
N(1)—C(2)	1.332(5)
N(1)—C(6)	1.356(4)
C(2)—C(3)	1.378(5)
C(3)—C(4)	1.373(6)
C(4)—C(5)	1.365(6)
C(5)—C(6)	1.386(5)
C(6)—C(7)	1.423(5)
C(7)—N(8)	1.282(4)
N(8)—C(9)	1.456(5)
C(9)—C(10)	1.505(6)
C(10)—O	1.410(5)
<b>Bond angles (°)</b>	
N(8)—Pt(1)—N(1)	80.11(11)
N(8)—Pt(1)—Cl(2)	95.30(8)
N(1)—Pt(1)—Cl(2)	175.41(8)
N(8)—Pt(1)—Cl(1)	175.45(8)
N(1)—Pt(1)—Cl(1)	95.41(8)
Cl(2)—Pt(1)—Cl(1)	89.17(4)
C(2)—N(1)—C(6)	118.4(3)
C(2)—N(1)—Pt(1)	128.1(2)
C(6)—N(1)—Pt(1)	113.4(2)
N(1)—C(2)—C(3)	122.4(4)
C(4)—C(3)—C(2)	119.1(4)
C(5)—C(4)—C(3)	119.3(4)
C(4)—C(5)—C(6)	119.3(4)

### Nuclease digest studies

Binding of the platinum complexes to DNA was investigated using enzymatic degradation of the DNA to nucleosides. The sequence of the model 20-base pair DNA strand used in this study (eq. [1]) has two predominant cisplatin binding sites, TGGT on one strand and AGGA on the complementary strand. Both the single and the double DNA strands were incubated with each platinum complex in a 1:3 DNA:Pt molar ratio at 37°C for 24 h in the dark. Samples (2.0 nmol of single-stranded and 1.0 nmol of double-stranded DNA) were digested in series with DNase I (Amersham Biosciences, 36 U for 4 h), nuclease P1 (Sigma, 12.5 U for 18 h), and alkaline phosphatase (Promega, 20 U for 4 h) at 37°C to convert the DNA strand into mononucleosides. The samples were heated to 90°C for 2 min, centrifuged at 10 000 g for 30 s and the protein pellet discarded. The nucleoside composition in each sample was analyzed at 254 nm on a C<sub>18</sub> column on a Pro-Star RP-HPLC (Varian). The isocratic solvent system used was 93% [Et<sub>3</sub>NH][OAc] (20 mM, pH 6.5) and 7% CH<sub>3</sub>CN at 1 mL min<sup>-1</sup>. The areas under the nucleoside peaks were inte-



**Fig. 4.** Chromatograms of nuclease digests of double-stranded model DNA (unplatinated DNA control (a) and DNA platinated with cisplatin (b)).



grated and the G:C ratio analyzed and compared with ANOVA followed by post-hoc multiple comparisons with Bonferonni's adjustment.



(Equation [1] shows the sequence of the DNA 20-mer used in the platination studies. Possible platinum binding sites are in bold).

## Results and discussion

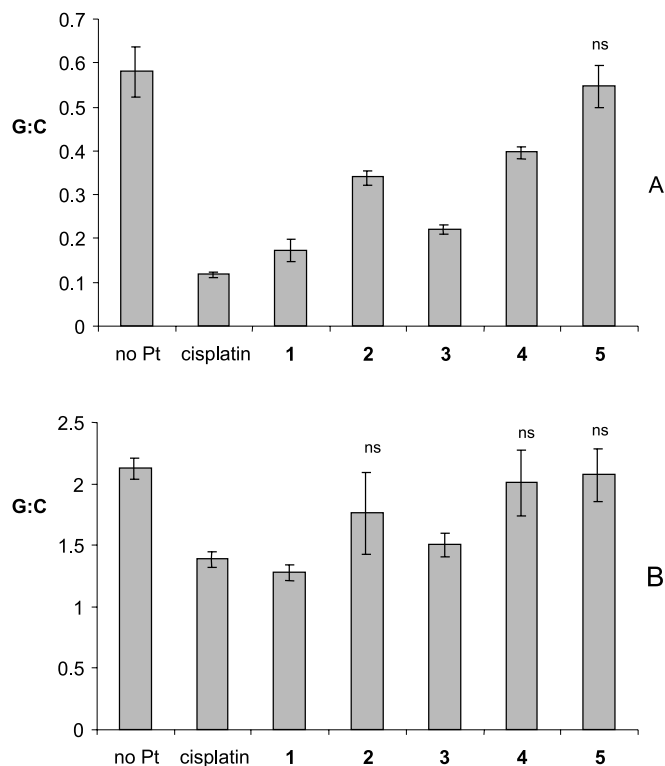
Addition of a primary amine to commercially available 2-pyridinecarboxaldehyde affords the corresponding pyridin-2-ylcarboxaldimine ligand in high yield (11–18, 22–31). Variation of the amine allows for the facile design of ligands and platinum complexes with different physical and chemical properties. In this study, the metal complexes **1–5** (Fig. 2) were prepared by the addition of the pyridin-2-ylcarboxaldimine ligands to  $\text{CH}_2\text{Cl}_2$  solutions of  $[\text{PtCl}_2(\text{coe})]_2$  (coe = *cis*-cyclooctene) (32). The ethanol and morpholine derivatives, **1** and **2**, respectively, were prepared in an attempt to

increase the hydrophilicity of the metal complexes as compared to cisplatin. The low solubility of cisplatin in water results in the administration of relatively high doses of the drug and accounts for many of the toxic side effects. Conversely, **3–5** were designed to increase the lipophilic nature of the complexes (6). Indeed, the oleyl compound **5** is soluble in common organic solvents such as  $\text{CHCl}_3$ . Compounds **3** and **4** are of special interest as recent studies have shown that structurally similar planar or semiplanar chromophores, such as acridine derivatives, play an important role in the class of DNA-intercalating anticancer drugs (33). In fact, the platinum complex derived from aniline (**3**) has been previously shown to display considerable activity against the hormone-independent human mammary carcinoma cell line MDA-MB 231 (18).

Complexes **1–5** have been characterized by a number of physical methods, including multinuclear NMR spectroscopy. A significant downfield shift in the  $^1\text{H}$  NMR is observed for the imine  $sp^2$  proton upon coordination of the ligand to the metal center. For instance, the singlet at  $\delta$  8.37 ppm for the free oleyl amine derived ligand shifts to 8.74 ppm in complex **5**. Platinum satellites are also observed for this resonance ( $J_{\text{H-Pt}} = 97$  Hz) upon complexation of the



**Fig. 5.** G:C ratios from the nuclease digests of single-stranded (A) and double stranded DNA (B). Mean values are  $\pm 95\%$  CI ( $n = 10$ ). ns = not significantly different from non-platinum control ( $p > 0.0001$ ).



ligand to the metal. Similar trends are observed for the pyridine hydrogen  $\alpha$  to the nitrogen atom as the chemical shift changes from  $\delta$  8.64 to 9.49 ppm ( $J_{\text{H-Pt}} = 38$  Hz).

Complex **1** has also been characterized by an X-ray diffraction study (Fig. 3). Crystallographic data are given in Table 1<sup>3</sup> and selected bond distances and angles shown in Table 2. The nitrogen—platinum bonds of 1.996(3) Å (pyridine) and 1.985(3) Å (imine) are similar to those reported in other iminopyridine platinum systems (34–36). Slightly longer Pt—N bond distances are observed in related five-coordinate Pt(II) (37, 38) and Pt(IV) complexes (39). The C(7)—N(8) distance is 1.282(4) Å which is in the range of accepted carbon—nitrogen double bonds (40). Although there is no considerable interaction of the hydroxy group with the metal center, as observed with AMD473, a network of hydrogen bonding is observed in the solid state with the OH group interacting with the Cl of an adjacent molecule ( $\text{OH}\cdots\text{Cl}(1') = 2.329$  Å and  $\text{O}\cdots\text{Cl}(1') = 3.145$  Å). Molecules are also linked by weak Pt(1) $\cdots$ N(8') (3.561 Å) and Cl(1) $\cdots$ Pt(1') (3.794 Å) interactions. Hydrogen bonding has been used recently to self-assemble related organometallic platinum complexes (41).

The efficacy of platinum complexes as anticancer agents is believed to arise, at least in part, from the ability of the metal center to coordinate to DNA. We therefore decided to

examine the *in vitro* activity of complexes **1–5** with a well-studied 20-base pair DNA strand (42). This DNA model strand contains one preferential binding site in the single strand, a TGGT motif, and a second binding site (AGGA) on the complementary strand. The degree of platination can be quantified by enzymatically degrading the DNA strand and separating the mononucleosides and Pt-containing dinucleotides using RP-HPLC (43–45). A typical chromatogram of nuclease digests derived from the double-stranded DNA treated with cisplatin is shown in Fig. 4. Cytosine is not affected by platination and is used as an internal standard so a decrease in the G:C ratio indicates a decrease in the amount of free guanosine. The amount of free guanosine can therefore be inversely correlated to the degree of platination, as binding will result in the formation of *cis*-[Pt(NH<sub>3</sub>)<sub>2</sub>{d(GpG)}] (**1**).

Complexes **1–5** were examined for their activity against both single- and double-stranded DNA, the results of the nuclease digest studies are shown in Fig. 5. Although the long-chain oleyl derivative **5** did not show significant binding to either type of strand, complexes **2** and **4** showed a small degree of binding specific to single-strand DNA. This selectivity is interesting as highly proliferating populations of cancer cells replicate their DNA continuously and are often in the single-stranded form, whereas in a normal healthy cell the usual state of DNA is the double-stranded form. As expected (18), complex **3** showed binding similar to that observed for cisplatin. More remarkable, however, is the observation that ethanol complex **1** also showed significant binding to both single- and double-stranded DNA, comparable to that observed for the control cisplatin. It is plausible that hydrogen bonding plays a role in how this complex interacts with DNA. These results show that complexes **1–5** show various degrees of binding to DNA. Future studies in this area will therefore relate the biochemical activities of these complexes to their cytotoxicities against cisplatin-sensitive and cisplatin-resistant cells. We are also investigating other iminopyridine analogues of AMD473, the results of which will be published in due course.

## Acknowledgements

Thanks are gratefully extended to the Research Corporation (Cottrell College Science Award, SAW), Natural Sciences and Engineering Research Council of Canada (SAW and RHEH), the Canada Research Chairs program (SAW), the University of Western Ontario, and Mount Allison University for financial support. We also thank Dan Durant for expert technical assistance and anonymous reviewers for helpful comments.

## References

1. E. Wong and C.M. Giandomenico. *Chem. Rev.* **99**, 2451 (1999).
2. R. Jamieson and S.J. Lippard. *Chem. Rev.* **99**, 2467 (1999).
3. P.J. Ferguson. *J. Otolaryngol. Jpn.* **24**, 242 (1995).
4. J. Reedijk. *Chem. Rev.* **99**, 2499 (1999).

<sup>3</sup>Supplementary data may be purchased from the Depository of Unpublished Data, Document Delivery, CISTI, National Research Council Canada, Ottawa, ON K1A 0S2, Canada ([http://www.nrc.ca/cisti/irm/unpub\\_e.shtml](http://www.nrc.ca/cisti/irm/unpub_e.shtml) for information on ordering electronically). CCDC 205640 contain the supplementary data for this paper. These data can be obtained, free of charge, via [www.ccdc.cam.ac.uk/conts/retrieving.html](http://www.ccdc.cam.ac.uk/conts/retrieving.html) (or from the Cambridge Crystallographic Data Centre, 12 Union Road, Cambridge, U.K.; fax +44 1223 336033 or [deposit@ccdc.cam.ac.uk](mailto:deposit@ccdc.cam.ac.uk)).



5. H. Rauter, R.D. Domencio, E. Menta, A. Oliva, Y. Qu, and N. Farrell. *Inorg. Chem.* **36**, 3919 (1997).
6. Y. Qu, J.A. Fitzgerald, H. Rauter, and N. Farrell. *Inorg. Chem.* **40**, 6324 (2001).
7. B. Lippert. *In Cisplatin*. Wiley-VCH, Zurich. 1999.
8. J. Reedijk. *Chem. Comm.* 801 (1996).
9. T.W. Hambley. *J. Chem. Soc., Dalton Trans.* 2711 (2001).
10. T. Okada, I.M. El-Mehasseb, M. Kodaka, T. Tomohiro, K. Okamoto, and H. Okuno. *J. Med. Chem.* **44**, 4661 (2001).
11. S.T. Sullivan, J.S. Saad, F.P. Fanizzi, and L.G. Marzilli. *Inorg. Chem.* **124**, 1558 (2002).
12. E.T. Martins, H. Baruah, J. Kramarczyk, G. Saluta, C.S. Day, G.L. Kucera, and U. Bierbach. *J. Med. Chem.* **44**, 4492 (2001) and refs. therein.
13. G. Tallen, C. Mock, S.B. Gangopadhyay, B. Kangarloo, B. Krebs, and J.E.A. Wolff. *Anticancer Res.* **20**, 445 (2000).
14. N. Poklar, D.S. Pilch, S.J. Lippard, E.A. Redding, S.U. Dunham, and K.J. Breslauer. *Proc. Natl. Acad. Sci. U.S.A.* **93**, 7606 (1996).
15. J.L. Butour and J.-P. Macquet. *Biochemistry*, **78**, 455 (1977).
16. K. Neplechová, J. Kašpárková, O. Vrána, O. Nováková, A. Habtemariam, B. Watchman, P.J. Sadler, and V. Brabec. *Mol. Pharmacol.* **56**, 20 (1999).
17. A.C.G. Hotze, Y. Chen, T.W. Hambley, S. Parsons, N.A. Kratochwil, J.A. Parkinson, V.P. Munk, and P.J. Sadler. *Eur. J. Inorg. Chem.* 1035 (2002).
18. H. Brunner, M. Schmidt, and H. Schönenberger. *Inorg. Chim. Acta*, **123**, 201 (1986).
19. SAINT 6.02. Bruker AXS, Inc., Madison, Wisconsin, U.S.A. 1997–1999.
20. G.M. Sheldrick. SADABS. Bruker AXS, Inc., Madison, Wisconsin, U.S.A. 1999.
21. G.M. Sheldrick. SHELXTL 5.1. Bruker AXS, Inc., Madison, Wisconsin, U.S.A. 1997.
22. P. Krumholz. *Inorg. Chem.* **4**, 609 (1965).
23. J. Burgess. *J. Chem. Soc. A*, 497 (1968).
24. H. Brunner, B. Reiter, and G. Riepl. *Chem. Ber.* **177**, 1330 (1984).
25. P. Pointeau, H. Patin, A. Mousser, and J.-Y. Le Marouille. *J. Organomet. Chem.* **312**, 263 (1986).
26. M. Crespo, X. Solans, and M. Font-BardRa. *Organometallics*, **14**, 355 (1995).
27. M. Crespo. *Polyhedron*, **15**, 1981 (1996).
28. J.H. Groen, M.J.M. Vlaar, P.W.N.M. van Leeuwen, K. Vrieze, H. Kooijman, and A.L. Spek. *J. Organomet. Chem.* **551**, 67 (1998).
29. M.L. Ferrara, I. Orabona, F. Ruffo, M. Funicello, and A. Panunzi. *Organometallics*, **17**, 3832 (1998).
30. S.-J. Kim, N. Yang, D.-H. Kim, S.O. Kang, and J. Ko. *Organometallics*, **19**, 4036 (2000).
31. A. Kundu and B.P. Buffin. *Organometallics*, **20**, 3635 (2001).
32. M.P. Shaver, C.M. Vogels, A.I. Wallbank, T.L. Hennigar, K. Biradha, M.J. Zaworotko, and S.A. Westcott. *Can. J. Chem.* **78**, 568 (2000).
33. I. Antonini, P. Polucci, A. Magnano, B. Gatto, M. Palumbo, E. Menta, N. Pescalli, and S. Martelli. *J. Med. Chem.* **45**, 696 (2002).
34. K.W. Nordquest, D.W. Phelps, W.F. Little, and D.J. Hodgson. *J. Am. Chem. Soc.* **98**, 1104 (1976).
35. J.G. Hinman, C.R. Baar, M.C. Jennings, and R.J. Puddephatt. *Organometallics*, **19**, 536 (2000).
36. C.R. Baar, H.A. Jenkins, M.C. Jennings, G.P.A. Yap, and R.J. Puddephatt. *Organometallics*, **19**, 4870 (2000).
37. C.R. Baar, M.C. Jennings, J.J. Vittal, and R.J. Puddephatt. *Organometallics*, **19**, 4150 (2000).
38. F. Di Bianca, G. Bandoli, A. Dolmella, S. Antonaroli, and B. Crociani. *J. Chem. Soc., Dalton Trans.* 212 (2002).
39. C.R. Baar, L.P. Carbray, M.C. Jennings, R.J. Puddephatt, and J.J. Vittal. *Organometallics*, **20**, 408 (2001).
40. A.I. Kitaigorodskii. *Organic chemical crystallography*. Consultants Bureau, New York. 1961.
41. C.S.A. Fraser, H.A. Jenkins, M.C. Jennings, and R.J. Puddephatt. *Organometallics*, **19**, 1635 (2000).
42. J.A. Rice, D.M. Crothers, A.L. Pinto, and S.J. Lippard. *Proc. Natl. Acad. Sci. U.S.A.* **85**, 4159 (1988).
43. A. Eastman. *Biochemistry*, **22**, 3927 (1983).
44. A.M.J. Fichtinger-Schepman, J.L. van der Veer, J.H.J. den Hartog, P.H.M. Lohman, and J. Reedijk. *Biochemistry*, **24**, 707 (1985).
45. M. Sharma, R. Jain, E. Ionescu, and H.K. Slocum. *Anal. Biochem.* **228**, 307 (1995).



# Solid-state $^{25}\text{Mg}$ NMR, X-ray crystallographic, and quantum mechanical study of bis(pyridine)-(5,10,15,20-tetraphenylporphyrinato)magnesium(II)

Gang Wu, Alan Wong, and Suning Wang

**Abstract:** We report solid-state  $^{25}\text{Mg}$  NMR, X-ray crystallographic, and quantum-mechanical calculation results for bis(pyridine)(5,10,15,20-tetraphenylporphyrinato)magnesium(II),  $\text{Mg}(\text{TPP})\cdot\text{Py}_2$ .  $\text{Mg}(\text{TPP})\cdot\text{Py}_2$  crystallizes in the triclinic form, in the space group  $P\bar{1}$ . The unit cell parameters are:  $a = 9.6139(13)$  Å,  $b = 11.0096(16)$  Å,  $c = 11.8656(15)$  Å;  $\alpha = 102.063(3)^\circ$ ,  $\beta = 103.785(3)^\circ$ ,  $\gamma = 114.043(2)^\circ$ ;  $Z = 1$ . The  $\text{Mg}(\text{II})$  ion is coordinated to four nitrogen atoms from the porphyrin ring and two nitrogen atoms from the axial pyridine ligands, forming a regular octahedron. The  $^{25}\text{Mg}$  quadrupole coupling constant ( $C_Q$ ) is  $15.32 \pm 0.02$  MHz, which represents the largest value so far observed for  $^{25}\text{Mg}$  nuclei. The electric field gradient tensor at the Mg site is axially symmetric,  $\eta_Q = 0.00 \pm 0.05$ . The  $^{25}\text{Mg}$  chemical shielding anisotropy is too small to be accurately determined. Quantum-mechanical calculations using a 6-31G(d) basis set reproduce reasonably well the observed  $^{25}\text{Mg}$  NMR data for  $\text{Mg}(\text{TPP})\cdot\text{Py}_2$ . The calculations also suggest that the span of the  $^{25}\text{Mg}$  chemical shift tensor is less than 50 ppm. Using a theoretical approach, we also investigate the dependence of the  $^{25}\text{Mg}$  quadrupole coupling constant on the  $\text{Mg}-\text{N}_{\text{ax}}$  bond distance. The calculation suggests that the  $^{25}\text{Mg}$  quadrupole coupling constant for an  $\text{Mg}(\text{II})$  ion at the center of a porphyrin ring without axial ligands is approximately 22 MHz, which may be treated as an upper limit of the  $^{25}\text{Mg}$  quadrupole coupling constant for all  $\text{Mg}$ -porphyrin complexes.

**Key words:**  $^{25}\text{Mg}$  NMR, crystal structure, quantum chemical calculation, quadrupole parameter, tetraphenylporphyrin.

**Résumé :** Dans ce travail, on rapporte les résultats d'études RMN du  $^{25}\text{Mg}$ , de diffraction des rayons X et de calculs théoriques de mécanique quantique sur la bis(pyridine)(5,10,15,20-tétraphénylporphyrinato)magnésium(II),  $\text{Mg}(\text{TPP})\cdot\text{Py}_2$ . Le  $\text{Mg}(\text{TPP})\cdot\text{Py}_2$  cristallise dans la forme triclinique, groupe d'espace  $P\bar{1}$ , avec  $a = 9,6139(13)$  Å,  $b = 11,0096(16)$  Å et  $c = 11,8656(15)$  Å;  $\alpha = 102,063(3)^\circ$ ,  $\beta = 103,785(3)^\circ$  et  $\gamma = 114,043(2)^\circ$  et  $Z = 1$ . L'ion  $\text{Mg}(\text{II})$  est coordonné à quatre atomes d'azote du noyau porphyrine et à deux atomes d'azote des ligands pyridine axiaux et il forme un octaèdre régulier. La constante de couplage quadripolaire du  $^{25}\text{Mg}$  ( $C_Q$ ) est de  $15,32 \pm 0,02$  MHz, ce qui correspond à la valeur la plus élevée jusqu'à maintenant pour le noyau  $^{25}\text{Mg}$ . Le tenseur du gradient du champ électrique au niveau du site Mg présente une symétrie axiale avec  $\eta_Q = 0,00 \pm 0,05$ . L'anisotropie de blindage chimique du  $^{25}\text{Mg}$  est trop faible pour être mesurée de façon fiable. Des calculs de mécanique quantique effectués à l'aide d'un ensemble de base 6-31G(d) permettent de reproduire raisonnablement les données observées par RMN du  $^{25}\text{Mg}$  pour le  $\text{Mg}(\text{TPP})\cdot\text{Py}_2$ . Les calculs suggèrent aussi que la plage du tenseur du déplacement chimique du  $^{25}\text{Mg}$  est inférieure à 50 ppm. Faisant appel à une approche théorique, on a aussi étudié la dépendance de la constante de couplage quadripolaire du  $^{25}\text{Mg}$  sur la longueur de la liaison  $\text{Mg}-\text{N}_{\text{ax}}$ . Les calculs suggèrent que la constante de couplage quadripolaire du  $^{25}\text{Mg}$  pour l'ion  $\text{Mg}(\text{II})$  au centre d'un noyau porphyrine sans ligands axiaux est d'environ 22 MHz, ce qui peut être considéré comme une limite supérieure pour la constante de couplage quadripolaire du  $^{25}\text{Mg}$  pour tous les complexes  $\text{Mg}$ -porphyrine.

**Mots clés :** RMN du  $^{25}\text{Mg}$ , structure cristalline, calculs de mécanique quantique chimique, paramètre quadripolaire, tétraphénylporphyrine.

[Traduit par la Rédaction]

## Introduction

Metalloporphyrins have been extensively studied for many years because of their biological and catalytic functions (1–3). Several spectroscopic techniques such as EPR (4), NMR (5), and Mössbauer spectroscopy (6) have been used to di-

rectly probe the metal centers in metalloporphyrin systems. Magnesium porphyrins represent an important class of metalloporphyrin compounds because of their relevance to chlorophyll (7). Until now it has not been possible to directly study the  $\text{Mg}(\text{II})$  ion in  $\text{Mg}$ -porphyrin complexes by  $^{25}\text{Mg}$  (spin:  $-5/2$ ) NMR. The  $^{25}\text{Mg}$  nucleus is among a group

Received 7 January 2003. Published on the NRC Research Press Web site at <http://canjchem.nrc.ca> on 9 April 2003.

Gang Wu,<sup>1</sup> Alan Wong, and Suning Wang. Department of Chemistry, Queen's University, Kingston, ON K7L 3N6, Canada.

<sup>1</sup>Corresponding author (e-mail: [gangwu@chem.queensu.ca](mailto:gangwu@chem.queensu.ca)).



of low- $\gamma$  quadrupolar nuclides that are known to be notoriously difficult to study by NMR. Although solution  $^{25}\text{Mg}$  NMR techniques have been applied to many chemical and biological systems, including proteins and nucleic acids (8), the scope of applications is severely restricted to cases where either the cation exchange is fast or the  $\text{Mg(II)}$  ion is at a symmetrical site, avoiding the unfavorable consequence of rapid  $^{25}\text{Mg}$  quadrupolar relaxation. When an  $\text{Mg(II)}$  ion is tightly bound to a biological macromolecule, the molecular rotational correlation time of the complex is determined by the macromolecule and may be on the order of tens of nanoseconds. Under such a circumstance, the quadrupolar relaxation is so efficient that  $^{25}\text{Mg}$  NMR signals may become too broad to be detected.

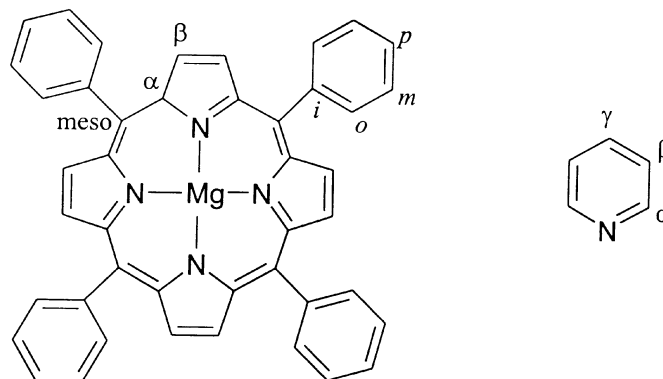
With recent advances in NMR methodology and high-field magnet technology, solid-state NMR has been recognized as a viable technique for studying half-integer quadrupolar nuclei. Previous solid-state  $^{25}\text{Mg}$  NMR studies have almost exclusively focused on inorganic systems (9). In addition, all reported  $^{25}\text{Mg}$  nuclear quadrupole coupling constants are relatively small (ca.  $<9$  MHz). Recently, two research groups have extended solid-state  $^{25}\text{Mg}$  NMR to organic systems. More specifically, Sham and Wu reported a solid-state  $^{25}\text{Mg}$  NMR study of several  $\text{Mg(II)}$  coordination complexes (10). These compounds were used as models for inner-sphere Mg binding often found in nucleic acids. Frydman and co-workers obtained solid-state  $^{25}\text{Mg}$  NMR spectra for an  $\text{Mg(II)}$  adenosine 5'-triphosphate (ATP) complex (11). These two studies demonstrate the great potential of solid-state  $^{25}\text{Mg}$  NMR in probing the  $\text{Mg(II)}$  binding environment in biomolecular systems. In this paper we report the first set of solid-state  $^{25}\text{Mg}$  NMR data for an  $\text{Mg(II)}$ -porphyrin system. To make the solid-state  $^{25}\text{Mg}$  NMR experiment feasible, we prepared  $^{25}\text{Mg}$  isotopically enriched bis(pyridine)(5,10,15,20-tetraphenylporphyrinato)magnesium(II),  $^{25}\text{Mg}(\text{TPP})\cdot\text{Py}_2$ . We also determined the molecular and crystal structures of  $\text{Mg}(\text{TPP})\cdot\text{Py}_2$  by single crystal X-ray crystallography. To better understand the  $^{25}\text{Mg}$  NMR properties and to examine their relationship to molecular structure, we carried out extensive quantum mechanical calculations for the electric field gradient and chemical shielding tensors in two  $\text{Mg}$ -porphyrin systems.

## Experimental details

### Sample preparation

Labeled  $^{25}\text{Mg}(\text{ClO}_4)_2$  (272 mg) was prepared by dissolving 50 mg of  $^{25}\text{MgO}$  ( $^{25}\text{Mg}$  99.1%, purchased from Trace Science International, Toronto, Canada) in  $\text{HClO}_4(\text{aq})$  and evaporating to dryness. The labeled  $^{25}\text{Mg}(\text{TPP})\cdot\text{Py}_2$  complex was prepared following the method described in the literature (12, 13). To a pyridine solution containing 310 mg of 5,10,15,20-tetraphenyl-21*H*, 23*H*-porphine (99+% obtained from Aldrich Chemicals Co., Canada) was added 225 mg of  $^{25}\text{Mg}(\text{ClO}_4)_2$ . The solution was gently refluxed for 12 h in

Scheme 1.



darkness and then evaporated to dryness in a rotary evaporator. The resulting purple precipitate was then washed three times with cold distilled water.  $^1\text{H}$  NMR (400.13 MHz,  $\text{CDCl}_3$ , 298 K) (ppm)  $\delta$ : 8.92 (s, 8H, pyrrole), 8.26 (d, 8H, *o*-phenyl), 7.75 (m, 12H, *m,p*-phenyl), 7.07 (t, 2H,  $\gamma$ -pyridine), 6.49 (t, 4H,  $\beta$ -pyridine), 5.92 (d, 4H,  $\alpha$ -pyridine).  $^{13}\text{C}$  NMR (100.61 MHz,  $\text{CDCl}_3$ , 298 K) (ppm)  $\delta$ : 150.25 (q,  $\alpha$ -pyrrole), 146.93 (t,  $\alpha$ -pyridine), 143.84 (q, *i*-phenyl), 135.87 (t,  $\gamma$ -pyridine), 134.68 (t, *o*-phenyl), 131.80 (t,  $\beta$ -pyrrole), 126.20 (t, *m*-phenyl), 127.03 (t, *p*-phenyl), 122.96 (t,  $\beta$ -pyridine), 121.65 (q, meso). The atomic labeling scheme is shown in Scheme 1.

### Solid-state NMR

Solid-state  $^{25}\text{Mg}$  NMR spectra were recorded on a Bruker Avance-500 (11.75 T) digital NMR spectrometer operating at 30.6 MHz for  $^{25}\text{Mg}$  nuclei. The radio frequency (RF) field strength at the  $^{25}\text{Mg}$  frequency was approximately 50 kHz. A single-channel wideline probe (5 mm insert) was used. A Hahn echo sequence (14) was employed to acquire static  $^{25}\text{Mg}$  NMR spectra:  $P_1(\phi_1) - \tau_1 - P_2(\phi_2) - \tau_2 - \text{Acq}(\phi_3)$ , where  $\phi_1 = x, x, x, x, y, y, y, y, -x, -x, -x, -x, -y, -y, -y, -y$ ;  $\phi_2 = 4 \times (x, y, -x, -y)$ ;  $\phi_3 = -y, y, -y, y, -x, x, -x, x, y, -y, y, -y, x, -x, x, -x$ . The radio-frequency (RF) pulse widths were  $P_1 = 1.50 \mu\text{s}$  and  $P_2 = 3.20 \mu\text{s}$ . The delay between the two RF pulses,  $\tau_1$ , was 400  $\mu\text{s}$ . A much shorter delay was chosen between  $P_2$  and acquisition ( $\tau_2 = 30 \mu\text{s}$ ) so that a whole echo signal could be obtained. Recycle delays of 1 and 2 s were used. To record the very short-lived free induction decay (FID) signals, a 12-bit fast digitizer was used with a dwell time of 0.5  $\mu\text{s}$ , corresponding to a spectral window of 1 MHz. A sample of  $\text{MgO(s)}$  was used as a secondary chemical-shift reference,  $\delta = 26$  ppm (15).

### X-ray crystallography

Crystallographic data for  $\text{Mg}(\text{TPP})\cdot\text{Py}_2$  were collected from a shiny red-purple, hexagonal-shaped crystal (0.1 mm  $\times$  0.2 mm  $\times$  0.4 mm) obtained by slow recrystallization from pyridine.<sup>2</sup> The X-ray diffraction data were col-

<sup>2</sup>Two tables containing hydrogen atom coordinates and anisotropic displacement parameters for  $\text{Mg}(\text{TPP})\cdot\text{Py}_2$  have been deposited as supplementary data. Supplementary data may be purchased from the Depository of Unpublished Data, Document Delivery, CISTI, National Research Council Canada, Ottawa, ON K1A 0S2, Canada ([http://www.nrc.ca/cisti/irm/unpub\\_e.shtml](http://www.nrc.ca/cisti/irm/unpub_e.shtml) for information on ordering electronically). CCDC 205592 contain the supplementary data for this paper. These data can be obtained, free of charge, via [www.ccdc.cam.ac.uk/conts/retrieving.html](http://www.ccdc.cam.ac.uk/conts/retrieving.html) (or from the Cambridge Crystallographic Data Centre, 12 Union Road, Cambridge, U.K.; fax +44 1223 336033; or [deposit@ccdc.cam.ac.uk](mailto:deposit@ccdc.cam.ac.uk)).



lected on a Siemens P4 single-crystal diffractometer with graphite-monochromated Mo K $\alpha$  radiation, operating at 50 kV and 40 mA at 296 K. Data were corrected for Lorentz and polarization effects and analyzed using the Siemens SHELXTL software package (16). The structure was solved by direct methods. Neutral atom scattering factors were taken from Cromer and Waber (17).

### Quantum mechanical calculations

All quantum mechanical calculations were performed on a SunFire 6800 symmetric multiprocessor system (24  $\times$  900 MHz processors and 24 GB of memory) using the Gaussian98 suite of programs (18). For each calculation, 4 or 8 processors were allocated. For  $^{25}\text{Mg}$  EFG calculations, the following convention was used for the nuclear quadrupole coupling constant ( $C_Q$ ) and the asymmetry parameter ( $\eta_Q$ ):

$$[1] \quad C_Q[\text{MHz}] = \frac{eQV_{ZZ}}{h} = -46.85 \times V_{ZZ} [\text{au}]$$

$$[2] \quad \eta_Q = \frac{V_{XX} - V_{YY}}{V_{ZZ}}$$

where  $V_{ZZ}$ ,  $V_{YY}$ , and  $V_{XX}$  are the principal components of the EFG tensor ( $|V_{ZZ}| \geq |V_{YY}| \geq |V_{XX}|$  and  $V_{ZZ} + V_{YY} + V_{XX} = 0$ ). The coefficient in eq. [1] is obtained using the  $^{25}\text{Mg}$  quadrupole moment value recommended by Pyykkö,  $Q(^{25}\text{Mg}) = 19.94 \times 10^{-30} \text{ m}^2$  (19). The computed EFG tensor components are reported in atomic units (1 au =  $9.717365 \times 10^{21} \text{ V m}^{-2}$ ).

To calculate  $^{25}\text{Mg}$  magnetic shielding tensors, the Gauge including atomic orbital (GIAO) method (20), as implemented in Gaussian98, was used. Because GIAO magnetic shielding calculations are in general more time consuming than EFG calculations, we employed a simplified molecular model to reduce computational time. In particular, the four phenyl groups in TPP were replaced by hydrogen atoms, resulting in a 59-atom model, which is significantly smaller than the total number of atoms in  $\text{Mg}(\text{TPP})\cdot\text{Py}_2$ , 99. To confirm the validity of the 59-atom model, we performed several tests in which calculations were done for both the complete molecule and the simplified model. The shielding tensor results are essentially the same for both clusters, while the computational cost for the 59-atom model was significantly smaller than that for the 99-atom cluster. For example, the HF/6-311G(2d,p) calculation gave  $\sigma_{11} = 571$ ,  $\sigma_{22} = 578$ , and  $\sigma_{33} = 616$  ppm for the 59-atom model with a CPU time of 23 h. In comparison, the CPU time for the complete 99-atom molecule at the same level of theory was 84 h and the  $^{25}\text{Mg}$  magnetic shielding tensor components were:  $\sigma_{11} = 571$ ,  $\sigma_{22} = 578$ , and  $\sigma_{33} = 613$  ppm. Therefore, we have assumed that the 59-atom model can be safely used for all shielding calculations.

## Results and discussion

### Crystal structure

$\text{Mg}(\text{TPP})\cdot\text{Py}_2$  crystallizes in triclinic form (space group,  $P\bar{1}$ ). The Mg(II) ion is located at the origin (0, 0, 0), which is also the center of inversion. The Mg(II) ion, lying in the approximate porphyrin plane, is coordinated to six nitrogen

**Table 1.** Crystallographic data and structure refinement for  $\text{Mg}(\text{TPP})\cdot\text{Py}_2$ .

Empirical formula	$\text{C}_{54} \text{H}_{38} \text{N}_6 \text{Mg}$
Formula weight	795.22
Temperature (K)	293(2)
Wavelength ( $\text{\AA}$ )	0.71073
Crystal system	Triclinic
Space group	$P\bar{1}$
Unit cell dimensions	$a = 9.6139(13) \text{ \AA}$ $b = 11.0096(16) \text{ \AA}$ $c = 11.8656(15) \text{ \AA}$ $\alpha = 102.063(3)^\circ$ $\beta = 103.785(3)^\circ$ $\gamma = 114.043(2)^\circ$
Volume ( $\text{\AA}^3$ )	1045.5(2)
Z	1
Density (calculated) ( $\text{g cm}^{-3}$ )	1.263
Absorption coefficient ( $\text{mm}^{-1}$ )	0.089
Max. and min. transmission	1.000 and 0.663
Crystal size ( $\text{mm}^3$ )	$0.1 \times 0.2 \times 0.4$
$\theta$ range for data collection ( $^\circ$ )	1.88–23.31
Index ranges	$-10 \leq h \leq 10$ , $-12 \leq k \leq 12$ , $-13 \leq l \leq 9$
Reflections collected	5436
Independent reflections	3019 ( $R_{\text{int}} = 0.0350$ )
Completeness to $\theta = 23.31^\circ$ (%)	99.7
Refinement method	Full-matrix least-squares on $F^2$
Data/restraints/parameters	3019/0/293
Goodness-of-fit on $F^2$	0.807
Final $R$ indices [ $I > 2\sigma(I)$ ]	$R_1 = 0.0426$ , $wR_2 = 0.0819$
$R$ indices (all data)	$R_1 = 0.0872$ , $wR_2 = 0.0911$

atoms in a distorted octahedral fashion. Detailed crystallographic data, atomic coordinates, and selected structural parameters are reported in Tables 1, 2, and 3, respectively. As shown in Fig. 1, the four equatorial nitrogen atoms are from the porphyrin moiety and the two remaining axial nitrogen ligands are pyridine molecules. The most important structural feature in  $\text{Mg}(\text{TPP})\cdot\text{Py}_2$  is that the  $\text{Mg}-\text{N}_{\text{eq}}$  bond lengths, 2.062 and 2.065  $\text{\AA}$ , are significantly shorter than that for the  $\text{Mg}-\text{N}_{\text{ax}}$  bond, 2.369  $\text{\AA}$ . Several precedents exist in the literature for long  $\text{Mg}-\text{N}_{\text{ax}}$  bonds in  $\text{Mg}$ -porphyrin systems. For example, the  $\text{Mg}-\text{N}_{\text{ax}}$  bond length in  $\text{Mg}(\text{TPP})\cdot(\text{piperidine})_2$  is 2.419  $\text{\AA}$  (21). For  $\text{Mg}(\text{octaethylporphyrin})\cdot\text{Py}_2$  and  $\text{Mg}(\text{TPP})\cdot(4\text{-picoline})_2$ , the  $\text{Mg}-\text{N}_{\text{ax}}$  bonds are 2.389 and 2.386  $\text{\AA}$ , respectively (21, 22), which are both very similar to that in  $\text{Mg}(\text{TPP})\cdot\text{Py}_2$ . In contrast, the  $\text{Mg}-\text{N}_{\text{ax}}$  distance for  $\text{Mg}(\text{TPP})\cdot(1\text{-methylimidazole})_2$  is much shorter, 2.297  $\text{\AA}$  (21). Because in all these systems the Mg(II) ion is at the center of the porphyrin ring, not surprisingly, the  $\text{Mg}-\text{N}_{\text{eq}}$  bond distances are essentially the same. The porphyrin core is slightly non-planar. The dihedral angle between the mean pyridine plane and the mean porphyrin plane is  $70^\circ$ . As seen from Fig. 1, the four phenyl groups exhibit two unique orientations with respect to the mean plane of the porphyrin core, 60 and  $80^\circ$ . Clearly, the two different orientations of the phenyl groups are related to the orientation of the pyridine ring. Other structural features regarding the TPP moiety are expected from previous exam-



**Table 2.** Atomic coordinates ( $\times 10^4$ ) and equivalent isotropic displacement parameters ( $\text{\AA}^2 \times 10^3$ ) for  $\text{Mg}(\text{TPP})\text{Py}_2$ .

	<i>x</i>	<i>y</i>	<i>z</i>	U(eq)
Mg(1)	0	0	0	47(1)
N(1)	436(3)	2304(2)	965(2)	54(1)
C(1)	-677(4)	2706(4)	608(3)	66(1)
N(2)	1040(2)	-180(2)	1647(2)	43(1)
C(2)	-424(4)	4065(4)	1006(3)	75(1)
N(3)	2296(2)	1007(2)	-82(2)	43(1)
C(3)	1072(5)	5096(4)	1827(3)	85(1)
C(4)	2245(4)	4720(4)	2214(3)	100(1)
C(5)	1870(4)	3336(4)	1769(3)	81(1)
C(6)	-2176(3)	-2404(3)	2728(2)	46(1)
C(7)	-2845(3)	-3851(3)	2371(3)	65(1)
C(8)	-3403(4)	-4572(3)	3125(3)	75(1)
C(9)	-3307(3)	-3861(4)	4245(3)	64(1)
C(10)	-2677(4)	-2437(4)	4613(3)	70(1)
C(11)	-2120(3)	-1712(3)	3852(3)	62(1)
C(12)	5632(3)	1499(3)	2713(2)	44(1)
C(13)	6186(3)	2428(3)	3908(2)	58(1)
C(14)	7800(4)	3042(3)	4685(3)	70(1)
C(15)	8850(4)	2696(4)	4278(3)	70(1)
C(16)	8323(3)	1745(3)	3135(3)	67(1)
C(17)	6721(3)	1159(3)	2344(3)	59(1)
C(18)	-1515(3)	-1623(3)	1926(2)	44(1)
C(19)	184(3)	-975(3)	2244(2)	43(1)
C(20)	1303(4)	-1097(3)	3203(3)	52(1)
C(21)	2796(4)	-384(3)	3188(2)	52(1)
C(22)	2650(3)	189(3)	2209(2)	43(1)
C(23)	3927(3)	976(3)	1856(2)	42(1)
C(24)	3759(3)	1363(3)	793(2)	42(1)
C(25)	5066(4)	2251(3)	474(3)	51(1)
C(26)	4408(3)	2430(3)	-570(2)	50(1)
C(27)	2672(3)	1657(3)	-917(2)	43(1)

### Solid-state NMR

Figure 2a shows the time-domain  $^{25}\text{Mg}$  free induction decay (FID) signal for a stationary powder sample of  $\text{Mg}(\text{TPP})\text{Py}_2$ . The whole echo can be clearly seen. As explained by Massiot et al. (23), the whole-echo approach leads to a signal-to-noise enhancement by a factor of  $\sqrt{2}$ . Figure 2b shows the direct FT of the whole echo. As expected, because of the long time delay used for obtaining the whole echo signal, a large phase distortion is present in the spectrum. This distortion can be readily corrected by a linear phase correction, as shown in Fig. 2c. The  $^{25}\text{Mg}$  NMR central-transition spectrum observed for  $\text{Mg}(\text{TPP})\text{Py}_2$  exhibits an extremely large line width, ca. 260 kHz at 11.75 T. Because the width of the NMR line shape is much larger than the strength of the  $B_1$  field (50 kHz), line shape distortions are observed. To obtain accurate values of  $C_Q$  and  $\eta_Q$ , it is important to determine the precise positions of the spectral singularities in a powder pattern. To overcome the so-called "rolling off" effect from a relatively weak RF field, we obtained several spectra with the RF transmitter being set to different frequency positions. As shown in Fig. 3, the entire  $^{25}\text{Mg}$  NMR line shape depends strongly on the position of the RF transmitter. For example, when the RF transmitter

was set close to one edge of the powder line shape, the other edge shows very low intensity, as a result of low RF excitation efficiency. Using the NMR spectra shown in Figs. 3a and 3c, we obtained  $C_Q = 15.32 \pm 0.02$  MHz and  $\eta_Q = 0.00 \pm 0.05$ . These values were confirmed by analyzing an  $^{25}\text{Mg}$  QCPMG NMR spectrum obtained at 9.40 T (data not shown). It is important to point out that the above  $^{25}\text{Mg}$  quadrupole parameters were extracted from the static  $^{25}\text{Mg}$  NMR spectra by considering the second-order quadrupole interaction alone. By comparing the spectra obtained at 11.75 and 9.40 T, we have estimated that the span of the  $^{25}\text{Mg}$  chemical shielding tensor ( $\Omega = \sigma_{33} - \sigma_{11}$ ) is less than 100 ppm for  $^{25}\text{Mg}(\text{TPP})\text{Py}_2$ . This estimate is confirmed by quantum mechanical calculations, as described in the next section.

The  $^{25}\text{Mg}$  quadrupole coupling constant observed for  $\text{Mg}(\text{TPP})\text{Py}_2$  is significantly larger than all previously reported  $C_Q$  values for  $^{25}\text{Mg}$  nuclei (9). Such a large  $C_Q$  value made it very challenging to record a satisfactory solid-state  $^{25}\text{Mg}$  NMR spectrum for  $\text{Mg}(\text{TPP})\text{Py}_2$ . The observed axial symmetry for the EFG tensor is expected from the crystal structure where an approximate axial symmetry is present at the Mg site. Because of the extremely large line width of the static  $^{25}\text{Mg}$  NMR spectrum, it is not possible to obtain a reliable value for the isotropic  $^{25}\text{Mg}$  chemical shift. It is also worth noting that our attempt to record  $^{25}\text{Mg}$  NMR spectra for  $\text{Mg}(\text{TPP})\text{Py}_2$  in  $\text{CDCl}_3$  solution was unsuccessful. This may be attributed to either the rapid relaxation due to a large  $^{25}\text{Mg}$  quadrupole coupling constant or the fast ligand exchange in solution. It is also possible that both of these factors are operative. Assuming that the molecular rotational correlation for the complex is approximately 200 ps, the value of  $T_1$  and  $T_2$  was estimated to be 5.6  $\mu\text{s}$  under the extreme narrowing condition. This was much shorter than the typical probe deadtime at low frequencies. This example further illustrates the advantage of solid-state NMR over traditional solution NMR for studying low- $\gamma$  quadrupolar nuclei.

### Quantum mechanical calculations

Because we have obtained both NMR and structural information for  $\text{Mg}(\text{TPP})\text{Py}_2$ , we decided to test whether quantum mechanical calculations can reproduce the experimental NMR parameters in this Mg-porphyrin system. This attempt is of particular interest because there has been no previous theoretical work on  $^{25}\text{Mg}$  NMR parameters in organic systems. The paucity of theoretical studies on  $^{25}\text{Mg}$  NMR parameters arises primarily from the fact that very little experimental  $^{25}\text{Mg}$  NMR data are available because of the practical difficulties mentioned earlier. For comparison, we also studied a closely related Mg-porphyrin compound,  $\text{Mg}(\text{TPP})\cdot(1\text{-MeIm})_2$ .  $\text{Mg}(\text{TPP})\cdot(1\text{-MeIm})_2$  crystallizes in the tetragonal space group  $P4_1/n$  with  $Z = 4$  (21). In this compound, the Mg(II) ion is also six-coordinated to nitrogen atoms. The Mg—N<sub>eq</sub> bonds, 2.082 and 2.074  $\text{\AA}$ , are very similar to those found in  $\text{Mg}(\text{TPP})\text{Py}_2$ . However, the Mg—N<sub>ax</sub> bond length in  $\text{Mg}(\text{TPP})\cdot(1\text{-MeIm})_2$ , 2.297  $\text{\AA}$ , is much shorter than that in  $\text{Mg}(\text{TPP})\text{Py}_2$ , 2.369  $\text{\AA}$ . The calculated results for the  $^{25}\text{Mg}$  quadrupole parameters and chemical shielding tensors in  $\text{Mg}(\text{TPP})\text{Py}_2$  and  $\text{Mg}(\text{TPP})\cdot(1\text{-MeIm})_2$  are summarized in Tables 4 and 5. The data shown in Table 4 indicate that, for a given basis set, the EFG calcula-



**Table 3.** Selected bond lengths (Å) and angles (°) for Mg(TPP)-Py<sub>2</sub>.

<b>Bond lengths (Å)</b>			
Mg(1)—N(2)	2.062(2)	C(9)—C(10)	1.353(4)
Mg(1)—N(3)	2.065(2)	C(10)—C(11)	1.387(4)
Mg(1)—N(1)	2.369(2)	C(12)—C(17)	1.377(3)
N(1)—C(5)	1.321(3)	C(12)—C(13)	1.390(3)
N(1)—C(1)	1.329(3)	C(12)—C(23)	1.498(3)
C(1)—C(2)	1.369(4)	C(13)—C(14)	1.385(3)
N(2)—C(22)	1.373(3)	C(14)—C(15)	1.367(4)
N(2)—C(19)	1.377(3)	C(15)—C(16)	1.356(4)
C(2)—C(3)	1.358(4)	C(16)—C(17)	1.385(3)
N(3)—C(27)	1.371(3)	C(18)—C(19)	1.401(3)
N(3)—C(24)	1.377(3)	C(18)—C(27)#1	1.409(3)
C(3)—C(4)	1.367(4)	C(19)—C(20)	1.438(3)
C(4)—C(5)	1.362(4)	C(20)—C(21)	1.333(4)
C(6)—C(11)	1.367(3)	C(21)—C(22)	1.438(3)
C(6)—C(7)	1.372(3)	C(22)—C(23)	1.401(3)
C(6)—C(18)	1.495(3)	C(23)—C(24)	1.408(3)
C(7)—C(8)	1.377(3)	C(24)—C(25)	1.435(3)
C(8)—C(9)	1.354(4)	C(25)—C(26)	1.344(3)
		C(26)—C(27)	1.432(3)
<b>Bond angles (°)</b>			
N(2)#1-Mg(1)-N(2)	180.00(11)	C(17)-C(12)-C(13)	117.9(2)
N(2)-Mg(1)-N(3)#1	90.83(7)	C(17)-C(12)-C(23)	122.5(2)
N(2)-Mg(1)-N(3)	89.17(7)	C(13)-C(12)-C(23)	119.5(3)
N(3)#1-Mg(1)-N(3)	180.00(10)	C(14)-C(13)-C(12)	121.0(3)
N(2)-Mg(1)-N(1)#1	86.47(8)	C(15)-C(14)-C(13)	119.3(3)
N(3)-Mg(1)-N(1)#1	94.07(8)	C(16)-C(15)-C(14)	120.8(3)
N(2)-Mg(1)-N(1)	93.53(8)	C(15)-C(16)-C(17)	120.0(3)
N(3)-Mg(1)-N(1)	85.93(8)	C(12)-C(17)-C(16)	120.9(3)
N(1)#1-Mg(1)-N(1)	180.00(14)	C(19)-C(18)-C(27)#1	127.4(2)
C(5)-N(1)-C(1)	114.7(3)	C(19)-C(18)-C(6)	116.1(2)
C(5)-N(1)-Mg(1)	122.5(2)	C(27)#1-C(18)-C(6)	116.4(2)
C(1)-N(1)-Mg(1)	122.1(2)	N(2)-C(19)-C(18)	125.4(2)
N(1)-C(1)-C(2)	125.0(3)	N(2)-C(19)-C(20)	109.0(2)
C(22)-N(2)-C(19)	106.5(2)	C(18)-C(19)-C(20)	125.5(2)
C(22)-N(2)-Mg(1)	127.15(17)	C(21)-C(20)-C(19)	107.7(3)
C(19)-N(2)-Mg(1)	124.96(16)	C(20)-C(21)-C(22)	107.6(3)
C(3)-C(2)-C(1)	118.4(3)	N(2)-C(22)-C(23)	124.8(2)
C(27)-N(3)-C(24)	106.6(2)	N(2)-C(22)-C(21)	109.2(2)
C(27)-N(3)-Mg(1)	125.75(16)	C(23)-C(22)-C(21)	126.0(2)
C(24)-N(3)-Mg(1)	126.81(17)	C(22)-C(23)-C(24)	126.0(2)
C(2)-C(3)-C(4)	118.1(4)	C(22)-C(23)-C(12)	117.0(2)
C(5)-C(4)-C(3)	119.0(3)	C(24)-C(23)-C(12)	116.9(2)
N(1)-C(5)-C(4)	124.7(3)	N(3)-C(24)-C(23)	125.1(2)
C(11)-C(6)-C(7)	117.2(3)	N(3)-C(24)-C(25)	108.6(2)
C(11)-C(6)-C(18)	121.7(3)	C(23)-C(24)-C(25)	126.1(2)
C(7)-C(6)-C(18)	121.1(3)	C(26)-C(25)-C(24)	108.2(2)
C(6)-C(7)-C(8)	121.4(3)	C(25)-C(26)-C(27)	106.7(3)
C(9)-C(8)-C(7)	120.4(3)	N(3)-C(27)-C(18)#1	124.7(2)
C(10)-C(9)-C(8)	119.5(3)	N(3)-C(27)-C(26)	109.8(2)
C(9)-C(10)-C(11)	120.0(3)	C(18)#1-C(27)-C(26)	125.4(2)
C(6)-C(11)-C(10)	121.4(3)		

**Note:** Symmetry transformations used to generate equivalent atoms: #1  $-x, -y, -z$ .

tions at the Hartree–Fock (HF), B3LYP, and MP2 levels of theory show very similar results. The calculations using the 6–31G(d) basis set seems to give the best agreement between the calculated and observed <sup>25</sup>Mg quadrupole param-

eters. The *C<sub>Q</sub>* values for Mg(TPP)·(1-MeIm)<sub>2</sub> are consistently smaller than those for Mg(TPP)·Py<sub>2</sub> by approximately 3–4 MHz. This is attributed to the shorter Mg—N<sub>ax</sub> bond length in Mg(TPP)·(1-MeIm)<sub>2</sub> (vide infra). Because no abso-



**Fig. 1.** Molecular structure of  $\text{Mg}(\text{TPP})\cdot\text{Py}_2$ . Hydrogen atoms are not shown for clarity.

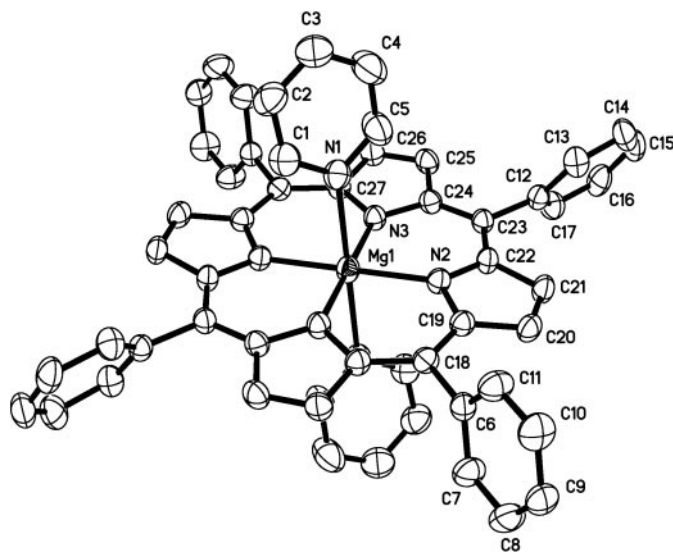
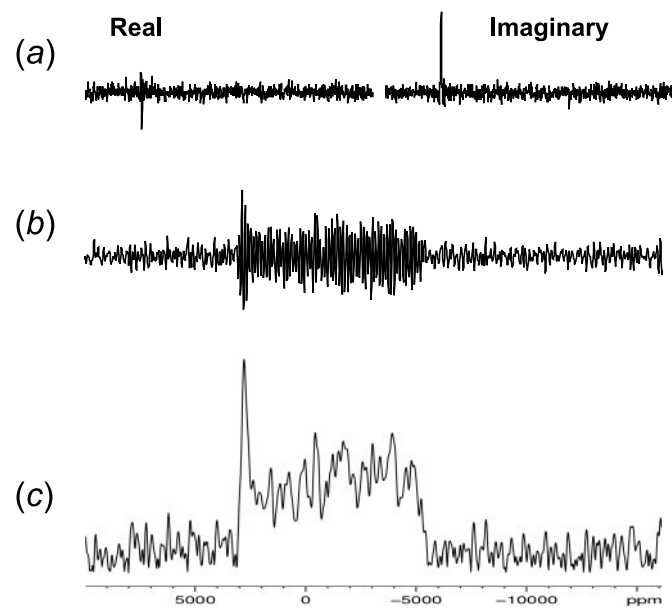
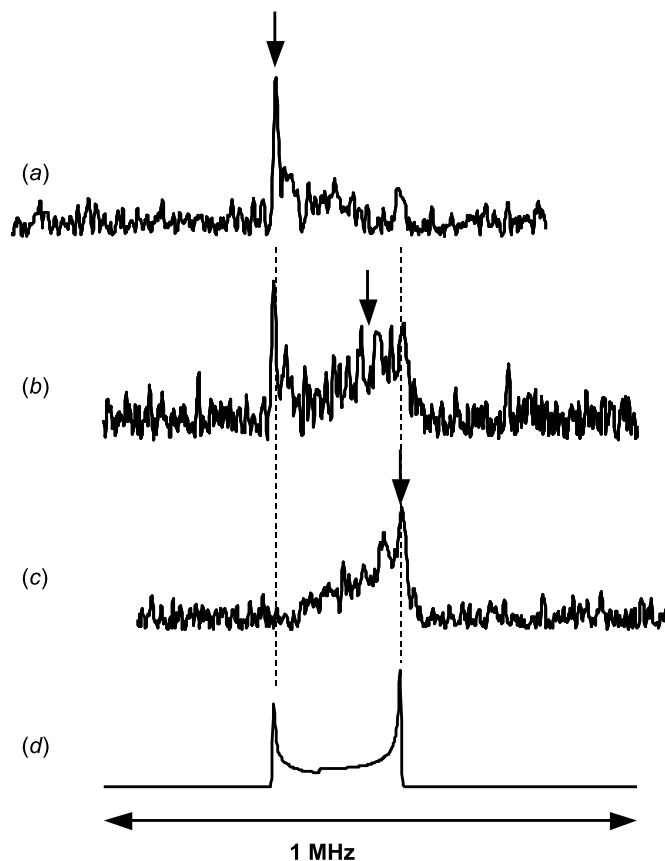


**Fig. 2.** (a) Real and imaginary parts of the  $^{25}\text{Mg}$  FID signal for  $^{25}\text{Mg}(\text{TPP})\cdot\text{Py}_2$ ; (b) Fourier transform of the whole-echo FID; (c) Phase-corrected  $^{25}\text{Mg}$  NMR spectrum. Detailed experimental parameters: transmitter offset =  $-3000$  ppm, 1 s recycle delay, 302 224 transients.



lute shielding scale for  $^{25}\text{Mg}$  is available in the literature, we decided to compute the chemical shielding constant for the referencing species,  $[\text{Mg}(\text{H}_2\text{O})_6]^{2+}$ . Using the shielding constant for  $[\text{Mg}(\text{H}_2\text{O})_6]^{2+}$ ,  $\sigma_{\text{ref}}$ , we were able to convert the calculated shielding values for  $\text{Mg}(\text{TPP})\cdot\text{Py}_2$  and  $\text{Mg}(\text{TPP})\cdot(1\text{-MeIm})_2$  into the “chemical shifts”,  $\delta_{\text{iso}} = \sigma_{\text{ref}} - \sigma_{\text{iso}}$ . The geometry of  $[\text{Mg}(\text{H}_2\text{O})_6]^{2+}$  was obtained by a full geometry optimization at the MP2/6-311G(d,p) level. The Mg—O distance is 2.105 Å and the O—H bond is 0.963 Å. The H—O—H angle for the water molecule is 105.3°. The  $[\text{Mg}(\text{H}_2\text{O})_6]^{2+}$  species has an  $O_h$  point group symmetry. To avoid the ap-

**Fig. 3.** Experimental (a, b, c) and simulated (d)  $^{25}\text{Mg}$  NMR spectra for  $^{25}\text{Mg}(\text{TPP})\cdot\text{Py}_2$ . The spectral width for each of the above spectra was 1 MHz. The arrows indicate the positions to which the RF transmitter was set. The dashed lines indicate the singularities of the powder line shape. Detailed experimental parameters are: (a) transmitter offset = 2700 ppm, 1 s recycle delay, 237 788 transients; (b) transmitter offset =  $-3000$  ppm, 1 s recycle delay, 425 216 transients; (c) transmitter offset =  $-5000$  ppm, 1 s recycle delay, 339 773 transients.



parent basis set dependence, we obtained  $\sigma_{\text{ref}}$  for each basis set. As seen from Table 5, the GIAO shielding calculations indicate that the span of the  $^{25}\text{Mg}$  chemical shielding tensor,  $\Omega = \sigma_{33} - \sigma_{11}$ , can be safely estimated to be less than 50 ppm for  $\text{Mg}(\text{TPP})\cdot\text{Py}_2$ . At 11.75 T, the line width contribution from a chemical shielding anisotropy of this magnitude would be expected to be less than 1.5 kHz in  $^{25}\text{Mg}$  NMR spectra. Since the experimental  $^{25}\text{Mg}$  NMR spectrum for  $\text{Mg}(\text{TPP})\cdot\text{Py}_2$  is 260 kHz wide at 11.75 T, it is not surprising that the  $^{25}\text{Mg}$  chemical shielding anisotropy can be ignored in our spectral analysis. For the same reason, it was also impossible to obtain experimentally a meaningful estimate for the isotropic  $^{25}\text{Mg}$  chemical shift for  $\text{Mg}(\text{TPP})\cdot\text{Py}_2$ . The GIAO shielding calculations suggest that the isotropic  $^{25}\text{Mg}$  chemical shift for an Mg(II) ion coordinated to six nitrogen ligands is approximately 10–20 ppm. We believe that this estimate is reasonably accurate; however, to our knowledge, no experimental  $^{25}\text{Mg}$  NMR data are available for six-coordinate  $\text{MgN}_6$  species.

Another piece of useful information obtained from the quantum mechanical calculations is the orientation of the



**Table 4.** Experimental and calculated  $^{25}\text{Mg}$  quadrupole parameters for  $\text{Mg}(\text{TPP})\cdot\text{Py}_2$  and  $\text{Mg}(\text{TPP})\cdot(1\text{-MeIm})_2$ .

	Method and (or) Basis set	$C_Q$ (MHz)	$\eta_Q$
$\text{Mg}(\text{TPP})\cdot\text{Py}_2$	Exptl.	$15.32 \pm 0.02$	$0.00 \pm 0.05$
	HF/6–31G(d)	15.013	0.034
	HF/6–311G(d,p)	18.524	0.047
	HF/6–311G(2d,p)	18.816	0.046
	B3LYP/6–31G(d)	14.763	0.018
	B3LYP/6–311G(d,p)	17.732	0.043
	B3LYP/6–311G(2d,p)	18.022	0.043
	MP2/6–31(d)	14.971	0.035
$\text{Mg}(\text{TPP})\cdot(1\text{-MeIm})_2$	HF/6–31G(d)	11.981	0.096
	HF/6–311G(d,p)	14.680	0.100
	HF/6–311G(2d,p)	14.969	0.103
	B3LYP/6–31G(d)	11.566	0.161
	B3LYP/6–311G(d,p)	14.164	0.103
	B3LYP/6–311G(2d,p)	14.456	0.104

**Table 5.** Calculated  $^{25}\text{Mg}$  magnetic shielding tensors for  $\text{Mg}(\text{TPP})\cdot\text{Py}_2$  and  $\text{Mg}(\text{TPP})\cdot(1\text{-MeIm})_2$ .<sup>a</sup>

	Method and (or) Basis set	$\sigma_{\text{ref}}^b$	$\delta_{\text{iso}}^c$	$\sigma_{11}$	$\sigma_{22}$	$\sigma_{33}$	$\Omega^d$
$\text{Mg}(\text{TPP})\cdot\text{Py}_2$	HF/6–31G(d)	621	11	595	603	631	36
	HF/6–311G(d,p)	609	20	572	580	616	44
	HF/6–311G(2d,p)	608	19	571	579	616	45
	B3LYP/6–31G(d)	599	9	578	589	602	24
	B3LYP/6–311G(d,p)	585	19	551	559	589	38
	B3LYP/6–311G(2d,p)	584	19	549	558	588	39
$\text{Mg}(\text{TPP})\cdot(1\text{-MeIm})_2$	HF/6–31G(d)	621	8	595	608	636	41
	HF/6–311G(d,p)	609	15	576	585	621	45
	HF/6–311G(2d,p)	608	15	574	583	621	47
	B3LYP/6–31G(d)	599	6	577	595	607	30
	B3LYP/6–311G(d,p)	585	14	555	565	594	39
	B3LYP/6–311G(2d,p)	584	14	554	563	593	39

<sup>a</sup>All magnetic shielding tensor components and isotropic chemical shifts are in ppm.<sup>b</sup> $\sigma_{\text{ref}}$  is calculated for  $[\text{Mg}(\text{H}_2\text{O})_6]^{+2}$  with an optimized geometry at the MP2/6–311G(d,p) level.<sup>c</sup> $\delta_{\text{iso}} = \sigma_{\text{ref}} - \sigma_{\text{iso}}$ .<sup>d</sup>Span  $\Omega = \sigma_{33} - \sigma_{11}$ .

NMR tensors in the molecular frame of reference. Figure 4 shows the orientations of both EFG and chemical shielding tensors for the  $^{25}\text{Mg}$  nucleus in  $\text{Mg}(\text{TPP})\cdot\text{Py}_2$ . The largest EFG tensor component,  $V_{\text{ZZ}}$ , is  $5.3^\circ$  off the  $\text{Mg}-\text{N}_{\text{ax}}$  bond direction. The smallest EFG component,  $V_{\text{XX}}$ , lies approximately in the porphyrin plane, making an angle of  $58.6^\circ$  with respect to one of the  $\text{Mg}-\text{N}_{\text{eq}}$  bonds. The chemical shielding tensor exhibits essentially the same orientation as the EFG tensor. In particular, the tensor component with the most shielding,  $\sigma_{33}$ , is approximately  $7.5^\circ$  off the  $\text{Mg}-\text{N}_{\text{ax}}$  direction, while the tensor component with the least shielding,  $\sigma_{11}$ , lies in the porphyrin plane and makes an angle of  $45.6^\circ$  relative to the same  $\text{Mg}-\text{N}_{\text{eq}}$  bond described for the EFG tensor.

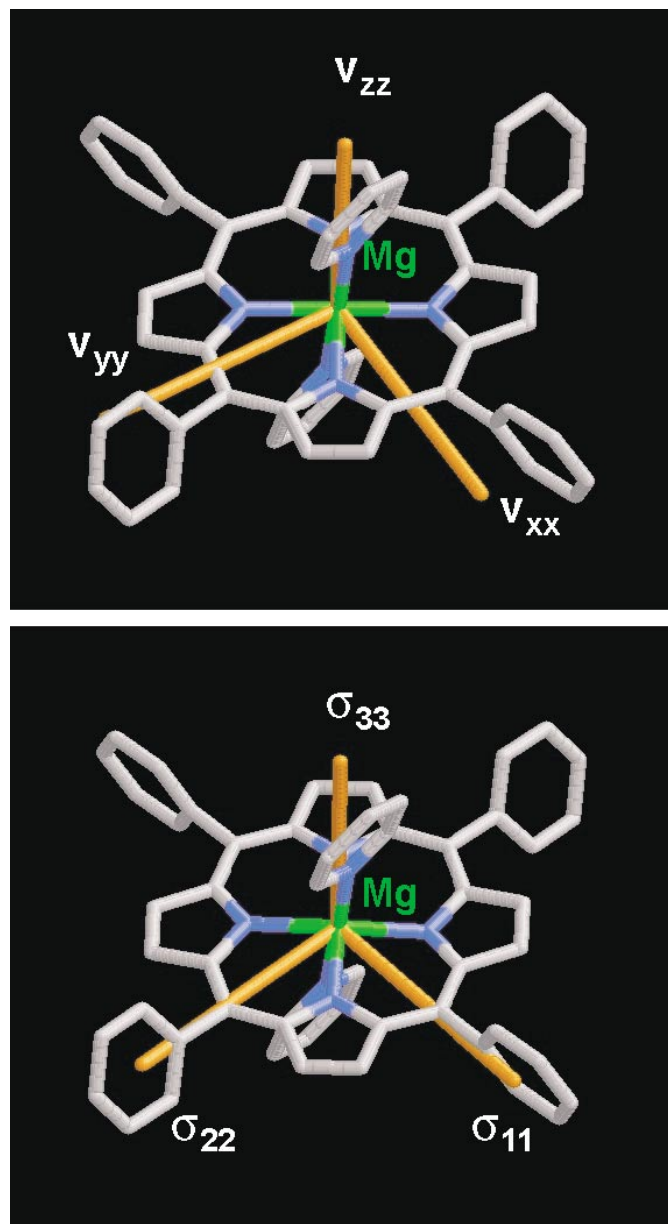
As mentioned earlier, one obvious structural feature that might be responsible for the observation of a large  $C_Q$  value at the Mg center in  $\text{Mg}(\text{TPP})\cdot\text{Py}_2$  is the large difference between  $\text{Mg}-\text{N}_{\text{eq}}$  and  $\text{Mg}-\text{N}_{\text{ax}}$  distances. To further explore the influence of the  $\text{Mg}-\text{N}_{\text{ax}}$  bond on the EFG at the Mg center, we performed a series of EFG calculations for a model where the position of the axial pyridine ligands is systematically varied. The geometry of the porphyrin core in

the model is identical to that in  $\text{Mg}(\text{TPP})\cdot\text{Py}_2$ . The results are shown in Table 6 and depicted in Fig. 5. It is interesting to see that the value of  $C_Q$  increases monotonically with the increase of  $\text{Mg}-\text{N}_{\text{ax}}$  bond distance. As shown in Table 6, the calculation also gave an estimate for an  $\text{Mg}(\text{II})$  ion in a square-planar binding geometry,  $C_Q \approx 22$  MHz. At 11.75 T, this  $C_Q$  value would correspond to a central-transition  $^{25}\text{Mg}$  NMR spectrum two times wider than the one shown in Fig. 2c. On the basis of these results, we believe that many  $\text{Mg}$ -porphyrin complexes should be accessible by solid-state  $^{25}\text{Mg}$  NMR at currently available high magnetic fields (from 11.75 to 21.15 T).

It is also of interest to compare the EFG tensor observed for  $\text{Mg}(\text{TPP})\cdot\text{Py}_2$  with those reported for two isostructural TPP complexes,  $\text{Fe}^{\text{II}}(\text{TPP})\cdot\text{Py}_2$  and  $\text{Co}^{\text{III}}(\text{TPP})\cdot\text{Py}_2$ . From a Mössbauer experiment, Kobayashi et al. (24) reported an  $^{57}\text{Fe}$  quadrupole splitting for  $\text{Fe}^{\text{II}}(\text{TPP})\cdot\text{Py}_2$  (low spin) at 300 K,  $\Delta E_Q = 1.22$  mm  $\text{s}^{-1}$ . This quadrupole splitting corresponds to  $V_{\text{ZZ}} = 0.75$  au, assuming  $Q(^{57}\text{Fe}) = 16.0 \times 10^{-30}$  m<sup>2</sup>. This EFG value is much larger than the corresponding value found at the Mg nucleus in  $\text{Mg}(\text{TPP})\cdot\text{Py}_2$ ,  $V_{\text{ZZ}} = 0.3202$  au. As illustrated in Fig. 5, the  $V_{\text{ZZ}}$  value is a function of the



**Fig. 4.** Orientations of the  $^{25}\text{Mg}$  EFG tensor (top) and the chemical shielding tensor (bottom) in the molecular frame of  $\text{Mg}(\text{TPP})\cdot\text{Py}_2$ . Quantum mechanical calculations were done at the HF/6-31G(d) level.



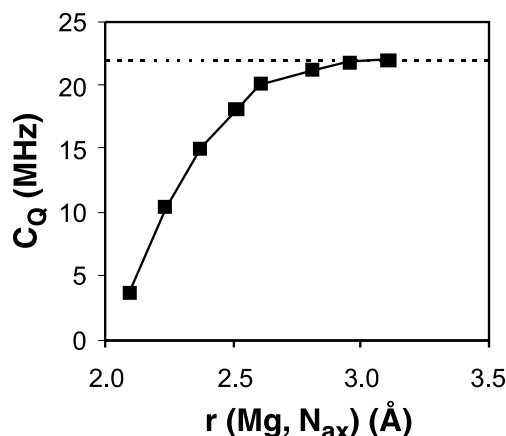
$\text{M}-\text{N}_{\text{ax}}$  distance. In  $\text{Fe}^{\text{II}}(\text{TPP})\cdot\text{Py}_2$ , however, the  $\text{Fe}-\text{N}_{\text{ax}}$  bond length, 2.039 Å, is similar to the  $\text{Fe}-\text{N}_{\text{eq}}$  bonds, 1.989 and 1.997 Å (25). This immediately suggests that the  $d^6$  metal TPP complexes behave differently as the  $\text{Mg}-\text{TPP}$  compounds. In  $\text{Co}^{\text{III}}(\text{TPP})\cdot\text{Py}_2$ , the  $V_{\text{ZZ}}$  value at the metal center is 0.167 au, as reported by Medek et al. from a solid-state  $^{59}\text{Co}$  NMR study (5g). This value is much smaller than that in  $\text{Fe}^{\text{II}}(\text{TPP})\cdot\text{Py}_2$ . This may be explained by a general trend, in which the  $\text{M}-\text{N}_{\text{ax}}$  distance is usually smaller in  $\text{Co}^{\text{III}}-\text{TPP}$  complexes than in  $\text{Fe}^{\text{II}}-\text{TPP}$  complexes (21). In this regard, the  $d^6$  metal-TPP compounds exhibit a similar  $\text{M}-\text{N}_{\text{ax}}$  dependence to that observed for  $\text{Mg}-\text{TPP}$  complexes.

**Table 6.** Calculated dependence of the  $^{25}\text{Mg}$  quadrupole parameters on the  $\text{Mg}-\text{N}_{\text{ax}}$  distance in  $\text{Mg}(\text{TPP})\cdot\text{Py}_2$  at the HF/6-31G(d) level.

$R(\text{Mg}-\text{N}_{\text{ax}})$ (Å)	$C_Q$ (MHz)	$\eta_Q$
2.091	3.677	0.070
2.233	10.502	0.042
2.369	15.013	0.034
2.510	18.056	0.032
2.604	20.094	0.032
2.807	21.151	0.033
2.952	21.716	0.034
3.103	21.987	0.036
$+\infty^a$	21.988	0.038

<sup>a</sup>Calculated without axial ligands.

**Fig. 5.** Calculated dependence of  $C_Q(^{25}\text{Mg})$  on the  $\text{Mg}-\text{N}_{\text{ax}}$  bond length in  $\text{Mg}(\text{TPP})\cdot\text{Py}_2$ . The dashed line indicates the  $C_Q(^{25}\text{Mg})$  value for an  $\text{Mg}-(\text{TPP})$  complex without axial ligands.



## Conclusion

We have reported solid-state  $^{25}\text{Mg}$  NMR, crystallographic, and computational results for an  $\text{Mg}(\text{II})$ -porphyrin complex,  $\text{Mg}(\text{TPP})\cdot\text{Py}_2$ . The  $^{25}\text{Mg}$  quadrupole coupling constant observed for  $\text{Mg}(\text{TPP})\cdot\text{Py}_2$ ,  $C_Q = 15.32 \pm 0.02$  MHz, is the largest so far reported for  $^{25}\text{Mg}$  nuclei. The  $^{25}\text{Mg}$  chemical shielding anisotropy is, however, too small to be measured reliably. We have performed quantum mechanical calculations for the  $^{25}\text{Mg}$  NMR tensors in two related  $\text{Mg}$ -porphyrin complexes:  $\text{Mg}(\text{TPP})\cdot\text{Py}_2$  and  $\text{Mg}(\text{TPP})\cdot(1-\text{MeIm})_2$ . Quantum mechanical calculations were carried out at various levels of theory including restricted Hartree-Fock, density functional theory, and MP2 with different basis sets. The calculations with a 6-31G(d) basis set have reproduced reasonably well the observed  $^{25}\text{Mg}$  NMR data for  $\text{Mg}(\text{TPP})\cdot\text{Py}_2$ . The calculations also suggest that the span of the  $^{25}\text{Mg}$  chemical shift tensor is less than 50 ppm for  $\text{Mg}(\text{TPP})\cdot\text{Py}_2$ .

To obtain an upper limit for the  $^{25}\text{Mg}$  quadrupole coupling constant in  $\text{Mg}$ -porphyrin systems, we have performed quantum mechanical calculations for an  $\text{Mg}(\text{II})$  ion at the center of a porphyrin moiety without axial ligands, which represents the most asymmetrical environment for the  $\text{Mg}$  cation. For such a model, the  $^{25}\text{Mg}$  quadrupole coupling



constant is approximately 22 MHz. This may suggest that most of Mg(II)–porphyrin complexes should be accessible by high-field  $^{25}\text{Mg}$  NMR. The present work represents the first solid-state  $^{25}\text{Mg}$  NMR study for an Mg(II)–porphyrin system. Extension of this research to chlorophyll models is under way in this laboratory.

## Acknowledgment

This work was supported by equipment and research grants from the Natural Sciences and Engineering Research Council (NSERC) of Canada (to G.W. and S.W.). G.W. thanks Queen's University for a Chancellor's Research Award (2000–2004) and the Province of Ontario for a Premier's Research Excellence Award (2000–2004). A.W. thanks Queen's University for an R.S. McLaughlin Fellowship (2000–2002) and the Province of Ontario for an Ontario Graduate Scholarship (OGS) (2002–2003). We are also grateful to Ramsey Ida for assistance in quantum mechanical calculations and to Professor Robert W. Schurko (University of Windsor) for obtaining an  $^{25}\text{Mg}$  QCPMG spectrum at 9.40 T. All quantum mechanical calculations were performed at the High Performance Computing Virtual Laboratory (HPCVL) at Queen's University.

## References

1. K.M. Kadish, K.M. Smith, and R. Guillard (*Editors*). The porphyrin handbook. Academic Press, Burlington, MA. 1999.
2. L.R. Milgrom. The colours of life: An introduction to the chemistry of porphyrins and related compounds. Oxford University Press, New York. 1997.
3. J.E. Falk. Porphyrins and metalloporphyrins. Elsevier, Amsterdam. 1975.
4. F.A. Walker. *Coord. Chem. Rev.* **185/186**, 471 (1999); and refs. therein.
5. (a) H.J. Jakobsen, P.D. Ellis, R.R. Inners, and C.F. Jensen. *J. Am. Chem. Soc.* **104**, 7442 (1982); (b) G.N. La Mar, C.M. Dellinger, and S.S. Sankar. *Biochem. Biophys. Res. Commun.* **128**, 628 (1985); (c) H.C. Lee, J.K. Gard, T.L. Brown, and E. Oldfield. *J. Am. Chem. Soc.* **107**, 4087 (1985); (d) L. Baltzer. *J. Am. Chem. Soc.* **109**, 3479 (1987); (e) M.A. Kennedy and P.D. Ellis. *J. Am. Chem. Soc.* **111**, 3195 (1989); (f) J. Chung, H.C. Lee, and E. Oldfield. *J. Magn. Reson.* **90**, 148 (1990); (g) A. Medek, V. Frydman, and L. Frydman. *J. Chem. Phys. B*, **101**, 8959 (1997).
6. (a) M.T. McMahon, A.C. deDios, N. Godbout, R. Salzmänn, D.D. Laws, H. Le, R.H. Havlin, and E. Oldfield. *J. Am. Chem. Soc.* **120**, 4784 (1998); (b) N. Godbout, L.K. Sanders, R. Salzmänn, R.H. Havlin, M. Wojdelski, and E. Oldfield. *J. Am. Chem. Soc.* **121**, 3829 (1999).
7. H. Scheer (*Editor*). Chlorophylls. CRC Press, Boca Raton, Florida. 1991.
8. (a) R.G. Bryant. *J. Magn. Reson.* **6**, 159 (1972); (b) S. Forsén, T. Andersson, T. Drakenberg, O. Teleman, and H.J. Vogel. *In Calcium binding proteins. Edited by B. de Bernad*. Elsevier, Amsterdam. 1983; (c) T. Shimizu and M. Hatano. *Inorg. Chem.* **24**, 2003 (1985); (d) M.-D. Tsai, T. Drakenberg, E. Thulin, and S. Forsén. *Biochemistry* **26**, 3635 (1987); (e) S.S. Reid and J.A. Cowan. *Biochemistry* **29**, 6025 (1990); (f) S.S. Reid and J.A. Cowan. *J. Am. Chem. Soc.* **113**, 673 (1991); (g) J.A. Cowan. *Inorg. Chem.* **30**, 2740 (1991); (h) J.A. Cowan. *J. Am. Chem. Soc.* **113**, 675 (1991); (i) E. Berggren, L. Nordenskiöld, and W.H. Braunlin. *Biopolymers*, **32**, 1339 (1992); (j) L. Wright and L.E. Lerner. *Biopolymers*, **34**, 691 (1994).
9. (a) M.E. Smith. *Ann. Rep. NMR Spectrosc.* **43**, 121 (2001) and refs. therein; (b) F.H. Larsen, J. Skibsted, H.J. Jakobsen, and N.C. Nielsen. *J. Am. Chem. Soc.* **122**, 7080 (2000).
10. S. Sham and G. Wu. *Inorg. Chem.* **39**, 4 (2000).
11. C.V. Grant, V. Frydman, and L. Frydman. *J. Am. Chem. Soc.* **122**, 11 743 (2000).
12. J.S. Lindsey and J.N. Woodford. *Inorg. Chem.* **34**, 1063 (1995).
13. S.J. Baum, B.F. Burnham, and R.A. Plane. *Proc. Natl. Acad. Sci. U.S.A.* **52**, 1439 (1964).
14. A.C. Kunwar, G.L. Turner, and E. Oldfield. *J. Magn. Reson.* **69**, 124 (1986).
15. R. Dupree and M.E. Smith. *Chem. Commun.* 1483 (1988).
16. Bruker AXS. 1995. SHELXTL Crystal structure analysis package [computer program]. Version 5. Bruker AXS, Analytical X-ray System, Siemens, Madison, WI.
17. D.T. Cromer and J.T. Waber. *International tables for X-ray crystallography*. Kynoch Press, Birmingham, U.K. 1974.
18. M.J. Frisch, G.W. Trucks, H.B. Schlegel, G.E. Scuseria, M.A. Robb, J.R. Cheeseman, V.G. Zakrzewski, J.A. Montgomery, R.E. Stratmann, J.C. Burant, S. Dapprich, J.M. Millam, A.D. Daniels, K.N. Kudin, M.C. Strain, O. Farkas, J. Tomasi, V. Barone, M. Cossi, R. Cammi, B. Mennucci, C. Pomelli, C. Adamo, S. Clifford, J. Ochterski, G.A. Petersson, P.Y. Ayala, Q. Cui, K. Morokuma, D.K. Malick, A.D. Rabuck, K. Raghavachari, J.B. Foresman, J. Cioslowski, J.V. Ortiz, B.B. Stefanov, G. Liu, A. Liashenko, P. Piskorz, I. Komaromi, R. Gomperts, R.L. Martin, D.J. Fox, T. Keith, M.A. Al-Laham, C.Y. Peng, A. Nanayakkara, C. Gonzalez, M. Challacombe, P.M.W. Gill, B. Johnson, W. Chen, M.W. Wong, J.L. Andres, M. Head-Gordon, E.S. Replogle, and J.A. Pople. 1998. Gaussian98 [computer program]. Revision A.6. Gaussian, Inc., Pittsburgh, PA.
19. P. Pykkö. *Mol. Phys.* **99**, 1617 (2001).
20. (a) R. Ditchfield. *Mol. Phys.* **27**, 789 (1974); (b) K. Wolinski, J.F. Hilton, and P. Pulay. *J. Am. Chem. Soc.* **112**, 8257 (1990).
21. V. McKee, C.C. Ong, and G.A. Rodley. *Inorg. Chem.* **23**, 4242 (1984).
22. R. Bonnett, M.B. Hursthouse, K.M.A. Malik, and B. Mateen. *J. Chem. Soc., Perkin Trans. 2*, 2072 (1977).
23. D. Massiot, I. Farnan, N. Gautier, D. Trumeau, A. Trokiner, and J.P. Coutures. *Solid State Nucl. Magn. Reson.* **4**, 241 (1995).
24. H. Kobayashi, Y. Maeda, and Y. Yanagawa. *Bull. Chem. Soc. Jpn.* **43**, 2342 (1970).
25. N. Li, V. Petricek, P. Coppens, and J. Landrum. *Acta Crystallogr. Sect. C*, **41**, 902 (1985).



# Insect toxins from spruce endophytes

John A. Findlay, Guoqiang Li, J. David Miller, and Taiwo O. Womiloju

**Abstract:** Extracts of fermentation cultures of a fungal endophyte (DAOM 221611) from spruce needles have afforded the known macrocyclic antibiotic vermiculin (**1**),  $7\alpha,8\beta,11$ -trihydroxydrimane (**2**), and eight novel 13-carbon  $\gamma$ -lactones, namely *trans*-3-methyldodec-*cis*-6-*en*-4-olide (**3**), *trans*-8-hydroxy-3-methyldodec-*cis*-6-*en*-4-olide (**4**), *trans*-8-acetoxy-3-methyldodec-*cis*-6-*en*-4-olide (**5**), *trans*-9-hydroxy-3-methyl-8-oxo-dodec-*trans*-6-*en*-4-olide (**6**), *trans*-8,9-dihydroxy-3-methyldodec-*cis*-6-*en*-4-olide (**7**), *trans*-9-hydroxy-8-oxo-3-methyldodecan-4-olide (**8**), *trans*-7,9-dihydroxy-3-methyl-8-oxo-dodecan-4-olide (**9**), and *trans*-6-hydroxymethyl-3-methyl-7-oxo-undecan-4-olide (**10**). A known JH III metabolism product, 10,11-dihydroxyfarnesenic acid (**11**), was also isolated and synthesized from farnesol. Other endophyte cultures from black spruce and white spruce afforded the novel 6,7-dihydroxy-2-propyl-2,4-octadien-4-olide (**16**), 5,6,8-trihydroxy-4-(1'-hydroxyethyl) isocoumarin (**17**) plus the known sescandelin (**18**), sescandelin B (**19**), and 4-hydroxy-2-methoxyacetanilide (**20**). Several of the  $\gamma$ -lactones showed toxicity to spruce budworm (*Choristoneura fumiferana* Clem.) larvae and vermiculin **1** and compound **16** were toxic to spruce budworm cells.

**Key words:** toxigenic endophytes, insect toxins,  $\gamma$ -lactones, isocoumarins.

**Résumé :** L'extraction des milieux de cultures de fermentation d'un champignon endophyte (DAOM 221611) des aiguilles d'épinette a permis d'isoler la vermiculine (**1**), un antibiotique macrocyclique connu, le  $7\alpha,8\beta,11$ -trihydroxydrimane (**2**) ainsi que huit nouvelles  $\gamma$ -lactones à 13 atomes de carbone, soit les *trans*-3-méthyldodéc-*cis*-6-*én*-4-olide (**3**), *trans*-8-hydroxy-3-méthyldodéc-*cis*-6-*én*-4-olide (**4**), *trans*-8-acétoxy-3-méthyldodéc-*cis*-6-*én*-4-olide (**5**), *trans*-9-hydroxy-3-méthyl-8-oxododéc-*cis*-6-*én*-4-olide (**6**), *trans*-8,9-dihydroxy-3-méthyldodéc-*cis*-6-*én*-4-olide (**7**), *trans*-9-hydroxy-8-oxo-3-méthyldodéc-*cis*-6-*én*-4-olide (**8**), *trans*-7,9-dihydroxy-3-méthyl-8-oxododéc-*cis*-6-*én*-4-olide (**9**) et *trans*-6-hydroxyméthyl-3-méthyl-7-oxoundéc-*cis*-6-*én*-4-olide (**10**). On a aussi isolé un produit connu de métabolisme JH III, l'acide 10,11-dihydroxyfarnésique (**11**) qu'on a synthétisé à partir du farnésol. D'autres milieux de cultures d'endophytes provenant d'épinettes noire ou blanche ont permis d'isoler de nouveaux produits, dont le 6,7-dihydroxy-2-propylocta-2,4-diène-4-olide (**16**) ainsi que la 5,6,8-trihydroxy-4-(1'-hydroxyéthyl)isocoumarine (**17**) en plus de produits connus comme la sescandéline (**18**), la sescandéline B (**19**) et le 4-hydroxy-2-méthoxyacétanilide (**20**). Plusieurs  $\gamma$ -lactones présentent de la toxicité pour les larves de la tordeuse des bourgeons d'épinette (*Choristoneura fumiferana* Clem.) alors que la vermiculine **1** et le composé **16** sont toxiques pour les cellules de la tordeuse des bourgeons d'épinette.

**Mots clés :** endophytes toxigènes, toxines d'insectes,  $\gamma$ -lactones, isocoumarines.

[Traduit par la Rédaction]

Recently, we reported that inoculation of white spruce, *Picea glauca* (Moench voss.), seedlings with a rugulosin-producing endophyte resulted in a significant reduction in larval growth rate of the destructive forest pest, the spruce budworm *Choristoneura fumiferana* Clem., in feeding experiments (1). This latter study followed from our pioneering discovery that some conifer needles are inhabited by insect-toxin-producing endophytes (2), consistent with the proposal of Carroll and Carroll that fungal endophytes recovered from conifer needles might be mutualistic symbionts (3). In our continuing studies in search of additional toxin-producing endophytic fungi from spruce needles we have encountered

cultures capable of producing an interesting array of novel  $\gamma$ -lactones (**3–10**), as well as 10,11-dihydroxyfarnesenic acid **11**, the macrocyclic antibiotic, vermiculin **1** (4), and the known sesquiterpene,  $7\alpha,8\beta,11$ -trihydroxydrimane **2** (5). Other spruce-needle-derived endophyte cultures gave the novel 2,4-dien-4-olide **16**, the novel isocoumarin **17**, plus the known sescandelin **18** (6), sescandelin B **19** (7), and 4-hydroxy-2-methoxyacetanilide **20** (Scheme 1). Both **18** and **19** have been previously isolated from the fungus *Sesquillium candelabrum*, and sescandelin **18** is reported to be a root-promoting agent (6). Compound **20** has recently been reported as a metabolite of a soil fungus (8).

The endophyte strain **5WS11I**, obtained from needles of a white spruce (*P. glauca* (Moench voss)), was cultured according to established protocols (9) using two different kinds of vessels. In the first case the fermentation was conducted in 250-mL Erlenmeyer flasks (2 L total), and in the second case Glaxo bottles (10 L total) were employed but no other changes in culturing procedures were made, and the fermentations proceeded simultaneously. The fermentation-medium filtrates were extracted with EtOAc, and crude extracts **E** (from Erlenmeyer flask culture) and **G** (from Glaxo bottle culture) were obtained by removal of solvent under vacuum

Received 12 December 2002. Published on the NRC Research Press Web site at <http://canjchem.nrc.ca> on 28 April 2003.

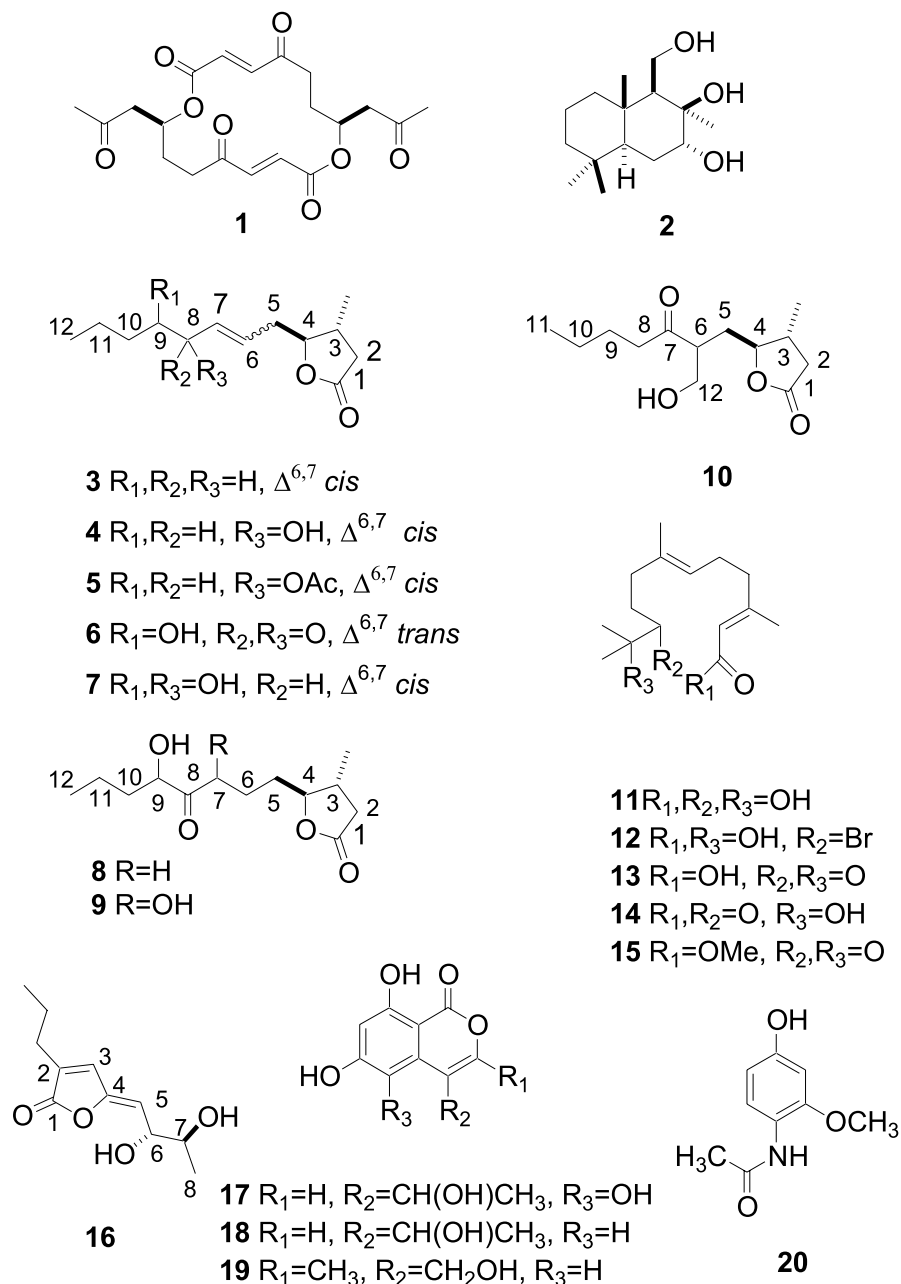
**J.A. Findlay<sup>1</sup>** and **G. Li**. Department of Chemistry, University of New Brunswick, Fredericton, NB E3B 6E2, Canada.

**J.D. Miller** and **T.O. Womiloju**. Ottawa-Carleton Institute of Chemistry, Department of Chemistry, Carleton University, Ottawa, ON K1S 5B6, Canada.

<sup>1</sup>Corresponding author (e-mail: [findlay@unb.ca](mailto:findlay@unb.ca))



Scheme 1.



at room temperature. From the crude extract **G**, a number of  $\gamma$ -lactones **3–10** and the sesquiterpenes **11** and 7 $\alpha$ ,8 $\beta$ ,11-trihydroxydrimane have been isolated and their structures elucidated by spectral data analyses. From the crude extract **E**, only the 16-membered ring dilactone, vermiculin, and 7 $\alpha$ ,8 $\beta$ ,11-trihydroxydrimane were isolated. The antibiotic vermiculin was previously reported from *Penicillium vermiculatum* (4) and a soil fungus *Talaromyces wortmannii* (10) while the  $\gamma$ -lactones **3–10** are closely related to a  $\gamma$ -decalactone (11) and *cis*-6-dodecen-4-olide (12), fungal metabolites previously reported from the cultures of *Sporobolomyces odoros*. Sesquiterpene **11** was previously reported as a biotransformation product of the corresponding 10,11-epoxide, an insect juvenile hormone (JHIII) homologue (13),

and 7 $\alpha$ ,8 $\beta$ ,11-trihydroxydrimane was isolated previously from the fungus, *Fomes annosus*, a destructive forest pathogen (5). Compounds **4**, **6–8**, **11** and 7 $\alpha$ ,8 $\beta$ ,11-trihydroxydrimane **2** were toxic to spruce budworm in a larval feeding bioassay, and vermiculin **1** and **16** were toxic to budworm cells.

Compound **3** was isolated as an optically active, oily substance from a nonpolar fraction of the crude extract **G**. Its molecular formula,  $C_{13}H_{22}O_2$ , was determined by HR-EI-MS. The IR spectrum is consistent with the presence of a lactone carbonyl group ( $1780\text{ cm}^{-1}$ ) and a vinyl group ( $1640\text{ cm}^{-1}$ ), and the  $^{13}C$  NMR and DEPT spectra (Table 1) indicate the presence of one carbonyl, four methines, six methylenes, and two methyls. A total of four downfield car-



Table 1. NMR data (CDCl<sub>3</sub>) for lactones 3–7.

Carbon	Compound 3		Compound 4		Compound 5		Compound 6		Compound 7	
	$\delta$	Proton ( <i>J</i> Hz)	$\delta$	Proton ( <i>J</i> Hz)	$\delta$	Proton ( <i>J</i> Hz)	$\delta$	Proton ( <i>J</i> Hz)	$\delta$	Proton ( <i>J</i> Hz)
1	176.7 (s)		176.3 (s)		176.6 (s)		175.5 (s)		176.2 (s)	
2	37.1 (t)	2.66 (dd, $\beta$ , 17.0, 9.2), 2.16 (dd, $\alpha$ , 17.0, 7.6)	36.9 (t)	2.64 (dd, $\beta$ , 17.2, 8.0), 2.15 (dd, $\alpha$ , 17.2, 9.2)	36.9 (t)	2.66 (dd, $\beta$ , 16.8, 8.0), 2.17 (dd, $\alpha$ , 16.8, 9.2)	36.7 (t)	2.67 (dd, $\beta$ , 15.6, 6.4), 2.20 (dd, $\alpha$ , 15.6, 10.0)	37.0 (t)	2.66 (dd, $\beta$ , 17.0, 7.6), 2.18 (dd, $\alpha$ , 17.0, 9.6)
3	35.1 (d)	2.25 (m, $\beta$ )	35.0 (d)	2.25 (m, $\beta$ )	35.7 (d)	2.26 (m, $\beta$ )	35.9 (d)	2.23 (m, $\beta$ )	35.1 (d)	2.30 (m, $\beta$ )
4	86.7 (d)	4.05 (ddd, $\alpha$ , 6.8, 6.8, 6.0)	86.1 (d)	4.06 (ddd, $\alpha$ , 7.2, 6.4, 4.8)	86.4 (d)	4.03 (ddd, $\alpha$ , 7.2, 7.2, 4.8)	84.6 (d)	4.13 (ddd, $\alpha$ , 12.0, 8.0, 4.4)	86.0 (d)	4.10 (ddd, $\alpha$ , 11.6, 6.4, 4.4)
5	31.3 (t)	2.42 (2H, m)	31.4 (t)	2.56 (m), 2.39 (m)	32.3 (t)	2.65 (m), 2.42 (m)	36.6 (t)	2.63 (m), 2.53 (m)	31.7 (t)	2.64 (m), 2.41 (m)
6	122.7 (d)	5.38 (dtt, 11.0, 7.2, 1.2)	124.7 (d)	5.49 (m)	127.7 (d)	5.58 (m),	127.8 (d)	6.98 (ddd, 15.6, 15.6, 7.2)	127.6 (d)	5.67 (ddd, 11.2, 7.6, 7.2)
7	133.9 (d)	5.55 (dtt, 11.0, 7.0, 1.6)	136.6 (d)	5.52 (m)	131.3 (d)	5.43 (m)	142.6 (d)	6.35 (ddd, 15.6, 1.2, 1.0)	132.7 (d)	5.59 (ddd, 11.2, 8.4, 1.2)
8	27.4 (t)	2.02 (2H, dt, 7.0, 6.8)	67.5 (d)	4.34 (m)	70.1 (d)	5.42 (m)	200.3 (s)		71.0 (d)	4.14 (dd, 8.4, 7.6)
9	29.1 (t)	1.34 (2H, m)	37.0 (t)	1.57 (m), 1.42 (m)	34.1 (t)	1.66 (m), 1.52 (m)	75.2 (t)	4.34 (dd, 6.8, 3.6)	74.5 (d)	3.46 (m)
10	31.5 (t)	1.29 (2H, m)	27.4 (t)	1.29 (2H, m)	27.2 (t)	1.28 (2H, m)	36.2 (t)	1.75 (m), 1.46 (m)	18.9 (t)	1.51 (m), 1.38 (m)
11	22.5 (t)	1.31 (2H, m)	22.6 (t)	1.29 (2H, m)	22.5 (t)	1.30 (2H, m)	18.1 (t)	1.48 (m), 1.40 (m)	34.9 (t)	1.42 (2H, m)
12	14.0 (q)	0.87 (3H, t, 7.2)	14.0 (q)	0.86 (3H, t, 7.2)	14.0 (q)	0.88 (3H, t, 6.8)	13.9 (q)	0.92 (t, 7.2)	14.0 (q)	0.91 (3H, t, 7.2)
13	17.7 (q)	1.13 (3H, d, 6.4)	17.6 (q)	1.11 (3H, d, 6.4)	17.4 (q)	1.14 (3H, d, 6.4)	17.1 (q)	1.15 (3H, d, 6.8)	17.6 (q)	1.14 (3H, d, 6.8)
14					170.7 (s)					
15					21.3 (q)	2.01 (3H, s)				



bon signals are assigned to an ester carbonyl, a double bond, and an oxygenated methine carbon. The proton and carbon chemical shifts were assigned on the basis of analysis of  $^1\text{H}$  NMR,  $^{13}\text{C}$  NMR, DEPT, HMQC,  $^1\text{H}$ - $^1\text{H}$  COSY, and HMBC spectra and NOE data, as were those of the other compounds reported here. The  $^1\text{H}$ - $^1\text{H}$  COSY spectrum displays a coupled spin system, which fully supports the sequence of protons from C-2 to C-8 and the methyl at C-3. The location of the  $\gamma$ -lactone is apparent from the chemical shifts of H-2 and H-4 and confirmed by HMBC correlations from the protons at C-2 to the C-1 carbonyl. The *trans* relationship of the two substituents on the  $\gamma$ -lactone ring is concluded on the basis of NOE enhancements between H-4 and methyl-13. The double bond is assigned the *cis* geometry based on the coupling constant ( $J = 11.0$  Hz) between H-6 and H-7 and the large NOE enhancements between them. We therefore assign the structure *trans*-3-methyldodec-*cis*-6-en-4-olide to **3**.

The optically active, oily  $\gamma$ -lactone alcohol **4** was the major metabolite isolated from the extract **G**. Its IR spectrum supports the presence of hydroxyl ( $3443\text{ cm}^{-1}$ ) and lactone ( $1777\text{ cm}^{-1}$ ) functional groups. The  $^{13}\text{C}$  NMR and DEPT spectra are very similar to those of  $\gamma$ -lactone **3** but feature one additional oxygenated methine in place of one methylene carbon. The molecular formula,  $\text{C}_{13}\text{H}_{22}\text{O}_3$ , was deduced on the basis of NMR spectral data and supported by an HR-EI-MS (found:  $m/z = 226.1584$ ; calculated for  $\text{C}_{13}\text{H}_{22}\text{O}_3$ :  $226.1569$ ,  $[\text{M}^+]$ ) The  $^1\text{H}$ - $^1\text{H}$  COSY spectrum shows an extended coupled spin system, similar to that of compound **3**, supporting the C-2 to C-8 substitution pattern. The  $\gamma$ -lactone ring is established by comparing the  $^{13}\text{C}$  chemical shifts with those of compound **3** and confirmed in detail by HMBC correlations. The relative stereochemistry of the five-membered ring lactone was resolved by the NOE enhancements between the methine proton at H-4 and methyl-13. The *cis* geometry of the double bond was apparent from the NOE enhancements between the homo-allylic protons H-8 and H-5, and thus we conclude **4** is *trans*-8-hydroxy-3-methyldodec-*cis*-6-en-4-olide.

The IR spectrum of optically active oil **5** shows the presence of vinyl ( $1641\text{ cm}^{-1}$ ), ester ( $1729\text{ cm}^{-1}$ ), and lactone ( $1781\text{ cm}^{-1}$ ) functional groups. The  $^1\text{H}$  NMR spectrum is nearly identical to that of  $\gamma$ -lactone alcohol **4** except for the presence of an additional methyl singlet at  $\delta$  2.01 and the downfield shift of H-8, indicating the presence of an acetate group. The mass spectral data support a molecular formula of  $\text{C}_{15}\text{H}_{24}\text{O}_4$  and show a major fragment corresponding to  $[\text{M}^+ - \text{C}_2\text{H}_2\text{O}]$ , typical for acetates. The  $^1\text{H}$ - $^1\text{H}$  COSY spectrum displays an extended coupling sequence, attesting to the C-2 to C-8 substitution pattern, and the stereochemistry of the double bond and lactone ring substituents were resolved by NOE and coupling constant data as in the case of **3**. We therefore conclude that **5** is *trans*-8-acetoxy-3-methyldodec-*cis*-6-en-4-olide.

The IR spectrum of the optically active oil **6** indicates the presence of hydroxyl ( $3459\text{ cm}^{-1}$ ), vinyl ( $1632\text{ cm}^{-1}$ ), ketone ( $1713\text{ cm}^{-1}$ ), and lactone ( $1777\text{ cm}^{-1}$ ) functional groups. Its  $^{13}\text{C}$  NMR spectrum and DEPT spectra are similar to those of compound **3** but feature one more carbonyl in place of a methylene carbon. The molecular formula,  $\text{C}_{13}\text{H}_{20}\text{O}_4$ , was determined on the basis of NMR data. The HR-EI-MS spectrum did not show a molecular ion, but major fragments of

$[\text{M}^+ - \text{C}_4\text{H}_8\text{O}]$  and  $[\text{M}^+ - \text{C}_4\text{H}_9\text{O}]$  correspond to cleavage at the C-8 — C-9 bond. The  $^1\text{H}$ - $^1\text{H}$  COSY spectrum displays two distinct coupled spin systems,  $\text{CH}_3\text{CH}_2\text{CH}_2\text{CHO}$ - and  $-\text{CH}=\text{CHCH}_2\text{CHCH}(\text{Me})\text{CH}_2$ -, establishing the connectivity and substitution pattern in **6**. The coupling constant ( $J = 15.6$  Hz) for H-6/H-7 indicates a *trans* double bond, and HMBC correlations of H-6 and H-9 to C-8 and of H-2 and H-4 to C-1 complete the structural analysis, and we conclude that **6** is *trans*-9-hydroxy-3-methyl-8-oxo-dodec-*trans*-6-en-4-olide.

Compound **7** was isolated as an optically active, oily substance whose IR spectrum is nearly identical to that of  $\gamma$ -lactone **4** and indicates the presence of hydroxyl ( $3430\text{ cm}^{-1}$ ), vinyl ( $1630\text{ cm}^{-1}$ ), and lactone ( $1775\text{ cm}^{-1}$ ) functions. The  $^{13}\text{C}$  NMR and DEPT spectra display one additional oxygenated methine relative to **4**. The molecular formula was determined as  $\text{C}_{13}\text{H}_{22}\text{O}_4$  on the basis of MS and NMR data. The  $^1\text{H}$ - $^1\text{H}$  COSY spectrum revealed an extended spin-coupling system containing the sequence  $-\text{CH}_2\text{CHCHCH}=\text{CHCH}_2\text{CHCH}(\text{Me})\text{CH}_2$ -, and the coupling constant ( $J = 11.2\text{ Hz}$ ) for H-6/H-7 established the *cis* geometry of the double bond. Thus lactone **7** is *trans*-8,9-dihydroxy-3-methyldodec-*cis*-6-en-4-olide.

Compound **8** was isolated as an optically active, oily substance whose IR spectrum indicates the presence of hydroxyl ( $3474\text{ cm}^{-1}$ ), lactone ( $1777\text{ cm}^{-1}$ ), and carbonyl ( $1711\text{ cm}^{-1}$ ) functionalities. Its molecular formula was determined as  $\text{C}_{13}\text{H}_{22}\text{O}_4$  on the basis of NMR and HR-EI-MS data (Table 2). The  $^1\text{H}$ - $^1\text{H}$  COSY spectrum shows the two independent spin coupling systems  $\text{CH}_3\text{CH}_2\text{CH}_2\text{CHO}$ - and  $-\text{CH}_2\text{CH}_2\text{CH}_2\text{CHCH}(\text{Me})\text{CH}_2$ - in agreement with formulation **8**. The HMBC correlations of H-7 and H-9 with C-8 and H-2 and H-4 with C-1 and NOE enhancements between H-4 and Me-13 support the conclusion that **8** is *trans*-9-hydroxy-3-methyl-8-oxo-dodecan-4-olide.

The minor compound **9** was isolated as an optically active oil and its IR spectrum indicates the presence of hydroxyl ( $3417\text{ cm}^{-1}$ ) and carbonyl ( $1777$  and  $1757\text{ cm}^{-1}$ ) functional groups. The  $^{13}\text{C}$  NMR and DEPT spectra are similar to those of  $\gamma$ -lactone **8** but feature an additional oxygenated methine in place of a methylene. The molecular formula,  $\text{C}_{13}\text{H}_{22}\text{O}_5$ , is assigned based on spectral data, including an EI-MS fragmentation pattern paralleling that of **6** with loss of  $\text{C}_4\text{H}_9\text{O}$  from the molecular ion due to cleavage at the C-8 — C-9 bond. The placement of the second oxygenated methine at C-7 follows from the  $^1\text{H}$ - $^1\text{H}$  COSY spectrum, which affirms the presence of the  $-\text{CH}(\text{O})\text{CH}_2\text{CH}_2\text{CH}(\text{O})\text{CH}(\text{Me})\text{CH}_2$ - moiety. HMBC correlations and NOE data confirm our conclusion that **9** is *trans*-7,9-dihydroxy-3-methyl-8-oxo-dodecan-4-olide.

The IR spectrum of the optically active, oily  $\gamma$ -lactone **10** indicates the presence of hydroxyl ( $3471\text{ cm}^{-1}$ ) and carbonyl ( $1778$ ,  $1723\text{ cm}^{-1}$ ) groups. The  $^{13}\text{C}$  NMR and DEPT spectra show a total of 13 carbons, comprising two methyls, six methylenes, three methines, and two quaternary carbons. The composition,  $\text{C}_{13}\text{H}_{22}\text{O}_4$ , was ascertained from EI-MS and NMR data. The two discreet spin coupling systems,  $\text{CH}_3\text{CH}_2\text{CH}_2\text{CH}_2$ - and  $\text{CH}_2(\text{O})\text{CHCH}_2\text{CHCH}(\text{Me})\text{CH}_2$ -, are apparent from the  $^1\text{H}$ - $^1\text{H}$  COSY spectrum. Comparison of spectral data with those for the similar compounds **8** and **9** led us to conclude that **10** is *trans*-6-hydroxymethyl-3-



**Table 2.** NMR data (CDCl<sub>3</sub>) for lactones **8–10**.

Compound <b>8</b>			Compound <b>9</b>			Compound <b>10</b>		
Carbon	$\delta$	Proton ( <i>J</i> Hz)	$\delta$	Proton ( <i>J</i> Hz)		$\delta$	Proton ( <i>J</i> Hz)	
1	176.2 (s)		176.2 (s)			177.2 (s)		
2	36.9 (t)	2.65 (m, $\beta$ ), 2.16 (m, $\alpha$ )	37.0 (t)	2.67 (m, $\beta$ ), 2.19 (m, $\alpha$ )		36.9 (t)	2.65 (m, $\beta$ ), 2.18 (m, $\alpha$ )	
3	36.1 (d)	2.19 (m, $\beta$ )	36.4 (d)	2.20 (m, $\beta$ )		37.0 (d)	2.19 (m, $\beta$ )	
4	87.0 (d)	3.97 (ddd, $\alpha$ , 10.8, 8.8, 3.2)	86.9 (d)	3.98 (m, $\alpha$ )		85.2 (d)	3.87 (ddd, $\alpha$ , 10.0, 7.2, 2.0)	
5	33.2 (t)	1.76 (m), 1.56 (m)	29.9 (t)	1.96 (m), 1.69 (m)		32.8 (t)	2.24 (m), 1.59 (m)	
6	19.9 (t)	1.81 (m), 1.76 (m)	31.0 (t)	2.09 (m), 1.55 (m)		50.4 (d)	3.04 (m)	
7	37.2 (t)	2.53 (t, 7.2), 2.51 (t, 6.8)	73.3 (d)	4.43 (m)		213.3 (s)		
8	211.8 (s)		213.5 (s)			43.5 (t)	2.57 (dt, 17.2, 7.6), 2.53 (dt, 17.2, 7.2)	
9	76.2 (d)	4.15 (ddd, 8.0, 4.8, 4.4)	73.6 (d)	4.45 (m)		25.4 (t)	1.54 (2H, m)	
10	35.9 (t)	1.75 (m), 1.47 (m)	36.4 (t)	1.76 (m), 1.51 (m)		22.3 (t)	1.31 (2H, m)	
11	18.2 (t)	1.48 (m), 1.37 (m)	18.1 (t)	1.49 (m), 1.42 (m)		13.9 (q)	0.89 (3H, t, 7.3)	
12	13.9 (q)	0.93 (3H, t, 7.3)	13.8 (q)	0.96 (3H, t, 7.2)		64.0 (t)	3.81 (dd, 11.2, 4.8), 3.75 (dd, 11.2, 5.2)	
13	17.3 (q)	1.12 (3H, d, 6.3)	17.1 (q)	1.14 (3H, d, 6.4)		16.9 (q)	1.12 (3H, d, 6.2)	

methyl-8-oxo-undecane-4-olide. This conclusion is fully consistent with HMBC and NOE experiments.

Compound **11** was isolated as an optically active oil whose IR spectrum supports the presence of hydroxyl,  $\alpha,\beta$ -unsaturated carboxyl (3500–2500, 1694 cm<sup>-1</sup>), and vinyl (1647 cm<sup>-1</sup>) groups. The composition, C<sub>15</sub>H<sub>26</sub>O<sub>4</sub>, follows from NMR spectral data and an HR-EI-MS that lacks a molecular ion but features prominent ions corresponding to [M<sup>+</sup> – C<sub>3</sub>H<sub>7</sub>O] and [M<sup>+</sup> – C<sub>3</sub>H<sub>7</sub>O – H<sub>2</sub>O]. The <sup>13</sup>C NMR and DEPT data attest to the presence of four methyls, four methylenes, two *sp*<sup>2</sup> methines and one *sp*<sup>3</sup> methine, three fully substituted *sp*<sup>2</sup> carbons, and one quaternary carbon. The <sup>1</sup>H-<sup>1</sup>H COSY spectrum shows the two separate coupling spin systems =CHCH<sub>2</sub>CH<sub>2</sub>- and -CH(O)CH<sub>2</sub>CH<sub>2</sub>-. The connection of these and the remaining structural units is readily achieved by an examination of the HMBC correlations (Fig. 1). The strong NOE correlations of H-2 with H-4 and H-6 with H-8 indicate the *trans* stereochemistry of the double bonds, and we conclude that **11** is *trans,trans*-10,11-dihydroxyfarnesenic acid.

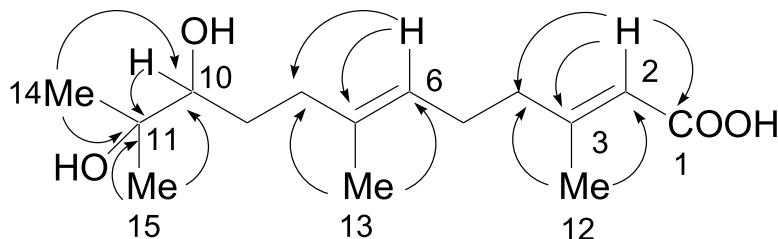
It should be noted that **11** is closely related to a *Cecropia* juvenile hormone (JHIII), methyl 10,11-epoxy-3,7,11-trimethyldodecanoate **15**, which profoundly affects metamorphoses of many insects and that **11** has been found to be a metabolic product of JHIII (13). The structure of this sesquiterpene was confirmed via synthesis. Farnesol was converted to farnesenic acid via a two-step oxidation by MnO<sub>2</sub> followed by NaClO<sub>2</sub>–NaH<sub>2</sub>PO<sub>4</sub>. The resulting acid was treated with *N*-bromosuccinimide, producing the corresponding 10,11-bromohydrin **12** in 74% isolated yield, which was then converted to the corresponding 10,11-epoxide **13**. Opening the epoxide ring under acidic conditions produced the racemic diol **11** in 46% yield from **12** plus the 11-membered lactone **14** in 36% yield from **12**. This lactone can be converted to the racemic diol **11** upon treatment with base.

The <sup>13</sup>C NMR data (Table 3) of compound **16** support the presence of five *sp*<sup>2</sup> carbons, two of which are protonated, together with two methyl, two methylene, and two oxygen-substituted methines. The <sup>1</sup>H-<sup>1</sup>H COSY spectrum attests to

the presence of an *n*-propyl group and the sequence CH<sub>3</sub>CH-CHCH- assigned to the side chains H-3', H-2', H-1' and H-8, H-7, H-6, H-5, respectively, in structure **16**. Furthermore, the signal for H-5 (5.34 ppm) shows a long-range coupling to the other vinylic proton H-3 ( $\delta$  7.37), while both of these show further couplings to the signal for H-1' ( $\delta$  2.31) consistent with their relationships in structure **16**. The placement of the lactone carbonyl follows from the HMBC correlations from H-1' and H-3 to C-1. The NOE difference spectrum displays significant correlations from H-3 to H-1' and H-5. The UV spectrum ( $\lambda_{\text{max}}$  = 272) is close to the calculated value ( $\lambda_{\text{max}}$  = 268) for this dienone chromophore. The HR-EI-MS showed an [M<sup>+</sup> – H<sub>2</sub>O] ion at *m/z* 194.0962 (calcd. 194.0943 for C<sub>11</sub>H<sub>14</sub>O<sub>3</sub>), which supports formulation **16**. Thus, we conclude compound **16** is 6,7-dihydroxy-2-propyl-octa-2,4-dien-4-olide. A conformational search of **16** (in acetone) revealed that four out of five of the lowest-energy conformations for the *threo* isomer displayed an H-6/H-7 dihedral angle near to 180°, whereas the *erythro* lowest-energy conformations favoured an H-5/H-6 dihedral angle near 70°, consistent with the observed coupling constant of 4.3 Hz. 2,4-Dien-4-olides have been reported from the gorgonians *Plexaura flava* (14) and *Euplexaura flava* (15) and from the liverwort *Marchantia paleacea* subsp. *diptera* (16) but not previously from a fungal source.

Compound **17** was isolated as an optically active, yellowish solid, and its molecular formula C<sub>11</sub>H<sub>10</sub>O<sub>6</sub> was determined by its HR-EI-MS molecular ion at *m/z* 238.0467 (calcd. 238.0477). The <sup>1</sup>H NMR spectrum of **17** (Table 4) closely resembles that of sescandelin **18** except for a signal corresponding to H-5. The <sup>13</sup>C NMR data attest to the presence of nine *sp*<sup>2</sup> carbons, two of which are protonated, plus a methine and a methyl group. There is a close correspondence in the chemical shift of signals for **17** assigned to C-1, C-3, C-4, C-8a, C-1', and C-2' and those of sescandelin **18** (6). The HMBC correlations of the signal at  $\delta$  11.47 with signals assigned to C-7, C-8, and C-8a establish the 5,6,8-substitution pattern of the aromatic ring, and correlations between the aromatic proton signal at  $\delta$  6.56 with signals assigned to C-5, C-6, C-8, and C-8a confirm this conclusion.



**Fig. 1.** Selected HMBC correlations for **11**.**Table 3.** NMR data (acetone- $d_6$ ) for compound **16**.

Carbon	$\delta$	Proton ( $J$ Hz)	HMBC (H to C)	NOE diff. (%)
1	170.8			
2	135.1			
3	138.7	7.37 (s)	C-1, C-4, C-1'	H-5 (3.1), H-1' (0.7), H-2' (1.0)
4	150.0			
5	114.0	5.34 (d, 9.0)	C-3, C-4, C-6, C-7	H-3 (4.0), H-6 (0.3), H-7 (0.8)
6	71.3	4.52 (dd, 9.1, 4.3)	C-4, C-7, C-8	H-5 (0.8), H-7 (1.1), H-8 (0.7)
7	71.0	3.83 (m)	C-5, C-6	H-5 (0.2), H-6 (1.9), H-8 (3.1)
8	19.0	1.09 (d, 6.7)	C-6, C-7	H-5 (0.5), H-6 (1.2), H-7 (1.7)
1'	27.9	2.31 (m)	C-1, C-2, C-3, C-2', C-3'	H-3 (0.8), H-2' (2.6)
2'	21.7	1.60 (m)	C-2, C-1', C-3'	H-3 (1.2), H-1' (2.1), H-3' (3.2)
3'	14.1	0.95 (t, 7.5)	C-1', C-2'	H-1' (0.8), H-2' (3.3)

**Table 4.** NMR data (acetone- $d_6$ ) for compound **17**.

Carbon	$\delta$	Proton ( $J$ Hz)	HMBC (H to C)	NOE diff. (%)
1	166.2			
3	140.1	7.36 (s)	C-1, C-4, C-1'	H-2' (0.7), H-1' (2.9)
4	119.5			
4a	119.6			
5	132.1			
6	155.9			
7	102.7	6.56 (s)	C-5, C-6, C-8, C-8a	
8	158.6			
8a	97.8			
1'	67.2	5.02 (q, 6.7)	C-3, C-4, C-2'	H-2' (4.0), H-3 (3.9)
2'	22.1	1.54 (d, 6.7)	C-4, C-1'	H-1' (1.1), H-3 (0.4)
8-OH		11.47 (s)	C-7, C-8, C-8a	
1'-OH		6.05 (bs) <sup>a</sup>		

<sup>a</sup>Measured in DMSO- $d_6$ .

The  $^{13}\text{C}$  NMR chemical shifts of C-4a, C-6, and C-8 in **17** are significantly downfield relative to the corresponding signals of sescandelin **18**, consistent with the presence of an hydroxyl at C-5. The absolute configuration of **17** is implied from the co-occurrence of *S*-(-)-6,8-dihydroxy-4-(1'-hydroxyethyl) isocoumarin **18** with the same sign of optical rotation. Isocoumarin derivatives are fairly common metabolites of plants, fungi, and insects and show a wide range of bioactivities (14). While 6,8-dihydroxylated variations are quite common, compound **17** is the first example of a 5,6,8-trihydroxyisocoumarin. Two 6,8-dihydroxy-5-methoxyisocoumarin derivatives have been reported from both *Aspergillus ustus* (17) and *Paecilmyces victoriae* (18).

Crude extracts and compounds **16–19** were tested for cytotoxicity against the spruce budworm (*C. fumiferana* Clem.) cell line CF-1 (9). Compound **16** was found to be

20–30% as toxic as the control, deoxynivalenol, while **17**, **18**, and **19** were individually weakly toxic. These findings may provide additional options for our ongoing development of insect resistance in conifers via inoculation of seedlings with toxin-producing endophytes (1).

## Experimental section

### General

High-resolution mass spectra (HR-EI-MS) were recorded on a Kratos MS-50 instrument. Optical rotations were measured on a PerkinElmer 241 polarimeter. Melting points were taken with a Kofler hot-stage apparatus and are uncorrected. The IR spectra were recorded as films on a Bruker IF-S25 spectrometer. UV spectra were determined on a PerkinElmer 330 spectrometer. Preparative thin layer chro-



matography (ptlc) was performed with precoated silica gel F<sub>254</sub> (1 mm) plates unless otherwise indicated. NMR data were recorded at room temperature in CDCl<sub>3</sub> (unless otherwise specified) on a Varian Unity 400 spectrometer operating at 399.944 MHz for <sup>1</sup>H and 100.575 MHz for <sup>13</sup>C. All 2D NMR were recorded non-spinning at 25°C using standard Varian software (VNMR 4.3).

### Fungal strain 5WS1111 (DAOM 221611)

The first fungal strain **5WS1111** was isolated from a white spruce (*P. glauca* (Moench) voss). This fungus was grown on 2% malt extract agar (MEA) in 250 mL Erlenmeyer flasks (2 L total) and Glaxo bottles (10 L total) according to the established protocols (6). There were no other changes in culturing procedures, and the fermentations proceeded simultaneously.

### Isolation of compounds 1–11

The culture filtrate, fermented in 250 mL Erlenmeyer flasks, was extracted with EtOAc (3 × 600 mL). The crude extract **E** (64.7 mg), obtained by removal of solvents under vacuum at room temperature, was purified on Kieselgel 60 F254 plates (1 mm) using CHCl<sub>3</sub>–MeOH (9:1). The fraction (23 mg, *R*<sub>f</sub> = 0.2–0.8) was further purified by ptlc using CHCl<sub>3</sub>–acetone (4:1) and yielded vermiculin **1** (1.7 mg) (Kieselgel 60 F254, 0.5 mm, *R*<sub>f</sub> = 0.70) and 7 $\alpha$ ,8 $\beta$ ,11-trihydroxydrimane **2** (3.4 mg) (Kieselgel 60 F254, 0.5 mm, *R*<sub>f</sub> = 0.11). The culture filtrate from the Glaxo bottles was extracted with EtOAc (3 × 3 L), and the total extract was evaporated to dryness at room temperature in vacuum to yield crude extract **G** (0.972 g). A portion of the crude extracts (0.800 g) was chromatographed on a silica column (Kieselgel 60G, 2.8 × 3.0 cm) and eluted with a discontinuous gradient of CHCl<sub>3</sub>–MeOH (1:0–0:1). The fractions (40 mL each) were combined on the basis of tlc scrutiny and further purified by repeated ptlc, yielding **3** (1.5 mg) (Baker Si-C18F, 0.20 mm, MeOH–H<sub>2</sub>O (4:1), *R*<sub>f</sub> = 0.22), **4** (40.0 mg) (Baker Si-C18F, 0.20 mm, acetone–H<sub>2</sub>O (3:2), *R*<sub>f</sub> = 0.43), **5** (2.5 mg) (0.25 mm, hexane–EtOAc (3:2), *R*<sub>f</sub> = 0.56), **6** (6.2 mg) (Baker Si-C18F, 0.20 mm, MeOH–H<sub>2</sub>O (7:3), *R*<sub>f</sub> = 0.62), **7** (6.3 mg) (Baker Si-C18F, 0.20 mm, MeOH–H<sub>2</sub>O (13:7), *R*<sub>f</sub> = 0.56), **8** (11.1 mg) (0.25 mm, CHCl<sub>3</sub>–acetone (17:3), *R*<sub>f</sub> = 0.62), **9** (5.7 mg) (Baker Si-C18F, 0.20 mm, acetone–H<sub>2</sub>O (3:2), *R*<sub>f</sub> = 0.69), and **10** (1.1 mg) (Baker Si-C18F, 0.20 mm, acetone–H<sub>2</sub>O (3:2), *R*<sub>f</sub> = 0.54), as well as sesquiterpenes **11** (12.0 mg), (0.25 mm, CHCl<sub>3</sub>–MeOH (9:1), *R*<sub>f</sub> = 0.47) and 7 $\alpha$ ,8 $\beta$ ,11-trihydroxydrimane **2** (4.0 mg) (Baker Si-C18F, 0.20 mm, MeOH–H<sub>2</sub>O (13:7), *R*<sub>f</sub> = 0.25).

### $\gamma$ -Lactone 3

An oil,  $[\alpha]_D^{25} = +25.3^\circ$  (CHCl<sub>3</sub>, 0.00075). IR (film, cm<sup>-1</sup>): 2959 (s), 1780 (s), 1640 (w), 1452 (m), 1382 (m), 1209 (s), 1157 (s), 940 (s), 748 (m). HR-EI-MS *m/z* (%): 210.1627 ([M<sup>+</sup>], 100) (calcd. for C<sub>13</sub>H<sub>22</sub>O<sub>2</sub>: 210.1620). EI-MS *m/z* (%): 210 (0.8), 209 (3.8), 166 (3.8), 149 (7.0), 99 (100), 96 (8.1), 81 (6.7), 71 (23.6).

### $\gamma$ -Lactone 4

An oil,  $[\alpha]_D^{25} = +47.7^\circ$  (CHCl<sub>3</sub>, 0.020). IR (film, cm<sup>-1</sup>): 3443 (br), 3020 (w), 2957 (s), 1777 (s), 1457 (s), 1210 (s),

1157 (s), 1007 (s), 920 (s), 733 (s). HR-EI-MS *m/z* (%): 226.1584 ([M<sup>+</sup>], 100) (calcd. for C<sub>13</sub>H<sub>22</sub>O<sub>3</sub>: 226.1569). EI-MS *m/z* (%): 226 ([M<sup>+</sup>], 9.0), 209 (13.6), 208 (8.8), 197 (11.1), 184 (46.3), 170 (18.7), 169 (75.6), 167 (15.0), 166 (35.8), 154 (24.7), 152 (55.7), 151 (100), 139 (66.1), 127 (40.3), 110 (83.3), 109 (85.7), 105 (54.0), 99 (98.1), 95 (77.6), 85 (72.9), 81 (70.9), 71 (75.1).

### $\gamma$ -Lactone 5

An oil,  $[\alpha]_D^{25} = +12.8^\circ$  (CHCl<sub>3</sub>, 0.0013). IR (film, cm<sup>-1</sup>): 2960 (s), 1781 (s), 1729 (s), 1641 (w), 1462 (m), 1370 (s), 1244 (s), 1014 (s), 943 (s), 747 (m), 668 (m). HR-EI-MS *m/z* (%): 226.1568 ([M<sup>+</sup> – CH<sub>2</sub>CO], 100) (calcd. for C<sub>13</sub>H<sub>22</sub>O<sub>3</sub>: 226.1569). EI-MS *m/z* (%): 226 (3.4), 225 (15.1), 208 (6.5), 207 (24.8), 168 (29.2), 165 (10.9), 150 (26.7), 138 (26.1), 110 (29.4), 99 (100), 81 (28.6), 71 (31.9).

### $\gamma$ -Lactone 6

An oil,  $[\alpha]_D^{25} = +105.8^\circ$  (CHCl<sub>3</sub>, 0.0031). IR (film, cm<sup>-1</sup>): 3459 (br), 2962 (s), 1777 (s), 1713 (s), 1632 (m), 1420 (m), 1384 (m), 1213 (s), 1158 (s), 1030 (m). HR-EI-MS *m/z* (%): 168.0776 ([M<sup>+</sup> – C<sub>4</sub>H<sub>8</sub>O], 5.0) (calcd. for C<sub>9</sub>H<sub>12</sub>O<sub>3</sub>: 168.0786), 167.0689 ([M<sup>+</sup> – C<sub>4</sub>H<sub>9</sub>O], 18.1) (calcd. for C<sub>9</sub>H<sub>11</sub>O<sub>3</sub>: 167.0708), 150 (31.0), 149 (20.1), 142 (13.0), 139 (73), 128 (23.6), 113 (16.1), 109 (30.4), 108 (26.9), 100 (19.9), 99 (100), 98 (12.1), 82 (91.6), 71 (82.7).

### $\gamma$ -Lactone 7

An oil,  $[\alpha]_D^{25} = +51.1^\circ$  (CHCl<sub>3</sub>, 0.0032). IR (film, cm<sup>-1</sup>): 3430 (br), 2959 (s), 1775 (s), 1630 (w), 1458 (m), 1211 (s), 1014 (s), 942 (m), 749 (m). EI-MS *m/z* (%): 242 ([M<sup>+</sup>], 0.4), 224 ([M<sup>+</sup> – H<sub>2</sub>O], 0.7), 206 ([M<sup>+</sup> – 2H<sub>2</sub>O], 6.5), 171 (9.6), 170 (15.5), 152 (51.8), 110 (63.2), 99 (47.2), 83 (100), 82 (16.1), 71 (43).

### $\gamma$ -Lactone 8

An oil,  $[\alpha]_D^{25} = +45.6^\circ$  (CHCl<sub>3</sub>, 0.0056). IR (film, cm<sup>-1</sup>): 3474 (br), 2960 (s), 1777 (s), 1711 (s), 1462 (m), 1368 (m), 1291 (m), 1214 (s), 1029 (s), 938 (s), 668 (s). HR-EI-MS *m/z* (%): 241.1410 ([M<sup>+</sup> – H], 6.8) (calcd. for C<sub>13</sub>H<sub>21</sub>O<sub>4</sub>: 241.1440), 226.1550 ([M<sup>+</sup> + H – OH], 20.2) (calcd. for C<sub>13</sub>H<sub>22</sub>O<sub>3</sub>: 226.1569), 225.1468 ([M<sup>+</sup> – OH], 22.8) (calcd. for C<sub>13</sub>H<sub>21</sub>O<sub>3</sub>: 225.1491), 224.1391 ([M<sup>+</sup> – H<sub>2</sub>O], 9.9) (calcd. for C<sub>13</sub>H<sub>20</sub>O<sub>3</sub>: 224.1412), 209 (23.5), 208 (12.2), 193 (16.3), 171 (16.4), 169 (31.5), 153 (22.2), 151 (30.5), 143 (30.7), 105 (28.9), 99 (79.4), 82 (51.8), 71 (38.4).

### $\gamma$ -Lactone 9

An oil,  $[\alpha]_D^{25} = +51.6^\circ$  (CHCl<sub>3</sub>, 0.0029). IR (film, cm<sup>-1</sup>): 3417 (br), 2961 (s), 1777 (s), 1757 (s), 1454 (m), 1383 (m), 1217 (m), 1078 (s), 983 (m). EI-MS *m/z* (%): 257 ([M<sup>+</sup> – H], 3.5), 256 ([M<sup>+</sup> – 2H], 4.5), 240 ([M<sup>+</sup> – H<sub>2</sub>O], 2.5), 186 ([M<sup>+</sup> – C<sub>4</sub>H<sub>8</sub>O], 6.5), 185 ([M<sup>+</sup> – C<sub>4</sub>H<sub>9</sub>O], 3.5), 169 (18.5), 155 (15.0), 139 (26.5), 110 (45.0), 99 (49.50), 97 (64.6), 83 (65.6), 69 (98.2), 55 (100).

### $\gamma$ -Lactone 10

An oil,  $[\alpha]_D^{25} = +65.5^\circ$  (CHCl<sub>3</sub>, 0.0006). IR (film, cm<sup>-1</sup>): 3471 (br), 2958 (s), 1778 (s), 1723 (s), 1462 (m), 1382 (m), 1215 (s), 1158 (s), 1035 (s), 940 (m), 668 (m). EI-MS *m/z* (%): 242 (2.8), 224 (4.9), 208 (14.6), 166 (10.2), 150 (25.9),



148 (13.1), 138 (10.6), 137 (13.1), 99 (100), 85 (22.4), 69 (41.6), 57 (29.4).

### Sesquiterpene 11

An oil,  $[\alpha]_D = +11.8^\circ$  ( $\text{CHCl}_3$ , 0.0039). IR (film,  $\text{cm}^{-1}$ ): 3391 (br, s), 2927 (s), 1694 (s), 1647 (s), 1381 (m), 1077 (m). HR-EI-MS  $m/z$  (%): 234.1636 ( $[\text{M}^+ - 2\text{H}_2\text{O}]$ , 3.5) (calcd. for  $\text{C}_{15}\text{H}_{22}\text{O}_2$ : 234.1612), 211.1359 ( $[\text{M}^+ - \text{C}_3\text{H}_7\text{O}]$ , 19.5) (calcd. for  $\text{C}_{12}\text{H}_{19}\text{O}_3$ : 211.1334), 206 (2.1), 194 (9.5), 193 (42.1), 163 (21.9), 143 (58.1), 123 (28.9), 100 (40.3), 93 (33.5), 81 (76.2), 59 (100).

### Synthesis of sesquiterpene 11

To a solution of 10-bromo-11-hydroxy-farnesyllic acid **12** (0.220 g, 0.660 mmole) in DMF- $\text{H}_2\text{O}$  (3:1) (12.5 mL), NaOH (0.055 g, 1.38 mmole) was added, and the solution was stirred at room temperature for 1.5 h before quenching with 0.01 M HCl. The mixture was extracted with  $\text{CHCl}_3$  ( $3 \times 10.0$  mL) and combined extracts washed with brine (15 mL) and evaporated at room temperature under vacuum to yield the crude epoxide **13** (0.197 g), which was dissolved in DMF- $\text{H}_2\text{O}$  (3:1) (12.5 mL), and *p*-toluenesulfonic acid (0.006 g, 0.003 mmole) was added. The solution was stirred for 2 h before addition of brine (10.0 mL). The mixture was extracted with  $\text{CHCl}_3$  ( $3 \times 10.0$  mL), and the combined extracts were washed with brine and evaporated under vacuum to give a crude mixture, which was purified by column to give sesquiterpene **11** (0.083 g, 46% from **12**) and the lactone **14** (0.060 g, 36% from **12**).

### Lactone 14

An oil. IR (film,  $\text{cm}^{-1}$ ): 3420 (s, br), 2972 (s), 1720 (s), 1640 (s), 1440 (s), 1376 (m), 1172 (s).  $^1\text{H}$  NMR ( $\text{CDCl}_3$ , ppm)  $\delta$ : 5.69 (s), 5.08 (m), 4.83 (dd), 2.20 (m, 4H), 2.15 (s, 3H), 2.05–1.90 (m, 2H), 1.80–1.6 (m, 2H), 1.58 (s, 3H), 1.20 (s, 6H).  $^{13}\text{C}$  NMR ( $\text{CDCl}_3$ , ppm)  $\delta$ : 162.64 (C), 161.23 (C), 134.98 (C), 123.89 (CH), 115.07 (CH), 79.56 (CH), 72.24 (C), 40.92 ( $\text{CH}_2$ ), 35.88 ( $\text{CH}_2$ ), 27.64 ( $\text{CH}_2$ ), 26.52 ( $\text{CH}_3$ ), 25.76 ( $\text{CH}_3$ ), 25.76 ( $\text{CH}_3$ ), 24.85 ( $\text{CH}_3$ ), 19.09 ( $\text{CH}_3$ ), 15.93 ( $\text{CH}_3$ ). EI-MS  $m/z$  (%): 252 ( $[\text{M}^+]$ , 4.5), 211 (28.7), 193 (62.9), 163 (37.64), 143 (100), 135 (65.4), 125 (53.1), 100 (52.4).

### Larval bioassays

Compounds **4**, **6**, **7**, **8**, **11**, and 7 $\alpha$ ,8 $\beta$ ,11-trihydroxydri-mane **2** were subjected to a budworm larval feeding bioassay according to established protocol (2) at a concentration of 0.0004 g g $^{-1}$  of diet, resulting in mortalities of 60, 76, 68, 72, 52, and 72% relative to control (42% mortality).

### Fungal strain 5WS26H1 (DAOM 229664)

Strains were transferred to slants containing 2% malt extract agar (Difco) and incubated at 20°C for at least one month. For each fermentation, the slant was macerated in sterile water (30 mL). An aliquot (2.5 mL) was used to inoculate each of six Erlenmeyer flasks (250 mL) containing 50 mL of medium (CZ Met) made from glucose (20 g),  $\text{NH}_4\text{Cl}$  (3 g),  $\text{KH}_2\text{PO}_4$  (2 g),  $\text{MgSO}_4$  (2g),  $\text{FeSO}_4 \cdot 7\text{H}_2\text{O}$  (0.2 g), yeast extract (2 g), malt extract (2 g), and peptone (2 g) per L of water. The flasks were put on a rotary shaker (3.81 cm throw) at 220 rpm at 20°C for 48 h in the dark.

The culture was then macerated, and 50 mL was used to inoculate three Glaxo bottles containing CZ Met medium (1 L) and three Glaxo bottles containing 2% malt extract medium (1 L). These were incubated at 20°C for 6 weeks. After incubation, each Glaxo bottle was filtered under vacuum through Whatman #1 filter paper and extracted with three portions of ethyl acetate (200 mL). The combined extract was dried with anhydrous sodium sulfate, filtered, and concentrated under vacuum at room temperature. The extracts were transferred into a pre-weighed vial using a small amount of ethyl acetate, which was then evaporated under nitrogen. Compounds **16–20** were variably isolated from a series of white spruce and black spruce strains, but all were produced by DAOM 229664 in CZ met medium incubated under the conditions described. This isolate and DAOM 221611 have been deposited in the Canadian Collection of Fungal Cultures (DAOM, Agriculture Agri-food Canada, Ottawa, ON K1A 0C6). They are preserved in liquid nitrogen.

### Isolation of compounds 16–20

Endophyte crude extract 5WS19B2-AMSF OCT 22/98 (73.8 mg) was fractionated by ptlc (two plates) using  $\text{CHCl}_3$ - $\text{C}_6\text{H}_{12}$ - $\text{CH}_3\text{OH}$  (7:2:1). Seven fractions A–G (in order of increasing polarity) were collected. Fraction E (20.8 mg,  $R_f$  0.34 to 0.40) was purified by ptlc using  $\text{C}_6\text{H}_6$ - $\text{CH}_3\text{COCH}_3$  (4:1) to afford pure compound **16** (0.65 mg,  $R_f$  0.51) and pure compound **17** (7.1 mg,  $R_f$  0.56). Fraction F (21.2 mg,  $R_f$  0.32) was purified by ptlc using  $\text{C}_6\text{H}_6$ - $\text{CH}_3\text{COCH}_3$  to afford compound **19** (5.5 mg,  $R_f$  0.20). Endophyte crude extracts 5BS21B1-ACZGF, 5BS21B1-BCZGF, and 5BS21B1-CCZGF NOV 30/98 were combined (257.3 mg) and fractionated by ptlc (six plates) using  $\text{CHCl}_3$ - $\text{C}_6\text{H}_{12}$ - $\text{CH}_3\text{OH}$  (7:2:1). Five fractions A–E (in order of increasing polarity) were collected. Fraction D (58.1 mg) was purified by ptlc with  $\text{CH}_3\text{COOC}_2\text{H}_5$ - $\text{C}_6\text{H}_{12}$  (4:1) to give two major fractions, one containing **18** (8.8 mg) and the other a mixture of **19** and **16** (8.4 mg). Compound **18** was further purified by ptlc with  $\text{CH}_3\text{COOC}_2\text{H}_5$ - $\text{C}_6\text{H}_{12}$  (3:2), (5.5 mg,  $R_f$  0.52). Further purification of the mixture by ptlc with  $\text{CHCl}_3$ - $\text{C}_6\text{H}_{12}$ - $\text{CH}_3\text{OH}$  (15:5:1) gave **19** (1.6 mg,  $R_f$  0.38) and **16** (2.7 mg,  $R_f$  0.42). Crude extract 5WS14G1-ACZGF NOV 10/98 (34.7 mg) was fractionated by ptlc (0.5 mm, two plates) using  $\text{CHCl}_3$ - $\text{C}_6\text{H}_{12}$ - $\text{CH}_3\text{OH}$  (7:2:1). The major fraction (8.1 mg) was further purified by ptlc using  $\text{CH}_3\text{COOC}_2\text{H}_5$ - $\text{C}_6\text{H}_{12}$  (4:1) to give pure compound **20** (3.1 mg,  $R_f$  0.30).

### 6,7-Dihydroxy-2-propyl-2,4-octadien-4-olide 16

A pale yellow oil;  $[\alpha]_D = +17.1^\circ$  (c 0.0021, MeOH). UV (EtOH)  $\lambda_{\text{max}}$  (nm) ( $\epsilon$ ): 272 (8600). HR-EI-MS  $m/z$  (%): 194.0962 ( $[\text{M}^+ - \text{H}_2\text{O}]$ , 1.6) (calcd. for  $\text{C}_{11}\text{H}_{14}\text{O}_3$ : 194.0943), 168 (100), 152 (11.6), 43 (29.8). See Table 3 for spectral data.

### 5,6,8-Trihydroxy-4-(1'-hydroxyethyl) isocoumarin 17

A yellow solid; mp 150–155°C;  $[\alpha]_D = -13.1^\circ$  (c 0.007,  $\text{CH}_3\text{COCH}_3$ ). UV (EtOH)  $\lambda_{\text{max}}$  (nm) ( $\epsilon$ ): 204 (8320), 238 (12 500), 252 (10 730), 272 (9820), 348 (9120). HR-EI-MS  $m/z$  (%): 238.0467 ( $[\text{M}^+]$ , 10.8) (calcd. for  $\text{C}_{11}\text{H}_{10}\text{O}_6$ : 238.0477), 220 ( $[\text{M}^+ - \text{H}_2\text{O}]$ , 100), 205 (36.9), 43 (16). See Table 4 for spectral data.



#### 4-Hydroxy-2-methoxyacetanilide 20

A yellow amorphous solid; mp 166–169°C (synthetic) 169–171°C.  $^1\text{H}$  NMR ( $\text{CD}_3\text{OD}$ , 400 MHz)  $\delta$ : 8.57, 7.53 (1H, br s, 4-OH and 1H, s, NH measured in  $\text{CDCl}_3$  + 5 drops of  $\text{DMSO}-d_6$ ), 7.48 (1H, d,  $J$  = 8.0 Hz, H-6), 6.45 (1H, d,  $J$  = 2.4, 9.6, H-5), 3.81 (1H, s,  $\text{OCH}_3$ ), 2.1 (1H, s,  $\text{CH}_3$ ).  $^{13}\text{C}$  NMR ( $\text{CD}_3\text{OD}$ , MHz)  $\delta$ : 170.4 (C=O), 155.6 (C-4), 152.4 (C-2), 124.5 (C-6), 118.3 (C-1), 105.9 (C-5), 98.7 (C-3), 54.6 ( $\text{OCH}_3$ ), 21.9 ( $\text{CH}_3$ ). HR-EI-MS  $m/z$  (%): 181.0740 ( $[\text{M}^+]$ , 60) (calcd. for  $\text{C}_9\text{H}_{11}\text{NO}_3$ : 181.0739), 139 (70), 124 (100).

#### Cell line assays

The spruce budworm cell line CF-1 was used according to the method of Clark et al. (9) to screen extracts and purified compounds for cytotoxicity. Deoxynivalenol ( $2\text{ }\mu\text{g mL}^{-1}$ , cell culture medium) was used as the positive control and ethanol ( $2\text{ }\mu\text{L mL}^{-1}$ ) as the negative control; no effect of ethanol on the CF-1 cells was detected at this concentration. Crude extracts were dissolved in ethanol and tested at 1, 2, and  $4\text{ }\mu\text{L mL}^{-1}$  culture medium. The crude extract arising from the non-sporulating strain 5WS26H1 (DAOM 229664) was as cytotoxic as the positive control solution. Compounds **16**–**19** were individually dissolved in ethanol and tested at  $2\text{ }\mu\text{g mL}^{-1}$  culture medium as above. Compound **17**, sescandelin **18**, and sescandelin B **19** were individually weakly cytotoxic. Compound **16** was ca. 20–30% as cytotoxic to CF-1 as deoxynivalenol at  $2\text{ }\mu\text{L mL}^{-1}$  culture medium.

#### Acknowledgments

Thanks are owing to the Natural Sciences and Engineering Research Council of Canada (NSERC), the Forestry Canada Green Plan (Research Network for the Discovery and Development of Natural Products for Integrated Forest Pest Management), the Industrial Research Assistance Program (IRAP) of the National Research Council of Canada (NRC), and JD Irving Ltd. Technical assistance was provided by Don Belilse, Kristina Bramwell, Regina de la Campa, Mark Foto, and Sabrena MacKenzie. The cell line

CF1 was a gift from Guido Caputo, Canadian Forestry Service, Sault Ste. Marie, Ontario, Canada. Thanks are also owing to Ghislain Deslongchamps for the Merck MMF 94 conformational search and to John A. Johnson for providing the larval bioassays.

#### References

1. J.D. Miller, S. Mackenzie, M. Foto, G.W. Adams, and J.A. Findlay. *Mycol. Res.* **106**(4), 471 (2002).
2. L.A. Calhoun, J.A. Findlay, J.D. Miller, and N.J. Whitney. *Mycol. Res.* **96**, 281 (1992).
3. G.C. Carroll and F.E. Carroll. *Can. J. Bot.* **56**, 3034 (1978).
4. P. Sedmera, J. Vokoun, M. Podojil, Z. Vanek, J. Fuska, P. Nemec, and I. Kuhr. *Tetrahedron Lett.* 1348 (1973).
5. D.M.X. Donnelly, J. Reilly, A. Chiaroni, and J. Polonski. *J. Chem. Soc. Perkin Trans. 1*, 2196 (1986).
6. Y. Kimura, H. Nakajima, and T. Hamasaki. *Agric. Biol. Chem.* **54**, 2477 (1990).
7. Y. Kimura, M. Nakadoi, H. Nakajima, T. Hamasaki, T. Nagai, K. Kohmoto, and A. Shimada. *Agric. Biol. Chem.* **55**, 1887 (1991).
8. Y. Zhang, T. Wang, Y. Pei, H. Hua, and B. Feng. *J. Chin. Pharm. Sci.* **10**(4), 190 (2001).
9. C.L. Clark, J.D. Miller, and N.J. Whitney. *Mycol. Res.* **93** (4), 508 (1989).
10. D. Jones and M.J. Wilson. *Trans. Br. Mycol. Soc.* **88** (2), 257 (1987).
11. S. Tahara, K. Fujiwara, H. Ishikaza, J. Mizutani, and Y. Obata. *Agric. Biol. Chem.* **36**, 2585 (1972).
12. S. Tahara, K. Fujiwara, and J. Mizutani. *Agric. Biol. Chem.* **37**, 2855 (1973).
13. A.F. White. *Life Sci.* **11**(4), (1972).
14. M. Inayat-Ur-Rahman, M. Arfan, and G.U.J. Khan. *J. Chem. Soc. Pak.* **20**, 76 (1998).
15. H. Kikuchi, Y. Tsukitani, H. Nakanishi, I. Shimizu, S. Saitoh, K. Iguchi, and Y. Yamada. *Chem. Pharm. Bull.* **31**, 1172 (1983).
16. M. Toyota, K. Mutsumi, N. Fumihito, H. Shitzu, and A. Yoshinori. *Phytochemistry*, **46**, 293 (1997).
17. H. Raistrick and C.E. Stickings. *Biochem. J.* **48**, 53 (1951).
18. V.C. Vora. *J. Sci. Ind. Res.* **13b**, 842 (1954).



# Convenient, tandem and one-reaction vessel synthesis of mixed dialkylated 2-naphthols from 2-tetralone

Amitabh Jha and Jonathan R. Dimmock

**Abstract:** A convenient acid-catalyzed method for the synthesis of 1-alkyl-2-alkoxynaphthalenes by one-reaction vessel mixed alkylation of 2-tetralone, using aryl or alkyl aldehydes and alcohols followed by aromatization, is described.

**Key words:** ethers, aromatization, rearrangement, alkylation, 2-alkoxynaphthalenes.

**Résumé :** On décrit une méthode pratique de synthèse acidocatalysée des 1-alkyl-2-alkoxynaphthalènes impliquant une réaction monotope d'alkylation mixte de la 2-tétralone à l'aide d'alcools et d'aldéhydes aliphatiques ou aromatiques suivie d'une aromatisation.

**Mots clés :** éthers, aromatisation, réarrangement, alkylation, 2-alkoxynaphthalènes.

## Introduction

A variety of methods are known for the synthesis of 2-alkoxy-1-arylmethylnaphthalenes (**1**, R = aryl), including the reduction of 1-(2-alkoxynaphthyl) aryl ketones (**1**) or the reduction of 1-(2-alkoxynaphthyl) aryl carbinols (**2**), Pd(II)-catalyzed C—C bond formation among 2-alkoxy-1-halonaphthalenes and substituted toluenes (**3**), and other procedures that are cumbersome (**4**, **5**). The C-1 alkylation and etherification of 2-naphthol using dialkyl sulfates leading to 2-alkoxy-1-alkylnaphthalenes (**1**, R = H, R' = CH<sub>3</sub>; R = CH<sub>3</sub>, R' = C<sub>2</sub>H<sub>5</sub>) is known (**6**). This procedure has at least two limitations: (i) the synthesis of the corresponding mixed dialkyl derivatives is not possible; and (ii) the unavailability of dialkyl sulfates limits the wider utility of this procedure. Another compound belonging to this class, namely 1-butyl-2-methoxynaphthylene (**1**, R = *n*-C<sub>3</sub>H<sub>7</sub>, R' = CH<sub>3</sub>), was made by a very lengthy and unwieldy procedure (**7**).

2-Alkoxy-1-arylmethylnaphthalenes (**1**, R = aryl, R' = alkyl) may also be obtained by the etherification of the corresponding 1-arylmethyl-2-naphthols (**1**, R = aryl, R' = H), for which a number of methods are known. These include a Fries-type rearrangement of 2-benzyloxynaphthalene (**8**), a base-catalyzed reaction between benzyl chloride or benzyl alcohol and 2-naphthol (**9–12**), as well as Zn-catalyzed transfer of a benzyl group from various benzyl aryl ethers to

2-naphthol (**8**). Some of these reactions yield side products (**5**, **8**, **9**, **11**).

Recently this research group reported a novel synthetic route to this class of compounds, which involved two simple reaction steps (**13**). 1-Arylmethylene-2-tetralones (**A**, R = aryl) (**14**) were converted to 2-alkoxy-1-arylmethylnaphthalenes (**1**, R = aryl, R' = alkyl) under anhydrous acidic conditions in common alcohols and the yields were generally satisfactory (**13**). As the synthesis of 1-arylmethylene-2-tetralones (**A**, R = aryl) can be carried out under anhydrous acidic conditions (**13–15**) and the subsequent reactions yielding the title compounds were also carried out under anhydrous acidic conditions (**13**), we thought that it should be possible to carry out these two reactions in the same pot, without isolating the corresponding intermediate 1-arylmethylene-2-tetralones (**A**, R = aryl). It was also realized that the success of this three-component reaction would depend on the sequence of occurrence of the two competing reactions, viz. condensation of the aldehyde group with the active methylene of 2-tetralone and the vinyl ether formation between the alcohol and the enolic form of 2-tetralone based on the reaction mechanism described previously (**13**) (and later in this paper). This could easily be verified by performing the reactions.

The formation of 2-alkoxy-1-alkylnaphthalenes **1a–1i** (Fig. 1) from a mixture of 2-tetralone, aryl or alkyl aldehydes, and an absolute alcohol under anhydrous acidic conditions (Scheme 1) is reported herein.

## Experimental section

### General

2-Tetralone and the substituted aldehydes were obtained from Aldrich Chemical Co. Column chromatography purifications were undertaken using silica gel (60–230 mesh) obtained from Aldrich Chemical Co. Hydrogen chloride gas was freshly generated in the laboratory by the action of con-

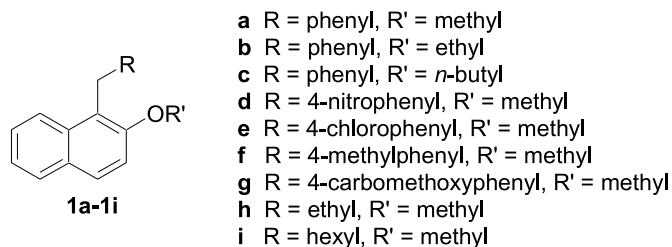
Received 18 November 2002. Published on the NRC Research Press Web site at <http://canjchem.nrc.ca> on 2 May 2003.

**A. Jha<sup>1,2</sup> and J.R. Dimmock.** College of Pharmacy and Nutrition, University of Saskatchewan, Saskatoon, SK S7N 5C9 Canada.

<sup>1</sup>Corresponding author (e-mail: [amitabh.jha@acadiau.ca](mailto:amitabh.jha@acadiau.ca)).

<sup>2</sup>Present address: Department of Chemistry, Acadia University, Wolfville, NS B4P 2R6, Canada.



**Fig. 1.** Chemical structures of compounds **1a–1i**.

concentrated sulfuric acid on the mixture of sodium chloride in concentrated hydrochloric acid in an appropriate apparatus.  $^1\text{H}$  NMR spectra were recorded on a Bruker AMX 300 NMR spectrometer at 300 MHz and HR-MS spectra were obtained on VG-Analytical (Manchester, U.K.) VG-70 SEQ spectrometer. Melting points were recorded on an electrothermal apparatus and are uncorrected.

### Syntheses of 2-alkoxy-1-alkylnaphthalenes (**1a–1i**)

#### General procedure

A mixture of 2-tetralone (3 mmol) and an appropriate aldehyde (3 mmol) in absolute alcohol (10 mL) was cooled by an ice bath to 0–5°C. Under anhydrous conditions, freshly generated dry hydrogen chloride gas was passed briskly through the solution for 20 min. The reaction mixture was stirred at room temperature for 24 h. Thin layer chromatography using precoated fluorescent silica gel and a developing solvent of hexane:chloroform (1:4) showed the formation of a faster moving product. The reaction mixture was evaporated to dryness under vacuum. Products (**1a–1c**, **1e**, **1f**, **1h**, **1i**) were purified using a silica gel (230–400 mesh) column with hexane as the eluent. Compounds **1d** and **1g** were obtained as solid powders from the reaction and were quite pure after filtration as viewed on TLC.

#### 2-Methoxy-1-phenylmethylnaphthalene (**1a**)

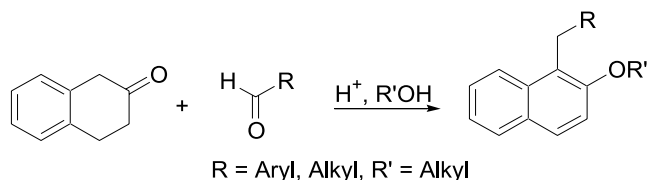
White crystalline solid (yield: 76%).  $R_f$  = 0.59 (10% EtOAc – hexane), mp 91 to 92°C (Lit. value (1) 81 to 82°C).  $^1\text{H}$  NMR (300 MHz,  $\text{CDCl}_3$ )  $\delta$ : 3.95 (3H, s,  $-\text{OCH}_3$ ), 4.50 (2H, s,  $\text{Ar}-\text{CH}_2-\text{Ar}'$ ), 7.10–7.22 (5H, m,  $\text{Ar}'\text{-Hs}$ ), 7.30–7.36 (2H, m, H-3, 6), 7.38–7.42 (1H, m, H-7), 7.79–7.82 (2H, m, H-4, 5), 7.91 (1H, d,  $J$  = 8.6 Hz, H-8). HR-MS calcd. for  $\text{C}_{18}\text{H}_{16}\text{O}$ : 248.1201; found: 248.1196. EI-MS (70 eV)  $m/z$  (% int.): 248 (100), 233 (16), 215 (39), 202 (24), 171 (21), 141 (17), 91 (14).

#### 2-Ethoxy-1-phenylmethylnaphthalene (**1b**)

White crystalline solid (yield: 71%).  $R_f$  = 0.67 (10% EtOAc – hexane), mp 74–76°C.  $^1\text{H}$  NMR (300 MHz,  $\text{CDCl}_3$ )  $\delta$ : 1.40 (3H, t,  $J$  = 7.0 Hz,  $\text{CH}_3$ ), 4.17 (2H, q,  $J$  = 7.0 Hz,  $\text{OCH}_2$ ), 4.49 (2H, s,  $\text{Ar}-\text{CH}_2-\text{Ar}'$ ), 7.10–7.21 (5H, m,  $\text{Ar}'\text{-Hs}$ ), 7.29–7.34 (2H, m, H-3, 6), 7.38–7.41 (1H, m, H-7), 7.75–7.80 (2H, m, H-4, 5), 7.92 (1H, d,  $J$  = 8.4 Hz, H-8). HR-MS calcd. for  $\text{C}_{19}\text{H}_{18}\text{O}$ : 262.1357; found: 262.1354. EI-MS (70 eV)  $m/z$  (% int.): 262 (100), 233 (44), 215 (34), 156 (19), 128 (21), 91 (31).

#### 2-Butoxy-1-phenylmethylnaphthalene (**1c**)

White crystalline solid (yield: 76%).  $R_f$  = 0.78 (10% EtOAc – hexane), mp 30–32°C.  $^1\text{H}$  NMR (300 MHz,

**Scheme 1.**

$\text{CDCl}_3$ )  $\delta$ : 0.95 (3H, t,  $J$  = 7.4 Hz,  $\text{CH}_2\text{CH}_3$ ), 1.44–1.54 (2H, m,  $\text{CH}_2$ ), 1.73–1.82 (2H, m,  $\text{CH}_2$ ), 4.11 (2H, t,  $J$  = 6.4 Hz,  $\text{OCH}_2$ ), 4.50 (2H, s,  $\text{Ar}-\text{CH}_2-\text{Ar}'$ ), 7.10–7.22 (5H, m,  $\text{Ar}'\text{-Hs}$ ), 7.30–7.34 (2H, m, H-3, 6), 7.38–7.42 (1H, m, H-7), 7.76–7.80 (2H, m, H-4, 5), 7.93 (1H, d,  $J$  = 8.5 Hz, H-8). HR-MS calcd. for  $\text{C}_{21}\text{H}_{22}\text{O}$ : 290.1670; found: 290.1677. EI-MS (70 eV)  $m/z$  (% int.): 290 (100), 234 (89), 215 (36), 202 (30), 156 (29), 128 (24), 91 (47).

#### 2-Methoxy-1-(4-nitrophenylmethyl)naphthalene (**1d**)

White solid (yield: 87%).  $R_f$  = 0.41 (10% EtOAc – hexane), mp 103–105°C (Lit. value (3) 106–108°C).  $^1\text{H}$  NMR data was found to be identical to that of the literature report (3). HR-MS calcd. for  $\text{C}_{18}\text{H}_{15}\text{NO}_3$ : 293.1052; found: 293.1058. EI-MS (70 eV)  $m/z$  (% int.): 293 (100), 278 (6), 262 (7), 231 (18), 215 (29), 202 (28), 171 (24), 141 (21), 128 (12), 101 (9).

#### 1-(4-Chlorophenylmethyl)-2-methoxynaphthalene (**1e**)

White crystalline solid (yield: 92%).  $R_f$  = 0.49 (10% EtOAc – hexane), mp 51 to 52°C.  $^1\text{H}$  NMR (300 MHz,  $\text{CDCl}_3$ )  $\delta$ : 3.94 (3H, s,  $\text{OCH}_3$ ), 4.44 (2H, s,  $\text{Ar}-\text{CH}_2-\text{Ar}'$ ), 7.10 (2H, d,  $J$  = 8.6 Hz, H-2', 6'), 7.16 (2H, d,  $J$  = 8.6 Hz, H-3', 5'), 7.32–7.36 (2H, m, H-3, 6), 7.39–7.47 (1H, m, H-7), 7.79–7.87 (3H, m, H-4, 5, 8). HR-MS calcd. for  $\text{C}_{18}\text{H}_{15}\text{ClO}$ : 282.0811; found: 282.0820. EI-MS (70 eV)  $m/z$  (% int.): 282 (100), 267 (13), 251 (20), 231 (26), 215 (49), 202 (31), 171 (29), 141 (20), 125 (18), 115 (14), 101 (17).

#### 2-Methoxy-1-(4-methylphenylmethyl)naphthalene (**1f**)

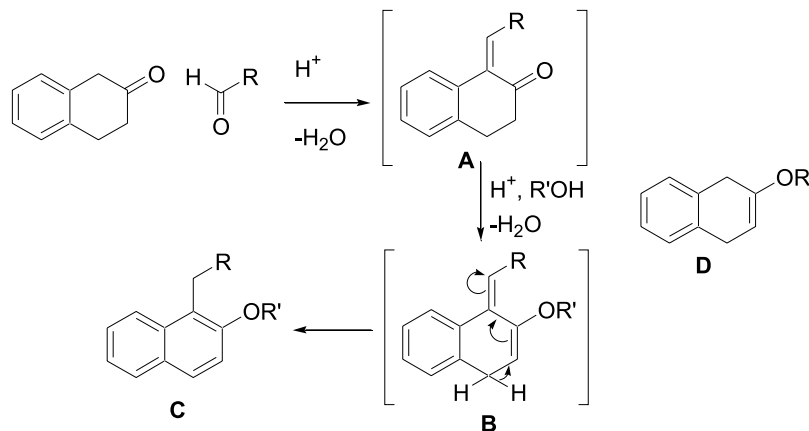
White crystalline solid (yield: 84%).  $R_f$  = 0.47 (10% EtOAc – hexane), mp 58 to 59°C.  $^1\text{H}$  NMR (300 MHz,  $\text{CDCl}_3$ )  $\delta$ : 2.27 (3H, s,  $\text{Ar}-\text{CH}_3$ ), 3.95 (3H, s,  $\text{OCH}_3$ ), 4.46 (2H, s,  $\text{Ar}-\text{CH}_2-\text{Ar}'$ ), 7.02 (2H, d,  $J$  = 8.0 Hz, H-2', 6'), 7.09 (2H, d,  $J$  = 8.2 Hz, H-3', 5'), 7.30–7.37 (2H, m, H-3, 6), 7.38–7.43 (1H, m, H-7), 7.78–7.82 (2H, m, H-4, 5), 7.93 (1H, d,  $J$  = 8.6 Hz, H-8). HR-MS calcd. for  $\text{C}_{19}\text{H}_{18}\text{O}$ : 262.1357; found: 262.1363. EI-MS (70 eV)  $m/z$  (% int.): 262 (100), 247 (25), 231 (34), 215 (34), 202 (19), 189 (8), 171 (15), 158 (10), 141 (14), 115 (13), 105 (16).

#### 1-(4-Carbomethoxyphenylmethyl)-2-methoxynaphthalene (**1g**)

White solid (yield: 90%).  $R_f$  = 0.28 (10% EtOAc – hexane), mp 88 to 89°C.  $^1\text{H}$  NMR (300 MHz,  $\text{CDCl}_3$ )  $\delta$ : 3.86 (3H, s,  $\text{CO}_2\text{CH}_3$ ), 3.94 (3H, s,  $\text{OCH}_3$ ), 4.52 (2H, s,  $\text{Ar}-\text{CH}_2-\text{Ar}'$ ), 7.21–7.25 (2H, d,  $J$  = 8.5 Hz, H-2', 6'), 7.32–7.44 (3H, m, H-3', 5', 6), 7.78–7.89 (5H, m,  $\text{Ar}'\text{-Hs}$ ). HR-MS calcd. for  $\text{C}_{20}\text{H}_{18}\text{O}$ : 306.1256; found: 306.1266. EI-MS (70 eV)  $m/z$  (% int.): 306 (100), 291 (4), 275 (14), 231 (15), 215 (27), 202 (14), 171 (13), 141 (12), 101 (7), 83 (27).



Scheme 2.



### 2-Methoxy-1-propylnaphthalene (**1h**)

Light brown viscous oil (yield: 30%).  $R_f$  = 0.61 (10% EtOAc – hexane).  $^1\text{H}$  NMR (300 MHz,  $\text{CDCl}_3$ )  $\delta$ : 1.02 (3H, t,  $J$  = 7.3 Hz,  $\text{CH}_2\text{CH}_3$ ), 1.63–1.70 (2H, m,  $\text{CH}_2\text{CH}_2\text{CH}_3$ ), 3.07 (2H, t,  $J$  = 7.9 Hz,  $\text{ArCH}_2$ ), 3.95 (3H, s,  $\text{OCH}_3$ ), 7.25–7.37 (2H, m, H-3, 6), 7.44–7.51 (1H, m, H-7), 7.70–7.81 (2H, m, H-4, 5), 7.97 (1H, d,  $J$  = 8.6, H-8).  $^{13}\text{C}$  NMR (75 MHz,  $\text{CDCl}_3$ )  $\delta$ : 14.70, 23.57, 27.20, 56.82, 113.75, 123.31, 123.64, 124.46, 126.26, 127.55, 128.70, 129.48, 133.28, 154.55. HR-MS calcd. for  $\text{C}_{14}\text{H}_{16}\text{O}$ : 200.1201; found: 200.1208. EI-MS (70 eV)  $m/z$  (% int.): 200 (44), 183 (26), 171 (100), 157 (96), 141 (66), 128 (56), 115 (24).

### 1-Heptyl-2-methoxynaphthalene (**1i**)

Colorless viscous oil (yield: 78%).  $R_f$  = 0.65 (10% EtOAc – hexane).  $^1\text{H}$  NMR (300 MHz,  $\text{CDCl}_3$ )  $\delta$ : 0.93 (3H, t,  $J$  = 6.8 Hz,  $\text{CH}_2\text{CH}_3$ ), 1.30–1.53 (8H, m,  $\text{ArCH}_2\text{CH}_2(\text{CH}_2)_4\text{CH}_3$ ), 1.63–1.69 (2H, m,  $\text{ArCH}_2\text{CH}_2\text{CH}_2$ ), 3.11 (2H, t,  $J$  = 7.7 Hz,  $\text{ArCH}_2$ ), 3.96 (3H, s,  $\text{OCH}_3$ ), 7.29 (1H, d,  $J$  = 9.0 Hz, H-3), 7.33–7.39 (1H, m, H-6), 7.47–7.52 (1H, m, H-7), 7.73 (1H, d,  $J$  = 9.0 Hz, H-4), 7.81 (1H, d,  $J$  = 8.1, H-5), 8.0 (1H, d,  $J$  = 8.5, H-8). HR-MS calcd. for  $\text{C}_{18}\text{H}_{24}\text{O}$ : 256.1827; found: 256.1825. EI-MS (70 eV)  $m/z$  (% int.): 256 (51), 171 (100), 141 (31), 115 (7).

## Results and discussion

It was found that when dry hydrogen gas was passed through a solution of 2-tetralone and benzaldehyde in absolute methanol for 20 min, and the reaction stirred at room temperature for 24 h, the TLC showed the formation of a faster moving spot. This product upon workup was characterized as 2-methoxy-1-phenylmethylnaphthalene (**1a**) in good yield.

The initial reactions in the present study were carried out in methyl alcohol (**1a**, **1d–1g**), but to confirm the generality of this procedure, one reaction in each of ethyl alcohol and *n*-butyl alcohol were also carried out under similar conditions. These attempts with 2-tetralone and benzaldehyde successfully yielded the compounds **1b** and **1c**. In the case of the reaction of 2-tetralone with 4-carboxybenzaldehyde in methanol, the obtained product (**1g**) had the carbomethoxy group as expected. We also found that this reaction worked for aliphatic aldehydes also and using propionaldehyde and heptaldehyde in methanol, we were able to make 2-methoxy-1-propylnaphthalene (**1h**) and 1-heptyl-2-methoxynaphthalene (**1i**) in 30 and 78% yield, respectively.

oxy-1-propylnaphthalene **1h** and 1-heptyl-2-methoxynaphthalene **1i** in 30 and 78% yield, respectively.

The likely mechanism of formation of these compounds seems similar to what was proposed in our previous paper (13) except that 1-arylidene-2-tetralone (**A**,  $\text{R} = \text{Ar}$ ) or 1-alkylidene-2-tetralone (**A**,  $\text{R} = \text{alkyl}$ ) are intermediates here. The formation of the enol ether **B** and subsequent rearrangement to **C** makes use of the extended conjugation (Scheme 2). Formation of an  $\alpha,\beta$ -unsaturated species from the corresponding active methylene compound and aldehyde is very common in anhydrous acidic conditions (14, 15). Enol ethers are also easily formed under similar conditions especially when the ketone has an  $\alpha$ -hydrogen atom (16), while hydronaphthalenes are quite amenable to aromatization (13, 17). Aromatization reactions usually require catalysts and harsh conditions (17), though highly facile aromatizations in different structural moieties are known (18). It was demonstrated by isotopic labeling studies in our previous work (13) that the rearrangement of protons does not take place by the less likely concerted 1,5-sigmatropic type rearrangement (for which a *cisoid* conformation is a prerequisite (19)) but follows the more favorable dissociation mechanism.

Based on these results, it can also be concluded that the condensation of the aldehyde group with the active methylene of 2-tetralone leading to the formation of **A** was favored over the formation of vinyl ether **D** as the highly predominant (or exclusive) intermediate. No efforts were made to detect the formation of **D** in the reaction mixture.

## Conclusions

In conclusion, we have devised an exceptionally simple method to perform efficient and selective mixed *C*- and *O*-alkylation leading to 2-alkoxy-1-alkylnaphthalenes from 2-tetralone using an aldehyde and an alcohol under anhydrous acidic conditions. This transformation could be of importance to synthetic and combinatorial chemists. We are working towards widening the scope of this procedure.

## Acknowledgement

Purdue Neuroscience Company, U.S.A., supported this work.



## References

1. W. Desai. *Proc. Indian Acad. Sci. Sect. A*, **24**, 382 (1947).
2. L.I. Lapkin, M.N. Rybakova, and B.V. Korionov. *J. Org. Chem. USSR*, **7**, 2366 (1971).
3. J.-I. Inoh, T. Satoh, S. Pivsa-Art, M. Miura, and M. Nomura. *Tetrahedron Lett.* **39**, 4673 (1998).
4. A.R. Katritzky, X. Lan, and J.N. Lam. *Chem. Ber.* **124**, 1819 (1991).
5. P.J. Bowman, B.R. Brown, M.A. Chapman, and P.M. Doyle. *J. Chem. Res. Miniprint*, 701 (1984).
6. M.R. Saidi. *Indian J. Chem. Sect. B: Org. Chem. Incl. Med. Chem.* **21**, 474 (1982).
7. E. Wenkert, R.D. Youssefyeh, and R.G. Lewis. *J. Am. Chem. Soc.* **82**, 4675 (1960).
8. O. Behaghel and H. Freiensehner. *Chem. Ber.* **67**, 1368 (1934).
9. M. Gomberg and C.C. Buchler. *J. Am. Chem. Soc.* **42**, 2059 (1920).
10. V.N. Setkina and D.N. Kursanov. *Izv. Akad. Nauk. SSSR, Ser. Khim.* 81 (1951); *Chem. Abstr.* 458 (1952).
11. T. Kito, K. Yoshinaga, S. Ohkami, K. Ikeda, and M. Yamaye. *J. Org. Chem.* **50**, 4628 (1985).
12. E.V. Dehmlow. *Izv. Akad. Nauk. Ser. Khim.* **11**, 2094 (1995); *Chem. Abstr.* **124**, 288 438 (1996).
13. A. Jha, M.P. Padmanilayam, and J.R. Dimmock. *Synthesis*, 463 (2002).
14. J.R. Dimmock, M.P. Padmanilayam, G.A. Zello, J.W. Quail, E.O. Oloo, J.S. Prisciak, H.-B. Kraatz, A. Cherkasov, J.S. Lee, T.M. Allen, C.L. Santos, E.K. Manavathu, E. De Clercq, J. Balzarini, and J.P. Stables. *Eur. J. Med. Chem.* **37**, 813 (2002).
15. (a) R. Pal, R.N. Handa, and H.K. Pujari. *Indian J. Chem. Sect. B: Org. Chem. Incl. Med. Chem.* **33**, 520 (1994); (b) J. March. *Advanced organic chemistry: Reactions, mechanism and structure*. 5th ed. John Wiley and Sons, New York. 2001. Chap. 16. p. 1222.
16. J. March. *Advanced organic chemistry: Reactions, mechanism and structure*. 5th ed. John Wiley and Sons, New York. 2001. Chap. 16. p. 1181.
17. P.P. Fu and R.G. Harvey. *Chem. Rev.* **78**, 317 (1978).
18. (a) W.J. Bailey and R.A. Baylouny. *J. Org. Chem.* **27**, 3476 (1962); (b) U. Weiss, C. Gilvarg, and E.S. Mingioli. *Science (Washington, D.C.)*, **119**, 774 (1954).
19. E.F. Kiefer and C.H. Tanna. *J. Am. Chem. Soc.* **91**, 4478 (1969).



# Corrosion et passivation de l'étain dans un milieu simulé à une eau industrielle

El Habib Ait Addi, Lahcen Bazzi, Mostafa Hilali, El Alami Zine, Rachid Salghi et Souad El Issami

**Résumé :** Le comportement à la corrosion de l'étain dans un milieu simulé à une eau industrielle a été étudié par emploi des méthodes électrochimiques (tracé des courbes potentiodynamiques et mesure de la résistance de polarisation). L'effet de la variation du pH, de la température et de la concentration des anions en solution a été étudié. Les résultats obtenus montrent que la variation du pH (autour de la valeur 8,2 du milieu synthétique) n'a pas d'effet sur la sensibilité à la piqûration de l'étain. Cependant, l'augmentation de la température de 20 à 70 °C accélère le processus de corrosion. La présence des anions  $\text{Cl}^-$  et  $\text{SO}_4^{2-}$  favorise le processus de piqûration de l'étain. Les ions  $\text{Cl}^-$  sont plus agressifs que les ions  $\text{SO}_4^{2-}$  alors que les ions  $\text{HCO}_3^-$  ont une action inhibitrice vis-à-vis de la corrosion par piqûre de l'étain dans le milieu étudié.

**Mots clés :** étain, corrosion, piqûration, eau industrielle.

**Abstract:** The corrosion behaviour of tin in a synthetic medium similar to an industrial water has been studied by using electrochemical methods (plotted potentiodynamic curves and polarization resistance measurement). The effect of pH variation, temperature and concentration of anions in solution has been investigated. The results obtained show that pH variation (around the value 8.2 of the synthetic medium) has no effect on the pitting sensitivity of tin. However, the increasing of temperature in the range of 20–70°C accelerates the corrosion process. The presence of anions  $\text{Cl}^-$  and  $\text{SO}_4^{2-}$  leads to pitting corrosion of tin.  $\text{Cl}^-$  ions are more aggressive than  $\text{SO}_4^{2-}$  ions, whereas  $\text{HCO}_3^-$  ions acted as an inhibitor for pitting corrosion of tin in the studied medium.

**Key words:** tin, corrosion, pitting, industrial water.

## Introduction

L'étain est un métal qui est largement utilisé dans l'industrie agro-alimentaire. Il permet le recouvrement superficiel des matériaux tel que l'acier pour les rendre plus résistants à la corrosion dans les eaux industrielles. Cependant, ce matériau est susceptible d'être attaqué par le milieu environnant. L'examen du diagramme potentiel-pH de l'étain (1) montre que ce métal peut être dans un état actif ou passif. Ainsi, l'étain réagit dans les milieux acides et basiques et il est relativement stable et résistant dans les milieux neutres. Sa dissolution est minimale pour une valeur de pH voisine de 8,5.

Plusieurs travaux ont été entrepris sur la corrosion de l'étain en milieux neutres ou légèrement alcalins (2–11).

Parmi ces travaux, nous citons ceux de Drogowska et al. (2) et de Brossard et al. (3) en milieu bicarbonate. Ces auteurs ont montré que l'étain présente dans ce milieu un phénomène de passivation sans rupture de passivité. Ils ont attribué ce phénomène à la formation d'un film passif constitué essentiellement par l'oxyde  $\text{SnO}_2$ . En présence des ions  $\text{Cl}^-$ , l'étain devient sensible à la piqûration. La valeur du potentiel de piqûration dépend à la fois de la teneur des ions  $\text{Cl}^-$  et des ions  $\text{HCO}_3^-$  en solution (3). Les travaux de Refaey (4) sur la corrosion de l'étain ont été entrepris dans une solution de borate de sodium (pH = 8,35). Il a montré que l'addition des ions  $\text{Cl}^-$  ou  $\text{Br}^-$  dans ce milieu provoque la corrosion par piqûre de ce matériau et que les ions  $\text{Cl}^-$  sont plus agressifs que les ions  $\text{Br}^-$ . Alvarez et al. (5) ont réalisé une étude sur le comportement anodique de l'étain dans une solution contenant soit les ions  $\text{HCO}_3^-$ – $\text{CO}_3^{2-}$  ou bien les ions  $\text{B}_4\text{O}_7^{2-}$ . Ces auteurs ont suggéré que l'oxydation successive de Sn en Sn(II) et de Sn(II) en Sn(IV) stabilise le film passif par le processus de déshydratation. Les mêmes auteurs ont étudié l'effet de la variation du pH entre 7,6 et 11,9 sur la dissolution de l'étain dans la solution de borate. Ils ont montré que la meilleure résistance à la corrosion est obtenue pour une valeur de pH égale à 11,9. Ils ont alors attribué ce phénomène à la formation d'un film compact et résistant.

Le but de ce travail est d'étudier le comportement à la corrosion de l'étain dans une solution simulée à une eau industrielle qui est utilisée dans l'industrie agroalimentaire à Agadir (sud du Maroc). Cette eau industrielle est caracté-

Reçu le 26 novembre 2002. Publié sur le site Web des Presses scientifiques du CNRC à <http://revcanchimie.cnrc.ca> le 7 Mai 2003.

**E.H.A. Addi, L. Bazzi<sup>1</sup>, M. Hilali et S. El Issami.** Équipe de chimie moléculaire et corrosion, Département de chimie, Faculté des sciences d'Agadir, B.P. 28/S, Agadir, Maroc.

**E.A. Zine.** Laboratoire de l'établissement autonome de contrôle et de coordination des exportations, Casablanca, Maroc.

**R. Salghi.** Laboratoire d'analyse agro-alimentaire, École Supérieure de Technologie d'Agadir (ESTA), Agadir, Maroc.

<sup>1</sup>Auteur correspondant (courriel : [lbazzi@caramail.com](mailto:lbazzi@caramail.com)).



risée par des teneurs en ions  $\text{Cl}^-$ ,  $\text{HCO}_3^-$  et  $\text{SO}_4^{2-}$  variables d'une unité de conserve à une autre. Nous évoquerons l'effet de la variation du pH, de la température et de la concentration des ions  $\text{Cl}^-$ ,  $\text{HCO}_3^-$  et  $\text{SO}_4^{2-}$  en solution. Notons l'absence à notre connaissance de travaux antérieurs dans de tels milieux contenant simultanément les trois anions précités.

## Conditions expérimentales

Au cours de ce travail, nous avons fait appel à deux méthodes électrochimiques. Il s'agit du tracé des courbes potentiodynamiques et la mesure de la résistance de polarisation.

Les essais électrochimiques ont été réalisés dans une cellule étanche thermostatée munie d'orifices permettant l'introduction de trois électrodes. L'électrode de référence est une électrode au calomel saturée (ECS). La contre électrode est en platine. L'électrode de travail est sous forme d'un disque de surface  $S = 0,5 \text{ cm}^2$  en étain enrobé dans une résine et fixé verticalement sur un porte-échantillon. Avant chaque essai, les échantillons subissent un polissage mécanique à l'aide de papier abrasif de granulométrie décroissante allant jusqu'à 1200, un dégraissage à l'acétone, un rinçage à l'eau bidistillée et un séchage à l'air comprimé. L'étude électrochimique est réalisée à l'aide d'un potentiostat-galvanostat PGP 201 piloté par ordinateur à l'aide du logiciel (VoltaMaster). La vitesse de balayage choisie est de 60 mV/min pour avoir des conditions quasi stationnaires (12,13). Avant chaque tracé de la courbe de polarisation, l'électrode de travail est maintenue à son potentiel libre pendant 30 min. La mesure de la résistance de polarisation  $R_p$  est réalisée dans les mêmes conditions que le tracé des courbes de polarisation. Une surtension de  $-10 \text{ mV/ECS}$  est imposée à l'électrode de travail. La valeur de  $R_p$  est alors déterminée à partir de la pente de droite obtenue. La solution électrolytique est préalablement désaérée par un barbotage continu d'azote et elle est soumise à une agitation constante. Le milieu synthétique (milieu témoin) contenant 0,01 M  $\text{Cl}^-$ , 0,008 M  $\text{SO}_4^{2-}$  et 0,003 M  $\text{HCO}_3^-$ , est préparé par dissolution dans l'eau bi-distillée de  $\text{NaCl}$ ,  $\text{Na}_2\text{SO}_4$  et  $\text{Na}_2\text{HCO}_3$  de grade pour analyse. La valeur du pH mesurée dans ces conditions est égale à 8,2.

## Résultats

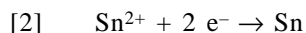
### Effet du pH

La variation du pH du milieu synthétique est assurée par ajout dans le milieu témoin (pH = 8,2) de quelques gouttes d'une solution de  $\text{NaOH}$  ou d'une solution de  $\text{H}_2\text{SO}_4$ . La variation de la concentration anionique provoquée par cet ajout reste négligeable. La température de la solution est fixée à 20 °C.

Les courbes de polarisation de l'étain enregistrées pour différentes valeurs de pH du milieu sont représentées à la figure 1. Nous constatons que l'allure générale de la courbe potentiodynamique est similaire pour les trois valeurs de pH. La branche cathodique est caractérisée par un domaine linéaire indiquant la réduction de l'eau selon un mécanisme d'activation pure (14) :



Pour des surtensions plus cathodiques, il y a apparition d'un palier de courant qui pourrait être attribué à la réduction des ions  $\text{Sn}^{2+}$  en solution.



L'examen de la branche anodique permet de conclure que l'étain présente un phénomène de passivation avec rupture de passivité par attaque localisée. En effet partant du potentiel de corrosion, la densité de courant anodique augmente avec le potentiel d'électrode pour atteindre un palier de courant appelé palier de passivation. La densité de courant de passivation  $I_p$  est alors déterminée par la mesure de la hauteur du palier de courant. Lorsqu'on atteint la valeur du potentiel de piqûration  $E_{\text{piq}}$ , la densité de courant anodique augmente brusquement. Il y a alors piqûration de l'étain.

L'examen de la figure 1 montre que lorsque la valeur du pH passe de 6,2 à 9,2, le potentiel de corrosion se déplace vers les valeurs plus actives; alors que la valeur du potentiel de piqûration reste sensiblement constante. Les densités de courant de corrosion  $I_{\text{cor}}$  et de passivation  $I_p$  subissent une légère augmentation. Ce résultat est corroboré par la décroissance subie par la résistance de polarisation lorsque le pH croît et traduit la faible tendance à la corrosion uniforme de l'étain.

### Effet de la concentration des ions sulfates

La variation de la teneur en ions  $\text{SO}_4^{2-}$  est réalisée par dissolution de la quantité correspondante de  $\text{Na}_2\text{SO}_4$  dans la solution contenant 0,01 M  $\text{Cl}^-$  et 0,003 M  $\text{HCO}_3^-$ . Le pH de la solution ainsi préparée reste voisin de la valeur 8,2 et la température est fixée à 20 °C.

Les courbes de polarisation de l'étain dans le milieu contenant les ions  $\text{SO}_4^{2-}$  à différentes concentrations sont représentées sur la figure 2. L'examen des résultats obtenus montre que l'augmentation de la concentration des ions sulfates de 0,0002 à 0,08 M a pour effet un déplacement du potentiel de piqûration vers des valeurs plus actives et du potentiel de corrosion vers des valeurs plus nobles. Ce résultat traduit la tendance de l'étain à la corrosion par piqûre en présence de ces ions. Notons que les densités de courant de corrosion  $I_{\text{cor}}$  et de passivation  $I_p$  ne subissent qu'une légère augmentation lorsque la teneur de ces ions croît en solution.

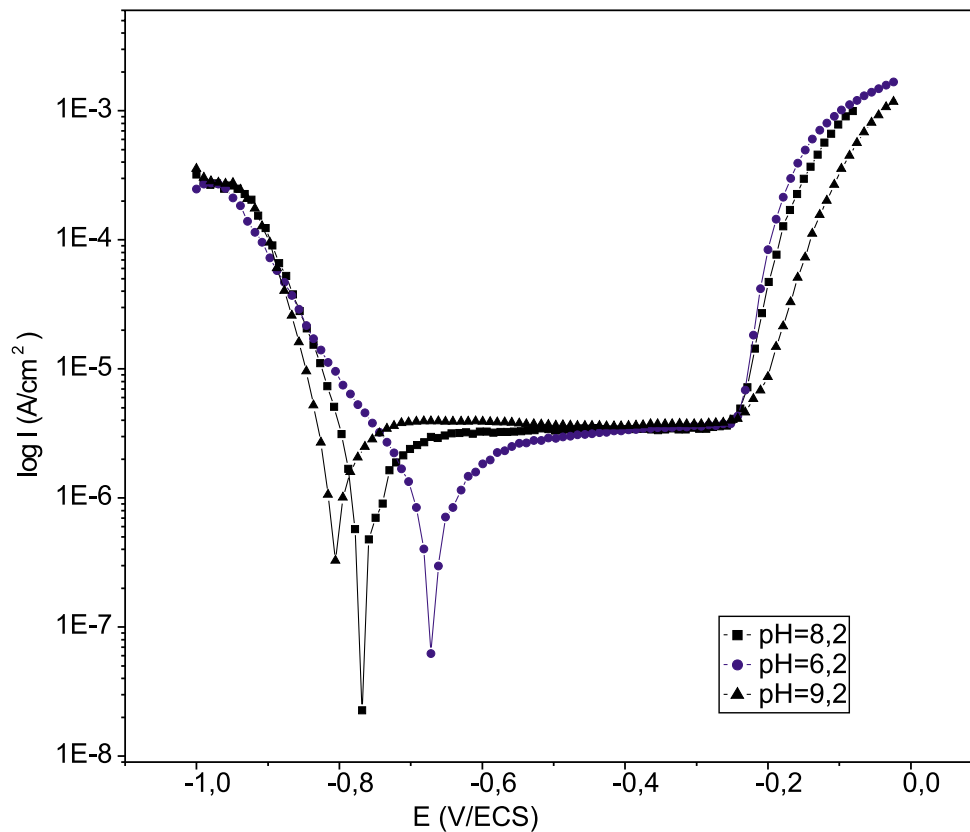
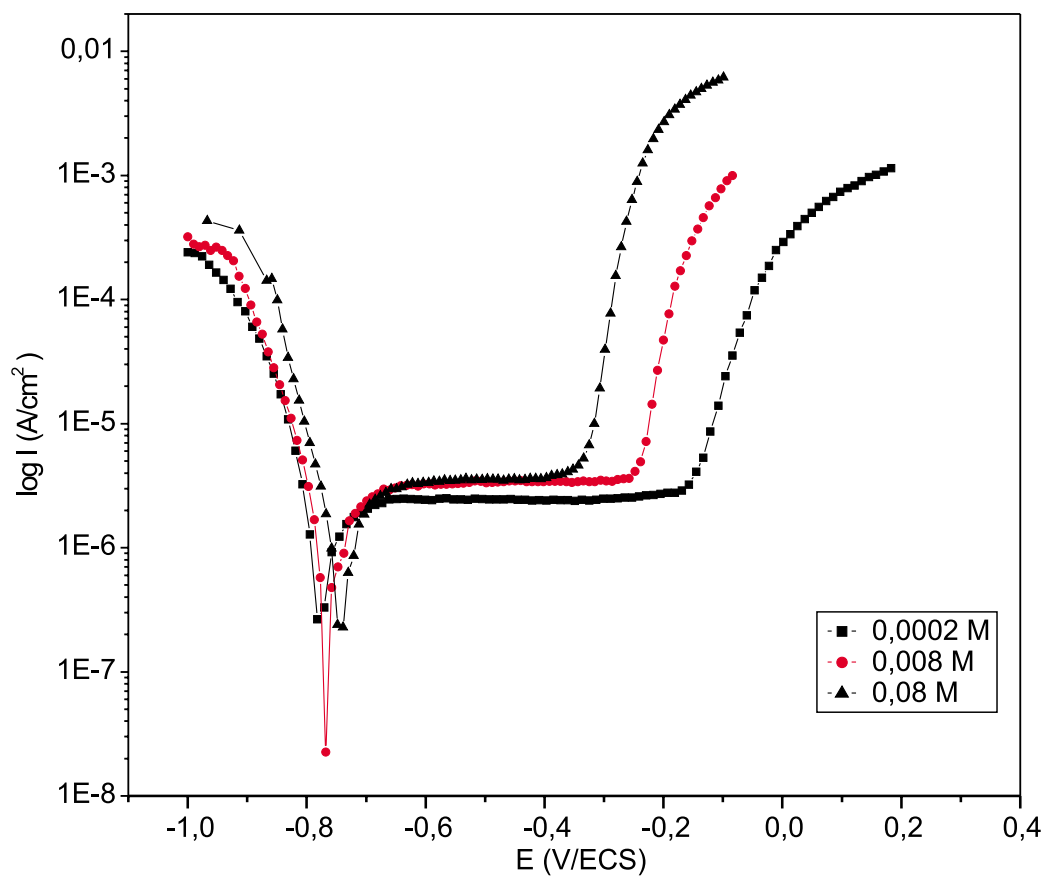
### Effet de la concentration des ions chlorures

Les essais concernant l'effet de la variation de la teneur en ions  $\text{Cl}^-$  sont réalisés dans une solution contenant 0,008 M  $\text{SO}_4^{2-}$  et 0,003 M  $\text{HCO}_3^-$  et  $x \text{ M}$  de  $\text{Cl}^-$ . La valeur de  $x$  désirée (entre 0,002 et 1 M) est obtenue par dissolution de cristaux de  $\text{NaCl}$  dans la solution contenant les ions  $\text{SO}_4^{2-}$  et  $\text{HCO}_3^-$ . Le pH de la solution obtenue est voisin de la valeur 8,2 et la température est maintenue à 20 °C.

La figure 3 représente les courbes de polarisation de l'étain enregistrées dans le milieu contenant différentes concentrations en ions chlorures.

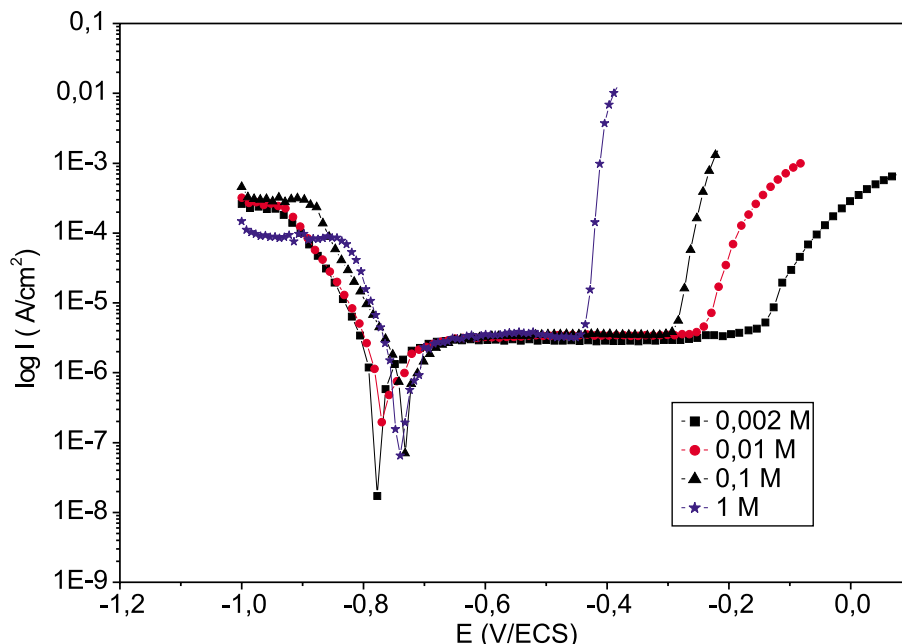
Dans la branche cathodique, nous constatons l'existence de la portion linéaire au voisinage du potentiel de corrosion. Ce qui traduit un comportement Tafelien pour la réduction de l'eau (réaction 1). Néanmoins, le palier de courant observé pour des surtensions plus cathodiques a tendance à s'élargir lorsque la teneur en ions  $\text{Cl}^-$  en solution croît. Dans la branche anodique, on assiste à un déplacement remar-



**Fig. 1.** Courbes de polarisation de l'étain dans le milieu témoin pour différentes valeurs de pH à 20 °C.**Fig. 2.** Courbes de polarisation de l'étain dans le milieu témoin pour différentes concentrations en ions sulfates à 20 °C.



**Fig. 3.** Courbes de polarisation de l'étain dans le milieu témoin pour différentes concentrations en ions chlorures à 20 °C.



quable du potentiel de piqûration vers des valeurs plus actives au fur et à mesure que la teneur des ions  $\text{Cl}^-$  en solution augmente. L'étain devient donc plus sensible à la piqûration à forte concentration en ions  $\text{Cl}^-$ . L'évolution du potentiel de piqûration  $E_{\text{piq}}$  en fonction du logarithme de la concentration des ions  $\text{Cl}^-$  ( $\log[\text{Cl}^-]$ ) est représentée à la figure 4. À titre de comparaison nous avons également représenté l'évolution de  $E_{\text{piq}}$  en fonction de  $\log[\text{SO}_4^{2-}]$ . Nous constatons que les deux variations sont sous forme de droites d'équations :

$$E_{\text{piq}1} = a_1 \log[\text{Cl}^-] + b_1$$

$$E_{\text{piq}2} = a_2 \log[\text{SO}_4^{2-}] + b_2$$

Où  $a_1$  et  $a_2$  représentent les pentes des deux droites,  $a_1 = -99$  et  $a_2 = -67$ ;  $b_1$  et  $b_2$  sont des constantes.

Ce résultat traduit le caractère agressif des ions  $\text{Cl}^-$  et  $\text{SO}_4^{2-}$  vis-à-vis de la corrosion par piqûre de l'étain dans le milieu étudié.

Notons que les valeurs des autres paramètres électrochimiques (tableau 1) ne subissent qu'une légère variation en présence des ions chlorures. Ces derniers n'ont pratiquement pas d'effet sur la valeur  $I_p$  de la densité de courant de passivation.

#### Effet de la concentration des ions hydrogénocarbonates

Les solutions contenant les ions  $\text{HCO}_3^-$  à différentes concentrations sont obtenues par dissolution de  $\text{NaHCO}_3$  dans le milieu contenant 0,008 M  $\text{SO}_4^{2-}$  et 0,01 M de  $\text{Cl}^-$ . Le pH de la solution est ensuite ramené à la valeur 8,2 par ajout de quelques gouttes de  $\text{NaOH}$  ou  $\text{H}_2\text{SO}_4$ . La température est fixée à 20 °C.

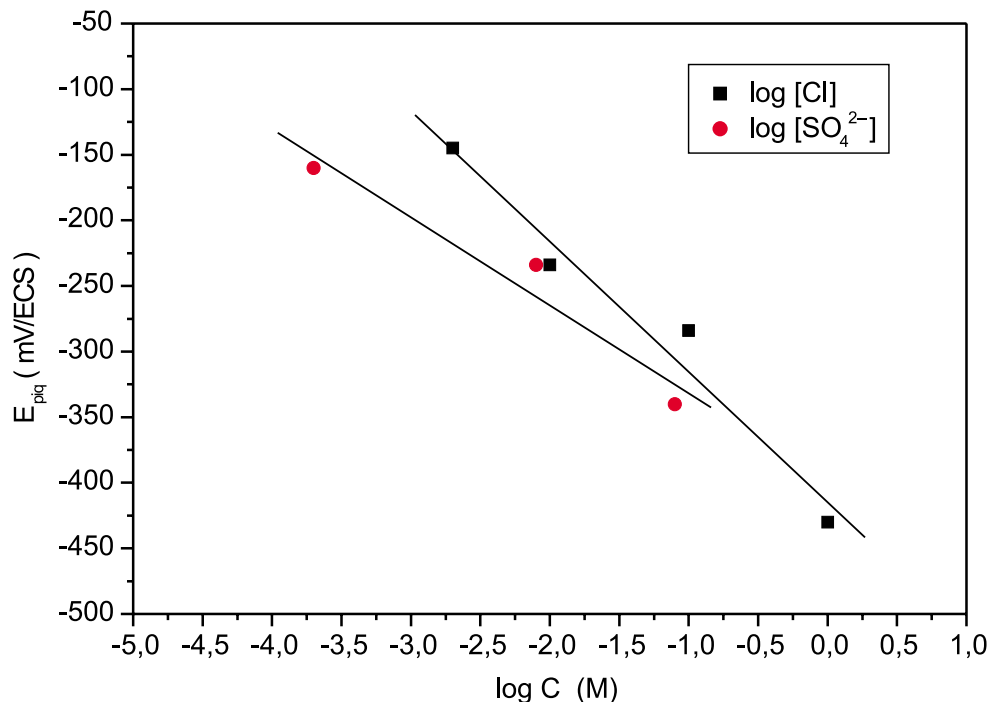
La figure 5 illustre l'effet de la variation de la teneur en ions hydrogénocarbonates sur les courbes de polarisation de l'étain dans le milieu synthétique. L'examen de cette figure révèle un changement remarquable dans la branche anodique. En effet, lorsque la teneur en ions hydrogénocarbonates augmente en solution, il y a apparition d'un domaine

d'activité au voisinage du potentiel de corrosion. Ce domaine est caractérisé par l'existence de deux pics I et II. Drogowska et al. (2), Brossard et al. (3) et Alvares et al. (5) ont observé le même phénomène dans des solutions contenant les ions  $\text{HCO}_3^-$ . Ces auteurs ont attribué les pics I et II à la formation de  $\text{Sn(II)}$  et  $\text{Sn(IV)}$  respectivement. Pour des surtensions plus anodiques, nous assistons à un large domaine de passivation avant d'atteindre la rupture de passivité par attaque localisée. Signalons que la position du potentiel de piqûration a tendance à se déplacer vers des valeurs plus nobles lorsque la concentration en ions hydrogénocarbonates augmente. Ce résultat traduit le caractère inhibiteur de ces ions vis-à-vis de la corrosion par piqûre de l'étain dans le milieu étudié (fig. 6). Cependant, l'examen des résultats présentés dans le tableau 2 révèle la tendance de l'étain à la corrosion uniforme lorsque la concentration des ions hydrogénocarbonates croît en solution. En effet, les densités de courant de corrosion  $I_{\text{cor}}$  et de passivation  $I_p$  augmentent avec la teneur de ces ions en solution. Ces résultats sont corroborés par les valeurs de  $R_p$  qui subissent une décroissance monotone.

Pour étudier l'effet des ions hydrogénocarbonates en présence des ions  $\text{Cl}^-$  à forte concentration, nous avons réalisé des essais avec une teneur en ions  $\text{Cl}^-$  égale à 1 M. La figure 7 représente les courbes de polarisation enregistrées dans le milieu contenant 1 M  $\text{Cl}^-$  à différentes concentrations en ions hydrogénocarbonates. Nous constatons que ces derniers ont un effet moins marqué sur l'inhibition de la corrosion par piqûre de l'étain. Le potentiel de piqûration n'est déplacé que de 230 mV vers des valeurs plus nobles pour une augmentation de la teneur en ions hydrogénocarbonates de 0,003 M. Signalons que pour le même intervalle,  $E_{\text{piq}}$  est déplacé de plus de 2434 mV lorsque la concentration des ions chlorures est égale à 0,01 M.

Les densités de courant de corrosion  $I_{\text{cor}}$  et de passivation  $I_p$  subissent quant à elles une nette augmentation (tableau 2) lorsque la teneur en ions  $\text{HCO}_3^-$  croît en solution. Ce résul-



**Fig. 4.** Variation du potentiel de piqûration  $E_{\text{piq}}$  en fonction de la concentration des ions chlorures et sulfates.**Tableau 1.** Effet de la concentration des ions chlorures sur les paramètres électrochimiques de l'étain dans le milieu synthétique à 20 °C.

$[\text{Cl}^-]$ (mol/L)	$E_{\text{cor}}$ (mV/ECS)	$E_{\text{piq}}$ (mV/ECS)	$I_{\text{cor}}$ ( $\mu\text{A}/\text{cm}^2$ )	$I_p$ ( $\mu\text{A}/\text{cm}^2$ )	$R_p$ ( $\text{k}\Omega\cdot\text{cm}^2$ )
0,002	-777	-145	1,5	3,3	16,10
0,01	-769	-234	1,4	3,1	16,94
0,1	-735	-284	1,3	3,4	17,61
1	-740	-430	1,0	3,4	28,11

tat traduit la tendance de l'étain à la corrosion généralisée en présence de ces ions.

### Effet de la température

Du fait que la température est l'un des facteurs susceptibles de modifier le comportement des matériaux dans un milieu corrosif, nous avons mené une étude potentiodynamique de l'étain dans le milieu synthétique (milieu témoin) à différentes températures comprises entre 20 et 70 °C. Les courbes de polarisation correspondantes sont représentées à la figure 8. Les paramètres électrochimiques sont regroupés dans le tableau 3. L'examen de ces résultats permet de faire les constatations suivantes :

L'allure générale des courbes de polarisation n'est pas modifiée par l'élévation de la température. En effet dans la branche cathodique et partant du potentiel de corrosion, nous constatons l'existence du domaine linéaire Tafelien qui traduit la réduction de l'eau selon un mécanisme d'activation pure (réaction 1). Pour des surtensions plus cathodiques, nous retrouvons le palier de courant attribué à la réduction des ions  $\text{Sn}^{2+}$  en solution (réaction 2) (15). L'élévation de la température a cependant pour effet un accroissement des densités de courant de corrosion et de passivation (tableau 3). Les potentiels de corrosion  $E_{\text{cor}}$  et de piqûration  $E_{\text{piq}}$  subissent un déplacement vers des valeurs plus actives. Les ré-

sultats présentés dans le tableau 3 montrent que la corrosion uniforme de l'étain dans le milieu étudié s'accroît avec l'augmentation de la température.

### Discussion

Dans ce travail, nous avons étudié le comportement à la corrosion de l'étain dans une eau synthétique simulée à une eau industrielle (pH = 8,2). Les résultats obtenus montrent que l'étain présente un phénomène de passivation avec rupture de passivité par attaque localisée. Le phénomène de passivation est probablement dû à la formation d'une couche passive protectrice qui limite la mise en solution de l'étain. En effet, les densités de courant de corrosion  $I_{\text{cor}}$  et de passivation  $I_p$  ne dépassent pas quelques micro-ampères ( $\approx 3 \mu\text{A}/\text{cm}^2$ ). Selon certains auteurs (2, 5), dans les milieux ayant des pH voisins du pH du milieu neutre, la formation de la couche passive suit le mécanisme réactionnel :

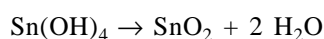
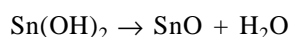
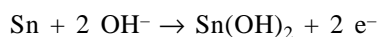




**Fig. 5.** Courbes de polarisation de l'étain dans le milieu témoin pour différentes concentrations en ions hydrogénocarbonates à 20 °C.

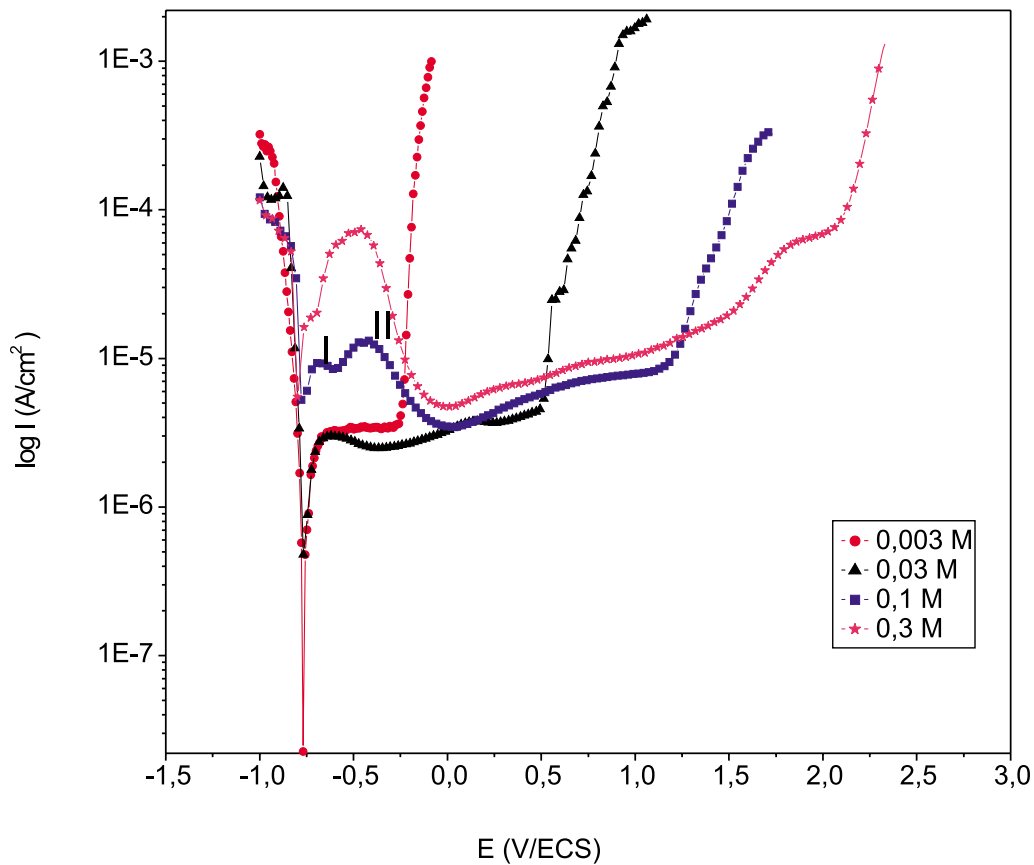


**Fig. 6.** Variation du potentiel de piqûre  $E_{\text{piq}}$  en fonction de la concentration des ions hydrogénocarbonates à différentes concentrations en ions chlorures à 20 °C.

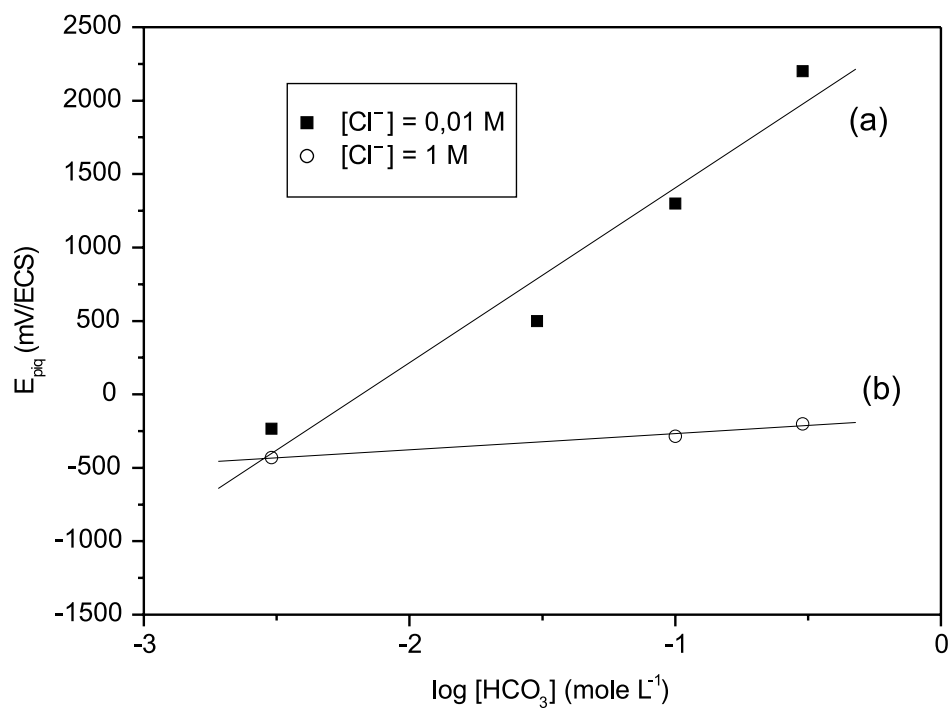




**Fig. 7.** Courbes de polarisation de l'étain dans le milieu témoin pour différentes concentrations en ions hydrogénocarbonates et pour une concentration en ions  $\text{Cl}^-$  égale à 1 M.

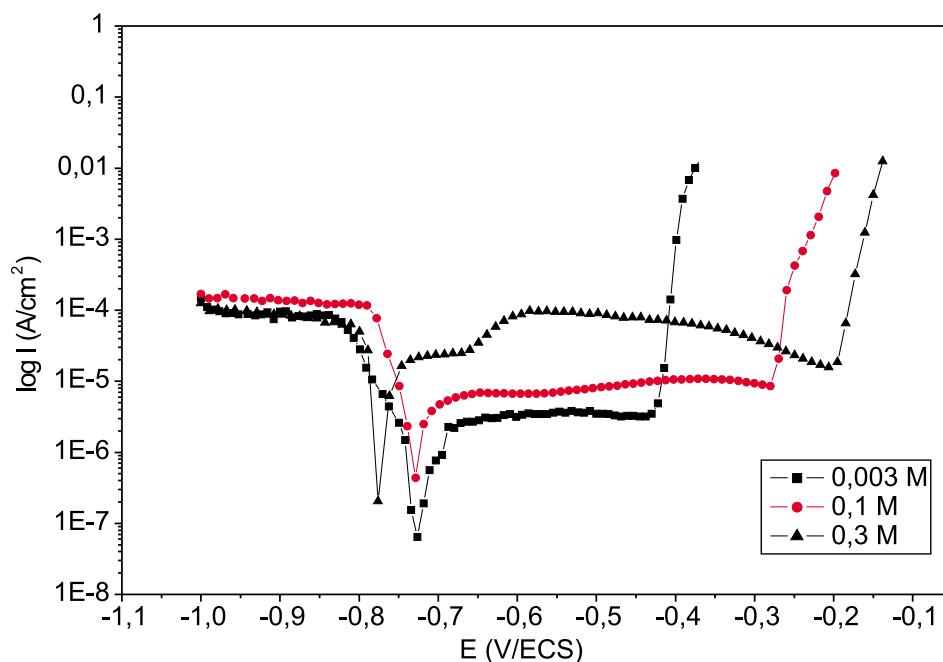
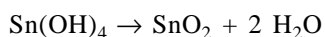
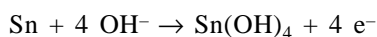


**Tableau 2.** Effet de la concentration des ions hydrogénocarbonates sur les paramètres électrochimiques de l'étain, à différentes concentrations en ions chlorures, dans le milieu synthétique à 20 °C.

$[\text{Cl}^-]$ (mol/L)	$[\text{HCO}_3^-]$ (mol/L)	$E_{\text{cor}}$ (mV/ECS)	$E_{\text{piq}}$ (mV/ECS)	$I_{\text{cor}}$ ( $\mu\text{A}/\text{cm}^2$ )	$I_p$ ( $\mu\text{A}/\text{cm}^2$ )	$R_p$ ( $\text{k}\Omega\cdot\text{cm}^2$ )
0,01	3	-765	-271	1,2	2,3	21,41
	0,003	-769	-234	1,4	3,1	16,94
	0,03	-763	500	1,8	3	14,21
	0,1	-771	1300	4	12	4,12
	0,3	-797	2200	13	66	0,90
1	0,003	-740	-430	1	3,4	28,10
	0,1	-747	-285	4,4	7,5	3,72
	0,3	-776	-200	17	90	1,12

Ces auteurs ont également évoqué la possibilité de l'oxydation directe de Sn (0) en Sn (IV) :



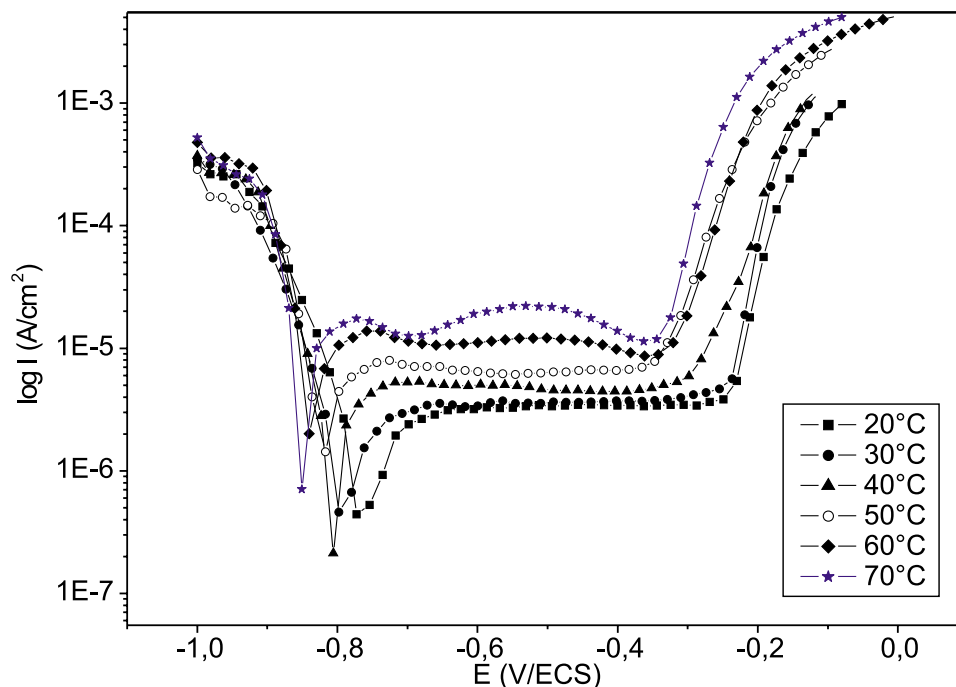
Dans le cas de notre milieu synthétique, la variation du pH autour de la valeur 8,2 n'affecte pas la sensibilité à la piqûration de l'étain. Le potentiel de piqûration demeure constant. Cependant, une légère augmentation des valeurs de  $I_{\text{cor}}$  et de  $I_p$  et un déplacement de  $E_{\text{cor}}$  vers des valeurs plus actives se produit lorsque le pH devient plus alcalin (pH = 9,2). Ce phénomène pourrait être attribué à la solubilité des oxydes et des hydroxydes de Sn (II) et Sn (IV) qui croît avec la teneur des ions  $\text{OH}^-$  en solution (4).

L'effet de la variation de la concentration des anions  $\text{SO}_4^{2-}$ ,  $\text{HCO}_3^-$  et  $\text{Cl}^-$  sur la résistance à la corrosion de l'étain dans le milieu synthétique a été étudié. Ainsi les ions  $\text{SO}_4^{2-}$  et  $\text{Cl}^-$  sont des stimulateurs de la corrosion par piqûre de l'étain. En effet, lorsque la concentration de ces ions croît

en solution, le potentiel de piqûration  $E_{\text{piq}}$  a tendance à se déplacer vers des valeurs plus actives. Les variations de  $E_{\text{piq}}$  en fonction de  $\log[\text{Cl}^-]$  et  $\log[\text{SO}_4^{2-}]$  sont des droites de pentes négatives  $a_1$  et  $a_2$ . Nous remarquons que la valeur de  $a_1$  est supérieure à celle de  $a_2$ ; ce qui montre que les ions  $\text{Cl}^-$  sont plus agressifs que les ions  $\text{SO}_4^{2-}$  vis-à-vis de la corrosion par piqûre de l'étain dans le milieu synthétique. Ce résultat pourrait être attribué à la taille des ions  $\text{Cl}^-$  plus petite que celle des ions  $\text{SO}_4^{2-}$ ; ce qui facilite leur adsorption à la surface du film passif puis leur pénétration à travers les défauts ponctuels et les pores. Il y a alors rupture de passivité (4). Notons que la densité de courant de corrosion est pratiquement indépendante de la concentration des ions  $\text{Cl}^-$  et  $\text{SO}_4^{2-}$ ; résultats en accord avec les travaux de Drogowska et al. (16).

Dans le cas des ions  $\text{HCO}_3^-$ , deux phénomènes antagonistes se produisent. Le premier est relatif au caractère inhibiteur de ces ions vis-à-vis de la corrosion par piqûre de l'étain dans le milieu étudié. Ce phénomène est clairement



**Fig. 8.** Courbes de polarisation de l'étain dans le milieu témoin à différentes températures.**Tableau 3.** Effet de la variation de la température sur les paramètres électrochimiques de l'étain dans le milieu synthétique.

Température (°C)	$E_{\text{cor}}$ (mV/ECS)	$E_{\text{piq}}$ (mV/ECS)	$I_{\text{cor}}$ ( $\mu\text{A}/\text{cm}^2$ )	$I_p$ ( $\mu\text{A}/\text{cm}^2$ )	$R_p$ ( $\text{k}\Omega\cdot\text{cm}^2$ )
20	-769	-234	1,4	3,1	16,94
30	-794	-240	2	3,7	14,10
40	-811	-275	3,1	5,4	7,22
50	-826	-330	4,4	7	3,72
60	-839	-320	6,9	11	2,04
70	-852	-327	9,2	18	1,58

démontré par l'évolution du potentiel de piqûration  $E_{\text{piq}}$  en fonction de  $\log [\text{HCO}_3^-]$  et qui présente une pente positive (fig. 6, tracé a). Cependant, la valeur de la pente de la droite décroît sans devenir négative lorsque la teneur des ions  $\text{Cl}^-$  en solution passe de 0,01 à 1 M (fig. 6, tracé b). Ce résultat montre que les ions  $\text{HCO}_3^-$  ont un caractère inhibiteur moins marqué vis-à-vis de la corrosion par piqûre à forte concentration en ions  $\text{Cl}^-$ .

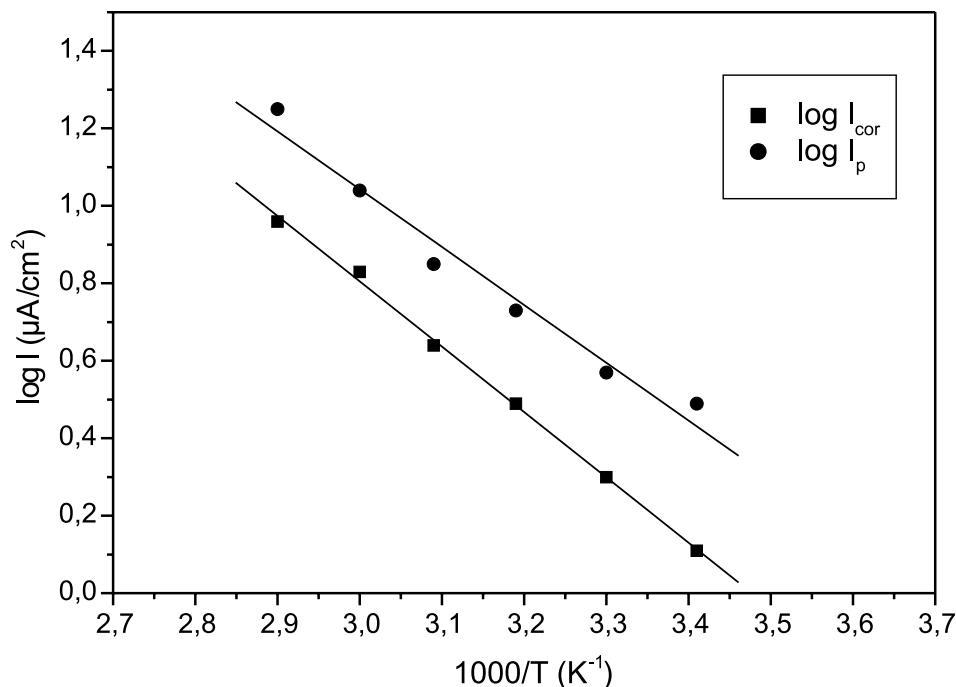
Le deuxième phénomène traduit le caractère agressif des ions  $\text{HCO}_3^-$  vis-à-vis de la corrosion uniforme de l'étain. En effet, les valeurs de  $I_{\text{cor}}$ , estimées par extrapolation des pentes de Tafel cathodiques au potentiel de corrosion, ont tendance à augmenter avec la concentration des ions  $\text{HCO}_3^-$ . Ce résultat est corroboré par la décroissance subie par la valeur de la résistance de polarisation  $R_p$  et pourrait être attribué à la stabilisation des cations  $\text{Sn}^{2+}$  et  $\text{Sn}^{4+}$  par leur complexation avec les anions  $\text{HCO}_3^-$ – $\text{CO}_3^{2-}$  en solution (3).

Pour des concentrations en ions  $\text{HCO}_3^-$  supérieures à 0,03 M, il y a apparition dans la branche anodique d'un domaine d'activité caractérisé par l'existence de deux pics d'oxydation I et II attribué à la formation de Sn (II) et Sn(IV) respectivement (2–5). La hauteur de ces deux pics a tendance à croître avec la concentration en ions  $\text{HCO}_3^-$  en solution. Ce

phénomène pourrait être expliqué par la participation directe de ces ions dans le processus de dissolution et la formation de certains complexes solubles en solution (2, 3, 4).

L'influence de la température sur la résistance à la corrosion de l'étain dans le milieu synthétique a été étudiée. L'intervalle de température choisi est compris entre 20 et 70 °C. Les résultats obtenus (fig. 8; tableau 5) montrent clairement l'effet défavorable de l'augmentation de la température sur la corrosion et la passivation de l'étain. Ceci se traduit par une croissance monotone des densités de courant de corrosion  $I_{\text{cor}}$  et de passivation  $I_p$ . Ce résultat est en accord avec la décroissance des valeurs de la résistance de polarisation  $R_p$ . Nous assistons également à un déplacement des potentiels de corrosion  $E_{\text{cor}}$  et de piqûration  $E_{\text{piq}}$  vers des valeurs plus actives lorsque la température augmente. L'évolution du logarithme des densités de courant de corrosion  $I_{\text{cor}}$  et de passivation  $I_p$  en fonction de l'inverse de la température absolue est représentée sur la figure 9. Nous constatons que la loi d'Arrhénius est vérifiée pour chacune des variations  $\log I_{\text{cor}}$  en fonction de  $(1/T)$  et  $\log I_p$  en fonction de  $(1/T)$ . Nous pouvons ainsi calculer les valeurs des énergies d'activation apparentes en utilisant les relations suivantes :



**Fig. 9.** Droites d'Arrhénius pour l'étain dans le milieu témoin.

$$I_{\text{cor}} = A \exp(-E/RT)$$

$$I_p = A' \exp(-E'/RT)$$

Où  $E$  et  $E'$  représentent les énergies d'activation apparentes,  $R$  la constante des gaz parfaits et  $A$  et  $A'$  sont des constantes.

Les valeurs des énergies d'activation apparentes trouvées sont :  $E = 14$  KJ/mole et  $E' = 20$  KJ/mole.

Nous remarquons que l'énergie d'activation  $E$  calculée à partir de la densité de courant de corrosion  $I_{\text{cor}}$  est inférieure à celle calculée à partir de la densité de courant de passivation  $I_p$ . Selon certains auteurs (3), les valeurs de  $E$  caractérisent le processus de dissolution de l'étain. Ainsi, lorsque le métal est au potentiel libre de corrosion, il y a probablement formation d'un film mince et poreux. Le processus de corrosion se fait alors à travers ce film. En appliquant une surtension anodique dans le domaine de passivation, le film passif devient compact et protecteur probablement à travers un mécanisme de dissolution-précipitation (3). La mise en solution de l'étain serait plus difficile; ce qui explique la valeur de  $E'$  plus importante par rapport à celle de  $E$ .

## Conclusion

Dans ce travail, nous avons étudié le comportement à la corrosion de l'étain dans une eau synthétique simulée à une eau industrielle. L'effet de la variation du pH du milieu, de la concentration des anions en solution et de la température a été évoqué. Ainsi :

L'étain présente dans le milieu synthétique un phénomène de passivation avec rupture de passivité par attaque localisée.

La variation du pH autour du pH du milieu synthétique (8,2) n'a pas d'effet sur la sensibilité à la piqûration de l'étain.

L'augmentation de la température provoque une accélération du processus de corrosion.

L'étain s'annonce très sensible aux variations de la concentration des anions en solution. En effet, les ions  $\text{Cl}^-$  et  $\text{SO}_4^{2-}$  stimulent la corrosion par piqûre mais restent sans effet notable sur la corrosion uniforme de l'étain. Par contre, les ions  $\text{HCO}_3^-$  réduisent la sensibilité à la piqûration de l'étain dans le milieu étudié.

## Bibliographie

1. M. Pourbaix. Atlas of electrochemical equilibria. Pergamon, Oxford. 1966. p. 475.
2. M. Drogowska, H. Ménard et L. Brossard. J. Appl. Electrochem. **21**, 84 (1991).
3. L. Brossard, M. Drogowska et H. Ménard. Trends Corros. Res. **1**, 209 (1993).
4. S.A.M. Refaey. Electrochim. Acta, **41**, 2545 (1996).
5. P.E. Alvarez, S.B. Ribota, M.E. Folquer, C.A. Gervasi et J.R. Vilche. Corros. Sci. **44**, 49 (2002).
6. C.A. Gervasi, F.E. Varela, J.R. Vilche et P.E. Alvarez. Electrochim. Acta, **42**, 537 (1997).
7. M. Drogowska, H. Ménard et L. Brossard. J. Appl. Electrochem. **140**, 1247 (1993).
8. A. El Rehim, A.A. El Samahi et A. El Sayed. Br. Corros. J. **20**, 196 (1985).
9. S.A.M. Refaey et G. Schwitzebel. Appl. Surf. Sci. **135**, 243 (1998).
10. S.A.M. Refaey. J. Appl. Electrochem. **26**, 503 (1996).
11. H.H. Hamdy, A.S. Sayed et F.M. Nobl. Corros. Sci. **44**, 37 (2002).
12. L. Bazzi, R. Salghi, A. Bouchtarte, Z. El Alami et S. Kertit. Rev.Métallurg. S.G.M. **98**, 189 (2002).
13. L. Bazzi, R. Salghi, E. Zine, S. El Issami et S. Kertit. Can. J. Chem. **80**, 106 (2002).



14. (a) L. Bazzi, S. Kertit et M. Hamdani. *Corrosion*, **51**, 811 (1995); (b) L. Bazzi, S. Kertit et M. Hamdani. *J. Chim. Phys.* **94**, 93 (1997).
15. K. Galic, M. Pavic et N. Cicovic. *Corros. Sci.* **36**, 785 (1994).
16. M. Drogowska, L. Brossard et H. Ménard. *J. Appl. Electrochem.* **19**, 231 (1989).



# Volumetric studies of ion solvation in propylene carbonate + *N,N*-dimethylformamide electrolyte solutions

Yang Zhao, Jianji Wang, Xiaopeng Xuan, and Ruisen Lin

**Abstract:** Apparent molar volumes  $V_{2,\phi}$  and standard partial molar volumes  $V_{2,\phi}^\circ$  for tetraethylammonium bromide ( $\text{Et}_4\text{NBr}$ ), tetrapropylammonium bromide ( $\text{Pr}_4\text{NBr}$ ), tetrabutylammonium bromide ( $\text{Bu}_4\text{NBr}$ ), and tetrahexylammonium bromide ( $\text{Hex}_4\text{NBr}$ ) have been determined at 298.15 K from precise density measurements in solvent mixtures of propylene carbonate (PC) with *N,N*-dimethylformamide (DMF). Combined with our previous data for  $\text{LiClO}_4$  and  $\text{LiBr}$  in the same solvents, ionic molar volumes of  $\text{Li}^+$ ,  $\text{Et}_4\text{N}^+$ ,  $\text{Pr}_4\text{N}^+$ ,  $\text{Bu}_4\text{N}^+$ ,  $\text{Hex}_4\text{N}^+$ , and related anions have been deduced from the extrapolation method suggested by Conway and co-workers. It is shown that the molar volumes of these cations are quite independent of the nature of the solvent and the composition of the solvent mixtures, in contrast to those of  $\text{ClO}_4^-$  and  $\text{Br}^-$  anions. This suggests that the Lewis-base-type solvents with similar molecular volumes have similar interactions with  $\text{Li}^+$ . The constancy in partial molar volume for tetraalkylammonium ions provides helpful evidence for the lack of solvation of large tetraalkylammonium cations in organic solvents. These findings have been interpreted using scaled-particle theory. The results are discussed in terms of ion solvation, packing effects of solvent molecules in the solvation shell, and the electrostriction of solvents.

**Key words:** ionic volumes, propylene carbonate, *N,N*-dimethylformamide, solvent mixtures, solvation, lithium batteries.

**Résumé :** Faisant appel à des mesures précises de densité faites à 298,15 K dans des mélanges de carbonate de propylène (CP) et de *N,N*-diméthylformamide (DMF) comme solvant, on a déterminé les volumes molaires apparents,  $V_{2,\phi}$ , et les volumes molaires partiels standards,  $V_{2,\phi}^\circ$ , du bromure de tétraéthylammonium ( $\text{Et}_4\text{NBr}$ ), du bromure de tétrapropylammonium ( $\text{Pr}_4\text{NBr}$ ), du bromure de tetrabutylammonium ( $\text{Bu}_4\text{NBr}$ ) et du bromure de tétrahexylammonium ( $\text{Hex}_4\text{NBr}$ ). Faisant appel à la méthode d'extrapolation suggérée par Conway et ses collaborateurs, on a combiné ces données avec celles obtenues antérieurement pour le  $\text{LiClO}_4$  et le  $\text{LiBr}$  dans les mêmes solvants pour en déduire les volumes molaires ioniques de  $\text{Li}^+$ ,  $\text{Et}_4\text{N}^+$ ,  $\text{Pr}_4\text{N}^+$ ,  $\text{Bu}_4\text{N}^+$ ,  $\text{Hex}_4\text{N}^+$  et des anions apparentés. Il est démontré que les volumes molaires de ces cations sont assez indépendants de la nature du solvant et de la composition des mélanges de solvants; ce comportement est en opposition à celui des anions  $\text{ClO}_4^-$  et  $\text{Br}^-$ . Ceci suggère que les solvants de type base de Lewis de volumes moléculaires semblables ont des interactions semblables avec le  $\text{Li}^+$ . La constance du volume molaire partiel des ions tétraalkylammonium fournit des indications utiles pour le manque de solvation des cations tétraalkylammonium volumineux dans les solvants organiques. Ces observations ont été interprétées à l'aide de la théorie de la particule scalaire. Les résultats sont discutés en fonction de la solvation des ions, des effets d'entassement des molécules de solvant dans la couche de solvation et de l'électrostriction des solvants.

**Mots clés :** volumes ioniques, carbonate de propylène, *N,N*-diméthylformamide, mélanges de solvants, solvation, batteries au lithium.

[Traduit par la Rédaction]

## Introduction

Molar volumes of electrolytes affect the properties of lithium-battery electrolyte solutions such as conductivity and viscosity, etc. (1). They also influence the behavior of the electrodes during cycling. Therefore, studies of volumetric properties are important for developing an understanding of

ion-solvent and ion-ion interactions in lithium-battery electrolyte solutions.

Literature surveys reveal that there have been numerous studies of conductivity, viscosity, and other properties for lithium-battery electrolyte solutions. However, very little investigation has been carried out on the related volumetric properties. Zana et al. (2) obtained the ionic volume of several electrolytes in PC from densities, ultrasonic vibration potentials, and transference numbers of electrolytes measured at 298.15 K. They compared their results with those deduced by other ionic scales and found that the electrostriction in PC is close to that for water, ethylene glycol, ethanol, and dimethyl sulfoxide. The apparent molar volumes of several electrolytes in solvent mixtures of PC with acetonitrile (AN), dimethoxyethane (DME), and tetrahydrofuran (THF) have been determined by Atkins et al. (3), but the

Received 25 October 2002. Published on the NRC Research Press Web site at <http://canjchem.nrc.ca> on 12 May 2003.

**Y. Zhao and R. Lin.** Department of Chemistry, Zhejiang University, Hangzhou, Zhejiang 310027, P.R. China.

**J. Wang<sup>1</sup> and X. Xuan.** Department of Chemistry, Henan Normal University, Xinxiang, Henan 453002, P.R. China.

<sup>1</sup>Corresponding author (e-mail: [Jwang@henannu.edu.cn](mailto:Jwang@henannu.edu.cn)).



volumes were measured at an electrolyte concentration of  $0.05 \text{ mol dm}^{-3}$ . No standard partial molar volumes were reported for these systems. Couture et al. (4) reported the volumes, heat capacities, and specific conductivities of  $\text{LiClO}_4$  and  $\text{LiBr}$  in mixtures of  $\gamma$ -butyrolactone (BL) with DME or PC. The properties of water in DME, BL, and their mixtures have been compared in the presence of  $\text{LiClO}_4$  and  $\text{LiBr}$ . Recently, Naejus et al. (5) determined the standard partial molar volumes of  $\text{LiClO}_4$ ,  $\text{LiCF}_3\text{SO}_3$ , and  $\text{LiPF}_6$  in PC, ethylene carbonate (EC), and DMC, and of  $\text{LiClO}_4$  in mixtures of EC with dimethyl carbonate (DMC) or PC. Partial molar volumes of  $\text{Li}^+$  and related anions in these solvents have been deduced and the effects are discussed in terms of ion-solvent interactions. The solvation of  $\text{LiAsF}_6$  in PC has been discussed by Afanas'ev et al. (6) on the basis of the dissolution heat, conductivity, and solution density and viscosity. It was shown that the donor-acceptor interaction between  $\text{Li}^+$  ions and the oxygen atoms of the carbonyl groups of PC makes the main contribution to the enthalpy. In a preliminary study (7), the standard partial molar volumes of  $\text{LiClO}_4$  and  $\text{LiBr}$  in solvent mixtures of PC with DMF, AN, THF, and methyl formate (MF) as a function of the mole fraction of the co-solvent have been reported by us. It was shown that these standard partial molar volumes are strongly dependent on the nature of the solvents and that the trends in  $V_{2,\phi}^\circ$  with changes in composition of the solvent mixtures are determined by the interaction volumes of electrolytes with solvents.

To study the solvation of  $\text{Li}^+$  and related anions in PC + DMF mixed solvents, which show potential as battery solvents (8), the partial molar volumes of tetraethylammonium bromide, tetrapropylammonium bromide, tetrabutylammonium bromide, and tetrahexylammonium bromide are reported here. The Conway extrapolation method (9) is used to separate the contribution of the anion and cation. The results are discussed in terms of ion-solvent interactions.

## Experimental

### Materials

$\text{Et}_4\text{NBr}$  (Shanghai Chem. Co., A.R.) was recrystallized from ethanol and dried at 333–353 K under vacuum for 2 days.  $\text{Pr}_4\text{NBr}$  (Fluka, A.T.) was recrystallized from acetone or methanol and dried at 383 K under vacuum for 2 days.  $\text{Bu}_4\text{NBr}$  (Shanghai Chem. Co., A.R.) was recrystallized from acetone or ethyl ether and dried at 333–353 K under vacuum for 2 days.  $\text{Hex}_4\text{NBr}$  (ACROS Organic, New Jersey, U.S.A.) was dried at room temperature under vacuum for 2 days before use.

Propylene carbonate (Luoyang Chemical Factory, A.R.) was dried over 4 Å molecular sieves for several days, refluxed for 5 h in the presence of sodium, and then distilled at reduced pressure. The middle fraction of the distillate was collected. *N,N*-Dimethylformamide (Tianjin Chemical Factory, A.R.) was mixed with 10% (by volume) of benzene (Beijing Chemical Factory, A.R.). The azeotrope was removed by distillation under atmosphere pressure at about 353 K. The product was dried over silica gel and distilled at reduced pressure.

Both solvents are highly hygroscopic, so the purified solvents were stored over  $\text{P}_2\text{O}_5$  in desiccators before use. The

water content, determined by the Karl Fischer method, was less than 100 ppm.

### Measurements

All solutions were prepared by weight, and the concentrations of the electrolytes are expressed as molalities ( $\text{mol kg}^{-1}$ ). Every precaution was taken to minimize contamination by water. The composition of the binary solvents is always represented by mole fraction ( $x$ ) of DMF in the solvent mixtures.

Solution densities accurate to  $\pm 1.5 \times 10^{-5} \text{ g cm}^{-3}$  were determined with an Anton Paar DMA 60/602 vibrating-tube densimeter. The temperature around the density meter cell was controlled to  $298.15 \pm 0.005 \text{ K}$  using a CT-1450 temperature controller and a CK-100 ultracryostat. The densimeter was calibrated with pure water and dry air every day. Other experimental details have been described previously (7, 10).

## Results and discussion

### Molar volume of electrolytes

Apparent molar volumes of tetraalkylammonium bromides in a given solvent were calculated from solution densities by

$$[1] \quad V_{2,\phi} = \frac{M}{\rho} - \frac{10^3(\rho - \rho_0)}{m\rho\rho_0}$$

where  $M$  and  $m$  are, respectively, molar mass and molality of the electrolytes;  $\rho$  and  $\rho_0$  are densities of the ternary solutions and the binary solvents, respectively, in units of  $\text{g cm}^{-3}$ . Apparent molar volumes of tetraalkylammonium bromides in PC + DMF solvent mixtures are given in Table 1.

It was found that  $V_{2,\phi}$  varied linearly with the square root of molalities of the salts in the studied concentration range ( $0.01 \text{ mol kg}^{-1} < m < 0.11 \text{ mol kg}^{-1}$ ).

$$[2] \quad V_{2,\phi} = V_{2,\phi}^\circ + S_V m^{1/2}$$

where  $V_{2,\phi}^\circ$  is the infinite-dilution apparent molar volume and  $S_V$  is the slope. Values of  $V_{2,\phi}^\circ$  obtained by least-squares fitting are listed in Table 2, along with their standard deviations. Our standard partial molar volumes for  $\text{Et}_4\text{NBr}$ ,  $\text{Pr}_4\text{NBr}$ , and  $\text{Bu}_4\text{NBr}$  in PC are, respectively, 166.16, 235.65, and  $304.09 \text{ cm}^3 \text{ mol}^{-1}$ , in excellent agreement with those reported by Zana et al. (2) (166.15, 235.64, and  $304.17 \text{ cm}^3 \text{ mol}^{-1}$ , respectively). No literature data can be found in regards to the mixed solvents.

It can be seen from Table 2 that the standard partial molar volumes of the tetraalkylammonium bromides in a given solvent increase with increasing number of carbon atoms ( $n_C$ ) in the alkyl chains of the cation of the electrolyte and decrease with increasing mole fraction of DMF in the mixtures. The dependence of  $V_{2,\phi}^\circ$  on  $n_C$  in every mixed solvent can be accurately fitted with the following series of linear equations:

$$[3] \quad x_{\text{DMF}} = 0.0000, \quad V_{\text{R}_4\text{NBr}}^\circ = 28.43 + 17.24 n_C$$

$$[4] \quad x_{\text{DMF}} = 0.2500, \quad V_{\text{R}_4\text{NBr}}^\circ = 26.88 + 17.22 n_C$$

$$[5] \quad x_{\text{DMF}} = 0.5000, \quad V_{\text{R}_4\text{NBr}}^\circ = 23.65 + 17.23 n_C$$

$$[6] \quad x_{\text{DMF}} = 0.7500, \quad V_{\text{R}_4\text{NBr}}^\circ = 18.89 + 17.29 n_C$$



**Table 1.** Solution density ( $\rho$ ) and apparent molar volume ( $V_2\phi$ ) for tetraalkylammonium salts in (1 -  $x$ )PC +  $x$ DMF mixtures at 298.15 K as a function of molality of the salts.

$x = 0.0000$			$x = 0.2500$			$x = 0.5000$			$x = 0.7500$			$x = 1.0000$		
$m$ (mol kg <sup>-1</sup> )	$\rho$ (g cm <sup>-3</sup> )	$V_2\phi$ (cm <sup>3</sup> mol <sup>-1</sup> )	$m$ (mol kg <sup>-1</sup> )	$\rho$ (g cm <sup>-3</sup> )	$V_2\phi$ (cm <sup>3</sup> mol <sup>-1</sup> )	$m$ (mol kg <sup>-1</sup> )	$\rho$ (g cm <sup>-3</sup> )	$V_2\phi$ (cm <sup>3</sup> mol <sup>-1</sup> )	$m$ (mol kg <sup>-1</sup> )	$\rho$ (g cm <sup>-3</sup> )	$V_2\phi$ (cm <sup>3</sup> mol <sup>-1</sup> )	$m$ (mol kg <sup>-1</sup> )	$\rho$ (g cm <sup>-3</sup> )	$V_2\phi$ (cm <sup>3</sup> mol <sup>-1</sup> )
<b>Et<sub>4</sub>NBr</b>														
0.0000	1.19933		0.0000	1.13858		0.0000	1.07669		0.0000	1.01091		0.0000	0.94396	
0.01233	1.19947	167.58	0.01348	1.13893	164.42	0.01576	1.07730	161.56	0.01569	1.01171	157.67	0.01438	0.94487	151.54
0.02923	1.19970	166.48	0.02485	1.13923	164.48	0.02729	1.07774	161.71	0.02594	1.01223	157.90	0.02883	0.94576	152.18
0.05273	1.19998	166.53	0.03436	1.13947	164.56	0.04300	1.07834	161.88	0.03625	1.01274	158.09	0.04892	0.94700	152.49
0.06294	1.20010	166.57	0.04901	1.13984	164.59	0.06182	1.07904	162.06	0.05029	1.01344	158.25	0.06429	0.94792	152.96
0.08042	1.20031	166.63	0.06764	1.14031	164.63	0.08194	1.07977	162.29	0.06670	1.01424	158.48	0.07842	0.94876	153.23
0.1020	1.20055	166.72	0.08346	1.14070	164.71	0.09924	1.08040	162.38	0.07984	1.01488	158.62	0.09299	0.94961	153.48
0.1181	1.20074	166.76	0.09066	1.14087	164.72				0.09780	1.01574	158.75	0.1151	0.95089	153.94
<b>Pr<sub>4</sub>NBr</b>														
0.0000	1.19933		0.0000	1.13856		0.0000	1.07681		0.0000	1.01108		0.0000	0.94395	
0.01298	1.19908	235.93	0.01419	1.13855	234.38	0.01458	1.07706	231.36	0.01501	1.01163	227.92	0.01306	0.94466	221.13
0.02428	1.19884	236.12	0.02380	1.13854	234.48	0.02114	1.07718	231.45	0.02408	1.01194	228.20	0.02436	0.94525	221.75
0.02950	1.19874	236.18	0.03882	1.13852	234.62	0.03406	1.07741	231.64	0.03323	1.01226	228.38	0.03940	0.94603	222.28
0.04445	1.19843	236.35	0.04810	1.13851	234.67	0.05035	1.07768	231.85	0.04692	1.01273	228.58	0.04850	0.94649	222.62
0.06718	1.19797	236.39	0.06499	1.13849	234.80	0.06233	1.07788	232.02	0.06594	1.01337	229.00	0.07980	0.94804	223.63
0.07557	1.19780	236.48	0.08030	1.13846	234.83	0.07504	1.07809	232.13	0.08201	1.01389	229.21	0.09928	0.94899	223.89
0.1005	1.19729	236.56	0.09243	1.13844	234.87	0.08783	1.07829	232.25	0.09916	1.01445	229.35			
<b>Bu<sub>4</sub>NBr</b>														
0.0000	1.19934		0.0000	1.13876		0.0000	1.07682		0.0000	1.01081		0.0000	0.94404	
0.01356	1.19865	304.28	0.01451	1.13839	302.77	0.01280	1.07681	300.18	0.01255	1.01110	295.98	0.009645	0.94449	289.47
0.02538	1.19805	304.44	0.02403	1.13815	302.82	0.02414	1.07679	300.31	0.02328	1.01134	296.31	0.01621	0.94478	289.80
0.03225	1.19769	304.79	0.04047	1.13768	302.90	0.03154	1.07678	300.41	0.03403	1.01157	296.73	0.02306	0.94509	290.27
0.04883	1.19688	304.48	0.04939	1.13751	302.94	0.05374	1.07675	300.56	0.05491	1.01201	297.21	0.04552	0.94610	290.18
0.06523	1.19606	304.53	0.05796	1.13729	302.98	0.06551	1.07672	300.66	0.06755	1.01227	297.31	0.06140	0.94672	291.75
0.08636	1.19502	304.62	0.06398	1.13709	303.00	0.08089	1.07670	300.70	0.08080	1.01255	297.37	0.07419	0.94724	292.06
0.1003	1.19434	304.70	0.07141	1.13696	303.01				0.1044	1.01303	297.43	0.1045	0.94847	292.52
<b>Hex<sub>4</sub>NBr</b>														
0.0000	1.19921		0.0000	1.13875		0.0000	1.07599		0.0000	1.01106		0.0000	0.94396	
0.009703	1.19810	442.28	0.008347	1.13812	440.21	0.01436	1.07543	437.32	0.01489	1.01099	434.37	0.009591	0.94424	428.05
0.02384	1.19650	442.35	0.02101	1.13717	440.29	0.02412	1.07506	437.44	0.02508	1.01094	434.46	0.02399	0.94464	428.35
0.03810	1.19491	442.41	0.02991	1.13651	440.36	0.03384	1.07469	437.61	0.03449	1.01090	434.56	0.03397	0.94491	428.74
0.04908	1.19370	442.45	0.05818	1.13444	440.45	0.04380	1.07431	437.64	0.04152	1.01086	434.64	0.04848	0.94529	429.10
0.05501	1.19305	442.45	0.08062	1.13283	440.53	0.04852	1.07413	437.70	0.05009	1.01082	434.69	0.06991	0.94584	429.45



**Table 2.** Standard partial molar volumes ( $V_{2,\phi}^\circ$ ) of tetraalkylammonium bromides and lithium salts in  $(1-x)$ PC +  $x$ DMF mixtures at 298.15 K as a function of the mole fraction of DMF.

$x$	$V_{2,\phi}^\circ$ ( $\text{cm}^3 \text{mol}^{-1}$ )					
	$\text{LiClO}_4^a$	$\text{LiBr}^a$	$(\text{Et})_4\text{NBr}$	$(\text{Pr})_4\text{NBr}$	$(\text{Bu})_4\text{NBr}$	$(\text{Hex})_4\text{NBr}$
0.0000	$37.15 \pm 0.08$	$15.26 \pm 0.11$	$166.16 \pm 0.05$	$235.65 \pm 0.06$	$304.09 \pm 0.05$	$442.16 \pm 0.01$
0.2500	$36.11 \pm 0.03$	$14.23 \pm 0.09$	$164.23 \pm 0.02$	$234.07 \pm 0.03$	$302.56 \pm 0.01$	$440.06 \pm 0.01$
0.5000	$34.30 \pm 0.10$	$11.19 \pm 0.12$	$160.98 \pm 0.03$	$230.71 \pm 0.03$	$299.83 \pm 0.03$	$436.80 \pm 0.06$
0.7500	$31.36 \pm 0.06$	$5.97 \pm 0.16$	$156.96 \pm 0.03$	$227.00 \pm 0.06$	$295.28 \pm 0.02$	$433.96 \pm 0.02$
1.0000	$25.97 \pm 0.20$	$-0.92 \pm 0.16$	$150.29 \pm 0.11$	$219.52 \pm 0.10$	$288.08 \pm 0.14$	$427.20 \pm 0.04$

<sup>a</sup>Reference 7.

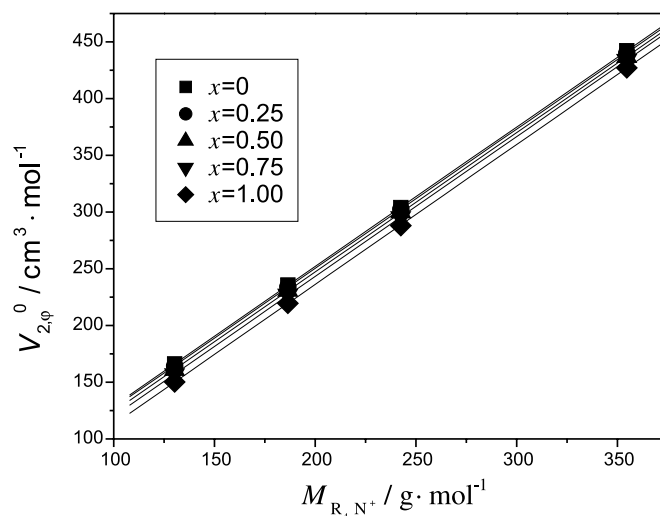
$$[7] \quad x_{\text{DMF}} = 1.0000, \quad V_{\text{R}_4\text{NBr}}^\circ = 11.74 + 17.30 n_{\text{C}},$$

with correlation coefficient  $r \geq 0.9999$ . Values of the slopes in these equations, which represent the contribution of  $-\text{CH}_2$ -groups to the partial molar volumes of tetraalkylammonium salts, are almost identical. However, the intercepts of the above equations, which represent the contribution of  $\text{N}^+\text{Br}^-$ , decrease with increasing mole fraction of DMF. The trend in the partial molar volume for  $\text{N}^+\text{Br}^-$  with changes in the composition of the solvent mixtures is the same as that for the tetraalkylammonium bromides. This indicates that it is the interactions of  $\text{N}^+\text{Br}^-$  with solvent molecules that play an important role in the molar volumes of the salts. It should be pointed out that the above equations can be used to predict the partial molar volumes of other tetraalkylammonium salts in PC + DMF mixed solvents. For example,  $V_{\text{Pen}_4\text{NBr}}^\circ = 373.21 \text{ cm}^3 \text{mol}^{-1}$  has been calculated for  $\text{Pen}_4\text{NBr}$  in PC by eq. [3]. It is in excellent agreement with the value ( $373.49 \text{ cm}^3 \text{mol}^{-1}$ ) reported in literature (2).

On the other hand, the standard partial molar volumes of  $\text{LiClO}_4$  and  $\text{LiBr}$  are also found to be dependent on the nature of the solvents and the composition of the solvent mixtures. To understand these experimental results, it is essential to divide the standard partial molar volumes of the electrolytes into individual ionic contributions.

### Molar volume of ions

The major methods for obtaining individual ionic standard partial molar volumes from whole electrolyte data in both aqueous and nonaqueous solutions were critically reviewed by Hefter and Marcus (11). Of the proposed methods, only the "direct" methods such as the ultrasonic vibration potential method, reference electrolyte methods, extrapolation methods, and the method involving crystal ionic radii of alkali metal and halide ions have either been widely used or may be considered to present relatively few theoretical difficulties. However, the reference electrolyte approach, using an electrolyte such as tetraphenylarsonium tetraphenylborate (TATB), appears to be the least objectionable of those available methods. On the other hand, the extrapolating method for the division of the standard partial molar volumes of the electrolyte into ionic contributions has been demonstrated to be more reliable (5), especially when organic solvents are used. Following the latter suggestion, the approach proposed by Conway et al. (9) has been employed in the present work. This approach was based on the assumption of the lack of solvation of large tetraalkylammonium ions in organic solvents. In the last few years, this method has been used more frequently. For example,

**Fig. 1.** Linear plots of  $V_{2,\phi}^\circ$  vs. the molar mass of  $\text{R}_4\text{N}^+$  ions in  $(1-x)$ PC +  $x$ DMF mixtures as a function of the mole fraction of DMF.

Saha and Das (12) used this method to separate the partial molar volumes of six symmetric tetraalkylammonium bromides in methanol + acetonitrile binary mixtures into ionic contributions. It has been found that  $V_{2,\phi}^\circ$  values for  $\text{R}_4\text{NX}$  are linear functions of the molar mass for the cation ( $M_{\text{R}_4\text{N}^+}$ ):

$$[8] \quad V_{\text{R}_4\text{NX}}^\circ = V_{\text{X}^-}^\circ + bM_{\text{R}_4\text{N}^+}$$

The intercept represents the standard partial molar volume of  $\text{X}^-$ , such as  $\text{Cl}^-$ ,  $\text{Br}^-$ , and  $\text{I}^-$ .

Figure 1 shows the linear plots between the partial molar volume for tetraalkylammonium bromides in PC + DMF mixtures and the molar mass of the corresponding tetraalkylammonium ions. From the standard partial molar volumes of  $\text{Br}^-$  in the mixtures obtained by least-squares analysis, the ionic molar volumes of  $\text{Li}^+$ ,  $\text{ClO}_4^-$ , and the tetraalkylammonium ions have been inferred based on the additivity law for electrolyte molar volumes and are reported in Table 3. It can be seen that  $V_{\text{Li}^+}^\circ$  is quite independent of the nature of the solvents under investigation. The mean value of  $9.5 \text{ cm}^3 \text{mol}^{-1}$  is different from that obtained in previous studies (3) using the TATB assumption ( $V_{\text{Li}^+}^\circ / V_{\text{TB}^-}^\circ = 1.000$ ):  $V_{\text{Li}^+}^\circ = -9 \text{ cm}^3 \text{mol}^{-1}$ . As the ratio  $V_{\text{TA}^+}^\circ / V_{\text{TB}^-}^\circ$  has been found to be solvent dependent, the TATB method may therefore sharply affect the volume of cation relative to those of anions. However, our result is in approximate agreement



**Table 3.** Ionic standard partial molar volume ( $V_{\text{ion}}^\circ$ ) at 298.15 K in  $(1-x)\text{PC} + x\text{DMF}$  mixtures as a function of the mole fraction of DMF.

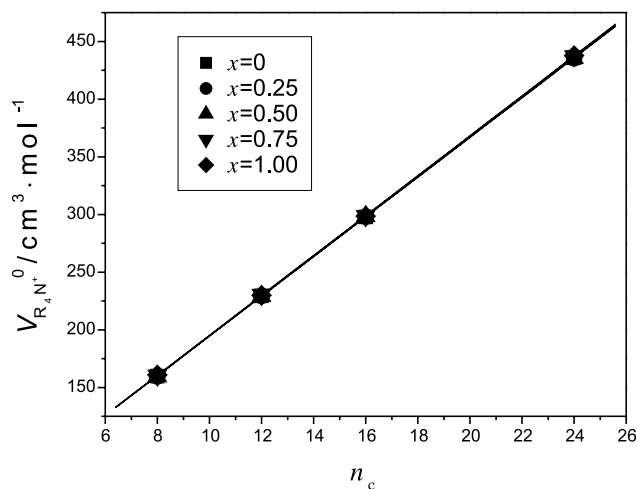
$x$	$V_{\text{ion}}^\circ$ ( $\text{cm}^3 \text{mol}^{-1}$ )						
	$\text{Li}^+$	$\text{Br}^-$	$\text{ClO}_4^-$	$(\text{Et})_4\text{N}^+$	$(\text{Pr})_4\text{N}^+$	$(\text{Bu})_4\text{N}^+$	$(\text{Hex})_4\text{N}^+$
0.0000	$9.1 \pm 0.4$	$6.2 \pm 0.4$	$28.1 \pm 0.4$	$160.0 \pm 0.4$	$229.5 \pm 0.4$	$297.9 \pm 0.4$	$436.0 \pm 0.4$
0.2500	$9.5 \pm 0.7$	$4.7 \pm 0.7$	$26.6 \pm 0.7$	$159.5 \pm 0.7$	$229.4 \pm 0.7$	$297.9 \pm 0.7$	$435.4 \pm 0.7$
0.5000	$9.7 \pm 0.9$	$1.5 \pm 0.9$	$24.6 \pm 0.9$	$159.5 \pm 0.9$	$229.2 \pm 0.9$	$298.3 \pm 0.9$	$435.3 \pm 0.9$
0.7500	$9.4 \pm 0.7$	$-3.4 \pm 0.7$	$22.0 \pm 0.7$	$160.4 \pm 0.7$	$230.4 \pm 0.7$	$298.7 \pm 0.7$	$437.4 \pm 0.7$
1.0000	$9.6 \pm 0.6$	$-10.5 \pm 0.6$	$16.4 \pm 0.6$	$160.8 \pm 0.6$	$230.0 \pm 0.6$	$298.6 \pm 0.6$	$437.7 \pm 0.6$

with the value of  $5.2 \text{ cm}^3 \text{mol}^{-1}$  obtained at 313.15 K using the King method (5). This is attributed to the fact that both the King and Conway methods have the same theoretical base.

It is interesting to find from Table 3 that the partial molar volumes for a given quaternary ammonium ion  $\text{R}_4\text{N}^+$  are almost constant in value from one solvent to another. Similar behavior has also been reported for tetraalkylammonium ions in other pure organic solvents (12, 13). The average values for the partial molar volumes of the tetraalkylammonium ions in PC + DMF mixtures at 298.15 K obtained are as follows:  $V_{\text{Et}_4\text{N}^+}^\circ = 160.0 \pm 0.9 \text{ cm}^3 \text{mol}^{-1}$ ,  $V_{\text{Pr}_4\text{N}^+}^\circ = 229.7 \pm 0.9 \text{ cm}^3 \text{mol}^{-1}$ ,  $V_{\text{Bu}_4\text{N}^+}^\circ = 298.3 \pm 0.9 \text{ cm}^3 \text{mol}^{-1}$ , and  $V_{\text{Hex}_4\text{N}^+}^\circ = 436.4 \pm 0.9 \text{ cm}^3 \text{mol}^{-1}$ . These values are in fair agreement with  $V_{\text{Et}_4\text{N}^+}^\circ = 160.8 \pm 1.0 \text{ cm}^3 \text{mol}^{-1}$ ,  $V_{\text{Pr}_4\text{N}^+}^\circ = 230.8 \pm 0.1 \text{ cm}^3 \text{mol}^{-1}$ ,  $V_{\text{Bu}_4\text{N}^+}^\circ = 298.6 \pm 1.3 \text{ cm}^3 \text{mol}^{-1}$ , and  $V_{\text{Hex}_4\text{N}^+}^\circ$  (at 313.15 K) =  $442.2 \pm 4.8 \text{ cm}^3 \text{mol}^{-1}$  reported by Krumgalz (14) with PC, EC, dimethylsulfoxide, formamide, and *N*-methyl acetamide as solvents at 298.15 K. This constancy in different solvents and solvent mixtures is evidence for the lack of solvation of large tetraalkylammonium cations in organic solvents. Furthermore, the proportionality of the partial molar volumes of tetraalkylammonium cations to the number of alkyl carbon atoms  $n_c$  (see Fig. 2) means that the contribution of  $-\text{CH}_2-$  to the partial molar volumes of these cations is constant. This contribution can be expressed by

$$[9] \quad V_{\text{R}_4\text{N}^+}^\circ = a + V_{\text{CH}_2}^\circ n_c$$

with correlation coefficient  $r \geq 0.9999$ . An average value for  $V_{\text{CH}_2}^\circ$  has been calculated to be  $17.26 \pm 0.04 \text{ cm}^3 \text{mol}^{-1}$ , which is in good agreement with the value of  $17.33 \pm 0.09 \text{ cm}^3 \text{mol}^{-1}$  reported for a series of organic solvents (14) at 298.15 K. Therefore, the contribution of the  $-\text{CH}_2-$  group to the volumes of tetraalkylammonium cation apparently has little to do with the nature of solvent and the composition of the solvent mixtures. The most likely explanation is that the  $-\text{CH}_2-$  group and, accordingly, the hydrocarbon chain for the cations are not solvated by the solvent molecules. The central meaning of the Conway method is fully embodied in these results. Moreover, it is surprising to note that the intercepts of the five straight lines, which are the contributions from  $\text{N}^+$ , are almost identical. An average value of  $22.22 \text{ cm}^3 \text{mol}^{-1}$  was obtained. This suggests that the contribution of  $\text{N}^+$  is also unrelated to the solvent properties. Therefore, it can be concluded that the contribution of  $\text{N}^+\text{Br}^-$  to the molar volumes of the electrolytes is mainly owing to the interaction of  $\text{Br}^-$  with the solvent molecules.

**Fig. 2.** Dependence of partial molar volumes of  $\text{R}_4\text{N}^+$  on the number of carbon atoms in  $(1-x)\text{PC} + x\text{DMF}$  mixtures as a function of the mole fraction of DMF.

### Interactions of ion with the solvents

At infinite dilution, where ion-ion interactions are absent, the partial molar volumes of ions are particularly appropriate for the study of ion-solvent interactions. IR and Raman spectra for PC + DMF mixtures investigated by us (15) indicated that PC and DMF molecules interact very weakly. Density and viscosity measurements (16) confirmed this observation. It can be concluded that the weak interaction between PC and DMF molecules would not affect the interaction of ions with solvents.

IR, Raman, and  $^7\text{Li}$  NMR data (15, 17) suggest that the interactions of  $\text{Li}^+$  with PC or DMF are strong in PC + DMF electrolyte solutions and that anions do not influence solvation of the  $\text{Li}^+$  ions. A coordination number of 4 has been reported for  $\text{Li}^+$  in PC (15) and DMF (17), reflecting the extent of ion solvation. Therefore, a similar solvation mechanism is operative in PC and DMF. Since no great difference in molecular size (molar volumes for PC and DMF at 298.15 K are  $85.2$  and  $77.4 \text{ cm}^3 \text{mol}^{-1}$ , respectively) and solvation properties toward  $\text{Li}^+$  was observed between PC and DMF, it is not surprising that the partial molar volume of  $\text{Li}^+$  is independent of the nature of the pure solvents and the composition of the solvent mixtures.

In a partial molar volume study of ions in carbonate solvents such as EC, DMC, and their mixtures, Naejus et al. (5) pointed out that the independence of  $\text{Li}^+$  volumes on the nature of these solvents could be attributed to the fact that  $\text{Li}^+$



is strongly coordinated by Lewis-base-type solvents. In our opinion, the solvent molar volumes are also an important factor for ion solvation in solvent mixtures. For example,  $\text{Li}^+$  is also solvated strongly by AN, as reported by Atkins et al. (3). However, the molar volume of AN ( $52.9 \text{ cm}^3 \text{ mol}^{-1}$ ) is significantly different from that of PC ( $85.2 \text{ cm}^3 \text{ mol}^{-1}$ ). It is expected that the standard partial molar volumes of  $\text{Li}^+$  in PC + AN mixtures should decrease with increasing mole fraction of AN. This expectation is supported by the results of Atkins et al. (3). Of course, this point should be confirmed by more experimental work.

Because the molar volume of  $\text{Li}^+$  is almost constant in the solvents studied, the dependence of the molar volumes for  $\text{Br}^-$  and  $\text{ClO}_4^-$  on the composition of the solvent mixtures is similar to those for  $\text{LiBr}$  and  $\text{LiClO}_4$  (see Fig. 3), showing a trend that decreases with increasing mole fraction of DMF in the mixtures. According to the Drude–Nernst equation, the electrostatic field of an ion can penetrate much deeper into a low-dielectric-constant solvent such as DMF than into PC, leading to the increased electrostriction of the solvents and the decreased partial molar volumes of ions. This is also responsible for the decreased intercept in eqs. [3–7], which is mainly the contribution of  $\text{Br}^-$ , with the addition of DMF in PC.

Since both PC and DMF have weak acceptor properties (acceptor number ( $A_N$ ) for PC and DMF is 18.3 and 13.6, respectively), anions are usually considered as non-coordinated in these solvents. Steric crowding of solvent molecules around anions will not occur to the same extent as with the cations because of the much larger size of the anions and the weaker interactions with the solvents. Thus, solvent molecules tend to collapse around the anion. It can be expected that the larger the anion, the less steric hindrance there would be to the packing of the solvent molecules, but this effect would be weakened by the decreased charge field around the larger anion ( $\text{ClO}_4^-$ ). Moreover, taking into account the structural differences between the tetrahedral  $\text{ClO}_4^-$  and linear  $\text{Br}^-$ , steric hindrance for the penetration of the solvent will occur for  $\text{ClO}_4^-$  in the bulky solvent molecules, and a higher molar volume than  $\text{Br}^-$  is expected.

### Interpretation by scaled particle theory

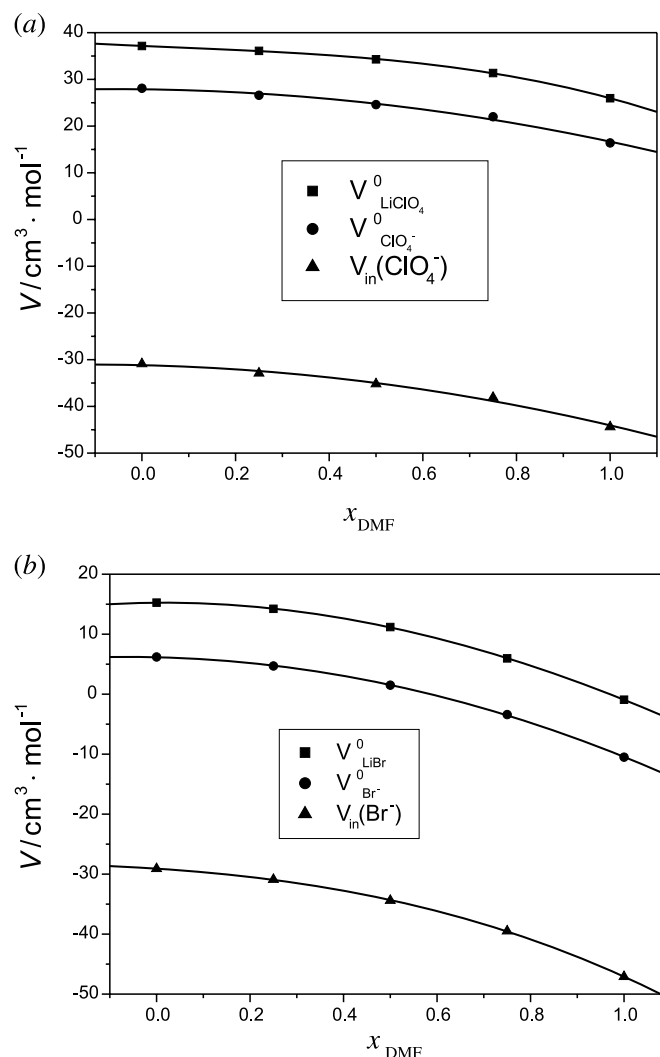
Volumetric properties are quite informative regarding solute–solvent interactions. Changes in the molar volumes of ions reflect the relative electrostriction (negative contribution) of solvent in the presence of a given ion. To see if the above experimental findings can be interpreted theoretically, scaled-particle theory (SPT) (18, 19) was used to evaluate the measured particle volume as a sum of the geometric volume of the ion and the change in the solvent due to its interaction with the ion. That is,

$$[10] \quad V_{2,\phi}^\circ = V_c + V_{\text{in}} + \beta RT,$$

where  $V_c$  is the partial molar volume of cavity formation and  $V_{\text{in}}$  is the interaction volume;  $\beta$  is the isothermal compressibility of the solvent. The term  $\beta RT$  describes the volume effect of the ideal part of the solute dissolution and is often neglected. Cavity volumes for  $\text{Li}^+$ ,  $\text{Br}^-$ , and  $\text{ClO}_4^-$  were calculated from

$$[11] \quad V_c = (4\pi N_0 / 3)(r_1 + \Delta)^3$$

**Fig. 3.** Dependence of the partial molar volume for  $\text{LiClO}_4$ ,  $\text{ClO}_4^-$ ,  $\text{LiBr}$ , and  $\text{Br}^-$  and the interaction volume for  $\text{ClO}_4^-$  and  $\text{Br}^-$  on the mole fraction of DMF in the mixtures.



$$[12] \quad \Delta = (3V_1 / 4\pi N_0)^{1/3} - r_2$$

on the basis of the small spherical ions in the study. Paulings crystal radii (20) are used as ionic radii ( $r_1$ ) in the calculations, and the radii of the solvents ( $r_2$ ) were calculated from the van der Waals volume using the method proposed by Bondi (21). Other details of the calculations can be found elsewhere (7).

The cavity volume of organic cations can be estimated by (22):

$$[13] \quad V_c^\circ(\text{R}_4\text{N}^+) = -33 + 1.42M_{\text{R}_4\text{N}^+}$$

The interaction volumes of these ions with solvent mixtures were then calculated by eq. [10] and reported in Table 4, along with the partial molar volumes of cavity formation.

It can be seen from Table 4 that values of  $V_c$  for  $\text{Li}^+$ ,  $\text{Br}^-$ , and  $\text{ClO}_4^-$  vary slightly with the mole fraction of DMF, whereas those for the tetraalkylammonium ions are constant in the studied mixtures. In fact,  $V_c$  consists of two terms:

$$[14] \quad V_c = V_g + V_v,$$



**Table 4.** Values of  $V_c$  ( $\text{cm}^3 \text{ mol}^{-1}$ ) and  $V_{in}$  ( $\text{cm}^3 \text{ mol}^{-1}$ ) for the ions in  $(1 - x)\text{PC} + x\text{DMF}$  mixed solvents calculated from SPT at 298.15 K.

$x$	$\text{Li}^+$		$\text{Br}^-$		$\text{ClO}_4^-$		$\text{Et}_4\text{N}^+$		$\text{Pr}_4\text{N}^+$		$\text{Bu}_4\text{N}^+$		$\text{Hex}_4\text{N}^+$	
	$V_c$	$V_{in}$	$V_c$	$V_{in}$	$V_c$	$V_{in}$	$V_c$	$V_{in}$	$V_c$	$V_{in}$	$V_c$	$V_{in}$	$V_c$	$V_{in}$
0.0000	3.0	6.1	35.3	-29.1	59.0	-30.9	151.6	8.4	231.1	-1.6	310.6	-12.7	469.7	-33.7
0.2500	3.1	6.4	35.6	-30.9	59.5	-32.9		7.9		-1.7		-12.7		-34.3
0.5000	3.1	6.6	35.9	-34.4	59.8	-35.2		7.9		-1.9		-12.3		-34.4
0.7500	3.2	6.2	36.1	-39.5	60.1	-38.1		8.8		-0.7		-11.9		-32.3
1.0000	3.3	6.3	36.6	-47.1	60.8	-44.4		9.2		-1.1		-12.0		-32.0

where  $V_g$  is the geometric volume occupied by the solute molecule itself and  $V_v$  is the “empty” volume, namely the volume of the void space surrounding the solute molecules (23), which is of the greatest importance for highly structured solvents such as water but is negligible in the case of unstructured solvents such as alkyl carbonates. As a first approximation for low-molecular-weight substances, the value of  $V_g$  can be taken as the van der Waals volume  $V_w$ , which is considered to be independent of the nature of the solvent and the composition of solvent mixtures. Therefore, it is understandable that no significant differences were observed in the  $V_c$  of the ions.

The most interesting result obtained from Table 4 is that the interaction volumes of  $\text{Li}^+$ ,  $\text{Et}_4\text{N}^+$ ,  $\text{Pr}_4\text{N}^+$ ,  $\text{Bu}_4\text{N}^+$ , and  $\text{Hex}_4\text{N}^+$  with the solvents are not sensitive to the nature of solvent and composition of the solvent mixtures, in contrast to the interaction volumes of  $\text{Br}^-$  and  $\text{ClO}_4^-$ . Because the standard partial volumes of ions can be viewed as the sum of the intrinsic volume of the ion (which is independent of the nature of solvents) and the volume resulting from the interaction of the ion with the solvents, the experimental findings for the ionic volumes represented in Table 3 have been interpreted qualitatively by scaled-particle theory.

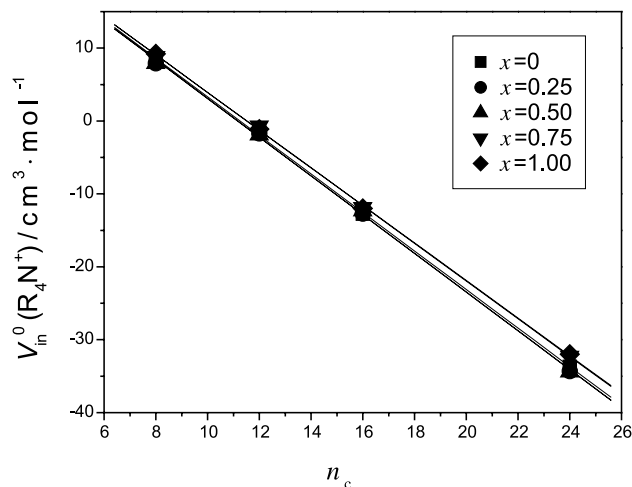
In Fig. 4,  $V_{in}$  values for tetraalkylammonium ions have been plotted vs. the number of carbon atoms in the alkyl chains ( $n_C$ ). Good linear relations are observed. The slopes of the straight lines, which denote the contribution of the  $\text{CH}_2$  groups to the interaction volumes of tetraalkylammonium cations, are nearly the same within experimental uncertainty. The increment per  $\text{CH}_2$  groups is approximately  $-2.6 \text{ cm}^3 \text{ mol}^{-1}$ . The same increment value has been inferred by Naejus et al. (5) in a study of the volumetric properties of electrolytes in mixed-carbonate solvents. The low magnitude of  $V_{in}$  shows that the electrostriction interaction of these solvents by the larger cations is very small. This is in accordance with the conclusion of the lack of solvation of tetraalkylammonium ions in the solvents investigated.

The mean value for  $V_{in}(\text{Li}^+)$  is  $6.3 \text{ cm}^3 \text{ mol}^{-1}$  in the investigated solvents. In the solvation shell, solvent molecules that are coordinated have only restricted motions and do not allow for tight packing of uncoordinated solvent molecules by electrostriction. The excluded volume owing to coordinated molecules tends to attenuate the electrostriction effect. Other solvent molecules belonging to the primary or secondary solvation shell of the ion are oriented by the field in a manner that is incompatible with the normal, mutual orientation in the bulk, producing a region of disorder around the ion. Therefore, the constancy in  $V_{in}(\text{Li}^+)$  values results from a compensation between the negative contribution of the electrostriction term and the positive contribution owing to the excluded volume of the coordinated molecules and the disordered volume around the ion.

Finally, the dependence of the interaction volume between the solvents and  $\text{ClO}_4^-$  or  $\text{Br}^-$  on the mole fraction of DMF in the mixtures is also included in Fig. 3 for the sake of comparison. It is clear that the interaction volumes of these anions determine the trends in the partial molar volume of the ions and even those of  $\text{LiClO}_4$ ,  $\text{LiBr}$ , and the tetraalkylammonium bromides with the changing composition of solvent mixtures. This suggests that anion-solvent interactions are important and interesting.



**Fig. 4.** The relation between the interaction volume  $V_{in}^{\circ} (R_4N^+)$  and the number of carbon atoms of tetraalkylammonium ions in  $(1-x)PC + xDMF$  mixtures as a function of the mole fraction of DMF.



## Conclusions

The ionic molar volumes of  $\text{Li}^+$ , tetraalkylammonium cations, and related anions in PC + DMF mixed solvents have been deduced by the extrapolation method of Conway. It was found that the partial molar volumes of the cations are not sensitive to the nature of solvents and the composition of the solvent mixtures, whereas those of  $\text{Br}^-$  and  $\text{ClO}_4^-$  are. These findings have been interpreted qualitatively by scaled-particle theory.

The constancy in the partial molar volumes of  $\text{Li}^+$  in the mixtures suggests that Lewis-base-type solvents with similar molecular sizes have similar and strong interactions with  $\text{Li}^+$ . The independence of the partial molar volumes of  $\text{Et}_4\text{N}^+$ ,  $\text{Pr}_4\text{N}^+$ ,  $\text{Bu}_4\text{N}^+$ , and  $\text{Hex}_4\text{N}^+$  on the composition of the solvent mixtures provides indirect evidence that these tetraalkylammonium cations are not associated and not solvated in the studied solvents. The central meaning of the Conway extrapolating method is embodied adequately in these results.

The trends in the partial molar volumes of  $\text{LiBr}$ ,  $\text{LiClO}_4$ , and the tetraalkylammonium bromides associated with changes in composition of the solvent mixtures are determined by the interaction volumes of  $\text{ClO}_4^-$  and  $\text{Br}^-$  with the

solvents, suggesting that anion solvation cannot be neglected in the ternary solutions investigated.

## Acknowledgments

We wish to acknowledge financial support from the National Natural Science Foundation of China (Grant No. 29 973 009) and the Research Foundation of Ministry of Education of China.

## References

1. G.E. Blomgren. In *Lithium batteries*. Edited by J.P. Gabano. Academic Press, New York. 1983. Chap. 2.
2. R. Zana, J.E. Desnoyers, G. Perron, R.L. Key, and K. Lee. *J. Phys. Chem.* **56**, 3996 (1982).
3. P. Atkins, G.T. Hefter, and P. Singh. *J. Solution Chem.* **20**, 1059 (1991).
4. L. Couture, J.E. Desnoyers, and G. Perron. *Can. J. Chem.* **74**, 153 (1996).
5. R. Naejus, R. Coudert, P. Willmann, and D. Lemordant. *Electrochim. Acta*, **43**, 275 (1998).
6. V.N. Afanas'ev, L.A. Zyat'kova, E. Yu. Tyunina, and M.D. Chekunova. *Russ. J. Electrochem.* **37**, 46 (2001).
7. J. Wang, Y. Zhao, K. Zhuo, and R. Lin. *Can. J. Chem.* **80**, 753 (2002).
8. V.R. Korch and J.H. Young. *Science*, **204**, 499 (1979).
9. B.E. Conway, R.E. Verall, and J.E. Desnoyers. *Trans. Faraday Soc.* **62**, 2738 (1966).
10. J. Wang, Z. Yan, K. Zhuo, and J. Lu. *Biophys. Chem.* **80**, 179 (1999).
11. G. Hefter and Y. Marcus. *J. Solution Chem.* **26**, 249 (1997).
12. N. Saha and B. Das. *J. Mol. Liq.* **89**, 169 (2000).
13. B. Das and D.K. Hazra. *Bull. Chem. Soc. Jpn.* **68**, 734 (1995).
14. B.S. Krumgalz. *J. Chem. Soc. Faraday. Trans. 1*, **76**, 1887 (1980).
15. X.P. Xuan, J.J. Wang, J.M. Tang, G.R. Qui, and J.S. Lu. *Spectrochim. Acta Part A*, **56**, 2131 (2000).
16. Y. Zhao, J. Wang, X. Xuan, and J. Lu. *J. Chem. Eng. Data*, **45**, 440 (2000).
17. I.S. Perelygin and M.A. Klimchuk. *Russ. J. Chem.* **47**, 1138 (1973).
18. H. Reiss. *Adv. Chem. Phys.* **9**, 1 (1964).
19. F.H. Stillinger. *J. Solution Chem.* **2**, 141 (1973).
20. F. Hirata and K. Arakawa. *Bull. Chem. Soc. Jpn.* **46**, 3367 (1973).
21. A. Bondi. *J. Phys. Chem.* **68**, 44 (1964).
22. R. Caminiti, G. Licheri, P. Piccaluga, and G. Pinna. *Rend. Semin. Fac. Sci. Univ. Cagliari*, XLVV Suppl. 19 (1977).
23. D.P. Kharakoz. *J. Solution Chem.* **21**, 569 (1992).



# Huperzines S, T, and U: New *Lycopodium* alkaloids from *Huperzia serrata*

Chang-Heng Tan, Xiao-Qiang Ma, Guo-Fu Chen, and Da-Yuan Zhu

**Abstract:** Three new *Lycopodium* alkaloids, huperzines S (**1**), T (**2**), and U (**3**), along with eight known compounds, were isolated from the total alkaloids of the whole plant of *Huperzia serrata* (Thunb) Trev. (Huperziaceae). Those novel alkaloids were identified as 2 $\beta$ ,13 $\beta$ -epoxyalopecuridine (**1**), 5 $\alpha$ -hydroxy-6-oxodihydrophlegmariurine A (**2**), and 2,3-dihydro-12-hydroxyhuperzine B (**3**), respectively, by means of spectral techniques including NMR studies.

**Key words:** *Huperzia serrata*, *Lycopodium* alkaloids, huperzines S, T, U.

**Résumé :** À partir des alcaloïdes totaux obtenus de toute la plante *Huperzia serrata* (Thumb) Trev., Huperziaceae, on a isolé trois nouveaux alcaloïdes du *Lycopodium*, les hupérezines S (**1**), T (**2**) et U (**3**) ainsi que huit composés connus. Sur la base de techniques spectrales impliquant des études de RMN, on a établi les structures des nouveaux alcaloïdes qui sont respectivement le 2 $\beta$ ,13 $\beta$ -époxyalopécouridine (**1**), la 5 $\alpha$ -hydroxy-6-oxodihydrophlégmariurine A (**2**) et la 2,3-dihydro-12-hydroxyhuperzine B (**3**).

**Mots clés :** *Huperzia serrata*, alcaloïdes du *Lycopodium*, huperzines S, T et U.

[Traduit par la Rédaction]

## Introduction

The genus *Lycopodium*, which produces a potential therapeutic agent, huperzine A, for treatment of Alzheimer's disease (1, 2), has been extensively studied in recent years (3). This work resulted in the isolation of several new *Lycopodium* alkaloids (4). Recently, we have reported the isolation of new alkaloids with novel frameworks, such as huperzines P (5), Q and its *N*-oxide (6), R (7), and W (8) from *Huperzia serrata* (Thunb.) Trev. (= *Lycopodium serratum* Thunb.). In the continuing search for new chemical constituents on this plant, we examined the low-polarity fraction of the crude alkaloids and isolated huperzines S (**1**), T (**2**), and U (**3**), three new alkaloids with fawcettimine-type, phlegmariurine B-type, and lycodine-type skeletons, respectively, along with eight known compounds, alopecuridine (4) (9), 4 $\alpha$ -hydroxyphlegmariurine A (lycposerramine-E, **5**) (10), des-*N*-methyl- $\alpha$ -obscurine (**6**) (11), phlegmariurine B (**7**) (12), lycodine (**8**) (13), fawcettimine (**9**) (14), huperzine B (**10**) (1), and huperzine (**11**) (15). Like most *Lycopodium* alkaloids, the above compounds exhibited far lower activity against AChE than huperzine A in biological tests. In this paper we report the isolation and structure elucidation of the above alkaloids.

## Results and discussion

Huperzine S (**1**) was obtained as white needles and showed a positive response with Dragendorff's reagent. Its HR-EI-MS spectrum gave the empirical molecular formula

as C<sub>16</sub>H<sub>23</sub>NO<sub>3</sub> (found: [M<sup>+</sup>] 277.1674; C<sub>16</sub>H<sub>23</sub>NO<sub>3</sub> requires 277.1678) with six double bond equivalents. IR bands pointed to the presence of a five-membered ring ketone (1747 cm<sup>-1</sup>) and a hydroxyl (3361 cm<sup>-1</sup>) group. In the <sup>13</sup>C NMR (Table 1) spectrum, two *sp*<sup>3</sup> quaternary carbons signals at  $\delta$  91.7 (C-13) and 46.9 (C-12) and a five-membered ring ketone signal at  $\delta$  217.8 (C-5), diagnostic of fawcettimine-type *Lycopodium* alkaloids (3), demonstrated that **1** was a fawcettimine analogue. Since no IR bands and <sup>13</sup>C NMR signals indicated a double bond, **1** must be pentacyclic, which suggested the possibility that a new ring was formed through an ether bond between two of the three oxygen-bearing carbons ( $\delta$  91.7, 76.6, and 70.0). Its <sup>1</sup>H-<sup>1</sup>H COSY and HMQC spectra displayed three isolated spin systems, -CH<sub>2</sub>CH<sub>2</sub>CH<sub>2</sub>- (C9-C10-C11), -CH<sub>2</sub>CH(OH)CH<sub>2</sub>- (C1-C2-C3), and -CH<sub>2</sub>CH(Me)CH<sub>2</sub>CH<sub>2</sub>- (C14-C15(C16)-C8-C7-C6). The fawcettimine-type skeleton and the presence of an O-atom connected with C-2 and C-13 were deduced by HMBC analysis, as shown in Fig. 1, which illustrated the long-range correlations for C-12/H<sub>2</sub>-11 and H-7, C-13/H<sub>2</sub>-14 and H<sub>2</sub>-11, C-4/H<sub>2</sub>-3, H-2 and H<sub>2</sub>-6, as well as C-5/H<sub>2</sub>-3 and H<sub>2</sub>-6. With the exception that the 4-OH group was assigned as  $\alpha$ -configuration on the basis of biogenetic consideration (from **4**), the relative configuration of huperzine S was elucidated as **1** by NOESY experiments (Fig. 1). Consequently, **1** was formulated as 2 $\beta$ ,13 $\beta$ -epoxyalopecuridine.

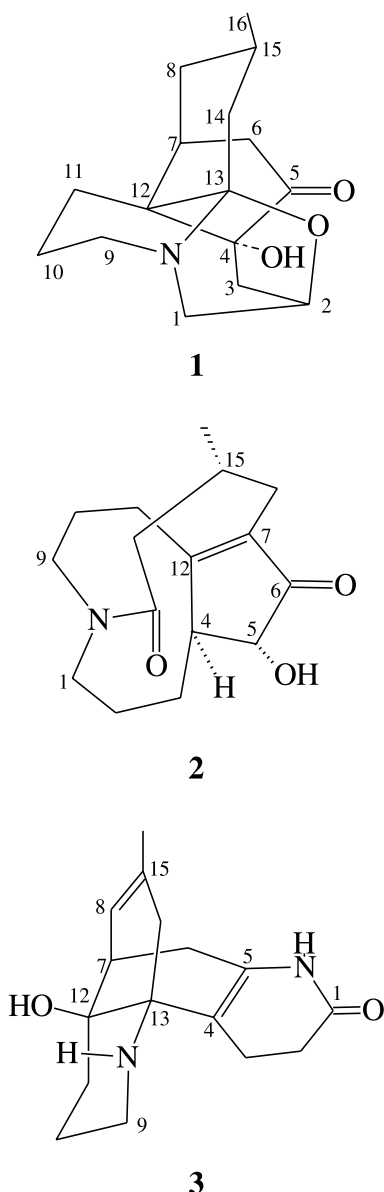
The molecular formula C<sub>16</sub>H<sub>23</sub>NO<sub>3</sub> for compound **2** was deduced from the HR-EI-MS spectrum. IR bands revealed a hydroxyl (3413 cm<sup>-1</sup>), a lactam (1622 cm<sup>-1</sup>), and an  $\alpha,\beta$ -un-

Received 10 December 2002. Published on the NRC Research Press Web site at <http://canjchem.nrc.ca> on 12 May 2003.

C.-H. Tan, X.-Q. Ma, G.-F. Chen, and D.-Y. Zhu.<sup>1</sup> State Key Laboratory of Drug Research, Shanghai Institute of Materia Medica, Shanghai Institutes for Biological Sciences, Chinese Academy of Sciences, 294 Taiyuan Road, Shanghai 200031, P.R. China.

<sup>1</sup>Corresponding author (e-mail: dyzhu@mail.shcnc.ac.cn).





saturated carbonyl ( $1712, 1689, 1456\text{ cm}^{-1}$ ) group. Its  $^{13}\text{C}$  NMR and DEPT (Table 1) spectra displayed signals for one methyl ( $\delta$  22.7, C-16), two N-bearing methylene ( $\delta$  49.8 and 50.5, C-1 and C-9), six high-field methylene ( $\delta$  21.1, 26.9, 30.2, 30.3, 31.9, and 40.0), three methine ( $\delta$  29.2, 50.6, and 73.6), and four  $sp^2$  quaternary carbons ( $\delta$  137.9, 172.7, 173.9, and 206.8), indicating a phlegmariurine B-type framework (12). By comparison with the  $^{13}\text{C}$  NMR data of phlegmariurine B (7) (12), **2** could be assigned a phlegmariurine B carbon skeleton with a rearranged five-membered ring either  $>\text{C}12=\text{C}4-\text{C}5(=\text{O})-\text{C}6(\text{OH})-\text{C}7(\text{H})<$  or  $>\text{C}12=\text{C}7-\text{C}6(=\text{O})-\text{C}5(\text{OH})-\text{C}4<$ . The latter structure was supported by 2D NMR ( $^1\text{H}-^1\text{H}$  COSY, TOCSY, HMQC, and HMBC) analysis (Fig. 2). The 5-OH group was positioned as  $\alpha$ -orientated based on the inspection of H-5 (d,  $J = 1.5\text{ Hz}$ ) and H-4 (br.s) combined with molecular modeling studies. Thus, the relative stereochemistry of huperzine T (**2**) was proved to be 5 $\alpha$ -hydroxy-6-oxodihydrophlegmariurine A.

Huperzine U (**3**) was isolated from the mother liquor that yielded huperzine B (**10**). Its EI-MS peaks at  $m/z$  274 ( $[\text{M}^+]$ ),

**Fig. 1.** Key 2D NMR correlations for **1**.

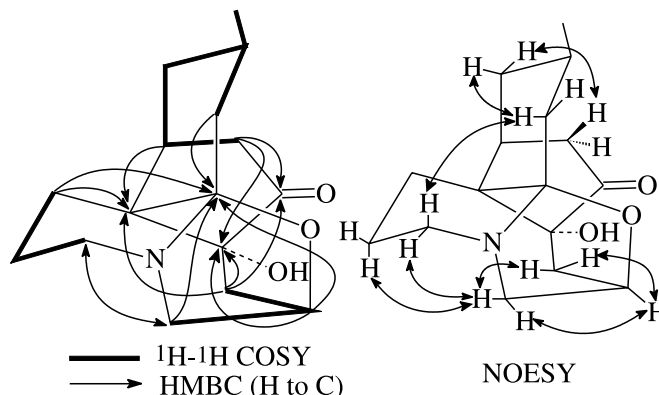


**Fig. 2.** Selected 2D NMR correlations for **2** and **3**.

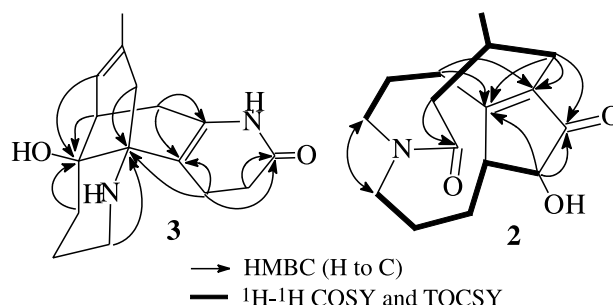


**Table 1.**  $^{13}\text{C}$  NMR chemical shifts for **1**–**3**.

Site	<b>1</b>	<b>2</b>	<b>3</b>
1	59.5 t	49.8 t	173.3 s
2	70.0 d	21.1 t	31.3 t
3	40.8 t	30.2 t	20.5 t
4	76.6 s	50.6 d	108.4 s
5	217.8 s	73.6 d	134.9 s
6	38.8 t	206.8 s	33.3 t
7	40.8 d	137.9 s	42.0 d
8	32.0 t	31.9 t	124.0 d
9	46.9 t	50.5 t	42.7 t
10	20.1 t	26.9 t	20.4 t
11	28.0 t	30.3 t	30.3 t
12	46.9 s	173.9 s	68.6 s
13	91.7 s	172.7 s	63.7 s
14	42.2 t	40.0 t	38.6 t
15	23.5 t	29.2 d	132.6 s
16	22.1 q	22.7 q	23.0 q

257 ( $[\text{M}^+ - 17]$ ), 219 ( $[\text{M}^+ - 55]$ ), and 203 ( $[\text{M}^+ - 71]$ ) indicated a hydroxylated lycodine-type *Lycopodium* alkaloid with a dedihydrogen bridge ring (16). An olefinic signal at  $\delta$  5.36 (br.d,  $J = 5.5\text{ Hz}$ , H-8) and a methyl signal at  $\delta$  1.66 (s, 16-Me) in the  $^1\text{H}$  NMR spectrum indicated the double bond of the bridge ring was localized between C-8 and C-15. In a comparison of the  $^{13}\text{C}$  NMR data of **3** with those of **10**, the main differences were the absence of two  $sp^2$  methines (C-2 and C-3) and an  $sp^3$  methine (C-12) and the presence of two additional methylenes ( $\delta$  31.3 and 20.5) and an O-bearing



**Table 2.**  $^1\text{H}$  NMR (400 MHz,  $J$  in Hz) data of **1–3**.

Site	<b>1</b> (in $\text{CDCl}_3$ )	<b>2</b> (in $\text{CDCl}_3$ )	<b>3</b> (in $\text{CD}_3\text{OD}$ )
1 $\alpha$	3.45 dd (8.7, 4.9)	2.45 td (13.8, 2.0)	—
$\beta$	2.58 d (8.7)	3.91 dt (13.8, 3.2)	—
2 $\alpha$	4.22 ddd (9.2, 5.0, 1.8)	2.10 <sup>a</sup>	2.52 td (10.7, 3.3)
$\beta$	—	1.51 <sup>a</sup>	2.41 dd (10.5, 6.5)
3 $\alpha$	2.96 dd (13.4, 2.6)	2.40 <sup>a</sup>	2.34 <sup>a</sup>
$\beta$	1.62 <sup>a</sup>	2.09 <sup>a</sup>	2.32 <sup>a</sup>
4	—	2.66 br.s	—
5	—	3.84 d (1.5)	—
6 $\alpha$	2.54 dd (18.6, 12.8)	—	2.49 br.d (17.2)
$\beta$	2.30 dd (18.6, 8.9)	—	1.96 d (17.2)
7	1.62 <sup>a</sup>	—	2.41 d (5.9)
8 <i>endo</i>	1.58 dd (13.8, 11.2)	2.44 dd (12.7, 2.0)	5.36 br.d (5.5)
<i>exo</i>	1.29 <sup>a</sup>	1.94 t (12.7)	—
9 $\alpha$	3.06 dt (14.2, 2.1)	3.11 br.d (13.9)	2.81 td (13.0, 3.1)
$\beta$	2.95 td (13.9, 2.6)	4.03 td (13.9, 3.3)	3.09 dt (13.0, 2.0)
10 $\alpha$	1.65 <sup>a</sup>	1.96 br.d (13.1)	1.67 br.d (14.0)
$\beta$	1.30 br.d (13.2)	2.40 qt (12.8, 4.4)	2.13 tt (13.5, 4.0)
11 $\alpha$	2.06 dq (13.5, 2.4)	2.41 br.d (13.7)	1.52 br.d (12.7)
$\beta$	1.52 td (13.5, 3.3)	2.99 td (13.7, 4.4)	1.97 dd (13.4, 4.4)
14 <i>endo</i>	1.62 <sup>a</sup>	1.95 br.d (13.6)	2.34 d (15.6)
<i>exo</i>	1.62 <sup>a</sup>	2.53 dd (13.6, 11.2)	2.02 d (15.8)
15	1.85 m	2.25 m	—
16	0.93 d (6.4)	1.09 d (6.8)	1.66 s

<sup>a</sup>Overlapped signals.

quaternary carbon ( $\delta$  68.6), respectively, in **3**. These data demonstrated that **3** is 2,3-dihydro-12-hydroxyhuperzine B. The postulated structure was further confirmed by HMBC (Fig. 2). Since its optical rotation was zero ( $c$  0.675, MeOH), **3** was considered to be a racemic compound.

As a corollary, we note that the  $^{13}\text{C}$  NMR assignments of C-9 and C-14 of **10** in the literature (1) need to be reversed. Carbon signals at  $\delta$  41.7 and 48.0 could easily be assigned to C-9 and C-14, respectively, via correlation with the distinguishable proton signals ( $\delta$  2.29 and 2.74,  $\text{H}_2$ -9;  $\delta$  2.02 and 1.83,  $\text{H}_2$ -14) in the HMQC spectrum of **10**. This result is in agreement with the  $\gamma$ -gauche effect exerted by the 12-OH of **3** ( $\Delta\delta(\mathbf{3-10})_{\text{C-14}}$ : -9.4;  $\Delta\delta(\mathbf{3-10})_{\text{C-10}}$ : -4.5) (17).

## Experimental

### General

All melting points were determined on a Fisher-Johns melting point apparatus and are uncorrected. The optical rotations were measured using a PerkinElmer 241 MC polarimeter in  $\text{CHCl}_3$  or MeOH. CD spectra were taken on a JASCO J-715 spectropolarimeter. IR spectra were recorded on a Nicolet Magna 750 FT-IR spectrophotometer. All NMR spectra were recorded on a Bruker AM-400 instrument (400 MHz for  $^1\text{H}$  and 100 MHz for  $^{13}\text{C}$ ) in  $\text{CDCl}_3$  or  $\text{CD}_3\text{OD}$  with TMS as internal standard. EI-MS and HR-EI-MS data were obtained with a MAT-95 mass spectrometer. Silica gel (200–300, 400 mesh) and precoated plates of silica gel (HSGF<sub>254</sub>) (Qingdao Haiyang Chemical Group Co. Ltd., Qingdao, P.R. China) were used for column chromatography (CC) and TLC, respectively.

### Plant material

Fresh whole plants of *H. serrata* (Thunb) Trev. (Huperziaceae) were collected in Zhejiang Province, China, in August 2000, and identified by Dr. X-Q. Ma. A voucher sample was deposited in the herbarium of this institute.

### Extraction and isolation

A large-scale isolation of huperzine A (HA) from 50 kg of dry *H. serrata*, as described in ref. 1, separated the total alkaloids into pre-HA, HA, and post-HA fractions in polar order. A part (86 g) of the pre-HA fraction was subjected to silica gel (1.5 kg) CC with petroleum ether, petroleum ether –  $\text{CHCl}_3$  (1:1), and a gradient  $\text{CHCl}_3$ –MeOH (1:0, 50:1, 25:1, 15:1, 10:1, 0:1) and gave 8 fractions in sequence. Fraction (fr.) 2 was chromatographed on silica gel to afford needle-shaped crystals of **1** (24 mg); fr. 3 gave **7** (1.2 g), **5** (560 mg), and **2** (8 mg), respectively, after CC on silica gel with EtOAc– $\text{Me}_2\text{CO}$  (2:1) as eluent and recrystallization ( $\text{Me}_2\text{CO}$ ). Further purification of fr. 4 on a silica gel column ( $\text{CHCl}_3$ –MeOH, 30:1) yielded needle-shaped crystals of **11** (210 mg). Fraction 6 yielded **8** (15 mg), **9** (34 mg), and **4** (5 mg) by repeated silica gel CC ( $\text{CHCl}_3$ –MeOH, 15:1). Compound **10** (1.0 g) was obtained as a powdery precipitate; the mother liquor gave **6** (24 mg) and **3** (18 mg) after repeated purification by silica gel CC ( $\text{CHCl}_3$ –MeOH, 10:1 and 5:1) and recrystallizations.

### Huperzine S (**1**)

White needles from petroleum ether – acetone; mp 146–148°C.  $[\alpha]_D^{25}$ : +156.6 ( $c$  1.345,  $\text{CHCl}_3$ ). IR (KBr)  $\nu_{\text{max}}$  ( $\text{cm}^{-1}$ ): 3361, 1747, 1460, 1054, 897.  $^1\text{H}$  ( $\text{CDCl}_3$ ) and  $^{13}\text{C}$  ( $\text{CDCl}_3$ ) NMR data: see Tables 2 and 1. EI-MS ( $m/z$ ): 277 ( $[\text{M}]^+$ ).



100), 260 (58), 249 (10), 221 (15), 220 (6). HR-EI-MS calcd. for  $C_{16}H_{23}NO_3$ : 277.1678; found: 277.1674 ( $[M^+]$ ).

#### Hyperzine T (2)

Amorphous powder.  $[\alpha]_D^{25}$ :  $-1.493$  ( $c$  0.075,  $CHCl_3$ ), CD ( $c$   $3.2 \times 10^{-3}$ ,  $CHCl_3$ ):  $[\theta]_{272} -1.9 \times 10^4$ . IR (KBr)  $\nu_{max}$  ( $cm^{-1}$ ): 3413, 2926, 2854, 1712, 1689, 1622, 1456.  $^1H$  ( $CDCl_3$ ) and  $^{13}C$  ( $CDCl_3$ ) NMR data: see Tables 2 and 1. EI-MS ( $m/z$ ): 263 ( $[M^+]$ , 10), 262 (4), 256 (4), 219 (5), 206 (43), 167 (3), 149 (9), 123 (6), 117 (9), 85 (64), 83 (100). HR-EI-MS calcd. for  $C_{16}H_{23}NO_3$ : 277.1678; found: 277.1697 ( $[M^+]$ ).

#### Hyperzine U (3)

Colorless powders, mp  $>300^\circ C$  (decomposition).  $[\alpha]_D^{25}$  0 ( $c$  0.675, MeOH), CD ( $c$   $1.8 \times 10^{-3}$ ,  $CH_3OH$ ):  $[\theta]_{240} +1.7 \times 10^4$ ,  $[\theta]_{313} -6.4 \times 10^2$ . IR (KBr)  $\nu_{max}$  ( $cm^{-1}$ ): 3311, 3209, 2679, 2357, 1676, 1653, 1585, 1464, 1433, 1377, 1226, 1124, 1012.  $^1H$  ( $CD_3OD$ ) and  $^{13}C$  NMR ( $CD_3OD$ ) data: see Tables 2 and 1. EI-MS ( $m/z$ ): 274 ( $[M^+]$ , 80), 257 (66), 246 (10), 219 (8), 203 (15), 190 (14), 164 (11), 83 (100). HR-EI-MS calcd. for  $C_{16}H_{22}N_2O_2$ : 274.1681; found: 274.1692 ( $[M^+]$ ).

### Acknowledgments

We are grateful to Professor X-C. Tang of our institute for bioactivity tests. This research was supported, in part, by grants from the National Natural Science Foundation of China (No. 39 900 013 to X-Q. Ma).

### References

1. J-S. Liu, Y-L. Zhu, C-M. Yu, Y-Z. Zhou, Y-Y. Han, F-W. Wu, and B-F. Qi. *Can. J. Chem.* **64**, 837 (1986).
2. X-C. Tang, Y-F. Han, X-P. Chen, and X-D. Zhu. *Acta Pharmacol. Sin.* **7**, 501 (1986).
3. (a) W.A. Ayer. *Nat. Prod. Rep.* **8**, 455 (1991); (b) W.A. Ayer and L.S. Trifonov. *In The alkaloids*. Vol. 45. Edited by G.A. Cordell and A. Brossi. Academic Press, New York. 1994. p 233.
4. (a) W-Y. Gao, Y-M. Li, B-D. Wang, and D-Y. Zhu. *Chin. Chem. Lett.* **10**, 463 (1999); (b) X-J. Tan, H-Q. Wang, H-L. Jiang, W-L. Zhu, S-H. Jiang, D-Y. Zhu, K-X. Chen, and R-Y. Ji. *Acta Chim. Sin.* **58**, 1386 (2000); (c) W-Y. Gao, Y-M. Li, S-H. Jiang, and D-Y. Zhu. *Planta Med.* **66**, 664 (2000); (d) J. Kobayashi, Y. Hirasawa, N. Yoshida, and H. Morita. *Tetrahedron Lett.* **41**, 9069 (2000); (e) M. Tori, T. Shimoji, E. Shimura, S. Takaoka, K. Nakashima, M. Sono, and W.A. Ayer. *Phytochemistry*, **53**, 503 (2000); (f) B-D. Wang, N-N. Teng, and D-Y. Zhu. *Chin. J. Org. Chem.* **20**, 812 (2000); (g) J. Kobayashi, Y. Hirasawa, N. Yoshida, and H. Morita. *J. Org. Chem.* **66**, 5901 (2001); (h) C-H. Tan, X-Q. Ma, S-H. Jiang, D-Y. Zhu. *Nat. Prod. Lett.* **16**, 149 (2002); (i) Y. Hirasawa, H. Morita, and J. Kobayashi. *Tetrahedron*, **58**, 5483 (2002); (j) C-H. Tan, X-Q. Ma, G-F. Chen, S-H. Jiang, and D-Y. Zhu. *J. Asian Nat. Prod. Res.* **4**, 227 (2002); (k) C-H. Tan, Wang B-D, G-F. Chen, S-H. Jiang, and D-Y. Zhu. *Planta Med.* **68**, 188 (2002).
5. C-H. Tan, S-H. Jiang, and D-Y. Zhu. *Tetrahedron Lett.* **41**, 5733 (2000).
6. C-H. Tan, X-Q. Ma, G-F. Chen, and D-Y. Zhu. *Helv. Chim. Acta*, **85**, 1058 (2002).
7. C-H. Tan, G-F. Chen, X-Q. Ma, S-H. Jiang, and D-Y. Zhu. *J. Nat. Prod.* **65**, 1021 (2002).
8. C-H. Tan, G-F. Chen, X-Q. Ma, S-H. Jiang, and D-Y. Zhu. *Chin. Chem. Lett.* **13**, 331 (2002).
9. W.A. Ayer, B. Altenkirk, and Y. Fukazawa. *Tetrahedron*, **30**, 4213 (1974).
10. H. Takayama, K. Katakawa, M. Kitajima, K. Yamaguchi, and N. Aimi. *Tetrahedron Lett.* **43**, 8307 (2002).
11. N. Miller, F. Mees, and J.C. Braekman. *Phytochemistry*, **10**, 1931 (1971).
12. (a) S-H. Tong and G-Q. Xiang. *Zhiwu Xuebao*, **26**, 411 (1984); (b) S-Q. Yuan, L. Feng, and G-M. Gu. *Zhongcaoyao*, **25**, 453 (1994).
13. F.A.L. Anet and M.V. Rao. *Tetrahedron Lett.* **20**, 9 (1960).
14. Y. Inubishi and T. Harayama. *Chem. Pharm. Bull.* **29**, 3418 (1981).
15. S-Q. Yuan and T-T. Wei. *Yaoxue Xuebao*, **23**, 516 (1988).
16. D.B. MacLean. *Can. J. Chem.* **41**, 2654 (1963).
17. T.T. Nakashima, P.P. Singer, L.M. Browne, and W.A. Ayer. *Can. J. Chem.* **53**, 1936 (1975).



# Thermodynamics of mixtures containing alkoxyethanols: Part XVII — ERAS characterization of alkoxyethanol + alkane systems

Juan Antonio González, Susana Villa, Nicolás Riesco, Isaías García de la Fuente, and José Carlos Cobos

**Abstract:** Alkoxyethanol + alkane systems have been examined in the framework of the ERAS model. An exact expression for the molar excess heat capacity at constant pressure,  $C_P^E$ , of solutions formed by a self-associated compound and an inert solvent has been derived. The  $C_P^E$  and the molar excess enthalpies ( $H^E$ ) and excess volumes ( $V^E$ ), as well as the molar enthalpies of vaporization of the pure alkoxyethanols, are represented accurately by ERAS. The calculated curves for  $H^E$  and  $V^E$  are skewed towards high mole fractions of the alkane. The experimental curves are more symmetrical. The opposite behaviour is observed for  $C_P^E$  in solutions with 2-ethoxyethanol, 2-propoxyethanol, or 2-butoxyethanol. The differences between the experimental and theoretical values arise because ERAS does not properly take into account the enhanced dipole–dipole interactions due to the formation of intramolecular H-bonds in alkoxyethanols. As in previous applications, ERAS cannot simultaneously represent molar excess Gibbs energies and liquid–liquid equilibria. DISQUAC, a purely physical theory, improves ERAS predictions for  $H^E$  (except at high temperatures and pressures) and for  $C_P^E$ . Liquid–liquid equilibria are also described more consistently. The self-association of alkoxyethanols via intramolecular H-bonds and the strong dipole–dipole interactions lead to values of the self-association enthalpy and of the adjustable parameter of the physical contribution to  $H^E$  and  $V^E$  that are higher than those of the homomorphic 1-alkanols. In contrast, the equilibrium constants are lower. There is good agreement between the partial molar excess enthalpies at 298.15 K and infinite dilution of 2-alkoxyethanol in 2-alkoxyethanol(1) + *n*-heptane(2) mixtures and the values of the self-association enthalpies.

**Key words:** alkoxyethanol, intermolecular, intramolecular, H-bond, dipole–dipole interactions.

**Résumé :** On a étudié les systèmes alkoxyéthanol + alcane dans le cadre du modèle ERAS. On a développé une expression exacte de la capacité calorifique molaire en excès à pression constante,  $C_P^E$ , des solutions formées par un composé autoassocié et un solvant inerte. Le modèle ERAS permet de faire une représentation exacte de  $C_P^E$ , des enthalpies molaires en excès ( $H^E$ ), des volumes molaires en excès ( $V^E$ ) ainsi que les enthalpies molaires de vaporisation d'alkoxyéthanol purs. Les courbes calculées pour  $H^E$  et  $V^E$  sont biaisées vers les fractions molaires élevées de l'alcane. Les courbes expérimentales sont plus symétriques. Le comportement opposé est observé pour les valeurs de  $C_P^E$  en solutions avec le 2-éthoxyéthanol, le 2-propoxyéthanol et le 2-butoxyéthanol. Les différences entre les valeurs expérimentales et théoriques découlent du fait que la méthode ERAS ne tient pas correctement compte des interactions dipôle–dipôle dont l'importance est augmentée en raison de la formation de liaisons hydrogènes intramoléculaires dans les alkoxyéthanol. Comme il a été observé dans des applications antérieures, ERAS ne permet pas de représenter simultanément les énergies molaires de Gibbs en excès et les équilibres liquide–liquide. DISQUAC, une théorie purement physique, améliore les prédictions d'ERAS pour  $H^E$  (excepté pour les pressions et les températures élevées) et pour  $C_P^E$ . Les équilibres liquide–liquide sont aussi décrits de façon plus cohérente. L'autoassociation des alkoxyéthanol par le biais de liaisons hydrogènes intramoléculaires et les fortes interactions dipôle–dipôle conduisent aux valeurs de l'enthalpie d'autoassociation et du paramètre ajustable de la contribution physique à  $H^E$  et  $V^E$  qui sont plus élevées que celles des 1-alkanols homomorphes. Par ailleurs, les constantes d'équilibre sont plus faibles. Il existe un bon accord entre les valeurs des enthalpies d'autoassociation et les enthalpies molaires partielles en excès à 298,15 K et à dilution infinie d'un 2-alkoxyéthanol dans des mélanges de 2-alkoxyéthanol(1) + *n*-heptane(2).

**Mots clés :** alkoxyéthanol, intermoléculaires, intramoléculaires, liaison hydrogène, interactions dipôle–dipôle.

[Traduit par la Rédaction]

Received 22 November 2002. Published on the NRC Research Press Web site at <http://canjchem.nrc.ca> on 14 May 2003.

J.A. González,<sup>1</sup> S. Villa, N. Riesco, I. García de la Fuente, and J.C. Cobos. G.E.T.E.F., Departamento de Termodinámica y Física Aplicada, Facultad de Ciencias, Universidad de Valladolid, 47071 Valladolid, Spain.

<sup>1</sup>Corresponding author (e-mail: [jagl@termo.uva.es](mailto:jagl@termo.uva.es))



## Introduction

The extended real associated solution (ERAS) model (1) combines the real association solution model (2–5) with Flory's equation of state (6). The excess functions are split into two additive terms that arise from hydrogen-bonding effects (the so-called chemical contribution) and non-polar van der Waals interactions, including free-volume effects (the so-called physical interactions). Moreover, it is assumed that only consecutive linear association occurs, which is described by a chemical equilibrium constant  $K_A$  independent of the chain length  $i$  of the associated species. Under these basic assumptions, ERAS has been applied successfully to the characterization of the following types of systems: self-associated component + inert solvent (alkanol + alkane (7–9), linear primary amine + alkane (10)); self-associated component + polar solvent (alkanol + linear or branched monoether (11–13) or + triethylamine (14)); or to solutions containing two self-associated compounds (1-alkanol + primary or secondary linear amine (15–16)).

Alkoxyethanols,  $\text{CH}_3-(\text{CH}_2)_n-\text{O}-(\text{CH}_2-\text{CH}_2\text{O})_m-\text{OH}$ , are a very interesting class of substances, owing to the presence of the O and OH groups in the same molecule, which allow self-association via inter- and intramolecular hydrogen bonds. The existence of intramolecular hydrogen bonds has been investigated using different spectroscopic techniques (17–22). For molecules of the type  $\text{CH}_3-(\text{CH}_2)_n-\text{O}-(\text{CH}_2-\text{CH}_2)_p-\text{OH}$ , 5-, 6-, and 7-membered rings are formed for  $p = 2, 3$ , and 4, respectively. The formation of intramolecular H-bonds is more favourable when the molecules are in gauche conformations. The stability of these conformations decreases with increasing  $p$ , resulting in a smaller number of rotational conformations favourable for intramolecular H-bonds. On the other hand, the increasing ring size of the intramolecularly H-bonded monomers results in greater restriction to internal rotation and is responsible for increasing the entropy changes involved in the interconversion of the mentioned species into free monomers. Alkoxyethanols with two ether groups and  $m = 1$  form 5-membered rings similar to those previously cited but can also form 8-membered rings of quite different properties. This can be ascribed to the replacement of a methylene group by a less bulky oxygen atom, which increases the stability of the ring system by decreasing the ring strain caused by crowding repulsions (20).

The formation of the intramolecular H-bonds leads to enhanced dipole–dipole interactions in solutions containing alkoxyethanols relative to those present in mixtures with homomorphic alkanols (23). This is supported by the following evidence: (i) The effective dipole moment (24) of alkoxyethanols is higher than that of the homomorphic 1-alkanol (23), and consequently, for a given alkane, the upper critical solution temperature (UCST) of the system including an alkoxyethanol is higher than that of the solution with the homomorphic 1-alkanol (23, 25, 26); (ii) The Trouton's constant of hydroxyethers (27),  $99.58 \text{ J mol}^{-1} \text{ K}^{-1}$ , is closer to the value of non-self-associated compounds (27),  $92.05 \text{ J mol}^{-1} \text{ K}^{-1}$ , than the value for 1-alkanols (27),  $110.88 \text{ J mol}^{-1} \text{ K}^{-1}$ ; (iii)  $H_1^{E,\infty}(\text{2-alkoxyethanol(1) + alkane(2)}) < H_1^{E,\infty}(\text{1-alkanol(1) + alkane(2)})$  (23, 28), where  $H_i^{E,\infty}$  is the excess partial enthalpy at infinite dilution of component  $i$ . This has been interpreted by assuming that the

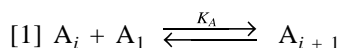
hydroxyether molecules become free via the destruction of the intermolecular H-bonds on addition of the solvent molecules and that each alkoxyethanol molecule forms an intramolecular H-bond between the O and the OH group of the same molecule and thus stabilizes itself (28); (iv) The  $H^E$  curves for alkoxyethanol + alkane mixtures are more symmetrical than those for alcoholic solutions, which are skewed towards low concentration of the self-associated compound. This also demonstrates that the contribution to the thermodynamic properties from the dipole–dipole interactions is higher in solutions with alkoxyethanols than in the corresponding mixtures with the homomorphic 1-alkanols (23).

All these features make the theoretical study of mixtures with alkoxyethanols very interesting. We have presented a complete treatment of hydroxyether + alkane systems (23) in terms of DISQUAC (dispersive-quasichemical) (29–30), a purely physical model based on the rigid lattice model developed by Guggenheim (31). In that work, we showed that the proximity effects between the O and OH groups of alkoxyethanols substantially change the interaction parameters of 1-alkanol +  $\text{CH}_3(\text{CH}_2)_u\text{O}(\text{CH}_2)_v\text{CH}_3$  systems (32).

The purpose of this work is to examine the ability of the ERAS model to represent the thermodynamic properties of alkoxyethanol + alkane mixtures. This is useful to gain insight into the interactions present in such solutions. 2-Methoxyethanol + alkane systems have been previously studied in terms of the MUNIQUAC-RAS model (33), which combines a modification (34) of the UNIQUAC equation (35) with the real-associated solution model (3).

## ERAS model

In this model, only consecutive, linear self-association of the alkoxyethanol is assumed, which can be described by a chemical equilibrium constant  $K_A$  independent of the chain length  $i$  of the associated species.



The dependence of  $K_A$  on temperature is given by the van't Hoff relation

$$[2] \quad K_A = K_{A_0} \exp \left[ -\frac{\Delta h_A^*}{R} \left( \frac{1}{T} - \frac{1}{T_0} \right) \right],$$

where  $\Delta h_A^*$  is the molar association enthalpy related to the intermolecular hydrogen bond formation.  $K_{A_0}$  is the association constant at temperature  $T_0$ . Values of the parameters  $\Delta h_A^*$  and  $K_A$  are required for calculating the chemical contribution to the excess properties. A further molecular parameter used in the ERAS model is the hydrogen bonding volume  $\Delta v_A^*$ , which is assumed to be a negative value, indicating that hydrogen bonding between alkoxyethanol molecules leads to a contraction of the hard-core volume of the molecules.  $K_A$  is a property of the individual alkoxyethanol. The chemical contributions to  $H^E$  and  $V^E$  are given by

$$[3] \quad H_{\text{chem}}^E = x_A K_A \Delta h_A^* (\phi_{1A} - \phi_{1A}^*) - \left[ \frac{P_M^* x_A \Delta v_A^* K_A (\phi_1 - \phi_{1A}^*)}{\bar{V}_M} \right]$$

$$[4] \quad V_{\text{chem}}^E = x_A \bar{V}_M K_A \Delta v_A^* (\phi_{1A} - \phi_{1A}^*)$$



**Table 1.** Physical constants of alkoxyethanols: thermal expansion coefficient,  $\alpha_P$ , isothermal compressibility,  $\kappa_T$ , molar volume,  $V_m$ , and reduction parameters for volume,  $V^*$ , and pressure,  $P^*$ , needed for ERAS calculations.

Alkoxyethanol	$T$ (K)	$\alpha_P$ ( $10^{-3}$ K $^{-1}$ )	$\kappa_T$ ( $10^{-9}$ Pa $^{-1}$ )	$V_m$ (cm $^3$ mol $^{-1}$ )	$V^*$ (cm $^3$ mol $^{-1}$ )	$P^*$ (J cm $^{-3}$ )
2-Methoxyethanol (2ME)	298.15	0.956 <sup>a</sup>	0.7008 <sup>a</sup>	79.25 <sup>b</sup>	66.38	479.8
	303.15	0.956 <sup>a</sup>	0.7199 <sup>a</sup>	79.64 <sup>a</sup>	66.59	474.6
	313.15	0.965 <sup>c</sup>	0.7586 <sup>c</sup>	80.40 <sup>c</sup>	66.88	472.1
	323.15	0.974 <sup>c</sup>	0.797 <sup>c</sup>	81.18 <sup>c</sup>	67.17	471.5
	348.15	0.998 <sup>c</sup>	0.894 <sup>c</sup>	83.21 <sup>c</sup>	67.89	474.2
	373.15	1.024 <sup>c</sup>	0.990 <sup>c</sup>	85.34 <sup>c</sup>	68.55	486.8
2-Ethoxyethanol (2EE)	298.15	1.033 <sup>d</sup>	0.7836 <sup>d</sup>	97.41 <sup>b</sup>	80.89	464.9
	303.15	1.04 <sup>d,e</sup>	0.815 <sup>c</sup>	97.92 <sup>d</sup>	81.03	460.6
	323.15	1.06 <sup>c</sup>	0.930 <sup>c</sup>	99.96 <sup>c</sup>	81.66	449.6
	328.15	1.07 <sup>c</sup>	0.945 <sup>c</sup>	100.47 <sup>c</sup>	81.72	458.9
2-Propoxyethanol (2PE)	298.15	1 <sup>d</sup>	0.792 <sup>d</sup>	114.75 <sup>b</sup>	94.39	491
	303.15	1.003 <sup>d</sup>	0.825 <sup>c</sup>	115.33 <sup>d</sup>	94.64	480.2
2-Butoxyethanol (2BE)	298.15	0.8815 <sup>d</sup>	0.7651 <sup>d</sup>	131.85 <sup>b</sup>	109.77	448.7
	303.15	0.885 <sup>d</sup>	0.810 <sup>f</sup>	132.45 <sup>f</sup>	110.0	432.4
2-(2-Methoxyethoxyethanol) (22MEE)	298.15	0.88 <sup>g</sup>	0.74 <sup>g</sup>	118.2 <sup>g</sup>	98.71	452.7
2-(2-Ethoxyethoxyethanol) (22EEE)	298.15	0.86	0.71	136.37	113.98	467.1
2-(2-Butoxyethoxyethanol) (22BEE)	298.15	0.82	0.67	171.14 <sup>h</sup>	143.56	477.2

<sup>a</sup>Reference 40.<sup>b</sup>Reference 41.<sup>c</sup>Estimated value.<sup>d</sup>Reference 42.<sup>e</sup>Reference 43.<sup>f</sup>Reference 44.<sup>g</sup>Reference 45.<sup>h</sup>Reference 46.**Table 2.** ERAS parameters (this work) and enthalpies of vaporization for alkoxyethanols.

Alkoxyethanol <sup>a</sup>	$K_A$ <sup>b</sup>	$\Delta h_a^*$ (kJ mol $^{-1}$ ) <sup>c</sup>	$\Delta v_A^*$ (cm $^3$ mol $^{-1}$ ) <sup>d</sup>	$s$ (nm $^{-1}$ ) <sup>e</sup>	$\Delta H_v$ (kJ mol $^{-1}$ ) <sup>f</sup>	
					Expl.	Calcd.
2ME	75	-18	-11	15.0	45.17	45.19
2EE	20	-16	-10	14.67	48.21	46.51
2PE	20	-13.5	-9	14.44	52.12	51.40
2BE	20	-13.5	-7	14.28	56.59	54.28
22MEE	20	-13.5	-7	14.53		50.60
22EEE	20	-13.5	-7	14.36		57.78
22BEE	20	-13.5	-7	14.33		70.74

<sup>a</sup>For symbols, see Table 1.<sup>b</sup>Equilibrium constant at 298.15 K for self-association of alkoxyethanol.<sup>c</sup>Self-association enthalpy of alkoxyethanol.<sup>d</sup>Self-association volume of alkoxyethanol.<sup>e</sup>Surface to volume ratio of alkoxyethanol, calculated according to the Bondi method (39).<sup>f</sup>Molar enthalpy of vaporization at 298.15 K (from ref. 49).

where  $\phi_{1A}$  and  $\phi_{1A}^*$  are the hard-core volume fractions of the monomeric species in the mixture and in the pure component, respectively. These volume fractions are related to the hard-core volume fraction  $\Phi_A$  ( $= 1 - \Phi_B = x_A V_A^*/(x_A V_A^* + x_B V_B^*)$ ) and  $K_A$

$$[5] \quad \phi_{1A} = \frac{2K_A\Phi_A + 1 - \sqrt{4K_A\Phi_A + 1}}{2K_A^2\Phi_A}$$

with  $\phi_{1A} \rightarrow \phi_{1A}^*$  as  $\Phi_A \rightarrow 1$ .

The physical contribution is derived from Flory's equation of state, which holds not only for pure components (index A or B) but also for the mixture (M)

$$[6] \quad \frac{\bar{P}_i \bar{V}_i}{\bar{T}_i} = \frac{\bar{V}_i^{1/3}}{\bar{V}_i^{1/3} - 1} - \frac{1}{\bar{V}_i \bar{T}_i}$$

with  $\bar{P}_i = P_i / P_i^*$ ,  $\bar{V}_i = V_i / V_i^*$ , and  $\bar{T}_i = T_i / T_i^*$  being the reduced pressure, volume, and temperature, respectively.  $P_i^*$ ,  $V_i^*$ , and  $T_i^*$  are the corresponding reduction parameters. For associating molecules, the procedure to obtain reduction parameters is somewhat different from the original one applied in Flory's model. In the ERAS model, the reduction parameters are calculated from  $P$ - $V$ - $T$  data (density, thermal expansion,  $\alpha_P$ , and isothermal compressibility,  $\kappa_T$ ), but they also depend on  $K_A$ ,  $\Delta h_A^*$ , and  $\Delta v_A^*$ . The method is explained elsewhere (36–38). The physical contribution is given by



$$[7] \quad H_{\text{phys}}^E = (x_A V_A^* + x_B V_B^*) \left( \frac{\Phi_A P_A^*}{\bar{V}_A} + \frac{\Phi_B P_B^*}{\bar{V}_B} - \frac{P_M^*}{\bar{V}_M} \right)$$

$$[8] \quad V_{\text{phys}}^E = (x_A V_A^* + x_B V_B^*) (\bar{V}_M - \Phi_A \bar{V}_A - \Phi_B \bar{V}_B)$$

The reduction parameters for the binary mixtures are calculated using the mixing rules

$$[9] \quad P_M^* = P_A^* \Phi_A + P_B^* \Phi_B - \Phi_A \theta_B X_{AB}$$

$$[10] \quad T_M^* = \frac{P_M^*}{\frac{P_A^* \Phi_A}{T_A^*} + \frac{P_B^* \Phi_B}{T_B^*}}$$

In eq. [9],  $\theta_B \left( = 1 - \theta_A = \frac{(s_B / S_A) \Phi_B}{\Phi_A + (s_B / S_A) \Phi_B} \right)$  is the surface

fraction of compound *B* calculated using the surface to volume ratios of molecules *B* and *A*,  $s_B$  and  $s_A$ , which are determined from the Bondi method (39) of molecular group contributions.  $X_{AB}$  is the only adjustable parameter of the physical contribution. It characterizes the differences in dispersive intermolecular interactions of molecules *A* and *B* in the mixture and in the pure liquids.

On the other hand, for the application of eqs. [3–4] and [7–8],  $\bar{V}_M$  must be determined. This is done using eq. [6] together with eqs. [9–10].

The chemical and physical contributions for  $C_P^E$  are represented by

$$[11] \quad C_{P,\text{chem}}^E = \frac{x_A K_A \Delta h_A^*}{RT^2} \left( \Delta h_A^* - \frac{P_M^* \Delta V_A^*}{\bar{V}_M} \right) \left[ \frac{\Phi_{1A}(1 - K_A \Phi_{1A})}{1 + K_A \Phi_{1A}} - \frac{\Phi_{1A}^*(1 - K_A \Phi_{1A}^*)}{1 + K_A \Phi_{1A}^*} \right] + x_A K_A (\Phi_{1A} - \Phi_{1A}^*) \Delta V_A^* \left( \frac{\Phi_A \theta_B \frac{dX_{AB}}{dt} + P_M^* \bar{\alpha}_M}{\bar{V}_M} \right)$$

$$[12] \quad C_{P,\text{phys}}^E = (x_A V_A^* + x_B V_B^*) \left( -\frac{\Phi_A P_A^* \bar{\alpha}_A}{\bar{V}_A} - \frac{\Phi_B P_B^* \bar{\alpha}_B}{\bar{V}_B} + \frac{P_M^* \bar{\alpha}_M + \Phi_A \theta_B \frac{dX_{AB}}{dT}}{\bar{V}_M} \right)$$

The expression usually employed for  $C_{P,\text{chem}}^E$  is (7, 11)

$$[13] \quad C_{P,\text{chem}}^E = \frac{x_A K_A \Delta h_A^*}{RT^2} \left[ \frac{\Phi_{1A}(1 - K_A \Phi_{1A})}{1 + K_A \Phi_{1A}} - \frac{\Phi_{1A}^*(1 - K_A \Phi_{1A}^*)}{1 + K_A \Phi_{1A}^*} \right],$$

which is obtained from eq. [11] when  $\Delta h_A^* > \Delta V_A^* P_M^* / \bar{V}_M$ , as in the case of 1-alkanols (7, 11), and it is recognized that  $\Phi_A - \Phi_{1A}^*$  is negligible.

In eqs. [11–12],  $\bar{\alpha}_A$ ,  $\bar{\alpha}_B$ , and  $\bar{\alpha}_M$  are calculated from the equation of state

$$[14] \quad \bar{\alpha}_i = \frac{3(\bar{V}_i^{1/3} - 1)}{T(4 - 3\bar{V}_i^{1/3})}$$

For the activity coefficients, the chemical contribution is written for each component as

$$[15] \quad \ln \gamma_{A,\text{chem}} = \ln \left( \frac{\Phi_{1A}}{x_A \Phi_{1A}^*} \right) - \frac{\Phi_{1A}}{1 - K_A \Phi_{1A}} - \frac{V_A^* \Phi_B}{V_B^*} + \frac{\Phi_{1A}^*}{1 - K_A \Phi_{1A}^*}$$

$$[16] \quad \ln \gamma_{B,\text{chem}} = \ln \left( \frac{\Phi_B}{x_B} \right) + \Phi_A - \frac{V_B^* \Phi_{1A}}{V_A^* (1 - K_A \Phi_{1A})},$$

while the physical contributions are given by the following expressions

$$[17] \quad \ln \gamma_{A,\text{phys}} = \frac{P_A^* V_A^*}{RT} 3\bar{T}_A \left[ \ln \left( \frac{\bar{V}_A^{1/3} - 1}{\bar{V}_M^{1/3} - 1} \right) + \frac{1}{\bar{V}_A} - \frac{1}{\bar{V}_M} \right] + \frac{X_{AB} - TQ_{AB}}{\bar{V}_M} + \frac{V_A^* \theta_B^2}{RT}$$

$$[18] \quad \ln \gamma_{B,\text{phys}} = \frac{P_B^* V_B^*}{RT} 3\bar{T}_B \left[ \ln \left( \frac{\bar{V}_B^{1/3} - 1}{\bar{V}_M^{1/3} - 1} \right) + \frac{1}{\bar{V}_B} - \frac{1}{\bar{V}_M} \right] + \frac{X_{AB} - TQ_{AB}}{\bar{V}_M} + \frac{V_B^* (1 - \theta_B)^2 (s_B / S_A)}{RT},$$

where  $Q_{AB}$  characterizes the entropic contribution to the different intermolecular interactions.

Finally, using the ERAS model, it is possible to evaluate the enthalpy of vaporization (7, 38) of the pure compounds

$$[19] \quad \Delta_m H_v = \frac{P_i^* V_i^*}{\bar{V}_i} - \frac{\Delta h_i^*}{2K_i} (2K_i + 1 - \sqrt{4K_i + 1}) + RT$$

Here, the first term arises from the van der Waals interactions and free volume effects, while the second term is owing to the intermolecular association due to hydrogen bonding.

### Estimation of the ERAS parameters

The reduction parameters  $P_i^*$  and  $V_i^*$  ( $i = A$ ) of the *n*-alkoxyethanols are listed in Table 1. For the alkanes, the reduction parameters were calculated from  $\alpha_p$  and  $\kappa_T$  data available in the literature (40, 47, 48) (Table A1 of Appendix A). The adjustable parameters are  $K_A$ ,  $\Delta h_A^*$ ,  $\Delta V_A^*$ ,  $X_{AB}$ ,  $Q_{AB}$ , and  $dX_{AB}/dT$ .  $K_A$ ,  $\Delta h_A^*$ ,  $\Delta V_A^*$ , and  $X_{AB}$  are fitted to  $H^E$  and  $V^E$  data at 298.15 K for *n*-alkoxyethanol + alkane mixtures. For the  $C_P^E$  calculations, it is necessary to evaluate  $dX_{AB}/dT$ . This was done by taking into account the available  $C_P^E$  and  $H^E$  data at  $T \neq 298.15$  K and assuming a linear dependence with  $T$  for  $X_{AB}$  (7). The entropic parameter  $Q_{AB}$  was obtained from  $G^E$  data (see below) (7, 9).



**Table 3.** ERAS parameters (this work) for the alkoxyethanol + alkane mixtures.

System <sup>a</sup>	<i>T</i> (K)	<i>K<sub>A</sub></i> <sup>b</sup>	<i>X<sub>AB</sub></i> <sup>c</sup> (J cm <sup>-3</sup> )	<i>Q<sub>AB</sub></i> <sup>d</sup> (J cm <sup>-3</sup> K <sup>-1</sup> )	( <i>dX<sub>AB</sub>/dT</i> ) <sup>e</sup> (J cm <sup>-3</sup> K <sup>-1</sup> )
2ME + <i>n</i> -C <sub>6</sub>	313.15	53	46.8	0.053	0.32
	323.15	43	50	0.057	0.32
	348.15	26	58		0.32
2ME + <i>n</i> -C <sub>7</sub>	298.15	75	42		0.32
	323.15	43	50	0.056	0.32
	348.15	26	58		0.32
2ME + <i>n</i> -C <sub>8</sub>	373.15	17	66		0.32
	348.15	26	51		0.32
	373.15	17	63		0.32
2ME + <i>n</i> -C <sub>10</sub>	348.15	26	51		0.32
	373.15	17	63		0.32
2ME + C <sub>6</sub> H <sub>12</sub>	298.15	75	48		0.60
	303.15	66.5	51	0.050	0.60
	323.15	43	63	0.067	0.60
2EE + <i>n</i> -C <sub>6</sub>	298.15	20	27		0.25
	303.15	18	28.2	0.020	0.25
	323.15	12	32	0.025	0.25
2EE + <i>n</i> -C <sub>7</sub>	298.15	20	26		0.25
	303.15	18	27	0.015	0.25
	323.15	12	32	0.02	0.25
2EE + <i>n</i> -C <sub>8</sub>	298.15	20	23		0.30
	303.15	18	24.5		0.30
	328.15	11	32		0.30
2EE + <i>n</i> -C <sub>10</sub>	298.15	20	18		
2EE + <i>n</i> -C <sub>12</sub>	298.15	20	18		
2EE + C <sub>6</sub> H <sub>12</sub>	298.15	20	34		0.35
	303.15	18	36	0.020	0.35
	323.15	12	43	0.025	0.35
	328.15	11	44.75		0.35
2PE + <i>n</i> -C <sub>7</sub>	298.15	20	23		
2PE + <i>n</i> -C <sub>8</sub>	298.15	20	22		0.30
	303.15	18	23.5		0.30
2BE + <i>n</i> -C <sub>6</sub>	303.15	18	22	0.030	0.25
2BE + <i>n</i> -C <sub>7</sub>	298.15	20	20		
	303.15	18	21.2		0.25
2BE + <i>n</i> -C <sub>8</sub>	298.15	20	19		0.25
	303.15	18	20.2		0.25
2BE + <i>n</i> -C <sub>10</sub>	298.15	20	18		
2BE + <i>n</i> -C <sub>12</sub>	298.15	20	18		
2BE + <i>n</i> -C <sub>14</sub>	298.15	20	18		
22BEE + <i>n</i> -C <sub>7</sub>	298.15	20	24		

<sup>a</sup>For symbols, see Table 1.<sup>b</sup>Equilibrium constant for self-association of alkoxyethanol at temperature *T*.<sup>c</sup>Physical interaction parameter in Flory's equation of state.<sup>d</sup>Entropy parameter needed for *G<sup>E</sup>* calculations.<sup>e</sup>Temperature dependence of *X<sub>AB</sub>*, required for calculations on *C<sub>P</sub><sup>E</sup>*.

The values used in this work for *K<sub>A</sub>*,  $\Delta h_A^*$ ,  $\Delta v_A^*$ , and *s* are listed in Table 2. The values of *X<sub>AB</sub>*, *Q<sub>AB</sub>*, and *dX<sub>AB</sub>/dT* are given in Table 3.

## Discussion

### ERAS results

The results of the calculations from the ERAS model for *H<sup>E</sup>*, *V<sup>E</sup>*, *C<sub>P</sub><sup>E</sup>*, and *G<sup>E</sup>* are presented in Tables 4–7 (see also

Figs 1–6). For *H<sup>E</sup>*, *C<sub>P</sub><sup>E</sup>*, and *G<sup>E</sup>*, these values are compared with those obtained using DISQUAC with the interaction parameters previously determined (23).

The composition dependence of *H<sup>E</sup>* is better represented by DISQUAC than by ERAS except when the measurements were carried out at very high temperatures and (or) pressures. See, for example, the results for the 2-methoxyethanol + *n*-heptane system at 373.15 K and 15 MPa (Table 4). In this case, the term  $\bar{P}_i \bar{V}_i / \bar{T}_i$  in the equation of



**Table 4.** Molar excess enthalpies,  $H^E$ , for alkoxyethanol(1) + alkane(2) mixtures at temperature  $T$  and equimolar composition.

System <sup>a</sup>	$T$ (K)	$N^b$	$H^E(x_1 = 0.5)$ (J mol <sup>-1</sup> )		dev( $H^E$ ) <sup>c</sup> (J mol <sup>-1</sup> )		DQ <sup>d</sup>	Ref.
			Expl.	ERAS	Expl.	ERAS		
2ME + <i>n</i> -C <sub>6</sub>	323.15	15	1367	1464	0.006	0.064	0.042	50
	348.15	13	1680 <sup>e</sup>	1705	0.009	0.091	0.035	50
2ME + <i>n</i> -C <sub>7</sub>	298.15	30	751 <sup>f</sup>	688	0.021	0.098	0.065	51
		7	697 <sup>g</sup>	629	0.004	0.190	0.067	28
	323.15	14	1470	1593	0.008	0.057	0.051	50
	348.15	14	1795 <sup>e</sup>	1847	0.007	0.066	0.044	50
2ME + <i>n</i> -C <sub>8</sub>	373.15	11	2146 <sup>e</sup>	2154	0.003	0.078	0.13	50
	348.15	11	1891	1923	0.006	0.063	0.030	50
	373.15	11	2270	2253	0.002	0.059	0.21	50
2ME + <i>n</i> -C <sub>10</sub>	348.15	10	1965	2127	0.006	0.090	0.061	50
	373.15	10	2451	2485	0.002	0.064	0.18	50
2ME + C <sub>6</sub> H <sub>12</sub>	298.15	19	1083	1154	0.010	0.076	0.068	52
		21	1064		0.008	0.095	0.090	40
	303.15	21	1140	1200	0.004	0.083	0.075	40
2EE + <i>n</i> -C <sub>7</sub>	298.15	21	1124	1156	0.004	0.045	0.052	53
2EE + <i>n</i> -C <sub>8</sub>	298.15	9	945	1172	0.014	0.180	0.018	54
		19	1130		0.003	0.052	0.043	55
2EE + C <sub>6</sub> H <sub>12</sub>	298.15	21	1072	1073	0.002	0.048	0.041	55
2PE + <i>n</i> -C <sub>7</sub>	298.15	21	974	987	0.003	0.050	0.033	28
2PE + <i>n</i> -C <sub>8</sub>	298.15	21	1023	1040	0.003	0.064	0.040	64
2BE + <i>n</i> -C <sub>7</sub>	298.15	21	903	918	0.004	0.045	0.036	28
		20	850		0.015	0.080	0.058	56
		28	904		0.007	0.076	0.066	57
2BE + <i>n</i> -C <sub>8</sub>	298.15	21	919	971	0.001	0.063	0.049	57
		19	965		0.005	0.068	0.051	64
2BE + <i>n</i> -C <sub>10</sub>	298.15	18	1076	1073	0.005	0.074	0.051	57
2BE + <i>n</i> -C <sub>12</sub>	298.15	20	1167	1191	0.003	0.071	0.048	57
2BE + <i>n</i> -C <sub>14</sub>	298.15	20	1270	1292	0.002	0.062	0.038	57
22BEE + <i>n</i> -C <sub>7</sub>	298.15	19	1008	1025	0.003	0.034	0.029	46

<sup>a</sup>For symbols, see Table 1.<sup>b</sup>Number of data points.<sup>c</sup>dev( $H^E$ ) = deviation( $H^E$ ) =  $\left\{ \sum [(H_{\text{exp}}^E - H_{\text{calc}}^E) / H_{\text{exp}}^E]^2 \right\}^{1/2}$ .<sup>d</sup>DISQUAC calculations using the interaction parameters given in ref. 23.<sup>e</sup>Experimental data at 15 bars (1 bar = 10<sup>5</sup> Pa).<sup>f</sup> $x_1 = 0.1101$ .<sup>g</sup> $x_1 = 0.1000$ .

state (eq. [6]), only negligible at atmospheric pressure, was included in the ERAS calculations.

ERAS provides  $V^E$  curves skewed towards high mole fractions of the alkane (Figs 3–4). Note that the predicted  $H^E$  curves are also slightly shifted towards that region (Fig. 2). The experimental curves are more symmetrical. Such behaviour may be interpreted, assuming that, for the solutions studied here, the model overestimates the chemical contribution to these thermodynamic properties. It should be noted that typically the experimental  $H^E$ ,  $V^E$ , and  $C_P^E$  curves are also shifted toward the region of high alkane mole fraction in solutions with 1-alkanols (24).

At 303.15 K, the experimental  $C_P^E$  curve for the 2-methoxyethanol(1) + cyclohexane(2) system is rather symmetrical (40) (Fig. 5). In contrast, the  $C_P^E$  curve is skewed towards low mole fractions of 2-alkoxyethanol in solutions of 2-ethoxyethanol, 2-propoxyethanol, or 2-butoxyethanol with

*n*-octane (64) (Fig. 6). In the case of the 2-methoxyethanol mixture, the different shape of the  $C_P^E$  curve may be ascribed to the existence of large fluctuations in concentration due to the proximity of the UCST (294.58 K (65)). Consequently, the importance of the self-association of 2-methoxyethanol becomes less relevant, and the model properly describes the  $C_P^E$  curve with  $C_{P,\text{phys}}^E > C_{P,\text{chem}}^E$ . For the same reason,  $H^E$  for 2-methoxyethanol + *n*-alkane mixtures is well represented at high temperatures and pressures. The inequality  $C_{P,\text{phys}}^E > C_{P,\text{chem}}^E$  is still valid for the 2-ethoxyethanol, 2-propoxyethanol, or 2-butoxyethanol + *n*-octane systems and leads to more symmetrical curves than the experimental ones (Fig. 6). That is, at room temperature the experimental data indicate that the more important contribution to  $C_P^E$  comes from the structure of the solution. ERAS cannot represent this behaviour because  $C_{P,\text{phys}}^E > C_{P,\text{chem}}^E$ . So, for the systems including 2-ethoxyethanol, 2-propoxyethanol, or 2-butoxy-



**Table 5.** Molar excess volumes,  $V^E$ , for alkoxyethanol(1) + alkane(2) mixtures at temperature  $T$  and equimolar composition.

System <sup>a</sup>	$T$ (K)	$V^E(x_1 = 0.5)$ (cm <sup>3</sup> mol <sup>-1</sup> )		
		Expl.	ERAS	Ref.
2ME + C <sub>6</sub> H <sub>12</sub>	298.15	0.910	0.878	40
	303.15	0.951	1.10	40
2EE + <i>n</i> -C <sub>6</sub>	298.15	0.368	0.351	58
	303.15	0.352	0.490	58
2EE + <i>n</i> -C <sub>7</sub>	298.15	0.635	0.613	58
		0.6147		59
2EE + <i>n</i> -C <sub>8</sub>	303.15	0.653	0.722	58
	298.15	0.708	0.745	58
		0.738		43
		0.753		42
	303.15	0.795	0.853	42
	328.15	1.004	1.167	43
2EE + <i>n</i> -C <sub>10</sub>	298.15	0.876	0.898	58
2EE + <i>n</i> -C <sub>12</sub>	298.15	0.898	1.060	58
2EE + C <sub>6</sub> H <sub>12</sub>	298.15	0.900	0.948	43
	328.15	1.087	1.340	43
2PE + <i>n</i> -C <sub>8</sub>	298.15	0.588	0.595	42
	303.15	0.625	0.709	42
2BE + <i>n</i> -C <sub>6</sub>	303.15	0.363	0.247	44
2BE + <i>n</i> -C <sub>7</sub>	303.15	0.470	0.462	44
2BE + <i>n</i> -C <sub>8</sub>	298.15	0.444	0.442	42
	303.15	0.461	0.616	42

<sup>a</sup>For symbols, see Table 1.

ethanol, the model cannot simultaneously describe their rather symmetrical  $H^E$  curves and the corresponding asymmetric  $C_P^E$  curves.

The composition dependence of  $C_P^E$  is also usually better represented by DISQUAC (Table 6, Figs. 5–6), although  $V^E = 0$  in terms of this rigid lattice theory. ERAS yields a quite satisfactory description for  $V^E$  (Table 5, Figs. 3–4).

Table 7 lists results for  $G^E$  using the entropic parameters  $Q_{AB}$  collected in Table 3. These parameters were determined from  $G^E$  data available in the literature. As in the case of 1-alkanol + alkane mixtures (7), the same  $Q_{AB}$  parameter cannot be used to simultaneously represent vapor–liquid equilibria and liquid–liquid equilibria. So, for 2-methoxyethanol + cyclohexane, the calculated UCST is 305 K using  $Q_{AB} = 0.07$  (DISQUAC gives 304 K for the UCST; the measured UCST (65) is 294.58 K). With this  $Q_{AB}$  value, ERAS predicts for the cited system  $G^E(x = 0.5, 305 \text{ K}) = 1339 \text{ J mol}^{-1}$ , which is quite different from the values given in Table 7 at 303.15 K and 323.15 K. This is one of the most important limitations of the ERAS model and of any association theory, as the type of association normally observed is not sufficient by itself to produce phase separation (66). Nevertheless, at temperatures far from the UCST, both models give similar results. This is the case for the 2-butoxyethanol + *n*-hexane system at 303.15 K (Table 7).

### The ERAS parameters

It is interesting to compare  $K_A$ ,  $\Delta h_A^*$ , and  $\Delta v_A^*$  for alkoxyethanols and homomorphic 1-alkanols. We note that  $\Delta h_A^*$  increases when passing from 1-alkanol (–25.1 kJ mol<sup>-1</sup>) to

**Table 6.** Molar excess heat capacities,  $C_P^E$ , for alkoxyethanol(1) + alkane(2) mixtures at temperature  $T$  and equimolar composition.

System <sup>a</sup>	$T$ (K)	$C_P^E(x_1 = 0.5)$ (J mol <sup>-1</sup> K <sup>-1</sup> )			Ref.
		Expl.	ERAS	DQ <sup>b</sup>	
2ME + C <sub>6</sub> H <sub>12</sub>	298.15	14.35	14.4	14.1	40
		13.0			60
	303.15	13.71	14.2	13.3	40
2EE + <i>n</i> -C <sub>8</sub>	298.15	11.14	12.6	11.1	64
2PE + <i>n</i> -C <sub>8</sub>	298.15	10.30	11.6	10.2	64
2BE + <i>n</i> -C <sub>8</sub>	298.15	9.38	10.4	8.3	64

<sup>a</sup>For symbols, see Table 1.<sup>b</sup>DISQUAC calculations using the interaction parameters given in ref. 23.**Table 7.** Molar excess Gibbs energies,  $G^E$ , for alkoxyethanol(1) + alkane(2) mixtures at temperature  $T$  and equimolar composition.

System <sup>a</sup>	$T$ (K)	$G^E(x_1 = 0.5)$ (J mol <sup>-1</sup> )			Ref.
		Expl.	ERAS	DQ <sup>b</sup>	
2ME + <i>n</i> -C <sub>6</sub>	313.15	1590	1514	1492	61
	323.15	1600	1537	1495	61
2ME + <i>n</i> -C <sub>7</sub>	323.15	1640	1563	1567	61
2ME + C <sub>6</sub> H <sub>12</sub>	303.15	1500	1426	1351	61
	323.15	1520	1479	1351	61
2EE + <i>n</i> -C <sub>6</sub>	303.15	1330	1249	1207	62
	323.15	1340	1261	1209	62
2EE + <i>n</i> -C <sub>7</sub>	303.15	1370	1282	1283	62
	323.15	1380	1337	1284	62
2EE + C <sub>6</sub> H <sub>12</sub>	303.15	1230	1210	1111	62
	323.15	1240	1252	1099	62
2BE + <i>n</i> -C <sub>6</sub>	303.15	1030	1025	1054	63

<sup>a</sup>For symbols, see Table 1.<sup>b</sup>DISQUAC calculations using the interaction parameters given in ref. 23.

alkoxyethanol (see Table 2). These increases in  $\Delta h_A^*$  indicate that the intermolecular H-bonds between 1-alkanol molecules are stronger than between alkoxyethanol molecules. In terms of the ERAS model, only consecutive linear self-association is assumed, while ring formation is neglected. That is, the model does not take into account the self-association via intramolecular hydrogen bonding characteristic of the alkoxyethanols. This means that ERAS probably overestimates the magnitude of  $\Delta h_A^*$ . In contrast,  $K_A(1\text{-alkanol}) > K_A(\text{alkoxyethanol})$ . So, at 298.15 K,  $K_A(1\text{-butanol}) = 175$  (37, 67) while  $K_A(2\text{-methoxyethanol}) = 75$  (Table 2) and  $K_A(1\text{-decanol}) = 88$  (37, 67);  $K_A(2\text{-(2-butoxyethoxyethanol)}) = 20$  (Table 2). The more relevant contribution of dipole–dipole interactions to the thermodynamic properties of alkoxyethanol + alkane mixtures is represented by the large values of the  $X_{AB}$  parameter. For example, at 298.15 K,  $X_{AB} = 5.42 \text{ J cm}^{-3}$  for 1-hexanol + *n*-hexane (7); for 2-propoxyethanol + *n*-heptane,  $X_{AB} = 23 \text{ J cm}^{-3}$ . Similar behaviour is observed in 1-alkanol + linear organic carbonate systems (67).

The value  $\Delta v_A^* = -5.6 \text{ cm}^3 \text{ mol}^{-1}$ , widely used for 1-alkanol + alkane mixtures (37, 67), differs from those listed in Table 2. A comparison of  $\Delta v_A^*$  values becomes difficult because other values of  $\Delta v_A^*$  have been used for 1-alkanols in order to provide a more accurate representation of the  $V^E$ .



**Fig. 1.**  $H^E$  for the 2-methoxyethanol(1) + *n*-heptane(2) system. Symbols, experimental data: (●)  $T = 298.15$  K (51); (■)  $T = 373.15$  K and 15 bar (1 bar =  $10^5$  Pa) (50). Solid lines, ERAS calculations. Dashed lines, chemical and physical contributions at 373.15 K and 15 bar.

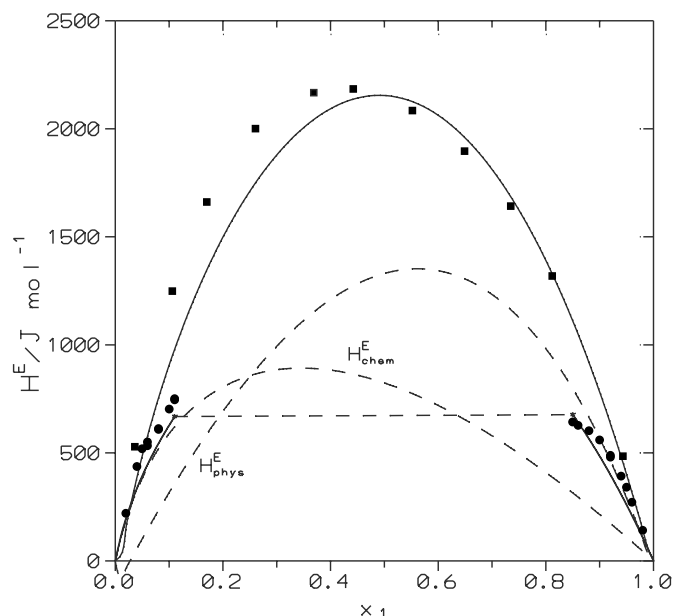
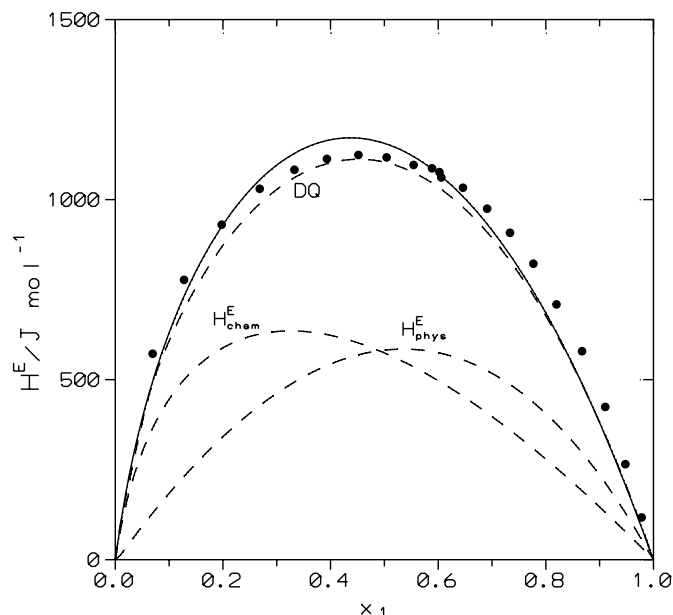


**Fig. 2.**  $H^E$  for the 2-ethoxyethanol(1) + *n*-heptane(2) system at 298.15 K. Symbols, experimental data (53). Solid lines, ERAS calculations. Dashed lines, chemical and physical contributions or DISQUAC (DQ) results (23).



So,  $\Delta v_A^* = -9 \text{ cm}^3 \text{ mol}^{-1}$  for ethanol when mixed with *n*-hexane (7); or  $-5.6 \text{ cm}^3 \text{ mol}^{-1}$  when mixed with *n*-hexadecane (7); or  $\Delta v_A^* = -6.9 \text{ cm}^3 \text{ mol}^{-1}$  for 1-hexanol when mixed with *n*-hexane (7). The  $\Delta v_A^*$  values determined in this work provide a reasonable description of the corresponding  $V^E$  curves.

**Fig. 3.**  $V^E$  for the 2-ethoxyethanol(1) + *n*-heptane(2) system at 298.15 K. Symbols, experimental data (59). Solid lines, ERAS calculations. Dashed lines, chemical and physical contributions.

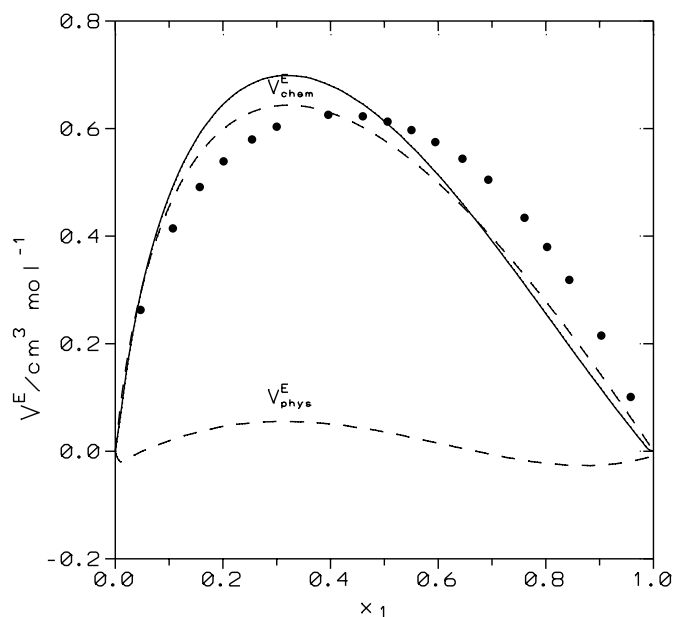
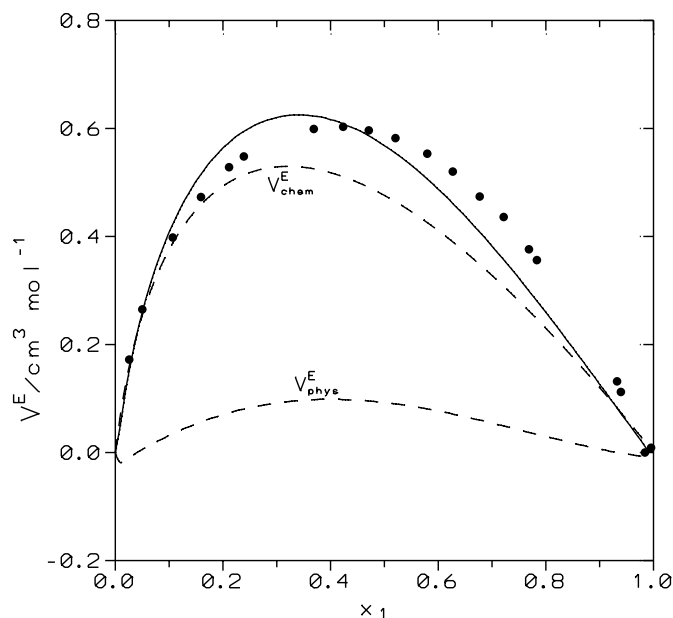


**Fig. 4.**  $V^E$  for the 2-propoxyethanol(1) + *n*-octane(2) system at 298.15 K. Symbols, experimental data (42). Solid lines, ERAS calculations. Dashed lines, chemical and physical contributions.



The  $K_A$ ,  $\Delta h_A^*$ , and  $\Delta v_A^*$  parameters for alkoxyethanols reported in this article are supported by the ERAS predictions for the molar enthalpy of vaporization (Table 2). In addition, the experimental  $H_1^{E,\infty}$  values (28) at 298.15 K for  $\text{CH}_3\text{-(CH}_2)_n\text{-O-CH}_2\text{-CH}_2\text{-OH(1) + } n\text{-heptane(2)}$  are in good agreement with our  $\Delta h_A^*$  values ( $H_1^{E,\infty}$  (kJ mol $^{-1}$ ) = 17.6, 15.5, 15.5, and 14.4, respectively, for  $n = 0, 1, 2$ , and 3)

Finally, it should be emphasized that the relative variation of the  $K_A$  and  $\Delta h_A^*$  parameters is consistent with the variation encountered previously for the enthalpic interchange coefficient.



**Fig. 5.**  $C_p^E$  for the 2-methoxyethanol(1) + cyclohexane(2) system at 303.15 K. Symbols, experimental data (40). Solid lines, ERAS calculations. Dashed lines, chemical and physical contributions or DISQUAC (DQ) results (23).

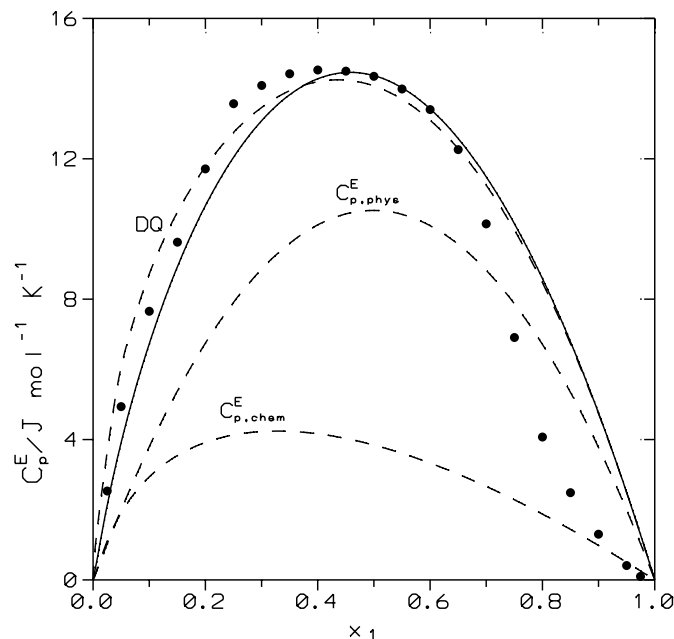
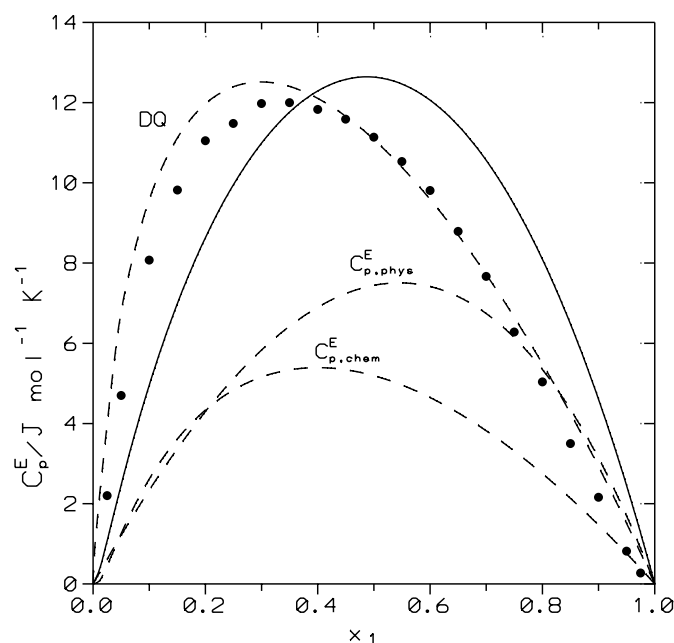
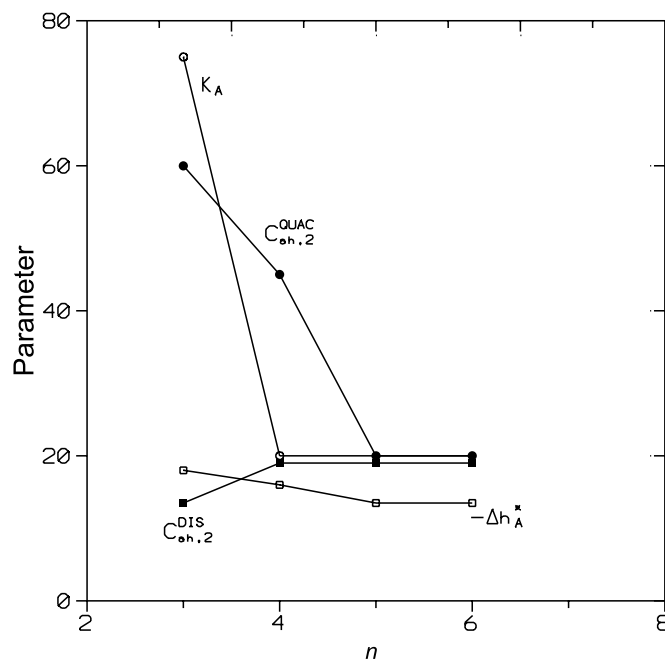


**Fig. 6.**  $C_p^E$  for the 2-ethoxyethanol(1) + *n*-octane(2) system at 298.15 K. Symbols, experimental data (64). Solid lines, ERAS calculations. Dashed lines, chemical and physical contributions or DISQUAC (DQ) results (23).



cients in the DISQUAC model (Fig. 7). For instance, the excellent results obtained for  $H^E$  for the 2-(2-butoxyethoxy)ethanol + heptane system (Table 4) using  $\Delta h_A^* = -13.5 \text{ kJ mol}^{-1}$  (the same value for 2-propoxyethanol or 2-butoxyethanol) are remarkable. Similarly, in the DISQUAC model, mixtures of 2-propoxyethanol, 2-butoxy-

**Fig. 7.** Parameters in the ERAS and DISQUAC models vs.  $n$ , the number of C atoms in 2-alkoxyethanol.



ethanol, or 2-(2-alkoxyethoxyethanol) with alkane are characterized by the same quasichemical enthalpic parameter (23).

## Conclusions

Alkoxyethanol + alkane systems have been examined in the framework of the ERAS model. The thermodynamic properties  $H^E$ ,  $V^E$ , and  $C_p^E$  are represented accurately. However, DISQUAC, a purely physical theory, improves the  $H^E$  (except at high temperatures and pressures) and  $C_p^E$  results from ERAS. The observed differences between experimental and theoretical values that can be ascribed to ERAS do not properly take into account the enhanced dipole-dipole interactions due to the intramolecular H-bonds of the alkoxyethanols. As in previous applications, ERAS cannot simultaneously represent  $G^E$  and liquid-liquid equilibria. There is good agreement between the partial molar excess enthalpies at 298.15 K and infinite dilution of 2-alkoxyethanol in 2-alkoxyethanol(1) + *n*-heptane(2) mixtures and  $\Delta h_A^*$ . The variation of  $K_A$  and of  $\Delta h_A^*$  with the molecular structure of alkoxyethanol is supported by that of the enthalpic interchange coefficients in DISQUAC.

## Acknowledgments

This work has been supported by the Ministerio de Ciencia y Tecnología, "Programa Nacional de Procesos y Productos Químicos" (Project reference PPQ2001-1664) y Unión Europea (F.E.D.E.R.) and by the Consejería de Educación y Cultura de la Junta de Castilla y León (Project reference VA039/01) y Unión Europea (F.S.E.).

## References

1. A. Heintz. Ber. Bunsenges. Phys. Chem. **89**, 172 (1985).
2. C.B. Kretschmer and R. Wiebe. J. Chem. Phys. **22**, 1697 (1954).



3. H. Renon and J.M. Prausnitz. *Chem. Eng. Sci.* **22**, 299 (1967).
4. H.V. Kehiaian. *Bull. Acad. Pol. Sci.* **16**, 165 (1968).
5. H.V. Kehiaian and A. Treszczanowicz. *Bull. Acad. Pol. Sci.* **16**, 171 (1968).
6. P.J. Flory. *J. Am. Chem. Soc.* **87**, 1833 (1965).
7. M. Bender and A. Heintz. *Fluid Phase Equilib.* **89**, 197 (1993).
8. H. Kaur, N.S. Samra, B.S. Mahl, J.R. Khurma, M. Bender, and A. Heintz. *Fluid Phase Equilib.* **67**, 241 (1991).
9. A. Cabañas, B. Coto, C. Pando, and J.A.R. Renuncio. *Ber. Bunsenges. Phys. Chem.* **98**, 777 (1994).
10. H. Funke, M. Wetzel, and A. Heintz. *Pure Appl. Chem.* **61**, 1429 (1989).
11. W. Mier, G. Oswal, E. Tusel-Langer, and R.N. Lichtenthaler. *Ber. Bunsenges. Phys. Chem.* **99**, 1123 (1995).
12. T.M. Letcher and P.U. Govender. *Fluid Phase Equilib.* **140**, 207 (1997).
13. R. Garriga, S. Martínez, P. Pérez, and M. Gracia. *Fluid Phase Equilib.* **147**, 195 (1998).
14. J.A. González, I. García de la Fuente, and J.C. Cobos. *Can. J. Chem.* **78**, 1272 (2000).
15. J.A. González, I. García de la Fuente, and J.C. Cobos. *Fluid Phase Equilib.* **168**, 31 (2000).
16. S. Villa, N. Riesco, I. García de la Fuente, J.A. González, and J.C. Cobos. *Fluid Phase Equilib.* **190**, 113 (2001).
17. L.P. Kuhn. *J. Am. Chem. Soc.* **74**, 2492 (1952).
18. L.P. Kuhn and R.A. Wires. *J. Am. Chem. Soc.* **86**, 2161 (1964).
19. P.J. Krueger and H.D. Mettee. *J. Mol. Spectrosc.* **18**, 131 (1965).
20. L.S. Prabhuminarishi. *J. Chem. Soc. Faraday Trans. 2*, **74**, 1567 (1978).
21. W. Caminati and E.B. Wilson. *J. Mol. Spectrosc.* **81**, 356 (1980).
22. R.L. Brinkley and R. Gupta. *Ind. Eng. Chem. Res.* **37**, 4823 (1998).
23. J.A. González, J.C. Cobos, F.J. Carmona, I. García de la Fuente, V.R. Bhethanabotla, and S.W. Campbell. *Phys. Chem. Chem. Phys.* **3**, 2856 (2001).
24. J.S. Rowlinson and F.L. Swinton. *Liquids and liquid mixtures*. 3rd ed. Butterworths, London. 1982.
25. F.J. Carmona, J.A. González, I. García de la Fuente, and J.C. Cobos. *J. Chem. Eng. Data*, **44**, 892 (1999).
26. R. Martínez, J.A. González, I. García de la Fuente, and J.C. Cobos. *J. Chem. Eng. Data*, **45**, 1036 (2000).
27. S.V. Vinogradov and R.H. Linnell. *Hydrogen bonding*. Van Nostrand, Reinhold, New York. 1971.
28. F. Kimura, S. Murakami, R. Fujishiro, and Y. Toshiyasu. *Bull. Chem. Soc. Jpn.* **50**, 791 (1977).
29. H.V. Kehiaian. *Fluid Phase Equilib.* **13**, 243 (1983).
30. H.V. Kehiaian. *Pure Appl. Chem.* **57**, 13 (1985).
31. E.A. Guggenheim. *Mixtures*. Oxford University Press, Oxford. 1952.
32. S. Delcros, J.R. Quint, J.-P.E. Grolier, and H.V. Kehiaian. *Fluid Phase Equilib.* **113**, 1 (1995).
33. W. Schulz and R.N. Lichtenthaler. *Fluid Phase Equilib.* **151**, 261 (1989).
34. H. Bilj, Th.W. de Loos, and R.N. Lichtenthaler. *Fluid Phase Equilib.* **14**, 157 (1983).
35. D.S. Abrams and J.M. Prausnitz. *AIChE J.* **21**, 116 (1975).
36. A. Heintz and D. Papaioannou. *Thermochim. Acta*, **310**, 69 (1998).
37. A. Heintz, P.K. Naicker, S.P. Verevkin, and R. Pfestorf. *Ber. Bunsenges. Phys. Chem.* **102**, 953 (1998).
38. D. Kulikov, S.P. Verevkin, and A. Heintz. *Fluid Phase Equilib.* **192**, 187 (2001).
39. A. Bondi. *Physical properties of molecular crystals, liquids and glasses*. Wiley, New York. 1968.
40. M. Nishimoto, S. Tabata, K. Tamura, and S. Murakami. *Fluid Phase Equilib.* **136**, 235 (1997).
41. J.A. Riddick, W.B. Bunger, and T.K. Sakano. *Organic solvents. Physical properties and methods of purification, techniques of chemistry. Edited by A. Weissberger. Vol. II*. John Wiley & Sons, New York. 1986.
42. K. Tamura, A. Osaki, S. Murakami, B. Laurent, and J.P.-E. Grolier. *Fluid Phase Equilib.* **173**, 285 (2000).
43. H. Ohji, H. Ogawa, S. Murakami, K. Tamura, and J.P.-E. Grolier. *Fluid Phase Equilib.* **156**, 101 (1999).
44. N.V. Sastry. *Fluid Phase Equilib.* **128**, 173 (1997).
45. N. Riesco, S. Villa, J.A. González, I. García de la Fuente, and J.C. Cobos. *Thermochim. Acta*, **362**, 89 (2000).
46. J.C. Cobos, I. García de la Fuente, and J.A. González. *Can. J. Chem.* **80**, 292 (2002).
47. M. Díaz Peña and G. Tardajos. *J. Chem. Thermodyn.* **10**, 19 (1978).
48. M. Díaz Peña, G. Tardajos, C. Mendiña, and R.L. Arenosa. *J. Chem. Thermodyn.* **11**, 67 (1979).
49. V. Majer and V. Svoboda. *Enthalpies of vaporization of organic compounds*. Blackwell, Oxford. 1985.
50. W. Schulz and R.N. Lichtenthaler. *Thermochim. Acta*, **151**, 261 (1989).
51. D.-Y. Peng, G.C. Benson, and B.C.-Y. Lu. *J. Chem. Thermodyn.* **30**, 1141 (1998).
52. J. Valero, M. Gracia, and C. Gutierrez Losa. *J. Chem. Thermodyn.* **11**, 1101 (1979).
53. R.J. Mayer and G.L. Giusti. *J. Chem. Thermodyn.* **9**, 1101 (1977).
54. P.S. Murti, M. Van Winkle, *AIChE J.* **3**, 517 (1957).
55. H. Ohji, A. Osaki, K. Tamura, S. Murakami, and H. Ogawa. *J. Chem. Thermodyn.* **30**, 761 (1998).
56. M.A. Villamañán, C. Casanova, A.H. Roux, and J.P.-E. Grolier. *J. Chem. Eng. Data*, **27**, 89 (1982).
57. J.C. Cobos, I. García, and C. Casanova. *Can. J. Chem.* **66**, 2618 (1988).
58. T.M. Aminabhavi and B. Gopalakrishna. *J. Chem. Eng. Data*, **40**, 632 (1995).
59. G.C. Benson, C.J. Halpin, and A.J. Treszczanowicz. *J. Chem. Thermodyn.* **13**, 1175 (1981).
60. G. Conti, P. Gianni, L. Lepori, E. Matteoli, and M.L. D'Amico. *J. Chem. Thermodyn.* **30**, 855 (1998).
61. F.J. Carmona, V.R. Bhethanabotla, S.W. Campbell, J.A. González, I. García de la Fuente, and J.C. Cobos. *J. Chem. Thermodyn.* **33**, 47 (2000).
62. F.J. Carmona, J.A. González, I. García de la Fuente, J.C. Cobos, V.R. Bhethanabotla, and S.W. Campbell. *J. Chem. Eng. Data*, **45**, 699 (2000).
63. F.J. Carmona. Personal communication.
64. K. Tamura, A. Osaki, S. Murakami, H. Ohji, H. Ogawa, B. Laurent, and J.P.-E. Grolier. *Fluid Phase Equilib.* **156**, 137 (1999).
65. M.A. Rubio, J.A. González, I. García de la Fuente, and J.C. Cobos. *Fluid Phase Equilib.* **143**, 111 (1998).
66. I. Prigogine and R. Defay. *Chemical thermodynamics*. Longmans Green and Co., Norwich. 1954.
67. J.A. González, M. Szurgocinska, and U. Domanska. *Fluid Phase Equilib.* **200**, 349 (2002).



## Appendix A

**Table A1.** Physical constants of alkanes: thermal expansion coefficient,  $\alpha_P$ , isothermal compressibility,  $\kappa_T$ , molar volume,  $V_m$ , and reduction parameters for volume,  $V^*$ , and pressure,  $P^*$ .

Alkane	$T$ (K)	$\alpha_P$ ( $10^{-3} \text{ K}^{-1}$ )	$\kappa_T$ ( $10^{-9} \text{ Pa}^{-1}$ )	$V_m$ ( $\text{cm}^3 \text{ mol}^{-1}$ )	$V^*$ ( $\text{cm}^3 \text{ mol}^{-1}$ )	$P^*$ ( $\text{J cm}^{-3}$ )
$n\text{-C}_6$	298.15	1.387	1.7039	131.57	99.52	424.2
	303.15	1.440	1.745	132.51	99.21	446.0
	313.15	1.46	1.925	134.45	99.76	431.4
	323.15	1.48	2.138	136.44	100.35	413.5
	348.15	1.54	2.82	141.71	101.86	368.0
$n\text{-C}_7$	298.15	1.256	1.4606	147.45	113.6	431.9
	303.15	1.289	1.501	148.32	113.4	445.5
	323.15	1.320	1.805	152.25	114.49	417.9
	348.15	1.360	2.184	157.45	116.03	399.2
	373.15	1.410	2.565	163.01	117.62	394.0
$n\text{-C}_8$	298.15	1.164	1.3024	163.50	127.70	436.8
	348.15	1.25	1.880	173.70	130.12	412.5
	373.15	1.29	2.183	179.30	131.70	408.7
$n\text{-C}_{10}$	298.15	1.051	1.1096	195.94	155.75	447.0
	348.15	1.11	1.546	206.76	158.38	426.0
	373.15	1.14	1.775	212.66	160.0	423.3
$n\text{-C}_{12}$	298.15	0.96	0.9876	228.55	184.40	445.2
$n\text{-C}_{14}$	298.15	0.886	0.872	261.32	213.52	453.7
$\text{C}_6\text{H}_{12}$	298.15	1.22	1.140	108.75	84.23	532.0
	303.15	1.31	1.172	109.41	83.39	583.3
	323.15	1.25	1.334	112.20	85.25	524.6
	328.15	1.26	1.374	112.86	85.37	525.9



# Catalysis by organotransition metal compounds: Synergism between the pure and the applied<sup>1</sup>

Michael C. Baird

**Abstract:** The modern era of transition-metal-catalyzed polymerization of alkenes began with the Nobel Prize winning work of Ziegler and Natta in the 1950s, but the field has exploded since the mid-1980s and anticipated applications of organometallic catalysts are being spectacularly realized. Our research in metal-catalyzed alkene polymerization began about ten years ago with an investigation of the catalytic applications of half-sandwich complexes of the Group 4 metals, and this lecture will describe our efforts to find both better initiators to make known commercial polymers and new initiators to make novel polymeric materials. Good luck, bad luck, blind alleys, and serendipity have all played key roles in our research, resulting ultimately in a very satisfying convergence of the motives for pure, and the needs of applied, research.

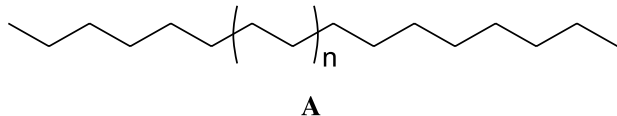
*Key words:* alkene, polymerization, Ziegler, catalysis, carbocationic, titanium.

**Résumé :** L'ère moderne de la polymérisation des alcènes à l'aide de catalyseurs à base de métaux de transition a débuté dans les années 1950 avec les travaux qui ont valu un prix Nobel à Ziegler et à Natta; toutefois, le champ a explosé depuis le milieu des années 1980 et des applications anticipées de catalyse par des organométalliques sont maintenant réalisées de façon spectaculaire. Nos travaux de recherches dans le domaine de la polymérisation des alcènes à l'aide de catalyseurs à base de métaux de transition ont débuté il y a une dizaine d'années avec une étude sur les applications catalytiques de complexes à demi-sandwich de métaux du groupe 4 et cette conférence décrira les efforts que nous avons déployés dans le but de trouver de meilleurs initiateurs pour faire des polymères commerciaux connus et de nouveaux initiateurs pour faire de nouveaux matériaux polymères. La chance, bonne et mauvaise, les voies sans issue et la sérendipité ont joué des rôles clés dans nos recherches qui ont permis éventuellement de conduire à une convergence satisfaisante des motifs de la recherche pure et des besoins de la recherche appliquée.

*Mots clés :* alcène, polymérisation, Ziegler, catalyse, carbocationique, titane.

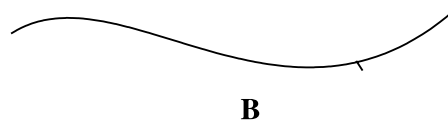
[Traduit par la Rédaction]

Transition-metal-based catalysts for alkene polymerization are — given the importance of plastics such as polyethylene and polypropylene — among the keystones of western civilization. For instance, current world production of polyethylene (PE) and polypropylene (PP) are  $>42 \times 10^6$  and  $>24 \times 10^6$  tonnes per annum (p.a.), respectively (1). The most important type (isomer) of PE is linear, i.e.,  $\text{Me}(\text{CH}_2)_n\text{Me}$  ( $n \geq 400$ ), and may be considered a long molecular strand, as in **A**.



This type of polymer was discovered serendipitously by Ziegler in the early 1950s and led quickly to the Nobel Prize in chemistry in 1955. The long chains of linear PE pack very effectively in the solid, resulting in a tough, high-melting

(~140°C), semi-crystalline material with a relatively high density (0.94–0.97 g mL<sup>-1</sup>); thus it is oft referred to as high-density PE or HDPE (1). Degrees of branching can also be induced in various ways to give products with a range of properties. For instance, the usual manufacturing processes can produce semi-crystalline material containing the occasional short methyl (or longer) branch, as in the cartoon drawing **B**.



The resulting materials exhibit slightly lower melting points (130–135°C), and hence offer greater ease of processability (1).

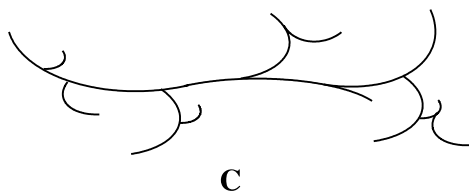
Received 7 March 2003. Published on the NRC Research Press Web site at <http://canjchem.nrc.ca> on 12 May 2003.

**M.C. Baird.** Department of Chemistry, Queen's University, Kingston, ON K7L 3N6, Canada. (e-mail: [bairdmc@chem.queensu.ca](mailto:bairdmc@chem.queensu.ca)).

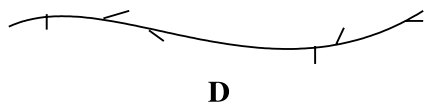
<sup>1</sup>2002 Catalysis Award Lecture. Presented at the 85th CSC Conference, Vancouver, BC, Canada.



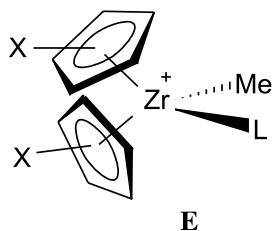
Isomeric with HDPE are highly branched forms of PE, which may be represented by **C**.



This type of material packs much less efficiently as a solid and thus is amorphous, low melting (106–112°C), and of relatively low density (0.915–0.935 g mL<sup>-1</sup>); hence LDPE (1). Not strictly isomeric but generally regarded as a third major classification of PE is a type of polymer obtained by copolymerizing ethylene with monomers such as propylene or 1-butene. The resulting material contains a random distribution of identical branches (**D**) and exhibits an intermediate melting temperature (~125°C) but low density (0.915–0.935 g mL<sup>-1</sup>). This material is referred to as linear low density PE or LLDPE (1).



The major commercial catalysts used for the manufacture of both PE and PP are generated by combining TiCl<sub>3</sub> with aluminum alkyls such as AlEt<sub>3</sub>, although Cr<sub>2</sub>O<sub>3</sub> is also an important catalyst for PE (1). These catalysts are heterogeneous, but there is currently a growing interest in applications of homogeneous catalysts based on metallocenes of titanium, zirconium, and hafnium (2). The most important class of homogeneous alkene polymerization initiators is of the type [Cp<sub>2</sub>ZrMeL]<sup>+</sup> (**E**).

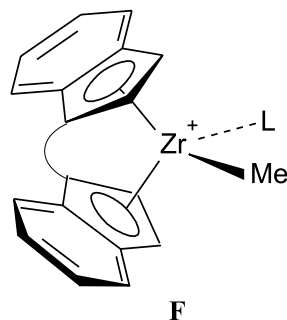


These contain a labile ligand *L*, *cis* to the alkyl ligand, important if a vacant site is to be made available for alkene coordination as shown in Scheme 1. The reactivity is also enhanced by the positive charge on the complex (2).

A very important sub-class of metallocene catalysts contains a dicyclopentadienyl ligand, which has local C<sub>2</sub> symmetry (**F**).

The strap between the Cp rings, which may be, e.g., a -(CH<sub>2</sub>)<sub>2</sub>- or an -SiMe<sub>2</sub>- group, maintains a chiral structure that induces molecules of a prochiral monomer such as propylene to coordinate via the same face almost every time. This has major implications for the stereochemistry of the polymer propagation process (2) (see discussion below concerning polypropylene).

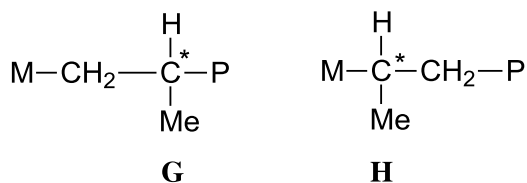
The mechanism of polymerization initiation and chain propagation for PP and most types of PE involves coordination of an alkene such as ethylene followed by repeated mi-



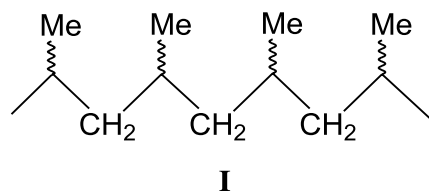
gratory insertion steps, as illustrated in Scheme 1 for a metallocene catalyst. Here (and below) the letter P is used to indicate a growing polymer chain.

As the HDPE originally discovered by Ziegler was the first example established as an application of this mechanism, the process is often referred to as Ziegler polymerization, although it is often known as coordination polymerization. Chain-termination and chain-transfer steps generally involve very similar chemistry, as in Scheme 2.

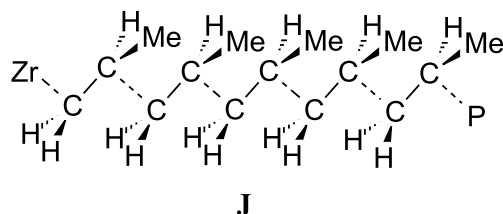
Polypropylene can also be obtained in isomeric forms, as regio- and stereoisomers rather than as structural isomers with varying degrees of branching. As a polymer chain grows, whether initiation and propagation involve 1,2- (**G**) or 2,1-insertion (**H**), incorporation of a molecule of monomer generates a new chiral centre (M = catalytic centre; ~P = growing polymer chain).



If the sense of handedness is decided purely randomly (mixture of *R*- and *S*-), the product is “atactic” polypropylene (**I**) (1).



With chiral, C<sub>2</sub>-symmetric catalysts of type **F**, the stereochemistry of insertion is often highly controlled (asymmetric induction) (1, 2). Each molecule of monomer inserts in the same way to give a stereoregular polymer, as in, e.g., **J**.

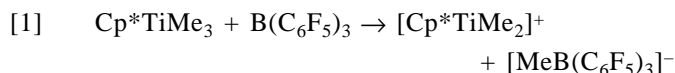


Chiral catalysts can therefore produce polymers with very high degrees of handedness at each step, i.e., for polypropy-

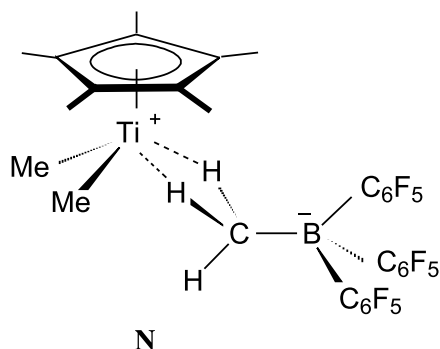




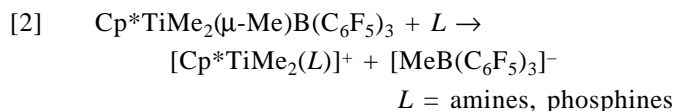




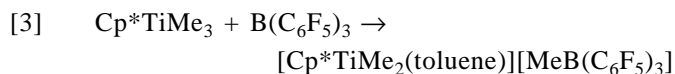
The resulting cationic complex has coordinated alkyl groups, vacant site(s), and a positive charge, as is important for metallocene catalysts (see above). However, it could be more active than metallocenes for both steric and electronic reasons. The structure of "[Cp\*TiMe<sub>2</sub>][MeB(C<sub>6</sub>F<sub>5</sub>)<sub>3</sub>]" actually involves a non-classical mode of coordination of the borate anion, as in **N**.



The chemistry of Cp\*TiMe<sub>2</sub>(μ-Me)B(C<sub>6</sub>F<sub>5</sub>)<sub>3</sub> proved to be very interesting. For instance, the borate anion is readily substituted in solution (eq. [2]) (4–6).

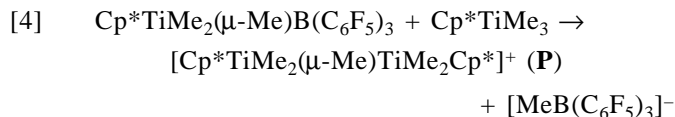


Similarly, arene complexes are formed in aromatic solvents (3, 6), e.g., in toluene:



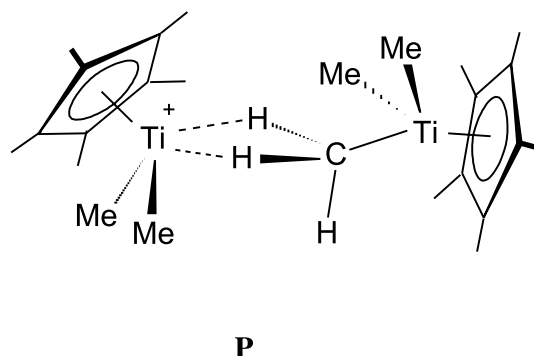
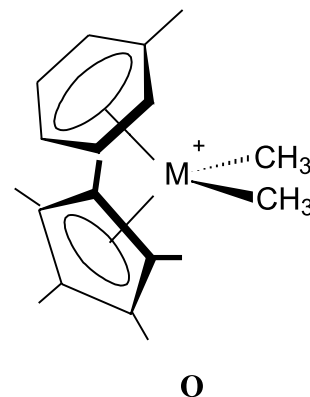
The products, which have been characterized for Ti, Zr, and Hf complexes, contain η<sup>6</sup>-bonded arene rings and thus are isoelectronic with the corresponding neutral dimethyl-metallocenes. The anticipated structure (**O**), has been demonstrated by an X-ray structure of a hafnium analogue (6).

The cationic moiety [Cp\*TiMe<sub>2</sub>]<sup>+</sup> also behaves as a Lewis acid towards Cp\*TiMe<sub>3</sub>, giving the dititanium species [Cp\*TiMe<sub>2</sub>(μ-Me)TiMe<sub>2</sub>Cp\*]<sup>+</sup> (**P**), as in eq. [4] (5).

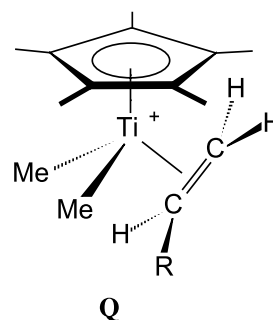


Thus the neutral Cp\*TiMe<sub>3</sub> is a better ligand than the anionic [MeB(C<sub>6</sub>F<sub>5</sub>)<sub>3</sub>]<sup>−</sup>!

We have found that Cp\*TiMe<sub>2</sub>(μ-Me)B(C<sub>6</sub>F<sub>5</sub>)<sub>3</sub> is an excellent alkene polymerization catalyst. Polymerizations of ethylene (4), propylene (7), and 1-hexene (8, 9) occur readily over a range of temperatures, and we obtain high-molecular-weight, linear polyethylene (HDPE), as well as high-molecular-weight, atactic polypropylene and poly-1-hexene. We can also make copolymers of ethylene with propylene (10) and 1-hexene (11) and commercially important terpolymers of ethylene, propylene, and 5-ethylidene-2-norbornene,



known as EPDM (10). These reactions undoubtedly involve Ziegler mechanisms and η<sup>2</sup>-alkene complexes of the type shown as **Q**.



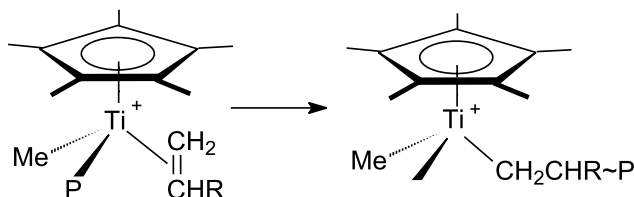
Initiation and the dominant mode of propagation involve 1,2-insertions, as shown in Scheme 3.

This was demonstrated using <sup>13</sup>C NMR spectroscopy and a labeled catalyst, as in Scheme 4 for 1-hexene ([Ti] = Cp\*TiMe<sub>2</sub>) (9).

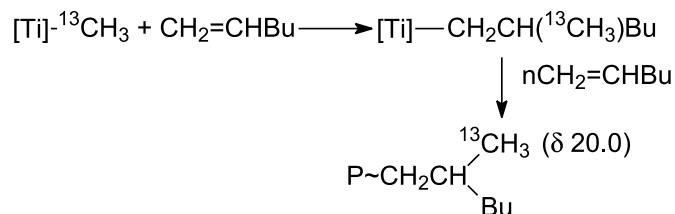
In situ <sup>13</sup>C NMR experiments of the reaction of Cp\*Ti-(<sup>13</sup>CH<sub>3</sub>)<sub>2</sub>(μ-<sup>13</sup>CH<sub>3</sub>)B(C<sub>6</sub>F<sub>5</sub>)<sub>3</sub> with 1-hexene in CD<sub>2</sub>Cl<sub>2</sub> at −50°C also give interesting mechanistic information. The resonance of the free borate [B(<sup>13</sup>CH<sub>3</sub>)(C<sub>6</sub>F<sub>5</sub>)<sub>3</sub>]<sup>−</sup> appeared, and thus the anion had clearly been displaced, as expected. Interestingly, the Ti–Me resonance also disappeared and no new ones appeared. Thus both methyl groups must become involved and polymerization must occur at two sites on the titanium, as expected although not previously demonstrated for any Ziegler-catalyst system. New resonances did appear at δ ~20 (methyl branch) and 10.5 (ethyl branch), and the latter implies an initial 2,1-insertion in CD<sub>2</sub>Cl<sub>2</sub> (Scheme 5).



Scheme 3.



Scheme 4.



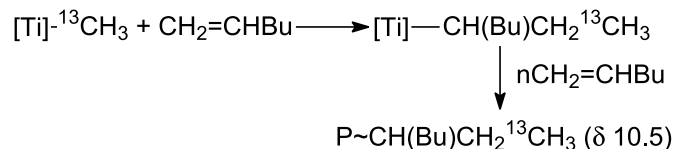
NMR analyses of end groups of low-molecular-weight polypropylene indicate two major modes of chain transfer for this olefin, as shown in Scheme 6. Following 2,1-insertion of 1-hexene,  $\beta$ -H elimination in the opposite direction also occurs (Scheme 7).

Very different chemistry was observed with styrene using  $\text{Cp}^*\text{Ti}(\text{CH}_3)_2(\mu\text{-CH}_3)\text{B}(\text{C}_6\text{F}_5)_3$ . For instance, we obtain only atactic polystyrene (PS) in toluene at temperatures below  $\sim 15^\circ\text{C}$  but highly (>98%) syndiotactic PS (*s*-PS) in neat styrene or in toluene above room temperature (reaction very rapid and exothermic) (4). Atactic PS is familiar as styrofoam, but *s*-PS is a hard solid (mp  $\sim 270^\circ\text{C}$ ), insoluble in all solvents at  $20^\circ\text{C}$ . It is therefore of great interest as a new plastic. That polymerization by  $\text{Cp}^*\text{Ti}(\text{CH}_3)_2(\mu\text{-CH}_3)\text{B}(\text{C}_6\text{F}_5)_3$  is initiated and proceeds via a Ziegler process involving 2,1-insertions is shown by NMR studies utilizing  $\text{Cp}^*\text{Ti}(^{13}\text{CH}_3)_2(\mu\text{-}^{13}\text{CH}_3)\text{B}(\text{C}_6\text{F}_5)_3$  (Scheme 8) (4).

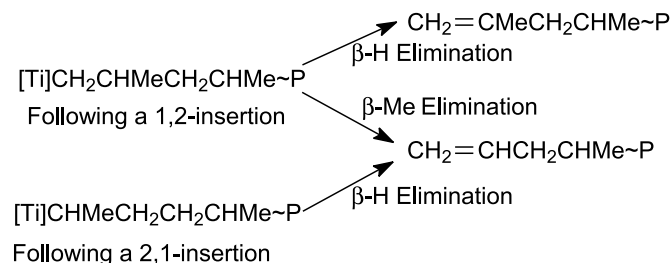
Chain propagation thus proceeds with an extremely high degree of stereoselectivity despite occurring at an achiral (!) metal centre. As it happens, the stereochemistry of insertion is under chain-end control, as the handedness at  $\text{C}_1$  (Scheme 8) controls the mode of insertion of the next monomer (12). There follow conventional termination – chain transfer processes ( $\beta$ -eliminations, migratory insertions). The nature of the catalytic species, possibly of  $\text{Ti}(\text{III})$ , is not known, although we and others have carried out considerable research on what is, at the time of writing, a very controversial issue (13).

It was during the early days of our research on the utilization of  $\text{Cp}^*\text{Ti}(\text{CH}_3)_2(\mu\text{-CH}_3)\text{B}(\text{C}_6\text{F}_5)_3$  to polymerize styrene that we carried out our initial experiments with propylene, a line of experimentation that through bad luck resulted in data misinterpretation. The consequences were at the time somewhat embarrassing, but resulted serendipitously in an avenue of exploration that we would not have otherwise taken but that led quickly to the development of a series of novel, quite unanticipated but very useful findings. During our earliest experiments, we had found that  $\text{Cp}^*\text{Ti}(\text{CH}_3)_2(\mu\text{-CH}_3)\text{B}(\text{C}_6\text{F}_5)_3$  was seemingly an excellent catalyst for the polymerization of ethylene and styrene to HDPE and *s*-PS, respectively, but a poor catalyst for the polymerization of propylene. This trend did not make sense for a Ziegler cata-

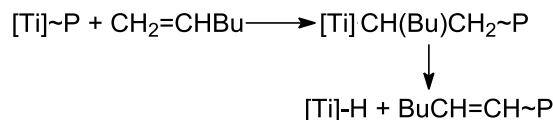
Scheme 5.



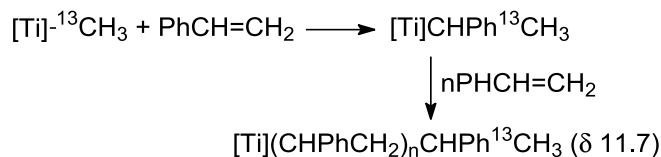
Scheme 6.



Scheme 7.



Scheme 8.



lyst, for which one would anticipate an order of activity ethylene > propylene > styrene, and we wondered if some other mechanism might be applicable in the formation of *s*-PS. A radical chain mechanism was clearly inappropriate as it is known to give *a*-PS (1), and we mistakenly gave serious consideration (14) to the possible role of carbocationic initiation (15).

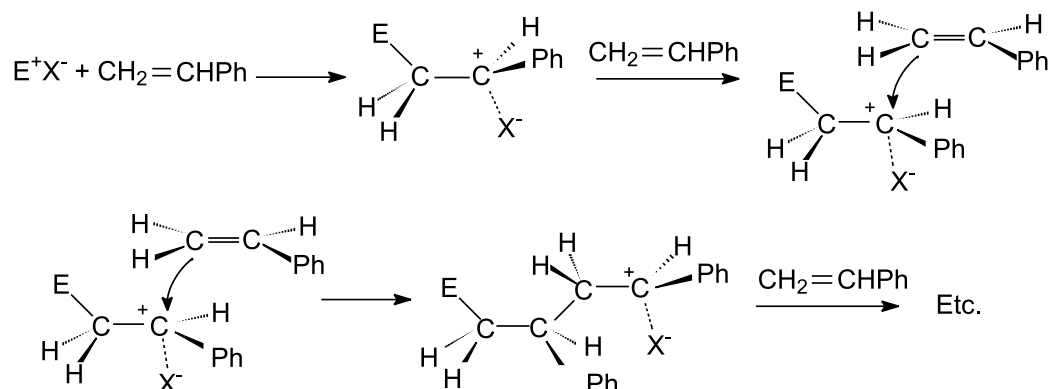
Carbocationic polymerization of alkenes involves activation of the monomer (initiation) by a good electrophile, as shown in Scheme 9 ( $\text{E}^+$  = electrophilic reagent) for styrene. The mechanism clearly requires a monomer that can form a stable cation (15).

When the electrophilic activator is  $[\text{Cp}^*\text{Ti}(\text{CH}_3)_2]^+$ , the process would involve  $\eta^1$ -coordination, as in Scheme 10.

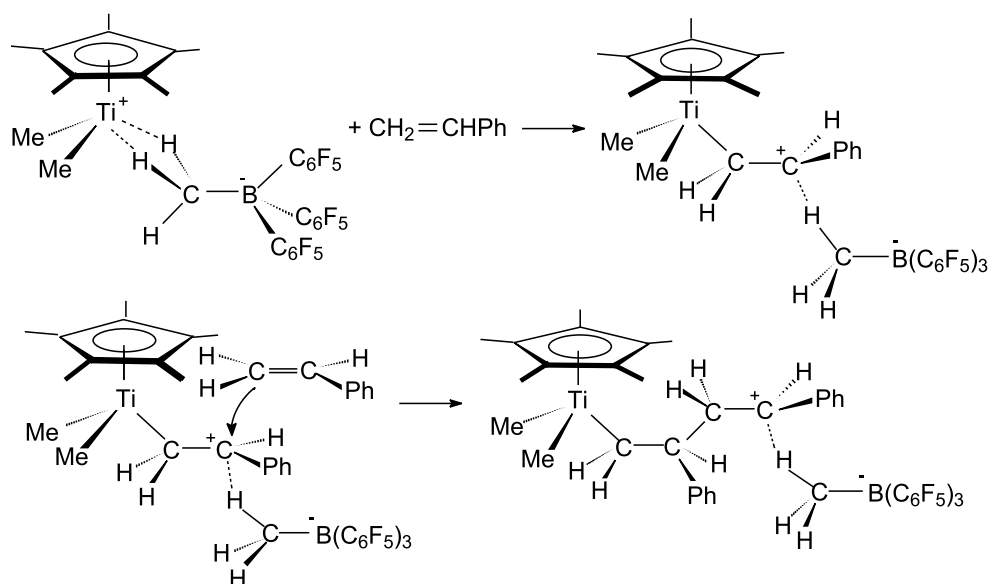
While we eventually found that this mode of activation does occur under certain circumstances (see below), we were soon disabused of the appropriateness of the mechanism for the synthesis of *s*-PS. We found that the propylene being used had not been dried appropriately and was killing the catalyst (4); indeed propylene is in fact polymerized quite effectively by  $\text{Cp}^*\text{Ti}(\text{CH}_3)_2(\mu\text{-CH}_3)\text{B}(\text{C}_6\text{F}_5)_3$  (7, 16). The results of the labeling experiment described above require a Ziegler mechanism, but, before we realized just what was going on, we investigated monomers that *prefer* to be polymerized via a carbocationic mechanism. In view of the undeniable novelty of an established Ziegler–Natta catalyst behaving preferentially as a carbocationic initiator, we



Scheme 9.



Scheme 10.



thought we would ascertain its possibly wider applicability. Obvious candidates were vinyl ethers, *N*-vinylcarbazole, and isobutene (15), shown in Scheme 11.

These are known to be polymerized only via a carbocationic mechanism, much as in Schemes 9 and 10, because their carbocationic centres are readily stabilized by the adjacent functionalities but never via a Ziegler mechanism (15).

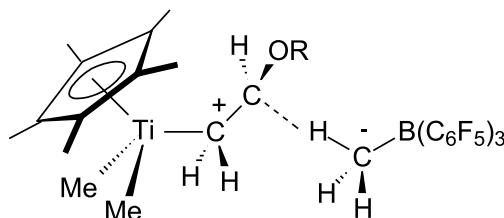
Much to our delight, polymers of vinyl ethers and *N*-vinylcarbazole are readily prepared using  $\text{Cp}^*\text{TiMe}_2(\mu\text{-Me})\text{B(C}_6\text{F}_5)_3$  (17). Low temperatures ( $-78^\circ\text{C}$ ) are required for high molecular weights to be achieved, as with conventional initiators, and in most cases the poly(vinyl ether) products exhibit tacticities very similar to those obtained with conventional Lewis-acid initiators and molecular weights comparable with the better literature results. Also in agreement with the postulated carbocationic mechanism, there is no reaction with 2,5-dihydrofuran (**R**), for which a carbocationic intermediate cannot be stabilized by a free electron pair on an adjacent oxygen atom.

While not in the commercial league of high-volume polymers such as PE and PP, polyvinyl ethers are important and are used as adhesives, plasticizers, hair spray, etc. Poly(*N*-vinylcarbazole) is also obtained with very high molecular

**R**

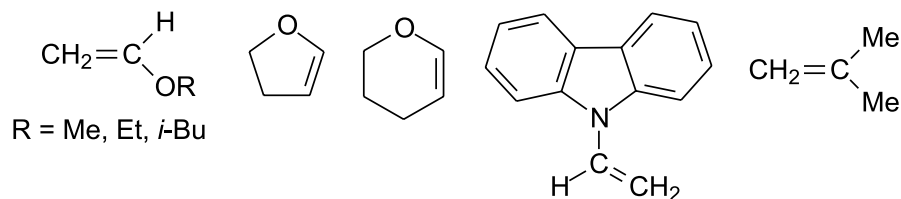
weights and is a material that forms interesting semiconductors when doped appropriately.

Polymerization by  $\text{Cp}^*\text{TiMe}_2(\mu\text{-Me})\text{B(C}_6\text{F}_5)_3$  presumably involves an  $\eta^1$  metal-alkene interaction, stabilized by a secondary interaction with the counteranion, as in **S**.

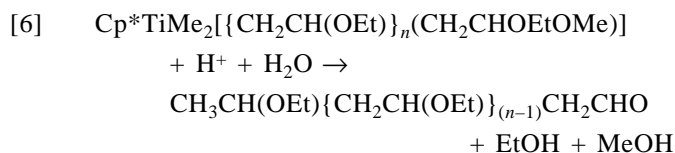
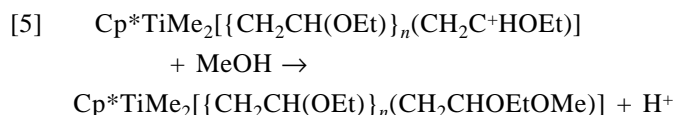
**S**



Scheme 11.



This is an unusual mode of metal—alkene bonding, but it resembles the transition state involved in nucleophilic attack on alkenes activated by coordination to electrophilic metals (18). Near- $\eta^1$  structures have precedent in a variety of known complexes of vinyl ethers, vinyl alcohol, and vinyl amine (19). By way of evidence that poly(vinyl ethers) are indeed formed via the carbocationic process, we found that the  $^1\text{H}$  NMR spectrum of poly(ethyl vinyl ether) formed exhibits a weak resonance at  $\delta$  9.88 attributable to an aldehyde end group, arising from hydrolysis of the acetal end group,  $-\text{CH}(\text{OMe})(\text{OEt})$ , formed by methanolysis (eqs. [5], [6]) (17).

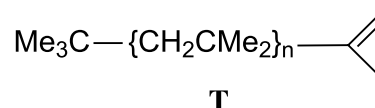


While carbocationic initiation is not a factor in the polymerization of styrene to *s*-PS, we did demonstrate its applicability to the formation of atactic PS in, e.g., toluene at temperatures below  $\sim -15^\circ\text{C}$ .  $^1\text{H}$  NMR monitoring of the polymerization reaction of styrene- $d_8$  to atactic polymer in  $\text{CD}_2\text{Cl}_2$  by  $\text{Cp}^*\text{Ti}(\text{CH}_3)_2(\mu\text{-CH}_3)\text{B}(\text{C}_6\text{F}_5)_3$  at  $-50^\circ\text{C}$  showed quite clearly that this process results in no measurable loss of initiator, consistent with a carbocationic mechanism. The  $^1\text{H}$  NMR spectrum of  $\text{Cp}^*\text{Ti}(\text{CH}_3)_2(\mu\text{-CH}_3)\text{B}(\text{C}_6\text{F}_5)_3$  before addition of styrene- $d_8$  and after polymerization of the latter was unchanged (4).

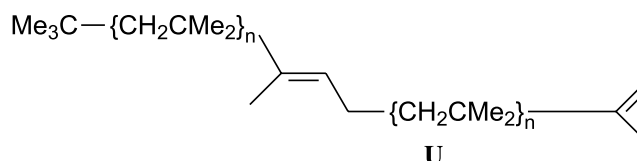
The remaining monomer of Scheme 11, which is known to insist on being polymerized only via carbocationic initiation, is isobutylene. We quickly found that this monomer is indeed polymerized by  $\text{Cp}^*\text{Ti}(\text{CH}_3)_2(\mu\text{-CH}_3)\text{B}(\text{C}_6\text{F}_5)_3$  in toluene and methylene chloride at temperatures in the range  $-78^\circ\text{C}$  to  $20^\circ\text{C}$  with conversions often  $>95\%$  (20, 21). The polymer forms as a high-molecular-weight ( $>700\,000$ ), rubbery solid at lowest temperatures and a viscous, oily liquid at room temperature, as with conventional Lewis-acid initiators. The  $^1\text{H}$  and  $^{13}\text{C}$  NMR spectra are also consistent with polymers (T) synthesized using conventional initiators. Polyisobutylene is useful in a large range of applications, depending on molecular weight (bicycle inner tubes, chewing gum, engine oil additives).

A related, very interesting, and useful material is isobutylene–isoprene copolymer (butyl rubber). We obtain a copolymer containing  $\sim 1\%$  isoprene at  $-78^\circ\text{C}$  if the monomer ratio is 99:1. Molecular weights are lower if polymerization is

carried out at higher temperatures and (or) with higher isoprene:isobutylene ratios. The  $^1\text{H}$  and  $^{13}\text{C}$  NMR spectra



suggest primarily trans-1,4-addition across the isoprene (U). This polymer is used primarily as inner lining for tubeless tires.



Virtually all production of this material worldwide is by Bayer and Exxon. Both use essentially the same technology; polymerization is carried out at cryogenic temperatures,  $\sim -100^\circ\text{C}$ , and chloromethane is the solvent of choice. Clearly higher temperatures and a more environmentally benign solvent are desirable for commercial processes, and we are currently focused on the development of initiators that form high-molecular-weight polyisobutylene and polyisobutylene–co-isoprene in hydrocarbon solvents at temperatures significantly higher than  $-100^\circ\text{C}$ .

## Summary

The 2002 Catalysis Award Lecture and this resulting article outline the early days and some of the resulting developments of our research into the utilization of  $\text{Cp}^*\text{Ti}(\text{CH}_3)_2(\mu\text{-CH}_3)\text{B}(\text{C}_6\text{F}_5)_3$  as an initiator of olefin polymerization. As has been shown,  $\text{Cp}^*\text{Ti}(\text{CH}_3)_2(\mu\text{-CH}_3)\text{B}(\text{C}_6\text{F}_5)_3$  is probably the most versatile of all olefin polymerization initiators in its effectiveness as both a very highly active Ziegler catalyst and as a very highly active carbocationic initiator. We have, of course, extended the above discussed research, including a variety of modifications of  $\text{Cp}^*\text{Ti}(\text{CH}_3)_2(\mu\text{-CH}_3)\text{B}(\text{C}_6\text{F}_5)_3$ , and some of these have resulted in more active species (22–29). Having succumbed to the thrills that can result from the convergence of organometallic chemistry and polymers, we have also explored a variety of other catalytic systems, in part to find better catalysts for known processes and new catalysts for new polymers, in part to better understand the mechanisms applicable to the various systems studied (30–36). However, while time restrictions required omission of these facets of our research from the Award Lecture, the reader is invited to peruse the publications cited.



## Acknowledgments

Financial and in-kind support from the Natural Sciences and Engineering Research Council of Canada (NSERC; Research, Strategic, and CRD Programs), Bayer Inc., Dupont Canada, Nova, Hoechst-Celanese Corp., Polymer Sheet Applications, and BASF Corp. made this research possible. Helpful suggestions and assistance from Ken Russell, Don Heyding, Warren Baker, Jim Hsu, Brian Hunter, and the late Almeria Natansohn are also much appreciated, as are of course the crucial contributions of my co-workers, cited below.

## References

1. For general discussions, see (a) A. Rudin. *The elements of polymer science and engineering*. 2nd ed. Academic Press, New York. 1999; (b) P. Rempp and E.W. Merrill. *Polymer synthesis*. 2nd ed. Hüthig & Wepf, Basel. 1991; (c) D. Feldman and A. Barbalata. *Synthetic polymers*. Chapman and Hall, London. 1996; (d) H.-G. Elias. *An introduction to polymer science*. VCH, Weinheim, 1997.
2. For useful reviews see: (a) P.C. Möhring and N.J. Coville. *J. Organomet. Chem.* **479**, 1 (1994); (b) V.K. Gupta, S. Satish, and I.S. Bhardwaj. *J. Macromol. Sci. Rev. Macromol. Chem. Phys.* **C34**, 439 (1994); (c) H.H. Brintzinger, D. Fischer, R. Mülhaupt, B. Rieger, and R.M. Waymouth. *Angew. Chem., Int. Ed. Eng.* **34**, 1143 (1995); (d) M. Bochmann. *J. Chem. Soc., Dalton Trans.* 255 (1996); (e) W. Kaminsky and M. Arndt. *Adv. Polym. Sci.* **127**, 143 (1997). The April 2000 issue of *Chemical Reviews* also contains many other important reviews on the general subject of applications of organometallic compounds to the catalysis of alkene polymerization.
3. D.J. Gillis, M.-J. Tudoret, and M.C. Baird. *J. Am. Chem. Soc.* **115**, 2543 (1993).
4. R. Quyoum, Q. Wang, D.J. Gillis, M.-J. Tudoret, D. Jeremic, B.K. Hunter, and M.C. Baird. *Organometallics*, **15**, 693 (1996).
5. Q. Wang, D.J. Gillis, R. Quyoum, D. Jeremic, and M.C. Baird. *J. Organomet. Chem.* **527**, 7 (1997).
6. D.J. Gillis, R. Quyoum, M.-J. Tudoret, Q. Wang, D. Jeremic, A. Roszak, and M. C. Baird. *Organometallics*, **15**, 3600 (1996).
7. M.J. Sarsfield, S.W. Ewart, T.L. Tremblay, E.F. Williams, and M.C. Baird. *Organometallics*, **17**, 1502 (1998).
8. M.C. Murray and M.C. Baird. *J. Mol. Catal.* **128**, 1 (1998).
9. M.C. Murray and M.C. Baird. *Can J. Chem.* **79**, 1012 (2001).
10. N. Bavarian, J.S. Parent, and M.C. Baird. *Macromol. Chem. Phys.* **202**, 3248 (2001).
11. M.C. Murray and M.C. Baird. *J. Polym. Sci. Part A Polym. Chem.* **A38**, 3966 (2000).
12. C. Pellecchia, D. Pappalardo, L. Oliva, and A. Zambelli. *J. Am. Chem. Soc.* **117**, 6593 (1995).
13. (a) E.F. Williams, M.C. Murray, and M.C. Baird. *Macromolecules*, **33**, 261 (2000); see also (b) C. Pellecchia and A. Grassi. *In Topics in catalysis*. Vol. 7. Edited by T.J. Marks and J.C. Stevens. Baltzer Science Publishers, Delft, The Netherlands. 1999. p 125; (c) A. Grassi, S. Saccheo, A. Zambelli, and F. Laschi. *Macromolecules*, **31**, 5588 (1998); (d) T.E. Ready, R. Gurge, J.C.W. Chien, and M.D. Rausch. *Organometallics*, **17**, 5236 (1998).
14. R. Quyoum, Q. Wang, M.-J. Tudoret, D.J. Gillis, and M.C. Baird. *J. Am. Chem. Soc.* **116**, 6435 (1994).
15. For general reviews of carbocationic initiation, see (a) J.P. Kennedy and E. Maréchal. *Carbocationic polymerization*. John Wiley and Sons, New York. 1982; (b) J.P. Kennedy and B. Iván. *Designed polymers by carbocationic macromolecular engineering, theory and practice*. Hanser Publishers, Munich. 1991; (c) M. Sawamoto. *Prog. Polym. Sci.* **16**, 111 (1991); for carbocationic initiation specifically by organometallic complexes, see (d) M.C. Baird. *Chem. Rev.* **100**, 1471 (2000).
16. J. Sassmannshausen and M. Bochmann. *J. Organomet. Chem.* **548**, 23 (1997).
17. Q. Wang and M.C. Baird. *Macromolecules*, **28**, 8021 (1995).
18. A.D. Cameron, V.H. Smith, and M.C. Baird. *J. Chem. Soc., Dalton Trans.* 1037 (1988) and refs. therein.
19. (a) F.A. Cotton, J.N. Francis, B.A. Frenz, and M. Tsutsui. *J. Am. Chem. Soc.* **95**, 2483 (1973); (b) T.C.T. Chang, B.M. Foxman, M. Rosenblum, and C. Stockman. *J. Am. Chem. Soc.* **103**, 7361 (1981); (c) N. Kuhn, H. Bohnen, D. Bläser, and R. Boese. *Chem. Ber.* **127**, 1405 (1994).
20. F. Barsan and M.C. Baird. *J. Chem. Soc., Chem. Commun.* 1065 (1995).
21. F. Barsan, A.R. Karam, M.A. Parent, and M.C. Baird. *Macromolecules*, **31**, 8439 (1998).
22. T.L. Tremblay, S.W. Ewart, M.J. Sarsfield, and M.C. Baird. *J. Chem. Soc., Chem Commun.* 831 (1997).
23. T.L. Tremblay, S.W. Ewart, M.J. Sarsfield, A. Roszak, and M.C. Baird. *J. Chem. Soc., Dalton Trans.* 3097 (1997).
24. Q. Wang, D. Jeremic, R. Quyoum, and M.C. Baird. *J. Organomet. Chem.* **497**, 143 (1995).
25. T.M. Liu, W.E. Baker, V. Schytt, T. Jones, and M.C. Baird. *J. Appl. Polym. Sci.* **62**, 1807 (1996).
26. C. Li Pi Shan, W.E. Baker, M.F. Cunningham, and M.C. Baird. *J. Appl. Polym. Sci.* **70**, 2679 (1998).
27. S.W. Ewart, M.J. Sarsfield, E.F. Williams, and M.C. Baird. *J. Organomet. Chem.* **579**, 106 (1999).
28. S.W. Ewart, M.A. Parent, and M.C. Baird. *J. Polym. Sci. Part A Polym. Chem.* **37**, 4386 (1999).
29. R. Kumar, A. Penciu, M.J. Drewitt, P.J. McInenly, and M.C. Baird. *J. Poly. Sci. A*, **40**, 3302 (2002).
30. S.Y. Desjardins, A.A. Way, D. Adirim, and M.C. Baird. *Organometallics*, **17**, 2382 (1998).
31. S.W. Ewart and M.C. Baird. *Topics in catalysis*. Edited by T.J. Marks and J.C. Stevens. Baltzer Science Publishers, Delft, The Netherlands. 1999. Chap 7. pp 1–8.
32. S.W. Ewart and M.C. Baird. *Preparation, properties and technology of metallocene-based polyolefins*. Vol. 1 (invited contribution). Edited by J. Scheirs and W. Kaminsky. John Wiley and Son, U.K. 1999. pp. 119–141.
33. M. Lin and M.C. Baird. *J. Organomet. Chem.* **619**, 62 (2001).
34. M.J. Drewitt, M. Niedermann, R. Kumar, and M.C. Baird. *Inorg. Chim. Acta*, **335**, 43 (2002).
35. M. Lin, G.J. Spivak, and M.C. Baird. *Organometallics*, **21**, 2350 (2002).
36. J.H. Brownie, L.N. Zakharov, A.L. Rheingold, and M.C. Baird. *Organometallics*, **22**, 33 (2003).



## ERRATUM

**Erratum: Taxanes in rooted cuttings vs. mature Japanese yew**

**Qing-Wen Shi, Tracy L. Petzke, Françoise Sauriol, Orval Mamer, and Lolita O. Zamir**

Ref.: Can. J. Chem. **81**(1): 64–74 (2003).

In this article the incorrect volume number was inadvertently published at the bottom of page 64. The corrected information should read:

Can. J. Chem. **81**: 64–74 (2003)

NRC Research Press apologizes for any inconvenience this error may have caused.

Received 28 March 2003. Published on the NRC Research Press Web site at <http://canjchem.nrc.ca> on 12 May 2002.

**Q.-W. Shi, T.L. Petzke, and L.O. Zamir.**<sup>1</sup> Université du Québec, INRS-Institut Armand-Frappier-Santé Humaine, 531 Boulevard des Prairies, Laval, QC H7V 1B7, Canada.

**F. Sauriol.** Department of Chemistry, Queen's University, Kingston, ON K7L 3N6, Canada.

**O. Mamer.** Biomedical Mass Spectrometry Unit, McGill University, 1130 Pine Avenue West, Montreal, QC H3A 1A3, Canada.

<sup>1</sup>Corresponding author (e-mail: [Lolita.Zamir@inrs-iaf.quebec.ca](mailto:Lolita.Zamir@inrs-iaf.quebec.ca)).



## AWARD LECTURE / CONFÉRENCE D'HONNEUR

## A fibre-optic biosensor for detection of microbial contamination<sup>1</sup>

Amer Almadidy, James Watterson, Paul A.E. Piunno, Inge V. Foulds,  
Paul A. Horgen, and Ulrich Krull

**Abstract:** A fibre-optic biosensor is described for detection of genomic target sequences from *Escherichia coli*. A small portion of the LacZ DNA sequence is the basis for selection of DNA probe molecules that are produced by automated nucleic acid synthesis on the surface of optical fibres. Fluorescent intercalating agents are used to report the presence of hybridization events with target strands. This work reviews the fundamental design criteria for development of nucleic acid biosensors and reports a preliminary exploration of the use of the biosensor for detection of sequences that mark the presence of *E. coli*. The research work includes consideration of the length of the strands and non-selective binding interactions that can potentially block the selective chemistry or create background signals. The biosensors were able to detect genomic targets from *E. coli* at a picomole level in a time of a few minutes, and dozens of cycles of use have been demonstrated. In a step towards the preparation of a completely self-contained sensor technology, a new intercalating dye known as SYBR 101 (Molecular Probes, Inc.) has been end-labelled to the LacZ nucleic acid probe, to examine whether dye tethered onto an oligonucleotide terminus could fluorimetrically transduce the formation of hybrids. The results obtained from experiments in solution indicate that the use of tethered dye provides fluorescence signals that are due to hybridization, and that this process is functional even in the presence of a high concentration of non-selective background DNA obtained from sonicated salmon sperm.

**Key words:** biosensor, DNA, fibre optic, hybridization, fluorescence, pathogen, *E. coli*.

**Résumé :** On décrit une fibre optique servant de biosenseur pour la détection du génome cible dans la séquence du *Escherichia coli*. Une petite portion de la séquence du LacZ-ADN sert de base pour la sélection des molécules sondes d'ADN obtenues par la synthèse automatique d'acides nucléiques à la surface des fibres optiques. On a utilisé des agents intercalants fluorescents pour mettre en évidence la présence de phénomènes d'hybridation avec la fibre cible. Ce travail passe en revue le critère de conception fondamental de développement de biosenseurs d'acides nucléiques, et rapporte également une exploration préliminaire de l'utilisation des biosenseurs pour détecter les séquences qui témoignent de la présence du *E.coli*. Les travaux de recherche tiennent compte de la longueur de la fibre et des interactions liantes non sélectives qui peuvent potentiellement bloquer la sélectivité chimique ou créer un bruit de fond. Les biosenseurs ont été capables de détecter le génome cible à partir du *E. coli* au niveau de la picomole et en quelques minutes, on a ainsi pu effectuer des douzaines de cycles d'études. Dans une étape en vue de la préparation de la technologie du senseur auto-contenu, on a marqué un nouveau colorant intercalaire connue sous le nom de SYBR 101 (Molecular Probes, Inc.) à l'extrémité de la sonde d'acide nucléique LacZ, pour voir si le colorant attaché dans l'oligonucléotide terminal peut fluorométriquement induire la formation d'hybrides. Les résultats obtenus à partir des expériences en solution indiquent que l'utilisation de colorant attaché fournit des signaux fluorescents qui sont dus à l'hybridation, et que ce processus est fonctionnel même en présence d'une forte concentration d'ADN d'arrière plan non sélectif obtenue à partir du sperme de saumon traité à l'ultrason.

**Mots clés :** biosenseur, ADN, fibre optique, hybridation, fluorescence, pathogène, *E. coli*.

Received 18 February 2003. Published on the NRC Research Press Web site at <http://canjchem.nrc.ca> on 29 May 2003.

**A. Almadidy, J. Watterson, and U. Krull.**<sup>2</sup> Department of Chemistry, University of Toronto at Mississauga, Mississauga, ON L5L 1C6, Canada.

**P.A.E. Piunno.** FONA Technologies, Inc., 785 Bridge Street, Waterloo, ON N2V 2K1, Canada.

**I.V. Foulds and P.A. Horgen.** Department of Biology, University of Toronto at Mississauga, Mississauga, ON L5L 1C6, Canada.

<sup>1</sup>MAXXAM Award Lecture. Presented by U.J. Krull at the Canadian Society for Chemistry Conference, 2002.

<sup>2</sup>Corresponding author (e-mail: [ukrull@utm.utoronto.ca](mailto:ukrull@utm.utoronto.ca)).



## Introduction

### Design of a nucleic acid biosensor

Methods that are suitable for the routine determination of the presence of bacterial species are of obvious importance in the quality control of foodstuff and water resources everywhere. Classical methods of nucleic acid hybridization assay are often time consuming and so may be inappropriate for laboratories that require rapid turnover of results and high sample throughput (1–6). As a result, significant research has been devoted to the development of biosensors in an attempt to generate assays that are reversible, reusable, sensitive, selective, and relatively simple to use. Methods of signal transduction to detect nucleic acid hybridization on biosensor surfaces include electrochemical, piezoelectric, and optical approaches (7–11) and compete favourably with the recent developments in wet-chemical methods such as those based on the polymerase chain reaction (12, 13).

The development of biosensors must take into consideration the effects of the local environment on the binding capacity of the immobilized selective molecular recognition elements. This involves careful consideration of the nature of the solid substrate used, the method of immobilization, solution conditions under which experiments will generally be done, and probe density and length. Each of these parameters has direct consequences on the reproducibility and sensitivity of signal generation (14–17).

To examine the effects of immobilization on nucleic acid hybridization, thermal denaturation experiments were done at the surface of fibre-optic nucleic acid biosensors to determine whether trends in hybridization observed in bulk solution could be extrapolated to describe nucleic acid hybridization in an interfacial environment (17).

The immobilization of oligonucleotide probes onto the surface of fused-silica optical fibre substrates was achieved by means of a modification using a silane reagent (15, 17). The modified optical fibre substrates were then subjected to standard  $\beta$ -cyanoethyl-phosphoramidite oligonucleotide synthesis protocols in order to undergo the stepwise synthesis of oligonucleotides at controlled densities onto the surface of the substrates.

To examine the energetics of interfacial hybridization, the van't Hoff enthalpy changes and temperature-corrected standard enthalpy changes were computed for a series of denaturation experiments, conducted based on the method developed by Piunno and co-workers (17). This model applies to denaturation occurring within a film of immobilized nucleic acids, with the complementary DNA freely able to float in and out of the membrane. The model assumes no interaction between neighbouring strands and that the denaturation is a two-state transition. The enthalpic change accompanying denaturation in an interfacial environment was significantly lower than that observed in experiments conducted in bulk solution. The sensitivities of  $\Delta H_{\text{vH}}(T_m)$  to changes in the characteristic melt temperature ( $T_m$ ) were a factor of 2–4 smaller for the transitions occurring at the interface of the optical biosensors relative to those observed for the experiments done in bulk solution and were usually opposite in sign. This suggested that the changes in heat capacity that accompanied the denaturation were not the same in an interfacial environment as they were in bulk solution.

This may be owing to local density changes in the nucleic acid films as a result of the denaturation. The results suggested that there may be significant differences in the nature of the base pairing in an interfacial environment compared with that which occurred in bulk solution. There did not appear to be a relationship between the packing density of immobilized oligonucleotides and the reduction in the endothermicity of the denaturation. The observed  $T_m$  values were still of comparable magnitude to those that were observed in experiments done in bulk solution, so it is likely that there is a significant difference in entropy changes accompanying hybridization and denaturation in an interfacial environment relative to those observed in experiments done in bulk solution.

The data further suggest that the selectivity of hybridization in an interfacial environment may be substantially different and advantageous in comparison with that observed in a bulk solution environment. Furthermore, the selectivity of hybridization does not necessarily follow the trend of  $T_m$ , which is seen as a function of ionic strength and oligonucleotide immobilization density. These results corroborate the notion that there is an ensemble of interactions that will occur, along with the hybridization–denaturation transition, in an interfacial environment. These interactions contribute to the overall stability of the binding of target DNA and therefore play an important role in defining the  $T_m$  values of a particular probe–target complex, as well as the shape of the thermal denaturation profile, and therefore ultimately affect the selectivity of hybridization.

The results of such work (15, 17) indicate that the choice of density of immobilized single-stranded DNA (ssDNA) does provide for control of selectivity. The optimization of the analytical function of a fibre-optic biosensor for any particular hybridization assay must consider both the issues of selectivity and the amount of fully complementary double-stranded DNA (dsDNA) that is formed, as this is the source of the analytical signal. A review of the data suggests that it is possible to select a combination of ssDNA density, solution ionic strength, and temperature that provides an improvement in the selectivity coefficient of about two orders of magnitude when comparing the formation of the fully complementary duplex to that which contains one central base-pair mismatch. Bulk solution experiments do not attain the same magnitude of selectivity coefficient. Importantly, only about 30% of the maximum amount of fully matched dsDNA is available under the conditions in bulk solution where the best case of selectivity is achieved. This does not compare favourably with the immobilized ssDNA system, where about 55% of the maximum amount of fully matched dsDNA is available under conditions where selectivity is maximized.

An important consideration in the evaluation of the sensitivity and selectivity of hybridization for a given sensor system is the nature of the sample that is being introduced. Samples may contain various levels of large, non-complementary genomic DNA and RNA molecules, which may interfere with analysis. Also, most nucleic acid sensor systems will be exposed to the target DNA of interest in double-stranded form. This imposes the requirement of denaturing these double-stranded targets so that selective hybridization may subsequently take place at the sensor



surface. In practice, this may result in a competition for hybridization of target strands in bulk solution between immobilized probe oligonucleotides and the complementary DNA in bulk solution. This competition for hybridization may impart some significant limitations on the sensitivity and selectivity of the assay. A balance can be struck between the desired sensitivity and selectivity of a given hybridization assay, and this balance is somewhat tunable by means of controlling the density of ssDNA immobilization. If non-selective adsorption occurs predominantly in regions between the immobilized oligonucleotide probes, then it may be that optimal assay sensitivity and selectivity would be achieved using a sensor with a higher density of probe molecules, where the number of exposed surface sites for non-selective adsorption is decreased.

To more accurately model the effects of interferences as experienced in a real sample, experiments were done to investigate the effects of the presence of large genomic DNA strands (20 kbp average size) on the response of the sensors to labeled oligonucleotides. The experiments were designed such that the relative concentrations of oligonucleotides and genomic DNA were adjusted. Experiments were done using concentration regimes where both fully complementary (cDNA) and non-complementary (ncDNA) oligonucleotide 20mers were introduced at a concentrations of about  $10^{15}$  molecules  $L^{-1}$ , while genomic DNA from *E. coli* was introduced at a concentration of  $10^{12}$  to  $10^{14}$  molecules  $L^{-1}$  (15). The results suggest that the presence of genomic DNA as a background species does not substantially block hybridization of very short target oligonucleotides or the extent of non-selective adsorption of short non-complementary oligonucleotides. This trend was observed for all concentration regimes used. Additionally, the presence of genomic DNA did not affect the response times of the sensors in the first few minutes of an analysis. Interestingly, the pretreatment of the sensor surface with genomic DNA for 10 min reduced the response time of the sensors to cDNA. It may be that the larger genomic DNA acted to reduce the effective solution volume near the sensor surface and to increase the effective analyte concentration. This effect was more significant at the lower analyte concentration, where response times were more sensitive to changes in analyte concentration. The response time of sensors to the addition of  $10^{15}$  molecules  $L^{-1}$  cDNA was  $224 \pm 5$  s, while the response time after pretreatment with genomic DNA was  $192 \pm 5$  s. The response time for addition of  $10^{16}$  molecules  $L^{-1}$  cDNA was  $28 \pm 1$  s, while the response time after pretreatment of the surface with genomic DNA was  $21 \pm 1$  s.

These results have ramifications for analyses of real-world samples. The preliminary results suggest that the process of non-selective adsorption by interfering short and long nucleic acid sequences in solution may not occur in such a manner as to substantially inhibit the extent of hybridization of a target sequence when early in an analytical experiment.

### A fibre-optic biosensor for *E. coli*

Coliforms are aerobic and facultatively anaerobic, gram-negative, non-spore forming bacilli, encompassing members of *Escherichia*, *Citrobacter*, *Klebsiella*, and *Enterobacter* (1–3). Although several of the coliform bacteria are not usually pathogenic themselves, they serve as an indicator of po-

tential bacterial pathogen contamination. Using such indicators, researchers in the U.S.A. estimate that 40% of private water supplies and 70% of spring-fed supplies contain coliform bacteria (4). Coliform bacteria concentrations are determined using methods specified by the Environmental Protection Agency (EPA) and those found in ref. 5. These methods can be slow, and new biosensor technologies may offer substantial advantages in providing analyses within seconds to minutes.

Currently, several methods are used for the detection or enumeration of *E. coli* cells in water, including microbiological, serological, and immunological procedures. Polymerase chain reaction (PCR) methods have been developed, where LacZ, lamB, and uid genes have been used as targets for the design of primers for coliform detection (6). False positive and negative results can arise when using these techniques, and only a very limited number of strains have been used to test for specificity of the primers. Standard PCR generally only provides information about detection, and even when using quantitative real-time PCR, the analyses still often require hours.

Herein we report the development of a fibre-optic biosensor for the detection of short sequences of oligonucleotides that indicate the presence of *E. coli*. Single-stranded DNA (ssDNA) was immobilized by covalent binding to a fused silica optical fibre. Hybridization on the solid surface was detected by use of the fluorescent intercalating dye, ethidium bromide (EB). Testing to detect coliform contamination of water was demonstrated using selective hybridization of nucleic acid sequences. A 25mer sequence on the LacZ gene of the *E. coli* was targeted using a 25mer ssDNA probe. The investigation has shown that the biosensor was capable of detecting minute amounts of synthetic cDNA and also genomic DNA that was extracted from *E. coli*. The biosensor could provide analytical information in less than 1 min and was regenerable for many cycles of application.

Preliminary work that targets the development of a self-contained biosensor has involved attachment of the intercalating fluorescent reporter dye to the probe by means of a short molecular tether. The intercalating fluorescing dye (SYBR 101) was covalently attached through a short tether to the 25mer ssDNA (labelled DNA, L-DNA), and the fluorescence changes caused by hybridization have been investigated in bulk solution using free L-DNA. In the design of a self-contained biosensor, this approach may help reduce background fluorescence from free dye in solution, will allow internal standardization, and will substantially reduce the risk of exposure of the operator to toxic chemicals by confining the intercalating dye to the surface of the device.

## Experimental

### Chemicals

SYBR 101, succinimidyl ester, was donated by Molecular Probes, Eugene, Oregon. Biosynthesis-grade solvents were purchased (EM Science, Toronto, ON) and further purified or dried by standard laboratory protocols. Reagents for DNA synthesis were purchased from Dalton Chemical Laboratories Inc. (Toronto, ON) and were used as received or were prepared as below. Anhydrous acetonitrile (EM Science) was pre-dried by distillation from  $P_2O_5$  and redistilled from



calcium hydride under dry argon. Tetrahydrofuran (EM Science) was pre-dried over  $\text{CaH}_2$ , filtered, and distilled immediately prior to use from sodium metal (Aldrich) / benzophenone (Aldrich). Water was double distilled in glass, treated with diethyl pyrocarbonate (Aldrich), and autoclaved. Molecular-biology-grade polyacrylamide gel electrophoresis reagents and apparatus were obtained through Bio-Rad (Hercules, California). Silica gel (Toronto Research Chemicals, Toronto, ON) had a particle size of 30–70 microns.

### Instrumentation

Fluorescence studies of LacZ-target hybridization onto the probe at the surface of the *E. coli* biosensors were done using an optic-fibre spectrofluorimeter operated in an intrinsic-mode configuration (17). The spectrofluorimeter was equipped with a fluid-handling system for stop-flow fluorescence investigations of nucleic acid hybridization. Preliminary fluorescence studies of LacZ target to the dye labelled ssDNA in solution were done using a spectrofluorimeter instrument.

### Attachment of SYBR 101 to ssDNA probe

The SYBR 101 – ssDNA probe consisted of three parts: the ssDNA, a C6 aminomodifier as a tether, and the fluorescent dye SYBR 101 (absorption 483 nm, emission 515 nm). The tether was attached to the ssDNA using an ABI 392 DNA/RNA synthesizer. C6 aminomodifier is a phosphoramidite synthon containing a six-carbon atom chain terminated by a protected amine moiety. The reagent was used in analogy to a phosphoroamidite nucleoside. The modifier was activated with tetrazole to form an active intermediate that coupled to the 5'-hydroxyl terminus of the oligonucleotide, which was bound to controlled pore glass (CPG) in the final coupling cycle. Oxidation and ammonium hydroxide cleavage – deprotection yielded the 5'-amine-modified oligonucleotide.

The ssDNA-linker at this stage bore a nucleophilic, unprotected primary amine group, which reacted with the electrophilic *N*-hydroxy succinamide group of the SYBR 101. SYBR 101 succinimidyl ester (reactive dye) was used to label the amine-modified oligonucleotide because it forms a very stable amide bond between the dye and the amine-modified oligonucleotide probe. The reactive dye is a hydrophobic molecule, so it was dissolved in high-purity dimethylsulfoxide before reaction with the amine-modified oligonucleotide probe. The reaction was done in a tetraborate buffer at pH 8.5, so that the reactive dye reacted with the non-protonated amine group on the modified oligonucleotide probe.

In this protocol, 250  $\mu\text{g}$  of the reactive dye was dissolved in 14  $\mu\text{L}$  dimethylsulfoxide. To this vial, 7  $\mu\text{L}$  of deionized, distilled  $\text{H}_2\text{O}$  was added followed by 75  $\mu\text{L}$  of the sodium tetraborate buffer and 4  $\mu\text{L}$  of a 25  $\mu\text{g } \mu\text{L}^{-1}$  of gel-purified 5'-amine-modified oligonucleotide. The vial was placed on an oscillating platform stirrer at low speed to insure that the reaction remained well mixed. The reaction was allowed to continue overnight. The labelled oligonucleotide (L-DNA) was purified from the reaction mixture by use of a Pharmacia NAP-10 column containing Sephadex G-25 me-

dium of DNA Grade, in distilled water containing 0.15% Kathone CG/ICP Biocide as a preservative.

### Preparation of optical fibres

The jacket material surrounding the fused silica optical fibres (400  $\mu\text{m}$  core diameter, 3M Power Core™ Series Optical Fibre, FT-400-URT or FP-400-UHT, distributed by Thor Labs Inc., Newton, NJ, U.S.A.) was mechanically removed by use of a fibre-stripping tool (Thor Labs Inc.) to reveal the fused silica core material and cladding layer. Optical fibre pieces 48 mm in length were then made by use of a custom-built, diamond-edged fibre-scoring device. The termini of the fibre pieces were visually inspected at 40  $\times$  magnifications to ensure the fibre termini were flat, orthogonal to the length of the fibre, and free of chips and nicks.

The fused silica fibre segments were cleaned prior to surface modification according to the published methods (14). CPG was used to grow ssDNA in tandem with fused silica fibres and was subsequently used for recovery of ssDNA to determine the quality and quantity of synthesis. CPG was treated identically to fused silica fibres. The fibre substrates were first immersed and gently agitated in a 1:1:5 (v/v) solution of 30% ammonium hydroxide – 30% hydrogen peroxide – water at 80°C for 5 min. The substrates were then recovered, washed with copious amounts of water, and then treated with 1:1:5 (v/v) concd. HCl – 30% hydrogen peroxide – water for 5 min at 80°C with gentle agitation. The substrates were recovered and washed with 100 mL portions of water, methanol, chloroform, and diethyl ether, respectively, dried under reduced pressure, and stored in vacuo and over  $\text{P}_2\text{O}_5$  until required.

### Functionalization of fused silica substrates with 3-glycidoxypropyltrimethoxysilane (GOPS)

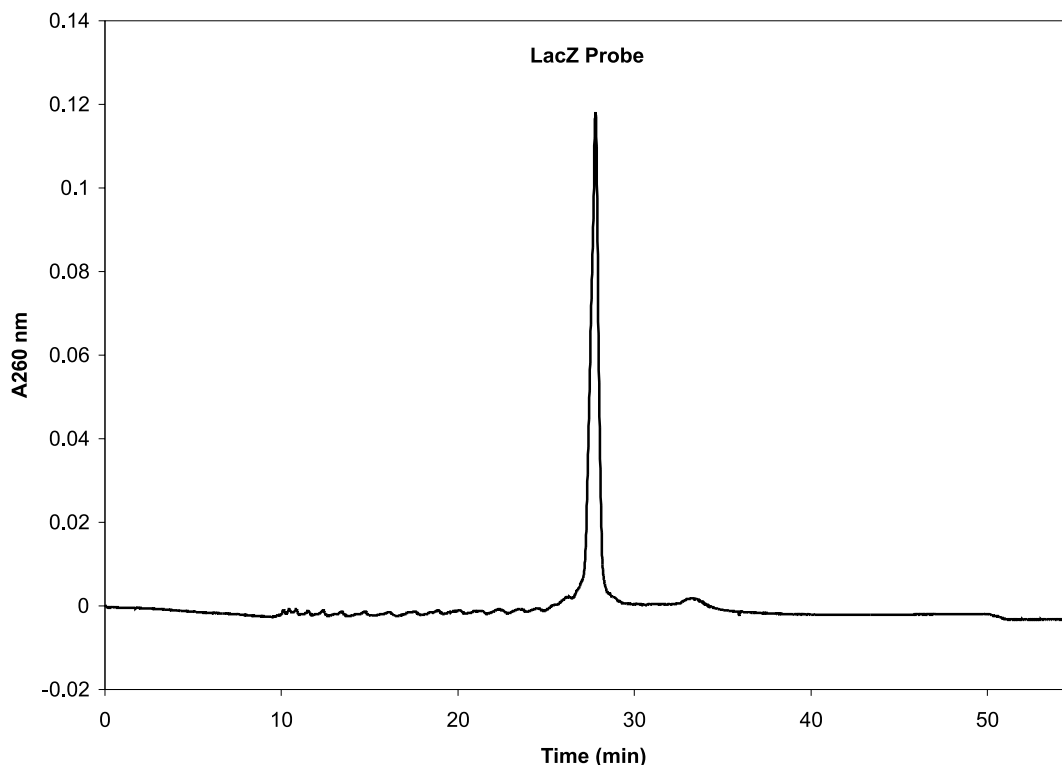
The cleaned fused silica substrates were suspended in an anhydrous solution of xylene – 3-glycidoxypropyltrimethoxysilane – diisopropylethylamine (100:30:1 v/v/v). The reaction was stirred under argon at 80°C for 24 h. The fibres were then collected and twice washed with 50 mL portions of methanol, chloroform, and diethyl ether, respectively, and then dried and stored in vacuo and over  $\text{P}_2\text{O}_5$  at room temperature until required.

### Synthesis of dimethoxytrityl hexaethylene glycol (DMT-HEG)

A solution of dimethoxytrityl chloride (7.1 g, 21 mmol) in dry pyridine (10 mL) was added dropwise to a stirred solution of hexaethylene glycol (5.6 mL, 21 mmol in 5 mL pyridine) under an argon atmosphere. Stirring was continued overnight, after which time the reaction mixture was combined with dichloromethane (50 mL). The mixture was shaken against 5% aqueous bicarbonate (2  $\times$  900 mL) and then with water (2  $\times$  900 mL) to remove unreacted HEG, pyridine, and salts. The organic layer was dried under reduced pressure to yield the crude product. The product was purified by liquid chromatography using a silica gel column and an eluent of 1:1 dichloromethane – diethyl ether containing 0.1% triethylamine (2.9 g, 24% yield).  $^1\text{H}$  NMR (200 MHz,  $\text{CDCl}_3$ )  $\delta$ : 7.47–7.19 (m, 9H), 6.81 (d, 4H,  $J$  = 8.8 Hz), 3.78 (s, 6H), 3.74–3.51 (m, 22H), 3.22 (t, 2H,  $J$  = 5.8 Hz). Purity DMT-HEG = 96%.



**Fig. 1.** HPLC anion-exchange chromatogram of the 25mer mixed-base LacZ probe that was grown on CPG and then quantitatively removed by base cleavage. The chromatogram indicates the synthetic purity of the sample used in this investigation.



#### Linkage of DMT-HEG onto GOPS-functionalized substrates

DMT-HEG (10 equiv relative to the quantity of surface hydroxyl moieties, 700 mg DMT-HEG – 100 mg CPG) that had been dried by extended storage in vacuo and over  $P_2O_5$  (>72 h) was dissolved in 20 mL of anhydrous pyridine and introduced to an excess of NaH (10 equiv) that had been thrice washed with dry hexane to remove the oil in which it had been suspended. The reaction was permitted to proceed with stirring for 1 h at room temperature under an argon atmosphere. The reaction mixture was filtered through a sintered glass frit under a positive pressure of argon and the filtrate immediately introduced to the reaction vessel containing the GOPS-functionalized substrates. One batch of GOPS-functionalized substrates containing both optical fibres and CPG was created, for which the DMT-HEG coupling reaction was permitted to proceed under a positive pressure of argon gas at room temperature with gentle agitation on an oscillating platform stirrer for durations of 4 h. Following the coupling reaction, the substrates were quickly recovered by filtration over a fritted glass funnel and washed with 150 mL portions of methanol, water, methanol, and diethyl ether, respectively, to quench the coupling reaction and remove non-specifically adsorbed reactants. The DMT-protected polyether-functionalized substrates were dried by placement in vacuo and over  $P_2O_5$  and were maintained under these conditions until further required.

#### Capping of unreacted silanol and hydroxyl functionalities with chlorotrimethylsilane

Sites on the surfaces of the fused silica fibres and CPG onto which undesired nucleotide synthon coupling could oc-

cur were capped prior to oligonucleotide assembly using chlorotrimethylsilane (TMS-Cl), as per the method of Watterson et al. (17). The substrates that had been dried by storage in vacuo and over  $P_2O_5$  for a minimum duration of 16 h were suspended in a solution of 1:10 (v/v) chlorotrimethylsilane–pyridine for 16 h under an argon atmosphere at room temperature. The fused silica substrates were thrice washed with 20 mL portions of pyridine, methanol, and diethyl ether, respectively, and stored in vacuo and over  $P_2O_5$  at 25°C until required.

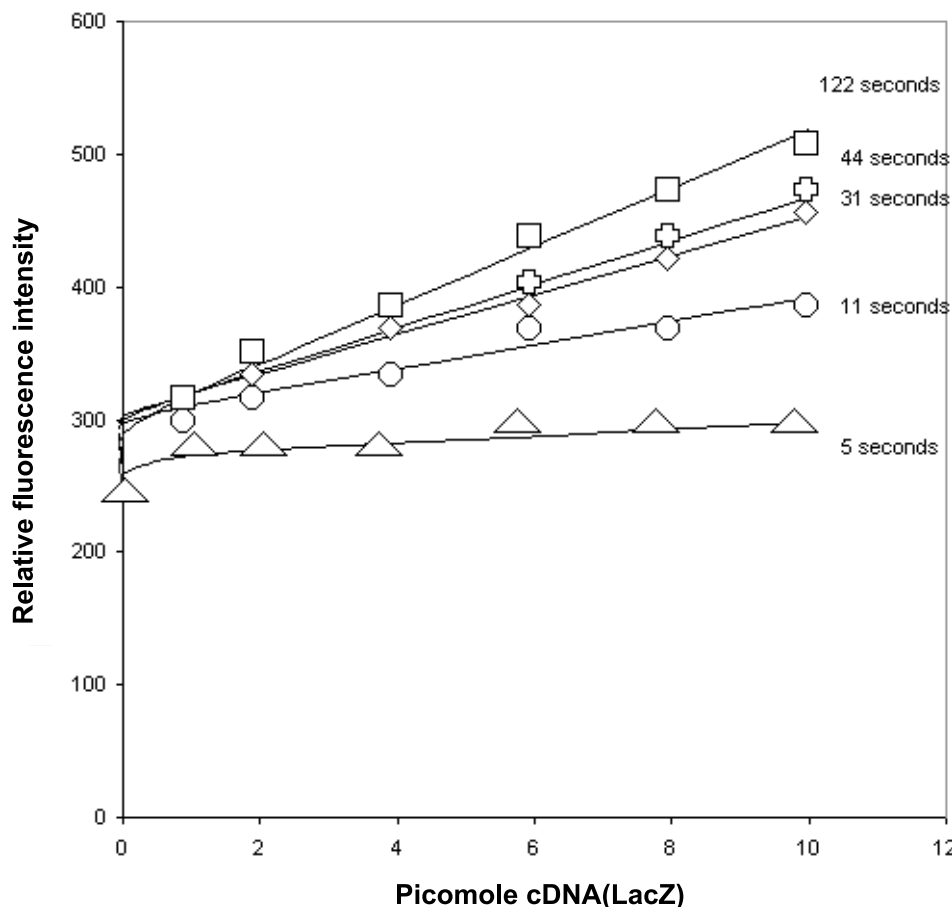
#### Solid-phase phosphoramidite synthesis of oligonucleotides

All oligonucleotide synthesis was done using a PE-ABI 391-EP DNA synthesizer (PerkinElmer Applied Biosystems, Foster City, CA, U.S.A.). The manufacturer-supplied synthesis cycles were employed for oligonucleotide assembly with modifications to the delivery times of the reagents as required to completely fill the synthesis columns that were used. Oligonucleotide synthesis onto optical fibres (400  $\mu\text{m}$  i.d.  $\times$  48 mm) was done in a custom-manufactured Teflon® synthesis column (6 mm i.d.  $\times$  50 mm) capable of holding 8 fibres in an evenly distributed and non-contacting fashion via cylindrical bores (400  $\mu\text{m}$  i.d.  $\times$  2 mm deep) machined into one of the end caps (9).

A nucleic acid oligonucleotide having the sequence (5')CAGGTAATGTGGCGGATGAGCGGCA(3') was synthesized onto the sensor surface as the ssDNA probe. The target nucleic acid (cDNA) used to challenge the probe was an oligonucleotide having the sequence (5')TGCCGC-TCATCCGCCACATATCCTA(3'), which was derived from a portion of the LacZ gene sequence. The 25mer



**Fig. 2.** *E. coli* biosensor response to serial dilutions of cDNA as a function of cDNA concentration at various times. Maximum response was observed at about 2 min for all concentrations of cDNA.



oligonucleotides were prepared by use of a phosphoramidite synthon (Dalton) and standard protocols for oligonucleotide assembly, purification, and quantitation, as have previously been reported (15).

Determination of the extent of surface coverage of CPG substrates with covalently immobilized oligonucleotide-polyether conjugates was done by anion-exchange HPLC using methods that have been reported elsewhere (16).

#### *E. coli* and salmon sperm DNA preparation

A 60 mL culture of *E. coli* was grown overnight at 37°C in LB media. Bacteria were harvested by centrifugation at 3000g for 10 min. Cells were lysed using TRIZOL reagent (Life Technologies, Canada) by repetitive pipetting, using 1 mL of the reagent per  $1 \times 10^7$  cells of the *E. coli*. The homogenized sample was incubated for 5 min at room temperature, and chloroform was then added (0.2 mL chloroform per 1 mL of TRIZOL). Sample tubes were capped and shaken vigorously for 15 s and incubated at room temp for 2–3 min. The sample tubes were then centrifuged at 12 000g for 15 min at 2–8°C, to separate the mixture into a lower, red phenol-chloroform phase, an interphase, and a colourless upper aqueous phase. DNA was precipitated from the interphase and the organic phase by the addition of 0.3 mL of 100% ethanol per 1 mL of TRIZOL reagent originally used. Samples were mixed by inversion and permitted to equilibrate at room temperature for a few minutes, followed

by precipitation of DNA by centrifugation at 2000g for 5 min at 2–8°C. Phenol-ethanol supernatant was removed and the DNA pellet was washed twice with ethanol and dried under vacuum. DNA was finally reconstituted by adding 1 mL of  $1 \times$  PBS and measurement of absorption at 260 nm showed that the DNA concentration of the resultant solution was about  $350 \mu\text{g mL}^{-1}$ . The extracted *E. coli* DNA was sheared by syringe and then by sonication for 5 min with a Vibra cell sonicator (Sonics & Materials, Inc.) equipped with a 5-mm tip and set to 125 W maximum power at 20 kHz. Samples were kept on ice at all times until they were used for examination of hybridization.

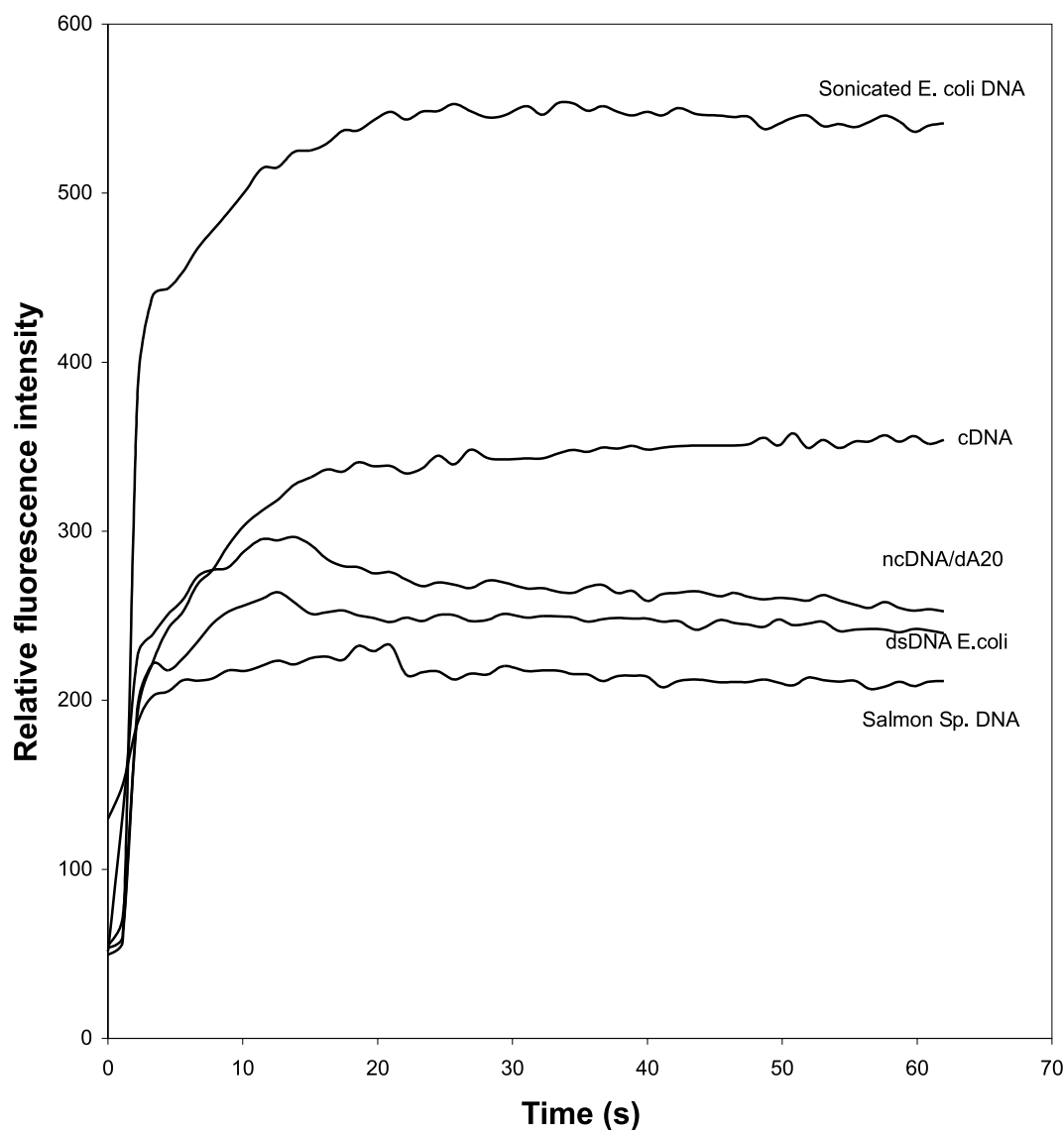
Lyophilized salmon sperm genomic DNA was reconstituted in 1 mL of  $1 \times$  PBS to a concentration of  $350 \mu\text{g mL}^{-1}$ , as indicated by measurement of absorption at 260 nm. This DNA was sheared by syringe and then by sonication for 5 min, as was done for the DNA from *E. coli*.

#### Hybridization assays of the *E. coli* biosensor

All sensors were cleaned by sonication in ethanol in a 40 W bath sonicator for 30 min to remove adsorbed contaminants from the sensor surface. In all cases, sensors were activated for hybridization by undergoing three consecutive thermal denaturation – re-annealing cycles, in which the sensors were exposed to a  $1 \times 10^{-7}$  M solution of the complementary 25mer oligonucleotide sequence (cDNA) in phosphate-buffered saline (PBS) hybridization buffer



**Fig. 3.** Chronofluorimetric response profile of a biosensor for *E. coli* using immobilized 25mer mixed-base probe on a fused silica optical fibre. Biosensor was exposed to 10 pmols of fully complementary LacZ 20mer (cDNA), 35 ng ssDNA from *E. coli* (prepared by treatment of whole genomic DNA by sonication and shearing), 35 ng of dsDNA from *E. coli*, and 35 ng ssDNA from salmon sperm (prepared by treatment of whole genomic DNA with sonication and shearing), in  $1 \times$  PBS containing  $10^{-7}$  M ethidium bromide at  $40^\circ\text{C}$  with full washing and chemical regeneration with water at  $90^\circ\text{C}$  and formamide solution (90% in TE buffer) between samples.



( $1.0 \text{ mol L}^{-1}$  NaCl,  $50 \text{ mmol L}^{-1}$  total phosphate ion, pH 7.0) and subsequently subjected to a temperature ramp of  $0.3^\circ\text{C per min}$ , over a range from  $20$  to  $80^\circ\text{C}$ . Hybridization assays were done for optical sensors that were exposed to solution-phase cDNA mixed with the staining intercalator ethidium bromide at a final concentration of  $0.1 \mu\text{mol L}^{-1}$ . Each sample solution had a total volume of  $26 \mu\text{L}$ , once in the reaction chamber. The flow was stopped and the signal was recorded over a period of up to 10 min. After reaction, the sensor was washed at a flow rate of  $3 \text{ mL min}^{-1}$ . Removal of the bound DNA that had associated with the sensor surface from the previous analysis was done prior to each experiment by flushing  $15 \text{ mL}$  of  $90^\circ\text{C}$  water through the flow cell ( $3 \text{ mL min}^{-1}$ , 5 min), followed by  $1 \text{ mL}$  of 95% ethanol, and final wash with 90% formamide in TE buffer ( $10 \text{ mm L}^{-1}$  Tris HCl,  $5 \text{ mmol L}^{-1}$  EDTA, pH = 8.3).

Salmon sperm DNA ( $0.1 \mu\text{mol L}^{-1}$ ) served as a control for genomic non-complementary DNA. Assays were performed using a solution temperature of  $40^\circ\text{C}$ . All hybridization assays were done in triplicate.

The L-DNA probe hybridization assays were done in bulk solution, by titrating the tethered SYBR 101-probe with a fully complementary synthetic LacZ sequence. A concentration range, from  $0.133$  to  $6.00 \mu\text{g mL}^{-1}$  of each sequence, was used in a total volume of  $700 \mu\text{L}$ .

## Results and discussion

The rapid detection of microbes in samples of water is becoming more critical as the population of the world increases. Our research group has focused on developing a biosensor that is rapid and sensitive for the detection of



**Fig. 4.** HPLC anion-exchange chromatogram of the mixed base 5' amine-modified LacZ probe that was grown on CPG and then quantitatively removed by base cleavage. The chromatogram indicates the high purity of the synthetic samples used in this investigation.

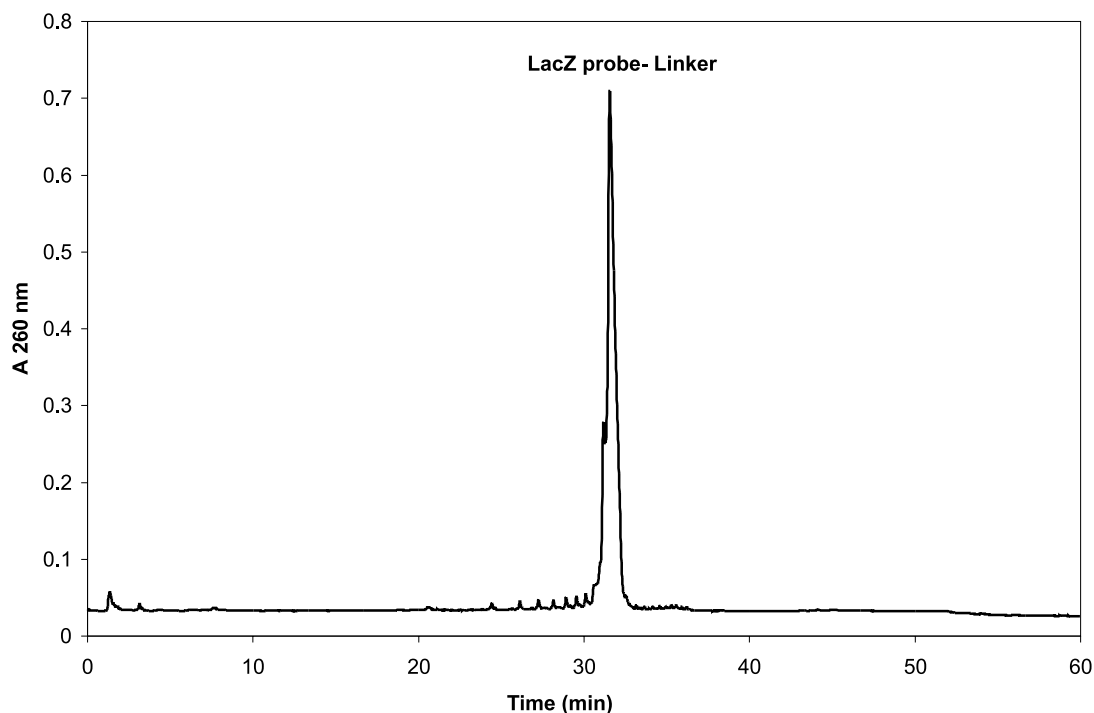
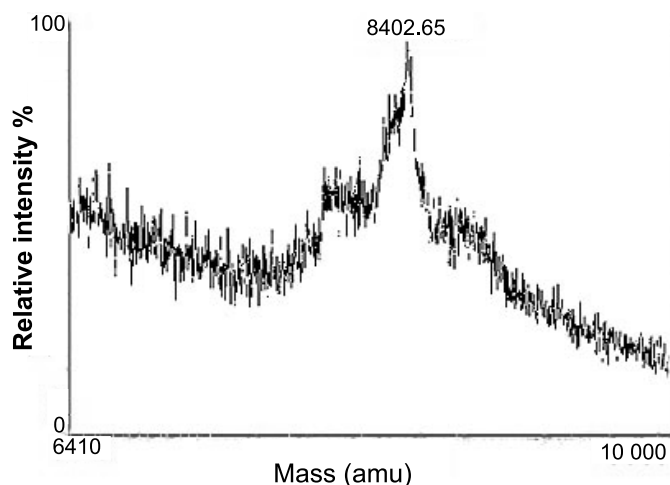


**Fig. 5.** MALDI-TOF mass spectrometric analysis of the mixed base SYBR 101-LacZ probe showing the molecular weight of the probe  $m/z$  (8402 amu). The results confirm the tethering of the dye to the probe.



coliforms as an indicator of microbial contamination in surface and ground water. Immobilized oligonucleotides on solid supports for use as molecular recognition elements in bioassays and biosensors are short sequences conjugated at

the strand terminus to a linker molecule, which in turn is covalently linked to the substrate. This strategy has proven advantageous in terms of the enhanced nucleotide coupling efficiency realized during solid-phase assembly of the oligonucleotide onto the linker and the rapid kinetics of hybrid formation of the immobilized strand with target sequences.

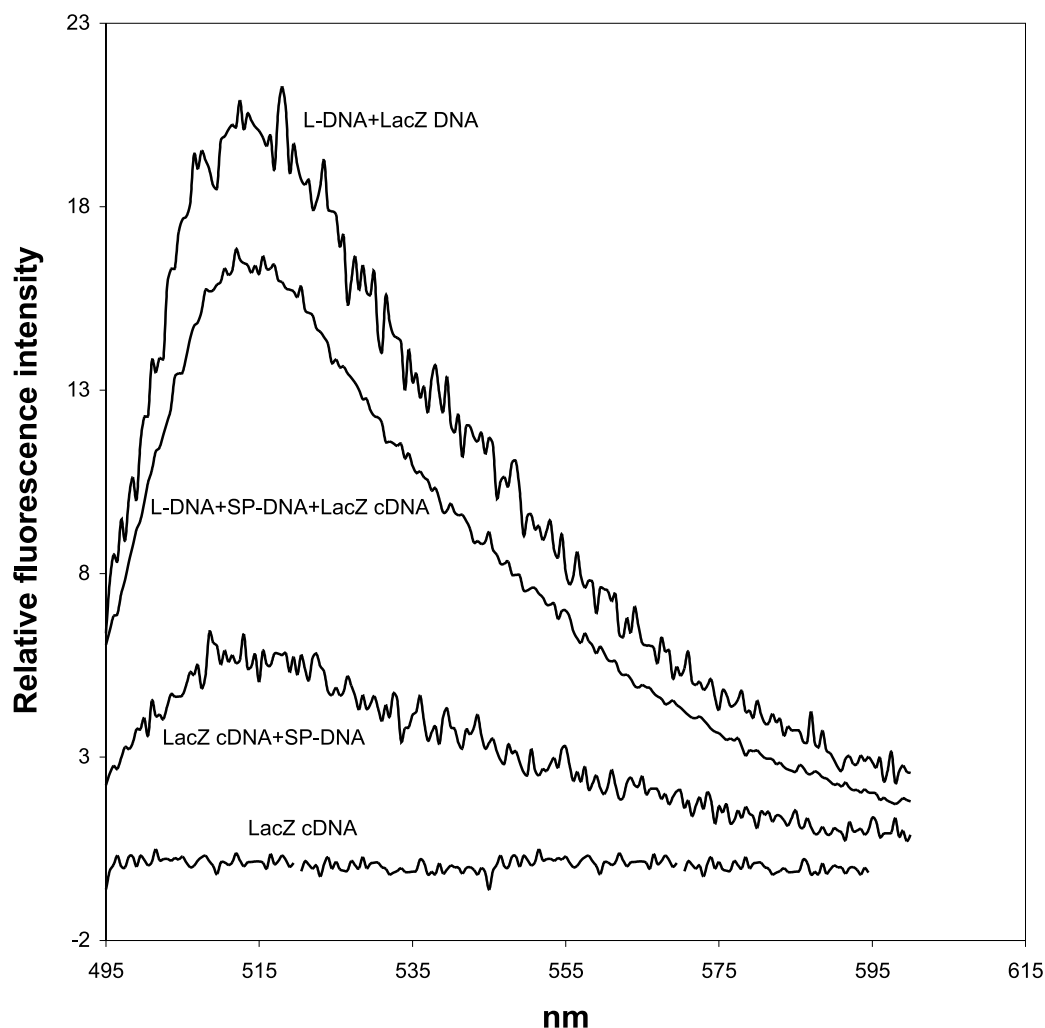
The single-stranded probe was immobilized via hexaethylene glycol linker (HEG) to functionalized fused silica substrates. This effectively provided an oligonucleotide surface where each molecule covered an approximate area of 400–1300 Å<sup>2</sup> when using linear co-polymer strands of ca. 100 Å lengths (18). This chemistry is highly stable toward water hydrolysis and physical cleavage, which can occur, owing to treatment of the surface by heating, cooling, and detergent washing. The use of HEG also provides advantages based on high solubility and hydrophilicity (19).

All sensors that were used were checked for quality of oligonucleotide immobilization by an indirect method based on concurrent immobilization of DNA on fibres and CPG. The material on the CPG was cleaved quantitatively from the surface with base, and anion exchange HPLC was then used for separation and analysis of recovered material (16). Figure 1 shows the HPLC analysis of the ssDNA LacZ probe that was synthesized on CPG. The chromatogram demonstrates the sequence integrity of the oligonucleotides that were used throughout this investigation.

Prior to hybridization, sensors were thermally activated by multiple cycles of heating (90°C) and cooling (30°C) in the presence of  $1 \times 10^{-7}$  M cDNA. The response of the biosensor to a series of samples introduced sequentially is shown in Fig. 2. The fluorescence signal was a function of the concentration of cDNA. In these experiments, the maximum signal was obtained at about 120 s after the cDNA was



**Fig. 6.** Spectrofluorimetric scan of SYBR 101-LacZ probe. The probe was treated with an equivalent amount of synthetic cDNA (LacZ) in the presence of an equivalent number of molecules of salmon sperm ssDNA, in  $1 \times$  PBS at 515 nm (room temperature). Salmon sperm ssDNA (SP-DNA) was prepared by treatment of whole genomic DNA with sonication.



introduced to the sensor. Figure 3 provides an indication of the shape of the curves and the speed of response. Quantities as low as about 100 fmole provided signals at the three-standard-deviation level. Fibres were washed and chemically regenerated using water at 90°C and 90% formamide solution in TE buffer between samples. The reproducibility was excellent, and dozens of cycles of use have been demonstrated.

Figure 3 shows that the sensor does respond selectively to the synthetic cDNA LacZ sequence in comparison to the non-complementary genomic sonicated DNA from salmon sperm. The fact that the signal for cDNA was present and reproducible after challenging the biosensor with sonicated genomic salmon sperm DNA provides an indication that, for real environmental samples, the possible co-existence of other non-complementary DNA would not block the biosensor from functioning. Upon challenging the biosensor with sonicated genomic *E. coli* DNA, the time dependence of the signal obtained demonstrates hybridization between the probe and the genomic LacZ.

Further results investigating the use of PCR products with the target sequences located in various positions within a

longer product have demonstrated that signal magnitude is somewhat dependent on the location of the target sequence (20), with the signals of greatest magnitude appearing when the target sequence is farthest removed from the biosensor surface.

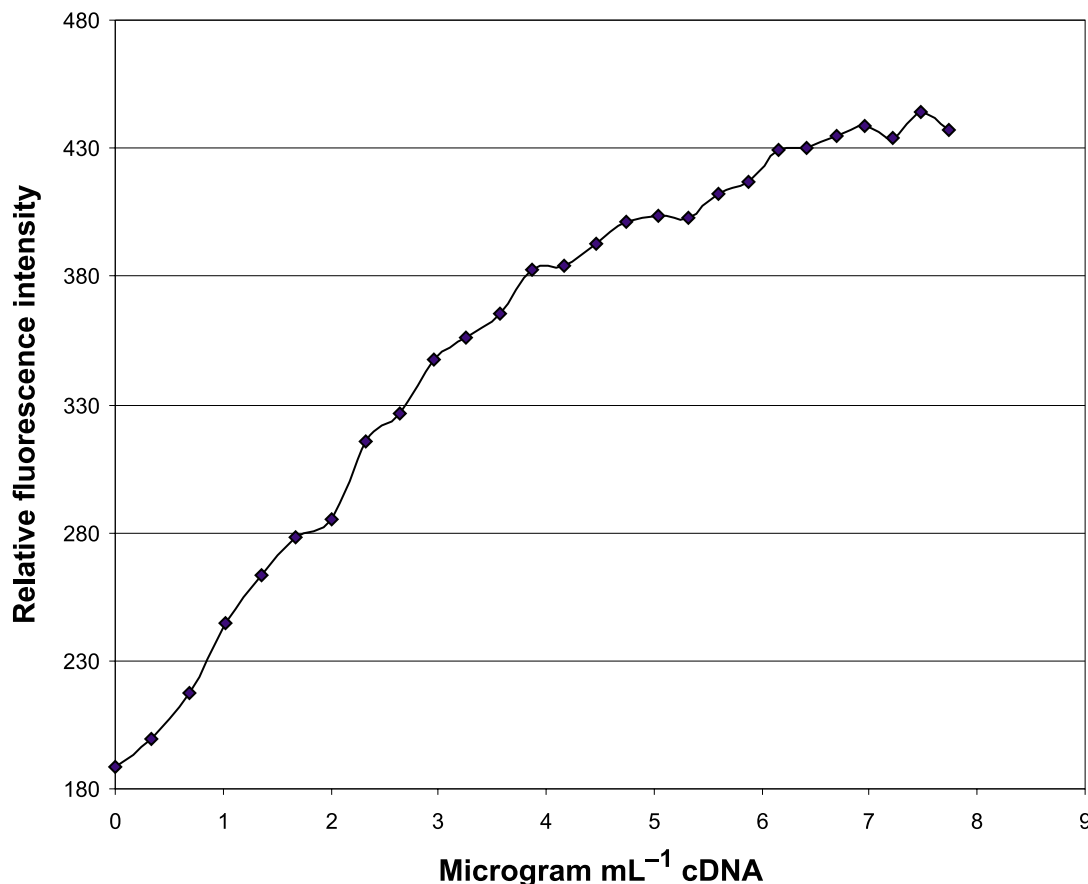
#### Tethered dye

In a preliminary experiment that was designed as a first step towards preparation of tethered dye, a second probe was constructed in which the fluorescent intercalator SYBR 101 was chemically conjugated to the probe via a tether. The dye-conjugated probe was purified and examined by anion exchange HPLC for purity (Fig. 4). The mass spectral analysis confirmed the formation of SYBR 101 labelled LacZ probe (Fig. 5).

The ability of the L-DNA to hybridize with fully complementary DNA was shown by the change in fluorescence when complementary, in comparison to non-complementary, DNA was added. Importantly, the results confirmed that the tethered dye could still bind into double-stranded DNA and achieve a substantial change in quantum yield. A second important observation was that the fully complementary target



**Fig. 7.** Spectrofluorimetric titration curve of SYBR 101-LacZ probe ( $5.7 \mu\text{g mL}^{-1}$ ) against concentrations of LacZ cDNA from  $0.1 \mu\text{g mL}^{-1}$  to  $7.7 \mu\text{g mL}^{-1}$  in  $1 \times \text{PBS}$  at 515 nm (room temperature).



could still be detected in the presence of a large background of salmon sperm DNA. Figure 6 provides spectral information about the tethered dye and a summary of the fluorescent signal due to binding events of the labelled probe at a concentration of  $1 \times 10^{14}$  molecules in  $700 \mu\text{L}$  PBS solution. When the probe was mixed with an equivalent number of molecules of salmon sperm DNA, the signal remained relatively high.

To observe the response to hybridization at different concentrations of target cDNA of the SYBR 101 labelled probe, a titration curve was generated using 25mer fully complementary target LacZ. In this experiment, a PBS solution of cDNA containing  $5.7 \mu\text{g mL}^{-1}$  ( $1 \times 10^{14}$  molecules) was titrated against the SYBR101-LacZ probe. A maximum of hybridization was achieved when a stoichiometrically equivalent amount of the labelled probe was added to the cell. The intensity of fluorescence did not substantially change beyond the 1:1 stoichiometric equivalence point, indicating that hybridization was necessary to bring the tethered dye into close proximity to a duplex for stable intercalation to occur (Fig. 7).

Preliminary work using tethered thiazole orange labels on short mixed nucleotide probes that were immobilized to the biosensor surface confirmed that such tethered dyes can report selective hybridization (21). The results also indicated that adsorption of non-complementary DNA had a significant effect on the environment of the tethered TO. This ap-

peared to be largely an electrostatic phenomenon where the positively charged dye interacted with the relatively concentrated DNA at the solid interface. The non-selective adsorption was largely eliminated by moving to high salt ( $3 \times \text{PBS}$ ), with the concurrent advantage being that the dsDNA stability was improved. The background intensity effect produced by non-complementary DNA could be reduced to less than 10%. Another limitation that was identified was sensitivity to photobleaching (21), which was easily ameliorated by use of gated detection. Further research has now demonstrated that a more complicated time-dependent chemical process, based on availability of intercalant after denaturation and biosensor regeneration, was the main cause of reduction in signal intensity as a series of experiments were done sequentially.

## Conclusions

A fibre-optic biosensor for a portion of the LacZ gene was constructed as a diagnostic device to provide a surface for the hybridization with markers from *E. coli*.

The LacZ gene of *E. coli* was selected because conventional coliform monitoring is based on detection of the activity of the gene product ( $\beta$  galactosidase) produced by coliform bacteria. Also, the LacZ sequence was selected as a target because it is specific to total coliforms, while the lamB gene is within *E. coli*, *Salmonella*, and *Shigella spp.*,



and the uid gene is within *E. coli* and *Shigella* spp. The 25mer length of the probe was shown to be sufficiently selective to hybridize genomic target from *E. coli* bacteria and was further investigated by searching within the GenBank nucleotide sequence data to insure that there were no other homologies with potential non-target sequences (22). The short length of the probe provides advantages in terms of reversibility and high speed of hybridization.

The LacZ probe was covalently attached through a C6 amino-modifier tether to SYBR 101 fluorescent intercalating dye. This labelled probe was used free in solution to investigate whether the dye could still participate in intercalation as hybridization with fully complementary target in the presence of a high concentration of non-complementary DNA (salmon sperm DNA) proceeded. The results are encouraging, as there was no indication that the fluorescent signal from hybridization was dramatically affected by the presence of the non-complementary material.

## Acknowledgments

This work was financially supported by the Natural Sciences and Engineering Research Council of Canada (NSERC). We would like to acknowledge Dr. Steven Yue and Dr. Nabi Malikzada of Molecular Probes Inc. for provision of the SYBR 101 reactive dye.

## References

1. R. Bordner and J. Winter. Microbiological methods for monitoring the environment: Water and wastes. EPA/600/8-78/017. Environmental Protection Agency, Washington, D.C. 1978.
2. A.F. Gaudy and E. T. Gaudy. Microbiology for environmental scientists and engineers. McGraw-Hill Book Co., New York. 1980.
3. American Water Works Association. Water quality and treatment. McGraw-Hill, Inc., New York. 1990.
4. P.B. Kubek and P.D. Robillard. Drinking water solutions 2.0: Computer information system. Pennsylvania State University Department of Agricultural and Biological Engineering., University Park, PA. 1990.
5. American Public Health Association. Standard methods for the examination of water and wastewater. 18th ed. Washington, D.C. 1992.
6. A.K. Bej, R.J. Steffan, L. Haff, and R.M. Atlas. Appl. Environ. Microbiol. **56**, 307 (1990).
7. M. Thompson and A.K. Deisingh. Analyst, **126**, 2153 (2001).
8. J. Wang. Nucleic Acids Res. **28**, 3011 (2000).
9. A. Bensimon, A. Simon, A. Chiffaudel, V. Croquette, F. Heslot, and D. Bensimon. Science, **265**, 2096 (1994).
10. F. Caruso, E. Rodda, D.N. Furlong, K. Niikura, and Y. Okahata. Anal. Chem. **69**, 2043 (1997).
11. A.P. Abel, M.G. Weller, G.L. Duveneck, M. Ehrat, and H.M. Widmer. Anal. Chem. **68**, 2905 (1996).
12. S. Fanning, J. O'Mullane, D. O'Meara, A. Ward, C. Joyce, M. Delaney, and B. Cryan. Br. J. Biomed. Sci. **52**, 317 (1995).
13. S. Iqbal, M. Mayo, J. Bruno, B. Bronk, C. Batt, and J. Chambers. Biosens. Bioelectron. **15**, 549 (2000).
14. A.H. Uddin, P.A.E. Piunno, R.H. Hudson, M.J. Damha, and U.J. Krull. Nucleic Acids Res. **25**, 4139 (1997).
15. J. Watterson, P.A.E. Piunno, C.C. Wust, S. Raha, and U.J. Krull. Fresenius J. Anal. Chem. **369**, 601 (2001).
16. B. Sojka, P.A.E. Piunno, C.C. Wust, and U.J. Krull. Anal. Chim. Acta, **395**, 273 (1999).
17. J.H. Watterson, P.A.E. Piunno, C.C. Wust, and U.J. Krull. Langmuir, **16**, 4984 (2000).
18. Z. Guo, R. Guilfoyle, A. Thiel, R. Wang, and L. Smith. Nucleic Acids Res. **22**, 5456 (1994).
19. M.S. Shchepinov, S.C. Case-Green, and E.M. Southern. Nucleic Acids Res. **25**, 1155 (1997).
20. A. Almadidy, J. Watterson, P.A.E. Piunno, S. Raha, I.V. Foulds, P.A. Horgen, A. Castle, and U.J. Krull. Anal. Chim. Acta, **461**, 37 (2002).
21. X. Wang and U.J. Krull. Anal. Chim. Acta, **470**, 57 (2002).
22. A.K. Bej, J.L. DiCesare, L. Haff, and R.M. Atlas. Appl. Environ. Microbiol. **57**, 1013 (1991).



# Benzotriazolium ylides: Experimental and theoretical study on the tautomeric equilibrium of monosubstituted benzotriazolium ylides

Neculai Doru Miron, Patrice Woisel, Georgiana G. Surpateanu, Gérard Vergoten, Ludovic Depature, and Gheorghe Surpateanu

**Abstract:** The biphenacyl benzotriazolium salts **12** give a tautomeric equilibrium **13**⇌**14** in the presence of triethylamine (TEA) or NaOH. The evaluation of this tautomeric equilibrium has been studied using a dynamic NMR analysis and a new synthetic procedure of disubstituted benzotriazolium ylides **15** and **16**, which have in their structures a picryl fragment. This study also includes a theoretical analysis on the reactivity of salts **12a–c** and the thermodynamic stability of tautomeric forms **13** and **14** by AM1 and PM3 procedure methods.

**Key words:** synthesis, salts, ylides, semiempirical calculations, kinetics.

**Résumé :** En présence de TEA ou de NaOH, les sels de biphénacylbenzotriazolium (**12**) donnent lieu à un équilibre tautomère. On a évalué cet équilibre tautomère par le biais d'une analyse RMN dynamique et on a mis au point une nouvelle méthode de synthèse des ylures de benzotriazolium disubstitués **15** et **16** comportant, dans leurs structures, un fragment picryle. Cette étude comporte aussi une analyse théorique, à l'aide des méthodes AM1 et PM3, de la réactivité des sels **12a–c** et de la stabilité thermodynamique des formes tautomères **13** et **14**.

**Mots clés :** synthèse, sels, ylures, calculs semiempiriques, cinétique.

[Traduit par la Rédaction]

## Introduction

The presence of the two tautomeric forms **1** and **2** for some triazolium ylides has been revealed by NMR spectroscopy and confirmed by trapping each monosubstituted ylide with picryl chloride (Scheme 1) (**1**, **2**).

The two tautomeric forms **1** and **2** were generated by addition of aqueous potassium carbonate on a suspension of the corresponding triazolium salt in DMSO-*d*<sub>6</sub>. The ratio of concentrations was evaluated at 23°C from the integration curves of the signals corresponding to the 5-H protons in the triazole ring.

Earlier, two different disubstituted carbanion triazolium ylides **3** and **4** (Scheme 2) had been isolated and characterized as stable compounds (**3**, **4**) by the reaction between tautomeric monosubstituted carbanion ylides **1** and **2** and picryl chloride. These two procedures, dynamic NMR spectra and chemical synthesis of the disubstituted ylides from their tautomeric forms and picryl chloride, represent the basic handling of the characterization of ylidic tautomers.

The synthetic utility of ylidic compounds is widely recognised (**5**, **6**). The reaction of this class of compounds with strong electrophiles such as picryl chloride (**7**) has also been described and used, in particular in the synthesis of a new azaheterocyclic framework as isoindoles (**3**, **4**).

In this paper, for the first time, the synthesis and characterization of tautomeric benzotriazolium ylides are reported. Systematically, molecular modelling has been used to explain the ratio and the chemical behaviour of ylidic tautomeric forms.

## Results and discussion

The monosubstituted benzotriazolium ylides reported in this paper are prepared using the well-known "salt method" (**8**). 1-Benzylbenzotriazole **5** is obtained from the commercially available benzotriazole via the corresponding anion and benzyl bromide. Thus, the 1-benzylbenzotriazole **5** treated with 4-substituted ω-bromoacetophenones **6** in dry boiling acetone furnish, after recrystallization (ethanol), the

Received 25 September 2002. Published on the NRC Research Press Web site at <http://canjchem.nrc.ca> on 15 May 2003.

**N.D. Miron.** Catedra CTPA, Facultatea de inginerie, Universitatea Bacau, Romania.

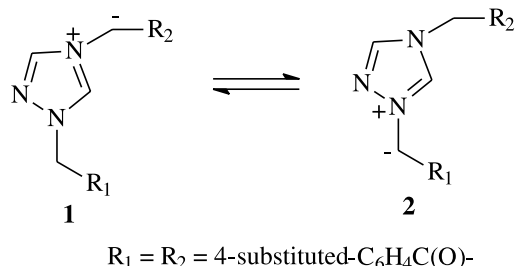
**P. Woisel, L. Depature, and G. Surpateanu.**<sup>1</sup> Laboratoire de Synthèse Organique et Environnement, EA 2599, MREID, 145, rue Maurice Schumann, 59140 Dunkerque, France.

**G.G. Surpateanu.** Departamentul de Chimie Organica si Biochimie, Facultatea de Chimie, Universitatea "Al.Cuza", B-dul Copou nr.11, Iasi, Romania.

**G. Vergoten.** CRESIMM Centre de Recherche et d'Etudes en Simulation et Modélisation Moléculaire, Université des Sciences et Technologies de Lille, Bâtiment C8, 59650 Villeneuve d'Ascq, France.

<sup>1</sup>Corresponding author (e-mail: [Surpatea@univ-littoral.fr](mailto:Surpatea@univ-littoral.fr)).



**Scheme 1.** Monosubstituted triazolium ylides.

corresponding salts **7** in good yields (Scheme 3). Next, these salts **7** in the presence of triethylamine (TEA) form “in situ” monosubstituted carbanion ylides **8**, which with picryl chloride offer directly benzotriazolium trinitrophenylmethyldes **9**. However, this reaction must be carried out under 10°C and without light to prevent cleavage of the  $\text{C}^-\text{N}^+$  bond.

By our experimental procedure only disubstituted benzotriazolium ylides **9** have been isolated. That corresponds to a single type of phenacylide structure (**8**). Another potential tautomeric benzyldic structure, **10**, could not be characterized. That is why we extended our synthesis to a new benzotriazolium ylide (Scheme 4) in which two phenacyl fragments are linked to nitrogen atoms 1 and 3 in a triazole ring. The general synthetic procedure is similar to those employed for the preparation of the benzotriazolium ylides **8**. Indeed, in this case two disubstituted benzotriazolium ylides **15** and **16** have been identified, in different ratios, as the final reaction mixture (Table 1).

Quantitative data were obtained by  $^1\text{H}$  NMR spectra, taking into account the chemical shifts and the integration of the signals belonging to the protons in the picryl fragments and methylene groups in every pair of corresponding benzotriazolium ylides **15** and **16**.

We supposed that this experimental result could be explained by the existence of a tautomeric equilibrium **13**⇌**14** between two monosubstituted benzotriazolium ylides.

Moreover, the absence of the ylide equilibrium **8**⇌**10** prompted us to develop a theoretical study on the reactivity of salts **7** and **12**, to generate the corresponding monosubstituted benzotriazolium ylides. Also, the reactivity of all tautomeric forms towards picryl chloride has been considered.

First, the semiempirical AM1 and PM3 calculations were performed using the PC-Spartan Plus package (9). For each compound, a multiconformational search has been developed. The employed method, which gave satisfactory results on our structures, has been described in recent papers (10, 11). Briefly, the procedure consists in studying the  $\Delta\text{H}$  (heat of formation variation) according to the variation of the dihedral angle by rotational increments of 15°. The minimum value of  $\Delta\text{H}$  is chosen according to the curve scribing. All constraints are removed and a new geometry optimization is made to obtain the most stable conformation. All single bonds have been taken in consideration.

In Table 2 the electrostatic and Mulliken charges of four methylenic hydrogens are given. Normally, the positive charges have similar values, as in the case of biphenacylide salts **12**. Otherwise, more important differences, especially

for the Mulliken charges, are observed, as in the case of benzylphenacyl salts **7**.

In this last case based on positive atomic charges, e.g., their acidities (12), we consider as more probable the formation of phenacylide system **8** than benzyldic system **10**. Qualitatively, the presence of a tautomeric equilibrium **13**⇌**14** and the absence of an equilibrium similar to the case of benzylphenacyl salts **5**⇌**7** seems to be an expected result.

Next, to evaluate the intervention of a possible thermodynamic factor in the generation of monosubstituted benzotriazolium ylides **8**, **10**, **13**, and **14**, we calculated the heats of formation of these monosubstituted ylides.

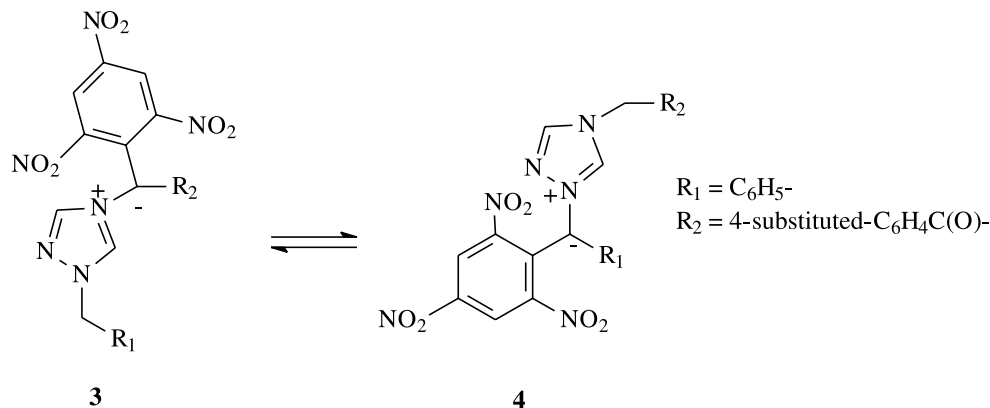
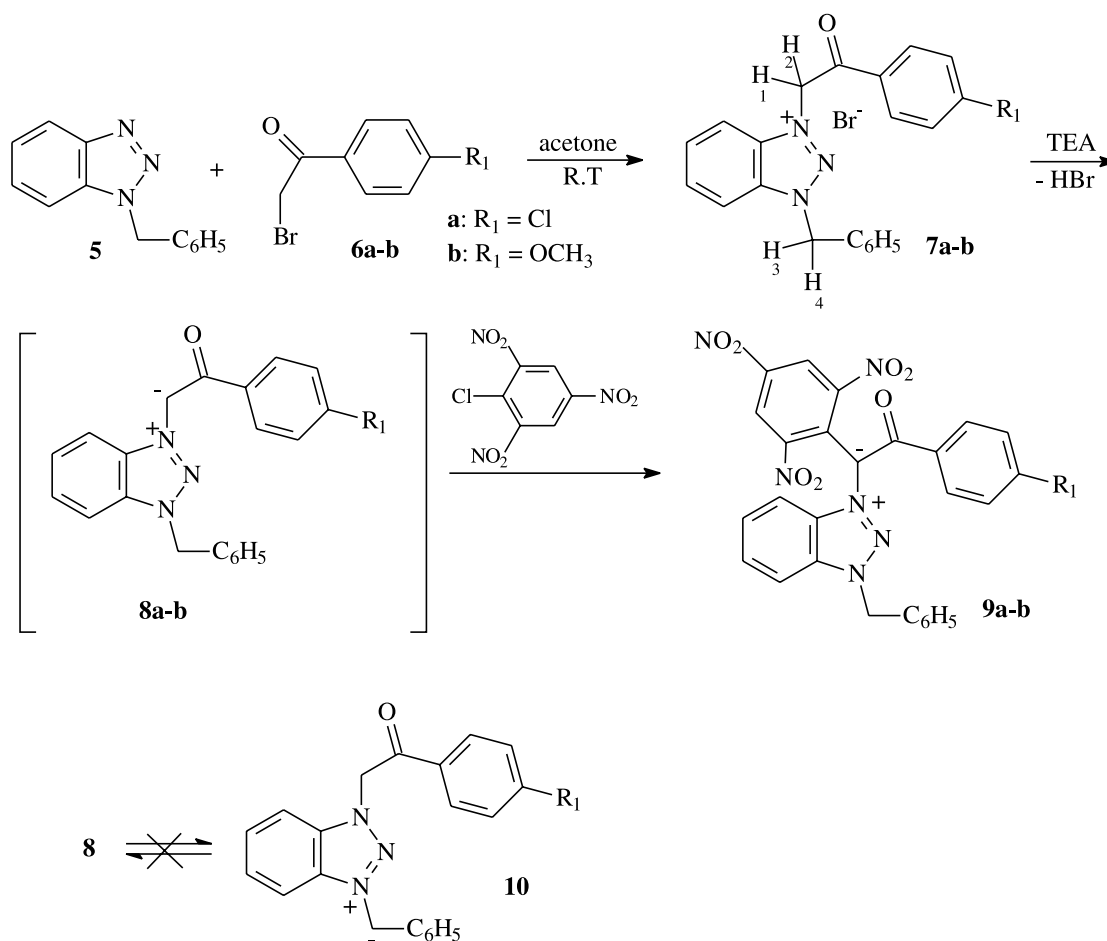
From the survey data in Table 3, some complementary conclusions could be extracted: (i) larger differences in the range of 2.03–2.81 kcal (AM1) and 1.08–1.68 kcal (PM3) in the case of ylide forms **8** and **10** and (ii) smaller differences of 0.21–0.65 kcal mol<sup>−1</sup> (AM1 and PM3) for ylide tautomeric forms **13** and **14**. In the first case, the formation of phenacylide forms **8** is favoured. Otherwise, in the second case the formation of both the tautomeric forms **13** and **14** is effective.

The reaction between a monosubstituted benzotriazolium ylide and picryl chloride could be considered to be proceeding as a donor–acceptor interaction, respectively. Thus, the atomic orbital coefficient of the ylide carbon atom in the HOMO (High occupied molecular orbital) could be taken into consideration as a chemical reactivity parameter (Table 4) (13–15).

By the absolute values of these coefficients, the reactivity of ylide carbon atoms in tautomeric benzotriazolium ylides **13** and **14** are comparable. Moreover, we proved experimentally that the reaction rate of monosubstituted ylides with picryl chloride is very important (the reaction is instantaneous). The visible disappearance of the colour (orange) of monosubstituted benzotriazole ylide **13** or **14** and the appearance of a deep purple colour corresponding to formation of the disubstituted benzotriazolium ylide have also been highlighted by UV–vis spectra and analytical thin layer chromatography.

Briefly, both experimental and theoretical results presented in this paper permit us to point out some conclusions: (i) the 1-phenacyl-3-benzyl benzotriazolium salt **7** in the presence of TEA gave a single monosubstituted benzotriazolium ylide **8**. The mobility of the methylenic hydrogens and the heat of formation of the hypothetical two tautomeric forms **8** and **10** reinforce the absence of an equilibrium; (ii) otherwise, the same theoretical parameters, e.g., the mobility of methylenic hydrogens in salt **12** and the heat of formation of the corresponding pair of forms **13** and **14** recommend the co-existence of tautomeric equilibrium of these two form; (iii) the small difference in the values of the charges of the two pairs of methylenic hydrogens in **12**, the closer heat of formation of **13** and **14**, and their comparable atomic orbital coefficients suggest formation of both these two tautomeric forms. At this stage of our experiments that is not proved. Experimentally, in all three analyzed equilibria, the form of **13** is the dominant one and much more so in the nitrophenacylide structure **13c**. The increasing trend of substituent constants —  $\sigma_{\text{Cl}}(0.22) < \sigma_{\text{OCH}_3}(0.22) < \sigma_{\text{NO}_2}(0.78)$  (12) — is also found from the ratio of concentrations of the tautomeric equilibrium **13**⇌**14**. Nevertheless,



**Scheme 2.** Reactivity of the monosubstituted triazolium ylides.**Scheme 3.** Preparation of the disubstituted benzotriazolium ylides.

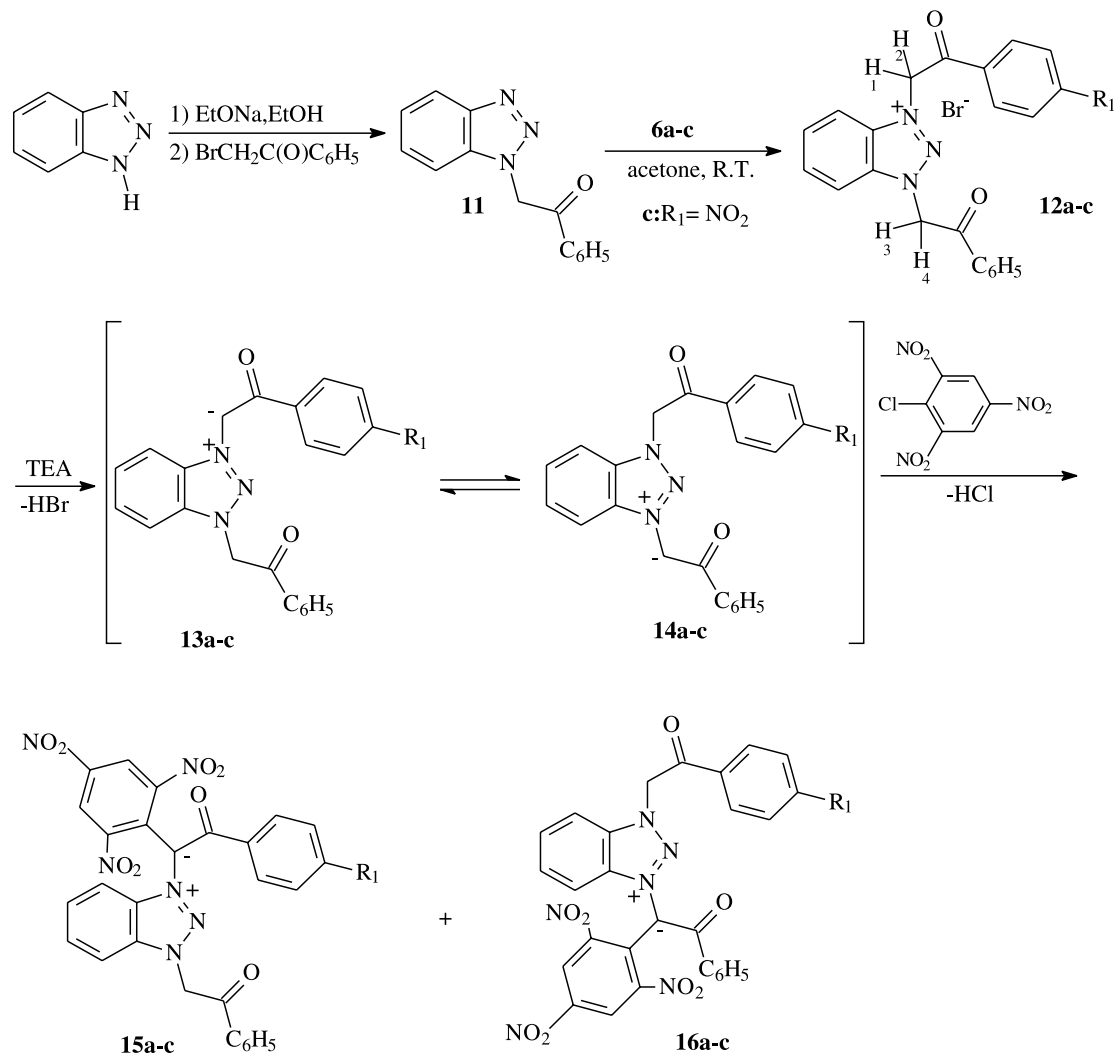
others factors (e.g., the nature of the solvent, the polarity of the reaction mixture) could influence the final concentrations of the two tautomeric forms. Next, we choose the equilibrium **13c**⇌**14c** (the extreme case) for a more detailed experimental study, monitoring the kinetics of the tautomeric equilibrium using  $^1\text{H}$  NMR. The analyses were directly performed in the NMR tube with addition of NaOD (2 equiv) –  $\text{D}_2\text{O}$  to the solution of benzotriazolium salt **12c** ( $2 \cdot 10^{-2} \text{ mol L}^{-1}$ ) –  $\text{D}_2\text{O}$ . The addition of NaOD was considered the starting time ( $t = 0$ ). The  $^1\text{H}$  NMR spectra unambig-

uously indicated the completion of the dehydrohalogenation reaction. The concentration of each tautomer was evaluated, as already mentioned, from the integrals of the remaining methylenic and picryl protons. The results are presented in Table 4.

After 15 min, equilibrium was achieved (no significant modification of involved signals was observed), but the degradation of the reaction mixture was growing significantly.

Finally, taking into account the quantitative data in Table 3, we imagined a new kind of synthesis of disubstituted



**Scheme 4.** Preparation of the disubstituted biphenacyl benzotriazolium ylides.**Table 1.** Mixture of ylides **15** and **16**.

Salt	Ylide <b>15</b>	Ylide <b>16</b>
<b>12a</b>	76	24
<b>12b</b>	75	25
<b>12c</b>	89	11

benzotriazolium ylides **15c** and **16c**. Always, the aim was to highlight the evolution of the equilibrium **13c**⇌**14c**.

Concretely, this equilibrium was generated by adding TEA in one step to the benzotriazolium salt **12c** in chloroform. Then a solution of picryl chloride in chloroform was added, also in one step, after 10 min. All other aspects concerning this new procedure are described in the experimental section of this paper.

Indeed, as we supposed, the ratio of disubstituted ylides **15c** and **16c** in the final reaction mixture was changed. Taking into account this new ratio, we could indirectly evaluate a corresponding equilibrium mixture of 78% **13c** and 22% **14c**.

Really, these values are slightly different with respect to those performed by dynamic NMR analysis at the same

time,  $t = 10$  min, but deeply different (89% **13c** and 11% **14c**) at time  $t = 0$  from those for the experiment described in the experimental section. Thus, we consider that the existence of a dynamic equilibrium **13c**⇌**14c** is undoubtedly proven by this new synthetic procedure. The developed dynamic NMR analysis and the new synthetic procedure involve different experimental conditions; NaOD or TEA as base and DMSO-*d*<sub>6</sub> or CHCl<sub>3</sub> as solvent, respectively, so that the quantitative differences on the concentrations of the tautomeric forms could be easily justified.

## Conclusion

The benzylphenacylbenzotriazolium salts **7** in the presence of TEA give exclusively one monosubstituted benzotriazolium ylide **8**.

The 1,3-biphenacylbenzotriazolium salts **12** under the same experimental condition form a tautomeric mixture of **13** and **14**.

The differences in these previous behaviours are proven by theoretical data, e.g., the mobility of methylenic groups and the thermodynamic stabilities of the tautomeric forms.



**Table 2.** Electrostatic (E) and Mulliken (M) charges (au) of benzotriazolium salts **7** and **12**.

Salt	Method	H1		H2		H3		H4	
		E	M	E	M	E	M	E	M
<b>7a</b>	AM1	0.15	0.16	0.15	0.15	0.17	0.13	0.18	0.14
	PM3	0.15	0.13	0.13	0.11	0.10	0.09	0.10	0.11
<b>12a</b>	AM1	0.17	0.17	0.16	0.15	0.18	0.17	0.17	0.15
	PM3	0.12	0.13	0.11	0.12	0.12	0.13	0.11	0.12
<b>7b</b>	AM1	0.17	0.16	0.17	0.15	0.13	0.13	0.13	0.15
	PM3	0.11	0.13	0.12	0.12	0.08	0.09	0.10	0.11
<b>12b</b>	AM1	0.14	0.16	0.12	0.15	0.17	0.16	0.16	0.15
	PM3	0.11	0.13	0.09	0.11	0.17	0.13	0.13	0.11
<b>12c</b>	AM1	0.17	0.17	0.16	0.15	0.18	0.17	0.16	0.15
	PM3	0.14	0.13	0.13	0.12	0.13	0.13	0.12	0.12

**Table 3.** Heat of formation ( $\Delta H$ ) and atomic orbital coefficient of monosubstituted benzotriazolium ylides **8**, **10**, **13**, and **14**.

Ylide	Method	$\Delta H$ (kcal mol <sup>-1</sup> )	HOMO ( $P_z$ )
<b>8a</b>	AM1	161.96	0.55
	PM3	114.76	0.43
<b>10a</b>	AM1	164.77	0.38
	PM3	116.44	0.39
<b>8b</b>	AM1	130.92	0.52
	PM3	83.37	-0.42
<b>10b</b>	AM1	132.95	0.48
	PM3	84.45	-0.40
<b>13a</b>	AM1	134.37	-0.64
	PM3	83.85	-0.57
<b>14a</b>	AM1	134.93	0.64
	PM3	83.64	-0.56
<b>13b</b>	AM1	103.25	-0.43
	PM3	51.81	0.36
<b>14b</b>	AM1	103.13	0.53
	PM3	52.43	0.48
<b>13c</b>	AM1	144.90	0.44
	PM3	81.72	-0.35
<b>14c</b>	AM1	147.18	0.42
	PM3	82.37	-0.38

In the case of tautomeric ylides **13** and **14**, their reactivities with picryl chloride are comparable (see the absolute values of atomic orbital coefficients of the ylide carbon atoms in HOMO).

The existence and the evolution of the equilibrium **13**⇌**14** was proven by a dynamic NMR analysis and by a new method of synthesis.

The slow rate of ylidic tautomeric equilibrium is due to a migration of a proton between two similar ylidic carbanion atoms.

## Experimental section

### General remarks

<sup>1</sup>H and <sup>13</sup>C NMR spectra were recorded with a Bruker AM 250 spectrometer with trimethylsilane as the internal standard. The abbreviations used are s (singlet), d (doublet), t (triplet), and m (multiplet). Mass spectra were measured

**Table 4.** The dynamic of equilibrium **13c**⇌**14c**.

Time (min)	<b>13c</b> (%)	<b>14c</b> (%)
5	80.3	19.7
10	69.5	31.5
15	60.5	39.5

using a Platform II Micromass Apparatus. IR spectra were recorded using a PerkinElmer instrument. Melting points were obtained with a Reichert Thermopan apparatus and are uncorrected. Chromatographic separations were carried out on SDS silica gel 60 (70–200  $\mu$ m). All reagents were used as purchased unless otherwise stated. Solvents were dried according to standard procedures. All reactions were performed under dry argon.

### General procedure for the synthesis of benzotriazolium salts **7** and **12**

The  $\omega$ -bromoacetophenone compounds **6a–c** are commercially available. A solution of  $\omega$ -bromoacetophenone **6** in anhydrous acetone (30 mL) was added, at room temperature under argon, to a solution of 1-benzyl-[1,2,3]benzotriazole **5** or 1-phenacyl-[1,2,3]benzotriazole **11** (10 mmol) in dry acetone (80 mL). The mixture was refluxed under stirring for 8 h. The crude product was filtered off and recrystallized from EtOH.

#### 3-Benzyl-1-[2-(4-chlorophenyl)oxoethyl]-3H-benzotriazol-1-ium bromide (**7a**)

Yield 3.13 g (71%), mp 158–159°C. IR (KBr) (cm<sup>-1</sup>): 3028, 1700, 1588, 1338, 1224, 1091, 986, 775. <sup>1</sup>H NMR (DMSO-TMS)  $\delta$ : 6.44 (s, 2H, CH<sub>2</sub>), 7.10 (s, 2H, CH<sub>2</sub>), 7.43–7.50 (m, 3 aromatic H), 7.55–7.63 (m, 2 aromatic H), 7.77 (d,  $J$  = 8.2 Hz, 2 aromatic H), 8.00–8.08 (m, 2 aromatic H), 8.16 (d,  $J$  = 8.2 Hz, 2 aromatic H), 8.40–8.45 (m, 1 aromatic H), 8.51–8.56 (m, 1 aromatic H). ES<sup>+</sup>-MS (cone 21)  $m/z$  (%): 364 ([M – Br], 32), 362 ([M – Br], 100). C<sub>21</sub>H<sub>17</sub>BrClN<sub>3</sub>O calcd.: C 57.14, H 3.88, N 9.53; found: C 56.88, H 3.84, N 9.39.

#### 3-Benzyl-1-[2-(4-methoxyphenyl)oxoethyl]-3H-benzotriazol-1-ium bromide (**7b**)

Yield 3.01 g (69%), mp 164–165°C. IR (KBr) (cm<sup>-1</sup>): 3035, 1684, 1602, 1575, 1184, 1028, 983, 775. <sup>1</sup>H NMR (DMSO-TMS)  $\delta$ : 3.92 (s, 3H, OCH<sub>3</sub>), 6.43 (s, 2H, CH<sub>2</sub>),



7.01 (s, 2H, CH<sub>2</sub>), 7.20 (d,  $J = 8.8$  Hz, 2 aromatic H), 7.43–7.51 (m, 3 aromatic H), 7.54–7.57 (m, 2 aromatic H), 7.98–8.05 (m, 2 aromatic H), 8.16 (d,  $J = 8.8$  Hz, 2 aromatic H), 8.37–8.39 (m, 1 aromatic H), 8.48–8.50 (m, 1 aromatic H). ES<sup>+</sup>-MS (cone 32)  $m/z$  (%): 358 ([M – Br], 100). C<sub>22</sub>H<sub>20</sub>BrN<sub>3</sub>O<sub>2</sub> calcd.: C 60.40, H 4.61, N 9.61; found: C 59.98, H 4.84, N 9.38.

**1-[2-(4-Chlorophenyl-oxoethyl)-3-(2-phenyl-oxoethyl)-3H-benzotriazol-1-ium bromide (12a)]**

Yield (80%), mp 158–159°C. IR (KBr) (cm<sup>-1</sup>)  $\bar{\nu}$ : 3094, 2968, 2830, 1700, 1588, 1233, 1087, 757. <sup>1</sup>H NMR (DMSO–TMS)  $\delta$  7.15 (s, 2H, CH<sub>2</sub>), 7.16 (s, 2H, CH<sub>2</sub>), 7.71–7.84 (m, 5 aromatic H), 8.04–8.07 (m, 2 aromatic H), 8.18 (m, 4 aromatic H), 8.45–8.49 (m, 2 aromatic H). ES<sup>+</sup>-MS (cone 31)  $m/z$  (%): 392 ([M – Br], 33), 390 ([M – Br], 100). C<sub>22</sub>H<sub>17</sub>BrClN<sub>3</sub>O<sub>2</sub> calcd.: C 56.29, H 3.65, N 8.96; found: C 56.20, H 3.84, N 9.08.

**1-[2-(4-Methoxyphenyl-oxoethyl)-3-(2-phenyl-oxoethyl)-3H-benzotriazol-1-ium bromide (12b)]**

Yield 3.47 g (74%), mp 159–160°C. IR (KBr) (cm<sup>-1</sup>)  $\bar{\nu}$ : 2909, 2836, 1683, 1600, 1356, 1237, 1176, 757. <sup>1</sup>H NMR (DMSO–TMS)  $\delta$  3.93 (s, 3H, OCH<sub>3</sub>), 7.04–7.24 (m, 6H, 2CH<sub>2</sub> + 2 aromatic H), 7.70 (t,  $J = 7.3$  Hz, 2 aromatic H), 7.84 (t,  $J = 7.3$  Hz, 1 aromatic H), 8.01–8.19 (m, 6 aromatic H), 8.43–8.50 (m, 2 aromatic H). ES<sup>+</sup>-MS (cone 20)  $m/z$  (%): 386 ([M – Br], 100). C<sub>23</sub>H<sub>20</sub>BrN<sub>3</sub>O<sub>3</sub> calcd.: C 59.35, H 4.33, N 9.03; found: C 59.34, H 4.41 N 9.11.

**1-[2-(4-Nitrophenyl-oxoethyl)-3-(2-phenyl-oxoethyl)-3H-benzotriazol-1-ium bromide (12c)]**

Yield 4.13 g (88%), mp 161–162°C. IR (KBr) (cm<sup>-1</sup>)  $\bar{\nu}$ : 2884, 1704, 1600, 1527, 1350, 1226, 994, 756. <sup>1</sup>H NMR (DMSO–TMS)  $\delta$  7.18 (s, 2H, CH<sub>2</sub>), 7.23 (s, 2H, CH<sub>2</sub>), 7.70 (d,  $J = 7.3$  Hz, 2 aromatic H), 7.83 (d,  $J = 7.3$  Hz, 2 aromatic H), 8.04–8.08 (m, 2 aromatic H), 8.18 (d,  $J = 7.3$ , 2 aromatic H), 8.38–8.53 (m, 5 aromatic H). ES<sup>+</sup>-MS (cone 25)  $m/z$  (%): 401 ([M – Br], 100). C<sub>22</sub>H<sub>17</sub>BrN<sub>4</sub>O<sub>4</sub> calcd.: C 55.00, H 3.57, N 11.67; found: C 59.94, H 3.62 N 11.71.

**General procedure for synthesis of disubstituted benzotriazolium ylides 9, 15, and 16**

To a mixture formed of salts **12** (2.8 mmol) in CHCl<sub>3</sub> (30 mL) and picryl chloride (2.8 mmol) was added gradually, at 0°C under Ar, a solution of freshly distilled Et<sub>3</sub>N (5.6 mmol) in dry CHCl<sub>3</sub> (10 mL) at 0°C under Ar. Then the mixture was stirred at room temperature for 3 h. Finally, the solvent was evaporated, and the deep purple crude product was chromatographed on SiO<sub>2</sub> using acetone–hexane (40:60) as the eluant.

**(3-Benzyl-3H-benzotriazol-1-io)(4-chlorobenzoyl)(2,4,6-trinitrophenyl)methanide 9a**

Yield 0.98 g (61%), mp 119–120°C. IR (KBr) (cm<sup>-1</sup>)  $\bar{\nu}$ : 2910, 1665, 1569, 1489, 1275, 1113, 1015, 766. <sup>1</sup>H NMR (CDCl<sub>3</sub>–TMS)  $\delta$  5.85 (s, 2H, CH<sub>2</sub>), 7.23–7.32 (m, 4 aromatic H), 7.45–7.57 (m, 6 aromatic H), 7.70–7.79 (m, 3 aromatic H), 8.60 (s, 2H, aromatic). ES<sup>+</sup>-MS (cone 30)  $m/z$  (%): 597 ([M + Na], 12), 595 ([M + Na], 40), 575 ([M + H], 31), 573 ([M + H], 100).

**(3-Benzyl-3H-benzotriazol-1-io)(4-methoxybenzoyl)(2,4,6-trinitrophenyl)methanide 9b**

Yield 0.87 g (55%), mp 139–140°C. IR (KBr) (cm<sup>-1</sup>)  $\bar{\nu}$ : 3077, 1603, 1558, 1527, 1258, 1252, 1027, 751. <sup>1</sup>H NMR (CDCl<sub>3</sub>–TMS)  $\delta$  3.85 (s, 3H, OCH<sub>3</sub>), 5.84 (s, 2H, CH<sub>2</sub>), 6.81 (d,  $J = 8.8$ , 2 aromatic H), 7.30–7.34 (m, 2 aromatic H), 7.47–7.49 (m, 3 aromatic H), 7.52–7.58 (m, 3 aromatic H), 7.66–7.76 (m, 3 aromatic H), 8.58 (s, 2H, aromatic). ES<sup>+</sup>-MS (cone 20)  $m/z$  (%): 569 ([M + H], 100).

**(3-(2-Phenyl-2-oxoethyl)-3H-benzotriazol-1-io)(4-chlorobenzoyl)(2,4,6-trinitrophenyl)methanide 15a and [(3-(2-(4-nitrophenyl)-2-oxoethyl)-3H-benzotriazol-1-io)(benzoyl)-(2,4,6-trinitrophenyl)methanide 16a]**

Yield 1.21 g (72%). IR (KBr) (cm<sup>-1</sup>)  $\bar{\nu}$ : 3077, 1603, 1558, 1527, 1258, 1252, 1027, 751. <sup>1</sup>H NMR (CDCl<sub>3</sub>–TMS)  $\delta$  6.95 (**15a**) and 6.93 (**16a**) (s, 2H, CH<sub>2</sub>), 7.22–7.26 (m, 4 aromatic H), 7.62–7.88 (m, 6 aromatic H), 8.09–8.12 (m, 2 aromatic H), 8.21–8.24 (m, 1 aromatic H), 8.60 (**15a**) and 8.64 (**16a**) (s, 2H, aromatic). ES<sup>+</sup>-MS (cone 42)  $m/z$  (%): 625 ([M + Na], 30), 623 ([M + Na], 70), 603 ([M + H], 20), 601 ([M + H], 60).

**[3-(2-Phenyl-2-oxoethyl)-3H-triazol-1-io](4-methoxybenzoyl)(2,4,6-trinitrophenyl)methanide 15b and [(3-(2-(4-methoxyphenyl)-2-oxoethyl)-3H-triazol-1-io)(benzoyl)-(2,4,6-trinitrophenyl)methanide 16b]**

Yield 0.93 g (56%). <sup>1</sup>H NMR (CHCl<sub>3</sub>–TMS)  $\delta$  3.71 (**16b**) and 3.90 (**16a**) (s, 3H, OCH<sub>3</sub>), 6.87 (**16b**) and 6.94 (**15b**) (s, 2H, CH<sub>2</sub>), 7.16–7.29 (m, 6 aromatic H), 7.64–7.88 (m, 4 aromatic H), 8.08–8.21 (m, 3 aromatic H), 8.58 (**15b**) and 8.61 (**16b**) (s, 2 aromatic H). ES<sup>+</sup>-MS (cone 35)  $m/z$  (%): 619 ([M + Na], 100), 597 ([M + H], 45).

**[3-(2-Phenyl-2-oxoethyl)-3H-triazol-1-io](4-nitrobenzoyl)-(2,4,6-trinitrophenyl)methanide 15c and [(3-(2-(4-nitroxyphenyl)-2-oxoethyl)-3H-triazol-1-io)(benzoyl)(2,4,6-trinitrophenyl)methanide 16c]**

Yield 1.11 g (65%). <sup>1</sup>H NMR (CHCl<sub>3</sub>–TMS)  $\delta$  6.92 (**15c**) and 6.94 (**16c**) (s, 2H, CH<sub>2</sub>), 7.40–7.43 (m, 2 aromatic H), 7.62–7.68 (m, 2 aromatic H), 7.77–7.92 (m, 4 aromatic H), 8.06–8.13 (m, 4 aromatic H), 8.23 (**15c**) and (**16c**) (d,  $J = 7.9$  Hz, 1 aromatic H), 8.61 (**16c**) and 8.72 (**15c**) (s, 2 aromatic H). ES<sup>+</sup>-MS (cone 30)  $m/z$  (%): 634 ([M + Na], 100), 612 ([M + H], 10).

## References

1. A. Couture, A. Lablache-Combier, P. Grandclaudon, and G. Surpateanu. *Heterocycles*, **31**(12), 2111 (1990).
2. G. Surpateanu, N.C. Lungu, N. Avarvari, A. Lablache-Combier, P. Grandclaudon, and A. Couture. *J. Chem. Phys.* **91**, 1648 (1994).
3. P. Woisel, M.L. Lehaire, and G. Surpateanu. *Tetrahedron*, **56**, 377 (2000).
4. P. Woisel, G. Surpateanu, F. Delattre, and M. Bria. *Eur. J. Org. Chem.* 1407 (2001).
5. Y. Karzazi and G. Surpateanu. *Heterocycles*, **51**, 863 (1999).
6. P. Woisel, G.G. Surpateanu, and G. Surpateanu. *Targets Heterocycl. Syst.* **5**, 461 (2001).
7. G.G. Surpateanu, G. Vergoten, A. Ellass, and G. Surpateanu. *Heterocycles*, **51**, 2213 (1999).



8. F. Kröncke. *Ber. Dtsch. Chem. Ges.* **68**, 1177 (1935).
9. Spartan 5.0. Wavefunction Inc., Irvine, CA. 1997.
10. G.G. Surpateanu, G. Vergoten, and G. Surpateanu. *J. Mol. Struct.* **526**, 143 (2000).
11. G.G. Surpateanu, G. Vergoten, and G. Surpateanu. *J. Mol. Struct.* **559**, 26 (2001).
12. L. Hansh and A. Leo. *In* Substituent constants for correlation analysis in chemistry and biology. John Wiley, New York. 1979.
13. G. Surpateanu, J.P. Catteau, P. Karafiloglou, and A. Lablache-Combier. *Tetrahedron*, **32**, 2647 (1976).
14. G. Surpateanu and A. Lablache-Combier. *Heterocycles*, **22**, 2079 (1984).
15. K.N. Houk, J. Sims, R.E. Duke, R.W. Storzier, and J.K. George. *J. Am. Chem. Soc.* **95**, 7287 (1973).



# Experimental values and ERAS model calculations for excess molar volumes and enthalpies of the ternary system 2-butanol + 1,3-dioxolane + cyclohexane

Ignacio Gascón, Santiago Martín, Beatriz Giner, Marta Haro, and Carlos Lafuente

**Abstract:** Densities and heats of mixing for the ternary system 2-butanol + 1,3-dioxolane + cyclohexane have been measured at 298.15 and 313.15 K. Excess molar volumes and excess molar enthalpies have been calculated from experimental data and fitted by the Redlich–Kister equation. The ERAS model has been used to calculate excess molar properties of the ternary mixture from parameters obtained from the constituent binary mixtures.

*Key words:* excess properties, ERAS model.

**Résumé :** On a mesuré à 298,15 et à 313,15 K les densités et les chaleurs de mélange du système ternaire : butan-2-ol + 1,3-dioxolane + cyclohexane. On a calculé les volumes molaires en excès, les enthalpies molaires en excès, à partir des données expérimentales et on les a ajustées à l'aide de l'équation de Redlich–Kister. On a utilisé le modèle ERAS pour calculer les propriétés molaires en excès du mélange ternaire à partir des paramètres obtenus des mélanges binaires de constituants.

*Mots clés :* propriétés en excès, modèle ERAS.

[Traduit par la Rédaction]

## Introduction

The study of the thermodynamic properties of binary mixtures containing cyclic polyethers has increased in recent years (1–6) because of industrial applications and theoretical interest in the structure of such solutions. However, experimental data for ternary mixtures of these compounds are scarce.

This work is a continuation of our previous investigations involving thermodynamic and transport properties of binary and ternary mixtures containing 1,3-dioxolane or 1,4-dioxane together with isomeric butanols, cyclohexane, and *n*-hexane (7–11). Here we report experimental excess molar volumes and excess molar enthalpies of the ternary mixture 2-butanol + 1,3-dioxolane + cyclohexane at 298.15 and 313.15 K. Experimental thermodynamic data of the mixtures provide a better understanding of the molecular interactions and can be used to test thermodynamic models. In the present paper the reported excess molar volumes and excess molar enthalpies are used to test the applicability of the ERAS model for describing excess molar properties of the ternary mixture at different temperatures from binary parameters.

## Experimental

2-Butanol (>99%), 1,3-dioxolane (>99%), and cyclohexane (>99.9%) were obtained from Aldrich. The purities of these compounds were checked by comparing the measured densities with those reported in the literature and also by a chromatographic method. This confirmed the absence of significant impurities. No further purification was considered necessary, but the 2-butanol was dried with 0.3 nm molecular sieves from Merck.

Properties of the pure compounds at 298.15 and 313.15 K, along with literature density values at 298.15 K (2, 12), are given in Table 1.

Densities,  $\rho$ , of the pure compounds and their mixtures were determined with an Anton Paar DMA-58 vibrating tube densimeter whose temperature was controlled within  $\pm 0.01$  K. The accuracy of the densimeter after proper calibration is  $\pm 1 \times 10^{-5}$  g cm<sup>-3</sup> and the precision of the density measurements was  $\pm 5 \times 10^{-6}$  kg m<sup>-3</sup>.

Mixtures were prepared by mass using a Mettler H20T balance. The uncertainty of mole fraction of the mixtures is estimated to be less than  $\pm 1 \times 10^{-4}$ .

Excess molar enthalpies were determined using a Thermo-metric 2277 thermal activity monitor with a combination measuring cylinder (LKB 2277–204) running under constant flow conditions (total flow rate =  $5 \times 10^{-3}$  mL s<sup>-1</sup>). During the experiments the temperature is kept constant within  $\pm 2 \times 10^{-4}$  K. Two Shimadzu LC-10ADVP HPLC pumps were used to drive the liquids. One of the pumps delivered pure 2-butanol while the other pump delivered a liquid mixture of 1,3-dioxolane and cyclohexane of known composition. Each pump was calibrated with pure 2-butanol or the binary mix-

Received 23 January 2003. Published on the NRC Research Press Web site at <http://canjchem.nrc.ca> on 20 May 2003.

I. Gascón, S. Martín, B. Giner, M. Haro, and C. Lafuente.<sup>1</sup> Departamento de Química Orgánica-Química Física, Facultad de Ciencias, Universidad de Zaragoza, Ciudad Universitaria, 50009 Zaragoza, Spain.

<sup>1</sup>Corresponding author (e-mail: celadi@posta.unizar.es).



**Table 1.** Physical properties and ERAS model parameters of the pure components at 298.15 and 313.15 K.

Property	T (K)		2-Butanol	1,3-Dioxolane	Cyclohexane
$\rho$ (g cm <sup>-3</sup> )	298.15	Exptl.	0.8022	1.05862	0.77372
		Lit.	0.80241 <sup>a</sup>	1.05866 <sup>b</sup>	0.77389 <sup>b</sup>
	313.15	Exptl.	0.78959	1.03997	0.75947
$V_m$ (cm <sup>3</sup> mol <sup>-1</sup> )	298.15		92.398	69.977	108.774
	313.15		93.874	71.232	110.815
$10^3 \alpha$ (K <sup>-1</sup> )	298.15		1.059	1.164	1.220
	313.15		1.105	1.226	1.257
$10^{12} \kappa_T$ (Pa <sup>-1</sup> )	298.15		1 006	758.3	1131.0
	313.15		1 114.7	862.7	1282.8
$C_{p,m}$ (J K <sup>-1</sup> mol <sup>-1</sup> )	298.15		196.9 <sup>c</sup>	122.21	156.2 <sup>d</sup>
	313.15		212.6 <sup>e</sup>	125.01	162.0 <sup>d</sup>
$s$ (Å <sup>-1</sup> )			1.484	1.230	0.961
$K_i^f$	298.15		72 <sup>g</sup>	4	—
	313.15		44	3.1	—
$\Delta v_i^*$ (cm <sup>3</sup> mol <sup>-1</sup> ) <sup>f</sup>			-5.6 <sup>h</sup>	-6.8	—
$\Delta h_i^*$ (J mol <sup>-1</sup> ) <sup>f</sup>			-25 100 <sup>h</sup>	-12 750	—
$V^{*0}$ (cm <sup>3</sup> mol <sup>-1</sup> )	298.15		74.951	57.422	84.267
	313.15		75.169	57.238	84.588
$P^*$ (J cm <sup>-3</sup> )	298.15		421	544	536
	313.15		423	557	527

<sup>a</sup>Reference (12).<sup>b</sup>Reference (2).<sup>c</sup>Reference (13).<sup>d</sup>Reference (14).<sup>e</sup>Reference (15).<sup>f</sup> $i = A$  for 2-butanol,  $i = B$  for 1,3-dioxolane.<sup>g</sup>Reference (16).<sup>h</sup>Reference (17).

ture, respectively, before calorimetric measurements were registered. The uncertainty in the mole fractions of the ternary mixture, calculated from the uncertainty in the flow delivered by the pumps, is  $\pm 0.001$ . The accuracy in the determination of the excess molar enthalpies could be expected to be  $\pm 1\%$ . More details about procedure and calibration can be found in a previous paper (18).

## Results and discussion

The experimental densities of the ternary system 2-butanol (1) + 1,3-dioxolane (2) + cyclohexane (3) at 298.15 and 313.15 K are shown in Table 2 along with calculated excess molar volumes. The excess molar enthalpies are presented in Table 3.  $H^E$  was determined according to the following relation:

$$[1] \quad H^E = \frac{\dot{Q} + (\dot{n}_2 + \dot{n}_3)H_{23}^E}{\dot{n}_1 + \dot{n}_2 + \dot{n}_3}$$

where  $\dot{Q}$  is the measured heat effect upon mixing,  $\dot{n}_i$  is the molar flow of the components ( $i = 1, 2, 3$ ), and  $H_{23}^E$  is the excess molar enthalpy of the binary mixture 1,3-dioxolane + cyclohexane delivered by one of the pumps. The  $H^E$  values for this binary mixture are given in Table 4.

The Redlich–Kister equation for ternary mixtures (19) was fitted to the measured excess molar volumes and enthalpies

$$[2] \quad Y^E = Y_{\text{bin}}^E + x_1 x_2 (1 - x_1 - x_2) [C + D_1 x_1 + D_2 x_2]$$

$Y^E$  is the excess molar property ( $V^E$  or  $H^E$ ) of the ternary mixture,  $x_i$  is the mole fraction of component  $i$  in the mixture,  $C$  and  $D_i$  are adjustable parameters obtained by the least-squares method, and  $Y_{\text{bin}}^E$  is the contribution to the excess molar property of the constituent binary mixtures given by

$$[3] \quad Y_{\text{bin}}^E = Y_{12}^E + Y_{13}^E + Y_{23}^E$$

Each binary contribution,  $Y_{ij}^E$ , is obtained by means of a Redlich–Kister polynomial equation for binary mixtures

$$[4] \quad Y_{ij}^E = x_i x_j \sum_{p=0}^n A_{p,ij} (x_i - x_j)^p$$

where  $x_i$  is the mole fraction of component  $i$  in the ternary mixture and  $A_{p,ij}$  are adjustable parameters obtained by least-squares fitting. Table 5 gives the parameters for the constituent binary mixtures obtained either from experimental measurements carried out in our laboratory or taken from previous papers (7, 9, 20). The standard deviations of the fits,  $\sigma$ , are also tabulated.

In Table 5 the parameters obtained for the excess molar enthalpies of the binary mixture 2-butanol + cyclohexane are included; these were fitted with the fractional equation proposed by Treszczanowicz and Benson (21)

$$[5] \quad H_{13}^E = x_1 x_3 \sum_{p=0}^m A_p x_1^{p/2}$$



**Table 2.** Densities and excess molar volumes of ternary 2-butanol (1) + 1,3-dioxolane (2) + cyclohexane (3) mixtures at 298.15 and 313.15 K.

$T = 298.15 \text{ K}$				$T = 313.15 \text{ K}$			
$x_1$	$x_2$	$\rho \text{ (g cm}^{-3}\text{)}$	$V^E \text{ (cm}^3 \text{ mol}^{-1}\text{)}$	$x_1$	$x_2$	$\rho \text{ (g cm}^{-3}\text{)}$	$V^E \text{ (cm}^3 \text{ mol}^{-1}\text{)}$
0.0528	0.0500	0.78114	0.447	0.0550	0.0642	0.76928	0.447
0.0525	0.1020	0.78998	0.609	0.0538	0.1071	0.77636	0.654
0.1009	0.0498	0.78166	0.541	0.1005	0.0513	0.76752	0.583
0.1042	0.0952	0.78936	0.704	0.1007	0.1039	0.77628	0.767
0.0957	0.1988	0.80853	0.930	0.1070	0.1895	0.79200	0.994
0.1937	0.0966	0.7914	0.802	0.1900	0.1014	0.77728	0.924
0.1020	0.2909	0.82806	1.040	0.0978	0.2975	0.81388	1.133
0.2059	0.1872	0.80914	0.986	0.1919	0.2066	0.79744	1.125
0.2958	0.0978	0.79419	0.854	0.2979	0.0987	0.77964	0.975
0.1025	0.3873	0.85063	1.070	0.1009	0.3979	0.83723	1.166
0.1961	0.2885	0.83074	1.067	0.2008	0.2946	0.81683	1.177
0.2985	0.2002	0.81494	1.000	0.2971	0.2028	0.80036	1.118
0.3940	0.0973	0.79707	0.848	0.3994	0.0970	0.78252	0.968
0.1052	0.4969	0.87952	1.020	0.1104	0.4907	0.86182	1.107
0.1916	0.3958	0.85669	1.056	0.1909	0.3988	0.84154	1.158
0.3010	0.2859	0.83440	1.035	0.2915	0.2960	0.82096	1.155
0.4119	0.1867	0.81641	0.930	0.3924	0.2090	0.80558	1.072
0.4929	0.0993	0.80091	0.803	0.4988	0.0979	0.78639	0.909
0.1011	0.5964	0.90889	0.885	0.1073	0.5925	0.89134	0.966
0.1981	0.4911	0.88313	0.963	0.2038	0.4924	0.86765	1.047
0.3037	0.3843	0.85948	0.974	0.2964	0.3916	0.84520	1.090
0.4044	0.2897	0.84028	0.939	0.3978	0.2938	0.82571	1.055
0.4968	0.1895	0.82073	0.853	0.4994	0.1887	0.80596	0.957
0.5971	0.1027	0.80591	0.695	0.5971	0.0991	0.79085	0.799
0.1046	0.6968	0.94266	0.686	0.0991	0.7022	0.92702	0.736
0.1951	0.6006	0.91677	0.783	0.1926	0.6023	0.90058	0.851
0.3008	0.4939	0.89052	0.839	0.2965	0.4991	0.87571	0.925
0.4042	0.3926	0.86761	0.841	0.4009	0.3910	0.85145	0.941
0.4875	0.3100	0.85014	0.800	0.4983	0.2926	0.83106	0.909
0.5920	0.2035	0.82878	0.717	0.5979	0.1910	0.81157	0.807
0.6942	0.0980	0.80926	0.561	0.6915	0.1091	0.79763	0.650
0.0498	0.8477	0.99573	0.366	0.0539	0.8460	0.97766	0.392
0.0986	0.7984	0.98051	0.431	0.1031	0.8098	0.96791	0.433
0.1979	0.7032	0.95302	0.535	0.1848	0.7170	0.94038	0.534
0.2928	0.6016	0.92492	0.618	0.2940	0.6019	0.90879	0.673
0.3974	0.4955	0.89806	0.667	0.3943	0.4979	0.88289	0.729
0.5037	0.3968	0.87539	0.664	0.4946	0.4066	0.86237	0.740
0.6051	0.2979	0.85414	0.597	0.5979	0.2979	0.83863	0.722
0.6934	0.2064	0.83532	0.517	0.7040	0.1861	0.81634	0.617
0.7972	0.0999	0.81483	0.385	0.8006	0.0957	0.80024	0.456
0.8440	0.0579	0.80763	0.287	0.8447	0.0505	0.79242	0.358
0.0517	0.8977	1.01741	0.216	0.0536	0.8941	0.99811	0.234
0.1012	0.8481	1.00118	0.294	0.1049	0.8433	0.98188	0.325
0.8423	0.1043	0.81815	0.313	0.8495	0.0989	0.80378	0.347
0.8952	0.0513	0.80873	0.189	0.8836	0.0603	0.79674	0.276

where  $H_{13}^E$  is the excess molar enthalpy of the binary mixture,  $x_1$  and  $x_3$  are the mole fractions of 2-butanol and cyclohexane, respectively, and  $A_p$  are adjustable parameters obtained by the least-squares method.

The  $C$  and  $D_i$  parameters of the Redlich–Kister equation for ternary mixtures are given in Table 6 along with the standard deviations of the fits.

Isolines at constant values of excess molar volumes and

enthalpies of the ternary mixture at 298.15 and 313.15 K are plotted in Figs. 1 and 2, respectively. The mixtures have relatively large positive excess molar volumes and enthalpies throughout the entire composition range. Both excess molar properties increase slightly with increasing temperature.

The observed behaviour of the excess molar properties can be interpreted in terms of molecular interactions. In particular, the mixtures show positive excess molar volumes



**Table 3.** Excess molar enthalpies of ternary 2-butanol (1) + 1,3-dioxolane (2) + cyclohexane (3) mixtures at 298.15 and 313.15 K.

$T = 298.15 \text{ K}$			$T = 313.15 \text{ K}$		
$x_1$	$x_2$	$H^E \text{ (J mol}^{-1}\text{)}$	$x_1$	$x_2$	$H^E \text{ (J mol}^{-1}\text{)}$
0.087	0.777	1440	0.044	0.815	1228
0.176	0.701	1788	0.087	0.778	1450
0.268	0.623	2011	0.176	0.702	1809
0.299	0.596	2056	0.268	0.624	2052
0.363	0.542	2121	0.363	0.543	2174
0.460	0.459	2128	0.460	0.460	2192
0.561	0.373	2023	0.561	0.374	2094
0.665	0.285	1797	0.665	0.286	1861
0.773	0.193	1413	0.773	0.194	1450
0.884	0.099	839	0.884	0.099	862
0.941	0.050	448	0.941	0.050	451
0.046	0.669	1679	0.046	0.669	1718
0.092	0.637	1823	0.092	0.637	1867
0.184	0.572	1993	0.184	0.572	2060
0.279	0.506	2043	0.279	0.506	2132
0.376	0.438	2004	0.376	0.438	2113
0.474	0.369	1901	0.474	0.369	2013
0.575	0.298	1733	0.575	0.298	1841
0.678	0.226	1488	0.678	0.226	1580
0.784	0.152	1127	0.783	0.152	1194
0.891	0.076	630	0.946	0.038	350
0.946	0.038	332	0.050	0.475	1973
0.050	0.475	1905	0.100	0.450	2073
0.100	0.450	1988	0.199	0.401	2122
0.199	0.401	2007	0.298	0.351	2044
0.298	0.351	1921	0.398	0.301	1898
0.398	0.301	1789	0.498	0.251	1731
0.498	0.251	1590	0.598	0.201	1507
0.598	0.201	1385	0.699	0.151	1230
0.699	0.151	1126	0.054	0.283	1817
0.800	0.100	809	0.107	0.267	1905
0.055	0.282	1710	0.212	0.236	1886
0.108	0.267	1752	0.316	0.205	1780
0.213	0.235	1694	0.418	0.175	1621
0.316	0.204	1591	0.518	0.144	1436
0.418	0.174	1436	0.617	0.115	1223
0.518	0.144	1264	0.715	0.085	968
0.617	0.114	1001	0.060	0.140	1400
0.715	0.085	765	0.118	0.131	1524
0.232	0.101	1305	0.231	0.115	1559
0.342	0.087	1255	0.341	0.098	1502
0.448	0.073	1157	0.447	0.082	1392
0.550	0.059	1016	0.549	0.067	1251
0.649	0.046	861	0.648	0.052	1068
0.745	0.034	670	0.744	0.038	843
0.838	0.021	457	0.837	0.024	583
0.928	0.010	230	0.928	0.011	296

and enthalpies, which result from the breaking up of alcohol agglomerates and ether–ether interactions that dominate over the negative contributions from heteromolecular interaction.

Although both  $H^E$  and  $V^E$  are related to molecular interactions,  $V^E$  is a better indicator of structural and packing effects. Maximum values of  $H^E$  appear for binary 2-butanol + 1,3-dioxolane mixtures, indicating that more bonds are bro-

**Table 4.** Excess molar enthalpies of binary 1,3-dioxolane (1) + cyclohexane (2) mixtures at 298.15 and 313.15 K.

$T = 298.15 \text{ K}$		$T = 313.15 \text{ K}$	
$x_1$	$H^E \text{ (J mol}^{-1}\text{)}$	$x_1$	$H^E \text{ (J mol}^{-1}\text{)}$
0.047	349	0.047	362
0.097	691	0.097	701
0.201	1201	0.201	1232
0.301	1522	0.301	1573
0.401	1703	0.401	1761
0.501	1746	0.501	1806
0.603	1677	0.603	1730
0.705	1489	0.705	1534
0.805	1165	0.805	1197
0.907	665	0.907	679
0.956	355	0.956	366

ken in 2-butanol + 1,3-dioxolane mixtures than in ternary 2-butanol + 1,3-dioxolane + cyclohexane mixtures. Maximum values of  $V^E$  appear at small mole fractions of 2-butanol where dissociation of the alcohol agglomerates is more extensive.

Comparing our results with those previously reported (7) for the ternary system 1-butanol + 1,3-dioxolane + cyclohexane, we observe that the composition dependence of the excess molar functions is very similar for both systems, but the  $H^E$  and  $V^E$  values are slightly larger in the ternary system containing 2-butanol.

## ERAS model calculations

The ERAS theory combines the real-associated solution model (22–25) with Flory's equation of state (26). The version of the ERAS model used here (17, 27) allows a description of the excess molar properties of mixtures containing two associating components, provided one of these shows a weak self-association. In the present work cyclohexane was assumed to be an inert component and 2-butanol presents a strong association, while 1,3-dioxolane is a weak-associated compound. Cross association between alcohol and ether was also considered.

The ERAS parameters of the pure compounds along with their physical properties are collected in Table 1. Molar volumes,  $V_m$ , and thermal expansion coefficients,  $\alpha$ , were derived from measured densities. Isothermal compressibilities,  $\kappa_T$ , at a given temperature  $T$  were calculated from molar volumes, thermal expansion coefficients, isentropic compressibilities,  $\kappa_S$ , and molar heat capacities,  $C_{p,m}$ , using the thermodynamic equation

$$[6] \quad \kappa_T = \kappa_S + \frac{TV_m\alpha^2}{C_{p,m}}$$

Values of  $\kappa_S$  were evaluated from experimental densities,  $\rho$ , and ultrasonic velocities,  $u$  (through the relation  $\kappa_S = (\rho u^2)^{-1}$ ). An Anton Paar DSA-48 density and sound analyzer was used to determine  $\rho$  and  $u$ .  $C_{p,m}$  values for 1,3-dioxolane were determined with a programmable, differential-scanning microcalorimeter (Setaram DSC II), while molar heat capacities of 2-butanol and cyclohexane were taken from literature



**Table 5.** Coefficients of the Redlich–Kister equation (eq. [4]) or the Treszczanowicz and Benson equation (eq. [5]),  $A_p$ , for  $V^E$ , and  $H^E$  of the constituent binary mixtures of the ternary system 2-butanol (1) + 1,3-dioxolane (2) + cyclohexane (3) at 298.15 and 313.15 K.

Property	$T$ (K)	$A_0$	$A_1$	$A_2$	$A_3$	$A_4$	$\sigma$ ( $Y^E$ )
<b>2-Butanol (1) + 1,3-dioxolane (2)</b>							
$V^E$ ( $\text{cm}^3 \text{mol}^{-1}$ ) <sup>a</sup>	298.15	1.731	0.352	0.251	0.072	—	0.003
	313.15	1.891	0.769	0.641	−0.089	—	0.002
$H^E$ ( $\text{J mol}^{-1}$ ) <sup>b</sup>	298.15	9 340	147	20	−1 065	—	16
	313.15	9 582	−45	509	725	—	17
<b>2-Butanol (1) + cyclohexane (3)</b>							
$V^E$ ( $\text{cm}^3 \text{mol}^{-1}$ ) <sup>c</sup>	298.15	2.521	−0.838	0.521	−0.403	—	0
	313.15	3.033	−1.048	0.336	0.321	—	0
$H^E$ ( $\text{J mol}^{-1}$ ) <sup>c</sup>	298.15	21 543	−95 233	203 597	−199 639	73 142	6
	313.15	27 593	−118 161	244 647	−235 593	86 063	7
<b>1,3-Dioxolane (2) + cyclohexane (3)</b>							
$V^E$ ( $\text{cm}^3 \text{mol}^{-1}$ ) <sup>d</sup>	298.15	3.698	−0.882	0.704	−0.183	—	0.003
	313.15	4.264	−0.622	0.061	−0.674	—	0.003
$H^E$ ( $\text{J mol}^{-1}$ )	298.15	6 987	−209	1 320	428	—	6
	313.15	7 224	−250	1 227	526	—	6

<sup>a</sup>Reference (7).<sup>b</sup>Reference (9).<sup>c</sup>Unpublished results.<sup>d</sup>Reference (20).**Table 6.** Coefficients of the Redlich–Kister equation (eq. [2]) for  $V^E$  and  $H^E$  of ternary 2-butanol (1) + 1,3-dioxolane (2) + cyclohexane (3) mixtures at 298.15 and 313.15 K.

Property	$T$ (K)	$C$	$D_1$	$D_2$	$\sigma$ ( $Y^E$ )
$V^E$ ( $\text{cm}^3 \text{mol}^{-1}$ )	298.15	4.426	−3.763	−0.957	0.013
	313.15	3.713	−3.299	−1.741	0.013
$H^E$ ( $\text{J mol}^{-1}$ )	298.15	−2920	−26 993	669	31
	313.15	−2098	−27 684	−4707	42

**Table 7.** ERAS model parameters for the constituent binary mixtures of ternary 2-butanol (1) + 1,3-dioxolane (2) + cyclohexane (3) mixtures at 298.15 and 313.15 K.

Mixture	$T$ (K)	$X_y$ ( $\text{J cm}^{-3}$ )	$K_{AB}$	$\Delta v_{AB}^*$ ( $\text{cm}^3 \text{mol}^{-1}$ )	$\Delta h_{AB}^*$ ( $\text{J mol}^{-1}$ )
2-Butanol (1) + 1,3-dioxolane (2)	298.15	7.2	3	−15	−3150
	313.15	12	2.8	−15	−3150
2-Butanol (1) + cyclohexane (3)	298.15	21.4	—	—	—
	313.15	26.9	—	—	—
1,3-Dioxolane (2) + cyclohexane (3)	298.15	50.3	—	—	—
	313.15	51.1	—	—	—

data (13–15). Finally, the surface to volume ratios,  $s$ , were estimated using Bondi's method (28).

The association parameters for 2-butanol ( $K_A$ ,  $\Delta v_A^*$ , and  $\Delta h_A^*$ ) were obtained from the literature (16, 17). For 1,3-dioxolane,  $K_B$ ,  $\Delta v_B^*$ , and  $\Delta h_B^*$  were obtained using the ERAS model equations (29) to fit, simultaneously, the experimental excess molar properties ( $V^E$  and  $H^E$ ) of 1,3-dioxolane +  $n$ -hexane mixtures (30) and the enthalpy of vaporization of the pure 1,3-dioxolane (13). In the ERAS model, the parameters  $\Delta v_i^*$  and  $\Delta h_i^*$  are considered to be temperature independent and the parameter  $K_i$  can be obtained at a given temperature using the van't Hoff equation from the corresponding  $K_i$  and  $\Delta h_i^*$  values at 298.15 K.

The adjustable parameters of the ERAS model are: the energetic interaction parameter ( $X_{ij}$ ) for the three binary mixtures and the cross-association parameters ( $K_{AB}$ ,  $\Delta v_{AB}^*$ ,  $\Delta h_{AB}^*$ ) for the 2-butanol + 1,3-dioxolane mixtures. For the 2-

butanol + 1,3-dioxolane mixtures at 313.15 K, it can be pointed out that the only adjustable parameter is  $X_{AB}$ , since  $\Delta v_{AB}^*$  and  $\Delta h_{AB}^*$  are temperature independent, and  $K_{AB}$  is calculated using the van't Hoff equation from  $K_{AB}$  and  $\Delta h_{AB}^*$  values at 298.15 K.

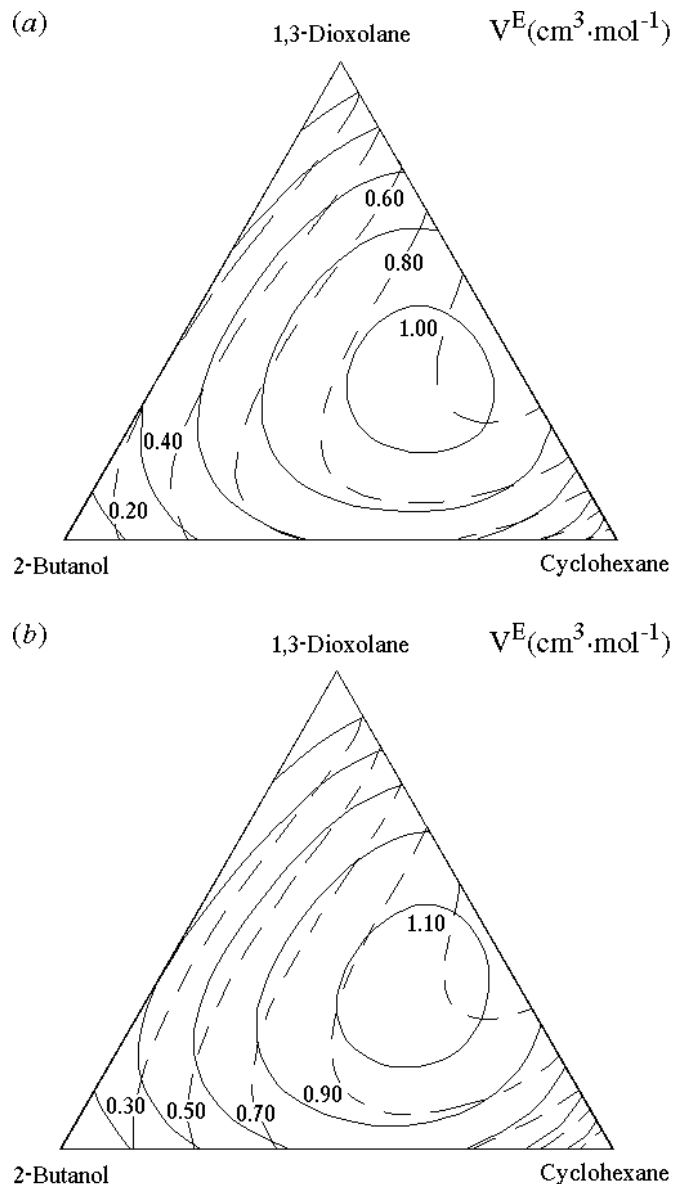
Evaluation of the parameters at each temperature was based on minimization, using the simulated annealing method (31, 32) of an objective function  $F$  defined in terms of experimental and calculated  $V^E$  and  $H^E$  values of the binary mixtures

$$[7] \quad F = \sum_{i=1}^{i=N} \left( \left( \frac{V_{\text{ERAS}}^E - V_{\text{exp}}^E}{V_{\text{exp}}^E} \right) + \left( \frac{H_{\text{ERAS}}^E - H_{\text{exp}}^E}{H_{\text{exp}}^E} \right)^2 \right)$$

where  $N$  is the number of experimental data. The parameter values are given in Table 7.



**Figure 1.** Isolines of constant excess molar volumes for ternary 2-butanol (1) + 1,3-dioxolane (2) + cyclohexane (3) mixtures: experimental correlation (continuous lines) and ERAS model predictions (dashed lines). (a) 298.15 K; (b) 313.15 K.



From these parameters, ERAS model calculations for the ternary system have been made. These calculations are graphically represented in Figs. 1 and 2. We have also obtained the corresponding mean relative standard deviations (MRSD) between experimental and calculated excess molar properties, defined as:

$$[8] \quad \text{MRSD} (\%) = \left[ \frac{1}{m} \sum \left( \frac{Y_{\text{ERAS}}^E - Y_{\text{exp}}^E}{Y_{\text{exp}}^E} \right)^2 \right]^{1/2} \times 100$$

where  $Y_{\text{exp}}^E$  and  $Y_{\text{ERAS}}^E$  are, respectively, the experimental and calculated excess molar properties of the ternary mixture ( $H^E$  or  $V^E$ ) and  $m$  is the number of experimental points. MRSD values are given in Table 8.

**Figure 2.** Isolines of constant excess molar enthalpies for ternary 2-butanol (1) + 1,3-dioxolane (2) + cyclohexane (3) mixtures: experimental correlation (continuous lines) and ERAS model predictions (dashed lines). (a) 298.15 K; (b) 313.15 K.

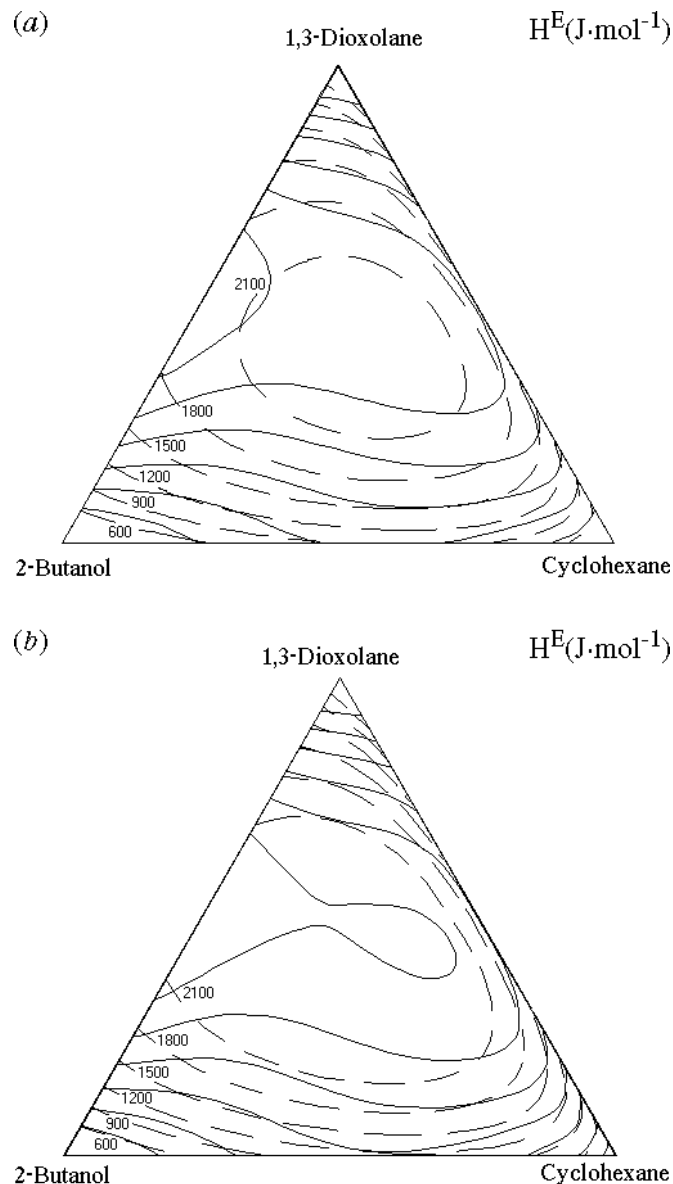


**Table 8.** ERAS model predictions for  $V^E$  and  $H^E$  of ternary 2-butanol (1) + 1,3-dioxolane (2) + cyclohexane (3) mixtures at 298.15 and 313.15 K.

Property	$T$ (K)	MRSD (%)
$V^E$ ( $\text{cm}^3 \text{ mol}^{-1}$ )	298.15	22.3
	313.15	24.6
$H^E$ ( $\text{J mol}^{-1}$ )	298.15	19.8
	313.15	20.9

In Figs. 1 and 2 we can see that the ERAS model correctly describes the variation with composition of the excess molar volumes and enthalpies of the ternary mixture at 298.15 and 313.15 K. In general, ERAS model predictions



could be considered satisfactory, since the model only uses parameters obtained from the constituent binary mixtures.

## Acknowledgments

We are grateful for financial assistance from Ministerio de Educación y Cultura (CICYT-INFR IN96-0191).

## References

1. E. Calvo, P. Brocos, R. Bravo, M. Pintos, A. Amigo, A.H. Roux, and G. Roux-Desgranges. *J. Chem. Eng. Data*, **43**, 105 (1998).
2. P. Brocos, E. Calvo, A. Amigo, R. Bravo, M. Pintos, A.H. Roux, and G. Roux-Desgranges. *J. Chem. Eng. Data*, **43**, 112 (1998).
3. P. Brocos, E. Calvo, R. Bravo, M. Pintos, A. Amigo, A.H. Roux, and G. Roux-Desgranges. *J. Chem. Eng. Data*, **44**, 67 (1999).
4. E. Calvo, P. Brocos, A. Piñeiro, M. Pintos, A. Amigo, R. Bravo, A.H. Roux, and G. Roux-Desgranges. *J. Chem. Eng. Data*, **44**, 948 (1999).
5. P. Brocos, E. Calvo, A. Piñeiro, R. Bravo, A. Amigo, A.H. Roux, and G. Roux-Desgranges. *J. Chem. Eng. Data*, **44**, 1341 (1999).
6. T.S. Banipal, A. Toor, and P.V.K. Rattan. *Indian J. Chem.* **39A**, 809 (2000).
7. I. Gascón, S. Martín, P. Cea, M.C. López, and F.M. Royo. *J. Solution Chem.* **31**, 905 (2002).
8. I. Gascón, H. Artigas, C. Lafuente, M.C. López, and F.M. Royo. *Fluid Phase Equilib.* **202**, 385 (2002).
9. I. Gascón, H. Artigas, S. Martín, P. Cea, and C. Lafuente. *J. Chem. Thermodyn.* **34**, 1351 (2002).
10. I. Gascón, J. Pardo, J. Santafé, M. Domínguez, and J.S. Urieta. *Fluid Phase Equilib.* **180**, 211 (2001).
11. I. Gascón, A.M. Mainar, L. Alvarez-Cerdeiría, F.M. Royo, and J.S. Urieta. *J. Chem. Eng. Data*, **45**, 751 (2000).
12. J.A. Riddick, W.B. Bunger, and T.K. Sanako. *Organic solvents. Physical properties and methods of purification* (Techniques of chemistry). Wiley-Interscience, New York. 1986.
13. D.R. Lide. *Handbook of chemistry and physics*. C.R.C. Press, Boca Ratón. 1992.
14. M. Frenkel (*Editor*). *T.R.C. thermodynamic tables hydrocarbons. Selected values of properties of chemical compounds*. Thermodynamic Research Center, Texas A&M University, College Station. 1999.
15. M. Frenkel (*Editor*). *T.R.C. thermodynamic tables non-hydrocarbons. Selected values of properties of chemical compounds*. Thermodynamic Research Center, Texas A&M University, College Station. 1984.
16. K. Kammerer and R.N. Lichtenthaler. *Thermochim. Acta*, **310**, 61 (1998).
17. H. Funke, M. Wetzel, and A. Heintz. *Pure Appl. Chem.* **61**, 1429 (1989).
18. C. Lafuente, H. Artigas, M.C. López, F.M. Royo, and J.S. Urieta. *Phys. Chem. Liq.* **39**, 665 (2001).
19. O. Redlich and A.T. Kister. *Ind. Eng. Chem.* **40**, 345 (1948).
20. C. Guzmán, C. Lafuente, J. Santafé, F.M. Royo, and J.S. Urieta. *Int. J. Thermophys.* **20**, 1435 (1999).
21. A.J. Treszczanowicz and G.C. Benson. *J. Chem. Thermodyn.* **9**, 1189 (1977).
22. C.B. Kretschmer and R. Wiebe. *J. Chem. Phys.* **22**, 1697 (1954).
23. H. Renon and J.M. Prausnitz. *Chem. Eng. Sci.* **22**, 299 (1967).
24. H. Kehiaian. *Bull. Acad. Pol. Sci.* **16**, 165 (1968).
25. H. Kehiaian and A.J. Treszczanowicz. *Bull. Acad. Pol. Sci.* **16**, 171 (1968).
26. P.J. Flory, R.A. Orwoll, and A. Vrji. *J. Am. Chem. Soc.* **86**, 3507 (1964).
27. M. Bender, J. Hauser, and A. Heintz. *Ber. Bunsen-Ges.* **95**, 801 (1991).
28. A. Bondi. *Physical properties of molecules. Liquids and gases*. Wiley, New York. 1968.
29. M. Bender and A. Heintz. *Fluid Phase Equilib.* **89**, 197 (1993).
30. I. Gascón. Ph.D. Thesis, Universidad de Zaragoza, Spain. 2002.
31. S. Kirkpatrick, C.D. Gelatt, and M.P. Vecchi. *Science*, **220**, 671 (1983).
32. S. Kirkpatrick. *J. Stat. Phys.* **34**, 975 (1984).



# Control of disaccharide conformation by $\pi$ -stacking

Jonathan Watts, Jesús Jiménez-Barbero, Ana Poveda, and T. Bruce Grindley

**Abstract:** The conformations of a series of derivatives of the disaccharide  $\alpha$ -L-fucopyranosyl-(1 $\rightarrow$ 3)-2-acetamido-2-deoxy-D-glucopyranoside, part of the Le<sup>x</sup> determinant, were studied by molecular modelling using the MM3\* forcefield and by <sup>1</sup>H NMR spectroscopy. Unusually shielded *O*-benzyl protons were observed in the <sup>1</sup>H NMR spectrum of phenyl 2,3,4-tri-*O*-benzyl- $\alpha$ -L-fucopyranosyl-(1 $\rightarrow$ 3)-2-deoxy-2-phthalimido-1-thio- $\alpha$ -D-glucopyranoside and assigned to the 2-*O*-benzyl group. This observation was explained by a shift in the population of the conformational mixture present about the glycosidic linkage from the positive  $\Psi$  region in the unsubstituted disaccharide to the negative  $\Psi$  region induced by  $\pi$ -stacking between the phthalimide and the 2-*O*-benzyl phenyl ring. The experimental nuclear Overhauser enhancements confirm the accuracy of the calculations.

**Key words:** disaccharide, conformation,  $\pi$ -stacking, Le<sup>x</sup> determinant, NOE measurements, MM3 calculations.

**Résumé :** Faisant appel à la modélisation moléculaire à l'aide du champ de force MM3\* et à la spectroscopie RMN du <sup>1</sup>H, on a étudié les conformations d'une série de dérivés du disaccharide  $\alpha$ -L-fucopyranosyl-(1 $\rightarrow$ 3)-2-acétamido-2-désoxy-D-glucopyranoside, une portion du déterminant Le<sup>x</sup>. Dans le spectre RMN du <sup>1</sup>H du 2,3,4-tri-*O*-benzyl- $\alpha$ -L-fucopyranosyl-(1 $\rightarrow$ 3)-2-désoxy-2-phthalimido-1-thio- $\alpha$ -D-glucopyranoside de phényle, on a observé des protons *O*-benzyliques exceptionnellement blindés qui ont été attribués au groupe 2-*O*-benzyle. Cette observation est expliquée par un déplacement dans la population du mélange conformationnel présent autour de la liaison glycosidique par rapport à la région  $\Psi$  positive dans le disaccharide non substitué à une région  $\Psi$  négative induite par un empilement  $\pi$  entre le phthalimide et le noyau phényle du groupe 2-*O*-benzyle. Des rehaussements expérimentaux d'effet Overhauser nucléaire confirment l'exactitude des calculs.

**Mots clés :** disaccharide, conformation, empilement  $\pi$ , déterminant Le<sup>x</sup>, mesures d'effets Overhauser nucléaire, calculs MM3.

[Traduit par la Rédaction]

## Introduction

Recognition of carbohydrate epitopes by protein depends on the conformation adopted by the carbohydrate chains. Normally, the most populated conformations are recognized (1–5), but often less populated conformers are the epitopes (6–8). Therefore, it is important to fully define the factors that influence conformational stability and also to determine the conformational potential energy surface of biologically active oligosaccharides completely.

The sequence  $\alpha$ -L-fucopyranosyl-(1 $\rightarrow$ 3)-2-acetamido-2-deoxy-D-glucose (**8**) is a principal constituent of Le<sup>x</sup>-bearing glycoconjugates, which mediate protein binding to the selectins and other proteins in several processes: inflammation (9), cancer, and others. As part of a project to synthesize conjugates of

the oligosaccharides present on mammalian zona pellucida as potential immunocontraceptives, we prepared a disaccharide, phenyl 2,3,4-tri-*O*-benzyl- $\alpha$ -L-fucopyranosyl-(1 $\rightarrow$ 3)-2-deoxy-2-phthalimido-1-thio- $\alpha$ -D-glucopyranoside (**4**). Fucose-containing oligosaccharides were targeted because of a report that the presence of fucose markedly enhanced sperm binding to the murine zona pellucida glycoprotein ZP3 (10). The conformation adopted by this disaccharide (**4**) appeared to be rather unusual because a signal of one of its benzyl protons appeared at 3.38 ppm in its <sup>1</sup>H NMR spectrum in chloroform-*d*, far from the normal region for benzyl protons, ~4.4–4.9 ppm (11). This report summarizes our determination of the cause of this unusual observation and provides additional information about the conformational energy surface for the very important disaccharide **8**.

## Results and discussion

### Synthesis

A summary of the synthetic procedures is shown in Scheme 1. Benzylation of phenyl 1-thio- $\alpha$ -L-fucopyranoside (**12**) gave the 2,3,4-tri-*O*-benzyl derivative (**1**), whose NMR spectra had not been fully assigned previously. Reaction of phenyl 2-deoxy-2-phthalimido-1-thio- $\alpha$ -D-glucopyranoside with benzaldehyde dimethyl acetal and *p*-toluenesulfonic acid in DMF afforded the 4,6-*O*-benzylidene acetal (**2**) in 80% yield,

Received 22 January 2002. Published on the NRC Research Press Web site at <http://canjchem.nrc.ca> on 20 May 2003.

*Dedicated to the late Professor R.U. Lemieux.*

**J. Watts and T.B. Grindley.**<sup>1</sup> Department of Chemistry, Dalhousie University, Halifax, NS B3H 4J3, Canada.

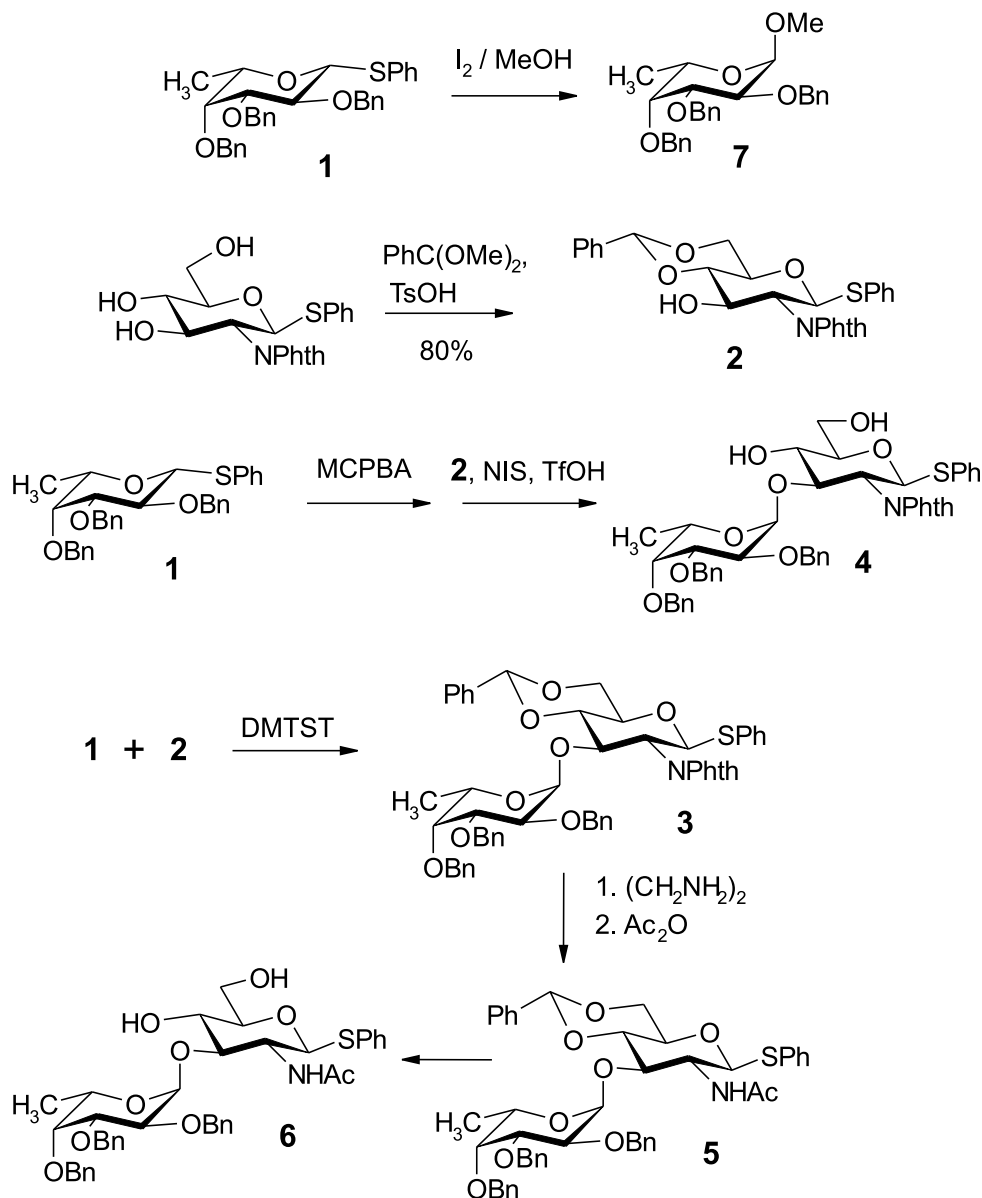
**J. Jiménez-Barbero.** Centro de Investigaciones Biológicas, CSIC, Velázquez 144, 28006 Madrid, Spain.

**A. Poveda.** Universidad Autonoma Madrid, 28049 Cantoblanco, Spain.

<sup>1</sup>Corresponding author (e-mail: [bruce.grindley@dal.ca](mailto:bruce.grindley@dal.ca)).



Scheme 1.



a compound prepared previously by a different method (13). Oxidation of **1** to a mixture of sulfoxide diastereomers with 3-chloroperbenzoic acid (14, 15) and glycosidation with **2** and triflic acid yielded the de-*O*-benzylidenated disaccharide **4** in 31% yield. Direct reaction of **1** with **2** catalyzed by *N*-iodosuccinimide and triflic acid gave a good yield of the succinimide derivative of the glycosyl donor. Such products have been observed previously when active glycosyl donors were reacted with inactive glycosyl acceptors in the presence of succinimide (16). Catalysis of the reaction of **1** and **2** by dimethyl(methylthio)sulfonium triflate (DMTST) (17, 18), a cationic catalyst with a non-nucleophilic counterion, yielded the expected disaccharide **3** in 73% yield. The *N*-acetyl analogs of **3** and **4**, compounds **5** and **6**, respectively, were obtained by removal of the phthalimide group from **4** with ethylenediamine, *N*-acetylation to give **5**, then de-*O*-benzylidenation with aqueous sulphuric acid to give **6**. Methyl 2,3,4-tri-*O*-benzyl- $\alpha$ -L-fucopyranoside (**7**) was ob-

tained from **1** by reaction with methanol and iodine (19). These latter three compounds were prepared in order to discover which interactions were critical in determining the conformations that caused the unusual chemical shift for the benzyl proton of **4** (Scheme 1).

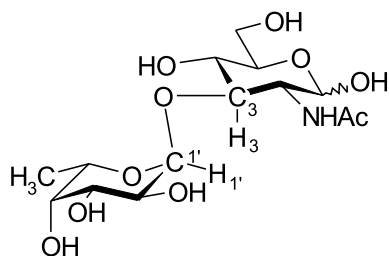
#### NMR spectroscopy and conformational analysis

Conformations about glycosidic bonds are discussed in terms of the  $\Phi$  and  $\Psi$  angles, defined as shown in Scheme 2 (20). In the following discussion, protons on the fucosyl residue are indicated by following the ring position by F, e.g., H1F is the fucosyl anomeric proton, while those on the *N*-acetylglucosaminyl residue are indicated by a following G. NMR chemical shifts of the compounds discussed are shown in Table 1, while details of the calculations and the NOE results are listed in Table 2.

Adiabatic potential energy surfaces for  $\alpha$ -L-fucopyranosyl-(1 $\rightarrow$ 3)-2-acetamido-2-deoxy-D-glucopyranoside (**8**) derivatives



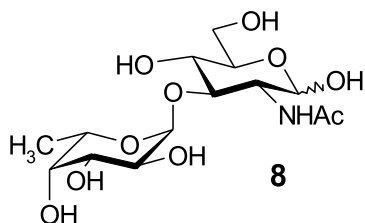
Scheme 2.



$$\Phi = \text{H1}'\text{-C1}'\text{-O-C3}$$

$$\Psi = \text{C1}'\text{-O-C3-H3}$$

have been explored previously using a variety of force fields (21, 22). The major low-energy region is centered in the so-called (23, 24) *syn*- $\Phi/\Psi$  energy region, where both  $\Phi$  and  $\Psi$  have absolute values  $<60^\circ$ . For **3** and **4**, MM3\* calculations indicate that the global minimum is located in the *syn*- $\Phi/\Psi$  region and has dihedral angles of ca.  $\Phi = 32^\circ$  and  $\Psi = -52^\circ$  (see Table 2). A second minimum was also found for **3** and **4** with positive  $\Psi$  angles, with  $\Phi$  ca.  $65^\circ$  and  $\Psi$  ca.  $40^\circ$  — about 9 kJ mol $^{-1}$  higher in energy than the global minimum. Obviously, low-amplitude motions around both glycosidic linkages may take place, as commonly found for oligosaccharide molecules. The computed  $\Phi/\Psi$  values are in agreement with those reported for the natural deprotected disaccharide **8** and its thioanalogue (22). However, for **8**, the  $\Psi$ -positive conformer was



calculated (22) to be more stable by about 3 kJ mol $^{-1}$ , the reverse of the preferences calculated for **3** and **4**.  $\Psi$ -positive conformers are also calculated (25, 26) and observed (25) to be more stable for the  $\alpha$ -L-fucopyranosyl linkage to O-3 of *N*-acetyl-D-glucosamine in Le $^x$ . Both conformers have  $\Phi$  values in the +*syn* region, in agreement with expectations based on the exo-anomeric effect (20). For **3** and **4**, the calculations indicate that the *anti* minima were, respectively, 24 and 31 kJ mol $^{-1}$  less stable than the global minimum, in contrast to those for **8** (22), where it was only 10 kJ mol $^{-1}$  less stable than the global minimum.

Analysis of the key structural factors present in both minima for **3** and **4** was performed. For the global minimum ( $\Psi$  negative), it is evident that the aromatic rings of the phthalimide moiety and the benzyl group at position C-2' are perfectly stacked (see Fig. 1). Short interresidue proton-proton distances between H1F-H3G (2.3 Å), H5F-H4G (2.5 Å), H6F-OH4G (2.7 Å), and H1F-OH4G (2.7 Å) are predicted for **4** (see Table 2). In addition, for **4**, a short distance was calculated between the hydroxyl hydrogen OH4G and O5F (2.7 Å), which suggests that a hydrogen bond may exist between them.

For the  $\Psi$ -positive minimum, the  $\pi$ -stacking between the phthalimide moiety and the benzyl group at position O2F disappears with a concomitant change in the interproton distances. The short interresidue distances from the global minimum conformer are calculated to be longer in this conformer of **4**: H1F-H3G is 3.0 Å; H5F-H4G is 4.0 Å; H6F-OH4G is 4.7 Å; and H1F-OH4G is 4.8 Å; and the two hydrogen atoms in the potentially hydrogen-bonded pair OH4G-O5F are now far apart (4.1 Å). In this conformer, the short interproton distances are H5F-H3G (2.5 Å) and H5F-OH4G (2.6 Å). As mentioned above, the calculated relative energy difference between the minima amounts to 10 kJ mol $^{-1}$ . This difference in stability results in the prediction that the population of the  $\Psi$ -positive minimum will be negligible.

NMR spectral data for **4** were recorded and scrutinized to assess the possible existence of both conformers (or conformational families). The most striking feature was the doublet in the spectrum of **4** due to an unusually shielded benzyl proton, which sparked this investigation (see Table 1); it was assigned to the O2F benzyl group through HMBC and NOESY experiments. This shielded position indicated that this benzylic proton is in the vicinity of an aromatic moiety. Obviously, this moiety could correspond to its vicinal OBn moiety at position C3F or to the interresidue phthalimide ring attached to C2G. The observation of normal chemical shifts for the benzyl groups of methyl 2,3,4-tri-*O*-benzyl- $\alpha$ -L-fucopyranoside (**7**) suggests that the vicinal OBn moiety at position C3F is not responsible for the shielding. As will be shown below, by using non-aromatic substituents at C2G, this latter hypothesis is valid.

Relevant interproton NOEs were observed for **4** (see Table 2). Thus, the methyl group of the Fuc residue gives an NOE to OH4G (see Fig. 2), and the H1F gives NOEs to H3G and to OH4G. These NOEs are consistent with the existence of a major conformation in the negative  $\Psi$  area, as predicted by the calculations. There was a peak that could also correspond to the fourth expected NOE, according to the short distances explained above, H5F-H4G, but the signal of H5F overlaps with the more deshielded of the benzylic protons at O2F and that of H4G overlaps with that of the other O2F benzylic proton (see Figs. 2 and 3), and the geminal O2F benzylic protons must have a large NOE. No NOEs were observed for H5F-H3G and H5-OH4G, consistent with the predicted negligible contribution from conformers around the positive  $\Psi$  area. The presence of the intramolecular O4G-H...O5F hydrogen bond was indirectly deduced from the appearance of the OH signal. This resonance is an unusually deshielded, slightly broadened signal (4.3 ppm) with a vicinal coupling smaller than 1.5 Hz. Therefore, the hydroxyl proton adopts a particular orientation with respect to its vicinal H4G and does not freely rotate in solution. Otherwise, a medium-size coupling of ca. 5–7 Hz would have been expected. This particular orientation may be due to its involvement in an intramolecular hydrogen bond to O5F, as deduced from the calculations.

In the  $^1\text{H}$  NMR spectrum of the 4,6-*O*-benzylidene derivative of **4**, compound **3**, a single benzyl proton (assigned to the 2-*O*-benzyl group) is again markedly shielded (3.84 ppm). This indicates that **3** also prefers  $\Psi$ -negative conformers, although probably not to the same extent as for **4**. The fucose methyl group was also shielded, appearing at 0.87 ppm,



**Table 1.** NMR spectral parameters for benzyl groups in chloroform-*d*.

Compound	C-2 OCH <sub>2</sub> Ph			C-3 OCH <sub>2</sub> Ph			C-4 OCH <sub>2</sub> Ph		
	$\delta_{\text{HA}}$	$\delta_{\text{HB}}$	$J_{\text{A,B}}$	$\delta_{\text{HA}}$	$\delta_{\text{HB}}$	$J_{\text{A,B}}$	$\delta_{\text{HA}}$	$\delta_{\text{HB}}$	$J_{\text{A,B}}$
<b>1</b>	4.73	4.79	10.3	4.732	4.745	12.0	4.67	5.01	11.6
<b>7</b>	4.69	4.82	12.1	4.73	4.87	11.9	4.65	4.98	11.6
<b>3</b>	3.84	4.26	12.6	4.38	4.43	11.6	4.49	4.79	11.6
<b>4</b>	3.38	4.13	13.0	4.64	4.84	11.5	4.55	4.89	11.4
<b>5</b>	4.61	4.93	11.5	4.75	4.75	— <sup>a</sup>	4.56	4.93	11.5
<b>6</b>	4.64	4.84	11.5	4.75	4.78	12.6	4.62	4.96	11.5

<sup>a</sup>Chemical shift difference too small to measure  $J_{\text{A,B}}$ .

compared to a shift of 1.11 ppm for the methyl of  $\alpha$ -L-fucopyranose (11), presumably because it is in the shielding cone of the benzylidene phenyl (see Fig. 1). In this case, the MM3\* calculations indicate again that the  $\Psi$ -negative region contains the global minimum, while the  $\Psi$ -positive and *anti* conformers are less stable by 8.6 and 23.9 kJ mol<sup>-1</sup>, respectively (see Table 2).

As a further step, the existence and importance of the  $\pi$ -stacking interaction between both aromatic rings located at the different GlcN and Fuc moieties was explored. Thus, the GlcNAc-containing analogs of compounds **3** and **4** were studied — disaccharides **5** and **6**, respectively. The molecular mechanics calculations on **5** and **6** also predict the occurrence of conformers with negative and positive  $\Psi$  values (see Table 2). However, in contrast with results of the MM3\* calculations for **4**, the energy preference for the  $\Psi$ -negative conformer is calculated to be much less, ca. 3 kJ mol<sup>-1</sup> for the unprotected derivative **6** and only 1 kJ mol<sup>-1</sup> for compound **5**. The *anti* conformers are also destabilized to a lesser extent, 14.1 and 12.8 kJ mol<sup>-1</sup> for **5** and **6** with respect to the global minima, respectively, but are still too energetic to contribute perceptibly to the conformational mixture. These relatively smaller values, in comparison to those of **3** and **4**, are probably owing to the significant stabilization provided by the Ar–Ar interaction in the phthalimide-containing molecules. Therefore, for both **5** and **6**, significant populations of the  $\Psi$ -positive conformers are calculated to be present in equilibrium mixtures in which the  $\Psi$ -negative conformers are most populated. The local minimum geometries in this area have  $\Phi/\Psi$  62°/43° for the unprotected derivative **6** and slightly different values,  $\Phi/\Psi$  45°/17°, for the benzylidene analogue **5**. For both compounds, the  $\Phi/\Psi$  values and the corresponding geometrical features in the  $\Psi$ -negative region are basically identical to those described above for **4** ( $\Phi/\Psi$  30°/–50°). In both cases, interactions between the aromatic rings of the 2-*O*-benzyl groups of the Fuc moieties and the methyl groups of the acetamide units of the GlcNAc residues are evident. The H1F–HNac distance is greater than 4 Å.

The expected distances for the secondary  $\Psi$ -positive minimum of the non-benzylidenated derivative **6** are analogous to those described above. One additional interresidue contact does appear: H1F–HNac (2.5 Å). Some changes in the distances take place for the benzylidene analogue **5**: H1F–H3G (2.4 Å); H5F–H4G (3.6 Å); H5F–H3G (3.4 Å); and H1F–HNac (2.5 Å).

In the <sup>1</sup>H NMR spectrum of the unprotected analogue **6**, the 2-*O*-benzylic protons of the Fuc residue have normal

chemical shifts, similar to those observed for the other CH<sub>2</sub> protons of the benzyl groups at positions 3 and 4 and very similar to those of the monosaccharide **7**. However, the methyl group of the acetamide unit is strongly shielded (1.61 ppm), in contrast with the chemical shift of 2.02 ppm for the acetamido methyl of phenyl 2-acetamido-2-deoxy-1-thio- $\beta$ -D-glucopyranoside, the related monosaccharide (**27**). These features provide evidence about two points, namely that the phthalimide moieties of **3** and **4** are  $\pi$ -stacked with the fucose O2 benzyl groups and that a conformer with an analogous Me–aromatic interaction is present for **6**. The NOESY experiments showed the presence of the short H1F–H3G, H5F–H4G, and H1F–OH4G distances, as expected for the presence of the negative  $\Psi$  conformer. However, additional crosspeaks appear in the spectrum that cannot be explained by the exclusive presence of conformers from the negative  $\Psi$  area. These are H5F–H3G and H1F–HNG NOEs that can only take place when conformers with positive  $\Psi$  values coexist in the conformational mixture.

Similar observations were made for the benzylidene derivative **5**. The acetamide methyl group was shielded (1.66 ppm), as was the methyl group of the fucose moiety (0.83 ppm), indicating the presence of conformers having interactions of these methyl groups with aromatic moieties. H1F–HNG and H1F–H3G NOEs were observed, indicating the presence of conformers in both positive and negative  $\Psi$  areas. The analysis of the geometry of the MM3\*-derived conformers indicate that the shielding of the methyl group of the fucose moiety is owing to the benzylidene unit of the GlcNAc moiety for both positive and negative  $\Psi$  angles, while that of the acetamide methyl group is owing to the 2-*O*-benzyl group of the Fuc unit only when  $\Psi$  adopts negative values.

In conclusion, a number of NMR observations assisted by MM3\* calculations have shown the importance of stacking interactions for the existence of conformational variations around the glycosidic torsion angles of oligosaccharides. It has been shown that the existence of  $\pi$ -stacking Ar–Ar interaction in the phthalimide derivatives (**3** and **4**) limits the populated conformers to the  $\Psi$ -negative region of the complete  $\Phi/\Psi$  map. In comparison with the unsubstituted disaccharide (**22**), this is a change of about 13 kJ mol<sup>-1</sup>. The stabilization provided by  $\pi$ -stacking of benzene rings is about 10  $\pm$  5 kJ mol<sup>-1</sup> (28–31), similar in magnitude to this change. The change of the phthalimide unit to an acetamide shifts the conformational equilibrium in a way that the positive  $\Psi$  area starts to be populated. Although an Me–Ar interaction is still evident and stabilizes the negative  $\Psi$  area, the removal of the Ar–Ar interaction changes the conform-



**Table 2.** Glycosidic torsional angles,<sup>a</sup> relative steric energy values,<sup>b</sup> and key interproton distances<sup>c</sup> for the three lowest-energy minima of compounds **3–6**.

Compound	Minimum ( $\Phi/\Psi$ ) <sup>a</sup>	$\Delta E$ (kJ mol <sup>-1</sup> )	H1F-H2G (Å)	H1F-H3G (Å)	H1F-H4G (Å)	H5F-H3G (Å)	H5F-H4G (Å)	H6F-OH4G (Å)	H1F-OH4G (Å)	H1F-HN (Å)
<b>3</b>	31/-51	0	4.4	2.4	3.8	4.3	2.6	—	—	—
	65/38	8.6	3.3	2.9	4.5	2.6	3.9	—	—	—
	23/172	23.9	2.3	3.7	2.2	3.7	5.0	—	—	—
	33/-52	0	4.5	<b>2.3</b>	3.8	4.3	<b>2.5</b>	2.7	2.7	—
	66/44	9.4	3.2	3.0	4.4	2.5	4.0	4.7	4.8	—
<b>4</b>	49/-150	30.7	3.5	3.5	2.1	4.1	2.6	6.7	3.0	—
	EXP		no	s	no	no	m	m	m	—
	NOE									
	29/-51	0.0	4.3	<b>2.3</b>	3.8	4.3	<b>2.7</b>	—	—	4.6
	45/17	0.8	3.7	<b>2.4</b>	4.5	3.4	3.6	—	—	<b>2.5</b>
<b>5</b>	28/178	14.1	2.5	3.7	2.0	3.8	5.0	—	—	4.5
	EXP		no	s	no	no	m	—	—	m
	NOE									
	31/-52	0.0	4.4	<b>2.3</b>	3.8	4.3	<b>2.6</b>	2.8	2.7	4.6
	62/43	3.4	3.2	3.0	4.4	<b>2.6</b>	4.0	4.7	4.8	<b>2.5</b>
<b>6</b>	23/173	12.8	2.3	3.7	2.1	3.7	5.0	8.0	4.3	4.4
	EXP		no	s	no	w	m	m	m	w
	NOE									
	31/-52	0.0	4.4	<b>2.3</b>	3.8	4.3	<b>2.6</b>	2.8	2.7	4.6
	62/43	3.4	3.2	3.0	4.4	<b>2.6</b>	4.0	4.7	4.8	<b>2.5</b>

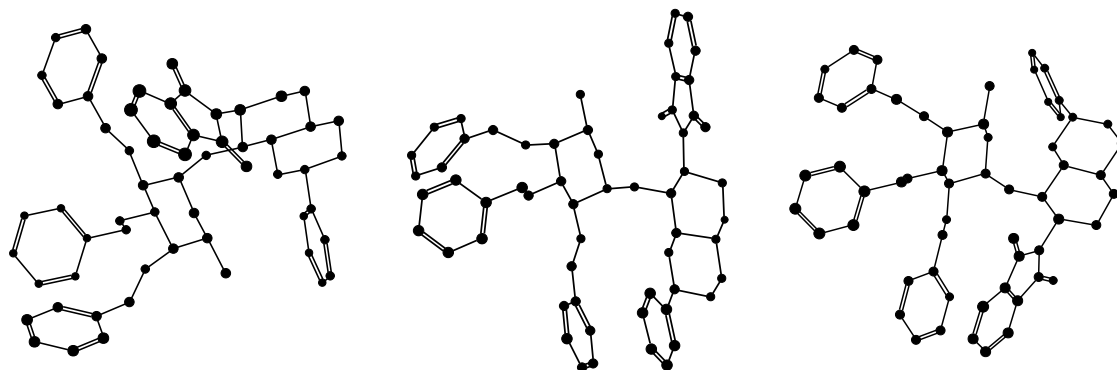
<sup>a</sup>Estimated by the MM3\* force field and the GB/SA solvent model for water. Values of  $\Phi/\Psi$  are approximate and may oscillate  $\pm 10^\circ$  between the GB/SA and the  $\epsilon = 80$  values, and the gg and gt rotamers of the hydroxymethyl group of the G moiety of **4** and **6**.

<sup>b</sup>Energy difference values vary less than 4 kJ mol<sup>-1</sup> between the GB/SA and the  $\epsilon = 80$  values, and between the gg and gt rotamers of the hydroxymethyl group of the G moiety of **4** and **6**.

<sup>c</sup>The expected distances, which are in agreement with the observed NOEs (given as experimental distances, EXP), are in bold. Experimental NOEs are given as strong (s), medium (m), weak (w), and not observed (no).



**Fig. 1.** From the left, positive, *anti*, and negative  $\Psi$  conformers of compound **3**. The more important stacking interactions take place in the negative  $\Psi$  conformer, although the positive  $\Psi$  conformer also shows a less energetically relevant 6-Me–benzylidene interaction. The conformers of compound **4** are similar. Torsion angle values and energies are given in Table 2.



ational distribution towards the “natural” one (more positive than negative) (22). The inclusion of a 4,6-*O*-benzylidene group on the GlcNAc moiety further shifts the equilibrium towards the positive  $\Psi$  area, possibly attributable to an additional stabilizing Me–Ar interaction, which is stronger for conformations within this region. Although the MM3\* force field used in this work only uses van der Waals interactions to model the Me–Ar or the Ar–Ar interactions, it provides models that satisfactorily explain the experimental observations.

The fact that a shift in conformational population to the negative  $\Psi$  area occurs on introducing benzyl substituents onto fucose provides experimental support for the conclusion, based on MM3\* calculations (22), that the potential energy surface for the natural disaccharide **8** contains a minimum in the negative  $\Psi$  area only slightly higher in energy than the global minimum.

## Experimental

### General methods

NMR spectra for synthetic purposes were recorded on Bruker AC-250 and Bruker AMX-400. The samples were made up in concentrations of approximately 10–15 mM in chloroform-*d* unless otherwise specified. Chemical shifts are given in parts per million (ppm) ( $\pm 0.01$  ppm) relative to TMS (tetramethylsilane) in the case of  $^1\text{H}$  NMR spectra and to the central line of  $\text{CDCl}_3$  ( $\delta$  77.16) for the  $^{13}\text{C}$  NMR spectra.  $^1\text{H}$  chemical shifts and coupling constants were obtained by first-order analyses. NMR experiments for conformational studies were recorded on Varian Unity 500 and Bruker DRX-500 spectrometers, using an approximately 5 mg mL $^{-1}$  solution of the disaccharides at different temperatures. Chemical shifts are reported in ppm, using external TMS (0 ppm) as references.  $\text{CDCl}_3$  and  $(\text{CD}_3)_2\text{CO}$  were used as solvents. The COSY spectra were performed with a data matrix of 256 \* 1K to digitize a spectral width of 4000 Hz. 16 scans were used with a relaxation delay of 1 s. The 2D TOCSY experiments were performed using a data matrix of 256 \* 2K to digitize a spectral width of 4000 Hz; 8 scans were used per increment with a relaxation delay of 2 s. MLEV 17 was used for the 70 ms isotropic mixing time. The one-bond proton–carbon correlation experiment was collected in the  $^1\text{H}$ -detection mode using the HSQC gradient-

enhanced sequence and an inverse probe. A data matrix of 256 \* 2K was used to digitize a spectral width of 4000 Hz in  $F_2$  and 15 000 Hz in  $F_1$ . Eight scans were used per increment with a relaxation delay of 1 s and a delay corresponding to a  $J$  value of 145 Hz.  $^{13}\text{C}$  decoupling was achieved by the WALTZ scheme. HMBC experiments were recorded using the gradient-enhanced sequence; 16 scans were used per increment (256), adjusting the long-range coupling evolution delay for values of  $J = 3, 4, 6, 8, 10$ , and 12 Hz. 2D NOESY and 2D-T-ROESY (32) experiments were performed with the standard sequences and with 600 ms of mixing time. Data matrices of 256 \* 2K were employed. The exact masses of compounds **1** and **2** were measured on a CEC 21–110B mass spectrometer using electron ionization (70 eV). The others were measured on a Micromass ZAB mass spectrometer at the University of Alberta using electrospray ionization. Thin layer chromatography was performed on 0.25-mm thick Whatman G/UV and Silicycle silica gel aluminum plates. Components were visualized by spraying with a 2% ceric sulfate solution in 1 M  $\text{H}_2\text{SO}_4$ , followed by heating on a hot plate until coloured spots formed. They were purified by flash chromatography on TLC standard grade (230–400 mesh) silica gel using mixtures of hexanes and ethyl acetate as eluents unless otherwise specified. Melting points were determined with a Fisher-Johns melting point apparatus and are uncorrected. Optical rotations were measured on a Digi-Pol model 781 polarimeter.

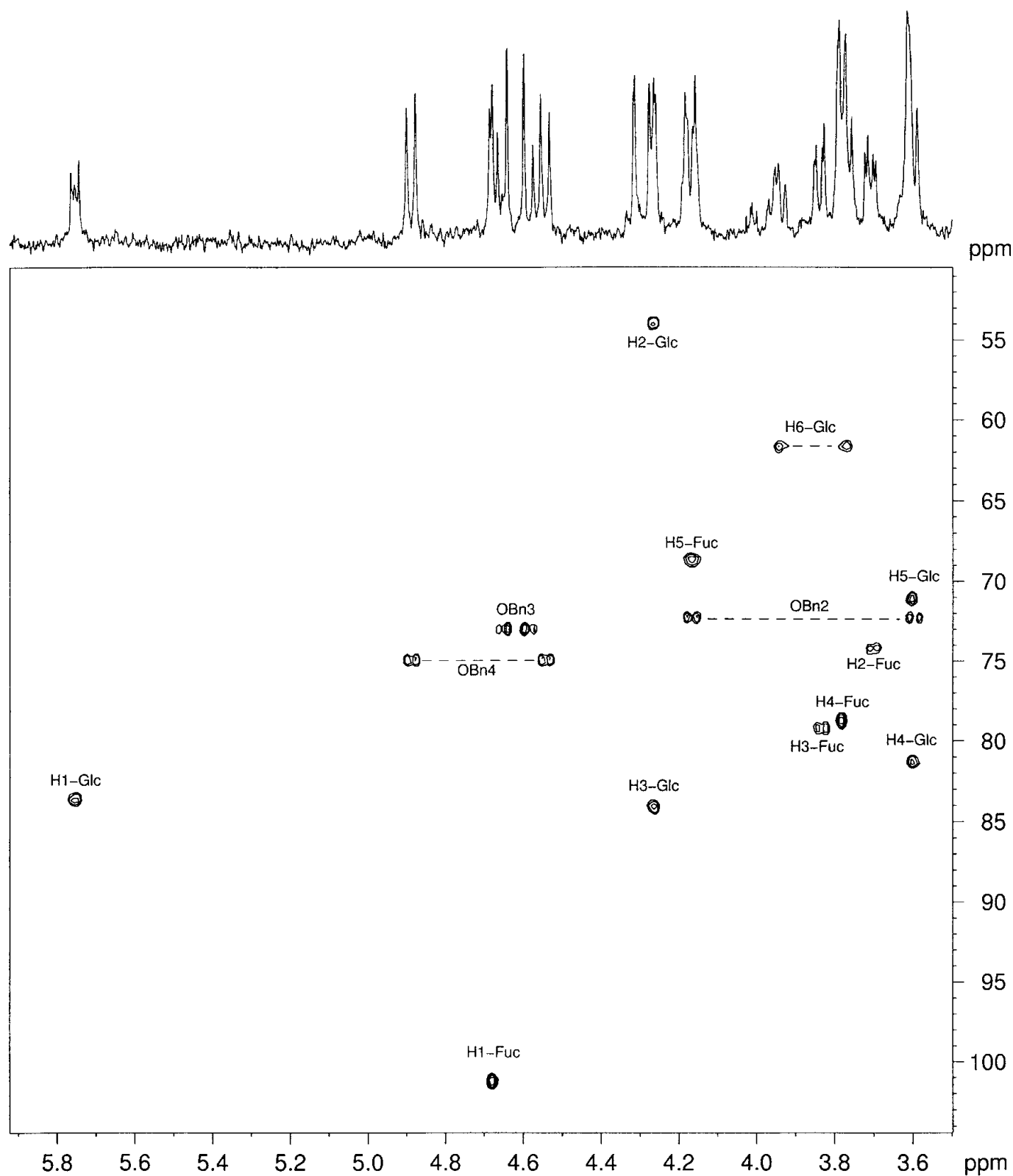
Pyridine was dried by reflux and distillation over calcium hydride. Dry methanol was obtained by distillation from magnesium turnings activated by iodine. *N,N*-Dimethylformamide was dried by distillation under reduced pressure from 4 Å molecular sieves onto fresh 4 Å molecular sieves. Toluene was stored over calcium hydride for 3 h and distilled onto 4 Å molecular sieves. Dichloromethane was distilled from calcium hydride and stored over 4 Å molecular sieves. All organic extracts were dried with anhydrous  $\text{MgSO}_4$ .

### Molecular mechanics calculations

Molecular mechanics calculations were performed using the MM3\* force field as implemented in MACROMODEL 4.5 (33). The MM3\* force field implemented in MACROMODEL differs from the original MM3 force field (34) in the treatment of the electrostatic term since it uses charge–charge instead of dipole–dipole interactions. Atoms from the



**Fig. 2.** Part of the 500 MHz NOESY spectrum of phenyl 2,3,4-tri-*O*-benzyl- $\alpha$ -L-fucopyranosyl-(1 $\rightarrow$ 3)-2 deoxy-2-phthalimido-1-thio- $\beta$ -D-glucopyranoside (**4**).

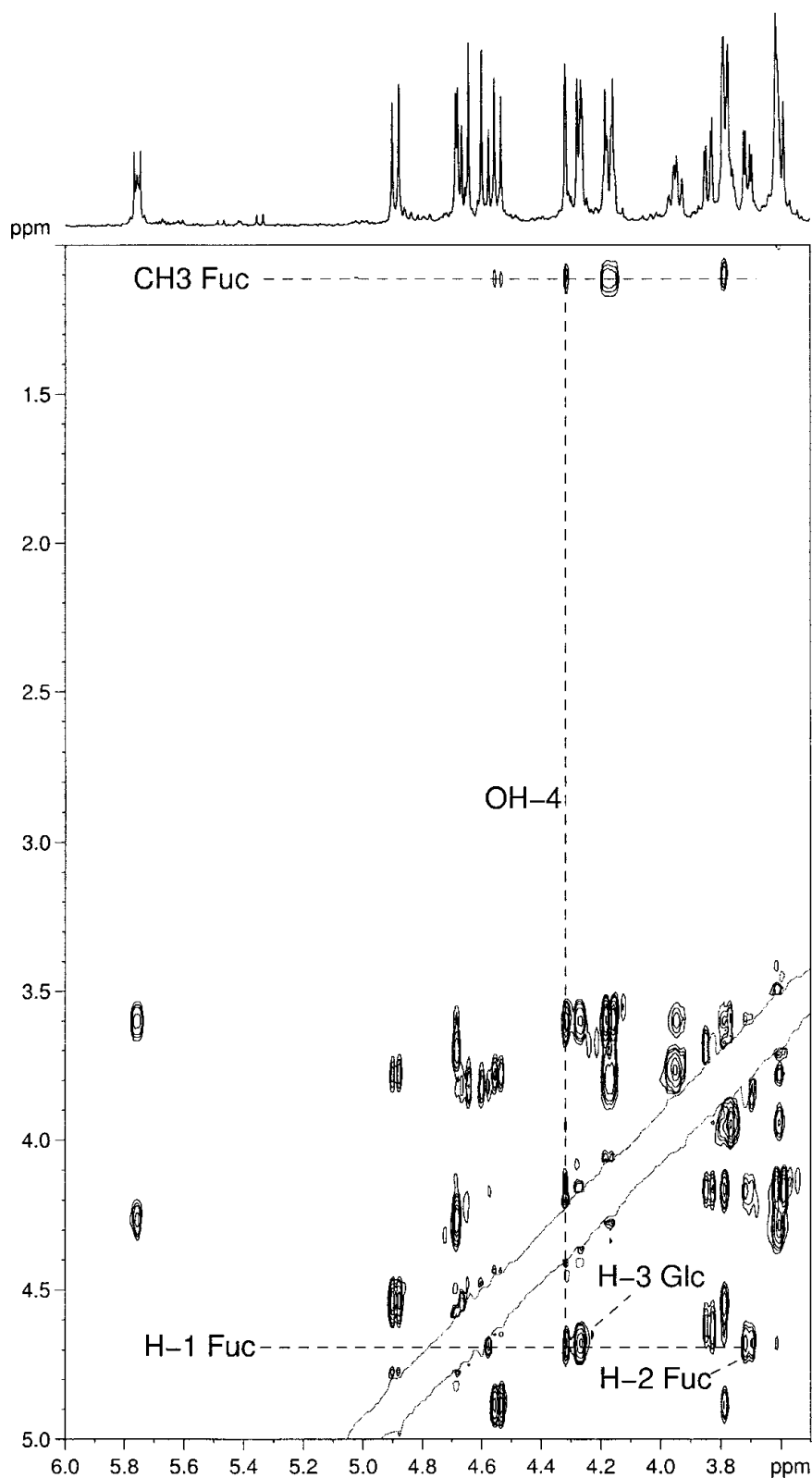


non-reducing monosaccharide are dubbed F and those of the reducing one, G. The torsional angle  $\Phi$  across the disacchar-

ide linkage is defined as  $H1F-C1F-O-C3G$  and  $\Psi$  as  $C1F-O-C3F-H3F$ .



**Fig. 3.** Part of the 500 MHz HSQC spectrum of phenyl 2,3,4-tri-*O*-benzyl- $\alpha$ -L-fucopyranosyl-(1 $\rightarrow$ 3)-2-deoxy-2-phthalimido-1-thio- $\beta$ -D-glucopyranoside (**4**).



MM3\* calculations either in vacuo or with the GB/SA solvent model for chloroform were performed. The minimizations were performed using 10 000 conjugate gradient iterations until

the rms derivative was better than  $0.03 \text{ kJ } \text{\AA}^{-1} \text{ mol}^{-1}$ . Eighteen different combinations of geometries of **4** and **6**, corresponding to the combination of the nine possible staggered rotamers



around  $\Phi/\Psi$  with the two major rotamers around C5–C6 (gg and gt) of the reducing end were built and submitted to energy minimizations under both dielectric conditions. For **5**, only the nine possible rotamers around  $\Phi/\Psi$  were considered. The S-phenyl group was set at a  $\Phi$  value of  $-60^\circ$ , in agreement with an exo-anomeric orientation (H1G-C1G-S-CPh). The phthalimide and the benzyl groups were set at positions where steric interactions with their corresponding rings were minimized and let free during the minimization process, after several trials with the corresponding monosaccharides. In particular, the starting position of the phthalimide group defined as H2G-C2G-N-CO was given an initial value of  $30^\circ$  and H2G-C2G-N-CO' was started at  $-150^\circ$ . For the 2-*O*-benzyl group, the starting orientation H2F-C2F-O-CH<sub>2</sub> was given a value of  $60^\circ$  and C2F-O-CH<sub>2</sub>-CPh was started in an *anti* arrangement. For the 3-*O*-benzyl group, the starting orientation H3F-C3F-O-CH<sub>2</sub> was  $60^\circ$  and C3F-O-CH<sub>2</sub>-CPh was also oriented *anti*. For the 4-*O*-benzyl group, the starting orientation H4F-C4F-O-CH<sub>2</sub> was  $-60^\circ$  and C4F-O-CH<sub>2</sub>-CPh was again *anti*. Depending on the compound, displacements of these groups from the original positions were found during the energy minimization steps, particularly for the 2-*O*-benzyl group. The HO-4 hydroxyl group of compounds **4** and **6** was set with a torsion angle (H-C-O-H) of  $60^\circ$ , pointing away from the glycosidic linkage and let free during the minimization process. From the  $\Phi/\Psi$  viewpoint, and for all of **3–6**, three conformers were always the most preferred ones: those with exo-anomeric orientations for the  $\Phi$  angle of F, combined with the three possible  $\Psi_+$ ,  $\Psi_-$ , and  $\Psi_{anti}$  orientations. In all cases, the  $\Psi_{anti}$  conformers displayed the highest energy values, in agreement with the experimental NOE results (see text). The non-anomeric ( $\Phi$  ca.  $-60^\circ$ ) starting conformers were not local minima and converged to the exo-anomeric region. The  $\Phi_{anti}$  conformers were stable, but highly destabilized (more than  $50 \text{ kJ mol}^{-1}$ ) with respect to the global minimum and were not considered for subsequent analysis. Values of  $\Phi/\Psi$  for the global and local minima oscillated  $\pm 10^\circ$  between the GB/SA and the  $\epsilon = 80$  values, and between the gg and gt rotamers of the hydroxymethyl group of the G moiety of **4** and **6**. Additionally, the relative steric energy values varied less than  $4 \text{ kJ mol}^{-1}$  between the GB/SA and the  $\epsilon = 80$  values, and between the gg and gt rotamers of the hydroxymethyl group of the G moiety of **4** and **6**. The most stable conformers, which agreed with the experimental NOEs, are depicted in the corresponding figures.

#### Phenyl 2,3,4-tri-*O*-benzyl-1-thio- $\beta$ -L-fucopyranoside (**1**)

A solution of phenyl 1-thio- $\beta$ -L-fucopyranoside (**12**) (1.00 g, 3.9 mmol) in DMF (30 mL) was cooled to  $0^\circ\text{C}$ . Sodium hydride (60% w/w oil suspension, 30 mmol) was added, and the mixture was allowed to stir for 30 min. Benzyl bromide (2.0 mL, 2.9 g, 17 mmol) was added, and the mixture was allowed to warm to room temperature, then stirred for a further 2 h. Methanol (1 mL) was added, and after 15 min, the mixture was concentrated under reduced pressure, then partitioned between ethyl acetate and water; the water layers were washed with ethyl acetate and discarded, and the combined ethyl acetate layers dried and concentrated. Recrystallization (ether–hexane) yielded colourless prisms (1.26 g, 61%); mp  $97\text{--}103^\circ\text{C}$  (lit. (**12**) mp  $107\text{--}109^\circ\text{C}$ );  $[\alpha]_D -7.0$  (*c* 1.58, CHCl<sub>3</sub>), (lit. (**12**)  $[\alpha]_D -14.0$  (*c* 0.7, CHCl<sub>3</sub>)). <sup>1</sup>H NMR (400.14 MHz, CDCl<sub>3</sub>)  $\delta$ : 1.27 (d, 3H,  $J_{5,6} = 6.4 \text{ Hz}$ , 3 H-6),

3.53 (dq, 1H,  $J_{5,6} = 6.4 \text{ Hz}$ ,  $J_{4,5} = 0.9 \text{ Hz}$ , H-5), 3.59 (dd, 1H,  $J_{3,4} = 2.8 \text{ Hz}$ ,  $J_{2,3} = 9.2 \text{ Hz}$ , H-3), 3.63 (dd, 1H,  $J_{4,5} = 0.9 \text{ Hz}$ ,  $J_{3,4} = 2.8 \text{ Hz}$ , H-4), 4.60 (d, 1H,  $J_{1,2} = 9.6 \text{ Hz}$ , H-1), 4.67 (d, 1H,  $J = 11.6 \text{ Hz}$ , 1 H of -CH<sub>2</sub>Bn on O-3), 4.73 and 4.79 (2 d (leaning), 2H,  $J = 10.2 \text{ Hz}$ , -CH<sub>2</sub>Bn on O-2), 4.74 (s with second-order side peaks, 2H, -CH<sub>2</sub>Bn on O-4), 5.01 (d, 1H,  $J = 11.5 \text{ Hz}$ , 1 H of -CH<sub>2</sub>Bn on O-3), 7.0–7.7 (m, 20H, 4 Ph). <sup>13</sup>C NMR (100.62 MHz, CDCl<sub>3</sub>)  $\delta$ : 17.43 (C6), 72.92 (CH<sub>2</sub> of 4-O Bn), 74.69 (C5 + CH<sub>2</sub> of 3-O Bn), 75.66 (CH<sub>2</sub> of 2-O Bn), 76.68 (C4), 77.19 (C2), 84.61 (C3), 87.60 (C1). EI-HR-MS calcd. for C<sub>33</sub>H<sub>34</sub>O<sub>4</sub>S ([M<sup>+</sup>]): 526.2178; found: 526.2178.

#### Phenyl 4,6-*O*-benzylidene-2-deoxy-2-phthalimido-1-thio- $\beta$ -D-glucopyranoside (**2**)

Anhydrous phenyl 2-deoxy-2-phthalimido-1-thio- $\beta$ -D-glucopyranoside (**13**) (31.1 g, 77.5 mmol) was dissolved in dry DMF (150 mL) in a 500-mL, round-bottomed flask. Benzaldehyde dimethyl acetal (12.3 g, 80.7 mmol) and *para*-toluenesulfonic acid hydrate (0.11 g, 0.58 mmol) were added. The solution was attached to a rotary evaporator, evacuated with a water aspirator, rotated, and lowered into a water bath at  $60 \pm 5^\circ\text{C}$ . After 140 min, another aliquot of benzaldehyde dimethyl acetal (10.1 g, 66.3 mmol) was added. After 220 min, about half the solvent was removed by reducing the pressure further with an oil pump, then a solution of NaHCO<sub>3</sub> (0.43 g) in water (50 mL) was added. A precipitate formed, and the mixture was concentrated to near-dryness. The reaction mixture was partitioned between dichloromethane (500 mL) and water (300 mL). The water layer was extracted with dichloromethane ( $3 \times 100 \text{ mL}$ ) and discarded. The combined organic layers were washed with water ( $2 \times 100 \text{ mL}$ ) and dried. These extractions were relatively difficult owing to the recurring formation of an emulsion layer. The organic layers were dried and concentrated, and the residue was purified by flash chromatography (5:2 Hex:EtOAc to 2:1 Hex:EtOAc), yielding **2** (30.2 g, 79.5%) as an amorphous solid:  $[\alpha]_D 35.0^\circ$  (*c* 2.04, CHCl<sub>3</sub>), lit. (**13**)  $[\alpha]_D 34.2^\circ$  (*c* 1.3, CHCl<sub>3</sub>). <sup>1</sup>H NMR (CDCl<sub>3</sub>)  $\delta$ : 2.84 (d, 1H,  $J_{\text{H-3,OH}} = 3.75 \text{ Hz}$ , OH), 3.54 (t, 1H,  $J_{3,4} \approx J_{4,5} = 9.2 \text{ Hz}$ , H-4), 3.63 (dt, 1H,  $J_{4,5} \approx J_{5,6\text{ax}} = 9.3 \text{ Hz}$ ,  $J_{5,6\text{eq}} = 4.6 \text{ Hz}$ , H-5), 3.78 (t, 1H,  $J_{6\text{ax},6\text{eq}} \approx J_{5,6} = 9.9 \text{ Hz}$ , H-6ax), 4.30 (t, 1H,  $J_{2,3} = J_{1,2} = 10.3 \text{ Hz}$ , H-2), 4.35 (dd, 1H,  $J_{5,6\text{eq}} = 4.5 \text{ Hz}$ ,  $J_{6\text{ax},6\text{eq}} = 10.2 \text{ Hz}$ , H-6eq), 4.59 (ddd, 1H,  $J_{\text{H3,OH}} = 3.8 \text{ Hz}$ ,  $J_{3,4} = 8.5 \text{ Hz}$ ,  $J_{2,3} = 9.9 \text{ Hz}$ , H-3), 5.53 (s, 1H, PhCH(O-)<sub>2</sub>), 5.65 (d, 1H,  $J_{1,2} = 10.5 \text{ Hz}$ ), 7.23–7.84 (m, 2 Ph + Phth). <sup>13</sup>C NMR (CDCl<sub>3</sub>)  $\delta$ : 55.6 (C-2), 68.6 (C-6), 69.7 (C-3), 70.3 (C-5), 81.9 (C-4), 84.3 (C-1), 102.0 (PhCH(OR)<sub>2</sub>). EI-HR-MS: calcd. for C<sub>27</sub>H<sub>23</sub>O<sub>6</sub>NS ([M<sup>+</sup>]): 489.1246; found: 489.1241.

#### First attempt to prepare phenyl 2,3,4-tri-*O*-benzyl- $\alpha$ -L-fucopyranosyl-(1 $\rightarrow$ 3)-4,6-*O*-benzylidene-2-deoxy-2-phthalimido-1-thio- $\beta$ -D-glucopyranoside (**3**)

Anhydrous compounds **1** (175 mg, 0.332 mmol) and **2** (115 mg, 0.236 mmol), along with *N*-iodosuccinimide (NIS, 85 mg, 0.378 mmol) and powdered 4 Å molecular sieves were placed in a 2-necked, round-bottomed flask, which was fitted with a rubber septum and an argon-filled balloon. The mixture was cooled to  $-40^\circ\text{C}$ , and dichloromethane (8 mL) was added via syringe. The stirred solution was allowed to warm up to  $-20^\circ\text{C}$  over 35 min, and triflic acid (0.3  $\mu\text{L}$ ,



0.5 mg, 0.0035 mmol) was added via syringe at 65 min. The cooling bath was removed after 100 min, and the reaction continued to stir and was monitored by TLC.

After 175 min, the reaction mixture was diluted with dichloromethane (10 mL) and filtered, then washed with saturated aqueous sodium bicarbonate (3 × 50 mL) and brine (50 mL), dried, and concentrated. The residue was purified by flash chromatography (4:1 to 2:1 Hex:EtOAc) to give *N*-(2,3,4-tri-*O*-benzyl-β-*L*-fucopyranosyl)succinimide as a syrup (132 mg, 77%). <sup>1</sup>H NMR (CDCl<sub>3</sub>) δ: 1.09 (d, *J*<sub>5,6</sub> = 6.4 Hz, 3 H-6), 2.55 (s, 2 CH<sub>2</sub> of succinimide), 3.71 (bd, *J*<sub>3,4</sub> = 2.6 Hz, H-4), 4.28 (bq, *J*<sub>5,6</sub> = 6.4 Hz, H-5), 4.49 (dd, *J*<sub>1,2</sub> = 7.5 Hz, *J*<sub>2,3</sub> = 9.8 Hz, H-2), 4.58 (dd, *J*<sub>2,3</sub> = 9.8 Hz, *J*<sub>3,4</sub> = 2.9 Hz, H-3), 4.48, 4.67 (2 leaning d, *J* = 11.7 Hz, CH<sub>2</sub>Bn), 4.66, 4.99 (2 leaning d, *J* = 11.6 Hz, CH<sub>2</sub>Bn), 4.76, 4.86 (2 leaning d, *J* = 11.8 Hz, CH<sub>2</sub>Bn), 6.13 (d, *J*<sub>1,2</sub> = 7.5 Hz, H-1), 7.25–7.33 (m, 3Ph). <sup>13</sup>C NMR (CDCl<sub>3</sub>) δ: 17.5 (C6), 28.3 (2 CH<sub>2</sub> of succinimide), 72.8 (C5), 73.3 (CH<sub>2</sub>Bn), 73.6 (CH<sub>2</sub>Bn), 74.9 (C2 + CH<sub>2</sub>Bn), 76.7 (C1), 77.7 (C4), 80.6 (C3), 127.6, 128.3, 128.4, 138.1, 138.6, 139.1 (aromatic), 178.0 (2 C=O of succinimide).

**Phenyl 2,3,4-tri-*O*-benzyl-α-*L*-fucopyranosyl-(1→3)-4,6-*O*-benzylidene-2-deoxy-2-phthalimido-1-thio-β-*D*-glucopyranoside (3)**

Anhydrous compounds **1** (670 mg, 1.28 mmol) and **2** (420 mg, 0.851 mmol) were dissolved in dichloromethane (40 mL) in a 2-necked, round-bottomed flask, which was fitted with a rubber septum and an argon-filled balloon. This solution was cooled to 0°C and a solution of dimethyl-(methylthio)sulfonium triflate (0.88 g, 3.4 mmol) in dichloromethane (40 mL) was added via syringe, with stirring. The reaction was monitored by TLC. After 1 h, the reaction was quenched by adding triethylamine (5 mL), then filtered through Celite. Dichloromethane (70 mL) was added, and the solution extracted with saturated aqueous sodium bicarbonate (2 × 100 mL) and water (100 mL), then dried and concentrated. The residue was separated by flash chromatography (5:1 hexanes: ethyl acetate) to give the title compound (0.47 g, 61%) plus a mixed fraction (0.18 g) in which **3** constituted 50%: total yield 0.56 g, 73%; [α]<sub>D</sub> 7.1° (c 2.04, CHCl<sub>3</sub>). <sup>1</sup>H NMR (400.13 MHz, CDCl<sub>3</sub>) δ: 0.87 (d, 3H, *J*<sub>5,6</sub> = 6.6 Hz, 3 H-6 Fuc), 3.47 (dd, 1H, *J*<sub>3,4</sub> = 2.37 Hz, *J*<sub>4,5</sub> = 1.27 Hz, H-4 Fuc), 3.66–3.76 (m, 4H, H-4 Glc, H-5 Glc, H-2 Fuc, H-3 Fuc), 3.83 (t, 1H, *J*<sub>5,6ax</sub> ≈ *J*<sub>6ax,6eq</sub> = 9.5 Hz, H-6ax Glc), 3.84, 4.26 (2 d, 2H, *J* = 12.6, CH<sub>2</sub>Ph), 4.04 (dq, 1H, *J*<sub>4,5</sub> = 1.1 Hz, *J*<sub>5,6</sub> = 6.6 Hz, H-5 Fuc), 4.38, 4.43 (2 d, 2H, *J* = 11.6 Hz, CH<sub>2</sub>Ph), 4.43 (dd, *J*<sub>1,2</sub> = 10.6 Hz, *J*<sub>2,3</sub> = 9.9 Hz, H-2 Glc), 4.43 (dd, 1H, H-6eq Glc), 4.49, 4.79 (2 d, 2H, *J* = 11.6 Hz, CH<sub>2</sub>Ph), 4.81 (d, 1H, *J*<sub>1,2</sub> = 2.9 Hz, H-1 Fuc), 5.55 (s, 1H, PhCH(OR)<sub>2</sub>), 5.74 (d, 1H, *J*<sub>1,2</sub> = 10.7 Hz, H-1 Glc), 7.0–7.8 (m, aromatics). <sup>13</sup>C NMR (100.62 MHz, CDCl<sub>3</sub>) δ: 16.57 (C6 Fuc), 54.98 (C4 Glc), 67.51 (C5 Fuc), 68.77 (C6 Glc), 70.79 (C5 Glc), 72.93 (CH<sub>2</sub>Bn), 73.29 (CH<sub>2</sub>Bn), 74.92 (CH<sub>2</sub>Bn), 75.84 (C4 Glc), 76.72 (C3 Glc), 78.28 (C4 Fuc), 79.83 (C2 Fuc), 82.12 (C3 Fuc), 84.45 (C1 Glc), 99.64 (C1 Fuc), 101.36 (PhCH(OR)<sub>2</sub>), 123.50, 126.30, 127.61, 127.66, 128.05, 128.28, 128.38, 128.40, 128.48, 128.57, 128.99, 129.15, 133.04, 134.06, 138.55 (aromatics), 167.76, 168.52 (2 C=O of phthalimide). HR-MS calcd. for C<sub>54</sub>H<sub>51</sub>NO<sub>10</sub>S + Na: 928.3131; found: 928.3130.

**Phenyl 2,3,4-tri-*O*-benzyl-α-*L*-fucopyranosyl-(1→3)-2-deoxy-2-phthalimido-1-thio-β-*D*-glucopyranoside (4)**

Compound **1** (473 mg, 0.955 mmol) was dissolved in dichloromethane (30 mL) in a 50-mL, round-bottomed flask fitted with a drying tube and a magnetic stirrer. The solution was cooled to –78°C using an ethyl acetate – liquid nitrogen slurry. *m*-Chloroperbenzoic acid (227 mg of 85% reagent, 1.12 mmol) was added to the stirring solution, and the reaction was monitored by TLC (eluent 2.5% acetone in CH<sub>2</sub>Cl<sub>2</sub>; *R*<sub>f</sub> sulfide = 0.92, *R*<sub>f</sub> sulfoxide = 0.51, 0.39 (*R* and *S* isomers), *R*<sub>f</sub> sulfone = 0.82). After 3.5 h, the reaction was allowed to warm up somewhat, then saturated aqueous sodium bicarbonate (15 mL) and dichloromethane (20 mL) were added. The aqueous layer was extracted with dichloromethane (2 × 20 mL). The combined organic layers were washed with water (30 mL), dried, and concentrated, yielding a residue that was purified by flash chromatography (2.5% acetone in CH<sub>2</sub>Cl<sub>2</sub>). The *R* and *S* isomers of phenyl 2,3,4-tri-*O*-benzyl-1-thio-α-*L*-fucopyranosyl sulfoxide (**1a**) were collected together and used for the next step.

Compounds **1a** (313 mg, 0.577 mmol) and **2** (200 mg, 0.408 mmol) were combined with 2,6-di-*tert*-butyl-4-methylpyridine (168 mg, 0.812 mmol) in a 2-necked, round-bottomed flask. One neck was stoppered and the mixture was azeotroped with toluene (3 × 10 mL), keeping the temperature low to avoid decomposition of the sulfoxide. The flask was fitted with a rubber septum and an argon-filled balloon. Dichloromethane (25 mL) was added by syringe, and the solution was cooled to –78°C using an ethyl acetate – liquid nitrogen slurry. To the cold, stirred solution was added triflic anhydride (0.08 mL, 130 mg, 0.45 mmol), dropwise, by syringe. Stirring was continued at –78°C, and the reaction was monitored by TLC. When the reaction neared completion, it was removed from the ethyl acetate slurry. The solution was extracted with saturated aqueous sodium bicarbonate (25 mL, 2 × 50 mL) and water (50 mL), then dried and concentrated. The residue was purified using flash chromatography (3:1 to 3:2 Hex:EtOAc). The main product was identified as phenyl 2,3,4-tri-*O*-benzyl-α-*L*-fucopyranosyl-(1→3)-2-deoxy-2-phthalimido-1-thio-β-*D*-glucopyranoside in 31% yield. <sup>1</sup>H NMR (500.13 MHz, CDCl<sub>3</sub>) δ: 1.09 (d, 3H, *J*<sub>5,6</sub> = 6.5 Hz, 3 H-6 Fuc), 3.38, 4.13 (2 leaning d, 2H, *J* = 13.0 Hz, –CH<sub>2</sub>Bn), 3.53 (dd, 1H, *J*<sub>3,4</sub> = 2.5 Hz, *J*<sub>4,5</sub> = 1.2 Hz, H-4 Fuc), 3.57 (bt, 1H, *J*<sub>3,4</sub> ≈ *J*<sub>4,5</sub> = 9.1 Hz, H-4 Glc), 3.64 (ddd, 1H, *J*<sub>5,6</sub> = 4.9 Hz, *J*<sub>5,6'</sub> = 3.4 Hz, *J*<sub>4,5</sub> = 8.3 Hz, H-5 Glc), 3.74 (dd, 1H, *J*<sub>1,2</sub> = 3.3 Hz, *J*<sub>2,3</sub> = 10.3 Hz, H-2 Fuc), 3.78 (dd, 1H, *J*<sub>2,3</sub> = 10.3 Hz, *J*<sub>3,4</sub> = 2.5 Hz, H-3 Fuc), 3.87 (dd, 1H, *J*<sub>5,6</sub> = 4.9 Hz, *J*<sub>6,6'</sub> = 11.8 Hz, H-6 Glc), 4.00 (dd, 1H, *J*<sub>5,6'</sub> = 3.4 Hz, *J*<sub>6,6'</sub> = 11.8 Hz, H-6' Glc), 4.07 (dq, 1H, *J*<sub>4,5</sub> = 1.0 Hz, *J*<sub>5,6</sub> = 6.6 Hz, H-5 Fuc), 4.25 (dd, 1H, *J*<sub>2,3</sub> = 10.4 Hz, *J*<sub>3,4</sub> = 8.1 Hz, H-3 Glc), 4.33 (t, 1H, *J*<sub>1,2</sub> = *J*<sub>2,3</sub> = 10.3 Hz, H-2 Glc), 4.55, 4.89 (2 leaning d, 2H, *J* = 11.4 Hz, –CH<sub>2</sub>Bn), 4.56, 4.63 (2 leaning d, 2H, *J* = 11.8 Hz, –CH<sub>2</sub>Bn), 4.62 (d, 1H, *J*<sub>1,2</sub> = 3.3 Hz, H-1 Fuc), 5.78 (d, 1H, *J*<sub>1,2</sub> = 10.3 Hz, H-1 Glc), 6.9–7.9 (m, aromatics). <sup>13</sup>C NMR (62.9 MHz, CDCl<sub>3</sub>) δ: 16.58 (C6 Fuc), 53.67 (C2 Glc), 62.77 (C6 Glc), 68.70 (C5 Fuc), 71.66 (C4 Glc), 72.55 (CH<sub>2</sub>Bn), 73.54 (CH<sub>2</sub>Bn), 73.88 (C2 Fuc), 74.86 (CH<sub>2</sub>Bn), 77.92 (C4 Fuc), 79.01 (C3 Fuc), 79.40 (C5 Glc), 83.33 (C1 Glc), 84.03 (C3 Glc), 101.04 (C1 Fuc), 123.15, 123.33, 127.65, 127.74, 128.29, 128.38, 128.49, 128.56, 129.12, 132.88,



133.90, 138.16, 138.36, 138.81 (aromatics), 167.80, 168.76 (2 C=O of phthalimide). HR-MS calcd. for  $C_{47}H_{47}NO_{10}S + Na$ : 840.2818; found: 840.2824.

**Phenyl 2,3,4-tri-*O*-benzyl- $\alpha$ -L-fucopyranosyl-(1 $\rightarrow$ 3)-2-acetamido-4,6-*O*-benzylidene-2-deoxy-1-thio- $\beta$ -D-glucopyranoside (5)**

To a stirred solution of **3** (0.43 g, 0.47 mmol) in anhydrous 1-butanol (80 mL) was added ethylenediamine (15 mL, 13.5 g, 220 mmol). Argon was bubbled through the solution and stirring continued for 5.5 h, monitoring the reaction by TLC with a ninhydrin spray reagent (0.25% in ethanol). The mixture was then evaporated to dryness. Toluene (2  $\times$  25 mL) and ethanol (25 mL) were in turn added and evaporated. To the residue was added methanol (60 mL), resulting in a heterogeneous mixture, which dissolved upon addition of triethylamine (1 mL, 7.2 mmol) and acetic anhydride (8 mL, 85 mmol) with stirring. After continued stirring for 19 h, the reaction was added to 250 mL ice water, which melted and was extracted with dichloromethane (3  $\times$  100 mL). The organic layers were dried and concentrated. Purification by flash chromatography yielded a white solid (0.22 g, 57%).  $^1H$  NMR (400.14 MHz,  $CDCl_3$ )  $\delta$ : 0.831 (d, 3H,  $J_{5,6}$  = 6.4 Hz, 3 H-6 Fuc), 1.659 (s, 3H, NAc), 3.5–3.65 (complex m, 4H, H-4 Fuc, H-2, H-4, H-5 Glc), 3.774 (t, 1H,  $J_{5,6ax}$  =  $J_{6ax,6eq}$  = 10.0 Hz, H-6ax Glc), 3.934 (dd,  $J_{2,3}$  = 10.1 Hz,  $J_{3,4}$  = 2.7 Hz, H-3 Fuc), 4.084 (dd, H-2 Fuc), 4.093 (br q, H-5 Fuc), 4.289 (br t,  $J_{2,3}$  =  $J_{3,4}$  = 9.0 Hz, H-3 Glc), 4.363 (dd,  $J_{5,6eq}$  = 4.5 Hz,  $J_{6ax,6eq}$  = 10.5 Hz, H-6eq), 4.562, 4.605 (2 d, 2H,  $J$  = 11.5, 2  $CH_2Ph$  H), 4.754 (s, 2H,  $CH_2Ph$ ), 4.931 (d, 2H,  $J$  = 11.5, 2  $CH_2Ph$  H), 5.102 (d, 1H,  $J_{1,2}$  = 3.5 Hz, H-1 Fuc), 5.193 (broad d, 1H,  $J_{1,2}$  = 10.4 Hz, H-1 Glc), 5.518 (s, 1H,  $O_2CHPh$ ), 5.741 (d, 1H,  $J_{1,2}$  = 7.7 Hz, NH), 7.2–7.6 (m, Ph H).  $^{13}C$  NMR (62.9 MHz,  $CDCl_3$ )  $\delta$ : 16.42 (C-6 Fuc), 23.53 ( $NCOCH_3$ ), 56.84 (C-2 Glc), 67.03 (C-5 Fuc), 68.79 (C-6 Glc), 70.64 (C-5 Glc), 72.67, 74.32, 75.04 (3  $OCH_2Ph$ ), 76.65 (C-3 Glc), 77.16 (C-2 Fuc), 77.55 (C-4 Fuc), 79.93 (C-3 Fuc), 80.64 (C-4 Glc), 86.70 (C-1 Glc), 98.39 (C-1 Fuc), 101.61 ( $O_2CHPh$ ), 126.3–129.0, 132.5 (PhCH), 137.3, 138.7 (quat C Ph), 170.6 (C=O). HR-MS calcd. for  $C_{48}H_{51}NO_9S + Na$ : 840.3182; found: 840.3188.

**Phenyl 2,3,4-tri-*O*-benzyl- $\alpha$ -L-fucopyranosyl-(1 $\rightarrow$ 3)-2-acetamido-2-deoxy-1-thio- $\beta$ -D-glucopyranoside (6)**

Compound **5** (0.13 g, 0.16 mmol) was dissolved in a solution of ethanol (150 mL) and water (1 mL). Sulfuric acid (0.18 g, 1.8 mmol) was added with stirring. The resulting solution was heated to reflux for 2 h, then cooled. Solid  $NaHCO_3$  (0.31 g, 3.7 mmol) was added and the solvent removed under reduced pressure. The residue was partitioned between water (100 mL) and  $CH_2Cl_2$  (100 mL) and the aqueous layer extracted with two further portions of  $CH_2Cl_2$  (100 mL each). Combined organic layers were dried and concentrated, and the product was purified by flash chromatography (2:1 to 1:1 hexanes:ethyl acetate) to yield a white solid (0.10 g, 86%).  $^1H$  NMR (250.13 MHz,  $CDCl_3$ )  $\delta$ : 1.155 (d, 3H,  $J_{5,6}$  = 6.6 Hz, 3 H-6 Fuc), 1.612 (s, 3H, NAc), 3.42 (complex m, H-5 Glc), 3.47 (t, 1H,  $J_{3,4}$  =  $J_{4,5}$  = 9.5 Hz, H-4 Glc), 3.58–3.73 (complex m, 3H, H-2, H-3 Glc, H-4 Fuc), 3.769 (dd, 1H,  $J_{5,6}$  = 4.7 Hz, H-6 Glc), 3.907 (dd,  $J_{5,6'}$  = 2.9 Hz,  $J_{6,6'}$  = 11.8 Hz, H-6' Glc), 3.932 (dd, 1H,  $J_{3,4}$  =

2.6 Hz,  $J_{2,3}$  = 10.2 Hz, H-3 Fuc), H-07–4.17 (complex m, H-2, H-5 Fuc), 4.618, 4.963 (2 d, 2H,  $J$  = 11.5 Hz,  $-CH_2Ph$ ), 4.750, 4.779 (AB quartet, 2H,  $J$  = 12.6 Hz,  $-CH_2Bn$ ), 4.636, 4.840 (2 d, 2H,  $J$  = 11.5,  $-CH_2Ph$ ), 4.946 (d, 1H,  $J_{1,2}$  = 3.2 Hz, H-1 Fuc), 5.056 (d, 1H,  $J_{1,2}$  = 9.4 Hz, H-1 Glc), 5.530 (d, 1H,  $J_{1,2}$  = 7.02 Hz, NH), 7.2–7.5 (m, aromatics).  $^{13}C$  NMR (100.62 MHz,  $CDCl_3$ )  $\delta$ : 16.88 (C-6 Fuc), 23.23 ( $NCOCH_3$ ), 54.55 (C-2 Glc), 63.00 (C-6 Glc), 68.63 (C-5 Fuc), 71.19 (C-4 Glc), 72.67, 74.32, 75.04 (3  $OCH_2Ph$ ), 76.65 (C-3 Glc), 76.48 (C-2 Fuc), 77.55 (C-4 Fuc), 79.33 (C-5 Glc), 79.39 (C-3 Fuc), 85.96 (C-3 Glc), 86.38 (C-1 Glc), 99.96 (C-1 Fuc), 127.9–129.2, 131.9 (PhCH), 133.66, 138.51, 138.45, 138.67 (quat C Ph), 171.16 (C=O). HR-MS calcd. for  $C_{41}H_{47}NO_9S + Na$ : 752.2869; found: 752.2877.

**Methyl 2,3,4-tri-*O*-benzyl- $\alpha$ -L-fucopyranoside (7)**

To a stirred solution of **1** (250 mg, 0.47 mmol) in dry methanol (2 mL) was added iodine (190 mg, 0.75 mmol). The flask was fitted with a silica gel drying tube and stirred for 4.5 h. Methanol (5 mL) and Rexyn 201 (OH) ion-exchange resin (4 mL) was added to the flask, and stirring was continued until the solution became virtually colorless. Filtration, concentration, and purification by flash chromatography yielded a syrup (150 mg, 70%).  $^1H$  NMR (400.14 MHz,  $CDCl_3$ )  $\delta$ : 1.114 (d, 3H,  $J_{5,6}$  = 6.6 Hz, 3 H-6 Fuc), 3.350 (s, 3H, OMe), 3.630 (dd, 1H,  $J_{3,4}$  = 2.8 Hz,  $J_{4,5}$  = 1.1 Hz, H-4), 3.828 (qd, 1H, H-5), 3.924 (dd, 1H,  $J_{2,3}$  = 10.1 Hz, H-3), 4.035 (dd, 1H,  $J_{1,2}$  = 3.7 Hz, H-2), 4.649, 4.978 (2 d, 2H,  $J$  = 11.6 Hz, C-4  $-OCH_2Ph$ ), 4.653 (d, 1H, H-1), 4.687, 4.821 (2d, 2H,  $J$  = 12.1 Hz, C-2  $-OCH_2Ph$ ), 4.730, 4.872 (2d, 2H,  $J$  = 11.9 Hz, C-3  $-OCH_2Ph$ ), 7.22–7.41 (m, Ph H).  $^{13}C$  NMR (62.9 MHz,  $CDCl_3$ )  $\delta$ : 16.63 (C-6), 55.31 (OMe), 66.08 (C-5), 73.36 (C3-  $OCH_2Ph$ ), 73.48 (C2-  $OCH_2Ph$ ), 74.83 (C4-  $OCH_2Ph$ ), 76.33 (C-2), 77.83 (C-4), 79.41 (C-3), 98.81 (C-1), 127.5–128.4 (PhC), 138.57 (C-2 quat PhC), 138.62 (C-4 quat PhC), 138.97 (C-3 quat PhC). HR-MS calcd. for  $C_{28}H_{32}O_5 + Na$ : 471.2147; found: 471.2147.

## Acknowledgments

JW thanks the Natural Sciences and Engineering Research Council of Canada (NSERC) for the award of an NSERC summer research assistantship. TBG is grateful to NSERC for a research grant and to the Atlantic Region Magnetic Resonance Centre for NMR time, and to Dr. Angelina Morales-Izquierdo at the University of Alberta for determining accurate masses. JJB thanks Direccion General de Investigacion Cientifica y Tecnica for financial support (BQU2000–1501-C02–01) and AP is grateful to Servicio Interdepartamental de Investigacion de la Universidad Autonoma de Madrid for the facilities provided.

## References

1. L. Poppe, G.S. Brown, J.S. Philo, P.V. Nikrad, and B.H. Shah. *J. Am. Chem. Soc.* **119**, 1727 (1997).
2. A. Poveda and J. Jiménez-Barbero. *Chem. Soc. Rev.* **27**, 133 (1998).
3. J. Jiménez-Barbero, J.L. Asensio, F.J. Cañada, and A. Poveda. *Curr. Opin. Struct. Biol.* **9**, 549 (1999).



4. R. Harris, G.R. Kiddle, R.A. Field, M.J. Milton, B. Ernst, J.L. Magnani, and S.W. Homans. *J. Am. Chem. Soc.* **121**, 2546 (1999).
5. J.F. Espinosa, F.J. Cañada, J.L. Asensio, H. Dietrich, M. Martín-Lomas, R.R. Schmidt, and J. Jiménez-Barbero. *Angew. Chem. Int. Ed. Eng.* **35**, 303 (1996).
6. J.F. Espinosa, E. Montero, A. Vian, J.L. Garcia, H. Dietrich, R.R. Schmidt, M. Martín-Lomas, A. Imberty, F.J. Cañada, and J. Jiménez-Barbero. *J. Am. Chem. Soc.* **120**, 1309 (1998).
7. M.J. Milton and D.R. Bundle. *J. Am. Chem. Soc.* **120**, 10 547 (1998).
8. T. Haselhorst, J.F. Espinosa, J. Jiménez-Barbero, T. Sokolowski, P. Kosma, H. Brade, L. Brade, and T. Peters. *Biochemistry*, **38**, 6449 (1999).
9. L.A. Lasky. *Science* (Washington, D.C.), **258**, 964 (1992).
10. D.S. Johnston, W.W. Wright, J.H. Shaper, C.H. Hokke, D.H. Van den Eijnden, and D.H. Joziassse. *J. Biol. Chem.* **273**, 1888 (1998).
11. K. Bock and H. Thøgersen. *Annu. Rep. NMR Spectrosc.* **13**, 1 (1982).
12. S. Komba, H. Ishida, M. Kiso, and A. Hasegawa. *Bioorg. Med. Chem.* **4**, 1833 (1996).
13. R.K. Jain and K.L. Matta. *Carbohydr. Res.* **226**, 91 (1992).
14. D. Kahne, S. Walker, Y. Cheng, and D. Van Engen. *J. Am. Chem. Soc.* **111**, 6881 (1989).
15. L. Yan and D. Kahne. *J. Am. Chem. Soc.* **118**, 9239 (1996).
16. Z. Zhang, I.R. Ollmann, X.-S. Ye, R. Wischnat, T. Baasov, and C.-H. Wong. *J. Am. Chem. Soc.* **121**, 734 (1999).
17. M. Ravenscroft, R.M.G. Roberts, and J.G. Tillett. *J. Chem. Soc., Perkin Trans. 2*, 1569 (1982).
18. F. Andersson, P. Fügedi, P.J. Garegg, and M.A. Nashed. *Tetrahedron Lett.* **27**, 3919 (1986).
19. K.P.R. Kartha, M. Aloui, and R.A. Field. *Tetrahedron Lett.* **37**, 5175 (1996).
20. T.B. Grindley. Structure and conformation of carbohydrates. *In* *Glycoscience: Chemistry and chemical biology. Edited by B. Fraser-Reid, K. Tatsuta, and J. Thiem. Springer-Verlag, Heidelberg.* 2001. p. 3.
21. A. Imberty, E. Mikros, J. Koca, R. Mollicone, R. Oriol, and S. Pérez. *Glycoconjugate J.* **12**, 331 (1995).
22. B. Aguilera, J. Jiménez-Barbero, and A. Fernández-Mayoralas. *Carbohydr. Res.* **308**, 19 (1998).
23. J. Dabrowski, T. Kozar, H. Grosskurth, and N.E. Nifant'ev. *J. Am. Chem. Soc.* **117**, 5534 (1995).
24. J.L. Asensio and J. Jiménez-Barbero. *Biopolymers*, **35**, 55 (1995).
25. T. Haselhorst, T. Weimar, and T. Peters. *J. Am. Chem. Soc.* **123**, 10 705 (2001).
26. G.I. Csonka, C.P. Sosa, and I.G. Csizmadia. *J. Phys. Chem. A*, **104**, 3381 (2000).
27. B. Guilbert, N.J. Davis, M. Pearce, R.T. Aplin, and S.L. Flitsch. *Tetrahedron: Asymmetry*, **5**, 2163 (1994).
28. C. Chipot, R. Jaffe, B. Maigret, D.A. Pearlman, and P.A. Kollman. *J. Am. Chem. Soc.* **118**, 11 217 (1996).
29. F. Tran, J. Weber, and T.A. Wesolowski. *Helv. Chim. Acta*, **84**, 1489 (2001).
30. V. Spirko, O. Engvist, P. Soldan, H.L. Selzle, E.W. Schlag, and P. Hobza. *J. Chem. Phys.* **111**, 572 (1999).
31. P. Hobza, H.L. Selzle, and E.W. Schlag. *J. Phys. Chem.* **100**, 18 790 (1996).
32. T.L. Hwang and A.J. Shaka. *J. Am. Chem. Soc.* **114**, 3157 (1992).
33. F. Mohamadi, N.G.J. Richards, W.C. Guida, R. Liskamp, M. Lipton, C. Caufield, G. Chang, T. Hendrickson, and W.C. Still. *J. Comput. Chem.* **11**, 440 (1990).
34. N.L. Allinger, Y.H. Yuh, and J.-H. Lii. *J. Am. Chem. Soc.* **111**, 8551 (1989).



# Derivatives of tetraphenylmethane and tetraphenylsilane: Synthesis of new tetrahedral building blocks for molecular construction

Jean-Hugues Fournier, Xin Wang, and James D. Wuest

**Abstract:** Useful derivatives of tetraphenylmethane and tetraphenylsilane have been synthesized by efficient methods that give crystalline products without chromatographic purification. New compounds include tetrakis(4-hydroxyphenyl)methane (**21**), tetrakis(4-formylphenyl)methane (**22**), tetrakis[(4-hydroxymethyl)phenyl]methane (**23**), tetrakis(4-bromophenyl)silane (**24**), tetrakis(4-iodophenyl)silane (**25**), tetrakis(4-hydroxyphenyl)silane (**26**), tetrakis[(4-hydroxymethyl)phenyl]silane (**27**), and tetrakis[(4-chloromethyl)phenyl]silane (**28**). These compounds are valuable precursors for the construction of complex molecules with tetrahedral geometries.

**Key words:** organic synthesis, molecular and supramolecular design and construction, tetraphenylmethane, tetraphenylsilane, tetrahedral building blocks.

**Résumé :** On a réalisé la synthèse de dérivés utiles du tétraphénylméthane et du tétraphénylsilane à l'aide de méthodes efficaces qui conduisent à des produits cristallins sans nécessité de purification chromatographique. Les nouveaux composés incluent les tétrakis(4-hydroxyphényl)méthane (**21**), tétrakis(4-formyl)méthane (**22**), tétrakis(4-hydroxyméthyl)méthane (**23**), tétrakis(4-bromophényl)silane (**24**), tétrakis(4-iodophényl)silane (**25**), tétrakis(4-hydroxyphényl)silane (**26**), tétrakis(4-hydroxyméthyl)silane (**27**) et tétrakis(4-chlorométhyl)silane (**28**). Ces composés sont des précurseurs précieux pour la construction de molécules complexes à géométries tétraédriques.

**Mots clés :** synthèse organique, ébauche et construction de molécules et de supramolécules, tétraphénylméthane, tétraphénylsilane, blocs tétraédriques de construction moléculaire.

[Traduit par la Rédaction]

## Introduction

Recent publications have underscored the importance of derivatives of tetraphenylmethane and tetraphenylsilane as subunits in molecular construction (1–39). Such tetrahedral building blocks have been successfully incorporated in supramolecular networks (1–13) and have also found use as precursors of dendrimers and polymers (14–22), nanoscale structures (23–25), optoelectronic materials (26–32), liquid crystals (33), and materials with other applications (34–39). Unfortunately, few syntheses of different functionalized derivatives of tetraphenylmethane and tetraphenylsilane have been reported. Currently known simple tetraphenylmethanes that are fully substituted in the *para* positions include compounds **1** (12, 21, 40), **2** (6, 19), **3** (41), **4** (42), **5** (42), **6** (12, 40, 41), **7** (40), **8** (40, 41), **9** (21), **10** (31, 43), **11** (43), **12** (19), and **13** (25), and analogous tetraphenylsilanes include compounds **14** (13, 44), **15** (8), **16** (13, 45), **17** (45), **18** (22), **19** (22), and **20** (1). To make a wider range of tetrahedral building blocks readily available for molecular construction, we now report efficient syntheses of a variety of new and

previously known *para*-substituted derivatives of tetraphenylmethane and tetraphenylsilane. Our syntheses use simple reactions and yield crystalline products without chromatographic purification. Newly characterized derivatives include tetrakis(4-hydroxyphenyl)methane (**21**), tetrakis(4-formylphenyl)methane (**22**), tetrakis[(4-hydroxymethyl)phenyl]methane (**23**), tetrakis(4-bromophenyl)silane (**24**), tetrakis(4-iodophenyl)silane (**25**), tetrakis(4-hydroxyphenyl)silane (**26**), tetrakis[(4-hydroxymethyl)phenyl]silane (**27**), and tetrakis[(4-chloromethyl)phenyl]silane (**28**).

## Results and discussion

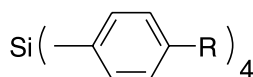
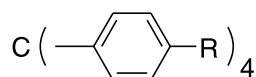
Our general approach to syntheses of derivatives of tetraphenylmethane and tetraphenylsilane is based on tetralithiation (41) of tetrakis(4-bromophenyl)methane (**1**) (12, 21, 40) or tetrakis(4-bromophenyl)silane (**24**) (4), followed by the addition of an appropriate electrophile. This approach has the advantage of providing a wide variety of derivatives simply by modifying the nature of the electrophile in a common experimental protocol. For example, treatment of tetrakis(4-bromophenyl)methane (**1**) with excess BuLi, followed by the addition of CH<sub>3</sub>I, afforded tetrakis(4-methylphenyl)methane (**3**) (41) in 60% yield after purification by recrystallization. Analogous procedures using B(OCH<sub>3</sub>)<sub>3</sub>–H<sub>2</sub>O<sub>2</sub> or *N,N*-dimethylformamide (DMF) provided the corresponding tetraphenol **21** and tetraaldehyde **22** in 62% and 46% yields, respectively, again after purification by re-

Received 7 September, 2002. Published on the NRC Research Press Web site at <http://canjchem.nrc.ca> on 23 May 2003.

J.-H. Fournier, X. Wang, and J.D. Wuest.<sup>1</sup> Département de Chimie, Université de Montréal, Montréal, PQ H3C 3J7, Canada.

<sup>1</sup>Corresponding author (e-mail: [wuest@chimie.umontreal.ca](mailto:wuest@chimie.umontreal.ca)).





- |                              |                              |
|------------------------------|------------------------------|
| 1 (R = Br)                   | 14 (R = CH <sub>3</sub> )    |
| 2 (R = I)                    | 15 (R = CN)                  |
| 3 (R = CH <sub>3</sub> )     | 16 (R = COOH)                |
| 4 (R = NO <sub>2</sub> )     | 17 (R = COOCH <sub>3</sub> ) |
| 5 (R = NH <sub>2</sub> )     | 18 (R = CH <sub>2</sub> Br)  |
| 6 (R = CN)                   | 19 (R = CH=CH <sub>2</sub> ) |
| 7 (R = COOH)                 | 20 (R = B(OH) <sub>2</sub> ) |
| 8 (R = COOCH <sub>3</sub> )  | 24 (R = Br)                  |
| 9 (R = B(OH) <sub>2</sub> )  | 25 (R = I)                   |
| 10 (R = COCH <sub>3</sub> )  | 26 (R = OH)                  |
| 11 (R = CH <sub>2</sub> Cl)  | 27 (R = CH <sub>2</sub> OH)  |
| 12 (R = CH=CH <sub>2</sub> ) | 28 (R = CH <sub>2</sub> Cl)  |
| 13 (R = C≡CH)                |                              |
| 21 (R = OH)                  |                              |
| 22 (R = CHO)                 |                              |
| 23 (R = CH <sub>2</sub> OH)  |                              |

crystallization. The reduction of tetraaldehyde **22** with NaBH<sub>4</sub> gave tetrakis[(4-hydroxymethyl)phenyl]methane (**23**) in 90% yield. Subsequent treatment with SOCl<sub>2</sub> gave a 94% yield of tetrakis[(4-chloromethyl)phenyl]methane (**11**), a known compound prepared previously by direct chloromethylation of tetraphenylmethane (43). Compounds **21–23** are useful new tetrahedral building blocks that can be subjected to further chemical modifications for use in molecular construction.

The corresponding tetraphenylsilanes were made in a similar way. Tetrakis(4-bromophenyl)silane (**24**) was prepared by the monolithiation of 1,4-dibromobenzene with BuLi, followed by the addition of SiCl<sub>4</sub> (4). This procedure provided target **24** in 45% yield after two recrystallizations. Alternatively, tetrakis(4-iodophenyl)silane (**25**) could be synthesized from 1,4-diiodobenzene by an analogous method in 56% yield (4). Tetrakis(4-methylphenyl)silane (**14**) (13, 44) and tetrakis(4-hydroxyphenyl)silane (**26**) could be prepared from tetrakis(4-bromophenyl)silane (**24**) in 65% and 59% yields, respectively, by tetralithiation and addition of appropriate electrophiles, using methods analogous to those used to make the corresponding tetraphenylmethanes. However, attempts to synthesize the aldehyde corresponding to compound **22** by use of DMF as electrophile resulted in complex mixtures that proved to be difficult to purify. Tetrakis(4-bromophenyl)silane (**24**) could be converted into the known tetraacid **16** (13, 45) by adding excess BuLi in THF and bubbling CO<sub>2</sub> through the resulting solution. This procedure gave compound **16** in 68% yield after purification by recrystallization. Previous syntheses of tetraacid **16** have been accomplished by oxidizing tetrakis(4-methylphenyl)silane (**14**) (13, 45). The tetraacid was subsequently reduced with LiAlH<sub>4</sub> in THF to afford tetrakis[(4-hydroxymethyl)phenyl]silane (**27**) in 80% yield. The reaction of tetraol **27**

with SOCl<sub>2</sub> then yielded tetrakis[(4-chloromethyl)phenyl]silane (**28**) in 76% yield.<sup>2</sup>

## Conclusions

The syntheses we describe provide convenient access to a wide variety of functionalized derivatives of tetraphenylmethane and tetraphenylsilane. The availability of these compounds creates many new opportunities for molecular and supramolecular construction using tetrahedral building blocks.

## Experimental

Tetrahydrofuran (THF) and ether were dried by distillation from the sodium ketyl of benzophenone. *N,N*-Dimethylformamide (DMF) was purified by distillation under reduced pressure and dried over 4 Å molecular sieves. All other reagents were commercial products that were used without further purification.

### Tetrakis(4-methylphenyl)methane (3) (41)

A solution of tetrakis(4-bromophenyl)methane (**1**; 635 mg, 0.998 mmol) (12, 21, 40) in THF (60 mL) was stirred at –78°C under dry N<sub>2</sub> and treated dropwise with a solution of butyllithium (3.20 mL, 2.5 M in hexane, 8.0 mmol). The resulting mixture was kept at –78°C for 30 min, and then CH<sub>3</sub>I (1.00 mL, 16.1 mmol) was added dropwise. The mixture was stirred overnight while the temperature was allowed to rise to 25°C. Saturated aqueous Na<sub>2</sub>S<sub>2</sub>O<sub>3</sub> was then added, and the resulting mixture was concentrated by partial evaporation under reduced pressure. The remaining aqueous concentrate was extracted with ethyl acetate, and the combined organic extracts were washed with brine and dried over MgSO<sub>4</sub>. Volatiles were removed by evaporation under reduced pressure, and the residue was recrystallized from ethyl acetate to afford tetrakis(4-methylphenyl)methane (41) (**3**; 226 mg, 0.600 mmol, 60%) as a colorless solid; mp 254–256°C (lit. (41) mp 254.5–255.5°C). <sup>1</sup>H NMR (300 MHz, CDCl<sub>3</sub>) δ: 7.12–7.03 (m, 16H), 2.31 (s, 12H). <sup>13</sup>C NMR (75 MHz, CDCl<sub>3</sub>) δ: 144.2, 135.0, 130.8, 128.0, 63.5, 20.8. FAB-MS (3-nitrobenzyl alcohol) *m/e*: 376. FAB-HR-MS (3-nitrobenzyl alcohol) calcd. for C<sub>29</sub>H<sub>28</sub> *m/e*: 376.21912; found: 376.22050. Anal. calcd. for C<sub>29</sub>H<sub>28</sub>: C 92.50, H 7.50; found: C 92.50, H 7.71.

### Tetrakis(4-hydroxyphenyl)methane (21)

A solution of tetrakis(4-bromophenyl)methane (**1**; 635 mg, 0.998 mmol) (12, 21, 40) in THF (60 mL) was stirred at –78°C under dry N<sub>2</sub> and treated dropwise with a solution of butyllithium (3.20 mL, 2.5 M in hexane, 8.0 mmol). The resulting mixture was kept at –78°C for 30 min, and then B(OCH<sub>3</sub>)<sub>3</sub> (1.80 mL, 16.1 mmol) was added dropwise. The mixture was stirred overnight while the temperature was allowed to rise to 25°C. To the solution was added 3 M aqueous NaOH (3 mL) followed by 30% aqueous H<sub>2</sub>O<sub>2</sub> (2 mL), and then the mixture was heated at reflux for

<sup>2</sup>Supplementary data (<sup>1</sup>H and <sup>13</sup>C NMR spectra of tetrakis[(4-chloromethyl)phenyl]silane (**28**)) may be purchased from the Depository of Unpublished Data, Document Delivery, CISTI, National Research Council Canada, Ottawa, ON K1A 0S2, Canada ([http://www.nrc.ca/cisti/irm/unpub\\_e.shtml](http://www.nrc.ca/cisti/irm/unpub_e.shtml) for information on ordering electronically).



1 h. The resulting mixture was acidified with 1 M aqueous HCl and concentrated by partial evaporation under reduced pressure. The aqueous concentrate was extracted with ethyl acetate, and the combined organic extracts were washed with water and brine, dried over  $\text{MgSO}_4$ , and filtered. Volatiles were removed by evaporation under reduced pressure, and the residue was recrystallized from ethyl acetate – hexane to afford tetrakis(4-hydroxyphenyl)methane (**21**; 238 mg, 0.619 mmol, 62%) as a colorless solid: mp > 300°C. IR (KBr) ( $\text{cm}^{-1}$ ): 3601, 3254.  $^1\text{H}$  NMR (400 MHz,  $\text{DMSO}-d_6$ )  $\delta$  9.30 (s, 4H), 6.82 (d, 8H,  $^3J = 8.8$  Hz), 6.61 (d, 8H,  $^3J = 8.8$  Hz).  $^{13}\text{C}$  NMR (100 MHz,  $\text{DMSO}-d_6$ )  $\delta$  154.9, 138.1, 131.5, 114.0, 61.5. FAB-MS (3-nitrobenzyl alcohol)  $m/e$ : 384. FAB-HR-MS (3-nitrobenzyl alcohol) calcd. for  $\text{C}_{25}\text{H}_{20}\text{O}_4$   $m/e$ : 384.13617; found: 384.13720. Anal. calcd. for  $\text{C}_{25}\text{H}_{20}\text{O}_4 \cdot 0.5 \text{ H}_2\text{O}$ : C 76.32, H 5.38; found: C 76.96, H 5.08.

#### Tetrakis(4-formylphenyl)methane (**22**)

A solution of tetrakis(4-bromophenyl)methane (**1**; 1.12 g, 1.76 mmol) (12, 21, 40) in THF (150 mL) was stirred at  $-78^\circ\text{C}$  under dry  $\text{N}_2$  and treated dropwise with a solution of butyllithium (6.4 mL, 2.5 M in hexane, 16 mmol). The resulting mixture was kept at  $-78^\circ\text{C}$  for 30 min, and then DMF (2.5 mL, 32 mmol) was added dropwise. The mixture was stirred overnight while the temperature was allowed to rise to  $25^\circ\text{C}$ . To the solution was added 1 M aqueous HCl (20 mL), and volatiles were partially removed by evaporation under reduced pressure. The remaining aqueous concentrate was extracted with ethyl acetate, and the combined organic extracts were washed with water and brine, dried over  $\text{MgSO}_4$ , and filtered. Volatiles were removed by evaporation under reduced pressure, and the residue was recrystallized from ethyl acetate to provide tetrakis(4-formylphenyl)methane (**22**; 350 mg, 0.809 mmol, 46%) as a light yellow solid: mp >  $180^\circ\text{C}$  decomposition (dec). IR (KBr) ( $\text{cm}^{-1}$ ): 1702.  $^1\text{H}$  NMR (400 MHz,  $\text{CDCl}_3$ )  $\delta$  10.01 (s, 4H), 7.84 (d, 8H,  $^3J = 8.7$  Hz), 7.44 (d, 8H,  $^3J = 8.7$  Hz).  $^{13}\text{C}$  NMR (100 MHz,  $\text{CDCl}_3$ )  $\delta$  191.6, 151.2, 135.1, 131.4, 129.8, 66.4. FAB-MS (3-nitrobenzyl alcohol)  $m/e$ : 433. FAB-HR-MS (3-nitrobenzyl alcohol) calcd. for  $\text{C}_{29}\text{H}_{20}\text{O}_4$  + H  $m/e$ : 433.14398; found: 433.14540.

#### Tetrakis[(4-hydroxymethyl)phenyl]methane (**23**)

A suspension of tetrakis(4-formylphenyl)methane (**22**; 90.3 mg, 0.209 mmol) in  $\text{CH}_3\text{OH}$  (10 mL) was stirred at  $0^\circ\text{C}$  and treated with  $\text{NaBH}_4$  (200 mg, 5.29 mmol) added in small portions. The resulting mixture was stirred at  $0^\circ\text{C}$  for 30 min and then at  $25^\circ\text{C}$  for 1 h. The mixture was poured into cold  $\text{H}_2\text{O}$  (150 mL), and the resulting precipitate was filtered, washed with water, and dried under vacuum. Recrystallization from ethyl acetate – hexane gave tetrakis[(4-hydroxymethyl)phenyl]methane (**23**; 83.4 mg, 0.189 mmol, 90%) as a colorless solid: mp >  $300^\circ\text{C}$ . IR (KBr) ( $\text{cm}^{-1}$ ): 3305.  $^1\text{H}$  NMR (300 MHz,  $\text{DMSO}-d_6$ )  $\delta$  7.21 (d, 8H,  $^3J = 8.5$  Hz), 7.09 (d, 8H,  $^3J = 8.5$  Hz), 5.12 (t, 4H,  $^3J = 5.6$  Hz), 4.44 (d, 8H,  $^3J = 5.6$  Hz).  $^{13}\text{C}$  NMR (100 MHz,  $\text{DMSO}-d_6$ )  $\delta$  145.2, 140.0, 130.2, 125.9, 63.7, 62.6. FAB-MS (3-nitrobenzyl alcohol)  $m/e$ : 440. FAB-HR-MS (3-nitrobenzyl alcohol) calcd. for  $\text{C}_{29}\text{H}_{28}\text{O}_4$   $m/e$ : 440.19876; found: 440.20030.

#### Tetrakis[(4-chloromethyl)phenyl]methane (**11**) (**43**)

A solution of tetrakis[(4-hydroxymethyl)phenyl]methane (**23**; 440 mg, 0.999 mmol) in dioxane (25 mL) was treated dropwise with  $\text{SOCl}_2$  (600  $\mu\text{L}$ , 8.2 mmol) under  $\text{N}_2$ , and the mixture was heated at reflux for 16 h. Volatiles were removed by evaporation under reduced pressure, and the residue was recrystallized from  $\text{CHCl}_3$ –hexane to give tetrakis[(4-chloromethyl)phenyl]methane (**43**) (**11**; 483 mg, 0.939 mmol, 94%) as light yellow needles: mp >  $250^\circ\text{C}$  (lit. (**43**) mp  $279^\circ\text{C}$ ).  $^1\text{H}$  NMR (400 MHz,  $\text{CDCl}_3$ )  $\delta$  7.28 (d, 8H,  $^3J = 8.6$  Hz), 7.20 (d, 8H,  $^3J = 8.6$  Hz), 4.57 (s, 8H).  $^{13}\text{C}$  NMR (100 MHz,  $\text{DMSO}-d_6$ )  $\delta$  147.2, 136.3, 131.5, 129.5, 65.0, 46.7. Anal. calcd. for  $\text{C}_{29}\text{H}_{24}\text{Cl}_4$ : C 67.72, H 4.70; found: C 67.31, H 4.79.

#### Tetrakis(4-bromophenyl)silane (**24**)

A solution of 1,4-dibromobenzene (23.6 g, 100 mmol) in ether (250 mL) was stirred at  $-10^\circ\text{C}$  under dry  $\text{N}_2$  and treated dropwise with a solution of butyllithium (40 mL, 2.5 M in hexane, 100 mmol). The resulting mixture was kept at  $-10^\circ\text{C}$  for 15 min, and then  $\text{SiCl}_4$  (2.85 mL, 24.9 mmol) was added dropwise. The mixture was stirred at  $-10^\circ\text{C}$  for 30 min and at  $25^\circ\text{C}$  for 1 h. Then 1 M aqueous HCl was added, and the resulting mixture was extracted with ether. The combined extracts were washed with  $\text{H}_2\text{O}$  and brine, dried over  $\text{MgSO}_4$ , and filtered. Volatiles were removed by evaporation under reduced pressure, and the residue was recrystallized twice from  $\text{CHCl}_3$ –ethanol to afford tetrakis(4-bromophenyl)silane (**24**; 7.28 g, 11.2 mmol, 45%) as a colorless solid: mp  $240$ – $241^\circ\text{C}$ .  $^1\text{H}$  NMR (300 MHz,  $\text{CDCl}_3$ )  $\delta$  7.55 (d, 8H,  $^3J = 8.4$  Hz), 7.35 (d, 8H,  $^3J = 8.4$  Hz).  $^{13}\text{C}$  NMR (75 MHz,  $\text{CDCl}_3$ )  $\delta$  137.6, 131.4, 131.4, 125.4. FAB-MS (3-nitrobenzyl alcohol)  $m/e$ : 652. Anal. calcd. for  $\text{C}_{29}\text{H}_{16}\text{Br}_4\text{Si}$ : C 44.21, H 2.47; found: C 43.83, H 2.45.

#### Tetrakis(4-iodophenyl)silane (**25**)

A solution of 1,4-diiodobenzene (13.2 g, 40.0 mmol) in THF (250 mL) was stirred at  $-78^\circ\text{C}$  under dry  $\text{N}_2$  and treated dropwise with a solution of butyllithium (16 mL, 2.5 M in hexane, 40 mmol). The resulting mixture was kept at  $-78^\circ\text{C}$  for 20 min, and then  $\text{SiCl}_4$  (1.15 mL, 10.0 mmol) was added dropwise. The mixture was stirred at  $-78^\circ\text{C}$  for 30 min and at  $25^\circ\text{C}$  for 1 h. Then 1 M aqueous HCl (100 mL) was added, and the phases were separated. The organic phase was washed with saturated aqueous  $\text{Na}_2\text{S}_2\text{O}_3$  (100 mL),  $\text{H}_2\text{O}$  (100 mL), and brine (100 mL), and then it was dried over  $\text{MgSO}_4$  and filtered. Volatiles were removed by evaporation under reduced pressure, and the residue was recrystallized twice from  $\text{CHCl}_3$ –ethanol to afford tetrakis(4-iodophenyl)silane (**25**; 4.70 g, 5.59 mmol, 56%) as a colorless solid: mp >  $310^\circ\text{C}$ .  $^1\text{H}$  NMR (300 MHz,  $\text{CDCl}_3$ )  $\delta$  7.75 (d, 8H,  $^3J = 7.9$  Hz), 7.20 (d, 8H,  $^3J = 7.9$  Hz).  $^{13}\text{C}$  NMR (75 MHz,  $\text{CDCl}_3$ )  $\delta$  137.5, 137.2, 131.7, 97.7. Anal. calcd. for  $\text{C}_{29}\text{H}_{16}\text{I}_4\text{Si}$ : C 34.31, H 1.92; found: C 34.17, H 1.78.

#### Tetrakis(4-methylphenyl)silane (**14**) (**13**, **44**)

A solution of tetrakis(4-bromophenyl)silane (**24**; 1.31 g, 2.01 mmol) in THF (150 mL) was stirred at  $-78^\circ\text{C}$  under dry  $\text{N}_2$  and treated dropwise with a solution of butyllithium (6.4 mL, 2.5 M in hexane, 16 mmol). The resulting mixture was kept at  $-78^\circ\text{C}$  for 30 min, and then  $\text{CH}_3\text{I}$  (2.00 mL,



32.1 mmol) was added dropwise. The mixture was stirred overnight while the temperature was allowed to rise to 25°C. Saturated aqueous  $\text{Na}_2\text{S}_2\text{O}_3$  was then added, and volatiles were partially removed from the resulting mixture by evaporation under reduced pressure. The aqueous concentrate was extracted with ethyl acetate, and the combined extracts were washed with brine, dried over  $\text{MgSO}_4$ , and filtered. Volatiles were removed by evaporation under reduced pressure, and the residue was recrystallized from toluene to afford tetrakis(4-methylphenyl)silane (**14**; 512 mg, 1.30 mmol, 65%) as a colorless solid. The spectroscopic data were identical to those reported in the literature (13, 44).

#### Tetrakis(4-hydroxyphenyl)silane (26)

A solution of tetrakis(4-bromophenyl)silane (**24**; 652 mg, 1.00 mmol) in THF (60 mL) was stirred at  $-78^\circ\text{C}$  under dry  $\text{N}_2$  and treated dropwise with a solution of butyllithium (3.20 mL, 2.5 M in hexane, 8.00 mmol). The resulting mixture was kept at  $-78^\circ\text{C}$  for 30 min, and then  $\text{B}(\text{OCH}_3)_3$  (1.80 mL, 16.1 mmol) was added dropwise. The mixture was stirred overnight while the temperature was allowed to rise to 25°C. To the solution was added 3 M aqueous NaOH (3 mL), followed by 30% aqueous  $\text{H}_2\text{O}_2$  (2 mL), and then the mixture was heated at reflux for 1 h. The resulting mixture was acidified with 1 M aqueous HCl and concentrated by partial evaporation of volatiles under reduced pressure. The aqueous concentrate was extracted with ethyl acetate, and the combined extracts were washed with water and brine, dried over  $\text{MgSO}_4$ , and filtered. Volatiles were removed by evaporation under reduced pressure, and the residue was recrystallized from ethyl acetate – hexane to afford tetrakis(4-hydroxyphenyl)silane (**26**; 238 mg, 0.594 mmol, 59%) as a colorless solid: mp  $274\text{--}278^\circ\text{C}$ . IR (KBr) ( $\text{cm}^{-1}$ ): 3607, 3300.  $^1\text{H}$  NMR (400 MHz,  $\text{DMSO}-d_6$ )  $\delta$ : 9.59 (s, 4H), 7.22 (d, 8H,  $^3J = 8.4$  Hz), 6.78 (d, 8H,  $^3J = 8.4$  Hz).  $^{13}\text{C}$  NMR (75 MHz,  $\text{DMSO}-d_6$ )  $\delta$ : 158.8, 137.5, 124.3, 115.4. FAB-MS (3-nitrobenzyl alcohol)  $m/e$ : 400. Anal. calcd. for  $\text{C}_{24}\text{H}_{20}\text{O}_4\text{Si}\cdot\text{H}_2\text{O}$ : C 68.88, H 5.30; found: C 69.16, H 5.12.

#### Tetrakis(4-carboxyphenyl)silane (16) (13, 45)

A solution of tetrakis(4-bromophenyl)silane (**24**; 2.6 g, 4.0 mmol) in THF (250 mL) was stirred at  $-78^\circ\text{C}$  under dry  $\text{N}_2$  and treated dropwise with a solution of butyllithium (8.0 mL, 2.5 M in hexane, 20 mmol). The resulting mixture was kept at  $-78^\circ\text{C}$  for 30 min, and then  $\text{CO}_2$  was bubbled through it. The mixture was stirred at  $-78^\circ\text{C}$  for 3 h and was then acidified with 1 M aqueous HCl (125 mL). The organic phase was separated, washed with  $\text{H}_2\text{O}$  (100 mL) and brine (100 mL), dried over  $\text{MgSO}_4$ , and filtered. Volatiles were removed by evaporation under reduced pressure, and the residue was recrystallized from ethyl acetate – hexane to afford tetrakis(4-carboxyphenyl)silane (13, 45) (**16**; 1.40 g, 2.73 mmol, 68%) as a white solid. The physical and spectroscopic data were identical to those reported in the literature (13, 45).

#### Tetrakis[(4-hydroxymethyl)phenyl]silane (27)

A suspension of tetrakis(4-carboxyphenyl)silane (**16**; 123 mg, 0.240 mmol) in THF (10 mL) was stirred at  $0^\circ\text{C}$  under  $\text{N}_2$  and treated with  $\text{LiAlH}_4$  (45 mg, 1.2 mmol) added in small portions. The resulting mixture was heated at reflux

overnight. The mixture was then cooled, treated carefully with 6 M aqueous NaOH and diluted with  $\text{H}_2\text{O}$ . The resulting mixture was filtered, and volatiles were removed by evaporation under reduced pressure. The solid residue was washed with water and dried under vacuum. Recrystallization from ethanol–hexane gave tetrakis[(4-hydroxymethyl)phenyl]silane (**27**; 87.6 mg, 0.192 mmol, 80%) as a colorless solid: mp  $298\text{--}299^\circ\text{C}$ . IR (KBr) ( $\text{cm}^{-1}$ ): 3339.  $^1\text{H}$  NMR (400 MHz,  $\text{DMSO}-d_6$ )  $\delta$ : 7.42–7.36 (m, 16H), 5.24 (bs, 4H), 4.52 (s, 8H).  $^{13}\text{C}$  NMR (75 MHz,  $\text{DMSO}-d_6$ )  $\delta$ : 144.4, 135.8, 132.1, 126.3, 63.0. Anal. calcd. for  $\text{C}_{24}\text{H}_{20}\text{O}_4\text{Si}\cdot 0.5\text{H}_2\text{O}$ : C 72.22, H 6.28; found: C 72.45, H 6.25.

#### Tetrakis[(4-chloromethyl)phenyl]silane (28)

A solution of tetrakis[(4-hydroxymethyl)phenyl]silane (**27**; 205 mg, 0.449 mmol) in dioxane (10 mL) was stirred at  $25^\circ\text{C}$  under  $\text{N}_2$  and treated dropwise with  $\text{SOCl}_2$  (260  $\mu\text{L}$ , 3.6 mmol). The resulting mixture was heated at reflux for 16 h. Volatiles were removed by evaporation under reduced pressure, and the residue was recrystallized from ethyl acetate to give tetrakis[(4-chloromethyl)phenyl]silane (**28**; 180 mg, 0.339 mmol, 76%) as a light yellow solid: mp  $251\text{--}253^\circ\text{C}$ .  $^1\text{H}$  NMR (300 MHz,  $\text{CDCl}_3$ )  $\delta$ : 7.55 (d, 8H,  $^3J = 8.1$  Hz), 7.42 (d, 8H,  $^3J = 8.1$  Hz), 4.61 (s, 8H).  $^{13}\text{C}$  NMR (100 MHz,  $\text{CDCl}_3$ )  $\delta$ : 139.1, 136.7, 133.8, 128.1, 46.0.

### Acknowledgments

We are grateful to the Natural Sciences and Engineering Research Council of Canada (NSERC), the Ministère de l'Éducation du Québec (MÉQ), Merck Frosst, the Canada Foundation for Innovation, and the Canada Research Chairs Program for financial support. In addition, acknowledgment is made to the donors of the Petroleum Research Fund, administered by the American Chemical Society, for support of this research. Jean-Hugues Fournier gratefully acknowledges fellowships from MÉQ (2000–2002) and NSERC (1998–2000).

### References

1. J.-H. Fournier, T. Maris, J.D. Wuest, W. Guo, and E. Galoppini, *J. Am. Chem. Soc.* **125**, 1002 (2003).
2. L. Vaillancourt, M. Simard, and J.D. Wuest, *J. Org. Chem.* **63**, 9746 (1998).
3. P. Brunet, M. Simard, and J.D. Wuest, *J. Am. Chem. Soc.* **119**, 2737 (1997).
4. D. Su, X. Wang, M. Simard, and J.D. Wuest, *Supramol. Chem.* **6**, 171 (1995).
5. X. Wang, M. Simard, and J.D. Wuest, *J. Am. Chem. Soc.* **116**, 12 119 (1994).
6. M. Simard, D. Su, and J.D. Wuest, *J. Am. Chem. Soc.* **113**, 4696 (1991).
7. R. Thaimattam, D.S. Reddy, F. Xue, T.C.W. Mak, A. Nangia, and G.R. Desiraju, *New J. Chem.* 143 (1998).
8. F.-Q. Liu and T.D. Tilley, *J. Chem. Soc., Chem. Commun.* 103 (1998).
9. E. Galoppini and R. Gilardi, *J. Chem. Soc., Chem. Commun.* 173 (1999).
10. G.P. Lorenzi, A. Manassis, N.C. Tirelli, and V. Gramlich, *Struct. Chem.* **8**, 435 (1997).



11. D. Venkataraman, S. Lee, J.S. Moore, P. Zhang, K.A. Hirsch, G.B. Gardner, A.C. Covey, and C.L. Prentice. *Chem. Mater.* **8**, 2030 (1996).
12. B.F. Hoskins and R. Robson. *J. Am. Chem. Soc.* **112**, 1546 (1990).
13. J.B. Lambert, Y. Zhao, and C.L. Stern. *J. Phys. Org. Chem.* **10**, 229 (1997).
14. G.M. Hübner, G. Nachtsheim, Q.Y. Li, C. Seel, and F. Vögtle. *Angew. Chem., Int. Ed. Engl.* **39**, 1269 (2000).
15. E.C. Constable, O. Eich, C.E. Housecroft, and D.C. Rees. *Inorg. Chim. Acta*, **300–302**, 158 (2000).
16. U.-M. Wiesler and K. Müllen. *J. Chem. Soc., Chem. Commun.* 2293 (1999).
17. R.J. Reid, H. Li, and M.J. Marsella. *Polym. Prepr. Am. Chem. Soc. Div. Polym. Chem.* **40**, 195 (1999).
18. S. Sengupta and S.K. Sadhukhan. *Tetrahedron Lett.* **40**, 9157 (1999).
19. D. Su and F.M. Menger. *Tetrahedron Lett.* **38**, 1485 (1997).
20. I. Sava, M. Bruma, B. Schulz, F. Mercer, V.N. Reddy, and N. Belomoina. *J. Appl. Polym. Sci.* **65**, 1533 (1997).
21. L.M. Wilson and A.C. Griffin. *J. Mater. Chem.* **3**, 991 (1993).
22. G. Drefahl and D. Lorenz. *J. Prakt. Chem.* **24**, 312 (1964).
23. J.P. Novak and D.L. Feldheim. *J. Am. Chem. Soc.* **122**, 3979 (2000).
24. E.C. Constable, O. Eich, D. Fenske, C.E. Housecroft, and L.A. Johnston. *Chem. Eur. J.* **6**, 4364 (2000).
25. O. Mongin and A. Gossauer. *Tetrahedron*, **53**, 6835 (1997).
26. C. Lambert, W. Gaschler, G. Nöll, M. Weber, E. Schmälzlin, C. Bräuchle, and K. Meerholz. *J. Chem. Soc., Perkin Trans. 2*, 964 (2001).
27. H.-C. Yeh, R.-H. Lee, L.-H. Chan, T.-Y.J. Lin, C.-T. Chen, E. Balasubramaniam, and Y.-T. Tao. *Chem. Mater.* **13**, 2788 (2001).
28. H. Zhao, C. Tanjutco, and S. Thayumanavan. *Tetrahedron Lett.* **42**, 4421 (2001).
29. M.R. Robinson, S. Wang, G.C. Bazan, and Y. Cao. *Adv. Mater.* **12**, 1701 (2000).
30. S. Wang, W.J. Oldham, Jr., R.A. Hudack, Jr., and G.C. Bazan. *J. Am. Chem. Soc.* **122**, 5695 (2000).
31. T.J. Zimmermann, O. Freundel, R. Gompper, and T.J.J. Müller. *Eur. J. Org. Chem.* 3305 (2000).
32. N. Armaroli, V. Balzani, J.-P. Collin, P. Gaviña, J.-P. Sauvage, and B. Ventura. *J. Am. Chem. Soc.* **121**, 4397 (1999).
33. A. Pegenau, T. Hegmann, C. Tschierske, and S. Diele. *Chem. Eur. J.* **5**, 1643 (1999).
34. R.K.R. Jetti, F. Xue, T.C.W. Mak, and A. Nangia. *J. Chem. Soc., Perkin Trans. 2*, 1223 (2000).
35. Y. Yao and J.M. Tour. *J. Org. Chem.* **64**, 1968 (1999).
36. H.W. Gibson, P.T. Engen, and S.-H. Lee. *Polymer*, **40**, 1823 (1999).
37. F.M. Raymo, K.N. Houk, and J.F. Stoddart. *J. Am. Chem. Soc.* **120**, 9318 (1998).
38. C. Pugh, J.-Y. Bae, J.R. Scott, and C.L. Wilkins. *Macromolecules*, **30**, 8139 (1997).
39. A.M.W. Cargill Thompson, J. Hock, J.A. McCleverty, and M.D. Ward. *Inorg. Chim. Acta*, **256**, 331 (1997).
40. M. Grimm, B. Kirste, and H. Kurreck. *Angew. Chem., Int. Ed. Engl.* **25**, 1097 (1986).
41. B. Kirste, M. Grimm, and H. Kurreck. *J. Am. Chem. Soc.* **111**, 108 (1989).
42. F.A. Neugebauer, H. Fischer, and R. Bernhardt. *Chem. Ber.* **109**, 2389 (1976).
43. T.J. Zimmermann and T.J.J. Müller. *Synthesis*, 1157 (2002).
44. M. Charissé, S. Roller, and M. Dräger. *J. Organomet. Chem.* **427**, 23 (1992).
45. H. Hopff, J.M. Deuber, and A. Said. *Helv. Chim. Acta*, **54**, 117 (1971).



# $\gamma$ -Irradiation route to photoluminescent CdS–CdSe with core–shell nanostructures under ambient conditions

Fen Xu, Xu Zhang, Jun Lu, Wang Xi, Jie Hong, and Yi Xie

**Abstract:** Photoluminescent CdS–CdSe nanocomposites with core–shell structures were obtained via a novel two-step  $\gamma$ -irradiation process followed by a simple ion-exchange reaction at room temperature and under ambient pressure. To fully characterize CdS–CdSe nanocomposites, X-ray photoelectron spectroscopy, UV–vis absorption spectra, and photoluminescence spectra were recorded, as well as powder X-ray diffraction, transmission electron microscopy, and high-resolution electron microscopy, to confirm the presence of the core–shell nanostructure.

**Key words:** core–shell nanostructure,  $\gamma$ -irradiation, ion-exchange reaction.

**Résumé :** On a obtenu des nanocomposés de CdS–CdSe, à structure conchoïdale avec un noyau central, en utilisant un nouveau processus en deux étapes comportant une irradiation  $\gamma$  suivie d'une réaction d'échange d'ion simple à température et pression ambiantes. Dans le but de caractériser complètement les nanocomposés de CdS–CdSe, on a enregistré les spectres de spectroscopie photoélectronique de rayons X, d'absorption UV–visible et de photoluminescence on a aussi utilisé la diffraction de poudres de rayons X, la microscopie par transmission d'électrons, la microscopie électronique à haute résolution, pour confirmer la présence de la nanostructure conchoïdale avec un noyau central.

**Mots clés :** nanostructure conchoïdale avec un noyau central, irradiation  $\gamma$ , réaction d'échange d'ion.

[Traduit par la Rédaction]

## Introduction

Recently, nanomaterials have become the focus of intensive research because of their numerous applications in diverse fields such as electro-optical and ultramodern electronic devices, super-magnets, photographic suspensions, and catalyst production, etc. (1). Tremendous advances in the preparation and characterization of semiconductor nanoparticles (2–4) have been made in that these materials exhibit strongly size-dependent optical and electrical properties when their dimensions are comparable to the Bohr radius. Because the surface of a nanocrystal is made up of atoms that are not fully coordinated, it is highly active and acts like it possesses defects unless passivated (5). To remove these defects, long-chain organic surfactants have been utilized to passivate these II–VI and III–V nanocrystals. However, it is generally very difficult to simultaneously passivate both anionic and cationic surface sites with the use of organic ligands, and there are always some dangling bonds on the surface. As for the nanocrystals, inorganic epitaxial growth, such as the growth of the shell on the core, can not only eliminate both the anionic and cationic surface dangling bonds but can also generate a new nanocrystal system with

novel properties. Furthermore, most of the properties of these “core–shell” systems are dependent on both core and shell materials (6). Hence, inorganic passivation has been explored in such core–shell structures as CdSe–ZnS (7), CdSe–ZnS or ZnS–CdSe (8), CdSe–ZnS (9), CdSe–ZnSe (10), CdS–HgS–CdS (11), CdSe–CdS (6, 12), CdS–CdSe (13), HgTe–CdS (14), CdSe–CdS–ZnS (15), and CdS–ZnO and CdS–Pb<sub>3</sub>O<sub>4</sub> (16). Apparently, the design and preparation of nanocomposites with core–shell structures has been an important, active research direction; these systems show reduced fluorescence lifetimes, exhibit high photoluminescence (PL) quantum yield, higher photoluminescence efficiency and superiority to some existing fluorophores, and other benefits (17) related to tailoring the band-gap positions between the two materials with respect to the uncoated dots due to the elimination of surface non-radiative recombination defects (6, 16, 18, 19).

Among these core–shell systems, the semiconductor pair of CdS and CdSe is the most attractive to focus attention on because of the similarities between the CdS and CdSe lattices (lattice mismatch is 4.26%), which dictated the choice of this semiconductor pair for the present investigation (20). Several synthesis routes (6, 12–13) have been applied to prepare the core–shell nanostructure; however, two limitations seem unavoidable: one is the necessary synthesis temperature (at least 100°C) and the other is the organic precursors. Here, we put forward a novel approach for the preparation of CdS–CdSe nanocomposites (with core–shell structures) at room temperature and under ambient pressure, based on our previous work on the  $\gamma$ -irradiation synthesis of various semiconductor nanoparticles and nanocomposites (21, 22). Using

Received 7 December 2002. Published on the NRC Research Press Web site at <http://canjchem.nrc.ca> on 27 May 2003.

**F. Xu, X. Zhang, J. Lu, W. Xi, J. Hong, and Y. Xie.<sup>1</sup>**  
Structure Research Lab and Department of Chemistry,  
University of Science & Technology of China, Hefei, Anhui  
230026, P.R. China.

<sup>1</sup>Corresponding author (e-mail: [xyielab@ustc.edu.cn](mailto:xyielab@ustc.edu.cn)).



this approach, a simple ion-exchange reaction followed with  $\gamma$ -irradiation can easily form a heterogeneous semiconductor shell on a certain core. For instance, after  $\gamma$ -irradiating a simple mixture system consisting of the chosen core and a suitable shell precursor solution, the core-shell nanostructure of the semiconductor pair of CdS–CdSe can be obtained easily via an ion-exchange reaction. This method may provide a simple and convenient route to synthesize for various metal chalcogenides with core-shell nanostructures; it is free of the use of complex and expensive organometallic precursors, and all procedures are carried out under ambient condition. Additionally, the chemistry of the core and (or) shell growth is clean — the  $\gamma$ -irradiation can offer a mass of reductive radicals, which are totally clean reductive agents from the point of view of green chemistry, and thus one can avoid the by-products from chemical reducing agents.

## Experimental

### Materials

All agents were analytically pure and were purchased from Shanghai Chemical Co. Ltd., including cadmium chloride ( $\text{CdCl}_2$ ), sodium thiosulfate ( $\text{Na}_2\text{S}_2\text{O}_3$ ), selenium (Se), sodium sulfite ( $\text{Na}_2\text{SO}_3$ ), and isopropyl alcohol ( $\text{CH}_3\text{CHOHCH}_3$ ).

### Synthesis of CdS–CdSe core-shell nanocomposites

In a typical process, two stepwise irradiation processes are required, and an ion-exchange reaction follows with the  $\gamma$ -irradiation processes. It is also worth mentioning that all operations were carried out at room temperature and under ambient pressure.

#### The formation of the CdS core

A typical solution, consisting of  $0.05 \text{ mol}\cdot\text{L}^{-1}$   $\text{CdCl}_2$ ,  $0.05 \text{ mol}\cdot\text{L}^{-1}$   $\text{Na}_2\text{S}_2\text{O}_3$ , and  $3 \text{ mol}\cdot\text{L}^{-1}$   $\text{CH}_3\text{CHOHCH}_3$  (as a scavenger for the hydroxyl radicals), was irradiated in the field of a  $2.59 \times 10^{15} \text{ Bq}$   $^{60}\text{Co}$   $\gamma$ -ray source with a radiation dose of  $3.0 \times 10^4 \text{ Gy}$  (21, 22). The yellow-orange CdS nanoparticles obtained were filtered off and washed with ethanol for the next step.

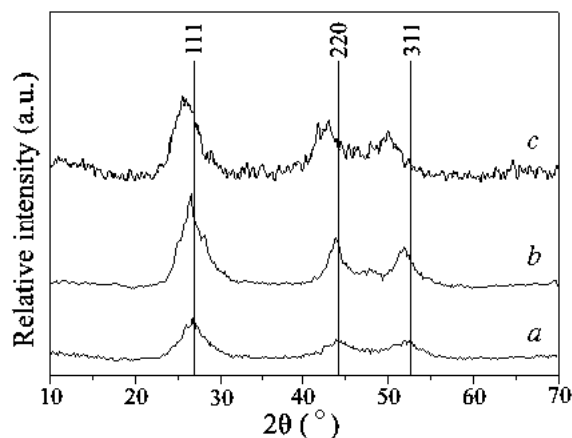
#### The growth of the CdSe shell on the CdS core

The prepared CdS nanoparticles,  $0.05 \text{ mol}\cdot\text{L}^{-1}$  sodium selenosulfate ( $\text{Na}_2\text{SeSO}_3$ ), and  $3 \text{ mol}\cdot\text{L}^{-1}$   $\text{CH}_3\text{CHOHCH}_3$  were added to 50 mL distilled water, ultrasonicated for 10 min, and further irradiated for several hours to produce the yellow-red products.  $\text{Na}_2\text{SeSO}_3$  can be synthesized by refluxing Se powders in an  $\text{Na}_2\text{SO}_3$  solution, according to the literature (23). The final yellow-red products were filtered off and washed with distilled water and ethanol successively and then dried for 6 h under vacuum at room temperature.

### Measurements

Powder X-ray diffraction (XRD) was performed on a Japan Rigaku D/Max rA rotation anode X-ray diffractometer, equipped with a Ni-filter Cu  $K\alpha$  radiation source ( $\lambda = 1.54178 \text{ \AA}$ ), 40 kV and 100 mA as the applied voltage and current, a scanning speed of  $8.00^\circ \text{ min}^{-1}$ , and a  $2\theta$  range of  $20^\circ$ – $70^\circ$ . The nanocrystal size and core-shell nanostructure

**Fig. 1.** XRD patterns of (a) CdS nanoparticles, (b) CdS–CdSe with core-shell nanostructure, and (c) CdSe nanoparticles.



investigations were measured by transmission electron microscopy (TEM) and high-resolution electron microscopy (HRTEM); measurements were taken on an H-800 transmission electron microscope with an accelerating voltage of 200 kV and a JEOL-2010 transmission electron microscope, respectively. Nanocrystals were dispersed in ethanol under ultrasonication, and 1 drop of the solution was deposited onto the grid before evaporating naturally. XPS was recorded on an ESCALab MKII instrument with Mg  $K\alpha$  radiation as the exciting source. The UV–vis absorption spectra were recorded on a JANA Spec200PC UV–vis spectrophotometer using quartz cells, and the PL spectra were obtained using a 970CRT-luminescence spectrophotometer with the excitation wavelength of 220 nm.

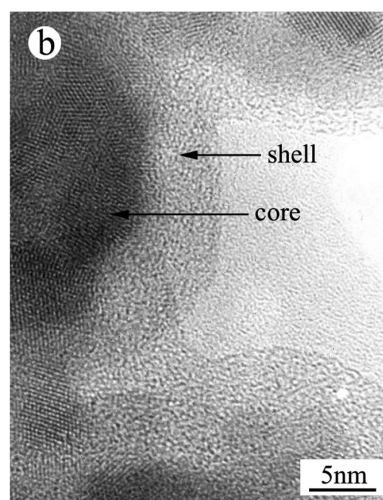
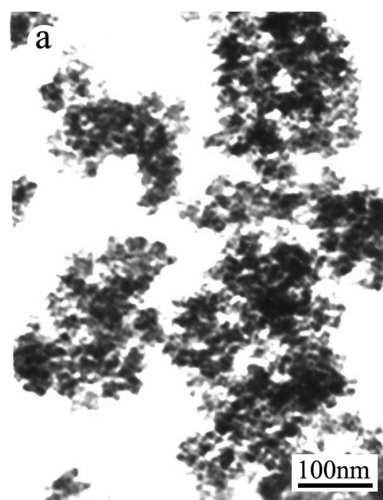
## Results and discussion

### Structural characterization

Powder X-ray diffraction (XRD) patterns of the three samples (shown in Fig. 1) give evidence that the final nanocomposites are CdS–CdSe with core-shell nanostructures. Figure 1a shows the XRD pattern for CdS nanoparticles, and Fig. 1c is the XRD pattern of CdSe nanoparticles, while Fig. 1b is the XRD pattern of the CdS–CdSe core-shell nanocomposites. The reflection peaks of the core-shell nanocomposites shift only a little from those characteristic of pure CdS and pure CdSe. As the shell is grown, the diffraction peaks shift towards a larger  $d$ -spacing (small  $2\theta$ ). Some evidence for a superposition of CdS and CdSe peaks forming the broader peaks can be observed in the nanocomposites, especially on their high-angle sides. If, considering the shifts in the peak positions alone, the XRD patterns may be indicative of alloying, however, a homogeneous alloy would show a significant narrowing of XRD peak widths with increasing size. But in this present case, this narrowing phenomenon is not observed (6). So, Fig. 1b implies the formation of CdS–CdSe with a core-shell nanostructure rather than that of a  $\text{CdS}_x\text{Se}_{1-x}$  alloy. X-ray photoelectron spectroscopy (XPS) was used to measure the composition of the core-shell nanocomposites, and the signal analysis gave an S:Se ratio of 13:1. To further ascertain the core-shell nano-



**Fig. 2.** (a) TEM image of CdS–CdSe core–shell nanocomposites and (b) a typical HRTEM image of CdS–CdSe with core–shell nanostructures.



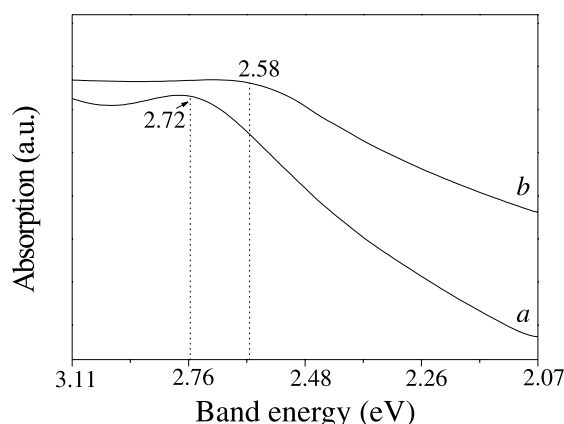
structure, transmission electron microscopy (TEM) and high-resolution electron microscopy (HRTEM) were employed.

The morphology and particle sizes are determined by transmission electron microscopy (TEM) and high-resolution electron microscopy (HRTEM). The TEM image of CdS–CdSe nanocomposites (shown in Fig. 2a) shows the spherical and congregated particles. Figure 2b shows a typical HRTEM micrograph of the CdS–CdSe nanoparticles, in which the core–shell structure can clearly be seen in the entire area, with the dark cores being surrounded by a light shell. In addition, the lattice planes of the CdS core are visible, indicating a high degree of crystallinity. It is also observed that the lattice fringes are continuous throughout the core and the shell. Furthermore, CdS nanoparticles have definitely been overcoated with a thick ( $>3$  nm) layer of CdSe. An increase of 4.00–5.00 nm in size testified to the successful growth of the CdSe shell on the CdS core.

### Optical characterization

The UV–vis absorption spectrum of the bare CdS nanoparticles and the CdS–CdSe core–shell nanocomposites dispersed in the distilled water are shown in Figs. 3a and 3b, respectively; these were carried out using distilled water as reference. A clear “excitonic” peak is visible for the bare CdS at 455 nm (2.72 eV), which clearly red-shifts 25 nm (0.14 eV) after the capping of CdSe is introduced, and this red shift is indicative of the formation of the core–shell structure. The nanocrystalline nature of the CdS and the CdS–CdSe nanocomposites are also reflected by their photoluminescence (PL) spectra, as shown in Fig. 4. When the excitation energy is 5.65 eV ( $\lambda_{\text{ex}} = 220$  nm), the luminescence spectrum of the pure CdS contains a shoulder peak at  $\sim 480$  nm (2.59 eV) (Fig. 4a) and the luminescence spectrum of the CdS–CdSe core–shell structure contains shoulders at  $\sim 456$  nm (2.72 eV) and 530 nm (2.36 eV), along with a peak at  $\sim 480$  nm (Fig. 4b). The peak of  $\sim 456$  nm and a peak of  $\sim 480$  nm may result from the CdS excitonic fluorescence. When the emission at  $\sim 480$  nm (2.59 eV) passes through a thin layer of CdSe, it would be absorbed by CdSe and would excite CdSe to emit luminescence light at  $\sim 530$  nm. In addition,

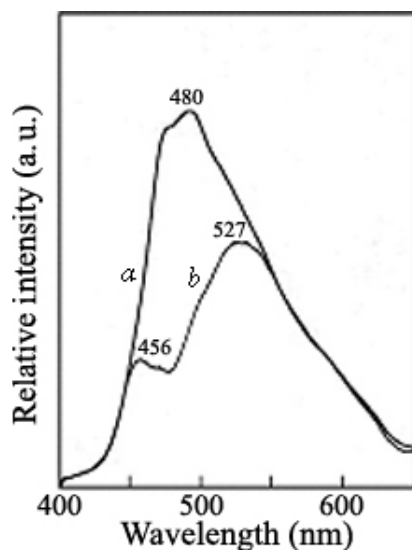
**Fig. 3.** UV–vis absorption spectra of (a) CdS nanoparticles and (b) CdS–CdSe core–shell nanocomposites.



tion, the excited energy used ( $\lambda_{\text{ex}} = 220$  nm) can also excite CdSe to emit luminescence. So, for this CdS–CdSe system, the luminescent intensity of CdS would decrease while that of CdSe would increase, as shown in Fig. 4b. In a comparison of Fig. 4a with Fig. 4b, there is little difference in the profile of the two spectra, probably because of the change in surface structure. The optical spectra are somewhat broadened, probably owing to the following two reasons: (i) Broadening may be caused by a gradual “ripening” of the nanocrystals with time; the effect of aging the core–shell samples in the experimental process is to red-shift and broaden the absorption spectra, and this effect has been reported in many cases, such as for HgTe–CdS core–shell nanoparticles (14). (ii) The shell growth results in a slight broadening while maintaining the optical spectra profile. Similarly, Peng et al. (6) reported the epitaxy growth of CdSe–CdS core–shell nanoparticles in which the absorption spectrum roughly maintains its profile with a slight broadening of feature. Meanwhile, the successful growth of the CdSe shell also causes the fluorescence changes, including the splitting of peaks and the red shift.

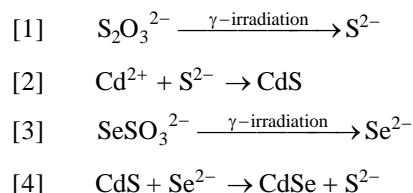


**Fig. 4.** Fluorescence emission spectra (excited at 220 nm) of (a) CdS nanoparticles and (b) CdS–CdSe core–shell nanocomposites.



#### Ion-exchange reaction mechanism

In this approach, the fundamental mechanism of the formation of CdS–CdSe core–shell nanostructure is an ion-exchange reaction followed by a two-step  $\gamma$ -irradiation process. It is known that sodium thiosulfate can homogeneously release  $S^{2-}$  upon  $\gamma$ -irradiation; thus, it is a good sulfur source to use in the formation of the CdS core. As to the formation of the CdSe shell, the selection of selenium source is critical, since the usual selenium source (selenium element) does not dissolve in distilled water, and this will limit the formation of the CdSe shell. Sodium selenosulfate ( $Na_2SeSO_3$ ) is a good selenium source, which may well dissolve in distilled water and homogeneously release  $Se^{2-}$  under  $\gamma$ -irradiation, owing to the similarity in the structures of the  $SeSO_3^{2-}$  and  $S_2O_3^{2-}$  (21, 22), which is propitious to the crystallization of the CdS–CdSe core–shell nanoparticles. The formation of CdSe shell on the CdS core can be described as a substitution-type process, considering the substantial difference between the solubility of the CdS ( $K_{sp} = 1.4 \times 10^{-19}$ ) and that of the CdSe ( $K_{sp} = 1.4 \times 10^{-35}$ ) in distilled water. The reactions for the whole process are as follows:



#### Conclusions

In general,  $\gamma$ -irradiation has been successfully used to prepare the CdS–CdSe core–shell nanocomposites for the first time. The keys to the reaction are the selection of the selenium source and the difference between the solubility of CdS and that of CdSe. Both the XRD pattern and the HRTEM image clearly ascertain the core–shell structure of

the nanocomposites. In addition, this approach is easily extended to the preparation of various metal chalcogenides by changing the core and shell precursor solution. It is reasonable to expand this method to the synthesis of other core–shell nanocomposites because of its ease, reproducibility, and versatility.

#### Acknowledgments

This work was supported by the Chinese National Foundation of Natural Science Research and the Chinese Ministry of Education.

#### References

1. G. Schmid. *Chem. Rev.* **92**, 1709 (1992).
2. A. Henglein. *Chem. Rev.* **89**, 1861 (1989).
3. H. Weller. *Adv. Mater.* **5**, 88 (1993).
4. L.E. Brus. *Appl. Phys. A – Solids Surf.* **53**, 465 (1991).
5. L. Spanhel, M. Haase, H. Weller, and A. Henglein. *J. Am. Chem. Soc.* **109**, 5649 (1987).
6. X.G. Peng, M.C. Schlamp, A.V. Kadavanich, and A.P. Alivisatos. *J. Am. Chem. Soc.* **119**, 7019 (1997).
7. B.O. Dabbousi, J. Rodriguez-Viejo, F.V. Mikulec, J.R. Heine, H. Mattoussi, R. Ober, K.F. Jensen, and M.G. Bawendi. *J. Phys. Chem. B*, **101**, 9463 (1997).
8. A.R. Kortan, R. Hull, R.L. Opila, M.G. Bawendi, M.L. Steigerwald, P.J. Carroll, and L.E. Brus. *J. Am. Chem. Soc.* **112**, 1327 (1990).
9. M.A. Hines and P. Guyot-Sionnest. *J. Phys. Chem.* **100**, 468 (1996).
10. M. Danek, K.F. Jensen, C.B. Murray, and M.G. Bawendi. *Chem. Mater.* **8**, 173 (1996).
11. A. Mews, A. Eychmüller, M. Giersig, D. Schooss, and H. Weller. *J. Phys. Chem.* **98**, 934 (1994).
12. N. Revaprasadu, M.A. Malik, P. O'Brien, and G. Wakefield. *Chem. Commun.* 1573 (1999).
13. Y. Xie, P. Yan, J. Lu, Y.T. Qian, and S.Y. Zhang. *Chem. Comm.* 1969 (1999).
14. M.T. Harrison, S.V. Kershaw, A.L. Rogach, A. Kornowski, A. Eychmüller, and H. Weller. *Adv. Mater.* **12**, 123 (2000).
15. L. Manna, E.C. Scher, L.-S. Li, and A. P. Alivisatos. *J. Am. Chem. Soc.* **124**, 7136 (2002).
16. M.W. Shao, Q. Li, B. Xie, J. Wu, and Y.T. Qian. *Mater. Chem. Phys.* **78**, 288 (2002).
17. M. Danek, K.F. Jensen, C.B. Murray, and M.G. Bawendi. *Appl. Phys. Lett.* **65**, 2795 (1994).
18. J. Rodriguez-Viejo, K.F. Jensen, H. Mattoussi, J. Michel, B.O. Dabbousi, and M.G. Bawendi. *Appl. Phys. Lett.* **70**, 2132 (1997).
19. S.M. Liu, H.Q. Guo, Z.H. Zhang, R. Li, W. Chen, and Z.G. Wang. *Physica E*, **8**, 174 (2000).
20. M.P. Halsall, J.E. Nicholls, J.J. Davies, B. Cockayne, and P.J. Wright. *J. Appl. Phys.* **71**, 907 (1992).
21. Z.P. Qiao, Y. Xie, X.J. Li, C. Wang, Y.J. Zhu, and Y.T. Qian. *J. Mater. Chem.* **9**, 735 (1999).
22. Y. Xie, Z.P. Qiao, M. Chen, X.M. Liu, and Y.T. Qian. *Adv. Mater.* **11**, 1512 (1999).
23. P. Pramanik and R.N. Bhattacharya. *J. Solid State Chem.* **44**, 425 (1982).



# Solubility of carbon dioxide in alkylcarbonates and lactones

F. Blanchard, B. Carré, F. Bonhomme, P. Biensan, and D. Lemordant

**Abstract:** The solubility of carbon dioxide in  $\gamma$ -butyrolactone (BL), caprolactone (CL), propylene carbonate (PC), ethylene carbonate (EC), dimethylcarbonate (DMC), diethylcarbonate (DEC), and mixtures of these components has been determined at temperatures from 275 to 333 K at atmospheric pressure. The Henry's law constant ( $k_H$ ) for the dissolution of  $\text{CO}_2$  in these solvents has been deduced from the solubility data. The value of  $k_H$  increases in the following order:  $\text{DEC} < \text{DMC} < \text{PC} < \text{CL} < \text{BL} < \text{EC}$ , which is identical to the order of the Hildebrand parameters ( $\delta$ ) of the corresponding solvents. The accuracy of classical theories for predicting gas solubilities in liquids has been examined. The best results are given by the Vilcu–Perisamu equation, which is derived from the Scatchard–Hildebrand theory but takes into account the polarizability of the solute and the permittivity of the solvent. A modified form of the Prausnitz and Shair equation is proposed to estimate the solubility of nonpolar molecules in strongly dipolar solvents. This equation fits the experimental data with improved precision.

**Key words:** alkylcarbonate, lactone, carbon dioxide, liquid–gas equilibrium, Henry's law, Hildebrand parameter.

**Résumé :** La solubilité du dioxyde de carbone dans la  $\gamma$ -butyrolactone (BL), la caprolactone (CL), le carbonate de propylène (PC), le carbonate d'éthylène (EC), le diméthylcarbonate (DMC), le diéthylcarbonate (DEC) et dans des mélanges de ces solvants a été déterminée à des températures comprises entre 275 K et 333 K et à pression atmosphérique. Les constantes de Henry ( $k_H$ ) relatives à la dissolution de  $\text{CO}_2$  dans les précédents milieux augmentent dans l'ordre:  $\text{DEC} < \text{DMC} < \text{PC} < \text{CL} < \text{BL} < \text{EC}$ . Les variations de  $k_H$  suivent celles du paramètres d'Hildebrand ( $\delta$ ). La validité des théories classiques pour la prévision de la solubilité des gaz dans les liquides a été examinée. Les meilleurs résultats ont été obtenus par application de la relation de Vilcu et Perisamu qui dérive de la théorie de Scatchard–Hildebrand tout en prenant en compte la polarisabilité du soluté et la permittivité du solvant. Une forme modifiée de l'équation de Prausnitz et Shair est proposée pour estimer la solubilité de molécules apolaires dans des solvants très polaires. Cette équation décrit les résultats expérimentaux avec une précision accrue.

**Mots clés :** alkylcarbonate, lactone, dioxyde de carbone, équilibre liquide–gaz, loi de Henry, paramètre de Hildebrand.

## Introduction

Liquid–gas equilibria play an important role in a wide range of natural and industrial processes. In rechargeable lithium cells, oxidation of the electrolyte, mainly composed of alkylcarbonates and lactones, leads to the formation of  $\text{CO}_2$  when high potentials are applied to the electrode. The resulting increase in pressure in the sealed cell container can be very large when the cell is overcharged. To estimate the total amount of  $\text{CO}_2$  generated at a given pressure, it is necessary to know the solubility of  $\text{CO}_2$  in the solvent or solvent mixture. For this reason it is of interest to determine the

solubility of  $\text{CO}_2$  as a function of temperature in lactones or alkylcarbonates such as  $\gamma$ -butyrolactone (BL), caprolactone (CL), propylene carbonate (PC), ethylene carbonate (EC), dimethylcarbonate (DMC), and diethyl carbonate (DEC) or mixtures of these components.

At low or moderate pressures, the solubility of a gas ( $i$ ) in a liquid solvent ( $s$ ) is given by Henry's law

$$[1] \quad x_i = \frac{P_i}{k_H^s}$$

where  $x_i$  represents the mole fraction of dissolved gas in the solvent,  $P_i$  its partial pressure, and  $k_H^s$  the Henry's law constant for the dissolution of gas  $i$  in solvent  $s$ .

If specific interaction effects (e.g., chemical bonds) between the dissolved molecule and the liquid solvent are negligible, cohesion parameters can be used to provide reasonable estimates of gas solubilities. For this reason, many attempts have been made to predict the solubility of gases in liquids using the Hildebrand solubility parameter ( $\delta$ ) (1–3). The Hildebrand solubility parameter is defined by the following equation:

Received 17 December 2002. Published on the NRC Research Press Web site at <http://canjchem.nrc.ca> on 28 May 2003.

**F. Blanchard, B. Carré, and D. Lemordant.**<sup>1</sup> Laboratoire de Physicochimie des Interfaces et Milieux Réactionnels (EA2098), Université de Tours, Faculté des Sciences et Techniques, Parc de Grandmont, F 37200 TOURS, France.

**F. Bonhomme and P. Biensan.** SAFT, Direction de la Recherche, 111 Boulevard A. Daney, 33074 Bordeaux, France.

<sup>1</sup>Corresponding author (e-mail: [lemordant@univ-tours.fr](mailto:lemordant@univ-tours.fr)).



$$[2] \quad \delta = c^{1/2} = \left( \frac{\Delta_{\text{vap}} U}{V_m} \right)^{1/2}$$

where  $c$  is the cohesive energy per unit volume, which can be calculated from the vaporization energy  $\Delta_{\text{vap}} U$  and the molar volume  $V_m$  of the liquid. Hildebrand and others (1–3) have pointed out that a close relationship exists between the logarithm of the gas solubility and the solvent parameter  $\delta$ . Most of the proposed equations connect the logarithm of the gas solubility to the difference in solubility parameters of the gas ( $\delta_g$ ) and the solvent ( $\delta_s$ ), as

$$[3] \quad \ln x_i = a - b [\delta_s - \delta_i]^2$$

Using relation [3], the numerical values of  $a$  and  $b$  can be deduced from the physical properties of the solute at a given temperature.

To estimate the solubility of gases in liquids, Lawson and co-workers (4–6) and Gjaldbaeck and co-workers (7–11) proposed the following equation based on the Hildebrand–Scatchard theory:

$$[4] \quad \ln x_i = -\ln x_i^{\text{id}} - \frac{V_i}{RT} [\delta_s - \delta_i]^2 - \ln \left( \frac{V_i}{V_s} \right) - \left( 1 - \frac{V_i}{V_s} \right)$$

where  $x_i^{\text{id}}$  is the ideal solubility of the gas,  $V_s$  the molar volume of the solvent, and  $V_i$  the partial molar volume of the gas at infinite dilution in the solvent.

Hildebrand, Prausnitz, and Shair (3, 12) considered a two-stage dissolving process, involving, as an intermediate, a hypothetical liquid state for the gas at room temperature. Using this process, the gas solubility is given by

$$[5] \quad \ln x_i = \ln(f_i / f_{i,l}) - \frac{V_{i,l}}{RT} [\delta_s - \delta_i]^2$$

where  $f_i / f_{i,l}$  is the ratio of the fugacities of the gas in its pure gaseous state to its hypothetical liquid state,  $V_{i,l}$  is the molar volume of the hypothetical liquid, and  $\delta_i$  is its solubility parameter. As  $V_{i,l}$  and  $\delta_i$  cannot be determined experimentally at room temperature, their values were obtained by fitting eq. [5] to available solubility data. The hypothetical fugacity  $f_{i,l}$  can be deduced from the vapour pressure of the dissolved gas and its critical temperature (3, 12). To the best of our knowledge, eq. [5] has never been applied to the dissolution of  $\text{CO}_2$  in strongly dipolar solvents such as carbonates or lactones.

Vilcu, Perisamu, and Cucuiat (13–15) applied eq. [4] to systems composed of a nonpolar gas and a polar solvent. To fit experimental data, they introduce a corrected solubility parameter,  $\delta_s^*$ , which is a function of the dielectric constant of the solvent ( $\epsilon_s$ ) and the polarizability of the solute ( $\alpha_i$ ). Using  $\delta_s^*$  instead of  $\delta_s$  in eq. [5], deviations between experimental and calculated solubilities do not exceed 20%. Nevertheless, when applied to  $\text{CO}_2$  as the dissolved gas, larger deviations are observed owing to the fact that polar solvents dissolve much more  $\text{CO}_2$  than predicted. To take into account the quadrupolar interaction of  $\text{CO}_2$  molecules with solvent dipoles, an extra term has been added ( $Q_{\text{CO}_2}$ ) in the definition of the corrected solubility parameter  $\delta_s^*$  (16)

**Table 1.** Parameters values used in eqs. [4–6] for  $\text{CO}_2$ .

Parameter	eq. [4]	eq. [5]	eqs. [5], [6]
$\delta$ ( $\text{MPa}^{1/2}$ )	6.8(4–6)	12.3(3–12)	10.63*
$10^6 V_i$ ( $\text{m}^3 \text{mol}^{-1}$ )	—	55 (3–12)	35*
$f_i$ (MPa)	—	4.12(17)	4.12 (17)
$\ln x^{\text{id}}$	–3.27 (4–6)	—	—
$10^6 V$ ( $\text{m}^3 \text{mol}^{-1}$ )	105 (4–6)	—	—
$10^{24} \alpha$ (esu)	—	—	2.65 (14–15)
$10^{26} Q$ (esu)	—	—	4.1 (18)

\*Values obtained by fitting.

$$[6] \quad \delta_s^* = \delta_s - (\epsilon_s - 1)(0.1225 - (8.43 \times 10^{21}) \alpha_{\text{CO}_2} + (2.52 \times 10^{24}) Q_{\text{CO}_2})$$

In eq. [6], the quadrupole moment of  $\text{CO}_2$ ,  $Q_{\text{CO}_2}$ , is given in esu and the solubility parameters  $\delta_s^*$  and  $\delta_s$  in  $\text{MPa}^{1/2}$ . Numerical factors have been chosen to fit the experimental results. Parameter values for eqs. [4–6] with  $\text{CO}_2$  as the solute are reported in Table 1.

The main advantage of using the Hildebrand parameter is that  $\delta$  values are available for a wide variety of solvents (19). Modern theories (20–22) make use of the Lennard-Jones potential ( $\lambda$ ) instead of the cohesive energy density. More precise equations are provided but, for practical reasons, simple empirical equation such as (22)

$$[7] \quad \ln x_i = a + b (\lambda / k)^{1/2}$$

are frequently used. Values of  $\lambda$  differ considerably according to the method used to determine them. Consequently,  $\lambda$  values are known less precisely than  $\delta$  values. The application of the Lennard-Jones potential to strongly dipolar solvent and molecules having a quadrupolar moment like  $\text{CO}_2$  is also questionable. We believe that these theories are better able to predict solubilities of nonpolar gases in nonpolar solvents than polar or nonpolar gases in polar solvents.

## Experimental

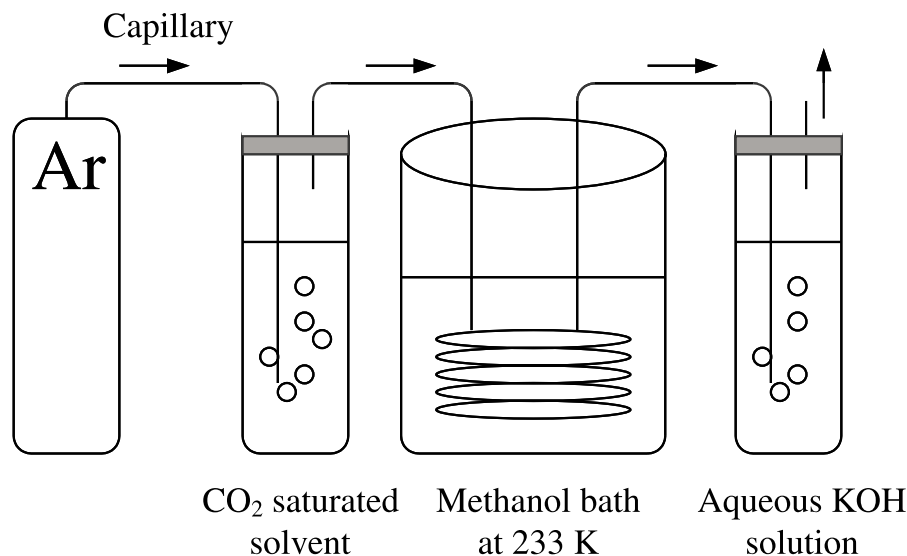
### Materials

Highly pure (99.99%) DMC, DEC, PC, EC, CL, and  $\gamma$ -BL were obtained from Aldrich and used as received. Three mixtures (EC–DMC 1:1 w/w, EC–DEC 1:1 w/w, EC–PC–DMC 1:1:3 w/w/w) were prepared by mixing pure solvent under a dry atmosphere in a glove box. KOH and HCl solutions, used to determine the amount of dissolved  $\text{CO}_2$  in the solvents, were prepared with distilled water. HCl solutions were standardized against KOH by potentiometric titration.

### Methods

The solubility of  $\text{CO}_2$  in each solvent was measured using the apparatus illustrated in Fig. 1. The solvent was first saturated with  $\text{CO}_2$  at atmospheric pressure by dissolving the gas in the liquid placed in a temperature-controlled vessel. When saturation was achieved, the dissolved  $\text{CO}_2$  was displaced from the saturation vessel by an argon flow. To remove the solvent vapors from the argon stream, the gas mixture was passed through a coil immersed in a cold methanol bath (233 K). The solvent-free gas mixture ( $\text{CO}_2 + \text{Ar}$ ) was then introduced into a vessel containing an aqueous KOH solution of known concentration, which was subsequently



**Fig. 1.** Equipment used for the determination of CO<sub>2</sub> solubilities.

titrated with HCl solution. Each measurement was run in triplicate. Henry's law constants at temperatures from 275 to 333 K were calculated from the CO<sub>2</sub> solubilities at atmospheric pressure using eq. [1]. The dielectric constants of the solvents were determined using an impedance spectrometer (Solartron SI 1260).

## Results

### CO<sub>2</sub> solubility in pure solvents

Henry's law constants for CO<sub>2</sub> in DMC, DEC, PC, EC, CL, and  $\delta$ -BL are reported in Table 2 for temperatures from 275 to 333 K. As expected for an exothermic dissolution process, the CO<sub>2</sub> solubility decreases as the temperature is raised. This is in accord with the van't Hoff relation applied to the dissolution of gas in liquids

$$[8] \quad \ln x_i = \frac{\Delta_{\text{dis}}H^\circ}{RT} + \frac{\Delta_{\text{dis}}S^\circ}{R}$$

In eq. [8],  $\Delta_{\text{dis}}H^\circ$  is the standard enthalpy of dissolution of the gas in the liquid,  $R$  is the ideal gas constant, and  $T$  is the temperature.  $\Delta_{\text{dis}}H^\circ$  can be determined by plotting  $\ln x_{\text{CO}_2}$  against  $1/T$  (Fig. 2). The linearity variation of  $\ln x_{\text{CO}_2}$  with  $1/T$  indicated that  $\Delta_{\text{dis}}H^\circ$  (and hence the standard entropy of dissolution  $\Delta_{\text{dis}}S^\circ$ ) can be considered to be independent of temperature in the range of temperatures investigated.

When  $\Delta_{\text{dis}}H^\circ$  is known, the Henry's law constant for CO<sub>2</sub> in each solvent can be calculated at 298 K. The standard entropy and Gibbs energy for the dissolution of CO<sub>2</sub> can be calculated by the following equations

$$[9] \quad \Delta_{\text{dis}}S^\circ = (\Delta_{\text{dis}}H^\circ - \Delta_{\text{dis}}G^\circ)/T$$

$$[10] \quad \Delta_{\text{dis}}G^\circ = RT \ln(k_H)$$

The values of  $k_H$ ,  $\Delta_{\text{dis}}G^\circ$ , and  $\Delta_{\text{dis}}S^\circ$  at 298 K are reported in Table 3 together with the boiling temperature of each solvent at atmospheric pressure. The value of  $k_H$  for PC at 298 K, obtained in the present study, agrees well with published values: 6.86 MPa (23), 7.98 MPa (24), 8.21 MPa (25), 8.22 MPa (26), 8.39 MPa (27), 10.01 MPa (28). Moreover,

**Table 2.** Henry's law constants ( $k_H$  in MPa) for CO<sub>2</sub> dissolution in pure solvents.

$T$ (K)	Cyclic carbonates		Linear carbonates		Lactones	
	EC	PC	DMC	DEC	BL	CL
275	<sup>a</sup>	5.33	<sup>a</sup>	4.05	7.18	6.63
283	<sup>a</sup>	—	5.41	—	—	—
291	16.08 <sup>b</sup>	8.29	6.17	5.39	9.85	8.81
313	20.47	—	—	—	—	11.78
316	—	13.06	10.95	7.99	16.50	—
333	27.51	—	—	—	—	—

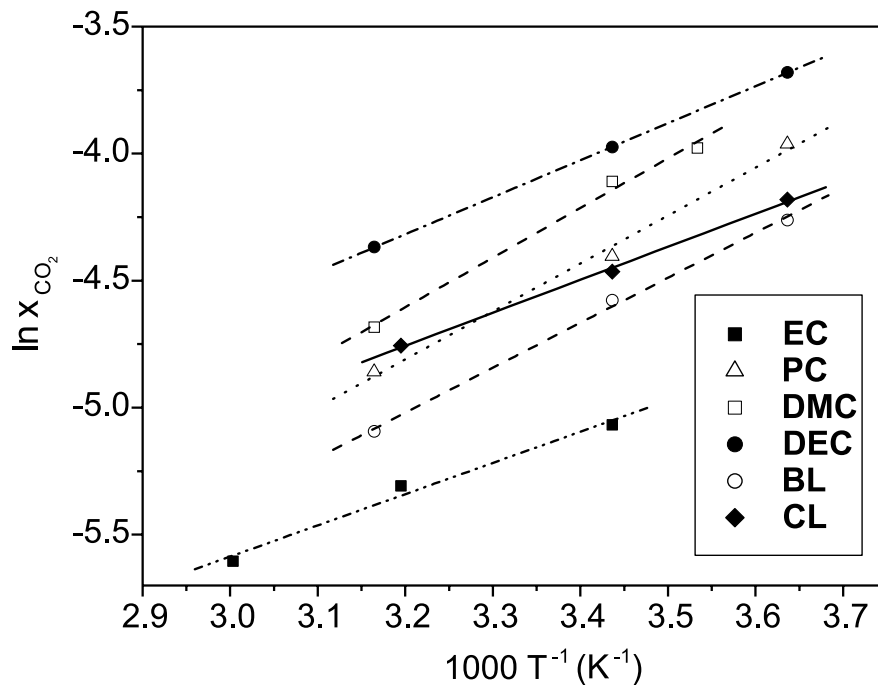
<sup>a</sup>Solid at this temperature.

<sup>b</sup>Extrapolated value, refer to text.

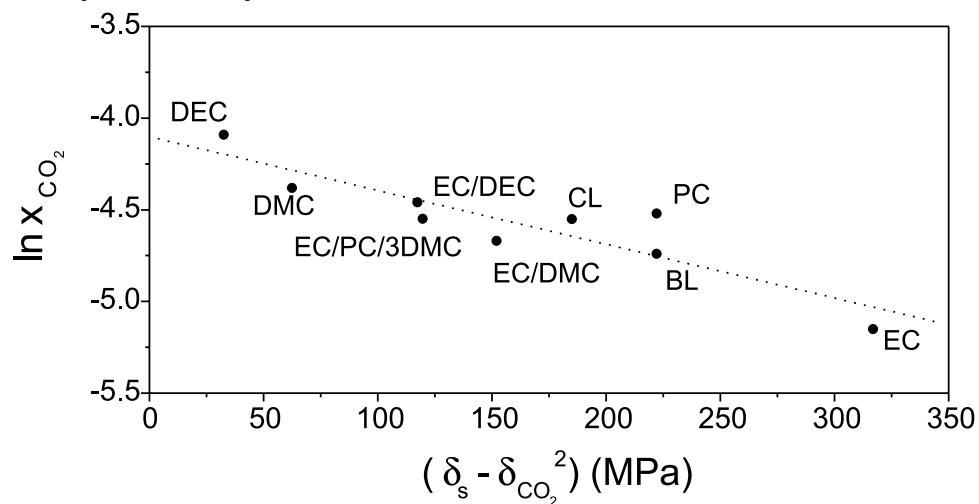
the standard enthalpy of dissolution of CO<sub>2</sub> in PC, deduced from the variations of  $k_H$  with temperature ( $-15.7 \text{ kJ mol}^{-1}$ ), is in excellent agreement with the value  $-15.9 \text{ kJ mol}^{-1}$  given by Murrieta-Guevara et al. (25). In the case of BL and EC, respectively, our results,  $k_H(\text{BL}, 298 \text{ K}) = 11.66 \text{ MPa}$  and  $k_H(\text{EC}, 313 \text{ K}) = 20.47 \text{ MPa}$ , are higher than those proposed by Kassim et al. (29):  $k_H(\text{BL}, 303 \text{ K}) = 6.33 \text{ MPa}$  or by Vilcu et al. (13):  $k_H(\text{EC}, 313 \text{ K}) = 14.41 \text{ MPa}$ . The origin of these discrepancies is not known, but one may remark that our values fit eq. [3] better, as seen on the graph in Fig. 3. Among the solvents investigated, DEC dissolves the largest quantity of CO<sub>2</sub> at atmospheric pressure and EC the smallest. It is noticeable that in each homologous series of solvents (acyclic carbonates, cyclic carbonates, and lactones), the solvent having the highest molecular weight dissolves the largest amount of CO<sub>2</sub>.

As expected for the dissolution of a gas like CO<sub>2</sub>, the dissolution enthalpies are all negative and increase with the boiling temperature of the solvent in all series. Following Hildebrand, Prausnitz, and Shair (3, 12), CO<sub>2</sub> dissolution may be interpreted as a two-step process that involves, as an intermediate, CO<sub>2</sub> in its hypothetical liquid state, as illustrated in Fig. 4. From this scheme, the following relation is easily inferred

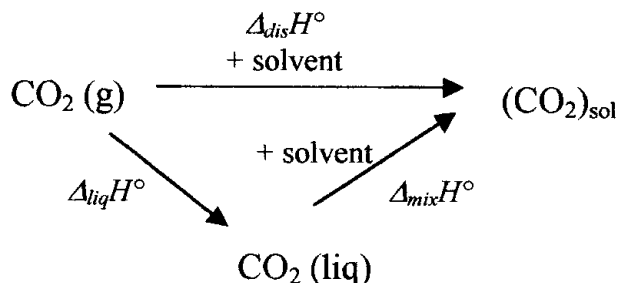


**Fig. 2.** Plot of  $\ln x_{\text{CO}_2}$  against  $1/T$  for  $\text{CO}_2$  dissolved in pure solvents.**Table 3.** Thermodynamic parameters and Henry's law constant at 298 K for pure solvents.

	EC	PC	DMC	DEC	BL	CL
$M (\text{g mol}^{-1})$	88.06	102.08	90.08	118.13	86.09	114.15
$T_{\text{vap}} (\text{K})$	517	513	363	400	477	508
$k_{\text{H}} (\text{MPa})$	17.46	9.27	7.48	6.07	11.64	9.63
$\Delta_{\text{dis}} H^{\circ} (\text{kJ mol}^{-1})$	-9.2	-15.7	-16.2	-11.9	-14.7	-10.8
$\Delta_{\text{mix}} H^{\circ} (\text{kJ mol}^{-1})$	7.7	1.2	0.7	5.0	2.2	6.1
$\Delta_{\text{dis}} G^{\circ} (\text{kJ mol}^{-1})$	12.8	11.2	10.6	10.1	11.7	11.3
$\Delta S^{\circ} (\text{J K}^{-1} \text{mol}^{-1})$	-73.8	-90.1	-89.9	-73.8	-88.6	-74.1

**Fig. 3.** Variations of  $\ln x_{\text{CO}_2}$  with  $(\delta_{\text{S}} - \delta_{\text{CO}_2})^2$  at 298 K.



**Fig. 4.** Scheme for CO<sub>2</sub> dissolution in liquids.

$$[11] \quad \Delta_{\text{dis}}H^\circ = \Delta_{\text{liq}}H^\circ + \Delta_{\text{mix}}H^\circ$$

In eq. [11],  $\Delta_{\text{liq}}H^\circ = -16.90 \text{ kJ mol}^{-1}$  is the standard enthalpy of liquefaction of CO<sub>2</sub> at 298 K and  $\Delta_{\text{mix}}H^\circ$  is the enthalpy of mixing of the solvent with CO<sub>2</sub> in its hypothetical liquid state. Calculated values of  $\Delta_{\text{dis}}H^\circ$  and  $\Delta_{\text{mix}}H^\circ$  are reported in Table 3.

The enthalpies of mixing are all positive, which clearly indicates a lack of specific interactions of CO<sub>2</sub> with these dipolar solvents. The largest  $\Delta_{\text{mix}}H^\circ$  value is observed for EC, which is known to be partially self-associated, as indicated by its Kirkwood factor ( $g = 1.2$ ) (30). The  $\Delta_{\text{dis}}S^\circ$  values are relatively large and negative, owing to the entropy of liquefaction of CO<sub>2</sub> in the first step, which is partially counterbalanced by the entropy of mixing that follows according to the scheme illustrated in Fig. 4.

### CO<sub>2</sub> solubility in mixed solvents

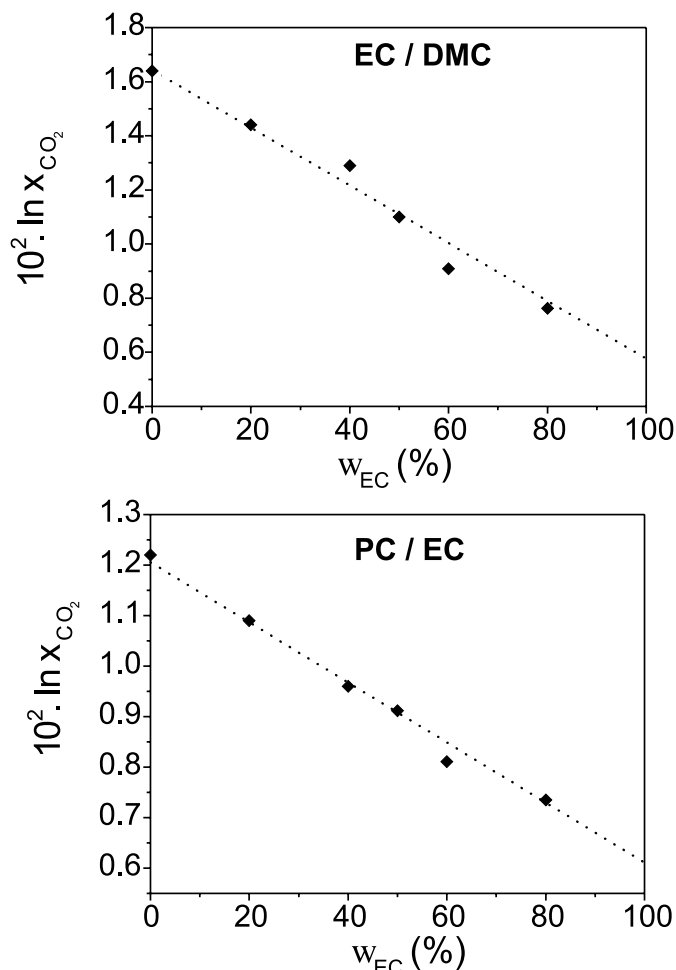
Solubilities of CO<sub>2</sub> at 291 K in PC–EC and EC–DMC mixtures are listed in Fig. 5 as a function of the weight fraction in EC ( $w_{\text{EC}}$ ). The variations in solubilities follow a linear relationship when the composition of the solvent is expressed in weight fractions. This result has been used for determining, by a linear extrapolation, the solubility of supercooled CO<sub>2</sub> in EC at 291 K (EC is solid below 311 K).

Henry law constants for the dissolution of CO<sub>2</sub> in EC–DMC (1:1), EC–DEC (1:1), and EC–PC–DMC (1:1:3), at 275, 291, and 316 K, are listed in Table 4. Values of  $k_{\text{H}}$ ,  $\Delta_{\text{dis}}H^\circ$ ,  $\Delta_{\text{mix}}H^\circ$ ,  $\Delta_{\text{dis}}G^\circ$ , and  $\Delta_{\text{dis}}S^\circ$  have been determined at 298 K by use of eqs. [8–11] and are reported in Table 5. The enthalpies of mixing of CO<sub>2</sub> in its hypothetical liquid state with those mixed solvents containing a large amount of DMC (EC–DMC and EC–PC–3DMC) are very weak.

### Comparison of measured and calculated CO<sub>2</sub> solubilities

Equation [3] has been used to estimate solubilities for the present CO<sub>2</sub> – dipolar solvent systems. As illustrated in Fig. 3, a linear relationship is obtained when  $\ln x_{\text{CO}_2}$  is plotted against  $(\delta_{\text{S}} - \delta_{\text{CO}_2})^2$ . For this purpose, the solubility parameters (19) given in Table 6 were used, and for CO<sub>2</sub>,  $\delta_{\text{CO}_2} = 12.3 \text{ MPa}^{1/2}$  has been adopted (3, 12). The solubility parameters of the three solvent mixtures are calculated by:

$$[12] \quad \delta = \sum_i^n \Phi_i \delta_i$$

**Fig. 5.** CO<sub>2</sub> solubility in EC–DMC (a) and PC–EC (b) mixed solvents as a function of the weight fraction in EC.**Table 4.** Henry's law constant in MPa for CO<sub>2</sub> in mixed solvents.

<i>T</i> (K)	EC–PC–3DMC	EC–DMC	EC–DEC
275	5.73	6.00	<sup>a</sup>
291	7.84	9.24	7.74
316	14.10	15.98	11.67

<sup>a</sup>Solid at this temperature.

**Table 5.** Thermodynamic parameters and Henry's law constant at 298 K for mixed solvents.

	EC–PC–3DMC	EC–DMC	EC–DEC
$k_{\text{H}}$ (MPa)	9.59	10.81	8.75
$\Delta_{\text{dis}}H^\circ$ (kJ mol <sup>-1</sup> )	-15.9	-17.2	-12.5
$\Delta_{\text{mix}}H^\circ$ (kJ mol <sup>-1</sup> )	1.0	-0.3	4.4
$\Delta_{\text{dis}}G^\circ$ (kJ mol <sup>-1</sup> )	11.3	11.6	11.0
$\Delta_{\text{dis}}S^\circ$ (J K <sup>-1</sup> mol <sup>-1</sup> )	-91.3	-96.6	-78.9

where  $\Phi_i$  and  $\delta_i$  represent, respectively, the volume fraction of component  $i$  and the solubility parameter of the pure solvent  $i$  (19). As shown in Fig. 3, only PC exhibits a positive deviation from the correlation.



**Table 6.** Hildebrand parameters and solvent dielectric constants.

	EC	PC	DEC	DMC	CL	BL	EC-PC-3DMC	EC-DMC	EC-DEC
$\delta$ (MPa <sup>1/2</sup> )	30.1	27.2	18	20.2	25.9	27.2	23.2	24.6	23.1
$\epsilon_r$	89.6	64.4	2.8	3.1	41.8	41.8	27.0	29.3	36.0

**Table 7.** Comparison of measured and predicted CO<sub>2</sub> solubilities.

$\log_{10}x_{\text{CO}_2}$	EC	PC	DMC	DEC	BL	CL	EC-PC-3DMC	EC-DMC	EC-DEC
Measured	-2.32	-1.96	-1.87	-1.78	-2.06	-1.98	-1.98	-2.03	-1.94
eq. [4]	-10.94	-9.08	-4.73	-3.73	-9.08	-8.14	-6.40	-7.28	-6.33
eq. [5]	-4.52	-3.75	-2.21	-1.92	-3.75	-3.39	-2.76	-3.08	-2.74
eqs. [5, 6]	-1.63	-1.70	-2.12	-1.91	-2.10	-1.92	-1.94	-2.04	-1.79
eqs. [5, 13]	-2.01	-1.96	-1.87	-1.70	-2.27	-2.08	-1.93	-2.07	-1.83

CO<sub>2</sub> solubilities given by eqs. [4–6] are reported in Table 7, together with our experimental results. The Perisamu equation, eqs. [5, 6], gives the best agreement, even though large deviations are observed in the case of PC and EC and to a lesser extent for DMC and DEC. Moreover, for EC and PC, the calculated solubilities are lower than the experimental values, but the reverse is true for DMC and DEC.

To obtain a better fit to the experimental results, the Prausnitz and Shair equation, eq. [5], has been modified by taking into account the quadrupolar interaction of the solute with the solvent. For this purpose a corrected solvent solubility parameter ( $\delta'$  in MPa<sup>1/2</sup>) has been introduced:

$$[13] \quad \delta' = \delta_s - (0.1\epsilon_s + 2.41)$$

Equation [13] is in fact identical to eq. [6], but the numerical values have been fitted to experimental data. This equation allows for reasonably good predictions of CO<sub>2</sub> solubilities when polar, as well as nonpolar, solvents are used (refer to eqs. [5] and [13] in Table 7).

## Conclusions

The solubilities of carbon dioxide in liquid lactones and alkylcarbonates have been determined at temperatures ranging from 275 to 333 K. In a homologous series of solvents (acyclic carbonate, cyclic carbonate, and lactone), the solubility increases with the molecular weight of the solvent. The standard enthalpies and entropies for the dissolution of CO<sub>2</sub> in these solvents have been deduced from the variations in the Henry's law constant with temperature.

Classical theories using the well-known Hildebrand parameter may be used for predicting CO<sub>2</sub> solubilities in liquids. The present results show that large discrepancies between calculated and experimental values are observed when dipolar aprotic solvents are used as dissolution media. The quadrupolar moment of CO<sub>2</sub>, interacting with the strong dipolar moment of the solvent molecules, may be invoked to explain these deviations. To take into account this specific intermolecular interaction and to fit experimental data with a better accuracy, a modified version of the Prausnitz and Shair equation has been proposed.

## References

1. J.H. Hildebrand and R.L. Scott. *In* Solubility of non-electrolytes. 3rd ed. Reinhold, New York. 1950.
2. J.H. Hildebrand and R.L. Scott. *In* Regular solutions. Prentice Hall, Englewood Cliffs. 1962.
3. J.H. Hildebrand and J.M. Prausnitz. *In* Regular and related solutions. Reinhold, Princeton. 1970.
4. H.A. Franck and D.D. Lawson. Methods for estimating the solubility of gases in electrolytes used in lithium batteries. *Proc. Electrochem. Soc.* 81 (1981); *Proc. Symp. Lithium Batteries*. p. 364-371.
5. D.D. Lawson, J. Moacanin, K.V. Jr. Scherer, T.F. Terranova, and J.D. Ingham. *J. Fluorine Chem.* **12**, 221 (1978).
6. D.D. Lawson. *Appl. Energy*, **6**, 241 (1980).
7. E.S. Thomsen and J.C. Gjaldbaek. *Acta Chem. Scand.* **17**, 127 (1963).
8. J.C. Gjaldbaek and J.H. Hildebrand. *J. Amer. Chem. Soc.* **71**, 3147 (1949).
9. J.C. Gjaldbaek. *Acta Chem. Scand.* **6**, 623 (1952).
10. A. Lannung and J.C. Gjaldbaek. *Acta Chem. Scand.* **14**, 1124 (1960).
11. J.C. Gjaldbaek and E.K. Anderson. *Acta Chem. Scand.* **8**, 1398 (1954).
12. J.M. Prausnitz and F.H. Shair. *AIChE J.* **7**, 682 (1961).
13. R. Vilcu, S.T. Perisanu, and M. Cucuiat. *Pol. J. Chem.* **54**, 2043 (1980).
14. R. Vilcu and S.T. Perisanu. *Pol. J. Chem.* **61**, 281 (1987).
15. R. Vilcu and S.T. Perisanu. *Rev. Roum. Chim.* **33**, 351 (1988).
16. S.T. Perisanu. *J. Solution Chem.* **30**, 183 (2001).
17. J.M. Prausnitz and T.F. Anderson. *In* Computer calculation for multicomponent vapor-liquid or liquid-liquid equilibria. Prentice Hall, Englewood Cliffs. 1980.
18. A.D. Buckingham and L. Dish. *Proc. R. Soc. A* **273**, 275 (1963).
19. F.M. Barton. *In* Handbook of solubility parameters and other cohesion parameters. CRC Press, Boca Raton, Florida. 1983.
20. E. Wilhelm and R. Battino. *J. Chem. Thermodyn.* **5**, 117 (1973).
21. R.A. Pierotti. *J. Phys. Chem.* **67**, 1840 (1963).
22. I.L. Leites. *Sep. Purif. Technol.* **12**, 201(1997).
23. J.Y. Lenoir, P. Renault, and H. Renon. *J. Chem. Eng. Data*, **16**, 340 (1971).
24. F. Murrieta-Guevara and A. Trejo Rodriguez. *J. Chem. Eng. Data*, **29**, 456 (1984).
25. F. Murrieta-Guevara, A. Romero Martinez, and A. Trejo. *Fluid Phase Equilib.* **44**, 105, 1988.



26. P.D. Mantor, O. Abib, K.Y. Song, and R. Kobayashi. *J. Chem. Eng. Data*, **27**, 243 (1982).
27. O.R. Rivas and J.M. Prausnitz. *AIChE J.* **25**, 975 (1979).
28. P. Schmack and H.J. Bittrich. *In Gas purification*. 2nd ed. Gulf, Houston. 1974.
29. D.M. Kassim, H.A. Zainel, S.A. Al-Asef, and E.K. Talib. *Fluid Phase Equilib.* **41**, 287 (1988).
30. R. Naejus, C. Damas, D. Lemordant, R. Coudert, and P. Willmann. *J. Chem. Thermodyn.* **34**, 795 (2002).



# UNIFAC calculation of thermodynamic properties of binary 1-chloroalkane + alkane and $\alpha,\omega$ -dichloroalkane + alkane mixtures: Comparison with Nitta–Chao and DISQUAC predictions

J. García, E.R. López, M.J.P. Comuñas, L. Lugo, and J. Fernández

**Abstract:** Data available in the literature for vapor–liquid equilibria, activity coefficients at infinite dilution, and enthalpies of mixing for binary mixtures of 1-chloroalkanes or dichloroalkanes with alkanes are used to determine interaction parameters for three versions of the UNIFAC model — the Tassios et al., Larsen et al., and Gmehling et al. versions. The interaction parameters for chlorine and methyl or methylene groups are calculated using data for the thermodynamic properties of 1-chloroalkane + alkane mixtures. In the case of the Gmehling version, the geometrical parameters for chlorine are also determined. In addition, structure-dependent interaction parameters for  $\alpha,\omega$ -dichloroalkane + alkane mixtures are presented, taking into account the proximity effect. When the two chlorine atoms of the dichloroalkane are more separated, they become more independent, and the reported values of the interaction parameters approach those of 1-chloroalkane. For all of the properties studied the mean deviation obtained with the new parameter values is lower than that obtained with older values. The results for the thermodynamic properties obtained using the new parameters of the three versions of UNIFAC are compared with those of DISQUAC and Nitta–Chao models.

**Key words:** alkanes, chloroalkanes, DISQUAC, excess thermodynamic properties, proximity effect, UNIFAC.

**Résumé :** Les données publiées dans la littérature de l'équilibre liquide vapeur, des coefficients d'activité à dilution infinie et de l'enthalpie de mélange des systèmes binaires 1-chloroalcane ou dichloroalcane + alcanes, ont été utilisées dans ce travail pour déterminer les paramètres d'interaction pour trois versions du modèle d'UNIFAC, celle de Tassios et al., Larsen et al., et Gmehling et al. Premièrement, les paramètres d'interaction pour les groupes chlorine, méthyle et méthylène ont été calculés en considérant des données des propriétés thermodynamiques des mélanges 1-chloroalcane + alcane. Pour la version de Gmehling, les paramètres géométriques du groupe chlorine ont été aussi déterminés. Secondement, les paramètres d'interaction pour les mélanges  $\alpha,\omega$ -dichloroalcane + alcane ont été calculés en considérant l'effet de proximité. Si les deux atomes chlorine du dichloroalcane sont de plus en plus écartés, ils sont plus indépendants et les valeurs retrouvées pour les paramètres d'interaction sont très proches à ceux du 1-chloroalcane. Pour toutes les propriétés thermodynamiques étudiées, la déviation moyenne obtenue avec les nouvelles valeurs des paramètres est inférieure à celle trouvée avec les anciennes valeurs. Finalement, les résultats obtenus dans ce travail avec les trois versions du modèle d'UNIFAC, ont été comparés aux résultats des modèles de Nitta–Chao et de DISQUAC.

**Mots clés :** alcanes, chloroalcanes, DISQUAC, propriété thermodynamique d'excès, effet proximité, UNIFAC.

## Introduction

Knowledge of the thermophysical properties of mixtures containing halogenated hydrocarbons is of considerable interest because these systems are widely used as solvents, blowing agents, and working fluids in refrigeration and in

air conditioning systems (1). Furthermore, from a theoretical point of view, these mixtures provide very interesting tests of group-contribution models because of the variety of the molecules and the availability of thermodynamic data.

The fundamental assumption of the group-contribution models is that the properties of a group and its interaction energies with other groups are molecule-independent. When a group is postulated, its contributions are estimated by correlating experimental data, and the group identification is tested by comparison with experimental data for other systems. On the basis of this comparison, the group is either accepted or redefined. The group as a whole should have approximately the same net charge, independent of the molecule in which it appears (2). The charge of a group can be affected by neighboring groups, which is known as the intramolecular proximity effect. Proximity effects are especially

Received 17 December 2002. Published on the NRC Research Press Web site at <http://canjchem.nrc.ca> on 28 May 2003.

J. García,<sup>1</sup> E.R. López, M.J.P. Comuñas, L. Lugo, and J. Fernández,<sup>2</sup> Laboratorio de Propiedades Termofísicas, Facultade de Física, Universidade de Santiago de Compostela, E-15782 Santiago de Compostela, Spain.

<sup>1</sup>Present address: Dpto. de Física Aplicada, Facultade de Ciencias, Universidade de Vigo, E-36200 Vigo, Spain.

<sup>2</sup>Corresponding author (e-mail: fajferna@usc.es).



important in cases where two or more polarizing atoms such as F, Cl, or Br are present in the same molecule. The proximity effect for molecules containing two identical polarizing groups (such as  $X(\text{CH}_2)X$ ) is called the homoproximity effect. The corresponding effect in molecules containing two different polarizing groups (such as  $X(\text{CH}_2)Y$ ) is called the heteroproximity effect. In 1989 Wu and Sandler (2) tested proximity effects in the UNIFAC model by analyzing predictions for mixtures of ether compounds. Wu et al. (3) confirmed that the predictions of the UNIFAC model are poor in systems containing morpholine because of important proximity effects.

Subsequently, Wu and Sandler (4, 5) proposed several rules for choosing the definition of groups, specifying that the groups must be approximately electroneutral. This method gives rise to an increase in the number of groups that must be employed and also requires quantum-mechanical analysis to identify the functional groups. However, until now, electronic charge contributions were calculated for only a few halogenated alkanes. Following this line, Storm (6), Kleiber (7, 8), and Jadot and Frère (9), among others, have given different group assignments for fluorocarbons, chlorocarbons, and hydrofluorocarbons. Recently, a new UNIFAC model, to be called KT-UNIFAC, was proposed by Kang et al. (10), to include proximity effects and to distinguish between isomers using contributions from first-order and second-order groups to predict vapor-liquid equilibria. The first-order functional groups are those currently applied in the estimation of mixture properties (i.e., the original UNIFAC), whereas the second-order functional groups involve molecular-structure data. The role of the second-order groups is to consider the proximity effects and to distinguish between isomers.

A solution to the above-mentioned problem has been proposed by Kehiaian and Marongiu (11) using the DISQUAC model. These authors keep the same definition of the groups and allow the interaction parameters to vary regularly with the molecular structure. This method is based on the fact that there is no a priori reason that the force field of an atom or group of atoms should be completely independent of the intramolecular environment. The results obtained by these authors are very good, especially for systems presenting proximity effects.

Following this point of view, in a previous study (12) we determined a set of Nitta-Chao interaction parameters that depend regularly on the chloroalkane length for  $\alpha,\omega$ -dichloroalkane +  $n$ -alkane mixtures. Furthermore, Ortega and Placido (13) have published interaction parameters, which depend on the alkane and dihalogenoalkane chain-lengths, in the framework of the Tassios version of the UNIFAC model for the  $\alpha,\omega$ -dihalogenoalkane (Cl, Br, I) +  $n$ -alkane binary mixtures. It is not clear, however, why the reported parameters can change with the alkane length, because the alkanes do not have polarizing atoms and therefore do not present the proximity effect. Owing to this fact, we prefer not to change the parameters with the alkane length.

For the Larsen et al. (14) and Gmehling et al. (15) UNIFAC versions (also called Lingby and Dortmund UNIFAC), no literature values are available for parameters that change regularly with molecular structure. Taking into account the proximity effect in the present article, we have

determined the interaction parameters of the Tassios, Larsen, and Gmehling versions of UNIFAC, as a function of the distance between the chlorine groups, for the  $\alpha,\omega$ -dichloroalkane + alkane mixtures. We have also determined, for 1-chloroalkane + alkane systems, a unique set of parameters for each version of the UNIFAC model. An updated database of experimental literature values of excess Gibbs energies (16–23), excess enthalpies (24–39), and infinite dilution activity coefficients (40–51) for these kinds of mixtures have been used.

## Application of the theoretical model

### The UNIFAC versions

The UNIFAC group-contribution model is based on the UNIQUAC equation. The activity coefficient is divided arbitrarily into two parts; the first is a combinatorial term that depends on the volume and surface area of each molecule, and the second, the residual term, is directly related to energy differences. In this sketch we will show only the main differences between the three versions of the UNIFAC model employed here.

The group interaction parameter between  $m$  and  $n$  groups,  $\Psi_{mn}$ , appearing in the residual contribution, is given by

$$[1] \quad \Psi_{mn} = \exp \left[ -\frac{a_{mn}}{T} \right]$$

In the original UNIFAC model,  $a_{mn}$  is assumed to be independent of the temperature, whereas in the Tassios version  $a_{mn}$  is given by

$$[2] \quad a_{mn} = \frac{z}{2} a'_{mn}$$

where  $z$  is the temperature function

$$[3] \quad z = 35.2 - 0.1272 T + 0.00014 T^2$$

and  $a'_{mn}$  are adjustable interaction parameters. This version can predict only excess enthalpies, using two fitting parameters,  $a'_{mn}$  and  $a'_{nn}$ , for each pair of groups. The Tassios version of the UNIFAC model was developed to predict excess enthalpies and to complement the original UNIFAC model that predicts only excess Gibbs energies ( $G^E$ ). Then the parameter values for the Tassios version are calculated only from experimental excess enthalpies.

In the Larsen version,  $a_{mn}$  depends on the temperature, as:

$$[4] \quad a_{mn} = a_{mn,1} + a_{mn,2} (T - T_0) + a_{mn,3} (T \ln (T_0/T) + T - T_0)$$

In the Larsen version,  $G^E$  at the temperature  $T_0$  depends only on the first interaction parameter coefficient,  $a_{mn,1}$ , while the excess enthalpy depends on the first and second coefficients,  $a_{mn,1}$  and  $a_{mn,2}$ . The excess heat capacity depends on the three coefficients,  $a_{mn,1}$ ,  $a_{mn,2}$ , and  $a_{mn,3}$ .

For the Gmehling version,  $a_{mn}$  is expressed as the following function of the temperature

$$[5] \quad a_{mn} = a_{mn,1} + a_{mn,2} T + a_{mn,3} T^2$$

The Larsen and Gmehling versions can predict excess enthalpies, excess Gibbs energies, and infinite dilution coef-



ficients with six parameters for each pair of groups,  $a_{mn,i}$  and  $a_{nm,i}$ , with  $i = 1, 2$ , and  $3$ . In addition, in the Gmehling modification the volume parameter of the group  $m$ ,  $R_m$ , and the surface parameter of the group  $m$ ,  $Q_m$ , are determined by fitting to experimental data.

The combinatorial contribution in the original UNIFAC model is given by the classical Guggenheim (52) approximation for athermal mixtures, whereas in the Larsen version the modification suggested by Kikic et al. (53) has been used. Gmehling et al. (15) changed the original combinatorial part of the UNIFAC model by introducing an empirical 3/4-exponent.

### Estimation of the characteristic parameters

Three types of groups form the components in the chloroalkane + alkane mixtures: chlorine groups (defined as Cl in the Tassios version and as  $\text{ClCH}_2$  for the Larsen and Gmehling versions) and both methyl and methylene groups (defined as  $\text{CH}_3$  and  $\text{CH}_2$ , respectively, for the three versions). As it is standard for the group-contribution models, the energetic parameters of the  $\text{CH}_3$  group will be considered here to be the same as those of the  $\text{CH}_2$  group. We have determined the interaction parameters for the 1-chloroalkane + alkane mixtures using a Marquardt algorithm. In the case of the Gmehling version, the structural parameters  $Q_{\text{Cl}}$  and  $R_{\text{Cl}}$  were also fitted, whereas  $Q_{\text{CH}_2}$ ,  $Q_{\text{CH}_3}$ ,  $R_{\text{CH}_2}$ , and  $R_{\text{CH}_3}$  were taken from the literature (15). The geometrical parameters for the other versions are determined, as usual, by the Bondi method. It must be pointed that the values of  $(z/2)Q_m$  coincide with that of  $Q_m$  for the original and Tassios versions. Tables 1–3 list the calculated parameters for the three versions.

Subsequently, for each dichloroalkane molecule, the energetic parameters were calculated using the database values and also the Marquardt optimization algorithm with the following constraints: (i) all the sets of parameters must present a regular dependence on the number of carbons in the dichloroalkane and (ii) according to the proximity effect, when the chloro groups of the dichloroalkane are more separated they become more independent, and therefore the values of the energetic parameters should approach those of the 1-chloroalkane. The parameters obtained in this manner are shown in Tables 4–6.

The databases employed to fit the parameters contained all of the experimental excess Gibbs energies listed in Table 7 and the enthalpy ( $H^E$ ) and activity coefficient at infinite dilution ( $\ln \gamma^\infty$ ) values marked with asterisks in Tables 8–10. One of the criteria used to choose a suitable database was the overall coherence of the experimental data. In addition, because the UNIFAC model fails for long-chain components, we have not introduced the activity coefficients at infinite dilution for systems containing compounds with more than 18 carbon atoms.

In Fig. 1 we have plotted the interaction parameters of the Tassios version against the number of carbons of the dichloroalkane. The interaction parameters for 1,8-dichlorooctane were guessed by following the regularity obtained with the dichloroalkane length. For this system, no experimental excess enthalpies — which could have been used to calculate the interaction parameters — were found in the literature. It is worth noting that the shapes of the interaction

**Table 1.** Geometrical ( $Q_m$ ) and interaction ( $a'_{mn}$  (K)) parameters of 1-chloroalkane + alkane systems for the Tassios version.

$Q_m$	Subgroup	Main group, $m$	$a'_{m\text{CH}_2}$	$a'_{m\text{Cl}}$
0.848	$\text{CH}_3$	$\text{CH}_2$	0.0	70
0.540	$\text{CH}_2$	$\text{Cl}$	140	0.0

**Fig. 1.** Plot of the interaction parameters of the Tassios version,  $a_{\text{CH}_2\text{Cl}}$  and  $a_{\text{ClCH}_2}$  for chloroalkane + alkane mixtures against  $n$ , the number of carbons in the dichloroalkane; (●) adjusted parameters, (○) guessed parameters.

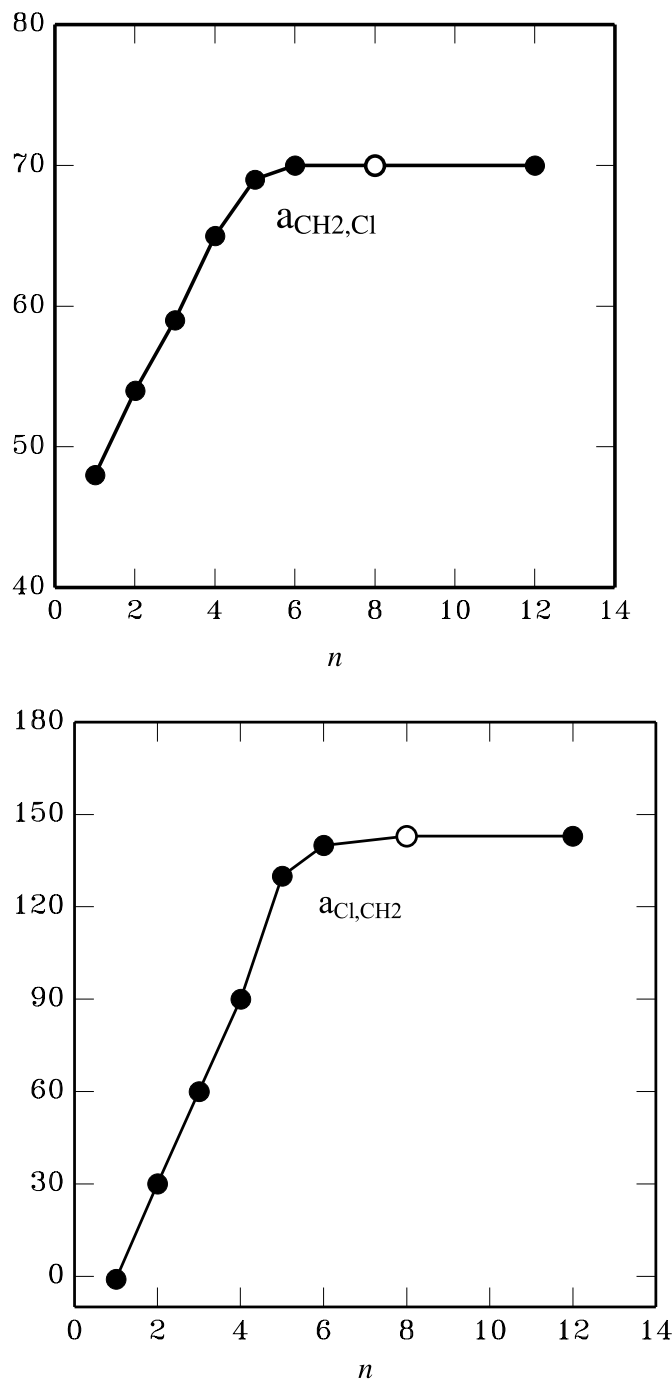




**Table 2.** Geometrical ( $R_m$ ,  $(z/2)Q_m$ ) and interaction ( $a_{mn,i}$ ,  $m = 1, 2, 3$ ) parameters of 1-chloroalkane + alkane systems for the Larsen version.

$z/2Q_m$	$R_m$	Subgroup	Main group, $m$	$a_{mCH_2,1}$ (K)	$a_{mClCH_2,1}$ (K)
				$a_{mCH_2,2}$	$a_{mClCH_2,2}$
				$a_{mCH_2,3}$	$a_{mClCH_2,3}$
0.848	0.9011	CH <sub>3</sub>	CH <sub>2</sub>	0.0	117
				0.0	-1.8
0.540	0.6744	CH <sub>2</sub>		0.0	-6.6
				130	0.0
1.264	1.4654	ClCH <sub>2</sub>	ClCH <sub>2</sub>	2.1	0.0
				12.1	0.0

**Table 3.** Geometrical ( $R_m$ ,  $Q_m$ ) and interaction parameters ( $a_{mn,i}$ ) of 1-chloroalkane + alkane systems for the Gmehling version.

$R_m$	$Q_m$	Subgroup	Main group, $m$	$a_{mCH_2,1}$ (K)	$a_{mClCH_2,1}$ (K)
				$a_{mCH_2,2}$	$a_{mClCH_2,2}$
				$a_{mCH_2,3}$ (K <sup>-1</sup> )	$a_{mClCH_2,3}$ (K <sup>-1</sup> )
0.6325	1.0608	CH <sub>3</sub>	CH <sub>2</sub>	0.0	430.0
				0.0	-0.8333
0.6325	0.7081	CH <sub>2</sub>		0.0	0.0008
				-99.0	0.0
1.3389	1.5998	ClCH <sub>2</sub>	ClCH <sub>2</sub>	0.2237	0.0
				-0.00060	0.0

**Table 4.** Interaction parameters ( $a'_{mn}$  (K)) for  $\alpha,\omega$ -dichloroalkane + alkane systems for the Tassios version.

$\alpha,\omega$ -Dichloroalkanes	$a'_{CH_2Cl}$	$a'_{ClCH_2}$
Cl-CH <sub>2</sub> -CH <sub>2</sub> -Cl	54	30
Cl-CH <sub>2</sub> -CH <sub>2</sub> -CH <sub>2</sub> -Cl	59	60
Cl-CH <sub>2</sub> -(CH <sub>2</sub> ) <sub>2</sub> -CH <sub>2</sub> -Cl	65	90
Cl-CH <sub>2</sub> -(CH <sub>2</sub> ) <sub>3</sub> -CH <sub>2</sub> -Cl	69	130
Cl-CH <sub>2</sub> -(CH <sub>2</sub> ) <sub>4</sub> -CH <sub>2</sub> -Cl	70	140
Cl-CH <sub>2</sub> -(CH <sub>2</sub> ) <sub>n-2</sub> -CH <sub>2</sub> -Cl <sup>a</sup> ( $n > 6$ )	70	140

<sup>a</sup>Disappearance of proximity effect, the same values as for 1-chloroalkane + alkane mixtures.

parameter curves are similar to those found by Kehiaian and Marongiu (11) for the quasichemical interchange coefficients of the DISQUAC model and by us (12) for the dispersive and chemical-energy parameters of the Nitta-Chao model. For the other versions of UNIFAC, similar trends of energetic parameters in relation to dichloroalkane length also exist.

## Results and discussion

The thermodynamic properties at equimolar compositions, calculated using the new and the older UNIFAC parameters, are shown in Tables 7–10. To compare the performance of the different analyzed group-contribution models, two quantities will be used: the absolute average deviation (AAD), defined by

$$[6] \quad AAD = \frac{100}{N_Y} \sum \frac{|Y_{\text{exp}} - Y_{\text{cal}}|}{Y_{\text{exp}}}$$

and the root mean square deviation (RMSD) given by

$$[7] \quad RMSD = \sqrt{\sum \frac{(Y_{\text{exp}} - Y_{\text{cal}})^2}{N_Y}}$$

where  $Y_{\text{exp}}$  and  $Y_{\text{cal}}$  are the experimental and the predicted values for each thermodynamic property and  $N_Y$  the number of the experimental values for this property. All the deviations were taken for the equimolecular mixtures listed in the relevant table. Owing to the fact that the logarithms of the infinite dilution coefficients are small quantities, their AADs are relatively high. For this reason we prefer to give the RMSD for this property instead of the AAD.

### 1-Chloroalkane + alkane mixtures

The predictive capacity of the three versions of the UNIFAC model has been increased with the new parameters, especially for the excess Gibbs energies when using the Gmehling version. Actually, for  $G^E$  (Table 7) the mean deviations using the new and the older parameters are, respectively: 12%, 14% for the Larsen version and 5% and 44% for the Gmehling version. Figure 2 shows how both sets of parameters for the Gmehling version predict the temperature dependence of  $G^E$  for the 1-chlorobutane + heptane system. In Fig. 3 it can be seen that the symmetry and the magnitude are well predicted for 1-chlorobutane + pentane using the new parameters.



**Table 5.** Interaction parameters ( $a_{mn,i}$ ) for  $\alpha,\omega$ -dichloroalkane + alkane systems for the Larsen version.

$\alpha,\omega$ -Dichloroalkanes	$a_{\text{CH}_2\text{Cl},1}$ (K)	$a_{\text{CH}_2\text{Cl},2}$	$a_{\text{CH}_2\text{Cl},3}$	$a_{\text{ClCH}_2,1}$ (K)	$a_{\text{ClCH}_2,2}$	$a_{\text{ClCH}_2,3}$
Cl-CH <sub>2</sub> -CH <sub>2</sub> -Cl	111.6	-0.2149	-3.5164	31.638	-0.2978	6.1452
Cl-CH <sub>2</sub> -CH <sub>2</sub> -CH <sub>2</sub> -Cl	113.6	-0.4451	-4.5	58.0	-0.0692	9.0
Cl-CH <sub>2</sub> -(CH <sub>2</sub> ) <sub>2</sub> -CH <sub>2</sub> -Cl	115.0	-0.8543	-5.5	90.0	0.4556	10.3
Cl-CH <sub>2</sub> -(CH <sub>2</sub> ) <sub>3</sub> -CH <sub>2</sub> -Cl	116.5	-1.5	-6.2	115.07	1.5	11.5
Cl-CH <sub>2</sub> -(CH <sub>2</sub> ) <sub>4</sub> -CH <sub>2</sub> -Cl	117	-1.7	-6.5	130	2.0	12.0
Cl-CH <sub>2</sub> -(CH <sub>2</sub> ) <sub><i>n-2</i></sub> -CH <sub>2</sub> -Cl <sup>a</sup> ( <i>n</i> > 6)	117	-1.8	-6.6	130	2.1	12.1

<sup>a</sup>Disappearance of proximity effect, the same values as for 1-chloroalkane + alkane mixtures.**Table 6.** Interaction parameters ( $a_{mn,i}$ ) for  $\alpha,\omega$ -dichloroalkane + alkane systems for the Gmehling version.

$\alpha,\omega$ -Dichloroalkanes	$a_{\text{CH}_2\text{Cl},1}$ (K)	$a_{\text{CH}_2\text{Cl},2}$	$a_{\text{CH}_2\text{Cl},3}$ (K <sup>-1</sup> )	$a_{\text{ClCH}_2,1}$ (K)	$a_{\text{ClCH}_2,2}$	$a_{\text{ClCH}_2,3}$ (K <sup>-1</sup> )
Cl-CH <sub>2</sub> -CH <sub>2</sub> -Cl	105.9	0.0056	-0.0003	-198.7	1.6941	-0.00320
Cl-CH <sub>2</sub> -CH <sub>2</sub> -CH <sub>2</sub> -Cl	343.3	-0.600	0.0005	-130.0	0.6256	-0.00120
Cl-CH <sub>2</sub> -(CH <sub>2</sub> ) <sub>2</sub> -CH <sub>2</sub> -Cl	419.0	-0.8111	0.0008	-110.0	0.3972	-0.00073
Cl-CH <sub>2</sub> -(CH <sub>2</sub> ) <sub>3</sub> -CH <sub>2</sub> -Cl	429.0	-0.8270	0.0008	-99.0	0.3000	-0.00065
Cl-CH <sub>2</sub> -(CH <sub>2</sub> ) <sub><i>n-2</i></sub> -CH <sub>2</sub> -Cl <sup>a</sup> ( <i>n</i> ≥ 6)	430.0	-0.8333	0.0008	-99.0	0.2237	-0.00060

<sup>a</sup>Disappearance of proximity effect, the same values as for 1-chloroalkane + alkane mixtures.**Table 7.** Excess Gibbs energies,  $G^E$ , for 1-chloroalkane + alkane and  $\alpha,\omega$ -dichloroalkane + alkane equimolar mixtures; (I) Experimental data; UNIFAC model: (II) and (IV) Larsen and Gmehling version with parameters of this work, (III) and (V) with older parameters.

		$G^E$ ( $T$ ; $x = 0.5$ ) (J mol <sup>-1</sup> )				
System (1)+(2)	$T$ (K)	I	II	III	IV	V
<b>1-Chlorobutane</b>						
Pentane	298.15	277 <sup>a</sup>	235	235	268	168
	348.35	250 <sup>a</sup>	195	188	231	124
	397.00	214 <sup>a</sup>	167	117	197	84
Hexane	300.15	266 <sup>b</sup>	246	248	266	170
	325.15	264 <sup>b</sup>	221	226	244	145
	350.15	239 <sup>b</sup>	202	197	222	121
Heptane	298.15	268 <sup>c</sup>	253	257	266	173
	303.15	257 <sup>b</sup>	247	253	261	168
	318.15	254 <sup>d</sup>	230	238	245	151
	323.15	247 <sup>b</sup>	225	233	240	146
	333.15	225 <sup>e</sup>	216	221	230	135
	338.15	256 <sup>d</sup>	211	215	225	129
	353.15	224 <sup>b</sup>	200	194	210	114
<b>1,2-Dichloroethane</b>						
Hexane	298.15	778 <sup>f</sup>	824	892	818	801
	303.15	790 <sup>g</sup>	809	877	804	785
Heptane	303.15	815 <sup>b</sup>	836	922	805	812
	343.15	709 <sup>b</sup>	647	747	625	659
		719 <sup>h</sup>				
<b>1,3-Dichloropropane</b>						
Hexane	298.15	886 <sup>f</sup>	775	760	899	651
	303.15	880 <sup>g</sup>	764	748	892	638
<b>1,4-Dichlorobutane</b>						
Hexane	298.15	858 <sup>f</sup>	725	651	909	546
	303.15	860 <sup>g</sup>	716	642	905	534

<sup>a</sup>Van Ness and Smith (16).<sup>b</sup>Gutsche and Knapp (17).<sup>c</sup>Sayegh et al. (18).<sup>d</sup>Ashraf and Vera (19).<sup>e</sup>Grolier (20).<sup>f</sup>Royo and Gutiérrez Losa (21).<sup>g</sup>Azpiaz et al. (22).<sup>h</sup>Eng and Sandler (23).



**Table 8.** Excess enthalpies,  $H^E$ , for 1-chloroalkane + alkane and  $\alpha,\omega$ -dichloroalkane + alkane equimolar mixtures; (I) Experimental data; UNIFAC model: (II), (IV), and (VI) Tassios, Larsen, and Gmehling versions with parameters of this work; (III), (V), and (VII) with older parameters.

		$H^E$ ( $T$ ; $x = 0.5$ ) (J mol <sup>-1</sup> )						
System (1)+(2)	$T$ (K)	I	II	III	IV	V	VI	VII
<b>1-Chlorobutane</b>								
Hexane	293.15	*502 <sup>a</sup>	533	542	559	459	541	482
	298.15	*511 <sup>b</sup>	519	526	559	473	540	480
		*496 <sup>c</sup>						
	308.15	*514 <sup>d</sup>	492	495	546	504	538	474
	323.15	*497 <sup>a</sup>	478	480	536	520	536	472
Heptane	298.15	*532 <sup>e</sup>	557	566	599	506	581	513
Octane	298.15	*553 <sup>c</sup>	590	601	633	535	618	541
Nonane	293.15	*608 <sup>a</sup>	638	652	668	544	653	571
	298.15	*604 <sup>b</sup>	620	632	665	561	651	567
	313.15	*582 <sup>a</sup>	567	573	631	615	644	556
Decane	298.15	*623 <sup>e</sup>	647	660	692	584	681	590
Dodecane	298.15	*668 <sup>c</sup>	693	709	740	623	732	628
Hexadecane	298.15	*828 <sup>e</sup>	764	785	812	684	811	687
		*815 <sup>c</sup>						
<b>1-Chloropentane</b>								
Hexane	298.15	*438 <sup>f</sup>	438	448	470	394	459	395
Heptane	298.15	*486 <sup>f</sup>	471	483	505	423	496	424
Octane	298.15	*499 <sup>f</sup>	501	514	536	448	529	449
Nonane	298.15	*531 <sup>g</sup>	528	543	564	471	559	472
Decane	298.15	*563 <sup>g</sup>	552	568	589	492	586	492
<b>1-Chlorohexane</b>								
Hexane	298.15	*365 <sup>f</sup>	374	386	401	333	395	331
Heptane	298.15	*396 <sup>f</sup>	404	417	432	359	428	357
Octane	298.15	*428 <sup>f</sup>	431	446	460	382	458	379
Nonane	298.15	*451 <sup>g</sup>	455	471	485	403	485	400
Decane	298.15	*477 <sup>g</sup>	477	495	507	421	509	418
Undecane	298.15	*507 <sup>g</sup>	497	516	528	439	532	435
<b>1-Chlorooctane</b>								
Hexane	298.15	*289 <sup>b</sup>	284	296	300	248	302	243
Octane	298.15	*334 <sup>b</sup>	330	345	348	288	354	282
<b>1-Chlorodecane</b>								
Hexane	298.15	*249 <sup>a</sup>	222	234	233	193	239	186
	313.15	*224 <sup>a</sup>	198	205	208	209	232	179
Nonane	293.15	*284 <sup>a</sup>	278	293	299	234	301	232
	303.15	*275 <sup>a</sup>	246	256	258	259	291	223
<b>1-Chlorododecane</b>								
Octane	298.15	*223 <sup>c</sup>	212	224	247	205	230	174
Dodecane	298.15	*249 <sup>c</sup>	264	280	272	226	288	216
Hexadecane	298.15	*302 <sup>c</sup>	303	323	311	259	332	247
<b>1-Chlorohexadecane</b>								
Octane	298.15	*233 <sup>c</sup>	148	158	151	126	162	118
Dodecane	298.15	*198 <sup>c</sup>	188	201	190	159	206	150
Hexadecane	298.15	*209 <sup>c</sup>	219	234	221	185	241	174
<b>1,2-Dichloroethane</b>								
Pentane	298.15	*1588 <sup>h</sup>	1536	1348	1551	1601	1510	1582
Hexane	288.15	1595 <sup>i</sup>	1680	1482	1470	1590	1450	1669
	298.15	*1618 <sup>i</sup>	1660	1486	1661	1737	1617	1725
		1548 <sup>j</sup>						
		1480 <sup>k</sup>						
	303.15	*1754 <sup>l</sup>	1646	1482	1757	1812	1703	1751
	308.15	1568 <sup>i</sup>	1630	1474	1855	1887	1792	1777
		1500 <sup>k</sup>						
	318.15	1562 <sup>i</sup>	1591	1450	2056	2038	1974	1825



Table 8 (continued).

System (1)+(2)	T (K)	$H^E$ (T; $x = 0.5$ ) (J mol <sup>-1</sup> )						
		I	II	III	IV	V	VI	VII
Heptane	288.15	1721 <sup>m</sup>	1792	1610	1559	1701	1532	1794
	293.15	*1705 <sup>n</sup>	1781	1612	1657	1778	1619	1822
	298.15	*1715 <sup>h</sup>	1768	1610	1755	1857	1708	1850
		1840 <sup>m</sup>						
		1520 <sup>k</sup>						
		1563 <sup>o</sup>						
	303.15	*1838 <sup>l</sup>	1752	1603	1855	1935	1798	1876
	308.15	*2007 <sup>m</sup>	1734	1593	1956	2015	1891	1902
		1230 <sup>k</sup>						
	313.15	1561 <sup>o</sup>	1713	1579	2059	2095	1986	1926
Octane	318.15	*2177 <sup>m</sup>	1691	1562	2165	2175	2083	1950
	303.15	*1936 <sup>l</sup>	1845	1712	1939	2045	1880	1986
Nonane	298.15	*1866 <sup>h</sup>	1947	1823	1909	2057	1853	2057
Decane	293.15	*1904	2041	1925	1868	2053	1815	2118
Undecane	298.15	*1994 <sup>h</sup>	2090	2000	2028	2218	1965	2223
Dodecane	293.15	*1991 <sup>n</sup>	2173	2092	1972	2195	1910	2269
Tridecane	298.15	*2110 <sup>h</sup>	2206	2149	2123	2350	2054	2358
Tetradecane	293.15	*2025 <sup>n</sup>	2282	2234	2056	2312	1987	2393
	298.15	1542 <sup>o</sup>	2257	2215	2164	2408	2092	2418
	313.15	1670 <sup>o</sup>	2167	2134	2053	2702	2423	2486
Pentadecane	298.15	*2222 <sup>h</sup>	2303	2277	2201	2461	2126	2471
Hexadecane	293.15	*2135 <sup>n</sup>	2373	2357	2126	2412	2049	2497
	298.15	1532 <sup>o</sup>	2346	2334	2235	2511	2157	2521
	308.15	2106 <sup>i</sup>	2283	2275	2460	2712	2381	2566
	318.15	1256 <sup>i</sup>	2212	2203	2702	2918	2617	2607
	328.15	2070 <sup>i</sup>	2133	2119	2967	3183	2864	2645
Heptadecane	298.15	*2311 <sup>h</sup>	2385	2387	2266	2556	2186	2566
<b>1,3-Dichloropropane</b>								
Pentane	298.15	*1423 <sup>h</sup>	1304	1182	1293	1319	1184	1324
Heptane	298.15	*1565 <sup>h</sup>	1521	1418	1488	1544	1410	1559
		1256 <sup>i</sup>						
		1460 <sup>p</sup>						
Nonane	298.15	*1677 <sup>h</sup>	1693	1611	1638	1723	1592	1744
Undecane	298.15	*1815 <sup>h</sup>	1832	1774	1758	1868	1742	1894
Tridecane	298.15	*1967 <sup>h</sup>	1948	1911	1854	1990	1867	2017
Pentadecane	298.15	*2106 <sup>h</sup>	2045	2030	1935	2092	1974	2120
	308.15	1834 <sup>i</sup>	2002	1965	2149	2254	2038	2143
	318.15	1799 <sup>i</sup>	1952	1891	2386	2421	2102	2163
	328.15	1743 <sup>i</sup>	1894	1808	2657	2594	2164	2181
Heptadecane	298.15	*2200 <sup>h</sup>	2128	2133	2003	2180	2065	2208
<b>1,4-Dichlorobutane</b>								
Pentane	298.15	*1305 <sup>h</sup>	1111	1043	1111	1109	1029	1121
Hexane	298.15	*1245 <sup>j</sup>	1219	1155	1214	1215	1143	1232
Heptane	298.15	*1437 <sup>h</sup>	1316	1256	1304	1309	1247	1329
		1540 <sup>p</sup>						
Nonane	298.15	*1549 <sup>h</sup>	1482	1433	1458	1470	1429	1495
Undecane	298.15	*1699 <sup>h</sup>	1620	1583	1583	1603	1582	1631
Tridecane	298.15	*1838 <sup>h</sup>	1737	1710	1867	1714	1712	1743
Pentadecane	298.15	*1976 <sup>h</sup>	1836	1821	1773	1809	1825	1838
Heptadecane	298.15	*2075 <sup>h</sup>	1921	1917	1847	1890	1923	1920
<b>1,5-Dichloropentane</b>								
Pentane	298.15	*1132 <sup>h</sup>	961	926	9711	949	952	961
Hexane	298.15	*1160 <sup>j</sup>	1062	1028	1075	1043	1060	1059
Heptane	298.15	*1262 <sup>h</sup>	1153	1120	1168	1127	1159	1146
		1280 <sup>p</sup>						
Nonane	298.15	*1380 <sup>h</sup>	1311	1283	1330	1273	1332	1296



Table 8 (concluded).

System (1)+(2)	T (K)	$H^E$ (T; x = 0.5) (J mol <sup>-1</sup> )						
		I	II	III	IV	V	VI	VII
Undecane	298.15	*1542 <sup>h</sup>	1444	1420	1465	1394	1479	1419
Tridecane	298.15	*1658 <sup>h</sup>	1557	1539	1579	1497	1605	1522
Pentadecane	298.15	*1785 <sup>h</sup>	1655	1642	1676	1585	1714	1610
Heptadecane	298.15	*1916 <sup>h</sup>	1740	1732	1761	1661	1810	1686
<b>1,6-Dichlorohexane</b>								
Pentane	298.15	*938 <sup>h</sup>	852	828	859	822	828	832
Hexane	298.15	*990 <sup>j</sup>	944	920	955	907	924	919
Heptane	298.15	*1097 <sup>h</sup>	1028	1005	1042	983	1012	998
		1190 <sup>p</sup>						
Nonane	298.15	*1210 <sup>h</sup>	1175	1154	1194	1116	1167	1133
Undecane	298.15	*1358 <sup>h</sup>	1299	1282	1323	1227	1299	1246
Tridecane	298.15	*1498 <sup>h</sup>	1406	1392	1433	1322	1414	1341
Pentadecane	298.15	*1592 <sup>h</sup>	1499	1488	1528	1403	1514	1422
Heptadecane	298.15	*1725 <sup>h</sup>	1580	1573	1610	1474	1602	1493

<sup>a</sup>Kohl and Heintz (24).  
<sup>b</sup>Doan-Nguyen and Vera (25).  
<sup>c</sup>Valero et al. (26).  
<sup>d</sup>Lai et al. (27).  
<sup>e</sup>Grolier et al. (28).  
<sup>f</sup>Paz Andrade and Bravo (29).  
<sup>g</sup>Núñez et al. (30).  
<sup>h</sup>Ortega and Plácido (31).  
<sup>i</sup>Baños et al. (32).  
<sup>j</sup>Polo et al. (33).  
<sup>k</sup>Nigam and Aggarwal (34).  
<sup>l</sup>Chaudhari and Katti (35).  
<sup>m</sup>Rhim and Bae (36).  
<sup>n</sup>Hahn and Svejda (37).  
<sup>o</sup>Svejda and Demiriz (38).  
<sup>p</sup>Grolier and Kehiaian (39).

Fig. 2. Comparison between the experimental values and the Gmehling predictions for the excess Gibbs energies,  $G^E$  (x = 0.5) of 1-chlorobutane + heptane at different temperatures. Experimental points: (●) (17), (□) (18), (○) (19), (■) (20); theoretical predictions: (—) new parameters, (---) older parameters.

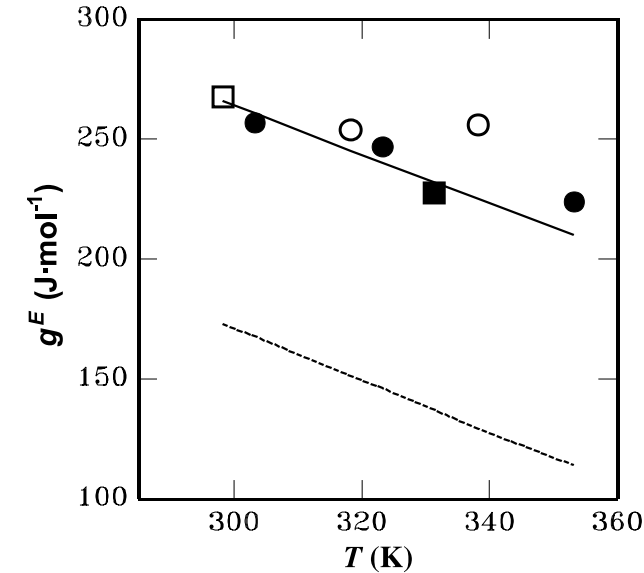
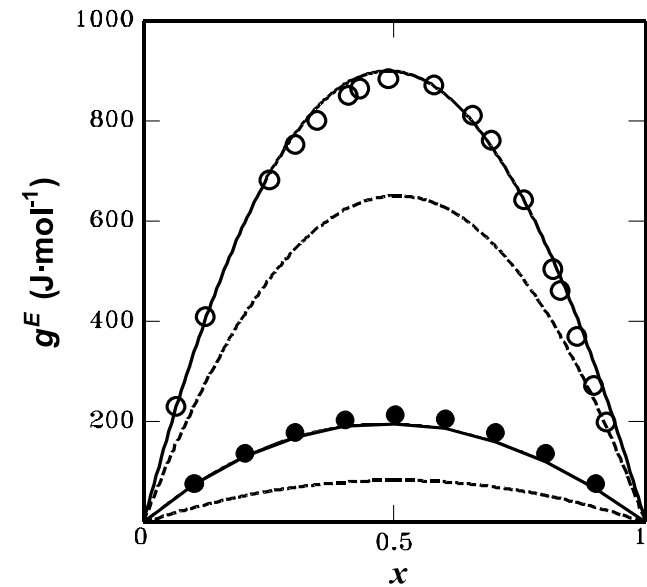


Fig. 3. Experimental excess molar Gibbs energies and theoretical predictions using the Gmehling version. Experimental points: (●) (x)1-chlorobutane + (1 - x)pentane at 397.15 K, (○) (x)1,3-dichloropropane + (1 - x)hexane at 298.15 K; theoretical predictions: (—) new parameters, (---) older parameters.





**Table 9.** Logarithm of activity coefficients at infinite dilution,  $\ln\gamma_1^\infty$ , for 1-chloroalkane + alkane and  $\alpha,\omega$ -dichloroalkane + alkane mixtures; (I) Experimental data; UNIFAC model: (II) and (IV) Larsen and Gmehling version with parameters of this work; (III) and (V) with older parameters.

		$\ln\gamma_1^\infty$				
System (1)+(2)	$T$ (K)	I	II	III	IV	V
<b>1-Chloropropane</b>						
Heptane	293.15	*0.385 <sup>a</sup>	0.414	0.453	0.463	0.293
Octane	293.15	*0.385 <sup>a</sup>	0.387	0.427	0.432	0.272
Eicosane	326.35	0.051 <sup>b</sup>	−0.014	0.029	0.001	−0.104
	333.15	−0.065 <sup>c</sup>	−0.03	0.009	−0.019	−0.120
	347.25	−0.003 <sup>b</sup>	−0.061	−0.034	−0.058	−0.151
Heneicosane	333.15	−0.059 <sup>d</sup>	−0.051	−0.012	−0.041	−0.141
<b>1-Chlorobutane</b>						
Hexane	301.0	*0.419 <sup>a</sup>	0.359	0.415	0.442	0.258
	315.3	0.405 <sup>a</sup>	0.319	0.038	0.398	0.223
	332.0	*0.358 <sup>a</sup>	0.280	0.332	0.352	0.188
	340.3	*0.336 <sup>a</sup>	0.264	0.310	0.332	0.172
Hexadecane	304.85	*0.166 <sup>e</sup>	0.139	0.196	0.176	0.049
	315.35	*0.148 <sup>e</sup>	0.110	0.138	0.144	0.024
	324.45	*0.113 <sup>e</sup>	0.088	0.143	0.118	0.004
Octadecane	324.55	0.020 <sup>e</sup>	0.047	0.102	0.074	−0.038
	334.55	0.030 <sup>e</sup>	0.026	0.080	0.048	−0.058
	343.65	0.050 <sup>e</sup>	0.009	0.052	0.026	−0.075
	353.65	−0.010 <sup>e</sup>	−0.007	0.026	0.003	−0.092
Eicosane	326.35	0.052 <sup>b</sup>	0.004	0.059	0.026	−0.082
	333.15	−0.038 <sup>c</sup>	−0.010	0.041	0.009	−0.096
	347.25	0.012 <sup>b</sup>	−0.036	0.004	−0.025	−0.122
Heneicosane	333.15	−0.051 <sup>d</sup>	−0.028	0.022	−0.012	−0.115
Tetracosane	324.45	−0.062 <sup>e</sup>	−0.063	−0.008	−0.048	−0.154
	333.75	−0.117 <sup>e</sup>	−0.083	−0.033	−0.072	−0.173
	343.55	−0.151 <sup>e</sup>	−0.101	−0.058	−0.096	−0.191
	349.15	−0.134 <sup>f</sup>	−0.111	−0.073	−0.109	−0.201
	353.45	−0.186 <sup>e</sup>	−0.117	−0.084	−0.118	−0.209
	361.15	−0.154 <sup>f</sup>	−0.129	−0.105	−0.135	−0.221
Triacontane	349.15	−0.274 <sup>f</sup>	−0.206	−0.168	−0.215	−0.305
	361.15	−0.307 <sup>f</sup>	−0.224	−0.200	−0.241	−0.325
Hexatriacontane	349.15	−0.414 <sup>f</sup>	−0.289	−0.252	−0.309	−0.397
	361.15	−0.439 <sup>f</sup>	−0.308	−0.283	−0.334	−0.417
<b>1-Chloropentane</b>						
Hexadecane	304.85	*0.174 <sup>e</sup>	0.143	0.204	0.185	0.060
	315.35	0.157 <sup>e</sup>	0.117	0.179	0.156	0.038
	324.45	*0.122 <sup>e</sup>	0.098	0.158	0.133	0.020
Octadecane	324.55	0.020 <sup>e</sup>	0.061	0.121	0.092	−0.018
	334.55	*0.049 <sup>e</sup>	0.043	0.097	0.069	−0.036
	343.65	*0.030 <sup>e</sup>	0.028	0.076	0.049	−0.050
	353.65	−0.020 <sup>e</sup>	0.014	0.053	0.029	−0.066
Eicosane	333.15	−0.024 <sup>c</sup>	0.010	0.065	0.033	−0.070
	349.15	−0.050 <sup>g</sup>	−0.015	0.028	−0.001	−0.096
Heneicosane	333.15	−0.020 <sup>d</sup>	−0.007	0.048	0.014	−0.088
Tetracosane	324.45	−0.062 <sup>e</sup>	−0.040	0.019	−0.021	−0.125
	333.75	−0.094 <sup>e</sup>	−0.058	−0.003	−0.043	−0.142
	343.55	−0.128 <sup>e</sup>	−0.073	−0.025	−0.064	−0.158
	349.15	−0.101 <sup>f</sup>	−0.081	−0.038	−0.075	−0.167
	353.45	−0.151 <sup>e</sup>	−0.087	−0.048	−0.084	−0.173
	361.15	−0.110 <sup>f</sup>	−0.097	−0.066	−0.098	−0.184
Triacontane	349.15	−0.248 <sup>f</sup>	−0.171	−0.128	−0.176	−0.264
	361.15	−0.272 <sup>f</sup>	−0.187	−0.156	−0.199	−0.281
Hexatriacontane	349.15	−0.355 <sup>f</sup>	−0.171	−0.128	−0.265	−0.352
	361.15	−0.380 <sup>f</sup>	−0.266	−0.235	−0.288	−0.369



**Table 9** (concluded).

		$\ln\gamma_1^\infty$					
System (1)+(2)	$T$ (K)	I	II	III	IV	V	
<b>1-Chlorohexane</b>							
Eicosane	333.15	−0.014 <sup>c</sup>	0.027	0.084	0.053	−0.046	
Heneicosane	333.15	−0.001 <sup>d</sup>	0.012	0.068	0.035	−0.063	
Tetracosane	349.15	−0.071 <sup>f</sup>	−0.056	−0.011	−0.047	−0.135	
	361.15	−0.078 <sup>f</sup>	−0.069	−0.036	−0.067	−0.150	
Triacontane	349.15	−0.224 <sup>f</sup>	−0.140	−0.095	−0.142	−0.226	
	361.15	−0.240 <sup>f</sup>	−0.153	−0.120	−0.162	−0.242	
Hexatriacontane	349.15	−0.322 <sup>f</sup>	−0.215	−0.170	−0.227	−0.310	
	361.15	−0.354 <sup>f</sup>	−0.229	−0.195	−0.247	−0.325	
<b>1-Chloroheptane</b>							
Eicosane	333.15	−0.006 <sup>d</sup>	0.042	0.098	0.070	−0.025	
Tetracosane	349.15	−0.051 <sup>f</sup>	−0.034	0.012	−0.022	−0.107	
	361.15	−0.063 <sup>f</sup>	−0.046	−0.011	−0.041	−0.120	
Triacontane	349.15	−0.189 <sup>f</sup>	−0.112	−0.067	−0.111	−0.193	
	361.15	−0.218 <sup>f</sup>	−0.125	−0.090	−0.130	−0.206	
Hexatriacontane	349.15	−0.301 <sup>f</sup>	−0.184	−0.138	−0.193	−0.272	
	361.15	−0.319 <sup>f</sup>	−0.196	−0.161	−0.211	−0.286	
<b>1,2-Dichloroethane</b>							
Hexane	298.0	*1.154 <sup>a</sup>	1.164	1.565	1.130	1.748	
	316.0	*1.004 <sup>a</sup>	1.018	1.382	0.989	1.005	
	332.2	*0.896 <sup>a</sup>	0.881	1.217	0.856	0.867	
	339.4	*0.842 <sup>a</sup>	0.818	1.144	0.795	0.810	
Heptane	293.15	*1.194 <sup>a</sup>	1.177	1.588	1.108	1.193	
Octane	293.15	*1.065 <sup>a</sup>	1.149	1.560	1.058	1.162	
Octadecane	353.15	0.285 <sup>g</sup>	0.381	0.690	0.221	0.362	
Eicosane	326.35	0.476 <sup>b</sup>	0.575	0.921	0.397	0.521	
	333.15	0.365 <sup>c</sup>	0.517	0.852	0.340	0.465	
	347.25	0.350 <sup>b</sup>	0.392	0.708	0.220	0.357	
Heneicosane	333.15	0.366 <sup>h</sup>	0.496	0.831	0.316	0.442	
Tetracosane	349.15	0.193 <sup>f</sup>	0.296	0.609	0.109	0.254	
	361.15	0.134 <sup>f</sup>	0.183	0.486	0.003	0.169	
Triacontane	349.15	0.040 <sup>f</sup>	0.193	0.507	−0.013	0.137	
	361.15	−0.030 <sup>f</sup>	0.081	0.384	−0.119	0.052	
Hexatriacontane	349.15	−0.019 <sup>f</sup>	0.105	0.418	−0.117	0.036	
	361.15	−0.159 <sup>f</sup>	−0.008	0.295	−0.223	−0.049	
<b>1,3-Dichloropropane</b>							
Eicosane	333.15	0.558 <sup>c</sup>	0.600	0.805	0.792	0.406	
Heneicosane	333.15	0.568 <sup>h</sup>	0.581	0.786	0.769	0.384	
<b>1,4-Dichlorobutane</b>							
Eicosane	333.15	0.668 <sup>c</sup>	0.674	0.763	1.007	0.370	
Heneicosane	333.15	0.706 <sup>h</sup>	0.656	0.745	0.985	0.350	
<b>1,5-Dichloropentane</b>							
Eicosane	333.15	0.818 <sup>h</sup>	0.672	0.726	0.882	0.346	

<sup>a</sup>Thomas et al. (40).<sup>b</sup>Martire and Pollara (41).<sup>c</sup>Meyer and Meyer (42).<sup>d</sup>Meyer and Baiocchi (43).<sup>e</sup>Alessi et al. (44).<sup>f</sup>Tewari et al. (45).<sup>g</sup>Harris and Prausnitz (46).<sup>h</sup>Meyer and Baiocchi (47).

Concerning the excess molar enthalpies, the overall AADs (Table 8) using the new and the older parameters are, respectively: 5%, 6% for the Tassios version; 7%, 11% for the Larsen version; and 7% and 12% for the Gmehling version. Again, the best improvements were obtained with the Gmehling version. Figure 4a shows  $H^E$  for the system 1-

chlorodecane + nonane using the Larsen version. The magnitude of  $H^E$  is better predicted with the new parameters. The experimental excess enthalpies increase as the alkane length increases and the 1-chloroalkane length decreases. This behavior is well predicted by all the versions of the UNIFAC model, but the experimental dependence is best



**Table 10.** Logarithm of activity coefficients at infinite dilution ( $\ln\gamma_2^\infty$ ) for 1-chloroalkane + alkane and  $\alpha,\omega$ -dichloroalkane + alkane mixtures; (I) Experimental data; UNIFAC model: (II) and (IV) Larsen and Gmehling version with parameters of this work; (III) and (V) with older parameters.

		$\ln\gamma_2^\infty$				
System (1)+(2)	$T$ (K)	I	II	III	IV	V
<b>1-Chlorononane</b>						
Hexane	303.65	*0.194 <sup>a</sup>	0.127	0.141	0.143	0.092
<b>1-Chlorohexadecane</b>						
Pentane	313.25	*0.039 <sup>b</sup>	0.037	0.048	0.047	0.028
	320.95	0.010 <sup>b</sup>	0.035	0.045	0.044	0.026
	328.35	0.010 <sup>b</sup>	0.033	0.043	0.042	0.024
	334.35	−0.010 <sup>b</sup>	0.032	0.041	0.040	0.022
Hexane	313.25	*0.058 <sup>b</sup>	0.043	0.055	0.055	0.032
	320.95	*0.030 <sup>b</sup>	0.041	0.052	0.052	0.030
	328.55	0.020 <sup>b</sup>	0.038	0.050	0.049	0.028
	334.55	0.020 <sup>b</sup>	0.037	0.047	0.047	0.026
Heptane	313.25	*0.077 <sup>b</sup>	0.050	0.063	0.063	0.037
	318.15	0.055 <sup>c</sup>	0.048	0.061	0.061	0.035
	320.95	*0.049 <sup>b</sup>	0.047	0.060	0.059	0.034
	328.35	0.049 <sup>b</sup>	0.044	0.057	0.056	0.032
	334.55	−0.039 <sup>b</sup>	0.042	0.054	0.053	0.030
<b>1-Chlorooctadecane</b>						
Pentane	315.55	−0.030 <sup>b</sup>	0.030	0.039	0.038	0.022
	323.95	*−0.041 <sup>b</sup>	0.028	0.036	0.036	0.020
	333.75	−0.041 <sup>b</sup>	0.026	0.034	0.033	0.018
	343.75	−0.041 <sup>b</sup>	0.024	0.031	0.031	0.016
Hexane	323.95	−0.010 <sup>b</sup>	0.032	0.042	0.042	0.023
	333.75	−0.030 <sup>b</sup>	0.030	0.039	0.039	0.021
	343.75	−0.040 <sup>b</sup>	0.028	0.036	0.036	0.019
Heptane	323.95	0.010 <sup>b</sup>	0.037	0.048	0.047	0.027
	343.75	−0.010 <sup>b</sup>	0.032	0.041	0.041	0.029
<b>1-Chloroeicosane</b>						
Hexane	333.15	−0.045 <sup>d</sup>	0.025	0.033	0.032	0.023
Heptane	333.15	−0.009 <sup>d</sup>	0.028	0.038	0.037	0.027
Octane	333.15	0.028 <sup>d</sup>	0.032	0.042	0.042	0.030
Nonane	333.15	0.056 <sup>d</sup>	0.035	0.047	0.046	0.033
<b>1,2-Dichloroethane</b>						
Pentane	293.15	*1.567 <sup>e</sup>	1.357	1.240	1.365	1.275
Hexane	293.15	*1.617 <sup>e</sup>	1.590	1.442	1.593	1.504
	304.15	*1.482 <sup>e</sup>	1.548	1.340	1.478	1.507
Heptane	318.5	*1.384 <sup>e</sup>	1.382	1.204	1.320	1.387
	337.2	*1.278 <sup>e</sup>	1.145	1.022	1.100	1.233
	354.2	*1.102 <sup>e</sup>	0.915	0.853	0.890	1.096
	318.5	*1.493 <sup>e</sup>	1.575	1.373	1.508	1.586
	337.2	*1.351 <sup>e</sup>	1.305	1.165	1.257	1.410
	354.2	*1.131 <sup>e</sup>	1.043	0.973	1.017	1.253

<sup>a</sup>Korol (48).

<sup>b</sup>Alessi et al. (49).

<sup>c</sup>Janini and Martire (50).

<sup>d</sup>Meyer and Baiocchi (47).

<sup>e</sup>Thomas et al. (51).

reproduced with the new parameters, as can be seen in Fig. 5a for the Tassios and Larsen versions.

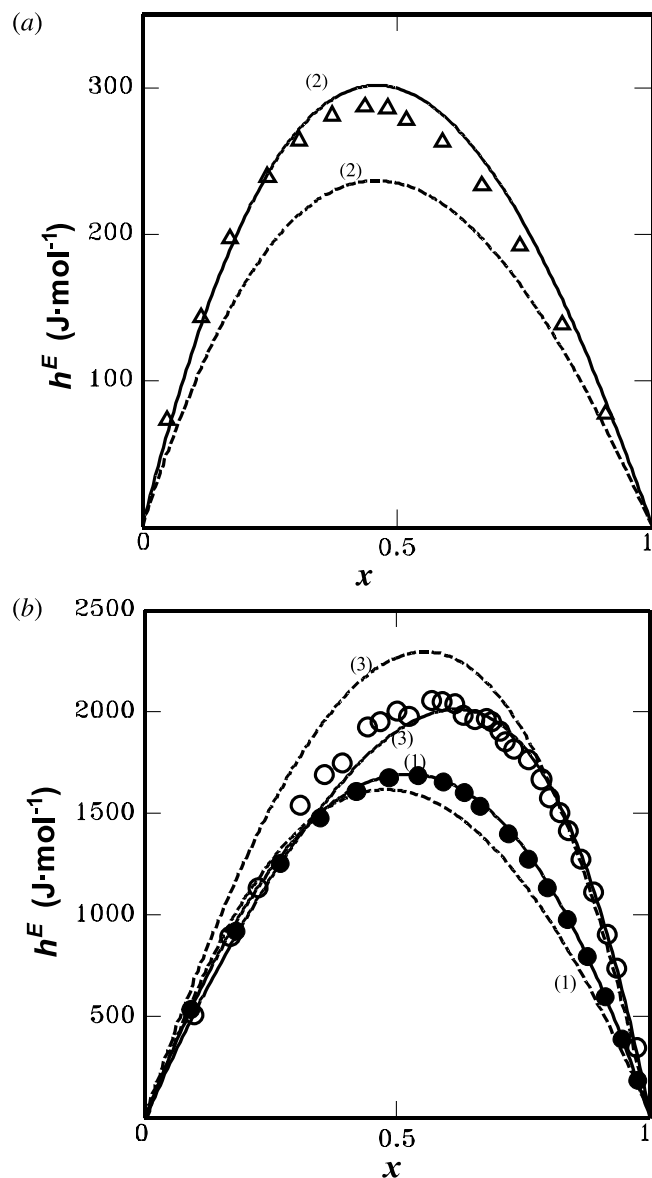
For the logarithm of the infinite-dilution activity coefficients, the RMSDs obtained using the new and the older parameters are, respectively: 0.060, 0.091 for the Larsen version and 0.059 and 0.074 for the Gmehling version (Tables 9 and 10). So, the results obtained with the new parameters are similar for both versions.

#### $\alpha,\omega$ -Dichloroalkane + alkane mixtures

These mixtures are very useful for studies of the intramolecular proximity effect. In these cases the intermolecular interactions (and of course their parameters) are affected by the changes in the net charge of the groups due to the proximity of polarizing atoms. This effect decreases when the spacing between the non-alkyl functional groups increases. This is in agreement with the values obtained in Tables 4–6



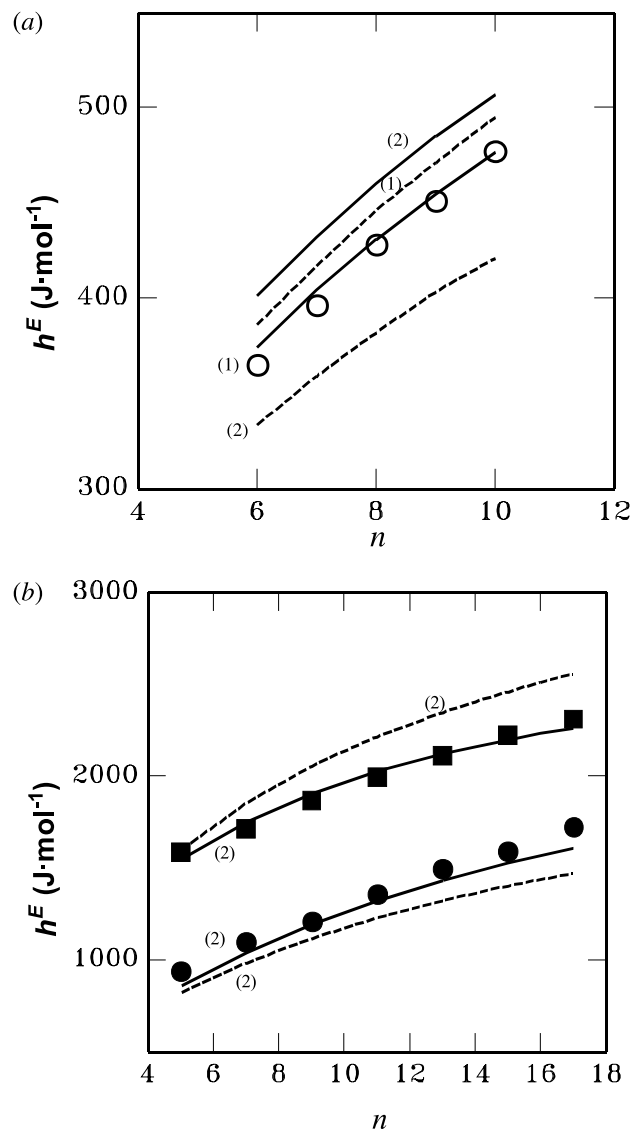
**Fig. 4.** Experimental excess molar enthalpies and theoretical predictions of some chloroalkane + alkane mixtures: (a) experimental points: ( $\Delta$ ) (x)1-chlorodecane + (1 - x)nonane at 293.15 K; theoretical predictions with Larsen version; (b) ( $\circ$ ) (x)1,2-dichloroethane + (1 - x)dodecane at 293.15 K, ( $\bullet$ ) (x)1,3-dichloropropane + (1 - x)nonane at 298.15 K; theoretical predictions: (1) Tassios version, (2) Larsen version, (3) Gmehling version; (—) new parameters, (---) older parameters.



for the three versions of UNIFAC, since the interaction parameters for the  $(\text{Cl}(\text{CH}_2)_n\text{Cl})$  dichloroalkanes with  $n > 6$  coincide with those of the 1-chloroalkane + alkane systems.

All of the properties that were considered for the  $\alpha,\omega$ -dichloroalkane + alkane mixtures are better predicted with the new parameters. The AADs for excess Gibbs energies using the new and the older parameters are, respectively: 10%, 14% for the Larsen version and 5%, 16% for the Gmehling version. As illustrated in Fig. 3, the calculated  $G^E$  vs. composition curves, using the Gmehling modification with the new parameters, agree quite well with the experimental data.

**Fig. 5.** Excess molar enthalpies  $H^E$  ( $x = 0.5$ ) of chloroalkane + alkane mixtures against  $n$ , the number of carbons in the alkane: experimental points: (a) ( $\circ$ ) 1-chlorohexane; (b) ( $\blacksquare$ ) 1,2-dichloroethane, ( $\bullet$ ) 1,6-dichlorohexane; theoretical predictions: (1) Tassios version, (2) Larsen version; (—) new parameters, (---) older parameters.

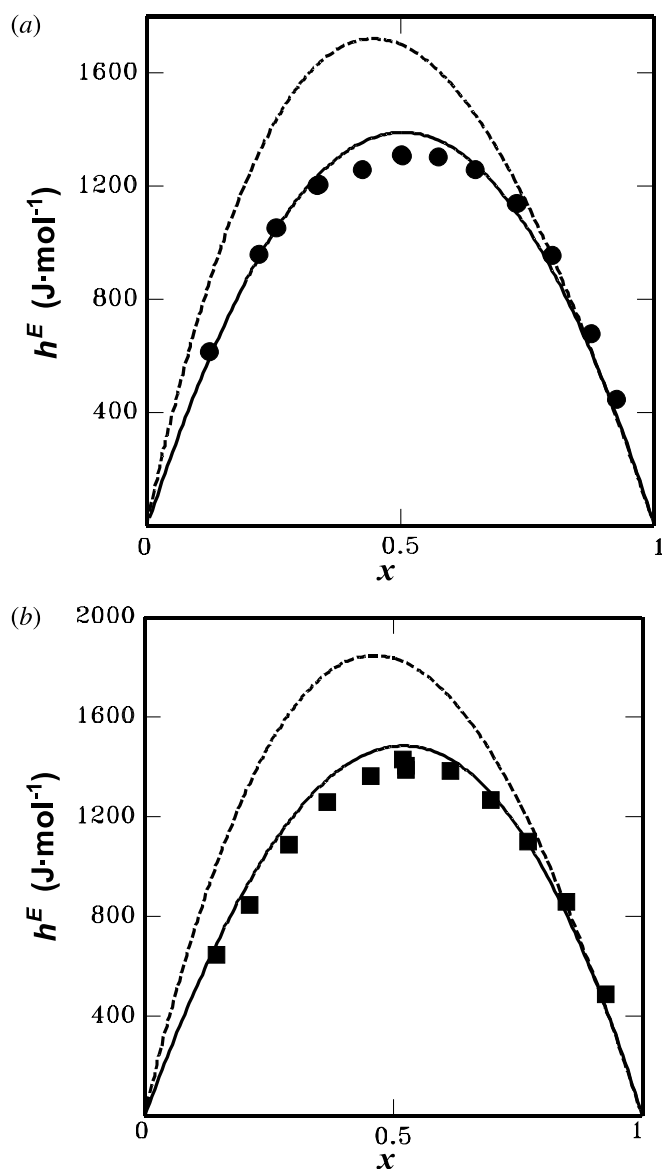


Concerning the excess enthalpies, the AADs obtained using the new and the older parameters are, respectively: 9%, 10% for the Tassios version; 11%, 15% for the Larsen version; and 11% and 14% for the Gmehling version. In Fig. 4b we compare the predictions of the Larsen and Tassios versions for two examples. The trend of  $H^E(0.5)$  with the alkane and dichloroalkane lengths seems to be fairly well reproduced with the Larsen modification, as can be seen in Fig. 5b.

In the case of the Tassios version, with the new parameters it is possible to predict the excess enthalpies of dichloromethane + alkane mixtures. Choosing Cl as a group instead of  $\text{CH}_2\text{Cl}$  allows the same group definition to be used for all chloroalkanes. The new parameters determined for these systems follow the trend previously obtained for the larger dichloroalkanes, as can be seen in Fig. 1. Figure 6



**Fig. 6.** Comparison between the experimental values  $H^E$  and the Tassios predictions for dichloromethane + alkane systems at 298.15 K: experimental points: (●) hexane, (■) heptane; theoretical predictions: (—) new parameters, (---) older parameters.



illustrates how the new parameters improve the predictions. The AAD is reduced from 30% to 6%. It is interesting to point out, however, that Larsen et al. (14) and Gmehling et al. (15) define dichloromethane as an independent group. Using the parameters recommended by these authors, the AADs are 2% and 24%, respectively, for the same systems.

The RMSDs for  $\ln\gamma^\infty$  using both the new and the older parameters are, respectively: 0.098, 0.334 for the Larsen version and 0.130, 0.184 for the Gmehling version for the dichloroalkane + alkane systems. For this type of system, a better representation of  $\ln\gamma^\infty$  is obtained using the Larsen version.

#### Comparison with other group-contribution models

Finally, we have compared the above-mentioned results using the UNIFAC model with the predictions of the Nitta–

Chao (12) and DISQUAC (11) models, using molecular-structure-dependent parameters. The conclusion of this comparison was that the different models have similar prediction accuracies. The AADs for the dichloroalkane + alkane mixtures are 6% and 8% for  $G^E$  and 10% and 6% for  $H^E$  using the DISQUAC and the Nitta–Chao models, respectively. The Gmehling version using the new parameters predicts slightly better excess Gibbs energies, and the DISQUAC model gives the smallest AADs for excess enthalpies. Similar results are obtained for 1-chloroalkane + alkane systems. For the infinite dilution activity coefficients, the best predictions for 1-chloroalkane + alkane mixtures are obtained using the Larsen and Gmehling versions. The corresponding AADs for the DISQUAC model are significantly larger (0.247), whereas for dichloroalkane + alkane mixtures the AADs are similar for the four models.

Based on our experience in fitting length-dependent parameters using several group-contribution models, we conclude that it is generally more difficult to find regular length-dependence with the UNIFAC model. This fact could be owing to the multiple solutions that are found in the minimization process for UNIFAC if there is no imposed limit on the range of the group interaction parameters. In the DISQUAC case the range of dispersive and quasichemical coefficients is small. Similar behavior is observed using the Nitta–Chao model, for which the hard core volumes must be close to their Bondi values, and their temperature-dependence parameter must be positive. The number of degrees of freedom of the groups is always between 0.1 and 1.0, and the dispersive and chemical energies have relatively narrow ranges.

#### Conclusions and future work

We have determined the interaction parameters between chlorine and methylene groups for three different versions of the UNIFAC model (Tassios et al., Larsen et al., and Gmehling et al.), taking into account the proximity effect. The  $H^E$ ,  $G^E$ , and  $\ln\gamma^\infty$  values of binary 1-chloroalkane + alkane and dichloroalkane + alkane systems are fairly well represented using the parameters proposed in this work. The results are similar to those obtained with the DISQUAC and the Nitta–Chao models.

In previous studies we determined the characteristic parameters representing the interaction of fluorine, bromine, and iodine with methylene groups for the UNIFAC and Nitta–Chao models in 1-fluoroalkane (54), 1-bromoalkane (55), and 1-iodoalkane (56) + alkane systems. We plan to extend this study to binary mixtures of alkanes with difluoroalkanes, dibromoalkanes, or diiodoalkanes to investigate the dependence of the interaction parameters on the distance between the halogen atoms. Furthermore, the halogen–methylene interaction parameters should follow a well-defined trend when the size of the halogen atom is varied.

#### Acknowledgments

This work was carried out under Research Project 20605B93 Xunta de Galicia and PPQ2001–3022 MCYT–Spain.



## References

1. J. Dymond and D. Richon. *Fluid Phase Equilib.* **199**, 1 (2002).
2. H.S. Wu and S.I. Sandler. *AIChE J.* **35**, 168 (1989).
3. H.S. Wu, W.E. Locke, and S.I. Sandler. *J. Chem. Eng. Data*, **36**, 127 (1991).
4. H.S. Wu and S.I. Sandler. *Ind. Eng. Chem. Res.* **30**, 881 (1991).
5. H.S. Wu and S.I. Sandler. *Ind. Eng. Chem. Res.* **30**, 889 (1991).
6. J. Storm. Ph.D. Thesis, Technischen Universität Carolo-Wilhelmina zu Braunschweig, Germany. (1989).
7. M. Kleiber. Ph.D. Thesis, Technischen Universität Carolo-Wilhelmina zu Braunschweig, Germany. (1994).
8. M. Kleiber. *Fluid Phase Equilib.* **107**, 161 (1995).
9. R. Jadot and M. Frere. *High Temp. High Pressures*, **25**, 491 (1993).
10. J.W. Kang, J. Abildskov, R. Gani, and J. Cobas. *Ind. Eng. Chem. Res.* **41**, 3260 (2002).
11. H.V. Kehiaian and B. Marongiu. *Fluid Phase Equilib.* **40**, 23 (1988).
12. J. García, E.R. López, J.L. Legido, and J. Fernandez. *Fluid Phase Equilib.* **110**, 31 (1995).
13. J. Ortega and J. Plácido. *Fluid Phase Equilib.* **109**, 205 (1995).
14. B.L. Larsen, P. Rasmussen, and A. Fredenslund. *Ind. Eng. Chem. Res.* **26**, 2274 (1987).
15. J. Gmehling, J. Li, and M. Schiller. *Ind. Eng. Chem. Res.* **32**, 178 (1993).
16. H.C. Van Ness and B.D. Smith. *Int. DATA Ser. Sel. Data Mixtures, Ser. A*, **3**, 21 (1983).
17. B. Gutsche and H. Knapp. *Fluid Phase Equilib.* **8**, 285 (1982).
18. S.O. Sayegh, J.H. Vera, and G.A. Ratcliff. *Can. J. Chem. Eng.* **57**, 513 (1979).
19. F.A. Ashraf and J.H. Vera. *Can. J. Chem. Eng.* **59**, 89 (1981).
20. B.J.-P.E. Grolier. *Int. DATA Ser. Sel. Data Mixtures, Ser. A*, **1**, 81 (1974).
21. F.M. Royo and C. Gutiérrez Losa. *J. Chem. Thermodyn.* **17**, 843 (1985).
22. Y. Azpiazu, F.M. Royo, and C. Gutiérrez Losa. *J. Chem. Thermodyn.* **16**, 561 (1984).
23. R. Eng and S.I. Sandler. *J. Chem. Eng. Data*, **29**, 156 (1984).
24. A. Kohl and A. Heintz. *Thermochim. Acta*, **94**, 79 (1985).
25. T.H. Doan-Nguyen and J.H. Vera. *J. Chem. Eng. Data*, **23**, 218 (1978).
26. J. Valero, M. Gracia, and C. Gutiérrez Losa. *J. Chem. Thermodyn.* **12**, 621 (1980).
27. T.T. Lai, T.H. Doan-Nguyen, J.H. Vera, and G.A. Ratcliff. *Can. J. Chem. Eng.* **56**, 358 (1978).
28. J.-P. E. Grolier, K. Sosnkowska-Kehiaian, and H.V. Kehiaian. *J. Chim. Phys.* **70**, 367 (1973).
29. M.I. Paz Andrade and R. Bravo. *Int. DATA Ser. Sel. Data Mixtures, Ser. A*, **1**, 71 (1977).
30. L. Núñez, F. Miguelez, L. Barral, and M.I. Paz-Andrade. *J. Chem. Thermodyn.* **21**, 495 (1989).
31. J. Ortega and J. Plácido. *Int. DATA Ser. Sel. Data Mixtures, Ser. A*, **21**, 1 (1993).
32. I. Baños, J. Valero, M. Gracia, and C. Gutierrez Losa. *Ber. Bunsen-Ges.* **87**, 866 (1983).
33. C. Polo, C. Gutiérrez Losa, M.-R. Kechavartz, and H.V. Kehiaian. *Ber. Bunsen-Ges.* **84**, 525 (1980).
34. R.K. Nigam and S. Aggarwal. *Fluid Phase Equilib.* **26**, 181 (1986).
35. S.K. Chaudhari and S.S. Katti. *Thermochim. Acta*, **158**, 99 (1990).
36. J.N. Rhim and S.Y. Bae. *Hwahak Konghak*, **17**, 201 (1979).
37. G. Hahn and P. Svejda. *Int. DATA Ser. Sel. Data Mixtures, Ser. A*, **2**, 143 (1985).
38. P. Svejda and A.M. Demiriz. Determination of the excess enthalpies of mixing of the liquid systems: 1,2-dichloroethane + *n*-alkanes by flow microcalorimetry. Presented at the Conferencia Internacional de Disoluciones de No Electrolitos, Santiago de Compostela, Spain. 1979. p. 137.
39. J.-P.E. Grolier and H.V. Kehiaian. *J. Chim. Phys.* **70**, 807 (1973).
40. E.R. Thomas, B.A. Newman, G.L. Nicolaides, and C.A. Eckert. *J. Chem. Eng. Data*, **27**, 233 (1982).
41. D.E. Martire and L.Z. Pollara. *J. Chem. Eng. Data*, **10**, 40 (1965).
42. E.F. Meyer and J.A. Meyer. *J. Phys. Chem.* **85**, 94 (1981).
43. E.F. Meyer and F.A. Baiocchi. *J. Am. Chem. Soc.* **99**, 6206 (1977).
44. P. Alessi, I. Kikic, A. Alessandrini, and M. Fermeglia. *J. Chem. Eng. Data*, **27**, 445 (1982).
45. Y.B. Tewari, J.P. Sheridan, and D.E. Martire. *J. Phys. Chem.* **74**, 3263 (1970).
46. H.G. Harris and J.M. Prausnitz. *J. Chromatogr. Sci.* **7**, 685 (1969).
47. E.F. Meyer and F.A. Baiocchi. *J. Chem. Thermodyn.* **10**, 249 (1978).
48. A.N. Korol. *Neftekhimiya* **3**, 635 (1963).
49. P. Alessi, I. Kikic, C. Nonino, and M.O. Visalberghi. *J. Chem. Eng. Data*, **27**, 448 (1982).
50. G.M. Janini and D.E. Martire. *J. Phys. Chem.* **78**, 1644 (1974).
51. E.R. Thomas, B.A. Newman, G.L. Nicolaides, and C.A. Eckert. *J. Chem. Eng. Data*, **27**, 399 (1982).
52. E.A. Guggenheim. *Mixtures*. Clarendon Press, Oxford. 1952.
53. I. Kikic, P. Alessi, P. Rasmussen, and A. Fredenslund. *Can. J. Chem. Eng.* **58**, 253 (1980).
54. J. García, E.R. Lopez, J. Fernández, and J.L. Legido. *High Temp. High Pressures*, **29**, 33 (1997).
55. J. García, M.J.P. Comuñas, L. Lugo, E.R. López, and J. Fernández. *Can. J. Chem.* **77**, 299 (1999).
56. J. García, E.R. Lopez, L. Lugo, and J. Fernandez. *Phys. Chem. Chem. Phys.* **3**, 5006 (2001).



# Canadensenes: Natural and semi-synthetic analogues

Qing-Wen Shi, Anastasia Nikolakakis, Françoise Sauriol, Orval Mamer, and Lolita O. Zamir

**Abstract:** The first bicyclic taxanes isolated in the needles of the Canadian yew were named canadensene **1** and 5-epi-canadensene **2**. Four additional analogues (**3–6**), isolated previously in *Taxus chinensis* and *Taxus mairei*, and a new natural 5-epi-canadensene analog **7** with a C-20-cinnamoyl group, were characterized for the first time in the needles of *Taxus canadensis*. A bicyclic derivative **8** with a docetaxel side chain on C-20 was synthesized using 5-epi-canadensene **2** as starting material. The lack of bioactivities of these bicyclic analogues (tubulin polymerization and cytotoxicities against human cancer cell lines) is discussed.

**Key words:** *Taxus canadensis*, Taxaceae, taxanes, natural products, semi-synthesis.

**Résumé :** Les premiers taxanes bicycliques isolés des aiguilles de l'if Canadien ont été nommés canadensene **1** et 5-épi-canadensene **2**. Quatre analogues additionnels (**3–6**) isolés auparavant dans *Taxus chinensis* et *Taxus mairei*, ainsi qu'un nouvel analogue **7** du 5-épi-canadensene avec un groupe cinnamoyl en C-20 ont été caractérisés pour la première fois dans les aiguilles du *Taxus canadensis*. Un dérivatif bicyclique **8** avec la chaîne latérale du docetaxel en C-20 a été synthétisé à partir du 5-épi-canadensene **2**. Le manque d'activité biologique de ces analogues bicycliques (polymérisation de la tubuline ainsi que cytotoxicités envers des cellules humaines cancérogènes) est discuté dans cette publication.

**Mots clés :** *Taxus canadensis*, Taxaceae, taxanes, produits naturels, semi-synthèse.

## Introduction

*Taxus canadensis* is a low-trailing bush abundant in the province of Quebec, with an unusual composition of taxane analogs (1–4). It is the only yew producing 9-dihydro-13-acetylbaccatin III in abundance in its needles (2, 3). The only other yew where it had been found is in the bark of *Taxus chinensis*, albeit only as traces (5). We reported the isolation of two bicyclic oxygenated taxanes in the Canadian yew that we named canadensene **1** and 5-epi-canadensene **2** (Fig. 1) in 1995 and 1998, respectively, to emphasize their origin (6, 7). Simultaneously, taxachitrienes **3–6** were reported in the needles of the Chinese and in the stems of the Japanese yews (8–11).

In the present work, the detailed structures of five 5-epi-canadensene analogs (**3–7**) differing in the substituents on C-2, C-5, C-13, or C-20 are reported from the needles of *T. canadensis*. Taxane **7**, which has a cinnamoyloxy group on C-20, is a new metabolite that has never been found in other

yews. It has been synthesized in our laboratory from cinnamoylation of 5-epi-canadensene (12). We are again reporting the high-resolution 2D NMR data of taxachitriene B (taxane **3**), since some signals had not been assigned. Taxanes **4** and **5** were characterized as 2-deacetyltaxachitriene A and 13,20-dideacetyltaxachitriene A, respectively. They had been previously identified in *Taxus mairei* needles (10, 11). Taxane **6** was identical to 5-deacetyltaxachitriene B previously isolated with taxachitriene B in *T. chinensis* needles (8, 9). In addition, we have semi-synthesized a 5-epi-canadensene analog to which the C-13 side chain of docetaxel was attached to C-20 (docecanadensene **8**, Fig. 1). Our hypothesis was that the canadensene derivative, being flexible because of its bicyclic structure, might allow for a long side chain on C-20 to reach the known active site of paclitaxel:  $\beta$ -tubulin (13–15). The lack of activity of these compounds toward tubulin polymerization and cytotoxicities against human cancer cell lines is discussed.

## Results and discussion

The methanolic extracts of *T. canadensis* needles were analyzed, and its taxanes were purified by repetitive chromatography, preparative or semi-preparative HPLC, and preparative TLC.

### Characterization of taxanes 3–6 (Fig. 1)

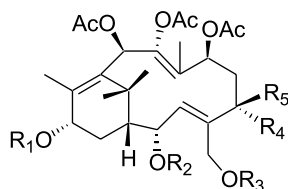
Taxanes **3–6** were identified as taxachitriene B (8), 2-deacetyltaxachitriene A (10), 13,20-dideacetyltaxachitriene A (11), and 5-deacetyltaxachitriene B (9), respectively, on the basis of 1D and (or) 2D spectral analysis and by comparison with the reported spectral data in the literature. Taxanes **3** and **6** have been previously isolated from *T. chinensis* needles.

Received 26 September 2002. Published on the NRC Research Press Web site at <http://canjchem.nrc.ca> on 29 May 2003.

Q.-W. Shi, A. Nikolakakis, and L.O. Zamir.<sup>1</sup> Human Health Research Center, INRS-Institut Armand-Frappier, Université du Québec, 531 Boulevard des Prairies, Laval, QC H7V 1B7, Canada.  
F. Sauriol. Department of Chemistry, Queen's University, Kingston, ON K7L 3N6, Canada.  
O. Mamer. Biomedical Mass Spectrometry Unit, McGill University, 1130 Pine Avenue West, Montreal, QC H3A 1A3, Canada.

<sup>1</sup>Corresponding author (e-mail: [Lolita.Zamir@inrs-iaf.quebec.ca](mailto:Lolita.Zamir@inrs-iaf.quebec.ca)).



**Fig. 1.** Canadensene analogs.

1	R <sub>1</sub> = Ac	R <sub>2</sub> = Ac	R <sub>3</sub> = H	R <sub>4</sub> = H	R <sub>5</sub> = OH
2	R <sub>1</sub> = Ac	R <sub>2</sub> = Ac	R <sub>3</sub> = H	R <sub>4</sub> = OH	R <sub>5</sub> = H
3	R <sub>1</sub> = Ac	R <sub>2</sub> = H	R <sub>3</sub> = H	R <sub>4</sub> = OAc	R <sub>5</sub> = H
4	R <sub>1</sub> = Ac	R <sub>2</sub> = H	R <sub>3</sub> = Ac	R <sub>4</sub> = OH	R <sub>5</sub> = H
5	R <sub>1</sub> = H	R <sub>2</sub> = Ac	R <sub>3</sub> = H	R <sub>4</sub> = OH	R <sub>5</sub> = H
6	R <sub>1</sub> = Ac	R <sub>2</sub> = H	R <sub>3</sub> = H	R <sub>4</sub> = OH	R <sub>5</sub> = H
7	R <sub>1</sub> = Ac	R <sub>2</sub> = Ac	R <sub>3</sub> = Cinn	R <sub>4</sub> = OH	R <sub>5</sub> = H
8	R <sub>1</sub> = Ac	R <sub>2</sub> = Ac	R <sub>3</sub> = docetaxel side chain	R <sub>4</sub> = OH	R <sub>5</sub> = H

dles (8, 9). Taxanes **4** and **5** have been previously isolated from *T. mairei* needles (10, 11). This is the first report of compounds **3–6** in the Canadian yew.

#### Characterization of 20-cinnamoyloxy-5-epi-canadensene **7** (Fig. 1, Table 1)

Compound **7** was obtained as a colorless, amorphous solid in a very small yield ( $\sim 0.4 \times 10^{-4}\%$ ) from dried needles of *T. canadensis*. The composition of **7**, C<sub>39</sub>H<sub>48</sub>O<sub>13</sub>, was established from combined analysis of high-resolution FAB-MS at  $m/z$  763.2734 ( $[M + K]^+$ ) and NMR spectral data. In a previous publication, 20-cinnamoyloxy-5-epi-canadensene was prepared from 5-epi-canadensene (12). In this publication, the <sup>1</sup>H NMR has been reported. A more comprehensive table of all NMR data for **7** is shown in Table 1. The relatively downfield signals of H-20a and H-20b in **7**, resonating at  $\delta$  4.93 and  $\delta$  4.55 compared with 5-epi canadensene **2** (**7**) at  $\delta$  4.56 and 3.46 or 5-cinnamoyloxy-epi-canadensene (12) at  $\delta$  4.65 and 3.55, implied that the cinnamoyloxy of **7** was positioned on C-20. The <sup>1</sup>H NMR data at  $\delta$  4.55 revealed that a hydroxy group was attached at C-5. This is in accord with the chemical shift at  $\delta$  4.64 for **2**, which has a free C-5-OH, whereas the chemical shift of 5-cinnamoyloxy-epi-canadensene for C-5-OH is further downfield at  $\delta$  5.91. The relative stereochemistry of **7** is the same as that of **2**, as confirmed by comparing their NOESY spectra. The structure of **7** is, therefore, (3*E*, 8*E*)-2 $\alpha$ ,7 $\beta$ ,9,10 $\beta$ ,13 $\alpha$ -pentaacetoxy-5 $\alpha$ -hydroxy-20-cinnamoyloxy-3,8-secotaxa-3,8,11-triene (Fig. 1).

#### Semi-synthesis of docecanadensene **8** (Scheme 1)

The semi-synthesis of docecanadensene (**8**) from **2** afforded a compound with a C-20 side chain. We postulated that the primary C-20 alcohol of **2** would be more reactive than the secondary alcohol at C-5. Direct esterification of **2** was realized with 2-(4-OMe)phenyl-1,3-oxazolidine of *N*-Boc phenylisoserine (**9**) (16); dicyclohexylcarbodiimide and 4-pyrrolidinopyridine in dichloromethane–toluene at 23°C afforded diastereomers **10** (79%). Deprotection of **10** with a stoichiometric amount of *p*-toluenesulfonic acid in MeOH gave **8** (67%). The downfield shift of H-20a/b at  $\delta$  4.56/3.46 in **2** (**7**) to  $\delta$  5.06/4.28 in **8** confirmed the attachment of the docetaxel side chain at C-20.

#### Bioactivity of canadensene analogs

The polymerization of tubulin into stable microtubules is the most characteristic mode of action of paclitaxel (17). According to our original hypothesis, when the configuration of the taxane is substantially altered, a side chain situated elsewhere than on C-13 might lead to bioactivity (13–15). Taxuspine D and taxagifine have a modified A ring. The former has a C12=C13 double bond while the latter has a C16–C12 ether linkage. Both taxuspine D and taxagifine have a cinnamoyl group attached to the C5-OH, and both promoted the polymerization of tubulin but to about 1/3 that of paclitaxel (13–15). Similar results were reported previously by Kobayashi and co-workers (18, 19). In this work, we wanted to test if the core skeleton of the taxane — that is, a 6-membered ring fused to two 8- and 6-membered rings — was essential. We therefore investigated the natural canadensene analogs as well as a synthetic canadensene analog **8**. In the Taxol® series the replacement of the 3'-*N* benzoyl group with a *t*-butoxycarbonyl group substantially increased the tubulin activity and the in vitro cytotoxicity of docetaxel, the 10-deacetyl-3'-*N*-*t*-butoxycarbonyl analog of Taxol® (20). Consequently, we chose to attach a docetaxel side chain to C-20 of 5-epi-canadensene (**8**). We proposed that the bicyclic structure of 5-epi-canadensene, being very flexible, would enable the C-20 side chain to reach the active site of  $\beta$ -tubulin, a known target of paclitaxel. Tubulin polymerization activities were investigated for 5-epicanadensene **2**, 20-cinnamoyloxy-5-epicanadensene **7**, and docecanadensene **8** compared with Taxol® (Fig. 2). Whereas Taxol® induced the initial rate of tubulin polymerization almost twice as much as the control, the analogs only showed comparable activities to the control. We tested the in vitro cytotoxicity of taxanes **2**, **7**, and **8** against breast cancer cell lines MCF7 and MCF7-ADR (adriamycin resistant), as compared with that of Taxol® (Table 2). The IC<sub>50</sub> (concentration killing 50% of cells) of compounds **2**, **7**, and **8** were comparable around the 700 nM range for the MCF7-wild-type cell line. However, paclitaxel was a more potent compound as its IC<sub>50</sub> was in the 2 nM range. Similarly for the MCF7-ADR cell line the IC<sub>50</sub> for compounds **2**, **7**, and **8** were 645 nM, 825 nM, and 882 nM, respectively, compared with the IC<sub>50</sub> for Taxol® at 5  $\mu$ M. Unfortunately, these canadensene analogs **2**, **7**, and **8** were inactive in both the tubulin assay as well as the two cytotoxicity assays. We would have liked to prepare two more synthetic analogs from 5-epi-canadensene, one having the side chain attached to C-13 and another analog with the side chain attached to C-5. Unfortunately 5-epi-canadensene can be isolated only in very small quantities, and therefore we were unable to prepare any more synthetic analogs. We cannot conclude, therefore, that the core skeleton (6/8/6 fused membered rings) is essential since we do not have the data pertaining to the compounds having a side chain on the C-13 or C-5 position. It is known, however, that 7,8-secotaxoids have excellent tubulin binding and cytotoxicity activity (21).

#### Experimental section

##### General experimental procedures

Optical rotations were recorded on a Jasco DIP-370 digital polarimeter. The NMR and HR-FAB-MS data were



**Table 1.**  $^1\text{H}$  and  $^{13}\text{C}$  NMR data for taxane **7** (500 MHz for  $^1\text{H}$ , 125 MHz for  $^{13}\text{C}$ ,  $\text{CDCl}_3$ ).

Position	$\delta$ ( $^1\text{H}$ ) multiplicity <sup>a</sup>	<i>J</i>	$\delta$ ( $^{13}\text{C}$ ) <sup>b</sup>	HMBC <sup>c</sup>	NOESY <sup>d</sup>
1	1.82 (dd)	6.5, 4.5	46.3	2, 3, 11, 14, 15, 16	2 <sup>s</sup> , 14a <sup>s</sup> , 14b <sup>w</sup> , 16 <sup>s</sup> , 17 <sup>m</sup>
2	5.84 (dd)	11.7, 4.7	68.9	1, 3, 4, 14, 170.0	1 <sup>s</sup> , 3 <sup>m</sup> , 17 <sup>s</sup> , 20a <sup>s</sup>
3	6.50 (d)	11.7	125.1	4, 5	2 <sup>m</sup> , 7 <sup>m</sup>
4			<b>137.4</b>		
5	4.55 (o.m)		68.2		6a <sup>s</sup> , 6b <sup>m</sup> , 19 <sup>w</sup> . See 20b <sup>w</sup>
6a	2.63 (ddd)	16.2, 7.8, 2.7	37.4		5/20b <sup>s</sup> , 6b <sup>s</sup> , 19 <sup>s</sup>
6b	2.03 (o.m)			3, 4, 5, 169.4	5/20b <sup>m</sup> , 6a <sup>s</sup> , 7 <sup>m</sup>
7	5.08 (d)	7.8	67.4	5, 6, 8, 9, 19, 172.7	3 <sup>s</sup> , 6b <sup>m</sup> , 10 <sup>s</sup> , 18 <sup>s</sup>
8			<b>123.6</b>		
9			<b>144.5</b>	168.1	
10	6.92 (s)		68.0	8, 9, 11, 12, 15, 168.1	7 <sup>s</sup> , 18 <sup>s</sup>
11			<b>136.7</b>		
12			<b>135.6</b>		
13	5.29 (d)	9.3	68.9	1, 11, 12, 14, 18, 170.9	14a <sup>s</sup> , 14b <sup>w</sup> , 16 <sup>w</sup> , 18 <sup>m</sup>
14a	2.52 (ddd)	16.6, 8.7, 7.6	25.1	1	1 <sup>s</sup> , 14b <sup>s</sup> , 13 <sup>s</sup> , 16 <sup>m</sup>
14b	2.17 (o.m)			1, 2/13, 12, 15	1 <sup>w</sup> , 3 <sup>w</sup> , 13 <sup>w</sup> , 14a <sup>s</sup>
15			<b>36.2</b>		
16	1.12 (s)		33.9	1, 11, 15, Me	1 <sup>s</sup> , 14a <sup>s</sup> , 13 <sup>w</sup>
17	1.29 (s)		24.6	1, 11, 15, Me	1 <sup>s</sup> , 2 <sup>s</sup> , 16 <sup>w</sup>
18	1.94 (s)		17.0	11, 12, 13, 15, 16	7 <sup>s</sup> , 10 <sup>s</sup> , 13 <sup>s</sup> , 16 <sup>m</sup>
19	1.67 (s)		12.9	7, 8, 9, 11, 168.1	5/20b <sup>w</sup> , 6a <sup>s</sup> , Ac(2.21) <sup>s</sup>
20a	4.93 (d)	12.9	59.6	3, 4, 5, 1'	2 <sup>s</sup> , 20b <sup>s</sup>
20b	4.55 (d)	12.9		3, 4, 5, 1'	20a <sup>s</sup> , see 5
OAc	2.21 (s)		20.3	168.1	
			<b>168.1</b>		
	2.18 (s)		21.2	170.9	
			<b>170.9</b>		
	2.09 (s)		21.6	172.5	
			<b>172.5</b>		
	1.97 (s)		21.2	169.9	
			<b>169.9</b>		
	1.96 (s)		20.7	168.1	
			<b>168.1</b>		
1'			<b>166.7</b>		
2'	6.37 (d)	16.1	117.3	1', 3', Ph-C1	
3'	7.64 (d)	16.1	145.2	1', 2', Ph-C1, Ph-o	
Ph'			134.3		
o	7.49 (m)		128.0		
m, p	7.38 (m)		128.8		
			130.3		

<sup>a</sup>Multiplicity: s, singlet; d, doublet; dd, doublet of doublets; ddd, doublets of doublets of doublets; m, multiplet; o, overlapped.<sup>b</sup>The  $^{13}\text{C}$  chemical shifts were extracted from the HMQC experiment ( $\pm 0.2$  ppm). The numbers in bold character represent quaternary carbons whose chemical shifts were obtained from the HMBC experiment ( $\pm 0.2$  ppm).<sup>c</sup>Italic font means weak HMBC correlations.<sup>d</sup>NOESY intensities are marked as strong (s), medium (m), or weak (w).

obtained with the instruments and conditions reported previously (4). Flash chromatography was performed on silica gel 60 (230–400 mesh EM Science). Thin layer chromatography was conducted on silica gel 60 F<sub>254</sub> pre-coated TLC plates (0.25 mm thickness for analytical, 0.25 and 0.5 mm for preparative, EM Science). The components were visualized on TLC plates using a UV illumination lamp (254 and 365 nm). The spraying reagent for TLC plates was 10% sulfuric acid in EtOH followed by heating the plates to visualize the spots. Analytical HPLC was performed on a Waters 600 FHU delivery system coupled to a PDA 996 detector. Preparative and semi-preparative HPLC were carried out on a

Waters Delta Prep 3000 instrument coupled to a UV 486 tunable absorbance detector (Waters). Peaks were detected between 210 and 320 nm, but most chromatograms were plotted at 227 or 278 nm. Analytical HPLC was performed with two Whatman partisl 10 ODS-2 analytical columns (4.6  $\times$  250 mm) in series. Semi-preparative HPLC was performed with two Whatman partisl 10 ODS-2 Mag-9 semi-preparative columns (9.4  $\times$  250 mm) in series. Preparative HPLC was performed with one partisl 10 ODS-2 MAG-20 preparative column (22  $\times$  500 mm). The products were eluted with a 50 min linear gradient of acetonitrile (25–100%) in H<sub>2</sub>O at a flow rate of 18 mL/min (preparative



**Scheme 1.** (a) **9**, DCC, 4-PP, CH<sub>2</sub>Cl<sub>2</sub>-toluene, 23°C, 2 h, taxane **10** 79%; (b) *p*-toluenesulfonic acid, methanol, 23°C, 45 min, taxane **8** 67%.

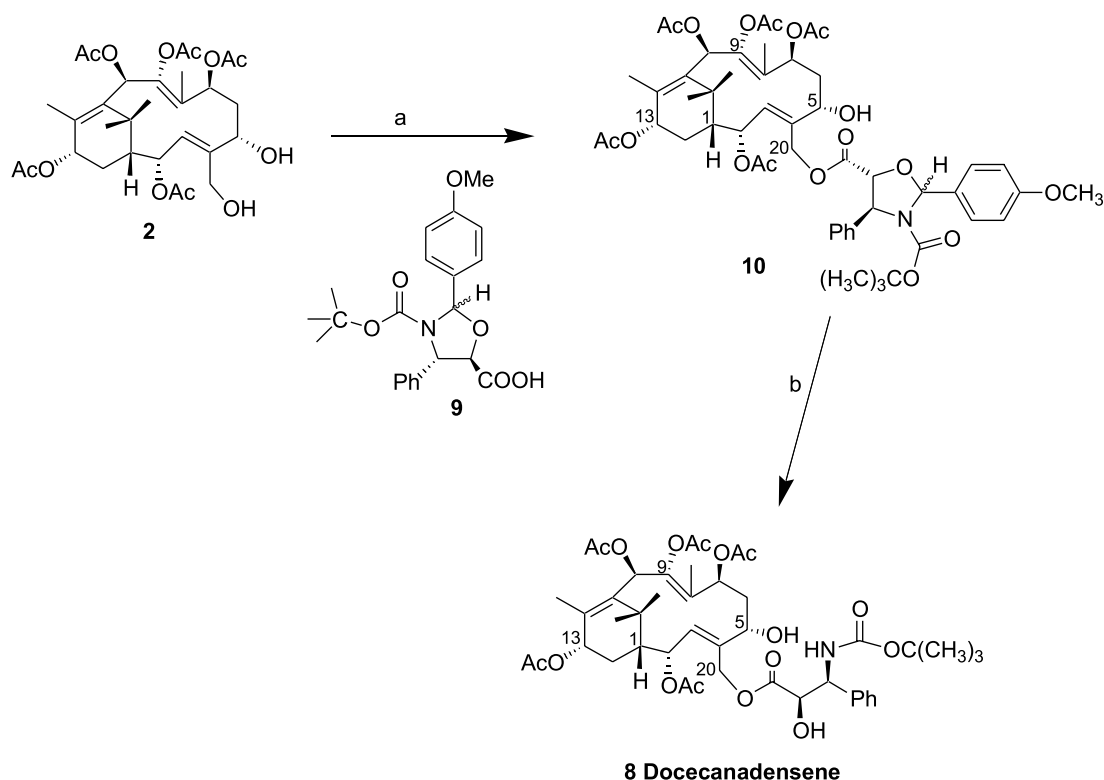
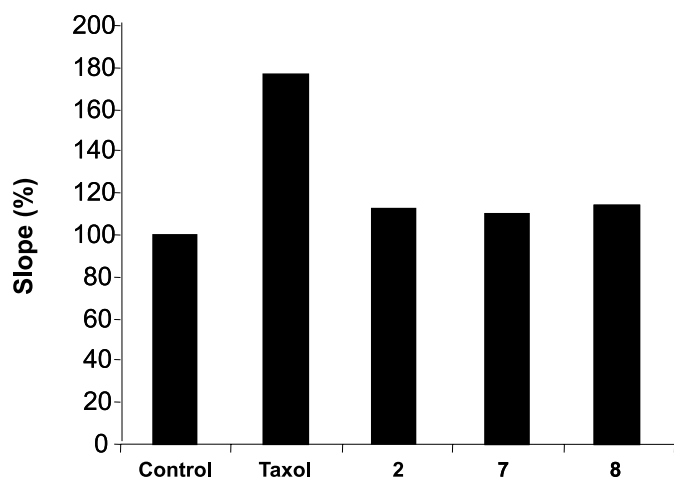


**Fig. 2.** Effect of canadensene analogs on tubulin assembly. Microtubule turbidity was evaluated at 340 nm by incubating tubulin (1 mg/mL) at 37°C in the presence or absence of taxanes. The slope percentage compared with control is depicted. The initial rate of tubulin polymerization was determined by initial slope detected during the first 3 min of tubulin assembly. This data represents mean  $\pm$  SEM (standard error mean) for separate experiments.



HPLC) and 3 mL/min (semi-preparative HPLC). All the reagents and solvents were of the best available commercial quality and were used without further purification.

## Plant material

*T. canadensis*, Marsh were collected in September 1997 at St-Jean-sur-Richelieu, Quebec, Canada. Several specimens (voucher # Iz97-03) have been deposited in the herbarium of the Montreal Botanical Garden.

## Extraction, isolation, and purification of taxanes (3–7)

Ground, air-dried needles of *T. canadensis* (4.0 kg) were extracted with 24 L of MeOH for 1 day at room temperature. The ground needles were filtered and extracted again with fresh solvent for another 3 days (8 L MeOH per day). The combined organic extracts were evaporated under reduced pressure. Water (3 L) was added and lipids were removed by stirring the mixture with hexane (3  $\times$  3 L). The hexane layer was removed and then condensed to 1500 mL and extracted with 80% MeOH (4  $\times$  500 mL). The 80% MeOH extract, after being re-extracted with hexane (2  $\times$  300 mL), was evaporated under reduced pressure, diluted with 1 L of H<sub>2</sub>O, and extracted with EtOAc (3  $\times$  700 mL). The combined EtOAc extracts were dried, filtered, and evaporated, yielding a dark brown extract (25 g). The aqueous phase was then saturated with 200 g NaCl and extracted with CH<sub>2</sub>Cl<sub>2</sub> (4  $\times$  3 L). The combined CH<sub>2</sub>Cl<sub>2</sub> extracts were dried, filtered, and evaporated, yielding a dark green extract (115 g).

A portion of the CH<sub>2</sub>Cl<sub>2</sub> extract (50 g) was absorbed onto 110 g silica gel. Purification by flash chromatography on 1320 g silica gel and successive elution with a CH<sub>2</sub>Cl<sub>2</sub>-MeOH gradient, with increasing amounts of MeOH from 5% to 45% (total 15 L), led to 45 fractions (Fr<sub>D-1</sub> to Fr<sub>D-45</sub>). Fractions Fr<sub>D-18</sub> to Fr<sub>D-24</sub>, after being monitored by TLC, were pooled (3.5 g) and chromatographed over silica gel



**Table 2.** Cytotoxicity of canadensene analogs.

Compound	Tumor cell cytotoxicity IC <sub>50</sub> (nM) <sup>a</sup>	
	MCF7-wild type	MCF7-ADR
Taxol®	2 ± 1.52	>5 <sup>b</sup>
5-Epicanadensene <b>2</b>	750 ± 5.38	645 ± 3.51
20-Cinnamoyloxy-5-epicanadensene <b>7</b>	655 ± 1.42	825 ± 2.14
Docecanadensene <b>8</b>	740 ± 3.99	882 ± 3.26

<sup>a</sup>Cytotoxicity of taxanes on the breast cancer cell lines MCF7-wild type and MCF7-ADR (adriamycin resistant). Exponentially growing cells were continuously exposed to taxanes at varying concentrations, and cell viability was evaluated by the MTT metabolic assay. Data represents mean ± SEM of three separate experiments. IC<sub>50</sub> is described as the concentration of agent required to inhibit cell proliferation to 50% vs. untreated cells.

<sup>b</sup>Unit is in µM.

(195 g, 4.2 × 32 cm) while eluting with hexane:EtOAc (1.2:1, 1.1 L; 1:1, 1.2 L; 1:1.2, 1.1 L; and 1:1.75, 1.1 L). Twenty-three fractions (Fr<sub>D-18-1</sub> to Fr<sub>D-18-23</sub>) were collected. The fraction Fr<sub>D-18-19</sub> (53 mg) was applied to a preparative TLC plate (hexane:acetone, 3:2) and cut into 5 bands as visualized under a UV lamp. The band with an *R<sub>f</sub>* = 0.30 (29 mg) was further separated by preparative HPLC and yielded **7** (7 mg, *t<sub>R</sub>* = 44.30 min).

The fractions Fr<sub>D-38</sub> to Fr<sub>D-41</sub> were combined (24 g) and chromatographed over silica gel (770 g) by eluting with hexane:acetone (3:2, 3 L; 1:1, 3 L; and 2:3, 3 L), affording 28 fractions (Fr<sub>D-38-1</sub> to Fr<sub>D-38-28</sub>). The fractions Fr<sub>D-38-19</sub> to Fr<sub>D-38-28</sub> were combined (2090 mg) and rechromatographed over silica gel (180 g, 4 × 35 cm) by elution with CH<sub>2</sub>Cl<sub>2</sub>:CH<sub>3</sub>CN (3:2, 2 L; 5:4, 1 L; and 1:1, 1 L), yielding 25 fractions (Fr<sub>D-38-19-1</sub> to Fr<sub>D-38-19-25</sub>). The fraction Fr<sub>D-38-19-8</sub> (280 mg) was fractionated by preparative HPLC. The peak at *t<sub>R</sub>* = 24.05 min was collected, concentrated (45 mg), and further purified by preparative TLC (hexane:acetone, 1:1) affording **3** (4.0 mg, *R<sub>f</sub>* = 0.32). The peak at *t<sub>R</sub>* = 25.18 min was collected (26 mg) and further purified by preparative TLC (hexane:acetone, 1:1), yielding **4** (3.4 mg, *R<sub>f</sub>* = 0.39). The fraction Fr<sub>D-38-19-20</sub> (112 mg) was subjected to preparative HPLC. The peak at *t<sub>R</sub>* = 24.08 min was collected (15 mg) and further purified by preparative TLC (CH<sub>2</sub>Cl<sub>2</sub>:CH<sub>3</sub>CN, 5:9), yielding **5** (4.0 mg, *R<sub>f</sub>* = 0.34).

The fractions Fr<sub>D-42</sub> to Fr<sub>D-45</sub> were combined (2.5 g), treated with activated charcoal, dissolved in EtOAc, and extracted three times with 10% HCl. The aqueous acid layer was adjusted to pH 9–10 and re-extracted with CH<sub>2</sub>Cl<sub>2</sub>. The organic layer was washed with H<sub>2</sub>O to neutrality, dried, filtered, and evaporated. The residue (200 mg) was fractionated by preparative TLC (hexane:EtOAc, 3:8). The band at *R<sub>f</sub>* = 0.15 was collected, washed with MeOH, and further purified by preparative TLC (hexane:acetone, 30:75), affording **6** (5 mg, *R<sub>f</sub>* = 0.15).

**(3E,8E)-5α,7β,9,10β,13α-Pentaacetoxy-2α,20-dihydroxy-3,8-secotaxa-3,8,11-triene (taxachitriene B) (3)**

<sup>1</sup>H NMR (500 MHz, CDCl<sub>3</sub>): H-1: 1.72 (dd, *J* = 7.5, 4.6 Hz); H-2: 4.65 (dd, *J* = 10.7, 4.4 Hz); H-3: 5.61 (d, *J* = 10.5 Hz); H-5: 5.53 (br.s); H-6a: 2.57 (o.m); H-6b: 2.05 (o.m); H-7: 5.29 (d, *J* = 9.3 Hz); H-10: 7.11 (s); H-13: 5.36 (br.d, *J* = 10.1 Hz); H-14a: 2.57 (o.m); H-14b: 2.05 (o.m); 16-Me: 1.06 (s); 17-Me: 1.19 (s); 18-Me: 2.08 (s); 19-Me: 1.57 (s); H-20a: 4.35 (d, *J* = 12.7 Hz); H-20b: 3.65 (br.d, *J* = 12.7); 5 × CH<sub>3</sub>CO-: 2.25 (s), 2.17 (s), 2.11 (s), 2.00 (s), 1.92

(s). <sup>13</sup>C NMR (125 MHz, CDCl<sub>3</sub>): C-1: 48.0; C-2: 66.1; C-3: 126.9; C-4: 134.5; C-6: 34.6; C-7: 66.9; C-8: 124.0; C-9: 143.2; C-10: 68.4; C-11: 135.2; C-12: 135.7; C-13: 69.9; C-14: 25.1; C-15: 36.2; C-16: 32.5; C-17: 25.6; C-18: 16.2; C-19: 12.5; C-20: 57.8; 5 × CH<sub>3</sub>CO-: 21.6, 20.4, 21.6, 21.1, 20.8; 5 × CH<sub>3</sub>CO-: 170.2, 167.5, 170.0, 169.2, 167.7. Assignments were achieved on the basis of 2D NMR spectra, including HMBC and HMQC.

**(3E,8E)-2α,7β,9,10β,13α-Pentaacetoxy-5α-hydroxy-20-cinnamoyloxy-3,8-secotaxa-3,8,11-triene (7)**

Amorphous gum. [α]<sub>D</sub><sup>22</sup> + 85° (*c* 0.005, CHCl<sub>3</sub>). <sup>1</sup>H and <sup>13</sup>C NMR, HMBC, and NOESY spectral data see Table 1. HR-FAB-MS *m/z*: 763.2734 ([M + K]<sup>+</sup>) (calcd. for C<sub>39</sub>H<sub>48</sub>O<sub>13</sub>K: 763.2732).

**Docecanadensene (8, Scheme 1)**

5-Epi-canadensene **2** (20 mg, 0.034 mmol) in toluene (0.6 mL) was treated with 2-(4-OMe)phenyl-1,3-oxazolidine of *N*-Boc phenylisoserine (**9**), (27 mg, 0.068 mmol) in 0.3 mL CH<sub>2</sub>Cl<sub>2</sub>, 4-pyrrolidinopyridine (4 mg, 0.027 mmol), and DCC (15 mg, 0.073 mmol) at 23°C for 2 h. The reaction mixture was diluted with ethyl acetate, washed with 5% NaHSO<sub>4</sub>, 5% NaHCO<sub>3</sub>, and then with brine to neutrality. The organic layer was dried, filtered, and evaporated. The residue was purified by flash chromatography on silica gel with hexane:ethyl acetate, 1:1, as eluent to give compound **10** (26 mg, 79%). The protected 5-epi-canadensene ester (22 mg, 0.023 mmol) in MeOH (4.3 mL) was treated with *p*-toluenesulfonic acid (4.3 mg, 0.023 mmol) at 23°C for 45 min. The methanol was evaporated, and the residue was diluted with EtOAc and washed with brine to neutrality. The organic layer was dried, filtered, and evaporated. The residue was purified by flash chromatography on silica gel with hexane:ethyl acetate, 35:65, as eluent to give compound **8** (13 mg, 67%). <sup>1</sup>H NMR (500 MHz, CDCl<sub>3</sub>) δ: 7.32 (m, 5H, Ph), 6.92 (br.s, 1H, H-10), 6.50 (d, *J* = 11.6 Hz, 1H, H-3), 5.73 (dd, *J* = 11.6, 4.5 Hz, 1H, H-2), 5.36 (br.d, *J* = 9.3 Hz, 1H, NH-4'), 5.28 (d, *J* = 9.2 Hz, 1H, H-13), 5.22 (br.d, *J* = 12.2 Hz, 1H, H-3'), 5.06 (o.br.d, *J* = 11.7 Hz, 2H, H-7, H-20a), 4.61 (br.s, 1H, H-2'), 4.41 (br.s, 1H, H-5), 4.28 (br.d, *J* = 11.7 Hz, 1H, H-20b), 3.76 (br.s, 1H, OH-5), 2.65 (m, 1H, H-6a), 2.52 (m, 1H, H-14a), 2.21 (s, 3H, OAc), 2.17 (s, 3H, OAc), 2.07 (s, 3H, OAc), 1.97 (s, 3H, OAc), 1.95 (s, 3H, OAc), 1.94 (s, 3H, H-18), 1.77 (t, *J* = 5.3 Hz, 1H, H-1), 1.65 (s, 3H, H-19), 1.39 (s, 9H, *t*-Bu), 1.23 (s, 3H, H-17),



1.12 (s, 3H, H-16). HR-FAB-MS  $m/z$ : 896.3467 ( $[M + K]^+$ ) (calcd. for  $C_{44}H_{59}N_1O_{16}K$ : 896.3471).

### Tubulin and bioactivity assay

Tubulin was extracted from cow brain according to a previously published procedure. The in vitro cytotoxicity activity determined on the MCF7 and MCF7-ADR cell lines with the MTT assay followed a previously published procedure (22).

### Acknowledgments

We thank the Natural Sciences and Engineering Research Council of Canada (NSERC) and the Canadian Breast Cancer Research Initiative for support via operating grants to L.O.Z. We thank the INRS-Institut Armand-Frappier for a postdoctoral fellowship to Q.W. Shi. Dr. Khadidja Haïdara is acknowledged for conducting the tubulin and cytotoxicity assays

### References

1. L.O. Zamir, M.E. Nedeia, S. Bélair, F. Sauriol, O. Mamer, E. Jacqmain, F.I. Jean, and F.X. Garneau. *Tetrahedron Lett.* **33**, 5173 (1992).
2. G.P. Gunawardana, U. Premachandran, N.S. Burres, D.N. Whittern, R. Henry, S. Spanton, and J.B. McAlpine. *J. Nat. Prod.* **55**, 1686 (1992).
3. L.O. Zamir, M.E. Nedeia, Z.-H. Zhou, S. Bélair, G. Caron, F. Sauriol, E. Jacqmain, F.I. Jean, F.X. Garneau, and O. Mamer. *Can. J. Chem.* **73**, 655 (1995).
4. J. Zhang, F. Sauriol, O. Mamer, X.L. You, M.A. Alaoui-Jamali, G. Batist, and L.O. Zamir. *J. Nat. Prod.* **64**, 450 (2001).
5. S. Zhang, W.M. Chen, and Y.H. Chen. *Yaoxue Xuebao*, **27**, 268 (1992).
6. (a) L.O. Zamir, Z.-H. Zhou, G. Caron, M.E. Nedeia, F. Sauriol, and O. Mamer. *J. Chem. Soc., Chem. Commun.* 529 (1995); (b) Y. Boulanger, A. Khiat, Z.-H. Zhou, G. Caron, and L.O. Zamir. *Tetrahedron*, **52**, 8957 (1996).
7. L.O. Zamir, J. Zhang, K. Kutterer, F. Sauriol, O. Mamer, A. Khiat, and Y. Boulanger. *Tetrahedron*, **54**, 15 845 (1998).
8. W.S. Fang, Q.C. Fang, X.T. Liang, Y. Lu, and Q.T. Zheng. *Tetrahedron*, **51**, 8483 (1995).
9. W.S. Fang, Q.C. Fang, and X.T. Liang. *Planta Med.* **62**, 567 (1996).
10. Q.W. Shi, T. Oritani, T. Sugiyama, and H. Kiyota. *J. Nat. Prod.* **61**, 1437 (1998).
11. Q.W. Shi, T. Oritani, and T. Sugiyama. *Phytochemistry*, **50**, 633 (1999).
12. J. Zhang, F. Sauriol, O. Mamer, and L.O. Zamir. *J. Nat. Prod.* **63**, 929 (2000).
13. J.H. Wu and L.O. Zamir. *Anti-Cancer Drug Des.* **15**, 73 (2000).
14. J.H. Wu, G. Batist, and L.O. Zamir. *Anti-Cancer Drug Des.* **15**, 441 (2000).
15. J.H. Wu, G. Batist, and L.O. Zamir. *Anti-Cancer Drug Des.* **16**, 129 (2001).
16. E. Didier, E. Fouque, I. Taillepié, and A. Commerçon. *Tetrahedron Lett.* **35**, 2349 (1994).
17. E. Nogales, S.G. Wolf, and K.H. Downing. *Nature (London)*, **391**, 199 (1998).
18. J. Kobayashi, H. Hosoyama, H. Shigemori, Y. Koiso, and S. Iwasaki. *Experientia*, **51**, 592 (1995).
19. J. Kobayashi and H. Shigemori. *Heterocycles*, **47**, 1111 (1998).
20. F. Lavelle, F. Guéritte-Voegelein, and D. Guénard. *Bull. Cancer*, **80**, 326 (1993).
21. G. Appendino, B. Danieli, J. Jakupovic, E. Belloro, G. Scambia, and E. Bombardelli. *Tetrahedron Lett.* **38**, 4273 (1997).
22. A. Nikolakakis, K. Haidara, F. Sauriol, O. Mamer, and L.O. Zamir. *J. Bioorg. Med. Chem.* **11**, 1551 (2003).



# The 30 year anniversary of a seminal paper on radical ions in solution (Radical ions in photochemistry. I. The 1,1-diphenylethylene cation radical)<sup>1</sup>

J.A. Pincock

**Abstract:** This article was written to serve as an introduction to this issue of the *Canadian Journal of Chemistry* that honors the contributions to chemistry of Professor D.R. Arnold. It summarizes the observations reported in a communication that appeared in the *Journal of the American Chemical Society* 30 years ago in June 1973. This historically important communication laid the foundation for his program on the photochemical generation and reactivity of radical ions in solution and also served as a guide for a developing area of interest of many other research groups.

**Key words:** photochemical electron transfer, radical cations, photo-NOCAS, benzylic radicals.

**Résumé :** Cet article se veut une introduction à ce numéro de la *Revue canadienne de chimie* qui souligne les réalisations du professeur D.R. Arnold en chimie. Il résume les observations rapportées dans une communication publiée dans la *Journal of the American Chemical Society* il y a de cela 30 ans, soit en juin 1973. Cette communication est très importante sur le plan historique puisqu'elle a non seulement servi de pierre d'assise au programme du professeur Arnold sur la génération et la réactivité photochimiques des ions radicaux en solution, mais aussi au développement d'un domaine d'intérêt pour de nombreux groupes de recherche.

**Mots clés :** transfert d'électron photochimique, cations radicaux, photo-NOCAS, radicaux benzyliques.

[Traduit par la Rédaction]

This issue of the *Canadian Journal of Chemistry* honours Professor Donald Arnold's contributions to chemistry. In September of 1972, I joined Don's research group at the University of Western Ontario as a PDF and began a project on cyclopropene photochemistry, vinyl diazo compounds, and the intermediate vinyl carbenes (1). The other PDF in the laboratory, Robert Neunteufel, had just discovered the first clear evidence from the Arnold research group of radical cation involvement in a photochemical reaction. The concise, seminal paper on these results (2) was published exactly 30 years ago in June 1973. Its impact on the larger chemistry community is indicated by its high citation count (over 300). Perhaps more indicative of its long-term importance is the fact that over two-thirds of these citations are from the more recent 15 years of the 30-year-period since its publication. The points<sup>2,3</sup> below summarize and highlight the importance of this paper which proved to be the founda-

tion for Don's program on the generation of radical ions in solution.

## Point 1: Introduction

As part of our effort to define the scope and limitations of the photocycloaddition of carbonyl compounds to olefins, our attention was attracted by the recent finding that aromatic esters ... can undergo this reaction.

In *benzene* as solvent, *p*-cyanobenzoate **1** had been shown to react by photochemical excitation in a bimolecular reaction with 1,1-diphenylethylene **2** to form the oxetane **3** (Scheme 1). Benzoates with other electron-withdrawing groups also reacted, but methyl benzoate itself did not. Don knew that these esters had lowest energy  $\pi,\pi^*$  triplet states (3). He had also written a review on oxetane formation (4) and knew that this observation was unusual because oxetanes are normally formed from  $n,\pi^*$  states of carbonyl compounds reacting with alkenes. An exciplex mechanism was therefore proposed.

## Point 2: The critical jump in understanding

When we irradiated solutions of **1** and 1,1-diphenylethylene **2**...in acetonitrile- $d_3$ ...A new product was isolated in 70% yield and identified as 1,1,4-triphenyl-1,2,3,4-tetrahydronaphthalene (**4**)...

The reaction was performed in *acetonitrile*, a polar solvent that allows separation of the exciplex into solvent separated ion pairs (Scheme 1) making other bimolecular

Received 16 April 2003. Published on the NRC Research Press Web site at <http://canjchem.nrc.ca> on 13 June 2003.

*Dedicated to Don Arnold. I enjoyed the ride(s!).*

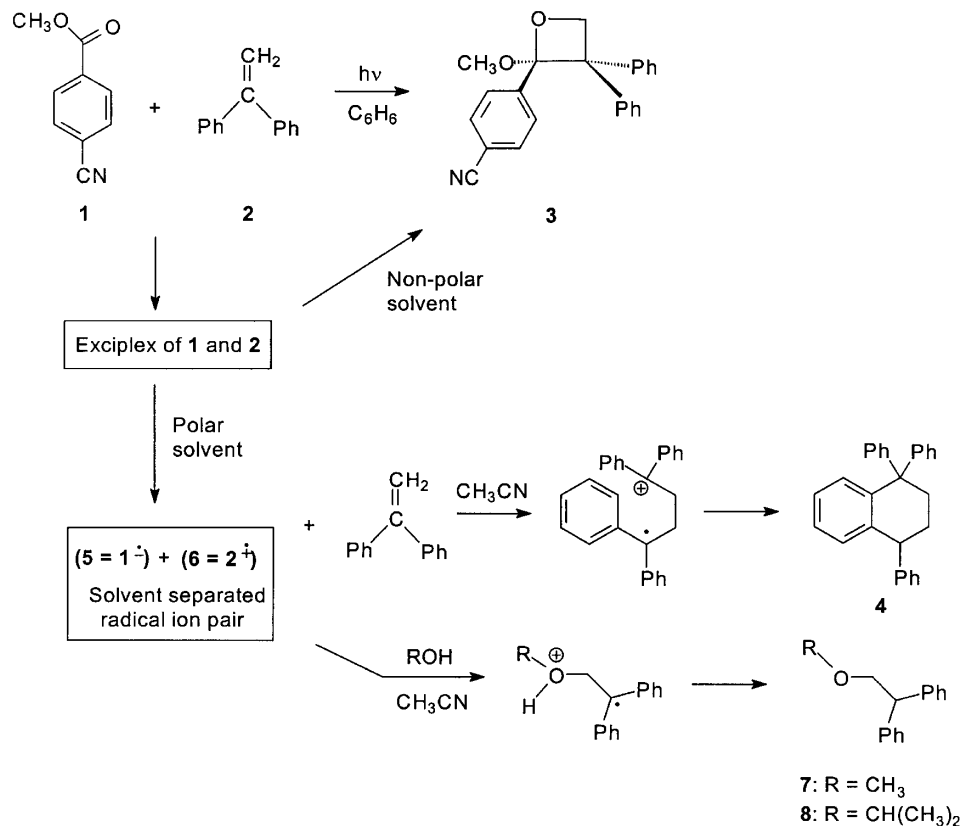
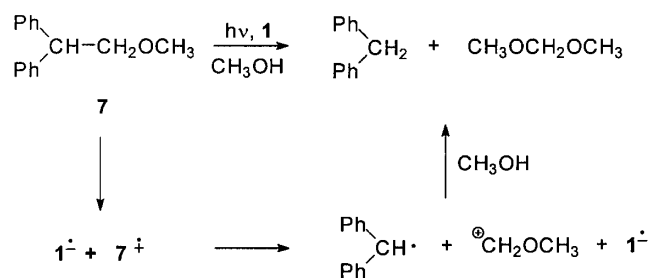
**J.A. Pincock.** Department of Chemistry, Dalhousie University, Halifax, NS B3H 4J3, Canada. (e-mail: james.pincock@dal.ca).

<sup>1</sup>R.A. Neunteufel and D.R. Arnold. *J. Am. Chem. Soc.* **95**, 4080 (1973).

<sup>2</sup>The text is from the original manuscript.

<sup>3</sup>Structure numbers used here are the same as those in the original manuscript.



**Scheme 1.** Reactions of the radical cation of 1,1-diphenylethylene **2** in acetonitrile and alcohols, methanol and 2-propanol.**Scheme 2.** Carbon-carbon bond cleavage of the radical cation of 1-methoxy-2,2-diphenylethane **7**.

reactions possible. Under these conditions, the tetralin **4** was now the major product. The important intermediates are the distonic radical cation and its precursor, **6** (the radical cation of **2**). These observations led directly to a series of papers on the generation of various distonic radical cations (**5**), other cycloadditions of radical cations (**6**), and *Z* to *E* configurational (**7**) and tautomeric deconjugative (**8**) isomerization of alkene radical cations.

### Point 3: The extension to a new reaction

Upon irradiation of **1** and **2** in methanol and 2-propanol ... we found formation of 2,2-diphenylethyl methyl ether (**7**) and 2,2-diphenylethyl isopropyl ether (**8**), respectively...

Changing the high dielectric constant solvent from acetonitrile to an alcohol, a better nucleophile, completely altered the pathway for the reactivity of the radical cation **6**.

This extension arose from the concept that if **6** reacted with the alkene **2** as a nucleophile, it should react with other nucleophiles. Now *anti*-Markovnikov addition of the alcohol occurred to give **7** and **8** (Scheme 1). This observation initiated a series of publications on additions to radical cations (**9**) and to the complementary radical anion of 1,1-diphenylethylene (**10**). More recently, the reactivity of radical cations with nucleophiles in solution (**11**) and other environments (**12**) has been directly observed by others using LFP techniques.

### Point 4: The importance of minor pathways

...irradiation in 2-propanol produced appreciable amounts of **3** (**3**:**8** = 1:3.2) besides small quantities of unidentified products.

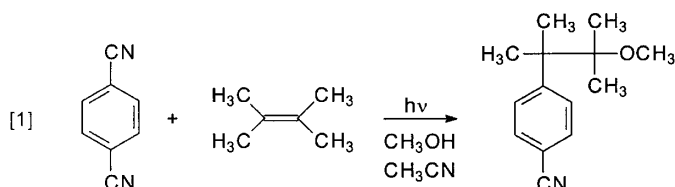
Don has always taken pride in insisting that even minor products must be characterized because they have often been good predictors of a new pathway which can become the major one by suitable choice of substrate and reaction conditions. The important phrase is "...besides small quantities of unidentified products" (**2**). These "unidentified products" from **7** were soon identified (**13**) as diphenylmethane and the dimethylacetal of formaldehyde. The proposed mechanism for their formation (Scheme 2), proceeds by cleavage of the radical cation of **7** to the diphenylmethyl radical and the methoxy methyl cation. This observation resulted in an extensive study of cleavage reactions of arylmethyl radical cations, including other carbon-carbon bond cleavages (**14**), carbon-oxygen bond cleavages (**15**), carbon-hydrogen bond



cleavages (16) reflecting the high acidity ( $\text{p}K_{\text{a}} \sim -11$ ) of protons on radical cations of benzylic substrates (17). The regiochemistry of the cleavage to the radical and cation fragment was shown to be controlled by the relative stability of the two fragments (oxidation potentials of radicals as a measure of cation stability (18), the  $\sigma_{\text{a}}$  scale as a measure of radical stability (19), merostabilization of radicals (20)) and by stereoelectronic requirements (21).

### The photo NOCAS reaction

Scheme 1 was later extended to studies on the variation in alkene structure. When 1,1-diphenylethylene **2** was replaced by 2,3-dimethyl-2-butene, the product obtained



resulted from nucleophile–olefin, combination, aromatic substitution and the photo NOCAS reaction was discovered (22) and developed extensively through the 1990s (23). The  $^1\text{H}$  NMR spectrum, taken from R. Borg's laboratory note book, of that first photo NOCAS product is reproduced on the cover of this issue of the *Canadian Journal of Chemistry*. The complementary process electrophile–olefin, combination, aromatic substitution (EOCAS) has also been recently explored (24).

### Conclusion

My colleagues (including Don) at Dalhousie have for many years taught a graduate class in organic photochemistry. In the section on excited-state electron transfer and radical ion chemistry, I have always used Don's manuscript summarized here as an example of how the right scientist at the right time and with the right background knowledge can make significant changes in our understanding of a research area. Some have called these events paradigm shifts (25). I think the students acquire an appreciation of that possibility from this example. I also think that both those who have contributed to this honorary issue and others have the same appreciation. Thanks Don.

### References

- J.A. Pincock, R. Morchat, and D.R. Arnold. *J. Am. Chem. Soc.* **95**, 7536 (1973).
- R.A. Neunteufel and D.R. Arnold. *J. Am. Chem. Soc.* **95**, 4080 (1973).
- D.R. Arnold, J.R. Bolton, and J.A. Pedersen. *J. Am. Chem. Soc.* **94**, 2872 (1972).
- D.R. Arnold. In *Advances in photochemistry*. Vol. 6. Edited by W.A. Noyes, Jr., G.S. Hammond, and J.N. Pitts. Interscience, New York. 1968. pp. 301–423.
- (a) D.R. Arnold and R.W.R. Humphreys. *J. Am. Chem. Soc.* **101**, 2743 (1979); (b) P.C. Wong and D.R. Arnold. *Tetrahedron Lett.* 2101 (1979); (c) D.D.M. Wayner and D.R. Arnold. *Chem. Commun.* 1087 (1982); (d) D.D.M. Wayner, R.J. Boyd, and D.R. Arnold. *Can. J. Chem.* **61**, 2310 (1983); (e) D.D.M. Wayner and D.R. Arnold. *Can. J. Chem.* **63**, 872 (1985); (f) D.D.M. Wayner, R.J. Boyd, and D.R. Arnold. *Can. J. Chem.* **63**, 3283 (1985); (g) D.R. Arnold, B.J. Fahie, L.J. Lamont, J. Wierzchowski, and K.M. Young. *Can. J. Chem.* **65**, 2734 (1987); (h) D.R. Arnold, L.J. Lamont, and A.L. Perrott. *Can. J. Chem.* **69**, 225 (1991).
- (a) A.J. Maroulis and D.R. Arnold. *Chem. Commun.* 351 (1979); (b) D.R. Arnold, P.C. Wong, A.J. Maroulis, and T.S. Cameron. *Pure Appl. Chem.* **52**, 2609 (1980); (c) D.R. Arnold, R.M. Borg, and A. Albini. *Chem. Commun.* 138 (1981).
- D.R. Arnold and P.C. Wong. *J. Am. Chem. Soc.* **101**, 1894 (1979).
- (a) D.R. Arnold and S.A. Mines. *Can. J. Chem.* **65**, 2312 (1987); (b) D.R. Arnold and S.A. Mines. *Can. J. Chem.* **67**, 689 (1989); (c) D. Mangion, J. Kendal and D.R. Arnold. *Org. Lett.* **3**, 45 (2001).
- (a) Y. Shigemitsu and D.R. Arnold. *Chem. Commun.* 407 (1975); (b) A.J. Maroulis, Y. Shigemitsu, and D.R. Arnold. *J. Am. Chem. Soc.* **100**, 535 (1978); (c) A.J. Maroulis and D.R. Arnold. *Synthesis*, 819 (1979).
- D.R. Arnold and A.J. Maroulis. *J. Am. Chem. Soc.* **99**, 7355 (1977).
- L.J. Johnston and N.P. Schepp. *Adv. Electron. Transfer Chem.* **5**, 41 (1996).
- H. Garcia and H.D. Roth. *Chem. Rev.* **102**, 3947 (2002).
- D.R. Arnold and A.J. Maroulis. *J. Am. Chem. Soc.* **98**, 5931 (1976).
- (a) D.R. Arnold and R.W.R. Humphreys. *J. Am. Chem. Soc.* **101**, 2743 (1979); (b) P.C. Wong and D.R. Arnold. *Tetrahedron Lett.* 2101 (1979); (c) A. Okamoto and D.R. Arnold. *Can. J. Chem.* **63**, 2340 (1985); (d) A. Okamoto, M.S. Snow, and D.R. Arnold. *Tetrahedron*, **42**, 6175 (1986); (e) R. Popielarz and D.R. Arnold. *J. Am. Chem. Soc.* **112**, 3069 (1990).
- (a) A. Albini and D.R. Arnold. *Can. J. Chem.* **56**, 2985 (1978); (b) D.R. Arnold and L.J. Lamont. *Can. J. Chem.* **67**, 2119 (1989); (c) L.J. Lamont and D.R. Arnold. *Can. J. Chem.* **68**, 390 (1990); (d) A.L. Perrott, H.J.P. de Lijser, and D.R. Arnold. *Can. J. Chem.* **75**, 384 (1997).
- (a) A.L. Perrott and D.R. Arnold. *Can. J. Chem.* **70**, 272 (1992); (b) D.R. Arnold, X. Du, and J. Chen. *Can. J. Chem.* **73**, 307 (1995).
- A.M. de P. Nicholas and D.R. Arnold. *Can. J. Chem.* **60**, 2165 (1982).
- (a) A.M. de P. Nicholas and D.R. Arnold. *Can. J. Chem.* **62**, 1850 (1984); (b) A.M. de P. Nicholas and D.R. Arnold. *Can. J. Chem.* **62**, 1960 (1984).
- (a) J.M. Dust and D.R. Arnold. *J. Am. Chem. Soc.* **105**, 1221 (erratum 6531) (1983); (b) D.D.M. Wayner and D.R. Arnold. *Can. J. Chem.* **62**, 1164 (1984); (c) D.R. Arnold, A.M. de P. Nicholas, and M.S. Snow. *Can. J. Chem.* **63**, 1150 (1985); (d) D.D.M. Wayner and D.R. Arnold. *Can. J. Chem.* **63**, 2378 (1985); (e) A.M. de P. Nicholas and D.R. Arnold. *Can. J. Chem.* **64**, 270 (1986); (f) D.R. Arnold, A.M. de P. Nicholas, and K.M. Young. *Can. J. Chem.* **64**, 769 (1986); (g) D.R. Arnold. In *Substituent effects in radical chemistry*. Edited by H.G. Viehe, Z. Janousek, and R. Merényi. D. Reidel Publishing Co., Dordrecht. NATO ASI Ser., Ser. C. 1986. pp. 171–188.
- (a) D.R. Arnold and R.W.R. Humphreys. *J. Chem. Soc. Chem. Commun.* 181 (1978); (b) R.W.R. Humphreys and D.R. Arnold. *Can. J. Chem.* **57**, 2652 (1979); (c) W.J. Leigh and D.R. Arnold. *Chem. Commun.* 406 (1980); (d) W.J. Leigh, D.R. Arnold, R.W.R. Humphreys, and P.C. Wong. *Can. J. Chem.* **58**, 2537 (1980); (e) W.J. Leigh and D.R. Arnold. *Can. J. Chem.* **59**, 609 (1981); (f) W.J. Leigh and D.R. Arnold. *Can. J. Chem.*



- 59**, 3061 (1981); (g) D.R. Arnold and M. Yoshida. Chem. Commun. 1203 (1981).
21. (a) D.R. Arnold, X. Du, and K.M. Henseleit. Can. J. Chem. **69**, 839 (1991); (b) A.L. Perrott and D.R. Arnold. Can. J. Chem. **70**, 272 (1992).
22. R.M. Borg, D.R. Arnold, and T.S. Cameron. Can. J. Chem. **62**, 1785 (1984).
23. D. Mangion and D.R. Arnold. Acc. Chem. Res. **35**, 297 (2002).
24. D. Mangion, M. Frizzle, D.R. Arnold, and T.S. Cameron. Synthesis, **8**, 1215 (2001).
25. N.J. Turro. Angew. Chem. Int. Ed. **39**, 2255 (2000).



# Photocycloaddition of cyclohex-2-enones to acrylonitrile

Lars Meyer, Nacira Alouane, Kerstin Schmidt, and Paul Margaretha

**Abstract:** The photocycloaddition of cyclohex-2-enones **1a**, **1b**, and **5a–5c** to acrylonitrile (**2**) in benzene has been studied. The reactions proceed with moderate regioselectivity and with preferential formation of diastereomeric mixtures of *endo*- and *exo*-5-oxobicyclo[4.2.0]octane-7-carbonitriles **3**, **4**, and **6–8**. Very similar relative rates of conversion to products are observed in the photocycloadditions of **1b**, **5a**, and **5b** to **2** and methacrylonitrile (**9**), respectively. In contrast, 5,5-dimethylcyclohex-2-enone (**1b**) forms cycloadducts with 2,3-dimethylbut-2-ene (**12**) as efficiently as with the unsaturated nitriles, but the 2,5,5-trialkylcyclohex-2-enones **5a** and **5b** do not react with this alkene at measurable rates of conversion. A dual path mechanism is presented that involves *either* exciplex formation between triplet-excited cyclohexenones and electron-rich alkenes *or* radical addition of the former to electron-deficient alkenes bearing a substituent, exercising a resonance effect.

**Key words:** [2+2]-photocycloaddition, cyclobutane, cyclobutanecarbonitrile, radical addition to unsaturated nitriles.

**Résumé :** On a étudié la photocycloaddition de cyclohex-2-énones (**1a**, **1b**, **5a–5c**) sur l'acrylonitrile (**2**) dans le benzène. Les réactions se produisent avec une régiosélectivité modérée impliquant la formation préférentielle de mélanges diastéréomères des *endo*- et *exo*-5-oxobicyclo[4.2.0]octane-7-carbonitriles (**3**, **4**, **6–8**). On a observé des vitesses relatives de conversion en produits très semblables pour les photoadditions des composés **1b**, **5a** et **5b** sur respectivement le composé **2** et sur le méthylacrylonitrile (**9**). Par ailleurs, la 5,5-diméthylcyclohex-2-énone (**1b**) forme des cycloadduits avec le 2,3-diméthylbut-2-ène (**12**) d'une façon pratiquement aussi efficace qu'avec les nitriles insaturés, mais les 2,5,5-trialkylcyclohex-2-énones **5a** et **5b** ne réagissent pas avec cet alcène à des vitesses de conversion mesurables. On propose un mécanisme réactionnel double impliquant soit la formation d'un exciplex entre les cyclohexénones excitées à l'état triplet et les alcènes riches en électrons soit l'addition du radical du premier sur les alcènes déficients en électron portant un substituant qui exerce un effet de résonance.

**Mots clés :** photocycloadditions [2+2], cyclobutanes, cyclobutanecarbonitriles, additions radicalaires sur des nitriles insaturés.

[Traduit par la Rédaction]

## Introduction

In the preparative application of [2+2]-photocycloadditions of cyclic enones to (substituted) alkenes two factors concerning product formation are of decisive relevance, namely the regioselectivity and the (overall) relative rate of conversion. Regarding the regioselectivity in the addition to mono- and 1,1-disubstituted alkenes, Corey et al. (1) had shown that the preferred addition mode of cyclohex-2-enone to isobutene or dimethoxyethylene was the one leading to both *cis*- and *trans*-fused bicyclo[4.2.0]octan-2-ones with substituents on C(7), while in the reaction with acrylonitrile the alternate orientation of addition, leading preferentially to only *cis*-fused — so-called *head-to-head* — cycloadducts was observed. Similar results were also reported for photocycloadditions of 3-methylcyclohex-2-enone to differently substituted alkenes by Cantrell et al. (2). No significant dif-

ferences in the overall relative rates of product formation for the different alkenes were observed in these studies.

To explain these observed regioselectivities it was assumed (1) that an *umpolung* occurs in the charge distribution of the C=C double bond in the triplet-excited cyclohexenone. Shortly thereafter, a mechanistic sequence was proposed by de Mayo (3), involving the formation of an exciplex between triplet-excited cyclohexenone and alkene (which should be the determining factor in the regiochemical outcome), followed by that of triplet 1,4-biradicals, which in turn, after intersystem crossing, afford the final product(s) via 1,4-cyclization. It was also assumed that the triplet-excited cyclohexenone exhibits an electrophilic behaviour and, therefore, reacts faster with electron-rich than with electron-deficient alkenes. This mechanistic description was corroborated by one of us in studies of the photocycloaddition of 4-oxacyclohex-2-enones to 2-chlorodifluoromethyl-

Received 4 February 2003. Published on the NRC Research Press Web site at <http://canjchem.nrc.ca> on 26 March 2003.

Dedicated to Prof. Donald R. Arnold in admiration of his expertise in both organic photochemistry and canoeing.

L. Meyer, N. Alouane, K. Schmidt, and P. Margaretha.<sup>1</sup> Institute of Organic Chemistry, University of Hamburg, M.L.King Platz 6, D-20146 Hamburg, Germany.

<sup>1</sup>Corresponding author (e-mail: Paul.Margaretha@chemie.uni-hamburg.de).



3-chloro-3,3-difluoropropene (4), which led to a very slow but exclusive formation of *head-to-head* cycloadducts, while the corresponding reaction with isobutene or 1,1-dimethoxyethylene afforded *head-to-tail* cycloadducts at much higher overall relative rates. It was pointed out (4) that in contrast to acrylonitrile this hexahalogenoalkene is not stabilized by conjugation between the C=C double bond and the substituent.

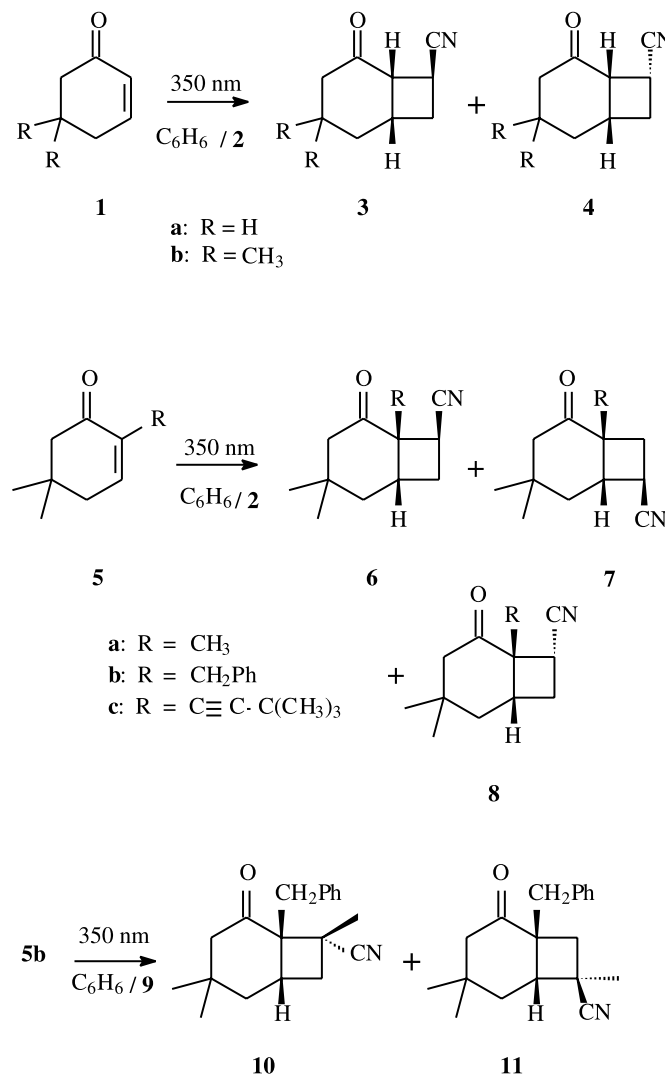
In a relevant paper describing triplet lifetime measurements using nanosecond flash photolysis, Schuster et al. (5) tackled the problem of describing "relative rates" for such reactions, since product yields in multistep processes depend on overall quantum efficiencies and not on the rate of a single specific step. The results, (a) that the rate constants for the quenching of enone triplets are much larger for electron-deficient alkenes than for those bearing electron-donor substituents, and (b) that no correlation whatsoever was seen between these quenching rates and the (overall) quantum yield for product formation, were found to be inconsistent with expectations based on the exciplex model described above. The direct formation of triplet biradicals from triplet enones and alkenes was therefore suggested as a plausible reaction step. Slightly later, based on results of photocycloaddition between cyclopent-2-enone and acrylonitrile, Weedon and co-workers (6) concluded that it was unnecessary to introduce an exciplex into the mechanism of the photocycloaddition reaction of cyclic enones with alkenes to explain the reaction regiochemistry.

We have recently (7) presented results on the photocycloaddition of cyclohex-2-enones to 2-alkylprop-2-enitriles, leading to the exclusive formation of cyclobutanecarbonitriles. The choice of these cyclohexenones came from (a) facilitated interpretation of the  $^1\text{H}$  NMR spectra of the photocycloadducts, owing to the geminal dimethyl group in the six-membered ring, and (b) variation of the substituent on C(2), regarding both size and radical stabilization. We now report on the photocycloaddition of these same cyclohex-2-enones to acrylonitrile.

## Results and discussion

All the photolyses described were run with benzene as solvent. Irradiation of cyclohexenone (**1a**) in the presence of acrylonitrile (**2**) afforded – as already described (6) – a mixture of six enone + alkene adducts, of which the two major products **3a** (41%) and **4a** (35%) were successfully isolated and analyzed. Similarly, irradiation of 5,5-dimethylcyclohex-2-enone (**1b**) in the presence of **2** gave a mixture of five enone + alkene adducts, of which, again, the two major products **3b** (35%) and **4b** (46%) were isolated and characterized. Irradiation of trialkylcyclohexenones **5a** and **5b** in the presence of **2** afforded almost equal mixtures of four cycloadducts. In both reactions the major components **6a** (50%) and **7a** (20%), and **6b** (40%) and **7b** (25%), respectively, were isolated, while one of the minor components, **8a** (17%) and **8b** (18%), respectively, was analyzed from the product mixture. In contrast, irradiation of **5c** with **2** gave only a 4:1 mixture of **6c** and **8c**. Irradiation of **5b** in the presence of methacrylonitrile (**9**) gave a 3:2 mixture of cycloadducts **10** and **11**, which were separated and fully characterized (Scheme 1).

Scheme 1.



Finally, to determine the relative rates of conversion to products, cyclohexenones **1b**, **5a**, and **5b** were irradiated in the presence of either acrylonitrile (**2**), methacrylonitrile (**9**), or 2,3-dimethylbut-2-ene (**12**) in a *merry-go-round* setup. The results of these measurements by GC analysis are summarized in Table 1.

The synthetic utility of cyclohexenone – unsaturated nitrile photocycloadditions definitively seems to be limited, as they proceed with rather moderate regio- and stereo-selectivities. The ratio of *HH*- vs. *HT*-photocycloadducts, both for acrylonitrile (**2**) and methacrylonitrile (**9**), is roughly 3:1 for the cyclohexenones bearing no substituents on C(2) (i.e., **1a** and **1b**), about 2:1 for **5a**, 3:2 for **5b**, and, finally, >20:1 for **5c**. Regarding the *exo:endo* selectivity in the formation of these 5-oxobicyclo[4.2.0]octane-7-carbonitriles, cyclohexenones **1a** and **1b** and acrylonitrile (**2**) afford roughly 1:1 mixtures of **3a,b** and **4a,b**, while cyclohexenones **5a–c** give preponderantly (>3:1) the *exo*-nitriles **6a–c**, respectively. In contrast, as observed earlier (7), all these cyclohexenones react with methacrylonitrile (**9**) to give almost exclusively the 7-*endo*-carbonitriles (e.g., **10**).



**Table 1.** Relative rates for the conversion of cyclohexenones **1b**, **5a**, and **5b** to products<sup>a</sup> upon irradiation in the presence of acrylonitrile (**2**), methacrylonitrile (**9**), or 2,3-dimethylbut-2-ene (**12**).

	Alkene	<b>2</b>	<b>9</b>	<b>12</b>
<b>Cyclohexenone</b>				
<b>1b</b>		1.00	1.13	0.67
<b>5a</b>		0.84	0.67	<0.01
<b>5b</b>		0.91	0.66	<0.01

<sup>a</sup>For comparative irradiations of cyclohexenones in the presence of alkenes **2**, **9**, and **12**, Ar-degassed solutions containing 0.1 mmol **1b**, **5a**, or **5b** and 2.0 mmol alkene in 2 mL benzene were irradiated in a merry-go-round setup, and the formation of products was monitored by GC, using dodecane as internal standard, after 15, 30, and 60 min, respectively.

The assignment of the *exo*-nitrile configuration in cycloadducts **3** and **6** and that of the *endo*-nitrile in **4** and **8** stems from NOE experiments, as well as from the fact that for all *exo*-nitriles **3** and **6** the chemical shift of H(1), in either CDCl<sub>3</sub> or C<sub>6</sub>D<sub>6</sub> solvent, is always larger than that of the corresponding H-atom in the *endo*-nitriles **4** and **8**, respectively. This is most probably due to the *cis*-relation between H(1) and the CN group in the former cycloadducts. Similarly, the *cis*-relation between the benzyl and the methyl groups on the cyclobutane ring in **10** is assigned again based on NOE experiments. Another difference between the acrylonitrile and methacrylonitrile cycloadducts is observed in the conformation of the six-membered ring. While in all methacrylonitrile cycloadducts the cyclohexanone ring adopts a twisted-boat conformation, its preferred alignment in cycloadducts **3**, **4**, **6**, and **8** is that of a boat, as reflected by the coupling constants between H(1) and the H-atoms on C(2), as well as by the much smaller chemical shift of one of the H-atoms on C(2) for which the orientation of the C—H bond is almost parallel to that of the carbonyl group.

The fact that the H-atoms of one of the cyclohexanone-methyl groups in **10** resonate at negative  $\delta$  values (−0.12 ppm in CDCl<sub>3</sub>, −0.35 ppm in C<sub>6</sub>D<sub>6</sub>) is also worth mentioning. Apparently, the axial methyl group on C(3), which is *cis* to the benzyl group, experiences a very strong deshielding effect by the aromatic ring. A more striking finding is the results of the measurements of relative rates of photocycloadduct formation between cyclohexenones and unsaturated nitriles, as the overall efficiency in these reactions is affected neither by the change of H vs. alkyl group on C(2) of the cyclohexenone nor by the replacement of H vs. CH<sub>3</sub> on C(2) in the nitrile. This contrasts the results of the cycloadditions of **1** and **5** to 2,3-dimethylbut-2-ene, where cycloadduct formation is totally prevented by the introduction of an alkyl group on the C(2) of the cyclohexenone. It should nevertheless be pointed out that bonding between tertiary C-atoms to afford cyclobutanes is a commonly encountered process for 3-alkylcyclohex-2-enones (**2**).

Although such overall relative rates have to be looked at with caution (**5**), qualitative conclusions can certainly be drawn, and the most straightforward one is that the addition of excited cyclohexenones to nitriles proceeds via a different path, which is less sensitive to steric interaction than that of electron-rich alkenes. While for this latter reaction there is substantial evidence for the interference of exciplexes (**3**, **4**,

**8**, **9**), the efficiency of the former can be attributed to the predominant interaction between the SOMO of a (nucleophilic) alkyl radical and the LUMO of the unsaturated nitrile (**10**). Indeed, it has been shown that alkyl radicals add to styrene about 23 times faster than to ethylene (**11**), and that cyclohexyl radicals add about 24 times faster to acrylonitrile than to styrene (**12**), i.e., the addition of C-centered radicals to alkenes experiences a 500-fold acceleration in going from ethylene to acrylonitrile. It seems therefore plausible to define ethylene as a “standard alkene” and to assume that cyclohexenone–alkene photocycloadditions are accelerated by either electron-donating (D) or — mesomerically — electron-withdrawing (A) substituents on the alkene, the former promoting exciplex formation and the latter radical addition (Scheme 2). If one neglects the cleavage of the intermediate biradicals formed by the addition of triplet-excited cyclohexenones, to unsaturated nitriles, back to starting materials, the regiochemical outcome of these reactions should correlate with the relative spin densities on C(2) and C(3) of the “cyclohexenone-1,2-biradical”, which should be quite similar for **1b**, **5a**, and **5b**, but significantly altered for **5c**.

This would explain, then, why no *HT*-cycloadduct is formed from **5c**, as the spin density on the propargylic C(2) is negligible.

## Experimental

### General

NMR spectra were recorded in either CDCl<sub>3</sub> or C<sub>6</sub>D<sub>6</sub> on a Bruker DRX 500 instrument at 500 and 125.8 MHz, respectively. GC coupled EI-MS was performed on a Varian MAT 311A spectrometer at 70 eV using a 30 m SE-30 capillary column. Photolyses were carried out in pyrex tubes using a Rayonet RPR 100 photochemical reactor equipped with 350 nm lamps (up to 16). The solvent (benzene) used for irradiations was of spectrophotometric grade. Cyclohex-2-enone (**1a**), acrylonitrile (**2**), methacrylonitrile (**9**), and 2,3-dimethylbut-2-ene (**12**) were purchased from Merck (Darmstadt). 5,5-Dimethylcyclohex-2-enone (**1b**) (**13**), 2,5,5-trimethylcyclohex-2-enone (**5a**) (**14**), 2-benzyl-5,5-dimethylcyclohex-2-enone (**5b**) (**15**), and 2-(3,3-dimethylbut-1-ynyl)-5,5-dimethylcyclohex-2-enone (**5c**) (**16**) were synthesized according to literature procedures.

### Photolyses: General procedures

In the preparative experiments, an Ar-degassed solution of cyclohexenone (1 mmol) and acrylonitrile (20 mmol) in benzene (10 mL) was irradiated for the time indicated and to the degree of conversion indicated (GC monitoring, peak percentages in increasing retention times) until maximum conversion of the enone was achieved. After evaporation, the residue was worked up using chromatography (CC) on SiO<sub>2</sub>. For comparative irradiations of cyclohexenones in the presence of alkenes **2**, **9**, and **12**, Ar-degassed solutions containing 0.1 mmol **1b**, **5a**, or **5b** and 2.0 mmol alkene in 2 mL benzene were irradiated in a merry-go-round setup, and the formation of products was monitored by GC, using dodecane as the internal standard, after 15, 30, and 60 min, respectively.



### Photolysis of 1a and 2

Irradiation for 2 h with up to 97% conversion led to 6 new product peaks (9% (unidentified (unident.)), 5% (unident.), 43% (**3a**), 7% (unident.), 5% (unident.), and 31% (**4a**)), in accordance with the product distribution reported in ref. (6), although no spectral data of the products are given. CC (Et<sub>2</sub>O:pentane:toluene:EtOAc = 85:5:5:5) afforded first 50 mg (34%) of **3a** (90% purity),  $R_f$  = 0.46, and then 25 mg (17%) of **4a** (95% purity),  $R_f$  = 0.32, both as colorless oils.

#### *1 $\alpha$ ,6 $\alpha$ -5-oxobicyclo[4.2.0]octane-7-exo-carbonitrile (3a)*

<sup>1</sup>H NMR (C<sub>6</sub>D<sub>6</sub>)  $\delta$ : 0.75 (m, 1H, H(2eq)), 1.10 (m, 1H, H(2ax)), 1.22 (m, 2H, H(3)), 1.44 (m, 1H, H(8)), 1.69 (m, 1H, H(4)), 1.70 (m, 1H, H(8)), 2.00 (m, 1H, H(4)), 2.57 (m, 1H, H(1)), 2.57 (m, 1H, H(6)), 2.96 (m, 1H, H(7)). <sup>13</sup>C NMR (C<sub>6</sub>D<sub>6</sub>)  $\delta$ : 23.2 (C(3)), 25.4 (C(7)), 26.1 (C(2)), 29.2 (C(8)), 35.6 (C(1)), 40.2 (C(4)), 48.2 (C(6)), 121.7 (CN), 208.5 (CO). MS (%): 149 ([M]<sup>+</sup>, 28), 55.

#### *1 $\alpha$ ,6 $\alpha$ -5-oxobicyclo[4.2.0]octane-7-endo-carbonitrile (4a)*

<sup>1</sup>H NMR (C<sub>6</sub>D<sub>6</sub>)  $\delta$ : 1.05 (m, 1H, H(2eq)), 1.16 (m, 1H, H(2ax)), 1.31 (m, 1H, H(3)), 1.49 (m, 1H, H(3)), 1.67 (m, 1H, H(8)), 1.78 (m, 1H, H(8)), 1.81 (m, 1H, H(4)), 2.21 (m, 1H, H(1)), 2.27 (m, 1H, H(4)), 2.59 (dd,  $J$  = 9.2, 9.1 Hz, 1H, H(6)), 2.75 (m, 1H, H(7)). <sup>13</sup>C NMR (C<sub>6</sub>D<sub>6</sub>)  $\delta$ : 20.4 (C(3)), 23.2 (C(7)), 26.3 (C(2)), 29.2 (C(8)), 33.6 (C(1)), 40.7 (C(4)), 45.8 (C(6)), 119.9 (CN), 207.9 (CO). MS (%): 149 ([M]<sup>+</sup>, 25), 55.

### Photolysis of 1b and 2

Irradiation for 2 h with up to 97% conversion led to five new product peaks (7% (unident.), 8% (unident.), 46% (**4b**), 5% (unident.), and 35% (**3b**)). CC (benzene:EtOAc = 85:15) afforded first 37 mg (21%) of **3b** (75% purity),  $R_f$  = 0.51, and then 57 mg (32%) of **4b** (80% purity),  $R_f$  = 0.43, both as colorless oils.

#### *1 $\alpha$ ,6 $\alpha$ -3,3-dimethyl-5-oxobicyclo[4.2.0]octane-7-exo-carbonitrile (3b)*

<sup>1</sup>H NMR (CDCl<sub>3</sub>)  $\delta$ : 0.94 (s, 3H, CH<sub>3</sub>), 1.06 (s, 3H, CH<sub>3</sub>), 1.43 (dd,  $J$  = 14.5, 10.1 Hz, 1H, H(2ax)), 1.82 (dd,  $J$  = 14.5, 7.5 Hz, 1H, H(2eq)), 2.10 (ddd,  $J$  = 11.6, 8.5, 4.5 Hz, 1H, H(8en)), 2.21 (d,  $J$  = 16.2 Hz, 1H, H(4eq)), 2.25 (d,  $J$  = 16.2 Hz, 1H, H(4ax)), 2.58 (ddd,  $J$  = 11.6, 8.5, 8.2 Hz, 1H, H(8ex)), 3.02 (m, 1H, H(1)), 3.25 (dd,  $J$  = 8.5, 8.4 Hz, 1H, H(6)), 3.36 (ddd,  $J$  = 8.6, 8.5, 8.4 Hz, 1H, H(7)). <sup>13</sup>C NMR (CDCl<sub>3</sub>)  $\delta$ : 23.9 (C(7)), 28.2 (CH<sub>3</sub>), 30.2 (C(3)), 30.9 (C(5)), 31.2 (C(1)), 31.4 (C(8)), 32.2 (CH<sub>3</sub>), 40.6 (C(2)), 47.3 (C(6)), 52.7 (C(4)), 121.9 (CN), 207.9 (CO). MS (%): 177 ([M]<sup>+</sup>, 13), 83.

#### *1 $\alpha$ ,6 $\alpha$ -3,3-dimethyl-5-oxobicyclo[4.2.0]octane-7-endo-carbonitrile (4b)*

<sup>1</sup>H NMR (CDCl<sub>3</sub>)  $\delta$ : 0.89 (s, 3H, CH<sub>3</sub>), 1.11 (s, 3H, CH<sub>3</sub>), 1.85 (dd,  $J$  = 12.5, 11.5 Hz, 1H, H(2ax)), 1.92 (ddd,  $J$  = 12.5, 7.8, 2.0 Hz, 1H, H(2eq)), 2.03 (ddd,  $J$  = 12.0, 3.5, 3.2 Hz, 1H, H(8en)), 2.31 (dd,  $J$  = 17.4, 2.0 Hz, 1H, H(4eq)), 2.46 (d,  $J$  = 17.4 Hz, 1H, H(4ax)), 2.73 (ddd,  $J$  = 12.0, 8.8, 8.7 Hz, 1H, H(8ex)), 2.82 (m, 1H, H(1)), 3.24 (dd,  $J$  = 9.8, 9.0 Hz, 1H, H(6)), 3.43 (dddd,  $J$  = 9.8, 8.8, 3.5, 1.4 Hz, 1H, H(7)). <sup>13</sup>C NMR (CDCl<sub>3</sub>)  $\delta$ : 25.9 (C(7)), 26.9 (CH<sub>3</sub>), 30.4 (C(3)), 30.8 (C(8)), 31.2 (C(1)), 31.7 (CH<sub>3</sub>),

42.1 (C(4)), 47.3 (C(6)), 54.1 (C(4)), 122.9 (CN), 208.4 (CO). MS (%): 177 ([M]<sup>+</sup>, 17), 83.

### Photolysis of 5a and 2

Irradiation for 2 h with up to 94% conversion led to four new product peaks (20% (**7a**), 17% (**8a**), 13% (unident.), and 50% (**6a**)). CC (pentane:Et<sub>2</sub>O = 60:40) afforded first 73 mg (38%) of **6a** (75% purity),  $R_f$  = 0.46, and then 19 mg (10%) of **7a** (90% purity),  $R_f$  = 0.38, both as colorless oils. The data for **8a** is obtained from the product mixture.

#### *1 $\alpha$ ,6 $\alpha$ -3,3,6-trimethyl-5-oxobicyclo[4.2.0]octane-7-exo-carbonitrile (6a)*

<sup>1</sup>H NMR (C<sub>6</sub>D<sub>6</sub>)  $\delta$ : 0.45 (s, 3H, CH<sub>3</sub>), 0.67 (dd,  $J$  = 14.2, 9.8 Hz, 1H, H(2ax)), 0.69 (s, 3H, CH<sub>3</sub>), 1.08 (dd,  $J$  = 14.2, 7.6 Hz, 1H, H(2eq)), 1.20 (ddd,  $J$  = 12.0, 9.1, 3.4 Hz, 1H, H(8en)), 1.25 (s, 3H, CH<sub>3</sub>), 1.70 (m, 2H, H(1) & H(4ax)), 1.90 (m, 2H, H(4eq) & H(8ex)), 2.72 (dd,  $J$  = 9.0, 8.8 Hz, 1H, H(7)). <sup>13</sup>C NMR (C<sub>6</sub>D<sub>6</sub>)  $\delta$ : 20.2 (CH<sub>3</sub>), 28.1 (C(7)), 28.5 (CH<sub>3</sub>), 29.2 (C(8)), 31.2 (CH<sub>3</sub>), 33.9 (C(3)), 39.2 (C(1)), 41.3 (C(2)), 50.5 (C(6)), 51.4 (C(4)), 118.7 (CN), 210.1 (CO). MS (%): 191 ([M]<sup>+</sup>, 4), 41.

#### *1 $\alpha$ ,6 $\alpha$ -1,4,4-trimethyl-2-oxobicyclo[4.2.0]octane-7-exo-carbonitrile (7a)*

<sup>1</sup>H NMR (C<sub>6</sub>D<sub>6</sub>)  $\delta$ : 0.53 (s, 3H, CH<sub>3</sub>), 0.69 (s, 3H, CH<sub>3</sub>), 0.72 (dd,  $J$  = 14.5, 8.0, 1H, H(5ax)), 1.05 (dd,  $J$  = 14.5, 4.6 Hz, 1H, H(5eq)), 1.06 (s, 3H, CH<sub>3</sub>), 1.65 (m, 2H, H(3eq) & H(8ex)), 1.82 (d,  $J$  = 14.8 Hz, 1H, H(3ax)), 2.02 (ddd,  $J$  = 9.8, 6.5, 6.3 Hz, 1H, H(7)), 2.27 (ddd,  $J$  = 8.0, 6.5, 4.6 Hz, 1H, H(6)), 2.30 (dd,  $J$  = 12.2, 9.8, 1H, H(8en)). <sup>13</sup>C NMR (C<sub>6</sub>D<sub>6</sub>)  $\delta$ : 23.5 (CH<sub>3</sub>), 24.2 (C(7)), 27.5 (CH<sub>3</sub>), 30.9 (C(4)), 31.2 (CH<sub>3</sub>), 33.9 (C(8)), 39.1 (C(5)), 44.8 (C(1)), 47.3 (C(6)), 51.2 (C(3)), 121.9 (CN), 210.2 (CO). MS (%): 191 ([M]<sup>+</sup>, 12), 83.

#### *1 $\alpha$ ,6 $\alpha$ -3,3,6-trimethyl-5-oxobicyclo[4.2.0]octane-7-endo-carbonitrile (8a)*

<sup>1</sup>H NMR (C<sub>6</sub>D<sub>6</sub>)  $\delta$ : 0.43 (s, 3H, CH<sub>3</sub>), 0.88 (s, 3H, CH<sub>3</sub>), 0.94 (s, 3H, CH<sub>3</sub>), 1.32 (m, 2H, H(2eq) & H(8en)), 1.53 (dd,  $J$  = 14.2, 8.5 Hz, 1H, H(2ax)), 1.65 (m, 1H, H(1)), 1.85 (ddd,  $J$  = 12.0, 9.1, 8.9, 1H, H(8ex)), 2.05 (m, 1H, H(7)), 2.15 (d,  $J$  = 17.3 Hz, 1H, H(4eq)), 2.45 (d,  $J$  = 17.3 Hz, 1H, H(4ax)). <sup>13</sup>C NMR (C<sub>6</sub>D<sub>6</sub>)  $\delta$ : 20.5 (CH<sub>3</sub>), 28.1 (C(8)), 28.5 (CH<sub>3</sub>), 31.0 (C(7)), 31.2 (CH<sub>3</sub>), 33.9 (C(3)), 39.2 (C(1)), 43.3 (C(2)), 52.1 (C(6)), 54.1 (C(4)), 119.7 (CN), 209.8 (CO). MS (%): 191 ([M]<sup>+</sup>, 4), 41.

### Photolysis of 5b and 2

Irradiation for 4 h with up to 85% conversion led to four new product peaks (25% (**7b**), 40% (**6b**), 17% (unident.), and 18% (**8b**)). CC (pentane:toluene:EtOAc = 70:15:15) afforded first 106 mg (40%) of **6b** (70% purity),  $R_f$  = 0.42, and then 40 mg (15%) of **7b** (95% purity),  $R_f$  = 0.32, both as colorless oils. The data for **8b** is obtained from the product mixture.

#### *1 $\alpha$ ,6 $\alpha$ -6-benzyl-3,3-dimethyl-5-oxobicyclo[4.2.0]octane-7-exo-carbonitrile (6b)*

<sup>1</sup>H NMR (CDCl<sub>3</sub>)  $\delta$ : 0.30 (s, 3H, CH<sub>3</sub>), 0.92 (s, 3H, CH<sub>3</sub>), 1.40 (dd,  $J$  = 14.3, 8.4 Hz, 1H, H(2ax)), 1.70 (dd,  $J$  = 14.3, 8.2 Hz, 1H, H(2eq)), 1.82 (d,  $J$  = 16.1 Hz, 1H, H(4ax)), 2.06



(d,  $J = 16.1$  Hz, 1H, H(4eq)), 2.09 (ddd,  $J = 11.6, 9.0, 4.5$  Hz, 1H, H(8en)), 2.57 (ddd,  $J = 11.6, 8.3, 8.2$  Hz, 1H, H(8ex)), 2.88 (m, 1H, H(1)), 3.41 (dd,  $J = 9.0, 8.3$  Hz, 1H, H(7)), 3.42 & 3.55 (AB,  $J = 13.2$  Hz, 2H, CH<sub>2</sub>Ph), 7.12–7.30 (m, 5H, arom). <sup>13</sup>C NMR (CDCl<sub>3</sub>)  $\delta$ : 28.0 (C(8)), 28.2 (C(7)), 28.7 (CH<sub>3</sub>), 31.0 (CH<sub>3</sub>), 34.5 (C(3)), 36.3 (C(1)), 40.3 (CH<sub>2</sub>Ph), 40.8 (C(2)), 52.7 (C(6)), 53.0 (C(4)), 119.6 (CN), 127.6–136.5 (arom), 211.9 (CO). MS (%): 267 ([M]<sup>+</sup>, 50), 91.

***1 $\alpha$ ,6 $\alpha$ -1-benzyl-4,4-dimethyl-2-oxobicyclo[4.2.0]octane-7-exo-carbonitrile (7b)***

<sup>1</sup>H NMR (CDCl<sub>3</sub>)  $\delta$ : 0.70 (s, 3H, CH<sub>3</sub>), 0.98 (s, 3H, CH<sub>3</sub>), 1.52 (dd,  $J = 14.1, 4.6$  Hz, 1H, H(5eq)), 1.77 (dd,  $J = 14.1, 7.6$  Hz, 1H, H(5ax)), 1.82 (d,  $J = 14.7$  Hz, 1H, H(3ax)), 2.05 (d,  $J = 14.7$  Hz, 1H, H(3eq)), 2.26 (dd,  $J = 12.0, 6.8$  Hz, 1H, H(8ex)), 2.78 (m, 2H, H(7) & H(8en)), 3.02 & 3.16 (AB,  $J = 13.2$  Hz, 2H, CH<sub>2</sub>Ph), 3.17 (m, 1H, H(6)), 7.10–7.30 (m, 5H, arom). <sup>13</sup>C NMR (CDCl<sub>3</sub>)  $\delta$ : 23.6 (C(7)), 29.4 (CH<sub>3</sub>), 31.4 (CH<sub>3</sub>), 32.9 (C(8)), 34.3 (C(4)), 39.2 (C(5)), 44.6 (CH<sub>2</sub>Ph), 45.4 (C(6)), 51.1 (C(1)), 52.8 (C(3)), 122.2 (CN), 127.6–136.4 (arom), 214.5 (CO). MS (%): 267 ([M]<sup>+</sup>, 20), 91.

***1 $\alpha$ ,6 $\alpha$ -6-benzyl-3,3-dimethyl-5-oxobicyclo[4.2.0]octane-7-endo-carbonitrile (8b)***

<sup>1</sup>H NMR (CDCl<sub>3</sub>)  $\delta$ : 0.39 (s, 3H, CH<sub>3</sub>), 1.04 (s, 3H, CH<sub>3</sub>), 1.52 (m, 1H, H(2ax)), 1.75 (m, 1H, H(2eq)), 1.94 (ddd,  $J = 12.0, 5.0, 4.6$  Hz, 1H, H(8en)), 2.02 (d,  $J = 17.4$  Hz, 1H, H(4eq)), 2.32 (d,  $J = 17.4$  Hz, 1H, H(4ax)), 2.46 (ddd,  $J = 12.0, 9.1, 9.0$  Hz, 1H, H(8ex)), 2.74 (m, 1H, H(1)), 3.00 (ddd,  $J = 9.1, 5.0, 1.3$  Hz, 1H, H(7)), 2.81 & 3.35 (AB,  $J = 13.2$  Hz, 2H, CH<sub>2</sub>Ph), 7.12–7.30 (m, 5H, arom). <sup>13</sup>C NMR (CDCl<sub>3</sub>)  $\delta$ : 27.7 (CH<sub>3</sub>), 27.9 (C(8)), 29.6 (CH<sub>3</sub>), 30.1 (C(7)), 32.1 (C(3)), 35.8 (C(1)), 41.7 (CH<sub>2</sub>Ph), 43.1 (C(2)), 53.8 (C(6)), 53.9 (C(4)), 120.9 (CN), 127.2–136.7 (arom), 211.1 (CO). MS (%): 267 ([M]<sup>+</sup>, 45), 91.

**Photolysis of 5c and 2**

Irradiation for 8 h with up to 80% conversion led to two new product peaks (82% (**6c**) and 18% (**7c**)). CC (pentane:Et<sub>2</sub>O = 70:30) afforded first 35 mg (18%) of a 1:1 mixture of **6c** and **8c**,  $R_f = 0.47$ , and then 101 mg (49%) of pure **6c**,  $R_f = 0.42$ , as light yellow solid, mp 33–35°.

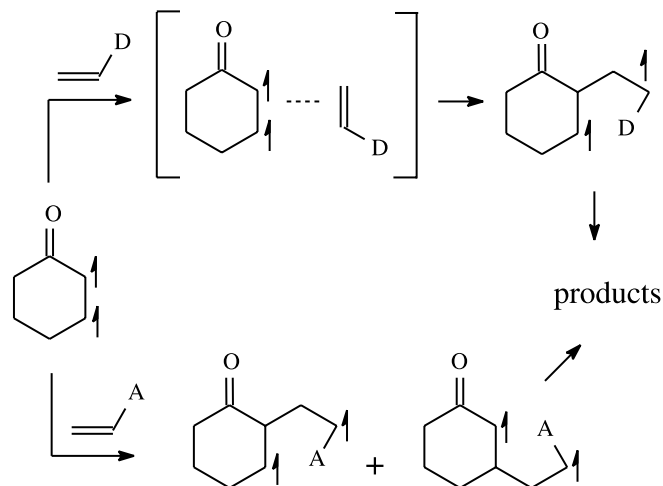
***1 $\alpha$ ,6 $\alpha$ -6-(3,3-dimethylbut-1-ynyl)-3,3-dimethyl-5-oxobicyclo[4.2.0]octane-7-exo-carbonitrile (6c)***

<sup>1</sup>H NMR (CDCl<sub>3</sub>)  $\delta$ : 0.96 (s, 3H, CH<sub>3</sub>), 1.13 (s, 3H, CH<sub>3</sub>), 1.17 (s, 9H, CH<sub>3</sub>), 1.24 (dd,  $J = 13.5, 7.0$  Hz, 1H, H(2eq)), 1.73 (dd,  $J = 13.5, 8.0$  Hz, 1H, H(2ax)), 1.99 (ddd,  $J = 12.0, 9.0, 6.0$  Hz, 1H, H(8en)), 2.07 (d,  $J = 14.6$  Hz, H(4ax)), 2.37 (ddd,  $J = 12.0, 9.0, 6.0$  Hz, 1H, H(8ex)), 2.59 (d,  $J = 14.6$  Hz, H(4eq)), 3.17 (m, 1H, H(1)), 3.61 (dd,  $J = 9.5, 6.0$  Hz, 1H, H(7)). <sup>13</sup>C NMR (CDCl<sub>3</sub>)  $\delta$ : 26.4 (CMe<sub>3</sub>), 27.1 (C(8)), 28.5 (CH<sub>3</sub>), 28.6 (CH<sub>3</sub>), 29.3 (C(7)), 29.6 ((CH<sub>3</sub>)<sub>3</sub>), 34.6 (C(3)), 37.7 (C(2)), 41.2 (C(1)), 48.6 (C(4)), 50.6 (C(6)), 74.5 & 95.9 (C $\equiv$ C), 118.0 (CN), 205.1 (CO). MS (%): 257 ([M]<sup>+</sup>, 2), 148.

***1 $\alpha$ ,6 $\alpha$ -6-(3,3-dimethylbut-1-ynyl)-3,3-dimethyl-5-oxobicyclo[4.2.0]octane-7-endo-carbonitrile (8c)***

<sup>1</sup>H NMR (CDCl<sub>3</sub>)  $\delta$ : 0.99 (s, 3H, CH<sub>3</sub>), 1.02 (s, 3H, CH<sub>3</sub>), 1.07 (s, 9H, CH<sub>3</sub>), 1.55 (dd,  $J = 13.0, 6.0$  Hz, 1H, H(2eq)),

**Scheme 2.**



1.81 (dd,  $J = 13.0, 8.0$  Hz, 1H, H(2ax)), 1.99 (ddd,  $J = 12.0, 6.0, 6.0$  Hz, 1H, H(8en)), 2.22 (d,  $J = 16.4$  Hz, H(4ax)), 2.48 (d,  $J = 16.4$  Hz, H(4eq)), 2.63 (ddd,  $J = 12.0, 9.0, 9.0$  Hz, 1H, H(8ex)), 2.87 (m, 1H, H(1)), 3.19 (ddd,  $J = 9.5, 6.0, 1.2$  Hz, 1H, H(7)). <sup>13</sup>C NMR (CDCl<sub>3</sub>)  $\delta$ : 26.7 (CMe<sub>3</sub>), 28.6 (C(8)), 28.7 (CH<sub>3</sub>), 28.8 (CH<sub>3</sub>), 29.5 ((CH<sub>3</sub>)<sub>3</sub>), 30.1 (C(7)), 32.5 (C(3)), 39.1 (C(2)), 40.7 (C(1)), 46.8 (C(6)), 50.6 (C(4)), 71.7 & 92.2 (C $\equiv$ C), 117.9 (CN), 203.3 (CO). MS (%): 257 ([M]<sup>+</sup>, 4), 41.

**Photolysis of 5b and 9**

Irradiation for 4 h with up to 75% conversion led to two new product peaks (54% (**10**) and 46% (**11**)). CC (pentane:toluene:EtOAc = 70:15:15) afforded first 84 mg (30%) of pure **11**,  $R_f = 0.47$ , as a light yellow oil and then 56 mg (20%) of pure **12**,  $R_f = 0.41$ , as a light yellow solid, mp 38–39°.

***1 $\alpha$ ,6 $\alpha$ -6-benzyl-3,3,7-trimethyl-5-oxobicyclo[4.2.0]octane-7-endo-carbonitrile (11)***

<sup>1</sup>H NMR (CDCl<sub>3</sub>)  $\delta$ : -0.12 (s, 3H, CH<sub>3</sub>), 0.91 (s, 3H, CH<sub>3</sub>), 1.55 (s, 3H, CH<sub>3</sub>), 1.72 (ddd,  $J = 14.2, 7.6, 2.6$  Hz, 1H, H(2eq)), 1.92 (dd,  $J = 18.6, 2.6$  Hz, 1H, H(4eq)), 1.95 (dd,  $J = 14.2, 10.7$  Hz, 1H, H(2ax)), 2.23 (dd,  $J = 12.0, 2.5$  Hz, 1H, H(8en)), 2.38 (d,  $J = 18.6$  Hz, 1H, H(4ax)), 2.45 (dd,  $J = 12.0, 8.5$  Hz, 1H, H(8ex)), 2.66 (m, 1H, H(1)), 2.66 & 3.49 (AB,  $J = 12.8$  Hz, 2H, CH<sub>2</sub>Ph), 7.17–7.37 (m, 5H, arom). <sup>13</sup>C NMR (CDCl<sub>3</sub>)  $\delta$ : 20.4 (CH<sub>3</sub>), 25.1 (CH<sub>3</sub>), 31.7 (C(3)), 32.5 (CH<sub>3</sub>), 32.8 (C(1)), 35.8 (C(8)), 37.7 (CH<sub>2</sub>Ph), 37.8 (C(7)), 39.5 (C(2)), 53.3 (C(4)), 55.0 (C(6)), 124.7 (CN), 126.5–136.9 (arom), 212.7 (CO). MS (%): 281 ([M]<sup>+</sup>, 30), 91.

***1 $\alpha$ ,6 $\alpha$ -1-benzyl-4,4,7-trimethyl-2-oxobicyclo[4.2.0]octane-7-exo-carbonitrile (12)***

<sup>1</sup>H NMR (CDCl<sub>3</sub>)  $\delta$ : 0.30 (s, 3H, CH<sub>3</sub>), 0.95 (s, 3H, CH<sub>3</sub>), 1.40 (s, 3H, CH<sub>3</sub>), 1.46 (dd,  $J = 13.6, 12.3$  Hz, 1H, H(5ax)), 1.55 (ddd,  $J = 13.6, 6.9, 2.2$  Hz, 1H, H(5eq)), 2.02 (dd,  $J = 17.6, 2.2$  Hz, 1H, H(3eq)), 2.10 (d,  $J = 17.6$  Hz, 1H, H(3ax)), 2.30 (d,  $J = 12.3$  Hz, 1H, H(8en)), 2.54 (dd,  $J = 12.3, 3.0$  Hz, 1H, H(8ex)), 3.13 (m, 1H, H(6)), 3.42 & 3.55 (AB,  $J = 13.2$  Hz, 2H, CH<sub>2</sub>Ph), 7.15–7.38 (m, 5H, arom). <sup>13</sup>C NMR (CDCl<sub>3</sub>)  $\delta$ : 20.5 (CH<sub>3</sub>), 25.6 (CH<sub>3</sub>), 32.5 (C(4)),



32.9 (CH<sub>3</sub>), 35.8 (C(5)), 40.8 (C(8)), 41.1 (C(7)), 42.3 (CH<sub>2</sub>Ph), 43.3 (C(6)), 48.2 (C(1)), 52.0 (C(3)), 126.7 (CN), 126.8–136.7 (arom), 214.7 (CO). MS (%): 281 ([M]<sup>+</sup>, 20), 91.

## References

1. E.J. Corey, J.D. Bass, R. LaMahieu, and R.B. Mitra. *J. Am. Chem. Soc.* **86**, 5570 (1964).
2. T.S. Cantrell, W.S. Haller, and J.C. Williams. *J. Org. Chem.* **34**, 509 (1969).
3. P. de Mayo. *Acc. Chem. Res.* **4**, 41 (1971)
4. P. Margaretha. *Helv. Chim. Acta*, **57**, 1866 (1974).
5. D.I. Schuster, G.E. Heibel, P.B. Brown, N.J. Turro, and C.V. Kumar. *J. Am. Chem. Soc.* **110**, 8261 (1988).
6. P. Krug, A. Rudolph, and A.C. Weedon. *Tetrahedron Lett.* **34**, 7221 (1993).
7. L. Meyer, B. Elsholz, I. Reulecke, K. Schmidt, P. Margaretha, and P. Wessig. *Helv. Chim. Acta*, **85**, 2065 (2002).
8. G. Cruciani, H.J. Rathjen, and P. Margaretha. *Helv. Chim. Acta*, **73**, 856 (1990).
9. B. Witte, L. Meyer, and P. Margaretha. *Helv. Chim. Acta*, **83**, 554 (2000).
10. I. Fleming. *Frontier orbitals and organic chemical reactions*. J. Wiley, New York. 1976.
11. K.U. Ingold. *In Free radicals*. Vol.1. *Edited by J.Kochi*. J. Wiley, New York. 1973. p. 92.
12. B. Giese, and J. Meixner. *Angew. Chem.* **91**, 167 (1979)
13. C. Wawrzenczyk and S. Lochynski. *Monatsh. Chem.* **116**, 99 (1985).
14. J.E. Ellis, J.S. Dutcher, and C.H. Heathcock. *J. Org. Chem.* **41**, 2677 (1976).
15. E. Negishi, Z. Tan, S.Y. Liou, and B. Liao. *Tetrahedron*, **56**, 10197 (2000).
16. P. Margaretha, S. Reichow, and W.C. Agosta. *J. Org. Chem.* **59**, 5393 (1994).



# Stereospecific Grignard reactions of cholesteryl 1-alkenesulfinate esters: Application of the Andersen Protocol to the preparation of non-racemic $\alpha,\beta$ -unsaturated sulfoxides

Rick R. Strickler, John M. Motto, Craig C. Humber, and Adrian L. Schwan

**Abstract:** Enantiomerically enriched  $\alpha,\beta$ -unsaturated sulfinate esters of (–)-cholesterol undergo stereospecific substitutions at sulfur when treated in benzene at 6°C with Grignard reagents. Sulfoxides with ees of 85–99.5% are obtained when enantiopure sulfinate esters are used. The substitution reactions proceed with inversion of sulfur configuration. Enantiomerically pure cholesteryl (*E*)-2-carbomethoxyethenesulfinate is not a suitable reactant under the Grignard reaction conditions. It is suggested that the ester group induces unwanted reactions significantly lowering both the yield and sulfur stereogenicity.

**Key words:** sulfinate, sulfoxide, Grignard reagents, stereospecific, unsaturated.

**Résumé :** Lorsqu'on les traite avec des réactifs de Grignard, dans le benzène à 6 °C, les sulfonates  $\alpha,\beta$ -insaturés énantiomériquement enrichis du (–)-cholestérol subissent des réactions de substitution stéréospécifiques au niveau du soufre. Des sulfoxydes avec des ee de 95 à 99,5 % sont obtenus lorsqu'on utilise des sulfonates énantiomériquement purs. Les réactions de substitution se produisent avec inversion de configuration au niveau du soufre. Le (*E*)-2-carbométhoxyéthènesulfinate de cholestéryle énantiomériquement pur n'est pas un réactif approprié dans les conditions utilisées avec les réactifs de Grignard. Il est suggéré que le groupe ester induit des réactions indésirables qui abaissent de façon significative tant le rendement que la stéréogénicité au niveau du soufre.

**Mots clés :** sulfinate, sulfoxyde, réactifs de Grignard, stéréospécifique, insaturé.

[Traduit par la Rédaction]

## Introduction

Enantioenriched sulfoxides can induce the introduction of carbon chirality into organic molecules by a number of means including carbanionic chemistry, Diels–Alder reactions and chiral ligand complexation (1–4). In these reactions it is the chirality at the sulfur center that plays a pivotal role in controlling the stereochemical outcome of the reaction. As such, a great deal of effort has gone into developing reliable and efficient methods for the synthesis of enantiopure sulfoxides. One mode of preparation of chiral sulfoxides that has enjoyed sustained popularity (4–7) is based on a protocol introduced by Andersen (8a). The original Andersen procedure involves treating a sulfinyl chloride with (–)-menthol to generate a diastereomeric mixture of menthyl sulfinate esters which, following a separation step, undergo organometallic substitution to afford enantiomerically pure sulfoxides (Scheme 1, R\*OH = menthol). Since the original Andersen method was first introduced several improvements have been advanced. These typically involve the use of other chiral alcohols such

as diacetone-*D*-glucose (DAG), (5b, 9) (1*R*,2*S*)-(–)-*trans*-2-phenyl-cyclohexanol (10), and cholesterol (7, 11). The majority of recent applications of this protocol have tended to employ either DAG (4, 5) or (–)-menthol (6).

To this point, the application of cholesterol to this chemistry has been focused on preparing methanesulfinate esters (11). The propensity of the large cholesteryl auxiliary to crystallize provided the driving force for the sulfinate separation by recrystallization and the eventual formation of enantiopure methanesulfonates and methyl sulfoxides (11). Our group has established a practical method for the synthesis of 1-alkenesulfinyl chlorides (12, 13) and while investigating their conversion to enantiopure  $\alpha,\beta$ -unsaturated sulfinate esters, has found that cholesterol is a preferred chiral alcohol (14). The aptitude for cholesterol derivatives to crystallize provided a benefit no other alcohols could equal. In that investigation the first collection of optically active 1-alkenesulfinate esters was reported (eq. [1]) (14). As part of our continuing interest in this area we investigated the nucleophilic conversion of these  $\alpha,\beta$ -unsaturated sulfinate esters to enantiopure or enriched  $\alpha,\beta$ -

Received 25 October 2002. Published on the NRC Research Press Web site at <http://canjchem.nrc.ca> on 7 April 2003.

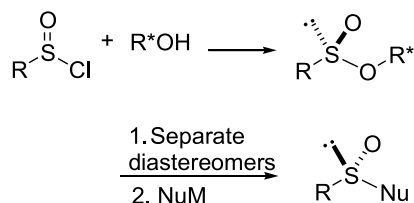
*Dedicated to Professor Don Arnold for his contributions to chemistry.*

**R.R. Strickler, J.M. Motto, C.C. Humber, and A.L. Schwan.**<sup>1</sup> Guelph-Waterloo Centre for Graduate Work in Chemistry and Biochemistry, Department of Chemistry and Biochemistry, University of Guelph, Guelph, ON N1G 2W1, Canada.

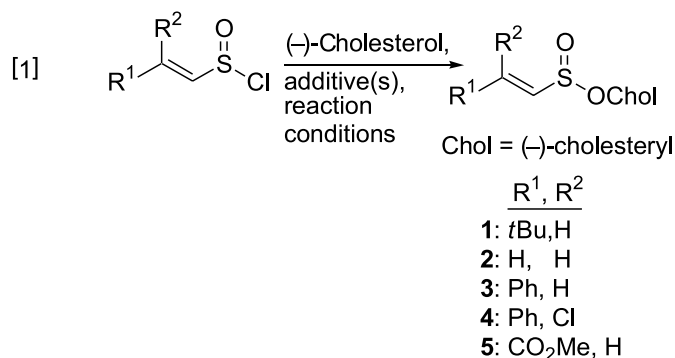
<sup>1</sup>Corresponding author (e-mail: [schwan@uoguelph.ca](mailto:schwan@uoguelph.ca)).



Scheme 1.



unsaturated sulfoxides, compounds that are well-established as useful sources of a variety of chiral derivatives (1, 15). Most of the existing chiral vinylic sulfoxide preparations either create the double bond after a chiral sulfoxide has been prepared, or treat a chiral arenesulfinate with a vinylic organometallic reagent (15c, 15d). No such syntheses have established the chirality once the C=C-S unit was already intact which is the strategy investigated by us. This paper reports the outcome of our investigation, a portion of which has already been communicated (7).



## Results and discussion

A synthetically useful organometallic displacement of the cholesteryl unit requires both high yield and maintenance of the stereogenicity at the sulfur. In work outlined in the preliminary communication (7), it was established using cyclohexyl analogs of the available enantioenriched sulfinate esters (14) that Grignard reagents (2 equiv) were readily found to be favored over organolithiums (16). To find the preferred conditions for maximum enantiomeric excesses, samples of [*R<sub>S</sub>*]-(-)-cholesteryl (*E*)-3,3-dimethyl-1-butenesulfinate (**1**) possessing 88–100% optical purity were treated with *n*-BuMgCl under various conditions.<sup>2</sup> The results directed us to perform all subsequent substitution reactions in benzene (17) at 6°C where possible, although ethyl ether was the original solvent for such reactions (8b, 18).

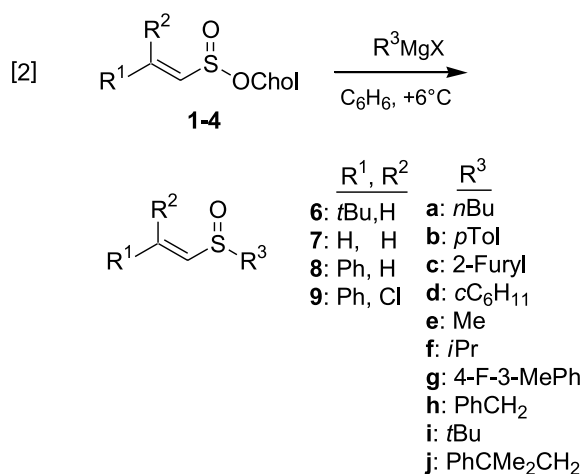
Using the reaction conditions found in those preliminary experiments, the reactions of enantiopure or enantioenriched selected [*R<sub>S</sub>*]- and [*S<sub>S</sub>*]-sulfates **1–4** with commercial and prepared Grignard reagents were proved to be efficient and chemoselective affording a wide variety of substituted α,β-unsaturated sulfoxides as outlined in Table 1 (eq. [2]). The enantiomeric excesses and the configurational assignments of the sulfoxides were determined using the chiral solvating

agent [*R*]-(-)-2,2,2-trifluoro-1-(9-anthryl)ethanol (**19**).<sup>3</sup> The sulfoxides possessing the highest ees arose from stereospecific reactions of sulfates **1**, **3**, and **4**. Simple ethenyl sulfoxides could not be produced with high ee, since the precursor (-)-cholesteryl ethenesulfinate (**2**) could only be formed with des as high as 47% (14). Nevertheless, Grignard reactions of **2** still proceeded with high stereospecificity and yield when aromatic Grignard reagents were employed. Aliphatic Grignard reagents afforded somewhat lower yield and brought on losses of stereogenicity. Utilizing the availability of [*S<sub>S</sub>*]-**1** (14) the corresponding Grignard reactions and the obtention of [*R<sub>S</sub>*]-sulfoxides confirms the stereospecificity of the substitution pathway and eliminates the possibility of stereoconvergent Grignard reactions.

It was decided that the <sup>1</sup>H NMR – solvating agent method (19) of ee determination had a detection limit of 98% for samples that had only one set of peaks evident: the <sup>1</sup>H NMR of solvated **6f** shows the minor isomer and the ee of the sample of **6f** was found to be 98%. A closer inspection of the rotation data for **8b** further corroborates the detection limit, and hence the optical purity of the sulfoxides. The literature reports a value of [α]<sub>D</sub><sup>25</sup> +166.0° (CHCl<sub>3</sub>) for **8b** with 100% optical purity (20) while we obtained [α]<sub>D</sub><sup>25</sup> +165.1° (CHCl<sub>3</sub>) meaning our isolated sample of **8b** possessed an ee of 99.5%.

Successful 2-furyl Grignard reactions were obtained after several attempts and it was found that 2-furylmgBr generated in THF by the reaction of 2-furyllithium with MgBr<sub>2</sub>·Et<sub>2</sub>O (**6d**, 21) reacts with [*R<sub>S</sub>*]-**1** in THF at -20°C in 78% yield and with >98% ee. Sulfoxides bearing the furyl group are important in organic synthesis and have been used in the synthesis of naturally occurring compounds (22). Also, noteworthy is that MeMgBr induced a 15% reduction in the measured ees of the sulfoxides obtained. Several repetitions and variations were performed but ees could not be improved and yields consistently ranged from 56 to 67%.

Many of the synthetic protocols for racemic and homo-



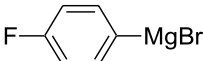
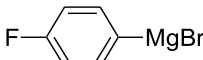
chiral α,β-unsaturated sulfoxides introduce the double bond in the last stage of the preparation and sometimes lead to

<sup>2</sup>The reader is referred to the table of preliminary data presented in the communication (ref. (7)).

<sup>3</sup>In some cases, one can gain confirmation of the assigned sulfur configuration by comparison of the sample's optical rotation with literature values.



**Table 1.** Grignard reactions of optically enriched  $\alpha,\beta$ -unsaturated sulfonates.

	Sulfonate and config.	Grignard reagent <sup>a</sup>	Sulfoxide			
			Structure	% Yield	$[\alpha]_D^{25b}$	% ee <sup>c</sup>
1	<b>2</b> : 42% [ <i>R<sub>S</sub></i> ]		<b>7g</b>	80	+153.4° ( <i>c</i> 1.09)	41 [ <i>R<sub>S</sub></i> ]
2	<b>2</b> : 22% [ <i>S<sub>S</sub></i> ]		<b>7g</b>	83	−79.9° ( <i>c</i> 1.42)	22 [ <i>S<sub>S</sub></i> ]
3	<b>2</b> : 22% [ <i>S<sub>S</sub></i> ]	<i>c</i> -C <sub>6</sub> H <sub>11</sub> MgCl	<b>7d</b>	42(63) <sup>d</sup>	−51.6° ( <i>c</i> 0.32)	23 [ <i>S<sub>S</sub></i> ]
4	<b>2</b> : 42% [ <i>R<sub>S</sub></i> ]	<i>p</i> -TolylMgBr	<b>7b</b>	77(85) <sup>d</sup>	+136.3° ( <i>c</i> , 1.08) <sup>e</sup>	42 [ <i>R<sub>S</sub></i> ]
5	<b>2</b> : 42% [ <i>R<sub>S</sub></i> ]	2-FurylMgBr <sup>f</sup>	<b>7c</b>	59	+72.3° ( <i>c</i> , 0.83)	41 [ <i>R<sub>S</sub></i> ]
6	<b>2</b> : 36% [ <i>R<sub>S</sub></i> ]	PhCMe <sub>2</sub> CH <sub>2</sub> MgCl	<b>7j</b>	39	+43.0° ( <i>c</i> 1.96)	28 [ <i>S<sub>S</sub></i> ]
7	<b>1</b> :100% [ <i>R<sub>S</sub></i> ]	<i>n</i> BuMgCl	<b>6a</b>	86	+130.7° ( <i>c</i> 1.57)	>98 [ <i>S<sub>S</sub></i> ]
8	<b>1</b> :100% [ <i>R<sub>S</sub></i> ]	MeMgBr	<b>6e</b>	56–67	+238.2° ( <i>c</i> 2.90)	85 to 86 [ <i>S<sub>S</sub></i> ]
9	<b>1</b> :100% [ <i>R<sub>S</sub></i> ]	<i>i</i> -PrMgCl	<b>6f</b>	85	+150.3° ( <i>c</i> 1.95)	98 [ <i>S<sub>S</sub></i> ]
10	<b>1</b> :100% [ <i>R<sub>S</sub></i> ]	<i>c</i> -C <sub>6</sub> H <sub>11</sub> MgBr	<b>6d</b>	86	+61.4° ( <i>c</i> 2.38)	>98 [ <i>S<sub>S</sub></i> ]
11	<b>1</b> :100% [ <i>R<sub>S</sub></i> ]	PhCH <sub>2</sub> MgBr <sup>g</sup>	<b>6h</b>	78	+142.0° ( <i>c</i> 1.31)	91 [ <i>S<sub>S</sub></i> ]
12	<b>1</b> :100% [ <i>R<sub>S</sub></i> ]	<i>p</i> -TolylMgBr	<b>6b</b>	86	+116.6° ( <i>c</i> 1.41) <sup>h</sup>	94 [ <i>R<sub>S</sub></i> ]
13	<b>1</b> :100% [ <i>R<sub>S</sub></i> ]	2-FurylMgBr <sup>f</sup>	<b>6c</b>	78	+125.8° ( <i>c</i> 1.69)	>98 [ <i>R<sub>S</sub></i> ]
14	<b>1</b> :71% [ <i>S<sub>S</sub></i> ]	<i>i</i> -PrMgCl	<b>6f</b>	76	−112.3° ( <i>c</i> 1.53)	72 [ <i>R<sub>S</sub></i> ]
15	<b>1</b> :71% [ <i>S<sub>S</sub></i> ]	<i>c</i> -C <sub>6</sub> H <sub>11</sub> MgBr	<b>6d</b>	79	−41.4° ( <i>c</i> 2.30)	71 [ <i>R<sub>S</sub></i> ]
16	<b>3</b> :42% [ <i>S<sub>S</sub></i> ]	<i>t</i> BuMgCl	<b>8i</b>	70	−46.6° ( <i>c</i> 1.08)	41.5 [ <i>S<sub>S</sub></i> ]
17	<b>3</b> :100% [ <i>R<sub>S</sub></i> ]	<i>t</i> -BuMgCl	<b>8i</b>	70	+109.8° ( <i>c</i> 0.96)	97 [ <i>R<sub>S</sub></i> ]
18	<b>3</b> :100% [ <i>R<sub>S</sub></i> ]	<i>i</i> -PrMgCl	<b>8f</b>	87	+116.7° ( <i>c</i> 1.69)	91 [ <i>S<sub>S</sub></i> ]
19	<b>3</b> :100% [ <i>R<sub>S</sub></i> ]	<i>c</i> -C <sub>6</sub> H <sub>11</sub> MgBr	<b>8d</b>	62	+62.3° ( <i>c</i> 1.61)	92 [ <i>S<sub>S</sub></i> ]
20	<b>3</b> :100% [ <i>R<sub>S</sub></i> ]	<i>n</i> -BuMgCl	<b>8a</b>	74	+62.1° ( <i>c</i> 0.89)	n/d <sup>i</sup>
21	<b>3</b> :100% [ <i>R<sub>S</sub></i> ]	PhCH <sub>2</sub> MgBr <sup>g</sup>	<b>8h</b>	56(87) <sup>c</sup>	−53.9° ( <i>c</i> 1.04)	91 [ <i>S<sub>S</sub></i> ]
22	<b>3</b> :100% [ <i>R<sub>S</sub></i> ]	PhCMe <sub>2</sub> CH <sub>2</sub> MgCl	<b>8j</b>	81	+125.3° ( <i>c</i> 0.64)	91 [ <i>S<sub>S</sub></i> ]
23	<b>3</b> :100% [ <i>R<sub>S</sub></i> ]	<i>p</i> -TolylMgBr	<b>8b</b>	76	+176.9° ( <i>c</i> , 1.03) <sup>j</sup>	>98 [ <i>R<sub>S</sub></i> ]
24	<b>3</b> :100% [ <i>R<sub>S</sub></i> ]		<b>8g</b>	82	+152.0° ( <i>c</i> 1.11)	95 [ <i>R<sub>S</sub></i> ]
25	<b>4</b> :86% [ <i>S<sub>S</sub></i> ]		<b>9g</b>	61	−49.5° ( <i>c</i> 2.52)	86 [ <i>S<sub>S</sub></i> ]
26	<b>4</b> :85% [ <i>S<sub>S</sub></i> ]	<i>c</i> -C <sub>6</sub> H <sub>11</sub> MgBr	<b>9d</b>	73	−28.0° ( <i>c</i> 1.17)	79 [ <i>R<sub>S</sub></i> ]

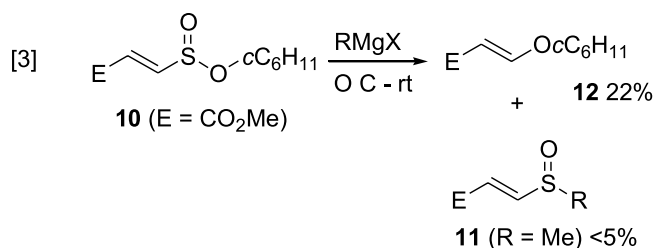
<sup>a</sup>Used 2 equiv of Grignard reagent unless otherwise noted. Reactions were performed in benzene at 6°C unless otherwise noted.<sup>b</sup>Optical rotations were obtained in acetone, unless otherwise noted.<sup>c</sup>Ees were determined using [*R*](−)-2,2,2-trifluoro-1-(9-anthryl)ethanol as an NMR solvating agent. See ref. (19).<sup>d</sup>Yield in brackets is based on recovered starting material.<sup>e</sup>Lit. (20) value +386° (ethanol, 94% [*R<sub>S</sub>*]).<sup>f</sup>Prepared from lithiated furanyl anion; see text and *Experimental* section for details.<sup>g</sup>Experiment was done with 1 equiv of Grignard reagent.<sup>h</sup>Lit. (23d) value +33° (acetone).<sup>i</sup>Not determinable.<sup>j</sup> $[\alpha]_D^{25}$  +165.1° (*c*, 1.03, CHCl<sub>3</sub>) (lit. (20) value +166.0°; (CHCl<sub>3</sub>, 100% [*R<sub>S</sub>*])).

mixtures of double bond isomers (6g, 20, 23, 24). At no point were the sulfoxides obtained herein contaminated with any *cis*-isomer. Our protocol establishes the geometry of the double bond at a very early stage of the chemistry, and the double bond configuration is never jeopardized thereafter. In this regard we are demonstrating the stereospecific transfer of selected chiral alkenesulfinyl units, while maintaining the double bond geometry. Hence, the sulfonates represent the first usage of an intact chiral [RCH=CHSO]<sup>+</sup> synthon.

### Reactions of cholesteryl (*E*)-2-carbomethoxyethenesulfinate

Grignard reactions of optically pure sulfinate **5** proved troublesome. Under our established conditions little or no sulfoxide was observed. Hence, cyclohexyl (*E*)-2-carbomethoxyethenesulfinate (**10**) (12) was enlisted as a model

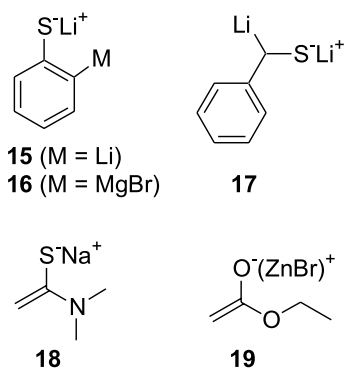
compound for **5** to employ in an investigation of the behavior of this unique sulfinate. The reaction of **10** with MeMgBr (eq. [3]) typifies the results of several trials. Sulfoxide **11** could only be obtained in 0–20% yield and the reaction mixture always contained vinyl ether **12**. Changing to other organometallic species such as organolithium and organocerium reagents offered little improvement.





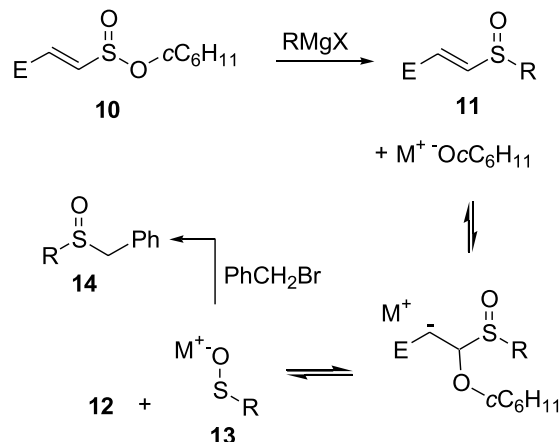
A mechanism to account for the observed results is offered in Scheme 2. It was felt that the sulfur substitution is indeed occurring, but the product is prone to counterattack by the displaced alkoxide. That attack occurs conjugate to the ester, the stronger electron-withdrawing group, and to conclude what appears to be an addition–elimination mechanism, a sulfenic acid anion (**13**) is released. To test this mechanism, sulfoxide **11** ( $R = \text{MeOC}_6\text{H}_4\text{CH}_2$ ), the precursor of sulfonates **5** (**14**) and **10** (**12**), was treated with lithium cyclohexylate and the mixture was quenched with benzyl bromide to capture any reactive sulfenate (e.g., **13**). The observation of **12** as a reaction constituent and the isolation of **14** ( $R = \text{MeOC}_6\text{H}_4\text{CH}_2$ ) in 47% purified yield from that mixture offer strong support for the proposed mechanism (Scheme 2).

A number of experiments were performed to see if the sulfoxide could be intercepted before the addition–elimination reaction took place. To this end, sulfinate **10** was treated with nucleophiles **15**–**19**. It was hoped that dianions **15** (**25**), **16**, and **17** (**26**) would effect sulfoxide formation and rapidly perform an intramolecular Michael addition. As an alternative strategy, it was suggested that **18** (**5d**) and **19** could achieve sulfoxide formation and the presence of a (thio)carbonyl group  $\beta$  to the sulfinyl unit would enhance the acidity of the intervening methylene hydrogens thereby providing the displaced alkoxide the recourse of deprotonation rather than Michael attack. None of these efforts provided significant sulfoxide and vinyl ether **12** was evident in the reaction mixtures.

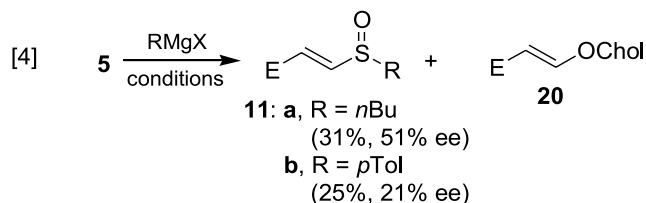


Not completely discouraged, we pursued several reactions of **5** with Grignard reagents. Equation [4] depicts the best results that could be achieved, and although the low yields of sulfoxide **11** and of vinyl ether **20** were foreseen, the loss of sulfur stereochemistry was unexpected. The loss of sulfur chirality is presumably because of the presence of the conjugating carboxylic ester group. It has recently been shown (**27**) that the presence of a vinylic ester conjugating to a sulfinyl lone pair and the consequent mesomeric donation of that lone pair toward the ester leads to a reduced inversion barrier for the sulfinyl group. Based on this behavior, it follows that the sulfinyl group in a compound such as **11** exhibits increased electrophilicity at sulfur. Hence, a reasonable explanation for the loss of sulfur stereochemistry entails attack of **11** by excess Grignard agent, a pseudorotation step of the intermediate sulfurane at which time loss of stereogenicity occurs followed by release of one of the two car-

Scheme 2.



bon-based ligands. Alternatively, attack by previously released cholesteryloxy anion on **5** would bring about a similar outcome, as preceded by counterattack and racemization by thiolate on chiral thiosulfonates (**28**). However, control experiments have shown that racemization of **5** by cholesteryloxy anion is minimal.



## Conclusions

Andersen, Mikolazczyk, and co-workers (**11**) have previously obtained optically pure cholesteryl [ $R_S$ ]- and [ $S_S$ ]-methanesulfonates in <5% yield. Although the behavior of cholesteryl ethenesulfonates would appear to be similar to those methanesulfonates, we were able to secure more substituted 1-alkenesulfonates in higher yield through recrystallization chemistry (**14**) and demonstrate in this paper that they are suitable 1-alkenesulfinyl transfer agents. Based on this observation, diastereomeric mixtures of cholesteryl sulfinate esters bearing large aryl and alkyl groups attached to sulfur may prove readily separable and hence worthy of investigation.

Those sulfinate esters that we have been able to secure undergo stereospecific substitution with inversion at sulfur yielding a range of  $\alpha,\beta$ -unsaturated sulfoxides. The presence of a carbomethoxy group trans to the sulfinate ester creates significant unwanted reactions under Grignard treatment conditions. The method outlined herein is not limited to vinylic sulfoxides bearing only a *p*-tolyl group, the preparations of which have been amply demonstrated in the literature, but allows for the preparation of a broader array of alkyl or aryl 1-alkenyl sulfoxides. It would appear that the collection of sulfoxides accessible by this protocol is only limited by the number of enantioenriched sulfonates available; we are currently exploring other means of pre-



paring a larger selection of enantiopure 1-alkene-sulfonates.

## Experimental

### General

Our general experimental methods have been outlined in a previous publication (12). Unless noted below, all Grignard reagents were purchased as stock solutions from Aldrich. Optical rotation measurements were performed on an Autopol III automatic polarimeter.

### Typical procedure for the conversion of optically enriched sulfonates 1–4 to sulfoxides

Diastereomerically pure cholesteryl 1-alkenesulfonate ester (1–4, 1 equiv) was dissolved in benzene (10 mL) and cooled to 6°C under N<sub>2</sub>. After 10 min the Grignard reagent (commercially available stock solution; 1 to 2 equiv) was added dropwise. The reaction mixture was stirred until complete by TLC analysis (1 to 2 h) and then quenched with NH<sub>4</sub>Cl (10 mL). The solution was diluted with EtOAc and the organic layer separated, washed with brine, dried with MgSO<sub>4</sub>, filtered, and concentrated under reduced pressure. The enantioenriched sulfoxides were isolated using silica gel flash chromatography, with EtOAc–hexanes as the eluent. Chemical yields, enantiomeric purities, and optical rotation data (in acetone) are presented in Table 1. All sulfoxides except **6c**, **7c**, **11a**, and **11b** were prepared by this protocol. Structural characterization of the sulfoxides follows.

#### [R<sub>S</sub>]-1-Ethenyl 4-methylphenyl sulfoxide (**7b**) (23c):

<sup>1</sup>H NMR (400 MHz) δ: 7.52 (d, *J* = 8.0 Hz, 2H), 7.32 (d, *J* = 8.4 Hz, 2H), 6.58 (dd, *J* = 16.4, 9.6 Hz, 1H), 6.19 (d, *J* = 16.4 Hz, 1H), 6.18 (d, *J* = 9.6 Hz, 1H), 2.41 (s, 3H).

#### [S<sub>S</sub>]-1-Ethenyl cyclohexyl sulfoxide (**7d**):

Mp: 48–50°C. IR (CH<sub>2</sub>Cl<sub>2</sub>) (cm<sup>-1</sup>): 3043, 2933, 2856, 1452, 1055. <sup>1</sup>H NMR (400 MHz) δ: 6.57 (dd, *J* = 16.5, 10.0 Hz, 1H), 6.07 (d, *J* = 16.5 Hz, 1H), 6.00 (d, *J* = 10.0 Hz, 1H), 2.57 (tt, *J* = 11.6, 3.6 Hz, 1H), 2.02–1.87 (m, 3H), 1.80–1.60 (m, 2H), 1.50–1.15 (m, 5H). <sup>13</sup>C NMR (100.6 MHz) δ: 138.6, 122.9, 60.2, 26.0, 25.5, 25.3, 24.2. MS (CI, NH<sub>3</sub>) *m/z* (%): 159 ([M + 1]<sup>+</sup>, 21), 108 (24), 91 (100), 90 (35), 74 (28), 73 (14). Anal. calcd. for C<sub>8</sub>H<sub>14</sub>OS: C 60.71, H 8.92; found: C 60.92, H 8.70.

#### [R<sub>S</sub>]-4-Fluoro-3-methylphenyl ethenyl sulfoxide (**7g**):

IR (neat) (cm<sup>-1</sup>): 3064, 3032, 2928, 1597, 1577, 1485, 1449, 1395, 1384, 1368, 1240, 1183, 1120, 1085, 1055, 1015, 986. <sup>1</sup>H NMR (400 MHz) δ: 7.48 (dd, *J* = 6.8, 1.6 Hz, 1H), 7.42 (m, 1H), 7.14 (t, *J* = 8.8 Hz, 1H), 6.57 (dd, *J* = 16.4, 9.6 Hz, 1H), 6.20 (d, *J* = 16.4 Hz, 1H), 6.91 (d, *J* = 9.6 Hz, 1H), 2.33 (s, 3H). <sup>13</sup>C NMR (100.6 MHz) δ: 162.9 (d, *J* = 250.6 Hz), 142.8, 138.1, 128.0 (d, *J* = 6.0 Hz), 126.9 (d, *J* = 18.5 Hz), 124.3 (d, *J* = 8.9 Hz), 120.6, 116.1 (d, *J* = 23.7 Hz), 14.5 (d, *J* = 3.2 Hz). MS (EI) *m/z* (%): 184 (M<sup>+</sup>, 11), 157 (21), 141 (18), 137 (11), 136 (100), 135 (21), 110 (18), 109 (33), 108 (10), 107 (12), 97 (11), 83 (20), 59 (10), 57 (13), 45 (19). Anal. calcd. for C<sub>9</sub>H<sub>9</sub>FOS: C 58.68, H 4.92; found: C 58.77, H 5.02.

#### [S<sub>S</sub>]-Ethenyl 1-(2-methyl-2-phenylpropyl) sulfoxide (**7j**):

IR (neat) (cm<sup>-1</sup>): 3089, 3034, 2967, 2932, 1497, 1444, 1370, 1047. <sup>1</sup>H NMR (400 MHz) δ: 7.31–7.24 (m, 3H), 7.17–7.14 (m, 2H), 6.25 (dd, *J* = 16.4, 9.6 Hz, 1H), 5.92 (d, *J* = 16.4 Hz, 1H), 5.73 (d, *J* = 9.6 Hz, 1H), 2.89 (AB<sub>q</sub>, *J* = 13.4 Hz, 2H), 1.16 (s, 3H), 0.78 (s, 3H). <sup>13</sup>C NMR (100.6 MHz) δ: 146.7, 141.5, 128.5, 126.6, 125.6, 120.7, 70.0, 37.8, 29.9, 27.2. MS (EI) *m/z* (%): 209, (82), 133 (91), 91(100), 55(20). Anal. calcd. for C<sub>12</sub>H<sub>16</sub>OS: C 69.19, H 7.74; found: C 69.38, H 7.59.

#### [S<sub>S</sub>]-(*E*)-3,3-Dimethyl-1-butenyl 1-butyl sulfoxide (**6a**):

IR (neat) (cm<sup>-1</sup>): 2959, 2932, 2906, 2870, 1625, 1465, 1364, 1265, 1074, 1039, 971. <sup>1</sup>H NMR (400 MHz) δ: 6.45 (d, *J* = 15.4 Hz, 1H), 6.09 (d, *J* = 15.4 Hz, 1H), 2.70 (t, *J* = 7.7 Hz, 2H), 1.68 (m, 2H), 1.48 (m, 2H), 1.11 (s, 9H), 0.96 (t, *J* = 7.3 Hz, 3H). <sup>13</sup>C NMR (100.6 MHz) δ: 151.1, 128.1, 53.8, 34.2, 28.8, 24.1, 22.0, 13.7. MS (EI) *m/z* (%): 188 (8), 171 (39), 132 (35), 118 (21), 117 (100), 115 (34), 101 (40), 99 (33), 97 (25), 85 (32), 84 (20), 83 (86), 79 (18), 74 (29), 71 (22), 69 (27), 67 (29), 65 (26), 59 (71), 57 (78), 56 (18), 55 (70), 53 (28), 51 (17). Anal. calcd. for C<sub>10</sub>H<sub>20</sub>OS: C 63.78, H 10.70; found: C 63.83, H 10.45.

#### [R<sub>S</sub>]-(*E*)-3,3-Dimethyl-1-butenyl 4-methylphenyl sulfoxide (**6b**) (29):

<sup>1</sup>H NMR (400 MHz) δ: 7.49 (d, *J* = 8.0 Hz, 2H), 7.31 (d, *J* = 8.0 Hz, 2H), 6.59 (d, *J* = 15.4 Hz, 1H), 6.11 (d, *J* = 15.4 Hz, 1H), 2.41 (s, 3H), 1.08 (s, 9H).

#### [S<sub>S</sub>]-(*E*)-3,3-Dimethyl-1-butenyl cyclohexyl sulfoxide (**6d**):

IR (CH<sub>2</sub>Cl<sub>2</sub>) (cm<sup>-1</sup>): 3029, 2935, 2855, 1622, 1474, 1463, 1451, 1365, 1264, 1055, 971. <sup>1</sup>H NMR (400 MHz) δ: 6.42 (d, *J* = 15.6 Hz, 1H), 6.04 (d, *J* = 15.6 Hz, 1H), 2.54 (m, 1H), 2.04 (m, 1H), 1.88 (m, 3H), 1.67 (m, 1H), 1.31 (m, 5H), 1.11 (s, 9H). <sup>13</sup>C NMR (100.6 MHz) δ: 152.2, 126.1, 60.5, 34.3, 28.9, 26.0, 25.6, 25.5, 25.3, 24.8. MS (EI) *m/z* (%): 214 (M<sup>+</sup>, 8), 198 (19), 183 (32), 132 (100), 117 (78), 115 (27), 101 (48), 83 (88), 81 (19), 74 (20), 67 (26), 59 (41), 53 (17), 55 (85). Anal. calcd. for C<sub>12</sub>H<sub>22</sub>OS: C 67.23, H 10.34; found: C 67.08, H 9.93.

#### [S<sub>S</sub>]-(*E*)-3,3-Dimethyl-1-butenyl methyl sulfoxide (**6e**) (23d):

<sup>1</sup>H NMR (400 MHz) δ: 6.47 (d, *J* = 15.4 Hz, 1H), 6.17 (d, *J* = 15.4 Hz, 1H), 2.61 (s, 3H), 1.11 (s, 9H). MS (EI) *m/z* (%): 146 (M<sup>+</sup>, 20), 131 (28), 130 (32), 117 (12), 115 (100), 83 (47), 81 (21), 71 (20), 58 (21), 57 (62), 53 (29), 51 (22). Anal. calcd. for: C<sub>7</sub>H<sub>14</sub>OS: C 57.49, H 9.65; found: C 57.45, H 9.52.

#### [S<sub>S</sub>]-(*E*)-3,3-Dimethyl-1-butenyl 2-propyl sulfoxide (**6f**):

IR (neat) (cm<sup>-1</sup>): 2961, 2932, 2905, 2868, 1628, 1475, 1463, 1365, 1266, 1062, 1024, 973. <sup>1</sup>H NMR (400 MHz) δ: 6.43 (d, *J* = 15.6 Hz, 1H), 6.01 (d, *J* = 15.6 Hz, 1H), 2.78 (m, *J* = 6.8 Hz, 1H), 1.24 (d, *J* = 6.8 Hz, 3H), 1.22 (d, *J* = 6.8 Hz, 3H), 1.10 (s, 9H). <sup>13</sup>C NMR (100 MHz) δ: 152.3, 125.4, 51.7, 34.3, 28.9, 15.2, 14.6. MS (EI) *m/z* (%): 174 (M<sup>+</sup>, 15), 158 (20), 143 (38), 132 (90), 117 (100), 115 (42), 101 (59), 99 (39), 83 (81), 74 (30), 67 (35), 65 (31), 59 (85), 57 (27). Anal. calcd. for C<sub>9</sub>H<sub>18</sub>OS: C 62.02, H 10.41; found: C 61.82, H 10.25.



*[S<sub>S</sub>]-(-E)-3,3-Dimethyl-1-butenyl benzyl sulfoxide (6h) (30):*

<sup>1</sup>H NMR (400 MHz) δ: 7.25–7.23 (m, 3H), 7.16–7.13 (m, 2H), 6.12 (d, *J* = 15.5 Hz, 1H), 5.89 (d, *J* = 15.4 Hz, 1H), 3.89 (AB<sub>q</sub>, *J* = 12.6 Hz, 2H), 0.90 (s, 9H).

*[R<sub>S</sub>]-(-E)-2-Phenylethenyl 1-butyl sulfoxide (8a):*

IR (CDCl<sub>3</sub>) (cm<sup>-1</sup>): 3084, 3030, 2961, 2933, 2875, 1615, 1494, 1467, 1070, 1039, 965. <sup>1</sup>H NMR (400 MHz) δ: 7.45 (m, 2H), 7.35 (m, 3H), 7.21 (d, *J* = 15.5 Hz, 1H), 6.82 (d, *J* = 15.5 Hz, 1H), 2.78 (m, 2H), 1.75 (m, 2H), 1.48 (m, 2H), 0.94 (t, *J* = 8 Hz, 3H). <sup>13</sup>C NMR (100.6 MHz) δ: 136.8, 133.8, 130.5, 129.6, 128.9, 127.6, 53.9, 24.0, 22.0, 13.7. MS (EI) *m/z* (%): 208 (4, M<sup>+</sup>), 192 (53), 152 (31), 136 (17), 135 (72), 94 (100). Anal. calcd. for C<sub>12</sub>H<sub>16</sub>OS: C 69.19, H 7.74; found: C 68.98, H 7.61.

*[R<sub>S</sub>]-(-E)-2-Phenylethenyl 4-methylphenyl sulfoxide (8b) (23c):*

<sup>1</sup>H NMR (400 MHz) δ: 7.58 (d, *J* = 6.8 Hz, 2H), 7.47–7.44 (m, 2H), 7.39–7.32 (m, 6H), 6.82 (d, *J* = 15.6 Hz, 1H), 2.41 (s, 3H).

*[S<sub>S</sub>]-(-E)-2-Phenylethenyl cyclohexyl sulfoxide (8d):*

Mp: 90 to 91°C. IR (CDCl<sub>3</sub>) (cm<sup>-1</sup>): 3088, 3055, 2936, 2857, 1449, 1263, 1253, 1234, 1167, 1159, 1032, 1015, 967. <sup>1</sup>H NMR (400 MHz) δ: 7.50–7.47 (m, 2H), 7.41–7.33 (m, 3H), 7.22 (d, *J* = 15.4 Hz, 1H), 6.81 (d, *J* = 15.4 Hz, 1H), 2.68 (tt, *J* = 11.8, 3.5 Hz, 1H), 2.09–1.96 (m, 2H), 1.91–1.87 (m, 2H), 1.73–1.70 (m, 1H), 1.55–1.40 (m, 2H), 1.40–1.15 (m, 3H). <sup>13</sup>C NMR (100.6 MHz) δ: 137.7, 134.0, 129.6, 128.9, 128.6, 127.5, 61.1, 26.1, 25.5 (2 C's), 25.3, 24.6. MS (EI) *m/z* (%): 234 (M<sup>+</sup>, 2), 152 (100), 135 (25), 104 (22), 91 (12), 83 (13), 77 (12), 73 (22), 55 (50), 45 (20), 41 (28). Anal. calcd. for C<sub>14</sub>H<sub>18</sub>OS: C 71.75, H 7.74; found: C 71.73, H 7.32.

*[S<sub>S</sub>]-(-E)-2-Phenylethenyl 2-propyl sulfoxide (8f):*

Mp: 50–52°C. <sup>1</sup>H NMR (400 MHz) δ: 7.49–7.47 (m, 2H), 7.41–7.34 (m, 3H), 7.23 (d, *J* = 15.6 Hz, 1H), 6.78 (d, *J* = 15.6 Hz, 1H), 2.92 (septet, *J* = 6.8 Hz, 1H), 1.33 (d, *J* = 6.8 Hz, 3H), 1.30 (d, *J* = 6.8 Hz, 1H). <sup>13</sup>C NMR (100.6 MHz) δ: 137.9, 134.0, 129.6, 128.9, 127.9, 127.5, 52.3, 15.4, 14.5. IR (CDCl<sub>3</sub>) (cm<sup>-1</sup>): 3056, 2973, 2932, 1625, 1449, 1262, 1255, 1167, 1159, 1148, 1121, 1032, 1014, 967. MS (EI) *m/z* (%): 194 (M<sup>+</sup>, 6), 152 (100), 135 (55), 134 (16), 104 (55), 91 (34), 77 (27), 73 (39), 51 (15), 45 (34), 43 (45), 41 (21). Anal. calcd. for C<sub>11</sub>H<sub>14</sub>OS: C 68.00, H 7.26; found: C 67.77, H 6.75.

*[R<sub>S</sub>]-(-E)-2-Phenylethenyl 4-fluoro-3-methylphenyl sulfoxide (8g):*

Mp: 58 to 59°C. IR (CDCl<sub>3</sub>) (cm<sup>-1</sup>): 3063, 3023, 3011, 2925, 1488, 1447, 1239, 1079, 1051, 1034. <sup>1</sup>H NMR (400 MHz) δ: 7.55–7.45 (m, 1H), 7.49–7.45 (m, 3H), 7.40–7.37 (m, 4H), 7.37 (d, *J* = 15.6 Hz, 1H), 7.14 (t, *J* = 8.8 Hz, 1H), 6.80 (d, *J* = 15.6 Hz, 1H), 2.33 (s, 3H). <sup>13</sup>C NMR (100.6 MHz) δ: 162.9 (d, *J* = 250 Hz), 138.8 (broad), 136.2, 133.6, 132.7, 129.8, 128.9, 128.0 (d, *J* = 5.9 Hz), 127.3, 126.9 (d, *J* = 18.4 Hz), 124.3 (d, *J* = 9.0 Hz), 116.1 (d, *J* = 23.6 Hz), 14.6. MS (CI, NH<sub>3</sub>) *m/z* (%): 261 ([M + H]<sup>+</sup>, 100), 212 (23), 91 (6). Anal. calcd. for C<sub>15</sub>H<sub>13</sub>SOF: C 69.21, H 5.03; found: C 69.40, H 5.07.

*[R<sub>S</sub>]-(-E)-2-Phenylethenyl benzyl sulfoxide (8h) (31):*

IR (CDCl<sub>3</sub>) (cm<sup>-1</sup>): 3032, 2359, 1576, 1497, 1455, 1052, 965. <sup>1</sup>H NMR (400 MHz) δ: 7.34 (m, 10H), 7.11 (d, *J* = 15.5 Hz, 1H), 6.76 (d, *J* = 15.5 Hz, 1H), 4.09 (AB<sub>q</sub>, *J* = 12.5 Hz, 2H). <sup>13</sup>C NMR (100.6 MHz) δ: 137.2, 133.8, 130.3, 129.8, 129.7, 129.4, 128.9, 128.8, 128.4, 127.6, 61.2.

*[R<sub>S</sub>]-(-E)-2-Phenylethenyl 1-(2-methyl-2-phenylpropyl) sulfoxide (8j):*

<sup>1</sup>H NMR (400 MHz) δ: 7.31 (m, 10H), 7.10 (d, *J* = 15.4 Hz, 1H), 6.48 (d, *J* = 15.4 Hz, 1H), 3.14 (AB<sub>q</sub>, *J* = 13.4 Hz, 2H), 1.71 (s, 3H), 1.56 (s, 3H). <sup>13</sup>C NMR (100.6 MHz) δ: 146.6, 135.5, 133.8, 131.3, 129.4, 128.8, 128.6, 127.5, 126.7, 125.7, 70.7, 37.8, 30.2, 27.2. IR (CDCl<sub>3</sub>) (cm<sup>-1</sup>): 3085, 3027, 2967, 2933, 2879, 1615, 1602, 1497, 1044, 1031, 965. Anal. calcd. for C<sub>18</sub>H<sub>20</sub>OS: C 76.01, H 7.09; found: C 76.22, H 7.10.

*[R<sub>S</sub>]-(-E)-2-Phenylethenyl 2,2-dimethylethyl sulfoxide (8i) (29):*

<sup>1</sup>H NMR (400 MHz) δ: 7.46 (m, 2H), 7.35 (m, 3H), 7.21 (d, *J* = 15.5 Hz, 1H), 6.78 (d, *J* = 15.5 Hz, 1H), 1.28 (s, 9H).

*[R<sub>S</sub>]-(-Z)-2-Chloro-2-phenylethenyl cyclohexyl sulfoxide (9d):*

IR (neat) (cm<sup>-1</sup>): 3058, 2933, 2855, 1625, 1594, 1489, 1454, 1296, 1066, 1063, 1030, 992. <sup>1</sup>H NMR (400 MHz) δ: 7.49–7.41 (m, 3H), 7.39–7.36 (m, 2H), 6.73 (s, 1H), 2.18 (tt, *J* = 12.0, 3.6 Hz, 1H), 1.90–1.32 (m, 7H), 1.28–1.11 (m, 3H). <sup>13</sup>C NMR (100.6 MHz) δ: 142.4, 130.0, 129.5, 129.0, 128.4, 122.8, 56.7, 27.3, 25.7, 25.2 (2 C's), 21.5. MS (EI) *m/z* (%): 270 (50), 269 (M<sup>+</sup>, 100), 188 (14), 186 (36), 185 (21), 83 (18), 55 (89), 54 (20). Anal. calcd. for C<sub>14</sub>H<sub>17</sub>ClOS: C 62.55, H 6.38; found: C 63.01, H 6.33.

*[S<sub>S</sub>]-(-Z)-2-Chloro-2-phenylethenyl 4-fluoro-3-methylphenyl sulfoxide (9g):*

IR (neat) (cm<sup>-1</sup>): 3060, 2927, 1580, 1488, 1444, 1239, 1184, 1081, 1060. <sup>1</sup>H NMR (400 MHz) δ: 7.35–7.28 (m, 3H), 7.20 (dd, *J* = 6.8, 1.6 Hz, 1H), 7.11 (s, 1H), 7.10–7.01 (m, 3H), 6.94 (t, *J* = 8.8 Hz, 1H). <sup>13</sup>C NMR (100.6 MHz) δ: 162.9 (d, *J* = 250.0 Hz), 147.4, 136.7, 129.4, 129.1, 129.0, 128.5, 128.1 (d, *J* = 6.1 Hz), 126.5 (d, *J* = 18.5 Hz), 124.6 (d, *J* = 9.0 Hz), 122.4, 115.7 (d, *J* = 23.8 Hz), 14.5 (d, *J* = 3.1 Hz). Anal. calcd. for C<sub>15</sub>H<sub>12</sub>ClFOS: C 61.12, H 4.10; found: C 61.32, H 4.24.

*Synthesis of [R<sub>S</sub>]-2-furyl ethenyl sulfoxide (7c):*

*n*-BuLi (360 μL, 0.73 mmol) was added to a solution of furan (50 μL, 0.65 mmol) in dry ether (5 mL) at –20°C under N<sub>2</sub>. After stirring for 20 min, MgBr<sub>2</sub> (180 mg, 0.98 mmol) dissolved in dry ether (5 mL) was added slowly with vigorous stirring over 20 min and then sulfinate [R<sub>S</sub>]-2 (301 mg, 0.65 mmol) in dry ether (5 mL) was added. After 1 h the reaction was quenched with NH<sub>4</sub>Cl. The organic layer was separated, and the aqueous layer was extracted with EtOAc. The combined organic layers were washed with brine, dried over MgSO<sub>4</sub>, and concentrated. Following flash chromatography (20% EtOAc – hexanes to elute cholesterol, 80% to elute sulfoxide) enantioenriched sulfoxide **7c** was isolated as an oil (42 mg, 59%). IR (neat) (cm<sup>-1</sup>): 3117, 3039, 3010, 2952, 1600, 1550, 1456, 1453, 1370, 1220, 1165, 1066, 1051. <sup>1</sup>H NMR (400 MHz) δ: 7.64 (m, 1H), 6.95 (dd, *J* = 3.8, 0.4 Hz, 1H), 6.76 (dd, *J* = 16.4, 9.6 Hz, 1H), 6.53 (dd, *J* = 3.8, 2.0 Hz, 1H), 6.34 (d, *J* = 16.4 Hz,



1H), 6.11 (d,  $J = 9.6$  Hz, 1H).  $^{13}\text{C}$  NMR (100.6 MHz)  $\delta$ : 137.4, 130.5, 130.2, 122.3, 116.4, 111.3. MS (EI)  $m/z$  (%): 142 (9), 126 (25), 115 (48), 99 (20), 97 (15), 94 (100), 83(15). Anal. calcd. for  $\text{C}_6\text{H}_6\text{O}_2\text{S}$ : C 50.69, H 4.25; found: C 50.77, H 4.42.

*Synthesis of  $[S_S]$ -(E)-3,3-dimethyl-1-butenyl 2-furyl sulfoxide (6c):*

As described for **7c**, *n*-BuLi (341  $\mu\text{L}$ , 0.68 mmol), furan (40  $\mu\text{L}$ , 0.57 mmol) in dry ether (5 mL),  $\text{MgBr}_2$  (125.8 mg, 0.68 mmol) in dry ether (5 mL) were all brought together and enantiopure sulfinate  $[R_S]$ -**1** (295 mg, 0.57 mmol, 100%  $[R_S]$ ) in dry ether (5 mL) was added. Work-up as for **7c** and flash chromatography (20% EtOAc – hexanes to elute cholesterol, 80% to elute sulfoxide) afforded enantioenriched sulfoxide **6c** as an oil (114.2 mg, 78%). Data for **6c**: IR (neat) ( $\text{cm}^{-1}$ ): 3114, 2961, 2905, 2868, 1625, 1475, 1366, 1266, 1218, 1128, 1066, 1008, 970.  $^1\text{H}$  (400 MHz)  $\delta$ : 7.63 (m, 1H), 6.88 (d,  $J = 3.6$  Hz, 1H), 6.66 (d,  $J = 15.4$  Hz, 1H), 6.51 (dd,  $J = 3.6, 1.6$  Hz, 1H), 6.35 (d,  $J = 15.4$  Hz, 1H), 1.13 (s, 9H).  $^{13}\text{C}$  NMR (100.6 MHz)  $\delta$ : 152.7, 151.7, 146.8, 125.9, 115.2, 111.3, 34.3, 28.7. MS (EI)  $m/z$  (%): 199 ( $[\text{M} + 1]^+$ , 6), 150 (51), 135 (69), 107 (11), 99 (15), 91 (10), 83 (17), 81 (16), 79 (15), 71 (14), 67 (11), 59 (22), 57 (57), 55 (82), 53 (17), 45 (32), 43 (37), 41 (100). Anal. calcd. for  $\text{C}_{10}\text{H}_{14}\text{O}_2\text{S}$ : C 60.57, H 7.12; found: C 60.69, H 7.06.

*Synthesis of (E)- $[S_S]$ -2-carbomethoxyethenyl 1-butyl sulfoxide (11a):*

The reaction of sulfinate **5** (336 mg, 0.65 mmol, 100%  $[R_S]$ ) with *n*-BuMgCl (388  $\mu\text{L}$ , 0.78 mmol, as a 2 M solution in  $\text{Et}_2\text{O}$ ) in anhydrous ether at  $-78^\circ\text{C}$  generated vinyl ether by-product **20** (117 mg, 38%) as a solid after chromatography (20% EtOAc – hexanes). Enantioenriched sulfoxide **11a** was isolated as a solid (37 mg, 30%, 51%  $[S_S]$ ) after additional chromatography (80% EtOAc – hexanes); mp: 53 to  $54^\circ\text{C}$ .  $[\alpha]_D^{25} +120.6^\circ$  ( $c$  0.73, acetone). IR ( $\text{cm}^{-1}$ ): 3030, 2959, 2932, 1719, 1621, 1292, 1223, 1146, 1041.  $^1\text{H}$  NMR (400 MHz)  $\delta$ : 7.58 (d,  $J = 15.0$  Hz, 1H), 6.66 (d,  $J = 15.0$  Hz, 1H), 3.81 (s, 3H), 2.87 (ddd,  $J = 13.2, 10.0, 5.8$  Hz, 1H), 2.74 (ddd,  $J = 13.2, 10.0, 5.8$  Hz, 1H), 1.81 (m, 1H), 1.69 (m, 1H), 1.48 (m, 2H), 0.96 (t,  $J = 7.2$  Hz, 3H).  $^{13}\text{C}$  NMR (100.6 MHz)  $\delta$ : 164.3, 149.7, 126.0, 52.6, 52.3, 24.0, 21.9, 6.6. MS (CI,  $\text{NH}_3$ )  $m/z$  (%): 191 ( $[\text{M} + 1]^+$ , 100), 175 (5.6), 151 (12), 141 (9), 135 (8), 121 (16), 107 (18), 57 (33). Anal. calcd. for  $\text{C}_7\text{H}_{14}\text{O}_2\text{S}$ : C 50.66, H 7.42; found: C 50.50, H 7.42.

*Synthesis of (E)- $[R_S]$ -2-carbomethoxyethenyl 4-methylphenyl sulfoxide (11b) (23f):*

The reaction of sulfinate **5** (471.5 mg, 0.91 mmol, 100%  $[R_S]$ ) with *p*-tolMgBr (1.09 mL, 1.09 mmol, as a 1 M solution in  $\text{Et}_2\text{O}$ ) in anhydrous ether warming from  $-78$  to  $-40^\circ\text{C}$  generated vinyl ether by-product **20** (76 mg, 18%) as a solid after chromatography (20% EtOAc – hexanes). Enantioenriched sulfoxide **11b** was isolated as a solid (50.5 mg, 25%, 21%  $[R_S]$ ) after additional chromatography (80% EtOAc – hexanes).  $[\alpha]_D^{25} +62.4^\circ$  ( $c$  0.22, acetone) (lit. (23f) value  $+421^\circ$ ) (acetone,  $>98\%$   $[R_S]$ ).  $^1\text{H}$  NMR (400 MHz)  $\delta$ : 7.52 (d,  $J = 8.0$  Hz, 2H), 7.48 (d,  $J = 15.0$  Hz, 1H), 7.33 (d,  $J = 8.0$  Hz, 2H), 6.73 (d,  $J = 15.0$  Hz, 1H), 3.77 (s, 3H), 2.47 (s, 3H).

*Characterization data for (–)-cholesteryl (E)-2-carbomethoxyethenyl ether (20):*

IR ( $\text{CH}_2\text{Cl}_2$ ) ( $\text{cm}^{-1}$ ): 2946, 2906, 2868, 2851, 1715, 1643, 1133, 959.  $^1\text{H}$  NMR (400 MHz)  $\delta$ : 7.55 (d,  $J = 12.4$  Hz, 1H), 5.40–5.39 (m, 1H), 5.26 (d,  $J = 12.4$  Hz, 1H), 3.84–3.76 (m, 1H), 3.69 (s, 3H), 2.38–2.35 (m, 2H), 1.01 (s, 3H), 0.91 (d,  $J = 6.5$ , 3H), 0.86 (d,  $J = 6.6$  Hz, 3H), 0.68 (s, 3H), 2.09–0.80 (remaining peaks for cholesteryl skeleton, 26H).  $^{13}\text{C}$  NMR (100.6 MHz)  $\delta$ : 168.6, 161.7, 139.3, 123.1, 97.0, 82.3, 56.7, 56.1, 51.0, 50.0, 42.3, 39.7, 39.5, 38.5, 36.8, 36.6, 36.2, 35.8, 31.9, 31.8, 28.2, 28.1, 28.0, 24.3, 23.8, 22.8, 22.6, 21.0, 19.3, 18.7, 11.8. MS (CI,  $\text{NH}_3$ )  $m/z$  (%): 471 ( $[\text{M} + \text{H}]^+$ , 37), 370 (29), 369 (100), 61 (13). Anal. calcd. for  $\text{C}_{31}\text{H}_{50}\text{O}_3$ : C 79.10, H 10.71; found: C 79.21, H 10.60.

## Acknowledgements

The authors thank the Petroleum Research Fund, administered by the American Chemical Society and the Natural Sciences and Engineering Research Council of Canada (NSERC) for generously funding this research. RRS also thanks NSERC and the Ontario government for graduate scholarships.

## References

1. M.C. Carreño. *Chem. Rev.* **95**, 1717 (1995).
2. A.J. Walker. *Tetrahedron: Asymmetry*, **3**, 961 (1992).
3. (a) N. Khair, I. Fernandez, A. Alcudia, and F. Alcudia. In *Advances in sulfur chemistry*. Vol. 2. Edited by C.M. Rayner. JAI Press, Stamford. 2000. pp. 57–115; (b) S.M. Allin and P.C. Bulman Page. In *Advances in sulfur chemistry*. Vol. 2. Edited by C.M. Rayner. JAI Press, Stamford. 2000. pp. 117–153.
4. N. Khair, C.S. Araújo, F. Alcudia, and I. Fernández. *J. Org. Chem.* **67**, 345 (2002).
5. (a) Y. Arroyo-Gómez, J.A. López-Sastre, J.F. Rodríguez-Amo, M. Santos-García, and M.A. Sanz-Tejedor. *J. Chem. Soc., Perkin Trans. 1*, 2177 (1994); (b) N. Khair, I. Fernandez, and F. Alcudia. *Tetrahedron Lett.* **35**, 5719 (1994); (c) V. Guerrero de la Rosa, M. Ordoñez, J.M. Llera, and F. Alcudia. *Synthesis*, 761 (1995); (d) C. Alayrac, S. Nowaczyk, M. Lemarié, and P. Metzner. *Synthesis*, 669 (1999); (e) N. Khair, F. Alcudia, J.-L. Espartero, L. Rodríguez, and I. Fernandez. *J. Am. Chem. Soc.* **122**, 7598 (2000); (f) S. Nakamura, M. Kuroyanagi, Y. Watanabe, and T. Toru. *J. Chem. Soc., Perkin Trans. 1*, 3143 (2000); (g) S. Nakamura, M. Oda, H. Yasuda, and T. Toru. *Tetrahedron*, **57**, 8469 (2001).
6. (a) K.H. Bell and L.F. McCaffery. *Aust. J. Chem.* **47**, 1925, (1994); (b) A.B. Bueno, M.C. Carreño, J.L. García Ruano, and J. Fischer. *Tetrahedron Lett.* **36**, 3737 (1995); (c) G. Solladié, C. Bauder, and L. Rossi. *J. Org. Chem.* **60**, 7774 (1995); (d) L.D. Girodier, C.S. Maignan, and F.P. Rouessac. *Tetrahedron: Asymmetry*, **6**, 2045 (1995); (e) G. Solladié and N. Huser. *Tetrahedron: Asymmetry*, **6**, 2679 (1995); (f) G. Solladié, L. Gressot, and F. Colobert. *Eur. J. Org. Chem.* 357 (2000); (g) W.E. Noland and B.L. Kedrowski. *Org. Lett.* **2**, 2109 (2000); (h) N. Maezaki, M. Izumi, S. Yuyama, H. Sawamoto, C. Iwata, and T. Tanaka, *Tetrahedron*, **56**, 7927 (2000); (i) C. Rolland, G. Hanquet, J.B. Ducep, and G. Solladié. *Tetrahedron Lett.* **42**, 9077 (2001); (j) S. Nakamura, H. Yasuda, Y. Watanabe, and T. Toru. *J. Org. Chem.* **65**, 8640 (2000); (k) S.G. Davies, T. Loveridge, M.F.C.C. Teixeira, and



- J.M. Clough. *J. Chem. Soc., Perkin Trans. 1*, 3405 (1999); (l) H. Yoshizaki, T. Tanaka, E. Yoshii, T. Koizumi, and K. Takeda. *Tetrahedron Lett.* **39**, 47 (1998).
7. R.R. Strickler and A.L. Schwan. *Tetrahedron: Asymmetry*, **10**, 4065 (1999).
8. (a) K.K. Andersen. *Tetrahedron Lett.* 93 (1962); (b) K.K. Andersen, W. Gaffield, N.E. Papanikolaou, J.W. Foley, and R.I. Perkins. *J. Am. Chem. Soc.* **86**, 5637 (1964); (c) M. Mikolajczyk, J. Drabowicz, and P. Kielbasinski. *Chiral sulfur reagents*. CRC Press, Boca Raton. 1997. pp. 7–28; (d) S. Allin. *In Organosulfur chemistry. Synthetic and stereochemical aspects. Vol. 2. Edited by P. Page*. Academic Press, San Diego. 1998. pp. 41–48.
9. (a) J.M. Llera, I. Fernández, and F. Alcudia. *Tetrahedron Lett.* **32**, 7299 (1991); (b) I. Fernández, N. Khair, A. Roca, A. Benabra, A. Alcudia, J.L. Espartero, and F. Alcudia. *Tetrahedron Lett.* **40**, 2029 (1999).
10. (a) J.K. Whitesell and M.S. Wong. *J. Org. Chem.* **56**, 4552 (1991); (b) J.K. Whitesell and M.S. Wong. *J. Org. Chem.* **59**, 597 (1994).
11. K.K. Andersen, B. Bujnicki, J. Drabowicz, M. Mikolajczyk, and J.B. O'Brien. *J. Org. Chem.* **49**, 4070 (1984).
12. A.L. Schwan, R.R. Strickler, Y. Lear, M.L. Kalin, T.E. Rietveld, T.-J. Xiang, and D. Brillon. *J. Org. Chem.* **63**, 7825 (1998).
13. A.L. Schwan, R.R. Strickler, R. Dunn-Dufault, and D. Brillon. *Eur. J. Org. Chem.* 1643 (2001).
14. R.R. Strickler and A.L. Schwan. *Tetrahedron: Asymmetry*, **11**, 4843 (2000).
15. (a) E. Lacôte, B. Delouvrié, L. Fensterbank, and M. Malacria. *Angew. Chem. Int. Ed.* **37**, 2116 (1998); (b) J.C. de la Rosa, N. Díaz, and J.C. Carretero. *Tetrahedron Lett.* **41**, 4107 (2000); (c) A.D. Westwell and C.M. Rayner. *In Organosulfur chemistry. Synthetic and stereochemical aspects. Vol. 2. Edited by P. Page*. Academic Press, San Diego. 1998. Chap. 5; (d) M. Mikolajczyk, J. Drabowicz, and P. Kielbasinski. *Chiral sulfur reagents*. CRC Press, Boca Raton. 1997. pp. 144–191.
16. R.R. Strickler. Ph.D Thesis, University of Guelph, Guelph, Ontario, 2000.
17. J. Drabowicz, B. Bujnicki, and M. Mikolajczyk. *J. Org. Chem.* **47**, 3325 (1982).
18. K. Mislow, M.M. Green, P. Laur, T.T. Mellilo, T. Simmons, and A.L. Ternay, Jr. *J. Am. Chem. Soc.* **87**, 1958 (1965).
19. (a) W.H. Pirkle and D.J. Hoover. *Top. Stereochem.* **13**, 263 (1982); (b) M. Mikolajczyk and J. Drabowicz. *Top. Stereochem.* **13**, 333 (1982).
20. M. Mikolajczyk, W. Midura, S. Grzejszczak, A. Zatorski, and J. Chęćzyska. *J. Org. Chem.* **43**, 473 (1978).
21. Y. Arroyo, M.C. Carreño, J.L. García Ruano, J.F. Rodríguez Amo, M. Santos, and M. Ascensión Sanz Tejedor. *Tetrahedron: Asymmetry*, **11**, 1183 (2000).
22. Y. Arai, T. Masuda, S. Yoneda, Y. Masaki, and M. Shiro. *J. Org. Chem.* **65**, 258 (2000).
23. (a) M. Mikolajczyk, W. Perlikowska, J. Omelanczuk, H.-J. Cristau, and A. Perraud-Darcy. *Synlett*, 913 (1991); (b) M. Mikolajczyk, W. Perlikowska, J. Omelanczuk, H.-J. Cristau, and A. Perraud-Darcy. *J. Org. Chem.* **63**, 9716 (1998); (c) J.H. van Steenis, J.J.G.S. van Es, and A. van der Gen. *Eur. J. Org. Chem.* 2787 (2000); (d) F. Chaigne, J.P. Gotteland, and M. Malacria. *Tetrahedron Lett.* **30**, 1803 (1989); (e) C. Cardellicchio, A. Iacuone, and F. Naso. *Tetrahedron Lett.* **36**, 6563 (1995); (f) K. Kokin, S. Tsuboi, J. Motoyoshiya, and S. Hayashi. *Synthesis*, 637 (1996).
24. (a) R. Tanikaga, N. Konya, T. Tamura, and A. Kaji. *J. Chem. Soc., Perkin Trans. 1*, 825 (1987); (b) R. Tanikaga, N. Konya, and A. Kaji. *Chem. Lett.* 1583 (1985).
25. E. Block, V. Eswarakrishnan, M. Gernon, G. Ofori-Okai, C. Saha, K. Tang, and J. Zubieta. *J. Am. Chem. Soc.* **111**, 658 (1989).
26. K.H. Geiss, D. Seebach, and B. Seuring. *Chem. Ber.* **110**, 1833 (1977).
27. F. Yuste, B. Ortiz, J.I. Pérez, A. Rodríguez-Hernández, R. Sánchez-Obregón, F. Walls, and J.L. García Ruano. *Tetrahedron*, **58**, 2613 (2002).
28. D.A. Cogan, G. Liu, K. Kim, B.J. Backes, and J.A. Ellman. *J. Am. Chem. Soc.* **120**, 8011 (1998).
29. J. Fawcett, S. House, P.R. Jenkins, N.J. Lawrence, and D.R. Russell. *J. Chem. Soc., Perkin Trans. 1*, 67 (1993).
30. A.L. Schwan and Y. Lear. *Sulfur Lett.* **23**, 111 (2000).
31. T. Kageyama, Y. Ueno, and M. Okawara. *Synthesis*, 815 (1983).



# Alkoxy radicals in the gaseous phase: $\beta$ -scission reactions and formation by radical addition to carbonyl compounds

Arvi Rauk, Russell J. Boyd, Susan L. Boyd, David J. Henry, and Leo Radom

**Abstract:** The structures and reactivities of the alkoxy radicals methoxy ( $\text{CH}_3\text{O}\cdot$ ), ethoxy ( $\text{CH}_3\text{CH}_2\text{O}\cdot$ ), 1-propoxy ( $\text{CH}_3\text{CH}_2\text{CH}_2\text{O}\cdot$ ), 2-propoxy ( $(\text{CH}_3)_2\text{CHO}\cdot$ ), 2-butoxy ( $\text{CH}_3\text{CH}_2\text{CH}(\text{CH}_3)\text{O}\cdot$ ), *tert*-butoxy ( $(\text{CH}_3)_3\text{CO}\cdot$ ), prop-2-enoxy ( $\text{CH}_2=\text{CHCH}_2\text{O}\cdot$ ), and but-3-en-2-oxy ( $\text{CH}_2=\text{CHCH}(\text{CH}_3)\text{O}\cdot$ ) have been investigated at the B3-LYP/6-31G(d) and CBS-RAD levels of theory. Enthalpies of formation ( $\Delta_f H_{298}^\circ$ ) were calculated with CBS-RAD for all the alkoxy radicals, the carbonyl and radical products of  $\beta$ -scission reactions, and the transition structures leading to them. The mean absolute deviation between the predicted and available experimental  $\Delta_f H_{298}^\circ$  values is  $5.4 \text{ kJ mol}^{-1}$ . Eyring ( $\Delta H_0^\ddagger$ ,  $\Delta H_{298}^\ddagger$ ,  $\Delta G_{298}^\ddagger$ ) and Arrhenius ( $\log A$ ,  $E_a$ ) activation parameters for both the forward ( $\beta$ -scission) and reverse (radical addition to carbonyl) pathways were calculated. Agreement with available experimental data is very good, generally within  $1\text{--}5 \text{ kJ mol}^{-1}$  for  $E_a$ , and  $0.5$  for  $\log A$ . The transition structures are found to be substantially polarized, with the departing radical slightly positive, the O atom negative, and the rest of the molecule positive. The barriers for the  $\beta$ -scission reactions decrease with decreasing endothermicity and with decreasing ionization energy of the departing radical.

**Key words:** alkoxy, alkoxy radical, radical, addition, carbonyl,  $\beta$ -scission, calculation, electronic structure, B3LYP, CBS-RAD, thermochemistry.

**Résumé :** Faisant appel à des calculs théoriques aux niveaux B3-LYP/6-31G(d) et CBS-RAD de la théorie, on a étudié les structures et les réactivités des radicaux alkoxy, méthoxy ( $\text{CH}_3\text{O}\cdot$ ), éthoxy ( $\text{CH}_3\text{CH}_2\text{O}\cdot$ ), 1-propoxy ( $\text{CH}_3\text{CH}_2\text{CH}_2\text{O}\cdot$ ), 2-propoxy [ $(\text{CH}_3)_2\text{CHO}\cdot$ ], 2-butoxy [ $\text{CH}_3\text{CH}_2\text{CH}(\text{CH}_3)\text{O}\cdot$ ], *tert*-butoxy [ $(\text{CH}_3)_3\text{CO}\cdot$ ], prop-2-énoxy ( $\text{CH}_2=\text{CHCH}_2\text{O}\cdot$ ) et but-3-én-2-oxy [ $\text{CH}_2=\text{CHCH}(\text{CH}_3)\text{O}\cdot$ ]. On a calculé les enthalpies de formation,  $\Delta_f H_{298}^\circ$ , au niveau CBS-RAD de la théorie pour tous les radicaux alkoxy, tous les produits carbonylés et tous les produits radicalaires provenant de réactions de  $\beta$ -scission et toutes les structures de transition qui y conduisent. La déviation absolue moyenne entre les valeurs prédites et les valeurs de  $\Delta_f H_{298}^\circ$  expérimentales disponibles est de  $5,4 \text{ kJ mol}^{-1}$ . On a aussi calculé les paramètres d'activation d'Eyring ( $\Delta H_0^\ddagger$ ,  $\Delta H_{298}^\ddagger$ ,  $\Delta G_{298}^\ddagger$ ) et d'Arrhenius ( $\log A$ ,  $E_a$ ) pour la réaction vers la droite ( $\beta$ -scission) et pour la réaction inverse (addition d'un radical sur le carbonyle). L'accord entre les valeurs calculées et les valeurs expérimentales disponibles est bon, généralement entre  $1$  et  $5 \text{ kJ mol}^{-1}$  pour les valeurs de  $E_a$  et de  $0,5$  pour le  $\log A$ . On a trouvé que les structures de transition sont assez polarisées alors que le radical qui se détache est légèrement positif, l'atome d'oxygène est négatif et que le reste de la molécule est positif. Les barrières aux réactions de  $\beta$ -scission diminuent avec une augmentation du caractère endothermique et avec une diminution de l'énergie d'ionisation du radical qui se détache.

**Mots clés :** alkoxy, alkoxy radical, radical, addition, carbonyle, scission- $\beta$ , calculs théoriques, structure électronique, B3LYP, CBS-RAD, thermochimie.

[Traduit par la Rédaction]

Received 24 October 2002. Published on the NRC Research Press Web site at <http://canjchem.nrc.ca> on 9 April 2003.

*Dedicated to Professor Don Arnold for his contributions to chemistry.*

**A. Rauk.**<sup>1</sup> Department of Chemistry, University of Calgary, Calgary, AB T2N 1N4, Canada.

**R.J. Boyd.** Department of Chemistry, Dalhousie University, Halifax, NS B3H 4J3, Canada.

**S.L. Boyd.** Department of Chemistry, Mount St. Vincent University, Halifax, NS B3M 2J6, Canada.

**D.J. Henry and L. Radom.** Research School of Chemistry, Australian National University, Canberra, ACT 0200, Australia.

<sup>1</sup>Corresponding author (e-mail: [rau@ucalgary.ca](mailto:rau@ucalgary.ca)).

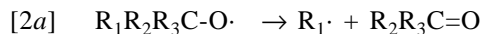


## Introduction

Alkoxy radicals ( $R_1R_2R_3C-O\cdot$ ) are important intermediate species in the combustion of hydrocarbons (1, 2), and in atmospheric chemistry (3–5). They can react by intramolecular hydrogen abstraction, or by intermolecular hydrogen abstraction from a suitable donor ( $R'-H$ ) to yield the corresponding alcohol:

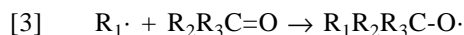


Alternatively, alkoxy radicals can undergo  $\beta$ -cleavage to yield an alkyl radical plus a ketone or aldehyde in up to three ways:



In proteins, production of such radicals by oxidative processes may lead to protein backbone cleavage (6). In general, the pathway that leads to the most stable radical is found to dominate the endothermic cleavage (7, 8) but exceptions have been noted in polycyclic systems (9) and have been investigated computationally (10).

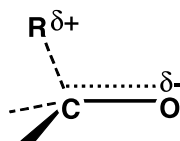
The reverse reaction, alkyl radical addition to the carbonyl double bond:



is hindered by an activation energy ( $E_{a(3)}$ ) which has empirically been found to depend on the ionization energy of the radical ( $IE(R_1\cdot)$ ) and the exothermicity of the reaction ( $\Delta H_{(3)}$ ) (11):

$$[4] \quad E_{a(3)} = 8.8[IE(R_1\cdot)] - 0.58|\Delta H_{(3)}| - 26$$

where the ionization energy is in units of eV and the enthalpy of the reaction is in  $\text{kJ mol}^{-1}$ . The relationship with the ionization energy was attributed (11) to a tight transition structure with substantial polarization in the sense:



Additional evidence for charge separation in the TS may be deduced from the observation of a large solvent effect for the  $\beta$ -scission of *tert*-butoxy radical (12). In a similar manner, barriers for the addition of alkyl and related radicals to alkenes have also been found to be dependent on the reaction enthalpy and the ionization energy of the radical but a multiplicative-type relationship is found to better describe this dependence (13).

We investigate here the factors affecting both the decomposition and radical-addition pathways for a systematic series of saturated and unsaturated alkoxy radicals, by using high-level quantum mechanical methods. A number of alkoxy radicals, including some of the systems of interest here, have been previously studied both experimentally, by means of laser flash photolysis – laser-induced fluorescence,

and computationally, by means of ab initio calculations, by Viskolcz and co-workers (14–18), and others (19, 20). Their work is discussed in the present context below.

## Theoretical methods

### Quantum mechanical calculations

Conventional ab initio (21) and density functional theory (22) calculations were carried out with the Gaussian 94 (23a), Gaussian 98 (23b), and Molpro 2000 (24) suites of electronic structure codes. Geometries and harmonic vibrational frequencies were obtained for all species at the B3-LYP/6-31G(d) level of theory. The vibrational frequencies were used, after appropriate scaling (25), in the calculation of thermodynamic and kinetic parameters including zero-point vibrational energies (ZPVEs), and to characterize each stationary point as a local minimum (no imaginary frequencies), or as a transition structure (one imaginary frequency). Higher-level energies were determined for all structures by the CBS-RAD procedure, which has been developed to provide accurate thermochemistry for radical species (26). The CBS-RAD(B3-LYP) combination employed here has been found to yield good reaction enthalpies and barriers for the addition of C-centered radicals to alkenes (13, 27).

### Thermochemical procedures

Gas-phase thermodynamic functions, including thermal enthalpy contributions ( $H^\circ - H_0^\circ$ ) (where  $H^\circ$  refers to 298.15 K) and entropies ( $S$ ) may be accurately calculated by application of standard statistical procedures (28). Values derived experimentally are available in standard sources (29–32).

Theoretical enthalpies of formation at 298.15 K for species  $C_aH_bO$  may be calculated from the energies of the atomization reactions:



by eqs. [6]–[8]:

$$[6] \quad \Delta_f H_{298}^\circ(C_aH_bO) = \Delta H_{(5)} + a\Delta_f H_{298}^\circ(C) + b\Delta_f H_{298}^\circ(H) + \Delta_f H_{298}^\circ(O)$$

where

$$[7] \quad \Delta H_{(5)}(298.15 \text{ K}) = \Delta H_{(5)}(0 \text{ K}) + (H^\circ - H_0^\circ)(C_aH_bO) - a(H^\circ - H_0^\circ)(C) - b(H^\circ - H_0^\circ)(H) - (H^\circ - H_0^\circ)(O)$$

and

$$[8] \quad \Delta H_{(5)}(0 \text{ K}) = E^{\text{CBS}}(C_aH_bO) - aE^{\text{CBS}}(C) - bE^{\text{CBS}}(H) - E^{\text{CBS}}(O)$$

In this procedure, the enthalpies of formation ( $\Delta_f H_{298}^\circ$ ) and the ( $H^\circ - H_0^\circ$ ) values for the gaseous atoms in their lowest electronic states are taken from experiment (29) ( $\text{kJ mol}^{-1}$ ): C (716.7, 6.535), H (218.0, 6.197), O (249.2, 6.724). The CBS-RAD energies ( $E^{\text{CBS}}(C_aH_bO)$ ) for all species discussed here are listed in Table 1. For the gaseous atoms in their



**Table 1.** CBS-RAD energies (0 K, hartrees), thermodynamic functions ( $H_{298}^{\circ} - H_0^{\circ}$  (kJ mol<sup>-1</sup>),  $S$  (J K<sup>-1</sup> mol<sup>-1</sup>), 298.15 K), and enthalpies of formation ( $\Delta_f H^{\circ}$  (kJ mol<sup>-1</sup>), 298.15 and 0 K).

Species	CBS-RAD <sup>a</sup>	$n^b$	$H_{298}^{\circ} - H_0^{\circ}$	$S_{(g)}$		$\Delta_f H_{298}^{\circ c}$		$\Delta_f H_0^{\circ}$
				Exptl.	Calcd.	Exptl.	Calcd.	Calcd.
H·	-0.49982	1	6.2	114.7 <sup>d</sup>	114.6	218.0		
CH <sub>3</sub> ·	-39.74402	1	10.6	194.2 <sup>d</sup>	195.4	146.4	150.0	153.1
CH <sub>3</sub> CH <sub>2</sub> ·	-78.96993	1	12.9	252.0 <sup>d</sup>	255.7	120.9	127.8	138.2
CH <sub>2</sub> =CH·	-77.74177	1	10.6		233.6	300.0	301.9	306.1
CH <sub>3</sub> O·	-114.87243	1	10.4		234.0 <sup>e,f</sup>	17.2, 21 <sup>g</sup>	21.0	28.7
CH <sub>3</sub> OH	-115.53807	1	11.1	239.7 <sup>d</sup>	237.7	-201.0	-201.8	-190.6
CH <sub>2</sub> =O	-114.34253	1	10.0	218.8 <sup>d</sup>	218.6	-108.6	-112.2	-108.3
H···CH <sub>2</sub> O·TS	-114.83531	1	11.5		243.9		119.6	126.2
CH <sub>3</sub> CH <sub>2</sub> O·	-154.10201	1	13.5		278.9 <sup>e</sup>	-15.5, -12 <sup>g</sup>	-9.9	4.2
CH <sub>3</sub> CH=O	-153.58023	1	12.7	264.2 <sup>h</sup>	262.3	-166.2	-164.8	-154.2
H···CH(CH <sub>3</sub> )O·TS	-154.06979	2	14.0		282.0		75.2	88.8
CH <sub>3</sub> ···CH <sub>2</sub> O·TS	-154.07668	1	14.9		285.9		58.0	70.7
CH <sub>3</sub> CH <sub>2</sub> CH <sub>2</sub> O·	-193.32697	3	16.1		316.3 <sup>e</sup>	-41.4	-29.3	-8.2
CH <sub>3</sub> CH <sub>2</sub> CH=O	-192.80566	3	15.6	304.7 <sup>h</sup>	301.5	-185.6	-185.2	-167.8
H···CH(CH <sub>2</sub> CH <sub>3</sub> )O·TS	-193.29559	3	17.1		316.4		54.1	74.2
CH <sub>3</sub> CH <sub>2</sub> ···CH <sub>2</sub> O·TS	-193.30643	3	17.8		326.6		26.4	45.8
(CH <sub>3</sub> ) <sub>2</sub> CHO·	-193.33181	1	16.1		305.4 <sup>e</sup>	-52.3, -46 <sup>g</sup>	-41.9	-20.9
(CH <sub>3</sub> ) <sub>2</sub> C=O	-192.81740	1	15.7 <sup>i</sup>	294.9 <sup>h</sup>	299.5	-217.1	-215.9	-198.6
H···C(CH <sub>3</sub> ) <sub>2</sub> O·TS	-193.30390	1	17.0		304.9		32.2	52.4
CH <sub>3</sub> ···CH(CH <sub>3</sub> )O·TS	-193.31051	2	17.8		319.7		15.7	35.0
CH <sub>3</sub> CH <sub>2</sub> CH(CH <sub>3</sub> )O·	-232.55793	6	19.6		351.4 <sup>e</sup>	-69.5	-63.4	-36.4
CH <sub>3</sub> CH <sub>2</sub> C(CH <sub>3</sub> )=O	-232.04323	1	19.8	338.1 <sup>h</sup>	337.1	-238.5	-235.9	-213.3
H···C(CH <sub>3</sub> )(CH <sub>2</sub> CH <sub>3</sub> )O·TS	-232.53034	6	20.3		350.5		9.7	36.1
CH <sub>3</sub> ···CH(CH <sub>2</sub> CH <sub>3</sub> )O·TS	-232.53579	2	21.2		351.8		-3.6	21.8
CH <sub>3</sub> CH <sub>2</sub> ···CH(CH <sub>3</sub> )O·TS	-232.54080	6	21.1		360.7		-16.9	8.6
(CH <sub>3</sub> ) <sub>3</sub> CO·	-232.56511	1	19.6		322.6 <sup>e,f</sup>	-90.8, -83 <sup>g</sup>	-82.2	-55.2
CH <sub>3</sub> ···C(CH <sub>3</sub> ) <sub>2</sub> O·TS	-232.54493	1	21.1		338.3		-27.8	-2.2
CH <sub>2</sub> =CHCH <sub>2</sub> O·	-192.11518	2	14.7		303.8 <sup>e</sup>		102.8	116.7
CH <sub>2</sub> =CHCH=O <sup>j</sup>	-191.59751	1	13.9		278.0	-77.0 <sup>k</sup>	-62.9	-52.4
H···CH(CH=CH <sub>2</sub> )O·TS	-192.08709	2	15.6		300.2		177.5	190.5
CH <sub>2</sub> =CH···CH <sub>2</sub> O·TS	-192.08108 <sup>l</sup>	3	17.6		328.7		195.2	206.3
CH <sub>2</sub> =CHCH(CH <sub>3</sub> )O·	-231.34649	6	18.2		342.8 <sup>e</sup>		67.6	87.7
CH <sub>2</sub> =CHC(CH <sub>3</sub> )=O	-230.83280	1	17.7		313.4	-138.0 <sup>k</sup>	-108.2	-92.0
H···C(CH <sub>3</sub> )(CH=CH <sub>2</sub> )O·TS	-231.32022	6	18.9		338.3		137.3	156.6
CH <sub>3</sub> ···CH(CH=CH <sub>2</sub> )O·TS	-231.32863 <sup>l</sup>	6	19.5		346.6		115.9	134.6
CH <sub>2</sub> =CH···CH(CH <sub>3</sub> )O·TS	-231.31577 <sup>l</sup>	6	20.6		362.1		150.7	168.3

<sup>a</sup>Energies for transition structures correspond to CBS-RAD-Scanmax values (see Table 2 and text) unless otherwise noted.<sup>b</sup>Number of significantly populated conformations (used to calculate entropies of mixing).<sup>c</sup>From ref. 32 unless otherwise noted.<sup>d</sup>Reference 29.<sup>e</sup>First excited state assumed to be significantly populated (adds  $R \ln 2$ ).<sup>f</sup>Rotational symmetry number = 3 assumed.<sup>g</sup> $\Delta_f H_{300}^{\circ}$  values from ref. 36.<sup>h</sup>Reference 34.<sup>i</sup>One methyl group rotation treated as a free rotation (contributes  $RT/2$ ).<sup>j</sup>Energies refer to *s-trans* conformation.<sup>k</sup>Reference 30.<sup>l</sup>Standard CBS-RAD value.

lowest electronic states, the CBS-RAD energies are  $E^{\text{CBS}}$  (hartrees): C (-37.785143), H (-0.499818), O (-74.987034).

Calculated enthalpies of formation are compared with available experimental values in Table 1. We have included

for convenience in Table 1 the enthalpies of formation for the transition structures, even though the  $\Delta_f H$  would be a somewhat artificial quantity for such species. In cases where a substance exists as an equilibrium mixture of two or more



conformers, the enthalpy of formation listed in Table 1 corresponds to that of the most stable conformer.

The entropy of a pure substance in the gas phase may be expressed as a weighted sum of the entropies of individual conformers, plus an entropy of mixing term (eq. [9]):

$$[9] \quad S^{\text{total}} = \sum_i x_i S_i - R \sum_i x_i \ln x_i \cong S_1 + R \ln n$$

where  $x_i$  is the mol fraction of conformer  $i$ ,  $S_1$  is the entropy of the most stable conformation, and  $n$  denotes the number of significantly populated conformations (33).

The alkoxy radicals investigated in this study exhibit Jahn–Teller distortions. We have accounted for the near degeneracy of the  $A'$  and  $A''$  states ( $C_s$  symmetry) by the addition of  $R \ln 2$  to the electronic entropy. In addition, for the methoxy and *tert*-butoxy radicals we have adopted a rotational symmetry number of 3. Calculated entropies are included in Table 1, together with experimental values where available.

### Rates of reaction

In the thermodynamic formulation of transition-state theory (TST) (34), the rate constant ( $k_T$ ) for a reaction at temperature  $T$  is related to the free energy barrier ( $\Delta G^\ddagger$ ) by eq. [10] (35):

$$[10] \quad k_T = (k_B T/h)(c^\circ)^{1-m} \exp(-\Delta G^\ddagger/RT)$$

where  $k_B$  and  $h$  are Boltzmann's and Planck's constants, respectively,  $R$  is the ideal gas constant,  $c^\circ$  is the standard unit of concentration ( $\text{mol L}^{-1}$ ), and  $m$  is the order of the reaction. The factor  $((c^\circ)^{1-m})$  provides the correct units for the rate constant of unimolecular ( $m = 1$ ) and bimolecular ( $m = 2$ ) reactions. In the gas-phase standard state ( $T = 298.15 \text{ K}$ ) the pressure is 1 atm and  $c^\circ = 0.0408 \text{ mol L}^{-1}$ . We apply eq. [10] for the calculation of both the (forward) unimolecular  $\beta$ -scission reaction (eq. [2]) and the (reverse) bimolecular radical-addition reaction (eq. [3]).

In Arrhenius rate theory, the rate constant is given by:

$$[11] \quad k_T = A \exp(-E_a/RT)$$

The Arrhenius activation energy ( $E_a$ ) is given by:

$$[12] \quad E_a = \Delta H^\ddagger + mRT$$

The Arrhenius frequency factor ( $A$ ) contains the entropy of activation ( $\Delta S^\ddagger$ ):

$$[13] \quad A = (k_B T/h)(c^\circ)^{1-m} e^m \exp(\Delta S^\ddagger/R)$$

Enthalpy barriers ( $\Delta H^\ddagger$  (generally referred to in the course of this paper simply as barriers)) are calculated directly from enthalpies of formation of the appropriate species (or equivalently from the calculated total energies and, if appropriate, the enthalpy temperature corrections). In the present study, we have not considered quantum mechanical tunneling. This could in principle be important in the reactions involving hydrogen-atom scission and (or) addition but preliminary calculations suggest that the effect is not particularly significant.

### Results and discussion

The energies of all species considered here are given in Table 1. The variation with the theoretical level of selected

properties of the transition structures are presented in Table 2. Table 3 gives the kinetic parameters ( $\Delta H^\ddagger$ ,  $\Delta G^\ddagger$ ,  $\log A$ , and  $E_a$ ) and the reaction enthalpies ( $\Delta H$ ) for  $\beta$ -scission reactions (eq. [2]), while corresponding data for the reverse reaction, radical addition to carbonyl (eq. [3]), are collected in Table 4.

### Enthalpies of formation

Enthalpies of formation, calculated from atomization energies as described above, are listed in Table 1. Comparison with experimental values may be made for 17 species. The largest discrepancy occurs for but-3-en-2-one ( $\text{CH}_2=\text{CHC}(\text{CH}_3)=\text{O}$ ) for which the calculated value ( $\Delta_f H_{298}^\circ = -108.2 \text{ kJ mol}^{-1}$ ) is  $29.8 \text{ kJ mol}^{-1}$  less negative than the experimental ( $\Delta_f H_{298}^\circ = -138.0 \text{ kJ mol}^{-1}$ ). For the remaining 16 species, the mean absolute deviation is  $3.8 \text{ kJ mol}^{-1}$ , consistent with the accuracy expected from CBS-RAD (26). The second-largest discrepancy ( $+14.1 \text{ kJ mol}^{-1}$ ) also occurs for an  $\alpha,\beta$ -unsaturated carbonyl compound, acrolein ( $(E)\text{-CH}_2=\text{CHCH}=\text{O}$ ). The calculated values for the heat of formation of the methoxy, ethoxy, 2-propoxy, and *tert*-butoxy radicals are in close agreement with the recent experimental results of Ramond et al. (36), and support these values over the older results (32) (which are generally less positive or more negative). Larger-than-average differences between theory and experiment occur for two alkoxy radicals 1-propoxy ( $\text{CH}_3\text{CH}_2\text{CH}_2\text{O}\cdot$ ,  $+12.1 \text{ kJ mol}^{-1}$ ) and 2-butoxy ( $\text{CH}_3\text{CH}_2\text{CH}(\text{CH}_3)\text{O}\cdot$ ,  $+6.1 \text{ kJ mol}^{-1}$ ), and for the ethyl radical ( $\text{CH}_3\text{CH}_2\cdot$ ,  $+6.9 \text{ kJ mol}^{-1}$ ). Experimental reexamination may be warranted in these instances. We are not aware of any experimental enthalpies of formation for the prop-2-en-1-oxy ( $\text{CH}_2=\text{CHCH}_2\text{O}\cdot$ ) or but-3-en-2-oxy ( $\text{CH}_2=\text{CHCH}(\text{CH}_3)\text{O}\cdot$ ) radicals.

### Sensitivity of calculated barriers to TS geometry and theoretical level

The barriers for the  $\beta$ -scission (forward, eq. [2]) and radical addition (reverse, eq. [3]) reactions are crucial for determining the kinetic fate of alkoxy radicals in atmospheric chemistry and for understanding the combustion of hydrocarbons. Columns 4 and 5 of Table 2 compare the B3-LYP/6-31G(d) and CBS-RAD barriers ( $\Delta H_0^\ddagger$ ) for  $\beta$ -scission of a number of the alkoxy radicals, in both cases using geometries and ZPVEs obtained at the B3-LYP/6-31G(d) level. It is evident that the B3-LYP values are significantly higher than the CBS-RAD values, by  $13\text{--}20 \text{ kJ mol}^{-1}$  for C-H scission, and by  $3\text{--}14 \text{ kJ mol}^{-1}$  for C-C scission. By either method, methyl-radical loss or ethyl-radical loss has a significantly lower barrier than H-atom loss in species where both channels are available.

The CBS-RAD procedure is expected to produce reasonably reliable estimates of the barriers provided that the geometries of the species derived at the B3-LYP/6-31G(d) level are adequate. The results should be most sensitive to the geometries of the transition structures. We have examined the appropriateness of the B3-LYP/6-31G(d) methodology for determining the transition structures by calculating the CBS-RAD energy at points along the bond-breaking coordinate for most of the  $\beta$ -scission reactions. The breaking C...H or C...C bond is stepped in  $0.02 \text{ \AA}$  increments from the B3-LYP/6-31G(d) transition structure with reoptimization of all the remaining geometric parameters. The zero-point vi-



**Table 2.** Dependence of transition structure bond length ( $r$ , Å) and reaction barrier ( $\Delta H_0^\ddagger$ , kJ mol<sup>-1</sup>) on theoretical level.

Alkoxy radical	Bond <sup>a</sup>	B3-LYP/6-31G(d)		CBS-RAD <sup>b</sup>	CBS-RAD-Scanmax <sup>c</sup>		Differences	
		<i>r</i>	$\Delta H_0^\ddagger$	$\Delta H_0^\ddagger$	<i>r</i>	$\Delta H_0^\ddagger$	$\Delta r^{d/}$	$\Delta H_0^{\ddagger e}$
<b>R<sub>1</sub>R<sub>2</sub>CHO• → H• + R<sub>1</sub>R<sub>2</sub>C=O</b>								
CH <sub>3</sub> O•	C...H	1.956	114.9	95.1	1.80	97.5	−0.16	2.4
CH <sub>3</sub> CH <sub>2</sub> O•	C...H	1.852	100.6	82.6	1.72	84.6	−0.13	2.0
CH <sub>3</sub> CH <sub>2</sub> CH <sub>2</sub> O•	C...H	1.851	98.4	80.6	1.72	82.4	−0.13	1.8
(CH <sub>3</sub> ) <sub>2</sub> CHO•	C...H	1.795	87.1	71.2	1.67	73.2	−0.13	2.0
CH <sub>3</sub> CH <sub>2</sub> CH(CH <sub>3</sub> )O•	C...H	1.797	85.6	70.8	1.70	72.4	−0.10	1.6
CH <sub>2</sub> =CHCH <sub>2</sub> O•	C...H	1.803	85.4	71.8	1.70	73.8	−0.10	2.0
CH <sub>2</sub> =CHCH(CH <sub>3</sub> )O•	C...H	1.763	80.3	67.1	1.66	69.0	−0.10	1.9
<b>R<sub>1</sub>R<sub>2</sub>(CH<sub>3</sub>)CO• → CH<sub>3</sub>• + R<sub>1</sub>R<sub>2</sub>C=O</b>								
CH <sub>3</sub> CH <sub>2</sub> O•	C...C	2.250	79.2	65.2	2.15	66.5	−0.10	1.3
(CH <sub>3</sub> ) <sub>2</sub> CHO•	C...C	2.182	65.2	55.0	2.10	55.9	−0.08	0.9
CH <sub>3</sub> CH <sub>2</sub> CH(CH <sub>3</sub> )O•	C...C	2.192	65.2	57.4	2.13	58.1	−0.06	0.7
(CH <sub>3</sub> ) <sub>3</sub> CO•	C...C	2.148	59.2	52.2	2.09	53.0	−0.06	0.8
<b>R<sub>1</sub>R<sub>2</sub>(CH<sub>3</sub>CH<sub>2</sub>)CO• → CH<sub>3</sub>CH<sub>2</sub>• + R<sub>1</sub>R<sub>2</sub>C=O</b>								
CH <sub>3</sub> CH <sub>2</sub> CH <sub>2</sub> O•	C...C	2.227	61.8	52.9	2.15	53.9	−0.08	1.0
CH <sub>3</sub> CH <sub>2</sub> CH(CH <sub>3</sub> )O•	C...C	2.153	47.2	44.6	2.11	45.0	−0.04	0.4

<sup>a</sup>Bond being broken in TS.<sup>b</sup>Calculated using B3-LYP/6-31G(d) geometries and (scaled) zero-point vibrational energies.<sup>c</sup>Calculated using the CBS-RAD-Scanmax procedure (see text); ZPVEs obtained with B3-LYP/6-31G(d) at the B3-LYP/6-31G(d) TS geometry.<sup>d</sup>CBS-RAD-Scanmax - B3-LYP/6-31G(d).<sup>e</sup>CBS-RAD-Scanmax - CBS-RAD.

brational energy is held constant at the TS value. The geometry at which the CBS-RAD energy, obtained in this manner, is a maximum, is an approximation to the CBS-RAD transition structure, while the corresponding  $\Delta H_0^\ddagger$  represents an improved CBS-RAD estimate of the barrier. This procedure has been referred to as Scanmax (37) and is closely related to the IRCMax procedure of Petersson and co-workers (38).

Table 2 lists the length ( $r$ ) of the bond being broken in the TS as obtained with B3-LYP/6-31G(d), the predicted B3-LYP/6-31G(d), and CBS-RAD values for  $\Delta H_0^\ddagger$  at the B3-LYP/6-31G(d) optimized geometry, and the values of  $r$  and  $\Delta H_0^\ddagger$  obtained using the CBS-RAD-Scanmax procedure. In each case, the CBS-RAD-Scanmax energy is a maximum at a value of  $r$  shorter than the B3-LYP/6-31G(d) optimized value, leading to an increase in the predicted  $\Delta H_0^\ddagger$ . The differences are listed in the last two columns of Table 2. Compared with CBS-RAD-Scanmax, B3-LYP/6-31G(d) overestimates the length of the breaking C—H bonds in the TS by 0.10–0.16 Å, leading to an underestimation of  $\Delta H_0^\ddagger$  by the standard CBS-RAD procedure by about 1.6–2.4 kJ mol<sup>-1</sup>. For C—C bond cleavage the corresponding differences in  $r$  and  $\Delta H_0^\ddagger$  are somewhat smaller, 0.04–0.10 Å and 0.4–1.3 kJ mol<sup>-1</sup>, respectively. Where available, we use the CBS-RAD-Scanmax values of  $\Delta H^\ddagger$  rather than standard CBS-RAD values in the remainder of this paper.

We note that a detailed analysis of the dependence of the results for some of the alkoxy radicals and their C—C unimolecular decomposition reaction characteristics on theoretical level and basis set, at levels comparable to those employed here, may be found in the study by Somnitz and Zellner (20). Their work is discussed further below. We note also that for most of the alkoxy radicals studied here, the barriers for the  $\beta$ -cleavage reactions have been previously determined at the CASSCF/6-31G(d) level of theory, without

zero-point energy correction (10). The values so obtained are uniformly 30–50 kJ mol<sup>-1</sup> higher than the values presented in Tables 3 and 4. In another study of  $\beta$ -scission reactions (39), AM1 theory was used to calculate barriers for a number of alkoxy radicals, only one of which is common to the present study. The AM1 barrier for the decomposition of the *tert*-butoxy radical decomposition is 13 kJ mol<sup>-1</sup> higher than the CBS-RAD value (Table 3).

### Individual alkoxy radicals

We discuss some of the individual alkoxy radicals prior to examination of the reactivity trends.

#### Methoxy radical

The CBS-RAD value of the bond dissociation enthalpy (BDE) of the O—H bond of methanol may be derived from the data in Table 1. The values at 0 and 298 K are 435.4 and 440.8 kJ mol<sup>-1</sup>, respectively, in good agreement with experimental values  $431 \pm 4$  and  $436 \pm 4$  kJ mol<sup>-1</sup>, respectively (40). Our calculated enthalpies of formation of the methoxy radical are  $\Delta_f H_0^\circ = 28.7$  kJ mol<sup>-1</sup> and  $\Delta_f H_{298}^\circ = 21.0$  kJ mol<sup>-1</sup>. Berkowitz et al. (40) reported  $\Delta_f H_0^\circ = 24.7 \pm 3.8$  kJ mol<sup>-1</sup> and  $\Delta_f H_{298}^\circ = 17.2 \pm 3.8$  kJ mol<sup>-1</sup> while Ramond et al. (36) reported  $\Delta_f H_{300}^\circ = 21 \pm 4$  kJ mol<sup>-1</sup>. Osborn et al. (41) reported  $\Delta_f H_0^\circ = 28.5 \pm 1.7$  kJ mol<sup>-1</sup>, in close agreement with our calculated value and also with the recent high-level theoretical value of Petraco et al. (19) ( $\Delta_f H_0^\circ = 27.2$  kJ mol<sup>-1</sup>).

The methoxy radical is predicted to undergo  $\beta$ -scission of a C—H bond with an Arrhenius activation energy ( $E_a = 101.1$  kJ mol<sup>-1</sup> (Table 3)) in close agreement with the value proposed by Dibble (42) ( $100 \pm 4$  kJ mol<sup>-1</sup>) on the basis of theoretical and experimental results. The length of the breaking C··H bond in the transition structure is 1.80 Å (Table 2), close to that found by Petraco et al. (19) (1.79 Å). The rate



**Table 3.** Enthalpy barriers ( $\Delta H^\ddagger$ , kJ mol<sup>-1</sup>), free energy barriers ( $\Delta G^\ddagger$ , kJ mol<sup>-1</sup>), frequency factors ( $A$ , s<sup>-1</sup>), activation energies ( $E_a$ , kJ mol<sup>-1</sup>), rate constants ( $s^{-1}$ , 298.15 K), reaction enthalpies ( $\Delta H$ , kJ mol<sup>-1</sup>) and reaction free energies ( $\Delta G$ ) for  $\beta$ -scission reactions calculated with CBS-RAD and B3-LYP/6-31G(d).<sup>a</sup>

Alkoxy radical	Reaction	$\Delta H^\ddagger_{298}$	$\Delta G^\ddagger_{298}$	log A	$E_a$	$k^b$	$\Delta H_0$	$\Delta H_{298}$	$\Delta G_{298}$
Methoxy	CH <sub>3</sub> O $\cdot$ $\rightarrow$ H $\cdot$ + CH <sub>2</sub> =O	98.6	95.7	13.74	101.1	$1.1 \times 10^{-5}$	79.0	84.8	55.2
Ethoxy	CH <sub>3</sub> CH <sub>2</sub> O $\cdot$ $\rightarrow$ H $\cdot$ + CH <sub>3</sub> CH=O	85.1	84.2	13.39	87.6	$1.1 \times 10^{-2}$	57.7	63.1	33.3
1-Propoxy	CH <sub>3</sub> CH <sub>2</sub> CH <sub>2</sub> O $\cdot$ $\rightarrow$ H $\cdot$ + CH <sub>3</sub> CH <sub>2</sub> CH=O	83.4	83.3	13.23	85.8	$1.6 \times 10^{-2}$	56.4	62.1	32.3
2-Propoxy	(CH <sub>3</sub> ) <sub>2</sub> CHO $\cdot$ $\rightarrow$ H $\cdot$ + (CH <sub>3</sub> ) <sub>2</sub> C=O	74.1	74.3	13.20	76.6	$6.0 \times 10^{-1}$	38.3	44.1	13.0
2-Butoxy	CH <sub>3</sub> CH <sub>2</sub> CH(CH <sub>3</sub> )O $\cdot$ $\rightarrow$ H $\cdot$ + CH <sub>3</sub> CH <sub>2</sub> C(CH <sub>3</sub> )=O	73.1	73.4	13.18	75.6	$8.6 \times 10^{-1}$	39.1	45.5	15.6
Prop-2-en-1-oxy	CH <sub>2</sub> =CHCH <sub>2</sub> O $\cdot$ $\rightarrow$ H $\cdot$ + (E)-CH <sub>2</sub> =CHCH=O	74.7	75.7	13.04	77.2	$3.3 \times 10^{-1}$	46.9	52.3	25.8
But-3-en-2-oxy	CH <sub>2</sub> =CHCH(CH <sub>3</sub> )O $\cdot$ $\rightarrow$ H $\cdot$ + (E)-CH <sub>2</sub> =CHC(CH <sub>3</sub> )=O	69.7	70.9	12.99	72.2	2.3	36.4	42.1	16.7
Ethoxy	CH <sub>3</sub> CH <sub>2</sub> O $\cdot$ $\rightarrow$ CH <sub>3</sub> $\cdot$ + CH <sub>2</sub> =O	67.9	65.8	13.60	70.4	$1.9 \times 10$	40.6	47.8	7.8
2-Propoxy	(CH <sub>3</sub> ) <sub>2</sub> CHO $\cdot$ $\rightarrow$ CH <sub>3</sub> $\cdot$ + CH <sub>3</sub> CH=O	57.7	53.4	13.96	60.1	$2.8 \times 10^3$	19.8	27.1	-18.5
2-Butoxy	CH <sub>3</sub> CH <sub>2</sub> CH(CH <sub>3</sub> )O $\cdot$ $\rightarrow$ CH <sub>3</sub> $\cdot$ + CH <sub>3</sub> CH <sub>2</sub> CH=O	59.8	59.6	13.25	62.3	$2.2 \times 10^2$	21.7	28.3	-14.8
tert-Butoxy	(CH <sub>3</sub> ) <sub>3</sub> CO $\cdot$ $\rightarrow$ CH <sub>3</sub> $\cdot$ + (CH <sub>3</sub> ) <sub>2</sub> C=O	54.5	49.7	14.06	56.9	$1.2 \times 10^4$	9.7	16.4	-33.3
But-3-en-2-oxy	CH <sub>2</sub> =CHCH(CH <sub>3</sub> )O $\cdot$ $\rightarrow$ CH <sub>3</sub> $\cdot$ + (E)-CH <sub>2</sub> =CHCH=O	48.2	47.1	13.43	50.7	$3.6 \times 10^4$	13.0	19.4	-19.2
1-Propoxy	CH <sub>3</sub> CH <sub>2</sub> CH <sub>2</sub> O $\cdot$ $\rightarrow$ CH <sub>3</sub> CH <sub>2</sub> $\cdot$ + CH <sub>2</sub> =O	55.7	52.6	13.77	58.1	$3.8 \times 10^3$	38.1	44.9	-1.2
2-Butoxy	CH <sub>3</sub> CH <sub>2</sub> CH(CH <sub>3</sub> )O $\cdot$ $\rightarrow$ CH <sub>3</sub> CH <sub>2</sub> $\cdot$ + CH <sub>3</sub> CH=O	46.5	43.7	13.72	48.9	$1.4 \times 10^5$	20.4	26.4	-22.8
Prop-2-en-1-oxy	CH <sub>2</sub> =CHCH <sub>2</sub> O $\cdot$ $\rightarrow$ CH <sub>2</sub> =CH $\cdot$ + CH <sub>2</sub> =O	92.4	85.0	14.53	94.8	$7.9 \times 10^{-3}$	81.0	87.0	42.7
But-3-en-2-oxy	CH <sub>2</sub> =CHCH(CH <sub>3</sub> )O $\cdot$ $\rightarrow$ CH <sub>2</sub> =CH $\cdot$ + CH <sub>3</sub> CH=O	83.1	77.3	14.24	85.6	$1.8 \times 10^{-1}$	64.3	69.5	23.2

<sup>a</sup>See text for details.<sup>b</sup>298.15 K.**Table 4.** Enthalpy barriers ( $\Delta H^\ddagger$ , kJ mol<sup>-1</sup>), free energy barriers ( $\Delta G^\ddagger$ , kJ mol<sup>-1</sup>), frequency factors ( $A$ , L mol<sup>-1</sup> s<sup>-1</sup>), activation energies ( $E_a$ , kJ mol<sup>-1</sup>), rate constants (L mol<sup>-1</sup> s<sup>-1</sup>, 298.15 K), reaction enthalpies ( $\Delta H$ , kJ mol<sup>-1</sup>), and reaction free energies ( $\Delta G$ ) for radical addition reactions calculated with CBS-RAD and B3-LYP/6-31G(d).<sup>a</sup>

Radical	IE <sup>b</sup>	Reaction	$\Delta H^\ddagger_{298}$	$\Delta G^\ddagger_{298}$	log A	$E_a$	$k^c$	$\Delta H_0$	$\Delta H_{298}$	$\Delta G_{298}$
H $\cdot$	13.6	H $\cdot$ + CH <sub>2</sub> =O $\rightarrow$ CH <sub>3</sub> O $\cdot$	13.8	40.5	10.37	18.7	$1.2 \times 10^7$	-79.0	-84.8	-55.2
		H $\cdot$ + CH <sub>3</sub> CH=O $\rightarrow$ CH <sub>3</sub> CH <sub>2</sub> O $\cdot$	22.0	50.9	9.99	27.0	$1.8 \times 10^5$	-57.7	-63.1	-33.3
		H $\cdot$ + CH <sub>3</sub> CH <sub>2</sub> CH=O $\rightarrow$ CH <sub>3</sub> CH <sub>2</sub> CH <sub>2</sub> O $\cdot$	21.3	51.0	9.84	26.2	$1.8 \times 10^5$	-56.5	-62.1	-32.3
		H $\cdot$ + (CH <sub>3</sub> ) <sub>2</sub> C=O $\rightarrow$ (CH <sub>3</sub> ) <sub>2</sub> CHO $\cdot$	30.1	61.3	9.58	35.0	$2.8 \times 10^3$	-38.3	-44.1	-13.0
		H $\cdot$ + CH <sub>3</sub> CH <sub>2</sub> C(CH <sub>3</sub> )=O $\rightarrow$ CH <sub>3</sub> CH <sub>2</sub> CH(CH <sub>3</sub> )O $\cdot$	27.6	57.8	9.76	32.6	$1.1 \times 10^4$	-39.1	-45.5	-15.6
		H $\cdot$ + (E)-CH <sub>2</sub> =CHCH=O $\rightarrow$ CH <sub>2</sub> =CHCH <sub>2</sub> O $\cdot$	22.4	50.0	10.22	27.4	$2.7 \times 10^5$	-46.9	-52.3	-25.9
		H $\cdot$ + (E)-CH <sub>2</sub> =CHC(CH <sub>3</sub> )=O $\rightarrow$ CH <sub>2</sub> =CHCH(CH <sub>3</sub> )O $\cdot$	27.5	54.3	10.36	32.5	$4.6 \times 10^4$	-36.4	-42.1	-16.7
Methyl	9.80	CH <sub>3</sub> $\cdot$ + CH <sub>2</sub> =O $\rightarrow$ CH <sub>3</sub> CH <sub>2</sub> O $\cdot$	20.1	58.0	8.41	25.1	$1.1 \times 10^4$	-40.6	-47.8	-7.8
		CH <sub>3</sub> $\cdot$ + CH <sub>3</sub> CH=O $\rightarrow$ (CH <sub>3</sub> ) <sub>2</sub> CHO $\cdot$	30.6	71.9	7.81	35.5	$3.8 \times 10$	-19.8	-27.1	18.5
		CH <sub>3</sub> $\cdot$ + CH <sub>3</sub> CH <sub>2</sub> CH=O $\rightarrow$ CH <sub>3</sub> CH <sub>2</sub> CH(CH <sub>3</sub> )O $\cdot$	31.5	74.4	7.53	36.5	$1.4 \times 10$	-21.7	-28.3	14.8
		CH <sub>3</sub> $\cdot$ + (CH <sub>3</sub> ) <sub>2</sub> C=O $\rightarrow$ (CH <sub>3</sub> ) <sub>3</sub> CO $\cdot$	38.1	83.0	7.18	43.0	$4.4 \times 10^{-1}$	-9.7	-16.4	33.3
Ethyl	8.12	CH <sub>3</sub> $\cdot$ + (E)-CH <sub>2</sub> =CHCH=O $\rightarrow$ CH <sub>2</sub> =CHCH(CH <sub>3</sub> )O $\cdot$	28.8	66.3	8.49	33.8	$3.8 \times 10^2$	-13.0	-19.4	19.3
		CH <sub>3</sub> CH <sub>2</sub> $\cdot$ + CH <sub>2</sub> =O $\rightarrow$ CH <sub>3</sub> CH <sub>2</sub> CH <sub>2</sub> O $\cdot$	10.7	53.8	7.52	15.7	$5.9 \times 10^4$	-38.1	-44.9	1.2
		CH <sub>3</sub> CH <sub>2</sub> $\cdot$ + CH <sub>3</sub> CH=O $\rightarrow$ CH <sub>3</sub> CH <sub>2</sub> CH(CH <sub>3</sub> )O $\cdot$	20.1	66.4	6.93	25.0	$3.5 \times 10^2$	-20.4	-26.4	22.8
Vinyl	8.25	CH <sub>2</sub> =CH $\cdot$ + CH <sub>2</sub> =O $\rightarrow$ CH <sub>2</sub> =CHCH <sub>2</sub> O $\cdot$	5.4	42.3	8.59	10.4	$5.9 \times 10^6$	-81.0	-86.9	-42.8
		CH <sub>2</sub> =CH $\cdot$ + CH <sub>3</sub> CH=O $\rightarrow$ CH <sub>2</sub> =CHCH(CH <sub>3</sub> )O $\cdot$	11.6	52.0	7.97	16.5	$1.2 \times 10^5$	-64.3	-69.5	-23.2

<sup>a</sup>See text for details.<sup>b</sup>Ionization energy of the radical (in eV).<sup>c</sup>298.15 K.



constant for unimolecular decomposition at 298 K is predicted to be  $1.1 \times 10^{-5} \text{ s}^{-1}$ .

The  $\beta$ -scission reaction (eq. [3]) is highly endothermic for the methoxy radical and the enthalpy change corresponds to the bond dissociation enthalpy (BDE) of the C—H bond ( $\Delta H_0^\circ = 79.0 \text{ kJ mol}^{-1}$  and  $\Delta H_{298}^\circ = 84.8 \text{ kJ mol}^{-1}$  (Table 3)). Our calculated 0 K value is slightly lower than that deduced experimentally by Osborn et al. (41) ( $82.8 \pm 1.7 \text{ kJ mol}^{-1}$ ) and that calculated by Petraco et al. (19) ( $84.1 \text{ kJ mol}^{-1}$ ).

The reverse reaction, addition of H atom to formaldehyde, has a predicted barrier height at 0 K ( $\Delta H_0^\ddagger$ ) of  $18.5 \text{ kJ mol}^{-1}$ , in good agreement with the recommended theoretical value of Petraco et al. (19) ( $19.7 \text{ kJ mol}^{-1}$ ). The reverse barrier is considerably smaller than the forward barrier because of the endothermicity of the  $\beta$ -scission reaction. Our Arrhenius parameters are  $\log A = 10.37$  and  $E_a = 18.7 \text{ kJ mol}^{-1}$ . The  $E_a$  value is somewhat lower than values reported by Walch (43) ( $22$  and  $26 \text{ kJ mol}^{-1}$ ), derived experimentally from rates for deuterium addition at room temperature ( $\log A = 10.30$  was assumed) and an RRKM analysis, respectively. Because of the large negative entropy of activation calculated for the addition reaction ( $-89.6 \text{ J mol}^{-1} \text{ K}^{-1}$ ) the free energy barrier ( $\Delta G_{298}^\ddagger = 40.5 \text{ kJ mol}^{-1}$ ) is substantially higher than the enthalpy barrier ( $\Delta H_{298}^\ddagger = 13.8 \text{ kJ mol}^{-1}$ ). Our calculated rate for the addition of H atom to formaldehyde is  $k = 1.2 \times 10^7 \text{ L mol}^{-1} \text{ s}^{-1}$ .

### Ethoxy radical

The calculated values for the enthalpy of formation of the ethoxy radical are  $\Delta_f H_0^\circ = 4.2 \text{ kJ mol}^{-1}$  or  $\Delta_f H_{298}^\circ = -9.9 \text{ kJ mol}^{-1}$  (Table 1). These are in fair agreement with the values recommended by Berkowitz et al. (40) ( $\Delta_f H_0^\circ = -1.7 \pm 3.8 \text{ kJ mol}^{-1}$  and  $\Delta_f H_{298}^\circ = -15.5 \pm 3.8 \text{ kJ mol}^{-1}$ , respectively). We find closer agreement with the experimental value of Ramond et al. (36) ( $\Delta_f H_{300}^\circ = -12 \pm 7 \text{ kJ mol}^{-1}$ ). Viskolcz and co-workers (15) used a variety of high theoretical levels to obtain  $\Delta_f H_{298}^\circ = 0 \pm 3 \text{ kJ mol}^{-1}$ , significantly higher than our CBS-RAD value and the experimental values.

Our calculated barrier for  $\beta$ -scission of the H atom from the ethoxy radical ( $\Delta H_{298}^\ddagger = 85.1 \text{ kJ mol}^{-1}$ ) is close to that obtained by Viskolcz and co-workers (15) ( $84.8 \text{ kJ mol}^{-1}$ ) at the QCISD(T)/6-311+G(3df,2p) level of theory. It is approximately  $14 \text{ kJ mol}^{-1}$  lower than for H-atom scission from the methoxy radical.

The barrier for the reverse reaction, addition of the H atom to acetaldehyde ( $\Delta H_{298}^\ddagger = 22.0 \text{ kJ mol}^{-1}$ ), is somewhat higher than that for addition to formaldehyde ( $\Delta H_{298}^\ddagger = 13.8 \text{ kJ mol}^{-1}$ ).

An activation energy of  $70.4 \text{ kJ mol}^{-1}$  is predicted for  $\beta$ -scission of  $\text{CH}_3^\cdot$  from the ethoxy radical, which is in close agreement with a recent experimental determination ( $E_a = 70.3 \text{ kJ mol}^{-1}$ ) measured by laser flash photolysis – laser-induced fluorescence (15). Our predicted rate constant ( $k = 19 \text{ s}^{-1}$ ) is higher than the experimental values of Viskolcz and co-workers (14) ( $5.2 \text{ s}^{-1}$ ) and Batt and Milne (44) ( $1.5 \text{ s}^{-1}$ ). This reaction has also been investigated by Somnitz and Zellner (20) at a modified G2 level of theory, using RRKM theory to derive Arrhenius activation parameters and reaction rate constants. Their  $E_a$  value ( $73.6 \text{ kJ mol}^{-1}$ ) is slightly higher than ours and their derived  $\log A$  value (12.99) is sig-

nificantly lower than ours (13.60). Their predicted rate constant at 300 K ( $1.46 \text{ s}^{-1}$ ) is in close agreement with the value of Batt and Milne (44).  $\beta$ -Scission of the ethoxy radical yielding  $\text{CH}_3^\cdot + \text{CH}_2=\text{O}$  is predicted to be endothermic by  $40.6 \text{ kJ mol}^{-1}$  at 0 K and  $47.8 \text{ kJ mol}^{-1}$  at 298 K (Table 3).

The experimentally determined activation energy for the addition of the methyl radical to formaldehyde is  $31.0 \text{ kJ mol}^{-1}$  (11), somewhat higher than that found in the present calculations ( $E_a = 25.1 \text{ kJ mol}^{-1}$ ) (Table 4).

### 1-Propoxy radical

The predicted values for the enthalpy of formation of the 1-propoxy radical are  $\Delta_f H_0^\circ = -8.2 \text{ kJ mol}^{-1}$  and  $\Delta_f H_{298}^\circ = -29.3 \text{ kJ mol}^{-1}$ , considerably less negative than the experimental value ( $\Delta_f H_{298}^\circ = -41.4 \text{ kJ mol}^{-1}$ ) (Table 1). In the light of the good agreement with recent experimental data (36) observed for other alkoxy radicals, we believe that experimental reexamination for 1-propoxy radical is desirable.

$\beta$ -Scission of the 1-propoxy radical yielding  $\text{CH}_3\text{CH}_2\text{CH}=\text{O} + \text{H}^\cdot$  has a predicted barrier ( $\Delta H_{298}^\ddagger$ ) of  $83.4 \text{ kJ mol}^{-1}$  (Table 3). This value is only slightly lower than that predicted for  $\beta$ -scission of the H atom from the ethoxy radical ( $\Delta H_{298}^\ddagger = 85.1 \text{ kJ mol}^{-1}$ ). The 0 K value ( $\Delta H_0^\ddagger = 82.4 \text{ kJ mol}^{-1}$ , Table 2) is  $13.1 \text{ kJ mol}^{-1}$  lower than that calculated by Viskolcz and co-workers (14) at the B3-LYP/SVP level of theory. The higher value of Viskolcz is consistent with our observations that the B3-LYP procedure tends to yield higher values for  $\beta$ -scission barriers than CBS-RAD (Table 2). The present results predict that the  $\beta$ -scission reaction of the 1-propoxy radical to give  $\text{CH}_3\text{CH}_2\text{CH}=\text{O} + \text{H}^\cdot$  is strongly endothermic by  $62.1 \text{ kJ mol}^{-1}$  ( $\Delta H_{298}^\circ$ ).

The predicted barrier for addition of the H atom to propanal is  $21.3 \text{ kJ mol}^{-1}$  (Table 4) which, not surprisingly, is close to the value for the addition to acetaldehyde ( $22.0 \text{ kJ mol}^{-1}$ ).

The present calculations predict that  $\beta$ -scission of the 1-propoxy radical yielding  $\text{CH}_3\text{CH}_2^\cdot + \text{CH}_2=\text{O}$ , is impeded by a barrier ( $\Delta H_{298}^\ddagger$ ) of  $55.7 \text{ kJ mol}^{-1}$  (Table 3) and is endothermic by  $44.9 \text{ kJ mol}^{-1}$  ( $\Delta H_{298}^\circ$ ). This reaction has also been investigated by Somnitz and Zellner (20). Their RRKM-derived  $E_a$  of  $62.4 \text{ kJ mol}^{-1}$  is slightly higher than ours ( $58.1 \text{ kJ mol}^{-1}$ ) and, as in the case of ethoxy, their  $\log A$  value (13.25) is somewhat lower than ours (13.77).

Our predicted barrier ( $\Delta H_{298}^\ddagger$ ) for addition of ethyl radical to formaldehyde is  $10.7 \text{ kJ mol}^{-1}$  (Table 4), approximately  $9 \text{ kJ mol}^{-1}$  lower than that for methyl-radical addition ( $\Delta H_{298}^\ddagger = 20.1 \text{ kJ mol}^{-1}$ ) and approximately  $3 \text{ kJ mol}^{-1}$  lower than that for H-atom addition ( $\Delta H_{298}^\ddagger = 13.8 \text{ kJ mol}^{-1}$ ).

### 2-Propoxy radical

The predicted values for the enthalpy of formation of 2-propoxy radical are  $\Delta_f H_0^\circ = -20.9 \text{ kJ mol}^{-1}$  and  $\Delta_f H_{298}^\circ = -41.9 \text{ kJ mol}^{-1}$ , somewhat less negative than the experimental ( $\Delta_f H_{298}^\circ = -52.3 \text{ kJ mol}^{-1}$  and  $\Delta_f H_{300}^\circ = -46 \pm 5 \text{ kJ mol}^{-1}$ ) and the value recommended by Sun and Bozzelli (45) ( $\Delta_f H_{298}^\circ = -49.6 \text{ kJ mol}^{-1}$ ).

Loss of the H atom from the 2-propoxy radical by  $\beta$ -scission is predicted to have a barrier ( $\Delta H_{298}^\ddagger$ ) of  $74.1 \text{ kJ mol}^{-1}$ , which is close to the G2(MP2) value of  $76.5 \text{ kJ mol}^{-1}$  obtained by Devolder et al. (16). It is somewhat lower than the barriers for H-atom loss from the ethoxy and propoxy radicals which have only a single  $\alpha$ -alkyl substituent ( $\text{CH}_3$



and  $\text{CH}_3\text{CH}_2$ , respectively). Conversely, the barrier for addition of the H atom to acetone ( $\Delta H_{298}^\ddagger = 30.1 \text{ kJ mol}^{-1}$ ) is somewhat higher than that for addition to the aldehydes  $\text{CH}_3\text{CH}=\text{O}$  and  $\text{CH}_3\text{CH}_2\text{CH}=\text{O}$  ( $\Delta H_{298}^\ddagger = 22.0$  and  $21.3 \text{ kJ mol}^{-1}$ , respectively).

$\beta$ -Scission of the 2-propoxy radical yielding  $\text{CH}_3\cdot + \text{CH}_3\text{CH}=\text{O}$  is predicted to be endothermic, with  $\Delta H_0 = 19.8 \text{ kJ mol}^{-1}$  and  $\Delta H_{298} = 27.1 \text{ kJ mol}^{-1}$  (Table 3). The barrier ( $\Delta H_{298}^\ddagger$ ) is predicted to be  $57.7 \text{ kJ mol}^{-1}$ . This value is similar to that found by Viskolcz and co-workers (16) at the G2(MP2) level ( $\Delta H_{298}^\ddagger = 61.2 \text{ kJ mol}^{-1}$ ). Our Arrhenius parameters  $\log A = 13.96$  and  $E_a = 60.1 \text{ kJ mol}^{-1}$ , are in moderate agreement with the experimental values, measured by laser flash photolysis – laser-induced fluorescence ( $\log A = 14.08$ ,  $E_a = 63.7 \text{ kJ mol}^{-1}$ ) (16). Our calculated rate at 298 K is  $k = 2.8 \times 10^3 \text{ s}^{-1}$ , somewhat higher than the experimental rate ( $k = 8.3 \times 10^2 \text{ s}^{-1}$ ). The corresponding theoretical RRKM values of Somnitz and Zellner (20) are  $E_a = 62.2 \text{ kJ mol}^{-1}$ ,  $\log A = 13.38$ , and  $k = 3.53 \times 10^2 \text{ s}^{-1}$  at 300 K, in somewhat better agreement with the experimental values of Viskolcz and co-workers (15).

Addition of the methyl radical to acetaldehyde is predicted to have a significantly higher barrier ( $\Delta H_{298}^\ddagger = 30.6 \text{ kJ mol}^{-1}$ ) than the addition of the H atom to acetaldehyde ( $\Delta H_{298}^\ddagger = 22.0 \text{ kJ mol}^{-1}$ ) or the addition of the methyl radical to formaldehyde ( $\Delta H_{298}^\ddagger = 20.1 \text{ kJ mol}^{-1}$ ).

### 2-Butoxy radical

$\beta$ -Scission of the 2-butoxy radical may proceed by three pathways: loss of the H atom, methyl radical, or ethyl radical. Loss of the H atom entails a very similar barrier ( $\Delta H_{298}^\ddagger = 73.1 \text{ kJ mol}^{-1}$ , Table 3) to that for H-atom loss from the 2-propoxy radical ( $\Delta H_{298}^\ddagger = 74.1 \text{ kJ mol}^{-1}$ ). Likewise the barrier for H atom addition to butan-2-one ( $\Delta H_{298}^\ddagger = 27.6 \text{ kJ mol}^{-1}$ , Table 4) is similar to that for the addition to acetone ( $\Delta H_{298}^\ddagger = 30.1 \text{ kJ mol}^{-1}$ ).

Loss of either of the two alkyl groups, methyl or ethyl, is hindered by smaller barriers than that for H-atom loss, with  $\Delta H_{298}^\ddagger = 59.8$  and  $46.5 \text{ kJ mol}^{-1}$ , respectively. Somnitz and Zellner (20) also investigated the two  $\beta$ -scission pathways involving alkyl group loss. Their theoretical RRKM values (methyl, ethyl) are  $E_a = (60.8 \text{ kJ mol}^{-1}, 50.0 \text{ kJ mol}^{-1})$ ,  $\log A = (12.26, 13.15)$ , and  $k = (46.0 \text{ s}^{-1}, 2.67 \times 10^4 \text{ s}^{-1})$  at 300 K. Our corresponding values from Table 3 are (methyl, ethyl)  $E_a = (62.3 \text{ kJ mol}^{-1}, 48.9 \text{ kJ mol}^{-1})$ ,  $\log A = (13.25, 13.72)$ , and  $k = (2.2 \times 10^2 \text{ s}^{-1}, 1.4 \times 10^5 \text{ s}^{-1})$  at 298 K. The  $E_a$  values are in good agreement, but the RRKM  $\log A$  values are lower than ours and that recommended by Fittschen et al. (17), who suggest a common value ( $\log A = 14 \pm 0.3$ ) for  $\beta$  C-C scission in alkoxy radicals. Experimental estimates of the rate constant for the dissociation to the ethyl radical plus acetaldehyde lie in the range  $7.5 \times 10^2$  to  $3 \times 10^4 \text{ s}^{-1}$  (see reference (20b) for a review and discussion). An experimental investigation in which both channels were observed found a difference of  $11.2 \text{ kJ mol}^{-1}$  between  $E_a$  values, and that the  $\log A$  value for the ethyl channel was higher by 0.6 (46). Both features are in reasonable agreement with the theoretical results.

The barrier for methyl-radical addition to propanal ( $\Delta H_{298}^\ddagger = 31.5 \text{ kJ mol}^{-1}$ ) is quite similar to that for the addition to acetaldehyde ( $\Delta H_{298}^\ddagger = 30.6 \text{ kJ mol}^{-1}$ ). However, the

barriers for both of these reactions are significantly greater than for ethyl-radical addition to acetaldehyde ( $\Delta H_{298}^\ddagger = 20.1 \text{ kJ mol}^{-1}$ ). The reaction enthalpies for all three processes are generally similar ( $\Delta H_{298} = -26.4$  to  $-28.3 \text{ kJ mol}^{-1}$ ).

### tert-Butoxy radical

The present calculations predict that  $\beta$ -scission of the *tert*-butoxy radical should occur with a barrier of  $54.5 \text{ kJ mol}^{-1}$ , only  $3.2 \text{ kJ mol}^{-1}$  lower than for  $\beta$ -scission of the methyl radical from 2-propoxy radical ( $\Delta H_{298}^\ddagger = 57.7 \text{ kJ mol}^{-1}$ ).

The calculated Arrhenius parameters for the scission reaction are  $\log A = 14.06$  and  $E_a = 56.9 \text{ kJ mol}^{-1}$ . Experimentally determined kinetics of *tert*-butoxy radical decomposition have been reported by Choo and Benson (11) ( $\log A = 14.1$ ,  $E_a = 64 \text{ kJ mol}^{-1}$ ), Batt et al. (47) ( $\log A = 14.04 \pm 0.37$ ,  $E_a = 62.5 \pm 0.6 \text{ kJ mol}^{-1}$ ), Viskolcz and co-workers (17) ( $\log A = 14.0$ ,  $E_a = 60.5 \text{ kJ mol}^{-1}$ ) and Blitz et al. (48) ( $\log A = 13.15$ ,  $E_a = 57 \pm 2 \text{ kJ mol}^{-1}$ ). While our  $E_a$  value is close to that of Blitz et al. (48), their  $\log A$  value is significantly lower. Our calculations support a value for  $A$  close to  $1 \times 10^{14}$ , which is also recommended by Viskolcz and co-workers (17).

As noted earlier for the corresponding H-atom additions to acetone, methyl-radical addition to acetone is hindered by a significantly higher barrier ( $\Delta H_{298}^\ddagger = 38.1 \text{ kJ mol}^{-1}$ ) than for the corresponding additions to acetaldehyde and propanal ( $\Delta H_{298}^\ddagger = 30.6$  and  $31.5 \text{ kJ mol}^{-1}$ , respectively).

### Prop-2-en-1-oxy and but-3-en-2-oxy radicals

The two unsaturated oxy radicals, prop-2-en-1-oxy and but-3-en-2-oxy, may undergo  $\beta$ -scission by losing a vinyl radical, or by losing a hydrogen atom or a methyl radical, respectively. The structures of the OCCC anticlinal conformers of these radicals, which are linked to the most stable (also OCCC anticlinal) conformations of the transition structures for H loss or  $\text{CH}_3$  loss, are shown in Fig. 1. In each case, the <OCCC dihedral angle is such as to orient one of the allylic groups (H and  $\text{CH}_3$ , respectively) approximately perpendicular to the plane of the vinyl group and well-positioned for  $\pi$ -bond-assisted departure.

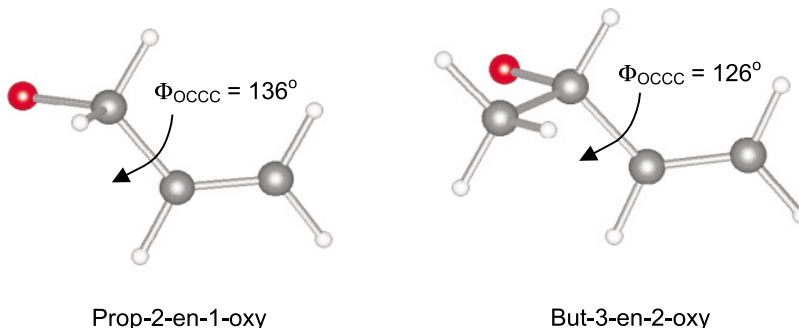
The barriers ( $\Delta H_{298}^\ddagger$ ) for H-atom loss from prop-2-en-1-oxy ( $74.7 \text{ kJ mol}^{-1}$ ) and but-3-en-2-oxy ( $69.7 \text{ kJ mol}^{-1}$ ) radicals are lower than those for the equivalent processes in the saturated analogues, 1-propoxy ( $83.4 \text{ kJ mol}^{-1}$ ) and 2-butoxy ( $73.1 \text{ kJ mol}^{-1}$ ), consistent with  $\pi$ -bond participation in the  $\beta$ -scission process for the unsaturated radicals. The lower barrier for the departure of the methyl radical from but-3-en-2-oxy ( $48.2 \text{ kJ mol}^{-1}$ ) as compared to methyl loss from 2-butoxy ( $59.8 \text{ kJ mol}^{-1}$ ) provides additional support for the  $\pi$ -bond assistance in the former case.

With the exception of H loss from methoxy, the loss of vinyl radicals are the most endothermic of those listed in Table 3. The barriers for vinyl group loss from the prop-2-en-1-oxy and but-3-en-2-oxy radicals are  $\Delta H_{298}^\ddagger = 92.4 \text{ kJ mol}^{-1}$  and  $83.1 \text{ kJ mol}^{-1}$ , respectively. The higher values for vinyl radical loss partly reflects the greater endothermicity in these cases.

### Influence of substituents in $\beta$ -scission reactions

The data in Table 3 are grouped according to the departing radical ( $\text{H}\cdot$ ,  $\text{CH}_3\cdot$ ,  $\text{CH}_3\text{CH}_2\cdot$ , or  $\text{CH}_2=\text{CH}\cdot$ ). It is apparent



**Fig. 1.** The unsaturated prop-2-en-1-oxy and but-3-en-2-oxy radicals.

that within any of these groupings, increasing alkyl substitution at the site of oxygen attachment promotes  $\beta$ -scission. Thus the barriers ( $\Delta H^\ddagger$ ) for  $\beta$ -scission of  $\text{H}\cdot$  decrease in the sequence:  $\text{CH}_3\text{O}\cdot \gg \text{CH}_3\text{CH}_2\text{O}\cdot \approx \text{CH}_3\text{CH}_2\text{CH}_2\text{O}\cdot > (\text{CH}_3)_2\text{CHO}\cdot \approx \text{CH}_3\text{CH}_2\text{CH}(\text{CH}_3)\text{O}\cdot$ . Likewise, the  $\Delta H^\ddagger$  values for  $\beta$ -scission of  $\text{CH}_3\cdot$  decrease in the sequence:  $\text{CH}_3\text{CH}_2\text{O}\cdot > (\text{CH}_3)_2\text{CHO}\cdot \approx \text{CH}_3\text{CH}_2\text{CH}(\text{CH}_3)\text{O}\cdot > (\text{CH}_3)_3\text{CO}\cdot$ . The two examples of loss of ethyl and vinyl groups also follow this pattern. These results are all consistent with a decrease in  $\Delta H^\ddagger$  accompanying a decrease in the reaction endothermicity  $\Delta H$ , as expected from the Bell–Evans–Polanyi relationship. The decreased endothermicity may in turn be associated with increased hyperconjugative stabilization of the product carbonyl compounds with increased alkyl substitution.

In addition to the reaction enthalpy effect, the barriers for  $\beta$ -scission (and for the reverse radical addition to carbonyl, see below) decrease as the ionization energy of the departing radical decreases, consistent with the development of positive charge at the incipient radical in the transition structure. Our calculated Mulliken charges indeed indicate that there is a small amount of positive charge of approximately +0.05–0.07 in the incipient radical moiety in the TS. The low net charge on the departing radical ( $\text{H}\cdot$ ,  $\text{CH}_3\cdot$ ,  $\text{CH}_3\text{CH}_2\cdot$ , or  $\text{CH}_2=\text{CH}\cdot$ ) is consistent with a loose (late) TS with more than 80% of the net spin on the radical. Interestingly, there is also a significant polarization of charge in the remainder of the transition structure, with a negative charge of approximately –0.4 on the incipient carbonyl oxygen and a positive charge of approximately +0.3 on the remainder of the molecule. The extent of this polarization increases with increasing alkyl substitution.

### Radical addition to the carbonyl group

The addition of radicals to alkenes has been extensively studied by high-level theoretical calculations (for example, see refs. 13 and 49). However, the addition of radicals to carbonyl compounds has received less attention (for example, see refs. 19 and 50). This reaction is the reverse of the  $\beta$ -scission reaction that we have discussed in detail above and we therefore make only a few brief comparative remarks here.

Table 4 contains our computed data for radical additions to carbonyl compounds, grouped according to the radical being added. An initial comment is that, because of the endothermicity of the  $\beta$ -scission reactions, the barriers for the reverse radical addition reactions are considerably smaller than the  $\beta$ -scission barriers.

Transition structures for the addition of hydrogen, methyl, ethyl, and vinyl radicals to acetaldehyde are shown in Fig. 2, along with the calculated Arrhenius activation parameters. A general plot of the calculated activation energies ( $E_a$ ) against reaction enthalpies ( $\Delta H_{298}$ ) is displayed in Fig. 3. It is clear that  $E_a$  generally decreases with increasing exothermicity, as expected from the Bell–Evans–Polanyi relationship. In addition, for a given exothermicity, the barriers tend to be lower for radicals with a lower ionization energy. These observations are qualitatively consistent with the empirical relationship (eq. [4]) of Choo and Benson (11), and with considerations based on a curve-crossing model (13, 51). Lower ionization energies enable greater participation of charge-transfer configurations of the type  $\text{radical}^+\text{carbonyl}^-$ , which in turn leads to a lowering of the barrier. The barriers follow the pattern  $(\text{CH}_3)_2\text{C}=\text{O} \approx \text{CH}_3\text{CH}_2\text{C}(\text{CH}_3)=\text{O} > \text{CH}_3\text{CH}=\text{O} \approx \text{CH}_3\text{CH}_2\text{CH}=\text{O} > \text{CH}_2=\text{O}$ , in line with the reaction exothermicity. Particularly low barriers are observed for the highly exothermic additions involving the vinyl radical.

An interesting observation, already noted above for the addition of  $\text{H}\cdot$  to  $\text{CH}_2=\text{O}$ , is that, in contrast to the situation for the  $\beta$ -scission reactions, the  $\Delta G_{298}^\ddagger$  values for the radical additions are considerably greater than the  $\Delta H_{298}^\ddagger$  values. This arises because of substantial negative entropies of activation, a result that is not unexpected for a bimolecular reaction. The differences between  $\Delta G_{298}^\ddagger$  and  $\Delta H_{298}^\ddagger$  depend on the radical that is added, and increase in the sequence  $\text{H}\cdot$  (26–31  $\text{kJ mol}^{-1}$ ) <  $\text{CH}_3\cdot$  (37–45  $\text{kJ mol}^{-1}$ )  $\approx$   $\text{CH}_2=\text{CH}\cdot$  (37–40  $\text{kJ mol}^{-1}$ ) <  $\text{CH}_3\text{CH}_2\cdot$  (43–46  $\text{kJ mol}^{-1}$ ).

Examination of the log  $A$  values shows that the frequency factors ( $A$ ) for  $\text{H}\cdot$  addition are close to  $1 \times 10^{10}$ , while those for alkyl radical addition are two to three orders of magnitude smaller. Frequency factors for vinyl-radical addition are close to those for methyl-radical addition.

### Conclusions

The structures of the alkoxy radicals methoxy ( $\text{CH}_3\text{O}\cdot$ ), ethoxy ( $\text{CH}_3\text{CH}_2\text{O}\cdot$ ), 1-propoxy ( $\text{CH}_3\text{CH}_2\text{CH}_2\text{O}\cdot$ ), 2-propoxy ( $(\text{CH}_3)_2\text{CHO}\cdot$ ), 2-butoxy ( $\text{CH}_3\text{CH}_2\text{CH}(\text{CH}_3)\text{O}\cdot$ ), *tert*-butoxy ( $(\text{CH}_3)_3\text{CO}\cdot$ ), prop-2-en-1-oxy ( $\text{CH}_2=\text{CHCH}_2\text{O}\cdot$ ), and but-3-en-2-oxy ( $\text{CH}_2=\text{CHCH}(\text{CH}_3)\text{O}\cdot$ ), and the products of their  $\beta$ -scission reactions, have been determined at the B3-LYP/6-31G(*d*) level of theory. CBS-RAD has been used to calculate the enthalpies of formation ( $\Delta_f H_{298}^\circ$ ). The predicted  $\Delta_f H_{298}^\circ$



**Fig. 2.** Calculated transition structures, bond lengths in (Å), and Arrhenius activation parameters (CBS-RAD, kJ mol<sup>-1</sup>) for the addition of hydrogen, methyl, ethyl, and vinyl radicals to acetaldehyde. Distances for hydrogen, methyl, and ethyl addition are by CBS-RAD–Scanmax; for vinyl group addition, the value is from B3-LYP/6-31G(d) optimization.

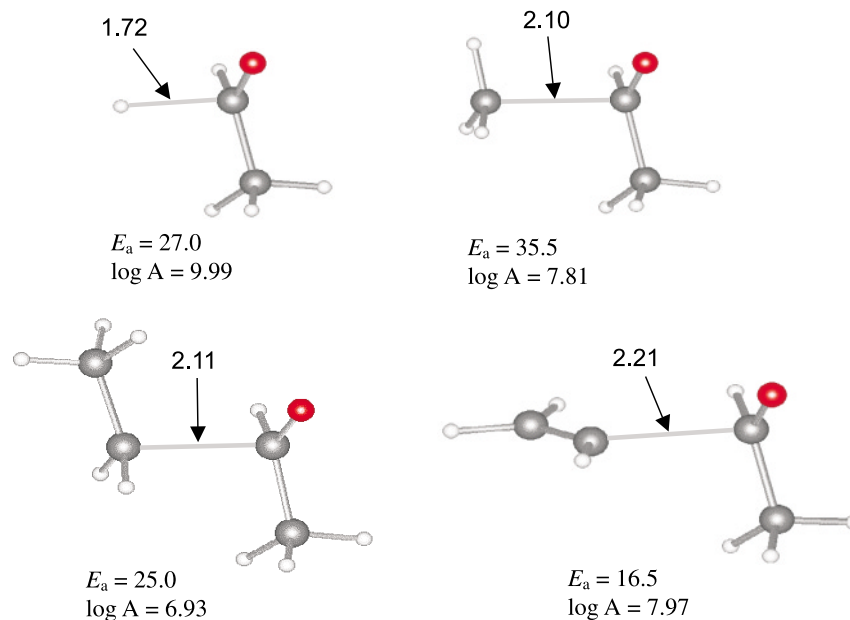
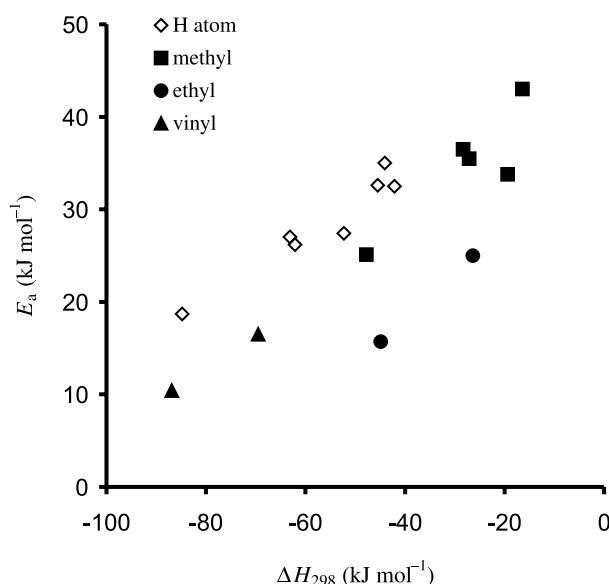


**Fig. 3.** Activation energies for the addition of hydrogen, methyl, ethyl, and vinyl radicals to carbonyl compounds vs. the reaction enthalpy.



values agree well with the available experimental data, with a mean absolute deviation of 5.4 kJ mol<sup>-1</sup>.

Transition structures (TS) for all the  $\beta$ -scission pathways were located at the B3-LYP/6-31G(d) level and, in most cases, at the CBS-RAD–Scanmax level. The bond being cleaved in the TS tends to be longer with B3-LYP by 0.10–0.16 Å (C–H) or 0.04–0.10 Å (C–C). At the B3-LYP geometry, the predicted B3-LYP barriers ( $\Delta H_0^\ddagger$ ) are 13–20 kJ mol<sup>-1</sup> higher than the CBS-RAD values for C–H scission, and 3–14 kJ mol<sup>-1</sup> higher for C–C bond breaking. The consequence of not reoptimizing the bond being broken at the

CBS-RAD level is an underestimation of  $\Delta H_0^\ddagger$  by 1.6–2.4 kJ mol<sup>-1</sup> (C–H) or 0.4–1.3 kJ mol<sup>-1</sup> (C–C).

Eyring ( $\Delta H_0^\ddagger$ ,  $\Delta H_{298}^\ddagger$ ,  $\Delta G_{298}^\ddagger$ ) and Arrhenius ( $\log A$ ,  $E_a$ ) activation parameters for both the forward ( $\beta$ -scission) and reverse (radical addition to carbonyl) pathways were calculated within the rigid rotor – harmonic oscillator model and transition-state theory. Most of the available experimental kinetic data refer to the  $\beta$ -scission pathway. Where direct comparison was possible, the agreement with the experimental is very good, generally within 1–5 kJ mol<sup>-1</sup> for  $E_a$ , and 0.5 for  $\log A$ .

The values of the barriers for either  $\beta$ -scission or radical addition to carbonyl are dominated by the reaction enthalpy: the barrier decreases with decreasing endothermicity ( $\beta$ -scission) or increasing exothermicity (radical addition). As a consequence, for example, alkyl or vinyl substituents in the alkoxy radical lower the barrier for  $\beta$ -scission of H $\cdot$ , CH<sub>3</sub> $\cdot$ , or CH<sub>3</sub>CH<sub>2</sub> $\cdot$  groups. In addition to the enthalpy effect, the barrier depends on the ionization energy of the departing radical in the  $\beta$ -scission reaction (or equivalently, the adding radical in the radical additions). Smaller barriers are associated with lower ionization energies. These results are consistent with expectations based on the curve-crossing model, the smaller ionization energies allowing greater participation of charge-transfer configurations of the type radical<sup>+</sup>carbonyl<sup>-</sup> in the transition structure. We find that in the transition structures, the departing radical carries a small positive charge while there is substantial charge polarization in the nascent carbonyl compound, the oxygen atom becoming negatively charged and the rest of the molecule becoming positively charged.

## Acknowledgements

Financial support by the Natural Sciences and Engineering Research Council of Canada (NSERC), the Australian Research Council (ARC), and the award of Visiting Fellowships



at the Australian National University (to AR, RJB, and SLB) are gratefully acknowledged. We also thank Professor Allan East for helpful discussions, and the Multimedia Advanced Computational Infrastructure (MACI) at the University of Calgary, the Australian Partnership for Advanced Computing, and the Australian National University Supercomputer Facility for generous allocations of computing resources.

## References

1. J.A. Miller, R.J. Knee, and C.I. Westbrook. *Annu. Rev. Phys. Chem.* **41**, 317 (1990).
2. J. Warantz. *In* Combustion chemistry. Edited by W.C. Gardiner, Jr. Springer, New York. 1984.
3. (a) R. Atkinson. *J. Phys. Chem. Ref. Data* **26**, 215 (1997); (b) R. Atkinson. *Int. J. Chem. Kinet.* **29**, 99 (1997); (c) E.S.C. Kwok, J. Arey, and R. Atkinson. *J. Phys. Chem.* **100**, 214 (1996).
4. D.M. Golden. *In* Chemical kinetic data needs for modeling the lower troposphere. NBS Special Publication 557, August 1979, pp. 51–61.
5. (a) L. Batt. *Int. Rev. Phys. Chem.* **6**, 53 (1987); (b) L. Batt. *Int. J. Chem. Kinet.* **11**, 977 (1979).
6. M.J. Davies. *Arch. Biochem. Biophys.* **336**, 163 (1996).
7. P. Gray and A. Williams. *Chem. Rev.* **59**, 239 (1959).
8. J.K. Kochi. *J. Am. Chem. Soc.* **84**, 1193 (1962).
9. W. Zhang and P. Dowd. *Tetrahedron*, **49**, 1965 (1993).
10. S. Wilsey, P. Dowd, and K.N. Houk. *J. Org. Chem.* **64**, 8801 (1999).
11. K.Y. Choo and S.W. Benson. *Int. J. Chem. Kinet.* **13**, 833 (1981).
12. M. Weber and H. Fischer. *J. Am. Chem. Soc.* **121**, 7381 (1999).
13. H. Fischer and L. Radom. *Angew. Chem. Int. Ed.* **40**, 1340 (2001).
14. H. Hippler, F. Striebel, and B. Viskolcz. *Phys. Chem. Chem. Phys.* **3**, 2450 (2001).
15. F. Caralp, P. Devolder, C. Fittschen, N. Gomez, H. Hippler, R. Mereau, M.T. Rayez, F. Striebel, and B. Viskolcz. *Phys. Chem. Chem. Phys.* **1**, 2935 (1999).
16. P. Devolder, C. Fittschen, A. Frenzel, H. Hippler, G. Poskrebyshev, F. Striebel, and B. Viskolcz. *Phys. Chem. Chem. Phys.* **1**, 675 (1999).
17. C. Fittschen, H. Hippler, and B. Viskolcz. *Phys. Chem. Chem. Phys.* **2**, 1677 (2000).
18. G. Lendvay and B. Viskolcz. *J. Phys. Chem. A*, **102**, 10 777 (1998).
19. N.D.K. Petraco, W.D. Allen, and H.F. Schaeffer, III. *J. Chem. Phys.* **116**, 10 229 (2002).
20. (a) H. Somnitz and R. Zellner. *Phys. Chem. Chem. Phys.* **2**, 1899 (2000); (b) H. Somnitz and R. Zellner. *Phys. Chem. Chem. Phys.* **2**, 1907 (2000).
21. (a) W.J. Hehre, L. Radom, P.v.R. Schleyer, and J.A. Pople. *Ab initio molecular orbital theory*. Wiley, New York. 1986; (b) F. Jensen. *Introduction to computational chemistry*. Wiley, New York. 1999.
22. W. Koch and M.C. Holthausen. *A chemist's guide to density functional theory*. Wiley-VCH, Weinheim. 2000.
23. (a) M.J. Frisch, G.W. Trucks, H.B. Schlegel, P.M.W. Gill, B.G. Johnson, M.A. Robb, J.R. Cheeseman, T.A. Keith, G.A. Petersson, J.A. Montgomery, K. Raghavachari, M.A. Al-Laham, V.G. Zakrzewski, J.V. Ortiz, J.B. Foresman, J. Cioslowski, B.B. Stefanov, A. Nanayakkara, M. Challacombe, C.Y. Peng, P.Y. Ayala, W. Chen, M.W. Wong, J.L. Andres, E.S. Replogle, R. Gomperts, R.L. Martin, D.J. Fox, J.S. Binkley, D.J. Defrees, J. Baker, J.P. Stewart, M. Head-Gordon, C. Gonzalez, and J.A. Pople. (1995) *Gaussian 94, (SGI-Revision B.3)*, Gaussian, Inc., Pittsburgh PA. (b) M.J. Frisch, G.W. Trucks, H.B. Schlegel, G.E. Scuseria, M.A. Robb, J.R. Cheeseman, V.G. Zakrzewski, J.A. Montgomery, Jr., R.E. Stratmann, J.C. Burant, S. Dapprich, J.M. Millam, A.D. Daniels, K.N. Kudin, M.C. Strain, O. Farkas, J. Tomasi, V. Barone, M. Cossi, R. Cammi, B. Mennucci, C. Pomelli, C. Adamo, S. Clifford, J. Ochterski, G.A. Petersson, P.Y. Ayala, Q. Cui, K. Morokuma, D.K. Malick, A.D. Rabuck, K. Raghavachari, J.B. Foresman, J. Cioslowski, J.V. Ortiz, A.G. Baboul, B.B. Stefanov, G. Liu, A. Liashenko, P. Piskorz, I. Komaromi, R. Gomperts, R.L. Martin, D.J. Fox, T. Keith, M.A. Al-Laham, C.Y. Peng, A. Nanayakkara, C. Gonzalez, M. Challacombe, P.M.W. Gill, B. Johnson, W. Chen, M.W. Wong, J.L. Andres, C. Gonzalez, M. Head-Gordon, E.S. Replogle, and J.A. Pople. *Gaussian 98*. Gaussian, Inc., Pittsburgh, Pennsylvania. 1998.
24. H.J. Werner, P.J. Knowles, R.D. Amos, A. Bernhardsson, A. Berning, P. Celani, D.L. Cooper, M.J.O. Deegan, A.J. Dobbyn, F. Eckert, C. Hampel, G. Hetzer, T. Korona, R. Lindh, A.W. Lloyd, S.J. McNicholas, F.R. Manby, W. Meyer, M.E. Mura, A. Nicklass, P. Palmieri, R. Pitzer, G. Rauhut, M. Schütz, H. Stoll, A.J. Stone, R. Tarroni, and T. Thorsteinsson. *Molpro 2000.6*. University of Birmingham, Birmingham. 1999.
25. A.P. Scott and L. Radom. *J. Phys. Chem.* **100**, 16 502 (1996). The scale factors used are 0.9806 (ZPVEs), 1.0015 (*S*), and 0.9989 ( $H^\circ - H_0^\circ$ ).
26. P.M. Mayer, P.J. Parkinson, D.M. Smith, and L. Radom. *J. Chem. Phys.* **108**, 604 (1998).
27. (a) M.W. Wong and L. Radom. *J. Phys. Chem.* **99**, 8582 (1995); (b) M.W. Wong and L. Radom. *J. Phys. Chem. A*, **102**, 2237 (1998).
28. D.A. McQuarrie. *Statistical thermodynamics*. Harper and Row, New York. 1973.
29. D.D. Wagman, W.H. Evans, V.B. Parker, R.H. Schumm, I. Halow, S.M. Bailey, K.L. Chyrney, and R.L. Nuttall. *J. Phys. Chem. Ref. Data*, **11** (Suppl. 2) (1982).
30. S.G. Lias, G.A. Bartmess, J.F. Liebman, J.L. Holmes, R.D. Levin, and W.G. Mallard. *J. Phys. Chem. Ref. Data* **17** (Suppl. 1) (1988).
31. J. Cioslowski, M. Schimeczek, G. Liu, and V. Stoyanov. *J. Chem. Phys.* **113**, 9377 (2000).
32. D.R. Lide (*Editor*). *CRC Handbook of chemistry and physics*. 82nd ed. CRC Press, West Palm Beach, Florida, U.S.A. 2001.
33. See for example: (a) J.P. Guthrie. *J. Phys. Chem. A*, **105**, 8495 (2001); (b) P.W. Atkins. *Physical Chemistry*. Oxford University Press, Oxford. 1998.
34. D.R. Stull, E.F. Westrum, Jr., and G.C. Sinke. *The thermodynamics of organic compounds*. John Wiley and Sons, New York. 1969.
35. P.J. Robinson. *J. Chem. Ed.* **55**, 509 (1978).
36. T.M. Ramond, G.E. Davico, R.L. Schwartz, and W.C. Lineberger. *J. Chem. Phys.* **112**, 1158 (2000).
37. M.L. Coote, G.P.F. Wood, and L. Radom. *J. Phys. Chem. A*, **106**, 12 124 (2002).
38. D.K. Malick, G.A. Petersson, and J.A. Montgomery. *J. Chem. Phys.* **108**, 5704 (1998).
39. O.M. Zarechnaya, I.A. Opeida, and A.F. Dmitruk. *Russ. J. Org. Chem.* **37**, 1405 (2001).
40. J. Berkowitz, G.B. Ellison, and D. Gutman. *J. Phys. Chem.* **98**, 2744 (1994).
41. D.L. Osborn, D.J. Leahy, E.R. Ross, and D.M. Neumark. *Chem. Phys. Lett.* **235**, 484 (1995).



42. T.S. Dibble. *J. Mol. Struct.* **485–486**, 67 (1999), and refs. therein.
43. S.P. Walch. *J. Chem. Phys.* **98**, 3076 (1993). (Analysis based on cited private communication by F. Temps).
44. L. Batt and R.T. Milne. *Int. J. Chem. Kinet.* **1**, 549 (1977).
45. H. Sun and J.W. Bozzelli. *J. Phys. Chem. A*, **106**, 3947 (2002).
46. R.M. Drew, J.A. Kerr, and J. Olive. *Int. J. Chem. Kinet.* **17**, 167 (1985).
47. L. Batt, M.W.M. Hisham, and M. Mackay. *Int. J. Chem. Kinet.* **21**, 535 (1989).
48. M. Blitz, M.J. Pilling, S.H. Robertson, and P.W. Seakins. *Phys. Chem. Chem. Phys.* **1**, 73 (1999).
49. C. Selcuki and V. Aviyente. *J. Mol. Model.* **7**, 398 (2001).
50. C. Gonzalez, C. Sosa, and H.B. Schlegel. *J. Phys. Chem.* **93**, 2435 (1989).
51. L. Radom, M.W. Wong, and A. Pross. *In* Controlled radical polymerization. *Edited by* K. Matyjaszewski. ACS Symposium Series 685. American Chemical Society, Washington, D.C. 1998. pp. 31–49.



# Regioselectivity of Meisenheimer complexation in reaction of oxygen-centred nucleophiles with picryl aryl ethers: Polar vs. SET mechanisms

Erwin Buncel, Julian M. Dust, Richard A. Manderville, and Richard M. Tarkka

**Abstract:** Picryl alkyl ethers react with hydroxide and methoxide ions to give regioisomeric Meisenheimer (anionic  $\sigma^-$ ) adducts; the C-3 adduct is kinetically favoured and the C-1 adduct is thermodynamically favoured (K3T1 behaviour). In the current 400 MHz NMR spectroscopic study of the reactions of two picryl aryl ethers, picryl phenyl ether (PicOPh, **1**) and picryl mesityl ether (PicOMes, **2**), the charge localized nucleophiles  $\text{OH}^-$  and  $\text{MeO}^-$  displayed the same K3 regioselectivity as found with picryl alkyl ethers; attachment at C-1 leads to  $\text{S}_{\text{N}}\text{Ar}$  displacement of the aryloxyde. In contrast, phenoxide ( $\text{PhO}^-$ ) and the sterically demanding 2,4,6-trimethylphenoxide (mesitoxide,  $\text{MesO}^-$ ) react with **1** and **2** to form the C-1 O-adduct as the product of kinetic control (i.e., K1 behaviour). These reactions were studied at low temperature ( $-40^\circ\text{C}$  in acetonitrile- $d_3$ :dimethoxyethane- $d_{10}$  1:1) and as a function of increasing temperature ( $-40^\circ\text{C}$  to ambient). On the thermodynamic side, the C-1  $\text{PhO}^-$  O-adduct of **1** is also the more stable of the possible phenoxide O-adducts; it shows T1 regioselectivity within the manifold of O-adducts (K1T1), but the C-3 C-adduct (via *para*-attack of  $\text{PhO}^-$ ) is the ultimate thermodynamic product. The C-1 O-adducts formed by  $\text{MesO}^-$  with **1** or **2** give way with time (or temperature increase) in favour of their C-3 regioisomers or a C-1,3-O-diadduct. Mesitoxide, therefore, displays K1T3 regioselectivity. Stereoelectronic stabilization is discussed as a factor influencing T1 regioselectivity in O-adduct formation. Frontier molecular orbital (FMO) interactions between the HOMO of the nucleophile and the LUMO of the picryl ether may play a role in the K1 preference of aryloxides. An alternative argument is presented based on a single electron (radical) transfer (SET) pathway for the aryloxyde nucleophiles rather than the polar ( $\text{S}_{\text{N}}\text{Ar}$ ) pathway for hydroxide and methoxide. The SET pathway also predicts a kinetic preference for C-1, as the C-1 position is of higher spin density than C-3 in the radical anion of the picryl ether and thus should be the preferred site for coupling by the aryloxyde radical.

**Key words:** anionic Meisenheimer adducts, regioselectivity, kinetic–thermodynamic control, FMO, stereoelectronic stabilization, single electron transfer (SET).

**Résumé :** Les oxydes de picryle et d'alkyle réagissent avec les ions hydroxydes et méthylates avec formation d'adduits (anioniques  $\sigma^-$ ) de Meisenheimer régioisomères; l'adduit en C-3 est favorisé d'un point de vue cinétique alors que l'adduit en C-1 est favorisé d'un point de vue thermodynamique (comportement K3T1). Dans l'étude courante, par spectroscopie RMN à 400 MHz, des réactions de deux oxydes de picryles et d'aryles, l'oxyde de picryle et de phényle (PicOPh, **1**) et l'oxyde de picryle et de mésityle (PicOMes, **2**), les nucléophiles à charge localisée,  $\text{OH}^-$  et  $\text{MeO}^-$ , présentent la même régiosélectivité K3 que celle observée avec les oxydes de picryle et d'alkyle; la fixation en C-1 conduit à un déplacement  $\text{S}_{\text{N}}\text{Ar}$  de l'aryloxyde. Par opposition, le phénolate ( $\text{PhO}^-$ ) et le 2,4,6-triméthylphénolate (mésitylate,  $\text{MesO}^-$ ) qui imposent des demandes stériques beaucoup plus importantes réagissent tous les deux avec les composés **1** et **2** pour former, comme produit de contrôle cinétique, un O-adduit en C-1 (comportement K1). On a étudié ces réactions à basse température ( $-40^\circ\text{C}$ , dans un mélange acétonitrile- $d_3$ :diméthoxyéthane- $d_{10}$  1:1) et en fonction d'une augmentation de la température ( $-40^\circ\text{C}$  à la température ambiante). D'un point de vue thermodynamique, le O-adduit du  $\text{PhO}^-$  en C-1 du produit **1** est aussi le plus stable des O-adduits possibles pour le phénolate; il présente du régiosélectivité T1 parmi les plusieurs O-adduits (K1T1); toutefois, le C-adduit C-3 (obtenu par une attaque en *para* du

Received 5 November 2002. Published on the NRC Research Press Web site at <http://canjchem.nrc.ca> on 17 April 2003.

*Dedicated to Prof. Don Arnold for his contributions to chemistry in Canada.*

**E. Buncel.**<sup>1</sup> Department of Chemistry, Queen's University, Kingston, ON K7L 3N6, Canada

**J.M. Dust.**<sup>2</sup> Departments of Chemistry and Environmental Science, Sir Wilfred Grenfell College, Corner Brook, NL A2H 6P9, Canada.

**R.A. Manderville.**<sup>3</sup> Department of Chemistry, Wake Forest University, Winston-Salem, NC 27109-7486, U.S.A.

**R.M. Tarkka.** Department of Chemistry, University of Central Arkansas, Conway, AR 72035, U.S.A.

<sup>1</sup>Corresponding author (e-mail: [buncele@chem.queensu.ca](mailto:buncele@chem.queensu.ca)).

<sup>2</sup>Corresponding author (e-mail: [jdust@swgc.mun.ca](mailto:jdust@swgc.mun.ca)).

<sup>3</sup>Corresponding author (e-mail: [manderra@wfu.edu](mailto:manderra@wfu.edu)).



PhO<sup>-</sup>) est le produit thermodynamique ultime. Les O-adduits C-1 qui se forment initialement entre le MeSO<sup>-</sup> et les produits **1** et **2** laissent la place, avec le temps ou une augmentation de la température, à leurs régioisomères C-3 ou à un C-1,3-O-diadduit. Le mésitylate présente donc une régiosélectivité K1T3. On discute de la stabilisation électronique comme facteur influençant la régiosélectivité T1 dans la formation des O-adduits. Les interactions des orbitales moléculaires frontières (OMF) entre l'OM haute occupée et la basse vacante de l'oxyde de picryle pourrait jouer un rôle dans la préférence K1 des aryloxydes. On présente un argument alternatif, basé sur une voie réactionnelle impliquant le transfert d'un seul (radical) électron (SET) pour les nucléophiles aryloxydes plutôt qu'une voie polaire (S<sub>N</sub>Ar) pour l'hydroxyde et le méthanolate. La voie SET permet aussi de prédire une préférence cinétique pour C-1 parce que cette position possède une densité de spin plus élevée que celle en C-3 dans l'anion radical de l'oxyde de picryle et qu'elle devrait donc être le site favorisé pour le couplage avec le radical aryloxyde.

**Mots clés :** adduits anioniques de Meisenheimer, régiosélectivité, contrôles cinétique et thermodynamique, OMF, stabilisation stéréoelectronique, transfert d'un seul électron (SET).

[Traduit par la Rédaction]

## Introduction

Reaction of a base (nucleophile) with an electron-deficient aromatic may give rise to diverse products, namely  $\pi$ -complexes (1), radical anions (2), aryl carbanions (3), and anionic  $\sigma$ -adducts (termed Meisenheimer complexes) (1–4). With 1-X-2,4,6-trinitrobenzenes, nucleophiles react to form Meisenheimer complexes according to an accepted general pattern of the initial formation of a C-3 adduct that gives way over time to a thermodynamically favoured C-1 adduct (5). This regioselectivity has been elaborated in a number of 1-X-2,4,6-trinitrobenzene-nucleophile reaction systems, notably with alkoxides and hydroxide as nucleophiles (5), and has been labelled K3T1 (6, 7) (cf. Fig. 1).

In a series of articles (6, 7), we have delineated a full range of regioselectivities in Meisenheimer complexation. Thus, while 2,4,6-trinitroanisole (TNA) reacts with methoxide according to the K3T1 pattern (cf. Fig. 1) (5*a–d*, 6*b*), TNA reacts with the oxygen centre of a phenoxide ion (PhO<sup>-</sup>) with K1T1 regioselectivity. In the latter case, a C-1 TNA·OPh<sup>-</sup> adduct was the first (and only) phenoxide O-adduct detected by 400 MHz <sup>1</sup>H NMR spectroscopy at –40°C in acetonitrile–dimethoxyethane (MeCN-*d*<sub>3</sub>:DME-*d*<sub>10</sub> 1:1) solvent (6*b*). The regioisomeric C-3 TNA·OPh<sup>-</sup> adduct was not observed, in accord with a previous stopped-flow UV-vis kinetic study in which the initially observed adduct was identified as the C-1 species (8). Furthermore, the structurally similar phenoxide O-adduct of 1,3,5-trinitrobenzene (i.e., TNB·OPh<sup>-</sup>) can be observed by <sup>1</sup>H NMR spectroscopy under the same conditions used in the TNA·PhO<sup>-</sup> study (9*a*). On this basis, the regioselectivity exhibited by the TNA·PhO<sup>-</sup> system was classified as K1T1, i.e., a system in which the C-1 adduct is favoured by both kinetics and thermodynamics (Fig. 1). However, the ultimate phenoxide product was the C-3 TNA·PhO(H)<sup>-</sup> *para* C-bonded adduct, consistent with the ambident (O- and C-) nucleophilic nature of PhO<sup>-</sup> (6*b*) and in agreement with results gleaned from related systems (9). The behaviour of phenoxide as a C-nucleophile corresponds to K3T3 regioselectivity wherein the C-3 C-adduct is the product of both kinetic and thermodynamic control. Our AM1 calculations on the regioisomeric adducts formed by TNA with OH<sup>-</sup> and CH<sub>3</sub><sup>-</sup> as prototypical O- and C-nucleophiles, respectively, confirm the thermodynamic preference for C-3 attack by carbon nucleophiles (6*d*). This K3T3 behaviour (Fig. 1) of C-nucleophiles is also im-

plicit in the synthetic results found in vicarious nucleophilic substitution (VNS) reactions, as documented by Makosza and co-workers (10). Finally, we have reported the results of the reaction of TNA with the bulky aryloxy nucleophile 2,4,6-trimethylphenoxide (mesitoxide, MesO<sup>-</sup>) (6*c*). In this system, attack at C-1 to yield a C-1 TNA·OMes<sup>-</sup> Meisenheimer complex is kinetically favoured at –40°C, but as the NMR probe temperature was raised, the C-1 adduct rapidly declined in concentration and was supplanted by the C-3 TNA·OMes<sup>-</sup> adduct, in accord with K1T3 behaviour (Fig. 1). This reactivity pattern is the inverse of the “normal” K3T1 isomerization pathway displayed by alkoxides and hydroxide.

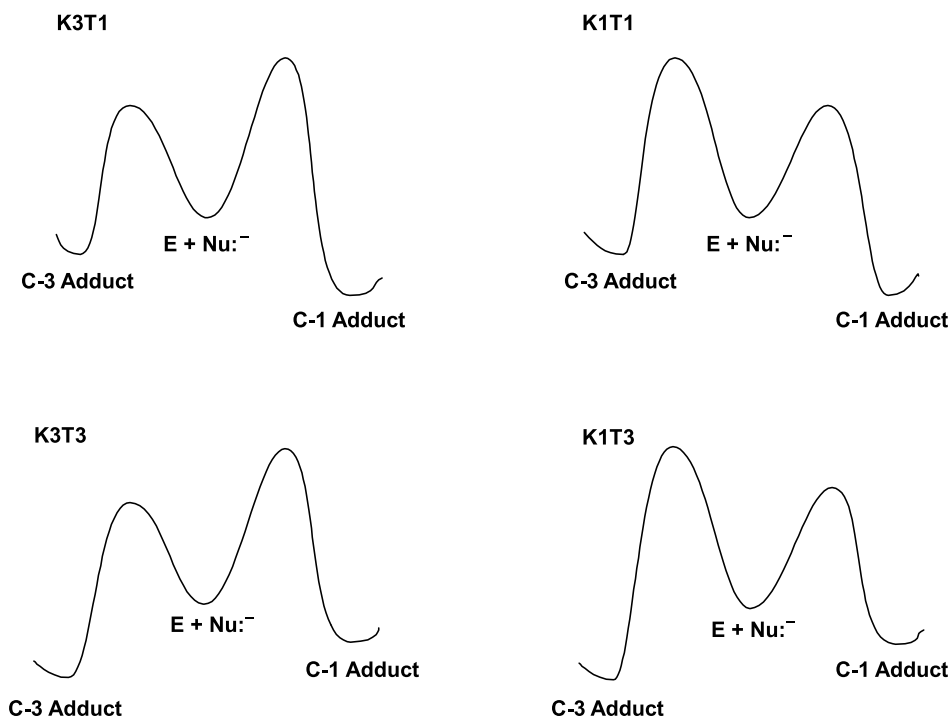
Although a wide range of kinetic and thermodynamic factors have been advanced (4, 5, 11, 12) to account for the regioselectivity found in picryl ether – base Meisenheimer complexation, our analysis has focused primarily on thermodynamics and has highlighted the contribution made by stereoelectronic stabilization of the relevant C-1 adducts (6*b–d*, 7, 9*a*). In this approach, C-1 adducts, as acetal analogues, can be stabilized by  $n \rightarrow \sigma^*$  donation from an oxygen lone pair of one RO group into the anti-bonding orbital of the C—OR bond (and vice versa); the interaction is maximized if the relevant lone pairs and C—OR fragment bonds can be arranged antiperiplanar to one another. Where stereoelectronic stabilization is negligible, the C-3 adduct may become the thermodynamic product (7).

The arguments concerning kinetic factors have either relied on assumptions made about the position of the transition state for adduct formation (5*d*, 6*b*) or have consisted of assessments of steric hindrance to attack at C-1 (F-strain) (11, 12*d*, 12*e*, 13, 14). In light of the K1T3 behaviour exhibited in the reaction of TNA with mesitoxide, a bulky nucleophile, the importance of F-strain in determining the regioselectivity of Meisenheimer complexation warrants re-examination.

The present article extends the study of picryl ether – nucleophile interactions to the picryl *aryl* ethers picryl phenyl ether (PicOPh, **1**) and picryl mesityl ether (PicOMes, **2**). The reactions of these ethers, **1** and **2**, with the aryloxy nucleophiles, phenoxide ion (PhO<sup>-</sup>) and mesitoxide (MesO<sup>-</sup>), were monitored in acetonitrile–dimethoxyethane (MeCN-*d*<sub>3</sub>:DME-*d*<sub>10</sub> 1:1 v/v) as a function of temperature (–40° to ambient), and the PicOPh–PhO<sup>-</sup> system was studied in dimethyl sulfoxide (DMSO-*d*<sub>6</sub>) at room temperature. Thus, the current study



**Fig. 1.** Qualitative comparative energy-reaction coordinate profiles for the four general patterns of regioselectivity. Barrier heights and relative stabilities are exaggerated for clarity. K3T1 describes those systems in which formation of the C-3 adduct is the product of *kinetic* control, but the C-1 adduct is the *thermodynamic* product. In the K1T1 profile the C-1 adduct is favoured by both kinetics and thermodynamics. The profile designated K3T3 represents the situation where the C-3 adduct is doubly preferred; that is by kinetics and by thermodynamics. The K1T3 profile describes the inverse behaviour from that indicated by K3T1; now the C-1 adduct is favoured kinetically but the C-3 adduct is the most stable product.



further probes the effect of steric hindrance at C-1 on the kinetics of these systems, particularly in the case of the highly hindered PicOMes reacting with the bulky MesO<sup>−</sup> anion.

The results are compared with those obtained in the related TNA–Nu<sup>−</sup> systems and are discussed with regard to possible frontier molecular orbital (FMO) interactions between the highest occupied molecular orbital (HOMO) of the aryloxide nucleophiles and the lowest unoccupied molecular orbital (LUMO) of the polynitroaromatic substrate. To model a 1-X-2,4,6-trinitrobenzene, we have carried out a semi-empirical (AM1) (15) molecular orbital calculation on TNA, and these results are included in this article. Finally, more recent suggestions that related reactions proceed through transition states having varying degrees of radical character (16) or via single electron transfer (SET) to give a radical–radical anion pair (2) are considered.

## Results

Reactions of the aryloxides PhO<sup>−</sup> and MesO<sup>−</sup> with the electrophiles PicOPh, **1**, and PicOMes **2**, were monitored by 400 MHz <sup>1</sup>H NMR in acetonitrile–dimethoxyethane (MeCN-*d*<sub>3</sub>-DME-*d*<sub>10</sub> 1:1 v/v), a solvent system that has proven useful in NMR studies down to temperatures of −50°C (6*b*, 6*c*, 9*a*). Reactions of **1** and **2** with OH<sup>−</sup> and MeO<sup>−</sup> were conducted in DMSO-*d*<sub>6</sub> at ambient temperature. Spectroscopic characteristics of the species (including coupling constants, *J*, in Hz) shown in Schemes 1 and 2 are listed in Table 1. In general, resonances are located at positions farther downfield

in the MeCN-*d*<sub>3</sub>:DME-*d*<sub>10</sub> medium than in DMSO-*d*<sub>6</sub>. <sup>13</sup>C NMR peak positions for some relevant σ-adducts measured in MeCN–DME and substrates measured in DMSO-*d*<sub>6</sub> are given in Table 2.

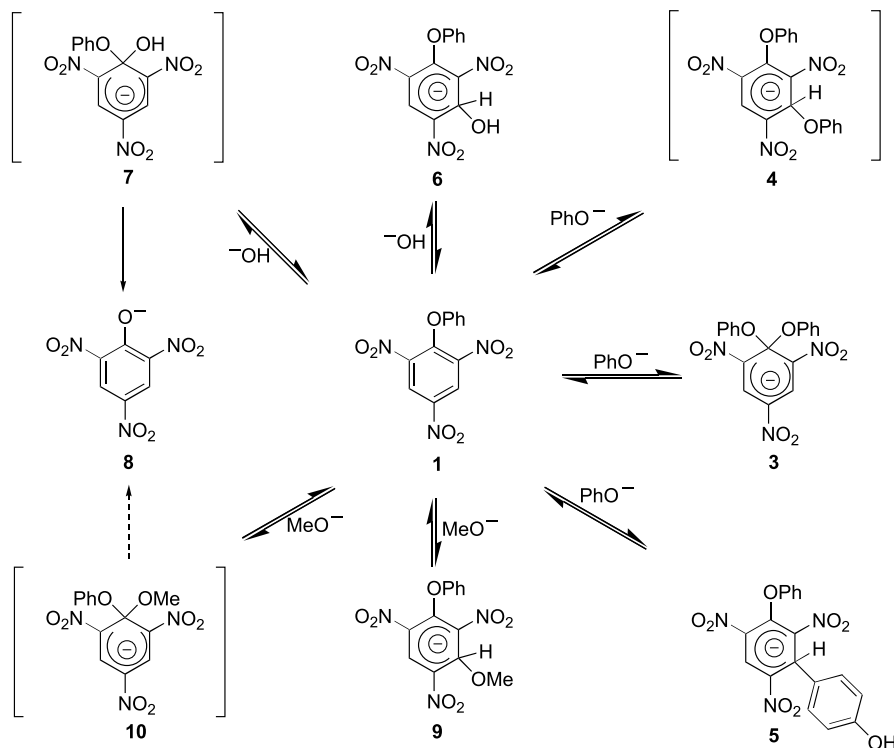
As in previous studies of the reaction of aryloxides with picryl systems (6*b*, 6*c*, 9), C-3 hydroxide adducts of **1** (i.e., **6**) and **2** (i.e., **15**) were observed also. The assignment of the signals of these adducts (**6** and **15**) was confirmed by control experiments that involved the electron-deficient substrates and tetramethylammonium hydroxide (Me<sub>4</sub>NOH) in DMSO. In general, these C-3 hydroxide adducts gave way over time to picrate anion (PicO<sup>−</sup>, **8**) following a pattern seen previously (6*b*, 6*c*, 9). Methoxide reacted with **1** and **2** to yield the respective C-3 adducts **9** and **17**, as the products of kinetic control; the corresponding C-1 adducts **10** and **18** were not observed. Relevant spectroscopic data for the observed adducts are given in Table 1.

### Reaction of **1** with excess PhOK in MeCN–DME

To an NMR tube that contained a solution of PicOPh (**1**) in MeCN-*d*<sub>3</sub>:DME-*d*<sub>10</sub> (1:1, v/v), cooled to −50°C, was injected 1.5 equiv of a similarly cooled MeCN-*d*<sub>3</sub>:DME-*d*<sub>10</sub> solution of phenoxide ion (PhOK; final concentrations of **1**:PhOK were 0.06:0.09 M). The first <sup>1</sup>H NMR spectrum recorded at −40°C contained a singlet at δ 8.63 that is consistent with the resonance for two equivalent ring protons (H<sub>3,5</sub>) of a C-1 O-adduct. Other signals in the spectrum are similarly attributable to the C-1 PicOPh·OPh<sup>−</sup> O-adduct, **3** (Scheme 1). The initial low-temperature spectrum was re-



Scheme 1.



markedly free from signals that would arise from formation of other adducts at this temperature. Therefore, a full assignment could be made for **3**: 8.63 (2H, s,  $H_{3,5}$ ), 7.15 (4H, m,  $H_m$ ), 6.95 (2H, m,  $H_p$ ), and 6.69 (2H, m,  $H_o$ ).<sup>4</sup> It is pertinent to note that the signals assigned to the ring protons of the attached phenoxy group are equivalent, indicating that the adduct is symmetrical. The <sup>13</sup>C NMR spectrum of **3** was also recorded (Table 2).

As the temperature was gradually raised, resonances of **3** began to broaden, and after ca. 1 h at 10°C a new set of doublets could be seen at 8.57 (1H,  $J = 1.9$ ) and 6.42 (1H,  $J = 1.9$ ). These peaks are assignable to  $H_5$  and  $H_3$ , respectively, of the C-3 PicOPh-OH<sup>-</sup> adduct, **6** (Scheme 1), that arises from equilibration of PhO<sup>-</sup> and adventitious water present in the solvent (cf. ref. 6b, 6c, 17). The OH resonance of **6** was not observed and its state of ionization is, therefore, uncertain.

As the temperature was further raised to ambient, a singlet was noted at 8.65. Comparison with related systems (**6**) shows that this singlet represents the two equivalent ring protons of picrate anion, i.e., PicO<sup>-</sup>, **8**. Eventually (>5 h) peaks appear that are ascribable to the C-3 *para*-bonded adduct, **5** (Scheme 1); resonances belonging to **5** are given in Table 1. The OH of the attached phenoxy group was not observed, so the state of ionization of this OH is uncertain. Moreover, the *para* proton ( $H_p$ ) of the C-1 phenoxy moiety of the C-3 PicOPh-PhO(H)<sup>-</sup> adduct, **5**, was apparently obscured by resonances of free PhOH (i.e.,  $H_m$ ,  $H_o$ ,  $H_p$ ).

In summary, as an O-nucleophile, PhO<sup>-</sup> reacts at C-1 of PicOPh, **1**, to yield the C-1 O-adduct, **3**, as the first phen-

oxide adduct. More significantly, at no time were peaks observed that could be attributed to a C-3 phenoxide O-adduct (i.e., **4**, Scheme 1). We have previously shown (9a) that the chemical shift of the diagnostic proton bonded to the  $sp^3$ -hybridized ring carbon in the phenoxide O-adduct of 1,3,5-trinitrobenzene, TNB·OPh<sup>-</sup>, is located 0.5–0.8 ppm downfield from the signal for the comparable proton in analogous TNB·OR<sup>-</sup> adducts. On this basis, the signal for the similar  $sp^3$ -bound proton in the putative C-3 PicOPh-OPh<sup>-</sup> adduct, **4**, should appear in a region of the spectrum well separated from the signals of the C-3 hydroxide adduct, **6**, and so should be readily identifiable. In fact, no such signal was seen before the appearance of the peaks assigned to the C-1 O-adduct, **3**, nor did it appear later in response to increasing temperature. As the temperature was raised, **6** and PicO<sup>-</sup>, **8**, were observed in the spectrum. Slowly, **6** gave way to **8** and free phenol, presumably through the intermediacy of a transient C-1 PicOPh-OH<sup>-</sup> adduct, **7**, that is not observed. Such adducts have been postulated in analogous reaction systems (6b–d). In accord with the ambident nature of phenoxide ion, the eventual product of phenoxide attack is the C-3 *para* C-bonded adduct, **5**.

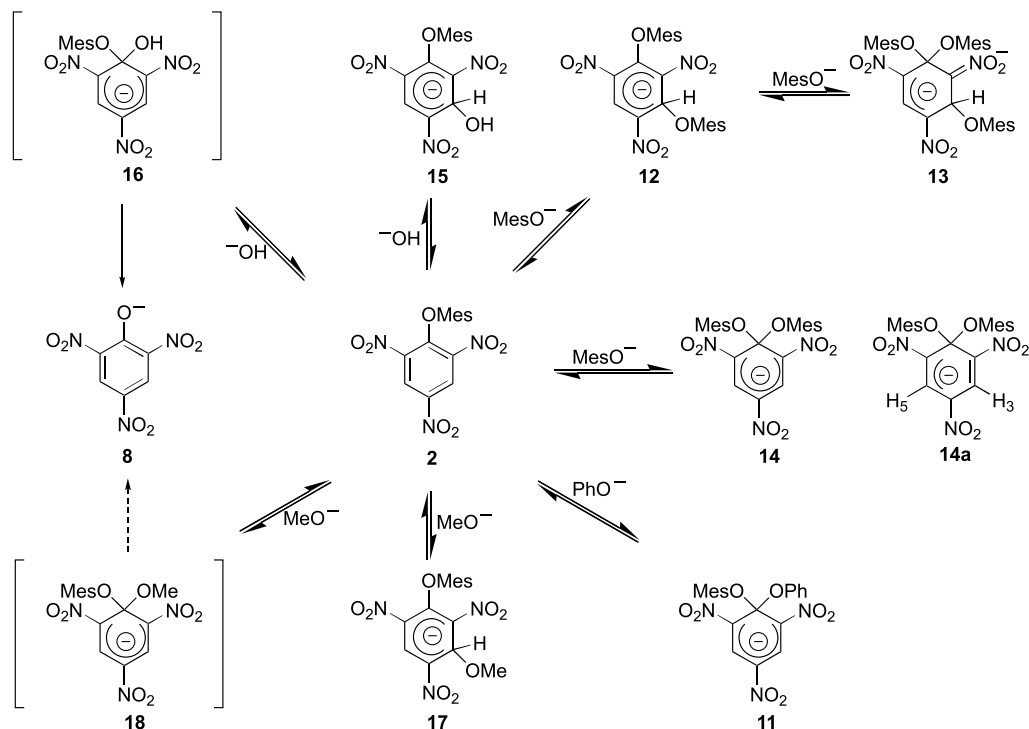
#### Reaction of **1** with equimolar MesOK in MeCN–DME

Upon addition of 1 equiv of potassium 2,4,6-trimethylphenoxide ion (potassium mesitoxide, MesOK) in MeCN-*d*<sub>3</sub>:DME-*d*<sub>10</sub> to the NMR tube that contained a cooled (–50°C) solution of **1** (final concentration 0.06 M), the sample turned a deep orange colour. Interestingly, the initial <sup>1</sup>H NMR spec-

<sup>4</sup>Signals assigned to the *para*, *meta*, and *ortho* ( $H_p$ ,  $H_m$ , and  $H_o$ ) protons typically appear as somewhat broadened triplets, and triplets and doublets, respectively. The broadening found is indicative of further unresolved coupling and so throughout this article the signals ascribed to attached phenoxy groups and to phenoxide ion or phenol will be listed as multiplets.



Scheme 2.



trum, recorded at  $-40^\circ\text{C}$ , showed the presence of *two*  $\sigma$ -complexes, the C-1 PicOPh-OMes<sup>-</sup> O-adduct, **11** (Scheme 2), and the C-1 PicOPh-OPh<sup>-</sup> adduct, **3** (Scheme 1). At this stage, peaks of **11** were found at  $\delta$  8.69 (2H, s,  $\text{H}_{3,5}$ ), 7.08 (2H, m,  $\text{H}_m$ ), 6.80 (1H, m,  $\text{H}_p$ ), 6.68 (2H, s,  $\text{H}_{3',5'}$ , mesitoxyl), 6.60 (2H, m,  $\text{H}_o$ ), 2.16 (3H, s, *p*-Me, mesitoxyl), and 1.97 (6H, s, *o*-Me) and were clearly distinguishable from the signals assigned to **3** (Table 1). The resonances of **11** were predominant in this initial spectrum: **11**:**3** = 2:1.

As the temperature of the system was slowly raised to  $-20^\circ\text{C}$ , broad resonances appeared, a set at ca. 8.60 and 6.80 and a signal at ca. 6.67; these resonances were ascribable to PicOMes, **2**, and mesitol (MesOH), respectively. Coincident with the appearance of the new signals, the resonances assigned to **11** declined in favour of those of **3**. With the increase to  $-10^\circ\text{C}$  and the passage of time (ca. 2 h), new resonances appeared that were assigned to C-3 aryloxide O-adducts. The  $sp^3$ -bound protons ( $\text{H}_3$ ) of the O-adducts were doublets at 6.90 ( $J = 2.2$ ) and 6.87 ( $J = 2.2$ ), whereas the  $sp^2$ -bound protons ( $\text{H}_5$ ) appeared as a single triplet that arises from overlapping doublets centred at 8.43. The downfield shift of the  $\text{H}_3$  protons (at 6.90 and 6.87) of these species relative to the shift of the corresponding proton established for the C-3 PicOPh-OH<sup>-</sup> adduct, **6**, was consistent with attachment of the O-centre of an aryloxide (6, 9a). Although additional signals that would be expected for these C-3 aryloxide O-adducts were obscured by the peaks of **2**, **3**, **11**, and MesOH, the signals at 6.90, 6.87, and 8.43 (as well as those for **3**, **6**, and **11**) do not survive acidification (trifluoroacetic acid, TFA; 5  $\mu\text{L}$ ); it is a characteristic of O-adducts that they are acid labile (4b, 6, 9). Tentative assignment of the structures of the C-3 O-adducts corresponding to the 6.90, 6.87, and 8.43 set of signals will be made below.

Subsequent monitoring of the reaction as a function of increasing temperature (from  $-10$  to  $0^\circ\text{C}$  in ca. 30 min) showed that the peaks due to **11** vanished while signals attributed to **3** and the C-3 aryloxide O-adducts remained in the spectrum. Furthermore, peaks assigned to the PicOPh-OH<sup>-</sup> adduct, **6**, were joined by those of the C-3 PicOMes-OH<sup>-</sup> adduct, **15** (Table 1, Scheme 2). At ambient temperature the signals attributed to **3** and the C-3 aryloxide O-adducts were no longer present; those of the OH<sup>-</sup> adducts, **6** and **11**, dominated the spectrum. Peaks for **2**, MesOH, and **8** were also found and a spectrum acquired after 2 days at ambient still contained peaks for **8** and mesitol as well as PhOH.

Thus, the results suggest that in the reaction of MesO<sup>-</sup> with **1**, initial attack gives the C-1 PicOPh-OMes<sup>-</sup> O-adduct, **11**. Breakdown of **11** via an  $\text{S}_{\text{N}}\text{Ar}$  pathway (18–20) leads to formation of PicOMes and PhO<sup>-</sup> and, therefore, to a system that contains two substrates (**1** and **2**) as well as two nucleophiles (PhO<sup>-</sup> and MesO<sup>-</sup>). The liberated PhO<sup>-</sup> ion reacts at C-1 of **1** to give **3**. As the reaction proceeds, peaks due to **11** decrease in intensity in tandem with growth of the resonances of **2**, MesOH and **3**. At no time are peaks of **1** and free PhOH observed at this early stage of the reaction.

The next observable  $\sigma$ -adducts appeared at  $-10^\circ\text{C}$  and were identifiable as C-3 aryloxide O-adducts (6, 9a). Although the exact assignment of these adducts is tentative, the spectroscopic evidence supports the assignment of the signals to C-3-type aryloxide O-adducts. Moreover, the C-3 adducts arise from attack of MesO<sup>-</sup> on **2** and are not C-3 adducts formed by attack of either PhO<sup>-</sup> or MesO<sup>-</sup> on **1**. First, the previous experiment (vide supra) confirmed PhO<sup>-</sup> attack at C-1 of **1** to give **3** as the only process that involves **1** and phenoxide as an O-nucleophile. Thus, none of the C-3 arylo-



**Table 1.**  $^1\text{H}$  NMR spectroscopic characteristics<sup>a</sup> of the C-1 and C-3 adducts formed by PicOPh, **1**, and PicOMes, **2**, with phenoxide, mesitoxide, hydroxide, and methoxide ions.

Adduct	H-5	H-3	Other signals	Adduct	H-5	H-3	Other signals
<b>3<sup>b,c</sup></b>	8.63, s	8.63, s	7.15 (m, Hm), 6.95 (m, Hp), 6.69 (m, Ho)	<b>12<sup>b,c</sup></b>	8.44, d $J = 2.0$	6.90, d $J = 2.0$	Obscured
<b>5<sup>b,d</sup></b>	8.57, d $J = 1.2$	5.77, d $J = 1.2$	7.08, 6.64 (A2X2, $J = 8.5$ ), 7.21 (m, C-1 Hm), 6.90 (m, C-1 Hp)	<b>13<sup>b,c</sup></b>	8.44, d $J = 2.0$	6.87, d $J = 2.0$	Obscured
<b>6<sup>e,f</sup></b>	8.47, d $J = 1.9$	6.30, d $J = 1.9$	7.27 (m, Hm), 6.98 (m, Hp), 6.91 (m, Ho)	<b>14<sup>b,f</sup></b>	8.63 br s	7.17 br s	6.50–6.80 (mesitoxyl), 1.9–2.2 (s, <i>o</i> - <i>p</i> -Me)
<b>9<sup>e,f</sup></b>	8.56, d $J = 1.9$	6.24, d $J = 1.9$	7.28 (m, Hm), 6.99 (m, Hp), 3.27 (s, C-3 OMe)	<b>15<sup>e,f</sup></b>	8.39 br s	6.13 br s	6.73, 6.71 (s, C-1 mesitoxyl), 2.16, 2.12, 1.96 (s, <i>o</i> - <i>p</i> -Me)
<b>11<sup>b,d</sup></b>	8.69, s	8.69, s	7.08 (m, Hm), 6.80 (m, Hp), 6.68 (s, mesitoxyl ring), 6.60 (m, Ho), 2.16 (s, <i>p</i> -Me), 1.97 (s, <i>o</i> -Me)	<b>17<sup>e,f</sup></b>	8.43, d $J = 2.0$	5.99, $J = 2.0$	6.76, 6.73 (s, C-1 mesitoxyl), 2.18, 2.16, 2.03 (s, <i>o</i> - <i>p</i> -Me)

<sup>a</sup>Chemical shifts were measured in ppm ( $\delta$ ) at 400.1 MHz; coupling constants are reported in Hz.<sup>b</sup>MeCN-*d*<sub>3</sub>:DME-*d*<sub>10</sub> (1:1, v/v).<sup>c</sup>Recorded at  $-40^\circ\text{C}$ .<sup>d</sup>Recorded at  $0^\circ\text{C}$ .<sup>e</sup>Recorded at room temperature.<sup>f</sup>DMSO-*d*<sub>6</sub>.

xide O-adducts can arise from interaction of **1** and  $\text{PhO}^-$ . Secondly, decomposition of the initially formed C-1 PicO-Ph-OMes<sup>-</sup> adduct, **11**, releases PicOMes, **2**, which could undergo further attack by mesitoxide. Note that **2** and MesOH are both observed in spectra acquired at this temperature. Further justification for the assignments was obtained from study of the PicOMes–MesO<sup>-</sup> system (vide infra). By the reasoning outlined, the peaks of the C-3 aryloxide O-adducts in the present system are ascribed to the C-3 PicOMes-OMes<sup>-</sup> adduct, **12**, and the C-1,3 PicOMes·(OMes)<sub>2</sub><sup>2-</sup> diadduct, **13**. The H<sub>3</sub> resonance at 6.90 (d,  $J = 2.2$ ) is attributed to **12**; that of **13** appears at 6.87 (d,  $J = 2.2$ ).

The final  $\sigma$ -adducts found in the system are the C-3 hydroxide complexes **6** and **15** that result from equilibration of  $\text{PhO}^-$  and MesO<sup>-</sup> with residual water in the medium that, in turn, generates OH<sup>-</sup>. Ultimately, these too give way to picrate ion, **8**, PhOH, and MesOH.

### Reaction of **2** with equimolar PhOK in MeCN–DME

The interaction of PicOMes, **2**, with PhOK in MeCN-*d*<sub>3</sub>:DME-*d*<sub>10</sub> (1:1 v/v) was found to give results similar to those for the PicOPh–MesO<sup>-</sup> reaction system described above. Consequently, after the addition of equimolar PhOK in MeCN-*d*<sub>3</sub>:DME-*d*<sub>10</sub> to a solution of **2** in the same medium (final concentrations: 0.06 M), cooled to  $-50^\circ\text{C}$ , the first spectrum (recorded at  $-40^\circ\text{C}$ ) includes resonances of the C-1 PicOMes-OPh<sup>-</sup> O-adduct, **11** (Scheme 2) as well as the C-1 PicOPh-OPh<sup>-</sup> O-adduct, **3** (Scheme 1). As the temperature is raised, peaks reappear for **2** and appear for MesOH, but at  $-10^\circ\text{C}$ , signals are observed that correspond to the C-3 mesitoxide adducts, **12** and **13**. Observation of the peaks for these species validates their observation and assignment in the PicOPh–MesO<sup>-</sup> reaction system.

Peaks due to **11** disappear from the spectrum at  $0^\circ\text{C}$  and resonances attributable to the C-3 hydroxide adducts, **6** and **15**, appear. At ambient temperature the signals for these hydroxide adducts, **6** and **15**, and for PicO<sup>-</sup> were dominant, whereas the peaks of **3**, **12**, and **13** diminish. Eventually (>12 h), the spectrum obtained at room temperature consists mainly of **8**, PhOH, and MesOH, although small extraneous, unidentified signals were also present.

### Reaction of **2** with equimolar MesOK in MeCN–DME

To a solution of **2**, cooled to  $-50^\circ\text{C}$ , was added a similarly cooled solution of MesOK in MeCN-*d*<sub>3</sub>:DME-*d*<sub>10</sub> (final concentration: 0.06 M). The major peaks in the initial  $^1\text{H}$  NMR spectrum measured at  $-40^\circ\text{C}$  (acquired within 5 min of mixing) were identified as belonging to unmodified **2** and MesOK. However, two equivalent broad singlets were also noted at  $\delta$  8.62 and 7.17. The 8.62 resonance could correspond to the H<sub>3,5</sub> protons of a C-1 MesO<sup>-</sup> adduct; comparison of the chemical shift with those for the H<sub>3,5</sub> protons of the related C-1 TNA·OMes<sup>-</sup> adduct, **18**, (i.e., 8.62 (6c)) and the C-1 PicOPh-OPh<sup>-</sup> adduct, **3** (i.e., 8.63) favours this assignment. However, in the present system the relative integrals link the 8.62 peak to the broad signal at 7.17 (i.e., 1:1 integral ratio). Moreover, peaks, albeit poorly resolved ones, are observed in the 6.5–6.8 and 1.9–2.2 ppm regions (other than those for **2** and MesOK) and are taken to represent the mesitoxyl protons of this initially formed species.



**Table 2.**  $^{13}\text{C}$  NMR spectral characteristics<sup>a</sup> of the C-1 PicOPh phenoxide adduct, **3**, and the C-1 TNA phenoxide adduct **10**,<sup>b</sup> in MeCN–glyme,<sup>c</sup> as well as the substrates, PicOMe (TNA), PicOPh (**1**), and PicOMes (**2**) in DMSO.<sup>d</sup>

Species	C-1	C-2,6	C-3,5	C-4	C-7	C-8,12	C-9,11	C-10
<b>3</b> <sup>c</sup>	104.4	130.8	130.5	119.9	155.1	120.8	130.4	124.0
<b>10</b> <sup>b,c</sup>	104.5	129.5	131.1	119.7	155.4	120.5	130.4	124.0
TNA <sup>d</sup>	151.5	144.3	125.0	141.7	65.2			
<b>1</b> <sup>d</sup>	145.2	144.0	125.5	143.3	156.4	115.8	130.1	124.6
<b>2</b> <sup>d,e</sup>	145.5	141.0	124.4	140.9	148.0	127.9	130.9	135.7

<sup>a</sup>Chemical shifts are given in ppm ( $\delta$ ) measured at 100 MHz.<sup>b</sup>Generated from reaction of TNA with 1 equiv  $\text{PhO}^-$ .<sup>c</sup> $\text{CD}_3\text{CN-DME-}d_{10}$  (1:1, v/v); obtained at  $-40^\circ\text{C}$ .<sup>d</sup>DMSO- $d_6$  at ambient temperature.<sup>e</sup>Mesitoxyl *o*-Me  $\delta$  15.9; *p*-Me 20.2.

Combination of these observations with the kinetic preference shown by aryloxides for attack at the C-1 position of picryl alkyl ethers (6, 7) leads to assignment of the resonances at 8.62 and 7.17 to the ring protons of the C-1 PicOMes·OMes<sup>−</sup> adduct, **14** (Scheme 2). In this case, the H<sub>3</sub> and H<sub>5</sub> protons are non-equivalent as a result of steric interactions between the C-1 mesitoxyl substituents and the flanking C-2,6 nitro groups. For example, if one of the C-2,6 NO<sub>2</sub> groups in **14** is twisted from the plane of the cyclohexadienyl ring to relieve the proposed steric strain, then the negative charge of **14** could only be delocalized to the C-4 and one of the C-2,6 NO<sub>2</sub> groups. Thus, assuming that the C-4 and C-6 nitro groups form part of the conjugated anionic system, the C-2 nitro group and the moiety to which it is bonded would resemble an isolated nitroalkene, and H<sub>3</sub>, in this example, would approximate a proton at the 2-position of a 1-nitroalkene (**14a**, Scheme 2). In this regard, it is noteworthy that the resonance for the olefinic proton at the 2-position of 1-nitrocyclohexene appears at 7.20 in DMSO- $d_6$  (21). Twisting of NO<sub>2</sub> groups out of the aromatic plane has been noted in numerous X-ray crystallographic studies of neutral nitroaromatic compounds that possess an alkoxy group adjacent to the nitro group (22).

As the temperature was gradually raised, the spectra obtained showed a sequential decline in the signals that represent **14** (Scheme 2). The spectrum acquired at  $-30^\circ\text{C}$  (recorded ca. 30 min after the initial spectrum acquired at  $-40^\circ\text{C}$ ) lacked peaks of **14**; signals of **2** were notably broad. Upon further warming, peaks sharpened, and at  $-10^\circ\text{C}$  the spectrum contained signals assigned to two C-3 MesO<sup>−</sup> adducts as follows: **12** at 8.44 (1H, d,  $J = 2.2$ , H<sub>5</sub>) and 6.90 (1H, d,  $J = 2.2$ , H<sub>3</sub>) and **13** at 8.44 (1H, d,  $J = 2.2$ , H<sub>5</sub> overlapped with H<sub>5</sub> of **12**) and 6.87 (1H, d,  $J = 2.2$ , H<sub>3</sub>). Observation of signals of these Meisenheimer complexes in this system was in accord with their previous identification in the PicOPh–MesO<sup>−</sup> and PicOMes–PhO<sup>−</sup> reactions and confirmed their assignment as adducts arising from attack of MesO<sup>−</sup> on PicOMes in all three studies.

At ambient temperature the peaks of **12** and **13** are replaced by those due to the C-3 PicOMes·OH<sup>−</sup> adduct, **15** (Scheme 2). After monitoring the reaction for 12 h at room temperature, the singlet for **8** at 8.65 is also seen.

## Discussion

### Reaction pathways and classification of regioselectivity

The interactions of the series of O-nucleophiles, phenoxide ( $\text{PhO}^-$ ), 2,4,6-trimethylphenoxide (mesitoxide, MesO<sup>−</sup>), hydroxide ( $\text{OH}^-$ ), and methoxide ( $\text{MeO}^-$ ) ions with the picryl aryl ethers PicOPh, **1**, and PicOMes, **2**, provide interesting insights into the variable regioselectivity of Meisenheimer complex formation. On the basis of comparison of the  $\text{p}K_{\text{a}}$  values of the parent phenols (23) in water and with the assumption that nucleophilicity follows basicity (24), MesO<sup>−</sup> as the more basic aryloxide of the two would be expected to be a more reactive nucleophile than  $\text{PhO}^-$  (i.e.,  $\text{p}K_{\text{a}}$  (PhOH) = 9.95;  $\text{p}K_{\text{a}}$  (MesOH) = 10.88, see also ref. 25). However,  $\text{PhO}^-$  may act as an ambident (C- and O-) nucleophile, whereas MesO<sup>−</sup> is restricted to O-attack. The *ortho*-Me groups in MesO<sup>−</sup> make it a sterically hindered nucleophile. This steric bulk would introduce further F-strain to attack at C-1, which would partly offset the higher nucleophilicity of MesO<sup>−</sup> compared with  $\text{PhO}^-$ . Therefore, the two aryloxides could display similar kinetic activity overall. Conversely, the steric factor may also render the resultant C-1 MesO<sup>−</sup> adduct significantly less stable than its C-1  $\text{PhO}^-$  oxygen-centred counterpart. Consequently, these nucleophiles would show different thermodynamic preferences while displaying the same kinetic preference for C-1 attachment.

The ambident nature of  $\text{PhO}^-$  also results in the formation and observation of C-centred adducts as the final, stable Meisenheimer complexes observed in the reaction systems involving phenoxide as nucleophile. In each case, C-adducts were identified as the C-3 regioisomers bonded via the *para* site of phenoxide.

In all of the aryloxide systems examined, hydroxide adducts also formed during the period of study as a result of reaction with adventitious H<sub>2</sub>O in the solvent systems. The assignments of these adducts was confirmed in separate control experiments that included reaction of **1** and **2** with tetramethylammonium hydroxide in DMSO and with potassium methoxide (in MeOH) in DMSO. As in other studies of picryl ether – alkoxide and picryl ether – hydroxide reactions (5), these localized O-nucleophiles reacted according to K3 classification in which attack at C-3 is kinetically pre-

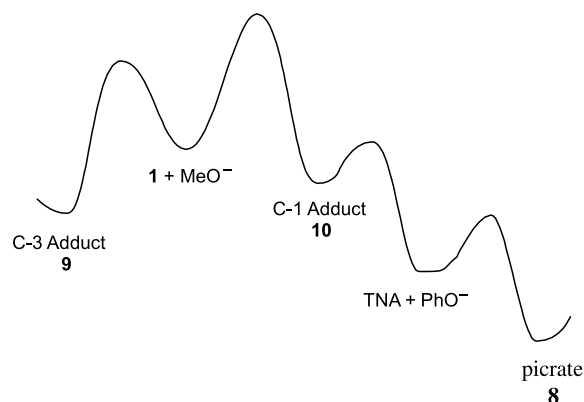


ferred. On the other hand, the C-1 O-adducts **7** and (or) **10** (Scheme 1) and **16** and (or) **18** (Scheme 2) are not detected and represent metastable intermediates in the  $S_NAr$  displacement reaction to yield picrate (**8**), TNA, and phenol or mesitol.

The situation in the picryl aryl ether – methoxide systems is particularly informative. Although the C-1 adducts PicOPh-OMe<sup>-</sup> (**10**) and PicOMes-OMe<sup>-</sup> (**18**) are observed in the TNA-PhO<sup>-</sup> (**6b**) and TNA-MesO<sup>-</sup> (**6c**) systems, respectively, these species are not observed in the present studies where the corresponding picryl aryl ethers react with methoxide to yield the C-3 adducts **9** and **17** as the only observable Meisenheimer complexes. It is important to note that in the TNA systems, **10** and **18** are the first and only adducts detected at -40°C in 1:1 MeCN–DME. Both adducts decompose to yield the C-3 hydroxide adduct of TNA via the thermodynamically unfavourable equilibrium between the aryloxide and adventitious water in the MeCN–DME medium (**6b–6d**, **9a**). This observation suggests that the C-3 TNA·OH<sup>-</sup> adduct is more stable than **10** and **18** and by extension the C-3 TNA·OMe<sup>-</sup> adduct should also be more stable. These arguments suggest strongly that the inability to detect **10** and **18** in reactions of **1** and **2** with MeO<sup>-</sup> stems from the fact that they are not as stable as the C-3 adducts **9** and **17**, respectively. The very slow rate of conversion of the C-3 PicOPh-OMe<sup>-</sup> adduct **9** and C-3 PicOMes-OMe<sup>-</sup> adduct **17** into the  $S_NAr$  products of TNA, PhO<sup>-</sup>, MesO<sup>-</sup>, and picrate (**8**) is consistent with this hypothesis. These arguments are summarized in the reaction coordinate diagram depicted in Fig. 2 for the reaction of PicOPh (**1**) with MeO<sup>-</sup>. Here the C-1 O-adduct **10** is shown to be less stable than the C-3 adduct **9**. However, the  $S_NAr$  product from decomposition of **10** (TNA, PhO<sup>-</sup>, and eventually picrate (**8**)) are the final products formed following irreversible processes. *Thus, even though the products from C-1 attack are thermodynamically favoured, the reactions of **1** and **2** with methoxide (and by extension hydroxide) can be designated as K3T3 on the basis of the kinetic and thermodynamic preferences in the initial reactions of **1** and **2** with the alkoxide (hydroxide) nucleophiles.*

Focusing on the aryloxide systems, PicOPh(**1**)–PhO<sup>-</sup> and PicOMes(**2**)–MesO<sup>-</sup> are regarded as symmetrical systems, as the nucleophile and leaving group in the  $S_NAr$  process are the same; conversely, PicOPh(**1**)–MesO<sup>-</sup> and PicOMes(**2**)–PhO<sup>-</sup> are regarded as nonsymmetric systems. In the symmetrical PicOPh(**1**)–PhO<sup>-</sup> system, it is clear that reaction of PhO<sup>-</sup> with **1** yields the C-1 PicOPh-OPh<sup>-</sup> adduct, **3**, as the first observable phenoxide O-adduct (at -40°C). No C-3 phenoxide O-adduct (i.e., **4**, Scheme 1) is detected either prior to observation of **3** or later in the reaction. In our previous study of the TNA-PhO<sup>-</sup> system we were able to demonstrate that a similar observation at low temperature indicated K1T1 regioselectivity (Fig. 1) in which formation of the corresponding C-1 TNA·OPh<sup>-</sup> Meisenheimer complex was favoured by both kinetics and thermodynamics (**6b**). However, the TNA-PhO<sup>-</sup> system had been previously examined by fast kinetic techniques that supported the assignment of the first formed O-adduct to the C-1 TNA·OPh<sup>-</sup> species (**8**). Further, it had been established that the related TNB·OPh<sup>-</sup> adduct could be identified and fully characterized by <sup>1</sup>H NMR spectroscopy under the same experimental conditions

**Fig. 2.** Qualitative reaction coordinate diagram for reaction of PicOPh (**1**) with MeO<sup>-</sup>.



(**9a**). Since the TNB·OPh<sup>-</sup> O-adduct is a reasonable model for a hypothetical C-3 TNA·OPh<sup>-</sup> O-complex, it follows that any C-3 phenoxide O-adduct would have been observed if it had formed. It is, therefore, important in following this train of logic to note that the TNB·OPh<sup>-</sup> adduct is also a structural analogue of the C-3 PicOPh·OPh<sup>-</sup> Meisenheimer complex, **4**, and that **4** would be expected to be observed if it formed during the course of the reaction. *Thus, in the symmetrical PicOPh–PhO<sup>-</sup> system, PhO<sup>-</sup> (as an O-nucleophile) follows K1T1 regioselectivity.*

The next observable species, as a function of increasing temperature, is **6**, the C-3 PicOPh·OH<sup>-</sup> complex. The necessary hydroxide is formed in low concentration via the thermodynamically unfavourable equilibrium between PhO<sup>-</sup> and adventitious water in the MeCN–DME medium (**6b–d**, **9a**). The timing of the appearance of the hydroxide adduct in these systems does not parallel the nucleophilicity of OH<sup>-</sup> relative to PhO<sup>-</sup> because of the expected significant difference in concentration of the two nucleophiles in these reaction systems. As the reaction proceeds, PicO<sup>-</sup> (picrate anion, **8**) and PhOH appear, presumably as decomposition products that arise from the transient C-1 PicOPh·OH<sup>-</sup> adduct, **7** (Scheme 1), whose existence has been postulated in a number of related systems (**6b–6d**).

The ultimate product of thermodynamic control is the C-3 para-bonded C-adduct, **5**. Formation of this C-3 PicOPh·PhO(H)<sup>-</sup> Meisenheimer complex further illustrates the ambident (O- and C-) nucleophilic nature of phenoxide; compound **5** is formed with effective irreversibility. It is apparent that this C-3 C-adduct is the product of kinetic preference for C-attack at the 3-position. AM1 calculations (**6d**) suggest that the C-3 C-adduct is also the product of thermodynamic control. The thermodynamic preference for C-3 attack by carbon nucleophiles is also implicit in the reaction scheme of the VNS reaction (**10**). *Thus, in the PicOPh–PhO<sup>-</sup> system, PhO<sup>-</sup> (as a C-nucleophile) follows K3T3 regioselectivity.*

In the nonsymmetric systems (PicOPh(**1**)–MesO<sup>-</sup> and PicOMes(**2**)–PhO<sup>-</sup>), reaction of **1** with MesO<sup>-</sup> forms the C-1 PicOPh-OMes<sup>-</sup> Meisenheimer complex, **11**, as the kinetically favoured species (Scheme 2). Although **11** is the dominant adduct observed in the first <sup>1</sup>H NMR spectrum acquired at -40°C, significant amounts of the C-1 PicOPh·OPh<sup>-</sup> adduct, **3**, were also present. This observation im-



plied that **11** broke down to yield low concentrations of **2** and free  $\text{PhO}^-$ , which could then attack **1** to yield **3**. In this sense, two nucleophiles ( $\text{MesO}^-$  and  $\text{PhO}^-$ ) and two substrates (**1** and **2**) must be simultaneously present here and, by extension, in the other nonsymmetric  $\text{PicOMes(2)-PhO}^-$  reaction system.

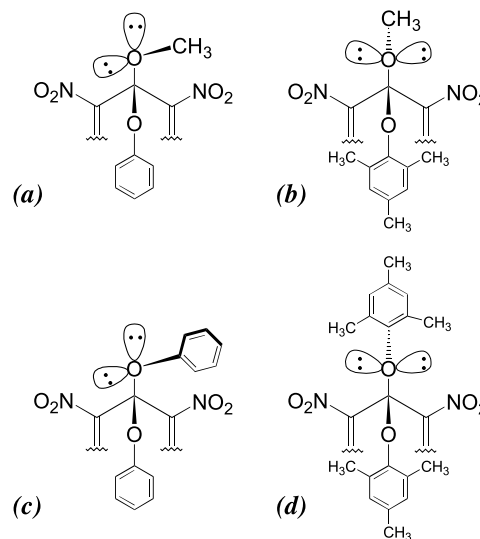
Importantly, the initially formed C-1 O-adducts of **1** and **2** eventually give way to the C-3 mesitoxide O-centred adducts C-3  $\text{PicOMes-OMes}^-$ , **12**, and the C-3 diadduct  $\text{PicOMes-(OMes)}_2^{2-}$ , **13**. The assignment of the structures of **12** and **13** as progeny of **2** was confirmed by the separate study of the symmetrical  $\text{PicOMes(2)-MesO}^-$  system. Here, the initially formed C-1  $\text{PicOMes-OMes}^-$  adduct, **14**, decomposes in favour of the C-3 species, **12** and **13**. Thus, the complexity of the nonsymmetric systems ( $\text{PicOPh-MesO}^-$  and  $\text{PicOMes-PhO}^-$ ) can render only a tentative classification as KIT3 (Fig. 1); however, as noted above, the simpler symmetrical  $\text{PicOMes-MesO}^-$  system can be definitively classified as following KIT3 regioselectivity.

### Stereoelectronic stabilization of the C-1 adducts

Of the factors that stabilize the respective C-1 picryl ether O-adducts, stereoelectronic  $n \rightarrow \sigma^*$  interactions have emerged from our analysis of the  $\text{TNA-PhO}^-$  and  $\text{TNA-MesO}^-$  systems as an important mechanism of stabilization of these adducts (6b–d, 7). In brief, full  $n \rightarrow \sigma^*$  stabilization is possible only when one O–R sigma bond is aligned antiperiplanar to one of the nonbonding lone pairs of the other C(1)–OR acetal-like group and vice versa (26), i.e., a “doubly antiperiplanar” conformation. We previously argued that in the C-1  $\text{TNA-OPh}^-$  adduct (i.e., **10**), rotameric forms that would permit single  $n \rightarrow \sigma^*$  interactions would be significantly populated in solution. Thus, as depicted in Fig. 3, Fig. 3a, which represents the most stable rotamer of **10**, will partake in this stereoelectronic stabilization through the antiperiplanar configuration of orbitals and consequently, adduct **10** is more stable than its C-3 counterpart (6b). However, from inspection of molecular models (Fieser or Darling) and on the basis of downfield  $^{13}\text{C}$  chemical shifts (6c) that suggested puckering of the cyclohexadienate ring of the  $\text{TNA}^-$  moiety, it became apparent that the rotamer shown in Fig. 3b was preferred for the mesitoxide C-1 adduct of TNA, even though it does not permit stereoelectronic stabilization (6c, 7). Consequently, the C-1  $\text{TNA-OMes}^-$  adduct is not as stable as its C-3 analogue (6c).

A further factor impinges on the degree of  $n \rightarrow \sigma^*$  stabilization provided to a given C-1 adduct that is geminally disubstituted by electronegative groups. Even if suitable doubly antiperiplanar conformers are readily accessible through rotation and even if such forms would be expected to be populated at a given temperature, the efficacy of the  $n \rightarrow \sigma^*$  stabilization will depend on the relative energies of the two  $\sigma^*$  fragment orbitals. Thus,  $n$  donation from OPh in adduct **10** to the  $\sigma^*$  orbital of the  $\text{OCH}_3$  fragment may be more or less effective than  $n$  donation from  $\text{OCH}_3$  to the  $\sigma^*$  orbital of OPh. In general then, unsymmetrical C-1 adducts should exhibit less stereoelectronic stabilization than their symmetrical counterparts regardless of whether their most favourable rotameric forms are accessible or not (7, 26, 27). Consequently, the C-1  $\text{PicOPh-OMe}^-$  adduct, **10**, the C-1  $\text{PicOMes-OMe}^-$  adduct, **18**, the C-1  $\text{PicOMes-OPh}^-$  adduct, **11**,

**Fig. 3.** (a) Illustration of the stereoelectronic stabilization of the C-1  $\text{TNA-OPh}^-$  adduct **10** through antiperiplanar interaction between the lone pair on the methoxy oxygen and the C—OPh bond; (b) Illustration of the  $\text{TNA-OMes}^-$  adduct, where stereoelectronic stabilization as in (a) is not possible; (c) Illustration of the C-1  $\text{PicOPh-OPh}^-$  adduct **3** where, as in (a), stereoelectronic stabilization is possible; (d) Illustration of the C-1  $\text{PicOMes-OMes}^-$  adduct **14** where, as in (b), stereoelectronic stabilization is not possible.



and the C-1 hydroxide adducts, **7** and **16**, would all be expected to partake of less stereoelectronic stabilization than their symmetrical analogues. This factor, no doubt, partly accounts for the inability to observe the hydroxide adducts, for example.

Focusing on the symmetrical aryloxide systems ( $\text{PicOPh(1)-PhO}^-$  and  $\text{PicOMes(2)-MesO}^-$ ), whose regioselectivity could be clearly defined, it would be expected that the C-1  $\text{PicOPh-OPh}^-$  adduct, **3**, if it could achieve suitable rotameric forms that would permit  $n \rightarrow \sigma^*$  donation, would be stabilized relative to its C-3 counterpart, **4**. Therefore, the  $\text{PicOPh-PhO}^-$  system would be expected to display thermodynamic preference for formation of the C-1 adduct, i.e., T1 in the observed KIT1 regioselectivity, and **4** would not be detected. Relating the C-1  $\text{PicOPh-OPh}^-$  adduct, **3**, to its TNA analogue (**10**, Fig. 3a), inspection of molecular models (Fieser or Darling) predicts that the rotamer represented in Fig. 3c would be the most stable for **3**. This configuration would be stabilized by  $n \rightarrow \sigma^*$  donation, and consequently **3** would be more stable than its C-3 analogue **4**. These expectations are borne out by the observation of **3** as the sole O-adduct in this system.

For the  $\text{PicOMes(2)-MesO}^-$  system, the rotamer represented in Fig. 3d is favoured for the C-1  $\text{PicOMes-OMes}^-$  adduct, **14**, on inspection of molecular models. This adduct is even more sterically congested than its TNA analogue (Fig. 3b), and **14** will be unable to derive any stabilization from  $n \rightarrow \sigma^*$  donation. In fact, the non-equivalence of the 2,4,6-trinitrocyclohexadienate ring protons of **14** showed that to accommodate the bulky mesitoxyl groups at C-1, the adduct must sacrifice delocalization of negative charge into one of the *ortho* nitro groups as indicated in structure **14a**.



The C-1 PicOMes-OMes<sup>-</sup> adduct (**14**) has a relatively short lifetime even at low temperatures (i.e., **14** is no longer present in the spectrum taken at -30°C, a temperature at which the analogous C-1 PicOPh-OPh<sup>-</sup> adduct (**3**) is the only adduct seen in the PicOPh-PhO<sup>-</sup> system). The lack of stereoelectronic stabilization and the consequent instability of **14** distinguishes the PicOMes-MesO<sup>-</sup> system that follows K1T3 regioselectivity from the PicOPh-PhO<sup>-</sup> system that exhibits K1T1 behaviour.

## Molecular orbital approaches to the kinetic preferences

### Frontier molecular orbital analysis

An important question arises from the above considerations. If the PicOMes-OMes<sup>-</sup> adduct, **14**, is inherently so unstable, why does mesitoxide attack at C-1 occur at all? Moreover, given the steric bulk of the mesitoxide nucleophile, why is C-1 attack by MesO<sup>-</sup>, particularly on the congested C-1 centre in PicOMes, **2**, favoured kinetically?

Molecular orbital theory, and, notably, the frontier molecular orbital (FMO) approach (28, 29), have been invoked to rationalize the regioselectivity in aromatic substitution reactions. As applied to the current systems, the FMO treatment holds that the preferred sites of attack will be those that permit maximum orbital overlap between the incoming (donor) nucleophile and the nitroaromatic (acceptor) substrate. In turn, this implies that the regioselectivity will be determined by the magnitude of the lowest unoccupied molecular orbital (LUMO) lobe at each ring carbon, as indicated by the orbital coefficients at each site, for a given nitroaromatic substrate.

Given the similarity in regioselectivity found for PicOPh, **1**, and PicOMes, **2**, in the current study and the behaviour of TNA with the same nucleophiles, namely PhO<sup>-</sup> (**6b**), MesO<sup>-</sup> (**6c**), and MeO<sup>-</sup> and OH<sup>-</sup> (**6b**, **6c**, **5a**, **5b**), TNA would appear to be an acceptable general model for all picryl ethers. In this regard, we have undertaken AM1 calculations on TNA (and some related compounds (**6d**)). The two degenerate LUMOs of 1,3,5-trinitrobenzene become split upon introduction of the C-1 methoxyl group to form TNA. The AM1 calculated LUMO and superjacent unoccupied molecular orbital (SUMO) are illustrated in Fig. 4. The energy of the LUMO is -2.50 eV according to the AM1 calculation, while the SUMO is higher in energy at -2.39 eV (a difference of 0.11 eV or 2.5 kcal mol<sup>-1</sup>).

Examination of the LUMO (Fig. 4) shows that C-1 is the site with the largest orbital coefficient. Interestingly, C-4, which bears a nitro group, is the site with the second highest orbital coefficient. The regioselectivity found should, in the FMO treatment, depend also on the energy of the highest occupied molecular orbital (HOMO) of the attacking nucleophile. The most favourable interaction will then be between nucleophile HOMO and substrate LUMO, when these are similar in energy.

Estimates of the HOMO energies of some of the anions have been made by Pearson (30) using the approximation that the electron affinity of the corresponding radicals (i.e., PhO<sup>•</sup>, OH<sup>•</sup>) represents the ionization potential (IP) of the anions that, according to Koopmans' theorem (31), is taken to be equal to the negative value of the HOMO energies. Therefore, the HOMO energy for PhO<sup>-</sup> and for OH<sup>-</sup> is estimated to be -2.35 and ca. -1.83 eV, respectively.

On the basis of the energetics, phenoxide (and, by extension, mesitoxide and other nucleophiles with relatively low-lying HOMO energies) may interact most strongly with the LUMO of TNA and, consequently, attack C-1, the site of highest orbital coefficient, preferentially. Conversely, hydroxide and methoxide may interact most strongly with the SUMO of TNA, which has its highest orbital coefficients at C-3 and C-5. Hence, aryloxides would show K1 behaviour while alkoxides and (or) hydroxide display K3 behaviour. However, such an analysis attributes significant changes in regioselectivity to relatively small energy differences; the energy gap between LUMO and SUMO is not large, and in fact, the HOMO of aryloxide nucleophiles would be expected to interact both with the LUMO and SUMO.

An alternative to the FMO approach is the configuration mixing model that is considered in the next section.

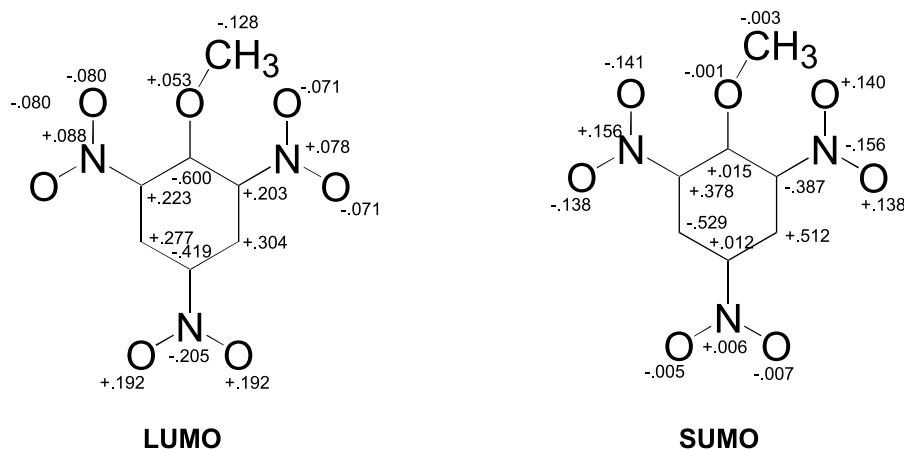
### Configuration mixing model: Polar vs. SET pathways

The configuration mixing model advanced by Shaik, Pross, and Hoz in a series of articles (32) and reviews (16) defines the full reaction profile for an organic reaction by assuming, in general, that transition states possess varying proportions of covalent-bonding and radical character. This model provides a mechanistic spectrum between a single electron transfer (SET) pathway and a polar one, where the polar process involves synchronous electron shift and bond formation through a radical coupling pathway. In the SET route, SET precedes bond formation. Thus, which particular pathway is followed in any given reaction depends on the feasibility of coupling of the two spin-paired electrons (bond formation) following the electron shift. Factors governing SET vs. polar pathways include effects of donor-acceptor ability, steric interactions, the donor-acceptor bond strength, and radical delocalization (16b). Taking these factors into consideration allows assessment of which donor-acceptor pair is likely to follow the SET pathway.

In the present system, single electron transfer from the nucleophile to the picryl aryl ether would produce the radical anion of the picryl aryl ether and the requisite radical of the nucleophile. Change in nucleophile from an alkoxide-HO<sup>-</sup> to an aryloxide may cause a shift from a polar to a SET pathway. Electrochemical measurements in acetonitrile show that the one-electron half-peak oxidation potential ( $E_{1/2}$ ) for the conversion of phenoxide into the phenoxyl radical is ~0.30 V vs. NHE. The corresponding value for HO<sup>-</sup> is ~0.6 V (33). The lower oxidation potential of phenoxide indicates that the phenoxyl radical is more stable than the hydroxyl radical as a consequence of the stabilizing effect exerted by the neighbouring aromatic ring on the radical centre. Further, since methyl substituents on a benzene ring are known to impart further stability to a benzylic (and presumably to an analogous aryloxide) radical, mesitoxyl radical would be expected to be more stable than phenoxyl radical and, therefore, to form even more readily (34, 35). Clearly the SET donor ability of the aryloxide is superior to that of alkoxides-HO<sup>-</sup>. In terms of steric interactions, it is equally clear that mesitoxide is a more sterically hindered nucleophile than methoxide-HO<sup>-</sup>. Steric hindrance favours the SET pathway since the polar pathway is energetically favourable when the reacting species can approach each other to within bonding distance. Steric repulsions will cancel en-



**Fig. 4.** Orbital coefficients ( $p_z$ ), according to a semi-empirical calculation (AM1), for the lowest unoccupied molecular orbital (LUMO) and for the superjacent unoccupied molecular orbital (SUMO) of 2,4,6-trinitroanisole (TNA), a model for picryl ethers, generally. (The  $p_x$  and  $p_y$  coefficients are negligibly small). The LUMO, which is calculated to be lower in energy ( $-2.50$  eV) than the SUMO ( $-2.39$  eV), has its largest ring orbital coefficient at C-1 (i.e.,  $-0.600$ ), whereas the largest ring orbital coefficients in the SUMO are located at C-3 and C-5 ( $0.512$  and  $-0.529$ , respectively).



ergy lowering because of bonding changes in the transition state, thus favouring the SET pathway, as SET processes take place at distances significantly greater than those at which incipient bonding takes place (16b). Furthermore, alkoxides and  $\text{HO}^-$  form strong bonds to give stable Meisenheimer complexes and generate localized radicals. These factors favour the polar pathway. In contrast, the aryloxides generate relatively unstable O-adducts that are transient in DMSO at room temperature (8, 9a) and delocalization of the aryloxide radical inhibits bond formation through radical coupling. These factors favour the SET pathway.

Shown in Fig. 5 is a schematic illustrating the relationship between the polar and SET reaction pathways (16b) for the present picryl aryl ether – nucleophile systems. The reactants are in the lower left corner where phenoxide and mesitoxide are represented as  $\text{ArO}^-$ . The polar process is indicated by the diagonal arrow, where both electron transfer and bond formation are synchronous.

The SET pathway depicted in Fig. 5 involves first electron transfer to generate the picryl aryl ether radical anion and the aryloxide radical ( $\text{ArO}^\cdot$ ) shown in the upper left corner. The second step involves bond formation. Now the regioselectivity (C-1 or C-3) of Meisenheimer complex formation would be controlled by the spin density at the C-1 or C-3 positions of the radical anion of the picryl aryl ether, an intermediate on the reaction pathway. The position of higher spin density would be expected to be the site where radical coupling will be most favoured. Calculation of the spin density of the radical anion of TNA, the model for picryl ethers, using the AM1 method shows that C-1 is the site of highest spin density. Thus, subsequent radical combination to form the Meisenheimer complex would be expected to occur at C-1.

The configuration mixing model provides a rationale for the regioselectivity observed in reactions of picryl ethers with O-centred nucleophiles. The regioselectivity depends on the degree of concertedness of electron shift and bond formation. When electron shift and bond formation are concerted, C-3 attachment is kinetically favoured because of

steric interactions at C-1. However, if the electron shift precedes bond formation, then the spin density of the picryl ether radical anion dictates C-1 attachment even though C-1 is clearly the more sterically hindered site.

In summary, on the basis of the above argument it can be concluded that *hydroxide and methoxide follow the polar ( $S_N\text{Ar}$ ) pathway; this will favour kinetically C-3 attachment due to F-strain at C-1. However, phenoxide and mesitoxide follow the SET pathway. In these cases, C-1 attachment is favoured kinetically due to the higher C-1 spin density in the radical anion of the picryl ether.*

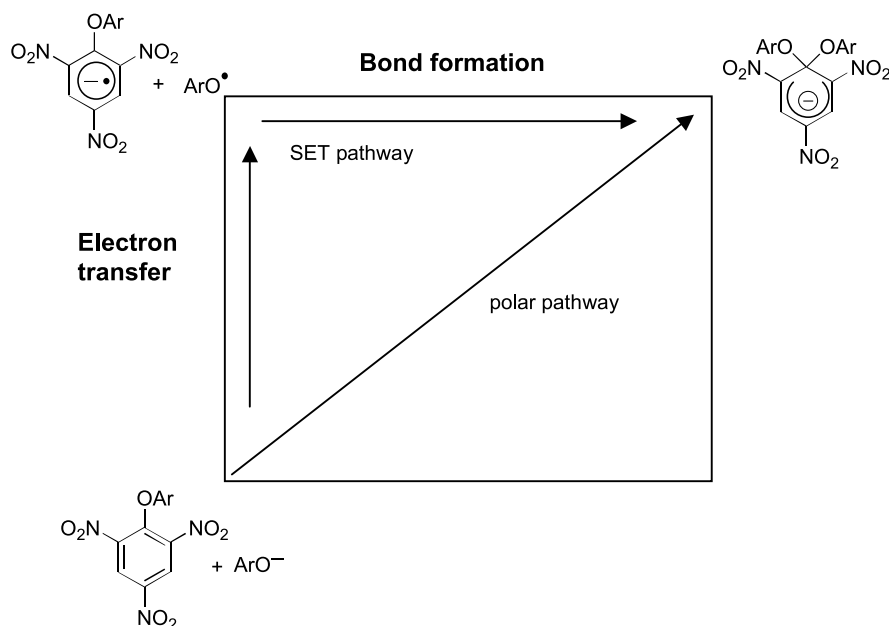
## Conclusions

The present results on the course of the reactions between picryl phenyl ether (PicOPh, **1**) and picryl mesityl ether (PicOMes, **2**) with the oxygen-nucleophiles, phenoxide, mesitoxide, hydroxide, and methoxide allow us to make the following conclusions.

The reactions of  $\text{HO}^-$  and  $\text{MeO}^-$  with **1** and **2** carried out in  $\text{DMSO}-d_6$  at ambient temperature show K3 behaviour, as documented in numerous picryl ether – alkoxide systems (5a–d). In contrast, phenoxide and mesitoxide display kinetic preference for C-1 attachment, i.e., K1 behaviour. This observation is analogous to the reactivity of these aryloxide nucleophiles towards 2,4,6-trinitroanisole (6b, 6c), and now appears to be a general trend for the reactions of aryloxide nucleophiles with picryl ethers. For the reaction of phenoxide with **1**, the C-1 O-adduct is also thermodynamically favoured for phenoxide acting as an O-nucleophile. Stereoelectronic stabilization of the C-1 PicOPh- $\text{OPh}^-$  adduct through  $n \rightarrow \sigma^*$  donation confers thermodynamic preference on this C-1 adduct relative to its C-3 oxygen-centred regioisomer. With mesitoxide ion, the C-1 adducts of both substrates are less stable than their C-3 counterparts. In these cases the steric congestion in the C-1 adducts associated with the presence of the *ortho* methyl groups of mesitoxyl moiety precludes significant stereoelectronic stabilization. Now the C-3 adducts of mesitoxide are more stable and the



**Fig. 5.** Schematic of a potential energy surface diagram illustrating the relationship between polar and SET reaction pathways for reaction of **1** and (or) **2** with aryoxide ( $\text{ArO}^-$ ) nucleophiles to give the C-1 Meisenheimer adducts.



initially formed C-1 adducts decline in favour of their C-3 regioisomers.

Although steric inhibition of stereoelectronic stabilization can account for the changeover in adduct stability (i.e., C-1  $\text{PhO}^-$  adduct of **1** are more stable than its C-3 counterpart, whereas the C-1  $\text{MesO}^-$  adducts of **1** and **2** are less stable than their C-3 isomers), there is still kinetic preference to formation of the C-1 adducts of **1** and **2** even when the attacking nucleophile is the bulky mesitoxide ion. Frontier molecular orbital considerations suggest that all nucleophiles would preferentially attack the C-1 site of picryl ethers, based on AM1 calculations of 2,4,6-trinitroanisole (TNA), as a general model for picryl ethers. An alternative explanation, which we propose, is that the reactions involving the aryloxides do not follow the polar  $\text{S}_{\text{N}}\text{Ar}$  pathway, but rather proceed according to the SET pathway outlined in Fig 5.

## Experimental

### Materials and methods

2,4,6-Trinitrophenyl phenyl ether (PicOPh, **1**) was prepared from picryl chloride and potassium phenoxide in ethanol as described by Dyall (36), mp 154–155°C (lit. (36) value mp 153–154°C). 2,4,6-Trinitrophenyl-2',4',6'-trimethylphenyl ether (PicOMes, **2**) was prepared from picryl chloride and ethanolic potassium mesitoxide, mp. 157–158°C (lit. (37) value mp 154–155°C). Picryl chloride used in these preparations resulted from the reaction of pyridinium picrate with  $\text{POCl}_3$  (38), mp. 80–81°C, after recrystallization from  $\text{CCl}_4$  (lit. (39) value mp 81°C). Acetonitrile- $d_3$  and dimethoxyethane- $d_{10}$  (Merck) were dried by sequential treatment with 4 Å molecular sieves as advocated by Burfield et al. (17). 1,4-Dibromobenzene (DBB; Eastman) was recrystallized from ethanol and dried in vacuo prior to use as an internal integration standard in the NMR experiments. Potassium phenoxide and mesitoxide were prepared from the re-

spective phenol and standard  $\text{MeOK-MeOH}$  in an  $\text{N}_2$ -filled glovebox as described previously (6b, 6c). 2,4,6-Trimethylphenol (mesitol; Aldrich) was recrystallized from petroleum ether and dried in vacuo before use. Trifluoroacetic acid (TFA; Aldrich) and tetramethylammonium hydroxide ( $\text{Me}_4\text{NOH}$ , 25 wt % solution in water; Aldrich) were used without further purification. Melting points were measured on a Thomas Hoover capillary apparatus and are not corrected.

### NMR experiments: General

NMR experiments were carried out using a Bruker AM-400 spectrometer ( $^1\text{H}$ : 400.1 MHz,  $^{13}\text{C}$ : 100.0 MHz) in  $\text{MeCN-}d_3\text{:DME-}d_{10}$  (1:1 v/v) or in dried  $\text{DMSO-}d_6$ . In the mixed solvent system,  $\text{CD}_2\text{HCN}$  served as chemical shift reference ( $^1\text{H}$ :  $\delta = 1.93$  ppm) and lock signal, whereas resonances found in spectra determined in DMSO were referenced to the peak for residual  $\text{CD}_3\text{SOCD}_2\text{-H}$  in the solvent ( $^1\text{H}$ :  $\delta = 2.50$  ppm). Chemical shifts are given in parts per million (ppm) and coupling constants ( $J$ ) are reported in hertz. Wilmad PP-507 NMR tubes (5 mm) were used in all experiments. All stock solutions were prepared in the appropriate solvents under a nitrogen atmosphere. NMR tubes were capped with rubber septa and swept out with dry  $\text{N}_2$  prior to injection of the reactants into the NMR tube with a gas-tight syringe.

### Low temperature NMR experiments in $\text{MeCN-DME}$ (1:1)

Typically, a weighed quantity of the aryoxide was dissolved in a 1:1 (v/v) mixture of  $\text{MeCN-}d_3\text{:DME-}d_{10}$  under a nitrogen atmosphere such that 300  $\mu\text{L}$  of this stock solution would yield 1–1.5 equiv of the aryoxide relative to the substrate. An aliquot of the stock solution (300  $\mu\text{L}$ ) was injected into the NMR tube, and the solution frozen by immersion in liquid  $\text{N}_2$ . To the frozen solution, 1 equiv of PicOPh or



PicOMes was injected by a gas-tight syringe (200  $\mu$ L; final concentrations 0.06–0.09 M). The final mixture was placed in a dry ice – acetone bath that had been maintained at  $-50^{\circ}\text{C}$ . The contents of the tube were allowed to mingle at this temperature. The tube was inverted several times to promote mixing and was then immersed again in liquid  $\text{N}_2$ . The tube was transferred to the spectrometer probe (at  $-40^{\circ}\text{C}$ ), the instrument was tuned as previously described (6b), and spectra were recorded at various intervals. A standard collection of FID would be made at 3, 5, 7, and 9 min and then as warranted by observed changes in the spectrum. Simultaneously, the temperature of the probe was gradually raised.

### Room temperature experiments in DMSO

A solution of the substrate was prepared in  $\text{DMSO}-d_6$  under an  $\text{N}_2$  atmosphere. An aliquot of this solution was transferred via syringe into an NMR tube and an initial spectrum run to ascertain the purity of the substrate. To this solution 1 equiv of nucleophile was injected through the septum and spectra were recorded as rapidly as possible initially and then at longer times as the reaction proceeded. 1,4-Dibromobenzene was present in the solution of the substrate and in the NMR tube as an internal integration standard.

### Molecular orbital calculations

Semi-empirical calculations were performed using AMPAC version 2.10 of AM1 (15a) on an IBM 3081 computer. The structure of 2,4,6-trinitroanisole (TNA) was calculated using the PRECISE option within the restricted Hartree–Fock (RHF; closed shell) scheme. The TNA structure was fully optimized following a Fletcher–Powell minimization (40) to a self-consistent field (SCF) that satisfied Herbert's test. The final structure was characterized as a local minimum when no negative force constants were obtained using the FORCE option.

### Acknowledgments

This research has been financed by a number of agencies. The support of the Natural Sciences and Engineering Research Council of Canada (NSERC) (to E.B.) and Wake Forest University (to R.A.M.) as well as the award of an R.T. Mohan Fellowship (to R.M.T.) is gratefully acknowledged. Discussions with Professors S. Hoz and F. Terrier were helpful, as always, and are appreciated.

### References

- (a) R.A. Foster. *J. Phys. Chem.* **84**, 2135 (1980); (b) M.A. Slifkin. *Mol. Interact.* **2**, 271 (1981).
- (a) R. Bacaloglu, C.A. Bunton, and G. Cerichelli. *J. Am. Chem. Soc.* **109**, 621 (1987); (b) R. Bacaloglu, C.A. Bunton, G. Cerichelli, and F. Ortega. *J. Am. Chem. Soc.* **110**, 3495 (1988); (c) R. Bacaloglu, C.A. Bunton, and F. Ortega. *Int. J. Chem. Kinet.* **20**, 195 (1988); (d) R. Bacaloglu, A. Blasko, C.A. Bunton, F. Ortega, and C. Zucco. *In Atual. Fis-Quim. Org. Conf. Latinoam. Fis-Quim. Org. 1st*, Edited by E. Humeres. 1991. p. 165; (e) R. Bacaloglu, A. Blasko, C.A. Bunton, E. Dorwin, F. Ortega, and C. Zucco. *J. Am. Chem. Soc.* **113**, 238 (1991); (f) R. Bacaloglu, A. Blasko, C.A. Bunton, F. Ortega, and C. Zucco. *J. Am. Chem. Soc.* **114**, 7708 (1992).
- (a) E.A. Symons and E. Buncel. *Can. J. Chem.* **50**, 1729 (1972); (b) E. Buncel and E.A. Symons. *J. Org. Chem.* **38**, 1201 (1973); (c) E. Buncel and A.W. Zabel. *Can. J. Chem.* **59**, 3168; 3177 (1981).
- (a) E. Buncel, J.M. Dust, K.T. Park, R.A. Renfrow, and M.J. Strauss. *In Nucleophilicity*. Edited by J.M. Harris and S.P. McManus. ACS Adv. in Chem. Ser. 215. American Chemical Society, Washington, D.C. 1987. pp 369–383; (b) E. Buncel, M.R. Crampton, M.J. Strauss, and F. Terrier. Electron deficient aromatic – and heteroaromatic – base interactions. The chemistry of anionic sigma complexes. Elsevier, Amsterdam. 1984; (c) E. Buncel. *In The chemistry of functional groups*. Supplement F. The chemistry of amino, nitro, and nitroso compounds. Edited by S. Patai. Wiley, London. 1982; (d) F. Terrier. *Chem. Rev.* **82**, 77 (1982); (e) F.A. Artamkina, M.P. Egorov, and I.P. Beletskaya. *Chem. Rev.* **82**, 427 (1982); (f) C.F. Bernasconi. *MTP Int. Rev. Sci. Org. Chem. Ser. One*, **3**, 33 (1973); (g) M.J. Strauss. *Chem. Rev.* **70**, 667 (1970); (h) E. Buncel, A.R. Norris, and K.E. Russell. *Quart. Rev. Chem. Soc. London*, **22**, 123 (1968).
- (a) K.L. Servis. *J. Am. Chem. Soc.* **87**, 5495 (1965); (b) K.L. Servis. *J. Am. Chem. Soc.* **89**, 1508 (1967); (c) R.A. Foster, C.A. Fyfe, P.H. Emslie, and M.I. Foreman. *Tetrahedron*, **23**, 227 (1967); (d) C.F. Bernasconi. *J. Am. Chem. Soc.* **92**, 4682 (1970); (e) G. Baldini, G. Doddi, G. Illuminati, and F. Stegel. *J. Org. Chem.* **41**, 2153 (1976); (f) M.P. Simonnin, M.J. Pouet, and F. Terrier. *J. Org. Chem.* **43**, 855 (1978); (g) A.D.A. Alaruri and M.R. Crampton. *J. Chem. Res. Synop.* 140 (1980); *J. Chem. Res. Miniprint*, 2157 (1980); (h) M.P. Simonnin, J.C. Halle, F. Terrier, and M.J. Pouet. *Can. J. Chem.* **63**, 866 (1985).
- (a) E. Buncel, S.K. Murarka, and A.R. Norris. *Can. J. Chem.* **62**, 534 (1984); (b) E. Buncel, J.M. Dust, A. Jonczyk, R.A. Manderville, and I. Onyido. *J. Am. Chem. Soc.* **114**, 5610 (1992); (c) R.A. Manderville and E. Buncel. *J. Am. Chem. Soc.* **115**, 8985 (1993); (d) E. Buncel, R.M. Tarkka, and J.M. Dust. *Can. J. Chem.* **72**, 1709 (1994).
- E. Buncel, J.M. Dust, and F. Terrier. *Chem. Rev.* **95**, 2261 (1995).
- C.F. Bernasconi and M.C. Muller. *J. Am. Chem. Soc.* **100**, 5530 (1978).
- (a) E. Buncel and R.A. Manderville. *J. Phys. Org. Chem.* **6**, 71 (1993); (b) E. Buncel and J.M. Dust. *Can. J. Chem.* **66**, 1712 (1988); (c) E. Buncel and W. Eggimann. *J. Am. Chem. Soc.* **99**, 5958 (1977); (d) E. Buncel, J.G.K. Webb, and J.F. Wiltshire. *J. Am. Chem. Soc.* **99**, 4429 (1977); (e) E. Buncel and W. Eggimann. *Can. J. Chem.* **54**, 2436 (1976); (f) E. Buncel, A. Jonczyk, and J.G.K. Webb. *Can. J. Chem.* **53**, 3761 (1975); (g) E. Buncel and J.G.K. Webb. *J. Am. Chem. Soc.* **95**, 328 (1973).
- (a) M. Makosza. *Pol. J. Chem.* **66**, 3 (1992); (b) M. Makosza, W. Daniekiewicz, and E. Wojciechowski. *Phosphorus Sulfur Silicon Relat. Elem.* **53**, 457 (1990); (c) M. Makosza and A. Kinowski. *Bull. Pol. Acad. Sci.* **37**, 127 (1989); (d) M. Makosza. *Russ. Chem. Rev.* **58**, 747 (1989); (e) M. Makosza and J. Winiarski. *Acc. Chem. Res.* **20**, 282 (1987).
- (a) M.R. Crampton and V. Gold. *J. Chem. Soc.* 4293 (1964); (b) M.R. Crampton and V. Gold. *J. Chem. Soc. B*, 893 (1966).
- (a) C.F. Bernasconi. *J. Am. Chem. Soc.* **93**, 6975 (1971); (b) M.R. Crampton and H.A. Khan. *J. Chem. Soc. Perkin Trans. 2*, 1173 (1972); (c) M.R. Crampton, B. Gibson, and F.W. Gilmore. *J. Chem. Soc. Perkin Trans. 2*, 91 (1979); (d) R. Destro, C. Grammicoli, and M. Simonetta. *Acta Crystallogr. Sect. B Struct. Crystallogr. Cryst. Chem.* **24**, 1369 (1968);



- (e) H. Ueda, N. Sakabe, J. Tanaka, and A. Furusaki. *Bull. Chem. Soc. Jpn.* **41**, 2866 (1968).
13. M.R. Crampton. *Adv. Phys. Org. Chem.* **7**, 211 (1969).
14. A. Cooney and M.R. Crampton. *J. Chem. Soc. Perkin Trans. 2*, 1973 (1984).
15. (a) M.J.S. Dewar, E.G. Zoeblich, E.F. Healy, and J.J.P. Stewart. *J. Am. Chem. Soc.* **107**, 3902 (1985); (b) M.J.S. Dewar and K.M. Dieter. *J. Am. Chem. Soc.* **108**, 8075 (1986).
16. (a) A. Pross and S.S. Shaik. *Acc. Chem. Res.* **16**, 363 (1983); (b) A. Pross. *Acc. Chem. Res.* **18**, 212 (1985); (c) S. Hoz. *Acc. Chem. Res.* **26**, 69 (1993).
17. D.R. Burfield and R.H. Smithers. *J. Org. Chem.* **43**, 3966 (1978).
18. (a) B. Gibson and M.R. Crampton. *J. Chem. Soc. Perkin Trans. 2*, 648, (1979); (b) C.F. Bernasconi, J. Fassberg, R.B. Killiom, Jr., D.F. Schuck, and Z. Rappoport. *J. Am. Chem. Soc.* **113**, 4937 (1991).
19. (a) J.F. Bunnett and R.E. Zahler. *Chem. Rev.* **49**, 273 (1951); (b) J.F. Bunnett. *Quart. Rev. Chem. Soc. London*, **12**, 1 (1958); (c) J.A. Orvik and J.F. Bunnett. *J. Am. Chem. Soc.* **92**, 2417 (1970).
20. (a) J. Miller. *Nucleophilic aromatic substitution*. Elsevier, Amsterdam. 1968; (b) F. Terrier. *Nucleophilic aromatic displacement. The influence of the nitro group*. VCH, New York. 1991.
21. C.J. Pouchert. *The Aldrich library of NMR spectra*. Vol. 1. Aldrich, Milwaukee, WI. 1986. p. 355
22. (a) J. Trotter. *Acta Crystallogr.* **12**, 605 (1959); (b) P. Coppens. *Acta Crystallogr.* **17**, 573 (1964); (c) F. Terrier, L. Xaio, P.G. Farrell, and D. Moskowitz. *J. Chem. Soc. Perkin Trans. 2*, 1259 (1992); and refs. cited therein.
23. G.R. Sprengling and C.W. Lewis. *J. Am. Chem. Soc.* **75**, 5709 (1953).
24. F. Bordwell, T.A. Cripe, and D.L. Hughes. *In Nucleophilicity. Edited by J.M. Harris and S.P. McManus. Adv. Chem. Ser.* **215**. American Chemical Society, Washington, D.C. 1987. pp 137–155.
25. (a) E.H. Baughman and M.M. Krevoy. *J. Phys. Chem.* **4**, 421 (1974); (b) F.G. Bordwell. *Acc. Chem. Res.* **21**, 456 (1988).
26. (a) A. J. Kirby. *The anomeric effect and related stereo-electronic effects at oxygen*. Springer-Verlag, Berlin. 1983. pp 9–11, 82, 90, 135–136; (b) P. Deslongchamps. *Stereoelectronic effects in organic chemistry*. Pergamon Press, New York. 1983. pp 5–20.
27. M.L. Sinnott. *Adv. Phys. Org. Chem.* **24**, 114 (1988).
28. K. Fukui, T. Yonezawa, C. Nagata, and H. Shingu. *J. Chem. Phys.* **22**, 1433 (1954).
29. I. Fleming. *Frontier orbitals and organic reactions*. Wiley. New York. 1976.
30. R.G. Pearson. *Inorg. Chem.* **27**, 734 (1988).
31. T. Koopmans. *Physica Utrecht*, **1**, 34 (1934).
32. (a) S.S. Shaik. *Prog. Phys. Org. Chem.* **15**, 197 (1985); (b) S.S. Shaik. *J. Am. Chem. Soc.* **103**, 3692 (1981); (c) A. Pross. *Isr. J. Chem.* **26**, 360 (1985).
33. P.K.S. Tsang, P. Cofre, and D.T. Sawyer. *Inorg. Chem.* **26**, 3604 (1987).
34. (a) J.M. Dust and D.R. Arnold. *J. Am. Chem. Soc.* **105**, 1221 (1983); (b) D.D.M. Wayner and D.R. Arnold. *Can. J. Chem.* **62**, 1164 (1984).
35. R.A. Jackson and M. Sharifi. *J. Chem. Soc. Perkin Trans. 2*, 775 (1996).
36. L.K. Dyal. *J. Chem. Soc.* 5160 (1960).
37. L.B. Clapp, H. Lacey, G.G. Beckwith, R.M. Srivastava, and N. Muhammad. *J. Org. Chem.* **33**, 4262 (1968).
38. R. Boyer, E.Y. Spencer, and G.F. Wright. *Can. J. Res.* **24B**, 200 (1946).
39. P.F. Frankland and F.H. Garner. *Chem. Ind. London*, **39**, 257 (1921).
40. R. Fletcher and M.J.D. Powell. *Comput. J.* **6**, 163 (1963).



# Singlet-oxygen reactions sensitized on solid surfaces of lignin or titanium dioxide: Product studies from hindered secondary amines and from lipid peroxidation

L.R.C. Barclay, M.-C. Basque, and M.R. Vinqvist

**Abstract:** Product analyses and kinetic methods were used to determine the role of singlet oxygen in lignin-catalyzed oxidations of organic substrates. Method **A** used the ESR analysis of nitroxide radicals formed by singlet oxygen (Type II) on 2,2,6,6-tetramethylpiperidine, **1**, or tetramethylpiperidone, **2**. Method **B** used HPLC analysis of the 9- and 13-linoleate chain hydroperoxides formed on oxidation of methyl linoleate to distinguish free-radical peroxidation (Type I) from singlet-oxygen oxidation (Type II) on the basis of different *cis,trans* (kinetic) to *trans,trans* (thermodynamic) product ratios. Applications of method **A** to solid dispersions of lignin or titanium dioxide (TiO<sub>2</sub>, a known singlet-oxygen sensitizer) indicated singlet-oxygen reactions. In addition to the nitroxide triplet, irradiation of lignin produces a persistent broad signal in the solid attributed to phenoxyl radicals. Benzophenone and 3,5-di-*tert*-butyl-*ortho*-benzoquinone, **5**, coated on silica gel were used as models to compare the effects of irradiating such compounds on the products and kinetics of methyl linoleate oxidation. Benzophenone acted as an initiator, giving free-radical peroxidation, whereas **5** or lignin coated with methyl linoleate acted as singlet-oxygen sensitizers, according to both product studies (method **B**) and the kinetic order in oxygen consumption during UV photolysis. Photolysis of phase-separated sensitizer (TiO<sub>2</sub> or lignin) and substrate (methyl linoleate) resulted in typical singlet-oxygen products. These results indicate that singlet oxygen plays a significant role in the photo-yellowing of high-lignin-content wood pulps.

**Key words:** lignin, singlet oxygen, mechanism, peroxidation, products.

**Résumé :** Faisant appel à des analyses de produit et à des méthodes cinétiques, on a déterminé le rôle de l'oxygène singulet dans les réactions d'oxydation catalysées par la lignine de substrats organiques. La méthode d'analyse **A** utilise la RPE des radicaux nitroxydes formés par l'action de l'oxygène singulet (Type II) sur la 2,2,6,6-tétraméthylpipéridine (**1**) ou la tétraméthylpipéridone (**2**). La méthode **B** est basée sur l'analyse par CLHP des hydroperoxydes des chaînes 9- et 13-linoléates qui se forment par oxydation du linoléate de méthyle; sur la base des divers rapports de produits (*cis, trans* (cinétique)) par rapport à (*trans, trans* (thermodynamique)), elle permet de distinguer entre la peroxydation radicalaire (Type I) et l'oxydation à l'aide d'oxygène singulet (Type II). Les applications de la méthode **A** à des dispersions solides de lignine ou de dioxyde de titane, TiO<sub>2</sub> bien connu comme sensibilisateur d'oxygène singulet, indiquent qu'elles se produisent par des réactions d'oxygène singulet. En plus du triplet nitroxyde, l'irradiation de la lignine produit dans le solide un large signal persistant qui est attribué aux radicaux phénoxyles. Des études modèles ont permis de comparer les effets sur la nature des produits et sur la cinétique de l'oxydation du linoléate de méthyle de l'irradiation de couches sur du gel de silice avec de benzophénone ou avec de la 3,5-di-*tert*-butyl-*ortho*-benzoquinone (**5**). La benzophénone agit comme initiateur d'une peroxydation radicalaire alors que, sur la base des études de produits (méthode **B**) et de l'ordre cinétique de la consommation d'oxygène au cours de la photolyse UV, le composé **5** et la lignine recouverte d'une couche de linoléate de méthyle agissent comme sensibilisateurs d'oxygène. La photolyse de photosensibilisateurs, TiO<sub>2</sub> ou lignine, en phases séparées du substrat, le linoléate de méthyle, conduisent à la formation des produits typiques de l'action d'oxygène singulet. Ces résultats indiquent que l'oxygène singulet joue un rôle significatif dans le photojaunissement des pulpes de bois contenant de fortes proportions de lignine.

**Mots clés :** lignine, oxygène singulet, mécanisme, peroxydation, produits.

[Traduit par la Rédaction]

Received 3 July 2002. Published on the NRC Research Press Web site at <http://canjchem.nrc.ca> on 16 April 2003.

*Dedicated to Professor Don Arnold for his contributions to chemistry.*

**L.R.C. Barclay<sup>1</sup>, M.-C. Basque, and M.R. Vinqvist.** Department of Chemistry, Mount Allison University, Sackville, NB E4L 1G8, Canada.

<sup>1</sup>Corresponding author (e-mail: [rbarclay@mta.ca](mailto:rbarclay@mta.ca))



## Introduction

Products from Canada's wood-pulping industry are the country's major export. The use of thermal mechanical pulps has provided more than 50% of the fibre for Canadian paper products (1). The high lignin content of these products has resulted in undesirable oxidative photo-yellowing, which can reduce the value of these products. Consequently, the inhibition of such yellowing is of major interest. The excited state of oxygen, singlet oxygen  $^1\Delta_g$ , is known to rapidly oxidize a wide variety of organic substrates (2 and refs. therein) and may be involved in photo-yellowing of thermal mechanical pulps. Singlet oxygen produced by dye sensitization *separately* from the substrates is known to react readily with lignin model compounds (3–8), lignin (9), high-yield pulps (10–12), and cellulose (13, 14). While these studies seem to implicate singlet oxygen as a possible mechanism for oxidative yellowing of lignin, controversy has continued about its significance in this process (5, 10, 11).

Lignin is a complex polymer of phenylpropyl units cross-linked and highly substituted by ether, carbonyl, hydroxyl, and methoxyl groups, as illustrated schematically in Fig. 1. Consequently, lignin is a paradox, in that the hydroxyl groups provide antioxidant activity against Type I free-radical oxidation, as observed for lignin-type monomers (15) and even in lignin itself (16); however, at the same time, the aromatic carbonyl chromophores could act as singlet-oxygen sensitizers and initiate singlet-oxygen (Type II) oxidations.

Earlier studies were limited by the lack of evidence for singlet-oxygen formation *directly* on lignin itself as its own sensitizer. Some evidence for the *direct* formation of singlet oxygen on lignin was given in our report, which showed that the light-induced, self-initiated oxidation of lignin was quenched by sodium azide, a known singlet-oxygen quencher (2). We now report in more detail on the issue of the role of singlet oxygen in lignin photo-oxidation. The structural complexity of lignin and the fact that lignin chromophores react readily with singlet oxygen (3–9) requires a multifaceted approach to the possible formation of singlet oxygen on lignin. Accordingly, we approached this problem in several ways, as follows. (a) Product studies: Two known methods of product analysis were used for gathering evidence of a singlet-oxygen reaction: (i) electron spin resonance (ESR) detection of nitroxide radicals formed by singlet-oxygen oxidation of hindered secondary amines and (ii) product profiles by high performance liquid chromatography (HPLC) of peroxidation of the lipid (methyl linoleate) by singlet oxygen compared with free-radical peroxidation. (b) Solid dispersions: A comparison was made of the products formed using a dispersion of titanium dioxide, a known singlet-oxygen sensitizer, with products formed by photolysis of lignin dispersions. (c) Kinetic studies: The kinetic orders in light intensity were determined for oxidation of methyl linoleate on silica gel in water catalyzed by the ketones, benzophenone (BP), and 3,5-di-*tert*-butyl-*ortho*-benzoquinone (DTBQ). The latter was selected as a simple lignin model compound because *ortho*-quinones are formed during the early photochemistry of mechanical pulps (17). These results were compared with the kinetics of oxidation of methyl linoleate "sensitized" by aqueous dispersions of lignin. The kinetic data and product analyses of linoleate peroxidation

provided a means of establishing the pathways; namely, free-radical oxidation (Type I) or singlet-oxygen reaction (Type II). (d) Phase-separated oxidation: A phase-separated system was used to mimic the natural lignin–air situation. In this technique, the substrate, methyl linoleate, is separated from the sensitizer by a narrow air gap. Product profiles (HPLC) of linoleate hydroperoxides are compared from irradiation experiments using, as sensitizers, titanium dioxide, benzophenone, and lignin. Structures for the main organic compounds employed are shown in Fig. 2.

## Results

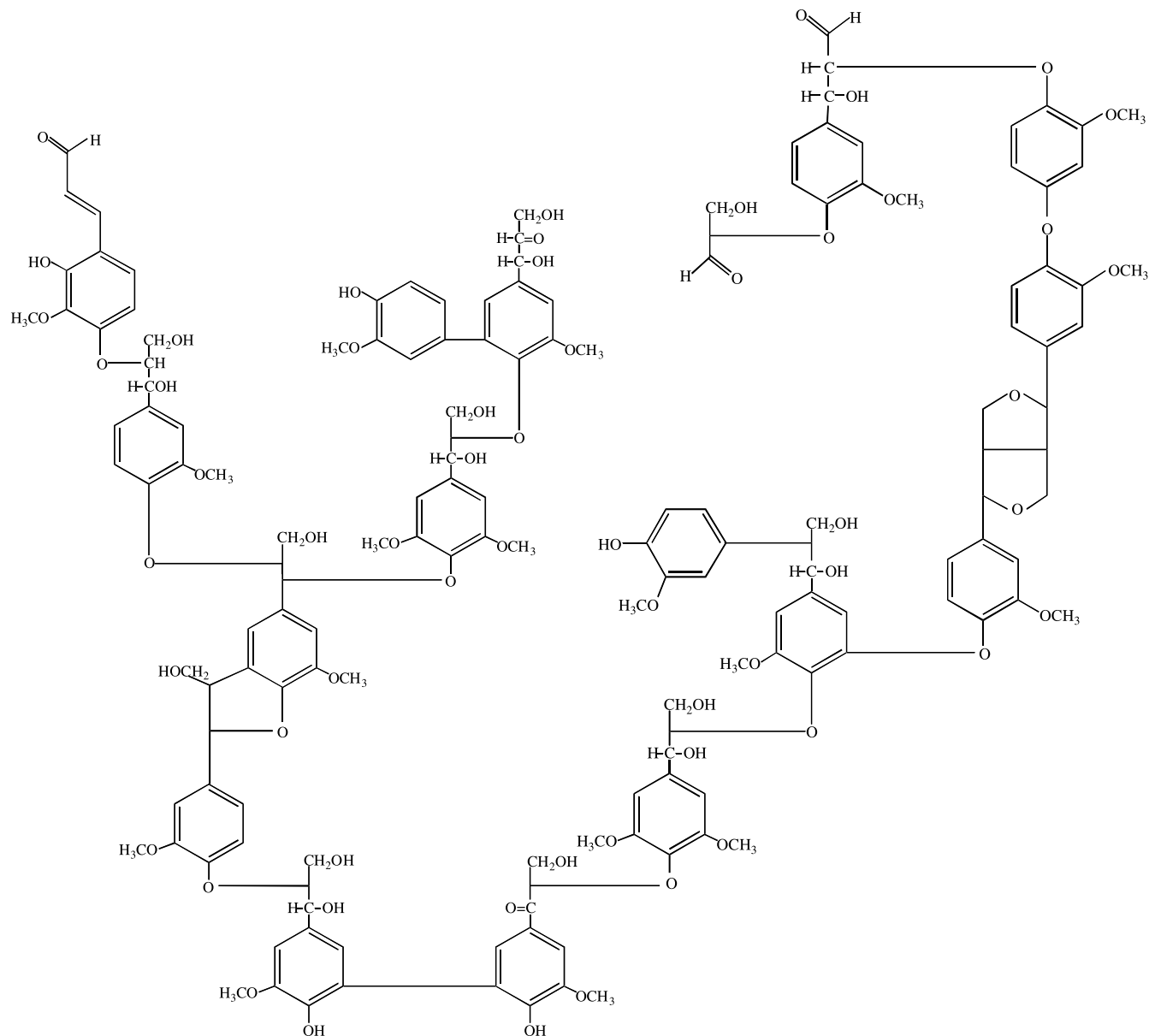
### Product studies from singlet-oxygen oxidation of hindered secondary amines or methyl linoleate

Product studies of (i) oxidation of hindered secondary (sec.) amines and (ii) peroxidation of methyl linoleate were carried out initially in solution to evaluate the employed methods and for comparison with the more complex heterogeneous systems containing lignin. The conversion by singlet oxygen of the hindered sec. amines, 2,2,6,6-tetramethylpiperidine (TMP, **1**) and its 4-oxo derivative (TMPO, **2**), to the corresponding nitroxide radicals, **3**, detected by ESR, have been used for many years and under various conditions as evidence of a singlet-oxygen reaction (18–30). The method is simple and very sensitive to ESR detection of the stable nitroxide radical. However, there are conflicting literature reports on its use. For example, there is at least one report that states that the TMP reaction with singlet oxygen "is highly specific" since it does not react with the superoxide anion nor with the hydroxyl radical (29), while others reported that these amines, **1** and **2**, are useful tools "for trapping hydroxyl radicals" (30).

We found that great care must be exercised when using the oxidation of these amines as evidence of singlet oxygen because nitroxide radicals are often present in commercial **1** and **2** (19, 25). For such work, the following precautions should be observed: (a) the traces of nitroxide radicals should be removed before commencing the singlet experiment to avoid ambiguous results. We found a convenient method to do this is to vortex stir the amine dissolved in hexane with aqueous hydrazine; (b) parallel control experiments should be done with a singlet-oxygen quencher; (c) the ESR signals observed should be intense, and the amount of conversion from the amine to nitroxide radical measured by integration of the ESR spectra. A typical example of the oxidation of TMP using a known singlet-oxygen sensitizer, methylene blue, and product studies by ESR is illustrated in Fig. 3b. This sample was not pretreated with hydrazine, and a trace of nitroxide radical is observed at higher receiver gain (Fig. 3a). However, the conversion on sensitization (approximately 2%) to the typical nitroxide triplet (hyperfine nitrogen coupling  $a_N = 16.0$  gauss) in agreement with literature values (23, 29), indicates reaction by singlet oxygen.

Product distribution of the hydroperoxides from peroxidation of the lipid, methyl linoleate (Fig. 2, structure **10**), is a useful method to distinguish between free-radical (Type I) and singlet-oxygen (Type II) reactions. Earlier reports described the separation and identification of the various isomers and related these to the two mechanisms involved (31–34). Type

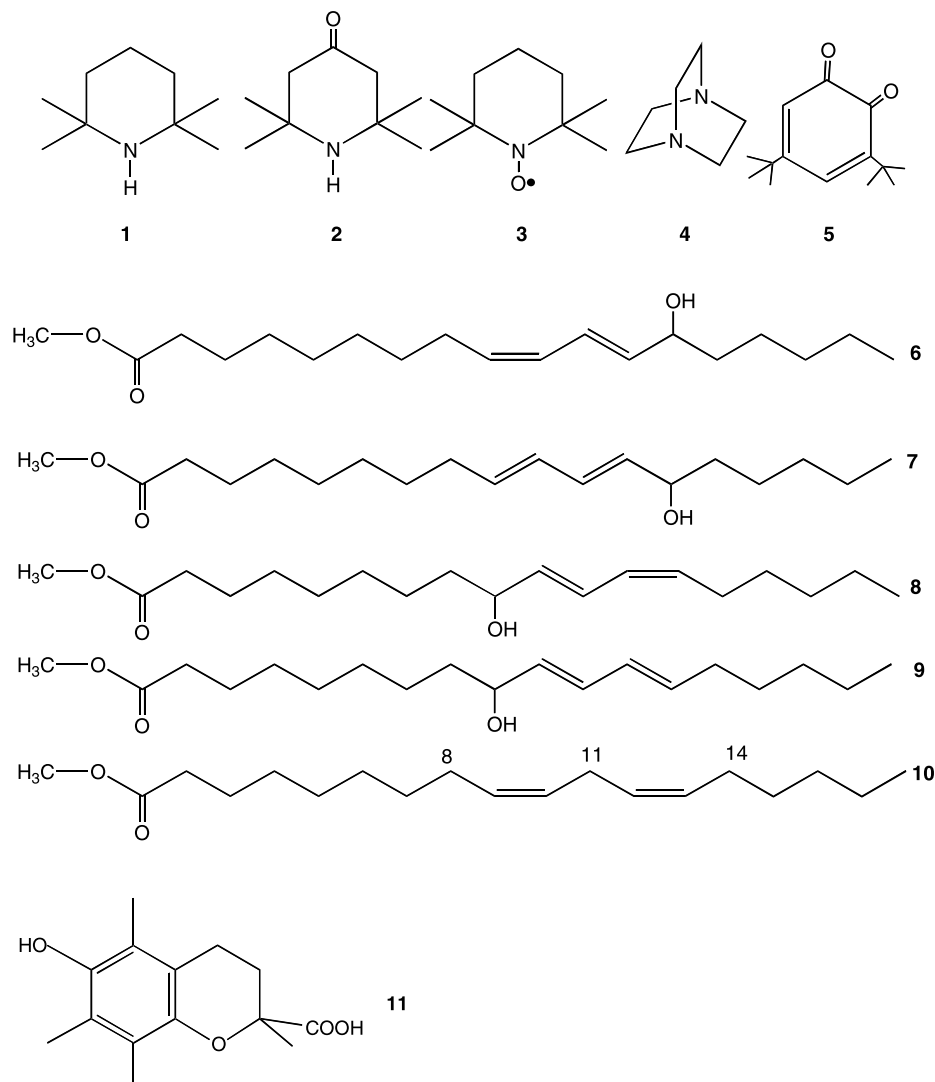


**Fig. 1.** Schematic illustration of the lignin polymer.

I reactions proceed by initial H-atom abstraction from position 11 on the linoleate chain, rapid reaction of the derived carbon-centered radical with oxygen, and rearrangement of the peroxy radicals, giving a distribution between the conjugated 9- and 13-substituted oxidation products, two with the *cis,trans* configuration (kinetic products **6** and **8**) and two with the *trans,trans* configuration (thermodynamic products **7** and **9**). A recent discovery (35) found that the *bis*-allylic 11-hydroperoxide is the kinetic product initially formed in the presence of  $\alpha$ -tocopherol, a powerful H-atom donor; however, this product was not detected in our experiments. These products are usually analyzed as their corresponding alcohols (Fig. 2) that are formed on reduction of the hydroperoxides. On the other hand, the singlet-oxygen reaction does not involve free radicals. Whether singlet oxygen reacts with linoleate by a concerted 'ene reaction or its reaction possibly involves other intermediates (36), the reaction is

kinetically controlled, producing an excess of the *cis,trans* over the *trans,trans* isomers (e.g., a high *cis,trans* to *trans,trans* ratio). So, a significantly higher *cis,trans* to *trans,trans* ratio is expected from a Type II reaction on linoleate compared with a Type I for the same linoleate concentration, bearing in mind that this ratio depends on the H-atom donating ability of the medium for Type I reactions (37, 38). In addition, the less selective singlet-oxygen reaction gives products of reaction at the 10 and 12 positions of linoleate, leading to two nonconjugated isomers, a total of 6 hydroperoxides (2, 31–34). These two pathways, Type I and Type II, are outlined in Scheme 1. An example singlet-oxygen product formation from the photolysis of methyl linoleate sensitized by methylene blue is shown in Fig. 4. In this case the *cis,trans* ratio was found to be 14.2 at 2.8% oxidation of linoleate. The HPLC method of separation and detection of the isomers at 234 nm shows the relative



**Fig. 2.** Structural formulas of the main compounds used.

composition of the conjugated isomers, but the non-conjugated ones will actually be more concentrated than they appear in the chromatogram, since they do not absorb as strongly as the conjugated isomers at 234 nm. Our results focus mainly on the conjugated products and their relative yields (e.g., the *cis,trans* to *trans,trans* ratios).

#### Sensitizations on solid dispersions: Titanium dioxide and lignin

Photolyses involving excited states and intermediates on solid surfaces are of continuing interest and the subject of several reviews (39–42). Solid titanium dioxide, like lignin (presumably), is classified as a *reactive surface* (40), since it is a known singlet-oxygen sensitizer (although despite that, it is also commonly used in cosmetic sunscreens). Irradiation of  $\text{TiO}_2$  with 320–400 nm light causes electronic excitation from a valence band to a conduction band, which allows energy transfer to oxygen (27). Because of the expected complexity of the excited state chemistry on the solid lignin polymer, we employed a comparative study of products formed from TMP when titanium dioxide sensitization was

used, contrasting these with the products formed from TMP (if any) when solid lignin was used.

A typical experiment using  $\text{TiO}_2$  dispersed in methylene chloride for photo-oxidation of TMP is shown in Fig. 5. The triplet, which formed only in the presence of  $\text{TiO}_2$ , is attributed to oxidation via singlet oxygen (Fig. 5b). This procedure was then applied to dispersions of solid lignin in solvents. Figs. 5c and 5d show the results of irradiation of lignin in methylene chloride containing TMP and a parallel experiment in the presence of the singlet-oxygen quencher 1,4-diazabicyclo[2.2.2]octane (Dabco). There was no nitroxide signal in the presence of the quencher (Fig. 5c), whereas the strong triplet appeared in its absence (Fig. 5d). In addition, a quantitative study of the radical concentration showed that it increased with time, as illustrated in Fig. 6. In a similar experiment, we found that extended irradiation of TMP in lignin–hexane dispersions (not shown) gave a 10% conversion to the nitroxide radical.

The ESR spectrum resulting from relatively short irradiation of lignin dispersed in hexane in the presence of 4-OXOTMP (2) was more complex, as shown in Fig. 7a, and



**Fig. 3.** ESR spectra from irradiation in PR-350 of tetramethylpiperidine (TMP), **1**, 7.7 mM, in methylene chloride for 15 min. (a) Without sensitizer, receiver gain (R.G.) of  $5.0 \times 10^5$ ; (b) with  $9.2 \times 10^{-8}$  mol methylene blue, R.G. =  $1.25 \times 10^5$ ,  $[R\cdot] = 0.14$  mM. The peak on the high field part of the triplet, which appears here and in other spectra, is due to a permanent cavity signal.



consisted of a very broad signal superimposed on the nitroxide triplet. The Lande  $g$ -factor for the broad signal was estimated to be  $g = 2.004$ – $2.005$  with reference to that of the nitroxide radical,  $g = 2.006$  (29). This  $g$ -factor for the broad signal is in the range of a wide variety of phenoxyl radicals substituted by alkyl, hydroxyl, methoxy, and keto groups, where  $g = 2.003$ – $2.005$  (43). The separated solution phase shows the spectrum of the nitroxide radical more clearly (Fig. 7b). The broad signal was also very persistent, and it could be observed in the lignin that was separated from TMP by filtration. Separate irradiation of lignin alone in hexane also produced this lignin signal (Fig. 7c), which on dissolution of the lignin in dioxane disappeared and did not reappear on further irradiation of the lignin–dioxane solution. It is also interesting to note that with irradiation of lignin, under these conditions but in the presence of Dabco, the broad signal appeared but *not* the nitroxide triplet (not shown).

#### Kinetic and product studies of methyl linoleate peroxidation sensitized by lignin in water: Comparisons with sensitizations by benzophenone and by 3,5-di-*tert*-butylbenzoquinone, **5**

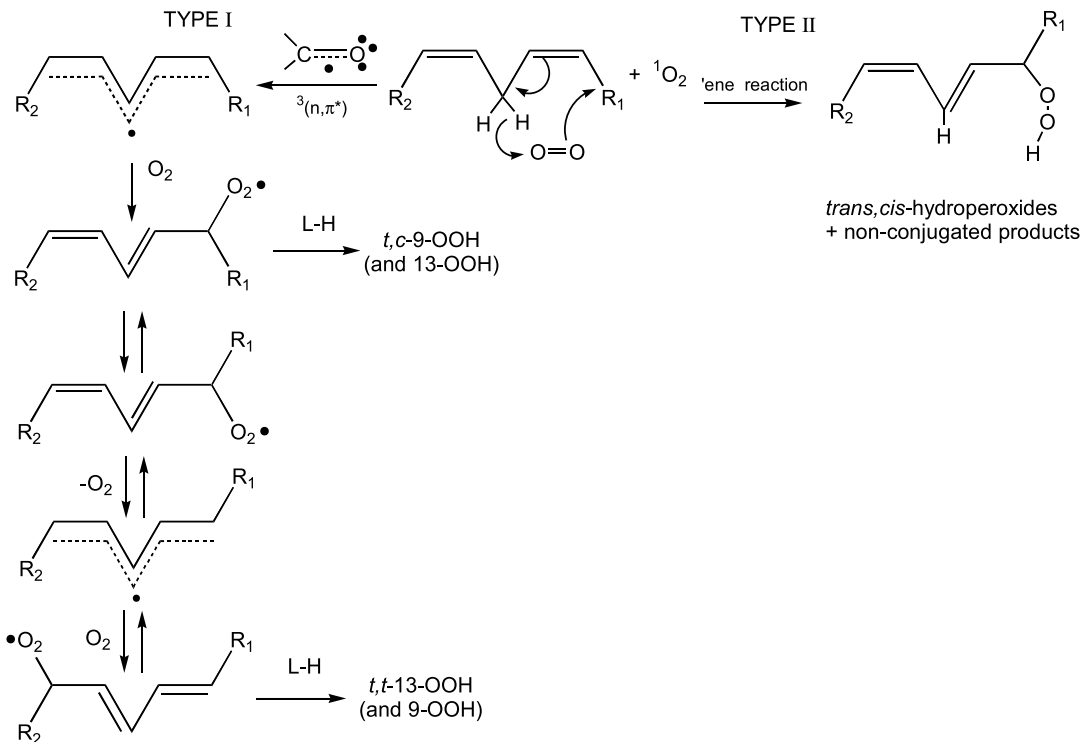
The kinetics of free-radical lipid peroxidation is known to follow the classical rate law for autoxidation (44) represented by the following equation (eq. [1]):

$$[1] \quad -d[O_2]/dt = k_p/(2k_t)^{1/2} \times [\text{lipid}] \times R_i^{1/2}$$

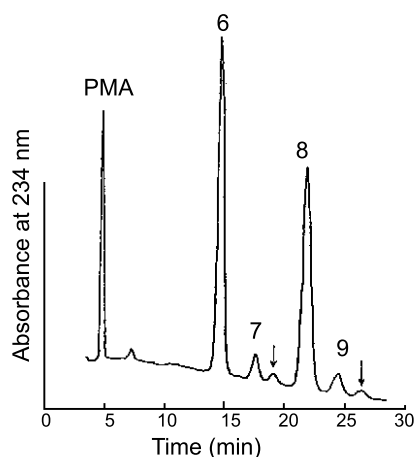
where  $k_p$  and  $2k_t$  are the rate constants for chain propagation and termination, respectively, and  $R_i$  is the rate of free-radical initiation. For photo-initiated H-atom abstraction by the  $n,\pi^*$  triplet state of ketones (Type I mechanism), the kinetic order in oxygen consumption is expected to be half-order in light intensity, since this controls the  $R_i$ , and this was observed earlier for benzophenone photo-initiated peroxidation of linoleate in heterogeneous aqueous micelles (44). On the other hand, the kinetic order for the peroxidation of linoleate photo-initiated by the coloured lignin model quinone (**5**) was approximately unity, indicative of a change in mechanism to Type II with this quinone as sensitizer (2). With these earlier results in mind, we determined the kinetic order in light intensity — together with the trends in product profiles — for oxidation of methyl linoleate initiated by benzophenone and by **5** in aqueous dispersions, for comparison with similar data using lignin in water. The ketones and methyl linoleate were used as films on silica gel since this is classed as a *non-reactive* surface (40); moreover, benzophenone is an effective H-atom abstractor when adsorbed on silica gel (45). Therefore, these two compounds, benzophenone and **5**, were expected to provide different kinetic orders of oxygen uptake in the oxidation of methyl linoleate. In an experiment using lignin, the lipid was evaporated directly onto the lignin. The results of typical experiments are shown in Fig. 8. The experiment using benzophenone (Fig. 8a) gave a kinetic order of 0.55, indicative of a Type I pathway, while with the quinone (**5**) the kinetic order (Fig. 8b) was significantly higher at 0.90. The oxygen uptake in the benzophenone – methyl linoleate experiment was inhibited by the active water-soluble antioxidant Trolox, **11**, which gave a distinct induction period (not shown) similar to that observed earlier for photolysis with this combination in micelles (44). It appears that Trolox can trap chain-propagating peroxy radicals generated on the methyl linoleate – silica gel surface, much like it does in other media. In contrast, Trolox gave no induction period during the photo-reaction combination of **5** – methyl linoleate. Lignin was also an effective photocatalyst for lipid oxidation and gave a kinetic order of 0.84 (Fig. 8c), similar to that observed with the quinone.

Product studies were carried out on oxidations of methyl linoleate under similar conditions to those in the kinetic runs. Typical product profiles from reactions using benzophenone and quinone, **5**, are shown in Figs. 9a and 9b. These product profiles are clearly different: the reaction using benzophenone gave the four conjugated isomers with a *cis,trans* to *trans,trans* isomer ratio of ca. unity (Fig. 9a), while six isomers were formed with a *cis,trans* to *trans,trans* ratio of ca. 32 when using quinone in the photolysis (Fig. 9b). The different kinetic orders together with different product profiles allow one to distinguish between the two possible mechanisms in these heterogeneous systems: a Type I free-radical oxidation initiated by H-atom abstraction by excited benzophenone vs. a Type II singlet-oxygen reaction sensitized by the quinone. Product analysis from oxidation of methyl linoleate on lignin (not shown) also showed an excess of the *cis,trans* isomers, but the chromatograms were very complex in the region where the *trans* isomers appear, preventing reliable calculations of the isomer ratios. However, these qualitative product studies, together with the kinetic order experiment, indicate the par-



**Scheme 1.** Free radical (Type I) and singlet-oxygen (Type II) pathways for lipid peroxidation.

**Fig. 4.** HPLC trace of photo-initiated oxidation products in air from methyl linoleate, 0.50 M in chloroform, with methylene blue,  $1.11 \times 10^{-2}$  M, using a 1000 W visible lamp for 10 min. Peaks labeled 6, 7, 8, and 9 are the 13 *cis,trans*, 13 *trans,trans*; 9 *cis,trans*, and 9 *trans,trans* isomers, respectively (see Fig. 2). The sample was 2.8% oxidized, giving a *cis,trans* to *trans,trans* product ratio = 14.2. Peaks marked by vertical arrows are non-conjugated isomers (see text). In this and other HPLC separations, PMA = 4-methoxyacetophenone, used as an internal standard for retention times and total hydroperoxides formed.



ticipation of singlet oxygen in the lignin – methyl linoleate photolysis.

#### Oxidations by separation of the sensitizer and substrate (phase separation, PS)

Physical separation of the sensitizer from the substrate should eliminate complications that are always present when

they are together in solution during singlet-oxygen oxidations, such as competing H-atom abstraction by the sensitizer or electron transfer reactions. In addition, the lifetime of singlet oxygen is much longer in the gas phase than in solution (46), which should make the reaction more efficient.

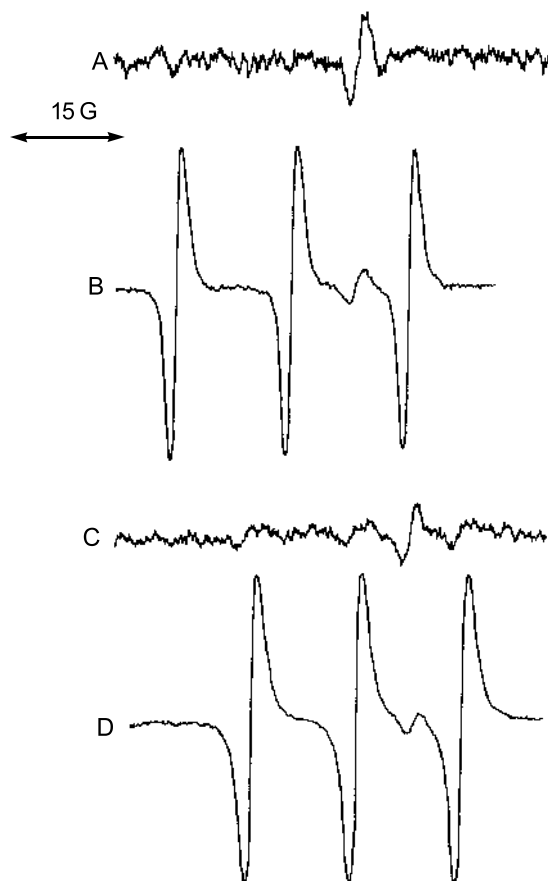
A simple apparatus was constructed for some experiments with the sensitizer and substrate separated 1 to 2 mm by an air gap (Fig. 10), a space that is expected to allow for diffusion of singlet oxygen across the gap (46, 47). The sensitizer was coated on the bottom of the top filter-petri dish either as a film (e.g., benzophenone) or as a powder on double-sided tape. The sensitizer and substrate were then separated by two microscope slides, and the assembly was mounted on a cold plate and moved into the photoreactor. In practice, our procedure had limitations because the coating of sensitizers often “screened” much of the light, making the process less efficient so that long irradiation times were needed, and this can result in thermal or photo-rearrangements of initially formed hydroperoxides in the products (see Discussion section).

We used benzophenone as a typical photo-initiator to test the effect of the PS procedure as compared with results obtained using a homogeneous solution. In the latter case, the classical free-radical reaction (Type I) is known to predominate (44), and this was confirmed in the present case, since the isomer distribution showed a predominance to *trans,trans* isomers (*cis,trans* to *trans,trans* ratio = 0.44, Fig. 11a). The PS experiment required longer irradiation times to obtain comparable product buildup for HPLC analysis, and typically the product profiles (Fig. 11b) from these experiments were quite different from reactions in solution, showing all six isomers and an excess of the *cis,trans* isomers (*cis,trans* to *trans,trans* ratio = 9.1).

To evaluate the effect that lignin might have in the PS procedure, experiments were carried out with titanium dioxide

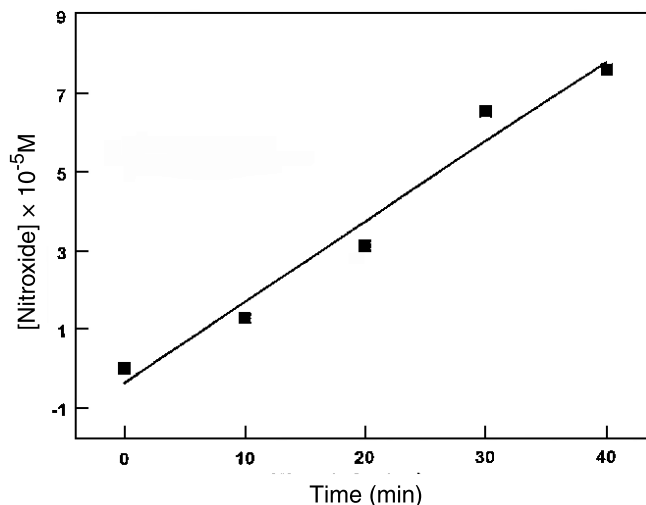


**Fig. 5.** ESR spectra from irradiation in air by PR-350 of methylene chloride solutions of TMP treated with hydrazine before irradiation. (a) With TMP, 0.40 M, and irradiated for 3 h, R.G. =  $2.0 \times 10^5$ ; (b) TMP, 0.40 M, in the presence of titanium dioxide dispersion, irradiated for 45 min., R.G. =  $4.0 \times 10^4$ ; (c) with TMP, 7.7 mM, Dabco quencher, 0.34 M, and 20 mg of lignin dispersion, irradiated for 40 min., R.G. =  $5.0 \times 10^5$ ; (d) TMP and lignin, as in (c) but without Dabco, irradiated for 40 min., R.G. =  $1.5 \times 10^5$ . The additional peak on the high field side of the triplet, which appears here and in other spectra, is due to a permanent cavity signal.



powder and with lignin powder for a comparison of the product profiles in the oxidation of methyl linoleate. These results are shown in Fig. 12. For similar relative conversions of the methyl linoleate (ca. 6%), the product profiles of the isomers are quite similar, with *cis,trans* to *trans,trans* ratios of 10.4 and 12.7 for the titanium dioxide sensitizer (Fig. 12a) and lignin as sensitizer (Fig. 12b), respectively. Both reactions appear to involve significant oxidation by singlet oxygen. This result indicates the specific advantage of phase separation to study a singlet-oxygen reaction. When the benzophenone and methyl linoleate were on separate silica gel surfaces but irradiated in the same glass vessel the product distribution (Fig. 9a) was similar to that found for a homogeneous solution (Fig. 11a). Presumably, this is because benzophenone and methyl linoleate were in close contact on the two silica gel surfaces, resulting in a process similar to a homogeneous system but with formation of a higher *cis,trans* to *trans,trans* ratio (on silica = 0.91 cf. in

**Fig. 6.** Plot of nitroxide concentration vs. time for irradiation of TMP, 1, 7.7 mM, with a dispersion of lignin, 15 mg, in methylene chloride in PR-350.



solution = 0.44), reflecting the effect of a higher substrate concentration for essentially neat substrate on silica gel.

## Experimental

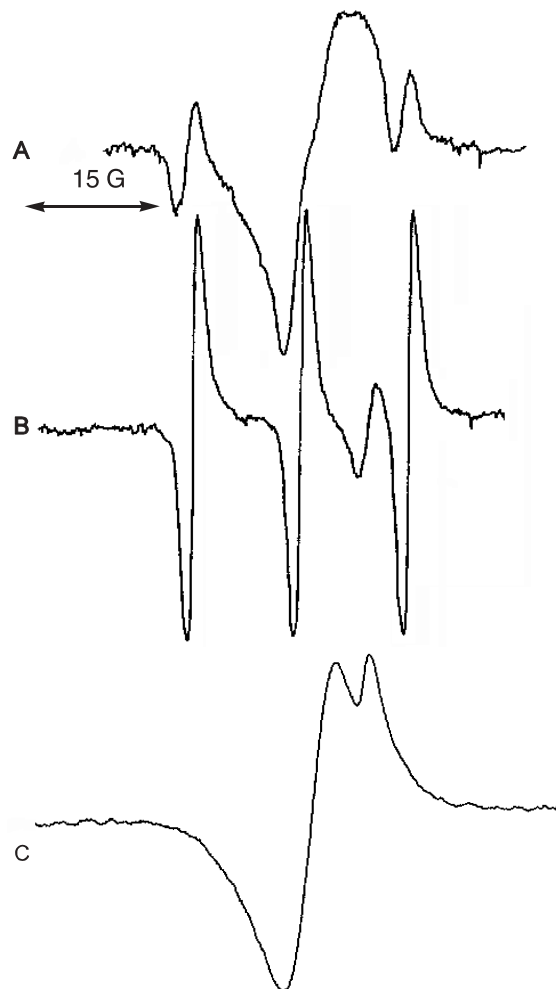
### Materials and preparations

The following chemicals used were the purest grade from Aldrich: 2,2,6,6-tetramethylpiperidine (TMP), 2,2,6,6-tetramethyl-4-piperidone (TMPO), 1,4-diazabicyclo[2.2.2]octane (Dabco), 3,5-di-*tert*-butyl-*ortho*-benzoquinone, 4-methoxyacetophenone, benzophenone, titanium dioxide (Anatase-powder), *N,N*-dimethyl-*p*-phenylene-2HCl (DMP-HCl), triphenylphosphine, and Trolox. Methyl linoleate (>99%) was obtained from Nu-Chek-Prep and silica gel (100–200 mesh) from Mallinckrodt. The lignin used was milled from unbleached softwood at Paprican, Pointe Claire, Quebec, Canada.

The TMP and TEMPO (sublimed in vacuo) were normally purified to remove nitroxide signals just before use in each experiment (see text). In a typical purification, an equal volume of TMP or TMPO and aqueous hydrazine (35%, Aldrich) in the solvent used (methylene chloride or hexane) were vortex stirred for 2–5 min. The mixture was centrifuged to separate the organic layer, which was dried over sodium sulfate and purged with argon, and the sample was checked for ESR signals before use. Commercial silica gels were washed free of traces of free metal ions before use. For this purpose the material was washed at least three times with distilled water then twice with methanol, and the samples were oven-dried overnight. Traces of hydroperoxides were removed from commercial methyl linoleate by column chromatography on silica gel under argon, and fractions free of hydroperoxides (by TLC analysis, as detected by a DMP-HCl spray) were used in experiments. Alternately, it was convenient to prepare hydroperoxide-free solutions of methyl linoleate by vortex stirring a solution of the ester in distilled hexane with silica gel (nominally: 200 mg of ester in 50 mL hexane and 70 mg of silica gel). The solutions were checked for hydroperoxides by UV absorption at 234 nm (conjugation) and by TLC before use.



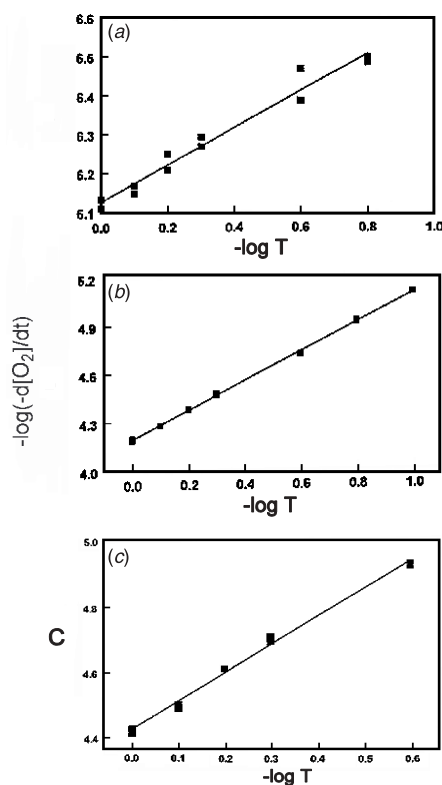
**Fig. 7.** ESR spectra from irradiation with a 200 W Hg arc lamp in air of hexane dispersions of lignin, 10 mg, in the probe of the spectrometer. Samples were purged with argon before recording spectra. (a) With TMPO, 6.7 mM, irradiated for 5 min., R.G. =  $5.0 \times 10^5$ ; (b) the spectrum of the solution after separation of the lignin, R.G. =  $2.0 \times 10^5$ ; (c) Irradiation of lignin dispersion alone in hexane for 12 min., R.G. =  $2.0 \times 10^5$ .



### Photolysis methods

Photolyses were carried out using pyrex filters. Irradiations at 350 nm were done in a photoreactor constructed in the laboratory of J.C. Scaiano, University of Ottawa, Canada, consisting of an air-cooled metal box (30 cm high  $\times$  35 cm  $\times$  35 cm) fitted with eight 25 W, 350 nm lamps, a prototype of a Luzchem Photoreactor, Inc. A cold plate (Stirr Kool Inc.), fitted into the reactor, permitted samples to be cooled to between 0 and  $-10^\circ\text{C}$ . This method, used for 350 nm photolysis, is referred to as PR-350 in the figure legends. A 200 W Oriel Hg-Xe lamp was used for photolyses undertaken in the probe of an electron spin resonance spectrometer (ESR); an Oriel 1000 W quartz-tungsten lamp was used for those experiments employing coloured dyes as sensitizers, such as methylene blue or 3,5-di-*tert*-butyl-*ortho*-quinone. A solution of the ester in an inert solvent (e.g., hydrocarbons, heptadecane, or dodecane) was used in the photo-irradiation of methyl linoleate by the phase sep-

**Fig. 8.** Plots of kinetic orders of oxygen uptake vs. light intensity for photo-initiated oxidation of methyl linoleate on silica gel in water at  $30^\circ\text{C}$ ; comparing the effects of the ketones, benzophenone, DTBQ, 5, and lignin. (a) Methyl linoleate, 54  $\mu\text{m}$ , on 125 mg silica gel with benzophenone, 5.6  $\mu\text{m}$ , on 100 mg silica gel, irradiated with 200 W Hg arc lamp; (b) methyl linoleate, 56  $\mu\text{m}$ , on 112 mg silica gel with DTBQ, 5, 8.7  $\mu\text{m}$ , on 185 mg silica gel irradiated with a 1000 W visible lamp; (c) methyl linoleate, 54  $\mu\text{m}$ , evaporated from methylene chloride on lignin, 92 mg, and irradiated with a 200 W Hg arc lamp.



aration (PS) method; it was mixed with silica gel (3 g per 500 mL) to hold the sample in the sample well close to the sensitizer (see Fig. 10 and text). In these cases, the silica gel was washed with methanol to remove the adsorbed oxidation products for reduction and HPLC analyses.

### Product analyses

#### Electron spin resonance (ESR)

ESR spectra were obtained on a Varian E-3 EPR Spectrometer operated generally at a power level of 3 to 3.2 mW and a modulation amplitude of 4 G to optimize signals. Quantitative analysis of nitroxide signals used double integration of the absorption curves and diphenylpicrylhydrazyl as a concentration standard (48). The integrations were corrected for ESR cavity response by the signal of a ruby installed in the probe.

#### HPLC method

The procedures for reduction of methyl linoleate hydroperoxides by triphenylphosphine and HPLC analysis of the resulting isomeric alcohols and their identification was described previously (2, 37). 4-Methoxyacetophenone was



**Fig. 9.** HPLC traces of oxidation products of methyl linoleate on silica gel in water at 30°C; comparing the effects of benzophenone and DTBQ, **5**. The quantities of methyl linoleate, benzophenone, and DTBQ were the same as in Fig. 8. (a) Benzophenone and irradiation with a 200 W Hg arc lamp. The *cis,trans* to *trans,trans* product ratio was 0.91 at 6.6% oxidation; (b) DTBQ and irradiation with a 1000 W visible lamp. The *cis,trans* to *trans,trans* product ratio was 32 at 9.4% oxidation. See Fig. 4 for identification of the HPLC peaks.

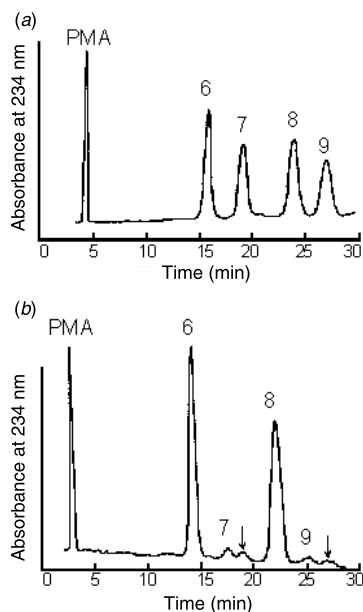
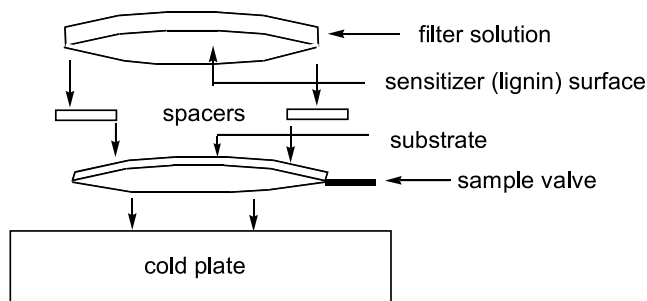


**Fig. 10.** Diagram of apparatus used for the phase separation (PS) method.



used as an internal standard to determine product concentrations, which are reported as “relative concentrations” of the total **6–9** isomeric compounds (Fig. 2).

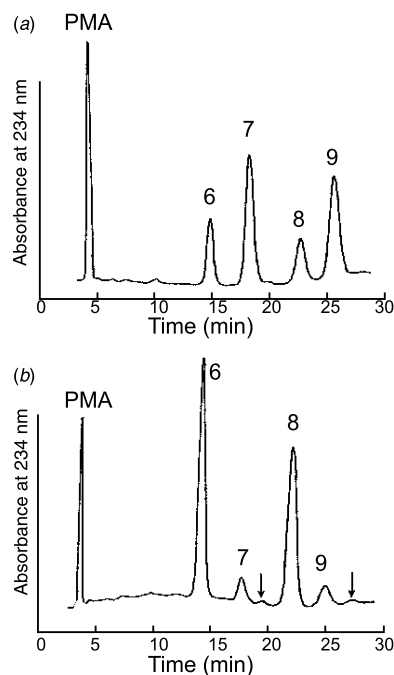
### Kinetic methods of oxygen uptake

Kinetic studies of oxidation were carried out at 30°C under 760 torr (1 torr = 133.322 Pa) of oxygen on a dual channel apparatus attached to a pressure transducer, as described previously (2). The kinetic order in oxygen uptake was determined by inserting seven neutral-density filters on a filter wheel into the light beam.

### Discussion

The combinations of product studies, kinetic measurements, and phase separations of sensitizer and substrate provide

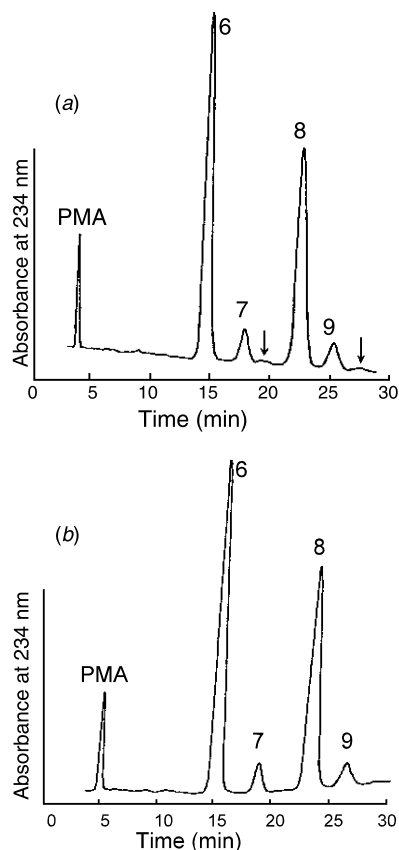
**Fig. 11.** HPLC traces of methyl linoleate oxidation products showing the result using “initiation” by benzophenone in solution compared with phase separation of benzophenone as “sensitizer”. (a) Methyl linoleate, 0.43 M, with benzophenone, 5.5 mM, in dodecane, irradiated in PR-350 for 1 h, giving 1.6% oxidation of methyl linoleate at a *cis,trans* to *trans,trans* product ratio = 0.44; (b) methyl linoleate, 0.69 M, in heptadecane and benzophenone powder, 29 mg, in the PS apparatus (Fig. 10) irradiated for 9 h, giving 2.2% oxidation at a *cis,trans* to *trans,trans* product ratio = 9.1. The identification of the peaks is given in Fig. 4.



quite conclusive results on the role of lignin in the generation of singlet oxygen. ESR studies of nitroxides from the oxidation of secondary amines **1** and **2** indicate singlet-oxygen generation by the photolysis of dispersions of solid lignin. A singlet-oxygen quencher inhibits the reaction, and in the absence of quencher the reaction products, nitroxides, increase in quantity with time. This ESR method has the advantage of high sensitivity, but the appearance of nitroxide radicals alone does not rule out the possible involvement of Type I reactions occurring simultaneously with singlet-oxygen oxidation. In this regard, the broad ESR signal produced during shorter irradiation times on lignin dispersion together with nitroxide formation is of special interest. Wan and co-workers observed similar broad, persistent signals ( $g = 2.0039$ ) on papers from mechanical pulps, attributed them to phenoxyl radicals formed by H-atom abstraction by excited chromophores (49), and showed their importance in the photo-yellowing of high lignin content pulps and paper (50, 51). Our results show that these radicals are formed from the photo-excited lignin component, presumably by H-atom abstraction by excited carbonyl groups. More importantly, the complex ESR spectrum (Fig. 7a) demonstrates that *both* Type I and Type II reactions are initiated from photo-excited lignin: one type by H-atom abstraction forming phenoxyl radicals, which are persistent in the polymer matrix, and the other by energy transfer to oxygen, resulting in nitroxide



**Fig. 12.** HPLC traces from oxidation of methyl linoleate using the PS method to compare the effect of lignin with that of titanium dioxide as “sensitizers”. (a) Methyl linoleate, 0.75 M, in heptadecane and titanium dioxide powder, 7.2 mg, irradiated for 8 h in PR-350, resulting in 6.2% oxidation and a *cis,trans* to *trans,trans* product ratio = 10.4; (b) methyl linoleate, 0.75 M, in heptadecane and lignin powder, 9.4 mg, irradiated for 1 h in PR-350, resulting in 6.3% oxidation and a *cis,trans* to *trans,trans* product ratio = 12.7. The identification of the peaks is given in Fig. 4.



radical formation by a singlet-oxygen reaction. The lignin-phenoxyl radicals were not observed in dioxane, probably owing to rapid radical–radical recombinations in solution.

The use of both kinetic experiments of oxygen uptake and product studies using methyl linoleate shows that the two mechanisms of peroxidation depend on the initiator or sensitizer used. Thus benzophenone, a known, excellent H-atom abstractor, showed a kinetic order of 0.55 when coated on silica gel, consistent with initiation by H-atom abstraction. The results with an *ortho*-quinone were quite different: the higher kinetic order indicates a change in mechanism and the HPLC product profile indicates a singlet-oxygen reaction. As observed before in homogeneous solution (2), kinetic orders for singlet-oxygen oxidation are close to unity, which is expected if one assumes that the oxygen uptake is directly related to the steady-state concentration of singlet oxygen. The somewhat lower kinetic orders, ca. 0.9 — actually observed for oxidations sensitized by the *ortho*-quinone, **5**, a known singlet-oxygen sensitizer, and for dispersions of lignin when coated on silica gel — could be due to some photo-

induced homolysis of the hydroperoxides that accumulate during prolonged irradiation times, resulting in some competing Type I reaction. In any event, lignin is an active “catalyst” for the oxidation of the lipid, methyl linoleate, on its surface (Fig. 8c). The reason for the difference in behavior of the two ketones — as shown by product profiles from the reactions on silica gel (Fig. 9a and 9b), where benzophenone causes initiation of a Type I reaction on methyl linoleate while the *ortho*-quinone acts as a sensitizer — probably lies in the nature and energy of two different excited states of these compounds. The  $^3(n,\pi^*)$  of benzophenone is a well-known, very reactive H-atom abstractor. Although the redox properties of **5** have been studied in detail, including reduction by ascorbic acid (52), details on its excited states are not available. However, the triplet states of 2- to 4-ring aromatic *ortho*-quinones exhibit “inversion” between  $n,\pi^*$  and  $\pi,\pi^*$  triplets where these were not active H-atom abstractors (53). Similarly, it appears that the excited state of quinone, **5**, is not an H-atom abstractor under our conditions but rather gives energy transfer, forming singlet oxygen.

We are well aware of the limitations of using hydroperoxide product studies as evidence for a singlet-oxygen reaction. In general, secondary photo reactions, especially by UV light, can cause further reactions on sensitive hydroperoxides and complicate the results, as pointed out by others (54–56). Consequently, in our results using geometric product ratios of the *cis,trans* and *trans,trans* isomers, it is not surprising that quite different ratios were observed even in reactions that apparently proceed via singlet oxygen. Most ratios were in the range of 9 to 14 (Figs. 4, 11b, 12a, and 12b), and the high ratio combined with the appearance of six isomers is taken as evidence for a pathway controlled by singlet oxygen, especially when compared with these ratios under conditions recognized to be a Type I reaction (Figs. 9a and 11a), where the highest ratio was ca. 1. In comparison, the ratio of ca. 33 when the *ortho*-quinone, **5**, was used as sensitizer in the visible region (Fig. 9a) is very different and suggests that the other examples may either indicate secondary photo rearrangements or a mixed Type I and Type II pathway. Triphenylphosphine (TPP) is used to rapidly reduce hydroperoxides to alcohols. Since it absorbs only weakly above 300 nm (57), we considered that photolysis experiments in the presence of TPP would reduce hydroperoxides as they form and simplify the product analysis. Unfortunately, other reactions of triphenyl phosphine — including those with excited states of ketones (58, 59) and with singlet oxygen (60) — actually complicate the system, and this procedure was abandoned.

Our experiments using lignin indicate that both Type I and Type II reactions can occur on photolysis. For example, the observation of two radicals following irradiation of **2** in the ESR cavity after a comparatively short irradiation time indicates that H-atom abstraction from phenolic hydroxyls (possibly by excited carbonyl groups) and singlet-oxygen reactions to generate nitroxide radicals occur simultaneously. The phase separation method does definitely show that singlet oxygen can be generated by the lignin surface (Fig. 12b). Overall we conclude that singlet oxygen plays an important role in the photo-yellowing of high-lignin-content materials, and consequently, this must be taken into consid-



eration in strategies for inhibition of photo-yellowing of high-lignin-content mechanical pulps.

## Acknowledgments

This research was supported by grants from the Mechanical and Chemimechanical Wood-Pulps Network (Canada) and the Natural Sciences and Engineering Research Council of Canada (NSERC). We thank Vanessa Stephenson for her assistance in the preparation of the manuscript.

## References

1. Mechanical and Chemimechanical Wood-Pulps Network. Annual Report. 1993.
2. L.R.C. Barclay, J.K. Grandy, H.D. MacKinnon, H.C. Nichol, and M.R. Vinqvist. *Can. J. Chem.* **76**, 1805 (1998).
3. C. Crestini and M. D'Auria. *Tetrahedron*, **53**, 7877 (1997).
4. K. Fischer, M. Beyer, and H. Koch. *Holzforschung*, **49**, 203 (1995).
5. H. Takagi, I. Forsskahl, H. Derakyla, S. Omori, and C.W. Dence. *Holzforschung*, **44**, 217 (1990).
6. S. Omori, H. Takagi, R.C. Francis, and C.W. Dence. *Holzforschung*, **46**, 47 (1992).
7. H. Tylli and C. Olkkonen. *J. Photochem. Photobiol. A*, **49**, 397 (1989).
8. I. Forsskahl. *J. Photochem.* **27**, 363 (1984).
9. M.G. Neumann and A.E.H. Machado. *J. Photochem. Photobiol. B*, **3**, 473 (1989).
10. J. Szabo, M. Fiserova, and M. Kosik. *Cellul. Chem. Technol.* **28**, 183 (1994).
11. I. Forsskahl, C. Olkkonen, and H. Tylli. *J. Photochem. Photobiol. A*, **43**, 337 (1988).
12. M. Beyer, Ch. Bäurich, and K. Fischer. *Papier (Darmstadt)*, **49**, 8 (1995).
13. J. Griffiths and C. Hawkins. *Polymer*, **17**, 1113 (1976).
14. B. Garston. *J. Soc. Dyers Color.* **96**, 535 (1980).
15. L.R.C. Barclay, F. Xi, and J.Q. Norris. *J. Wood Chem. Technol.* **17**, 73 (1997).
16. J.A. Schmidt, C.S. Rye, and N. Gurnagul. *Polym. Degrad. Stab.* **49**, 291 (1995).
17. D.S. Argyropoulos, C. Heitner, and J. A. Schmidt. *Res. Chem. Intermed.* **9**, 263 (1995).
18. Y. Lion, M. Delmelle and A. Van de Vorst. *Nature (London)*, **263**, 442 (1976).
19. J. Moan and E. Wold. *Nature (London)*, **279**, 450 (1979).
20. S. Cannistraro, A. Van de Vorst, and G. Jori. *Photochem. Photobiol.* **28**, 257 (1978).
21. Y. Lion, E. Gandin, and A. Van de Vorst. *Photochem. Photobiol.* **31**, 305 (1980).
22. C. M. Krishna, Y. Lion, and P. Riesz. *Photochem. Photobiol.* **45**, 1 (1987).
23. T. Kondo and P. Riesz. *Radiat. Res.* **127**, 11 (1991).
24. T. Michalska, K. Lichszeld, I. Kruk, and S. Marczyński. *J. Photochem. Photobiol. B*, **19**, 55 (1993).
25. C.M. Krishna and A.K. Roy. *Indian J. Biochem. Biophys.* **30**, 7 (1993).
26. S. Dzwigaj and H. Pezerat. *Free Radical Res.* **23**, 103 (1995).
27. R. Konaka, E. Kasahara, W.C. Dunlap, Y. Yamamoto, K. Chang Chien, and M. Inoue. *Free Radical Biol. Med.* **27**, 294 (1999).
28. B.F. Sels, D.E. De Vos, P.J. Grobet, F. Pierard, F. Kirsh-De Mesmaeker, and P.A. Jacobs. *J. Phys. Chem. B*, **103**, 11 114 (1999).
29. L.-Y. Zang, F.J.G.M. van Kuijk, B.R. Misra, and H.P. Misra. *Biochem. Mol. Biol. Int.* **37**, 283 (1995).
30. I. Rosenthal, C. Murali Krishna, G.C. Yang, T. Kondo, and P. Riesz. *FEBS Lett.* **222**, 75 (1987).
31. M.J. Thomas and W.A. Pryor. *Lipids*, **15**, 544 (1980).
32. J. Terao and S. Matsushita. *J. Am. Oil Chem. Soc.* **54**, 234 (1977).
33. E.N. Frankel, W.E. Neff, E. Selke, and D. Weisleder. *Lipids*, **17**, 11 (1982).
34. H.W.-S. Chan and G. Levett. *Lipids*, **12**, 99 (1977).
35. A. Brash. *Lipids*, **35**, 947 (2000).
36. M. Prein and W. Adam. *Angew. Chem. Int. Ed. Engl.* **35**, 477 (1996).
37. N.A. Porter and D.G. Wujek. *J. Am. Chem. Soc.* **106**, 2626 (1984).
38. X.-H. Wang, T. Ohshima, H. Ushio, and C. Koizumi. *Lipids*, **34**, 675 (1999).
39. J.C. Scaiano and H. Garcia. *Acc. Chem. Res.* **32**, 783 (1999).
40. P.V. Kamat. *Chem. Rev.* **93**, 267 (1993).
41. J.K. Thomas. *Chem. Rev.* **93**, 301 (1993).
42. V. Ramamurthy. *Tetrahedron*, **42**, 5753 (1986).
43. W.T. Dixon, P.M. Kok, and D. Murphy. *J. Chem. Soc. Faraday Trans. 2*, **74**, 1528 (1978).
44. L.R.C. Barclay, K.A. Baskin, S.J. Locke, and T.D. Schaeffer. *Can. J. Chem.* **65**, 2529 (1987).
45. S. Kazanis, A. Azarani, and L.J. Johnson. *J. Phys. Chem.* **95**, 4430 (1991).
46. W.R. Midden and S.Y. Wang. *J. Am. Chem. Soc.* **105**, 4129 (1983).
47. W.R. Midden and T.A. Dahl. *Biochim. Biophys. Acta.* **1117**, 216 (1992).
48. J.E. Wertz and J.R. Bolton. *Electron spin resonance: Elementary theory and practical applications*. McGraw-Hill Inc., New York. 1972. pp. 462–463.
49. J.K.S. Wan, M.Y. Tse, and C. Heitner. *J. Wood Chem. Technol.* **13**, 327 (1993).
50. I.A. Shkrob, M.C. Depew, and J.K.S. Wan. *Res. Chem. Intermed.* **17**, 271 (1992).
51. J.K.S. Wan and M.C. Depew. *Res. Chem. Intermed.* **22**, 241 (1996).
52. S.V. Jovanovic, K. Konya, and J.C. Scaiano. *Can J. Chem.* **73**, 1803 (1995).
53. M. Barra, E.D. Harderr, and J.P. Balfe. *J. Chem. Soc. Perkin Trans. 2*, 1439 (1999).
54. C. Taniellan, R. Mechin, R. Seghrouchni, and C. Schweitzer. *Photochem. Photobiol.* **71**, 12 (2000).
55. F. Bosca, M.A. Miranda, I.M. Morera, and A. Samadi. *J. Photochem. Photobiol. B*, **58**, 1 (2000).
56. C. Taniellian and R. Mechin. *Photochem. Photobiol.* **59**, 263 (1994).
57. P. Changenet, P. Plaza, M.M. Martin, Y.H. Meyer, and W. Rettig. *Chem. Phys.* **221**, 311 (1997).
58. Y.L. Chow and B. Marciniak. *J. Org. Chem.* **48**, 2910 (1983).
59. L.D. Wescott, H. Sellers, and P. Poh. *Chem. Commun.* 586 (1970).
60. S. Tsuji, M. Kondo, K. Ishiguro, and Y. Sawaki. *J. Org. Chem.* **58**, 5055 (1993).



# The synthesis and structural characterization of linear and macrocyclic bis(dinitrosyliron) complexes supported by bis(phosphine) bridging ligands

Lijuan Li, Nada Reginato, Michael Urschey, Mark Stradiotto, and John D. Liarakos

**Abstract:** Reactions involving  $\text{Fe}(\text{NO})_2(\text{CO})_2$  and the bis(phosphine) ligands bis(diphenylphosphino)methane (DPPM), bis(diphenylphosphino)acetylene (DPPA), 1,6-bis(diphenylphosphino)hexane (DPPH), and 1,4-bis(diphenylphosphino)benzene (DPPB) have been examined. From these reactions, the mononuclear complex,  $\text{Fe}(\kappa^1\text{-DPPM})(\text{NO})_2(\text{CO})$  **3**, linear dinuclear species of the type  $\text{Fe}_2(\mu\text{-}L)(\text{NO})_4(\text{CO})_2$  ( $L = \text{Ph}_2\text{PCH}_2\text{PPh}_2$  **4**,  $\text{Ph}_2\text{PC}\equiv\text{CPh}_2$  **5**,  $\text{Ph}_2\text{PCH}_2(\text{CH}_3)_4\text{CH}_2\text{PPh}_2$  **6**, and  $\text{Ph}_2\text{P}(p\text{-C}_6\text{H}_4)\text{PPh}_2$  **7**), and macrocyclic dinuclear species of the type  $\text{Fe}_2(\mu\text{-}L)_2(\text{NO})_4$  ( $L = \text{Ph}_2\text{PCH}_2\text{PPh}_2$  **8** and  $\text{Ph}_2\text{PC}\equiv\text{CPh}_2$  **9**) were isolated and spectroscopically characterized. For **4**, **5**, **8**, and **9**, the solid-state molecular structures of the products were determined by use of single-crystal X-ray diffraction techniques.

**Key words:** dinitrosyliron, iron nitrosyls, dinuclear macrocycles, bis(phosphine) complexes.

**Résumé :** On a étudié des réactions impliquant le  $\text{Fe}(\text{NO})_2(\text{CO})_2$  et les ligands bis(phosphines), bis(diphénylphosphino)méthane (DPPM), bis(diphénylphosphino)acétylène (DPPA), 1,6-bis(diphénylphosphino)hexane (DPPH), et 1,4-bis(diphénylphosphino)benzène (DPPB). À partir de ces réactions on a isolé le complexe mononucléaire  $\text{Fe}(\kappa^1\text{-DPPM})(\text{NO})_2(\text{CO})$  (**3**), les espèces dinucléaires linéaires du type  $\text{Fe}_2(\mu\text{-}L)(\text{NO})_4(\text{CO})_2$  ( $L = \text{Ph}_2\text{PCH}_2\text{PPh}_2$  (**4**);  $\text{Ph}_2\text{PC}\equiv\text{CPh}_2$  (**5**);  $\text{Ph}_2\text{PCH}_2(\text{CH}_3)_4\text{CH}_2\text{PPh}_2$  (**6**) et  $\text{Ph}_2\text{P}(p\text{-C}_6\text{H}_4)\text{PPh}_2$  (**7**)) et les espèces dinucléaires macrocycliques de type  $\text{Fe}_2(\mu\text{-}L)_2(\text{NO})_4$  ( $L = \text{Ph}_2\text{PCH}_2\text{PPh}_2$  (**8**);  $\text{Ph}_2\text{PC}\equiv\text{CPh}_2$  (**9**)) et on les a caractérisés par spectroscopie. Les structures moléculaires à l'état solide des produits **4**, **5**, **8** et **9** ont été déterminées par la technique de diffraction des rayons X par un cristal unique.

**Mots clés :** dinitrosylfer, nitrosyles de fer, macrocycles dinucléaires, complexes de bis(phosphine).

[Traduit par la Rédaction]

## Introduction

Dinitrosyliron-based compounds are known to participate in a variety of important chemical processes ranging from the transfer of molecular oxygen to alkenes or phosphines (1, 2) to the polymerization of olefins (3–6). Some non-heme iron nitrosyl complexes have also been identified as nitric oxide storage substances within biological systems; these have been detected by EPR studies, both as products

after the biosynthetic evolution of NO in vitro and from the addition of NO to iron-centered proteins (7). As part of our ongoing study of this class of chemically and biologically important complexes, we reported on the synthesis, structural characterization, and electrochemical behavior of compounds such as **1** that are derived from the reaction of  $\text{Fe}(\text{NO})_2(\text{CO})(\text{PR}_3)$  with tetracyanoethylene (8–10). These molecules represent the first crystallographically characterized examples of dinitrosyliron-based complexes containing  $\pi$ -bound olefinic ligands. Subsequently, we have prepared and studied the non-heme iron complex, **2**, which comprises imidazole and nitrosyl ligands (Scheme 1) (11, 12).

Building upon this research, we have recently turned our focus to the preparation of both linear and macrocyclic bis(dinitrosyliron) complexes bridged by either one or two bis(phosphine) ligands, respectively, in the anticipation that these dinuclear species may exhibit interesting and unusual properties related to the proximal nature of the two metal fragments (13). The pioneering work of Cowie and co-workers (14), Puddephatt and co-workers (15), and others demonstrates the reactivity advantages that can be brought about by connecting late metal fragments with bridging bis(phosphine) ligands such as DPPM (DPPM = bis(diphenylphosphino)methane). Moreover, Hong and co-workers have shown that dinuclear Group

Received 10 February 2003. Published on the NRC Research Press Web site at <http://canjchem.nrc.ca> on 17 April 2003.

*We dedicate this article to Professor Don Arnold, in recognition of his remarkable contributions to chemical research in Canada.*

**L. Li<sup>1</sup> and J.D. Liarakos.** Department of Chemistry and Biochemistry, California State University, Long Beach, CA 90840, U.S.A.

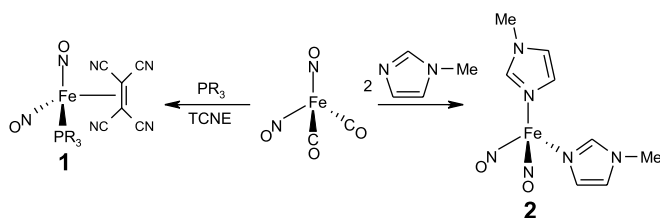
**N. Reginato and M. Urschey.** Department of Chemistry, McMaster University, Hamilton, ON L8S 4M1, Canada.

**M. Stradiotto,<sup>2</sup>** Department of Chemistry, Dalhousie University, Halifax, NS B3H 4J3, Canada.

<sup>1</sup>Corresponding author (e-mail: [lli@csulb.edu](mailto:lli@csulb.edu)).

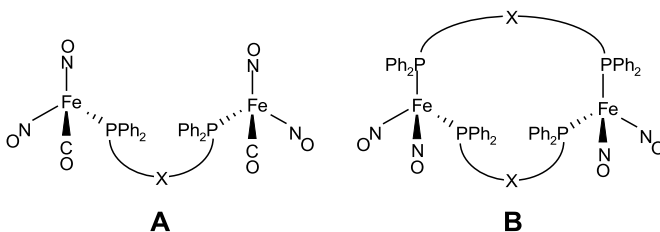
<sup>2</sup>Corresponding author (e-mail: [mark.stradiotto@dal.ca](mailto:mark.stradiotto@dal.ca)).



**Scheme 1.** Substitution reactions of  $\text{Fe}(\text{NO})_2(\text{CO})_2$ , yielding **1** and **2**.

10 complexes of the type  $\text{cyclo}[\text{M}(\kappa^2\text{-DPPM})]_2(\mu\text{-DPPA})_2$  (DPPA = bis(diphenylphosphino)acetylene) exhibit interesting photoluminescent behavior (16). Despite the well-established history of dinuclear bis(phosphine) complexes in the field of inorganic chemistry, bis(dinitrosyliron) derivatives of this class are still rare, and their reactivity properties remain essentially unexplored (17).

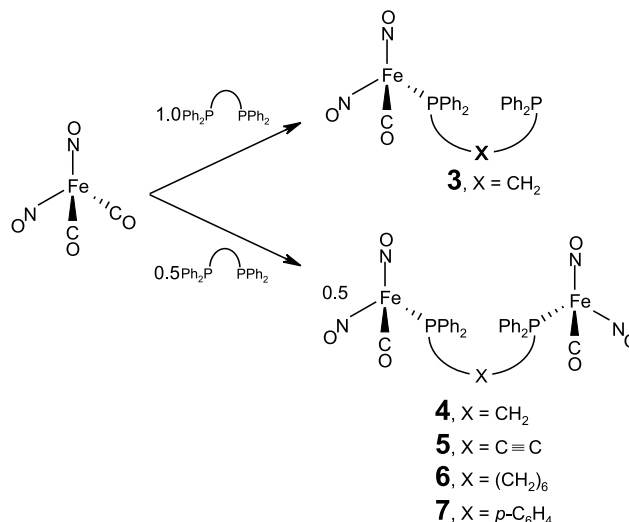
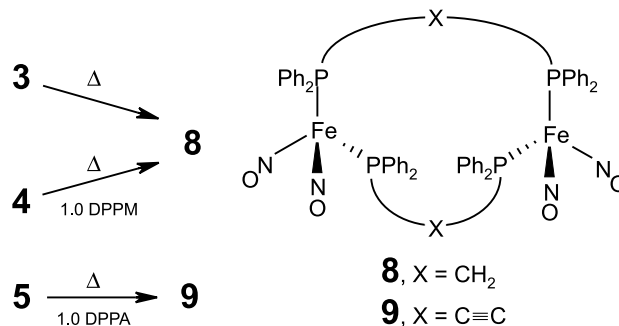
Herein we report the synthesis and structural characterization of bis(dinitrosyliron) complexes spanned by a structurally diverse series of bis(phosphine) ligands, including: (a) DPPM; (b) DPPH (DPPH = 1,6-bis(diphenylphosphino)hexane); (c) DPPA; and (d) DPPB (DPPB = 1,4-bis(diphenylphosphino)benzene). Depending on the reaction conditions employed, either linear diiron constructs connected by one bis(phosphine) linker,  $(\text{NO})_2\text{FeP}\sim\text{PFe}(\text{NO})_2$  (**A**), or macrocyclic species spanned by two bridging ligands,  $[(\text{NO})_2\text{Fe}]_2(\text{P}\sim\text{P})_2$  (**B**), are obtained.



## Results and discussion

The mononuclear complex, **3**, and the linear diiron species, **4–7**, were readily prepared from  $\text{Fe}(\text{NO})_2(\text{CO})_2$  via addition of the desired bis(phosphine), as depicted in Scheme 2. For compounds **3–5**, these could then be converted into the corresponding cyclic compounds **8** (from either **3** or **4**) and **9** (from **5**) (Scheme 3). Compounds **3–9** are air sensitive and undergo complete decomposition after several hours. Decomposition also occurs (albeit more slowly) when these complexes are stored either in degassed solvents or as pure solids under dinitrogen at ambient temperature. Interestingly, Braunstein et al. have previously observed the formation of both **3** and **8** as side products in the process of preparing Pt–Fe clusters (18), while Atkinson et al., in examining the reaction between  $[\text{Fe}_2(\mu\text{-I})_2(\text{NO})_4]$  and DPPM, were able to isolate compound **8** as the corresponding tetrahydrofuran-solvated complex (19). However, in both cases no X-ray crystallographic structural data were provided.

The conversion of  $\text{Fe}(\text{NO})_2(\text{CO})_2$  into compounds **3–7** and subsequently into **8** or **9** is readily monitored by use of infrared spectroscopy; selected FT-IR data are listed in Table 1. The decrease in stretching frequencies observed for the car-

**Scheme 2.** Generalized synthetic pathway to compounds **3–7**.**Scheme 3.** Preparation of compounds **8** and **9**.

bonyl and the two nitrosyl ligands in **3–7** relative to  $\text{Fe}(\text{NO})_2(\text{CO})_2$  is characteristic of phosphine-substituted dinitrosyliron complexes (9). In turn, the nitrosyl stretching frequencies observed for both **8** and **9** appear at an even lower wavenumber. The macrocyclic DPPM-supported complex, **8**, exhibits four distinct IR absorptions (1733, 1721, 1687, and 1668  $\text{cm}^{-1}$ ) in the solid and in solution (spectra obtained from samples dissolved in  $\text{CH}_2\text{Cl}_2$  match previously reported values (19)), possibly arising from the interaction of the  $\text{Fe}(\text{NO})_2$  centers, as has been observed in other cyclic systems (19, 20). This phenomenon appears to depend on ring size, as the related ten-membered ring compound, **9**, displays only two nitrosyl stretching signals (1723 and 1679  $\text{cm}^{-1}$ ) in both the solid and liquid states. Based on the observed IR frequencies, the nitrosyl groups are best described as linear, donating  $\text{NO}^+$  fragments (vide infra) (21, 22). The formation of **3–9** was also followed by use of NMR spectroscopy, and each of the dinuclear compounds (**4–9**) exhibit a single  $^{31}\text{P}$  NMR resonance in the range of 33–57 ppm, consistent with a disubstituted bis(phosphine) complex.

In an attempt to evaluate how altering the characteristics of the bridging bis(phosphine) ligand impacts the structural topology of these linear and macrocyclic bis(dinitrosyliron) complexes, an X-ray crystallographic study of compounds **4**, **5**, **8**, and **9** was conducted. Crystallographic collection and refinement parameters and selected metrical parameters ap-



**Table 1.** Nitrosyl and carbonyl IR stretching frequencies for **3–9** (KBr pellet).

Compounds	$\nu_{\text{CO}}$ ( $\text{cm}^{-1}$ )	$\nu_{\text{NO}}$ ( $\text{cm}^{-1}$ )
[Fe(DPPM)(NO) <sub>2</sub> (CO)], <b>3</b>	2014, 1994; 2005 <sup>a</sup>	1763, 1720 (s), 1700; 1761, <sup>a</sup> 1718 <sup>a</sup>
[Fe <sub>2</sub> ( $\mu$ -DPPM)(NO) <sub>4</sub> (CO) <sub>2</sub> ], <b>4</b>	2005; 2004 <sup>a</sup>	1760, 1719 (s), 1702; 1764, <sup>a</sup> 1718 <sup>a</sup>
[Fe <sub>2</sub> ( $\mu$ -DPPA)(NO) <sub>4</sub> (CO) <sub>2</sub> ], <b>5</b>	2020, 2005	1767, 1716
[Fe <sub>2</sub> ( $\mu$ -DPPH)(NO) <sub>4</sub> (CO) <sub>2</sub> ], <b>6</b>	1999	1755, 1701
[Fe <sub>2</sub> ( $\mu$ -DPPB)(NO) <sub>4</sub> (CO) <sub>2</sub> ], <b>7</b>	2009, 1999	1760, 1707
[Fe <sub>2</sub> ( $\mu$ -DPPM) <sub>2</sub> (NO) <sub>4</sub> ], <b>8</b>	—	1733, 1721, 1687, 1668
[Fe <sub>2</sub> ( $\mu$ -DPPA) <sub>2</sub> (NO) <sub>4</sub> ], <b>9</b>	—	1723, 1679

<sup>a</sup>Measured in THF solution.**Table 2.** Crystallographic collection and refinement parameters for **4**, **5**, **8**, and **9·CH<sub>2</sub>Cl<sub>2</sub>**.

	<b>4</b>	<b>5</b>	<b>8</b>	<b>9·CH<sub>2</sub>Cl<sub>2</sub></b>
Empirical formula	C <sub>27</sub> H <sub>22</sub> P <sub>2</sub> N <sub>4</sub> Fe <sub>2</sub> O <sub>6</sub>	C <sub>28</sub> H <sub>20</sub> P <sub>2</sub> N <sub>4</sub> Fe <sub>2</sub> O <sub>6</sub>	C <sub>50</sub> H <sub>44</sub> P <sub>4</sub> N <sub>4</sub> Fe <sub>2</sub> O <sub>4</sub>	C <sub>53</sub> H <sub>42</sub> P <sub>4</sub> N <sub>4</sub> Fe <sub>2</sub> O <sub>4</sub> Cl <sub>2</sub>
Molecular weight	672.13	682.12	1000.47	1105.39
Description	Red needle	Dark red plate	Dark red prism	Dark red prism
Size (mm <sup>3</sup> )	0.42 × 0.09 × 0.03	0.3 × 0.16 × 0.08	0.25 × 0.15 × 0.14	0.28 × 0.25 × 0.12
Temperature (K)	213(2)	213(2)	213(2)	213(2)
Crystal system	Triclinic	Triclinic	Monoclinic	Monoclinic
Space group	$P\bar{1}$	$P\bar{1}$	$P2_1/c$	$P2_1/c$
<i>a</i> (Å)	8.3037(1)	8.714(23)	21.2512(1)	21.3908(2)
<i>b</i> (Å)	10.9324(3)	9.539(28)	12.3414(1)	13.8839(1)
<i>c</i> (Å)	17.6037(2)	9.959(25)	22.2870(2)	17.8203(2)
$\alpha$ (°)	78.43(2)	114.52(8)	90.000	90.000
$\beta$ (°)	77.318(1)	96.13(16)	112.49(1)	101.463(1)
$\gamma$ (°)	82.198(2)	97.76(12)	90.000	90.000
Volume (Å <sup>3</sup> )	1520.35(5)	734.1(34)	5400.69(7)	5186.84(8)
<i>Z</i>	2	1	4	4
<i>D</i> <sub>calcd</sub> (g cm <sup>-3</sup> )	1.468	1.543	1.230	1.416
Scan mode	$\omega$ -scans	$\omega$ -scans	$\omega$ -scans	$\omega$ -scans
<i>F</i> (000)	684	346	2064	2264
Absorption coefficient (mm <sup>-1</sup> )	1.105	1.145	0.698	0.834
$\theta$ -range (°)	1.20 to 22.50	2.29 to 27.34	1.04 to 22.50	0.97 to 22.50
Index ranges	-10 ≤ <i>h</i> ≤ 10 -13 ≤ <i>k</i> ≤ 13 -21 ≤ <i>l</i> ≤ 21	-11 ≤ <i>h</i> ≤ 11 -12 ≤ <i>k</i> ≤ 12 -12 ≤ <i>l</i> ≤ 12	-27 ≤ <i>h</i> ≤ 27 -16 ≤ <i>k</i> ≤ 16 -28 ≤ <i>l</i> ≤ 20	-27 ≤ <i>h</i> ≤ 27 -17 ≤ <i>k</i> ≤ 17 -22 ≤ <i>l</i> ≤ 22
Reflections collected	11 146	5231	31 207	28 244
Independent reflections	3892	2673	6976	6769
Data/restraints/parameters	3851/0/370	2673/0/190	6922/0/577	6763/12/656
GoF on <i>F</i> <sup>2</sup> (all)	1.011	0.938	1.120	1.017
Final <i>R</i> ( <i>I</i> > 2σ( <i>I</i> ))	<i>R</i> <sub>1</sub> = 0.0658; <i>wR</i> <sub>2</sub> = 0.1162	<i>R</i> <sub>1</sub> = 0.0772; <i>wR</i> <sub>2</sub> = 0.1810	<i>R</i> <sub>1</sub> = 0.0885; <i>wR</i> <sub>2</sub> = 0.2818	<i>R</i> <sub>1</sub> = 0.1134; <i>wR</i> <sub>2</sub> = 0.2865
<i>R</i> indices (all data)	<i>R</i> <sub>1</sub> = 0.1384; <i>wR</i> <sub>2</sub> = 0.1466	<i>R</i> <sub>1</sub> = 0.1462; <i>wR</i> <sub>2</sub> = 0.2146	<i>R</i> <sub>1</sub> = 0.1201 <i>wR</i> <sub>2</sub> = 0.3163	<i>R</i> <sub>1</sub> = 0.1451 <i>wR</i> <sub>2</sub> = 0.3264
Transmittance (max., min.)	0.9098, 0.7914	0.8722, 0.1802	0.8944, 0.6976	0.8577, 0.2080
Largest diff. peak (e Å <sup>-3</sup> )	0.338	0.971	2.932	2.605
Largest diff. hole (e Å <sup>-3</sup> )	-0.302	-0.405	-0.444	-1.606

pear in Tables 2 and 3, respectively. Thermal ellipsoid plots of the refined molecular structures of the DPPM compounds, **4** and **8**, and the DPPA compounds, **5** and **9**, appear in Figs. 1 to 4, respectively.

The iron centers in all four of the crystallographically characterized compounds possess distorted tetrahedral geometries, a structural feature that is common to dinitrosyliron complexes (12, 22). The iron—iron distances in both the linear (**4**, ~5.2 Å; **5**, ~7.6 Å) and macrocyclic (**8**, ~4.4 Å; **9**, ~7.0 Å) compounds are all significantly longer than the

related distances found in other structurally characterized bis(dinitrosyliron) species described as possessing a metal—metal bond (23). The crystallographically determined structures of the linear species, **4** and **5**, can be compared with that of [Fe(NO)<sub>2</sub>Cl]<sub>2</sub>( $\mu$ -DPPE) (DPPE = 1,2-bis(diphenylphosphino)ethane), where DPPE stands as a single bridge joining the two metal centers (17).

Despite the range in N-Fe-N angles (115.6(4)° to 126.5(4)°), all eight of the Fe(NO)<sub>2</sub> units in compounds **4**, **5**, **8**, and **9** exhibit “attracto” conformations (N-Fe-N > O-Fe-



**Table 3.** Selected bond lengths (Å) and angles (°) for **4**, **5**, **8**, and **9**·CH<sub>2</sub>Cl<sub>2</sub>.

	<b>4</b>	<b>5</b>	<b>8</b>	<b>9</b> ·CH <sub>2</sub> Cl <sub>2</sub>
<b>Bond lengths (Å)</b>				
Fe—Fe	5.21	7.60	4.35	7.01
Fe(1)—N(1)	1.693(8)	1.680(7)	1.643(9)	1.66(1)
Fe(1)—N(2)	1.654(6)	1.73(1)	1.644(8)	1.65(1)
Fe(2)—N(3)	1.675(8)	—	1.668(9)	1.67(1)
Fe(2)—N(4)	1.705(8)	—	1.644(9)	1.646(9)
N(1)—O	1.171(8)	1.169(7)	1.19(1)	1.19(1)
N(2)—O	1.175(6)	1.164(9)	1.20(1)	1.19(1)
N(3)—O	1.182(8)	—	1.18(1)	1.16(1)
N(4)—O	1.163(8)	—	1.19(1)	1.20(1)
<b>Bond angles (°)</b>				
Fe(1)-N(1)-O	177.8(7)	175.9(6)	174(1)	176.2(8)
Fe(1)-N(2)-O	174.8(7)	178.1(7)	168.9(8)	172.9(7)
Fe(2)-N(3)-O	175.0(7)	—	166.6(8)	174.5(9)
Fe(2)-N(4)-O	177.1(8)	—	177.1(9)	179.6(8)
N(1)-Fe(1)-N(2)	122.1(8)	115.6(4)	117.0(4)	120.5(4)
N(3)-Fe(2)-N(4)	118.1(9)	—	116.8(4)	126.5(4)
*O-Fe(1)-O*	119.9	114.1	109.6	116.4
*O-Fe(2)-O*	116.2	—	110.3	124.3

\*Nitrosyl oxygen atoms.

O) (24–26). The observation of contracted Fe—N distances (~1.64 to ~1.73 Å) and lengthened N—O bonds (~1.16 to ~1.20 Å) in these complexes indicates significant iron–nitrosyl multiple bond character, arising owing to appreciable back-donation from the iron fragment into the  $\pi^*$ -orbital on the nitrosyl ligand (22). By comparison, Ray et al. reported crystallographic data for a series of trigonal bipyramidal iron nitrosyl complexes, in which the Fe—N(O) and N—O distances are in the range of ~1.73–1.75 Å and ~1.12–1.15 Å, respectively (27). These X-ray structural data, in addition to the observation of nearly linear Fe–N–O linkages, corroborate the IR spectroscopic results and suggest that the NO units in **4**, **5**, **8**, and **9** function as three-electron donors.

Compounds **5** and **9** represent the first examples of crystallographically characterized species containing the Fe(NO)<sub>2</sub>( $\mu$ -DPPA) fragment, and as such are worthy of further commentary. The “*anti*” orientation of the Fe(NO)<sub>2</sub> groups, coupled with the presence of a crystallographic inversion center, results in an interesting solid-state molecular geometry for the linear bis(dinitrosyliron) species, **5**, in which ten of the non-hydrogen atoms (O(1), N(2), Fe(1), P(1), C(1), C(1A), P(1A), Fe(1A), N(2A), and O(1A)) are essentially coplanar (mean deviation from the plane ~0.32 Å). The non-linear nature of the P–C $\equiv$ C fragment in **5** (P(1)–C(1)–C(1A) 172.9(8)°) parallels other crystallographically characterized compounds of the type  $L_nM$ -DPPA- $ML_n$  (28–34) and presumably arises because of steric congestion in the vicinity of the triple bond. Interestingly, such steric demands do not result in a lengthening of the alkyne bonds in either **5** (1.21(1) Å) or **9** (C(1)–C(2) 1.198(4) Å; C(3)–C(4) 1.20(1) Å), which remain essentially unchanged relative to free DPPA (35).

The overall molecular structure of the macrocyclic DPPA compound, **9**, can be described as a severely twisted ten-membered ring, a geometry that is similar to Mo<sub>2</sub>( $\mu$ -DPPA)<sub>2</sub>(CO)<sub>8</sub> (36), but different from the nearly planar

structure found for PdPtCl<sub>4</sub>( $\mu$ -DPPA)<sub>2</sub> (37). The puckering of the ring framework in **9** gives rise to a “bow-tie” orientation of the alkyne units, in which these fragments are twisted by approximately 49° with respect to one another (Fig. 5). As was observed for **5**, the two P–C $\equiv$ C–P units in **9** exhibit concave bowing; however, one P–C $\equiv$ C–P fragment is only slightly bent (P(3)–C(3)–C(4) 173.9(9)°; P(4)–C(4)–C(3) 175.5(9)°), while the other exhibits more pronounced asymmetric bending (P(1)–C(1)–C(2) 170.8(9)°; P(2)–C(2)–C(1) 165.8(9)°). Upon viewing the structure of **9** down the Fe–Fe vector, it is evident that the DPPA ligands can be loosely classified as “staggered” (P(1)–C(1)–C(2)–P(2)) and “eclipsed” (P(3)–C(3)–C(4)–P(4)), with the former experiencing greater strain and subsequently more pronounced deviation from linearity than the latter. It is interesting to note that although Mo<sub>2</sub>( $\mu$ -DPPA)<sub>2</sub>(CO)<sub>8</sub> possesses similarly “staggered” and “eclipsed” DPPA ligands (36), a correlation between the degree of nonlinearity of the DPPA ligands and their relative orientation does not exist in this Mo-based system.

## Experimental

### General

All manipulations were carried out in an atmosphere of dry dinitrogen using freshly distilled and degassed solvents. Unless otherwise stated, all chemicals, including bis(diphenylphosphino)methane (DPPM, Aldrich), 1,6-bis(diphenylphosphino)hexane (DPPH, Aldrich), bis(diphenylphosphino)acetylene (DPPA, Strem Chemicals), and 1,4-bis(diphenylphosphino)benzene (DPPB, Organometallics Inc.) were used as supplied. Fe(NO)<sub>2</sub>(CO)<sub>2</sub> was prepared following a published procedure (38). The <sup>1</sup>H, <sup>13</sup>C, and <sup>31</sup>P NMR spectral data were acquired using either a Bruker AC-200 or AC-300 spectrometer in deuterated chloroform, unless otherwise stated. All <sup>13</sup>C and <sup>31</sup>P NMR spectra were recorded in proton-decoupled mode with phosphorus chem-



**Fig. 1.** The X-ray structure of **4**, showing the atomic numbering scheme. Anisotropic thermal displacement ellipsoids are shown at the 30% probability level.

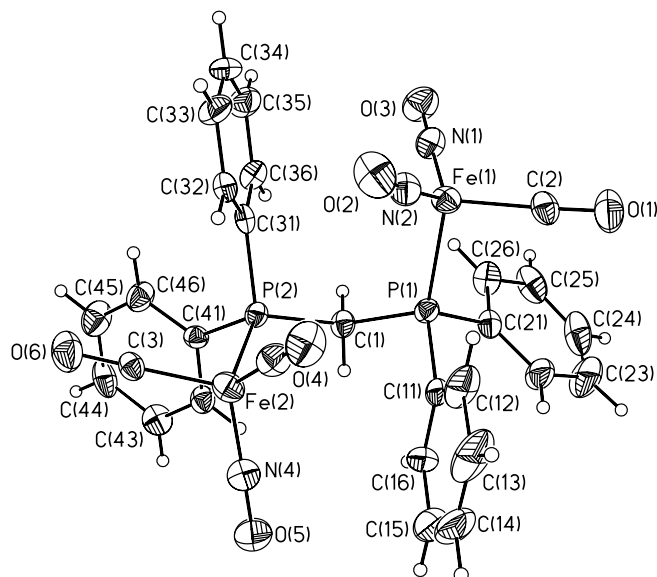
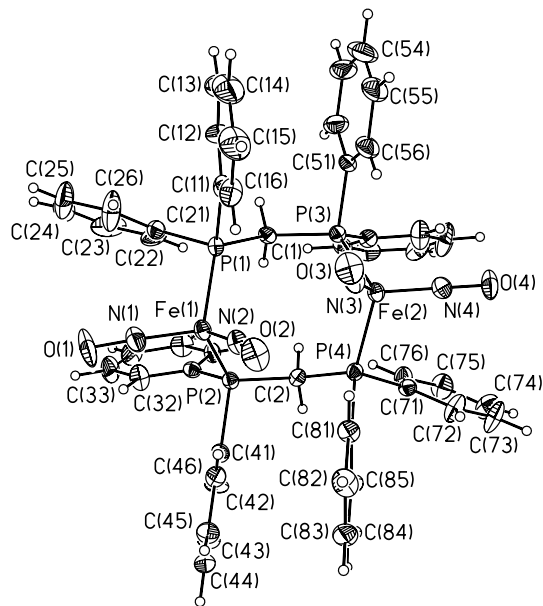
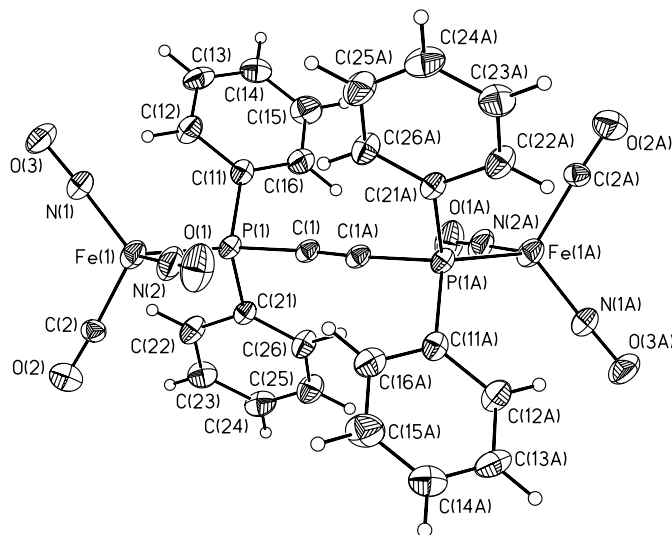


**Fig. 2.** The X-ray structure of **8**, showing the atomic numbering scheme. Anisotropic thermal displacement ellipsoids are shown at the 30% probability level.



ical shifts externally referenced relative to 85%  $\text{H}_3\text{PO}_4$  in  $\text{D}_2\text{O}$ . Melting and decomposition points were measured using differential scanning calorimetry performed on a DSC 2910 instrument (TA instruments). IR spectra were recorded on a Bio-Rad FTS-40 single-beam spectrometer using KBr pellets, unless otherwise stated. Mass spectra were recorded on a Micromass Quattro LC instrument using positive electrospray ionization (ESI+). Despite repeated attempts, satisfactory elemental analysis data for the compounds reported herein could not be obtained.

**Fig. 3.** The X-ray structure of **5**, showing the atomic numbering scheme. Anisotropic thermal displacement ellipsoids are shown at the 30% probability level.

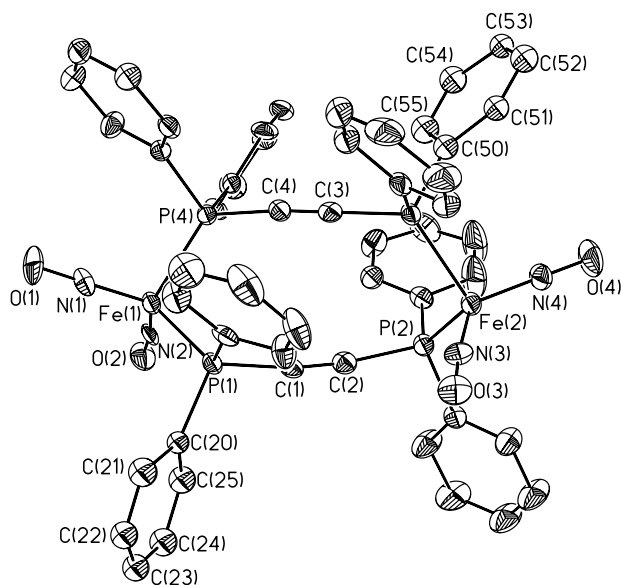


### X-Ray crystallography

Crystallographic data for **4**, **5**, **8**, and **9-CH<sub>2</sub>Cl<sub>2</sub>** were collected from suitable samples mounted on glass fibers. The instrument used for the collection of diffraction data was a Siemens P4 diffractometer equipped with a Siemens SMART 1K CCD Area Detector (using the program SMART) and a rotating anode using graphite-mono-chromated Mo  $\text{K}\alpha$  radiation ( $\lambda = 0.71073 \text{ \AA}$ ). Data processing was carried out by use of the program SAINT, while the program SADABS was utilized for the scaling of diffraction data, the application of a decay correction, and an empirical absorption correction based on redundant reflections. Structures were solved by using the direct methods procedure in the Siemens SHELXTL program library and refined by full-matrix least squares methods on  $F^2$ . All non-hydrogen atoms, with the exception of the disordered atoms in **9-CH<sub>2</sub>Cl<sub>2</sub>**, were refined using anisotropic thermal parameters. Hydrogen atoms were added as fixed contributors at calculated positions, with isotropic thermal parameters based on the bonded carbon atom. Compound **5** crystallizes in the space group  $P\bar{1}$  with half a molecule per asymmetric unit; the other half of the molecule may be generated by a crystallographic inversion center, resulting in the observation of only one molecule per unit cell ( $Z = 1$ ). Combustion analysis, previously obtained by others (39), for compound **8** (similarly prepared in tetrahydrofuran) suggested the presence of one solvated tetrahydrofuran per molecule of **8** in the crystalline lattice. However, despite the fact that the data readily allow for a complete anisotropic refinement of the target molecule, attempts to resolve atomic positions for the disordered solvate were unsuccessful, leading to rather high values for the residual electron density and the refinement statistics. In the case of **9-CH<sub>2</sub>Cl<sub>2</sub>**, the final refined structure involved a disordered model in which the phenyl rings containing C(20)–C(25) and C(50)–C(55) could exist in either of two orientations resulting from rotation about the P–C(*ipso*) bond. Based on the observed thermal displacement



**Fig. 4.** The X-ray structure of **9**·CH<sub>2</sub>Cl<sub>2</sub>, with thermal displacement ellipsoids shown at the 30% probability level. For clarity, hydrogen atoms and the dichloromethane solvate have been omitted, and only the most highly populated components of the disordered phenyl rings are shown.

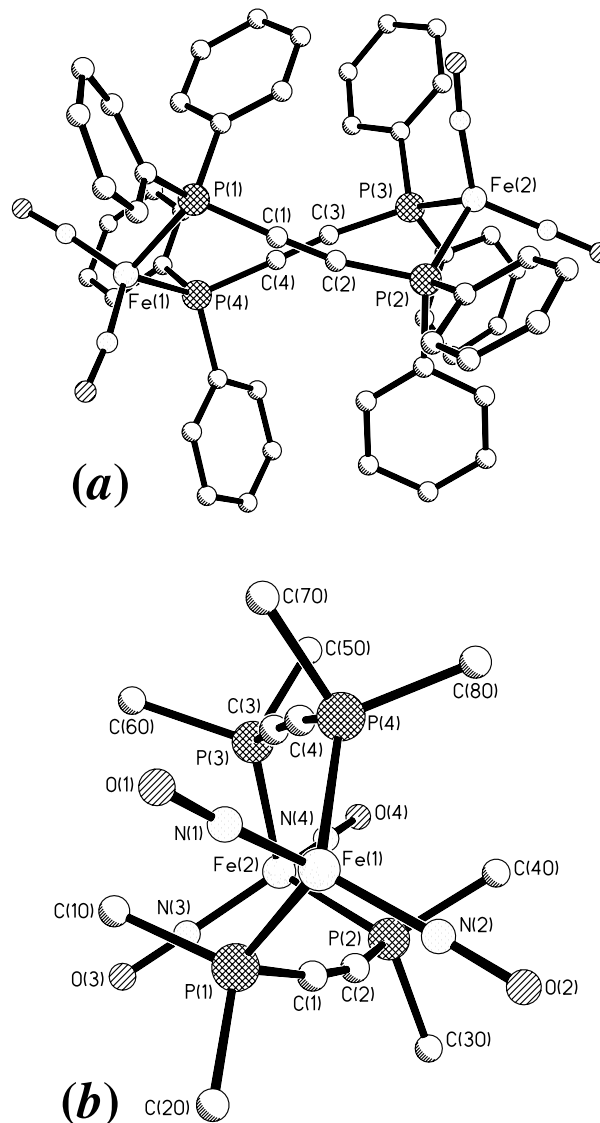


ellipsoids, it was assumed that only these carbon atoms were significantly affected by this disorder process. The occupancies for each of the two orientations were each allowed to be refined as a free variable (final ratio of approximately 55:45 for both of the phenyl units). Moreover, during the refinement of **9**·CH<sub>2</sub>Cl<sub>2</sub>, a disordered molecule of dichloromethane was located in the asymmetric unit. Given the magnitude, location, and number of electron density difference peaks observed in the region of the solvate, the final refined structure was based on a disordered model that involved two possible orientations generated by rotation about a fixed and non-disordered (fully occupied) central methylene carbon. The occupancies for each of the two orientations were each allowed to be refined as a free variable (final ratio of approximately 90:10). Hydrogen atoms for each unique component of the disordered phenyl and dichloromethane units were added at calculated positions with occupancy factors equal to the occupancy factor of the associated carbon atom. The hydrogen atoms were refined using a riding model with isotropic displacement parameters equal to 1.2 times the equivalent isotropic displacement parameter of the attached carbon (40–43).<sup>3</sup>

### General preparation of compounds 3–7

Method (a): To an Erlenmeyer flask containing Fe(NO)<sub>2</sub>(CO)<sub>2</sub> was added a suspension of the phosphine ligand in pentane at room temperature. After stirring the solution for 18 h, the precipitate generated was filtered and washed with pentane. Method (b): To an Erlenmeyer flask containing the

**Fig. 5.** Views of the crystallographically determined structure of **9**·CH<sub>2</sub>Cl<sub>2</sub>: (a) highlighting the “bow-tie” orientation of the alkyne units and (b) down the Fe(1)–Fe(2) vector (selected atoms omitted for clarity).



phosphine ligand in THF was added Fe(NO)<sub>2</sub>(CO)<sub>2</sub> at room temperature. After stirring the solution for 18 h, the solvent was removed under reduced pressure and the remaining solid washed with pentane.

### General preparation of compounds 8 and 9

Method (c): A solution of the reactants was filtered into a sealable tube, degassed by use of freeze-pump-thaw procedures, flame-sealed under vacuum, and subsequently heated to 75°C.

<sup>3</sup>Supplementary data may be purchased from the Depository of Unpublished Data, Document Delivery, CISTI, National Research Council Canada, Ottawa, ON K1A 0S2, Canada ([http://www.nrc.ca/cisti/irm/unpub\\_e.shtml](http://www.nrc.ca/cisti/irm/unpub_e.shtml) for information on ordering electronically). CCDC 205068 (4), 205069 (5), 205070 (8), and 205071 (9·CH<sub>2</sub>Cl<sub>2</sub>) contain the supplementary data for this paper. These data can be obtained, free of charge, via [www.ccdc.cam.ac.uk/conts/retrieving.html](http://www.ccdc.cam.ac.uk/conts/retrieving.html) (or from the Cambridge Crystallographic Data Centre, 12 Union Road, Cambridge, U.K.; fax +44 1223 336033; or [deposit@ccdc.cam.ac.uk](mailto:deposit@ccdc.cam.ac.uk)).



**[Fe( $\kappa^1$ -DPPM)(NO) $_2$ (CO)] 3**

Method (a): Fe(NO) $_2$ (CO) $_2$  (0.1 mL, 0.9 mmol) and DPPM (170 mg, 0.44 mmol) in pentane (8 mL) produced **3** as bright orange-red powder (70 mg, 30%). Method (b): DPPM (170 mg, 0.44 mmol), Fe(NO) $_2$ (CO) $_2$  (0.05 mL, 0.45 mmol), and THF (6 mL) produced **3** (160 mg, 69%), m.p. 119°C (with decomposition). IR (KBr) (cm $^{-1}$ )  $\nu$ : 2014 (CO), 1994 (CO), 1763 (NO), 1720 (shoulder) (NO), 1700 (NO). IR (THF-solution) (cm $^{-1}$ )  $\nu$ : 2005 (CO), 1761 (NO), 1718 (NO).  $^1\text{H}$  NMR (200 MHz)  $\delta$ : 3.21 (d, 2H,  $^2J_{\text{HP}} = 8.7$  Hz, CH $_2$ ), 7.27–7.49 (m, 20H, Ph).  $^{13}\text{C}$  NMR (50 MHz)  $\delta$ : 31.7 (m, CH $_2$ ), 127.9–137.6 (Ph), 221.3 (s, CO).  $^{31}\text{P}$  NMR (121 MHz)  $\delta$ : –25.0 (d, 1P,  $^2J_{\text{PP}} = 105.6$  Hz), 48.0 (d, 1P,  $^2J_{\text{PP}} = 105.6$  Hz, P-Fe).

**[Fe $_2$ ( $\mu$ -DPPM)(NO) $_4$ (CO) $_2$ ] 4**

Method (a): Fe(NO) $_2$ (CO) $_2$  (0.34 mL, 3.1 mmol) was added to a suspension of DPPM (120 mg, 0.31 mmol) in pentane (10 mL). During the course of the reaction the DPPM dissolved, and a dark red - brown powder precipitated, which was filtered and washed with pentane (190 mg, 92%). Method (b): DPPM (500 mg, 1.3 mmol), Fe(NO) $_2$ (CO) $_2$  (0.3 mL, 2.7 mmol), and THF (10 mL) produced **4** (690 mg, 79%), m.p. 144°C (with decomposition). IR (KBr) (cm $^{-1}$ )  $\nu$ : 2005 (CO), 1760 (NO), 1719 (shoulder) (NO), 1702 (NO). IR (THF-solution) (cm $^{-1}$ )  $\nu$ : 2004 (CO), 1764 (NO), 1718 (NO).  $^1\text{H}$  NMR (300 MHz, CD $_2$ Cl $_2$ )  $\delta$ : 3.76 (t, 2H,  $^2J_{\text{HP}} = 9.7$  Hz, CH $_2$ ), 7.41–7.44 (m, 20H, Ph).  $^{13}\text{C}$  NMR (75 MHz)  $\delta$ : 32.6 (t,  $^1J_{\text{CP}} = 11.4$  Hz, CH $_2$ ), 129.3 (t,  $J_{\text{CP}} = 5.2$  Hz, C $_o$  or C $_m$ ), 131.1 (s, C $_p$ ), 132.6 (t,  $J_{\text{CP}} = 6.5$  Hz, C $_m$  or C $_o$ ), 134.3 (t,  $J_{\text{CP}} = 22.2$  Hz, C $_i$ ), 221.1 (s, CO).  $^{31}\text{P}$  NMR (121 MHz)  $\delta$ : 45.6 (s). Single crystals suitable for X-ray diffraction studies were grown from pentane by slow evaporation under an atmosphere of dinitrogen.

**[Fe $_2$ ( $\mu$ -DPPA)(NO) $_4$ (CO) $_2$ ] 5**

Method (b): DPPA (300 mg, 0.76 mmol), Fe(NO) $_2$ (CO) $_2$  (0.18 mL, 1.6 mmol), and THF (6 mL) yielded **5** (370 mg, 71%). IR (KBr) (cm $^{-1}$ )  $\nu$ : 2020 (CO), 2005 (CO), 1716 (NO), 1767 (NO).  $^1\text{H}$  NMR (300 MHz)  $\delta$ : 7.43–7.64 (m, 20H, Ph).  $^{13}\text{C}$  NMR (50 MHz)  $\delta$ : 129.1 (d,  $J_{\text{CP}} = 11.5$  Hz, C $_o$  or C $_m$ ), 131.1 (s, C $_p$ ), 131.8 (d,  $J_{\text{CP}} = 14.4$  Hz, C $_m$  or C $_o$ ), 132.0 (d,  $J_{\text{CP}} = 47.9$  Hz, C $_i$ ), 218.7 (s, C $\equiv$ O).  $^{31}\text{P}$  NMR (121 MHz)  $\delta$ : 33.1 (s). Single crystals suitable for X-ray diffraction studies were grown from pentane by slow evaporation under an atmosphere of dinitrogen.

**[Fe $_2$ ( $\mu$ -DPPH)(NO) $_4$ (CO) $_2$ ] 6**

Method (b): DPPH (500 mg, 1.2 mmol), Fe(NO) $_2$ (CO) $_2$  (0.3 mL, 2.8 mmol), and THF (15 mL) produced **6** (500 mg, 56%). IR (KBr) (cm $^{-1}$ )  $\nu$ : 1999 (CO), 1755 (NO), 1701 (NO).  $^1\text{H}$  NMR (200 MHz)  $\delta$ : 1.0–1.4 (m, 8H, PCH $_2$ (CH $_2$ ) $_4$ -CH $_2$ P), 2.29 (m, 4H, PCH $_2$ (CH $_2$ ) $_4$ CH $_2$ P), 7.40–7.42 (m, 20H, Ph).  $^{13}\text{C}$  NMR (50 MHz)  $\delta$ : 24.1 (s, 2  $\times$  CH $_2$ ), 30.0 (d,  $^1J_{\text{CP}} = 8.4$  Hz, 2  $\times$  PCH $_2$ ), 30.5 (s, 2  $\times$  CH $_2$ ), 128.7 (d,  $J_{\text{CP}} = 9.5$  Hz, C $_o$  or C $_m$ ), 130.0 (s, C $_p$ ), 131.8 (d,  $J_{\text{CP}} = 11.8$  Hz, C $_m$  or C $_o$ ), 134.0 (d,  $J_{\text{CP}} = 39.6$  Hz, C $_i$ ), 222.0 (s, CO).  $^{31}\text{P}$  NMR (121 MHz)  $\delta$ : 49.2 (s).

**[Fe $_2$ ( $\mu$ -DPPB)(NO) $_4$ (CO) $_2$ ] 7**

Method (b): DPPB (500 mg, 1.1 mmol), Fe(NO) $_2$ (CO) $_2$  (0.27 mL, 2.5 mmol), and THF (25 mL) yielded **7** (760 mg, 94%); m.p. 301°C (with decomposition). IR (KBr pellet) (cm $^{-1}$ )  $\nu$ : 2009 (CO), 1999 (CO), 1760 (NO), 1707 (NO).  $^1\text{H}$  NMR (200 MHz)  $\delta$ : 7.34–7.42 (m, Ph).  $^{13}\text{C}$  NMR (50 MHz)  $\delta$ : 129.0 (d,  $J_{\text{CP}} = 10.8$  Hz, C $_o$  or C $_m$  and *o*-C $_6$ H $_4$ ), 130.8 (s, C $_p$ ), 132.3 (d,  $J_{\text{CP}} = 24.6$  Hz, *i*-C $_6$ H $_4$ ), 133.2 (d,  $J_{\text{CP}} = 13.6$  Hz, C $_m$  or C $_o$ ), 136.9 (d,  $J_{\text{CP}} = 38.2$  Hz, C $_i$ ), 221.0 (s, CO).  $^{31}\text{P}$  NMR (121 MHz)  $\delta$ : 57.1 (s).

**[Fe $_2$ ( $\mu$ -DPPM) $_2$ (NO) $_4$ ] 8**

Method (c): After stirring DPPM (72 mg, 0.19 mmol) and **4** (125 mg, 0.19 mmol) in THF (6 mL) for 18 h, the solution gradually turned black. After 24 h a red crystalline product (**8**) was isolated by filtration (45 mg, 24%); these crystals were used for X-ray diffraction studies. Alternative route using method (c): **3** (150 mg, 0.28 mmol) in THF (5 mL) (35 mg, 13%); m.p. 167°C. IR (KBr) (cm $^{-1}$ )  $\nu$ : 1733 (NO), 1721 (NO), 1687 (NO), 1668 (NO); the spectrum run in CH $_2$ Cl $_2$  matches previously reported values (19).  $^1\text{H}$  NMR (200 MHz)  $\delta$ : 3.7 (t,  $^2J_{\text{HP}} = 6.5$  Hz, 2  $\times$  CH $_2$ ), 7.5–7.3 (m, Ph, 40H).  $^{31}\text{P}$  NMR (121 MHz)  $\delta$ : 43.5 (s). MS-MS (90:10 CH $_2$ Cl $_2$ /MeOH, *m/z*, (%)): 1000 ([M] $^+$ , 100), 970 ([M – NO] $^+$ , 2), 500 ([M/2] $^+$ , 45).

**[Fe $_2$ ( $\mu$ -DPPA) $_2$ (NO) $_4$ ] 9**

Method (c): After stirring **5** (100 mg, 1.5 mmol) and DPPA (58 mg, 1.5 mmol) in THF (5 mL) for 18 h, the solution gradually turned black. After 72 h the tube was opened, the solvent removed under reduced pressure, and the remaining brown solid (**9**) washed with pentane (90 mg, 64%). Single crystals suitable for X-ray analysis were grown from CH $_2$ Cl $_2$  by slow evaporation of the solvent under an atmosphere of dinitrogen. IR (KBr) (cm $^{-1}$ )  $\nu$ : 1723 (NO), 1679 (NO).  $^1\text{H}$  NMR (200 MHz)  $\delta$ : 7.51–7.09 (m, Ph, 40H).  $^{31}\text{P}$  NMR (121 MHz)  $\delta$ : 38.6 (s).

**Summary**

The results described herein demonstrate that both linear and macrocyclic organometallic complexes containing a pair of dinitrosyliron fragments spanned by either one or two bis(phosphine) ligands can be selectively prepared from Fe(NO) $_2$ (CO) $_2$ . The X-ray crystallographic characterization of four members of this series reveals that the choice of bridging bis(phosphine) ligand used in these syntheses has a profound influence on the molecular structure of the resulting diiron framework. This preliminary synthetic and structural investigation provides the groundwork for exploring the chemical, physical, and reactivity properties of this class of molecules. These studies are underway and will be the focus of future reports.

**Acknowledgments**

Support of this work by the Natural Sciences and Engineering Research Council of Canada (NSERC), Research Corporation (CC5392), and the Petroleum Research Fund administered by the American Chemical Society (37034-GB3) is gratefully acknowledged. We would also like to



thank Dr. James F. Britten (McMaster University, Canada) for his assistance in the acquisition of X-ray crystallographic data.

## References

1. H. Li Kam Wah, M. Postel, and M. Pierrot. *Inorg. Chim. Acta*, **165**, 215 (1989).
2. V. Munyejabo, P. Guillaume, and M. Postel. *Inorg. Chim. Acta*, **221**, 133 (1994).
3. D. Ballivet-Tkatchenko, M. Riveccie, and N. El-Murr. *J. Am. Chem. Soc.* **101**, 2763 (1979).
4. D. Ballivet-Tkatchenko, C. Billard, and A. Revillon. *J. Polym. Sci.* **19**, 1697 (1981).
5. D. Ballivet. *J. Organomet. Chem.* **124**, C9 (1977).
6. G.E. Gadd, M. Poliakoff, and J.J. Turner. *Organometallics*, **6**, 391 (1987).
7. B. Muller, A.L. Kleschjov, and J.C. Stoclet. *Br. J. Pharmacol.* **119**, 1281 (1996).
8. L. Li, G.D. Enright, and K.F. Preston. *Organometallics*, **13**, 4686 (1994).
9. A. Hörsken, G. Zheng, M. Stradiotto, C.T.C. McCrory, and L. Li. *J. Organomet. Chem.* **558**, 1 (1998).
10. L. Li, J.R. Morton, and K.F. Preston. *Mag. Res. Chem.* **33**, S14 (1995).
11. N. Reginato, C.T.C. McCrory, D. Pervitsky, and L. Li. *J. Am. Chem. Soc.* **121**, 10 217 (1999).
12. L. Li. *Comm. Inorg. Chem.* **23**, 335 (2002).
13. (a) D.W. Stephan. *Coord. Chem. Rev.* **95**, 42 (1989); (b) N. Wheatley and P. Kalck. *Chem. Rev.* **99**, 3379 (1999).
14. S.J. Trepanier, B.T. Sterenberg, R. McDonald, and M. Cowie. *J. Am. Chem. Soc.* **121**, 2613 (1999) and refs. cited therein.
15. Y. Gao, M.C. Jennings, R.J. Puddephatt, and H.A. Jenkins. *Organometallics*, **20**, 3500 (2001) and refs. cited therein.
16. D. Xu, H.J. Murfee, W.E. van der Veer, and B. Hong. *J. Organomet. Chem.* **596**, 53 (2000).
17. For a crystallographically characterized example, see: P. Guillaume, H. Li Kam Wah, and M. Postel. *Inorg. Chem.* **30**, 1828 (1991).
18. P. Braunstein and J. Richert. *J. Chem. Soc., Dalton Trans.* 3801 (1990).
19. F.L. Atkinson, H.E. Blackwell, N.C. Brown, N.G. Connelly, J.G. Crossley, A.G. Orpen, A.L. Rieger, and P.H. Rieger. *J. Chem. Soc., Dalton Trans.* 3491 (1996).
20. K.S. Chong, S.J. Rettig, A. Storr, and J. Trotter. *Can. J. Chem.* **57**, 3119 (1979).
21. T.R. Bryar and D.R. Eaton. *Can. J. Chem.* **70**, 1917 (1992).
22. W. Harrison and J. Trotter. *J. Chem. Soc. A*, 1542 (1971) and refs. cited therein.
23. J.T. Thomas, J.H. Robertson, and E.G. Cox. *Acta Cryst.* **11**, 599 (1958).
24. G.B. Richter-Addo and P. Legzdins. *Metal nitrosyls*. Oxford University Press, New York. 1992. p. 81.
25. J.H. Enemark and R.D. Feltham. *Coord. Chem. Rev.* **13**, 339 (1974).
26. R.D. Feltham and J.H. Enemark. *In Topics in stereochemistry*. Vol. 12. Edited by G.L. Geoffroy. John Wiley & Sons, New York. 1981. p. 155.
27. M. Ray, A.P. Bolombek, M.P. Hendrich, G.P.A. Yap, L.M. Liable-Sands, A.L. Rheingold, and A.S. Borovik. *Inorg. Chem.* **38**, 3110 (1999).
28. R.J. Puddephatt. *Chem. Soc. Rev.* **12**, 99 (1983).
29. M. Semmelmann, D. Fenske, and J.F. Corrigan. *J. Chem. Soc., Dalton Trans.* 2541 (1998).
30. T.M. Layer, J. Lewis, A. Martin, P.R. Raithby, and W.T. Wong. *J. Chem. Soc., Dalton Trans.* 3411 (1992).
31. C.J. Adams, M.I. Bruce, B.W. Skelton, and A.H. White. *J. Organomet. Chem.* **447**, 91 (1993).
32. J. Lee, M.G. Humphrey, D.C.R. Hockless, B.W. Skelton, and A.H. White. *Organometallics*, **12**, 3468 (1993).
33. G. Hogarth and T. Norman. *J. Chem. Soc., Dalton Trans.* 1077 (1996).
34. E. Louattani, J. Suades, K. Urriaga, M.I. Arriortua, and X. Solans. *Organometallics*, **15**, 468 (1996).
35. J.C.J. Bart. *Acta Cryst.* **B25**, 489 (1969).
36. G. Hogarth and T. Norman. *Polyhedron*, **15**, 2859 (1996).
37. H.C. Clark, G. Ferguson, P.N. Kapoor, and M. Parvez. *Inorg. Chem.* **24**, 3924 (1985).
38. W. Hieber and H.Z. Beutner. *Anorg. Allg. Chem.* **320**, 101 (1963).
39. R.J. Mawby, D. Morris, E.M. Thortinson, and F. Basolo. *Inorg. Chem.* **5**, 27 (1966).
40. G.M. Sheldrick. 1996. SMART [computer program]. Release 4.05. Siemens Energy And Automation Inc., Madison, WI 53719.
41. G.M. Sheldrick. 1996. SAINT [computer program]. Release 4.05. Siemens Energy And Automation Inc., Madison, WI 53719.
42. G.M. Sheldrick. 1996. SADABS (Siemens area detector absorption corrections) [computer program].
43. G.M. Sheldrick. 1994. Siemens SHELXTL [computer program]. Version 5.03. Siemens Crystallographic Research Systems, Madison, WI 53719.



# Dimethylplatinum(IV) chemistry: Stannyl, hydride, hydroxide, and aqua complexes

Ernest M. Prokopchuk and Richard J. Puddephatt

**Abstract:** The dimethylplatinum(II) complex  $[\text{PtMe}_2(\text{Me}_3\text{TACN})]$  ( $\text{Me}_3\text{TACN}$  = 1,4,7-trimethyl-1,4,7-triazacyclononane) reacts easily with  $\text{Me}_3\text{SnCl}$ ,  $\text{Me}_2\text{SnCl}_2$ , or  $\text{HX}$  ( $\text{X} = \text{CF}_3\text{CO}_2$ ,  $\text{CF}_3\text{SO}_3$ ,  $\text{BF}_4$ ) to give the thermally stable cationic dimethylplatinum(IV) complexes  $[\text{Pt}(\text{SnMe}_3)\text{Me}_2(\text{Me}_3\text{TACN})]^+$ ,  $[\text{Pt}(\text{SnMe}_2\text{Cl})\text{Me}_2(\text{Me}_3\text{TACN})]^+$ , or  $[\text{PtHMe}_2(\text{Me}_3\text{TACN})]^+$ . The complexes  $[\text{PtMe}_2(\text{Me}_3\text{TACN})]$  and  $[\text{PtHMe}_2(\text{Me}_3\text{TACN})]^+$  are oxidized by moist air to give the hydroxo complex  $[\text{PtMe}_2(\text{OH})(\text{Me}_3\text{TACN})]^+$ , which can then be protonated reversibly to form the aqua complex  $[\text{PtMe}_2(\text{OH}_2)(\text{Me}_3\text{TACN})]^{2+}$ . The structures of the hydroxo complex  $[\text{PtMe}_2(\text{OH})(\text{Me}_3\text{TACN})]^+$ , as both the  $\text{BF}_4^-$  or  $\text{CF}_3\text{SO}_3^-$  salt, and of the mixed hydroxo, aqua complex  $[\text{PtMe}_2(\text{OH})(\text{Me}_3\text{TACN})][\text{PtMe}_2(\text{OH}_2)(\text{Me}_3\text{TACN})][\text{BF}_4]_3$  have been determined and the complexes are shown to display interesting hydrogen bonding.

**Key words:** platinum, oxidation, organometallic, tin, hydride.

**Résumé :** Le complexe de diméthylplatine(II)  $[\text{PtMe}_2(\text{Me}_3\text{TACN})]$  ( $\text{Me}_3\text{TACN}$  = 1,4,7-triméthyl-1,4,7-triazacyclononane) réagit facilement avec le  $\text{Me}_3\text{SnCl}$ , le  $\text{Me}_2\text{SnCl}_2$  ou  $\text{HX}$  ( $\text{X} = \text{CF}_3\text{CO}_2$ ,  $\text{CF}_3\text{SO}_3$ ,  $\text{BF}_4$ ) pour conduire à la formation des complexes cationiques thermiquement stables du diméthylplatine(IV)  $[\text{Pt}(\text{Sn}(\text{Me}_3)\text{Me}_2)(\text{Me}_3\text{TACN})]^+$ ,  $[\text{Pt}(\text{Sn}(\text{Me}_2\text{Cl})\text{Me}_2)(\text{Me}_3\text{TACN})]^+$  ou  $[\text{PtHMe}_2](\text{Me}_3\text{TACN})]^+$ . Les complexes  $[\text{PtMe}_2(\text{Me}_3\text{TACN})]$  et  $[\text{PtHMe}_2](\text{Me}_3\text{TACN})]^+$  sont oxydés à l'air humide et fournissent le complexe hydroxo  $[\text{PtMe}_2(\text{OH})(\text{Me}_3\text{TACN})]^+$  qui peut ensuite être protoné d'une façon réversible pour former le complexe aqua  $[\text{PtMe}_2(\text{OH}_2)(\text{Me}_3\text{TACN})]^{2+}$ . On a déterminé les structures des complexes hydroxo  $[\text{PtMe}_2(\text{OH})(\text{Me}_3\text{TACN})]^+$  sous les formes de sels de  $\text{BF}_4^-$  ou de  $\text{CF}_3\text{SO}_3^-$  et du complexe mixte hydroxo, aqua  $[\text{PtMe}_2(\text{OH})(\text{Me}_3\text{TACN})][\text{PtMe}_2(\text{OH}_2)(\text{Me}_3\text{TACN})][\text{BF}_4]_3$  et on a pu montrer que les complexes présentent des liaisons hydrogènes intéressantes.

**Mots clés :** platine, oxydation, organométallique, étain, hydrure.

[Traduit par la Rédaction]

## Introduction

Aryl and alkyl(hydrido)platinum(IV) complexes are believed to be the intermediates in arene and alkane activation by electrophilic organoplatinum(II) complexes (1–6), and their chemistry has been the subject of much research (7–22). Octahedral methyl(hydrido)platinum(IV) complexes are stabilized by the presence of a strongly coordinating ligands that do not allow formation of the five-coordinate intermediate from which the reductive elimination of methane occurs (12, 13, 15, 18d). Facially coordinating tridentate ligands are ideal for stabilizing methyl(hydrido)platinum(IV) complexes and some stable examples **A**, **B** are shown in Chart 1 (12–15). In particular, the simple cyclic ligand 1,4,7-triazacyclononane (TACN) gave the stable cationic dimethyl(hydrido)platinum(IV) complex  $[\text{PtHMe}_2(\text{TACN})]^+$  (**A**) which was slowly oxidized by air to give the hydroxo complex  $[\text{PtMe}_2(\text{OH})-$

(TACN)]<sup>+</sup> (14). The oxidation of methylplatinum(II) complexes or hydrido(methyl)platinum(IV) complexes is of interest because it would be a key step in potential catalytic oxidation of methane to methanol, and there have been several studies of such reactions (14, 19–22). The dimethyl-(peroxo)platinum(IV) complex  $[\text{PtMe}_2(\text{OOH})(\text{Tp}^*)]$ ,  $\text{Tp}^*$  = hydridotris(3,5-dimethylpyrazolyl)borate is isolated from the reaction of  $[\text{PtHMe}_2(\text{Tp}^*)]$  (**B**) with oxygen and decomposes only slowly to the hydroxo complex  $[\text{PtMe}_2(\text{OH})(\text{Tp}^*)]$  (19). The reaction of  $[\text{PtMe}_2(\text{tmeda})]$  (tmeda = tetramethylethylenediamine) with dioxygen in methanol gives a mixture of  $[\text{PtMe}_2(\text{OH})(\text{OMe})(\text{tmeda})]$  and  $[\text{PtMe}_2(\text{OOH})(\text{OMe})(\text{tmeda})]$  (20), and several complexes  $[\text{PtMe}_2(\text{OH})(\text{OMe})(\text{NN})]$  have been obtained with NN = diimine (20–22).

The work described in this paper involves dimethylplatinum complexes of the ligand 1,4,7-trimethyl-1,4,7-triazacyclononane ( $\text{Me}_3\text{TACN}$ ), and extends earlier studies using the ligand TACN (14). The ligands are similar but also different in several respects. The NH groups in TACN can cause complications by undergoing H,D-exchange with deuteriated reagents and solvents, while the methyl substituents in  $\text{Me}_3\text{TACN}$  are bulkier and more electron-releasing than the hydrogen atoms in TACN thus leading to significantly different steric and electronic effects. In addition to this comparative study, the ability of the ligand  $\text{Me}_3\text{TACN}$  to stabilize stannylplatinum(IV) complexes has been investigated. As background, it is noted that the oxidative addition

Received 26 October 2002. Published on the NRC Research Press Web site at <http://canjchem.nrc.ca> on 29 April 2003.

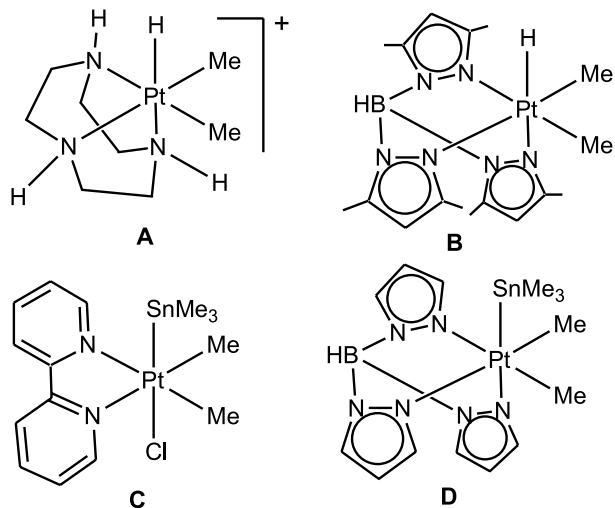
*This paper is dedicated to Professor Don Arnold in recognition of his outstanding research in organic photochemistry, much of which was reported in the Canadian Journal of Chemistry.*

**E.M. Prokopchuk and R.J. Puddephatt.**<sup>1</sup> Department of Chemistry, University of Western Ontario, London, ON N6A 5B7 Canada.

<sup>1</sup>Corresponding author (e-mail: [pudd@uwo.ca](mailto:pudd@uwo.ca)).



Chart 1.



of organotin halides to complexes  $[\text{PtMe}_2(\text{NN})]$  (NN = diimine) to give **C** (Chart 1) are easily reversible (23, 24) whereas the reactions with complexes of the type  $[\text{PtMe}_2(\text{HBpz}_3)]^-$  to give **D** (Chart 1) are irreversible (25).

## Results

### Preparation of $[\text{PtMe}_2(\text{Me}_3\text{TACN})]$

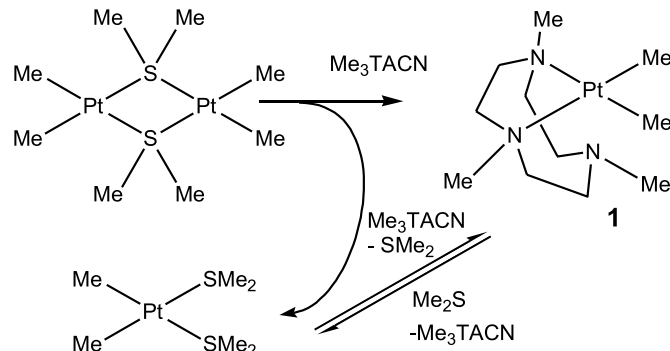
The synthesis is shown in Scheme 1. The reaction of  $[\text{Pt}_2\text{Me}_4(\mu\text{-SMe}_2)_2]$  with 2 equiv of the ligand  $\text{Me}_3\text{TACN}$  in deuterated acetone slowly gave the desired product  $[\text{PtMe}_2(\text{Me}_3\text{TACN})]$  (**1**). The reaction did not go to completion but gave an equilibrium with some  $[\text{PtMe}_2(\text{SMe}_2)_2]$ . NMR analysis indicated that a typical reaction over 1 day gave about 90% **1** and 10%  $[\text{PtMe}_2(\text{SMe}_2)_2]$  and unreacted ligand. For this reason, complex **1** was normally prepared and used in situ, without isolation. Since **1** is much more reactive towards electrophilic reagents than  $[\text{PtMe}_2(\text{SMe}_2)_2]$ , the removal of **1** from the equilibrium mixture led to an equilibrium shift and the subsequent products with  $\text{Me}_3\text{TACN}$  ligands were formed in good yield and were not contaminated by dimethylsulfide complex impurities.

Complex **1** was readily identified by its methylplatinum resonance at  $\delta = 0.18$ ,  $^2J(\text{PtH}) = 90$  Hz, in the  $^1\text{H}$  NMR spectrum, and  $\delta = -22.50$ ,  $^1J(\text{PtC}) = 869$  Hz, in the  $^{13}\text{C}$  NMR spectrum. At room temperature, the  $\text{CH}_2$  and  $\text{CH}_3\text{N}$  resonances in the  $^1\text{H}$  NMR spectrum appeared as broad peaks because of fluxionality involving exchange between free and coordinated N-donors of the ligand. At  $-50^\circ\text{C}$ , the  $\text{CH}_2$  resonances appeared as complex, overlapping multiplets in the region  $\delta = 4.61\text{--}2.58$ , while the  $\text{CH}_3\text{N}$  resonances were resolved at  $\delta = 2.62$ ,  $^3J(\text{PtH}) = 22$  Hz, and  $\delta = 2.26$  in a 2:1 ratio, corresponding to the two coordinated MeN groups and one free MeN group, respectively.

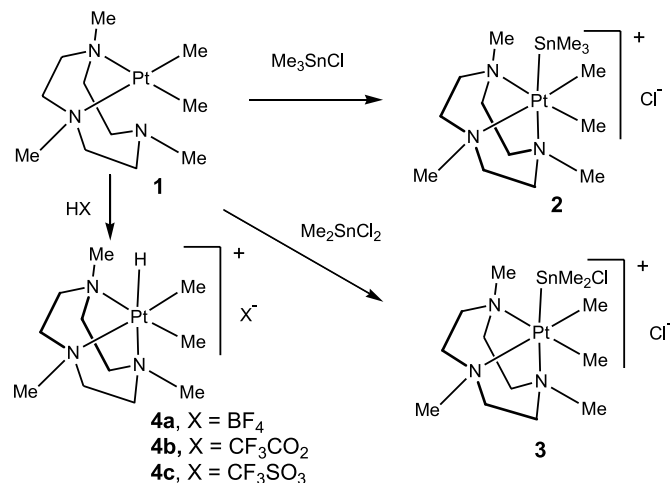
### Reactions of complex **1** with organotin halides

The new reactions are shown in Scheme 2. The reactions with  $\text{Me}_3\text{SnCl}$  and  $\text{Me}_2\text{SnCl}_2$  gave the ionic platinum(IV) complexes  $[\text{PtMe}_2(\text{SnMe}_3)(\text{Me}_3\text{TACN})]\text{Cl}$  (**2**) and  $[\text{PtMe}_2(\text{SnMe}_2\text{Cl})(\text{Me}_3\text{TACN})]\text{Cl}$  (**3**), respectively. Both complexes **2** and **3** are colourless, air-stable solids that were readily characterized by their NMR spectra. For example, complex

Scheme 1.



Scheme 2.



**2** gave methylplatinum and methyltin resonances in the  $^1\text{H}$  NMR at  $\delta = 0.47$  (s, 6H,  $^2J(\text{PtH}) = 59$  Hz) and  $0.16$  (s, 9H,  $^2J(\text{SnH}) = 45$  Hz,  $^3J(\text{PtH}) = 6$  Hz) and in the  $^{13}\text{C}$  NMR at  $\delta = -10.11$  ( $^1J(\text{PtC}) = 609$  Hz,  $^2J(\text{SnC}) = 36$  Hz) and  $-8.65$  ( $^2J(\text{PtC}) = 54$  Hz), respectively. The observation of long-range couplings  $J(\text{SnPtMe})$  and  $J(\text{PtSnMe})$  clearly shows that there is a tin–platinum bond in **2**. There were two MeN resonances in the  $^1\text{H}$  NMR at  $\delta = 2.87$  ( $^3J(\text{PtH}) = 23$  Hz, PtNMe *trans* Me) and  $2.49$  ( $^3J(\text{PtH}) = 14$  Hz, PtNMe *trans* Sn) and in the  $^{13}\text{C}$  NMR at  $\delta = 52.61$  ( $^2J(\text{PtC}) = 15$  Hz, PtNMe *trans* to Me) and  $45.16$  ( $^2J(\text{PtC}) = 10$  Hz, PtNMe *trans* to Sn). In both cases the trend in coupling constants reflects the higher *trans*-influence of the stannyl compared to the methyl group. Complex **3** gave similar NMR spectral features as described for complex **2** and details are in the experimental section.

In solution in dichloromethane, there was no evidence for dissociation of the stannyl group and sealed solutions of **2** or **3** were stable for several months, though they did decompose slowly in the presence of air. The complexes thus have comparable properties as the corresponding tripyrazolylborate complexes, and have much higher thermal stability than the complexes with diimine ligands (23–25).

### Protonation of complex **1** to give a dimethyl(hydrido)-platinum(IV) complex cation

Complex **1** reacted with acids HX (X =  $\text{BF}_4$ ,  $\text{CF}_3\text{CO}_2$ ,  $\text{CF}_3\text{SO}_3$ ) in THF solution to form the corresponding dimethyl-



(hydrido)platinum(IV) complexes  $[\text{PtHMe}_2(\text{Me}_3\text{TACN})]\text{X}$  (**4a–4c**) (Scheme 2). The tetrafluoroborate complex **4a** ( $\text{X} = \text{BF}_4$ ) precipitated as it was formed, while the other complexes **4b** ( $\text{X} = \text{CF}_3\text{CO}_2$ ) and **4c** ( $\text{X} = \text{CF}_3\text{SO}_3$ ) were precipitated as colourless solids on addition of pentane. As expected (14), these hydridoplatinum(IV) complexes have high thermal stability, and solid samples or solutions in acetone were stable for at least 2 months at room temperature in the absence of air. Thermogravimetric analysis under nitrogen atmosphere showed that complex **4a**, in the solid state, does not begin to decompose until over 190°C.

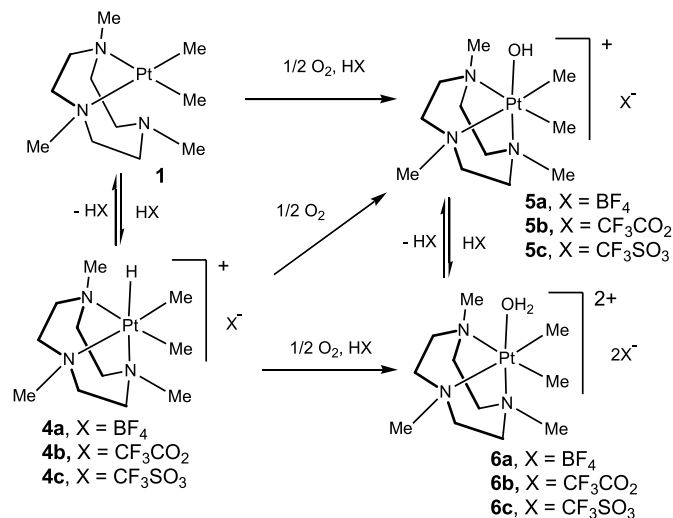
The hydride resonance for the cation **4** was observed at  $\delta = -20.99$  with  $^1J(\text{PtH}) = 1406$  Hz, and the methylplatinum resonance was present at  $\delta = 0.62$  with  $^2J(\text{PtH}) = 66$  Hz, both in the range found for platinum(IV) complexes with hydride and methyl groups *trans* to nitrogen (9–15). The methylamine resonances were at  $\delta = 3.02$  ( $^3J(\text{PtH}) = 22$  Hz) and 2.63 ( $^3J(\text{PtH}) = 17$  Hz), in the expected 2:1 ratio for the methylamine groups *trans* to the methyl and hydride, respectively. It is clear that the ligand is rigidly bound to the platinum centre, that there is no easy ligand exchange, and that hydride has a higher *trans*-influence than methyl in the complex cation **4**.

For a solution of **4a** in acetone- $d_6$ , slow exchange of the hydride ligand by deuteride occurred as monitored by  $^1\text{H}$  NMR. As the exchange occurred, the hydride resonance of **4** decreased in intensity and a slight isotope effect on the chemical shift led to a new methylplatinum resonance at  $\delta = 0.625$ ,  $^2J(\text{PtH}) = 66$  Hz. However, there was no deuterium incorporation into the methylplatinum groups of **4**, indicating that there is no reversible formation of a methane complex (7, 10, 14–17). The complexes **4** were stable in the presence of excess acid HX, and no deuterium incorporation into the methylplatinum groups was observed with deuterio acids DX. All of these results indicate that the strong *fac*-tridentate coordination of the ligand  $\text{Me}_3\text{TACN}$  does not allow easy formation of a five-coordinate intermediate from complex **4** that could lead to either reversible or irreversible reductive elimination of methane. Hence, the hydrido complex cation **4** has good thermal stability and does not give H–D exchange into the methylplatinum groups. It is also noteworthy that the cation **4** is stable in the presence of free acid, while the neutral complex  $[\text{PtHMe}_2(\text{Tp}^*)]$  (**B**) (Chart 1), which has similar thermal stability to **4** in the solid state (12), is decomposed in the presence of acid. This decomposition involves protonation of one Pt–N bond with partial ligand dissociation, thus allowing reductive elimination of methane (12). The analogous reaction is not observed with the cationic complex **4**, presumably because it is less basic and the Pt–N bonds are not susceptible to electrophilic attack.

### Reactions of the complexes **1** and **4** with air

Exposure of a solution of the dimethylplatinum(II) complex **1** to the atmosphere led to rapid oxidation, with formation of the cationic dimethyl(hydroxo)platinum(IV) complex **5** (Scheme 3) as the hydroxide salt. The reaction was complete within minutes at room temperature. The cationic complex **4** reacted more slowly, but reaction was complete within 1 day at room temperature to give the same complex cation **5**, with little dependence on the anion. In the presence of excess acid, the product of air oxidation was the

Scheme 3.



dicationic aqua complex **6**. In either case, the rate of reaction of **4** with air was not significantly different if carried out in the presence or absence of light and no long-lived intermediates were detected in reactions monitored by  $^1\text{H}$  NMR. Using pure **4a**, the reaction accelerated with time, but rate data were difficult to reproduce. The product complexes **5** and **6** were easily interconverted by adjusting the solution pH.

### Characterization of the hydroxo and aqua complexes **5** and **6**

Complexes **5** and **6** had distinct  $^1\text{H}$  NMR spectra that were essentially independent of the nature of the anion. Thus, the methylplatinum resonance for **5** and **6** was at  $\delta = 1.00$  ( $^2J(\text{PtH}) = 68$  Hz) and 1.48 ( $^2J(\text{PtH}) = 65$  Hz), respectively, and proton exchange between **5** and **6** was slow enough that separate resonances of the two complexes were observed when both were present. The  $\text{CH}_3\text{N}$  resonances for **5** appeared in a 2:1 ratio at  $\delta = 2.80$  ( $^3J(\text{PtH}) = 12$  Hz, *trans* to Me) and 2.86 ppm ( $^3J(\text{PtH}) = 32$  Hz, *trans* to OH).

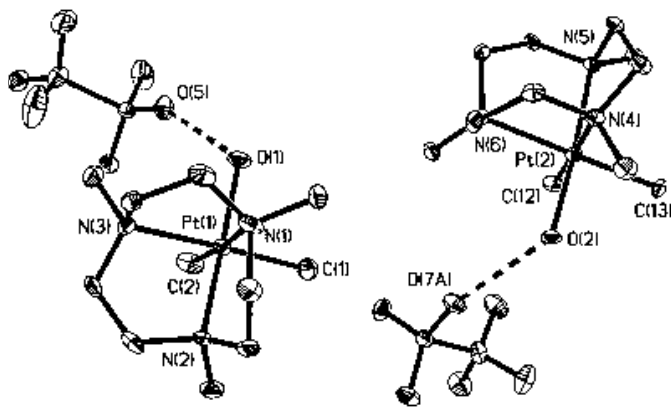
The complex cation  $[\text{PtMe}_2(\text{OH})(\text{Me}_3\text{TACN})]^+$  (**5**) was structurally characterized as both the tetrafluoroborate and triflate salt, **5a** and **5c**, respectively. Selected bond distances and angles are listed in Table 1. There were two independent but similar molecules of **5c** as shown in Fig. 1. In each case, there is a *fac*-tridentate  $\text{Me}_3\text{TACN}$  ligand, two methyl groups, and a hydroxo ligand at the platinum(IV) centre of the cation. The Pt–N distances *trans* to the hydroxo ligand are shorter than those *trans* to methyl (Table 1), reflecting the difference in the *trans*-influence of these ligands. In both molecules, there is hydrogen bonding between the triflate anion and the hydroxo ligand with  $\text{O}(1)\cdots\text{O}(5) = 3.18(1)$  Å and  $\text{O}(2)\cdots\text{O}(7A) = 2.99(1)$  Å.

The structure of the cation  $[\text{PtMe}_2(\text{OH})(\text{Me}_3\text{TACN})]^+$  in the tetrafluoroborate salt **5a** is very similar to that in **5c** but a more complex form of hydrogen bonding is present (Table 1, Fig. 2). There is a molecule of water of crystallization that is also involved in hydrogen bonding. The hydroxo ligand acts as a hydrogen bond donor to the  $\text{BF}_4^-$  anion with  $\text{O}(1)\cdots\text{F}(1A) = 2.91(1)$  Å, while the water molecule acts as a



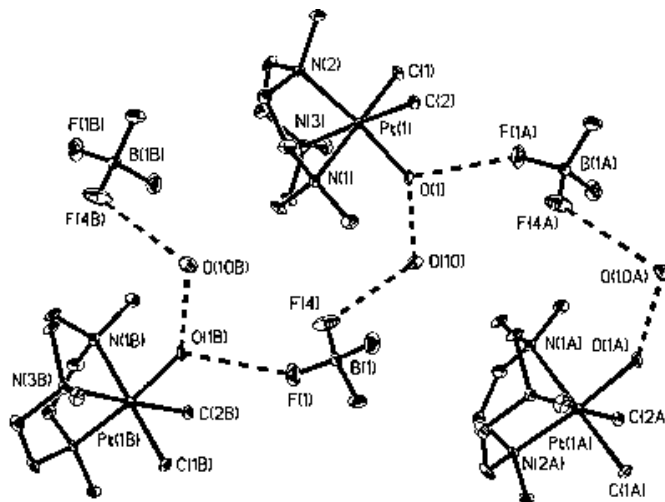
**Table 1.** Selected bond lengths (Å) and angles (°) for [PtMe<sub>2</sub>(OH)(Me<sub>3</sub>TACN)]<sup>+</sup> in complexes **5a** and **5c**.

Molecule	<b>5c</b> (No. 1)	<b>5c</b> (No. 2)	<b>5a</b> ·H <sub>2</sub> O
<b>Bond lengths (Å)</b>			
Pt(1)—O(1)	1.999(5)	Pt(2)—O(2)	1.992(5)
Pt(1)—C(2)	2.049(8)	Pt(2)—C(13)	2.041(9)
Pt(1)—C(1)	2.06(1)	Pt(2)—C(12)	2.060(8)
Pt(1)—N(2)	2.100(6)	Pt(2)—N(5)	2.101(5)
Pt(1)—N(1)	2.178(7)	Pt(2)—N(6)	2.202(7)
Pt(1)—N(3)	2.193(7)	Pt(2)—N(4)	2.212(6)
<b>Bond angles (°)</b>			
O(1)—Pt(1)—C(1)	88.2(3)	O(2)—Pt(2)—C(13)	87.7(3)
O(1)—Pt(1)—C(2)	90.2(3)	O(2)—Pt(2)—C(12)	90.2(3)
C(2)—Pt(1)—C(1)	87.2(5)	C(13)—Pt(2)—C(12)	85.9(4)
C(1)—Pt(1)—N(1)	97.8(4)	C(12)—Pt(2)—N(6)	96.3(3)
C(1)—Pt(1)—N(2)	95.1(3)	C(12)—Pt(2)—N(5)	95.7(3)
C(2)—Pt(1)—N(2)	96.8(3)	C(13)—Pt(2)—N(5)	97.2(3)
C(2)—Pt(1)—N(3)	94.3(4)	C(13)—Pt(2)—N(4)	96.1(3)
O(1)—Pt(1)—N(1)	88.8(2)	O(2)—Pt(2)—N(4)	90.3(2)
O(1)—Pt(1)—N(3)	93.7(3)	O(2)—Pt(2)—N(6)	92.0(2)
N(1)—Pt(1)—N(2)	83.9(2)	N(5)—Pt(2)—N(4)	83.7(2)
N(2)—Pt(1)—N(3)	82.9(3)	N(5)—Pt(2)—N(6)	82.9(2)
N(1)—Pt(1)—N(3)	80.7(3)	N(6)—Pt(2)—N(4)	81.7(2)
Pt(1)—O(1)	2.024(7)	Pt(1)—C(1)	2.068(8)
Pt(1)—C(1)	2.069(8)	Pt(1)—N(2)	2.096(7)
Pt(1)—N(2)	2.166(6)	Pt(1)—N(3)	2.184(7)

**Fig. 1.** A view of the structure of complex [PtMe<sub>2</sub>(OH)(Me<sub>3</sub>TACN)]<sup>+</sup>CF<sub>3</sub>SO<sub>3</sub><sup>−</sup> (**5c**) showing the two independent cations, each hydrogen-bonded to a triflate anion. Hydrogen atoms, except for those involved in the H-bonding, are omitted for clarity.

hydrogen bond donor to both the hydroxo group and the BF<sub>4</sub><sup>−</sup> anion with O(10)···O(1) = 2.69(1) Å and O(10)···F(4) = 3.11(1) Å. The O···H···O hydrogen bonding is strong, and we note that the data could be interpreted as involving an aqua complex of platinum(IV) that is hydrogen bonded to a hydroxide ion, though this is considered a less accurate formulation. The same argument has been applied for hydrogen bonding in the complex [PtMe<sub>2</sub>(OH)(Bpz<sub>4</sub>)]·H<sub>2</sub>O in which there is hydrogen bonding between the hydroxo ligand and water of crystallization (13). The Pt—O distance is slightly longer in **5a** than in either molecule of **5c** (Table 1), probably as a result of the stronger hydrogen bonding in **5a**. The hydrogen bonding in **5a** leads to the formation of helical chains with repeating units  $\cdots(\text{OH}\cdots\text{FBF}\cdots\text{HOH})_n\cdots$ , as shown in Fig. 2.

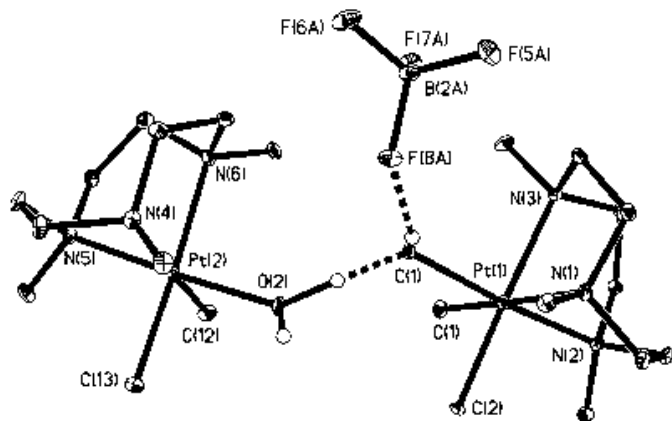
It was not possible to grow single crystals of the aqua complex [PtMe<sub>2</sub>(OH<sub>2</sub>)(Me<sub>3</sub>TACN)]<sup>2+</sup> (**6**) but crystallization

**Fig. 2.** A view of the structure of [PtMe<sub>2</sub>(OH)(Me<sub>3</sub>TACN)]<sup>+</sup>BF<sub>4</sub><sup>−</sup>·H<sub>2</sub>O (**5a**) showing part of an infinite helical chain formed by H-bonding. Hydrogen atoms are omitted for clarity.

from a solution of the tetrafluoroborate salt containing both **5a** and **6a** gave a complex formulated as the mixed hydroxo-aqua salt [PtMe<sub>2</sub>(OH)(Me<sub>3</sub>TACN)][PtMe<sub>2</sub>(OH<sub>2</sub>)(Me<sub>3</sub>TACN)][BF<sub>4</sub>]<sub>3</sub> (**7**) in which there is strong hydrogen bonding involving both cations and one anion (Fig. 3). The hydrogen atoms for the hydroxo and aqua ligands were located and refined isotropically and their locations are shown in Fig. 3. The platinum centres have distorted octahedral geometry, with stereochemistry and bond parameters similar to those in the hydroxo complexes **5a** and **5c** (compare Tables 1 and 2). There is very strong hydrogen bonding between the hydroxo and aqua ligands of the two cations with O(1)···O(2) = 2.421(7) Å and weaker hydrogen bonding between the hydroxo ligand and tetrafluoroborate anion with O(1)···F(8A) = 2.806(6) Å (Fig. 3). The assignment of Pt(1)



**Fig. 3.** A view of the structure of the hydrogen bonded unit  $[\text{PtMe}_2(\text{OH})(\text{Me}_3\text{TACN})]^+[\text{PtMe}_2(\text{OH}_2)(\text{Me}_3\text{TACN})]^{2+}\text{BF}_4^-$  in complex **7**·MeOH. Hydrogen atoms are omitted for clarity.



as the hydroxo complex and Pt(2) as the aqua complex is based only on the difference in the OH distances for the  $\text{OH}\cdots\text{O}$  hydrogen bonded unit ( $\text{O}(2)\text{H}(88) = 1.10(9)$  Å,  $\text{O}(1)\text{H}(88) = 1.34(9)$  Å,  $\text{O}(2)\text{H}(88)\text{O}(1) = 164(7)^\circ$ , Fig. 3) and, since the location of hydrogen atoms in the presence of heavy atoms like platinum is always uncertain and the difference in OH distances is less than  $3\sigma$  of the distances, the opposite assignment cannot be ruled out. Indeed, analysis of the minor differences in Pt—O distances and Pt—N distances *trans* to O suggests the other assignment. In the limit of very strong hydrogen bonding the combined aqua and hydroxide ligands could be considered as symmetrical  $[\text{H}_3\text{O}_2]^-$  bridging between two platinum(IV) centres.

## Discussion

The ligand  $\text{Me}_3\text{TACN}$  is shown to give particularly stable organoplatinum(IV) complexes, even compared to the similar ligand TACN (14). This is attributed to the greater tendency of the bowl-shaped  $\text{Me}_3\text{TACN}$  ligand to act as a facial tridentate ligand than TACN (23, 24), and to the greater electron-releasing properties of the methyl substituents in  $\text{Me}_3\text{TACN}$  than the hydrogen substituents in TACN. For bidentate TACN in a square-planar platinum(II) complex, the free nitrogen atom can be accommodated with the nitrogen lone pair away from platinum, but steric effects in bidentate  $\text{Me}_3\text{TACN}$  lead to a strong preference for the bowl conformation with the free nitrogen directed towards the platinum atom (26, 27), and the oxidation to platinum(IV) with synchronous formation of *fac*-tridentate  $\text{Me}_3\text{TACN}$  is very favorable. Hence, the cationic platinum(IV) complexes  $[\text{PtMe}_2(\text{SnMe}_3)(\text{Me}_3\text{TACN})]^+$ ,  $[\text{PtMe}_2(\text{SnMe}_2\text{Cl})(\text{Me}_3\text{TACN})]^+$ , and  $[\text{PtHMe}_2(\text{Me}_3\text{TACN})]^+$  are all thermally stable complexes. Similarly, the complex  $[\text{PtMe}_2(\text{Me}_3\text{TACN})]$  (**1**) is more easily oxidized by molecular oxygen than the TACN analog, almost certainly by the same mechanism, as shown in Scheme 4 (14). A related mechanism has been suggested recently for the reaction of  $[\text{PtMe}_2(\text{tmeda})]$  with oxygen in methanol to give  $[\text{PtMe}_2(\text{OOH})(\text{OMe})(\text{tmeda})]$  and  $[\text{PtMe}_2(\text{OH})(\text{OMe})(\text{tmeda})]$ , and in this case the hydroperoxo complex could be isolated from reactions carried out at high dilution (20). No hydroperoxide was detected in the reac-

**Table 2.** Selected bond lengths (Å) and angles ( $^\circ$ ) for **7**·MeOH.

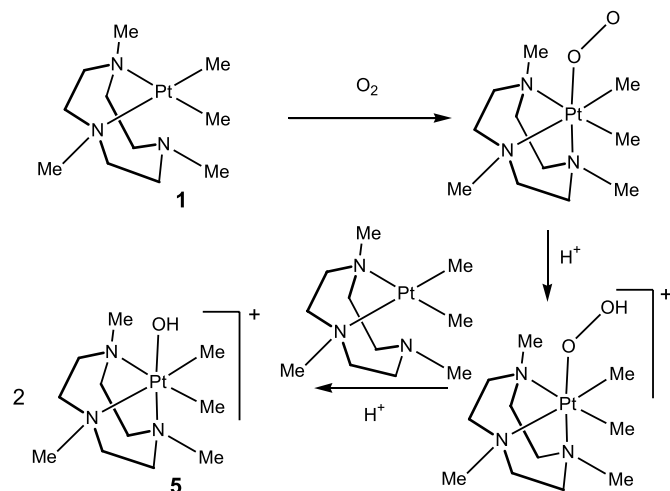
Bond lengths ( $^\circ$ )	
Pt(1)—O(1)	2.040(4)
Pt(1)—C(1)	2.044(6)
Pt(1)—C(2)	2.052(7)
Pt(1)—N(2)	2.054(5)
Pt(1)—N(1)	2.196(5)
Pt(1)—N(3)	2.199(6)
Pt(2)—O(2)	2.023(5)
Pt(2)—C(12)	2.064(6)
Pt(2)—C(13)	2.064(7)
Pt(2)—N(5)	2.063(5)
Pt(2)—N(6)	2.186(6)
Pt(2)—N(4)	2.197(5)
Bond angles ( $^\circ$ )	
C(1)—Pt(1)—N(3)	97.1(3)
O(1)—Pt(1)—N(1)	96.7(2)
O(1)—Pt(1)—N(3)	92.3(2)
N(2)—Pt(1)—N(1)	83.7(2)
N(2)—Pt(1)—N(3)	83.2(2)
N(1)—Pt(1)—N(3)	81.0(2)
O(2)—Pt(2)—C(12)	87.1(3)
O(2)—Pt(2)—C(13)	87.4(3)
C(13)—Pt(2)—C(12)	87.1(3)
N(5)—Pt(2)—C(12)	95.4(3)
N(5)—Pt(2)—C(13)	95.3(3)
C(12)—Pt(2)—N(6)	95.8(3)
C(13)—Pt(2)—N(4)	95.7(3)
O(2)—Pt(2)—N(6)	94.1(2)
O(2)—Pt(2)—N(4)	94.2(2)
N(5)—Pt(2)—N(6)	83.1(2)
N(5)—Pt(2)—N(4)	83.1(2)
N(6)—Pt(2)—N(4)	81.4(2)

tions of Scheme 4, so it presumably reacts faster than it is formed under all conditions studied.

The complex cation  $[\text{PtHMe}_2(\text{Me}_3\text{TACN})]^+$  (**4**) is also somewhat more easily oxidized by  $\text{O}_2$  than its TACN analog, but the mechanism of reaction is not clear. In neutral solution, oxidation of **4** is complete in 1 day whereas the oxidation of the TACN analog is only about one-third complete in this time (14). It has been shown that oxygen insertion into the Pt—H bond of  $[\text{PtHMe}_2(\text{Tp}^*)]$  gives  $[\text{PtMe}_2(\text{OOH})(\text{Tp}^*)]$  by a radical chain mechanism, and that subsequent decomposition gives  $[\text{PtMe}_2(\text{OH})(\text{Tp}^*)]$  (19). This reaction is greatly accelerated by light whereas the rate of reaction of **4** with  $\text{O}_2$  was not significantly affected by light, and no hydroperoxide intermediate was detected. An alternate mechanism might involve deprotonation of **4** to give **1**, followed by oxidation as described above (Scheme 5). This is consistent with the observation that oxidation of **4** is faster in neutral than in acid solution. It is also consistent with the observation of increased rate with time since the hydroxo, peroxo, and hydroperoxo complexes **5**, **8**, and **9** (Scheme 5) will all be more basic than **4**. Scheme 5 shows only the proposed deprotonation of **4** by the most basic peroxo complex **8**, but the overall effect should be that the relative concentration of **1b**:**4** should increase as reaction proceeds and so the



Scheme 4.



rate should increase. However, one might expect complete inhibition of oxidation under acid conditions if this were the sole mechanism, and this was not observed. It is possible that more than one mechanism might operate under different conditions, with a radical mechanism (19) operating when the catalysis by **1** cannot occur. The hydroxo and aqua complexes form interesting supramolecular structures through hydrogen bonding, as seen in Figs. 1–3. Finally, it is noted that the formation of hydroxo(methyl)platinum(IV) complexes is important for modelling potential intermediates in the formation of methanol from methane and air (2, 10), and that the characterization of the hydroxo and aqua complexes **5a**, **5c**, and **7** adds substantially to the understanding of these potential intermediates (13, 20).

## Experimental

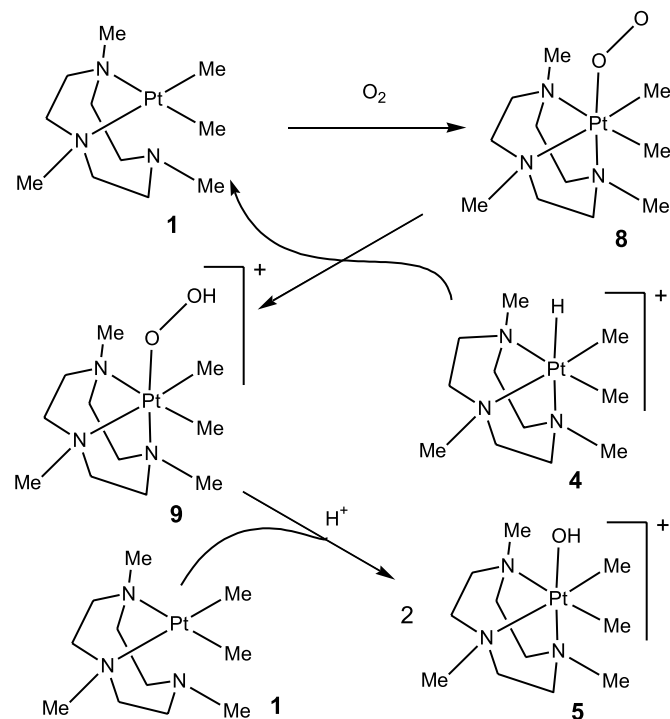
NMR spectra were obtained by using a Varian Inova 400 MHz spectrometer. The complex  $[Pt_2Me_4(\mu-SMe_2)_2]$  was prepared according to the literature method (28). Solvents were dried and distilled immediately before use. Except when noted, reactions were carried out under nitrogen atmosphere by using either Schlenk or drybox techniques.

### $[PtMe_2(Me_3TACN)]$ (**1**)

To a solution of  $[Pt_2Me_4(\mu-SMe_2)_2]$  (20.0 mg, 0.0348 mmol) in acetone- $d_6$  (0.5 mL) was added  $Me_3TACN$  (14  $\mu$ L, 0.0696 mmol). After 20 h, the solution contained the product **1** (ca. 90%) and  $[PtMe_2(SMe_2)_2]$  (ca. 10%). For **1**:  $^1H$  NMR (acetone- $d_6$ , 20°C)  $\delta$ : 2.83 (br, 6H,  $CH_2$ ), 2.56 (br, 9H,  $NCH_3$ ), 0.18 (s, 6H,  $^2J(PtH) = 90$  Hz, PtMe).  $^{13}C$  NMR  $\delta$ : 57.32 (s,  $CH_2$ ), 46.28 (s, NMe),  $-22.50$  (s,  $^1J(PtC) = 869$  Hz, PtMe).  $^1H$  NMR ( $-50^\circ C$ )  $\delta$ : 4.61 (m, 2H,  $CH_2$ ), 3.39 (m, 4H,  $CH_2$ ), 2.70–2.58 (m, 6H,  $CH_2$ ), 2.62 (s, 6H,  $^3J(PtH) = 21$  Hz, Pt–NMe), 2.26 (s, 3H, NMe), 0.17 (s, 6H,  $^2J(PtH) = 90$  Hz, Pt–Me).

For most synthetic reactions, a solution of  $[Pt_2Me_4(\mu-SMe_2)_2]$  (75.0 mg, 0.131 mmol) and  $Me_3TACN$  (52  $\mu$ L, 0.262 mmol) in THF (10 mL) was stirred for 20 h to give a solution of **1**. This solution was used in situ in reactions of **1**.

Scheme 5.



### $[PtMe_2(SnMe_3)(Me_3TACN)]Cl$ (**2**)

A mixture of **1** (0.39 mmol) and  $Me_3SnCl$  (0.39 mmol) in THF (5 mL) was stirred for 1 h. A white precipitate of the product formed. Pentane (30 mL) was added, the solvent was removed by cannula, and the product was dried under vacuum. Yield: 68%.  $^1H$  NMR ( $CD_2Cl_2$ )  $\delta$ : 3.83 (m, 2H,  $CH_2$ ), 3.67 (m, 4H,  $CH_2$ ), 3.01 (m, 2H,  $CH_2$ ), 2.82 (m, 4H,  $CH_2$ ), 2.87 (s, 6H,  $^3J(PtH) = 23$  Hz, PtNMe *trans* Me), 2.49 (s, 3H,  $^3J(PtH) = 14$  Hz, PtNMe *trans* Sn), 0.47 (s, 6H,  $^2J(PtH) = 59$  Hz, PtMe), 0.16 (s, 9H,  $^2J(SnH) = 45$  Hz,  $^3J(PtH) = 6$  Hz, SnMe).  $^{13}C$  NMR  $\delta$ : 61.56 (s,  $CH_2$ ), 61.28 (s,  $CH_2$ ), 58.22 (s,  $CH_2$ ), 52.61 (s,  $^2J(PtC) = 15$  Hz, PtNMe *trans* to Me), 45.16 (s,  $^2J(PtC) = 10$  Hz, PtNMe *trans* to Sn),  $-8.65$  (s,  $^2J(PtC) = 54$  Hz, SnMe),  $-10.11$  (s,  $^1J(PtC) = 609$  Hz,  $^2J(SnC) = 36$  Hz, PtMe). Anal. calcd. for  $C_{14}H_{36}ClN_3PtSn$  (%): C 28.23, H 6.09, N 7.05; found: C 27.80, H 6.44, N 7.05.

### $[PtMe_2(SnMe_2Cl)(Me_3TACN)]Cl$ (**3**)

A mixture of **1** (0.38 mmol) and  $Me_2SnCl_2$  (0.38 mmol) in THF (10 mL) was stirred for 5 h. A white precipitate of the product formed. Pentane (20 mL) was added, the solvent was removed by cannula, and the product was dried under vacuum. Yield: 67%.  $^1H$  NMR ( $CD_2Cl_2$ )  $\delta$ : 3.79 (m, 6H,  $CH_2$ ), 3.45 (m, 2H,  $CH_2$ ), 2.89 (m, 4H,  $CH_2$ ), 3.04 (s, 6H,  $^3J(PtH) = 23$  Hz, PtNMe *trans* Me), 2.58 (s, 3H,  $^3J(PtH) = 19$  Hz, PtNMe *trans* Sn), 0.64 (s, 6H,  $^2J(SnH) = 47$  Hz, SnMe), 0.53 (s, 6H,  $^2J(PtH) = 55$  Hz, PtMe).  $^{13}C$  NMR  $\delta$ : 61.90 (s,  $CH_2$ ), 61.70 (s,  $CH_2$ ), 59.53 (s,  $CH_2$ ), 52.87 (s,  $^2J(PtC) = 15$  Hz, PtNMe *trans* to Me), 45.85 (s,  $^2J(PtC) = 9$  Hz, PtNMe *trans* to Sn),  $-1.57$  (s,  $^1J(SnC) = 315$  Hz,  $^2J(PtC) = 83$  Hz, SnMe),  $-9.27$  (s,  $^1J(PtC) = 565$  Hz,  $^2J(SnC) = 49$  Hz, PtMe). Anal. calcd. for  $C_{13}H_{33}Cl_2N_3$



**Table 3.** Crystal data and structure refinement for the complexes.

Complex	<b>5a</b> ·H <sub>2</sub> O	<b>5c</b>	<b>7</b> ·MeOH
Formula	C <sub>11</sub> H <sub>28</sub> BF <sub>4</sub> N <sub>3</sub> O <sub>2</sub> Pt	C <sub>12</sub> H <sub>28</sub> F <sub>3</sub> N <sub>3</sub> O <sub>4</sub> PtS	C <sub>23</sub> H <sub>61</sub> B <sub>3</sub> F <sub>12</sub> N <sub>6</sub> O <sub>3</sub> Pt <sub>2</sub>
Formula wt	516.26	562.52	1120.38
Temperature (K)	200(2)	200(2)	200(2)
Wavelength (Å)	0.71073	0.71073	0.71073
Crystal system	Orthorhombic	Monoclinic	Monoclinic
Space group	<i>Pna</i> 2(1)	<i>P</i> 2 <sub>1</sub> / <i>c</i>	<i>P</i> 2 <sub>1</sub> / <i>c</i>
Cell dimensions: <i>a</i> (Å)	16.9041(4)	16.4314(6)	8.7633(1)
<i>b</i> (Å)	8.9856(2)	15.1084(5)	16.0313(2)
<i>c</i> (Å)	11.4332(3)	15.3976(5)	26.5750(3)
β (°)	90	103.083(1)	95.9070(6)
Volume (Å <sup>3</sup> ), <i>Z</i>	1736.63(7), 4	3723.3(2), 8	3713.62(8), 4
<i>D</i> (calc.) (Mg m <sup>-3</sup> )	1.975	2.007	2.004
Abs. coeff. (mm <sup>-1</sup> )	8.126	7.699	7.621
<i>F</i> (000)	1000	2192	2176
Reflns., Ind. reflns.	25 448, 3781	35 907, 8357	48 754, 10 860
Abs. correction	Integration	Integration	Integration
Data/restr./param.	3781/1/206	8357/0/445	10 860/0/466
Gof on <i>F</i> <sup>2</sup>	1.020	1.023	0.934
<i>R</i> indices ( <i>I</i> > 2σ( <i>I</i> ))	<i>R</i> 1 = 0.0332 <i>wR</i> 2 = 0.0756	<i>R</i> 1 = 0.0471 <i>wR</i> 2 = 0.1117	<i>R</i> 1 = 0.0475 <i>wR</i> 2 = 0.0832

PtSn·H<sub>2</sub>O (%): C 24.62, H 5.48, N 6.72; found: C 24.87, H 5.88, N 6.44.

#### [PtHMe<sub>2</sub>(Me<sub>3</sub>TACN)]CF<sub>3</sub>SO<sub>3</sub> (**4c**)

To a solution of **1** (0.26 mmol) in THF (10 mL) was added triflic acid (23.5 μL, 0.265 mmol) and the colourless solution was stirred for 2 h. The volume of solvent was reduced under vacuum and pentane (30 mL) was added to precipitate the product. The solvent was removed by cannula and the solid product was dried under vacuum. Yield: 108.8 mg, 76%. IR (Nujol) ν(PtH) (cm<sup>-1</sup>): 2245. <sup>1</sup>H NMR (acetone-*d*<sub>6</sub>) δ: 3.42 (m, 2H, CH<sub>2</sub>), 3.27 (m, 6H, CH<sub>2</sub>), 3.06 (m, 4H, CH<sub>2</sub>), 3.02 (s, 6H, <sup>3</sup>*J*(PtH) = 22 Hz, PtNMe *trans* Me), 2.63 (s, 3H, <sup>3</sup>*J*(PtH) = 17 Hz, PtNMe *trans* H), 0.62 (s, 6H, <sup>2</sup>*J*(PtH) = 66 Hz, PtMe), -20.99 (s, 1H, <sup>1</sup>*J*(PtH) = 1406 Hz, PtH). <sup>13</sup>C NMR δ: 60.81 (s, CH<sub>2</sub>), 60.45 (s, CH<sub>2</sub>), 58.55 (s, CH<sub>2</sub>), 51.50 (s, <sup>2</sup>*J*(PtC) = 15 Hz, PtNMe *trans* to Me), 46.05 (s, <sup>2</sup>*J*(PtC) = 8 Hz, PtNMe *trans* to H), -13.02 (s, <sup>1</sup>*J*(PtC) = 628 Hz, PtMe). Anal. calcd. for C<sub>12</sub>H<sub>28</sub>F<sub>3</sub>N<sub>3</sub>O<sub>3</sub>PtS (%): C 26.37, H 5.16, N 7.69; found: C 26.30, H 5.13, N 7.57.

#### [PtHMe<sub>2</sub>(Me<sub>3</sub>TACN)]BF<sub>4</sub> (**4a**)

To a solution of **1** (0.43 mmol) in THF (10 mL) was added HBF<sub>4</sub> (54% in ether, 60 μL, 0.435 mmol) to give a colourless solution that was stirred for 2 h. Pentane (30 mL) was added, to give a white precipitate. The solvent was removed by cannula and the product was dried under vacuum. Yield: 170 mg, 82%. Decomposition at 193°C. The NMR parameters are as described for the triflate salt. Anal. calcd. for C<sub>11</sub>H<sub>28</sub>BF<sub>4</sub>N<sub>3</sub>Pt: C 27.28, H 5.83, N 8.68; found: C 27.09, H 5.98, N 8.63.

#### [PtMe<sub>2</sub>(OH)(Me<sub>3</sub>TACN)]CF<sub>3</sub>SO<sub>3</sub> (**5c**)

A solution of [PtHMe<sub>2</sub>(Me<sub>3</sub>TACN)]CF<sub>3</sub>SO<sub>3</sub> (0.045 mmol) in acetone-*d*<sub>6</sub> (0.5 mL) was exposed to the atmosphere for

24 h, resulting in 97% conversion to **5c**, as monitored by NMR. <sup>1</sup>H NMR (acetone-*d*<sub>6</sub>) δ: 3.48 (m, 2H, CH<sub>2</sub>), 3.36 (m, 4H, CH<sub>2</sub>), 3.26 (m, 2H, CH<sub>2</sub>), 3.19 (m, 4H, CH<sub>2</sub>), 2.86 (s, 3H, <sup>3</sup>*J*(PtH) = 32 Hz, NMe *trans* OH), 2.80 (s, 6H, <sup>3</sup>*J*(PtH) = 12 Hz, NMe *trans* Me), 1.00 (s, 6H, <sup>2</sup>*J*(PtH) = 68 Hz, PtMe). <sup>13</sup>C NMR δ: 64.12 (s, <sup>2</sup>*J*(PtC) = 10 Hz, CH<sub>2</sub>), 58.79 (s, CH<sub>2</sub>), 57.21 (s, CH<sub>2</sub>), 50.82 (s, Pt-NMe *trans* OH), 46.12 (s, Pt-NMe *trans* Me), -1.01 (s, <sup>1</sup>*J*(PtC) = 665 Hz).

#### [PtMe<sub>2</sub>(OH)(Me<sub>3</sub>TACN)]BF<sub>4</sub> (**5a**)

To a solution of **1** (0.576 mmol) in THF (5 mL) was added H[BF<sub>4</sub>] (54% in ether, 79.5 μL, 0.577 mmol) to precipitate **4a**. The mixture was stirred for 30 min, then the nitrogen atmosphere was replaced with air. After 20 h, the solvent was evaporated to give the product **5a** as a white solid that was crystallized from acetone. Yield: 139 mg, 48%. NMR data were identical with those of the triflate analogue. The product analyzed as 0.8[PtMe<sub>2</sub>(OH)(Me<sub>3</sub>TACN)]BF<sub>4</sub>; 0.2[PtMe<sub>2</sub>-(OH<sub>2</sub>)(Me<sub>3</sub>TACN)][BF<sub>4</sub>]<sub>2</sub>. Anal. calcd. for C<sub>11</sub>H<sub>28.2</sub>B<sub>1.2</sub>F<sub>4.8</sub>N<sub>3</sub>-OPt (%): C 25.51, H 5.49, N 8.12; found: C 25.50, H 5.25, N 7.82.

#### [PtMe<sub>2</sub>(OH<sub>2</sub>)(Me<sub>3</sub>TACN)][CF<sub>3</sub>SO<sub>3</sub>]<sub>2</sub> (**6c**)

To a solution of [PtMe<sub>2</sub>(Me<sub>3</sub>TACN)] (0.07 mmol) in acetone-*d*<sub>6</sub> (0.5 mL) was added triflic acid (0.14 mmol) to give a solution containing **6c**. <sup>1</sup>H NMR (acetone-*d*<sub>6</sub>) δ: 4.30 (br, 2H, OH<sub>2</sub>), 3.8–3.3 (m, br, CH<sub>2</sub>), 3.03 (br s, 6H, NMe *trans* to Me), 2.95 (br s, 3H, NMe *trans* to OH<sub>2</sub>), 1.48 [s, 6H, <sup>2</sup>*J*(PtH) = 65 Hz, PtMe]. On attempted isolation, partial deprotonation to **5c** occurred as determined by NMR analysis.

#### Structure determinations

Crystals of **5a**, **5c**, and **7** were grown from saturated THF (**5c**), acetone (**5a**), and methanol (**7**) solutions, and were mounted on glass fibres. Data were collected at -73°C by using a Nonius Kappa-CCD diffractometer with COLLECT



software (Nonius B.V., 1998). The unit cell parameters were calculated and refined from the full data set. Crystal cell refinement and data reduction were carried out using DENZO (Nonius B.V., 1998). The data were scaled using SCALEPACK (Nonius B.V., 1998). The crystal data and refinement parameters are listed in Table 3.

The SHELXTL V5.1 suite of programs was used to solve the structures by Patterson methods, followed by successive difference Fouriers. All of the non-hydrogen atoms in all three structures were refined with anisotropic thermal parameters. The hydrogen atom positions were calculated geometrically and were included as riding on their respective carbon atoms, except for H81, H82, and H88 on the hydroxo and aqua ligands in the structure of **7**, which were refined with isotropic thermal parameters. The water molecule in **5a** was modelled as an anisotropic oxygen (no hydrogen atoms added).

## Acknowledgements

We thank Dr. M.C. Jennings for the X-ray data and the Natural Sciences and Engineering Research Council of Canada (NSERC) for financial support and for a scholarship to EP. RJP thanks the government of Canada for a Canada Research Chair.

## Supporting information

X-ray crystallographic files, in CIF format for the structure determinations of three complexes. Supplementary data may be purchased from the Depository of Unpublished Data, Document Delivery, CISTI, National Research Council Canada, Ottawa, ON K1A 0S2, Canada ([http://www.nrc.ca/cisti/irm/unpub\\_e.shtml](http://www.nrc.ca/cisti/irm/unpub_e.shtml) for information on ordering electronically). CCDC 196122–196124 contain the supplementary data for this paper. These data can be obtained, free of charge, via [www.ccdc.cam.ac.uk/conts/retrieving.html](http://www.ccdc.cam.ac.uk/conts/retrieving.html) (or from the Cambridge Crystallographic Data Centre, 12 Union Road, Cambridge, U.K., CB2 1E2; fax: +44 1223 336033; or deposit@ccdc.cam.ac.uk).

## References

1. A.E. Shilov and G.B. Shul'pin. *Chem. Rev.* **97**, 2879 (1997).
2. S.S. Stahl, J.A. Labinger, and J.E. Bercaw. *Angew. Chem., Int. Ed. Engl.* **37**, 2181 (1998).
3. (a) R.A. Periana, D.J. Taube, S. Gamble, H. Taube, T. Satoh, and H. Fujii. *Science (Washington, D.C.)*, **280**, 560 (1998); (b) J. Kua, X. Xu, R.A. Periana, and W.A. Goddard, III. *Organometallics*, **21**, 511 (2002).
4. R.H. Crabtree. *J. Chem. Soc., Dalton Trans.* 2437 (2001).
5. (a) K. Mylvaganam, G.B. Bacskay, and N.S. Hush. *J. Am. Chem. Soc.* **121**, 4633 (1999); (b) K. Mylvaganam, G.B. Bacskay, and N.S. Hush. *J. Am. Chem. Soc.* **122**, 2041 (2000); (c) T.M. Gilbert, I. Hristov, and T. Ziegler. *Organometallics*, **20**, 1183 (2001).
6. (a) M. Lin, C. Shen, E.A. Garcia-Zayas, and A. Sen. *J. Am. Chem. Soc.* **123**, 1000 (2001); (b) A. Sen. *Acc. Chem. Res.* **31**, 550 (1998).
7. R.J. Puddephatt. *Coord. Chem. Rev.* **219–221**, 157 (2001).
8. D.P. Arnold and M.A. Bennett. *Inorg. Chem.* **23**, 2110 (1984).
9. V. de Felice, A. de Renzi, A. Panunzi, and D. Tesaro. *J. Organomet. Chem.* **488**, C13 (1995).
10. (a) S.S. Stahl, J.A. Labinger, and J.E. Bercaw. *J. Am. Chem. Soc.* **117**, 9371 (1995); (b) S.S. Stahl, J.A. Labinger, and J.E. Bercaw. *J. Am. Chem. Soc.* **118**, 5961 (1996); (c) M.W. Holtcamp, J.A. Labinger, and J.E. Bercaw. *Inorg. Chim. Acta*, **265**, 117 (1997).
11. G.S. Hill, L.M. Rendina, and R.J. Puddephatt. *Organometallics*, **14**, 4966 (1995).
12. (a) S.A. O'Reilly, P.S. White, and J.L. Templeton. *J. Am. Chem. Soc.* **118**, 5684 (1996); (b) S. Reinartz, P.S. White, M. Brookhart, and J.L. Templeton. *Organometallics*, **19**, 3854 (2000); (c) S. Reinartz, P.S. White, M. Brookhart, and J.L. Templeton. *Organometallics*, **20**, 1709 (2001).
13. (a) A.J. Canty, A. Dedieu, H. Jin, A. Milet, and M.K. Richmond. *Organometallics*, **15**, 2845 (1996); (b) A.J. Canty, S.D. Fritsche, H. Jin, J. Patel, B.W. Skelton, and A.H. White. *Organometallics*, **16**, 2175 (1997).
14. E.M. Prokopchuk, H.A. Jenkins, and R.J. Puddephatt. *Organometallics*, **18**, 2861 (1999).
15. (a) H.A. Jenkins, G.P.A. Yap, and R.J. Puddephatt. *Organometallics*, **16**, 1946 (1997); (b) U. Fekl, A. Zahl, and R. van Eldik. *Organometallics*, **18**, 4156 (1999).
16. J.G. Hinman, C.R. Baar, M.C. Jennings, and R.J. Puddephatt. *Organometallics*, **19**, 563 (2000).
17. (a) L. Johansson and M. Tilset. *J. Am. Chem. Soc.* **123**, 739 (2001); (b) L. Johansson, M. Tilset, J.A. Labinger, and J.E. Bercaw. *J. Am. Chem. Soc.* **122**, 10 846 (2000).
18. (a) K.L. Bartlett, K.I. Goldberg, and W.T. Borden. *Organometallics*, **20**, 2669 (2001); (b) H. Heiberg, O. Swang, O.B. Ryan, and O. Gropen. *J. Phys. Chem.* **103**, 10 004 (1999); (c) A.N. Vedernikov, G.A. Shamov, and B.N. Solomonov. *Russ. J. Gen. Chem.* **69**, 1102 (1999); (d) G.S. Hill and R.J. Puddephatt. *Organometallics*, **17**, 1478 (1998).
19. D.D. Wick and K.I. Goldberg. *J. Am. Chem. Soc.* **121**, 11 900 (1999).
20. V.V. Rostovtsev, L.M. Henling, J.A. Labinger, and J.E. Bercaw. *Inorg. Chem.* **41**, 3608 (2002).
21. P.K. Monaghan and R.J. Puddephatt. *Organometallics*, **3**, 444 (1984).
22. V.V. Rostovtsev, J.A. Labinger, J.E. Bercaw, T.L. Lasseter, and K.I. Goldberg. *Organometallics*, **17**, 4530 (1998).
23. J. Kuyper. *Inorg. Chem.* **16**, 2171 (1977).
24. (a) C.J. Levy, R.J. Puddephatt, and J.J. Vittal. *Organometallics*, **13**, 1559 (1994); (b) C.J. Levy, R.J. Puddephatt, and J.J. Vittal. *Organometallics*, **15**, 35 (1996); (c) C.J. Levy, R.J. Puddephatt, and J.J. Vittal. *Organometallics*, **15**, 2108 (1996).
25. (a) A.J. Canty, and H. Jin. *J. Organomet. Chem.* **565**, 135 (1998); (b) A.J. Canty, H. Jin, B.W. Skelton, and A.H. White. *Aust. J. Chem.* **52**, 417 (1999).
26. P. Chaudhuri and K. Wieghardt. *Prog. Inorg. Chem.* **35**, 330 (1987).
27. N.F. Curtis. *In Coordination chemistry of macrocyclic compounds. Edited by G.A. Melson. Plenum Press, New York. 1979. p. 234.*
28. G.S. Hill, M.J. Irwin, C.J. Levy, and R.J. Puddephatt. *Inorg. Synth.* **32**, 149 (1998).



# Photogeneration of a diene template for surface Diels–Alder reactions: Photoenolization of an *ortho*-methyl-benzophenone-modified Au cluster

Arnold J. Kell, Christopher C. Montcalm, and Mark S. Workentin

**Abstract:** A series of monolayer-protected clusters (MPCs) modified with a photoreactive [4-(11-mercaptoundecyl)-phenyl](2-methylphenyl)methanone (**1**) moiety have been prepared where **1** is co-absorbed to the MPC surface with dodecanethiol, octadecanethiol, or 11-mercaptoundecanoic acid methyl ester. Upon irradiation the MPC-anchored **1** reacts efficiently through its triplet excited states, yielding 1,4-biradicals that collapse to synthetically useful, long-lived photodienol intermediates, which can be efficiently trapped in Diels–Alder type chemistry by dienophiles — namely, dimethyl acetylenedicarboxylate (DMAD). In all cases the Diels–Alder trapping of the dienol occurred efficiently resulting in >60% conversion to the Diels–Alder adduct. This indicates that the local environment surrounding **1** did not influence its ability to react via the Diels–Alder reaction; however, the reaction could not be taken to completion. The inability to react completely is attributed to **1** binding to distinct sites on the MPC core; there are edge, vertice, and terrace sites. Selective population of these specific sites and the subsequent irradiations show that MPCs with **1** anchored predominantly at edge and vertice sites results in an extent of reaction of  $85 \pm 3\%$ , whereas selectively populating the terrace sites results in an extent of reaction of  $36 \pm 2\%$ . These results suggest that **1** anchored to edge and vertice sites is more reactive to the Diels–Alder reaction than that involving terrace sites.

**Key words:** monolayer protected cluster, site selective reactivity, Diels–Alder, photochemistry.

**Resume :** On a préparé une série d'agrégats protégés en monocouches (« MPC »), modifiés par une portion photoréactive de [4-(11-mercaptoundécyl)phényl](2-méthylphényl)méthanone (**1**) coabsorbée sur la surface des « MPC » avec du dodécaneéthiol, de l'octadécaneéthiol ou du 11-mercaptoundécanoate de méthyle. Par irradiation, le composé **1** attaché au « MPC » réagit de façon efficace, par le biais de ses états excités, pour donner des 1,4-biradicaux qui se décomposent en intermédiaires photodiénoles utiles d'un point de vue synthétique et qui peuvent être piégés d'une façon efficace par des diénoles tels l'acétylènedicarboxylate de diméthyle (ADCM), dans des réactions de type Diels–Alder. Dans tous les cas, le piégeage de type Diels–Alder du diénole se fait d'une façon efficace conduisant à plus de 60 % de conversion en adduit de Diels–Alder. Ce résultat indique que l'environnement local autour du composé **1** n'influence pas sa facilité à réagir par le biais de la réaction de Diels–Alder; toutefois, il n'a pas été possible d'obtenir une réaction complète. On attribue cette inhabilité du composé **1** à réagir complètement à la nature des sites auxquels il est attaché sur les « MPC » qui comportent des sites en bordures, aux sommets et sur des terrasses. Une population sélective de chacun de ces sites spécifiques suivie d'irradiations montrent que le degré de réaction s'élève à  $85 \pm 3\%$  lorsque le composé **1** s'est fixé sur des sites en bordures ou aux sommets des « MPC » mais qu'il n'est que de  $36 \pm 2\%$  lorsque le composé **1** s'est fixé sur des sites des terrasses des « MPC ». Ces résultats suggèrent que le composé **1** fixé sur des sites en bordure ou aux sommets sont plus réactifs vis-à-vis de la réaction de Diels–Alder que ceux des terrasses.

**Mots clés :** agrégat protégé en monocouche, réactivité sélective d'un site, Diels–Alder, photochimie.

[Traduit par la Rédaction]

## Introduction

The irradiation of *ortho*-alkylated benzophenones generates synthetically useful *ortho*-quinodimethane enol intermediates (1, 2). This reaction, first described by Yang and Rivas (3), involves an intramolecular  $\gamma$ -hydrogen atom ab-

straction from the *ortho*-alkyl substituent by the  $n,\pi^*$  excited state of the carbonyl group, which generates a 1,4-biradical that subsequently collapses to the respective *E* and *Z*-dienols (Scheme 1). The lifetime of the *Z*-dienol is very short (0.03–1  $\mu$ s) whereas that of the *E*-dienol is significantly longer (3 s). The *Z*-dienol has a short lifetime because its orienta-

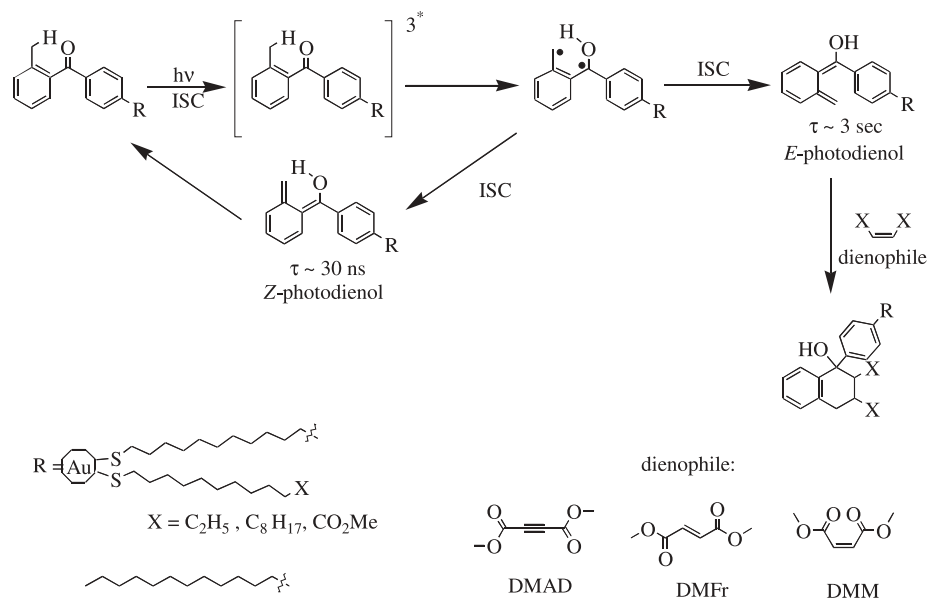
Received 7 March 2003. Published on the NRC Research Press Web site at <http://canjchem.nrc.ca> on 29 April 2003.

Dedicated to Professor Don Arnold for his many contributions to chemistry in Canada.

A.J. Kell, C.C. Montcalm, and M.S. Workentin.<sup>1</sup> Department of Chemistry, The University of Western Ontario, London, ON N6A 5B7, Canada.

<sup>1</sup>Corresponding author (e-mail: [mworkent@uwo.ca](mailto:mworkent@uwo.ca)).



**Scheme 1.** The generation of the photodienol and its subsequent Diels–Alder reaction.

tion allows reketonization and re-aromatization to occur easily through a 1,5-hydrogen shift; the reketonization process for the *E*-dienol requires acid or base catalysis. The long-lived *E*-dienol provides an intermediate that can be efficiently trapped by Diels–Alder dienophiles to yield, exclusively, the endo products, with excellent regioselectivity (1, 2). In this report we extend this photoinitiated Diels–Alder reaction to monolayer-protected gold clusters or MPCs. While there are a variety of reported photoinduced reactions on planar metal surfaces (4–15), there are surprisingly few reports of photochemical reactions (16, 17) or photophysical properties (18–20) of organic molecules anchored to MPCs even though these substrates are emerging as important new materials (21, 22). In recent studies we reported the intramolecular Norrish–Yang Type II photoreaction of an aryl ketone in this type of MPC environment (23, 24); those studies illustrated, among other things, that unimolecular carbonyl photoreactions can be efficient in MPCs and can lead to surface modifications. Here we report the photodienolization of an *ortho*-methyl-benzophenone-modified gold MPC and the subsequent trapping of the dienol by a model dienophile (Scheme 1). To the best of our knowledge, this study represents the first example of a bimolecular photochemical reaction on an MPC. Mrksich and co-workers recently reported elegant studies of an electrochemically generated quinone-immobilized dienophile on planar gold using Diels–Alder chemistry and showed that the reaction can be used for selective modification with proteins (25–28).

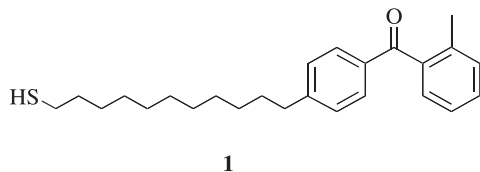
Little has been done to elucidate the dynamics (29) and reactivity associated with substrates anchored to MPC surfaces, considering that the MPC core is well known to be inhomogeneous (21, 30): there are edge, vertice, and terrace sites on each MPC. These distinct sites may display different reactivity; we have found evidence for this in our earlier studies (23). It is of interest to observe how efficiently a photo-induced bimolecular reaction, such as the Diels–Alder trapping of the *E*-dienol, can occur on the MPC surface and what factors associated with the MPC environment influence

its reactivity. The Diels–Alder reaction between the photodienol and a dienophile is a versatile probe of the MPC environment. This reaction allows for the study of (i) the ability of the ketone to be excited to the dienol in the MPC environment, (ii) the ability to trap the dienol, and (iii) the effects that co-absorbed substrates on the MPC surface have on the ability of the photodienol to react with a dienophile (will the photodienol in the monolayer environment be too sterically hindered to allow the subsequent Diels–Alder reaction?). Additionally, because the MPC core contains a number of distinct sites, selectively populating the different sites with **1** will help elucidate where these bimolecular reactions occur most efficiently on the MPC surface.

To address our interests in MPC reactivity we have prepared a series of MPCs designed to probe a variety of properties within the MPC environment (Fig. 1). A [4-(11-mercaptopundecyl)phenyl](2-methylphenyl)methanone (**1**) (Scheme 2) substrate was “place-exchanged” onto the surface of previously prepared dodecanethiolate ( $\text{C}_{12}\text{MPC}$ ), octadecanethiolate ( $\text{C}_{18}\text{MPC}$ ), and 11-mercaptopundecanoic acid methyl ester ( $\text{MeO}_2\text{CC}_{10}\text{MPC}$ ) MPCs. The corresponding MPCs, defined as **1**- $\text{C}_{12}\text{MPC}$ , **1**- $\text{C}_{18}\text{MPC}$ , and **1**- $\text{MeO}_2\text{CC}_{10}\text{MPC}$ , respectively, where, for example, **1**- $\text{C}_{12}\text{MPC}$  represents the place-exchange of **1** onto an original  $\text{C}_{12}\text{MPC}$ , were then irradiated in the presence of a dienophile, namely dimethyl acetylenedicarboxylate (DMAD). The majority of this report makes use of DMAD as the dienophile, but the reaction was also shown to occur efficiently with other dienophiles such as dimethyl fumarate (DMFr) and dimethyl maleate (DMM). The dienophiles were selected because they were symmetric, making product identification more straightforward, and because the solution photochemistry involving *ortho*-methyl benzophenone with these dienophiles is well known to occur efficiently and regioselectively (i.e., where possible, only the endo product is generated) (3, 31–33).

The base MPCs were chosen so that a variety of effects associated with the Diels–Alder reaction between the photodienol and a dienophile could be studied. If we assume that



**Scheme 2.** The probe molecule incorporated into the MPC.

the methylene chains of both **1** and the dilutant chain (or the substrate on the original MPC, namely C<sub>12</sub>, C<sub>18</sub>, or MeO<sub>2</sub>CC<sub>10</sub>) pack similarly, then the mixed **1**-C<sub>12</sub>MPC will allow for the photochemical generation of the dienol directly at the interface. In the case of **1**-C<sub>18</sub>MPC, the resulting photodienol is expected to be embedded within the monolayer. This is of interest because embedding the dienol may hinder its ability to react with a dienophile. Both of these mixed MPCs bear nonpolar terminal methyl groups on the dilutant chain. Because the terminal groups on MPCs are known to influence some of their physical properties (21) — MPCs containing terminal carboxylic acid groups are soluble in methanol and water, whereas MPCs containing terminal methyl groups are soluble only in nonpolar solvents such as chloroform, dichloromethane, benzene, and hexanes — we were also interested in employing a dilutant chain containing a terminal ester. The terminal ester would serve to change the local polarity at the interface and may allow the polar dienophile to be incorporated into the interface (because both are polar), possibly allowing the Diels–Alder reaction to occur more efficiently. We were also interested in determining if the reactivity of **1** is influenced by its location on the MPC surface. As mentioned earlier, MPCs have distinct sites. Selective population of the different sites of the MPC surface with **1** will allow for the determination of differences in the efficiency of the Diels–Alder reaction when it occurs at edge and vertice sites, as compared with terrace sites. The extent of this bimolecular reaction within the MPC environment will be a valuable tool, employed in determining how steric and environmental effects introduced by the monolayer affect the ability of the dienophile to react with the surface-bound dienol.

## Results and discussion

The **1**-MPCs were prepared from a [4-(11-mercaptopoundecyl)phenyl](2-methylphenyl)methanone (**1**) precursor (Scheme 2). The synthesis of **1** started from (11-bromoundecyl)benzene, prepared by the addition of phenyl lithium to a large excess of 1,11-dibromoundecane. A Friedel–Crafts acylation reaction between (11-bromoundecyl)benzene generated in the mixture and *o*-toluoyl chloride in the presence of AlCl<sub>3</sub> generated 4-(11-bromoundecyl)phenyl(2-methylphenyl)methanone. The bromide was then converted to thiol through the reaction of potassium thioacetate and the hydrolysis of the resulting thioester with ethanolic K<sub>2</sub>CO<sub>3</sub>. The resulting thiol (**1**) was purified via column chromatography using 3:1 dichloromethane:hexanes as eluant and characterized by <sup>1</sup>H NMR, <sup>13</sup>C NMR, and IR spectroscopy and mass

spectrometry. Details of the synthetic transformations are provided in the experimental section.

Generally MPCs are prepared by the reduction of hydrogen tetrachloroaurate in the presence of a thiol (34, 35). This protocol is incompatible with **1** because the presence of a reducing agent will convert the carbonyl functionality to an alcohol. So, to prepare the desired **1**-MPC, we employ the place-exchange reaction (36, 37) developed by Murray and co-workers starting from well-defined base MPCs (35). The place-exchange reaction is an equilibrium-based reaction involving the replacement of free thiol from solution onto the MPC surface (36, 37). It is accomplished by stirring an excess of a thiol that is to be exchanged onto the MPC surface in the presence of an already prepared base MPC for 4–5 days. As mentioned earlier, the MPC core consists of different sites. It has been suggested that the place-exchange reaction populates the edge and vertice sites quickly (within 1 h) and population of the terrace occurs over a much longer timescale (36). This means that depending on the timescale of the place-exchange reaction, **1** can populate predominantly the edge and vertice sites (1 h), or all sites (the terrace, edge, and vertice sites) can be populated over much longer exchange times (4–5 days). This is an important property of the place-exchange reaction that was exploited and will be addressed later. The base MPCs were prepared according to procedures outlined by Murray and co-workers, as they are known to produce relatively monodisperse MPCs with a core diameter of 2.0 nm and general stoichiometry of Au<sub>314</sub>(X)<sub>108</sub>, where there are 314 gold atoms comprising the MPC core and X is the thiolate surrounding the MPC core (35).

Proton NMR spectroscopy was used to determine the purity and the extent of exchange (stoichiometry) of the resulting mixed MPCs (**1**-C<sub>12</sub>MPC, **1**-C<sub>18</sub>MPC, and **1**-MeO<sub>2</sub>CC<sub>10</sub>MPC, respectively). The purity of the MPC is judged by the amount of free thiol or disulfide remaining in solution after work-up and isolation of the MPC. Any free thiol or disulfide would appear as sharp resonances in the <sup>1</sup>H NMR spectrum. Figures 2a and 3a are typical <sup>1</sup>H NMR spectra, recorded in benzene-*d*<sub>6</sub>, of the **1**-C<sub>12</sub>MPC and **1**-MeO<sub>2</sub>CC<sub>10</sub>MPC, respectively, isolated after place-exchange; of particular note is the absence of sharp resonances assignable to free thiol (or disulphide in solution). The <sup>1</sup>H NMR spectrum of **1**-C<sub>18</sub>MPC is not shown, but is similar to these (see supplemental information).<sup>2</sup> All of the spectra exhibit distinctive broad resonances (38, 39) at the chemical shifts measured for pure **1** in benzene-*d*<sub>6</sub> solution, confirming that the place-exchange has occurred. These resonances include those of the aromatic protons on the phenyl rings *ortho* to the carbonyl at 7.85 (2H) and 7.22 (1H) ppm, the protons on the methyl function *ortho* to the carbonyl at 2.29 ppm, and the CH<sub>2</sub> protons of the alkyl spacer  $\alpha$  to the benzophenone function at 2.57 ppm (Figs. 2a and 3a). The remaining methylene protons of the alkyl chain for **1** appear between 1.15 and 1.90 ppm along with those of the dilutant chain, either C<sub>12</sub>, C<sub>18</sub>, or MeO<sub>2</sub>CC<sub>10</sub>. The resonance signal at 0.9 ppm in Fig. 2a is due to the terminal methyl protons of the remaining dodecanethiolate present on the MPC after the place-

<sup>2</sup>Supplementary data may be purchased from the Depository of Unpublished Data, Document Delivery, CISTI, National Research Council Canada, Ottawa, ON K1A 0S2, Canada ([http://www.nrc.ca/cisti/irm/unpub\\_e.shtml](http://www.nrc.ca/cisti/irm/unpub_e.shtml) for information on ordering electronically).



**Fig. 1.** Cartoon depictions of the various MPCs studied, showing that the photodienol will be (a) at the interface, (b) embedded within the monolayer, or (c) near a more polar co-absorbed substrate.

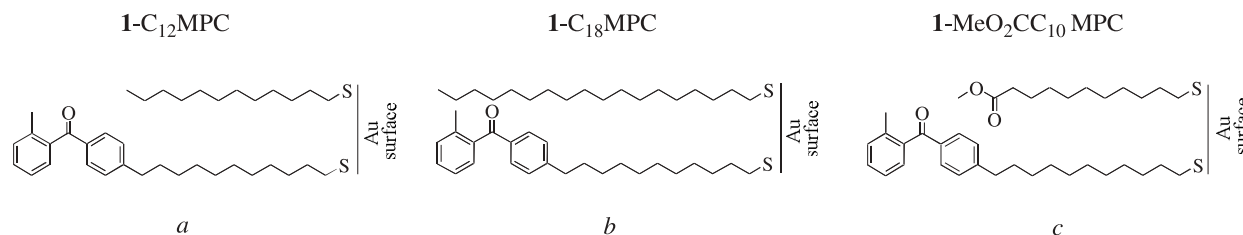
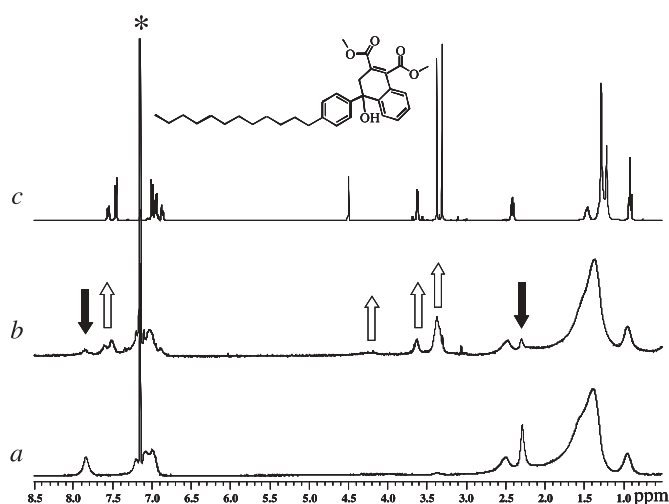
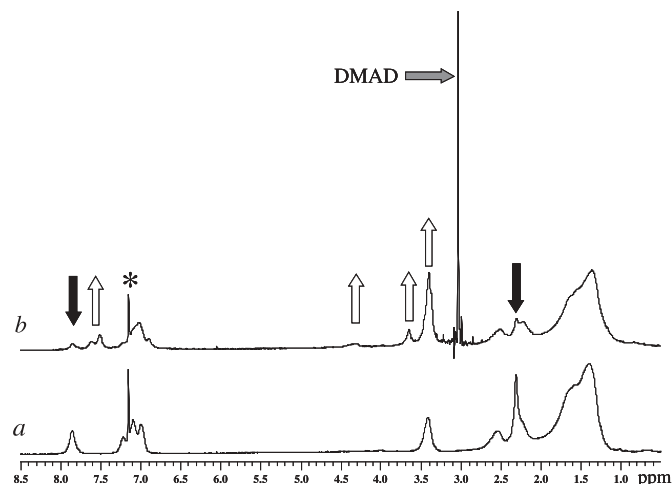


**Fig. 2.** The irradiation of  $\text{Au}_{314}(\text{C}_{12}\text{S})_{50}(\mathbf{1})_{58}$  in benzene- $d_6$  (\*) before irradiation (a) and after an irradiation period of 80 h in the presence of a 3-times molar excess of DMAD (b). The filled arrows indicate the decrease in intensity for the resonances associated with  $\text{Au}_{314}(\text{C}_{12}\text{S})_{50}(\mathbf{1})_{58}$  while the hollow arrows indicate an increase in the resonances associated with the product, namely  $\text{Au}_{314}(\text{C}_{12}\text{S})_{50}(\mathbf{1})_{26}(\mathbf{1}\text{-DMAD})_{32}$ . Note: the DMAD has been washed away before the final  $^1\text{H}$  NMR spectra was acquired. The  $^1\text{H}$  NMR spectrum of an authentic sample of the model compound (2-DMAD) in benzene- $d_6$  is shown in (c) (actual molecule pictured).



exchange reaction (or in the case of  $\mathbf{1}\text{-C}_{18}\text{MPC}$ , the resonance at 0.9 ppm is due to the terminal methyl group of octadecanethiolate). As expected, the resonances associated with the protons  $\alpha$ ,  $\beta$ , and  $\gamma$  to the thiolate moiety are not observed: because the substrates are anchored to the MPC surface they are unable to rotate freely, and the signal broadens into the baseline. There is some overlap of the broad resonances attributed to the terminal methyl group of the dilutant chain and those of the methylene groups of both  $\mathbf{1}$  and the dilutant chain in the  $\mathbf{1}\text{-C}_{12}$  and  $\mathbf{1}\text{-C}_{18}\text{MPC}$ s. This necessitates the use of an  $\text{I}_2$  decomposition reaction that quantitatively liberates any thiolate bound to the MPC surface as disulfide and reduces the MPC core to elemental gold, allowing accurate integration to determine their stoichiometries (40). As mentioned above, the MPCs employed in the study have a general stoichiometry of  $\text{Au}_{314}(\text{X})_{108}$ , where X is either  $\text{C}_{12}\text{S}$ ,  $\text{C}_{18}\text{S}$ , or  $\text{MeO}_2\text{CC}_{10}\text{S}$ . The total number of substrates bound to the MPC surface is expected to remain constant after place-exchange, so the stoichiometry is based on the  $\mathbf{1}\text{:X}$  ratio. The stoichiometries of the MPCs were  $\text{Au}_{314}\text{-}$

**Fig. 3.** The irradiation of  $\text{Au}_{314}(\text{MeO}_2\text{CC}_{10}\text{S})_{59}(\mathbf{1})_{49}$  in benzene- $d_6$  (\*) before irradiation (a) and after an irradiation period of ~96 h in the presence of a 3-times molar excess of DMAD (b). The filled arrows indicate the decrease in intensity for the resonances associated with  $\text{Au}_{314}(\text{MeO}_2\text{CC}_{10}\text{S})_{59}(\mathbf{1})_{49}$  while the hollow arrows indicate an increase in the resonances associated with the product, namely  $\text{Au}_{314}(\text{MeO}_2\text{CC}_{10}\text{S})_{59}(\mathbf{1})_{15}(\mathbf{1}\text{-DMAD})_{34}$ .



$(\text{C}_{12}\text{S})_{50}(\mathbf{1})_{58}$  and  $\text{Au}_{314}(\text{C}_{18}\text{S})_{74}(\mathbf{1})_{34}$  for the  $\mathbf{1}\text{-C}_{12}\text{MPC}$  and the  $\mathbf{1}\text{-C}_{18}\text{MPC}$ , respectively. These stoichiometries were determined in deuteriochloroform solution by comparison of the integrations for the resonance signal at 7.72 ppm attributed to the aromatic protons  $\alpha$  to the carbonyl in  $\mathbf{1}$  and the resonance signal at 0.86 ppm attributed to the terminal methyl group of either  $\text{C}_{12}$  or  $\text{C}_{18}$  after  $\text{I}_2$  decomposition of the appropriate MPC.

In Fig. 3a, the resonance signal at 3.35 ppm and the shoulder at 2.28 ppm are due to the terminal methyl protons of the ester and the methylene protons  $\alpha$  to the ester, respectively, on the  $\text{MeO}_2\text{CC}_{10}$  moiety. The stoichiometry of the mixed  $\mathbf{1}\text{-MeO}_2\text{CC}_{10}\text{MPC}$  was determined directly from the  $^1\text{H}$  NMR spectrum of the MPC in benzene- $d_6$  by taking the ratio of the integrations for the resonance at 3.35 ppm (from  $\text{MeO}_2\text{CC}_{10}$ ) and 7.85 ppm (from  $\mathbf{1}$ ) and was found to be  $\text{Au}_{314}(\text{MeO}_2\text{C}_{10}\text{S})_{59}(\mathbf{1})_{49}$ . This was possible because there was no overlap in these resonance signals, allowing accurate integration directly from the MPC.

Irradiations were carried out in argon- or  $\text{N}_2$ -purged benzene- $d_6$  solutions in Pyrex NMR tubes using a Rayonet photochemical reactor fitted with 350 nm bulbs and a merry-go-round apparatus. Generally, the solutions contained ~15–20 mg of  $\mathbf{1}\text{-C}_{12}\text{MPC}$ ,  $\mathbf{1}\text{-C}_{18}\text{MPC}$ , or  $\mathbf{1}\text{-MeO}_2\text{CC}_{10}\text{MPC}$  dis-

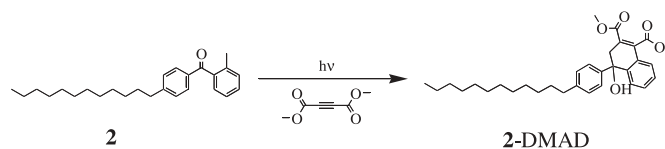


solved in 0.5 mL benzene- $d_6$  (~0.008–0.012 M with respect to **1**), with a three-times molar excess of the dienophile, namely dimethyl acetylenedicarboxylate (DMAD). Irradiation under these conditions produced MPCs consistent with the trapping of the photodienol (Scheme 1). The reaction can be monitored directly by NMR spectroscopy; this is illustrated in Figs. 2 and 3 for **1**-C<sub>12</sub>MPC and **1**-MeO<sub>2</sub>CC<sub>10</sub>MPC, respectively, where the MPCs were irradiated in the presence of DMAD as the dienophile. The <sup>1</sup>H NMR and IR spectra of the MPCs irradiated in the presence of DMAD can be compared with those of an authentic sample of the Diels–Alder products made from irradiation of [4-(dodecyl)phenyl](2-methylphenyl)methanone (**2**), with DMAD as dienophile (Scheme 3). The irradiation product of **2** with DMAD was characterized via <sup>1</sup>H NMR, <sup>13</sup>C NMR, and IR spectroscopy, as well as mass spectrometry. The <sup>1</sup>H NMR spectrum of **2**-DMAD is shown in Fig. 2c. The key spectral changes that occur upon irradiation of **1**-C<sub>12</sub>MPC, **1**-C<sub>18</sub>MPC, and **1**-MeO<sub>2</sub>CC<sub>10</sub>MPC with DMAD are consistent with the formation of the Diels–Alder product. These include the appearance of two overlapping, broad aromatic peaks at 7.6 and 7.5 ppm and another aromatic resonance signal at 6.87 ppm, as well as broad peaks at 4.15 (the hydroxyl H), 3.62 (the methylene H's), and 3.35 ppm (the methyl ester H's), concomitant with a decrease in the intensity of broad aromatic peaks at 7.85, 7.22, and 7.05, along with the broad resonance at 2.39 ppm (the *ortho* methyl group of **1**) (Figs. 2 and 3). The <sup>1</sup>H NMR spectra comparing **1**-C<sub>12</sub>MPC, **1**-DMADC<sub>12</sub>MPC, and the model compound **2**-DMAD are shown in Figs. 2a–c, respectively. The IR spectra of the irradiated MPCs are consistent with the product as well, evidenced by the growth of peaks between 1715–1730 cm<sup>-1</sup> (consistent with an ester functionality) and between 3434–3468 cm<sup>-1</sup> (consistent with a hydroxyl moiety). Product formation was generally complete after 48–60 h with no sign of further reaction on extended irradiation. The success of these trapping experiments allows us to formulate some ideas about the reactivity and steric constraints of substrates confined to the MPC surface.

We begin our analysis of the Diels–Alder trapping of the photodienol by comparing the extents of reaction for the cases where the photodienol is directly at the interface (**1**-C<sub>12</sub>MPC), when it is embedded within the monolayer (**1**-C<sub>18</sub>MPC), and when the local polarity of the interface is varied (**1**-MeO<sub>2</sub>CC<sub>10</sub>MPC). The reaction proceeds efficiently, generating only one product on extensive irradiation on all of the MPCs studied. Irradiation of Au<sub>314</sub>(C<sub>12</sub>S)<sub>50</sub>(**1**)<sub>58</sub>, Au<sub>314</sub>(C<sub>18</sub>S)<sub>74</sub>(**1**)<sub>34</sub>, and Au<sub>314</sub>(MeO<sub>2</sub>CC<sub>10</sub>S)<sub>59</sub>(**1**)<sub>49</sub> produces MPCs with final stoichiometries of Au<sub>314</sub>(C<sub>12</sub>S)<sub>50</sub>(**1**)<sub>26</sub>(**1**-DMAD)<sub>32</sub> (64 ± 2% conversion to the Diels–Alder adduct), Au<sub>314</sub>(C<sub>18</sub>S)<sub>74</sub>(**1**)<sub>13</sub>(**1**-DMAD)<sub>21</sub> (60 ± 2%), and Au<sub>314</sub>-(MeO<sub>2</sub>CC<sub>10</sub>S)<sub>59</sub>(**1**)<sub>15</sub>(**1**-DMAD)<sub>34</sub> (69%), respectively. The irradiations were carried out at least twice for Au<sub>314</sub>(C<sub>12</sub>S)<sub>50</sub>(**1**)<sub>58</sub> and Au<sub>314</sub>(C<sub>18</sub>S)<sub>74</sub>(**1**)<sub>34</sub>, whereas Au<sub>314</sub>(MeO<sub>2</sub>CC<sub>10</sub>S)<sub>59</sub>(**1**)<sub>49</sub> was irradiated only once in parallel with Au<sub>314</sub>(C<sub>12</sub>S)<sub>50</sub>(**1**)<sub>58</sub> (Table 1).

These conversions are essentially identical, suggesting that the ability of the reaction to proceed is not affected by the length or the polarity of the dilutant chain co-absorbed to

**Scheme 3.** The photochemical generation of **2**-DMAD from **2**, which serves as the model for this reaction on the MPC surface.



the MPC with **1**. The extent of reaction was also not affected by the relative concentration of DMAD: the concentration was varied from 1 to 10 times the molar excess of **1**. Though the physical environment of the MPC was different in each of these MPCs studied, the reaction only proceeds to ~65% conversion in all cases. Assuming that the substrates bound to the MPC are distributed over the entire MPC surface because the place-exchange reaction employed was carried out over 5 days, the extent of reaction may be related to the number of **1** bound at the edge and vertice positions of the MPC as compared with the number bound to the terrace. That is, there may be a site-dependent reactivity associated with the substrates bound to the MPC surfaces.

As mentioned above, in the MPCs studied **1** should be positioned in each of the three distinct sites (i.e., on the edge, vertice, or terrace) (Fig. 4). It is assumed that every **1** bound to the MPC is capable of forming the photodienol. If this is the case, there must be certain sites on the MPC surface where the photodienol can be more efficiently trapped as the Diels–Alder adduct and others where the reaction is less efficient. It is intriguing to propose that there is a correlation between the position of substrates on the MPC core and the extent of reaction. To investigate this, the place-exchange reaction was exploited to selectively populate either the edge and vertice sites or the terrace sites with **1**.

Selective population of the edge and vertice sites occurs if short (~1 h) place-exchange reactions are carried out (36). Using this strategy, C<sub>12</sub>MPC was stirred in the presence of **1** in toluene for 1 h under a nitrogen atmosphere, generating **1**(edge)-C<sub>12</sub>MPC, where **1**(edge) implies that the **1** is positioned predominantly at the edge and vertice sites of a C<sub>12</sub>MPC, as suggested by Murray and co-workers.<sup>3</sup> The MPC was purified and I<sub>2</sub> decomposition was utilized to determine the stoichiometry of this MPC, which was Au<sub>314</sub>(C<sub>12</sub>S)<sub>71</sub>(**1**)<sub>37</sub>. The MPC was then weighed out (~15 mg), dissolved in benzene- $d_6$ , and irradiated in the presence of DMAD (three-times excess) until there were no further change in the <sup>1</sup>H NMR spectrum (Fig. 5). The spectral changes were similar to those explained for the above MPCs. Upon purification to remove the excess DMAD, the stoichiometry of the irradiated MPC was found to be Au<sub>314</sub>(C<sub>12</sub>S)<sub>71</sub>(**1**)<sub>5</sub>(**1**-DMAD)<sub>32</sub>, which translates to an 85 ± 3% conversion to Diels–Alder adduct based on two irradiations. This is a significant increase in the conversion of **1** to the Diels–Alder adduct, suggesting that **1** positioned at the edge and vertice more readily undergo the reaction. However, this result does not indicate if **1** bound to the terrace is less reactive towards the Diels–Alder reaction. This can only be determined by preparing an MPC where **1** has been selectively positioned on the terrace.

<sup>3</sup>This is known to populate some of the terrace as well; see ref. 36.



**Table 1.** Stoichiometries of the original MPCs and the extents of reaction for their irradiations in the presence of DMAD.

MPC <sup>a</sup>	Stoichiometry (before irradiation)	Stoichiometry (after irradiation in presence of DMAD) <sup>b</sup>	Conversion (%) <sup>c</sup>
1-C <sub>12</sub> MPC	Au <sub>314</sub> (C <sub>12</sub> S) <sub>50</sub> (1) <sub>58</sub> <sup>d</sup>	Au <sub>314</sub> (C <sub>12</sub> S) <sub>50</sub> (1) <sub>26</sub> (1-DMAD) <sub>32</sub>	64 ± 2
1-C <sub>18</sub> MPC	Au <sub>314</sub> (C <sub>18</sub> S) <sub>74</sub> (1) <sub>34</sub> <sup>d</sup>	Au <sub>314</sub> (C <sub>18</sub> S) <sub>74</sub> (1) <sub>13</sub> (1-DMAD) <sub>21</sub>	60 ± 2
1-C <sub>10</sub> CO <sub>2</sub> MeMPC	Au <sub>314</sub> (MeO <sub>2</sub> CC <sub>10</sub> S) <sub>59</sub> (1) <sub>49</sub> <sup>e</sup>	Au <sub>314</sub> (MeO <sub>2</sub> CC <sub>10</sub> S) <sub>59</sub> (1) <sub>15</sub> (1-DMAD) <sub>34</sub>	69
1(edge)-C <sub>12</sub> MPC	Au <sub>314</sub> (C <sub>12</sub> S) <sub>71</sub> (1) <sub>37</sub> <sup>d</sup>	Au <sub>314</sub> (C <sub>12</sub> S) <sub>71</sub> (1) <sub>5</sub> (1-DMAD) <sub>32</sub>	85 ± 3
1(terrace)-C <sub>12</sub> MPC	Au <sub>314</sub> (C <sub>12</sub> S) <sub>90</sub> (1) <sub>18</sub> <sup>d</sup>	Au <sub>314</sub> (C <sub>12</sub> S) <sub>90</sub> (1) <sub>11</sub> (1-DMAD) <sub>7</sub>	36 ± 2

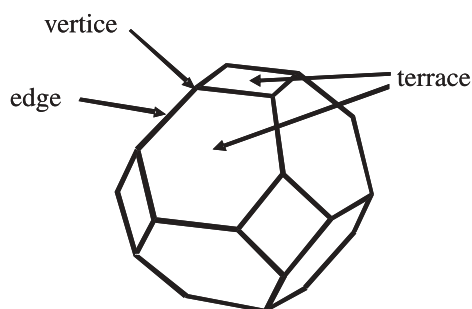
<sup>a</sup>For example, 1-C<sub>12</sub>MPC represents 1 place exchanged onto an original dodecanethiolate MPC.

<sup>b</sup>Determined via ratio integrations for resonances attributed to 1 (7.85 ppm) and 1-DMAD (7.6–7.5 ppm) in the <sup>1</sup>H NMR spectrum, uncertainty is ±5%.

<sup>c</sup>Conversion determined as (the number of 1-DMAD ligands generated)/(number of 1 ligands on starting MPC).

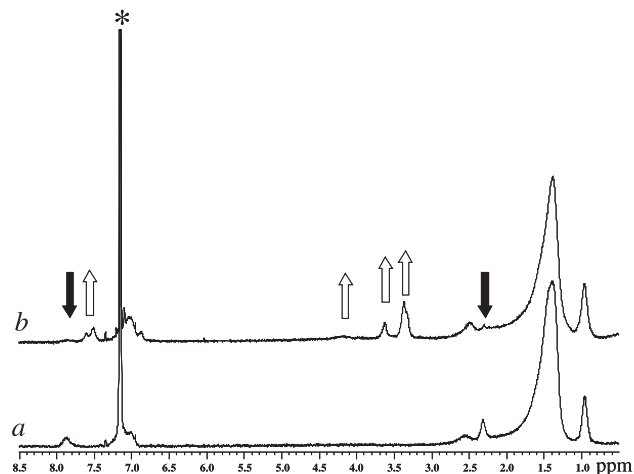
<sup>d</sup>Determined via ratio of integrations for the mixed disulfides generated upon I<sub>2</sub> decomposition of the MPC; uncertainty is ±5%.

<sup>e</sup>Determined via ratio of integrations for the substrates on the actual MPC in solution; uncertainty is ±5%.

**Fig. 4.** A cartoon representation of the MPC core and the assignments of the edge, vertex, and terrace sites.

Selectively populating the terrace with 1 is not as straightforward as populating the edge and vertex sites. The procedure involves initial preparation 1-C<sub>12</sub>MPC in a place-exchange reaction carried out over 5 days. This should populate the terrace, edge, and vertex sites with 1. The resulting MPC (with a stoichiometry of Au<sub>314</sub>(C<sub>12</sub>S)<sub>50</sub>(1)<sub>58</sub>) is then subjected to a subsequent place-exchange reaction in the presence of an excess of dodecanethiol (C<sub>12</sub>SH) for 1 h, which should populate predominantly the edge and vertex sites with dodecanethiol and displace any 1 positioned there. Conveniently, any 1 on the terrace should be trapped, allowing for the study of the reaction between its photodieneol and DMAD. The stoichiometry of the resulting MPC was determined as for the other MPCs and found to be Au<sub>314</sub>(C<sub>12</sub>S)<sub>90</sub>(1)<sub>18</sub> and will be referred to as 1(terrace)-C<sub>12</sub>MPC, where 1(terrace) implies that 1 is predominantly at the terrace and the dilutant chain is C<sub>12</sub>S. Upon irradiation of 1(terrace)-C<sub>12</sub>MPC in the presence of a three-times molar excess of DMAD, similar spectral changes were observed as for the previous MPCs, and the final stoichiometry of the MPC was Au<sub>314</sub>(C<sub>12</sub>S)<sub>90</sub>(1)<sub>11</sub>(1-DMAD)<sub>7</sub>, which translates to a 36 ± 2% conversion to the Diels–Alder adduct based on two irradiations (Fig. 6). This conversion is much lower than that for the MPCs containing 1 at the edge and vertex positions, suggesting that the reactivity on the MPC surface is position dependent.

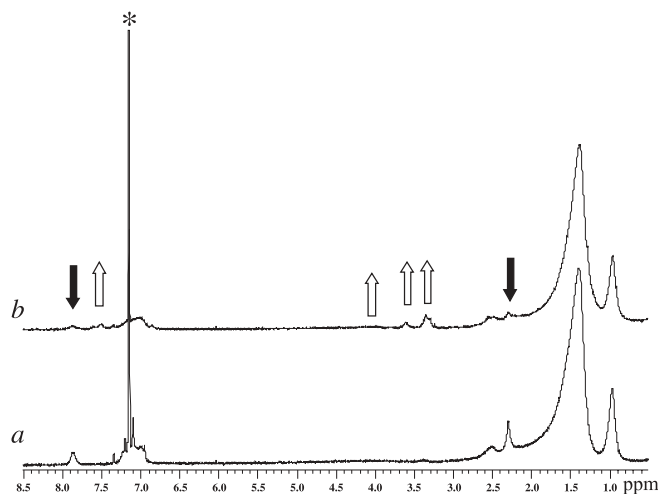
It is reasonable to assume that the edge and vertex sites, which may provide more room for a bimolecular reaction to occur based on the highly faceted shape of the MPC core (Fig. 4), are the positions on the MPC surface where the Diels–Alder reaction is occurring more efficiently. The idea of the edge and vertex sites anchoring substrates with less

**Fig. 5.** The irradiation of Au<sub>314</sub>(C<sub>12</sub>S)<sub>71</sub>(1)<sub>37</sub> (where 1 is positioned predominantly at the edge and vertex sites on the MPC surface) in benzene-*d*<sub>6</sub> (\*) before irradiation (a) and after an irradiation period for 96 h in the presence of a 3-times molar excess of DMAD (b). The filled arrows indicate the decrease in intensity for the resonances associated with Au<sub>314</sub>(C<sub>12</sub>S)<sub>71</sub>(1)<sub>37</sub> while the hollow arrows indicate an increase in the resonances associated with the product, namely Au<sub>314</sub>(C<sub>12</sub>S)<sub>71</sub>(1)<sub>5</sub>(1-DMAD)<sub>32</sub>. Note: the DMAD was washed away before the <sup>1</sup>H NMR spectrum was acquired for (b).

order has been reported recently through an investigation that described how intracuster hydrogen bonding decreases the rate of cyanide-induced MPC decomposition (41), presumably because the highly faceted gold core prohibits effective intracuster chain interactions directly at the edge and vertex sites in the absence of substrates capable of hydrogen bonding. Our own work also suggests that mobility constraints imposed by aryl ketones anchored to terrace sites on MPCs prevent the unimolecular Norrish–Yang Type II reaction from occurring, whereas the reaction occurs more readily at the edge and vertex sites (23, 24). Also of note is a study involving the S<sub>N</sub>2 reaction of amines and MPC-bound terminal bromides (40). The authors found the S<sub>N</sub>2 reaction proceeds quite efficiently (at least 80% completion) regardless of the bulkiness of the amine. Though the product conversions for this simple reaction are higher than we report, the authors employed MPCs smaller (~140 gold atoms in the MPC core) than those we used. The smaller MPC



**Fig. 6.** The irradiation of  $\text{Au}_{314}(\text{C}_{12}\text{S})_{90}(\mathbf{1})_{18}$  (where  $\mathbf{1}$  is positioned predominantly at terrace sites on the MPC surface) in benzene- $d_6$  (\*) before irradiation (a) and after an irradiation period for 96 h in the presence of a 3-times molar excess of DMAD (b). The filled arrows indicate the decrease in intensity for the resonances associated with  $\text{Au}_{314}(\text{C}_{12}\text{S})_{90}(\mathbf{1})_{18}$  while the hollow arrows indicate an increase in the resonances associated with the product, namely  $\text{Au}_{314}(\text{C}_{12}\text{S})_{71}(\mathbf{1})_{11}(\mathbf{1}\text{-DMAD})_7$ . Note: the DMAD was washed away before the  $^1\text{H}$  NMR spectrum was acquired for (b).



cores may result in more disordered monolayers. There have also been studies carried out on 2-D self-assembled monolayers (SAMs) suggesting that if edge sites are produced within the monolayer, the substrates at the edge sites are much more mobile and floppy, as evidenced by their ability to “trap” embedded groups (42, 43).

If the conversion were related to the number of edge and vertex sites on an MPC one may assume that it would be directly related to the percentage of edge and vertex sites on the MPC itself. Our results indicate that the conversion to Diels–Alder adduct is ~65%. A rough calculation<sup>4</sup> indicates that, assuming equal distribution over all sites on the MPC, 41% of  $\mathbf{1}$  should reside at the edge and vertex sites. If the substrates at the edge and vertex sites and one atom row adjacent to the edge and vertex sites were able to undergo the reaction, this would account for 86% of the sites on the MPC surface. Because the conversion lies somewhere between these numbers, we offer the following explanation: there is the possibility that there is not an equal distribution of  $\mathbf{1}$  over the entire surface of the MPC and slightly more  $\mathbf{1}$  is concentrated at the edge and vertex sites. If this were true, it could explain why the conversion to Diels–Alder adduct is higher than the percentage of edge and vertex sites on the MPC surface. It is also possible that some of the  $\mathbf{1}$  directly adjacent to the edge and vertex is capable of reacting, which would increase the conversion as well. We prefer the former explanation, based on the mechanism of place-exchange. At the beginning of the place-exchange reaction there is much more  $\mathbf{1}$  than dodecanethiol in solution. The

edge and vertex sites are populated with  $\mathbf{1}$  quickly, resulting in the displacement of dodecanethiol into solution. Consequently, both dodecanethiol and  $\mathbf{1}$  will be in solution, but excess  $\mathbf{1}$  is employed in the place-exchange reaction, so there will always be a higher concentration of  $\mathbf{1}$  in solution. Because population of the MPC during the place-exchange reaction is dependent on the concentration of thiol in solution, and because the edge and vertex sites are populated most easily, they may be populated to a greater extent with  $\mathbf{1}$ . This could account for the conversion of the  $\text{Au}_{314}(\text{C}_{12}\text{S})_{50}(\mathbf{1})_{58}$ ,  $\text{Au}_{314}(\text{C}_{18}\text{S})_{74}(\mathbf{1})_{34}$ , and  $\text{Au}_{314}(\text{MeO}_2\text{CC}_{10})_{59}(\mathbf{1})_{49}$  to  $\text{Au}_{314}(\text{C}_{12}\text{S})_{50}(\mathbf{1})_{26}(\text{DMAD-}\mathbf{1})_{32}$  ( $64 \pm 2\%$  conversion to Diels–Alder adduct),  $\text{Au}_{314}(\text{C}_{18}\text{S})_{74}(\mathbf{1})_{13}(\text{DMAD-}\mathbf{1})_{21}$  ( $62 \pm 2\%$ ), and  $\text{Au}_{314}(\text{MeO}_2\text{CC}_{10})_{59}(\mathbf{1})_{15}(\mathbf{1}\text{-DMAD})_{34}$  (69%), respectively, being slightly higher than expected.

Also of note are the results of irradiations of  $\mathbf{1}\text{-C}_{12}$  and  $\mathbf{1}\text{-C}_{18}$  MPCs in the presence of DMFr and DMM. The spectral changes observed in the  $^1\text{H}$  NMR spectra are consistent with the generation of the Diels–Alder adducts, with the final stoichiometry of the photolysed MPCs being  $\text{Au}_{314}(\text{C}_{12}\text{S})_{50}(\mathbf{1})_{21}(\mathbf{1}\text{-DMFr})_{37}$  (64% conversion),  $\text{Au}_{314}(\text{C}_{18}\text{S})_{74}(\mathbf{1})_{13}(\mathbf{1}\text{-DMFr})_{21}$  (63% conversion),  $\text{Au}_{314}(\text{C}_{12}\text{S})_{50}(\mathbf{1})_{22}(\mathbf{1}\text{-DMM})_{36}$  (61% conversion), and  $\text{Au}_{314}(\text{C}_{18}\text{S})_{74}(\mathbf{1})_{15}(\mathbf{1}\text{-DMM})_{19}$  (58% conversion), respectively. The average conversion for these reactions is  $62 \pm 4\%$ , which is, within experimental error, what we would expect based on the results of the analogous reaction with DMAD. These reactions show a variety of dienophiles can be employed in this reaction, and we are working on exploiting this aspect of the chemistry. The spectral data for the DMFr- and DMM-modified MPCs are provided in the supplemental information.

## Experimental

### Commercial solvents and reagents used

The compounds dodecanethiol, octadecanethiol, hydrogen tetrachloroaurate(III), tetraoctylammonium bromide, sodium borohydride, 1,11-dibromoundecane, 1.8 M phenyl lithium in cyclohexane-ether, *o*-toluoyl chloride, potassium thioacetate, dimethyl acetylenedicarboxylate, dimethyl maleate, and dimethyl fumarate were all purchased from Aldrich and used as received. Potassium carbonate (Caledon), aluminum chloride (BHD), benzene- $d_6$  (Cambridge Isotope Laboratories), and iodine (BDH) were also used as received. Acetone, dichloromethane, benzene, toluene, methanol, diethyl ether, and hexanes were purchased from either Caledon or EM Science and used as received. Tetrahydrofuran was dried by distillation from sodium/benzophenone. Ethanol (both anhydrous and 95%) was purchased from Commercial Alcohols Inc. Silica gel was purchased from EM Science.

### General instrumentation

$^1\text{H}$  NMR spectra were recorded on a Varian Mercury 400 (400.087 MHz) spectrometer in either deuteriochloroform or benzene- $d_6$  solutions and are reported in parts per million (ppm) with respect to chloroform or benzene peaks at 7.26 ppm or 7.15 ppm, respectively.  $^{13}\text{C}$  NMR spectra were

<sup>4</sup>Our calculation assumes equal distribution of the substrate over the entire surface and involves dividing the number of atoms directly at edge and vertex sites and by the total number of surface atoms (41%) or dividing the number of atoms at the edge and vertex sites and those directly adjacent to the edge and vertex sites by the total number of surface atoms (86%).



recorded on a Varian Mercury 400 (100.602 MHz) spectrometer in either deuteriochloroform or benzene- $d_6$  solution and are reported in parts per million with respect to chloroform or benzene peaks at 77.0 or 128.02 ppm. UV-vis absorption spectra were recorded on a Cary 100Bio spectrometer in spectrometry-grade benzene. Mass spectra and exact masses were recorded on a MAT 8200 Finnigan high resolution mass spectrometer; the latter employed a mass of 12.0000 for carbon. IR spectra were recorded on a Bomem MB-Series or a Bruker Vector 33 spectrometer using a dropcasting technique on NaCl plates and are reported in wavenumbers ( $\text{cm}^{-1}$ ).

### Steady-state photolysis experiments

Steady-state irradiation experiments were carried out in septa-sealed Pyrex NMR tubes using benzene- $d_6$  as solvent or 5 mL Pyrex photolysis cells using reagent-grade benzene as solvent. The light source was a Rayonet photochemical reactor fitted with bulbs that emitted UV light in the 300–400 nm range, with a maximum at 350 nm and a merry-go-round apparatus to ensure an equal amount of radiation was received. In a typical procedure, ~15–20 mg of MPC was weighed out and placed under vacuum to ensure all solvent was removed. The MPC was then dissolved in ~0.5 mL benzene- $d_6$ , degassed for 15 min with either argon or nitrogen gas, and sealed with a rubber septum and Parafilm. An  $^1\text{H}$  NMR spectrum was recorded prior to the addition of dienophile and at intermittent reaction times until the reaction was complete. The temperature of the solutions was typically  $38 \pm 2^\circ\text{C}$ .

### [4-(11-Mercaptoundecyl)phenyl](2-methylphenyl)methanone (1)

To a solution of 1,11-dibromoundecane (5.2 g, 16.5 mmol) in dry THF (25 mL) was added phenyl lithium (3.7 mL of a 1.8 M solution, 6.7 mmol) dropwise, generating 11-phenyl-1-bromoundecane in situ. After aqueous workup and drying, the 11-phenylbromoundecane – 1,11-dibromoundecane mixture was redissolved with 25 mL dichloromethane and cooled in a salted ice bath. When the flask was cooled, *o*-toluoyl chloride (1.12 g, 7.26 mmol) and aluminum chloride (1.01 g, 7.59 mmol) were added, and the mixture was stirred for 4 h, maintaining a temperature of  $0^\circ\text{C}$ . Upon aqueous workup and drying with  $\text{MgSO}_4$ , the resulting [4-(11-bromoundecyl)phenyl](2-methylphenyl)methanone was purified via gradient column chromatography on silica gel, beginning with 10:1 hexanes:dichloromethane to elute the unreacted dibromoundecane and ending with 2:1 hexanes:dichloromethane which eluted [4-(11-bromoundecyl)phenyl](2-methylphenyl)methanone (0.90 g) as a clear colorless oil. The bromide was converted to the thioacetate through a reaction with potassium thioacetate in acetone, quantitatively generating [4-(11-acetylsulfanylundecyl)phenyl](2-methylphenyl)methanone. The thioacetate (0.72 g, 1.7 mmol) was then transferred to a 100-mL round-bottom flask fitted with a reflux condenser, dissolved in absolute ethanol, and the solution degassed with argon for 15 min after which time the solution was charged with potassium carbonate (0.24 g, 2.07 mmol) and heated to reflux for 3 h. The ethanol was removed via rotary evaporation, and the resulting liquid was redissolved in dichloromethane and washed with saturated

ammonium chloride (30 mL), washed with  $3 \times 30$  mL of distilled water, and dried over  $\text{MgSO}_4$  for 20 min. Concentration yielded a yellowish oil that was purified by column chromatography using silica gel and 3:1 dichloromethane:hexanes as eluant; a colorless oil (0.5 g, 1.30 mmol) was produced in 76% yield. UV-vis (benzene) (nm) ( $\epsilon$  ( $\text{M}^{-1}\text{cm}^{-1}$ )): 339 ( $9.790 \times 10$ ), 277 ( $7.832 \times 10^3$ ). IR ( $\text{cm}^{-1}$ ) (dropcast on NaCl): 2925, 2853, 1661, 1604, 1267.  $^1\text{H}$  NMR (400 MHz,  $\text{CDCl}_3$ ) (ppm)  $\delta$ : 7.73 (d,  $J = 7.8$  Hz, 2H), 7.38 (m, H), 7.28 (m, 5H), 2.67 (t,  $J = 7.8$  Hz, 2H), 2.52 (quartet,  $J = 7.0$  Hz, 2H), 2.33 (s, 3H), 1.61 (m, 4H), 1.44–1.19 (m, 15H (includes SH proton)).  $^{13}\text{C}$  NMR (400 MHz,  $\text{CDCl}_3$ ) (ppm)  $\delta$ : 198.36, 148.99, 138.90, 136.45, 135.24, 130.82, 130.29, 129.94, 128.51, 128.28, 125.08, 36.06, 34.05, 31.16, 29.51, 29.48, 29.45, 29.40, 29.25, 29.02, 28.34, 24.63, 19.91. EI-MS  $m/z$  (%): 382 (20), 364 (6), 223 (8), 195 (100), 119 (23), 84 (20), 49 (33). Exact mass calcd.: 382.2330; found: 382.2329.

### [4-(11-Dodecyl)phenyl](2-methylphenyl)methanone (2)

To a flame-dried, 10-mL round-bottom flask fitted with an argon inlet and condenser was added aluminum chloride (1.8 g, 13.5 mmol), dichloromethane (7 mL), and phenyldodecane (2.5 g, 10.0 mmol), and the mixture was cooled in a salted ice bath. A solution containing *o*-toluoyl chloride (1.7 g, 11.0 mmol) in 2 mL of dichloromethane was then added to the mixture over 1 min. This mixture was left stirring for 3 h while warming to room temperature. The reaction was then quenched by pouring the entire contents of the flask into a beaker containing 40 mL of distilled water cooled in an ice bath. The organic layer was diluted with 20 mL dichloromethane, washed with  $4 \times 50$  mL of distilled water, and dried over  $\text{MgSO}_4$  for 30 min. Concentration of the dried organic phase yielded a yellow oil, which was purified by column chromatography using silica gel and 1:1 hexanes:dichloromethane as eluant, generating a clear, colorless liquid (1.83 g, 5.02 mmol) in 50% yield. IR ( $\text{cm}^{-1}$ ) (dropcast on NaCl): 2926, 2853, 1662, 1605, 1264.  $^1\text{H}$  NMR (400 MHz,  $\text{CDCl}_3$ ) (ppm)  $\delta$ : 7.72 (d,  $J = 7.8$  Hz, 2H), 7.37 (t, H), 7.30–7.21 (m, 5H), 2.65 (t,  $J = 2\text{H}$ ), 2.31 (s, 3H), 1.62 (quintet, 2H), 1.37–1.21 (m, 18H), 0.86 (t, 3H).  $^1\text{H}$  NMR (400 MHz,  $\text{C}_6\text{D}_6$ ) (ppm)  $\delta$ : 7.84 (d, 2H  $J = 8.6$  Hz), 7.20 (t,  $J = 7.8$  Hz, H), 7.07 (m, H), 7.01–6.89 (m, 4H), 2.40 (t,  $J = 7.8$  Hz, 2H), 2.28 (s, 3H), 1.45 (broad quintet, 2H), 1.36–1.16 (m, 18H), 0.91 (t,  $J = 7.0$  Hz, 3H).  $^{13}\text{C}$  NMR (400 MHz,  $\text{CDCl}_3$ ) (ppm)  $\delta$ : 198.36, 149.04, 138.95, 136.48, 135.26, 130.85, 130.30, 129.95, 128.49, 128.25, 125.09, 36.04, 31.90, 31.11, 29.64, 29.61, 29.54, 29.45, 29.33, 29.28, 22.67, 14.11. EI-MS  $m/z$  (%): 364 (3.5), 195 (100), 119 (9), 91 (8). Exact mass calcd.: 364.2766; found: 364.2765.

### Dodecanethiolate MPC ( $\text{C}_{12}\text{MPC}$ )

Following the procedures of Brust et al. (34) and Murray and co-workers (35): to a 250-mL round-bottom flask was added hydrogen tetrachloroaurate(III) trihydrate (0.30 g, 0.768 mmol) dissolved in 28 mL distilled water (resulting in a bright yellow solution) and tetraoctylammonium bromide (2.01 g, 0.369 mmol) dissolved in 70 mL toluene (a clear and colorless solution). The contents were rapidly stirred for 30 min at room temperature to facilitate the phase transfer of



the hydrogen tetrachloroaurate(III) trihydrate into the toluene layer, which resulted in the organic layer turning a dark orange color and the aqueous layer becoming clear and colorless. After phase transfer, the aqueous layer was removed and dodecanethiol (0.15 g, 0.18 mL, 0.762 mmol) was added via a volumetric pipet to the solution, which was allowed to stir at room temperature while a fresh solution of sodium borohydride (0.33 g, 8.68 mmol) in 18 mL water was prepared. The aqueous sodium borohydride was added to the toluene solution over ~5 s and the mixture was allowed to stir at room temperature overnight (~18 h). The organic layer was washed with 3 × 20 mL distilled water, dried with  $\text{MgSO}_4$ , and concentrated. The concentrated MPC was then suspended in 200 mL of 95% ethanol and placed in the freezer overnight, during which time the  $\text{C}_{12}\text{MPC}$  precipitated from solution. The ethanol was then decanted and the MPC was dissolved in benzene and concentrated, resulting in the formation of a film in the round-bottom flask. This film was washed repeatedly with 10 × 15 mL of 95% ethanol warmed to 40°C. The MPC was pure, according to the  $^1\text{H}$  NMR spectrum, which showed no signs of dodecanethiol, dodecyl disulfide, or tetraoctylammonium bromide.

#### Octadecanethiolate MPC ( $\text{C}_{18}\text{MPC}$ )

The octadecanethiolate MPC was synthesized as described above for the dodecanethiolate MPC. The procedure involved 0.20 g (0.51 mmol) hydrogen tetrachloroaurate, 1.32 g (2.41 mmol) tetraoctylammonium bromide, 0.20 g (5.59 mmol) sodium borohydride, and 0.146 g (0.51 mmol) octadecanethiol.

#### 11-Mercaptoundecanoic acid methyl ester MPC ( $\text{MeO}_2\text{-CC}_{10}\text{MPC}$ )

The MPC was synthesized as described above for the dodecanethiolate MPC. The procedure involved 0.30 g (0.76 mmol) hydrogen tetrachloroaurate, 2.04 g (3.42 mmol) tetraoctylammonium bromide, 0.32 g (8.36 mmol) sodium borohydride, and 0.177 g (0.76 mmol) 11-mercaptoundecanoic acid methyl ester. The MPC was purified by washing with hexanes.

#### [4-(11-Mercaptoundecyl)phenyl](2-methylphenyl)methanone – dodecanethiolate MPC ( $1\text{-C}_{12}\text{MPC}$ )

Following the procedure outlined by Murray and co-workers (36, 37),  $\text{C}_{12}\text{MPC}$  (0.11 g, 0.136 mmol of dodecanethiol) was dissolved in 34 mL toluene in a 100-mL round-bottom flask fitted with an argon inlet. Excess [4-(11-mercaptoundecyl)phenyl](2-methylphenyl)methanone (0.0629 g, 0.163 mmol) was then added to the flask and the mixture was stirred for 4–5 days under argon. After 4–5 days the solution was concentrated and the mixed MPC was washed with warm (35–40°C) 95% ethanol to remove excess [4-(11-mercaptoundecyl)phenyl](2-methylphenyl)-methanone and dodecanethiol. The  $^1\text{H}$  NMR (400 MHz,  $\text{C}_6\text{D}_6$ ) spectra indicated that the [4-(11-mercaptoundecyl)-phenyl](2-methylphenyl)methanone was incorporated onto the MPC, and iodine-induced decomposition indicated that the MPC had a composition of  $\text{Au}_{314}(\text{C}_{12}\text{S})_{50}(\mathbf{1})_{58}$ . Population of the edge and vertex sites with **1** was accomplished using the same conditions but with a decreased time period over which the exchange reaction took place (1 h) (36). The resulting MPC

had a stoichiometry of  $\text{Au}_{314}(\text{C}_{12}\text{S})_{71}(\mathbf{1})_{37}$ . Population of the terrace with **1** was accomplished by stirring the  $\text{Au}_{314}(\text{C}_{12}\text{S})_{50}(\mathbf{1})_{58}$  (0.050 g) (prepared via the 5 day place-exchange reaction described above) dissolved in 10 mL toluene with an excess of dodecanethiol (0.10 g) under a nitrogen atmosphere for 1 h. The resulting MPC had a stoichiometry of  $\text{Au}_{314}(\text{C}_{12}\text{S})_{90}(\mathbf{1})_{18}$ .

#### [4-(11-Mercaptoundecyl)phenyl](2-methylphenyl)methanone – octadecanethiolate MPC ( $1\text{-C}_{18}\text{MPC}$ )

Following the procedure outlined above for  $\text{Au}_{314}(\text{SC}_{12})_{50}(\mathbf{1})_{58}$ ,  $\text{C}_{18}\text{MPC}$  (0.05 g, 0.044 mmol octadecanethiolate) was dissolved in 15 mL toluene in a 100-mL round-bottom flask fitted with an argon inlet, to which [4-(11-mercaptoundecyl)phenyl](2-methylphenyl)-methanone (0.0226 g, 0.059 mmol) dissolved in ~3 mL toluene was added. After stirring for 4 days, the toluene was removed by rotary evaporation, and the mixed MPC was washed with a warmed (35–40°C) 6:1 ethanol:toluene solution to remove excess [4-(11-mercaptoundecyl)phenyl](2-methylphenyl)methanone and octadecanethiol. The resulting MPC had a composition of  $\text{Au}_{314}(\text{C}_{18}\text{S})_{74}(\mathbf{1})_{34}$ , as determined via iodine decomposition.

#### [4-(11-Mercaptoundecyl)phenyl](2-methylphenyl)methanone – 11-mercaptoundecanoic acid methyl ester MPC ( $1\text{-MeO}_2\text{CC}_{10}\text{MPC}$ )

Following the procedure outlined above for  $\text{Au}_{314}(\text{SC}_{12})_{50}(\mathbf{1})_{58}$ ,  $\text{MeO}_2\text{CC}_{10}\text{MPC}$  (0.15 g, 0.16 mmol 11-mercaptoundecanoic acid methyl ester) was dissolved in 40 mL toluene in a 100-mL round-bottom flask fitted with an argon inlet, to which [4-(11-mercaptoundecyl)phenyl](2-methylphenyl)methanone (0.073 g, 0.19 mmol) was added. After stirring for 4 days, the toluene was removed by rotary evaporation, and the mixed MPC was washed with ethanol to remove excess [4-(11-mercaptoundecyl)phenyl](2-methylphenyl)methanone and 11-mercaptoundecanoic acid methyl ester. The resulting MPC had a composition of  $\text{Au}_{314}(\text{MeO}_2\text{CC}_{10}\text{S})_{59}(\mathbf{1})_{49}$ , as determined by direct integration of the aromatic resonances at 7.85 ppm (resonances from protons  $\alpha$  to carbonyl) and 3.42 ppm (resonances from protons of the terminal ester) in benzene- $d_6$  solution.

#### MPC decomposition procedure

As reported by Murray and co-workers (40), approximately 10 mg of mixed MPC was placed in a 10-mL round-bottom flask and dissolved in 2 mL dichloromethane. A small crystal of iodine (~1 mg) was added, and the solution was stirred until the originally brown, opaque solution became clear and a light purple colour with a black precipitate (20 min). The dichloromethane was rotary evaporated, and 0.5 mL deuteriochloroform was added to redissolve the resulting mixed disulfide. This was placed in an NMR tube by first passing it through a pipette equipped with a Kimwipe filter to remove the precipitate. The sample was then analyzed by  $^1\text{H}$  NMR spectroscopy, where the integrations for the appropriate resonance signals were compared.

#### Generation of 2-methyl-4'-(dodecyl)benzophenone Diels-Alder adducts

In a typical procedure, [4-(11-dodecyl)phenyl](2-methylphenyl)methanone (**2**) (0.1 g, 0.41 mmol) was dissolved in



5 mL of benzene, transferred to a 5 mL Pyrex photolysis cell sealed with a septum, and the solution was degassed with argon for 20 min. The dienophile (namely dimethyl acetylenedicarboxylate, dimethyl fumarate, or dimethyl maleate) (0.41 mmol) was then added to the degassed solution via syringe, and the mixture was irradiated for 12 h. The product was purified via column chromatography, employing 1% methanol in dichloromethane as eluant.

### 2-DMAD Diels–Alder adduct

IR (cm<sup>-1</sup>) (dropcast on NaCl): 3474, 2924, 2853, 1732. <sup>1</sup>H NMR (400 MHz, C<sub>6</sub>D<sub>6</sub>) (ppm) δ: 7.55 (d, *J* = 8.6 Hz, 1H), 7.49 (d, *J* = 8.6 Hz, 2H), 6.9–7.05 (m, 4H), 6.82 (d, *J* = 7.8 Hz, 1H), 4.26 (s, 1H), 2.61 (s, 2H), 3.34 (s, 3H), 3.28 (s, 3H), 2.95 (t, *J* = 5.5 Hz, 2H), 2.46 (t, *J* = 7.0 Hz, 2H), 1.38–1.60 (m, 4H), 1.0–1.3 (br, 14H) 0.85 (t, *J* = 7.0 Hz, 3H). <sup>13</sup>C NMR (400 MHz, C<sub>6</sub>D<sub>6</sub>) (ppm) δ: 168.06, 166.66, 143.40, 142.09, 141.84, 140.41, 130.78, 128.51, 127.50, 127.36, 126.13, 74.67, 52.17, 36.12, 32.59, 32.01, 31.20, 30.39, 30.36, 30.28, 30.19, 30.09, 30.00, 23.40, 14.69. EI-MS *m/z* (%): 554 (45), 552 (42), 303 (6), 223 (8), 195 (100), 119 (23), 84 (20), 49 (33). Exact mass calcd.: 506.3032; found: 506.3028.

### Conclusions

The Diels–Alder reaction of the photodienol generated from **1** in the MPC environment is shown to proceed efficiently, with similar extents of reaction regardless of the local environment surrounding the reactive group. In addition, this reaction exhibited evidence suggesting site-dependant reactivity. It appears as though there are properties inherent to substrates bound at specific sites on the MPC core that render them more or less reactive toward the Diels–Alder reaction. This is evidenced by the general trend observed with respect to the reactivity of **1** on the MPC surface: in the comparison of the reactivity of the multi-site-populated MPC — where all of the sites on the MPC are populated (**1**-C<sub>12</sub>MPC) — placing **1** predominantly at terrace sites (**1**(terrace)-C<sub>12</sub>MPC) results in significantly lower conversions, while placing **1** predominantly at edge and vertice sites (**1**(edge)-C<sub>12</sub>MPC) results in significantly higher conversions. In fact, quantitatively speaking, the same amount of **1** reacts efficiently when the entire MPC is populated (**1**-C<sub>12</sub>MPC) as when the majority of **1** is at the edge and vertice sites (**1**(edge)-C<sub>12</sub>MPC); the number of **1** converted to **1**-DMAD is 32 in each case. Qualitatively, we attribute a more hindered environment within the terrace of the MPC as the main cause of the lowered extent of conversion. The most accessible sites — those at the edge and vertice — on the MPCs can undergo this rather complex bimolecular reaction more efficiently. Those within the terrace (where the monolayer is very well packed and more accurately mimics that of a 2-D SAM) are more hindered and less likely to undergo the rather complex bimolecular reaction. It is difficult to predict if the decreased ability for the terrace-bound dienol to react is due to steric constraints that do not allow the dienophile to reach the photodienol or if the dienophile is able to reach the dienol but cannot achieve the geometry required for the reaction to occur. The inability for these bimolecular reactions to reach completion is similar to what

we have found for unimolecular reactions carried out on identical MPC cores (23, 24). However, the reasons for the lowered extents of reaction are not expected to be the same. Mobility constraints play a definitive role in the efficiency of unimolecular reactions carried out on MPCs, but in this investigation, which involves bimolecular reactivity, sterics and the ability to adopt specific orientations play key roles in the efficiency of the reaction.

It is intriguing to propose that there are differences in reactivity and dynamics associated with the distinct sites on the MPC surface. We are currently investigating the effect that increasing and decreasing the size of the MPC core has on the extent of reaction, because the size of the terrace can be easily manipulated by increasing or decreasing the size of the metal core. This study will provide more insight on the physical properties inherent to substrates when they are anchored to specific sites on these highly faceted gold cores.

### Acknowledgments

Financial support for this research from the Natural Sciences and Engineering Research Council of Canada (NSERC), the Academic Development Fund (UWO), the Canadian Foundation for Innovation, and the Ontario Research and Development Challenge Fund is gratefully acknowledged. MSW thanks the Government of Ontario for a Premier's Research Excellence Award, and AJK thanks NSERC for a graduate scholarship. We also thank Dr. Robert Donkers for helpful suggestions.

### References

1. A.C. Weedon. In *The chemistry of enols*. Edited by Z. Rappoport. John Wiley and Sons, Toronto, Ont., Canada. 1990. p. 615.
2. R.M. Wilson. In *Organic photochemistry*. Edited by A. Padwa. Marcel Dekker Inc., New York. 1985. p. 339.
3. N.C. Yang and C. Rivas. *J. Am. Chem. Soc.* **83**, 2213 (1961).
4. G.J. Jocsys and M.S. Workentin. *J. Chem. Soc., Chem. Commun.* 839 (1999).
5. J.L. Pitters, M. Kovar, K. Griffiths, P.R. Norton, and M.S. Workentin. *Angew. Chem., Int. Ed.* **39**, 2144 (2000).
6. L.F. Rozsnyai and M.S. Wrighton. *J. Am. Chem. Soc.* **116**, 5993 (1994).
7. E.W. Wollman, D. Kang, C.D. Frisbie, I.M. Lorkovic, and M.S. Wrighton. *J. Am. Chem. Soc.* **116**, 4395 (1994).
8. M.O. Wolf and M.A. Fox. *J. Am. Chem. Soc.* **117**, 1845 (1995).
9. M.O. Wolf and M.A. Fox. *Langmuir*, **12**, 955 (1996).
10. I. Willner, A. Doron, and E. Katz. *J. Phys. Org. Chem.* **11**, 546 (1998).
11. T. Kim, K.C. Chan, and R.M. Crooks. *J. Am. Chem. Soc.* **119**, 189 (1997).
12. W. Li, V. Lynch, H. Thompson, and M.A. Fox. *J. Am. Chem. Soc.* **119**, 7211 (1997).
13. M.A. Fox and M.D. Wooten. *Langmuir*, **13**, 7099 (1997).
14. S. Sortino, S. Petralia, G. Compagnini, S. Conoci, and G. Condorelli. *Angew. Chem. Int. Ed.* **41**, 1914 (2002).
15. O. Prucker, C.A. Naumann, J. Rühe, W. Knoll, and C.W. Frank. *J. Am. Chem. Soc.* **121**, 8766 (1999).
16. J. Zhang, J.K. Whitesell, and M.A. Fox. *Chem. Mater.* **13**, 2323 (2001).
17. J. Hu, J. Zhang, F. Liu, K. Kittredge, J.K. Whitesell, and M.A. Fox. *J. Am. Chem. Soc.* **123**, 1464 (2001).



18. H. Imahori, M. Arimura, T. Hanada, Y. Nishimura, I. Yamazaki, Y. Sakata, and S. Fukuzumi. *J. Am. Chem. Soc.* **123**, 335 (2001).
19. T. Wang, D. Zhang, W. Xu, J. Yang, R. Han, and D. Zhu. *Langmuir*, **18**, 1840 (2002).
20. A. Aguila and R.W. Murray. *Langmuir*, **16**, 5949 (2000).
21. A.C. Templeton, W.P. Wuelfing, and R.W. Murray. *Acc. Chem. Res.* **33**, 27 (2000).
22. V. Chechik, R.M. Crooks, and C.J.M. Stirling. *Adv. Mater.* **12**, 1161 (2000).
23. A.J. Kell and M.S. Workentin. *Langmuir*, **17**, 7355 (2001).
24. A.J. Kell, D.L.B. Stringle, and M.S. Workentin, *Org. Lett.* **2**, 3381 (2000).
25. Y. Kwon and M. Mrksich. *J. Am. Chem. Soc.* **124**, 806 (2002).
26. M.N. Yousaf, E.W.L. Chan, and M. Mrksich. *Angew. Chem. Int. Ed.* **39**, 1943 (2000).
27. M.N. Yousaf and M. Mrksich. *J. Am. Chem. Soc.* **121**, 4286 (1999).
28. E.W.L. Chan, M.N. Yousaf, and M. Mrksich. *J. Phys. Chem. A*, **104**, 9315 (2000).
29. A. Badia, R.B. Lennox, and L. Reven. *Acc. Chem. Res.* **33**, 475 (2000).
30. R.L. Whetten, J.T. Khoury, M.M. Alvarez, S. Murthy, I. Vezmar, Z.L. Wang, P.W. Stephens, C.L. Cleveland, W.D. Luedtke, and U. Landman. *Adv. Mater.* **8**, 428 (1996).
31. M. Pfau, E.W. Sarver, and N.D. Heindel. *Bull. Soc. Chim. Fr.* **1**, 183 (1973).
32. M. Pfau, S. Combrisson, J.E. Rowe, and N.D. Heindel. *Tetrahedron*, **34**, 3459 (1978).
33. E. Block and R. Stevenson. *J. Chem. Soc. Perkin Trans. 1*, 308 (1973).
34. M. Brust, M. Walker, D. Bethell, D.J. Schiffrin, and R.J. Whyman. *J. Chem. Soc., Chem. Commun.* 801 (1994).
35. M.J. Hostetler, J.E. Wingate, C.-J. Zhong, J.E. Harris, R.W. Vachet, M.R. Clark, J.D. Londono, S.J. Green, J.J. Stokes, G.D. Wignall, G.L. Glish, M.D. Porter, N.D. Evans, and R.W. Murray. *Langmuir*, **14**, 17 (1998).
36. Y. Song and R.W. Murray. *J. Am. Chem. Soc.* **124**, 7096 (2002).
37. M.J. Hostetler, A.C. Templeton, and R.W. Murray. *Langmuir*, **15**, 3782 (1999).
38. R.H. Terrill, T.A. Postlethwaite, C.-h. Chen, C.-D. Poon, A. Terzis, A. Chen, J.E. Hutchison, M.R. Clark, G. Wignall, J.D. Londono, R. Superfine, M. Falvo, C.S. Johnson, Jr., E.T. Samulski, and R.W. Murray. *J. Am. Chem. Soc.* **117**, 12 537 (1995).
39. A. Badia, W. Goa, S. Singh, L. Demers, L. Cicca, and L. Reven. *Langmuir*, **12**, 1262 (1996).
40. A.C. Templeton, M.J. Hostetler, C.T. Kraft, and R.W. Murray. *J. Am. Chem. Soc.* **120**, 1906 (1998).
41. R. Paulini, B.L. Frankcamp, and V.M. Rotello. *Langmuir*, **18**, 2368 (2002).
42. W. Fudickar, J. Zimmermann, L. Ruhlmann, J. Schneider, B. Röder, U. Siggel, and J.-H. Fuhrhop. *J. Am. Chem. Soc.* **121**, 9539 (1999).
43. M. Lahav, E. Katz, and I. Willner. *Langmuir*, **17**, 7387 (2001).



# Potentiometric titration of metal ions in methanol

Graham Gibson, Alexei A. Neverov, and R.S. Brown

**Abstract:** The potentiometric titrations of nine lanthanide<sup>III</sup> triflates, Zn<sup>II</sup> and Cu<sup>II</sup> triflate, and the Ni<sup>II</sup>, Co<sup>II</sup>, Mg<sup>II</sup>, and Ti<sup>IV</sup> perchlorates were obtained in methanol to determine the titration constants (defined as the  $s\text{pH}$  at which the  $[\text{OCH}_3^-]/[\text{M}^{x+}]_t$  ratios are 0.5 and 1.5) as well as the apparent  $s\text{p}K_a$  values for deprotonation of the metal-bound solvent molecules. The titrations were performed under various conditions with and without added salts as electrolytes, and the variations in the titration constants are discussed. In selected cases (La<sup>3+</sup>, Zn<sup>2+</sup>) the titration profiles were analyzed using a complex fitting program to obtain information about the species present in solution.

**Key words:** potentiometric titration, methanol,  $s\text{pH}$ , metal ion, lanthanides, apparent  $s\text{p}K_a$ .

**Résumé :** Opérant en solution méthanolique, on a effectué des titrages potentiométriques de neufs triflates de lanthanides<sup>III</sup>, des triflates de Zn<sup>II</sup> et de Cu<sup>II</sup> et des perchlorates de Ni<sup>II</sup>, de Co<sup>II</sup>, de Mg<sup>II</sup> et de Ti<sup>IV</sup> afin de déterminer les constantes de titrage (définies comme le  $s\text{pH}$  auquel les rapports  $[\text{OCH}_3^-]/[\text{M}^{x+}]_t$  sont égaux à 0,5 et 1,5) ainsi que les valeurs apparentes de  $s\text{p}K_a$  pour la déprotonation des molécules de solvant fixées au métal. On a effectué les titrages sous diverses conditions, avec et sans addition de sels comme électrolytes, et on discute des variations dans les constantes de titrage. Dans des cas choisis (La<sup>3+</sup>, Zn<sup>2+</sup>) on a analysé les profils de titrage à l'aide d'un programme complexe d'ajustement des données afin d'en tirer de l'information sur les espèces présentes en solution.

**Mots clés :** titrage potentiométrique, méthanol,  $s\text{pH}$ , ion métallique, lanthanides,  $s\text{p}K_a$  apparent.

[Traduit par la Rédaction]

## Introduction

Recently we reported mechanistic aspects of di- and trivalent metal ion catalysis of the methanolysis of activated amides like acetylimidazole (*1a*) and  $\beta$ -lactams (*1b*), phosphate diesters (*1c*, *1g*), and carbon-based esters (*1d*, *1f*). Certain metal ions, notably La<sup>3+</sup> and Eu<sup>3+</sup>, give impressive rate enhancements for methanolysis of the substrates, in some cases several million- (*1d*, *1f*) and billion-fold (*1c*, *1g*). These studies revealed a number of interesting aspects about the M<sup>x+</sup>/methanol system that proves of practical and fundamental interest in developing other useful catalytic systems for alcoholysis reactions. Among organic solvents, methanol is closest to water in terms of structure and solvation, but its lower dielectric constant of 31.5 vs. 78.5 at 25°C (*2*) allows a much greater organic substrate solubility than does water and promotes ion-pairing (ion association) of the M<sup>x+</sup> and negatively charged substrates. Furthermore, unlike the situation in water where precipitation of M<sup>x+</sup>(OH)<sub>*n*</sub> is a problem above the p*K*<sub>a</sub> of the metal-coordinated waters (*3*), we have observed a greater solubility of most metal ions in MeOH throughout the entire pH region where ionization of M<sup>x+</sup>(HOMe)<sub>*y*</sub> occurs.

While there are several advantages to the M<sup>x+</sup>/methanol system, it became evident to us that detailed kinetic and

mechanistic analyses required reliable methods for determining and controlling “pH” in methanol as well as determining equilibrium constants and “p*K*<sub>a</sub>” values for the various ionizations of M<sup>x+</sup>(HOMe)<sub>*y*</sub>. Potentiometric titration methods are relatively simple and effective ways to obtain metal-ion complex stability constants and acid dissociation constants and, under favourable conditions, the speciation of complex mixtures in solution can be estimated with fair confidence (*4*). Potentiometric titrations have traditionally been done in aqueous solvents (*5*) and extensive tabulated data are available (*6*) but titrations in nonaqueous solvents have seen less use, particularly in the cases with metal ions (*7a*, *7b*). A major reason for using nonaqueous solvents has been to determine acidity constants for compounds that could not be reliably measured in the relatively narrow range offered by amphiprotic water, or to better resolve ionizations (*8*). Since there was no simple way to reliably convert potentiometric readings to absolute pH in nonaqueous solvents referenced to that solvent (denoted  $s\text{pH}$ ),<sup>2</sup> nonaqueous solvents were generally inconvenient to use (*8c*) and apply, particularly in studies of reaction mechanism. Some years ago, deLigny and Rehbach (*9a*) empirically determined a method for measuring the  $s\text{pH}$  in methanol by adding a correction constant of 2.34 (on the molality scale) to a measured electrode reading. More recently Bosch and co-workers (*10*) have reported

Received 13 January 2003. Published on the NRC Research Press Web site at <http://canjchem.nrc.ca> on 22 May 2003.

*Dedicated to Professor Don Arnold for his contributions to chemistry.*

**G. Gibson, A.A. Neverov, and R.S. Brown.**<sup>1</sup> Department of Chemistry, Queen's University, Kingston, ON K7L 3N6, Canada.

<sup>1</sup>Corresponding author (e-mail: [rsbrown@chem.queensu.ca](mailto:rsbrown@chem.queensu.ca)).

<sup>2</sup> $s\text{pH}$  notation is based on the recommendations of the IUPAC, Compendium of analytical nomenclature, definitive rules 1997. 3rd ed. Blackwell, Oxford, U.K. 1998.



a method for determining  ${}^s\text{pH}$  on the molarity scale which for our purposes is relatively simple: if a glass electrode is calibrated using standard aqueous buffers but the potentiometric measurements are taken in a nonaqueous solvent, the values are termed  ${}^s\text{pH}$ . Subsequently, one computes  ${}^s\text{pH} = {}^w\text{pH} - \delta$ , where  $\delta$  is a correction factor of  $-2.24$  on the molarity scale for measurements made as above in methanol (10). Although dependent on the junction potential of the electrode, there was found to be little difference between readings taken with different electrodes. Rived et al. (10c) have presented an extensive tabulation of  ${}^s\text{pK}_a$  values in methanol for many organic acids and bases that can be used as buffers to control  ${}^s\text{pH}$ , and where previously unknown  ${}^s\text{pK}_a$  values for materials are needed, these can be determined by titration according to the methods presented.

The titration of metal ions, however, is not as straightforward and forms the subject of the present report concerning the potentiometric titration of five common divalent metal ions ( $\text{Zn}^{\text{II}}$ ,  $\text{Co}^{\text{II}}$ ,  $\text{Mg}^{\text{II}}$ ,  $\text{Cu}^{\text{II}}$ ,  $\text{Ni}^{\text{II}}$ ) and nine  $\text{Ln}^{\text{III}}$  ions, as well as  $\text{Ti}^{\text{IV}}$  in MeOH. We have analyzed the potentiometric data in two ways depending upon the level of information required concerning the  ${}^s\text{pH}$ -dependent species formed in solution. In addition we have determined qualitatively the effect on titrations of some added counterions often used as anionic components of buffers used for pH control in kinetic experiments and as supporting electrolytes.

## Experimental

### Materials

Methanol (anhydrous) was obtained in a SureSeal™ bottle (Aldrich) and used as received. Sodium methoxide was received in a SureSeal™ bottle as a  $0.5\text{ M}$  solution in methanol which was diluted to make stock solutions ( $4 \times 10^{-3}$  –  $2 \times 10^{-2}\text{ M}$ ). Stock  $\text{Na}^+\text{OMe}^-$  solutions were stored under argon atmosphere and used within 5 days. All  $\text{Ln}^{\text{III}}$  metal ions were purchased as trifluoromethanesulfonate ( $\text{OTf}^-$ ) salts from Aldrich. Stock solutions were prepared in methanol ( $1 \times 10^{-2}$  or  $5 \times 10^{-2}\text{ M}$ ) and used within 2 days.  $\text{Ti}(\text{OMe})_4$  was purchased from Aldrich and a  $2 \times 10^{-3}\text{ M}$  stock solution was prepared in methanol and converted to the perchlorate salt in situ by the addition of 4 equiv of perchloric acid.  $\text{Zn}(\text{OTf})_2$ ,  $\text{Cu}(\text{OTf})_2$ ,  $\text{Co}(\text{ClO}_4)_2 \cdot 6\text{H}_2\text{O}$ , and  $\text{Ni}(\text{ClO}_4)_2 \cdot 6\text{H}_2\text{O}$  were obtained from Aldrich while  $\text{Mg}(\text{ClO}_4)_2$  was obtained from Alfa Aesar; all were used as received. Tetrabutylammonium salts were used as purchased from Sigma-Aldrich (except the chloride, from Fluka) to prepare stock solutions in methanol ( $5 \times 10^{-3}$  –  $2 \times 10^{-2}\text{ M}$ ).

### Potentiometric titrations

Titrations were performed using a Radiometer Vit90 Autotitrator equipped with an ABU91 Autoburette. The electrodes were Radiometer combination glass electrodes with a double junction design (model pH2201 had a sleeve junction, and pH2501 a porous ceramic pin, the latter type being recommended in reference (8a) and found to be most reliable in our studies). The lower reservoir of the pH electrode in contact with the test solution was filled with a  $1\text{ M}$  solution of  $\text{LiClO}_4$  in methanol. The temperature was kept at  $25.0^\circ\text{C}$  using a water bath and all titrations were conducted under Ar in a jacketed titration cell.

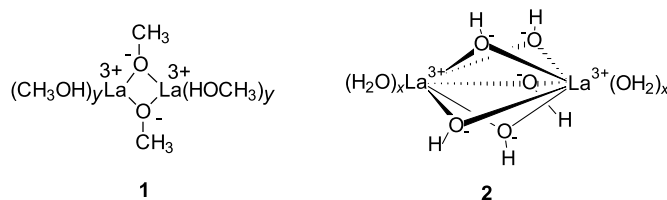
The metal ion concentration ranged from  $1 \times 10^{-4}$  to  $4 \times 10^{-3}\text{ M}$ , and ionic strength was controlled with  $0.01\text{ M}$   $\text{Bu}_4\text{NClO}_4$  unless otherwise noted. Sodium methoxide titrant was standardized by titrating an aliquot of Fisher certified aq HCl, with the endpoint taken to be pH 7.0. Electrode calibration was accomplished by the so-called “practical method” (11), immersing it in standardized aqueous buffers at pH 4.0 and 10.0 followed by rinsing the electrode in anhydrous methanol. Subsequent acidity measurements in methanol gave experimental  ${}^w\text{pH}$  readings very close to the actual hydrogen ion concentration, usually  $\sim 0.03$  units higher (11) which was sufficient for our purposes. To the  ${}^w\text{pH}$  readings was added the constant 2.24 to give the  ${}^s\text{pH}$  as described by Bosch and co-workers (10). Titration data were analyzed by standard computer treatments provided within the program PKAS (4) and, in two selected cases, Hyperquad 2000 (version 2.1 NT) (12) as well, with the autoprotolysis constant of pure methanol taken to be  $1 \times 10^{-16.77}$  at  $25^\circ\text{C}$  (10).

Since the stated water content of the Aldrich anhydrous methanol is  $<0.002\%$ , the maximum water content for the metal ion solutions containing  $2 \times 10^{-3}\text{ M}$   $\text{Ni}(\text{ClO}_4)_2 \cdot 6\text{H}_2\text{O}$  and  $\text{Co}(\text{ClO}_4)_2 \cdot 6\text{H}_2\text{O}$  was  $\sim 1.2 \times 10^{-2}\text{ M}$  or  $0.05\%$ . For metal salts that were not used as hydrates, the water content of the methanol solution would be  $<0.01\%$ . The inclusion of such a small amount of water did not significantly alter the characteristics of the solution relative to pure methanol, and therefore the correction factor of  $+2.24$  was sufficiently precise for our purposes (9).

## Results and discussion

### Speciation of $\text{La}^{3+}$

Our initial titration studies focused on  $\text{La}^{3+}$  because it was the first ion we studied as a catalyst of the methanolysis of acetylimidazole (1a) and esters (1d) where the kinetic studies pointed to a catalytically active  $(\text{La}^{3+}(\text{OMe}))_2$  dimer, formulated as **1**. Previously reported studies also support lanthanide hydroxy-bridged dimer formation in aqueous solution, both in the presence of special ligands (5b, 5d–5g, 5m) and in bare solvent (3, 5h, 5n, 7b), an example being the  $\text{La}_2(\text{OH})_5^+$  dimer **2** proposed to be important in the hydrolysis of an RNA model (5h). It is also known that lanthanide ions form polymeric species over extended periods in water, a process termed “ageing” (5e, 5f, 7b).

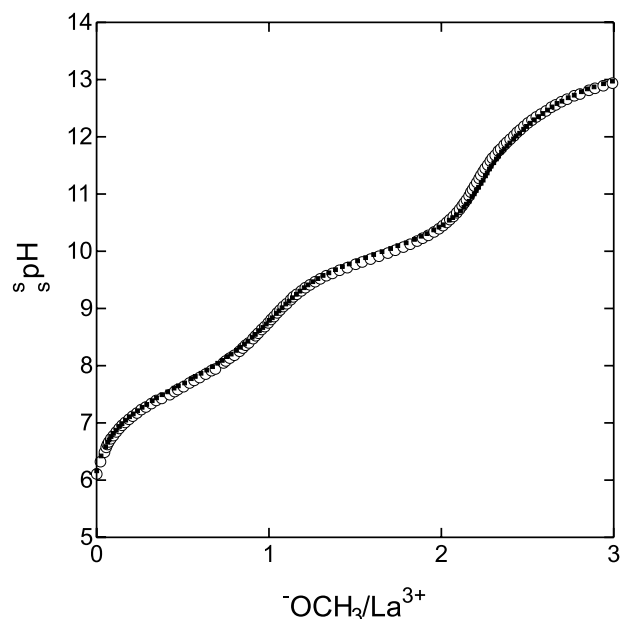


Shown in Fig. 1 are duplicate titration profiles of  $2 \times 10^{-3}\text{ M}$   $\text{La}(\text{OTf})_3$  in methanol with no added counterions, similar to the titration conditions in our first investigations of the  $\text{La}^{3+}$ -catalyzed methanolysis of esters (1d) and acetyl imidazole (1a).

Visual inspection of the curve indicates a consumption of  $\sim 2.5$  equiv of methoxide per metal ion by  ${}^s\text{pH}$  11, comprising two regions having, what we will term for the moment, apparent titration values of  $\sim 7.8$  (consuming 1 equiv of methoxide) and 10 (consuming  $\sim 1.5$  equiv of methoxide).



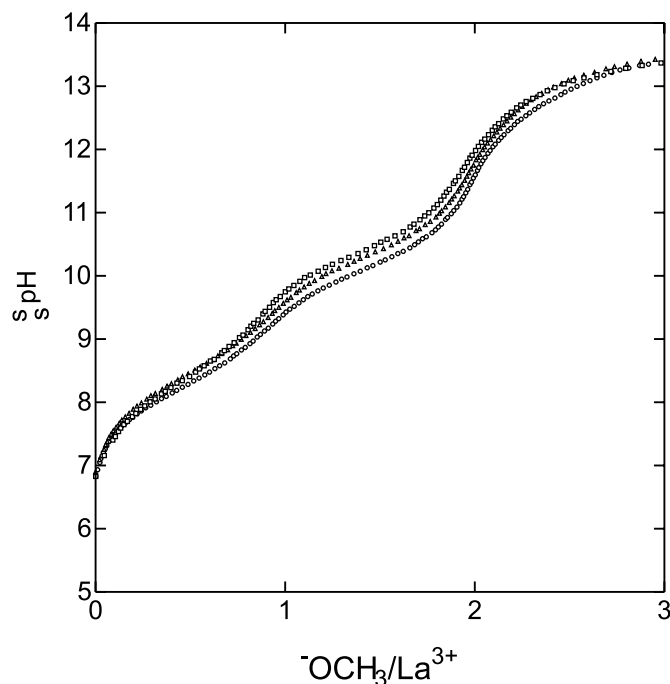
**Fig. 1.** Two overlaid potentiometric titration profiles for  $2 \times 10^{-3}$  M  $\text{La}(\text{OTf})_3$  in methanol (no added electrolyte,  $T = 25.0^\circ\text{C}$ ).



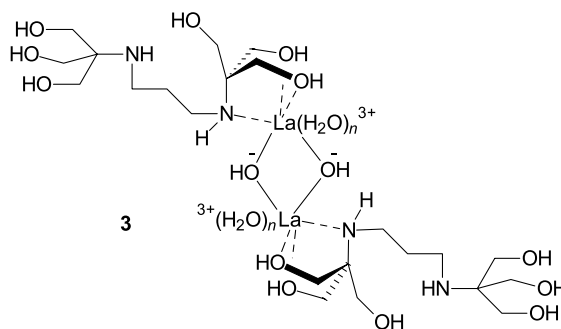
Notable is the fact that the titration curve is somewhat steeper in terms of  $\delta[\text{OCH}_3]/\delta[\text{s pH}]$  than expected for a simple ionization. This behaviour is consistent with the intervention of cooperative processes such as the formation of dimers or higher order aggregates (3, 13), or a change in the metal coordination number (14, 15) accompanying coordination of the methoxide. Indeed, as shown in Fig. 2 for  $(1-4) \times 10^{-3}$  M  $[\text{La}(\text{OTf})_3]$  conducted in the presence of 0.01 M  $\text{Bu}_4\text{NClO}_4$  (to hold the ionic strength approximately constant), the shapes of the three titration curves change and move to lower apparent titration values with increasing  $[\text{La}(\text{OTf})_3]$ .

There are several standard methods for obtaining equilibrium constants from titrimetric data, one of the most sophisticated and current being the Hyperquad 2000 computer program (12) which allows one to calculate stability constants for suggested multispecies equilibrium situations. Through its use we have been able to obtain a satisfactory fit of the potentiometric data in Fig. 1 to a proposed multi-equilibrium process involving several sequential associations of  $\text{OCH}_3$  to  $\text{La}^{3+}$  to form  $\text{La}_2(\text{OCH}_3)_n$  dimers where  $n$  (the number of associated methoxides) varies from 1–5. The best fit stability constants are given in Table 1, and illustrated in Fig. 3 is a speciation diagram calculated on the basis of those constants which shows the distribution of species as a function of  $\text{s pH}$ . According to this treatment, the two dominant species have even numbers of attached methoxides, e.g.,  $\text{La}_2(\text{OMe})_2$  between  $\text{s pH}$  8 and 10 (maximum concentration of ~80% at  $\text{s pH}$  8.9), and  $\text{La}_2(\text{OMe})_4$  between  $\text{s pH}$  10 and 12 (maximum concentration of ~80% at  $\text{s pH}$  11). Species with odd numbers of methoxides ( $\text{La}_2(\text{OCH}_3)_1$  and  $\text{La}_2(\text{OCH}_3)_3$ ) are also present to a lesser extent (maximum concentrations of ~25% in each reached at respective  $\text{s pH}$  values of 7.5 and 10). It is of note that the analogous  $\text{Ln}_2(\text{OH})_2$  (suggested structure **3** in the  $\text{La}^{3+}$  cases) and  $\text{Ln}_2(\text{OH})_4$  species, complexed to two molecules of bis-tris propane (BTP), are observed to be the dominant forms in

**Fig. 2.** Potentiometric titration profiles for  $[\text{La}(\text{OTf})_3] = 1 \times 10^{-3}$  M ( $\square$ ),  $2 \times 10^{-3}$  M ( $\triangle$ ), and  $4 \times 10^{-3}$  M ( $\circ$ ) in methanol in the presence of 0.01 M  $\text{NBu}_4\text{ClO}_4$ .



aqueous solution (5f). In that case it was suggested that the BTP stabilizes the dinuclear core and prevents the formation of complexes with higher nuclearity and, eventually, the metal hydroxide precipitation. Apparently methanol solvent serves a similar role in stabilizing the dinuclear core, at least in the case of  $\text{La}^{3+}$ .



Knowledge of the species distribution, when combined with kinetic behaviour as a function of  $\text{s pH}$  and  $[\text{M}^{x+}]$ , allows an insight into a complex multiequilibrium system where the different components may have different catalytic activity. Such an approach has been applied by Martell and co-workers (5d) and Gómez-Tagle and Yatsimirsky (5f) to  $\text{Ln}^{3+}$ -catalyzed hydrolysis of phosphate diesters in water. Previously we determined the kinetic constants for the  $\text{La}^{3+}$ -catalyzed methanolysis of the simple carbon-based ester *p*-nitrophenyl acetate (1d) as a function of both  $[\text{La}^{3+}]_t$  and  $\text{s pH}$ . The second-order rate constants for the  $\text{La}^{3+}$ -catalyzed reaction are superimposed on the speciation plot in Fig. 3, and coincide nicely with the bell-shaped concentration profile for  $\text{La}_2(\text{OMe})_2$  lending further support to our original

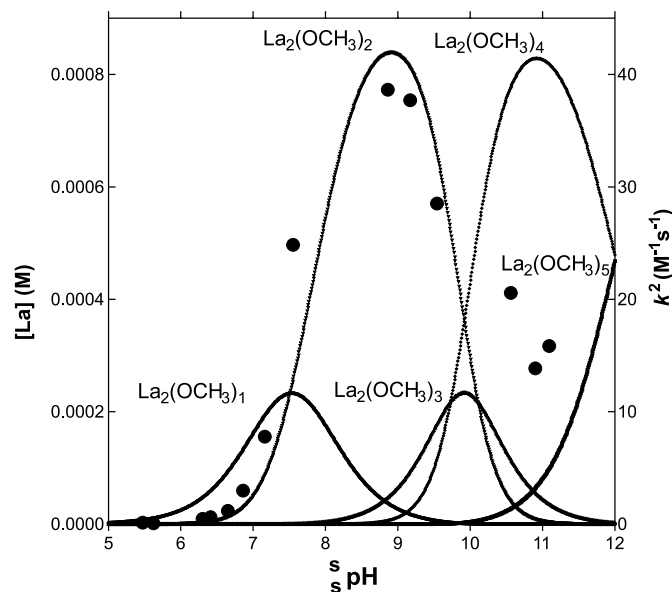


**Table 1.** Stability constants ( $\log {}^sK$  for the formation of  $\text{La}_2(\text{OMe})_n$  species in methanol (25.0°C).

Equilibrium	$\log {}^sK^a$	Microscopic ${}^s\text{p}K_a^b$
$[\text{La}_2(\text{OMe})_1]/[\text{La}]^2[\text{OMe}]$	$10.99 \pm 0.42^c$	
	$11.66 \pm 0.04^d$	
$[\text{La}_2(\text{OMe})_2]/[\text{La}]^2[\text{OMe}]^2$	$19.62 \pm 0.23^c$	${}^s\text{p}K_a^2 = 8.13 \pm 0.22^c$
	$20.86 \pm 0.07^d$	$7.56 \pm 0.10^d$
$[\text{La}_2(\text{OMe})_3]/[\text{La}]^2[\text{OMe}]^3$	$26.08 \pm 0.15^c$	${}^s\text{p}K_a^3 = 10.32 \pm 0.12^c$
	$27.52 \pm 0.09^d$	$10.11 \pm 0.02^d$
$[\text{La}_2(\text{OMe})_4]/[\text{La}]^2[\text{OMe}]^4$	$32.60 \pm 0.16^c$	${}^s\text{p}K_a^4 = 10.25 \pm 0.09^c$
	$34.56 \pm 0.20^d$	$9.73 \pm 0.11^d$
$[\text{La}_2(\text{OMe})_5]/[\text{La}]^2[\text{OMe}]^5$	$37.07 \pm 0.24^c$	${}^s\text{p}K_a^5 = 12.29 \pm 0.08^c$
	$39.32 \pm 0.26^d$	$12.00 \pm 0.07^d$

<sup>a</sup>Derived from fits of the potentiometric titration data using the program Hyperquad (12).<sup>b</sup>Defined as  $-\log {}^sK_a$  for  $\text{La}_2(\text{OMe})_n(\text{HOMe})_x \rightleftharpoons \text{La}_2(\text{OMe})_{n+1}(\text{HOMe})_y + \text{H}^+$ , calculated from the data in column 2 as  $16.77 - ({}^s\text{p}K^n - {}^s\text{p}K^{n-1})$  where 16.77 is the  $-\log$  (auto protolysis constant) for pure methanol.<sup>c</sup>Averages of duplicate titrations of three  $[\text{La}(\text{OTf})_3]$  (1, 2,  $4 \times 10^{-3}$  M) in the presence of 0.01 M  $\text{Bu}_4\text{NClO}_4$ .

Errors are calculated as the standard deviations of the mean of all six titrations.

<sup>d</sup>Averages of duplicate titrations of  $\text{La}(\text{OTf})_3$  ( $2 \times 10^{-3}$  M) with no added electrolyte. Errors calculated as the standard deviation of the mean.**Fig. 3.** Speciation diagram for  $1.0 \times 10^{-3}$  M  $\text{La}^{3+}$  in methanol as a function of  ${}^s\text{pH}$ . Data superimposed on the figure as (●) are second-order rate constants for  $\text{La}^{3+}$ -catalyzed methanolysis of *p*-nitrophenyl acetate (1d).

suggestions of its intermediacy based exclusively on treatment of the kinetic data.<sup>3</sup>

Analogous Hyperquad fits of the Fig. 2 titration data for the three  $[\text{La}^{3+}]$  determined in the presence of 0.01 M  $\text{Bu}_4\text{NClO}_4$  provide the average stability constants reported in Table 1 which can also be used to find the sequential microscopic acid dissociation constants of the  $\text{La}^{3+}$ -coordinated methanols ( ${}^s\text{p}K_{a_2}$  to  ${}^s\text{p}K_{a_5}$ ). It is of note that the constants determined in the presence of added  $\text{Bu}_4\text{NClO}_4$  are some-

what different than those determined in its absence indicating that the overall equilibria depend upon the conditions and particularly on the presence of counterions which we show later can associate with the  $\text{La}^{3+}$ . In fact this introduces some limitations to the interpretation of the equilibrium constants. These must be considered conditional since they are derived from titrations determined under various conditions where the concentrations of  $\text{La}(\text{OTf})_3$  and supporting electrolyte, the activities, and the degree of ion pairing of the various species are not constant. It is important to realize that the low concentration or absence of supporting electrolyte is a technical necessity since high concentrations of anions can seriously impair the catalytic ability of the metal ion, and our goal is to achieve titration conditions that approximate as closely as possible the kinetic conditions.

We have not undertaken additional Hyperquad (12) treatment of these data to account for the various  $\text{La}^{3+}/\text{ClO}_4^-$  or  $\text{La}^{3+}/\text{OTf}^-$  equilibria because the inclusion of such will inevitably lead to mathematically acceptable results, but in the end this becomes a fitting exercise and does not provide useful chemical insight. Indeed it is possible to treat any of the potentiometric titration data for the lanthanides to various schemes involving complex equilibria similar to those used for  $\text{La}^{3+}$ , adding or removing various proposed components to obtain satisfactory fits. However, unless one has additional information for the presence or absence of specific species in any given case, the whole process has inherent uncertainties because alternative schemes can produce fits of similar quality implicating species for which there is no confirmatory evidence.

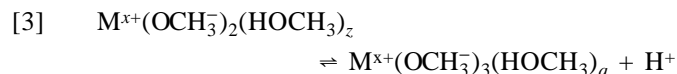
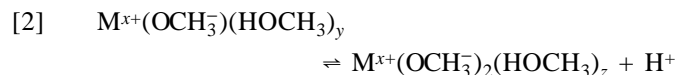
### Simplification of analysis

Owing to the above limitations, we sought to analyze the titration data by simpler methods that identify ionization events associated with the consumption of  $\text{CH}_3\text{O}^-$  by the metal ions.

<sup>3</sup>Our previous work (1a) indicated that  $\text{La}_2(\text{OCH}_3)_2$  and some higher order species ( $\text{La}_2(\text{OCH}_3)_n$  where  $n$  is uncertain but  $>2$ ) were involved in the catalysis. Fitting of the  $k_2$  kinetic data shown in Fig. 3 as a linear combination of rate constants for the various  $\text{La}_2(\text{OCH}_3)_n$  species provides a rate constant of  $(91.8 \pm 8.8) \text{ M}^{-1}\text{s}^{-1}$  for the  $\text{La}_2(\text{OCH}_3)_2$  and  $(38.0 \pm 5.6) \text{ M}^{-1}\text{s}^{-1}$  for the  $\text{La}_2(\text{OCH}_3)_4$  species with no involvement of  $\text{La}_2(\text{OCH}_3)_3$ .



Following Simms (16), we define the titration constants  ${}^sG'_1$ ,  ${}^sG'_2$ ,  ${}^sG'_3$ , ... etc., which are obtained as half neutralization points determined as if the solution contained monovalent, noninteracting acids. In our case, for the hypothetical metal ion methanolysis process shown in eqs. [1–3], the  ${}^sG'_1$ ,  ${}^sG'_2$ , and  ${}^sG'_3$  values are simply interpreted as the solution  ${}^s\text{pH}$  at which the  $[\text{OCH}_3^-]/[\text{M}^{x+}]$  is 0.5, 1.5, and 2.5.



The  ${}^sG'_n$  values are not the individual  ${}^sK'_n$  values (defined as the dissociation constants of the polyvalent acid, not corrected for activities) pertaining to the three stepwise hypothetical ionizations in eqs. [1–3], but are related to them through the application of eqs. [4–6]:

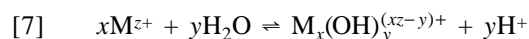
$$[4] \quad {}^sK'_1 = {}^sG'_1 + {}^sG'_2 + {}^sG'_3$$

$$[5] \quad {}^sK'_1 {}^sK'_2 = {}^sG'_1 {}^sG'_2 + {}^sG'_1 {}^sG'_3 + {}^sG'_2 {}^sG'_3$$

$$[6] \quad {}^sK'_1 {}^sK'_2 {}^sK'_3 = {}^sG'_1 {}^sG'_2 {}^sG'_3$$

This method identifies the half neutralization points, but it cannot accommodate the overall appearance of a titration curve that is too steep to be explained by sequential unconnected ionizations. This is because the method does not allow for situations where there is a cooperativity (e.g.,  $\text{p}K'_2 - \text{p}K'_1 < 0.6$ ), such as is observed where there is dimerization of the metal ions accompanying the ionizations.

Baes, Jr. and Mesmer (3a) describe the application of potentiometric titration to quantifying hydrolysis of cations in water according to the simplified process in eq. [7].



The ligand number ( $\bar{n}$ ) is defined by the mol ratio of bound  $\text{OH}^-$  to the metal ions in solution and is given as:

$$[8] \quad \bar{n} = \sum y[\text{M}_x(\text{OH})_y^{(xz-y)+}] / m_{\text{M}}$$

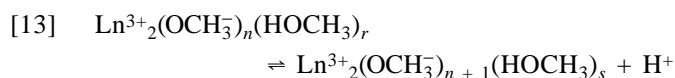
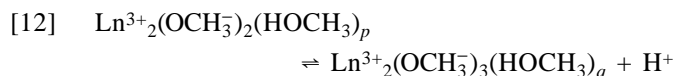
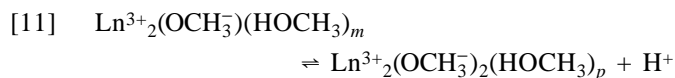
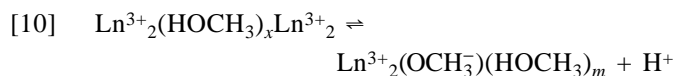
where  $m_{\text{M}}$  is the total metal ion concentration including non-bound forms or:

$$[9] \quad m_{\text{M}} = \sum x[\text{M}_x(\text{OH})_y^{(xz-y)+}]$$

In principle it is possible to determine the ligand number  $\bar{n}$  as a function of both the pH and metal ion concentration and thereby determine the formula of each hydroxide complex in eq. [7]. This should also be applicable to titrations performed in methanol, although such an exact treatment is unreliable at present because of the ion pairing and lack of ionic strength control. Nevertheless, it is possible to provide some valuable conditional constants which pertain to the average number of  $\text{CH}_3\text{O}^-/\text{M}^{x+}$ . From the forms of eqs. [8] and [9], it can be seen that when  $\bar{n} = 0.5, 1.5$ , or  $2.5$ , the observed  ${}^s\text{pH}$  would correspond to the Simms' titration constants or half-neutralization

points,  ${}^s\text{p}G'_1$ ,  ${}^s\text{p}G'_2$ , and  ${}^s\text{p}G'_3$ . The  ${}^s\text{p}G'_1$ ,  ${}^s\text{p}G'_2$  values for various  $\text{Ln}^{3+}$  ions are listed in Table 2.

Since the half neutralization constants do not define the overall shape of the titration profile we applied the program PKAS (4) to determine the apparent  ${}^s\text{p}K_{a_i}$  values pertaining to the overall titration curves. Simple fitting of the titration data to a di- or tribasic acid model failed, in most of the cases, to reproduce the steeper-than-normal shape of the titration profiles for the  $\text{Ln}^{3+}$  species. However, satisfactory fits can be obtained under the assumption that the  $\text{Ln}^{3+}$  ions exist predominantly as dimers having 1, 2, 3, ...,  $n$  associated ionizations as depicted in eqs. [10–13] (an assumption that is probably valid in the case of  $\text{La}^{3+}$  itself as determined by the Hyperquad fits described above). The so-determined apparent  ${}^s\text{p}K_{a_1}$  to  ${}^s\text{p}K_{a_n}$  values listed in columns 4–7 of Table 2 incorporate all microscopic equilibrium constants (such as those for dimerization, and association with counterions) that may affect the consumption of  $\text{CH}_3\text{O}^-$  by  $\text{Ln}^{3+}$ .



The average of the best fit apparent ( ${}^s\text{p}K_{a_1} + {}^s\text{p}K_{a_2}$ ) and ( ${}^s\text{p}K_{a_3} + {}^s\text{p}K_{a_4}$ ) values is within experimental error of the two titration constants ( ${}^s\text{p}G'_1$  and  ${}^s\text{p}G'_2$ ) for these events. In addition, the fits of this model to the experimental titration curves were much better than obtained with a simple dibasic acid model. Cases where cooperative interactions are at play are readily identified by the visual steepness of the curve. This situation invariably leads to a fit having computed apparent  ${}^s\text{p}K_{a_2} - {}^s\text{p}K_{a_1} < 0.6$  suggesting that the second ionization of the dimer is easier than the first, perhaps because of bridging the ensuing methoxide between the two metal ions as in 1 and 2.

### Some trends among the lanthanide ions

Across the lanthanide series the titration curves all show consumption of between 2 and 2.5 equiv methoxide per metal ion comprising two distinct events, a first consuming 1 equiv  $\text{OME}^-/\text{Ln}^{3+}$  followed by a second event consuming 1 to 1.5 equiv  $\text{OME}^-/\text{Ln}^{3+}$  at higher  ${}^s\text{pH}$ . Among the trends across the series, one of the most interesting is the shape of the titration profile, three examples belonging to  $\text{Pr}^{3+}$ ,  $\text{Eu}^{3+}$ , and  $\text{Yb}^{3+}$  being given in Fig. 4. The difference between the  ${}^s\text{p}G'_1$  and  ${}^s\text{p}G'_2$  values of the two ionization events decreases with atomic number, with  $\text{La}^{3+}$ ,  $\text{Pr}^{3+}$ , and  $\text{Nd}^{3+}$  having curves with clearly distinct steps,  $\text{Sm}^{3+}$  and  $\text{Eu}^{3+}$  to a lesser extent, and  $\text{Gd}^{3+}$  and all elements right of it in the series having a small difference between  ${}^s\text{p}G'_1$  and  ${}^s\text{p}G'_2$ . This effect may be related to the so-called “gadolinium break”, which refers to trends in complex formation constants across



**Table 2.** Observed titration constants ( ${}^s\text{p}G'_1$ ,  ${}^s\text{p}G'_2$ ) and best fit  ${}^s\text{p}K_a$  values for acid dissociation of  $\text{Ln}^{3+}(\text{HOCH}_3)_m$  in methanol ( $T = 25.0^\circ\text{C}$ ).

$\text{M}^{x+}$	Titration constant		${}^s\text{p}K_a$ s as fitted by PKAS (4) software to a dimer model				Conditions
	${}^s\text{p}G'_1$	${}^s\text{p}G'_2$	${}^s\text{p}K_{a_1}$	${}^s\text{p}K_{a_2}$	${}^s\text{p}K_{a_3}$	${}^s\text{p}K_{a_4}$	
$\text{La}^{3+}$	7.8	10.0	7.45	8.19	10.60	9.44	<i>a</i>
$\text{La}^{3+b}$	7.7	9.9	7.46	8.13	10.04	9.85	<i>c</i>
$\text{La}^{3+b}$	8.4	10.4	8.17	8.73	10.26	10.41	<i>d</i>
$\text{La}^{3+b}$	8.3	10.2	8.13	8.61	10.15	10.26	<i>e</i>
$\text{Pr}^{3+}$	6.7	9.5	6.26	7.01	9.73	9.10	<i>a</i>
$\text{Nd}^{3+}$	7.0	9.1	6.58	7.51	8.89	9.18	<i>a</i>
$\text{Sm}^{3+}$	6.3	8.5	6.24	6.49	8.07	8.91	<i>a</i>
$\text{Eu}^{3+}$	6.0	7.9	6.02	6.08	7.34	8.12	<i>a</i>
$\text{Gd}^{3+}$	6.6	8.0	6.36	6.91	7.54	8.03	<i>a</i>
$\text{Tb}^{3+}$	6.8	7.9	6.86	6.68	7.90	7.76	<i>f</i>
$\text{Ho}^{3+}$	6.6	7.8	6.65	6.77	7.36	8.04	<i>f</i>
$\text{Yb}^{3+}$	5.3	6.8	5.28	5.49	6.52	7.00	<i>a</i>

*a*  $5 \times 10^{-4}$  M  $\text{Ln}(\text{OTf})_3$  ( $5 \times 10^{-3}$  M  $\text{Bu}_4\text{NClO}_4$  added).

*b* Average of two independent titrations.

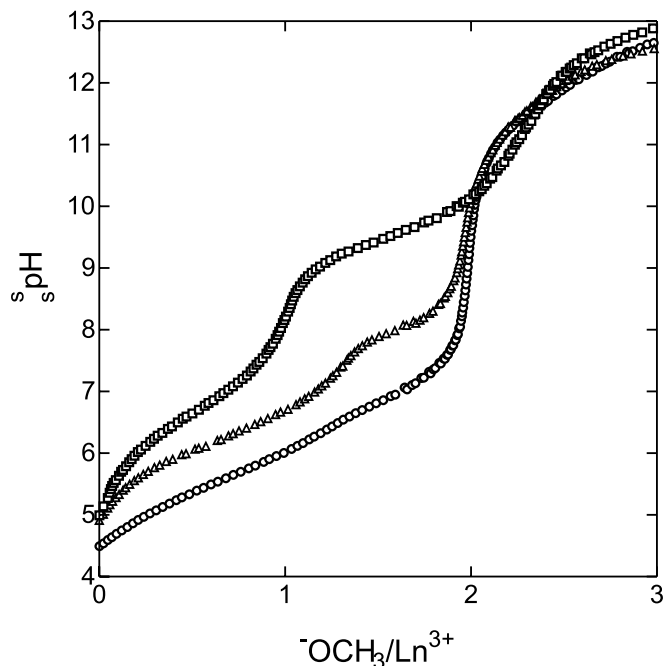
*c*  $2 \times 10^{-3}$  M  $\text{Ln}(\text{OTf})_3$  (no added salt).

*d*  $2 \times 10^{-3}$  M  $\text{Ln}(\text{OTf})_3$  (0.01 M  $\text{Bu}_4\text{NClO}_4$  added).

*e*  $4 \times 10^{-3}$  M  $\text{Ln}(\text{OTf})_3$  (0.01 M  $\text{Bu}_4\text{NClO}_4$  added).

*f*  $1 \times 10^{-3}$  M  $\text{Ln}(\text{OTf})_3$  (no added salt).

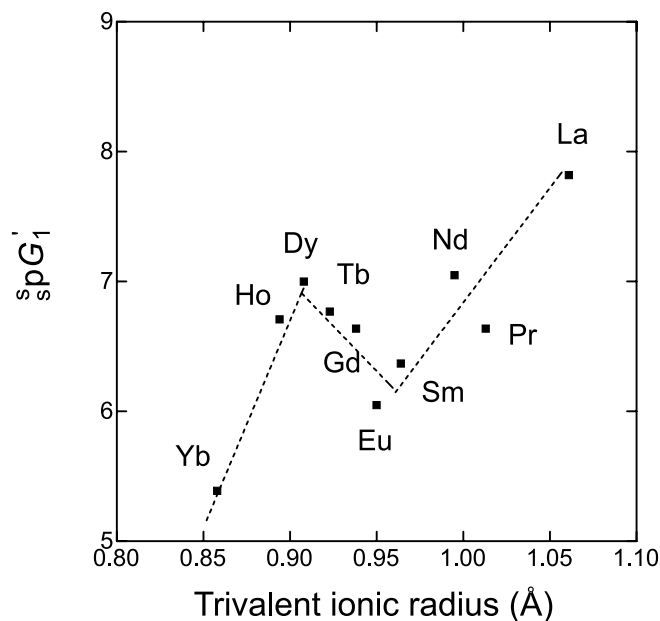
**Fig. 4.** Titration profiles for  $5 \times 10^{-4}$  M  $\text{Pr}(\text{OTf})_3$  ( $\square$ ),  $\text{Eu}(\text{OTf})_3$  ( $\triangle$ ), and  $\text{Yb}(\text{OTf})_3$  ( $\circ$ ) in methanol containing  $5 \times 10^{-3}$  M  $\text{Bu}_4\text{NClO}_4$  ( $T = 25.0^\circ\text{C}$ ).



the series and has been explained in part by a possible change in coordination number from 9 to 8 around gadolinium (3, 5*k*, 7*a*, 7*b*).

For the various lanthanide ions tested here, the  ${}^s\text{p}G'_1$  values range from 5.3 ( $\text{Yb}^{3+}$ ) to 7.8 ( $\text{La}^{3+}$ ) and, in general, the methanols associated with the lighter lanthanides (like  $\text{La}^{3+}$ ) are less acidic than the heavier lanthanides. Shown in Fig. 5 is

**Fig. 5.** Relationship of  ${}^s\text{p}G'_1$  for ionization of  $\text{Ln}^{3+}$ -bound methanol (Table 2) as a function of  $\text{Ln}^{3+}$  ionic radius (17).



a plot of  ${}^s\text{p}G'_1$  values vs.  $\text{Ln}^{3+}$  ionic radii (17) which follows the expected Lewis acidity trends where electrostatic association between  $\text{OCH}_3^-$  and the metal ion is stronger for the heavier cations because of their smaller ionic radii, stabilizing the species  $(\text{Ln}^{3+})_{1,2}(\text{OCH}_3^-)_{1,2}$  (3*a*). This argument suggests more extensive oligomerization for the heavier  $\text{Ln}^{3+}$  ions, which is consistent with the general reduction of the  ${}^s\text{p}G'_2$  across the row and smaller differences between  ${}^s\text{p}G'_1$  and  ${}^s\text{p}G'_2$  for the heavier ions. The plot in Fig. 5 shows breaks in the middle that may also result from the gadolinium break.



**Table 3.** Observed titration constants ( ${}^s\text{p}G'_1$ ,  ${}^s\text{p}G'_2$ ) and best fit  ${}^s\text{p}K_a$  values for dissociation of  $\text{M}^{2+}(\text{HOCH}_3)_m$  in methanol ( $T = 25.0^\circ\text{C}$ ).

$\text{M}^{2+}$	Titration constant		${}^s\text{p}K_a$ s as fitted by PKAS (4) software		Conditions
	${}^s\text{p}G'_1$	${}^s\text{p}G'_2$	${}^s\text{p}K_{a_1}$	${}^s\text{p}K_{a_2}$	
$\text{Zn}^{2+}$	9.7	10.2	10.64 (10.66) <sup>a</sup>	9.30 (8.94) <sup>a</sup>	<i>b, c</i>
$\text{Ni}^{2+}$	10.9	11.6	11.24	11.07	<i>d</i>
$\text{Mg}^{2+}$	N.A.	N.A.	13.67	12.60	<i>d, e</i>
$\text{Co}^{2+}$	11.1	11.6	12.84	9.96	<i>d</i>

**Note:** N.A. = not detected visually in the titration curve.

<sup>a</sup>Values in brackets determined as microscopic  ${}^s\text{p}K_{a_1}$  and  ${}^s\text{p}K_{a_2}$  from Hyperquad fit to model containing  $\text{Zn}^{2+}(\text{OCH}_3^-)$  and  $\text{Zn}^{2+}(\text{OCH}_3^-)_2$ .

<sup>b</sup> $2 \times 10^{-3}$  M  $\text{M}(\text{OTf})_2$  (no added salt).

<sup>c</sup> $2 \times 10^{-3}$  M  $\text{M}(\text{OTf})_2$  (0.01 M  $\text{Bu}_4\text{NClO}_4$  added).

<sup>d</sup> $1 \times 10^{-3}$  M  $\text{M}(\text{ClO}_4)_2$  (no added salt).

<sup>e</sup> $2 \times 10^{-3}$  M  $\text{M}(\text{ClO}_4)_2$  (no added salt).

### Other metal ions

We have applied the above titration analysis to other metal ions, notably  $\text{Ti}^{\text{IV}}$ ,  $\text{Zn}^{\text{II}}$ ,  $\text{Co}^{\text{II}}$ ,  $\text{Cu}^{\text{II}}$ ,  $\text{Mg}^{\text{II}}$ , and  $\text{Ni}^{\text{II}}$ , and the various titration constants (except for  $\text{Cu}^{\text{II}}$  discussed later) are given in Table 3. The titration profile for  $\text{Ti}^{4+}$  (not shown) shows exactly 3 equiv  $\text{OMe}^-/\text{Ti}^{4+}$  consumed before  ${}^s\text{pH}$  4 followed by a fourth equivalent having an apparent  ${}^s\text{p}K_a$  of 5.8. This result indicates that the  $\text{Ti}^{4+}$  ion is most likely mononuclear throughout the titration, and is very acidic in methanol largely because of its tetravalent nature and small ionic radius which makes it a better Lewis acid than any of the  $\text{Ln}^{3+}$  ions. The formation of  $\text{Ti}(\text{OH})_2^{2+}$  even in a 1.5 M aq  $\text{HClO}_4$  solution provides further evidence of the extreme acidity of ROH attached to this metal ion (3a).

The titration curves for the divalent transition metal ions  $\text{Zn}^{2+}$ ,  $\text{Co}^{2+}$ , and  $\text{Ni}^{2+}$  are remarkably similar, as shown in Fig. 6. Each consumes 2 equiv  $\text{OMe}^-/\text{M}^{2+}$  in one step, and shows cooperativity where  ${}^s\text{p}K_{a_2} < {}^s\text{p}K_{a_1}$ . In the case of  $\text{Zn}^{2+}$ , we have determined through Hyperquad fitting of the potentiometric data that only the inclusion of  $\text{Zn}^{2+}(\text{OCH}_3^-)$  and  $\text{Zn}^{2+}(\text{OCH}_3^-)_2$  is required to explain the data, and that the microscopic  ${}^s\text{p}K_{a_1}$  and  ${}^s\text{p}K_{a_2}$  values are 10.66 and 8.94, close to the values determined by the PKAS fitting. Thus, the likely source of the cooperativity stems not from dimerization as was the case with the  $\text{La}^{3+}$  ions, but from a change in the  $\text{M}^{2+}$ -coordination number following the first association of methoxide to form  $\text{M}^{2+}(\text{OCH}_3^-)$ . It has been shown that for the similar process of  $\text{ZnCl}_2$  formation in methanol, a change in coordination number from 6 or 5 to 4 following the association of the first  $\text{Cl}^-$  results in a cooperativity such that the second association of  $\text{Cl}^-$  proceeds more easily than the first (15). All three metal ions are only weakly acidic, with acid strength increasing in the order  $\text{Co} < \text{Ni} < \text{Zn}$  as ionic size decreases, a trend that is expected on the basis of Lewis acidity. The titration profile for  $\text{Cu}^{2+}$  is also shown on Fig. 6, and is quite different from those of the other transition metal ions in that it shows two separate titration steps, the first having a  ${}^s\text{p}G'_1$  of 6.5 consuming exactly 1 equiv of  $\text{OCH}_3^-/\text{Cu}^{2+}$ . However, the second titration step with an apparent  ${}^s\text{p}G'_2$  of 8.1 is extremely steep indicative of an oligomerization process, which, when fit with the PKAS program has computed  ${}^s\text{p}K_{a_3}$  and  ${}^s\text{p}K_{a_4}$  values of 11.4 and 4.5, respectively. Ultimately, when the titra-

tion mixture containing  $\text{Cu}(\text{OCH}_3)_2$  is allowed to stand for some time, a heavy precipitate is formed consistent with the proposed oligomerization to form  $(\text{Cu}(\text{OCH}_3)_2)_n$ .

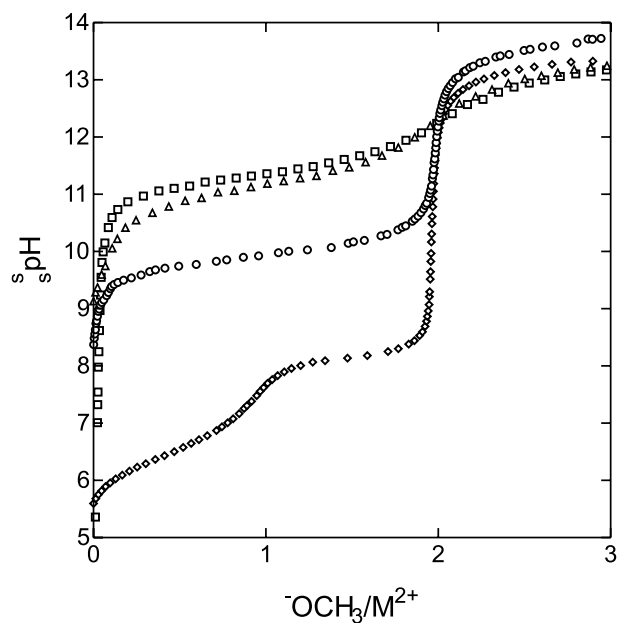
### Qualitative salt effects

As has been observed in aqueous systems (4, 5d, 7a), certain anions can associate with  $\text{M}^{x+}$  in solution and the low dielectric constant of methanol (31.5 at  $25^\circ\text{C}$  (2)) solvent will increase ion pairing or association (18, 19). Bunzli and co-workers (20) showed that counterions normally considered “inert”, such as triflate and perchlorate, coordinate to lanthanide ions in methanol as do  $\text{Br}^-$ ,  $\text{Cl}^-$ , and  $\text{NO}_3^-$ . Gómez-Tagle and Yatsimirsky (5f) have noted that counterions, specifically perchlorate, inhibited the activity of their dimeric lanthanide catalyst **3** in  $\text{H}_2\text{O}$ . We have earlier observed that the  $\text{M}^{x+}$ -catalyzed methanolysis of acetyl imidazole and  $\beta$ -lactams is inhibited by the presence of certain counterions such as  $\text{Cl}^-$  (1a, 1b, 21). Thus, all our subsequent studies of the  $\text{Ln}^{3+}$  catalysis were undertaken in media containing as low concentrations of weakly coordinating counterions such as triflate and perchlorate as possible and, to better approximate our kinetic conditions, initial titrations were performed without added salts to limit ion pairing.

The addition of added salts does have profound effects on the titration profiles as exemplified by the profiles shown in Fig. 7 for  $1 \times 10^{-3}$  M  $\text{La}(\text{OTf})_3$  in the presence of 0.04 M  $\text{Bu}_4\text{NX}$  salts. Since the cationic portion is constant and incapable of direct binding to the metal, the effects noticed are largely due to the chemical nature of the anion. Of the anions investigated, nitrate perturbs the titration profiles most, moving the  ${}^s\text{p}G'_1$  value upward by about 3.6 units. Even though nitrate is not considered to be a strong binding ligand to most metal ions, it does have a special propensity to bind to lanthanides forming a mixture of inner and outer sphere complexes in aqueous solution, depending on concentration (22). It has also been noted that in a nonaqueous solvent, inner sphere complexes are formed which serve as a basis for the extraction of  $\text{Ln}^{\text{III}}$  (23). In our study in methanol its association constant with  $\text{La}^{3+}$  can be estimated to be at least  $1 \times 10^5 \text{ M}^{-1}$  under the assumption of competitive binding of a single nitrate, probably indicative of a bidentate binding as has been observed in several crystal structures of Ln–nitrate



**Fig. 6.** Potentiometric titration of  $2 \times 10^{-3}$  M  $\text{Zn}(\text{OTf})_2$  ( $\circ$ ),  $(\text{Ni}(\text{ClO}_4)_2$  ( $\Delta$ ),  $\text{Co}(\text{ClO}_4)_2$  ( $\square$ ), and  $\text{Cu}(\text{OTf})_2$  ( $\diamond$ ) in methanol (no added electrolyte).



species (24). For the halide series, the perturbation on  ${}^s\text{p}G'_1$  follows the order  $\text{Cl}^- > \text{Br}^- > \text{I}^-$ . This trend is not surprising as the notoriously hard cation  $\text{La}^{3+}$ , which binds via predominantly electrostatic interactions, is expected to bind more weakly to the softer halides ( $\text{I}^-$  and  $\text{Br}^-$ ) that have significant covalent character in their bonds (5i, 7a).

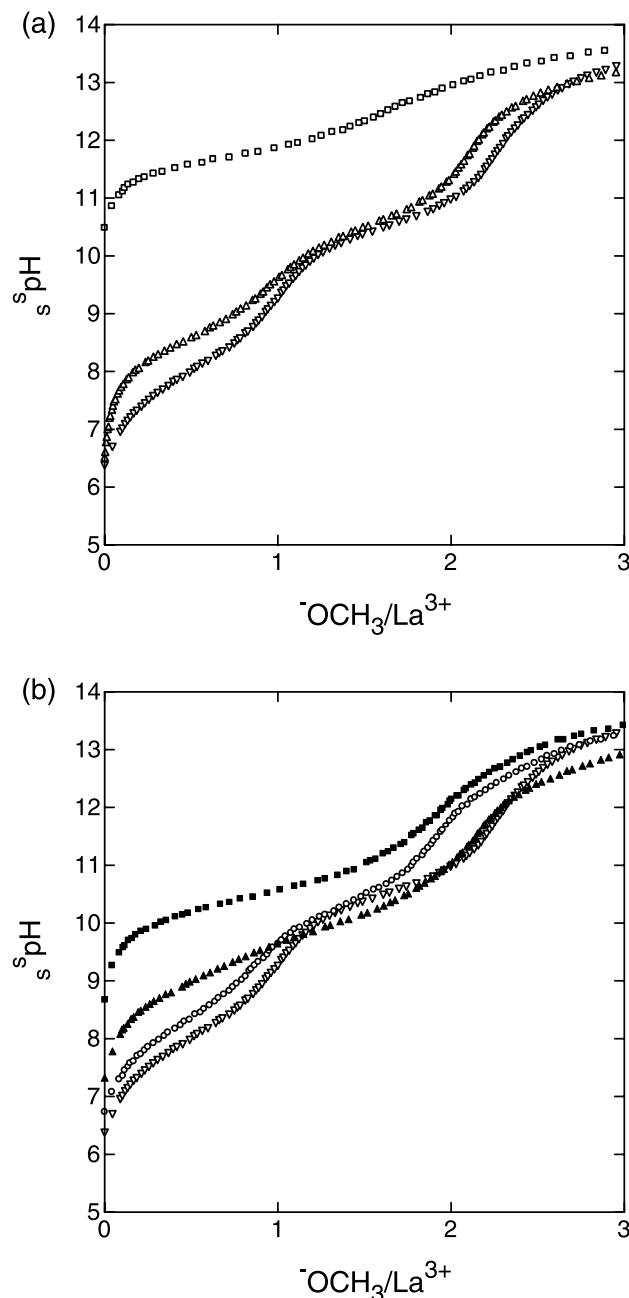
While we have tried to minimize the salt effects by using weakly nucleophilic anions such as  $\text{ClO}_4^-$  and  $\text{CF}_3\text{SO}_3^-(\text{OTf}^-)$ , these too raise the  ${}^s\text{p}G'_1$  to a certain extent. To investigate further the extent of perturbation of the  ${}^s\text{p}G'_1$  we titrated  $1 \times 10^{-3}$  M  $\text{La}(\text{OTf})_3$  solutions containing  $1$ ,  $2$ , and  $4 \times 10^{-2}$  M  $\text{Bu}_4\text{NOTf}$  (titration curves not shown). Both the  ${}^s\text{p}G'_1$  ( ${}^s\text{p}G'_2$ ) values increase, from  $8.0$  ( $10.3$ ) in the absence of added salt to  $8.3$  ( $10.3$ ),  $8.4$  ( $10.4$ ), and  $8.6$  ( $10.5$ ) at the three concentrations employed. This upward shift likely results from an ion association of the triflate with the  $\text{La}^{3+}$  which reduces its affinity for  $\text{OCH}_3^-$ , possibly by decreasing the Lewis acidity of the metal ion or by acting as a competitive inhibitor of methoxide binding in the various metal containing species. Perchlorate ion behaves similarly as judged by comparison of the titration  ${}^s\text{p}G'_1$  and  ${}^s\text{p}G'_2$  values given in Table 2, rows 2 and 3.

The divalent transition metal ions, already found to be less acidic than any of the trivalent metal ions studied, are also much less affected by association with added counterions. The titration profiles of  $2 \times 10^{-3}$  M  $\text{Zn}(\text{OTf})_2$  without and with  $0.01$  M added  $\text{Bu}_4\text{NClO}_4$  (not shown) were essentially superimposable indicating a lack of ion association in this case.

## Conclusions

The objective of this study was to find a convenient method to obtain titration constants for various metal ions in methanol solution, including the lanthanides and certain transition metal ions. The titration constants are crucial elements for determin-

**Fig. 7.** Potentiometric titration curves of  $1 \times 10^{-3}$  M  $\text{La}(\text{OTf})_3$  in the presence of  $0.04$  M  $\text{Bu}_4\text{NX}$  salts. (a) ( $\square$ )  $\text{X} = \text{NO}_3^-$ , ( $\Delta$ )  $\text{X} = \text{OTf}^-$ , ( $\nabla$ ) no added electrolyte; (b) ( $\blacksquare$ )  $\text{X} = \text{Cl}^-$ , ( $\blacktriangle$ )  $\text{X} = \text{Br}^-$ , ( $\circ$ )  $\text{X} = \text{I}^-$ , ( $\nabla$ ) no added electrolyte.



ing the  ${}^s\text{pH}$  values at which species with a known  $[\text{OCH}_3^-]/\text{M}^{x+}$  ratio exist. As such they are essential for interpreting our findings that  $\text{La}^{3+}$ ,  $\text{Eu}^{3+}$ , and  $\text{Zn}^{2+}$  are remarkably active in catalyzing certain methanolysis reactions (1, 21). We have undertaken three different approaches for analyzing the titration data. We have applied the simplified method of Simms for determining certain titration constants, defined as half neutralization constants or  ${}^s\text{p}G'_1$ , conveniently interpreted as the solution  ${}^s\text{pH}$  where the average  $\text{OCH}_3^-/\text{M}^{x+}$  ratio is  $0.5$  and  $1.5$ . This allows one to define approximately the  ${}^s\text{pH}$  regions where one can form the maximum concentrations of



certain species that may have kinetic activity. However, this approach does not reveal the intricate details of the acid–base equilibria involved and the constants are complicated composites of various equilibria including ion-pairing between the  $M^{x+}$  and solution counterions and metal dimerizations and (or) oligomerizations which can affect the ionizations of  $(M^{x+})_n(HOCH_3)_m$  forms. Through subsequent application of a computer program (PKAS), the shape of the titration profile can be modeled, and apparent  ${}^s pK_a$  values can be derived. While these are also complicated functions of the various equilibria in solution, one can identify quickly situations where metal ion association exists because the titration profiles are much steeper than expected for a simple ionization.

When necessary, additional detailed information concerning the speciation of the  $M^{x+}/OCH_3^-$  forms can be obtained through fits of the potentiometric titration curves to multi-equilibrium models using the computer program Hyperquad which gives the microscopic stability constants for the various species in solution. This type of fit is best undertaken for metal ions shown to be catalytically active, and where additional information concerning the likely speciation in solution is available. Through an extensive fitting of the  $La^{3+}$  titration data and comparison with our previous kinetic results for the catalyzed methanolysis of *p*-nitrophenyl acetate, we have confirmed that the active form of the catalyst is a previously proposed  $La_2(OCH_3)_2$  dimer, giving further credence to the applicability of the titration and (or) kinetic treatment. Moreover, this method reveals a much more complex situation where another dimeric form ( $La_2(OCH_3)_4$ ) is present and reactive. As such, the advantage of this approach when applied to metal ion catalysis of methanolyses, is the ability to analyze complex kinetic behaviour attributable to a multiequilibrium system which may be difficult, if not impossible, to analyze by standard kinetic approaches. Further work from these laboratories will be aimed at extending the titration and kinetic methodology to other reactions, metal ions, and alcohol solvents.

## Acknowledgements

The authors acknowledge the financial assistance of Queen's University and the Natural Sciences and Engineering Research Council of Canada (NSERC). Also acknowledged are Mr. Todd McDonald and Dr. Pedro Montoya-Pelaez for their assistance in determining reliable methods for performing the titrations in methanol.

## References

- (a) A.A. Neverov and R.S. Brown. *Can. J. Chem.* **78**, 1247 (2000); (b) A.A. Neverov, P. Montoya-Pelaez, and R.S. Brown. *J. Am. Chem. Soc.* **123**, 210 (2001); (c) A.A. Neverov and R.S. Brown. *Inorg. Chem.* **40**, 3588 (2001); (d) A.A. Neverov, T. McDonald, G. Gibson, and R.S. Brown. *Can. J. Chem.* **79**, 1704 (2001); (e) R.S. Brown and A.A. Neverov. *J. Chem. Soc. Perkin Trans. 2*, 1039 (2002); (f) A.A. Neverov, G. Gibson, and R.S. Brown. *Inorg. Chem.* **42**, 228 (2003); (g) J.S.W. Tsang, A.A. Neverov, and R.S. Brown. *J. Am. Chem. Soc.* **125**, 1559 (2003).
- H.S. Harned and B.B. Owen. *The physical chemistry of electrolytic solutions*. 3rd Ed. ACS Monograph Series 137, Reinhold Publishing, New York. 1957. pp. 161.
- (a) C.F. Baes, Jr. and R.E. Mesmer. *The hydrolysis of cations*. John Wiley and Sons, New York. 1976; (b) C.F. Baes, Jr. and R.E. Mesmer. *The hydrolysis of cations*. John Wiley and Sons, New York. 1976. pp. 51–59.
- A.E. Martell and R.J. Motekaitis. *Determination and use of stability constants*. VCH Publishers, New York. 1988.
- (a) R. Delgado, Y. Sun, R.J. Motekaitis, and A.E. Martell. *Inorg. Chem.* **32**, 3320 (1993); (b) Z. Wang, J. Reibenspies, and A.E. Martell. *Inorg. Chem.* **36**, 629 (1997); (c) H. He, A.E. Martell, R.J. Motekaitis, and J.H. Reibenspies. *Inorg. Chem.* **39**, 1586 (2000); (d) P.E. Jurek, A.M. Jurek, and A.E. Martell. *Inorg. Chem.* **39**, 1016 (2000); (e) P. Gómez-Tagle and A.K. Yatsimirsky. *J. Chem. Soc., Dalton Trans.* 2663 (2001); (f) P. Gómez-Tagle and A.K. Yatsimirsky. *Inorg. Chem.* **40**, 3786 (2001); (g) B.K. Takasaki and J. Chin. *J. Am. Chem. Soc.* **115**, 9337 (1993); (h) P. Hurst, B.K. Takasaki, and J. Chin. *J. Am. Chem. Soc.* **118**, 9982 (1996); (i) F. Arnaud-Neu. *Chem. Soc. Rev.* **23**, 235 (1994); (j) I. Yoshida, N. Yamamoto, F. Sagara, K. Ueno, D. Ishii, and S. Shinkai. *Chem. Lett.* 2105 (1991); (k) J. Massaux and J.F. Desreux. *J. Am. Chem. Soc.* **104**, 2967 (1982); (l) J. Huskens, H. van Bekkum, J.A. Peters, and G.R. Choppin. *Inorg. Chim. Acta*, **245**, 51 (1996); (m) C.W. Yoon, S.J. Oh, Y.J. Jeon, Y.-S. Choi, Y.-K. Son, S. Hwangbo, J.K. Ku, and J.W. Park. *Bull. Korean Chem. Soc.* **22**, 199 (2001); (n) L. Ciavatta, M. Iuliano, and R. Porto. *Polyhedron*, **6**, 1283 (1987).
- A.E. Martell and R.M. Smith. *Critical stability constants*. Vols. 1–6. Plenum Press, New York. 1974.
- (a) T. Moeller, D.F. Martin, L.C. Thompson, R. Ferrús, G.R. Feistel, and W.J. Randall. *Chem. Rev.* **65**, 1 (1965); (b) J. Burgess. *Metal Ions in solution*. John Wiley and Sons, New York. 1978.
- (a) J.S. Fritz. *Acid-base titrations in nonaqueous solvents*. Allyn and Bacon, Inc., Boston, Mass. 1973; (b) W. Huber. *Titration in nonaqueous solvents*. Academic Press, New York. 1967; (c) I. Gyenes. *Titration in non-aqueous media*. D. Van Nostrand Company, Inc., New Jersey. 1967.
- (a) C.L. deLigny and M. Rehbach. *Recl. Trav. Chim. Pays-Bas*, **79**, 727 (1960); (b) R.G. Bates, M. Paabo, and R.A. Robinson. *J. Phys. Chem.* **67**, 1833 (1963); (c) R.G. Bates. *Determination of pH: Theory and practice*. 2nd ed. John Wiley and Sons, New York. 1964. p. 245.
- (a) I. Canals, J.A. Portal, E. Bosch, and M. Rosés. *Anal. Chem.* **72**, 1802 (2000); (b) E. Bosch, F. Rived, M. Rosés, and J. Sales. *J. Chem. Soc., Perkin Trans. 2*, 1953 (1999); (c) F. Rived, M. Rosés, and E. Bosch. *Anal. Chim. Acta*, **374**, 309 (1998); (d) E. Bosch, P. Bou, H. Allemann, and M. Rosés. *Anal. Chem.* **68**, 3651 (1996).
- H. Sigel, A.D. Zuberbühler, and O. Yamauchi. *Anal. Chim. Acta*, **255**, 63 (1991).
- P. Gans, A. Sabatini, and A. Vacca. *Talanta*, **43**, 1739 (1996).
- R.D. Porasso, J.C. Benegas, and M.A.G.T. van den Hoop. *J. Phys. Chem.* **103**, 2361 (1999).
- (a) S. Ahrland and N.-O. Björk. *Acta Chem. Scand. Ser. A*, **30**, 265 (1976); (b) S. Ahrland, N.-O. Björk, and R. Portanova. *R. Acta Chem. Scand. Ser. A*, **30**, 270 (1976).
- (a) H. Doe and T. Kitagawa. *Inorg. Chem.* **21**, 2272 (1982); (b) H. Doe, A. Shibagaki, and T. Kitagawa. *Inorg. Chem.* **22**, 1639 (1983).
- H.S. Simms. *J. Am. Chem. Soc.* **48**, 1239 (1926).
- T. Moeller. *The chemistry of the lanthanides*. Reinhold Publishing Corp., New York. 1963. p. 20.
- Y. Marcus. *Ion solvation*. John Wiley and Sons, New York. 1986. pp. 245–284.



19. (a) H.B. Silber and A. Pezzica. *J. Inorg. Nucl. Chem.* **38**, 2053 (1976); (b) H. Suganuma, M. Nakamura, T. Katoh, I. Satoh, and T. Omori. *J. Radioanal. Nucl. Chem.* **223**, 167 (1997); (c) D.W. James and R.E. Mayes. *J. Phys. Chem.* **88**, 637 (1984).
20. (a) J.C.G. Bünzli, A.E. Merbach, and R.E. Nielson. *Inorg. Chim. Acta*, **139**, 151 (1987); (b) F. Pilloud and J.C.G. Bünzli. *Inorg. Chim. Acta*, **139**, 153 (1987).
21. P.J. Montoya-Pelaez and R.S. Brown. *Inorg. Chem.* **41**, 309 (2002).
22. (a) I. Abrahamer and Y. Marcus. *Inorg. Chem.* **6**, 2103 (1967); (b) G.R. Choppin and W.F. Strazik. *Inorg. Chem.* **4**, 1250 (1965).
23. L.I. Katzin and M.L. Barnett. *J. Phys. Chem.* **68**, 3779 (1964).
24. J. Petrova, S. Momchilova, E.T.K Haupt, J. Kopf, and G. Eggers. *Phosphorus Sulfur Silicon Relat. Elem.* **177**, 1337 (2002).



# New potential dendritic cores: Selective chemistry of dipentaerythritol

Hussein Al-Mughaid, T. Bruce Grindley, Katherine N. Robertson, and T. Stanley Cameron

**Abstract:** Methods were developed to convert dipentaerythritol efficiently into di-*O*-benzylidene, di-*O*-cyclohexylidene, di-*O*-1-ethylpropylidene, and di-*O*-methylene diacetals. The known di-*O*-benzylidene acetal, considered to be a single isomer, was shown to be close to a statistical mixture of the *cis,cis*-, *cis,trans*-, and *trans,trans*-isomers. Structures were established by a combination of NMR spectroscopy and X-ray crystallography. Reaction of the di-*O*-benzylidene acetals with benzyl chloride and potassium hydroxide surprisingly gave good to excellent yields of the monobenzyl ethers. An explanation for this observation was advanced. The dibenzyl derivatives of the di-*O*-benzylidene acetals were formed by reaction of their dianions with benzyl bromide in DMF. Selective reduction of the di-*O*-benzylidene acetals with triethylsilane and boron trifluoride etherate gave 2,6'-di-*O*-benzylidipentaerythritol. A crown ether was formed in modest yield (12%) by reaction of the dianion of the di-*O*-methylene acetal with  $\alpha,\alpha'$ -dibromo-*m*-xylene in DMF.

**Key words:** dipentaerythritol, pentaerythritol, acetals, dendrimer, selective benzylation, crown ether.

**Résumé :** On a mis au point des méthodes qui permettent de transformer efficacement le dipentaérythritol en diacétals di-*O*-benzylidène, di-*O*-cyclohexylidène, di-*O*-1-éthylpropylidène et di-*O*-méthylène. On a démontré que l'acétal connu di-*O*-benzylidène, qui était considéré comme un seul isomère, est en fait un mélange pratiquement statistique des trois isomères *cis,cis*-, *cis,trans*- et *trans,trans*-. On a déterminé les structures par une combinaison de spectroscopie RMN et de diffraction des rayons X. La réaction des acétals du di-*O*-benzylidène avec le chlorure de benzyle en présence d'hydroxyde de potassium conduit d'une façon surprenante à des rendements allant de bons à excellents des éthers monobenzylés. On propose une explication pour cette observation. Les dérivés dibenzylés des acétals du di-*O*-benzylidène se forment par réaction de leurs dianions avec le bromure de benzyle dans le DMF. Une réduction sélective des acétals du di-*O*-benzylidène par le triéthylsilane et l'éthérate de trifluorure de bore conduit au 2,6'-di-*O*-benzylidipentaérythritol. La réaction du dianion de l'acétal du di-*O*-benzylidène avec le  $\alpha,\alpha'$ -dibromo-*m*-xylène, dans le DMF, conduit à la formation d'un éther couronne avec un rendement modeste (12%).

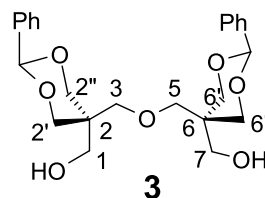
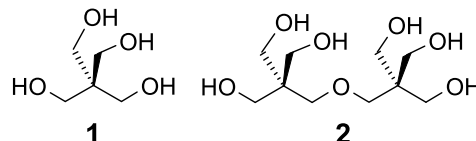
**Mots clés :** dipentaérythritol; pentaérythritol; acétals; dendrimer; benzylation sélective; éther couronne.

[Traduit par la Rédaction]

## Introduction

Dendrimers have become the subject of intense interest in the last few years (1–7). One of the molecules that has attracted the most attention as either the central core or a branching point of clusters and dendrimers is pentaerythritol (1) (8–19). In contrast, dipentaerythritol (2), an inexpensive commercially available compound with many of the favorable characteristics of pentaerythritol, has been almost totally neglected. Moreover, little is known about the regioselective substitution of 2, whereas pentaerythritol has been extensively investigated and there are now methods available to selectively prepare a wide range of derivatives (20–29).

Dipentaerythritol has  $C_{2v}$  symmetry making its six primary hydroxyl groups identical. As a result, it has considerable potential as a core or a branching point for the formation of clusters and dendrimers. It is also a promising headgroup for gemini surfactants (30). In order for this potential to be achieved, the fundamental chemistry of this compound must be established. In this paper, we report studies of the selective formation of acetals of 2 and examine some further chemistry of these acetals.



Received 01 October 2002. Published on the NRC Research Press Web site at <http://canjchem.nrc.ca> on 14 May 2003.

Dedicated to Professor Don Arnold for his contributions to chemistry.

H. Al-Mughaid, T.B. Grindley,<sup>1</sup> K.N. Robertson, and T.S. Cameron. Department of Chemistry, Dalhousie University, Halifax, N.S. B3H 4J3, Canada.

<sup>1</sup>Corresponding author (e-mail: [Bruce.Grindley@Dal.Ca](mailto:Bruce.Grindley@Dal.Ca)).



Scheme 1.

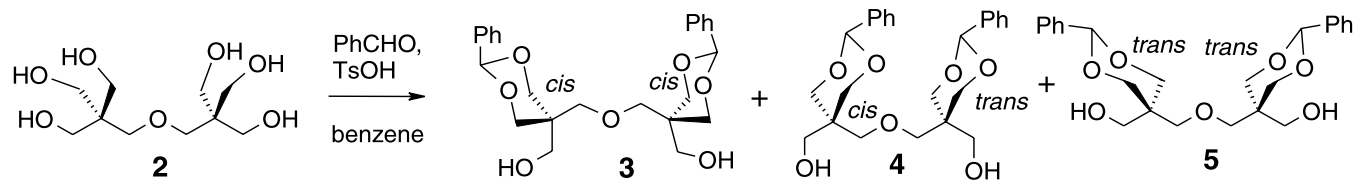


**Fig. 1.** ORTEP diagram for 1,7-di-*O*-benzoyl-*cis,cis*-2,2':6,6'-di-*O*-benzylidene-2,2',6,6'-tetra(hydroxymethyl)-4-oxa-1,7-heptanediol (**3b**).

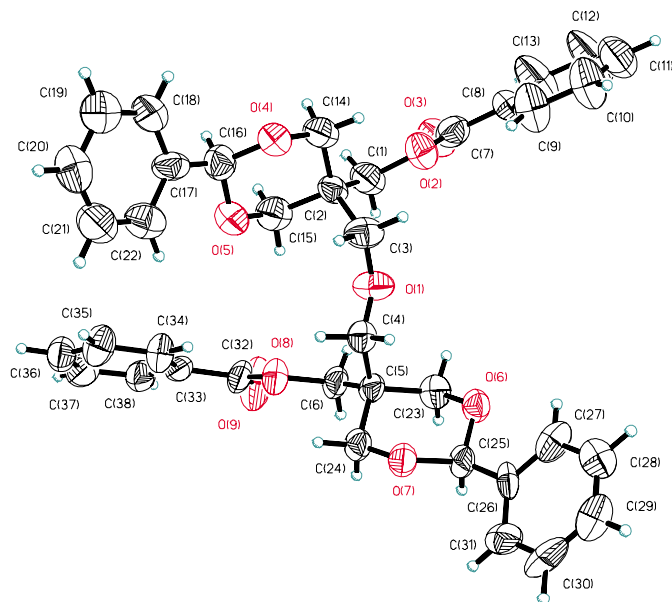
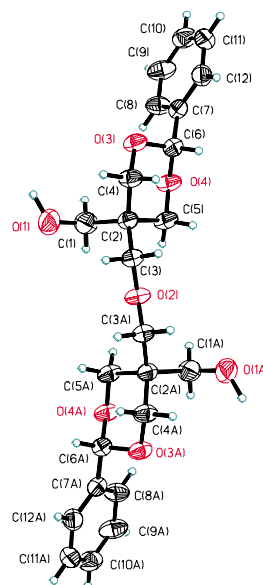


**Fig. 2.** ORTEP diagram for *trans,trans*-2,2':6,6'-di-*O*-benzylidene-2,2',6,6'-tetra(hydroxymethyl)-4-oxa-1,7-heptanediol (**5**).



There are two previous reports of acetals of dipentaerythritol (**2**). In 1950, Bograchov (31) reported that **2** reacted with benzaldehyde in benzene to form a di-*O*-benzylidene acetal with a sharp mp (166°C) in 60% yield, but did not discuss the possibility of stereoisomerism. He also reported di-*p*-methoxybenzylidene and di-*p*-nitrobenzylidene acetals. Later, Cabasso et al. (32) performed a transacetalization reaction of dipentaerythritol with diethyl 2,2-diethoxyethylphosphonate and obtained a bis-*O*-(2,2-diethyl phosphonoethylidene) diacetal in 90% yield, again without discussion of stereoisomerism. For all acetals derived from dipentaerythritol, 1,3-dioxane derivatives are produced that have single substituents at C-2 of the 1,3-dioxane ring and two different substituents at C-5. In these compounds, the 1,3-dioxane C-5 substituents are similar, both being CH<sub>2</sub>OR groups, and the A-values of substituents at C-5 in 1,3-dioxane rings are small (33). Therefore, under the equilibrium conditions used above, mixtures of stereoisomers should have been produced and the results herein are in accord with this expectation.

## Results and discussion

### Acetal formation

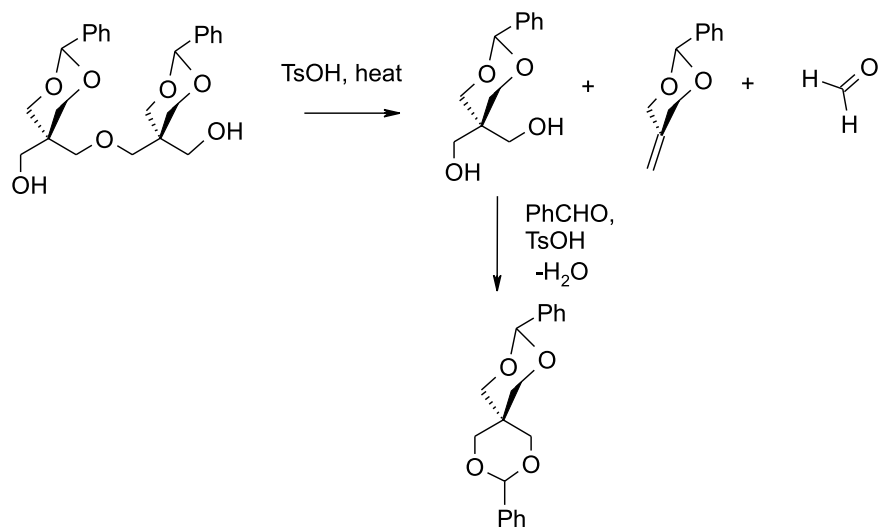
Bograchov's procedure for the preparation of the di-*O*-benzylidene acetal of dipentaerythritol (**2**) in benzene did not specify reaction time or the precise amount of the catalytic *p*-toluenesulfonic acid used (31). Under conditions sim-

ilar to those used by Bograchov, a reaction time of 10 h at reflux in benzene with removal of water was found to give the best yield of the dibenzylidene acetals of 85%. Longer reaction times gave faster moving compounds (see later) on TLC; shorter reaction times resulted in lower consumption of dipentaerythritol. The use of toluene as the solvent under azeotropic conditions gave lower yields of the di-*O*-benzylidene acetals as will also be discussed later. The product was found to be a mixture of the three possible stereoisomers, the *cis,cis*-, *cis,trans*-, and *trans,trans*-isomers (Scheme 1). One isomer (**3**, mp 164–166°C) had a smaller *R<sub>f</sub>* value on TLC on silica gel and it was separated by flash column chromatography. The other two isomers (**4** (mp 123–125°C), **5** (mp 170–173°C)) had very similar *R<sub>f</sub>* values but were obtained individually by acetylation, separation of the diacetates (**4a** and **5a**) by chromatography, and deacetylation. Based on their melting points, the compound isolated by Bograchov was the *cis,cis*-isomer.

In the 1,3-dioxane rings of the acetals and their derivatives discussed in this publication, there are two very similar groups at C-5 of the 1,3-dioxane rings, CH<sub>2</sub>OCH<sub>2</sub>C groups and CH<sub>2</sub>OH groups, or derived CH<sub>2</sub>OR groups. The selection of which groups are used to determine *cis* or *trans* for all benzylidene acetals described here is based on the Cahn–Prelog–Ingold priorities (34) for the parent acetal, that is, at C-5 in each 1,3-dioxane ring, the arrangement of the CH<sub>2</sub>OCH<sub>2</sub>C group with respect to the phenyl group is used to name the configuration present. This has the advantage



Scheme 2.

**Table 1.** Chemical shifts (ppm) of diols **3–5**.<sup>a–c</sup>

Compound		<i>cis</i>					<i>trans</i>					
		Ring						Ring				
	H1	H2'a	H2'e	H3	PhCH		H1	H2'a	H2'e	H3	PhCH	
3	3.44	3.72 <sup>d</sup>	4.13 <sup>d</sup>	3.97	5.41							
4	3.41	3.70	4.11 <sup>e</sup>	3.82	5.41	4.00	3.79 <sup>f</sup>	4.11 <sup>f</sup>	3.32	5.39		
5						3.98	3.74 <sup>g</sup>	4.11 <sup>g</sup>	3.21	5.42		
	C1	C2	C3	C2'	PhCH		C1	C2	C3	C2'	PhCH	
3	64.5	39.3	71.8	70.5	102.2							
4	64.2	39.4	71.6	70.6	102.1	62.3	39.3	72.4	70.2	102.1		
5						62.4	39.4	72.7	70.1	102.1		

<sup>a</sup>Numbering shown on structures.<sup>b</sup>The assignment of H2'a and H2'e based on chemical shifts (35) was supported by a larger NOESY cross-peak between the signal of H2'a and that of the acetal proton than that of H2'e and the acetal proton.<sup>c</sup>Aromatic protons and carbons are not shown.<sup>d</sup> $J_{2'a'2'e} = J_{6'a'6'e} = 11.9$  Hz.<sup>e</sup> $J_{2'a'2'e} = 12.5$  Hz.<sup>f</sup> $J_{6'a'6'e} = 12.2$  Hz.<sup>g</sup> $J_{2'a'2'e} = J_{6'a'6'e} = 11.6$  Hz.**Table 2.** Chemical shifts (ppm) of acetates **3a–5a**.<sup>a–c</sup>

Compound		<i>cis</i>					Ring					<i>trans</i>		Ring					
	H1	H2'a	H2'e	H3	PhCH	Ac	H1	H2'a	H2'e	H3	PhCH	Ac		H1	H2'a	H2'e	H3	PhCH	Ac
3a	3.94	3.81 <sup>d</sup>	4.10 <sup>d</sup>	3.84	5.43	2.06													
4a	3.95	3.84 <sup>e</sup>	4.08 <sup>e</sup>	3.74	5.44	2.10	4.46	3.91 <sup>f</sup>	4.11 <sup>f</sup>	3.32	5.42	2.05							
5a							4.47	3.90 <sup>f</sup>	4.11 <sup>f</sup>	3.20	5.44	2.09							
	C1	C2	C3	C2'	PhCH	Ac	C1	C2	C3	C2'	PhCH	Ac		C1	C2	C3	C2'	PhCH	Ac
3a	64.1	38.2	69.9	69.8	101.1	20.8													
4a	63.9	38.2	70.1	69.7	101.9	21.0	63.3	38.2	71.3	69.9	102.1	20.9							
5a							63.1	38.2	71.4	69.8	102.2	21.0							

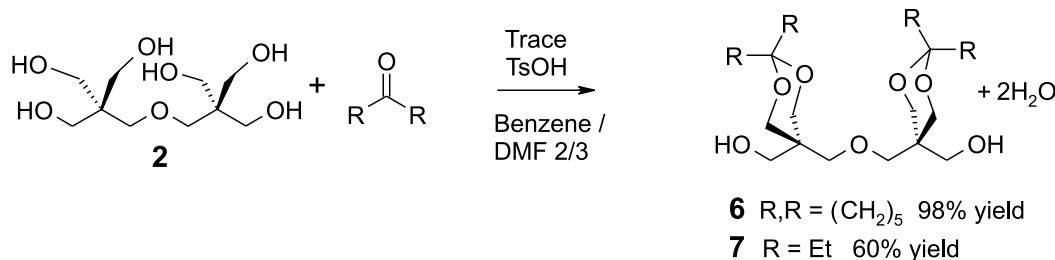
<sup>a</sup>The assignment of H2'a and H2'e based on chemical shifts (35) was supported by a larger NOESY cross-peak between the signal of H2'a and that of the acetal proton than that of H2'e and the acetal proton.<sup>b</sup>Aromatic protons and carbons are not shown.<sup>c</sup> $J_{2'a'2'e} = J_{6'a'6'e} = 11.90$  Hz.<sup>d</sup> $J_{2'a'2'e} = J_{6'a'6'e} = 11.90$  Hz.<sup>e</sup> $J_{2'a'2'e} = 11.75$  Hz.<sup>f</sup> $J_{6'a'6'e} = 11.90$  Hz.

that substitution does not change the description of the stereoisomer. All numbering of atoms in these compounds in

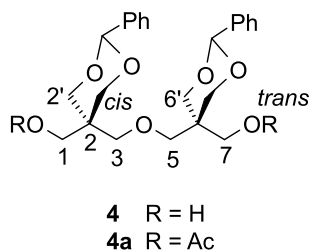
this publication is based on that of the parent 4-oxa-1,7-heptanediol system as illustrated in the structure of **3**, except



Scheme 3.



where features related to 1,3-dioxane rings are discussed. Carbons directly attached to carbon-2 are designated carbon-2' and carbon-2''.



Compound **4** was assigned the  $C_s$  symmetric *cis,trans*-structure from the observation of two sets of signals in the NMR spectra of it and its diacetate (**4a**), arising from the two diastereotopic halves of the molecules (see Tables 1 and 2). The structures of the two  $C_{2v}$  symmetric isomers (**3** and **5**) were obtained from their X-ray structures and from that of the di-*O*-benzoyl derivative of **3**, **3b**. ORTEP diagrams of the structures of **3b** and **5** are shown in Figs. 1 and 2 and the crystal data is given in Table 3. The X-ray structure of the *cis,cis*-structure **3** contains interesting hydrogen-bonding features that are discussed in detail elsewhere.<sup>2</sup> The crystal structures of it and of its di-*O*-benzoyl derivative (**3b**) (see Fig. 1) establish that **3** has the *cis,cis*-configuration and that of **5** confirms its assignment as the *trans,trans*-isomer.

The <sup>1</sup>H NMR chemical shifts of the exocyclic CH<sub>2</sub> groups do not fit the normal pattern (35) in which the signals of equatorial groups on six-membered rings are more deshielded than those of axial groups (see Tables 1 and 2). In the spectrum of the *cis,cis* isomer **3**, the methylene protons in the equatorial CH<sub>2</sub>OH group appear at 3.44 ppm, while those in the axial CH<sub>2</sub>OC group appear at 3.97 ppm; in the spectrum of the *trans,trans* isomer **5**, the methylene protons in the equatorial CH<sub>2</sub>OC group appear at 3.21 ppm, while those in the axial CH<sub>2</sub>OH group appear at 3.98 ppm. Weber had previously assigned signals for analogous pentaerythritol signals in the same way (25) and it is well-known that axial substituents at C-5 of 1,3-dioxane derivatives are more deshielded than equatorial substituents (36–38).

The <sup>13</sup>C NMR chemical signals of the CH<sub>2</sub>OH groups are particularly useful for assignments, appearing in an other-

Table 3. Crystal data for **3b** and **5**.<sup>a</sup>

Compound	<b>3b</b>	<b>5</b>
Empirical formula	C <sub>38</sub> H <sub>38</sub> O <sub>9</sub>	C <sub>12</sub> H <sub>15</sub> O <sub>3.5</sub>
FW	638.71	215.25
<i>T</i> (K)	293(2)	293(2)
Wavelength (Å)	1.5418	1.5418
Crystal system	Triclinic	Monoclinic
Space group	<i>P</i> 1	<i>C</i> 2
<i>a</i> (Å)	14.547(4)	19.760(4)
<i>b</i> (Å)	19.069(4)	5.847(3)
<i>c</i> (Å)	6.004(2)	10.553(3)
$\alpha$ (°)	91.70(2)	90
$\beta$ (°)	100.07(2)	115.03(2)
$\gamma$ (°)	90.02(2)	90
<i>V</i> (Å <sup>3</sup> )	1639.0(7)	1104.8(6)
<i>Z</i>	2	4
<i>D</i> <sub>calcd.</sub> (Mg m <sup>-3</sup> )	1.294	1.294
$\mu$ (mm <sup>-1</sup> )	0.756	0.781
<i>F</i> (000)	676	460
No. of reflns. collected	4575	1033
No. of indep. reflns., <i>R</i> <sub>int</sub>	4342, 0.1200 <sup>b</sup>	999, 0.0432
<i>S</i> (GoF) on <i>F</i> <sup>2</sup>	0.925	1.108
<i>R</i> [ <i>I</i> > 2 <i>F</i> ( <i>I</i> )]	0.0373	0.0431
<i>wR</i> (all data)	0.1431	0.1255
Largest diff. peak, hole (e Å <sup>-3</sup> )	0.168, -0.197	0.227, -0.242

<sup>a</sup>Crystallographic information deposited with the Cambridge Crystallographic Data Centre<sup>3</sup> and CISTI<sup>4</sup>.

<sup>b</sup>0.0279 for the 5*F* data (136 reflections).

wise unoccupied region. Those of equatorially oriented carbons in *cis* rings appear at 64 to 65 ppm while the axial ones in *trans* rings appear at 62.0 to 62.5 ppm. In contrast to the observations made about for the <sup>1</sup>H NMR spectra above, this trend is opposite to what has been observed for 2-substituted-5-methyl-1,3-dioxanes; axial methyl carbons are more deshielded than those of their equatorial counterparts (37–39).

The individual proportions of the isomers in the 85% total yield of di-*O*-benzylidene isomers were obtained by taking the isolated yields of the diacetates of **4** and **5** and extrapo-

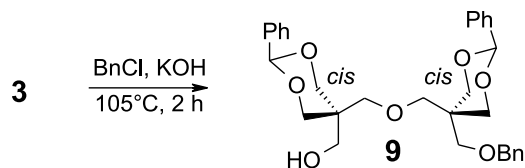
<sup>2</sup>T.B. Grindley, H. Al-Mughaid, K.N. Robertson, T.S. Cameron, M.D. Lumsden, D. MacLaren, and M.A. White. In preparation.

<sup>3</sup>Crystallographic information has been deposited with the Cambridge Crystallographic Data Centre (CCDC Nos. 199279 and 199280 for **3b** and **5**, respectively). Copies of the data can be obtained free of charge via [www.ccdc.cam.ac.uk/conts/retrieving.html](http://www.ccdc.cam.ac.uk/conts/retrieving.html) (or from the Cambridge Crystallographic Data Centre, 12 Union Road, Cambridge CB2 1EZ, U.K.; fax: +44 1223 336033; or [deposit@ccdc.cam.ac.uk](mailto:deposit@ccdc.cam.ac.uk)).

<sup>4</sup>Supplementary data, which includes further X-ray data and NMR spectra, may be purchased from the Depository of Unpublished Data, Document Delivery, CISTI, National Research Council of Canada, Ottawa, ON K1A 0S2, Canada ([http://www.nrc.ca/cisti/irm/unpub\\_e.shtml](http://www.nrc.ca/cisti/irm/unpub_e.shtml) for information on ordering electronically).



Scheme 4.



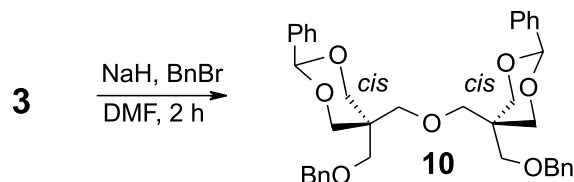
lating back to the original mixture. These were 34:41:24% for **3**:**4**:**5**, respectively, fairly close to a statistical distribution. As expected from the similarity of the substituents at the two C-5 positions of each 1,3-dioxane ring, the differences in stability between the *cis*- and *trans*-isomers are very small.

Murguía et al. (40) recently introduced the use of DMF–benzene mixtures as solvents for the formation of acetals from diols and polyols that are very insoluble in benzene or toluene, particularly from pentaerythritol. Azeotropic removal of water from this solvent mixture can be performed exactly as with pure benzene. Application of this procedure to the formation of benzylidene acetals of **2** gave about the same yield of di-*O*-benzylidene acetals as obtained under the conditions described above, that is, using benzene alone as a solvent. The stereoisomeric distribution, measured from the intensities of the  $^{13}\text{C}$  NMR peaks for the C-2',2'',6',6'' carbons (70 to 71 ppm), was also very close to statistical.

Use of toluene or DMF–toluene mixtures for this reaction under conditions for the azeotropic removal of water was less satisfactory in that lower yields of the di-*O*-benzylidene acetals were obtained. Under these conditions, the product mixture always contained products that moved faster than the di-*O*-benzylidene acetals on TLC. The compound giving the most intense fast-moving spot was isolated and identified as di-*O*-benzylidenepentaerythritol (23, 41). This product probably arises from a fragmentation reaction, for which one possibility is shown in Scheme 2. Intermediates resulting from dehydration of compounds resulting from the aldol condensation of formaldehyde and acetaldehyde are thought to lead to the by-product dipentaerythritol during the preparation of pentaerythritol (42). A fragmentation reaction, such as that observed here, is expected to be aided by a large positive entropy of reaction and thus to be strongly favored by increased reaction temperature. It appears that the approximately 30°C increase in reaction temperature on changing the solvent from benzene to toluene is sufficient to make fragmentation a significant process.

In the report (32) of the transacetalization reaction of **2** with diethyl 2,2-diethoxyethylphosphonate, 10.2 g of **2** were stirred with 2.02 equiv of the acetal and 20 mL of concentrated hydrochloric acid at room temperature for 8 days. The product, a syrup, was obtained in 90% yield after neutralization and extraction. These were equilibrium conditions. As for the benzylidene acetals, there is no reason to believe that the *cis*- and *trans*-isomers would have significantly different stabilities. Therefore, this product should be a mixture of the three possible stereoisomers. The  $^1\text{H}$  NMR and  $^{13}\text{C}$  NMR spectra of the product were recorded at either 60 MHz or 100 MHz and at 25.2 MHz, respectively (32). In the  $^1\text{H}$  NMR spectra (32), the methylene units in the  $\text{CH}_2\text{OH}$  groups were reported to appear as doublets ( $J = 7.5$  Hz) with no identified coupling partner (the OH peak was a singlet).

Scheme 5.



Similarly, the methylene units in the  $\text{CCH}_2\text{OCH}_2\text{C}$  group were reported (32) to appear as a doublet ( $J = 6.0$  Hz) with no identified coupling partner. Since neither of these two groups gave rise to doublets in individual isomers, this is clear evidence that a mixture was present. We conclude that the expected mixture was present in this literature product, even though the reported (32) spectral data cannot be interpreted fully. It should be noted that the spectra of the initial di-*O*-benzylidene acetal mixture are difficult to interpret, even on higher field spectrometers.

Reaction of dipentaerythritol with cyclohexanone in the presence of a 0.1 mol equiv (based on cyclohexanone) of *p*-toluenesulfonic acid monohydrate in benzene–DMF (40:60, v/v) for 6 h at reflux (the conditions of Murguía et al. (40)) afforded the diacetal **6** in 98% yield (Scheme 3). The amount of *p*-toluenesulfonic acid used is important; the reaction proceeded very slowly in the presence of <1 mol% but occurred rapidly when >2 mol% was added, again based on the ketone. Under the same conditions, 3-pentanone gave the corresponding diacetal **7** in 60% yield. The di-*O*-methylene acetal (**8**) derivative of dipentaerythritol was formed in 41% yield by stirring with 37% aqueous formaldehyde and concentrated hydrochloric acid at 85°C for 14 h.

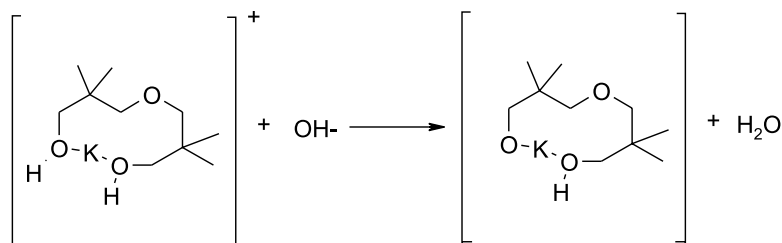
It is interesting to note that the chemical shift differences between the two sets of signals for H'2, H2'', H6', and H6'' were very small in the  $^1\text{H}$  NMR spectra of **6**–**8** in chloroform-*d* (0 (0.034 in pyridine-*d*<sub>5</sub>), 0, and 0.025 ppm, respectively) but were much larger in those of **3**–**5** (0.42, 0.41 and 0.32 (*trans*-ring), and 0.37 ppm, respectively). These differences reflect the conformational properties of the two sets of compounds. In the benzylidene acetals, the 2-phenyl group in each 1,3-dioxane ring fixes the chair conformer giving rise to distinct equatorial and axial orientations for the two protons on C-2', C-2'', C-6', and C-6''. In contrast, the 1,3-dioxane rings of **6**–**8** were present in both chair conformers in approximately equal amounts, also reflected in the small chemical shift difference between the acetal protons of the di-*O*-methylene acetal **8** (0.046 ppm).

## Formation of benzyl ethers

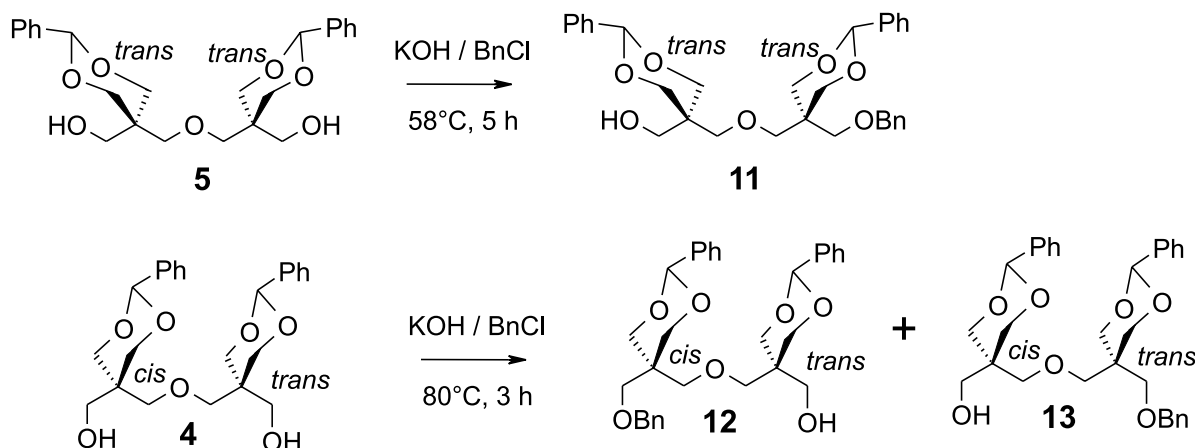
Benzylation of diol **3** by stirring with potassium hydroxide in benzyl chloride as the solvent for 2 h at 105°C surprisingly afforded the monobenzyl ether (**9**) in 83% yield (Scheme 4). This high selectivity was reproduced a number of times in reactions performed at temperatures ranging from room temperature up to 105°C. Selective formation of a monoether from a diol in good yield is highly unusual and is only possible if the rate of the first substitution is substantially faster than that of the second. Neither allowing the reaction to proceed longer nor raising the reaction temperature produced the di-*O*-benzyl derivative. However, this latter compound (**10**) could be made by reaction with sodium hy-



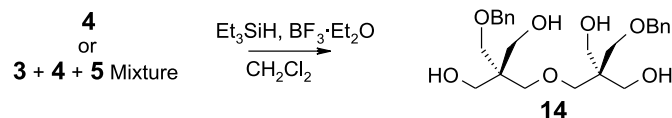
Scheme 6.



Scheme 7.



Scheme 8.



dride and benzyl bromide in *N,N*-dimethylformamide (see Scheme 5).

The normal outcome of attempts to form monosubstituted products from two identical isolated reactive sites are mixtures of unsubstituted, monosubstituted, and disubstituted products because the site remaining after the first substitution has about the same reactivity as those in the original compound (43–47). Selective monobenzylation of these diols can arise in two ways: the reactivity of one diol hydroxyl group under these conditions may be greater than that of an isolated alcohol or the introduction of the first benzyl may have decreased the reactivity of the unreacted hydroxyl. The latter possibility could occur if the monobenzyl derivative existed mainly in conformations where the remaining hydroxymethyl group was shielded by the benzyl group. This possibility was investigated by measuring 1D-NOEs in chloroform. There were no substantial NOEs between the methylene hydrogens of the hydroxymethyl group and either the methylene hydrogens or the phenyl hydrogens of the benzyl group. We thus concluded that acceleration of the initial benzylation must be the cause of this effect.

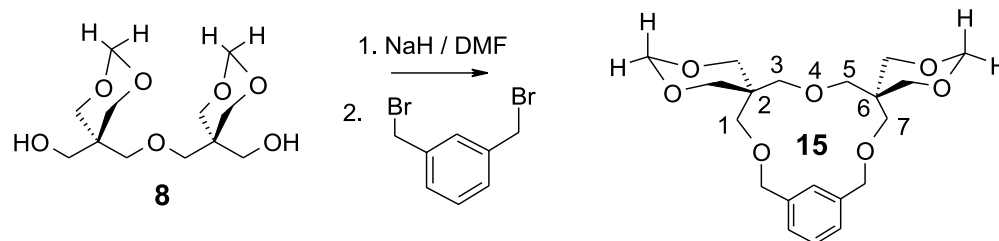
To confirm this hypothesis, a competition reaction was performed in the presence of two equivalents of an unhindered primary alcohol (1-octanol) (equivalent number of hydroxyl groups) at room temperature for about the same time as nor-

mally taken for reaction completion with **3**. Surprisingly, these conditions yielded, after work-up, an approximately 2:1:1 mixture of the mono-*O*-benzyl derivative, the di-*O*-benzyl derivative, and 1-octanol benzyl ether with no indication of the presence of 1-octanol. The benzylation of the monobenzyl ether was much faster in the presence of 1-octanol than in its absence. This observation indicates that complexation of the potassium cation to at least two hydroxyl groups is key to the selectivity of this reaction. A tentative hypothesis is that complexation of the second hydroxyl to a potassium cation makes both hydroxyl protons sufficiently acidic that one can be removed easily, generating a more potent nucleophile (see Scheme 6). In the absence of 1-octanol, when one oxygen atom becomes hindered by formation of the monobenzyl ether, the remaining hydroxyl becomes too insufficiently acidic to be competitive as a nucleophile.

Bessodes and Boukarim (47) have obtained selective monobenzylation of 1,*n*-diols with benzyl bromide in tetrahydrofuran containing a catalytic amount of crown ether, using as base potassium hydroxide or sodium hydroxide, but not lithium hydroxide. They attributed the selectivity to a surface effect under their heterogeneous reaction conditions because the ineffective base (lithium hydroxide) was the only one to dissolve in the reaction medium. The selectivity obtained here was obtained under fairly similar conditions to those of these authors. However, the current selectivity cannot be attributed to surface reactions because selectivity was obtained under both homogeneous (higher temperatures) and heterogeneous conditions. Bouzide and Sauvé (46) obtained selective monobenzylation of symmetrical diols using silver oxide and benzyl bromide in dichloromethane and other nonpolar solvents. They attributed the selectivity to ease of



Scheme 9.



initial deprotonation from an intermediate similar to that proposed here.

Treatment of the *trans,trans*-isomer (**5**) under the same conditions also gave a mono-*O*-benzyl derivative (**11**) (69%). However, the *cis,trans*-isomer (**4**) can form two different monobenzyl ethers. Both isomers were formed; substitution on the equatorial hydroxymethyl group in the *cis*-ring to give compound **12** (54% yield) was preferred to substitution on the axial hydroxymethyl group in the *trans*-ring to give compound **13** (16% yield) (see Scheme 7).

### Other reactions

Benzylidene acetals can be reduced to hydroxy benzyl ethers with a variety of reducing agents, most commonly  $\text{LiAlH}_4\text{-AlCl}_3$  (48, 49),  $\text{NaCNBH}_3\text{-HCl}$  (50), and  $\text{Et}_3\text{SiH-TFA}$  (51). Recently, Debenham and Toone (52) have reported a facile procedure for the regioselective reductive cleavage of the benzylidene group to the corresponding benzyl ether with  $\text{Et}_3\text{SiH-BF}_3\cdot\text{Et}_2\text{O}$ . Reduction of **4** under these latter conditions in dichloromethane for 12 h resulted in the clean formation of the dibenzyl ether of dipentaerythritol (**14**) in 64% yield. Application of the same procedure to the chromatographically purified mixture of di-*O*-benzylidene acetals (**3-5**) also gave **14** in similar yield (68%) (see Scheme 8).

Reaction of the di-*O*-methylene acetal with sodium hydride in DMF followed by  $\alpha,\alpha$ -dibromo-*m*-xylene yielded a crown ether (**15**) in modest yield (12%) (Scheme 9). The observation of small chemical shift differences between the two sets of protons on C2', C2'', C6', and C6'' (0.034 ppm) and also between the two acetal protons (0.024 ppm) indicates that the chair conformers of the 1,3-dioxane rings in this crown ether are still inverting rapidly on the NMR time scale.

We have now developed efficient methods for the formation of di-*O*-cyclohexylidene and di-*O*-benzylidene and other acetals of dipentaerythritol. We have established that all diacetals of dipentaerythritol derived from aldehydes, as exemplified by the di-*O*-benzylidene acetals, will be present as mixtures of the *cis,cis*-, *cis,trans*-, and *trans,trans*-isomers and have developed a method to separate and identify them. We have demonstrated that these latter acetals can be converted either into monobenzyl ethers or dibenzyl ethers efficiently and have demonstrated other chemistry of these diacetals. The ability to form selectively substituted dipentaerythritol derivatives has allowed us to make both novel clusters with carbohydrate end groups (glycoclusters) and novel gemini surfactants which will be reported in subsequent publications.

## Experimental section

### General methods

Melting points were determined with a Fisher-Johns melting point apparatus and are uncorrected.  $^1\text{H}$  and  $^{13}\text{C}$  NMR spectra were recorded at 300 K in 5 mm NMR tubes on Bruker AC-250 MHz or AMX-400 NMR spectrometers operating at 250.13 or 400.13 and 62.9 or 100.08 MHz, respectively, on solutions in chloroform-*d*, unless otherwise indicated. Chemical shifts are given in parts per million (ppm) ( $\pm 0.01$  ppm) relative to that of tetramethylsilane (TMS) (0.00 ppm) in the case of  $^1\text{H}$  NMR spectra, and to the central line of chloroform-*d* ( $\delta$  77.23) for the  $^{13}\text{C}$  NMR spectra. All assignments were confirmed by COSY, HETCOR, HMQC, or HMBC experiments. The exact masses of compounds **3**, **3a**, **4**, **4a**, **5**, **5a**, **8**, and **15** were measured on a CEC 21-110B mass spectrometer using electron ionization (70 eV). The exact masses of compounds **6**, **7**, **9**, and **14** were measured by positive ion mode electrospray ionization on a Micromass ZabSpec Hybrid Sector-TOF mass spectrometer. The liquid carrier (methanol) was infused into the electrospray source by means of a Harvard syringe pump at a flow rate of  $10\ \mu\text{L min}^{-1}$ . The masses of **10**, **11**, and **13** were measured on a Micromass MALDI-TOF mass spectrometer calibrated with a Sigma ProteoMass Peptide MALDI-MS calibration kit. Pyridine was dried by refluxing over calcium hydride followed by distillation. Dichloromethane was refluxed over calcium hydride for 1 h, then distilled over 3 Å molecular sieve. Chloroform was dried with magnesium sulfate, then distilled and stored over 4 Å molecular sieve. Cyclohexanone and 3-pentanone were distilled prior to use. *N,N*-Dimethylformamide was stored over activated 4 Å molecular sieve for 72 h. It was distilled under reduced pressure over freshly activated 4 Å molecular sieve. Benzyl chloride was dried with magnesium sulfate, refluxed over calcium hydride, and then fractionally distilled under reduced pressure, collecting the middle fraction. It was stored over calcium hydride. Benzylidene acetals were visualized by quenching of fluorescence or by spraying the plate with a solution (53) of 0.2% *p*-methoxyphenol in ethanol – 2 N  $\text{H}_2\text{SO}_4$  (1:1, v/v) and heating on a hot plate until colour developed. The di-*O*-methylene acetal was located by spraying (54) with an acidic solution of anisaldehyde in ethanol (ethanol (9 mL), anisaldehyde (0.5 mL), and concentrated sulfuric acid (0.5 mL)) and heating on a hot plate until colour developed. Other compounds were visualized by UV where applicable and (or) were located by spraying with a solution of 2% ceric sulfate in 1 M sulfuric acid followed by heating on a hot plate until colour developed. Compounds



were purified on silica gel (TLC standard grade, 230–400 mesh) by flash chromatography using specified eluents. Analyses were performed by the Canadian Microanalytical Service, Delta, B.C.

### X-ray structure determinations

Crystals of **3b** ( $1.50 \times 0.10 \times 0.10$  mm) and **5** ( $0.70 \times 0.25 \times 0.10$  mm) were mounted on glass fibres. All measurements were made at room temperature on a Rigaku AFC5R diffractometer equipped with a 12 kW rotating anode generator and using graphite-monochromated Cu-K $\alpha$  radiation. For each structure, cell constants and an orientation matrix for data collection were obtained from a least-squares refinement using the setting angles of a minimum of 24 reflections. During the data collections the intensities of three representative reflections were measured after every 150 reflections. Over this time the standards decreased by 3.9% for compound **5** so a polynomial decay correction was applied. An empirical absorption correction was also applied in each case; this resulted in transmission factors ranging from 0.665 to 1.000 (**3b**) or 0.660 to 1.000 (**5**). In both determinations, the data were corrected for Lorentz and polarization effects and a correction for secondary extinction was applied. The structures were solved by direct methods (55) and expanded using Fourier techniques. Full-matrix least-squares refinement on  $F^2$  data was carried out using the program SHELXL97 (56). The non-hydrogen atoms were refined anisotropically. In general, the hydrogen atoms were included in geometrically calculated positions but were not refined. The only exception was H(O1) of compound **5**. The position of H(O1) was located in the Fourier difference map and was refined isotropically. Crystal data are summarized in Table 3.<sup>3,4</sup>

### *cis,cis*-, *cis,trans*-, and *trans,trans*-2,2':6,6'-Di-O-benzylidene-2,2',6,6'-tetra(hydroxymethyl)-4-oxa-1,7-heptanediol (**3**, **4**, and **5**, respectively)

A suspension of dipentaerythritol (**2**) (12.71 g, 0.05 mol), benzaldehyde (11.2 mL, 0.11 mol, 2.2 equiv), and *p*-toluenesulfonic acid monohydrate (0.1 g) in benzene (270 mL) was refluxed for 2 h then allowed to cool to room temperature. Additional benzene (250 mL) and *p*-toluenesulfonic acid monohydrate (0.4 g) were then added and the mixture was refluxed for 8 h using a Dean–Stark apparatus. After being cooled to room temperature, the homogeneous reaction mixture was stirred with calcium carbonate (5 g) and filtered. The filtrate was dried over MgSO<sub>4</sub> and concentrated to an oily residue (18.28 g), which solidified upon standing. Part of the above residue (3.85 g) was separated by flash column chromatography using ethyl acetate – hexanes (1:1) as the eluent. A mixture (1.77 g) of isomers **4** and **5** eluted first ( $R_f$  = 0.32) (eluent ethyl acetate – hexanes, 2:1). The second component was isomer **3** ( $R_f$  = 0.15) (eluent ethyl acetate – hexanes, 2:1) as an amorphous solid (1.32 g, 34%), which was then recrystallized from 1-propanol to afford pure colorless needles, mp 164–166°C, lit. value (31) 166°C. For <sup>1</sup>H and <sup>13</sup>C NMR data, see Table 1. EI-HR-MS calcd. for C<sub>24</sub>H<sub>30</sub>O<sub>7</sub>: 430.1991; found: 430.1985.

The first eluting fraction (1.77 g) from the previous column was dissolved in pyridine (128 mL). The stirred solution was cooled to 0°C and acetic anhydride (128 mL) was added dropwise. After being allowed to warm to room tem-

perature, the solution was stirred for 12 h, then poured into ice water (500 mL). The resulting mixture was extracted with dichloromethane (4 × 50 mL). The combined extracts were dried over MgSO<sub>4</sub> and concentrated to an oily residue. The residue was separated by flash column chromatography on silica gel (ethyl acetate – hexanes, 1:5).

First to elute was 1,7-di-*O*-acetyl-*cis,trans*-2,2':6,6'-di-*O*-benzylidene-2,2',6,6'-tetra(hydroxymethyl)-4-oxa-1,7-heptanediol (**4a**), an amorphous solid (2.2 g).  $R_f$  0.74 (ethylacetate – hexanes, 1:1), mp 108 to 109°C. For <sup>1</sup>H and <sup>13</sup>C NMR data, see Table 2. EI-HR-MS calcd. for C<sub>28</sub>H<sub>34</sub>O<sub>9</sub>: 514.2202; found: 514.2210.

The second component was 1,7-di-*O*-acetyl-*trans,trans*-2,2':6,6'-di-*O*-benzylidene-2,2',6,6'-tetra(hydroxymethyl)-4-oxa-1,7-heptanediol (**5a**), an amorphous solid (1.35 g) that crystallized from acetone–methanol as microcrystalline needles.  $R_f$  0.66 (ethyl acetate – hexanes, 1:1), mp 139 to 140°C. For <sup>1</sup>H and <sup>13</sup>C NMR data, see Table 2. EI-HR-MS calcd. for C<sub>28</sub>H<sub>34</sub>O<sub>9</sub>: 514.2202; found: 514.2211.

A solution of **4a** (2.2 g, 0.004 mol) in dry chloroform (100 mL) was cooled to 0°C and 1 M sodium ethoxide (2 mL) was added dropwise. The mixture was then stirred until TLC indicated the disappearance of the starting material (3 h). The chloroform solution was washed with water (6 × 30 mL), dried over MgSO<sub>4</sub>, and concentrated to afford the de-*O*-acetylated *cis,trans*-isomer **4** (1.53 g, 83%), which was recrystallized from 1-propanol; mp 126 to 127°C. For <sup>1</sup>H and <sup>13</sup>C NMR data, see Table 1. EI-HR-MS calcd. for C<sub>24</sub>H<sub>30</sub>O<sub>7</sub>: 430.1991; found: 430.1987.

1,7-Di-*O*-acetyl-*trans,trans*-2,2':6,6'-di-*O*-benzylidene-2,2',6,6'-tetra(hydroxymethyl)-4-oxa-1,7-heptanediol (**5a**) (1.35 g, 0.0026 mol) was de-*O*-acetylated as above, to give the *trans,trans*-isomer **5** as an amorphous solid (0.77 g, 82%), which was then recrystallized from 1-propanol to afford thin colorless plates; mp 170–173°C. For <sup>1</sup>H and <sup>13</sup>C NMR data, see Table 1. EI-HR-MS calcd. for C<sub>24</sub>H<sub>30</sub>O<sub>7</sub>: 430.1991; found, 430.1978. For X-ray data, see Table 3.<sup>3,4</sup>

### 1,7-Di-*O*-acetyl-*cis,cis*-2,2':6,6'-di-*O*-benzylidene-2,2',6,6'-tetra(hydroxymethyl)-4-oxa-1,7-heptanediol (**3a**)

Compound **3** (50 mg) was acetylated as for the **4**, **5** mixture above. Colorless crystals (55 mg, 92%) were obtained that were recrystallized from acetone–methanol; mp 104 to 105°C. For <sup>1</sup>H and <sup>13</sup>C NMR data, see Table 2. EI-HR-MS calcd. for C<sub>28</sub>H<sub>34</sub>O<sub>9</sub> (M<sup>+</sup>): 514.2202; found: 514.2176. Calcd. for C<sub>28</sub>H<sub>33</sub>O<sub>9</sub>: 513.2124; found: 513.2117.

### Alternative method of preparation of *cis,cis*-, *cis,trans*-, and *trans,trans*-2,2':6,6'-di-*O*-benzylidene-2,2',6,6'-tetra(hydroxymethyl)-4-oxa-1,7-heptanediol (**3**, **4**, and **5**, respectively)

A suspension of dipentaerythritol (**2**) (1.0 g, 3.9 mmol), benzaldehyde (0.90 mL, 8.8 mmol, 2.2 equiv), and *p*-toluenesulfonic acid monohydrate (0.45 g, 2.6 mmol) in dry benzene (60 mL) and *N,N*-dimethylformamide (90 mL) was refluxed for 5 h with azeotropic removal of water. After being cooled to room temperature, the homogeneous reaction mixture was stirred with calcium carbonate (2 g) and filtered. The filtrate was dried over MgSO<sub>4</sub> and concentrated to an oily residue, which was purified by flash column chroma-



tography on silica gel (ethyl acetate – hexane, 1:2) to give a mixture of compounds **3**, **4**, and **5** (1.46 g, 85%).

**Preparation of *cis,cis*-, *cis,trans*-, and *trans,trans*-2,2':6,6'-di-*O*-benzylidene-2,2',6,6'-tetra(hydroxymethyl)-4-oxa-1,7-heptanediol (**3**, **4**, and **5**, respectively) in toluene**

A suspension of dipentaerythritol (5 g, 19.7 mmol), benzaldehyde (4.4 mL, 43.3 mol, 2.2 equiv), and *p*-toluenesulfonic acid monohydrate (0.5 g) in toluene (650 mL) was refluxed for 8 h using a Dean–Stark apparatus. After cooling to room temperature, the unreacted material (1.55 g) was filtered off. The filtrate was stirred with calcium carbonate (2 g) and filtered, dried over  $\text{MgSO}_4$  and concentrated to dryness. The oily residue was separated by flash column chromatography using ethyl acetate – hexanes (1:1) as the eluent. First to elute was di-*O*-benzylidenepentaerythritol (0.19 g, 3.3%), mp 155–158°C, lit. value (57) 160°C.  $^1\text{H}$  NMR spectrum was identical to that of Clark (41). The second component was a mixture (2.81 g) of isomers **4** and **5**. The third component was isomer **3** (0.94 g).

**1,7-Di-*O*-benzoyl-*cis,cis*-2,2':6,6'-di-*O*-benzylidene-2,2',6,6'-tetra(hydroxymethyl)-4-oxa-1,7-heptanediol (**3b**)**

Benzoyl chloride (0.1 mL) was added dropwise to a stirred solution of the *cis,cis*-isomer (**3**, 100 mg, 0.230 mmol) in dry pyridine (3 mL) and stirring was continued for 1 h. The reaction mixture was poured into ice water (20 mL) and the resulting mixture was extracted with dichloromethane (3 × 15 mL). The combined extracts were dried ( $\text{MgSO}_4$ ) and concentrated to a solid residue (178 mg, 70%) which was then recrystallized from ethanol to afford fine colorless needles, mp 165–167°C.  $^1\text{H}$  NMR  $\delta$ : 7.97–8.02 (m, 4 × PhH, 20H), 5.45 (s, 2 × PhCH), 4.24 (s, 2 ×  $\text{CCH}_2\text{OCO}$ ), 4.23, 3.93 (AB q, 8H,  $J = 11.9$  Hz, H2', H2'', or H6', H6''), 4.00 ( $\text{CCH}_2\text{OCH}_2\text{C}$ ).  $^{13}\text{C}$  NMR  $\delta$ : 166.25 (2 × PhCO), 128.45–138.11 (4 × PhC), 102.07 (2 × acetal C), 70.13 ( $\text{CCH}_2\text{OCH}_2\text{C}$ ), 69.89 (C2', C2'', C6', C6''), 64.40 ( $\text{CCH}_2\text{OCO}$ ). For X-ray data, see Table 3.<sup>3,4</sup>

**2,2':6,6'-Di-*O*-cyclohexylidene-2,2',6,6'-tetra(hydroxymethyl)-4-oxa-1,7-heptanediol (**6**)**

Dipentaerythritol (2.60 g, 0.010 mol), freshly distilled cyclohexanone (0.025 mol, 2.5 equiv), and *p*-toluenesulfonic acid (0.45 g, 2.6 mmol) were stirred in a refluxing mixture of dry benzene and dry dimethylformamide (130 mL, 4:6 (v/v)) for 6 h with removal of water. After being cooled to room temperature, the homogeneous reaction mixture was stirred with calcium carbonate (2 g) and filtered. The filtrate was dried over  $\text{MgSO}_4$  and concentrated to give the title compound (4.02 g, 98%) as a pure colorless solid that was recrystallized from ethyl acetate, mp 116–118°C.  $^1\text{H}$  NMR  $\delta$ : 3.70 (s, 2 × H2', H2'', H6', H6'', 8H), 3.64 (s,  $\text{CH}_2\text{OH}$ , 4H), 3.49 ( $\text{CCH}_2\text{OCH}_2\text{C}$ , 4H), 1.42–1.74 (complex m, 2 × cyh H, 20H).  $^1\text{H}$  NMR (pyridine- $d_5$ , 400.13 MHz)  $\delta$ : 4.05 (AB quartet, 2 × H2', H2'', H6', and H6''),  $\Delta\nu = 0.0336$  ppm,  $J = 11.6$  Hz, 8H), 4.03 (s,  $\text{CH}_2\text{OH}$ , 4H), 3.73 ( $\text{CCH}_2\text{OCH}_2\text{C}$ , 4H), 1.35–1.90 (complex m, 2 × cyh H, 20H).  $^{13}\text{C}$  NMR  $\delta$ : 98.66 (2 × acetal C), 72.55 ( $\text{CCH}_2\text{OCH}_2\text{C}$ ), 63.86 (2 ×  $\text{CH}_2\text{OH}$ ), 62.21 (C2', C2'', C6', C6''), 39.63 (2 × C2), 32.72,

32.51 (2 × cyh C2, C6), 25.73 (2 × cyh C4), 22.63 (2 × cyh C3, C5). ES-HR-MS calcd. for  $\text{C}_{22}\text{H}_{38}\text{O}_7 + \text{Na}$ : 437.2515; found: 437.2511.

**2,2':6,6'-Di-*O*-(1-ethylpropylidene)-2,2',6,6'-tetra(hydroxymethyl)-4-oxa-1,7-heptanediol (**7**)**

Dipentaerythritol (2.60 g, 0.010 mol) was reacted with freshly distilled 3-pentanone (2.15 g, 2.6 mL, 0.025 mol) as above, to give the title compound (60%) as a colorless solid, mp 123–126°C.  $^1\text{H}$  NMR  $\delta$ : 3.67 (s, 2 × H2', H2'', H6', H6'', 8H), 3.63 (s,  $\text{CH}_2\text{OH}$ , 4H), 3.49 ( $\text{CCH}_2\text{OCH}_2\text{C}$ , 4H), 1.71 (q, 4 ×  $\text{CH}_3\text{CH}_2$ -, 8H,  $J = 7.32$  Hz), 0.88 (t, 4 ×  $\text{CH}_3\text{CH}_2$ -, 12H,  $J = 4.88$  Hz).  $^{13}\text{C}$  NMR  $\delta$ : 101.71 (2 × C ( $\text{CH}_2\text{CH}_3$ )<sub>2</sub>), 72.32 ( $\text{CCH}_2\text{OCH}_2\text{C}$ ), 63.60 (2 ×  $\text{CH}_2\text{OH}$ ), 62.36 (C2', C2'', C6', C6''), 39.25 (2 × C quat), 25.80, 25.53 (4 ×  $\text{CH}_3\text{CH}_2$ -), 7.62 (4 ×  $\text{CH}_3\text{CH}_2$ -). H-ES-MS calcd. for  $\text{C}_{20}\text{H}_{38}\text{O}_7 + \text{Na}$ : 413.2515; found: 413.2517.

**2,2':6,6'-Di-*O*-methylene-2,2,6,6-tetrahydroxymethyl-4-oxa-1,7-heptanediol (**8**)**

2,2,6,6-Tetrahydroxymethyl-4-oxa-1,7-heptanediol **2** (26.0 g) was stirred with 37% aqueous formaldehyde (26 mL) and concentrated hydrochloric acid (26 mL) at 85°C for 14 h, then cooled to room temperature. Sodium hydroxide pellets were added slowly until the solution was basic (12.5 g) and the cooled solution was filtered. The filtrate was extracted with dichloromethane (3 × 50 mL) and the combined extracts were washed with water (10 mL), dried ( $\text{MgSO}_4$ ), and concentrated to a syrupy residue (25.76 g). The residue was taken up in chloroform (50 mL). When hexanes (75 mL) were added, a colorless amorphous precipitate (7.3 g after air drying) was obtained and concentration followed by repetition yielded more precipitate (2.0 g). The residue (14.0 g) was separated by flash column chromatography on silica gel using ethyl acetate – hexanes (3:1) as the eluant and a further 2.26 g were obtained. Total yield 11.56 g, 40.6%.  $R_f$  0.34 (ethyl acetate – hexanes, 4:1). Recrystallization from chloroform–hexanes yielded lustrous colorless plates, mp 95 to 96°C.  $^1\text{H}$  NMR (400.13 MHz)  $\delta$ : 3.08 (br t, 2 H,  $J = 5.8$  Hz, OH), 3.51 (s, 4 H, H-3,5), 3.64 (d, 4H, H-1,7), 3.72 (AB q, 8H,  $J_{AB} = 11.25$  Hz,  $\Delta\delta_{AB} = 0.025$ ,  $\text{CH}_2\text{S}$  on C-2',2'',6,6'), 4.80 (AB q, 4H,  $J_{AB} = 6.08$  Hz,  $\Delta\delta_{AB} = 0.036$ , acetal  $\text{CH}_2$ ).  $^{13}\text{C}$  NMR (62.9 MHz)  $\delta$ : 39.89 (C-2,6), 62.54 (C-1,7), 69.74 (C-2',2'',6,6'), 71.14 (C-3,5), 94.27 (acetal C). HR-EI-MS calcd. for  $\text{C}_{12}\text{H}_{21}\text{O}_7$  ( $M - 1$ ): 277.1287; found: 277.1270.

***cis,cis*-2,2':6,6'-Di-*O*-benzylidene-7-benzoyloxy-2,2',6,6'-tetra(hydroxymethyl)-4-oxa-1-heptanol (**9**)**

Powdered potassium hydroxide (0.3 g, 5 mmol) was dissolved in a stirred solution of dry benzyl chloride (11.0 g, 10.0 mL, 86.9 mmol) over 20 min as the temperature was raised to 105°C. *cis,cis*-Diol **4** (100 mg, 0.23 mmol) was added and the solution was stirred for 2 h at 105°C. The reaction mixture was allowed to cool to room temperature and chloroform (25 mL) and water (25 mL) were added. The organic layer was washed with water (2 × 25 mL) and dried ( $\text{MgSO}_4$ ) and concentrated to a colorless syrup, that was purified by column chromatography on silica gel using ethyl acetate – hexanes (1:1) as the eluant. Yield: 100 mg, 83%.  $^1\text{H}$  NMR  $\delta$ : 7.23–7.77 (m, 3 × PhH, 15H), 5.41 (2 × PhCH),



4.45 (s,  $\text{PhCH}_2\text{O}$ , 2H), 4.14, 3.73 (AB q, 4H,  $J = 12.5$  Hz,  $\text{H}_2'$ ,  $\text{H}_2''$  or  $\text{H}_6'$ ,  $\text{H}_6''$ ), 4.11, 3.85 (AB q, 4H,  $J = 12.5$  Hz,  $\text{H}_6'$ ,  $\text{H}_6''$  or  $\text{H}_2'$ ,  $\text{H}_2''$ ), 3.97, 3.92 (s,  $\text{CCH}_2\text{OCH}_2\text{C}$ , 4H), 3.45 (s,  $\text{CH}_2\text{OH}$ , 2H), 3.27 (s,  $\text{CCH}_2\text{OCH}_2\text{Ph}$ , 2H).  $^{13}\text{C}$  NMR  $\delta$ : 126.14–138.20 ( $3 \times \text{PhC}$ ), 101.94, 102.08 ( $2 \times \text{PhC}$ ), 73.64 ( $\text{PhCH}_2\text{O}$ ), 72.80, 70.67 ( $\text{CCH}_2\text{OCH}_2\text{C}$ ), 70.53, 70.35 ( $\text{C}_2'$ ,  $\text{C}_2''$ ,  $\text{C}_6'$ ,  $\text{C}_6''$ ), 70.43 ( $\text{CCH}_2\text{OCH}_2\text{Ph}$ ), 65.44 ( $\text{CH}_2\text{OH}$ ), 39.06, 39.12 ( $2 \times \text{C quat}$ ). HR-ES-MS calcd. for  $\text{C}_{31}\text{H}_{36}\text{O}_7 + \text{Na}$ : 543.2359; found: 543.2360.

**1,7-Di-*O*-benzyl-*cis,cis*-2,2':6,6'-di-*O*-benzylidene-2,2',6,6'-tetra(hydroxymethyl)-4-oxa-1,7-heptanediol (10)**

After a solution of *cis,cis*-diol **3** (100 mg, 0.23 mmol) in DMF (20 mL) was cooled to  $0^\circ\text{C}$ , a 60% oil suspension of sodium hydride (50 mg, 1.2 mmol) was added and the mixture was allowed to stir for 30 min. Benzyl bromide (0.2 mL) was added and the mixture was allowed to warm to room temperature, then stirred for a further 3 h. Methanol (1 mL) was added. After 15 min the mixture was concentrated under reduced pressure, then partitioned between ethyl acetate (25 mL) and water (25 mL); the aqueous layer was extracted with ethyl acetate (25 mL), and the combined ethyl acetate layers were dried over  $\text{MgSO}_4$  and concentrated. The residue was purified by column chromatography on silica gel (ethyl acetate – hexane (1:5),  $R_f = 0.37$ ) to give the title compound (**10**) as a colorless oil (77 mg, 54%).  $^1\text{H}$  NMR  $\delta$ : 7.30–7.50 (m,  $4 \times \text{PhH}$ , 20H), 5.42 ( $2 \times \text{PhCH}$ , 2H) 4.43 (s,  $2 \times \text{PhCH}_2\text{O}$ , 4H), 4.11, 3.90 (AB q, 8H,  $J = 11.6$  Hz,  $\text{H}_2'$ ,  $\text{H}_2''$ ,  $\text{H}_6'$ ,  $\text{H}_6''$ ), 3.87 (s,  $\text{CCH}_2\text{OCH}_2\text{C}$ , 4H), 3.29 (s,  $\text{CCH}_2\text{OCH}_2\text{Ph}$ , 4H).  $^{13}\text{C}$  NMR  $\delta$ : 126.36–138.59 ( $4 \times \text{PhC}$ ), 101.99 (acetal C), 73.71 ( $\text{CH}_2\text{Ph}$ ), 70.57 ( $\text{CCH}_2\text{OCH}_2\text{C}$ ), 70.32 ( $\text{C}_2'$ ,  $\text{C}_2''$ ,  $\text{C}_6'$ ,  $\text{C}_6''$ ) 70.32 ( $\text{CH}_2\text{OCH}_2\text{Ph}$ ), 39.38 ( $\text{C quat}$ ). MALDI-TOF HR-MS calcd. for  $\text{C}_{38}\text{H}_{42}\text{O}_7 + \text{Na}$ : 633.283; found: 633.274.

***trans,trans*-2,2':6,6'-Di-*O*-benzylidene-7-benzoyloxy-2,2',6,6'-tetra(hydroxymethyl)-4-oxa-1-heptanol (11)**

Powdered potassium hydroxide (0.3 g, 5 mmol) dissolved partially in a stirred solution of dry benzyl chloride (11.0 g, 10.0 mL, 86.9 mmol) over 20 min as the temperature was raised to  $58^\circ\text{C}$ . *trans,trans*-Diol **6** (100 mg, 0.23 mmol) was added and the mixture was stirred for 5 h at  $58^\circ\text{C}$ . The reaction mixture was allowed to cool to room temperature and chloroform (25 mL) and water (25 mL) were added. The organic layer was washed with water ( $2 \times 25$  mL) and dried ( $\text{MgSO}_4$ ) and concentrated. The residue was purified by column chromatography on silica gel (ethyl acetate – hexane (1:1),  $R_f = 0.72$ ) to give the title compound (**11**). Yield: 83 mg, 69%. Recrystallization from diethyl ether – hexanes afforded an amorphous solid, mp  $100$  to  $101^\circ\text{C}$ .  $^1\text{H}$  NMR  $\delta$ : 7.26–7.60 (m,  $3 \times \text{PhH}$ , 15H), 5.41, 5.40 ( $2 \times \text{PhCH}$ ), 4.58 (s,  $\text{PhCH}_2\text{O}$ , 2H), 4.13, 3.82 (AB q, 4H,  $J = 11.6$  Hz,  $\text{H}_2'$ ,  $\text{H}_2''$  or  $\text{H}_6'$ ,  $\text{H}_6''$ ), 4.07, 3.76 (AB q, 4H,  $J = 11.9$  Hz,  $\text{H}_6'$ ,  $\text{H}_6''$  or  $\text{H}_2'$ ,  $\text{H}_2''$ ), 3.97 (d,  $\text{CH}_2\text{OH}$ ,  $J = 4.9$  Hz, 2H), 3.81 (s,  $\text{CCH}_2\text{OCH}_2\text{Ph}$ , 2H), 3.26, 3.21 (2s,  $\text{CCH}_2\text{OCH}_2\text{C}$ , 4H), 1.27 (t, 1H, OH).  $^{13}\text{C}$  NMR  $\delta$ : 126.25–138.59 ( $3 \times \text{PhC}$ ), 102.08 ( $2 \times \text{PhC}$ ), 73.70 ( $\text{PhCH}_2\text{O}$ ), 72.85, 72.11 ( $\text{CCH}_2\text{OCH}_2\text{C}$ ), 70.22, 70.00 ( $\text{C}_2'$ ,  $\text{C}_2''$ ,  $\text{C}_6'$ ,  $\text{C}_6''$ ), 69.03 ( $\text{CCH}_2\text{OCH}_2\text{Ph}$ ), 62.81 ( $\text{CH}_2\text{OH}$ ), 39.37, 39.23 ( $2 \times \text{C quat}$ ). MALDI-TOF HR-MS calcd. for  $\text{C}_{31}\text{H}_{36}\text{O}_7 + \text{Na}$ : 543.236; found: 543.217.

***trans,cis*-2,2':6,6'-Di-*O*-benzylidene-7-benzoyloxy-2,2',6,6'-tetra(hydroxymethyl)-4-oxa-1-heptanol (12) and *cis,trans*-2,2':6,6'-di-*O*-benzylidene-7-benzoyloxy-2,2',6,6'-tetra(hydroxymethyl)-4-oxa-1-heptanol (13)**

Powdered potassium hydroxide (0.3 g, 5 mmol) was partially dissolved in a stirred solution of dry benzyl chloride (11.0 g, 10.0 mL, 86.9 mmol) over 20 min as the temperature was raised to  $80^\circ\text{C}$ . *cis,trans*-Diol **4** (100 mg, 0.23 mmol) was added and the mixture was stirred for 3 h at  $80^\circ\text{C}$ . The reaction mixture was allowed to cool to room temperature and chloroform (25 mL) and water (25 mL) were added. The organic layer was washed with water ( $2 \times 25$  mL) then dried ( $\text{MgSO}_4$ ) and concentrated. The oily residue was separated by flash column chromatography on silica gel (ethyl acetate – hexanes, 1:2). First to elute was compound **12**, an amorphous solid. Yield: 63 mg, 52%.  $R_f = 0.4$  (ethyl acetate – hexanes, 1:2). It was recrystallized from 1-propanol; mp  $124$  to  $125^\circ\text{C}$ .  $^1\text{H}$  NMR  $\delta$ : 7.32–7.48 (m,  $3 \times \text{PhH}$ , 15H), 5.44, 5.41 ( $2 \times \text{PhCH}$ ), 4.50 (s,  $\text{PhCH}_2\text{O}$ , 2H), 4.14, 3.78 (AB q, 4H,  $J = 12.21$  Hz,  $\text{H}_2'$ ,  $\text{H}_2''$  or  $\text{H}_6'$ ,  $\text{H}_6''$ ), 4.12, 3.87 (AB q, 4H,  $J = 11.6$  Hz,  $\text{H}_6'$ ,  $\text{H}_6''$  or  $\text{H}_2'$ ,  $\text{H}_2''$ ), 4.01 (d,  $\text{CH}_2\text{OH}$ , 2H,  $J = 6.1$  Hz), 3.80 (s, 2H,  $\text{CCH}_2\text{OCH}_2\text{C}$  from the *cis*-ring), 3.35, 3.27 (2s, 4 H,  $\text{CCH}_2\text{OCH}_2\text{Ph}$  from the *cis*-ring,  $\text{CCH}_2\text{OCH}_2\text{C}$  from the *trans*-ring), 2.15 (t, 1 H, OH).  $^{13}\text{C}$  NMR  $\delta$ : 126.08–138.06 ( $3 \times \text{PhC}$ ), 102.10, 102.07 ( $2 \times \text{PhC}$ ), 73.76 ( $\text{PhCH}_2\text{O}$ ), 73.20, 70.66 ( $\text{CCH}_2\text{OCH}_2\text{C}$ ), 70.22, 70.18 ( $\text{C}_2'$ ,  $\text{C}_2''$ ,  $\text{C}_6'$ ,  $\text{C}_6''$ ), 70.44 ( $\text{CCH}_2\text{OCH}_2\text{Ph}$ ), 63.33 ( $\text{CH}_2\text{OH}$ ), 39.16, 39.33 ( $2 \times \text{C quat}$ ). Anal. calcd. for  $\text{C}_{31}\text{H}_{36}\text{O}_7$ : C 71.52, H 6.97; found: C 71.64, H 7.08.

The second component was also an amorphous solid (**13**, 19 mg, 16%).  $R_f = 0.25$  (ethyl acetate – hexanes, 1:2), mp  $90$ – $92^\circ\text{C}$ .  $^1\text{H}$  NMR  $\delta$ : 7.25–7.39 (m,  $3 \times \text{PhH}$ , 15H), 5.43, 5.40 ( $2 \times \text{PhCH}$ ), 4.58 (s,  $\text{PhCH}_2\text{O}$ , 2H), 4.16, 3.77 (AB q, 4H,  $J = 11.9$  Hz,  $\text{H}_2'$ ,  $\text{H}_2''$  or  $\text{H}_6'$ ,  $\text{H}_6''$ ), 4.14, 3.82 (AB q, 4H,  $J = 11.9$  Hz,  $\text{H}_6'$ ,  $\text{H}_6''$  or  $\text{H}_2'$ ,  $\text{H}_2''$ ), 3.86, 3.84 (2s, 4H,  $\text{CH}_2\text{OCH}_2\text{Ph}$  in the *trans*-ring,  $\text{CCH}_2\text{OCH}_2\text{C}$  in the *cis*-ring), 3.47 (d, 2H,  $J = 5.8$  Hz,  $\text{CH}_2\text{OH}$ ), 3.41 (s,  $\text{CCH}_2\text{OCH}_2\text{C}$  in the *trans*-ring), 2.33 (t, 1H, OH).  $^{13}\text{C}$  NMR  $\delta$ : 126.06–138.36 ( $3 \times \text{PhC}$ ), 102.24, 102.13 ( $2 \times \text{PhC}$ ), 73.77 ( $\text{PhCH}_2\text{O}$ ), 73.06, 72.43 ( $\text{CCH}_2\text{OCH}_2\text{C}$ ), 70.60, 70.37 ( $\text{C}_2'$ ,  $\text{C}_2''$ ,  $\text{C}_6'$ ,  $\text{C}_6''$ ), 69.37 ( $\text{CCH}_2\text{OCH}_2\text{Ph}$ ), 65.49 ( $\text{CH}_2\text{OH}$ ), 39.24, 39.14 ( $2 \times \text{C quat}$ ). HR-ES-MS calcd. for  $\text{C}_{31}\text{H}_{36}\text{O}_7 + \text{Na}$ : 543.236; found: 543.259.

**2,6-Bis(benzoyloxymethyl)-4-oxa-1,7-heptanediol (14)**

(a) From compound **4**. To a stirred solution of the *cis,trans*-diol **4** (0.16 g, 0.37 mmol, dried under vacuum for 12 h) in dry dichloromethane (5 mL) at  $0^\circ\text{C}$  was added triethylsilane (2.13 mL, 4.5 mmol, 36 equiv) and freshly distilled boron trifluoride etherate (0.56 mL, 1.5 mmol, 12 equiv). After being allowed to warm to room temperature, the solution was stirred for 12 h. The mixture was then diluted with dichloromethane (30 mL), washed with a saturated sodium hydrogen carbonate solution (40 mL), dried ( $\text{MgSO}_4$ ), and concentrated. The residue was purified by flash column chromatography (ethyl acetate – hexanes (2:1),  $R_f = 0.21$ ) to afford the title compound (**14**) as a colorless solid. Yield: 0.10 g, 64%, mp  $95$ – $97^\circ\text{C}$ .  $^1\text{H}$  NMR  $\delta$ : 7.26–7.33 (m,  $2 \times \text{PhH}$ , 10H), 4.46 (s,  $2 \times \text{PhCH}_2\text{O}$ , 4H), 3.61 (s,  $4 \times \text{CH}_2\text{OH}$ , 8H), 3.46 (s,  $2 \times \text{CCH}_2\text{OCH}_2\text{Ph}$ , 4H), 3.40 (s,  $\text{CCH}_2\text{OCH}_2\text{C}$ , 4H).  $^{13}\text{C}$  NMR  $\delta$ : 127.68–137.93 ( $2 \times \text{PhC}$ ),



73.82 ( $2 \times \text{PhCH}_2\text{O}$ ), 71.96 ( $\text{CCH}_2\text{OCH}_2\text{C}$ ), 71.75 ( $2 \times \text{CCH}_2\text{OCH}_2\text{Ph}$ ), 64.23 ( $4 \times \text{CH}_2\text{OH}$ ), 45.42 ( $2 \times \text{C quat}$ ). HR-ES-MS calcd. for  $\text{C}_{24}\text{H}_{34}\text{O}_7 + \text{Na}$ : 457.2202; found: 457.2202.

(b) From the mixture of compounds **3–5**. Application of the procedure from part (a) to the mixture of diols **3–5** (50 mg, 0.12 mmol) gave the same product (**14**) (36 mg, 68%).

### Reaction of 2',2':6',6''-di-*O*-methylene-2,2,6,6-tetrahydroxymethyl-4-oxa-1,7-heptanediol (**8**) with 1,3-di(bromomethyl)benzene

To a solution of sodium hydride (60% oil dispersion, 320 mg, 8 mmol) in dry DMF (50 mL) magnetically stirred in a three-necked round-bottomed flask under nitrogen was added dropwise, simultaneously, solutions of compound **8** (1.113 g, 4 mmol) in DMF (20 mL) and 1,3-di(bromomethyl)benzene (1.056 g, 4 mmol) in DMF (15 mL) from pressure-equalized dropping funnels. After two-thirds of the addition had been made, more 60% sodium hydride (400 mg, 10 mmol) was added before the dropwise addition was complete. The mixture was stirred 3 days, then concentrated. The residue was taken up in dichloromethane (30 mL) and the solution was washed with water ( $3 \times 10$  mL), dried ( $\text{MgSO}_4$ ), and concentrated. Crystals of the title compound (**15**) were deposited which were recrystallized from chloroform–hexanes. Yield: 180 mg, 12%.  $R_f = 0.81$  (ethyl acetate — hexanes, 3:1), mp 197–199°C.  $^1\text{H}$  NMR (400.13 MHz)  $\delta$ : 3.30 (s, 4H, H-1,7), 3.53 (s, 4H, H-3,5), 3.69 (AB q, 8H,  $J_{AB} = 11.31$  Hz,  $\Delta\delta_{AB} = 0.0344$ ,  $\text{CH}_2\text{s}$  on C-2',2'',6',6''), 4.64 (s, 4H, Bn H), 4.80 (AB q, 4H,  $J_{AB} = 6.08$  Hz,  $\Delta\delta_{AB} = 0.027$ , acetal  $\text{CH}_2$ ), 7.03 (dd, 2H,  $J_{ortho} = 7.48$  Hz,  $J_{meta} = 1.45$  Hz, Ph H-4,6), 7.251 (t, 1H, Ph H-5), 7.512 (br s, Ph H-2).  $^{13}\text{C}$  NMR (62.9 MHz)  $\delta$ : 39.29 (C-2,5), 66.91 (C-1,7), 69.27 (Bn  $\text{CH}_2$ ), 70.40 (C-2',2'',6',6''), 71.96 (C-3,5), 94.49 (acetal C), 123.11 (Ph C-2), 126.13 (Ph C-4,6), 128.17 (Ph C-5), 139.24 (Ph C-1,3). HR-EI-MS calcd. for  $\text{C}_{20}\text{H}_{28}\text{O}_7$  ( $\text{M}^+$ ): 380.1835; found: 380.1817.

### Competition experiment

Powdered potassium hydroxide (0.15 g, 2.5 mmol) was suspended in dry benzyl chloride (5.5 g, 5 mL, 43.5 mmol) and this mixture was stirred at room temperature for 15 min. *cis,cis*-Diol **5** (50 mg, 0.12 mmol) was added followed by 1-octanol (0.23 mmol, 2 equiv, 0.036 mL) and the mixture was stirred for 2.5 h at room temperature. The solution was concentrated and the residue was examined by NMR.

### Acknowledgements

TBG and TS thank the Natural Sciences and Engineering Research Council of Canada (NSERC) for support. We thank Mike Potvin for EI-MS, Dr. Angelina Morales-Izquierdo of the University of Alberta for high resolution ES-MS, and Bob Whitehead of IMB/NRC in Halifax for measuring MALDI-TOF mass spectra. We thank ARMRC for the NMR time.

### References

1. M. Fischer and F. Vögtle. *Angew. Chem. Int. Ed. Eng.* **38**, 885 (1999).
2. O.A. Matthews, A.N. Shipway, and J.F. Stoddart. *Prog. Polym. Sci.* **23**, 1 (1998).
3. F.W. Zeng and S.C. Zimmerman. *Chem. Rev.* **97**, 1681 (1997).
4. N. Ardoin and D. Astruc. *Bull. Soc. Chim. Fr.* **132**, 875 (1995).
5. D.A. Tomalia, A.M. Naylor, and W.A. Goddard. *Angew. Chem. Int. Ed. Eng.* **29**, 138 (1990).
6. D.A. Tomalia and H.D. Durst. *Top. Curr. Chem.* **165**, 193 (1993).
7. S.K. Grayson and J.M.J. Fréchet. *Chem. Rev.* **101**, 3819 (2001).
8. A.B. Padias, H.K. Hall, D.A. Tomalia, and J.R. McConnell. *J. Org. Chem.* **52**, 5305 (1987).
9. S. Hanessian, D.X. Qiu, H. Prabhanjan, G.V. Reddy, and B.L. Lou. *Can. J. Chem.* **74**, 1738 (1996).
10. S. Hanessian, H.K. Huynh, G.V. Reddy, R.O. Duthaler, A. Katopodis, M.B. Streiff, W. Kinzy, and R. Oehrlein. *Tetrahedron*, **57**, 3281 (2001).
11. T.K. Lindhorst, M. Dubber, U. Krallmann-Wenzel, and S. Ehlers. *Eur. J. Org. Chem.* 2027 (2000).
12. E.C. Constable, C.E. Housecroft, M. Cattalini, and D. Phillips. *New J. Chem.* **22**, 193 (1998).
13. C.-M. Dong, K.-Y. Qiu, Z.W. Cu, and X.-D. Feng. *Macromolecules*, **34**, 4691 (2001).
14. C.-M. Dong, K.-Y. Qiu, Z.-W. Gu, and X.-D. Feng. *Polymer*, **42**, 6891 (2001).
15. M.C. Murguía and R.J. Grau. *Synlett*, 1229 (2001).
16. A. Halabi and M.C. Strumia. *J. Org. Chem.* **65**, 9210 (2000).
17. M. Schmidt, B. Dobner, and P. Nuhn. *Eur. J. Org. Chem.* 669 (2002).
18. B.C. Liu and R. Roy. *Chem. Commun.* 594 (2002).
19. J. Esnault, J.M. Mallet, Y.M. Zhang, P. Sinay, T. Le Bouar, F. Pincet, and E. Perez. *Eur. J. Org. Chem.* 253 (2001).
20. S. David. *Carbohydr. Res.* **331**, 327 (2001).
21. T.J. Dunn, W.L. Neumann, M.M. Rogic, and S.R. Woulfe. *J. Org. Chem.* **55**, 6368 (1990).
22. A.-R. Abdun-Nur and C.H. Issidorides. *J. Org. Chem.* **27**, 67 (1962).
23. M. Apel and B. Tollens. *Ann.* **289**, 34 (1896).
24. E. Bograchov. *J. Am. Chem. Soc.* **72**, 2268 (1950).
25. E. Weber. *J. Org. Chem.* **47**, 3478 (1982).
26. C.H. Issidorides and R.C. Gulen. *Monobenzalpentacerythritol. In Organic syntheses collected. Vol. IV. Edited by N. Rabjohn. John Wiley and Sons, New York. 1963. p. 679.*
27. M. Schmidt, B. Dobner, and P. Nuhn. *Synlett*, 1157 (2000).
28. S. Hanessian, H. Prabhanjan, D.X. Qiu, and S. Nambiar. *Can. J. Chem.* **74**, 1731 (1996).
29. P. Westerduin, G.H. Veeneman, J.E. Marugg, G.A. van der Marel, and J.H. van Boom. *Tetrahedron Lett.* **27**, 1211 (1986).
30. F.M. Menger and V.A. Migulin. *J. Org. Chem.* **64**, 8916 (1999).
31. E. Bograchov. *J. Am. Chem. Soc.* **72**, 2274 (1950).
32. I. Cabasso, S.K. Sahni, and D. Vofsi. *J. Polym. Sci. Part A: Polym. Chem.* **26**, 2997 (1988).
33. F.G. Riddell. *The conformational analysis of heterocyclic compounds. Academic Press Inc., London. 1980.*
34. E.L. Eliel, S.H. Wilen, and L.N. Mander. *Stereochemistry of organic compounds. John Wiley and Sons, New York. 1994.*
35. L.M. Jackman and S. Sternhell. *Applications of nuclear magnetic resonance spectroscopy in organic chemistry. Pergamon Press, Oxford. 1969. pp. 238–241.*
36. E.L. Eliel and R.J.L. Martin. *J. Am. Chem. Soc.* **90**, 682 (1968).



37. T.A. Crabb, M. Porssa, and N.F. Elmore. *Magn. Reson. Chem.* **29**, 613 (1991).
38. J.Q. Cai, A.G. Davies, and C.H. Schiesser. *J. Chem. Soc., Perkin Trans. 2*, 1151 (1994).
39. A.J. Jones, E.L. Eliel, D.M. Grant, M.C. Knoeber, and W.F. Bailey. *J. Am. Chem. Soc.* **93**, 4772 (1971).
40. M.C. Murguía, S.E. Vaillard, and R.J. Grau. *Synthesis*, 1093 (2001).
41. T.J. Clark. *J. Chem. Ed.* **72**, 375 (1995).
42. S. Wawzonek and D.A. Rees. *J. Am. Chem. Soc.* **70**, 2433 (1948).
43. L. Börjesson, I. Csöreg, and C.J. Welch. *J. Org. Chem.* **60**, 2989 (1995).
44. K.C. Nicolaou, C.K. Hwang, B.E. Marron, S.A. DeFrees, E.A. Couladouros, Y. Abe, P.J. Carroll, and J.P. Snyder. *J. Am. Chem. Soc.* **112**, 3040 (1990).
45. J.A. Marshall, S. Beaudoin, and K. Lewinski. *J. Org. Chem.* **58**, 5876 (1993).
46. A. Bouzide and G. Sauvé. *Tetrahedron Lett.* **38**, 5945 (1997).
47. M. Bessodes and C. Boukarim. *Synlett*, 1119 (1996).
48. A. Lipták, I. Jodál, J. Harangi, and P. Nánási. *Acta Chim. Hung.* **113**, 415 (1983).
49. A.H. Haines. *Adv. Carbohydr. Chem. Biochem.* **39**, 13 (1981).
50. P.J. Garegg, H. Hultberg, and S. Wallin. *Carbohydr. Res.* **108**, 97 (1982).
51. M.P. Deninno, J.B. Etienne, and K.C. Duplantier. *Tetrahedron Lett.* **36**, 669 (1995).
52. S.D. Debenham and E.J. Toone. *Tetrahedron: Asymmetry*, **11**, 385 (2000).
53. H. Herzner, T. Reipen, M. Schultz, and H. Kunz. *Chem. Rev.* **100**, 4495 (2000).
54. E. Stahl and U. Kaltenbach. *J. Chromatogr.* **5**, 351 (1961).
55. A. Altomare, G. Cascarano, C. Giacovazzo, and A. Guagliardi. *J. Appl. Crystallogr.* **26**, 343 (1993).
56. G.M. Sheldrick. *SHELXL97*. Program for crystal structure refinement. University of Göttingen, Göttingen, Germany. 1997.
57. J. Read. *J. Chem. Soc.* **101**, 2090 (1912).



# An unusual abnormal Wolff rearrangement<sup>1</sup>

Howard E. Zimmerman and Pengfei Wang

**Abstract:** An unusual example of the abnormal Wolff rearrangement was studied. The bicyclic structure of the reactant and intermediates precluded some mechanistic possibilities of this unusual abnormal Wolff rearrangement. The study involved the photochemical rearrangement of diazodehydronorbornone bearing phenyl and 2-pyridyl groups at C-7. A number of examples of interesting stereoselectivity were encountered. The mechanism was investigated by use of ab initio QST type computations, which located a unique transition structure species accounting for the reaction mechanism.

**Key words:** abnormal-Wolff, carbene, rearrangement, QM computations, reaction mechanism.

**Résumé :** On a étudié un exemple inhabituel d'un réarrangement anormal de Wolff. La structure bicyclique du réactif et des intermédiaires ne permettaient pas certaines possibilités mécanistiques de cet exemple inhabituel d'un réarrangement anormal de Wolff. L'étude implique le réarrangement photochimique d'une diazodéhydronorbornone portant des groupes phényle et 2-pyridyle au niveau du C-7. On a rencontré un certain nombre d'exemples de stéréosélectivité intéressante. On a étudié le mécanisme sur la base de calculs théoriques ab initio de type QST qui ont permis de localiser la structure d'une espèce définie de transition permettant d'expliquer le mécanisme réactionnel.

**Mots clés :** réaction anormale de Wolff, carbène, réarrangement, calculs de type QM, mécanisme réactionnel.

[Traduit par la Rédaction]

## Introduction and background

The Wolff rearrangement has been a valuable synthetic tool. Interestingly, in the special case of  $\beta,\gamma$ -unsaturation in the reactant diazoketone, there is a dramatic alteration of the reactivity (1). Remarkably, this rather interesting reactivity went unnoticed until the simultaneous efforts of our research group (2), that of Smith (3), and Lokensgard (4). The extensive studies by Smith established the generality and synthetic utility of the reaction.

Our own research was initiated with the idea of providing housone reaction intermediates involved in the photochemical rearrangement of 4,4-diphenylcyclopentenone (2a) which had been found to afford an unexpected unsaturated ketene. Indeed, it was found that at low temperature housones were formed (2) but fragmented on warming to afford ketenes of structure 5. From room temperature irradiations only the ketene 5 was observed and isolated as methyl ester 6. The mechanisms considered are shown in Scheme 1.

An independent generation of the intermediates was sought in the reaction of the stilbenyl diazoketone 7 which was observed to afford the same housone 4, ketene 5, and methyl ester 6 (Scheme 2). Parallel results were observed in the study of Smith (3) who obtained a large number of examples of the diazoketone reaction.

Recently, in connection with our studies of intramolecular proton transfer, we found closely related results in the Wolff rearrangement of dehydronorbornyl diazoketones. However, as a consequence of the bicyclic nature of the system, a number of mechanistic aspects, originally proposed, needed modification for this system.

## Results

### Synthesis of the diazoketones

The synthesis of the two diazoketones (**12-syn** and **12-anti**) of interest is outlined in Scheme 3. The reactant norbornenones, **10-syn** and **10-anti** derived from our earlier studies (5), and provided convenient starting points. In the case of the syn ketone **10-syn**, the initially formed lithium enolate was obtained as a solid and could be used directly rather than isolating the formylated ketone. Both diazoketone diastereomers (**12-syn** and **12-anti**) were obtained as yellow crystalline solids.

## Results

### The abnormal Wolff rearrangement

In contrast to the ordinary Wolff rearrangement of the saturated 7,7-diaryldiazonorbornyl ketones (5), the dehydronorbornyl counterparts **12-syn** and **12-anti** reacted to give

Received 6 December 2002. Published on the NRC Research Press Web site at <http://canjchem.nrc.ca> on 12 May 2003.

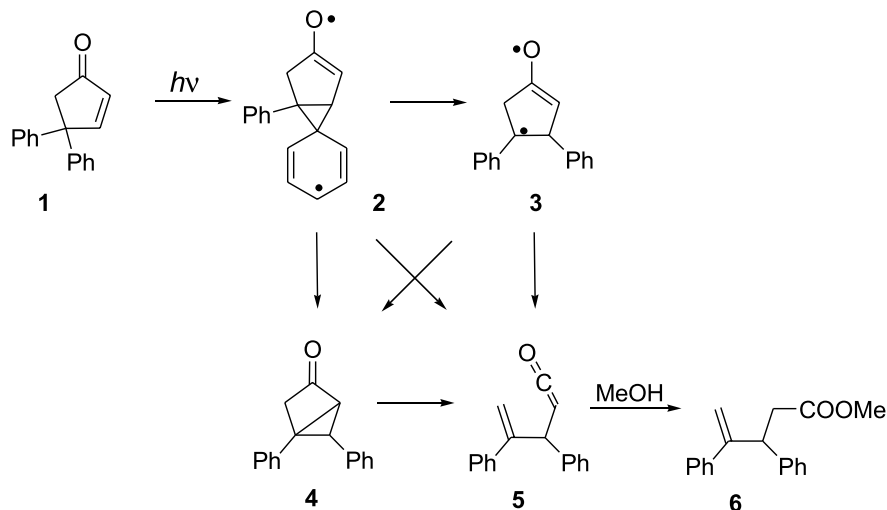
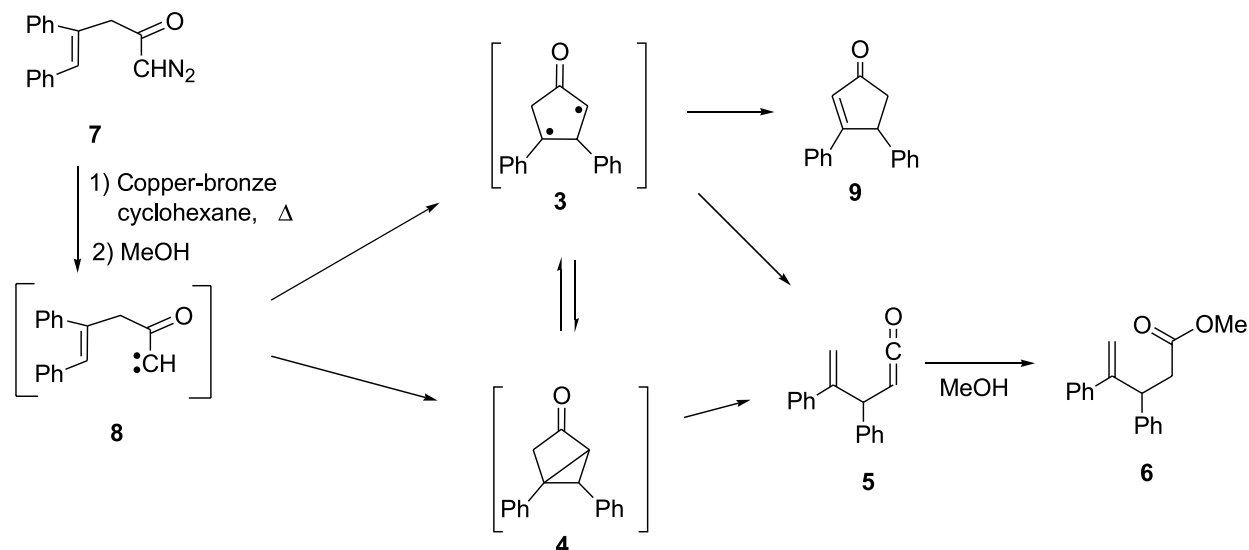
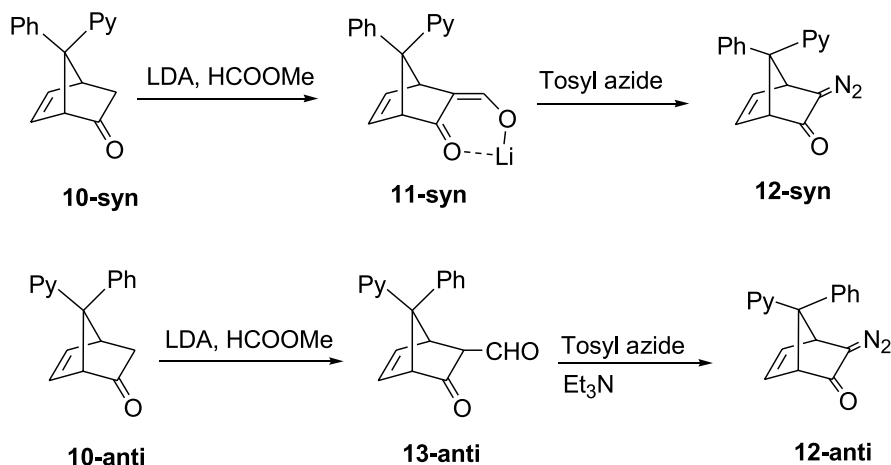
In honor of Professor Donald Arnold for his superb contribution to organic photochemistry.

**H.E. Zimmerman<sup>2</sup> and P. Wang.** Chemistry Department, University of Wisconsin, Madison, WI 53706, U.S.A.

<sup>1</sup>(a) This is paper 269 of our general series and 204 of our photochemical series; (b) For No. 268 see: H.E. Zimmerman and P. Wang. *J. Org. Chem.* **67**, 9216 (2002).

<sup>2</sup>Corresponding author (e-mail: [Zimmerman@Chem.Wisc.Edu](mailto:Zimmerman@Chem.Wisc.Edu)).

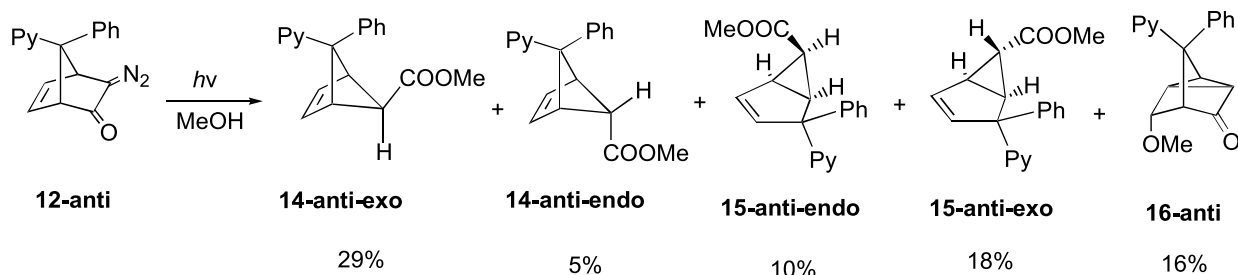


**Scheme 1.** Original reaction mechanisms considered.**Scheme 2.** Reaction mechanism variations.**Scheme 3.** Synthesis of the diastereomeric dehydronorbornyl diazocompounds.

unanticipated photoproducts. The reaction course of the *syn*-phenyl diastereomer (**12-anti**) is outlined in Scheme 4. In

addition to the expected normal Wolff rearrangement products (**14-anti-exo** and **14-anti-endo**) there were three rather



**Scheme 4.** Reaction of the *anti*-pyridyl diazoketone.

interesting but unexpected photoproducts — **15-anti-endo**, **15-anti-exo**, and **16-anti**.

The photolysis of **12-syn** led, in addition to the anticipated Wolff rearrangement products **14-syn-exo** and **14-syn-endo**, to two abnormal Wolff products (**15-syn-endo** and **16-syn**) (Scheme 5). These structures derived from proton NMR and NOE experiments. Further, the structures of **14-anti-exo**, **15-anti-exo** (see Table 1 for crystal data and structure refinement), and **16-anti** (see Table 2 for crystal data and structure refinement) were established by X-ray analysis. Details are given in the *Experimental section*. Also, the independent synthesis of **15-syn-exo**, which was not a photoproduct, but which was helpful in the structure determination of **15-syn-endo**, is outlined in Scheme 6. Also, Scheme 6 outlines the epimerization of **15-syn-endo** to **15-syn-exo**. This conversion favors the thermodynamically more stable diastereomer.

## Discussion

### Stereochemistry of the ethyl diazoacetate addition to the pyridyl cyclopentadiene; the unusual syn-endo addition to the pyridyl phenyl cyclopentadiene

Before proceeding to discussion of the abnormal Wolff mechanisms, we need to consider the unusual reaction depicted in Scheme 6. Thus, two facets of the cyclopropanation, utilized in the synthesis, are of interest and one is unique. In this highly stereoselective reaction, the preferential *exo* configuration of the product is anticipated on the basis of lesser steric repulsions than in an *endo* addition. In contrast, the kinetic preferences for the totally stereoselective *syn* addition to afford **15-syn-exo** is not so easily rationalized. However, copper-catalyzed addition of ethyl diazoacetate to alkene  $\pi$  bonds has been suggested (6) to proceed with the carbethoxy carbene  $sp^2$ -hybrid bonding as a ligand to copper while the electrophilic carbene  $p$ -orbital attacks the alkene  $\pi$  bond. In the present instance, analogous coordination of cupric ion to the pyridyl nitrogen and the carbene  $sp^2$  orbital forces the carbene to bond *syn* (i.e., *cis* to the pyridyl group). Also LDA epimerization under thermodynamic conditions of **15-syn-endo**, available from the Wolff rearrangement as described above, led to **15-syn-exo**. However, the mixture of the two diastereomers favored the *exo* diastereomer.

### The normal Wolff rearrangement and the stereochemistry of kinetic protonation

The stereochemistry of the normal Wolff rearrangement of the *syn* phenyl diazoketone **12-anti**, affords the rearrange-

ment products **14-anti-exo** and **14-anti-endo** (note Scheme 4). The observed 6:1 preference for formation of the *exo* product stereoisomer clearly arises from less hindered protonation of the intermediate enol **18-anti** as anticipated from the ubiquitous phenomenon originally reported by one of us (7a) and described in a long list of our publications (5, 7) (Scheme 7).

Interestingly, in the case of the **12-syn** diazoketone, although the Wolff rearrangement product from this diastereomer also gave the same preference for less hindered protonation, the stereoselectivity had dropped to 2:1. This is outlined in Scheme 8. The diminished stereoselectivity may be attributed to the intervention of some intramolecular hydrogen transfer from methanol hydrogen bonded to the pyridyl group. This was the dominant process in our study of the dihydro analog of the present system (5).

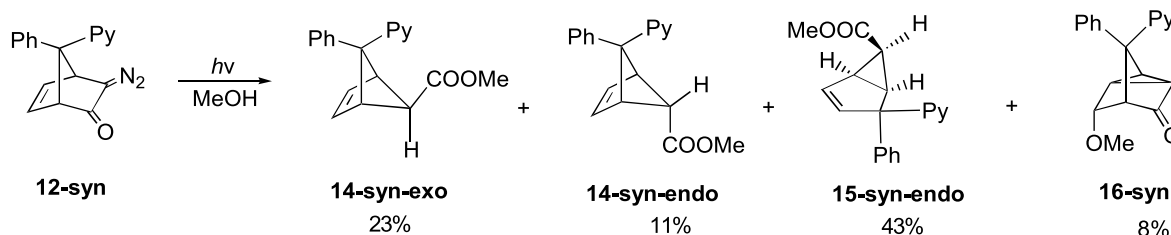
### The abnormal Wolff rearrangement

In comparing our present results with those we and others carried out much earlier (2–4), we recognize that the housone (note species **4** of Scheme 2) of the earlier studies cannot be involved in the bicyclic system currently under study. Secondly, in contrast to species **3** (Scheme 2 again) there can be no delocalization in a diradical counterpart of **3** of the earlier study because of Bredt's rule limitations. Such a diradical would have an unstable structure discussed below as **26**. Yet housone intermediates were observed in the acyclic studies and thus must be taken as possible but not necessary for the abnormal Wolff rearrangement.

Turning now to the abnormal Wolff rearrangement products let us consider the *anti*-pyridyl reactivity first. Here, in the formation of **15-anti-endo** and **15-anti-exo**, we note that a species of generalized structure such as **20-anti** in Scheme 9 is likely to be involved. Thus, we know that, in proceeding to the ketene **21-anti**, bond 1—2 is severed and a new bond (4—6) is formed as well as  $\pi$  bond 3—4 being weakened. Also, the formation of methoxy product **16** involves formation of that same bond, 4—6, and pickup of methanol at C-3.

To provide some further light on this proposal, we proceeded with some computational efforts. Gaussian98 RHF/6-31G\* optimization of the S0 carbene **19** and ketene **21** established these as energy minima. We next proceeded to QST2 and QST3 computations on the truncated system as outlined in Scheme 10. With singlet carbene **23** as reactant and ketene **25** as product species, with or without interposition of a species of geometry close to that depicted as a truncated **20-anti**, a transition structure of geometry **24** was obtained. This species was close in structure to that of **26**



**Scheme 5.** Reaction of the *syn*-pyridyl diazoketone.**Table 1.** Crystal data and structure refinement for **15-anti-exo**.

Identification code	<b>15-anti-exo</b>
Empirical formula	C <sub>19</sub> H <sub>17</sub> NO <sub>2</sub>
Formula weight	291.34
Temperature (K)	293(2)
Wavelength (Å)	0.71073
Crystal system	Monoclinic
Space group	P2(1)
Unit cell dimensions: <i>a</i> (Å)	9.5203(11)
<i>b</i> (Å)	7.1738(7)
<i>c</i> (Å)	11.2914(12)
$\alpha$ (°)	90
$\beta$ (°)	92.251(2)
$\gamma$ (°)	90
Volume (Å <sup>3</sup> )	770.57(14)
<i>Z</i>	2
Density (calculated) (Mg m <sup>-3</sup> )	1.256
Absorption coefficient (mm <sup>-1</sup> )	0.081
<i>F</i> (000)	308
Crystal size (mm <sup>3</sup> )	0.50 × 0.40 × 0.40
$\theta$ Range for data collection (°)	1.80–26.35
Index ranges	−11 ≤ <i>h</i> ≤ 11, −4 ≤ <i>k</i> ≤ 8, −12 ≤ <i>l</i> ≤ 13
Reflections collected	3708
Independent reflections	2373 ( <i>R</i> (int) = 0.0118)
Completeness to $\theta = 26.35^\circ$ (%)	96.9
Refinement method	Full-matrix least-squares on <i>F</i> <sup>2</sup>
Data/restraints/parameters	2373/1/267
Goodness-of-fit on <i>F</i> <sup>2</sup>	1.064
Final <i>R</i> indices ( <i>I</i> > 2 $\sigma$ ( <i>I</i> ))	<i>R</i> 1 = 0.0330, <i>wR</i> 2 = 0.0791
<i>R</i> indices (all data)	<i>R</i> 1 = 0.0396, <i>wR</i> 2 = 0.0826
Absolute structure parameter	1.8(14)
Largest diff. peak and hole (e Å <sup>-3</sup> )	0.116 and −0.164

**Table 2.** Crystal data and structure refinement for **16-anti**.

Identification code	<b>16-anti</b>
Empirical formula	C <sub>19</sub> H <sub>17</sub> NO <sub>2</sub>
Formula weight	291.34
Temperature (K)	100(2)
Wavelength (Å)	0.71073
Crystal system	Orthorhombic
Space group	P2(1)2(1)2(1)
Unit cell dimensions: <i>a</i> (Å)	6.1964(14)
<i>b</i> (Å)	13.703(3)
<i>c</i> (Å)	16.864(4)
$\alpha$ (°)	90
$\beta$ (°)	90
$\gamma$ (°)	90
Volume (Å <sup>3</sup> )	1432.0(5)
<i>Z</i>	4
Density (calculated) (Mg m <sup>-3</sup> )	1.351
Absorption coefficient (mm <sup>-1</sup> )	0.088
<i>F</i> (000)	616
Crystal size (mm <sup>3</sup> )	0.32 × 0.12 × 0.08
$\theta$ Range for data collection (°)	1.91–26.40
Index ranges	−7 ≤ <i>h</i> ≤ 7, −17 ≤ <i>k</i> ≤ 17, −21 ≤ <i>l</i> ≤ 21
Reflections collected	11 569
Independent reflections	2929 ( <i>R</i> (int) = 0.0580)
Completeness to $\theta = 26.40^\circ$ (%)	99.8
Absorption correction	None
Refinement method	Full-matrix least-squares on <i>F</i> <sup>2</sup>
Data/restraints/parameters	2929/0/267
Goodness-of-fit on <i>F</i> <sup>2</sup>	1.051
Final <i>R</i> indices ( <i>I</i> > 2 $\sigma$ ( <i>I</i> ))	<i>R</i> 1 = 0.0498, <i>wR</i> 2 = 0.1133
<i>R</i> indices (all data)	<i>R</i> 1 = 0.0614, <i>wR</i> 2 = 0.1189
Absolute structure parameter	1.8(18)
Largest diff. peak and hole (e Å <sup>-3</sup> )	0.287 and −0.226

except that bond 1—2 was elongated while the distance between atoms 4 and 6 approached normal single bond length.

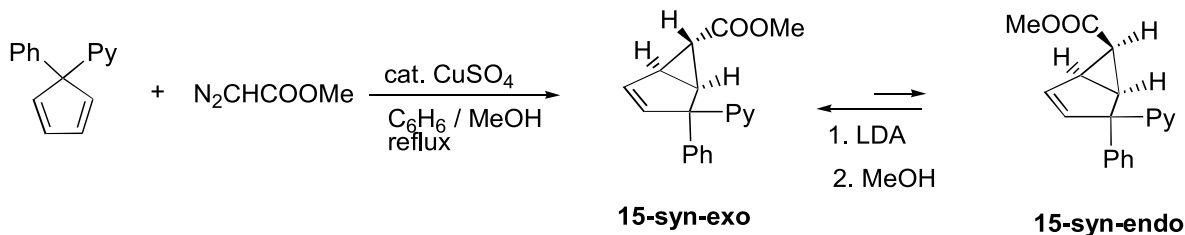
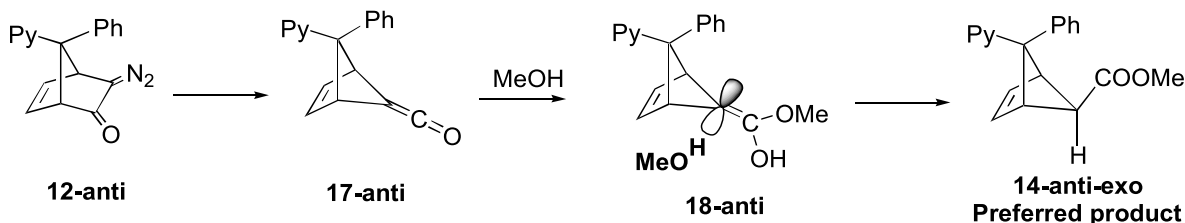
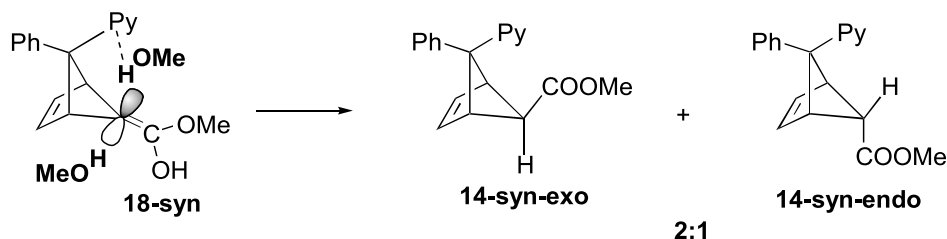
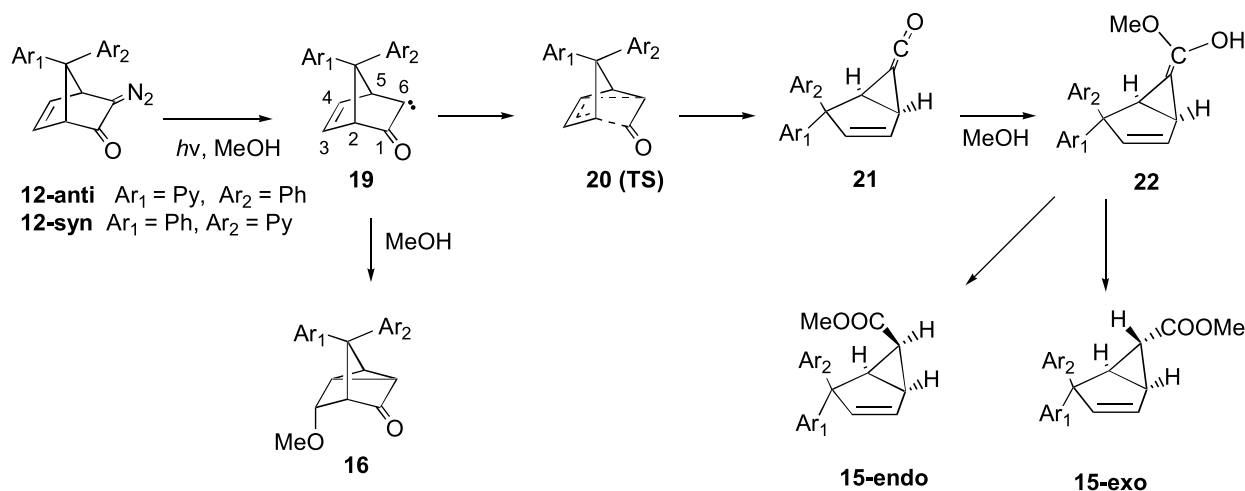
Interestingly, structure **26** proved not to be an energy minimum and stable. Rather, geometry optimization with RHF/6-31G\* of this starting species led to the carbene **23**. A further point of interest was the behavior of species **23** when a proton, placed in the vicinity (ca. 5 Å) of C-6, was included in the optimization. This reactant (i.e., **23**) then picked up the proton to afford cation **27** which proved to be an energy minimum. When a methanol molecule was introduced close to C-3, methoxyketone **28** resulted.

Thus, the truncated QST system behaved quite parallel to the experimental sequence suggested in Scheme 9. However,

there is an additional possibility in the case of formation of **15-syn-endo**, this deriving from species **27**. This alternative does not involve ketonization and is outlined in Scheme 11.

Finally, we need to consider the stereochemical outcome of several of the reactions in leading to photoproducts. In the case of **14-anti-exo** and **14-anti-endo** being formed in a ratio of ca. 6:1, compared with **14-syn-exo** and **14-syn-endo** in a ratio of 2:1 (note Schemes 4 and 5) the preference for the *exo* isomers is understood as a consequence of less hindered protonation of the enolic precursors. The lower diastereoselectivity in the *syn*-pyridyl seems possibly to arise



**Scheme 6.** Stereoselective carbomethoxycarbene addition.**Scheme 7.** Less hindered protonation of the normal Wolff rearrangements.**Scheme 8.** Diminished selectivity of the *syn*-pyridyl diastereomer due to intramolecular protonation.**Scheme 9.** Mechanism of the abnormal Wolff rearrangement.

from the 2-pyridyl group delivering hydrogen-bonded methanol to a minor extent.

The preferential formation of **15-anti-exo** relative to **15-anti-endo** (Scheme 4) in a ca. 2:1 ratio, does not seem a consequence of less hindered protonation of their enolic precursor. Rather, there is some evidence (8) that methanol may  $\pi$  bond to the face of a phenyl group, thus delivering protons to the enolic precursor.

## Conclusion

This study revealed an unanticipated but remarkable difference between the ordinary Wolff rearrangement of the satu-

rated norbornyl system previously studied and the dehydro counterpart. As this research proceeded, a number of stereochemical and mechanistic aspects were uncovered. One of the most interesting derived from the QST computations.

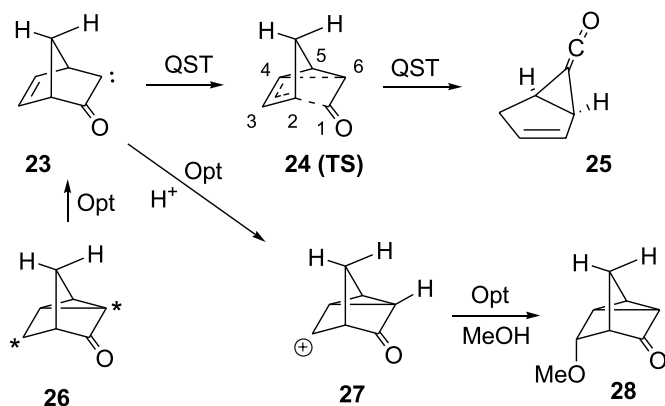
## Experimental section

### 3-Diazo-7-*syn*-phenyl-7-*anti*-pyridin-2-yl-bicyclo[2.2.1]-hept-5-en-2-one (**12-anti**)

To diisopropylamine (0.78 mL, 5.2 mmol) dissolved in 2.5 mL of freshly distilled THF under nitrogen at  $-78^\circ\text{C}$  was added 3.80 mL of *n*-BuLi (1.37 M) and stirred for 35 min at



Scheme 10. Computational mechanisms.



$-78^{\circ}\text{C}$ . **10-anti** dissolved in 25 mL of freshly distilled THF at room temperature was cooled to  $-78^{\circ}\text{C}$ , LDA was added, and the mixture was stirred for 2 h.  $\text{HCOOMe}$  (2.4 mL, 14 mmol) was then added and the mixture was stirred overnight with the temperature gradually rising to ambient and then stirred for one more day. The suspension was filtered, and the solid was dissolved in 20 mL of 10% KOH, washed with 20 mL dichloromethane. The aqueous solution was adjusted to pH ca. 8 by addition of dilute HCl, and then extracted with dichloromethane. The combined organic layers were dried over  $\text{Na}_2\text{SO}_4$  and concentrated to yield 1.0 g (79%) of **13-anti** as a light yellow solid: mp  $178$  to  $179^{\circ}\text{C}$ .  $^1\text{H}$  NMR ( $\text{CDCl}_3$ )  $\delta$ : 9.43 (d,  $J = 0.6$  Hz, 1H), 8.47 (d,  $J = 5.0$  Hz, 1H), 7.51 (td,  $J = 7.5$ , 2.0 Hz, 1H), 7.40 (d,  $J = 8.0$  Hz, 2H), 7.28 (t,  $J = 7.5$  Hz, 2H), 7.18 (m, 2H), 7.02 (ddd,  $J = 7.5$ , 5.0, 1.0 Hz, 1H), 6.84 (dd,  $J = 5.5$ , 3.0 Hz, 1H), 5.84 (m, 1H), 4.37 (m, 1H), 4.33 (m, 1H), 3.15 (m, 1H).  $^{13}\text{C}$  NMR ( $\text{CDCl}_3$ )  $\delta$ : 202.1, 196.4, 160.9, 149.0, 142.7, 140.4, 136.2, 129.2, 127.5, 126.8, 125.9, 122.0, 121.3, 74.9, 62.5, 61.2, 47.7.

The formyl ketone **13-anti** (1.0 g, 3.46 mmol) was stirred with tosyl azide (0.68 g, 3.46 mmol) in 23 mL of dichloromethane in an ice bath and triethylamine (1.0 mL, 6.92 mmol) was added. The reaction mixture was stirred overnight in the dark and allowed to warm up to ambient temperature. The mixture was concentrated in vacuo; the yellow residue was subjected to chromatography on neutral alumina (pH ca. 7.5). Elution with dichloromethane yielded 0.744 g (75%) of **12-anti** as yellow crystals:  $R_f$  0.57 (dichloromethane–ether, 9:1), mp  $155^{\circ}\text{C}$  (decomposed). UV ( $\text{CDCl}_3$ ): 260 nm ( $\epsilon = 17\,027$ ), 322 nm ( $\epsilon = 1622$ ), 432 nm ( $\epsilon = 22$ ). IR ( $\text{CDCl}_3$ ) ( $\text{cm}^{-1}$ ): 2076 (strong), 1693 (strong).  $^1\text{H}$  NMR ( $\text{CDCl}_3$ )  $\delta$ : 8.45 (d,  $J = 5.0$  Hz, 1H), 7.55–7.00 (m, 8H), 6.90 (dd,  $J = 5.0$ , 3.0 Hz, 1H), 6.30 (m, 1H), 5.00 (s, 1H), 4.25 (t,  $J = 3.0$  Hz, 1H).  $^{13}\text{C}$  NMR ( $\text{CDCl}_3$ )  $\delta$ : 200.5, 161.3, 148.9, 143.2, 141.0, 136.3, 132.9, 128.9, 127.1, 127.0, 121.6, 121.2, 81.8, 63.8, 51.9. HR-MS-ESI  $m/z$  ( $[\text{M} + \text{MeOH} + \text{Na}]^+$ ) calcd. for  $\text{C}_{19}\text{H}_{17}\text{N}_3\text{O}_2\text{Na}$ : 342.1218; found: 342.1199.

### 3-Diazo-7-*anti*-phenyl-7-*syn*-pyridin-2-yl-bicyclo[2.2.1]-hept-5-en-2-one (**12-syn**)

To diisopropylamine (2.2 mmol, 0.33 mL) dissolved in 1.0 mL of freshly distilled THF at  $-78^{\circ}\text{C}$  was added  $n\text{-BuLi}$  (2.2 mmol, 1.6 M). The reaction mixture was stirred at  $-78^{\circ}\text{C}$  for 1 h. The *syn* ketone **10-syn** (1.9 mmol, 0.5 g) in 14 mL of freshly distilled THF was stirred at room temperature until a clear solution was obtained, then the solution was cooled to  $-78^{\circ}\text{C}$ , and LDA was added. The reaction mixture became brown, and was stirred at  $-78^{\circ}\text{C}$  for 2.5 h. Methyl formate (1.0 mL, 6.0 mmol) was then added, and the resulting mixture was stirred at  $-78^{\circ}\text{C}$  for 2 h and allowed to warm to room temperature during stirring overnight. The resulting brown suspension was filtered and washed with ether to give **11-syn** (0.51 g) as a gray solid. To the crude **11-syn** (372 mg) dissolved in 8.0 mL of dichloromethane and cooled in an ice bath, was added tosyl azide (248 mg, 1.26 mmol); the reaction mixture was stirred overnight in the dark and allowed to warm to room temperature. The mixture was then concentrated in vacuo and the residue was subjected to chromatography on neutral alumina (pH ca. 7.5). Elution with dichloromethane yielded 170 mg of **12-syn** as nice yellow crystals:  $R_f$  0.57 (dichloromethane–ether, 9:1). IR ( $\text{CDCl}_3$ ) ( $\text{cm}^{-1}$ ): 2082 (strong), 1679 (strong).  $^1\text{H}$  NMR ( $\text{CDCl}_3$ )  $\delta$ : 8.53 (d,  $J = 5.0$  Hz, 1H), 7.55 (td,  $J = 8.0$ , 2.0 Hz, 1H), 7.32–7.10 (m, 7H), 6.82 (dd,  $J = 5.0$ , 2.5 Hz, 1H), 6.35 (ddd,  $J = 5.0$ , 3.0, 1.0 Hz, 1H), 4.94 (m, 1H), 4.22 (m, 1H).  $^{13}\text{C}$  NMR ( $\text{CDCl}_3$ )  $\delta$ : 200.2, 161.2, 149.6, 141.6, 140.7, 136.6, 128.4, 127.4, 126.5, 121.7, 82.0, 64.1, 51.8. HR-MS-ESI  $m/z$  ( $[\text{M} + \text{Na}]^+$ ) calcd. for  $\text{C}_{18}\text{H}_{13}\text{N}_3\text{ONa}$ : 310.0956; found: 310.0959.

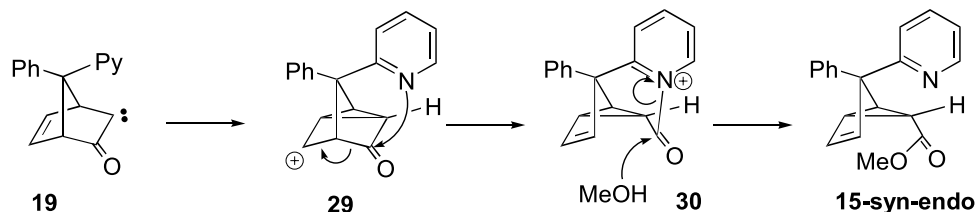
### Irradiation of *anti*-pyridyl diazoketone (**12-anti**)

*anti*-Pyridyl diazoketone (**12-anti**) (644 mg, 2.23 mmol) in 200 mL of MeOH was irradiated with a 400 W medium pressure mercury lamp for 70 min through 0.50 cm of 0.20 M  $\text{CuSO}_4$  as a filter solution. Methanol was then removed, and the brown residue was subjected to chromatography on silica gel. Elution with dichloromethane–ether (9:1) gave 116 mg (18%) of **15-anti-exo**, 66 mg (10%) of **15-anti-endo**. The next three fractions were combined and chromatographed on a second silica gel column, eluted with hexane–dichloromethane–ether (2:2:1) to yield **16-anti** (16%), **14-anti-exo** (29%), and **14-anti-endo** (5%). The combined yield was 78%.

Data for **15-anti-exo**:  $R_f$  0.6 (dichloromethane–ether, 9:1). IR ( $\text{CDCl}_3$ ) ( $\text{cm}^{-1}$ ): 1722.9.  $^1\text{H}$  NMR ( $\text{CDCl}_3$ )  $\delta$ : 8.60 (ddd,  $J = 5.0$ , 2.0, 1.0 Hz), 7.55 (t,  $J = 8.0$  Hz, 1H), 7.30–7.10 (m, 7H), 6.15 (m, 2H), 3.20 (m, 1H), 2.66 (dtd,  $J = 6.5$ , 2.5, 0.7 Hz, 1H), 1.29 (dd,  $J = 3.5$ , 2.5 Hz, 1H).  $^{13}\text{C}$  NMR ( $\text{CDCl}_3$ )  $\delta$ : 172.6, 165.3, 149.1, 144.7, 136.4, 136.1, 132.4, 128.4, 127.7, 126.3, 121.8, 121.3, 65.9, 51.7, 34.7, 34.3, 31.2. HR-MS-EI  $m/z$  ( $[\text{MH}]^+$ ) calcd. for  $\text{C}_{19}\text{H}_{18}\text{NO}_2$ : 292.1337; found: 292.1340. The structure was proved by X-ray analysis.<sup>3</sup>

<sup>3</sup>Supplementary data may be purchased from the Depository of Unpublished Data, Document Delivery, CISTI, National Research Council Canada, Ottawa, ON K1A 0S2, Canada ([http://www.nrc.ca/cisti/irm/unpub\\_e.shtml](http://www.nrc.ca/cisti/irm/unpub_e.shtml) for information on ordering electronically). CCDC 199230 and 199231 contain the supplementary data for this paper. These data can be obtained, free of charge, via [www.ccdc.cam.ac.uk/conts/retrieving.html](http://www.ccdc.cam.ac.uk/conts/retrieving.html) (or from the Cambridge Crystallographic Data Centre, 12 Union Road, Cambridge CB2 1EZ, U.K.; fax +44 1223 336033; or [deposit@ccdc.cam.ac.uk](mailto:deposit@ccdc.cam.ac.uk)).



**Scheme 11.** Unique mechanism of the *exo*-product.

Data for **15-anti-endo**:  $R_f$  0.5 (dichloromethane–ether, 9:1). IR (CDCl<sub>3</sub>) (cm<sup>-1</sup>): 1737.1. <sup>1</sup>H NMR (CDCl<sub>3</sub>)  $\delta$ : 8.56 (ddd,  $J = 5.0, 2.0, 1.0$  Hz, 1H), 7.52 (td,  $J = 8.0, 2.0$  Hz, 1H), 7.37–7.09 (m, 6H), 7.09 (ddd,  $J = 7.5, 5.0, 1.0$  Hz, 1H), 6.34 (dd,  $J = 5.5, 1.5$  Hz, 1H), 6.12 (dd,  $J = 5.5, 2.0$  Hz, 1H), 3.25 (ddd,  $J = 9.0, 6.0, 1.5$  Hz, 1H), 2.57 (ddd,  $J = 7.0, 6.0, 2.0$  Hz, 1H), 2.05 (dd,  $J = 9.0, 7.0$  Hz, 1H). <sup>13</sup>C NMR (CDCl<sub>3</sub>)  $\delta$ : 169.7, 166.0, 148.8, 144.2, 136.3, 135.6, 129.9, 127.9, 127.9, 126.0, 121.9, 121.1, 64.0, 50.9, 33.1, 30.1, 27.9. HR-MS-EI  $m/z$  ([MH]<sup>+</sup>) calcd. for C<sub>19</sub>H<sub>18</sub>NO<sub>2</sub>: 292.1337; found: 292.1342.

Data for **16-anti**: IR (CDCl<sub>3</sub>) (cm<sup>-1</sup>): 1761.2. <sup>1</sup>H NMR (CDCl<sub>3</sub>)  $\delta$ : 8.58 (m, 1H), 7.62 (td,  $J = 8.0, 2.0$  Hz, 1H), 7.45–7.09 (m, 7H), 3.81 (t,  $J = 2.0$  Hz, 1H), 3.22 (td,  $J = 5.0, 1.5$  Hz, 1H), 3.11 (s, 1H), 2.56 (m, 1H), 1.79 (t,  $J = 5.0$  Hz, 1H). <sup>13</sup>C NMR (CDCl<sub>3</sub>)  $\delta$ : 208.9, 162.3, 149.2, 141.29, 136.7, 128.5, 127.2, 127.0, 121.7, 121.3, 82.6, 58.0, 57.2, 50.9, 28.3, 25.8, 20.5. HR-MS-EI  $m/z$  ([MH]<sup>+</sup>) calcd. for C<sub>19</sub>H<sub>18</sub>NO<sub>2</sub>: 292.1337; found: 292.1323. The structure was proved by X-ray analysis.<sup>3</sup>

Data for **14-anti-exo**: IR (CDCl<sub>3</sub>) (cm<sup>-1</sup>): 1723.0. <sup>1</sup>H NMR (CDCl<sub>3</sub>)  $\delta$ : 8.40 (d,  $J = 5.0$  Hz, 1H), 7.58 (d,  $J = 7.5$  Hz, 2H), 7.42 (td,  $J = 8.0, 2.0$  Hz, 1H), 7.24 (t,  $J = 7.5$  Hz, 2H), 7.12 (m, 1H), 6.95 (d,  $J = 7.5$  Hz, 1H), 6.88 (ddd,  $J = 7.5, 5.0, 1.0$  Hz, 1H), 6.72 (t,  $J = 2.0$  Hz, 2H), 3.98 (t,  $J = 2.0$  Hz, 2H), 3.35 (s, 1H), 3.07 (s, 3H). <sup>13</sup>C NMR (CDCl<sub>3</sub>)  $\delta$ : 170.8, 166.2, 148.6, 142.0, 141.6, 135.8, 128.5, 127.6, 126.7, 121.5, 120.1, 92.2, 74.7, 51.4, 50.7. HR-MS-EI  $m/z$  ([MH]<sup>+</sup>) calcd. for C<sub>19</sub>H<sub>18</sub>NO<sub>2</sub>: 292.1337; found: 292.1341. The structure was further proved by preliminary X-ray analysis.

Data for **14-anti-endo**: IR (CDCl<sub>3</sub>) (cm<sup>-1</sup>): 1733.1. <sup>1</sup>H NMR (CDCl<sub>3</sub>)  $\delta$ : 8.43 (ddd,  $J = 5.0, 2.0, 1.0$  Hz, 1H), 7.60–7.45 (m, 3H), 7.35–7.20 (m, 4H), 6.91 (ddd,  $J = 7.5, 5.0, 1.0$  Hz, 1H), 6.55 (t,  $J = 2.0$  Hz, 2H), 3.81 (q,  $J = 2.0$  Hz, 2H), 3.75 (t,  $J = 2.0$  Hz, 1H), 3.60 (s, 3H). <sup>13</sup>C NMR (CDCl<sub>3</sub>)  $\delta$ : 172.9, 164.3, 148.7, 142.9, 138.4, 128.5, 127.0, 126.6, 122.2, 120.5, 88.0, 71.5, 51.4, 51.3. HR-MS-EI  $m/z$  ([MH]<sup>+</sup>) calcd. for C<sub>19</sub>H<sub>18</sub>NO<sub>2</sub>: 292.1337; found: 292.1332.

#### Photolysis of *syn*-pyridyl diazoketone (12-*syn*)

*syn*-Pyridyl diazoketone (**12-*syn***) (59 mg, 0.20 mmol) dissolved in 40 mL of MeOH was irradiated for 255 min using the CuSO<sub>4</sub> filter solution (vide supra). Methanol was then removed, and the residue was subjected to column chromatography on silica gel. Elution with dichloromethane–hexane–ether (2:2:1) yielded **14-*syn*-endo** (11%), **15-*syn*-endo** (43%), **14-*syn*-exo** (23%), and **16-*syn*** (8%), with a combined yield of 85%.

Data for **14-*syn*-endo**: IR (CDCl<sub>3</sub>) (cm<sup>-1</sup>): 1735.3. <sup>1</sup>H NMR (CDCl<sub>3</sub>)  $\delta$ : 8.55 (ddd,  $J = 4.5, 1.8, 1.0$  Hz, 1H), 7.58

(td,  $J = 7.5, 1.8$  Hz, 1H), 7.41 (d,  $J = 7.5$  Hz, 1H), 7.20–7.05 (m, 6H), 6.57 (t,  $J = 2.0$  Hz, 2H), 3.86 (q,  $J = 2.5$  Hz, 2H), 3.59 (s, 3H), 3.58 (t,  $J = 2.5$  Hz, 1H). <sup>13</sup>C NMR (CDCl<sub>3</sub>)  $\delta$ : 172.7, 163.6, 149.3, 143.8, 138.3, 136.4, 128.0, 127.8, 125.8, 121.5, 121.3, 88.0, 72.1, 51.7, 51.4, 29.7. HR-MS-EI  $m/z$  ([MH]<sup>+</sup>) calcd. for C<sub>19</sub>H<sub>18</sub>NO<sub>2</sub>: 292.1337; found: 292.1325.

Data for **15-*syn*-endo**: IR (CDCl<sub>3</sub>) (cm<sup>-1</sup>): 1738.1. <sup>1</sup>H NMR (CDCl<sub>3</sub>)  $\delta$ : 8.58 (ddd,  $J = 5.0, 2.0, 1.0$  Hz, 1H), 7.61 (td,  $J = 7.5, 2.0$  Hz, 1H), 7.35 (dt,  $J = 8.0, 1.0$  Hz, 1H), 7.30–7.10 (m, 6H), 6.40 (d,  $J = 5.5$  Hz, 1H), 6.05 (dd,  $J = 5.5, 2.0$  Hz, 1H), 3.16 (s, 3H), 2.68–2.58 (m, 2H), 2.11 (t,  $J = 8.0$  Hz, 1H). <sup>13</sup>C NMR (CDCl<sub>3</sub>)  $\delta$ : 169.7, 163.5, 148.7, 147.2, 137.8, 135.9, 128.4, 127.6, 126.8, 126.4, 122.9, 121.0, 64.3, 50.9, 34.6, 31.2, 29.7, 28.0. HR-MS-EI  $m/z$  ([MH]<sup>+</sup>) calcd. for C<sub>19</sub>H<sub>18</sub>NO<sub>2</sub>: 292.1337; found: 292.1324.

Data for **14-*syn*-exo**: IR (CDCl<sub>3</sub>) (cm<sup>-1</sup>): 1732.0. <sup>1</sup>H NMR (CDCl<sub>3</sub>)  $\delta$ : 8.52 (ddd,  $J = 5.0, 2.0, 1.0$  Hz, 1H), 7.53 (td,  $J = 7.5, 2.0$  Hz, 1H), 7.46 (dt,  $J = 8.0, 1.0$  Hz, 1H), 7.20–7.00 (m, 6H), 6.75 (t,  $J = 2.0$  Hz, 2H), 4.05 (t,  $J = 2.0$  Hz, 2H), 3.40 (s, 1H), 3.16 (s, 3H). <sup>13</sup>C NMR (CDCl<sub>3</sub>)  $\delta$ : 170.6, 162.7, 148.6, 146.4, 141.9, 135.6, 128.5, 128.4, 127.9, 127.3, 126.8, 126.6, 125.4, 123.4, 121.3, 92.1, 75.2, 51.8, 50.9, 29.8. HR-MS-EI  $m/z$  ([MH]<sup>+</sup>) calcd. for C<sub>19</sub>H<sub>18</sub>NO<sub>2</sub>: 292.1337; found: 292.1324.

Data for **16-*syn***: <sup>1</sup>H NMR (CDCl<sub>3</sub>)  $\delta$ : 8.51 (ddd,  $J = 5.0, 2.0, 1.0$  Hz, 1H), 7.57 (td,  $J = 7.5, 2.0$  Hz, 1H), 7.46–7.20 (m, 6H), 7.07 (ddd,  $J = 7.5, 5.0, 1.0$  Hz, 1H), 3.82 (t,  $J = 2.0$  Hz, 1H), 3.32 (s, 3H), 3.23 (td,  $J = 5.0, 1.0$  Hz, 1H), 3.05 (s, 1H), 2.58 (tdd,  $J = 5.0, 2.0, 1.0$  Hz, 1H), 1.74 (t,  $J = 5.0, 1.0$  Hz).

#### Synthesis of 4-*anti*-phenyl-4-*syn*-pyridin-2-yl-bicyclo-[3.1.0]hex-2-ene-6-carboxylic acid methyl ester (15-*syn*-*exo*)

5-Phenyl-5-pyridylcyclohexadiene (238 mg, 1.09 mmol) and methyl diazo acetate (250 mg, 2.50 mmol) and 12 mg of anhyd CuSO<sub>4</sub> was refluxed in 1 mL of benzene for 75 min. The reaction mixture was concentrated and the residue was subjected to column chromatography, eluted with hexane–ether (3:1) to give **15-*syn*-exo** (15%) as the only adduct:  $R_f$  0.17. IR (CDCl<sub>3</sub>) (cm<sup>-1</sup>): 1723.8. <sup>1</sup>H NMR (CDCl<sub>3</sub>)  $\delta$ : 8.56 (ddd,  $J = 4.5, 2.0, 1.0$  Hz, 1H), 7.67 (td,  $J = 7.5, 2.0$  Hz, 1H), 7.40 (dt,  $J = 8.0, 1.0$  Hz, 1H), 7.32–7.12 (m, 6H), 6.23 (dd,  $J = 5.5, 1.0$  Hz, 1H), 6.09 (dd,  $J = 5.5, 2.0$  Hz, 1H), 3.65 (s, 3H), 2.80 (m, 1H), 2.71 (dt,  $J = 6.0, 2.5$  Hz, 1H), 1.27 (dd,  $J = 3.5, 2.5$  Hz, 1H). <sup>13</sup>C NMR (CDCl<sub>3</sub>)  $\delta$ : 172.4, 164.2, 149.1, 146.3, 137.7, 136.6, 130.9, 128.4, 126.8, 126.5, 122.8, 121.4, 65.9, 51.7, 36.0, 34.7, 31.6, 29.7. HR-MS-ESI  $m/z$  ([MH]<sup>+</sup>) calcd. for C<sub>19</sub>H<sub>18</sub>NO<sub>2</sub>: 292.1337; found: 292.1328.



## Acknowledgement

Support of this research by the National Science Foundation is gratefully acknowledged with special appreciation for its support of basic research.

## References

1. Some precedent is found in the early studies of Wilds et al. (1*a*); (a) A.L. Wilds, J. van der Berghe, C.H. Winestock, R.L. von Trebra, and N.F. Woolsey. *J. Am. Chem. Soc.* **84**, 1503 (1962); (b) A.L. Wilds, R.L. von Trebra, and N.F. Woolsey. *J. Org. Chem.* **34**, 2401 (1969).
2. (a) H.E. Zimmerman and R.D. Little. *J. Chem. Soc., Chem. Commun.* 699 (1972); (b) H.E. Zimmerman and R.D. Little. *J. Am. Chem. Soc.* **96**, 4623 (1974).
3. (a) A.B. Smith. *J. Chem. Soc. Chem. Commun.* 695 (1974); (b) A.B. Smith, B.H. Toder, and S.J. Branca. *J. Am. Chem. Soc.* **106**, 3995 (1985); (c) A.B. Smith, B.H. Toder, R.E. Richmond, and S.J. Branca. *J. Am. Chem. Soc.* **106**, 4001 (1985).
4. J.P. Lokensgard, J. O'Dea, and E.A. Hill. *J. Org. Chem.* **39**, 3355 (1974).
5. (a) H.E. Zimmerman and P. Wang. *Helv. Chim. Acta*, **84**, 1342 (2001); (b) H.E. Zimmerman and P. Wang. *J. Org. Chem.* **67**, 9216 (2002).
6. (a) J.M. Fraile, J.I. Garcia, V. Martinez-Merino, J.A. Mayoral, and L. Salvatella. *J. Am. Chem. Soc.* **123**, 7616 (2001); (b) M.M. Diaz-Requejo, A. Cabellero, T.R. Belderrain, M.L. Nicasio, S. Trofilimenko, and P.J. Perez. *J. Am. Chem. Soc.* **124**, 978 (2002).
7. (a) H.E. Zimmerman. *J. Org. Chem.* **20**, 549 (1955); (b) H.E. Zimmerman. *Acc. Chem. Res.* **20**, 263 (1987), and refs. cited therein; (c) H.E. Zimmerman and L.W. Linder. *J. Org. Chem.* **48**, 1637 (1985); (d) H.E. Zimmerman. *J. Am. Chem. Soc.* **78**, 1168 (1956); (e) H.E. Zimmerman and A. Ignatchenko. *J. Org. Chem.* **64**, 6635 (1999).
8. J.F. Malone, C.M. Murray, M.H. Charlton, R. Docherty, and A.J. Lavery. *J. Chem. Soc. Faraday Trans.* **93**, 3424 (1997).



# An ab initio and AIM study on the decomposition of phosphite ozonides

Jeff L. Langeland and Nick H. Werstiuk

**Abstract:** DFT calculations at the Becke3PW91/6–31+G(d) level of theory provided optimized geometries, transition states, and wave functions suitable for the study of the reactivity and molecular structure with Atoms-in-molecules (AIM) of phosphite ozonide complexes. These calculations also provided activation energies for the extrusion of singlet oxygen from the ozonides, which occurs in a concerted manner. The molecular species investigated were trimethyl phosphite ozonide (**1**), triphenyl phosphite ozonide (**2**), trifluoromethyl phosphite ozonide (**3**), trifluoroethyl phosphite ozonide (**4**), 4-ethyl-1-phospha-2,6,7-trioxabicyclo[2.2.2]octane ozonide (**5**), 1-phospha-2,6,7-trioxabicyclo[2.2.2]octane ozonide (**6**), 1-phospha-2,8,9-trioxadamantane ozonide (**7**), and propylene phenyl phosphite ozonide (**8**). Single-point calculations at the Becke3PW91/6–311++G(d,p) level on the geometries obtained from the lower level theory yielded activation energies of 15.1 and 16.4 kcal mol<sup>-1</sup> for the nonconstrained complexes **1** and **2**, respectively. These values differed from the electronegative trifluoro derivatives **3** and **4**, which had much higher barriers of 23.5 and 20.8 kcal mol<sup>-1</sup>, respectively. The activation energies of the bicyclic complexes **5–7** were significantly higher than **1** and **2** and comparable to **3** and **4**, ranging from 23 to 26 kcal mol<sup>-1</sup>. An intermediate barrier of 20.5 kcal mol<sup>-1</sup> was computed for **8**. AIMPAC studies showed no direct correlation between the AIM atomic charges on the phosphorus or oxygen atoms of the ozonide ring with the ease of decomposition of **1–8** to singlet oxygen and the corresponding phosphate.

**Key words:** phosphite ozonide complexes, decomposition, DFT methods, AIM, activation energy.

**Résumé :** Des calculs de types « DFT » effectués au niveau Becke3PW91/6–31+G(d) de la théorie ont permis d'obtenir des géométries optimisées, des états de transition et des fonctions d'onde convenables pour l'étude de la réactivité et la structure moléculaire de complexes d'ozonides de phosphite par la méthode des atomes dans les molécules (« AIM »). Ces calculs ont aussi permis d'obtenir les énergies d'activation pour l'extrusion d'un atome d'oxygène singulet à partir des ozonides qui se fait d'une manière concertée. Les espèces moléculaires étudiées sont les ozonides du phosphite de triméthyle (**1**), du phosphite de triphényle (**2**), du phosphite de trifluorométhyle (**3**), du phosphite de trifluoroéthyle (**4**), du 4-éthyl-1-phospha-2,6,7-trioxabicyclo[2.2.2]octane (**5**), du 1-phospha-2,6,7-trioxabicyclo[2.2.2]octane (**6**), du 1-phospha-2,8,9-trioxadamantane (**7**) et du phosphite de propylène et de phényle (**8**). Des calculs ponctuels au niveau Becke3PW91/6–311++G(d,p) effectués sur les géométries obtenues au niveau inférieur de la théorie ont permis d'évaluer à 15,1 et 16,4 kcal mol<sup>-1</sup> les énergies d'activation respectives pour les complexes sans contraintes **1** et **2**. Ces valeurs diffèrent de celles des dérivés trifluoro électro-négatifs, **3** et **4**, pour lesquels les valeurs étaient beaucoup plus élevées, soit 23,5 et 20,8 kcal mol<sup>-1</sup> respectivement. Les énergies d'activation pour les complexes bicycliques **5–7** sont beaucoup plus élevées que celles des composés **1** et **2** ainsi que celles des composés comparables **3** et **4**; elles s'étalent de 23 à 26 kcal mol<sup>-1</sup>. Pour le composé **8**, on a calculé que sa valeur est intermédiaire à 20,5 kcal mol<sup>-1</sup>. Des études de type « AIMPAC » ont montré qu'il n'existe aucune corrélation directe entre les charges atomiques « AIM » des atomes de phosphore ou d'oxygène de l'ozonide et la facilité avec laquelle les composés **1–8** se décomposent en oxygène singulet et en phosphate correspondant.

**Mots clés :** complexes d'ozonides de phosphite, décomposition, méthodes « DFT », « AIM », énergie d'activation.

[Traduit par la Rédaction]

## Introduction

Thompson (1) was the first to observe the reaction of ozone with triaryl and trialkyl phosphites at low temperatures. The phosphite ozonide complex (POC) that is pro-

duced from the reaction is thermally unstable and yields the corresponding phosphate and, as later discovered (2), singlet oxygen, as shown in Scheme 1.

This reaction was important because the ozonide complex can react with certain alkenes through a direct bimolecular reaction (3–5) or by first releasing <sup>1</sup>O<sub>2</sub> that can react with the alkene (6–8). The direct attack shows different regioselectivity — with the reaction appearing to occur in a stepwise fashion — as opposed to the concerted attack of singlet oxygen (3, 9). The product distribution depends on the mode of attack with allylic hydroperoxides, cyclic peroxides, and 1,2-dioxetanes being formed (8). Various structures were proposed for the ozonide complex, including several penta-coordinated monomeric and dimeric species (1, 10). From

Received 11 December 2002. Published on the NRC Research Press Web site at <http://canjchem.nrc.ca> on 20 May 2003.

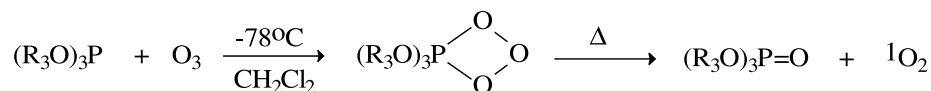
*We dedicate this paper to Professor Don Arnold for his contributions to chemistry.*

**J.L. Langeland and N.H. Werstiuk.**<sup>1</sup> Department of Chemistry, McMaster University, Hamilton, ON L8S 4M1, Canada.

<sup>1</sup>Corresponding author (e-mail address: [werstiuk@mcmaster.ca](mailto:werstiuk@mcmaster.ca)).

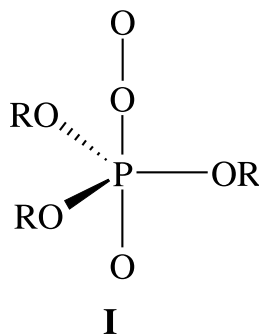


Scheme 1.



the  $^{31}P$  NMR chemical shift at  $\delta = -63$  ppm (1) relative to  $H_3PO_4$  and from freezing point depression experiments on triphenyl phosphite ozonide (2) in  $CHCl_3$ , Bartlett and Chu (11) suggested that the ozonide is monomeric with a penta-coordinated phosphorus atom. Recently, Dimitrov and Seppelt (12) confirmed this hypothesis by obtaining a crystal structure of 4-ethyl-1-phospha-2,6,7-trioxabicyclo[2.2.2]octane ozonide (5).

There have been several kinetic studies involving the rates of decomposition of various POCs (6, 8, 10, 13). For bicyclic POCs 5 and 7, Stephenson and McClure (13) observed that the rate of decomposition varied slightly with substituent. Amazingly, Ramos et al. (6) observed that there was significant variation in the rate of oxygen evolution from bridge-head-substituted derivatives of bicyclic ozonide 6 (for example with the substituent  $-CH_2OCO-C_6H_5$  vs  $-CH_2OSO_2-p-CH_3C_6H_4$ ), even though the change in the  $R$  group was five atoms away from the phosphorus atom. For ozonides 1–4 that have rotational freedom about the  $P-OR$  bond, the rate constants varied by more than two orders of magnitude in some cases (13). A reactive intermediate displayed as **I** was first suggested by Stephenson and McClure (13) ( $R = Ph$ ) for the decomposition of 2, to account for the differences in rate constants for unrestrained ozonide complexes 1–4 vs. the restrained POCs 5–8.



These authors did not speculate as to the electronic distribution of this species. It was suggested that the intermediate has apical oxygen atoms and equatorial phenoxy groups derived from pseudorotation, which occurs after the cleavage of an  $O-O$  bond. There has been conflicting evidence that **I** is a viable species. Mendenhall et al. (10) suggested that the mode of decay would be through a bimolecular reaction if an intermediate such as **I** existed. Bartlett and Chu (11) gave some evidence that **I** was not likely because they found no significant changes in rate constants between hindered and non-hindered POCs with reactive olefins. However, Bartlett and Lonsetta (14) rationalized that **I** ( $R = CH_3$ ) was plausible, as the methoxy groups would preferentially occupy the equatorial positions (rather than the phenoxy groups of 2 ( $R = Ph$ )).

Our interest in using POCs as a source of singlet oxygen ( ${}^1O_2$ ) for study by photoelectron spectroscopy and the variation in the mechanistic proposals presented to date led us to a computational study of these molecules and their decomposition to phosphate and  ${}^1O_2$ . To our knowledge there have been no computational studies on this unusual family of molecules at any level of theory. We undertook a DFT and Atoms-in-molecules (AIM) (15) study to investigate and clarify the mechanism of extrusion of  ${}^1O_2$  and to obtain information on the molecular structure of selected POCs and transition states, as well as the role of structure in determining the activation energy. A brief investigation of the molecular orbitals was also undertaken to examine the consequence of substituent effects and to draw conclusions as to why these ozonides are thermally unstable. The results are presented in this paper.

## Methods

Optimized equilibrium geometries of the POCs — displayed in Fig. 1 — and transition states (TSs) were obtained at the Becke3PW91/6–31+G(d) level, which includes the three-parameter Becke-Perdew-Wang, (Becke3PW91) exchange-correlation potential (16), using either Gaussian 94 or Gaussian 98 (17). The transition states were found by stretching one of the  $O-O$  bonds in the optimized geometry of a POC from 1.44 to 1.75 Å. These geometries were then optimized with a restraint on that bond distance at the PM3 level, which was followed by removal of the restraints and a TS search. Final TS structures were obtained at the Becke3PW91/6–31+G(d) level by performing an opt=TS calculation, by reading in the force constants from the PM3 level. Selected geometrical parameters of 5 and 5-TS are collected in Table 1. The Z-matrices of the other optimized geometries and transition states are included as Supplementary information.<sup>2</sup> Frequency calculations, to characterize the optimized geometries or TSs as well as the zero point energies (ZPE), were performed for all structures. Single-point calculations were carried out at the Becke3PW91/6–311++G(d,p) on the lower-level optimized geometries. The Becke3PW91 functional was used because it has been shown to estimate energies of ionization potentials, proton affinities, and other chemical properties within acceptable values compared with G2 theory but without the computational cost (18). Diffuse functions were included with the expectation that a better description of phosphorus-containing ozonides and their transition states would be realized. The activation energies ( $E_a$ ), calculated from eq. [1], are collected in Table 2.

$$[1] \quad E_a = \{ [ (TS)_{Energy} + (TS)_{ZPE} ] - [ (POC)_{Energy} + (POC)_{ZPE} ] \} + RT$$

<sup>2</sup>Supplementary data may be purchased from the Depository of Unpublished Data, Document Delivery, CISTI, National Research Council Canada, Ottawa, ON K1A 0S2, Canada ([http://www.nrc.ca/cisti/irm/unpub\\_e.shtml](http://www.nrc.ca/cisti/irm/unpub_e.shtml) for information on ordering electronically).



**Fig. 1.** Optimized equilibrium geometries of ozonides investigated: trimethyl phosphite ozonide (**1**), triphenyl phosphite ozonide (**2**), trifluoromethyl phosphite ozonide (**3**), trifluoroethyl phosphite ozonide (**4**), 4-ethyl-1-phospha-2,6,7-trioxabicyclo[2.2.2]octane ozonide (**5**), 1-phospha-2,6,7-trioxabicyclo[2.2.2]octane ozonide (**6**), 1-phospha-2,8,9-trioxadamantane ozonide (**7**), and propylene phenyl phosphite ozonide (**8**).

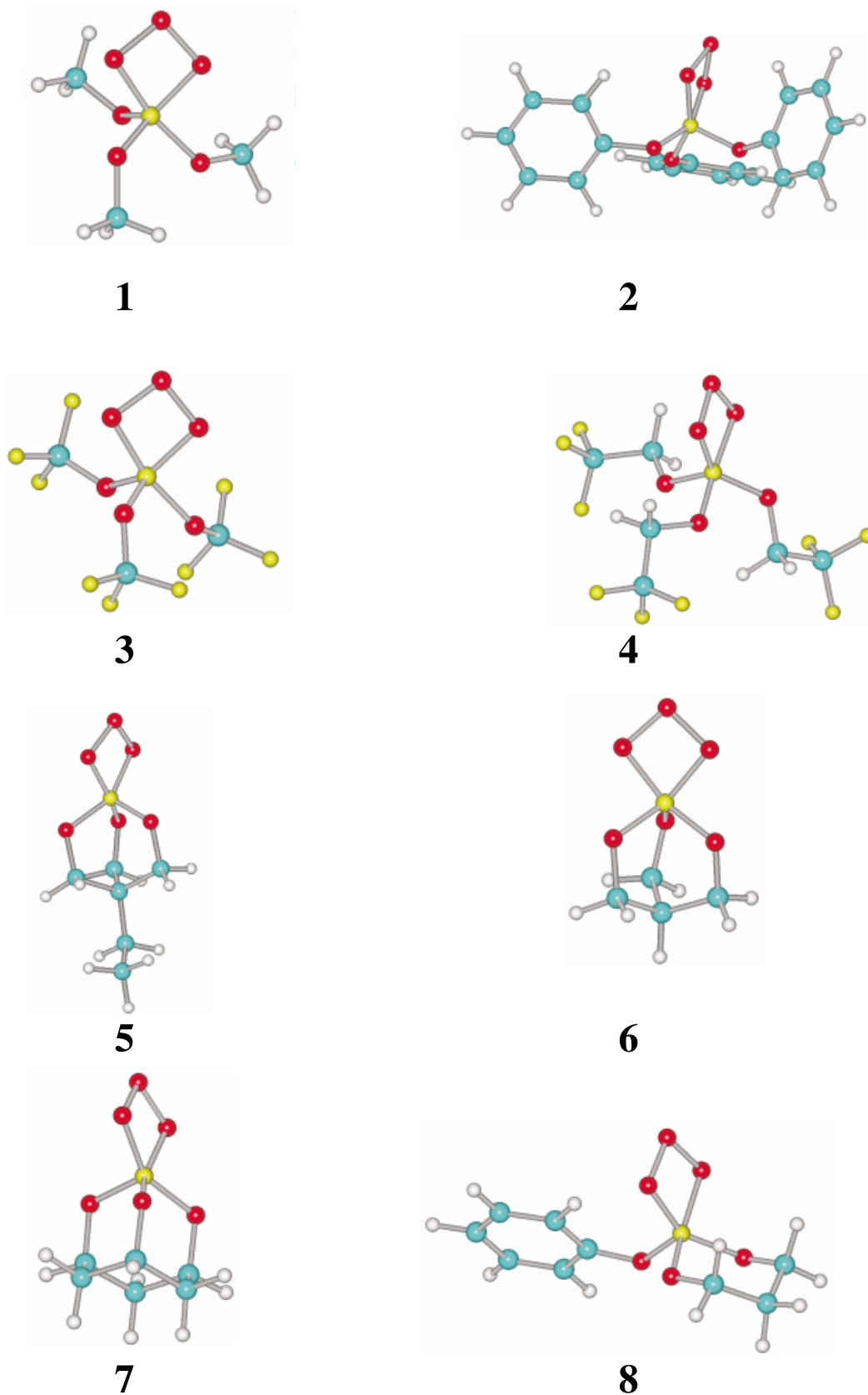




**Table 1.** Selected calculated (Becke3PW91/6-31+G(d)) and experimental geometrical parameters of **5** and its transition state.

Parameter <sup>a</sup>	Calculated	X-ray <sup>b</sup>	TS
P <sub>1</sub> —O <sub>3</sub>	1.69	1.67	2.14
O <sub>3</sub> —O <sub>4</sub>	1.44	1.46	1.31
O <sub>4</sub> —O <sub>5</sub>	1.44	1.46	1.74
O <sub>5</sub> —P <sub>1</sub>	1.68	1.67	1.57
P <sub>1</sub> -O <sub>3</sub> -O <sub>4</sub>	93.8	94.4	46.2
O <sub>3</sub> -O <sub>4</sub> -O <sub>5</sub>	93.8	92.1	97.3
O <sub>4</sub> -O <sub>5</sub> -P <sub>1</sub>	94.3	94.6	84.4
O <sub>5</sub> -P <sub>1</sub> -O <sub>3</sub>	77.2	78.2	74.8
P <sub>1</sub> -O <sub>3</sub> -O <sub>4</sub> -O <sub>5</sub>	7.4	7.0	31.7

<sup>a</sup>Distance units are in Å; bond and torsional angle units are in degrees (°).<sup>b</sup>Reference 12.

Bond critical points and molecular graphs were obtained with AIM2000 (19). Integrations over atomic basins to obtain electron populations — the *L* values (15) were less than 10<sup>-2</sup> — and net atomic charges (included as Supplementary information)<sup>2</sup> were carried out with PROAIM or PROMEGA of the AIMPACK (20) suite of programs. The hydrogens of **2** and **4** were not integrated.

## Results and discussion

Selected geometrical parameters of **5** and **5-TS** are collected in Table 1. The results for **5** agree well with crystal-structure data obtained recently (12). The geometrical parameters of the other POCs are very similar to those found for **5** (see the Z-matrices of the Supplementary information).<sup>2</sup> The ozonide ring conformation was virtually identical in all optimized geometries.

The ozonide ring torsional angle varied only slightly, from a low of 11.0° for **1** to a high of 13.6° for **8**. All other bond distances were essentially the same in the POCs with other bond and torsional angles varying only as a function of substituent. For example, in comparing the bicyclic structures of **5** and **6**, the equilibrium geometries were almost identical. This was expected because of the rigidity of these molecules, their overall similarity, and the lack of rotational freedom in the P-OR groups.

In all cases, it was found that the <sup>1</sup>O<sub>2</sub> is preferentially extruded between two P—OR bonds, as opposed to directly over one of the oxygens. For example, in the case of **5**, singlet oxygen arises from O<sub>3</sub> and O<sub>4</sub> and is extruded between and slightly above atoms O<sub>7</sub> and O<sub>8</sub>, thus forming a new P<sub>1</sub>=O<sub>5</sub> double bond (see Fig. 3 for numbering). This preferential mode for dissociation can easily be rationalized since the O<sub>5</sub>-P<sub>1</sub>-O<sub>3</sub> group of atoms rotates slightly downward and bonds P<sub>1</sub>—O<sub>3</sub> and O<sub>4</sub>—O<sub>5</sub> stretch, giving rise to the new P<sub>1</sub>=O<sub>5</sub> double bond and <sup>1</sup>O<sub>2</sub>. Since this process is concerted, a large amount of structural organization would be required if the singlet oxygen would be extruded over atom O<sub>6</sub>. The transition states also showed little variation in the conformation of the ozonide ring. The torsional angle of the ozonide ring for **1** was computed at 16° while the values for all the other POCs ranged between 22–25°. For the non-ozonide portion of the molecule, the transition states of **5–7** showed little variation from their equilibrium geometries. For the

**Table 2.** Experimental and calculated activation energies (kcal mol<sup>-1</sup>).

POC	Experimental <i>E</i> <sub>a</sub> <sup>a</sup>	B3PW91/6-31+G(d)	B3PW91/6-311++G(d,p)
<b>1</b>	N/A	17.8	15.1
<b>2</b>	14.4 <sup>b</sup>	18.5	16.4
<b>3</b>	N/A	27.9	23.5
<b>4</b>	N/A	22.9	20.8
<b>5</b>	4.4 <sup>c</sup>	26.0	23.9
<b>6</b>	N/A	26.2	24.1
<b>7</b>	19.1 <sup>d</sup>	27.6	25.8
<b>8</b>	N/A	22.6	20.5

<sup>a</sup>Numerous rate constants have been found experimentally for various POCs. Very few have been determined at more than one temperature, so *E*<sub>a</sub> could not always be calculated.<sup>b</sup>Reference 2.<sup>c</sup>See discussion section.<sup>d</sup>Reference 6.

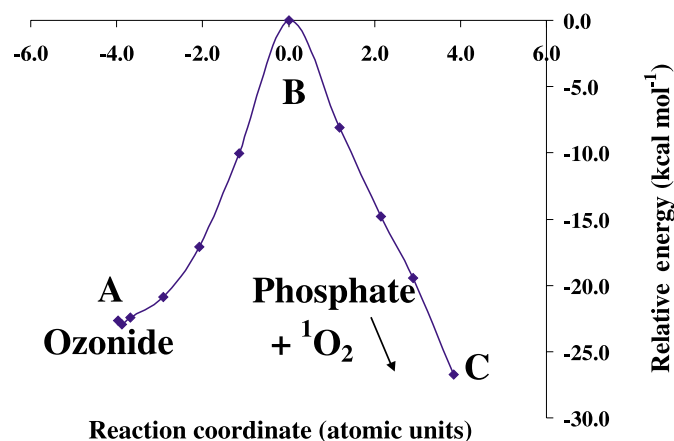
bicyclic structure **5**, very little structural rearrangement is permitted along the reaction coordinate from ozonide to products. Points A, B, and C in Fig. 2 corresponded to selected geometries along the Intrinsic reaction coordinate (IRC). This calculation was performed to ensure that **5-TS** connected the ozonide to the products. Because all of the calculated transition states appeared to exhibit little variation from one another, only one IRC was calculated. Fig. 3 displays the geometries A, B, and C of the **5-TS** IRC, showing both the ozonide (negative reaction coordinate) and the phosphate plus singlet oxygen (positive reaction coordinate) being formed. The increase in the O<sub>5</sub>-P<sub>1</sub>-O<sub>3</sub> angle and the twisting of the ozonide dihedral angle, as well as P<sub>1</sub>—O<sub>3</sub> and O<sub>4</sub>—O<sub>5</sub> bond distances, clearly indicate that the TS (point B of Fig. 2) is on the reaction coordinate.

The intermediate of the type **I** proposed by Stephenson and McClure (13) was not found in our study (when we studied **I** with *R* = Me) for computational efficiency. However, the *E*<sub>a</sub> for the formation of such an intermediate would be expected to be quite large. The calculated TSs exhibited very little structural displacement of the P—OR groups. A great deal of internal re-organization involving both steric and electronic factors would be required if an ozonide such as trimethyl phosphite ozonide (**1**) was transformed to a structure that resembles the previously described intermediate. An “optimized” structure was found for **I** but the O—O ligand migrated more than 6 Å away from the phosphorus atom. Therefore, **I** with *R* = Me is not a stationary point on the potential energy surface.

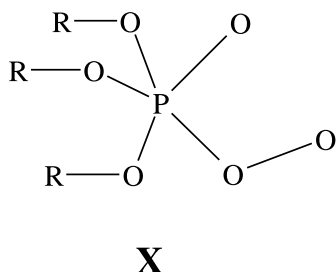
One imaginary frequency between 400i to 600i cm<sup>-1</sup> was calculated for all POC transition states. With the aid of the molecular visualization package MOLEKEL (21), these negative frequencies were animated. The exaggerated animation showed that, starting with a P<sub>1</sub>-O<sub>3</sub>-O<sub>4</sub>-O<sub>5</sub> ozonide torsional angle of approximately 22° in the TS, the evolving <sup>1</sup>O<sub>2</sub> would twist to an almost 90° torsional angle (see the side view of Fig. 3 for a partial sequence) when these atoms were at the furthest point away from the reaction centre. The exaggerated animated imaginary frequencies clearly exhibited the correct normal mode for the dissociation to singlet oxygen and phosphate as well as the return to starting material.



**Fig. 2.** IRC for **5** from the TS (**B**), to the ozonide **A**, and to the product side **C**. The energies of the ozonide and phosphate and singlet oxygen relative to the TS (point **B**) are  $-23.5$  and  $-44.6$  kcal mol $^{-1}$ , respectively.

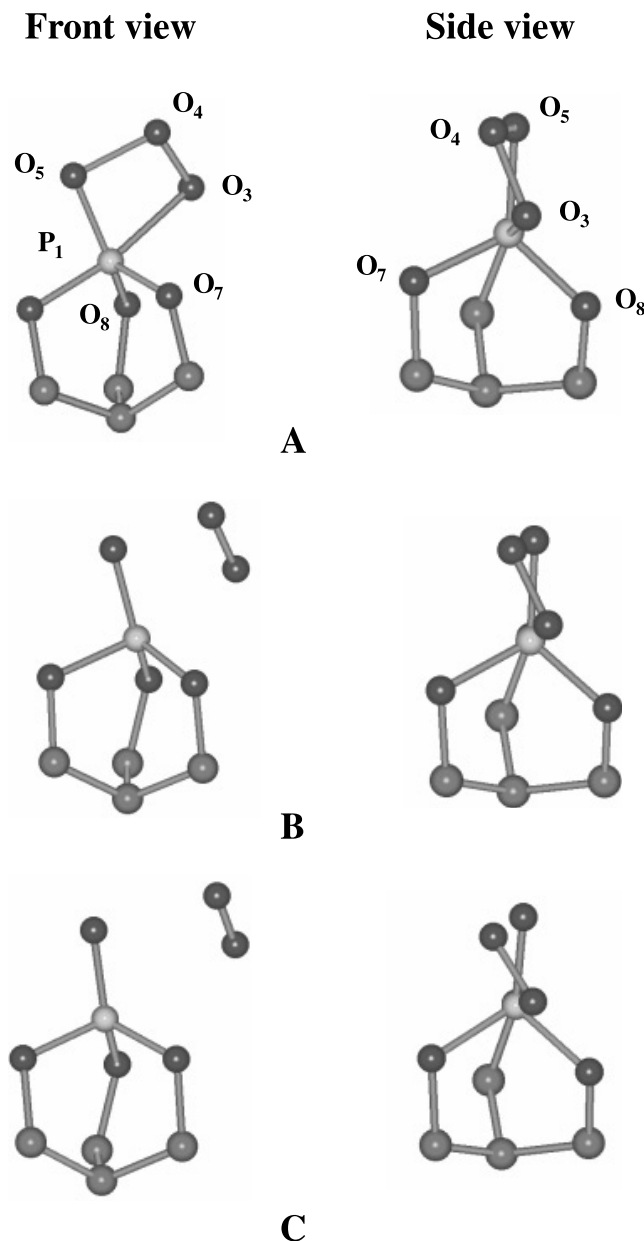


Stephenson and McClure (13) also suggested that a pre-equilibrium of an ozonide before decomposition could occur to give a structure similar to **X**. They rationalized **X** from thermochemical analysis that Benson and Shaw (22) performed, which indicated a maximum oxygen—oxygen bond strength of only 2 kcal mol $^{-1}$  — compared with the relatively high  $E_a$ s for **1–8**. However, the analysis by Benson and Shaw (22) was based on the assumptions that: (a) the O—O bond would be similar to that of other trioxides; (b) the ring strain was similar to that in 4-membered rings containing sulphur, and (c) the solvation enthalpy of  $^1\text{O}_2$  in solvent was small. We are unaware of any recent calculations or experimental evidence of these ozonides to prove otherwise. However, low temperature  $^{31}\text{P}$  NMR (11) revealed only one sharp peak  $\delta = -63$  ppm (relative to  $\text{H}_3\text{PO}_4$ ), suggesting no equilibrium to **X**.



Also, recent calculations (23) on polyoxides of the type  $\text{H}(\text{O})_n\text{H}$  ( $n > 2$ ) suggest that the bond dissociation energy for  $n = 3$  was 33 kcal mol $^{-1}$  and the minimum barrier for any  $n > 2$  would be 6.4 kcal mol $^{-1}$ . Mendenhall et al. (10) discounted both a diradical and zwitterionic intermediate of type **X** based on the lack of observation of bimolecular self-reactions. A TS or intermediate structure resembling **X** at the uBecke3PW91/6–31+G(d) level was not found in our study. At the semiempirical level (PM3), a TS was found for the above, but when the transition state search was performed at the ab initio level by reading in the force constants from the PM3 calculation, the TS that we described above was obtained. The “intermediate” for **X**, found at the PM3

**Fig. 3.** Front and side view of geometries **A**, **B**, and **C** along the reaction coordinate for the decomposition of 4-ethyl-1-phospha-2,6,7-trioxabicyclo[2.2.2]octane ozonide (**5**). The side view is a 90° rotation and tilted forward slightly to show the twisting of the extruding singlet oxygen. For clarity, the ethyl substituent and hydrogens have been omitted. Atom  $\text{O}_6$  lies behind the carbon atom in the side view.



level by restraining the  $\text{O}_3\text{—O}_4$  and  $\text{P}_1\text{—O}_5$  bonds, also converted to a structure resembling the TSs that we described above when calculated at the uBecke3PW91/6–31+G(d) level of theory. The  $\text{P}_1\text{—O}_5$  bond would significantly stretch (approximately 0.5 Å) and the ozonide ring torsion would twist (approximately 10°). If the  $\text{O}_3\text{—O}_4$  bond was not stretched far enough (less than 0.2 Å from equilibrium distance) then the **X** intermediate would return to the ozonide at the uBecke3PW91/6–31+G(d) level of theory. Therefore,



we were unable to locate a stable structure that resembled **X** ( $R = \text{Me}$ ) either as a TS or an intermediate.

The computed activation energies are collected in Table 2. Several identifiable patterns are in the data. The greater the size and the more electronegative the  $R$  substituent of the POC, the higher is the barrier for extrusion of  $^1\text{O}_2$ . Generally, the single-point calculations at the Becke3PW91/6-311++G(d,p) level gave  $E_a$ s (eq. [1]) of 2.0 to 4.5 kcal mol $^{-1}$  less than the value obtained at the Becke3PW91/6-31+G(d) level. The unconstrained POCs **1–4** showed a substantial variation in their  $E_a$ s. Trimethyl phosphite ozonide (**1**) had the lowest calculated activation energy of the POCs at 15.1 kcal mol $^{-1}$ . An experimental  $E_a$  is not known, as the lifetime, even at  $-88^\circ\text{C}$ , is extremely short (14). The calculated  $E_a$  for **2**, 16.5 kcal mol $^{-1}$ , was in good agreement with the experimental value (2) of 14.4 kcal mol $^{-1}$ . Steric factors might play a small role in determining the  $E_a$  of **2** vs. **1** in that the methoxy ligands pose less steric hindrance than the phenoxy groups of **2**. There was only a small increase in activation energy for **2**, as the singlet oxygen tends to extrude above the P–OR ligands and was not substantially affected by the phenoxy groups of **2** relative to the methoxy groups of **1**.

For trifluoromethyl phosphite ozonide (**3**) and trifluoroethyl phosphite ozonide (**4**) the calculated activation energies were approximately 10 and 5 kcal mol $^{-1}$  higher than that of the trimethyl analogue. The equilibrium geometries of **1**, **3**, and **4** had similar geometry of the P–OR groups and would be best described as trigonal pyramidal (as well as the other POCs studied). The transition states of **1**, **3**, and **4** also showed this same type of geometry. However, there was a variation in the torsional angle within the ozonide ring (15.9, 25.2, and  $26.2^\circ$ , respectively), and the P–OR conformations differed somewhat. The substituent effect of the electronegative fluorine groups that caused the large separation of  $E_a$  values between **1** and **3** will be explained qualitatively though the AIM molecular graphs in the next section. Ozonide **4** was similar in conformation to **3**. The phosphorus and oxygen atoms in the P–OR ligands are buffered through an additional methylene group. This buffering relative to **3** appears to be a major factor as to why the  $E_a$  of **4** was only 20.4 kcal mol $^{-1}$ , approximately 3 kcal mol $^{-1}$  less than the  $E_a$  for **3**.

For the bicyclic POCs **5–7** the calculated activation energies were in the range of 23–26 kcal mol $^{-1}$ , much higher than those found experimentally. The experimental values for the  $E_a$  of **5** were found to be only 8.5 kcal mol $^{-1}$  with acetone as the solvent (10) and 4.4 kcal mol $^{-1}$  calculated from rate constants obtained in  $\text{CH}_2\text{Cl}_2$  at two different temperatures (13). These results do not compare well with the computed value of 26.0 kcal mol $^{-1}$  (Becke3PW91/6-31+G(d)) or 23.5 kcal mol $^{-1}$  obtained at the Becke3PW91/6-311++G(d,p) level. However, the experimental (13) first-order rate constant was found to be  $9.75 \times 10^{-5} \text{ s}^{-1}$  for **5** compared with  $740 \times 10^{-5} \text{ s}^{-1}$  for **2** in dichloromethane at  $-5^\circ\text{C}$ . This suggests that **2** would have a lower activation barrier than **5**. For this reason we suggest that the experimental  $E_a$  of **5** should have been higher than that observed. We therefore arrive at the same conclusion that Schaap et al. (8) reached, in that “additional experiments on the thermal stability of **5** seem to be required”. In comparing **5** and **6** there was no

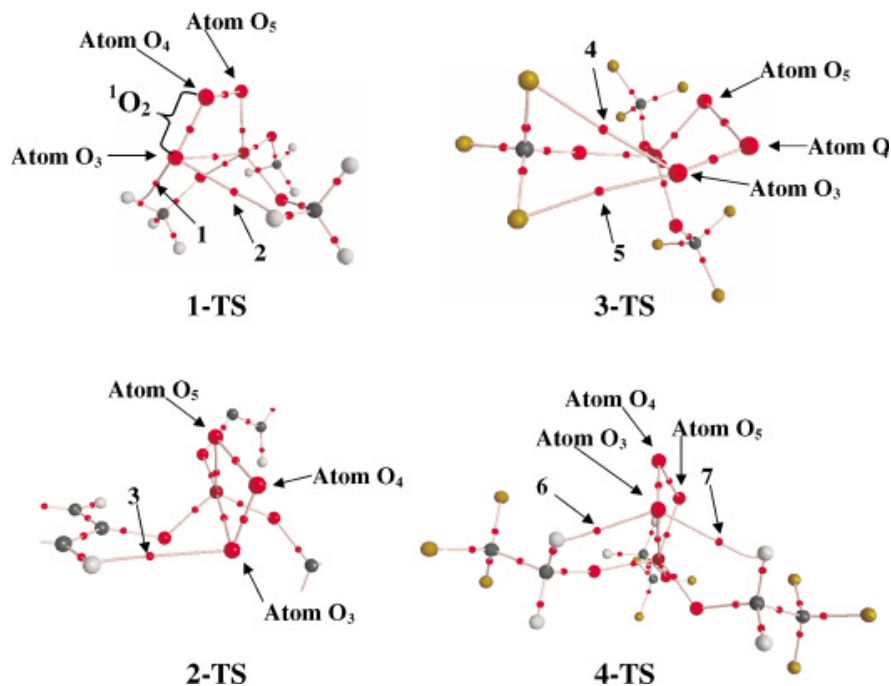
substitution effect noted, as the computed  $E_a$  for **5** was only 0.2 kcal mol $^{-1}$  higher than the value for **6**. This was expected, since the change was small and the substitution was five atoms away from the reaction centre. As noted earlier, Ramos et al. (6) saw a variation of one order of magnitude in rate constants for derivatives of **6** in some cases. They argued that the remote-substituent effect was perhaps a spatial, steric, or electronic effect, which affects the stability of the POCs. Others (13) observed an average rate constant of  $k = 1.4 \pm 0.4 \times 10^{-4} \text{ s}^{-1}$  for a total of eight constrained POCs, which varied dramatically in their structure. At the semi-empirical level (PM3) we found no stable conformation for some of the ozonides studied by Ramos et al. (6) that would suggest a spatial or electronic effect to account for the variation they saw in the rate constants. The calculated value for **7** was more than 6 kcal mol $^{-1}$  higher than the experimental value (8) of  $19.1 \pm 1.2 \text{ kcal mol}^{-1}$ . The experimental value was derived from rate constants obtained at five different temperatures with a small error, so it would appear to be correct. However, the precautions necessary for the reproducibility experiments using  $\text{CH}_2\text{Cl}_2$  as the solvent has also been voiced (10). Ozonide **8** showed an approximate 5 kcal mol $^{-1}$  decrease in  $E_a$  compared with POCs **5–7**. The explanation offered here is that there is at least some flexibility within **8**. This seems reasonable since the flexibility and  $E_a$  of **8** is generally in between that of **1–4** and **5–7**. The ease of rotation about the P–OR bond along with electronegative substituents seems to be the determining factors in the  $E_a$ s of the complexes studied. A referee suggested that the binding energy of ozone to the phosphate should have been investigated for completeness of this study. However, we feel that this would have no bearing on the interpretation of the results. Justification for this arises from the fact that the ozonides are prepared at  $-78^\circ\text{C}$  and decompose quantitatively to phosphate and singlet oxygen (6, 10) above this temperature. We therefore conclude that there is no competing reaction or equilibrium that involves the dissociation of the POCs to phosphite and ozone; no ozonolysis products of alkenes have been found in the reactions.

### AIM analysis

We carried out AIM analyses with the wave functions obtained at the Becke3PW91/6-31+G(d) level. Bond critical points and bond paths were obtained for all POCs. With the exception of **1-**, **2-**, **3-**, and **4-TS**, as well as propylene phenyl phosphate derived from **8**, the POCs showed no anomalies. However, what was truly interesting about these TSs were the hydrogen and fluorine bond paths from the P–OR groups ( $R = \text{CH}_3$ , Ph,  $\text{CF}_3$ , or  $\text{CH}_2\text{CF}_3$ ) to the lower oxygen (atom  $\text{O}_3$ ) of the extruding singlet oxygen (Fig. 4). Since atom  $\text{O}_3$  was found to have a negative charge of  $-0.74e$  in the optimized geometry and  $-0.34e$  in the TS (discussed later), the two hydrogen atoms appear to show a favourable interaction with sufficient electron density, which may stabilize the TS somewhat. At the unexpected bond critical points **1** and **2** for the **1-TS** in Fig. 4, the electron densities,  $\rho(\mathbf{r})$ , were 0.016 and 0.018 au, respectively. Similar values were found for the critical points in the **2-**, **3-**, and **4-TS**s. For points **3–7** in Fig. 4, the  $\rho(\mathbf{r})$  values were 0.010, 0.012, 0.013, 0.025, and 0.016 au, respectively. These electron density values were much less than for the other bond critical points within



**Fig. 4.** Molecular graphs with selected bond critical points of the transition states for POCs **1**, **2**, **3**, and **4**. The lines that connect the atoms are bond paths, and the points between atoms are the bond critical points. For clarity, the phenyl rings of **2-TS** have been truncated.



the molecule. For comparison, the density values for some other bond critical points in **1-TS** were;  $P_1-O_3 = 0.046$ ,  $P_1-O_5 = 0.195$ ,  $P_1-O_{6-8} = 0.184-0.187$ ,  $O_3-O_4 = 0.377$ ,  $O_4-O_5 = 0.172$ ,  $O_6-C_{11} = 0.232$ , and  $C_{11}-R$  ( $R = H$ ) =  $0.280-0.285$  au. There have been several recent reports on molecules that show similar, unusual molecular graphs. Koch and Popelier (24) studied four van der Waals complexes, including formaldehyde–chloroform and benzene–formaldehyde systems. They suggested that the intermolecular interaction energy would be less than  $0.5 \text{ kJ mol}^{-1}$  for the complexes. Others (25) suggested a much higher intramolecular stabilization energy occurs in ribonucleosides. These ribonucleosides exhibited several  $CH\cdots O$  interactions, which accounted for approximately  $5-18 \text{ kcal mol}^{-1}$  in stability vs. the conformations in which these interactions were not present. Our intent was not to describe a full quantitative analysis of these interactions, as there are eight hydrogen-bonding criteria within the AIM formalism (24, 26, 27). However, we would like to suggest that, since **1-** and **2-TS** exhibit such a molecular graph, the lower activation energy compared with POCs **5-7** might result from the stabilization of the transition state through these weak hydrogen-bonding interactions. This type of stabilization could result in a lowering of the  $E_a$ . Similar interactions, which had activation barriers moderately higher than **1** or **2**, were also noted for the **3-** and **4-TS**s. The bond paths in **3-TS** connect two fluorine atoms in one of the  $P-OCF_3$  groups to atom  $O_3$  in the extruding singlet oxygen (Fig. 4). It is possible that the extrusion of singlet oxygen is hindered through electrostatic repulsion by the fluorine atoms (typically bearing a negative charge of  $-0.67$  to  $-0.69e$ ) with atom  $O_3$ , which also carries a net negative charge (approximately  $-0.33$  to  $-0.34e$ ). This is contrasted to the slight positive charge (typically

$0.05$  to  $0.06e$ ) found on the hydrogen atoms of **1** and **2**. Because the hydrogen atoms are somewhat electron deficient, interactions with the partially negatively charged  $O_3$  atom would tend to lower the energy of the TSs. We would suggest that the  $E_a$  for **3** would be slightly lower than calculated if the repulsive interactions between the fluorine atoms and the oxygen atom of the extruding singlet oxygen were not present. Similarly, we would suggest that the activation energies of the POCs **1** and **2** would be slightly higher if these weak hydrogen interactions with atom  $O_3$  were not present. It is difficult to account for the elevated  $E_a$  of **4** relative to **1**, as there are two similar bond paths (points 6 and 7 in Fig. 4) with relatively high  $\rho$  values compared with the previous points, as discussed in the case of **1-TS**. It would be expected that these weak interactions would stabilize the **4-TS** and lower the  $E_a$ , as described for **1-TS**. The electronegative fluorine groups may play a role in determining the  $E_a$  of **4** relative to **1**, although no unusual bond critical points between the fluorines and the extruding singlet oxygen were observed. Still, the  $E_a$  for **4** was almost  $4 \text{ kcal mol}^{-1}$  less than that for **3**, which suggests that the electronegative fluorine groups, combined with  $CH\cdots O$  interactions, give the intermediate  $E_a$  of **4** relative to **1** or **3**. However, at this time, it is difficult to quantify a precise explanation as to why the activation energy of **4** had this intermediate value. Since POCs **5-8** did not exhibit any of the above-mentioned anomalous molecular graphs, there is no stabilization or destabilization of the TSs that leads to the calculated activation energies, which are very similar (especially for **5-7**, where the  $E_a$ s differed by less than  $2 \text{ kcal mol}^{-1}$ ).

The AIM-PAC results for the atomic charges for the atoms within the POCs, TSs, and selected phosphates are collected in Table 3. On the whole, there was little variation in the net



**Table 3.** AIM net charges of selected atoms of phosphite ozonides and transition states.

Species <sup>a</sup>	P <sub>1</sub>	O <sub>3</sub>	O <sub>4</sub>	O <sub>5</sub>	O <sub>6</sub>	O <sub>7</sub>	O <sub>8</sub>	C <sub>9</sub>	C <sub>10</sub>	C <sub>11</sub>
<b>1</b>	3.61	-0.69	-0.05	-0.74	-1.32	-1.31	-1.30	0.42	0.43	0.42
<b>2</b>	3.58	-0.71	-0.04	-0.73	-1.31	-1.33	-1.31	0.43	0.44	0.47
<b>3</b>	3.63	-0.69	0.00	-0.73	-1.29	-1.29	-1.28	2.42	2.41	2.41
<b>4</b>	3.60	-0.70	-0.01	-0.71	-1.29	-1.27	-1.28	0.48	0.47	0.46
<b>5</b>	3.48	-0.68	-0.03	-0.67	-1.25	-1.24	-1.24	0.43	0.45	0.45
<b>6</b>	3.59	-0.69	-0.03	-0.70	-1.27	-1.29	-1.27	0.44	0.45	0.44
<b>7</b>	3.59	-0.70	-0.04	-0.70	-1.27	-1.27	-1.29	0.45	0.43	0.44
<b>8</b>	3.59	-0.70	-0.04	-0.74	-1.29	-1.29	-1.29	0.44	0.43	0.47
<b>1-TS</b>	3.50	-0.48	-0.04	-0.94	-1.28	-1.27	-1.27	0.41	0.42	0.44
<b>2-TS</b>	3.58	-0.41	0.03	-1.03	-1.33	-1.35	-1.33	0.41	0.44	0.44
<b>3-TS</b>	3.56	-0.29	-0.03	-1.09	-1.29	-1.28	-1.28	2.42	2.41	2.42
<b>4-TS</b>	3.61	-0.46	-0.02	-1.00	-1.32	-1.30	-1.31	0.47	0.46	0.49
<b>5-TS</b>	3.56	-0.37	-0.02	-1.03	-1.28	-1.28	-1.28	0.40	0.41	0.44
<b>6-TS</b>	3.56	-0.36	-0.01	-1.03	-1.28	-1.27	-1.27	0.41	0.41	0.45
<b>7-TS</b>	3.56	-0.37	-0.02	-1.03	-1.28	-1.27	-1.27	0.41	0.41	0.45
<b>8-TS</b>	3.57	-0.35	-0.03	-1.07	-1.29	-1.30	-1.33	0.44	0.41	0.44
<b>1-P</b>	3.66			-1.47	-1.32	-1.32	-1.32	0.41	0.41	0.41
<b>3-P</b>	3.66			-1.42	-1.30	-1.30	-1.30	2.41	2.41	2.42
<b>5-P</b>	3.62			-1.45	-1.29	-1.28	-1.29	0.42	0.42	0.42
<b>8-P</b>	3.55			-1.43	-1.30	-1.28	-1.26	0.43	0.41	0.43

<sup>a</sup>**1-P**, **3-P**, **5-P**, and **8-P** are the corresponding phosphates derived from **1**, **3**, **5**, and **8**.

atomic charges for individual atoms from the optimized geometries to the TSs and then to the phosphates of the POCs studied.

The equilibrium geometries exhibited a highly electron-deficient phosphorus atom, with the charges varying from 3.48e for **5** to 3.63e for **3**. In going to the TS, the phosphorus atom essentially retains its net charge, as do the remaining atoms in the molecule with the exception of atoms O<sub>3</sub> and O<sub>5</sub>. Atom O<sub>3</sub> exhibits a nominal one-half decrease in negative charge while atom O<sub>5</sub> tends to double its negative charge. From the TS to the phosphate, essentially only atoms O<sub>5</sub> and O<sub>3</sub> are affected. For example, from **1-TS** to the phosphate (**1-P**) and singlet oxygen we see that atom O<sub>5</sub> increases its negative charge from -0.94 to -1.47e while atom O<sub>3</sub> changes from -0.48e to zero in singlet oxygen. All other atoms show almost complete retention of atomic populations from ozonide to TS to phosphate.

It was suggested (12) that the more electropositive the phosphorus atom in the cyclic and bicyclic systems, the stronger the O—O bond in the ozonide portion of the molecule, thus resulting in an elevated  $E_a$ . However, in the case of POC **1**, the phosphorus atom had a positive charge of +3.61e, which was marginally higher than the values found for the bicyclic structures but slightly lower than **3**. For **1** and **2**, the charges on the phosphorus atom had an intermediate value compared with the other POCs **3–8**. Ozonides **1** and **2** are the most reactive of the series (2, 12) and have significantly lower calculated  $E_a$ s relative to **3**. But, since the atomic charges on the phosphorus atom for **1** and **2** were intermediate in their values, there does not seem to be a direct correlation between atomic charges on the phosphorus atom and activation parameters. This argument is substantiated by noting that the atomic charges on the phosphorus atom were very similar in the starting materials, TSs, and phosphates for all of the POCs, as seen from Table 3. The electron-withdrawing fluorine groups, as in **3** and **4**, for the most part

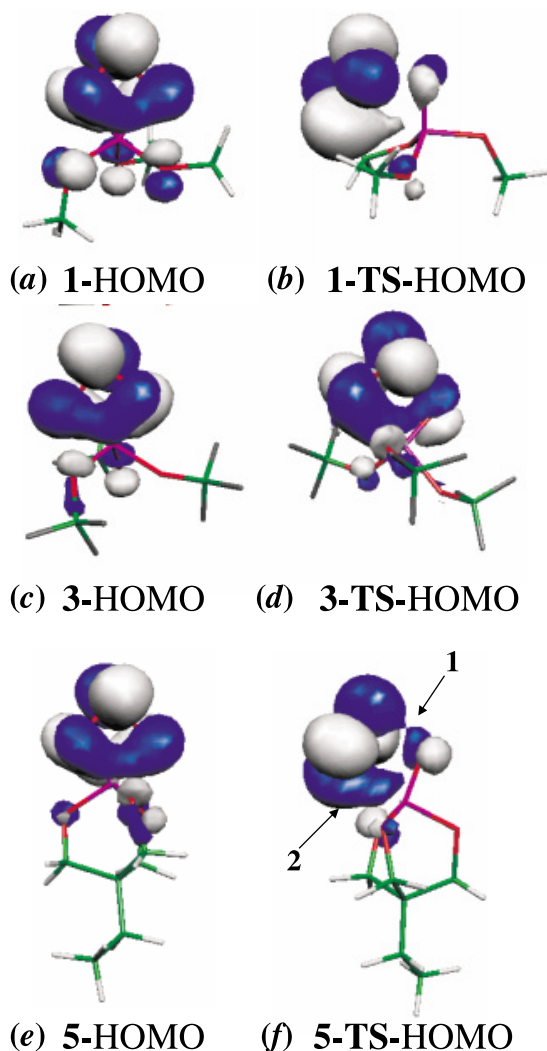
did not affect the net atomic charge on the phosphorus. The substituted trifluoromethyl carbon atoms (C<sub>9</sub>–C<sub>11</sub>) in **3** had substantial positive charges of approximately +2.4e in the optimized geometry, TS, and phosphate. However, the neighbouring oxygens to the trifluoromethyl substituent in **3** had no change to their net charges compared with the other POCs. The bicyclic ozonides (**5–7**) and **8** had virtually identical atomic charges in the ozonides and TSs (Table 3). However, the  $E_a$  of **8** was approximately 5 kcal mol<sup>-1</sup> less than **5–7**. Therefore, from the above results, we draw the conclusion that there is no direct correlation with net atomic charges of individual atoms in the POCs with an increase or decrease in activation energy.

Because these complexes decompose at low temperatures, the frontier MOs of the ozonide ring were investigated. It was found that a large degree of antibonding character existed in the ozonide ring. For POCs **1**, **3**, and **5** the molecular orbitals were investigated to see why the ozonides might be unstable and why there was “twisting” of the evolving singlet oxygen in all the transition states. The HOMOs of these POCs and their TSs immediately shed light on the above two questions. Figure 5 illustrates the HOMO of ozonides **1**, **3**, and **5** and their associated TSs. The large antibonding character of the *p*-orbitals of the oxygen atoms in the ozonide ring, along with minor contributions from the *p*-orbitals of the bicyclic ring oxygens, is evident. Of note is the bonding interaction seen between atoms O<sub>3</sub> and O<sub>5</sub>. Also, the HOMO showed no bonding interactions between the phosphorus and the oxygen atoms in the ozonide ring. Thus, this result would suggest that the O<sub>5</sub>—O<sub>4</sub> bonds would break first, followed by the simultaneous cleavage of the P<sub>1</sub>—O<sub>3</sub> bond, with formation of singlet oxygen and the phosphate.

With the antibonding character associated with their occupied MOs, it is easy to rationalize why these molecules readily decompose. Upon heating, POC **5** would go to the



**Fig. 5.** Highest occupied molecular orbitals of POCs **1**, **3**, and **5** (*a*, *c*, *e*) and the corresponding transition states (*b*, *d*, *f*).



TS, as depicted above. The twisting of the  $^1\text{O}_2$  occurs to create more bonding character between  $\text{O}_3$  and  $\text{O}_4$ , within the HOMO of the TS (Fig. 5, points (e) and (f)). The MOs of **1** and **3** were also investigated and were somewhat similar to those found for **5**. Qualitatively, there did not appear to be any significant deviation to rationalize the 10 kcal mol $^{-1}$  difference in the  $E_a$ s for **1** and **3**. The illustration for the **5-TS** HOMO at points 1 and 2 in Fig. 5f appears to exhibit more bonding interaction of the oxygen and phosphorus atoms than does **1**. A similar interaction, as for the **5-TS** HOMO, is noted for the **3-TS** HOMO, only more substantial (Fig. 5d). However, the internuclear distances of  $\text{P}_1\text{--O}_3$  and  $\text{P}_1\text{--O}_4$  in **1-TS** were greater than those of **5-TS** and even greater than in **3-TS**. Therefore, conclusions as to the relative lowering of the activation barrier through these weak additional bonding interactions are difficult to quantify.

As a final note, the decomposition of the POC TSs described above exhibited similar characteristics to an oxaphosphetane transition state (OP-TS) from a Wittig reaction decomposing to the phosphine oxide and alkene products. The mechanism for the Wittig decomposition remains somewhat controversial, especially when considering the non-

stabilized and stabilized ylides (28, 29). However, recent calculations (30) at the Becke3PW91/6–31G(d) show the OP-TS has a dihedral angle of approximately 7–29° (*trans* route) for the four atoms that make up the ring in the TS. The puckering of the OP-TS is similar to the TSs that we calculated, and the varying angles may be attributed to the substituents on the aldehyde examined by Vedejs and Marth (29). These calculations also showed imaginary frequencies that ranged between 300i to 400i cm $^{-1}$ , similar to the ones we described.

## Conclusions

Plausible optimized geometries and transition states for the POCs investigated gave the calculated activation energies. The computed  $E_a$ s for the extrusion of singlet oxygen from the ozonides were within reasonable agreement with experimental results, with the exception of 4-ethyl-1-phospha-2,6,7-trioxabicyclo[2.2.2]octane ozonide. The activation energies ranged from a low of 15.1 kcal mol $^{-1}$  for trimethyl phosphite ozonide to a high of 25.6 kcal mol $^{-1}$  for 1-phospha-2,8,9-trioxadamantane ozonide from single point calculations at the Becke3PW91/6–31++G(d,p) level of theory. A nice correlation was found: the more hindered and electronegative the P–OR groups, the higher the activation barriers. The AIM results indicated that there is no correlation between the atomic charges on the atoms near the reaction centre and the reactivity of the POCs. We have discounted structures **I** and **X**, which were proposed to be likely intermediates or TSs, as no suitable geometries were found in our study. Weak electrostatic interactions — both attractive and repulsive — that either lower or raise the  $E_a$  may occur in POCs in which the TSs are stabilized or destabilized by such interactions. Qualitative arguments were presented from a frontier molecular orbital description to account for the thermal instability of these ozonides.

## Acknowledgments

We gratefully acknowledge grants of CPU time on the SGI Origin 2000 computer at the Université de Montréal, a centre of the Réseau Québécois de Calcul de Haute Performance (RQCHP). We thank the Shared Hierarchical Academic Research Computing Network of Ontario (SHARCNET) for providing computing resources at McMaster University. We gratefully acknowledge financial support by the Natural Sciences and Engineering Research Council of Canada (NSERC).

## References

1. Q.E. Thompson. *J. Am. Chem. Soc.* **83**, 845 (1961).
2. R.W. Murray and M.L. Kaplan. *J. Am. Chem. Soc.* **90**, 5356 (1968).
3. A. Maranzana, G. Ghigo, and G. Tonachini. *J. Am. Chem. Soc.* **122**, 1414 (2000).
4. P.H. Dussault and K.R. Woller. *J. Org. Chem.* **62**, 1556 (1997).
5. P.A. Schaap and P.D. Bartlett. *J. Am. Chem. Soc.* **92**, 6055 (1970).
6. S.M. Ramos, J.C. Owrutsky, and P.M. Keehn. *Tetrahedron Lett.* **26**, 5895 (1985).



7. L.M. Stephenson and M.B. Zielinski. *J. Am. Chem. Soc.* **104**, 5819 (1982).
8. P.A. Schaap, K. Kees, and A.L. Thayer. *J. Org. Chem.* **40**, 1185 (1975).
9. P.D. Bartlett and A.P. Schaap. *J. Am. Chem. Soc.* **92**, 3223 (1970).
10. G.D. Mendenhall, R.F. Kesseck, and M.J. Dobrzelewski. *J. Photochem.* **25**, 227 (1984).
11. P.D. Bartlett and H.-K. Chu. *J. Org. Chem.* **45**, 3000 (1980).
12. A. Dimitrov and K. Seppelt. *Eur. J. Inorg. Chem.* **8**, 1929 (2001).
13. L.M. Stephenson and D.E. McClure. *J. Am. Chem. Soc.* **95**, 3074 (1973).
14. P.D. Barlett and C.M. Lonzeta. *J. Am. Chem. Soc.* **105**, 1984 (1983).
15. R.F.W. Bader. *Atoms in molecules – A quantum theory*. Oxford University Press, Oxford. 1990.
16. J.P. Perdew and Y. Wang. *Phys. Rev. Sect. B*, **45**, 13 244 (1992).
17. M.J. Frisch, G.W. Trucks, H.B. Schlegel, G.E. Scuseria, M.A. Robb, J.R. Cheeseman, V.G. Zakrzewski, J.A. Montgomery, Jr., R.E. Stratmann, J.C. Burant, S. Dapprich, J.M. Millam, A.D. Daniels, K.N. Kudin, M.C. Strain, O. Farkas, J. Tomasi, V. Barone, M. Cossi, R. Cammi, B. Mennucci, C. Pomelli, C. Adamo, S. Clifford, J. Ochterski, G.A. Petersson, P.Y. Ayala, Q. Cui, K. Morokuma, D.K. Malick, A.D. Rabuck, K. Raghavachari, J.B. Foresman, J. Cioslowski, J.V. Ortiz, A.G. Baboul, B.B. Stefanov, G. Liu, A. Liashenko, P. Piskorz, I. Komaromi, R. Gomperts, R.L. Martin, D.J. Fox, T. Keith, M.A. Al-Laham, C.Y. Peng, A. Nanayakkara, M. Challacombe, P.M.W. Gill, B. Johnson, W. Chen, M.W. Wong, J.L. Andres, C. Gonzalez, M. Head-Gordon, E.S. Replogle, and J.A. Pople. 1998. Gaussian 98 [computer program]. Revision A.9. Gaussian Inc., Pittsburgh, PA.
18. F. Jensen. *Introduction to computational chemistry*. John Wiley and Sons Ltd., New York. 1999. pp. 177–193.
19. F.W. Biegler-Konig. 1998–2000. AIM 2000 [computer program]. University of Applied Science, Bielefeld, Germany.
20. F.W. Biegler-Konig, R.F.W. Bader, and T.H. Tang. *J. Comput. Chem.* **3**, 317 (1982).
21. P. Flükiger, H.P. Lüthi, S. Portmann, and J. Weber. 2000. MOLEKEL 4.0 [computer program]. Swiss Center for Scientific Computing, Manno, Switzerland).
22. S. Benson and R. Shaw. *Org. Peroxides*, **1**, 105 (1970).
23. D.J. Mckay and J.S. Wright. *J. Am. Chem. Soc.* **120**, 1003 (1998).
24. U. Koch and P.L.A. Popelier. *J. Phys. Chem.* **99**, 9747 (1995).
25. G. Louit, A. Hocquet, and M. Ghomi. *Phys. Chem. Chem. Phys.* **4**, 3843 (2002).
26. P.L.A. Popelier. *J. Phys. Chem. A*, **102**, 1873 (1998).
27. A. Hocquet. *Phys. Chem. Chem. Phys.* **3**, 3192 (2001).
28. H. Yamataka, K. Nagareda, T. Takatsuka, K. Ando, T. Hanafusa, and S. Nagase. *J. Am. Chem. Soc.* **115**, 8570 (1993).
29. E. Vedejs and C. Marth. *J. Am. Chem. Soc.* **110**, 3948 (1988).
30. H. Yamataka and S. Nagase. *J. Am. Chem. Soc.* **120**, 7530 (1998).



# An ab initio molecular orbital study of the geometry of the dicationic Wallach rearrangement intermediate<sup>1</sup>

Robin A. Cox, David Y.K. Fung, Imre G. Csizmadia, and Erwin Buncel

**Abstract:** Ab initio calculations have been performed on several different structures for the dicationic intermediate proposed for the Wallach rearrangement of aromatic azoxy compounds to hydroxy-substituted azo systems in strongly acidic media. For the unsubstituted parent compound azoxybenzene, these calculations reveal that the preferred structure for the intermediate is planar, as previously assumed, but bent rather than linear as we have formulated it. The presence of two methyl groups at the *para* positions of both aromatic rings does not change this situation, but six methyl groups at all *para* and *ortho* ring positions lead to a different preferred structure — still bent but with the two aromatic rings now at 90° to one another rather than being coplanar — undoubtedly due to steric interference between the *ortho* methyl groups. In all the cases examined the two positive charges reside primarily in the aromatic rings rather than on the nitrogens, which are  $sp^2$  hybridized and still have their lone pairs. The overall structures can best be regarded as two six-electron  $\pi$  systems joined together, with little communication between the two rings. For the most part the calculations are in good agreement with experimental observations. Recent calculations on other possible reaction intermediates by other groups are also discussed.

**Key words:** Ab initio calculations, Wallach rearrangement, azoxyarenes, reaction intermediate, acid catalysis, intermediate structure, reaction mechanism.

**Résumé :** On a effectué de calculs théoriques sur plusieurs structures différentes d'intermédiaires dicationiques proposés pour le réarrangement de Wallach, en milieu fortement acide, de composés azoxy aromatiques en systèmes azo portant des substituants hydroxy. Pour le composé azoxybenzène parent, ne comportant pas de substituant, ces calculs mettent en évidence que la structure privilégiée de l'intermédiaire est planaire comme on le croyait antérieurement, mais qu'elle est repliée et non pas linéaire comme on l'avait formulé. La présence de deux groupes méthyles dans les positions *para* des deux noyaux aromatiques ne modifie pas cette situation, mais si le composé azo comporte six groupes méthyles, un dans chacune des positions *ortho* et *para*, la structure privilégiée est différente tout en demeurant repliée; les deux noyaux aromatiques sont toutefois maintenant à 90° l'un par rapport à l'autre plutôt que d'être coplanaires et cette situation est probablement causée par l'interférence entre les groupes méthyles en *ortho*. Dans tous les cas examinés, les deux charges positives se retrouvent principalement sur les noyaux aromatiques plutôt que sur les atomes d'azote dont les hybridations sont  $sp^2$  alors qu'ils portent toujours leurs paires d'électrons non paillés. La meilleure façon de visualiser les structures globales est de les considérer comme deux systèmes à six électrons  $\pi$  reliés sans grande communication entre les deux noyaux. Dans l'ensemble, les calculs sont en bon accord avec les observations expérimentales. On discute aussi d'autres calculs récents relatifs à d'autres intermédiaires réactionnels possibles par d'autres groupes.

**Mots clés :** calculs ab initio, réarrangement de Wallach, azoxyarènes, intermédiaire réactionnel, catalyse acide, structure de l'intermédiaire, mécanisme réactionnel.

[Traduit par la Rédaction]

Received 06 January 2003. Published on the NRC Research Press Web site at <http://canjchem.nrc.ca> on 7 May 2003.

*This paper is dedicated to Professor Don Arnold, in recognition of his many contributions to chemistry in Canada.*

**Robin A. Cox,<sup>2,3</sup> David Y.K. Fung, and Imre G. Csizmadia.** Department of Chemistry, University of Toronto, 80 St. George St., Toronto, ON M5S 3H6, Canada.

**Erwin Buncel.<sup>4</sup>** Department of Chemistry, Queen's University, Kingston, ON K7L 3N6, Canada

<sup>1</sup>Presented in part at the 85th Canadian Society for Chemistry Conference, Vancouver, B.C., June 2002, no. 899. Part 26 of the series 'Mechanistic studies in strong acids', of which part 25 is R.A. Cox, Can. J. Chem. **77**, 709 (1999), and part 26 of the series 'Studies of azo and azoxy dyestuffs', of which part is 25 is K.-S. Cheon, Y.S. Park, P.M. Kazmaier, and E. Buncel. Dyes Pigm. **53**, 3 (2002).

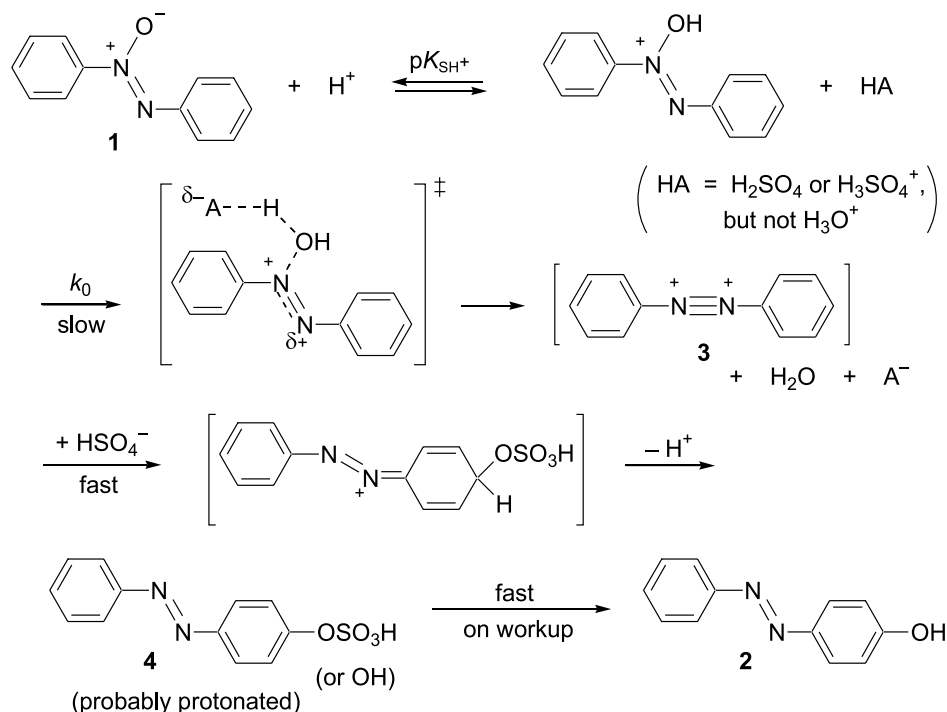
<sup>2</sup>Corresponding author (e-mail: [robin.a.cox@sympatico.ca](mailto:robin.a.cox@sympatico.ca)).

<sup>3</sup>Present address: 16 Guild Hall Drive, Scarborough, ON M1R 3Z8, Canada.

<sup>4</sup>Corresponding author (e-mail: [buncel@chem.queensu.ca](mailto:buncel@chem.queensu.ca)).

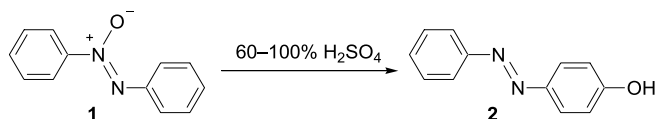


Scheme 1.



## Introduction

The Wallach rearrangement, originally discovered by Wallach and Belli in 1880 (1), is the rearrangement of aromatic azoxy compounds in strong aqueous acidic media to azo compounds having an hydroxy group elsewhere in the molecule (normally in a *para* position), as shown below for the parent compound azoxybenzene **1** rearranging to *p*-hydroxyazobenzene **2**.

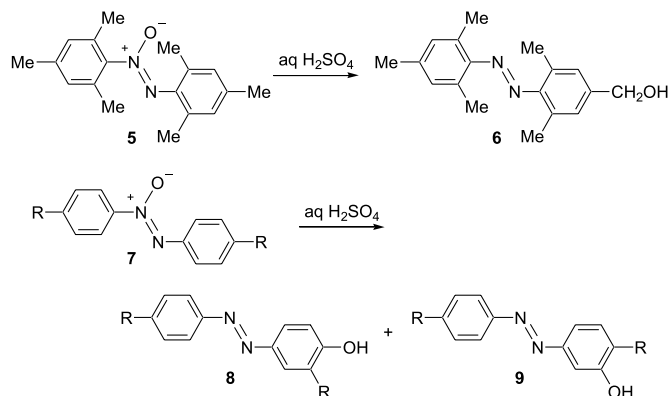


The reaction mechanism for the rearrangement of **1** and of related aromatic azoxy compounds has been the subject of a considerable amount of work by various research groups; we have carried out a number of careful kinetic and other studies of this process over several decades (2–7). Despite comments in advanced-level textbooks about the mechanism being “not completely settled” (8), the mechanism that we proposed originally (2) has essentially stood the test of time.

This mechanism has been given in several review articles (9–13); for **1** itself in concentrated sulfuric and other acids it is given in Scheme 1. In brief, pre-equilibrium protonation of **1** gives a species that is stable in the strong acid reaction media (2); this is then attacked by a second molecule of acid in the rate-determining step, only the strongest acids in the medium being capable of reacting in this general-acid-catalysis process (4). The result is a dicationic intermediate, which we have been writing as having the structure **3** (and which could be called 1,2-diaza-1,2-diphenylethyne). Subsequent fast processes give the observed reaction product **2** on workup, as shown; if **4** is the first-formed product it is

known to hydrolyze rapidly to **2** as the reaction mixture is diluted (14).

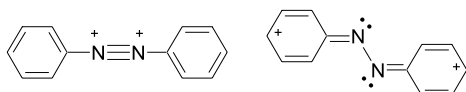
In general, aromatic azoxy compounds appear to react via the mechanism in Scheme 1 if the acidity of the medium is high (**1** and some azoxypyridines (7)). However, at lower acidities the more reactive compounds (several azoxynaphthalenes (**6**) and hexamethylazoxybenzene (**5**)) can react via a quinonoid intermediate mechanism as well (10); this will be discussed below.



While compiling information for a recent review (10) we became aware of an apparent discrepancy in the products formed from different alkyl-substituted compounds. Hexamethylazoxybenzene **5** gives the hydroxymethyl product **6** (5), whereas the 4,4'-dialkyl compounds **7** give at least some of the rearranged products **8** and **9** (15). Admittedly the reaction conditions in these two cases were quite different. The reaction of **5** was carried out under highly dilute kinetic conditions of some  $10^{-4}$  M where intermolecular reactions are quite unlikely; products equivalent to **8** and **9** were



searched for but not found, **6** being the only product observed (16). The reaction of **7** took place under synthesis conditions at much higher concentrations (>1 M), and much byproduct formation was observed, some of it clearly by intermolecular processes (15). Nevertheless the discrepancy seems to be real, and we thought that it might be due to the dicationic intermediate having different geometries in the two cases — the *ortho* methyl groups perhaps causing steric interference in the case of **5** — thus driving the reaction in a different direction.



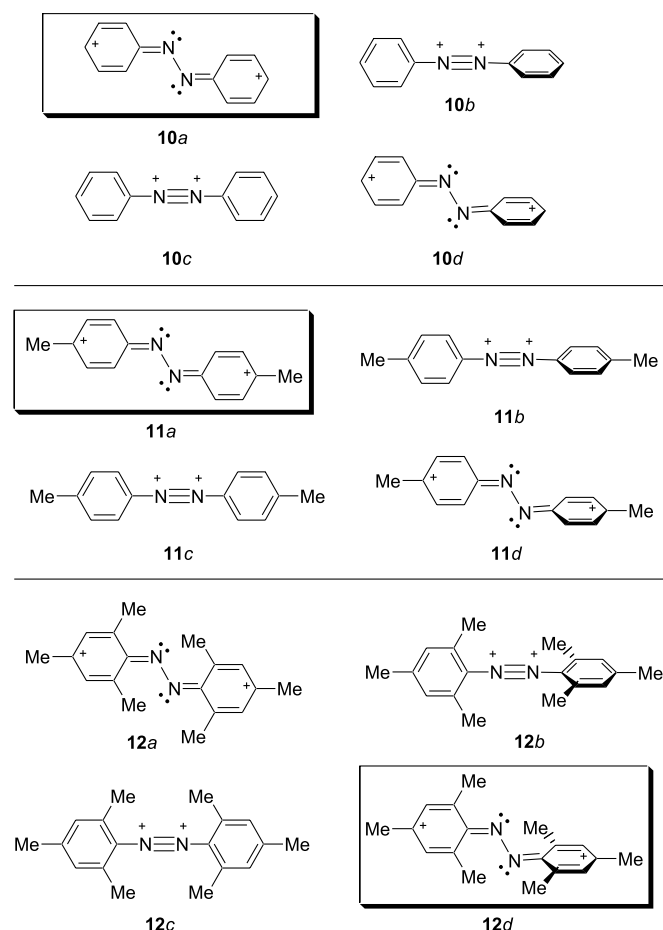
There are no recent theoretical calculations on these dicationic intermediates. Many years ago we performed simple Hückel MO calculations on the two possible structures for **3** given above (17); the calculations showed that both geometries were possible but were unable to distinguish between them in terms of energy. More recent semi-empirical AM1 calculations on several possible Wallach rearrangement intermediates (18) did not include these, which is surprising since **3** has actually been observed by NMR at  $-78^\circ\text{C}$  in  $\text{SbF}_5\text{--HF--SO}_2$  (19). While this observation does not necessarily mean that **3** really is an intermediate in concentrated aqueous sulfuric acid and related reaction media, it does make it more probable than other unobserved intermediates. Consequently we decided to perform some up-to-date *ab initio* calculations on possible structures for the dicationic intermediates in the reactions of **1**, **7** (with  $R = \text{Me}$  for **7**), and **5**; these are given as **10**, **11**, and **12** below, with the four different structures calculated for each one being designated as *a*, *b*, *c*, and *d*.

## Calculations

Gaussian 94/98 (20) was used to perform Hartree–Fock (HF) calculations using the standard 3–21G and 6–31G\* basis sets on the structures of interest, as has been done before for cationic intermediates (21) and other species (22–23). Recently it has been shown that HF/3–21G calculations give results comparable with those obtained using the higher-order MP2/6–311++G\*\* level of theory (24), and thus it was not deemed necessary to use this theory level on these quite large species. Frequency calculations were performed on optimized structures to determine whether the geometry of the structures found were local minima ( $\lambda = 0$ ) or saddle points ( $\lambda = 1, 2, \dots, 3N - 6$ , where  $N$  is the number of atoms in the molecule) of their potential energy surfaces. (The index  $\lambda$  represents the number of negative values of the Hessian matrix (corresponding to the number of imaginary frequencies) for a given critical point.) Surface points generated by scan calculations were plotted using Axum 5.0C and Microsoft Excel 97; these plots are not provided as they add little information to that given in the tables and structures in this paper. The results of the calculations are summarized for the various structures in Tables 1 and 2, and calculated Mulliken charges on the relevant atoms of those structures found to be minima are given in Table 3.

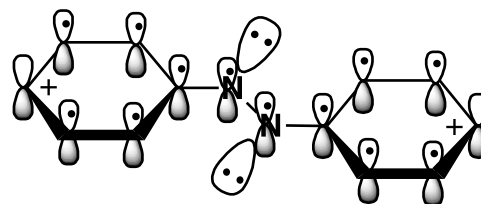
## Results

The results of our calculations can be summarized in the structure diagrams given below; in all the left-hand structures the two phenyl rings are coplanar, and in all the right-hand ones they are perpendicular to one another. Both levels of theory used gave the same results.



In each case the most stable (lowest energy) structure found for that species is boxed. Not all of the structures were found to be energy minima; see Tables 1 and 2. Energy differences between the structures (for each of the three species **10**, **11**, and **12**) calculated at the two levels of theory are given in the Tables. Calculated Mulliken charges on relevant atoms of those structures found to be minima at the RHF/6–31G\* level are given in Table 3.

## Discussion



The global minimum structures, **10a**, **11a**, and **12d**, are all bent, not linear; the C–N–N bond angles are near  $120^\circ$  ( $115^\circ$



**Table 1.** Computed energies, bond angles, and torsional angles of the Wallach rearrangement dicationic intermediate at the RHF/3–21G level of theory.

Structure number	Index of critical point ( $\lambda$ )	Bond angle (C–N–N) ( $^\circ$ )	Torsional angle (between rings) ( $^\circ$ )	Energy (Hartrees)	$\Delta E$ (kcal mol $^{-1}$ )
<b>10a</b>	0	115.12	0	–565.2234531	0.00
<b>10b</b>	0	180	90	–565.2208280	1.65
<b>10c</b>	1	180	0	–565.2009733	14.11
<b>10d</b>	(No energy minimum found)				
<b>11a</b>	0	115.07	0	–642.9060893	0.00
<b>11b</b>	0	180	90	–642.8902219	9.96
<b>11c</b>	1	180	0	–642.8651809	25.67
<b>11d</b>	(No energy minimum found)				
<b>12a</b>	(No energy minimum found)				
<b>12b</b>	2	180	90	–798.2084115	5.08
<b>12c</b>	(No energy minimum found)				
<b>12d</b>	0	131.18	104.93	–798.2165135	0.00

**Table 2.** Computed energies, bond angles, and torsional angles of the Wallach rearrangement dicationic intermediate at the RHF/6–31G\* level of theory.

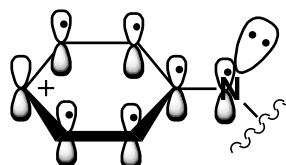
Structure number	Index of critical point ( $\lambda$ )	Bond angle (C–N–N) ( $^\circ$ )	Torsional angle (between rings) ( $^\circ$ )	Energy (Hartrees)	$\Delta E$ (kcal mol $^{-1}$ )
<b>10a</b>	0	115.26	0	–568.4326391	0.00
<b>10b</b>	0	179.99	90	–568.4188955	8.62
<b>10c</b>	(No energy minimum found)				
<b>10d</b>	(No energy minimum found)				
<b>11a</b>	0	115.22	0.39	–646.5462712	0.00
<b>11b</b>	0	179.83	90.03	–646.5192632	16.95
<b>11c</b>	(No energy minimum found)				
<b>11d</b>	(No energy minimum found)				
<b>12a</b>	(No energy minimum found)				
<b>12b</b>	2	179.84	90	–802.6989699	10.66
<b>12c</b>	(No energy minimum found)				
<b>12d</b>	0	129.10	105.94	–802.7159544	0.00

**Table 3.** Mulliken charges for the dicationic intermediate computed at the RHF/6–31G\* level of theory.

Structure number	Atom position	Mulliken charge
<b>10a</b>	C(4), C(4')	–0.018327
<b>10b</b>	C(4), C(4')	–0.081163
<b>11a</b>	C(4), C(4')	0.175532
	H(9), H(9')	0.261925
	H(10), H(10')	0.280308
	H(11), H(11')	0.260623
<b>11b</b>	C(4), C(4')	0.127457
	H(9), H(9')	0.244912
	H(10), H(10')	0.261886
	H(11), H(11')	0.244915
<b>12b</b>	C(4), C(4')	0.147703
	H(9), H(9')	0.256877
	H(10), H(10')	0.240342
	H(11), H(11')	0.240347
<b>12d</b>	C(4), C(4')	0.176930
	H(9), H(9')	0.266567
	H(10), H(10')	0.251396
	H(11), H(11')	0.249100

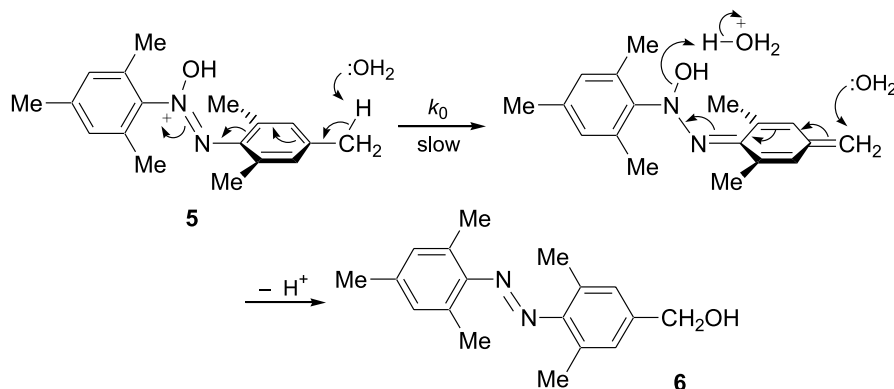
for **10a** and **11a** and  $131^\circ$  for **12d**). The conclusion must be that the positive charges in the molecules reside primarily on the rings and not on the nitrogens, which, with these bond angles, must be  $sp^2$  hybridized with the lone pairs still present, as shown above (**10a** was also found to be the most stable structure according to simple Hückel MO calculations (17)).

Communication between the two aromatic rings seems not to be important. Compound **12d** is the global minimum structure for **12** despite having a torsional angle between the two rings of close to  $90^\circ$  (actually  $105^\circ$ ), undoubtedly caused by *ortho* methyl steric interference, whereas **10a** and **11a** are flat ( $0^\circ$ ). There is precedence for this, insofar as the azine  $R_2C=N-N=CR_2$  species studied by Rademacher and co-workers have also been shown to consist of two essentially planar halves (25).

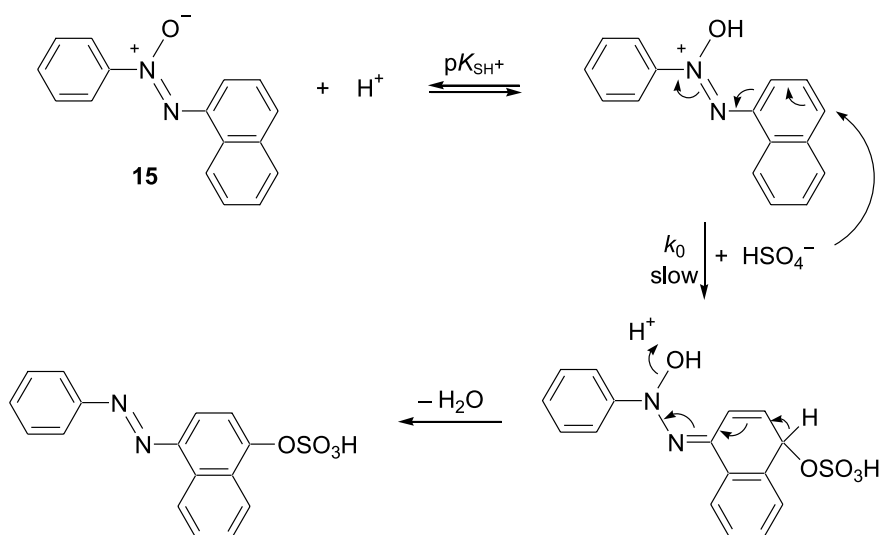




Scheme 2.



Scheme 3.



Thus the intermediates can probably best be regarded as two six-electron  $\pi$  systems joined together, as indicated for the partial structure above, with the torsional angle between them being of little consequence. Rademacher finds that in his cases the nitrogen lone pairs are in conjugation with the opposite part of the molecule (25); there is some evidence for that here (in Table 3 the charge densities at the 4 and 4' carbons in **10a** are actually very slightly negative), but his systems did not involve aromatic electron sextets as ours do, and lone-pair delocalization would add very little extra stabilization in our case. Zuman and Ludvík state that "the delocalization is either minimal or absent" in both cyclic and acyclic compounds containing the  $\text{C}=\text{N}-\text{N}=\text{C}$  grouping, according to electrochemically determined reduction potentials (26).

With methyl groups present, the calculated charge density on the rings is higher than it is in their absence (Table 3), and this is consistent with the experimental observation that alkylated azoxybenzenes react faster than does azoxybenzene itself (5). Much of this charge is delocalized onto the hydrogens of the methyl groups (by hyperconjugation), see Table 3, which become acidic as a consequence, explaining why **6** is formed from **5** by base attack on the methyl hydrogens (5) rather than the rearranged phenols equivalent to

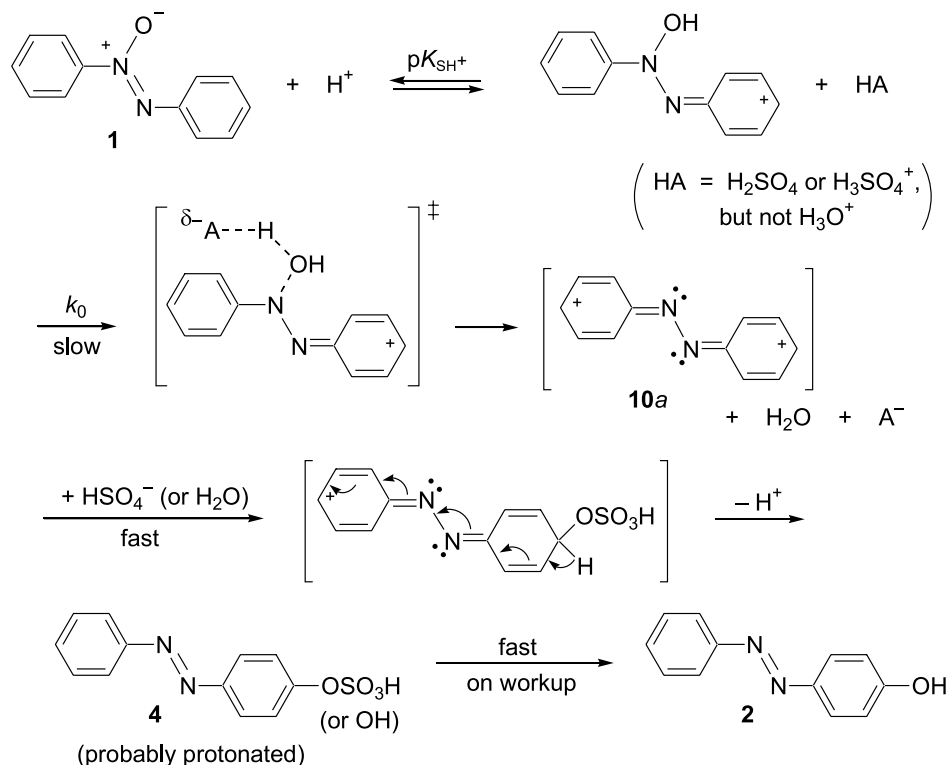
**8** and **9** that would result from nucleophilic attack on carbon, as in Scheme 1 above for **1**. It also makes it likely that the formation of **8** and **9** from **7** is a secondary reaction of some sort under the high concentration reaction conditions used (15); this reaction needs to be re-examined under reaction conditions corresponding to those used for **5** (5). We hope to be able to undertake a study of this type in the future.

Consistent with the higher charge density on the methyl hydrogens found for **5** is the fact that **5** also undergoes a quinonoid-intermediate mechanism at low acidity, see Scheme 2 (5); the regular dication mechanism takes over from this at acidities higher than 80%  $\text{H}_2\text{SO}_4$ . Even one positive charge in the molecule is sufficient to make the methyl hydrogens acidic enough to react.

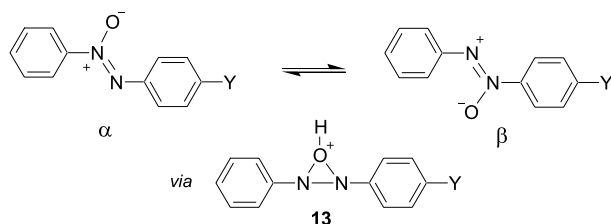
Recent semi-empirical AM1 calculations concerning the Wallach rearrangement involved many other postulated reaction intermediates (18). Though the authors state that  $\alpha$ - $\beta$  interconversions of aromatic azoxy compounds in acid (from either direction) are low-energy processes taking place via species like **13** (various states of protonation of **13** being possible), this is at variance with the experimental facts, i.e., that these interconversions are not significant under controlled Wallach rearrangement reaction conditions (13). Only



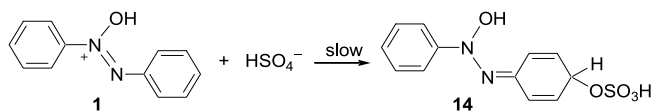
Scheme 4.



one such reaction has been properly investigated, the  $\beta$ - $\alpha$  isomerization of the 4- $\text{NO}_2$  compound (27), and that requires protonation of the  $\text{NO}_2$  group first, certainly not a low-energy process (13).



Another conclusion of these AM1 studies (18) was that “the quasiplanarity of the azoxybenzene ring is destroyed during the reaction”. According to the present work this is clearly not the case for the intermediates formed from azoxybenzene **1** itself or from **7** — the torsional angles between the rings found here being  $0^\circ$  — although the rings do not have to be coplanar; we find **12d** with a torsional angle of  $105^\circ$  to be the stable form for the intermediate formed from **5**.



The major conclusion to which Özen et al. came (18) was that the reaction mechanism for **1** involved quinonoid intermediate **14**, a mechanism originally proposed by Duffey and Hendley (28). This is also certainly at variance with the experimental facts, since isotopic substitution studies have clearly shown that the two nitrogens become equivalent dur-

ing the reaction (12, 13). Interestingly, we know that some reactive azoxybenzenes can indeed use this mechanism, e.g., **5** as in Scheme 2 above and the azoxynaphthalene **15** as shown in Scheme 3 (6), but not azoxybenzene itself! Apart from the isotopic substitution results the kinetics are also at variance with this mechanism, since the correct mechanism clearly requires the involvement of two acid molecules, not one (4).

Thus we have shown that the mechanism of the Wallach rearrangement in strong acid media clearly involves dicationic intermediates such as **10a**. Insofar as this has a bent structure rather than the linear one **3** as given in Scheme 1, the overall mechanistic scheme requires slight modification, as shown in Scheme 4. (For clarity, only one of the possible resonance forms is given for several structures in Scheme 4.) Note that the azo-azoxy function remains in the same bent format throughout in this mechanism, which is satisfying in terms of the principle of least nuclear motion. This principle states that those reactions are favoured that require the least amount of relative atom displacement in going from reactant to product (29).

## Acknowledgments

Financial support of this research through a grant by the Natural Sciences and Engineering Research Council of Canada (NSERC) (to EB) is gratefully acknowledged. We thank Professor Heidi Muchall of Concordia University for helpful discussions.

## References

1. O. Wallach and E. Belli. *Chem. Ber.* **13**, 525 (1880).



2. E. Buncl and B.T. Lawton. *Chem. Ind. (London)*, 1835 (1963); *Can. J. Chem.* **43**, 862 (1965).
3. E. Buncl and W.M.J. Strachan. *J. Chem. Soc., Chem. Commun.* 765 (1969); *Can. J. Chem.* **48**, 377 (1970).
4. R.A. Cox. *J. Am. Chem. Soc.* **96**, 1059 (1974).
5. R.A. Cox and E. Buncl. *J. Am. Chem. Soc.* **97**, 1871 (1975).
6. R.A. Cox, A.J. Dolenko, and E. Buncl. *J. Chem. Soc., Perkin Trans. 2*, 471 (1975).
7. E. Buncl and S.-R. Keum. *J. Chem. Soc., Chem. Commun.* 578 (1983).
8. M.B. Smith and J. March. *March's advanced organic chemistry: reactions, mechanisms and structure*. 5th ed. Wiley, New York. 2001. pp. 1464–5. Also in earlier editions.
9. E. Buncl. *Can. J. Chem.* **78**, 1251 (2000).
10. R.A. Cox and E. Buncl. *In The chemistry of the hydrazo, azo and azoxy groups*. Vol. 2. *Edited by S. Patai*. Wiley, London. 1997. pp. 569–602.
11. R.A. Cox. *Adv. Phys. Org. Chem.* **35**, 1 (2000).
12. E. Buncl. *Acc. Chem. Res.* **8**, 132 (1975); R.A. Cox and E. Buncl. *In The chemistry of the hydrazo, azo and azoxy groups*. Vol. 1. *Edited by S. Patai*. Wiley, London. 1975. pp. 775–859; A.J. Dolenko and E. Buncl. *In The chemistry of the hydrazo, azo and azoxy groups*. Vol. 1. *Edited by S. Patai*. Wiley, London. 1975. pp. 725–773.
13. E. Buncl. *In Mechanisms of molecular migrations*. Vol. 1. *Edited by B.S. Thyagarajan*. Wiley, New York. 1968. pp. 61–119.
14. E. Buncl and W.M.J. Strachan. *Can. J. Chem.* **47**, 911 (1969).
15. I. Shimao and S. Matsumura. *Bull. Chem. Soc. Jpn.* **49**, 2294 (1976).
16. E. Buncl and R.A. Cox. *J. Chem. Soc., Chem. Commun.* 1259 (1972); R.A. Cox and E. Buncl. *Can. J. Chem.* **51**, 3143 (1973).
17. E. Buncl, A. Dolenko, I.G. Csizmadia, J. Pincock, and K. Yates. *Tetrahedron*, **24**, 6671 (1968).
18. A.S. Özen, S.S. Erdem, and V. Aviyente. *Struct. Chem.* **9**, 15 (1998).
19. G.A. Olah, K. Dunne, D.P. Kelly, and Y.K. Mo. *J. Am. Chem. Soc.* **94**, 7438 (1972).
20. M.J. Frisch, G.W. Trucks, H.B. Schlegel, P.M.W. Gill, B.G. Johnson, M.A. Robb, J.R. Cheesman, T. Keith, G.A. Petersson, J.A. Montgomery, K. Raghavachari, M.A. Al-Laham, V.G. Zakrzewski, J.V. Ortiz, J.B. Foresman, J. Cioslowski, B.B. Stefanov, A. Nanayakkara, M. Challacombe, C.Y. Peng, P.Y. Ayala, W. Chen, M.W. Wong, J.L. Andres, E.S. Replogle, R. Gomperts, R.L. Martin, D.J. Fox, J.S. Binkley, D.J. Defrees, J. Baker, J.P. Stewart, M. Head-Gordon, C. Gonzalez, and J.A. Pople. 1995. GAUSSIAN 94 [computer program]. Revision E.2. Gaussian, Inc., Pittsburgh PA. As updated.
21. J.C.Y. Yeung, G.A. Chasse, E.J. Frondoza, L.L. Torday, and J.G. Papp. *THEOCHEM*, **546**, 143 (2001).
22. M.A. Berg, S.J. Salpietro, A. Perczel, Ö. Farkas, and I.G. Csizmadia. *THEOCHEM*, **504**, 127 (2000).
23. I.A. Topol, S.K. Burt, E. Deretey, T.-H. Tang, A. Perczel, A. Rashin, and I.G. Csizmadia. *J. Am. Chem. Soc.* **123**, 6054 (2001).
24. G. Endrédi, A. Perczel, Ö. Farkas, M.A. McAllister, G.I. Csonka, J. Ladik, and I.G. Csizmadia. *THEOCHEM*, **391**, 15 (1997).
25. G. Korber, P. Rademacher, and R. Boese. *J. Chem. Soc., Perkin Trans. 2*, 761 (1987).
26. P. Zuman and J. Ludvík. *Tetrahedron Lett.* **41**, 7851 (2000).
27. M.M. Shemyakin, T.E. Agadzhanyan, V.I. Maimind, R.V. Kudryavtsev, and D.N. Kursanov. *Dokl. Akad. Nauk SSSR*, **135**, 346 (1960); *Chem. Abs.* **55**, 11 337d (1961); M.M. Shemyakin, V.I. Maimind, and T.E. Agadzhanyan. *Chem. Ind. (London)*, 1223 (1961).
28. D. Duffey and E.C. Hendley. *J. Org. Chem.* **33**, 1918 (1968); E.C. Hendley and D. Duffey. *J. Org. Chem.* **35**, 3579 (1970).
29. O.S. Tee. *J. Am. Chem. Soc.* **91**, 7144 (1969); J. Hine. *Adv. Phys. Org. Chem.* **15**, 1 (1977).



# Acrylonitrile (AN)-Cu<sub>9</sub>(100) interfaces: Electron distribution and nature of bonded interactions

Petar M. Mitrasinovic

**Abstract:** There is a fundamental interest in the investigation of the interfacial interactions and charge migration processes between organic molecules and metallic surfaces from a theoretical standpoint. Quantum mechanical (QM) concepts of bonding are contrasted, and the vital importance of using combined QM methods to explore the nature of the interfacial interactions is established. At the one-electron level, the charge distribution and nature of bonded interactions at the AN-Cu<sub>9</sub>(100) (neutral and charged (-1)) interfaces are investigated by both the Becke (B) – Vosko (V) – Wilk (W) – Nusair (N)/DZVP density functional theory (DFT) method and the MP2/6-31+G\* strategy within the conceptual framework provided by natural bond orbital (NBO) – natural atomic orbital (NAO) population analysis and Atoms-In-Molecules (AIM) theory. By this approach, the interfacial interactions are given physical definitions free of any assumptions and are visualized by using the topological features of the total electron density. A natural link between the electron density on the one side and the shapes (not energies) of the highest occupied molecular orbital (HOMO) and lowest unoccupied molecular orbital (LUMO) on the other side is clarified. The question of whether the spatial extents of the HOMO and LUMO resemble the corresponding spatial maps of the negative (charge locally concentrated) and positive (charge locally depleted) Laplacian of the total electron density in [AN-Cu<sub>9</sub>(100)]<sup>-1</sup> is addressed.

**Key words:** AN-Cu<sub>9</sub>(100) interfaces, NBO-NAO population, electron distribution, AIM, bonded interactions.

**Résumé :** D'un point de vue théorique, il existe un intérêt fondamental pour les recherches sur les interactions interfaciales et les processus de migration de charge entre des molécules organiques et les surfaces métalliques. On met en relief les concepts de la mécanique quantique (MQ) de liaison et on démontre l'importance vitale d'utiliser des méthodes de MQ pour explorer la nature des interactions interfaciales. Au niveau d'un électron, on a étudié la distribution de la charge et la nature des interactions de liaison aux interfaces AN-Cu<sub>9</sub>(100) (neutres ou portant une charge de (-1)) par la théorie de la densité fonctionnelle (TDF) de Becke (B) – Vosko (V) – Wilk (W) – Nusair (N)/DZVP ainsi qu'en faisant appel à la stratégie MP2/6-31+G\* dans le cadre conceptuel fournit par l'analyse des populations d'orbitale liante naturelle (OLN) et d'orbitale atomique naturelle (OAN) ainsi que la théorie des atomes dans la molécule (ADM). Par cette approche, on donne des définitions physiques des interactions interfaciales qui sont exemptes de toute hypothèse et qui sont visualisées en faisant appel à des caractéristiques topologiques de la densité totale d'électron. On a clarifié un lien naturel entre d'une part la densité électronique et d'autre part les formes (non pas les énergies) de l'orbitale moléculaire haute occupée (OH) et de la basse vacance (BV). On a essayé de déterminer si, dans [AN-Cu<sub>9</sub>(100)]<sup>-1</sup>, les distributions spatiales des orbitales moléculaires OH et BV ressemblent aux cartes spatiales correspondantes des laplaciens négatifs (charge ponctuellement concentrée) et positifs (charge ponctuellement appauvrie) de la densité électronique totale.

**Mots clés :** interfaces AN-Cu<sub>9</sub>(100), population OLN-OAN, distribution électronique, ADM, interactions liées.

[Traduit par la Rédaction]

## Introduction

The semiconductor industry is facing difficulties with respect to its ultimate goal: to maintain a stable growth of the density of packing on a single chip. The permanent trend for reducing the size of conventional MOS (metal-oxide-semiconductor) components, followed by the significant rise in the costs needed for producing integrated circuits of a larger

scale, reflects the difficulties in the best possible sense (1). In this context, the potential of molecular electronics to become an alternative to the semiconductor industry is growing rapidly. Many experimental and theoretical studies have been addressing the question of identifying the functional abilities of single molecules or molecular self-assemblies to behave as wires, diodes, transistors, and rectifiers. An experiment performed by Reed et al. (2) has shown that phenyl-

Received 5 September 2002. Published on the NRC Research Press Web site at <http://canjchem.nrc.ca> on 23 May 2003.

*Dedicated to Professor Don Arnold for his contributions to chemistry.*

**P.M. Mitrasinovic.**<sup>1</sup> Laboratory for Chemistry of Novel Materials, Center for Research on Molecular Electronics and Photonics, The University of Mons-Hainaut, B-7000 Mons, Belgium, Europe.

<sup>1</sup>Corresponding author (e-mail: [pmitrasi68@yahoo.com](mailto:pmitrasi68@yahoo.com)).



ene-based derivatives are capable of behaving as a conducting wire when inserted into a metallic break junction. There are indications that some molecules such as nanotubes (3) and DNA (4) conduct a current when inserted between two metal electrodes. An ancient idea — dating back to Aviram and Ratner (5) — that organic moieties linked by a saturated spacer between two metallic electrodes can act as a rectifier has recently been verified experimentally (6, 7). Mujica et al. (8) have noticed that molecular rectification is rare because the interplay between different transport regimes (for a specific interface) such as tunneling, hopping, and diffusion is temperature dependent. The authors (8) have also indicated that the current of the charge-carrying particles in the coherent tunneling regime depends strongly on the following factors: (i) the nature of the molecular bridge and the contacts; (ii) the strength of the surface–molecule interaction; (iii) the position of the Fermi energy; and (iv) the profile of the electrochemical potential across the interface. The density of states within the HOMO–LUMO gap (HLG) makes the precise position of the Fermi energy level sensitive to a small amount of charge transfer. Thus, the Fermi energy level should be viewed as a fitting parameter inside a reasonable range. Several theoretical investigations (9–14) devoted to the understanding of the conducting mechanisms through molecular wires have shown that the electronic structure of the molecule and the geometry of the metal–organic interfaces, as well as the nature of the chemical interactions, are crucial. By modifying original contacts between a conjugated molecule and a metallic surface by the addition of the sulfur and gold atoms to a terminal carbon of the molecule, Seminario et al. (15) have shown that the character of the organic–metal interactions is local. The authors of ref. 1 have stated on p. 10 077: “...there is still a fundamental interest from a theoretical standpoint to address separately, at least in the case of long molecular wires, the charge injection mechanism (i.e., the interfacial interactions between molecules and metallic surfaces 32, 33) and the charge migration process...” (1). The present study opens the question of the nature of bonded interaction at organic–metal interfaces from a more rigorous (in a physical sense) point of view.

There have been theoretical attempts to rationalize the experimental results that characterize the organic–metal interfaces. Although useful, there are well-known problems associated with such attempts, which have been quite extensively reviewed (16). The partitioning schemes of the molecular interaction energy used are arbitrary, and the definitions of additive contributions to the energy are obscure. The divisions of the molecular interaction energy into classically interpretable segments do not distinguish different aspects of electron behavior. The charge transfer and electrostatic components do not have the usual physical meanings considered in the Mulliken and Morokuma analyses, respectively (17(a)). The descriptions of bonded interactions have also been sought in orbitals that are not invariant (17(b)). This study readily makes the distinctions.

Seminario et al. (18, p. 3017) have noticed that most previous work dedicated to the understanding of conduction mechanism has been based on “...the orbital energetics

without considering the spatial extent of the conduction channels...” (18). To predict the electronic transport of a charged molecule when some unoccupied orbitals of the neutral molecule become occupied following application of an external voltage, the spatial profile of the LUMO and the HLG have been observed, because the HLG may be viewed as a measure of the hardness of the electron density (18–20). It has been proposed that a prerequisite for a satisfactory charge transmission through a molecular junction is the delocalization of the LUMO without referring to the total electron density (21). This study is a fundamental reformulation of this qualitative approach for a deeper reason that the success of frontier molecular orbital theory to rationalize the interfacial charge migration process may depend on if the spatial maps of the HOMO and LUMO resemble those determined by negative and positive values of the Laplacian of the total electron density, which determines the reactivity.<sup>2</sup>

Becke and Edgecombe (22) have noted that physically meaningful descriptions of electron behavior must be sought in the density matrix (or related functions) and not in the orbitals. Wave functions (or more generally density matrices) are therefore indispensable for the interpretation of electron behavior. At the one-electron level, the density matrix may be diagonalized by using the natural orbitals (NOs) (23, 24). By writing the NOs as linear combinations of the atomic orbitals, an invariant description of electron behavior can be related to a localized picture of the atomic orbitals involved in bonding. On one hand, NBO analysis (25, 26) is often in good agreement with such descriptions (27). On the other hand, Bader et al. (28) recognized an alternative orbital-independent description of electron localization based on the electron density. A bond path, as defined by Bader in his AIM theory (29, 30), is a universal indicator of bonded interactions (31). In this study, the behavior of the electrons in the AN–Cu<sub>9</sub>(100) complexes in terms of the charge distribution and nature of bonded interactions is described by use of the NBO–NAO–AIM strategy.

The plan of this paper is as follows. The theoretical background is given in the following section. The primary intention of this part is to emphasize the importance of using combined theoretical methods in investigating the organic–metal bonded interactions. By using NBO–NAO (23) population analysis and AIM (29, 30) theory, the electron distribution and nature of bonded interactions between AN and Cu<sub>9</sub>(100) are explored in the “Electron distribution” and “Nature of bonded interaction” sections, respectively. The initial parts of nucleophilic reactions in the complexes are quantitatively expressed by use of the Fukui function  $f_+$  (32). In the “[AN–Cu<sub>9</sub>(100)]<sup>−1</sup>: Laplacian of total electron density and spatial extents of HOMO and LUMO” section, the spatial extents of the HOMO and LUMO are contrasted to those of the negative and positive Laplacian in [AN–Cu<sub>9</sub>(100)]<sup>−1</sup>, respectively. Finally, the present qualitative approach is contrasted to those used in various contributions to this topic.

## Background

It is difficult to explore the nature of bonded interactions at organic–metal interfaces without the concept of bonding

<sup>2</sup>P.M. Mitrasinovic. Unpublished data.



and the association of atoms in molecules. Bonds are implicit in the very notion of association. An appropriate question to be raised, which is not entirely metaphysical, is whether the bonds hold the atoms together or whether the bonds are the outcome of other processes. In the context of this question, the key quantum mechanical concepts of bonding are contrasted below, indicating the importance of the use of NBO analysis and AIM theory to characterize bonded interactions.

Quantum mechanical descriptions of bonding can be classified into three groups. The first is based on the partition of the molecular interaction energy (33–39). The strength of the arbitrary partitioning schemes to divide the molecular interaction energy into classically interpretable segments is less pronounced than their weakness to ignore different aspects of electron behavior. The determination of electron behavior is crucial. The second interprets bonding by using density matrices (22, 27, 40). Ruedenberg (40) sought to extract physically meaningful descriptions of bonding, but Fulton (27) fully succeeded in his attempt of this kind at the one-electron level. Due to computational costs, the one-electron density matrices of good quality for organic–metal complexes are unattainable at the present time. The intention of this study is, still, to investigate the interfacial interactions by use of theoretical techniques capable of producing qualitative interpretations, which are comparable to those rooted in the density matrices. NBO analysis fulfils the requirement (25, 26). The third description of bonding takes advantage of the characteristics of the electron density within the molecule to interpret bonding (28–31). Note that the electronic charge density distribution determines the three-dimensional arrangements of the negative charge of an atom or a molecule, the sizes and shapes of molecules, and the electric moments. In other words, the electron density, as a physically measurable quantity, determines all chemical and physical properties of atoms and molecules. The actual distribution of charge within the molecule allows us to classify ionic and covalent bonding patterns, but they are given physical definitions free of any assumptions. AIM theory (28–31) is of particular interest for characterizing the organic–metal bonded interactions.

The original definition of natural orbitals was given by using the density matrix from a full configuration interaction (CI) wave function (24). The wave function is the best one constructed for a given basis set. The idea contained in the NAO and NBO analyses is that the one-electron density matrix can be used for defining the shape of the atomic orbitals in the molecules and for deriving chemical bonds from electron density between atoms (23). The first-order density matrix can be diagonalized by the eigenvectors called NOs and the eigenvalues called Occupation Numbers. The summation of all contributions from orbitals on a specific atom gives the atomic charge. The NAOs usually contribute more than 99% to the electron density, giving a compact expression of the wave function in terms of atomic orbitals. Since the NAOs are defined from the one-electron density matrix, the electron occupation is between 0 and 2, and the NAOs converge to defined values as the size of the basis set is increased. NAO and NBO analyses may be run for correlated wave functions. On the basis of computational considerations, the NAO procedure is an attractive choice for analysis purposes,

involving only matrix diagonalization of small subsets of the density matrix.

The charge density distribution in the donor and acceptor molecules and in intermolecular regions can be used to characterize weak bonds within AIM theory (28–31). A line of the highest electron density linking any bonded pair of atoms is called a bond path. The existence of a bond path is a necessary and sufficient condition for the existence of a bond. The point of a line of the highest electron density where the gradient,  $\nabla\rho(r)$ , of the density  $\rho(r)$  is equal to zero is the bond critical point (CP). The properties of the density at this point give quantitative information about the characteristics of that bond. A bond path between a pair of nonchemically bonded atoms is termed an interaction line. The Laplacian of the electron density ( $\nabla^2\rho(r)$ ) indicates where the electron density is locally concentrated ( $\nabla^2\rho(r) < 0$ ) and depleted ( $\nabla^2\rho(r) > 0$ ) and, therefore, contains a large amount of chemical information. Note also that the electronic charge operator is simply the negative of the number operator ( $-1$  for an electron) in the quantum mechanical sense. The problem is in the definition of an atom in a molecule. The most rigorous division of a molecular volume into atomic subspaces is given by Bader and co-workers (28–31).

In general, a reaction is followed by a change in the electron density that may be quantified by the Fukui function (32).

$$[1] \quad f(r) = \frac{\partial\rho(r)}{\partial N}$$

The Fukui function indicates the change in the electron density at a given position when the number of electrons  $N$  is changed. A finite difference of the function associated with the addition of an electron is

$$[2] \quad f_+(r) = \rho_{N+1}(r) - \rho_N(r).$$

The function is expected to be the initial part of a nucleophilic reaction, and the reaction will probably occur where the function is large (41). The function may be written in terms of orbital contributions as

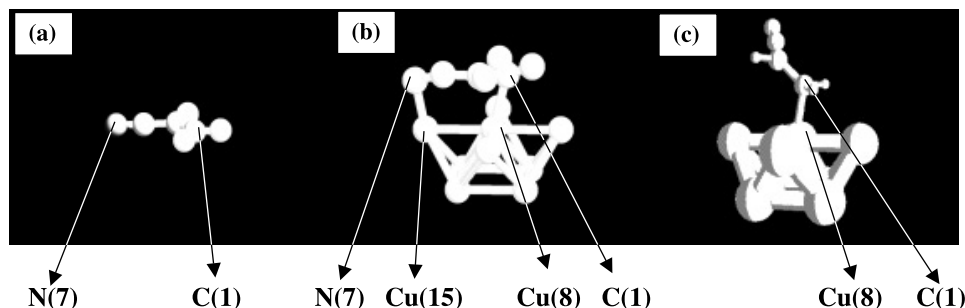
$$[3] \quad f_+(r) = \phi_{\text{LUMO}}^2(r) + \sum_{i=1}^N \frac{\partial\phi_i^2(r)}{\partial n_i}$$

The last terms become zero in the frozen molecular orbital approximation, and the Fukui function contains only the contribution from LUMO (32).

## Electron distribution

In this section, analysis of the charge distribution and charge-transfer processes at the AN–Cu<sub>9</sub>(100) interfaces is performed using the NBO–NAO partitioning scheme. The natural charges obtained in this way were shown to be sufficiently reliable and stable to computational parameters (23). A two-layer Cu<sub>9</sub>(100) cluster was used to simulate the actual surface. The following are recommendations in the literature: that the geometry of AN is not affected by the size of the clusters (9 atoms) and that the use of smaller clusters (<9 atoms) will affect the binding energy (42). Also, the use of larger clusters would mimic the density of states of the actual surface (43). The chosen cluster size may be viewed



**Fig. 1.** Optimized geometries: (a) AN; (b) AN-Cu<sub>9</sub>(100); (c) [AN-Cu<sub>9</sub>(100)]<sup>-1</sup>.

both as a compromise among the recommendations and as representative of the problems being addressed. A static electric field of  $-0.015$  atomic units (au) was chosen to simulate the driving voltage between the electrode and the molecule. The results reported below are based on calculations done at the B-VWN/DZVP(DFT) (44–46) and MP2/6–31+G\* levels of approximation. The optimized geometries (Fig. 1) were generated using the program DMol (17, 47, 48). The interatomic distances of the Cu<sub>9</sub>(100) clusters were frozen at the bulk values (17). The natural population analysis was carried out by use of the Gaussian 98 suite of programs (49).

### B-VWN/DZVP(DFT)

The NBO analysis shows the high percentage (>99%) contribution of the NAOs to the molecular charge distribution, i.e., 99.58% of 20 in the AN valence, 99.48% of 119 in the AN-Cu<sub>9</sub>(100) valence, and 99.52% of 120 in the [AN-Cu<sub>9</sub>(100)]<sup>-1</sup> valence. AN is set as a standard against which the changes in the charge distribution caused by the formation of the bonds can be measured. The identified sites between which the bonding occurs are C(1)—Cu(8) and N(7)—Cu(15) in AN-Cu<sub>9</sub>(100), as well as C(1)—Cu(8) in [AN-Cu<sub>9</sub>(100)]<sup>-1</sup>. The NECs of these atomic sites, given in Table 1, contain only those valence NAOs that have been substantially modified in terms of the electron distribution by incorporating the isolated AN into the AN-Cu<sub>9</sub>(100) complexes. In comparison to the standard, the natural charges indicate that the C(1) and N(7) sites become more negative by  $-0.41$  and  $-0.27$  in AN-Cu<sub>9</sub>(100) and that the C(1) site gains a negative charge of  $-0.40$  in [AN-Cu<sub>9</sub>(100)]<sup>-1</sup>. The Cu(8) and Cu(15) atoms have the overall natural charges of  $+0.15$  and  $+0.32$  in AN-Cu<sub>9</sub>(100), while the Cu(8) site is essentially neutral (slightly negative,  $-0.08$ ) in [AN-Cu<sub>9</sub>(100)]<sup>-1</sup>. The C(1)—Cu(8) and N(7)—Cu(15) bonds in AN-Cu<sub>9</sub>(100) should be looked upon as being ionic (charge separated) as far as the natural charges are concerned. The changes in the electron distribution are most pronounced in the second shells of C(1) and N(7) and in the 3d and 4s NAOs of Cu(8) and Cu(15) in AN-Cu<sub>9</sub>(100), as given in Table 1. By adding an electron to the neutral complex AN-Cu<sub>9</sub>(100), the C(1) site does not experience any substantial change while Cu(8) gains a negative charge of  $-0.23$ , of which  $-0.21$  is assigned to the 4s. After applying an electric field to the neutral complex AN-Cu<sub>9</sub>(100), the N(7) atom in [AN-Cu<sub>9</sub>(100)]<sup>-1</sup> becomes more positive, by  $+0.14$ , than N(7) in AN-Cu<sub>9</sub>(100), of which  $+0.16$  is assigned to the 2p NAO and  $-0.02$  to the 2s and has an overall natural charge of  $-0.45$ . The Cu(15) atom in [AN-

**Table 1.** B-VWN/DZVP(DFT): natural charges and electron configurations (NECs) at interaction sites.

Molecule	Atom (site)	Natural charge	Configuration
AN	C(1)	$-0.29$	$2s(1.04)2p(3.24)$
	N(7)	$-0.32$	$2s(1.62)2p(3.67)$
AN-Cu <sub>9</sub> (100)	C(1)	$-0.70$	$2s(1.12)2p(3.53)$
	Cu(8)	$+0.15$	$4s(0.84)3d(9.88)$
	N(7)	$-0.59$	$2s(1.59)2p(3.96)$
	Cu(15)	$+0.32$	$4s(0.81)3d(9.83)$
[AN-Cu <sub>9</sub> (100)] <sup>-1</sup>	C(1)	$-0.69$	$2s(1.13)2p(3.52)$
	Cu(8)	$-0.08$	$4s(1.05)3d(9.90)$

Cu<sub>9</sub>(100)]<sup>-1</sup> becomes more negative by  $-0.46$  than the Cu(15) atom in AN-Cu<sub>9</sub>(100), of which  $-0.12$  is distributed into the 3d NAO and  $-0.34$  into the 4s and has an overall natural charge of  $-0.14$ .

It is also possible to determine the molecule(AN)-cluster(Cu<sub>9</sub>) charge separation by simply summing the appropriate natural charges of atoms. The molecule-cluster natural charge separation is AN( $-0.79$ )-Cu<sub>9</sub>( $+0.79$ ) in the neutral complex. In some respects the C(1)—Cu(8) and N(7)—Cu(15) bonds in AN-Cu<sub>9</sub>(100) can be considered as charge separated, as far as the molecule-cluster natural charge separation is concerned. The molecule-cluster natural charge separation in [AN-Cu<sub>9</sub>(100)]<sup>-1</sup> is AN( $-0.67$ )-Cu<sub>9</sub>( $-0.33$ ). Thus, the AN molecule as a whole becomes more positive by  $+0.12$  while the Cu<sub>9</sub> cluster as a whole becomes more negative by  $-1.12$ , after applying an external voltage to the neutral complex AN-Cu<sub>9</sub>(100).

Additional information about the nature of bonded interactions is provided by Tables 2 and 3, containing the spin-separated NAOs at the interaction sites. The letters “a” and “b” used in the analysis mean “alpha (spin up)” and “beta (spin down)”, respectively. Since the valence electrons tend to be chemically active, the total occupancies of the spin-separated NAOs at the interaction sites in AN-Cu<sub>9</sub>(100) involved in the bonding are 2.33a and 2.31b at C(1), 2.77a and 2.74b at N(7), 5.4a and 5.34b at Cu(8), and 5.3a and 5.34b at Cu(15). The occupancies of the  $\sigma$ -bonding and antibonding C(1)—Cu(8) NOs of the alpha spin are 0.79 (72.4% at C(1)) and 0.28 (27.6% at C(1)) in AN-Cu<sub>9</sub>(100). The occupancies of the  $\sigma$ -bonding and antibonding N(7)—Cu(15) NOs of the alpha spin are 0.77 (81.5% at N(7)) and 0.28 (18.5% at N(7)) in AN-Cu<sub>9</sub>(100). Table 3 shows that the valence occupancies of the spin-separated NAOs are 2.36a and 2.27b at C(1), as well as 5.59a and 5.38b at Cu(8), in



**Table 2.** B-VWN/DZVP(DFT): AN-Cu<sub>9</sub>(100) — spin-separated valence natural atomic orbitals.

Atom (site)	Atomic orbital	Type (atomic orbital) <sup>a</sup>	Occupancy
C(1)	<i>s</i>	Val (2 <i>s</i> )a	0.56121
C(1)	<i>px</i>	Val (2 <i>p</i> )a	0.54971
C(1)	<i>py</i>	Val (2 <i>p</i> )a	0.58395
C(1)	<i>pz</i>	Val (2 <i>p</i> )a	0.64153
N(7)	<i>s</i>	Val (2 <i>s</i> )a	0.79381
N(7)	<i>px</i>	Val (2 <i>p</i> )a	0.69440
N(7)	<i>py</i>	Val (2 <i>p</i> )a	0.62876
N(7)	<i>pz</i>	Val (2 <i>p</i> )a	0.68147
Cu(8)	<i>s</i>	Val (4 <i>s</i> )a	0.43659
Cu(8)	<i>dxy</i>	Val (3 <i>d</i> )a	0.99714
Cu(8)	<i>dxz</i>	Val (3 <i>d</i> )a	0.99631
Cu(8)	<i>dyz</i>	Val (3 <i>d</i> )a	0.99553
Cu(8)	<i>dx<sup>2</sup>y<sup>2</sup></i>	Val (3 <i>d</i> )a	0.99814
Cu(8)	<i>dz<sup>2</sup></i>	Val (3 <i>d</i> )a	0.95938
Cu(15)	<i>s</i>	Val (4 <i>s</i> )a	0.39141
Cu(15)	<i>dxy</i>	Val (3 <i>d</i> )a	0.99159
Cu(15)	<i>dxz</i>	Val (3 <i>d</i> )a	0.96475
Cu(15)	<i>dyz</i>	Val (3 <i>d</i> )a	0.99007
Cu(15)	<i>dx<sup>2</sup>y<sup>2</sup></i>	Val (3 <i>d</i> )a	0.99123
Cu(15)	<i>dz<sup>2</sup></i>	Val (3 <i>d</i> )a	0.98031
C(1)	<i>s</i>	Val (2 <i>s</i> )b	0.56002
C(1)	<i>px</i>	Val (2 <i>p</i> )b	0.54942
C(1)	<i>py</i>	Val (2 <i>p</i> )b	0.58261
C(1)	<i>pz</i>	Val (2 <i>p</i> )b	0.62381
N(7)	<i>s</i>	Val (2 <i>s</i> )b	0.79309
N(7)	<i>px</i>	Val (2 <i>p</i> )b	0.68505
N(7)	<i>py</i>	Val (2 <i>p</i> )b	0.62175
N(7)	<i>pz</i>	Val (2 <i>p</i> )b	0.64960
Cu(8)	<i>s</i>	Val (4 <i>s</i> )b	0.40603
Cu(8)	<i>dxy</i>	Val (3 <i>d</i> )b	0.99695
Cu(8)	<i>dxz</i>	Val (3 <i>d</i> )b	0.99246
Cu(8)	<i>dyz</i>	Val (3 <i>d</i> )b	0.99374
Cu(8)	<i>dx<sup>2</sup>y<sup>2</sup></i>	Val (3 <i>d</i> )b	0.99420
Cu(8)	<i>dz<sup>2</sup></i>	Val (3 <i>d</i> )b	0.95658
Cu(15)	<i>s</i>	Val (4 <i>s</i> )b	0.41956
Cu(15)	<i>dxy</i>	Val (3 <i>d</i> )b	0.99059
Cu(15)	<i>dxz</i>	Val (3 <i>d</i> )b	0.96412
Cu(15)	<i>dyz</i>	Val (3 <i>d</i> )b	0.99007
Cu(15)	<i>dx<sup>2</sup>y<sup>2</sup></i>	Val (3 <i>d</i> )b	0.99126
Cu(15)	<i>dz<sup>2</sup></i>	Val (3 <i>d</i> )b	0.98030

<sup>a</sup>a = alpha (spin up); b = beta (spin down); Val = valence.

[AN-Cu<sub>9</sub>(100)]<sup>-1</sup>. The occupancies of the  $\sigma$ -bonding and antibonding C(1)—Cu(8) NOs of the “up” spin are 0.96 (57.6% at C(1)) and 0.32 (42.4% at C(1)) in [AN-Cu<sub>9</sub>(100)]<sup>-1</sup>.

#### MP2/6-31+G\*

The NBO analysis shows the high percentage (>99%) contribution of the NAOs to the molecular charge distribution, that is, 99.40% of 20 in the AN valence, 99.28% of 119 in the AN-Cu<sub>9</sub>(100) valence, and 99.56% of 120 in the [AN-Cu<sub>9</sub>]<sup>-1</sup> valence. The summary of NO population analysis is given in Table 4. By incorporating the isolated AN into the AN-Cu<sub>9</sub>(100) complex, the natural charges indicate that the C(1) and N(7) sites become more negative by -0.41, of which -0.25 is distributed into 2*p* and -0.11 into 2*s* at C(1) and -0.46 into 2*p* and +0.06 into 2*s* at N(7). The Cu(8) and

Cu(15) atoms have the natural charges of -0.05 and +0.49 in AN-Cu<sub>9</sub>(100), respectively. As far as the natural charges are concerned, the N(7)—Cu(15) bond is charge separated (ionic), while the C(1)—Cu(8) bond is not, in AN-Cu<sub>9</sub>(100). By adding an electron to the neutral complex, the C(1) site becomes slightly more negative by -0.05 while the Cu(8) site gains a negative natural charge of -0.56, of which -0.55 is assigned to 4*s*. In comparison to the neutral complex, the change of the Cu(8) natural charge of -0.56 is substantial. The overall natural charges of the C(1) and Cu(8) sites in [AN-Cu<sub>9</sub>(100)]<sup>-1</sup> are -0.78 and -0.61, respectively.

By summing the appropriate natural charges of atoms, the molecule-cluster natural charge separation is AN(-0.94)—Cu<sub>9</sub>(+0.94) in the neutral complex. In some respects the C(1)—Cu(8) and N(7)—Cu(15) bonds in AN-Cu<sub>9</sub>(100) can be considered as charge separated, as far as the molecule-



**Table 3.** B-VWN/DZVP(DFT):  $[\text{AN}-\text{Cu}_9(100)]^{-1}$  — spin-separated valence natural atomic orbitals.

Atom (site)	Atomic orbital	Type (atomic orbital) <sup>a</sup>	Occupancy
C(1)	<i>s</i>	Val (2 <i>s</i> )a	0.57052
C(1)	<i>px</i>	Val (2 <i>p</i> )a	0.57445
C(1)	<i>py</i>	Val (2 <i>p</i> )a	0.58371
C(1)	<i>pz</i>	Val (2 <i>p</i> )a	0.64184
Cu(8)	<i>s</i>	Val (4 <i>s</i> )a	0.61215
Cu(8)	<i>dxy</i>	Val (3 <i>d</i> )a	0.99702
Cu(8)	<i>dxz</i>	Val (3 <i>d</i> )a	0.97963
Cu(8)	<i>dyz</i>	Val (3 <i>d</i> )a	0.99810
Cu(8)	<i>dx<sup>2</sup>y<sup>2</sup></i>	Val (3 <i>d</i> )a	0.99138
Cu(8)	<i>dz<sup>2</sup></i>	Val (3 <i>d</i> )a	0.99665
C(1)	<i>s</i>	Val (2 <i>s</i> )b	0.56195
C(1)	<i>px</i>	Val (2 <i>p</i> )b	0.55757
C(1)	<i>py</i>	Val (2 <i>p</i> )b	0.58376
C(1)	<i>pz</i>	Val (2 <i>p</i> )b	0.57474
Cu(8)	<i>s</i>	Val (4 <i>s</i> )b	0.44150
Cu(8)	<i>dxy</i>	Val (3 <i>d</i> )b	0.99094
Cu(8)	<i>dxz</i>	Val (3 <i>d</i> )b	0.97103
Cu(8)	<i>dyz</i>	Val (3 <i>d</i> )b	0.98665
Cu(8)	<i>dx<sup>2</sup>y<sup>2</sup></i>	Val (3 <i>d</i> )b	0.98857
Cu(8)	<i>dz<sup>2</sup></i>	Val (3 <i>d</i> )b	0.99678

<sup>a</sup>a = alpha (spin up); b = beta (spin down); Val = valence.**Table 4.** MP2/6–31+G\*: natural electron charges, natural electron configurations, and Mulliken charges.

Molecule	Atom (site)	Natural charge	Configuration <sup>a</sup>	Spin natural charge		Mulliken charge <sup>b</sup>
				Up	Down	
AN	C(1)	–0.32	2 <i>s</i> (1.00)2 <i>p</i> (3.30)	–0.16	–0.16	–0.08
	N(7)	–0.28	2 <i>s</i> (1.62)2 <i>p</i> (3.63)	–0.14	–0.14	–0.22
AN–Cu <sub>9</sub> (100)	C(1)	–0.73	2 <i>s</i> (1.11)2 <i>p</i> (3.55)	–0.57	–0.16	–0.40
	Cu(8)	–0.05	4 <i>s</i> (1.02)3 <i>d</i> (9.40)4 <i>p</i> (0.44)	–0.09	+0.04	–0.28
	N(7)	–0.69	2 <i>s</i> (1.56)2 <i>p</i> (4.09)	+0.25	–0.94	–0.45
	Cu(15)	+0.49	4 <i>s</i> (0.71)3 <i>d</i> (9.53)4 <i>p</i> (0.15)	+0.18	+0.31	+0.25
$[\text{AN}-\text{Cu}_9(100)]^{-1}$	C(1)	–0.78	2 <i>s</i> (1.13)2 <i>p</i> (3.59)	+0.49	–1.27	–0.04
	Cu(8)	–0.61	4 <i>s</i> (1.57)3 <i>d</i> (9.35)4 <i>p</i> (0.48)	–0.71	+0.10	–0.71

<sup>a</sup>The given NAOs have been substantially modified in terms of the charge distribution by incorporating AN into AN–Cu<sub>9</sub>(100).<sup>b</sup>The Mulliken charges are only to be used to demonstrate the arbitrary and unpredictable behavior of this partitioning scheme.

cluster natural charge separation is concerned. The molecule–cluster natural charge separation in  $[\text{AN}-\text{Cu}_9(100)]^{-1}$  is AN(–0.36)–Cu<sub>9</sub>(–0.64). Therefore, the AN molecule as a whole becomes more positive by +0.58 while the Cu<sub>9</sub> cluster as a whole becomes more negative by –1.58 after applying an external voltage to the neutral complex AN–Cu<sub>9</sub>(100).

Additional information about the nature of bonded interactions is provided by Tables 5–7, containing the valence NAOs at the interaction sites in AN and the spin separated valence NAOs at the interaction sites in AN–Cu<sub>9</sub>(100) and  $[\text{AN}-\text{Cu}_9(100)]^{-1}$ , respectively. The total occupancies involved in the bonding in AN are 4.30 at C(1) and 5.26 at N(7). The total occupancies involved in the bonding in AN–Cu<sub>9</sub>(100) are 2.53a and 2.13b at C(1), 2.22a and 3.42b at N(7), 5.27a and 5.15b at Cu(8), and 5.18a and 5.06b at Cu(15). By bonding AN to Cu<sub>9</sub>(100), the site C(1) gains a bonding NAO occupancy of 0.38a and loses that of 0.02b, while the site N(7) loses a bonding NAO occupancy of 0.41 having the “up” spin and gains that of 0.79 having the “down” spin. The occupancies of the  $\sigma$ -bonding and anti-

bonding C(1)—Cu(8) NOs of the alpha spin are 0.73 (66.83% at C(1)) and 0.26 (33.17% at C(1)) in AN–Cu<sub>9</sub>(100), respectively. The occupancies of the  $\sigma$ -bonding and antibonding N(7)—Cu(15) NOs of the alpha spin are 0.62 (65.31% at N(7)) and 0.22 (34.69% at N(7)) in AN–Cu<sub>9</sub>(100), respectively. Table 7 also shows that the valence occupancies of the spin-separated NAOs are 1.48a and 3.24b at C(1) and 5.7a and 5.05b at Cu(8) in  $[\text{AN}-\text{Cu}_9(100)]^{-1}$ . By adding an electron to the neutral complex, the C(1) site loses an alpha-bonding occupancy of 1.05 and gains a beta one of 1.11, while the Cu(8) site gains an alpha-valence occupancy of 0.43 and loses a beta one of 0.1. The occupancies of the  $\sigma$ -bonding and antibonding C(1)—Cu(8) NOs of spin “up” are 0.6 (36.12% at C(1)) and 0.2 (63.88% at C(1)) in  $[\text{AN}-\text{Cu}_9(100)]^{-1}$ .

The AN molecule retains its planarity in AN–Cu<sub>9</sub>(100) while it becomes distorted after applying an external voltage, as given in Fig. 1. The C(1)—C(2), C(3)—N(7), and C(2)—C(3) geometric bond lengths (GBLs) in AN are 2.52 au, 2.21 au, and 2.66 au, respectively. The C(1)—C(2) and



**Table 5.** MP2/6-31+G\*: AN — valence natural atomic orbitals at the C(1) and N(7) sites.

Atom (site)	Atomic orbital	Type (atomic orbital) <sup>a</sup>	Occupancy
C(1)	<i>s</i>	Val(2 <i>s</i> )	1.00396
C(1)	<i>px</i>	Val(2 <i>p</i> )	1.14970
C(1)	<i>py</i>	Val(2 <i>p</i> )	1.11966
C(1)	<i>pz</i>	Val(2 <i>p</i> )	1.02730
N(7)	<i>s</i>	Val(2 <i>s</i> )	1.61634
N(7)	<i>px</i>	Val(2 <i>p</i> )	1.14945
N(7)	<i>py</i>	Val(2 <i>p</i> )	1.40741
N(7)	<i>pz</i>	Val(2 <i>p</i> )	1.07615

<sup>a</sup>a = alpha (spin up); b = beta (spin down); Val = valence.**Table 6.** MP2/6-31+G\*: AN-Cu<sub>9</sub>(100) — spin-separated valence natural atomic orbitals.

Atom (site)	Atomic orbital	Type (atomic orbital) <sup>a</sup>	Occupancy
C(1)	<i>s</i>	Val (2 <i>s</i> )a	0.56951
C(1)	<i>px</i>	Val (2 <i>p</i> )a	0.58950
C(1)	<i>py</i>	Val (2 <i>p</i> )a	0.61067
C(1)	<i>pz</i>	Val (2 <i>p</i> )a	0.76383
N(7)	<i>s</i>	Val (2 <i>s</i> )a	0.75370
N(7)	<i>px</i>	Val (2 <i>p</i> )a	0.53719
N(7)	<i>py</i>	Val (2 <i>p</i> )a	0.32182
N(7)	<i>pz</i>	Val (2 <i>p</i> )a	0.61095
Cu(8)	<i>s</i>	Val (4 <i>s</i> )a	0.53980
Cu(8)	<i>dxy</i>	Val (3 <i>d</i> )a	0.95956
Cu(8)	<i>dxz</i>	Val (3 <i>d</i> )a	0.96381
Cu(8)	<i>dyz</i>	Val (3 <i>d</i> )a	0.96291
Cu(8)	<i>dx<sup>2</sup>y<sup>2</sup></i>	Val (3 <i>d</i> )a	0.95701
Cu(8)	<i>dz<sup>2</sup></i>	Val (3 <i>d</i> )a	0.89262
Cu(15)	<i>s</i>	Val (4 <i>s</i> )a	0.43380
Cu(15)	<i>dxy</i>	Val (3 <i>d</i> )a	0.96544
Cu(15)	<i>dxz</i>	Val (3 <i>d</i> )a	0.90644
Cu(15)	<i>dyz</i>	Val (3 <i>d</i> )a	0.96552
Cu(15)	<i>dx<sup>2</sup>y<sup>2</sup></i>	Val (3 <i>d</i> )a	0.96028
Cu(15)	<i>dz<sup>2</sup></i>	Val (3 <i>d</i> )a	0.95151
C(1)	<i>s</i>	Val (2 <i>s</i> )b	0.54128
C(1)	<i>px</i>	Val (2 <i>p</i> )b	0.54188
C(1)	<i>py</i>	Val (2 <i>p</i> )b	0.60240
C(1)	<i>pz</i>	Val (2 <i>p</i> )b	0.44503
N(7)	<i>s</i>	Val (2 <i>s</i> )b	0.80284
N(7)	<i>px</i>	Val (2 <i>p</i> )b	0.86106
N(7)	<i>py</i>	Val (2 <i>p</i> )b	0.89021
N(7)	<i>pz</i>	Val (2 <i>p</i> )b	0.86922
Cu(8)	<i>s</i>	Val (4 <i>s</i> )b	0.47945
Cu(8)	<i>dxy</i>	Val (3 <i>d</i> )b	0.94021
Cu(8)	<i>dxz</i>	Val (3 <i>d</i> )b	0.93111
Cu(8)	<i>dyz</i>	Val (3 <i>d</i> )b	0.95569
Cu(8)	<i>dx<sup>2</sup>y<sup>2</sup></i>	Val (3 <i>d</i> )b	0.95266
Cu(8)	<i>dz<sup>2</sup></i>	Val (3 <i>d</i> )b	0.88607
Cu(15)	<i>s</i>	Val (4 <i>s</i> )b	0.27714
Cu(15)	<i>dxy</i>	Val (3 <i>d</i> )b	0.96607
Cu(15)	<i>dxz</i>	Val (3 <i>d</i> )b	0.92352
Cu(15)	<i>dyz</i>	Val (3 <i>d</i> )b	0.97039
Cu(15)	<i>dx<sup>2</sup>y<sup>2</sup></i>	Val (3 <i>d</i> )b	0.96129
Cu(15)	<i>dz<sup>2</sup></i>	Val (3 <i>d</i> )b	0.96313

<sup>a</sup>a = alpha (spin up); b = beta (spin down); Val = valence.



**Table 7.** MP2/6-31+G\*: [AN-Cu<sub>9</sub>(100)]<sup>-1</sup> — spin-separated valence natural atomic orbitals.

Atom (site)	Atomic orbital	Type (atomic orbital) <sup>a</sup>	Occupancy
C(1)	<i>s</i>	Val (2 <i>s</i> )a	0.46816
C(1)	<i>px</i>	Val (2 <i>p</i> )a	0.42184
C(1)	<i>py</i>	Val (2 <i>p</i> )a	0.56532
C(1)	<i>pz</i>	Val (2 <i>p</i> )a	0.01859
Cu(8)	<i>s</i>	Val (4 <i>s</i> )a	0.9988
Cu(8)	<i>dxy</i>	Val (3 <i>d</i> )a	0.95234
Cu(8)	<i>dxz</i>	Val (3 <i>d</i> )a	0.90209
Cu(8)	<i>dyz</i>	Val (3 <i>d</i> )a	0.95399
Cu(8)	<i>dx<sup>2</sup>-y<sup>2</sup></i>	Val (3 <i>d</i> )a	0.94188
Cu(8)	<i>dz<sup>2</sup></i>	Val (3 <i>d</i> )a	0.95919
C(1)	<i>s</i>	Val (2 <i>s</i> )b	0.65702
C(1)	<i>px</i>	Val (2 <i>p</i> )b	0.71899
C(1)	<i>py</i>	Val (2 <i>p</i> )b	0.65700
C(1)	<i>pz</i>	Val (2 <i>p</i> )b	1.20373
Cu(8)	<i>s</i>	Val (4 <i>s</i> )b	0.40021
Cu(8)	<i>dxy</i>	Val (3 <i>d</i> )b	0.94093
Cu(8)	<i>dxz</i>	Val (3 <i>d</i> )b	0.88619
Cu(8)	<i>dyz</i>	Val (3 <i>d</i> )b	0.92084
Cu(8)	<i>dx<sup>2</sup>-y<sup>2</sup></i>	Val (3 <i>d</i> )b	0.93905
Cu(8)	<i>dz<sup>2</sup></i>	Val (3 <i>d</i> )b	0.95498

<sup>a</sup>a = alpha (spin up); b = beta (spin down); Val = valence.

C(3)—N(7) GBLs in both AN-Cu<sub>9</sub>(100) and [AN-Cu<sub>9</sub>(100)]<sup>-1</sup> are 2.7 au and 2.27 au, while those of the C(2)—C(3) bonds are 2.57 au and 2.59 au, respectively. The elongation of the C(1)—C(2) and C(3)—N(7) bonds and the shortening of the C(2)—C(3) bonds with reference to AN confirm electron transfer from Cu<sub>9</sub> to AN. The calculated value of the ionization potential (IP) of 4.43 electron volts (eV) for Cu<sub>9</sub> confirms recent measurements of 4.2 eV, which is comparable with the IPs of Na (5.14 eV) and K (4.34 eV) (50). A similar electron transfer in NO population has been reported for an AN molecule with an Na atom, as well as for an acrolein molecule with an Na atom (51, 52).

### Nature of bonded interactions

In this section, the nature of the AN-Cu<sub>9</sub>(100) interfacial interactions is investigated by use of AIM theory at the B-VWN/DZVP(DFT) and MP2/6-31+G\* levels of theory. The calculations pertaining to the topological features of the electron density were performed by use of the program EXTREM (53). The figures were created by use of the program MOLDEN (54).

#### B-VWN/DZVP(DFT)

The Bader (AIM) (29, 30) analysis shows the existence of the C(1)—Cu(8) and N(7)—Cu(15) through-space interactions in AN-Cu<sub>9</sub>(100), as well as that between the C(1) and the Cu(8) in [AN-Cu<sub>9</sub>(100)]<sup>-1</sup>; that is, bond paths — lines of the highest electron density linking the pairs of the atoms — exist. The total bond path lengths (TBPLs) are in agreement with the geometric bond lengths. For example, the TBPLs of the C(1)—Cu(8) and the N(7)—Cu(15) in AN-Cu<sub>9</sub>(100) are 3.9223 au and 3.5795 au, while the corresponding GBLs are 3.9204 au and 3.5779 au, respectively. Also, the TBPL of the C(1)—Cu(8) bond in [AN-Cu<sub>9</sub>(100)]<sup>-1</sup> is 4.1189 au while the C(1)—Cu(8) GBL is 4.1172 au. The bond critical point is

determined by the condition that the gradient of the electron density is equal to zero, and the properties of the density at this point provide quantitative characteristics of a bond. The bond CPs have a small electron density of 0.0829 *ea*<sub>0</sub><sup>-3</sup> between C(1) and Cu(8) and of 0.1093 *ea*<sub>0</sub><sup>-3</sup> between N(7) and Cu(15) in AN-Cu<sub>9</sub>(100), as well as of 0.0669 *ea*<sub>0</sub><sup>-3</sup> between C(1) and Cu(8) in [AN-Cu<sub>9</sub>(100)]<sup>-1</sup>. The positions of the bond CPs are clear as pronounced minima of the electron density in the regions between the corresponding nuclei in Fig. 2. The Laplacian (the second derivative of the density) of the bond CPs has values of +0.1189 (C(1)—Cu(8)) and +0.3184 (N(7)—Cu(15)) in AN-Cu<sub>9</sub>(100) and of +0.1095 (C(1)—Cu(8)) in [AN-Cu<sub>9</sub>(100)]<sup>-1</sup>, characteristic of a donor-acceptor bond.

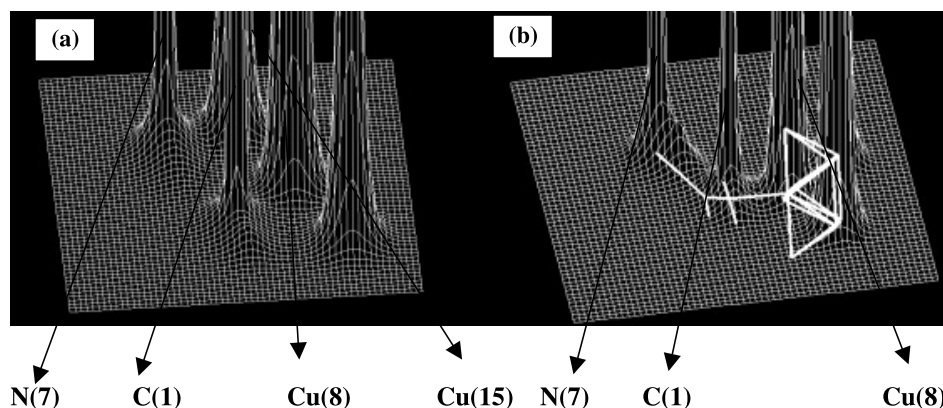
Applying an external voltage to the neutral complex caused a change in the number of electrons, from 289 in AN-Cu<sub>9</sub>(100) to 290 in [AN-Cu<sub>9</sub>(100)]<sup>-1</sup>. The Fukui function *f*<sub>+</sub> has values of -0.43 at C(1), +0.39 at Cu(8), -0.02 at N(7), and +30.18 at Cu(15), respectively. The changes of the electron density at C(1), Cu(8), and N(7) are not substantial, and therefore, a nucleophilic reaction may not be expected to occur in the vicinity of the interaction sites. Such a reaction may be possible in the vicinity of Cu(15).

#### MP2/6-31+G\*

The Bader analysis shows that the total bond path lengths are in agreement with the geometric bond lengths (i.e., AN-Cu<sub>9</sub>(100): C(1)—Cu(8) TBPL = 3.9265 au, GBL = 3.9205; N(7)—Cu(15) TBPL = 3.5809 au, GBL = 3.5779 au; [AN-Cu<sub>9</sub>(100)]<sup>-1</sup>: C(1)—Cu(8) TBPL = 4.1214 au, GBL = 4.1172). The bond CPs have a small total electron density of 0.0805 *ea*<sub>0</sub><sup>-3</sup> between C(1) and Cu(8) and of 0.1076 *ea*<sub>0</sub><sup>-3</sup> between N(7) and Cu(15) in AN-Cu<sub>9</sub>(100), as well as of 0.0657 *ea*<sub>0</sub><sup>-3</sup> between C(1) and Cu(8) in [AN-Cu<sub>9</sub>(100)]<sup>-1</sup>. The values of the spin electron densities at the bond CPs are



**Fig. 2.** Electron density. B-VWN/DZVP(DFT). (a) AN-Cu<sub>9</sub>(100); (b) [AN-Cu<sub>9</sub>(100)]<sup>-1</sup>.



0.0414  $ea_0^{-3}$  (C(1)—Cu(8)) and 0.0554  $ea_0^{-3}$  (N(7)—Cu(15)) in AN-Cu<sub>9</sub>(100), as well as 0.0338  $ea_0^{-3}$  (C(1)—Cu(8)) in [AN-Cu<sub>9</sub>(100)]<sup>-1</sup>. The Laplacian of the bond CPs has values of +0.0892 (C(1)—Cu(8)) and +0.3704 (N(7)—Cu(15)) in AN-Cu<sub>9</sub>(100) and of +0.0867 (C(1)—Cu(8)) in [AN-Cu<sub>9</sub>(100)]<sup>-1</sup>, characteristic of a donor-acceptor bond.

The Fukui function  $f_+$  has values of -0.49 at C(1), +133.2 at Cu(8), +2.84 at N(7), and +172.17 at Cu(15), respectively. The changes of the electron density of the Cu(8) and Cu(15) sites are substantial, indicating that a nucleophilic reaction may be expected to occur in the vicinity of the interaction sites.

### [AN-Cu<sub>9</sub>(100)]<sup>-1</sup>: Laplacian of total electron density and spatial extents of HOMO and LUMO

In this section, the Laplacian of the electron density is analyzed and contrasted to the spatial extents of the HOMO and LUMO in [AN-Cu<sub>9</sub>(100)]<sup>-1</sup>.

The Laplacian itself contains features such as bonds and lone pairs, which are not observable in the density itself. The cut of the Laplacian of the electron density is given in Figs. 3 and 4. From left to right, the nuclei in the plane of the cut are N(7), C(1), and Cu(8). The electron density is locally concentrated in spatial regions determined by a negative Laplacian and locally depleted in those regions determined by a positive Laplacian. Having a slightly positive value of the Laplacian, the position of the bond critical point is nicely visible in the region between C(1) and Cu(8).

In most previous work, the HLG has been observed as a crucial parameter for understanding conductance mechanisms through molecular junctions. The ability of a molecule to rearrange its electron density under the presence of an external electron underlies such observations. If the ability is not that pronounced, the molecular admittance to the incoming electron is less recognizable and, therefore, a molecule is more stable. As the first consequence, by employing the electronegativity equalization theorem and a relative alignment of the Fermi energy level with respect to the HLG (20, 55–59), the barrier to electron transfer is proportional to the HLG to the first approximation. As the second consequence, the size of the HLG may be regarded as a measure of the hardness of the electron density. The relative alignment of

**Fig. 3.** [AN-Cu<sub>9</sub>(100)]<sup>-1</sup> — Laplacian of electron density. B-VWN/DZVP(DFT).

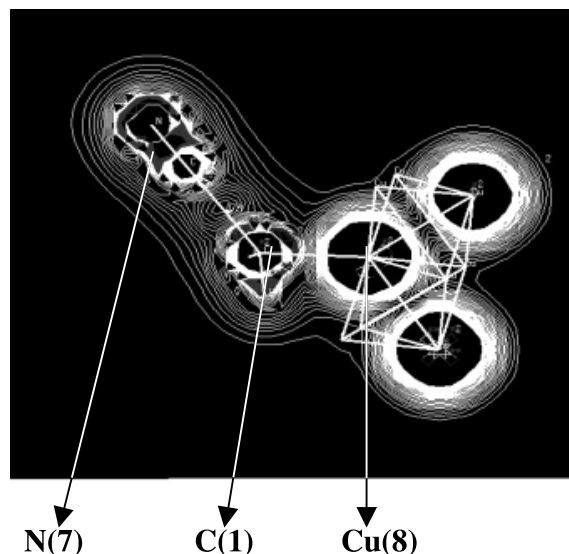
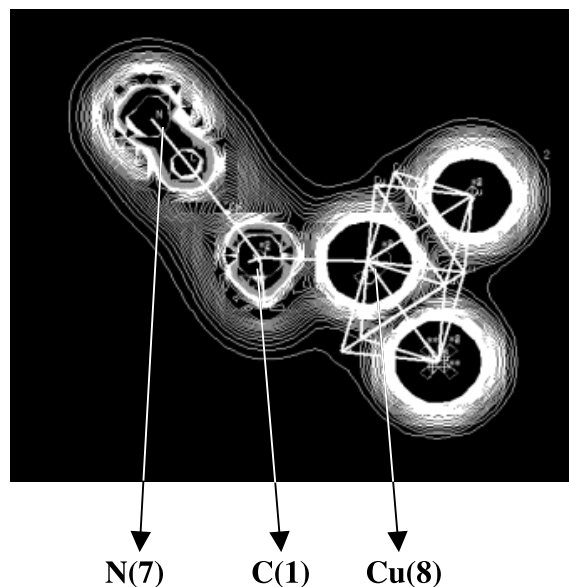


**Fig. 4.** [AN-Cu<sub>9</sub>(100)]<sup>-1</sup> — Laplacian of electron density. MP2/6-31+G\*.





the Fermi energy level is strongly dependent upon the density of states within the HLG and is sensitive to a small amount of charge transfer. Thus, the physical essence is contained in the electron density distribution.

Electron transfer, from  $\text{Cu}_9$  to AN, leads to substantial change in the molecular structure according to the nature of the LUMO in AN. Electrons occupy some unoccupied orbitals of the neutral complex after the action of an external voltage. An area with locally concentrated electron density is susceptible to attack by an electrophile while an area with locally depleted electron density is susceptible to attack by a nucleophile. In general, it has been found that a map of negative values of the Laplacian of the total electron density resembles a spatial extent of the HOMO while that of positive values of the Laplacian resembles a spatial extent of the LUMO (60). The spatial extent of the LUMO or, more conceivably, the extent of its electron delocalization may be employed to describe electronic molecular transport of a charged molecule qualitatively if and only if (according to this study) a spatial extent of the LUMO resembles a map of positive values of the Laplacian of the total electron density. What do the spatial extents of the HOMO and LUMO in  $[\text{AN-Cu}_9(100)]^{-1}$  indicate?

#### B-VWN/DZVP(DFT)

The cut of the HOMO in  $[\text{AN-Cu}_9(100)]^{-1}$  is given in Fig. 5. The plane of the cut is the same as that of the Laplacian in Fig. 3. Note the contour map of the negative Laplacian (Fig. 3). The contours encompass C(1) and N(7), showing roughly circular curvatures, but those around C(1) are not fully closed. Note the contour lines of the HOMO residing in the same regions in Fig. 5. In its immediate vicinity, C(1) is encompassed by the negative contours. The contours are also shifted behind C(1) where the corresponding lines of the Laplacian are not fully closed. In the vicinity of N(7), the negative contours encircle N(7) towards C(1) but not fully behind the N(7) nucleus, in Fig. 5. Regardless of the qualitative differences, the area determined by negative values of the Laplacian spreads roughly in the same spatial regions as that of the HOMO.

The cut of the LUMO in  $[\text{AN-Cu}_9(100)]^{-1}$  is given in Fig. 6. The plane of the cut is the same as that of the Laplacian in Fig. 3. Focus on the region between C(1) and Cu(8). The contour lines of the LUMO in this region are negative, spreading both toward the left and the right with respect to the C(1)—Cu(8) bond line. In contrast to it, the contour lines of the Laplacian in the same region are positive. It is clear that the spatial extent of the LUMO does not resemble that of the positive Laplacian.

#### MP2/6-31+G\*

The cut of the HOMO in  $[\text{AN-Cu}_9(100)]^{-1}$  is given in Fig. 7. The plane of the cut is the same as that of the Laplacian given in Fig. 4. The negative contours of the HOMO show a circular curvature in the immediate vicinity of C(1), which spreads right under the C(1)—Cu(8) inter-nuclear axis. In contrast to the Laplacian, there are some positive contours of the HOMO in the immediate vicinity of C(1), which are still edged by the negative ones right above the C(1)—Cu(8) interaction line. The N(7) site is also surrounded by two concentric spatial profiles of the negative

Fig. 5.  $[\text{AN-Cu}_9(100)]^{-1}$  — HOMO. B-VWN/DZVP(DFT).

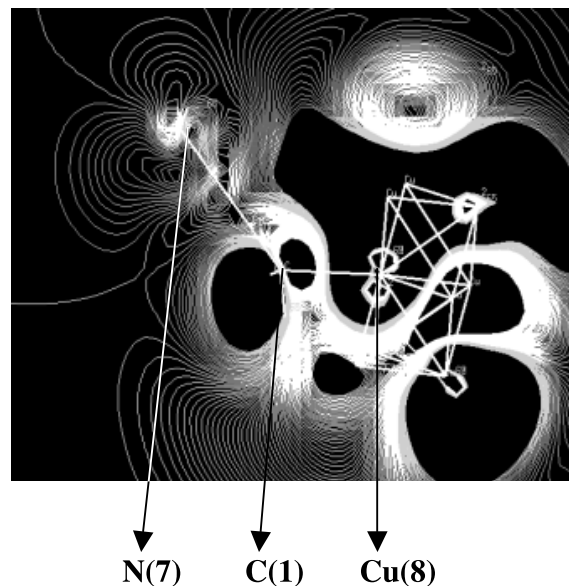
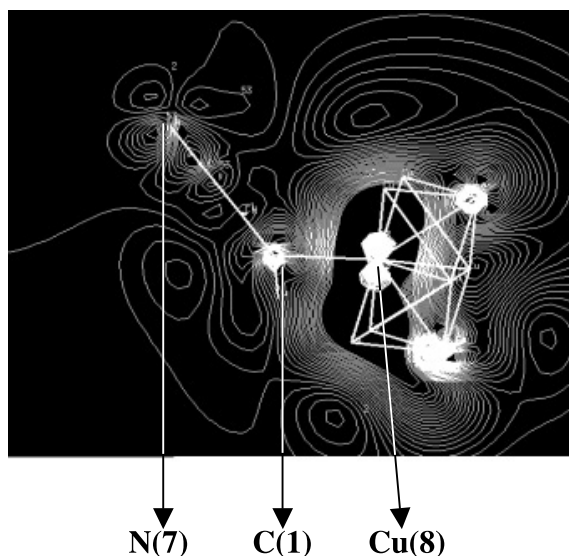


Fig. 6.  $[\text{AN-Cu}_9(100)]^{-1}$  — LUMO. B-VWN/DZVP(DFT).

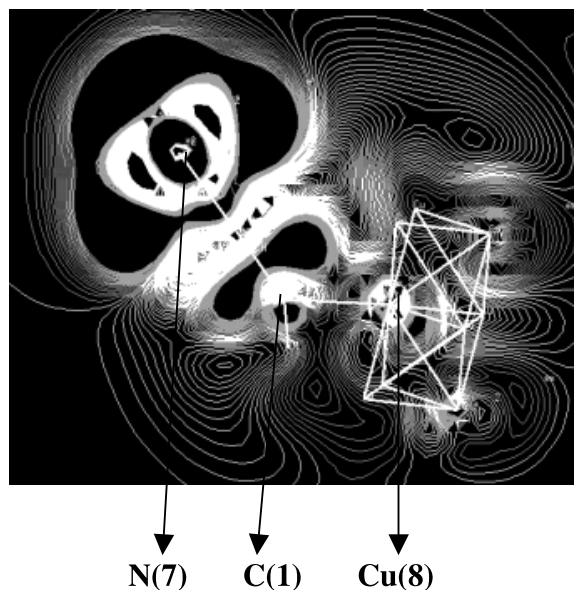
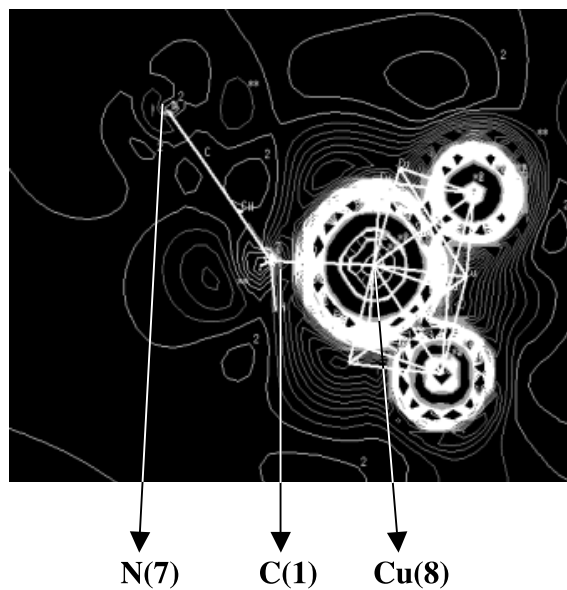


contours, of which the outer one is substantially extended both toward the left and the right with respect to N(7). Regardless of the qualitative differences, the area determined by negative values of the Laplacian spreads roughly in the same spatial regions as that of the HOMO.

The cut of the LUMO in  $[\text{AN-Cu}_9(100)]^{-1}$  is given in Fig. 8. The plane of the cut is the same as that of the Laplacian in Fig. 4. Focus on region between C(1) and Cu(8). It is clear that the map of the LUMO resembles that determined by positive values of the Laplacian conspicuously.

The fundamental question related to the essential origin of the electron distribution in the AN- $\text{Cu}_9$  systems is not yet resolved.



**Fig. 7.**  $[\text{AN}-\text{Cu}_9(100)]^{-1}$  — HOMO. MP2/6-31+G\*.**Fig. 8.**  $[\text{AN}-\text{Cu}_9(100)]^{-1}$  — LUMO. MP2/6-31+G\*.

## Discussion

Most results related to the characterizations of the interfacial interactions are strongly dependent on the molecular geometries used. The first aspect is that considerable effects of the increase of the cluster size and the choice of metal surface on the molecular properties are well known. The second aspect is that methods chosen to generate the optimized geometries need to be computationally efficient with respect to the number of atoms involved in such calculations. The third aspect is that a satisfactory basis set is required, providing that the structure is qualitatively correct. In contrast to the  $\text{Cu}_9$  cluster, the problems associated with the clusters having the open-shell characters are well known. The strong dependence of degenerate open-shell atomic energies on the occupancy of the atomic orbitals within DFT is associated with the different densities of the degenerate atomic orbitals. The degenerate atomic orbitals can be populated in different ways. It is difficult to reproduce the exact degeneracy of these states within the average thermo chemical accuracy ( $2 \text{ kcal mol}^{-1}$ ) by using approximate exchange-correlation functionals that depend on density gradient (61). There are recommendations that the local spin-density (LSD) approximation, in combination with some improved optimization algorithms (62, 63), is capable of generating reliable adsorption structures of adsorbates (64, 65).

The questions that have been previously addressed regarding the nature of the organic—metal-bonded interactions can be summarized as follows (17, 66–68). Where is the energetically preferable adsorption site for a molecule on different metal surfaces? How are the structures for a molecule at different adsorption sites on different metal surfaces? What are the different contributions to the bond between interaction sites? What are the differences for the adsorption of a molecule to different metal surfaces? The extraction of orbitals important in the bonding to the metal surfaces has been the key objective, but simplified structures have been needed for the construction of the orbitals. The simplified structures

sometimes had all atoms except those in the top layer removed (66). There are two reasons for these implications. First, the energetic requirements are based on the arbitrary partition of the molecular interaction energy. Second, the descriptions of bonded interactions are sought in orbitals. The physics underlying these results is not clear for two primary reasons. In a pure physical sense, the general trend contradictory to the investigations is to have the clusters of larger sizes involved in calculations to mimic the density of states of the actual surface. If the analysis of tracing bond paths between the atoms in the  $\text{AN}-\text{Cu}_9$  systems is carried out in a greater detail, it is possible to intuitively predict the directions of “hypothetical” bond paths linking the atoms of the organic molecule to those of a “hypothetical” cluster possessing a size that is larger or smaller than the actual one. In other words, the existence of possible bond paths is physically independent of increasing or decreasing the cluster size. This is the essence of the understanding that the bond path is a universal indicator of bonded interactions, as noted by Bader in 1990 when his AIM theory was released (29).

The question raised at the very end of the previous section is fundamentally profound. Possible DFT analyses of the density of states and band structures would probably indicate that the origin of the electron distribution in this system is more complicated than that based solely on classical interpretations. The first quantitative measurement of the 2D band structure at a self-assembling interface between a thiolate and a silver surface by use of two-photon photoemission may be an appropriate guidance for some future work (69). Experimental and theoretical investigations converging to the same answer are worth being pursued.

## Summary

The electron distribution around the nuclei and the nature of bonded interactions at the  $\text{AN}-\text{Cu}_9$  interfaces need to be investigated by combining different quantum mechanical methods. The QM methods include ab initio electron corre-



lation effects and lead toward the invariant descriptions of the interfacial interactions.

The success of frontier molecular orbital theory to rationalize the organic-metal charge migration process may depend on whether the spatial extents of the HOMO and LUMO support the corresponding topological features of the total electron density, which determines the reactivity.

The essential origin of the electron transfer in the AN-Cu<sub>9</sub> system is not yet described.

The message of this study is best described by C.A. Coulson, "In a profound sense the description of the bonds in a molecule is simply the description of the distribution of electrons around the nuclei", as quoted from p. 2 of ref. 34.

## Acknowledgments

This work in Mons, Belgium was supported by the European Commission project SANEME (IST-1999-10323).

## References

1. Karzazi, J. Cornil, and J.L. Bredas. *J. Am. Chem. Soc.* **123**, 10 076 (2001).
2. M.A. Reed, C. Zhou, C.J. Muller, T.P. Burgin, and J.M. Tour. *Science* (Washington, D.C.), **278**, 252 (1997).
3. S.J. Trans, M.H. Devoret, H. Dai, A. Thess, R.E. Smalley, L.J. Geerligs, and C. Dekker. *Nature*, **386**, 474 (1997).
4. D. Porath, A. Bezryadin, S. de Vries, and C. Dekker. *Nature*, **403**, 635 (2000).
5. A. Aviram and M.A. Ratner. *Chem. Phys. Lett.* **29**, 277 (1974).
6. R.M. Metzger. *Acc. Chem. Res.* **32**, 950 (1999).
7. R.M. Metzger, B. Chen, U. Hopfner, M.V. Lakshmikantham, D. Vuillaume, T. Kawai, X. Wu, H. Tachinaba, T.V. Hughes, H. Sakurai, J.W. Baldwin, C. Hosch, M.P. Cava, L. Brehmer, and G.J. Ashwell. *J. Am. Chem. Soc.* **119**, 10 455 (1997).
8. V. Mujica, M.A. Ratner, and A. Nitzan. *Chem. Phys.* **281**, 147 (2002).
9. S.N. Yaliraki, M. Kemp, and M.A. Ratner. *J. Am. Chem. Soc.* **121**, 3428 (1999).
10. V. Mujica, M. Kemp, and M.A. Ratner. *J. Chem. Phys.* **101**, 6849 (1994).
11. M.P. Samanta, W. Tian, S. Datta, J.I. Henderson, and C.P. Kubiak. *Phys. Rev. B*, **53**, 7626 (1996).
12. S. Datta, W. Tian, S. Hong, R. Reifenberger, J.I. Henderson, and C.P. Kubiak. *Phys. Rev. Lett.* **79**, 2530 (1997).
13. M. Magoga and C. Joachim. *Phys. Rev. B*, **56**, 4722 (1996).
14. E.G. Emberly and G. Kirczenow. *Phys. Rev. B*, **58**, 10 911 (1998).
15. J.M. Seminario, A.G. Zacarias, and P.A. Derosa. *J. Phys. Chem. A*, **105**, 792 (2001).
16. F. Zahid, M. Paulsson, and S. Datta. *Advanced semiconductors and organic nano-techniques*. Edited by H. Markoc. Academic Press. In publication. Chap 2.
17. (a) X. Crispin, V. Geskin, A. Crispin, J. Cornil, R. Lazzaroni, W.R. Salaneck, and J.L. Bredas. *J. Am. Chem. Soc.* **124**, 8131 (2002); (b) X. Crispin, C. Bureau, V. Geskin, R. Lazzaroni, W.R. Salaneck, and J.L. Bredas. *J. Chem. Phys.* **111**, 3237 (1999).
18. J.M. Seminario, A.G. Zacarias, and J.M. Tour. *J. Am. Chem. Soc.* **122**, 3015 (2000).
19. R.G. Parr and R.G. Pearson. *J. Am. Chem. Soc.* **105**, 7512 (1983).
20. R.G. Par and W. Yang. *Density-functional theory of atoms and molecules*. Oxford University Press, New York. 1989.
21. J. Cornil, Y. Karzazi, and J.L. Bredas. *J. Am. Chem. Soc.* **124**, 3516 (2002).
22. A.D. Becke and K.E. Edgecombe. *J. Chem. Phys.* **92**, 5397 (1990).
23. A.E. Reed, L.A. Curtiss, and F. Weinhold. *Chem. Rev.* **88**, 899 (1988).
24. P.O. Löwdin. *Phys. Rev.* **97**, 1474 (1955).
25. P.M. Mitrasinovic. *J. Comput. Chem.* **22**, 1387 (2001).
26. P.M. Mitrasinovic. *J. Phys. Chem. A*, **106**, 7026 (2002).
27. R.L. Fulton. *J. Phys. Chem.* **97**, 7516 (1993).
28. R.F.W. Bader and H. Essén. *J. Chem. Phys.* **80**, 1943 (1984).
29. R.F.W. Bader. *Atoms in molecules*. Clarendon Press, Oxford. 1990.
30. R.F.W. Bader. *Chem. Rev.* **91**, 893 (1991).
31. R.F.W. Bader. *J. Phys. Chem. A*, **102**, 7314 (1998).
32. R.G. Par and W. Yang. *J. Am. Chem. Soc.* **106**, 4049 (1984).
33. C.A. Coulson. *Research*, **10**, 149 (1957).
34. R. McWeeny. *Coulson's valence*. 3rd. ed. Oxford University Press, NY. 1990.
35. K. Morokuma. *J. Chem. Phys.* **55**, 1236 (1971).
36. K. Morokuma and H. Umeyama. *J. Am. Chem. Soc.* **99**, 1316 (1977).
37. K. Morokuma. *Acc. Chem. Res.* **10**, 294 (1977).
38. E.D. Glendening and A. Streitwieser. *J. Chem. Phys.* **100**, 2900 (1994).
39. M. Martinov and J. Cioslowski. *Mol. Phys.* **85**, 121 (1995).
40. K. Ruedenberg. *Rev. Mod. Phys.* **34**, 326 (1962).
41. Y. Li and J.N.S. Evans. *J. Am. Chem. Soc.* **117**, 7756 (1995).
42. X. Crispin, V. Geskin, R. Lazzaroni, C. Bureau, W. Salaneck, and J.L. Bredas. *J. Chem. Phys.* **111**, 3237 (1999).
43. X. Crispin, V. Geskin, R. Lazzaroni, C. Bureau, and J.L. Bredas. *Eur. J. Inorg. Chem.* **349** (1999).
44. A.D. Becke. *Phys. Rev. Sect. A*, **38**, 3098 (1988).
45. S.H. Vosko, L. Wilk, and M. Nusair. *Can. J. Phys.* **58**, 1200 (1980).
46. N. Godbout, D.R. Salahub, J. Andzelm, and E. Wimmer. *Can. J. Chem.* **70**, 560 (1992).
47. B. Delley. *J. Chem. Phys.* **92**, 508 (1990).
48. B. Delley. *New J. Chem.* **16**, 1103 (1992).
49. M.J. Frisch, G.W. Trucks, H.B. Schlegel, G.E. Scuseria, M.A. Robb, J.R. Cheeseman, V.G. Zakrzewski, J.A. Montgomery, Jr., R.E. Stratmann, J.C. Burant, S. Dapprich, J.M. Millam, A.D. Daniels, K.N. Kudin, M.C. Strain, O. Farkas, J. Tomasi, V. Barone, M. Cossi, R. Cammi, B. Mennucci, C. Pomelli, C. Adamo, S. Clifford, J. Ochterski, G.A. Petersson, P.Y. Ayala, Q. Cui, K. Morokuma, D.K. Malick, A.D. Rabuck, K. Raghavachari, J.B. Foresman, J. Cioslowski, J.V. Ortiz, A.G. Baboul, B.B. Stefanov, G. Liu, A. Liashenko, P. Piskorz, I. Komaromi, R. Gomperts, R.L. Martin, D.J. Fox, T. Keith, M.A. Al-Laham, C.Y. Peng, A. Nanayakkara, M. Challacombe, P.M.W. Gill, B. Johnson, W. Chen, M.W. Wong, J.L. Andres, C. Gonzalez, M. Head-Gordon, E.S. Replogle, and J.A. Pople. 1998. Gaussian 98. Revision A.9. Gaussian, Inc., Pittsburgh PA. NBO Version 3.1, E.D. Glendening, A.E. Reed, and F. Weinhold.
50. M. Muhlhauser, G.E. Froudakis, and S.D. Peyerimhoff. *Chem. Phys. Lett.* **336**, 171 (2001).
51. K. Ohshimo. *J. Phys. Chem. A*, **104**, 765 (2000).
52. K. Ohshimo. *Int. J. Mass. Spectrom.* **216**, 29 (2002).
53. F.W. Biegler-König, R.F.W. Bader, and T.H. Tang. *J. Comput. Chem.* **3**, 317 (1982).



54. G. Schaftenaar. 2000. Molden 3.7 [computer program]. CAOS/CAMM Center, Nijmegen, Netherlands.
55. R.T. Sanderson. *Science* (Washington, D.C.), **114**, 670 (1951).
56. R.T. Sanderson. *Chemical bonds and bond energy*. Academic Press, New York. 1976.
57. G. Margaritondo. *Rep. Prog. Phys.* **62**, 765 (1999).
58. M. Peressi, N. Binggeli, and A. Baldereschi. *J. Phys. D Appl. Phys.* **31**, 1273 (1998).
59. R. Hoffman. *Solid and surfaces: A chemist view of bonding in extended structures*. Wiley VCH, New York. 1988.
60. F. Jensen. *Introduction to computational chemistry*. John Wiley & Sons, Inc., New York. 352 (2001).
61. A.D. Becke. *J. Chem. Phys.* **117**, 6935 (2002).
62. J. Baker and W.J. Hehre. *J. Comput. Chem.* **12**, 606 (1991).
63. J. Baker. *J. Comput. Chem.* **14**, 1085 (1993).
64. T. Ziegler. *Chem. Rev.* **91**, 651 (1991).
65. X. Crispin, R. Lazzaroni, V. Geskin, N. Baute, P. Dubois, R. Jerome, and J.L. Bredas. *J. Am. Chem. Soc.* **121**, 176 (1999).
66. J. Clausen and T. Lund-Olesen. An investigation of self assembled monolayers formed by thiol-modified molecules on metal surfaces. Microelectronic Center, Danish Institute of Fundamental Meteorology, Copenhagen. PMP. 2002.
67. A. Johansson and S. Stafstrom. *Chem. Phys. Lett.* **322**, 301 (2002).
68. W. Andreoni, A. Curioni, and H. Gronbeck. *Int. J. Quantum Chem.* **80**, 598 (2000).
69. A.D. Miller, K.J. Gaffney, S.H. Liu, P. Szymanski, S. Garrett-Roe, C.M. Wong, and C.B. Harris. *J. Phys. Chem. A*, **106**, 7636 (2002).



# Photo aldol reactions with 5-methoxyoxazoles: Highly regio- and diastereoselective synthesis of $\alpha$ -amino $\beta$ -hydroxy carboxylic acid derivatives

Axel G. Griesbeck and Samir Bondock

**Abstract:** A versatile route to derivatives of  $\alpha$ -amino  $\beta$ -hydroxy carboxylic acids, either with tertiary (from a corresponding glycine equivalent) or a quaternary  $\alpha$ -carbon center is described. The key reaction is the cycloaddition of electronically excited carbonyl compounds (aromatic and aliphatic aldehydes, respectively) to oxazoles. To make the products hydrolytically more labile, a methoxy substituent at position C-5 was introduced leading to the formation of cycloadducts with an orthoester substructure. The photocycloaddition, either with triplet excited (aromatic) carbonyls or with singlet excited (aliphatic) carbonyls, led to the formation of mixtures of *endo*- and *exo*-diastereoisomers with moderate to very high *exo*-selectivities. The 4-unsubstituted 5-methoxyoxazole **1** (glycine equivalent) gave the [2 + 2]-adducts **3a–3f** with aldehydes **2a–2f** in high yields and excellent diastereoselectivities. Hydrolysis of these compounds resulted in the  $\alpha$ -amino  $\beta$ -hydroxy esters **4a–4f** with preferred *erythro* ( $S^*,S^*$ ) configuration. As an extension of this process, 4-alkylated 5-methoxyoxazoles **5a–5f** were applied as alkene components and the corresponding cycloadducts with benzaldehyde **6a–6f** were obtained. Again, the *exo*-diastereoisomers were formed as the major products in diastereoselectivities from 73:27 (*exo:endo*) up to >95:5. Hydrolysis of these adducts resulted in the formation of  $\alpha$ -amino  $\beta$ -hydroxy esters **7a–7f** with *like* ( $S^*,S^*$ ) configuration of the major diastereoisomers.

**Key words:** photo aldol reaction, oxazoles, oxetanes, photocycloaddition, amino acids, hydroxy acids.

**Résumé :** On décrit une voie versatile pour obtenir des acides  $\alpha$ -amino- $\beta$ -hydroxycarboxyliques portant des centres  $\alpha$ -carbonés tertiaire (à partir de la glycine équivalente correspondante) ou quaternaire. La réaction clé est une cycloaddition de composés carbonylés électroniquement excités (aldéhydes aromatiques et aliphatiques respectivement) à des oxazoles. Afin de que les produits soient plus facilement hydrolysables, on a introduit un substituant méthoxyle en position C-5 afin d'obtenir des cycloadduits comportant une structure orthoester. La photocycloaddition, avec des carbonyles (aromatiques) excités à l'état triplet ou avec des carbonyles (aliphatiques) excités à l'état singulet, conduit à la formation de mélanges de diastéréomères *endo*- et *exo*- dans lesquels la sélectivité en faveur de l'*exo*- est de modérée à très élevée. La réaction du 5-méthoxyoxazole non substitué en position 4 (**1**) (équivalent de la glycine) avec les aldéhydes **2a–2f** donne les adduits [2 + 2] **3a–3f** avec des rendements élevés et d'excellentes diastéréosélectivités. L'hydrolyse de ces composés conduit aux  $\alpha$ -amino- $\beta$ -hydroxyesters **4a–4f** avec la configuration *érythro* ( $S^*,S^*$ ) préférée. Comme extension de ce procédé, on a utilisé les 5-méthoxyoxazoles alkylées en position 4 (**5a–5f**) comme composants alcéniques et, par réaction avec les benzaldéhyde, on a obtenu les cycloadduits correspondants **6a–6f**. Une fois de plus, les diastéréoisomères se forment comme produits majeurs, avec des diastéréosélectivités allant de 73:27 (*exo:endo*) jusqu'à >95:5. L'hydrolyse de ces produits conduit à la formation des  $\alpha$ -amino- $\beta$ -hydroxyesters **7a–7f** dans lesquels les diastéomères de configuration apparentée à ( $S^*,S^*$ ) sont prépondérants.

**Mots clés :** réaction photoaldolique, oxazoles, oxétanes, photocycloaddition, acides aminés, hydroxyacides.

[Traduit par la Rédaction]

## Introduction

The photochemical aldol addition route has been developed by Schreiber (1) as a powerful photochemical tool for the synthesis of  $\beta$ -hydroxy carbonyl compounds. This concept is surprising because electronic excitation leads, in most cases, to an *umpolung* effect, i.e., the regioselectivity of the

carbonyl addition to enolate analogues is expected to be reversed. This is in fact the case for monoalkenes such as 2,3-dihydrofuran (2). The Paternò-Büchi reaction of furan and furan derivatives, however, with electronically excited aliphatic as well as aromatic aldehydes proceeds highly regioselective to give the 2,7-dioxabicyclo[3.2.0]hept-3-enes with the substituent at C-6 preferentially in the *exo*-position.

Received 19 September 2002. Published on the NRC Research Press Web site at <http://canjchem.nrc.ca> on 22 May 2003.

Dedicated to Don Arnold on the occasion of his 65th birthday in recognition of his remarkable and influential contributions to organic photochemistry.

A.G. Griesbeck<sup>1</sup> and S. Bondock. University of Cologne, Institute of Organic Chemistry, Greinstr. 4, D-50939 Köln, Germany.

<sup>1</sup>Corresponding author (e-mail: [griesbeck@uni-koeln.de](mailto:griesbeck@uni-koeln.de)).



In these cases, the heteroaromatic dienes operate as vinylogue enolate equivalents. The *exo-endo* selectivity is unusually high (e.g., 212:1 for the benzaldehyde–furan case) for a *two-step triplet* photocycloaddition (2). Aliphatic aldehydes react with slightly lower *exo*-selectivity and a weak spin-selectivity effect (3) was determined; singlets favor the formation of the *exo*-diastereoisomer less pronounced than the corresponding triplets (4).<sup>2</sup> These photocycloadditions have been extensively used for synthetic applications especially because of the extraordinarily high degree of diastereocontrol (5–12). Several other five-membered aromatic heterocycles were used as alkene components in the Paternò–Büchi photocycloaddition (13–19) and recently the oxazole-based route to  $\alpha$ -amino  $\beta$ -hydroxy ketones was added by us (20). As substrate, the commercially available 2,4,5-trimethyloxazole was used and excellent (*exo*-)diastereoselectivities were observed for the photocycloaddition with aldehydes. An attractive family of target compounds, which might be available by this route, consists of derivatives of  $\alpha$ -amino  $\beta$ -hydroxy carboxylic acids (21–26), either with tertiary (from a corresponding glycine equivalent) or quaternary  $\alpha$ -carbon centers (Fig. 1).

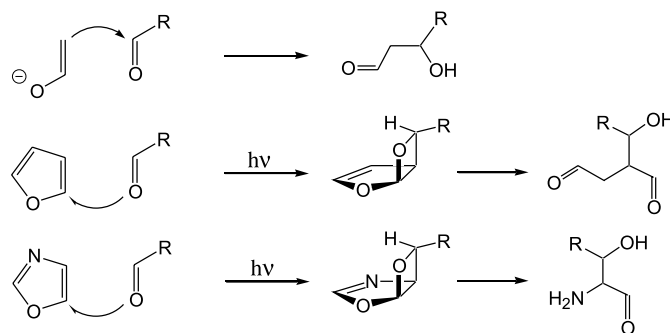
## Results and discussion

To investigate this concept, we first applied the 4-unsubstituted 5-methyloxazole **1** (27) as a diene and as the glycine equivalent in the photocycloaddition with aldehydes **2a–2f**. In all cases only one regioisomeric bicyclic oxetane (**3a–3f**) was detected in the crude photolysis mixture and, in most cases, only one diastereoisomer (Scheme 1). From the comparison with the results from the trimethyloxazole experiment (20) and NMR comparison with the hydrolysis products, the *exo*-configuration of the cycloadducts could be determined. Especially, the strong ring-current-induced upfield shift for the phenylated product **3a** is indicative of the *exo*-configuration of the aryl substituent; for **3a**: <sup>1</sup>H NMR (H-1)  $\delta$ : 4.58 ppm; for **3d**: <sup>1</sup>H NMR (H-1)  $\delta$ : 5.04 ppm. The ring-current effects detected for the phenylated compound **3a** were analogous in size to effects detected in  $\beta$ -lactams which resulted from the Yang cyclization of amino-acid-derived chiral butyrophenone derivatives (28). The primary photoproducts (**3a–3f**) were hydrolytically unstable and underwent twofold ring opening to give the  $\beta$ -hydroxy amino acid esters **4a–4f** (Table 1). In most cases, the diastereoisomeric ratio (d.r.) of the ring-opened products matched the d.r. of the oxetane precursors.

The relative configuration of the methyl esters of phenylserine (**4a**) (29) and  $\beta$ -hydroxyleucine (**4e**) (30) were already elucidated in the literature and by comparison with our data, the *erythro* (*S\*,S\**) configuration for the major diastereoisomers of **4a–4f** was established, e.g., for the  $\beta$ -hydroxyleucine derivative **4e**: <sup>13</sup>C NMR for the  $\beta$ -carbon  $\delta$ : 77.2 ppm for *R\*,S\** (29); 69.8 ppm for the major diastereoisomer (*S\*,S\**) obtained via the photo aldol route.

Subsequently, we investigated a series of 5-methoxy oxazoles (**5a–5f**) as substrates with an additional substituent at C-4. These substrates were easily available from the amino acids alanine,  $\alpha$ -amino butyric acid, valine, norvaline,

**Fig. 1.** The aldol and photo aldol route to  $\beta$ -hydroxy carbonyl compounds.



leucine, and isoleucine (31–33). The photocycloadditions of **5a–5f** with benzaldehyde were performed using equimolar amounts of the substrates in benzene. The primary photo-adducts (**6a–6f**) were formed with excellent diastereoselectivities except for additions to oxazole substrates with bulky substituents  $R^2$ . Again, the strong ring-current-induced upfield shifts for the phenylated products were indicative of the *exo*-configuration of the aryl substituent. Because of the less-pronounced diastereoselectivities of the benzaldehyde additions in these cases, both *endo*- and *exo*-isomers could be compared. The isopropyl-substituted oxazole **5d** gave in 80% yield a mixture of diastereoisomers (regioisomeric purity >98% in all cases) (**6d**). The <sup>1</sup>H NMR chemical shifts of the methyl groups for *i*-Pr in *exo*-**6d** were 0.52 and 0.73 ppm, and in *endo*-**6d** were 0.93 and 0.98 ppm, again analogous to effects detected for photochemically synthesized  $\beta$ -lactams (28).

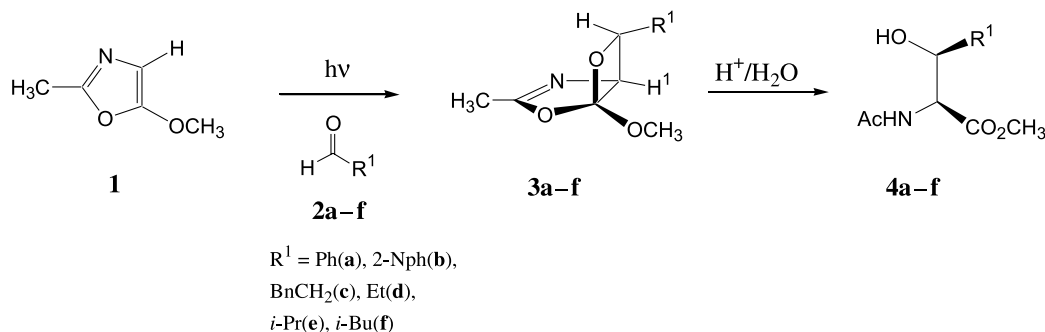
Upon chromatography, most of the products were hydrolyzed to give the (*S\*,S\**)  $\alpha$ -acylamino  $\beta$ -hydroxy carboxylic acid esters **7a–7f** (Scheme 2, Table 2). The relative configuration of the oxetanes (**6**) was confirmed by NMR spectroscopy and spectral comparison with representative literature-known products (*anti*-**7**) (34–37).

Whereas the high *exo*-selectivity of the photocycloaddition of electronically excited aldehydes to the C4-unsubstituted oxazole **1** is analogous to the furan case, the high diastereoselectivity for the trisubstituted oxazoles **5a–5f** deserves a comment. In the triplet photocycloaddition to cycloalkenes (38), ring alkylation leads to a *decrease* in selectivity and, in some cases, to selectivity inversion because of interference with the spin-orbit-coupling geometries (39). This is obviously not the case for the oxazoles **5a–5f** which indicates that the secondary orbital interaction model originally applied for the benzaldehyde–furan reaction is operating (2). Figure 2 shows the triplet 1,4-biradical conformers **A–C** with reactive spin-orbit-coupling geometries (40). If most of the spin inversion process is directed through the channel **C**, high *exo*-selectivity is expected. The *endo*-contribution from **A** becomes only relevant for bulky groups  $R^2$  (as for **5d–5f**).

An alternative interpretation, proposed by Abe, for the high *exo*-selectivities observed in triplet photocycloadditions

<sup>2</sup>A.G. Griesbeck, M. Fiege, and S. Bondock. Unpublished results.



**Scheme 1.** Photo aldol reaction with oxazole **1**.**Table 1.** Photocycloaddition of aldehydes (**2**) with 5-methoxy-oxazole (**1**) and subsequent ring opening.

No.	R <sup>1</sup> =	d.r. ( <b>3</b> ) <sup>a</sup>	Yield ( <b>3</b> ) <sup>b</sup>	d.r. ( <b>4</b> ) <sup>a</sup>	Yield ( <b>4</b> ) <sup>c</sup>
<b>a</b>	Ph	>98:2	87	>98:2	70
<b>b</b>	β-Naph	>98:2	85	>98:2	75
<b>c</b>	BnCH <sub>2</sub>	>98:2	87	>98:2	65
<b>d</b>	Et	>98:2	90	95:5	72
<b>e</b>	<i>i</i> -Pr	>98:2	86	>98:2	78
<b>f</b>	<i>i</i> -Bu	>98:2	88	>98:2	74

<sup>a</sup>Based on the integration of characteristic signals in the <sup>1</sup>H NMR spectrum of the crude product mixture (±2%).

<sup>b</sup>Yield (%) based on converted oxazole of the isolated mixture of diastereoisomers **3**.

<sup>c</sup>Yield (%) of the isolated mixture of diastereoisomers.

of aldehydes to heterocyclic dienes was recently proposed by Abe.<sup>3</sup> It is also based on the comparison of the intermediate 1,4-triplet biradical conformers as depicted in Fig. 2, however, with emphasis on the additional anomeric stabilization in structure **C** and **B** that is not present in **A** (no lone pair at oxygen antiperiplanar to the ring oxygen). This small difference in energy is sufficient to explain the high *exo*-selectivities and the cleavage competition as expressed in the quantum yields (**3**).

## Conclusions

In summary, an efficient stereoselective photochemical protocol for the synthesis of α-amino β-hydroxy carboxylic acid derivatives was developed. The major advantage of these light-induced reactions in comparison with classical thermal aldol processes is the high diastereocontrol in the (triplet as well as singlet) photocycloaddition. As a plausible explanation for the high *exo*-selectivity, secondary orbital effects are postulated at the stage of the ISC (intersystem crossing)-active triplet-1,4-biradical conformers. The adducts of the Paternò-Büchi reactions were hydrolytically unstable and ring-opened to give α-*N*-acylamino β-hydroxy carboxylic acid methyl esters. As major diastereoisomers, the *erythro*-products with tertiary α-carbon centers and the *like* (*S*\*,*S*\*) products with quaternary α-carbon centers were formed.

## Experimental

### General remarks

All reactions were carried out in oven-dried glassware (100°C). All solvents were dried before use. Ether was distilled from sodium-benzophenone, chloroform, and dichloromethane from calcium hydride. Aldehydes were purchased from Aldrich and were distilled before use. Mixtures of ethyl acetate and *n*-hexane were used as eluents. TLC: commercially precoated polygram<sup>®</sup> SIL-G/UV 254 plates (Macherey-Nagel). Spots were detected with UV light in an iodine chamber. <sup>1</sup>H NMR: Bruker AC 300 (300 MHz). <sup>13</sup>C NMR: Bruker AC 300 (75.5 MHz), carbon multiplicities were determined by DEPT. UV-vis: Hitachi U-3200. Mass spectroscopy (EI or CI): Finnigan Incos 500; *m/z* (rel. %). HR-MS (FAB): Finnigan MAT H-SQ 30. Preparative TLC: silica gel (2–25 μm) on TLC plates (Fluka) (layer thickness 0.25 mm, medium pour diameter 60 Å, 20 × 20 on glass plates). All melting points were determined with a Büchi melting point apparatus (type Nr. 535) and are uncorrected. Combustion analyses: Elementar Vario EL. Rayonet<sup>®</sup> chamber photoreactors RPR-208 (8 × 3000 Å lamps, ca. 800 W, λ = 300 ± 10 nm) were used for irradiation.

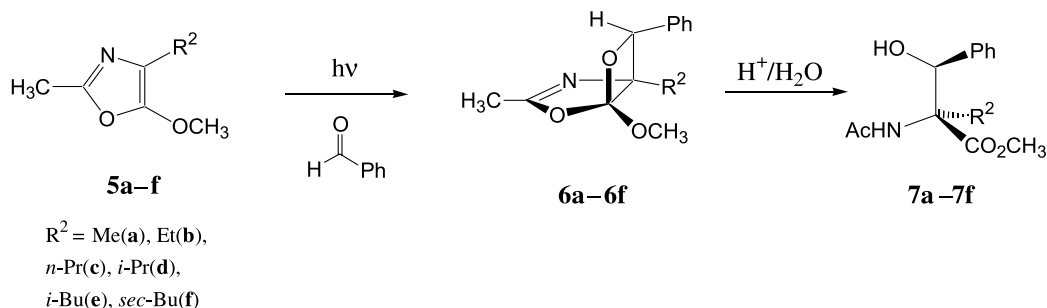
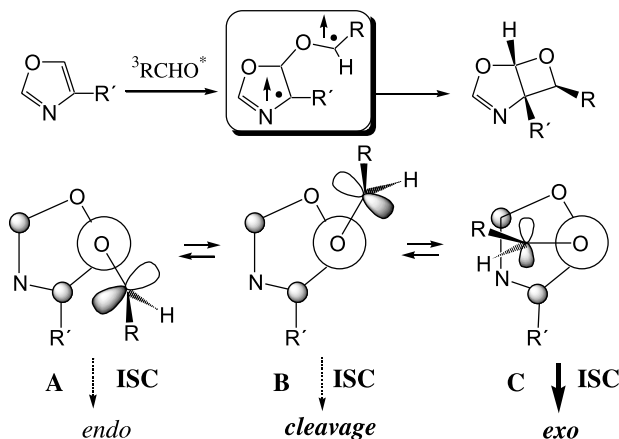
### Synthesis of 5-methoxyoxazoles

#### General procedure

*N*-Acetyl-L-amino acid methyl ester (0.1 mol) was dissolved in 20 mL of chloroform in a 250 mL flask; 20.8 g (0.1 mol) of phosphorous pentachloride were added and the flask was fitted with a calcium chloride tube. The solution was gently warmed by means of a water bath (ca. 60°C) with stirring until the HCl gas evolution ceased and the solution became an intense yellow. Then, the flask was cooled by an ice-salt bath and 50 mL of absolute ether were added. To the cooled mixture, 20% aq KOH was added dropwise with vigorous stirring until neutralization. The mixture was stirred at room temperature for 30 min. The organic layer was subsequently separated and the aqueous layer was extracted with 2 × 200 mL of ether. The combined organic extracts were washed with water and brine and dried over anhyd MgSO<sub>4</sub>. After removal of the solvents under vacuum, the remaining oil was distilled by a Büchi Kugelrohr apparatus to give the product.

<sup>3</sup>M. Abe. Personal communication and poster contribution at the XIXth IUPAC Symposium on Photochemistry, Budapest, 14–19 August 2002.



**Scheme 2.** Photo aldol reaction with 5-methoxyoxazoles **5a–5f**.**Fig. 2.** 1,4-Biradical geometries in oxazole – triplet carbonyl photocycloadditions.

### Photolyses of 5-methoxyoxazoles with aldehydes

#### General procedure

A mixture of the 5-methoxyoxazole (5 mmol) and the aldehyde (5 mmol) was dissolved in 50 mL benzene, the solution transferred to a vacuum jacket quartz tube, and degassed with a steady stream of  $\text{N}_2$  gas. The reaction mixture was irradiated at  $10^\circ\text{C}$  in a Rayonet photoreactor (RPR-208,  $\lambda = 300 \pm 10$  nm) for 24 h. The solvent was evaporated ( $40^\circ\text{C}$ , 20 torr (1 torr = 133.322 Pa)) and the residue was purified by preparative thick layer chromatography (EA = ethyl acetate, H = hexane).

#### exo-5-Methoxy-3-methyl-7-phenyl-4,6-dioxo-2-azabicyclo[3.2.0]heptene-2-ene (exo-3a)

A solution of benzaldehyde (0.53 g, 5 mmol) and 2-methyl-5-methoxyoxazole (0.57 g, 5 mmol) in 50 mL of benzene was irradiated for 24 h according to the general procedure. The crude product was purified by preparative thick layer chromatography (EA:H = 1:4) to give 0.55 g (65%) of the oxetane as a colorless oil.  $R_f = 0.43$  (EA:H = 1:4). IR (film) ( $\text{cm}^{-1}$ ): 2987 (C–H), 1635 (C=N), 1600 (Ph), 1440 (CH), 1012 (C–O).  $^1\text{H}$  NMR (300 MHz,  $\text{CDCl}_3$ )  $\delta$ : 2.11 (s, 3H,  $\text{CH}_3$ ), 3.79 (s, 3H,  $\text{OCH}_3$ ), 4.58 (d,  $J = 7.7$  Hz, 1H, 1-H), 5.68 (d,  $J = 7.7$  Hz, 1H, 7-H), 7.26–7.31 (m, 5H,  $\text{H}_{\text{arom}}$ ).  $^{13}\text{C}$  NMR (75.5 MHz,  $\text{CDCl}_3$ )  $\delta$ : 15.9 (q), 52.8 (q), 76.2 (d, C-1), 83.0 (d, C-7), 122.9 (s, C-5), 125.4 (d), 126.2 (d), 128.1 (d), 134.3 (s), 167.7 (s, C-3). HR-MS calcd. ( $\text{C}_{12}\text{H}_{13}\text{NO}_3$ ): 219.0892; found: 219.0886.

**Table 2.** Diastereoselective photocycloaddition of benzaldehyde with 5-methoxyoxazoles **5a–5f** and subsequent ring opening.

No.	$\text{R}^2 =$	d.r. (6) <sup>a</sup>	Yield (6) <sup>b</sup>	d.r. (7) <sup>a</sup>	Yield (7) <sup>c</sup>
a	Me	>98:2	85	>98:2	65
b	Et	>98:2	84	93:7	73
c	<i>n</i> -Pr	>98:2	86	90:10	58
d	<i>i</i> -Pr	73:27	80	90:10	48
e	<i>i</i> -Bu	87:13	78	90:10	57
f	<i>sec</i> -Bu	85:15	81	92:8	58

<sup>a</sup>Based on the integration of characteristic signals in the  $^1\text{H}$  NMR spectrum of the crude product mixture ( $\pm 2\%$ ).

<sup>b</sup>Yield (%) based on converted oxazole of the isolated mixture of diastereoisomers **6**.

<sup>c</sup>Yield (%) of the isolated mixture of diastereoisomers **7**.

#### exo-5-Methoxy-1,3-dimethyl-7-phenyl-4,6-dioxo-2-azabicyclo[3.2.0]heptene-2-ene (exo-6a)

A solution of benzaldehyde (0.53 g, 5 mmol) and 2,4-dimethyl-5-methoxyoxazole (0.64 g, 5 mmol) in 50 mL benzene was irradiated for 24 h according to the above general procedure. The crude product was purified by preparative thick layer chromatography (EA:H = 1:4) to give 0.59 g (72%) of the oxetane as a colorless oil.  $R_f = 0.51$  (EA:H = 1:4). IR (film) ( $\text{cm}^{-1}$ ): 2987, 2894 (C–H), 1615 (C=N), 1605 (Ph), 1445 (CH), 1008 (C–O).  $^1\text{H}$  NMR (300 MHz,  $\text{CDCl}_3$ )  $\delta$ : 0.79 (s, 3H,  $\text{CH}_3$ ), 1.99 (s, 3H,  $\text{CH}_3$ ), 3.52 (s, 3H,  $\text{OCH}_3$ ), 5.19 (s, 1H, 7-H), 7.21–7.25 (m, 5H,  $\text{H}_{\text{arom}}$ ).  $^{13}\text{C}$  NMR (75.5 MHz,  $\text{CDCl}_3$ )  $\delta$ : 13.4 (q), 14.8 (q), 51.2 (q), 75.8 (s, C-1), 89.3 (d, C-7), 124.9 (s, C-5), 125.7 (d), 128.2 (d), 129.1 (d), 136.3 (s), 164.9 (s, C-3). HR-MS calcd. ( $\text{C}_{13}\text{H}_{15}\text{NO}_3$ ): 233.0762; found: 233.0758.

#### Synthesis of erythro (2S\*,3S\*)-α-acetamido-β-hydroxy esters

##### General procedure

To a solution of bicyclic oxetanes (2 mmol) in 20 mL methylene chloride, 0.5 mL of concd HCl was added. The mixture was stirred in an open flask at room temperature for 2 h and the reaction was controlled by TLC. The reaction mixture was quenched by being poured into water and extracted with methylene chloride (3 × 20 mL). The organic layer was washed with 5%  $\text{NaHCO}_3$  and brine and dried over anhyd  $\text{MgSO}_4$ . The solvent was removed in vacuo and the residual oil was purified by preparative thick layer chromatography.



**Methyl (2S\*,3S\*) 2-(N-acetylamino)-3-hydroxy-3-phenylpropionate (erythro-4a)**

According to the above general procedure, bicyclic oxetane **3a** (0.44 g, 2 mmol) was cleaved hydrolytically in 3 h. Preparative chromatography yielded 0.33 g (70%) of the product as a colorless oil.  $R_f = 0.34$  (EA:H = 1:4). IR (film) ( $\text{cm}^{-1}$ ): 3500 (OH), 3370 (NH), 2983, 2894 (C-H), 1725 (COO), 1675 (CON), 1605 (Ph), 1445 (CH), 1018 (C-O).  $^1\text{H}$  NMR (300 MHz,  $\text{CDCl}_3$ )  $\delta$ : 2.07 (s, 3H,  $\text{CH}_3\text{CO}$ ), 3.97 (s, 3H,  $\text{OCH}_3$ ), 4.45 (d,  $J = 9.7$  Hz, 1H, CHN), 5.85 (d,  $J = 9.7$  Hz, 1H, CHOH), 6.37 (bs, 1H, NH), 7.28–7.35 (m, 5H,  $\text{H}_{\text{arom}}$ ).  $^{13}\text{C}$  NMR (75.5 MHz,  $\text{CDCl}_3$ )  $\delta$ : 23.7 (q), 52.4 (q), 75.4 (d, C-2), 81.6 (d, C-3), 126.2 (s, C-5), 128.9 (d), 129.6 (d), 134.3 (s), 169.3 (s, CON), 170.3 (s, COO). Anal. calcd. ( $\text{C}_{12}\text{H}_{15}\text{NO}_4$ ): C 60.75, H 6.37, N 5.90; found: C 60.65, H 6.42, N 5.85.

**Methyl (2S\*,3S\*) 2-(N-acetylamino)-3-hydroxy-3-phenylpropionate (erythro-7a)**

According to the above general procedure, bicyclic oxetane **6a** (0.47 g, 2 mmol) was cleaved hydrolytically in 4 h. Preparative chromatography yielded 0.32 g (65%) of the product as a colorless oil.  $R_f = 0.33$  (EA:H = 1:4). MS (EI, 70 eV)  $m/z$  (%): 249 ( $\text{M}^+ - \text{H}_2$ , 4), 236 ( $\text{M}^+ - \text{Me}$ , 8), 202 (8), 192 ( $\text{M}^+ - \text{CO}_2\text{Me}$ , 15), 191 (78), 160 (10), 131 (100), 105 (50), 91 (20), 77 (30), 51 (10). IR (film) ( $\text{cm}^{-1}$ ): 3500 (OH), 3320 (NH), 2988 (C-H), 1720 (COO), 1680 (CON), 1580 (Ph), 1440 (CH), 1025 (C-O).  $^1\text{H}$  NMR (300 MHz,  $\text{CDCl}_3$ )  $\delta$ : 1.23 (s, 3H,  $\text{CH}_3$ ), 2.12 (s, 3H,  $\text{CH}_3\text{CO}$ ), 3.79 (s, 3H,  $\text{OCH}_3$ ), 4.06 (s, 1H, CHOH), 7.28–7.35 (m, 5H,  $\text{H}_{\text{arom}}$ ).  $^{13}\text{C}$  NMR (75.5 MHz,  $\text{CDCl}_3$ )  $\delta$ : 13.5 (q), 21.4 (q), 21.4 (q), 23.4 (q), 47.7 (s, C-2), 49.1 (d, C-3), 52.9 (q), 127.6 (s, C-5), 128.4 (d), 129.6 (d), 133.5 (s), 169.9 (s, CON), 179.4 (s, COO). HR-MS calcd. ( $\text{C}_{13}\text{H}_{17}\text{NO}_4$ ): 251.1254; found: 251.1249.

**Acknowledgements**

This work has been financially supported by the Deutsche Forschungsgemeinschaft, the Fonds der Chemischen Industrie. Amino acids were obtained as gifts from Degussa AG. Samir Bondock expresses his thanks to the Egyptian government for a Ph.D. grant (1999–2003).

**References**

1. S.L. Schreiber. *Science* (Washington, D.C.), **111**, 5367 (1989).
2. A.G. Griesbeck, S. Buhr, M. Fiege, H. Schmickler, and J. Lex. *J. Org. Chem.* **63**, 3847 (1998).
3. A.G. Griesbeck, S. Bondock, and M.S. Gudipati. *Angew. Chem. Int. Ed.* **40**, 4684 (2001).
4. A.G. Griesbeck, M. Fiege, S. Bondock, and M.S. Gudipati. *Org. Lett.* **2**, 3623 (2000).
5. S.L. Schreiber and K. Satake. *J. Am. Chem. Soc.* **105**, 6723 (1983).
6. S.L. Schreiber and K. Satake. *J. Am. Chem. Soc.* **106**, 4186 (1984).
7. S.L. Schreiber, A.H. Hoveyda, and H.-J. Wu. *J. Am. Chem. Soc.* **105**, 660 (1983).
8. S.L. Schreiber and A.H. Hoveyda. *J. Am. Chem. Soc.* **106**, 7200 (1984).
9. H.A.J. Carless and A.F.E. Halfhide. *J. Chem. Soc., Perkin Trans. 1*, 1081 (1992).
10. S.L. Schreiber, D. Desmaele, and J.A. Porco, Jr. *Tetrahedron Lett.* **29**, 6689 (1988).
11. S.L. Schreiber and J.A. Porco, Jr. *J. Org. Chem.* **54**, 4721 (1989).
12. R. Hambalek and G. Just. *Tetrahedron Lett.* **31**, 4693 (1990).
13. C. Rivas and R.A. Bolivar. *J. Heterocycl. Chem.* **13**, 1037 (1976).
14. G. Jones, II, H.M. Gilow, and J. Low. *J. Org. Chem.* **44**, 2949 (1979).
15. T. Matsuura, A. Banba, and K. Ogura. *Tetrahedron*, **27**, 1211 (1971).
16. T. Nakano, C. Rivas, C. Perez, and J.M. Larrauri. *J. Heterocycl. Chem.* **13**, 173 (1976).
17. C. Rivas, D. Pacheco, F. Vargas, and J. Ascanio. *J. Heterocycl. Chem.* **18**, 1065 (1981).
18. T. Nakano, W. Rodriguez, S.Z. de Roche, J. Larrauri, C. Rivas, and P. Pérez. *J. Heterocycl. Chem.* **17**, 1777 (1980).
19. Y. Ito, M. Ji-Ben, S. Suzuki, Y. Kusunaga, T. Matsuura, and K. Fukuyama. *Tetrahedron Lett.* **26**, 93 (1985).
20. A.G. Griesbeck, M. Fiege, and J. Lex. *Chem. Commun.* 589 (2000).
21. As components in vancomycin and related cyclopeptides: A.V.R. Rao, M.K. Gurjar, K.L. Reddy, and A.S. Rao. *Chem. Rev.* **95**, 2135 (1995).
22. T. Kimura, V.P. Vassilev, G.-J. Shen, and C.-H. Wong. *J. Am. Chem. Soc.* **119**, 11 734 (1997).
23. M.A. Blaskovich, G. Evindar, N.G.W. Rose, S. Wilkinson, Y. Luo, and G.A. Lajoie. *J. Org. Chem.* **63**, 3631 (1988).
24. F.A. Davis, V. Srirajan, D.L. Fanelli, and P. Portonovo. *J. Org. Chem.* **65**, 7663 (2000).
25. J.S. Panek and C.E. Masse. *Angew. Chem. Int. Ed.* **38**, 1093 (1999).
26. D.A. Evans, J.M. Janey, N. Magomedov, and J.S. Tedrow. *Angew. Chem. Int. Ed.* **40**, 1884 (2001).
27. R.S. Singh and R.M. Singh. *Indian J. Chem. Sect. B: Org. Chem. Incl. Med. Chem.* **39**, 688 (2000).
28. A.G. Griesbeck and H. Heckroth. *Synlett*, 131 (2002).
29. J. Legters, L. Thijs, and B. Zwanenburg. *Recl. Trav. Chim. Pays-Bas*, **111**, 16 (1992).
30. G. Cardillo, L. Gentilucci, M. Gianotti, and A. Tolomelli. *Tetrahedron: Asymmetry*, **12**, 563 (2001).
31. P. Karrer and C. Gränacher. *Helv. Chim. Acta*, 763 (1924).
32. N.D. Doktorova, L.V. Ionova, M.Y.A. Karpeisky, N.S. Padyukova, K.F. Turchin, and V.L. Florentiev. *Tetrahedron*, **25**, 3527 (1969).
33. G.A. Tolstikov and E.E. Shul'ts. *J. Org. Chem. USSR* **20**, 2032 (1984).
34. R. Grandel, U. Kazmaier, and B. Nuber. *Liebigs Ann.* 1143 (1996).
35. R. Gandel and U. Kazmaier. *Eur. J. Org. Chem.* 409 (1998).
36. R.O. Duthaler. *Tetrahedron*, **50**, 1539 (1994).
37. D. Seebach, A.R. Sting and M. Hoffmann. *Angew. Chem. Int. Ed. Engl.* **35**, 2708 (1996).
38. A.G. Griesbeck and S. Stadtmüller. *J. Am. Chem. Soc.* **113**, 6923 (1991).
39. A.G. Griesbeck, H. Mauder, and S. Stadtmüller. *Acc. Chem. Res.* **27**, 70 (1994).
40. A.G. Kutateladze. *J. Am. Chem. Soc.* **123**, 9279 (2001).



# TiO<sub>2</sub>-photocatalyzed reactions of some benzylic donors

Laura Cermenati, Maurizio Fagnoni, and Angelo Albini

**Abstract:** TiO<sub>2</sub>-photocatalyzed oxidation of toluene (**1a**), benzyltrimethylsilane (**1b**), and 4-methoxybenzyltrimethylsilane (**1c**) has been carried out in acetonitrile under oxygen, under nitrogen, and in the presence of electrophilic alkenes under various conditions (using Ag<sub>2</sub>SO<sub>4</sub> as electron acceptor, adding 2.5% H<sub>2</sub>O, changing solvent to CH<sub>2</sub>Cl<sub>2</sub>). Benzyl radicals, formed via electron transfer and fragmentation, are trapped. A good material balance is often obtained. The overall efficiency of the process depends on the donor  $E_{ox}$ , on the rate of fragmentation of the radical cation, and on the acceptor present (Ag<sup>+</sup> is an efficient oxidant, an electrophilic alkene a poor one, O<sub>2</sub> is intermediate). With ring-unsubstituted benzyl derivatives **1a** and **1b**, oxidative fragmentation occurs mainly close to the catalyst surface. The benzyl radicals form at a high local concentration and give benzaldehyde under O<sub>2</sub>, bibenzyl under N<sub>2</sub> and dibenzylated derivatives by attack on the alkenes (acrylonitrile, fumaronitrile, maleic acid). In this case, using CH<sub>2</sub>Cl<sub>2</sub>-O<sub>2</sub> enhances the yield of benzaldehyde. With methoxylated **1c**, however, the radical cation migrates into the solution before fragmentation and, therefore, the free benzyl radical is formed. This radical in part is oxidized to the cation, giving a considerable amount of benzylacetamide (or of the alcohol with water), and in part is trapped by the alkenes. The last reaction is less efficient in this case and yields monobenzyl derivatives.

**Key words:** photocatalysis, oxidation, alkylation.

**Résumé :** On a effectué l'oxydation photocatalysée du toluène (**1a**), du benzyltriméthylsilane (**1b**) et du 4-méthoxybenzyltriméthylsilane (**1c**) par le TiO<sub>2</sub> dans l'acétonitrile, sous atmosphère d'azote ou d'oxygène, et en présence d'alcènes électrophiles et sous diverses conditions (faisant appel au Ag<sub>2</sub>SO<sub>4</sub> comme accepteur d'électron, avec addition de 2,5% d'eau et en changeant le solvant pour le CH<sub>2</sub>Cl<sub>2</sub>). On a piégé les radicaux benzyles qui se forment par transfert d'électron et fragmentation. On a souvent obtenu une bonne balance pour les produits ayant réagi. L'efficacité globale du processus dépend du  $E_{ox}$  du donneur, de la vitesse de fragmentation du cation radical et de la présence d'un accepteur (Ag<sup>+</sup> est un oxydant efficace, un alcène électrophile est mauvais alors que O<sub>2</sub> est intermédiaire). Avec les dérivés **1a** et **1b** comportant un noyau benzyle non substitué, la fragmentation oxydante se produit relativement près de la surface du catalyseur. Les radicaux benzyles se forment à une concentration locale élevée et conduisent à la formation de benzaldéhyde en présence de O<sub>2</sub>, en bibenzyle sous N<sub>2</sub> et en dérivés dibenzylés par attaque sur les alcènes (acrylonitrile, fumaronitrile, acide maléique). Dans ce cas, l'utilisation de CH<sub>2</sub>Cl<sub>2</sub>-O<sub>2</sub> conduit à une augmentation du rendement en benzaldéhyde. Toutefois, avec le dérivé méthoxy **1c**, le cation radical migre en solution avant la fragmentation et on observe la formation d'un radical libre. Ce radical est partiellement oxydé en cation conduisant à la formation de benzaldéhyde et à une quantité considérable de benzylacétamide (ou d'alcool avec l'eau); il est aussi piégé par les alcènes. La dernière réaction est moins efficace dans ce cas et elle conduit aux dérivés monobenzyliques.

**Mots clés :** photocatalyse, oxydation, alkylation.

[Traduit par la Rédaction]

## Introduction

Titanium dioxide is extensively used for the photoinduced mineralization of organic contaminants in polluted water (1). Under these conditions, photoinduced charge separation is followed by hole and electron transfer to water and oxygen, respectively, and the reaction of the organic molecule mainly involves hydrogen abstraction by the thus formed hydroxyl radicals; the organic radicals then react with oxygen or the

superoxide anion. The alternative possibility that the organic substrate is directly oxidized at the semiconductor surface is of interest in two respects. First, because it has been shown that, at least with reasonable donors, this mechanism participates in the TiO<sub>2</sub> photocatalytic oxidation in water (2) and second, because, particularly in nonaqueous solvents, such a path may lead to the controlled oxidation of the substrate, rather than to the complete oxidation to CO<sub>2</sub> that is the target when photocatalysis is used for the recovery of polluted

Received 7 January 2003. Published on the NRC Research Press Web site at <http://canjchem.nrc.ca> on 23 May 2003.

*Dedicated to Professor Don R. Arnold, the pioneer of electron transfer photochemistry.*

L. Cermenati, M. Fagnoni, and A. Albini.<sup>1</sup> Dep. Organic Chemistry, University of Pavia, v. Taramelli 10, 27100 Pavia, Italy.

<sup>1</sup>Corresponding author (e-mail: [albini@chifis.unipv.it](mailto:albini@chifis.unipv.it)).



water. With reference to the second aspect, a number of positive results have been obtained. As an example,  $\text{TiO}_2$ -photocatalyzed oxygenation of cyclohexane neat or mixed with organic solvents gives useful yields of products from the intermediate oxidation, e.g., of cyclohexanone (3, 4). Substituting a different electron acceptor for oxygen, e.g., the silver cation, adds flexibility (5). In this case different radical reactions, e.g., radical dimerization, occur in nitrogen-flushed solution while controlled oxygenation takes place in the presence of oxygen. Furthermore, the acceptor can be an organic molecule, e.g., an electrophilic alkene, which functions also as a radical trap and is alkylated (6). More generally, photocatalysis in organic solvents may have some synthetic interest (7), as opposed to the destructive mineralization occurring in water.

Both controlled oxygenation and alkylation reactions have been carried out successfully with benzylic derivatives. This is not surprising because the pioneering work by Arnold has shown that these compounds are both susceptible to photo-induced single electron oxidation and prone to fragmentation at the radical cation stage (8). In particular, benzylic oxygenation and benzylic coupling in acetonitrile and in aqueous media by  $\text{TiO}_2\text{-Ag}^+$  have been described by Baciocchi and Sebastiani and co-workers (5, 9) in several reports. We were curious to compare such a reaction with the  $\text{TiO}_2$ -photocatalyzed alkylation of alkenes (6, 10) through a systematic examination. We surmised that this comparison may give information about the mode of reaction, in particular with regard to the formation of the radicals either as solvated species or close to the semiconductor surface, a difference that is important for synthetic applications.

Therefore, we chose a small group of benzyl derivatives and compared the effect of some key experimental parameters as well as the effect of trapping by electrophilic alkenes. As described in the following, this examination indeed revealed new facets and demonstrated the versatility of the system.

## Results and discussion

### Photocatalysis of benzylic derivatives

Three benzylic derivatives were examined under standard conditions (0.02 M solutions in, 3.5 mg  $\text{mL}^{-1}$  Degussa  $\text{TiO}_2$ , 3 h irradiation) in tightly stoppered vessels, after flushing either with oxygen or with nitrogen. Scheme 1 shows the products formed and Table 1 reports the % conversion of starting material and the % yield (calculated on the converted substrate) of products formed.

The effects of adding silver sulfate and of a small percentage of water on the reaction in acetonitrile as well as of changing the solvent to dichloromethane are compared. For each condition, the results with the three substrates are listed in sequence. No significant reaction took place over this time when  $\text{TiO}_2$  was omitted.

Toluene (**1a**) reacted sluggishly in oxygen-flushed acetonitrile and gave only traces of benzaldehyde **2a**. Both conversion and yield of the aldehyde increased in the presence of 2.5% water, and further some benzyl alcohol (**3a**) and phenylpropionitrile (**6a**) were formed. Adding 0.01 M  $\text{Ag}_2\text{SO}_4$  or having both this salt and water present at the

same time did not increase the rate of conversion, but enhanced the yield of the aldehyde (35–45%), accompanied, in the latter case, by some benzyl alcohol. Carrying out the photoreaction in oxygen-flushed dichloromethane rather than in MeCN caused more extensive oxidation leading to the aldehyde (59% at a 42% conversion of **1a**), but also to a large amount of benzoic acid (**4a**, 29%).

No appreciable reaction took place in nitrogen-flushed acetonitrile (not reported), but it did in the presence of silver sulfate, where the main product was bibenzyl (**5a**, 65% for a 16% conversion) accompanied by minor amounts of aldehyde **2a** and nitrile **6a**, as well as traces of **3a** and of benzylacetamide (**7a**). No significant reaction occurred in the presence of 2.5% water in MeCN nor upon irradiation in nitrogen-flushed  $\text{CH}_2\text{Cl}_2$  (not reported; the other substrates examined likewise did not react under these conditions).

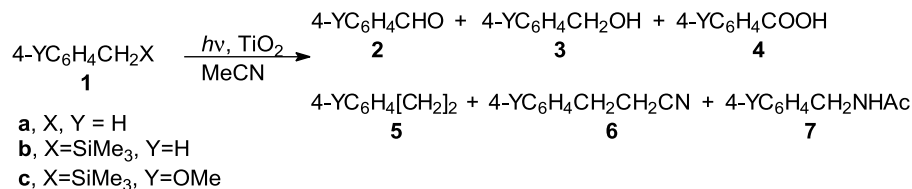
Compared with **1a**, benzyltrimethylsilane (**1b**) was more easily photooxidized in  $\text{MeCN-O}_2$  (25% conversion, 66% aldehyde, compare entries 2 and 1). Adding water had little effect (except for the formation of a small amount of propionitrile), while adding  $\text{Ag}_2\text{SO}_4$  did not increase the rate of oxidation but improved selectivity for the formation of benzaldehyde (92%, entry 8). In dichloromethane the reaction was faster than in MeCN, with a similar product distribution.

Again, no reaction took place under nitrogen in MeCN,  $\text{MeCN} - 2.5\% \text{H}_2\text{O}$  or  $\text{CH}_2\text{Cl}_2$ . However, **1b** was quite reactive in deoxygenated MeCN in the presence of  $\text{Ag}^+$ . The conversion was larger than under oxygen (64 rather than 25%, entry 17) and bibenzyl was the main product (70%). Also formed were small amounts of alcohol, aldehyde, and propionitrile, as well as compounds resulting, as indicated by mass spectrometry, from the benzylation of bibenzyl and the starting benzylsilane. The experiment with both water and  $\text{Ag}^+$  gave somewhat less of bibenzyl and more of benzyl alcohol.

With 4-methoxybenzylsilane (**1c**) the rate of photooxidation in MeCN further increased (85% conversion) and the aldehyde (**2c**, 77%) was accompanied by a significant amount of the alcohol (**3c**, 6%), which increased in the presence of water (12%, entry 6). The presence of the silver salt made the reaction more selective for the aldehyde (83%, entry 9). This time, in dichloromethane the oxidation was slower than in MeCN (55% rather than 85%, entry 15) and led to both aldehyde and alcohol. Compound **1c** was reactive under nitrogen, though somewhat slower than under oxygen, provided, as with the previous donors, that  $\text{Ag}^+$  was present; the main product was the bibenzyl derivative (**5c**, 55%), but 4-methoxybenzylacetamide (**7c**, 25%) was also important (entry 18). In the presence of both water and  $\text{Ag}^+$ , 4-methoxybenzyl alcohol (**3c**) was the main product (36%, entry 21). The solution became acidic during the irradiation and was neutralized with triethylamine before work-up. If this precaution was omitted, further benzylation reactions via the benzylic cation formed from the alcohol led to the formation of small amount of diphenylmethanes, a fact that has been previously noted (9a), but is an artifact due to the acidity developed (compare to 11). Small amounts (0.5 to 1%) of 4-methoxytoluene were detected in all the photocatalytic experiments with **1c**. The photooxidation of **1c** was tested at a somewhat large scale (0.78 g) in an immersion well appara-



## Scheme 1.

Table 1. TiO<sub>2</sub> photocatalytic oxidation of benzylic donors.<sup>a</sup>

			Conversion (%)	Products (%) <sup>b</sup>					
	Donor	Conditions	1	2	3	4	5	6	7
1	1a	MeCN, O <sub>2</sub>	8	12					
2	1b		25	66	3	16			
3	1c <sup>c</sup>		85	77	6	3			
4	1a	O <sub>2</sub> , H <sub>2</sub> O <sup>d</sup>	20	35	5			4	
5	1b		31	66	9	11		1	
6	1c		76	72	12	4			
7	1a	O <sub>2</sub> , Ag <sup>+e</sup>	10	35					
8	1b		25	92	4	3			
9	1c		90	83	2	3			
10	1a	O <sub>2</sub> , H <sub>2</sub> O, Ag <sup>+</sup>	11	45	11				
11	1b		32	86	8	6			
12	1c		75	80	2	3			
13	1a	CH <sub>2</sub> Cl <sub>2</sub> , O <sub>2</sub>	42	59	2	36			
14	1b		57	63	5	1			
15	1c		55	55	29	1			
16	1a	MeCN, N <sub>2</sub> , Ag <sup>+</sup>	16	8	1		65	12	2
17	1b		64	6	1		70		
18	1c <sup>f</sup>		66		tr		53	tr	25
19	1a	N <sub>2</sub> , H <sub>2</sub> O, Ag <sup>+</sup>	—						
20	1b <sup>f</sup>		59	2	8		58	6	
21	1c		56	1	36	1	7		6

<sup>a</sup>Upon irradiation of 0.02 M suspensions of the benzylic derivatives **1** (140 mg TiO<sub>2</sub>, 40 mL acetonitrile) for 3 h.<sup>b</sup>% Yields on converted **1**.<sup>c</sup>Small amounts (0.5–1%) of 4-methoxytoluene formed in all experiments with **1c**.<sup>d</sup>H<sub>2</sub>O (2.5%).<sup>e</sup>Ag<sub>2</sub>SO<sub>4</sub> (0.01 M).<sup>f</sup>Small amounts (up to 3%) of (4-methoxybenzylbenzyl)trimethylsilane and 4-methoxybenzyltoluenes revealed by GC–MS.

tus and it gave 90% conversion (of which 91% was the aldehyde) after 8 h irradiation.

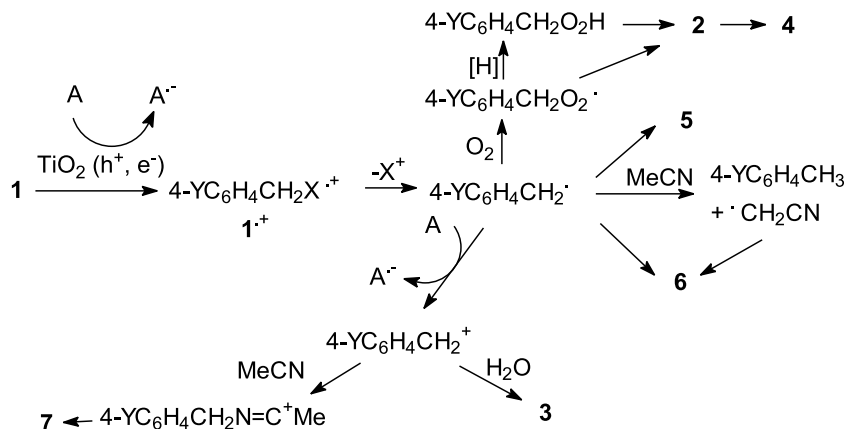
These results clearly support the role of radical cations formed by hole transfer at the surface of the semiconductor in the photooxidation of benzylic substrates (see Scheme 2), adding to previous evidence by Baciocchi and Sebastiani and co-workers (5, 9), showing that Ag<sup>+</sup> can be a substitute for oxygen in the role of electron acceptor. Favorable conditions for the process are that the reagent is reasonably easily oxidized and bears a good electrofugal group that makes fragmentation of the radical cation competitive with back electron transfer to the semiconductor. Thus, a moderate donor such as toluene (*E*<sub>ox</sub> 2.2 V vs. SCE) with a poor leaving group is slowly oxidized; in MeCN, cleavage of a proton from the toluene radical cation (**1a**<sup>+</sup>) is more than 100 times slower than cleavage of a trimethylsilyl cation from **1b**<sup>+</sup> (12). Introduction of a silyl group in α and of a methoxy group on the ring both make the reagents better donors such as **1b** (*E*<sub>ox</sub> 1.78 V) and **1c** (*E*<sub>ox</sub> 1.31 V) (13) and offer a good

electrofugal cation Me<sub>3</sub>Si<sup>+</sup> from the radical cation. These compounds react much faster than **1a** and give consistently a good material balance. Fragmentation is no longer the rate-limiting step. With these highly reactive radical cations, it can be appreciated that Ag<sup>+</sup> is a superior oxidant to O<sub>2</sub> (with **1b**, an increase in the rate of reaction by a factor of 2.5 in MeCN/Ag<sup>+</sup> in comparison with the experiments under oxygen).

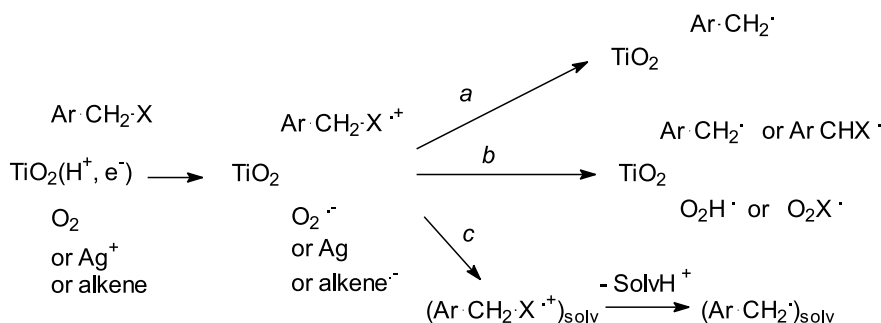
Fragmentation leads to benzyl radicals (Scheme 2). In nitrogen-flushed solution, these mainly dimerize to bibenzyls **5a**, **5c**. A minor process is hydrogen abstraction from the solvent, which generates ·CH<sub>2</sub>CN radicals revealed by the presence of arylpropionitriles **6a**, **6c** and is consistent with the formation of a small amount of methylanisole from **1c**. The ratio of nitrile (**6**) – bibenzyl (**5**) is larger with toluene (0.2) than with silane **1b** (<0.02 in neat MeCN, though it grows to 0.1 with 2.5% H<sub>2</sub>O), consistently with the fast desilylation and thus the higher local concentration of radicals in the latter case.



Scheme 2.



Scheme 3.



Also with **1c** only traces of nitrile are formed, but there another reaction competes. This is oxidation of the benzyl radical to the cation (Scheme 2). This process is revealed both by addition to acetonitrile, resulting after reaction with adventitious water, in the formation of amide **7c**, and, in the presence of 2.5% water, in the formation of alcohol **3c**. As previously proposed (9), the radical is oxidized by silver cations (0.4 V in MeCN) (14). Accordingly, from **1c** the yield of amide is 25%, and with the better nucleophile H<sub>2</sub>O the sum of the alcohol + amide is 42%, because oxidation of the 4-methoxybenzyl radical, with  $E_{ox}$  0.23 V (15), is fast. In contrast, no amide is formed from **1b** and only traces from **1a**, since oxidation of the unsubstituted benzyl radical ( $E_{ox}$  0.73 V) (15) is slow.

In the presence of oxygen, benzyl radicals are trapped by oxygen or the superoxide anion formed in the initial electron transfer (Scheme 2). Decomposition of the hydroperoxides or of the peroxy radicals leads to the aldehydes (Ag<sup>+</sup> when present makes the decomposition faster). In the case of **1c**, the presence of the hydroperoxide was revealed by an enhancement of the yield of alcohol **3c** (by a factor of 2) upon treatment of the irradiated solution by triphenylphosphine. When this process is efficient, secondary oxidation to benzoic acids is less important. Thus the aldehyde:acid ratio grows when the SET path is favored by the electron donating characteristics of the reagent (the ratio is 4 with **1b**, 25 with **1c**) or by the use of a better acceptor, such as Ag<sup>+</sup>, which allows better transient charge separation at the semiconductor surface (the ratio is ca. 30 for both **1b** and **1c**). Water is oxidized competitively with the aromatic substrate in the case of poorly reacting toluene and the increased yield

of aldehyde and the formation of some propionitrile (entry 4) are indicative of the participation of OH• radicals. However, competitive oxidation of water does not occur in the case of silanes **1b** and **1c**. With these compounds, the result is not affected by the presence of 2.5% water, except for the formation of more alcohol with the latter one, another indication of the increased role of the benzyl cation in this case.

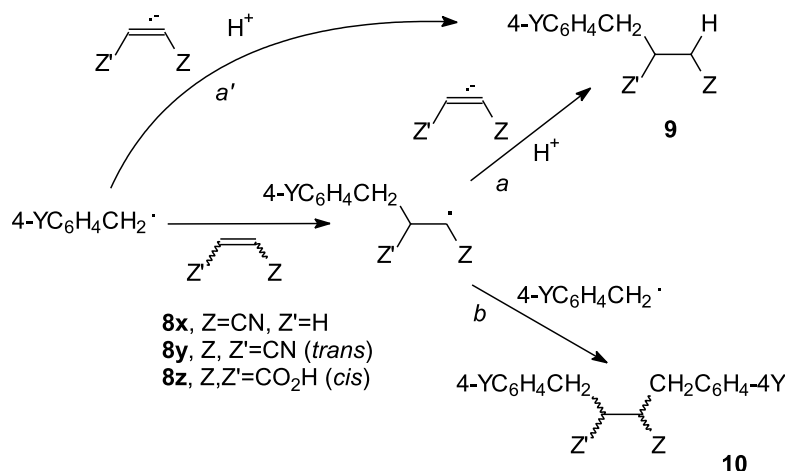
Using dichloromethane in the place of acetonitrile obliterates the difference in the rate of oxidation in the series **1a**–**1c**, enhancing the rate of the first two substrates and slightly lowering the rate for the last one. This remarkable effect can again be rationalized on the basis of the electron transfer mechanism for the fragmentation. A less polar solvent increases absorption of the substrate on the surface, thus facilitating oxidation. Furthermore, superoxide anion is expected to be a stronger base in less polar CH<sub>2</sub>Cl<sub>2</sub> than in MeCN (compare to 16), and assists deprotonation of the radical cation (and apparently also desilylation, since some alcohol is formed from the silanes), adding to the action of basic centres on TiO<sub>2</sub>. This offers an alternative mechanism of reaction (path *b* in Scheme 3) for substrates for which fragmentation of the *free* radical cation is unimportant (see below).

#### Photocatalysis of benzylic derivatives in the presence of electrophilic alkenes

Previous work had shown that TiO<sub>2</sub> photocatalysis in the presence of electrophilic alkenes leads to efficient alkylation (6, 10). In that case, the alkene functions both as electron ac-



Scheme 4.

**Table 2.** TiO<sub>2</sub> photocatalytic reactions of benzylic donors in the presence of alkenes **8** and 0.01 M silver sulfate.<sup>a</sup>

			Conversion (%)	Products (%) <sup>b</sup>				
	Donor	Alkene	<b>1</b>	<b>2</b>	<b>5</b>	<b>7</b>	<b>9</b>	<b>10</b>
1	<b>1b</b>	<b>8x</b> (0.02 M)	30	3	60			5
2	<b>1a</b>	<b>8x</b> (0.1 M)	9	7	33	2		5
3	<b>1b</b>		65	4	39			15
4	<b>1a</b>	<b>8y</b> (0.02 M)	20	4	30	3		28
5	<b>1b</b>		67	6	43			33
6	<b>1c</b>		66		13	32	8	3
7	<b>1b</b>	<b>8z</b> (0.02 M)	60	3	34		2	34
8	<b>1c</b>		60		10	33	8	

<sup>a</sup>Upon irradiation of 0.02 M suspensions of the benzylic derivatives **1** (140 mg TiO<sub>2</sub>, 40 mL acetonitrile) for 3 h.<sup>b</sup>% Yield on converted **1**.

ceptor and as radical trap, and we were curious to compare the present system with Ag<sup>+</sup> as the oxidant.

As shown in Table 2 and Scheme 4, with TiO<sub>2</sub>-Ag<sup>+</sup> the percentage conversion of donors **1a–1c** was similar to that observed in the absence of the alkene, but even a poor trap such as acrylonitrile (**8x**, 0.1 M) led to the formation of a certain amount of adduct. As an example, from **1b** 15% of the bibenzylated propionitrile **10ax** was formed at the expense of bibenzyl (dropping from 70% to 39%, entry 3). A lower amount of **10ax** (5%) was formed from **1b** with a lower trap concentration (0.02 M **8x**, entry 1) as well as from a poorer radical precursor such as toluene and 0.1 M **8x** (entry 2). However, a better trap such as fumaronitrile (**8y**) was effective at the 0.02 M concentration with both **1a** and **1b**, making the yield of bibenzylated **10ay** (28–33%, mixture of the two diastereoisomers) comparable to that of bibenzyl (30–43%, entries 4, 5). Bibenzylation was obtained in a similar yield (34%) also from **1b** and maleic acid (**8z**, entry 7).

The result was different with the methoxybenzylsilane **1c**. In this case, the yield of bibenzyl was much reduced when the alkenes **8** were present (while the yield of amide **7c**, if anything, slightly increased), but trapping by the alkene was inefficient, giving a small amount of the mono derivatives **9cy**, **9cz**, and with **8y** only traces of bisadduct **10cy** (entries 6, 8).

As compared with our previous data on the benzylation reaction in the absence of the silver salt (**6**), a large difference in rate and product distribution is now observed. In the absence of Ag<sup>+</sup>, the reaction of **1b** with e.g., **8z** required 20 h for a 15% conversion and gave 7% bibenzyl, 80% monoadduct, and 5% bisadduct, rather than 60% conversion in 3 h and 34, 2, and 34%, respectively, of the products in the present experiment. In the presence of the alkene alone, the conversion of **1b** reached 35% after 60 h and that of **1c** 100% after 30 h; it was 10–50 times slower than in the presence of Ag<sup>+</sup> and the monoadducts were by far the major products (50–80%). No useful result was obtained from **1a**.

The difference is due to the double role of 1,2-electron-withdrawing substituted alkenes such as **8y** and **8z**. These act both as electron acceptors (**8y**,  $E_{\text{red}} -1.63$  V vs. Ag/Ag<sup>+</sup>) (**17**) and as radical traps. In the absence of other acceptors, the alkene radical anions build up and either directly trap the radicals or reduce the radical adducts, thus leading to the monobenzylation of alkenes (path *a*, *a'*, Scheme 4).

With the silver cation the two functions are separated, the inorganic cation being the main oxidant and the alkene functioning as radical trap because Ag<sup>+</sup> is a better acceptor. Under these conditions photoinduced fragmentation of the donors is much faster with **1b** and **1c**, and even with **1a** some reaction occurs, while none was observed in the absence of Ag<sup>+</sup>. Furthermore, the radical anion **8<sup>-</sup>** does not



build up in this case, and the relatively stable ( $\alpha$ -cyano or carboxyl) adduct radicals have no easy path for reduction. Thus, these couple with a benzyl radical to give the bisadduct (path *b*, Scheme 4, see below). This path requires a high concentration of benzyl radicals, a situation that applies in the vicinity of the photocatalyst surface with donors **1a**, **1b**. The nonstabilized radical cations of these substrates do not migrate and fragment (with different efficiency) close to the surface (path *a* in Scheme 3), generating a high local concentration of the radicals.

On the contrary, migration of the longer lived stabilized radical cation from **1c** precedes fragmentation; thus, the free benzyl radical is formed from the solvated radical cation (path *c* in Scheme 3). The solvated radical is in part oxidized by  $\text{Ag}^+$  (soluble in MeCN), and thus, is not available for trapping. A part is trapped, as revealed by the strong decrease of bibenzyl in the presence of alkenes, but the radical adduct has little opportunity both for coupling with benzyl radicals (because of the low concentration in solution) and for reduction (since no reducing  $\mathbf{8}^-$  builds up). Presumably higher molecular weight products are formed and the yield of isolated products (monoadducts **9** and traces of bisadducts **10**) is far from balancing the amount of radicals trapped.

Thus, trapping by alkenes gives an indication about the mode of  $\alpha$ -cleavage, in solution or close to the surface. On the other hand, the photoinduced reaction becomes much faster with  $\text{Ag}^+$ , but the yield of the useful process, alkylation of the electron-withdrawing substituted alkene is decreased by the competing oxidation of the radical, and from the synthetic point of view the reaction in the absence of silver salts (6) is preferable.

## Conclusions

The  $\text{TiO}_2$  photocatalytic oxidation of benzylic donors gives products resulting from the trapping of benzyl radicals (benzaldehydes, bibenzyl or alkylated derivatives), sometimes with satisfactory material balance. The efficiency of the electron transfer oxidation of these substrates depends on the oxidation potential of the donor, on the presence of an electrofugal group in the  $\alpha$  position, and on the presence of a good electron acceptor that allows exploitation of the transient charge separation on the semiconductor surface. Among these,  $\text{Ag}^+$  is more efficient than  $\text{O}_2$ , and both of these are much better than an electrophilic alkene. On the other hand, the presence of a strong oxidant such as silver sulfate causes partial further oxidation of the radical to the cation and limits the benzylation of electrophilic alkenes since it hinders a required step, reduction of the adduct radical.

Comparing photocatalysis for the substrates **1a–1c** suggests that the reaction occurs via two main mechanisms. The stabilized radical cation  $\mathbf{1c}^+$  is solvated and fragments in solution (path *c*, Scheme 3). The free radical formed can be trapped. Further oxidation of the radical to the cation also has an important role. The shorter lived, less stable analogues  $\mathbf{1a}^+$ ,  $\mathbf{1b}^+$  do not migrate and mainly fragment close to the surface of the catalyst (path *a*), e.g., yielding bibenzyl or bibenylation of added electrophilic alkenes. Deprotonation of  $\mathbf{1a}^+$  is slow, so that with 2.5% water the

cosolvent is competitively oxidized. This process is faster in  $\text{CH}_2\text{Cl}_2$ , probably via a  $\text{O}_2^-$  assisted reaction (path *b*).

## Experimental

### Reagents

Degussa P25 titanium dioxide was dried in a oven at  $110^\circ\text{C}$  for 24 h and acetonitrile was distilled over calcium hydride and stored over molecular sieves. The chemicals were commercially available or prepared through conventional procedures for the case of **1c**.

### Irradiations

Irradiations were carried out on magnetically stirred solutions contained in 4.5 cm diameter serum-capped Pyrex cylindrical reactors. Suspensions (40 mL) containing the benzylic derivatives (0.02 M), the appropriate additives (see Tables 1 and 2) and 140 mg  $\text{TiO}_2$  were used. These were sonicated for 1 min and then stirred and flushed with either oxygen or purified nitrogen (through needles) in the dark for 20 min. The tubes were put in the centre of four 15 W phosphor-coated lamps (centre of emission, 360 nm) and irradiated for 3 h while maintaining slow gas flow and stirring. The suspension was then filtered over a  $0.2\ \mu\text{m}$  porosity filter under vacuum and either directly analyzed or rotary evaporated and taken up to a fixed volume.

The products were identified by comparison of their GC–MS spectra with authentic samples (compounds **9cy**, **9az**, **9cz** and diastereoisomeric **10ax**, **10ay**, **10cy**, **10az** were previously reported) (6) and quantified by GC on the basis of calibration curves using dodecane or cyclododecane as the internal standard. Gas chromatography analyses were carried out by using an HP 5890 apparatus with a  $0.3\ \text{mm} \times 30\ \text{m}$  capillary column with a flame ionization detector. Gas chromatography – mass spectrometry determination was performed using an HP 5970B instrument operating at a ionizing voltage of 70 eV, connected to an HP 5890 instrument equipped with the same column as above.

A larger scale irradiation was carried out with **1c** (0.78 g, 0.02 M) in a suspension of  $\text{TiO}_2$  (0.7 g) in MeCN (200 mL) in an immersion well apparatus fitted with a Pyrex-filtered, water-cooled medium pressure mercury arc (150 W). The suspension was magnetically stirred and flushed with argon during irradiation (8h).

## Acknowledgement

Partial support of this work by MIUR (Ministerio dell'Istruzione Universitaria e Ricerca), Rome, is gratefully acknowledged.

## References

- (a) A. Mills and S. Le Hunte. *J. Photochem. Photobiol.* **A**, **108**, 1 (1997); (b) P. Pichat. *In Handbook of heterogeneous catalysis. Edited by G. Ertl, H. Knoezinger, and J. Weitkamp.* Academic Press, New York. 1997. p. 2111; (c) D. Bahnemann, J. Cunningham, M.A. Fox, E. Pelizzetti, P. Pichat, and N. Serpone. *In Aquatic and surface photochemistry. Edited by G.R. Helz, R.G. Zepp, and D.G. Crosby.* Lewis Publ., Orlando. 1994. p. 261; (d) M.R. Hoffmann, S.T. Martin, W. Choi, and D.W. Bahnemann. *Chem. Rev.* **93**, 671 (1993); (e) O. Legrini,



- E. Oliveros, and A.M. Braun. *Chem. Rev.* **93**, 671 (1993); (f) P. Pichat. *Catal. Today*, **19**, 313 (1994); (g) N. Serpone. *In* Kirk-Othmer encyclopedia of chemical technology. Vol. 18. Wiley, New York. 1996. p. 820; (h) M. Sturini, F. Soana, and A. Albini. *Tetrahedron*, **58**, 2943 (2002).
2. (a) L. Cermenati, P. Pichat, C. Guillard, and A. Albini. *J. Phys. Chem.* **101**, 2650 (1998); (b) M. Ranchella, C. Rol, and G.V. Sebastiani. *J. Chem. Soc., Perkin Trans. 2*, 311 (2000); (c) F. Soana, M. Sturini, L. Cermenati, and A. Albini. *J. Chem. Soc., Perkin Trans. 2*, 699 (2000).
3. P. Boarini, V. Carassiti, A. Maldotti, and R. Amadelli. *Langmuir*, **14**, 2081 (1998).
4. C.B. Almquist and P. Biswas. *Appl. Catal. A*, **214**, 252 (2001).
5. E. Baciocchi, C. Rol, G.C. Rosato, and V. Sebastiani. *J. Chem. Soc., Chem. Commun.* 59 (1992).
6. L. Cermenati, M. Mella, and A. Albini. *Tetrahedron*, **54**, 2575 (1998).
7. (a) H. Kisch and M. Hopfner. *In* Electron transfer in chemistry. Vol. 4. Edited by V. Balzani, Wiley-VCH, Weinheim. 2001. p. 232; (b) H. Kisch. *Adv. Photochem.* **26**, 93 (2001); (c) M.A. Fox and M.T. Dulay. *Chem. Rev.* **93**, 341 (1993); (d) A. Maldotti, A. Molinari, and R. Amadelli. *Chem. Rev.* **102**, 3811 (2002).
8. (a) A.M.P. Nicholas and D.R. Arnold. *Can. J. Chem.* **60**, 2165 (1982); (b) X. Du, D.R. Arnold, R.J. Boyd, and Z. Shi. *Can. J. Chem.* **69**, 1365 (1991).
9. (a) E. Baciocchi, C. Rol, G.V. Sebastiani, and L. Taglieri. *J. Org. Chem.* **59**, 5272 (1994); (b) E. Baciocchi, M. Biotti, M.I. Ferrero, C. Rol, and G.V. Sebastiani. *Acta Chem. Scand.* **52**, 160 (1998); (c) E. Baciocchi, G.C. Rosato, C. Rol, and G.V. Sebastiani. *Tetrahedron Lett.* **33**, 5437 (1992); (d) L. Amori, T. Del Giacco, C. Rol, and G.V. Sebastastiani. *J. Chem. Res.* 644 (1998).
10. (a) L. Cermenati, C. Richter, and A. Albini. *Chem. Commun.* 85 (1998); (b) L. Cermenati and A. Albini. *J. Adv. Oxid. Technol.* **5**, 58 (2002).
11. (a) E.F. Pratt and H.J.E. Seagrave. *J. Am. Chem. Soc.* **81**, 5369 (1981); (b) K.A. Rutheford, O.A. Mamer, J.M. Prokipcak, and R.A. Jobin. *Can. J. Chem.* **44**, 2337 (1966).
12. (a) M. Freccero, A.C. Pratt, A. Albini, and C. Long. *J. Am. Chem. Soc.* **120**, 284 (1998); (b) N. d'Alessandro, A. Albini, and P. S. Mariano. *J. Org. Chem.* **58**, 937 (1993).
13. J.P. Dinnocenzo, S. Farid, J.L. Goodman, I.R. Gould, W.P. Todd, and S.L. Mattes. *J. Am. Chem. Soc.* **111**, 8973 (1989).
14. C.K. Mann and K.K. Barnes. *Electrochemical reactions in nonaqueous systems*. M. Dekker, New York. 1970. p. 479.
15. D.D.M. Wayner, B.A. Sim, and J.J. Dannenberg. *J. Org. Chem.* **56**, 4853 (1991).
16. (a) C.P. Andrieux, P. Hapiot, and J.M. Savéant. *J. Am. Chem. Soc.* **109**, 3768 (1987); (b) D.T. Sawyer and M.J. Gibian. *Tetrahedron*, **35**, 1471 (1979).
17. D.R. Arnold and P.C. Wong. *Can. J. Chem.* **57**, 1037 (1979).



# Application of time-resolved linear dichroism spectroscopy: Intensity borrowing in charge transfer complex absorption spectra

Dustin Levy and Bradley R. Arnold

**Abstract:** Time-resolved linear dichroism spectroscopy has been used to study the influence of solvent on the charge transfer complex formed between hexamethylbenzene and 1,2,4,5-tetracyanobenzene. It was shown that cyano-substituted solvents induce a  $1500\text{ cm}^{-1}$  increase in the charge transfer transition energies relative to those observed in chlorinated solvents. Furthermore, the angle between the charge transfer absorption transition moments and the photochemically produced radical anion absorption transition moment, after relaxation, has been measured for this complex in several solvents. A simple model was used to correlate the angles measured using time-resolved linear dichroism spectroscopy with the extent of localized excitation mixed into the charge transfer transitions. These measurements reveal that different charge transfer transitions borrow intensity from the localized excitation to different extents. By using different excitation wavelengths, the partitioning of the borrowed intensity among the charge transfer transitions of this complex could be evaluated for the first time.

**Key words:** 1,2,4,5-tetracyanobenzene, hexamethylbenzene, donor–acceptor complex, photoinduced electron transfer, photoselection.

**Résumé :** On a fait appel à la spectroscopie de dichroïsme linéaire résolu en fonction du temps pour étudier l'influence du solvant sur le complexe de transfert de charge qui se forme entre l'hexaméthylbenzène et le 1,2,4,5-tétracyanobenzène. On a trouvé que, les solvants portant des groupes cyano induisent une augmentation de  $1500\text{ cm}^{-1}$  dans les énergies de transition du transfert de charge par comparaison avec celles observées par les solvants chlorés. De plus, on a mesuré dans plusieurs solvants l'angle entre les moments de la transition d'absorption de transfert de charge et le moment de transition d'absorption de l'anion radical produit photochimiquement, après relaxation. On a utilisé un modèle simple pour établir une corrélation entre les angles mesurés en faisant appel à la spectroscopie de dichroïsme linéaire résolu en fonction du temps et le degré d'excitation localisée qui se mêle aux transitions de transfert de charge. Ces mesures révèlent que les diverses transitions de transfert de charge emprunte à des degrés différents de l'intensité de l'excitation localisée. En utilisant des longueurs d'onde d'excitation différentes, on a pu évaluer pour la première fois le niveau d'intensité emprunté par les diverses transitions de transfert de charge de ce complexe.

**Mots clés :** 1,2,4,5-tétracyanobenzène, hexaméthylbenzène, complexe donneur–accepteur, transfert d'électron photoinduit, photosélection.

[Traduit par la Rédaction]

## Introduction

An important class of intermolecular interactions leads to the formation of charge transfer (CT) complexes. These complexes are characterized by the appearance of a weak electronic absorption that is not present in the spectrum of the isolated reaction partners. The CT complex ground state wave function is usually depicted as a mixture of the wave functions for nonbonded interactions and of the ion-pair state (1–5). Several recent spectroscopic studies have sug-

gested that this two-state model is severely oversimplified and that the contribution of localized excited states must also be considered (6–13). Our studies of the CT complexes formed between 1,2,4,5-tetracyanobenzene (TCNB) as acceptor and methylated benzene donors have shown conclusively that the two-state model is not uniformly applicable to all CT complexes (6, 7, 14). Significant intensity borrowing from the localized excitation band (LE) of the acceptor was proven in the case of several TCNB complexes (14) and has been proposed for many other types of CT complexes (15, 16).

A clarification is required on this point. It has been customary to call the transition that appears when an acceptor and donor are combined a CT transition. For many CT complexes the transition of interest will not be purely CT in nature and in some cases may not even be dominated by a CT contribution. For the sake of simplicity and continuity with the established literature it should be understood that the term CT transition, as used herein, simply identifies the new transition and is not making a statement about its character.

Received 7 January 2003. Published on the NRC Research Press Web site at <http://canjchem.nrc.ca> on 23 May 2003.

*Dedicated to Professor Don Arnold for his contributions to chemistry.*

**D. Levy and B.R. Arnold.**<sup>1</sup> Department of Chemistry and Biochemistry, University of Maryland Baltimore County, 1000 Hilltop Circle, Baltimore, MD, U.S.A.

<sup>1</sup>Corresponding (e-mail: [barnold@umbc.edu](mailto:barnold@umbc.edu)).



Presently, a distinction between the pure CT transition moment and the observed CT transition moment, which may include a contribution from LE states, will be made clear.

Little is known about the nature of the CT excited states or how the LE contribution influences the processes that lead to photoinduced charge separation and the formation of contact radical ion-pairs (CRIP). The effects of mixing LE and CT states on the CT emission spectrum and rate constants for return electron transfer have been studied (17). It was shown that a small contribution from the LE dominates the photophysical behavior of the resultant CRIP–exciplex. We believe that the rapid relaxation observed for several CT complexes (6–13) is also a result of the mixing of LE intensity into the CT transition. It is therefore desirable to examine ways in which the extent of LE mixing may be influenced and how LE mixing affects the photophysics of these complexes.

The decrease in the integrated absorption intensities (oscillator strengths) of the localized bands within CT complex absorption spectra has been used as a measure of the degree of intensity borrowing (14). These measurements require the CT absorption spectra to be free from the contributions of unbound acceptor and donor, which in turn requires knowledge of the association constant for complex formation. The difficulties in determining the association constants for weakly bound complexes are now well known (15, 16, 18, 19). Such analysis assumes the LE band shape remains constant within the complex when compared to the free chromophore, (14) which is not true in all solvents. Furthermore, these measurements do not allow the partitioning of the borrowed oscillator strengths among the multiple CT transitions to be determined.

Time-resolved linear dichroism (TRLD) has been used to study CT complexes in detail (6, 7). The angle between the CT absorption transition moment and the photochemically produced radical anion absorption transition moment, after relaxation, has been measured for several complexes. A simple theoretical model was developed which correlated the extent of localized excitation mixed into the CT transitions with the results of TRLD measurements. One shortcoming of the initial study (7) was that the partitioning of the LE intensity among the multiple CT bands could not be determined because of the severely overlapping CT transitions. The following report examines the influence of different solvent environments on CT absorption spectra where the borrowing of LE intensity and the partitioning of this intensity among the possible CT transitions are determined.

## Experimental

### Methods

The ps pump-probe apparatus used in these time-resolved linear dichroism experiments has been described in detail elsewhere (20). A Continuum PY61C Nd:YAG laser was used to produce 1064-nm pulses of ca. 35 ps in duration. The 1064-nm fundamental was doubled and subsequently tripled to produce 355-nm pulses for sample excitation. Focusing the 355-nm light into a 10-cm solution cell and isolating the stimulated Raman emission at 404 nm ( $\text{H}_2\text{O}$ ) or 446 nm (cyclohexane) allowed different excitation wavelengths to be used. Continuum was generated by focusing

12 mJ of the residual 1064-nm light into a 10-cm quartz cell containing a 1:1 mixture of  $\text{D}_2\text{O}$ – $\text{H}_2\text{O}$ . The resultant continuum pulse was spatially filtered, collimated, passed through a polarizer, and split into two beams, one of which was used as a reference beam while the other passed through the sample. The sample and reference beams were coupled into separate legs of a bifurcated fiber-optic bundle and dispersed using a 0.3 m spectrograph. Transient absorption spectra were obtained using a dual diode array and single wavelength kinetic measurements were performed using matched PMT detectors. An IBM compatible computer allowed automated control of the experiment through serial and general-purpose interface bus (GPIB) interfaces in addition to data storage and analysis.

Solutions of TCNB and hexamethylbenzene (HMB) (both approximately  $1 \times 10^{-2}$  M) were placed in a quartz cuvette with the appropriate solvent. Ground-state absorption spectra were recorded using a Beckman DU 640 UV–vis spectrometer. During data collection, the samples were stirred using a magnetic stirrer and 200 pulse pairs were averaged to obtain a  $\Delta\text{OD}$  measurement at each delay setting. The resultant traces were fit using a simplex computer program to find the nonlinear least-squares minimum of the error between a model function and the observed data.

### Materials

TCNB was purchased from Aldrich Chemical Co. and purified by passing it through silica gel twice with methylene chloride as the eluting solvent, followed by recrystallization from chloroform. HMB was purchased from Aldrich and purified by passing it through alumina with 1,2-dichloroethane as the eluting solvent followed by recrystallization from ethanol. Chloroform (CLF), methylene chloride (MCL), and 1,2-dichloroethane (DCLE) were purchased from VWR as HPLC grade and were used as received. Acetonitrile (ACN) was obtained as HPLC grade from Aldrich and was used without further purification. Butyronitrile (BCN), pentanenitrile (PCN), and octanenitrile (OCN) (all from Aldrich) were purified by fractional distillation and passed twice through activated alumina prior to use.

## Results

### Absorption spectra

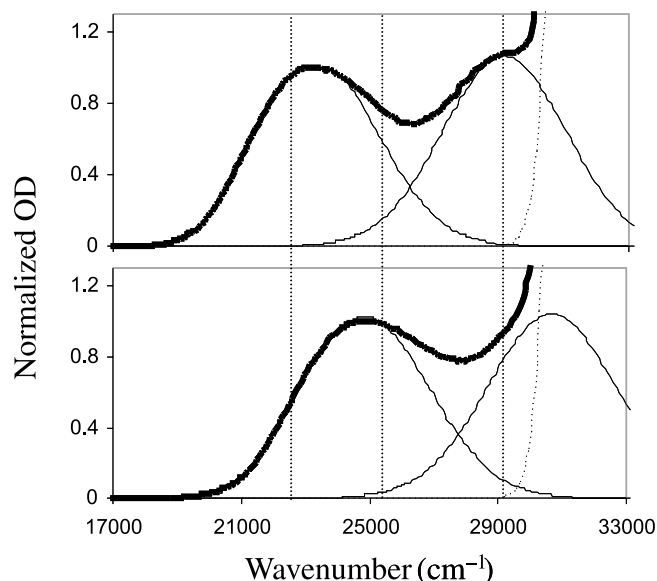
The ground-state absorption spectra of mixtures of HMB and TCNB in CLF or OCN as solvent are shown in Fig. 1. The observed spectra demonstrate the characteristics of CT complex formation when two new absorption bands are observed upon mixing the individual acceptor and donor. The positions of the first absorption maximum observed in several solvents are included in Table 1.

### Time-resolved spectroscopy

Excitation of the TCNB–HMB complex in CLF solvent with 355-nm light results in the observation of a new species that absorbs at 468 nm. This new species has been assigned previously to the TCNB radical anion produced within the laser pulse. The production and decay of the radical anion are recorded in the trace shown in Fig. 2. The excitation was linearly polarized along the laboratory Z-axis and the probe beam was linearly polarized at  $54.7^\circ$  with respect to the lab-



**Fig. 1.** Normalized absorption spectra of the HMB–TCNB CT complex in chloroform (top panel) and octanenitrile (bottom panel). Both spectra can be described using two CT bands (solid lines) and a LE band (dashed line). The resulting predicted spectrum coincides with the experimental spectrum (dark line) in all cases. The excitation wavelengths used to excite these complexes, 22 420  $\text{cm}^{-1}$  (446 nm), 24 750  $\text{cm}^{-1}$  (404 nm), and 28 170  $\text{cm}^{-1}$  (355 nm) are included on the diagram (vertical dashed lines).



oratory Z-axis. In this configuration the observed trace is due to the formation and decay of the ion pair convoluted with the instrument response function and does not contain dichroic information. The currently accepted model for the dynamics of photochemically produced ion-pairs gives the ion-pair decay as a two-exponential function with a constant offset and requires five adjustable parameters. In an effort to reduce the number of adjustable parameters, the magic angle trace was analyzed as a single-exponential decay. A rapid relaxation process has been reported for this complex with a lifetime of 5 ps in ACN (10). This process is too rapid to be resolved by our apparatus and need not be included in the kinetic scheme. Least-squares analysis yielded the following parameters:  $A_{\text{MA}} = 0.125$  (OD),  $k_{\text{MA}} = 1.40 \times 10^9 \text{ s}^{-1}$  with an instrument response of 35 ps assuming a Gaussian profile. The fitted line is included in Fig. 2 and the parameters obtained are collected in Table 1.

Two additional decay traces were recorded as shown in Fig. 3. In the first trace (open squares) the probe beam was linearly polarized along the laboratory Z-axis (i.e., parallel to the excitation) and in the second (filled squares) the probe beam was polarized within the laboratory XY-plane (i.e., perpendicular to the excitation). Except for the polarization of the probe beam, all three traces (Figs. 2 and 3) were collected under identical conditions. The shapes of the traces shown in Fig. 3 are due to a composite of the ion-pair decay and the randomizing rotations of the ion-pairs in solution superimposed on the instrument response profile of the laser system. The set of dichroic traces were fit assuming a single exponential anisotropy time constant, along with two anisotropy preexponential factors, one for each trace. The param-

eters obtained from the magic angle traces are used to describe the production and decay of the ion-pair and were used as fixed parameters in the fitting of the dichroism data. For the traces shown in Fig. 3, the dichroism decay rate constant obtained was  $k_{\text{OR}} = 3.37 \times 10^{10} \text{ s}^{-1}$  and the pre-exponential factors were  $A_{(\parallel)} = -0.038$  (OD units) for the parallel trace and  $A_{(\perp)} = 0.0107$  (OD units) for the perpendicular trace.

Similar sets of traces were obtained for the 355-nm excitation of HMB–TCNB CT complexes in MCL, DCLE, OCN, PCN, BCN, and ACN. The analysis of these data followed the procedure as described above and led to the fit parameters collected in Table 1.

The effect of excitation wavelength was also studied where Raman shifting of 355-nm light was used to allow excitation at 404 nm (water) or 446 nm (cyclohexane). The magic angle trace for the 446-nm excitation of the HMB–TCNB complex in OCN solvent is shown in Fig. 4 and the set dichroic traces is shown in Fig. 5. Additional traces for HMB–TCNB in DCLE and BCN excited using these wavelengths were also measured. The fit parameters resulting from the analysis of these data are also collected in Table 1.

## Discussion

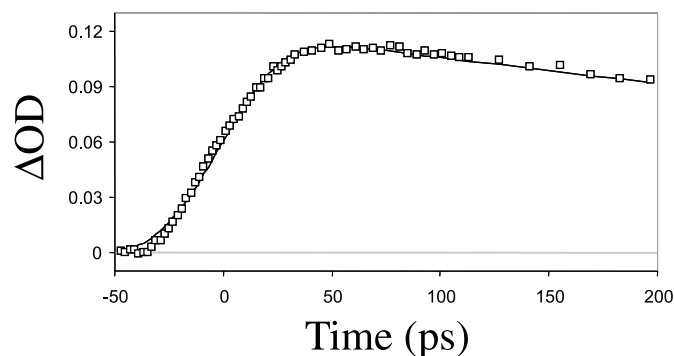
Multiple absorption bands are frequently observed within CT spectra and examination of Fig. 1 shows this to be true for the HMB–TCNB complex. These bands arise when multiple states participate in CT interactions. HMB has a doubly degenerate ground state and the weak interactions associated with complex formation are unlikely to split these states significantly. On the other hand, TCNB has two low lying excited states that are separated by 5800  $\text{cm}^{-1}$  (14). Both of these excited states can participate in CT interactions and two CT absorption bands are expected for the HMB–TCNB complex as indicated in the diagram in Fig. 6. Each band should have approximately the same oscillator strength with the second absorption band 5800  $\text{cm}^{-1}$  higher in energy than the first. For convenience these transitions will be designated CT1 for the low-energy transition and CT2 for the high-energy transition to distinguish between them and to reflect the possibility that they may include a significant contribution from the LE.

Examination of the ground-state spectra in Fig. 1 reveals that the absorption bands are relatively broad and significant overlap of the transitions occurs. Band shape analysis was performed on the CT spectra to help identify band maxima and to allow the band overlap at the excitation wavelengths to be assessed. In this analysis two Gaussian band profiles were assumed with a set width of 2820  $\text{cm}^{-1}$  and a constant energy difference of 5800  $\text{cm}^{-1}$ . These values are consistent with those found for complexes between TCNB and several methyl-substituted benzene donors (14). Fig. 1 shows the HMB–TCNB CT spectra in CLF and OCN, including the predicted absorption bands. The predicted spectrum, obtained as the sum of the two CT bands along with the LE, is included in Fig. 1 and it coincides with the experimental spectrum at all wavelengths in all solvents. Excellent agreement between the experimental and expected spectra was achieved for all solvents, which justifies the use of the parameters assumed.



**Table 1.** Spectroscopic characterization of hexamethylbenzene–1,2,4,5-tetracyanobenzene CT complexes in various solvents.

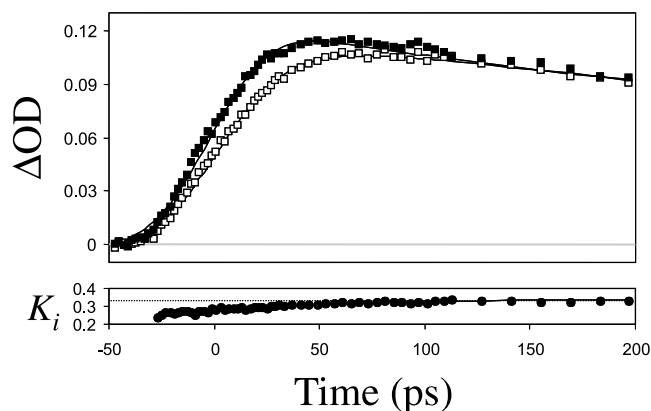
Solvent	$\bar{\nu}_{\text{CT1}}$ (cm <sup>-1</sup> ) <sup>a</sup>	$\lambda_{\text{EX}}$ (nm) <sup>b</sup>	$A_{\text{MA}}$ (OD) <sup>c</sup>	$k_{\text{MA}}$ (s <sup>-1</sup> ) <sup>d</sup>	$A_{\parallel}$	$A_{\perp}$	$k_{\text{OR}}$ (s <sup>-1</sup> )
CLF	23 360	355	0.125	$1.40 \times 10^9$	-0.038	0.011	$3.37 \times 10^{10}$
MCL	23 420	355	0.171	$6.20 \times 10^9$	-0.053	0.012	$6.69 \times 10^{10}$
DCLE	23 580	355	0.136	$6.16 \times 10^9$	-0.040	0.012	$2.49 \times 10^{10}$
		404	0.464	$5.83 \times 10^9$	-0.118	0.069	$3.09 \times 10^{10}$
		446	0.275	$6.20 \times 10^9$	-0.078	0.030	$2.20 \times 10^{10}$
OCN	24 880	355	0.144	$6.72 \times 10^9$	-0.016	0.017	$1.29 \times 10^{10}$
		404	0.389	$7.09 \times 10^9$	-0.010	0.029	$2.22 \times 10^{10}$
		446	0.251	$6.98 \times 10^9$	-0.066	0.027	$1.70 \times 10^{10}$
PCN	24 880	355	0.219	$13.1 \times 10^9$	-0.037	0.012	$2.32 \times 10^{10}$
BCN	25 000	355	0.179	$17.6 \times 10^9$	-0.032	0.008	$3.80 \times 10^{10}$
		404	0.228	$19.1 \times 10^9$	-0.052	0.016	$4.75 \times 10^{10}$
		446	0.240	$19.3 \times 10^9$	-0.054	0.039	$2.59 \times 10^{10}$
ACN	24 940	355	0.143	$28.9 \times 10^9$	-0.028	0.006	$5.90 \times 10^{10}$

<sup>a</sup>Wavenumber corresponding to the maximum absorbance of CT1. CT2 is 5800 cm<sup>-1</sup> higher in energy in each case.<sup>b</sup>Wavelength used to excite sample.<sup>c</sup>Preexponential factor corresponding to analysis of the magic angle traces ( $A_{\text{MA}}$ ) and the dichroic pair of traces ( $A_{\parallel}$  and  $A_{\perp}$ ). Please see text.<sup>d</sup>Rate constants for decay of the TCNB radical anion ( $k_{\text{MA}}$ ) and the decrease in dichroism ( $k_{\text{OR}}$ ).**Fig. 2.** Picosecond pump-probe transient absorption decay trace of the HMB–TCNB CT complex in chloroform excited at 355 nm and observed with 468-nm light polarized at the magic angle (open squares). The solid line indicates the best fit of the observed trace using a single exponential decay convoluted with a 35 ps instrument response.

Continuum models are generally used to describe the influence of solvent on absorption spectra (15, 21, 22). One such model predicts a linear relationship between the frequency of maximum absorbance ( $\bar{\nu}_{\text{MAX}}$ ) and the solvent parameter  $f$ , given by eq. [1] where  $D$  and  $n$  are the solvent dielectric constant and refractive index, respectively (22).

$$[1] \quad f = \left( \frac{D-1}{D+2} - \frac{n^2-1}{n^2+2} \right)$$

A plot of ( $\bar{\nu}_{\text{MAX}}$ ) for CT1 of the HMB–TCNB complex vs.  $f$  is shown in Fig. 7. Clearly, the chlorinated and cyano-substituted solvents fall into distinct groups where the transition energies are lower in chlorinated solvents by 1500 cm<sup>-1</sup> relative to cyano-substituted solvents. Similar observations have been reported previously for chloranil (15, 23), 1,3,5-trinitrobenzene (15, 23, 24), and tetracyanoethylene (15, 25) complexes with various donors when the CT absorption maxima were compared in hydrocarbons, alcohols, and halogenated solvents. Specific solvent–solute interactions have been invoked to account for the large differences in transi-

**Fig. 3.** Top panel: ps pump-probe transient absorption decay trace of the HMB–TCNB CT complex in chloroform excited at 355 nm and observed using 468-nm light polarized parallel (open squares) and perpendicular (filled squares) to the excitation. The solid lines indicate the best fit of the dichroic traces assuming a single-exponential anisotropy decay in addition to the parameters obtained by fitting the magic angle trace (see text (Fig. 2)). Bottom panel: plot of the orientation factor as a function of time calculated using the above dichroic traces. The solid line indicates the fit of the orientation factor based on the parameters obtained from the fit of the individual traces above. The dashed line indicates the isotropic  $K_i$  value of 0.333.

tion energy with changing solvent, although the exact nature of the interaction is not well understood. Germane to the present discussion is that solvent can be used to significantly alter the energies of the CT transitions and the LE transitions are not affected appreciably. These solvent effects will facilitate a test of the hypothesis that the magnitude of intensity borrowing will be sensitive to the energy difference between the CT and LE excited states.

Descriptions of TRLD and the methods of analysis of dichroic data have been published (6, 7). Recall that the anisotropic nature of light absorption can be used to produce partially oriented samples of excited states by a process



**Fig. 4.** Picosecond pump-probe transient absorption decay trace of the HMB–TCNB CT complex in octanenitrile excited at 446 nm and observed with 468-nm light polarized at the magic angle (open squares). The solid line indicates the best fit of the observed trace using a single-exponential decay convoluted with a 45 ps instrument response.

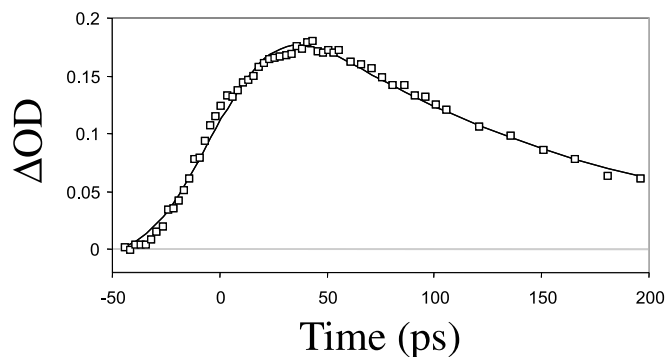
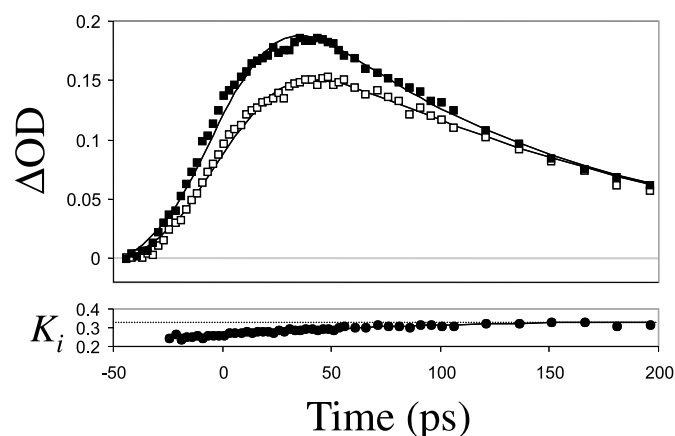
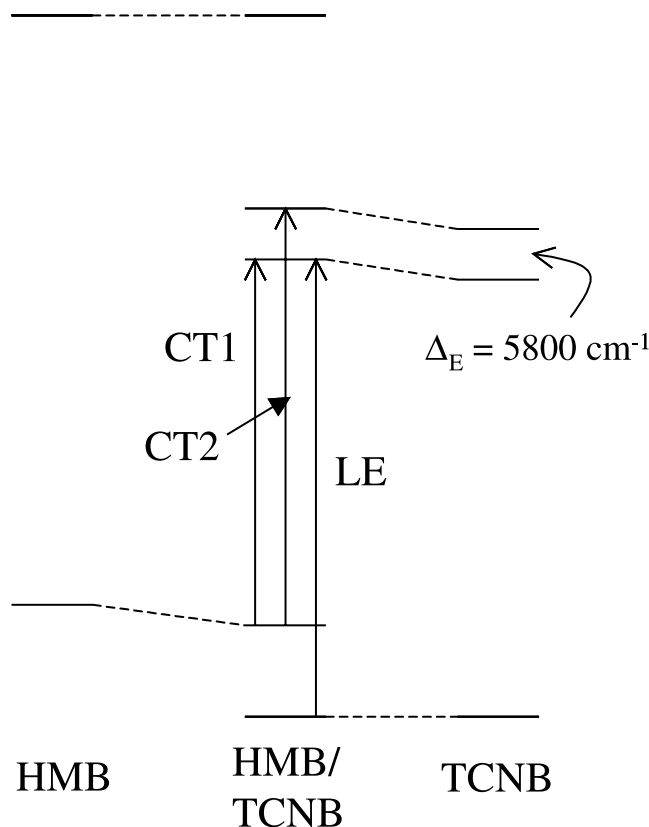


**Fig. 5.** Top panel: ps pump-probe transient absorption decay trace of the HMB–TCNB CT complex in octanenitrile excited at 446 nm and observed with 468-nm light polarized parallel (open squares) and perpendicular (filled squares) to the excitation. The solid lines indicate the best fit of the dichroic traces assuming a single-exponential anisotropy decay in addition to the parameters obtained by fitting the magic angle trace (see text (Fig. 4)). Bottom panel: plot of the orientation factor as a function of time calculated using the above dichroic traces. The solid line indicates the fit of the orientation factor based on the parameters obtained from the fit of the individual traces above. The dashed line indicates the isotropic  $K_i$  value of 0.333.



known as photoselection (26–30). Two sets of axes systems are required in the following discussion. The first is the laboratory frame of reference in which three mutually perpendicular axes are depicted using the upper case letters  $X$ ,  $Y$ , and  $Z$ . The second is the molecular frame in which mutually perpendicular axes will be depicted using the lower case letters  $x$ ,  $y$ , and  $z$ . The configuration of the TRLD apparatus allows the excitation beam to be linearly polarized with the electric vectors of the photons directed along the laboratory  $Z$ -axis. When the sample absorbs these photons and the excited states produced are subsequently probed with a second beam of linearly polarized light, the measured absorbance obtained when the electric vector of the probe beam is paral-

**Fig. 6.** Molecular orbital depiction of the CT1, CT2, and LE transitions associated with the HMB–TCNB complex.



lel ( $OD_Z$ ) compared to the absorbance perpendicular ( $OD_Y$ ) to the laboratory  $Z$ -axis may be different. The ratio of the parallel and perpendicular absorbance at wavelength  $\lambda$ , at any time, is defined as the dichroic ratio ( $d_\lambda = OD_{Z(\lambda)}/OD_{Y(\lambda)}$ ). It is particularly convenient to describe the observed orientation in terms of orientation factors as opposed to other, perhaps better known, order parameters (29, 30). The orientation factor of the probe transition ( $K_i$ ) is obtained directly from the dichroic ratio ( $K_i = d_\lambda/(d_\lambda + 2)$ ). The magnitude of  $K_i$  reflects both the degree of alignment of the sample within the laboratory frame and the angle between the ground-state absorption transition moment vector (TMV) and the probe TMV within the molecular frame. The alignment of the sample is described by the magnitude of the principal orientation factors ( $K_X$ ,  $K_Y$ ,  $K_Z$ ) which can be predicted using photoselection theory (29, 30).

Photoselection of linear absorbers results in uniaxial orientation of excited states with the principal orientation factors:  $K_Z = 0.60$  and  $K_X = K_Y = 0.20$  (29, 30). In this case the unique axis of the sample, the average orientation of the ground state CT TMV within the molecular frame and the direction of the electric vector of the excitation beam will all coincide with the laboratory  $Z$ -axis. The measured value of  $K_i$  is then related to the average angle between the ground state CT TMV (and the laboratory  $Z$ -axis) and the TCNB radical anion transition moment vector after relaxation to the CRIP. Equation [2] allows the absolute value of this angle to be calculated and the values obtained are collected in Table 2.



**Fig. 7.** Plot of the energy of the first CT absorption band ( $\bar{\nu}_{\text{MAX}}$ ) vs. the solvent polarity function ( $f$ ) defined in eq. [1]. Chlorinated solvents are indicated by filled squares and cyano-substituted solvents are indicated using open squares.

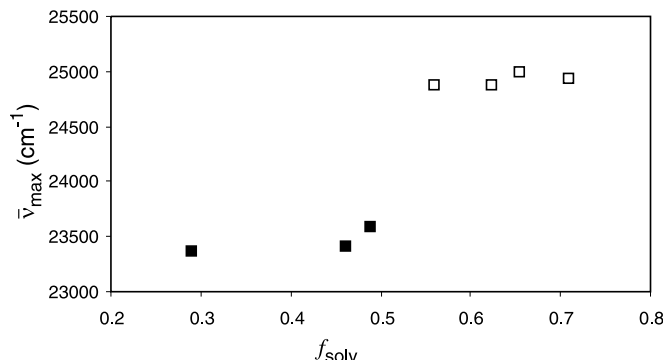


**Table 2.** Observed transition moment vector directions for hexamethylbenzene-1,2,4,5-tetracyanobenzene CT complexes in various solvents.

Solvent	$\lambda_{\text{EX}}$ (nm) <sup>a</sup>	Transition <sup>b</sup>	$K_i^c$	$\phi^d$ (°)
CLF	355	CT2	0.242	71
MCL	355	CT2	0.244	71
DCLE	355	CT2	0.246	70
	404	0.90 CT1 + 0.10 CT2	0.245	70
	446	CT1	0.244	71
OCN	355	0.35 CT1 + 0.65 CT2	0.284	63
	404	0.95 CT1 + 0.05 CT2	0.252	69
	446	CT1	0.249	70
PCN	355	0.35 CT1 + 0.65 CT2	0.282	63
BCN	355	0.35 CT1 + 0.65 CT2	0.282	63
	404	0.95 CT1 + 0.05 CT2	0.266	66
	446	CT1	0.250	69
ACN	355	0.35 CT1 + 0.65 CT2	0.277	64

<sup>a</sup>Wavelength used to excite sample.

<sup>b</sup>Transition(s) excited at the excitation wavelength used.

<sup>c</sup>Orientation factor.

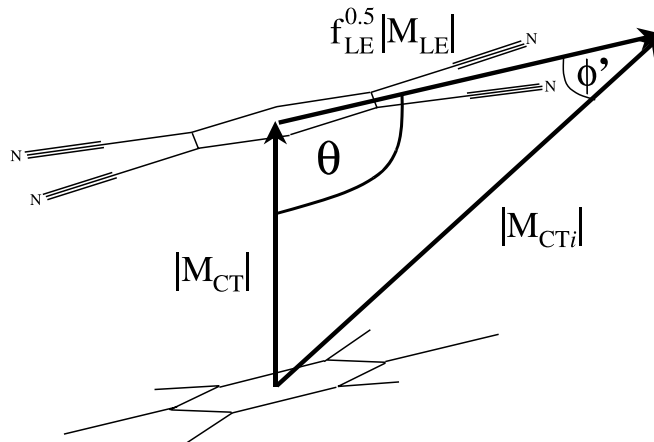
<sup>d</sup>Measured angle between the ground state CT transition moment(s) and the relaxed CRIP transition moment.

$$[2] \quad |\phi_i| = \tan^{-1} \sqrt{\frac{(K_Z - K_i)}{(K_i - K_Y)}}$$

A vector addition scheme has been described (6, 7) and is reproduced in Fig. 8, in which the pure CT transition moment ( $\mathbf{M}_{\text{CT}}^2$ ) and the contribution of the LE transition moment ( $f_{\text{LE}}\mathbf{M}_{\text{LE}}^2$ ) are added, resulting in the observed transition moment ( $\mathbf{M}_{\text{CT}i}^2$ ).

To see how these angles relate within the molecular frame, knowledge of the transition moment vector directions is required. According to calculations the LE TMV is directed along the long in-plane axis of TCNB. The pure CT TMV will be directed between the centers of charge density of the donor and acceptor. For centrosymmetric molecules like HMB and TCNB the centers of charge density will coincide with the centers of mass. The angle  $\theta = 100 \pm 4^\circ$ , was estimated from crystallographic data and calculated structures of the CT complex (6, 7). The last TMV direction

**Fig. 8.** Diagram depicting the vector addition of the pure CT TMV ( $\mathbf{M}_{\text{CT}}$ ) with a contribution for the LE TMV ( $f_{\text{LE}}^{0.5}\mathbf{M}_{\text{LE}}$ ) to obtain the observed CT TMV ( $\mathbf{M}_{\text{CT}i}$ ). The angle  $\theta$  is the angle between the pure CT TMV and the long in-plane axis of TCNB. The angle  $\phi'$  is the angle between the observed CT TMV and the TCNB radical anion TMV which coincides with the long in-plane axis of TCNB.



needed is that of the TCNB radical anion absorption at 468 nm, which, according to calculations, also coincides with the long in-plane axis of TCNB, as shown in Fig. 8. Finally, the angle  $\phi'$ , also depicted in Fig. 8, will be the angle obtained using TRLD spectroscopy assuming that relaxation of the complex does not lead to an observable rotation. Numerical evaluation of  $\phi'$  is possible using eq. [3].

$$[3] \quad \sin(\phi') = \frac{\mathbf{M}_{\text{CT}} \sin(180 - \theta - \phi)}{f_{\text{LE}}^{0.5} \mathbf{M}_{\text{LE}}}$$

Inspection of eq. [3] reveals that the magnitude of  $\phi'$  will depend on the ground-state geometry of the CT complex, the magnitude of LE intensity borrowed within the specific CT transition under consideration, and the geometry of the CRIP.

Consider the limiting case when intensity borrowing is negligible. The predicted angle is  $\phi' = 80^\circ$ . A measured value of  $|\phi| = 70^\circ$  was reported for HMB-TCNB complexes in DCLE where intensity borrowing was known to be negligible. It was proposed that the difference between the predicted and measured angles was due to rotation of the complex as a result of a small geometry change between the ground state and the relaxed CRIP (6, 7). Assuming this to be true, the model predicts the angles before relaxation occurs but the measured angles are those observed after relaxation to the CRIP. A topochemical increment to the observed orientation must be assessed to account for the relaxation. Based on the measured rotation of several methylbenzene complexes with TCNB an average value of  $7^\circ$  is expected (7). Therefore, the measured angles can be compared with the predicted angles only after the topochemical increment of  $7^\circ$  has been added ( $\phi' = |\phi| + 7^\circ$ ).

Three excitation wavelengths were used in the current study (355, 404, and 446 nm). The relevant excitation energies are shown pictorially in Fig. 1 where it is observed that different fractions of CT1 and CT2 are excited using these different wavelengths. In all solvents, 446 nm excites only



CT1 and the measured angles are consistently  $|\phi| = 70^\circ$ . The magnitude of the angle is comparable with the limiting case in which CT1 is pure CT in nature. The consistency of the measured angle in all solvents studied suggests that solvent does not change the ground-state geometry.

A dramatic difference between the solvent groups is observed when 355-nm light is used to excite the samples. At this wavelength CT2 is responsible for all of the absorption in chlorinated solvents and the measured angle remains  $|\phi| = 70^\circ$ . Thus, it can be concluded that in chlorinated solvents CT2 is a pure CT transition. In cyano-substituted solvents 355-nm light excites both CT1 (35%) and CT2 (65%) based on the band shape analysis. In these solvents the measured angle falls to  $|\phi| = 63^\circ$ . Figure 9 shows that the orientation factors for 355- and 446-nm excitation of the HMB–TCNB complex in OCN are indeed measurably different. Based on the ratios of CT1 and CT2 excited at 355 nm and assuming CT1 is pure CT, as the results of 446-nm excitation suggest, the measured angle if CT2 were excited alone would be closer to  $|\phi| = 59^\circ$ .

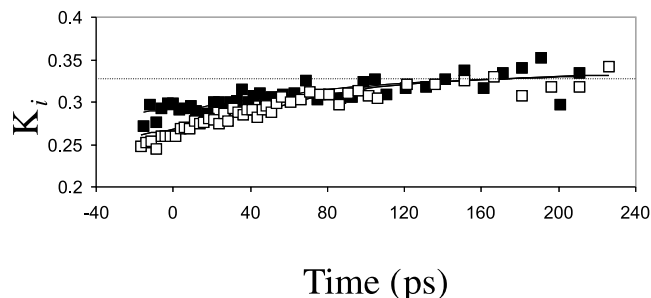
Having already ruled out differences in ground-state geometry in these solvents, LE intensity borrowing in the CT2 transitions is the most probable explanation for the variation in the observed angles. The energy difference between the LE and CT2 transitions is less than  $200\text{ cm}^{-1}$  in cyano-substituted solvents as compared to  $1700\text{ cm}^{-1}$  in chlorinated solvents. The energy differences between the CT1 and LE transitions are even greater, being about  $6000$  and  $8000\text{ cm}^{-1}$  in cyano-substituted and chlorinated solvents, respectively. It appears that the solvent interaction lowers the energy gap between the LE and CT transitions sufficiently to allow the two states to mix and intensity borrowing to occur.

Assuming the observed deviation in the angle is indeed the result of LE intensity borrowing, it is possible to calculate the fraction of LE that must be incorporated into CT2 in the cyano-substituted solvents to produce the observed angle. Given the measured angle of  $|\phi| = 59^\circ$ , and taking into account the topochemical increment of  $7^\circ$ , the percentage of LE oscillator strength incorporated into CT2 can be calculated based on the geometric constraints given by the model depicted in Fig. 8. In cyano-substituted solvents the observed higher energy CT transition, CT2, is 10–20% LE in character.

## Conclusions

Time-resolved linear dichroism spectroscopy has been used to study the influence of solvent on intensity borrowing in the charge transfer complex formed between hexamethylbenzene and 1,2,4,5-tetracyanobenzene. For the HMB–TCNB CT complex two CT transitions are observed. It was shown that cyano-substituted solvents induce a  $1500\text{ cm}^{-1}$  increase in the charge transfer transition energies relative to those observed in chlorinated solvents. Furthermore, the angle between the charge transfer absorption transition moments and the photochemically produced TCNB radical anion absorption transition moment, after relaxation, has been measured for this complex in several solvents. A simple model was used to correlate the angles measured using time-resolved linear dichroism spectroscopy with the extent of localized excitation mixed into the charge transfer transi-

**Fig. 9.** Plot of orientation factor ( $K_i$ ) as a function of time for the HMB–TCNB CT complex in octanenitrile observed at 468 nm after 355-nm excitation (filled squares) and 446-nm excitation (open squares). The solid lines indicate the best fit of the orientation factor assuming a single-exponential anisotropy decay. The dashed line indicates the isotropic  $K_i$  value of 0.333.



tion excited. These measurements reveal that the different CT transitions borrow LE intensity to different extents. It was shown that both CT transitions of the HMB–TCNB complex in chlorinated solvents are pure CT in nature. In cyano-substituted solvents, the lower energy CT transitions are pure CT in nature but the higher energy transition must include a significant contribution, as much as 20%, due to LE oscillator strength.

## Acknowledgements

The authors are grateful for the support of this work by NSF (CHE-9985299) and by University of Maryland, Baltimore County through a CBI Fellowship to DL.

## References

1. R.S. Mulliken. *J. Am. Chem. Soc.* **72**, 600 (1950).
2. R.S. Mulliken. *J. Am. Chem. Soc.* **72**, 4493 (1950).
3. R.S. Mulliken. *J. Chem. Phys.* **19**, 514 (1951).
4. R.S. Mulliken. *J. Am. Chem. Soc.* **74**, 811 (1952).
5. R.S. Mulliken. *J. Chem. Phys.* **23**, 397 (1955).
6. B.R. Arnold, A.W. Schill, and P.V. Poliakov. *J. Phys. Chem. A*, **105**, 537 (2001).
7. B.R. Arnold, A. Euler, P.V. Poliakov, and A.W. Schill. *J. Phys. Chem. A*, **105**, 10 404 (2001).
8. H. Miyasaka, S. Ojima, and N. Mataga. *J. Phys. Chem.* **93**, 3380 (1989).
9. S. Ojima, H. Miyasaka, and N. Mataga. *J. Phys. Chem.* **94**, 4147 (1990).
10. S. Ojima, H. Miyasaka, and N. Mataga. *J. Phys. Chem.* **94**, 5834 (1990).
11. N. Mataga and Y. Murata. *J. Am. Chem. Soc.* **91**, 3144 (1969).
12. T. Kobayashi, K. Yoshihara, and S. Nagakura. *Bull. Chem. Soc. Jpn.* **44**, 2603 (1971).
13. I.R. Gould, D. Noukakis, L. Gomez-Jahn, R.H. Young, J.L. Goodman, and S. Farid. *Chem. Phys.* **179**, 439 (1993).
14. B.R. Arnold, R.Y. Zaini, and A. Euler. *Spectrosc. Lett.* **33**, 595 (2000).
15. R. Foster. *Organic charge transfer complexes*. Academic Press, New York. 1969.
16. R.S. Mulliken and W.B. Person. *Molecular complexes*. Wiley, New York. 1969.
17. I.R. Gould, R.H. Young, L.J. Mueller, A.C. Albrecht, and S. Farid. *J. Am. Chem. Soc.* **116**, 8188 (1994).



18. R. Zaini, A.C. Orcutt, and B.R. Arnold. *Photochem. Photobiol.* **69**, 443 (1999).
19. B.R. Arnold, A. Euler, K. Fields, and R.Y. Zaini. *J. Phys. Org. Chem.* **13**, 729 (2000).
20. P.V. Poliakov and B.R. Arnold. *Spectrosc. Lett.* **32**, 747 (1999).
21. N. Mataga and T. Kubota. *Molecular interactions and electronic spectra*. Marcel Dekker, Inc., New York. 1970.
22. A.Y. Yu, C.A. Tolbert, D.A. Farrow, and D.M. Jonas. *J. Phys. Chem. A*, **106**, 9407 (2002).
23. K.M.C. Davis and M.C.R. Symons. *J. Chem. Soc.* 2079 (1965).
24. C.C. Thompson, Jr. and P.A.D. de Maine. *J. Phys. Chem.* **69**, 2766 (1965).
25. H.M. Rosenberg, E. Eimutis, and D. Hale. *Can. J. Chem.* **44**, 2405 (1966).
26. D. Magde. *J. Chem. Phys.* **68**, 3717 (1978).
27. A. Ansari and A. Szabo. *Biophys. J.* **64**, 838 (1993).
28. A. Szabo. *J. Chem. Phys.* **81**, 150 (1984).
29. E.W. Thulstrup and J. Michl. *Spectroscopy with polarized light. Solute alignment by photoselection in liquid crystals, polymers, and membranes*. VCH Publishers, Deerfield Beach. 1986.
30. E.W. Thulstrup and J. Michl. *Elementary polarization spectroscopy*. VCH Publishers, Deerfield Beach. 1989.



# Substituent effects in oxime radical cations. 1.

## Photosensitized reactions of acetophenone oximes

H.J. Peter de Lijser, Jason S. Kim, Suzanne M. McGrorty, and Erin M. Ulloa

**Abstract:** A variety of *ortho*-, *meta*-, and *para*-substituted (-H, -F, -Cl, -CF<sub>3</sub>, -CN (*meta* and *para* only), -CH<sub>3</sub>, -OCH<sub>3</sub>, and -NO<sub>2</sub>) acetophenone oximes were synthesized and studied using laser flash photolysis (LFP) and steady-state photolysis experiments in acetonitrile with chloranil as the photosensitizer. In addition, semi-empirical (AM1) calculations were performed on the neutral species, the radical cations, and the corresponding iminoxyl radicals. The data was analyzed in terms of the electrochemical peak potentials of the oximes, the quenching rates of triplet chloranil (LFP), the calculated ionization potentials, and the measured conversions of the oximes in the steady-state photolysis experiments. Photolysis of the oximes in the presence of chloranil results in the formation of the chloranil radical anion, which reacts rapidly with the oxime radical cation to form the semiquinone radical and an iminoxyl radical. Evidence for the formation of the chloranil radical anion and the semiquinone radical was obtained from LFP studies. The measured quenching rates from the LFP studies represent the rates of electron transfer from the oximes to triplet chloranil. This data was correlated to various radical and polar substituent constants. The Hammett studies suggest that steric, polar, and radical effects are important for *ortho*-substituted acetophenone oximes, polar effects are important for *para*-substituted oximes, and radical stabilization is more important than polar effects for the *meta*-substituted substrates. The calculated ionization potentials of the oximes show an excellent correlation with the measured quenching rates supporting the electron transfer pathway. On the basis of calculated charge densities, we conclude that the measured substituent effects are transition state effects rather than ground state effects. At this point all of the available data suggests that the conversion of the oximes is controlled by two energetically opposing reactions, namely oxidation of the neutral oxime, which is favorable for oximes with electron-donating substituents, and deprotonation of the oxime radical cation, which is favorable for oximes with electron-withdrawing substituents. The overall result is a reaction with little selectivity as far as substituent effects are concerned.

**Key words:** oxime, radical cation, iminoxyl radical, electron transfer, substituent effect.

**Résumé :** On a synthétisé une grande variété d'oximes d'acétophénonnes substituées en *ortho*-, *méta*- et *para*- (-H, -F, Cl, -CF<sub>3</sub>, -CN (uniquement en *méta*- et *para*-), -CH<sub>3</sub>, -OCH<sub>3</sub> et -NO<sub>2</sub>) qu'on a étudiées par des expériences de photolyse éclair au laser (PEL) et de photolyse à l'état stationnaire dans l'acétonitrile, en utilisant le chloranile comme photosensibilisateur. De plus, on a effectué des calculs semiempiriques (AM1) sur les espèces neutres, les cations radical et les radicaux iminoxyles correspondants. On a analysé les données en fonction des potentiels électrochimiques maximaux des oximes, les vitesses de désactivation du chloranile triplet (PEL), des potentiels d'ionisation calculés et des conversions mesurées des oximes dans les expériences de photolyse à l'état stationnaire. La photolyse des oximes en présence de chloranile conduit à la formation de l'anion radical du chloranile qui réagit rapidement avec le cation radical de l'oxime pour conduire à la formation du radical de la semiquinone et à un radical iminoxyle. On a obtenu des indications relatives à la formation de l'anion radical du chloranile et du radical de la semiquinone à partir des études de PEL. Les vitesses mesurées de désactivation obtenues à partir des études de PEL correspondent aux vitesses de transfert d'électron des oximes vers le chloranile triplet. On a pu établir une corrélation entre ces données et diverses constantes de radicaux et de substituants polaires. Les études de Hammett suggèrent que les effets stériques, polaires et radicalaires sont importants pour les oximes des acétophénonnes substituées en *ortho*-, que les effets polaires sont importants pour les oximes des acétophénonnes substituées en *para*- et que la stabilisation radicalaire est plus importante que les effets polaires pour les substrats substitués en *méta*-. Les potentiels d'oxydation calculés des oximes présentent une excellente corrélation avec les vitesses de désactivation mesurées ce qui supporte une voie de transfert électronique. Sur la base des densités de charge calculées, on en conclut que les effets de substituants mesurés sont des effets liés aux états de transition plutôt que des effets liés aux états fondamentaux. À ce point, toutes les données disponibles

Received 16 December 2002. Published on the NRC Research Press Web site at <http://canjchem.nrc.ca> on 21 May 2003.

This paper is dedicated to Professor Donald R. Arnold for his contributions to chemistry.

H.J.P. de Lijser,<sup>1</sup> J.S. Kim, S.M. McGrorty, and E.M. Ulloa. Department of Chemistry and Biochemistry, California State University Fullerton, Fullerton, CA 92834, U.S.A.

<sup>1</sup>Corresponding author (e-mail: [pdelijser@fullerton.edu](mailto:pdelijser@fullerton.edu)).



suggèrent que la conversion des oximes est contrôlée par deux réactions énergétiquement opposées, soit l'oxydation de l'oxime neutre qui est favorable aux oximes portant des substituants électrodonneurs ou la déprotonation du cation radical de l'oxime qui est favorable aux oximes portant des substituants électroattracteurs. Le résultat global est une réaction qui, du point de vue des effets de substituants, ne présente pas beaucoup de sélectivité.

*Mots clés* : oxime, cation radical, radical iminoxyle, transfert d'électron, effet de substituant.

[Traduit par la Rédaction]

## Introduction

Oximes and oxime ethers have found use as protection groups for carbonyl compounds (1). The regeneration of carbonyl compounds from oximes can be achieved using a variety of methods, including oxidative, reductive, and photochemical techniques (2, 3). Of specific interest to us are the photochemical techniques (3) as well as other studies focusing on the photochemical behavior of these compounds (4). Haley and Yates (3) studied the photohydrolysis of oximes and concluded that the reactive excited state was the lowest singlet state since triplet sensitization did not result in the formation of any products, with the exception of *syn-anti* isomerization. The latter observation is consistent with Padwa and Albert's (4j) work on the triplet-sensitized photolysis of oxime ethers. It is interesting to note, however, that the measured quantum yields in the aqueous photohydrolysis reactions were typically low and certain substituted substrates did not react at all. We recently reported on our studies involving the photosensitized regeneration of carbonyl compounds from oximes (5). Photolysis of oximes in the presence of the triplet sensitizer chloranil resulted in formation of the corresponding carbonyl compounds in reasonable to good yields. The data is most consistent with an electron transfer mechanism and we have proposed that the oxime radical cation reacts rapidly with the sensitizer (chloranil) radical anion to form the iminoxyl radical and the hydrochloranil (semiquinone) radical (Scheme 1).

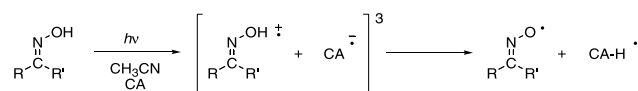
An important issue that has not yet been addressed is whether the formation of the iminoxyl radicals from oximes via an electron transfer pathway is a two-step process or a concerted proton-coupled electron transfer (PCET) process (6). Both oxime radical cations and iminoxyl radicals are important intermediates in chemical and biochemical processes (7), however, despite the large amount of data available on the structure of these species (7, 8), little is known about their reactivity. A complete understanding of the mechanistic aspects of these reactions and the intermediates involved is therefore desirable.

The electronic structure of iminoxyl radicals has been proposed as that shown in Scheme 2a (8c, 8f).

According to this description, which is based on ESR measurements, no spin density is available on carbon. Several other mechanistic interpretations involving iminoxyl radicals have suggested the possibility of a resonance structure as shown in Scheme 2b (9a, 9c).

Although the formation of carbonyl compounds from oxime radical cations (Scheme 3) can be most easily explained on the basis of the resonance structure shown in

Scheme 1.



Scheme 2b, more detailed studies are necessary to support this hypothesis.

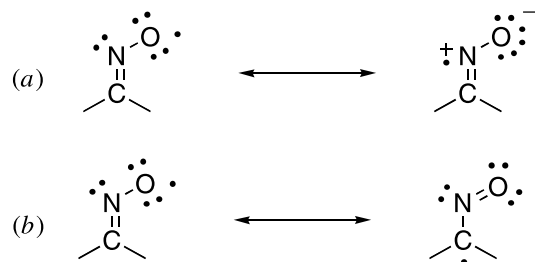
Structure-reactivity studies have been of great value for the exploration of mechanistic problems and the involvement of reactive intermediates (10). A number of linear free energy relationships (LFERs) for dealing with different intermediates (cations, anions, radicals) in both ground state and excited state reactions have been developed over the past decades (11). It is well established that when studying aromatic substrates, only the *meta*- and *para*-substituted compounds are considered. In general, steric effects and hydrogen bonding prohibit the true electronic nature of *ortho*-substituent effects and, therefore, are most often not considered when discussing substituent effects. A variety of specific scales for dealing with *ortho*-substituents have been developed (12). For example, Tribble and Traynham (12c) reported a method for measuring electronic effects of *ortho*-substituents by means of NMR in DMSO solution using *ortho*-substituted phenols. This scale is known as the  $\sigma_o^-$  or  $\Delta\delta_o$  scale. A value for *o*-NO<sub>2</sub> was not available as it did show significant hydrogen bonding even in DMSO solution, however, a value of 1.20 was reported earlier by Dietrich et al. (13). Separation of steric and electronic effects has been an active field of study, initiated by Taft (14) who proposed  $E_s$  and  $E_s^\circ$  values. Charton (15) indicated that the Taft  $E_s$  values are a linear function of the van der Waals radii and independent of electronic effects, whereas the  $E_s^\circ$  values are a function of electronic effects only without any significant contribution of steric effects. A new steric parameter ( $E_s^e$ ) which was corrected for electronic effects, was introduced by Unger and Hansch (16).

Although reasonable correlations are obtained for most ionic reactions by using the traditional polar substituent constants such as  $\sigma_m$ ,  $\sigma_p$  (referred to here as  $\sigma_{pol}$ ), and  $\sigma^+$ , those involving radicals are often much poorer. To deal more effectively with this problem, a variety of new scales that specifically deal with free radicals (e.g.,  $\sigma_{\alpha^\bullet}$  (17a–17d),  $\sigma_{rad}$  (17e, 17f),  $\sigma_{J^\bullet}$  (17g–17j), and  $\sigma_{JJ^\bullet}$  (17l)) were developed. Typically, dual parameter correlations are done for free radical reactions, which then reveal the relative importance of the substituent effect on the radical species (17).

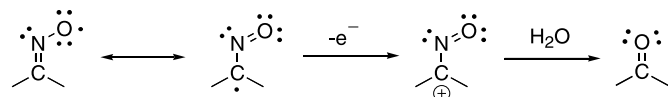
The use of LFER studies in radical ion reactions is much more limited and no specific scales have been developed.



Scheme 2.



Scheme 3.



For reactions involving a radical cation species, the observed rates are most often correlated with the Brown–Okamoto  $\sigma^+$  parameter (18), owing to the fact that stabilization of the positive charge is typically more important than that of the radical. The effect depends on the type of reaction studied, and both small and large effects have been reported (19). For example, Nave and Trahanovsky (19a) found a  $\rho$ -value of  $-2.0$  for the one-electron oxidative cleavage of 2-aryl-1-phenylethanols using cerium(IV), whereas Fox and Chen (19e) found a relatively small reaction constant ( $\rho^+ = -0.56$ ) for the  $\text{TiO}_2$ -photocatalyzed oxidative cleavage of olefins. Clearly, the use of a structure–reactivity study is expected to aid in the development of an understanding of complicated mechanistic problems.

Here, we report on a detailed Hammett study involving a series of *ortho*-, *meta*-, and *para*-substituted acetophenone oximes to examine the effects of substituents on the reactivity of the oxime radical cations and iminoxyl radicals. To obtain as much detailed information as possible, we have included all but one (4-*tert*-butyl) of the groups necessary for a complete assessment of the reactivity for both radical and ionic reactions, as suggested by Exner (20) and Dust and Arnold (17a), respectively.

## Results and discussion

### Laser flash photolysis studies of oximes

Formation of iminoxyl radicals from oximes via photosensitized reactions can potentially result from three pathways: (i) electron transfer followed by proton transfer; (ii) proton-coupled electron transfer; or (iii) hydrogen atom transfer. If the intermediate radical cation – radical anion pair has a long enough lifetime, it should be possible to distinguish among pathways (i) and (ii) or (iii) using spectroscopic methods. A nanosecond laser flash photolysis experiment would most likely not be able to differentiate between pathways (ii) and (iii). The intermediates of interest, triplet chloranil, chloranil radical anion, and semiquinone radical, were each generated separately and their spectra were recorded. The chloranil radical anion was obtained by photolysis of a chloranil–biphenyl mixture (in acetonitrile) and the semiquinone radical was obtained from photolysis of a chloranil–toluene mixture. The spectrum of triplet chloranil shows a maximum of 508 nm and a shoulder at 480 nm. The

chloranil radical anion shows a sharp absorption around 445 nm, whereas the semiquinone radical is observed at 433 nm. These spectra are consistent with those reported in the literature (21). Attempts to observe the oxime radical cation directly via photoionization (308 nm) were unsuccessful and a direct kinetic analysis (observing the rate of disappearance of the oxime radical cation) was therefore not possible.

Photolysis of an argon-purged solution containing acetophenone oxime and chloranil resulted in the formation of the chloranil triplet, which was rapidly quenched by acetophenone oxime (Fig. 1). At approximately 400 ns after the pulse, two new species were formed. We assigned these two signals to the chloranil radical anion (445 nm) and the semiquinone radical (433 nm). At longer times, the strong signal of the semiquinone radical was obvious, however, the shoulder at 445 nm indicated the presence of the chloranil radical anion. Similar spectra were obtained for a variety of other oximes, suggesting that the mode of action for the initial steps is always the same. On the basis of these results, we concluded that the initial steps involved in the chloranil-sensitized photolysis of oximes are electron transfer from the oxime to triplet chloranil to form a triplet radical ion pair, followed by deprotonation to form the iminoxyl radical and the semiquinone radical. Because of the presence of the chloranil radical anion in these spectra, we believe that neither hydrogen atom transfer nor proton-coupled electron transfer are important pathways in these reactions.

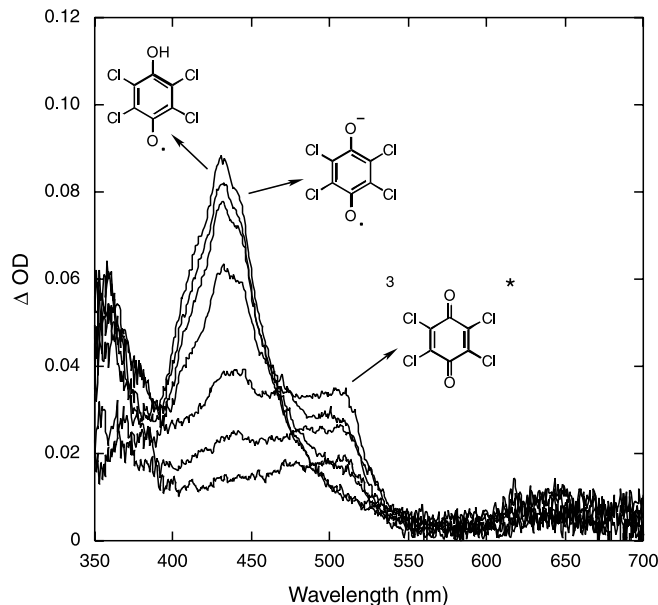
### Photosensitized reactions of *ortho*-, *meta*-, and *para*-substituted acetophenone oximes

The results of the photosensitized reactions of the *ortho*-, *meta*-, and *para*-substituted acetophenone oximes are listed in Table 1. Accurate peak potentials ( $E_p$ ) could not be obtained for the *o*- $\text{CF}_3$ , *o*-Cl, and *o*- $\text{CH}_3$  derivatives. Reasonable numbers (based on electronic properties) were obtained for *o*-F, *o*- $\text{OCH}_3$ , and *o*- $\text{NO}_2$  acetophenone oximes. A possible reason for the large positive numbers for the *o*- $\text{CF}_3$ , *o*-Cl, and *o*- $\text{CH}_3$  derivatives is a steric effect. These three groups are unable to orient themselves in such a manner that the oxime moiety can become coplanar with the aromatic ring upon ionization. This was confirmed by semiempirical (AM1) calculations (22). The calculated dihedral angles for these three radical ions are  $33.7^\circ$  ( $\text{CF}_3$ ),  $28.9^\circ$  (Cl), and  $33.5^\circ$  ( $\text{CH}_3$ ). This is significantly larger than acetophenone oxime ( $7.9^\circ$ ) or the *o*-F derivative ( $17.3^\circ$ ). The exception is *o*- $\text{NO}_2$  acetophenone oxime for which the calculated dihedral angle is  $70.3^\circ$ . Further analysis of the structure revealed that the  $\text{NO}_2$  group is coplanar with the aromatic ring and lined up such that one of the oxygens of the nitro group is directed towards the carbon of the oxime moiety (distance is 2.5 Å) providing some stabilization. This particular orientation results in the presence of large charge and spin densities on the oxime carbon.

The calculated  $\Delta G_{\text{ET}}$  values (using the Weller equation (23)) for several of the substituted oximes are positive (endothermic) suggesting that electron transfer is not favorable. However, the results from nanosecond laser flash photolysis experiments do not agree with that conclusion. Quenching of the excited triplet state of chloranil (monitored at 510 nm) is fast ( $4 \times 10^7 - 1 \times 10^{10} \text{ M}^{-1} \text{ s}^{-1}$ ) for all *ortho*-substituted



**Fig. 1.** Time-resolved (ns) spectra resulting from the quenching of triplet chloranil by acetophenone oxime in argon-purged acetonitrile solution showing the spectral bands of triplet chloranil ( $\lambda_{\text{max}} = 508$  nm), chloranil radical anion (shoulder at  $\lambda_{\text{max}} = 445$  nm), and the semiquinone radical ( $\lambda_{\text{max}} = 433$  nm). Delay times are 380, 390, 400, 425, 450, 475, and 500 ns (increasing curves).



acetophenone oximes (Table 1). A typical decay trace and quenching plot are shown in Fig. 2. The discrepancy between the  $\Delta G_{\text{ET}}$  and quenching rates ( $k_q$ ) can (in part) be clarified by the results of the product studies. Previously, it was suggested that the photochemistry (photohydrolysis) of oximes occurs via their singlet states as triplet sensitization did not result in the formation of products (3). Results obtained by us<sup>2</sup> and others (3, 4j), suggest that triplet sensitization (energy transfer) results in *syn-anti* isomerization in oximes, whereas electron transfer results in the formation of carbonyl compounds and other products<sup>3</sup> (5). Similar to our previous studies on the photosensitized electron transfer reactions of oximes, the major product formed in these reactions is the corresponding carbonyl compound (5). However, it is important to note that photolysis of the *o*-NO<sub>2</sub>, *o*-CH<sub>3</sub>, and *o*-Cl oximes also resulted in large amounts of *syn-anti* isomerization, suggesting that both electron transfer and energy transfer pathways are important in these reactions. The fact that two of these oximes had peak potentials more positive than 2.5 V and all three oxime radical cations had large dihedral angles is consistent with the idea that in order for electron transfer to take place favorably, the substituent must be able to become coplanar with the aromatic ring upon ionization.

Analysis of the laser flash photolysis (LFP) data reveals that it is consistent with substituent effects as predicted on the basis of electronic properties, i.e., oximes with electron-withdrawing groups such as -NO<sub>2</sub> and -CF<sub>3</sub> are expected to

react slower than oximes with electron-donating groups such as -OCH<sub>3</sub>. To explore the behavior of these substituted oximes further, the energy required for ionization of the neutral oxime ( $\Delta\Delta H_f$ ) was calculated for each oxime. The results are listed in Table 1 and a plot of the calculated ionization potentials against the measured  $k_q$  values (Fig. 3) reveals that there is an excellent correlation ( $r^2 = 0.85$ ). It must be noted that some of the measured rates are close to the diffusion-controlled limit, however, there is no sign of these rates leveling off. One could argue that the value of *p*-OCH<sub>3</sub> is probably the closest to that limit, however, when that point is omitted the slope of the line does not change significantly, nor does the  $r^2$  value change much. This correlation supports the idea that the diffusion-controlled limit is not reached and we are confident that the measured rate constants reflect the influence of the substituent on the initial electron transfer process. Comparison of the *ortho*- and *para*-values of  $\Delta\Delta H_f$  (Table 1) is also consistent with a steric effect. The  $\Delta\Delta H_f$  values for the *ortho*-substituted oximes are consistently higher than those of the *para*-substituted oximes (with the exception of the nitro-substituted oximes).

Analysis of the data for the *meta*-substituted oximes in Table 1 indicates that no correlation exists between the measured peak potentials and the quenching rates ( $k_q$ ). The exact reason for this is unclear and at this point we will not discuss these observations. There is an excellent correlation between the measured  $k_q$  values and the calculated  $\Delta\Delta H_f$  values. The initial (electron transfer) reaction is fast for all the *meta*-substituted oximes and the differences are clearly due to electronic effects. An energy transfer pathway is ruled out as no *syn-anti* isomerization was observed for any of these oximes. Interesting electronic effects were observed for the *m*-OCH<sub>3</sub> derivative. Analysis of the spin and charge distributions from the AM1 calculations reveals that there is an unusually large (positive) spin density and negative charge on the carbon of the oxime moiety. In addition, the dihedral angle ( $-33.2^\circ$ ) is larger than for all the other substituents, which suggests that the large peak potential (measured) is possibly due to the fact that coplanarity cannot be achieved (as was observed for certain *ortho*-substrates). The calculated C=N bond length is much shorter than in any of the other oximes, the N—O bond length is much longer, and the O—H bond length is shorter than in the other oxime radical cations. Also, the calculated charge density on the hydroxyl proton is smaller than usual and is only slightly larger than that of the hydroxyl proton in the neutral oxime. These results suggest that oxidation does not occur on the oxime moiety but rather somewhere else in the molecule. Several other conformers were examined as well, all of which displayed the same characteristics, suggesting that electronic effects rather than conformational effects cause this phenomenon.

The data obtained for the *para*-substituted oximes clearly shows that the major trends are different from those of the *ortho*- and *meta*-substituted oximes and actually reflect the true (polar) nature of the substituents much better. This is not unexpected; many radical ion reactions correlate well

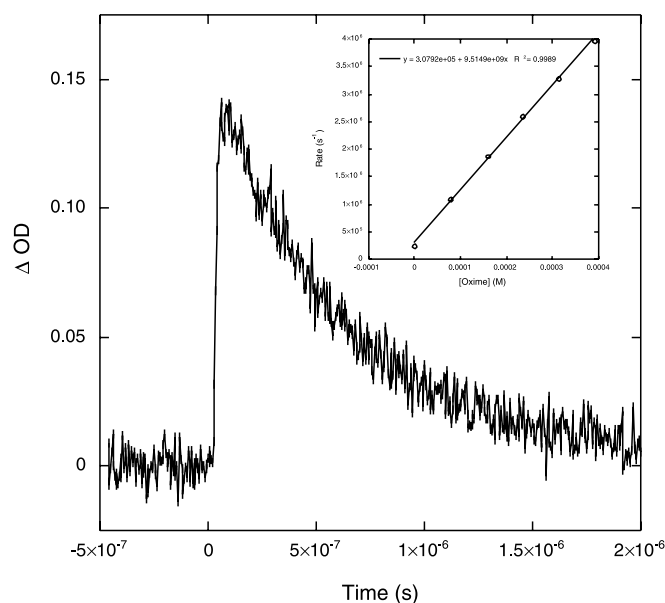
<sup>2</sup>S.E. Ng'wono, B.V. Marquez, A. Park, and H.J.P. de Lijser. Unpublished results.

<sup>3</sup>H.J.P. de Lijser, J.S. Kim, S.M. McGrorty, and E.M. Ulloa. More detailed studies on the product formation under these conditions are underway and will be published elsewhere. Manuscript in preparation.

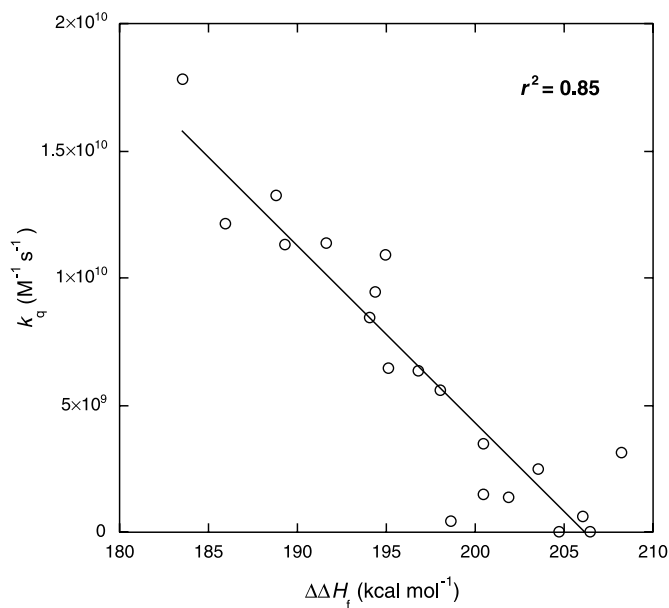


**Table 1.** Reactivity data for *ortho*-substituted acetophenone oximes.

Substituent		$E_p^a$ (V)	$\Delta G_{ET}$ (kcal mol <sup>-1</sup> )	$k_q^b$ (M <sup>-1</sup> s <sup>-1</sup> )	Conversion (%) <sup>c</sup>	$\Delta\Delta H_f$ (kcal mol <sup>-1</sup> ) <sup>d</sup>
H		1.65	-11.5	$9.5 \times 10^9$	18	193.04
CF <sub>3</sub>	<i>o</i>	>2.50	>8.0	$4.7 \times 10^7$	43	204.63
	<i>m</i>	2.20	+1.2	$1.4 \times 10^9$	14	201.81
	<i>p</i>	2.05	-2.3	$2.5 \times 10^9$	20	203.54
Cl	<i>o</i>	>2.50	>8.0	$4.5 \times 10^9$	48	198.57
	<i>m</i>	2.06	-2.1	$6.4 \times 10^9$	21	196.73
	<i>p</i>	1.93	-5.1	$9.4 \times 10^9$	28	194.35
F	<i>o</i>	2.26	+3.7	$1.1 \times 10^{10}$	80	194.92
	<i>m</i>	2.26	+2.5	$5.6 \times 10^9$	19	198.04
	<i>p</i>	1.95	-4.6	$8.5 \times 10^9$	23	194.01
CH <sub>3</sub>	<i>o</i>	>2.50	>8.0	$6.5 \times 10^9$	54	195.10
	<i>m</i>	1.95	-4.6	$1.1 \times 10^{10}$	18	191.60
	<i>p</i>	1.50	-15.0	$1.1 \times 10^{10}$	14	189.25
OCH <sub>3</sub>	<i>o</i>	1.52	-14.5	$1.2 \times 10^{10}$	92	185.92
	<i>m</i>	2.19	+0.9	$1.3 \times 10^{10}$	22	188.73
	<i>p</i>	1.27	-20.3	$1.8 \times 10^{10}$	55	183.47
NO <sub>2</sub>	<i>o</i>	1.99	-3.7	$6.7 \times 10^7$	33	206.45
	<i>m</i>	2.16	+0.2	$6.5 \times 10^8$	20	206.04
	<i>p</i>	2.03	-2.8	$3.2 \times 10^9$	17	208.19
CN	<i>m</i>	2.15	0.0	$1.5 \times 10^9$	56	200.43
	<i>p</i>	2.19	+0.9	$3.5 \times 10^9$	26	200.41

<sup>a</sup>Peak potential measured by cyclic voltammetry.<sup>b</sup>Rate of triplet chloranil quenching.<sup>c</sup>Conversion determined by calibrated GC-FID after 20 min of photolysis except for *ortho*-substituted oximes which were subjected to 2 h photolysis.<sup>d</sup>Calculated using semiempirical (AM1) methods; the number is the difference between the calculated heats of formation of the radical cation and the neutral species.**Fig. 2.** Decay of the chloranil triplet signal (at 510 nm) in the presence of acetophenone oxime ( $1.6 \times 10^{-4}$  M). (Inset) Determination of the rate constant for quenching triplet chloranil by acetophenone oxime.

with the  $\sigma^+$  parameter (18), suggesting a strong polar effect in these reactions. A reasonable correlation ( $r^2 = 0.84$ ) is observed between the measured  $E_p$  and  $k_q$  values. Electron-donating substituents activate the molecule (i.e., less posi-

**Fig. 3.** Correlation between the measured quenching rates (LFP) of triplet chloranil and the calculated (AM1) ionization potentials ( $\Delta\Delta H_f$ ) of the acetophenone oximes.

tive peak potentials are obtained relative to the unsubstituted compound) and electron-withdrawing substituents deactivate the molecule; the overall range ( $\Delta\Delta G_{ET}$ ) spans more than 21 kcal mol<sup>-1</sup>. On the basis of the measured peak potentials, calculated  $\Delta G_{ET}$  values, the measured  $k_q$  values, and the



calculated  $\Delta\Delta H_f$  values, we conclude that quenching of triplet chloranil proceeds predominantly via an electron transfer process to form the oxime radical cation. However, as indicated above, a competitive energy transfer pathway for the *o*-NO<sub>2</sub>, *o*-CH<sub>3</sub>, and *o*-Cl derivatives cannot be ruled out.

At this point we believe that the measured  $k_q$  values most accurately represent the substituent effect on the initial electron transfer process. As such, we have used this particular set of data to determine the influence of steric ( $E_s^e$ ), polar ( $\sigma_o^-$ ,  $\sigma_{mb}$ ,  $\sigma_{pol}$ ), and radical ( $\sigma_\alpha$ ,  $\sigma_{rad}$ ,  $\sigma_{JJ\cdot}$ ) effects on this initial process. Since no *ortho*-substituent constants are available for these scales, we have opted to use the data available for the *para*-substituents. The substituent constants used in this study are listed in Table 2.

Correlation of the quenching rates with the  $\sigma_o^-$  substituent constants for *ortho*-substituents reveals a reasonable correlation ( $\rho = -1.76$ ,  $r^2 = 0.81$ ; Table 3) and suggests that there is a significant polar *electronic* contribution from the *ortho*-substituents. Correlation of the data with the steric parameter  $E_s^e$  shows that steric effects are important ( $\rho = +1.00$ ,  $r^2 = 0.81$ ), however, a dual parameter fit using both  $E_s^e$  and  $\sigma_o^-$  does not improve the correlation. To determine if there was a radical stabilization effect in these reactions, the data was correlated with both  $\sigma_o^-$  and the (*para*) radical substituent coefficients  $\sigma_{rad}$ ,  $\sigma_{JJ\cdot}$ , and  $\sigma_\alpha$ ; however, the correlations were significantly worse when including  $\sigma_{rad}$  or  $\sigma_{JJ\cdot}$  and only a small improvement was observed when using  $\sigma_o^-$  and  $\sigma_\alpha$  ( $\rho/\rho_o = 3.3$ ,  $r^2 = 0.81$ ) suggesting that radical effects are potentially important for *ortho*-substituents. Care has to be taken to interpret this data, as no *ortho*-substituent constants are available. The fact that better correlations are observed when using the  $\sigma_\alpha$  constants rather than the  $\sigma_{rad}$  or  $\sigma_{JJ\cdot}$  constants is most likely due to the fact that the  $\sigma_\alpha$  constants are derived from benzylic substrates and take into account the deviation of the half-empty orbital from the plane of the aromatic ring and the resulting decreasing spin delocalization. If this is correct, it would suggest that a resonance structure such as shown in Scheme 2b has a significant contribution.

Correlation of the log of the relative rate ( $\log(k_X/k_H)$ ) for the *meta*-substituted oximes with a variety of substituent constants reveals that both polar and radical stabilizing effects are important, however, the magnitude of the radical stabilization constant is much larger (Table 3). These analyses indicate that both polar substituent constants ( $\sigma_{pol}$  and  $\sigma_{mb}$ ) give similar results, whereas the results from the radical substituent constants are significantly different. The best results are obtained when using Creary's radical ( $\sigma_{rad}$ ) substituent constants. A dual parameter correlation using  $\sigma_{pol}$  and  $\sigma_{rad}$  gives a value of 4.2 for the ratio  $\rho_{rad}/\rho_{pol}$ . Similarly, a value of 6.2 is obtained when using  $\sigma_{mb}$  and  $\sigma_{rad}$ . All of these data clearly indicate that radical effects are important in stabilizing the transition states of the electron transfer reactions of *meta*-substituted acetophenone oximes. This is consistent with the observation by Jiang and Ji (17) who noted a *meta*-(radical) substituent effect in the thermal cycloaddition reactions of  $\alpha,\beta,\beta$ -trifluorostyrenes, which was independent of a polar effect.

Correlation of the quenching rates ( $k_q$ ) for the *para*-substituted oximes with the familiar polar and radical substituent constants shows that good results are obtained when using polar substituent constants (Table 3). The slope is typically

small, which is not unusual for radical ion reactions, and supports the formation of a positively charged species in the transition state. Poor correlations are observed when using the radical substituent constants. Clearly, radical stabilizing effects are not of significant importance for these derivatives. Dual parameter correlations do not significantly improve these results, however, there is some variation in the  $\rho_{rad}/\rho_{pol}$  ratios. Using  $\sigma^+$  and  $\sigma_{rad}$  gives  $\rho_{rad}/\rho_{pol} = 1.0$ , whereas using  $\sigma^+$  and  $\sigma_\alpha$  gives  $\rho_{rad}/\rho_{pol} = 3.7$ .

When analyzing kinetic data of this kind it is common practice to combine the results of the *meta*- and *para*-substituents. When doing so for the data presented here (Table 4), the results emphasize the observed trends for the individual series; however, overall the correlations are worse than for the individual series. This is most likely due to the fact that different stabilizing effects are important for each series of compounds. Poor correlations are observed when using  $k_q$  and the radical substituent constants and good correlations when using polar substituent constants or a dual parameter correlation. However, as stated above, a much better insight into these reactions is obtained when using individual series rather than a mixed set.

It has been suggested that substituent effects are often ground state effects rather than an effect on the transition state of the reaction under investigation, especially when considering phenols and similar species (24). To see if this is also true for these oximes, we have calculated the spin and charge distributions in the ground state (neutral) and in the radical cation species. The calculations show that both sets of compounds are affected by the substituents. In general, the radical ion species is more susceptible to these effects, however, large effects are also seen in the calculated charge densities for the neutral ground state species with -NO<sub>2</sub> and -OCH<sub>3</sub> substituents. The calculated charge densities on the carbon of the oxime moiety of the radical ion seem to accurately reflect the substituent effects. For the *ortho*-substituted substrates, a plot of the charge density against the  $\sigma_o^-$  values gives an excellent correlation ( $r^2 = 0.90$ ), whereas a plot of charge density of the neutral compound against the same  $\sigma_o^-$  values gives a poor correlation (Fig. 4a). The slopes of the two lines (0.13 vs. 0.01) are significantly different and we conclude that for the *ortho*-substrates ground state effects are less important than the effect of the substituent in the transition state of the electron transfer reaction. The calculations for the *meta*-substituted oximes show the familiar pattern of larger (more positive) charge densities on the carbon of the oxime moiety when electron-withdrawing groups are present, as can be seen from the correlation (slope = 0.08) between these calculated charge densities and the polar  $\sigma$  values ( $\sigma_{pol}$ ), which is acceptable when the *m*-OCH<sub>3</sub> point is omitted (Fig. 4b). A better correlation is observed when using the ground state charge densities of the same carbon and plotting them against  $\sigma_{pol}$  ( $r^2 = 0.91$ ), however, the slope (0.008) is smaller by a factor of 10. This clearly demonstrates that polar effects are more important for the radical ions of the *meta*-substituted oximes but not as much for the neutral ground state molecules. A reasonable correlation ( $r^2 = 0.80$ ) also exists between the calculated spin densities at the carbon of the oxime moiety and the  $\sigma_{rad}$  constants (ignoring the *m*-OCH<sub>3</sub> point). The slope in this case (-0.84) is much larger than that observed for the charge density,



**Table 2.** Substituent constants used for Hammett studies of *ortho*-, *meta*-, and *para*-substituted acetophenone oximes.

	$\sigma_o^a$	$E_s^{eb}$	$\sigma_{rad}^c$		$\sigma_{pol}^d$		$\sigma_{JJ}^e$		$\sigma_{mb}^e$		$\sigma_{\alpha}^f$	
	<i>o</i>	<i>o</i>	<i>m</i>	<i>p</i>	<i>m</i>	<i>p</i>	<i>m</i>	<i>p</i>	<i>m</i>	<i>p</i>	<i>m</i>	<i>p</i>
H	0	0	0	0	0	0	0	0	0	0	0	0
CH <sub>3</sub>	-0.13	-1.24	0.03	0.11	-0.069	-0.17	0	0.15	-0.2	-0.29	-0.001	0.001
OCH <sub>3</sub>	-0.37	-0.55	-0.02	0.24	0.115	-0.268	0.1	0.23	-0.11	-0.77		0.034
CF <sub>3</sub>	0.81	-2.4	-0.07	0.08	0.43	0.54	-0.07	-0.01	0.39	0.49	-0.014	0.001
NO <sub>2</sub>	1.20 <sup>g</sup>	-2.52	-0.11	0.57	0.71	0.778	0.001	0.36	0.69	0.86		
Cl	0.50	-0.97	-0.04	0.12	0.373	0.227	-0.05	0.22	0.12	0.11	-0.001	0.017
CN	1.18	-0.51	-0.12	0.46	0.56	0.66	0.11	0.42	0.89	0.86	-0.039	0.043
F	0.29	-0.46	-0.05	-0.08	0.337	0.062	0.03	-0.02	0.23	-0.24	-0.018	-0.011

<sup>a</sup>M.T. Tribble and J.G. Traynham. J. Am. Chem. Soc. **91**, 379 (1969).<sup>b</sup>S.H. Unger and C. Hansch. Prog. Phys. Org. Chem. **12**, 91 (1976).<sup>c</sup>X. Creary. J. Org. Chem. **45**, 280 (1980); X. Creary, M. Mehrsheikh-Mohammadi, and S. McDonald. J. Org. Chem. **52**, 3254 (1987).<sup>d</sup>D.H. McDaniel and H.C. Brown. J. Org. Chem. **23**, 420 (1958).<sup>e</sup>X.-K. Jiang and G.-Z. Ji. J. Org. Chem. **57**, 6051 (1992).<sup>f</sup>J.M. Dust and D.R. Arnold. J. Am. Chem. Soc. **105**, 1221 (1983); D.D.M. Wayner and D.R. Arnold. Can. J. Chem. **62**, 1167 (1984); D.D.M. Wayner and D.R. Arnold. Can. J. Chem. **63**, 2378 (1985); A.M. de P. Nicholas and D.R. Arnold. Can. J. Chem. **64**, 270 (1986).<sup>g</sup>M.W. Dietrich, J.S. Nash, and R.E. Keller. Anal. Chem. **38**, 1479 (1966).**Table 3.** Hammett data for *ortho*-, *meta*-, and *para*-substituted acetophenone oximes.

Parameter	<i>ortho</i>	<i>meta</i>	<i>para</i>
$\sigma_o^-$	-1.76 (0.81)		
$E_s^e$	+1.00 (0.81)		
$\sigma_{pol}$		-1.63 (0.79)	-0.73 (0.88)
$\sigma_{mb}$		-1.15 (0.82)	-0.49 (0.83)
$\sigma^+$			-0.54 (0.91)
$\sigma_{JJ}^+$		+1.08 (0.02)	-0.36 (0.04)
$\sigma_{rad}$		+8.46 (0.79)	-0.62 (0.20)
$\sigma_{\alpha}^+$		+20.0 (0.59)	+0.20 (0.00)

**Table 4.** Hammett data for *meta*- and *para*-substituted acetophenone oximes (combined).

Parameter	$\rho_{rad}$	$\rho_{JJ}$	$\rho_{pol}$	$\rho_{mb}$	$\rho_{\alpha}^+$	$r^2$
$\sigma_{pol}$			-1.06			0.70
$\sigma_{mb}$				-0.70		0.68
$\sigma_{rad}$	+0.29					0.02
$\sigma_{jj}^+$		+0.50				0.19
$\sigma_{\alpha}^+$					+7.37	0.21
$\sigma_{pol} + \sigma_{jj}^+$		-1.21	-2.49			0.71
$\sigma_{mb} + \sigma_{jj}^+$		-1.32		-1.78		0.69
$\sigma_{pol} + \sigma_{\alpha}^+$			-0.94		+4.26	0.79
$\sigma_{mb} + \sigma_{\alpha}^+$				-0.61	+2.98	0.76

suggesting that radical effects are more important than polar effects for the *meta*-substituted acetophenone oximes. These results are in good agreement with the Hammett correlations discussed above. Similar results are obtained for the *para*-substituted oximes. The calculated charge densities follow the trends as expected for typical electron-donating and electron-withdrawing groups. Correlation of the calculated charge densities with the polar parameters  $\sigma_{pol}$  and  $\sigma_{mb}$  revealed that there is a reasonable relationship between these in the ground state ( $r^2 = 0.92$  and  $0.91$ , respectively) as well

as for the radical ions ( $r^2 = 0.70$  and  $0.79$ , respectively), however, the slopes are significantly different (Fig. 4c). Good correlations are also found when using the  $\sigma^+$  constants. These results suggest that both ground state effects and stabilization of the transition state of the electron transfer pathways are important. Similar to the results for the *ortho*- and *meta*-substituted oximes, the ground state effects are less important than the transition state effects. This observation is consistent with O—H bond dissociation energy (BDE) data for a series of substituted benzaldehyde oximes as calculated by Bordwell and Ji (9a). The BDE values show little variation with different substituents (e.g., *p*-OCH<sub>3</sub> (87.8 kcal mol<sup>-1</sup>), *p*-CN (87.8 kcal mol<sup>-1</sup>, *p*-CF<sub>3</sub> (87.9 kcal mol<sup>-1</sup>)), which would be expected for compounds for which ground state effects are not important. Although it is not obvious from any of these correlations, the *p*-OCH<sub>3</sub> substituted oxime shows a somewhat abnormal behavior, similar to that observed for the *m*-OCH<sub>3</sub> derivative. The C=N bond length is significantly shorter than for most other *para*-substituted oxime radical cations and the calculated N—O bond length is much longer. These results are not as drastic as those observed for the *meta*-derivative, however, it seems to suggest that oxidation elsewhere in the molecule is competitive with oxidation of the oxime moiety. These results are supported by a plot of the log of the relative charge or spin densities against the different substituent constants. In all cases, the point for the *p*-OCH<sub>3</sub> derivative substantially deviates from the best-fit line.

In contrast to these observations are the results from the calculations on the iminoxyl radicals. The calculated spin densities on the carbon of the oxime moiety are all quite similar and do not reflect any significant substituent effects. A large amount of (negative) spin density is present on the carbon and large amounts of positive spin density are present on both the nitrogen and the oxygen. Similar results were obtained for the *meta*- and *para*-substituted iminoxyl radicals. The fact that all of the calculated parameters for the *m*-OCH<sub>3</sub> derivative are similar to those of the other *meta*-substituted oximes, confirms that the unusual behavior noted before is due to electronic effects in the radical cation. Deprotonation of the *meta*-methoxyacetophenone oxime radical

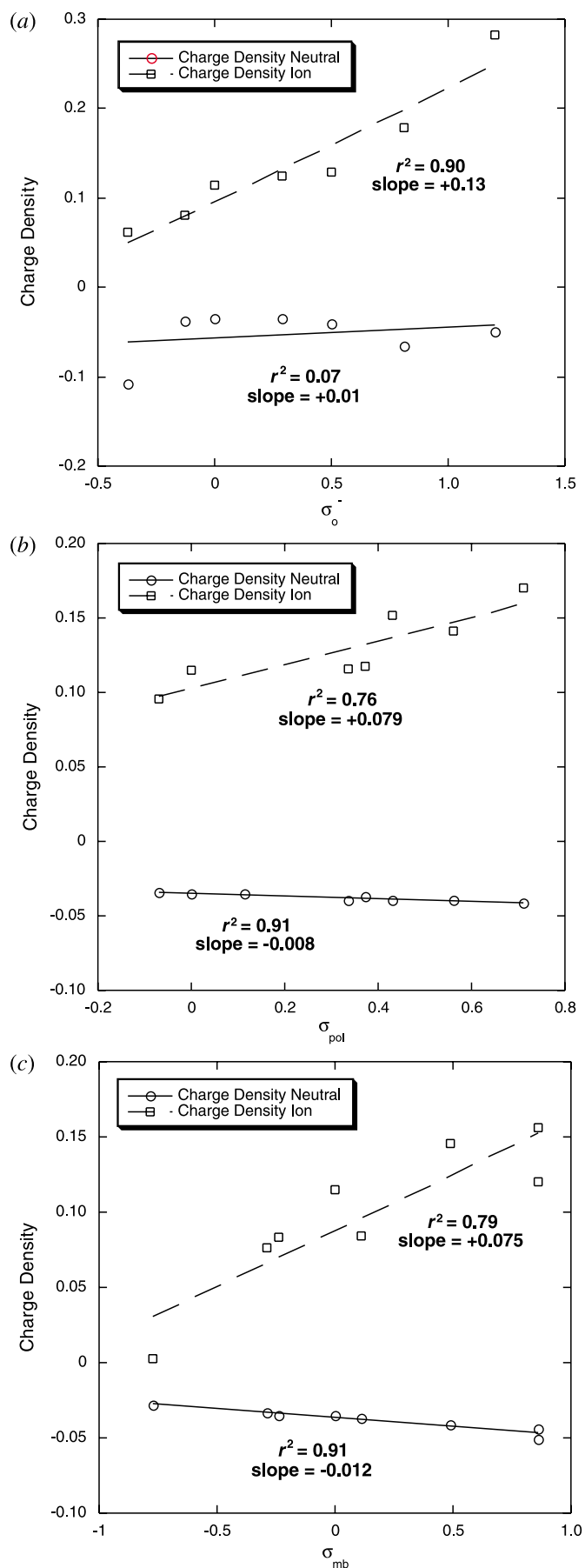


**Fig. 4.** Correlation between (a) the *ortho*-substituent constant  $\sigma_o^-$  and the calculated (AM1) charge density on the iminoxyl carbon of the *ortho*-substituted acetophenone oximes; (b) the polar (*meta*) substituent constant  $\sigma_{\text{pol}}$  and the calculated charge density on the iminoxyl carbon of the *meta*-substituted acetophenone oximes; (c) the polar (*para*) substituent constant  $\sigma_{\text{mb}}$  and the calculated charge density on the iminoxyl carbon of the *para*-substituted acetophenone oximes.

cation leads to an iminoxyl radical with electronic properties similar to those of other iminoxyl radicals. These results indicate that: (i) substituent effects are not important for iminoxyl radicals; and (ii) a complete electronic structure of iminoxyl radicals must include both configurations as shown in Scheme 2.

#### Steady-state photolysis of *meta*- and *para*-substituted acetophenone oximes

Steady-state photolysis of the oximes was carried out in a Rayonet photochemical reactor. In a typical experiment, the oxime (0.015 M) and chloranil (0.005 M) were irradiated using black lights ( $\lambda_{\text{max}} = 350$  nm) for 20 min to keep the conversion low. The progress of the reaction was followed by gas chromatography with flame ionization detection (GC-FID) and the conversion of the oximes was determined by calibrated GC-FID. Analysis of the data in Table 1 indicates that even at these short irradiation times significant conversion occurs. No obvious relationship among conversion and any other parameter ( $k_q$ ,  $E_p$ ,  $\Delta\Delta H_f$ , etc.) was found and correlation of the log of the relative conversion with the usual substituent parameters failed as well. These results can be explained on the basis of the proposed mechanism and additional data available in the literature. Several pieces of information are available. First, the measured quenching rates for the reactions of the substituted oximes with triplet chloranil are believed to represent the initial electron transfer reaction between these two species and the variation in the measured rate constants is due to substituent effects. As expected on the basis of electronic properties of these substituents, the presence of electron-donating groups increases the quenching rate and the presence of electron-withdrawing groups slows it down. Second, calculations have shown that (i) the ionization potentials correlate well with the measured rate constants (supporting the electron transfer pathway), (ii) the effects are not due to ground state effects, and (iii) the substituents have no significant effect on the spin distribution of the iminoxyl radicals. Third, Bordwell and Ji (9a) calculated the  $\text{p}K_a$  values of a variety of oximes, including several substituted benzaldehyde oximes and acetophenone oxime itself. For example, the calculated  $\text{p}K_a$  values of the oxidized *p*-CH<sub>3</sub>, *p*-OCH<sub>3</sub>, and *p*-NO<sub>2</sub> benzaldehyde oximes are -11, 0.7, and -22, respectively. Benzaldehyde oxime radical cation and acetophenone oxime radical cation both have a  $\text{p}K_a$  value of -13. These results demonstrate that electron-donating groups (-CH<sub>3</sub>, -OCH<sub>3</sub>) decrease the acidity, whereas electron-withdrawing groups (-NO<sub>2</sub>) increase the acidity of the radical ions. Combining all this data and applying it to the working mechanism of the first steps of these reactions (electron transfer followed by deprotonation of the oxime radical cation) can explain the observed conversions. Compounds with electron-donating groups are more easily oxidized and ex-





hibit fast quenching rates, however, the resulting radical ions must overcome larger barriers for the deprotonation step. The opposite is true for oximes with electron-withdrawing substituents, which have slower quenching rates but will undergo a faster deprotonation step because the resulting radical cations are more acidic. Clearly, this is a simplified picture and many more factors are likely to be important in the overall reactions of these substrates. For example, this explanation does not yet include the follow up steps, which are likely to be important. Oxidation of the iminoxyl radical (Scheme 3) would result in the formation of a carbocation species, which would be expected to show a large substituent effect. We continue to investigate the scope and limitations of the photosensitized electron transfer reactions of oximes as well as the structure and reactivity of iminoxyl radicals.

## Conclusions

This study has shown that quenching of the excited photosensitizer (chloranil) by substituted acetophenone oximes is typically fast except in those cases where there is a significant steric effect. This steric effect is only observed with the substituent in the *ortho*-position reactions and can also be noticed from the measured peak potentials. It is believed that bulky *ortho*-substituents such as  $-\text{CH}_3$ ,  $-\text{CF}_3$ ,  $-\text{NO}_2$ , and  $-\text{Cl}$  prevent the oxime moiety and aromatic ring from becoming coplanar so that conjugation is minimized. Under these conditions, energy transfer can be competitive with electron transfer as shown by significant *syn-anti* isomerization. The measured quenching rates correlate well with the calculated (AM1) ionization potentials for the radical ions, suggesting that the quenching represents an electron transfer pathway. Correlation of the quenching rates with Hammett substituent constants revealed that for the *ortho*-substituted oximes, steric ( $E_s^\circ$ ), polar electronic ( $\sigma_p^\circ$ ), and radical ( $\sigma_{\alpha\cdot}^\circ$ ) effects are important. For *meta*-substituted oximes, both polar and radical effects dominate the quenching rates, however, the large magnitude of the radical reaction constants suggests that radical effects dominate. As expected, polar effects dominate the *para*-substituted oximes. It seems clear that to predict the influence of a substituent on the photosensitized electron transfer reactions of acetophenone oximes, the best results will be obtained by analysis of the quenching rates and when studying individual series of compounds. On the basis of the correlation between calculated (AM1) charge densities on the carbon of the oxime moiety and polar substituent constants it is concluded that ground state effects are relatively unimportant and the observed substituent effects represent transition state effects. Also of importance is the observation that the quenching rates do not correlate with the measured conversions of the oximes. This is explained in terms of two important but energetically opposing steps: oxidation and deprotonation. Whether this process consists of two individual steps (oxidation followed by deprotonation) or a single proton-coupled electron transfer step is unclear, although the LFP studies currently favor the

former pathway. The latter pathway is certainly a possibility in the electrochemical experiments because of the timescale in these reactions. In the photochemical experiments it would be possible if the energetics are favorable, and on the basis of the results obtained so far, we predict that it would be more likely to occur in the case of oximes with electron-withdrawing substituents as their acidity (upon one-electron oxidation) is much larger and the deprotonation step is expected to be much faster. Future experiments will have to clarify this issue.<sup>4</sup>

## Experimental

### Materials

All chemicals other than the oximes were commercially available. Acetonitrile (Fisher) was HPLC grade and used as received. All oximes were prepared via standard procedures (25) from the corresponding ketones (Aldrich or Lancaster Synthesis, Inc.). A typical procedure consisted of combining equal amounts (~1 g) of hydroxylamine hydrochloride and the appropriate acetophenone with 5 mL of water and 3 mL of 3 M NaOH. Ethanol (95%) was used to create a clear solution, which was then refluxed for 60 min. The reaction solution was allowed to cool, and the product was extracted with diethyl ether. The solvent was evaporated and the crude product collected and purified by recrystallization or column chromatography. The purity was checked by GC-FID (> 98% peak area), GC-MS, <sup>1</sup>H NMR, FT-IR, and melting point determination.

### Steady-state photolysis experiments and sample analysis

Appropriate amounts of the *ortho*-substituted acetophenone oxime (0.025 M) and chloranil (0.025 M) were weighed out and dissolved in 5 mL of acetonitrile. The studies on the *meta*- and *para*-substituted oximes utilized 0.015 M oxime and 0.005 M chloranil. The solution was placed in a Pyrex tube and photolyzed in a Rayonet RPR-100 photochemical reactor, equipped with 16 RPR-3500A (black light phosphor) bulbs ( $\lambda = 350$  nm) for up to 3 h. The progress of the reactions was followed by GC-FID and the products were identified by GC-MS. Conversion of the starting material and product yields were determined by calibrated GC-FID. Sample analyses were performed on a Hewlett-Packard 5890 series II gas chromatograph coupled to a Hewlett-Packard 5971 series mass selective detector (MSD) and on a Perkin-Elmer (PE) Autosystem equipped with a flame ionization detector (FID). The HP GC-MS was equipped with an HP-5 capillary column (30 m  $\times$  0.25 mm i.d., film thickness 0.25 mm). The PE GC-FID was equipped with a Chrompack CP-Sil-5-Cb capillary column (30 m  $\times$  0.32 mm i.d., film thickness 0.25 mm).

### Cyclic voltammetric measurements

Cyclic voltammetry at a sweep rate of 100 mV s<sup>-1</sup> was used to obtain the oxidation potential of the oximes. All electrochemical experiments were performed using a BAS CV-50 voltammetric analyzer and a BAS C3 electrochemis-

<sup>4</sup>Supplementary data may be purchased from the Depository of Unpublished Data, Document Delivery, CISTI, National Research Council Canada, Ottawa, ON K1A 0S2, Canada ([http://www.nrc.ca/cisti/irm/unpub\\_e.shtml](http://www.nrc.ca/cisti/irm/unpub_e.shtml) for information on ordering electronically). These data can be obtained, free of charge, via [www.ccdc.cam.ac.uk/conts/retrieving.html](http://www.ccdc.cam.ac.uk/conts/retrieving.html) (or from the Cambridge Crystallographic Data Centre, 12 Union Road, Cambridge CB2 1EZ, U.K.; fax +44 1223 336033; or [deposit@ccdc.cam.ac.uk](mailto:deposit@ccdc.cam.ac.uk)).



try cell stand. The working electrode (BAS MF-2013) consisted of a platinum disk (1.6 mm diameter) embedded in a CTFE plastic rod. The counter electrode was a platinum wire (BAS MF-1032). The reference electrode was a BAS RE-5B Ag/AgCl (MF-2079) electrode. Tetraethylammonium perchlorate (TEAP, 0.1 M solution in acetonitrile) was used as the electrolyte; the oxime concentration was ca. 0.005 M. The reported potentials were referenced to the  $\text{Fc}^+/\text{Fc}$  couple. All measurements were carried out under an argon atmosphere.

### Theoretical calculations

AM1 calculations (22) were performed using the program MacSpartan Pro 1.0.4 (26) on a PowerMac G4. The lowest energy conformers were obtained from a conformer distribution search. Geometry optimizations were performed at the AM1 level of theory.

### Laser flash photolysis

The apparatus used for the kinetic laser flash photolysis (LFP) experiments was of standard design (27) and the details have been described elsewhere (28). The quenching rates were obtained as follows. An acetonitrile (spectrophotometric grade) solution containing chloranil (CA, OD ~ 0.5–1) in a glass cuvet was purged with argon for about 5 min. The sample was subjected to the laser pulse (355 nm, 10 Hz, 0.5–2 mJ/pulse, 4 ns pulse width) and the decay of  $^3\text{CA}$  at 510 nm was observed. Small amounts (10–25  $\mu\text{L}$ ) of the quencher (~0.015 M oxime standard solutions in acetonitrile) were added to the solution after which the decay was measured. The quenching rate was obtained from a plot of the measured decay rates against the quencher concentration.

Detailed descriptions of the nanosecond transient absorption apparatus used for the spectral studies are given elsewhere (29). Spectra were obtained by flash photolysis (343 nm, 15 ns, 3 mJ) of argon-saturated acetonitrile solutions (3 mL) in a quartz cuvet containing the oxime (10 mM) and chloranil (OD ~ 0.5–1).

### Acknowledgements

Acknowledgement is made to the donors of the Petroleum Research Fund, administered by the American Chemical Society, and to the Research Corporation for support of this work. Part of this work is based upon work supported by the National Science Foundation under Grant No. 0097795. We are grateful to Professors J.P. Dinnocenzo (University of Rochester) and I.R. Gould (Arizona State University) for the use of their laser flash photolysis equipment.

### References

- (a) G.W. Kabalaka, R.D. Pace, and P.P. Wadgaonkar. *Synth. Commun.* **20**, 2453 (1990); (b) S.R. Sandler and W. Karo. *Organic functional group preparation*. Academic Press, Inc., San Diego. 1989. pp. 430–481.
- (a) C.H. DePuy and B.W. Ponder. *J. Am. Chem. Soc.* **81**, 4629 (1959); (b) E.B. Hershberg. *J. Org. Chem.* **13**, 542 (1948); (c) M.P. Cava, R.L. Little, and D.R. Napier. *J. Am. Chem. Soc.* **80**, 2257 (1958); (d) S.H. Pines, J.M. Chemerda, and M.A. Kozlowski. *J. Org. Chem.* **31**, 3446 (1966); (e) P.M. Pojer. *Aust. J. Chem.* **32**, 201 (1979); (f) J.W. Bird and D.G. Diaper. *Can. J. Chem.* **47**, 145 (1969); (g) H.C. Araujo, G.A.L. Ferreira, and J.R. Mahajan. *J. Chem. Soc., Perkin Trans. 1*, 2257 (1974); (h) A. McKillop, J.D. Hunt, R.D. Naylor, and E.C. Taylor. *J. Am. Chem. Soc.* **93**, 4918 (1971); (i) G.A. Olah, Y.D. Vankar, and G.K.S. Prakash. *Synthesis*, 113 (1997); (j) J.R. Maloney, R.E. Lyle, J.E. Saavedra, and G.L. Lyle. *Synthesis*, 212 (1974); (k) J. Drabowicz. *J. Chem. Soc., Chem. Commun.* 125 (1980).
- M.F. Haley and K. Yates. *J. Org. Chem.* **52**, 1817 (1987).
- (a) J.H. Amin and P. de Mayo. *Tetrahedron Lett.* 1585 (1963); (b) G. Just and C. Pace-Asciak. *Tetrahedron*, **22**, 1069 (1966); (c) R.T. Taylor, M. Douek, and G. Just. *Tetrahedron Lett.* 4143 (1966); (d) G. Just and L.S. Ng. *Can. J. Chem.* **46**, 3381 (1968); (e) T. Oine and T. Mukai. *Tetrahedron Lett.* 157 (1969); (f) M. Cunningham, L.S. Ng Lim, and G. Just. *Can. J. Chem.* **49**, 2891 (1971); (g) G. Just and M. Cunningham. *Tetrahedron Lett.* 1151 (1971); (h) H. Sugimoto, K. Furukawa, and K. Orito. *J. Chem. Soc., Perkin Trans. 1*, 917 (1991); (i) Y. Ogata, K. Takagi, and K. Mizuno. *J. Org. Chem.* **47**, 3684 (1982); (j) A. Padwa and F. Albrecht. *J. Am. Chem. Soc.* **96**, 4849 (1974).
- H.J.P. de Lijser, F.H. Fardoun, J.R. Sawyer, and M. Quant. *Org. Lett.* **4**, 2325 (2002).
- For a recent investigation on proton-coupled electron transfer (PCET) see: R.I. Cukier. *J. Phys. Chem. A*, **103**, 5989 (1999), and refs. therein.
- (a) S.A. Everett, M.A. Naylor, M.R.L. Stratford, K.B. Patel, E. Ford, A. Mortensen, A.C. Ferguson, B. Vojnovic, and P. Wardman. *J. Chem. Soc., Perkin Trans. 2*, 1989 (2001); (b) L. Benchariff, A. Tallec, and R. Tardivel. *Electrochim. Acta*, **42**, 3509 (1997); (c) C.J. Rhodes and H. Agirbas. *J. Chem. Soc., Faraday Trans. 86*, 3303 (1990); (d) D.G. Horne and R.G.W. Norrish. *Proc. R. Soc. London Ser. A*, **315**, 287 (1970); (e) D.J. Edge and R.O.C. Norman. *J. Chem. Soc. B*, 182 (1969); (f) P. Smith and W.M. Fox. *Can. J. Chem.* **47**, 2227 (1969); (g) J.Q. Adams. *J. Am. Chem. Soc.* **89**, 6022 (1967); (h) R.N. Butler, F.L. Scott, and T.A.F. O'Mahony. *Chem. Rev.* **73**, 93 (1973); (i) J.W. Lown. *J. Chem. Soc. B*, 441 (1966); (j) G. Just and K. Dahl. *Tetrahedron Lett.* 2441 (1966); (k) H. Lemaire and A. Rassat. *Tetrahedron Lett.* 2245 (1964); (l) J.W. Bird and D.G.M. Diaper. *Can. J. Chem.* **47**, 145 (1969); (m) T. Cai, M. Xian, and P.G. Wang. *Bioorg. Med. Chem. Lett.* **12**, 1507 (2002); (n) Y. Sanakis, C. Goussias, R.P. Mason, and V. Petrouleas. *Biochemistry*, **36**, 1411 (1997).
- (a) K.U. Ingold and S. Brownstein. *J. Am. Chem. Soc.* **97**, 1817 (1975); (b) L.R. Mahoney, G.D. Mendenhall, and K.U. Ingold. *J. Am. Chem. Soc.* **95**, 8610 (1973); (c) J.L. Brokenshire, J.R. Roberts, and K.U. Ingold. *J. Am. Chem. Soc.* **94**, 7040 (1972); (d) J.L. Brokenshire, G.D. Mendenhall, and K.U. Ingold. *J. Am. Chem. Soc.* **93**, 5278 (1971); (e) G.D. Mendenhall and K.U. Ingold. *J. Am. Chem. Soc.* **95**, 627 (1973); (f) G.D. Mendenhall and K.U. Ingold. *J. Am. Chem. Soc.* **95**, 2963 (1973).
- (a) F.G. Bordwell and G.-Z. Ji. *J. Org. Chem.* **57**, 3019 (1992); (b) F.G. Bordwell, X.-M. Zhang, A.V. Satish, and J.-P. Cheng. *J. Am. Chem. Soc.* **116**, 6605 (1994); (c) F.G. Bordwell and S. Zhang. *J. Am. Chem. Soc.* **117**, 4858 (1995); (d) F.G. Bordwell, Y. Zhao, and J.-P. Cheng. *J. Phys. Org. Chem.* **11**, 10 (1998).
- (a) J.E. Leffler and E. Grunwald. *Rates and equilibria of organic reactions*. John Wiley, New York. 1963; (b) L.P. Hammett. *Physical organic chemistry*. 2nd ed. McGraw-Hill, New York. 1970; (c) N.B. Chapman. *In Advances in linear free energy relationships*. Edited by J. Shorter. Plenum Press, New York.



- 1972; (d) N.B. Chapman and J. Shorter. Correlation analysis in chemistry. Plenum Press, New York. 1978.
11. Excited state  $\sigma$  scales: A.L. Pincock, J.A. Pincock, and R. Stefanova. *J. Am. Chem. Soc.* **124** (2002), and refs. therein.
12. (a) D.A.D. Jones and G.G. Smith. *J. Org. Chem.* **29**, 3531 (1964); (b) N.B. Chapman, M.G. Rodgers, and J. Shorter. *J. Chem. Soc. B*, 157 (1968); (c) M.T. Tribble and J.G. Traynham. *J. Am. Chem. Soc.* **91**, 379 (1969); (d) T. Fujita. *Anal. Chim. Acta*, **133**, 667 (1981).
13. M.W. Dietrich, J.S. Nash, and R.E. Keller. *Anal. Chem.* **38**, 1479 (1966).
14. R.W. Taft, Jr. *In steric effects in organic chemistry. Edited by M.S. Newman.* John Wiley and Sons, Inc., New York. 1965.
15. M. Charton. *J. Am. Chem. Soc.* **91**, 615 (1969).
16. S.H. Unger and C. Hansch. *Prog. Phys. Org. Chem.* **12**, 91 (1976).
17. (a) J.M. Dust and D.R. Arnold. *J. Am. Chem. Soc.* **105**, 1221 (1983); (b) D.D.M. Wayner and D.R. Arnold. *Can. J. Chem.* **62**, 1167 (1984); (c) D.D.M. Wayner and D.R. Arnold. *J. Chem.* **63**, 2378 (1985); (d) A.M. de P. Nicholas and D.R. Arnold. *Can. J. Chem.* **64**, 270 (1986); (e) X. Creary. *J. Org. Chem.* **45**, 280 (1980); (f) X. Creary, M. Mehrsheikh-Mohammadi, and S. McDonald. *J. Org. Chem.* **52**, 3254 (1987); (g) S. Dinçtürk, R.A. Jackson, and M. Townson. *J. Chem. Soc. Chem Commun.* 172 (1979); (h) Dinçtürk, R.A. Jackson, M. Townson, H. Agirbas, N.C. Billingham, and G. March. *J. Chem. Soc., Perkin Trans. 2*, 1121 (1981); (i) S. Dinçtürk and R.A. Jackson. *J. Chem. Soc., Perkin Trans. 2*, 1127 (1981); (j) H. Agirbas and R.A. Jackson. *J. Chem. Soc., Perkin Trans. 2*, 739 (1983); (k) T.H. Fisher and A.W. Meierhofer. *J. Org. Chem.* **443**, 224 (1978); (l) X.-K. Jiang and G.-Z. Ji. *J. Org. Chem.* **57**, 6051 (1992); (m) H.G. Viehe, Z. Janousek, and R. Merényi (*Editors*). *Substituent effects in radical chemistry.* NATO ASI Ser., Ser. C. Vol. 189. Reidel, Dordrecht, The Netherlands. 1986.
18. H.C. Brown and Y. Okamoto. *J. Am. Chem. Soc.* **80**, 4979 (1958).
19. (a) P.M. Nave and W.S. Trahanovsky. *J. Am. Chem. Soc.* **90**, 4755 (1968); (b) F.A. Carroll, M.T. McCall, and G.S. Hammond. *J. Am. Chem. Soc.* **95**, 315 (1973); (c) D.D. Tanner, J.A. Plambeck, D.W. Reed, and T.W. Mojelsky. *J. Org. Chem.* **45**, 5177 (1980); (d) S. Oae, Y. Watanabe, and K. Fujimori. *Tetrahedron Lett.* **23**, 1189 (1982); (e) M.A. Fox and C.-C. Chen. *Tetrahedron Lett.* **24**, 547 (1983); (f) S. Oae, K. Asada, and T. Yoshimura. *Tetrahedron Lett.* **24**, 1265 (1983); (g) K.E. O'Shea and C. Cardona. *J. Org. Chem.* **59**, 5005 (1994); (h) N.L. Bauld and W. Yueh. *J. Am. Chem. Soc.* **116**, 8845 (1994); (i) N.L. Bauld, J.T. Aplin, W. Yueh, and A. Loinaz. *J. Am. Chem. Soc.* **119**, 11 381 (1997).
20. O. Exner. *In Advances in linear free energy relationships. Edited by J. Shorter.* Plenum Press, New York. 1972. p. 50.
21. (a) T.M. Bockman and J.K. Kochi. *J. Chem. Soc., Perkin Trans. 2*, 1633 (1996); (b) G. Jones, II, N. Mouli, W.A. Haney, and W.R. Bergmark. *J. Am. Chem. Soc.* **119**, 8788 (1997).
22. M.J.S. Dewar, E.G. Zoebisch, E.F. Healy, and J.J.P. Stewart. *J. Am. Chem. Soc.* **107**, 3902 (1985).
23. D. Rehm and A. Weller. *Isr. J. Chem.* **8**, 259 (1970).
24. K.B. Clark and D.D.M. Wayner. *J. Am. Chem. Soc.* **113**, 9363 (1991).
25. A.I. Vogel, B.S. Furniss, A.J. Hannaford, P.W.G. Smith, and A.R. Tatchell. *Vogel's textbook of practical organic chemistry.* 5th ed. Longman, New York. 1989.
26. MacSpartan [computer program], version 1.0.4. 2001. Wavefunction, Inc., 18401 Von Karman Avenue, Suite 370, Irvine, CA 92715, U.S.A.
27. W.G. Herkstroeter and I.R. Gould. *In Physical methods of chemistry series. Vol. 8. 2nd ed. Edited by B. Rossiter and R. Baetzold.* Wiley, New York. 1993. p. 225.
28. E.D. Lorange, W.H. Kramer, and I.R. Gould. *J. Am. Chem. Soc.* **124**, 15 225 (2002).
29. L. Chen, M.S. Farahat, E.R. Gaillard, S. Farid, and D.G. Whitten. *J. Photochem. Photobiol. A*, **95**, 21 (1996).



# Chemistry of photogenerated $\alpha$ -hydroxy-*p*-nitrobenzyl carbanions in aqueous solution: protonation vs. disproportionation

James Morrison, Peter Wan, John E.T. Corrie, and V. Ranjit N. Munasinghe

**Abstract:** The photochemistry of *p*-nitrobenzyl derivatives **6–10** has been studied in aqueous solution as a function of pH, using product analysis, UV–vis spectrophotometry, and laser flash photolysis (LFP). The compounds were chosen with the aim of further exploring the propensity of these systems to give rise to  $\alpha$ -hydroxy-*p*-nitrobenzyl carbanions on photolysis, and to study their mechanisms of subsequent reaction.  $\alpha$ -Hydroxy-substituted carbanions are anions that cannot be readily formed using thermal routes but which are believed to have some interesting chemistry. Three methods were employed for photogenerating these carbanions: (i) decarboxylation; (ii) retro-Aldol reaction; and (iii) carbon acid deprotonation. All three methods proved to be successful using the *p*-nitrobenzyl chromophore. Photogenerated  $\alpha$ -hydroxy-*p*-nitrobenzyl carbanions react via disproportionation, giving rise to oxidized and reduced products; simple protonation of the anion was undetectable.

**Key words:** photodecarboxylation, nitrobenzyl carbanions, photoredox, nitroaromatic compounds, excited-state carbon acids.

**Résumé :** Opérant en solutions aqueuses en fonction du pH et faisant appel à l'analyse des produits, à la spectrophotométrie UV–vis et à la photolyse éclair au laser, on a étudié la photochimie des dérivés *p*-nitrobenzyles (**6–10**). On a choisi les composés dans le but de pouvoir explorer plus à fond la propension de ces systèmes de donner naissance à des carbanions  $\alpha$ -hydroxy-*p*-nitrophényles par photolyse et d'étudier les mécanismes de leur réaction subséquente. Les carbanions portant un substituant  $\alpha$ -hydroxy sont des anions qui ne peuvent pas se former facilement par les voies thermiques, mais que l'on soupçonne d'avoir des propriétés chimiques intéressantes. On a utilisé trois méthodes pour la photogénération de ces carbanions: (i) la décarboxylation; (ii) la réaction rétroaldolique et (iii) la déprotonation d'un acide carbonique. Ces trois méthodes ont été couronnées de succès avec le chromophore *p*-nitrobenzyle. Les carbanions  $\alpha$ -hydroxy-*p*-nitrobenzyles photogénérés réagissent par une réaction de métathèse qui conduit à la formation de produits oxydés et de produits réduits; on n'a pas pu mettre en évidence de protonation simple de l'anion.

**Mots clés :** photodécarboxylation, carbanions nitrobenzyles, photorédox, composés nitroaromatiques, état excité d'acides carbonés.

[Traduit par la Rédaction]

## Introduction

Carbanions are synthetically useful and fundamentally important reactive intermediates in organic chemistry (1). The reactivity of carbanions as either nucleophiles, bases, or as electron donors is well-known and substituents strongly influence their stability and reactivity. This is exemplified by the enormous range of carbon acid  $pK_a$  values (1) and these data are useful in predicting the conditions necessary to generate a carbanion and its subsequent reactivity. Substituent effects on the negatively charged intermediate may be manifested through resonance, inductive effects, or by providing a new reaction pathway.  $\alpha$ -Hydroxy carbanions **1**, in which

an hydroxy group (an oxygen acid) is directly attached to the carbanion, are an interesting type of carbanion whose formation and stability has been the subject of theoretical interest (2, 3). However, for obvious reasons, the breadth of experimental knowledge of these carbanions is quite limited. Nonetheless,  $\alpha$ -hydroxy carbanions have been proposed as intermediates in photochemical (4–6) and enzymatically catalyzed (7, 8) reactions.



Received 3 January 2003. Published on the NRC Research Press Web site at <http://canjchem.nrc.ca> on 26 May 2003.

*Dedicated to Professor Don Arnold for his contributions to chemistry.*

**J. Morrison and P. Wan.**<sup>1</sup> Department of Chemistry, Box 3065, University of Victoria, Victoria, BC V8W 3V6, Canada.

**J.E.T. Corrie<sup>2</sup> and V.R.N. Munasinghe.** National Institute for Medical Research, The Ridgeway, Mill Hill, London, NW7 1AA, U.K.

<sup>1</sup>Corresponding author (e-mail: [pwan@uvic.ca](mailto:pwan@uvic.ca)).

<sup>2</sup>Corresponding author (e-mail: [jcorrie@nimr.mrc.ac.uk](mailto:jcorrie@nimr.mrc.ac.uk)).

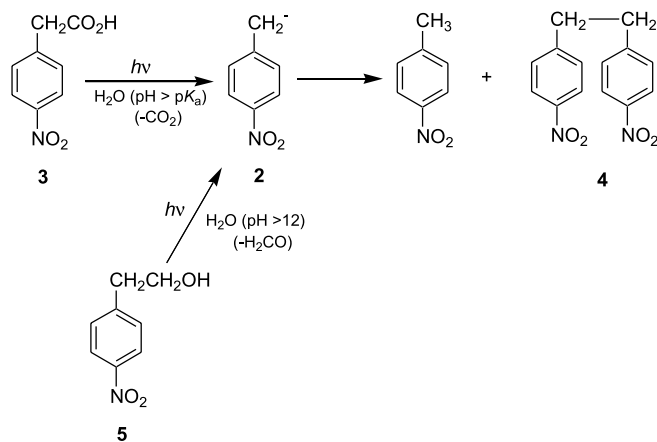


To study “free” carbanions in solution it is advantageous to generate appreciable amounts of these intermediates quickly. A well-known route is via photochemical reaction (9), preferably one that is fast and efficient. The simplest conceivable photochemical route to a carbanion is via a heterolytic C—C or C—H bond cleavage, for example via photodecarboxylation or photodeprotonation, respectively. Nitrobenzyl compounds, with their electron-withdrawing nitro group, are particularly adept at inducing these photochemical reactions, generally via the triplet excited state (10, 11). While it is well-known that *o*-nitrobenzyl systems are highly photoreactive (generally via initial transfer of the benzylic hydrogen to the nitro group), the *m*- and *p*-isomers also display a range of photochemical reactivity not often reported for the *o*-isomer (10, 11). Both *m*- and *p*-nitrobenzyl compounds are known to undergo a variety of photofragmentation reactions, such as photodecarboxylation (12), photodeprotonation (4), and photoretro-aldol reaction (13), all of which have been proposed to generate *m*- and *p*-nitrobenzyl carbanions as intermediates. However, prior to our studies, only the parent *p*-nitrobenzyl carbanion was observed by transient methods (vide infra).

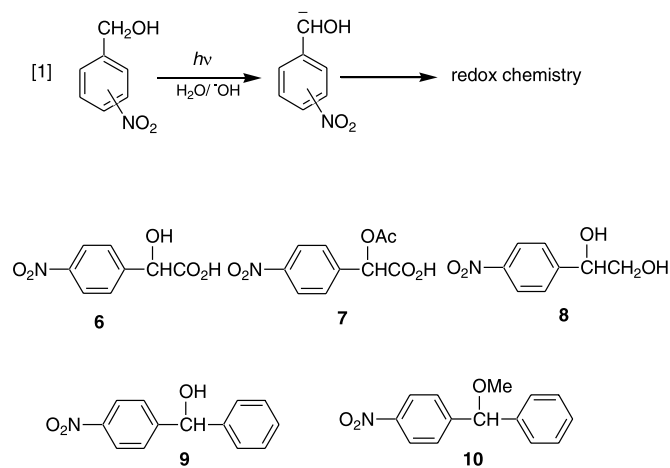
Margerum and Petrusis (12) were the first to investigate the chemistry of photogenerated *p*-nitrobenzyl carbanion (**2**), which they prepared by photodecarboxylation of *p*-nitrophenylacetic acid (**3**) (Scheme 1). The observed chemistry of photogenerated **2**, to give *p*-nitrotoluene (simple protonation) and *p,p'*-dinitrobenzyl (**4**) (disproportionation product), may be described as “conventional” *p*-nitrobenzyl carbanion chemistry since thermally generated **2** (formed by deprotonation of *p*-nitrotoluene in *tert*-butyl alcohol – KOH) has also been observed to give **4** (14–16). Carbanion **2** is strongly stabilized by the *p*-nitrophenyl ring and is thus readily observable by UV–vis spectrophotometry as well as by  $\mu$ s and faster laser flash photolysis (LFP) ( $\lambda_{\text{max}}$  358 nm;  $\tau$  = 53 s at pH 13) (12). The complex decay kinetics of carbanion **2** (mixed first- and second-order) were studied in some detail by Craig et al. (17, 18), who explained the data as arising via two competing pathways of reaction: (i) a simple protonation pathway to give *p*-nitrotoluene; and (ii) a bimolecular coupling pathway (of two molecules of **2**), followed by loss of two electrons (the final fate of which was not determined) to form **4**. Wan and Muralidharan (13) discovered a second method for generating carbanion **2**, by base-catalyzed photoretro-aldol reaction of **5**, with subsequent chemistry identical to that reported above.

The chemistry of  $\alpha$ -hydroxy-nitrobenzyl carbanions is not as well understood. Wan and Yates (4) first proposed water and hydroxide-mediated photodeprotonation of the benzylic proton of *m*- and *p*-nitrobenzyl alcohols, to give the corresponding  $\alpha$ -hydroxy nitrobenzyl carbanions (eq. [1]). In retrospect, the proposal of C—H bond deprotonation in the excited (triplet) state as a primary step was unusual, as there was no precedent for such a pathway at the time. In addition, reprotonation of these carbanions apparently does not occur, as shown by the absence of deuterium exchange, but instead redox chemistry was observed (4). *p*-Nitrobenzyl alcohol was found to give a simple intramolecular redox product in base (*p*-nitrosobenzaldehyde), whereas *m*-nitrobenzyl alcohol gave a mixture of *m*-nitrobenzaldehyde (60–70%) and *m*-azoxybenzaldehyde (40–30%) (in neutral, acid, and basic

Scheme 1.



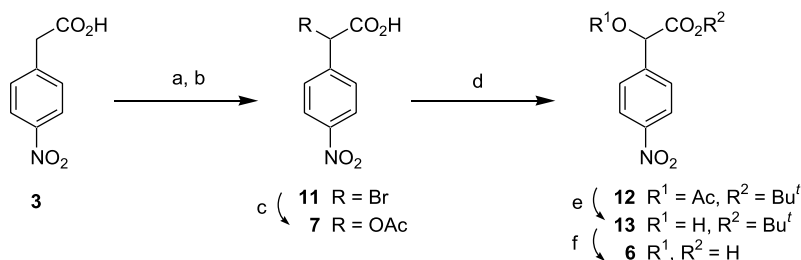
solutions), via an apparent disproportionation of the photo-generated carbanion. Disproportionation chemistry has also been observed for photogenerated  $\alpha$ -hydroxy-*p*-(*p*-nitrophenyl)benzyl carbanion in neutral solution (6). The observation of disproportionation and redox pathways is perhaps not unexpected considering that even the parent *p*-nitrobenzyl carbanion (**2**) displays this kind of reactivity. Moreover, theoretical calculations (3) have shown that simple anions (in the gas phase) such as  $^-\text{CH}_2\text{OH}$  and  $^-\text{CH}_2\text{NH}_2$  are unstable with respect to their radicals. This suggests that carbanions of this kind have an intrinsic propensity for disproportionation chemistry (for example, via initial electron transfer). Some of the products described above (4, 6) are consistent with this pathway.



The aim of this work is to study in more detail the chemistry of a variety of photogenerated  $\alpha$ -hydroxy-*p*-nitrobenzyl carbanions (**1**,  $\text{R}' = p\text{-nitrophenyl}$ ) and related species, using product studies and LFP. For this purpose *p*-nitromandelic acid (**6**) and its *O*-acetyl derivative **7** are obvious initial substrates since it is anticipated that these compounds will undergo efficient photodecarboxylation, to give the corresponding  $\alpha$ -hydroxy and  $\alpha$ -acetoxy-*p*-nitrobenzyl carbanions. *p*-Nitrophenylethylene glycol (**8**) would be expected to undergo base-catalyzed photoretro-aldol reaction to give the parent  $\alpha$ -hydroxy-*p*-nitrobenzyl carbanion in basic medium. Finally, *p*-nitrobenzhydrol (**9**), and the corresponding methyl



**Scheme 2.** Synthesis of **6** and **7**. Reagents and conditions: (a)  $\text{SOCl}_2$ ; (b)  $\text{Br}_2$ ; (c)  $\text{Hg}(\text{OAc})_2$ ,  $\text{HOAc}$ ; (d)  $\text{Cl}_3\text{C}(\text{NH})\text{O}-t\text{-Bu}$ ,  $\text{CH}_2\text{Cl}_2$ ; (e)  $\text{CsCO}_3$ ,  $\text{MeOH}$ ; (f)  $\text{TFA}$ .



ether **10** are expected to give  $\alpha$ -hydroxy (or methoxy)  $p$ -nitrobenzyl carbanions via photodeprotonation.

## Results and discussion

### Materials

$p$ -Nitromandelic acid (**6**) is only sporadically reported in the literature and its synthesis, unlike that of the corresponding  $o$ -nitro isomer (**19**), is surprisingly difficult. In our hands the complex procedure described by Carrara et al. (20), based on formation of  $p$ -nitromandelonitrile and subsequent acidic hydrolysis, was not reproducible. We, therefore, adopted the route shown in Scheme 2 which yielded first the  $O$ -acetyl derivative **7**. Because of concerns about the stability of **6** under basic conditions and possible difficulties of isolation, we chose to prepare it via the *tert*-butyl ester **12**. Subsequent mild base treatment ( $\text{CsCO}_3$  in methanol) gave the alcohol **13**, from which **6** was obtained by  $\text{TFA}$ -mediated cleavage of the *tert*-butyl group.

Glycol **8** was available from a previous study (21).  $p$ -Nitrobenzhydrol (**9**) and its methyl ether derivative **10** were made by standard methods (see *Experimental*).

### Product studies

UV-vis spectrophotometry was used as a quick and informative tool to monitor the photochemistry of substrates **6–10** under various conditions and preparative photolyses were used to identify products formed. Photolysis of  $p$ -nitromandelic acid (**6**) as its carboxylate salt ( $\sim 100\%$   $\text{H}_2\text{O}$ , pH 7, Ar purged, Rayonet photoreactor, 300 nm) in a UV cuvette resulted in formation of new (permanent) absorption bands at 289 and 308 nm (Fig. 1). No transient species was observed on this time scale. Strikingly different spectral changes that imply different photochemistry were observed upon photolysis of the  $O$ -acetyl derivative **7** (Fig. 2). A strong absorption band at 369 nm that was observed immediately after brief irradiation (Ar purged) decayed via complex kinetics over the course of several minutes (Fig. 3; the decay cannot be satisfactorily fitted to either first- or second-order kinetics; it is assumed to be a mixture of these components). The overall decay was slower in  $\text{D}_2\text{O}$ , consistent with a component of the processes involving proton (deuteron) transfer from solvent. The 369 nm absorption band was not observed using this technique upon photolysis of **7** in oxygen-saturated solution ( $\tau < 10$  s). These observations are very similar to those reported for the 358 nm absorption band of the parent  $p$ -nitrobenzyl carbanion (**2**) (12, 17, 18).

Therefore, the 369 nm transient is assigned to  $\alpha$ -acetoxy- $p$ -nitrobenzyl carbanion (**14**).

Preparative photolysis of **6** and **7** ( $1 \times 10^{-3}$  M, 1:1  $\text{H}_2\text{O}-\text{CH}_3\text{CN}$ , Rayonet photoreactor, 300 nm) confirmed the observations from UV-vis spectrophotometry that indicated different reaction pathways for these compounds. Low conversion runs ( $< 30\%$ ) of **6** at pH 7 (Ar purged) followed by product isolation gave  $p$ -nitrobenzaldehyde (**15**) and  $p,p'$ -azoxybisbenzaldehyde (**16**) (Scheme 3). The relative yields of **15** and **16** (60–70% and 40–30%, respectively) were independent of conversion (up to  $\sim 40\%$ ), consistent with both being primary photoproducts. These are the expected disproportionation products of an  $\alpha$ -hydroxy- $p$ -nitrobenzyl carbanion intermediate, analogous to the reported products of the photochemistry of  $m$ -nitrobenzyl alcohol (**4**) and  $p$ -( $p$ -nitrophenyl)benzyl alcohol (**6**). At high conversion ( $> 50\%$ ) insoluble orange precipitates and some soluble (but unidentified) secondary photoproducts were observed. Photolysis of **6** in oxygen-saturated solution gave mostly **15** ( $> 90\%$ ) and some minor unidentified products. At pH 13 (Ar purged), low conversion ( $\sim 15\%$ ) runs gave **15** and **16** (60–70% and 40–30%, respectively, as at pH 7). Photolysis at pH 3 gave the intramolecular redox product  $p$ -nitrosobenzaldehyde (**17**) in addition to **15** and **16** (relative yields 28:50:22). The formation of **17** in acidic solution is reminiscent of the intramolecular photoredox chemistry reported for  $p$ -nitrobiphenyl systems (6). We were not able to enhance the relative yield of **17** since the photodecarboxylation quantum yield becomes negligible in solutions below pH 3, because ionization of the carboxylic acid is suppressed. For example, irradiation of **6** at pH 1 resulted in quantitative recovery of substrate. These observations are consistent with a mechanism in which **17** must arise via initial decarboxylation of the ionized form of **6**. The requirement of an acidic solution for formation of **17** will be discussed later.

Preparative photolysis of **7** (pH 7, Ar purged) gave the product of simple decarboxylation, i.e.,  $p$ -nitrobenzyl acetate (**18**) and the expected disproportionation product,  $\alpha,\alpha'$ -bisacetoxy- $p,p'$ -dinitrobenzyl (**19**) (eq. [2]). The relative yield of **18** to **19** was  $\sim 1:1$  in  $\text{H}_2\text{O}-\text{CH}_3\text{CN}$  but this ratio was dramatically altered in 1:1  $\text{D}_2\text{O}-\text{CH}_3\text{CN}$  ( $\sim 5\%$   $\alpha$ -deuterated **18** and  $\sim 95\%$  **19**). Thus, when the protonation pathway (**14**  $\rightarrow$  **18**) is retarded in  $\text{D}_2\text{O}$  by a primary solvent isotope effect, the disproportionation pathway that gives **19** becomes dominant. Photolysis of **7** in oxygen-saturated solution gave **15** (60%) and  $p$ -nitrobenzoic acid (40%); neither **18** nor **19** was observed. This indicates that interception of



**Fig. 1.** UV-vis traces observed on photolysis of **6** in ~100% H<sub>2</sub>O ( $6.6 \times 10^{-5}$  M, 0.01 M pH 7 phosphate buffer, Ar purged). Each trace represents 15 s irradiation at 300 nm (4 lamps). Arrows indicate changes in absorbance.

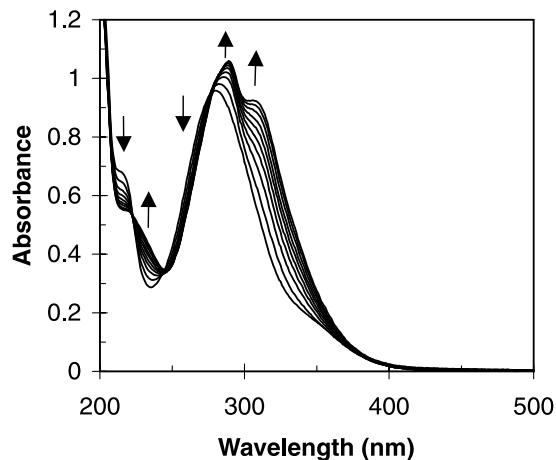
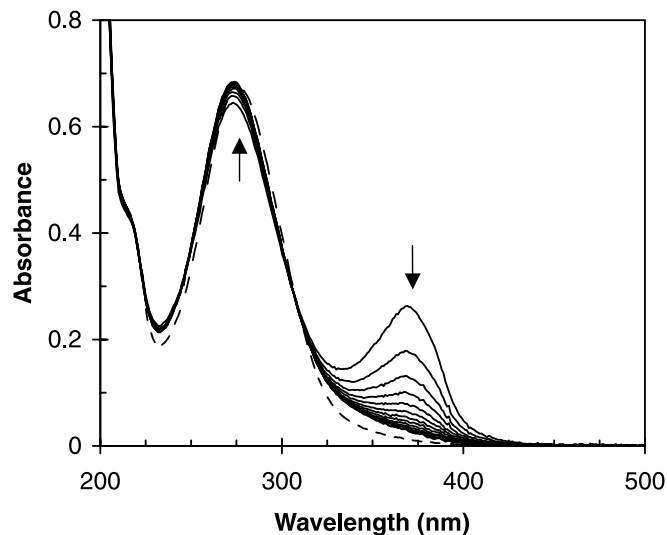
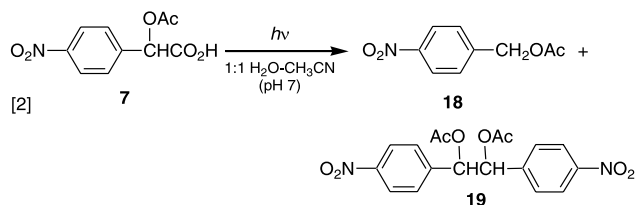


**Fig. 2.** UV-vis traces observed before (dashed line) and immediately following 15 s photolysis (300 nm, 16 lamps) of **7** in ~100% H<sub>2</sub>O (solid lines) ( $6.7 \times 10^{-5}$  M, 0.01 M pH 7 phosphate buffer, Ar purged). Each trace of the dark reaction is separated by 30 s. Arrows indicate changes in absorbance during the dark reaction.

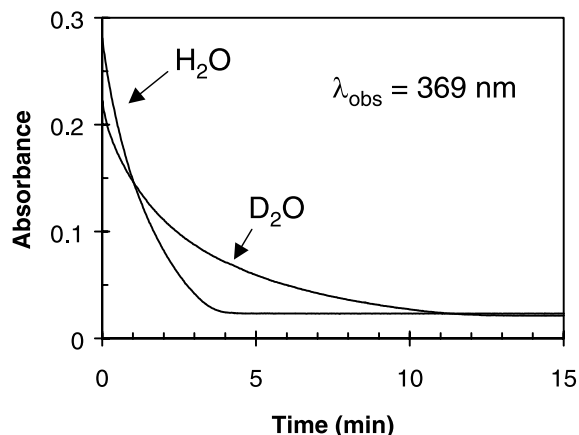


**14** by dissolved oxygen is much more efficient than either protonation or disproportionation.

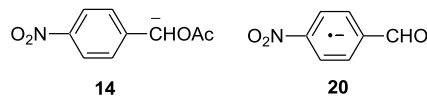


*p*-Nitrophenylethylene glycol (**8**) was found to be photo-reactive only in basic solution. UV-vis traces of the reaction (~100% H<sub>2</sub>O, pH 13, Ar purged) allowed observation of a

**Fig. 3.** Decay in absorbance of **14** photogenerated from **7** in ~100% H<sub>2</sub>O (complete within 5 min) or ~100% D<sub>2</sub>O (complete within 15 min) measured at 369 nm immediately following 15 s photolysis ( $6.7 \times 10^{-5}$  M, 300 nm, 16 lamps, pH(D) 7, Ar purged). Neither trace could be fitted satisfactorily to a first- or second-order kinetic equation.



strong transient absorption band at  $\lambda_{\text{max}}$  403 nm that decayed within 1 h (Fig. 4) with complex kinetics (Fig. 4, inset). The initial decay appears to obey first-order kinetics; however, after approximately 20 min the decay becomes (reproducibly) more complex, suggestive of contributions from competing reactions. This transient was observed only in basic solution (Fig. 5); no spectral changes were observed in neutral or acidic solution (below pH 11), even on prolonged irradiation. The transient was also not observed in oxygen-saturated basic solution.



Preparative photolysis of **8** ( $1 \times 10^{-3}$  M, pH 13, Ar) gave **15** and **16** (60–70% and 40–30%, respectively), as observed for **6** in neutral or basic solution. In keeping with the cuvette results above, no reaction was observed at pH 7. Base catalysis of the reaction of **8** is in line with observations made for **5** (13), although the latter is not known to give an observable 403 nm transient. In a previous study of **8** in our laboratory (21), a long-lived radical anion species was photogenerated and assigned from its ESR spectrum as *p*-nitrobenzaldehyde radical anion (**20**). Its lifetime in the ESR spectrum was similar to that observed for the transient 403 nm absorption band. Radical anion **20** has previously been reported to have an absorption maximum of ~400 nm (22) and the present data are in good agreement with this.

Irradiation of *p*-nitrobenzhydrol (**9**) at pH 13 (~100% H<sub>2</sub>O, Ar purged, 300 nm) in a UV cuvette resulted in initial spectral changes that were consistent with formation of **21**. However, other components were evidently present, as the initial spectrum was not stable over time and underwent complex changes over the course of 10–30 min in the absence of light, indicating that relatively slow dark processes were occurring. No spectral changes were observed at pH 7, consistent with base catalysis of photoreaction. Preparative



## Scheme 3.

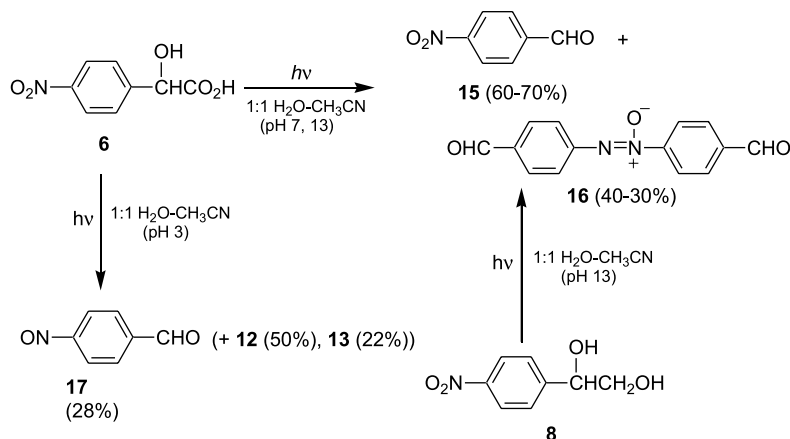
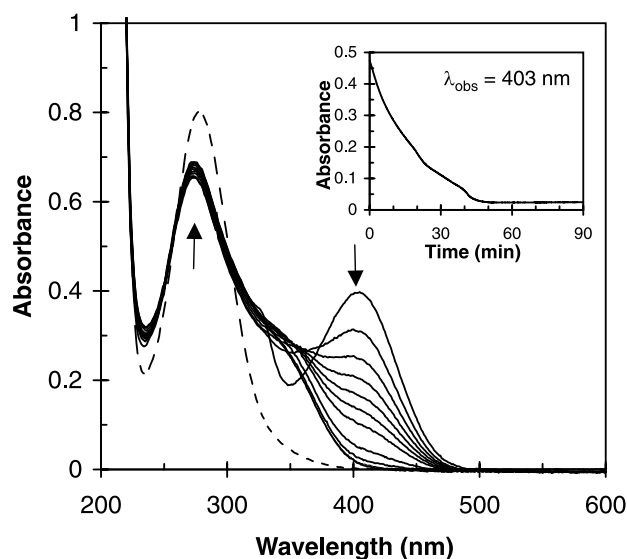
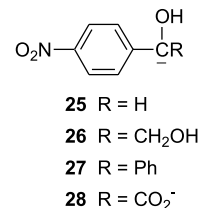
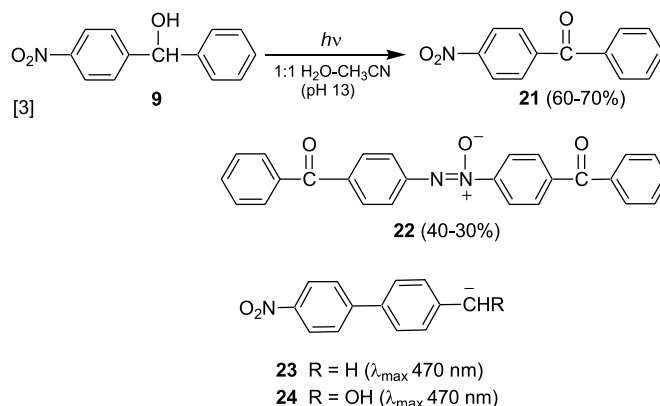


**Fig. 4.** UV-vis traces observed before (dashed line) and immediately following 30 s photolysis (300 nm, 16 lamps) of **8** in ~100% pH 13 H<sub>2</sub>O ( $7.4 \times 10^{-5}$  M, Ar purged). Each trace is separated by 5 min (solid lines). Arrows indicate changes in absorbance during the dark reaction. Inset: observed decay of the 403 nm absorption band.



photolysis of **9** ( $1 \times 10^{-3}$  M, 1:1 H<sub>2</sub>O-CH<sub>3</sub>CN, pH 13) gave two isolable disproportionation products, *p*-nitrobenzophenone (**21**) and *p,p'*-azoxybisbenzophenone (**22**) (60–70 and 40–30% relative yield, respectively), and a third minor (<10%, relative to **21**) product that has not been fully characterized but is believed to be derived from further reduction of **22** (see *Experimental*) (eq. [3]). Observation of base-catalyzed products from **9**, which is reminiscent of the photochemistry of *m*- and *p*-nitrobenzyl alcohol (**4**), suggests that the reaction pathway involves initial deprotonation from the benzylic position of **9**. However, attempts to trap the  $\alpha$ -hydroxybenzyl carbanion intermediate from **9** with D<sub>2</sub>O (at pD 13) were unsuccessful. Thus, extended photolysis of **9** in 1:1 D<sub>2</sub>O-CH<sub>3</sub>CN (pD 13) to >80% conversion followed by recovery of unreacted substrate showed complete absence of deuterium incorporation at the methine position (as monitored by <sup>1</sup>H NMR integration of this signal relative to the ar-

omatic signals). This is in agreement with previous studies of *m*- and *p*-nitrobenzyl alcohols (**4**), in which the corresponding photogenerated carbanions were also found not to undergo deuterium incorporation at the benzylic position. *p*-Nitrobenzhydryl methyl ether (**10**) might be expected to display “conventional” *p*-nitrobenzyl carbanion chemistry upon photodeprotonation, which would lead to deuterium incorporation. However, prolonged irradiation of **10** (pD 13, 10 h) resulted in complete recovery of substrate, with no evidence of deuterium exchange.



The quantum yield for reaction of **6** was estimated using *p*-nitrophenylacetic acid (**3**) ( $\Phi = 0.6$ ) (**12**, **17**) as secondary actinometer. Comparative photolysis of **3** and **6** to low conversion (<20%) gave a quantum yield for the reaction of **6** in 100% H<sub>2</sub>O (pH 6) of  $0.4 \pm 0.1$ . Quantum yields for reaction of **7** (pH 7), **8** (pH 14), and **9** (pH 13) were also estimated using product analysis and were 0.4, 0.5, and 0.02, respectively.



**Fig. 5.** Initial change in 403 nm absorbance ( $\Delta OD = OD$  immediately after irradiation minus  $OD$  before irradiation) upon irradiation of **8** in ~100%  $H_2O$ , pH 1–14 (300 nm, 16 lamps, 15 s photolysis time,  $7.4 \times 10^{-5}$  M, Ar purged).

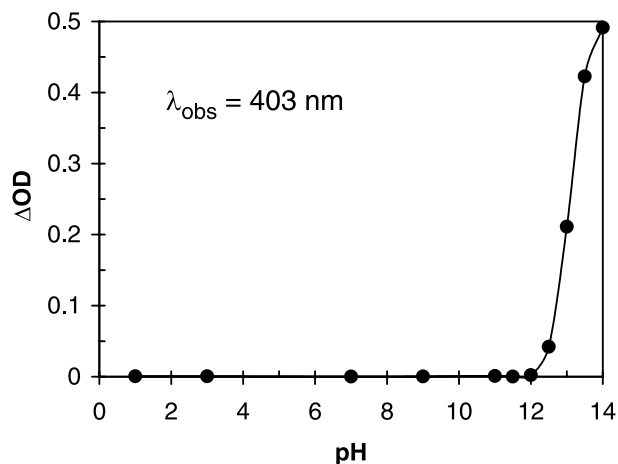
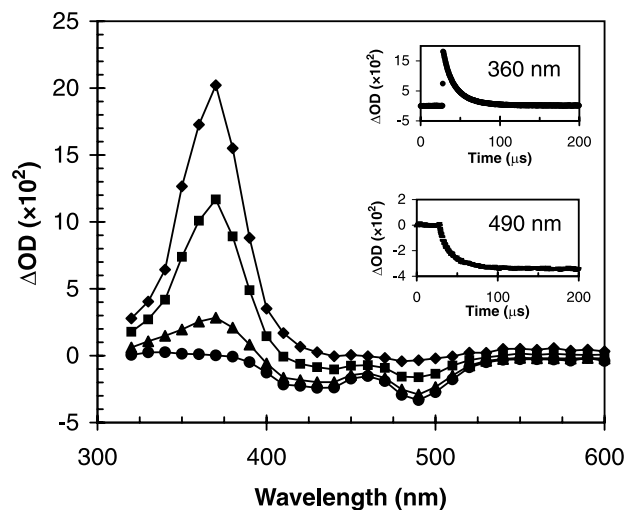


**Fig. 6.** LFP traces for **7** ( $4.7 \times 10^{-5}$  M) with  $1 \times 10^{-4}$  M  $IrCl_6^{2-}$  in ~100%  $H_2O$  (pH 7,  $N_2$  purged,  $\lambda_{ex}$  308 nm). Diamonds represent the spectrum sampled 1.8  $\mu s$  after the laser pulse, which includes carbanion **14** at 369 nm. Squares and triangles (sampled at 9.2 and 34  $\mu s$ ) represent the decay of the 369 nm band simultaneous with the bleaching of the  $IrCl_6^{2-}$  absorption bands at 430 and 490 nm to the final spectrum (at 130  $\mu s$ ) represented by circles. Top inset: decay of carbanion **14** ( $k_{obs} = 6.2 \times 10^4$  s $^{-1}$ , monitored at 360 nm). Bottom inset: bleaching of  $IrCl_6^{2-}$  ( $k_{obs} = 6.2 \times 10^4$  s $^{-1}$ , monitored at 490 nm).



### Laser flash photolysis

*p*-Nitrobenzyl carbanion **2** (which absorbs strongly at  $\lambda_{max}$  358 nm) has been extensively studied by transient methods (12, 17). Its lifetime is sensitive to pH but not to oxygen and is shortened in the presence of  $IrCl_6^{2-}$  that acts as a one-electron acceptor (23–25). When the  $\pi$  system is further extended with another phenyl ring, as is the case for *p*-(*p*'-nitrophenyl)benzyl carbanion (**23**), the absorption maximum is at much longer wavelength ( $\lambda_{max}$  470 nm) (6). Further

**Fig. 7.** LFP traces for **6** in ~100%  $H_2O$ , pH 6.0 ( $4.6 \times 10^{-5}$  M, 0.01 M phosphate buffer,  $N_2$  purged,  $\lambda_{ex}$  266 nm). Diamonds represent the spectrum sampled 700 ns after the laser pulse, which includes  $\alpha$ -hydroxy carbanion **25** at 360 nm. Squares and triangles represent the decay of the spectrum at 2.6 and 6.9  $\mu s$  after the laser pulse, respectively. Final spectrum after the decay (sampled at 36  $\mu s$ ) of **25** to the product at 340 nm is represented by circles. Top inset: decay of carbanion **25** ( $k_{obs} = 2.6 \times 10^5$  s $^{-1}$ , monitored at 360 nm). Bottom inset: growth of product ( $k_{obs} = 3.1 \times 10^5$  s $^{-1}$ , monitored at 290 nm).

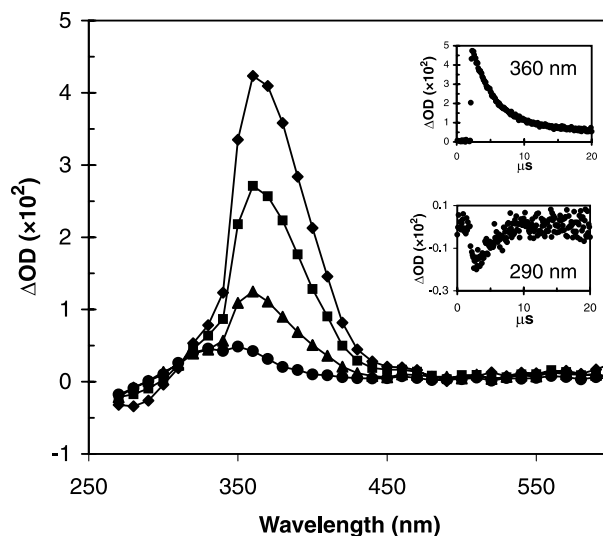
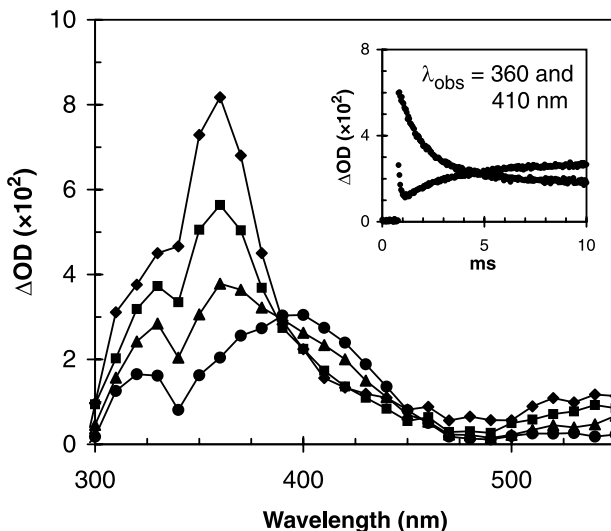


**Fig. 8.** LFP traces for **8** in ~100%  $H_2O$ , pH 13.0 ( $5.7 \times 10^{-5}$  M,  $N_2$  purged,  $\lambda_{ex}$  266 nm) which includes  $\alpha$ -hydroxy carbanion **25** at 360 nm. Squares and triangles represent decay of the spectrum at 900  $\mu s$  and 2.8 ms, respectively. After the decay of **25** was complete, the spectrum of radical anion **20** was observed; represented by circles, sampled at 14 ms after the laser pulse. Inset: Decay of **25** ( $k_{obs} = 6.7 \times 10^{-2}$  s $^{-1}$ , monitored at 360 nm) is simultaneous with the growth of radical anion **20** ( $k_{obs} = 4.2 \times 10^{-2}$  s $^{-1}$ , monitored at 410 nm).



substitution of the carbanion with an  $\alpha$ -hydroxy group does not shift the absorption maximum, as  $\alpha$ -hydroxy-*p*-(*p*'-nitro-



**Fig. 9.** LFP traces observed for **9** in ~100% H<sub>2</sub>O, pH 13.0 ( $5.3 \times 10^{-5}$  M, N<sub>2</sub> purged,  $\lambda_{\text{ex}}$  266 nm). Diamonds represent the spectrum sampled 1.7  $\mu$ s after the laser pulse, which includes carbanion **27** at 460 nm. Squares and triangles represent decay of the spectrum, sampled at 8.6 and 28  $\mu$ s, respectively. Circles represent spectrum after the decay of **27** at 77  $\mu$ s. Inset: decay of **27** ( $k_{\text{obs}} = 5.2 \times 10^4$  s<sup>-1</sup>, observed at 460 nm).

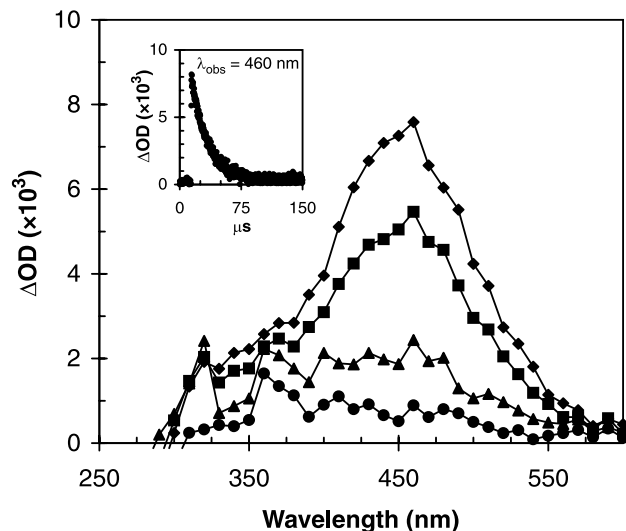
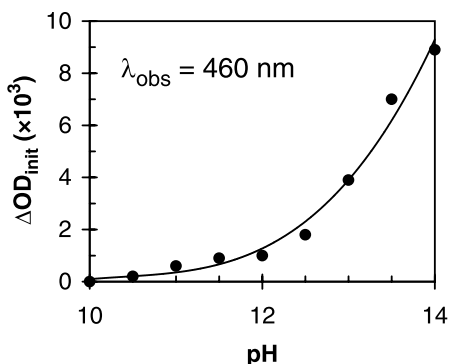


**Fig. 10.** Plot of the initial change in absorbance ( $\Delta\text{OD}_{\text{init}}$ ) at 460 nm upon LFP of **9** at pH 10–14 ( $5.3 \times 10^{-5}$  M, ~100% H<sub>2</sub>O, N<sub>2</sub> purged,  $\lambda_{\text{ex}}$  266 nm). Each point represents the average initial  $\Delta\text{OD}$  observed for 10 shots, assigned to carbanion **27** formed by photodeprotonation of **9**.



phenyl)benzyl carbanion (**24**) was also observed at 470 nm (**6**). Thus, it was anticipated that the *p*-nitrobenzyl carbanions generated from **6–8** should also have absorption maxima near 360 nm. This indeed was found to be the case for carbanion **14** formed from **7** ( $\lambda_{\text{max}}$  369 nm, vide supra), which was sufficiently long-lived to allow detection by conventional UV-vis spectrophotometry. LFP of **7** (266 nm, pH 7, ~100% H<sub>2</sub>O, N<sub>2</sub> purged) also gave **14** ( $\lambda_{\text{max}}$  369 nm) which did not decay within the 150 ms (longest possible) time window of our LFP system, consistent with it being a very long-lived species (vide supra). However, LFP of **7** in the presence of IrCl<sub>6</sub><sup>2-</sup> (308 nm, N<sub>2</sub> purged) showed an accelerated decay of the 369 nm transient that was simultaneous with bleaching of IrCl<sub>6</sub><sup>2-</sup> bands at 430 and 490 nm (Fig. 6).

**Fig. 11.** LFP traces observed for **6** in ~100% H<sub>2</sub>O, pH 13.0 ( $4.6 \times 10^{-5}$  M, N<sub>2</sub> purged,  $\lambda_{\text{ex}}$  266 nm). Diamonds represent the spectrum sampled 5.1  $\mu$ s after the laser pulse, which includes carbanion **28** (420 nm) formed by photodeprotonation of **6**, and carbanion **25** (360 nm) formed by photodecarboxylation of **6**. Squares and triangles represent partial decay of the spectrum (decay of **28** and not **25**), sampled at 26 and 69  $\mu$ s, respectively. Circles represent the spectrum after **28** has completely decayed, leaving **25** and possible products from **28**. Top inset: decay of **28** ( $k_{\text{obs}} = 2.1 \times 10^4$  s<sup>-1</sup>, monitored at 420 nm). Bottom inset: growth of product from **28** ( $k_{\text{obs}} = 2.2 \times 10^4$  s<sup>-1</sup>, monitored at 350 nm).

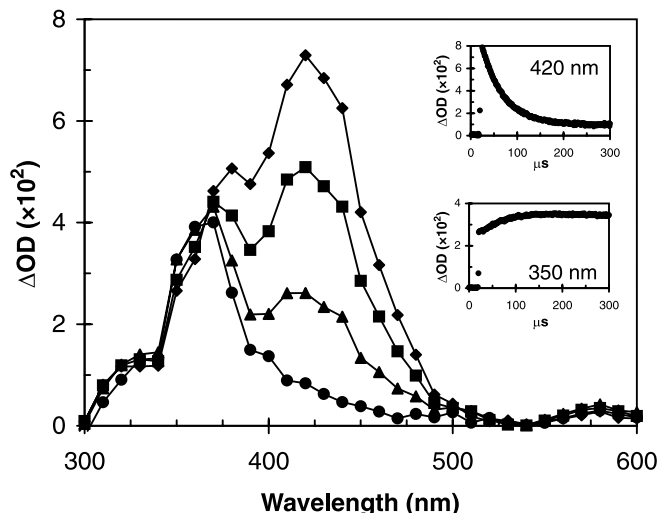
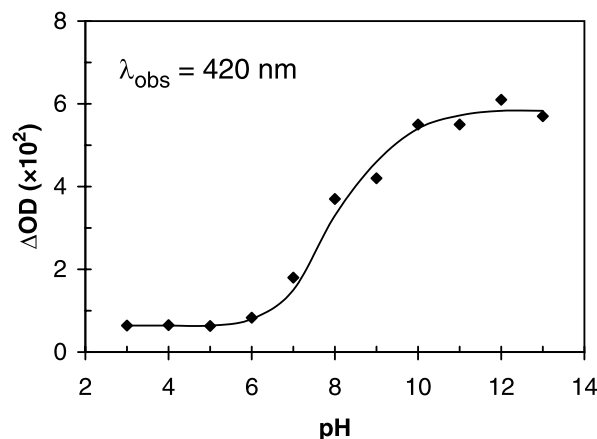


**Fig. 12.** Plot of the initial change in absorbance ( $\Delta\text{OD}_{\text{init}}$ ) at 420 nm upon LFP of **6** at pH 3–13 ( $4.6 \times 10^{-5}$  M, ~100% H<sub>2</sub>O, N<sub>2</sub> purged,  $\lambda_{\text{ex}}$  266 nm). Each point represents the average initial  $\Delta\text{OD}$  observed for 10 shots. Above pH 7  $\Delta\text{OD}_{\text{init}}$  is mostly attributed to carbanion **28** formed by direct carbon acid deprotonation. At pH 7 and below  $\Delta\text{OD}_{\text{init}}$  is mostly attributed to **25** formed by photodecarboxylation which has weak absorption at 420 nm (assignment based on lifetimes).



LFP of **6** (266 nm) at pH 6 gave a transient at ~360 nm with a similar absorption profile as that of carbanion **14** (Fig. 7). It decayed via first-order kinetics ( $\tau = 3.8$   $\mu$ s, 0.01 M phosphate buffer, pH 6) to a weaker but permanent absorption in the range 300–340 nm, assignable as a mixture



of **15** and **16**. Assignment of the 360 nm transient to **25** is based on its similarity to **14**. Additionally, LFP of **6** in the presence of  $\text{IrCl}_6^{2-}$  showed an accelerated decay of the 360 nm band in synchrony with bleaching of the  $\text{IrCl}_6^{2-}$  bands at 430 and 490 nm.

LFP of **8** at pH 13 also gave carbanion **25** ( $\tau = 1.5$  ms) as a transient (Fig. 8). No transients were observed at pH 7 consistent with its lack of photochemical reactivity in neutral solution (vide supra). Decay of **25** (at pH 13) was concomitant with the growth of a band at 400 nm, which did not decay within 150 ms (Fig. 8, inset). The long-lived 400 nm transient (not observed in the presence of oxygen) is assigned to radical anion **20**, which was also observed by UV-vis spectrophotometry (Fig. 4). Closer examination of the kinetic trace at 410 nm (Fig. 8, inset) also showed evidence of a shorter-lived species ( $\tau = 63$   $\mu\text{s}$ ) absorbing in this region, the identity of which is not known with certainty but which we have tentatively assigned to carbanion **26**, arising via benzylic deprotonation of **8**.

LFP of **9** at pH 13 gave a broad absorption band at 460 nm (Fig. 9) that decayed by first-order kinetics to baseline (Fig. 9, inset). The intensity of the 460 nm absorption was strongest at pH 14 and was progressively weaker at lower pH values; at pH 10 no signal was observable (Fig. 10). This apparent base catalysis of transient formation supports its assignment as carbanion **27**. Its absorption maximum is red-shifted by 100 nm compared to carbanion **25** ( $\lambda_{\text{ex}}$  360 nm) which is compatible with the extended conjugation available from the additional phenyl ring.

The LFP spectrum of **6** at pH 13 was dominated by a band at 420 nm (Fig. 11), which decayed ( $\tau = 47$   $\mu\text{s}$ ) to a long-lived ( $\tau > 150$  ms) 360 nm band. The  $\Delta\text{OD}$  of the 420 nm band as a function of pH is shown in Fig. 12, which has an apparent titration plot, suggesting that the 420 nm transient is carbanion **28** (with an excited state  $\text{pK}_a$  of  $\sim 8$  for the benzylic proton of **6**). This seems reasonable considering the analogous photodeprotonation observed for **9** at high pH.

### Mechanisms of reaction

Our study of the photochemistry of *p*-nitrobenzyl derivatives **6–10**, by a combination of product studies, UV-vis spectrophotometry, and LFP, has provided additional insights into their mechanisms of reaction. It seems clear that the aqueous photochemistry for all of **6–9** involves *p*-nitrobenzyl carbanions. Indeed, several  $\alpha$ -hydroxy-*p*-nitrobenzyl carbanions, generated by C—H bond deprotonation or by decarboxylation (or deformylation), were observed for the first time. With the present data, an overall mechanistic picture of the photochemistry of these compounds is now available.

Photodecarboxylation of **6** (assumed to be via  $T_1$ ) occurs with appreciable quantum efficiency at pH 3–13 to generate **25** (Scheme 4). The lack of photoreactivity of **6** and absence of an LFP signal attributable to **25** at pH values 1 and 2 indicate that photodecarboxylation only occurs via the carboxylate form of **6**. The necessary steps to generate products **15** and **16** from **25** most likely involve overall loss of an electron and a proton (sequentially or via one-step loss of a hydrogen atom), to generate radical anion **20** ( $\lambda_{\text{max}}$  403 nm, vide supra), which is known to be long-lived at high pH but undetectable at lower pH (21). Radical ion **20** has been

shown to lead to reduction product **16** (21), while scavenging of the electron of **20** by residual oxygen or on work-up would lead to **15**. The formation of **17** at pH 3 suggests an alternate pathway involving an overall intramolecular redox reaction for **25**. This new pathway is observed at a pH that coincides with significant protonation of the nitro group of **25**, to give **29** (similar *aci*-nitrobenzyl compounds have  $\text{pK}_a \sim 3$ , (6, 17, 26)). Net dehydration of **29** gives **17**.

At pH values  $> 8$ , photoionization of the benzylic proton of **6** (to give **28**) apparently competes with photodecarboxylation, as shown in LFP studies, although to what extent is not entirely clear with the data available. We have not isolated any product at high pH that might be expected to arise via **28**, but only compounds **15** and **16** as seen at pH values in the range  $\sim 4$ –7. The possibility of facile reprotonation of **28** to give back **6** (in the ground-state reaction) is a distinct possibility. However, we have not attempted any deuterium incorporation experiments at these high pHs because of the obvious complication of thermal background exchange in basic  $\text{D}_2\text{O}$ . Thus, further understanding of the competing benzylic C—H deprotonation of **6** requires additional studies.

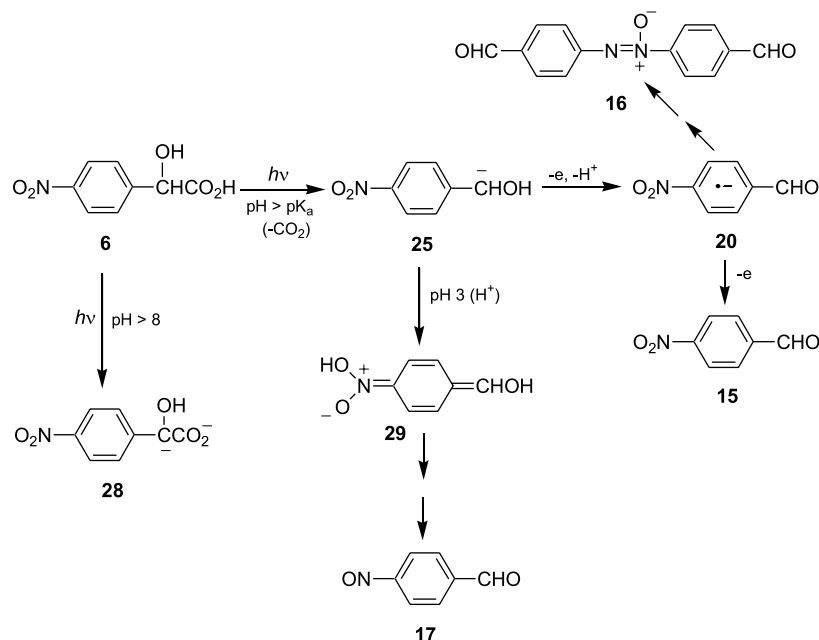
The proposed reaction pathway for **8** (pH  $> 12$ ) (Scheme 5) is simpler. LFP observations at pH 13 indicate that generation of **25** from **8** occurs much more cleanly, with no significant photoionization at the benzylic position. Carbanion **25** (from **8**) gives radical anion **20** (via overall loss of an electron and a proton), as shown by growth of the radical anion absorption band ( $\lambda_{\text{max}}$  403 nm) concomitantly with decay of the absorption band of **25** ( $\lambda_{\text{max}}$  360 nm) (Fig. 8). The subsequent decay of **20** appears to be more complex, after a phase with initial first-order kinetics (Fig. 4, inset), and is suggestive of multistep pathways for subsequent formation of **16**.

The  $\alpha$ -acetoxy carbanion **14** generated via photodecarboxylation of **7** behaves as a conventional *p*-nitrobenzyl carbanion (mimicking **2**, Scheme 1). The two observed products, **18** and **19**, arise via protonation and coupling pathways (giving a dianion, which subsequently loses two electrons to give **19**) (18). Given that the observed lifetime of **14** is very long compared to that of **25**, both its protonation and coupling processes must be slow. In contrast, the lifetime of **25** at pH 6 is more than 7 orders of magnitude shorter ( $\mu\text{s}$  vs. min). Clearly the disproportionation pathway available to **25** is sufficiently fast that protonation or coupling cannot compete. Comparison of the pseudo-first-order rate constants for reaction of these carbanions with  $\text{IrCl}_6^{2-}$  (**25** reacts only about 2 times faster than **14**) suggests that the oxidation potentials of **14** and **25** are roughly equivalent. Thus, the key structural feature that allows the efficient disproportionation pathway observed for **25** is the  $\alpha$ -hydroxyl proton. This is consistent with gas-phase theoretical calculations (3) that have shown anions such as  $^-\text{CH}_2\text{OH}$  and  $^-\text{CH}_2\text{NH}_2$  to be unstable with respect to their radicals.

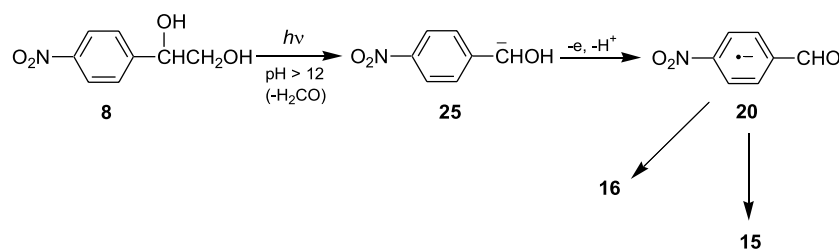
The reaction pathway of **9** is similar in essence to those of **6** and **8**. It differs in that the carbanion **27** is formed by direct C—H bond heterolysis, and is the only *p*-nitrobenzyl carbanion that could form in this case. To our knowledge, only one other example of LFP observation of a carbanion generated by photoionization has been reported (6). The subsequent product-forming steps from **27** are believed to be similar to those proposed for **6** and **8**; i.e., the carbanion for-



Scheme 4.



Scheme 5.



ally loses a hydrogen atom to form the corresponding radical anion, which subsequently disproportionates to products **21** and **22**. The complete absence of photochemistry from **10** indicates the sensitive nature of excited-state deprotonation with respect to substituents. Further work will be needed to understand the factors that influence the operation of these substituent effects, which may be quite subtle.

## Experimental

### General

$^1\text{H}$  NMR spectra were obtained on Bruker AC300 or JEOL FX90Q instruments in  $\text{CDCl}_3$  unless otherwise specified. Low-resolution mass spectra were obtained on a Finnigan 3300 (CI) and HR-MS were obtained on a Kratos Concept H (EI) instrument. UV-vis spectra were recorded on a Varian Cary 5 instrument. Acetonitrile (HPLC grade) and distilled water were used for product studies and LFP experiments. Reagent grade  $\text{CH}_2\text{Cl}_2$  was redistilled before use for work-up protocols. The following buffers (0.01 M) were used for some product studies and LFP static and flow cell experiments: potassium phosphate – phosphoric acid (pH 3), acetate – acetic acid (pH 4 and 5), potassium phosphate (pH 6–8), sodium carbonate – sodium bicarbonate (pH 9–11). Aqueous  $\text{H}_2\text{SO}_4$  and NaOH were used for solutions at other pH values.

### Materials

*p*-Nitrobenzaldehyde (**15**) and *p*-nitrobenzophenone (**21**) (Aldrich) were recrystallized (ethanol– $\text{H}_2\text{O}$ ) prior to use. Sodium hexachloroiridate(IV) hexahydrate 99.9+% (Strem) was used without further purification. Product **18** was prepared by substitution of *p*-nitrobenzyl bromide with sodium acetate. An authentic sample of product **22** was prepared by reduction of **21** with paraformaldehyde–KOH, as described elsewhere (27).

### O-Acetyl *p*-nitromandelic acid (7)

A stirred suspension of 4-nitrophenylacetic acid (15.3 g, 84.5 mmol) in thionyl chloride (6.66 mL, 91.3 mmol) was refluxed for 1 h. The solution was allowed to cool and bromine (14.9 g, 93 mmol) was added in one portion. The mixture was heated at  $70^\circ\text{C}$  for 5.5 h and stirred overnight at room temperature. Ice water was added and the mixture was extracted with  $\text{Et}_2\text{O}$ . The organic phase was washed with brine, dried and evaporated to a brown oil (22 g) that was dissolved in a mixture of THF (230 mL) and water (100 mL) and stirred for 6 h at room temperature. The solution was concentrated under reduced pressure to remove most of the THF and water (50 mL) was added. The mixture was extracted with  $\text{Et}_2\text{O}$  and the ethereal extract was washed with brine, dried and evaporated to give a solid (18.5 g) that contained the starting nitrophenylacetic acid and the product **11** (typical ratio  $\sim 1:4$ ). After two crystallizations from



benzene–hexanes, the contamination by starting material was reduced to 8% and this material (11.7 g) was used without further processing. Within the mixture, **11** had  $^1\text{H}$  NMR  $\delta$ : 8.22 (d,  $J = 8.8$  Hz, 2H, Ar-H), 7.73 (d,  $J = 8.8$  Hz, 2H, Ar-H), 5.40 (s, 1H, CHBr).

A mixture of the impure bromo compound **11** (11.49 g, 41.65 mmol) and mercury(II) acetate (28.2 g, 88.4 mmol) in glacial acetic acid (88 mL) was refluxed for 0.5 h. The solution was cooled, diluted with water, and extracted with  $\text{Et}_2\text{O}$ . The ether phase was washed with water and brine, dried and evaporated under reduced pressure. The residue was crystallized from water to give the acetate **7** (7.5 g, 37%), mp 153 to 154°C (lit. mp (28) 157–159°C).  $^1\text{H}$  NMR  $\delta$ : 8.25 (d,  $J = 8.8$  Hz, 2H, Ar-H), 7.69 (d,  $J = 8.8$  Hz, 2H, Ar-H), 6.04 (s, 1H, CHOAc), 2.23 (s, 3H, Me).

#### **p-Nitromandelic acid (6)**

*tert*-Butyl 2,2,2-trichloroacetimidate (4.0 g, 18.3 mmol) in  $\text{CH}_2\text{Cl}_2$  (32 mL) was added in one portion to a solution of **7** (2.73 g, 11.4 mmol) in  $\text{CH}_2\text{Cl}_2$  (69 mL) and the solution was stirred overnight at room temperature. The mixture was diluted with  $\text{CH}_2\text{Cl}_2$ , washed with saturated  $\text{NaHCO}_3$ , water, and brine, dried and evaporated. The residue was dissolved in  $\text{Et}_2\text{O}$  (~10 mL) and most of the trichloroacetamide was precipitated by the addition of hexanes (~40 mL). The filtrate was evaporated and purified by flash chromatography (EtOAc–hexanes, 3:17) to give *tert*-butyl acetoxy-(4-nitrophenyl)acetate (**12**) as a yellow solid, (2.56 g, 76%). A sample crystallized from hexanes had mp 80 to 81°C (lit. mp (28) 82°C).  $^1\text{H}$  NMR  $\delta$ : 8.24 (d,  $J = 8.8$  Hz, 2H, Ar-H), 7.66 (d,  $J = 8.8$  Hz, 2H, Ar-H), 5.91 (s, 1H, CHOAc), 2.23 (s, 3H, Me), 1.41 (s, 9H,  $\text{CMe}_3$ ).

A solution of **12** (2.53 g, 8.6 mmol) in methanol (25 mL) was treated with cesium carbonate (0.14 g, 0.43 mmol) in methanol (5 mL) and stirred for 0.5 h at room temperature. The solution was diluted with EtOAc, washed with satd.  $\text{NaHCO}_3$  and brine, dried and evaporated under reduced pressure. The residue was purified by flash chromatography (EtOAc–hexanes, 3:17) to give *tert*-butyl hydroxy-(4-nitrophenyl)acetate (**13**) (1.51 g, 70%), mp 91.5–93°C (hexanes).  $^1\text{H}$  NMR  $\delta$ : 8.21 (d,  $J = 8.8$  Hz, 2H, Ar-H), 7.63 (d,  $J = 8.8$  Hz, 2H, Ar-H), 5.16 (d,  $J_{\text{H,OH}} = 4.5$  Hz, 1H, CHOH), 3.72 (d,  $J_{\text{H,OH}} = 4.5$  Hz, 1H, OH), 1.42 (s, 9H,  $\text{CMe}_3$ ). Anal. calcd. for  $\text{C}_{12}\text{H}_{15}\text{NO}_5$ : C 56.91, H 5.97, N 5.53; found: C 56.75, H 5.97, N 5.38.

The *tert*-butyl ester **13** (1.8 g, 7.1 mmol) was stirred with trifluoroacetic acid (36 mL) for 1 h at room temperature, then evaporated under reduced pressure to a brown gum which solidified on trituration with  $\text{Et}_2\text{O}$ . The solid was crystallized twice from toluene to give **6** as yellow needles (0.7 g, 48%), mp 128.5–130°C (lit. mp (29) 126 to 127°C).  $^1\text{H}$  NMR ( $\text{CD}_3\text{OD}$ )  $\delta$ : 8.25 (d,  $J = 8.8$  Hz, 2H, Ar-H), 7.69 (d,  $J = 8.8$  Hz, 2H, Ar-H), 5.26 (s, 1H, CHOH).

#### **p-Nitrobenzhydrol (9)**

Reduction of *p*-nitrobenzophenone (**21**) (Aldrich) with  $\text{NaBH}_4$  gave a white solid, which upon recrystallization from ethanol– $\text{H}_2\text{O}$  gave white crystals of *p*-nitrobenzhydrol (**9**), mp 69 to 70°C. IR (KBr disc,  $\text{cm}^{-1}$ ): 1190 (m), 1340 (s), 1450 (m), 1510 (s), 1600 (m), 3300–3500 (s).  $^1\text{H}$  NMR (300 MHz)  $\delta$ : 2.37 (s, 1H, exchanges with  $\text{D}_2\text{O}$ , OH), 5.90 (s, 1H, methine), 7.33 (m, 5H, arom.), 7.56 (d,  $J = 8.8$  Hz,

2H, arom.), 8.17 (d,  $J = 8.8$  Hz, 2H). HR-MS (EI) calcd. for  $\text{C}_{13}\text{H}_{11}\text{NO}_3$ : 229.0739; found: 229.0739.

#### **p-Nitrobenzhydrol methyl ether (10)**

A solution of **9** (300 mg) in methanol (50 mL) (in the presence of 10% concd  $\text{H}_2\text{SO}_4$ ) was refluxed for 24 h. Addition of ether and washing with  $\text{H}_2\text{O}$  resulted in extraction of a light yellow oil which by  $^1\text{H}$  NMR was found to contain 5% **9** and 95% **10**. Preparative TLC ( $\text{CH}_2\text{Cl}_2$  and silica gel) allowed isolation of a colourless oil ( $R_f$  0.9) *p*-nitrobenzhydrol methyl ether (**10**). IR (neat,  $\text{cm}^{-1}$ ): 1090 (s), 1190 (m), 1350 (s), 1450 (m), 1520 (s), 1600 (m).  $^1\text{H}$  NMR (300 MHz)  $\delta$ : 3.38 (s, 3H, methyl), 5.29 (s, 1H, methine), 7.30 (m, 5H, arom.), 7.51 (d,  $J = 8.8$  Hz, 2H, arom.), 8.16 (d,  $J = 8.8$  Hz, 2H, arom.). HR-MS (EI) calcd. for  $\text{C}_{14}\text{H}_{13}\text{NO}_3$ : 243.0896; found: 243.0893.

#### **$\alpha,\alpha'$ -Bisacetoxy-*p,p'*-dinitrobibenzyl (19)**

Esterification of the corresponding diol (0.5 g), which was available from a previous study (21), in refluxing (10 h) glacial acetic acid (in the presence of 10% concd  $\text{H}_2\text{SO}_4$ ) gave 89% yield of an approximate 1:1 mixture of *cis*- and *trans*- $\alpha,\alpha'$ -bisacetoxy-*p,p'*-dinitrobibenzyl (**19**). Recrystallization from ethyl acetate – hexanes enriched one of the diastereomers, thus allowing distinction between the  $^1\text{H}$  NMR signals of the two diastereomers. IR (mixture of diastereomers, KBr disc,  $\text{cm}^{-1}$ ): 1220 (s), 1350 (s), 1460 (w), 1530 (s), 1610 (m), 1750 (s).  $^1\text{H}$  NMR (300 MHz) diastereomer A (40%)  $\delta$ : 2.07 (s, 6H,  $\text{COCH}_3$ ), 6.14 (s, 2H, methine), 7.34 (d,  $J = 8.8$  Hz, 4H, arom.), 8.16 (d,  $J = 8.8$  Hz, 4H, arom.).  $^1\text{H}$  NMR (300 MHz) diastereomer B (60%)  $\delta$ : 2.10 (s, 6H,  $\text{COCH}_3$ ), 6.11 (s, 2H, methine), 7.33 (d,  $J = 8.8$  Hz, 4H, arom.), 8.13 (d,  $J = 8.8$  Hz, 4H, arom.). MS (mixture of diastereomers, + LSI-MS) 389 *m/e* ( $\text{M}^+ + 1$ ).

#### **Product studies**

UV–vis photolyses were carried out for 3 mL of the appropriate solution in Suprasil quartz cuvettes. Immediately before photolysis, each sample was Ar or  $\text{O}_2$  purged for 5 min, then quickly sealed with a Teflon stopper. During the photolysis the cuvette sat on top of an inverted 1 L beaker inside the Rayonet reactor (300 nm, 4–16 lamps) and was cooled with an internal fan. Irradiations did not exceed 10 min (total photolysis time); no heating of the samples was observed.

Preparative photolyses were carried out with the substrate (20–100 mg) dissolved in the appropriate solvent (100 mL) in a quartz tube. The solution was irradiated at 300 nm (Rayonet reactor, 4–16 lamps) with continuous cooling (by a cold finger) and purging by a stream of Ar for approximately 15 min before and continuously during irradiation (via a long stainless steel needle). Photolysis times ranged from 1 min to 20 h, depending on the conversion desired, the efficiency of the reaction, and the amount of substrate used. After photolysis, aqueous samples were acidified to pH 1 to 2 and extracted with  $\text{CH}_2\text{Cl}_2$ . Typical experiments are described below.

#### **Photolysis of *p*-nitromandelic acid (6) in 1:1 $\text{H}_2\text{O}$ – $\text{CH}_3\text{CN}$ (pH 7)**

A solution of **6** (20 mg) in 1:1  $\text{H}_2\text{O}$ – $\text{CH}_3\text{CN}$  (100 mL, pH adjusted to 7 with NaOH, Ar purged) was photolyzed for



2 min (300 nm, 16 lamps). After work-up,  $^1\text{H}$  NMR of the photolysate allowed observation of two aldehyde products (60% **15**, 40% **16**) and **6** (36% total conversion). Preparative TLC ( $\text{CH}_2\text{Cl}_2$  and silica gel) allowed isolation of the two products, one of which was identified as **15** ( $R_f$  0.5) by comparison with an authentic sample; the other ( $R_f$  0.3) identified as *p,p'*-azoxybisbenzaldehyde (**16**), mp 192°C. IR (KBr disc,  $\text{cm}^{-1}$ ): 1200 (m), 1320 (m), 1460 (m), 1600 (m), 1700 (s).  $^1\text{H}$  NMR  $\delta$ : 8.01 (d,  $J$  = 8.1 Hz, 2H, arom.), 8.05 (d,  $J$  = 8.1 Hz, 2H, arom.), 8.26 (d,  $J$  = 8.1 Hz, 2H, arom.), 8.49 (d,  $J$  = 8.1 Hz, 2H, arom.), 10.05 (s, 1 H, CHO), 10.14 (s, 1 H, CHO). HR-MS (EI) calcd. for  $\text{C}_{14}\text{H}_{10}\text{N}_2\text{O}_3$ : 254.0692; found: 254.0689.

#### Photolysis of *p*-nitromandelic acid (**6**) in 1:1 $\text{H}_2\text{O}$ - $\text{CH}_3\text{CN}$ (pH 3)

A solution of **6** (20 mg) in 1:1  $\text{H}_2\text{O}$ - $\text{CH}_3\text{CN}$  (100 mL, pH 3, 0.01 M phosphate buffer, Ar purged) was photolyzed for 5 min (300 nm, 16 lamps). Following work-up,  $^1\text{H}$  NMR allowed observation of the aldehyde peaks of **15** and **16**, as well as an aldehyde signal which had not been present in the pH 7 product studies. Based on integration the relative yields of these products were 50% (**15**), 22% (**16**) and 28% of the new aldehyde product, and the total conversion from substrate was 61%. This procedure was repeated until approximately 90 mg of photolysate had been collected. An initial attempt to separate the new product via preparative TLC ( $\text{CH}_2\text{Cl}_2$  and silica gel) resulted in recovery of **15** and the new product in one band ( $R_f$  0.6). A second attempt (1:9 ethyl acetate:hexanes and silica gel) succeeded in separating **15** ( $R_f$  0.2) from the new light yellow product ( $R_f$  0.3), identified as *p*-nitrosobenzaldehyde (**17**) (based on identical  $^1\text{H}$  NMR with that reported in the literature (30)). IR (KBr disc,  $\text{cm}^{-1}$ ): 1200 (m), 1260 (s), 1390 (m), 1460 (w), 1595 (m), 1690 (s).  $^1\text{H}$  NMR  $\delta$ : 8.03 (d,  $J$  = 8.8 Hz, 2H, arom.), 8.17 (d,  $J$  = 8.1 Hz, 2H, arom.), 10.20 (s, 1H, CHO). HR-MS (EI) calcd. for  $\text{C}_7\text{H}_5\text{NO}_2$ : 135.0321; found: 135.0323.

#### Photolysis of *O*-acetyl *p*-nitromandelic acid (**7**) in 1:1 $\text{H}_2\text{O}$ - $\text{CH}_3\text{CN}$ (pH 7)

A solution of **7** (20 mg) in 1:1  $\text{H}_2\text{O}$ - $\text{CH}_3\text{CN}$  (100 mL, pH adjusted to 7, Ar purged) was photolyzed for 20 min (300 nm, 4 lamps). Following work-up,  $^1\text{H}$  NMR of the photolysate revealed 23% conversion to **18** and **19** (47 and 53%, respectively), each of which were identified by addition of an authentic sample (vide supra) which enhanced the  $^1\text{H}$  NMR signals.

#### Photolysis of *p*-nitrophenylethylene glycol (**8**) in 1:1 $\text{H}_2\text{O}$ - $\text{CH}_3\text{CN}$ (pH 13)

A solution of **8** (100 mg) in 1:1  $\text{H}_2\text{O}$ - $\text{CH}_3\text{CN}$  (100 mL, pH 13, Ar purged) was photolyzed for 30 min (300 nm, 16 lamps). Following work-up  $^1\text{H}$  NMR of the photolysate revealed 69% conversion to **15** and **16** (60 and 40%, respectively), identified as above (vide supra).

#### Photolysis of *p*-nitrobenzhydrol (**9**) in 1:1 $\text{H}_2\text{O}$ - $\text{CH}_3\text{CN}$ (pH 13)

A solution of **9** (20 mg) in 1:1  $\text{H}_2\text{O}$ - $\text{CH}_3\text{CN}$  (100 mL, pH 13, Ar purged) was photolysed for 60 min (300 nm, 16 lamps). After photolysis the solution turned a deep red color

that did not dissipate for up to several hours. Upon acidification to pH 2 with aq HCl, the color turned to yellow (between pH 10 and 11), with formation of a yellow precipitate. Extraction of the whole mixture with  $\text{CH}_2\text{Cl}_2$  gave a  $^1\text{H}$  NMR that showed ~15% conversion of **9** to **21** and **22** (70 and 30%, respectively), and a third, unidentified product. In a separate experiment, the precipitate formed during acidification was isolated by suction filtration and found to contain **22** and the unidentified product (in a ~1:1 mixture), while the filtrate contained **9** and **21**. Preparative TLC ( $\text{CH}_2\text{Cl}_2$  and silica gel) failed to separate **22** from the unidentified product. Based on analysis of the  $^1\text{H}$  NMR pattern of the unidentified product (as a mixture with **22**), we have tentatively identified it as a secondary photoproduct of **22**, i.e., a hydroxyazobenzene derived from **22**, consistent with the known photo-Wallach rearrangement of aromatic azoxy compounds (31).

#### Quantum yields

The quantum yield of **6** was measured by preparative photolysis and  $^1\text{H}$  NMR using **3** as secondary actinometer ( $\Phi$  = 0.6) (12). Photolysis of **3** (20 mg, pH 7, 100 mL 100% 0.01 M phosphate buffer, 300 nm, 4 lamps, 2 min, Ar purged) followed by assessment of the conversion to product (10–15%) allowed calculation of the number of photons emitted by the apparatus. In a following photolysis of **6** (100% pH 6 0.01 M phosphate buffer) using identical conditions, assessment of conversion (5–10%) allowed calculation of the quantum yield for the reaction. These photolyses were repeated four times, and the average quantum yield was calculated.

#### Laser flash photolysis (LFP)

LFP data was acquired using either a Nd:YAG laser (Spectra-Physics Quanta-Ray GCR-11,  $\lambda_{\text{ex}}$  266 nm; this laser was used for most LFP experiments) or a Lumonics excimer laser (EX-510,  $\lambda_{\text{ex}}$  308 nm; this laser was used for experiments using  $\text{IrCl}_6^{2-}$ ) with pulse widths ~20 ns and power attenuated to ~20 mJ/pulse. Signals were digitized with a Tektronix TDS 520 recorder. Solutions with OD = 0.3 at  $\lambda_{\text{ex}}$  were used to ensure even penetration of the laser light. Quartz flow cells were used for all studies except for the measurement of  $\Delta\text{OD}_{\text{init}}$  at various pH values (Figs. 10 and 12), where quartz static cells were used. Samples in flow cells were continuously purged with a stream of  $\text{N}_2$  or  $\text{O}_2$  for 15 min before and during the experiment. Samples in static cells were purged with  $\text{N}_2$  or  $\text{O}_2$  for 5 min and subsequently sealed prior to the experiment. The contents of static cells were mixed between each laser shot to avoid depletion of the solution in the irradiated volume.

#### Acknowledgments

We thank the Natural Sciences and Engineering Research Council of Canada (NSERC) for continued support of this research, and Mr. Xigen Xu for the initial studies on compound **8**.



## References

1. D.J. Cram. Fundamentals of carbanion chemistry. Academic Press Inc., New York. 1965. p. 289.
2. P.M. Mayer and L. Radom. *J. Phys. Chem. A*, **102**, 4918 (1998).
3. K.M. Downard, J.C. Sheldon, J.H. Bowie, D.E. Lewis, and R.N. Hayes. *J. Am. Chem. Soc.* **111**, 8112 (1989).
4. P. Wan and K. Yates. *Can. J. Chem.* **64**, 2076 (1986).
5. P. Wan and X. Xu. *Tetrahedron Lett.* **31**, 2809 (1990).
6. J. Morrison, H. Osthoff, and P. Wan. *Photochem. Photobiol. Sci.* **1**, 384 (2002).
7. M. St. Maurice and S.L. Bearne. *Biochemistry*, **39**, 13324 (2000).
8. M. Garcia-Viloca, A. Gonzalez-Lafont, and J.M. Lluch. *J. Am. Chem. Soc.* **123**, 709 (2001).
9. P.K. Das. *Chem. Rev.* **93**, 119 (1993).
10. T.-I. Ho and Y.L. Chow. *In* The chemistry of amino, nitroso and related groups. Vol. 1. *Edited by* S. Patai. John Wiley and Sons, Toronto. 1996. p. 747.
11. D. Döpp. *In* CRC handbook of organic photochemistry and photobiology. *Edited by* W.M. Horspool and P.-S. Song. CRC Press, Boca Raton. 1995. Chap. 81. p. 1019.
12. J.D. Margerum and C.T. Petrusis. *J. Am. Chem. Soc.* **91**, 2467 (1969).
13. P. Wan and S. Muralidharan. *J. Am. Chem. Soc.* **110**, 4336 (1988).
14. G.A. Russell, A.J. Moye, E.G. Janzen, S. Mak, and E.R. Talaty. *J. Org. Chem.* **32**, 137 (1967).
15. G.A. Russell and E.G. Janzen. *J. Am. Chem. Soc.* **89**, 300 (1967).
16. E. Buncel and B.C. Menon. *J. Am. Chem. Soc.* **102**, 3499 (1980).
17. B.B. Craig, R.G. Weiss, and S.J. Atherton. *J. Phys. Chem.* **91**, 5906 (1987).
18. B.B. Craig and S.J. Atherton. *J. Chem. Soc., Perkin Trans. 2*, 1929 (1988).
19. A. McKenzie and P.A. Stewart. *J. Chem. Soc.* 104 (1935).
20. G. Carrara, F. Fava, C. Martinuzzi, and A. Vecchi. *Gazz. Chim. Ital.* **82**, 674, (1952).
21. S. Muralidharan and P. Wan. *J. Photochem. Photobiol. A*, **57**, 191 (1991).
22. T. Shida. *Electronic absorption spectra of radical ions*. Elsevier, New York. 1988.
23. S. Steenken and P. Neta. *J. Am. Chem. Soc.* **104**, 1244 (1982).
24. J. Halpern, R.J. Legare, and R. Lumry. *J. Am. Chem. Soc.* **85**, 680 (1963).
25. J.Y. Chen, H.C. Gardner, and J.K. Kochi. *J. Am. Chem. Soc.* **98**, 6150 (1976).
26. M. Schwörer and J. Wirz. *Helv. Chim. Acta*, **84**, 1441 (2001).
27. R.B. Davis and J.D. Benigni. *J. Org. Chem.* **27**, 1605 (1962).
28. K. Schank. *Chem. Ber.* **103**, 3093 (1970).
29. G. Heller. *Chem. Ber.* **46**, 280 (1913).
30. X. Creary, P.S. Engel, N. Kavaluskas, L. Pan, and A. Wolf. *J. Org. Chem.* **64**, 5634 (1999).
31. N.J. Bunce, J.P. Schoch, and M.C. Zerner. *J. Am. Chem. Soc.* **99**, 7986 (1977).



# Intramolecular reactions of dialkoxycarbene with a carbonyl group

Małgorzata Dawid and John Warkentin

**Abstract:** Thermolysis of 5,5-dimethyl-2-methoxy-2-(2-oxocyclohexylmethoxy)- $\Delta^3$ -1,3,4-oxadiazoline (**3a**) in benzene at 110°C generated a carbonyl ylide intermediate that gave, in a minor side reaction, a product of 1,3-dipolar cycloaddition to the carbonyl group. The major fate of the ylide was fragmentation to acetone and a dialkoxycarbene, MeO-(RCH<sub>2</sub>O)C:, where R = 2-oxocyclohexyl. The carbene, in turn, underwent overall [2 + 1] cycloaddition to the carbonyl group, presumably to afford diastereomeric dialkoxyoxiranes that could not be isolated. A product of methanolysis of the presumed oxiranes was isolated by GC and its structure was determined by means of X-ray diffraction. Methanol is believed to result from reaction of an intermediate or product with adventitious water. Deliberate hydrolysis of the product of methanolysis gave a hydroxy lactone, the structure of which was also secured by means of single crystal X-ray diffraction. Those structures indicated the likely structures of the oxirane precursors. A second, and major, product from the carbene was a bicyclic ketone. Similar products were obtained from intramolecular reactions of a carbene tethered to cyclopentanone through a two-carbon or a one-carbon tether. Some compounds that are apparently “dimers” of the oxiranes were also isolated and identified by means of X-ray diffraction. These dimers are thought to originate from the reaction of a ring-opened oxirane (a dipole or a cation from electrophilic opening of the oxirane) with a molecule of the oxirane rather than from bimolecular reaction between two oxirane molecules. The oxiranes open by cleavage of the (RO)<sub>2</sub>C—O bond rather than the oxirane C—C bond, the normally observed sense of thermal ring opening. The properties of the carbenes and the presumed oxiranes serve to point out the options available to such intermediates and suggest that some new, synthetically useful reactions may become possible.

**Key words:** bicyclic ketone, dialkoxycarbene, dialkoxyoxirane, hydroxylactone, “oxirane dimers”.

**Résumé :** La thermolyse de la 5,5-diméthyl-2-méthoxy-2-(2-oxocyclohexylméthoxy)- $\Delta^3$ -1,3,4-oxadiazoline (**3a**), dans le benzène, à 110 °C, génère la formation d'un ylure de carbonyle comme intermédiaire qui réagit, dans une réaction latérale mineure, pour former un produit de cycloaddition 1,3-dipolaire sur le groupe carbonyle. La réaction principale de l'ylure est une fragmentation en acétone et en dialkoxycarbène, MeO(RCH<sub>2</sub>O)C:, dans lequel R = 2-oxocyclohexyle. Par la suite, le carbène subit une réaction globale de cycloaddition [2 + 1] sur le groupe carbonyle qui fournit probablement les dialkoxyoxiranes diastéréomères qui n'ont pas été isolés. Faisant appel à la CG, on a toutefois pu en isoler un produit de méthanolyse et on a déterminé sa structure par diffraction des rayons X. On croit que le méthanol est issu de la réaction d'un intermédiaire ou d'un produit avec de l'eau présente de façon fortuite. L'hydrolyse délibérée du produit de méthanolyse conduit à une hydroxylactone dont la structure a été déterminée par diffraction des rayons X sur un cristal unique. Ces structures suggèrent celles des oxiranes qui leur ont donné naissance. Un deuxième et le plus important produit provenant du carbène est une cétone bicyclique. Des produits semblables ont été obtenus par le biais de réactions intramoléculaires d'un carbène auquel on a attaché une cyclopentanone par le biais de rallonges à un ou deux atomes de carbones. On a aussi isolé des composés qui sont apparemment des dimères d'oxiranes et on les a identifiés par le biais de la diffraction des rayons X. On croit que ces dimères trouvent leur origine dans la réaction d'un oxirane à cycle ouvert (un dipôle ou un cation résultant de l'ouverture électrophile de l'oxirane) avec une molécule d'oxirane plutôt par une réaction bimoléculaire entre deux molécules d'oxirane. Les oxiranes s'ouvrent par rupture de la liaison (RO)<sub>2</sub>C—O plutôt que par ouverture de la liaison C—C de l'oxirane, le sens d'ouverture normalement observé dans l'ouverture thermique du cycle. Les propriétés des carbènes et des oxiranes suggérés permettent de préciser les diverses options ouvertes à ces intermédiaires et de suggérer que de nouvelles réactions utiles en synthèse puissent se développer.

**Mots clés :** cétone bicyclique, dialkoxycarbène, dialkoxyoxirane, hydroxylactone, dimères d'oxirane.

[Traduit par la Rédaction]

Received 8 August 2002. Published on the NRC Research Press Web site at <http://canjchem.nrc.ca> on 22 May 2003.

*Dedicated to Professor Don Arnold, for his exemplary devotion to excellence in chemistry.*

**M. Dawid and J. Warkentin.**<sup>1</sup> Department of Chemistry, McMaster University, 1280 Main St. West, Hamilton, ON L8S 4M1, Canada.

<sup>1</sup>Corresponding author (e-mail: [warkent@mcmaster.ca](mailto:warkent@mcmaster.ca)).



## Introduction

The nucleophilicity of dialkoxycarbenes was first reported by Hoffmann's group, and other examples followed (1). Relative nucleophilicities of various carbenes have been quantified by Moss et al. (2). The nucleophilic characteristics of dialkoxycarbenes are evident from their sluggish reactions with simple alkenes, such as cyclohexene (1*b*, 3) and their greater reactivity toward Michael acceptors such as isocyanates and diphenylketene (1*d*), for example. Donor-atom-substituted carbenes are also capable of bimolecular nucleophilic displacements. Nucleophilic substitution at unsaturated carbon occurs between an imidazolylidene and 2,3,4,5,6-pentafluoropyridine (4) and in reactions of dimethoxycarbene (DMC) with hexachlorocyclopentadiene (5), 1-fluoro-2,4-dinitrobenzene, and hexafluorobenzene (6), for example, although the yields can be very low (6).

A common reaction of nucleophiles with carbonyl compounds is addition, to change the geometry at the carbonyl carbon from planar to tetrahedral. Diaminocarbenes were known to attack at the carbonyl carbon atom of aldehydes (7), and DMC appears to add to the carbonyl group of hexafluoroacetone (Scheme 1) (8), fluorenone (9), and cyclohexanone (10). Recently it was shown that DMC reacts to effect insertion into the bond between the carbonyl carbon and the  $\alpha$ -oxygen atom of anhydrides (11) and a lactone (12). Similar apparent insertion into the bond between a carbonyl carbon and the  $\alpha$ -carbon of strained cyclic ketones was reported (12) (Scheme 2). Such reactions could be concerted or they could involve tetrahedral intermediates with dipolar or diradical characteristics. Either of those intermediates could rearrange by ring enlargement or cyclize to isolable dialkoxoxiranes, as in the case of addition of dimethoxycarbene to cyclohexanone (Scheme 3) (10). Dimethoxycarbene also reacts with thiocarbonyl compounds to form dimethoxythiiranes (13). Although imidazolylidenes are known to form stable dipolar intermediates by forming a single bond to carbon disulfide (14), carbon dioxide (15), or sulfur trioxide (16), attack of a less-nucleophilic dialkoxycarbene at a carbonyl or thiocarbonyl group could be concerted, leading directly to a dialkoxoxirane or a dialkoxythiirane.

The nucleophilic reactivity of dialkoxycarbenes was suggested by the previously demonstrated reactions of vinylogous dialkoxycarbenes with ketones (17–19). It is not surprising that vinylogous dialkoxycarbenes are better nucleophiles than saturated analogues because the former carbenes are presumably more polarizable and can disperse positive charge better in a stepwise or nonsynchronous concerted reaction. The stepwise pathway for vinylogous dialkoxycarbenes is illustrated in Scheme 4.

It was of interest to us to explore further the possible intramolecular reactions of non-vinylogous dialkoxycarbenes with a tethered carbonyl group. Previously only one case of such a process had been reported and that was for reaction with the carbonyl group of a tethered cyclobutanone (12). We now report reactions of a dialkoxycarbene with the carbonyl group of a cyclohexanone tethered at the  $\alpha$ -position with a one-carbon tether to the carbene, as well as reactions of dialkoxycarbenes tethered analogously to cyclopentanone with a one- or two-carbon tether.

## Methods, results, and discussion

The oxadiazoline precursors (3) of dialkoxycarbenes were prepared from 2-hydroxyalkyl cyclanones (2) and 2-acetoxy-2-methoxy-5,5-dimethyl- $\Delta^3$ -1,3,4-oxadiazoline (1) by the exchange method (19), as illustrated in Scheme 5. The exchange had to be done carefully to minimize dehydration of 2*a* or destruction of 3 subsequent to their formation. Protection of the carbonyl group of 2*a* with 1,2-ethane dithiol and subsequent exchange followed by deprotection was achieved but that route did not offer any improvement of the yield of 3*a*. Compounds 3 were isolated by chromatography on silica.

After purification of 3*a* by chromatography, a benzene solution was heated for 24 h at 110°C in a sealed glass tube. Products isolated by chromatography on silica included 4 (7%) and 1-methoxy-8-oxa-9-oxobicyclo[4.2.1]nonane (5, 31%), as shown in Scheme 6. Acetal 6 (16%), which had two methoxy signals in the  $^1\text{H}$  NMR spectrum and the correct mass for 6-OMe, was isolated by means of GC. Despite many attempts the material could not be crystallized. Structure 6 was inferred from the structure of the single product of hydrolysis of the material (below). In addition, diastereomers 7*a* and 7*b*, both crystalline solids, were isolated by means of radial chromatography on silica. Compound 7*a* was identified completely by means of single crystal X-ray diffraction and 7*b* was assigned on the basis of its NMR spectra, which closely resembled those of 7*a*.

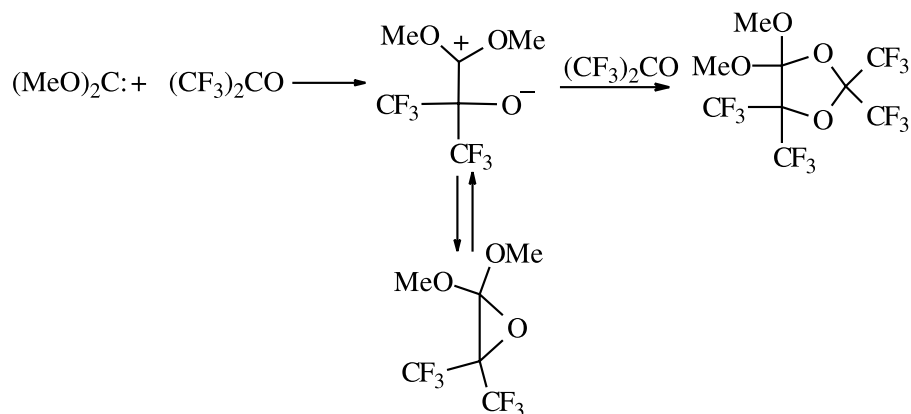
The products can be accounted for as follows. Oxadiazoline 3*a* loses  $\text{N}_2$  in the first step to generate carbonyl ylide 8 (Scheme 7). Intramolecular cycloaddition of the ylide to the carbonyl group leads to 4, the stereochemistry of which was assigned on the basis of the structure of the product of acid-catalyzed hydrolysis of 4, hydroxy lactone 9. The structure of 9 was secured by means of single crystal X-ray diffraction.

A major fate of the carbonyl ylide must be the well-precedented loss of acetone (1*k*) to afford carbene intermediate 10, which attacks the carbonyl group of the cyclohexanone to generate intermediate 11 or, possibly, the oxiranes 12 (Scheme 7). The intermediacy of diastereomers 12 is speculative because many attempts to isolate a sample by gas chromatography gave material that contained 6 and, possibly, the diastereomers 12. Deliberate hydrolysis of such samples led to hydroxy lactone 9 only. The structure of 9 means that both the ylide 8 (precursor of 4) and the carbene 10 (precursor of 11) react from that conformation in which the side chain is axial, as shown in Scheme 7.

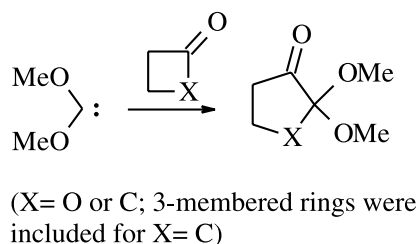
Although the rearrangement of 10 to 5 amounts to an insertion (overall) of the carbene into a C—CO bond of the carbonyl group, the reaction is not necessarily concerted. Reactions of cyclic ketones with diazomethane, leading to products of ring expansion, are believed to be stepwise (20). Those reactions are reasonable models for ring expansion of cyclic ketones by reaction with dialkoxycarbenes. It was shown previously that migration of the more-substituted carbon is preferred when  $\alpha$ -alkylcyclobutanones react with dimethoxycarbene to afford corresponding dimethoxycyclopentanones (12). In the case of postulated intermediate 11, in which migration of the more-substituted carbon would lead to a four-membered ring (Scheme 7), the less-substituted  $\alpha$ -carbon migrated to expand the ring from six-



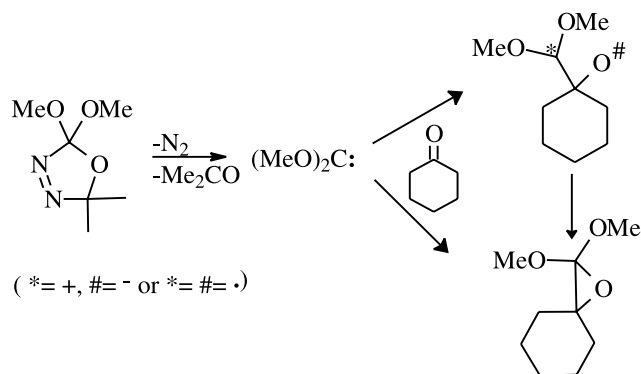
Scheme 1.



Scheme 2.



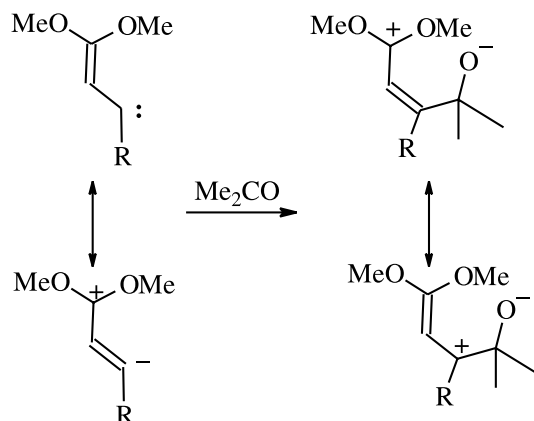
Scheme 3.



to seven-membered. A simple model that aids in visualization of the transition state charge separation is the enolate alkylation model (12) shown in Scheme 8. It should perhaps be emphasized that such structures, with enolate and cation character, are simply models for actual transition states or intermediates.

An additional product from thermolysis of **3a** was the complex compound **13**, consisting essentially of 3 equiv of the proposed oxirane intermediate. Its structure was determined by means of single crystal X-ray diffraction. Scheme 9 is a rationalization for its formation from reaction of the ring-opened oxirane with the oxirane. It should be emphasized that the mechanism, involving intermediates **11** and **13**, is speculative. Instead of the dipolar species **11**, one could invoke a cationic intermediate formed by protonation (by adventitious water) and subsequent ring-opening of an oxirane **12**. That cation could then act as an electrophile to

Scheme 4.



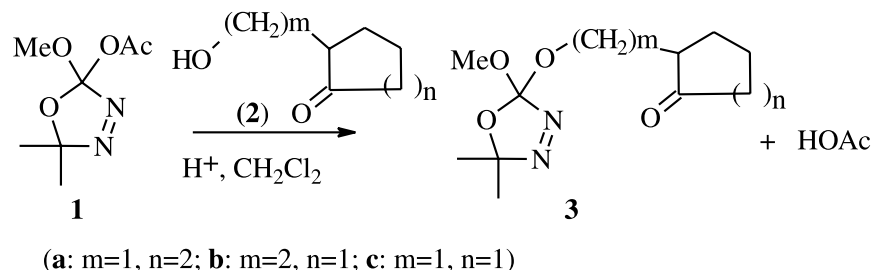
open a second molecule of oxirane. The connectivity of **14** does require that the oxirane intermediates *do not open to carbonyl ylides*; the usual sense of thermal ring opening of oxiranes. Presumably there were other compounds, analogous to **14**, that we were unable to isolate.

Heating of a solution of **3b** in benzene afforded similar products. A major product (33%) was 1-methoxy-2-oxa-8-oxobicyclo[3.3.1]nonane (**17**). Again there was indirect evidence for isomeric oxirane intermediates, probably **15** and **16** (Scheme 10), although they were too unstable to be isolated. Preparative gas chromatography gave fractions that changed during the collection process, probably because of hydrolysis. Two stable compounds (**18** and **19**) were also isolated by means of GC and identified by means of single crystal X-ray diffraction. Compound **18** is probably formed by the methanolysis of **15** and **16**. The source of methanol is again assumed to be hydrolysis of an intermediate by adventitious water.

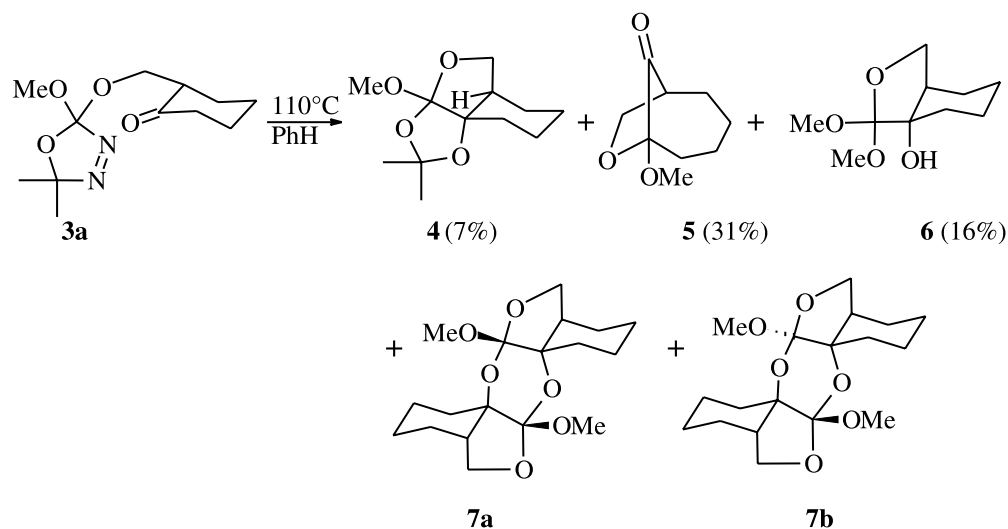
The hexahydropyranyl ring of **19** is fused *trans* to the 1,4-dioxanyl ring and the ring juncture of the hexahydropyranyl and cyclopentyl rings is *cis*. It is analogous to compound **11** that was obtained from **3a**, and it appears, at first sight, to be a head-to-tail dimer of the dipolar intermediate that would result from stepwise addition of the nucleophilic carbene center to the carbonyl group (Scheme 10). Such a dimerization is unlikely, of course, because reactive intermediates are not expected to accumulate to concentrations that



Scheme 5.



Scheme 6.



could lead to bimolecular reactions between them. We are therefore led to propose, again, that there is a bimolecular reaction between a dipolar species, in equilibrium with the oxirane precursor and the oxirane. Alternatively, a cationic species, from electrophile-catalyzed ring opening of the oxirane, reacts with the oxirane to generate **19**. Isomers of **19** might be expected, given that isomeric oxiranes such as **15** and **16** could result from the carbene. The GC trace showed compounds with retention times similar to that of **19**, and we assume that isomers of **19** were generated and that they account for some of material imbalance.

Thermolysis of **3c** gave products analogous to those from **3a** and **3b** (Scheme 11). Compound **22** (2%) can be attributed to dipolar cycloaddition of the ylide from **3c** to the carbonyl group, and the carbene from **3c** afforded **23** and **24**, because we were able to isolate a product (**25**) of apparent methanolysis of **24**. Lactone **26** was also obtained as was bicyclic ketone **28** (28%), possibly from rearrangement of a dipolar intermediate **23**. In the case of **3c**, two dimers (**29** and **30**) of the putative oxirane intermediate could be obtained in crystalline form suitable for single crystal X-ray diffraction. Compound **27** is apparently the product of hydrolysis of a product like **29**. In diastereomer **29** the 1,4-dioxanyl ring is in the chair conformation, and it is fused *cis* to the tetrahydrofuran rings. In diastereomer **30** the 1,4-dioxanyl ring is in a boat conformation, and both tetrahydrofuran rings are again fused *cis* to it. As in cases of **3a** and

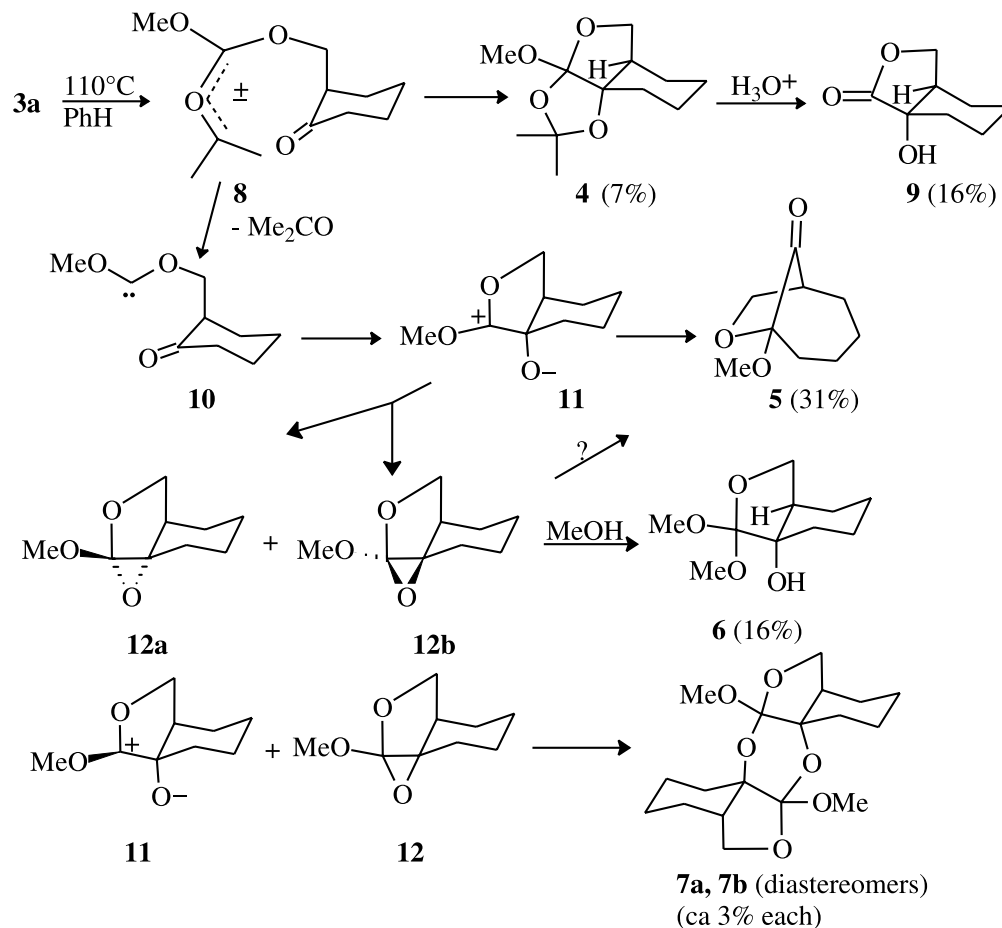
**3b**, there were other products with GC retention times similar to those of **29** and **30**. Those products were probably also dimers, isomers of **29** and **30**.

In order to trap a possible intermediate, thermolysis of **3a** was carried out in the presence of dimethyl acetylenedicarboxylate (DMAD). The yield of **5** was reduced by a factor greater than two, and there were formed, instead, two products isolated in essentially equal amounts, ca. 3% each, with greater GC retention times. It was possible to isolate those compounds, by means of semipreparative GC followed by MPLC, and to determine that they were diastereomers **32** and **33** (Scheme 12). Structure **32** was secured by means of single crystal X-ray diffraction while **33** was inferred from its NMR spectrum, which was very similar to that of **32**. It is clear from the connectivity that DMAD *had not intercepted a carbonyl ylide* such as **30**, which is the intermediate that is normally obtained from thermal, conrotatory ring opening of an oxirane, but something like dipole **31** or the cation from protonation of **31**. The cation mechanism appears to fit best because a cationic intermediate would not be likely to attack the triple bond but it could coordinate instead to carbonyl oxygen.

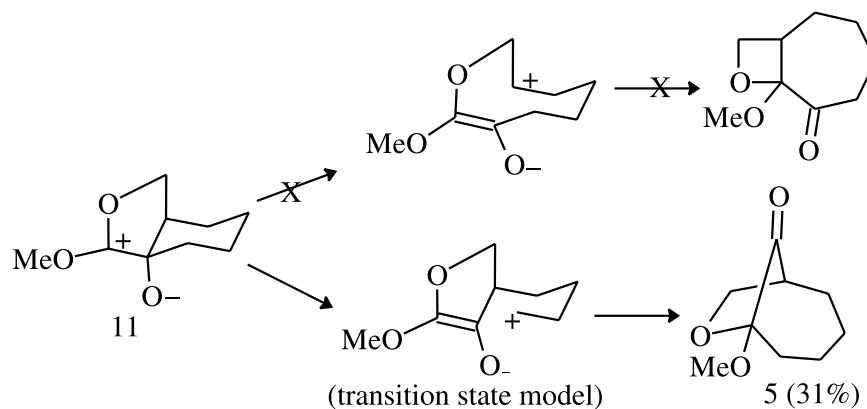
In summary dialkoxycarbenes, tethered *alpha* to the carbonyl group of cyclohexanone or cyclopentanone, react intramolecularly with the carbonyl group to generate an intermediate with a new five- or six-membered ring. Dialkoxycarbenes could not be isolated but they were



Scheme 7.



Scheme 8.



inferred from products of their ring opening by methanol or water. Some novel oxirane dimers were isolated, as well as, in each case, a bicyclic ketone.

## Experimental

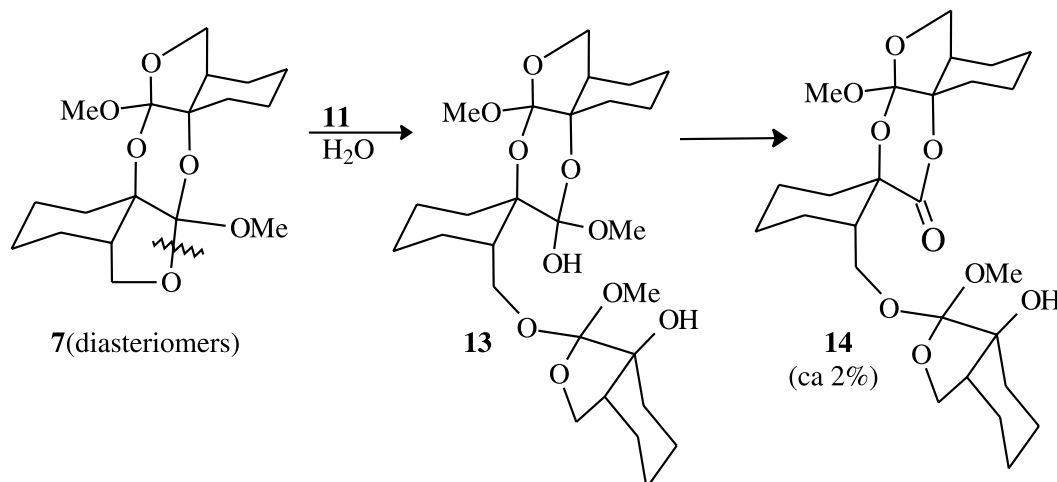
### Preparation of oxadiazoline **3a**

A solution of 2-acetoxy-2-methoxy-5,5-dimethyl- $\Delta^3$ -1,3,4-oxadiazoline (**1**) in  $\text{CH}_2\text{Cl}_2$ , containing about 30% of an acy-

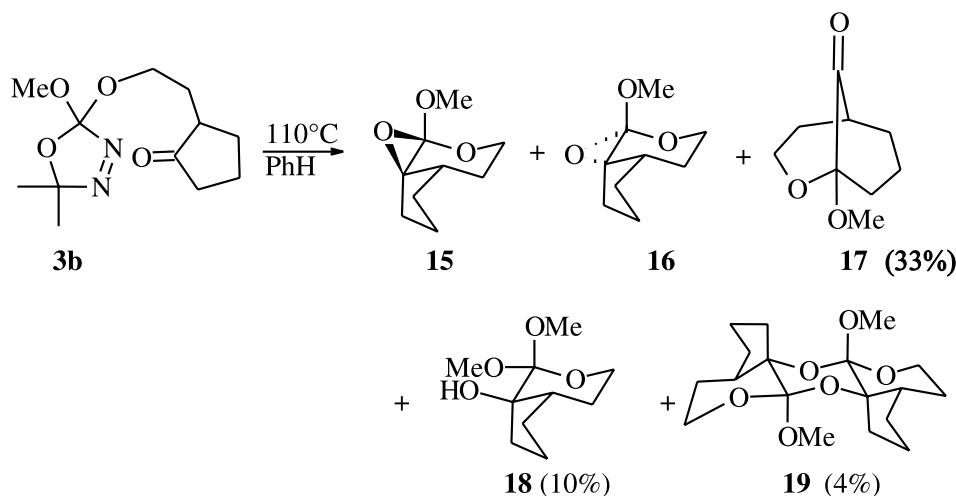
clic isomer (**19**), was treated with hydroxy ketone **2a** (**21**) and trifluoroacetic acid in dichloromethane. After washing with dilute base, the organic layer was dried and the solvent was evaporated. Chromatography of the residue (silica gel, hexane:ethyl acetate: $\text{Et}_3\text{N}$  (85:15:0.5)) gave oxadiazoline **3a** (67% of pure product) as a colourless oil. IR (neat, KBr) ( $\text{cm}^{-1}$ ): 2989, 2944, 2865, 1711, 1452, 1211, 1167, 1136, 914.  $^1\text{H}$  NMR (300 MHz,  $\text{CDCl}_3$ , 1:1 mixture of two diastereoisomers)  $\delta$ : 4.14 (dd,  $J = 9.9, 5.1$  Hz, 1H,  $\text{OCH}_a$ ),



Scheme 9.



Scheme 10.



4.04 (dd,  $J = 9.9, 5.1$  Hz, 1H,  $\text{OCH}_a$ ), 3.71 (dd,  $J = 9.9, 7.7$  Hz, 1H,  $\text{OCH}_b$ ), 3.59 (dd,  $J = 9.9, 7.7$  Hz, 1H,  $\text{OCH}_c$ ), 3.45 (s, 6H), 2.65 (m, 2H), 2.34 (m, 6H), 2.03 (m, 2H), 1.90 (m, 2H), 1.67 (m, 4H), 1.54 (s, 12H), 1.44 (m, 2H).  $^{13}\text{C}$  NMR (75 MHz,  $\text{CDCl}_3$ )  $\delta$ : 210.7, 137.1, 119.3, 63.9, 52.0, 50.4, 42.2, 31.4, 24.7, 24.2, 24.1. EI-MS  $m/z$  (%): molecular ion not observed, 225 ( $[\text{M} - \text{OMe}]^+$ , 3), 170 (7), 129 (15), 111 (59), 94 (47), 73 (60), 55 (100). CI-MS ( $\text{NH}_3$ )  $m/z$ : 274 ( $[\text{M} + \text{NH}_4]^+$ , 28).

#### Thermolysis of **3a** in benzene

A solution of **3a** (0.51 g, 2 mmol) in benzene (20 mL) in a sealed tube was heated at  $110^\circ\text{C}$  for 18 h. Evaporation of the solvent left a residue that was chromatographed on silica (hexane:ethyl acetate, 90:10) to afford bicyclic ketone **5** (31%), hydroxy orthoester **6** (16%), **4** (7%), and compounds **7** (<5%).

Semipreparative gas chromatography (OV-17, 5%, helium at  $50 \text{ mL min}^{-1}$ ; temperature program,  $80^\circ\text{C}$  for 5 min, increased at  $4^\circ\text{C min}^{-1}$  to  $250^\circ\text{C}$ ; retention time 26–29 min) gave **6**, which is probably a product of oxirane methanolysis,

as a semicrystalline material. A crystal suitable for X-ray crystallography could not be obtained. Exposure of the sample to the atmosphere led to its slow hydrolysis to **9**.

#### Product **4**

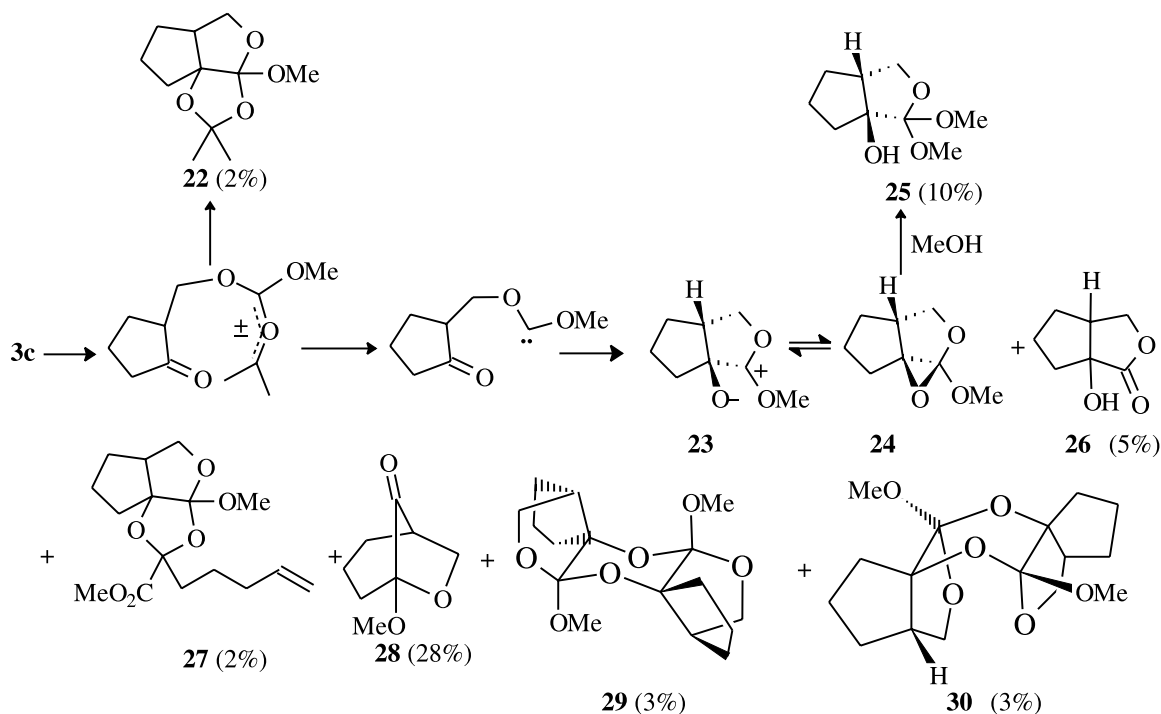
Yield: 7%, colourless oil.  $^1\text{H}$  NMR (300 MHz,  $\text{CDCl}_3$ )  $\delta$ : 4.12 (dd,  $J = 8.3, 4.7$  Hz, 1H), 3.57 (d,  $J = 8.3$  Hz, 1H), 3.35 (s, 3H), 2.20 (m, 1H), 2.03 (m, 1H), 1.44 (s, 6H), 1.4–1.85 (m, 7H).  $^{13}\text{C}$  NMR (75 MHz,  $\text{CDCl}_3$ )  $\delta$ : 126.5, 108.8, 87.6, 71.0, 51.4, 44.6, 32.1, 29.3, 28.1, 28.0, 23.5, 23.0. EI-MS  $m/z$  (%): 229 ( $[\text{M} + 1]^+$ , 4), 213 (55), 154 (45), 153 (48), 111 (41), 93 (100), 81 (66), 55 (84), 43 (80). Compound **4** in  $\text{CDCl}_3$  was converted rapidly to lactone **9** during storage.

#### 1-Methoxy-8-oxa-9-oxobicyclo[4.2.1]nonane (**5**)

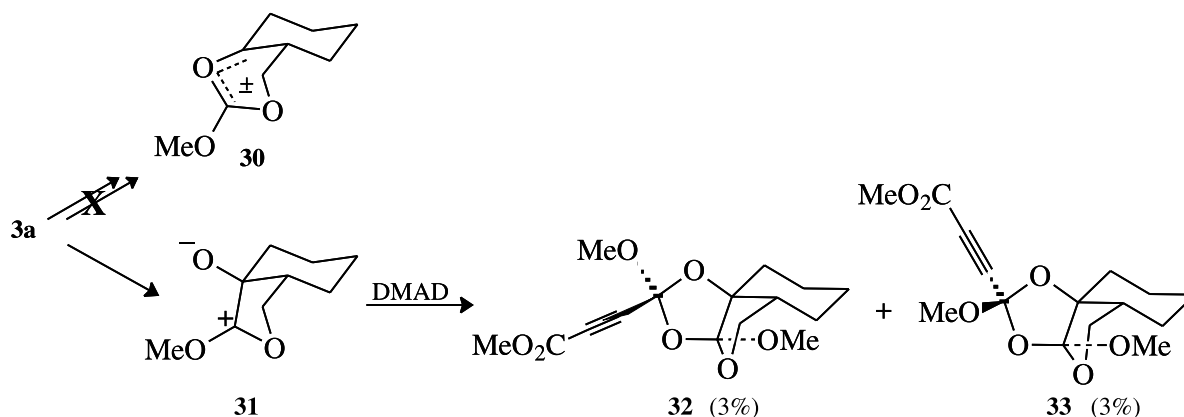
Yield: 31%, colourless oil. IR (neat) ( $\text{cm}^{-1}$ ): 2938, 2866, 1767, 1456, 1189, 1158, 1075, 998.  $^1\text{H}$  NMR (200 MHz,  $\text{CDCl}_3$ )  $\delta$ : 4.34 (dd,  $J = 8.8, 5.2$  Hz, 1H), 4.07 (d,  $J = 8.8$  Hz, 1H), 3.28 (s, 3H), 2.67 (m, 1H), 1.15–1.90 (m, 8H).  $^{13}\text{C}$  NMR (50 MHz,  $\text{CDCl}_3$ )  $\delta$ : 216.0, 104.9, 70.3, 51.1, 45.6, 33.0, 31.2, 23.7, 22.6. EI-MS  $m/z$  (%): 171 ( $[\text{M} + 1]^+$ , 15),



Scheme 11.



Scheme 12.



142 (42), 110 (68), 83 (55), 74 (100), 53 (92), 41 (100). CI-MS ( $\text{NH}_3$ )  $m/z$ : 188 ( $[\text{M} + \text{NH}_4]^+$ , 100).

#### Product 6

Semicrystalline.  $^1\text{H}$  NMR (500 MHz,  $\text{CDCl}_3$ )  $\delta$ : 3.80 (dd,  $J = 14.4$ ,  $J = 2.5$  Hz, 2H), 3.39 (s, 3H), 3.35 (s, 3H), 2.43 (d,  $J = 1.4$ , 1H), 2.37 (m, 1H), 1.44–1.90 (m, 6H). EI-MS  $m/z$  (%): 171 ( $[\text{M} - \text{OMe}]^+$ , 100), 147 (18), 112 (73), 97 (56), 83 (23), 69 (14). Compound 6 was rapidly converted to lactone 9 during storage.

#### Product 7a

Colourless crystals, mp 118°C.  $^1\text{H}$  NMR (200 MHz,  $\text{C}_6\text{D}_6$ )  $\delta$ : 4.02 (t,  $J = 7.8$  Hz, 2H), 3.50 (dd,  $J = 7.8$ , 4.1 Hz, 2H), 3.45 (s, 6H), 2.68 (m, 2H), 2.13 (m, 2H), 1.94 (m, 2H), 1.69–1.55 (m, 6H), 1.40–1.26 (m, 6H).  $^{13}\text{C}$  NMR (50 MHz,  $\text{C}_6\text{D}_6$ )  $\delta$ : 116.7, 79.6, 68.9, 48.7, 42.5, 29.9, 25.2, 22.3, 22.2.

EI-MS  $m/z$  (%): 341 ( $[\text{M} + 1]^+$ , 100), 340 ( $[\text{M}]^+$ , 78), 339 (46), 154 (100), 153 (22), 139 (19), 109 (21), 95 (29), 79 (30). The connectivity and stereochemistry of 7a were established by means of single crystal X-ray diffraction.

#### Product 7b

Colourless crystals, mp 148°C.  $^1\text{H}$  NMR (200 MHz,  $\text{C}_6\text{D}_6$ )  $\delta$ : 4.21 (t,  $J = 7.7$  Hz, 2H), 3.45 (s, 6H), 3.21 (dd,  $J = 7.7$ , 3.3 Hz, 2H), 2.25 (m, 2H), 1.44–1.98 (m, 16H).  $^{13}\text{C}$  NMR (50 MHz,  $\text{C}_6\text{D}_6$ )  $\delta$ : 117.6, 80.0, 70.1, 48.1, 43.4, 31.6, 28.6, 23.5, 23.3.

#### Hydroxy lactone 9

Yield: 16% (formed during chromatography), colourless crystals, mp 129°C. IR (neat, KBr) ( $\text{cm}^{-1}$ ): 3420 (br), 2972, 2879, 1769, 1439, 1372, 1211, 1161, 1011, 970.  $^1\text{H}$  NMR (200 MHz,  $\text{CDCl}_3$ )  $\delta$ : 4.40 (dd,  $J = 8.6$ , 7.0 Hz, 1H), 4.05



(dd,  $J = 8.6, 7.5$  Hz, 1H), 2.68 (br s 1H), 2.50 (m 1H), 1.32–1.93 (m, 8H).  $^{13}\text{C}$  NMR (50 MHz,  $\text{CDCl}_3$ )  $\delta$ : 179.1, 73.2, 69.2, 41.0, 31.6, 23.6, 21.8, 21.0. EI-MS  $m/z$  (%): molecular ion not observed, 154 (13), 112 (42), 97 (57), 83 (78), 55 (100). CI-MS ( $\text{NH}_3$ )  $m/z$ : 174 ( $[\text{M} + \text{NH}_4]^+$ , 100). The connectivity and stereochemistry of **9** were established by means of single crystal X-ray diffraction.

### Synthesis of **3b**

A solution in  $\text{CH}_2\text{Cl}_2$  of 2-acetoxy-2-methoxy-5,5-dimethyl- $\Delta^3$ -1,3,4-oxadiazoline (**1**), containing about 40% of an acyclic isomer (**19**), was treated with hydroxy ketone **2b** and trifluoroacetic acid in dichloromethane. After washing with dilute base, the organic layer was dried and the solvent was evaporated. Chromatography of the residue gave pure oxadiazoline **3b** (57%) as a colorless oil. IR (neat) ( $\text{cm}^{-1}$ ): 2961, 2885, 1744, 1449, 1212, 1136, 1125, 1108, 921.  $^1\text{H}$  NMR (300 MHz,  $\text{CDCl}_3$ , 1:1 mixture of two diastereomers)  $\delta$ : 3.70–3.85 (m, 4H,  $-\text{OCH}_2$ ), 3.43 (s, 3H,  $-\text{OCH}_3$ ), 3.42 (s, 3H,  $-\text{OCH}_3$ ), 2.43–1.50 (m, 18H), 1.53 (s, 12H).  $^{13}\text{C}$  NMR (75 MHz,  $\text{CDCl}_3$ )  $\delta$ : 220.7, 137.1, 119.2, 63.1, 52.0, 46.4, 38.0, 29.8, 29.6, 24.3, 24.2, 20.9. EI-MS  $m/z$  (%): molecular ion not observed, 181, 153 (100), 129, 112, 111, 83 (100). CI-MS ( $\text{NH}_3$ )  $m/z$ : 274 ( $[\text{M} + \text{NH}_4]^+$ ).

### Thermolysis of **3b**

A solution of **3b** (0.51 g, 2 mmol) in benzene (20 mL) in a sealed tube was heated at  $110^\circ\text{C}$  for 20 h. Evaporation of the solvent left a residue that was chromatographed on silica (hexane:ethyl acetate, 90:10) to afford bicyclic ketone **17** (33%), hydroxyorthoester **18** (~10% after thermolysis), and dimer **19** (ca. 4%).

### Product **17**

Yield: 33%, colourless oil. IR (neat) ( $\text{cm}^{-1}$ ): 2946, 2861, 1740, 1464, 1452, 1164, 1064, 1044.  $^1\text{H}$  NMR (300 MHz,  $\text{CDCl}_3$ )  $\delta$ : 4.09 (dd,  $J = 11.8, 6.1$  Hz, 1H), 3.60 (d,  $J = 12.2, J = 4.4$ , Hz, 1H), 3.39 (s 3H), 2.86 (m, 1H), 1.51–2.26 (m, 8H).  $^{13}\text{C}$  NMR (75 MHz,  $\text{CDCl}_3$ )  $\delta$ : 212.8, 102.5, 65.0, 50.4, 45.4, 40.5, 35.9, 32.0, 17.9. HR-MS  $m/z$  calcd. for  $\text{C}_9\text{H}_{14}\text{O}_3$ : 170.0943; found: 170.0969.

### Product **18**

Only a few colourless crystals could be obtained for X-ray diffraction. The compound hydrolysed spontaneously to the corresponding hydroxylactone.

### Product **19**

Colourless crystals, yield ca. 3%.  $^1\text{H}$  NMR (200 MHz,  $\text{CDCl}_3$ )  $\delta$ : 3.77 (m, 4H), 3.28 (s, 6H,  $-\text{OCH}_3$ ), 2.73 (m, 2H), 2.18–1.32 (m, 16H).  $^{13}\text{C}$  NMR (75 MHz,  $\text{CDCl}_3$ )  $\delta$ : 108.9, 84.9, 61.4, 47.9, 42.6, 33.5, 27.8, 27.2, 20.9. The structure and stereochemistry were confirmed by means of single crystal X-ray diffraction.

### Synthesis of **3c**

A solution in  $\text{CH}_2\text{Cl}_2$  of 2-acetoxy-2-methoxy-5,5-dimethyl- $\Delta^3$ -1,3,4-oxadiazoline (**1**), containing about 40% of an acyclic isomer (**19**), was treated with hydroxy ketone **2c** and trifluoroacetic acid in dichloromethane. After washing with dilute base, the organic layer was dried and the solvent

was evaporated. Chromatography of the residue gave pure oxadiazoline **3c** (60%) as a colorless oil. IR (neat) ( $\text{cm}^{-1}$ ): 2959, 2888, 1742, 1458, 1211, 1140, 1104, 917.  $^1\text{H}$  NMR (300 MHz,  $\text{CDCl}_3$ , mixture of two diastereoisomers)  $\delta$ : 3.81–4.02 (overlapping multiplets, 4H), 3.43 (s, 3H), 3.42 (s, 3H), 1.60–2.42 (m, 14H), 1.54 (s, 6H), 1.53 (s, 3H), 1.52 (s, 3H).  $^{13}\text{C}$  NMR (75 MHz,  $\text{CDCl}_3$ )  $\delta$ : 218.5, 136.9, 119.5, 63.6, 63.5, 52.0, 48.8, 38.7, 27.0, 24.3, 24.1, 20.9. EI-MS  $m/z$  (%): molecular ion not observed, 211 ( $[\text{M} - \text{OMe}]^+$ , 9), 173 (38), 139 (11), 129 (10), 97 (100), 84 (26), 69 (100). CI-MS ( $\text{NH}_3$ )  $m/z$ : 260 ( $[\text{M} + \text{NH}_4]^+$ , 58).

### Thermolysis of **3c**

A solution of **3c** (0.51 g, 2 mmol) in benzene (20 mL) in a sealed tube was heated at  $110^\circ\text{C}$  for 20 h. Evaporation of the solvent left a residue that was chromatographed on silica (hexane:ethyl acetate, 90:10) to afford bicyclic ketone **28** (28%), **25** (10% isolated, unstable compound, hydrolysing, in part, to hydroxylactone **26** during the separation procedure), product **22** (2% isolated, undergoes hydrolyses to  $\alpha$ -hydroxylactone **26**), hydroxylactone **26**, product **27**, some of which could have hydrolysed to **26** during TLC separation (5% isolated), and dimers **29** and **30** (about 3% each).

### Product **22**

Colourless oil.  $^1\text{H}$  NMR (200 MHz,  $\text{C}_6\text{D}_6$ )  $\delta$ : 4.09 (dd,  $J = 9.0$  Hz,  $J = 6.4$  Hz, 1H), 3.62 (s, 3H), 3.47 (dd,  $J = 9.0, J = 2.9$  Hz, 1H), 2.57 (m, 1H), 2.32 (m, 1H), 2.0–1.55 (m, 4H), 1.54 (s, 3H), 1.50 (s, 3H), 1.27 (m, 1H).  $^{13}\text{C}$  NMR (50 MHz,  $\text{C}_6\text{D}_6$ )  $\delta$ : 124.8, 109.4, 98.1, 70.9, 51.1, 50.1, 34.2, 31.3, 28.1, 27.7, 25.5. Product **22** hydrolysed easily to **26**.

### Product **25**

Colourless oil. IR (neat) ( $\text{cm}^{-1}$ ): 3510 (br), 2954, 2881, 1449, 1365, 1168, 1135, 1113, 1045, 982.  $^1\text{H}$  NMR (500 MHz,  $\text{CDCl}_3$ )  $\delta$ : 3.92 (t,  $J = 10.1$  Hz, 1H), 3.37 (dd,  $J = 10.2, J = 5.6$  Hz, 1H), 3.34 (s, 3H), 3.31 (s, 3H), 2.88 (br. s, 1H), 2.34 (m, 1H), 1.98–2.10 (m, 2H), 1.72–1.80 (m, 3H), 1.45 (m, 1H).  $^{13}\text{C}$  NMR (125 MHz,  $\text{CDCl}_3$ )  $\delta$ : 118.2, 90.6, 69.6, 51.5, 50.7, 47.9, 35.1, 32.6, 26.1. EI-MS  $m/z$  (%): 189 ( $[\text{M} + 1]^+$ , 5), 157 ( $[\text{M} - \text{OMe}]^+$ , 100), 98 (10), 75 (8).

### Product **26**

Colourless oil. IR (neat) ( $\text{cm}^{-1}$ ): 3425 (br), 2962, 2876, 1765, 1446, 1383, 1211, 1156, 1008, 978.  $^1\text{H}$  NMR (200 MHz,  $\text{C}_6\text{D}_6$ )  $\delta$ : 3.74 (t,  $J = 9.3$  Hz, 1H), 3.04 (dd,  $J = 9.4, J = 5.8$  Hz, 1H), 2.91 (br s, 1H), 2.29 (m, 1H), 2.00–0.85 (m, 6H).  $^{13}\text{C}$  NMR (50 MHz,  $\text{C}_6\text{D}_6$ )  $\delta$ : 179.5, 83.6, 71.1, 46.4, 39.0, 31.3, 24.8. EI-MS  $m/z$  (%): 143 ( $[\text{M} + 1]^+$ , 41), 112 (10), 98 (94), 97 (100), 83 (19). CI-MS ( $\text{NH}_3$ )  $m/z$ : 160 ( $[\text{M} + \text{NH}_4]^+$ , 100).

### Product **27**

Colourless oil. IR (neat) ( $\text{cm}^{-1}$ ): 3051, 2954, 2875, 1754, 1642, 1441, 1364, 1202, 1074, 1018, 929.  $^1\text{H}$  NMR (200 MHz,  $\text{C}_6\text{D}_6$ )  $\delta$ : 5.69 (m, 1H), 4.97 (m, 2H), 4.04 (dd,  $J = 9.1, J = 6.2$  Hz, 1H), 3.69 (s, 3H), 3.43 (dd,  $J = 9.1, J = 1.6$  Hz, 1H), 3.37 (s, 3H), 2.47 (m, 1H), 1.50–2.25 (m, 12H).  $^{13}\text{C}$  NMR (125 MHz,  $\text{C}_6\text{D}_6$ )  $\delta$ : 171.1, 138.4, 127.1, 115.2, 106.8, 98.7, 71.7, 51.7, 50.1, 36.0, 33.8, 32.7, 31.6, 25.9, 22.1. EI-MS  $m/z$  (%): 264 (9), 254 (100), 253 ( $[\text{M} - \text{CO}]$



(OCH<sub>3</sub>)<sup>+</sup>, 45). HR-MS *m/z* calcd. for C<sub>16</sub>H<sub>24</sub>O<sub>6</sub>: 312.1573; found: 312.1555. Compound **27** hydrolysed readily to **26**.

#### Product 28

Colourless oil. IR (neat) (cm<sup>-1</sup>): 2947, 2888, 1774, 1449, 1330, 1178, 1094, 959, 721. <sup>1</sup>H NMR (200 MHz, CDCl<sub>3</sub>) δ: 4.28 (dd, *J* = 8.4 Hz, *J* = 4.5 Hz, 1H), 4.21 (t, *J* = 8.4 Hz, 1H), 3.36 (s, 3H), 2.60 (m, 1H), 1.60–2.15 (m, 6H). <sup>13</sup>C NMR (125 MHz, CDCl<sub>3</sub>) δ: 211.9, 102.5, 67.8, 52.0, 45.3, 40.8, 34.6, 18.6. EI-MS *m/z* (%): 157 ([M + 1]<sup>+</sup>, 5), 128 (58), 113 (10), 97 (32), 84 (20), 74 (100). CI-MS (NH<sub>3</sub>) *m/z*: 174 ([M + NH<sub>4</sub>]<sup>+</sup>, 100).

#### Product 29

<sup>1</sup>H NMR (200 MHz, C<sub>6</sub>D<sub>6</sub>) δ: 4.22 (t, *J* = 8.6 Hz, 2H), 3.38 (s, 6H), 3.32 (dd, *J* = 8.6, *J* = 5.3 Hz, 2H), 2.87 (m, 2H), 2.27 (m, 2H), 1.45–2.05 (m, 10H). <sup>13</sup>C NMR (50 MHz, C<sub>6</sub>D<sub>6</sub>) δ: 115.2, 92.1, 69.6, 49.2, 47.3, 36.4, 31.5, 25.4. EI-MS *m/z* (%): 312 ([M]<sup>+</sup>, 2), 281 ([M – OCH<sub>3</sub>]<sup>+</sup>, 9), 141 (81), 140 (100), 139 (63), 112 (62), 111 (42), 79 (27). The structure and stereochemistry were secured by means of single crystal X-ray diffraction. The structure of **30**, an isomer of **29**, was also determined by means of single crystal X-ray diffraction.

#### Thermolysis of 3a in the presence of dimethyl acetylenedicarboxylate (DMAD)

A solution of **3a** (0.26 g, 1 mmol) and DMAD (1.3 mmol) in benzene (10 mL) in a sealed tube was heated at 110°C for 20 h. Evaporation of the solvent left a residue that was chromatographed on silica (hexane:ethyl acetate, 90:10) to afford a mixture of diastereomers **32** and **33**. The diastereomers were separated with a Merck (LOBAR, MPLC) silica column, eluent EtOAc–hexane, 10:90).

#### Product 32

Colourless oil, yield: 3%. IR (neat) (cm<sup>-1</sup>): 2950, 2860, 2248, 1724, 1439, 1254, 1062, 909. <sup>1</sup>H NMR (300 MHz, CDCl<sub>3</sub>) δ: 4.28 (dd, *J* = 8.5, *J* = 4.6 Hz, 1H), 3.77 (s, 3H), 2.69 (d, *J* = 8.5 Hz, 1H), 3.34 (s, 3H), 3.55 (s, 3H), 3.47 (s, 3H), 2.3 (br. m, 1H), 2.12 (m, 1H), 1.30–1.85 (m, 8H). <sup>13</sup>C NMR (75 MHz, CDCl<sub>3</sub>) δ: 153.2, 126.8, 111.5, 90.2, 80.9, 72.8, 71.8, 52.9, 51.8, 51.4, 43.4, 29.8, 27.8, 23.1, 22.6. EI-MS *m/z* (%): molecular ion not observed, 281 ([M – CO]<sup>+</sup>, 32), 229 (13), 140 (35), 111 (100), 93 (64).

#### Product 33

Colourless crystals, yield: 3%, mp 68°C. <sup>1</sup>H NMR (300 MHz, CDCl<sub>3</sub>) δ: 4.19 (dd, *J* = 8.6, *J* = 4.3 Hz, 1H), 3.77 (s, 3H), 3.61 (d, *J* = 8.7 Hz, 1H), 3.56 (s, 3H), 3.40 (s, 3H), 2.25 (br m, 1H), 2.14 (m, 1H), 1.30–1.90 (m, 8H). <sup>13</sup>C NMR (75 MHz, CDCl<sub>3</sub>) δ: 153.0, 127.0, 112.0, 88.8, 79.5, 72.8, 71.3, 52.9, 52.0, 51.5, 43.8, 30.6, 27.7, 23.1, 22.7. The structure of **33** (Scheme 12) was determined by means of single crystal X-ray diffraction.

#### Acknowledgments

Financial support from the Natural Sciences and Engineering Research Council of Canada (NSERC) is gratefully

acknowledged. We thank Dr. Jim Britten for the X-ray crystallography and Professor Paul Harrison for the use of his MPLC equipment.

#### References

- (a) R.W. Hoffmann and H. Häuser. *Tetrahedron*, **21**, 891 (1965); (b) D.M. Lemal, E.P. Gosselink, and S.D. McGregor. *J. Am. Chem. Soc.* **88**, 582 (1966); (c) R.W. Hoffmann. *Angew. Chem. Int. Ed. Engl.* **10**, 529 (1971); (d) R.W. Hoffmann, K. Steinbach, and B. Dittrich. *Chem. Ber.* **106**, 2174 (1973); (e) R.W. Hoffmann and M. Reiffen. *Chem. Ber.* **109**, 2565 (1976); (f) R.A. Moss and J.K. Huselton. *J. Chem. Soc., Chem. Commun.* 950 (1976); (g) G. Hömberger, W. Kirmse, and R. Lelgemann. *Chem. Ber.* **124**, 1867 (1991); (h) G. Frenzen, M. Rischke, and G. Seitz. *Chem. Ber.* **126**, 2317 (1993); (i) C. Gerninghaus, A. Kümmell, and G. Seitz. *Chem. Ber.* **126**, 733 (1993); (j) P. Couture, D.L. Pole, and J. Warkentin. *J. Chem. Soc., Perkin Trans. 2*, 1565 (1997); (k) J. Warkentin. *J. Chem. Soc., Perkin Trans. 1*, 2161 (2000).
- (a) R.A. Moss, C.B. Mallon, and C.-T. Ho. *J. Am. Chem. Soc.* **99**, 4105 (1977); (b) R.A. Moss. *Acc. Chem. Res.* **13**, 58 (1980); (c) R.A. Moss, C.M. Young, L.A. Perez, K. Krogh-Jespersen. *J. Am. Chem. Soc.* **103**, 2413 (1981).
- N.G. Rondan, K.N. Houk, and R.A. Moss. *J. Am. Chem. Soc.* **102**, 1770 (1980).
- N. Kuhn, J. Fahl, R. Boese, G. Henkel. *Z. Naturforsch.* **53b**, 881 (1998).
- J.A. Dunn, J.P. Pezacki, M.J. McGlinchey, and J. Warkentin. *J. Org. Chem.* **64**, 4344 (1999).
- J.P. Ross, P. Couture, and J. Warkentin. *Can. J. Chem.* **75**, 1331 (1997).
- (a) H.-W. Wanzlick. *Angew. Chem. Int. Ed. Engl.* **1**, 75 (1962); (b) G. Doleschall. *Tetrahedron Lett.* **21**, 4183 (1980).
- R.A. Braun. *J. Am. Chem. Soc.* **87**, 5516 (1965).
- D.L. Pole and J. Warkentin. *J. Org. Chem.* **62**, 4065 (1997).
- (a) M. Dawid, P.C. Venneri, and J. Warkentin. *Can. J. Chem.* **79**, 110 (2001); (b) M. Dawid, P.C. Venneri, and J. Warkentin. *Can. J. Chem.* **79**, 1294 (2001).
- D.L. Pole and J. Warkentin. *Liebigs Ann.* 1907 (1995).
- P.C. Venneri and J. Warkentin. *Can. J. Chem.* **78**, 1194 (2000).
- M. Dawid, G. Mloston, and J. Warkentin. *Org. Lett.* **3**, 2455 (2001).
- N. Kuhn, H. Bohnen, and G. Henkel. *Z. Naturforsch.* **49b**, 1473 (1994).
- N. Kuhn, M. Steimann, and G. Weyers. *Z. Naturforsch.* **54b**, 427 (1999).
- N. Kuhn, K. Eichele, and M. Walker. *Z. Anorg. Allg. Chem.* **627**, 2565 (2001).
- D.L. Boger and C.E. Brotherton. *Tetrahedron Lett.* **25**, 5611 (1984).
- K. Kassam and J. Warkentin. *J. Org. Chem.* **59**, 5071 (1994).
- K. Kassam, D.L. Pole, M. El-Saidi, and J. Warkentin. *J. Am. Chem. Soc.* **116**, 1161 (1994).
- H.N.C. Wong. *Houben-Weyl: Methods of organic chemistry*. Vol. E17e. Edited by A. deMeijere. Georg Thieme Verlag, Stuttgart. 1998. pp. 513–514.
- H.E. Zimmerman and J. English. *J. Am. Chem. Soc.* **76**, 2285 (1954).



# Generation of 6-methylene-2,4-cyclohexadienyli-deneketene by flash photolysis of benzocyclobutenone in aqueous solution and study of the reactions of this ketene in that medium

Y. Chiang, A.J. Kresge, and H.-Q. Zhan

**Abstract:** Flash photolysis of benzocyclobutenone in aqueous solution produced a transient species with a microsecond lifetime whose rates of decay were measured in perchloric acid, sodium hydroxide, and buffer solutions over the acidity range  $[H^+] 1 \times 10^{-13} - 10^0$  M. This produced a rate profile, isotope effects, and buffer behaviour typical of ketene reactions, and that, together with product identification, served to identify this transient as 6-methylene-2,4-cyclohexadienyli-deneketene, formed by electrocyclic opening of the four-membered ring of benzocyclobutenone. Comparison of rates of reaction of this ketene with those of its saturated analog, pentamethyleneketene, produced some expected as well as some unexpected results.

**Key words:** cyclobutenone chemistry, electrocyclic ring opening, ketene hydration, rate profile, solvent isotope effects.

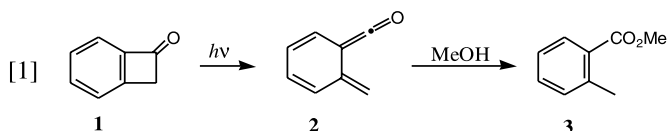
**Résumé :** La photolyse éclair de la benzocyclobuténone en solution aqueuse produit une entité transitoire de temps de vie de la microseconde dont on a mesuré les vitesses de décroissance dans l'acide perchlorique, l'hydroxyde de sodium et des solutions tampons dont l'acidité  $[H^+]$  s'étale de  $1 \times 10^{-13}$  à  $10^0$ . Sur la base de ces données, on a établi que le profil de vitesse de réaction, les effets isotopiques et le comportement vis-à-vis des tampons sont typiques des réactions des cétones et, en les combinant à l'identification du produit, on a pu établir que cette entité transitoire est le 6-méthylèncyclohexa-2,4-diénylidènekétène qui se forme par une ouverture électrocyclique du cycle à quatre chaînons de la benzocyclobuténone. Une comparaison des vitesses de réaction de ce cétène avec celles de son analogue saturé, pentaméthylènekétène, a conduit à des résultats dont quelques-uns étaient attendus alors que d'autres étaient inattendus.

**Mots clés :** chimie de la cyclobuténone, ouverture électrocyclique de cycle, hydratation d'un cétène, profil de vitesse de réaction, effets isotopiques de solvant.

[Traduit par la Rédaction]

## Introduction

Three decades ago, Don Arnold, studying the photochemistry of benzocyclobutenone (**1**) (1) corroborated an earlier observation (2) that irradiation of this ketone in methanol solution produced methyl 2-methylbenzoate (**3**). He then postulated that this reaction occurred through electrocyclic opening of the four-membered ring to give 6-methylene-2,4-cyclohexadienyli-deneketene (**2**) followed by the well-known addition of alcohols to ketenes to form the ester product (eq. [1]).



Support for this hypothesis was provided by subsequent observations (3) that irradiation of benzocyclobutenone in low-temperature hydrocarbon matrices converts it into an unstable but observable substance with UV and IR spectral properties expected of 6-methylene-2,4-cyclohexadienyli-deneketene. Additional evidence for this structural assignment came from a room-temperature flash photolytic study of benzocyclobutenone in ether solution that showed generation and decay of a transient species whose pattern of reactivity with added reagents agreed with expectation for this ketene (4).

We now add to these previous investigations a flash photolytic study of benzocyclobutenone in aqueous solution. This has allowed comparison of rates of hydration of 6-methylene-2,4-cyclohexadienyli-deneketene with those of other ketenes, and that has revealed some interesting features concerning the reactivity of this substance.

Received 17 December 2002. Published on the NRC Research Press Web site at <http://canjchem.nrc.ca> on 23 May 2003.

This paper is dedicated to Professor Don Arnold in appreciation for his many contributions to organic photochemistry.

Y. Chiang, A.J. Kresge,<sup>1</sup> and H.-Q. Zhan. Department of Chemistry, University of Toronto, Toronto, ON M5S 3H6, Canada.

<sup>1</sup>Corresponding author (e-mail: [akresge@chem.utoronto.ca](mailto:akresge@chem.utoronto.ca)).



## Experimental section

### Materials

Benzocyclobutenone, a gift from Dr. P. Schiess, was made by flash vacuum pyrolysis of 2-methylbenzoyl chloride (5). 2-Methylbenzamide was prepared by treating 2-methylbenzoyl chloride (6) with concentrated aqueous ammonia (7). All other materials were the best available commercial grades.

### Kinetics

Rate measurements were made using a nanosecond, eximer laser flash photolysis system operating at  $\lambda_{\text{exc}} = 248$  nm that has already been described (8), and reactions were followed by monitoring absorbance decay at  $\lambda = 400$  nm. Initial substrate (benzocyclobutenone) concentrations were ca.  $1 \times 10^{-5}$  M, and the temperature of all reacting solutions was controlled at  $25.0 \pm 0.05^\circ\text{C}$ . The rate data so obtained conformed to the first-order rate law well, and observed first-order rate constants were obtained by least-squares fitting of a single exponential function.

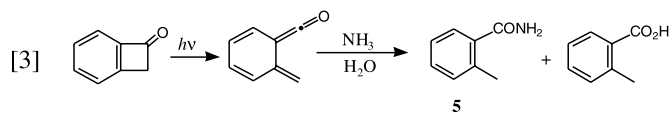
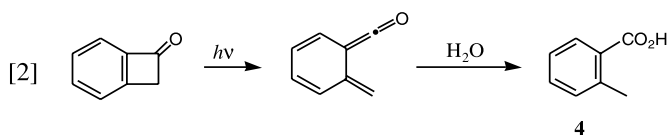
### Product analyses

Product compositions were determined by HPLC using a Varian Vista 5500 instrument with a NovoPak C<sub>18</sub> reverse-phase column and methanol–water (50:50, v/v) as the eluent. Reaction solutions containing substrate at similar concentrations as used for the kinetic measurements (ca.  $1 \times 10^{-5}$  M) were subjected to a single pulse from a microsecond flash photolysis system (9), and products were identified by comparing retention times and UV spectra with those of authentic samples.

## Results and discussion

### Reaction identification

Flash photolysis of benzocyclobutenone in aqueous solution produced a transient species with strong absorbance at  $\lambda = 400$  nm. This is the wavelength at which 6-methylene-2,4-cyclohexadienylideneketene showed a strong absorption band when generated in low-temperature matrices (3) or in ether solution at room temperature (4), which indicates that this ketene is generated by irradiation of this precursor in an aqueous solvent just as in these other media. Additional support for this conclusion comes from the fact that 2-methylbenzoic acid (4) was found to be the only product formed by flash photolysis of benzocyclobutenone in unbuffered water and in 0.001 M aqueous perchloric acid solution (eq. [2]) consistent with the known proclivity of ketenes to react with water giving carboxylic acid products (10a).



In aqueous ammonium ion – ammonia buffers, 2-methylbenzamide (5) was formed as well (eq. [3]) which again is consistent with the known reaction of ketenes with ammonia and amines to give amide products (10b, 11).

### Rate profile

Rates of decay of 6-methylene-2,4-cyclohexadienylideneketene were measured in aqueous perchloric acid and sodium hydroxide solutions and in acetic acid, biphosphate ion, tris-(hydroxymethyl)methylammonium ion, and ammonium ion buffers. The ionic strength of these solutions was maintained at 0.10 M through the addition of sodium perchlorate as required, except in the case of perchloric acid solutions at concentrations greater than 0.1 M, where the ionic strength was equal to the acid concentration. These data are summarized in Tables S1–S3.<sup>2</sup>

The measurements in buffers were made using series of solutions of varying buffer concentration but constant buffer ratio and therefore, because the ionic strength was constant, constant hydronium ion concentration. In each solution series, observed first-order rate constants proved to be linear functions of buffer concentration, and the data were therefore analyzed by least-squares fitting of the buffer dilution expression shown as eq. [4]. The zero-buffer-

$$[4] \quad k_{\text{obs}} = k_{\text{intcpt}} + k_{\text{buff}}[\text{buffer}]$$

concentration intercepts obtained in this way ( $k_{\text{intcpt}}$ ), together with the rate constants obtained in perchloric acid and sodium hydroxide solutions, are displayed as the rate profile shown in Fig. 1. Hydronium ion concentrations of the buffer solutions needed for this purpose were obtained by calculation using acidity constants of the buffer acids from the literature and activity coefficients recommended by Bates (12).

This rate profile shows a long uncatalyzed portion extending from  $[\text{H}^+] = 1 \times 10^{-1}$  to  $[\text{H}^+] = 1 \times 10^{-11}$ , with weak hydroxide ion catalysis and even weaker hydronium ion catalysis. Such behavior is typical of ketene hydrations, where the hydroxide ion reaction is only moderately faster than uncatalyzed hydration and acid catalysis is often not observed.<sup>3</sup> This profile therefore provides further evidence that the transient species observed is a ketene.

As is often the case for acid-catalyzed reactions in concentrated acid solutions, rates of hydration of 6-methylene-2,4-cyclohexadienylideneketene in perchloric acid solutions more concentrated than 0.1 M increased more steeply than in direct linear proportion to acid concentration. The data were therefore treated by the Cox–Yates method using the  $X_0$  excess acidity function (14). The analysis was done by least-squares fitting of eq. [5], where  $\text{H}^+$

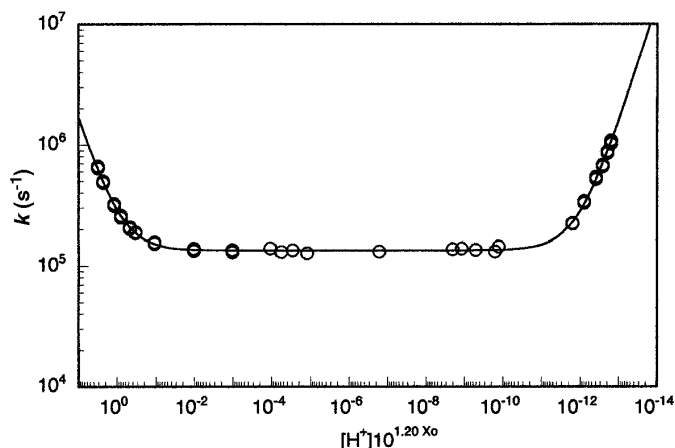
$$[5] \quad k_{\text{obs}} = k_{\text{uc}} + k_{\text{H}^+}[\text{H}^+]10^{mX_0}$$

<sup>2</sup>Tables of rate data (Tables S1–S4) have been deposited and may be purchased from the Depository of Unpublished Data, Document Delivery, CISTI, National Research Council Canada, Ottawa ON, K1A 0S2, Canada ([http://www.nrc.ca/cisti/irm/unpub\\_e.shtml](http://www.nrc.ca/cisti/irm/unpub_e.shtml) for information on ordering electronically).

<sup>3</sup>See, for example, ref. (13).



**Fig. 1.** Rate profile for the hydration of 6-methylene-2,4-cyclohexadienylideneketene in aqueous solution at 25°C.



represents the hydronium ion, with  $[H^+]$  and  $X_0$  as independent variables, and  $k_{uc}$ ,  $k_{H^+}$ , and  $m$  as parameters to be determined by the fit. This gave  $k_{uc} = (1.35 \pm 0.01) \times 10^5 \text{ s}^{-1}$ ,  $k_{H^+} = (1.45 \pm 0.03) \times 10^5 \text{ M}^{-1} \text{ s}^{-1}$ , and  $m = 1.20 \pm 0.03$ . This value of  $m$  was then used to calculate the quantity  $[H^+]10^{mX_0}$ , which was used as the abscissa for the rate profile of Fig. 1. Because  $X_0$  becomes equal to zero at hydronium ion concentrations less than 0.1 M, and  $10^{mX_0}$  consequently becomes equal to unity,  $[H^+]10^{mX_0}$  differs from  $[H^+]$  only at  $[H^+] > 0.1$ .

With this definition of the abscissa, the rate law that applies to the rate profile of Fig. 1 is the expression shown in eq. [6]. Least-squares fitting of this expression gave  $k_{H^+} = (1.44 \pm 0.01) \times 10^5 \text{ M}^{-1} \text{ s}^{-1}$ ,  $k_{uc} = (1.35 \pm 0.01) \times 10^5 \text{ s}^{-1}$ , and  $k_{HO^-} = (9.26 \pm 0.06) \times 10^6 \text{ M}^{-1} \text{ s}^{-1}$ . It is

$$[6] \quad k_{\text{obs}} = k_{H^+}[H^+]10^{mX_0} + k_{uc} + k_{HO^-}[HO^-]$$

gratifying that the values of  $k_{H^+}$  and  $k_{uc}$  obtained in this way are in excellent agreement with those produced by the Cox–Yates analysis of the perchloric acid data.

It has been observed that substituent effects on the rates of uncatalyzed ketene hydration ( $k_{uc}$ ) are remarkably similar to those on the rates of hydroxide-ion catalyzed hydration ( $k_{HO^-}$ ) and this similarity has been used to support a common nucleophilic reaction mechanism for both processes (10a). It has also led to the good correlation of rate constants for these two reactions illustrated in Fig. 2 (15). This figure also shows that the presently determined data fit this correlation well, thus substantiating identification of the presently observed transient species as 6-methylene-2,4-cyclohexadienylideneketene.

### Isotope effects

Rates of hydration of 6-methylene-2,4-cyclohexadienylideneketene were also measured in moderately concentrated solutions of HCl in  $H_2O$  and DCl in  $D_2O$ . These data are summarized in Table S4<sup>2</sup> and are displayed in Fig. 3.

Once again, observed rate constants increased more steeply than in direct proportion to acid concentration, and the Cox–Yates method (14) using the  $X_0$  scale for HCl (16) was used to analyze the data. The  $X_0$  scale has not been determined for DCl in  $D_2O$  solution, but other acidity func-

**Fig. 2.** Correlation of rates of uncatalyzed ( $k_{uc}$ ) and hydroxide-ion-catalyzed ( $k_{HO^-}$ ) ketene hydration; 6-methylene-2,4-cyclohexadienylideneketene (●), other ketenes (○).

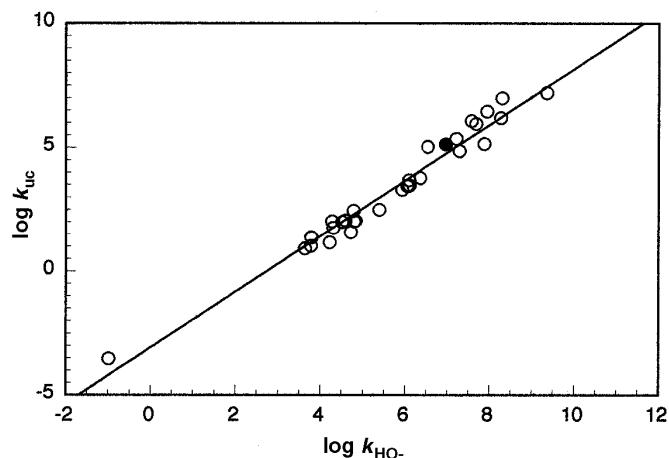
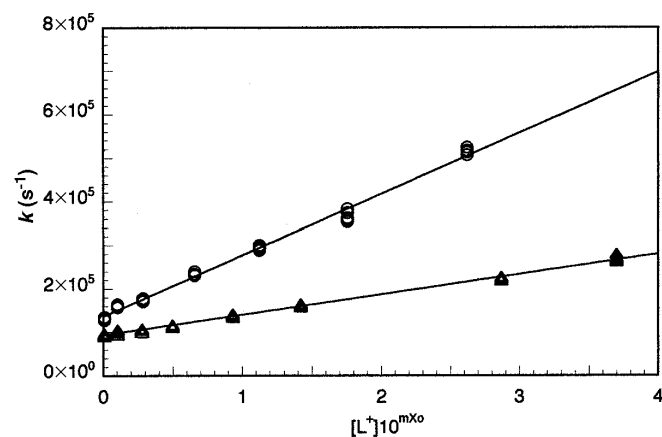


**Fig. 3.** Reaction of 6-methylene-2,4-cyclohexadienylideneketene in aq HCl– $H_2O$  (○) and DCl– $D_2O$  (Δ) solutions at 25°C.



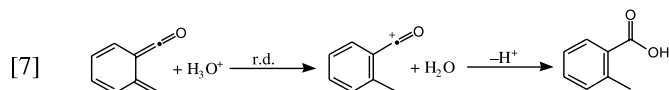
tions are known to be the same for  $D_2O$  as for  $H_2O$  solutions of hydrochloric (17) and perchloric (18) acids when the comparison is made at the same molar acid concentration. It seems reasonable to assume that the same would be true for the  $X_0$  scale, and values of  $X_0$  for HCl in  $H_2O$  were therefore used for the  $D_2O$  solutions.

Least-squares analysis using eq. [5] gave  $k_{uc} = (1.37 \pm 0.02) \times 10^5 \text{ s}^{-1}$ ,  $k_{H^+} = (1.39 \pm 0.09) \times 10^5 \text{ M}^{-1} \text{ s}^{-1}$ , and  $m = (1.64 \pm 0.17)$  for the  $H_2O$  solutions and  $k_{uc} = (9.35 \pm 0.01) \times 10^4 \text{ s}^{-1}$ ,  $k_{D^+} = (4.66 \pm 0.02) \times 10^5 \text{ M}^{-1} \text{ s}^{-1}$ , and  $m = (1.40 \pm 0.10)$  for the  $D_2O$  solutions. These values of  $k_{uc}$  and  $k_{H^+}$  agree well with those determined for  $H_2O$  solutions of  $HClO_4$  (vide supra). The difference between the HCl and  $HClO_4$  values of  $m$ , on the other hand, is somewhat greater than their combined standard deviations, suggesting that medium effects are not quite the same in concd HCl as in concd  $HClO_4$  solutions.

These data provide the isotope effects  $k_{H^+}/k_{D^+} = 2.98 \pm 0.25$  and  $(k_{uc})_{H_2O}/(k_{uc})_{D_2O} = 1.46 \pm 0.03$ . Acid-catalyzed hydration of ketenes is known to occur by rate-determining protonation of the  $\beta$ -carbon atom of the ketene, followed by rapid reaction of the acylium ion thus formed with water

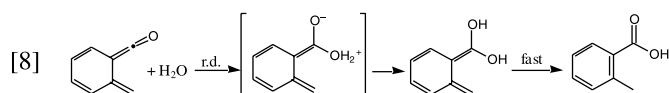


(10c, 19). In the present case, protonation is more likely to occur on the *exo*-carbon atom of the methylene group, because that will regenerate a benzene ring and benefit from a gain of benzene resonance energy (eq. [7]). In any event, there will be a hydron in flight in



the rate-determining step of this reaction and the isotope effect will consequently have a primary component. It will, however, have an inverse secondary component as well, produced by tightening of the hydrogen–oxygen bonds of the transition state moiety on its way to becoming a water molecule. The isotope effect observed ( $k_{\text{H}^+}/k_{\text{D}^+} = 2.98$ ) is in fact a typical value for such a process (20).

Uncatalyzed hydration of ketenes, on the other hand, occurs through nucleophilic attack of a water molecule on the carbon atom of the ketene carbonyl group, generating an enol intermediate, which then ketonizes in a fast subsequent step (10a, 15) (eq. [8]). Formation of the



enol could occur either through a zwitterion, or the zwitterion could be avoided by simultaneous proton shuffling. In either case, the solvent isotope effect would be small because there would be no primary component; in zwitterion formation because no hydron transfer takes place, and in simultaneous proton shuffling because the hydron transfer here is between oxygen atoms with the hydron lying in a stable potential well at the transition state and consequently not being in flight (21). The isotope effect observed ( $k_{\text{H}}/k_{\text{D}} = 1.46$ ) is a typical value for such a process (15).

### Reaction in buffers

The rate measurements in acetic acid and ammonium ion buffers were each made at four different buffer ratios, which allowed separation of the buffer-dependent rate constants of eq. [4] ( $k_{\text{buff}}$ ) into their buffer base ( $k_{\text{B}}$ ) and buffer acid ( $k_{\text{HA}}$ ) components. This was done through the use of eq. [9], in which  $f_{\text{A}}$  is the fraction of buffer present in the acid form.

$$[9] \quad k_{\text{buff}} = k_{\text{B}} + (k_{\text{HA}} - k_{\text{B}})f_{\text{A}}$$

Least-squares fitting of this equation gave  $k_{\text{B}} = (1.23 \pm 0.07) \times 10^6 \text{ M}^{-1} \text{ s}^{-1}$  and  $k_{\text{HA}} = -(8.84 \pm 5.26) \times 10^4 \text{ M}^{-1} \text{ s}^{-1}$  for the acetic acid buffers, and  $k_{\text{B}} = (1.72 \pm 0.11) \times 10^6 \text{ M}^{-1} \text{ s}^{-1}$  and  $k_{\text{HA}} = (1.76 \pm 8.99) \times 10^4 \text{ M}^{-1} \text{ s}^{-1}$  for the ammonium ion buffers. In both cases, therefore, the buffer-dependent reaction was wholly of the basic type.

A similar analysis could not be carried out for the biphosphate and tris-(hydroxymethyl)methylammonium ion buffers because measurements here were made at only one buffer ratio. It seems fair to assume, however, that the buffer-dependent reaction here was also wholly of the basic type, inasmuch as the acid and base strengths of the components of these buffers lie between those (acetic acid and ammonium ion) for which analysis using eq. [9] showed only a

**Table 1.** Buffer base rate constants ( $k_{\text{B}}$ ) for the reaction of 6-methylene-2,4-cyclohexadienylideneketene in aqueous solution at 25°C.<sup>a</sup>

Base	p <i>K</i> <sub>a</sub> (BH)	<i>k</i> <sub>B</sub> (10 <sup>6</sup> M <sup>-1</sup> s <sup>-1</sup> )
CH <sub>3</sub> CO <sub>2</sub> <sup>-</sup>	4.76	1.23
HPO <sub>4</sub> <sup>2-</sup>	7.20	1.01
(CH <sub>2</sub> OH) <sub>3</sub> CNH <sub>2</sub>	8.07	0.283
NH <sub>3</sub>	9.25	1.72

<sup>a</sup>Ionic strength = 0.10 M (NaClO<sub>4</sub>).

**Table 2.** Comparison of rates of hydration of 6-methylene-2,4-cyclohexadienylideneketene with those of an analogous ketene not having a cyclohexadienyl structure.<sup>a</sup>

Substrate	<i>k</i> <sub>HO<sup>-</sup></sub> (M <sup>-1</sup> s <sup>-1</sup> )	<i>k</i> <sub>uc</sub> (s <sup>-1</sup> )	<i>k</i> <sub>H<sup>+</sup></sub> (M <sup>-1</sup> s <sup>-1</sup> )
	$9.26 \times 10^6$	$1.35 \times 10^5$	$1.44 \times 10^5$
	$6.24 \times 10^3$	$2.30 \times 10^1$	$2.78 \times 10^3$

<sup>a</sup>Aqueous solution, 25°C; data for pentamethyleneketene from ref. (15).

base reaction. Using this reasonable assumption, the buffer-dependent rate constants for the biphosphate and tris-(hydroxymethyl)methylammonium buffers ( $k_{\text{buff}}$ ) were transformed into buffer base rate constants. The results, together with the buffer base rate constants obtained from acetic acid and ammonium ion buffers, are listed in Table 1.

Inspection of Table 1 shows that the reactivity of the buffer bases does not increase regularly with buffer base strength, as it would if the buffer bases were acting as proton transfer agents. Tris-(hydroxymethyl)methylamine, for example, is a stronger base than either acetate or hydrogen phosphate ions, and yet its rate of reaction is only a quarter of that of the ions. The reactivity order shown by Table 1, on the other hand, is what might be expected if the buffer bases were reacting as nucleophiles: tris-(hydroxymethyl)methylamine, with its large bulk, should be a poorer nucleophile than the other smaller bases of this table. Bases, of course, react with ketenes as nucleophiles and not as proton transfer agents (11), and the data in Table 1, therefore, provide still more evidence that the substance produced by photolysis of benzocyclobutenone is 6-methylene-2,4-cyclohexadienylideneketene.

### Reactivity

Rates of hydration of the presently studied ketene are considerably faster than those of other ketenes whose reactions do not convert a cyclohexadienyl structure into an aromatic benzene ring. The data assembled in Table 2 provide a comparison with pentamethyleneketene (15), a substrate also possessing a six-membered carbocyclic ring. It may be seen that the present ketene is the much more reactive substance, by a factor of 1500, corresponding to a free energy of activation difference of  $\delta G^\ddagger = 4.3 \text{ kcal mol}^{-1}$ , for the hydroxide-ion-catalyzed process and by a factor of 5900 or  $\delta \Delta G^\ddagger = 5.1 \text{ kcal mol}^{-1}$  for the uncatalyzed reaction. The greater difference for the slower uncatalyzed hydration is of course



understandable as operation of the reactivity–selectivity principle.

The hydronium-ion-catalyzed reaction of 6-methylene-2,4-cyclohexadienylideneketene is also faster than that of pentamethyleneketene, but now the difference, a factor of 52 or  $\delta\Delta G^\ddagger = 2.3 \text{ kcal mol}^{-1}$ , is much less than those for the hydroxide ion and uncatalyzed processes. This is surprising, because the hydronium ion catalysis of 6-methylene-2,3-cyclohexadienylideneketene hydration presumably takes place by rate-determining proton transfer to the *exo*-carbon atom of the methylene group, as shown in eq. [7]. This immediately converts a cyclohexadienyl structure into an aromatic ring and profits from a gain in benzene resonance energy. The hydroxide-ion-catalyzed and uncatalyzed reactions, on the other hand, occur by nucleophilic attack on the ketene's carbonyl carbon atom (10a, 15), as illustrated for the uncatalyzed process in eq. [8]. Because this nucleophilic attack occurs in the ketene molecular plane (4), it puts negative charge into an orbital that is orthogonal to the cyclohexadienyl  $\pi$  system. Delocalization of this charge into the  $\pi$  system therefore does not occur, and this suggests that aromatization of the cyclohexadienyl ring in the reaction's rate-determining transition state does not take place; the reaction therefore does not benefit from a gain in benzene resonance energy.

These arguments lead to the expectation that hydronium-ion-catalyzed hydration of 6-methylene-2,4-cyclohexadienylideneketene should be faster than that of pentamethyleneketene by an amount greater than those for the hydroxide-ion-catalyzed and uncatalyzed reactions, contrary to the data presented in Table 2. The reason for this unexpected difference is not clear.

## Acknowledgements

We are grateful to the Natural Sciences and Engineering Research Council of Canada (NSERC) for financial support of this research.

## References

1. D.R. Arnold, E. Hedeya, V.Y. Merritt, L.A. Karnitsky, and M.E. Kent. *Tetrahedron Lett.* 3917 (1972).
2. M.P. Cava and R.J. Spangler. *J. Am. Chem. Soc.* **89**, 4550 (1967).
3. (a) A. Krantz. *J. Am. Chem. Soc.* **96**, 4992 (1974); (b) N.P. Hacker and N.J. Turro. *J. Photochem.* **22**, 131 (1983).
4. P. Schiess, M. Eberle, M. Huys-Francotte, and J. Wirz. *Tetrahedron Lett.* **25**, 2201 (1984).
5. P. Schiess and M. Heitzmann. *Angew. Chem. Int. Ed. Engl.* **16**, 469 (1977).
6. H.G. Tanner and P.A. Lasselle. *J. Am. Chem. Soc.* **48**, 2163 (1926).
7. R.L. Shriner and R.C. Fuson. *The systematic identification of organic compounds*. Wiley, New York. 1948. pp. 157–158.
8. J. Andraos, Y. Chiang, C.G. Huang, A.J. Kresge, and J.C. Scaiano. *J. Am. Chem. Soc.* **115**, 10 605 (1993).
9. Y. Chiang, M. Hojatti, J.R. Keeffe, A.J. Kresge, N. P. Schepp, and J. Wirz. *J. Am. Chem. Soc.* **109**, 4000 (1987).
10. (a) T.T. Tidwell. *Ketenes*. Wiley-Interscience, New York. 1995; pp. 571–587; (b) T.T. Tidwell. *Ketenes*. Wiley-Interscience, New York. 1995. pp. 589–590; (c) T.T. Tidwell. *Ketenes*. Wiley-Interscience, New York. 1995. 585–587.
11. J. Andraos and A.J. Kresge. *J. Am. Chem. Soc.* **114**, 5643 (1992).
12. R.G. Bates. *Determination of pH theory and practice*. Wiley-Interscience, New York. 1973. p. 49.
13. Y. Chiang, A.J. Kresge and V.V. Popik. *J. Am. Chem. Soc.* **117**, 9165 (1995).
14. R.A. Cox. *Adv. Phys. Org. Chem.* **35**, 1 (2000).
15. J. Andraos and A.J. Kresge. *Can. J. Chem.* **78**, 508 (2000).
16. R.A. Cox and K. Yates. *Can. J. Chem.* **59**, 2116 (1981).
17. E. Hogfeldt and J. Bigeleisen. *J. Am. Chem. Soc.* **82**, 15 (1960).
18. R.A. Cox, S.-O. Lam, R.A. McClelland, and T.T. Tidwell. *J. Chem. Soc., Perkin Trans. 2*, 272 (1979).
19. (a) J. Andraos and A.J. Kresge. *J. Photochem. Photobiol. A.* **57**, 165 (1991); (b) J. Andraos, A. J. Kresge, and N. P. Schepp. *Can. J. Chem.* **73**, 539 (1995).
20. A.J. Kresge, D.S. Sagatys and H.L. Chen. *J. Am. Chem. Soc.* **99**, 7228 (1977).
21. C.G. Swain, D.A. Kuhn, and R.L. Schowen. *J. Am. Chem. Soc.* **87**, 1553 (1965).



# Compounds of chromium(VI): The pyridine – chromic anhydride complex, benzimidazolinium dichromate, and three 2-alkyl-1*H*-benzimidazolinium dichromates

T. Stanley Cameron, Jason A.C. Clyburne, Pramod K. Dubey, J. Stuart Grossert, K. Ramaiah, J. Ramanatham, and Sergei V. Sereda

**Abstract:** Pyridine, when allowed to react with chromic anhydride under strictly anhydrous conditions, gives the known, very air-sensitive, crystalline 2:1 Lewis acid–base complex **1**. The crystal structure has now been successfully determined. When benzimidazole and three 2-alkyl-1*H*-benzimidazoles were treated with chromium trioxide in aqueous acetic acid, crystalline dichromate salts (**2–5**) were readily formed. These salts consist of dichromate anions linked to the cations by hydrogen bonds of the type N—H...O. The chromium atoms have distorted tetrahedral environments, with the Cr—O distances being typical for dichromate anions. In the cases of the 2-methyl and 2-ethyl salts, the anions are disordered about a centre of inversion. The hydrogen bonding arrangements are discussed and the structures are compared with other oxygenated chromium(VI) species. The dichromate salts are useful selective oxidants for a range of primary and secondary alcohols; examples of these reactions are reported.

**Key words:** chromium(VI), pyridine – chromium trioxide complex, benzimidazolinium dichromate salts, controlled oxidation of alcohols.

**Résumé :** La réaction de la pyridine avec de l'anhydride chromique dans des conditions strictement anhydres fournit le complexe acide–base de Lewis 2:1 (**1**), un composé cristallin bien connu et très sensible à l'air. On en a maintenant déterminé la structure cristalline. Le traitement du benzimidazole et de trois 2-alkyl-1*H*-benzimidazoles par le trioxyde de chrome en solution acétique aqueuse conduit à la formation facile de dichromates cristallins (**2–5**). Ces sels sont constitués d'anions dichromates liés à des cations par des liaisons hydrogènes du type N—H...O. Les atomes de chrome se trouvent dans des environnements tétraédriques déformés dans lesquels les distances Cr—O sont typiques pour des anions de dichromate. Dans les cas des sels comportant des substituants 2-méthyle ou 2-éthyle, les anions sont désordonnés autour d'un centre d'inversion. On discute des arrangements des liaisons hydrogènes et on compare les structures avec celles d'autres espèces oxygénées du chrome(VI). Les dichromates sont utiles comme oxydants sélectifs pour tout un éventail d'alcools primaires et secondaires; on rapporte des exemples de telles réactions.

**Mots clés :** chrome(VI), complexe pyridine – trioxyde de chrome, dichromate de benzimidazolinium, oxydation contrôlée d'alcools.

[Traduit par la Rédaction]

## Introduction

Benzimidazoles constitute an important group of heterocyclic compounds which possess a wide spectrum of biological activity. There have been few reports of 2-substituted benzimidazoles containing sulphur and recent work towards this goal (1, 2) has involved an attempted oxidization at the

benzylic position of 2-ethyl-1*H*-benzimidazole to form 2-acetyl-1*H*-benzimidazole, using chromium trioxide in aqueous acetic acid. Instead of a ketone, the substance isolated was a yellow-orange crystalline material containing chromium. Similar materials were formed from three other benzimidazoles. A review of the literature describing nitrogen heterocycles forming complexes and salts with oxygenated

Received 24 September 2002. Published on the NRC Research Press Web site at <http://canjchem.nrc.ca> on 26 May 2003.

*Dedicated to the honour of Professor Donald R. Arnold, a valued colleague and friend.*

**T.S. Cameron,<sup>1</sup> J.A.C. Clyburne,<sup>2</sup> J.S. Grossert,<sup>3</sup> and S.V. Sereda.** Department of Chemistry, Dalhousie University, Halifax, NS B3H 4J3, Canada.

**P.K. Dubey, K. Ramaiah, and J. Ramanatham.** Department of Chemistry, Jawaharlal Nehru Technological University, Kukatpally, Hyderabad (AP), India 500 872.

<sup>1</sup>Corresponding author (e-mail: Stanley.Cameron@Dal.ca).

<sup>2</sup>Present address: Department of Chemistry, Simon Fraser University, Burnaby, BC V5G 1S6, Canada.

<sup>3</sup>Corresponding author (e-mail: J.S.Grossert@Dal.ca).



**Table 1.** Crystallographic data for (Py)<sub>2</sub>·CrO<sub>3</sub> (**1**) and for bis(1*H*-benzimidazolium) dichromate (**2**).

	<b>1</b>	<b>2</b>
Empirical formula	C <sub>10</sub> H <sub>10</sub> CrN <sub>2</sub> O <sub>3</sub>	C <sub>14</sub> H <sub>14</sub> Cr <sub>2</sub> N <sub>4</sub> O <sub>7</sub>
Formula weight	258.20	454.28
Description	Dark brown block	Orange block
Crystal dimensions (mm)	0.15 × 0.27 × 0.33	0.35 × 0.20 × 0.15
Crystal system	Monoclinic	Triclinic
Space group	<i>Cc</i> (No. 9)	<i>P</i> -1 (No. 2)
Cell determination	19 (7.3–26.4°)	24 (20.1–26.8°)
<i>a</i> (Å)	11.998(2)	10.068(3)
<i>b</i> (Å)	10.884(1)	11.749(2)
<i>c</i> (Å)	8.467(1)	8.306(2)
α (°)	90	100.44(2)
β (°)	97.64(1)	112.73(2)
γ (°)	90	77.95(2)
<i>V</i> (Å <sup>3</sup> )	1095.9(2)	880.7(4)
<i>Z</i> value, <i>D</i> <sub>calc</sub> (Mg m <sup>-3</sup> )	4, 1.565	2, 1.713
<i>F</i> <sub>000</sub>	528.00	460.00
μ (MoKα) (cm <sup>-1</sup> )	10.36	12.80
2θ <sub>max</sub> (°)	46.0	50.0
No. reflns measured	854	3279
Unique reflns ( <i>R</i> <sub>int</sub> )	802 (0.021)	3085 (0.039)
No. with <i>I</i> > 2σ( <i>I</i> )	565	2141
<i>h</i>	0 → 13	0 → 11
<i>k</i>	0 → 11	–13 → 13
<i>l</i>	–9 → 9	–9 → 9
No. of variables	87	245
<i>R</i> 1, <sup>a</sup> <i>wR</i> 2 <sup>b</sup>	0.040, 0.1125	0.036, 0.131
Goodness of fit <sup>c</sup>	1.06	0.95
(Δ/σ) <sub>max</sub>	0.00	0.00
Δρ <sub>max</sub> , Δρ <sub>min</sub> (e <sup>-</sup> Å <sup>-3</sup> )	0.41, –0.41	0.57, –0.48

<sup>a</sup>Full-matrix least-squares refinement on *F*<sup>2</sup>, *R*1 = Σ||*F*<sub>o</sub>| – |*F*<sub>c</sub>||/Σ|*F*<sub>o</sub>|.

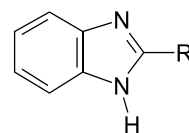
<sup>b</sup>*wR*2 = [Σ(*w*(*F*<sub>o</sub><sup>2</sup> – *F*<sub>c</sub><sup>2</sup>)<sup>2</sup>)/Σ(*w*(*F*<sub>o</sub><sup>2</sup>)<sup>2</sup>)]<sup>1/2</sup>.

<sup>c</sup>GoF = [Σ(*w*(*F*<sub>o</sub><sup>2</sup> – *F*<sub>c</sub><sup>2</sup>)<sup>2</sup>)/(*N*<sub>o</sub> – *N*<sub>v</sub>)]<sup>1/2</sup> (*N*<sub>o</sub> = no. of observations, *N*<sub>v</sub> = no. of variables).

chromium(VI) species revealed that a considerable range of substances has been described, many of which were intended as selective oxidants for organic substrates (3–5). It was apparent that many of these reagents had not been thoroughly characterized, such as by X-ray diffraction techniques. Also, many papers are not cross-referenced to each other. The parent pyridine–chromic anhydride complex [(C<sub>5</sub>H<sub>5</sub>N)<sub>2</sub>·CrO<sub>3</sub>] (**1**) was first described by Sisler et al. (6) over 50 years ago. It was suggested that an X-ray crystal structure of the compound would be forthcoming, but to our knowledge the structure has never been published. The complex was reported by Collins et al. (7) as being labile towards aqueous hydrolysis, yielding a species suggested to be dipyridinium dichromate ([C<sub>5</sub>H<sub>5</sub>NH]<sub>2</sub>Cr<sub>2</sub>O<sub>7</sub>). Other dichromate salts which have been reported include pyridinium (8), quinolinium (9), and 2- and 4-benzylpyridinium (10) and a complex between benzotriazole and chromic anhydride was claimed to be a versatile oxidant (11).

A limited number of nitrogen heterocyclic dichromate salts have been characterized by X-ray crystal diffraction techniques. These include bis(1*H*<sup>+</sup>-pyrazinium N<sup>4</sup>-oxide) dichromate (12), bis(2-amino-5-nitropyridinium) dichromate (13), ethylenediaminium dichromate (14), and a series of bipyridyl dichromate salts (15). A significant paper by Pressprich et al. (16) reported on the crystal structure of

dipyrazinium trichromate ([C<sub>4</sub>H<sub>4</sub>N<sub>2</sub>H]<sub>2</sub>Cr<sub>3</sub>O<sub>10</sub>) and reviewed the bonding in a range of chromate anions. The present work extends this series, correlates work on these species with that on chromic anhydride complexes, introduces another oxidizing agent which showed selectivity for the conversion of primary alcohols into aldehydes, and provides a compact collection of the literature in this area.



**2:** R = H

**3:** R = Me

**4:** R = Et

**5:** R = (*n*)-Pr

**6:** see Table 4

## Experimental

### Preparation of the pyridine – chromic anhydride complex (dipyridinetrioxochromium(VI)) (**1**)

Caution! Chromic anhydride, a suspected carcinogen, is a powerful oxidizing agent which can react explosively with



**Table 2.** Crystallographic data for bis(2-methyl-1*H*-benzimidazolinium) dichromate (**3**) and for bis(2-ethyl-1*H*-benzimidazolinium) dichromate (**4**).

	<b>3</b>	<b>4</b>
Empirical formula	C <sub>8</sub> H <sub>9</sub> CrN <sub>2</sub> O <sub>3.50</sub>	C <sub>9</sub> H <sub>11</sub> CrN <sub>2</sub> O <sub>3.50</sub>
Formula weight	241.17	255.19
Description	Orange plate	Orange needle
Crystal dimensions (mm)	0.50 × 0.30 × 0.10	0.20 × 0.20 × 0.50
Crystal system	Monoclinic	Monoclinic
Space group	<i>P</i> 2 <sub>1</sub> / <i>a</i> (No. 14)	<i>P</i> 2 <sub>1</sub> / <i>n</i> (No. 14)
Cell determination	25 (34.5–40.7°)	20 (33.0–39.0°)
<i>a</i> (Å)	7.569(2)	7.166(4)
<i>b</i> (Å)	16.662(2)	15.094(2)
<i>c</i> (Å)	8.463(2)	9.909(1)
β (°)	112.95(1)	98.60(2)
<i>V</i> (Å <sup>3</sup> )	982.9(3)	1059.6(4)
<i>Z</i> value, <i>D</i> <sub>calc</sub> (Mg m <sup>−3</sup> )	4, 1.630	4, 1.600
<i>F</i> <sub>000</sub>	492.00	524.00
μ (MoKα) (cm <sup>−1</sup> )	11.52	10.74
2θ <sub>max</sub> (°)	50.0	46.0
No. reflns measured	1935	1683
Unique reflns ( <i>R</i> <sub>int</sub> )	1724 (0.037)	1474 (0.024)
No. with <i>I</i> > 2σ( <i>I</i> )	1035	1113
<i>h</i>	0 → 9	0 → 7
<i>k</i>	0 → 19	0 → 16
<i>l</i>	−10 → 9	−10 → 10
No. of variables	146	155
<i>R</i> 1, <sup>a</sup> <i>wR</i> 2 <sup>b</sup>	0.040, 0.143	0.037, 0.110
Goodness of fit <sup>c</sup>	0.96	1.05
(Δ/σ) <sub>max</sub>	0.00	0.00
Δρ <sub>max</sub> (e <sup>−</sup> Å <sup>−3</sup> )	0.36	0.45
Δρ <sub>min</sub> (e <sup>−</sup> Å <sup>−3</sup> )	−0.52	−0.30

<sup>a</sup>Full-matrix least-squares refinement on *F*<sup>2</sup>, *R*1 = Σ||*F*<sub>o</sub>| − |*F*<sub>c</sub>||/Σ|*F*<sub>o</sub>|.<sup>b</sup>*wR*2 = [Σ(*w*(*F*<sub>o</sub><sup>2</sup> − *F*<sub>c</sub><sup>2</sup>)/Σ(*w*(*F*<sub>o</sub><sup>2</sup>))<sup>1/2</sup>].<sup>c</sup>GoF = [Σ(*w*(*F*<sub>o</sub><sup>2</sup> − *F*<sub>c</sub><sup>2</sup>)/(*N*<sub>o</sub> − *N*<sub>v</sub>))] <sup>1/2</sup> (*N*<sub>o</sub> = no. of obs, *N*<sub>v</sub> = no. of variables).

reducible species. The complex **1** was prepared using a modification of the original method (6). Pyridine (30 mL, dried by distillation from CaH<sub>2</sub>), was distilled in a vacuum line (17) on to CrO<sub>3</sub> (0.27 g). After 20 min, a yellow precipitate formed in the stirred mixture which was then allowed to stand overnight. Filtration in a nitrogen atmosphere gave a crop of bright red, extremely air-sensitive needles (0.31 g). The IR spectrum (Nujol, Nicolet FT-IR) had ν<sub>max</sub> 1602, 1246, 1207, 1074, 926 (broad, very strong), 763, 697, 638, 333, 323 cm<sup>−1</sup> and was similar to a published spectrum (18). The extreme air sensitivity of the complex could account for the fact that its crystal structure has not yet been published — indeed it is the most air-sensitive compound encountered by one of us (TSC) in over 35 years of X-ray crystallography.

#### Preparation of the benzimidazole–dichromate salts (2–5)

A solution of chromic anhydride or potassium chromate (10 mmol) in aq acetic acid (5% v/v, 10 mL) was added to a solution of the required benzimidazole (10 mmol, commercially unavailable compounds were prepared by the method of Phillips (19)) in aq AcOH (5% v/v, 10 mL) and the mix-

ture was stirred for 15 min. The separated product was filtered, washed (water), and recrystallized twice from dilute aqueous acetic acid to give yellow-orange crystals, with physical data as follows: bis(1*H*-benzimidazolinium) dichromate (**2**) prisms, mp 150–152°; bis(2-methyl-1*H*-benzimidazolinium) dichromate (**3**) plates, mp 148–150°; bis(2-ethyl-1*H*-benzimidazolinium) dichromate (**4**) needles, mp 155–157°; and bis(2-propyl-1*H*-benzimidazolinium) dichromate (**5**) plates, mp 140–143°. IR (KBr) of **4** (cm<sup>−1</sup>): 2870, 2745, 2630, 1620, 1559, 1455, 1410, 954, 921, 770, 616. <sup>1</sup>H NMR (*d*<sub>6</sub>-DMSO) of **4** δ: 1.4, 3.0, 6.0, 7.3, 7.6 (all broad, s, approx. ratio = 3:2:4:2:2). EI-MS of **4** gave the same mass spectrum as 2-ethyl-1*H*-benzimidazole. Classical analyses on **2**–**5** indicated a 1:1 heterocycle:Cr stoichiometric ratio.

#### X-ray data collection and structure refinement

An X-ray structural study of **1**–**5** was performed with a Rigaku AFC5R diffractometer, using a 12 kW rotating anode and graphite-monochromated Mo-K<sub>α</sub> radiation. The crystal of **1** was sealed into a glass capillary while the others were mounted on glass fibers. Data were collected at 296 ±



**Table 3.** Crystallographic data for bis(2-propyl-1*H*-benzimidazolium) dichromate (**5**).

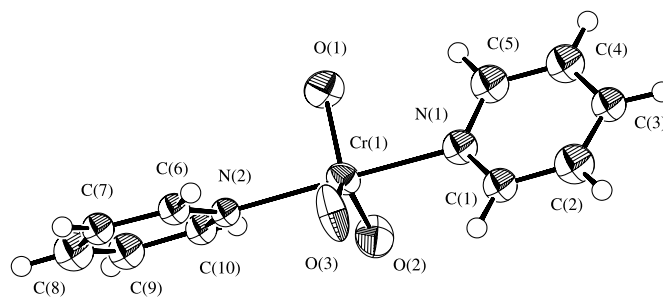
Empirical formula	C <sub>20</sub> H <sub>26</sub> Cr <sub>2</sub> N <sub>4</sub> O <sub>7</sub>
Formula weight	538.44
Description	Yellow plate
Crystal dimensions (mm)	0.05 × 0.30 × 0.30
Crystal system	Monoclinic
Space group	<i>P</i> 2 <sub>1</sub> / <i>n</i> (No. 14)
Cell determination	6 (11.1–13.3°)
<i>a</i> (Å)	7.864(8)
<i>b</i> (Å)	18.65(1)
<i>c</i> (Å)	16.161(7)
β (°)	96.80(6)
<i>V</i> (Å <sup>3</sup> )	2354(3)
<i>Z</i> value, <i>D</i> <sub>calc</sub> (Mg m <sup>−3</sup> )	4, 1.519
<i>F</i> <sub>000</sub>	1112.00
μ (MoKα) (cm <sup>−1</sup> )	9.71
2θ <sub>max</sub> (°)	46.3
No. reflns measured	3696
Unique reflns ( <i>R</i> <sub>int</sub> )	3276 (0.088)
No. with <i>I</i> > 3σ( <i>I</i> )	838
<i>h</i>	0 → 8
<i>k</i>	0 → 20
<i>l</i>	−17 → 17
No. of variables	179
<i>R</i> , <sup>a</sup> <i>R</i> <sub>w</sub> <sup>b</sup>	0.058, 0.060
Goodness of fit <sup>c</sup>	1.18
(Δ/σ) <sub>max</sub>	0.02
Δρ <sub>max</sub> , Δρ <sub>min</sub> (e <sup>−</sup> Å <sup>−3</sup> )	0.38, −0.26

<sup>a</sup>Full-matrix least-squares refinement on *F*, *R* = Σ||*F*<sub>o</sub>| − |*F*<sub>c</sub>||/Σ|*F*<sub>o</sub>|.<sup>b</sup>*R*<sub>w</sub> = [Σw(|*F*<sub>o</sub>| − |*F*<sub>c</sub>|)<sup>2</sup>/Σw*F*<sub>o</sub><sup>2</sup>]<sup>1/2</sup>.<sup>c</sup>GoF = [Σw(|*F*<sub>o</sub>| − |*F*<sub>c</sub>|)<sup>2</sup>/(*N*<sub>o</sub> − *N*<sub>p</sub>)]<sup>1/2</sup>.**Table 4.** Controlled oxidation of alcohols using bis(2-ethyl-1*H*-benzimidazolium) dichromate (**4**).

Entry	Alcohol	Product <sup>a</sup>	Yield (%) <sup>b</sup>
1	1-Butanol	Butanal	91
2	1-Pentanol	Pentanal	90
3	Isopentanol	Isopentanal	90
4	Glycolic acid	Glyoxylic acid	89
5	Cyclohexanol	Cyclohexanone	86
6	Benzyl alcohol	Benzaldehyde	92
7	<b>6</b> , R = CH <sub>2</sub> OH	<b>6</b> , R = CHO	67
8	<b>6</b> , R = CHOHCH <sub>3</sub>	<b>6</b> , R = COCH <sub>3</sub>	65

<sup>a</sup>Entries 1–6 run at room temperature; entries 7, 8 heated to 100° for 5 min, then kept at room temperature for 30 min.<sup>b</sup>Isolated yields; products were characterized as 2,4-dinitrophenylhydrazones, all of which gave melting points within ±2° of literature values.

1 K. Summaries of the crystallographic data and structure refinements are given in Tables 1–3. Complete details are available upon request.<sup>4</sup>

**Fig. 1.** The structure of dipyridinetrioxochromium(VI) (**1**) showing 50% probability thermal ellipsoids.**Table 5.** Bond distances (Å) and selected bond angles (°) for the non-hydrogen atoms of [C<sub>5</sub>H<sub>5</sub>N]<sub>2</sub>CrO<sub>3</sub> (**1**).

Bond distances (Å)	
Cr1—O1	1.617(16)
Cr1—O2	1.631(16)
Cr1—O3	1.630(6)
Cr1—N1	2.147(5)
Cr1—N2	2.152(5)
N1—C1	1.330(3)
N1—C5	1.329(3)
N2—C6	1.330(3)
N2—C10	1.330(3)
C1—C2	1.365(3) <sup>a</sup>
Selected bond angles (°)	
O1—Cr1—O3	121.5(11)
O3—Cr1—O2	118.8(11)
O3—Cr1—N1	88.0(9)
O1—Cr1—N2	91.2(8)
O2—Cr1—N2	90.0(8)
C5—N1—C1	119.9(4)
C1—N1—Cr1	122.3(7)
C10—N2—Cr1	122.6(6)
O1—Cr1—O2	119.7(4)
O1—Cr1—N1	90.2(8)
O2—Cr1—N1	91.8(9)
O3—Cr1—N2	88.8(9)
N1—Cr1—N2	176.9(2)
C5—N1—Cr1	117.6(7)
C10—N2—C6	119.5(4)
C6—N2—Cr1	117.6(6)

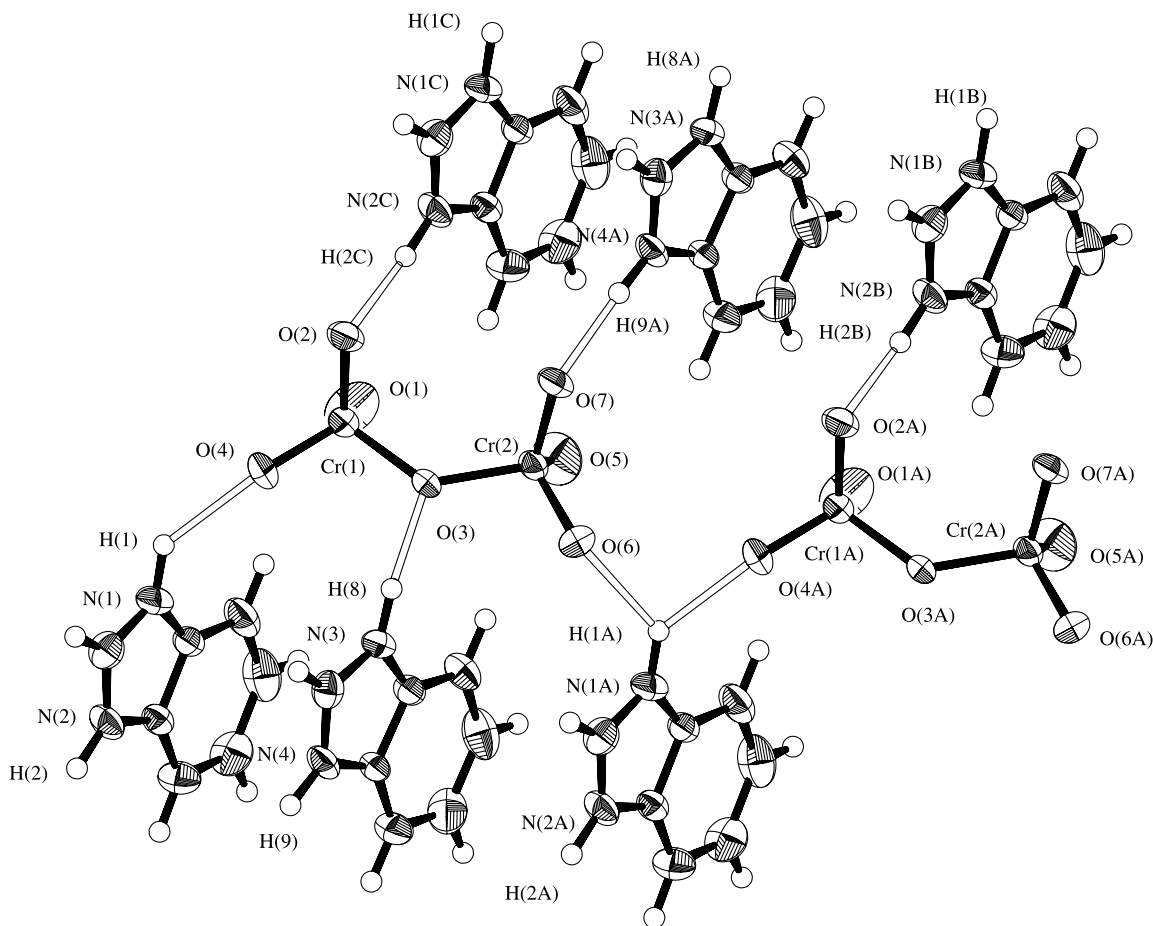
<sup>a</sup>Other C—C bond distances were in the range of 1.364(3)–1.367(3) Å.

Structures were solved by direct methods (SIR92 for **1**, **3**, **4** (20), SHELXS97 for **2**, **5** (21)), expanded using Fourier techniques (DIRDIF-94) (22), and refined by full-matrix least-squares techniques in a fully anisotropic approximation for **2–4** and a partial anisotropic approximation for **1** and **5**. It should be noted that the crystal of **5** was a very weak scatterer. Structures for **1–4** were refined on *F*<sup>2</sup> using

<sup>4</sup>Supplementary data may be purchased from the Depository of Unpublished Data, Document Delivery, CISTI, National Research Council Canada, Ottawa, ON K1A 0S2, Canada ([http://www.nrc.ca/cisti/irm/unpub\\_e.shtml](http://www.nrc.ca/cisti/irm/unpub_e.shtml) for information on ordering electronically). CCDC 191250–191254 contain the supplementary crystallographic data for this paper. These data can be obtained, free of charge, via [www.ccdc.cam.ac.uk/conts/retrieving.html](http://www.ccdc.cam.ac.uk/conts/retrieving.html) (or from the Cambridge Crystallographic Data Centre, 12 Union Road, Cambridge CB2 1EZ, U.K.; fax +44 1223 336033; or deposit@ccdc.cam.ac.uk).



**Fig. 2.** The structure of bis(1*H*-benzimidazolium) dichromate (**2**) showing 50% probability thermal ellipsoids, together with the hydrogen bonding network in the crystal.



SHELXL97 (21) whereas that for **5** was refined on *F* using teXsan (23). Extinction parameters were refined for all structures and the Flack parameter was refined for **1**. Hydrogen atoms were not located in Fourier difference maps; they were set geometrically and included in the final refinement with fixed positional and thermal parameters. Corrections for Lorentz and polarization effects were applied. An absorption correction ( $\psi$  scan) was applied to **3** and **5** and a decay correction was applied to **5** (decay  $-38.4\%$ ). Neutral atom scattering factors were from Cromer and Waber (24), anomalous dispersion effects were included in  $F_{\text{calc}}$  (25), the values for the values for  $\Delta f'$  and  $\Delta f''$  were those of Creagh and McAuley (26), and the values for the mass attenuation coefficients are those of Creagh and Hubbell (27).

#### Controlled oxidation of alcohols using **4**

A solution of the alcohol (2.5 mM) in glacial acetic acid was added in portions to a stirred suspension of **4** (1.25 g, 2.5 mM) in glacial acetic acid at room temperature. After 30 min the colour had changed from orange-yellow to green and the reaction was worked up by pouring into water, followed by a regular extraction procedure with diethyl ether. The residual benzimidazole could be recovered from the aqueous layer by adjusting the pH. A selection of results is presented in Table 4.

## Results and discussion

The preparation of compound **1** proved to be challenging owing to its great air sensitivity. However, nicely crystalline material was obtained, which resulted in the well-defined crystal structure depicted in Fig. 1, with selected geometrical parameters for **1** being given in Table 5. The chromium atom is bonded to five ligands in an almost perfect trigonal bipyramid. It should be noted that this structure can be refined in either of the space groups *C2* or *C2/c*. In *C2/c* the Cr—O(3) bond should be coincident with a twofold axis, but this results in the anisotropic thermal parameters of O(3) being unreasonably distorted with the ratio 4.3:1 of the displacement parameters across and along the Cr—O(3) bond. The mean  $\text{abs}(E^2 - 1)$  value for all general reflections *hkl* was 0.809, where the values predicted for centric and acentric cells are 0.968 and 0.736, respectively. Nevertheless, with the structure being so nearly centrosymmetric, the distinction between *Cc* and *C2/c* will be a matter of opinion. The structure was therefore refined in *C2*, the refinement proceeding routinely, without recourse to disorder.

The mean chromium—oxygen bond length at 1.626 Å is slightly longer than the mean nonbridging chromium—oxygen bond length of 1.599(5) Å in the parent  $(\text{CrO}_3)_\infty$  (28) and is intermediate between the single (1.736(2) Å) and double



**Table 6.** Selected bond distances (Å) and bond angles (°) for the non-hydrogen atoms of  $[\text{C}_7\text{H}_7\text{N}_2]_2\text{Cr}_2\text{O}_7$  (**2**).

Bond distances (Å)	
Cr1—O1	1.586(3)
Cr1—O2	1.627(3)
Cr1—O3	1.794(2)
Cr1—O4	1.599(3)
N1—C1	1.328(5)
N1—C2	1.391(4)
N2—C1	1.324(5)
N2—C7	1.396(4)
C2—C7	1.391(5)
Bond angles (°)	
O1—Cr1—O2	110.60(17)
O1—Cr1—O3	109.04(16)
O1—Cr1—O4	112.0(2)
O2—Cr1—O3	108.99(13)
O2—Cr1—O4	109.50(15)
O3—Cr1—O4	106.61(14)
Cr1—O3—Cr2	129.25(14)
O3—Cr2—O5	109.38(16)
O3—Cr2—O6	105.98(13)
O3—Cr2—O7	108.86(13)
O5—Cr2—O6	110.97(17)
O5—Cr2—O7	110.90(17)
O6—Cr2—O7	110.60(15)
N1—C1—N2	110.2(3)

(1.578(2) Å) bonds in the chromate ester ( $\text{CrO}_2(\text{OCPh}_3)_2$ ) (**29**). The mean of the two chromium—nitrogen bonds at 2.150 Å can be compared with typical lengths of 2.158–2.178 Å for the nitrogen—chromium(VI) bond (**30**). More specifically, comparison can be made with the lengths of the chromium—nitrogen bonds in oxodiperoxopyridinechromium(VI) ( $[\text{CrO}_5\text{-C}_5\text{-H}_5\text{N}]$ ) at 2.047(13) Å (**31**, **32**) and in the complex with chromyl chloride of a secondary amine chlorodioxo-(2,2,6,6-tetramethylpiperidine)chromium(VI) ( $[\text{CrO}_2\text{Cl}(\text{NC}_9\text{H}_{18})]$ ) at 1.81(1) Å (**33**). The latter compound is not actually a complex, but has a formal N—Cr bond. It is also instructive to make comparisons with some other Lewis acid–base complexes involving pyridine. Three examples, with the N—X bond distance in brackets, are pyridine–boron trichloride (1.592(3) Å) and pyridine–boron trifluoride (1.604(5) Å) (**34**), examples of strongly bound complexes to a small electrophilic atom, with the third example, pyridine 1-sulphonate (1.829 Å) (**35**), being a strongly bound larger electrophile.

Another noteworthy feature of **1** is that the planes of the two pyridine rings are twisted at an angle of ca. 60° with respect to each other, as would be expected if electron-pair repulsions are to be minimized. These data are overall in accord with the bonding between the pyridine rings and the chromic anhydride being a classic example of a Lewis acid–base complex. A trigonal pyramidal structure for **1** was originally proposed by Sisler et al. (**36**). The IR spectrum of **1** is not especially informative, although the strong band at 926  $\text{cm}^{-1}$  likely results from Cr—O stretching vibrations (**31**). Confirmation that the pyridine–chromic anhydride complex is monomeric is consistent with its solubility prop-

erties in organic solvents (**37**), with dissolution in dichloromethane avoiding the pyrophoric nature of the complex dissolved in pyridine. This complex has been used for many years as a selective oxidant for organic alcohols, although many procedures and stoichiometric ratios have been published, especially for the selective oxidation of primary alcohols to aldehydes (**37**).

The isolation of the dichromate salts **2–5** offered the opportunity to explore their chemistry and to supplement the limited literature on the structural features of heterocyclic chromate salts. A picture of compound **2** (50% probability thermal ellipsoids) is given in Fig. 2 while selected geometrical parameters are given in Table 6.

In compounds **3** and **4**, the chromate anions are disordered about  $\bar{1}$ , with oxygen atom O(2) occupying two positions and the two  $\text{CrO}_3$  groups being staggered with respect to each other. The geometry of chromate anions, associated with heterocyclic cations, of general form  $[\text{R}^+]_2[\text{Cr}_n\text{O}_{3n+1}]^{2-}$ , continues to attract attention (**12**, **16**, **38**, **39**). A smooth correlation of terminal and bridging Cr—O distances with increasing degree of polymerization has been noted (**16**). The lengths of the bridging Cr—O bonds in **2** are 1.794(2) and 1.795(2) Å, but are 1.78(1) and 1.80(1) Å in **5** for a mean of 1.79 Å; the terminal bonds of both **2** and **5** are clustered around a mean value of 1.60 Å. These may be compared with the literature values of 1.780(7) and 1.615(18) Å, respectively (**16**). The nonbridging bond angles are close to tetrahedral at 105.98(13)–112.0(2)° in **2** and 106.7(7)–112.3(8)° in **5**, whereas the bridging bond angles are 129.25(14), 130.4(3), 134.0(4), and 123.2(6)° for the four salts, respectively. Again, these are comparable to literature values, namely, 127.0(4)° (**12**), 122.7(1)° (**13**), 124.7(8)° (**14**), and 135.3(5)° (**15**). These numbers show that there is considerable flexibility in the bonding about the bridging oxygen atom. The ability of dichromate anions to build an acentric polar framework has been studied by Pecaut and Masse (**13**) in connection with attempts to design efficient organic–inorganic nonlinear optical crystals. Compounds **2–5** have nonpolar space groups, with symmetrical molecular arrangements. The dimensions of the dichromate anions in **3** and **4** are similar to those of **2** and **5** but the structures of **3** and **4** are disordered.

Hydrogen bonds, of the type N—H...O, play a crucial role in determining the molecular packing in these systems. Interestingly, the hydrogen bonding networks in the four structures are different, as outlined in Table 7. These values are in general agreement with published values for such hydrogen bonds (40–42). In **2**, each dichromate anion is linked to five benzimidazolium cations through three strong hydrogen bonds and a pair of bifurcated hydrogen bonds (Fig. 2). Five of the seven oxygen atoms are involved in the hydrogen bonding, but oxygen atoms O(1) (and by symmetry, O(5)) are not. These two oxygen atoms, therefore, have larger thermal parameters than the other four terminal oxygen atoms. These facts are mirrored in the chromium—oxygen bond lengths (Table 6). The molecular structure thus takes on the form of an infinite molecular chain along *a*, which is joined together by the fifth hydrogen bond (N(1)—H(9)...O(4)) in a molecular layer in plane (010). In contrast to this, structure **3** has two hydrogen bonds which create a molecular sheet in plane (201), while in **4** there is a bimolecular chain along



**Table 7.** Hydrogen bond distances (Å) and bond angles (°) in the bis(1*H*-benzimidazolinium) dichromates **2–5**.

Compound	D—H...A	<i>d</i> <sub>D-H</sub>	<i>d</i> <sub>H-A</sub>	<i>d</i> <sub>D-A</sub>	D—H—A (°)
<b>2</b>	N1—H1...O4	0.95	2.06	2.829(5)	136.3
	N2—H2...O2	0.96	1.79	2.746(4)	174.3
	N3—H8...O3	0.95	1.86	2.774(4)	161.0
	N4—H9...O7	0.95	1.83	2.769(4)	167.3
<b>3</b>	N1—H1...O6	0.95	2.12	2.835(5)	130.2
	N1—H8...O4	0.95	1.90	2.780(5)	151.7
<b>4</b>	N2—H9...O1	0.94	1.77	2.701(5)	169.1
	N1—H1...O4	0.95	1.83	2.728(4)	156.6
<b>5</b>	N2—H2...O1	0.95	1.83	2.763(5)	164.9
	N1—H1...O2	0.95	1.88	2.82(2)	171.2
	N2—H2...O4	0.95	1.87	2.79(2)	165.3
	N3—H14...O3	0.96	1.77	2.72(2)	171.4
	N4—H15...O7	0.95	2.03	2.95(3)	163.4

(001) and in **5** there is simply a three-dimensional network. When the alkyl side chain is a methyl or ethyl group, a larger cavity than for **2** is created for the dichromate anion and the hydrogen bonding occurs only to two of the terminal oxygen atoms. Since there is no hydrogen bond to the bridging oxygen atom, the anion can become disordered. When the alkyl side chain is a propyl group, the cavity for the anion is again smaller with hydrogen bonding to both terminal and bridging oxygen atoms. The anion is now no longer disordered. In some cases (structures **2** and **3**) the cations are unfavourably stacked with nearly parallel directions of their dipoles, the interplane distances being in the range 3.45 to 3.60 Å. Thus, hydrogen bonding plays an important role in these structures, compensating for the repulsions between the adjacent cations.

Finally, these dichromate salts appear to have some useful chemical properties. We have found that the selective oxidation process described in this work, using equimolar amounts of **4** and the alcohol in glacial acetic acid, is simple to carry out and does not require rigorously anhydrous conditions. Work up is straightforward and the reaction is efficient in terms of reagent use since the benzimidazole can be recovered. Studies were carried out using the other benzimidazolinium salts, **2**, **3**, and **5** as oxidants, but **4** gave somewhat superior results. Compounds **3–5**, but not **2**, gradually and irreversibly darkened on standing in the air, presumably because of a slow surface oxidation of the heterocyclic side chain. However, the process did not appear to yield any synthetically useful quantities of oxidized heterocycles.

## Conclusions

Crystals of the strong oxidant CrO<sub>3</sub>·Pyr<sub>2</sub> were prepared and characterized by X-ray crystallography more than 50 years after the compound was first prepared. A series of benzimidazolinium dichromate salts was prepared and characterized, their crystal structures were studied and their utility as selective oxidants for alcohols was explored.

## Acknowledgments

The authors gratefully acknowledge financial support from the Natural Sciences and Engineering Research Council of Canada (NSERC) and the University Grants Commis-

sion (New Delhi); their respective universities provided laboratory and instrumentation support. Thanks are due to Professor O. Knop for helpful discussions and to Dr. K.N. Robertson for assistance.

## References

1. K. Ramaiah, P.K. Dubey, J. Ramanatham, J.S. Grossert, and D.L. Hooper. *Indian J. Chem. Sect B: Org. Chem. Incl. Med. Chem.* **38**, 302 (1999).
2. K. Ramaiah, J.S. Grossert, D.L. Hooper, P.K. Dubey, and J. Ramanatham. *J. Indian Chem. Soc.* **76**, 140 (1999).
3. M.K. Mahanti and K.K. Banerji. *J. Indian Chem. Soc.* **79**, 31 (2002).
4. M. Hudlický. *Oxidations in organic chemistry*, A.C.S. Monograph No. 186. American Chemical Society, Washington, D.C. 1990.
5. G. Cainelli and G. Cardillo. *Chromium oxidations in organic chemistry*. Springer-Verlag, Berlin. 1984.
6. H.H. Sisler, J.D. Bush, and O.E. Accountius. *J. Am. Chem. Soc.* **70**, 3827 (1948).
7. (a) J.C. Collins, W.W. Hess, and F.J. Frank. *Tetrahedron Lett.* 3363 (1968); (b) J.C. Collins and W.W. Hess. *Org. Synth.* **52**, 5 (1972).
8. E.J. Corey and G. Schmidt. *Tetrahedron Lett.* 399 (1979).
9. K. Balasubramanian and V. Prathiba. *Indian J. Chem.* **25B**, 326 (1986).
10. K.G. Akamanchi, L.G. Iyer, and R. Meenakahi. *Synth. Commun.* **21**, 419 (1991).
11. E.J. Parish, H. Honda, and D.L. Hileman. *Synth. Commun.* **20**, 3359 (1990).
12. M.R. Pressprich, R.D. Willett, R.M. Sheets, W.W. Paudler, and G.L. Gard. *Acta Crystallogr. Sect. C: Cryst. Struct. Commun.* **C46**, 1635 (1990).
13. J. Pecaut and R. Masse. *Acta Crystallogr. Sect. B: Struct. Crystallogr. Cryst. Chem.* **B49**, 277 (1993).
14. P.A. Lorenzo-Luis, P. Martín-Zarza, P. Gili, J.M. Arrieta, G. Germain, and L. Dupont. *Acta Crystallogr. Sect. C: Cryst. Struct. Commun.* **51**, 1073 (1995).
15. P. Martín-Zarza, P. Gili, F.V. Rodriguez-Romero, C. Ruiz-Pérez, and X. Solans. *Polyhedron*, **14**, 2907 (1995).
16. M.R. Pressprich, R.D. Willett, R.D. Poshusta, S.C. Sauders, H.B. Davis, and G.L. Gard. *Inorg. Chem.* **27**, 260 (1988).
17. N. Burford, J. Müller, and T.M. Parks. *J. Chem. Ed.* **71**, 807 (1994).



18. M. Camelot. *Rev. Chim. Miner.* **6**, 853 (1969).
19. M.A. Phillips. *J. Chem. Soc.* 1409 (1930).
20. A. Altomare, M. Cascarano, C. Giacovazzo, and A. Guagliardi. *J. Appl. Crystallogr.* **26**, 343 (1994).
21. G.M. Sheldrick. SHELXS97 and SHELXL97. Institute of Inorganic Chemistry, University of Göttingen, Germany. 1997.
22. P.T. Beurskens, G. Admiraal, G. Beurskens, W.P. Bosman, R. de Gelder, R. Israel, and J.M.M. Smits. The DIRDIF-94 program system. Technical Report of the Crystallography Laboratory, University of Nijmegen, The Netherlands. 1994.
23. teXsan for Windows. Version 1.06. Crystal structure analysis package. Molecular Structure Corporation, The Woodlands, Texas. 1997–1999.
24. D.T. Cromer and J.T. Waber. International tables for X-ray crystallography. Vol. IV. The Kynoch Press, Birmingham, U.K. 1974. Table 2.2 A.
25. J.A. Ibers and W.C. Hamilton. *Acta Crystallogr.* **17**, 781 (1964).
26. D.C. Creagh and W.J. McAuley. International tables for crystallography. Vol. C. *Edited by* A.J.C. Wilson. Kluwer Academic Publishers, Boston. 1992. Table 4.2.6.8. pp. 219–222.
27. D.C. Creagh and J.H. Hubbell. International tables for crystallography. Vol. C. *Edited by* A.J.C. Wilson. Kluwer Academic Publishers, Boston. 1992. Table 4.2.4.3. pp. 200–206.
28. J.S. Stephens and D.W.J. Cruickshank. *Acta Crystallogr. Sect. B: Struct. Crystallogr. Cryst. Chem.* **B26**, 222 (1970).
29. P. Stavropoulis, N. Bryson, M.-T. Youinou, and J.A. Osborn. *Inorg. Chem.* **29**, 1807 (1990).
30. A.G. Orpen, L. Brammer, F.H. Allen, O. Kennard, D.G. Watson, and R. Taylor. *In* International tables for crystallography. Vol. C. *Edited by* A.J.C. Wilson. Kluwer Academic Publishers, Dordrecht, The Netherlands. 1992. p. 738.
31. R. Stomberg. *Ark. Kemi*, **22**, 29 (1964).
32. M.H. Dickman and M.T. Pope. *Chem. Rev.* **94**, 569 (1994).
33. H. Lam, G. Wilkinson, B. Hussain-Bates, and M.B. Hursthouse. *J. Chem. Soc., Dalton Trans.* 1477 (1993).
34. K. Töpel, K. Hensen, and J.W. Bats. *Acta Crystallogr. Sect. C: Cryst. Struct. Commun.* **C40**, 828 (1984).
35. S. Brownstein, E.J. Gabe, F. Lee, and B. Louie. *J. Org. Chem.* **53**, 951 (1988).
36. H.H. Sisler, Wan Chen Loh Ming, E. Metter, and F.R. Hurley. *J. Am. Chem. Soc.* **75**, 446 (1953).
37. A.H. Haines. Methods for the oxidation of organic compounds: Alcohols, alcohol derivatives, alkyl halides, nitroalkanes, alkyl azides, carbonyl compounds, hydroxyarenes and aminoarenes. Academic Press, London. 1988. Section 2.1.3. pp. 17–42.
38. M. Cygler, M.J. Grabowski, A. Stępień, and E. Wajsman. *Rocz. Chem.* **50**, 1587 (1976).
39. A. Stępień and M.J. Grabowski. *Acta Crystallogr. Sect. B: Struct. Crystallogr. Cryst. Chem.* **B33**, 2924 (1977).
40. I. Olovsson and P.-G. Jönsson. *In* The hydrogen bond. Vol. II. *Edited by* P. Schuster, G. Zundel, and C. Sandorfy. North Holland, Amsterdam. 1976. pp. 394–456.
41. M. Middlemiss and C. Calvo. *Can. J. Chem.* **54**, 2025 (1976).
42. A. Mirčeva and L. Golič. *Acta Crystallogr. Sect. C: Cryst. Struct. Commun.* **C51**, 798 (1995).



# Alkali metal ion controlled product selectivity during photorearrangements of 1-naphthyl phenyl acylates and dibenzyl ketones within zeolites

M. Warrier, Lakshmi S. Kaanumalle, and V. Ramamurthy

**Abstract:** Photochemical behaviors of 1-naphthyl phenyl acylates and dibenzyl ketones included in zeolites have been compared. 1-Naphthyl phenyl acylates while in solution produce eight photoproducts; within NaY it gives a single product. The selectivity is attributed to the restriction brought on the mobility of the primary radical pair by the alkali metal ions present in zeolites. Photochemistry of dibenzyl ketones within NaY reveals that the intersystem crossing in caged radical pairs could be influenced by the heavy alkali metal ions. Structures of complexes among  $\text{Li}^+$  ion and the guest 1-naphthyl phenyl acetates and dibenzyl ketone computed at the B3LYP level have been useful to understand the origin of the observed product selectivity within zeolites.

**Key words:** photo-Fries reaction, zeolites, cation- $\pi$  interaction, spin-orbit coupling, heavy atom effect.

**Résumé :** On a comparé les comportements photochimiques des phénylacylates de 1-naphtyle et des dibenzylcétones inclus dans des zéolites. Les phénylacylates de 1-naphtyle en solution conduisent à huit photoproduits alors qu'il ne s'en forme qu'un lorsqu'ils sont inclus dans NaY. On attribue la sélectivité à la restriction imposée à la paire de radicaux primaires par les ions des métaux alcalins présents dans les zéolites. La photochimie des dibenzylcétones dans NaY révèle que le passage entre systèmes dans une paire de radicaux en cage peut être influencé par les ions des métaux alcalins lourds. Les structures des complexes entre l'ion  $\text{Li}^+$  et les molécules de phénylacétates de 1-naphtyle et de dibenzylcétones qui ont été calculées au niveau B3LYP se sont avérées utiles pour comprendre l'origine de la sélectivité des produits qui a été observée pour les réactions dans les zéolites.

**Mots clés :** réaction de photo-Fries, zéolites, interaction cation- $\pi$ , couplage spin-orbite, effet d'atome lourd.

[Traduit par la Rédaction]

## Introduction

Photo-Fries rearrangement of phenylacetate and photo-Claisen rearrangement of allylphenyl ether yield *ortho*-hydroxy and *para*-hydroxy isomers as products (Scheme 1) (1). In solution, independent of the polarity of the medium, one obtains a mixture. On the other hand, within alkali metal ion exchanged X and Y zeolites, *ortho*-hydroxy isomers are obtained as the major products from phenylacetate and allylphenyl ether (2). Selectivity obtained within zeolites was very high even during the photo-Fries rearrangement of 1-naphthyl acetate and 1-naphthyl benzoate (Scheme 1) (3). The results with 1-naphthyl esters suggested that zeolites could favor the formation of a single product (2-acetyl-1-naphthol and 2-benzoyl-1-naphthol) by discriminating among three possible photoproducts, all of which may be formed with equal probability in isotropic media.

Both photo-Fries and photo-Claisen rearrangements proceed via a similar mechanism (1). Promotion to the excited singlet state results in fragmentation of the ester and the ether. Cage escape, recombination, and hydrogen migration

result in both the *ortho*- and the *para*-isomers (Scheme 2). However, the factors that control the outcome of the products vary with the nature of the medium. In solution, it is the electron densities at various aromatic carbons in the aryloxy radical which control the regioselectivity. We suggested that the selectivity within zeolites resulted from the restriction imposed on the mobility of the aryloxy and the acetyl fragments by the cations present in zeolites (2). Vasenkov and Frei (4) provided support for the existence of  $\text{Na}^+$ -acetyl radical interaction within solvent-free NaY through time-resolved FT-IR spectroscopy. They also confirmed that only 2-acetyl-1-naphthol is formed upon photolysis of 1-naphthyl acetate within solvent-free NaY. The acetyl radicals generated by photolysis of 1-naphthyl acetate (reacting from excited singlet state) within NaY decay following a single exponential law with a lifetime of  $71 \pm 15 \mu\text{s}$ . The acetyl radical generated from pinacolone (reacting from triplet state) has a much longer lifetime ( $315 \pm 30 \mu\text{s}$ ). The difference in lifetime between singlet and triplet radical pairs suggested that the reactivity of the reactive radical generated from the excited singlet and triplet states of the precursors

Received 13 January 2003. Published on the NRC Research Press Web site at <http://canjchem.nrc.ca> on 28 May 2003.

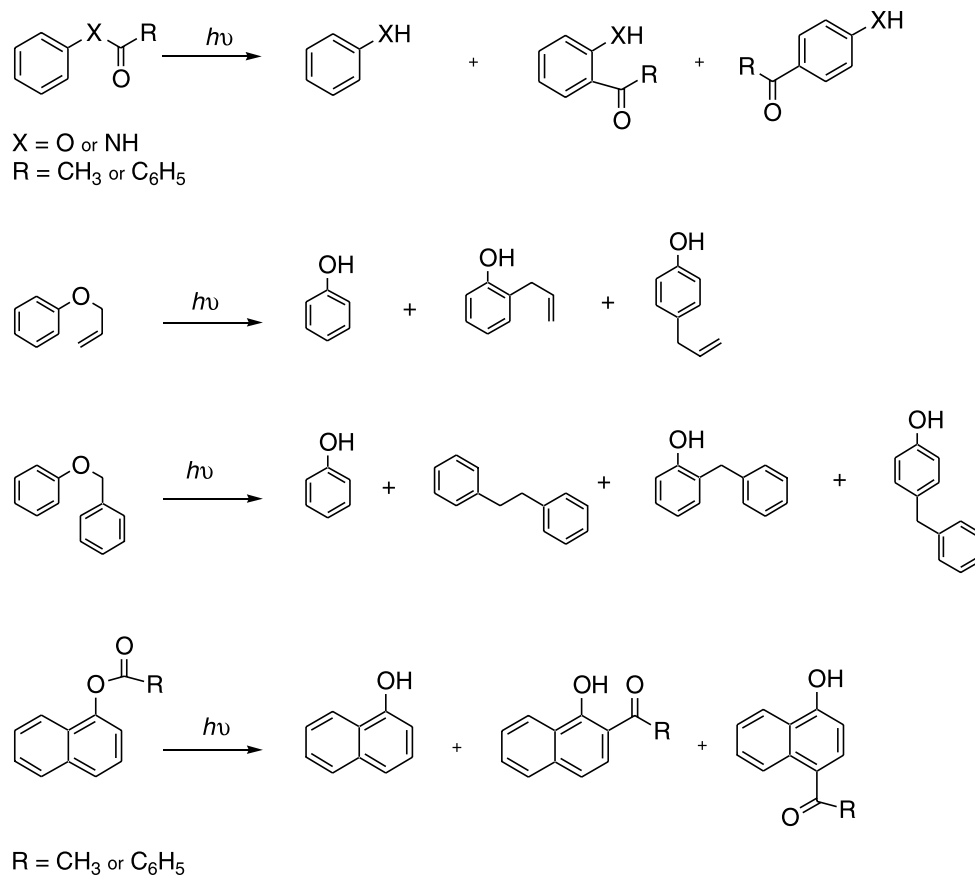
Dedicated to Professor Donald R. Arnold for his contributions to Chemistry.

M. Warrier, L.S. Kaanumalle, and V. Ramamurthy.<sup>1</sup> Department of Chemistry, Tulane University, New Orleans, LA 70118 U.S.A.

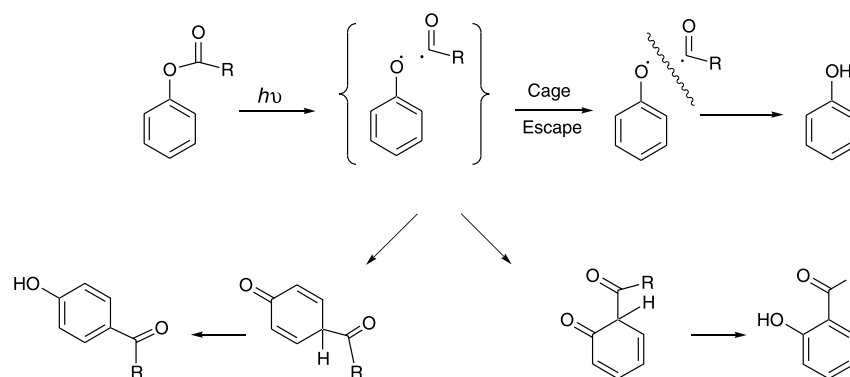
<sup>1</sup>Corresponding author (e-mail: [murthy@tulane.edu](mailto:murthy@tulane.edu)).



Scheme 1.



Scheme 2.



would behave differently. Further, the long lifetime ( $\mu\text{s}$ ) of the acetyl radical suggested that the *ortho* and (or) *para* selectivity in photo-Fries reaction would depend on the nature of the “spin” of the primary radical pair. To test these possibilities and to further explore the selectivity in photo-Fries reactions in naphthyl systems we have examined the photobehavior of three 1-naphthyl phenylacetyl esters **1a–1c** and three dibenzyl ketones **2a–2c** (Scheme 3) (5). The study mainly consisted of photoproducts analysis. To gain an insight into the alkali ion binding to the reactants within zeolites density functional theory (DFT) calculations were performed. Results of these studies are presented in this report.

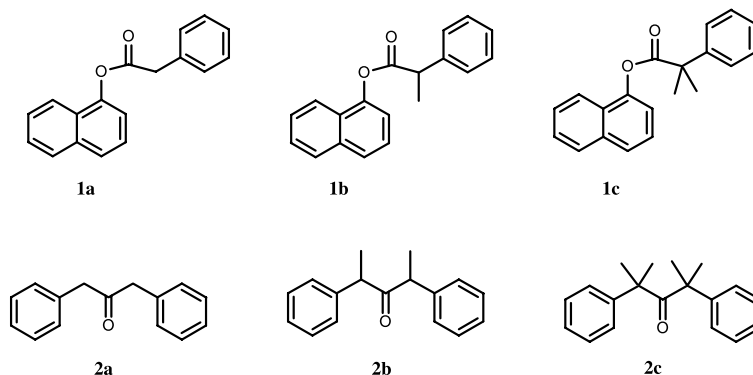
## Results

### Photolysis of 1-naphthyl phenylacetyl esters **1a–1c**

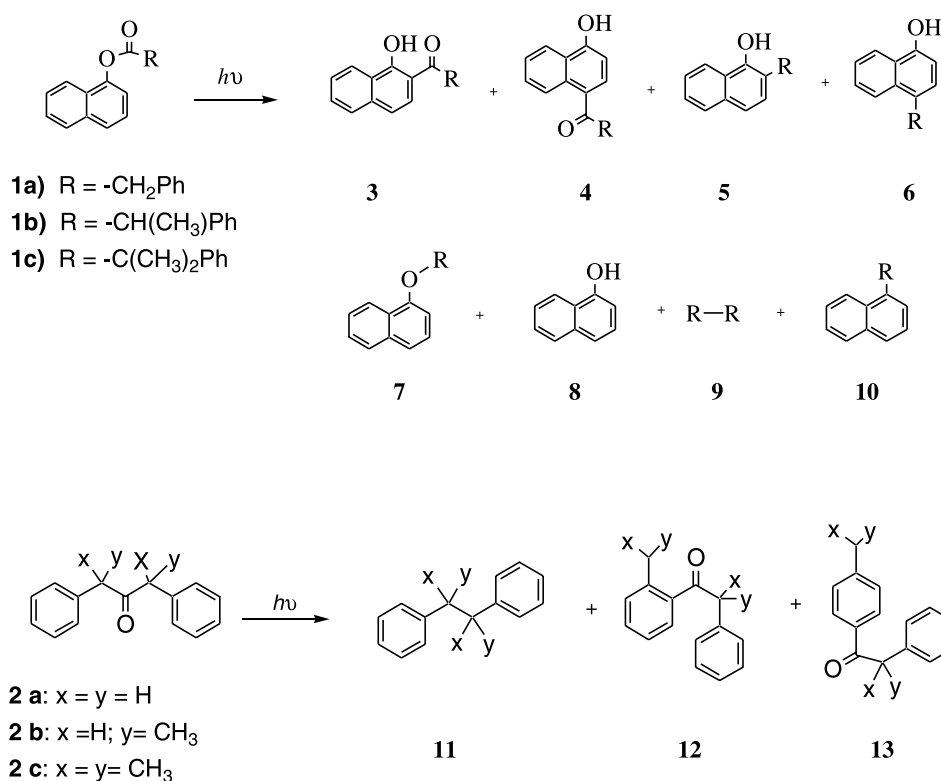
Photolysis of 1-naphthyl phenylacetyl esters **1a–1c** in hexane resulted in a mixture of products (Scheme 4), yields of which are presented in Table 1. The product distributions obtained in this study is identical to the ones reported by Gu and Weiss (6) recently. Photolysis of **1a–1c** within different cation-exchanged zeolites, however, showed formation of mainly the *ortho*-rearrangement product (2-phenylacetyl-1-naphthol (**3**)) accompanied by minor amounts of 1-naphthol (**8**) (Table 2). Percentage conversion for the same length of



Scheme 3.



Scheme 4.



irradiation and for the same loading level of **1a–1c** within zeolites decreased from light alkali metal ion-exchanged zeolites (e.g., LiY) to heavy alkali metal ion-exchanged zeolites (e.g., TiY) (Table 2). Based on our earlier studies (7), facile intersystem crossing leading the reactive excited singlet esters into their unreactive triplet state was suspected for the decrease in reactivity within heavy alkali metal ion-exchanged zeolites. To ascertain this possibility, emission spectra of **1a–1c** in different alkali metal ion-exchanged zeolites at 77 K were recorded. As seen in Fig. 1 for 1-naphthyl phenylacetate, the emission was mainly fluorescence in LiY and NaY and mainly phosphorescence in CsY and TiY. Similar emission behavior was obtained in the case of **1b** and **1c**.

#### Photolysis of dibenzyl ketones **2a–2c**

Photolysis of dibenzyl ketones **2a–2c** in hexane yielded only the decarbonylation products 1,2-diphenyl ethane, 2,3-diphenyl butane, 2,3-diphenyl 2,3-dimethylbutane, respectively (Scheme 4, Table 3). These results are consistent with the original reports by Engel (8a), Robbins and Eastman (8b), and Turro and co-workers (8c, 8d). The same products obtained in hexane were formed upon photolysis of **2a** and **2b** in light-atom-exchanged zeolites (e.g., LiY and NaY) (Table 3). Photolysis of **2a** and **2b** in heavy-atom-exchanged zeolites such as CsY and TiY resulted in rearrangement products, 2-methyl-phenyl benzyl ketone and 4-methyl-phenyl benzyl ketone, and 2-ethyl-phenyl  $\alpha$ -methyl benzyl ketone and 4-ethyl-phenyl  $\alpha$ -methyl benzyl ketone in addi-



**Table 1.** Product distribution upon photolysis of substrates **1a–1c** in hexane.

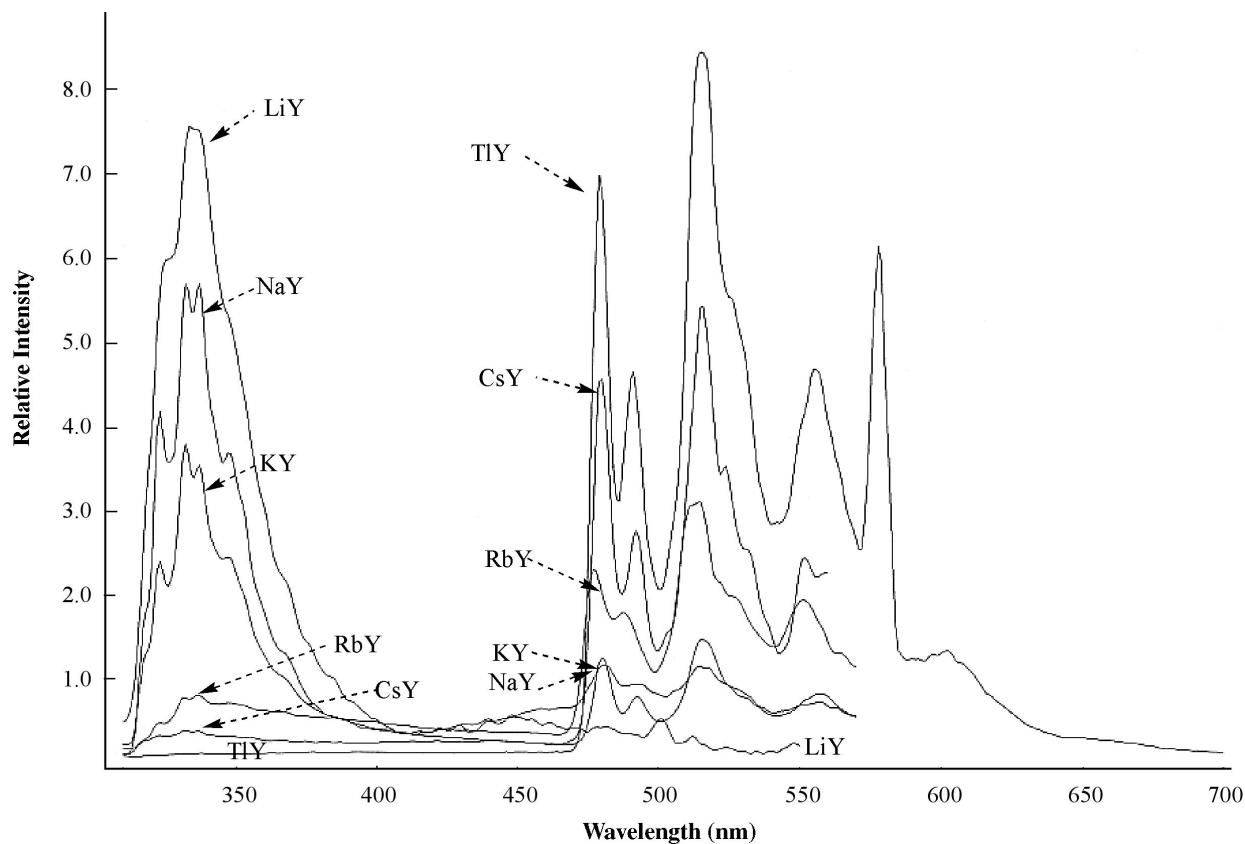
Compound	Product yields <sup>a</sup>							
	3	4	5	6	7	8	9	10
<b>1a</b>	59	6	7	11	1	9	2	5
<b>1b</b>	59	9	9	17	1	2	2	1
<b>1c</b>	28	15	9	14	—	13	15	6

<sup>a</sup>Irradiations were conducted to about 40% conversion. The conversion was achieved in 15 min. All yields presented are an average of at least five independent runs. Error limits on yields were  $\pm 5\%$ .

**Table 2.** Product distribution upon photolysis of 1-naphthyl phenyl acylates (**1a–1c**) within zeolites.

Medium	Conversion <sup>a</sup> (%)	<b>3a</b> (%)	<b>8a</b> (%)	Conversion <sup>a</sup> (%)	<b>3b</b> (%)	<b>8b</b> (%)	Conversion <sup>a</sup> (%)	<b>3c</b> (%)
LiY	27	97	3	19	>99	—	46	>99
NaY	24	97	3	26	>99	—	24	>99
KY	15	96	4	11	93	7	35	>99
RbY	9	92	8	7	95	5	<1	—
CsY	3	—	—	2	87	13	<1	—
TIY	<1	—	—	<1	—	—	—	—

<sup>a</sup>All irradiations were carried out for 2 h in a hexane slurry. The ratio of products were independent of the conversion in the range 15–90%. All yields are an average of at least five independent runs. Error limit on yields were  $\pm 5\%$ .

**Fig. 1.** Emission spectra of 1-naphthyl phenylacetyl ester (**1a**) in various cation exchanged zeolites at 77 K.

tion to 1,2-diphenylethane and 2,3-diphenylbutane, respectively (Scheme 4) (9). The relative yields of the rearrangement products (2-alkyl and 4-alkyl-phenyl benzyl ketone) with respect to the decarbonylated products were dependent on the rates of decarbonylation of the phenyl acyl

radical which in turn depended on the stability of the benzylic radicals formed. For example, in the case of dibenzyl ketone (**2a**), which forms, after decarbonylation, a primary benzyl radical, yield of the rearrangement products was as high as 79% in TIY zeolite (Table 3). In the case of



**Table 3.** Product distribution upon photolysis of dibenzyl ketones (**2a–2c**) in hexane and Y zeolites.

Medium	<b>11a</b> <sup>a</sup> (%)	<b>12a</b> (%)	<b>13a</b> (%)	<b>11b</b> <sup>a</sup> (%)	<b>12b</b> (%)	<b>13b</b> (%)	<b>11c</b> <sup>b</sup> (%)
Hexane	100	—	—	100	—	—	>99
LiY	95	1	4	>99	—	—	>99
NaY	76	2	8	>99	—	—	>99
KY	90	7	17	>99	—	—	>99
RbY	79	3	18	95	—	5	>99
CsY	33	13	54	76	—	24	>99
TIY	21	57	22	75	7	18	>99

<sup>a</sup>All yields are an average of at least five independent runs. Error limit on yields were  $\pm 5\%$ .

<sup>b</sup>In addition to **11c**, cumene and  $\alpha$ -methylstyrene are formed as minor products. The yield on this column represents all three.

$\alpha,\alpha,\alpha',\alpha'$ -tetramethyl dibenzyl ketone (**2c**), where a stable substituted tertiary benzyl radical is formed, the yield of the rearrangement products was <1% in TIY (Table 3).

### Alkali metal ion interaction with 1-naphthyl phenylacetyl esters and dibenzyl ketones probed through computations

To gain a better insight on the role of cations (present within zeolite supercages) on the observed photobehavior of naphthyl esters and dibenzyl ketones within zeolites, density functional theory (DFT) calculations on  $\text{Li}^+$  binding to 1-naphthyl phenyl acetate and dibenzyl ketone were carried out (10). The polarized 6-31G\* basis set was used for C, H, O, and Li. In view of the complexities involved in the reactions inside the zeolite cage, the goals of the computational work were necessarily limited to a few specific aspects. First, the magnitude of the interaction energies among  $\text{Li}^+$  and 1-naphthyl phenyl acetate and dibenzyl ketone were quantified. This provided a measure of the potential role of different cations in altering the reactivity of 1-naphthyl phenyl acetate and dibenzyl ketone. In addition to the energy, the structures of lithium ion – 1-naphthyl phenyl acetate and lithium ion – dibenzyl ketone complexes were analyzed. Interaction energies of  $\text{Li}^+$  were determined based on gas-phase optimized geometries of metal ion complexes with 1-naphthyl phenyl acetate and dibenzyl ketone.

The computed geometries of 1-naphthyl phenyl acetate and dibenzyl ketone are shown in Figs. 2 and 3. In both the cases, two low energy conformers were identified and these were used for complexation with lithium ion. Intuitively, binding of  $\text{Li}^+$  is expected to be higher with the substrate when it interacts simultaneously with either two aryl rings or an aryl ring and a carbonyl chromophore. Thus, we have chosen initial guess geometry with the  $\text{Li}^+$  positioned between the two functional groups. During the calculation the cations were free to move to find the most stable position. Calculations did not include any structural moiety from the zeolite. In the case of 1-naphthyl phenyl acetate, three geometry-optimized structures obtained upon metal ion complexation along with their interaction energies are shown in Fig. 2. Interaction energies of  $\text{Li}^+$  to 1-naphthyl phenyl acetate were almost similar in all three structures. Two geometry-optimized structures for the lithium ion complex with dibenzyl ketone were obtained (Fig. 3). Since within a zeolite, the cations are bound to oxygen counter ions, the metal ions are likely to interact less effectively with 1-naphthyl phenyl acetate and dibenzyl ketone than the com-

puted values. Nevertheless, the interaction between the alkali metal ion and the substrates is expected to be significant within zeolites.

### Discussion

Details of the photo-Fries reaction of 1-naphthyl phenylacetyl esters in solution and polymer medium have recently been discussed by Gu, Weiss, and co-workers (5). Product distributions obtained upon photolysis of esters **1a–1c** in hexane could be understood based on the mechanism provided in Scheme 5. Homolytic cleavage of the esters occurs from their excited singlet state to yield singlet geminate radical pair **A**. It is followed by in-cage recombination (giving rearranged products **3** and **4**) or cage escape. Decarbonylation of phenylacetyl radical within the cage results in the radical pair **B** and outside the cage leads to naphthoxy and benzyl free radicals. Reactions of these two radicals either within or outside the cage result in products **5–8**, and product **9** is the result of coupling between two alkyl radicals outside the cage. In this study we make use of the photo-Fries reaction of 1-naphthyl phenylacetyl esters to establish that zeolites are capable of influencing the product distributions in a reaction that gives as many as eight products. Further, the reaction allows us to probe the characteristics of zeolite cages, knowledge of which could be further used to control photoreactions. All our conclusions are based on photoproduct distributions and attempts to monitor the rates of reactions through time-resolved diffuse reflectance laser techniques were not successful. The following aspects of the mechanism presented in Scheme 5 are noteworthy. The relative ratio of products **3** to **4**, and **5** to **6** provide information about the rotational mobility of reactive fragments present in cages **A** and **B** (Scheme 5). The relative yields of products **8** and **9** give an indication about the translational mobility of radical fragments. The relative selectivity observed in the photo-Fries products **3** and **4** and the decarbonylated products **5** and **6** provides valuable information concerning restrictions imposed by the zeolite on different time scales.

When 1-naphthyl phenylacetyl esters **1a–1c** were irradiated in hexane, eight photoproducts (shown in Scheme 4) were formed and the relative yields remained the same independent of the conversion in the range 5–40% (Table 1). Upon photolysis of 1-naphthyl phenylacetyl esters **1a–1c** within LiY, NaY, and KY zeolites led essentially to a single product **3** (Table 2). The selectivity was dramatic, going from eight products in hexane solution to a single product (2-phenylacetyl 1-naphthol (**3**)) in zeolites. For this to happen,



**Fig. 2.** Conformations of 1-naphthyl phenylacetyl ester (top 2 structures) and its complex with  $\text{Li}^+$  (bottom three) as computed at the RB3LYP/6-31G(d) level.

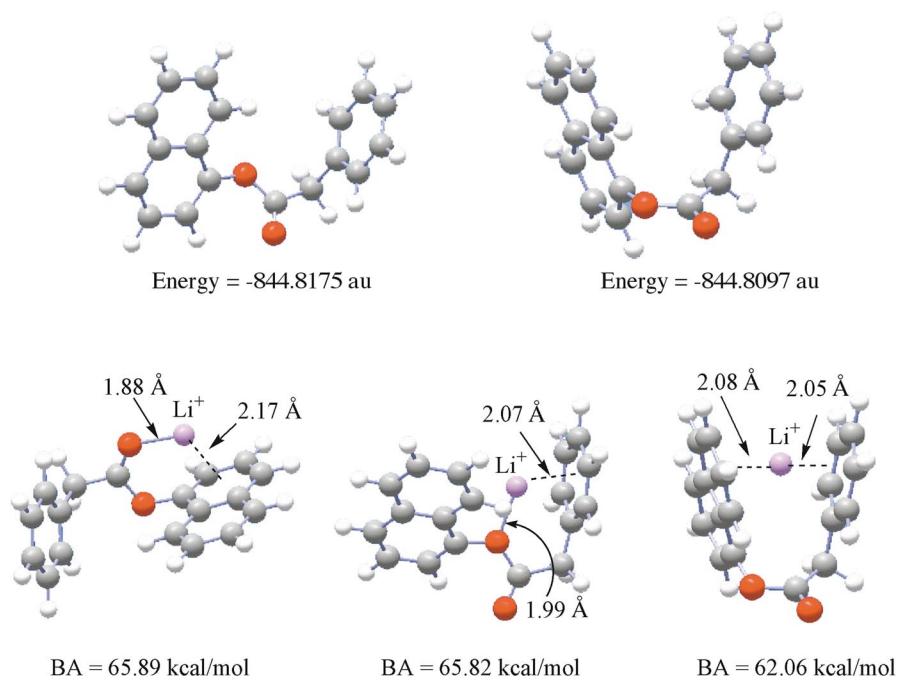
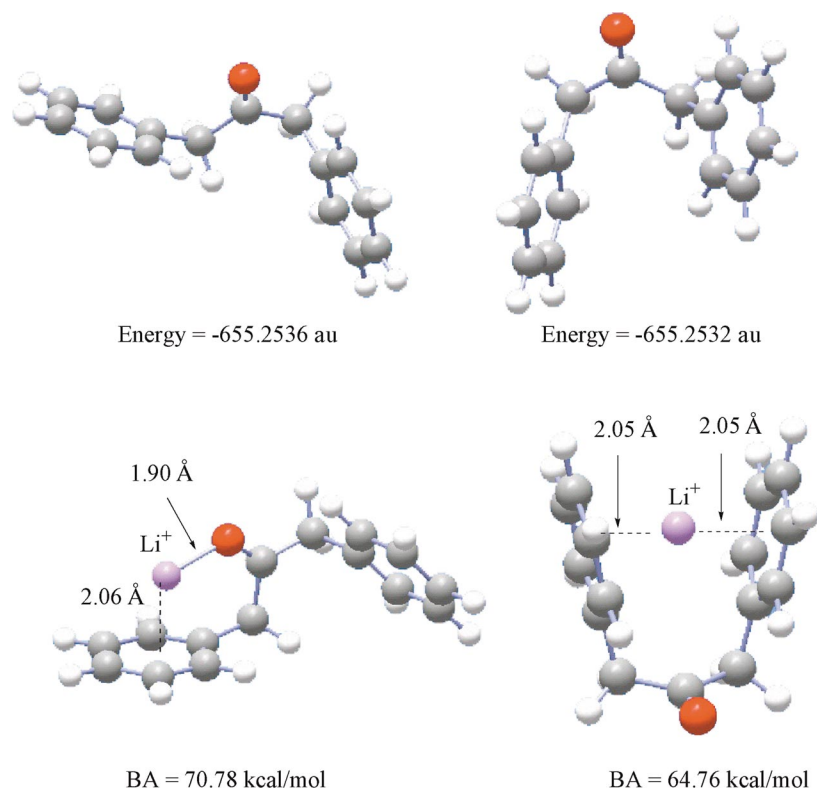


**Fig. 3.** Conformations of dibenzyl ketone (top 2 structures) and its complex with  $\text{Li}^+$  (bottom two) as computed at the RB3LYP/6-31G(d) level.

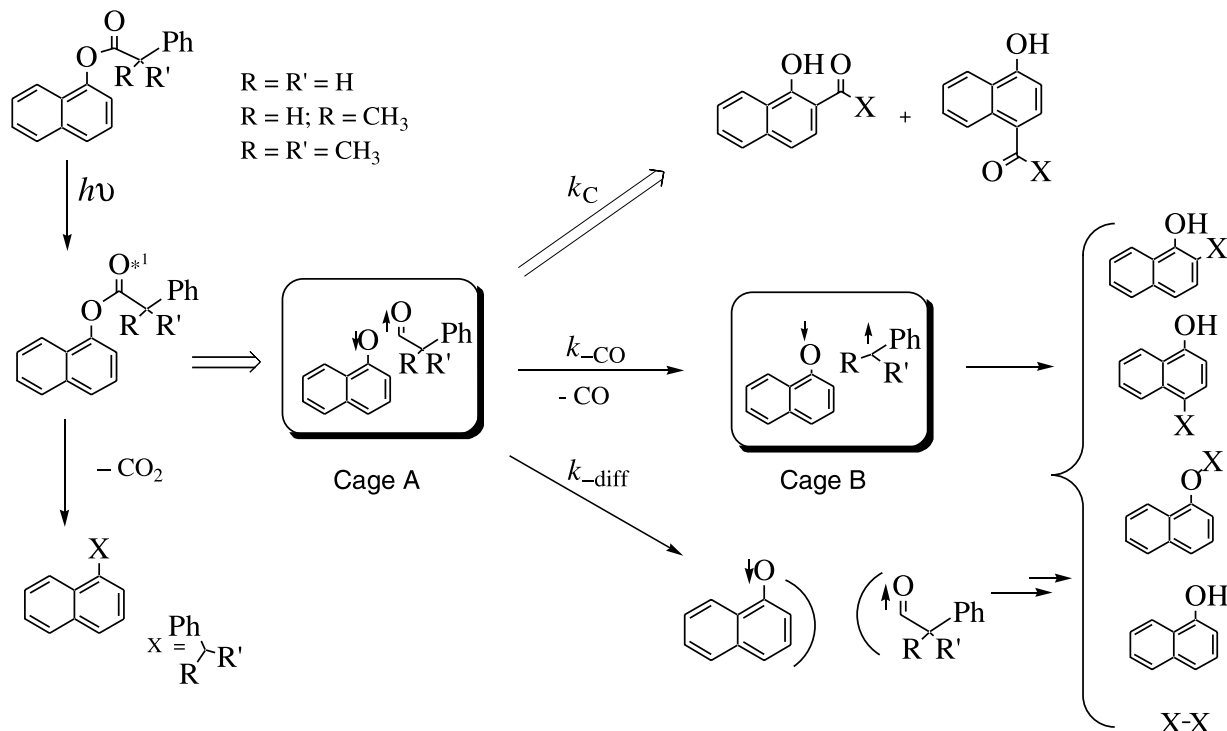


the two primary radicals in **A** formed upon photofragmentation must be coupling before the decarbonylation of phenylacetyl radical. Thus, two questions need to be addressed: (a) Why is the *ortho*-isomer (2-phenylacetyl 1-naphthol **3**)

alone formed?; and (b) Why do the primary phenylacetyl (and related) radicals not decarbonylate within zeolites, or why is the coupling of radical in cage **A** faster than decarbonylation?



Scheme 5.



If one accepts that the two reactive fragments, naphthoxy and phenylacyl radicals, would be held close to each other by the intrazeolite cations, preference for ortho coupling to yield **3a–3c** over the para coupling to yield **4a–4c** is understandable. This suggestion is based on the optimized structures for the  $Li^+$  – 1-naphthyl phenyl acetate complex shown in Fig. 2. Photofragmentation of the  $Li^+$  – 1-naphthyl phenyl acetate complex present in these structural forms would lead to naphthoxy and phenylacyl radicals being held close to each other by the alkali metal ion. Lack of separation enforced by the zeolite wall and the alkali metal ion would place the two radicals, having opposite electronic spins (favorable for bond formation), close to one another. Due to restricted mobility enforced by the alkali metal ion, the attack of the acyl fragment would occur at the nearest available position on the aromatic ring, namely the 2-position of the naphthoxy ring.

The lack of formation of products **5–9** implies that the primary radical pair **A** do not proceed to the radical pair **B**. This suggests that the recombination of the naphthoxy and phenylacyl radicals within a zeolite must be rapid compared with cage diffusion and decarbonylation of the phenylacyl radical. The rates of decarbonylation of phenylacyl and 1-methyl 2-phenylacyl and 1,1'-dimethyl 2-phenylacyl radicals have been estimated to be  $4.8 \times 10^6 \text{ s}^{-1}$ ,  $4.0 \times 10^7 \text{ s}^{-1}$ , and  $1.5 \times 10^8 \text{ s}^{-1}$ , respectively (11). It is important to note that even in **1c** where the intermediate 1,1'-dimethyl 2-phenylacyl radical decarbonylates ~30 times faster than phenylacyl radical, no decarbonylation products were obtained within zeolites and the only product obtained was 2-phenylacyl 1-naphthol **3c**. Given this, the rate of diffusion of the radical pair **A** out of the cage must be smaller than the maximum rate of decarbonylation observed in the case of 1,1'-dimethyl

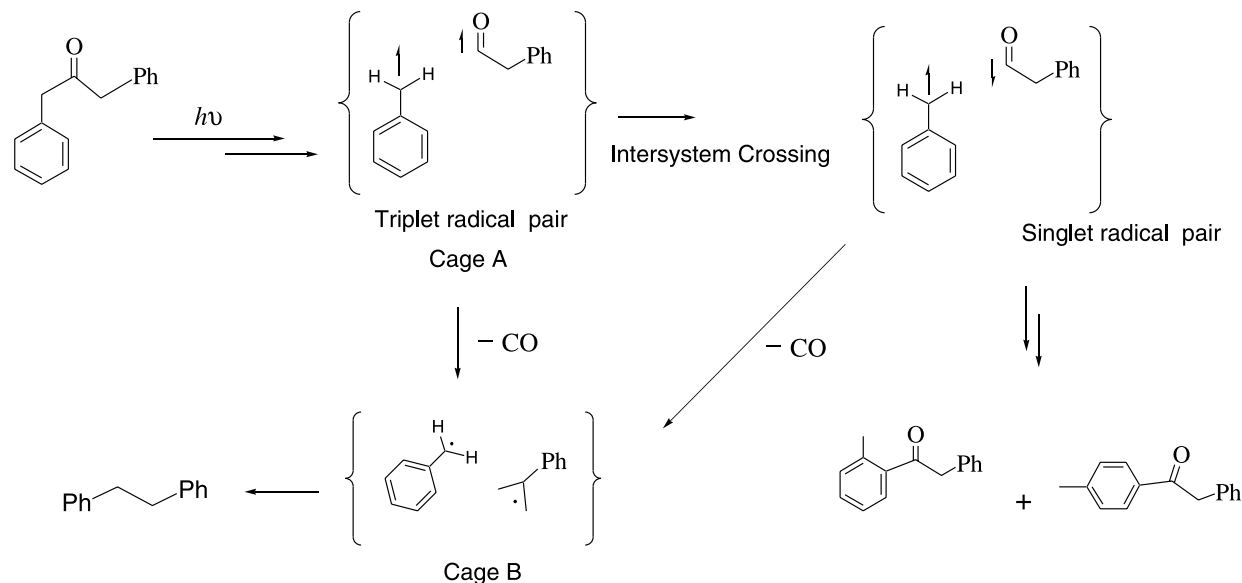
2-phenylacyl radical ( $1.5 \times 10^8 \text{ s}^{-1}$ ). In the absence of data relating to the rate of decarbonylation within zeolites, we can only speculate that the lack of products due to decarbonylation and radical pair **B** is most likely due to the fact that the rate of recombination in the case of cage pair **A** is faster than the rates of decarbonylation and cage escape. Intuitively then, if the recombination step can be slowed the decarbonylation could become competitive. This led us to explore the photochemistry of dibenzyl ketones, where the same phenylacyl radical would be produced as part of a triplet radical pair. Results of these are discussed below.

At this point, a discussion on the lack of reactivity of the naphthyl esters within heavy alkali metal ion exchanged zeolites is appropriate. An important observation within CsY and TiY was that no photoproducts from **1a–1c** were observed in these zeolites. Enhanced intersystem crossing efficiency in heavy cation exchanged zeolites and the fact that these esters are unreactive in their triplet states explain the lack of reactivity within CsY and TiY. Evidence for intersystem crossing can be found in the emission spectra for the ester **1a** in different cation exchanged zeolites shown in Fig. 1. Fluorescence predominates in light atom zeolites like LiY and NaY. Within KY and RbY, phosphorescence increases at the expense of fluorescence. In TiY there is only phosphorescence, suggesting complete population of the triplet state. Consistent with this, naphthyl esters **1a–1c** were unreactive within TiY.

Upon excitation, dibenzyl ketones similar to 1-naphthyl phenylacyl esters, yield products via two stages of radical pair formation,  $\alpha$ -cleavage to yield primary caged radical pair **A** and decarbonylation to give the secondary free radicals (or radical pair **B**) (Scheme 6) (12). An important difference among 1-naphthyl esters and dibenzyl ketones is that



Scheme 6.



the former reacts from  $S_1$  to give the singlet radical pair and the latter from  $T_1$  to give the triplet radical pair. The radical pair **A** resulting from dibenzyl ketones following intersystem crossing can undergo coupling to yield the rearrangement products 4-methylphenyl benzyl ketone and 2-methylphenyl benzyl ketone or decarbonylate (following or prior to intersystem crossing) to yield the caged radical pair **B** or diffuse apart to give two free radicals. Since intersystem crossing is required for the formation of rearrangement products, relative yields of 4-methylphenyl benzyl ketone and 2-methylphenyl benzyl ketone with respect to decarbonylated products (diphenylethanes) provides information concerning the extent of restriction imposed by zeolite cages on longer time scales (compared with 1-naphthyl phenylacetyl esters chemistry) on the radical pair **A**. Further, the dibenzyl ketone systems allow us to probe the influence of heavy cations on the intersystem crossing process in radical pairs.

Decarbonylation to give diphenylethanes is the only reaction upon irradiation of dibenzyl ketones **2a–2c** in hexane solution (Scheme 4) (12). Decarbonylation accounted for >90% of the products when the dibenzyl ketones **2a–2c** included in zeolites LiY, NaY, and KY were photolyzed. This behavior was distinctly different from that of the naphthyl esters **1a–1c** which did not decarbonylate within the same zeolites. We had indicated above that if we could slow the rate of recombination of the geminate radical pair it might be possible to observe decarbonylation of phenylacetyl radicals within zeolites. Results with the dibenzyl ketones suggest that we have achieved this goal. Because of the triplet character of the radical pair, even close proximity and lack of mobility are unable to favor the recombination of the radical pair over the decarbonylation process. The fact that the “spin” prevents the recombination of the radical pair is evident from the dependence of the product distribution on the alkali metal ion present in zeolites. Higher yields of rearrangement products (4-methylphenyl benzyl ketone and 2-methylphenyl benzyl ketone) from dibenzyl ketone were obtained within heavy alkali metal ion exchanged zeolites (Ta-

ble 3). Similar dependence of product distribution on the alkali metal ion was observed in the case of  $\alpha,\alpha'$ -dimethyldibenzyl ketone **2b**. Significantly, the ketone **2c** gave only 2,3-diphenyl-2,3-dimethyl butane,  $\alpha$ -methyl styrene, and cumene in all zeolites.

Turro and Zhang (13) rationalized the variations in the yield of the rearrangement products from **2a** within MX zeolites on the basis of “cation size effect”. Within X zeolites the yield of the rearranged products 4-methylphenyl benzyl ketone and 2-methylphenyl benzyl ketone were dependent on the size of the cation; larger the size, higher the yield. They proposed that smaller free volume within a cage would restrict the mobility of enclosed radicals and thus prolong the lifetime of the triplet radical pair. Long lifetime would favor intersystem crossing and recombination to yield the rearranged products. Thus, cations with larger sizes are predicted to yield more rearrangement products. This feature is unlikely to play a role in Y zeolites, which contain fewer cations. The supercage of X zeolites contains four type II and ~3.5 type III cations whereas Y zeolites contain four type II cations and no type III cations. Absence of type III cations makes more room for the guest molecules. Also, if cage free volume was a major factor, cation size would influence product distributions accordingly. Ionic radii of different cations are shown in Table 4. Product distributions in KY and TIY provide an ideal case to compare and discuss size effects on product formations during the photolysis of **2a**. Both cations  $K^+$  and  $Tl^+$  are of the same size but differ in their spin orbit coupling parameters by 2 orders of magnitude (Table 4). Rearrangement products are produced in much larger yields in TIY than in KY. This suggests that size is not the most important parameter in deciding selectivity within Y zeolites.

A comparison of the results observed with dibenzyl ketones and 1-naphthyl phenylacetyl esters provides an insight into how a zeolite may be influencing the reactivity of intermediates generated within its cages. First, let us compare the behavior of dibenzyl ketone **2a** and 1-naphthyl phenylacetyl ester **1a**. Both systems upon photolysis generate phenylacetyl



**Table 4.** Ionic radii and spin-orbit coupling constants for different cations exchanged into the zeolites.

Cation	Ionic radius of the cation <sup>a</sup>	Spin-orbit coupling constants <sup>b</sup> for the corresponding atom $\zeta$ cm <sup>-1</sup>
Li <sup>+</sup>	0.86	0.23
Na <sup>+</sup>	1.12	11.5
K <sup>+</sup>	1.44	38
Rb <sup>+</sup>	1.58	160
Cs <sup>+</sup>	1.84	370
Tl <sup>+</sup>	1.40	3410

<sup>a</sup>See F.A. Cotton and G. Wilkinson. *Advanced Inorganic Chemistry*. V ed. Wiley-Interscience, New York. 1988. p. 124 and 209.

<sup>b</sup>Numbers taken from S.L. Murov, I. Carmichael, and G.L. Hug. *Handbook of photochemistry*. Marcel Dekker, New York. 1988. pp. 338–341.

radical. In NaY while **1a** quantitatively rearranged to **3**, **2a** gave only 10% of the rearranged products **12** and **13** (Scheme 4). Clearly, in the later case, the phenylacyl radical decarbonylates before it has a chance to recombine to form the rearranged products. This difference, we believe, is the result of the spin state of the geminate radical pair. When a mechanism to spin interconversion is provided as with TIY, the yields of the rearranged products from **2a** increased to ~79%, suggesting that the spin barrier is the main reason for the lack of rearrangement in **2a**. An insight into the process is gained by comparing the behaviors of naphthyl ester **1c** and dibenzyl ketone **2c**. While the former gives the rearranged product **3** quantitatively, the latter gives only the corresponding decarbonylated product **11c**. In this case due to the presence of  $\alpha$ -methyl groups, the decarbonylation occurs 30 times faster than in unsubstituted phenyl acyl radical (compare the rates of decarbonylation of phenylacyl and 1,1'-dimethyl 2-phenylacyl radicals:  $4.8 \times 10^6$  s<sup>-1</sup> and  $1.5 \times 10^8$  s<sup>-1</sup>) (11). Since we would have detected 1% of the rearranged product by GC, we believe that the rate of Tl<sup>+</sup> induced ISC in the geminate pair (**A**<sup>3</sup> to **A**<sup>1</sup>, Scheme 6) must be  $<1 \times 10^6$  s<sup>-1</sup>. Thus, a comparison of the results observed with dibenzyl ketones and naphthyl esters suggest that lack of products due to decarbonylation in the case of naphthyl esters **1a–1c** is due to the fact that the primary radical pair **A** is formed in the singlet state. Based on the computed structures for lithium ion – dibenzyl ketone complexes (Fig. 3), one would expect that the radical pairs resulting from fragmentation of dibenzyl ketone would be held close to each other within a zeolite cage. The structures of the complexes being similar in dibenzyl ketone and 1-naphthyl phenyl acetate one would expect the primary radical pair to be positioned in a similar manner from the two systems within a zeolite cage facilitating the formation of the rearranged products. The lack of rearranged products in the dibenzyl ketone system within LiY and NaY suggests that restricting the mobility of the radical pair near one another alone is not sufficient. Coupling between the two radicals can occur only when they have the singlet spin. In dibenzyl ketone systems where the radical pair is produced in the triplet state the limiting factor for coupling is the spin. When the mechanism for spin interconversion becomes available as within heavy cation exchanged zeolites the rearranged products are formed. Thus, the cations serve two roles: they restrict the

mobility of the radical pair and provide a mechanism for spin interconversion.

## Summary

Photochemistry of a series of 1-naphthyl phenylacyl esters and dibenzyl ketones were investigated in different cation exchanged zeolites. Naphthyl esters which give eight products in isotropic solution give essentially a single product within light alkali metal ion exchanged zeolites. Consistent with the known triplet reactivity of these molecules, within heavy alkali metal ion exchanged zeolites no photoproducts were obtained. Most importantly, within light alkali metal ion exchanged zeolites these molecules do not undergo decarbonylation. The reaction stops at the stage of the primary radical pair and observed products are formed from this radical pair. Alkali metal ion binding to the reactant ester in a cooperative fashion to two parts of the reactant molecule is suggested to favor recombination of the primary radicals (**A**) at the nearest possible site, namely the 2-position of the naphthoxy ring. Such effects fail to stop decarbonylation when the primary radical pair is formed in the triplet state. A comparison of the photobehavior of dibenzyl ketones with that of naphthyl esters reveals this facet of the mechanism. Results presented here suggest that it is possible to steer the course of a photoreaction and direct the formation of a specific photoproduct by using zeolites as reaction media.

## Experimental

NaY zeolite was obtained from Zeolyst International, the Netherlands. Monovalent cation exchanged (Li<sup>+</sup>, K<sup>+</sup>, Rb<sup>+</sup>, Cs<sup>+</sup>, and Tl<sup>+</sup>) zeolites were prepared by stirring 10 g of NaY with 100 mL of a 10% solution (in water) of the corresponding metal nitrate for 12 h with continuous refluxing. The zeolite was filtered and washed thoroughly with distilled water. This procedure was repeated three times. The zeolite was then heated in an oven at 120°C for about 6 h to obtain the cation exchanged zeolite used for photolysis. The exchange levels were estimated by ICP analysis and they were in the range 60–85%.

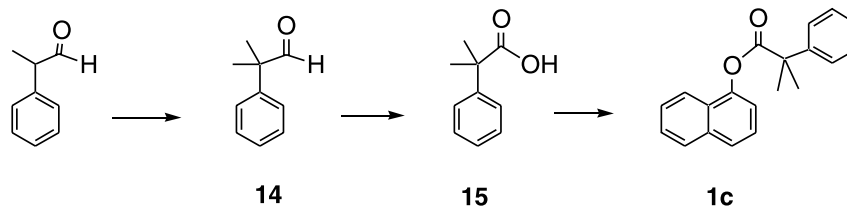
1-Naphthyl phenylacyl esters **1a** and **1b** were gifts from W. Gu and R.G. Weiss of Georgetown University. 1-Naphthyl phenylacyl ester **1c** was synthesized as per Scheme 7 (14).

### Step a

Lithium diisopropyl amide (0.02 mol) in dry THF (100 mL) was stirred under nitrogen at –78°C. To this 2 g (0.015 mol) of 2-phenyl propionaldehyde in dry THF was added dropwise with continuous stirring. To the resulting orange dispersion 2.7 g (0.02 mol) of methyl iodide was added dropwise. The mixture was stirred for 12 h and then poured over an ice water mixture and extracted with three 20 mL portions of diethyl ether. The ether layer was dried with anhyd MgSO<sub>4</sub>, filtered, and evaporated to give a crude mixture of the product aldehyde (**14**). Pure **14** was obtained by purification using column chromatography (silica gel and hexane); yield: 35%. MS data: 148 (M<sup>+</sup>, 6.5), 119 (97.8), 103 (14.1), 91 (100), 77 (28.3), 65 (8.7), 51 (27.2), 41 (54.3).



Scheme 7.

**Step b**

Silver oxide was prepared by adding a solution of 5.1 g (0.03 mol) of  $\text{AgNO}_3$  in 10 mL of water to a solution of 2.4 g (0.06 mol) of NaOH in 10 mL of water. Continuous shaking during the addition ensured complete reaction and resulted in a brown semisolid mixture. This mixture was cooled with an ice bath and 2 g (0.014 mol) of the aldehyde **14** was added slowly with continuous stirring. The oxidation reaction was allowed to proceed for 2 h. The black silver suspension was removed by suction filtration and was washed with warm water. The combined filtrate was allowed to cool and the washings were acidified with concentrated hydrochloric acid precipitating about 1.8 g of the corresponding acid (**15**); yield: 70%. MS data: 164 ( $\text{M}^+$ , 23.5), 119 (100), 103 (12.2), 91 (73.5), 77 (20.4), 65 (6.1), 51 (17.3), 41 (30.6).

**Step c**

The acid, **15** (2 g) (0.012 mol), 1.76 g (0.012 mol) of 1-naphthol, 2.5 g (0.012 mol) of DCC, and 0.15 g (0.0012 mol) of DMAP were mixed together in 50 mL of dry methylene chloride. The mixture was stirred under nitrogen for 12 h. The resulting suspension was then filtered to remove the white residue. The filtrate was washed with water and aqueous acetic acid (5%). The resulting methylene chloride solution was then dried with anhydrous  $\text{MgSO}_4$  giving a crude mixture of the product ester **1c**. The mixture was purified by column chromatography, eluting with petroleum ether, then with 5% methylene chloride in petroleum ether, and finally with 1% ethyl acetate in petroleum ether. Yield: 23%. The resulting ester was a thick viscous colourless liquid.  $^1\text{H}$  NMR ( $\text{CDCl}_3$ , 400 MHz)  $\delta$ : 1.89 (s, H), 7.18 (1H, d), 7.35–7.55 (7H, m), 7.6 (2H, d), 7.73 (2H, d), 7.85 (2H, d).  $^{13}\text{C}$  NMR ( $\text{CDCl}_3$ , 100 MHz)  $\delta$ : 26.4, 47, 118, 121, 125.5, 126 (Ar-C), 126.5, 127, 127.3, 128, 128.8, 134.8, 144, 146.8, 175.2. MS data  $m/e$  (relative intensity): 290 ( $\text{M}^+$ , 14.7), 144 (75), 119 (100), 115 (41.2), 103 (10.3), 91 (51.5), 77 (13.2), 63 (10.3), 41 (32.4).

Dibenzyl ketone (**2a**) was used as obtained from Aldrich. Dibenzyl ketones **2b** and **2c** were synthesized following the procedure described below.

**Synthesis of  $\alpha,\alpha'$ -dimethyl dibenzyl ketone (2b) (15)**

Dibenzyl ketone (**2a**) (1 g, 0.005 mol) dissolved in 15 mL of dry THF was added dropwise to the cooled solution ( $-10^\circ\text{C}$ ) of potassium hydride (0.4 g, 0.01 mol) in 15 mL dry THF. The resulting light yellow suspension was allowed to stir for 30 min and then 0.62 mL (0.01 mol) of methyl iodide was added dropwise. The white suspension formed was allowed to stir for 12 h, acidified with dil. HCl and extracted with diethyl ether. The ether layer was dried with anhydrous  $\text{MgSO}_4$  and evaporated to give a crude product mixture. Pure **2b** was

obtained by column chromatography eluting with 2% ethyl acetate in petroleum ether. The product was a colorless oil; yield 31%.  $^1\text{H}$  NMR ( $\text{CDCl}_3$ , 400 MHz)  $\delta$ : 1.35, 1.45 (d, 3H), 3.9, 4 (q, 1H), 7–7.5 (10 H, m).  $^{13}\text{C}$  NMR ( $\text{CDCl}_3$ , 100 MHz)  $\delta$ : 18.5, 19, 51, 51.7, 140.2, 141, 141.8, 143.2, 210.3, 211.3. MS data  $m/e$  (relative intensity): 238 ( $\text{M}^+$ , 4.4), 133 (10.3), 128 (2.9), 105 (100), 89 (1.5), 77 (17.6), 63 (1.5), 51 (5.9), 39 (2.9).

**Synthesis of  $\alpha,\alpha',\alpha',\alpha'$ -tetramethyl dibenzyl ketone (2c) (15)**

Dibenzyl ketone (**2a**) (1 g, 0.005 mol) dissolved in 15 mL of dry THF was added dropwise to the cooled solution ( $-10^\circ\text{C}$ ) of potassium hydride (0.8 g, 0.02 mol) in 15 mL dry THF. The resulting light yellow suspension was allowed to stir for 30 min and then 1.24 mL (0.02 mol) of methyl iodide was added to the solution dropwise. The white suspension formed was allowed to stir for 12 h at room temperature, acidified with dil. HCl, and extracted with diethyl ether. The ether layer was dried with anhydrous  $\text{MgSO}_4$  and evaporated to give a crude product mixture. Pure **2c** was obtained by column chromatography, eluting on a silica gel column with 2% ethyl acetate in petroleum ether. The product was a white solid; yield 81%.  $^1\text{H}$  NMR ( $\text{CDCl}_3$ , 400 MHz)  $\delta$ : 1.3 (s, 12 H), 7.18–7.3 (10H, m, Ar-H).  $^{13}\text{C}$  NMR ( $\text{CDCl}_3$ , 100 MHz)  $\delta$ : 28 ( $-\text{CH}_3$ ), 53.2 ( $-\text{C}(\text{CH}_3)_2$ ), 125.8 (Ar-C), 126.5 (Ar-C), 128.5 (Ar-C), 144.5 (Ar-C), 213.4 ( $\text{C}=\text{O}$ ). MS data  $m/e$  (relative intensity): 266 ( $\text{M}^+$ , 0.9), 147 (6.8), 119 (100), 103 (4.5), 91 (45.5), 77 (9), 51 (4.5), 41 (18).

**Identification of photoproducts**

Photoproducts from **1a** and **1b** have been identified previously by W. Gu and R.G. Weiss of Georgetown University. The spectra of the photoproducts **3a–10a** and **3b–10b** agreed with the reported data. Authentic samples provided by Gu and Weiss were used to identify the GC peaks. Irradiation of **1c** in hexane gave 1-naphthol, **9c**, and **3c** as the major products. An authentic sample obtained from Aldrich was used to identify 1-naphthol. The spectral data for **9c** and **3c** are shown below: For **9c**:  $^1\text{H}$  NMR ( $\text{CDCl}_3$ , 400 MHz)  $\delta$ : 1.34 (s), 7.06–7.5 (10 H, m).  $^{13}\text{C}$  NMR ( $\text{CDCl}_3$ , 100 MHz)  $\delta$ : 25.2, 43.6, 125.5, 126.8, 128.6, 146.8. MS data  $m/e$  (relative intensity): 238 ( $\text{M}^+$ , 0.5), 128 (0.5), 119 (100), 91 (50), 77 (9.2), 65 (2.6), 51 (3.9), 41 (17). The other photoproducts from ester **1c** were assigned by comparing their GC retention times with similar products from the photolysis of esters **1a** and **1b**.

Photoproducts upon photolysis of dibenzylketones namely diphenylethane (**11**), cumene (**17**), and  $\alpha$ -methyl styrene (**18**) were compared to the original samples obtained from Aldrich. Products **14** and **19** were prepared by preparative photolysis of **2b** and **2c**, respectively, in hexane. Spectral data for **14**:  $^{13}\text{C}$  NMR ( $\text{CDCl}_3$ , 400 MHz)  $\delta$ : 18.5, 19, 46.5,



47.5, 126.2, 127.9, 128.5, 146. MS data  $m/e$  (relative intensity): 210 (4.4), 106 (8.9), 105 (100), 91 (3.3), 77 (15.6), 65 (2.2), 51 (5.6), 39 (3.3). For **19**:  $^1\text{H}$  NMR ( $\text{CDCl}_3$ , 400 MHz)  $\delta$ : 1.34 (s), 7.06–7.5 (10 H, m).  $^{13}\text{C}$  NMR ( $\text{CDCl}_3$ , 100 MHz)  $\delta$ : 25.2, 43.6, 125.5, 126.8, 128.6, 146.8. MS data  $m/e$  (relative intensity): 238 (0.5), 128 (0.5), 119 (100), 91 (50), 77 (9.2), 65 (2.6), 51 (3.9), 41 (17).

#### Synthesis of 2-methyl phenyl benzyl ketone (12) and 4-methyl phenyl benzyl ketone (13)

In a small round-bottomed flask, 0.5 g (0.003 mol) of the corresponding acid chloride (2-methyl benzoyl chloride or 4-methyl benzoyl chloride) was added to 15 mL dry THF. This mixture was kept stirring at  $-10^\circ\text{C}$  under a nitrogen atmosphere. A benzyl magnesium chloride (0.0025 mol) suspension in THF was added dropwise to the above solution. The light yellow solution was allowed to stir for 12 h at room temperature ( $25^\circ\text{C}$ ) followed by addition of satd  $\text{NH}_4\text{Cl}$  solution in water and extraction with three 20 mL portions of diethyl ether. The ether layers were combined, dried with anhyd  $\text{MgSO}_4$ , and evaporated to give a crude product mixture. Pure **12** or **13** was then obtained by column chromatography, eluting on a silica gel column with 2% ethyl acetate in petroleum ether. For **12**:  $^1\text{H}$  NMR ( $\text{CDCl}_3$ , 400 MHz)  $\delta$ : 2.45 (s), 4.23 (s), 7.2–7.4 (8H, m), 7.74 (1H, d).  $^{13}\text{C}$  NMR ( $\text{CDCl}_3$ , 100 MHz)  $\delta$ : 21.3, 48.5, 125.5, 126.8, 128.5, 130, 132, 133, 134.5, 136.6, 137.6, 138.8, 201.5. MS data  $m/e$  (relative intensity): 210 (2.7), 165 (1.1), 119 (100), 91 (69.4), 65 (48.6), 51 (8.3), 39 (25). For **13**:  $^1\text{H}$  NMR ( $\text{CDCl}_3$ , 400 MHz)  $\delta$ : 2.42 (s), 4.28 (s), 7.22–7.38 (7H, m), 7.94 (2H, d).  $^{13}\text{C}$  NMR ( $\text{CDCl}_3$ , 100 MHz)  $\delta$ : 21.7, 45.4, 127.6, 129.4, 129.6, 130.1, 130.2, 135, 135.6, 144.9, 198.5. MS data  $m/e$  (relative intensity): 210 (2.7), 165 (1.4), 119 (100), 91 (48.6), 65 (37.8), 51 (6.8), 39 (17.6).

#### Synthesis of 2-ethyl phenyl $\alpha$ -methyl benzyl ketone (15) and 4-ethyl phenyl $\alpha$ -methyl benzyl ketone (16)

Ethyl benzene (10 g) (0.09 mol) and 14.5 g (0.094 mol) of phenyl acetyl chloride were placed in a small round-bottomed flask. Into a conical flask, 12.5 g (0.09 mol) of  $\text{AlCl}_3$  was weighed out and this solid was added with frequent shaking to the contents of the round-bottomed flask. The mixture turned dark green with evolution of HCl gas during the addition. After addition was complete, a reflux condenser was attached and the round-bottomed flask was heated on a water bath for 3 h. The contents of the flask were poured into a mixture of crushed ice and concd HCl with continuous stirring. The resultant water layer was extracted with five 25 mL portions of diethyl ether. The ether layers were combined, dried with anhyd  $\text{MgSO}_4$ , and evaporated to give a crude product mixture. The non-methylated precursors to **15** and **16** could be isolated by column chromatography, eluting on a silica gel column with a 5% ethyl acetate in petroleum ether mixture. They were then methylated using the procedure used for the ketones **2b** and **2c** described earlier. Purification by silica gel chromatography, eluting with 2% ethyl acetate in petroleum ether afforded pure **15** and **16**. Spectral data for **15**: white colored solid.  $^1\text{H}$  NMR ( $\text{CDCl}_3$ , 400 MHz)  $\delta$ : 1.25 (t), 1.6 (d), 2.7 (q), 4.7 (q), 7.23–7.45 (8H, m), 7.76 (1H, d).  $^{13}\text{C}$  NMR: ( $\text{CDCl}_3$ , 100 MHz)  $\delta$ : 16, 20, 29, 48, 127, 128.2, 128.5, 129, 130.2,

134.5, 142, 149.8, 200. MS data  $m/e$  (relative intensity): 238 (1.9), 165 (1.3), 133 (100), 119 (3.7), 105 (22.2), 91 (5.6), 77 (18.2), 51 (5.6), 39 (3.7). For **16**: light orange colored solid.  $^1\text{H}$  NMR ( $\text{CDCl}_3$ , 400 MHz)  $\delta$ : 1.25 (t, 3H), 1.6 (d, 3H), 2.7 (q, 2H), 4.7 (q, 1H), 7.2–7.4 (7H, m), 7.95 (2H, d).  $^{13}\text{C}$  NMR ( $\text{CDCl}_3$ , 100 MHz)  $\delta$ : 16, 20, 29, 48, 127, 128.2, 128.5, 129, 130.2, 134.5, 142, 149.8, 200. MS data  $m/e$  (relative intensity): 238 (1.6), 165 (1.6), 133 (100), 105 (21.8), 89 (4.7), 77 (15.6), 51 (6.3), 39 (3.1).

#### Photolysis

Known amounts of substrate (3 mg) and activated ( $450^\circ\text{C}$ , air oven) zeolite (300 mg) were stirred together in hexane for at least 6 h, filtered, and washed with excess hexane. GC analysis of the hexane layer made sure that all substrate was loaded into the zeolite. The loading level was kept about 1 molecule per 12 supercages for the esters **1a–1c** and 1 molecule in 7 supercages for the ketones **2a–2c**. The “loaded” zeolite sample was transferred to fresh hexane solvent (10 mL) and photolyzed (Pyrex tubes, 450 W medium pressure mercury lamp) as a hexane slurry. A continuous nitrogen purge was maintained through the slurry during the irradiation of ketones **2a–2c**. For the esters **1a–1c**, 30% conversion was achieved upon 2 h of photolysis in zeolites LiY, NaY, and KY. The reaction proceeded very slowly in zeolites RbY and CsY and was almost completely absent in TiY. A 30% conversion was achieved after 2 h of irradiation for ketone **2a**, 1 h of irradiation for ketone **2b**, and 30 min of irradiation for ketone **2c**. GC analysis of the hexane layer of the irradiated slurry confirmed that all the products and the reactant remained within the zeolite. After irradiation, the samples were extracted with a 5% water in THF solution and analyzed on a GC (Hewlett-Packard 5890 (FID detector), column SPB-5 (30 m, 0.32 mm i.d., 1.0 mm film thickness)). The conditions used for the GC run for esters **1a–1c** were: initial temperature ( $100^\circ\text{C}$ ), initial time (1 min), rate ( $5^\circ\text{C}$  per min), final temperature ( $250^\circ\text{C}$ ), final time (10 min). The GC conditions used for ketone **2a** were: initial temperature ( $100^\circ\text{C}$ ), initial time (1 min), rate ( $2^\circ\text{C}$  per min), final temperature ( $160^\circ\text{C}$ ), final time (10 min), rate A ( $10^\circ\text{C}$  per min), final temperature A ( $250^\circ\text{C}$ ), final time A (1 min). GC conditions used for ketones **2b** and **2c** were: initial temperature ( $100^\circ\text{C}$ ), initial time (1 min), rate ( $5^\circ\text{C}$  per min), final temperature ( $250^\circ\text{C}$ ), final time (10 min). In general, mass balance as followed by using a calibration compound on a GC was found to be  $\sim 85\%$ . The calibration compound used for the esters **1a–1c** was 1-naphthyl acetate and for the ketones **2a–2c** was phenyl phenyl acetate.

#### Absorption spectra

Absorption spectra were recorded using a Shimadzu 2101 PC UV–vis spectrophotometer with a diffuse reflectance accessory attachment. The dried zeolite samples were packed into a 2 mm quartz cuvette (in a dry box) and sealed with teflon tape. Conversion of the reflectance spectra to the absorption spectra was carried out using a Kubelka–Munk program supplied with the instrument.

#### Emission spectra

Emission spectra were recorded for the three naphthyl esters **1a–1c**. The spectra were recorded on a Edinburgh FS-



900 CDT spectrofluorimeter. Solid zeolite samples were taken in quartz ESR tubes placed in a quartz cylindrical Dewar, and the emissions collected at right angles were recorded. The ester samples were excited at 290 nm. The fluorescence  $\lambda_{\text{max}}$  was 340 nm and the phosphorescence  $\lambda_{\text{max}}$  was 525 nm. Lifetime measurements were carried out on an Edinburgh FL-900 CDT single photon counter using a hydrogen filled ns flashlamp (40 KHz) as the light source. The samples were excited at 290 nm, and the emitted photons were collected at the peak maximum of the fluorescence bands of the adsorbed substrates. The lamp profile was collected with ludox as the scattering medium. The observed decays were fitted using the distribution or the exponential analysis program supplied with the instrument. The lifetimes were fitted to an exponential fit. The suitability of the fit was ascertained by a  $\chi^2$  value close to unity. The decays within the zeolites were usually biexponential.

### Computations

Geometry optimizations were carried out using the restricted hybrid Hartree–Fock density functional theory (RB3LYP) with Becke three parameter exchange functional in conjunction with correlation functional by Lee, Yang, and Parr (LYP). The 6-31G(d) basis set was used for C, H, O, Li. Stationary points have been characterized as true minima by frequency calculations. All of the calculations were carried out using the Gaussian 98 series of programs (10).

### Acknowledgement

It is a pleasure to thank Professors R.G. Weiss and N.J. Turro for very useful and stimulating discussions. We also thank W. Gu and R.G. Weiss for providing authentic samples at the beginning and at various stages of the project. The authors thank the National Science Foundation (CHE-9904187 and CHE-0212042) for support of the research summarized here.

### References

- (a) D. Bellus. *Adv. Photochem.* **8**, 109 (1971); (b) D. Bellus and P. Hrdlovic. *Chem. Rev.* **67**, 599 (1967); (c) V.I. Stenborg. *Org. Photochem.* **1**, 127 (1967); (d) M.A. Miranda. *In Handbook of organic photochemistry and photobiology. Edited by W.M. Horspool and P.S. Song.* CRC Press, Boca Raton. 1995. pp. 570.
- (a) K. Pitchumani, M. Warrier, and V. Ramamurthy. *J. Am. Chem. Soc.* **118**, 9428 (1996); (b) K. Pitchumani, M. Warrier, and V. Ramamurthy. *Res. Chem. Intermed.* **25**, 623 (1999); (c) W. Gu, M. Warrier, B. Schoon, V. Ramamurthy, and R.G. Weiss. *Langmuir*, **16**, 6977 (2000).
- K. Pitchumani, M. Warrier, C. Cui, R.G. Weiss, and V. Ramamurthy. *Tetrahedron Lett.* 6251 (1996).
- (a) S. Vasenkov and H. Frei. *J. Am. Chem. Soc.* **120**, 4031 (1998); (b) S. Vasenkov and H. Frei. *J. Phys. Chem. A*, **104**, 4327 (2000).
- (a) W. Gu, M. Warrier, V. Ramamurthy, and R.G. Weiss. *J. Am. Chem. Soc.* **121**, 9467 (1999); (b) M. Warrier, N.J. Turro, and V. Ramamurthy. *Tetrahedron Lett.* **41**, 7163 (2000).
- (a) W. Gu and R.G. Weiss. *Tetrahedron*, **56**, 6913 (2000); (b) W. Gu and R.G. Weiss. *J. Photochem. Photobiol. C*, **2**, 117 (2001).
- V. Ramamurthy, J.V. Caspar, D.F. Eaton, E.W. Kuo, and D.R. Corbin. *J. Am. Chem. Soc.* **114**, 3882 (1992).
- (a) P.S. Engel. *J. Am. Chem. Soc.* **92**, 6074 (1970); (b) W.K. Robbins and R.H. Eastman. *J. Am. Chem. Soc.* **92**, 6076 (1970); (c) N.J. Turro and W.R. Cherry. *J. Am. Chem. Soc.* **100**, 7431 (1978); (d) N.J. Turro and B. Kraeutler. *Acc. Chem. Res.* **13**, 369 (1980).
- Such rearrangement products were first reported by Turro, de Mayo, and co-workers: (a) N.J. Turro, D.R. Anderson, and B. Kraeutler. *Tetrahedron Lett.* **21**, 3 (1980); (b) B. Frederick, L.J. Johnston, P. de Mayo, and S.K. Wong. *Can. J. Chem.* **62**, 403 (1984).
- M.J. Frisch, G.W. Trucks, H.B. Schlegel, G.E. Scuseria, M.A. Robb, J.R. Cheeseman, V.G. Zakrzewski, J.A. Montgomery, Jr., R.E. Stratmann, J.C. Burant, S. Dapprich, J.M. Millam, A.D. Daniels, K.N. Kudin, M.C. Strain, O. Farkas, J. Tomasi, V. Barone, M. Cossi, R. Cammi, B. Mennucci, C. Pomelli, C. Adamo, S. Clifford, J. Ochterski, G.A. Petersson, P.Y. Ayala, Q. Cui, K. Morokuma, D.K. Malick, A.D. Rabuck, K. Raghavachari, J.B. Foresman, J. Cioslowski, J.V. Ortiz, B.B. Stefanov, G. Liu, A. Liashenko, P. Piskorz, I. Komaromi, R. Gomperts, R.L. Martin, D.J. Fox, T. Keith, M.A. Al-Laham, C.Y. Peng, A. Nanayakkara, C. Gonzalez, M. Challacombe, P.M.W. Gill, B. Johnson, W. Chen, M.W. Wong, J.L. Andres, C. Gonzalez, M. Head-Gordon, E.S. Replogle, and J.A. Pople. *Gaussian 98, Revision A.9.* Gaussian, Inc., Pittsburgh, Penn. 1998.
- (a) L. Lunazzi, K.U. Ingold, and J.C. Scaiano. *J. Phys. Chem.* **87**, 529 (1983); (b) N.J. Turro, I.R. Gould, and B.H. Baretz. *J. Phys. Chem.* **87**, 531 (1983).
- (a) I.R. Gould, N.J. Turro, and M.B. Zimmt. Magnetic field and magnetic isotope effects on the product of organic reactions. *In Advances in physical organic chemistry. Vol. 20. Edited by V. Gold and D. Bethell.* Academic Press, H.B. Jovanovich, London. 1984. pp. 1; (b) N.J. Turro. *Pure Appl. Chem.* **67**, 199 (1995); (c) N.J. Turro. *Acc. Chem. Res.* **33**, 637 (2000); (d) N.J. Turro. *Pure Appl. Chem.* **58**, 1219 (1986).
- N.J. Turro and Z. Zhang. *Tetrahedron Lett.* **28**, 5637 (1987).
- (a) E. Campaigne and W.M. Leuser. *In Organic syntheses Coll. IV. Edited by N. Rabjohn.* John Wiley and Sons, New York. pp. 919; (b) A. Hassner and V. Alexanian. *Tetrahedron Lett.* 4475 (1978).
- A.A. Millard and M.W. Rathke. *J. Org. Chem.* **43**, 1834 (1978).



# A generally applicable synthetic approach for heteroleptic thiolate complexes of bismuth

Lisa Agocs, Glen G. Briand, Neil Burford, Melanie D. Eelman, Nadia Aumeerally, Deanna MacKay, Katherine N. Robertson, and T. Stanley Cameron

**Abstract:** As part of a systematic development of bismuth coordination chemistry, we are exploiting the thermodynamic and hydrolytic stability of Bi—S bonds. A series of heteroleptic thiolate bismuth complexes have been isolated and characterized. The generally applicable synthetic methodology involves the use of hetero-bifunctional ligands containing a thiolate moiety as an anchor to facilitate coordinate interaction of weak donors (carbonyls, amines, hydroxyls) with bismuth. The bifunctional nature of the ligands is manifested in chelating roles. Important comparisons with established thiolate complexes of bismuth are discussed.

**Key words:** bismuth, thiolate, heteroleptic, crystallography.

**Résumé :** Dans le cadre d'un développement systématique de la chimie de coordination du bismuth, on essaye d'exploiter la stabilité thermodynamique et hydrolytique des liaisons Bi—S. On a isolé et caractérisé une série de complexes hétéroleptiques de thiolate de bismuth. La méthode de synthèse généralement applicable implique l'utilisation de ligands hétéro-bifonctionnels comportant une portion thiolate agissant comme ancre pour faciliter l'interaction du coordinaat des donneurs faibles (carbonyles, amines, hydroxyles) avec le bismuth. La nature bifonctionnelle des ligands se manifeste dans les rôles d'agents chélatant. On discute d'importantes comparaisons avec des complexes bien établis de thiolate de bismuth.

**Mots clés :** bismuth, thiolate, hétéroleptique, cristallographie.

[Traduit par la Rédaction]

## Introduction

Bismuth compounds have been used to treat a variety of medical disorders for over 200 years (1). Most obvious is the widespread gastrointestinal application of the commercially available preparations Pepto-Bismol® and De-Nol®, which contain “bismuth subsalicylate” (BSS) and “colloidal bismuth subcitrate” (CBS), respectively. However, the mechanisms of bioactivity are not understood and chemical characterization of these compounds remains incomplete. Indeed, the chemical database for bismuth is still superficially developed.

The high thermal and hydrolytic stability of the sulfur–bismuth bond are responsible for the fact that sulfur compounds represent the most extensive series of bismuth complexes for which there is a reliable set of data (2). We have recently developed a series (3, 4) of bismuth thiolates. Their antimicrobial behaviour (5) and ulcer healing capabilities (6) suggest a structure–bioactivity relationship for the bismuth environment. In this context, it is interesting to see that BSS and bismuth nitrate react readily with thiol-based biomolecules to give predictable complexes (7), leading us to specu-

late that the biochemical fate of bismuth pharmaceuticals begins with thiolation.

It is now necessary to devise universally applicable synthetic procedures that enable rational development of the thiolate coordination chemistry for bismuth in the presence of other donors. To this end, we have examined complexes with hetero-bifunctional ligands bearing a thiolate functionality that serves as an anchor to promote or assist interaction of weaker tethered donors with bismuth. This has enabled us to control the reaction stoichiometry, giving access to series of complexes bearing one (1), two (2), and three (3) thiolate ligands (4, 8). Molecular drawings 1–11 illustrate connectivity only, as drawings of these complexes aimed at describing bonding features (e.g., Lewis) are not meaningful or are misleading.

We now report the first systematic preparation and comprehensive characterization of heteroleptic thiolate complexes of bismuth. Facile synthesis and isolation of the chlorodithiolate complexes 4 and 5 (9) highlights their suitability as precursors to dithiolate–aminothiolates 6a (R = Me) and 7a, dithiolate–hydroxythiolates 6b and 7b, and the dithiolate–esterthiolate 8. Compound 1b is also versatile and

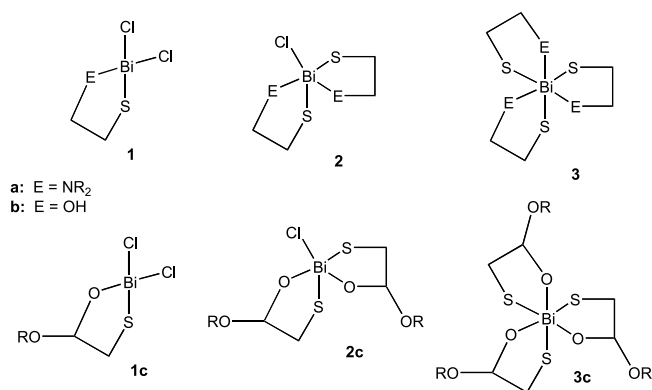
Received 4 February 2003. Published on the NRC Research Press Web site at <http://canjchem.nrc.ca> on 28 May 2003.

This article is dedicated to Professor Donald Arnold in recognition of his outstanding contributions to chemistry in Canada.

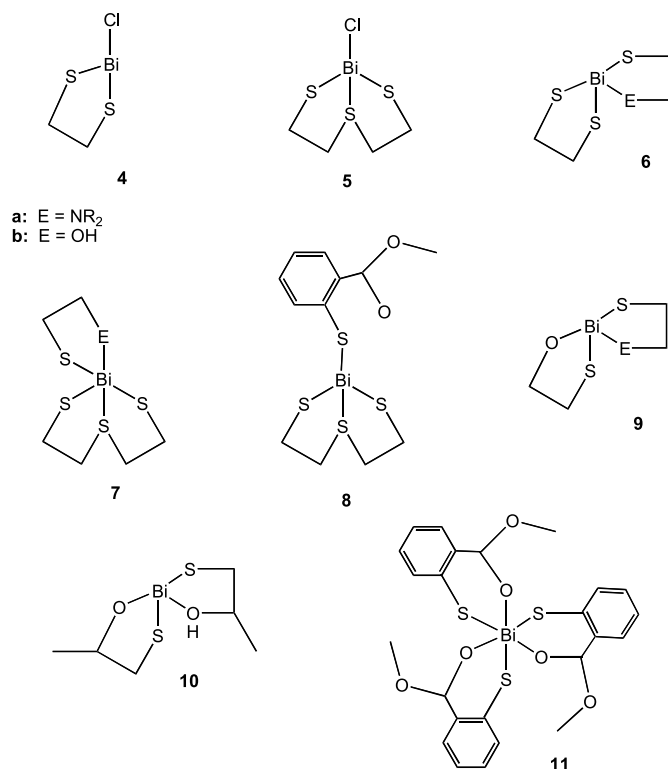
L. Agocs, G.G. Briand, N. Burford,<sup>1</sup> M.D. Eelman, N. Aumeerally, D. MacKay, K.N. Robertson, and T.S. Cameron.  
Department of Chemistry, Dalhousie University, Halifax, NS B3H 4J3, Canada.

<sup>1</sup>Corresponding author (e-mail: [neil.burford@dal.ca](mailto:neil.burford@dal.ca)).





has allowed for the isolation of an oxothiolate–aminothiolate **9a** (R = H). The compounds are rare, resilient examples of amino-, alkoxo-, and ester-complexes of bismuth.



## Experimental

### General

Bismuth chloride, 2-mercaptoethanol, 2-aminoethanethiol hydrochloride, *N,N*-dimethylaminoethanethiol hydrochloride, *N,N*-diethylaminoethanethiol hydrochloride, methyl thio-salicylate, and 1,2-ethanedithiol were used as received from Aldrich. Potassium hydroxide was used as received from BDH. All reactions were performed at room temperature under an atmosphere of nitrogen. All isolated products are air stable. Melting points were recorded on an Electro-thermal melting point apparatus. IR spectra were recorded as Nujol mulls on CsI plates using a Nicolet 510P spectrometer or a Bruker Vector 22 spectrometer. Raman spectra were obtained for powdered and crystalline samples on a Bruker RFS 100 spectrometer. Vibrational spectra are presented as

wavenumber (cm<sup>-1</sup>) maxima with ranked intensities for each absorption given in parentheses (the most intense peak is given a ranking of 1). Chemical analyses were performed by Canadian Microanalytical Service Ltd., Delta, British Columbia.

### Synthetic procedures

Compounds **6–8** were prepared according to a general procedure involving the dropwise addition of an ethanolic solution (50 mL) of thiol and KOH to a stirred slurry of **4** or **5** in ethanol (50 mL). The resulting reaction mixtures were allowed to stir overnight at room temperature. The precipitates were suction filtered using a Buchner funnel and washed with two 10 mL aliquots of water. Reagents are presented in Table 1 along with yields, elemental analyses, melting points, and vibrational spectroscopic data for each compound.

Compound **6b** was also obtained by the dropwise addition of 1,2-ethanedithiol to an aqueous solution of bis(2-hydroxy-ethanethiolato)bismuth(III) chloride (**2b**) (**3**) (100 mL). The reaction was stirred overnight at room temperature and suction filtered.

Compound **9a** was prepared by addition of a solution of KOH and 2-mercaptoethanol in ethanol (50 mL) to a slurry of bismuth chloride in ethanol (50 mL). The resulting yellow reaction mixture was stirred for 3 h at which point an ethanolic solution (50 mL) containing KOH and 2-amino-ethanethiol chloride was added dropwise. This reaction mixture was allowed to stir overnight at room temperature. The reaction mixture was suction filtered.

Compounds **6a–9a** were crystallized from filtrates reduced in volume on a rotary evaporator and cooled in the refrigerator (4°C) for 1 day to give yellow needles (**6a**) or left to evaporate slowly over a period of 4 days to give yellow needles (**7a**, **8**) or green-gold plates (**9a**). Compound **6b** was isolated as an analytically pure powder and was recrystallized as green-gold cubic crystals from hot DMF.

### X-ray crystallography

Data were collected on a Rigaku AFC5R diffractometer with graphite-monochromated Cu-K $\alpha$  radiation ( $\lambda$  = 1.54178 Å) and a 12 kW rotating anode generator. The structures were solved by direct methods (SHELXS86 (**6a**), SIR92 (**6b**, **7a**, and **9a**)) or Patterson methods (SIR92 (**8**)). They were refined by full-matrix least-squares on *F* using 1435 (**6a**) and 468 (**9a**) reflections with  $I > 3.00\sigma(I)$  or on  $F^2$  using 1298 (**6b**), 1970 (**7a**), and 1397 (**8**) unique reflections (SHELXL97) (10). Unit cell parameters were obtained from the setting angles of high angle centred reflections. The choice of space groups was based on systematically absent reflections and was confirmed by the successful solution and refinement of the structures.

All data were collected using the  $\omega$ -2 $\theta$  scan technique. The intensities of three representative reflections were measured after every 150 reflections. No decay corrections were applied. Data were corrected for Lorentz and polarization effects, and an empirical absorption correction was applied for each structure. Secondary extinction was refined for **6–8**. All of the heavy atoms were refined anisotropically for each structure except **9a**, where only Bi and S atoms were made anisotropic (the remainder being refined isotropically). Hy-



**Table 1.** Reagents, yields, elemental analyses, melting points, distinctive IR and Raman bands (ranked intensities) for **6–9a**.

Cpd	Reagents (g, mmol)	Yield (g, mmol, %)	Elemental analysis (% calcd. (found))	mp [dp] (°C)	IR bands (cm <sup>-1</sup> )	Raman (cm <sup>-1</sup> )
<b>6a</b>	<b>4</b> (3.36, 9.97), HSCH <sub>2</sub> CH <sub>2</sub> NMe <sub>3</sub> ·HCl (1.41, 9.94), KOH (1.46, 26.0)	1.56, 3.85, 39	C: 17.78 (17.50) H: 3.46 (3.38) N: 3.46 (3.27)	[165–184]	758(1), 994(2), 835(3), 1215(4), 1274(5), 919(6), 1248(7), 1270(8), 946(9), 432(10), 1166(11), 1099(12), 1054(13), 1040(14), 421(15), 1407(16), 1428(17), 528(18), 1143(19), 1123(20)	306(1), 104(2), 2891(3), 131(4), 251(5), 291(6), 76(7), 153(8), 179(9), 89(10), 265(11), 197(12), 2801(13), 357(14), 2918(15), 1157(16), 1288(17), 2945(18), 2833(19), 2966(20)
<b>6b</b>	(1) <b>4</b> (1.98, 5.89), HSCH <sub>2</sub> CH <sub>2</sub> OH (0.60, 7.66), KOH (0.43, 7.70) (2) <b>2b</b> (3.87, 9.46), HSCH <sub>2</sub> CH <sub>2</sub> SH (0.89, 9.40)	2.12, 5.62, 96  3.36, 8.89, 95	C: 12.69 (12.72) H: 2.40 (2.38)	112–114	1054(1), 988(2), 272(3), 331(4), 3222(5), 1293(6), 1279(7), 1413(8), 674(9), 440(10), 643(11), 482(12), 440(13), 1236(14), 1012(15), 929(16),	283(1), 137(2), 123(3), 301(4), 100(5), 185(6), 212(7), 159(8), 79(9), 667(11), 482(12), 644(13)
<b>7b</b>	<b>5</b> (0.375, 0.946), HSCH <sub>2</sub> CH <sub>2</sub> NH <sub>3</sub> · HCl (0.135, 1.19), KOH (0.151, 2.69)	0.21, 0.48, 51	C: 16.51 (16.56) H: 2.98 (3.19) N: 3.21 (3.16)	[107–145]	269(1), 839(2), 893(3), 1641(4), 811(5), 1166(6), 724(7), 530(8), 1269(9), 414(10), 451(11), 966(12), 1133(13), 1560(14), 1049(15), 657(16)	291(1), 253(2), 315(3), 274(4), 165(4), 2888(5), 2917(6), 178(7), 150(8), 225(9), 204(10), 98(11), 2836(12), 1403(13), 2815(14), 2944(15)
<b>8</b>	<b>5</b> (2.00, 5.15), MeOCOC <sub>6</sub> H <sub>4</sub> SH (0.85, 5.08), KOH (0.34, 6.08), BiCl <sub>3</sub> (0.952, 3.02)	1.56, 3.00, 59	C: 27.27 (27.39) H: 2.86 (3.06)	138–140	273(1), 866(2), 875(3), 1716(4), 1423(5), 1136(6), 1274(7), 1437(8), 532(9), 749(10), 307(11), 970(11), 1041(12), 1123(13), 1309(14)	
<b>9a</b>	HSCH <sub>2</sub> CH <sub>2</sub> OH (0.276, 3.53), KOH (0.350, 6.24), HSCH <sub>2</sub> CH <sub>2</sub> NH <sub>3</sub> · HCl (0.278, 3.60), KOH (0.207, 3.68)	0.625, 1.74, 50	C: 13.30 (13.51) H: 2.79 (2.89) N: 3.88 (3.57)	168–173	1035(1), 334(2), 1275(3), 1005(4), 510(5), 1366(6), 317(7), 964(8), 381(9), 833(10), 1052(11), 1418(12), 1205(13), 288(14), 925(15), 1084(16), 271(17), 1160(18), 663(19), 721(20)	

drogen atoms were placed in geometrically calculated positions and not refined, in all cases (Table 2).

A final difference-Fourier map yielded  $\rho$  (max) = 1.71 e<sup>-</sup> Å<sup>-3</sup> and  $\rho$  (min) = -1.89 e<sup>-</sup> Å<sup>-3</sup> (**6a**),  $\rho$  (max) = 1.89 e<sup>-</sup> Å<sup>-3</sup> and  $\rho$  (min) = -3.22 e<sup>-</sup> Å<sup>-3</sup> (**6b**),  $\rho$  (max) = 1.72 e<sup>-</sup> Å<sup>-3</sup> and  $\rho$  (min) = -1.96 e<sup>-</sup> Å<sup>-3</sup> (**7a**),  $\rho$  (max) = 1.65 e<sup>-</sup> Å<sup>-3</sup> and  $\rho$  (min) = -1.43 e<sup>-</sup> Å<sup>-3</sup> (**8**), and  $\rho$  (max) = 1.46 e<sup>-</sup> Å<sup>-3</sup> and  $\rho$  (min) = -1.53 e<sup>-</sup> Å<sup>-3</sup> (**9a**). Atomic coordinates, bond

lengths and angles, and thermal parameters have been deposited.<sup>2</sup>

## Results and discussion

Facile hydrolysis of many bismuth element bonds typically results in essentially quantitative precipitation of bismuthyl (BiO<sup>+</sup>) salts, and this has impeded studies aimed at

<sup>2</sup>Supplementary data may be purchased from the Depository of Unpublished Data, Document Delivery, CISTI, National Research Council Canada, Ottawa, ON K1A 0S2, Canada ([http://www.nrc.ca/cisti/irm/unpub\\_e.shtml](http://www.nrc.ca/cisti/irm/unpub_e.shtml) for information on ordering electronically). CCDC 207453–207457 contain the supplementary data for this paper. These data can be obtained, free of charge, via [www.ccdc.cam.ac.uk/conts/retrieving.html](http://www.ccdc.cam.ac.uk/conts/retrieving.html) (or from the Cambridge Crystallographic Data Centre, 12 Union Road, Cambridge CB2 1EZ, U.K.; fax +44 1223 336033; or [deposit@ccdc.cam.ac.uk](mailto:deposit@ccdc.cam.ac.uk)).



**Table 2.** Crystallographic data for compounds **6–9a**.

	<b>6a</b>	<b>6b</b>	<b>7a</b>	<b>8</b>	<b>9a</b>
Formula	C <sub>6</sub> H <sub>14</sub> BiNS <sub>3</sub>	C <sub>4</sub> H <sub>9</sub> BiOS <sub>3</sub>	C <sub>6</sub> H <sub>14</sub> BiNS <sub>4</sub>	C <sub>12</sub> H <sub>15</sub> BiO <sub>2</sub> S <sub>4</sub>	C <sub>4</sub> H <sub>10</sub> BiNOS <sub>2</sub>
fw	405.34	378.27	437.40	528.47	361.23
$\lambda$ (Å) (CuK $\alpha$ )	1.54178	1.54178	1.54178	1.54178	1.54178
Space group	<i>P</i> -1	<i>P</i> 2 <sub>1</sub> / <i>a</i>	<i>P</i> 2 <sub>1</sub> / <i>n</i>	<i>P</i> 2 <sub>1</sub>	<i>P</i> 2 <sub>1</sub> / <i>c</i>
<i>a</i> (Å)	9.121(2)	9.158(1)	11.748(2)	8.147(2)	8.233(3)
<i>b</i> (Å)	9.266(2)	11.872(2)	5.365(2)	8.736(2)	6.492(4)
<i>c</i> (Å)	7.6099(5)	8.037(1)	19.5313(9)	11.941(2)	16.738(3)
$\alpha$ (°)	104.722(9)	90	90	90	90
$\beta$ (°)	101.996(9)	90.09(1)	98.354(6)	103.54(2)	111.96(2)
$\gamma$ (°)	63.51(1)	90	90	90	90
<i>V</i> (Å <sup>3</sup> )	553.4(2)	873.9(2)	1217.9(3)	826.3(3)	829.6(5)
<i>Z</i>	2	4	4	2	4
<i>T</i> (°C)	23 ±1	23 ±1	23 ±1	23 ±1	23 ±1
<i>D</i> <sub>c</sub> (Mg m <sup>-1</sup> )	2.432	2.875	2.374	2.124	2.892
$\mu$ (cm <sup>-1</sup> )	362.44	458.81	345.69	257.12	460.18
<i>R</i> <sup>a</sup>	0.049	0.050	0.033	0.044	0.0570
	(obs 3 $\sigma$ data)	(obs 2 $\sigma$ data)	(obs 2 $\sigma$ data)	(obs 2 $\sigma$ data)	(obs 3 $\sigma$ data)
<i>R</i> <sub>w</sub> <sup>b</sup>	0.047				0.073
	(obs 3 $\sigma$ data)				(obs 3 $\sigma$ data)
<i>wR</i> <sup>c</sup>		0.164	0.125	0.124	
		(all data)	(all data)	(all data)	

$$^a R = \Sigma |F_o| - |F_c| / \Sigma |F_o|$$

$$^b R_w = \{[\Sigma w(|F_o| - |F_c|)^2] / \Sigma w |F_o|^2\}^{1/2}$$

$$^c wR^2 = \{[\Sigma w(F_o^2 - F_c^2)^2] / \Sigma w F_o^2\}^{1/2}$$

**Table 3.** Selected bond lengths (Å) listed in order of increasing bond length (i.e., A < B < C < D) for compounds **1–11**.

	Reference	Bi—S <sub>A</sub>	Bi—S <sub>B</sub>	Bi—S <sub>C</sub>	Bi—S <sub>D</sub>	Bi—N <sub>A</sub>	Bi—N <sub>B</sub>	Bi—N <sub>C</sub>	Bi—O <sub>A</sub>	Bi—O <sub>B</sub>	Bi—O <sub>C</sub>
<b>1a</b>	4	2.530(7)				2.52(2)					
<b>1c</b>	11	3.021(2)							2.562(6)		
<b>2a</b>	4	2.569(3)	2.608(3)			2.398(8)	2.528(9)		2.86(1)		
<b>2b</b>	3	2.558(4)	2.595(3)						2.80(1)	2.86(1)	
<b>2b</b>	13	2.663(6)	2.853(6)						2.58(2)	2.64(2)	
<b>2c</b>	8	2.849(7)	2.884(6)						2.68(2)	2.77(2)	
<b>3a</b>	4	2.567(5)	2.654(5)	2.748(7)		2.64(2)	2.81(2)	2.83(2)			
<b>3c</b>	8	2.568(2)	2.574(2)	2.608(2)					2.807(5)	2.861(5)	3.071(7)
<b>4-2py</b>	9	2.542(6)	2.545(4)								
<b>6a*</b>		2.542(4)	2.572(4)	2.589(5)		2.72(1)					
		Bi-S3	Bi-S2	Bi-S1		Bi-N1					
<b>6b*</b>		2.532(5)	2.558(5)	2.639(6)					2.77(2)		
		Bi-S1	Bi-S2	Bi-S3					Bi-O1		
<b>5</b>	9	2.541(6)	2.849(5)	3.534(7)							
<b>7a*</b>		2.574(2)	2.592(3)	2.621(3)	3.248(3)	2.723(9)					
		Bi-S1	Bi-S4	Bi-S3	Bi-S2	Bi-N1					
<b>8*</b>		2.543(5)	2.550(5)	2.602(5)	3.068(4)				3.55(2)		
		Bi-S3	Bi-S1	Bi-S4	Bi-S4				Bi-O1		
<b>11</b>	14	2.597(5)2	2.602(6)	2.606(5)					2.72(2)	2.84(1)	3.08(2)
<b>9a*</b>		2.57(2)	2.58(2)			2.41(7)			2.22(4)		
		Bi-S1	Bi-S2			Bi-N1			Bi-O1		
<b>9b</b>	13	2.527(3)	2.564(3)						2.195(9)	2.577(9)	
<b>10</b>	15	2.582(1)	2.560(1)						2.197(4)	2.589(4)	

**Note:** Bi-E bond labels are given below the bond distances where distinction is necessary.

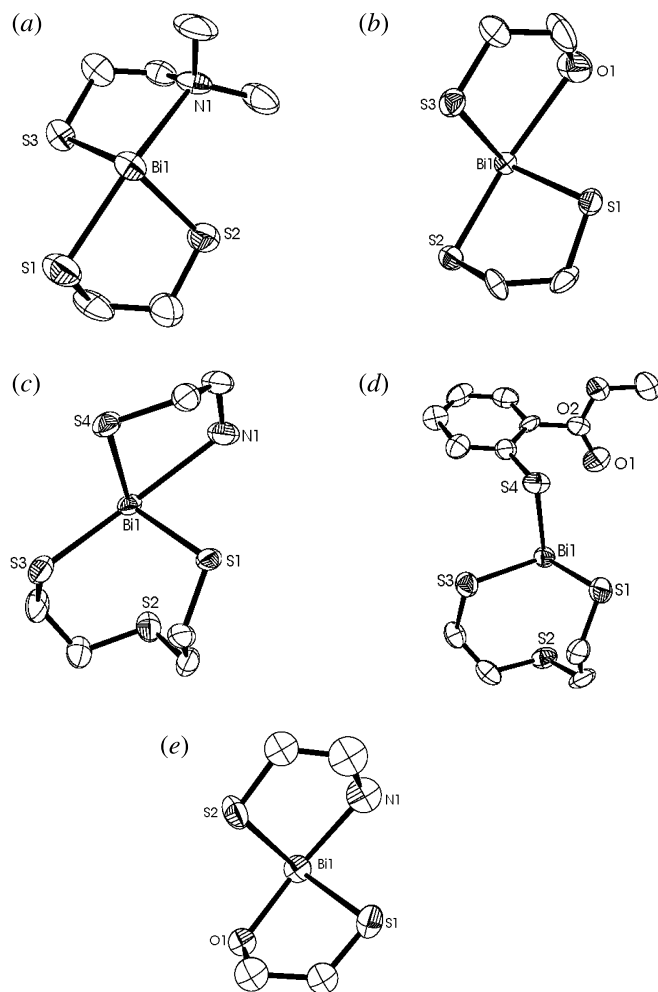
\*Structures reported in this article.

rational and systematic development of bismuth chemistry. Some complexes involving weakly donating functionalities have been isolated in the absence of moisture, but many

conventional types of ligands have yet to be observed coordinated to bismuth. As a result, numerous complexes of bismuth represent unique examples for a particular ligand,



**Fig. 1.** Crystallographic views of (a) **6a**, (b) **6b**, (c) **7a**, (d) **8**, (e) **9a**. Thermal ellipsoids are drawn to 50% probability. Hydrogen atoms have been omitted for clarity.



rather than a series of related compounds and general synthetic procedures have not been established to allow for assessment of physical and chemical properties.

A wide range of bismuth thiolate complexes are known due to the high thermal and hydrolytic stability of the sulfur–bismuth bond (2), however, most complexes involve multi-thiolation. Hetero-bifunctional ligands containing a thiolate moiety and an auxiliary donor have proven effective for developing complexes of bismuth with new donors. Moreover, the chelate interaction of the weaker donor mediates the thiophilicity of the bismuth centre and it is possible to isolate kinetically stable, partially thiolated complexes, so that all three stoichiometric combinations (**1**, **2**, **3**) have been prepared for aminoethanethiolate (**4**) and esterthiolate (**8**, **11**) complexes.

We have now exploited the features of bifunctional thiolate ligands to develop synthetic procedures for heteroleptic bismuth complexes. The starting materials **4** (12) and **5** (9) that are readily obtained via precipitation, react slowly at room temperature with potassium thiolate solutions in a slurry with little or no change in the visual appearance of the reaction mixture. Nevertheless, the precipitates are characterized as analytically pure metathesis products formed in

reasonable yield. Some yields are relatively low, however, conditions to optimize them have not yet been assessed.

Compounds **6–9a** have been crystallographically and spectroscopically characterized. Molecular structures are shown in Fig. 1 and selected bond lengths are compared with those of compounds **1–5** in Table 3. The spirocyclic environments observed for bismuth in **6a**, **6b**, **7a**, and **9a** confirm auxiliary coordination of the hydroxyl (**6b**), amino (**6a**, **7a**, and **9a**) and alkoxide (**9a**) functional groups to the bismuth centre in each respective example. The structures are consistent with the homoleptic thiolate series **1–3** (3, 4, 13), except for compound **8** in that the ester functionality is terminal (Bi–O, 3.55(2) Å; cf. Bi–O 2.56–2.86 Å (**8**, **11**)), showing no evidence of interaction with bismuth. This is an unexpected structural feature, when one compares the structure of tris(thiosalicylato)bismuth **11**, which exhibits a definitively hexacoordinate site for bismuth and typical Bi–O coordinate bond distances (Bi–O 2.72(2)–3.08(2) Å) (14). Although the cross-ring S2–Bi distance is relatively long (3.0688 (4) Å) in **8**, we speculate that this interaction lowers the Lewis acidity of the bismuth center to render the carbonyl donation ineffective.

The structural features of compounds **6–9a** represent a useful contribution to the developing database for the chelate–thiolate coordination chemistry of bismuth, as documented in Table 3. Mono-, bis-, and tris-thiolate complexes of bismuth exhibit a narrow range of Bi–S bond distances. The geometry at bismuth varies considerably throughout the series of complexes including a variety of coordination numbers. Nevertheless, most complexes are observed to have Bi–S bond lengths within a narrow range (2.5 to 2.6 Å), so that the thiolate interaction is essentially independent of the number of thiolate ligands, the presence of auxiliary intramolecular coordination to bismuth, or the number of intermolecular interactions at bismuth. The unusually long Bi–S bonds in **1c**, **2b**, and **2c** are likely due to strong intermolecular interactions in the solid state that provide for a dimeric arrangement for **1c** and a polymeric (ribbon-like) structure for **2b** and **2c** (3, 8). The fourth Bi–S contact in **7a** and **8** represent the intramolecular cross-ring thioether donation, which is predictably weaker than those of the thiolates. The relatively weak interactions of the amines are likely made possible by the chelate arrangement. The Bi–N distances are comparable to those of the thiolates despite the smaller size of nitrogen. These observations are consistent with the realization that amine complexes of bismuth are extremely rare and the most reliable comparative data comes from complexes of pyridine derivatives (2), which are in the range of the Bi–N distances listed in Table 3. The relative Bi–O distances are in agreement with the relative Lewis basicity of the oxygen donor in that interactions of hydroxyl (**2b**, **6b**, **9b**, **10**) and carbonyl (**1c**, **2c**, **3c**, **8**, **11**) ligands are longer than interactions with alkoxide (**9a**, **9b**, **10**) functionalities.

## Conclusion

The use of thiolates in bifunctional ligands offers a synthetically versatile approach to bismuth complexes involving weak Lewis donors and provides for a general systematic and comprehensive development of bismuth chemistry.



## Acknowledgements

We thank the Natural Sciences and Engineering Research Council of Canada (NSERC), the Killam Trusts, the Canada Research Chairs program, the Canada Foundation for Innovation, the Nova Scotia Research and Innovation Trust Fund and MDS Sciex for funding, the Dalhousie Mass Spectrometry Center for the use of instrumentation, and Douglas Jackson for performing some of the preparative work.

## References

1. G.G. Briand and N. Burford. *Chem. Rev.* **99**, 2601 (1999).
2. G.G. Briand and N. Burford. *Adv. Inorg. Chem.* **50**, 285 (2000).
3. L. Agocs, G.G. Briand, N. Burford, T.S. Cameron, W. Kwiatkowski, and K.N. Robertson. *Inorg. Chem.* **36**, 2855 (1997).
4. G.G. Briand, N. Burford, T.S. Cameron, and W. Kwiatkowski. *J. Am. Chem. Soc.* **120**, 11 374 (1998).
5. D.E. Mahony, S. Lim-Morrison, L. Bryden, G. Faulkner, P.S. Hoffman, L. Agocs, G.G. Briand, N. Burford, and H. Maguire. *Antimicrob. Agents Chemother.* **43**, 582 (1999).
6. G.S. Sandha, R. LeBlanc, S.J.O.V. van Zanten, T.D. Sitland, L. Agocs, N. Burford, L. Best, D. Mahony, P. Hoffman, and D.J. Leddin. *Dig. Dis. Sci.* **43**, 2727 (1999).
7. N. Burford, M.D. Eelman, D. Mahony, and M. Morash. *Chem. Commun.* 146 (2003).
8. G.G. Briand, N. Burford, and T.S. Cameron. *Chem. Commun.* 13 (2000).
9. L. Agocs, N. Burford, T.S. Cameron, J.M. Curtis, J.F. Richardson, K.N. Robertson, and G.B. Yhard. *J. Am. Chem. Soc.* **126**, 895 (1996).
10. G.M. Sheldrick. *SHELXL97: Program for the solution of crystal structures [computer program]*. Version 2. University of Göttingen, Göttingen, Germany. 1997.
11. G.G. Briand, N. Burford, M.D. Eelman, T.S. Cameron, and K.N. Robertson. *Inorg. Chem.* **42**, 3136 (2003).
12. P. Powell. *J. Chem. Soc. A*, 2587 (1968).
13. E. Asato, K. Kamamuta, Y. Akamine, T. Fukami, R. Nukada, M. Mikuriya, S. Deguchi, and Y. Yokota. *Bull. Chem. Soc. Jpn.* **70**, 639 (1997).
14. N. Burford, M.D. Eelman, and T.S. Cameron. *Chem. Commun.* 1402 (2002).
15. P.C. Andrews, G.B. Deacon, W.R. Jackson, M. Maguire, N.M. Scott, B.W. Skelton, and A.H. White. *J. Chem. Soc., Dalton Trans.* 4634 (2002).



# Variation of the ease of $\alpha$ -sulfonyl carbanion formation with the orientation of different $\beta$ -substituents: Experimental evidence for the generality of negative hyperconjugation as an important substituent effect

James F. King, Manqing Li, Allan Zijun Cheng, Vinod Dave, and  
Nicholas C. Payne

**Abstract:** Following up on our previous observation that the rate of formation of a  $\beta$ -alkoxy-substituted  $\alpha$ -sulfonyl carbanion depends on the stereochemistry of the alkoxy group, we have found similar behaviour when the  $\beta$ -substituent is  $R_2N$ ,  $RS$ , or  $R_3N^+$ . With each substituent, the variation of  $k_N$  (defined by  $k_N = (k_{\text{exch}})_X / (k_{\text{exch}})_{\text{model}}$ ) is consistent with an equation of the form  $\log k_N = a + b \cos^2 \theta$ , where  $\theta$  is the H-C-C-X torsion angle. We propose that the  $a$  term describes the polar (field plus inductive) effect and the  $b$  term the negative hyperconjugative effect of the substituent; we show how the variations in  $a$  and  $b$  may be readily accommodated within this framework. Some features of the trialkylammonio group previously postulated in the literature are discussed in the light of our results.

**Key words:** negative hyperconjugation, substituent effects, stereoelectronic factors, sulfonyl carbanions, anomeric effect.

**Résumé :** Suite à notre observation antérieure à l'effet que la vitesse de formation d'un carbanion  $\alpha$ -sulfonyl portant un substituant  $\beta$ -alkoxy dépend de la stéréochimie du groupe alkoxy, on a observé un comportement semblable avec les substituants  $\beta$  sont  $R_2N$ ,  $RS$  ou  $R_3N^+$ . Avec chacun de ces substituants, la variation de la valeur  $k_N$  (où  $k_N = (k_{\text{éch}})_X / (k_{\text{éch}})_{\text{modèle}}$ ) peut être calculée par une équation de la forme  $k_N = a + b \cos^2 \theta$  dans laquelle  $\theta$  correspond à l'angle de torsion H-C-C-X. On suggère que le terme  $a$  correspond à l'effet polaire (champ plus inductif) et alors que le terme  $b$  serait associé à l'effet d'hyperconjugaison négative du substituant et on montre comment les variations dans les termes  $a$  et  $b$  peuvent facilement être accomodés dans ce cadre. À la lumière de nos résultats, on discute de certaines caractéristiques du groupe trialkylammonio postulées antérieurement dans la littérature.

**Mots clés :** hyperconjugaison négative, effets de substituants, facteurs stéréoelectroniques, carbanions sulfonyles, effet anomère.

[Traduit par la Rédaction]

## Introduction

We have recently reported (1) on an extended investigation, which showed that the ease of deprotonation of a sulfone to form the  $\alpha$ -sulfonyl carbanion can be influenced strongly not only by the presence of a  $\beta$ -alkoxy substituent but also by its geometry. Specifically, we investigated a series of  $\beta$ -alkoxy sulfones of the general formula **A** ( $X = RO$ )

(Scheme 1), and observed a dependence of the ease of carbanion formation (**A**  $\rightarrow$  **B**) on  $\theta$ , the  $H_{\alpha}-C_{\alpha}-C_{\beta}-X$  torsion angle. More precisely, if we define  $(k_{\text{exch}})_X$  as the second-order rate constant for the H-D exchange of the  $\beta$ -substituted substrate (**A**),  $(k_{\text{exch}})_{\text{model}}$  as the rate constant for H-D exchange in an appropriate model (e.g., **A** with  $X = H$  or  $CH_3$ ), and  $k_N = (k_{\text{exch}})_X / (k_{\text{exch}})_{\text{model}}$ , then we observed the relation summarized by eq. [1]

$$[1] \log k_N = a + b \cos^2 \theta$$

where  $a = 1.70$  and  $b = 2.62$ .

This result was interpreted in terms of a (more or less) angle-independent combination of field and inductive effects responsible for the  $a$  term taken with torsion angle dependent negative hyperconjugation, leading to the  $b \cos^2 \theta$  component. This term is maximal at  $\theta = 0^\circ$  and  $\theta = 180^\circ$  and in reactions of molecules with these torsion angles is responsible for the *major* part of the electronic effect of the  $\beta$ -alkoxy group on the ease of formation of a  $\beta$ -alkoxy  $\alpha$ -sulfonyl carbanion. The negative hyperconjugation was identified as  $\pi$ -type donation of the incipient carbanionic electrons into the

Received 28 October 2002. Published on the NRC Research Press Web site at <http://canjchem@nrc.ca> on 18 June 2003.

*Dedicated to Professor Donald R. Arnold for his contributions to chemistry.*

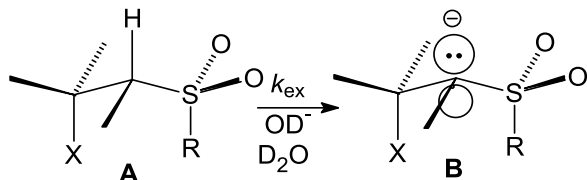
J.F. King,<sup>1</sup> M. Li, A.Z. Cheng, V. Dave, and N.C. Payne,<sup>2</sup>  
Department of Chemistry, The University of Western Ontario,  
London, ON N6A 5B7, Canada.

<sup>1</sup>Corresponding author concerning the organic chemistry  
(e-mail: [scijfk@uwo.ca](mailto:scijfk@uwo.ca)).

<sup>2</sup>Corresponding author concerning the X-ray crystallography  
(e-mail: [noggin@uwo.ca](mailto:noggin@uwo.ca)).



Scheme 1.



antibonding orbital,  $\sigma^*_{\text{CO}}$ . Such hyperconjugation would be expected to be smallest at  $\theta = 90^\circ$  with values increasing from  $90^\circ$  to maxima at  $0^\circ$  and  $180^\circ$ .

Related negative hyperconjugative interactions have been treated theoretically (2–5). Especially relevant to the present study is the paper by Schleyer and Kos (5) who calculated  $\Delta E$  for the conversion of two conformations of  $\text{ROCH}_2\text{CH}_2^-$ : (i) that with the  $p$ -orbital on the carbon atom coplanar with the C—O bond (in our terminology,  $\theta = 180^\circ$ ); and (ii) that with the  $p$ -orbital at  $90^\circ$  to the C—O bond ( $\theta = 90^\circ$ ). They estimated that the perpendicular conformation was less stable than the coplanar by  $13.2 \text{ kcal mol}^{-1}$  and assigned the energy difference to negative hyperconjugation. For the reaction  $\text{CH}_3\text{CH}_2^- + \text{ROCH}_2\text{CH}_3 \rightarrow \text{CH}_3\text{CH}_3 + \text{ROCH}_2\text{CH}_2^-$  with the carbanion in the coplanar conformation they estimated  $\Delta E = -23.5 \text{ kcal mol}^{-1}$ . Note that the stabilization assigned to hyperconjugation ( $13.2 \text{ kcal mol}^{-1}$ ) is somewhat greater than that of the polar effect ( $11.3 \text{ kcal mol}^{-1}$ ), i.e., our conclusions based on the experiment are in full accord with those of Schleyer and Kos (5), derived from ab initio MO calculations.

It was reasonable to expect that other substituents, especially those that are highly electronegative or have a low-lying antibonding C—X orbital ( $\sigma^*_{\text{CX}}$ ), would show the same behaviour as  $\beta$ -alkoxy substituents, though this expectation could not be taken for granted. We therefore set out to examine a further set of  $\beta$ -substituted sulfones with two aims in mind: (i) to provide experimental evidence for the generality of the effect shown by the alkoxy group; and (ii) in the event that this proved to be the case, to obtain a set of  $a$  and  $b$  parameters (see eq. [1]) for each substituent to determine if our hypotheses about the contributions of negative hyperconjugation and field and inductive effects would withstand the light of the additional information.

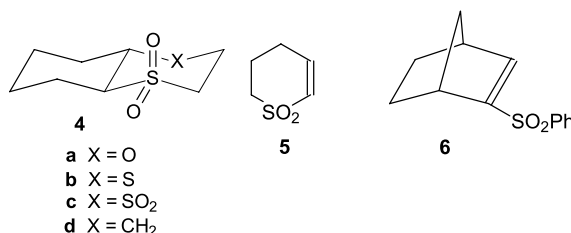
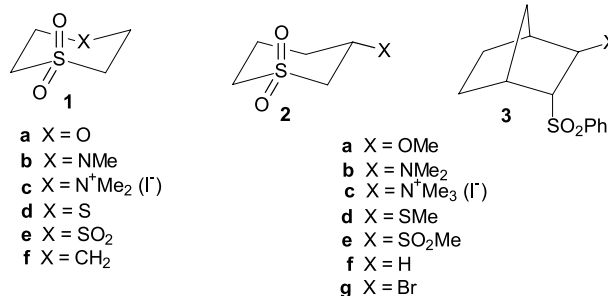
## Results and discussion

### Materials and methods

In our previous study (1) the  $\beta$ -alkoxysulfones **1a**, **2a**, and **3a** (Scheme 2) had proved both convenient and well behaved. Accordingly, we set out to explore the effect of other substituents by examining the analogues **1b–1e**, **2b–2e**, and **3b–3e**. The low solubility of **1e** rendered kinetic studies impossible in our hands and, in view of the satisfactory results previously obtained with the heterodecalins **4a** and **4d** turned instead to the disulfone **4c**.

The monocyclic substrates (**1** and **2**) varied from commercially available (**1b**), previously known (**1d**), to readily prepared by straightforward routes from known precursors, as

Scheme 2.



described in the *Experimental* section. Conjugate addition of dimethylamine to the unsaturated sulfone (**5**), for example, proved a convenient route to **2b** and thence to **2c**. Analogous conjugate addition of dimethylamine and methanethiol to **6** led to the bicyclic substrates, **3b** and **3d**, respectively, and these in turn were converted easily into **3c** and **3e**. The present study requires a firm assignment of the stereochemistry of each substrate, and we postulate the following picture.

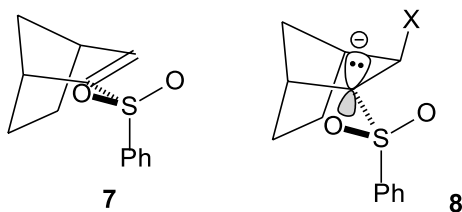
The conjugate addition is believed to take place by attack of the nucleophile on the less-hindered *exo* face of the sulfone (**6**) in the arrangement shown in **7** with formation of the sulfonyl carbanion with the phenylsulfonyl group *endo* (Scheme 3); the usual stereospecific protonation of the carbanion (**8**) leads directly to **3**. Evidence for this pathway was obtained by treating **6** with sodium methoxide in methanol to obtain **3a**, which had been previously obtained by another route (1). The structure and stereochemistry of **3a** had been firmly established by its mode of synthesis and by single crystal X-ray structure determination. The generality of the stereochemistry of this addition was then secured by X-ray structure determination of **3c**.<sup>3</sup>

The H-D exchange rates were determined by following the disappearance of the <sup>1</sup>H NMR signal of the  $\alpha$ -sulfonyl hydrogen with time, as described earlier (1). A 1:1 mixture of D<sub>2</sub>O and dioxane-*d*<sub>8</sub> was the most frequently used solvent medium, though solubility reasons or the availability of rate data for the model compounds sometimes led to other media. The second-order rate constants for the substrates (**1b–1d**, **2b–2e**, **3b–3d**, and **4c**) together with those of the corresponding model compounds (**1f**, **2f**, and **3f**) are given in Table 1. Missing from the table is compound **3e** for which a combination of low solubility, signal overlap, and apparent reaction complexity has frustrated our efforts to obtain rate

<sup>3</sup> Iodide salt, **3c**;  $a = 16.208(3)$ ,  $b = 17.347(4)$ ,  $c = 26.370(5)$ ,  $\beta = 106.30(3)^\circ$ ,  $T = -100^\circ\text{C}$ , space group  $C2/c$ ,  $Z = 16$ ,  $R = 0.037$  for 9762 data with  $F_{\text{obs}} > 4\sigma(F_{\text{obs}})$ . Full details of this and supporting analyses will be published elsewhere.



Scheme 3.



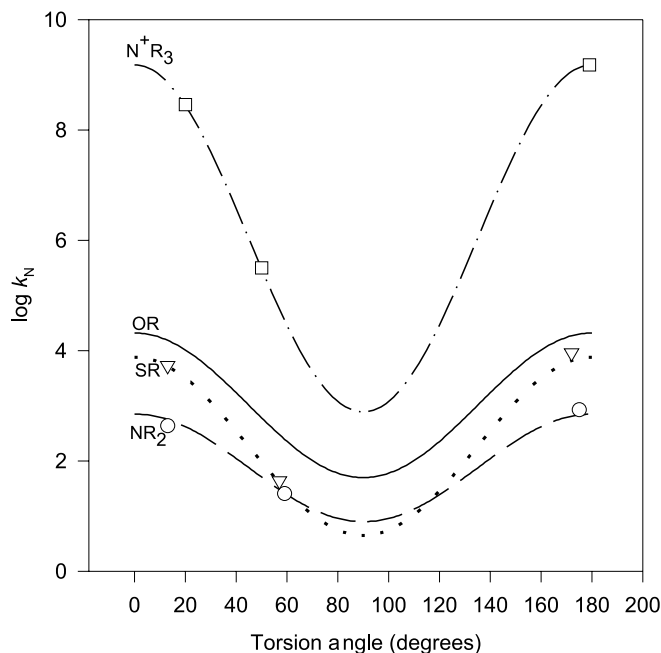
constants to date. For two of the substrates in Table 1, namely the quaternary ammonium salts **2c** and **3c**, the reaction showed no sign of any initial H-D exchange but, rather, gave the unsaturated sulfones, **5** and **6**, respectively. This, of course, is simply a Hofmann elimination and is the expected result whenever one generates a carbanion vicinal to a quaternary ammonium centre. Since this reaction consumes a molecule of base for each reaction it was necessary to modify the experimental procedure to include the use of a buffer system. The reaction gave the same second-order rate constant with buffer concentrations differing by 400-fold, pointing to specific base catalysis. One simple mechanism is that the initially-formed carbanion undergoes rapid unimolecular extrusion of the tertiary amine, i.e., that the process is an irreversible E1cB reaction. The reversible E1cB is excluded by lack of H-D exchange in the starting material, but the possibility remains for a *cis*-E2 reaction of **3c** and a similar reaction from a twist form in **2c**. To check this point we have plotted the  $\log k_N$  values for **2a–2e** (the  $\sim 60^\circ$  series) vs. **1a–1e** (the  $\sim 180^\circ$  series). The  $\sim 180^\circ$  set and all but **2c** in the  $\sim 60^\circ$  series showed only H-D exchange and can be expected to show a reasonably linear correlation in such a plot. In the event we obtained a fair straight line with no sign of positive deviation of the point for **2c**. The same features were also found in a similar plot of **3a–3d** (the  $\sim 0^\circ$  set) vs. **1a–1d**. These observations are in accord with the simple picture that all of the reactions with rate constants listed in Table 1 involve rate-determining carbanion formation.

### Kinetic results

The  $\log k_N$  values for the dialkylamino, trialkylammonio, and thioalkyl substituents in Table 1 are presented in Fig. 1, along with the line for the alkoxy substituents obtained earlier (1). The two points for the alkylsulfonyl groups are not plotted, but it is evident that they fall close to the corresponding points for the trialkylammonio function. From the curves in Fig. 1 it is evident that the torsion angle dependence originally observed with the alkoxy group is also found with the other substituents, i.e., the phenomenon is general. The parameters for eq. [1] obtained by a nonlinear least-squares fit of the data to eq. [1], along with the parameters for eq. [1] that fit the two alkylsulfonyl points, are presented in Table 2. Shown also are  $\sigma^*_0$  (which is identical to  $\sigma^*_{180}$ ) and  $\sigma^*_{90}$  values, as defined by the equations in the footnotes to Table 2 (cf. ref. (1)). We note specifically that  $\sigma^*_{90}$  (because  $\cos^2 90 = 0$ ) is given simply by  $\sigma^*_{90} = a/4.9$  and discussions of the trends in  $\sigma^*_{90}$  and  $a$  values are equivalent.

First we note that the  $a$  parameters (and the  $\sigma^*_{90}$  values) follow the order  $RS < R_2N < RO < RSO_2 < R_3N^+$ , precisely the order of the electronegativities of the heteroatoms (modified where appropriate by formal or actual charges). We note

**Fig. 1.** Plot of  $\log k_N$  vs. the  $H-C_\alpha-C_\beta-X$  torsion angle ( $\theta$ ) for  $\beta$ -substituted sulfones **1b**, **2b**, **3b** (circles), **1c**, **2c**, **3c** (squares), and **1d**, **2d**, **3d** (triangles). The points are experimental (Table 1), and each line derived from a nonlinear least-squares fit to eq. [1]; the  $a$  and  $b$  parameters are listed in Table 2. The solid line is for  $X = RO$  and is taken from ref. (1).



explicitly that this is not the order of the usual Taft  $\sigma^*$  or  $\sigma_1$  values, parameters which have long been regarded as describing the polar effect alone, although the fact that  $\sigma^*_{CH_2X}$  for  $X = MeS$  is greater than that for  $X = Me_2N$  (see Table 2) has long been a difficult point to reconcile with a simple polar (field and (or) inductive) effect. The picture presented in the current paper, that the polar effect is augmented by hyperconjugation, is, by contrast, highly satisfactory; when the hyperconjugation is not present (i.e., when  $\theta \approx 90^\circ$ ) then the  $\sigma^*_{90}$  values follow the expected polar-effect order as noted above.

It is also of interest to note that even the upper range of the  $\sigma^*$  values from the literature is less than the  $\sigma^*_{180}$  ( $= \sigma^*_0$ ) value. Though individual  $\sigma^*$  determinations may well be subject to factors unique to the system, it seems likely that one reason why  $\sigma^*_{180}$  is greater than  $\sigma^*$  as commonly measured is that in many instances the substrate being examined does not consist of a conformationally homogeneous material with all molecules having the  $H-C_\alpha-C_\beta-X$  angle (or its analogue) at  $180^\circ$  (or  $0^\circ$ ). A mixture of two (or more) conformations would show Winstein-Holness kinetics, which would reflect the population of the less reactive (or unreactive) conformer and the substituent constant ( $\sigma^*$ ) would be correspondingly reduced. As a simple illustration we point to structure **A** in which the torsion angle ( $\theta$ ) is at the favourable angle of  $180^\circ$ . At the same time, simple conformational considerations point to a strong nonbonding interaction between the  $X$  and  $R$  groups that can be alleviated, for example, by rotating around the  $C_\alpha-C_\beta$  bond to place the  $X$  group antiplanar to the  $C_\alpha-S$  bond. In an unconstrained system this conformation can be expected



**Table 1.** Rate constants for base-promoted formation of  $\alpha$ -sulfonyl carbanions from  $\beta$ -substituted sulfones with fixed  $H_{\alpha}-C_{\alpha}-C_{\beta}-X$ 

Substituted sulfone	$\theta$ (deg) <sup>a</sup>	$(k_{\text{exch}})_X$ ( $M^{-1}s^{-1}$ ) (conditions) <sup>b</sup>	Model	$(k_{\text{exch}})_{\text{model}}$ ( $M^{-1}s^{-1}$ ) (conditions) <sup>b</sup>	$\log k_N^c$
<b>1b</b>	175	$2.60 \times 10^{-3}$ (A) ( $5.20 \times 10^{-3}$ ) <sup>d</sup>	<b>1f</b>	$3.1 \times 10^{-6}$ (A) ( $6.2 \times 10^{-6}$ ) <sup>d,e</sup>	2.92
<b>2b</b>	59	$1.60 \times 10^{-4}$ (A)	<b>1f</b>	$3.1 \times 10^{-6}$ (A) ( $6.2 \times 10^{-6}$ ) <sup>d,e</sup>	1.41
<b>3b</b>	14	$1.60 \times 10^{-4}$ (B)	<b>3f</b>	$4.5 \times 10^{-8}$ (B) <sup>e</sup>	2.64
<b>1c</b>	179	$1.50 \times 10^3$ (C) ( $3.00 \times 10^3$ ) <sup>d</sup>	<b>1f</b>	$1.0 \times 10^{-6}$ (C) ( $2.0 \times 10^{-6}$ ) <sup>d,e</sup>	9.18
<b>2c</b>	50	$6.3 \times 10^{-1}$ (C)	<b>1f</b>	$1.0 \times 10^{-6}$ (C) ( $2.0 \times 10^{-6}$ ) <sup>d,e</sup>	5.50
<b>3c</b>	20 (20.1, 17.3)	$1.2 \times 10^1$ (B)	<b>3f</b>	$4.5 \times 10^{-8}$ (B) <sup>e</sup>	8.4
<b>1d</b>	172	$2.8 \times 10^{-2}$ (A) ( $5.6 \times 10^{-2}$ ) <sup>d</sup>	<b>1f</b>	$3.1 \times 10^{-6}$ (A) ( $6.2 \times 10^{-6}$ ) <sup>d,e</sup>	3.96
<b>2d</b>	57	$2.7 \times 10^{-4}$ (A)	<b>1f</b>	$3.1 \times 10^{-6}$ (A) ( $6.2 \times 10^{-6}$ ) <sup>d,e</sup>	1.64
<b>3d</b>	13	$2.4 \times 10^{-4}$ (B)	<b>3f</b>	$4.5 \times 10^{-8}$ (B) <sup>e</sup>	3.73
<b>4c</b>	177	$2.6 \times 10^2$ (B)	<b>1f</b>	$9.0 \times 10^{-7}$ (B) ( $1.8 \times 10^{-6}$ ) <sup>d,e</sup>	8.16
<b>2e</b>	54	$1.1 \times 10^{-1}$ (C)	<b>4d</b>	$1.2 \times 10^{-6}$ (B) <sup>e</sup>	8.34
			<b>1f</b>	$1.0 \times 10^{-6}$ (C) ( $2.0 \times 10^{-6}$ ) <sup>d,e</sup>	4.75

<sup>a</sup>H-C-C-S-X torsion angle estimated by PCModel (PCM4); values in parentheses are from the X-ray crystal structure determination.<sup>b</sup>Reaction conditions: A: D<sub>2</sub>O:dioxane-*d*<sub>8</sub> (1:1, 25°C); B: D<sub>2</sub>O:CD<sub>3</sub>CN (1:1, 21°C); C: D<sub>2</sub>O (20°C). The reactions of the ammonium salts and the disulfones were carried out using phosphate buffers (see ref. (1)); no sign of buffer catalysis was apparent.<sup>c</sup> $k_N = (k_{\text{exch}})_X / (k_{\text{exch}})_{\text{model}}$ , see text.<sup>d</sup>The rate constant is that for H-D exchange *per hydrogen*, i.e., in the present cases the measured rate constant multiplied by 2 (cf. ref. (1)).<sup>e</sup>Taken from ref. (1).



**Table 2.** Substituent parameters.

Substituent	eq. [1] Parameters <sup>a</sup>		$\sigma^*_{90}$ <sup>b</sup>	$\sigma^*_0 (= \sigma^*_{180})$ <sup>b</sup>	$\sigma^*_{\text{CH}_2\text{X}}$ range <sup>c</sup> (R = Me)
	<i>a</i>	<i>b</i>			
RS	0.65	3.23	0.13	0.79	0.29–0.69
R <sub>2</sub> N	0.90	1.95	0.18	0.58	0.13–0.42
RO	1.70	2.62	0.35	0.88	0.51–0.76
(RSO <sub>2</sub> )	2.72	5.66	0.56	1.71) <sup>d</sup>	1.22–1.42
R <sub>3</sub> N <sup>+</sup>	2.89	6.29	0.59	1.87	1.62–2.98

<sup>a</sup>Equation [1]:  $\log k_N = a + b \cos^2 \theta$  where  $\theta$  is the H-C<sub>α</sub>-C<sub>β</sub>-X torsion angle.

<sup>b</sup> $\sigma^*_{90} = \sigma^*_\theta$  for  $\theta = 90^\circ$  and  $\sigma^*_0 = \sigma^*_{180} = \sigma^*_\theta$  for  $\theta = 0^\circ$  or  $180^\circ$ ;  $\sigma^*_\theta = (a + b \cos^2 \theta)/4.9$ , see ref. (1).

<sup>c</sup>Values for  $(\sigma_i)_X$  taken from ref. (6), transformed using the relation  $\sigma^*_{\text{CH}_2\text{X}} = (\sigma_i)_X/0.45$ .

<sup>d</sup>Values for *a* and *b* and derived values of  $\sigma^*_\theta$  for RSO<sub>2</sub> were calculated from the two points in Table 1 assuming eq. [1] applies.

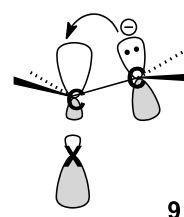
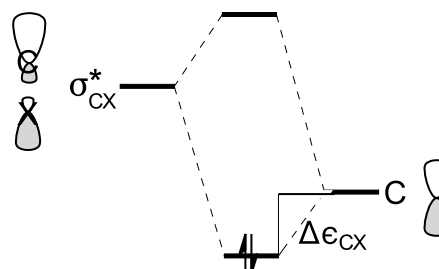
to be (i) an important conformer, and (ii) less reactive than the original conformer shown as **A**, and a value of  $\sigma^*$  obtained with such a conformational mixture would be smaller than  $\sigma^*_{180}$ .

The second parameter in eq. [1], namely *b*, describes the sensitivity of the rate constant to change in the torsion angle ( $\theta$ ). According to our interpretation the parameter *b* measures the extent of the hyperconjugation in each system, and the question immediately arises, does the extent of the hyperconjugation as measured by *b* concur with theory? The hyperconjugation that we are invoking involves  $\pi$ -type donation of the electrons of the incipient carbanion into a  $\sigma^*_{\text{C-X}}$  orbital. For simplicity we shall restrict further discussion to the stabilization of the (full) carbanion derived from the H-C<sub>α</sub>-C<sub>β</sub>-X torsion angle of  $180^\circ$  as indicated by **9** (Scheme 4). The general orbital interaction diagram, patterned on those given by Rauk (7a), is shown in Fig. 2.<sup>4</sup> To the extent that the hyperconjugative overlap shown in **9** occurs, the energy of the carbanion is lowered; the lowering is shown in Fig. 2 as  $\Delta\epsilon_{\text{CX}}$ . The value of  $\Delta\epsilon_{\text{CX}}$  is given approximately by eq. [2], where  $h^2_{\text{AB}}$  is the interaction matrix element and  $\epsilon_A$  and  $\epsilon_B$  are the energies of the interacting orbitals (7b).

$$[2] \quad \Delta\epsilon_{\text{CX}} \approx \frac{h^2_{\text{AB}}}{\epsilon_A - \epsilon_B}$$

For the hyperconjugative interaction itself, the  $h^2_{\text{AB}}$  term, which involves in the present cases  $\pi$ -type interaction of two carbon atoms (C<sub>α</sub> and C<sub>β</sub>), is not expected to change much from one molecule to another, and the variation in  $\epsilon_A - \epsilon_B$  is the chief source of the change in the energy of hyperconjugation and, hence, in the magnitude of parameter *b*.

We should recall that the magnitude of *b* reflects a variation in  $\log k_N$  and that  $k_N$  is defined as  $(k_{\text{exch}})_X/(k_{\text{exch}})_{\text{model}}$ , where, for simplicity in the comparison of the orbital interactions, we take X = C as the model system. The energies of hyperconjugation in the model (carbon) and substituted system are given by eq. [2], specifically the respective approximations  $\Delta\epsilon_{\text{CC}} \approx h^2_{\text{AB}}/(\epsilon_{\sigma^*_{\text{CC}}} - \epsilon_{\text{C}})$  and  $\Delta\epsilon_{\text{CX}} \approx h^2_{\text{AB}}/(\epsilon_{\sigma^*_{\text{CX}}} - \epsilon_{\text{C}})$ . As it happens (and as will be shown below), all of the values for the energy levels for the antibonding C-X orbitals ( $\epsilon_{\sigma^*_{\text{CX}}}$ ) of the substituents in this study are lower in energy than that for the antibonding C-C orbital ( $\epsilon_{\sigma^*_{\text{CC}}}$ ) and hence for each of the examples in this paper  $\Delta\epsilon_{\text{CX}}$  is greater than  $\Delta\epsilon_{\text{CC}}$ , i.e., the hyperconjugative interactions from these X substituents

**Scheme 4.****Fig. 2.** Orbital interaction diagram for hyperconjugative stabilization of an electron pair in a *p*-orbital on carbon by  $\pi$ -type interaction with an adjacent antibonding C-X orbital ( $\sigma^*_{\text{C-X}}$ ) as illustrated in **9**.

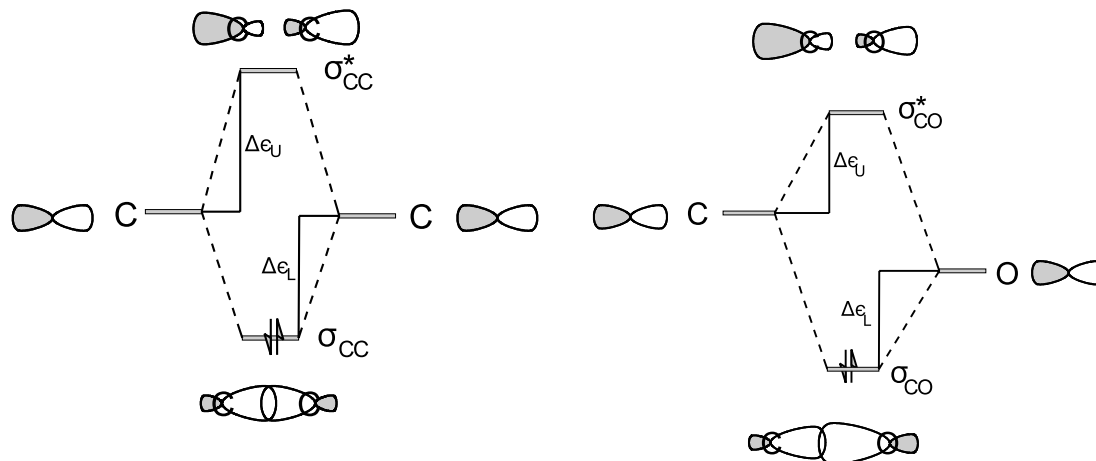
are all stabilizing relative to the carbon model. That the energy levels of the  $\sigma^*_{\text{CX}}$  orbitals are lower than that of  $\sigma^*_{\text{CC}}$  arises in most of the present cases because the heteroatom of the substituent is more electronegative than carbon. Taking oxygen as the example, we see from the familiar orbital interaction diagrams in Fig. 3 that the lower energy of  $\sigma^*_{\text{CO}}$  vs.  $\sigma^*_{\text{CC}}$  arises because of the lower energy of the oxygen atomic orbital relative to carbon (taken with eq. [2] and the analogous expression required for the homopolar C—C bond). When X = R<sub>2</sub>N, one may readily determine by interpolation that the energy difference between  $\sigma^*_{\text{CC}}$  and  $\sigma^*_{\text{CN}}$  is rather less than that with oxygen. Addition of the full positive charge on nitrogen, as in R<sub>3</sub>N<sup>+</sup>, sharply lowers the energy of the nitrogen atomic orbital, which substantially lowers the energy of  $\sigma^*_{\text{CX}}$  when X = R<sub>3</sub>N<sup>+</sup>, leading to a very large value of the parameter *b* for this substituent.

The effect of the RS group depends less on electronegativity differences than on the smaller overlap in a  $\sigma$ -bond between carbon and sulfur as compared with carbon and

<sup>4</sup>It may be helpful at this stage to note explicitly that the symbol  $\sigma^*$  in this paper (unavoidably) refers to two different things: (i) the Taft substituent constant; and (ii) an antibonding  $\sigma$  orbital.



**Fig. 3.** Orbital interaction diagram showing  $\sigma$ -bond formation leading to  $\sigma^*_{\text{CO}}$  having lower energy than  $\sigma^*_{\text{CC}}$ .



carbon (or oxygen). This feature is reflected in eq. [2] by the  $h_{\text{AB}}^2$  term that is smaller with the C—S bond than C—C or C—O; this leads to a smaller value of  $\Delta\epsilon_{\text{U}}$  (and  $\Delta\epsilon_{\text{L}}$ ) for the C-S array than that for the C-O system shown in Fig. 3. This in turn results in a lower value for the energy of  $\sigma^*_{\text{CS}}$  than for  $\sigma^*_{\text{CC}}$  or  $\sigma^*_{\text{CO}}$  and hence, by the argument given above using eq. [2], to a greater hyperconjugative stabilization with RS than with RO, i.e., to a larger  $b$  parameter for RS than RO. The still larger value for  $\text{RSO}_2$  is a simple reflection of the effect of the formal positive charge on the sulfur atom. The qualitative orbital interaction picture therefore predicts the following sequences for  $b$ : (i)  $\text{R}_2\text{N} < \text{RO} < \text{R}_3\text{N}^+$ ; and (ii)  $\text{RO} < \text{RS} < \text{RSO}_2$ . These patterns are, of course, observed, and, in our view, this agreement of theory and experiment provides a strong case for the basic hypothesis that negative hyperconjugation is at the root of the torsion angle dependence of the heteroatom substituents observed in our investigation.

### The trialkylammonio group: a perfectly normal substituent?

#### The role of the field effect

On occasion, trialkylammonio groups, and indeed quaternary ammonio functions in general, have been implicated in controversy concerning their role as substituents. The present study has yielded some relevant information and a few comments seem in order. It is necessary to recall that unlike most substituents on the standard roster, the trialkylammonio group is monopolar and its interaction with a developing charge at a reacting centre via the field effect (i.e., through space) is not the same as that of a dipolar substituent such as the alkoxy group. This becomes apparent when one looks at the results of a brief study in which we compared the field effect of the methoxy and trimethylammonio groups using the classic treatment of Bjerrum (8) and Eucken (9) and Kirkwood and Westheimer (10, 11). Specifically, we looked at the variation in energy as a function of the H-C-C-X torsion angle of the species  $\text{X}-\text{C}_\beta-\text{C}_\alpha^\delta\cdots\text{H}$  bearing a partial charge on  $\text{C}_\alpha$  obtained by partial deprotonation of the  $\text{C}_\alpha$ -hydrogen. The study is presented in detail elsewhere (12), but we will mention three points here: (i) the variation of the

energy of the interaction of the charges with change in torsion angle yields a curve (superficially rather like a simple cosine curve, i.e.,  $+\cos \theta$ ) with the principal changes in energy around  $\theta = 90 \pm 50^\circ$ ; (ii) more strikingly, the curves for the dipolar and monopolar groups are reversed, i.e., the largest stabilizing effect of the  $\text{Me}_3\text{N}^+$  group is found at  $\theta \approx 0^\circ$  (at which point the interaction between the positive nitrogen and the incipient negative charge is maximal), whereas the stabilization due to the (dipolar) alkoxy substituent is greatest when  $\theta \approx 180^\circ$  (at which point the destabilization due to the interaction of the incipient negative charge and the  $\delta^-$  on the alkoxy oxygen atom is minimal). (Note that the interaction of the incipient negative charge with the *positive* end of the dipole, i.e.,  $\text{C}_\beta$ , is unaffected by change in the torsion angle ( $\theta$ )); (iii) the magnitude of the energy of interaction with the monopolar trimethylammonio group is distinctly larger (typically by a factor of about five times) than that with the dipolar (alkoxy) group. If the Bjerrum–Eucken–Kirkwood–Westheimer picture is correct in principle, the simple observation that the trialkylammonio group shows qualitatively the same behaviour as the dipolar substituents establishes beyond reasonable doubt that the field effect cannot be the major contributor to the effect of a  $\beta$ -substituent on the ease of formation of an  $\alpha$ -sulfonyl carbanion. This, of course, adds further weight to the conclusion drawn previously that the principal interaction is negative hyperconjugation. The question remains, how much influence, if any, does the field effect have in this system?

One way of looking at the matter takes one along the following lines of thought. Our observation of a reasonable fit of our  $\log k$  values to a simple  $a + b \cos^2 \theta$  relationship could be merely a fortuitous simplification, i.e., the reality may be more complex than first appearance would suggest. One might imagine, for example, that with more (and more accurate)  $k_{\text{N}}$  values the “true”  $\log k_{\text{N}}$  vs.  $\theta$  relationship requires another term,  $-c \cos \theta$ , such that the resulting curve for the negative hyperconjugation energy would look more like the familiar Karplus curve describing NMR coupling constants vs. torsion angle; the key change with the negative  $\cos \theta$  term is that the value of  $\log k_{\text{N}}$  at  $0^\circ$  becomes distinctly smaller than that at  $180^\circ$ . Lambert’s curves for the stabilization of incipient carbocations by the  $\text{Me}_3\text{Si}$  group show such



an appearance with the effect at  $0^\circ$  much weaker than that at  $180^\circ$  (13). Such a difference between  $0$  and  $180^\circ$  is usually ascribed to poorer  $\pi$ -type overlap in the  $0^\circ$  array vs. that at  $180^\circ$ . Is it possible that the field effect of the trialkylammonio group is just the correct magnitude to cancel any effect of a  $\cos \theta$  term? Such a picture is not inconceivable, but if the field effect were of real importance with  $R_3N^+$ , at least some sign would be expected to show up with a dipolar group. With the latter any field effect term would have the *same* sign as the  $\cos \theta$  component, and one would expect to see a clear sign of a lower value for  $\log k_N$  at  $0$  vs.  $180^\circ$ . Careful inspection of the curves for the RO, RS, and  $R_2N$  groups shows little, if any, sign of such a result, suggesting that the combined influence of the field effect and any  $\cos \theta$  term cannot be large. In summary, the results from the present study are most simply accounted for by a primary negative hyperconjugation energy with, as a first approximation, a  $\cos^2 \theta$  dependence on the torsion angle ( $\theta$ ). In addition, there is also an inductive effect totally independent of  $\theta$  and a field effect sufficiently small that the expected variation with  $\theta$  is not clearly evident to us; the possibility of a more substantial field effect is not rigorously excluded.

#### Any reverse anomeric effect?

Perrin (14) has defined the reverse anomeric effect as “the tendency for cationic substituents on a tetrahydropyran ring to take the equatorial position”. This notion had its roots in a 1965 report by Lemieux and Morgan (15) who noted that the  $^1H$  NMR spectra of glycosylpyridinium ions pointed to an equatorial orientation for the ammonio group and not the usual axial conformation expected from the normal anomeric effect. They suggested that the putative effect might arise from field-effect interactions of the free electron pairs on the anomeric oxygen with the monopolar quaternary ammonio group. The considerable array of experiments, up to about 1995, designed to assess this proposal has been nicely summarized by Perrin (14). A relatively recent report by Kirby et al. (16) points to “a preference — though not a strong preference — for the conformation ... favoured by the normal anomeric effect”. Perrin et al. (17), in a recent report on the effect of protonation in *N*-glycopyranosyl imidazoles, found a small preference for the axial orientation of the protonated imidazolyl group relative to the unprotonated group. They concluded that “there is no firm evidence for [the reverse anomeric] effect” and that “previous evidence for this effect is not reliable” (17).

The present study is in qualitative accord with these recent investigations of the reverse anomeric effect in that we see a substantial negative hyperconjugative stabilization with all electron-withdrawing groups whether dipolar or monopolar. We must note, however, that there is a very sizable difference in magnitude of the hyperconjugative effect in our carbanionic system and in the glycoside ammonium salts. The *N*-methylation of the amines (e.g., **1b**  $\rightarrow$  **1c**) is accompanied by a change in hyperconjugative stabilization of the incipient carbanion of about  $5.9 \text{ kcal mol}^{-1}$  (i.e.,  $2.303RT(6.29 - 1.95)/1000$ ). The changes in the *A* value accompanying protonation of the nitrogen reported by Perrin are all less than  $0.3 \text{ kcal mol}^{-1}$ . This difference between the carbanionic and carbohydrate systems is expected on the basis of eq. [2]. The energy of the electrons of the (incipient)

negative charge on carbon is much higher than that of the free electron pair on the tetrahydropyran oxygen atom, with the result that the denominator in eq. [2] ( $\epsilon_A - \epsilon_B$ ) is relatively small in the carbanionic species and much higher in the carbohydrates.

#### The supposed inability of the trialkylammonio group to stabilize by delocalization

It has long been recognized that “the  $(CH_3)_3N^+$  group cannot enter into conjugation in a conventional manner” (18), and the conclusion that has commonly been drawn is that the trialkylammonio group exerts its electronic effect exclusively by the polar (i.e., field plus inductive) effect. Our present results point to negative hyperconjugation of a  $\beta$ -trialkylammonio group in  $\alpha$ -sulfonyl carbanion formation, and hence, any study that explicitly depends on the assumption that the trialkylammonio group functions only via the field and inductive effects probably requires reexamination.

Swain and co-workers (19, 20) based an important analysis of substituent effects on the possibility of assigning unique field and resonance parameters to every substituent. One of its cornerstones is that the large substituent effect of the trimethylammonio group has no resonance component and is entirely a polar effect. Bordwell et al. (21) have also invoked the same basic picture to assign the respective polar and resonance effects to electron-withdrawing groups. These pictures are, at the very least, incomplete in that they both ignore the possibility of hyperconjugation. In light of our work, it is tempting to suggest that our  $\sigma_{90}^*$  parameter would be the place to start in assigning the simple polar (field plus inductive) effect of any group.

## Experimental

The experimental procedures are as described earlier (1), except that some of the rates in the **3** series were measured with a Varian Mercury 400 MHz instrument. Mass spectra: (a) electron impact (EI) and chemical ionization (CI) spectra were recorded using a direct-exposure probe at 70 eV with the source temperature at  $150$ – $175^\circ\text{C}$  and isobutane as the gas for the CI measurements; (b) fast atom bombardment (FAB) were recorded using a glycerol – oxalic acid matrix at room temperature with xenon at 8 kV. New compounds were purified until  $^1H$  and  $^{13}C$  NMR spectra showed only signals appropriate to the assigned structure. Camag DF-5 silica gel was used for chromatography. *N*-Methylthiomorpholine 1,1-dioxide (**1b**) was obtained from Lancaster Synthesis Ltd.

#### 4,4-Dimethyltetrahydro-1,4-thiazinium iodide 1,1-dioxide (**1c**)

A solution of **1b** (50 mg, 0.34 mmol) and MeI (238 mg, 1.68 mmol) in MeOH (1 mL) was allowed to stand overnight at room temperature. Ether (5 mL) was added and the precipitate filtered off and washed with ether giving **1c** as a white solid, mp  $315^\circ\text{C}$  (with decomposition (decomp.)) (80 mg, 82% yield).  $^1H$  NMR ( $D_2O$ )  $\delta$ : 3.2, (s, 6H), 3.5–3.7 (m, 4H), 3.8–4.0 (m, 4H). HR-MS calcd. for  $C_6H_{14}NO_2S$ : 164.0745; found (FAB)  $m/z$ : 164.0739.



**3-(Dimethylamino)tetrahydrothiapyran 1,1-dioxide (2b)**

4*H*-2,3-Dihydrothiapyran-1,1-dioxide (**5**) (22) (50 mg, 0.38 mmol) and dimethylamine (1 mL) were sealed in an NMR tube. After 2 days at room temperature, the tube was cooled in an ice bath and opened carefully and warmed to room temperature to let the excess Me<sub>2</sub>NH evaporate. The residue was dissolved in CH<sub>2</sub>Cl<sub>2</sub> and washed with 10% hydrochloric acid, 5% sodium chloride, and satd. NaCl and dried over MgSO<sub>4</sub>. Removal of the solvent gave **2b** as a white solid, mp 84–86°C, in almost quantitative yield. <sup>1</sup>H NMR (CDCl<sub>3</sub>) δ: 1.25–1.50 (m, 2H), 1.80–2.02 (m, 2H), 2.23 (s, 6H), 2.70–2.85 (m, 2H), 2.90–3.05 (m, 2H), 3.10–3.20 (m, 1H). <sup>13</sup>C NMR (CDCl<sub>3</sub>) δ: 20.9, 27.3, 40.5, 51.1, 52.2, 60.4. HR-MS calcd. for C<sub>7</sub>H<sub>15</sub>NO<sub>2</sub>S: 177.0822; found (EI) *m/z*: 177.0821.

**3-(Trimethylammonio)tetrahydrothiapyran 1,1-dioxide iodide (2c)**

A solution of **2b** (20 mg, 0.11 mmol) and MeI (100 mg, 0.70 mmol) in MeOH (2 mL) treated as in the preparation of **1c** gave **2c** as a white solid, mp 315°C (with decomp.) (31 mg, 86% yield). <sup>1</sup>H NMR (CDCl<sub>3</sub>) δ: 1.50–1.85 (m, 2H), 2.15–2.40 (m, 2H), 2.90 (s, 9H), 2.85–3.20 (m, 2H), 3.36–3.52 (m, 1H), 3.66–3.80 (m, 2H). HR-MS calcd. for C<sub>8</sub>H<sub>18</sub>NO<sub>2</sub>S: 192.1058; found (FAB) *m/z*: 192.1058.

**endo-2-(Phenylsulfonyl)-3-exo-(dimethylamino)norbornane (3b)**

The reaction of (**6**) (23) (100 mg, mmol) in CDCl<sub>3</sub> (0.5 mL) containing excess Me<sub>2</sub>NH in a sealed NMR tube was monitored by <sup>1</sup>H NMR. After 24 h the volatile material was evaporated under reduced pressure and the residue chromatographed on a 20 g silica gel plate (benzene–ether, 1:1) giving **3b** (100 mg, 83%) as a colourless solid, mp 105–107°C. IR (Nujol) *v*<sub>max</sub>: 1307 (s), 1292 (s), 1158 (s). <sup>1</sup>H NMR (CDCl<sub>3</sub>) δ: 1.14 (m, 3H), 1.50–1.64 (m, 2H), 2.13 (s, 6H), 2.17–2.20 (br s, 2H), 2.44 (d, 1H, *J* = 5 Hz), 2.75 (d, 1H, *J* = 4 Hz), 3.22–3.24 (m, 1H), 7.42–7.59 (m, 3H), 7.79–7.87 (m, 2H). <sup>13</sup>C NMR (CDCl<sub>3</sub>) δ: 23.2, 26.2, 37.1, 39.5, 39.9, 43.0, 69.5, 70.3, 127.8, 128.8, 133.1, 140.2. HR-MS calcd. for C<sub>15</sub>H<sub>21</sub>NO<sub>2</sub>S: 279.1293; found (EI) *m/z*: 279.1297.

**Trimethyl-*exo*-3-[endo-2-(phenylsulfonyl)norbornyl]ammonium iodide (3c)**

A diethyl ether solution (5 mL) of **3b** (200 mg, 0.71 mmol) and excess MeI was refluxed for 24 h. The volatile material was evaporated and the residue rinsed several times with ether leaving **3d** as a colourless solid, mp 209–211°C (250 mg, 85%). IR (Nujol): 1387 (s), 1312 (s), 1158 (s). <sup>1</sup>H NMR (D<sub>2</sub>O) δ: 1.10–1.40 (m, 3H), 1.50–1.90 (m, 3H), 2.10 (br s, 1H), 2.86 (d, 1H, *J* = 4 Hz), 3.07 (s, 9H), 3.87 (d, 1H, *J* = 6 Hz), 4.33 (br s, 1H), 7.54–7.63 (m, 2H), 7.66–7.75 (m, 1H), 7.85–7.91 (m, 2H). <sup>13</sup>C NMR (CDCl<sub>3</sub>) δ: 24.5, 29.7, 39.7, 43.1, 44.3, 55.6, 70.5, 80.0, 130.6, 132.5, 137.8, 139.5. HR-MS calcd. for C<sub>16</sub>H<sub>24</sub>NO<sub>2</sub>S: 294.1528; found (FAB) *m/z*: 294.1529.

**1,4-Dithiane 1,1-dioxide (1d)**

Literature preparation (24), mp 202–204°C. <sup>1</sup>H NMR (CDCl<sub>3</sub>) δ: 3.05–3.20 (m, 4H), 3.20–3.30 (m, 4H). <sup>13</sup>C NMR (CDCl<sub>3</sub>) δ: 27.7, 54.1.

**3-(Methylthio)tetrahydrothiapyran 1,1-dioxide (2d)**

A solution of 3-bromotetrahydrothiapyran 1,1-dioxide (**25**) (350 mg, 1.64 mmol) and NaSMe (173 mg, 2.46 mmol) in 2-butanol (30 mL) was refluxed for 1 h under N<sub>2</sub>. Work up and recrystallization from EtOAc–hexane gave **2d** as white needles (210 mg, 71%), mp 94 to 95°C. <sup>1</sup>H NMR (CDCl<sub>3</sub>) δ: 1.3–1.5 (m, 1H), 2.0–2.5 (m, 3H), 2.14 (s, 3H), 2.5–3.2 (m, 4H), 3.2–3.5 (m, 1H). <sup>13</sup>C NMR (CDCl<sub>3</sub>) δ: 13.5, 23.1, 30.8, 41.1, 50.8, 56.8. HR-MS calcd. for C<sub>6</sub>H<sub>12</sub>O<sub>2</sub>S: 180.0279; found (EI) *m/z*: 180.0276.

**3-(Methylsulfonyl)tetrahydrothiapyran 1,1-dioxide (2e)**

A mixture of **2d** (230 mg, 1.28 mmol), glacial HOAc (~1 mL), and 30% H<sub>2</sub>O<sub>2</sub> (~2 mL) was heated at 100°C for 15 min. The mixture was cooled, water (30 mL) was added, and the mixture extracted with CH<sub>2</sub>Cl<sub>2</sub> (5 × 40 mL). The combined extracts were then washed with 5% aq NaOH (2 × 30 mL) and satd. NaCl (2 × 60 mL). Evaporation of the solvent and recrystallization from EtOH gave **2e** as white crystals (57 mg, 21%), mp 210.5–212°C. <sup>1</sup>H NMR (CDCl<sub>3</sub>) δ: 1.20–1.30 (m, 1H), 2.05–2.50 (m, 3H), 2.94 (s, 3H), 3.05–3.25 (m, 2H), 3.40–3.60 (m, 2H), 4.0–4.2 (m, 1H). <sup>13</sup>C NMR (CDCl<sub>3</sub>) δ: 22.0, 23.5, 38.6, 49.8, 50.8, 59.1. HR-MS calcd. for C<sub>6</sub>H<sub>13</sub>O<sub>4</sub>S ([M + 1]): 213.0255; found (CI) *m/z*: 213.0261.

**endo-2-(Phenylsulfonyl)-*exo*-3-(methylthio)norbornane (3d)**

*endo*-2-Chloro-*exo*-3-(phenylsulfonyl)norbornane (**23**) (230 mg, 0.85 mmol) and sodium methoxide (92 mg, 1.3 mmol) in dry MeOH (5 mL) were refluxed for 5 h. The MeOH was evaporated and the residue taken up in CH<sub>2</sub>Cl<sub>2</sub>. The solution was washed with water and evaporated. Chromatography on a silica gel plate (20 g, 20 × 20 cm) developing with benzene–ether (3:1) gave **3d** (190 mg, 79%) as a colourless solid, mp 119–121°C. IR (Nujol) (cm<sup>-1</sup>) *v*<sub>max</sub>: 1387 (s), 1158 (s). <sup>1</sup>H NMR (CDCl<sub>3</sub>) δ: 1.34–1.49 (m, 3H), 1.64–1.82 (m, 2H), 2.04 (s, 3H), 2.26–2.37 (m, 1H), 2.39 (d, 1H, *J* = 5 Hz), 2.55 (br s, 1H), 3.10–3.22 (m, 2H), 7.20–7.58 (m, 2H), 7.59–7.66 (m, 1H), 7.87–7.97 (m, 2H). <sup>13</sup>C NMR (CDCl<sub>3</sub>) δ: 16.0, 23.3, 27.6, 37.8, 40.3, 43.8, 49.8, 73.5, 128.01, 128.06, 133.4, 140.1. HR-MS calcd. for C<sub>14</sub>H<sub>18</sub>O<sub>2</sub>S<sub>2</sub>: 282.0748; found (EI) *m/z*: 282.0742.

**endo-2-(Phenylsulfonyl)-*exo*-3-(methylsulfonyl)norbornane (3e)**

A solution of **3d** (130 mg, 0.46 mmol) in MeOH (8 mL) at 0°C was added with stirring to a solution of OXONE® (847 mg, 1.4 mmol) in H<sub>2</sub>O (5 mL) at 0°C, and the mixture allowed to come to room temperature. After 4.5 h the mixture was extracted with excess CH<sub>2</sub>Cl<sub>2</sub>, the organic layer dried, and the solvent evaporated. The residue was chromatographed on a 20 g silica gel plate (benzene–ether, 3:1) giving the sulfone (**3e**) as a colourless solid (123 mg, 85%), mp 190 to 191°C. IR (Nujol) *v*<sub>max</sub>: 1297 (s), 1148 (s). <sup>1</sup>H NMR (CDCl<sub>3</sub>) δ: 1.25–1.60 (m, 3H), 1.70–1.90 (m, 2H), 2.27 (br s, 2H), 3.04 (s, 3H), 3.04–3.15 (br s, 1H), 3.50 (d, 1H, *J* = 4 Hz), 3.89 (br s, 1H), 7.56–7.68 (m, 2H), 7.65–7.73 (m, 1H), 7.85–7.97 (m, 2H). <sup>13</sup>C NMR (CDCl<sub>3</sub>) δ: 22.5, 28.0, 38.1, 39.8, 40.6, 41.1, 64.7, 67.3, 128.3, 134.1, 136.2,



138.2. HR-MS calcd. for  $C_{14}H_{19}O_4S_2$  ( $[M + 1]$ ): 315.0725; found (CI)  $m/z$ : 315.0730.

#### 1,4-Dithia-*trans*-decalin 1,1,4,4-tetroxide (4c)

Literature preparation (26), mp 289–291°C (sealed capillary), lit. (26) mp value 288°C.  $^1H$  NMR ( $CDCl_3$ )  $\delta$ : 1.25–1.45 (m, 2H), 1.55–1.75 (m, 2H), 1.88–2.05 (m, 2H), 2.24–2.38 (m, 2H), 3.29–3.42 (m, 2H), 3.40–3.53 (m, 2H), 3.68–3.88 (m, 2H).  $^{13}C$  NMR ( $CDCl_3$ )  $\delta$ : 20.2, 23.3, 49.0, 61.6.

#### Acknowledgement

We thank the Natural Sciences and Engineering Research Council of Canada (NSERC) for support of this work.

#### References

1. J.F. King, R. Rathore, Z. Guo, M. Li, and N.C. Payne. *J. Am. Chem. Soc.* **122**, 10 308 (2000).
2. R. Hoffmann, L. Radom, J.A. Pople, P.v.R. Schleyer, W.S. Hehre, and L. Salem. *J. Am. Chem. Soc.* **94**, 6221 (1972).
3. S. David, O. Eisenstein, W.J. Hehre, L. Salem, and R. Hoffmann. *J. Am. Chem. Soc.* **95**, 3806 (1973).
4. R.C. Bingham. *J. Am. Chem. Soc.* **97**, 6743 (1975).
5. P.v.R. Schleyer and A.J. Kos. *Tetrahedron*, **39**, 1141 (1983).
6. O. Exner. *In* Correlation analysis in chemistry: Recent advances. *Edited by* N.B. Chapman and J. Shorter. Plenum Press, New York. 1978. Chap. 10. pp. 439–540.
7. (a) A. Rauk. *Orbital interaction theory of organic chemistry*. Wiley-Interscience, New York. 2001. pp. 83–84; (b) A. Rauk. *Orbital interaction theory of organic chemistry*. Wiley-Interscience, New York. 2001. p. 44.
8. N. Bjerrum. *Z. Phys. Chem.* **106**, 219 (1923).
9. A. Eucken. *Z. Angew. Chem.* **45**, 203 (1932).
10. J.G. Kirkwood and F.H. Westheimer. *J. Chem. Phys.* **6**, 506 (1938).
11. F.H. Westheimer and J.G. Kirkwood. *J. Chem. Phys.* **6**, 513 (1938).
12. M. Li. Ph.D thesis, The University of Western Ontario, London, Ontario, Canada. 1999. pp. 71–79, 142–150.
13. J.B. Lambert and X. Liu. *J. Organomet. Chem.* **521**, 203 (1996); J.B. Lambert, Y. Zhao, R.W. Emblidge, L.A. Salvador, X. Liu, J.-H. So, and E.C. Chelius. *Acc. Chem. Res.* **32**, 183 (1999).
14. C.L. Perrin. *Tetrahedron*, **51**, 11901 (1995).
15. R.U. Lemieux and A.R. Morgan. *Can. J. Chem.* **43**, 2205 (1965).
16. A.J. Kirby, I.V. Komarov, P.D. Wothers, N. Feeder, and P.G. Jones. *Pure Appl. Chem.* **71**, 385 (1999).
17. C.L. Perrin, M.A. Fabian, J. Brunckova, and B.K. Ohta. *J. Am. Chem. Soc.* **121**, 6911 (1999).
18. F.G. Bordwell and P.J. Boutan. *J. Am. Chem. Soc.* **78**, 87 (1956).
19. C.G. Swain and E.C. Lupton, Jr. *J. Am. Chem. Soc.* **90**, 4328 (1968).
20. C.G. Swain, S.H. Unger, N.R. Rosenquist, and M.S. Swain. *J. Am. Chem. Soc.* **105**, 492 (1983).
21. (a) F.G. Bordwell, M. Van Der Puy, and N.R. Vanier. *J. Org. Chem.* **41**, 1883 (1976); (b) 1885 (1976).
22. S.M. Liebowitz, J.B. Lombardini, and C.I. Allen. *Biochem. Pharmacol.* **38**, 399 (1989).
23. P.B. Hopkins and P.L. Fuchs. *J. Org. Chem.* **43**, 1208 (1978).
24. E.L. Clennan, D.X. Wang, K. Yang, D.J. Hodgson, and A.R. Oki. *J. Am. Chem. Soc.* **114**, 3021 (1992).
25. E.A. Fehnel. *J. Am. Chem. Soc.* **74**, 1569 (1952).
26. C.C.J. Culvenor, W. Davies, D.G. Hawthorne, P.L. MacDonald, and A.V. Robertson. *Aust. J. Chem.* **20**, 2207 (1967).



# Influence of alkali metal cations on the photoheterolysis of 9-cyclopropyl-9-fluorenone and the reactivity of the 9-cyclopropyl-9-fluorenyl cation in non-acidic zeolites

Melanie A. O'Neill and Frances L. Cozens

**Abstract:** Alkali metal cation regulation of carbocation formation and reactivity in non-acidic zeolites is probed using the photoheterolysis reaction of 9-cyclopropyl-9-fluorenone. Nanosecond time-resolved diffuse reflectance is employed to directly observe the 9-cyclopropyl-9-fluorenyl cation as a transient species within the non-acidic zeolites. The efficiency of carbocation formation via photoheterolysis and the dynamics of other reaction pathways available to photoexcited 9-cyclopropyl-9-fluorenone are found to be strongly dependent on the zeolite alkali metal counterion. In particular, the yield of carbocation decreases with increasing counterion size in a manner consistent with the zeolite assisting the excited state C—O bond cleavage via Lewis acid catalysis involving the metal cation. Zeolite encapsulation is also found to modulate the ability of water and methanol to assist photoheterolysis. For instance, the influence of coadsorbed water on the photoheterolysis reaction within zeolites is found to be highly sensitive to the alkali metal cation. The rate constant for intrazeolite decay of the 9-cyclopropyl-9-fluorenyl cation increases significantly as the alkali metal cation size increases and as the Si—Al ratio decreases. These reactivity trends suggest that the intrazeolite decay of the 9-cyclopropyl-9-fluorenyl cation involves nucleophilic addition at the active site [Si—O—Al]<sup>−</sup> bridges of the zeolite framework. In addition, the reactivity of the 9-cyclopropyl-9-fluorenyl cation within alkali metal zeolites can be regulated by the co-inclusion of reagents such as methanol, water, and 1,1,1,3,3,3-hexafluoro-2-propanol.

**Key words:** cation-exchanged zeolites, 9-cyclopropyl-9-fluorenyl cation, laser photolysis, reactivity.

**Résumé :** La formation de carbocation contrôlée par les cations de métaux alcalins, et la réactivité dans les zéolites non acides sont mises en évidence en utilisant la réaction de photohétérolyse du 9-cyclopropyl-9-fluorénone. On a employé le pouvoir réflecteur diffus résolu dans des temps de l'ordre de la nanoseconde, pour observer directement le cation 9-cyclopropyl-9-fluorényle comme une espèce intermédiaire dans les zéolites non acides. On a trouvé que l'efficacité de la formation du carbocation via la photohétérolyse ainsi que la dynamique d'autres chemins réactionnels disponibles pour exciter photochimiquement le 9-cyclopropyl-9-fluorénone dépendent fortement du contre-ion métal alcalin zéolite. En particulier, le rendement de carbocation décroît avec l'augmentation de la taille du contre-ion d'une manière qui suggère une influence de la zéolite sur l'état excité résultant du clivage de la liaison C—O via une catalyse acide de Lewis impliquant le cation métallique. On a également trouvé que l'encapsulation de la zéolite module la capacité de l'eau et du méthanol à assister la photohétérolyse. Par exemple, on a trouvé que l'influence de l'eau coadsorbée sur la réaction de photohétérolyse dans la zéolite dépend fortement du cation de métal alcalin. La constante de vitesse pour la décroissance de la zéolite encapsulée dans le cation 9-cyclopropyl-9-fluorényle augmente de façon significative lorsque la taille du cation de métal alcalin augmente et lorsque le ratio Si—Al diminue. Ces réactivités suggèrent que la décroissance de la zéolite encapsulée dans le cation 9-cyclopropyl-9-fluorényle implique une addition nucléophile au niveau des ponts [Si—O—Al]<sup>−</sup> du site actif du squelette de la zéolite. De plus la réactivité du cation 9-cyclopropyl-9-fluorényle à l'intérieur des zéolites de métal alcalin peut être contrôlée par la co-inclusion de réactifs tels le méthanol, l'eau et le 1,1,1,3,3,3-hexafluoro-2-propanol.

**Mots clés :** zéolites à échange de cation, cation 9-cyclopropyl-9-fluorényle, photolyse au laser, réactivité.

[Traduit par la Rédaction]

Received 7 February 2003. Published on the NRC Research Press Web site at <http://canjchem.nrc.ca> on 10 June 2003.

*This paper is dedicated to Professor Don Arnold in recognition of his many fine contributions to the world of chemistry.*

**M.A. O'Neill and F.L. Cozens.**<sup>1</sup> Department of Chemistry, Dalhousie University, Halifax, NS B3H 4J3, Canada.

<sup>1</sup>Corresponding author (e-mail: [fcozens@dal.ca](mailto:fcozens@dal.ca)).

## Introduction

Zeolites (1–3) continue to demonstrate their potential as unique and versatile host materials for a variety of chemical transformations (4–10). The efficient catalytic activity of zeolites and the important role of cationic intermediates in these reactions have been the impetus for much research aimed at understanding the chemistry of carbocations (11–18) and radical cations (8, 16, 19–25) within the cavities and channels of zeolites. However, to date, most studies of



carbocations within zeolite hosts have focused on proton-exchanged Brønsted zeolites, or zeolites with divalent metal ions such as  $\text{Ca}^{2+}$  that possess strong acidic properties upon thermal activation (26–29). In the highly acidic environment of acid zeolites a wide number of carbocations can be readily generated and, more importantly, are thermodynamically and kinetically stabilized to the extent that they can be readily examined by steady-state techniques such as solid-state NMR (12, 15, 30–34), UV–vis diffuse reflectance (9, 35–39), and UV–vis absorption spectroscopy (40, 41). This research has contributed to the emerging picture of Brønsted zeolites not as superacid solid materials as once envisioned, but as strong acids whose ability to stabilize and influence the reactivity of cationic species is closely linked to the dynamic role of the zeolite framework in carbocation chemistry (12). Thus, although several types of relatively stabilized carbocations such as triarylmethyl (38), xanthylum (11, 36), indanyl (30), and cyclopentenyl cations (33) can be detected as stable ions in acidic zeolites, more reactive species such as phenethyl cations (30) do not persist within these environments.

In addition to strong Brønsted and Lewis acid sites, stabilization of positively charged intermediates in acidic zeolites has been attributed to the high electrostatic fields associated with the intrazeolite environment and the tight confinement provided by the zeolite micropore, which protects the ion from nucleophilic attack (9, 42, 43). Consequently, non-protic zeolites have also been shown to be useful media for the photochemical generation and stabilization of radical cations (8, 19, 23, 24), and more recently have been shown to be unique hosts for the study of reactive carbocations (17, 18). Further insights into carbocation-mediated reactions can be obtained from studies investigating the behavior of carbocations within non-protic, alkali metal cation-exchanged zeolites. For example, using alkali metal cation zeolites, the influence of the counterion on the generation and kinetic stability of the carbocation can be readily explored. In this way it is possible to examine the effect of properties such as electrostatic field strength and exchangeable counterion size on the chemistry of carbocations within the cavities of alkali metal cation zeolites. While the negatively charged framework in proton-exchanged zeolites is generally presumed to act as a large, relatively non-nucleophilic counterion, the possibility that localized sites of electron density in these zeolite frameworks, namely the  $[\text{Si-O-Al}]^-$  bridges, may be reactive towards carbocation intermediates can also be explored.

9-Fluorenol derivatives are attractive probe molecules for investigating within non-acidic zeolites carbocation formation and reactivity, both of which have been studied extensively in solution (44–49). In solution the absorption spectra and absolute reactivity of a wide range of 9-substituted-9-fluorenyl cations have been well characterized as a function of substituent and solvent conditions (50–53). In addition, the formation of 9-fluorenyl cations by photoheterolysis of 9-fluorenols is an interesting probe reaction, particularly since considerable experimental evidence suggests that photoheterolysis of the C—O bond of 9-fluorenols is assisted by proton sources (44–46, 49). Therefore, generation of 9-fluorenyl cations in non-protic zeolites addresses questions concerning the existence and nature of acidic sites

within these frameworks and their potential to catalyze heterolysis reactions. Since 9-fluorenols are known to undergo both heterolysis and ionization upon photoexcitation in solution (48), the competition between carbocation and radical cation formation can be directly examined as a function of the local zeolite environment. This can afford new insights into the dynamics of carbocation formation within non-acidic zeolites.

Herein we report on the dynamics of photoexcited 9-cyclopropyl-9-fluorenol (cPrFOH) and on the reactivity of the photogenerated 9-cyclopropyl-9-fluorenyl cation in alkali metal cation zeolites. The presence of the cyclopropyl substituent at the 9-position affords a significant degree of stability to the 9-fluorenyl cation without introducing unwanted steric bulk or structural changes associated with a 9-aryl substituent (50). In the present work the photogeneration and reactivity of the 9-cyclopropyl-9-fluorenyl cation is used to investigate the internal environment within non-protic Y and X zeolites in terms of their ability to mediate photoheterolysis and to influence the reactivity of cationic intermediates. Particular emphasis is placed on the rather dramatic role the alkali metal cation plays in defining both the reactivity of photoexcited cPrFOH towards photoheterolysis and the lifetime of the corresponding 9-cyclopropyl-9-fluorenyl cation. In addition, the presence of protic co-reagents, such as methanol, water and 1,1,1,3,3,3-hexafluoro-2-propanol (HFIP), on the efficiency of both photoheterolysis and the reactivity of the carbocation was investigated.

## Results

### Laser photolysis of 9-cyclopropyl-9-fluorenol in dry NaY

The transient diffuse reflectance spectrum obtained upon 308 nm laser irradiation of cPrFOH in evacuated ( $1 \times 10^{-4}$  torr, 1 torr = 133.322 Pa) dry NaY has three distinct absorption bands at 380, 445, and 640 nm and a well-defined shoulder at 330 nm (Fig. 1a). The absorption bands located at 380 and 445 nm, together with the shoulder at 330 nm bear a close resemblance to the known absorption spectrum of the 9-cyclopropyl-9-fluorenyl cation previously generated photochemically in 2,2,2-trifluoroethanol (TFE) (50). The similarities between the diffuse reflectance spectrum in NaY and the known absorption spectrum of the 9-cyclopropyl-9-fluorenyl cation strongly suggest that this carbocation contributes significantly to the absorption bands observed at 330, 380, and 445 nm in NaY. In addition, the transient species observed at 380 and 445 nm is unreactive towards oxygen, but decays more rapidly in the presence of nucleophiles such as water and methanol (vide infra), consistent with its identification as a cationic intermediate. Furthermore, the absorption at these wavelengths decays (Fig. 1 inset) with a first-order rate constant of  $3.8 \times 10^5 \text{ s}^{-1}$  (Table 1) that lies in the range expected for the 9-cyclopropyl-9-fluorenyl cation based on the reactivity of other 9-fluorenyl cations (18) within NaY. These observations are all consistent with the presence of the 9-cyclopropyl-9-fluorenyl cation generated by photoheterolysis of cPrFOH within the cavities of NaY (Scheme 1, path (a)).

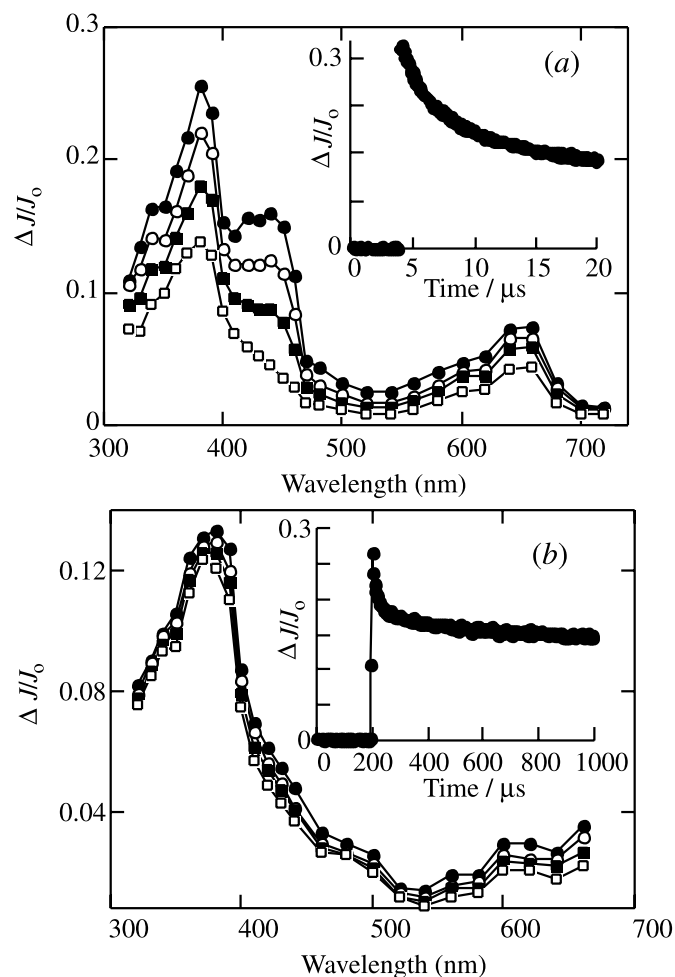
A significant long-lived absorption remains at 380 nm after the decay of the 9-cyclopropyl-9-fluorenyl cation is



**Table 1.** Decay rate constants for the 9-cyclopropyl-9-fluorenyl cation in dry and hydrated alkali metal cation Y zeolites, ratio of carbocation decay rate constant observed under hydrated and dry conditions, and increase in carbocation yield upon hydration.

Zeolite	$k_{\text{dry}}$ ( $10^5 \text{ s}^{-1}$ )	$k_{\text{hyd}}$ ( $10^5 \text{ s}^{-1}$ )	$k_{\text{hyd}}/k_{\text{dry}}$	Increase in carbocation yield upon hydration (%)
LiY	$0.64 \pm 0.01$	$2.5 \pm 0.1$	3.9	3
NaY	$3.8 \pm 0.1$	$7.2 \pm 0.1$	1.8	10
KY	$8.0 \pm 0.1$	$10.6 \pm 0.3$	1.4	32
RbY	$10.4 \pm 0.2$	$22.7 \pm 0.2$	1.6	54
CsY	Not observed	Not observed	—	—
NaX	$7.9 \pm 0.1$	—	—	—

**Fig. 1.** (a) Transient diffuse reflectance spectra generated 700 ns (●), 2.40  $\mu\text{s}$  (○), 7.00  $\mu\text{s}$  (■), and 34.0  $\mu\text{s}$  (□) after 308 nm laser irradiation of cPrFOH in evacuated NaY. Inset shows the decay trace monitored at 445 nm over a short time scale. (b) Transient diffuse reflectance spectra generated 16.8  $\mu\text{s}$  (●), 294  $\mu\text{s}$  (○), 440  $\mu\text{s}$  (■), and 684  $\mu\text{s}$  (□) after 308 nm laser irradiation of cPrFOH in evacuated NaY. Inset shows the decay trace monitored at 380 nm over a long time scale.



complete (Fig. 1b). This suggests the presence of an additional species upon laser photolysis of cPrFOH in NaY. The spectral appearance of this species is closely similar to that previously observed upon laser irradiation of other 9-fluorenols in alkali metal cation zeolites (18) and in solution

(47) and is identified as the triene isomer generated by photoinduced rearrangement of cPrFOH within NaY (Scheme 1, path (b)). Evidence to support the identification of the long-lived 380 nm band to the rearranged triene isomer is the lack of dependence on the addition of oxygen to the zeolite sample and the long lifetime where virtually no decay is observed at time scales as long as 1 ms after the laser pulse (54). Both observations are consistent with the expected behavior for the rearranged triene isomer.

The transient diffuse reflectance spectrum shown in Fig. 1a also has long wavelength absorption with a maximum at 640 nm and a shoulder near 600 nm. This absorption band is not associated with either the 9-cyclopropyl-9-fluorenyl cation or the triene isomer, but is highly characteristic of fluorene-type radical cations (46, 48, 55). The detection of the cPrFOH radical cation following laser photolysis of cPrFOH in NaY is anticipated based on the observation that other 9-alkyl-9-fluorenols undergo photoionization in alkali metal zeolites to generate the corresponding radical cation (18). Thus, the absorption band at 640 nm is attributed to the cPrFOH radical cation produced by photoionization of cPrFOH within NaY (Scheme 1, path (c)).

The cPrFOH radical cation decays over a broad range of time scales from a few  $\mu\text{s}$  to several hundreds of  $\mu\text{s}$  and thus exhibits notable fast and slow components. Although the decay kinetics of the radical cation are somewhat complex, the decay of the fast component at 640 nm can be represented by a first-order process described by the rate constants given in Table 2. As fluorene-type radical cations are known to have a second absorption band in this region following laser photolysis of cPrFOH within NaY must also contain a contribution from the cPrFOH radical cation. The 380 nm band is therefore very complex, with three species contributing to the absorption at that wavelength. As a result, detailed examination of the reactivity of the 9-cyclopropyl-9-fluorenyl cation focussed on the 445 nm region where only the carbocation has significant absorption.

#### Laser photolysis of 9-cyclopropyl-9-fluorenyl in dry alkali metal cation MY zeolites

Laser photolysis of cPrFOH incorporated within other alkali metal cation (LiY, KY, RbY, and CsY) zeolites was carried out to examine the effect of the zeolite environment on the generation and reactivity of the 9-cyclopropyl-9-fluorenyl cation. The transient diffuse reflectance spectra obtained upon 308 nm excitation of cPrFOH in the MY zeolites under dry vacuum conditions ( $1 \times 10^{-4}$  torr, 1 torr =



Scheme 1.

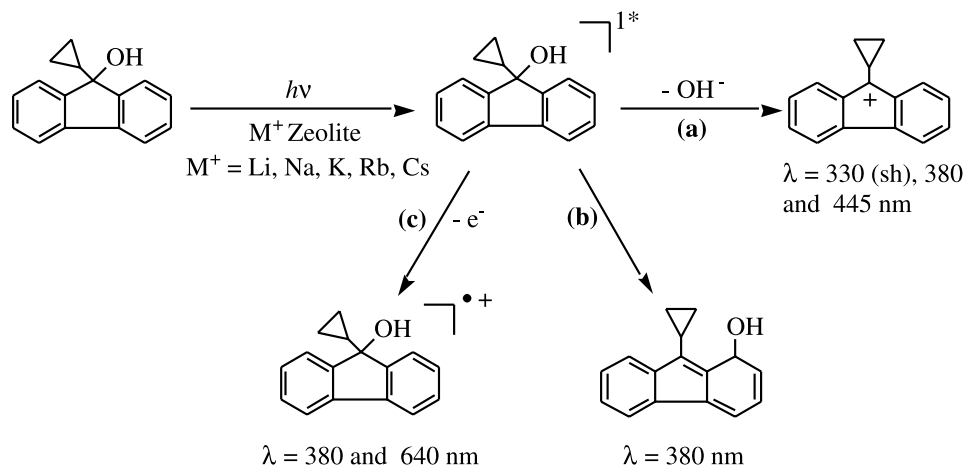


**Fig. 2.** Transient diffuse reflectance spectra generated (a) 320 ns (●), 2.96  $\mu\text{s}$  (○), 6.00  $\mu\text{s}$  (■), and 14.8  $\mu\text{s}$  (□) after photolysis in LiY and 320 ns (●), 800 ns (○), 2.00  $\mu\text{s}$  (■), and 14.0  $\mu\text{s}$  (□) after photolysis in (b) KY, (c) RbY, and (d) CsY. Insets show decay traces monitored at 445 nm (top  $\Delta J/J_0 = 0.35$  in each case).

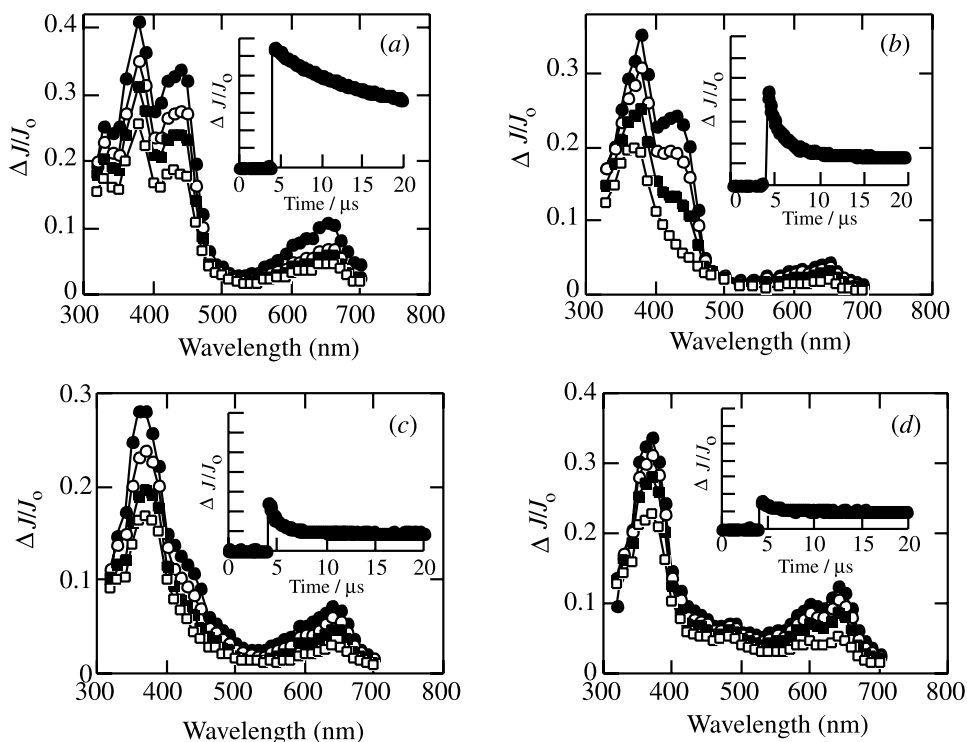


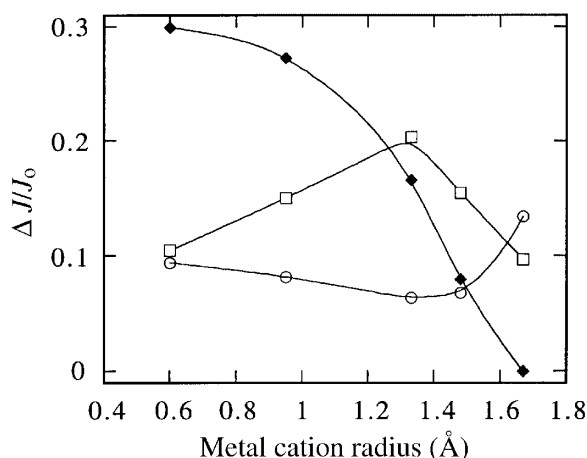
**Table 2.** First-order rate constants for the decay of the 9-cyclopropyl-9-fluorenyl radical cation observed at 640 nm in dry alkali metal cation zeolites.

Zeolite	$k_{\text{obs}}$ ( $10^5 \text{ s}^{-1}$ )
LiY	$6.7 \pm 0.3$
NaY	$8.7 \pm 0.3$
KY	$9.2 \pm 0.5$
RbY	$8.5 \pm 0.5$
CsY	$5.6 \pm 0.2$

133.322 Pa) are shown in Fig. 2. Each spectrum clearly exhibits distinct features, especially with regard to the 9-cyclopropyl-9-fluorenyl cation probed at 445 nm, which shows a dramatic dependence on the zeolite counterion both in terms of yield and absolute reactivity (Fig. 2 insets). For instance, as the size of the alkali metal counterion increases upon going from  $\text{Li}^+$  to  $\text{Rb}^+$ , the observed rate constant for the disappearance of the 9-cyclopropyl-9-fluorenyl cation increases significantly from  $k = 6.4 \times 10^4 \text{ s}^{-1}$  in LiY to  $k = 1.04 \times 10^6 \text{ s}^{-1}$  in RbY (Table 1). In addition, the intensity of the absorption at 445 nm, which is proportional to the yield of carbocation formation, decreases significantly along the zeolite series and is not detected at all in CsY. Thus, the



**Fig. 3.** Variation in the yield of the 9-cyclopropyl-9-fluorenyl cation (◆), cPrFOH radical cation (○), and rearranged triene isomer (□) as a function of alkali metal cation radius following laser photolysis of cPrFOH in evacuated LiY, NaY, KY, RbY, and CsY zeolites.



alkali metal counterion exerts two distinct effects: it modulates both the efficiency of the photoheterolysis reaction and carbocation formation (Fig. 3) and the reactivity of the resulting 9-cyclopropyl-9-fluorenyl cation.

In addition to carbocation formation via heterolysis, the efficiencies of ionization and rearrangement are also strongly influenced by the nature of the zeolite counterion (Fig. 3). The yield of the triene isomer was evaluated from the absorption at 380 nm after the other transients with absorption at that wavelength had completely decayed. The yield of the triene isomer initially increases with increasing alkali cation size to a maximum in KY where subsequent increases in counterion size result in an overall decrease in the yield of the triene isomer. Correspondingly, the yield of radical cation, as determined from the intensity of absorption observed at 640 nm immediately following the laser pulse, decreases slightly upon going from Li<sup>+</sup> to K<sup>+</sup> and then increases in the larger alkali metal cation zeolites and is the major transient formed in CsY.

The transient diffuse reflectance spectrum generated upon laser photolysis of cPrFOH within the cavities of dry, evacuated NaX is characterized by three absorption maxima at 380, 445, and 640 nm, and closely resembles the spectra observed in the alkali metal cation Y zeolites, in particular KY. The first-order decay rate constant for the carbocation at 445 nm in NaX of  $k = 7.9 \times 10^5 \text{ s}^{-1}$  is twice as large as in NaY where  $k = 3.8 \times 10^5 \text{ s}^{-1}$  (Table 1). At longer times scales after the carbocation has completely decayed (>20 μs), and most of the radical cation has disappeared (>200 μs), an intense absorption band at 380 nm due to the triene isomer is observed and exhibits no decay in NaX over times as long as 1 ms.

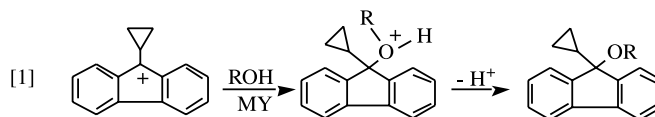
#### Co-adsorption of water and methanol in NaY

Water has been shown to strongly influence the photoheterolysis of 9-fluorenol derivatives in solution and tends to increase the efficiency of photoheterolysis relative

to non-protic solvents such as acetonitrile (45, 49). The effect of such reagents on the microenvironment of the zeolite cavity can be examined by investigating how co-adsorbates influence both the photochemistry of cPrFOH and reactivity of the 9-cyclopropyl-9-fluorenyl cation.

The transient diffuse reflectance spectra obtained upon laser photolysis of cPrFOH in NaY containing 6% water and 6% methanol<sup>2</sup> along with the corresponding decay traces at 445 nm are shown in Fig. 4. The first-order rate constants  $k = 7.2 \times 10^5 \text{ s}^{-1}$  and  $k = 9.9 \times 10^5 \text{ s}^{-1}$  obtained for the decay of the carbocation at 445 nm in NaY containing 6% water and 6% methanol, respectively, are considerably faster than that observed under dry conditions ( $k = 3.8 \times 10^5 \text{ s}^{-1}$ ). In addition, upon coinorporation of these protic reagents, the transient spectra more closely resemble that observed upon photolysis of the same precursor in neat TFE where carbocation formation is the dominant reaction pathway. In particular, the long-lived absorption at 380 nm because of the rearranged triene isomer and long wavelength absorption because of the cPrFOH radical cation are attenuated in the zeolite hosts containing a proton source. The attenuation of these absorption bands suggests that photoheterolysis of the C—O bond is now the dominant reaction pathway and that water and methanol co-adsorbed within the zeolite framework strongly influences the behaviour of photoexcited cPrFOH. The spectra show that the influence of methanol is not as dramatic as the influence of water on the relative yield of carbocation with respect to the other processes that are available to photoexcited cPrFOH within the zeolite environment. As such, the transient spectrum observed in NaY containing methanol continues to possess visible absorption because of the triene isomer at 380 nm and cPrFOH radical cation at 640 nm.

The rate constant for the decay of the 9-cyclopropyl-9-fluorenyl cation at 445 nm increases as a function of the concentration of methanol and water (Fig. 5a). The increase in the rate constant upon the addition of methanol or water to the zeolite cavity is in agreement with a mechanism involving nucleophilic attack of the carbocation via co-incorporated methanol or water (eq. [1]). The greater dependence on methanol concentration as compared to water is consistent with the greater nucleophilicity of methanol as compared to water towards reactive carbocations within zeolites (17, 18).

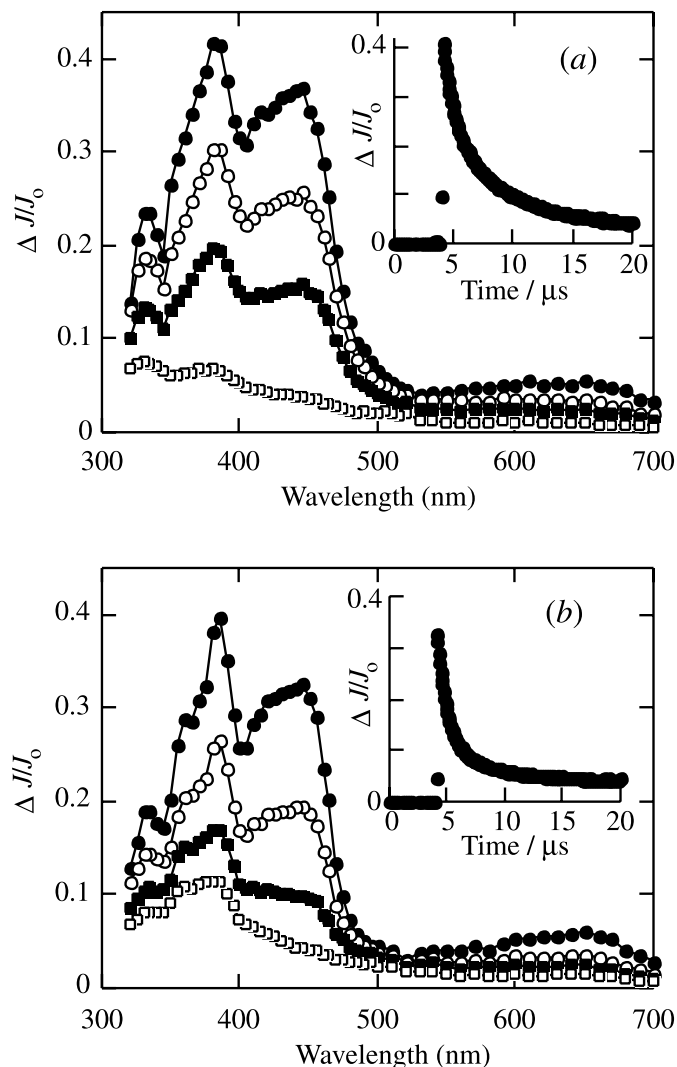


When the change in diffuse reflectance ( $\Delta J/J_0$ ) is monitored at 445 nm following photolysis of cPrFOH in NaY as a function of water or methanol content, a steady increase in the yield of carbocation with increasing adsorbate concentration is revealed (Fig. 5b). This clearly demonstrates that C—O bond heterolysis of excited cPrFOH in NaY is progressively enhanced by co-adsorption of increasingly higher concentrations of either water or methanol. Notably, the increase in photoheterolysis within NaY is more substantial

<sup>2</sup>The % additive content is given in terms of weight %.



**Fig. 4.** Transient diffuse reflectance spectra generated at 280 ns (●), 1.00  $\mu$ s (○), 2.64  $\mu$ s (■), and 14.9  $\mu$ s (□) after 308 nm laser irradiation of cPrFOH in NaY containing 6% (by weight) (a) co-adsorbed water and (b) co-adsorbed methanol.

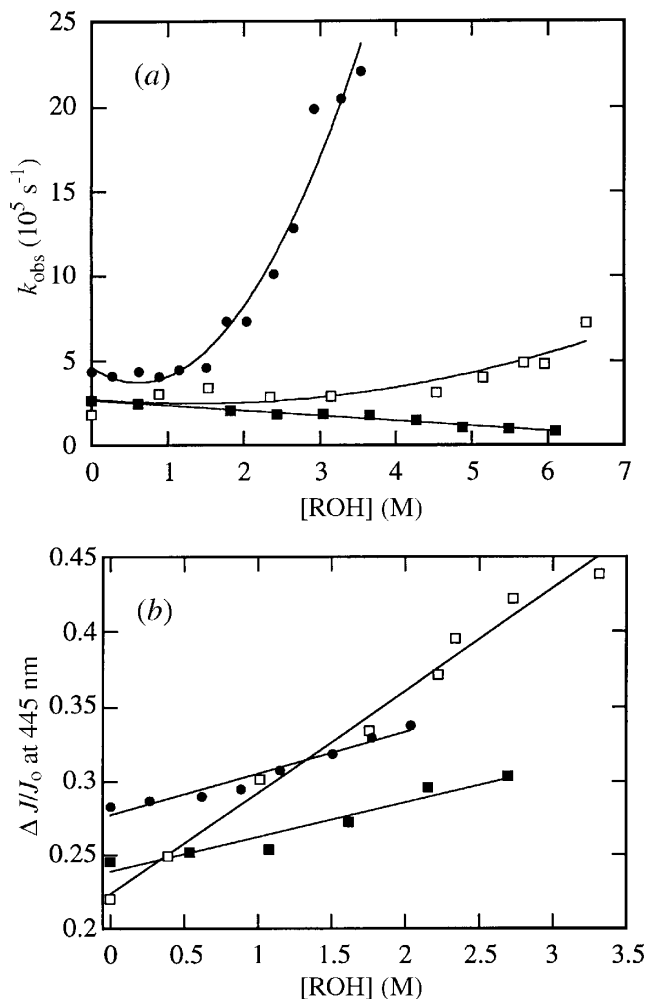


using water as a protic additive as compared to methanol. This is consistent with the higher efficiency of water as a reagent to promote photolysis of 9-fluorenols in solution.

#### Co-adsorption of 1,1,1,3,3,3-hexafluoro-2-propanol in NaY

We previously reported that the inclusion of small amounts of HFIP within alkali metal cation zeolites enhances the yield and the lifetime of the 9-methyl-9-fluorenyl and 9-fluorenyl cations (18). Similarly, the inclusion of small amounts of HFIP within NaY influences both the yield and the lifetime of the 9-cyclopropyl-9-fluorenyl cation generated by laser photolysis of cPrFOH in NaY. Thus, the inclusion of progressively larger concentrations of HFIP leads

**Fig. 5.** (a) Observed first-order rate constant for the decay of the 9-cyclopropyl-9-fluorenyl cation in dry NaY as a function of increasing water (□), methanol (●), or HFIP (■) concentration. (b) Variation in the change in diffuse reflectance observed at 445 nm immediately following 308 nm laser photolysis of cPrFOH in NaY as a function of the concentration of water (□), methanol (●), or HFIP (■).



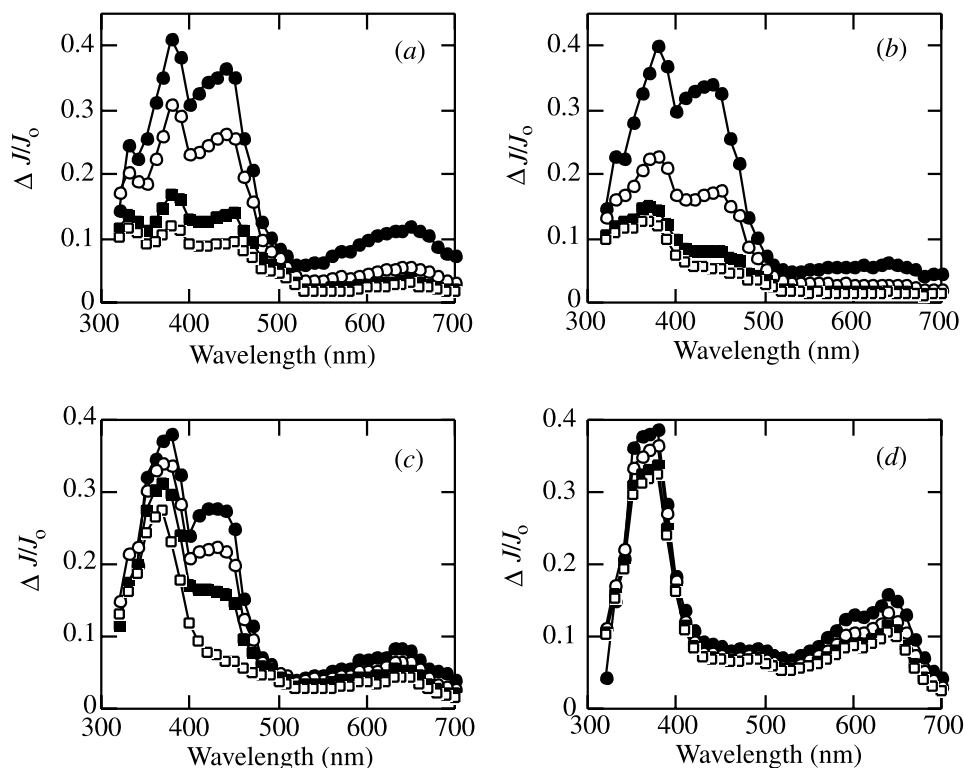
to a progressive increase in the yield of the 9-cyclopropyl-9-fluorenyl cation (Fig. 5b). The magnitude by which HFIP enhances photolysis is less than that achieved using water as a co-adsorbate, but is similar to the enhancement obtained via the addition of methanol to the zeolite sample. In addition, the rate constants for decay of the 9-cyclopropyl-9-fluorenyl cation exhibit a progressive decrease with increasing concentrations of HFIP (Fig. 5a). This contrasts with the influence of methanol or water and is consistent with the known kinetic stabilizing effect of HFIP on the reactivity of reactive carbocations in solution (56, 57).

#### Co-adsorption of water in MY zeolites

The transient diffuse reflectance spectrum obtained upon 308 nm laser photolysis of cPrFOH in hydrated LiY (Fig. 6a) closely resembles the absorption spectrum of the 9-cyclopropyl-9-fluorenyl cation in TFE. Weak absorption due



**Fig. 6.** Transient diffuse reflectance spectra generated at 200 ns (●), 1.76  $\mu$ s (○), 7.40  $\mu$ s (■), and 14.0  $\mu$ s (□) after 308 nm laser irradiation of cPrFOH in hydrated (a) LiY and (b) KY; transient diffuse reflectance spectra generated at 50 ns (●), 180 ns (○), 380 ns (■), and 3.46  $\mu$ s (□) after 308 nm laser irradiation of cPrFOH in hydrated (c) RbY and (d) CsY.



to the cPrFOH radical cation at 640 nm persists under hydrated conditions, but little long-lived absorption at 380 nm due to the rearranged triene isomer is evident. Increased carbocation generation is also apparent from the transient diffuse reflectance spectra obtained in hydrated KY and hydrated RbY (Figs. 6b and 6c and Table 1) where the transient spectra show a significantly enhanced yield of the 9-cyclopropyl-9-fluorenyl cation upon the absorption of water into the zeolite. In each case the addition of water into the MY framework caused an increase in the observed rate constant for the decay of the 9-cyclopropyl-9-fluorenyl cation compared to dry conditions (Table 1). Notably, the relative reactivity of the carbocation in hydrated alkali metal cation zeolites is the same as observed in the absence of water. Thus, the 9-cyclopropyl-9-fluorenyl cation is longest lived in hydrated LiY and becomes progressively shorter lived as the counterion size increases. In addition, the long-lived absorption because of the triene isomer continues to contribute to the absorption at 380 nm in hydrated KY, and particularly in hydrated RbY where the isomer is still a very dominant species. Interestingly, the transient diffuse reflectance spectrum observed in hydrated CsY is very similar to that in dry CsY. The spectrum does not contain any significant contribution from the 9-cyclopropyl-9-fluorenyl cation but instead strongly resembles that of the cPrFOH radical cation in combination with the triene isomer (Fig. 6d). Thus, heterolytic cleavage of the hydroxy group does not seem to be a facile process for photoexcited cPrFOH in CsY under either dry or hydrated conditions. The

rate constants for the decay of the cPrFOH radical cation in dry MY zeolites are given in Table 2.

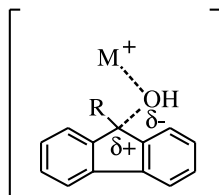
## Discussion

### Influence of alkali metal cations on the 9-cyclopropyl-9-fluorenyl cation formation

Photoexcitation of cPrFOH encapsulated within dry alkali metal cation zeolites leads to the formation of the 9-cyclopropyl-9-fluorenyl cation via photoheterolysis of the C—O bond (48, 50). As the photohydroxylation reaction of 9-fluorenols is thought to occur predominately from the singlet excited state in the presence of a proton source (45, 46), which is needed to assist in the cleavage of the hydroxyl group, it is of interest to ascertain the mechanism of interaction between the intrazeolite environment and the leaving hydroxide ion. One possible explanation is that the zeolite framework actually aids the photodehydroxylation reaction where the metal cation assists the excited state C—O bond cleavage via Lewis-acid-type catalysis (Scheme 2). In this case, interaction of the alkali metal cation stabilizes the hydroxide ion as the C—O bond cleaves in the excited state. A weak interaction between the alcohol functionality of cPrFOH and the zeolite alkali metal cation is expected even in the ground state, based on similar interactions between alkali metal cations and methanol within zeolites (58–63). Once an interaction is established in the ground state, cPrFOH will likely be oriented appropriately for Lewis-acid-assisted



Scheme 2.



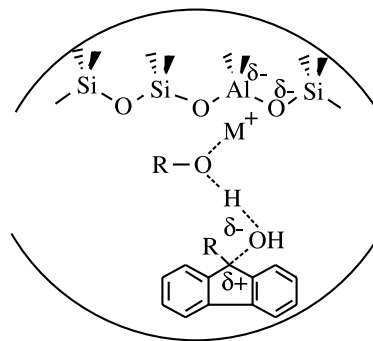
heterolysis upon photoexcitation. The ground state interaction should be highly dependent on the cation size. For instance the calculated binding energies of methanol at the bare alkali metal cations are  $150 \text{ kJ mol}^{-1}$  for  $\text{Li}^+$  and  $61 \text{ kJ mol}^{-1}$  for  $\text{Cs}^+$  (63). The binding energies of methanol within the alkali-metal-exchanged zeolites have been estimated to be about half as large as those associated with the bare cations, which correlates with the lower positive charge of the cations at zeolite clusters (63).

The notion that the zeolite counterion facilitates the cleavage of the hydroxyl group from photoexcited cPrFOH is supported by the distinct variation in photoheterolysis efficiency as a function of zeolite counterion (Fig. 3). For instance, the overall yield (absolute and relative) of the 9-cyclopropyl-9-fluorenyl cation decreases dramatically as the Y zeolite counterion is varied from  $\text{Li}^+$  to  $\text{Cs}^+$ . In fact, although carbocation formation is the dominant reaction pathway of photoexcited cPrFOH in LiY, no carbocation is detected in CsY. The large variation in the yield of carbocation as a function of alkali metal cation size is most consistent with a reduction in the efficiency of the photoheterolysis reaction as the counterion size increases from  $\text{Li}^+$  to  $\text{Cs}^+$ . This is the anticipated trend in efficiency for a heterolysis reaction involving Lewis acid catalysis within the zeolite cavities (Scheme 2) since the Lewis acidity of the counterion, and of the zeolite interior, decreases significantly within increasing alkali metal cation size (64, 65).

### Influence of protic reagents on the 9-cyclopropyl-9-fluorenyl cation formation

In alkali metal cation zeolites both the absolute yield of carbocation formation and the yield relative to competing processes such as ionization and rearrangement increase upon inclusion of protic reagents such as water, methanol, and HFIP, within the zeolite. The concentration of reagent needed to observe this effect is relatively small, often only a few molecules per zeolite cavity. Under these conditions, the surrounding environment experienced by the photoexcited 9-fluorenyl is not comparable to a solvent cage of these reagents, as would be the case, for instance, at much higher concentrations, or in a slurry of zeolite and cosolvent. Instead, the intrazeolite environment is akin to that observed under dry conditions with the exception that additional guest molecules, the protic reagent, are present within the zeolite cavities. Therefore, the ability of these protic guest molecules to enhance photoheterolysis is likely a consequence of the combined influences of both the zeolite matrix and the proton source, with the protic reagent actively participating in the C—OH bond cleavage of the excited state 9-fluorenyl. The protic reagent incorporated within the zeolite cavity can interact with the oxygen of the excited 9-fluorenyl and stabilize the incipient charge on the developing hydroxide ion

Scheme 3.



(Scheme 3). Direct assistance of the photodehydroxylation of 9-methyl-9-fluorenyl and 9-fluorenyl by zeolite-encapsulated HFIP has been previously demonstrated from studies of isotope effects using HFIP-OD (18).

The experimental results obtained within hydrated alkali metal cation zeolites support the notion that Lewis acid catalysis is an important interaction for carbocation generation. The dependence of carbocation yield on the alkali metal cation size is maintained even under hydrated conditions, where the carbocation yield is the highest in hydrated LiY and decreases dramatically with cation size such that no carbocation is observed in hydrated CsY. Thus, even under conditions where small amounts of water are included within the zeolite cavities, the distinct influence of the zeolite microenvironment continues to control the efficiency of carbocation formation. This is noteworthy considering the powerful ability of water to regulate the efficiency of photoheterolysis of 9-fluorenyl derivatives in homogeneous aqueous acetonitrile solutions. These observations provide further evidence that the zeolite framework and, particularly the alkali metal counterions, plays a direct and defining role in intrazeolite photoheterolysis, and that carbocation formation is likely a consequence of Lewis-acid-type interactions between the excited state 9-fluorenyl and the framework alkali metal cation.

In this regard, it is interesting to consider the magnitude by which hydration influences the efficiency of photoheterolysis within different zeolite environments. In LiY, where heterolysis is the favored reaction pathway of photoexcited cPrFOH in the absence of a proton source, the inclusion of water does little to further enhance the excited-state bond cleavage. Conversely, in RbY, where the absolute and relative yield of photoheterolysis is very low compared to other reaction pathways, the inclusion of water dramatically increases the yield of the photoheterolysis reaction. However, in this case the spectrum still has significant contributions from the triene isomer and the cPrFOH radical cation. Thus, in the strongest Lewis acid zeolite (LiY),  $\text{Li}^+$ -assisted photoheterolysis dominates the chemistry of photoexcited cPrFOH and the co-adsorbed water participates little in the heterolysis reaction. Conversely, in RbY,  $\text{Rb}^+$ -assisted heterolysis is a relatively minor pathway for photoexcited cPrFOH, and water has a much greater opportunity to participate in photoheterolysis. In CsY, the ability of the zeolite to facilitate photoheterolysis of cPrFOH, even under hydrated conditions, is too small to compete with the other photochemical processes taking place within CsY, particularly



photoionization to the cPrFOH radical cation. These observations suggest that the zeolite framework continues to directly influence the heterolysis reaction and that the ability of water to modulate heterolysis is determined by combined effects of the co-adsorbed water and the specific zeolite environment (66, 67).

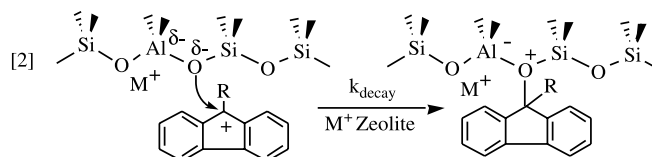
The enhanced photoheterolytic generation of the 9-cyclopropyl-9-fluorenyl cation observed in alkali metal cation zeolites upon inclusion of protic reagents is more significant for water than for methanol. This trend in relative efficiencies is not surprising considering that water is superior in its ability to facilitate photoheterolysis of 9-fluorenols in homogeneous solution (44–46). However, the observation that inclusion of small amounts of methanol increases the efficiency of intrazeolite photoheterolysis is contrary to results observed in homogeneous solution where carbocation formation is extremely inefficient in neat methanol. For instance, from product studies and time-resolved experiments, it has been shown that the 9-methyl-9-fluorenyl cation is not generated to a significant extent upon excitation of 9-methyl-9-fluorene (MeFOH) in neat methanol, but is readily formed in methanol–water mixtures, with the efficiency of photoheterolysis increasing at higher water content (44–46). As described above the current observation that the addition of small amounts of methanol can help induce photoheterolysis of 9-fluorenols within zeolite cavities is likely due to an association of the included protic reagent with the zeolite framework (Scheme 3). A binding of this nature should increase the acidity of the alcohol and thereby elevate the ability of the proton to assist C–O bond cleavage.

### Absolute reactivity of the 9-cyclopropyl-9-fluorenyl cation in alkali metal cation zeolites

A fundamental impetus for studying reactive carbocations in non-acidic zeolites is to develop an understanding of the mechanisms by which non-protic zeolites interact with positive ion species and to assess their potential as hosts for these reactive intermediates. Recent studies of reactive carbocations within non-acidic zeolites in our laboratory have shown that the environment within these zeolites can support the generation and stabilization of reactive carbocations as transient species. The detection in the  $\mu$ s time regime of the 9-cyclopropyl-9-fluorenyl cation in alkali metal zeolites further supports these ideas. The significant lifetime of carbocations in alkali metal cation zeolites is not due to a thermodynamic effect, like that present in acid zeolites where the highly acidic environment shifts an otherwise unfavorable equilibrium to the side of the carbocation. Similarly, it is not due to a situation in which the strength of the nucleophilic sites of the zeolite framework is reduced by protonation. The ability to observe reactive carbocations on the ns to  $\mu$ s time scale in alkali metal cation zeolites is instead attributed to the unique intrazeolite environment, specifically the confined environment, polar, anionic matrix, and large electrostatic fields within the zeolite cages.

The carbocation lifetime depends dramatically on the nature of the zeolite environment, specifically on the identity of the alkali metal counterion and the Si–Al ratio. As shown in Table 1, the lifetime of the 9-cyclopropyl-9-fluorenyl cation decreases systematically as the alkali counterion is varied from  $\text{Li}^+$  to  $\text{Rb}^+$ . This trend is consistent with an increase

in the nucleophilicity of the zeolite framework as the alkali cation size is increased. Several recent studies have demonstrated that one effect of cation exchange in Y zeolites is modification of the electron donating ability, or Lewis basicity of the  $[\text{Si-O-Al}]^-$  active sites within the framework (23, 65, 68–71). This effect can be rationalized by a progressive decrease in interaction strength between the zeolite counterion and the electron-rich framework oxygen sites as the counterion becomes larger and more charge diffuse. Similarly, the tight interaction of a small, charge dense cation such as  $\text{Li}^+$  with  $[\text{Si-O-Al}]^-$  framework sites will render these sites considerably less nucleophilic than similar framework sites interacting more loosely with a large, charge diffuse cation such as  $\text{Rb}^+$ . Decreased cation–framework interactions are thus manifested as increased framework nucleophilicity, and correspondingly enhanced rate constants for nucleophilic addition to encapsulated carbocations as the counterion size is increased (eq. [2]). In fact, the variation in lifetime of the 9-cyclopropyl-9-fluorenyl cation with zeolite structure parallels that previously observed for the *p*-methoxycumyl cation where intrazeolite decay via nucleophilic addition of the framework has been established (17).



The 9-cyclopropyl-9-fluorenyl cation decays significantly faster, by almost an order of magnitude, in NaX (Si/Al = 1.2) than in NaY (Si/Al = 2.4). This observation is also consistent with a decay mechanism involving addition of nucleophilic framework sites. Considerable research has shown that the Lewis basicity of zeolites increases as the Si–Al ratio decreases (65, 68, 69, 72, 73). An increase in Lewis base strength results in an increase in the nucleophilicity of each site thereby enhancing the reactivity of these sites towards carbocation addition. The increased reactivity of the 9-cyclopropyl-9-fluorenyl cation in NaX as compared to NaY correlates nicely with this expectation. It must also be recognized that NaX possesses a significantly larger number of  $[\text{Si-O-Al}]^-$  bridges than NaY.

Infrared (74–76) and NMR (12, 77–81) investigations of alkoxy intermediates indicate that framework-bound carbocations covalently attach to  $[\text{Si-O-Al}]^-$  sites. In addition, theoretical investigations indicate that the oxygen atoms within  $[\text{Si-O-Al}]^-$  bridges bind carbocations more tightly than oxygen atoms within  $[\text{Si-O-Si}]$  bridges (82, 83). Such observations indicate that the  $[\text{Si-O-Al}]^-$  bridges are the dominant nucleophilic sites within the zeolite lattice. As a result, the smaller Si–Al ratio of NaX as compared to NaY renders the number of potential nucleophilic sites available for attack on encapsulated carbocations to be higher in NaX. Thus, in addition to the enhanced nucleophilicity associated with individual sites, the increased concentration of such sites also contributes to the higher reactivity of the carbocation in NaX relative to NaY. Thus, the notion that the decay of the 9-cyclopropyl-9-fluorenyl cation observed in alkali metal cation zeolites proceeds via direct nucleophilic



addition of the zeolite to yield a framework-bound alkoxy intermediate is consistent with the current view of carbocation behaviour in acid zeolites.

Further evidence that nucleophilic addition of the zeolite framework is responsible for the disappearance of 9-cyclopropyl-9-fluorenyl cation within alkali metal cation zeolites can be obtained by correlating the lifetime of the carbocation with the nucleophilicity of the zeolite framework. As previously described (17), it is possible to discuss the nucleophilicity of the zeolite in terms of the electron density associated with the active nucleophilic sites, the zeolite lattice oxygen atoms bound to aluminum. One method for obtaining the average electron density at these sites is to calculate the partial negative charge on the framework oxygen atom using Sanderson electronegativity principles (84–86). While calculation of the average charge on a zeolite framework atom is an oversimplification that masks the heterogeneous nature of the zeolite environment, it has proved successful in rationalizing a number of physicochemical characteristics (87, 88), including Brønsted acidity and catalytic efficiency (89), Lewis and Brønsted basicity (65, 70, 72, 73), and redox properties (23). For the purpose of the current work, Sanderson electronegativity principles provide a means to correlate the observed variation in carbocation lifetime with a measure of zeolite nucleophilicity (17). The Sanderson electronegativity and partial charge on the framework oxygen atoms of the alkali metal Y zeolites used in this study are given in Table 3. A plot of the log of the lifetime of the 9-cyclopropyl-9-fluorenyl cation in alkali metal cation Y zeolites vs. the charge on the framework oxygen yields a linear relationship (Fig. 7). The correlation between the lifetime of the carbocation and the charge on the framework oxygen is consistent with a mechanism of carbocation decay involving addition of the zeolite framework. Furthermore, it is significant to note that the slope of the correlation is virtually identical to that obtained for the *p*-methoxycumyl cation (17) (Fig. 7). The close match in lifetime variation as a function of the zeolite microenvironment strongly supports the notion that both carbocations decay via the same mechanism within alkali metal cation zeolites.

Beyond lending support to a decay mechanism characterized by nucleophilic addition, the observed variation in lifetime of the 9-cyclopropyl-9-fluorenyl cation with framework oxygen charge provides good evidence that this carbocation is not generated by photoheterolysis within CsY. As shown in Fig. 7, the correlation between the carbocation lifetime and the oxygen charge leads to an estimated lifetime for the 9-cyclopropyl-9-fluorenyl cation in CsY of 280 ns, which is within the time resolution of the ns diffuse reflectance system. Thus, the inability to detect the 9-cyclopropyl-9-fluorenyl cation in CsY is presumably not due to rapid decay of this carbocation within the laser pulse, but instead it is more likely due to inefficient photoheterolysis of cPrFOH within CsY.

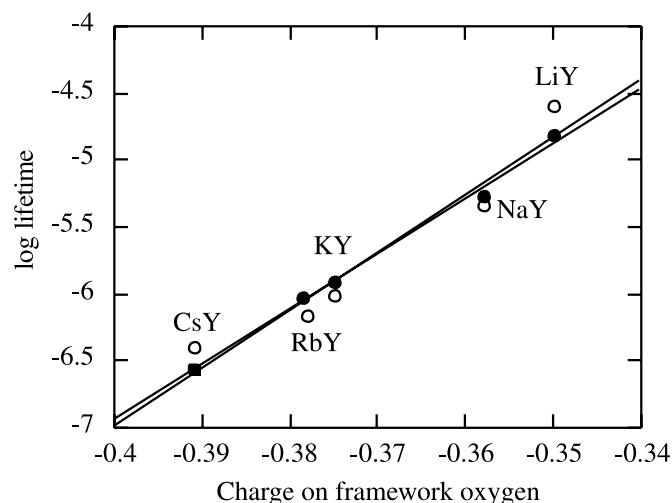
### Reactivity trends of carbocations in MY zeolites

The 9-cyclopropyl-9-fluorenyl cation is significantly less reactive within alkali metal cation zeolites than the 9-alkyl-9-fluorenyl and unsubstituted 9-fluorenyl cations previously investigated (18). This parallels the relative reactivity of these carbocations in solution, where the lifetime of the 9-

**Table 3.** Unit cell composition, equalized electronegativity ( $S_{\text{zeolite}}$ ), and partial charge on the framework oxygen atoms ( $\delta_{\text{O}}$ ) of alkali metal zeolites.

Unit cell composition	$S_{\text{zeolite}}$	$\delta_{\text{O}}$
$\text{Li}_{26}\text{Na}_{30}\text{Al}_{56}\text{Si}_{136}\text{O}_{384}$	2.60	−0.350
$\text{Na}_{56}\text{Al}_{56}\text{Si}_{136}\text{O}_{384}$	2.58	−0.358
$\text{K}_{54}\text{Na}_2\text{Al}_{56}\text{Si}_{136}\text{O}_{384}$	2.53	−0.375
$\text{Rb}_{25}\text{Na}_{31}\text{Al}_{56}\text{Si}_{136}\text{O}_{384}$	2.52	−0.378
$\text{Cs}_{26}\text{Na}_{30}\text{Al}_{56}\text{Si}_{136}\text{O}_{384}$	2.48	−0.391

**Fig. 7.** Variation in the log of the lifetime of the 9-cyclopropyl-9-fluorenyl cation (●) and the 4-methoxycumyl cation (○) as a function of the charge on the framework oxygen atom. The extrapolated lifetime for the 9-cyclopropyl-9-fluorenyl cation in CsY is included and indicated with (■). Data for the 4-methoxycumyl cation (○) were taken from ref. (17).



cyclopropyl-9-fluorenyl cation is several orders of magnitude larger than the lifetimes of 9-alkyl-9-fluorenyl and the 9-fluorenyl cation (50, 51). This difference is attributed to the strong stabilization of the carbocation center provided by the cyclopropyl substituent (90), where the order of 9-fluorenyl cation reactivity is due to the ability of the substituent to stabilize the carbocation center. However, an interesting observation can be made by considering the reactivity range exhibited by 9-fluorenyl cations in zeolites as compared to solution (Table 4). In particular, it is observed that the unstable 9-fluorenyl cation is significantly longer lived within the zeolites LiY and NaY as compared to water, or even the weakly nucleophilic solvent TFE. Conversely, the more stabilized 9-cyclopropyl-9-fluorenyl cation is actually one to two orders of magnitude more reactive in these alkali metal cation zeolites than in TFE, and exhibits somewhat similar lifetimes in NaY and water. The net result is that the environment within the zeolite cavities exerts a dramatic *leveling effect*, whereby the relative reactivity of carbocations is significantly less sensitive to the relative thermodynamic stability than observed in solution. This further suggests that the zeolite plays a significant role in



**Table 4.** Lifetimes of 9-R-9-fluorenyl cations in LiY, NaY, TFE, and water, and the reactivity range exhibited by these cations in each environment.

R	Lifetime (ns)			
	LiY	NaY	Water	TFE
H	345	145	<0.02 <sup>a</sup>	1.1 <sup>b</sup>
Methyl	540	290	0.275 <sup>a</sup>	120 <sup>c</sup>
Cyclopropyl	15 600	2600	150 <sup>d</sup>	140 000 <sup>e</sup>
<b>Reactivity range:</b>	45	18	>7500	120 000

<sup>a</sup>Data taken from ref. (46).<sup>b</sup>Data taken from ref. (51).<sup>c</sup>Data taken from ref. (52).<sup>d</sup>Data taken from footnote 3.<sup>e</sup>Data taken from ref. (50).

carbocation-mediated reactions and is more than merely an inert, non-nucleophilic reaction vessel.

## Summary

In dry LiY, NaY, KY, and RbY zeolites cPrFOH undergoes photoheterolysis to yield the 9-cyclopropyl-9-fluorenyl cation as a transient intermediate. Both the photoheterolysis reaction and the reactivity of the resultant 9-cyclopropyl-9-fluorenyl cation are strongly dependent on the nature of the intrazeolite environment. The dramatic influence of the alkali metal cation on photoheterolysis efficiency demonstrates the importance of the zeolite environment to the efficiency of heterolysis and suggests that the zeolite assists the excited state C—O bond cleavage via Lewis acid catalysis involving the metal cation. In addition, carbocation formation within these zeolites is enhanced by coincluded protic reagents in a manner that is consistent with direct participation of these reagents in the C—O bond cleavage. The observations that methanol can effectively increase the efficiency of photoheterolysis in zeolites, but not in solution, and that water is inefficient at effecting heterolysis in CsY but very efficient at inducing heterolysis in solution, suggest that the zeolite plays a defining role in the photoheterolysis even in cases where the cleavage is directly assisted by a co-adsorbed reagent. This is attributed to the interplay between the zeolite, the protic reagent and the 9-fluorenyl substrate, and the influences of such interactions on heterolysis and other reaction pathways available to photoexcited 9-fluorenyls in zeolites.

Trends in the absolute reactivity of the 9-cyclopropyl-9-fluorenyl cation as a function of the nature of the charge balancing cation and the Si—Al ratio suggest that intrazeolite decay of the carbocation involves nucleophilic addition of lattice oxygen atoms in [Si—O—Al]<sup>−</sup> bridges. Consequently, the lifetime of the 9-cyclopropyl-9-fluorenyl cation can be correlated to the charge on the framework oxygen atom as has previously been reported for the 4-methoxycumyl cation. Due to the distinct influences of zeolite encapsulation on photoheterolysis efficiency and carbocation reactivity, it is possible to control the yield and lifetime of the 9-cyclopropyl-9-fluorenyl cation by simple zeolite modifications such as alkali metal exchange.

Our current understanding, based on the study of reactive carbocations in non-acidic zeolites, is that the application of zeolitic systems to controlling and catalyzing positive-ion-mediated processes may not be derived from the ability of these materials to enhance carbocation lifetimes over what can be achieved in certain solvents. Instead, the use of zeolites in carbocation chemistry may more aptly be directed towards modifying carbocation reactivity and the efficiency of carbocation formation relative to competitive processes in ways which are distinct from those observed in homogeneous environments.

## Experimental

### Materials

9-Cyclopropyl-9-fluorenyl was synthesized by Grignard addition of the cyclopropyl bromide to fluorenone, purified by recrystallization three times from 95% ethanol, and fully characterized using <sup>1</sup>H and <sup>13</sup>C NMR spectroscopy. Spectroscopic grade solvents were used in zeolite sample preparation and laser experiments and were commercially available from BDH or Aldrich and used without additional purification. NaY, Si/Al = 2.4, and NaX, Si/Al = 1.2, were purchased from Aldrich and used as received. The exchanged zeolites were prepared as previously described (17). The percent exchange is typically 47% for LiY, 97% for KY, 44% for RbY, and 47% for CsY. It is known that for the larger cations such as Rb<sup>+</sup> and Cs<sup>+</sup>, only the accessible Na<sup>+</sup> which occupy type II and type III sites can be readily exchanged (2). Thus, the maximum cation exchange is ~70%. Values of ~50% exchange indicate that a small percentage of type II cations are not completely exchanged. The low percent exchange for the LiY sample is because hydrated Li<sup>+</sup> also does not readily exchange the type III cations.

### Zeolite samples

9-Cyclopropyl-9-fluorenyl was incorporated into alkali metal zeolites using hexane as a carrier solvent to achieve a loading level of approximately one molecule in every 10 supercages. A general procedure for sample preparation is as follows. Zeolites (typically 300–400 mg) are activated for at least 12 h at 450°C to remove the co-adsorbed water. The dehydrated zeolite is removed from the oven and placed in approximately 20 mL of anhydrous hexane in a sample tube and sealed with a septum. A small quantity (typically <250 µL) of a relatively concentrated (typically 1 × 10<sup>−1</sup> to 1 × 10<sup>−2</sup> M) dichloromethane solution of cPrFOH is then added to the zeolite–hexane slurry, the mixture is stirred for 1 to 2 h, and then the carrier solvent is separated from the zeolite solid by centrifuge. An additional 20 mL aliquot of hexane is then added to the material and the mixture is again stirred for approximately 30 min to remove surface adsorbates, centrifuged, and the zeolite sample is separated from the supernatant liquid. To remove the remaining hexane the zeolite–substrate complex is placed in a desiccator that is evacuated with a vacuum pump (1 × 10<sup>−3</sup> torr, 1 torr = 133.322 Pa) for 8–12 h. The sealed desiccator containing the zeolite powder is placed in a glove bag under an inert atmosphere of dry nitrogen to transfer the dried zeolite composite

<sup>3</sup>F.L. Cozens and M.A. O'Neill. Unpublished results.



to a  $3 \times 7$  mm<sup>2</sup> quartz laser cell. This is attached to a vacuum line equipped with a diffusion pump ( $1 \times 10^{-4}$  torr, 1 torr = 133.322 Pa) for an additional 12 h to remove any oxygen and any residual hexane, which may be present.

During the incorporation procedure, the utmost care is taken to keep the zeolite sample dry. In particular, all manipulations of dried composites are carried out in an atmosphere of dry nitrogen. UV analysis of the combined decants indicated that 100% of the organic precursor was incorporated within NaY. The initial amount of cPrFOH was adjusted to account for the reduced % incorporation in the larger alkali cation zeolites, such that the final concentration was approximately one molecule in every 10 supercages for all zeolites examined.

Hydration of 9-cyclopropyl-9-fluorenyl-zeolite composites was carried out by exposing a known quantity of the vacuum dried 9-cyclopropyl-9-fluorenyl-zeolite composite to the atmosphere. The sample was spread into a thin layer in a petri dish to allow efficient hydration, and the changes in sample mass because of water uptake were monitored. The uptake of water by the zeolite was dependent on the charge balancing cation and Si–Al ratio. Typical values of water uptake (expressed as weight percent) by the 9-cyclopropyl-9-fluorenyl-zeolite composites are ca. 12%, 10%, 6%, 3% and 2% for the alkali metal zeolites LiY through CsY respectively, and ca. 5% for NaX.

The coadsorbed alcohols, methanol and HFIP, were introduced after substrate incorporation and evacuation. In this case the laser cells containing the zeolite composites were preweighed before putting the samples into the cells in the glove bag. In this manner the mass of the zeolite samples within the cells could be accurately determined. The typical zeolite mass used in studies with coadsorbed reagents was ca. 100 to 200 mg. To inject the coadsorbate, the laser cells were sealed with a rubber septum. A small quantity of the neat alcohol (typically 1  $\mu$ L) was then injected into the top of the cell using a syringe. Care was taken to ensure that the zeolite powder did not come into direct contact with the alcohol. The sample was then gently heated with hot air to vaporize the alcohol, during which time the cell was rotated to ensure an even distribution of reagent throughout the sample. The sample was then allowed to cool and thoroughly mixed before laser experiments were conducted.

### Nanosecond laser flash photolysis

A computer-controlled ns laser flash photolysis system was employed in this study and has been previously described (17). The excitation source was a pulsed Lambda-Physik excimer laser containing a Xe–HCl–He gas mixture (308 nm,  $\leq 100$  mJ/pulse,  $< 10$  ns pulse). Diffuse reflectance experiments involve measuring the fraction of reflected light absorbed by the transient, denoted as the reflectance change ( $\Delta J/J_0$ ), where  $J_0$  is the reflectance intensity before laser excitation and  $\Delta J$  is the change in reflectance intensity after excitation due to absorption by photogenerated transients. The diffuse reflected light is focused through a grating monochromator into a photomultiplier system before being captured with a Tektronix 620A digitizing oscilloscope and transferred via a GPIB interface to a Power Macintosh 7100 computer which controls the laser system using a program written with LabView<sup>TM</sup> 3.0 software. The resulting appara-

tus couples relatively short laser pulse widths with a rapid and efficient detection system so that reactive intermediates with lifetimes = 20 ns can be studied in opaque samples.

### Acknowledgments

F.L.C. gratefully acknowledges the Natural Sciences and Engineering Research Council of Canada (NSERC) for financial support of this research. M.A.O. thanks NSERC and the Izaak Walton Killam Memorial Foundation for postgraduate scholarships. We also thank Don Arnold for many enlightening discussions.

### References

1. D.W. Breck. Zeolite molecular sieves: Structure, chemistry and use. John Wiley and Sons, New York. 1974.
2. H. van Bekkum, E.M. Flanigen, and J.C. Jansen (*Editors*). Introduction to zeolite science and practice. Elsevier Science Ltd., Amsterdam. 1991.
3. A. Dyer. An introduction to zeolite molecular sieves. John Wiley and Sons, Bath. 1988.
4. V. Ramamurthy, R.J. Robbins, K.J. Thomas, and P.H. Lakshminarasimhan. In Organized molecular assemblies in the solid state. *Edited by* J.K. Whitesell. John Wiley and Sons Ltd., New York. 1999. p. 63.
5. J.C. Scaiano and H. García. *Acc. Chem. Res.* **32**, 783 (1999).
6. N.J. Turro. *Acc. Chem. Res.* **33**, 637 (2000).
7. K.B. Yoon. *Chem. Rev.* **93**, 321 (1993).
8. J.K. Thomas. *Chem. Rev.* **93**, 301 (1993).
9. A. Corma. *Chem. Rev.* **95**, 559 (1995).
10. V. Ramamurthy. In Photochemistry in organized and constrained media. *Edited by* V. Ramamurthy. VCH, New York. 1991. p. 429.
11. M.L. Cano, A. Corma, V. Fornes, and H. Garcia. *J. Phys. Chem.* **99**, 4241 (1995).
12. J.F. Haw, J.B. Nicholas, T. Xu, L.W. Beck, and D.B. Ferguson. *Acc. Chem. Res.* **29**, 259 (1996).
13. J.B. Nicholas and J.F. Haw. *J. Am. Chem. Soc.* **120**, 11 804 (1998).
14. L. Fernández, V. Marti, and H. García. *Phys. Chem. Chem. Phys.* **1**, 3689 (1999).
15. T. Tao and G.E. Maciel. *Langmuir*, **15**, 1236 (1999).
16. W. Adam, I. Casades, V. Fornés, H. García, and O. Weichold. *J. Org. Chem.* **65**, 3947 (2000).
17. M.A. O'Neill, F.L. Cozens, and N.P. Schepp. *J. Am. Chem. Soc.* **122**, 6017 (2000).
18. M.A. O'Neill, F.L. Cozens, and N.P. Schepp. *Tetrahedron*, **56**, 6969 (2000).
19. F.L. Cozens, R. Bogdanov, M. Regimbald, H. Garcia, V. Marti, and J.C. Scaiano. *J. Phys. Chem. B*, **101**, 6821 (1997).
20. L. Brancalione, D. Brousmiche, V.J. Rao, L. Johnston, and V. Ramamurthy. *J. Am. Chem. Soc.* **120**, 4926 (1998).
21. R.A. van Santen and G.J. Kramer. *Chem. Rev.* **95**, 637 (1995).
22. M.L. Cano, F.L. Cozens, H. Garcia, V. Marti, and J.C. Scaiano. *J. Phys. Chem.* **100**, 18 152 (1996).
23. X. Liu, K. Iu, and J.K. Thomas. *J. Phys. Chem.* **98**, 7877 (1994).
24. V. Ramamurthy, J.V. Caspar, and D.R. Corbin. *J. Am. Chem. Soc.* **113**, 594 (1991).
25. I.K. Lednev, N. Mathivanan, and L.J. Johnston. *J. Phys. Chem.* **98**, 11 444 (1994).



26. K. Pitchumani, P.H. Lakshminarasimhan, G. Turner, M.G. Bakker, and V. Ramamurthy. *Tetrahedron Lett.* **38**, 371 (1997).
27. H. Kao, C.P. Grey, K. Pitchumani, P.H. Lakshminarasimhan, and V. Ramamurthy. *J. Phys. Chem. A*, **102**, 5627 (1998).
28. K. Pitchumani and V. Ramamurthy. *Chem. Commun. (Cambridge)*, 2763 (1996).
29. K. Pitchumani, P.H. Lakshminarasimhan, N. Prevost, D.R. Corbin, and V. Ramamurthy. *Chem. Commun. (Cambridge)*, 181 (1997).
30. T. Xu and J.F. Haw. *J. Am. Chem. Soc.* **116**, 10 188 (1994).
31. T. Xu and J.F. Haw. *J. Am. Chem. Soc.* **116**, 7753 (1994).
32. T. Tao and G.E. Maciel. *J. Am. Chem. Soc.* **117**, 12 889 (1995).
33. J.F. Haw, J.B. Nicholas, W. Song, F. Deng, Z. Wang, T. Xu, and C.S. Heneghan. *J. Am. Chem. Soc.* **122**, 4763 (2000).
34. T. Xu, D.H. Barich, P.W. Goguen, W. Song, Z. Wang, J.B. Nicholas, and J.F. Haw. *J. Am. Chem. Soc.* **120**, 4025 (1998).
35. F.L. Cozens, H. García, and J.C. Scaiano. *J. Am. Chem. Soc.* **115**, 11 134 (1993).
36. F.L. Cozens, H. García, and J.C. Scaiano. *Langmuir*, **10**, 2246 (1994).
37. A. Sanjuan, A. Mercedes, G. Aguirre, H. García, and J.C. Scaiano. *J. Am. Chem. Soc.* **120**, 7351 (1998).
38. M.L. Cano, A. Corma, V. Fornes, H. García, M.A. Miranda, C. Baerlocher, and C. Lengauer. *J. Am. Chem. Soc.* **118**, 11 006 (1996).
39. M.L. Cano, V. Fornes, H. García, M.A. Miranda, and J. Perez-Prieto. *J. Chem. Soc., Chem. Commun.* 2477 (1995).
40. I. Kiricsi, H. Forster, G. Tasi, and J.B. Nagy. *Chem. Rev.* **99**, 2085 (1999).
41. I. Kiricsi, G. Tasi, P. Fejes, and H. Förster. *J. Chem. Soc., Faraday Trans.* **89**, 4221 (1993).
42. M.L. Cano, F.L. Cozens, M.A. Esteves, F. Márquez, and H. García. *J. Org. Chem.* **62**, 7121 (1997).
43. A. Corma and H. García. *Top. Catal.* **6**, 127 (1998).
44. P. Wan and E. Krogh. *J. Chem. Soc., Chem. Commun.* 1207 (1985).
45. P. Wan and E. Krogh. *J. Am. Chem. Soc.* **111**, 4887 (1989).
46. S.L. Mecklenburg and E.F. Hilinski. *J. Am. Chem. Soc.* **111**, 5471 (1989).
47. E. Gaillard, M.A. Fox, and P. Wan. *J. Am. Chem. Soc.* **111**, 2180 (1989).
48. R.A. McClelland, N. Mathivanan, and S. Steenken. *J. Am. Chem. Soc.* **112**, 4857 (1990).
49. A. Blazek, M. Pungente, E. Krogh, and P. Wan. *J. Photochem. Photobiol. A*, **64**, 315 (1992).
50. F.L. Cozens. Ph.D. Thesis, University of Toronto, Toronto, Ontario, Canada, 1992.
51. F.L. Cozens, N. Mathivanan, R.A. McClelland, and S. Steenken. *J. Chem. Soc., Perkin Trans. 2*, 2083 (1992).
52. C.S.Q. Lew, R.A. McClelland, L.J. Johnston, and N.P. Schepp. *J. Chem. Soc., Perkin Trans. 2*, 395 (1994).
53. A.D. Allen, J.D. Colomvakos, O.S. Tee, and T.T. Tidwell. *J. Org. Chem.* **59**, 7185 (1994).
54. F.L. Cozens, A. Pincock, J.A. Pincock, and R. Smith. *J. Org. Chem.* **63**, 434 (1998).
55. M.O. Delcourt and M.J. Rossi. *J. Phys. Chem.* **86**, 3233 (1982).
56. R.A. McClelland, R.A. Chan, F.L. Cozens, A. Modro, and S. Steenken. *Angew. Chem. Int. Ed. Engl.* **30**, 1337 (1991).
57. R.A. McClelland. *Tetrahedron*, **52**, 6823 (1996).
58. A.V. Kiselev, L. Kubelkova, and V.I. Lygin. *Russ. J. Phys. Chem.* **38**, 1480 (1964).
59. K.T. Geodakyan, A.V. Kiselev, and V.I. Lygin. *Russ. J. Phys. Chem.* **41**, 227 (1967).
60. G. Mirth, J.A. Lercher, M.W. Anderson, and J. Klinowski. *J. Chem. Soc., Faraday Trans.* **86**, 3039 (1990).
61. B. Hunger, S. Matysik, M. Heuchel, and W. Einicke, *Langmuir*, **13**, 6249 (1997).
62. M. Rep, A.E. Palomares, G. Eder-Mirth, J.G. van Ommen, N. Rösch, and J.A. Lercher. *J. Phys. Chem. B*, **104**, 8624 (2000).
63. G.N. Vayssilov, J.A. Lercher, and N. Rösch. *J. Phys. Chem. B*, **104**, 8614 (2000).
64. J.W. Ward. *J. Catal.* **10**, 34 (1968).
65. D. Barthomeuf. *J. Phys. Chem.* **88**, 42 (1984).
66. A. Kirmse, J. Karger, F. Stallmach, and B. Hunger. *Appl. Catal. A*, **188**, 241 (1999).
67. C.E.A. Kirschhock, B. Hunger, J. Martens, and P.A. Jacobs. *J. Phys. Chem. B*, **104**, 439 (2000).
68. Y. Okamoto, M. Ogawa, A. Maezawa, and T. Imanaka. *J. Catal.* **112**, 427 (1988).
69. M. Huang, A. Adnot, and S. Kaliaguine. *J. Catal.* **137**, 322 (1992).
70. S.Y. Choi, Y.S. Park, S.B. Hong, and K.B. Yoon. *J. Am. Chem. Soc.* **118**, 9377 (1996).
71. J. Lavalley, J. Lamotte, A. Travert, J. Czyzniewska, and M. Ziolek. *J. Chem. Soc., Faraday Trans.* **94**, 331 (1998).
72. H. Hattori. *Chem. Rev.* **95**, 537 (1995).
73. D. Barthomeuf. *In Acidity and basicity of solids. Edited by J. Fraissard and L. Petrakis. Kluwer Academic Publishers, Dordrecht, the Netherlands. 1994. p. 181.*
74. T.R. Forester and R.F. Howe. *J. Am. Chem. Soc.* **109**, 5076 (1987).
75. J.N. Kondo, H. Ishikawa, E. Yoda, F. Wakabayashi, and K. Domen. *J. Phys. Chem. B*, **103**, 8538 (1999).
76. H. Ishikawa, E. Yoda, J.N. Kondo, F. Wakabayashi, and K. Domen. *J. Phys. Chem. B*, **103**, 5681 (1999).
77. F.G. Oliver, E.J. Munson, and J.F. Haw. *J. Am. Chem. Soc.* **96**, 8106 (1992).
78. C.E. Bronnimann and G.E. Maciel. *J. Am. Chem. Soc.* **108**, 7154 (1986).
79. A.G. Stepanov, K.I. Zamaraev, and J.M. Thomas. *Catal. Lett.* **13**, 407 (1992).
80. V. Bosáček. *J. Phys. Chem.* **97**, 10 732 (1993).
81. V. Bosáček. *Z. Phys. Chem. (Muenchen)*, **189**, 241 (1995).
82. C.J.A. Mota, P.M. Esteves, and M.B. de Amorim. *J. Phys. Chem.* **100**, 12 418 (1996).
83. G.J. Kramer and R.A. van Santen. *J. Am. Chem. Soc.* **115**, 2887 (1993).
84. R.T. Sanderson. *J. Chem. Ed.* **65**, 112 (1988).
85. R.T. Sanderson. *J. Am. Chem. Soc.* **105**, 2259 (1983).
86. R.T. Sanderson. *J. Chem. Ed.* **65**, 227 (1988).
87. W. Mortier. *J. Catal.* **55**, 138 (1978).
88. W. Mortier. *Compilation of extra-framework sites in zeolites. Butterworth Scientific Limited, Guildford, U.K. 1982.*
89. P.A. Jacobs, W.J. Mortier, and J.B. Uytterhoeven. *J. Inorg. Nucl. Chem.* **40**, 1919 (1978).
90. W. Kirmse, B. Krzoss, and S. Steenken. *J. Am. Chem. Soc.* **118**, 7473 (1996).



# Intramolecular sensitization within steroids: Excited-state interaction of C-17 $\alpha$ and $\beta$ carbon- bromine bonds with a C-6 carbonyl group

Wen-Shan Li, Lokman Torun, and Harry Morrison

**Abstract:** The synthesis, photochemistry, and photophysics of 17 $\alpha$ -bromo-3 $\alpha$ -(triphenylsilyloxy)-5 $\alpha$ -androstan-6-one (**1**) and 17 $\beta$ -bromo-3 $\beta$ -(triphenylsilyloxy)-5 $\alpha$ -androstan-6-one (**2**) have been studied in aqueous tetrahydrofuran. The 17 $\alpha$ -bromo isomer gives evidence (reduced  $\phi_f$ ,  $\tau_1$ , and  $\phi_{isc}$  for the ketone) for interaction between the ketone and C–Br moieties in the excited singlet state. Some photodehalogenation is also observed upon excitation of the ketone chromophore. This interaction seems to be absent or minimal for the 17 $\beta$ -bromo isomer.

**Key words:** photodehalogenation, bromosteroid, ketosteroid, intramolecular singlet–singlet energy transfer (ISSET).

**Résumé :** On a réalisé la synthèse et on a étudié la photochimie et la photophysique de la 17 $\alpha$ -bromo-3 $\alpha$ -(triphenylsilyloxy)-5 $\alpha$ -androstan-6-one (**1**) et de la 17 $\beta$ -bromo-3 $\beta$ -(triphenylsilyloxy)-5 $\alpha$ -androstan-6-one (**2**) dans le tétrahydrofurane. Avec l'isomère 17 $\alpha$ -bromo, on a observé des résultats (valeurs réduites de  $\phi_f$ ,  $\tau_1$  et  $\phi_{isc}$  pour la cétone) suggèrent l'existence d'une interaction entre les portions cétone et C–Br dans l'état singulet excité. On a aussi observé la présence de photodéshalogénation lors de l'excitation du chromophore de la cétone. Cette interaction semble être absente ou minimale dans l'isomère 17 $\beta$ -bromo.

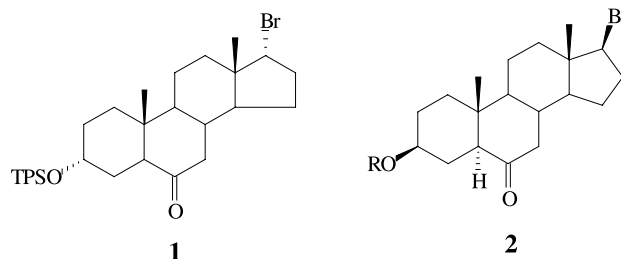
**Mots clés :** photodéshalogénation, bromostéroïde, cétostéroïde, transfert d'énergie singulet–singlet intramoléculaire (TESSI).

## Introduction

For many years chemists have evinced interest in the use of rigid, well-defined hydrocarbon skeletons to study the photophysical and photochemical consequences of excited-state intramolecular energy transfer between distal functional groups. The most extensively studied frameworks have involved norbornylogous (**1**) and steroidal (**2**) backbones. The use of steroids to study intramolecular singlet–singlet and triplet–triplet energy transfer dates back to the 1960s (**3**). Though most efforts in the field have emphasized photophysics, we have had a particular interest in the capability of the steroid skeleton to facilitate the photochemical activation of a reactive, non-light absorbing, functional group (**2**). Both through-space and through-bond interactions can effect such a result. Given the interchromophore distances involved, chemistry resulting from triplet–triplet intramolecular energy transfer involving rings A and D of the steroid skeleton most convincingly makes the case for coupling through the hydrocarbon framework (**4**, **5**).

In general, our program has explored the chemistry of unsaturated (e.g., ketone and olefin) acceptor groups resulting from the transfer of energy from an absorbing (“antenna”) chromophore. However, in a preliminary communication, we recently presented evidence that a  $\sigma$ -bonded (e.g., C–Br) functionality attached to the steroid framework could be activated by interaction with a ketone antenna (**2**). Specifically, photonic excitation (directly or indirectly) of a 6-keto (i.e., ring B) functionality can effect the photochemical cleavage of an  $\alpha$  C-17 (ring D) C–Br bond in the androstane **1**. We now present the details of this chemistry and extend the earlier study to include the  $\beta$  C-17 analogs (**2**). (Note that TPS and TBDMS in **2** are triphenylsilyl and *tert*-butyldimethylsilyl, respectively).

The somewhat surprising outcome of our most recent observations is that the interaction between the C-6 ketone and the C-17 C–Br bond appears to be specific to the 17 $\alpha$  isomer.



(a) R = TPS  
(b) R = TBDMS  
(c) R = Me

Received 6 January 2003. Published on the NRC Research Press Web site at <http://canjchem.nrc.ca> on 18 June 2003.

*Dedicated to Professor Don Arnold for his contributions to chemistry.*

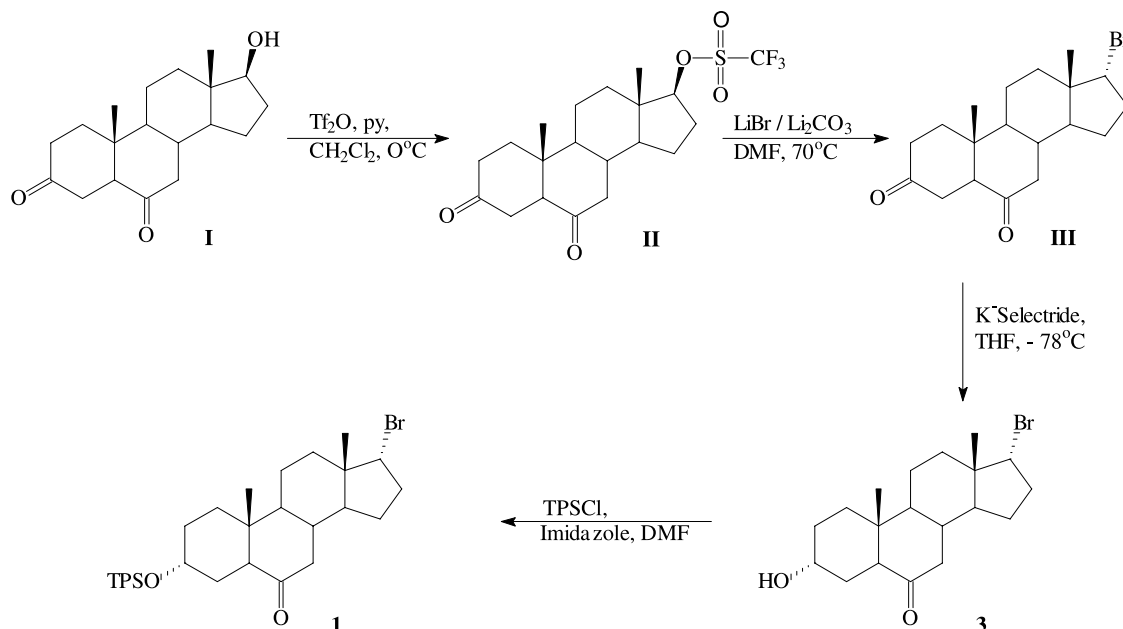
W.-S. Li,<sup>1</sup> L. Torun, and H. Morrison.<sup>2</sup> Department of Chemistry, Purdue University, 560 Oval Drive, West Lafayette, IN 47907-2038, U.S.A.

<sup>1</sup>Present address: Institute of Chemistry, Academia Sinica, 128 Academia Road, Taipei 11529, Taiwan.

<sup>2</sup>Corresponding author (e-mail: [hmmorrison@purdue.edu](mailto:hmmorrison@purdue.edu)).



Scheme 1.



## Results and discussion

### Preparation of steroid substrates

#### 17 $\alpha$ -Bromo-3 $\alpha$ -(triphenylsilyloxy)-5 $\alpha$ -androstane-6-one (**1**; 3 $\alpha$ -TPSO-6ketone-17 $\alpha$ -Br)

This substrate was prepared as outlined in Scheme 1, starting with 17 $\beta$ -hydroxy-5 $\alpha$ -androstane-3,6-dione that had itself been prepared from 17 $\beta$ -hydroxyandrost-4-en-3-one (6).

The assignment of structure to **1** was confirmed by X-ray analysis which clearly established the  $\alpha$  orientations of both the 3-TPSO and 17-Br functionalities (2).

#### 17 $\beta$ -Bromo-3 $\beta$ -(triphenylsilyloxy)-5 $\alpha$ -androstane-6-one (**2a**; 3 $\beta$ -TPSO-6ketone-17 $\beta$ -Br)

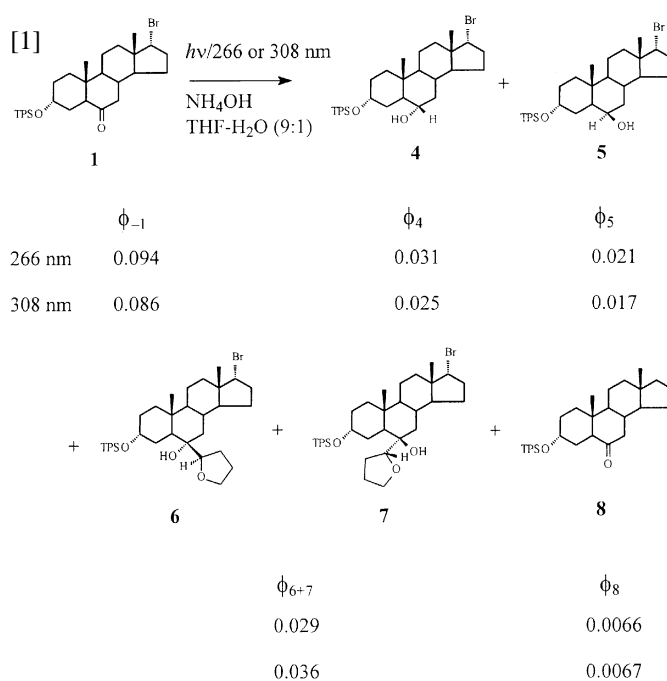
The title compound was prepared in six steps from commercially available 5-androsten-3 $\beta$ -ol-17-one (dehydroisoandrosterone) as outlined in Scheme 2. The selective reduction of the vinylbromide in ring D in the presence of the cycloalkene in ring B is noteworthy. The conversion to the cycloalkyl bromide is virtually quantitative. An expanded discussion of this reaction as a synthetic tool will be presented elsewhere. As with compound **1**, X-ray analysis (Fig. 1) was employed to confirm the  $\beta$  bromide stereochemistry at C-17 as well as the  $\beta$  configuration of the 3-TPSO group. The latter was a matter of convenience in the availability of starting material. The stereochemistry in ring A is of no consequence to the photophysics discussed in this paper. The axial and pseudo-axial configurations of the methine protons at C-3 and C-17, respectively, were also evident in the chemical shifts of their resonances at 3.6–3.8  $\delta$ , characteristically upfield of the resonances for their equatorial and pseudo-equatorial counterparts in **1** that appear at 4.2–4.3  $\delta$  (7).

Two analogs of **2a** were also prepared. One was 17 $\beta$ -bromo-3 $\beta$ -(*tert*-butyldimethylsilyloxy)-5 $\alpha$ -androstane-6-one (**2b**),

using a route totally analogous to that used for **2a**. The other was 17 $\beta$ -bromo-3 $\beta$ -methoxy-5 $\alpha$ -androstane-6-one (**2c**), wherein the 3-ol was methylated prior to the reduction of ring D and hydroboration–oxidation in ring B.

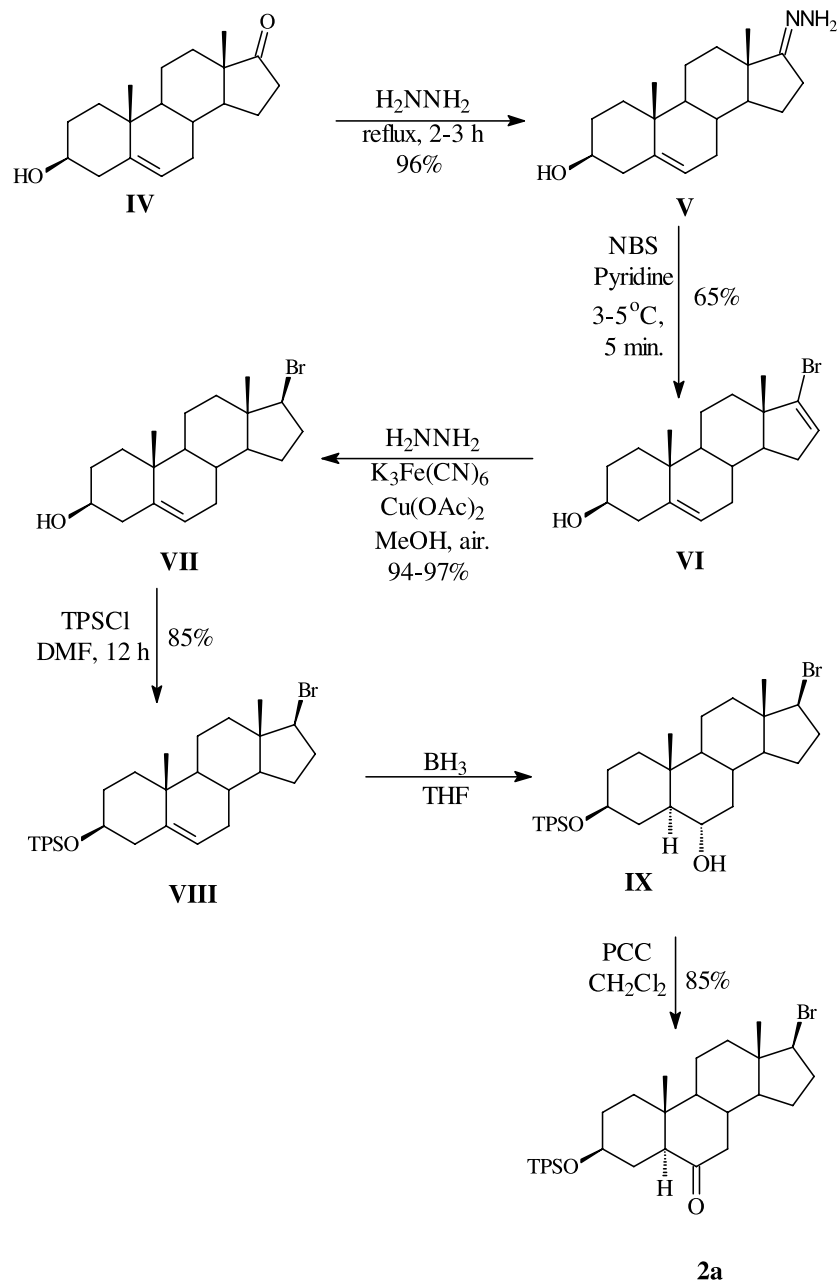
### Photochemistry of compounds **1** and **2a–2c**

The photolysis of **1** was studied using both 266 and 308 nm laser light. A mixture of THF and water was employed to facilitate solubility and ammonium hydroxide was present to neutralize released HBr. A summary of our observations, reproduced from our communication (2), is presented in eq. [1].





Scheme 2.



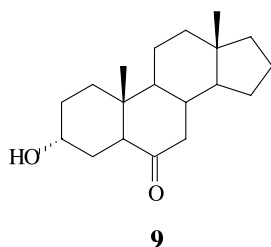
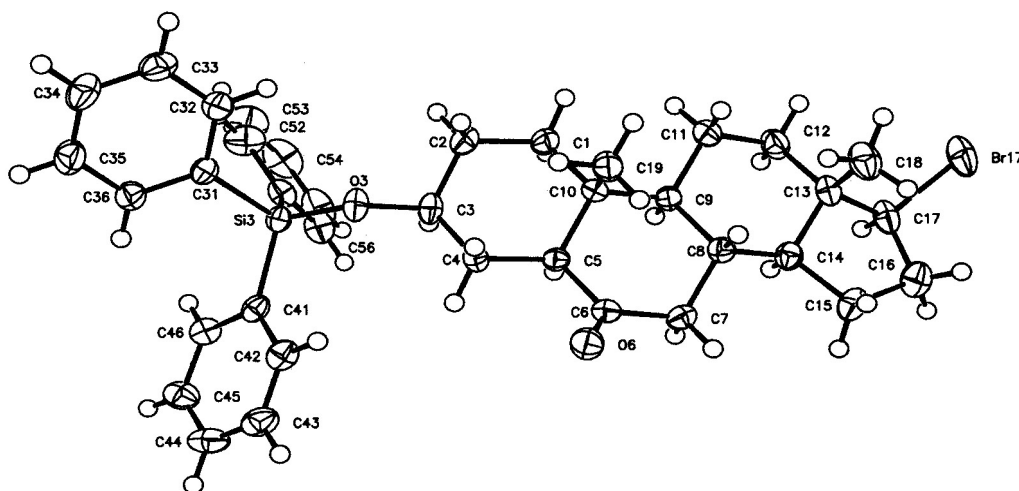
The assignment of **4** and **5** as the 6 $\alpha$  and 6 $\beta$  alcohols, respectively, rests on the (axial) 6H resonance (3.14–3.28  $\delta$ ) in **4** being located well upfield of the (equatorial) 6H resonance (3.54–3.60  $\delta$ ) in **5** (7). The debromination characteristic of **8** was readily evident in the mass spectrum and in the disappearance of the downfield C-17 methine proton and C-17 carbon resonances characteristic of **1**. Compounds **4**, **5**, and **8** were independently synthesized, the alcohols by sodium borohydride reduction of **1**, and **8** by reduction of 5 $\alpha$ -androstan-3,6-dione with K-Selectride followed by silylation. Compounds **6** and **7** were inseparable and handled as a mixture. The mass spectrum confirms the net addition of THF to **1** and the proton NMR is consistent with the assignment. These products are expected consequences of hydrogen abstraction from THF by the 6-keto group followed by

bond formation by the radical pair. We cannot distinguish among the possible diastereomers that could result from such a mechanism.

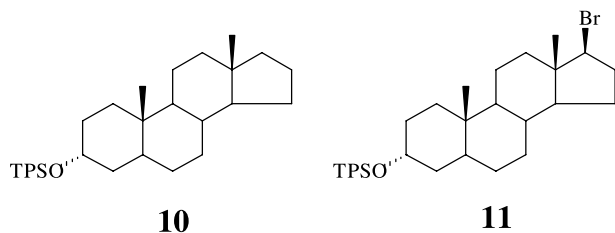
Among the products shown in eq. [1], the most interesting is the debrominated steroid (**8**). To confirm that cleavage of the C-17 C—Br bond is occurring by intramolecular sensitization, we photolysed the 3 $\alpha$ -OH-17 $\alpha$ -Br steroid, both alone and in conjunction with **1**, using both 266 and 300 nm irradiation. No debromination was observed in any of these cases. Nor could debromination of this steroid be sensitized by the 3 $\alpha$ -OH-6ketone (**9**) or by acetone (as solvent) using 300 nm irradiation.

Quantum efficiencies are included in eq. [1]. Note that the data for 266 vs. 308 nm irradiation are essentially identical within experimental error. The former deposits energy in the



Fig. 1. X-ray structure of **2a**.

aryl chromophore while the latter selectively excites the carbonyl group. The lack of any significant dependence on the initial site of excitation is reasonable, since we have earlier demonstrated that singlet-singlet energy transfer from an  $\alpha$ -arylsilyloxy group at C-3 to a ketone at C-6 is 90% efficient (8). (The efficiency drops to 77% when the arylsilyloxy group is  $\beta$  at C-3 (8)). These efficiencies are readily calculated from eq. [2] (or an analogous equation utilizing singlet lifetimes) (8). Inserting the TPSO fluorescence quantum efficiency for **1** of  $9.5 \times 10^{-4}$ , and using either that for **10** ( $1.0 \times 10^{-2}$ ) or **11** ( $9.3 \times 10^{-3}$ ) as the reference ("r"), likewise provides an efficiency of singlet energy transfer from C-3 to C-6 ( $\phi_{\text{intra3} \rightarrow 6}^1$ ) of 90%.



$$[2] \quad \phi_{\text{intra3} \rightarrow 6}^1 = [\phi_{f(r)} - \phi_{f(1)}] / \phi_{f(r)}$$

The highly efficient transfer of singlet energy to C-6 from the TPSO group, and the ability of the ketone, when directly excited, to initiate cleavage of the C-17 C—Br bond, argue for activation of the C—Br bond as involving the 6-keto group as the sensitizing chromophore. We return to this

point, and address the question of the excited-state multiplicity of the ketone as sensitizer, later in the discussion.

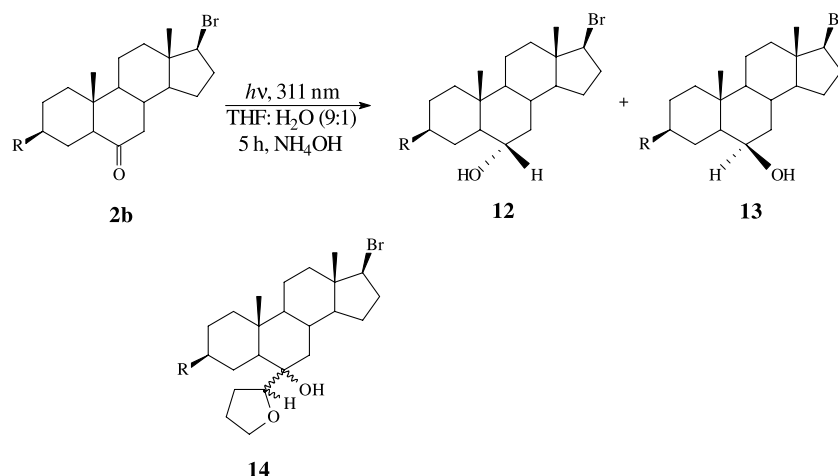
The photochemistry of the  $\beta$  17-Br series was studied in a manner identical to that outlined above for **1**. We began with the  $3\beta$ -TPSO derivative (**2a**) but quickly found that the photolysis mixture was less readily resolved by the usual analytical techniques than had been the case with **1**. Recognizing that the aryl chromophore at C-3 was, in fact, superfluous for sensitization at C-17, we turned to the two analogs (**2b** and **2c**), which retained the requisite 6-keto functionality and proved more amenable to study by GLC. The photolysis of **2b** is outlined in eq. [3]. Note that only direct photolysis of the ketone with 311 nm light was employed since the TBDMSO functionality is transparent to 266 nm light.

The products proved to be analogous to those reported in eq. [1], with the exception that *no dehalogenated steroid could be detected*. The alcohols (**12** and **13**) were formed in a ca 1:1 ratio and together constituted 73% of the product mixture by area count. They were each identified by GC-MS spectrometry as a 6-ol but the spectral data in hand did not permit a specific assignment of stereochemistry to a specific peak. Three other peaks, totaling 27% of the product, were also resolvable by GLC. Each gave molecular ions by GC-MS corresponding to a THF adduct and are assigned as such, but again the data in hand did not allow one to differentiate among the possible diastereoisomers and they are grouped in eq. [3] as **14**.

Compound **2c** was likewise photolyzed with 311 nm light (see eq. [4]). Again, no dehalogenated steroid was detectable. In this case only a single peak, constituting 41% of the product area count, could be attributed to a 6 hydroxy product (**15**); the GC-MS spectrum did not allow us to distinguish between the two possible diastereomers. Four peaks at longer retention times, which together constituted 53% of the product, each gave mass spectra consistent with a THF adduct. They are grouped in eq. [4] as the mixture of isomers (**16**). Finally, a sixth peak (**17**, 6%) was detected with a retention time intermediate between the alcohols and the

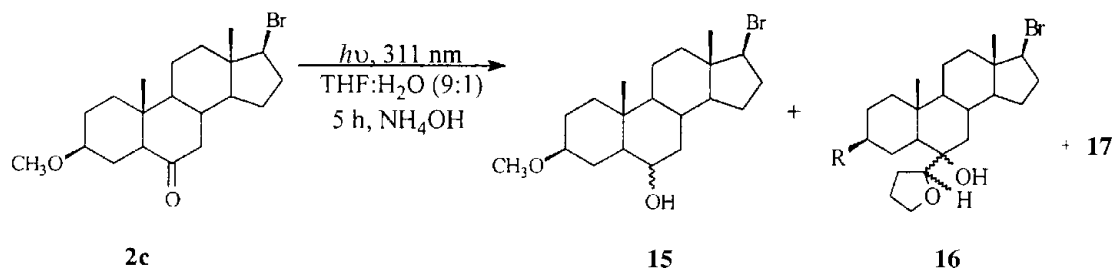


[3]



R = TBDMSO-

[4]



THF adducts that has not been identified. Its mass spectrum indicates that it still retains bromine.

In summary, much of the photochemistry of the two C-17 stereoisomers derives from reactions at C-6 that one would anticipate as resulting from initial hydrogen abstraction from the THF by the ketone excited state. Only in **1** do we see any indication of activation at C-17. Mechanistic and photophysical studies were conducted to further clarify the nature and extent of this interaction.

### Mechanistic and photophysical studies

Our first concern was to establish the multiplicity of the ketone excited state(s) responsible for the chemistry depicted in eq. [1]. This was done using *cis*-piperylene (1.2 mM) as a potential triplet quencher for the 300 nm photolysis of 6 mM **1**. The contrasting effects on the products were striking; 50–70% of the alcohol and THF adduct (**4–7**) formation was quenched whereas there was no effect on the formation of the C-17 cleavage product (**8**). That the hydrogen abstraction chemistry should derive from the ketone triplet state is to be expected. What was not so obvious is that the C-17 cleavage chemistry would involve the ketone excited singlet state.

Nevertheless, this conclusion is supported by singlet lifetime data obtained for a pair of 3 $\alpha$ -OH 6-keto steroids in which the C-6 ketone is the only emitting chromophore, i.e., compounds **3** (with Br at C-17) and **9** (no Br at C-17). Values of  $2.5 \pm 0.2$  and  $3.6 \pm 0.1$  ns were measured for these two compounds, respectively. We attribute the ca 31% reduction in ketone singlet lifetime in **3** to interaction between

the carbonyl singlet excited state and the C-Br functionality. The reduction in singlet lifetime should also be manifested in the relative quantum efficiencies for intersystem crossing at C-6 ( $\phi_{isc}$ ) in these two steroids. Knowing that the reduction products at C-6 derive from the triplet state, and assuming that the ketone  $\phi_{isc}$  would be ca 1.0 in the model (**9**), the relative conversions to C-6 reduction products (at identical photon flux) should provide the  $\phi_{isc}$  for C-6 in **3**. In the event, we observed a 37% diminution (by GLC) of alcohols and THF adducts from photolysis of the halogen-containing steroid (**3**) relative to that observed with the model (**9**), thus leading us to estimate that  $\phi_{isc}$  for **3** is 0.63. The ratio of 1.6 for the relative  $\phi_{isc}$ s for **9:3** compares well with the ratio of 1.4 for their respective singlet lifetimes. The two sets of data, taken together, lead to the conclusion that there is an additional mode of singlet decay present in **3** that causes a reduction in this compound's singlet lifetime and  $\phi_{isc}$ .

Perhaps most notable in this series of studies is that the measured singlet lifetime for the C-6 ketone in the 17 $\beta$  C-Br steroid (**2c**) is  $3.2 \pm 0.2$  ns. It is debatable as to whether the 11% reduction relative to **9** is statistically significant, but it seems clear that the  $\alpha$  C-17 C-Br functionality in **3** has a much greater effect on the C-6 ketone singlet state than does a  $\beta$  C—Br bond in the same location. This conclusion is supported by a comparison of the photoreactivity of **2c** relative to the non-brominated model (**9**) as was done for the  $\phi_{isc}$  study for **3** described above. We found that the relative photoreactivities of compounds **2c** vs. **9** was 1.06, essentially identical within experimental error. It is also interest-



ing to note that the C-6 ketone triplet seems to be ineffective in sensitizing cleavage of the C-17 C—Br bond, despite the fact that its estimated (using cyclohexanone) energy of ca 78 kcal mol<sup>-1</sup> (9) should be well in excess of the estimated (using isopropyl bromide) bond energy for the C—Br bond of ca 68 kcal mol<sup>-1</sup> (10). Additional studies in a solvent less capable of intercepting the carbonyl triplet state are necessary to confirm that triplet energy remains totally localized at the ketone. The challenge, of course, will be to do this while simultaneously efficiently trapping the C-17 radical generated by C-Br homolysis.

#### Further consideration of the interaction between the C-6 carbonyl group and the C-17 C—Br bond in **1**

Given that the singlet lifetime of the C-6 ketone has been shortened from 3.6 to 2.5 ns by the presence of an  $\alpha$  C-17 C—Br bond (see above), if one assumes that this shortening is entirely due to new decay involving an interaction between the two moieties, one calculates a rate constant for this decay mode of  $1.2 \times 10^8$  s<sup>-1</sup>. An analogous calculation using the 37% reduction in  $\phi_{isc}$  yields a rate of singlet decay because of interaction of  $1.5 \times 10^8$  s<sup>-1</sup>. We have already estimated that ca 37% of the ketone singlets are diverted from intersystem crossing by this interaction. Only 0.0066 (the quantum yield for formation of **8** (eq. [1])) is accounted for by product formation resulting from C-Br cleavage. Clearly, a very small fraction (ca 2%) of the diverted singlets surface as product, either because cleavage of the interacting C—Br bond is minimal or because there is efficient cleavage but also efficient radical-pair recombination.

As to the specific nature of the ketone—C-Br interaction, we suggest that this may occur through TBI coupling of the ketone  $n, \pi^*$  singlet state with the C-Br  $n, \sigma^*$  state, by analogy with the proposed explanation for the sensitized photoactivation of a  $\beta$  C—Cl bond in chloronorbornenes (11) and chlorobenzobicyclics (12). The strong stereoelectronic dependence of the interaction is not surprising, there being ample precedent in systems having fewer  $\sigma$  bonds between the two moieties (13). However, the apparent preference for interaction with the  $\alpha$ , pseudo-axial C—Br bond at C-17 was unexpected, since the “all trans” rule is generally accepted as leading to enhanced coupling of  $\sigma$ -bonded equatorial vs. axial substituents with the steroid framework (14). Nevertheless, though we have likewise observed a greater rate of intramolecular triplet–triplet energy transfer (intraTTET) from an equatorial (DPSO) donor at C-3 to an olefin at C-17, relative to its axial C-3 counterpart (4), the inverse was observed when the donor was  $\sigma$ -bonded to C-17. In that event, intraTTET from C-17 to C-3 was found to be almost 10-fold faster from the  $\alpha$ -DPSO group (15). Thus, the evaluation of additional steroidal ketobromides, both by experiment and by theory, is needed to determine whether the stereoelectronics associated with the C-6—C-17 interaction studied here is prototypical or peculiar to the specific placement of the C—Br bond at C-17 in ring D.

## Experimental

### General

A considerable amount of the experimental details is available in the doctoral dissertation of L. Torun (16) or as supplemental material for the preliminary communication (2). Thus, only the most salient features are presented below or as supplemental material.<sup>2</sup>

<sup>13</sup>C NMR spectra were obtained in CDCl<sub>3</sub> with a Varian spectrometer operating at 50 MHz with chemical shifts relative to the residual chloroform peak at 77 ppm unless otherwise noted. <sup>1</sup>H NMR spectra were obtained in CDCl<sub>3</sub> with a Varian spectrometer operating at 200 MHz with chemical shifts relative to the residual chloroform peak at 7.24 ppm. In the case of two synthetic intermediates, the proton count in the steroid aliphatic region read ca 5–10% high relative to the downfield protons; this is indicated in the listing of the proton spectra. Mass spectrometry utilized a Finnigan 4000 mass spectrometer operating at a source temperature of 250°C. Electron impact (EI) mass spectra and chemical ionization (CI) mass spectra were recorded at an ionization energy of 70 eV, with the latter utilizing isobutane at a pressure of 0.30 torr (1 torr = 133.322 Pa). Elemental analysis was done by HR-MS using either FAB or EI ionization on samples analytically pure by GLC. Ultraviolet absorption spectra were recorded using 1-cm quartz cells on a dual beam Cary model 100 UV–vis spectrophotometer interfaced to a computer using Cary software. Steady-state fluorescence spectra were obtained with 1 cm square fluorescence cells on a SLM Aminco SPF-500 spectrophotometer using a 250 W xenon arc lamp operating in the A/B mode. Fluorescence quantum efficiencies were obtained using toluene as the reference. The fluorescence lifetime measurements were obtained using a PTI model 100 spectrophotometer at room temperature. All the fluorescence samples were purged with argon for 20 min prior to analysis. For the X-ray structural analysis, crystals of 17 $\alpha$ -bromo-3 $\alpha$ -(triphenylsilyloxy)-5 $\alpha$ -androstane-6-one (**1**) were prepared by recrystallization of column-purified material from hexane–CH<sub>2</sub>Cl<sub>2</sub>. A colorless plate with dimensions of 0.41  $\times$  0.35  $\times$  0.22 mm was placed on a glass fiber in a random orientation. X-ray data were collected with MO K $\alpha$  radiation ( $\lambda$  = 0.71073 Å) on a Nonius Kappa CCD computer-controlled diffractometer equipped with a graphite crystal, incident beam monochromator. Cell constants and an orientation matrix for data collection were obtained from least-squares refinement, using the setting angle of 17 224 reflections in the range  $4 < \theta < 27^\circ$ . Data were collected at a temperature of  $173 \pm 1^\circ\text{C}$  to a maximum of  $2\theta$  of  $55.8^\circ$ . Melting points were determined with a Fisher-Johns melting point apparatus and are uncorrected. Laser irradiations were conducted at 266 nm using a Continuum NY-61 Nd:YAG laser equipped with a frequency quadrupler (10 Hz, ca 3.0 mJ/pulse). Samples (3 mL, 10.0 mM) were degassed with argon for at least 25 min prior to irradiation

<sup>2</sup>Supplementary data may be purchased from the Depository of Unpublished Data, Document Delivery, CISTI, National Research Council Canada, Ottawa, ON K1A 0S2, Canada ([http://www.nrc.ca/cisti/irm/unpub\\_e.shtml](http://www.nrc.ca/cisti/irm/unpub_e.shtml) for information on ordering electronically). These data can be obtained, free of charge, via [www.ccdc.cam.ac.uk/conts/retrieving.html](http://www.ccdc.cam.ac.uk/conts/retrieving.html) (or from the Cambridge Crystallographic Data Centre, 12 Union Road, Cambridge CB2 1EZ, U.K.; fax +44 1223 336033; or [deposit@ccdc.cam.ac.uk](mailto:deposit@ccdc.cam.ac.uk)).



and kept closed with septa. They were photolyzed in square vycor photolysis cells with continuous stirring using a 2 mm stirring bar. The power of the laser was measured with an OPHIR power meter, model AN/2. Data were corrected for scatter and reflectance of light from the cell walls. For 311 nm irradiations, a reactor was equipped with 8 × 311 nm Phillips TL01 (20 W) lamps and a merry-go-round turntable apparatus that positioned 8 cylindrical quartz tubes (10 mm i.d.) approximately 2 cm from the lamps. The 300 nm irradiation employed a Rayonet Reactor (New England Ultraviolet Co.) equipped with lamps having maximal output at 300 nm. All solutions were deoxygenated with a stream of argon prior to photolysis. Uranyl oxalate actinometry was used for the quantum efficiency determinations. 4-Androsten-3,17-dione, 3 $\beta$ -hydroxy-5 $\alpha$ -androstan-17-one, 17 $\beta$ -hydroxy-5 $\alpha$ -androstan-3-one, 3 $\beta$ -hydroxy-5 $\alpha$ -androsten-17-one, 5-androsten-3 $\beta$ -ol-17-one (dehydroisoandrosterone), and testosterone were purchased from Sigma.

#### 17-Bromo-3 $\beta$ -hydroxy-androsta-5,16-diene (VI)

3 $\beta$ -Hydroxy-5-androsten-17-hydrazone (V) (2.0 g, 6.57 mmol), prepared from commercially available 3 $\beta$ -hydroxy-5-androsten-17-one (IV), was dissolved in pyridine (30 mL) and the solution cooled in an ice bath. NBS (2.0 g, 16.85 mmol) dissolved in 15 mL of pyridine was added dropwise to the solution over 5 min. After stirring the yellow-colored solution at ice bath temperature for 5 min, the solution was poured into 50 mL of ice water and the mixture extracted with ether. The combined ether layers were washed with 10% HCl (3 × 20 mL), NaHCO<sub>3</sub> solution (3 × 20 mL), and water (2 × 20 mL) and dried over Na<sub>2</sub>SO<sub>4</sub>. The crude product was chromatographed on silica gel with 2% EtOAc in hexane to give a white solid product in 48–65% yield; mp: 163 to 164°C. <sup>1</sup>H NMR (CDCl<sub>3</sub>, 200 MHz)  $\delta$ : 5.90–5.80 (dd, 1H), 5.4–5.3 (m, 1H), 3.6–3.4 (m, 1H), 2.4–0.85 (m, ca 24 H). <sup>13</sup>C NMR (CDCl<sub>3</sub>, 50 MHz)  $\delta$ : 141.2, 135.6, 129.0, 121.1, 71.6, 55.5, 50.4, 48.5, 42.2, 37.1, 36.7, 34.5, 31.8, 31.5, 31.3, 30.7, 20.6, 19.3, 15.0. CI (*m/z*): (M + H)<sup>+</sup>: 351/353 (base peak). EI: 350/352 (M)<sup>+</sup>; 91 (base peak).

#### 17 $\beta$ -Bromo-5-androsten-3 $\beta$ -ol (VII)

Hydrazine monohydrate (3.0 mL) was added to a flask containing 17-bromo-3 $\beta$ -hydroxy-androsta-5,16-diene (VI) (0.7 g, 1.99 mmol) dissolved in 30 mL of methanol. To this solution was added K<sub>3</sub>Fe(CN)<sub>6</sub> (1.2 g, 3.64 mmol) and a catalytic amount of Cu(OAc)<sub>2</sub> (~10 mg). The resulting solution was stirred at room temperature with continuous monitoring by GC. Hydrazine monohydrate (3.0 mL each time) was added as needed to eliminate all starting material in the solution. A total of 9 to 10 mL was added over 3 days. The milky white solution was filtered and MeOH was removed in vacuo. The resulting aqueous residue was partitioned between dichloromethane and water and extracted with dichloromethane. The solvent was dried over Na<sub>2</sub>SO<sub>4</sub>, concentrated, and purified by column chromatography on silica gel using 15% EtOAc in hexane to afford a white solid in 85–92% yield; mp: 145–147°C. <sup>1</sup>H NMR (CDCl<sub>3</sub>, 200 MHz)  $\delta$ : 5.4–5.2 (d, 1H), 3.85–3.65 (t, 1H), 3.65–3.40 (m, 1H), 2.40–0.75 (m, 26H). <sup>13</sup>C NMR (CDCl<sub>3</sub>, 50 MHz)  $\delta$ : 140.88, 121.10, 71.59, 61.94, 51.34, 50.01, 43.82, 37.21,

36.54, 36.19, 32.82, 32.44, 31.50, 24.53, 20.63, 19.38, 13.96. EI (*m/z*): 352/354 (M)<sup>+</sup>.

#### 17 $\beta$ -Bromo-3 $\beta$ -(triphenylsilyloxy)-5-androsten (VIII)

17 $\beta$ -Bromo-5-androsten-3 $\beta$ -ol (VII) (52 mg, 0.14 mmol) was added to a round-bottomed flask containing DMF (2.0 mL). To this solution was added triphenylsilyl chloride (0.65 mg, 0.22 mmol), imidazole (20 mg, 0.28 mmol), and a catalytic amount of 4(dimethylamino)pyridine, and the solution was stirred under argon for 12 h. Water (10 mL) was added and the solution was extracted with ether. The organic extracts were washed with water. After drying and concentrating, the crude product was chromatographed on a Chromatotron plate prepared with silica gel using hexane to obtain 0.27 g (80%) as an oily product. <sup>1</sup>H NMR (CDCl<sub>3</sub>, 200 MHz)  $\delta$ : 7.65–7.58 (m, 6H), 7.48–7.32 (m, 9H), 5.25–5.10 (bs, 1H), 3.85–3.65 (m, 2H), 2.60–0.80 (m, ca 25H). <sup>13</sup>C NMR (CDCl<sub>3</sub>, 50 MHz)  $\delta$ : 141.24, 135.40, 134.94, 134.89, 130.10, 129.97, 127.90, 127.76, 73.31, 62.03, 51.34, 49.96, 43.82, 42.30, 37.16, 36.56, 36.19, 32.80, 32.45, 31.77, 31.53, 24.53, 20.59, 19.40, 13.97. EI (*m/z*): 610/612 (M<sup>+</sup>), 259 (Ph<sub>3</sub>Si)<sup>+</sup> base peak. HR-MS (EI) calcd. for C<sub>37</sub>H<sub>43</sub>BrOSi: 610.2267; found: 610.2250.

#### 17 $\beta$ -Bromo-3 $\beta$ -triphenylsilyoxy-5 $\alpha$ -androstan-6 $\alpha$ -ol (IX)

The general procedure used for hydroboration was to add the silylated bromoandrosterone (ca 0.5 to 0.6 mmol) to a flask containing 10 mL of dry THF, cool to ice bath temperature, and then add a borane solution (1 M) in THF (0.8 mL) under argon. After stirring in an ice bath for 1 h, and then at room temperature for 12 h, the excess borane was destroyed with water. A 2 N solution of NaOH (1.5 mL) and 30% H<sub>2</sub>O<sub>2</sub> (1.5 mL) was added and the resulting mixture stirred at 50°C for 1 h. After cooling to room temperature, the crude product was extracted with ether (3 × 15 mL). The combined organic layers were washed with water and dried over Na<sub>2</sub>SO<sub>4</sub>, and concentrated under reduced pressure. The residue was chromatographed on a column using CH<sub>2</sub>Cl<sub>2</sub>:hexanes (1:2) to obtain the products as white solids in >90% yield. For 17 $\beta$ -bromo-3 $\beta$ -triphenylsilyoxy-5 $\alpha$ -androstan-6 $\alpha$ -ol: <sup>1</sup>H NMR (CDCl<sub>3</sub>, 200 MHz)  $\delta$ : 7.72–7.6 (m, 6H), 7.50–7.30 (m, 9H), 3.85–3.65 (t, 2H), 3.45–3.3 (m, 1H), 2.40–0.50 (m, 27 H). <sup>13</sup>C NMR (CDCl<sub>3</sub>, 50 MHz)  $\delta$ : 135.38, 134.85, 129.85, 127.74, 72.88, 69.14, 61.83, 53.60, 51.81, 50.79, 44.04, 40.90, 37.22, 36.18, 35.06, 32.39, 32.10, 31.34, 24.30, 20.58, 14.09, 13.38. CI (*m/z*): 353/355 (M – Ph<sub>3</sub>SiO)<sup>+</sup>. HR-MS (FAB) calcd. for C<sub>37</sub>H<sub>45</sub>BrO<sub>2</sub>Si: 628.2372; found: 628.2352.

#### 17 $\beta$ -Bromo-3 $\beta$ -(triphenylsilyloxy)-5 $\alpha$ -androstan-6-one (2a)

17 $\beta$ -Bromo-3 $\beta$ -triphenylsilyoxy-5 $\alpha$ -androstan-6 $\alpha$ -ol (IX) (0.24 g, 0.38 mmol) was dissolved in 5 mL of dichloromethane and added to a stirred suspension of pyridinium chlorochromate (0.123 g, 0.58 mmol) and sodium acetate (0.031 g, 0.44 mmol). The solution was stirred at room temperature for 3 h, filtered, concentrated, and chromatographed on a silica gel column using hexane to afford 0.16 g (85% yield) of an oily product that solidified over several days; mp 186–190°C. <sup>1</sup>H NMR (CDCl<sub>3</sub>, 200 MHz)  $\delta$ : 7.70–7.55 (m, 6 H), 7.50–7.30 (m, 9H), 3.80–3.60 (m, 2H), 2.40–2.17 (m, 2H), 2.15–1.50 (m, 12H), 1.50–0.96 (m, 6H), 0.89 (s,



3H), 0.84 (s, 3H).  $^{13}\text{C}$  NMR ( $\text{CDCl}_3$ , 50 MHz)  $\delta$ : 210.14, 135.40, 129.92, 127.79, 72.21, 61.17, 56.75, 53.77, 51.45, 48.25, 44.44, 40.73, 38.58, 36.88, 35.96, 32.28, 30.97, 28.91, 24.25, 20.99, 14.11, 13.15. CI ( $m/z$ ): 627/629 ( $\text{M}^+$ ), 351/353 (base peak). HR-MS (FAB) calcd. for  $\text{C}_{37}\text{H}_{43}\text{BrO}_2\text{Si}$ : 627.2294; found: 627.22267.

### 17 $\beta$ -Bromo-3 $\beta$ -(*tert*-butyldimethylsilyloxy)-5 $\alpha$ -androstan-6-one (2b)

The methods used for this preparation were analogous to those described above for **2a**. It was obtained as a white crystalline material, mp 172 to 173°C.  $^1\text{H}$  NMR ( $\text{CDCl}_3$ , 200 MHz)  $\delta$ : 3.83–3.67 (t, 1H), 3.59–3.40 (m, 1H), 2.40–0.95 (m, 20H), 0.85 (s, 9H), 0.80 (s, 3H), 0.74 (s, 3H), 0.01 (s, 6H).  $^{13}\text{C}$  NMR ( $\text{CDCl}_3$ , 50 MHz)  $\delta$ : 210.31, 71.26, 61.21, 56.95, 53.91, 51.48, 46.27, 44.46, 40.78, 38.58, 36.83, 36.01, 32.30, 31.24, 30.18, 25.84, 24.27, 21.04, 18.18, 14.13, 13.18, –4.63, –4.71. HR-MS (CI) calcd. for  $\text{C}_{25}\text{H}_{43}\text{BrO}_2\text{Si}$  ( $\text{M} + \text{H}$ ) $^+$ : 483.2294; found: 483.2309.

### 17 $\beta$ -Bromo-3 $\beta$ -methoxy-5 $\alpha$ -androstan-6-one (2c)

The methods used for this preparation were analogous to those described above for **2a**.  $^1\text{H}$  NMR ( $\text{CDCl}_3$ , 200 MHz)  $\delta$ : 3.85–3.65 (t, 1H), 3.32 (s, 3H), 3.20–2.90 (m, 1H), 2.40–1.50 (m, 11 H), 1.50–0.95 (m, 7 H), 0.81 (s, 3H), 0.74 (s, 3H).  $^{13}\text{C}$  NMR ( $\text{CDCl}_3$ , 50 MHz)  $\delta$ : 210.05, 78.92, 61.14, 56.62, 55.60, 53.80, 51.39, 46.18, 44.41, 40.98, 38.50, 36.57, 35.92, 32.25, 27.44, 25.80, 24.22, 21.00, 14.10, 13.06. CI ( $m/z$ ): 383/385 ( $\text{M} + \text{H}$ ) $^+$ . EI: 382/384 ( $\text{M}^+$ ), 353/355 (base peak). HR-MS calcd. for  $\text{C}_{20}\text{H}_{29}\text{BrO}_2$ : 382.1507; found: 382.1507.

### Photolyses

The details for the preparative photolysis of compound **1** have been presented (2). For the study of 17 $\beta$ -bromo-3 $\beta$ -(*tert*-butyldimethylsilyloxy)-5 $\alpha$ -androstan-6-one (**2b**), 5.0 mM solutions in THF:H<sub>2</sub>O (9:1) containing ca 5 mM of NH<sub>4</sub>OH were degassed with argon for 20 min and irradiated in quartz tubes with 311 nm light for 5 h. The reactions were analyzed by GLC using a 30 m DB-5 column at 280°C under isocratic conditions. The starting material, with a retention time of 11.9 min, was the major component of the reaction mixtures and constituted 65% of the total area counts. Five photoproducts were also observed in the chromatograms. Two major photoproducts appeared with retention times of 11.1 and 11.2 min in a 12.1:13.6 relative ratio. There were three other peaks with retention times of 20.5, 21.5, and 21.9, with relative ratios of 6.0:1.51:1.5. The five products were characterized by GC–MS analyses. The two major photoproducts had very similar EI and CI mass spectra, with a ( $\text{M} + \text{H}$ ) $^+$  molecular ion evident in the CI mass spectrum at  $m/z$  485/487. Loss of water was evident at 467/469. There were three additional photoproducts with retention times of 20.5, 21.5, and 21.9 min. One (20.5 min) exhibited a small molecular ion peak in the CI spectrum at  $m/z$  = 555/557 corresponding to the addition of THF to **2b**. The spectrum also contained a fragment ion peak at  $m/z$  = 537/539 as the base peak, corresponding to the loss of water. The other two products had very similar EI and CI mass spectra but lacked the small molecular ion peak.

Photolysis of 17 $\beta$ -bromo-3 $\beta$ -methoxy-5 $\alpha$ -androstan-6-one (**2c**) was conducted in a similar manner. Five photoproducts were detectable by GLC in addition to unreacted starting material (6.3 min) that made up 69% of the total GLC area count. The first photoproduct had a retention time at 6.2 min and constituted 10% of the total area count. The EI mass spectrum showed a molecular ion peak at  $m/z$  = 384/386 corresponding to reduction of the ketone. Fragment ions were observable at 366/368 ( $\text{M} - \text{H}_2\text{O}$ ) $^+$  and 353/355 (base peak;  $\text{M} - \text{OCH}_3$ ) $^+$ . The other four photoproducts had relatively long GLC retention times (11.9, 12.2, 12.4, and 12.7 min), were formed in a ratio of 4.5:4.9:1.7:1.6, respectively, and had a combined area count constituting 13% of the total area. All four products had identical EI mass spectra and very similar CI mass spectra. The former contained the THF fragment ion ( $m/z$  = 71) as the base peak, and included fragment ion peaks at  $m/z$  = 383/385 ( $\text{M} - \text{THF}$ ) $^+$  and  $m/z$  = 351/353 ( $\text{M} - \text{THF} - \text{CH}_3\text{OH}$ ) $^+$ . The base peak in the CI spectra appeared at  $m/z$  = 437/439 [( $\text{M} + \text{H}$ ) – H<sub>2</sub>O] $^+$ . A sixth photoproduct (9.0 min) constituted 1.3% of the total area count. Its CI mass spectrum exhibited a fragment ion at  $m/z$  = 368/370 as the base peak.

### Acknowledgements

We thank Professor Mary Boyd of Loyola University for the use of her PTI instrument. We are grateful to Phil Fanwick and Karl Wood for their assistance in obtaining the X-ray and mass spectral data, respectively.

### References

1. T.A. Smith, N. Lokan, N. Cabral, S.R. Davies, M.N. Paddon-Row, and K.P. Ghiggino. *J. Photochem. Photobiol. A*, **149**, 55 (2002), and refs. therein.
2. W.-S. Li and H. Morrison. *Org. Lett.* **2**, 15 (2000), and refs. therein.
3. (a) D.E. Breen and R.A. Keller. *J. Am. Chem. Soc.* **90**, 1935 (1968); (b) R.A. Keller. *J. Am. Chem. Soc.* **90**, 1940 (1968); (c) R.A. Keller and L.J. Dolby. *J. Am. Chem. Soc.* **91**, 1293 (1969).
4. L.D. Timberlake and H. Morrison. *J. Am. Chem. Soc.* **121**, 3618 (1999).
5. (a) C.-H. Tung, L.-P. Zhang, Y. Li, H. Cao, and Y. Tanimoto. *J. Phys. Chem.* **100**, 4480 (1996); (b) C.-H. Tung, L.-P. Zhang, Y. Li, H. Cao, and Y. Tanimoto. *J. Am. Chem. Soc.* **119**, 5348 (1997).
6. J.H. Fried, A.N. Natile, and G.E. Arth. *J. Am. Chem. Soc.* **82**, 5704 (1960).
7. J.E. Bridgeman, P.C. Cherry, A.S. Clegg, J.M. Evans, E.R.H. Jones, A. Kasal, V. Kumar, G.D. Meakins, Y. Morisawa, E.E. Richards, and P.D. Woodgate. *J. Chem. Soc. C*, 250 (1970).
8. J.K. Agyin, L.D. Timberlake, and H. Morrison. *J. Am. Chem. Soc.* **119**, 7945 (1997).
9. N.J. Turro. *Modern molecular photochemistry*. Benjamin/Cummings, Menlo Park, Calif. 1978. p. 290.
10. S.W. Benson. *Thermochemical kinetics*. Wiley, New York. 1968.
11. D.M. Pearl, P.D. Burrow, J.J. Nash, H. Morrison, and K.D. Jordan. *J. Am. Chem. Soc.* **115**, 9876 (1993); J.J. Nash, D.V. Carlson, A.M. Kaspar, D.E. Love, K.D. Jordan, and H. Morrison. *J. Am. Chem. Soc.* **115**, 8969 (1993); B.D. Maxwell, J.J.



- Nash, H.A. Morrison, M.L. Falcetta, and K.D. Jordan. *J. Am. Chem. Soc.* **111**, 7914 (1989).
12. A.J. Post, J.J. Nash, D.E. Love, K.D. Jordan, and H. Morrison. *J. Am. Chem. Soc.* **117**, 4930 (1995), and other papers in this series.
13. H. Morrison, T.-V. Singh, L. De Cardenas, D. Severance, K. Jordan, and W. Shaefer. *J. Am. Chem. Soc.* **108**, 3862 (1986).
14. N. Liang, J.R. Miller, and G.L. Closs. *J. Am. Chem. Soc.* **112**, 5353 (1990), and preceding papers in this series.
15. L. Timberlake. Doctoral Dissertation, Purdue University, W. Lafayette, Indiana, December 1998.
16. L. Torun. Doctoral Dissertation, Purdue University, W. Lafayette, Indiana, December 2001.



# Intramolecular photosensitization of the pinene-ocimene rearrangement

Kevin McMahon and Peter J. Wagner

**Abstract:** Bonding of nopol to the para position of acetophenone produces 5,5-dimethyl-2-(2-(*p*-acetylphenoxy)ethyl)bicyclo[3.1.1]hept-2-ene **1**, which contains two chromophores: a *para*-alkoxyacetophenone and an  $\alpha$ -pinene, connected by a single methylene group. UV irradiation of **1** in both benzene and methanol produces none of the intramolecular [2 + 2] cycloaddition that most *para*-(3-buten-1-oxy)acetophenones undergo. Instead, the pinene unit rearranges to a triene skeleton identical to that of ocimene, a known photoproduct of pinene. At modest conversion the diene portion of the triene is *cis* but gradually is converted to a 52:48 *trans*:*cis* ratio. It is concluded that intramolecular triplet energy transfer from the excited ketone chromophore forms the 1,2-biradical triplet state of the pinene moiety, which then undergoes cyclobutylcarbiny ring opening to a 1,4-biradical that cleaves to the 1,3,6-triene structure of ocimene. This mechanism is suggested to be responsible for the earlier reported intermolecularly sensitized rearrangement of  $\alpha$ -pinene to the ocimene isomers.

**Key words:** intramolecular energy transfer, triplet pinene, cyclobutylcarbiny ring opening, photosensitization.

**Résumé :** La fixation du nopol en position para de l'acétophénone produit le 5,5-diméthyl-2-(2-(*p*-acétylphénoxy)éthyl)bicyclo[3.1.1]hept-2-ène **1** qui contient deux chromophores : la *para*-alkoxyacétophénone et l' $\alpha$ -pinène, reliés par un seul groupe méthylène. L'irradiation UV du composé **1** dans le benzène et dans le méthanol ne donne aucun des produits de cycloaddition intramoléculaire [2 + 2] que les *para*-(3-buten-1-oxy)acétophénone donnent généralement. L'unité pinène se réarrange de préférence en un triène dont le squelette est identique à celui de l'ocimène, un photoproduit connu du pinène. A un taux modéré de transformation la portion diène du triène est *cis*, mais elle se transforme graduellement pour donner un rapport *trans* : *cis* de 52 : 48. On en conclut que le transfert d'énergie intramoléculaire du triplet à partir du chromophore cétone excitée forme l'état triplet 1,2-biradical de l'unité pinène qui, par ouverture subséquente du cycle du cyclobutylcarbiny, donne un 1,4-biradical qui s'ouvre à son tour pour donner la structure 1,3,6-triène de l'ocimène. On suggère que ce mécanisme est responsable du réarrangement intermoléculaire sensibilisé de l' $\alpha$ -pinène en isomères de l'ocimène rapporté antérieurement.

**Mots clés :** transfert d'énergie intramoléculaire, pinène triplet, ouverture du cycle du cyclobutylcarbiny, photosensibilisation.

[Traduit par la Rédaction]

## Introduction

Many years ago two papers were published reporting the acetophenone-photosensitized isomerization of  $\alpha$ -pinene to *cis*- and *trans*-ocimene (Scheme 1) (1, 2). Both authors suggested triplet energy transfer from the ketone as the initiator of pinene's rearrangement; but given the incomplete understanding of excited-state reactivity in those years, neither could provide a compelling mechanism describing how triplet pinene rearranges. Frank suggested the possibility of thermal rearrangement following intersystem crossing of the triplet pinene to a vibrationally excited ground state, a then relatively popular notion already subject to suspicion. Kropp merely noted that rearrangement must be facile since other-

wise, as in norbornene, the biradical triplet would have abstracted hydrogen atoms from the solvent. Both authors noted that the initially formed *cis*-ocimene undergoes sensitized *cis*  $\rightarrow$  *trans* isomerization, gradually forming a nearly 1:1 equilibrium.

This paper describes our discovery of an intramolecular version of the photosensitized pinene rearrangement and a simple mechanism for the rearrangement based on the 1,2-biradical nature of triplet alkenes (3). To test whether intramolecular [2 + 2] cycloaddition of remote double bonds to triplet benzenes (4) works with cyclic alkenes, nopol was attached para to acetophenone to form **1**. Irradiation of **1** caused rearrangement of the dimethylbicyclo[3.1.1]heptene ring to a mixture of the *cis*- and *trans*-isomers of 3-(2-(*p*-

Received 20 March 2003. Published on the NRC Research Press Web site at <http://canjchem.nrc.ca> on 17 June 2003.

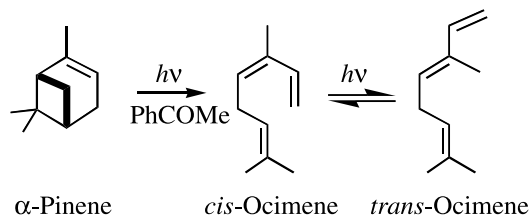
*This paper is dedicated to Don Arnold for his many important contributions to chemistry in North America, and just as important, for his long-time friendship.*

K. McMahon<sup>1</sup> and P.J. Wagner,<sup>2</sup> Chemistry Department, Michigan State University, East Lansing, MI 48824, U.S.A.

<sup>1</sup>Present address: Department of Chemistry and Biochemistry, Carroll College, Waukesha, WI 53186, U.S.A.

<sup>2</sup>Corresponding author (e-mail: [wagnerp@msu.edu](mailto:wagnerp@msu.edu)).

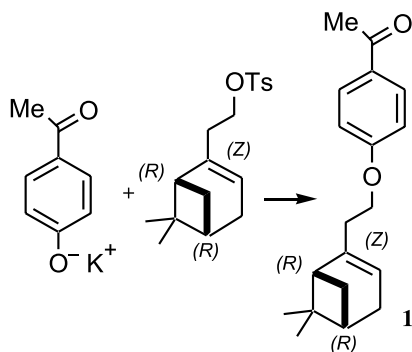


**Scheme 1.** Photosensitized rearrangement of  $\alpha$ -pinene.

acetylphenoxy)ethyl)-7-methylocta-1,3,6-triene, the same transformation that  $\alpha$ -pinene itself undergoes (Scheme 2).

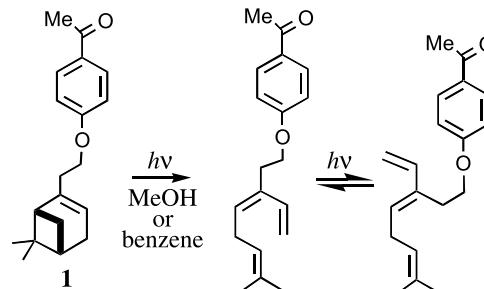
## Results

Compound **1** was prepared via  $S_N2$  reaction of the tosylate of nopol with potassium *p*-acetylphenoxide in DMF as described in the *Experimental section*.



**1** was irradiated in the same way that other *p*-alkenoxyacetophenones had been (**4**). Preliminary experiments were run in deaerated NMR tubes containing benzene- $d_6$  or methanol- $d_4$  solutions 0.02 M in both **1** and methyl benzoate (as an internal standard). Similar results were obtained in both solvents. NMR spectra at various conversions revealed no significant changes in the alkoxyacetophenone portion of the molecule, and the UV spectrum of the product mixture was dominated by an intense peak at 270 nm characteristic of *p*-alkoxyphenyl ketone chromophores. However, changes in the NMR spectrum for the pinene portion of the molecule were consistent with the formation of an ocimene-like triene. Only tiny traces of peaks ascribable to other unidentified products were noted, but it was obvious that no significant amount of cycloaddition of the pinene double bond to the benzene ring occurred. As with the early studies on pinene itself, the *cis*-ocimene unit was the only product at low conversions but it gradually equilibrated to a 48:52 *cis*–*trans* ratio in 73% combined yield at 84% conversion of starting **1**. The products of larger scale reactions were purified by preparative TLC. That the pinene portion of **1** was no longer present was indicated by the lack of significant optical activity in the product solutions at high conversion.

The conversion of the pinene moiety to a triene was demonstrated by the addition of four vinyl proton peaks (6.8 or 6.3 and 5.30–5.06 ppm) to the single vinyl proton peak at 5.34 ppm as well as the increase in  $^{13}\text{C}$  vinyl peaks (110–122 ppm) from two to six. The chemical shifts and coupling constants of the nonaromatic protons correspond very closely to those reported for ocimene (**2**), including the dif-

**Scheme 2.** Photoinduced rearrangement of compound **1**.

ference between the *cis* and *trans* isomers, most notably the 0.5 ppm difference between the  $\text{H}_2$  peaks (see *Experimental*).

## Discussion

This experiment has revealed that triplet energy transfer from the excited acylbenzene chromophore to a tethered alkene can occur at the expense of possible cycloaddition. That such energy transfer could occur was not unexpected, given the early bimolecular examples, although no such total quenching of cycloaddition occurs for acetophenone with a *para* 3-methyl-3-penten-1-oxy tether (**5**), which also has a trialkyl-substituted double bond. Caldwell and co-workers' (**6**) measurement of the triplet energies of various olefins indicate an  $E_T$  of 77 kcal/mol for 2-methyl-2-butene, but only 75 kcal/mol for 1-methylcyclohexene, a better model for  $\alpha$ -pinene. Both  $E_T$ s are higher than that of *p*-acetylanisole (~71 kcal/mol (**7**)), so any energy transfer is quite endothermic. The apparent lack of much if any energy transfer to the trisubstituted acyclic double bond undoubtedly reflects its higher endothermicity. We should note that the lowest triplet of *p*-alkoxy alkanophenones is  $\pi, \pi^*$ , whereas acetophenone itself has a  $n, \pi^*$  lowest triplet. However, there appear to be only slight differences between  $n, \pi^*$  and  $\pi, \pi^*$  ketones in rate constants for intramolecular energy transfer (**8**).

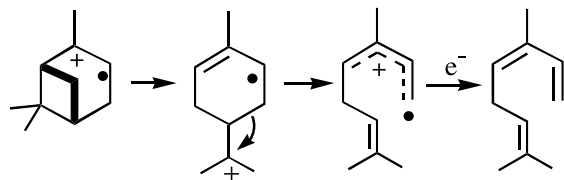
It must be noted that we cannot distinguish quantitatively between intermolecular and intramolecular energy transfer in the case of **1**, although its low concentration should have minimized any intermolecular interactions. The 4 kcal endothermicity of energy transfer to pinene would be expected to slow down a bimolecular process to a rate constant  $\sim 1 \times 10^7 \text{ M}^{-1} \text{ s}^{-1}$  (**9**). Intramolecular reactions usually enjoy rate enhancement, but it has been shown that compounds with a three-atom chain between triplet donor and acceptor have an effective molarity near 1, with very similar first- and second-order rate constants (**10**). That being the case, energy transfer to the pinene moiety should be only about 10% as fast as the  $\sim 1 \times 10^8 \text{ s}^{-1}$  rate constant for [2 + 2] cycloaddition by acylbenzenes with simple acyclic alkenoxy tethers (**4**). The lack of cycloaddition in **1** then probably involves some form of steric hindrance to proximity between the pinene unit and the benzene ring, either at the charge transfer stage or at the C—C bonding stage.

Ab initio computations at the 3-21G and 6-31G\*/UHF levels affirm the 1,2-biradical character of triplet  $\alpha$ -pinene, with the two *p*-like SOMOs at a roughly 45° angle and the one on the carbon next to the bridgehead nearly parallel to

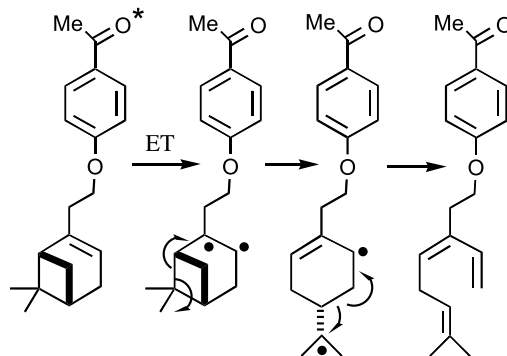


the bridgehead—Me<sub>2</sub>C bond. This alignment should provide for efficient cleavage of the four-membered ring to yield a 1,4-biradical that can then cleave to two double bonds. Scheme 3 depicts this chain of events for **1**. We suspect that this same biradical double cleavage occurs in pinene itself. The ring-opening of cyclobutylcarbinyl radicals to 4-penten-1-yl radicals was not widely recognized and studied until the early 1980s, although Scheme 4 shows an early example of this same ring opening in the benzoyl-peroxide-initiated addition of carbon tetrachloride to  $\beta$ -pinene (11). The rate constant for cyclobutylmethyl ring opening has been measured as  $4 \times 10^3 \text{ s}^{-1}$  in Australia (12) and  $1.5 \times 10^4 \text{ s}^{-1}$  in Canada (13). A comparable rate constant for opening of the four-membered ring in triplet  $\alpha$ -pinene would seem unable to compete with measured triplet decay rates in the  $1 \times 10^7 \text{ s}^{-1}$  range for alkenes (6). However, in this case radical ring-opening involves loss of both electronic excitation and bicyclic ring strain, as well as formation of a tertiary radical site and thus, may be sufficiently exothermic to be quite rapid. Whatever the exact kinetics, the likelihood that the rearrangement begins with a known radical reaction further confirms the biradical nature of triplet alkenes (3, 6).

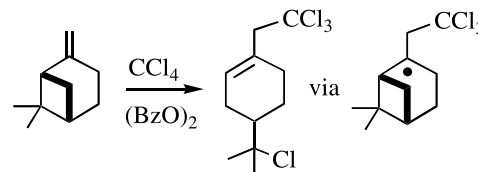
Another possibility is that charge transfer interaction between the bicycloheptene double bond and the triplet phenone produces enough radical-cation character in the pinene to allow ring opening with spread of the radical-cation character between tertiary and allylic sites. Further bond cleavage could then generate a diene radical-cation that collapses to an ocimene structure after back electron transfer. This possibility deserves further study.



**Scheme 3.** Mechanism for triplet pinene rearrangement.

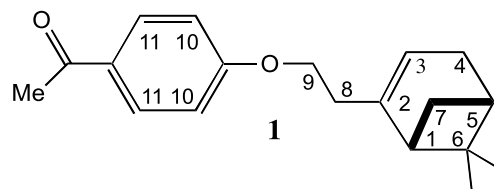


**Scheme 4.** Radical cyclobutylcarbinyl ring opening in pinene.



6.00, 1.50 Hz), 1.21 (s, 3H, Me), 1.05 (d, 1H, 8.40 Hz), 0.74 (s, 3H, Me). <sup>13</sup>C NMR (CDCl<sub>3</sub>, 75.5 MHz)  $\delta$ : 144.63, 142.61, 133.28, 129.77, 127.85, 119.67, 68.57, 45.53, 40.56, 37.99, 36.08, 31.50, 31.27, 26.16, 21.62, 21.04

**5,5-Dimethyl-2-(2-(*p*-acetylphenoxy)ethyl)bi-cyclo[3.1.1]hept-2-ene (1)**



Nopol tosylate (2.00 g, 0.00675 mol), *p*-hydroxy-acetophenone (1.38 g, 0.0101 mol), and K<sub>2</sub>CO<sub>3</sub> (2.80 g, 0.0202 mol) were added to DMF (50 mL) and heated to 60°C under argon for 15 h. The mixture was then cooled to room temperature and water (50 mL) was added. The solution was extracted with ether (3  $\times$  30 mL). The combined organic layer was washed with 2 N NaOH (2  $\times$  30 mL) and aq NaCl (2  $\times$  30 mL), and then dried over MgSO<sub>4</sub>. After removal of the ether at reduced pressure, the desired product was obtained without further purification as a colorless oil (1.35 g, 0.0047 mol, 71%). [ $\alpha$ ]<sup>25°C</sup> (CHCl<sub>3</sub>, *c* = 0.0273): −27.56 (589 nm), −28.66 (578 nm), −32.56 (546 nm), −54.77 (436 nm), −84.82 (365 nm). UV (CH<sub>3</sub>OH)  $\lambda_{\text{max}}$ : 275 (14 789), 216 (11 668), 204 (11 965). MS *m/z*: 284 (<1%), 241 (18), 137 (25), 121 (15), 105 (100), 93 (21), 91 (29), 79 (23), 77 (22), 43 (44). <sup>1</sup>H NMR (CDCl<sub>3</sub>, 300 MHz)  $\delta$ : 7.90 (d, 2H, 9.00 Hz, H<sub>11</sub>), 6.88 (d, 2H, 9.00 Hz, H<sub>10</sub>), 5.34 (br s, 1H, H<sub>3</sub>), 4.01 (t, 2H, 7.05 Hz, H<sub>9</sub>), 2.53 (s, 3H, COMe), 2.44 (tdd, 2H, 7.05, 1.2, 1.2 Hz, H<sub>8</sub>), 2.36 (ddd, 1H, 8.70, 5.62, 5.62 Hz, H<sub>5</sub>), 2.23 (br d, 2H, 8.40 Hz, H<sub>7</sub>), 2.08 (br d, 2H, 5.40 Hz, H<sub>4</sub>), 1.26 (s, 3H, 6-Me), 1.16 (d, 1H, 8.40 Hz, H<sub>1</sub>), 0.80 (s, 3H, 6-Me). <sup>13</sup>C NMR (CDCl<sub>3</sub>, 75.5 MHz)  $\delta$ : 196.74, 162.90, 144.17, 130.56, 130.18, 118.90, 114.15, 66.56,

## Experimental

### Preparation of reactant

#### Nopol tosylate

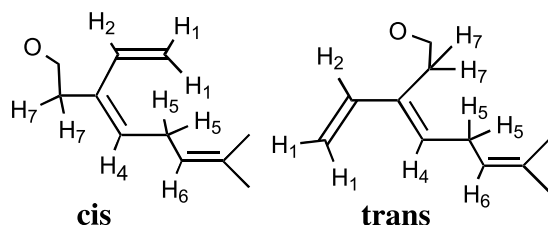
(1R)-(−)-Nopol (Aldrich, 20.00 g, 0.11 mol) in pyridine (32 mL) was cooled to 0°C. Tosyl chloride (13.65 g, 0.0716 mol) was added portion-wise under argon over 1 h. The mixture was stirred mechanically for a further 5 h at low temperature. Then H<sub>2</sub>SO<sub>4</sub> (2 N, 100 mL) was added to the mixture. The resulting solution was extracted using ether (3  $\times$  100 mL). The combined organic extracts were washed with 2 N NaOH, NaHCO<sub>3</sub>, and NaCl. After drying over MgSO<sub>4</sub>, the ether was removed by distillation at reduced pressure. The crude product was purified by dry column flash chromatography (silica gel, CH<sub>2</sub>Cl<sub>2</sub>), to give a colorless oil (13.33 g, 0.045 mol, 63%). [ $\alpha$ ]<sup>25°C</sup> (CHCl<sub>3</sub>, *c* = 0.0273): −23.81 (589 nm), −24.94 (578 nm), −28.46 (546 nm), −48.02 (436 nm), −75.46 (365 nm). <sup>1</sup>H NMR (CDCl<sub>3</sub>, 300 MHz)  $\delta$ : 7.76 (d, 2H, 8.40 Hz, Tos), 7.32 (d, 2H, 7.80 Hz, Tos), 5.22 (br s, 1H, =CH), 4.01 (t, 2H, 6.90 Hz, O-CH<sub>2</sub>), 2.43 (s, 3H, Tos), 2.32–2.24 (m, 3H), 2.17–2.15 (m, 2H), 2.04–2.01 (m, 1H), 1.91 (td, 1H, 6.00,



45.89, 40.73, 38.08, 36.33, 31.64, 31.37, 26.28 21.17. HR-MS calcd. for  $C_{19}H_{24}O_2$ : 284.1770; found: 284.1776.

### Irradiation procedures

Samples of **1** were irradiated in both benzene and methanol solutions. Solutions of **1** (0.0047 g,  $1.65 \times 10^{-5}$  mol) and methyl benzoate (0.0020 g,  $1.47 \times 10^{-5}$  mol) in deuterated solvent (0.75 mL) were placed in an NMR tube. These were irradiated at room temperature in a Rayonet reactor with 300 nm lights. After 1 h and 84% conversion of starting ketone, NMR analysis indicated that the pinene portion of **1** had been converted to two ocimene structures in a 48:52 (cis–trans) ratio in 73% combined yield. This ratio was based on the relative intensities of the 6.77 and 6.34 ppm proton peaks. In the early stages of the reaction, only the cis-isomer was observed. Further irradiation led to equilibration of the two isomers. No optical rotation was observed for the product mixture. Larger scale reactions were purified by PTLC (silica gel,  $CHCl_3$ ).



The isomer mixture obtained at full conversion was analyzed by  $^{13}C$  NMR, UV, and MS. Italicized data represent the NMR peaks for the aryl ketone portion of the molecules, which remain nearly identical to their analogs in the reactant. The mass spectrum indicated that the products are isomers of the reactant **1**, while an intense 270 nm UV peak indicated that the alkoxyacetophenone portion of the molecule survived irradiation unscathed.

### 3-(2-(p-Acetylphenoxy)ethyl)-7-methyl-cis-octa-1,3,6-triene and 3-(2-(p-acetylphenoxy)ethyl)-7-methyl-trans-octa-1,3,6-triene

UV ( $CH_3OH$ )  $\lambda_{max}$ : 270. MS  $m/z$ : 284 (6), 241 (7), 137 (20), 133 (48), 121 (53), 105 (100), 79 (62), 77 (56), 69 (27), 55 (27), 43 (73).  $^{13}C$  NMR ( $CDCl_3$ , 75.5 MHz, DEPT)  $\delta$ : 196.62, 162.83, 162.77, 139.86 (CH), 134.60 (CH), 133.38, 132.53, 132.40 (CH), 131.77, 131.69 (CH), 130.50 (CH), 130.49 (CH), 130.21, 130.16, 121.97 (CH), 121.71 (CH), 114.16 (CH), 114.07 (CH), 113.64 ( $CH_2$ ), 110.81 ( $CH_2$ ), 67.34 ( $CH_2$ ), 66.61 ( $CH_2$ ), 32.90 ( $CH_2$ ), 27.43 ( $CH_2$ ), 26.57 ( $CH_2$ ), 26.24 ( $CH_3$ ), 26.11 ( $CH_2$ ), 25.61 ( $CH_3$ ), 17.75 ( $CH_3$ ), 17.72 ( $CH_3$ ).

$^1H$  NMR spectra of the individually isolated isomers were measured to compare chemical shifts and coupling constants

to those reported for ocimene (2). Italicized data again represent NMR peaks for the aryl ketone portion of the molecules, which remain nearly identical to their analogs in the reactant.

### 3-(2-(p-Acetylphenoxy)ethyl)-7-methyl-cis-octa-1,3,6-triene

$^1H$  NMR ( $CDCl_3$ , 300 MHz, COSY)  $\delta$ : 7.94 (*d*, 2H, 9.00 Hz), 6.95 (*d*, 2H, 9.00 Hz), 6.77 (dd, 1H, 17.70, 11.40 Hz,  $H_2$ ), 5.47 (t, 1H, 7.80 Hz,  $H_4$ ), 5.32 (*d*, 1H, 17.70 Hz,  $H_1$ ), 5.15–5.06 (m, 1H,  $H_6$ ), 5.15 (*d*, 1H, 9.60 Hz,  $H_1$ ), 4.13 (t, 2H, 6.90 Hz,  $O-CH_2$ ), 2.88 (dd, 2H, 7.20 Hz,  $2H_5$ ), 2.69 (t, 2H, 6.90 Hz,  $2H_7$ ), 2.54 (*s*, COMe), 1.68 (br s, Me), 1.63 (br s, Me).

### 3-(2-(p-Acetylphenoxy)ethyl)-7-methyl-trans-octa-1,3,6-triene

$^1H$  NMR ( $CDCl_3$ , 300 MHz, COSY)  $\delta$ : 7.94 (*d*, 2H, 9.00 Hz), 6.95 (*d*, 2H, 9.00 Hz), 6.34 (dd, 1H, 17.40, 10.5 Hz,  $H_2$ ), 5.60 (t, 1H, 7.65 Hz,  $H_4$ ), 5.20 (*d*, 1H, 17.70 Hz,  $H_1$ ), 5.15–5.06 (m, 1H,  $H_6$ ), 4.97 (*d*, 1H, 10.80 Hz,  $H_1$ ), 4.09 (t, 2H, 7.20 Hz,  $O-CH_2$ ), 2.90 (t, 2H, 7.20 Hz,  $2H_5$ ), 2.80 (t, 2H, 6.90 Hz,  $2H_7$ ), 2.54 (*s*, COMe), 1.68 (br s, Me), 1.63 (br s, Me).

### Acknowledgment

This work was supported by National Institute of Health (U.S.A.) grant GM-39821.

### References

1. G. Frank. J. Chem. Soc. B, 130 (1968).
2. P.A. Kropp. J. Am. Chem. Soc. **91**, 5783 (1969).
3. R.A. Caldwell. Pure Appl. Chem. **56**, 1167 (1984); R.A. Caldwell and L. Zhou. J. Am. Chem. Soc. **116**, 2271 (1994).
4. P.J. Wagner. Acc. Chem. Res. **32**, 1 (2001), and refs. therein.
5. P.J. Wagner and K.-L. Cheng. Tetrahedron Lett. **34**, 907 (1993).
6. T. Ni, R.A. Caldwell, and L.A. Melton. J. Am. Chem. Soc. **111**, 457 (1989).
7. P.J. Wagner, A.E. Kemppainen, and H.N. Schott. J. Am. Chem. Soc. **95**, 5604 (1973).
8. P.J. Wagner and P. Klán. J. Am. Chem. Soc. **121**, 9625 (1999).
9. P.J. Wagner. J. Am. Chem. Soc. **89**, 2820 (1967); P.J. Wagner and I. Kochevar. J. Am. Chem. Soc. **90**, 2232 (1968); P.J. Wagner. Mol. Photochem. **1**, 71 (1969).
10. G.L. Closs, P. Piotrowiak, J.M. MacInnis, and G.R. Fleming. J. Am. Chem. Soc. **110**, 2652 (1988).
11. D.M. Oldroyd, G.S. Fisher, and L.A. Goldblatt. J. Am. Chem. Soc. **72**, 2407 (1950).
12. A.L.J. Beckwith and G. Moad. J. Chem. Soc., Perkin Trans. 2, 1083 (1980).
13. K.U. Ingold, B. Maillard, and J.C. Walton. J. Chem. Soc., Perkin Trans. 2, 970 (1981).



# Stereoselective O<sub>2</sub>-induced photoisomerization of all-*trans*-1,6-diphenyl-1,3,5-hexatriene

Jack Saltiel, Govindarajan Krishnamoorthy, Zhennian Huang, Dong-Hoon Ko, and Shujun Wang

**Abstract:** Irradiation of all-*trans*-1,6-diphenyl-1,3,5-hexatriene (*ttt*-DPH) in degassed acetonitrile (AN) gives *ctt*- and *tct*-DPH, relatively inefficiently, mainly via isomerization in the singlet excited state. The triplet contribution to the photoisomerization is small due to a very low intersystem crossing yield ( $\phi_{\text{is}} = 0.01$ ). Central bond isomerization is quenched in the presence of air by a factor of 1.4, consistent with the expected quenching of the lowest singlet and triplet excited states by oxygen. However, the presence of air enhances terminal bond photoisomerization by nearly twofold. Triplet-sensitized *ttt*-DPH photoisomerization favors *tct*-DPH formation and is quenched by oxygen. It follows that the interaction of singlet-excited *ttt*-DPH with O<sub>2</sub> suppresses isomerization to *tct*-DPH but opens a new isomerization pathway to *ctt*-DPH. The presence of dimethylfuran, a singlet O<sub>2</sub> trap, has no effect on the photoisomerization, eliminating the possible involvement of singlet O<sub>2</sub> in this new reaction. *ttt*-DPH radical cations are ruled out as intermediates because the presence of fumaronitrile, which leads to their formation, suppresses both central and terminal bond photoisomerizations. In contrast to acetonitrile, *ctt*-DPH formation is quenched by oxygen in methylcyclohexane, suggesting the requirement of a polar environment. Strikingly different deuterium isotope effects distinguish the direct and O<sub>2</sub>-induced photoisomerization pathways. A comparative study of *ttt*-DPH-*d*<sub>0</sub> with *ttt*-DPH-*d*<sub>2</sub> and *ttt*-DPH-*d*<sub>4</sub>, involving deuteration of one and both terminal double bonds, reveals an inverse kinetic isotope effect ( $k_{\text{H}}^{\text{ox}}/k_{\text{D}}^{\text{ox}} = 0.92$ ) for the O<sub>2</sub>-induced reaction. An attractive mechanism for the new oxygen-induced photoisomerization involves charge transfer from the S<sub>1</sub> state of *ttt*-DPH to oxygen followed by collapse of the exciplex to either a zwitterionic or a biradicaloid species through bonding at one of the benzylic positions. Rotation about the new single bond in this intermediate followed by reversion to DPH and O<sub>2</sub> gives the observed result.

**Key words:** diphenylhexatrienes, trans-cis photoisomerization, oxygen sensitization.

**Résumé :** L'irradiation du 1,6-diphénylhexa-1,3,5-triène complètement *trans* (*ttt*-DPH), dans de l'acétonitrile dégazé (AN) conduit d'une façon relativement inefficace à la formation des *ctt*- et *tct*-DPH, principalement par le biais d'une isomérisation dans l'état excité singulet. La contribution triplet à la photoisomérisation est faible en raison du très faible rendement du passage intersystème ( $\phi_{\text{is}} = 0,01$ ). L'isomérisation de la liaison centrale est piégée en présence d'air par un facteur de 1,4 qui est en accord le piégeage par l'oxygène des états excités singulet et triplet les plus bas. Toutefois, la présence d'air augmente la photoisomérisation de la liaison terminale par un facteur égal pratiquement à deux. La photoisomérisation du *ttt*-DPH sensibilisée au niveau triplet favorise la formation de *tct*-DPH et elle est piégée par l'oxygène. Il en découle que l'interaction de l'oxygène avec le *ttt*-DPH excité à l'état singulet supprime l'isomérisation en *tct*-DPH mais qu'elle conduit à une nouvelle voie d'isomérisation conduisant au *ctt*-DPH. La présence de diméthylfurane, un piège pour O<sub>2</sub> à l'état singulet, n'a pas d'effet sur la photoisomérisation ce qui élimine la possibilité d'implication du O<sub>2</sub> à l'état singulet dans cette nouvelle réaction. On a éliminé la possibilité d'une implication des cations radicaux *ttt*-DPH comme intermédiaires sur la base du fait que la présence de fumaronitrile qui conduit à leur formation supprime les photoisomérisations des liaisons tant terminale que centrale. Par opposition à ce qui est observé avec l'acétonitrile, la formation de *ctt*-DPH est piégée par l'oxygène dans le méthylcyclohexane ce qui suggère la nécessité d'un environnement polaire. Des effets isotopiques du deutérium très différents distinguent les voies de photoisomérisations directe et induite par O<sub>2</sub>. Une étude comparative des *ttt*-DPH-*d*<sub>0</sub>, *ttt*-DPH-*d*<sub>2</sub> et *ttt*-DPH-*d*<sub>4</sub> impliquant la deutération d'une et des deux doubles liaisons terminales permet de mettre en évidence un effet isotopique cinétique inverse,  $k_{\text{H}}^{\text{ox}}/k_{\text{D}}^{\text{ox}} = 0,92$ , pour la réaction induite par O<sub>2</sub>. Un mécanisme intéressant pour la nouvelle photoisomérisation induite par l'oxygène implique un transfert de charge de l'état S<sub>1</sub> du *ttt*-DPH vers l'oxygène, suivi d'une décomposition de l'exciplex en espèces soit zwitterionique ou biradicaloïde par le biais de la formation d'une liaison à l'une des positions benzyliques. Une rotation autour de la nouvelle liaison simple de cette intermédiaire, suivie d'une

Received 24 February 2003. Published on the NRC Research Press Web site at <http://canjchem.nrc.ca> on 17 June 2003.

Dedicated to Professor Don Arnold for his contributions to chemistry.

J. Saltiel,<sup>1</sup> G. Krishnamoorthy, Z. Huang, D.-H. Ko, and S. Wang. Department of Chemistry and Biochemistry, Florida State University, Tallahassee, FL 32306-4390, U.S.A.

<sup>1</sup>Corresponding author (e-mail: saltiel@chem.fsu.edu).



réversion en DPH et en O<sub>2</sub>, conduit au résultat observé.

**Mots clés :** diphénylhexatriènes, photoisomérisation trans-cis, sensibilisation par l'oxygène.

[Traduit par la Rédaction]

## Introduction

all-*trans*-1,6-Diphenyl-1,3,5-hexatriene (*ttt*-DPH) has been used as a model for the long polyenes related to the retinols and vitamin A. It is the first member of the  $\alpha,\omega$ -diphenylpolyene vinylogous family whose all-*s-trans* conformer exhibits fluorescence both from the initially excited  $1^1B_u$  state and from a lower energy singlet excited state that, following Hudson and Kohler, is identified as the forbidden doubly excited  $2^1A_g$  state (1–3). The lowest singlet excited states of all longer diphenylpolyenes (1–3) and of all conjugated polyenes starting with 1,3-butadiene (4–7), have also been identified as  $2^1A_g$  states. In degassed solutions the *trans*  $\rightarrow$  *cis* photoisomerization of *ttt*-DPH following direct excitation occurs inefficiently by a combination of singlet and triplet pathways (8). In the triplet state, the ground state isomers of DPH exist as a mixture of freely equilibrating conformers in which *ttt*, *tct*, and *ctt* geometries dominate (9). In the absence of oxygen, triplet excitation transfer events between relatively long-lived DPH triplets and DPH ground states of different geometry are links in quantum chain processes that enhance the contribution of triplets to the photoisomerization, compensating somewhat for the low intersystem crossing yields. The quenching of the triplets by oxygen significantly decreases their lifetime and prevents their participation in quantum chain events (9).

Changing the solvent from methylcyclohexane (MCH) to acetonitrile (AN) increases the rates of photoisomerization in the singlet excited state manifold, the increase being especially pronounced (20-fold) at the terminal double bonds (8, 10), thereby decreasing the singlet excited state lifetime and the contribution of the competing decay channels of fluorescence ( $\phi_f = 0.65$  and  $0.27$  at  $20^\circ\text{C}$  in MCH (11) and AN (10), respectively) and intersystem crossing ( $\phi_{is} = 0.029$  and  $0.010$  at  $20^\circ\text{C}$  in MCH (12) and AN (13, 14), respectively). Photoisomerization in the *ttt*  $\rightarrow$  *ctt* direction in AN is almost entirely a singlet excited state process (98%) that is attenuated by a factor of 1.36 on deuteration of the olefinic hydrogens of the terminal double bond (10).

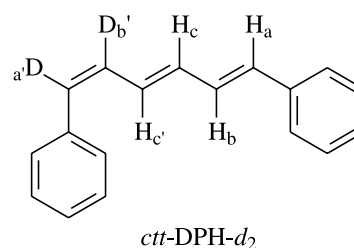
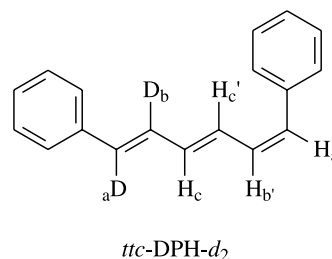
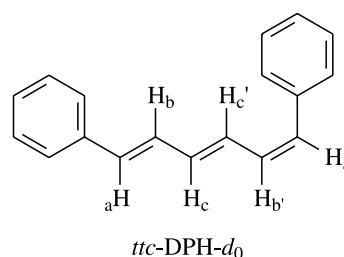
We report here the effect of oxygen on the photoisomerization of *ttt*-DPH and its 1,2-dideuterio and 1,2,5,6-tetradeuterio derivatives upon direct excitation in AN. In contrast to the central bond whose photoisomerization is attenuated, consistent with oxygen quenching of singlet and triplet excited states, oxygen enhances photoisomerization at the terminal double bonds. The mechanism of this new photoisomerization pathway is addressed in this paper.

## Experimental section

### Materials

Sources and purification procedures for all-*trans*-1,6-diphenyl-1,3,5-hexatriene (100.0%, HPLC), benzophenone, *trans*-stilbene, anthracene, and acetonitrile have been described (8, 10). Acetonitrile was used as received or purified

using a known procedure (15). Lithium perchlorate (Spectrum, anhydrous ACS reagent) was used as received. The syntheses of 1,2-dideuterio- (*ttt*-DPH-*d*<sub>2</sub>, 99.9%, HPLC) and 1,2,5,6-tetradeuterio-all-*trans*-1,6-diphenyl-1,3,5-hexatriene (*ttt*-DPH-*d*<sub>4</sub>, 98.0%, HPLC, 1.7% *tcc*-DPH-*d*<sub>4</sub>, major contaminant) have been described (10). Prior to use in this study, *ttt*-DPH-*d*<sub>4</sub> was recrystallized three times to a final purity of 99.4% with 0.5% *tcc*-DPH-*d*<sub>4</sub>, the major contaminant.



### Irradiation procedure

Irradiations were carried out in a Moses merry-go-round (16) apparatus immersed in a thermostated water bath. A heating coil connected to a thermoregulator (Polyscience Corporation) was used to control the temperature to  $20 \pm 0.1^\circ\text{C}$ . The benzophenone-sensitized photoisomerization of *trans*-stilbene was used for actinometry ( $\phi_{t \rightarrow c} = 0.55$ ) (17, 18). A Hanovia medium pressure Hg lamp (200 W, Ace Glass, Inc.) and Corning CS 7-37 and 0-52 filters were used for excitation at 366 nm. Aliquots of actinometer solutions (3.0 mL) were pipetted into Pyrex ampoules (13 mm o.d.), degassed, and flame-sealed at a constriction. Air-saturated DPH solutions ( $1.0 \times 10^{-3}$  M in AN, 3 mL aliquots) were



irradiated in 13 mm o.d. Pyrex ampoules lightly stoppered with Teflon-tape-covered rubber stoppers. In some instances, the ampoules were provided with fritted disks at the bottom for bubbling air or oxygen throughout the irradiation. Sample preparation, degassing, and analysis were performed in almost complete darkness (red light).

### Analytical procedures

Actinometer solutions were analyzed by GLC and DPH solutions by HPLC ( $\lambda_{\text{mon}} = 350 \text{ nm}$ ) as previously described (8, 9), except that on replacing AN with hexanes prior to HPLC analyses, a stream of argon was used to evaporate the solvent and care was exercised to avoid taking samples to dryness (10). This procedure minimizes *ctt*-DPH losses.

### Fluorescence measurements

Fluorescence spectra were measured with a Hitachi/PerkinElmer MPF-2A fluorescence spectrophotometer as previously described (19), or with a Hitachi F4500 fluorimeter. Fluorescence spectra were recorded for both air-saturated and Ar-bubbled solutions of DPH in AN in standard  $1 \text{ cm}^2$  quartz cells. Temperature was maintained at  $20.0 \pm 0.1^\circ\text{C}$  using a Neslab-RTE 4DD constant temperature circulation bath, and was monitored continuously during each scan with an Omega Engineering Model 199 RTD digital thermometer in a reference cell placed in the same constant temperature cell holder. Fluorescence lifetimes were measured with a phase modulation Fluorolog- $\tau 2$  lifetime spectrofluorometer (SPEX) equipped with a 450 W Xe arc source, a Hamamatsu R928P photomultiplier tube, and a Lasermetrics BNC1072FW Pockel cell ( $\text{KD}_2\text{PO}_4$ ). The Fluorolog- $\tau 2$  modulates the frequency of the excitation light from 0.5 to 300 MHz. A glycogen solution ( $\tau = 0 \text{ ns}$ , scattered light) was used as reference. Temperature was maintained at  $20.0 \pm 0.1^\circ\text{C}$  and was monitored continuously during each scan as described above. Air-saturated *ttt*-DPH solutions ( $2.0 \times 10^{-6} \text{ M}$ ) were employed. Software (DMF 3000F Spectroscopy) provided by the manufacturer was used to analyze the data. Determinations of the quality of the lifetimes were based on examination of the statistics of the fit (a plot of the residual deviations vs. frequency) and reduced  $\chi^2$  values that were all close to unity.

## Results

### Photochemical observations

Photostationary states were approached from the *ttt*-DPH- $d_n$  ( $n = 2$  and 4) side. Degassed DPH samples ( $1.0 \times 10^{-3} \text{ M}$ ) in air-saturated AN were irradiated for different time intervals at  $20.0^\circ\text{C}$  until HPLC analysis revealed no further change in the isomer composition. Photostationary state fractions are shown in Table 1. Overall conversions for quantum yield measurements were kept below 8% and were corrected for back reaction as has been described (10). Quantum yields are also shown in Table 1. The effect of additives was studied for *ttt*-DPH- $d_0$ . The presence of up to  $0.40 \text{ M LiClO}_4$  had no effect on *ctt*/*tct* conversion ratios for both air-saturated and degassed AN solutions. The presence of  $0.188 \text{ M}$  2,5-dimethylfuran (DMF) had no significant effect on photoisomerization quantum yields of  $1.38 \times 10^{-3} \text{ M}$  *ttt*-DPH- $d_0$  in air-saturated AN. Similarly, addition of up to

**Table 1.** PSS fractions and photoisomerization quantum yields for *ttt*-DPH- $d_n$  in air-saturated AN (366 nm,  $20.0^\circ\text{C}$ ).<sup>a</sup>

DPH	<i>ctt</i> + <i>ttc</i>	<i>tct</i>	<i>ttt</i>
<b>PSS fractions</b>			
$d_0$	0.430(0.239)	0.095(0.106)	0.400(0.635)
$d_2$	0.419(0.206)	0.100(0.106)	0.401(0.667)
$d_4$	0.395(0.183)	0.109(0.115)	0.402(0.661)
<b>Quantum yields</b>			
	$\phi_{\text{ctt}+\text{ttc}}$	$\phi_{\text{tct}}$	
$d_0$	0.121 (0.062)	0.025 (0.035)	
$d_2$	0.119 (0.054)	0.026 (0.036)	
$d_4$	0.114 (0.046)	0.028 (0.038)	

<sup>a</sup>Values in parentheses are corresponding values under degassed conditions from ref. (10); estimated uncertainties in absolute quantum yields are  $\pm 5\%$ .

$1.2 \times 10^{-3} \text{ M}$  diethylamine (DEA) to  $1.00 \times 10^{-3} \text{ M}$  *ttt*-DPH- $d_0$  in degassed or air-saturated AN solutions did not alter the photoisomerization quantum yields.

### Fluorescence measurements

The fluorescence of  $1.0 \times 10^{-3} \text{ M}$  *ttt*-DPH- $d_0$  in degassed and air-saturated AN was found to be independent of [DEA] up to  $1.5 \times 10^{-3} \text{ M}$ . Fluorescence lifetimes at different temperatures for air-saturated solutions are compared in Table 2 with those for degassed solutions (10). Excellent fits to the single exponential decay model were obtained ( $\chi^2 \leq 1.2$ ) and the lifetimes were independent of excitation and monitoring wavelengths, within experimental uncertainty. Reproducibility in independent measurements was better than  $\pm 0.1 \text{ ns}$ .

## Discussion

### Background

The ground state of molecular oxygen is generally a very effective quencher of electronically excited molecules (20). Rate constants for oxygen quenching of singlet excited states of aromatic hydrocarbons in hydrocarbon solvents are often close to the diffusion-controlled limit. Corresponding values for triplet state quenching are usually an order of magnitude smaller owing to restrictions by spin statistical factors (20–22). These quenching events are commonly associated with formation of the lowest singlet state of the oxygen molecule  $\text{O}_2^*(^1\Delta_g)$ , sometimes through the intermediacy of the higher energy state  $\text{O}_2^*(^1\Sigma_g^+)$ . In the case of singlet excited states of aromatic hydrocarbons, induced intersystem crossing has been shown to accompany oxygen quenching in hydrocarbon media (23), a pathway to triplets that is diminished by polar solvents such as acetonitrile (23–25). The importance of a charge transfer (CT) quenching pathway by oxygen was first established by Kikuchi et al. (26) who showed that, for anthracenecarbonitriles and acridinium salts, fluorescence quenching rate constants in acetonitrile decrease as the free energy for full electron transfer ( $\Delta G_s^{\text{CT}}$ ) increases from negative to positive values. A comprehensive systematic study of the contribution of CT in the quenching of aromatic hydrocarbon singlet and triplet states by oxygen in AN was described by Abdel-Shafi and Wilkinson (27). With the exception of tetracene that undergoes significant chemical degradation, the net rate constants for the triplet quenching



**Table 2.** O<sub>2</sub> effect on *ttt*-DPH-*d<sub>n</sub>* fluorescence lifetimes (366 nm).<sup>a</sup>

<i>T</i> (°C)	$\tau$ (Air, ns)	$\tau$ (Deg, ns) <sup>b</sup>
10.0	3.9	5.3
20.0	3.5	4.7
30.0	2.9	4.1
40.0	2.5	3.6
50.0	2.2	3.2

<sup>a</sup>Reproducibility in independent measurements was better than  $\pm 0.1$  ns.<sup>b</sup>From ref. (10).

pathway involving CT were shown to correlate well with  $\Delta G_T^{CT}$ , indicating a transition state with 13.5% CT character (27). Net rate constants for the analogous process involving excited singlet states were as high as  $1.6 \times 10^{10} \text{ M}^{-1} \text{ s}^{-1}$  but could not be determined over a sufficiently large  $\Delta G_S^{CT}$  range to establish a meaningful logarithmic dependence on this quantity (27). Except in the case of 2,6-dimethoxynaphthalene (DMN) for which the quenching event is accompanied by a small yield of <sup>2</sup>DMN<sup>+</sup> ( $3 \times 10^{-3}$ ) (25), attempts to detect the radical cations of the donors and <sup>2</sup>O<sub>2</sub><sup>•−</sup> have failed, despite the exothermicity of full electron transfer in AN for most of the excited singlet donors studied (25, 27).

Energy transfer from the triplet state of *ttt*-DPH to O<sub>2</sub> in air-saturated solutions yields O<sub>2</sub><sup>•−</sup>(<sup>1</sup>Δ<sub>g</sub>) with unit efficiency (28). Quenching of the singlet state of *ttt*-DPH leads to O<sub>2</sub><sup>•−</sup>(<sup>1</sup>Δ<sub>g</sub>) less efficiently and the efficiency decreases with increasing solvent polarity (0.5 and 0.3 in cyclohexane and methanol, respectively) (29). Competing with O<sub>2</sub><sup>•−</sup>(<sup>1</sup>Δ<sub>g</sub>) formation is O<sub>2</sub>-induced intersystem crossing leading to as much as a 10-fold increase in  $\phi_{is}$  (0.015 to 0.15 for degassed vs. air-saturated methanol (12)).

Two-photon laser excitation of *ttt*-DPH gives the radical cation (<sup>2</sup>*ttt*-DPH<sup>+</sup>) in a variety of solvents (30, 31). In AN the lifetime of the radical cation (7.3 μs) is insensitive to the presence of air (31, 32). The radical cation is also observed on quenching of <sup>1</sup>*ttt*-DPH\* by electron acceptors in polar solvents including AN (12, 13). It isomerizes to a new transient, assigned as a product of *trans* → *cis* photoisomerization, which reverts thermally to <sup>2</sup>*ttt*-DPH<sup>+</sup>, and reacts efficiently with electron donors to give back the starting *ttt*-DPH (31).

### Oxygen effects on *ttt*-DPH photoisomerization

We reported earlier that the fluorescence quantum yields and lifetimes of *ttt*-DPH-*d<sub>n</sub>* (*n* = 0, 2, and 4) in AN are nearly independent of deuterium substitution at the terminal double bonds (10). It was not surprising, therefore, that oxygen in air-saturated AN solutions at 20°C attenuates fluorescence quantum yields and lifetimes of the three *ttt*-DPH-*d<sub>n</sub>* (*n* = 0, 2, and 4) by the same  $1.31 \pm 0.01$  factor, within experimental uncertainty (10). The 1.3<sub>4</sub> ratio of the lifetimes at 20°C in Table 2 is in reasonable agreement with the quantum yield measurements and the effect is similar at different temperatures. Use of  $1.9 \pm 0.2 \times 10^{-3}$  for the oxygen concentration in air-saturated AN (33) gives  $k_{qox} = (3.5 \pm 0.4) \times 10^{10} \text{ M}^{-1} \text{ s}^{-1}$  for the quenching of the excited singlet states of

*ttt*-DPH-*d<sub>n</sub>* (*n* = 0, 2, and 4) by molecular oxygen, a value close to the diffusion-controlled limit.

The range of attenuations of  $\phi_{ttt \rightarrow tct}$  values by oxygen is slightly larger (1.36 to 1.40) than the attenuations of fluorescence quantum yields and lifetimes, because in addition to quenching the singlet excited state, oxygen dramatically shortens the lifetime of DPH triplets, effectively eliminating quantum chain contributions to the photoisomerization (9b). Oxygen interferes with the photoisomerization of the central bond of *ttt*-DPH-*d<sub>n</sub>* (*n* = 0, 2, and 4) only in so far as it deactivates *ttt*-DPH-*d<sub>n</sub>* excited singlet (primarily) and triplet states. Photoisomerization quantum yields in the presence of FN in degassed and air-saturated AN solutions are consistent with an O<sub>2</sub> induced sixfold (compared with factors of 7 and 10 reported for cyclohexane and methanol, respectively, (12, 29)) enhancement of  $\phi_{is}$  (34). In this case, however, this is a minor perturbation because it only raises  $\phi_{is}$  from 0.01 to 0.06.

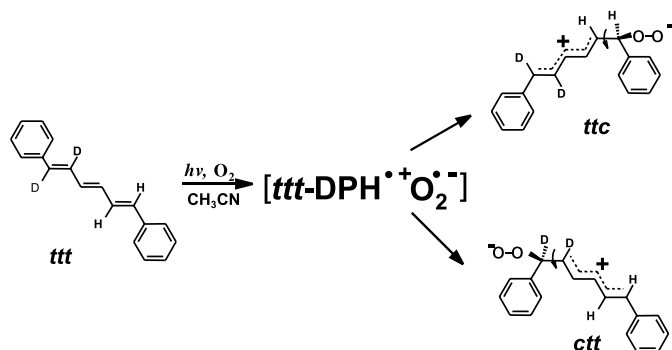
The results in Table 1 reveal a strikingly different O<sub>2</sub> effect on terminal bond photoisomerization. Instead of the expected ~1.3-fold attenuation,  $\phi_{ctt}$  values are enhanced by factors of 2 to 2.5, progressively increasing with terminal bond deuteration. Correspondingly, the presence of air strongly shifts photostationary state (PSS) compositions to larger *ctt*-DPH contributions at the expense of *ttt*-DPH. Oxygen enhanced *trans* to *cis* 1,2-diarylethene photoisomerization quantum yields have previously been observed, but were generally attributed to O<sub>2</sub> induced intersystem crossing (35–38). For instance, in the case of *trans*-4,4'-diphenylstilbene, quenching of the highly fluorescent singlet excited state by  $\sim 1 \times 10^{-2} \text{ M}$  O<sub>2</sub> in methylcyclohexane increases  $\phi_{t \rightarrow c}$  18-fold from 0.0025 to 0.045. However, because DPH triplets in AN favor decay to *tct*-DPH over decay to *ctt*-DPH by at least a factor of 5 (9a), O<sub>2</sub>-catalyzed intersystem crossing would be expected to increase  $\phi_{tct}$  more than  $\phi_{ctt}$ . Instead, we observe enhancement of the latter and quenching of the former. We conclude that the differential O<sub>2</sub> effects on central and terminal bond photoisomerization rule out the O<sub>2</sub>-induced intersystem crossing pathway in *ttt*-DPH.

In the *Background* section, we reviewed evidence for the formation of radical cations (<sup>2</sup>*ttt*-DPH<sup>+</sup>) in AN solutions. We recently evaluated and ruled out their possible involvement in the photoisomerization of *ttt*-DPH following direct excitation in degassed AN (8). Briefly, fluorescence and photoisomerization quantum yields, measured as a function of fumaronitrile (FN) concentration, show that <sup>2</sup>*ttt*-DPH<sup>+</sup> radical cations formed from the <sup>1</sup>(*ttt*-DPH-FN)\* exciplex (13) undergo no photoisomerization (8). It is not surprising, therefore, that we find that addition of up to 0.015 M diethylamine (DEA) has no effect on the photoisomerization quantum yields and, in particular, on the  $\phi_{ctt}:\phi_{ct}$  ratio in either degassed or air-saturated AN. At the high concentrations employed, DEA, a known, effective quencher of <sup>2</sup>*ttt*-DPH<sup>+</sup> radical cations,  $k_q = 1.05 \times 10^9 \text{ M}^{-1} \text{ s}^{-1}$  (31a), should have intercepted them all, in view of their long lifetime (7.3 μs) (31). In the unlikely event that electron transfer from <sup>1</sup>*ttt*-DPH\* to O<sub>2</sub> contributes to the formation of <sup>2</sup>*ttt*-DPH<sup>+</sup> radical cations, they are not involved in *trans* → *cis* photoisomerization.

The possibility that O<sub>2</sub> opens a thermal free radical isomerization process can be ruled out because the observed



Scheme 1.



formation of more cis double bonds moves the system up hill thermodynamically (9b). We are left with addition followed by elimination starting from  ${}^1\text{ttt-DPH}^*-\text{O}_2$  interaction, as a viable Schenck-type mechanism (39) for the  $\text{O}_2$ -induced photoisomerization (Scheme 1). Although the adduct (adducts for  $\text{ttt-DPH-d}_2$ ) in Scheme 1 is shown as a zwitterionic species because this process is much more pronounced in AN than in MCH,<sup>2</sup> the possibility that the adduct is biradicaloid cannot be ruled out. Bond formation at the benzylic positions should be favored because it leads to the more delocalized carbon-centered cation or radical intermediate. Rotation about the new single bond followed by loss of  $\text{O}_2$  would explain enhanced  $\text{ctt-DPH}$  formation. In principle, the intermediate could form either from the interaction of  ${}^1\text{ttt-DPH}^*$  with ground state  $\text{O}_2$  ( ${}^3\Sigma_g^-$ ) or by the addition of singlet  ${}^1\text{O}_2^*$  ( ${}^1\Delta_g$ ) to ground state  $\text{ttt-DPH}$ . However, if  ${}^1\text{O}_2^*$  were responsible for enhanced values under direct excitation conditions, then  $\text{O}_2$  would enhance  $\phi_{\text{ctt}}$  values even more under triplet-sensitized conditions because the efficiency of  ${}^1\text{O}_2^*$  formation is higher when  ${}^3\text{ttt-DPH}^*$  is quenched by  ${}^3\text{O}_2$  (28, 29). It follows that the involvement of  ${}^1\text{O}_2^*$  can be ruled out because we have found no photoisomerization enhancement of any kind under triplet-sensitized conditions in air-saturated AN (9). As a further precaution, we now report that addition of 0.188 M 2,5-dimethylfuran (DMF), a very efficient  ${}^1\text{O}_2^*$  scavenger (28, 41), has no effect on the  $\phi_{\text{ctt}}:\phi_{\text{tct}}$  ratio in air-saturated AN.

### Deuterium isotope effect

The small increasing trend in  $\phi_{\text{tct}}$  values under both degassed and air-saturated conditions with increasing deuterium substitution is consistent with the effect of deuterium on the lifetime of  ${}^1\text{ttt-DPH}^*$  (10). Terminal bond deuterium substitution does not affect rate constants for central bond isomerization. In contrast,  $\phi_{\text{ctt}}$  values decrease strongly in degassed solutions and show a less-pronounced decrease in the presence of air. The torsional relaxation rate constants for dihydro- and dideuterio-terminal bonds in  ${}^1\text{ttt-DPH}^*$  are subject to a normal deuterium isotope effect ( $k_{\text{H}}/k_{\text{D}} = 1.36$ )

**Table 3.** Dissection of quantum yields for terminal bond photoisomerization into normal and oxygen pathways.

DPH	$(1 - f_{\text{ox}})$	$\phi_{\text{ctt}+\text{tct}}^{\text{S}}$	$\phi_{\text{ctt}+\text{tct}}^{\text{ox}}$	$k_{\text{H}}^{\text{ox}}/k_{\text{D}}^{\text{ox}}$	$f_{\text{ad}}$
$\text{d}_0$	0.76 <sub>2</sub>	0.047	0.074		0.62
$\text{d}_2$	0.75 <sub>9</sub>	0.041	0.078	0.90	0.65
$\text{d}_4$	0.75 <sub>9</sub>	0.035	0.079	0.94	0.66

(10). Analysis of  $\phi_{\text{ctt}}$  values in the presence of air is accomplished by dissecting them into contributions from the normal pathway, involving the fraction of  ${}^1\text{ttt-DPH}^*$  not intercepted by oxygen ( $1 - f_{\text{ox}}$ ), and the new pathway, involving the fraction of  ${}^1\text{ttt-DPH}^*$  that is intercepted by oxygen ( $f_{\text{ox}}$ ) and follows the pathway in Scheme 1. Since nearly all terminal bond isomerization in degassed solution is a singlet excited state reaction, we expect that, in the presence of air, the normal pathway will experience the same attenuation as fluorescence. Substitution of  $k_{\text{qox}} = 3.5 \times 10^{10} \text{ M}^{-1} \text{ s}^{-1}$  for the quenching of the excited singlet states of  $\text{ttt-DPH-d}_n$  ( $n = 0, 2$ , and 4),  $[\text{O}_2] = 1.9 \times 10^{-3} \text{ M}$ , and the singlet excited state lifetimes ( $\tau_{\text{f}}^0$ ) (10) in eq. [1] gives the  $(1 - f_{\text{ox}})$  values listed in

$$[1] \quad (1 - f_{\text{ox}}) = k_{\text{qox}}\tau_{\text{f}}^0[\text{O}_2]/(1 + k_{\text{qox}}\tau_{\text{f}}^0[\text{O}_2])$$

Table 3. Quantum yields for terminal bond isomerization by the normal singlet excited state pathway ( $\phi_{\text{ctt}+\text{tct}}^{\text{S}}$ ) obtained by multiplying the values under degassed conditions (given in parentheses in Table 1) by the  $(1 - f_{\text{ox}})$  attenuation factors, were subtracted from observed quantum yields in the presence of air to obtain  $\phi_{\text{ctt}+\text{tct}}^{\text{ox}}$ , the quantum yields for the  $\text{O}_2$ -induced pathway (Table 3). Assuming that Scheme 1 applies, the ratio of the rate constant for bond formation at a benzylic position bearing hydrogen ( $k_{\text{H}}^{\text{ox}}$ ), to the analogous rate constant for a benzylic position bearing deuterium ( $k_{\text{D}}^{\text{ox}}$ ) is given by

$$[2] \quad k_{\text{H}}^{\text{ox}}/k_{\text{D}}^{\text{ox}} = (\alpha_{\text{D}}/\alpha_{\text{H}})(\phi_{\text{ctt}}^{\text{d0}}/\phi_{\text{ctt}}^{\text{d4}})(\tau_{\text{d4}}^{\text{ox}}/\tau_{\text{d0}}^{\text{ox}})$$

where the  $\alpha$ s are decay fractions to  $\text{ctt-DPH}$  for the deuterated and undeuterated  $\text{DPH-O}_2$  adducts, the quantum yields are the values for the  $\text{O}_2$ -induced pathway from Table 3, and the fluorescence lifetimes are in the presence of air. Taking  $\alpha_{\text{D}} = \alpha_{\text{H}}$  and substituting for the other quantities in eq. [2] using the data for  $\text{ttt-DPH-d}_0$  and  $\text{ttt-DPH-d}_4$  gives  $k_{\text{H}}^{\text{ox}}/k_{\text{D}}^{\text{ox}} = 0.94$ . This requires that formation of the  $\text{DPH-O}_2$  exciplex be somewhat reversible, as no intermolecular deuterium isotope effect would be expected if exciplex formation were irreversible and product determining. A similar treatment using the data for  $\text{ttt-DPH-d}_0$  and  $\text{ttt-DPH-d}_2$  gives  $k_{\text{H}}^{\text{ox}}/k_{\text{D}}^{\text{ox}} = 0.90$ . The inverse secondary deuterium isotope effect is consistent with the expected  $sp^2$  to  $sp^3$  rehybridization in the transition states leading to the adducts (42, 43).

Significant fractions of  ${}^1\text{ttt-DPH}^*-\text{O}_2$  quenching interactions must follow the adduct pathway to isomerization. These fractions ( $f_{\text{ad}}$ ) can be estimated from  $f_{\text{ox}}/(\alpha\phi_{\text{ctt}+\text{tct}}^{\text{ox}})$  by assuming equal partitioning of the adducts to cis and trans double bonds ( $\alpha = 0.5$ ). The resulting values are rela-

<sup>2</sup>In MCH, the presence of air attenuates  $\text{tct-}$  and  $\text{ctt-DPH}$  formation by factors of 0.35 and 0.58, respectively (34, 40).



tively insensitive to deuterium substitution falling in a narrow 0.62 to 0.66 range (Table 3).

### Trapping the exciplex

Initial indications that the  $O_2$ -induced photoisomerization pathway is quenched when  $Li^+ClO_4^-$  is included in AN (34), were not confirmed when great care was taken to avoid *ctt*-DPH loss in sample preparation for HPLC analysis. Because no changes in  $\phi_{ctt}:\phi_{ict}$  ratios were observed even when a saturated  $Li^+ClO_4^-$  solution (~0.4 M) was used in air-saturated AN, we can conclude that  $Li^+$  fails to intercept an ion pair in this case. This approach has been shown to succeed in several instances (44). Apparently, in our case, either charge transfer is not complete in the exciplex, or the exciplex is too short-lived. An interesting anomaly is our preliminary observation that on attempting to increase the contribution of the  $O_2$ -induced photoisomerization pathway by increasing the  $O_2$  concentration (bubbling  $O_2$  during the irradiation) we were surprised to find lower  $\phi_{ctt}:\phi_{ict}$  ratios than in the presence of air. If the mechanism in Scheme 1 is correct, this result suggests that, at the higher concentration, oxygen quenches the *ttt*-DPH- $O_2$  exciplex. While oxygen quenching of singlet exciplexes is well-known (45), quenching of an exciplex is unprecedented and remains to be established.

### Acknowledgments

The National Science Foundation, most recently by Grant CHE 9985895, supported this research. JS dedicates this paper to his friend Don Arnold as an expression of his admiration for Don's many seminal contributions to photochemistry.

### References

- B.S. Hudson and B.E. Kohler. *Annu. Rev. Phys. Chem.* **25**, 437 (1974).
- B.S. Hudson, B.E. Kohler, and K. Schulten. *In Excited states*. Vol. 6. Edited by E.C. Lim. Academic Press, New York. 1982. pp. 1–95.
- J. Saltiel and Y.-P. Sun. *In Photochromism, molecules and systems*. Edited by H. Dürr and H. Bouas-Laurent. Elsevier, Amsterdam. 1990. pp. 64–164.
- W. Fuß, S. Lochbrunner, W.E. Schmid, and K.L. Kompa. *J. Phys. Chem. A*, **102**, 9334 (1998).
- W. Fuß, W.E. Schmid, and S.A. Trushin. *J. Chem. Phys.* **112**, 8347 (2000).
- For a recent review of polyene photophysics, see: W. Fuß, Y. Haas, and S. Zilberg. *Chem. Phys.* **259**, 273 (2000).
- (a) S.H. Pullen, N.A. Anderson, L.A. Walker, II, and R.J. Sension. *J. Chem. Phys.* **108**, 556 (1998); (b) N.A. Anderson, J.J. Shiang, and R.J. Sension. *J. Phys. Chem. A*, **103**, 10 730 (1999).
- J. Saltiel, S. Wang, L.P. Watkins, and D.-H. Ko. *J. Phys. Chem. A*, **104**, 11 443 (2000).
- (a) J. Saltiel, S. Wang, D.-H. Ko, and D.A. Gormin. *J. Phys. Chem. A*, **102**, 5383 (1998); (b) J. Saltiel, J.M. Crowder, and S. Wang. *J. Am. Chem. Soc.* **121**, 895 (1999).
- J. Saltiel, G. Krishnamoorthy, Z. Huang, D.-H. Ko, and S. Wang. *J. Phys. Chem. A*, **107**, 3178 (2003).
- E.D. Cehelnik, R.B. Cundall, J.R. Lockwood, and T.J. Palmer. *J. Phys. Chem.* **79**, 1369 (1975).
- S.K. Chattopadhyay, P.K. Das, and G.L. Hug. *J. Am. Chem. Soc.* **104**, 4507 (1982).
- F.W. Schael. Ph.D. Dissertation, Technische Universität, Carlo-Wilhelmina zu Braunschweig, Germany, 1995.
- (a) F.W. Schael and H.-G. Löhmansröben. *Chem. Phys.* **206**, 193 (1996); (b) F.W. Schael, J. Kühster, and H.-G. Löhmansröben. *Chem. Phys.* **218**, 175 (1997). (c) F.W. Schael and H.-G. Löhmansröben. *J. Photochem. Photobiol. A*, **105**, 317 (1997).
- J.F. O'Donnell, J.T. Ayres, and C.K. Mann. *Anal. Chem.* **37**, 1161 (1965).
- F.G. Moses, R.S.H. Liu, and B.M. Monroe. *Mol. Photochem.* **1**, 245 (1969).
- H.A. Hammond, D.E. DeMeyer, and J.L.R. Williams. *J. Am. Chem. Soc.* **91**, 5180 (1969).
- D. Valentine, Jr. and G.S. Hammond. *J. Am. Chem. Soc.* **94**, 3449 (1972).
- J. Saltiel, D.F. Sears, Jr., J.-O. Choi, Y.-P. Sun, and D.W. Eaker. *J. Phys. Chem.* **98**, 35 (1994); **98**, 8260 (1994).
- (a) I.B. Berlman. *Handbook of fluorescence spectra of aromatic molecules*. 2nd ed. Academic Press, New York. 1971; (b) J. Saltiel and B.W. Atwater. *Adv. Photochem.* **14**, 1 (1988); (c) F. Wilkinson, W.P. Helman, and A.B. Ross. *J. Phys. Chem. Ref. Data*, **22**, 113 (1993).
- (a) G. Porter and M.R. Wright. *Discuss. Faraday Soc.* **27**, 18 (1959); (b) B. Stevens and B.E. Algar. *Ann. N. Y. Acad. Sci.* **171**, 50 (1970).
- O.L.J. Gijzeman, F. Kaufman, and G. Porter. *J. Chem. Soc., Faraday Trans. 2*, **69**, 708 (1973).
- R. Potashnik, C.R. Goldschmidt, and M. Ottolenghi. *Chem. Phys. Lett.* **9**, 424 (1971).
- (a) F. Wilkinson, D.J. McGarvey, and A.F. Olea. *J. Am. Chem. Soc.* **115**, 12 144 (1993); (b) A.F. Olea and F. Wilkinson. *J. Phys. Chem.* **99**, 4518 (1995).
- C. Sato, K. Kikuchi, C. Sato, Y. Takahashi, and T. Miyashi. *J. Phys. Chem.* **99**, 16 925 (1995).
- K. Kikuchi, K. Okamura, M. Watabe, H. Ikeda, Y. Takahashi, and T. Miyashi. *J. Am. Chem. Soc.* **115**, 5180 (1993).
- A.A. Abdel-Shafi and F. Wilkinson. *J. Phys. Chem. A*, **104**, 5747 (2000).
- K.C. Wu and A.M. Trozzolo. *J. Phys. Chem.* **83**, 3180 (1979).
- S.K. Chattopadhyay, C.V. Kumar, and P.K. Das. *J. Phys. Chem.* **89**, 670 (1985).
- M. Almgren and J.K. Thomas. *Photochem. Photobiol.* **31**, 329 (1980).
- (a) Z. Wang and W.G. McGimpsey. *J. Phys. Chem.* **97**, 3324 (1993); (b) Z. Wang and W.G. McGimpsey. *J. Phys. Chem.* **97**, 5054 (1993).
- H. Görner. *J. Photochem.* **19**, 343 (1982).
- W.D.K. Clark and C. Steel. *J. Am. Chem. Soc.* **93**, 6347 (1971).
- S. Wang. Ph.D. Dissertation, Florida State University, Tallahassee, Florida, 1998.
- P. Bortolus and G. Galiazzi. *J. Photochem.* **2**, 361 (1974).
- G. Fischer and E. Fischer. *Mol. Photochem.* **6**, 463 (1974).
- G.G. Aloisi, U. Mazzucato, J.B. Birks, and L. Minuti. *J. Am. Chem. Soc.* **99**, 6340 (1977).
- For a review see: J. Saltiel, J.L. Charlton. *In Rearrangements in ground and excited states*. Vol. 3. Edited by P. de Mayo. Academic Press, New York. 1980. Essay 14.
- G.O. Schenck and R. Steinmetz. *Bull. Soc. Chim. Belg.* **71**, 781 (1962).
- D.-H. Ko. Ph.D. Dissertation, Florida State University, Tallahassee, Florida, 1997.



41. K. Gollnick, T. Franken, G. Schade, and G. Dorhofer. *Ann. N.Y. Acad. Sci.* **171**, 89 (1970).
42. A. Streitwieser, Jr., R.H. Jagow, R.C. Fahey, and S. Suzuki. *J. Am. Chem. Soc.* **80**, 2326 (1958).
43. For relevant early examples, see: M. Matsuoka and M. Szwarc. *J. Am. Chem. Soc.* **83**, 1260 (1961).
44. (a) J. Gersdorf and J. Mattay. *J. Photochem.* **28**, 405 (1985);  
(b) M. Mac and J. Wirz. *Chem. Phys. Lett.* **211**, 20 (1993);  
(c) M. Mac, P. Kwiatkowski, and A.M. Turek. *Chem. Phys. Lett.* **250**, 104 (1996); (d) M. Mac and J. Wirz. *Photochem. Photobiol. Sci.* **1**, 24 (2002).
45. For a typical example, see: J.L. Charlton, D.E. Townsend, B.D. Watson, P. Shannon, J. Kowalewska, and J. Saltiel. *J. Am. Chem. Soc.* **99**, 5992 (1977).



# The effect of central bond torsional mobility on the Rydberg state ring opening of alkylcyclobutenes

Bruce H.O. Cook and William J. Leigh

**Abstract:** The stereochemistry of the  $\pi, R(3s)$  excited state ring opening of a series of bicyclic alkylcyclobutenes has been studied in hydrocarbon solution with 228 nm excitation. In these compounds, the C=C bond is shared between the cyclobutene ring and a five-, six-, or seven-membered ancillary ring, which has the effect of restricting the torsional mobility about the central C—C bond in the isomeric diene products. It has previously been shown that monocyclic alkylcyclobutenes undergo stereospecific *conrotatory* ring opening upon excitation at the long wavelength edge of the  $\pi, R(3s)$  absorption band (228 nm), and nonstereospecific ring opening upon irradiation at shorter wavelengths (within the  $\pi, \pi^*$  absorption band). Different behaviour is observed for the bicyclic systems studied in the present work. The bicyclo[3.2.0]hept-1-ene, bicyclo[4.2.0]oct-1-ene, and one of the bicyclo[5.2.0]non-1-ene derivatives yield nearly the same mixtures of *E,E*- and *E,Z*-diene isomers upon irradiation at 214 and 228 nm, with the product mixtures being heavily weighted in favor of the isomer(s) corresponding to disrotatory ring opening. The results may indicate that the stereochemical characteristics of the Rydberg-derived ring opening of alkylcyclobutenes depends on the ability of the molecule to twist about the “central” bond (i.e., the C=C bond in the cyclobutene) as ring opening proceeds. It is proposed that restricting the torsional mobility about the central bond activates internal conversion from the  $\pi, R(3s)$  to the  $\pi, \pi^*$  potential energy surface, from which predominant disrotatory ring opening ensues.

**Key words:** cyclobutene, Rydberg, ring opening, photopericyclic, electrocyclic.

**Résumé :** Opérant en solution dans des hydrocarbures et avec une excitation à 228 nm, on a étudié la stéréochimie de l'ouverture de cycle dans l'état excité  $\pi, R(3s)$  d'une série d'alkylcyclobutènes bicycliques. Dans ces composés, la liaison C=C est partagée entre le cycle du cyclobutène et un cycle ancillaire à cinq-, six- ou sept-membres qui a pour effet de restreindre la mobilité torsionnelle autour de la liaison C—C centrale des produits diéniques isomères. Il a été démontré antérieurement que les alkylcyclobutènes monocycliques subissent une ouverture de cycle *conrotatoire* stéréospécifique lors de leur excitation dans la portion de grande longueur d'onde de la bande d'absorption  $\pi, R(3s)$  (228 nm) et une ouverture de cycle non stéréospécifique par irradiation à des longueurs d'onde plus faibles (dans la bande d'absorption  $\pi, \pi^*$ ). Dans le présent travail, on observe un comportement différent pour les systèmes bicycliques. Lors de leur irradiation à 214 ou à 228 nm, le bicyclo[3.2.0]hept-1-ène, le bicyclo[4.2.0]oct-1-ène et un des dérivés du bicyclo[5.2.0]non-1-ène conduisent pratiquement tous aux mêmes mélanges *E,E*- et *E,Z*- de diènes isomères; les mélanges contiennent principalement les isomères résultant d'une ouverture disrotatoire du cycle. Les résultats suggèrent que les caractéristiques stéréochimiques de l'ouverture de cycle d'alkylcyclobutènes se produisant dans la région de Rydberg dépend de la facilité de la molécule à se retourner autour de la liaison centrale (c'est-à-dire la liaison C=C du cyclobutène) lorsque l'ouverture de cycle se produit. On suggère qu'une restriction de la mobilité torsionnelle autour de la liaison centrale active la conversion interne de  $\pi, R(3s)$  à la surface d'énergie potentielle  $\pi, \pi^*$  à partir de laquelle il résulte une ouverture de cycle disrotatoire.

**Mots clés :** cyclobutène, Rydberg, ouverture de cycle, photopériodique, électrocyclique.

[Traduit par la Rédaction]

## Introduction

The direct irradiation of simple alkylcyclobutenes in the gas phase or solution results in electrocyclic ring opening and stereospecific [2 + 2]-cycloreversion to yield the corre-

sponding alkyne and alkene (1–4). It has been known for several years that contrary to early indications (5), the ring opening reaction proceeds *nonstereospecifically* (6, 7), in apparent violation of simple orbital symmetry selection rules for photoelectrocyclic reactions (8) as well as the results of

Received 6 January 2003. Published on the NRC Research Press Web site at <http://canjchem.nrc.ca> on 17 June 2003.

*Dedicated to Professor Don Arnold for his contributions to chemistry.*

**B.H.O. Cook<sup>1</sup> and W.J. Leigh,<sup>2</sup>** Department of Chemistry, McMaster University, 1280 Main Street West, Hamilton, ON L8S 4M1, Canada.

<sup>1</sup>Present address: 3M Canada Company, 1840 Oxford St. E., London, ON N6A 4T1, Canada.

<sup>2</sup>Corresponding author (e-mail: [leigh@mcmaster.ca](mailto:leigh@mcmaster.ca)).

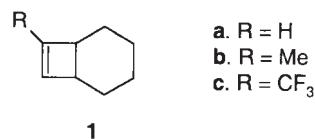


high level ab initio calculations (9, 10), all of which predict that the process should proceed with preferred *disrotatory* stereochemistry when initiated by population of the lowest  $\pi,\pi^*$  excited singlet state of the molecule. Assuming that orbital symmetry selection rules are, in fact, obeyed in the  $\pi,\pi^*$  reaction, there are at least three possible explanations for this behaviour (6): (i) ring opening proceeds *adiabatically*, yielding the photochemically allowed (disrotatory) diene isomer(s) in the lowest  $\pi,\pi^*$  excited singlet state, from which the forbidden (thermally allowed, conrotatory) isomer(s) are formed via *E,Z*-isomerization; (ii) the conrotatory isomers are formed via reaction from upper vibrational levels of the ground state of the cyclobutene, populated by internal conversion in competition with disrotatory  $\pi,\pi^*$  state ring opening; and (iii) the conrotatory isomers are formed via competing reaction of the radical-cation-like  $\pi,R(3s)$  Rydberg excited singlet state, which is known to be of similar energy to the  $\pi,\pi^*$  (valence) singlet state in alkylcyclobutenes (4, 11, 12), just as it is in other aliphatic alkenes (13–15).<sup>2</sup>

Much of our work in this area over the past 15 years has been directed at attempting to distinguish between these possibilities, through studies of the effects of substituents, excitation wavelength, and various structural constraints on the stereochemistry of the reaction (4, 6, 12, 16–23). By the mid-1990s, we had concluded: (i) that the  $\pi,R(3s)$  state is responsible for the [2 + 2]-cycloreversion reaction but is not involved in ring opening (12, 24); and (ii) that the adiabatic,  $\pi,\pi^*$  state ring opening mechanism most adequately accounts for the nonstereospecificity of the reaction (19, 21, 22).

The first conclusion was based on an analysis of the photochemistry of a series of 7-substituted bicyclo[4.2.0]oct-7-ene derivatives (**1**), in which the energy of the  $\pi,R(3s)$  state varies systematically as a function of the non-conjugating substituent attached to the cyclobutenyl C=C bond (12). The quantum yield of ring opening products is highest in the case of the 7-trifluoromethyl derivative **1c**, in which the  $\pi,R(3s)$  state is significantly higher in energy than the  $\pi,\pi^*$  singlet state, and the yields of ring opening relative to cycloreversion products increase with increasing excitation wavelength between 193 and 214 nm (the opposite is true for **1a**, **1b**). Furthermore, the degree of nonstereoselectivity associated with ring opening is roughly constant throughout the series of compounds, and does not vary with excitation wavelength. It was thus concluded that the  $\pi,\pi^*$  state alone is responsible for ring opening, and hence, that the nonstereospecificity of the reaction somehow originates in the specific manner in which ring opening proceeds on the potential energy surface of this electronic state. However, it is difficult to rule out the possibility that the trifluoromethyl substituent in **1c** might also affect excited state dynamics in addition to altering the relative energies of the  $\pi,R(3s)$  and  $\pi,\pi^*$  states, and perhaps cause a fundamental

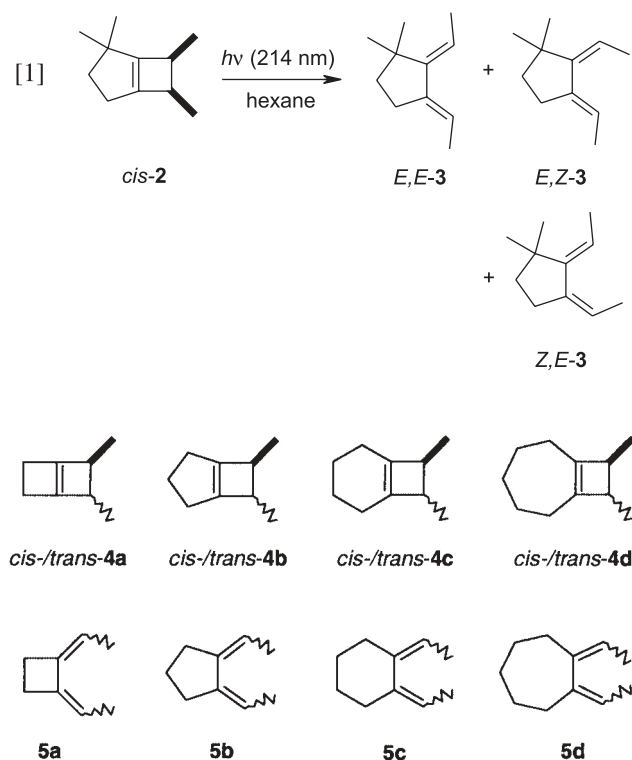
change in the reactivity of the  $\pi,\pi^*$  state compared to that in the parent compound. Indeed, recent ultrafast time-resolved experiments (25, 26), as well as detailed theoretical calculations (27–29), strongly suggest that such possibilities *cannot* be ignored in other cycloalkenes such as cyclohexene and norbornene. Thus, there may be other viable explanations for the observed trends in the photoreactivity of **1a–1c** that go well beyond simple arguments based on the effects of the substituents on the relative energies of the  $\pi,R(3s)$  and  $\pi,\pi^*$  excited states in these molecules. One possibility is that in **1a** and **1b**, ring opening proceeds from both the  $\pi,R(3s)$  and  $\pi,\pi^*$  states, each with a high degree of stereoselectivity (conrotatory from the Rydberg state and disrotatory from the  $\pi,\pi^*$  state); in **1c**, ring opening proceeds only from the  $\pi,\pi^*$  state, but with a lower degree of disrotatory stereoselectivity owing to a fundamental change in excited-state dynamics caused by the strongly polarizing trifluoromethyl substituent. Such alternatives are difficult to rule out solely on the basis of simple product studies.



The second conclusion was based on an examination of the photochemistry of the series of constrained cyclobutenes **2** and **4**, comparing the relative yields of isomeric dienes obtained upon 214-nm photolysis of these compounds to values predicted from the quantum yields for direct *E,Z*-photoisomerization of the corresponding isomeric dienes (19, 21, 22). For example, 214 nm irradiation of *cis*-2,2,6,7-tetramethylbicyclo[3.2.0]hept-1-ene (*cis*-**2**) in hydrocarbon solution yields a mixture of three diene isomers, *E,E*-, *E,Z*-, and *Z,E*-**3** (eq. [1]); the two *E,Z*-isomers are formed in a ratio that is *identical* (within experimental error) to that obtained from direct (254 nm) irradiation of the photochemically allowed (*E,E*) diene isomer (21). Reasonable (but not perfect) agreement was also observed between the isomeric diene ratios obtained from 214-nm photolysis of the symmetrically substituted bicyclic cyclobutenes **4**, and values calculated from the quantum yields for *E,Z*-photoisomerization of their isomeric dienes **5** (19, 22). This series of compounds bears the important feature that the dienes **3** and **5a–5d** are constrained to exist in the *s-cis* conformation, similar to that which would (presumably) be formed directly in the electrocyclic ring opening reaction. This allows one to independently determine the excited state torsional decay characteristics of the product in the conformation in which it is initially formed from ring opening of the corresponding cyclobutene derivative. Acyclic dienes generally prefer the *s-trans* conformation, so such analyses are more problematic with monocyclic cyclobutenes.

<sup>2</sup>There is a long-standing debate, which to our knowledge has never been resolved, as to the identity of the excited state responsible for the weak long-wavelength absorptions in the condensed phase UV absorption spectra of tetraalkyl-substituted alkenes — whether they are the Rydberg absorptions, substantially reduced in intensity and blue-shifted relative to their character in the gas phase spectrum, or those corresponding to a very weak transition to a low-lying valence state such as the  $\pi,\sigma^*$  state (13). We favour the Rydberg state assignment because of the similarities between the photochemistry of alkenes in hydroxylic solvents and the chemistry of the corresponding radical cations under similar conditions (14, 15). The photochemistry of 1,2-dimethylcyclobutene in methanol exhibits similar features as that of other alkenes in hydroxylic media (4).



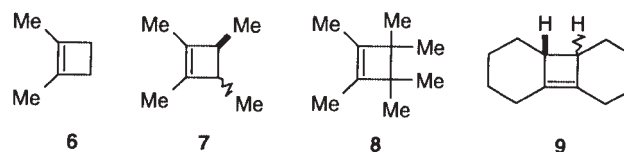


Thus, the mechanism that emerged from these studies is one in which the  $\pi,\pi^*$  excited singlet state of the cyclobutene undergoes purely disrotatory ring opening, but with internal conversion to the ground state potential energy surface occurring *after* the diene is fully formed rather than at a geometry intermediate between reactant and product (19, 21, 22); a mixture of diene isomers is formed not because the reaction itself is nonstereospecific, but because the product is formed in an excited singlet state whose main avenue for relaxation to the ground state is *cis,trans*-isomerization.

This mechanism is fully compatible with orbital symmetry selection rules, as well as with high level theoretical studies that indicate that within the first ~50 fs after excitation to the  $\pi,\pi^*$  ( $1^1B_2$ ) state, ring opening is initiated with the disrotatory stereochemistry that is predicted by orbital symmetry (9, 10). Mathies and co-workers (30, 31) had previously reached the same conclusion on the basis of an analysis of the resonance Raman spectrum of cyclobutene. However, the vibrational assignments on which their analysis was based have been refuted (32), and it appears that a different experimental approach will be required to define the stereochemistry of the process on this timescale (10, 32). To date, however, neither theory nor ultrafast spectroscopic methods have been able to address the question of why, if  $\pi,\pi^*$  state ring opening proceeds with a high degree of stereochemical integrity in its very early stages, mixtures of both *dis*- and *conrotatory* dienes are *ultimately* formed upon irradiation of stereo-labelled cyclobutene derivatives in solution.

More recent results from our laboratory strongly suggest that the adiabatic ring opening mechanism, with only the  $\pi,\pi^*$  state being involved in the reaction, may be incorrect, or at least not general (4). If the  $\pi,R(3s)$  excited state of cyclobutene is really not involved in ring opening, as was concluded on the basis of the photochemistry of **1a–1c** (12),

then it would be predicted that photolysis of cyclobutene derivatives with especially low Rydberg state energies, under conditions where the Rydberg state is selectively and exclusively excited, should lead *only* to cycloreversion. This premise was tested with the monocyclic, 1,2-disubstituted cyclobutene derivatives **6** and **7**, whose gas phase UV absorption spectra indicate to have spectroscopic  $\pi,R(3s)$  excited singlet states of substantially lower energies than the valence ( $\pi,\pi^*$ ) state (4). Indeed, photolysis of the three compounds at the long-wavelength edge of their Rydberg absorptions (228 nm) leads mainly to [2 + 2]-cycloreversion in both the gas phase and solution, consistent with the previous assignment of this reaction mode to the  $\pi,R(3s)$  Rydberg state. Surprisingly however, all three derivatives also undergo ring opening upon excitation under these conditions, and furthermore, the stereochemically labelled derivatives *cis*- and *trans*-**7** appear to do so with clean, *conrotatory* stereochemistry — the stereochemistry associated with the *ground state* ring opening reaction. In a subsequent paper, we showed that high yields of ring opening products are obtained upon 228 nm photolysis of other 1,2-dialkylcyclobutenes (**8** and **9**) as well, and by comparing the quantum yields for product formation to values calculated on the basis of RRKM theory, demonstrated that the process is most likely a discrete reaction of the Rydberg excited state, rather than being the result of internal conversion to upper vibrational levels of the ground state of the cyclobutene, from which thermal ring opening would ensue (23).



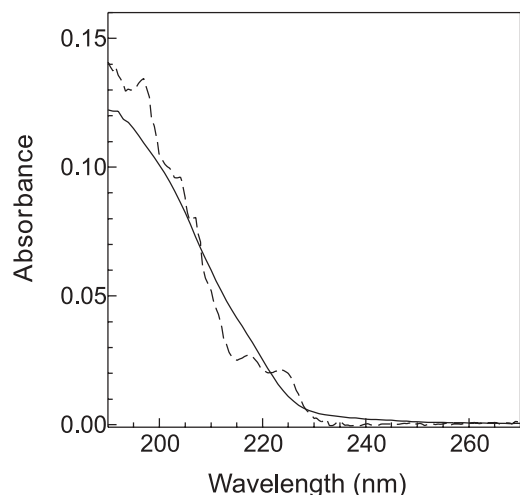
These latest discoveries require that we reconsider the possibility that the overall nonstereospecificity observed with shorter wavelength excitation, where the valence and Rydberg absorptions overlap, is in fact due to competing *stereospecific* reactions from the  $\pi,\pi^*$  and  $\pi,R(3s)$  excited states. As a first step in this reanalysis, we have chosen to have a closer look at the possible role of the Rydberg state in the ring opening of some of the compounds that led us in the first place to conclude that the  $\pi,\pi^*$  state reacts adiabatically (22). We thus report the results of a study of the photolysis of the *cis*- and *trans*-isomers of the bicyclic cyclobutene derivatives **4b–4d** at 228 nm, where the  $\pi,R(3s)$  Rydberg absorptions are well-isolated from the higher energy  $\pi,\pi^*$  absorption band and can be excited selectively.

## Results

The UV absorption spectra of *cis*-7,8-dimethylbicyclo[4.2.0]oct-1-ene (*cis*-**4c**) in the gas phase (1 atm = 101.325 kPa, SF<sub>6</sub> buffer) and in hexane solution are shown in Fig. 1. The spectra and the differences between them are very similar to those reported earlier for *cis*-1,2,3,4-tetramethylcyclobutene (*cis*-**7**) (4); they clearly show both that the  $\pi,R(3s)$  excited state is significantly lower in energy than the valence ( $\pi,\pi^*$ ) state in this compound, and that it should be populated selectively upon photolysis with



**Fig. 1.** UV absorption spectra of *cis*-**4c** in the gas phase (---) and in hexane solution (—).



monochromatic 228-nm light, at the long-wavelength edge of the absorption spectrum. As expected, the fine structure associated with the gas phase Rydberg absorptions in *cis*-**4c** is washed out in the solution phase spectrum, leaving behind a weak, featureless absorption that tails out to >230 nm. Similar features are observed in the spectra of *trans*-**4c** and the *cis*- and *trans*-isomers of **4b** and **4d** in hexane solution under similar conditions (22).

Photolyses of *cis*- and *trans*-**4b–4d** were carried out using the light from 16 W Zn (214 nm) and Cd (228 nm) resonance lamps, on argon-saturated solutions containing 0.06 M substrate and 0.001 M of *n*-octane as an internal GC standard. The solutions were analyzed by capillary gas chromatography between ca. 0.2 and 2–5% conversion of substrate (except in the case of *trans*-**4b** with 214 nm light, which was analyzed between 3.5 and 9% conversion). The photolyses produced mixtures of *E,E*- and *E,Z*-**5b–5d** as the only detectable products under the analytical conditions employed in this work (eqs. [2] and [3]), except in the case of *trans*-**4d**, which also afforded small amounts of *Z,Z*-**5d**. Relative product yields were determined from the intercepts of plots

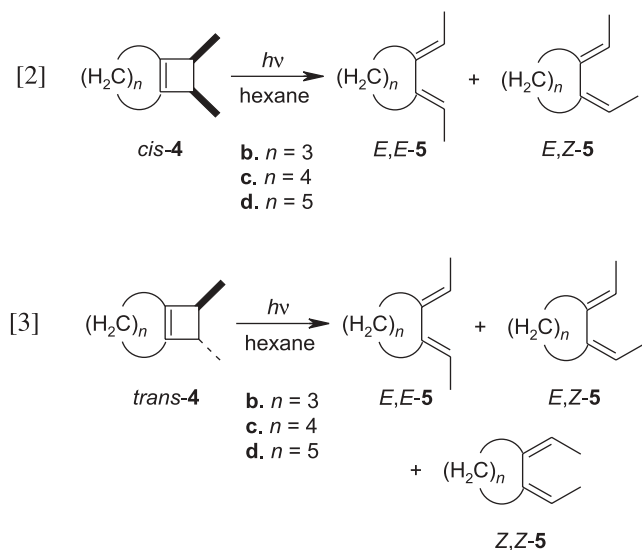
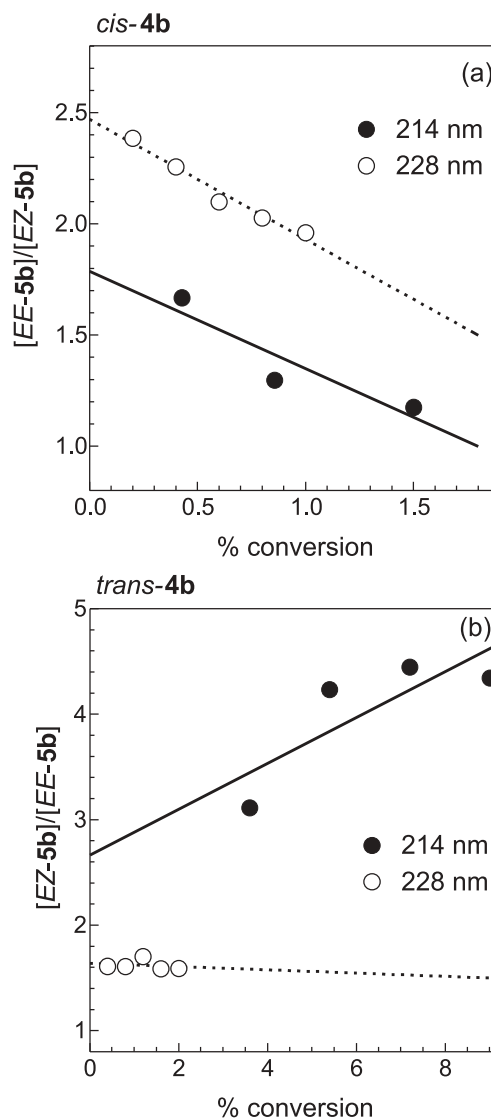


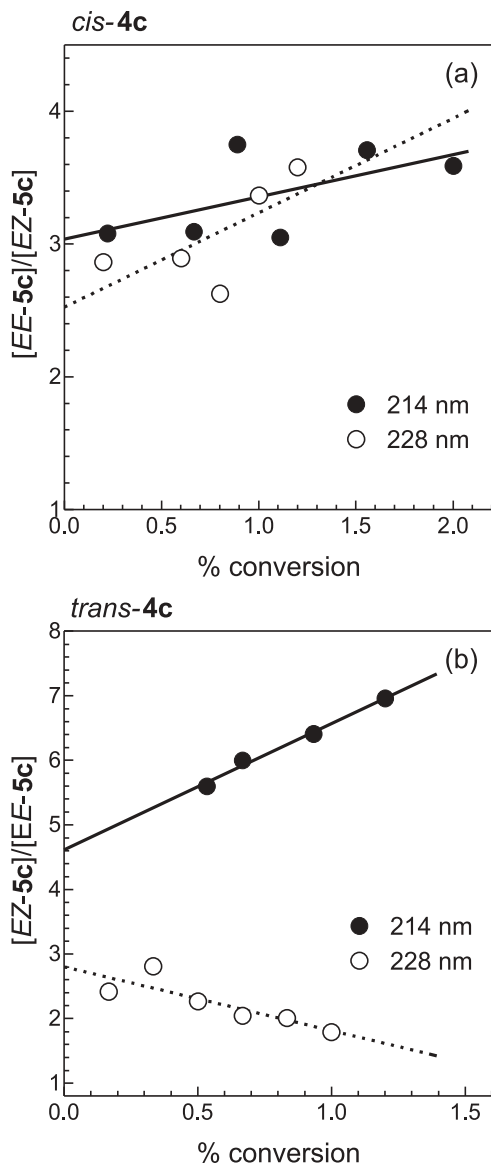
**Fig. 2.** Plots of DIS:CON diene isomer ratios vs. % conversion of **4**, for the photolysis of (a) *cis*- and (b) *trans*-6,7-dimethylbicyclo[3.2.0]hept-1(5)-ene (*cis*- and *trans*-**4b**) in deoxygenated hexane solution at 214 nm (●, —) and 228 nm (○, ---).



of relative product concentrations (e.g.,  $[E,E]/[E,Z]$ -**5** in the case of the *cis*-isomers, and the inverse for the *trans*-isomers) vs. % conversion of starting material, which are shown in Figs. 2–4 for the 214 and 228 nm photolyses of *cis*- and *trans*-**4b–4d**. Plotting the data in this way magnifies the effects of secondary photolysis on the primary isomeric diene yields (as well as the errors associated with the measurement of relatively small GC peak areas); the plots for all six of the compounds studied in this work generally had nonzero slopes, indicative of significant secondary photolysis effects throughout the course of the experiments. Thus, the intercepts represent the best estimates of the true primary isomeric diene yields in the photolyses. Table 1 summarizes the results of these experiments, where the isomeric diene ratios are expressed as the relative yields of disrotatory:conrotatory isomers as defined above. It should be noted that while error bars were not specifically calcu-



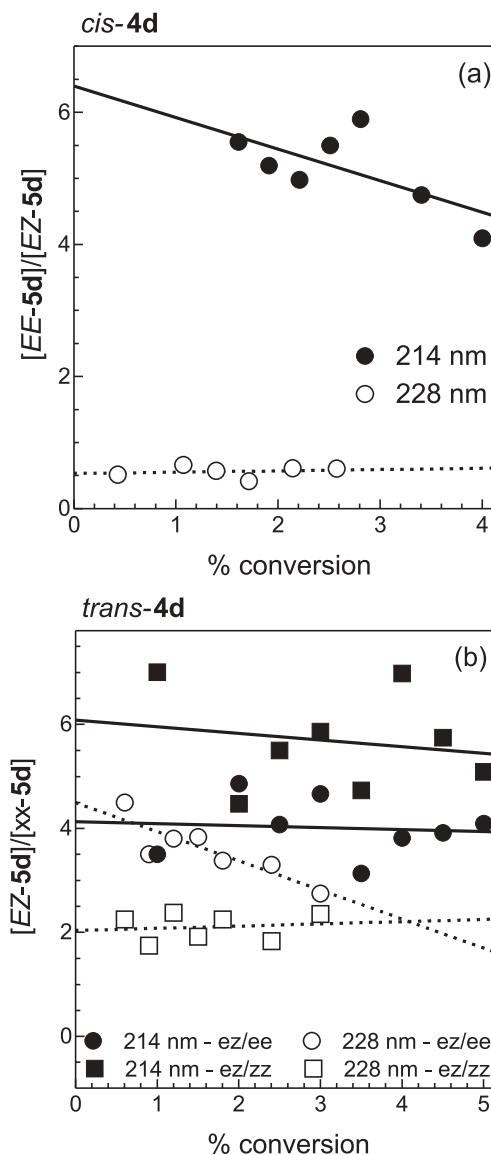
**Fig. 3.** Plots of DIS:CON diene isomer ratios vs. % conversion of **4**, for the photolysis of (a) *cis*- and (b) *trans*-7,8-dimethylbicyclo[4.2.0]oct-1(6)-ene (*cis*- and *trans*-**4c**) in deoxygenated hexane solution at 214 nm (●, —) and 228 nm (○, - - -).



lated for each of the data points shown in the plots of Figs. 2–4, they will naturally be largest at low conversions and decrease in size with increasing conversion. This is of particular concern for the results of photolysis of *trans*-**4b** at 214 nm, which was carried out with a more dilute sample (and to higher conversion of starting material) than the other experiments. Thus, the *E,Z/E,E*-ratio reported for this experiment in Table 1 should be considered a lower limit, with the true value of *E,Z*-**5b**/*E,E*-**5b** being a maximum of about 4.0 (as previously reported (22)). Also included in the table are the analogous product ratios obtained with 193 nm excitation, from previous work (22). The 214 nm product ratios obtained in the present work are in satisfactory agreement with those reported previously (22).

Table 1 also contains the photostationary state (pss) compositions for direct irradiation of **5b–5d** with 228 nm light,

**Fig. 4.** Plots of DIS:CON diene isomer ratios vs. % conversion of **4**, for the photolysis of (a) *cis*- and (b) *trans*-8,9-dimethylbicyclo[5.2.0]non-1(7)-ene (*cis*- and *trans*-**4d**) in deoxygenated hexane solution at 214 nm (filled symbols, —) and 228 nm (open symbols, - - -).



which were determined under the same conditions as those employed above for photolysis of the cyclobutenes. These ratios were determined by exhaustive photolysis of samples of *E,E*- and *E,Z*-**5**, which led to the formation of complex mixtures of *cis*- and *trans*-**4** and other isomeric products, but common mixtures of *E,E*-, *E,Z*-, and *Z,Z*-**5**. Comparison of the diene photostationary state ratios to the isomeric diene ratios from photolysis of the cyclobutenes verifies that the latter more or less accurately represent the true primary product ratios from photolysis of *cis*- and *trans*-**4b** and **4c**. The situation is less clear for *cis*- and *trans*-**4d**, in particular that of the *cis*-isomer, where the relative yields of *E,E*-, *E,Z*-, and *Z,Z*-**5d** are very similar to the diene pss ratio at 228 nm. The extinction coefficient at 228 nm is significantly lower for this compound than for the others studied in this work



**Table 1.** Isomeric diene ratios from direct irradiation of bicyclic cyclobutenes *cis*- and *trans*-**4b-d** as deoxygenated solutions in hexane at 25°C, expressed as the ratios of disrotatory:conrotatory isomers.

Wavelength (nm)	<i>cis</i> - <b>4b</b> ( <i>EE/EZ</i> )	<i>trans</i> - <b>4b</b> ( <i>EZ/EE</i> )	<i>cis</i> - <b>4c</b> ( <i>EE/EZ</i> )	<i>trans</i> - <b>4c</b> ( <i>EZ/EE</i> )	<i>cis</i> - <b>4d</b> ( <i>EE/EZ</i> )	<i>trans</i> - <b>4d</b> ( <i>EZ/EE+ZZ</i> ) [ <i>EE:EZ:ZZ</i> ]
193 <sup>a</sup>	2.5 ± 0.4	9.1 ± 1.2	3.4 ± 0.4	5.6 ± 0.7	9.1 ± 0.9	3.6 ± 0.4
214	1.8 ± 0.6	2.7 ± 1.4 <sup>b</sup>	3.0 ± 0.5	4.6 ± 0.3	6.9 ± 1.0	1.8 ± 0.4 [1.0:3.7:1.0]
228	2.47 ± 0.07	1.64 ± 0.11	2.5 ± 0.8	2.8 ± 0.4	0.54 ± 0.12	1.4 ± 0.2 [1.0:4.5:2.3]
pss <sup>c</sup>	5.0:4.1:1.0		2.3:2.0:1.0		2.1:4.1:1.0	

**Note:** The ratios reported correspond to *E,E/E,Z-5* ratios from the *cis*-isomers and *E,Z/E-5* ratios from the *trans*-isomers. The *Z,Z*-isomers were not detected at conversions less than ~2% in any of the photolyses except that of *trans*-**4d**, which contained small amounts of all three diene isomers at *t* = 0. The DIS:CON ratios for the latter compound are thus expressed as *E,Z/(E,E + Z,Z)*. The values listed for the 214 and 228 nm photolyses, which were carried out on 0.06 M solutions in all cases but one, are the intercepts from the plots of product ratio vs. %conversion shown in Figs. 2–4. Those for 193 nm photolyses are reproduced from ref. 22, and were determined using 0.02 M solutions of **4**.

<sup>a</sup>From ref. 22.

<sup>b</sup>From photolysis of a 0.02 M solution of *trans*-**4b**.

<sup>c</sup>Photostationary state compositions from photolysis of the corresponding dienes (**5**) at 228 nm, expressed as *EE:EZ:ZZ*.

(22), and thus, we cannot rule out the possibility that secondary photolysis effects distort the true product ratios in this case.

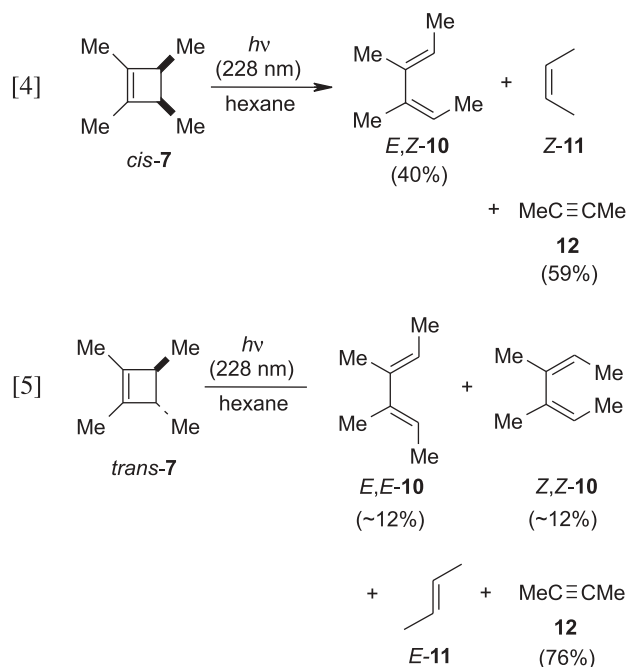
## Discussion

The solution phase absorption spectra of monocyclic 1,2-dialkylcyclobutenes such as *cis*- and *trans*-**7** consist of a dominant  $\pi,\pi^*$  absorption band with maximum below 195 nm, and a weak tail absorption that extends out to ~230 nm (4, 16). In the corresponding gas phase spectra, the latter is intensified considerably and takes on distinctive fine structure, characteristic of olefinic  $\pi,\text{R}(3s)$  absorptions (13). The gas and solution phase spectra of *cis*-**4c** show similar characteristics to those of **7** in this regard (22). Interestingly, the solution phase UV spectra of *cis*- and *trans*-**4b** show enhanced (though weak) absorption in the 220–240 nm range compared with the other compounds in the series, and are virtually identical to one another. The solution phase spectra of *cis*- and *trans*-**4c** and **4d**, on the other hand, show the similarities and differences characteristic of monocyclic 1,2-dialkylcyclobutenes of corresponding stereochemistry at C-3 and C-4 (4, 16, 22). It can thus be concluded that the relative energies of the (spectroscopic) valence and Rydberg excited states are unaffected by the structural constraints imposed by the ancillary cycloalkyl ring in these compounds.

Direct irradiation of *cis*-**7** with 228 nm light in hydrocarbon solution or in the gas phase at 1 atm (1 atm = 101.325 kPa) results in stereospecific conrotatory ring opening, affording the isomeric diene *E,Z*-**10** in ca. 40% overall yield, along with *Z*-2-butene (*Z*-**11**) and 2-butyne (**12**) in ca. 60% yield (eq. [4]) (4). Direct irradiation of the *trans*-isomer under the same conditions, on the other hand, yielded a mixture of all three diene isomers (25% total), *E*-**11**, and **12** (ca. 75%), with the yield of *E,Z*-**10** relative to those of the *E,E*- and *Z,Z*-isomers increasing continuously over the 0.15–0.4% conversion range. However, control experiments showed the relative isomeric diene yields to be distorted by secondary photolysis effects, and demonstrated that the yields of *E,Z*-**10** observed under these conditions are consistent with the actual formation of a ca. 1:1 mixture of *E,E*- and *Z,Z*-**10**. We thus concluded that ring opening of *trans*-**7** at 228 nm very likely exhibits similar conrotatory selectivity to that of the

*cis*-isomer, producing a nearly equal mixture of the *E,E*- and *Z,Z*-dienes.

The product distributions obtained upon irradiation at this wavelength, where the  $\pi,\text{R}(3s)$  states of the cyclobutenes are selectively populated, are much different than those obtained with shorter wavelength (193–214 nm) excitation, where both conrotatory and disrotatory diene isomers are formed in similar amounts. Since both excited states are populated in the 193–214 nm wavelength range, it was concluded that the  $\pi,\pi^*$  state must be responsible for ring opening to yield the disrotatory diene isomer(s), and that reaction competes effectively with internal conversion to the lower energy Rydberg state. At short excitation wavelengths, the conrotatory isomers may arise because the  $\pi,\pi^*$  process occurs adiabatically, as we previously concluded (22), or because the  $\pi,\text{R}(3s)$  excited state is also populated (by direct excitation and (or) by internal conversion from the  $\pi,\pi^*$  state), or both.



The present work shows that in contrast, the mixtures of diene isomers formed upon ring opening of the fused



bicyclic cyclobutenes *cis*- and *trans*-**4b** and **4c** at 228 nm are only modestly different from those obtained with shorter wavelength excitation, where in each case there is a very distinct preference for the formation of the disrotatory diene isomers. In all cases but *cis*-**4b**, there appears to be a consistent wavelength dependence in the product ratios, with the yield of conrotatory product(s) increasing modestly as the excitation wavelength increases. As we found previously in our studies of the photochemistry of **7** at this wavelength (and as the data of Figs. 2–4 clearly show), secondary photolysis effects are generally very difficult to control, and thus, the product ratios reported cannot be considered to be quantitatively accurate. Nevertheless, the trends are clear; the corresponding disrotatory diene isomers are the major products of irradiation of both isomers of **4b** and **4c** at 228 nm, just as they are at shorter irradiation wavelengths.

Assuming that the Rydberg state is indeed *exclusively* excited in these compounds upon absorption of a 228 nm photon, the fact that similar distributions of diene isomers are observed for **4b** and **4c** as with shorter excitation wavelengths (where the  $\pi,\pi^*$  state is also directly populated) suggests either that ring opening within the Rydberg state exhibits similar characteristics to  $\pi,\pi^*$  state ring opening in these compounds or that (conrotatory) Rydberg state ring opening is less efficient than in monocyclic derivatives, allowing internal conversion to the  $\pi,\pi^*$  state (at a non-Franck–Condon geometry), from which ring opening occurs with predominant disrotatory stereochemistry, to compete more effectively.

One interpretation of the results for **4b** and **4c** is that Rydberg state ring opening, in addition to proceeding with preferred conrotatory stereochemistry, also involves twisting about the “central” C=C bond as ring opening proceeds; accordingly, incorporating the cyclobutenyl C=C bond in a second ancillary ring would be expected to result in a structurally induced barrier to Rydberg state ring opening. Scheme 1 shows a hypothetical reaction coordinate diagram for dis- and conrotatory ring opening on the  $\pi,\pi^*$  and  $\pi,R(3s)$  excited state surfaces, which incorporates these ideas and illustrates their possible ramifications on the stereochemical characteristics of the reaction. Disrotatory ( $\pi,\pi^*$  state) ring opening is assumed to proceed, at least initially, with little deviation of the 4-carbon system from planarity, since short wavelength ( $\leq 214$  nm) irradiation of **4a–4d** proceeds with high efficiency, with no real variation in quantum yield throughout the series (22); the  $\pi,\pi^*$  surface falls in energy along this reaction coordinate, as predicted both by simple orbital symmetry considerations (8) and recent *ab initio* calculations (9, 10). If the  $\pi,R(3s)$  surface rises in energy along the disrotatory reaction coordinate, the result will be a thermally activated crossing of the two surfaces at some intermediate geometry (A). The conrotatory reaction coordinate is represented as projecting perpendicularly to the disrotatory one, as it involves both conrotatory twisting about C1—C4 and C2—C3 and torsion about the central C1—C2 bond, leading eventually to *s-trans*-diene. In monocyclic cyclobutenes, the  $\pi,R(3s)$  surface is proposed to fall in energy along this reaction coordinate, while the  $\pi,\pi^*$  surface increases in energy owing to orbital symmetry effects, thus resulting in preferred conrotatory ring opening upon selective population of the Rydberg state. In **4b–4d** on the other hand,

motions along the conrotatory (+ central bond torsion) reaction coordinate in the  $\pi,R(3s)$  state encounter the structurally induced barrier, possibly allowing the excited molecule to traverse the (presumably somewhat smaller) barrier to the  $\pi,\pi^*$  surface along the disrotatory reaction coordinate, from which ring opening proceeds with the characteristics of that excited state. It might further be expected that the structurally induced barrier to Rydberg state conrotatory ring opening should decrease as the size and flexibility of the ancillary ring increases, and thus, allow reaction via this pathway to be more competitive with internal conversion to the  $\pi,\pi^*$  state, where ring opening proceeds with preferred disrotatory stereochemistry. Unfortunately, the data for *cis*- and *trans*-**4d** are not sufficiently reliable to address this possibility in a conclusive way; certainly, there is no evidence for it in the wavelength dependence associated with the ring openings of *cis*- and *trans*-**4b** and **4c**.

It is relevant to point out the analogy between cyclobutene Rydberg state ring opening and the ring opening of cyclobutene radical cations ( $CB^+$ ), to the extent that the latter species constitutes a reasonable model for the “semi-ionized” olefinic  $\pi,R(3s)$  Rydberg state (14, 15). The reaction has been extensively studied in recent years (33–42), and is known to proceed with the preferred conrotatory stereochemistry (36) that theory predicts (39, 43–47). Calculations indicate that the reaction proceeds via two competing conrotatory pathways: a nonsynchronous concerted pathway leading to *s-cis*-1,3-butadiene (*s-cis*- $BD^+$ ) radical cation, and one involving rotation about the ionized double bond leading to *s-trans*- $BD^+$  via a transition state exhibiting structural characteristics of the cyclopropylcarbinyl radical cation (43, 45–47). Interestingly, photolysis of  $CB^+$  in a low-temperature matrix has been reported to yield *s-trans*- $BD^+$  exclusively (39).

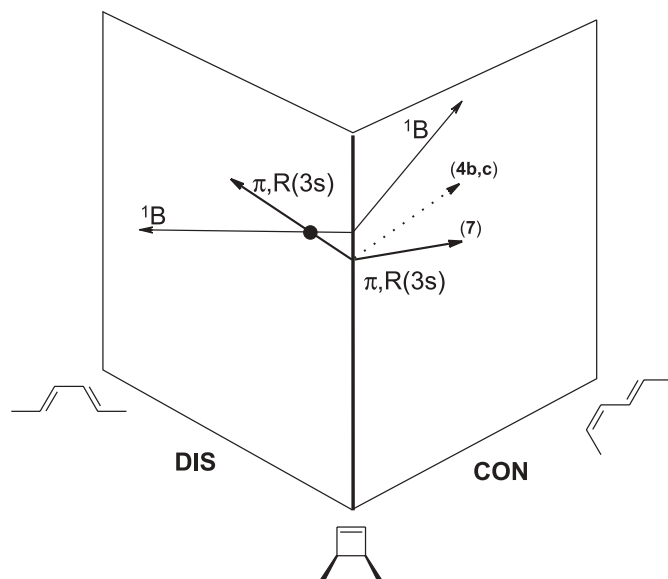
This explanation is obviously highly speculative, and undoubtedly not the only one possible. Nevertheless, it contains a number of features that might be tested experimentally. For example, the idea that ring opening on the  $\pi,R(3s)$  potential energy surface can be impeded by the introduction of a structurally induced barrier might be tested through studies of the temperature dependence of the reaction stereochemistry in these and monocyclic cyclobutenes as a function of excitation wavelength. Ultrafast time-resolved studies, along the lines of those recently reported for other aliphatic alkenes (25, 26), would also offer potentially invaluable information on the mechanism. Finally, it still remains to be established to what extent the  $\pi,R(3s)$  state contributes to the ring opening of alkylcyclobutenes at shorter excitation wavelengths (185–214 nm), where the  $\pi,\pi^*$  excited singlet state is also populated. Further work in this area is clearly necessary.

## Summary and conclusions

Alkylcyclobutenes have two low-lying excited singlet states of similar energy, the  $\pi,\pi^*$  (valence) and  $\pi,R(3s)$  (Rydberg) state, and both lead to electrocyclic ring opening to the isomeric 1,3-dienes. The Rydberg state is markedly lower in energy than the  $\pi,\pi^*$  state in 1,2-dialkylcyclobutenes, a characteristic that allows the photochemistry associated with this excited state to be studied under conditions of selective excitation.



Scheme 1.



In such compounds, excitation at the short wavelengths necessary for population of the  $\pi,\pi^*$  state results in non-stereospecific ring opening, and the yields of formally allowed (disrotatory) diene isomers relative to the formally forbidden (conrotatory) ones vary with excitation wavelength and the stereochemistry and other structural characteristics of the substrate. On the other hand, selective excitation at the long-wavelength edge of the absorption band, where the  $\pi,R(3s)$  Rydberg state absorptions appear in the gas phase spectrum, results in reaction characteristics that vary much more dramatically with substrate structure; monocyclic derivatives open with clean conrotatory stereospecificity, while bicyclic derivatives, in which the cyclobutenyl C=C bond is shared with a second ancillary ring, appear to exhibit predominant disrotatory stereoselectivities, similar to what is observed upon shorter wavelength ( $\pi,\pi^*$ ) excitation. These results are interpreted as suggesting that the Rydberg state process involves both conrotatory motions about the cyclobutenyl C1—C4 and C2—C3 bonds and twisting about the C=C bond as the reaction is initiated on the excited-state surface. Impeding the latter motions through appropriate structural constraints has the effect of directing the molecule over a barrier and onto the  $\pi,\pi^*$  state surface, in which ring opening with predominant disrotatory stereochemistry ensues. The wavelength dependent stereoselectivities that have been observed with most of the compounds that have now been studied suggest that internal conversion from the  $\pi,\pi^*$  state to the lower-lying Rydberg state is slow relative to ring opening, or at best competitive with it.

The true degree of disrotatory stereoselectivity that is associated with the  $\pi,\pi^*$  state reaction unfortunately remains poorly defined, though it is clear that in some cases at least, it is very high. At least two viable mechanisms remain which could explain the non-stereospecificity observed upon excitation of alkylcyclobutenes in the region of the  $\pi,\pi^*$  absorption: adiabatic ring opening within the  $\pi,\pi^*$  state, and the competing involvement of the Rydberg state, populated either by direct absorption or (incomplete) internal conver-

sion from the  $\pi,\pi^*$  state. Further study of the reaction will be necessary to conclusively distinguish between these possibilities.

## Experimental

The cyclobutenes studied in this work were prepared and purified as previously reported (22), while photoproducts were identified by GC coinjection with authentic samples or after isolation from semipreparative scale photolyses of the corresponding cyclobutene derivative. The cyclobutenes were purified to >99% purity by semipreparative gas chromatography (20% TCEP on 80/100 Chromosorb PNAW, 0.25"  $\times$  6", stainless steel, Chromatographic Specialties, Inc.), followed where necessary by passage through a 1:5 (silver nitrate:silica gel) microcolumn using pentane as the eluant. Only the sample of *trans*-4d remained contaminated with isomeric dienes after this treatment, but the amounts were small (ca. 1% in total by GC), and were accounted for in the analyses of the 214 and 228 nm photolyses of this compound. Hexanes (BDH Omnisolv) and *n*-octane (Aldrich) were used as received from the suppliers. UV absorption spectra were recorded using a Cary 50 UV-vis spectrophotometer in 1 cm Suprasil cells. Analytical gas chromatographic separations were carried out using a Hewlett-Packard 5890 gas chromatograph equipped with a flame ionization detector and a 0.22 mm  $\times$  15 m DB-1 fused silica microbore capillary column (Chromatographic Specialties, Inc.). FID response factors were determined for all compounds by construction of standard working curves from mixtures of stock solutions of the pure compounds.

Samples for photolysis contained the cyclobutene (ca. 0.06 M) and *n*-octane (0.001 M) in hexane solution. Aliquots (ca. 0.3 mL) were placed in 5 mm quartz tubes containing a micro stirring bar, sealed with rubber septa, and deoxygenated with a stream of dry argon. Photolyses were carried out using 16 W Philips 93106E zinc or 16 W Philips 93107E cadmium resonance lamps for irradiation at 214 or 228 nm, respectively, with constant agitation of the solutions with a magnetic stirrer. Aliquots were removed from the cells by microlitre syringe at suitable photolysis intervals and analysed by GC. Product formation was monitored as a function of photolysis time in all cases.

## Acknowledgments

We wish to thank the Natural Sciences and Engineering Research Council of Canada (NSERC) for financial support of this work and Don Arnold for his enthusiasm, encouragement, and mentorship over the past 30 years. *Ille est noster pater in spiratu.*

## References

1. W.J. Leigh. *Can. J. Chem.* **71**, 147 (1993).
2. W.J. Leigh. *Chem. Rev.* **93**, 487 (1993).
3. W.J. Leigh. In *CRC handbook of organic photochemistry and photobiology*. Edited by W.G. Horspool and P.-S. Song. CRC Press, Boca Raton. 1995. p. 123.
4. W.J. Leigh and B.H.O. Cook. *J. Org. Chem.* **64**, 5256 (1999).
5. J. Saltiel and L.S. Ng Lim. *J. Am. Chem. Soc.* **91**, 5404 (1969).



6. K.B. Clark and W.J. Leigh. *J. Am. Chem. Soc.* **109**, 6086 (1987).
7. W.G. Dauben and J.E. Haubrich. *J. Org. Chem.* **53**, 600 (1988).
8. R.B. Woodward and R. Hoffmann. *The conservation of orbital symmetry*. Verlag-Chemie, Weinheim. 1970.
9. M. Ben-Nun, J. Quenneville, and T.J. Martinez. *J. Phys. Chem. A*, **104**, 5161 (2000).
10. M. Ben-Nun and T.J. Martinez. *J. Am. Chem. Soc.* **122**, 6299 (2000).
11. B.B. Loeffler, E. Eberlin, and L.W. Pickett. *J. Chem. Phys.* **28**, 345 (1958).
12. W.J. Leigh, K. Zheng, N. Nguyen, N.H. Werstiuk, and J. Ma. *J. Am. Chem. Soc.* **113**, 4993 (1991).
13. M.B. Robin. *Higher excited states of polyatomic molecules*. Vol. II. Academic Press, New York. 1975.
14. P.J. Kropp. *In CRC handbook of organic photochemistry and photobiology*. Edited by W.G. Horspool and P.-S. Song. CRC Press, Boca Raton. 1995. p. 16.
15. P.J. Kropp. *Org. Photochem.* **4**, 1 (1979).
16. W.J. Leigh, K. Zheng, and K.B. Clark. *Can. J. Chem.* **68**, 1988 (1990).
17. W.J. Leigh, K. Zheng, and K.B. Clark. *J. Org. Chem.* **56**, 1574 (1991).
18. W.J. Leigh and K. Zheng. *J. Am. Chem. Soc.* **113**, 2163 (1991).
19. W.J. Leigh and K. Zheng. *J. Am. Chem. Soc.* **113**, 4019 (1991).
20. W.J. Leigh and J.A. Postigo. *J. Am. Chem. Soc.* **117**, 1688 (1995).
21. W.J. Leigh, J.A. Postigo, and P.C. Venneri. *J. Am. Chem. Soc.* **117**, 7826 (1995).
22. W.J. Leigh, J.A. Postigo, and K.C. Zheng. *Can. J. Chem.* **74**, 951 (1996).
23. B.H.O. Cook, W.J. Leigh, and R. Walsh. *J. Am. Chem. Soc.* **123**, 5188 (2001).
24. K.B. Clark and W.J. Leigh. *Can. J. Chem.* **66**, 1571 (1988).
25. W. Fuss, W.E. Schmid, and S.A. Trushin. *J. Am. Chem. Soc.* **123**, 7101 (2001).
26. W. Fuss, K.K. Pushpa, W.E. Schmid, and S.A. Trushin. *J. Phys. Chem. A*, **105**, 10 640 (2001).
27. S. Wilsey and K.N. Houk. *J. Am. Chem. Soc.* **124**, 11182 (2002).
28. S. Wilsey, K.N. Houk, and A.H. Zewail. *J. Am. Chem. Soc.* **121**, 5772 (1999).
29. S. Wilsey and K.N. Houk. *J. Am. Chem. Soc.* **122**, 2651 (2000).
30. M.K. Lawless, S.D. Wickham, and R.A. Mathies. *J. Am. Chem. Soc.* **116**, 1593 (1994).
31. M.K. Lawless, S.D. Wickham, and R.A. Mathies. *Acc. Chem. Res.* **28**, 493 (1995).
32. F. Negri, G. Orlandi, F. Zerbetto, and M.Z. Zgierski. *J. Chem. Phys.* **103**, 5911 (1995).
33. C. Dass, T.M. Sack, and M.L. Gross. *J. Am. Chem. Soc.* **106**, 5780 (1984).
34. M.L. Gross and D.H. Russell. *J. Am. Chem. Soc.* **101**, 2082 (1979).
35. Y. Kawamura, M. Thurnauer, and G.B. Schuster. *Tetrahedron*, **42**, 6195 (1986).
36. T. Miyashi, K. Wakamatsu, T. Akiya, K. Kikuchi, and T. Mukai. *J. Am. Chem. Soc.* **109**, 5270 (1987).
37. B.-E. Brauer and M. Thurnauer. *Chem. Phys. Lett.* **133**, 207 (1987).
38. F. Gerson, X.-Z. Qin, T. Bally, and J.-N. Aebischer. *Helv. Chim. Acta*, **71**, 1069 (1988).
39. J.N. Aebischer, T. Bally, K. Roth, E. Haselbach, F. Gerson, and X.-Z. Qin. *J. Am. Chem. Soc.* **111**, 7909 (1989).
40. A. Faucitano, A. Buttafava, F. Martinotti, R. Sustmann, and H.G. Korth. *J. Chem. Soc., Perkin Trans. 1*, 865 (1992).
41. A. Marcinek, J. Michalak, J. Rogowski, W. Tang, T. Bally, and J. Gebicki. *J. Chem. Soc., Perkin Trans. 1*, 1353 (1992).
42. J. Gebicki, A. Marcinek, J. Michalak, J. Rogowski, T. Bally, and W. Tang. *J. Mol. Struct.* **275**, 249 (1992).
43. O. Wiest. *J. Am. Chem. Soc.* **119**, 5713 (1997).
44. D.J. Bellville, R. Chelsky, and N.L. Bauld. *J. Comput. Chem.* **3**, 548 (1982).
45. G.N. Sastry, T. Bally, V. Hroudá, and P. Carsky. *J. Am. Chem. Soc.* **120**, 9323 (1998).
46. V. Barone, N. Rega, T. Bally, and G.N. Sastry. *J. Phys. Chem. A*, **103**, 217 (1999).
47. D.J. Swinarski and O. Wiest. *J. Org. Chem.* **65**, 6708 (2000).



# The conformational behaviour of methylenecyclohexanes revisited

Heidi M. Muchall, Petrina R.N. Kamy, and Jean Lessard

**Abstract:** Conformational analyses on 2-substituted (methoxy, vinyloxy, and acetoxy) methylenecyclohexanes have been performed computationally with HF, B3LYP, PBE0, and MP2 and the 6-31G(d) basis set. The global minimum for the methoxy substituent is an axial conformer. For the vinyloxy substituent, except with PBE0, an axial conformer is determined as the global minimum. The acetoxy substituent prefers the equatorial orientation. This sequence is in keeping with the operation of an "unsaturation effect" in addition to an anomeric effect. For a full conformational analysis, torsional potentials for the substituents have been generated, which show further low-energy minima, which affect the equilibrium composition. In general, axial conformers dominate the equilibria. To reproduce the experimentally observed predominance of equatorial conformers for vinyloxy and acetoxy substituents, PBE0 has to be employed. CSGT isotropic shielding tensors at the B3LYP/6-311+G(d,p)//B3LYP/6-31G(d) level have been employed for comparison with experimentally observed  $^{13}\text{C}$  chemical shifts.

**Key words:** conformational analysis, methylenecyclohexanes, anomeric effect, unsaturation effect.

**Résumé :** On a réalisé une analyse conformationnelle de méthylèncyclohexanes portant des substituants (méthoxy, vinyloxy et acétoxy) en position 2 en faisant appel à des méthodes de calcul théorique à l'aide de HF, B3LYP, PBE0, MP2 et l'ensembles de bases 6-31G(d). Le minimum global pour le substituant méthoxy est le conformère axial. Pour le substituant vinyloxy, tous les ensembles à l'exception du PBE0 attribuent le minimum global au conformère axial alors que le substituant acétoxy occupe préférentiellement l'orientation équatoriale. Cette séquence est en accord avec l'opération de l'effet d'insaturation en plus de l'effet anomère. Pour une analyse conformationnelle complète, on a généré les potentiels de torsion des substituants qui mettent en évidence d'autres minima de basse énergie qui affectent la composition de l'équilibre. En général, les conformères axiaux prédominent à l'équilibre. Afin de reproduire la prédominance des conformères équatoriaux observée expérimentalement pour les substituants vinyloxy et acétoxy, il faut utiliser l'ensemble PBE0. Pour pouvoir faire une comparaison avec les valeurs observées expérimentalement pour les déplacements chimiques  $^{13}\text{C}$ , on a utilisé des tenseurs de blindage isotrope CSGT au niveau B3LYP/6-311+G(d,p)//B3LYP/6-31G(d).

**Mots clés :** analyse conformationnelle, méthylèncyclohexanes, effet anomère, effet d'insaturation.

[Traduit par la Rédaction]

## Introduction

2-Substituted oxanes exhibit an anomeric effect, i.e., a substituent  $-\text{OR}$  prefers the axial (*gauche*) rather than the equatorial (*anti*) position. The commonly accepted reason for this is a stabilizing  $n_{\text{O}}-\sigma^*_{\text{C-O}}$  interaction in the axial orientation, but electrostatic (dipole-dipole) interactions destabilizing the equatorial orientation are most probably involved as well (1, 2). If the heteroatom of the oxane ring is replaced by a double bond, such as in 3-methoxycyclohexene and 2-methoxymethylenecyclohexane (**1**), the methoxy group also prefers the pseudoaxial or axial orientation, and this preference has been explained by a stabilizing  $\pi-\sigma^*_{\text{C-O}}$  interaction, electrostatic (dipole-quadrupole) interactions being considered less impor-

tant than the orbital interaction (3). The axial preference is larger for an acetoxy group than for a methoxy group in 2-substituted oxanes (4–6) and in 3-substituted cyclohexenes (5, 6), as expected from larger  $n_{\text{O}}-\sigma^*_{\text{C-O}}$  or  $\pi-\sigma^*_{\text{C-O}}$  interactions of the axial conformer in the case of the acetoxy group, which is more electron withdrawing and thus a better electron acceptor (i.e.,  $\sigma^*_{\text{C-O}}$  is lower in energy) than the methoxy group (1, 7).

In 1979, dynamic  $^{13}\text{C}$  NMR studies of 2-substituted methylenecyclohexanes, such as and including **1–3**, revealed an unexpected conformational behaviour (5). From low-temperature experiments (3% solutions in  $\text{CH}_2\text{Cl}_2\text{-CD}_2\text{Cl}_2$  (4:1 v/v) at  $-110^\circ\text{C}$ ), the chemical shifts of  $\text{C}^4$  of the axial (ax) and equatorial (eq) species were determined. The assignment of the observed chemical shifts as belonging to the

Received 17 January 2003. Published on the NRC Research Press Web site at <http://canjchem.nrc.ca> on 17 June 2003.

*Dedicated to Professor Don Arnold for his contributions to chemistry.*

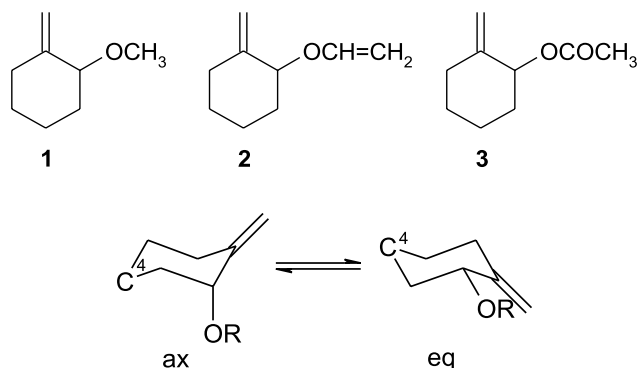
**H.M. Muchall<sup>1</sup>** and **P.R.N. Kamy**. Department of Chemistry and Biochemistry, Concordia University, Montreal, QC H3G 1M8, Canada.

**J. Lessard**. Département de Chimie, Université de Sherbrooke, Sherbrooke, QC J1K 2R1, Canada.

<sup>1</sup>Corresponding author (e-mail: [muchall@alcor.concordia.ca](mailto:muchall@alcor.concordia.ca)).



axial or equatorial conformer was based on the  $\gamma$ -effect, in that a  $^{13}\text{C}$  nucleus in the  $\gamma$ -position from the substituent is shielded by 4.5 ppm in the axial relative to the equatorial conformer. From the individual chemical shifts and the observed averaged  $\text{C}^4$  chemical shift  $\delta_{\text{m}}$  at  $0^\circ\text{C}$ , the proportion  $x$  of the equatorial conformer was calculated as  $\delta_{\text{m}} = x\delta_{\text{eq}} + (1 - x)\delta_{\text{ax}}$ . With a  $\delta_{\text{m}}$  of 22.6 ppm for **1**, 23.3 ppm for **2**, and 23.9 ppm for **3**, it was concluded that the equatorial orientation is preferred for unsaturated substituents: **1** 41% eq, **2** 61% eq, and **3** 80% eq. At  $-110^\circ\text{C}$ , by integration of the signals, the proportion of the equatorial conformer was determined to be 33% for **1** and more than 95% for **3** (6). This unexpected substituent behaviour was termed the “unsaturation effect” (5, 6).

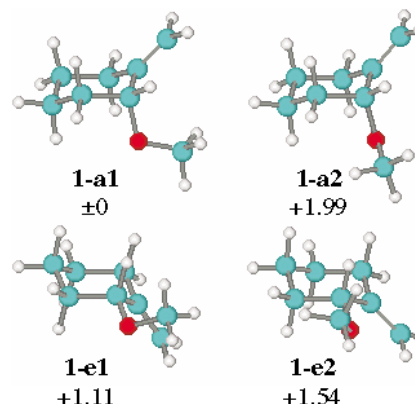


As was pointed out in a contribution by Forsyth and Seabag (8), even though chemists are nowadays able to accurately calculate  $^{13}\text{C}$  chemical shifts of organic compounds by ab initio methods, this is still not being done routinely. Accurate geometries are needed for calculated chemical shifts to be useful, and for a conformationally flexible system this means establishing the important conformers and evaluating their contribution to an equilibrium. To our knowledge, there are no computational studies as to the conformational behaviour of 2-substituted methylenecyclohexanes. Here we present a computational study of the conformational behaviour of the three representative species, **1**, **2**, and **3**, that illustrates the importance of a full conformational analysis that takes the rotamers of the substituent into account.

### Computational details

The Gaussian 98 program package was employed in all calculations (9). All minimum-energy conformations were initially optimized at HF/6-31G(d) and followed with optimizations at B3LYP/6-31G(d) (10, 11). Optimizations were also performed with the “parameter free” density functional PBE0 (12, 13) (Gaussian keyword PBE1PBE) and for **3** also with MP2(full). If not stated otherwise, representative geometry parameters in the text are given for B3LYP/6-31G(d), but the optimized species from all levels are virtually superposable. Frequency calculations were performed at HF/6-31G(d) and PBE0/6-31G(d) for zero-point vibrational (ZPV) energies, which are reported unscaled. Torsional analyses (relaxed scans) were performed at HF/6-31G(d) and in one case (for  $\phi_1$  in **3**, see below) also at B3LYP/6-31G(d) (partial optimizations in the gas phase) and PBE0/6-31G(d) (partial optimizations in dichloromethane). In our torsional analyses, minima with a relative energy of more than

**Fig. 1.** Low-energy conformers (**a** axial, **e** equatorial) of 2-methoxymethylenecyclohexane (**1**). Relative energies (B3LYP/6-31G(d)) are given in kcal/mol.



2.5 kcal/mol were not studied further, as the corresponding conformers do not contribute significantly to an overall equilibrium.

For an evaluation of a solvent influence, HF/6-31G(d)//HF/6-31G(d) and PBE0/6-31G(d)//PBE0/6-31G(d) calculations were carried out with dichloromethane (dielectric constant 9.08) and the self-consistent isodensity polarized continuum model (SCI-PCM) at an isodensity value of 0.0004. Isotropic shielding tensors were calculated with B3LYP/6-311+G(d,p)//B3LYP/6-31G(d) using the CSGT (continuous set of gauge transformations) method (14). To obtain chemical shifts, the values were corrected for the calculated absolute shielding for carbon in tetramethylsilane (181.98; the experimental value is 188.1 (15)) at this level of theory.

## Results

### Conformations

#### 2-Methoxymethylenecyclohexane (**1**)

To locate all relevant minima on the potential energy surface, the H-C-O-C torsion angle  $\phi$  was twisted through  $360^\circ$  in both the axial and equatorial forms in  $30^\circ$  steps. Four low-energy conformations of **1** were identified. These were fully optimized at HF/6-31G(d), B3LYP/6-31G(d), and PBE0/6-31G(d). The B3LYP-optimized conformers are given in Fig. 1; all energies are listed in Table 1.

As expected from a possible, stabilizing  $\pi\text{-}\sigma^*_{\text{C-O}}$  interaction and in analogy to the anomeric effect, the global minimum is an axial species, **1-a1** ( $\phi -50^\circ$ ). A low-energy barrier ( $\phi 0^\circ$ ) connects rotamers **1-a1** and **1-a2** ( $\phi +43^\circ$ ). Similarly, a low-energy barrier connects **1-e1** ( $\phi -34^\circ$ ) and **1-e2** ( $\phi +37^\circ$ ). All model chemistries agree on one order of stability for the four conformers, and the relative energies indicate that all four are populated significantly at  $0^\circ\text{C}$ . We have calculated the equilibrium populations at 273 K at all levels of theory employed (Table 1). As can be seen from Table 1, the relative energies and the resulting equilibrium composition are virtually identical for the gas-phase calculations. The population of the axial conformers is about 80%; that of the equatorial conformers is about 20%. As expected, the use of free energies does not show a significant change from these values (data not given). In contrast, the inclusion of solvent



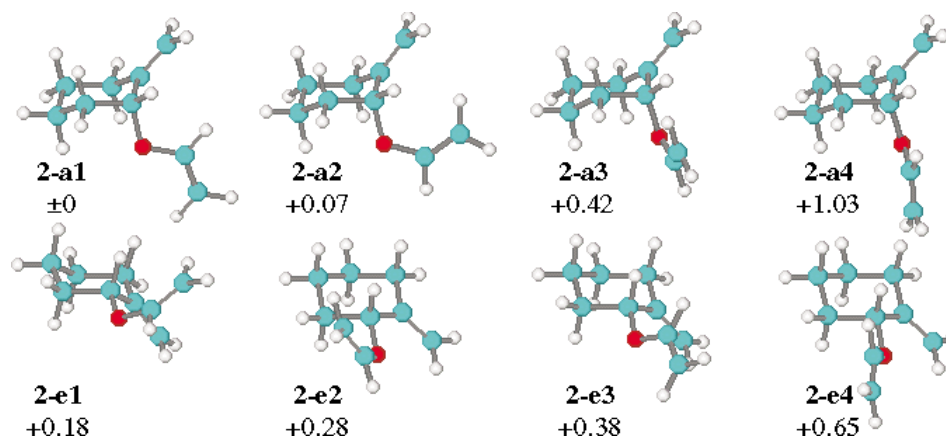
**Table 1.** Total energies (hartrees ( $1 \text{ hartree} = 4.359 \times 10^{-18} \text{ J}$ )) for axial (a) and equatorial (e) conformers of **1**.

	1-a1	1-a2	1-e1	1-e2
HF/6-31G(d)	–385.933163 (0) 84.0%	–385.930019 (1.97) 2.5%	–385.931364 (1.13) 10.1%	–385.930367 (1.75) 3.4%
+ZPVE	–385.709792 (0) 82.0%	–385.706806 (1.87) 2.5%	–385.708085 (1.07) 11.5%	–385.707265 (1.59) 4.1%
SCI-PCM	–385.935232 <sup>a</sup> (0) 69.9%	–385.932664 (1.61) 3.5%	–385.934164 <sup>b</sup> (0.67) 20.3%	–385.933124 (1.32) 6.3%
B3LYP/6-31G(d)	–388.480611 (0) 82.0%	–388.477433 (1.99) 2.5%	–388.478850 (1.11) 10.7%	–388.478163 (1.54) 4.9%
PBE0/6-31G(d)	–388.017400 (0) 79.4%	–388.014048 (2.10) 1.6%	–388.015907 (0.94) 14.3%	–388.014994 (1.51) 4.8%
+ZPVE	–387.807388 (0) 76.9%	–387.804235 (1.98) 2.3%	–387.805965 (0.89) 14.6%	–387.805213 (1.36) 6.2%
SCI-PCM	–388.019239 (0) 64.9%	–388.016446 (1.75) 2.6%	–388.018368 (0.55) 23.4%	–388.017552 (1.06) 9.1%

**Note:** Relative energies (kcal/mol) in parentheses, equilibrium populations at 273 K.

<sup>a</sup>Total energy from an optimization that includes solvent at this level is –385.935274 hartrees.

<sup>b</sup>Total energy from an optimization that includes solvent at this level is –385.934210 hartrees.

**Fig. 2.** Low-energy conformers (**a** axial, **e** equatorial) of 2-vinyloxymethylenecyclohexane (**2**). Relative energies (B3LYP/6-31G(d)) are given in kcal/mol.

does not change the order of stability of the four conformers but decreases all energy differences. This causes an almost doubling of the equatorial population in the equilibrium, and the sum of the axial conformers decreases to about 70%. In the dynamic  $^{13}\text{C}$  NMR experiments of **1**, the equilibrium composition at  $0^\circ\text{C}$  was estimated to be 59% axial in  $\text{CHFCl}_2\text{-CD}_2\text{Cl}_2$  (5, 6) and 65% axial in the less polar  $\text{CF}_2\text{Br}_2\text{-CD}_2\text{Cl}_2$  (6), which is in reasonable agreement with our calculated data.

### 2-Vinyloxymethylenecyclohexane (**2**)

Energy profiles were obtained for two torsion angles, H-C-O-C ( $\phi_1$ ) and C-O-C-C ( $\phi_2$ ). From the information in these profiles, eight low-energy conformations were identi-

fied and optimized at HF/6-31G(d), B3LYP/6-31G(d), and PBE0/6-31G(d). The B3LYP-optimized conformers are given in Fig. 2, energies are listed in Table 2.

Torsion angles  $\phi_1$  in all eight conformers are in the range of either  $+50^\circ$  or  $-50^\circ$ , which are similar values to those found in **1**. While the conformer with  $\phi_1$  near  $180^\circ$  is a high-energy minimum, **2** does not exhibit a significant preference ( $0^\circ$  over  $180^\circ$ ) for  $\phi_2$ . All model chemistries, except for the uncorrected (ZPV energies not included) PBE0/6-31G(d) and the solvent calculations at this level, agree on an axial species, **2-a1**, as the global minimum. This is in contrast to the interpretation from the NMR experiments and in line with a stabilizing  $\pi^*\text{-}\sigma_{\text{C-O}}$  interaction. For the two PBE0 calculations, **2-e1** is the global minimum. The other seven con-



**Table 2.** Total energies (hartrees) for axial (a) and equatorial (e) conformers of **2**.

	<b>2-a1</b>	<b>2-a2</b>	<b>2-a3</b>	<b>2-a4</b>
HF/6-31G(d)	–423.781976 (0) 37.3%	–423.781181 (0.50) 14.9%	–423.780530 (0.91) 7.1%	–423.780096 (1.18) 4.1%
+ZPVE	–423.553742 (0) 45.5%	–423.552335 (0.88) 9.1%	–423.551635 (1.32) 4.1%	–423.551861 (1.18) 5.0%
SCI-PCM	–423.784806 (0) 34.2%	–423.783538 (0.80) 7.9%	–423.783100 (1.07) 4.8%	–423.783368 (0.90) 6.5%
B3LYP/6-31G(d)	–426.566617 (0) 21.7%	–426.566507 (0.07) 19.1%	–426.565948 (0.42) 10.0%	–426.564977 (1.03) 3.3%
PBE0/6-31G(d)	–426.057756 (0.31) 13.3%	–426.058144 (0.07) 20.9%	–426.057470 (0.49) 9.5%	–426.055928 (1.46) 1.7%
+ZPVE	–425.843308 (0) 21.6%	–425.842983 (0.20) 14.9%	–425.842322 (0.62) 6.9%	–425.841385 (1.21) 2.4%
SCI-PCM	–426.060355 (0.30) 12.6%	–426.060401 (0.27) 14.0%	–426.059870 (0.60) 7.6%	–426.058919 (1.20) 2.5%
	<b>2-e1</b>	<b>2-e2</b>	<b>2-e3</b>	<b>2-e4</b>
HF/6-31G(d)	–423.780962 (0.64) 11.6%	–423.780455 (0.95) 6.3%	–423.781090 (0.56) 13.4%	–423.780247 (1.08) 5.2%
+ZPVE	–423.552241 (0.94) 8.2%	–423.551650 (1.31) 4.1%	–423.552893 (0.53) 16.8%	–423.552163 (0.99) 7.3%
SCI-PCM	–423.783722 (0.68) 9.6%	–423.783172 (1.03) 5.1%	–423.784482 (0.20) 23.6%	–423.783576 (0.77) 8.2%
B3LYP/6-31G(d)	–426.566326 (0.18) 15.6%	–426.566172 (0.28) 13.0%	–426.566017 (0.38) 10.9%	–426.565581 (0.65) 6.5%
PBE0/6-31G(d)	–426.058253 (0) 23.7%	–426.058007 (0.15) 17.8%	–426.057416 (0.53) 9.0%	–426.056760 (0.94) 4.3%
+ZPVE	–425.843259 (0.03) 20.3%	–425.842876 (0.27) 13.2%	–425.842902 (0.25) 13.4%	–425.842414 (0.56) 7.6%
SCI-PCM	–426.060832 (0) 22.9%	–426.060563 (0.17) 16.7%	–426.060514 (0.20) 15.8%	–426.059926 (0.57) 8.0%

Note: Relative energies (kcal/mol) in parentheses, equilibrium populations at 273 K.

formers lie within 1.5 kcal/mol for all methods, but the model chemistries do not agree on the order of stability. In particular, gas-phase HF/6-31G(d) calculations give a relatively large energy difference between **2-a1** and **2-e3**, the most stable of the equatorial conformers (Table 2), which results in an equilibrium concentration of the axial conformers of over 60%. Relative energies from B3LYP and from HF solvent calculations lead to a sum of the axial conformers that is significantly smaller at about 50%. The sum of axial conformers only drops below 50% with PBE0, in accord with experiment. All model chemistries reproduce the experimentally observed increase in equatorial conformer concen-

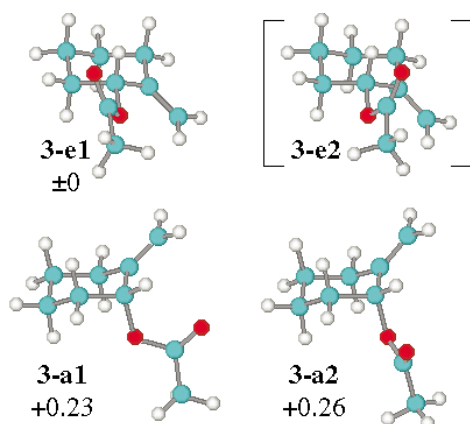
tration from **1** and therefore the “unsaturation effect”. At the PBE0 level this trend is reproduced particularly well, with the experimental equilibrium composition of **2** at 0°C of 39% axial and 61% equatorial (5).

### 2-Acetoxymethylenecyclohexane (**3**)

Energy profiles were obtained for two torsion angles, H-C-O-C ( $\phi_1$ ) and C-O-C-O ( $\phi_2$ ). From the information in these profiles, four low-energy conformations were identified and optimized with HF/6-31G(d) and MP2(full)/6-31G(d). With B3LYP/6-31G(d) and PBE0/6-31G(d), only three conformers, **3-e1**, **3-a1**, and **3-a2** were identified. The



**Fig. 3.** Low-energy conformers (**a** axial, **e** equatorial) of 2-acetoxymethylenecyclohexane (**3**). Relative energies (B3LYP/6-31G(d)) are given in kcal/mol. Compound **3-e2** was obtained with PBE0/6-31G(d) (geometry optimization in CH<sub>2</sub>Cl<sub>2</sub>, SCI-PCM).



B3LYP-optimized conformers are given in Fig. 3, energies are listed in Table 3.

For **3**, the model chemistries agree on neither the order nor the number of the conformers. In agreement with the interpretation of the NMR studies (5, 6), in the gas phase, HF, B3LYP, and PBE0 give an equatorial species, **3-e1**, as the global minimum. With MP2, **3-a1** is most stable. Yet while there are four low-energy conformers at the HF and MP2 levels, there are only three with B3LYP and PBE0. With HF and MP2, in addition to the three conformers shown in Fig. 3, the fourth conformer **3-e2** has a torsion angle  $\phi_1$  of  $-18^\circ$  (with  $\phi_2$  at  $0^\circ$ ), in analogy to **1-e1**, **2-e1**, and **2-e3**; for B3LYP and PBE0 (gas-phase geometries), the potential energy surface does not possess a stationary point in that region. This is evident from the torsional analysis of  $\phi_1$  using B3LYP/6-31G(d) and starting with the optimized **3-e1** (diamonds in Fig. 4). The equilibrium composition varies widely with the model chemistry chosen. At MP2 and furthest from experiment, the composition shows about 80% axial conformers. With HF and B3LYP this value drops to just above 50%. The experimentally observed equatorial predominance (5, 6) is only reproduced with PBE0. But even there, the equatorial conformer (gas-phase geometry) is only present with just over 50%, instead of the estimated 80% at  $0^\circ\text{C}$  from experimental data.

In an attempt to identify the source of this discrepancy between experiment and theory for **3**, which is absent for both **1** and **2**, we obtained the torsional profile for **3** with an equatorial substituent using PBE0/6-31G(d), performing geometry optimizations in the solvent, and covering the region of  $\phi_1$  in which the “missing” conformer **3-e2** should be. The result is given in Fig. 4 (squares). Obviously, while the relative energy is increasing monotonously from the optimized **3-e1** at  $30^\circ$  for the gas phase species (diamonds), there is an additional minimum with the inclusion of solvent. A subsequent

geometry optimization at PBE0/6-31G(d) in this region confirmed that the fourth conformer **3-e2** is recovered when the solvent is considered in the geometry optimization (Table 3). This conformer is given in Fig. 3 in brackets.

Unfortunately, we were not able to optimize **3-a1** or **3-a2** with the inclusion of solvent (at any level), which would be needed to determine the equilibrium composition.<sup>2</sup> At this point, an assumption seems feasible. Checks on selected species (**1-a1**, **1-e1**, and **3-e1**) at the HF level have revealed that it matters little in which manner the solvent is considered in the calculations. Regardless of whether the geometry is optimized in the solvent cavity (the total energies for the three species are given in Tables 1 and 3) or whether the energy is just evaluated for the gas-phase geometry in the solvent cavity, the magnitude of the stabilization due to the solvent is about the same. If we thus assume that the solvent-optimized conformers **3-a1** and **3-a2** are also both 0.45 kcal/mol less stable than **3-e1** (Table 3), then the equilibrium exhibits 67% equatorial species, which finally is in much better agreement with the experimental value.

## Chemical shifts

### $\gamma$ -Effect

We tested our choice level of theory for NMR calculations by checking for the reproducibility of the  $\gamma$ -effect (16) in methylcyclohexane (**4**). With B3LYP/6-31G(d), **4-a** is 2.15 kcal/mol higher in energy than **4-e**, in good agreement with the experimental A value of 1.74 kcal/mol (17). The calculated relative energy leads to an equilibrium composition at 273 K of 98% **4-e** : 2% **4-a** or 97% **4-e** : 3% **4-a** at room temperature. The experimental and calculated chemical shifts for the ring carbon atoms of **4-e**, **4-a**, and cyclohexane are given in Fig. 5.

As expected, with our choice of model chemistry, the experimental chemical shifts are reproduced well. For cyclohexane, there is a difference between calculated and experimental chemical shifts  $\Delta\delta$  of 5.5 ppm. A difference of this magnitude is also found for **4**. The averaged calculated values for the equilibria at 0 and  $25^\circ\text{C}$  are C<sup>1</sup> 40.5 ( $\Delta\delta$  = 7.5 ppm), C<sup>2</sup> 39.9 ( $\Delta\delta$  = 4.3 ppm), C<sup>3</sup> 32.0 ( $\Delta\delta$  = 5.4 ppm), and C<sup>4</sup> 31.6 ppm ( $\Delta\delta$  = 5.0 ppm).

As can be seen from Fig. 5, the  $\gamma$ -effect is reproduced qualitatively: C<sup>3</sup> in **4-a** is shielded by 6.0 ppm in comparison to **4-e**.

### Methylenecyclohexanes

The calculated chemical shifts for C<sup>4</sup> of all conformers of **1–3** are given in Table 4. The chemical shift for **3-e2** was estimated as follows: chemical shifts were determined for **3-e1** and **3-e2** at B3LYP/6-311+G(d,p)//HF/6-31G(d); for **3-e1**, the difference from the B3LYP/6-311+G(d,p)//B3LYP/6-31G(d) value was determined and the chemical shift for **3-e2** was adjusted accordingly. Within an axial or equatorial series, the C<sup>4</sup> chemical shift varies little with the choice of substituent at C<sup>2</sup>, while it is systematically larger for those

<sup>2</sup>We have since been able to optimize the geometries of all conformers of **1–3** and of several 7-substituted **1** in dichloromethane using PBE0 and COSMO, and the equilibrium composition based on zero-point corrected total energies agrees exceedingly well with experiment for all three compounds. The compositions based on free energy differences again do not differ significantly from these. A manuscript is in preparation.



**Table 3.** Total energies (hartrees) for axial (a) and equatorial (e) conformers of **3**.

	<b>3-a1</b>	<b>3-a2</b>	<b>3-e1</b>	<b>3-e2</b>
HF/6-31G(d)	-498.703311 (0.03) 28.5%	-498.703327 (0.02) 29.1%	-498.703355 (0) 30.0%	-498.702586 (0.48) 12.3%
+ZPVE	-498.469487 (0.03) 28.4%	-498.469459 (0.04) 27.5%	-498.469529 (0) 29.9%	-498.468873 (0.41) 14.1%
SCI-PCM	-498.708810 (0.08) 23.7%	-498.708936 (0) 27.6%	-498.708882 <sup>a</sup> (0.03) 25.9%	-498.708770 (0.10) 22.6%
MP2/6-31G(d)	-500.265666 (0) 45.0%	-500.265520 (0.09) 38.3%	-500.264408 (0.79) 10.4%	-500.263959 (1.07) 6.3%
B3LYP/6-31G(d)	-501.842427 (0.23) 28.7%	-501.842370 (0.26) 27.0%	-501.842792 (0) 44.2%	— <sup>b</sup>
PBE0/6-31G(d)	-501.261429 (0.47) 22.9%	-501.261397 (0.49) 22.4%	-501.262174 (0) 54.6%	— <sup>b</sup>
+ZPVE	-501.041563 (0.51) 21.5%	-501.041618 (0.48) 23.2%	-501.042375 (0) 55.2%	— <sup>b</sup>
SCI-PCM	-501.266027 (0.45) 23.5%	-501.266026 (0.45) 23.0%	-501.266744 (0) 53.5%	— <sup>b</sup>
SCI-PCM opt.	— <sup>c</sup>	— <sup>c</sup>	-501.266799 (0)	-501.266626 (0.11)

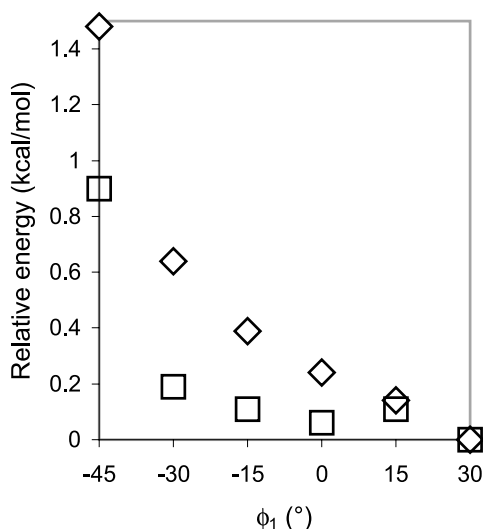
**Note:** Relative energies (kcal/mol) in parentheses, equilibrium populations at 273 K.

<sup>a</sup>Total energy from an optimization that includes solvent at this level is -498.708974 hartrees.

<sup>b</sup>Not a stationary point.

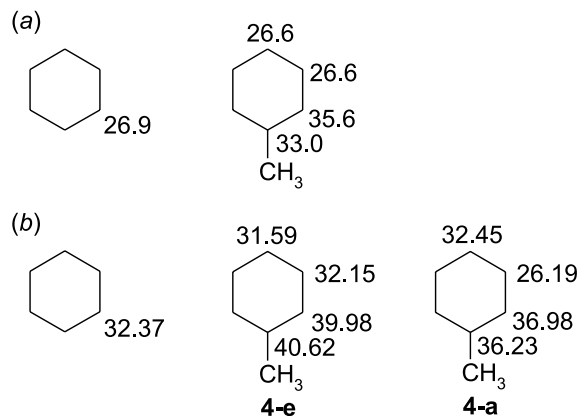
<sup>c</sup>Could not be determined.

**Fig. 4.** Torsional energy profile for  $\phi_1$  in **3** with the substituent in equatorial orientation (with  $\phi_2$  at about  $0^\circ$ , relaxed scan). Shown are energies for gas phase geometries from B3LYP/6-31G(d) ( $\diamond$ ) and solvent-optimized geometries from PBE0/6-31G(d) ( $\square$ ).



rotamers with a negative  $\phi$  (or  $\phi_1$ ) than for rotamers with a positive value for this torsion angle. This also holds for our estimated value of **3-e2**. We have estimated the  $\gamma$ -effect

**Fig. 5.** (a) Experimental and (b) calculated (B3LYP/6-311+G(d,p)/B3LYP/6-31G(d))  $^{13}\text{C}$  chemical shifts for the ring carbon atoms of cyclohexane and methylcyclohexane in ppm.



from separately weighted averages of axial and equatorial conformers. In this way, the  $\gamma$ -effect ( $\delta_{\text{eq}} - \delta_{\text{ax}}$ ) for **1** is about 5 ppm, for **2** about 4.5 ppm, and for **3** about 4 ppm, the actual values depending little on the specific energy differences used in the weighting. This reduction in the  $\gamma$ -effect results from a progressively more shielded averaged chemical shift for the equatorial species (for example, 30.80 ppm in **1**, 30.35 ppm in **2**, 29.73 ppm in **3**, from the PBE0 solvent



**Table 4.** Chemical shifts (ppm) for C<sup>4</sup> in conformers of **1–3** from B3LYP/6-311+G(d,p)//B3LYP/6-31G(d).

<b>1-a1</b>	<b>1-a2</b>	<b>1-e1</b>	<b>1-e2</b>
25.88	25.24	31.04	30.18
<b>2-a1</b>	<b>2-a2</b>	<b>2-a3</b>	<b>2-a4</b>
25.77	25.94	25.45	24.81
<b>2-e1</b>	<b>2-e2</b>	<b>2-e3</b>	<b>2-e4</b>
30.76	29.69	30.61	30.05
<b>3-a1</b>	<b>3-a2</b>	<b>3-e1</b>	<b>3-e2</b>
26.09	25.74	29.73	30.46 <sup>a</sup>

<sup>a</sup>Value estimated as described in the text.**Table 5.** Calculated (weighted average at 273 K) and experimental chemical shifts  $\delta_m$  (ppm) for C<sup>4</sup> in **1–3**.

	Calculated	Experimental
<b>1</b>		
HF/6-31G(d)	26.53	22.6
+ZPVE	26.66	
SCI-PCM	27.18	
B3LYP/6-31G(d)	26.65	
PBE0/6-31G(d)	26.84	
+ZPVE	26.89	
SCI-PCM	27.46	
<b>2</b>		
HF/6-31G(d)	27.40 (0.9) <sup>a</sup>	23.3 (0.7) <sup>a</sup>
+ZPVE	27.45 (0.8) <sup>a</sup>	
SCI-PCM	27.85 (0.7) <sup>a</sup>	
B3LYP/6-31G(d)	27.86 (1.2) <sup>a</sup>	
PBE0/6-31G(d)	28.31 (0.5) <sup>a</sup>	
+ZPVE	28.33 (0.4) <sup>a</sup>	
SCI-PCM	28.68 (1.2) <sup>a</sup>	
<b>3</b>		
HF/6-31G(d)	27.59 (0.2) <sup>b</sup>	23.9 (0.6) <sup>b</sup>
+ZPVE	27.67 (0.2) <sup>b</sup>	
SCI-PCM	27.87 (0.0) <sup>b</sup>	
MP2/6-31G(d)	26.61	
B3LYP/6-31G(d)	27.58 (−0.3) <sup>b</sup>	
PBE0/6-31G(d)	27.97 (−0.3) <sup>b</sup>	
+ZPVE	27.99 (−0.3) <sup>b</sup>	
SCI-PCM	27.96 (−0.7) <sup>b</sup>	
SCI-PCM opt.	28.68	

<sup>a</sup>Difference to **1**.<sup>b</sup>Difference to **2**.

calculations) and an essentially stable chemical shift for the axial species (25.86 ppm in **1**, 25.76 ppm in **2**, 25.92 ppm in **3**).

The weighted averages  $\delta_m$  for an equilibrium consisting of all axial and equatorial species at 0°C and the experimental chemical shifts at this temperature are listed in Table 5. The difference  $\Delta\delta_m$  that results from a change of substituent at C<sup>2</sup> is also given. Replacing methoxy at C<sup>2</sup> with vinyloxy leads to an experimentally observed  $\Delta\delta_m$  of 0.7 ppm, and this is reproduced well with all model chemistries. If we also consider that the difference between experimental and calculated values  $\delta$  for cyclohexane and methylcyclohexane is about 5.5 ppm, the chemical shifts determined using relative energies from PBE0 solvent calculations give the best agree-

ment with experiment for both **1** and **2**. The experimentally observed deshielding of 0.6 ppm as vinyloxy is exchanged for acetoxy, on the other hand, is not reproduced by any of the model chemistries listed (Table 5). Instead, the calculated  $\delta_m$  for **2** and **3** is about the same (or even slightly smaller) at all levels, as can be seen from the  $\Delta\delta_m$  in Table 5. This of course is in accord with the calculated equilibrium composition for **2** and **3**, which is also similar and lies, for the equatorial conformers, at about 60% at the DFT level.

As discussed above, for **3**, the observed equatorial preference is only reproduced with PBE0, and the equilibrium is estimated to contain about 67% equatorial conformers when the solvent-optimized conformers are considered. The estimated  $\delta_m$  of 28.68 ppm reflects the fact that even this equilibrium is not rich enough in equatorial conformers.

## Conclusions

The unexpected increase in equatorial conformer upon introducing unsaturation in the 2-substituent of methylenecyclohexanes that was observed experimentally (**1** 41% eq, **2** 61% eq, and **3** 80% eq in CHFC1<sub>2</sub>-CD<sub>2</sub>Cl<sub>2</sub> at 0°C) and was termed the “unsaturation effect” was qualitatively reproduced. For **1** (methoxy substituent), the equilibrium was well described already at the HF level when relative energies from single-point solvent calculations were employed. For **2** (vinyloxy substituent), to reproduce the observed equatorial preference, PBE0 had to be employed, and again single-point solvent calculations gave the best results. Agreement with the large equatorial preference in the equilibrium of **3** (acetoxy substituent) was only obtained with relative energies from solvent-optimized conformers at the PBE0 level, even though the equilibrium composition could only be estimated because of the lack of data for the axial conformers. <sup>13</sup>C chemical shifts for C<sup>4</sup> (in  $\gamma$ -position to the substituent), which were calculated as weighted averages from all equilibrium species, confirmed the progressively increased deshielding in the methoxy–vinyloxy–acetoxy series that was observed experimentally.

In this study, we have shown that the experimentally observed “unsaturation effect” can indeed be reproduced computationally. We will now focus on studies towards an explanation of this effect.

## Acknowledgments

We thank Dr. R.C. Mawhinney for helpful discussions. Calculations were performed at the Center for Research in Molecular Modeling (CERMM), which was established with the financial support of the Concordia University Faculty of Arts and Science, the Ministère de l'Éducation du Québec (MEQ) and the Canada Foundation for Innovation (CFI). This work was supported by a research grant from the Natural Sciences and Engineering Research Council (NSERC) of Canada.

## References

1. I. Tarovzka and T. Bleha. Can. J. Chem. **57**, 424 (1979).
2. P. Deslongchamps. Stereoelectronic effects in organic chemistry. Pergamon Press, New York. 1983. p. 6.



3. J. Lessard, M.T. Phan Viet, R. Martino, and J.K. Saunders. *Can. J. Chem.* **55**, 1015 (1977).
4. C.B. Anderson and D.T. Sepp. *Tetrahedron*, **24**, 1707 (1968).
5. M.T. Phan Viet, J. Lessard, and J.K. Saunders. *Tetrahedron Lett.* 317 (1979).
6. A. Ouedraogo, M.T. Phan Viet, J.K. Saunders, and J. Lessard. *Can. J. Chem.* **65**, 1761 (1987).
7. A.J. Kirby. *The anomeric effect and related stereoelectronic effects at oxygen*. Springer Verlag, New York. 1983. p. 71.
8. D.A. Forsyth and A.B. Sebag. *J. Am. Chem. Soc.* **119**, 9483 (1997).
9. M.J. Frisch, G.W. Trucks, H.B. Schlegel, G.E. Scuseria, M.A. Robb, J.R. Cheeseman, V.G. Zakrzewski, J.A. Montgomery Jr., R.E. Stratmann, J.C. Burant, S. Dapprich, J.M. Millam, A.D. Daniels, K.N. Kudin, M.C. Strain, O. Farkas, J. Tomasi, V. Barone, M. Cossi, R. Cammi, B. Mennucci, C. Pomelli, C. Adamo, S. Clifford, J. Ochterski, G.A. Petersson, P.Y. Ayala, Q. Cui, K. Morokuma, D.K. Malick, A.D. Rabuck, K. Raghavachari, J.B. Foresman, J. Cioslowski, J.V. Ortiz, A.G. Baboul, B.B. Stefanov, G. Liu, A. Liashenko, P. Piskorz, I. Komaromi, R. Gomperts, R.L. Martin, D.J. Fox, T. Keith, M.A. Al-Laham, C.Y. Peng, A. Nanayakkara, C. Gonzalez, M. Challacombe, P.M.W. Gill, B. Johnson, W. Chen, M.W. Wong, J.L. Andres, C. Gonzalez, M. Head-Gordon, E.S. Replogle, and J.A. Pople. 1998. Gaussian 98 [computer program]. Revision A.7. Gaussian, Inc., Pittsburgh, PA.
10. A.D. Becke. *J. Chem. Phys.* **98**, 5648 (1993).
11. C. Lee, W. Yang, and R.G. Parr. *Phys. Rev. B Condens. Matter*, **37**, 785 (1988).
12. J.P. Perdew, K. Burke, and M. Ernzerhof. *Phys. Rev. Lett.* **77**, 3865 (1996); *Phys. Rev. Lett.* **78**, 1396 (1997) (E).
13. C. Adamo and V. Barone. *J. Chem. Phys.* **110**, 6158 (1999).
14. T.A. Keith and R.F.W. Bader. *Chem. Phys. Lett.* **210**, 223 (1993).
15. A.K. Jameson and C.J. Jameson. *Chem. Phys. Lett.* **134**, 461 (1987).
16. D.K. Dalling and D.M. Grant. *J. Am. Chem. Soc.* **96**, 1827 (1974).
17. H. Booth and J.R. Everett. *J. Chem. Soc. Perkin Trans. 2*, 255 (1980).



# Cyclization of 5-hexenyl radicals from nitroxyl radical additions to 4-pentenylketenes and from the acyloin reaction

Huda Henry-Riyad and Thomas T. Tidwell

**Abstract:** Photochemical Wolff rearrangements were used to form 5-substituted-4-pentenylketenes **1a–1d** ( $\text{RCH}=\text{CHCH}_2\text{X}-\text{CH}_2\text{CH}=\text{C}=\text{O}$ : **1a** R = H, X =  $\text{CH}_2$ ; **1b** R = Ph, X =  $\text{CH}_2$ ; **1c** R = *c*-Pr, X =  $\text{CH}_2$ ; **1d** R = H, X = O), which were observed by IR at 2121, 2120, 2119, and 2126  $\text{cm}^{-1}$ , respectively, as relatively long-lived species at room temperature in hydrocarbon solvents. These reacted with the nitroxyl radical tetramethylpiperidinyloxy (TEMPO, TO $\cdot$ ) forming carboxy-substituted 5-hexenyl radicals **3**, which were trapped by a second nitroxyl radical forming 1,2 diaddition products **4a–4d**. On thermolysis, **4a–4d** underwent reversible reformation of the radicals **3**, which underwent cyclization forming cyclopentanecarboxylic acid derivatives **6** or **11** as the major products. However, in the case of **1b**, the cyclopentane derivative was formed reversibly and on prolonged reaction times the only product isolated was  $\text{PhCH}=\text{CH}-(\text{CH}_2)_4\text{CO}_2\text{H}$  (**8b**) from hydrogen transfer to  $\text{C}_\beta$  and cleavage of the TEMPO group. Cyclopropylcarbinyl radical ring opening in the cyclized radical **5c** from **1c** led to the 2-(4-*N*-tetramethylpiperidinyloxybut-1-enyl)cyclopentane derivative **11** as the major product. In a test for 5-hexenyl radical ring closure in the radical anion intermediate of the acyloin condensation, the ester  $\text{CH}_2=\text{CH}(\text{CH}_2)_3\text{CO}_2\text{Et}$  (**12a**) gave the acyloin **13a** (76%) as the only observed product, while  $\text{PhCH}=\text{CH}(\text{CH}_2)_3\text{CO}_2\text{CH}_3$  (**12b**) with Na in toluene gave 21% of the acyloin product **13b** and 42% of 2-benzylcyclopentanol (**15**) from cyclization of the intermediate radical anion.

**Key words:** ketenes, free radical cyclization, TEMPO, acyloin condensation.

**Résumé :** On a utilisé les réarrangements photochimiques de Wolff pour produire des 4-penténylcétènes substitués en position 5 **1a–1d** ( $\text{RCH}=\text{CHCH}_2\text{XCH}_2\text{CH}=\text{C}=\text{O}$  : **1a** R = H, X =  $\text{CH}_2$  ; **1b** R = Ph, X =  $\text{CH}_2$  ; **1c** R = *c*-Pr, X =  $\text{CH}_2$  ; **1d** R = H, X = O). On a observé ces produits en IR à 2121, 2120, 2119 et 2126  $\text{cm}^{-1}$  respectivement, comme étant relativement des espèces à longue durée de vie dans des solvants hydrocarbonés à la température ambiante. Ces produits substitués réagissent avec le radical nitroxyle tétraméthylpipéridinoxyle (TEMPO, TO $\cdot$ ) en formant des radicaux 5-hexényles portant un substituant carboxy **3**, qui sont piégés par un deuxième radical nitroxyle pour donner des produits de diaddition 1,2 **4a–4d**. Par thermolyse, ces produits **4a–4d** redonnent de façon réversible le radical **3** qui par cyclisation forme les dérivés de l'acide cyclopentanecarboxylique **6** ou **11** comme produits majoritaires. Toutefois dans le cas du composé **1b** le dérivé cyclopentane se forme de façon réversible, et en prolongeant les temps de réaction le seul produit obtenu est le :  $\text{PhCH}=\text{CH}(\text{CH}_2)_4\text{CO}_2\text{H}$  (**8b**) résultant du transfert d'hydrogène sur  $\text{C}_\beta$  et du clivage du groupe TEMPO. L'ouverture du cycle du radical cyclopropylcarbinyle dans le radical cyclisé **5c** obtenu à partir du composé **1c** conduit au dérivé 2-(4-*N*-tétraméthylpipéridinyloxybut-1-ényl)cyclopentane **11** comme produit majoritaire. Dans un essai de cyclisation du radical 5-hexényle de l'anion radicalaire intermédiaire de la condensation acyloïne, l'ester  $\text{CH}_2=\text{CH}(\text{CH}_2)_3\text{CO}_2\text{Et}$  (**12a**) donne l'acyloïne **13a** (76%) comme seul produit observé, tandis que le composé  $\text{PhCH}=\text{CH}(\text{CH}_2)_3\text{CO}_2\text{CH}_3$  (**12b**) avec le Na dans le toluène donne 21% de l'acyloïne **13b** et 42% de 2-benzylcyclopentanol (**15**) à partir de la cyclisation de l'anion radicalaire intermédiaire.

**Mots clés :** cétènes, radical libre, cyclisation, TEMPO, condensation acyloïne.

[Traduit par la Rédaction]

## Introduction

As part of our studies of the reactions of ketenes with aminoxyl radicals (1), we have examined the reactivity of 4-pentenylketenes **1a**, **1b** with TEMPO (TO $\cdot$ ) (1a). For **1a** (R = H, X =  $\text{CH}_2$ ) and **1b** (R = Ph, X =  $\text{CH}_2$ ) generated from

diazo ketones **2** (eq. [1]) these reactions were found to proceed by radical attack at the carbonyl carbon forming enolic radicals **3** which then were trapped by a second TEMPO giving the 1,2-diaddition products **4** (eqs. [2] and [3]). Cyclization of the intermediate 5-hexenyl radicals **3** forming cyclopentylmethyl radicals **5** and capture as cyclopentanes **6** was

Received 8 January 2003. Published on the NRC Research Press Web site at <http://canjchem.nrc.ca> on 18 June 2003.

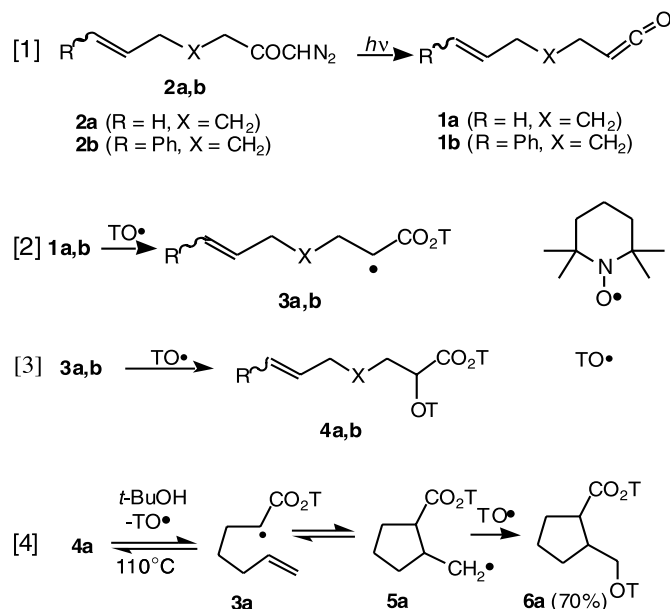
This paper is dedicated to Professor Don Arnold in recognition of his many achievements in chemistry.

H. Henry-Riyad and T.T. Tidwell.<sup>1</sup> Department of Chemistry, University of Toronto, Toronto, ON M5S 3H6, Canada.

<sup>1</sup>Corresponding author (e-mail: [ttidwell@chem.utoronto.ca](mailto:ttidwell@chem.utoronto.ca)).



evidently too slow to compete with capture of **3** by TEMPO at these concentrations. However, on thermolysis of **4a** in *tert*-butyl alcohol according to the protocol of Studer (2a) cyclization forming **6a** was successful, indicating that upon equilibration of **3a** and **4a** cyclization to **5a** was followed by capture by TEMPO forming **6a** as a *cis-trans* mixture (eq. [3]).



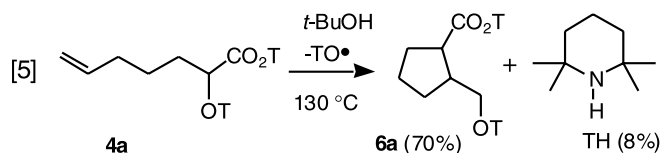
However, when the 1, 2-bis(TEMPO) addition product **4b** from 5-phenyl-4-pentenylketene (**1b**) was heated as in eq. [4], the corresponding cyclization product **6b** was not observed, and other reactions appeared to be taking place (**1a**). Further investigations have now been carried out to elucidate the behavior of **4b**, and the reactivity of 5-cyclopropyl-4-pentenylketene **1c** as well as the 2-oxa-4-pentenylketene analogue **1d** have been studied, and the results are reported here.

The reactions of ketenes with TEMPO and the reactions of these substrates are of interest because of current studies of the reactions of TEMPO with free radicals and the chemistry of the adducts (2, 3), especially in living free radical polymerization (4). Free radical rearrangements are also of wide applicability in organic synthesis (5, 6). In other recent studies designed to examine the formation and reaction of TEMPO esters, we have reported the thermal reactivity of  $\text{Ph}_3\text{CCO}_2\text{T}$  (**1j**) and the addition of TEMPO to the unreactive ketenes  $\text{CH}_2=\text{C}=\text{O}$  and  $\text{PhMe}_2\text{SiCH}=\text{C}=\text{O}$  (**1k**).

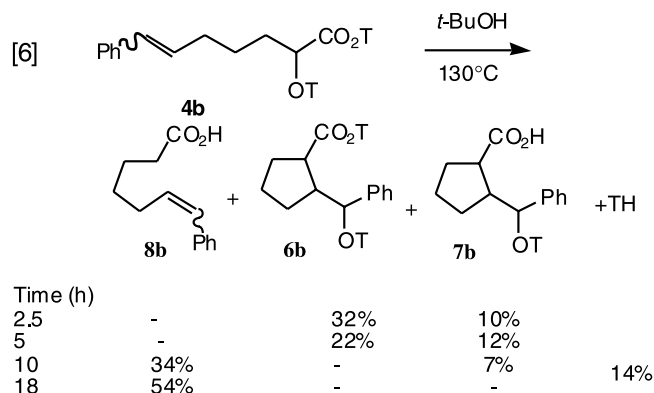
## Results

The thermolysis reaction of the bis(TEMPO) adduct **4a** (**1a**) from **1a** in *tert*-butyl alcohol by the protocol of Studer (2a) was reexamined, and, in addition to the cyclized TEMPO ester **6a** (70%), tetramethylpiperidine (TH, 8%) was also identified (eq. [5]). The presence of carboxylic acid absorption in the IR was also detected in the crude product, but the acid was not isolated.

Heating the bis(TEMPO) adduct **4b** (**1a**) of 5-phenyl-4-pentenylketene **1b** at 130°C for 18 h in *tert*-butyl alcohol

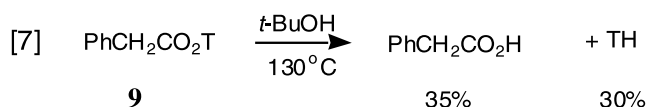


gave no detectable cyclized product, but instead the carboxylic acid **8b** was isolated (54%), along with TH (14%). Experiments at shorter time intervals revealed that **8b** was not the first formed product, but the cyclized ester **6b** (mixture of stereoisomers) was present early in the reaction, as well as the cyclized acid **7b** (eq. [6]).

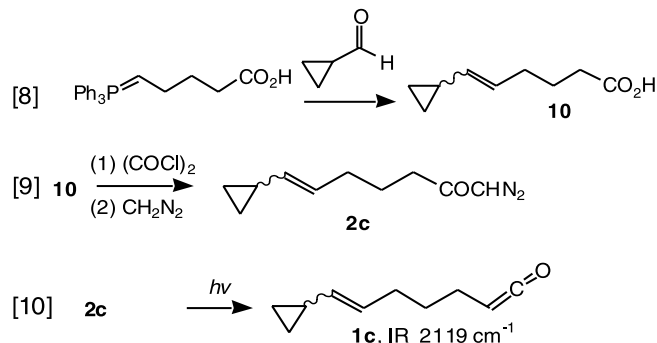


As a test of the source of carboxylic acids and TH in these reactions, the thermolysis of the ester **9** of phenylacetic acid and 2,2,6,6-tetramethylpiperidinol under Studer's conditions was examined. This reaction was found to give phenylacetic acid (35%) and TH (30%) after 7 days at 130°C (eq. [7]).

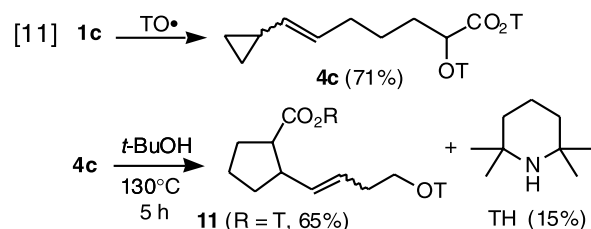
The cyclopropyl group serves as a useful clock for investi-



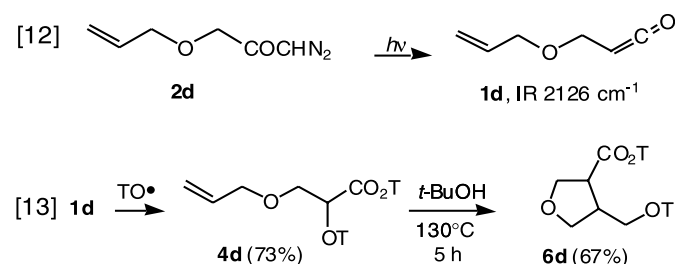
gating the presence of free radicals and so the new 5-cyclopropyl-substituted 4-pentenyl diazomethyl ketone **2c** was prepared as shown (eqs. [8] and [9]). Photolysis of **2c** gave the ketene **1c** as identified by the IR absorption at  $2119\text{ cm}^{-1}$  (eq. [10]), and addition of TEMPO to the pre-formed ketene gave the 1,2-diaddition product **4c** in 71% yield (eq. [11]). Thermolysis of **4c** resulted in the formation of the cyclized ester **11** (mixture of stereoisomers) in 65% yield, along with TH in 15% yield (eq. [11]).



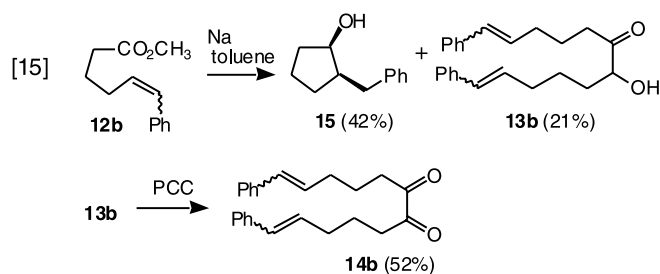
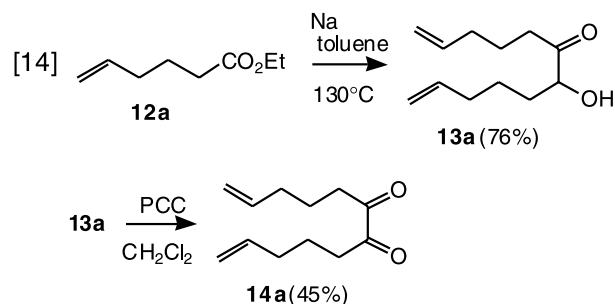




The incorporation of hetero atoms in 5-hexenyl radical chains is a method to enhance their propensity for cyclization to cyclopentylmethyl radicals (4), and so the ketene precursor 2-oxa-4-pentenyl diazomethyl ketone **2d** was prepared from 3-oxa-5-hexenoic acid (**7h**) by conversion to the acyl chloride and reaction with diazomethane. Photolysis of **2d** in pentane at room temperature gave the ketene **1d**, as identified by its ketenyl IR absorption at  $2126\text{ cm}^{-1}$  (eq. [12]), and upon reaction with TEMPO this gave the product **4d** of 1,2-addition of two molecules of TEMPO to the ketenyl moiety (eq. [13]). Thermolysis of **4d** in *tert*-butanol at  $130^\circ\text{C}$  gave the cyclized product **6d** (*cis-trans* mixture) in 67% yield (eq. [13]).



The acyloin condensation (8) is a reaction proposed to involve radical anion intermediates formed by electron transfer from sodium to esters, but we are unaware of examples of radical cyclization under these conditions. As a further test of the cyclization of 5-hexenyl radicals, the acyloin condensations of ethyl 5-hexenoate (**12a**) (**7j**) and methyl 6-phenyl-5-hexenoate (**12b**) (**7b**, **7i**) were investigated. Reaction of **12a** with sodium in toluene gave the acyloin **13a** in 76% yield as the only isolated product (eq. [14]), and for further characterization this was oxidized to the diketone **14a** (45%). Similar reaction of **12b** gave the cyclized product *cis*-2-benzylcyclopentane **15** (42%) along with the acyloin **13b** (21%) (eq. [15]). Oxidation of **13b** formed the corresponding  $\alpha$ -diketone **14b** (52%). The stereochemistry of **15** was assigned by comparison with the reported spectra (**7j**).

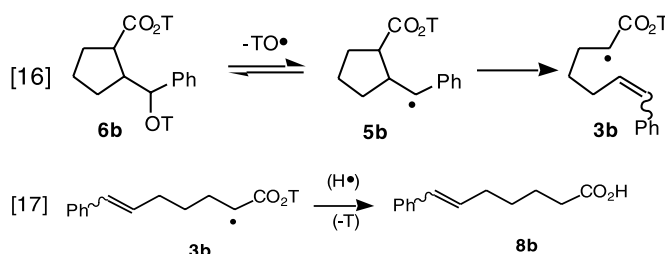


## Discussion

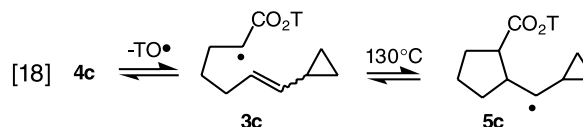
As already reported (**1a**), the formation of the cyclized product **6a** (eq. [4]) is in accord with the mechanism in which the initially formed product **4a** of 1,2-diaddition of TEMPO reforms the radical **3a** upon heating, and this undergoes cyclization leading to **6a**, which is stable to ring opening. The formation of carboxylic acids and TH as observed from **4a–4c** and from  $\text{PhCH}_2\text{CO}_2\text{T}$  (**9**) under these conditions is however unusual, and this reaction is under further investigation.

2-Oxa-4-pentenylketene (**1d**) reacted similarly to **1a** with TEMPO (eq. [12]), and formed the cyclized product **6d** upon thermolysis in an analogous manner (eq. [13]). However, no improved efficiency of cyclization was observed compared to the carbon analogue **1a**.

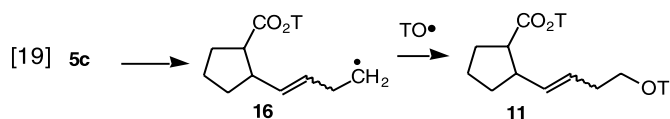
The initial 1,2-diaddition of TEMPO to 5-phenyl-pentenylketene **1b** (eqs. [2] and [3]) was also reported previously (**1a**). Upon heating this is also found to form the cyclized product **6b** at short reaction time, analogously to the previously observed formation of **6a** (eq. [4]). However, **6b** is reactive under these conditions, and is gradually converted to **8b**, evidently by reforming the intermediate radical **5b** which reopens to **3b**, which abstracts hydrogen and also undergoes loss of the TEMPO group as found for  $\text{PhCH}_2\text{CO}_2\text{T}$  (eqs. [16] and [17]).



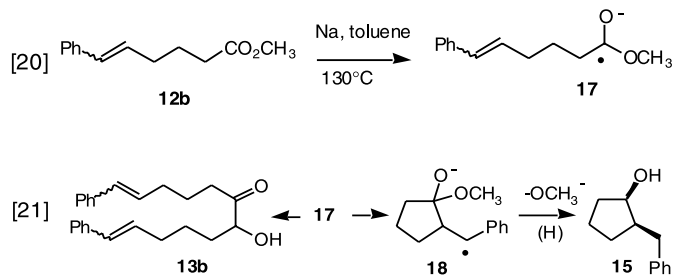
The formation of **11** (eq. [11]) in the reaction of TEMPO with 5-cyclopropyl-4-pentenylketene (**1c**) indicates that radical **3c** is formed by TEMPO dissociation from **4c**, and then undergoes cyclization to **5c** (eq. [18]). Ring opening of **5c** gives **16** which is captured by TEMPO forming **11** (eq. [19]).







The possibility of 5-hexenyl radical cyclization during the acyloin condensation does not appear to have been previously examined, but acyloin reactions of linoleic and oleic esters gave the normal acyloin products, and did not undergo the potential radical cyclization which would form 10-membered rings (**8a**). In this study, ethyl 5-hexenoate (**12a**), which could form a five-membered ring by radical cyclization, gave the normal acyloin product (eq. [14]). However, when the double bond is activated with a phenyl substituent cyclization does occur with the formation of **15** from **12b** (eq. [15]). Evidently the intermediate radical anion **17** from single electron transfer to **12b** (eq. [20]) undergoes competitive acyloin condensation, forming **13b**, and cyclization leading to **15** via **18** (eq. [21]). Related radical cyclizations of radical anions from ketones are known (**5b**). The scope and mechanism of this interesting reaction are under further study.



In summary, radical cyclization of the 5-hexenyl radicals **3** resulting from TEMPO addition to 4-pentenylketenes **1** does not compete with the addition of a second TEMPO forming the 1,2-diaddition products **4**. However, upon heating under the conditions of Studer (**2a**) the products **4** reversibly reform **3**, which cyclize to cyclopentylmethyl radicals **5** which are captured by TEMPO for **1a** and **1d**, and for **1b** are in equilibrium with **3b**, which eventually reacts by hydrogen abstraction. The cyclopropyl derivative **5c** undergoes cyclopropylcarbinyl radical ring opening forming **11** after addition of TEMPO. Degradation of TEMPO esters to carboxylic acids and TH is noted, and is under further study. 5-Hexenyl radical cyclization is observed in the radical ion intermediate of the acyloin condensation when the double bond is activated with a phenyl substituent.

## Experimental

Chromatography was carried out on silica gel. Solutions for reactions of TEMPO products were degassed and kept under argon or nitrogen. Gas chromatography (GC) was carried out with a flame ionization detector and a Simplicity 5 column (poly-5% diphenylsiloxane – 95% dimethylsiloxane). The disubstituted alkenes studied were *cis-trans* isomers that were not separated but the NMR spectra were assigned from the mixtures.

Lithium hexamethyldisilazide was prepared, by addition to a solution of 1,1,1,3,3,3-hexamethyldisilazane (1.04 equiv) in

1 to 2 mL THF cooled in an ice water bath, of a hexane solution of *n*-butyllithium (1.0 equiv) via syringe, followed by stirring the mixture at room temperature for 15–30 min prior to use (**7d**).

(4-Carboxybutyl)triphenylphosphonium bromide (**7c**, **7f**, **7g**) was prepared by addition of  $\text{Ph}_3\text{P}$  (5.06 g, 19.3 mmol) to a solution of 5-bromovaleric acid (3 g, 16.6 mmol) in acetonitrile (7.5 mL). The resulting mixture was stirred at  $80^\circ\text{C}$  under reflux for 24 h, concentrated, and the residue was washed with benzene, hexane, and ether and dried giving (4-carboxybutyl)triphenylphosphonium bromide (6.75 g, 92%) as a white solid.  $^1\text{H}$  NMR (400 MHz,  $\text{CDCl}_3$ )  $\delta$ : 1.70 (m, 2,  $\text{CH}_2\text{CH}_2\text{CH}_2$ ), 1.91 (m, 2,  $\text{CHCH}_2\text{CH}_2$ ), 2.90 (t, 2,  $\text{CH}_2\text{CO}$ ,  $J = 6.9$  Hz), 3.68 (m, 1,  $\text{Ph}_3\text{PCH}$ ), 7.73–7.78 (m, 15, Ar).

## Thermolysis of **4a**

The bis-TEMPO adduct **4a** (20 mg, 0.047 mmol) in degassed *t*-BuOH (4 mL) was heated 24 h in a sealed ampoule at  $130^\circ\text{C}$ , and GC analysis indicated the presence of 2,2,6,6-tetramethylpiperidine ( $8 \pm 1\%$ ). The solvent was removed under reduced pressure and chromatography ( $\text{CHCl}_3$ –MeOH, 9:1) gave a product containing carboxylic acid based on the IR spectrum ( $\text{CDCl}_3$ ) 3516, 1745,  $1700\text{ cm}^{-1}$ . Base extraction and rechromatography ( $\text{CHCl}_3$ –MeOH, 9:1) afforded **6a** (14 mg, 70%, *E:Z* (45:55)) (**1a**). The carboxylic acid product was not recovered from the aqueous layer.

## Thermolysis of *N*-2,2,6,6-tetramethylpiperidinyl 2-(*N*-2,2,6,6-tetramethyl piperidinyl-7-phenyl-5-heptenoate (**4b**))

The bis-TEMPO adduct **4b** (20 mg, 0.040 mmol) under nitrogen in degassed *t*-BuOH (4 mL) was sealed in an ampoule and heated 18 h at  $132$ – $135^\circ\text{C}$  in a refluxing xylene bath. Gas chromatography showed the presence of TH ( $14 \pm 2\%$ ). The solvent was removed under reduced pressure and chromatography ( $\text{CHCl}_3$ –MeOH, 9:1) gave the known (**7b**) uncyclized acid **8b**  $\text{PhCH}=\text{CH}(\text{CH}_2)_4\text{CO}_2\text{H}$  (54%). IR ( $\text{CDCl}_3$ ) ( $\text{cm}^{-1}$ ): 1703, 3518.  $^1\text{H}$  NMR (400 MHz,  $\text{CDCl}_3$ )  $\delta$ : 1.54–1.83 (m, 4,  $\text{CH}_2\text{CH}_2\text{CO}_2\text{H}$ ), 2.23 (m, 2,  $\text{CHCH}_2\text{CH}_2$ ), 2.42 (m, 2,  $\text{CH}_2\text{CH}_2\text{CO}_2\text{H}$ ), 5.66 (m, 1, *cis*- $\text{PhCH}=\text{CH}$ ), 6.18 (m, 1, *trans*- $\text{PhCH}=\text{CH}$ ), 6.37 (m, 1,  $\text{PhCH}=\text{CH}$ ), 7.33 (m, 5, Ar).  $^{13}\text{C}$  NMR (100 MHz,  $\text{CDCl}_3$ )  $\delta$ : 24.5, 28.9, 32.8, 33.9, 126.2, 127.1, 128.7, 128.8, 128.9, 129.6, 130.4, 130.5, 131.3, 132.5, 137.6, 137.9, 178.8 (CO). EI-MS ( $m/z$ ): 204 ( $\text{M}^+$ ), 186, 157, 144, 130, 117, 104, 91, 77, 65. HR-EI-MS ( $m/z$ ) calcd. for  $\text{C}_{13}\text{H}_{16}\text{O}_2$ : 204.1143; found: 204.1150.

Heating of **4b** with shorter reaction times gave *N*-2,2,6,6-tetramethyl-piperidinyl 2-(phenyl-*N*-2,2,6,6-tetramethylpiperidinyl-oxymethyl)cyclopentanecarboxylate (**6b**) which was purified by chromatography ( $\text{CH}_2\text{Cl}_2$ ).  $^1\text{H}$  NMR (500 MHz,  $\text{CDCl}_3$ )  $\delta$ : 2.66–2.85 (m, 44), 3.25–3.28 (m, 1,  $\text{CHCO}_2\text{T}$ ), 4.76 (d, 1,  $\text{CHPhOT}$ ,  $J = 6.8$  Hz), 7.22–7.39 (m, 5, Ar).  $^{13}\text{C}$  NMR (125 MHz,  $\text{CDCl}_3$ )  $\delta$ : 17.2, 17.3, 20.5, 20.6, 23.4, 24.8, 28.7, 29.1, 29.7, 31.1, 31.9, 32.1, 32.2, 32.3, 32.7, 39.0, 39.1, 39.2, 39.25, 45.7, 47.3, 59.8, 60.1, 87.7  $\text{CH}(\text{OT})\text{Ph}$ , 126.0, 127.2, 127.5, 128.5, 128.9, 131.0, 137.7, 140.9, 175.5 (CO). EI-MS ( $m/z$ ): 499 ( $\text{M}^+$ ), 326, 187, 157, 140, 117, 91, 69, 55. HR-EI-MS ( $m/z$ ) calcd. for  $\text{C}_{31}\text{H}_{51}\text{N}_2\text{O}_3$ : 499.3907; found: 499.3900. IR ( $\text{CDCl}_3$ ) ( $\text{cm}^{-1}$ ): 1751. Further chromatography ( $\text{EtOAc}$ –MeOH, 3:7) gave 2-(phenyl-*N*-2,2,6,6-tetramethylpiperidinyl-oxymethyl)cyclo-



pentane carboxylic acid (**7b**). IR (CDCl<sub>3</sub>) (cm<sup>-1</sup>): 3513, 1701. <sup>1</sup>H NMR (500 MHz, CDCl<sub>3</sub>) δ: 1.06–2.38 (m, 24), 2.78–2.80 (m, 1, CHCHOTPh), 2.98–3.02 (m, 1, CHCO<sub>2</sub>H), 4.80 (d, 1, CHOTPh) *J* = 8.9 Hz, 7.23–7.36 (m, 5, Ar). <sup>13</sup>C NMR (125 MHz, CDCl<sub>3</sub>) δ: 17.4, 21.5, 22.9, 25.4, 30.3, 31.8, 38.5, 40.0, 46.9, 47.7, 53.7, 61.2, 88.8 (CHOTPh), 126.5, 127.6, 128.0, 128.6, 129.1, 130.1, 130.4, 139.7, 178.9 (CO). EI-MS (*m/z*): 360 (M<sup>+</sup>), 293, 239, 203, 185, 157, 142, 125, 91, 69, 55. HR-EI-MS (*m/z*) calcd. for C<sub>22</sub>H<sub>34</sub>NO<sub>3</sub>: 360.2534; found: 360.2539.

### 6-Cyclopropyl-5-hexenoic acid (**10**)

4-Carboxy-*n*-butyltriphenylphosphonium bromide (5 g, 11.3 mmol) in THF (15 mL) was treated with lithium hexamethyldisilazide (23.7 mmol) in THF (4 mL) at 25°C with stirring. After 15 min, cyclopropanecarboxaldehyde (0.79 g, 11.3 mmol) in THF (5 mL) was added at 25°C, rapidly decolorizing the red-orange mixture. After 15 min, water (25 mL) and ether (25 mL) were added. The organic phase was rinsed with 20 mL of water. The combined aqueous solution was washed with EtOAc (25 mL), acidified with 10% HCl, and extracted with EtOAc. The united EtOAc extracts were rinsed with H<sub>2</sub>O, dried with Na<sub>2</sub>SO<sub>4</sub>, and concentrated. Kugelrohr distillation gave **10** (1.12 g, 64%) (*E/Z* isomers, 1:1). <sup>1</sup>H NMR (400 MHz, CDCl<sub>3</sub>) δ: 0.30–0.32 (m, 2), 0.63–0.67 (m, 2, *E*-isomer), 0.69–0.73 (m, 2, *Z*-isomer), 1.49–1.58 (m, 1), 1.65–2.41 (m, 6), 4.80 (dd, 1, *J* = 10.6, 9.8 Hz, *c*-PrHCH=CH, *Z*-isomer), 5.02 (dd, 1, *J* = 15.2, 8.2 Hz, *c*-PrHCH=CH, *E*-isomer), 5.30 (dt, 1, *J* = 10.6, 6.2 Hz, CH=CHCH<sub>2</sub>, *Z*-isomer), 5.45 (dt, 1, *J* = 15.2, 6.4 Hz, CH=CHCH<sub>2</sub>, *E*-isomer).

### 6-Cyclopropyl-5-hexenoyl chloride

Oxalyl chloride (1.05 g, 8 mmol) was added dropwise to a stirred solution of 6-cyclopropyl-5-hexenoic acid (**10**, 0.76 g, 4 mmol) in CCl<sub>4</sub> (10 mL) and stirred for 2 h. The solvent was removed in vacuo to give 6-cyclopropyl-5-hexenoyl chloride as a dark brown oil (1.20 g, 92%) containing *E/Z* (50:50), used subsequently without further purification. <sup>1</sup>H NMR (400 MHz, CDCl<sub>3</sub>) δ: 0.31–0.32 (m, 2), 0.71–0.73 (m, 2, *E*-isomer), 0.74–0.79 (m, 2, *Z*-isomer), 1.52–1.6 (m, 1), 1.90 (distorted q, 2, CH<sub>2</sub>CH<sub>2</sub>CH<sub>2</sub>), 2.32 (dt, 2, CHCH<sub>2</sub>CH<sub>2</sub>), 3.05 (t, 2, *J* = 7.2 Hz, CH<sub>2</sub>COCl), 4.84 (dd, 1, *J* = 10.5, 8.4 Hz, *c*-PrHCH, *Z*-isomer), 5.20 (dd, 1, *J* = 13.2, 7.7 Hz, *c*-PrHCH=CH, *E*-isomer), 5.35 (dt, 1, *J* = 9.4, 7.5 Hz, CH=CHCH<sub>2</sub>, *Z*-isomer), 5.50 (dt, 1, *J* = 11.4, 8.5 Hz, CH=CHCH<sub>2</sub>, *E*-isomer).

### 1-Diazo-7-cyclopropyl-6-hepten-2-one (**2c**)

6-Cyclopropyl-5-hexenoyl chloride (1.20 g, 7.0 mmol) in ether (5 mL) was added dropwise over a period of 0.5 h to a stirring cooled solution of 0.018 mol of diazomethane (3 equiv) in ether (60 mL) which the solution was stirred at 0°C for 2 h. Excess diazomethane was removed by evacuating with a water aspirator through an empty Erlenmeyer flask and quenched in acetic acid, and the solution was concentrated. Chromatography (EtOAc–hexane, 3:7) gave **2c** (0.92 g, 5.2 mmol, 74%) as a yellow oil containing *E/Z* isomers (47:53). IR (pentane) (cm<sup>-1</sup>): 2102, 1662. <sup>1</sup>H NMR (400 MHz, CDCl<sub>3</sub>) δ: 0.29–0.32 (m, 2), 0.63–0.66 (m, 2, *E*-isomer), 0.69–0.74 (m, 2, *Z*-isomer), 1.32–1.34 (m, 1, *E*-iso-

mer), 1.48–1.53 (m, 1, *Z*-isomer), 1.73 (distorted q, 2, CH<sub>2</sub>CH<sub>2</sub>CH<sub>2</sub>), 2.00–2.35 (m, 4), 4.80 (dd, 1, *J* = 10.6, 6.3 Hz, *c*-PrHCH=CH, *Z*-isomer), 4.98 (dd, 1, *J* = 12.3, 8.2 Hz, *c*-PrHCH=CH, *E*-isomer), 5.23 (s, 1, COCHN<sub>2</sub>), 5.28 (dt, 1, *J* = 10.4, 9.9 Hz, CH=CHCH<sub>2</sub>, *Z*-isomer), 5.45 (dt, 1, *J* = 13.2, 6.4 Hz, CH=CHCH<sub>2</sub>, *E*-isomer). <sup>13</sup>C NMR (100 MHz, CDCl<sub>3</sub>) δ: 7.2, 10.0, 13.9, 25.4, 27.2, 32.2, 126.9 (CH=CHCH<sub>2</sub>), 135.3 (*c*-PrCH=CH), 195.2 (CO). EI-MS *m/z*: 179 (MH<sup>+</sup>), 149 (M<sup>+</sup> – N<sub>2</sub>), 135, 121, 107, 91. HR-EI-MS *m/z* calcd. for C<sub>10</sub>H<sub>14</sub>N<sub>2</sub>O: 179.1186; found: 179.1184.

### 5-Cyclopropyl-4-pentenylketene (**1c**) and reaction with TEMPO

1-Diazo-7-cyclopropyl-6-hepten-2-one (**2c**, 100 mg, 0.56 mmol) in pentane (75 mL) was photolyzed for 30 min with 250-nm light to give ketene **1c** (IR: 2119 cm<sup>-1</sup>). TEMPO (183 mg, 1.18 mmol, 2.1 equiv) was added to the preformed ketene and the solution was left stirring at room temperature for 24 h. Chromatography with CH<sub>2</sub>Cl<sub>2</sub> gave **4c** (191 mg, 0.40 mmol, 71%) *E/Z* isomers (50:50). IR (CDCl<sub>3</sub>) (cm<sup>-1</sup>): 1770. <sup>1</sup>H NMR (400 MHz, CDCl<sub>3</sub>) δ: 0.28–0.31 (m, 2), 0.62–0.65 (m, 2, *E*-isomer), 0.68–0.72 (m, 2, *Z*-isomer), 1.08–2.20 (m, 43), 4.48 (distorted t, 1, CH<sub>2</sub>CHOT), 4.75 (dd, 1, *J* = 10.2, 7.3 Hz, *c*-PrHCH=CH, *Z*-isomer), 4.92 (dd, 1, *J* = 9.4, 8.2 Hz, CH=CHCH<sub>2</sub>, *E*-isomer), 5.31 (dt, 1, *c*-PrHCH=CH, *Z*-isomer), 5.45 (dt, 1, *J* = 13.9, 7.5 Hz, CH=CHCH<sub>2</sub>, *E*-isomer). <sup>13</sup>C NMR (100 MHz, CDCl<sub>3</sub>) δ: 6.6, 7.1, 9.8, 13.7, 17.2, 17.4, 20.8, 20.9, 24.7, 24.9, 27.8, 32.1, 32.3, 32.4, 32.6, 34.8, 39.5, 40.7, 60.2, 60.5, 83.7 (CHOT), 127.6, 127.7 (CH=CHCH<sub>2</sub>), 134.6, 134.7 (*c*-PrCH=CH), 171.9 (CO<sub>2</sub>T). EI-MS *m/z*: 464 (MH<sup>+</sup>), 448 (M<sup>+</sup> – CH<sub>3</sub>), 322 (M<sup>+</sup> – T), 306, 278, 182, 156 (TO<sup>+</sup>), 140 (T<sup>+</sup>), 126, 83, 55. HR-EI-MS *m/z* calcd. for MH<sup>+</sup> C<sub>28</sub>H<sub>51</sub>N<sub>2</sub>O<sub>3</sub>: 463.3869; found: 463.3899.

### Thermolysis of **4c**

The bis-TEMPO adduct **4c** (50 mg, 0.108 mmol) in degassed *t*-BuOH (5 mL) was heated in a sealed ampoule at 130°C for 18 h. GC analysis indicated the presence of 2,2,6,6-tetramethylpiperidine (15 ± 2%). Concentration and chromatography (CHCl<sub>3</sub>–MeOH, 9:1) afforded the cyclized ester **11** containing carboxylic acid. IR (CDCl<sub>3</sub>) (cm<sup>-1</sup>): 3512, 1740, 1702. Base extraction and chromatography (CH<sub>2</sub>Cl<sub>2</sub>–MeOH, 9:1) afforded ester **11** (32 mg, 0.069 mmol, 65%). IR (CDCl<sub>3</sub>) (cm<sup>-1</sup>): 1750. <sup>1</sup>H NMR (500 MHz, CDCl<sub>3</sub>) δ: 1.08–2.00 (m, 42), 2.22 (dt, 2, CH<sub>2</sub>CH<sub>2</sub>OT), 2.51 (m, 1, *Z*-CHCO<sub>2</sub>T), 2.79 (m, 1, *E*-CHCO<sub>2</sub>T), 3.71–3.74 (t, 2, *J* = 6.71 Hz, CH<sub>2</sub>OT), 5.43–5.48 (m, 1, *c*-PnCH=CH), 5.52–5.56 (m, 1, *c*-PnCH=CH). <sup>13</sup>C NMR (125 MHz, CDCl<sub>3</sub>) δ: 17.4, 20.4, 20.8, 24.2, 24.8, 25.0, 30.0, 30.4, 31.5, 32.2, 33.3, 33.6, 39.8, 47.7, 50.4, 56.0, 76.5 (CH<sub>2</sub>OT), 127.5 (CH=CHCH<sub>2</sub>), 133.9 (*c*-PnCH=CH), 180.6 (CO<sub>2</sub>T). EI-MS *m/z*: 463 (MH<sup>+</sup>), 447 (M<sup>+</sup> – CH<sub>3</sub>), 306 (M<sup>+</sup> – OT), 278 (M<sup>+</sup> – CO<sub>2</sub>T), 182, 156 (TO), 140 (T), 126, 109, 93, 83, 69, 55. HR-EI-MS *m/z* calcd. for C<sub>28</sub>H<sub>50</sub>N<sub>2</sub>O<sub>3</sub>: 462.3816; found: 462.3821.

### Allyloxyacetyl chloride

Oxalyl chloride (3.99 g, 2.7 mL, 0.03 mol) was added dropwise to a stirred solution of allyloxyacetic acid (7 h, 1.75 g, 0.015 mol) in dichloromethane (20 mL) followed by



stirring at room temperature for 2 h. The solvent was removed in vacuo to give allyloxyacetyl chloride as a yellow oil (1.85 g, 0.0137 mol, 92%) used subsequently without further purification.  $^1\text{H}$  NMR (400 MHz,  $\text{CDCl}_3$ )  $\delta$ : 4.12–4.23 (m, 4,  $\text{CH}_2\text{OCH}_2\text{COCl}$ ), 5.26–5.39 (m, 2,  $\text{CH}_2=\text{CH}$ ), 5.85–5.98 (m, 1,  $\text{CH}_2=\text{CH}$ ).

### 1-Diazo-4-oxa-6-hexen-2-one (2d)

Allyloxyacetyl chloride (1 g, 7 mmol) was dissolved in ether (5 mL) and added dropwise over 0.5 h to a stirring cooled solution of diazomethane (0.018 mol, 2.5 equiv) in ether (100 mL), and the solution was stirred cold for 2 h. The excess diazomethane was removed by evacuating with a water aspirator pump and quenched into acetic acid. Concentration and chromatography (EtOAc–hexane, 1:3) gave **2d** (0.71 g, 5.1 mmol, 69%) as a yellow oil. IR (pentane) ( $\text{cm}^{-1}$ ): 2107, 1661.  $^1\text{H}$  NMR (400 MHz,  $\text{CDCl}_3$ )  $\delta$ : 3.95–4.04 (m, 4,  $\text{CH}_2\text{OCH}_2\text{COHN}_2$ ), 5.17–5.37 (m, 2,  $\text{CH}_2=\text{CH}$ ), 5.73 (s, 1,  $\text{COCHN}_2$ ), 5.79–5.92 (m, 1,  $\text{CH}_2=\text{CH}$ ).  $^{13}\text{C}$  NMR (100 MHz,  $\text{CDCl}_3$ )  $\delta$ : 53.3, 57.3, 67.2, 76.4, 118.1 ( $\text{CH}=\text{CHCH}_2$ ), 133.7 ( $\text{CH}=\text{CH}$ ), 193.9 (CO). EI-MS  $m/z$ : 141 ( $\text{MH}^+$ ), 84, 69, 55. HR-EI-MS  $m/z$  calcd. for  $\text{MH}^+$   $\text{C}_6\text{H}_9\text{N}_2\text{O}_2$ : 141.0657; found: 141.0664.

### (2-Oxa-4-pentenyl)ketene (1d) and reaction with TEMPO

1-Diazo-3-allyloxy-2-propanone (**2d**, 250 mg, 1.8 mmol) in 75 mL of pentane was photolyzed for 60 min with 250-nm light to give the corresponding ketene (IR:  $2126\text{ cm}^{-1}$ ). TEMPO (585 mg, 3.8 mmol, 2.1 equiv) was added to the preformed ketene and the solution was stirred at room temperature for 6 h. Concentration and chromatography ( $\text{CH}_2\text{Cl}_2$ ) gave the bis-adduct **4d** (562 mg, 1.32 mmol, 73%). IR ( $\text{CDCl}_3$ ) ( $\text{cm}^{-1}$ ): 1773.  $^1\text{H}$  NMR (400 MHz,  $\text{CDCl}_3$ )  $\delta$ : 1.22–1.82 (m, 36), 3.94–4.05 (m, 2,  $\text{OCH}_2\text{CHOT}$ ), 4.11 (d, 2,  $J = 4.2\text{ Hz}$ ,  $\text{CH}_2=\text{CHCH}_2\text{O}$ ), 4.68 (t, 1,  $J = 5.5\text{ Hz}$ ,  $\text{CHOT}$ ), 5.15–5.31 (m, 2,  $\text{CH}_2=\text{CH}$ ), 5.83–5.94 (m, 1,  $\text{CH}_2=\text{CH}$ ).  $^{13}\text{C}$  NMR (100 MHz,  $\text{CDCl}_3$ )  $\delta$ : 17.4, 17.5, 20.6, 20.8, 21.0, 21.1, 32.4, 34.0, 34.4, 39.6, 39.7, 40.8, 60.5, 60.7, 70.1, 72.8, 83.6 ( $\text{CHOT}$ ), 117.7 ( $\text{CH}_2=\text{CH}$ ), 135.0 ( $\text{CH}_2=\text{CH}$ ), 170.5 ( $\text{CO}_2\text{T}$ ). EI-MS  $m/z$ : 410 ( $\text{MH}^+ - \text{CH}_3$ ), 308, 285 ( $\text{M}^+ - \text{T}$ ), 268 ( $\text{M}^+ - \text{TO}$ ), 240 ( $\text{M}^+ - \text{CO}_2\text{T}$ ), 156 ( $\text{TO}^+$ ), 140 (T), 126, 83, 69, 58. ES-MS  $m/z$  425 ( $\text{MH}^+$ ), 447 ( $\text{MNa}^+$ ), 463 ( $\text{MK}^+$ ).

The bis-TEMPO adduct **4d** (100 mg, 0.23 mmol) in degassed *t*-BuOH (5 mL) was heated for 5 h at  $135^\circ\text{C}$  in a refluxing xylene bath. After concentration chromatography ( $\text{CHCl}_3$ –MeOH, 9:1) gave the cyclized product **6d** (67 mg, 0.16 mmol, 67%). IR ( $\text{CDCl}_3$ ) ( $\text{cm}^{-1}$ ): 1756.  $^1\text{H}$  NMR (500 MHz,  $\text{CDCl}_3$ )  $\delta$ : 1.04–1.70 (m, 36), 2.74–2.97 (m, 2), 3.72–4.10 (m, 6,  $\text{CH}_2$ ).  $^{13}\text{C}$  NMR (125 MHz,  $\text{CDCl}_3$ )  $\delta$ : 17.3, 17.5, 20.2, 20.3, 20.4, 20.9, 23.0, 30.0, 32.2, 32.4, 32.5, 33.4, 33.5, 39.3, 39.4, 39.9, 41.5, 43.2, 46.1, 59.9, 60.2, 60.3, 74.9 ( $\text{CH}_2\text{OT}$ ), 172.9 ( $\text{CO}_2\text{T}$ ). EI-MS  $m/z$ : 341, 311, 270, 216, 156, 142, 126, 83, 69. ES-MS  $m/z$ : 447 ( $\text{MNa}^+$ ), 463 ( $\text{MK}^+$ ).

### 6-Phenyl-5-hexenoic acid (7b)

4-Carboxybutyltriphenylphosphonium bromide (2.0 g, 4.5 mmol) in dry THF (6 mL), under nitrogen, was treated with lithium hexamethyldisilazide (1.8 mL, 9.48 mmol). Af-

ter 15 min, water and ether were added, the organic phase was rinsed with water (20 mL) and the combined aqueous solution was washed with EtOAc (25 mL), acidified with 10% HCl, and extracted with EtOAc. The united EtOAc extracts were rinsed with  $\text{H}_2\text{O}$ , dried with  $\text{Na}_2\text{SO}_4$ , and concentrated. Kugelrohr distillation gave 6-phenyl-5-hexenoic acid (0.68 g, 80%) containing *trans/cis* isomers (87:13).  $^1\text{H}$  NMR (400 MHz,  $\text{CDCl}_3$ ) *trans*-isomer  $\delta$ : 1.70–2.56 (m, 6), 6.15 (m, 1,  $\text{PhCH}=\text{CH}$ ), 6.45 (m, 1,  $\text{PhCH}=\text{CH}$ ), 7.20 (m, 5, Ar), 10.65 (br s, 1,  $\text{CO}_2\text{H}$ ); *cis*-isomer  $\delta$ : 1.70–2.56 (m, 6), 5.60 (m, 1,  $\text{PhCH}=\text{CH}$ ), 6.45 (m, 1,  $\text{PhCH}=\text{CH}$ ), 7.20 (m, 5, Ar), 10.65 (br s, 1,  $\text{CO}_2\text{H}$ ).

### 6-Phenyl-5-hexenoyl chloride (7b)

Oxalyl chloride (1.05 g, 8 mmol) was added dropwise to a stirred solution of 6-phenyl-5-hexenoic acid (0.76 g, 4.0 mmol) in  $\text{CCl}_4$  (10 mL) followed by stirring at room temperature for 2 h. The solvent was removed in vacuo to give 6-phenyl-5-hexenoyl chloride as a yellow oil (0.81 g, 3.9 mmol, 97%) containing *E/Z* isomers (85:15), used subsequently without further purification.  $^1\text{H}$  NMR (400 MHz,  $\text{CDCl}_3$ )  $\delta$ : 1.89 (distorted q, 2,  $\text{CH}_2\text{CH}_2\text{CH}_2$ ), 2.29 (dt, 2,  $\text{CHCH}_2\text{CH}_2$ ), 2.95 (t, 2,  $J = 6.8\text{ Hz}$ ,  $\text{CH}_2\text{COCl}$ ), 6.16 (m, 1,  $\text{PhCH}=\text{CH}$ , *Z*-isomer), 5.61 (m, 1,  $\text{PhCH}=\text{CH}$ , *E*-isomer), 6.41 (m, 1,  $\text{PhCH}=\text{CH}$ , *E* and *Z* isomers), 7.31–7.36 (m, 5H, Ar).

### Methyl 6-phenylhex-5-enoate (12b) (7i)

To a stirred mixture of methanol (0.2 mL, 4.9 mmol) and triethylamine (0.62 mL, 4.9 mmol) in  $\text{CH}_2\text{Cl}_2$  (30 mL) at  $0^\circ\text{C}$  was added of 6-phenyl-5-hexenoyl chloride (1 g, 4.9 mmol). The reaction mixture was stirred for 20 min then 2 M HCl (10 mL) was added. The organic layer was washed with  $\text{NaHCO}_3$  and brine, dried, and concentrated. Chromatography ( $\text{CH}_2\text{Cl}_2$ ) yielded **12b**, (0.90 g, 4.4 mmol, 90%) as a yellow oil (*E/Z* isomers, 93:7).  $^1\text{H}$  NMR (400 MHz,  $\text{CDCl}_3$ ) *trans*-**12b**  $\delta$ : 1.82–1.88 (q, 2,  $\text{CH}_2\text{CH}_2\text{CH}_2$ ), 2.25–2.32 (dt, 2,  $\text{CHCH}_2\text{CH}_2$ ), 2.37–2.42 (t, 2,  $J = 4.9\text{ Hz}$ , 2,  $\text{CH}_2\text{CO}_2\text{CH}_3$ ), 3.69 (s, 3, *E*- $\text{OCH}_3$ ), 3.94 (s, 3, *Z*- $\text{OCH}_3$ ), 6.22 (m, 1,  $\text{PhCH}=\text{CH}$ ), 6.39 (m, 1,  $\text{PhCH}=\text{CH}$ ), 7.31–7.36 (m, 5, Ar).

### Acyloin reaction of 12a

Sodium metal (0.64 g, 28 mmol) and toluene (100 mL) were refluxed for 1 h with vigorous stirring, and ethyl hex-5-enoate (**7j**) (**12a**, 0.20 g, 20 mmol) in toluene (10 mL) was added dropwise over 20 min, and stirred a further 2 h. The solution was cooled and MeOH (15 mL) was added, the mixture was poured into water–EtOAc and acidified with 10% HCl, extracted with EtOAc, washed with water and  $\text{NaHCO}_3$ , dried, and concentrated. Chromatography (hexane–EtOAc, 7:3) gave **13a** (7-hydroxydodeca-1,11-diene-6-one, 2.08 g, 76%). IR ( $\text{CDCl}_3$ ) ( $\text{cm}^{-1}$ ): 1707, 3519.  $^1\text{H}$  NMR (400 MHz,  $\text{CDCl}_3$ )  $\delta$ : 1.61–1.82 (m, 6,  $\text{CH}_2\text{CH}_2\text{CH}_2$  and  $\text{CHOHCH}_2$ ), 2.04–2.18 (m, 4  $\text{C}=\text{CHCH}_2$ ), 2.40 (t, 2,  $J = 7.4\text{ Hz}$ ,  $\text{CH}_2\text{CO}$ ), 4.96–5.09 (m, 4,  $\text{CH}_2=\text{C}$ ), 5.75–5.85 (m, 2  $\text{CH}_2=\text{CH}$ ).  $^{13}\text{C}$  NMR (100 MHz,  $\text{CDCl}_3$ )  $\delta$ : 23.0, 23.9, 33.2, 33.5, 33.9, 38.9, 77.6 ( $\text{CHOH}$ ), 115.1, 115.8, 137.7, 138.5, 180.1 (CO). EI-MS  $m/z$ : 196 ( $\text{M}^+$ ), 182, 169, 167, 149, 125, 107, 99, 97, 81, 69, 55. HR-EI-MS  $m/z$  calcd. for  $\text{C}_{12}\text{H}_{20}\text{O}$ : 97.0656; found: 97.0653.



### Oxidation of 13a

Pyridinium chlorochromate (1.6 g, 7 mmol) and **13a** (1.0 g, 5.1 mmol) in  $\text{CH}_2\text{Cl}_2$  (20 mL) were heated at reflux for 1.5 h. The mixture was filtered through Celite, washed with ether, and the filtrate was concentrated. Chromatography (hexane–EtOAc, 7:3) gave dodeca-1,11-diene-6,7-dione (**14a**) as a yellow oil (0.44 g, 2.3 mmol, 45%). IR ( $\text{CDCl}_3$ ) ( $\text{cm}^{-1}$ ): 1711.  $^1\text{H}$  NMR (400 MHz,  $\text{CDCl}_3$ )  $\delta$ : 1.63–1.78 (m, 4,  $\text{CH}_2\text{CH}_2\text{CH}_2$ ), 2.08–2.19 (m, 4,  $\text{CHCH}_2$ ), 2.37 (t, 4,  $J = 7.2$  Hz,  $\text{CH}_2\text{CO}$ ), 4.98–5.12 (m, 4,  $\text{CH}_2=\text{CH}$ ), 5.77–5.83 (m, 2,  $\text{CH}_2=\text{CH}$ ).  $^{13}\text{C}$  NMR (100 MHz,  $\text{CDCl}_3$ )  $\delta$ : 24.6, 34.5, 52.0, 115.8, 138.7, 200.0 (CO). EI-MS  $m/z$ : 195 ( $\text{MH}^+$ ), 167, 153, 149, 140, 125, 97, 81, 69, 55. HR-EI-MS  $m/z$  calcd. for  $\text{C}_{12}\text{H}_{19}\text{O}_2$ : 195.1380; found: 195.1385.

### Acyloln reaction of 12b

Sodium metal (0.2 g, 8.6 mmol) and toluene (20 mL) were heated to reflux with vigorous stirring for 1 h. To this was added methyl 6-phenylhex-5-enoate (**12b**, 0.88 g, 4.3 mmol) in toluene (10 mL) dropwise over 20 min. Stirring was continued for a further 2 h. The solution was cooled and MeOH (2 mL) was added. The mixture was poured into water–EtOAc and acidified with 10% HCl, extracted with EtOAc, washed with water and  $\text{NaHCO}_3$ , dried, and concentrated. Chromatography (hexane–EtOAc, 7:3) afforded the cyclized product *cis*-**15** (**7j**) as a colourless oil (0.32 g, 1.8 mmol, 42%). IR ( $\text{CDCl}_3$ ) ( $\text{cm}^{-1}$ ): 3608.  $^1\text{H}$  NMR (400 MHz,  $\text{CDCl}_3$ )  $\delta$ : 1.25–2.14 (m, 8,  $3\text{CH}_2$ ,  $\text{CHCH}_2\text{Ph}$ , and  $\text{OH}$ ), 2.52–2.57 (m, 1,  $\text{CHHAr}$ ), 2.74–2.79 (m, 1,  $\text{CHHAr}$ ), 3.90–3.93 (m, 1,  $\text{CHOH}$ ), 7.28–7.37 (m, 4, Ar).  $^{13}\text{C}$  NMR (100 MHz,  $\text{CDCl}_3$ )  $\delta$ : 21.7, 30.1, 34.4, 40.0, 50.1, 78.8 ( $\text{CHOH}$ ), 126.2, 128.5, 128.6, 129.1, 141.3. EI-MS  $m/z$ : 176 ( $\text{M}^+$ ), 158 ( $\text{M}^+ - \text{H}_2\text{O}$ ), 143, 129, 117, 104, 98, 85, 67, 57. HR-EI-MS  $m/z$  calcd. for  $\text{C}_{12}\text{H}_{16}\text{O}$ : 176.1199; found: 176.1201. 1,12-Diphenyl-7-hydroxy-dodeca-1,11-dien-6-one (**13b**) was obtained as a yellow oil (0.31 g, 21%) 78:22 double bonds of *E/Z* isomers. IR ( $\text{CDCl}_3$ ) ( $\text{cm}^{-1}$ ): 1705, 3522.  $^1\text{H}$  NMR (400 MHz,  $\text{CDCl}_3$ )  $\delta$ : 1.79–1.84 (m, 6,  $2\text{CH}_2\text{CH}_2\text{CH}_2$  and  $\text{CHOHCH}_2$ ), 2.24–2.28 (m, 2,  $\text{CH}_2\text{CH}_2\text{CO}$ ), 2.33–2.36 (m, 4,  $2\text{CHCH}_2\text{CH}_2$ ), 5.59–5.63 (m, *Z*- $\text{PhCH}=\text{CH}$ ), 6.17–6.23 (m, *E*- $\text{PhCH}=\text{CH}$ ), 6.38–6.44 (m, 2,  $2\text{PhCH}=\text{CH}$ ), 7.21–7.39 (m, 10, Ar).  $^{13}\text{C}$  NMR (100 MHz,  $\text{CDCl}_3$ )  $\delta$ : 24.5, 27.4, 28.7, 32.4, 33.5, 37.5, 50.2, 79.4 ( $\text{CHOH}$ ), 126.2, 127.3, 128.4, 128.6, 128.7, 128.9, 129.6, 130.4, 131.2, 133.9, 137.8, 179.6 (CO). EI-MS  $m/z$ : 244 ( $\text{M}^+ - \text{PhCH}=\text{CH}$ ), 210, 190, 130, 117, 105, 91, 77. HR-EI-MS  $m/z$  calcd. for  $\text{C}_{16}\text{H}_{22}\text{O}_2$ : 244.1456; found: 244.1454.

### Oxidation of 13b

Pyridinium chlorochromate (0.35 g, 1.6 mmol) and **13b** (0.32 g, 1 mmol) in dry  $\text{CH}_2\text{Cl}_2$  (5 mL) were heated at reflux for 1.5 h. The black mixture was filtered through Celite, washed with ether, and the filtrate was concentrated. Chromatography (hexane–EtOAc, 7:3) gave 1,12-diphenyldodeca-1,11-diene-6,7-dione (**14b**) as a yellow oil (0.18 g, 52%), 81:19 *E/Z* double bonds. IR ( $\text{CDCl}_3$ ) ( $\text{cm}^{-1}$ ): 1711.  $^1\text{H}$  NMR

(400 MHz,  $\text{CDCl}_3$ )  $\delta$ : 1.81–1.94 (m, 4,  $\text{CH}_2\text{CH}_2\text{CH}_2$ ), 2.37–2.41 (m, 4,  $\text{CHCH}_2\text{CH}_2$ ), 2.43 (t, 4,  $\text{CH}_2\text{CH}_2\text{CO}$ ),  $J = 7.6$  Hz), 5.61–5.72 (m, *Z*- $\text{PhCH}=\text{CH}$ ), 6.18–6.28 (m, *E*- $\text{PhCH}=\text{CH}$ ), 6.40–6.58 (m, 2,  $\text{PhCH}=\text{CH}$ ), 7.17–7.45 (m, 10, Ar).  $^{13}\text{C}$  NMR (100 MHz,  $\text{CDCl}_3$ )  $\delta$ : 24.5, 29.9, 32.5, 126.2, 127.4, 128.2, 128.4, 128.7, 129.6, 130.5, 131.2, 197.0 (CO). EI-MS  $m/z$ : 243 ( $\text{M}^+ - \text{PhCH}=\text{CH}$ ), 215 ( $\text{M}^+ - \text{C}_{10}\text{H}_{11}$ ), 202 ( $\text{M}^+ - \text{C}_{11}\text{H}_{13}$ ), 190 ( $\text{M}^+ - \text{C}_{12}\text{H}_{13}$ ), 174 ( $\text{M}^+ - \text{C}_{12}\text{H}_{13}\text{O}$ ), 146 ( $\text{M}^+ - \text{C}_{13}\text{H}_{13}\text{O}_2$ ), 130, 117, 105, 91, 77. HR-EI-MS  $m/z$  calcd. for  $\text{C}_{16}\text{H}_{19}\text{O}_2$ : 243.1177; found: 243.1192.<sup>2</sup>

### Acknowledgements

Financial support by the Natural Sciences and Engineering Research Council of Canada, The Petroleum Research Fund administered by the American Chemical Society, and the Killam Foundation for the Arts for a Fellowship to T.T.T. is gratefully acknowledged.

### References

- (a) A.D. Allen, M.H. Fenwick, H. Henry-Riyad, and T.T. Tidwell. *J. Org. Chem.* **66**, 5759 (2001); (b) W. Huang, H. Henry-Riyad, and T.T. Tidwell. *J. Am. Chem. Soc.* **121**, 3939 (1999); (c) A.D. Allen, B. Cheng, M.H. Fenwick, W. Huang, S. Missiha, D. Tahmassebi, and T.T. Tidwell. *Organic Lett.* **1**, 693 (1999); (d) A.D. Allen, B. Cheng, M.H. Fenwick, B. Givehchi, H. Henry-Riyad, V.A. Nikolaev, E.A. Shikova, D. Tahmassebi, T.T. Tidwell, and S. Wang. *J. Org. Chem.* **66**, 2611 (2001); (e) J. Carter, M.H. Fenwick, W. Huang, V.V. Popik, and T.T. Tidwell. *Can. J. Chem.* **77**, 806 (1999); (f) A.D. Allen, H. Henry-Riyad, J. Porter, D. Tahmassebi, T.T. Tidwell. *J. Org. Chem.* **66**, 7420 (2001); (g) M.H. Fenwick and T.T. Tidwell. *Eur. J. Org. Chem.* **66**, 3415 (2001); (h) A.D. Allen, H. Rangwalla, K. Saidi, T.T. Tidwell, and J. Wang. *Russ. Chem. Bull.* 2130 (2001); (i) K. Sung and T.T. Tidwell. *J. Org. Chem.* **63**, 9690 (1998); (j) H. Henry-Riyad and T.T. Tidwell. *J. Phys. Org. Chem.* In press (2003); (k) A.D. Allen, H. Henry-Riyad, and T.T. Tidwell. *Arkivoc.* JM-597F (2002).
- (a) A. Studer. *Angew. Chem. Int. Ed.* **39**, 1108 (2000); (b) S. Marque, H. Fischer, E. Baier, and A. Studer. *J. Org. Chem.* **66**, 1146 (2001); (c) A.J. McCarroll and J.C. Walton. *J. Chem. Soc., Perkin Trans. 2*, 2399 (2000); (d) S. Marque, C. Le Mercier, P. Tordo, and H. Fischer. *Macromolecules*, **33**, 4403 (2000); (e) M.V. Ciriano, H.-G. Korth, W. van Scheppingen, and P. Mulder. *J. Am. Chem. Soc.* **121**, 6375 (1999); (f) J. Sobek, R. Martschke, and H. Fischer. *J. Am. Chem. Soc.* **123**, 2849 (2001); (g) T. Kothe, S. Marque, R. Martschke, M. Popov, and H. Fischer. *J. Chem. Soc., Perkin Trans. 2*, 1553 (1998).
- (a) D. Benoit, V. Chaplinski, and C.J. Hawker. *J. Am. Chem. Soc.* **121**, 3904 (1999); (b) R. Braslau, L.C. Burrill, II, M. Siano, N. Naik, R.K. Howden, and L.K. Mahal. *Macromolecules*, **30**, 6445 (1997); (c) T. Kothe, S. Marque, R. Martschke, M. Popov, and H. Fischer. *J. Chem. Soc., Perkin Trans. 2*, 1553 (1998); (d) U. Jahn. *J. Org. Chem.* **63**, 7130 (1998).
- (a) M.K. Georges, R.P.N. Veregin, P.M. Kazmaier, and G.K. Hamer. *Macromolecules*, **26**, 2987 (1993); (b) C.J. Hawker. *Acc. Chem. Res.* **30**, 373 (1997); (c) T.E. Patten and K. Matyjaszewski. *Acc. Chem. Res.* **33**, 895 (1999).

<sup>2</sup>Supplementary data ( $^1\text{H}$  NMR spectra) may be purchased from the Depository of Unpublished Data, Document Delivery, CISTI, National Research Council Canada, Ottawa, ON K1A 0S2, Canada ([http://www.nrc.ca/cisti/irm/unpub\\_e.shtml](http://www.nrc.ca/cisti/irm/unpub_e.shtml) for information on ordering electronically).



5. (a) A.L.J. Beckwith and K.U. Ingold. Free-radical rearrangements. In *Rearrangements in ground and excited states*. Vol. 1., Academic Press, New York. 1980. Chap. 4. pp. 161–310; (b) B. Geise, B. Kopping, T. Göbel, J. Dickhaut, G. Thoma, K.J. Kulicke, and F. Trach. *Org. React. N.Y.*, **48**, 301 (1996); (c) D.P. Curran, N.A. Porter, and B. Giese. *Stereochemistry of radical reactions*. VCH, New York. 1996. Chap. 2.
6. (a) M. Newcomb, T.R. Varick, C. Ha, M.B. Manek, and X. Yue. *J. Am. Chem. Soc.* **114**, 8158 (1992); (b) S.-U. Park, S.-K. Chung, and M. Newcomb. *J. Am. Chem. Soc.* **108**, 240 (1986); (c) C.-K. Sha, F.-K. Lee, and C.-J. Chang. *J. Am. Chem. Soc.* **121**, 9875 (1999); (d) D.P. Curran and C.-T. Chang. *J. Org. Chem.* **54**, 3140 (1989); (e) D.P. Curran, M.-H. Chen, E. Spletzer, C.M. Seong, and C.-T. Chang. *J. Am. Chem. Soc.* **111**, 8872 (1989); (f) M. Newcomb, J.H. Horner, M.A. Filipkowski, C. Ha, and S.-U. Park. *J. Am. Chem. Soc.* **117**, 3674 (1995).
7. (a) P. Ceccherelli, M. Curini, M.C. Marcotullio, and O. Rosati. *Tetrahedron*, **48**, 9767 (1992); (b) M.M. Fawzi and C.D. Gutsche. *J. Org. Chem.* **31**, 1390 (1966); (c) M.D.L.A. Rey, J.A. Martínez-Pérez, A. Fernández-Gacio, K. Halkes, Y. Fall, J. Granja, and A. Mourino. *J. Org. Chem.* **64**, 3196 (1999); (d) D.J. Hart, K. Kanai, D.G. Thomas, and T.-K. Yang. *J. Org. Chem.* **48**, 289 (1983); (e) E. Juaristi and H.A. Jiménez-Vázquez. *J. Org. Chem.* **56**, 1623 (1991); (f) B.E. Maryanoff and B.A. Duhl-Emswiler. *Tetrahedron Lett.* **22**, 4185 (1981); (g) S. Nagumo, A. Matsukuma, H. Suemune, and K. Sakai. *Tetrahedron*, **49**, 10 501 (1993); (h) M.J. Broadhurst, S.J. Brown, J.M. Percy, and M.E. Prime. *J. Chem. Soc., Perkin Trans 1*, 3217 (2000); (i) J. Lee, C.H. Kang, H. Kim, and J.K. Cha. *J. Am. Chem. Soc.* **118**, 291 (1996); (j) A.F. Simpson, C.D. Bodkin, C.P. Butts, M.A. Armitage, and T. Gallagher. *J. Chem. Soc., Perkin Trans. 1*, 3047 (2000).
8. (a) J.J. Bloomfield, D.C. Owsley, and D.M. Nelke. *Org. React. (N.Y.)*, **23**, 259 (1976); (b) T.S. Daynard, P.S. Eby, J.H. Hutchinson. *Can. J. Chem.* **71**, 1022 (1993); (c) M.J. Crossley, S. Gorjian, S. Sternhell, and K.M. Tansey. *Aust. J. Chem.* **47**, 723 (1994).



# The photochemistry of *trans*-1,4,4,4-tetraphenylbut-2-en-1-one: A highly efficient aryl migration (type B) enone photorearrangement

John R. Scheffer and Kodumuru Vishnumurthy

**Abstract:** Photolysis of *trans*-1,4,4,4-tetraphenylbut-2-en-1-one (**3**) in acetonitrile or benzene leads to *trans*-*cis* isomerization (**7**) along with rearrangement to *trans*-1-benzoyl-2,2,3-triphenylcyclopropane (**8**). Formation of the latter product represents a new example of the aryl migration (type B) enone photorearrangement reaction first reported by Zimmerman and co-workers for 4,4-diphenylcyclohex-2-en-1-one (**1**). The quantum yield in the case of enone **3** (0.4) is approximately 10 times greater than that for 4,4-diphenylcyclohex-2-en-1-one, a result that is ascribed to steric acceleration of phenyl migration from the triphenylmethyl group plus greater resonance stabilization of the intermediate biradical.

**Key words:** photochemistry, mechanism, rearrangement, aryl migration, enone, di- $\pi$ -methane.

**Résumé :** La photolyse de la *trans*-1,4,4,4-tétraphénylbut-2-én-1-one (**3**) dans l'acétonitrile ou le benzène conduit à une isomérisation *trans*-*cis* (**7**) ainsi qu'à un réarrangement en *trans*-1-benzoyl-2,2,3-triphenylcyclopropane (**8**). La formation de ce dernier produit représente un nouvel exemple de réaction de photoréarrangement d'énone avec migration d'aryle (type B) qui avait été observé pour la première fois par Zimmerman et ses collaborateurs pour la 4,4-diphénylcyclohex-2-én-1-one (**1**). Le rendement quantique dans le cas de l'énone **3** (0,4) est approximativement dix fois plus grand que celui observé avec la 4,4-diphénylcyclohex-2-én-1-one; on attribue cette différence à l'accélération stérique associée à la migration du phényle à partir du groupe triphénylméthyle ainsi qu'à la plus grande stabilisation par résonance du biradical intermédiaire.

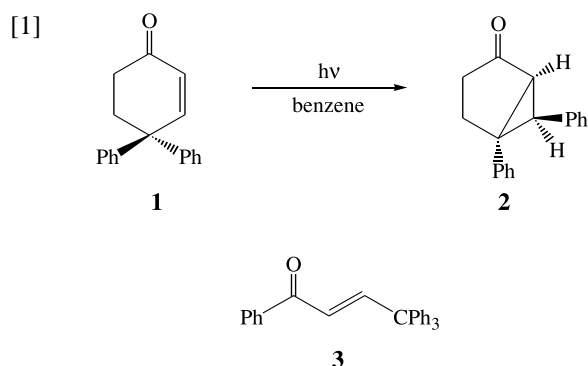
**Mots clés :** photochimie, mécanisme, réarrangement, migration d'un groupe aryle, énone, di- $\pi$ -méthane.

[Traduit par la Rédaction]

## Introduction

Many of the principles of organic photochemistry with which we are familiar today rest on early studies of the light-induced behavior of enones and dienones (**1**). As an example, consider the case of 4,4-diphenylcyclohex-2-en-1-one (**1**) (eq. [1]), whose photochemistry was first reported by Zimmerman and Wilson (**2**) in 1964 and subsequently investigated in more detail by Zimmerman and Hancock (**3**) in 1968. In these studies, irradiation of ketone **1** in solution was shown to afford *trans*-5,6-diphenylbicyclo[3.1.0]hexan-2-one (**2**) in rather low quantum efficiency ( $\Phi = 0.043$ ) but excellent chemical yield; trace amounts of *cis*-5,6-diphenylbicyclo[3.1.0]hexan-2-one and 3,4-diphenylcyclohex-2-en-1-one were also formed. Formally a di- $\pi$ -methane process involving the enone double bond and a double bond on one of the phenyl groups, the formation of photoproduct **2** takes place in the triplet state via a 1,2-phenyl shift accompanied

by cyclopropane ring closure. Subsequent studies by the Zimmerman group used the aryl migration cyclohexenone photorearrangement reaction to investigate the relative excited-state migratory aptitudes of aryl groups bearing electron-donating and electron-withdrawing substituents (**4**).



Received 10 December 2002. Published on the NRC Research Press Web site at <http://canjchem.nrc.ca> on 18 June 2003.

Dedicated to Professor Donald R. Arnold for his contributions to Chemistry.

**J.R. Scheffer<sup>1</sup>** and **K. Vishnumurthy**, Department of Chemistry, University of British Columbia, 2036 Main Mall, Vancouver, BC V6T 1Z1, Canada.

<sup>1</sup>Corresponding author (e-mail: [scheffer@chem.ubc.ca](mailto:scheffer@chem.ubc.ca)).

In seeking variations of the aryl migration enone photorearrangement for the purpose of investigating asymmetric induction in organic photochemical reactions, we chose *trans*-1,4,4,4-tetraphenylbut-2-en-1-one (**3**, eq. [1]) as a potential target molecule. This choice is attractive from several points of view. For one, we anticipated that modification of the benzoyl group to accept ionic chiral auxiliaries (**5**) would be relatively easy. A second, unrelated motivation was that preparation of analogs of enone **3** in which the

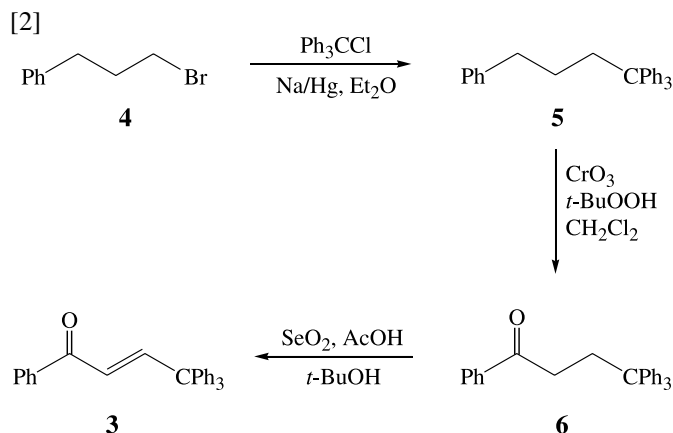


three terminal aryl groups are, for example, phenyl, *p*-methoxyphenyl, and *p*-cyanophenyl, offers the possibility of investigating the relative excited-state migratory aptitude of three aryl groups simultaneously, rather than only two at a time as in the case of cyclic enones. In the present article we outline the synthesis of the parent compound (**3**) and describe its basic photochemical behavior in solution.

## Results

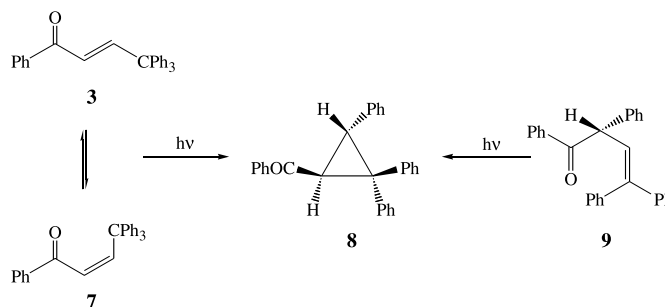
The synthesis of enone **3** was accomplished in straightforward fashion through the known intermediates **5** and **6** (eq. [2]). The final step, selenium dioxide oxidation of ketone **6**, proceeded in 94% overall yield to afford the target enone **3** as a colorless crystalline solid, mp 133–136°C. The assignment of *trans* stereochemistry to enone **3** followed from its proton NMR spectrum, which showed the vinyl hydrogens as doublets at 8.00 and 6.67 ppm with a 15.6 Hz coupling constant between them. By way of contrast, the *cis* isomer of enone **3** (i.e., compound **7**, eq. [3]), which could be isolated in small amounts when **3** was irradiated for relatively short periods of time (vide infra), exhibited an NMR spectrum in which the vinyl doublets appeared at 6.79 and 6.32 ppm with a mutual coupling constant of 12 Hz. The photochemistry of enone **3** was examined in both ben-

zene and acetonitrile solution and the progress of the reaction monitored by gas chromatography. This showed the formation of two photoproducts, subsequently shown to be *cis*-enone **7** and *trans*-1-benzoyl-2,2,3-triphenylcyclopropane (**8**) (eq. [3]). Photolysis was stopped when GC analysis indicated the complete disappearance of enone **3**, at which point the **7**:**8** ratio was approximately 1:3; chromatography of this reaction mixture allowed small amounts of *cis*-enone **7** to be isolated and characterized. Continuing the photolysis until no further enone **7** could be detected by GC analysis (ca. 2 h) and subsequent silica gel column chromatography allowed cyclopropyl ketone **8** to be isolated in 96% yield. The structure and *trans* stereochemistry of photoproduct **8** were assigned on the basis of a comparison of its mp and spectroscopic properties with those reported in the literature for the



zene and acetonitrile solution and the progress of the reaction monitored by gas chromatography. This showed the formation of two photoproducts, subsequently shown to be *cis*-enone **7** and *trans*-1-benzoyl-2,2,3-triphenylcyclopropane (**8**) (eq. [3]). Photolysis was stopped when GC analysis indicated the complete disappearance of enone **3**, at which point the **7**:**8** ratio was approximately 1:3; chromatography of this reaction mixture allowed small amounts of *cis*-enone **7** to be isolated and characterized. Continuing the photolysis until no further enone **7** could be detected by GC analysis (ca. 2 h) and subsequent silica gel column chromatography allowed cyclopropyl ketone **8** to be isolated in 96% yield. The structure and *trans* stereochemistry of photoproduct **8** were assigned on the basis of a comparison of its mp and spectroscopic properties with those reported in the literature for the

[3]

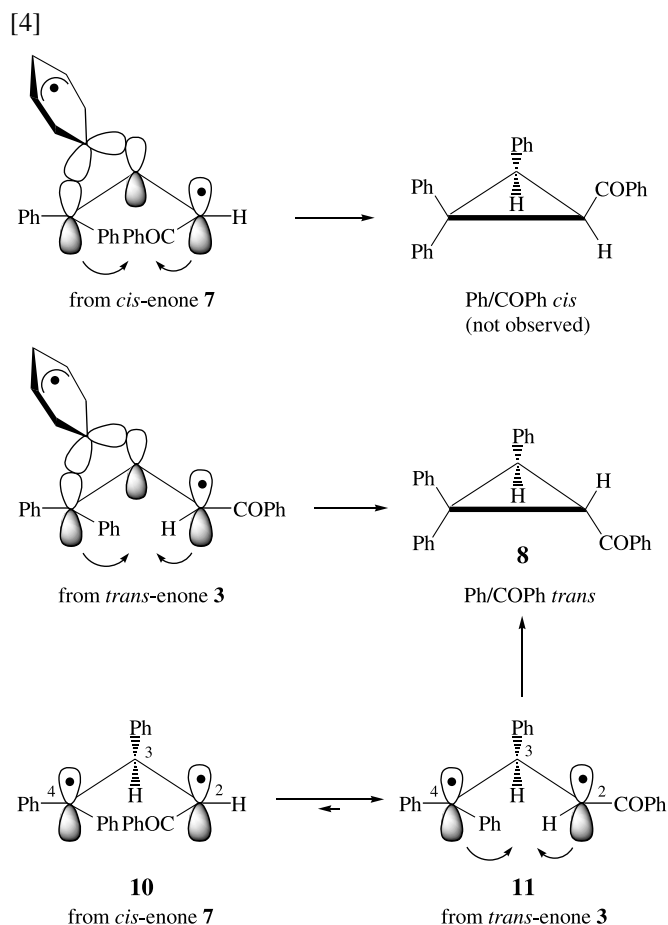


## Discussion

While cyclopropyl ketone **8** has the gross structure expected of a straightforward 1,2-phenyl migration photorearrangement of enone **3**, its stereochemistry differs from that of the major product **2** formed in the photolysis of 4,4-diphenylcyclohex-2-en-1-one. In the latter case, the migrating phenyl group ends up *cis* to the carbonyl group, whereas in ketone **8** there is a *trans* relationship between these two moieties. Both results are consistent with the concerted mechanism proposed by Zimmerman and Hancock (3) in which phenyl migration is synchronous with cyclopropane ring formation. As depicted in eq. [4], this mechanism predicts that *cis*-enones (e.g., **1** and **7**) will form products in which the migrating group (Ar) and the C=O group are *cis* to one another (e.g., **2**), and that *trans*-enones (e.g., **3**) will lead to products having a *trans*-Ar – C=O relationship (e.g., **8**). There is a problem with this picture, however, in that independent photolysis of *cis*-enone **7** did not form the expected *cis*-Ar – C=O diastereomer; only photoproduct **8** was observed. This indicates that either the concerted photorearrangement of *cis*-enone **7** is slower than its isomerization to *trans*-enone **3** (no **3** could be detected, however), or that both enones rearrange by a non-concerted mechanism through a common, conformationally equilibrated intermediate such as **11** (eq. [4]) in which ring closure with clockwise rotation about the C-2—C-3 bond is favored, leading to photoproduct **8**.<sup>2</sup> Zimmerman and Hancock (3) also concluded that a non-concerted mechanism is capable of rationalizing the stereochemical course of the photorearrangement of cyclohexenone **1**. At the moment, therefore, a definitive choice between the concerted and non-

<sup>2</sup>Biradical **11** is expected to be more stable than its conformer **10** in which the benzoyl group interferes with a phenyl group on C-4. Clockwise rotation around C-2—C-3 during ring closure of biradical **11** is favored over counterclockwise rotation, since the latter pathway leads to increased nonbonded interactions between the benzoyl group and the phenyl group on C-3.





concerted pathway cannot be made, although it could be argued that the triplet nature of the photorearrangement favors the latter.

A final point of discussion concerns the 10-fold higher quantum yield for the photorearrangement of acyclic enone **3** compared with that of cyclic enone **1**. Although quantum yields are not always a reflection of rates of reaction, it is tempting to equate the higher quantum yield for the photorearrangement of enone **3** with relief of steric crowding in the triphenylmethyl group as well as greater resonance stabilization of the intermediate biradical **10**.

Work is continuing in our laboratory on developing methods for carrying out the aryl migration enone photorearrangement enantioselectively as well as synthesizing triarylmethane analogs of enone **3** for use in excited-state migratory aptitude studies.

## Experimental

### Instrumentation and general procedures

Commercial spectral grade solvents were used for photochemical experiments unless otherwise noted. Infrared spectra were recorded on a Perkin-Elmer 1710 Fourier transform spectrometer. Solid samples were ground in KBr (1–5%) and liquid samples were run neat as thin films. Melting points were determined on a Fisher-Johns hot stage apparatus and are uncorrected.  $^1\text{H}$  NMR spectra were recorded in deuterated solvents as noted on a Varian AV-300 (300 MHz) instrument.  $^{13}\text{C}$  NMR spectra were run on the same instrument at

75 MHz under broadband  $^1\text{H}$  decoupling. Low- and high-resolution mass spectra were obtained from a Kratos MS 50 instrument using electron impact (EI) ionization at 70 eV or the chemical ionization (CI) method; intensities of the ions are given in parentheses. Ultraviolet spectra were recorded on a PerkinElmer Lambda-4B spectrophotometer in the solvent indicated. Gas chromatographic analyses were performed on a Hewlett-Packard HP 5890 instrument.

### 1,1,1,4-Tetraphenylbutane (**5**)

The known compound **5** (**6**) was synthesized by a modified procedure of Brook and Pierce (6) (8). Mercury (36.5 g, 182 mmol) was placed in a 100 mL two-necked round-bottomed flask equipped with a magnetic stirrer and a reflux condenser and the system thoroughly flushed with anhydrous nitrogen. Sodium (0.365 g, 15.9 mmol) was carefully added in several small pieces to the mercury under nitrogen with cooling by means of a water bath. A solution of 2.0 g (7.2 mmol) of triphenylmethyl chloride (Aldrich) in 50 mL of anhydrous ether was then added to the sodium amalgam under nitrogen with stirring, whereupon a blood red color developed over a period of approximately 1 h. Stirring was continued for an additional 2 h after which 1.78 g (8.9 mmol) of 3-phenyl-1-bromopropane (**4**) (Aldrich) was added. The red color disappeared immediately and the resulting solution was stirred at room temperature for 4 h. The reaction mixture was worked up by hydrolysis with 20 mL of distilled water followed by extraction with diethyl ether. The ether layers were combined, dried over anhydrous sodium sulphate, and concentrated in vacuo to afford a non-crystalline residue that was subjected to silica gel column chromatography using 2% ethyl acetate in petroleum ether as the eluting solvent. This afforded 1.70 g (53%) of compound **5** as a colorless solid. Recrystallization from ether:petroleum ether (2:1) gave colorless needles, mp 94 to 95°C (lit. (6) mp 92 to 93.5°C).

### 1,4,4,4-Tetraphenylbutan-1-one (**6**)

The known compound **6** (**6**) was prepared using an oxidation procedure of Muzart (9). To a solution of 0.89 g (2.5 mmol) of compound **5** in 4.2 mL of dichloromethane was added 0.074 g (0.74 mmol) of chromium trioxide (Aldrich) and 6.6 mL of a 70% aqueous solution of *tert*-butylperoxide (Aldrich) and the resulting mixture stirred for 36 h at room temperature. The biphasic reaction mixture was worked up by addition of 8 mL of saturated aqueous sodium thiosulphate solution until no longer oxidizing to starch-iodide paper and then extracted with dichloromethane (2 × 15 mL). The combined organic layers were washed with water and brine and then dried over anhydrous magnesium sulphate. Removal of the solvent in vacuo followed by radial chromatography over silica gel (2% ethyl acetate in petroleum ether) afforded 0.7 g (75%) of ketone **6** as a colorless solid. Recrystallization from ethyl acetate gave small prisms, mp 141–143°C (lit. (6) mp 139 to 140.5°C).

### *trans*-1,4,4,4-Tetraphenylbut-2-en-1-one (**3**)

Following an oxidation procedure of Bernstein and Littell (10), a solution of 1.0 g (2.7 mmol) of ketone **6** and 1.2 g (10.8 mmol) of selenium dioxide (Aldrich) in 125 mL of *tert*-butanol and 5.6 mL of glacial acetic acid was refluxed



with stirring for 48 h. The reaction mixture was diluted with 25 mL of ethyl acetate, filtered, and the filtrate washed with water, 10% aqueous sodium hydroxide, water again, brine, and then dried over anhydrous sodium sulphate. Removal of the solvent in vacuo followed by GC analysis of the residue revealed the presence of both ketone **3** and ketone **6** in a 2:1 ratio. This mixture was subjected to a second oxidation identical to the first but on half the scale until GC analysis indicated the complete disappearance of starting material **6**. Workup as before afforded a crude reaction mixture that was subjected to radial chromatography over silica gel (5% ethyl acetate in petroleum ether) to afford 0.94 g (94%) of solid enone **3**. Recrystallization from ethyl acetate:hexane (3:1) gave colorless needles, mp 133–136°C. IR (KBr) ( $\text{cm}^{-1}$ ): 3054, 1667, 1610, 1490, 1445, 1326, 1304, 1291, 1223, 1179, 1033, 1004, 757, 702, 590.  $^1\text{H}$  NMR ( $\text{CDCl}_3$ , 300 MHz)  $\delta$ : 8.0 (d, 1H,  $J = 15.6$  Hz, vinyl), 7.79–7.76 (m, 2H), 7.51–7.46 (m, 1H), 7.4–7.35 (m, 2H), 7.30–7.19 (m, 9H), 7.09–7.06 (m, 6H), 6.67 (d, 1H,  $J = 15.6$  Hz, vinyl).  $^{13}\text{C}$  NMR ( $\text{CDCl}_3$ , 75 MHz)  $\delta$ : 190.7, 154.4, 144.4, 137.9, 132.8, 130.1, 129.1, 128.6, 128.1, 126.9, 126.6, 125.5, 61.3. LR-MS (EI)  $m/z$ : 374 ( $\text{M}^+$ ), 269, 191, 165, 105, 91, 77, 51. HR-MS (EI)  $m/z$  calcd. for  $\text{C}_{28}\text{H}_{22}\text{O}$ : 374.1671; found: 374.1672. Anal. calcd. for  $\text{C}_{28}\text{H}_{22}\text{O}$ : C 89.80, H 5.93; found: C 89.81, H 5.95.

### Photolysis of enone **3**

Enone **3** (0.1 g, 0.27 mmol) was dissolved in 30 mL of acetonitrile and the solution purged with nitrogen for 30 min. The solution was then irradiated for 2 h through Pyrex using the output of a Hanovia 450 W medium pressure mercury lamp. GC analysis of an aliquot revealed the complete consumption of starting material and the formation of a single photoproduct. Removal of the solvent in vacuo followed by radial chromatography over silica gel (2% ethyl acetate in petroleum ether) afforded 0.096 g (96%) of photoproduct **8** as a colorless solid. Recrystallization from a mixture of diethyl ether and petroleum ether afforded small prisms, mp 126–128°C (lit. (7) mp 125–127°C). The methine hydrogens of compound **8** exhibited a mutual 6 Hz coupling in the  $^1\text{H}$  NMR, thus confirming their *trans* relationship (11). When 0.02 g of enone **3** in 15 mL of benzene was irradiated through Pyrex for 1 h, GC analysis indicated the presence of a mixture of *trans*-enone **3**, its *cis* isomer **7**, and cyclopropyl ketone **8** in a 3:10:20 ratio. Photolysis was continued for an additional 15 min until GC analysis showed the complete consumption of starting material **3**. Subsequent removal of solvent in vacuo followed by radial chromatography as before afforded 0.012 g of photoproduct **8** and 0.004 g of *cis*-enone **7**, mp 136–139°C (from ethyl acetate). IR (KBr): 3058, 2974, 1672, 1597, 1581, 1494, 1447, 1226, 1175, 1036, 991, 901, 842, 738, 702.  $^1\text{H}$  NMR ( $\text{C}_6\text{D}_6$ , 300 MHz)  $\delta$ : 7.59–7.56 (m, 2H), 7.32–7.29 (m, 6H), 7.12–6.91 (m, 12H), 6.79 (d, 1H,  $J = 12$  Hz, vinyl), 6.32 (d, 1H,  $J = 12$  Hz, vinyl).  $^{13}\text{C}$  NMR ( $\text{CDCl}_3$ , 75 MHz)  $\delta$ : 192.4, 147.4, 145.5, 136.7, 132.7, 130.4, 129.6, 128.6, 128.4, 128.1, 128.0, 127.7, 126.4, 61.7. LR-MS (EI)  $m/z$ : 374 ( $\text{M}^+$ ), 269, 191, 165, 105, 91, 77, 51. HR-MS (EI)  $m/z$  calcd. for

$\text{C}_{28}\text{H}_{22}\text{O}$ : 374.1671; found: 374.1669. Anal. calcd. for  $\text{C}_{28}\text{H}_{22}\text{O}$ : C 89.80, H 5.93; found: C 89.78, H 5.97.

### Quantum yield determination

The quantum yield for formation of cyclopropyl ketone **8** in benzene was determined using valerophenone actinometry ( $\Phi = 0.33$ ) (12) according to the standard protocol used in our group (13). *n*-Tetradecane and *n*-nonadecane were used as internal standards for the solutions of actinometer and ketone **8**, respectively. Quantum yields were determined at varying conversions and plotted against conversion; the reported quantum yield of 0.4 represents the value extrapolated to 0% conversion.

### Acknowledgement

We thank the Natural Sciences and Engineering Research Council of Canada (NSERC) for financial support.

### References

- (a) O.L. Chapman. In *Advances in photochemistry*. Vol. 1. Edited by W.A. Noyes, G.S. Hammond, and J.N. Pitts. Wiley Interscience, New York. 1963. pp. 323–420; (b) K. Schaffner. In *Advances in photochemistry*. Vol. 4. Edited by W.A. Noyes, G.S. Hammond, and J.N. Pitts. Wiley-Interscience, New York. 1966. pp. 81–112; (c) D.I. Schuster. In *Rearrangements in ground and excited states*. Edited by P. de Mayo. Academic Press, New York. 1980. pp. 167–279; (d) D.I. Schuster. In *The chemistry of enones*. Edited by S. Patai and Z. Rappoport. Wiley, Chichester, U.K. 1989. Chap. 15. pp. 623–756; (e) D.I. Schuster. In *CRC handbook of organic photochemistry and photobiology*. Edited by W. Horspool and P.-S. Song. CRC Press, Boca Raton, Florida. 1994. pp. 579–592.
- H.E. Zimmerman and J.W. Wilson. *J. Am. Chem. Soc.* **86**, 4036 (1964).
- H.E. Zimmerman and K.G. Hancock. *J. Am. Chem. Soc.* **90**, 3749 (1968).
- (a) H.E. Zimmerman, R.D. Rieke, and J.R. Scheffer. *J. Am. Chem. Soc.* **89**, 2033 (1967); (b) H.E. Zimmerman and N. Lewin. *J. Am. Chem. Soc.* **91**, 879 (1969).
- For a recent review on the use of ionic chiral auxiliaries for the purpose of asymmetric induction in organic photochemistry, see: J.R. Scheffer. *Can. J. Chem.* **79**, 349 (2001).
- A.G. Brook and J.B. Pierce. *Can. J. Chem.* **42**, 298 (1964).
- L.P. Tenney, D.W. Boykin, and R.E. Lutz. *J. Am. Chem. Soc.* **88**, 1835 (1966).
- Triphenylmethylsodium was prepared according to the procedure of: W.B. Renfrow, Jr. and C.R. Hauser. *Organic synthesis*. Coll. Vol. II. Wiley, New York. 1943. p. 607.
- J. Muzart. *Tetrahedron Lett.* **28**, 2131 (1987).
- S. Bernstein and R. Littell. *J. Am. Chem. Soc.* **82**, 1235 (1960).
- R.M. Silverstein, G.C. Bassler, and T.C. Morrill. *Spectrometric identification of organic compounds*. 5th ed. Wiley, New York. 1991. Chap. 4. p. 221.
- P.J. Wagner, I.E. Kochevar, and A.E. Kempainen. *J. Am. Chem. Soc.* **94**, 7489 (1972).
- M. Leibovitch, G. Olovsson, J.R. Scheffer, and J. Trotter. *J. Am. Chem. Soc.* **120**, 12 755 (1998).



# The photochemistry of 1-(3,5-dimethoxyphenyl)-2-(4-methoxyphenyl)ethyl ethanoate in alcohol solvents: A search for carbocation rearrangements

J.C. Roberts and J.A. Pincock

**Abstract:** The photochemistry of the title compound **1** in methanol and 2,2,2-trifluoroethanol has been examined. In both solvents two ether products were obtained: one (**18**) resulting from trapping of the carbocation **2** (expected from photosolvolysis of **1**), and the other (**19**) from the carbocation **3** (expected after rearrangement by hydride migration of cation **2**). The substituted *trans*- and *cis*-stilbene derivatives **20** and **21** were also primary photoproducts. Analysis of product yields as a function of time revealed that the ether product **19** was formed by secondary photolysis of the stilbene derivatives, presumably by a pathway involving excited state protonation. Nanosecond laser flash photolysis results demonstrated that substituted *trans*-stilbene **20** was produced on the same time scale as the laser pulse.

**Key words:** ester photochemistry, stilbene photoadditions, carbocation rearrangements.

**Résumé :** On a étudié la photochimie du composé mentionné dans le titre **1** dans le méthanol et dans le 2,2,2-trifluoroéthanol. Dans les deux solvants on obtient deux éthers : L'un deux (**18**) résulte du piégeage du carbocation **2** (produit attendu de la photolyse du composé **1**), et l'autre (**19**) provient du carbocation **3** (produit attendu d'un réarrangement par migration d'un ion hydrure du cation **2**). Les dérivés *trans* et *cis* des stilbènes substitués **20** et **21** sont également des photoproduits primaires. L'analyse des produits obtenus en fonction du temps, révèle que l'éther **19** résulte d'une photolyse secondaire des dérivés du stilbène, vraisemblablement selon un chemin impliquant la protonation de l'état excité. Les résultats de la photolyse éclair au laser, avec des impulsions de l'ordre de la nanoseconde, démontrent que le *trans*-stilbène substitué **20** est produit dans la même échelle de temps que l'impulsion laser.

**Mots clés :** photochimie d'un ester, photoadditions du stilbène, réarrangements de carbocations.

[Traduit par la Rédaction]

## Introduction

The photochemical generation of carbocations by cleavage of arylmethyl leaving group  $\sigma$  bonds ( $\text{ArCR}_2\text{-LG}$ ) is currently of considerable interest (1). One focus has been on the mechanism for formation of the arylmethyl cation with the two possibilities being either (i) direct heterolytic cleavage to an ion pair from the excited singlet state, or (ii) excited state homolytic cleavage followed by rapid redox electron transfer converting the first formed radical pair to an ion pair (2). Product studies have been extensively used to probe these two possible pathways. Another focus has been the direct observation of arylmethyl cations by laser flash photolysis (LFP) techniques (3), which has provided information regarding the reactivity of these species, in particular

their rates of reaction with various nucleophiles and solvents.

The observation of products resulting from rearrangements of carbocations is a well-established phenomenon in ground state chemistry and appears in early chapters of all modern text books on introductory organic chemistry. The driving force for these rearrangements is formation of a more stable cation from a less stable one, with both 1,2-carbon and hydrogen migrations as well-known examples. We hoped to apply the above two photochemical techniques to observe a hydride shift by both product studies and directly by LFP. We chose the substrate **1** and the cations **2** and **3** as targets (eq. [1]).

The idea behind this choice is that the 3,5-dimethoxyphenyl chromophore efficiently promotes the photochemical

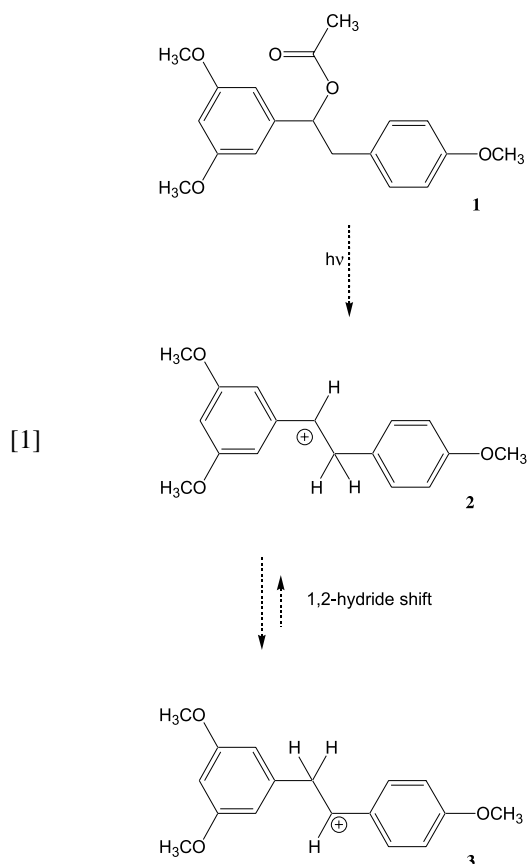
Received 13 January 2003. Published on the NRC Research Press Web site at <http://canjchem.nrc.ca> on 23 June 2003.

*Dedicated to Professor Don Arnold for his contributions to chemistry. We have both enjoyed and benefited from our many interactions with him as a colleague, friend, and research supervisor (JAP, 1972–1973; JCR, 1997–1998).*

**J.C. Roberts and J.A. Pincock.**<sup>1</sup> Department of Chemistry, Dalhousie University, Halifax, NS B3H 4J3, Canada.

<sup>1</sup>Corresponding author (e-mail: [james.pincock@dal.ca](mailto:james.pincock@dal.ca)).





generation of carbocations via C—O bond cleavage (4, 5). For instance, the yield of ion-derived products from the photolysis of 3,5-dimethoxybenzyl acetate in methanol is 60% with a quantum yield of 0.37 (6). A rate constant for this excited state bond cleavage has not been determined because the lack of fluorescence precludes determination of the excited singlet state lifetime, but we estimate that the rate constant is greater than  $1 \times 10^9 \text{ s}^{-1}$ . If it is formed, carbocation **2** is expected to rearrange rapidly to the more stable isomer **3** by a hydride shift. The difference in stability for the two cations can be demonstrated by the relative rates of solvolysis for 4-methoxybenzyl tosylate and 3,5-dimethoxybenzyl tosylate ( $1:1 \times 10^5$  in 80% aqueous acetone at  $25^\circ\text{C}$ ) (7). Finally, the 4-methoxybenzyl cation has a characteristic absorption band at 340 nm that has been used previously to study its reactivity by LFP (8). Therefore, if **3** is formed from **2**, the time evolution of its growth could be observable.

A similar approach has been reported recently by Lee-Ruff and co-workers (9). In the first example (9), photolysis of the vicinal diol **4** in acetonitrile, methanol, and 2,2,2-trifluoroethanol (TFE) gave the radical-derived product **5**, along with the pinacol rearrangement product **6** (Scheme 1). The proposed mechanism proceeds through the cations **7** and **8**. The efficient formation of **7** results from the previously reported high photochemical reactivity of 9-hydroxyfluorene derivatives to give fluorenyl cations which are not stabilized by aromatic delocalization because they have  $4n \pi$  electrons (10). The cation **7** was observed by LFP, and its unimolecular rearrangement to **8** (not observed) was found to have a

rate constant of  $5 \times 10^5 \text{ s}^{-1}$  in 1,1,1,3,3,3-hexafluoroisopropanol (HFIP). In a second example (11), the irradiation of the 9-fluorenol derivative **9** in methanol gave the ether **10** (28%) and the elimination product **11** (7%). However, the ether **12** (which would have been formed after a 1,2-hydride shift converting **13** to **14**) was not detected in the reaction mixture (Scheme 2). When **9** was submitted to strong acid conditions at  $-78^\circ\text{C}$ , **13** was detected spectroscopically, but **14** was not observed until the solution was warmed to room temperature. Quenching of the cold or warmed solution with methanol gave **10** or **12**, respectively. The authors rationalized these observations by suggesting that cation **14** is not formed by a 1,2-hydride shift, but rather by a deprotonation–protonation sequence involving the by-product **11** (a process which is only possible in the strong acid experiments). This suggests that the activation barrier for rearrangement of **13** to **14** is high enough to prevent the process from competing with rapid quenching by methanol when **13** is generated photochemically.

## Results

### Synthesis of ester **1**

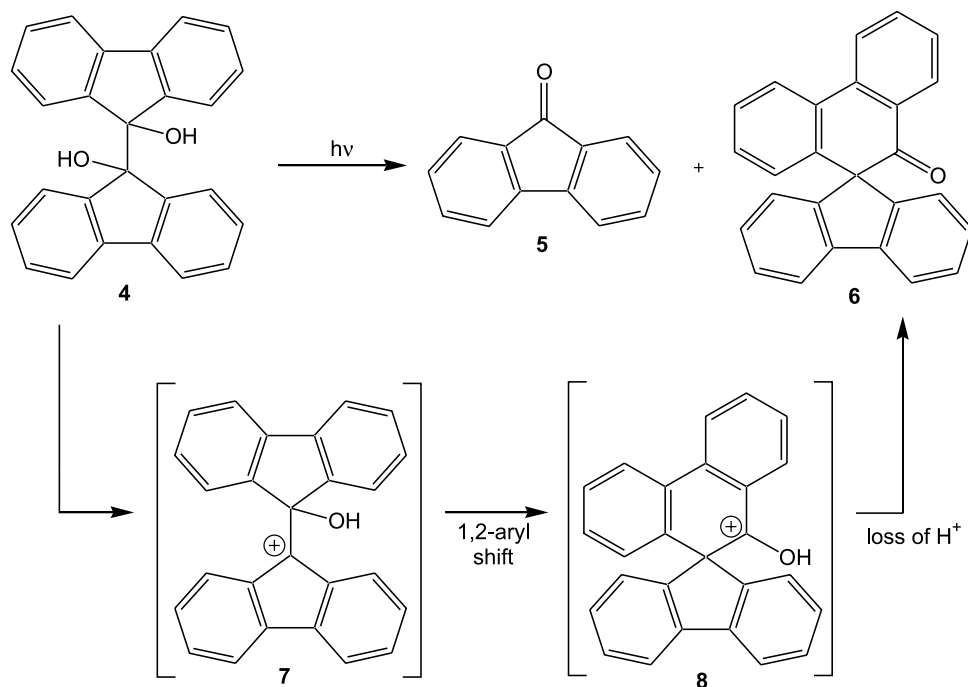
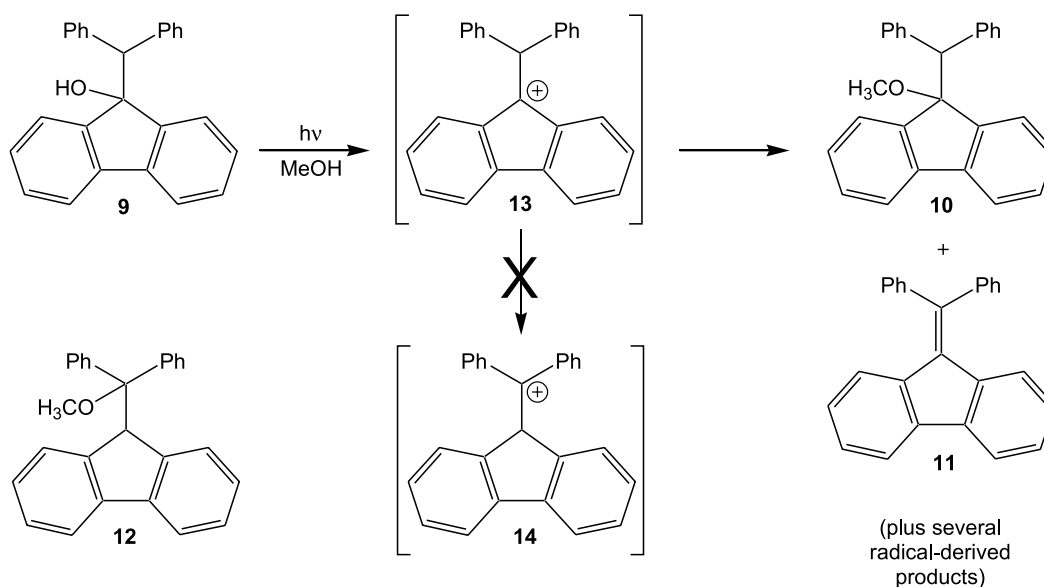
Arylmethyl esters such as **1** are easily accessed by esterification of the corresponding alcohols, and therefore, alcohol **15** was identified as the direct precursor that was required for the preparation of **1**. For the synthesis of **15**, a Grignard reaction between 3,5-dimethoxy-bromobenzene **16** and 2-(4-methoxyphenyl)ethanal **17** was chosen. As shown in Scheme 3, the bromide **16** was synthesized by a Sandmeyer reaction (12) in a low yield (33%) that is consistent with literature precedent (13). The aldehyde **17** was prepared in 74% yield over three steps by Darzens' sequence from 4-methoxybenzaldehyde as reported by Macchia and co-workers (14). Grignard coupling of **16** with **17** gave **15** (96% yield), and esterification by the procedure of Steglich and Neises (15) gave the desired ester **1** (70% yield). Details of the procedures are in the *Experimental* section.

A methanolic solution of ester **1** had absorption maxima at 274 nm ( $\epsilon = 3600 \text{ M}^{-1} \text{ cm}^{-1}$ ) and 280 nm ( $\epsilon = 3300 \text{ M}^{-1} \text{ cm}^{-1}$ ). Excitation of **1** at 274 nm results in fluorescence with  $\lambda_{\text{max}}$  at 298 nm, and the 0,0 band is at 288 nm ( $415 \text{ kJ mol}^{-1}$ ). Since 3,5-dimethoxybenzyl acetate itself does not fluoresce, this observation is attributed to the 4-methoxyphenyl chromophore, which will absorb competitively with the more reactive portion of the molecule. To check for any interaction between the two chromophores, the absorption spectra of 4-methylanisole and 1-(3,5-dimethoxyphenyl)ethyl ethanoate were recorded and normalized. Summation of the normalized spectra resulted in a slightly higher absorption (8%) than was observed at the  $\lambda_{\text{max}}$  of **1** (274 nm). No increased absorption was observed at longer wavelengths. Therefore, the competitive absorption between the two chromophores may decrease the quantum yield of the reaction, but there does not appear to be any strong ground-state interaction between them.

### Photolysis of ester **1** in methanol

Photolysis of a nitrogen-saturated solution of **1** in methanol using a Rayonet reactor and 254 nm lamps afforded a



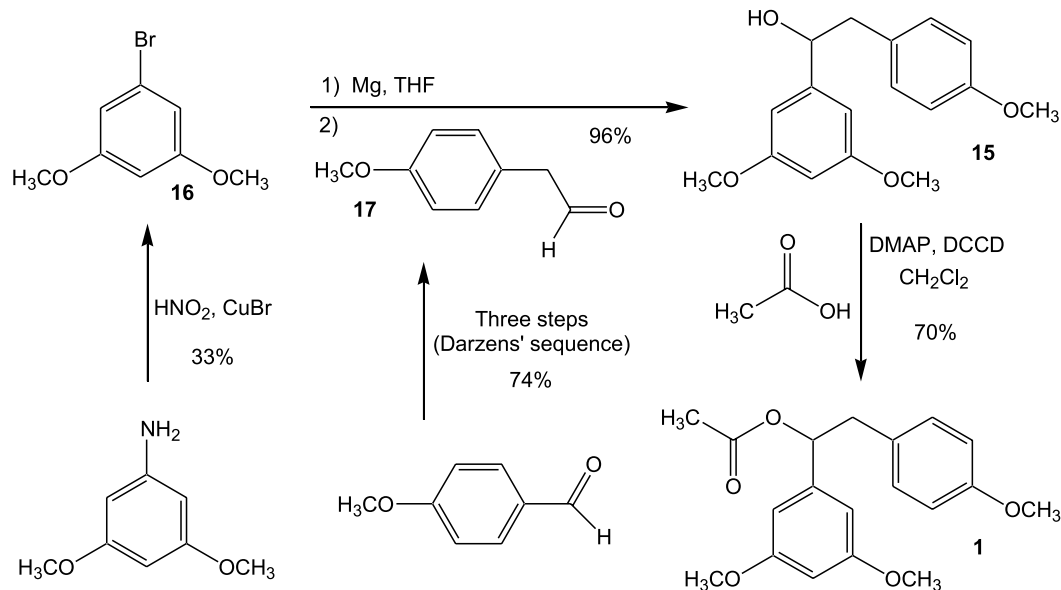
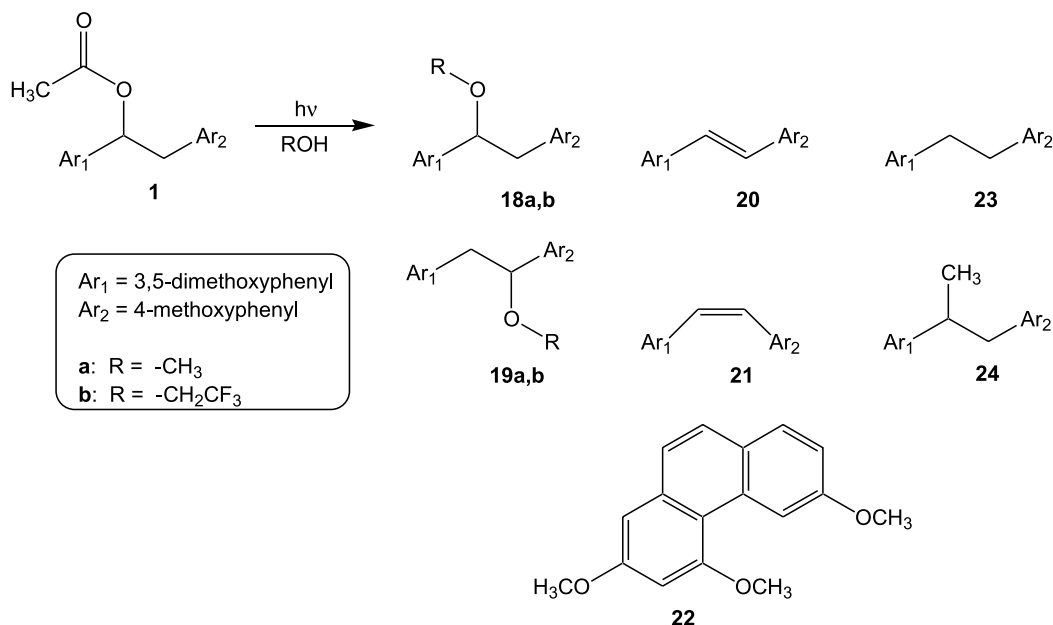
**Scheme 1.** Formation of ketone **6** via the photochemical pinacol rearrangement of cation **7**.**Scheme 2.** The photochemistry of fluorenol **9** in methanol.

mixture of seven products after irradiation for 1 h (Scheme 4). Figure 1 shows the normalized product yields as a function of time. Preliminary identification of the products was made on the basis of their mass spectra (GC-MS). Pure samples were obtained either by independent syntheses or by isolation following photochemical reactions (*vide infra*). The reaction was also monitored by gas chromatography with a flame ionization detector (GC-FID). The GC-FID response was calibrated using each of the pure samples, allowing the accurate calculation of product yields (Table 1). Further details on the methods used to obtain accurate val-

ues for the product yields can be found in the *Experimental* section.

As shown in Fig. 1 and Table 1, almost 90% of **1** is consumed after 1 h of irradiation, and by this time there is very little change in the relative percentages of the products over time. For the purposes of the current project, the methyl ethers **18a** and **19a** ( $\text{R} = \text{CH}_3$ ) are of the greatest interest, since they are the products that would be formed from nucleophilic attack of the solvent on carbocations **2** and **3**. Although the yield of **19a** is difficult to measure at low conversions, the ratio of **18a** to **19a** appeared to decrease with



**Scheme 3.** The synthesis of 1-(3,5-dimethoxyphenyl)-2-(4-methoxyphenyl)ethyl ethanoate **1**.**Scheme 4.** Products detected following the photolysis of ester **1** in methanol and TFE.

time until a steady state ratio of 21:1 was reached; after only 10 min, however, **18a**:**19a** = 33:1.

The substituted stilbenes **20** and **21** are clearly primary photoproducts, but at low conversions the *trans* isomer is formed in higher yield than the *cis* (*trans*:*cis* = 2:1 at 2% conversion). The two isomers then photoequilibrate to a ratio of 1:1 at high conversion of **1**. The substituted phenanthrene **22** is produced by secondary photochemistry — a photochemically allowed conrotatory electrocyclic reaction of the *cis*-stilbene **21**, followed by oxidation of the dihydrophenanthrene intermediate. This reaction has been well-established for the photochemistry of other electron-rich

stilbene derivatives (**16**). Finally, products **23** and **24** are radical-derived by-products of the reaction.

As noted above, the identification of most products was made by comparison with authentic samples. Ether **18a** was synthesized by reaction of alcohol **15** with sodium hydride and iodomethane. To produce **19a** in a similar alkylation method, the required alcohol **25** was synthesized by Grignard coupling of 4-bromoanisole and 2-(3,5-dimethoxyphenyl)ethanal **26** (the aldehyde, in turn, was prepared by the Darzens' sequence from 3,5-dimethoxy-benzaldehyde). The substituted *trans*-stilbene **20** was produced by dehydration of **15** with *p*-toluenesulfonic acid in benzene. Photo-



**Fig. 1.** Product yields as a function of time for the photolysis of ester **1** in methanol (Note: compounds **23** and **24** have been removed for improved clarity).

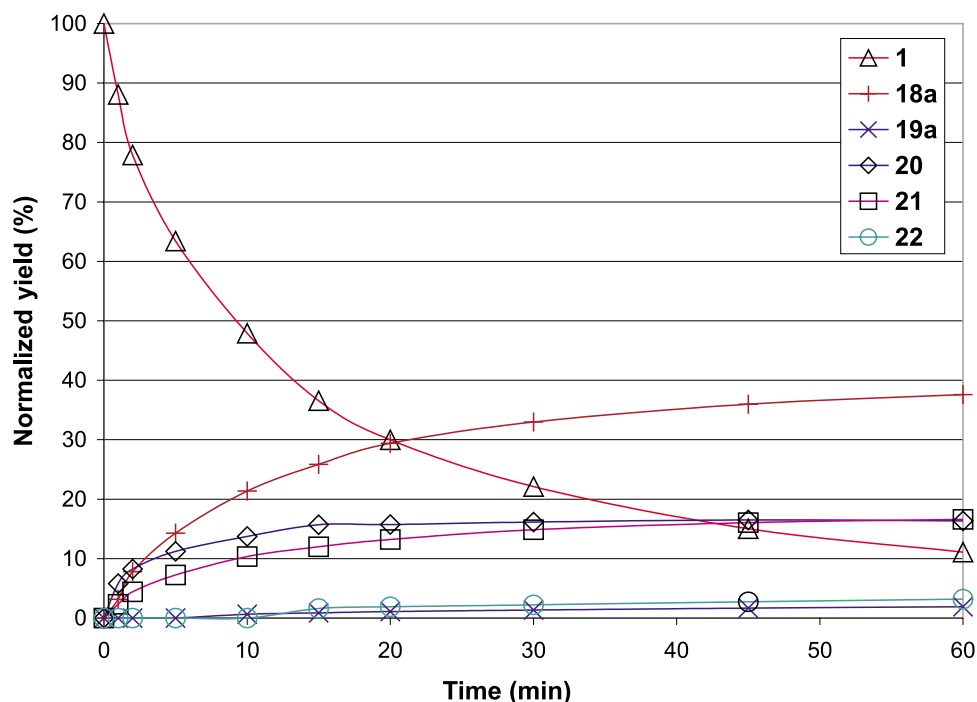


**Table 1.** Product yields after photolysis of ester **1** for 1 h in methanol and TFE.

Solvent	% Conversion <sup>a</sup>	<b>18</b> <sup>b</sup>	<b>19</b> <sup>b</sup>	<b>20</b>	<b>21</b>	<b>22</b>	<b>23</b>	<b>24</b>
Methanol (R = CH <sub>3</sub> )	89	42	2	18	19	4	5	10
TFE (R = CH <sub>2</sub> CF <sub>3</sub> )	82	30	27	13	13	5	4	7

<sup>a</sup>Product yields are normalized to 100% because mass balances were essentially quantitative; see the *Experimental* section for complete analysis details.

<sup>b</sup>For R = CH<sub>3</sub>, products are designated **18a** and **19a**. For R = CH<sub>2</sub>CF<sub>3</sub>, products are designated **18b** and **19b**.

chemical *cis-trans* isomerization of **20** in acetonitrile provided access to the substituted *cis*-stilbene **21** in a steady-state ratio of *trans*:*cis* = 1:2 (Pyrex filter, 280 nm cut-off). Finally, irradiation of **20** in an aerated solution of methanol gave the substituted phenanthrene **22** after purification by column chromatography. Complete synthetic procedures for all of these compounds are included in the *Experimental* section.

An issue of some concern was whether or not **18a** could react by secondary photochemistry, and thereby revert to carbocation **2**. To this end, a nitrogen-saturated solution of **18a** in methanol was irradiated. Although the ether was consumed (25% conversion after 1 h, 47% after 5 h), only the reduction product **23** was detected. This is clearly a result of radical, not cation, intermediates. Column chromatography of the reaction mixture after a high-conversion photolysis of **18a** provided a convenient method for isolating larger amounts of pure **23** than were obtained following photolysis of **1** in methanol.

#### Photolysis of ester **1** in TFE

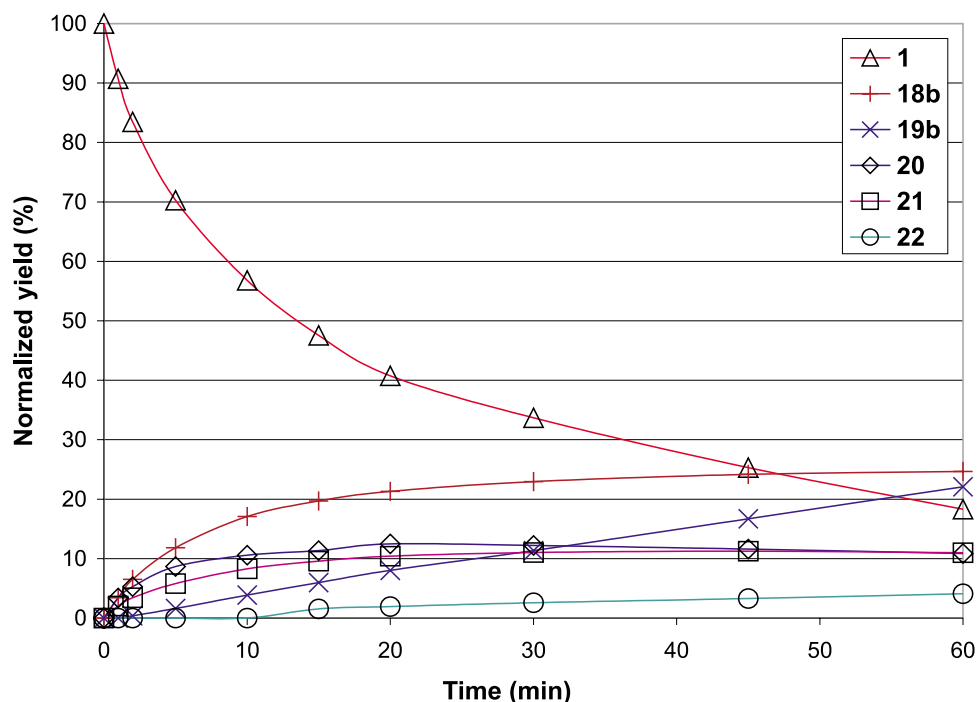
With hopes of prolonging the lifetime of cation **2**, and thereby allowing more time for the rearrangement to **3**, the

photochemistry of **1** in TFE was examined under the same conditions as the experiments in methanol. Figure 2 shows the normalized product yields as a function of time. As indicated in Scheme 4 and Table 1, the same photoproducts were formed, keeping in mind that the addition of TFE to cations **2** and **3** leads to the ethers **18b** and **19b** (i.e., with R = CH<sub>2</sub>CF<sub>3</sub>). The synthesis of both trifluoroethyl ethers was accomplished from alcohols **15** and **25** using a modification of the Mitsunobu reaction developed by Falck and co-workers (17). Attempts to alkylate either **15** or **25** using NaH–DMSO and 2-bromo-1,1,1-trifluoroethane gave no detectable amounts of the desired ethers. Just as in the case of the ether **18a** (R = CH<sub>3</sub>), **18b** (R = CH<sub>2</sub>CF<sub>3</sub>) was also checked for its photochemical reactivity (this time in TFE). Consumption of the ether was observed (29% conversion after 1 h), and compound **23** was again the only product detected. None of the isomeric ether **19b** was detected, confirming that **18b** is not sufficiently reactive to give carbocation intermediates.

Although the % conversion of **1** over 1 h is essentially the same in methanol and TFE (89 vs. 82%) the product yields do show some significant differences. As discussed earlier for the reaction in methanol (R = CH<sub>3</sub>), the ratio of the ether



**Fig. 2.** Product yields as a function of time for the photolysis of ester **1** in TFE (Note: compounds **23** and **24** have been removed for improved clarity).



product derived from cation **2** (**18a**) to the product derived from cation **3** (**19a**) is 21:1 after 1 h. The analogous ratio for **18b:19b** (the reaction in TFE,  $R = \text{CH}_2\text{CF}_3$ ) is 30:27 (approximately 1:1), supporting the possibility that the less nucleophilic solvent (TFE) perhaps allows more time for the 1,2-hydride shift to occur. However, examination of Fig. 2 reveals that the ratio of **18b:19b** is not constant. In fact, the changes in the relative amounts of the ether products during the photolysis of **1** are much more pronounced in TFE (**18b:19b** = 16:1 after 2 min; 1:1 after 1 h) than in methanol (**18a:19a** = 33:1 after 10 min, 21:1 after 1 h).

With the intention of observing the growth of cation **3** directly, a solution of **1** in TFE was subjected to LFP at 266 nm. As shown in the representative spectrum (Fig. 3), an intense absorption band was observed from 280 (the lowest wavelength used) to 350 nm, with a maximum of approximately 300 nm. Importantly, the signal did not decay over any time window investigated with the laser system (10 ns to 50  $\mu\text{s}$ ). The same signal was observed in solutions that were purged with either oxygen or nitrogen. To explore the idea that the signal might be due to a transient species that decays over a much longer time period, a solution of **1** in TFE was submitted to 50 laser pulses, and monitored using a conventional UV-vis spectrometer. The signal did not decay after 30 min, indicating that this signal is not due to a reactive intermediate, but rather to a strongly absorbing photoproduct. Comparison of the laser spectrum with the UV absorption spectra of the isolated products **18–23** suggests that *trans*-stilbene **20** ( $\lambda_{\text{max}} = 303 \text{ nm}$ ,  $\epsilon_{\text{max}} = 29\,000 \text{ M}^{-1} \text{ cm}^{-1}$ ) is the compound responsible for the absorption (Fig. 4).

Also shown in Fig. 4 is the absorption spectrum of **1**. At the maximum light output of the lamp used for the photolysis experiments ( $\lambda = 254 \text{ nm}$ ), the extinction coefficient

of **20** ( $\epsilon_{254} = 3030 \text{ M}^{-1} \text{ cm}^{-1}$ ) is more than three times larger than that of **1** ( $\epsilon_{254} = 800 \text{ M}^{-1} \text{ cm}^{-1}$ ). Furthermore, **20** absorbs much more strongly than **1** at longer wavelengths. This means that when the photolysis of **1** has proceeded to the point that  $[\mathbf{1}] < 3[\mathbf{20}]$ , the majority of the light will be absorbed by **20**. The results from the photolysis of **1** in the two solvents suggest that this condition would be met between 10 and 15 min after starting the photolysis.

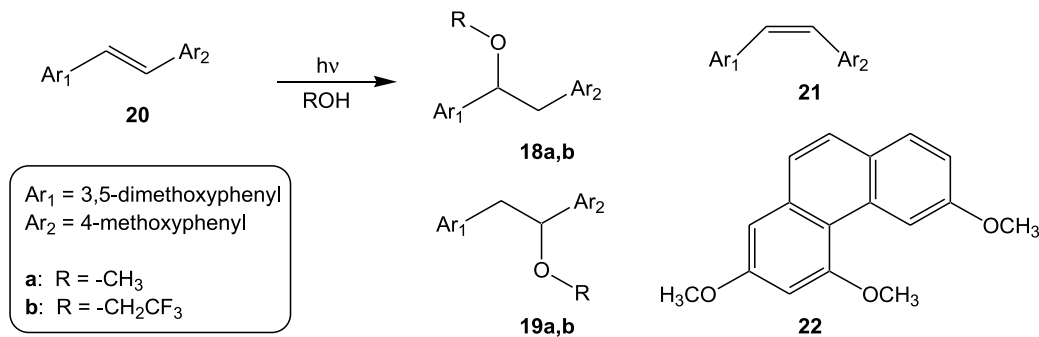
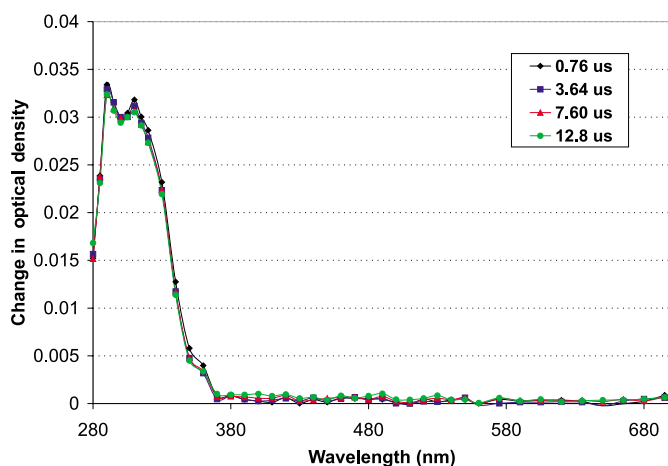
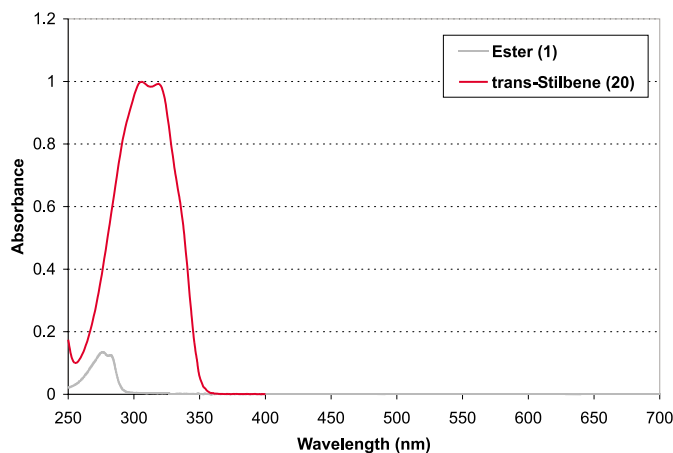
At this point, an important issue must be addressed. Because the formation of **20** during LFP of the ester **1** makes the direct observation of cations **2** and **3** virtually impossible, the use of product yields in assessing the importance of rearrangement becomes critical. If the excited state of **20** is sufficiently reactive to photochemical addition of the alcohol solvent to give the ethers **18** and **19**, then any conclusions about cation rearrangements will be incorrect. To address this point, the photochemistry of **20** in methanol and TFE was examined.

#### Photolysis of substituted *trans*-stilbene **20** in methanol and TFE

The formation of **20** during the photolysis of **1** corresponds to the loss of acetic acid from the parent ester. For this reason, 1 equiv of acetic acid was added to the solution of **20** in either solvent before irradiation, so as to reproduce the reaction conditions as accurately as possible. No product formation was observed after stirring the solutions of **20** in methanol or TFE with added acetic acid for 48 h in the dark, thus, ensuring that **20** does not react by ground-state chemistry during the time frame of the photolysis experiment.

Photolysis of **20** in the two solvents gave a mixture of four products (Scheme 5). All of the products have already been observed during the photolysis of **1**, and so calibrated



**Scheme 5.** Products detected following the photolysis of substituted *trans*-stilbene **20** in methanol and TFE.**Fig. 3.** Change in optical density following LFP at 266 nm of ester **1** in TFE.**Fig. 4.** Comparison of the absorption spectra of ester **1** and substituted *trans*-stilbene **20** (both  $3.45 \times 10^{-5}$  M in methanol).

product yields were calculated (Table 2). The normalized product yields as a function of time are shown in Figs. 5 (methanol) and 6 (TFE). In striking contrast to the ester **1**, which exhibits very similar reactivity in either methanol or TFE, **20** reacts much faster in TFE than in methanol. After 1 h, the % conversion of **20** in methanol is 48%, whereas the % conversion is 80% after the same time in TFE. In both solvents, the substituted stilbene isomers approach the steady state composition of 1:1 and then disappear simultaneously, although this process occurs much more rapidly in TFE. Another important observation is that the ether products observed require the formation of both carbocations **2** and **3** by photochemical protonation of **20**. Furthermore, in contrast to the results for **1**, the ethers produced from nucleophilic attack on the rearranged carbocation **3** (i.e., **19a** and **19b**) are formed in greater yield than their isomeric counterparts (**18a** and **18b**). In fact, **18a** was not detected even after 5 h of irradiation. These results strongly suggest that cation **3** is formed rapidly upon photolysis of **20** in methanol and TFE.

## Discussion and conclusions

The general mechanism that has been developed for ester photochemistry seems to hold for ester **1**. Both ion- and radical-derived products are formed. The results from the photolysis of **1** in methanol and TFE initially suggested that the desired 1,2-hydride shift occurred as was predicted

(eq. [1]). This was based on the idea that TFE, being a less nucleophilic solvent, would promote the formation of carbocation **3** from carbocation **2**. The difference in the final product ratios (**18**:**19**) seemed to support this idea. However, closer inspection of the data revealed that this ratio is not constant over the course of the experiment. For the reaction in methanol, **18a**:**19a** = 33:1 after 10 min, and 20:1 after 60 min. The change is even more drastic for the photolysis in TFE: after 2 min **18b**:**19b** = 16:1, but after 1 h the ratio is **18b**:**19b** = 1:1. The change in the relative amounts of the products that result from nucleophilic attack on carbocations **2** and **3** indicates that a secondary photochemical reaction occurs during the steady-state photolysis of **1**. One possible explanation is that the ethers **18** decay over the course of the photolysis experiments involving **1**. Although these ethers were shown to be photochemically active in the control experiments, they appear to react too slowly to account for the observed change in the **18**:**19** ratio. Furthermore, the presence of several strongly absorbing compounds in the same reaction mixture will make absorption by the ethers **18** even less likely. Indeed, the only experiment in which decay of either **18a** or **18b** was detected was during the photolysis of **20** in TFE (Fig. 4). The yield of **18b** does decrease over the final 2 h of the experiment (4 to 2%), but only after most of the substituted stilbenes have been converted to products.

A much more satisfying explanation of the observed change in the **18**:**19** ratio is that secondary photochemistry provides an alternative pathway for the formation of the

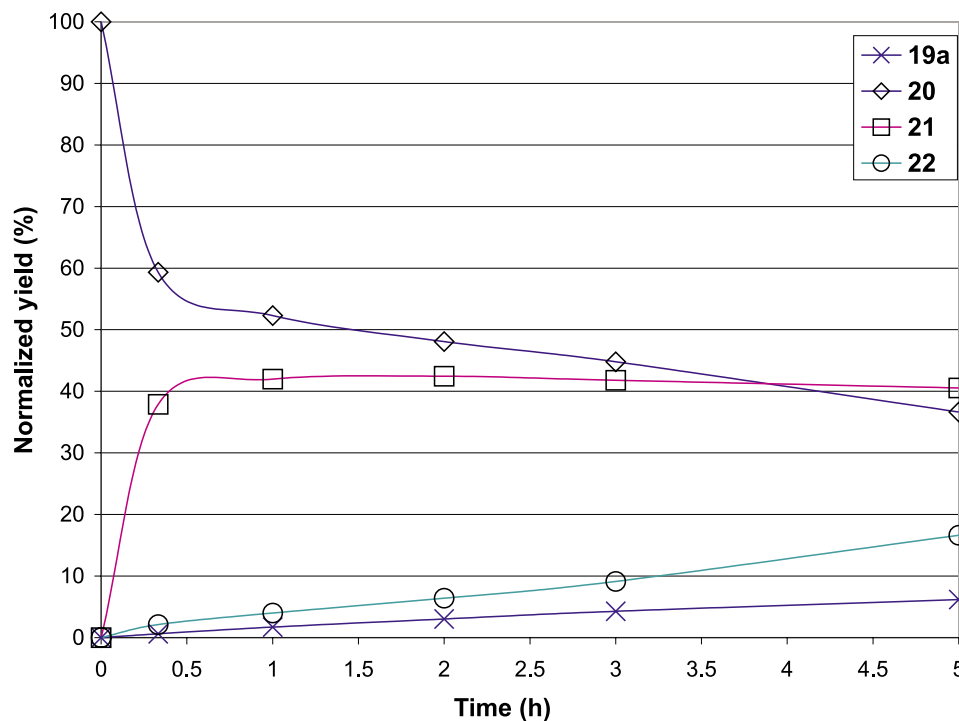


**Table 2.** Product yields after photolysis of substituted *trans*-stilbene **20** in methanol and TFE.

Solvent	Time (h)	% Conversion <sup>a</sup>	<b>18</b> <sup>b</sup>	<b>19</b> <sup>b</sup>	<b>21</b>	<b>22</b>
Methanol (R = CH <sub>3</sub> )	1	48	0	4	88	8
Methanol (R = CH <sub>3</sub> )	5	63	0	10	64	26
TFE (R = CH <sub>2</sub> CF <sub>3</sub> )	1	80	4	60	27	9
TFE (R = CH <sub>2</sub> CF <sub>3</sub> )	4	95	2	87	3	8

<sup>a</sup>Product yields are normalized to 100% because mass balances were essentially quantitative; see the *Experimental* section for complete analysis details.

<sup>b</sup>For R = CH<sub>3</sub>, products are designated **18a** and **19a**. For R = CH<sub>2</sub>CF<sub>3</sub>, products are designated **18b** and **19b**.

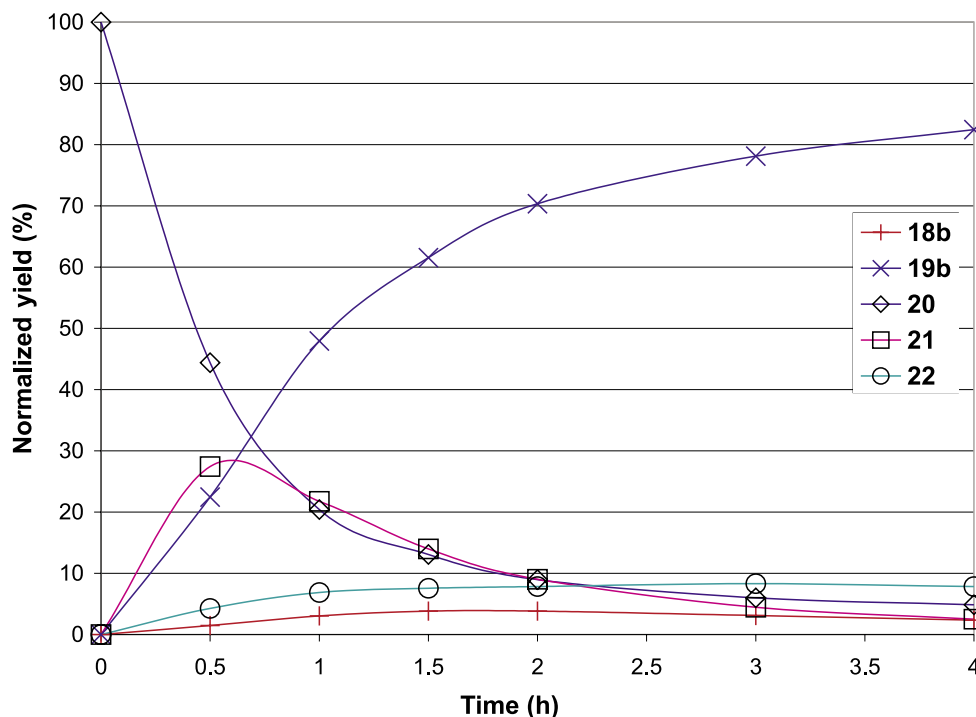
**Fig. 5.** Product yields as a function of time for the photolysis of substituted *trans*-stilbene **20** in methanol.

products derived from the cation **3**, specifically the ethers **19**. As shown in the control experiments involving **18a** and **18b**, there is no pathway for converting **18** to **19**. Rather, the secondary photochemical reaction is addition of the solvent to the excited state of the substituted *trans*-stilbene **20**. As clearly shown by the steady-state photolysis results, cation-derived products (i.e., **18** and **19**) can be formed in reasonable efficiency from **20** under the same reaction conditions used for the photolysis of ester **1**. Furthermore, this reaction favours the ethers **19** over **18**, which is the reverse of the regiochemistry observed for the photolysis of **1**. The LFP experiments demonstrate that **20** is formed rapidly upon irradiation of **1**, and will be available to absorb competitively with **1** very early in the photolysis experiments involving the ester. Therefore, as the substituted *trans*-stilbene **20** accumulates during the photolysis of **1**, the photochemistry of **20** will become more important, and **19** (formed primarily from **20**) will eventually be formed more rapidly than **18** (formed primarily from **1**). Indeed, even if the formation of **20** did not make the observation of benzylic carbocations by LFP impossible (by obscuring the wavelengths of interest), the observation of a signal corresponding to cation **3** would not be conclusive evidence for the rearrangement of interest.

Unfortunately, the rapid formation of **20** upon photolysis of **1** makes the ester a poor substrate for the investigation of cation rearrangements. Our results are similar to those of Lee-Ruff and co-workers (11) (Scheme 2), where the desired cation rearrangement is too unfavourable to compete with rapid quenching by the alcohol solvent (either by nucleophilic attack or by deprotonation). However, the photochemistry of **1** is further complicated by the fact that the by-products themselves react by secondary photochemistry, making reliable assessment of the rearrangement extremely difficult.

There are several other points that need to be addressed for a thorough understanding of the photochemistry of **1** and its photoproducts. Firstly, although deprotonation of cation **2** or **3** appears to be the most likely pathway for formation of **20**, more study is needed to rule out other mechanisms. Work is in progress to examine the possibility that substituted stilbenes **20** and **21** are produced by either a radical pathway or by concerted photochemical elimination of acetic acid from **1**. In addition, the 1,2,2-trimethyl derivative of **1** is currently being synthesized. This substrate may allow the observation of a rearrangement without the complications present for **1** because rearrangement and nucleophilic trap-



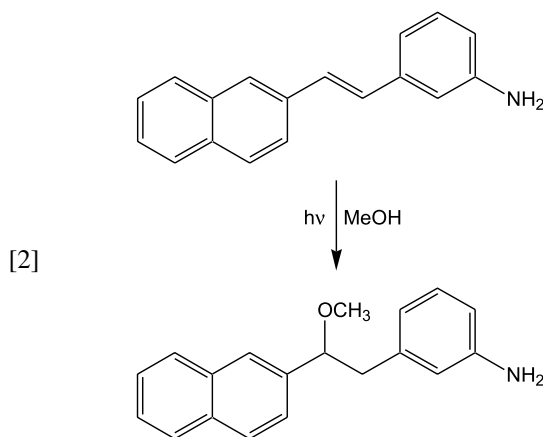
**Fig. 6.** Product yields as a function of time for the photolysis of substituted *trans*-stilbene **20** in TFE.

ping may be the only reactions available for the initial carbocation.

Secondly, the photochemical addition of alcohols to substituted stilbenes needs to be investigated in much greater detail. At first, the reaction appears to be analogous to the photohydration of substituted styrenes that has been studied extensively by McEwen and Yates (18), who demonstrated that excitation of 3-methoxystyrene in water gave the Markovnikov addition product faster than 4-methoxystyrene (another example of the photochemical meta effect). Additional support for the presence of a carbocation intermediate in such photochemical additions was provided by McClelland and co-workers (19), who found that laser flash photolysis of 4-methoxystyrene in TFE produced a transient absorption signal at 340 nm that was attributed to the corresponding cation. However, the presence of a second aromatic ring in the single chromophore of the substituted stilbenes makes the assessment of substituent effects much more complicated than for substituted styrenes (with regards to both the rate of the reaction and the regiochemistry of the addition).

A survey of the literature indicates that the photochemical addition of methanol to a variety of substituted stilbenes was first observed by Laarhoven and co-workers (20). In contrast to the results for substituted styrenes, the yield of stilbene-solvent adduct was found to be independent of acid concentration. This suggested that protonation of the singlet excited state is not the rate-limiting step in the photochemical addition of methanol to substituted stilbenes. With the aid of experiments conducted in deuterated methanol, the authors concluded that the addition of methanol to stilbenoid systems occurs via two competing mechanisms: (i) direct addition across the central bond; and (ii) rearrangement of the excited state via a 1,2-hydride shift to give a carbene inter-

mediate, which then inserts directly to the methanol O—H(D) bond. However, the influence of electron-rich substituents in the meta position was never addressed (the only compound examined with meta substituents was the symmetric 3,3'-dimethylstilbene). In more recent work, Lewis et al. (21, 22) have made several detailed studies of the effect of electron-donating substituents (mostly amino) on the fluorescence behaviour of substituted stilbenes and related compounds. These results indicate that stilbenes with electron-donating meta-substituents have longer singlet lifetimes and higher fluorescence quantum yields than the para-substituted analogues. Furthermore, the authors attribute this observation to a higher barrier for bond torsion in the meta-substituted cases. Addition of methanol was only observed in one case (21) (eq. [2]). However, methanol was not employed as a solvent for many of the photophysical studies that were of interest to the authors, so the reaction may in fact be more general.





From the results of the current study, just how the photochemistry of **20** fits with the examples in the literature is not yet clear. The rapid addition of the solvent (TFE in particular) appears to be because of the two meta substituents (the 3,5-dimethoxyphenyl ring), while the preferred regiochemistry is governed by the para substituent (4-methoxyphenyl ring). We had originally believed that the increased reactivity of **20** in TFE compared to methanol could be attributed to the greater effective acidity of the former solvent, which might lead to more rapid protonation of the excited state. However, the study by Laarhoven and co-workers (20) seems to indicate that the mechanism of solvent addition may be even more complicated. Clearly, a larger set of stilbene derivatives is required to confidently assess the factors controlling the reaction. This work is currently in progress.

## Experimental

### General procedures

Melting points were determined on a Fisher-Johns apparatus and are uncorrected.  $^1\text{H}$  and  $^{13}\text{C}$  NMR spectra were recorded in deuterated chloroform on a Bruker AC 250F instrument, and chemical shifts are reported as parts per million (ppm) relative to tetramethylsilane internal standard. The coupling constants of the ABX systems observed in several compounds were analysed by matching the line positions with those of simulated spectra. Gas chromatography was performed on a Perkin-Elmer Autosystem XL instrument (controlled by a computer with TurboMass and TurboChrom software) with one Turbomass detector and one FID (both columns: Supelco 30 m/0.25 mm MDN-5S 5% phenyl methylsiloxane, film thickness 0.50  $\mu\text{m}$ ). For GC-MS, the injection volume was 1  $\mu\text{L}$ ; mass spectral data are reported in units of mass over charge ( $m/z$ ) with intensities relative to the base peak (in brackets). For GC-FID, an injection volume of 2.5  $\mu\text{L}$  was used. The same temperature program was used for both detectors: 60°C for 1 min, ramp at 20°C/min to 240°C, hold at 240°C for 20 min. Ultraviolet spectra were recorded on a Varian-Cary Bio 100 spectrometer.

Methanol, water, ethyl acetate, and hexanes were all distilled prior to use. Dichloromethane, benzene, dimethylsulfoxide (DMSO), TFE, pentane, and the deuterated solvents were all reagent grade, while acetonitrile was HPLC grade (these solvents were used without extra purification). Tetrahydrofuran (THF) was distilled from sodium-benzophenone, and then a second time from lithium aluminium hydride before being kept under nitrogen. All starting materials were supplied by Aldrich Chemicals, with the exception of 3,5-dimethoxyaniline and 3,5-dimethoxybenzaldehyde (Avocado Chemicals). Thin layer chromatography was performed using plates from Eastman-Kodak. Preparative chromatography was performed using 60–250 mesh silica gel from Silicycle.

### Synthetic procedures

#### 3,5-Dimethoxybromobenzene (**16**)

This compound was prepared from the diazonium ion made from 3,5-dimethoxyaniline using the procedure described (12) for the synthesis of *o*-bromochlorobenzene,

yield 33%: mp 64–65°C, lit. (13) mp 64–66°C.  $^1\text{H}$  NMR  $\delta$ : 6.66 (d, 2H,  $J = 2.4$  Hz), 6.37 (t, 3H,  $J = 2.4$  Hz), 3.76 (s, 6H).  $^{13}\text{C}$  NMR  $\delta$ : 161.2, 123.0, 109.8, 99.8, 55.5. GC-MS  $m/z$ : 218 (82.6), 216 (100.0), 108 (69.7), 79 (41.6), 77 (56.2), 63 (48.9), 51 (26.3).

#### 2-(4-Methoxyphenyl)ethanal (**17**)

This compound was prepared from 4-methoxybenzaldehyde by glycidic ester condensation as described (14), yield of 74% over three steps:  $^1\text{H}$  NMR  $\delta$ : 9.66 (d, 1H,  $J = 2.4$  Hz), 7.09 (d, 2H,  $J = 8.5$  Hz), 6.88 (d, 2H,  $J = 8.5$  Hz), 3.75 (s, 3H), 3.57 (d, 2H,  $J = 2.4$  Hz).  $^{13}\text{C}$  NMR  $\delta$ : 199.8, 159.0, 130.8, 123.9, 144.4, 55.2, 49.6. GC-MS  $m/z$ : 121 (100), 91 (20.5), 78 (23.9), 77 (31.2), 51 (12.2).

#### 1-(3,5-Dimethoxyphenyl)-2-(4-methoxyphenyl)ethan-1-ol (**15**)

For this reaction, all glassware was dried in an oven and purged with nitrogen gas prior to use. Liquid transfers were performed using a cannula needle under positive pressure. A solution of 3,5-dimethoxybromobenzene **16** (4.00 g, 18.4 mmol) in THF (20 mL) was prepared, and then transferred to a dropping funnel atop a three-necked 100 mL round-bottomed flask containing magnesium turnings (2.68 g, 110 mmol) in THF (5 mL). Approximately 10% of the aryl halide solution was run into the flask, along with a small crystal of iodine. After 15 min of stirring, the yellow colour of the iodine disappeared, and the mixture began to reflux. The remaining solution in the dropping funnel was added to the magnesium over 15 min, and the mixture was refluxed for 30 min after the addition was complete. After cooling to room temperature, the resulting orange solution was transferred under nitrogen to a clean three-necked flask.

A solution of 2-(4-methoxyphenyl)ethanal **17** (2.76 g, 18.4 mmol, distilled under vacuum prior to use) in THF (20 mL) was prepared. The solution was then added dropwise to the solution containing the Grignard reagent, and the resulting mixture was refluxed for 30 min after the addition was complete. After cooling to room temperature, the yellow solution was poured into a separatory funnel containing saturated ammonium chloride solution (100 mL) and dichloromethane (50 mL). The layers were separated, and the aqueous portion was extracted with dichloromethane (2  $\times$  50 mL). The combined organic extracts were washed with distilled water and saturated sodium chloride solution (2  $\times$  75 mL each). After drying over anhydrous magnesium sulfate and filtering, the solvent was removed under reduced pressure to give 5.10 g of the product alcohol (96%). Further reactions were performed using the crude material, although characterization was performed using a sample recrystallized from ethyl acetate – hexanes, mp: 97–99 °C.  $^1\text{H}$  NMR  $\delta$ : 7.09 (d, 2H,  $J = 8.6$  Hz), 6.83 (d, 2H,  $J = 8.6$  Hz), 6.49 (d, 2H, 2.4 Hz), 6.36 (t, 1H,  $J = 2.4$  Hz), 4.76 (m, 1H,  $J_1 = 8.5$  Hz,  $J_2 = 4.9$  Hz,  $J_3 = 2.4$  Hz), 3.77 (s, 9H), 2.95 (m, 1H,  $J_1 = 13.7$  Hz,  $J_2 = 4.9$  Hz), 2.89 (m, 1H,  $J_1 = 13.7$  Hz,  $J_2 = 8.5$  Hz), 2.07 (d, 1H,  $J = 2.4$  Hz).  $^{13}\text{C}$  NMR  $\delta$ : 160.8, 158.4, 146.5, 130.5, 130.0, 113.9, 103.8, 99.6, 75.4, 55.4, 55.3, 45.1. GC-MS  $m/z$ : 271 (5.6), 270 (35.8), 167 (13.1), 139 (35.8), 122 (100.0), 121 (49.9), 77 (16.0). HR-MS calcd.: 288.1361; found: 288.1357  $\pm$  0.0008.



**1-(3,5-Dimethoxyphenyl)-2-(4-methoxyphenyl)ethyl ethanoate (1)**

This compound was prepared using the method of Steglich and Neises (15). A solution of *N,N*-dimethyl-4-aminopyridine (63 mg, 0.52 mmol) and acetic acid (312 mg, 5.2 mmol) in dichloromethane (25 mL) was prepared, and then added to a solution of 1-(3,5-dimethoxyphenyl)-2-(4-methoxyphenyl)ethan-1-ol **15** (1.5 g, 5.2 mmol) in dichloromethane (30 mL). After the resulting solution was cooled in an ice bath, 1,3-dicyclohexylcarbodiimide (1.17 g, 5.67 mmol) was added in one portion. The resulting mixture was stirred at 0°C for 5 min, and then allowed to stir at room temperature for 3 h. The urea precipitate was filtered off, the solvent was removed under reduced pressure, and the residue was taken up in dichloromethane (50 mL) and filtered again. The clear solution was then washed with 0.5 M hydrochloric acid and distilled water (2 × 25 mL each). The organic material was then dried with anhydrous magnesium sulfate, filtered, and the solvent removed under reduced pressure to give a clear oil. The oil was adsorbed onto silica for column chromatography. Using 5% ethyl acetate – hexanes as the eluant provided 1.5 g of a solid product, which was recrystallized from the same solvent mixture to give 1.2 g of colourless crystals (70%), mp: 68–69°C. <sup>1</sup>H NMR δ: 7.03 (d, 2H, *J* = 8.6 Hz), 6.78 (d, 2H, *J* = 8.6 Hz), 6.40 (d, 2H, *J* = 2.4 Hz), 6.37 (t, 1H, *J* = 2.4 Hz), 5.81 (m, 1H, *J*<sub>1</sub> = 7.9 Hz, *J*<sub>2</sub> = 6.1 Hz), 3.77 (s, 3H), 3.75 (s, 6H), 3.08 (m, 1H, *J*<sub>1</sub> = 14.0 Hz, *J*<sub>2</sub> = 7.9 Hz), 2.97 (m, 1H, *J*<sub>1</sub> = 14.0 Hz, *J*<sub>2</sub> = 6.1 Hz), 2.02 (s, 3H). <sup>13</sup>C NMR δ: 170.1, 160.7, 158.3, 142.6, 130.5, 129.1, 113.6, 104.6, 99.7, 76.7, 55.3, 55.2, 42.1, 21.2. GC–MS *m/z*: 270 (41.5), 167 (49.1), 139 (20.3), 121 (100), 77 (14.9). HR–MS calcd.: 330.1467; found: 330.1461 ± 0.0008.

**1-(3,5-Dimethoxyphenyl)-2-(4-methoxyphenyl)-1-methoxyethane (18a)**

A 60% sodium hydride – oil suspension (0.08 g of suspension, 0.002 mmol NaH) was washed with hexane to remove the oil. After decanting the washes, the residue was taken up in DMSO (2 mL) and added to a solution of 1-(3,5-dimethoxyphenyl)-2-(4-methoxyphenyl)ethan-1-ol **15** (0.288 g, 1.00 mmol) in DMSO (5 mL). The mixture was stirred at room temperature for 30 min, and then a solution of methyl iodide (0.284 g, 2.00 mmol) in DMSO (5 mL) was added dropwise. After stirring the solution for 3.5 h, distilled water (12 mL) was added slowly to quench the reaction. The organic layer was drawn off, and the aqueous portion was extracted with dichloromethane (3 × 10 mL). The combined organic material was washed with distilled water (3 × 25 mL), dried with anhydrous magnesium sulfate, and filtered. Removal of the solvent under reduced pressure gave 0.25 g of material, which was adsorbed onto silica for column chromatography. Elution using 2.5% ethyl acetate – hexanes gave the pure ether (0.098 g, 32%). Characterization was performed on a sample that was further purified by bulb-to-bulb distillation. <sup>1</sup>H NMR δ: 7.03 (d, 2H, *J* = 6.7 Hz), 6.78 (d, 2H, *J* = 6.7 Hz), 6.38 (m, 3H), 4.21 (dd, 1H, *J*<sub>1</sub> = 5.5 Hz, *J*<sub>2</sub> = 7.6 Hz), 3.77 (s, 3H), 3.75 (s, 6H), 3.20 (s, 3H), 3.01 (dd, 1H, *J*<sub>1</sub> = 7.6 Hz, *J*<sub>2</sub> = 13.7 Hz), 2.82 (dd, 1H, *J*<sub>1</sub> = 5.5 Hz, *J*<sub>2</sub> = 13.7 Hz). <sup>13</sup>C NMR δ: 160.8,

158.0, 144.4, 130.4, 113.5, 104.6, 99.6, 85.4, 56.9, 55.3, 55.2, 43.8. GC–MS *m/z*: 303 (0.8), 302 (4.4), 271 (1.5), 270 (6.3), 182 (10.4), 181 (100.0), 121 (12.1). HR–MS calcd.: 302.1518; found: 302.1522 ± 0.0008.

**1-(3,5-Dimethoxyphenyl)-2-(4-methoxyphenyl)-1-(trifluoroethoxy)ethane (18b)**

This compound was prepared using the method of Falck et al. (17). To a solution of 1-(3,5-dimethoxyphenyl)-2-(4-methoxyphenyl)ethan-1-ol **15** (0.300 g, 1.04 mmol) in benzene (20 mL) was added 1,1'-(azodicarbonyl)dipiperidine (0.525 g, 2.08 mmol). The flask was purged with nitrogen for 10 min, and tri(*n*-butyl)phosphine (0.421 g, 2.08 mmol) was added. After stirring the reaction mixture for another 15 min, TFE (1.04 g, 10.4 mmol) was added. The mixture was stirred at room temperature for 1 h, and the solvent was then removed under reduced pressure. The residue was taken up in dichloromethane, filtered, and the liquid then adsorbed onto silica gel for column chromatography. Elution with 5% ethyl acetate – hexanes gave the desired product (0.154 g, 40% yield). <sup>1</sup>H NMR δ: 7.03 (2H, d, *J* = 8.6 Hz), 6.78 (d, 2H, *J* = 8.6 Hz), 6.38 (s, 3H), 4.43 (dd, 1H, *J*<sub>1</sub> = 5.5 Hz, *J*<sub>2</sub> = 7.3 Hz), 3.77 (s, 3H), 3.75 (s, 6H), 3.64 (m, 2H), 3.09 (dd, 1H, *J*<sub>1</sub> = 14.0 Hz, *J*<sub>2</sub> = 7.3 Hz), 2.86 (dd, 1H, *J*<sub>1</sub> = 14.0 Hz, *J*<sub>2</sub> = 5.5 Hz). <sup>13</sup>C NMR δ: 161.0, 158.2, 142.6, 130.5, 129.7, 124.0 (q, *J* = 278.6 Hz), 113.5, 104.6, 100.1, 84.9, 66.0 (q, *J* = 34.3 Hz), 55.3, 55.2, 43.5. GC–MS (*m/z*): 371 (1.5), 370 (7.9), 270 (6.8), 250 (11.6), 249 (100.0), 166 (22.1), 121 (81.1). HR–MS calcd.: 370.1392; found: 370.1392 ± 0.0008.

**2-(3,5-Dimethoxyphenyl)ethanal (26)**

The sodium salt of 3-(3,5-dimethoxyphenyl)glycidic acid was prepared in two steps (62% yield) using the same procedures as described for the synthesis of 2-(4-methoxyphenyl)ethanal **17** (14). Decarboxylation of the sodium salt was accomplished using the method of Bullimore et al. (23), giving the desired aldehyde in 20% yield (12% over three steps). <sup>1</sup>H NMR δ: 9.69 (t, 1H, *J* = 2.4 Hz), 6.40 (t, 1H, *J* = 1.8 Hz), 6.35 (d, 2H, *J* = 1.8 Hz), 3.77 (s, 6H), 3.58 (d, 2H, *J* = 2.4 Hz). <sup>13</sup>C NMR δ: 199.2, 161.3, 134.0, 107.6, 99.3, 55.3, 50.7.

**1-(4-Methoxyphenyl)-2-(3,5-dimethoxyphenyl)ethan-1-ol (25)**

A solution of 4-bromoanisole (1.04 g, 5.55 mmol) in THF (10 mL) was prepared under nitrogen, and then transferred to a dropping funnel atop a three-necked 100 mL round-bottomed flask containing magnesium turnings (0.81 g, 33.3 mmol). Approximately 10% of the aryl halide solution was added to the magnesium along with an iodine crystal, and the reaction began within 10 min. The remaining aryl halide solution was added over 5 min, and the resulting mixture was heated to reflux for 30 min after the addition was complete. After cooling to room temperature, the resulting orange solution was transferred under nitrogen to a clean three-necked flask.

A solution of 2-(3,5-dimethoxyphenyl)ethanal **26** (1.00 g, 5.55 mmol) in THF (10 mL) was added dropwise to the Grignard reagent, and the resulting mixture was refluxed gently for 30 min. The mixture was then cooled, and added to a separatory funnel containing saturated ammonium chlo-



ride (50 mL) and dichloromethane (25 mL). The layers were separated, and the aqueous portion was extracted with dichloromethane (2 × 50 mL). The combined organic extracts were washed with water and saturated sodium chloride (2 × 25 mL each), and then dried with anhydrous magnesium sulfate. Removal of solvent under reduced pressure gave a crude oil, which was purified by column chromatography (10% ethyl acetate – hexanes, eluant) to give the desired product (1.00 g, 63% yield).  $^1\text{H}$  NMR  $\delta$ : 7.26 (d, 2H,  $J$  = 8.5 Hz), 6.87 (d, 2H,  $J$  = 8.5 Hz), 6.33 (s, 3H), 4.81 (dd, 1H,  $J_1$  = 8.5 Hz,  $J_2$  = 4.9 Hz), 3.78 (s, 3H), 3.73 (s, 6H), 2.92 (m, 2H,  $J_1$  = 8.5 Hz,  $J_2$  = 4.9 Hz,  $J_3$  = 13.7 Hz), 2.12 (s, 1H).  $^{13}\text{C}$  NMR  $\delta$ : 160.7, 159.0, 140.6, 136.1, 127.2, 113.7, 107.4, 98.6, 74.7, 55.3, 55.2, 46.3.

#### 2-(3,5-Dimethoxyphenyl)-1-(4-methoxyphenyl)-1-methoxyethane (19a)

A 60% sodium hydride – oil suspension (0.083 g of suspension, 2.08 mmol NaH) was washed with hexane to remove the oil. After decanting the washes, the residue was taken up in DMSO (5 mL) and added to a solution of 2-(3,5-dimethoxyphenyl)-1-(4-methoxyphenyl)ethan-1-ol **25** (0.300 g, 1.00 mmol) in DMSO (10 mL). The mixture was stirred at room temperature for 30 min, and then a solution of methyl iodide (0.295 g, 2.08 mmol) in DMSO (5 mL) was added dropwise. After stirring the solution for 5 h, distilled water (15 mL) was added slowly to quench the reaction. The organic layer was drawn off, and the aqueous portion was extracted with dichloromethane (3 × 20 mL). The combined organic material was washed with distilled water and saturated sodium chloride solution (2 × 20 mL each), dried with anhydrous magnesium sulfate, and filtered. Removal of the solvent under reduced pressure gave 0.34 g of material, which was adsorbed onto silica for column chromatography. Elution using 5% ethyl acetate – hexanes gave the pure ether (0.24 g, 32%). Characterization was performed on a sample that was further purified by bulb-to-bulb distillation.  $^1\text{H}$  NMR  $\delta$ : 7.15 (d, 2H,  $J$  = 8.5 Hz), 6.87 (d, 2H,  $J$  = 8.5 Hz), 6.29 (t, 1H,  $J$  = 1.8 Hz), 6.26 (d, 2H,  $J$  = 1.8 Hz), 4.27 (dd, 1H,  $J_1$  = 6.2 Hz,  $J_2$  = 7.4 Hz), 3.80 (s, 3H), 3.71 (s, 6H), 3.17 (s, 3H), 3.06 (dd, 1H,  $J_1$  = 13.4 Hz,  $J_2$  = 7.4 Hz), 2.80 (dd, 1H,  $J_1$  = 13.4 Hz,  $J_2$  = 6.2 Hz).  $^{13}\text{C}$  NMR  $\delta$ : 160.4, 159.1, 140.9, 133.6, 128.0, 113.7, 107.4, 98.3, 84.4, 56.5, 55.2 (two signals), 45.0. GC–MS ( $m/z$ ): 302 (not observed), 286 (9.3), 270 (6.7), 165 (11.5), 151 (29.8), 122 (9.2), 121 (100.0). HR–MS calcd.: 302.1518; found: 302.1526 ± 0.0008.

#### 2-(3,5-Dimethoxyphenyl)-1-(4-methoxyphenyl)-1-(trifluoroethoxy)ethane (19b)

This compound was prepared using the method of Falck et al. (17). To a solution of 2-(3,5-dimethoxyphenyl)-1-(4-methoxyphenyl)ethan-1-ol **25** (0.300 g, 1.04 mmol) in benzene (20 mL) was added 1,1'-(azodicarbonyl)dipiperidine (0.525 g, 2.08 mmol). The flask was purged with nitrogen for 10 min, and tri(*n*-butyl)phosphine (0.421 g, 2.08 mmol) was added. After stirring the reaction mixture for another 15 min, TFE (1.04 g, 10.4 mmol) was added. The mixture was stirred at room temperature for 1 h, and the solvent was then removed under reduced pressure. The residue was taken up in dichloromethane, filtered, and the liquid then adsorbed onto silica gel for column chromatography. Elution with 5% ethyl acetate – hexanes gave the desired product (0.210 g,

55% yield).  $^1\text{H}$  NMR  $\delta$ : 7.16 (d, 2H,  $J$  = 9.2 Hz), 6.30 (d, 2H,  $J$  = 9.2 Hz), 6.31 (t, 1H,  $J$  = 1.8 Hz), 6.29 (d, 2H,  $J$  = 1.8 Hz), 4.50 (dd, 1H,  $J_1$  = 5.5 Hz,  $J_2$  = 7.3 Hz), 3.80 (s, 3H), 3.72 (s, 6H), 3.62 (m, 2H), 3.14 (dd, 1H,  $J_1$  = 14.0 Hz,  $J_2$  = 7.3 Hz), 2.83 (dd, 1H,  $J_1$  = 14.0 Hz,  $J_2$  = 5.5 Hz).  $^{13}\text{C}$  NMR  $\delta$ : 160.5, 159.6, 140.1, 132.0, 128.1, 124.0 (q,  $J$  = 278.6 Hz), 114.0, 107.4, 98.8, 84.1, 65.8 (q,  $J$  = 34.3 Hz), 55.3, 55.2, 44.8. GC–MS ( $m/z$ ): 370 (1.1), 271 (5.8), 270 (27.6), 220 (10.6), 219 (100.0), 135 (27.3). HR–MS calcd.: 370.1392; found: 370.1389 ± 0.0008.

#### trans-1-(3,5-Dimethoxyphenyl)-2-(4-methoxyphenyl)ethene (20)

A solution of 1-(3,5-dimethoxyphenyl)-2-(4-methoxyphenyl)ethan-1-ol **15** (4.00 g, 13.9 mmol) in benzene (600 mL) was prepared in a three-necked round-bottomed flask. A portion of *p*-toluenesulfonic acid (0.29 g, 1.5 mmol) was added, and the solution was heated to reflux with stirring. Water was removed from the mixture by way of a Dean–Stark trap. After 6 h, analysis by GC–MS indicated that 97% of the starting material had reacted, and the reaction mixture was allowed to cool to room temperature. The solution was then washed with distilled water, and saturated sodium chloride solution (2 × 200 mL each). A portion of benzene (100 mL) was used to reextract the aqueous washes. The combined organic material was then dried with anhydrous magnesium sulfate, filtered, and the solvent was removed under reduced pressure to give an orange oil. Isolation of the desired product was achieved using column chromatography with 20% ethyl acetate – hexanes (eluant). Recrystallization of the resulting product from pentane gave white crystals (1.27 g, 34% yield), mp 55–57°C, lit. (24) mp 53–54°C.  $^1\text{H}$  NMR  $\delta$ : 7.43 (d, 2H,  $J$  = 8.6 Hz), 7.05 (d, 1H,  $J$  = 16.5 Hz), 6.91 (d, 1H,  $J$  = 16.5 Hz), 6.90 (d, 2H,  $J$  = 8.6 Hz), 6.65 (d, 2H,  $J$  = 2.4 Hz), 6.38 (t, 1H,  $J$  = 2.4 Hz), 3.83 (s, 9H).  $^{13}\text{C}$  NMR  $\delta$ : 161.0, 159.4, 139.7, 129.9, 128.7, 127.8, 126.6, 114.1, 104.3, 99.6, 55.4, 55.3. GC–MS ( $m/z$ ): 271 (17.6), 270 (100.0), 269 (15.5), 239 (19.7), 224 (13.0), 196 (12.7), 195 (12.33), 165 (10.3), 153 (12.4), 152 (17.6), 141 (10.5). HR–MS calcd.: 270.1256; found: 270.1263 ± 0.0008.

#### cis-1-(3,5-Dimethoxyphenyl)-2-(4-methoxyphenyl)ethene (21)

A solution of *trans*-1-(3,5-dimethoxyphenyl)-2-(4-methoxyphenyl)ethene **20** (0.40 g, 1.5 mmol) in acetonitrile (340 mL) was prepared in a large photolysis reaction vessel, and purged with nitrogen for 30 min. A 450 W, medium-pressure Hanovia mercury lamp with a Pyrex filter (300 nm cut-off) was employed to irradiate the solution for 30 min. Analysis by GC–FID indicated that by this time the mixture had achieved a photostationary state consisting of a 2:1 ratio of the *cis* and *trans* isomers. The solvent was removed under reduced pressure, and the residue was prepared for column chromatography. Separation of the isomers was achieved using 2.5% ethyl acetate – hexanes (eluant), and the pure *cis* isomer was isolated as a clear oil (0.15 g, 38% yield).  $^1\text{H}$  NMR  $\delta$ : 7.19 (d, 2H,  $J$  = 8.5 Hz), 6.78 (d, 2H,  $J$  = 8.5 Hz), 6.52 (d, 1H,  $J$  = 12.2 Hz), 6.44 (d, 1H,  $J$  = 12.2 Hz), 6.43 (d, 2H,  $J$  = 2.4 Hz), 6.32 (t, 1H,  $J$  = 2.4 Hz), 3.78 (s, 3H), 3.67 (s, 6H).  $^{13}\text{C}$  NMR  $\delta$ : 160.6, 158.7, 139.5, 130.3, 130.2, 129.6, 128.7, 113.5, 106.6, 99.7, 55.2. GC–MS ( $m/z$ ): 271



(16.44), 270 (100.0), 269 (17.5), 239 (22.5), 224 (14.5), 165 (10.6), 153 (12.7), 152 (18.6), 141 (10.6), 127 (11.2), 115 (14.6). HR-MS calcd.: 270.1256; found: 270.1254  $\pm$  0.0008.

### 2,4,6-Trimethoxyphenanthrene (22)

A solution of *trans*-1-(3,5-dimethoxyphenyl)-2-(4-methoxyphenyl)ethene **20** (0.30 mg, 1.1 mmol) in methanol (340 mL) was prepared in a large photolysis reaction vessel. To promote the formation of the desired product, no nitrogen was used. A 450 W, medium-pressure Hanovia mercury lamp with a Pyrex filter (280 nm cut-off) was employed to irradiate the solution for 7 h. The solvent was removed under reduced pressure, and the residue was adsorbed onto silica and placed at the top of a dry-flash column (2 cm diameter, 7.5 cm length). Elution with 2.5% ethyl acetate – hexanes gave 0.10 g of a white solid. Recrystallization from methanol gave the desired product as clear crystals (0.076 g, 25% yield), mp 111–113°C.  $^1\text{H}$  NMR  $\delta$ : 9.08 (d, 1H,  $J$  = 2.8 Hz), 7.76 (d, 1H,  $J$  = 8.8 Hz), 7.65 (d, 1H,  $J$  = 8.6 Hz), 7.49 (d, 1H,  $J$  = 8.8 Hz), 7.17 (dd, 1H,  $J_1$  = 2.8 Hz,  $J_2$  = 8.6 Hz), 6.88 (d, 1H,  $J$  = 2.7 Hz), 6.74 (d, 1H,  $J$  = 2.7 Hz), 4.10 (s, 3H), 3.99 (s, 3H), 3.95 (s, 3H).  $^{13}\text{C}$  NMR  $\delta$ : 161.9, 160.0, 158.2, 158.1, 136.0, 131.6, 129.4, 128.1, 124.5, 115.4, 114.7, 109.6, 101.3, 99.0, 55.8, 55.4, 55.3. GC-MS ( $m/z$ ): 269 (18.1), 268 (100.0), 225 (16.4), 210 (22.7), 152 (15.6), 139 (18.2). HR-MS calcd.: 268.1099; found: 268.1112  $\pm$  0.0008.

### 1-(3,5-Dimethoxyphenyl)-2-(4-methoxyphenyl)ethane (23)

A solution of 1-(3,5-dimethoxyphenyl)-2-(4-methoxyphenyl)-1-methoxyethane **18a** (0.0523 g, 0.173 mmol) in methanol (50 mL) was prepared and poured into a quartz reaction vessel. After purging with nitrogen gas for 30 min, the stirred solution was irradiated for 5 h at 25°C. The solvent was removed under reduced pressure, and the residue was purified by column chromatography (2.5% ethyl acetate – hexanes, eluant) to give the desired product (0.020 g, 42% yield).  $^1\text{H}$  NMR  $\delta$ : 7.10 (d, 2H,  $J$  = 8.5 Hz), 6.83 (d, 2H,  $J$  = 8.5 Hz), 6.33 (s, 3H), 3.79 (s, 3H), 3.77 (s, 6H), 2.84 (s, 2H).  $^{13}\text{C}$  NMR  $\delta$ : 160.7, 157.87, 144.3, 133.8, 129.4, 113.8, 106.5, 97.9, 55.3, 55.2, 38.5, 36.8. GC-MS ( $m/z$ ): 273 (2.1), 272 (11.4), 151 (2.0), 122 (9.1), 121 (100.0).

### 2-(3,5-Dimethoxyphenyl)-1-(4-methoxyphenyl)propane (24)

This photoproduct was not synthesized or isolated; thus, the identification rests solely on the GC-MS spectrum ( $m/z$ ): 287 (2.3), 286 (12.0), 165 (15.0), 122 (10.2), 121 (100.0). The molecular ion of  $m/z$  286 and the major fragment ions of  $m/z$  165 and  $m/z$  122 (the two possible benzylic carbocations that may be formed by cleavage of the molecular ion) strongly support the assignment.

### Photolysis procedures

In all four photolysis reactions, a similar procedure was used. The solid starting material (**1**: 100 mg, 0.30 mmol; **20**: 50 mg, 0.20 mmol) was placed in a 100 mL volumetric flask, and the flask was filled to the mark with the solvent of interest. After the substrate was fully dissolved, the solution was poured into a quartz reaction vessel and purged with nitrogen for 30 min. The solution was thermostated at 25°C with an immersion circulating water tube, and mixed with a magnetic stirrer. In the reactions involving **20**, an equimolar

amount of acetic acid (11  $\mu\text{L}$ , 0.20 mmol) was added to the solution, and the solution was stirred overnight to check for the presence of ground-state reactions (none were found). The photolyses were performed using a Rayonet reactor with 10 low-pressure mercury lamps (254 nm emission). While the reaction was in progress, 1 mL samples were analyzed using the GC conditions outlined above.

The purified photoproducts were used to obtain calibrations for the GC-FID response of each compound as a function of concentration. These calibrations were then used to convert the peak areas from the reaction chromatograms to concentrations. The concentrations of the components were then converted to percentages based on the initial concentration of the starting material and the amount of material consumed during the reaction.

Laser flash photolysis of **1** was performed using a  $2.28 \times 10^{-4}$  M solution in TFE, which had an absorbance of 0.45 at 266 nm. A portion of this solution was excited using a Continuum Nd:Yag NY-61 laser (266 nm, <8 ns/pulse,  $\leq 15$  mJ/pulse). Several time domains (10 ns to 50  $\mu\text{s}$ ) were used, as well as three different conditions: air-saturated, nitrogen-saturated, and oxygen-saturated.

### Acknowledgments

We thank the Natural Sciences and Engineering Research Council of Canada (NSERC) for financial support and Sepracor Canada Ltd., Windsor, Nova Scotia, for the donation of chemicals. J.C.R. also thanks NSERC for a postgraduate scholarship.

### References

1. S.A. Fleming and J.A. Pincock. Organic molecular photochemistry. Vol. 3. Marcel Dekker, New York. 1999. p. 211.
2. J.A. Pincock. Acc. Chem. Res. **30**, 43 (1997).
3. R.A. McClelland. Tetrahedron, **52**, 6823 (1996).
4. J.A. Pincock and P.J. Wedge. J. Org. Chem. **59**, 5587 (1994).
5. H.E. Zimmerman and V.R. Sandel. J. Am. Chem. Soc. **85**, 915 (1963).
6. D.P. DeCosta, N. Howell, A.L. Pincock, J.A. Pincock, and S. Rifai. J. Org. Chem. **65**, 4698 (2000).
7. M. Fujio, M. Goto, T. Susuki, I. Akasaka, M. Mishima, and Y. Tsuno. Bull. Chem. Soc. Jpn. **63**, 1146 (1990).
8. R.A. McClelland, C. Chan, F. Cozens, A. Modro, and S. Steenken. Angew. Chem. Int. Ed. Engl. **30**, 1337 (1991).
9. M. Hoang, T. Gadosy, G. Hedieh, D.F. Hou, A.C. Hopkinson, L.J. Johnston, and E. Lee-Ruff. J. Org. Chem. **63**, 7168 (1998).
10. P. Wan and E. Krogh. J. Am. Chem. Soc. **111**, 4887 (1989).
11. G. Mladenova, L. Chen, C.F. Rodriguez, K.W.M. Sui, L.J. Johnston, A.C. Hopkinson, and E. Lee-Ruff. J. Org. Chem. **66**, 1109 (2001).
12. A. Vogel. Vogel's textbook of organic chemistry. Longman Scientific and Technical, London. 1989. p. 935.
13. M.R. Detty and B.J. Murray. J. Am. Chem. Soc. **105**, 883 (1983).
14. P. Crotti, M. Ferreti, F. Macchia, and A. Stoppioni. J. Org. Chem. **51**, 2759 (1986).
15. W. Steglich and B. Neises. Angew. Chem. Int. Ed. Engl. **17**, 522 (1978).



16. K. Noller, F. Dosteyn, and H. Meier. *Chem. Ber.* **121**, 1609 (1988).
17. J.R. Falck, J. Yu, and H.S. Cho. *Tetrahedron Lett.* **35**, 5997 (1994).
18. J. McEwen and K. Yates. *J. Phys. Org. Chem.* **4**, 193 (1991).
19. F.L. Cozens, V.M. Kanagasabapathy, R.A. McClelland, and S. Steenken. *Can. J. Chem.* **77**, 2069 (1999).
20. J. Woning, A. Oudenampsen, and W.H. Laarhoven. *J. Chem. Soc. Perkin Trans. II*, 2147 (1989).
21. F.D. Lewis and J.S. Yang. *J. Am. Chem. Soc.* **119**, 3834 (1997).
22. F.D. Lewis, W. Weigel, and X. Zuo. *J. Phys. Chem. A*, **105**, 4691 (2001).
23. B.K. Bullimore, J.F.W. McOmie, A.B. Turner, M.N. Galbraith, and W.B. Whalley. *J. Chem. Soc. C*, 1289 (1967).
24. E. Mannila, A. Talvitie, and E. Kolehmainen. *Phytochemistry*, **33**, 813 (1993).



# The photo-NOCAS reaction: Trapping an intermediate

Robert M. Borg, Danielle Franke, and Adrian Vella

**Abstract:** Irradiation of a mixture of 1,4-dicyanobenzene, phenanthrene, and 2,3-dimethyl-2-butene in acetonitrile–methanol solvent in the presence of acrylonitrile or methyl acrylate leads to a diversion from the usual photo-NOCAS product formation towards products that result from the formal addition of methanol and electrophilic alkenes to the butene.

**Key words:** photo-NOCAS, photoinduced electron transfer, photosubstitution, photoaddition, redox photosensitization, alkene, 2-methoxyalkyl radical.

**Résumé :** L'irradiation d'un mélange de 1,4-dicyanobenzène, de phénanthrène et de 2,3-diméthylbut-2-ène dans un mélange d'acétonitrile et de méthanol, en présence d'acrylonitrile ou d'acrylate de méthyle conduit à la formation d'un produit de photo-NOCAS qui diffère du produit usuel et qui résulte de l'addition formelle de méthanol et d'alcènes électrophiles au butène.

**Mots clés :** photo-NOCAS, transfert d'électron photoinduit, photosubstitution, photoaddition, photosensibilisation redox, alcène, radical 2-méthoxyalkyle.

[Traduit par la Rédaction]

## Introduction

The photo-NOCAS reaction is a well-established one with numerous examples having appeared in the literature (1). The acronym stands for nucleophile-olefin combination aromatic substitution, and was proposed by Arnold (2) to represent a class of photosubstitution reactions that was first discovered in his laboratories almost 20 years ago (3). Such a reaction is depicted in Scheme 1. As the mechanistic scheme illustrates, irradiation of the redox photosensitizer phenanthrene (**1**) leads to electron transfer between the first excited singlet state of **1** and 1,4-dicyanobenzene (**2**). The ensuing radical cation of **1** then serves to generate the radical cation of 2,3-dimethyl-2-butene (**3**) by means of a secondary electron transfer step. Nucleophilic interception of the radical cation of **3** by methanol, followed by deprotonation and coupling of the resulting radical **4** with the radical anion of **2** and loss of cyanide ion, leads to the photo-NOCAS product **5** in high yield (3).

The alkoxy-substituted radical **4** is a proposed key intermediate in the reaction, and does not undergo reductive back electron transfer (BET) upon encountering the radical anion of **2**, since it is well-known that tertiary alkyl radicals are more difficult to reduce than **2**.<sup>2</sup> This is in contrast with similar phenylated radicals, where BET *does* occur,<sup>3</sup> and is followed by protonation, leading to the overall *anti-Markovnikov* addition of methanol (and no NOCAS-type products), as illustrated for 1,1-diphenylethene (**6**) in Scheme 2 (5). For this reason, reports on the photosensitized (electron transfer) simple addition of nucleophiles to alkylated olefins are few, and in those cases involve strained alkenes (**1b**, **1c**, **6**).

It occurred to us that it might be possible to intercept radical intermediates such as **4** before coupling with the cyanoaromatic radical anion takes place. We now wish to describe the trapping of the alkoxy-substituted radical **4** by means of electron-poor olefins.

## Results and discussion

A mixture of phenanthrene (**1**), 1,4-dicyanobenzene (**2**), 2,3-dimethyl-2-butene (**3**), and acrylonitrile (**8a**) dissolved in acetonitrile:methanol (3:1 by volume) was irradiated for 16 h by means of a 400 W medium pressure mercury lamp through Pyrex ( $\lambda > 280$  nm). Monitoring of the reaction by gas chromatography (GC) revealed that formation of the usual photo-NOCAS product (**5**) had been suppressed, and that a major new peak at shorter retention time had appeared. Evaporation of solvent in vacuo, followed by hexane extraction of the photolysates, resulted in the isolation of a yellow liquid which was vacuum distilled to afford a colourless oil. Repetition of the above procedure in the presence of methyl acrylate (**8b**), instead of acrylonitrile, resulted in the

Received 10 February 2003. Published on the NRC Research Press Web site at <http://canjchem.nrc.ca> on 19 June 2003.

*Dedicated to Professor Donald R. Arnold for his contributions to chemistry.*

**R.M. Borg,<sup>1</sup> D. Franke, and A. Vella.** Department of Chemistry, University of Malta, Msida, Malta MSD 06.

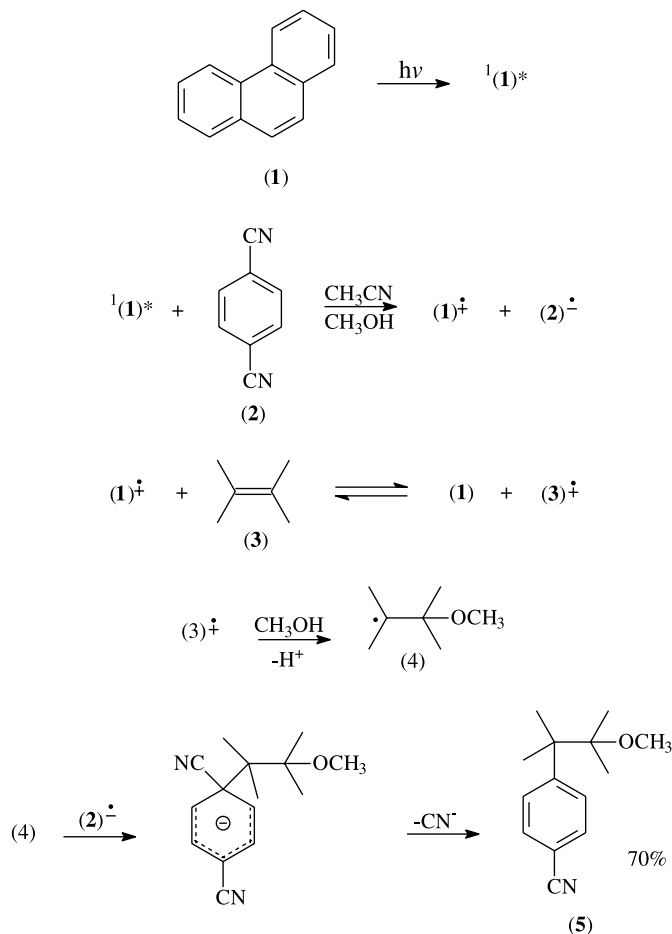
<sup>1</sup>Corresponding author (e-mail: [robert.m.borg@um.edu.mt](mailto:robert.m.borg@um.edu.mt)).

<sup>2</sup>The reduction potential for the *tert*-butyl radical has been estimated to be around  $-2.5$  V vs. Ag (4). In comparison, the reduction potential for **2** has been measured as  $-2.0$  V vs. Ag (3).

<sup>3</sup>The reduction potential for the 1,1-diphenylethyl radical has been measured as  $-1.61$  V vs. Ag (4).



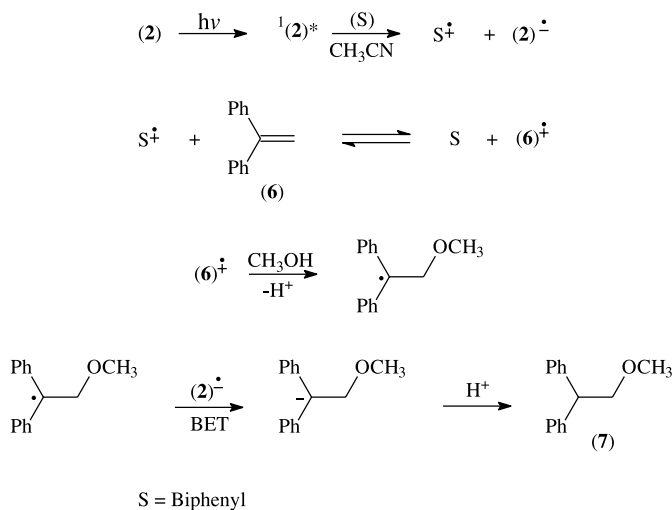
Scheme 1.



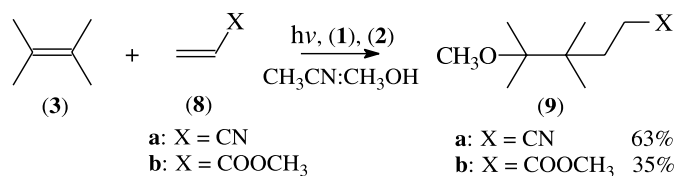
isolation of another colourless oil. Dark control experiments established the photochemical nature of the process; furthermore, the products were not formed in the absence of **2**, and yields were lower and the reactions inefficient in the absence of phenanthrene (**1**).

The two major new photoproducts were identified as 5-cyano-2-methoxy-2,3,3-trimethylpentane (**9a**) and methyl 5-methoxy-4,4,5-trimethylhexanoate (**9b**), respectively, (Scheme 3), by spectroscopic techniques. Thus, for example, the 250 MHz  $^1\text{H}$  NMR spectrum obtained for **9a** exhibits, besides three singlets for the methyl and methoxy groups, an AA'BB' non-first-order system of two multiplets at  $\delta$  1.76 and 2.39. This is typical of adjacent methylene groups where the geminal protons in each group are magnetically nonequivalent (7). The spectrum for **9b** is practically identical, except for an additional sharp singlet at  $\delta$  3.67. The presence of a cyano group is clearly indicated by the sharp absorption peak at  $2244\text{ cm}^{-1}$  in the IR spectrum of **9a**, whilst **9b** gives an ester carbonyl stretch signal at  $1740\text{ cm}^{-1}$ . Other spectro-

Scheme 2.



Scheme 3.



scopic data (given below) are also in accordance with the proposed structures.

When the above irradiations were attempted with 1,1-diphenylethene (**6**) as the electron-rich alkene, instead of 2,3-dimethyl-2-butene (**3**) (and with biphenyl as the redox photosensitizer), only the anti-Markovnikov adduct 2,2-diphenylethyl methyl ether (**7**, Scheme 2) was formed (**5**), both in the absence and presence of either acrylonitrile (**8a**) or methyl acrylate (**8b**). No products analogous to **9a** and **9b** could be detected.

In accordance with the established mechanism (3) for the photo-NOCAS reaction (Scheme 1) we are suggesting that the introduction of electron-poor alkenes into the reaction mixture allows the interception of the alkoxy-substituted radical **4**.<sup>4,5</sup> This results in the formation of a cyano- (or carboxymethyl-) centered radical intermediate (**10**) whose reduction potential clearly is less negative than that of **4**.<sup>6</sup> Upon encounter with the dicyanobenzene radical anion, therefore, BET to **10** occurs in preference to addition as occurs with **4**. Protonation of the resulting anion leads to the final products (Scheme 4).

At first glance, it seems remarkable that the reactions being reported here proceeded as desired, in view of the complex nature of the reaction mixture. In fact, the material balance is not a good one. The electron-poor alkenes had to be replenished several times during the photolysis, as it was

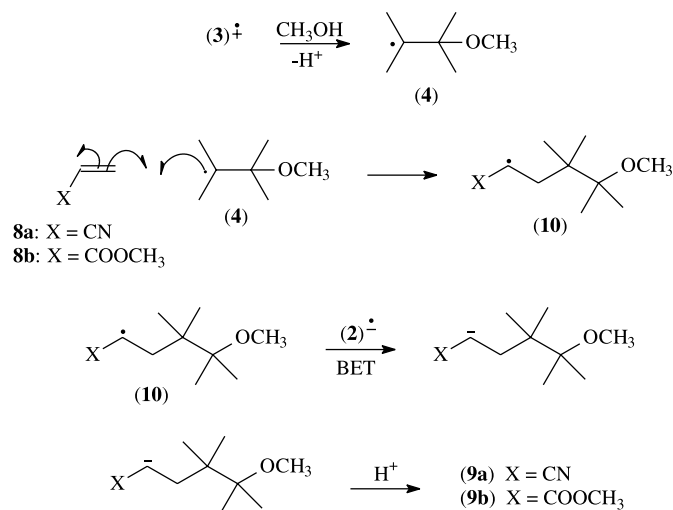
<sup>4</sup>The alternative scenario, i.e., interception of the radical cation of **3** by **8a** or **8b**, followed by nucleophilic attack by methanol cannot be ruled out. However, since the bimolecular rate constant for attack by methanol on phenylated alkene radical cations has been estimated to be as high as  $1 \times 10^9\text{ M}^{-1}\text{ s}^{-1}$  (8), then with methanol at solvent concentrations, nucleophilic capture should compete easily with other processes.

<sup>5</sup>Albini has described the similar trapping of radicals generated via photoinduced electron transfer (9).

<sup>6</sup>The reduction potential of the cyanomethyl radical has been estimated to be  $-0.97\text{ V}$  vs. Ag (1c).



Scheme 4.



observed that they were being consumed at a much faster rate than that for product formation. Inspection of the photolysates and distillation residues by <sup>1</sup>H NMR spectroscopy revealed the presence of complex aliphatic mixtures that could not be analysed by GC. Presumably, these might be polymers and (or) oligomers of acrylonitrile (8a) or methyl acrylate (8b). A reaction mixture in which radical ions are formed might involve the electrophilic alkenes at a stage other than that shown in Scheme 4. For example, upon excitation of phenanthrene (1) to the first excited singlet state, electron transfer might occur to 8a or 8b in competition with transfer to 1,4-dicyanobenzene (2). The radical anions of these alkenes might even be formed via electron transfer from the dicyanobenzene radical anion. Either of these processes seems unlikely. The reduction potentials of both 8a ( $E_{1/2}^{\text{red}} = -2.7$  V, vs. Ag) (10) and 8b ( $E_{1/2}^{\text{red}} = -2.6$  V, vs. Ag) (10) are substantially more negative than that for 2 ( $E_{1/2}^{\text{red}} = -2.0$  V, vs. Ag) (3). Use of these values in the Weller equation (11) gives theoretical free energy changes for electron transfer from the excited singlet of 1 to either 8a or 8b that are appreciably positive.<sup>7</sup> However, it has been reported (12) that acrylonitrile (8a) quenches the excited state of anthracene with a (albeit low) rate constant of ca.  $1 \times 10^7 \text{ M}^{-1} \text{ s}^{-1}$ , in an initiation step leading to polymerization. Conceivably, a similar pathway involving phenanthrene might lead to oligomers and (or) polymers in the current systems. This is reinforced by the observation that irradiation of 8a or 8b in the presence of phenanthrene in acetonitrile-methanol solution leads to the formation of a gummy residue whose <sup>1</sup>H NMR spectrum closely resembles that obtained in the above photolysis.

The negative results obtained with 1,1-diphenylethene might be interpreted as an indication that back electron transfer from the dicyanobenzene radical anion to the 1,1-diphenylethyl-2-methoxy radical intermediate (Scheme 2) is fast. This is probably both a consequence of the relatively

high reduction potential of 2 and the relative ease of reduction of this radical.<sup>3</sup> Attempts to lessen the rate of this BET step through the use of a cyanoaromatic with a lower reduction potential such as 9,10-dicyanoanthracene ( $E_{1/2}^{\text{red}} = -1.2$  V vs. Ag (13)) proved unsuccessful.

## Experimental

Phenanthrene (BDH Chemicals Ltd.) and 1,4-dicyanobenzene (Aldrich Chemical Co. Ltd.) were recrystallized three times from 96% ethanol. Acrylonitrile (Aldrich) and methyl acrylate (BDH) were distilled before use. 2,3-Dimethyl-2-butene and 1,1-diphenylethene (both Aldrich) were used as received. Acetonitrile (Rathburn, HPLC grade) was purified by elution through an activated alumina column, followed by reflux and distillation over calcium hydride. Methanol (Aldrich, analytical grade) was used as received.

Irradiations were carried out in Pyrex tubes at  $15^\circ\text{C} \pm 5^\circ$  by means of a water-cooled 400 W medium pressure mercury lamp (Photochemical Reactors Ltd.). Typically, 0.3 g of 1, 1.1 g of 2, and 1 g of 3 were dissolved in 25 mL of a 3:1 mixture of acetonitrile:methanol containing either 1.4 g of 8a or 2.2 g of 8b. During irradiation of the mixture, the progress of the reaction was monitored by GC (BP1, 50 m  $\times$  0.22 mm). At ca. 4-h intervals, the rapidly decreasing concentration of the trapping alkene 8a (or 8b) was restored by the addition of 0.5 g aliquots. When product formation had ceased, the solvent was removed in vacuo, and the resulting mixture of oil and solid was extracted with hexane. Evaporation of the hexane extracts, followed by vacuum distillation of the resulting yellow oil, led to the isolation of the product as a colourless oil.

### 5-Cyano-2-methoxy-2,3,3-trimethylpentane (9a)

Yield: 1.27 g (63%),<sup>8</sup> bp  $88\text{--}96^\circ\text{C}$  (ca. 0.1 mmHg (1 mmHg = 133.322 Pa)). IR (NaCl)  $\text{cm}^{-1}$  v: 2977, 2950, 2888, 2827, 2244, 1476, 1377, 1368, 1148, 1131, 1070. <sup>1</sup>H NMR (250 MHz, CDCl<sub>3</sub>-TMS)  $\delta$ : 3.15 (s, 3H), 2.39 (m, 2H), 1.76 (m, 2H), 1.08 (s, 6H), 0.89 (s, 6H). <sup>13</sup>C NMR (62.9 MHz, CDCl<sub>3</sub>-TMS)  $\delta$ : 121.3, 79.2, 49.0, 40.2, 34.0, 22.2, 19.1, 13.5. MS (EI)  $m/z$  (%): 169 (1), 154 (8), 138(2), 115 (2), 96 (2), 83 (4), 73 (100), 69 (3), 55 (9), 30 (8). HR-MS (FAB) calcd. for C<sub>10</sub>H<sub>20</sub>NO (i.e., M + 1): 170.15447; found: 170.15438.

### Methyl 5-methoxy-4,4,5-trimethylhexanoate (9b)

Yield: 0.86 g (35%),<sup>8</sup> bp  $84\text{--}106^\circ\text{C}$  (ca. 0.1 mmHg (1 mmHg = 133.322 Pa)). IR (NaCl)  $\text{cm}^{-1}$  v: 2975, 2952, 2826, 1740, 1476, 1392, 1375, 1366, 1248, 1195, 1147, 1123, 1073. <sup>1</sup>H NMR (250 MHz, CDCl<sub>3</sub>-TMS)  $\delta$ : 3.67 (s, 3H), 3.16 (s, 3H), 2.33 (m, 2H), 1.69 (m, 2H), 1.09 (s, 6H), 0.86 (s, 6H). <sup>13</sup>C NMR (62.9 MHz, CDCl<sub>3</sub>-TMS)  $\delta$ : 175.3, 79.2, 51.5, 49.1, 40.1, 32.3, 30.3, 21.8, 19.1. MS (EI)  $m/z$  (%): 202 (3), 187 (19), 178 (16), 171 (13), 123 (21), 115 (10), 95 (20), 83 (13), 74 (25), 73 (100), 69 (16), 51 (17), 30

<sup>7</sup> $\Delta G$  was estimated to be +41 and +31 kJ mol<sup>-1</sup>, respectively, using the value of 346 kJ mol<sup>-1</sup> for the first singlet of 1, and an oxidation potential of +1.31 V vs. Ag (3).

<sup>8</sup>Due to its volatility, unconsumed residual 2,3-dimethyl-2-butene (3) (as revealed by GC) was not recovered during work-up. These are therefore minimum yields, based upon the theoretical total consumption of (3).



(17). HR-MS (FAB) calcd. for  $C_{11}H_{22}NaO_3$  (i.e.,  $M + Na$ ): 225.14665; found: 225.14662.

## Conclusion

It has been demonstrated that the photo-NOCAS reaction can be diverted from the final substitution step by interception with electron-poor alkenes. In spite of the poor material balance, the reactions described here not only provide further evidence for the proposed mechanism of the photo-NOCAS reaction, but lead to convenient yields of products that are not trivially synthesized by other routes.<sup>9</sup> Ongoing studies in our laboratories are focusing on other alkene-nucleophile systems so as to further define the scope and limitations of these reactions.

## Acknowledgement

We thank the University of Malta Research Grants Committee for providing financial support for this work.

## References

1. (a) For a recent review of the photo-NOCAS reaction, see: D. Mangion and D.R. Arnold. *Acc. Chem. Res.* **35**, 297 (2002), and refs. cited therein; (b) D. Zhou, J. Chou, and H.D. Roth. *J. Phys. Org. Chem.* **12**, 867 (1999); (c) H. Weng and H.D. Roth. *J. Org. Chem.* **60**, 4136 (1995).
2. D.R. Arnold and M. Snow. *Can. J. Chem.* **66**, 3012 (1988).
3. R.M. Borg, D.R. Arnold, and T.S. Cameron. *Can. J. Chem.* **62**, 1785 (1984).
4. D.D.M. Wayner, D.J. McPhee, and D. Griller. *J. Am. Chem. Soc.* **110**, 132 (1988).
5. (a) R.A. Neunteufel and D.R. Arnold. *J. Am. Chem. Soc.* **95**, 4080 (1973); (b) D. Mangion and D.R. Arnold. *Can. J. Chem.* **77**, 1655 (1999).
6. P.G. Gassman and K.D. Olson. *Tetrahedron Lett.* **24**, 19 (1983).
7. D.H. Williams and I. Fleming. *In Spectroscopic methods in organic chemistry*. 5th ed. McGraw-Hill, London. 1995. p. 91.
8. S.L. Mattes and S. Farid. *J. Am. Chem. Soc.* **108**, 7356 (1986).
9. M. Fagnoni, M. Mella, and A. Albini. *J. Org. Chem.* **63**, 4026 (1998).
10. D.R. Arnold, R.M. Borg, and A. Albini. *J. Chem. Soc., Chem. Commun.* 138 (1981).
11. D. Rehm and A. Weller. *Isr. J. Chem.* **8**, 259 (1970).
12. H.-J. Timpe. *In Topics in current chemistry*. Vol. 156: Photoinduced electron transfer I. Springer-Verlag, Berlin. 1990. p.174.
13. S.L. Mattes and S. Farid. *In Organic photochemistry*. Vol. 6. Edited by A. Padwa. Marcel Dekker, New York. 1983. p. 237.
14. B. Giese and K. Heuck. *Tetrahedron Lett.* **21**, 1829 (1980).

<sup>9</sup>Giese (14) has described the synthesis of similar compounds via the methoxymercuration reaction of alkenes, followed by reduction in the presence of methyl acrylate. However, his method fails with tetra-substituted alkenes.



# C-H...H-C interactions in organoammonium tetraphenylborates: another look at dihydrogen bonds

Katherine N. Robertson, Osvald Knop, and T. Stanley Cameron

**Abstract:** The crystal structures of the tetraphenylborates of the dabcoH<sup>+</sup>, guanidinium (MeCN solvate), and biguanidinium cations are shown to contain a variety of C-H...H-C dihydrogen (DB) bonds of nominally zero polarity, as well as a variety of N-H...N, C-H...N, N-H...Ph, and C-H...Ph hydrogen (HB) bonds. These intermolecular bonds have been characterized topologically after multipole refinement of the structures. The coexistence of the DBs and HBs in each of the structures makes it possible to establish their relative strength hierarchy. It also illustrates the importance of the DBs in satisfying the tendency of these structures to maximize the total intermolecular bonding engagement. To compare the above DBs with other DBs, the results of an extensive set of MP2/6-31G(d,p) calculations (supplied by I. Alkorta) were analyzed for reference correlations between the bond-critical parameters. Thus, for an X-H...H-Y bond, the difference  $\Delta\epsilon(H)_m$  between the Mulliken charges on the H atoms in the uncomplexed X-H and H-Y components correlates quite well with the X-H...H-Y parameters and can be used for predicting the topological strength of an X-H...H-Y bond. The use of the difference  $\Delta\epsilon(H)_c$  in the bond does not appear to change the correlation significantly; closer correlations are observed when the amount of charge transferred on formation of the H...H bond is used instead of  $\Delta\epsilon(H)_m$  or  $\Delta\epsilon(H)_c$ . Bonding interactions are obtained even between like or symmetry-related H atoms as a consequence of induced-dipole interactions, which accounts for the existence of the above intermolecular C-H...H-C bonds with  $d(H...H) = 2.18\text{--}2.57$  Å, electron density at the bond-critical point of  $\sim 0.05\text{--}0.08$  e/Å<sup>3</sup>, and a rough estimate of the H...H binding energy of  $\sim 1\text{--}5$  kcal/mol. Examination of the bond-critical parameters of X-H...H-Y bonds also suggests a criterion of stability of these bonds with respect to the transition from non-shared (closed-shell) X-H...H-Y interaction to covalent (shared-shell) X...H-H...Y interaction. This transition appears to be discontinuous.

**Key words:** bond-critical parameters, bond topology, dihydrogen bonds, hydrogen bonds, organoammonium tetraphenylborates.

**Résumé :** On a démontré que les structures cristallines des tétraphénylborates des cations dabcoH<sup>+</sup>, guanidinium (solvaté avec du MeCN) et biguanidinium comportent une variété de liaisons dihydrogènes (DB) C-H...H-C de polarité nominale nulle ainsi que des liaisons hydrogène (HB) de N-H...H, C-H...H, N-H...Ph et C-H...Ph. On a caractérisé ces liaisons intermoléculaires d'une façon topologique après un affinement multipolaire des structures. La coexistence de DB et de HB dans chacune de ces structures permet d'établir la hiérarchie de leurs forces relatives. Elle illustre aussi l'importance des DB pour satisfaire la tendance de ces structures à maximiser l'engagement de liaison intermoléculaire total. Dans le but de comparer les DB observées plus haut avec d'autres DB, on a analysé les résultats d'un grand nombre de calculs effectués au niveau MP2/6-31G(d,p) (fournis par I. Alkorta) pour trouver des corrélations de référence entre des paramètres critiques pour les liaisons. Ainsi, pour une liaison X-H...H-Y, il existe une bonne corrélation entre la différence  $\Delta\epsilon(H)_m$  entre les charges de Mulliken sur les atomes dans les composants X-H et H-Y non complexés et les paramètres X-H...H-Y et elle peut être utilisée pour faire des prédictions relatives à la force topologique d'une liaison X-H...H-Y. Il ne semble pas que la corrélation change de façon significative si on utilise la différence  $\Delta\epsilon(H)_c$  dans la liaison; de meilleures corrélations peuvent être obtenues par l'utilisation de la quantité de charge transférée lors de la formation de la liaison H...H au lieu des  $\Delta\epsilon(H)_m$  ou  $\Delta\epsilon(H)_c$ . On obtient des interactions de liaison même avec des atomes H semblables ou apparentés par symétrie en raison des interactions entre dipôles induits qui expliquent l'existence des liaisons intermoléculaires C-H...H-C rapportées plus haut avec un  $d(H...H) = 2,18\text{--}2,57$  Å, la densité électronique au point critique de liaison d'environ  $0,05\text{--}0,08$  e/Å<sup>3</sup> et une évaluation approximative de l'énergie de liaison H...H d'environ 1,5 kcal/mol. L'examen des paramètres critiques de liaison des liaisons X-H...H-Y suggère aussi un critère de stabilité de ces liaisons par rapport à la transition d'interaction non partagée (couche fermée) X-H...H-Y à interaction covalente (couche partagée) X...H-H...Y. Cette transition semble discontinue.

Received 16 April 2003. Published on the NRC Research Press Web site at <http://canjchem.nrc.ca> on 30 June 2003.

*Dedicated to Professor Donald R. Arnold on the occasion of his retirement.*

K.N. Robertson, O. Knop, and T.S. Cameron<sup>1</sup>. Department of Chemistry, Dalhousie University, Halifax, NS B3H 4J3, Canada.

<sup>1</sup>Corresponding author (e-mail: [stanley.cameron@dal.ca](mailto:stanley.cameron@dal.ca)).



**Mots clés :** paramètres critiques de liaison, topologie de liaison, liaisons dihydrogènes, liaisons hydrogène, tétraphénylborates d'organoammonium.

[Traduit par la Rédaction]

## Introduction

In this paper we describe and discuss features that are observed in the electron-density distributions of C-H...H-C groupings in the recently determined<sup>2</sup> crystal structures of three organoammonium tetraphenylborates, and which point to the existence of bonding interactions between the hydrogen atoms. Numerous examples of presumed X-H...H-Y bonding interactions (termed “dihydrogen bonds”, DB, in ref. 2 and provisionally referred to as “bonds” in the following) have been reported previously (cf. refs. 3–9 for comprehensive reviews). These rely almost entirely on the evidence provided by unusually short H...H distances rather than on detailed topological criteria, or by *ab initio* energies of formation (cf. refs. 10–38 for mostly experimental results and refs. 39–67 for theoretical aspects). It has been largely (though not always, e.g., refs. 8 and 39) assumed that these interactions depend for their existence and strength on the “polarity” of the H...H group, i.e., on the observed or postulated non-negligible difference  $|\Delta\epsilon(\text{H})|$  between the net (usually Mulliken) charges  $\epsilon(\text{H})$  on the two H atoms. There is thus a “donor”  $\text{H}_\text{d}$  and an “acceptor”  $\text{H}_\text{a}$  atom in the pair. In the tetraphenylborates, the distinctive feature of the C-H...H-C bonds is the *smallness* of  $|\Delta\epsilon(\text{H})|$ . With one exception, the bonds are formed between C-H groups of phenyl rings on neighbouring  $\text{BPh}_4^-$  anions; the net charges on the H atoms are very small to begin with (68) and so their differences are even smaller. This contrasts with the previously reported examples of DBs, in most of which  $|\Delta\epsilon(\text{H})|$  is appreciable (but see ref. 38). In the following we report details of our observations and discuss geometric and topological arguments for and against interpreting these interactions as *bonds*.

The interatomic distances  $d$  in this paper are in Å, the electron density  $\rho_\text{c} = \rho(\mathbf{r}_\text{c})$  at the bond-critical point (BCP) is in  $\text{e}/\text{\AA}^3$ , the Laplacian  $\nabla_\text{c}^2 = \nabla^2\rho(\mathbf{r}_\text{c})$  is in  $\text{e}/\text{\AA}^5$ , and the net (Mulliken) atom charge on H,  $\epsilon(\text{H})$ , is in e. Standard deviations  $\sigma_f$  of fit (for  $f$  degrees of freedom) are quoted also as a percent of the observed range of the dependent variable, thus  $\sigma_{25} = 0.063 \sim 3.5\%$ . The following shorthand notation is used:  $d_\text{H} = d(\text{H}\cdots\text{H})$ ,  $\rho_\text{H} = \rho_\text{c}(\text{H}\cdots\text{H})$ ,  $\nabla_\text{H}^2 = \nabla_\text{c}^2(\text{H}\cdots\text{H})$ , etc. Where these quantities refer exclusively to the *ab initio* values in Table 1, they are designated as  $d_\text{A}$ ,  $\rho_\text{A}$ , etc. In composite plots, where parameters from two or more data sets are included, a non-discriminatory common parameter label (e.g.,  $\rho_\text{c}$ ) stands for any of the set-specific labels, such as  $\rho_\text{H}$ ,  $\rho_\text{A}$ , etc. The optimizations listed in Table 1 with A as the sole reference were carried out at the MP2/6-31G(d,p) level, without basis set superposition error (BSSE) corrections and were not checked by frequency calculations.

## Evidence of H...H (set H) and other (set E) intermolecular bonding interactions

It is now widely accepted that, for a chemical bond between two atoms X and Y to exist, the electron-density dis-

tribution between X and Y has to satisfy certain requirements. These requirements have been formulated by Bader in his “Atoms in Molecules” (AIM) theory (69–72). They are, for the purposes of this investigation, concisely summarized in refs. 48 and 71. The principal topological requirement is the existence of a clearly characterized bond path BP between X and Y and of a (3,–1) BCP in this path. Association of the BP with an actual *bond* and the corresponding bond energy is easily demonstrated for classical chemical bonds but not so easily for very weak hydrogen bonds and a fortiori for DBs (5). The evidence for the existence of C-H...H-C bonds, presented in the following, is essentially geometric and topological in nature.

The three salts we have investigated are 1-azonia-4-azabicyclo[2.2.2]octane tetraphenylborate,  $(\text{dabcoH}^+)\text{BPh}_4$  (DTB); guanidinium tetraphenylborate solvate,  $[\text{C}(\text{NH}_2)_3]\text{BPh}_4 \cdot \text{MeCN}$  (GTB); and biguanidinium tetraphenylborate,  $\{[(\text{H}_2\text{N})_2\text{C}-]_2\text{N}\}\text{BPh}_4$  (BTB). Their crystal structures and topological features are described in detail separately,<sup>2</sup> as are particulars of the multipole refinements. Briefly, high-resolution X-ray diffraction data were collected at  $-120^\circ\text{C}$  (or lower) using  $\text{Mo K}\alpha$  radiation. After data processing, a preliminary least-squares refinement with the conventional spherical model led to the determination of a scale factor, starting positions, and thermal parameters for the multipole refinement of each structure. The multipole refinements were performed using the XD software package (cited in ref. 2) and are described in detail elsewhere. Since neutron data were not available, hydrogen atom positions were constrained such that all X-H bond lengths corresponded to appropriate neutron values. The program XDGEOM of the XD package was used to search for the intermolecular (interion) contacts of 3 Å or less in each of the structures. The XDPROP program of the XD package was then used to search for critical points in the electron density distribution, generated from the final multipole model of each compound, for each of the located short contacts. Bond paths were also calculated using the XDPROP function of the XD package.

The structures were searched, among other things, for inter-ion and ion–solvent contacts (with H...Y distances shorter than 3 Å) between a hydrogen atom and any possible acceptor Y. The search included all inter-ion/solvent contacts but not intra-ion contacts. All eligible geometric contacts were then subjected to a topological investigation, which involved searching for BCPs and associated BPs between the atoms. Of the 43 geometrically close C-H...Y contacts investigated, all but one were found to have associated BCPs and BPs. Two new contacts were located in the topological search, for a total of 44 interactions of various types being studied. The interactions could be characterized in two ways:

(i) *Geometry*. Criteria have been developed to determine, with confidence, interaction type based solely on the geometry of the interaction.<sup>2</sup> For example, if in a C-H...Ph interac-

<sup>2</sup>Ref. 1 and K. N. Robertson, W. Kwiatkowski, O. Knop, and T. S. Cameron, to be published.



**Table 1.** Bond-critical parameter values for the H...H bonds in MP2/6-31G(d,p) optimized linear X-H<sub>d</sub>...H<sub>a</sub>-Y complexes.<sup>a</sup>

Complex	$d_A$	$x_A$	$\xi_A$	$\rho_A$	$\nabla_A^2$	$\Delta\epsilon(H)_m^b$	$\epsilon(H_X)_A^c$	$\epsilon(H_Y)_A^c$	$\Delta\epsilon(H)_c^c$	$\Delta q_A$	Ref. <sup>d</sup>
1 LiH...HNF <sub>3</sub> <sup>+</sup>	0.738	0.399	0.5407	1.802	-32.8	0.625					A
2 LiH...HNH <sub>3</sub> <sup>+</sup>	0.805	0.463	0.5743	1.458	-22.0	0.579					42, A
3 LiH...HNC	1.579	0.905	0.5730	0.192	0.964	0.506	-0.267	0.355	0.622	0.0801	A, 66
4 LiH...HCN	1.866	1.041	0.5578	0.111	0.815	0.399	-0.231	0.247	0.478	0.0489	42, 47, 66
5 LiH...HNLi <sub>3</sub> <sup>+</sup>	2.027	1.104	0.5445	0.088	0.728	0.420	-0.221	0.309	0.529	0.0930	A
6 LiH...HCCSiH <sub>3</sub>	2.035	1.127	0.5535	0.078	0.672	0.371	-0.191	0.250	0.447	0.0323	A
7 LiH...HCCF	2.046	1.134	0.5545	0.078	0.656	0.370	-0.200	0.239	0.439	0.0311	A, 66
8 LiH...HCCH	2.080	1.151	0.5530	0.074	0.631	0.364	-0.197	0.236	0.433	0.0288	42, 47, 62, 66
9 LiH...HCCCH <sub>3</sub>	2.134	1.180	0.5526	0.066	0.583	0.369	-0.191	0.250	0.441	0.0248	A
10 LiH...HCCLi	2.399	1.316	0.5484	0.041	0.371	0.298	-0.168	0.184	0.352	0.0133	A
11 HBeH...HNF <sub>3</sub> <sup>+</sup>	1.166	0.669	0.5740	0.506	-0.251	0.547	-0.213	0.347	0.560	0.2604	A
12 HBeH...HNH <sub>3</sub> <sup>+</sup>	1.591	0.896	0.5631	0.153	0.940	0.501	-0.220	0.372	0.592	0.0933	42, A
13 HBeH...HNC	1.864	1.033	0.5540	0.085	0.827	0.428	-0.150	0.334	0.483	0.0339	A
14 HBeH...HCN	2.115	1.138	0.5381	0.055	0.588	0.321	-0.129	0.222	0.351	0.0196	42
15 HBeH...HCCF	2.242	1.198	0.5343	0.042	0.470	0.291	-0.110	0.201	0.311	0.0130	A
16 HBeH...HCCSiH <sub>3</sub>	2.252	1.201	0.5331	0.042	0.465	0.293	-0.111	0.205	0.316	0.0129	A
17 HBeH...HCCH	2.272	1.211	0.5328	0.040	0.448	0.285	-0.109	0.197	0.306	0.0120	A
18 HBeH...HCCCH <sub>3</sub>	2.315	1.232	0.5322	0.036	0.412	0.291	-0.104	0.207	0.311	0.0105	A
19 HBeH...HNLi <sub>3</sub> <sup>+</sup>	2.429	1.277	0.5255	0.033	0.350	0.342	-0.142	0.266	0.408	0.0250	A
20 HBeH...HCCLi	2.472	1.299	0.5256	0.028	0.301	0.220	-0.091	0.139	0.230	0.0054	A
21 H <sub>2</sub> BH...HCCF	2.383	1.255	0.5268	0.028	0.347	0.260	-0.089	0.201	0.290	0.0025	A
22 H <sub>2</sub> BH...HCCLi	2.509	1.299	0.5178	0.023	0.271	0.188	-0.063	0.131	0.194	0.0012	A
23 H <sub>3</sub> BH...HNC	1.385	0.795	0.5734	0.280	1.070	0.587	-0.220	0.342	0.563	0.1407	A
24 H <sub>3</sub> BH...HCCH	1.802	0.995	0.5521	0.118	0.887	0.444	-0.190	0.219	0.409	0.0710	A
25 H <sub>3</sub> BH...HCCLi	2.086	1.137	0.5448	0.068	0.595	0.378	-0.204	0.200	0.404	0.0378	A
26 LiCCH...HNH <sub>3</sub> <sup>+</sup>	1.775	0.995	0.5605	0.084	0.995	0.281	-0.086	0.455	0.542	0.0019	A
27 LiCCH...HNC	2.356	1.254	0.5322	0.019	0.323	0.208	0.074	0.351	0.277	0.0001	A
28 LiCCH...HCN	2.357	1.219	0.5174	0.021	0.351	0.102	0.084	0.223	0.140	0.0013	A
29 LiCCH...HCCF	2.396	1.221	0.5096	0.021	0.306	0.072	0.100	0.195	0.096	0.0001	A
30 LiCCH...HCCH	2.436	1.238	0.5083	0.020	0.282	0.066	0.102	0.192	0.090	0.0001	A
31 H <sub>3</sub> CH...LiCCH	2.514	1.239	0.5072	0.020	0.253	0.010	0.123	0.124	0.001	0.0015	A
32 H <sub>3</sub> CH...HCCH	2.539	1.230	0.5157	0.018	0.234	0.076	0.106	0.191	0.085	0.0019	A
33 H <sub>3</sub> CH...HCH <sub>3</sub> ( <i>D</i> <sub>3d</sub> )	2.661	1.330	1/2	0.016	0.195	0	0.118	0.118	0	0.00001	A
H <sub>2</sub> <sup>e</sup>	0.7337	0.3669	1/2	1.857	-34.15	0	0	0	0	0	

<sup>a</sup> $d_A = d(H...H)_A$ ,  $x_A = d(H_X...BCP)$ ,  $\xi_A = x_A/d_A$ ,  $\rho_A = \rho_c(H...H)_A$ ,  $\nabla_A^2 = \nabla^2(\rho_A)$ .

<sup>b</sup> $\Delta\epsilon_m = \Delta\epsilon(H)_m = |\epsilon(H_d)_m - \epsilon(H_a)_m|$ ;  $\epsilon(H_d)_m$ ,  $\epsilon(H_a)_m$ , Mulliken charges on the H<sub>d</sub> and H<sub>a</sub> atom, respectively, in the XH and HY molecules before complexation: H<sub>3</sub>BH<sup>-</sup>, -0.252; LiH, -0.171; HBeH, -0.093; H<sub>2</sub>BH, -0.062; H<sub>3</sub>CH, 0.117; HCCLi, 0.127; HCCH, 0.192; HCCCH<sub>3</sub>, 0.198; HCCF, 0.199; HCCSiH<sub>3</sub>, 0.200; HCN, 0.228; Li<sub>3</sub>NH<sup>+</sup>, 0.249; HNC, 0.335; H<sub>3</sub>NH<sup>+</sup>, 0.408; F<sub>3</sub>NH<sup>+</sup>, 0.454.

<sup>c</sup> $\epsilon(H_X) = \epsilon(H_X)_A$ ,  $\epsilon(H_Y) = \epsilon(H_Y)_A$ , Mulliken charges on the H atoms in the X-H...H-Y complex;  $\Delta\epsilon(H)_c = |\epsilon(H_X)_A - \epsilon(H_Y)_A|$ .

<sup>d</sup>A: these results were supplied, at the authors' request, by Dr. I. Alkorta by way of extension of ref. 42.<sup>4</sup> Remko's (47) MP2(Full)/6-31G(d)  $d(H...H)$  values for linear **4**, **8**, **14**, and **17** are 1.889, 2.105, 2.116, and 2.271 Å, respectively (no imaginary frequencies).

<sup>e</sup>Optimized in MP2/6-31G(d,p);  $G_c(H-H) = 0.58466$  au,  $K_c(H-H) = 0.58471$  au.

tion the minimum H<sub>C</sub>...C<sub>ring</sub> distance is longer than the corresponding H<sub>C</sub>...H<sub>ring</sub> distance by 0.40 Å or more, then an H...H contact would be expected to occur.

(ii) *Bond path.* As described more completely elsewhere,<sup>2</sup> the H...H contacts always have BPs that begin at one H<sub>C</sub> atom and terminate at another H<sub>C</sub> atom, although they may follow either C-H bond for a portion of its distance.

Generally, there was good agreement between the two classification methods. For example, a total of 15 H...H con-

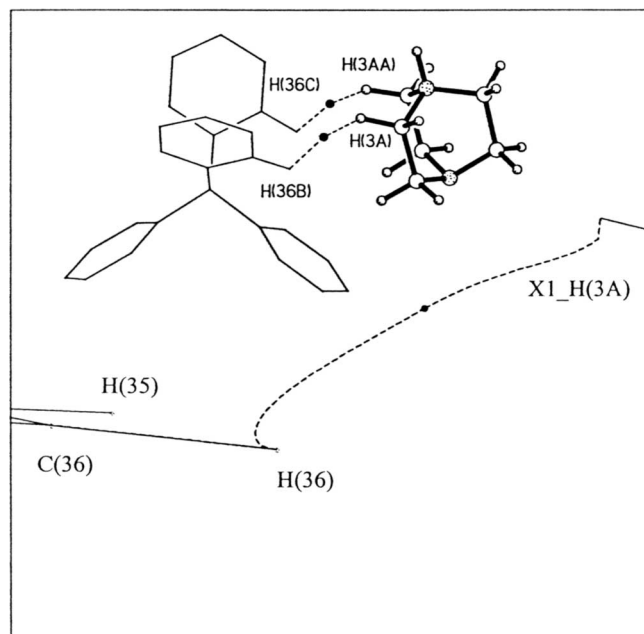
tacts were located by each method in the three structures: two in DTB, five in GTB, and eight in BTB (set **H**). They are reported in Table 2 (and in more detail in Table A), according to the C-H<sub>d</sub>...H<sub>a</sub>-C description that gives the best (largest) C-H...H angle. Only one H<sub>anion</sub>...H<sub>cation</sub> contact was found (in DTB) and no H<sub>ion</sub>...H<sub>solvent</sub> contact; the rest were of the H<sub>anion</sub>...H<sub>anion</sub> type. Other types of contact identified in the structures included (N-)H...N, (N-)H...Ph, and (C-)H...Ph hydrogen bonds (set **E**,  $n = 27$ ).<sup>3</sup> The bond-critical parameters of all the interactions studied are listed in Table B for

<sup>3</sup>In addition, nine (C-)H...N contacts were also found, and four of a type intermediate between H...H contacts and C-H...Ph bonds; these are not discussed here.



**Table 2.** Bond-critical parameters for the C-H...H'-C' contacts in the tetraphenylborates studied (set **H**).

	Type <sup>a</sup>	$d_{\text{H}}^{b,c}$	$\angle(\text{C-H}\cdots\text{H}')^c$	$\angle(\text{H}\cdots\text{H}'-\text{C}')^c$	$\rho_{\text{H}}$	$\nabla^2_{\text{H}}$	$\Delta\epsilon(\text{H})_{\text{m}}^d$	Structure
<b>a</b>	<i>o-m</i>	2.179	165.8	103.1	0.078(1)	0.703(1)	0.026	BTB
<b>b</b>	<i>o-m</i>	2.205	175.5	117.3	0.056(1)	0.583(1)	0.026	BTB
<b>c</b>	<i>o-o</i>	2.261	115.1	115.1	0.057(1)	0.782(1)	0	BTB
<b>d</b>	cation- <i>o</i>	2.262	132.8	120.9	0.056(0)	0.413(1)		DTB
<b>e</b>	<i>m-o</i>	2.337	154.8	112.4	0.051(1)	0.442(1)	0.026	GTB
<b>f</b>	<i>m-m</i>	2.347	151.1	106.7	0.053(1)	0.626(1)	0	BTB
<b>g</b>	<i>m-o</i>	2.354	159.6	105.7	0.065(0)	0.441(0)	0.026	DTB
<b>h</b>	<i>p-m</i>	2.357	121.3	114.3	0.061(2)	0.504(1)	0.003	GTB
<b>i</b>	<i>m-o</i>	2.391	173.7	113.3	0.043(1)	0.423(1)	0.026	BTB
<b>j</b>	<i>o-p</i>	2.446	166.0	106.7	0.045(1)	0.406(1)	0.029	BTB
<b>k</b>	<i>m-o</i>	2.454	124.0	108.9	0.058(1)	0.467(1)	0.026	GTB
<b>l</b>	<i>p-m</i>	2.454	149.5	103.4	0.045(1)	0.479(1)	0.003	BTB
<b>m</b>	<i>o-m</i>	2.464	167.9	103.1	0.049(1)	0.439(1)	0.026	GTB
<b>n</b>	<i>p-m</i>	2.508	115.1	105.2	0.040(1)	0.533(1)	0.003	BTB
<b>o</b>	<i>p-o</i>	2.574	151.6	98.3	0.046(1)	0.405(1)	0.029	GTB
	Mean	2.37[11]			0.054[10]	0.51[12]	0.018[12]	

<sup>a</sup>Type of H atom on the phenyl ring.<sup>b</sup>Internuclear H...H distance.<sup>c</sup>In the multipole refinements the hydrogen atoms were placed at the appropriate neutron bond lengths; error estimates on distances and angles are not available. The standard error on the C-C bond lengths in the structures ranged from 0.001–0.005 Å and the standard error on the corresponding C-C-C bond angles ranged from 0.1–0.3°.<sup>d</sup>Approximate  $\Delta\epsilon(\text{H})_{\text{m}}$  from B3LYP/6-31G(d,p) optimization of  $\text{BPh}_4^-$  (68).**Fig. 1.** C-H<sub>cation</sub>...H<sub>anion</sub>-C interaction in DTB (**d** in Table 2). Black dots indicate positions of the bond-critical points in the H...H contacts. Note that the X<sub>n</sub>-atom label in the bond path diagrams refer to symmetry-generated atoms. Details for the generation of these atoms are given in the deposited material (Table A).

comparison.<sup>4</sup> All these contacts are fully described elsewhere;<sup>2</sup> here we give only a summary of the H...H parameters (Table 2) and a sample of interaction diagrams showing projections of the H...H BPs (Figs. 1–4).

The internuclear distances  $d_{\text{H}}$  in **H** are all shorter than 2.6 Å, the shortest being 2.18 Å (Table 2). The H...H contacts occur between all three types of phenyl hydrogens. The C-H...H angles vary from approximately 115° to 176°, without a detectable trend with  $d_{\text{H}}$  (cf. a similar observation for B-H...H and N-H...H angles, ref. 29). The observed H...H BPs always start at one H atom and end on another, but sometimes they are appreciably curved (Figs. 1–4).<sup>5</sup> In extreme cases the path starts out in the direction of the midpoint of a C-H bond, but just before its completion it veers sharply toward the H atom (cf. Fig. 4). The length of the BP then differs significantly from the internuclear H...H distance in Table 2. It is not simple to trace the actual length of a BP as the path curves in space, and its length projected on a plane containing the two H atoms provides only a minimum estimate of the actual length. Inspection of the complete BPs has shown that, on the average, the internuclear H...H distances underestimate the actual length by some 5–10%, i.e., ~0.22–0.25 Å. For a BP as curved as that in Fig. 4 there is also the question: how exactly should its length be measured? To the terminating H atom (BP longer) or to the point where the bond path first approaches the C-H bond (BP shorter)?

<sup>4</sup>Supplementary data may be purchased from the Depository of Unpublished Data, Document Delivery, CISTI, National Research Council Canada, Ottawa, ON K1A 0S2, Canada ([http://www.nrc.ca/cisti/irm/unpub\\_e.shtml](http://www.nrc.ca/cisti/irm/unpub_e.shtml) for information on ordering electronically). Tables deposited: A. Geometric and bond-critical parameters for the H...H interactions in the tetraphenylborates studied. B. Bond-critical parameters for all intermolecular interactions of 3 Å or less in the tetraphenylborates studied. Figures deposited: A to I. Bond path diagrams for all the experimental H...H interactions.

<sup>5</sup>Intramolecular C-H...H-C BPs with similar features have recently been observed in a variety of ab initio structures of benzenoid and other hydrocarbons by Matta et al. (38). For these, differences between the internuclear H...H distance and the actual BP length are reported to amount to as much as ~0.27 Å (i.e., ca. 13%; converted from au).



**Fig. 2.** C-H<sub>anion</sub>...H<sub>anion</sub>-C contacts to ring 1 in GTB (H23...H12, e; H13...H12, k; H14...H15, h in Table 2). The ring-critical points are not shown. Note one C-H...Ph HB is also formed.

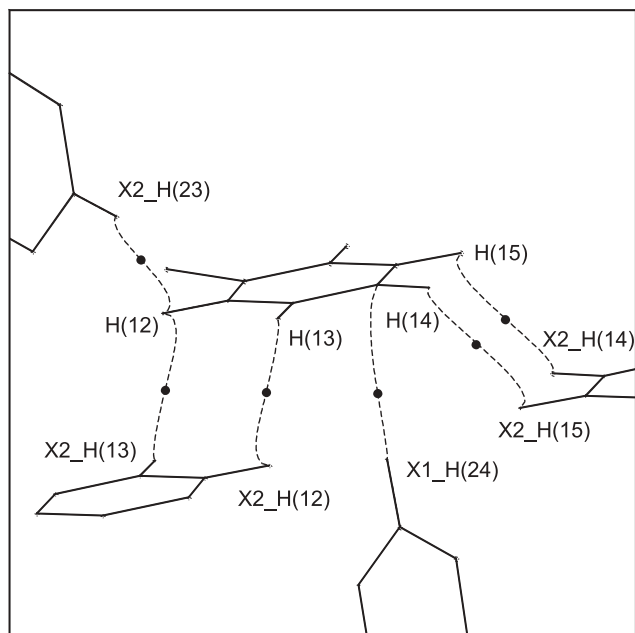
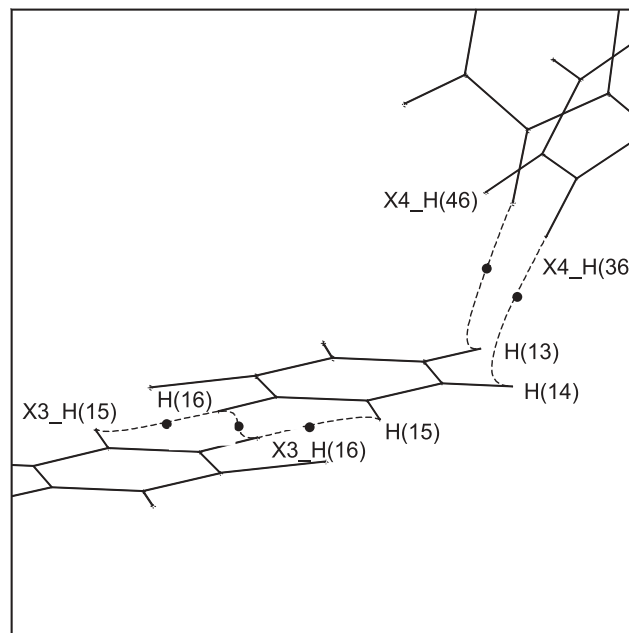


**Fig. 3.** C-H<sub>anion</sub>...H<sub>anion</sub>-C contacts to ring 1 in BTB (H16...H15, b; H16...H16, c; H46...H13, a; H36...H14, j in Table 2). The ring-critical points are not shown.



### Establishing a comparison norm (set A)

To position the DB parameters of Table 2 in the body of known DBs, it is desirable to establish some kind of reference norm. Experimental determinations of such parameters have been spotty (cf. ref. 28), and ab initio calculations are not always available at the same theory level, thus precluding systematic comparisons on equal footing. For our purposes a suitable norm is conveniently established with recourse to the ab initio calculations of Alkorta et al. (42), who studied, among other species, a number of linear X-H...H-Y complexes (Table 1). Additional calculations by Alkorta<sup>6</sup> have expanded the original MP2/6-31G(d,p) set to that presented in Table 1 and named set A.<sup>7</sup> Examination of A permits the following observations to be made:

(a) As would be expected,  $\rho_A$  increases monotonically with decreasing  $d_A$  (Fig. 5). This non-linear dependence can be represented by a power or an exponential function. A power regression yields

$$[1] \quad \rho_A = 0.717d_A^{-3.113}, \quad r^2 = 0.996, \\ \sigma_{31} = 0.0240 \sim 1.3\%,$$

as against the exponential regression

$$[2] \quad \rho_A = 13.28 \exp(-2.727d_A), \quad r^2 = 0.997, \\ \sigma_{31} = 0.0204 \sim 1.1\%.$$

Although eq. [2] has a smaller  $\sigma$ , neither fit is entirely satisfactory, as, in modelling  $\rho_A$ , eq. [1] overestimates and eq. [2] underestimates  $\rho_A$  at large  $d_A$ , i.e., for weak DBs. The empirical hybrid function related to  $\rho_A = 1/2(\text{eq. [1]} + \text{eq. [2]})$  but independently refined,

$$[3] \quad \rho_A = 0.313d_A^{-3.001} + 8.038 \exp(-2.789d_A)$$

( $r^2 = 0.999$ ,  $\sigma_{29} = 0.0124 \sim 0.7\%$ ), gives a better result. It also closely accommodates the matching data point for the H<sub>2</sub> molecule (Table 1). Although eq. [3] provides an acceptable overall fit to  $d_A \cdot \rho_A$ , a more detailed examination shows that the  $d_A \cdot \rho_A$  set in fact has a structure that cannot be entirely ignored and that may be important.

(b) The  $\nabla_A^2$  vs.  $d_A$  plot (Fig. 6) is of the type observed for the (N-)H...N<sup>8</sup> and (F-)H...F (74) hydrogen bonds. The variation of  $\nabla_A^2$  with  $d_A$  over the considerable data range is approximated very well by the difference of two exponentials,

$$[4] \quad \nabla_A^2 = 57.52 \exp(-2.163d_A) \\ - 1779.4 \exp(-4.996d_A),$$

$r^2 = 1.000$ ,  $\sigma_{29} = 0.119 \sim 0.35\%$ .<sup>9</sup> The regression line has a maximum of 1.253 at  $d_A = 1.507$  and crosses the  $\nabla_A^2 = 0$  line at  $d_A = 1.212$ . However, for  $d_A > 1.3 \text{ \AA}$  (which would amply cover the present experimental range), the A set is more closely fitted by

<sup>6</sup>The authors are indebted to Dr. Ibon Alkorta for supplying, at their request, the MP2/6-31G(d,p) results for the complexes listed in Table 1 but not examined in ref. 42.

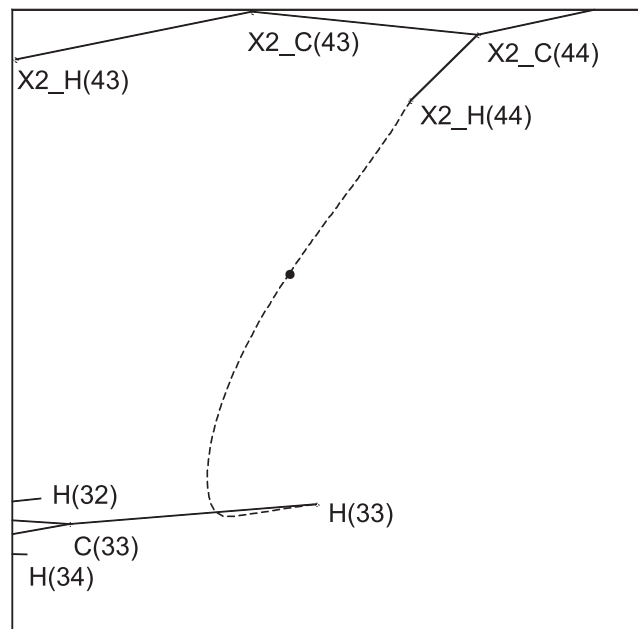
<sup>7</sup>MP2/6-31G(d,p) optimizations of CNH...HCN, HCCCH...HCCF, HCCH...HCN, HCCH...HF, and H<sub>3</sub>BH...<sup>+</sup>HNF<sub>3</sub> were also attempted but failed to yield results suitable for inclusion in A.

<sup>8</sup>Ref. 73 and O. Knop, K.N. Rankin, and R.J. Boyd, to be published.

<sup>9</sup>This fit, while close, might perhaps be improved somewhat, arithmetically, by including a join function to bridge the low and the high  $d_A$  regions, analogous to (though conceptually different from) that employed in ref. 74 for fitting  $d_c \cdot \nabla_c^2$  of F-H...F hydrogen bonds.



**Fig. 4.** One of the C-H<sub>anion</sub>...H<sub>anion</sub>-C interactions in BTB (H44...H33, 1 in Table 2). The H...H bond path first heads toward the midpoint of the C33-H33 bond but then changes course and terminates at H33.



$$[5] \quad \nabla_A^2 = -4.270 + 8.916d_A - 4.706(d_A)^2 + 0.7461(d_A)^3$$

( $r^2 = 0.986$ ,  $\sigma_{26} = 0.0329 \sim 3.9\%$ ). This partial regression appears to be better suited to the experimental range of  $d_c, \nabla_c^2$  values for H...H bonds. The statistical model function eq. [4] may be regarded as *formally* representing two opposing tendencies, which compensate each other at  $\nabla_c^2 = 0$ .

(c) An excellent cubic correlation over the entire  $\rho_A, \nabla_A^2$  data range is

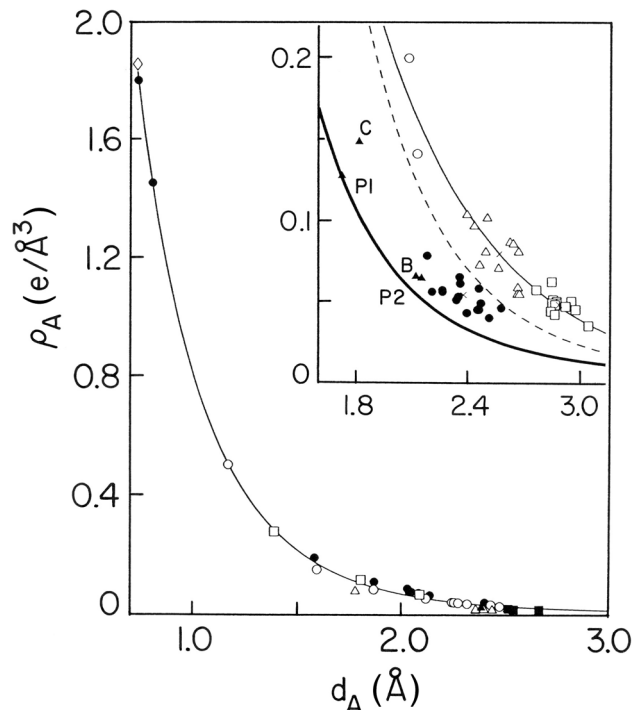
$$[6] \quad \nabla_A^2 = 0.0743 + 9.859\rho_A - 23.61(\rho_A)^2 + 4.450(\rho_A)^3$$

( $r^2 = 1.000$ ,  $\sigma_{29} = 0.078 \sim 0.2\%$ ; Fig. 7), with a maximum of 1.139 at  $\rho_A = 0.224$  and  $\nabla_A^2 = 0$  at  $\rho_A = 0.465$ . The regression line constrained to pass through the origin is only slightly worse:

$$[7] \quad \nabla_A^2 = 10.58\rho_A - 24.57(\rho_A)^2 + 4.78(\rho_A)^3$$

( $r^2 = 1.000$ ,  $\sigma_{29} = 0.092 \sim 0.3\%$ ; Fig. 7), with a  $\nabla_A^2$  maximum of 1.165 at  $\rho_A = 0.231$  and  $\nabla_A^2 = 0$  at  $\rho_A = 0.474$ . These regressions are compared with the corresponding regression for the (N-)H...N hydrogen bonds (set N,  $n = 54$ , MP2/6-31G(d,p);<sup>8</sup> Fig. 7),

**Fig. 5.** Correlation of  $d_A$  and  $\rho_A$  (eq. [3]). Solid circles, LiH...HY; open circles, HBeH...HY; open squares, H<sub>3</sub>BH...HY; open triangles, LiCCH...HY; solid triangles, H<sub>2</sub>BH...HY; solid squares, H<sub>3</sub>CH...HY; open diamond, H<sub>2</sub>. Inset: location of the data points for sets E and H relative to the correlation lines A (thick), E (eq. [9], thin), and N (eq. [10], broken line). Solid circles, H...H (set H); open circles, (N-)H...N; open triangles, (N-)H...Ph; open squares, (C-)H...Ph; solid triangles B, C, P1, P2 (see text; footnote 10). Positions of group centroids are indicated by X.



$$[8] \quad \nabla_A^2 = 16.89\rho_N'' - 25.69(\rho_N'')^2, \quad r^2 = 0.983, \\ \sigma_{51} = 0.531 \sim 3.8\%.$$

Relative to the N curve, the A curves cross the  $\nabla_A^2 = 0$  line sooner and fall off less sharply in the  $\nabla_c^2 < 0$  region.

Each of the three heterocorrelations a–c thus finds its counterpart in the (N-)H...N (set N) and (F-)H...F (74) *hydrogen* bonds, so that, formally, there is no qualitative difference in the functional dependence between hydrogen and dihydrogen bonds.

#### Experiment vs. the ab initio norm

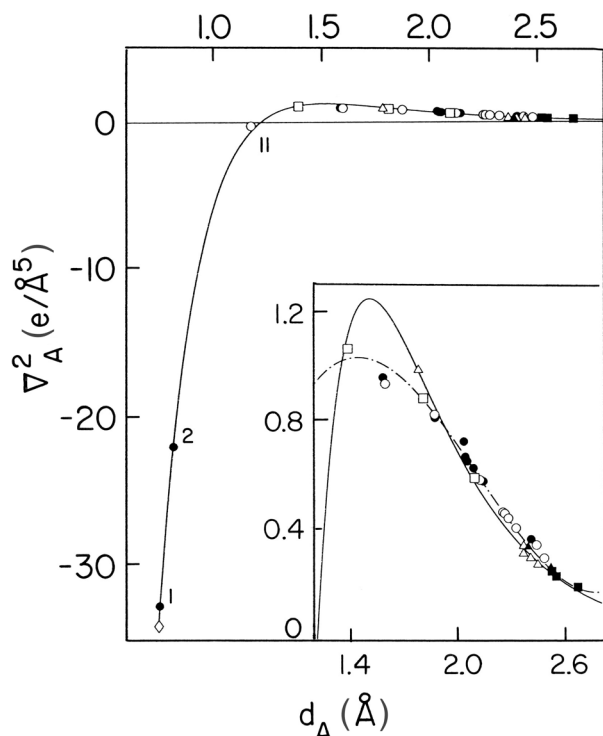
With the ab initio norm a–c established we can relate A to the experimental sets H and E, as well as to other experimental and ab initio results.<sup>10</sup>

The inset of Fig. 5 contains two kinds of comparison. First, it shows the experimental  $d_A, \rho_A$  data points of set E, i.e., for the topologically qualified (N-)H...N, (N-)H...Ph,

<sup>10</sup>There still is, in the literature, a scarcity of bond-critical parameter values for H...H bonds fully characterized by their BPs and BCPs, but the following (B, C, P1, and P2 in the plots; Figs. 5, 8, and 9) can be quoted for comparison. Point B refers to the (C-)H...H(-Mn) bond in CABNIC01 and CABNIC02 (28):  $d_c = 2.12(1)$ ,  $\rho_c = 0.066(5)$ ,  $\nabla_c^2 = 0.79(3)$ . Point C refers to the H9...H12 bond in the MP2/6-31G(d,p) optimized [Ir(H)<sub>3</sub>(PH<sub>3</sub>)<sub>2</sub>(NHCHNH<sub>2</sub>)] (60):  $d_c = 1.818$ ,  $\rho_c = 0.149$ ,  $\nabla_c^2 = 1.060$ . Point P1 refers to the (B1-)H3...H12(-N10) and point P2 to the (B9-)H15...H5(-N2) bond in the MP2/6-31G(d,p) optimized (H<sub>3</sub>BNH<sub>3</sub>)<sub>2</sub> dimer (48). For P1,  $d_c = 1.726$ ,  $\rho_c = 0.128$ ,  $\nabla_c^2 = 1.118$ ; for P2,  $d_c = 2.149$ ,  $\rho_c = 0.065$ ,  $\nabla_c^2 = 0.836$ . The charges on the H atoms for P1 and P2 are AIM rather than Mulliken charges; they cannot be used with the latter in our correlations (personal communication from P.L.A. Popelier and refs. 76 and 77; cf. also ref. 52).



**Fig. 6.** Correlation of  $d_A$  and  $\nabla_A^2$  (eq. [4]). Inset: enlargement of the main plot for large  $d_A$ . The local cubic approximation eq. [5] is represented by the broken line. Symbols as in caption of Fig. 5.



and (C-)H...Ph hydrogen bonds of Table B. Each group of contacts is cleanly separated from the other two and there is clear visual evidence that the (C-)H...Ph hydrogen bonds are weaker than the (N-)H...Ph bonds.<sup>2</sup> The 27  $d_E\rho_E$  data points can be fitted by a common exponential regression

$$[9] \quad \rho_E = 5.306 \exp(-1.639d_E), \quad r^2 = 0.901, \\ \sigma_{25} = 0.0114 \sim 6.9\%.$$

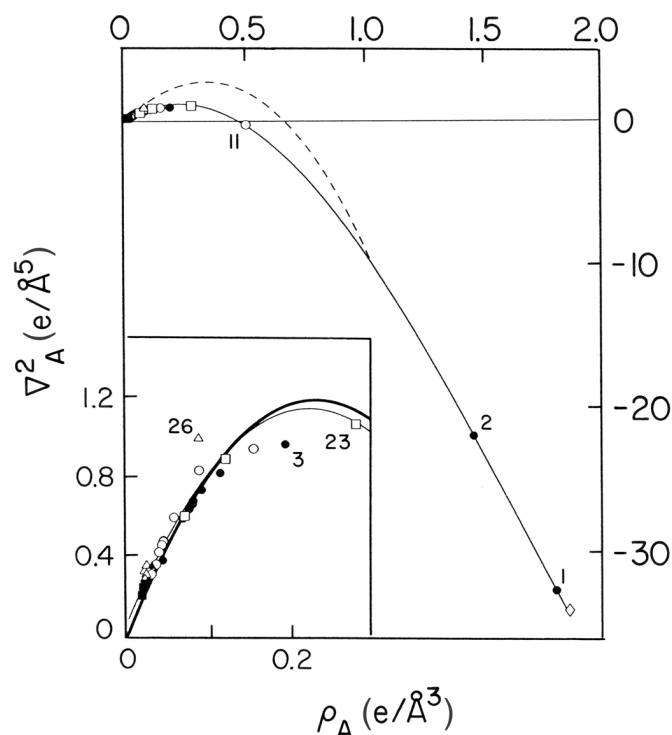
Second, the  $d_H\rho_H$  points for the H...H contacts are compared with the ab initio norm (set A). They all fall above the A curve, but visually it is obvious that, as a group, they are closer to the A than to the E curve and, as measured by  $\rho_c$ , correspond to weaker interactions than do the hydrogen bonds of E. The experimental point B and the ab initio points C, P1, and P2 are consistent with the H set.<sup>10</sup> The regression line N for the ab initio set N,

$$[10] \quad \rho_N = 1.308d_N^{-3.928} + 13.32 \exp(-2.580d_N)$$

( $r^2 = 0.990$ ,  $\sigma_{50} = 0.0334 \sim 3.3\%$ ) is below the E line, the difference arising partly from the underestimation of N in the MP2/6-31G(d,p) optimization.

The parallel comparison for  $d_H, \nabla_H^2$  is shown in Fig. 8. The H points (Fig. 8b) are somewhat above line A (eq. [5]), but they and points B, C, P1, and P2 otherwise follow more or less the trend of line A. The disposition of the E points about their common regression line (Fig. 8a) again reveals a clean separation of the three classes of HBs, in the strength sequence (N-)H...N, (N-)H...Ph, (C-)H...Ph. The exponential regression shown for E,

**Fig. 7.** Correlation of  $\nabla_c^2$  and  $\rho_c$  for sets A (eq. [7]) and N (eq. [8], broken line). The N line terminates at the  $\rho_S = 1.026$ ,  $\nabla_S^2 = -10.22$  point for the symmetric hydrogen bond (75). Inset: enlargement for small  $\rho_A$ . Thin line, unconstrained regression eq. [6]; thick line, eq. [7]. Symbols as in caption of Fig. 5.



$$[11] \quad \nabla_E^2 = 60.18 \exp(-1.733d_E), \quad r^2 = 0.92, \\ \sigma_{25} = 0.095 \sim 6.8\%,$$

coincides, over the data range, quite closely with the corresponding local cubic approximation eq. [5] (Fig. 6, inset). As in Fig. 5 (inset), the regression line for the N set in Fig. 8a,

$$[12] \quad \nabla_N^2 = 427.8 \exp(-2.671d_N'') \\ - 44515 \exp(-5.935d_N'')$$

( $r^2 = 0.985$ ,  $\sigma_{50} = 0.515 \sim 3.7\%$ ), is below the E line.

For  $\rho_E, \nabla_E^2$  (Fig. 9a) the separation of (N-)H...N, (N-)H...Ph, and (C-)H...Ph is also clean. The regression line E for this data set,

$$[13] \quad \nabla_E^2 = 8.91\rho_E, \quad r^2 = 0.90, \quad \sigma_{25} = 0.110 \sim 8.0\%,$$

is significantly below the ab initio curve N for the (N-)H...N bonds.<sup>8</sup> Unlike in Figs. 5 and 8, the H points in Fig. 9 are mixed up considerably with the points of E, mainly with those for the (C-)H...Ph bonds; points B, C, P1, and P2, not included in the regressions, appear to correspond to stronger H...H interactions. The lack of separation is consistent with the essentially similar character of the H...H and weak HBs.

At comparable  $d_c$  (Fig. 5, inset),  $\rho_c$  in set H is about half that in the (N-)H...Ph HBs. The  $\rho_H$  values that are observed at, say,  $\sim 0.05 \text{ e/Å}^3$  in H...H bonds of ca. 2.4 Å length are comparable to the  $\rho_c$  values in (C-)H...Ph HBs of ca. 2.9 Å



**Fig. 8.** Location of the  $d_c \nabla_c^2$  data points for sets **E** (a) and **H** (b) relative to the correlation lines A (eq. [4], thick), E (eq. [11], thin), and N (eq. [12], broken line). Symbols as in caption of Fig. 5 (inset).

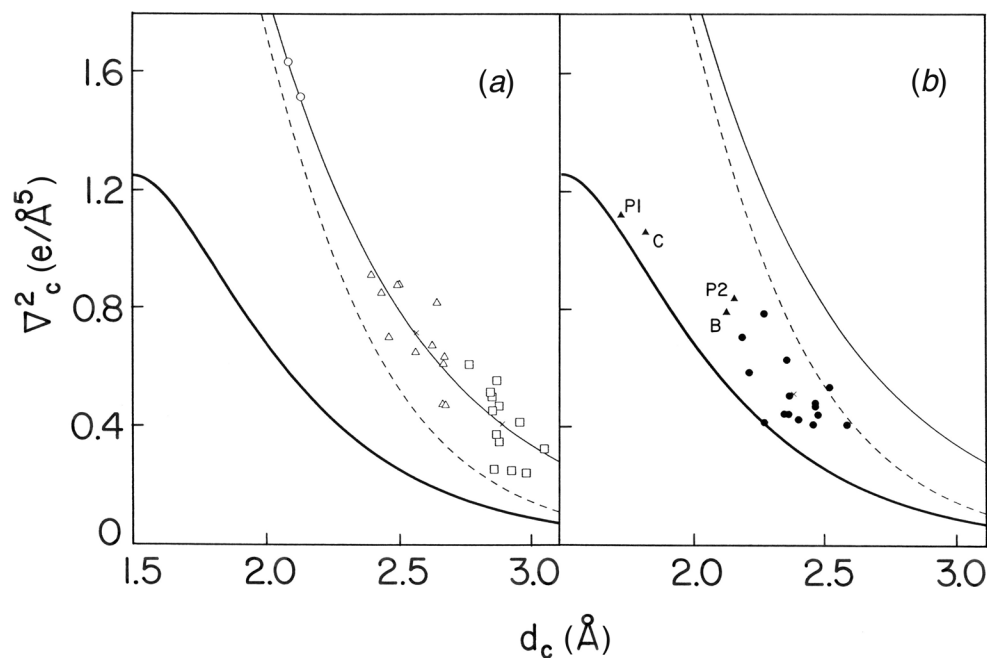
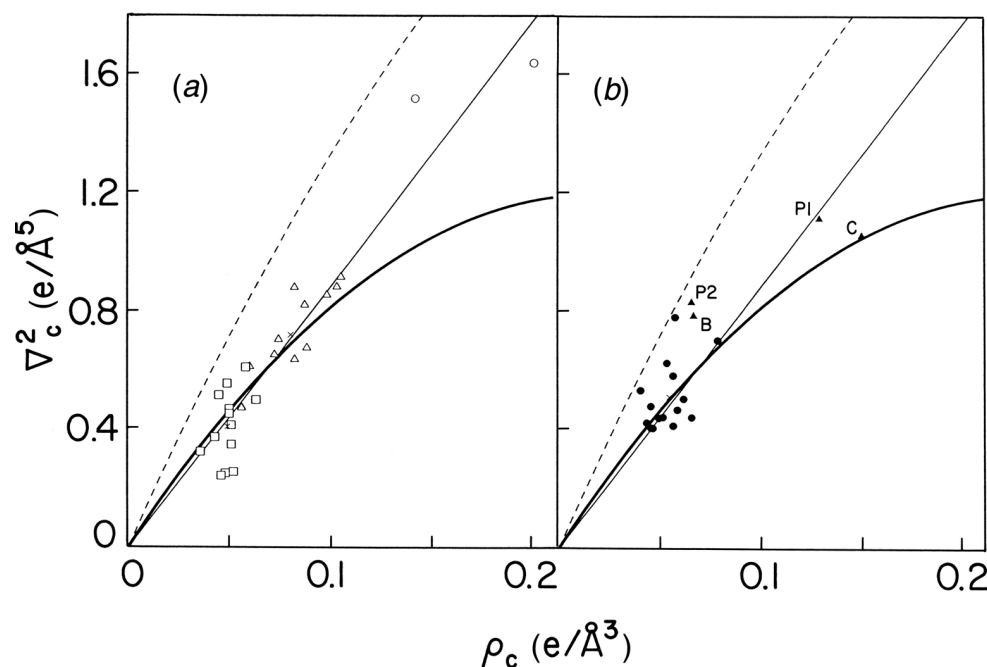


**Fig. 9.** Location of the  $\rho_c \nabla_c^2$  data points of sets **E** (a) and **H** (b) relative to the correlation lines A (eq. [7], thick), E (eq. [13], thin), and N (eq. [8], broken line). Symbols as in caption of Fig. 5 (inset).



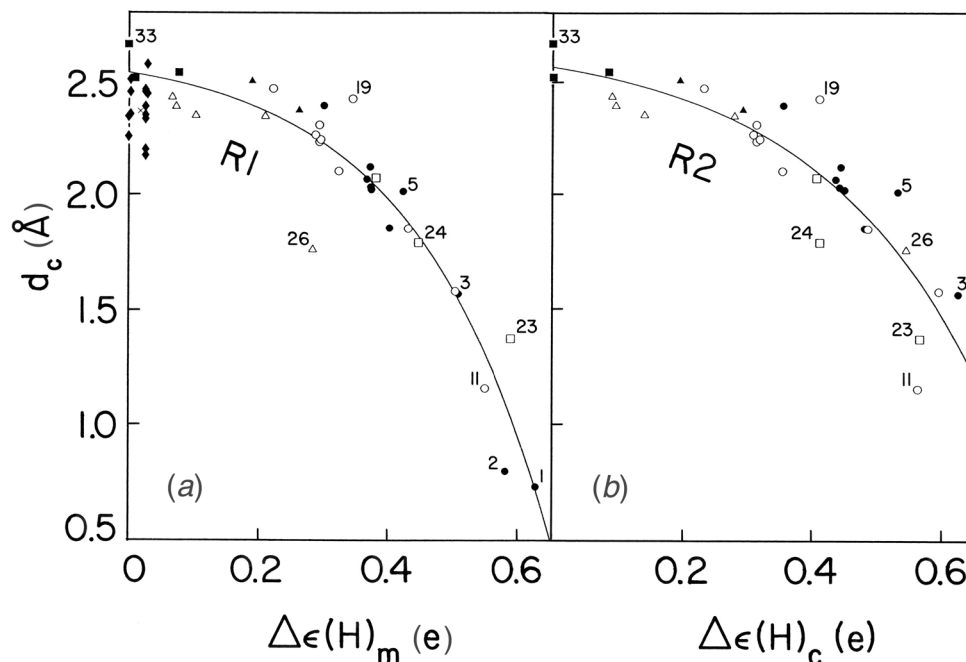
length. The DBs are thus significantly weaker than the (N-)H...Ph or the (C-)H...Ph bonds in the three structures and weaker also than the H...H bonds in B, C, P1, and P2.<sup>10</sup> This is reflected more quantitatively in the positions of the centroids of the three groups of data points for sets **H** and **E** (Figs. 5 (inset), 8, and 9):<sup>11</sup>

	Type	<i>n</i>	$\bar{d}_c$	$\bar{\rho}_c$	$\bar{\nabla}_c^2$
Set <b>H</b>	(C-)H...H(-C)	15	2.37[11]	0.054[10]	0.51[12]
Set <b>E</b>	(N-)H...Ph	12	2.56[10]	0.079[17]	0.72[16]
	(C-)H...Ph	13	2.89[7]	0.048[7]	0.41[12]

<sup>11</sup>The corresponding centroids for the nine (C-)H...N hydrogen bonds (not discussed here;<sup>3</sup> Table B) are  $\bar{d}_c = 2.82[12]$ ,  $\bar{\rho}_c = 0.053[10]$ , and  $\bar{\nabla}_c^2 = 0.54[9]$ , respectively.



**Fig. 10.** (a) Correlation of  $d_A$  with  $\Delta\epsilon(H)_m$ . Regression line R1, eq. [14]. Solid diamonds, set **H**. (b) Correlation of  $d_A$  with  $\Delta\epsilon(H)_c$ . Regression line R2:  $d_A = 2.673 - 0.115 \exp[3.922\Delta\epsilon(H)_c]$ ,  $r^2 = 0.81$ ,  $\sigma_{28} = 0.163 \sim 11\%$ . Symbols as in caption of Fig. 5.



All three comparisons thus confirm the strength hierarchy<sup>2</sup> of the three types of HBs in **E** and testify to the non-negligible strength of the observed H...H interactions.

In Fig. 5 (inset) the **H** data points fall above their ab initio reference line A by roughly a similar amount as the **E** data points fall above the comprehensive ab initio reference line N for the (N-)H...N bonds<sup>8</sup> if N is taken as a common estimate of points of the **E** set. The discrepancy between the experimental points and the reference curve appears thus to arise mainly from inadequacies of the MP2/6-31G(d,p) model.

The lengths of the H...H contacts in **H** are not unusual among those reported from experiment for main-group X and Y. Ref. 9 suggests 1.7–2.2 Å for  $d(H\cdots H)$  and 90–135° for X-H...H or H...H-Y as the overall range for DBs, with an upper limit of 2.65 Å in C-H...H-B bonds. More specifically, in adducts of LiBH<sub>4</sub> (27), NaBH<sub>4</sub> (25), and NaCNBH<sub>3</sub> (25), the range of (corrected) intermolecular distances is 1.62–2.28 Å. As for intramolecular H...H contacts, Matta et al. (38) find, in documented ab initio BPs in a variety of benzenoid and other hydrocarbons,  $d(H\cdots H) < 2.12$  Å between hydrogens on benzenoid carbons and  $d(H\cdots H) > 2.17$  Å and up to ~2.70 Å between hydrogens of Me groups (distances converted from au; van der Waals radius of H assumed to be ~2.39 Å). Similarly, the 16 bifurcated, highly bent B-H(...H-C)<sub>2</sub> intramolecular H...H bonds in TARNOP, TARNUV, TARPAD, TARPEH, and TARPIL (not characterized topologically) are reported (21) to have a range of 2.22(4)–2.94(5) Å and an unweighted grand mean of 2.51[18] Å compared with the intermolecular  $d_H(\mathbf{H})$  of 2.38[11] Å and a range of 2.18–2.57 Å (Table 2).

#### Do bond-critical parameters of DBs depend on $\Delta\epsilon(H)$ ?

As pointed out in the Introduction, the Mulliken charges  $\epsilon(H)$  on the phenyl hydrogens of **H** are very small (68) and their differences  $\Delta\epsilon(H)$  are even smaller. Yet in spite of their

almost negligible polarity the H...H contacts have topological characteristics that suggest kinship with authenticated DBs. To investigate to what extent  $\Delta\epsilon(H)$  is a determinative factor in the formation of an H...H bond,  $d_A$ ,  $\rho_A$ , and  $\nabla_A^2$  have been plotted against  $\Delta\epsilon(H)_m = |\epsilon(H_d)_m - \epsilon(H_a)_m|$ , the difference between the Mulliken charges on the pertinent H atoms in the two species XH and HY prior to complexation (Figs. 10–12). In none of these plots are the data points cleanly separated into an LiH and an HBeH set (Table 1) or even more finely, but it is evident that the parameters correlate significantly with  $\Delta\epsilon(H)_m$ .

As might be anticipated, the  $d_A$  values decrease with increasing  $\Delta\epsilon(H)_m$ , and the decrease is steep (Fig. 10a). In spite of the considerable scatter the  $\Delta\epsilon(H)_m, d_A$  pairs are quite well fitted by

$$[14] \quad d_A = 2.635 - 0.096 \exp[4.787\Delta\epsilon(H)_m], \\ r^2 = 0.91, \sigma_{30} = 0.153 \sim 8.0\%.$$

With the outlier **26** removed,  $r^2$  increases to 0.94,  $\sigma_{29} = 0.125 \sim 6.5\%$ , but the new regression line differs from that of eq. [14] only insignificantly.

The range of  $\rho_A$  is too large to display the features of a  $\Delta\epsilon(H)_m, \rho_A$  plot in sufficient detail directly. However, a  $\Delta\epsilon(H)_m, \ln \rho_A$  plot (Fig. 11a) can be fitted reasonably well by

$$[15] \quad \ln \rho_A = -4.442 + 0.376 \exp[4.088\Delta\epsilon(H)_m], \\ r^2 = 0.93, \sigma_{30} = 0.329 \sim 7.0\%.$$

The functional form of this regression reveals that even at  $\Delta\epsilon(H)_m = 0$  the  $\rho_A$  value is still about 0.018 e/Å<sup>3</sup> (compare this with Bader's (69)  $\rho_c$  in Ne...HF and Ar...HF, 0.067 and 0.052 e/Å<sup>3</sup>, respectively).

The sign inversion of  $\nabla_A^2$  within the observed  $\Delta\epsilon(H)_m$  range lends the  $\nabla_A^2$  vs.  $\Delta\epsilon(H)_m$  plot (Fig. 12a) a particularly informative character. For  $\Delta\epsilon(H)_m$  up to ca. 0.52,  $\nabla_A^2$  shows



**Fig. 11.** (a) Correlation of  $\ln \rho_A$  with  $\Delta\epsilon(H)_m$ . Regression line R1, eq. [15]. Solid diamonds, set **H**. (b) Correlation of  $\ln \rho_A$  with  $\Delta\epsilon(H)_c$ . Regression line R2:  $\ln \rho_A = -4.827 + 0.686 \exp[2.648\Delta\epsilon(H)_c]$ ,  $r^2 = 0.84$ ,  $\sigma_{28} = 0.360 \sim 7.8\%$ . Symbols as in caption of Fig. 5.

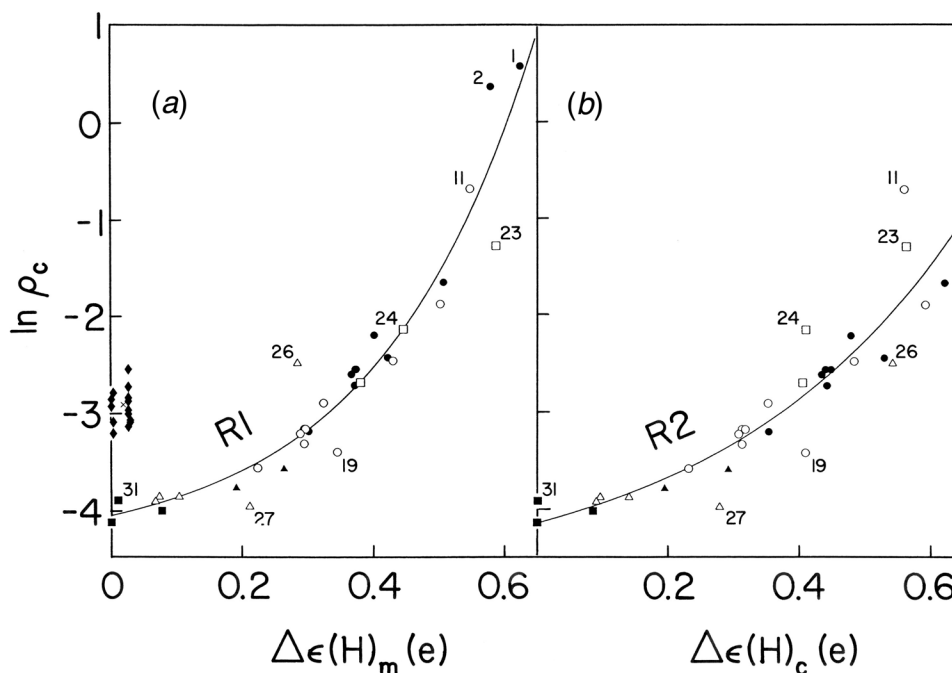
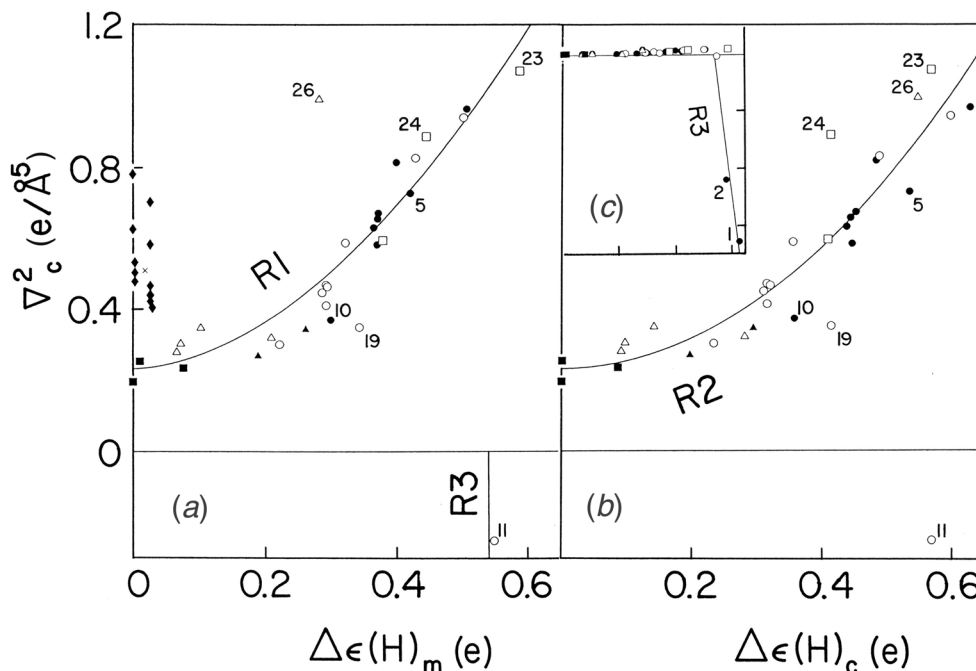


**Fig. 12.** (a) Correlation of  $\nabla_A^2$  with  $\Delta\epsilon(H)_m$ . Regression line R1, eq. [16]. (b) Correlation of  $\nabla_A^2$  with  $\Delta\epsilon(H)_c$ . Regression line R2:  $\nabla_A^2 = 0.231 + 2.19[\Delta\epsilon(H)_c]^{2.00}$ ,  $r^2 = 0.86$ ,  $\sigma_{27} = 0.102 \sim 12\%$ . (c) Correlation of  $\nabla_A^2$  with  $\Delta\epsilon(H)_m$ , all data pairs shown. Regression line R3:  $\nabla_A^2 = 218 - 405\Delta\epsilon(H)_m$ ,  $r^2 = 0.92$ ,  $\sigma = 6.8\%$ . Symbols as in caption of Fig. 5; solid diamonds, set **H**.



a steady non-linear increase with  $\Delta\epsilon(H)_m$ . This portion of the plot can be represented by

$$[16] \quad \nabla_A^2 = 0.232 + 2.390[\Delta\epsilon(H)_m]^{1.790}, \quad r^2 = 0.78, \\ \sigma_{27} = 0.127 \sim 12\%,$$

i.e.,  $\Delta\epsilon(H)_m$  and  $\nabla_A^2$  in this region are correlated, and the variation is monotonic. However, the  $\nabla_A^2$  values for **1**, **2**, and

**11** are negative, and at the same time the magnitudes of  $\nabla_A^2$  of **1** and **2** are also dramatically large relative to  $\nabla_A^2 < 0.52$  (Fig. 12c). This indicates a change-over from an essentially electrostatic to a covalent bond character and suggests that the sign of  $\nabla_c^2$  can be used as a diagnostic of the X-H...H-Y/X...H-H...Y instability (see below). This change of the interaction regime occurs at  $\Delta\epsilon(H)_m \sim 0.54$ . There is some uncertainty concerning **23**, which has a positive Laplacian and



a  $\Delta\epsilon(\text{H})_{\text{m}}$  value larger than that of **11**. Possibly this has to do with the negative charge on the complex.

To compare the experimental parameters of **H** with those of the **A** set, estimates of  $\epsilon(\text{H})$  for the phenyl hydrogens are required. These are obtained from the  $\epsilon(\text{H})_{\text{m}}$  for the free  $\text{BPh}_4^-$  anion in its ground-state  $S_4$  conformation (B3LYP/6-31G(d,p), ref. 68: 0.064[2] e for the *ortho*, 0.038[1] e for the *meta*, and 0.035 e for the *para* hydrogens). Thus  $\Delta\epsilon(\text{H})_{\text{m}} = 0$  for like hydrogens,  $\sim 0.026$  e for *ortho*–*meta*,  $\sim 0.029$  e for *ortho*–*para*, and  $\sim 0.003$  e for *meta*–*para* H···H contacts. These values, even for the *ortho* interactions, are 10–20 times smaller than the  $\Delta\epsilon(\text{H})_{\text{m}}$  in Table 1. One would therefore expect BPs in the tetraphenylborates, if any, only for the *ortho* interactions, but in fact BPs are observed even *between like H atoms* (Table 2).

In Fig. 10a the centroid of **H** is at  $d_{\text{H}} = 2.37[11]$  Å,  $\Delta\epsilon(\text{H})_{\text{m}} = 0.016[13]$  e, i.e., only ca. 0.13 Å below the regression line and thus well within  $1\sigma$  of the fit. The  $\nabla_{\text{H}}^2$  values in **H** (Fig. 12a) stretch over a wider interval than might be expected but otherwise are consistent with the general location anticipated for (C-)H···H(-C) interactions. Only very small differences are observed between the *o*, *m*, and *p* types of the phenyl hydrogens. In **H** there is a small  $\rho_{\text{H}}$  at the BCP even at  $\Delta\epsilon(\text{H})_{\text{m}}$  nominally zero (**c** and **f**) or close to zero (Table 2). These “residual”  $\rho_{\text{H}}$  values are commented upon in the Discussion.

#### Differences between $\Delta\epsilon(\text{H})_{\text{m}}$ and $\Delta\epsilon(\text{H})_{\text{c}}$

The use of  $\Delta\epsilon(\text{H})_{\text{m}}$  in the correlation plots is anticipatory, i.e., it is expected that the correlation will depend on the difference of the  $\epsilon(\text{H})_{\text{m}}$  charges in the respective “monomers”, without consideration of the a priori unknown extent of the variation of  $\epsilon(\text{H})$  on complexation. Figure 13 compares the differences  $\Delta\epsilon(\text{H})_{\text{m}}$  and  $\Delta\epsilon(\text{H})_{\text{c}}$ , i.e., before and after the formation of the DB (Table 1). Constrained linear regression ( $\epsilon(\text{H})_{\text{c}}$  values were not obtained for **1** and **2**, both of the  $\text{Li}^+\cdots\text{H}-\text{H}\cdots\text{NX}_3$  type) yields

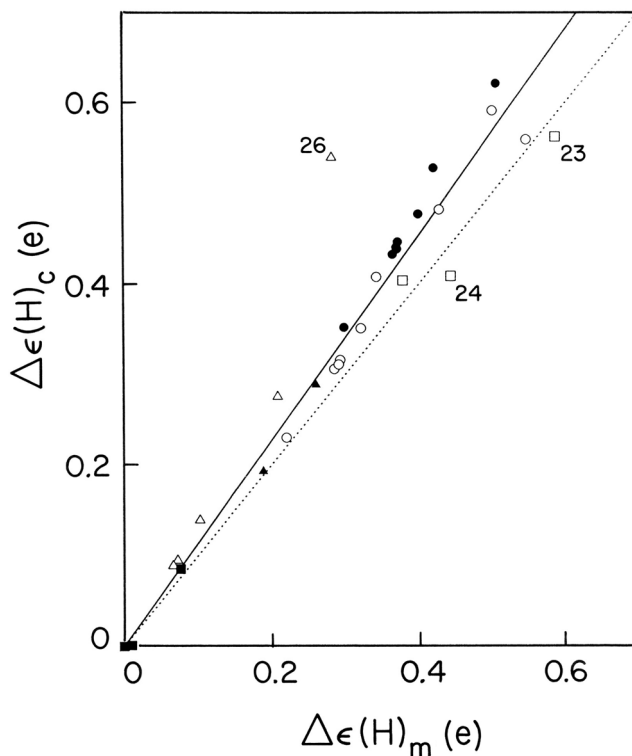
$$[17] \quad \Delta\epsilon(\text{H})_{\text{c}} = 1.136\Delta\epsilon(\text{H})_{\text{m}}, \quad r^2 = 0.90, \\ \sigma_{29} = 0.055 \sim 8.8\%.$$

With **26** not included,

$$[18] \quad \Delta\epsilon(\text{H})_{\text{c}} = 1.118\Delta\epsilon(\text{H})_{\text{m}}, \quad r^2 = 0.96, \\ \sigma_{28} = 0.036 \sim 5.8\%.$$

Thus the difference  $\Delta\epsilon(\text{H})_{\text{c}} - \Delta\epsilon(\text{H})_{\text{m}}$  increases quasilinearly with  $\Delta\epsilon(\text{H})_{\text{m}}$ . Replotting Figs. 10a–12a in terms of  $\Delta\epsilon(\text{H})_{\text{c}}$  does not produce major qualitative changes in the trends (Figs. 10b–12b), although the shifts in the positions of *individual* data points may be large (cf. **19**, **23**, **24**, **26**).

**Fig. 13.** Correlation of  $\Delta\epsilon(\text{H})_{\text{m}}$  and  $\Delta\epsilon(\text{H})_{\text{c}}$  (Table 1). Solid line, all  $\Delta\epsilon(\text{H})_{\text{m}}\Delta\epsilon(\text{H})_{\text{c}}$  pairs, regression line (eq. [17]) constrained to pass through the origin; dotted line,  $\Delta\epsilon(\text{H})_{\text{c}} = \Delta\epsilon(\text{H})_{\text{m}}$ . Symbols as in caption of Fig. 5.



#### Is there a bond-critical criterion of H···H/H<sub>2</sub> instability?

With decreasing  $d(\text{H}\cdots\text{H})$  the two atoms will eventually come sufficiently close for the covalent component of the H···H interaction to dominate, and formation of a perturbed H<sub>2</sub> molecule,  $\text{X}\cdots\text{H}-\text{H}\cdots\text{Y}$ , will then become energetically favourable. As a consequence, loss of H<sub>2</sub> from the DB complex may occur in the course of its formation from XH and HY during the optimization process.<sup>12</sup> Thus, for example, MP2/6-31G(d,p) optimization of the linear complex  $\text{H}_3\text{BH}\cdots\text{H}\cdots\text{H}\cdots\text{NH}_3$  ( $\Delta\epsilon(\text{H})_{\text{m}} = 0.659$ ) has been described (5, 42) as dissociative,<sup>13</sup> with liberation of H<sub>2</sub>, and an attempted similar optimization of  $\text{H}_3\text{BH}\cdots\text{H}\cdots\text{H}\cdots\text{NF}_3$  ( $\Delta\epsilon(\text{H})_{\text{m}} = 0.705$ ) resulted in the formation of BH<sub>3</sub>, H<sub>2</sub>, and NF<sub>3</sub> (I. Alkorta, personal communication).<sup>14</sup> At which point the instability begins to occur can, in our context, be investigated only in geometric/topological terms, as we have not examined the energy aspects of the problem. However, it is noted that the  $\nabla_{\text{A}}^2$  values of the three species with very short H···H contacts, viz. **1**, **2**, **11** (and of course H<sub>2</sub>), are all negative and thus indicative of covalent bonding interactions.

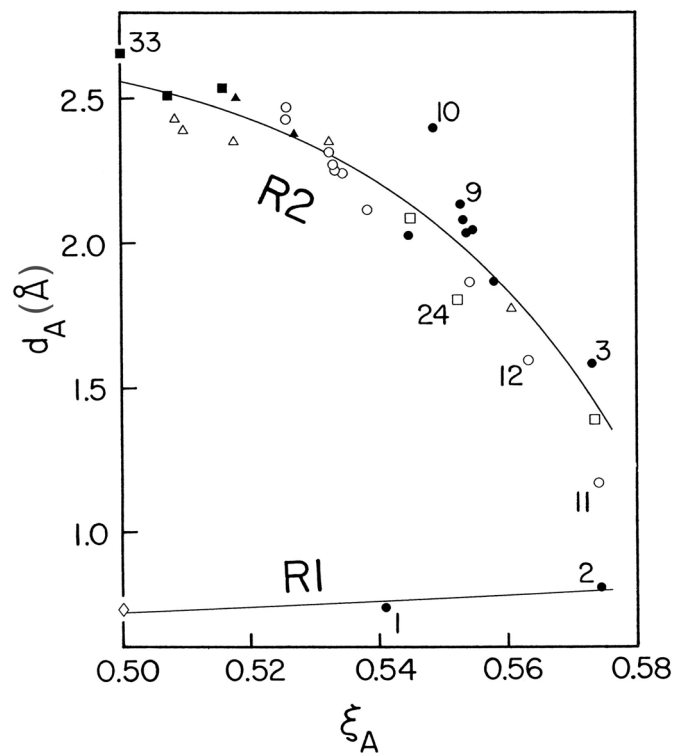
<sup>12</sup>Under experimental conditions, loss of H<sub>2</sub> from a DB complex already formed need not occur even at very short H···H distances (**24**, **25**, **27**, **30**; also **44**, **46**, **50–53**), although such loss has been reported in some cases (**78–80**).

<sup>13</sup>Interestingly, crystalline ammonium borohydride  $\text{NH}_4^+\text{BH}_4^-$  has been reported to be stable below  $-20^\circ\text{C}$  and to liberate H<sub>2</sub> at higher temperatures (**81**, **82**).

<sup>14</sup>The position of the  $\text{X}-\text{H}\cdots\text{H}-\text{Y}/\text{X}\cdots\text{H}-\text{H}\cdots\text{Y}$  equilibrium can be shifted by application of an external electric field (**44**). By choosing the strength and direction of the field (ab initio calculations) it was possible to displace the two H atoms along the bond and thus to manipulate the equilibrium in the  $\text{LiH}/\text{HF}$ ,  $\text{H}_3\text{BH}/\text{H}\cdots\text{H}\cdots\text{NH}_3$ , and  $\text{HBeH}/\text{H}\cdots\text{H}\cdots\text{NH}_3$  bond systems from a DB, via a coordinated H<sub>2</sub> molecule, to H<sub>2</sub> and vice versa. In set **A** the variation of the bond type is achieved by “chemical” manipulation of X and Y, without external fields. The results of ref. **44** emphasize the difference between DB stability in the ab initio calculation and in the crystal environment (cf. also ref. **65**).<sup>13</sup>



**Fig. 14.** Variation of  $d_A$  with the relative position  $\xi_A = d(\text{H}_d \cdots \text{BCP})/d_A$  of the BCP in the  $\text{H}_d \cdots \text{H}_a$  bond. Regression line R1, eq. [20]; regression line R2, eq. [19]. Symbols as in caption of Fig. 5; open diamond,  $\text{H}_2$ .



Plotting  $d_A$  against the relative position  $\xi_A = d(\text{H}_d \cdots \text{BCP})/d_A$  of the BCP in the  $\text{H} \cdots \text{H}$  bond (Fig. 14), we see that, for  $d_A > 1.1$  Å,  $d_A$  decreases steadily with increasing  $\xi_A$ :

$$[19] \quad d_A = 2.759 - 0.195 \exp[25.96(\xi_A - 1/2)],$$

$$r^2 = 0.89, \sigma_{27} = 0.354 \sim 28\%$$

(regression R2, **11** not included); at the  $\xi_A = 1/2$  limit,  $d_A = 2.564$  Å. In contrast, the two data points with  $d_A < 1$  Å, **1** and **2**, do not fall on an extension of line R2. They and the point for  $\text{H}_2$  can be accommodated by R1:

$$[20] \quad d_A = 0.596/(1.324 - \xi_A), r^2 = 0.77,$$

$$\sigma_1 = 0.016 \sim 23\%,$$

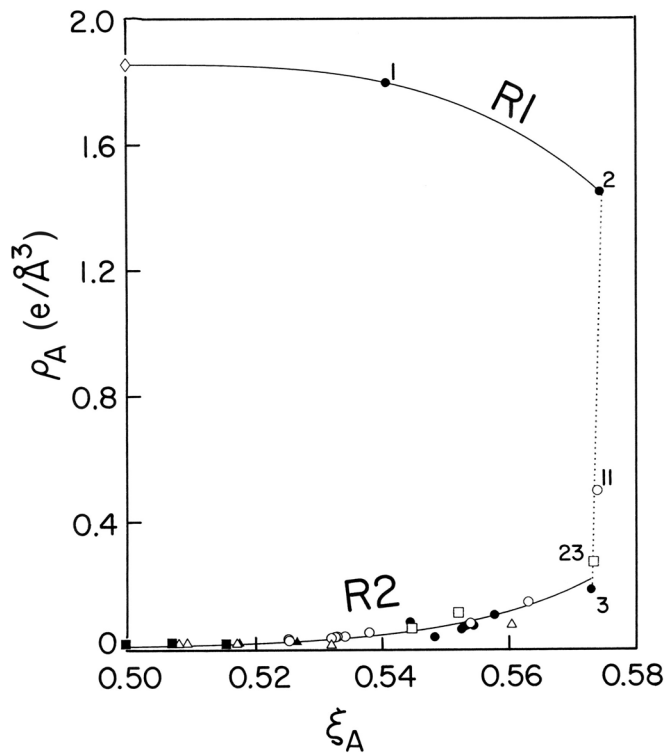
i.e., by an entirely different regression function. The gap in  $d_A$  between the two groups of data points indicates that a change takes place somewhere between  $d_A \sim 0.85$  and  $\sim 1.1$  Å. This change involves the manner in which  $d(\text{H} \cdots \text{H})$  determines the relative position of the BCP and with it the character of the interaction. While this plot involves only geometric parameters,  $d_A$  and  $\xi_A = x_A/d_A$ , the existence of the gap is confirmed by the presence of parallel features in the  $\xi_A \cdot \rho_A$  (Fig. 15) and  $\xi_A \cdot \nabla_A^2$  (Fig. 16) plots, both of which involve the non-geometric parameters  $\rho_A$  and  $\nabla_A^2$ .

In Fig. 15 the electron density  $\rho_A$  at the BCP,

$$[21] \quad \rho_A = 0.0165 + 0.00278 \exp[59.66(\xi_A - 1/2)],$$

$$r^2 = 0.91, \sigma_{27} = 0.0186 \sim 7\%,$$

**Fig. 15.** Variation, with  $\xi_A = x_A/d_A$ , of  $\rho_A$  in the  $\text{H} \cdots \text{H}$  bonds. Regression line R1:  $\rho_A = 1.857 - 2130(\xi_A - 1/2)^{3.30}$  (exact fit). Regression line R2, eq. [21]. Symbols as in caption of Fig. 5; open diamond,  $\text{H}_2$ .



increases with  $\xi_A$  to ca.  $0.2 \text{ e}/\text{\AA}^3$  at  $\xi_A \sim 0.573$ , at which point it jumps suddenly (catastrophically?) to  $\sim 1.45 \text{ e}/\text{\AA}^3$  with very little change in  $\xi_A$  but with a considerable contraction of  $d_A$ , from  $1.385$  Å in **23** to  $0.805$  Å in **2**. After this,  $\rho_A$  continues to increase but now with decreasing  $\xi_A$ . At the same time the Laplacian  $\nabla_A^2$  at the BCP of **1** and **2** changes sign, indicating the now strongly covalent nature of the  $\text{H} \cdots \text{H}$  interaction. This contraction process ends at the  $\text{H}_2$  molecule with  $\xi_A = 1/2$ . Corresponding features are observed in the  $\xi_A \cdot \nabla_A^2$  plot of Fig. 16 (cf. also Fig. 12).

The number of data points in the  $\xi_A = 0.573\text{--}0.575$  interval unfortunately is too small for elucidating the features of the plot in this region in more detail, but it seems that **11**, with its small negative Laplacian of  $-0.25 \text{ e}/\text{\AA}^5$ , represents the incipient stage of the change in the  $\text{H} \cdots \text{H}$  regime.

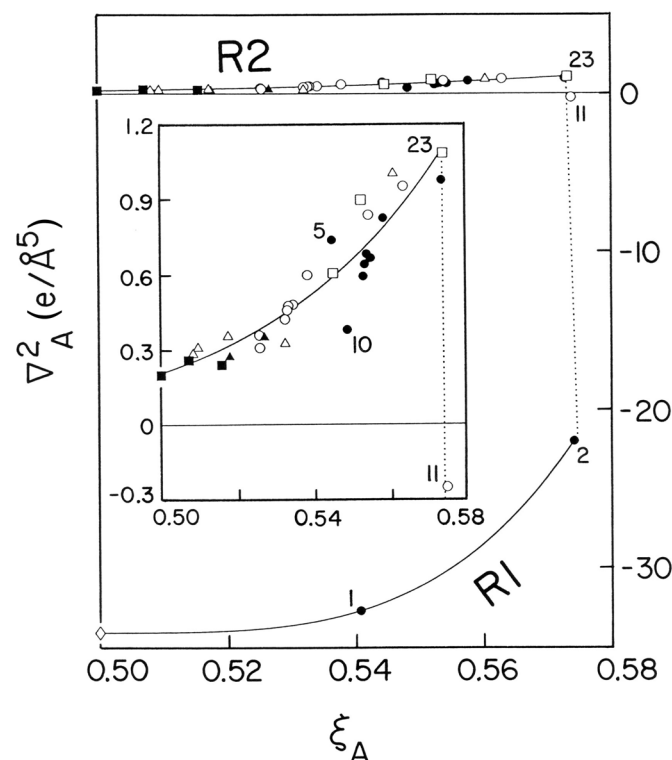
The regression value  $\rho_A \sim 0.02 \text{ e}/\text{\AA}^3$  at  $\xi_A = 1/2$  (eq. [21]) is within  $1\sigma$  (eq. [21]), i.e., statistically  $\rho_A(\xi_A = 1/2) = 0$  cannot be dismissed. However, the observed  $\rho_H$  values, all with  $\xi_A$  close to  $1/2$ , are all larger than  $0.04 \text{ e}/\text{\AA}^3$  (Table 2), i.e., non-zero and thus compatible with the regression value of  $\rho_A$  from eq. [21].

## Discussion

Unlike many of the crystal structures reported to contain DBs, the structures of the three organoammonium tetraphenylborates offer the advantage of containing, beside at least two distinct intermolecular  $\text{H} \cdots \text{H}$  contacts shorter than  $3$  Å in each structure, a variety of weak  $\text{N-H} \cdots \text{Y}$  and  $\text{C-H} \cdots \text{Y}$  hydrogen bonds (Table B). Thus, coming from the



**Fig. 16.** Variation, with  $\xi_A$ , of  $\nabla_A^2$  at the BCP in the H...H bonds. Regression line R1:  $\nabla_A^2 = -34.15 + 146283(\xi_A - 1/2)^{3.617}$  (exact fit). Regression line R2:  $\nabla_A^2 = 0.2219 + 73.58(\xi_A - 1/2)^{1.708}$ ,  $r^2 = 0.87$ ,  $\sigma_{27} = 0.096 \sim 11\%$ . Inset: expansion of the R2 plot. Symbols as in caption of Fig. 5; open diamond,  $H_2$ .

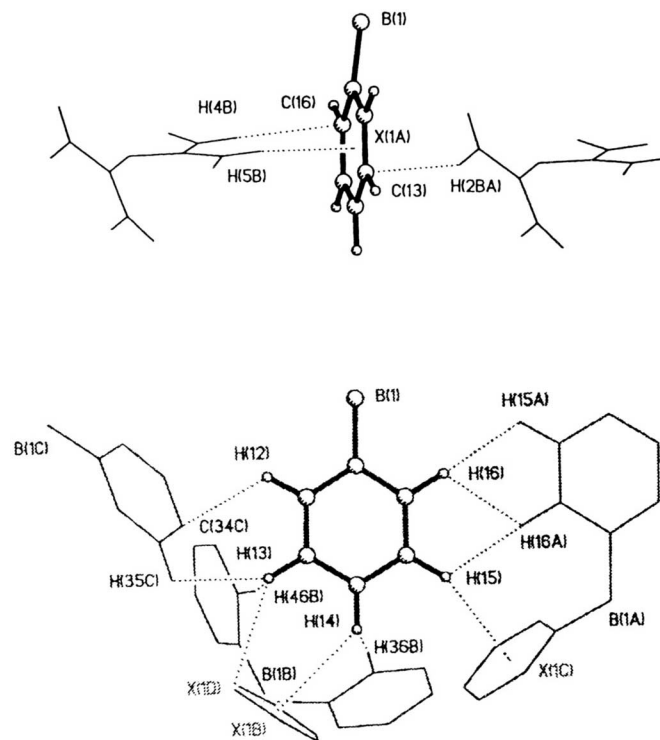


same structure, the DBs and the corresponding HBs can be compared on equal footing in terms of bonding engagement and bond-critical parameters.

There are numerous short (i.e., less than the sum of the van der Waals radii) H...H contacts reported in the literature and presumed to be bonding even though their characterization is incomplete, being based on no more evidence than the  $d(H\cdots H)$  distance instead of on complete topology. In the present case, each of the 15 observed intermolecular H...H contacts (set **H**) has a clearly characterized BP and a BCP, thus satisfying the most important of the criteria of the H...H bonding interaction (48, 71). The BPs are all somewhat curved (Figs. 1–4), which makes it difficult to establish their “true” lengths; the internuclear H...H distances  $d_H$  are therefore used instead in describing the contacts. The  $d_H$  and the associated  $\rho_H$  and  $\nabla_H^2$  values are listed in Table 2.

The simultaneous presence of intermolecular HBs and H...H contacts in the three structures demonstrates also the important principle of exhaustive (saturation) bonding in crystal structures containing such bonds. The schematic view of the bonding engagement of phenyl ring 1 in BTB (Fig. 17) serves as an instructive illustration of the importance of the total intermolecular interaction. Here *every phenyl hydrogen* is either a donor or an acceptor of a proton in a DB and (or) an HB bond, and the DBs, while weaker than the HBs, are not unimportant.<sup>15</sup> Another excellent ex-

**Fig. 17.** Intermolecular bonding engagement of phenyl ring 1 in BTB (DBs and HBs up to 3 Å). (Bottom) Projection on the plane of ring 1: phenyl – ring 1 interactions. (Top) Projection roughly perpendicular to the plane of ring 1: cation – ring 1 interactions. X indicates either the centroid of a phenyl ring (X(1B), X(1C)) or of a ring bond (X(1D)).



ample of exhaustive intermolecular bonding is found in the dabcoH<sup>+</sup> cation in DTB, but it is difficult to present all the bonding interactions of the cation satisfactorily in a 2D projection.

### Comparison norm for bond-critical parameters

To compare  $d_H$ ,  $\rho_H$ , and  $\nabla_H^2$  with the corresponding parameters of other H...H and (X-)H...Y bonds, it was convenient to establish a comparison norm utilizing Alkorta's<sup>6</sup> extensive ab initio data listed in Table 1 (set **A**). As the  $d_A\rho_A$ ,  $d_A\nabla_A^2$ , and  $\rho_A\nabla_A^2$  plots (Figs. 5–7) show, these parameters are strongly and smoothly pairwise correlated. The correlation curves give no indication of discontinuities or other features that would point to the existence of a qualitative differentiation in the nature of the H...H bonds in set **A** with respect to their length.

However, when the relative position  $\xi_A = d(H_d\cdots BCP)/d_A = x_A/d_A$  of the BCP in the H...H bond is plotted against  $d_A$  (Fig. 14), the data points are seen to fall in two groups (separated by a gap at  $d_A$  between approximately 0.9 and 1.15 Å), and *two* correlation curves with quite different slopes are required to represent the complete data set when the subset with  $d_A < 0.9$  Å is augmented by the  $d_A, \xi_A$  point for the  $H_2$  molecule. The existence of the gap is confirmed in Fig. 15, where  $\rho_A$ , which is not a purely geometric param-

<sup>15</sup>Cf. also the  $NaBH_4 \cdot N(CH_2CH_2OH)_3$  adduct, in which there is no conventional hydrogen bonding, but all the OH groups are engaged in H...H bonds to the anion (25).



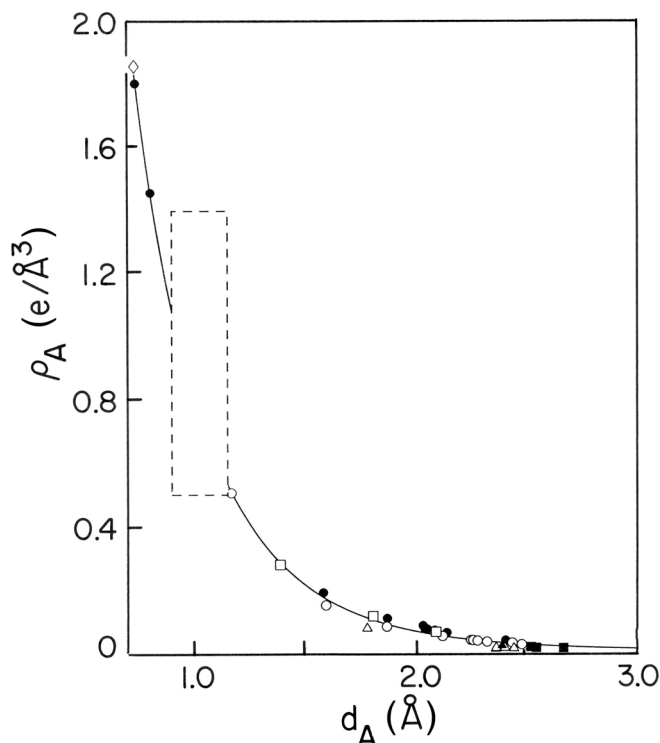
eter, is plotted against  $\xi_A$ . The gap in this plot occurs between  $d_A \sim 0.5\text{--}1.4 \text{ e}/\text{\AA}^3$  and at  $\xi_A \sim 0.575$ . The corresponding exclusionary, “taboo” domain is shown in Fig. 18, from which it is evident that the smoothness of the  $d_A\rho_A$  correlation curve in Fig. 5 is only apparent (in spite of the excellent statistical figures of merit, eq. [3]) and that the failure to detect the gap in the  $d_A\rho_A$  plot arises from the paucity or nonexistence of data points in the taboo domain. It is precisely in this domain that complications involving existence or stability of DB-containing species have been reported (24, 30, 46, 50, 51, 78, 80, 83). The data points of **H** all have  $d_A$  values above  $2 \text{ \AA}$ , so the existence of the taboo domain does not interfere with our discussion of the experimental results.

The sudden jump in  $\rho_A$  from R1 to R2, at practically constant  $\xi_A$  at **23** and **2** but with considerable concomitant contraction of  $d(\text{H}\cdots\text{H})$  (Fig. 15), invites speculation about a possible connection with the unexpected observation (50) on the perpendicular  $\text{H}_2$  ligand in the “elongated” dihydrogen complex,  $\text{OsCl}_2(\eta^2\text{-H}_2)(\text{NH}=\text{CPh}_2)(\text{P-}i\text{-Pr}_3)_2$  (**Os1**), modelled by  $\text{OsCl}_2(\eta^2\text{-H}_2)(\text{NH}=\text{CH}_2)(\text{PH}_3)_2$  (**Os2**). While B3LYP optimization of **Os2** resulted in  $d(\text{H}\cdots\text{H}) = 1.294 \text{ \AA}$ , close to that obtained from the NMR  $J(\text{H},\text{D})$  coupling in **Os1**, further examination revealed that the total energy of **Os2** was practically independent of  $d(\text{H}\cdots\text{H})$  between 0.90 and 1.60  $\text{\AA}$ . This means that in this complex the oxidative addition and its reverse, the reductive elimination of  $\text{H}_2$ , occur in the coordination sphere of the complex without any activation barrier, i.e., the two hydrogen atoms move freely in a wide region of the Os coordination sphere.

### Do the $\text{H}\cdots\text{H}$ BPs represent bonds?

For an  $\text{H}\cdots\text{H}$  contact characterized by a BP and a BCP to qualify as a dihydrogen bond, additional criteria must be satisfied. According to Popelier (48, 71; cf. also ref. 5), these additional criteria are the same as those that apply to hydrogen bonds. The  $\text{H}\cdots\text{H}$  contacts in the ab initio set **A** appear to satisfy the first four (geometric/topological) criteria of the eight listed tentatively by Popelier (Table 10.2 of ref. 71), as well as the fifth, the shift of the electronic charge from  $\text{H}_a$  to  $\text{H}_d$  on formation of the bond from the fragments, i.e.,  $\varepsilon(\text{H}_d)_c < \varepsilon(\text{H}_d)_m$ . Compliance with criteria 6–8 cannot be tested explicitly with the limited data at our disposal at present. However, the linear complexes **4**, **8**, **12**, and **14** (42) correspond to global minima on their respective MP2/6-31G(d,p) potential energy surfaces, which guarantees that these criteria also are satisfied. These stable, equilibrium-geometry complexes are used to construct and calibrate the various correlation curves described above. Because of the smooth continuity of most of the correlation curves it is reasonable to assume that when data points for other, less-well documented  $\text{H}\cdots\text{H}$  complexes are accommodated by these curves, the  $\text{H}\cdots\text{H}$  contacts in the latter also correspond to  $\text{H}\cdots\text{H}$  bonds. This conjecture is particularly useful when dealing with  $\text{H}\cdots\text{H}$  complexes for which only information from crystallography is available, which means practically all complexes with experimentally determined  $d_H$ ,  $\rho_H$ , and  $\nabla_H^2$  values. The conjecture is further

**Fig. 18.** The presumed exclusionary domain in the  $d_A\rho_A$  plot (cf. Fig. 5). DB complexes with  $d_A\rho_A$  points falling inside the broken-line rectangle are unstable (evolution of  $\text{H}_2$ ) or nonexistent.



supported by the remarkable self-consistence of all the **A** and other data.

On this argument the  $\text{H}\cdots\text{H}$  contacts in the organoammonium tetraphenylborates should be regarded as  $(\text{C-})\text{H}\cdots\text{H}(\text{-C})$  bonds. Furthermore, by the same token, the  $(\text{N-})\text{H}\cdots\text{N}$ ,  $(\text{N-})\text{H}\cdots\text{Ph}$ , and  $(\text{C-})\text{H}\cdots\text{Ph}$  contacts in the three salts (set **E**) also constitute hydrogen bonds, even though some of them are quite weak.

The DBs of set **H** are weak as  $\text{H}\cdots\text{H}$  bonds go. Of particular interest is the almost negligible polarity of the  $\text{H}\cdots\text{H}$  group. The  $\text{H}\cdots\text{H}$  bonds between like phenyl hydrogens have  $\Delta\varepsilon(\text{H})_c$  values that should in principle be zero but for their crystallographic nonequivalence. The classical precedent for a non-covalent  $\text{H}\cdots\text{H}$  bond between like atoms is the methane dimer  $(\text{CH}_4)_2$ . The dimer was not formed in SCF calculations, which would suggest that its  $\text{C-H}\cdots\text{H-C}$  contact interactions are repulsive. However, a detailed post-HF investigation (ref. 39 and references therein) showed that it was bound in all six configurations examined:  $\text{H}_3\text{CH}\cdots\text{H}_2\text{CH}_2$  ( $C_s$ ),  $\text{H}_2\text{CH}_2\cdots\text{H}_2\text{CH}_2$  ( $D_{2h}$  and  $D_{2d}$ )<sup>16</sup>,  $\text{HCH}_3\cdots\text{H}_3\text{CH}$  ( $D_{3h}$  and  $D_{3d}$ ), and  $\text{H}_3\text{CH}\cdots\text{HCH}_3$  ( $D_{3h}$ ).<sup>17</sup> The attractive nature of the interactions is consistent with the results of  $\text{CH}_4\text{-CH}_4$  scattering experiments (crossed molecular beams, cited in ref. 39). In fact, they are weak van der Waals interactions of induced dipole – induced dipole type. The  $\text{H}_3\text{CH}\cdots\text{HCH}_3$  ( $D_{3h}$ ) configuration was the one associated with  $\text{C}\cdots\text{C}$  distances longer than ca. 4.5  $\text{\AA}$ . The optimized

<sup>16</sup>The  $\text{H}_2\text{CH}_2\cdots\text{H}_2\text{CH}_2$  ( $D_{2d}$ ) configuration 3b (Fig. 3 of ref. 39) is erroneously labelled as being of  $D_{2h}$  symmetry.

<sup>17</sup>The configuration of most interest to us,  $\text{H}_3\text{CH}\cdots\text{HCH}_3$  ( $D_{3d}$ ), was not examined, but it may be assumed that, qualitatively, the general result obtained for  $\text{H}_3\text{CH}\cdots\text{HCH}_3$  ( $D_{3h}$ ) would for our purposes serve also for the  $D_{3d}$  configuration.



H...H distance in the MP2/6-31G\*\* calculation was 2.699 Å compared with the best (lowest energy) MP2/6-311G(2d,2p) calculation, 2.686 Å. The value found for H<sub>3</sub>CH...HCH<sub>3</sub> (*D*<sub>3d</sub>, **33**) is somewhat smaller, *d*<sub>A</sub> = 2.661 Å, the difference, if it is of consequence, being probably attributable to the repulsion of the non-bonded, eclipsed hydrogens in the *D*<sub>3h</sub> configuration. The “finite” ρ<sub>A</sub> values of 0.016 e/Å<sup>3</sup> at Δε(H)<sub>c</sub> = 0 in **33** and the experimental values ρ<sub>H</sub> = 0.04–0.08 e/Å<sup>3</sup> at Δε(H)<sub>c</sub> ~ 0 and *d*(C...C) ~ 4.2–4.6 Å for the DBs of the **H** set (Fig. 11) are therefore not surprising. On a conservative estimate, the H...H interactions at *d*<sub>A</sub> > 2 Å, being a continuous mix of Coulombic and dipolar contributions, are qualitatively of the same type and are to be viewed as constituting dihydrogen *bonds*, regardless of the convergence to zero of Δε(H)<sub>c</sub>, the estimator of the “Coulombic” component of the interaction.

### Involvement of Δε(H)

Although the plots of Figs. 10–12 show appreciable “chemical” scatter, there is little doubt that correlations exist in all these cases (eqs. [14–16]; eqs. [17] and [18]; Fig. 13). At Δε(H) = 0 the regression values of *d*<sub>A</sub>, ρ<sub>A</sub>, and ∇<sub>A</sub><sup>2</sup> are non-zero, in agreement with both observation (set **H**) and calculation (methane dimer, ref. 39).

By their nature, the Δε(H) should not be expected to give *close* correlations. Better results in this respect can be obtained using different charge measures (see below). However, Δε(H)<sub>m</sub> has a rough predictive value, as the ε(H)<sub>m</sub> values in the XH and HY fragments may already be available, and the a priori likelihood of existence of an X-H...H-Y complex can be estimated without calculation.

It is not clear at present how Δε(H)<sub>m</sub> relates, quantitatively, to the stability of an X-H...H-Y complex vis-à-vis the corresponding X...H-H...Y complex. Investigating this matter in some detail might well repay the extra effort.

### Estimating the H...H binding energy

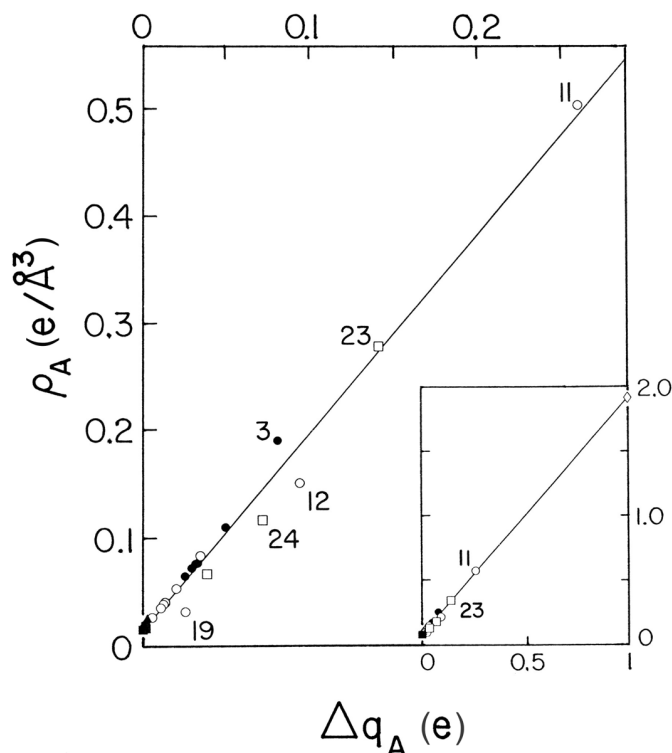
In a paper that came to our attention only quite recently (66) the authors investigate, among other things, relationships between the binding energy *E*<sub>b</sub> and the bond-critical parameters of DB-containing complexes. From the results of their MP2/aug'-cc-pVTZ (MP\* for short) calculations they find that, for several M-H...H'-Y (M = Li, Na) complexes, linear relationships exist between *E*<sub>b</sub> and ρ<sub>c</sub>\* (Fig. 4, ref. 66; also ref. 32) and between *E*<sub>b</sub> and the charge Δ*q*\* transferred from MH to the H...H bond (Fig. 3, ref. 66). These important findings offer a discussion of the H...H bonds in a way alternative to that based on Δε(H) and a possibility of estimating *E*<sub>b</sub> for the complexes in Table 1 from the data at our disposal at present.

Since the complexes LiH...HCN, LiH...HCCH, LiH...HCCF, and LiH...HNC (this last-named is non-linear in MP\*, H-N-Li = 149.4°) are common to both ref. 66 and set **A**, the following empirical correspondences can be established:

$$d_c^* = 0.619 + 1.856 \ln d_A, r^2 = 1.000,$$

$$\sigma_2 = 0.003 \sim 0.6\%$$

**Fig. 19.** Correlation of ρ<sub>A</sub> and Δ*q*<sub>A</sub>. All Δ*q*<sub>A</sub>, ρ<sub>A</sub> pairs, eq. [24]; with **5** and **26** not included, eq. [25].



$$\Delta q^* = 6.36 \Delta q_A^{1.744}, r^2 = 0.997, \sigma_2 = 0.0017 \sim 3\%$$

$$\rho_c^* = -0.015 + 1.333 \rho_A, r^2 = 0.997, \sigma_2 = 0.005 \sim 3\%.$$

From the linearity of ρ<sub>c</sub>\*, *E*<sub>b</sub> and Δ*q*\*, *E*<sub>b</sub> it follows that Δ*q*\*·ρ<sub>c</sub>\* also is linear. From the parameter values for complexes **1**\*–**8**\* of ref. 66 one obtains

$$[22] \quad \rho_c^* = 0.066 + 1.867 \Delta q^*, r^2 = 0.996, \sigma_6 = 0.007 \sim 2.5\%.$$

Furthermore,

$$[23] \quad E_b = -0.59 - 89.6 \Delta q^* - 36.34 \rho_c^*, r^2 = 0.984, \sigma_5 = 1.3 \sim 6\%$$

(ρ<sub>c</sub>\* in e/Å<sup>3</sup>, Δ*q*\* in e, *E*<sub>b</sub> in kcal/mol), i.e., loci of equal *E*<sub>b</sub> in the Δ*q*\*·ρ<sub>c</sub>\* plot will form a system of parallel straight lines with negative slopes.

Treating the bond-critical parameters of set **A** in a similar manner, we have

$$[24] \quad \rho_A = 0.018 + 1.753 \Delta q_A$$

(all Δ*q*<sub>A</sub>, ρ<sub>A</sub> pairs, *r*<sup>2</sup> = 0.94, σ<sub>29</sub> = 0.025 ~ 5.0%) and, with **5** and **26** not included,

$$[25] \quad \rho_A = 0.016 + 1.843 \Delta q_A, r^2 = 0.985, \sigma_{27} = 0.012 \sim 2.4\%$$

(Fig. 19). The intercept 0.016(12) ~ 1.4σ<sub>27</sub> is non-zero. Interestingly, when Δ*q*<sub>A</sub> = 1, then ρ<sub>A</sub> is 1.857 e/Å<sup>3</sup>, which reproduces exactly the ρ<sub>A</sub> value for H<sub>2</sub> (Table 1).



The rough estimate of  $E_b$  that can be obtained for the DBs of **H** by combining the above relations leads to values between ~1 and ~5 kcal/mol, i.e., of an order comparable to the recently quoted estimates (38) for intramolecular (C-)H...H(-C) bonds in benzenoid and other hydrocarbons.

## Conclusions

A number of intermolecular (C-)H...H(-C) contacts with  $d(\text{H} \cdots \text{H}) \leq 3 \text{ \AA}$  in the crystal structures of the three organoammonium tetraphenylborates studied are characterized by well-defined bond paths and bond-critical points. These contacts exist primarily between phenyl hydrogens of neighbouring  $\text{BPh}_4^-$  anions. The Mulliken charges  $\epsilon(\text{H})$  on these H atoms are very small and their differences  $\Delta\epsilon(\text{H})$  are estimated to range from nominally zero to ca. 0.03 e. To determine whether the H...H contacts (set **H**) correspond to actual (C-)H...H(-C) dihydrogen bonds, their topological bond-critical parameters  $\rho_c$  and  $V_c^2$  have been compared with an ab initio norm constructed from Alkorta's MP2/6-31G(d,p) values of the parameters for a variety of linear X-H...H-Y complexes. This detailed comparison leads to the conclusion that the observed H...H contacts indeed represent dihydrogen bonds. The simultaneous presence of a number of (N-)H...N, (N-)H...Ph, and (C-)H...Ph hydrogen bonds in the three crystal structures (set **E**) makes it possible to establish relative topological strengths of the (C-)H...H(-C) DBs and the hydrogen bonds. The sequence is (N-)H...N, (N-)H...Ph, (C-)H...Ph, with the dihydrogen bonds weaker than any of these hydrogen bonds (but see text).

Examination of the various bond-critical parameters in the Alkorta set (set **A**) reveals a remarkable self-consistence of the binary parameter correlations. Discontinuities in certain of the correlations demonstrate the existence of a transition from a mainly unshared-shell X-H...H-Y to a mainly shared-shell (covalent) X...H-H...Y regime, as a consequence of the "chemical" effect of the choice of the X,Y pair (and the charges on X and Y) on the H...H distance. In the limit this transition ends in liberating  $\text{H}_2$  from the complex or in preventing a stable complex from forming in the first place.

## Acknowledgments

We are indebted to Dr. Ibon Alkorta for extending, at our request, the ab initio calculations in ref. 42 and making the results available to us for use in this investigation, and for his helpful comments in general. We also thank Rigaku/MSU, The Woodlands, Texas, for the provision of the low-temperature data collection facilities during a Sabbatical Leave Fellowship to TSC. Financial support from the Natural Sciences and Engineering Research Council of Canada is acknowledged.

## References

1. K.N. Robertson. Doctoral thesis. Dalhousie University, Nova Scotia, Canada. 2001.
2. T.B. Richardson, S. de Gala, R.H. Crabtree, and P.E.M. Siegbahn. *J. Am. Chem. Soc.* **117**, 12 875 (1995).
3. R.H. Crabtree. *Acc. Chem. Res.* **23**, 95 (1990).
4. R.H. Crabtree. *Science*, **282**, 2000 (1998).
5. I. Alkorta, I. Rozas, and J. Elguero. *Chem. Soc. Rev.* **27**, 163 (1998).
6. D. Braga, F. Grepioni, E. Tedesco, M.J. Calhorda, and P.E.M. Lopes. *New J. Chem.* **23**, 219 (1999).
7. G.R. Desiraju. *J. Chem. Soc. Dalton Trans.* 3745 (2000).
8. M.J. Calhorda. *J. Chem. Soc. Chem. Commun.* 801 (2000).
9. R. Custelcean and J.E. Jackson. *Chem. Rev.* **101**, 1963 (2001).
10. S.J. La Placa, W.C. Hamilton, J.A. Ibers, and A. Davison. *Inorg. Chem.* **8**, 1928 (1969).
11. E.A. McNeill and F.R. Scholer. *J. Am. Chem. Soc.* **99**, 6243 (1977).
12. R.C. Stevens, R. Bau, D. Milstein, O. Blum, and T.F. Koetzle. *J. Chem. Soc. Dalton Trans.* 1429 (1990).
13. A.J. Lough, S. Park, R. Ramachandran, and R.H. Morris. *J. Am. Chem. Soc.* **116**, 8356 (1994).
14. S. Park, R. Ramachandran, A.J. Lough, and R.H. Morris. *J. Chem. Soc. Chem. Commun.* 2201 (1994).
15. J.C. Lee, Jr., E. Peris, A.L. Rheingold, and R.H. Crabtree. *J. Am. Chem. Soc.* **116**, 11 014 (1994).
16. E. Peris, J.C. Lee, Jr., J.R. Rambo, O. Eisenstein, and R.H. Crabtree. *J. Am. Chem. Soc.* **117**, 3485 (1995).
17. J. Wessel, J.C. Lee, Jr., E. Peris, G.P.A. Yap, J.B. Fortin, J.S. Ricci, G. Sini, A. Albinati, T.F. Koetzle, O. Eisenstein, A.L. Rheingold, and R.H. Crabtree. *Angew. Chem. Int. Ed. Engl.* **34**, 2507 (1995).
18. G.A. Luinstra, U. Rief, and M.H. Prosenc. *Organometallics*, **14**, 1551 (1995).
19. R.H. Crabtree, P.E.M. Siegbahn, O. Eisenstein, A.L. Rheingold, and T.F. Koetzle. *Acc. Chem. Res.* **29**, 348 (1996).
20. T.B. Richardson, T.F. Koetzle, and R.H. Crabtree. *Inorg. Chim. Acta*, **250**, 69 (1996).
21. I.I. Padilla-Martínez, M.J. Rosalez-Hoz, H. Tlahuext, C. Camacho-Camacho, A. Ariza-Castolo, and R. Contreras. *Chem. Ber.* **129**, 441 (1996).
22. Wenbin Yao and R.H. Crabtree. *Inorg. Chem.* **35**, 3007 (1996).
23. E.S. Shubina, N.V. Belkova, A.N. Krylov, E.V. Vorontsov, L.M. Epstein, D.G. Gusev, M. Niedermann, and H. Berke. *J. Am. Chem. Soc.* **118**, 1105 (1996).
24. J.A. Ayllón, C. Gervaux, S. Sabo-Etienne, and B. Chaudret. *Organometallics*, **16**, 2000 (1997).
25. R. Custelcean and J.E. Jackson. *J. Am. Chem. Soc.* **120**, 12 935 (1998).
26. L.M. Epstein, E.S. Shubina, E.V. Bakhmutova, L.N. Saitkulova, V.I. Bakhmutov, A.L. Chistyakov, and I.V. Stankevich. *Inorg. Chem.* **37**, 3013 (1998).
27. R. Custelcean and J.E. Jackson. *Angew. Chem. Int. Ed. Engl.* **38**, 1661 (1999).
28. Yu.A. Abramov, L. Brammer, W.T. Klooster, and R.M. Bullock. *Inorg. Chem.* **37**, 6317 (1998).
29. W.T. Klooster, T.F. Koetzle, P.E.M. Siegbahn, T.B. Richardson, and R.H. Crabtree. *J. Am. Chem. Soc.* **121**, 6337 (1999).
30. S. Gründemann, S. Ulrich, H.-H. Limbach, N.S. Golubev, G.S. Denisov, L.M. Epstein, S. Sabo-Etienne, and B. Chaudret. *Inorg. Chem.* **38**, 2550 (1999).
31. S.H. Park, A.J. Lough, G.P.A. Yap, and R.H. Morris. *J. Organomet. Chem.* **609**, 110 (2000).
32. S.J. Grabowski. *J. Phys. Chem. A*, **104**, 5551 (2000).
33. Q. Fu, L. Li, and R.F. Hicks. *Phys. Rev. B*, **61**, 11 034 (2000).
34. R. Custelcean, M. Vlassa, and J.E. Jackson. *Angew. Chem. Int. Ed. Engl.* **39**, 3299 (2000).
35. Zhengkun Yu, J.M. Wittbrodt, A. Xia, M.J. Heeg, H.B. Schlegel, and C.H. Winter. *Organometallics*, **20**, 4301 (2001).



36. M. Güizado-Rodríguez, A. Ariza-Castolo, G. Merino, A. Vela, H. Noth, V.I. Bakhmutov, and R. Contreras. *J. Am. Chem. Soc.* **123**, 9144 (2001).
37. G.N. Patwari, T. Ebata, and N. Mikami. *Chem. Phys.* **283**, 193 (2002).
38. C.F. Matta, J. Hernández-Trujillo, Ting-Hua Tang, and R.F.W. Bader. *Chem. Eur. J.* **9**, 1940 (2003).
39. J.J. Novoa, M.-H. Whangbo, and J.M. Williams. *J. Chem. Phys.* **94**, 4835 (1991).
40. U. Koch and P.L.A. Popelier. *J. Chem. Phys.* **99**, 9747 (1995).
41. Q. Liu and R. Hoffmann. *J. Am. Chem. Soc.* **117**, 10 108 (1995).
42. I. Alkorta, J. Elguero, and C. Foces-Foces. *J. Chem. Soc. Chem. Commun.* 1633 (1996).
43. J.E. Del Bene, W.B. Person, and K. Szczepaniak. *Mol. Phys.* **89**, 47 (1996).
44. I. Rozas, I. Alkorta, and J. Elguero. *Chem. Phys. Lett.* **275**, 423 (1997).
45. I. Rozas, I. Alkorta, and J. Elguero. *J. Phys. Chem. A*, **101**, 4236 (1997).
46. A. Milet, A. Dedieu, and A. Canty. *Organometallics*, **10**, 5331 (1997).
47. M. Remko. *Mol. Phys.* **94**, 839 (1998).
48. P.L.A. Popelier. *J. Phys. Chem. A*, **102**, 1873 (1998).
49. D. Braga, P. De Leonardis, F. Grepioni, E. Tedesco, and M.J. Calhorda. *Inorg. Chem.* **37**, 3337 (1998).
50. G. Barea, M.A. Esteruelas, A. Lledós, A.M. López, and J.I. Tolosa. *Inorg. Chem.* **37**, 5033 (1998).
51. R. Gelabert, M. Moreno, J.M. Lluch, and A. Lledós. *J. Am. Chem. Soc.* **120**, 8168 (1998).
52. G. Orlova and S. Scheiner. *J. Phys. Chem. A*, **102**, 260 (1998).
53. G. Orlova and S. Scheiner. *J. Phys. Chem. A*, **102**, 4813 (1998).
54. S.A. Kulkarni. *J. Phys. Chem. A*, **102**, 7704 (1998).
55. S.A. Kulkarni and A.K. Srivastava. *J. Phys. Chem. A*, **103**, 2836 (1999).
56. S.J. Grabowski. *Chem. Phys. Lett.* **312**, 542 (1999).
57. S.J. Grabowski. *Chem. Phys. Lett.* **327**, 203 (2000).
58. S.J. Grabowski. *J. Mol. Struct.* **553**, 151 (2000).
59. J. Lundell, S. Berski, and Z. Latajka. *Phys. Chem. Chem. Phys.* **2**, 5521 (2000).
60. M.J. Calhorda and P.E.M. Lopes. *J. Organomet. Chem.* **609**, 53 (2000).
61. S.J. Grabowski. *Chem. Phys. Lett.* **338**, 361 (2001).
62. S.J. Grabowski. *J. Phys. Chem. A*, **105**, 10 739 (2001).
63. J. Li, F. Zhao, and F. Jing. *J. Chem. Phys.* **116**, 25 (2002).
64. J.E. Del Bene, S.A. Perera, R.J. Bartlett, I. Alkorta, J. Elguero, O. Mó, and M. Yáñez. *J. Phys. Chem. A*, **106**, 9331 (2002).
65. G. Merino, V.I. Bakhmutov, and A. Vela. *J. Phys. Chem. A*, **106**, 8491 (2002).
66. I. Alkorta, J. Elguero, O. Mó, M. Yáñez, and J.E. Del Bene. *J. Phys. Chem. A*, **106**, 9325 (2002).
67. M.J. Calhorda and P.J. Costa. *Cryst. Eng. Comm.* **4**, 368 (2002).
68. O. Knop, K.N. Rankin, T.S. Cameron, and R.J. Boyd. *Can. J. Chem.* **80**, 1351 (2002).
69. R.F.W. Bader. *Atoms in molecules: a quantum theory*. Clarendon Press, Oxford. 1990.
70. P. Coppens. *X-ray charge densities and chemical bonding*. International Union of Crystallography. Oxford University Press, Oxford. 1997.
71. P.L.A. Popelier. *Atoms in molecules. An introduction*. Prentice Hall, Pearson Education Ltd., Harlow, England. 2000.
72. R.J. Gillespie and P.L.A. Popelier. *Chemical bonding and molecular geometry*. Oxford University Press, New York. 2001.
73. O. Knop, K.N. Rankin, and R.J. Boyd. *J. Phys. Chem. A*, **105**, 6552 (2001).
74. E. Espinosa, I. Alkorta, J. Elguero, and E. Molins. *J. Chem. Phys.* **117**, 5529 (2002).
75. O. Knop, K.N. Rankin, and R.J. Boyd. *J. Phys. Chem. A*, **107**, 272 (2003).
76. D.S. Kosov and P.L.A. Popelier. *J. Phys. Chem. A*, **104**, 7339 (2000).
77. D.S. Kosov and P.L.A. Popelier. *J. Chem. Phys.* **113**, 3969 (2000).
78. H.S. Chu, C.P. Lau, K.Y. Wong, and W.T. Wong. *Organometallics*, **17**, 2768 (1998).
79. J.A. Ayllón, S.F. Sayers, S. Sabo-Etienne, B. Donnadiu, B. Chaudret, and E. Clot. *Organometallics*, **18**, 3981 (1999).
80. H.S. Chu, Z. Xu, S.M. Ng, C.P. Lau, and Z. Lin. *Eur. J. Inorg. Chem.* 993 (2000).
81. R.W. Parry, D.R. Schultz, and P.R. Girardot. *J. Am. Chem. Soc.* **80**, 1 (1958).
82. D.R. Schultz and R.W. Parry. *J. Am. Chem. Soc.* **80**, 4 (1958).
83. N.B. Okulik, R. Pis Diez, A.H. Jubert, P.M. Esteves, and C.J.A. Mota. *J. Phys. Chem. A*, **105**, 7079 (2001).



# Controlling parameters for radical cation fragmentation reactions: Origin of the intrinsic barrier

Deepak Shukla, Guanghua Liu, Joseph P. Dinnocenzo, and Samir Farid

**Abstract:** C—C bond cleavages of radical cations of 2-substituted benzothiazoline derivatives were investigated to determine the parameters controlling the fragmentation rate constants. In spite of the low oxidation potentials of the compounds, fragmentation rate constants greater than  $1 \times 10^6 \text{ s}^{-1}$  could be achieved through weakening of the fragmenting bond by substituents that stabilize the radical fragment and exert steric crowding. A quantitative assessment of the relative roles of radical stabilization vs. steric effects to weaken the fragmenting C—C bond was achieved through DFT calculations. The calculated activation enthalpies matched reasonably well with the experimentally determined values. A thermokinetic analysis revealed that the fragmentations of benzothiazoline radical cations have relatively large intrinsic kinetic barriers, ascribed to the delocalized nature of the product radical and cation fragments. Interestingly, the same factors that lead to the large intrinsic barriers led, simultaneously, to large thermodynamic driving forces for the fragmentations, which should lead to lower activation barriers. These effects oppose each other kinetically and provide important insight into the design of fast radical ion fragmentation reactions.

**Key words:** benzothiazoline, radical cation, fragmentation, steric effects, DFT.

**Résumé :** Dans le but de déterminer les paramètres qui contrôlent la constante de vitesse de fragmentation, on a étudié la rupture de la liaison C—C des cations radicalaires des dérivés de la benzothiazoline substituée en position 2. En dépit du faible potentiel d'oxydation de ces composés, on peut obtenir des constantes de vitesse de fragmentation supérieures à  $1 \times 10^6 \text{ s}^{-1}$  en affaiblissant la liaison qui subit la fragmentation à l'aide de substituants qui stabilisent le fragment radicalaire tout en exerçant un encombrement stérique. Faisant appel aux calculs DFT, on a évalué quantitativement le rôle relatif de la stabilisation du radical par rapport aux effets stériques dans l'affaiblissement de la liaison C—C qui se fragmente. Les enthalpies de liaisons calculées correspondent assez bien aux valeurs expérimentales. Une analyse thermocinétique a révélé que les fragmentations des cations radicalaires de la benzothiazoline ont une large barrière cinétique intrinsèque relative, attribuable à une délocalisation du radical et des fragments de cations obtenus. Il est intéressant de noter que les mêmes facteurs qui conduisent à une large barrière intrinsèque, conduisent simultanément à de très grandes forces motrices thermodynamiques pour la fragmentation, ce qui devrait provoquer une diminution de la barrière d'activation. Cinétiquement, ces effets qui s'opposent l'un à l'autre fournissent une connaissance plus profonde du processus impliquant les réactions rapides de fragmentation de l'ion radical.

**Mots clés :** benzothiazoline, cation radical, fragmentation, effets stériques, DFT.

[Traduit par la Rédaction]

## Introduction

One-electron oxidation can decrease bond dissociation energies of otherwise stable molecules to such an extent that fast fragmentation can occur readily. This effect is best understood in terms of a thermodynamic cycle, pioneered by Arnold and co-workers (1). According to the cycle, the higher the oxidation potential of the molecule, the lower the

bond dissociation energy of the radical cation and, in general, the more likely that fast fragmentation of the corresponding radical cation would be achieved. Conversely, as the oxidation potential is lowered, the bond dissociation energy (BDE) of the radical cation increases and will eventually reach a point where the fragmentation will be too slow to be competitive with other reactions of the radical cation. Fragmentations of C—C bonds of several radical cations

Received 20 March 2003. Published on the NRC Research Press Web site at <http://canjchem.nrc.ca> on 26 June 2003.

*Dedicated to Donald R. Arnold, a pioneer in the chemistry of photoinduced electron transfer.*

**G. Liu and J.P. Dinnocenzo.**<sup>1</sup> Department of Chemistry, University of Rochester, Rochester, NY 14627-0216, U.S.A.  
**D. Shukla<sup>2</sup> and S. Farid.**<sup>3</sup> Research Laboratories, Eastman Kodak Company, Rochester, NY 14650-2109, U.S.A.

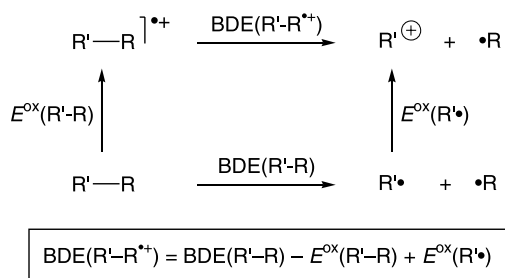
<sup>1</sup>Corresponding author (e-mail: [jpd@chem.rochester.edu](mailto:jpd@chem.rochester.edu)).

<sup>2</sup>Corresponding author (e-mail: [deepak.shukla@kodak.com](mailto:deepak.shukla@kodak.com)).

<sup>3</sup>Corresponding author (e-mail: [samir.farid@kodak.com](mailto:samir.farid@kodak.com)).



have been investigated and it has been confirmed that the fragmentation rate constants indeed depend strongly on the oxidation potential of the substrate (2).



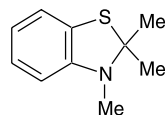
It is conceivable that compounds with low oxidation potentials could yield radical cations that rapidly fragment if the fragmenting bonds are weakened through proper substitution. There are, in principle, two ways to weaken such bonds: (1) by having substituents on the fragments (the radical and the cation) that stabilize these species; and (2) by steric crowding in the reactants. There are a number of reported examples where fragmentation of radical cations derived from low oxidation potential compounds have been achieved by such weakening of the fragmenting bonds (3).

Herein, we report a new class of low oxidation potential compounds — substituted benzothiazolines — that undergo rapid fragmentation when oxidized to their radical cations. Pulsed laser techniques were used to generate and characterize the benzothiazoline radical cations, as well as to measure their fragmentation kinetics. In addition, DFT calculations were performed to estimate the BDEs of the radical cations as well as their activation barriers for fragmentation. Finally, the relative contributions to bond weakening in the radical cations from stabilization of the fragments vs. steric crowding were determined.

## Results and discussion

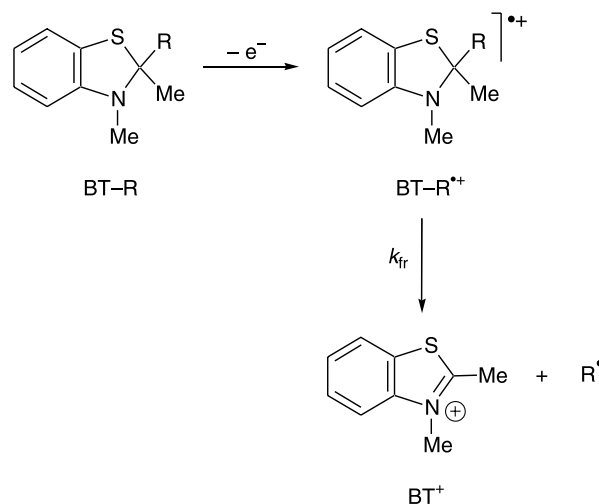
### Structural features and synthesis

The initial aim of this work was to choose an electrophore with such a low oxidation potential that cleavage of a non-stabilized radical fragment upon one-electron oxidation would be very slow. Systematic structural changes to increase the stability of the radical fragment would then be tested with the aim of achieving fragmentation of the radical cation with a rate constant of  $1 \times 10^5$  to  $1 \times 10^7 \text{ s}^{-1}$ , a convenient range for transient kinetics. Substituted benzothiazoline (2,3-dihydrobenzothiazole) derivatives, BT-R (eq. [1]) appeared to be well-suited for this study. They have low oxidation potentials (e.g., 0.77 V vs. SCE for R = Me), the cation fragment (BT<sup>+</sup>) is highly stabilized, and derivatives with varying R — the cleaving radical fragment — can be readily synthesized.



1

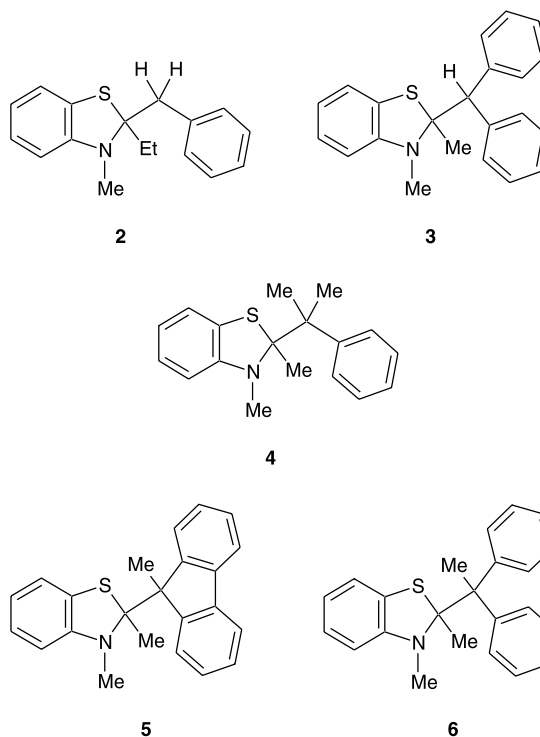
[1]



Compound **1** was used as a model nonfragmenting analogue to determine the absorption spectrum of the main chromophore of the radical cation.

Five other derivatives (**2–6**) with varying substitution of R to promote fragmentation, were synthesized to test the effect of increasing stabilization of the radical R<sup>•</sup> and of weakening of the bond on the fragmentation rate constant.

The benzothiazoline derivatives were prepared from 2-methylamino-benzenethiol according to reported procedures (eq. [2]) (4, 5) through direct condensation with the appropriate ketone (compounds **2** and **3**) or through reaction with an acid chloride to give a thiazolium salt, followed by the addition of CH<sub>3</sub>MgBr (compounds **1** and **4–6**).

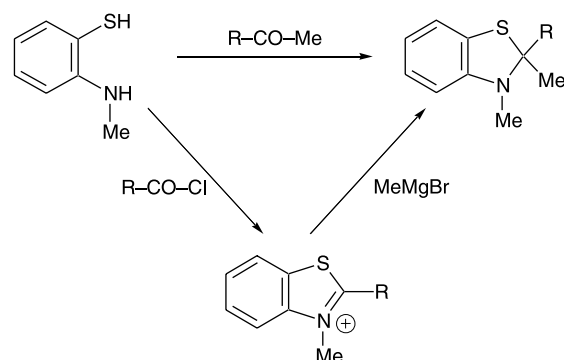


5

6



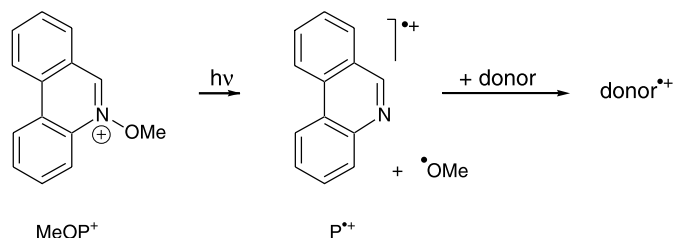
[2]



### Experimental approach

Different approaches were considered to generate and study the fragmentation kinetics of the radical cations of the benzothiazoline derivatives ( $\text{BT-R}^{\bullet+}$ ), by flash photolysis. In one approach, an excited sensitizer reacts with a donor (acting as a cosensitizer, C) to form the radical cation of the latter ( $\text{C}^{\bullet+}$ ) in high quantum yield (6). Next, a secondary electron transfer from  $\text{BT-R}$  to  $\text{C}^{\bullet+}$  generates  $\text{BT-R}^{\bullet+}$ . To avoid direct excitation of the reactant, it is desirable for the sensitizer to absorb at longer wavelength than the  $\text{BT-R}$  derivative. The absorption of  $\text{BT-R}$  derivatives below 350 nm renders sensitizers such as 1,4-dicyanonaphthalene and *N*-methylquinolinium of limited use. The dynamics of the radical cations  $\text{BT-R}^{\bullet+}$  are most conveniently studied at their absorption maxima, which, as shown below, are near 420 nm. Thus, sensitizers such as 9,10-dicyanoanthracene that have strong absorptions in this region are also of limited use.

Because of the lack of a suitable electron transfer sensitizer with absorption in the  $370 \pm 10$  nm window that would meet the above requirements, we applied a different approach to generate the radical cations  $\text{BT-R}^{\bullet+}$ . This approach is based on the chemistry of *N*-methoxyphenanthridinium ( $\text{MeOP}^+$ ), which is reported to undergo photochemical N—O bond cleavage to yield phenanthridine radical cation ( $\text{P}^{\bullet+}$ ) and a methoxy radical (eq. [3]) (7). The radical cation of phenanthridine is a powerful oxidant (oxidation potential of phenanthridine is  $\sim 1.9$  V vs. SCE) that can be used in a subsequent bimolecular reaction to generate the radical cation of an added donor (eq. [3]).

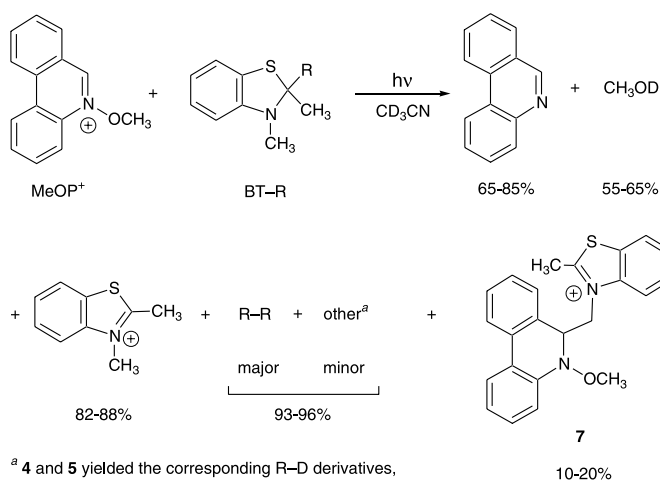


[3]

### Steady state photolysis and reaction products

To correlate the decay of the radical cations to their fragmentations, it was important to first confirm that the products of these reactions are those expected according to eqs. [1] and [3]. The photoreactions of  $\text{MeOP}^+$  with the benzothiazolines **3–6** at equimolar concentrations in  $\text{CD}_3\text{CN}$  were followed by  $^1\text{H}$  NMR and the products were identified by comparison with authentic samples (see *Experimental section* for details). The products were indeed those expected from the N—O fragmentation of  $\text{MeOP}^+$  (phenanthridine and methanol) and those of the C—C fragmentation of the radical cations  $\text{BT-R}^{\bullet+}$  (2,3-dimethylbenzothiazolium and products of the cleaved radical  $\text{R}^{\bullet}$ ). In each case the main product of the radical  $\text{R}^{\bullet}$  was the dimer  $\text{R-R}$  ( $\sim 70$  to  $>90\%$ ). In some cases the deuterated product  $\text{R-D}$  (via deuterium abstraction from the solvent), and (or) the corresponding olefin (via loss of hydrogen atom) were formed (eq. [4]) (see *Experimental section*).

[4]



<sup>a</sup> **4** and **5** yielded the corresponding  $\text{R-D}$  derivatives, **4** and **6** yielded the corresponding olefins:  $\alpha$ -methylstyrene and 1,1-diphenylethylene, respectively.

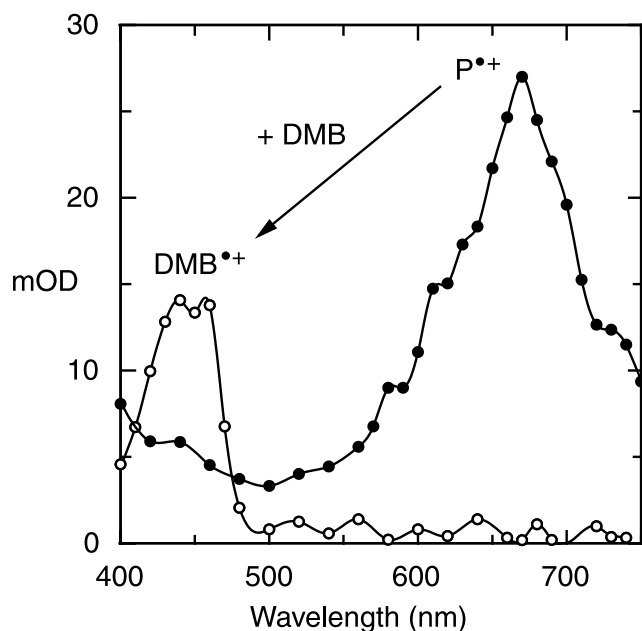
An unexpected, minor photolysis product of these reactions was adduct **7** (eq. [4]).<sup>4</sup> This compound was formed in all reactions of **3–6** in  $\sim 12$ – $20\%$  yield. The structure of this compound, which has not yet been isolated in pure form, was based on  $^1\text{H}$  NMR spectral analysis. Importantly, the alternative assignment of the isomeric structure **8** to this compound was ruled out by independent synthesis of **8** via the base-catalyzed reaction of  $\text{MeOP}^+$  with dimethylbenzothiazolium (eq. [5]). Assignment of the NMR signals of compound **8** was based on several 2D NMR and NOE experiments, which establish the connectivity of the two moieties.

Photolysis of  $\text{MeOP}^+$  in the presence of the benzyl derivative (**2**) yielded, in addition to phenanthridine and methanol, 2-methyl-3-ethylbenzothiazolium, an expected fragmentation product of  $\text{2}^{\bullet+}$ . However, none of the likely products of benzyl

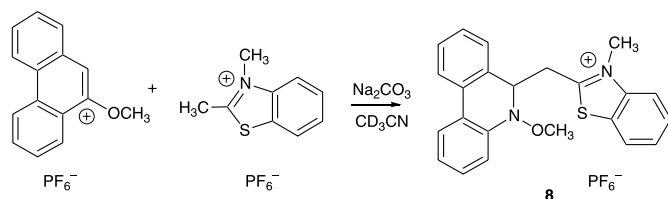
<sup>4</sup> The mechanism for formation of **7** has not been investigated. One possibility involves initial reaction of  $\text{MeO}^{\bullet}$  with  $\text{BT-R}$  by hydrogen atom abstraction from the N-Me group. The resulting  $\alpha$ -amino radical might then add to  $\text{MeOP}^+$  at C-6 to give a *N*-alkoxy amine radical cation. Subsequent intramolecular electron transfer from the benzothiazoline moiety to the *N*-alkoxy amine radical cation followed by fragmentation of the resulting benzothiazoline radical cation would produce **7**. Further experiments are required to test this hypothesis.



**Fig. 1.** Absorption spectrum of phenanthridine radical cation ( $P^{\bullet+}$ ) obtained from photolysis of  $\text{MeOP}^+$  in acetonitrile (closed circles) and that obtained in the presence of 1,4-dimethoxybenzene (DMB) (open circles), which matches the spectrum of an independently generated  $\text{DMB}^{\bullet+}$ .<sup>5</sup>



[5]

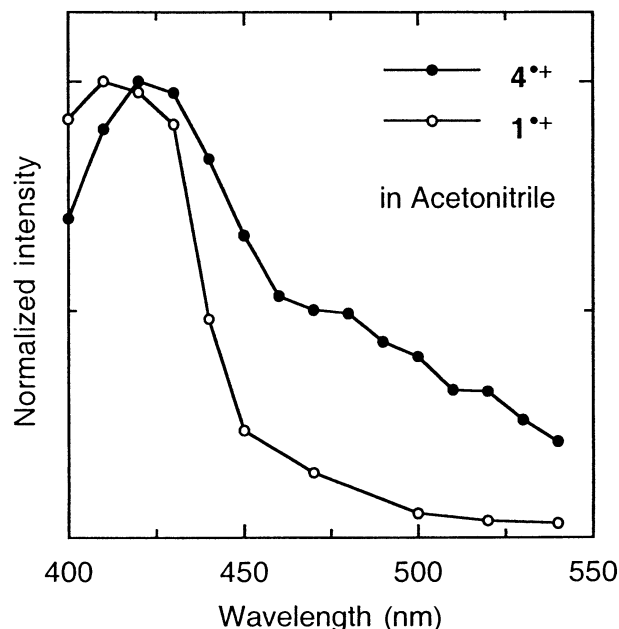


radical, such as 1,2-diphenylethane or toluene were formed in this reaction. There is also no indication that either benzyl methyl ether (a coupling product between benzyl and methoxy radicals) or *N*-benzylacetamide (an addition product of benzyl cation to acetonitrile, followed by hydrolysis) is formed. In spite of the fact that not all fragmentation products have been identified in this case, the clear evidence for formation of the benzothiazolium salt suggests that fragmentation of  $2^{\bullet+}$  does take place. Additional support for this conclusion is provided by the fact that the activation enthalpy calculated for fragmentation of  $2^{\bullet+}$  agrees well with that measured experimentally for its disappearance (see *Density functional calculations*).

#### Characterization of the radical cations BT- $R^{\bullet+}$

The following experiments were carried out to probe the applicability of  $\text{MeOP}^+$  photochemistry (eq. [2]) to generate and study the reactivity of radical cations by flash photo-

**Fig. 2.** Absorption spectra of the radical cations of compounds **1** and **4**, obtained from photolysis (380 nm) of  $\text{MeOP}^+$  in the presence of these electron donors in acetonitrile. The spectra were obtained after a delay time of  $>2 \mu\text{s}$  to avoid contributions owing to the secondary transient species produced from photolysis of  $\text{MeOP}^+$  (see text).



lysis. Irradiation of  $\text{MeOP}^+$  in acetonitrile gave a transient ( $\lambda_{\text{max}}$  at 670 nm), which was assigned to  $P^{\bullet+}$  based on the lack of quenching by dioxygen and on its efficient quenching by 1,4-dimethoxybenzene (DMB,  $E^{\text{ox}} = 1.3 \text{ V vs. SCE}$ ). In the presence of 0.1 M DMB, the 670 nm absorption is completely replaced by that shown in Fig. 1 ( $\lambda_{\text{max}} = 440$  and 458 nm), which corresponds to the spectrum of DMB radical cation generated independently.<sup>5</sup> Using the benzothiazoline derivatives as donors (eq. [3]) this approach provided a convenient method to generate their radical cations and to study their fragmentation kinetics.

As expected, the phenanthridine radical cation ( $P^{\bullet+}$ ) is efficiently intercepted by the benzothiazoline derivatives ( $k_q \approx 6 \times 10^9 \text{ M}^{-1} \text{ s}^{-1}$ ). Thus, 355 or 380 nm laser excitation of  $\text{MeOP}^+$  in the presence of 5–10 mM of **1** in aerated or in argon-saturated acetonitrile led to a long-lived species ( $\sim 200$ – $250 \mu\text{s}$ ) with an absorption maximum at  $\sim 410 \text{ nm}$  (Fig. 2). Support for assigning this absorption to  $1^{\bullet+}$  was obtained from a number of experiments. Excitation of 1,4-dicyanophthalene at 343 nm in the presence of 0.3 M biphenyl as a cosensitizer in acetonitrile led to the formation of biphenyl radical cation, characterized by the strong absorption at 670 and 380 nm. Absorption due to the sensitizer radical anion was removed by purging the samples with dioxygen, where electron transfer leads to the formation of  $\text{O}_2^{\bullet-}$ , which does not absorb in the visible region. Addition of **1** (0.5 to 1.5 mM) led to quenching of the biphenyl radical cation with a bimolecular rate constant of  $1.8 \times 10^{10} \text{ M}^{-1} \text{ s}^{-1}$  and concomitant appearance of an absorption identical to that

<sup>5</sup> An authentic spectrum of  $\text{DMB}^{\bullet+}$  was obtained in aerated acetonitrile by 355 nm excitation of DCA ( $\text{OD}_{355} = 0.6$ ) in the presence of 0.15 M biphenyl (as a cosensitizer) and 0.01 M DMB.



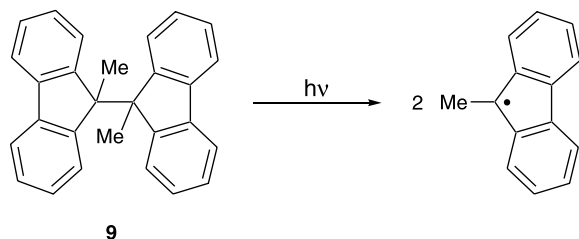
obtained in the above mentioned experiment with  $\text{MeOP}^+$ .<sup>6</sup> Similarly, 343 nm excitation of *N*-methylquinolinium with toluene (1.5 M) as a cosensitizer in dioxygen-purged 1,2-dichloroethane generated the toluene radical cation ( $\lambda_{\text{max}} = 450$  nm), which was efficiently quenched by **1** (~2 mM). The transient spectrum recorded after complete quenching of the toluene radical cation was also very similar to that obtained in the other experiments mentioned above.

Assigning the ~410 nm absorbing transient to  $\mathbf{1}^+$  was further confirmed through electron transfer interception by a lower-oxidation-potential compound. The transient obtained from the reaction of  $\text{MeOP}^+$  with **1** in acetonitrile was readily quenched by tri-*p*-anisylamine ( $E^{\text{ox}} = 0.52$  V vs. SCE) with the concomitant formation of the radical cation of the latter, characterized by its absorption maximum at 720 nm (6). Plots of the rate constants for the transient decays and for growth of the trianisylamine radical cation vs. amine concentration were linear. Slopes of the plots provided a quenching rate constant of  $4.1 \times 10^9 \text{ M}^{-1} \text{ s}^{-1}$ .

Shown also in Fig. 2 is the spectrum of  $\mathbf{4}^+$  obtained using  $\text{MeOP}^+$  as described above for  $\mathbf{1}^+$ . Clearly the absorption spectra of the radical cations are not the same in spite of the fact that the low-oxidation-potential electrophore (the benzothiazoline moiety) is the same. The weak absorption that appears as a shoulder at ~470 nm in the spectrum of the nonfragmenting  $\mathbf{1}^+$  seems to be considerably enhanced in the spectrum of  $\mathbf{4}^+$ . The spectra of  $\mathbf{2}^+$  (not shown) and of  $\mathbf{5}^+$  (Fig. 3) are similar to that of  $\mathbf{4}^+$ .

Additional support for the spectral assignment of the benzothiazole radical cations was derived from the transient assigned to  $\mathbf{5}^+$ , whose decay was concomitant with formation of the 9-methylfluorenyl radical. Unlike the radicals resulting from the fragmentation of the other radical cations mentioned in this work, which lack absorptions in the visible region, the methylfluorenyl radical could be readily identified by its absorption ( $\lambda_{\text{max}} = 485$  nm) (see Fig. 3) (8). This absorption matches that of an authentic sample, also shown in Fig. 3, generated from photolysis of the dimer (compound **9**) (eq. [6]). As expected, in aerated solution this absorption band is suppressed as a result of quenching by dioxygen.

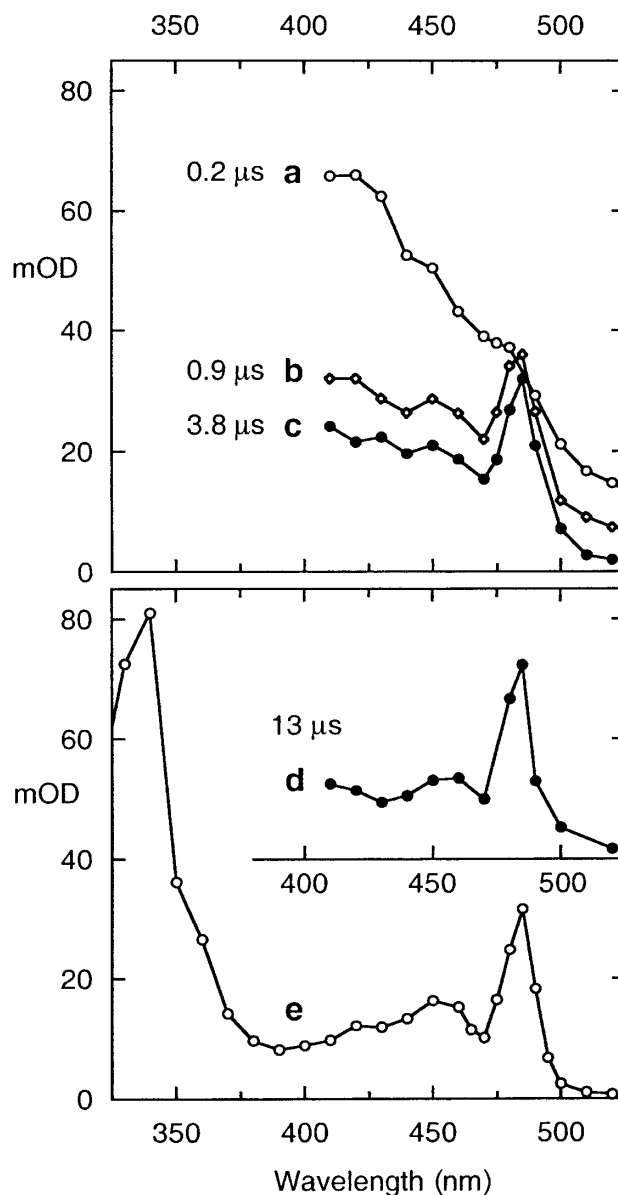
[6]



#### Fragmentation rate constants and activation energies

The fragmentation rate constants of the radical cations  $\text{BT-R}^+$ , obtained via 355 or 380 nm excitation of  $\text{MeOP}^+$ , were determined from the decay kinetics in acetonitrile. The use of  $\text{MeOP}^+$  in these flash photolysis experiments allowed for a high enough concentration (10–15 mM) of the reactants to ensure fast interception of the phenanthridine radical cation. Under these conditions the growth rates of the radical

**Fig. 3.** (Top) Transient spectra from photolysis (380 nm) of  $\text{MeOP}^+$  in the presence of the methylfluorenyl derivative **5** (0.01 M) in acetonitrile at different delay times after the pulse. The spectrum after (a) 0.2  $\mu\text{s}$  is essentially that of the radical cation  $\mathbf{5}^+$ , with increasing delay times ((b) and (c)) this spectrum is gradually replaced by that of methylfluorenyl radical. (Bottom) Spectrum after (d) 13  $\mu\text{s}$  delay and spectrum of methylfluorenyl radical obtained from direct photolysis of the dimer (**9**) (e) at 308 nm in acetonitrile. The spectra from photolysis of  $\text{MeOP}^+$  could not be measured below 400 nm because of absorption by  $\text{MeOP}^+$ .



cations are faster than their decay. For all samples the radical cation decays were somewhat complicated by the presence of a second transient species. The decay rate constant for this latter species was the same in all samples and had the same temperature dependency. The nature of this second transient has not been established, but it is likely to

<sup>6</sup>Compound **1** absorbs at the excitation wavelength and concentrations higher than 1.5 mM and could not be used in these experiments.



**Table 1.** Comparison of fragmentation rate constants ( $k_{\text{fr}}$  at 25°C) and activation enthalpies for substituted benzothiazoline radical cations  $2^+$ – $6^+$  and R-H bond dissociation energies.

Compound (R·)	$k_{\text{fr}}$ ( $\text{s}^{-1}$ )	$\Delta H^\ddagger$ (BT–R $^+$ ) <sup>a</sup>	BDE (R–H) <sup>b</sup>
<b>2</b> (PhCH <sub>2</sub> ·)	1	~16 <sup>c</sup>	89.8
<b>3</b> (Ph <sub>2</sub> CH·)	$9.8 \times 10^4$	$9.5 \pm 0.9$	85.8
<b>4</b> (PhCMe <sub>2</sub> ·)	$1.9 \times 10^5$	$9.6 \pm 0.5$	87.3
<b>5</b> (9-MeFl·)	$5.0 \times 10^6$	$3.9 \pm 0.7$	79.7
<b>6</b> (Ph <sub>2</sub> CMe·)	$6.1 \times 10^6$	$4.4 \pm 0.6$	82.8

**Note:** All energies in kcal/mol.

<sup>a</sup>From nonlinear least-squares fit of the temperature-dependent rate data; reported errors are one standard deviation.

<sup>b</sup>Reference (9).

<sup>c</sup>This value was estimated from the room temperature fragmentation rate constant for  $2^+$  assuming that the activation entropy was the same as for  $3^+$ .

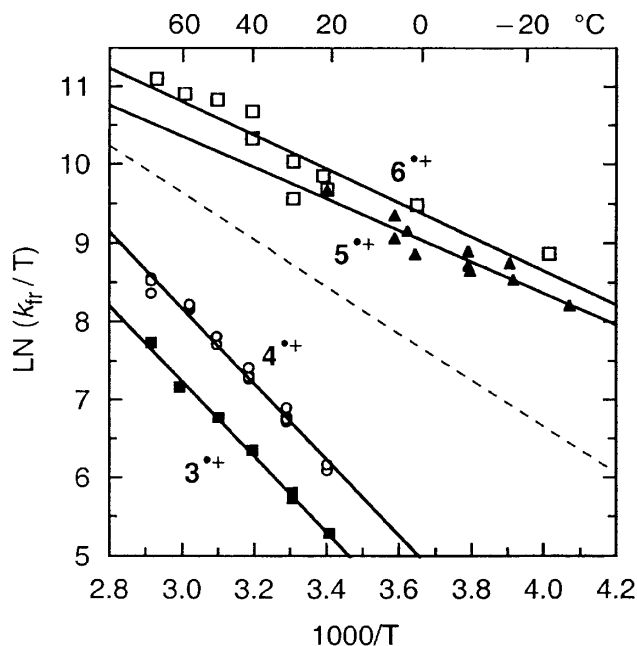
be due to a species resulting from MeOP<sup>+</sup> chemistry because of its independence on the added BT–R derivative. Thus, although this experimental approach suffered from the need to analyze the data as a sum of two exponentials, it offered the best option to obtain the desired kinetic data.

The fragmentation rate constants of  $3^+$ – $6^+$  were in the range that could be readily determined by laser flash photolysis. The rate constants of these reactions were also measured as a function of temperature (see Fig. 4). Listed in Table 1 are the fragmentation rate constants at 25°C and the activation enthalpies, which were derived from nonlinear least-squares fitting of the kinetic data in Fig. 4.

Unlike the fragmentations of  $3^+$ – $6^+$ , which could be readily investigated by flash photolysis, the radical cation  $2^+$  had a lifetime of ~50–60  $\mu\text{s}$  and, importantly, its decay showed only a slight temperature dependence. This behavior suggests that the decay may be largely due to other deactivation processes rather than being a measure of the fragmentation rate constant. Indeed, based on cyclic voltammetry, a rate constant of only  $1 \pm 0.2 \text{ s}^{-1}$  was obtained for the fragmentation of  $2^+$  (see *Experimental section*).

From the above mentioned data it is evident that the fragmentation rate constants for  $2^+$ – $6^+$  fall into three groups. Cleavage resulting in formation of the primary, benzyl radical (from  $2^+$ ) is particularly slow (~1  $\text{s}^{-1}$ ). The cleavages to form both the secondary, diphenylmethyl radical (from  $3^+$ ) and of the tertiary, cumyl radical (from  $4^+$ ) are in the range of  $\sim 1 \times 10^5 \text{ s}^{-1}$ . The cleavages to form the tertiary, methylfluorenyl, and diphenylethyl radicals (from  $5^+$  and  $6^+$ ) are in the range of  $5 \times 10^6 \text{ s}^{-1}$ . The increased substitution on the radical fragment clearly increases the fragmentation rate constant.

Although the activation energies for the fragmentation of  $2^+$ – $6^+$  roughly correlate with increasing stability of the radical fragment, further analysis reveals that other factors must also play a role in controlling the fragmentation barriers. The relative radical (R·) stabilities can be estimated from the R–H bond dissociation energies (BDE (R–H)) of the corresponding hydrocarbons, as shown in Table 1. The data show clear discontinuities in the correlation of BDE (R–H) and  $\Delta H^\ddagger$ . For example,  $\Delta H^\ddagger$  for  $3^+$  and  $4^+$  are identical within experimental error yet, as judged by BDE (R–H), the radical formed from  $4^+$  is less stabilized than from  $3^+$  by 1.5 kcal/mol. Similarly,  $\Delta H^\ddagger$  ( $5^+$ ) is 0.5 kcal/mol lower than  $\Delta H^\ddagger$  ( $6^+$ ), however, based on radical stability one would ex-

**Fig. 4.** Plot of the logarithm of fragmentation rate constants divided by the absolute temperature ( $\ln(k_{\text{fr}}/T)$ ) for the radical cations of compounds **3**–**6** vs. the reciprocal of the absolute temperature ( $1000/T$ ) in acetonitrile. The negative slopes of the linear plots obtained by least-squares fitting are: 4.82, 4.84, 2.00, and 2.15, respectively. The dashed line (negative slope of 2.98) corresponds to the decay rate constant of another intermediate from the photolysis of MeOP<sup>+</sup> detected in all cases (see text).

pect the radical formed from  $5^+$  to be ca. 3 kcal/mol more stabilized than that formed from  $6^+$ . These data clearly reveal that radical stability is not the sole determinant of the relative energetic barriers for radical cation fragmentation; it seems likely that differential steric effects also play a crucial role. To gain insight into the relative contributions of these two factors, we decided to use density functional theory to calculate both the bond dissociation energies and the activation energies for C–C bond fragmentation of  $2^+$ – $6^+$ .

### Density functional calculations

The thermodynamic and kinetic properties of the substituted benzothiazoline radical cations were modeled with density functional calculations. The B3LYP functional was chosen because it has been shown to be particularly well-suited to radical cation calculations (10). Computations were performed with the Gaussian 98 series of programs (11). All geometries were fully optimized using a 6-31G\* basis set and all optimized species were determined to be either minima or saddle points by frequency calculations. The radical cation carbon–carbon BDEs for  $2^+$ – $6^+$  were determined as the differences between the energies of the benzothiazolium cation (BT<sup>+</sup>) and the radical fragments (R·) and that of the most stable radical cation conformer, unless otherwise noted. The energy differences include electronic energies, zero point energy corrections, and thermal corrections (at 298.15 K). In several cases, BDEs from higher energy radical cation conformers were calculated to compare with the transition state energies for conformational interconversion.



### Activation energies

The activation energies for fragmentation of  $2^{+}$ – $6^{+}$  were sought for comparison with the experimentally determined values. The relative energies of the conformational isomers of the radical cations were first computed to determine the lowest energy conformer for each compound. The energetic barriers for conformational interconversion were also computed. The results are graphically illustrated in Fig. 5.

The activation energies for fragmentation were computed from the lowest energy conformer for each radical cation. For the radical cations with the lowest activation energies for fragmentation, activation energies were also computed for the higher energy conformers. The results are shown in Fig. 5.

The highest computed barrier for fragmentation (14.4 kcal/mol) was found for  $2^{+}$ . This value is in line with the observed fragmentation rate constant for  $2^{+}$  of  $\sim 1 \text{ s}^{-1}$ , which corresponds to an activation barrier of  $\sim 16 \text{ kcal/mol}$ ,  $\sim 2 \text{ kcal/mol}$  higher than the computed value. The computed barriers for  $3^{+}$  (7.8 kcal/mol) and  $4^{+}$  (7.0 kcal/mol) are substantially lower. Gratifyingly, the computed barriers for  $3^{+}$  and  $4^{+}$  are also consistent with those determined experimentally (9.5 and 9.6 kcal/mol). Again, as in the case of  $2^{+}$ , the measured barriers for  $3^{+}$  and  $4^{+}$  are higher than the computed values by ca. 2 to 3 kcal/mol.

As shown in Fig. 5, the computed activation energies for fragmentation of  $3^{+}$  and  $4^{+}$  begin to become comparable to the activation energies for conformational interconversion. This trend continues as one progresses toward the most reactive radical cations ( $5^{+}$  and  $6^{+}$ ). In these latter cases, the activation energies computed for fragmentations from the lowest energy conformers are both lower than for conformational interconversion, particularly for  $6^{+}$ . The computed activation energy for fragmentation of  $6^{+}$  (4.7 kcal/mol) is in excellent agreement with the experimental value (4.4 kcal/mol) and is ca. 3 kcal/mol less than for  $3^{+}$  and  $4^{+}$ , in reasonable agreement with the experimental results ( $\Delta\Delta H^{\ddagger} \approx 5 \text{ kcal/mol}$ ).

Interestingly, the computed fragmentation barrier from the lowest energy conformer of  $5^{+}$  (6.4 kcal/mol) is intermediate between those calculated for  $4^{+}$  and  $6^{+}$ . This contrasts with the measured activation enthalpy for fragmentation of  $5^{+}$  (3.9 kcal/mol), which is more similar to that of  $6^{+}$  (4.4 kcal/mol) than to that of  $4^{+}$  (9.6 kcal/mol). A possible origin of this apparent discrepancy was discovered when comparing the relative energies of the conformers for  $2^{+}$ – $6^{+}$  with those for the corresponding neutral molecules (2–6). Calculations revealed that the lowest energy conformers for radical cations  $2^{+}$ – $6^{+}$  also corresponded to the lowest energy conformers for the neutral molecules 2–6, except for

the  $5^{+}/5$  pair.<sup>7</sup> The lowest energy conformer for  $5^{+}$  is predicted to be *n* (see Fig. 5), whereas the lowest energy conformer of **5** is predicted to be *c* ( $E_{\text{rel}}(\mathbf{5}_n) = 2.3$ ;  $E_{\text{rel}}(\mathbf{5}_s) = 1.4 \text{ kcal/mol}$ ). The relative energies of the calculated conformers for **5** suggest that over the temperature range used to measure the fragmentation kinetics of  $5^{+}$  ( $-35$  to  $+21^{\circ}\text{C}$ ),  $>90\%$  of **5** should be present as  $\mathbf{5}_c$ . Making the reasonable assumption that one-electron oxidation of **5** does not result in simultaneous oxidation and conformational interconversion, one would expect **5** to be oxidized to initially form  $\mathbf{5}_c^{+}$ , i.e., *not* the lowest energy conformer of the radical cation ( $\mathbf{5}_n^{+}$ ). Consequently, if the energy barrier for fragmentation from  $\mathbf{5}_c^{+}$  is less than the barrier for conformational interconversion to the lower energy  $\mathbf{5}_n^{+}$  conformer, then the experimental activation barrier for fragmentation of  $5^{+}$  should be compared to the computed fragmentation barrier predicted from  $\mathbf{5}_c^{+}$  not from  $\mathbf{5}_n^{+}$ .

Figure 5 shows that the computed activation enthalpy for fragmentation of  $\mathbf{5}_c^{+}$  (4.4 kcal/mol) is in good agreement with the experimental value (3.9 kcal/mol). Interestingly, the computations also show that the energy of the fragmentation transition state from  $\mathbf{5}_c^{+}$  is equal to that for conformational interconversion to  $\mathbf{5}_n^{+}$ . Thus, the calculational results predict that a significant fraction of  $\mathbf{5}_c^{+}$  should partition to the  $\mathbf{5}_n^{+}$  conformer, which is predicted to have a significantly larger barrier to fragmentation (6.4 kcal/mol). As illustrated in Fig. 5, if  $\mathbf{5}_c^{+}$  partitions between fragmentation and conformational interconversion, one would expect the experimental decay of  $5^{+}$  to show biexponential behavior, i.e., a fast component due to fragmentation from  $\mathbf{5}_c^{+}$  and a slow component due to fragmentation from  $\mathbf{5}_n^{+}$ . Unfortunately, the presence of the unknown species resulting from MeOP<sup>+</sup> chemistry masked our ability to establish whether the fragmentation of  $5^{+}$  was biexponential. Finally, it is worth noting that all of the calculated transition state energies refer to activation enthalpies, whereas the kinetics are obviously determined by the lowest activation free energies. It seems plausible that the activation entropies for the radical cation fragmentations might be significantly lower than  $\Delta S^{\ddagger}$  for the conformational interconversions. If so, the activation free energy for fragmentation of  $\mathbf{5}_c^{+}$  might be lower than for conformational interconversion to  $\mathbf{5}_n^{+}$ . This also would be consistent with our kinetic data.

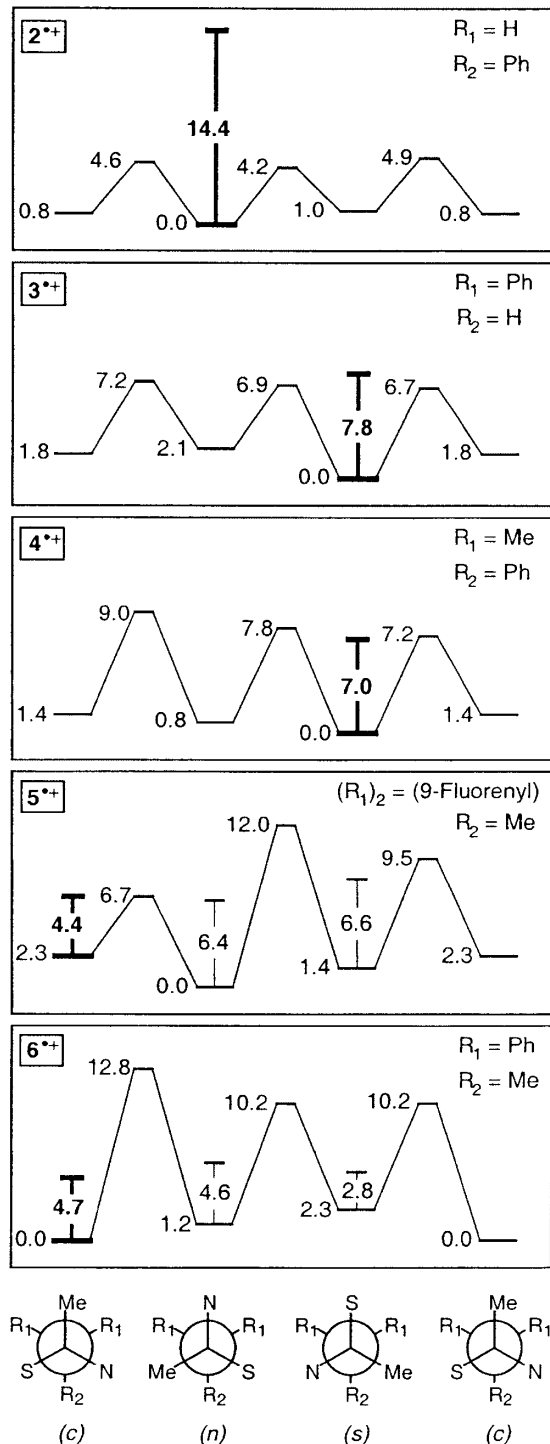
### Bond dissociation energies

Gas phase and solution phase bond dissociation energies were calculated for the benzothiazoline radical cations  $2^{+}$ – $6^{+}$ . The gas phase bond dissociation energies (BDE ( $\text{BT-R}^{+}$ )<sub>g</sub>), were determined using B3LYP/6-31G\* calculations as the sum of the enthalpies of the benzothiazolium cation ( $\text{BT}^{+}$ )

<sup>7</sup>The origin of the reversal in conformer stability for **5** vs.  $5^{+}$  can be traced to two factors: (i) a change in the geometry at nitrogen upon one-electron oxidation; and (ii) the conformational inflexibility of the fluorenyl ring. The calculations on neutral molecules **1**–**6** showed that the nitrogen atom is strongly pyramidalized. In contrast, the nitrogen is much less pyramidalized in the corresponding radical cations and is actually planar for  $1^{+}$ . The planarization of the nitrogen in radical cations causes the N-CH<sub>3</sub> group to move closer to the R groups at C-2, resulting in increased, destabilizing nonbonded interactions. For  $5/5^{+}$ , planarization of the nitrogen upon one-electron oxidation resulted in a severe steric interaction between the N-CH<sub>3</sub> group and syn-C-1 hydrogen on the fluorenyl ring for the  $\mathbf{5}_c^{+}$  conformer, which caused a significant bow in the ring. In **5** this interaction is greatly diminished by pyramidalization at nitrogen which moves the N-CH<sub>3</sub> group away from the fluorenyl ring. We attribute the interchange in the relative stabilities of the *c* and *n* conformers of **5** vs.  $5^{+}$  to this structural reorganization. Interestingly, in the otherwise structurally similar pair  $6/6^{+}$ , a similar steric interaction between the N-CH<sub>3</sub> group and one of the hydrogens in the syn-phenyl group of  $6^{+}$  is relieved by rotation of the phenyl group. A comparable structural relaxation for  $\mathbf{5}_c^{+}$  is not possible because rotation of the syn-phenyl ring is constrained by its linkage to the other phenyl group that makes up the fluorenyl ring.



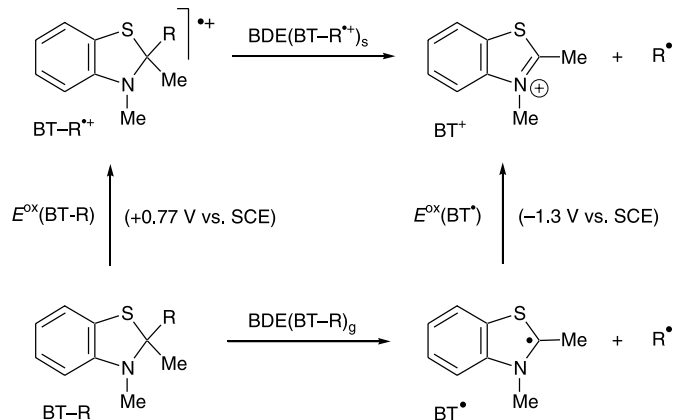
**Fig. 5.** Results of density functional calculations showing the relative potential energies (kcal/mol) for the ground state conformers of  $2^+-6^+$  and for the transition states that interconnect them. Also shown are activation enthalpies for fragmentation from selected radical cation conformers (vertical lines). Shown in bold are the ground and transition states for the proposed, reacting conformers.



and the radical fragments ( $R\cdot$ ) minus the enthalpy of the most stable radical cation conformer. For  $5^+$ , the enthalpy of the  $5_c^+$  conformer was used for the reasons described above.

The results are shown in Table 2, along with the experimental and calculated activation energies for radical cation fragmentation. The data show that there is a general correlation of  $\Delta H^\ddagger$  with the radical cation BDEs.

Table 2 also lists estimates of the solution phase bond dissociation energies for  $2^+-6^+$  ( $BDE(BT-R^+)_s$ ) which were obtained by using Arnold's thermodynamic cycle method (1), as shown below. For these estimates we have used the approximation that the oxidations of **2–6** are similar to the reversible oxidation potential measured of **1** (0.77 V vs. SCE in  $CH_3CN$ ). The oxidation of the 2,3-dimethylbenzothiazolium radical was estimated from the (irreversible) reduction of the corresponding cation ( $\sim -1.3$  V vs. SCE in  $CH_3CN$ ). Finally, the bond dissociation energies of the neutral benzothiazolines **2–6** ( $BDE(BT-R)_g$ ), were estimated by DFT calculations. The results shown in Table 2 reveal that the estimated solution phase, radical cation bond dissociation energies are ca. 7–9 kcal/mol lower than those calculated for the gas phase. The lower solution phase BDEs would be consistent with greater solvation of the benzothiazolium cation than that of the radical cations.



The relative  $BT-R$  bond dissociation energies for  $2^+-6^+$  presumably reflect contributions from differences in both the stabilization of the radicals and the steric crowding present in the radical cations. We sought to estimate the comparative contributions of these factors to the relative BDEs. Relative radical stabilization energies of  $R\cdot$  can be defined in a number of ways. One of the most general definitions has been pioneered by Rüchardt, who has compared the difference in stability between a pure hydrocarbon radical and its substituted analogue in which one or more alkyl groups are replaced by substituents (12). The advantage of this approach is that it provides radical stabilization increments for substituents that are transferable between different radicals because the intrinsic differences in stabilities for primary, secondary, and tertiary radicals are factored out. To assess the relative effects of radical stabilities on the BDEs for  $2^+-6^+$ , however, we *do* want to include the differences in stabilities between primary, secondary, and tertiary radicals. Therefore, we have adopted the more traditional approach to assessing radical stabilities by comparing the relative  $R-H$  BDEs to a reference compound. We are primarily interested in only the *relative* contributions to radical stability along the series, therefore, we have chosen the least stabilized radical in this series ( $PhCH_2\cdot$ ) as our reference. Thus, we define



**Table 2.** Experimental ( $\Delta H_{\text{exp}}^\ddagger$ ) and calculated ( $\Delta H_{\text{calcd}}^\ddagger$ ) activation energies for fragmentation of  $2^+-6^+$ , gas phase C-R bond dissociation energies calculated for  $2-6$  (BDE (BT-R)<sub>g</sub>), gas phase (BDE (BT-R<sup>+</sup>)<sub>g</sub>), and solution phase (BDE (BT-R<sup>+</sup>)<sub>s</sub>) bond dissociation energies calculated for  $2^+-6^+$ .

Compound (R-)	$\Delta H_{\text{exp}}^\ddagger$	$\Delta H_{\text{calcd}}^\ddagger$ <sup>a</sup>	BDE (BT-R) <sub>g</sub> <sup>a</sup>	BDE (BT-R <sup>+</sup> ) <sub>g</sub> <sup>a</sup>	BDE (BT-R <sup>+</sup> ) <sub>s</sub> <sup>b</sup>
<b>2</b> (PhCH <sub>2</sub> -)	~16	14.4	52.2	11.6	~5
<b>3</b> (Ph <sub>2</sub> CH-)	9.6	7.8	37.8	-0.6	~-10
<b>4</b> (PhCMe <sub>2</sub> -)	9.6	7.0	38.4	-0.7	~-9
<b>5</b> (9-MeFl-)	3.9	4.4	32.1	-8.5	~-16
<b>6</b> (Ph <sub>2</sub> CMe-)	4.3	4.7	28.3	-10.3	~-19

**Note:** All energies in kcal/mol.

<sup>a</sup>From density functional calculations.

<sup>b</sup>BDE (BT-R)<sub>g</sub> -  $E^{\text{ox}}$  (BT-R) +  $E^{\text{ox}}$  (BT); based on the approximation that  $E^{\text{ox}}$  (BT-R) is the same for **2-6**.

**Table 3.** Estimates of the contributions of radical stability and steric effects on the gas phase and solution BT-R bond dissociation energies for  $3^+-6^+$  relative to those for  $2^+$ .

Radical Cation	R-	Relative radical stabilization <sup>a</sup>	Relative steric effect (gas phase) <sup>b</sup>	Relative steric effect (solution) <sup>c</sup>
<b>2</b> <sup>+</sup>	PhCH <sub>2</sub> -	(0)	(0)	(0)
<b>3</b> <sup>+</sup>	Ph <sub>2</sub> CH-	-4	-8	-11
<b>4</b> <sup>+</sup>	PhCMe <sub>2</sub> -	-3	-10	-11
<b>5</b> <sup>+</sup>	9-MeFl-	-10	-10	-11
<b>6</b> <sup>+</sup>	Ph <sub>2</sub> CMe-	-7	-15	-17

**Note:** All energies in kcal/mol.

<sup>a</sup>BDE (PhCH<sub>2</sub>-H) - BDE (R-H); see Table 1 for values.

<sup>b</sup>{[BDE (BT-CH<sub>2</sub>Ph<sup>+</sup>)<sub>g</sub> - BDE (BT-R<sup>+</sup>)<sub>g</sub>] - [BDE (PhCH<sub>2</sub>-H) - BDE (R-H)]}.

<sup>c</sup>{[BDE (BT-CH<sub>2</sub>Ph<sup>+</sup>)<sub>s</sub> - BDE (BT-R<sup>+</sup>)<sub>s</sub>] - [BDE (PhCH<sub>2</sub>-H) - BDE (R-H)]}.

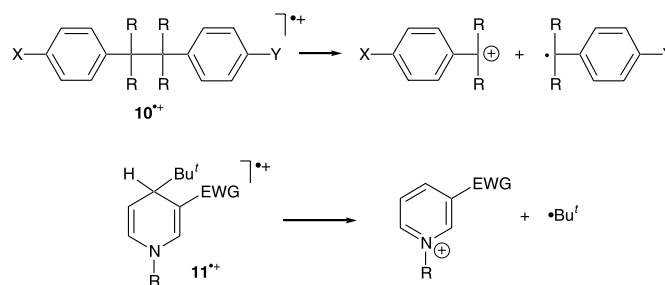
relative radical stabilities for the present purpose as BDE (PhCH<sub>2</sub>-H) - BDE (R-H).<sup>8</sup> For the relative steric contributions to the BDEs for  $2^+-6^+$ , we also use the benzyl substituted radical cation as a reference. Thus, the relative steric effects are estimated by subtracting the radical stabilization contribution from the difference in radical cation BDEs, i.e., {BDE (BT-CH<sub>2</sub>Ph<sup>+</sup>) - BDE (BT-R<sup>+</sup>)} - [BDE (PhCH<sub>2</sub>-H) - BDE (R-H)]. The results of this analysis are shown in Table 3. Note that the relative steric effects estimated from the gas phase and solution BDEs for  $2^+-6^+$  are in good agreement.

The results in Table 3 show that, relative to  $2^+$ , the BDEs for  $3^+-6^+$  roughly fall into two classes. For  $5^+$ , the relative contributions owing to radical stabilization and steric effects are nearly equal, 10 and 11 kcal/mol, respectively. For radical cations  $3^+$ ,  $4^+$ , and  $6^+$ , the relative radical stabilization and steric contributions to bond weakening are 3-7 kcal/mol and 11-17 kcal/mol, respectively, i.e., the steric effects dominate.

### Origin of the radical cation fragmentation barriers

Estimates of the BDEs for radical cations  $3^+-6^+$  in Table 2 show that all are predicted to be exothermic in solution. Nonetheless, the radical cations have substantial activation barriers to fragmentation. It is of interest to compare this behavior to that observed for the fragmentations of substituted bibenzyl radical cations (**10**<sup>+</sup>) reported by Maslak et al. (3a) and to the alkylated NADH radical cations (**11**<sup>+</sup>) reported by Savéant and co-workers (13). These radical cation fragmentations were found to have very small in-

trinsic barriers for fragmentation ( $\leq 4$  kcal/mol), showing that the internal and solvent reorganization energies for the reactions are quite small. In this respect the fragmentations of  $3^+-6^+$  are clearly different. Based on the fact that  $3^+$  and  $4^+$  have substantial activation energies for fragmentation ( $\Delta H^\ddagger \approx 10$  kcal/mol) despite the reactions being exothermic by 9 to 10 kcal/mol in solution, one can conclude that the intrinsic barriers for fragmentation of the substituted benzothiazine radicals studied here are  $>10$  kcal/mol.



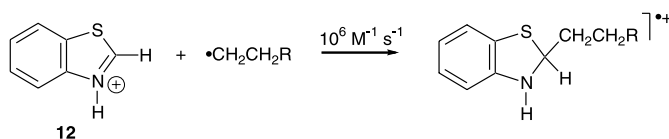
What is the origin of the difference in the intrinsic barriers for fragmentation of **10**<sup>+</sup> and **11**<sup>+</sup> vs.  $2^+-6^+$ ? We propose that the difference is related to the relative internal reorganization energies of the fragmentations. It is perhaps easier to think about the problem by considering the origin of the barrier for the reverse reaction, i.e., cation + radical recombination. The barrier for the recombination reaction will be directly related to the extent of delocalization of the cation and radical fragments. The greater the degree of delocali-

<sup>8</sup> Although it would have been desirable to use BDE (R-CH<sub>3</sub>) rather than BDE (R-H) to estimate relative radical stabilities, the former values are not well determined for the systems studied here.



zation, the greater will be the degree of electronic, internal reorganization, and, therefore, the greater will be the reaction barrier. When comparing the cation and radical fragments produced from fragmentation of  $10^+$  vs.  $2^+-6^+$ , the primary difference is likely related to the extent of delocalization of the cation, i.e., the benzyl cation (in the case of  $10^+$ ) vs. the benzothiazolium cation (in the case of  $2^+-6^+$ ). The benzothiazolium cation is expected to have significantly less carbocation character at the recombination site than a benzyl cation, which would lead to a larger internal reorganization energy for the benzothiazolium cation + radical recombination. In addition, for benzothiazoline radical cations  $3^+-6^+$ , the radicals produced by fragmentation are more delocalized than a simple benzyl radical, which will also lead to greater internal reorganization energies for recombination and, consequently, for fragmentation too. For the fragmentation of  $11^+$  vs.  $2^+-6^+$ , we presume that delocalization of the cation fragments for the two systems is somewhat similar. However, the relative extent of radical delocalization is clearly different. For  $11^+$ , the radical fragment —  $\cdot t\text{-Bu}$  — is clearly much more localized than any of the radicals formed from fragmentation of  $2^+-6^+$ . Thus, cation + radical recombination to form  $11^+$  should have a lower internal reorganization energy than the recombinations to form  $2^+-6^+$ .

The proposition that the cation + radical recombination reactions to form  $2^+-6^+$  should have significant barriers is supported by the fact that even addition of a localized, primary radical to benzothiazolium cation **12** has a rate constant of only  $1 \times 10^6 \text{ M}^{-1} \text{ s}^{-1}$  at  $25^\circ\text{C}$  (14). It should be clear that addition of the delocalized radicals, such as those derived from fragmentation of  $2^+-6^+$ , would have significantly lower rate constants. Consequently, the fragmentations of  $2^+-6^+$  are expected to have significant intrinsic barriers.



## Conclusions

There are three main conclusions from this work. First, we have demonstrated that benzothiazoline derivatives, which are among the lowest oxidation potential compounds yet investigated as candidates for radical cation fragmentation, can undergo rapid fragmentation upon one-electron oxidation if the fragmenting bond is sufficiently weakened by a combination of stabilizing the radical fragment and by steric crowding in the reactants. These two factors allow the rate constants for fragmentation of benzothiazoline radical cations to be tuned by over 6 orders of magnitude. Second, benzothiazoline radical cations were found to have considerably large intrinsic activation barriers ( $>10 \text{ kcal/mol}$ ) for fragmentation. The barriers were attributed to large reorganization energies of the product fragments, the benzothiazolium cation and the resonance-delocalized radicals. Consequently, the same factors that lead to the thermodynamic driving forces for the fragmentations — the stabilities of the benzothiazolium cation and the resonance-delocalized radicals — simultaneously result in large intrinsic barriers.

These factors lead to opposing kinetic effects. On the one hand, the natural exothermicities of the reactions should decrease the activation barriers for fragmentation according to the Bell–Evans–Polanyi principle. On the other hand, the large intrinsic barriers increase the activation energies. This analysis reveals a fundamental limitation of using delocalized cation and radical products in the design of fast radical cation fragmentation reactions. As shown in the present work, steric effects are the more attractive structural feature to utilize for designing fast radical ion fragmentations because they do not increase the intrinsic barrier. Third, for relatively fast radical ion fragmentations of sterically congested systems such as those described in this work, one should keep in mind that the energetic barriers for fragmentation can be lower than the barriers for conformational interconversion. In these cases, the possibility exists that the most stable radical ion conformer may not necessarily be the reactive conformer.

## Experimental section

### General method

$^1\text{H}$  NMR spectra were recorded with either a General Electric/Nicolet QE-300 spectrometer or a Bruker Avance-400 spectrometer.  $^{13}\text{C}$  NMR spectra were recorded with an Avance-400 spectrometer. Proton chemical shifts ( $\delta$ ) are reported in parts per million (ppm) downfield from tetramethylsilane or in ppm relative to the singlet at 7.24 ppm for the residual  $\text{CHCl}_3$  in the chloroform- $d$  or the multiplet at 1.93 ppm for the residual  $\text{CHD}_2\text{CN}$  in the acetonitrile- $d_3$ . Reported proton–proton coupling constants assume first-order behavior. Splitting patterns are designated as singlet (s), doublet (d), triplet (t), quartet (q), multiplet (m), and broad (br). The meta- and para-couplings are ignored. Ortho-, meta-, and para-hydrogens of phenyl groups are designated *o*-, *m*-, and *p*-; for magnetically nonequivalent phenyl groups the signals of the second phenyl group are designated *o'*-, *m'*-, and *p'*-. The aromatic hydrogens of the benzothiazoline and benzothiazolium derivatives are numbered 4–7 from the  $\alpha$  position to N. Carbon chemical shifts are reported in ppm relative to internal acetonitrile- $d_3$  (117.61 and 0.60 ppm) or chloroform- $d$  (77.34 (t) ppm).

Acetonitrile was refluxed over  $\text{CaH}_2$  for 24 h and distilled fresh prior to use under an atmosphere of nitrogen. Anhydrous diethyl ether and tetrahydrofuran were freshly distilled from benzophenone ketyl under nitrogen.

### Electrochemical measurements

Cyclic voltammetric measurements were carried out on a glassy carbon disk electrode using a CHI660 electrochemical analyzer (CH Instruments, Inc.) in acetonitrile with tetrabutylammonium perchlorate as electrolyte. 2,3-Dimethylbenzothiazolium showed irreversible reduction with a peak potential of  $-1.30 \text{ V}$  vs. SCE. A reversible oxidation potential was obtained for compound **1** ( $0.77 \text{ V}$  vs. SCE, 3 mm electrode at  $0.5 \text{ V/s}$ ). Compounds **3** and **6** showed irreversible oxidation with peak potentials at  $0.63$  and  $0.65 \text{ V}$  vs. SCE, respectively.

Using a  $33 \mu\text{m}$  carbon electrode at a scan rate  $\geq 25 \text{ V/s}$ , compound **2** showed a quasi-reversible oxidation of  $0.70 \text{ V}$  vs. SCE. Scanning at slower rates ( $2.5$ – $10 \text{ V/s}$ ) and with



varying delays, a rate constant of  $1 \pm 0.2 \text{ s}^{-1}$  was obtained for the follow-up chemical reaction, presumably the fragmentation of  $2^{+}$ .

### Laser flash photolysis

Nanosecond laser flash photolysis experiments were carried out using either 380 or 355 nm excitations. For 380 nm excitation, a Lambda Physik Lextra 50 excimer laser (XeCL, 308 nm; <180 mJ/pulse; 10 ns pulses) and a Lambda Physik LPD 3002 pumped-dye laser (Exciton-384 dye for 380 nm; <10 mJ/pulse; 7 ns pulses) were used. For 355 nm excitation, the frequency-tripled output from an OPOTEK Vibrant Q-switched Nd:YAG laser system (pulse width 4 ns, 2–8 mJ) was used. The excitation pulses were attenuated, when necessary, using neutral density filters.

Transient absorption was monitored at right angles to the excitation. A pulsed Oriel 150 W xenon lamp (Model 66007) was used as the monitoring beam. The analyzing beam was collected and focused on the entrance slit (2 nm) of an Instrument S. A. H-20 monochromator. A Hamamatsu R-446 photomultiplier tube (PMT) in a custom housing (Products for Research) was attached to the exit slit of the monochromator. A computer-controlled Stanford Research Systems high voltage power supply (model PS310) was used with the PMT. The signals from the PMT were digitized using a Tektronix TDS 620 oscilloscope and transferred to a PC, via a GPIB interface, for data storage and processing. A Quantum Composer pulse generator (Model 9318) provided TTL trigger pulses to control the timing for the laser, lamp, and oscilloscope.

Appropriate long pass filters were placed on either side of the sample to prevent photolysis by the analyzing light.

### Spectral measurements

To acetonitrile solutions of *N*-methoxyphenanthridinium hexafluorophosphate ( $\text{MeOP}^+$ ) with an OD of 0.5–0.77 at the excitation wavelength (380 or 355 nm) were added benzothiazolines 2–6 (5–15 mM). The samples were thoroughly purged with either dioxygen or argon (~10 min) before passing them through a  $1 \times 1 \text{ cm}^2$  quartz flow cell. The flow rate was adjusted so that fresh sample was available for each laser shot.

### Kinetics measurements

The samples were purged with either dioxygen or nitrogen prior to, and during, laser irradiation. Typically, a solution of  $\text{MeOP}^+$  in acetonitrile (OD at 380 nm = 0.6–0.8) was exposed to 380 nm laser excitation (0.5–0.6 mJ/pulse) in the presence of the benzothiazoline derivative (6 to 7 mM), and the decay of the radical cation was followed between 420–450 nm on the ns to  $\mu\text{s}$  time scale. For temperature dependence studies, fresh samples were equilibrated at each temperature for 15–20 min prior to the measurement. Each set of experiments was repeated at least three times.

### Materials

2-Methylamino-benzenethiol was prepared according to a literature procedure by reductive ring opening of 2,3-dihydro-1,3-benzothiazole (Aldrich) using lithium aluminum hydride (15). Methyl iodide, trimethyloxonium tetrafluoroborate, acetophenone, 1-phenyl-2-butanone, 1,1-diphenyl-

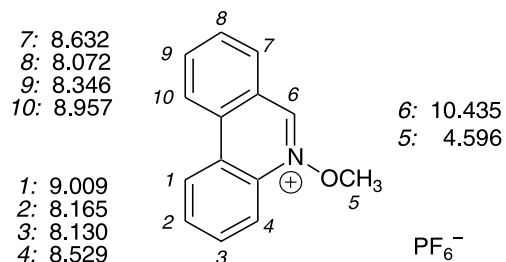
acetone, cumene,  $\alpha$ -methylstyrene, 1,1-diphenylethylene, and fluorene were all obtained from Aldrich Chemical Company and used without further purification. 1,1,2,2-Tetraphenylethane (16), 2,2,3,3-tetraphenylbutane (17), 2,3-dimethyl-2,3-diphenylbutane (18), and compound 9 (19) were prepared following previously reported methods. 2-Phenyl-2-methylpropionoyl chloride was prepared from the corresponding acid (20a) by reaction with  $\text{PCl}_5$  using a procedure analogous to that described in ref. (20b). Products of the cleaved radicals were identified by comparison with  $^1\text{H}$  NMR spectra of authentic samples.

### 2,3-Dimethylbenzothiazolium hexafluorophosphate

This material was prepared by modification of a literature procedure (4). To a stirred solution of acetyl chloride (5.0 g, 63.7 mmol) in benzene (dry, 200 mL), a solution of 2-methylamino-benzenethiol (8.84 g, 63.7 mmol) in benzene (20 mL) was added dropwise at room temperature. The reaction mixture was refluxed for 1 h. Solvent removal provided a pale yellow solid that was dissolved in water (200 mL) followed by addition of potassium hexafluorophosphate (7.0 g in 100 mL  $\text{H}_2\text{O}$ ) to afford a white precipitate (19 g, 79%).  $^1\text{H}$  NMR ( $\text{CD}_3\text{CN}$ )  $\delta$ : 8.24 (d,  $J = 8 \text{ Hz}$ , 1H), 8.05 (d,  $J = 9 \text{ Hz}$ , 1H), 7.92 (t,  $J = 8 \text{ Hz}$ , 1H), 7.82 (t,  $J = 8 \text{ Hz}$ , 1H), 4.15 (s, 3H), 3.09 (s, 3H).

### *N*-Methoxyphenanthridinium hexafluorophosphate

*N*-Methoxyphenanthridinium tetrafluoroborate was prepared from the reaction of phenanthridine-*N*-oxide with trimethyloxonium tetrafluoroborate in dichloromethane (7). A solution of the  $\text{BF}_4$  salt (1 g) in ~15 mL water was added to an aqueous solution of potassium hexafluorophosphate (2 g in ~10 mL). The mixture was cooled and the precipitate was recrystallized from water as a crystalline pale yellow solid.  $^1\text{H}$  NMR ( $\text{CD}_3\text{CN}$ )  $\delta$ : 10.09 (s, 1H), 9.06 (d, 1H), 9.02 (d, 1H), 8.57 (t, 2H), 8.43 (t, 1H), 8.24–8.13 (m, 3H), 4.61 (s, 3H).



### 2,2,3-Trimethylbenzothiazoline (1)

This compound was prepared according to a literature procedure (5). To a stirred suspension of 2,3-dimethylbenzothiazolium toluene-4-sulfonate (5.0 g, 14.32 mmol) in anhydrous diethyl ether (125 mL) at  $-40^\circ\text{C}$ , methylmagnesium bromide (2.87 M solution in diethyl ether, 5.3 mL, 15 mmol) was added dropwise over 5 min under an atmosphere of  $\text{N}_2$ . The reaction mixture was refluxed for 2 h and then quenched with aqueous ammonium chloride solution (70 mL). The organic layer was separated and the aqueous layer was extracted with ether ( $3 \times 50 \text{ mL}$ ). The organic extracts were combined, washed successively with water ( $2 \times 100 \text{ mL}$ ) and with brine solution ( $2 \times 100 \text{ mL}$ ), and dried



over anhydrous magnesium sulfate. Filtration and removal of the solvent yielded a red oil (2.2 g, 77%). The crude product was distilled under reduced pressure, bp 80°C at 10 mmHg (1 mmHg = 133.322 Pa) (lit. (5c) bp 75–80°C at 10 mmHg (1 mmHg = 133.322 Pa)) to yield a colorless oil (2.0 g, 76%). MS  $m/z$ : 179 ( $M^+$ , calculated for  $C_{11}H_{15}NS$ ).  $^1H$  NMR ( $CDCl_3$ )  $\delta$ : 7.05 (d,  $J$  = 7.4 Hz, H-7), 6.99 (t,  $J$  = 7.6 and 7.8 Hz, H-5), 6.64 (t,  $J$  = 7.4 and 7.6 Hz), 6.31 (d,  $J$  = 7.8 Hz, H-4), 2.72 (s,  $NCH_3$ ), 1.65 (s,  $C(CH_3)_2$ ).  $^{13}C$  NMR ( $CDCl_3$ )  $\delta$ : 146.64, 124.17, 121.70, 117.55, 106.31, 61.03, 37.28, 28.58, 28.40.

## 2-Benzyl-2-ethyl-3-methyl-benzothiazoline (2)

A solution of 2-methylamino-benzenethiol (1.0 g, 7.2 mmol) and 1-phenyl-2-butanone in absolute ethanol (7 mL) was refluxed for 48 h under an atmosphere of  $N_2$ . The reaction mixture was cooled and kept at –40°C for 3 h. A precipitate came out of solution, which rapidly melted at room temperature to afford a yellow oil. The latter was distilled under reduced pressure (165–167°C at 0.04 mmHg (1 mmHg = 133.322 Pa)) to obtain a very pale yellow oil (1.2 g, 63%). MS  $m/z$ : 269 ( $M^+$ , calculated for  $C_{17}H_{19}NS$ ).  $^1H$  NMR ( $CDCl_3$ )  $\delta$ : 7.36–7.26 (m, 5H), 7.04 (d,  $J$  = 7.4 Hz, 1H), 7.00 (t,  $J$  = 7.6 and 7.8 Hz, 1H), 6.64 (t,  $J$  = 7.4 and 7.6 Hz, 1H), 6.30 (d,  $J$  = 7.8 Hz, 1H), 3.28 (d,  $J$  = 13.4 Hz, 1H), 3.10 (d,  $J$  = 13.4 Hz, 1H), 2.86 (s, 3H), 2.10 (sextet,  $J$  = 14.9 and 7.2 Hz, 1H), 1.72 (sextet,  $J$  = 14.9 and 7.2 Hz, 1H), 1.05 (t,  $J$  = 7.2 Hz, 3H).  $^{13}C$  NMR ( $CDCl_3$ )  $\delta$ : 148.17, 136.36, 131.10, 127.74, 126.62, 125.17, 124.17, 121.09, 117.60, 105.48, 85.78, 45.46, 30.19, 29.04, 9.15.  $^{13}C$  DEPT135 NMR ( $CDCl_3$ )  $\delta$ : 131.10, 127.74, 125.17, 121.09, 117.60, 105.48, 45.46 (negative peak), 30.19 (negative peak), 29.04, 9.15.

## 2,3-Dimethyl-2-diphenylmethyl-benzothiazoline (3)

A solution of 2-methylamino-benzenethiol (2.0 g, 14.38 mmol) and 1,1-diphenylacetone (3.02 g, 14.38 mmol) in absolute ethanol (15 mL) was refluxed for 52 h under an atmosphere of  $N_2$ . Upon cooling to –40°C, a colorless solid (2.3 g, 48%) formed which was recrystallized twice from ethanol to yield colorless plates (2.0 g, 42%), mp 82°C. MS  $m/z$ : 331.0 ( $M^+$ , calculated for  $C_{22}H_{21}NS$ ).  $^1H$  NMR ( $CDCl_3$ )  $\delta$ : 7.67 (*o*-H, 2H), 7.53 (*o'*-H, 2H), 7.33 (*m'*-H, 2H), 7.27 (*p'*-H, 1H), 7.20 (*m*-H, 2H), 7.14 (*p*-H, 1H), 6.99 (d,  $J$  = 7.4 Hz, 1H), 6.92 (t,  $J$  = 7.5 and 7.8 Hz, 1H), 6.59 (t,  $J$  = 7.4 and 7.5 Hz, 1H), 6.14 (d,  $J$  = 7.8 Hz, 1H), 4.51 (s,  $CHPh_2$ ), 2.69 (s,  $N-CH_3$ ), 1.75 (s,  $CH_3$ ).  $^{13}C$  NMR ( $CDCl_3$ )  $\delta$ : 147.71, 140.69, 129.89, 128.23, 127.70, 127.03, 126.31, 125.25, 124.06, 121.00, 117.51, 105.99, 83.77, 59.53, 29.14, 27.81.  $^{13}C$  DEPT45 NMR ( $CDCl_3$ ) (only CH and  $CH_3$  carbons)  $\delta$ : 129.89, 129.83, 128.23, 127.70, 127.03, 126.31, 125.25, 121.00, 117.51, 105.99, 59.53, 29.14, 27.81.

## 2-Cumyl-2,3-dimethyl-benzothiazoline (4)

To a stirred solution of 2-phenyl-2-methylpropionoyl chloride (4.8 g, 26.3 mmol) in benzene (dry, 80 mL), a solution of 2-methylamino-benzenethiol (3.7 g, 26.4 mmol) in benzene (20 mL) was added dropwise at room temperature. The reaction mixture was refluxed for 1.5 h. Solvent removal gave an oil that was dissolved in  $CH_2Cl_2$  (100 mL). The resulting solution was added dropwise to rapidly stirred

diethyl ether (dry, 850 mL) to form a yellow precipitate. The precipitate was dissolved in water (400 mL) at 70–80°C and an aqueous solution of potassium hexafluorophosphate (4.8 g in 100 mL  $H_2O$ ) was added. Upon cooling the solution, a pale yellow precipitate formed. Recrystallization from acetonitrile – diethyl ether (1:10) gave a colorless solid of the 2-cumyl-3-methyl-benzothiazolium salt (9.0 g, 83%).  $^1H$  NMR ( $CD_3CN$ )  $\delta$ : 8.35 (d,  $J$  = 8.0 Hz, H-7), 8.02 (d,  $J$  = 8.3 Hz, H-4), 7.94 (t,  $J$  = 7.3 and 8.3 Hz, H-5), 7.88 (t,  $J$  = 7.3 and 8.0 Hz, H-6), 7.5–7.42 (m, *m*- and *p*-H, 3H), 7.37–7.35 (m, *o*-H, 2H), 3.75 (s,  $NCH_3$ ), 2.04 (s,  $C(CH_3)_2$ ).  $^{13}C$  NMR ( $CD_3CN$ )  $\delta$ : 142.10, 130.10, 129.62, 128.25, 125.82, 123.79, 117.30, 116.75, 45.72, 37.92, 28.73.  $^{13}C$  DEPT45 NMR ( $CD_3CN$ )  $\delta$ : 130.10, 129.62, 128.91, 128.25, 125.82, 123.79, 116.75, 37.92, 28.73.

To a stirred suspension of 2-cumyl-3-methyl-benzothiazolium hexafluorophosphate (1.0 g, 2.42 mmol) in tetrahydrofuran (80 mL) under an atmosphere of  $N_2$ , methylmagnesium bromide (2.73 M solution in ether, 7.5 mL, 22 mmol) was added dropwise over 15 min at –70°C. The reaction was stirred at –70°C for an additional 30 min, followed by 4 h at room temperature, and then refluxed for 15 min. The reaction was quenched with aqueous ammonium chloride solution (50 mL, pH ~ 4) and extracted with diethyl ether (3  $\times$  50 mL). The ether extracts were washed with brine solution (2  $\times$  50 mL), dried over anhydrous magnesium sulfate, filtered, and the solvent removed to afford a pale yellow oil (0.54 g, ~79%). The crude material was recrystallized from aqueous methanol to yield a pale yellow solid, mp 70–71°C. MS  $m/z$ : 283 ( $M^+$ , calculated for  $C_{18}H_{21}NS$ ).  $^1H$  NMR ( $CDCl_3$ )  $\delta$ : 7.56 (d, *o*-H, 2H), 7.34 (t, *m*-H, 2H), 7.27 (t, *p*-H, 1H), 6.99–6.95 (m, 2H), 6.62 (t, 1H), 6.31 (d, 1H), 2.54 (s, 3H), 1.78 (s, 3H), 1.62 (s, 3H), 1.54 (s, 3H).  $^{13}C$  ( $CDCl_3$ )  $\delta$ : 149.95, 144.51, 128.81, 127.23, 126.31, 125.66, 124.90, 119.81, 117.74, 107.0, 87.03, 49.99, 34.06, 24.76, 24.64, 23.49.  $^{13}C$  DEPT135 ( $CDCl_3$ ) (only CH and  $CH_3$  carbons observed)  $\delta$ : 128.81, 127.23, 126.31, 124.90, 119.81, 117.74, 106.99, 34.07, 24.76, 24.64, 23.49.

## 2-(1,1-Diphenylethyl)-2,3-dimethyl-benzothiazoline (5)

Reaction of 2,2-diphenylpropionyl chloride with 2-methylamino-benzenethiol, as described above for compound **4** (reflux time of 5 h), gave the corresponding benzothiazolium chloride in 70% yield as colorless cubes from acetonitrile – diethyl ether (1:10).  $^1H$  NMR ( $CDCl_3$ )  $\delta$ : 8.57 (d, 1H), 8.12 (d, 1H), 7.87 (t, 1H), 7.72 (t, 1H), 7.48–7.44 (m, 6H), 7.25–7.21 (m, 4H), 4.29 (s, 3H), 2.66 (s, 3H).  $^{13}C$  NMR ( $CDCl_3$ )  $\delta$ : 186.79, 144.05, 143.36, 141.55, 130.76, 129.17, 127.79, 123.25, 118.27, 53.64, 40.54, 27.68.

Similarly, compound **5** was prepared from the reaction of 2-(1,1-diphenylethyl)-3-methylbenzothiazolium chloride with  $MeMgBr$  as described above for compound **4**. Compound **5** was obtained in 46% yield as colorless crystals from ethanol, mp 58–62°C. MS  $m/z$ : 345 ( $M^+$ , calculated for  $C_{23}H_{23}NS$ ).  $^1H$  NMR ( $CDCl_3$ )  $\delta$ : 7.37–7.17 (m, 10H), 6.98 (d,  $J$  = 7.4 Hz, 1H), 6.97 (t,  $J$  = 7.5 and 7.8 Hz, 1H), 6.63 (t,  $J$  = 7.4 and 7.5 Hz, 1H), 6.31 (d,  $J$  = 7.8 Hz, 1H), 2.20 (br. s, 3H), 2.06 (s, 3H), 1.98 (s, 3H).  $^{13}C$  NMR ( $CDCl_3$ )  $\delta$ : 153.83, 149.34, 133.55, 130.81, 129.35, 127.39, 127.09, 126.51, 125.68, 125.05, 119.85, 107.62, 34.32, 27.58, 25.65.



### 2,3-Dimethyl-2-(9-methylfluoren-9-yl)-benzothiazoline (6)

9-Methylfluorene-9-carbonyl chloride (prepared in an analogous manner to 2-phenyl-2-methylpropionoyl chloride, see above) was reacted with 2-methylamino-benzenethiol, as described above under compound **4** (1 h reflux time), to give the corresponding benzothiazolium hexafluorophosphate salt as colorless crystals in 96% yield.  $^1\text{H}$  NMR ( $\text{CDCl}_3$ )  $\delta$ : 8.89 (d,  $J \approx 8$  Hz, 1H), 8.30 (d,  $J \approx 8$  Hz, 1H), 7.91 (d,  $J \approx 7.6$  Hz, 2H), 7.79 (t,  $J \approx 7$  and 8 Hz, 1H), 7.71 (t,  $J \approx 7$  and 8 Hz, 1H), 7.54 (t, 2H), 7.41–7.36 (m, 4H), 3.30 (s, 3H), 2.22 (s, 3H).  $^{13}\text{C}$  NMR ( $\text{CDCl}_3$ )  $\delta$ : 181.55, 144.38, 143.32, 139.78, 130.70, 130.07, 129.51, 128.87, 128.73, 125.57, 123.88, 121.70, 117.01, 54.21, 36.37, 29.06.

The benzothiazolium salt was treated as described above for compound **4** to give compound **6** as a colorless viscous oil in 40% yield after flash chromatography (silica gel, 60% hexane – diethyl ether). MS  $m/z$ : 343 ( $\text{M}^+$ , calculated for  $\text{C}_{23}\text{H}_{21}\text{NS}$ ).  $^1\text{H}$  NMR ( $\text{CDCl}_3$ )  $\delta$ : 7.89 (d,  $J = 7.6$  Hz, 1H), 7.78 (d,  $J = 7.7$  Hz, 1H), 7.74 (d,  $J \approx 7.5$  Hz, 1H), 7.72 (d,  $J \approx 7.5$ , 1H), 7.41 (t,  $J = 7.5$  Hz, 1H), 7.36 (t,  $J = 7.5$  Hz, 1H), 7.30 (t,  $J = 7.4$  Hz, 1H), 7.22 (t,  $J = 7.5$  Hz, 1H), 7.01 (d,  $J = 7.4$  Hz, H-4), 6.95 (t,  $J = 7.4$  and 7.9 Hz, H-6), 6.66 (t,  $J = 7.4$ , 7.4 Hz, H-5), 6.32 (d,  $J = 7.9$  Hz, H-7), 2.61 (s, 3H), 1.79 (s, 3H), 1.62 (s, 3H).  $^{13}\text{C}$  NMR ( $\text{CDCl}_3$ )  $\delta$ : 150.21, 148.91, 148.58, 141.215, 140.97, 127.68, 127.52, 126.85, 126.77, 126.45, 126.01, 125.02, 125.98, 119.84, 119.61, 119.17, 118.49, 108.36, 85.96, 61.87, 34.58, 23.35, 20.75.

### General procedure for photolysis of benzothiazolines in acetonitrile- $d_3$

An equimolar (~0.01 M) solution of the benzothiazoline and  $\text{MeOP}^+$  in acetonitrile- $d_3$  was purged with nitrogen for 5–10 min and then irradiated for 5–10 min in a Rayonet reactor equipped with 400 nm lamps. The color of the reaction mixture changed from pale yellow to slightly darker yellow during the photolysis. After photolysis, a known amount of internal standard, viz., tetrachloroethane was added into the reaction mixture and  $^1\text{H}$  NMR recorded. Products were identified by comparison with  $^1\text{H}$  NMR spectra of authentic samples prepared independently. The yields of products were determined by  $^1\text{H}$  NMR integration of diagnostic proton signals of products relative to the area of peak due to internal standard tetrachloroethane ( $\delta$  6.3, s, 2H).

### Photolysis products of 3

2,3-Dimethylbenzothiazolium (82%, 8.25 (d,  $J = 8.2$  Hz, H-7), 8.09 (d,  $J = 8.5$  Hz, H-4), 7.92 (t,  $J = 7.2$  and 8.5 Hz, H-5), 7.83 (t,  $J = 7.2$  and 8.2 Hz, H-6), 4.16 (s, 3H), 3.10 (s, 3H)), phenanthridine, 1,1,2,2-tetraphenylethane (93%), adduct **7** (27%),  $\text{CH}_3\text{OH(D)}$  (54%).

### Photolysis products of 4

2,3-Dimethylbenzothiazolium (87%), phenanthridine (85%), 2,3-dimethyl-2,3-diphenylbutane (70%),  $\alpha$ -methylstyrene (5%), cumene (18%), adduct **7** (13%),  $\text{CH}_3\text{OH(D)}$  (63%).

### Photolysis products of 5

2,3-Dimethylbenzothiazolium (88%), phenanthridine (83%), bis-(9-methyl-9-fluorenyl) (**9**) ((85%)  $\delta$ : 7.49 (d,  $J = 7.5$  Hz, 4H), 7.23 (t, average  $J = 7.4$  Hz, 4H), 7.06 (t, average  $J = 7.4$  Hz, 4H), 6.88 (very broad, 4H), 1.91 (s, 6H)), 9-methylfluorene (11%), adduct **7** (13%),  $\text{CH}_3\text{OH(D)}$  (66%).

### Photolysis products of 6

2,3-Dimethylbenzothiazolium (88%), phenanthridine (65%), 2,2,3,3-tetraphenylbutane (82%), 1,1-diphenylethylene (12%), adduct **7** (22%),  $\text{CH}_3\text{OH(D)}$  (63%).

### Attempted isolation of adduct 7

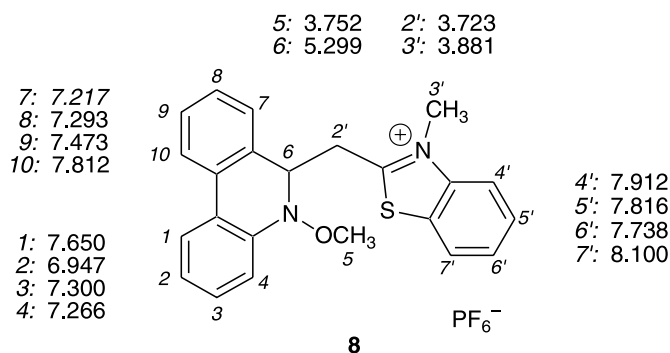
An equimolar (0.01 M) solution of benzothiazoline **3** and  $\text{MeOP}^+$  in acetonitrile (25 mL) was irradiated under nitrogen for 20 min in a Rayonet reactor equipped with 400 nm lamps. The solution was concentrated to ~2 mL and diluted with diethyl ether (~50 mL). A precipitate formed which was collected and identified by  $^1\text{H}$  NMR as 2,3-dimethylbenzothiazolium. Upon addition of hexane to the ethereal solution the mixture turned turbid and, upon standing, resulted in formation of an oil. The supernatant liquid was decanted and the oil was repeatedly washed with hot hexane to further remove phenanthridine and 1,1,2,2-tetraphenylethane. Analysis of the hexane-washed solid by  $^1\text{H}$  NMR showed that it was a mixture of primarily 2,3-dimethylbenzothiazolium salt and adduct **7**, along with traces of 1,1,2,2-tetraphenylethane and phenanthridine.

### Compound 7

$^1\text{H}$  NMR ( $\text{CD}_3\text{CN}$ )  $\delta$ : 8.18 (d,  $J = 6.3$  Hz, 1H), 7.85–7.77 (m, 5H), 7.48 (t,  $J = 7.7$  Hz, 1H), 7.37 (t,  $J = 7.7$  Hz, 1H), 7.24 (d,  $J \approx 8$  Hz, 1H), 7.21 (t,  $J = 7.5$  Hz, 1H), 7.10 (t,  $J = 7.4$  Hz, 1H), 7.89 (br d, 6.4, 1H), 5.30 (dd,  $J = 4.8$  and 7.4 Hz, 1H), 4.96 (dd,  $J = 4.8$  and 14.6, 1H), 4.75 (dd,  $J = 7.4$  and 14.6 Hz, 1H), 3.80 (s, 3H), 2.53 (s, 3H).

### Preparation of adduct 8

To an equimolar solution of *N*-methoxyphenanthridinium hexafluorophosphate (35.5 mg, 0.1 mmol) and 2,3-dimethylbenzothiazolium hexafluorophosphate (30.9 mg, 0.1 mmol) in 4 mL  $\text{CD}_3\text{CN}$ , ~30 mg anhydrous sodium carbonate was added. The solution was stirred at room temperature and the reaction was monitored by  $^1\text{H}$  NMR. After ~8 h, the conversion was nearly complete yielding almost exclusively compound **8**, which was identified by its NMR spectrum ( $\text{CD}_3\text{CN}$ ). The chemical shifts of the  $^1\text{H}$  NMR were assigned based on NOE, COSY, and TOCSY experiments using a 500 MHz spectrometer; those of strongly overlapping signals were further confirmed by comparison with simulated spectra. The NOE experiment indicated the proximity of H-6 (methine triplet at 5.299 ppm) to H-7 (aromatic hydrogen at 7.217 ppm) and of H-3' (methyl singlet at 3.881 ppm) to H-4' (aromatic hydrogen at 7.912 ppm).





## Acknowledgments

Financial support was provided by the National Science Foundation (CHE-9812719). We are grateful to Ralph Young (University of Rochester) for help in analyzing the kinetic data. We also thank Shihua S. Chen (Eastman Kodak Company) for the electrochemical measurements and James M. Hewitt (Eastman Kodak Company) for the 2D NMR measurements.

## References

1. (a) A. Okamoto, M.S. Snow, and D.R. Arnold. *Tetrahedron*, **42**, 6175 (1986); (b) D.R. Arnold and L.J. Lamont. *Can. J. Chem.* **67**, 2119 (1989); (c) R. Popielarz and D.R. Arnold. *J. Am. Chem. Soc.* **112**, 3068 (1990); (d) X. Du, D.R. Arnold, R.J. Boyd, and Z. Shi. *Can. J. Chem.* **69**, 1365 (1991).
2. (a) A. Okamoto and D.R. Arnold. *Can. J. Chem.* **63**, 2340 (1985); (b) P. Maslak. *Top. Curr. Chem.* **168**, 1 (1993); (c) A. Albin, M. Mella, and M. Freccero. *Tetrahedron*, **50**, 575 (1994); (d) E.R. Gaillard and D.G. Whitten. *Acc. Chem. Res.* **29**, 292 (1996); (e) R.D. Burton, M.D. Bartberger, Y. Zhang, J.R. Eyler, and K.S. Schanze. *J. Am. Chem. Soc.* **118**, 5655 (1996); (f) K.P. Dockery, J.P. Dinnocenzo, S. Farid, J.L. Goodman, I.R. Gould, and W.P. Todd. *J. Am. Chem. Soc.* **119**, 1876 (1997); (g) J.P. Dinnocenzo, H. Zuilhof, D.R. Lieberman, T.R. Simpson, and M.W. McKechney. *J. Am. Chem. Soc.* **119**, 994 (1997); (h) Z. Su, P.S. Mariano, D.E. Falvey, U.C. Yoon, and S.W. Oh. *J. Am. Chem. Soc.* **120**, 10 676 (1998).
3. (a) P. Maslak, W.H. Chapman, Jr., T.M. Vallombroso, Jr., and B.A. Watson. *J. Am. Chem. Soc.* **117**, 12 380 (1995). (b) H. Gan, U. Leinhos, I.R. Gould, and D.G. Whitten. *J. Phys. Chem.* **99**, 3566 (1995).
4. H. Chikashita, S. Komazawa, N. Ishimoto, K. Inoue, and K. Itoh. *Bull. Chem. Soc. Jpn.* **62**, 1215 (1989).
5. (a) P. Kiprianow. *Zh. Obshch. Khim.* **19**, 1515 (1949); (b) E. Davin-Pretelli, M. Guiliano, G. Mille, J. Chouteau, R. Guglielmetti, and C. Gelebart. *Helv. Chim. Acta*, **60**, 215 (1977); (c) J. Metzger, H. Larivé, R. Dennilaule, R. Baralle, and C. Gaurat. *Bull. Soc. Chim. Fr.* 2868 (1964).
6. I.R. Gould, D. Ege, J.E. Moser, and S. Farid. *J. Am. Chem. Soc.* **112**, 4290 (1990).
7. J.D. Mee, D.W. Heseltine, and E.C. Taylor. *J. Am. Chem. Soc.* **92**, 5814 (1970).
8. D.A. Falvey and G.B. Schuster. *J. Am. Chem. Soc.* **108**, 7419 (1986).
9. (a) BDE (PhCH<sub>2</sub>-H) from: G.B. Ellison, G.E. Davico, V. Bierbaum, and C.H. DePuy. *Int. J. Mass. Spectrom. Ion Processes*, **156**, 109 (1996); (b) all other BDEs from: J.J. Brocks, H.-D. Beckhaus, A.L.J. Beckwith, and C. Rüchardt. *J. Org. Chem.* **64**, 1935 (1998).
10. T. Bally and W.T. Borden. *Rev. Comput. Chem.* **13**, 1 (1999).
11. M.J. Frisch, G.W. Trucks, H.B. Schlegel, G.E. Scuseria, M.A. Robb, J.R. Cheeseman, V.G. Zakrzewski, J.A. Montgomery, Jr., R.E. Stratmann, J.C. Burant, S. Dapprich, J.M. Millam, A.D. Daniels, K.N. Kudin, M.C. Strain, O. Farkas, J. Tomasi, V. Barone, M. Cossi, R. Cammi, B. Mennucci, C. Pomelli, C. Adamo, S. Clifford, J. Ochterski, G.A. Petersson, P.Y. Ayala, Q. Cui, K. Morokuma, P. Salvador, J.J. Dannenberg, D.K. Malick, A.D. Rabuck, K. Raghavachari, J.B. Foresman, J. Cioslowski, J.V. Ortiz, A.G. Baboul, B.B. Stefanov, G. Liu, A. Liashenko, P. Piskorz, I. Komaromi, R. Gomperts, R.L. Martin, D.J. Fox, T. Keith, M.A. Al-Laham, C.Y. Peng, A. Nanayakkara, M. Challacombe, P.M.W. Gill, B. Johnson, W. Chen, M.W. Wong, J.L. Andres, C. Gonzalez, M. Head-Gordon, E.S. Replogle, and J.A. Pople. *Gaussian 98 (Revision A.11)*. Gaussian, Inc., Pittsburgh, Pa. 2001.
12. C. Rüchardt and H.-D. Beckhaus. *Top. Curr. Chem.* **130**, 1 (1985).
13. A. Anne, S. Fraoua, J. Moiroux, and J.-M. Savéant. *J. Am. Chem. Soc.* **118**, 3938 (1996).
14. A. Citterio, F. Minisci, O. Porta, and G. Sesana. *J. Am. Chem. Soc.* **99**, 7960 (1977).
15. P. Jacob, W. Richter, and I. Ugi. *Liebigs Ann. Chem.* 519 (1991).
16. J. Protasiewicz and G.D. Mendenhall. *J. Org. Chem.* **50**, 3220 (1985).
17. I. Granoth, Y. Segall, H. Leader, and R. Alkabetz. *J. Org. Chem.*, **41**, 3682 (1976).
18. R.H. Farmer and C.G. More. *J. Chem. Soc.* 131 (1951).
19. K. Rakus, S.P. Verevkin, J. Shätzer, H.-D. Beckhaus, and C. Rüchardt. *Chem. Ber.* **127**, 1095 (1994).
20. (a) H. Kuntzel, H. Wolf, and K. Schaffner. *Helv. Chim. Acta*, **54**, 868 (1954); (b) G.V. Boyd and M.D. Harms. *J. Chem. Soc. C*, 807 (1970).



# Metallocene-catalyzed olefin polymerizations using triphenylcyclopropenium tetrakis(pentafluorophenyl)borate as the activator

Huiying Li and Douglas C. Neckers

**Abstract:** Triphenylcyclopropenium (TPCP) tetrakis(pentafluorophenyl)borate activates bis(cyclopentadienyl)dimethyl titanium resulting in a highly reactive initiating system for the polymerization of styrene. In contrast to triphenylmethyl tetrakis(pentafluorophenyl)borate which is quite active in the absence of the metallocene, TCPB shows no activity for styrene polymerization in the absence of bis(cyclopentadienyl)dimethyl titanium. TCPB is the most efficient activator in the carbonium ion – borate class. We propose, based on  $^1\text{H}$  NMR evidence that reaction of  $\text{Cp}_2\text{TiMe}_2$  and TCPB borate leads to the formation of the cationic Ti complex  $[\text{Cp}_2\text{TiMe}]^+\text{B}(\text{C}_6\text{F}_5)_4^-$ . Evidence for the latter is also provided by UV–vis spectroscopy in that we found a bathochromic shift of the  $\text{Cp}_2\text{TiMe}_2$  LMCT absorption band from 361 to 482 nm in  $\text{CH}_2\text{Cl}_2$  and 487 nm in toluene, respectively. Thermal decomposition of the cationic complex  $[\text{Cp}_2\text{TiMe}]^+\text{B}(\text{C}_6\text{F}_5)_4^-$  leads to less activity. The systems are good catalysts for ethylene polymerization as well, but are less active when using propylene. A conventional Ziegler–Natta coordination polymerization mechanism accounts for ethylene and propylene polymerization while a carbocationic polymerization mechanism is proposed for styrene.

**Key words:** triphenylcyclopropenium tetrakis(pentafluorophenyl)borate, bis(cyclopentadienyl)dimethyl titanium, activator, olefin polymerization.

**Résumé :** Le tétrakis(pentafluorophényl)borate de triphénylcyclopropénium (TPCP) active le bis(cyclopentadiényl)diméthyltitane qui conduit à un système très réactif pour initier la polymérisation du styrène. Par opposition au tétrakis(pentafluorophényl)borate de triphénylméthyle qui est très actif en l'absence de métallocène, le borate de TCPB ne présente aucune activité vis-à-vis de la polymérisation du styrène en l'absence du bis(cyclopentadiényl)diméthyltitane. Le TCPB est l'activateur le plus efficace de la classe borate – ion carbonium. On suggère, sur la base de données de RMN du  $^1\text{H}$ , que la réaction du  $\text{Cp}_2\text{TiMe}_2$  et du borate de TCPB conduit à la formation du complexe cationique du Ti,  $[\text{Cp}_2\text{TiMe}]^+\text{B}(\text{C}_6\text{F}_5)_4^-$ . Ce résultat est également appuyé par des mesures effectuées par spectrométrie UV–vis qui démontrent un déplacement bathochrome de la bande d'absorption du LMCT du  $\text{Cp}_2\text{TiMe}_2$  de 361 nm vers 482 nm pour le  $\text{CH}_2\text{Cl}_2$  et vers 487 nm pour le toluène, respectivement. Une décomposition thermique du complexe cationique  $[\text{Cp}_2\text{TiMe}]^+\text{B}(\text{C}_6\text{F}_5)_4^-$  conduit à une perte d'activité. Les systèmes sont aussi de bons catalyseurs pour la polymérisation de l'éthylène, mais ils sont moins réactifs pour le propylène. Un mécanisme de polymérisation conventionnel de Ziegler–Natta par coordination permet d'expliquer la polymérisation de l'éthylène et du propylène alors qu'on propose un mécanisme de polymérisation carbocationique pour le styrène.

**Mots clés :** tétrakis(pentafluorophényl)borate de triphénylcyclopropénium, bis(cyclopentadiényl)diméthyltitane, activateur, polymérisation d'oléfine.

[Traduit par la Rédaction]

## Introduction

Metallocene coordination polymerization catalyst systems for olefins are an important research and development topic

(1). Successful catalysts invariably consist of transition metal complexes called *catalyst precursors* and activators also called *co-catalysts*. The partners react forming an active species that is comprised of a cation–anion ion pair. The struc-

Received 9 January 2003. Published on the NRC Research Press Web site at <http://canjchem.nrc.ca> on 23 June 2003.

*It is a sincere pleasure to recognize the career-long contributions to the photochemical sciences of Professor Don Arnold on the occasion of his retirement. Through the application of the principles of physical organic chemistry to the study of the emerging field of reactions catalyzed by ultraviolet light, Professor Arnold and his students enhanced predictive power in organic photochemistry. His colleagues are most grateful for his insights.*

**H. Li and D.C. Neckers.**<sup>1,2,3</sup> Center for Photochemical Sciences, Bowling Green State University, Bowling Green, OH 43403, U.S.A.

<sup>1</sup>Corresponding author (e-mail: [neckers@photo.bgsu.edu](mailto:neckers@photo.bgsu.edu)).

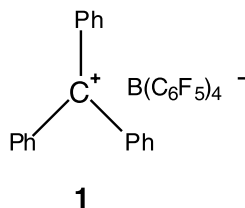
<sup>2</sup>Contribution number 500 from the Center for Photochemical Sciences.

<sup>3</sup>Dedicated to Professor Dr. J.W. Neckers, on the occasion of his 101st birthday.



ture of the activator significantly influences catalytic activity, the character of the polymerization, and polymer properties.

The number of viable co-catalysts for metallocene polymerizations is rather limited (2). Methylaluminoxane (MAO) is an important industrial co-catalyst, but must be used in huge excess to achieve high activity. Triphenylmethyl carbenium ion ("trityl") if paired with  $B(C_6F_5)_4^-$  (1) has been reported to be a highly efficient activator for group 4 dimethylmetallocenes (3) at low co-catalyst to catalyst ratios (1:1). A number of other borates have also been developed to improve properties such as solubility in organic solvents and thermal stability (4).



We have recently discovered that triarylcyclopropenium salts may be used as cationic initiators for both the thermal and photochemical polymerization of epoxides (5, 6). Triphenylcyclopropenium (TPCP) cation is a strong electrophile (7) and when TCPC salts paired with weakly nucleophilic anions tetrakis(pentafluorophenyl)gallate are dissolved in ketones with active  $\alpha$ -hydrogens such as cyclohexanone we found that super acids (presumably  $H-Ga(C_6F_5)_4$ ) form. Super acids also result from irradiation of  $TPCP^+Ga(C_6F_5)_4^-$  in various solvents (8).

In view of this new discovery we wished to explore further the advantages of cyclopropenium salts in various polymerization reactions. We report herein results of olefin polymerization catalyzed by bis(cyclopentadienyl)dimethyl titanium (3) using TCPC borate (2) as the activator (Fig. 1).

## Experimental section

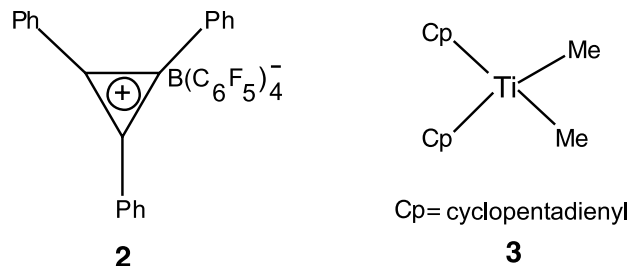
### Materials

All chemicals were used as received from Aldrich unless otherwise noted. Benzene and toluene were distilled over sodium under argon.  $CH_2Cl_2$  was freshly distilled over  $CaH_2$  under argon.  $\alpha,\alpha$ -Dichlorotoluene was purchased from Acros Organics and used as received. Bis(cyclopentadienyl)titanium dichloride was purchased from Strem Chemicals Inc. and used as received. Styrene was distilled over  $CaH_2$  at  $50^\circ C$  under vacuum and kept over molecular sieves ( $4 \text{ \AA}$ ) under argon in a refrigerator. Potassium tetrakis(pentafluorophenyl)borate was prepared as reported (9). Bis(cyclopentadienyl)dimethyltitanium (3) was prepared according to the literature (10) and kept in a freezer as a solution (~36%) in toluene.

### Measurements

$^1H$  and  $^{19}F$  NMR spectra were recorded either with a Varian Gemini 200 NMR or a Varian Unity plus 400 NMR spectrometer. Chemical shifts are in ppm with TMS as the internal standard ( $^1H$  NMR) or  $CFCl_3$  as the external standard ( $^{19}F$  NMR). Melting points were determined with a Thomas Hoover capillary melting point apparatus and were uncorrected. UV-vis spectra were recorded on a Shimadzu

**Fig. 1.** Structure of the activator and the catalyst.



UV-2401PC UV-vis recording spectrophotometer. Number- and weight-average molecular weights ( $M_n$  and  $M_w$ ) and polydispersity ratios ( $M_w/M_n$ ) were estimated by gel permeation chromatography (GPC) on a Shimadzu HPLC system equipped with a Plgel  $5 \mu m$  MIXED-C  $300 \times 7.5 \text{ mm}$  column (Polymer Laboratories), using THF as the eluent with a flow rate of  $1.0 \text{ mL min}^{-1}$  by polystyrene calibration, and a RID-10A refractive index (RI) detector.

### Synthesis of TCPC tetrakis(pentafluorophenyl)borate (2)

To a suspension of TCPC chloride (11) (1.51 g, 5 mmol) in acetonitrile (25 mL) was added a solution of potassium tetrakis(pentafluorophenyl)borate (4.00 g, 5 mmol) in acetonitrile (15 mL) and the reaction mixture stirred at room temperature for 2 h. The solid thus formed was removed by filtration and the filtrate concentrated to give a brown viscous substance that was further purified using a silica gel column with  $CH_2Cl_2$  as the eluent. After washing with pentane, the product was obtained as white crystals (62%), mp  $209$  to  $210^\circ C$ .  $^1H$  NMR ( $CDCl_3$ )  $\delta$ : 7.88 (dd,  $^3J_{H-H} = 7.6$ , 7.8 Hz, 6H, 3,5-H on phenyl), 8.06 (t,  $^3J_{H-H} = 7.8$  Hz, 3H, 4-H on phenyl), 8.42 (d,  $^3J_{H-H} = 7.6$  Hz, 6H, 2,6-H on phenyl).  $^{19}F$  NMR ( $CDCl_3$ )  $\delta$ :  $-133.12$  (s, 2, 6-F on  $C_6F_5$ ),  $-163.40$  (sm, 4-F on  $C_6F_5$ ),  $-167.20$  (s, 3,5-F on  $C_6F_5$ ). Anal. calcd. for  $C_{45}H_{15}F_{20}B$ : C 57.11, H 1.60; found: C 57.02, H 1.66.

### Polymerization of styrene

In a typical polymerization, 2 (0.03 mmol) was dissolved in solvent (2 mL) (TCPC tetrakis(pentafluorophenyl)borate dissolved in  $CH_2Cl_2$  and is partially soluble in toluene) and the solution degassed (freeze-thaw) for three cycles. 3 (0.03 mmol, 36% in toluene) was also dissolved in styrene (2 mL) and the solution degassed as above. The catalyst solution in styrene was then transferred into the solution of 2 under dry argon at room temperature and the mixture stirred for 30 min. Subsequently, the polymerization mixture was quenched with MeOH (containing 1% HCl). The resulting polymer was purified twice from  $CH_2Cl_2$ -MeOH or until a white powder of the polymer was obtained. The polymer was dried under vacuum overnight. The activity of the catalyst system was calculated by the following:

Activity = weight of polymer (g)/(Ti (mol) monomer (mol) time (h))

### Polymerization of styrene with preactivated initiating systems

In a typical polymerization run, 3 (36% in toluene) was mixed with  $CH_2Cl_2$  (2 mL), and the solution degassed using freeze-thaw techniques for three cycles. This initiating solu-



tion in  $\text{CH}_2\text{Cl}_2$  was then transferred into the polymerization tube (prevacuum evacuated) containing **2** under dry argon (the reactions are quite sensitive to spurious moisture) at room temperature and the mixture stirred (aged) for 10 min. The mixture turned from yellow to dark red. Styrene (predegassed) was next introduced into the system, and the polymerization mixture stirred at room temperature for 15–30 min. It was next quenched by MeOH (containing 1% HCl). The resulting polystyrene (PS) was purified twice from  $\text{CH}_2\text{Cl}_2$ –MeOH or until a white powder of the polymer was obtained, and the polymer then dried under vacuum overnight.

### Polymerization of ethylene

In a typical polymerization run, a solution of **3** (1.5–3.0 mmol, 36% in toluene) in  $\text{CH}_2\text{Cl}_2$  (2 mL) was degassed for three cycles and then transferred into a polymerization tube (25 mL, prevacuumed) containing **2** (1.5–3.0 mmol) under an ethylene atmosphere. The catalyst system was preactivated for 10 min at room temperature and then ethylene at 1 atm (1 atm = 101.325 kPa) was bubbled through the solution. Polyethylene (PE) precipitated from the solution immediately. After 5 min, the polymerization reaction was quenched with MeOH (containing 1% HCl, 5 mL). The polymer was collected by filtration. After washing with MeOH, the polymer was dried under vacuum overnight. The resulting polymer did not dissolve in THF or in 1,1,2,2-tetrachloroethane.

### Polymerization of propylene

Polymerization of propylene resulted if a similar procedure to that used for ethylene polymerization was employed. Propylene was bubbled through the catalyst solution at 1 atm (1 atm = 101.325 kPa) for 30 min at room temperature. After quenching with MeOH (1% HCl), the resulting polypropylene (PP) (viscous oil) was collected by carefully decanting the solvent and subsequently dried under vacuum overnight.

### $^1\text{H}$ NMR studies

To complete the reaction of  $\text{Cp}_2\text{TiMe}_2$  with TPCP salts, a mol ratio of 1.1:1.0 for TPCP:Ti was used in this experiment. In a typical experiment,  $\text{CD}_2\text{Cl}_2$  was vacuum distilled over  $\text{CaH}_2$ , trapped at 78 K, and then degassed by freeze-thaw techniques for three cycles. The catalyst (0.03 mmol, 36% solution in toluene) was dissolved in the above  $\text{CD}_2\text{Cl}_2$  and the solution transferred to a vacuum evacuated tube containing TPCPB (0.032 mmol) at  $-78^\circ\text{C}$ . The solution was subsequently warmed to room temperature and held there for 5 min. During this period, the catalyst system turned from yellow to dark red. The dark red solution was next transferred into an NMR tube that had been degassed by passing dry argon through it for 30 min. The NMR tube was cooled to  $-78^\circ\text{C}$  again and taken to the NMR. The sample temperature was equilibrated for 1 h at  $0^\circ\text{C}$  and the NMR data collected.

### UV-vis studies

Absorption spectra of the catalyst systems were recorded under dry argon in a quartz cuvette (1.0 cm path length). In a typical experiment, a solution of **3** ( $4.2 \times 10^{-4}$  M) in

$\text{CH}_2\text{Cl}_2$  (containing traces of toluene) was degassed for three cycles. **2** was placed in a quartz cuvette and the cuvette degassed with bubbling dry argon for 20 min. Catalyst solution was introduced using a two-tipped needle and the vessel sealed under dry argon. UV-vis spectra of the resulting solutions were recorded at room temperature at various times.

## Results and discussion

### Synthesis of TPCP borate

Anion exchange of TPCP chloride with  $\text{KB}(\text{C}_6\text{F}_5)_4^-$  afforded triphenylcyclopropenium tetrakis(pentafluorophenyl)borate **2** as a white solid, mp 209 to  $210^\circ\text{C}$ . **2** is stable under air at room temperature and soluble in  $\text{CH}_2\text{Cl}_2$  but only slightly soluble in toluene.

### Polymerization of styrene

Styrene polymerizations were carried out in toluene or  $\text{CH}_2\text{Cl}_2$  at  $23^\circ\text{C}$  under dry argon (Table 1). Control experiments show neither **2** nor **3** had significant activity when used alone in  $\text{CH}_2\text{Cl}_2$  or toluene. Following the prescribed period of preactivation, **2** was among the most active activators for styrene polymerization (entry 6) of the type carbonium ion – borate (12). The solvent had little effect on initiation activity (entries 1 and 2), but polystyrene obtained from toluene solution was of lower weight average molecular weight ( $M_w$ ), presumably because of the limited solubility of **2** and the active species. The activity of a preactivated initiating system was much higher than that without preactivation. If the preactivation time was increased to 20 min (entry 4), the activity of the initiating system was reduced by about 50%. We presume this is due to the thermal decomposition of the catalytic cationic complex at room temperature.

The efficiency of **2** in the polymerization of styrene is compared to that of the trityl salt **1** in toluene. Titanocene **3** shows a high activity of  $6.04 \times 10^6$  g (PS)/mol (Ti)  $\times$  mol (styrene)  $\times$  h in the presence of **1** (entry 11), however, from control experiments, **1** itself is a rather active initiator for the polymerization of styrene with the activity of  $5.60 \times 10^6$  g (PS)/mol (Ti)  $\times$  mol (styrene)  $\times$  h (entry 12). This is not the case with **2**.

All polystyrene samples obtained in our reactions are soluble in 2-butanone indicating only atactic polystyrene (a-PS) is formed. This was confirmed by  $^{13}\text{C}$  NMR spectroscopy (13).

### Polymerization of ethylene and propylene

Polymerization was carried out at room temperature by bubbling of ethylene (1 atm, (1 atm = 101.325 kPa)) through a preactivated solution of **4** (1.5–3.0 mmol) formed by reaction of an equimolar concentration of **2** and **3** in  $\text{CH}_2\text{Cl}_2$  (2 mL) (Table 1). PE immediately precipitated from the solution. After 5 min, quenching the reaction mixture with acidic methanol yielded lightly yellow polymers with  $T_m$  127 ~  $130^\circ\text{C}$ . The PE obtained was not soluble in organic solvents such as  $\text{CH}_2\text{Cl}_2$ , THF, and 1,1,2,2-tetrachloroethane.

Bubbling of propylene into the catalyst system for 30 min, followed by quenching of the polymerization mixture with acidic methanol, gave polypropylene as a viscous oil of relatively low molecular weight ( $4.0$ – $7.2 \times 10^3$  g mol $^{-1}$ ). Though the quantity of catalyst used had little effect on the yield of



**Table 1.** Polymerization of styrene, ethylene, and propylene by  $\text{Cp}_2\text{TiMe}_2\text{-TPCP}^+\text{B}(\text{C}_6\text{F}_5)_4^-$  in  $\text{CH}_2\text{Cl}_2$ .<sup>a</sup>

Run	Catalyst (mmol)	Polymerization time (min)	Monomer	Yield (g)	Activity ( $\times 10^6$ ) <sup>b</sup>	$M_w$ (kg mol <sup>-1</sup> )	$M_w/M_n$
1 <sup>c</sup>	3.0	30	Styrene	1.23	4.68	20.6	2.13
2	3.0	30	Styrene	1.06	4.05	65.3	1.93
3 <sup>d</sup>	3.0	30	Styrene	1.80	7.15	50.8	2.31
4 <sup>e</sup>	3.0	30	Styrene	0.92	3.50	50.5	2.14
5 <sup>d</sup>	3.0	15	Styrene	1.78	13.5	40.2	2.38
6 <sup>d</sup>	1.5	15	Styrene	1.43	21.8	54.8	2.27
7 <sup>d</sup>	3.0	5	Ethylene	0.17	0.068	— <sup>f</sup>	—
8 <sup>d</sup>	1.5	5	Ethylene	0.17	0.14	—	—
9 <sup>d</sup>	3.0	30	Propylene	0.037	0.0035	3.97	1.46
10 <sup>d</sup>	5.0	30	Propylene	0.038	0.0015	7.18, 5.56	2.68, 2.14
11 <sup>c</sup>	3.0 <sup>g</sup>	30	Styrene	1.59	6.04	6.3	2.48
12 <sup>c</sup>	— <sup>h</sup>	30	Styrene	1.46	5.60	8.3	4.14

<sup>a</sup>Polymerization conditions: Styrene polymerization: temperature = 23°C, styrene = 2 mL, solvent = 2 mL, [Styrene] = 4.4 M. Ethylene and propylene polymerization: temperature = 23°C, solvent = 2 mL, monomer pressure = 1 atm (1 atm = 101.325 kPa).

<sup>b</sup>Unit: g (PS)/(mol Ti  $\times$  mol styrene  $\times$  h); g (PE or PP)/(mol Ti  $\times$  atm  $\times$  h) (1 atm = 101.325 kPa).

<sup>c</sup>Toluene was used as the solvent.

<sup>d</sup>Preactivation time: 10 min.

<sup>e</sup>Preactivation time: 20 min.

<sup>f</sup>The polymers were not soluble in  $\text{CH}_2\text{Cl}_2$ , THF, and  $\text{CHCl}_2\text{CHCl}_2$  for  $M_w$  measurement.

<sup>g</sup>Trityl tetrakis(pentafluorophenyl)borate was used as the activator.

<sup>h</sup>Only trityl tetrakis(pentafluorophenyl)borate was used.

PE and PP, the use of a large amount of catalyst (5.0 mmol) for propylene resulted in polymers that exhibited a bimodal molecular weight distribution pattern.

### Formation of the cationic complex

The dimethyl Ti(IV) complex reacts with a stoichiometric amount of TPCPB at room temperature to yield the cationic titanium – monomethyl complex  $[\text{Cp}_2\text{TiMe}]^+[\text{B}(\text{C}_6\text{F}_5)_4]^-$  (**4**) as a dark red solution. If the reaction is carried out at 0 or –23°C, it takes longer (>30 min) to form the red solution. On the basis of its NMR spectrum taken at 0°C, the cationic complex **4** exhibits resonances at  $\delta$  6.38 (s, 10H), 1.30 (s, 3H) attributed to the Cp and Ti-Me hydrogens, respectively. The spectrum of **4** differs from that of the parent  $\text{Cp}_2\text{TiMe}_2$  ( $^1\text{H}$  NMR in  $\text{CD}_2\text{Cl}_2$  at 25°C  $\delta$ : 6.07 (s, 10H), –0.15 (s, 6H)) and the integrated ratio of Cp to methyl evolved to 10:3 in the activated complex as compared to a value for the parent compound of 10:6. Bochmann et al. (14) reported a similar complex was generated by reaction of the parent complex with dimethylanilinium tetraphenylborate and that it exhibits resonances at  $\delta$  6.28 (s, 10H), 1.26 (s, 3H). We presume that the resonance differences from the two cationic complexes are due to differences in ion pairing. There were also small resonances in the ranges of 0.20–2.00 and 6.40–6.70 which could not be assigned.

If the catalyst solution is warmed to 25°C and equilibrated for 30 min, the resonances at  $\delta$  6.38 and 1.30 decrease slightly, and the resonances at  $\delta$  0.22 and 6.56, 6.64, 6.72 grow presumably because of decomposition of the cationic complex. One of the deactivation processes of the metallocenium cation that may occur results from  $\text{Cl}^-$  abstraction from the solvent if the reaction is carried out in  $\text{CH}_2\text{Cl}_2$  (15). During our NMR studies no by-products such as  $\text{CH}_3\text{-CD}_2\text{Cl}$  were observed.

### UV–vis spectroscopy

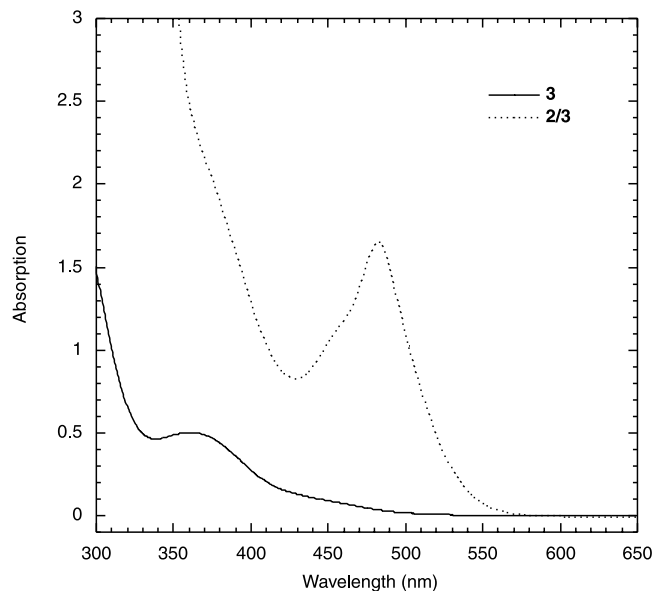
There are a number of reports of spectroscopic studies of the reactions of zirconocene precursors with MAO (16) and  $\text{PhMe}_2\text{NH}^+\text{B}(\text{C}_6\text{F}_5)_4^-$  (17) but few such reports with activated titanocene catalysts (18). In the zirconocene studies, the activated complex formed is easily distinguished by changes in the positions of the ligand-to-metal charge transfer (LMCT) bands in the optical spectra. Though UV–vis spectroscopy is not suitable for catalyst systems containing trityl cation owing to the overlap of absorption of the cation with the LMCT bands of the complexes formed in the activation process (Fig. 2), TPCP cation has no absorption beyond 320 nm. Thus, one may examine the LMCT bands formed from catalyst systems containing TPCP cation using UV–vis spectroscopy.

In the absence of **2**, **3** shows a LMCT band at 361 nm in both  $\text{CH}_2\text{Cl}_2$  and toluene. The LMCT absorption band of **3** is shifted to 482 nm in  $\text{CH}_2\text{Cl}_2$  in the presence of **2** and to 487 nm in toluene, respectively, corresponding to a decrease of electron density on the metal center (16a). This is consistent with the formation of cationic Ti(IV) complex observed by NMR spectroscopy. During styrene polymerization, we found that with preactivation, a deep approximately dark red solution of initiator was required in order for the system to exhibit the highest activity. Yellow solutions showed little or no activity as polymerization initiators. Therefore, the corresponding species, which absorbs at 482 nm, must be the actual active species.

In the case of the **2**, **3** couple, formation of the active species **4** was followed by observing the absorption changes in dichloromethane at 482 nm (Fig. 3). In the absence of monomer at fixed concentrations of reagents, the maximum concentration of **4** was observed after 17 min (Fig. 3a). The absorption then decayed presumably because of the thermal



**Fig. 2.** UV-vis spectra of catalyst  $\text{Cp}_2\text{TiMe}_2$  (**3**) and a mixture of **2** and **3** in  $\text{CH}_2\text{Cl}_2$ . Concentration of catalyst and activator:  $[\mathbf{3}] = 4.2 \times 10^{-4} \text{ M}$ ,  $[\mathbf{2}] = 4.8 \times 10^{-4} \text{ M}$ ; spectrum of the mixture of **2** and **3** was taken after being mixed for 17 min.



decomposition of the active cationic complex. Consistent with results obtained in the polymerization of styrene in that if the initiation system was preactivated for times greater than 17 min (e.g., 20 min, entry 4, Table 1), one observes decreased activity. Consistent with the lower activity observed for the polymerization of styrene when the initiator is prepared in its presence, the growing in of the absorption at 482 nm was much slower in the presence of styrene than in its absence (Fig. 3b). This can be explained if styrene consumes the active species during its formation. A rapid decay of **4** also results from the addition of styrene to the initiation system (Fig. 3c). We presume this to be from the reaction of styrene at the Ti center resulting in a decreased concentration of the cationic complex **4** (Scheme 1).

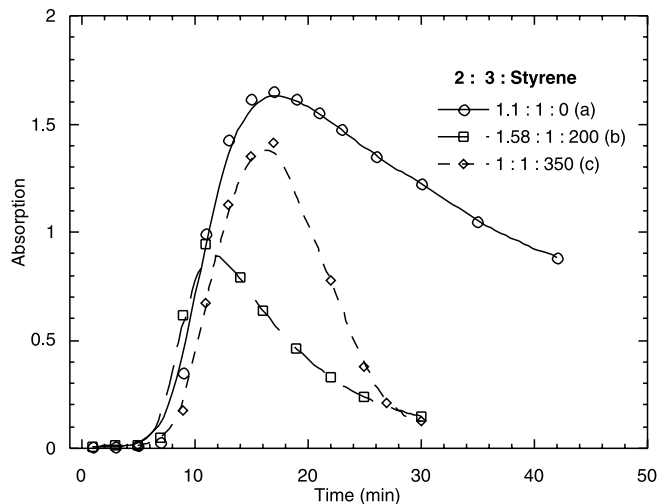
The formation and decay of cationic complex **4** was studied by following the absorption changes at 482 nm. The formation and decay lifetimes of the active species were obtained by fitting the experimental data to a double exponential decay function using ORIGIN 6.1 software. The species grew in rapidly with  $\tau_1$  of 7.96 min and then decayed slowly with  $\tau_2$  of 28.9 min.

### Mechanism of olefin polymerization

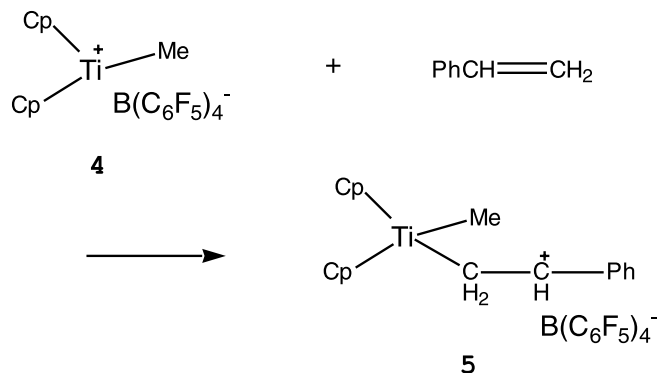
The mechanism we propose for olefin polymerization is that dimethyl Ti(IV) complex reacts with a stoichiometric amount of TPCPB at room temperature to yield the cationic titanium – monomethyl complex  $[\text{Cp}_2\text{TiMe}]^+[\text{B}(\text{C}_6\text{F}_5)_4]^-$  (**4**). The system is active for nonfunctionalized olefins like ethylene, propylene, and styrene with polymerization of ethylene and styrene being much faster in  $\text{CH}_2\text{Cl}_2$  at room temperature than the polymerization of propylene. That ethylene polymerization is faster than that of propylene is consistent with a coordination polymerization mechanism (Scheme 2).

It has recently been found that some well-characterized Ziegler–Natta catalysts can also initiate carbocationic poly-

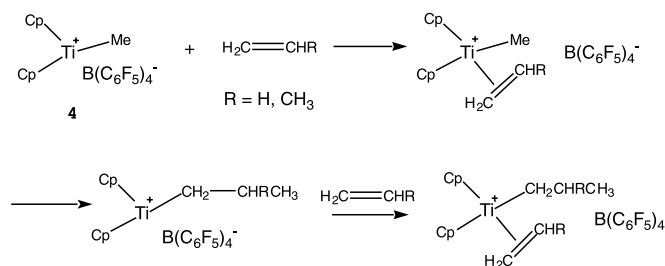
**Fig. 3.** Variation of the absorption of **2** and **3** at 482 nm with time in  $\text{CH}_2\text{Cl}_2$ .  $[\mathbf{3}] = 4.2 \times 10^{-4} \text{ M}$ , ratio of **2**:**3**:styrene in mol (a) in the absence of styrene; (b) in the presence of styrene; and (c) styrene added at 17 min.



**Scheme 1.** Electrophilic attack of **4** on styrene.

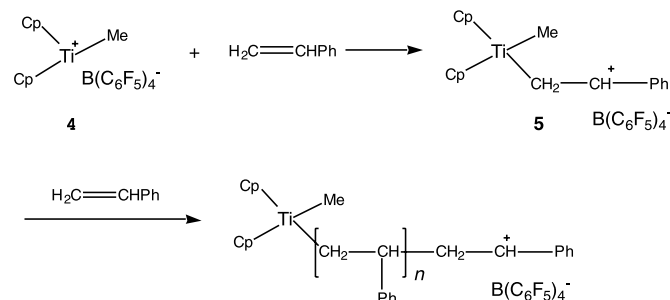


**Scheme 2.** Coordination polymerization pathway.



merization of olefins (19) and that styrene may undergo polymerization via both coordination and carbocationic mechanisms. Using  $\text{Cp}^*\text{TiMe}_3\text{--B}(\text{C}_6\text{F}_5)_3$  as the catalyst and if the polymerization is carried out at a low temperature, only atactic polystyrene was produced. If the polymerization temperature rises to above  $-10^\circ\text{C}$ , highly syndiotactic polystyrene is obtained (20). At high temperature Ti(III) complex formed by reductive decomposition was confirmed to be the active catalyst for production of syndiotactic polystyrene (21). At lower temperatures, cationic Ti(IV) complex



**Scheme 3.** Cationic polymerization of styrene.

initiates a carbocationic process for the production of atactic polystyrene.

Our spectroscopic studies indicate that cation  $[\text{Cp}_2\text{TiMe}]^+$  is more stable than  $[\text{Cp}^*\text{TiMe}_2]^+$  but that it decomposes, though moderately, at room temperature on the polymerization time scale. The decay lifetime of the cationic complex is 28.9 min indicating that most of the cationic complex survived during the polymerization process. Each of the PS samples prepared using our initiating system is soluble in 2-butanone, suggesting no syndiotactic PS (s-PS) forms. Therefore, we assume that the cationic Ti(IV) complex is the actual active species in the system reacting as a carbocationic initiator with styrene and producing atactic polystyrene (Scheme 3). The relatively narrow polydispersities of the resulting PS samples (1.92–2.56) is further evidence for a carbocationic polymerization process.

In summary, TPCP borate efficiently reacts with bis(cyclopentadienyl) dimethyltitanium to form cationic Ti complex  $[\text{Cp}_2\text{TiMe}]^+\text{B}(\text{C}_6\text{F}_5)_4^-$  (4). The formation of cationic Ti complex 4 was confirmed by NMR spectroscopy. The reaction was also studied using UV–vis spectroscopy and observed the bathochromic shift of the  $\text{Cp}_2\text{TiMe}_2$  LMCT main absorption band from 361 to 482 nm in  $\text{CH}_2\text{Cl}_2$ . The kinetic profile showed the cationic species grew in rapidly and then decayed slowly. Though the cationic complex  $[\text{Cp}_2\text{TiMe}]^+\text{B}(\text{C}_6\text{F}_5)_4^-$  was observed to be thermally unstable and its activity in the polymerization of styrene decreased with time, the system shows generally high polymerization activity for both ethylene and styrene. It is less active for the polymerization of propylene. The cationic Ti(IV) complex is proposed to be a conventional Ziegler–Natta coordinative catalyst for ethylene and propylene polymerization, while it acts as a carbocationic initiator for styrene polymerization.

## Acknowledgments

We would like to thank the United Soybean Board for financial support. We also thank Dr. Kangtai Ren and Ms. Priya Hewavitharanage for helpful discussions.

## References

- For recent reviews see: (a) J.A. Gladysz. *Chem. Rev.* **100**, 4 (2000); (b) Y. Imanishi and N. Naga. *Prog. Polym. Sci.* **26**, 1147 (2001); (c) G.J.P. Britovsek, V.C. Gibson, and D.F. Wass. *Angew. Chem. Int. Ed.* **38**, 428 (1999); (d) G.W. Coates, P.D.

- Hustad, and S. Reinartz. *Angew. Chem. Int. Ed.* **41**, 2236 (2002).
- E.Y.-X. Chen and T.J. Marks. *Chem. Rev.* **100**, 1391 (2000), and refs. cited therein.
- J.C.W. Chien, W.-M. Tsai, and M.D. Rausch. *J. Am. Chem. Soc.* **113**, 8570 (1991).
- (a) V.C. Williams, G.J. Irvine, W.E. Piers, Z. Li, S. Collins, W. Clegg, M.R.J. Elsegood, and T.B. Marder. *Organometallics*, **19**, 1619 (2000); (b) F.A.R. Kaul, G.T. Puchta, H. Schneider, M. Grosche, D. Mihalios, and W.A. Herrmann. *J. Organomet. Chem.* **621**, 177 (2001); (c) S.J. Lancaster, A. Rodriguez, A. Lara-Sanchez, M.D. Hannant, D.A. Walker, D.H. Hughes, and M. Bochman. *Organometallics*, **21**, 451 (2002).
- (a) H. Li, K. Ren, W. Zhang, J.H. Malpert, and D.C. Neckers. *Macromolecules*, **34**, 2019 (2001); (b) H. Li, K. Ren, and D.C. Neckers. *Macromolecules*, **34**, 8637 (2001).
- D.C. Neckers and W. Zhang. U.S. Patent 6 420 460, July 16, 2002.
- (a) R. Breslow. *J. Am. Chem. Soc.* **79**, 5318 (1957); (b) R. Breslow and C. Yuan. *J. Am. Chem. Soc.* **80**, 5991 (1958).
- H. Li, K. Ren, and D.C. Neckers. *J. Org. Chem.* **66**, 8556 (2001).
- F. Castellanos, J.P. Fouassier, C. Priou, and J. Cavezzan. *J. Appl. Polym. Sci.* **60**, 705 (1996).
- L.M. Dollinger, A.J. Ndakala, M. Hashemzadeh, G. Wang, Y. Wang, I. Martinez, J.T. Arcari, D.J. Galluzzo, and A.R. Howell. *J. Org. Chem.* **64**, 7074 (1999).
- In this procedure  $\text{HCl(g)}$  was used instead of  $\text{HBr(g)}$ . R. Xu and R. Breslow. *Synth.* **74**, 72 (1997).
- G. Xu. *Macromolecules*, **31**, 586 (1998).
- H.N. Cheng. *Int. J. Polym. Anal. Charact.* **2**, 439 (1996).
- M. Bochmann, A.J. Jahhar, and J. Nicholls. *Angew. Chem. Int. Ed. Engl.* **29**, 780 (1990).
- (a) R. Gomez, M.L. Green, and J.L. Haggitt. *J. Chem. Soc. Dalton Trans.* 939 (1996); (b) T. Guenca, M. Galakhov, G. Jiménez, E. Royo, P. Royo, and M. Bochmann. *J. Organomet. Chem.* **543**, 209 (1997).
- (a) P.J.J. Pieters, J.A.M. van Beek, and M.F.H. van Tol. *Macromol. Rapid Commun.* **16**, 463 (1995); (b) D. Coevoet, H. Cramail, and A. Deffieux. *Macromol. Chem. Phys.* **199**, 1451 (1998); (c) D. Coevoet, H. Cramail, and A. Deffieux. *Macromol. Chem. Phys.* **199**, 1459 (1998); (d) J.-N. Pédeutour, D. Coevoet, H. Cramail, and A. Deffieux. *Macromol. Chem. Phys.* **200**, 1215 (1999); (e) J.-N. Pédeutour, H. Cramail, and A. Deffieux. *J. Mol. Catal. A: Chem.* **174**, 81 (2001); (f) J.-N. Pédeutour, H. Cramail, and A. Deffieux. *J. Mol. Catal. A: Chem.* **176**, 87 (2001).
- U. Wieser and H.H. Brintzinger. *Organometallic catalysts and olefin polymerization*. Springer-Verlag, Berlin, Germany. 2001. pp. 3–13.
- (a) J. Kim, K.H. Kim, J.E. Cho, S. Kwak, K.U. Kim, W.H. Jo, H.S. Yoon, and D.S. Lim. *J. Polym. Sci. Part A: Polym. Chem.* **36**, 1733 (1998); (b) A. Anderson, H.G. Cordes, J. Herwig, W. Kamisky, A. Merk, R. Mottweiler, J.H. Sinn, and H.-J. Vollmer. *Angew. Chem. Int. Ed. Engl.* **15**, 630 (1976).
- M.C. Baird. *Chem. Rev.* **100**, 1471 (2000), and refs. cited therein.
- (a) Q. Wang, R. Quyoum, D.J. Gillis, M.-J. Tudoret, D. Jeremic, B.K. Hunter, and M.C. Baird. *Organometallics*, **15**, 693 (1996); (b) C. Pellecchia, D. Pappalardo, L. Oliva, and A. Zambelli. *J. Am. Chem. Soc.* **117**, 6593 (1995).
- C. Pellecchia and A. Grassi. *Top. Catal.* **7**, 125 (1999).



# Oxidation of cyclohexane using a novel RuO<sub>2</sub>-zeolite nanocomposite catalyst

Bi-Zeng Zhan, Mary Anne White, James A. Pincock, Katherine N. Robertson, T. Stanley Cameron, and Tsun-Kong Sham

**Abstract:** We report the synthesis, using an organic-template-free hydrothermal crystallization method, and catalysis of a new type of nanocomposite material, 1.3 nm-sized RuO<sub>2</sub> particles confined in faujasite zeolite. The zeolite-confined RuO<sub>2</sub> composites were fully characterized with X-ray powder diffraction, Ru K-edge X-ray absorption, and high-resolution transmission electron microscopy. XRD and X-ray fluorescence analysis indicate that the framework is faujasite zeolite with a Si:Al ratio of 1.25. Ru K-edge X-ray absorption near-edge structures indicate that the ruthenium species in the zeolite is Ru(IV) with nearest-neighbor octahedral environments similar to hydrous RuO<sub>2</sub>, i.e., distorted "RuO<sub>6</sub>". The *k*<sup>2</sup>-weighted extended X-ray absorption fine structure indicates that the Ru(IV) species anchored in the zeolite likely form amorphous RuO<sub>2</sub> with a 2D-chain structure, in which RuO<sub>6</sub> units are connected together by two shared oxygen atoms. TEM shows that the particle size of RuO<sub>2</sub> encapsulated inside the supercages of FAU is about 1.3 nm. The RuO<sub>2</sub>-FAU composites display significant catalytic activity in the oxidation of cyclohexane with *t*BHP under mild (room temperature and 1 atm (1 atm  $\equiv$  101.325 kPa)) conditions. The ketone and alcohol concentration can be as high as 0.26 mol L<sup>-1</sup> in 5 h with 48% peroxide efficiency. The catalyst is stable and reusable. Possible oxidation mechanisms are also discussed.

**Key words:** nanocomposite, ruthenium oxide, catalysis, oxidation, zeolite.

**Résumé :** Faisant appel à une méthode de cristallisation hydrothermique sans gabarit organique on a effectué la synthèse d'un nouveau matériau nanocomposite, des particules de RuO<sub>2</sub> d'une taille de 1,3 nm confinées dans un zéolite de faujasite, et on a examiné ses propriétés comme catalyseur. Les composites de RuO<sub>2</sub> confinées dans le zéolite ont été caractérisés par diffraction des rayons X sur des poudres, absorption de rayons X par l'arête K du Ru et par microscopie électronique de transmission à haute résolution. L'analyse de la diffraction et de la fluorescence des rayons X indiquent que le squelette est le zéolite de faujasite avec un rapport de Si:Al de 1,25. Les structures près des rebords obtenues par absorption de rayons X par l'arête K du Ru indiquent que l'espèce ruthénium du zéolite est le Ru(IV) avec un environnement octaédrique pour les voisins immédiats, comme dans le cas du RuO<sub>2</sub> hydratée c'est-à-dire du « RuO<sub>6</sub> » déformé. La structure fine d'absorption étalée des rayons X indique que l'espèce Ru(IV) ancrée dans le zéolite forme vraisemblablement du RuO<sub>2</sub> amorphe avec une structure en chaîne bidimensionnelle dans laquelle les unités de RuO<sub>6</sub> sont reliées entre elles par deux atomes d'oxygène partagés. La méthode « TEM » montre que la taille des particules de RuO<sub>2</sub> encapsulées dans les supercages de FAU est d'environ 1,3 nm. Les composites RuO<sub>2</sub>-FAU présentent une activité catalytique significative dans l'oxydation du cyclohexane par le *t*BHP dans des conditions douces (température ambiante et 1 atm (1 atm  $\equiv$  101.325 kPa)). Les concentrations de cétone et d'alcool peuvent atteindre une valeur de 0,26 mol L<sup>-1</sup> en 5 h, avec une efficacité de peroxyde de 48%. Le catalyseur est stable et peut être réutilisé. On discute aussi des mécanismes d'oxydation possibles.

**Mots clés :** nanocomposite, oxyde de ruthénium, catalyse, oxydation, zéolite.

[Traduit par la Rédaction]

## Introduction

Oxidation of cyclohexane under mild conditions is one of the most interesting and challenging topics in oxidation chemistry (1–4). Considerable effort has been made to develop novel homogeneous and heterogeneous catalysts and

catalytic processes for the oxidation of cyclohexane to cyclohexanol and cyclohexanone (1–9). To achieve satisfactory selectivity (>80%), yield usually must be sacrificed (~4% conversion) because of free-radical autooxidation processes (5). Incorporation of transition metal compounds into molecular sieves offers one of the most promising ap-

Received 19 December 2002. Published on the NRC Research Press Web site at <http://canjchem.nrc.ca> on 24 June 2003.

*Dedicated to Professor Don Arnold for his contributions to chemistry.*

**B.-Z. Zhan, M.A. White,<sup>1</sup> J.A. Pincock, K.N. Robertson, and T.S. Cameron.** Department of Chemistry and Institute for Research in Materials, Dalhousie University, Halifax, NS B3H 4J3, Canada.

**T.-K. Sham.** Department of Chemistry, The University of Western Ontario, London, ON N6A 5B7, Canada.

<sup>1</sup>Corresponding author (e-mail: [Mary.Anne.White@dal.ca](mailto:Mary.Anne.White@dal.ca)).



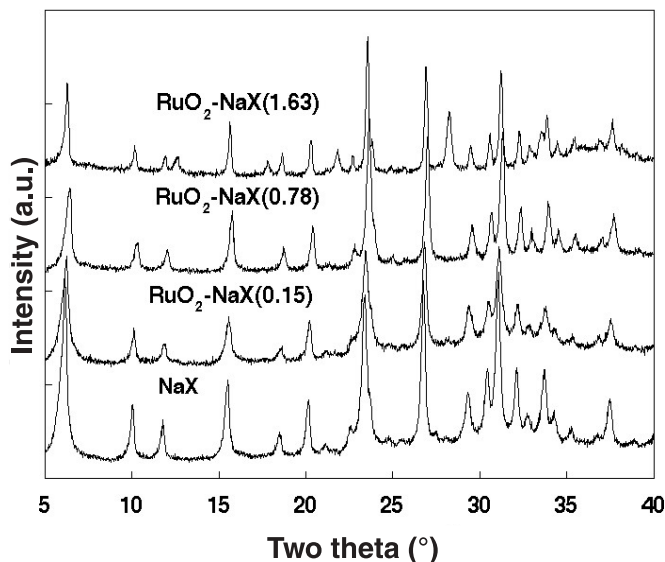
proaches to enhance the selectivity because the free radicals generated by autooxidation are constrained by the well-defined porous system. Various metals and metallo-complexes have been incorporated into zeolites, silicates, SAPO, ALPO, and mesoporous materials and used as catalysts for alkanes and alkenes oxidation (5–10). Among them, zeolite-confined metallophthalocyanines have displayed the attractive activity of cyclohexane oxidation with *t*BHP at room temperature (8, 9). However, there are several drawbacks in these systems, such as the complicated synthetic procedures and the use of expensive metallo-complexes. Development of an efficient and recyclable catalyst for alkane oxidation under mild conditions is still a significant challenge.

Ruthenium compounds have considerable potential for oxidation of alkanes and alkenes because of their rich redox properties (11 oxidation states, ranging from Ru<sup>II</sup> to Ru<sup>VIII</sup>) (11–13). Recently, RuO<sub>2</sub>, especially RuO<sub>2</sub>(110), has been receiving considerable attention for its extraordinarily high catalytic activity (14–18). The outstanding catalytic ability of the RuO<sub>2</sub>(110) surface is attributed to the existence of coordinatively unsaturated ruthenium atoms (14–16). Interestingly, a structure similar to RuO<sub>2</sub>(110) was found in amorphous hydrous RuO<sub>2</sub> (19). Nanomaterials can be novel catalysts because of the large surface area and the high density of active sites (20–21). Thus, it is expected that zeolite-confined hydrous nano-RuO<sub>2</sub> could exhibit favourable oxidation chemistry. Recently, we have reported the synthesis of faujasite zeolites (FAU) with controllable particle size and surface properties by using an organic-additive-free hydrothermal crystallization approach (22, 23). This organic-additive-free synthetic method makes it possible to synthesize zeolite-based host–guest materials in a simple one-step modification or build-the-bottle-around-the-ship approach (10), namely directly adding guest molecules into the fresh-prepared aluminosilicate gel before hydrothermal crystallization. Furthermore, FAU zeolites have a unique and well-defined pore system: ~1.3 nm supercages are tetrahedrally connected by 12-membered-ring channels with ~0.74 nm openings (24). Therefore, physically trapped nanoparticles or molecules with sizes between about 0.74 and 1.3 nm cannot diffuse out of the supercages unless the strict framework of the zeolite is destroyed (8–10). In this paper, we report the synthesis and catalysis of novel nanocomposite materials, viz. faujasite zeolites with confined RuO<sub>2</sub> nanoclusters (abbreviated as RuO<sub>2</sub>–FAU) with a one-step modification of the hydrothermal synthetic method for FAU. The catalytic results indicate that these materials are very efficient and stable catalysts for cyclohexane oxidation at room temperature.

## Results and discussion

All the synthesized zeolite-confined hydrous RuO<sub>2</sub> samples were characterized by X-ray powder diffraction as shown in Fig. 1. The XRD patterns of as-synthesized RuO<sub>2</sub>–FAU samples match very well with simulated XRD results for faujasite zeolites (25). For our sample with the highest RuO<sub>2</sub> loading, RuO<sub>2</sub>–FAU(1.63) (where the number in brackets refers to RuO<sub>2</sub> concentration in mmol g<sup>−1</sup>; see the *Experimental* section for details), a few weak peaks appear

**Fig. 1.** XRD patterns for synthetic RuO<sub>2</sub>–FAU composites and pure FAU. The numbers in parentheses are RuO<sub>2</sub> concentrations in the FAU zeolites in mmol g<sup>−1</sup>.



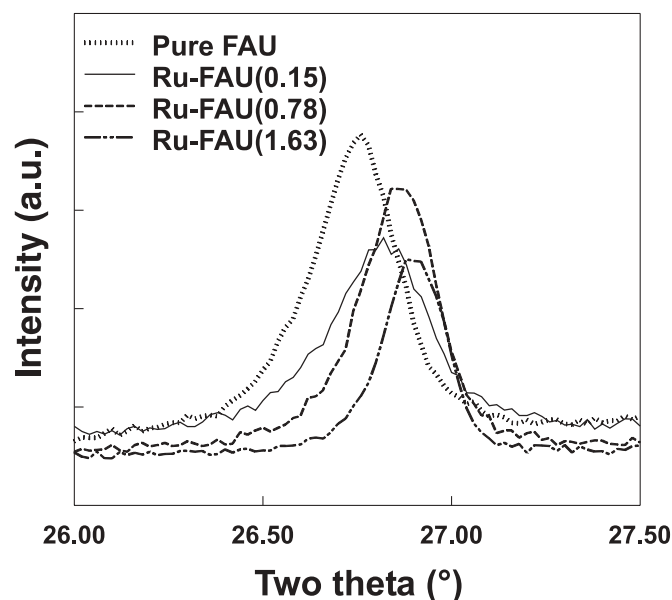
at  $2\theta$  values of 12.6°, 18.6°, 21.8°, 28.2°, and 33.5°, indicating the presence of small amounts of NaP-1 zeolite impurity (25). In comparison with the XRD pattern of pure FAU zeolite, the  $2\theta$  values of the diffraction peaks of RuO<sub>2</sub>–FAU composites are slightly higher, and they increase with increased RuO<sub>2</sub> loading. Figure 2 gives an example of the shift of the *hkl*(642) diffraction peak as a function of RuO<sub>2</sub> loading. This shift demonstrates encapsulation of RuO<sub>2</sub> inside the cages of FAU zeolite using our hydrothermal crystallization method. No new diffraction peaks belonging to RuO<sub>2</sub> compounds were found, indicating that the RuO<sub>2</sub> in the zeolite is amorphous.

The Ru K-edge X-ray absorption near-edge structures of all the RuO<sub>2</sub>–FAU composites resemble those of hydrous RuO<sub>2</sub> (26). This indicates that the ruthenium species in the zeolite is Ru(IV) with nearest-neighbor octahedral environments similar to hydrous RuO<sub>2</sub>, i.e., distorted “RuO<sub>6</sub>” (19). It also shows that all the Ru(III) species are oxidized to Ru(IV) under the hydrothermal synthetic conditions. Furthermore, the *k*<sup>2</sup>-weighted extended X-ray absorption fine structure of RuO<sub>2</sub>–FAU composites is virtually the same as that of amorphous RuO<sub>2</sub>·2.32H<sub>2</sub>O (26) indicating that the Ru(IV) species anchored in the FAU zeolite likely form amorphous RuO<sub>2</sub> with a 2D-chain structure, in which RuO<sub>6</sub> units are connected together by two shared oxygen atoms (19). This is consistent with the XRD results. A schematic structure of a RuO<sub>2</sub> nanocluster in FAU zeolite is given in Scheme 1.

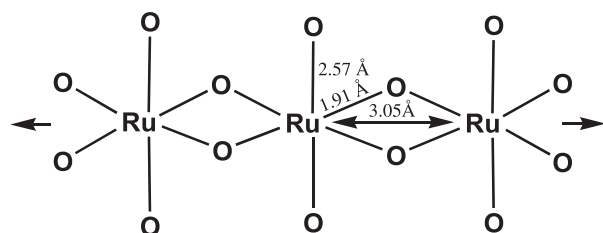
Figure 3 shows a typical high-resolution transmission electron microscopy (TEM) image taken at the RuO<sub>2</sub>–FAU(0.78) sample. The dark spots, homogeneously distributed through the sample and not seen in the pure FAU, are reasonably attributed to the RuO<sub>2</sub> particles. Figure 3 clearly indicates that these particles are very uniform, in the size range 1.3 ± 0.2 nm. This is the same size as the supercages of FAU zeolite. Likely the RuO<sub>2</sub> nanoclusters are incorporated into the supercages of FAU zeolite during the hydro-



**Fig. 2.** XRD pattern showing the shift of the  $hkl(642)$  diffraction peak of FAU zeolites as a function of  $\text{RuO}_2$  loading.



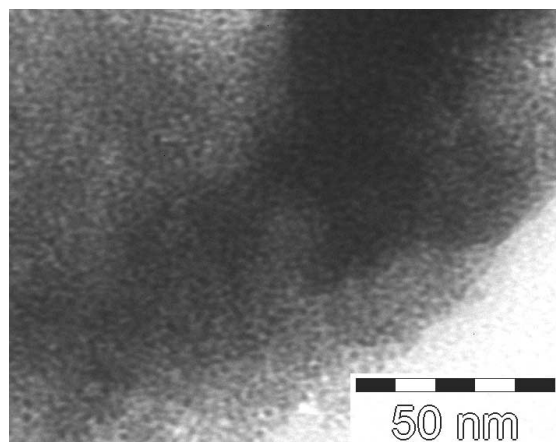
**Scheme 1.** The 2D-chain structure of  $\text{RuO}_2$  in zeolite.



thermal crystallization process and the growth of  $\text{RuO}_2$  clusters is strictly constrained by the rigid zeolitic framework. The encapsulation of nano- $\text{RuO}_2$  inside the zeolite is further confirmed by catalytic results (vide infra). It is estimated that, on average, every 1.3 nm  $\text{RuO}_2$  cluster contains five Ru atoms, as deduced from the bond lengths.

All the synthetic  $\text{RuO}_2$ -FAU nanocomposites were employed as catalysts for cyclohexane oxidation at room temperature using *tert*-butyl hydroperoxide (*t*BHP) as the oxidant. The catalytic oxidation results are given in Table 1, along with the results of the FePcY-PDMS catalyst (8). Several control experiments were carried out to determine the catalytically active sites of  $\text{RuO}_2$ -FAU catalysts: no catalytic products were observed when unmodified FAU zeolite was used as the "catalyst" (entry 1, Table 1), showing that pure FAU does not have any catalytic activity at room temperature even in the presence of *t*BHP. No oxidation products were detected on mixing cyclohexane with  $\text{RuO}_2$ -FAU without *t*BHP. In the absence of cyclohexane, *t*BHP is decomposed to *tert*-butyl alcohol,  $\text{O}_2$ , and a very small amount of *tert*-butyl peroxide (*t*-BuOO*t*-Bu). Very high catalytic activity of cyclohexane oxidation was observed using  $\text{RuO}_2$ -FAU composites as catalysts. Furthermore, cyclohexane conversion was found to increase with increased  $\text{RuO}_2$  nanocluster

**Fig. 3.** Typical TEM image of the  $\text{RuO}_2$ -FAU(0.78) composite.



loading in the FAU zeolites (entries 2, 3, and 5, Table 1). This clearly demonstrates that  $\text{RuO}_2$  incorporated in the zeolitic framework provides the catalytically active sites for the alkane oxidation. The turnover number (TON) of  $\text{RuO}_2$ -FAU(0.15) is about 630, which is close to the best results (990) achieved with FePcY-PDMS as the catalyst (entry 6, Table 1), although our oxidation reaction was carried out in a simple batch reactor (8). Higher  $\text{RuO}_2$  concentrations can increase catalytic activity, i.e., cyclohexane conversion, but give lower TONs because of the partial blockage of zeolitic channels by the  $\text{RuO}_2$  nanoclusters. Comparing the cyclohexane conversion, TON value, and peroxide efficiency, we conclude that the optimum concentration of  $\text{RuO}_2$  in  $\text{RuO}_2$ -FAU is ca. 0.78 mmol  $\text{g}^{-1}$ , e.g., about one  $\text{RuO}_2$  nanocluster in every two to three supercages.

Cyclohexanol (*ol*) and cyclohexanone (*one*) are the predominant products (about 90 mol%). The *one:ol* ratio increases from 1.3 in  $\text{RuO}_2$ -FAU(0.15) to 3.3 in  $\text{RuO}_2$ -FAU(1.63) (entries 2 and 5, Table 1), showing that higher  $\text{RuO}_2$  concentration can lead to further oxidation of the alcohol to the ketone. The high oxidation activity of  $\text{RuO}_2$ -FAU is also revealed from the low proportion (<8 mol%) of cyclohexyl hydroperoxide (CHHP) in the products. The only observed side product, *tert*-butyl cyclohexyl peroxide, is relatively minor (<5 mol%). No over-oxidation products, such as adipic acid, were found. Furthermore, no dicyclohexyl by-product was found in the oxidation mixture, which contrasts with the Ce/silicate catalysts (27). It appears that, because of the steric constraints imposed by the zeolitic channels and (or) cages, two cyclohexyl radicals cannot be created in one channel and (or) cage at the same time. This provides strong evidence that  $\text{RuO}_2$  is indeed confined in the supercages of FAU zeolite. The shape-selectivity of  $\text{RuO}_2$ -FAU nanocomposites to both substrates and products is also observed in other catalysis experiments such as the oxidation of alcohols (26) and alkyl-aromatics.<sup>2</sup>

If we assume that 1 mol of ketone product is formed for every 2 mol of peroxide, the peroxide efficiency is about 48% for both  $\text{RuO}_2$ -FAU(0.78) and  $\text{RuO}_2$ -FAU(1.63) catalysts (entries 3 and 5, Table 1), which is higher than the observed 35% efficiency in FePcY-PDMS (8). The concen-

<sup>2</sup>B.-Z. Zhan, M.A. White, J.A. Pincok. To be submitted.



**Table 1.** Catalytic results for cyclohexane oxidation.

No.	Catalyst	Products (mol%) <sup>a</sup>				Conv. (%) <sup>b</sup>		TON <sup>c</sup>	Conc. (mol L <sup>-1</sup> ) <sup>d</sup>	Effic. (%) <sup>e</sup>
		<i>ol</i>	<i>one</i>	CHHP	<i>t</i> BCP	<i>ane</i>	<i>t</i> BHP			
1	FAU	—	—	—	—	—	—	—	—	—
2	RuO <sub>2</sub> -FAU(0.15)	39	50	8	3	4.5	47	630	0.13	36
3	RuO <sub>2</sub> -FAU(0.78)	25	66	5	5	8.6	74	190	0.23	48
4	RuO <sub>2</sub> -FAU(0.78) <sup>f</sup>	33	56	7	5	7.6	68	170	0.21	44
5	RuO <sub>2</sub> -FAU(1.63)	21	69	5	5	9.4	84	100	0.26	48
6	FePcY-PDMS (8) <sup>g</sup>	(main products are <i>ol</i> + <i>one</i> )				—	—	990	—	35

<sup>a</sup>*ol* = cyclohexanol, *one* = cyclohexanone, CHHP = cyclohexyl hydroperoxide, *t*BCP = *tert*-butyl cyclohexyl peroxide.

<sup>b</sup>Conversion (*ane* = cyclohexane, *t*BHP = *tert*-butyl hydroperoxide).

<sup>c</sup>TON = turnover number on *t*BHP per RuO<sub>2</sub> nanocluster in 5 h.

<sup>d</sup>Concentration of *ol* + *one* after 5 h of reaction.

<sup>e</sup>Efficiency of *tert*-butyl hydroperoxide, i.e., the percentage of peroxide used for substrate oxidation.

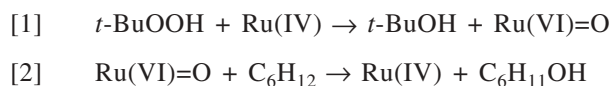
<sup>f</sup>Catalytic results from a third run. After each run, the solid catalyst was separated by centrifugation and then fully washed with acetone and reused for a next run under the same conditions.

<sup>g</sup>Reaction was carried out with 0.32 g of FePcY-PDMS in a counter-current membrane reaction with 40 mmol of *t*BHP as a 7% solution in water, 300 mmol of cyclohexane.

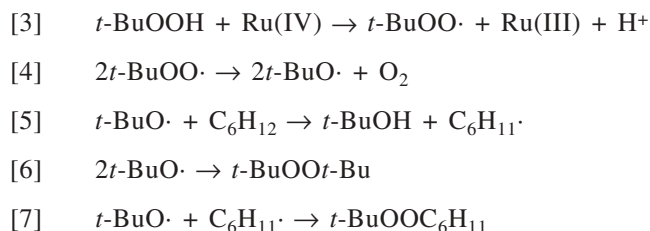
tration of *one* + *ol* with RuO<sub>2</sub>-FAU(1.63) reached 0.26 mol L<sup>-1</sup> in 5 h at RT (entry 5). Furthermore, RuO<sub>2</sub> is physically occluded in the zeolite supercage, making the catalyst reusable. After reaction, a clear, colorless organic phase was separated by centrifugation. Leaching of RuO<sub>2</sub> in the filtrate is negligible: the concentration of Ru in the organic phase is less than 30 ppb (ICP analysis). Further stirring of the organic phase with *t*BHP did not change the product composition, showing that trace amounts of Ru did not cause any oxidation under the experimental conditions, e.g., RT and 1 atm (1 atm  $\equiv$  101.325 kPa). About 90% of the reactivity, e.g., the conversion of both *ane* and *t*BHP, remained in the third run (entries 3 and 4, Table 1).

The high activity of RuO<sub>2</sub>-FAU can be related to the oxidation mechanism. A competitive oxidation of C<sub>6</sub>H<sub>12</sub>-C<sub>6</sub>D<sub>12</sub> over RuO<sub>2</sub>-FAU(0.78) catalyst at RT showed an isotopic effect of  $k_H/k_D = 8.3 \pm 0.2$  (extrapolated to 0% conversion). This indicates the existence of an electrophilic oxo-species (e.g., eqs. [1] and [2]) (8, 28). The relative reactivity of primary, secondary, and tertiary C—H bonds provides further evidence for the presence of Ru-oxo species. In adamantane oxidation over RuO<sub>2</sub>-FAU(0.78) zeolite, we found the tertiary C—H bonds to be 9.7 times more reactive than secondary C—H bonds (secondary:tertiary product ratio of 0.31; statistical factor of 3). This product ratio is significantly higher than 0.05 with Fenton chemistry and 0.14 for hydroxyl radicals (29), but remains in the range required for oxo-chemistry as observed in P-450 and its model systems (8, 30, 31). However, we cannot rule out a small contribution from a free-radical pathway (e.g., eqs. [3]–[7]), as we observe a small amount of CHHP, *t*BCP, and O<sub>2</sub> products in the cyclohexane oxidation. Quite likely, two competitive oxidation pathways are involved since there are different Ru(IV) environments in the RuO<sub>2</sub>-FAU composite catalyst. Looking at the 2D-chain RuO<sub>2</sub> structure, two different coordination environments of Ru(IV) are found: in a five-Ru-atom RuO<sub>2</sub> nanocluster, the two end Ru atoms are completely different from those three Ru in the middle. Two types of oxygen, e.g., bridged and terminal, could also be involved in the oxidation process.

### Ru-oxo oxidation mechanism



### Free-radical oxidation mechanism



### Conclusions

We have synthesized a new type of nanocomposite material, nanosized RuO<sub>2</sub> in a faujasite zeolite, using an organic-template-free hydrothermal crystallization approach. The ruthenium encapsulated inside the supercages of FAU is amorphous hydrous RuO<sub>2</sub> with a particle size of 1.3 nm. It has a 2D-chain structure in which RuO<sub>6</sub> units are connected together by sharing two oxygen atoms (26). The RuO<sub>2</sub>-FAU composites display significant catalytic activity in the oxidation of cyclohexane with *t*BHP under mild (room temperature and 1 atm (1 atm  $\equiv$  101.325 kPa)) conditions. The ketone and alcohol concentration can be as high as 0.26 mol L<sup>-1</sup> in 5 h with 48% peroxide efficiency. Furthermore, RuO<sub>2</sub> is physically trapped in the zeolite supercage, making the catalyst potentially reusable.

### Experimental details

Chemical reagents included fumed silica (11 nm, Sigma), tetraethylorthosilicate (Aldrich), NaOH (Aldrich), NaAlO<sub>2</sub> (Allied Chemical), Al(OH)<sub>3</sub> (McArthur Chemical), RuCl<sub>3</sub>·3H<sub>2</sub>O (Aldrich), and RuO<sub>2</sub> (A.D. Mackay). All other organic and inorganic chemicals were reagent grade and were used without further purification.



### Synthesis of pure faujasite zeolite

The pure faujasite zeolite was synthesized by hydrothermal crystallization in an oil bath with both controllable temperature and stirring rate. Unmodified faujasite zeolite was synthesized using hydrothermal crystallization methods reported previously (22, 23). Aluminosilicate gel was prepared by mixing freshly prepared aluminate and silicate solutions together in the molar ratio  $5.5\text{Na}_2\text{O}:1.0\text{Al}_2\text{O}_3:4.0\text{SiO}_2:190\text{H}_2\text{O}$ . The powdered products were recovered with centrifugation and washed with deionized (DI) water until  $\text{pH} < 8$ , and then dried at room temperature for 24 h for further characterization. X-ray fluorescence analysis showed that the Si:Al ratio for the 4-day crystallization sample was 1.25, within the range of 1.0 ~ 1.5 for faujasite-X zeolite.

### Synthesis of $\text{RuO}_2$ -FAU composites

The  $\text{RuO}_2$ -FAU nanocomposites were synthesized with one-step modification to the method for pure FAU, namely adding  $\text{RuCl}_3 \cdot 3\text{H}_2\text{O}$  into the freshly prepared aluminosilicate gel, before hydrothermal crystallization. A measured amount of  $\text{RuCl}_3 \cdot 3\text{H}_2\text{O}$  was added to an aluminosilicate gel containing 5.34 g NaOH, 2.42 g  $\text{NaAlO}_2$ , 3.43 g  $\text{SiO}_2$ , and 50.0 g  $\text{H}_2\text{O}$ . The gel was aged for 2 days and then crystallized at  $90^\circ\text{C}$  for 15 h with stirring. The resultant black powder was separated from solution by centrifugation and then washed thoroughly with DI water to remove any physically absorbed species. All the synthesized samples were dried at room temperature for further characterization and catalytic investigations. ICP-MS analysis indicated that three  $\text{RuO}_2$ -FAU samples with different  $\text{RuO}_2$  loadings were synthesized:  $\text{RuO}_2$ -FAU(0.15),  $\text{RuO}_2$ -FAU(0.78), and  $\text{RuO}_2$ -FAU(1.63), where the numbers in the parentheses are  $\text{RuO}_2$  concentrations in the FAU zeolites in  $\text{mmol g}^{-1}$ . These correspond, respectively, to one  $\text{RuO}_2$  nanocluster in every ca. 10, 2.2, and 1.1 supercages of FAU (on average, every 1.3 nm  $\text{RuO}_2$  nanocluster contains five Ru atoms, as deduced from the bond lengths).

### Cyclohexane oxidation

The oxidation reactions were carried out in sealed vials containing a mixture of 0.1 g  $\text{RuO}_2$ -FAU catalyst, 10 mmol cyclohexane, 4 mmol *t*BHP, and 2 mL acetone as solvent. The reaction products were analyzed and quantified by GC after 5 h of room-temperature reaction, and identified by either GC-MS or GC with standard samples. All the reactions were run under aerobic conditions. All the GC analyses were performed on a Supelco MDN-55 column ( $30\text{ m} \times 0.25\text{ mm} \times 0.50\text{ }\mu\text{m}$ ) with a Perkin-Elmer Auto System GC equipped with an FID. GC-MS for the product identification was conducted using a Perkin-Elmer Auto System XL GC with a Perkin-Elmer TurboMass mass spectrometer. Chlorobenzene was chosen as the internal standard for GC analyses. Cyclohexyl peroxide was converted to cyclohexanol for quantification. This was done by reacting the oxidation mixture with excess triphenyl phosphine at room temperature for 20 min, followed by GC analysis. The consumption of *tert*-butyl hydroperoxide was directly calculated from the GC results.

### Control reactions

Pure FAU as catalyst: 0.1 g FAU was used as the "catalyst" instead of 0.1 g  $\text{RuO}_2$ -FAU composite. All other con-

ditions are the same as described above. Without *t*BHP: the mixture of 0.1 g  $\text{RuO}_2$ -FAU catalyst, 10 mmol cyclohexane, and 2 mL acetone was stirred for 5 h. Without cyclohexane: 0.1 g  $\text{RuO}_2$ -FAU catalyst, 4 mmol *t*BHP, and 2 mL acetone were mixed together and stirred for 5 h at room temperature. Reaction products were analyzed with GC.

### Isotope effect

The reaction was conducted in sealed vials containing a mixture of 0.1 g  $\text{RuO}_2$ -FAU catalyst, 5 mmol  $\text{C}_6\text{H}_{12}$ , 5 mmol  $\text{C}_6\text{D}_{12}$ , 4 mmol *t*BHP, and 2 mL acetone as solvent. The reaction products taken at different reaction times were analyzed and quantified by GC.

### Adamantane reaction

The reaction was conducted in sealed vials containing a mixture of 0.1 g  $\text{RuO}_2$ -FAU catalyst, 2 mmol adamantane, 4 mmol *t*BHP, and 2 mL acetone as solvent. The reaction products taken at different reaction times were analyzed and quantified by GC and identified by GC-MS.

### Characterization

X-ray powder diffraction patterns were recorded on a Rigaku Miniflex System using  $\text{Cu-K}\alpha$  radiation, 30 kV, 15 mA with a scanning speed of  $1^\circ (2\theta) \text{ min}^{-1}$ ,  $T = 20^\circ\text{C}$ . Ru K-edge XAFS measurements were made at the Bending Magnet Beamline of the PNC (Pacific Northwest Consortium)-CAT (Collaborative Access Team) at the Advanced Photon Source (APS) at Argonne National Laboratory. APS is a 7 GeV, third-generation electron storage ring, operating typically at 100 mA injection current. All the measurements were conducted in fluorescence mode using a Xe-filled ion chamber with filter and solar slit arrangements. High-resolution TEM images were recorded with a FEI Tecnai-12 operated at 80 kV.

### Acknowledgements

The authors thank K.V.R. Rao for XAFS assistance. This work was financially supported by the Natural Sciences and Engineering Research Council of Canada (NSERC) and the Killam Trusts (the latter for a postdoctoral research fellowship to BZZ and research professorship to MAW).

### References

1. J. Halpern. *Discuss. Faraday Soc.* **46**, 7 (1968).
2. R.A. Sheldon and J.K. Kochi. *Metal catalyzed oxidation of organic compounds*. Academic Press, New York. 1981.
3. C.L. Hill. *Activation and functionalization of alkanes*. Wiley, New York. 1989.
4. G.W. Parshall and S.D. Ittel. *Homogeneous catalysis*. 2nd ed. Wiley, New York. 1992.
5. U. Schuchardt, D. Cardoso, R. Sercheli, R. Pereira, R.S. da Cruz, M.C. Guerreiro, D. Mandelli, E.V. Spinace, and E.L. Pires. *Appl. Catal. A*, **211**, 1 (2001), and refs. therein.
6. J.M. Thomas and R. Raja. *Chem. Commun.* 675 (2001), and refs. therein.
7. R. Raja and J.M. Thomas. *J. Mol. Catal. A: Chem.* **181**, 3 (2002).



8. R.F. Parton, I.F.J. Vankelecom, M.J.A. Casselman, C.P. Bezoukhanova, J.B. Uytterhoeven, and P.A. Jacobs. *Nature* (London), **370**, 541 (1994).
9. K.J. Balkus, Jr., M. Eissa, and R. Levado. *J. Am. Chem. Soc.* **117**, 10 753 (1995).
10. B.-Z. Zhan and X.-Y. Li. *Chem. Commun.* 349 (1998).
11. T. Naota, H. Takaya, and S.-I. Murahashi. *Chem. Rev.* **98**, 2599 (1998).
12. E.A. Seddon and K.R. Seddon. *The chemistry of ruthenium*. Elsevier, New York. 1984. Chaps. 3–7.
13. G.A. Barf and R.A. Sheldon. *J. Mol. Catal. A: Chem.* **102**, 23 (1995).
14. H. Over, Y.D. Kim, A.P. Seitsonen, S. Wendt, E. Lundgren, M. Schmid, P. Varga, A. Morgante, and G. Ertl. *Science* (Washington, D.C.), **287**, 1474 (2000).
15. H. Over, A.P. Seitsonen, E. Lundgren, M. Schmid, and P. Varga. *J. Am. Chem. Soc.* **123**, 11 807 (2001).
16. K. Reuter and M. Scheffler. *Phys. Rev. B: Condens. Matter*, **65**, 35 406 (2001).
17. L. Zang and H. Kisch. *Angew. Chem. Int. Ed.* **39**, 3921 (2000).
18. H. Madhavaram, H. Idriss, S. Wendt, Y.D. Kim, M. Knapp, H. Over, J. Aßmann, E. Löffler, and M. Muhler. *J. Catal.* **202**, 296 (2001).
19. D.A. Mckeown, P.L. Hagans, L.P.L. Carette, A.E. Russell, K.E. Swider, and D.R. Rolison. *J. Phys. Chem. B*, **103**, 4825 (1999).
20. A.N. Goldstein. *Handbook of nanophase materials*. Marcel Dekker, Inc., New York. 1997.
21. K.J. Klabunde (*Editor*). *Nanoscale materials in chemistry*. Wiley-Interscience, New York. 2001.
22. B.-Z. Zhan, M.A. White, K.N. Robertson, T.S. Cameron, and M. Gharghour. *Chem. Commun.* 1176 (2001).
23. B.-Z. Zhan, M.A. White, M. Lumsden, J. Mueller-Neuhaus, K.N. Robertson, T.S. Cameron, and M. Gharghour. *Chem. Mater.* **14**, 3636 (2002).
24. R. Szostak. *Molecular sieves: principles of synthesis and identification*. Van Nostrand Reinhold, New York. 1989.
25. <[www.iza-online.org/databases](http://www.iza-online.org/databases)> (accessed June 12, 2003).
26. B.-Z. Zhan, M.A. White, T.-K. Sham, J.A. Pincock, R.J. Doucet, K.V.R. Rao, K.N. Robertson, and T.S. Cameron. *J. Amer. Chem. Soc.* **125**, 2195 (2003).
27. E.L. Pires, U. Arnold, and U. Schuchardt. *J. Mol. Catal. A: Chem.* **169**, 157 (2001).
28. A.M. Khenkin and A.E. Shilov. *New J. Chem.* **13**, 659 (1989).
29. W. Nam and J.S. Valentine. *New J. Chem.* **13**, 677 (1989).
30. V. Ullrich. *Top. Curr. Chem.* **83**, 67 (1979).
31. D. Mansuy and P. Battioni. *In Activation and functionalization of alkanes. Edited by C.T. Hill*. Wiley, New York. 1989. Chap. 5. p. 195.



# Intramolecular excimer fluorescence from folded ground state rotamers of *N,N'*-dimethyl-*N,N'*-dipyrenylurea protophanes

Frederick D. Lewis and Todd L. Kurth

**Abstract:** The molecular structure, absorption, and fluorescence spectra of *N,N'*-dimethyl-*N,N'*-di-1-pyrenylurea and *N,N'*-dimethyl-*N,N'*-di-2-pyrenylurea have been investigated and compared to the properties of *N,N,N'*-trimethyl-*N'*-pyrenylurea model compounds. Di-1-pyrenylurea exists as a mixture of folded (*E,E*) syn- and anti-rotamers that interconvert via flipping of one of the pyrene rings to an unfolded (*E,Z*) rotamer geometry. The symmetric di-2-pyrenylurea exists as a single folded (*E,E*) conformation which is in equilibrium with a less-stable, unfolded (*E,Z*) rotamer. The absorption and fluorescence spectra of the dipyrenylureas at 77 K in a rigid glass are similar to those of monopyrenylurea model compounds. However, in fluid solution, the dipyrenylureas exhibit excimer fluorescence and very weak monomer fluorescence which have identical decay times. This behavior is attributed to fast rotational equilibrium between folded rotamers which exhibit excimer fluorescence and unfolded rotamers which exhibit monomer fluorescence. The behavior of the dipyrenylureas is compared with that of other systems that form intramolecular pyrene excimers and diarylureas.

**Key words:** excited state rotamers, dipyrenylureas, pyrene excimers, ureaphane.

**Résumé :** On a étudié la structure moléculaire et les spectres d'absorption et de fluorescence de la *N,N'*-diméthyl-*N,N'*-di-1-pyrénylurée et de la *N,N'*-diméthyl-*N,N'*-di-2-pyrénylurée et on les a comparés aux propriétés correspondantes de composés modèles de la famille des *N,N,N'*-triméthyl-*N'*-pyrénylurée. La di-1-pyrénylurée existe sous la forme de mélange de rotamères syn- et anti- repliés (*E,E*) qui donnent lieu à une interconversion par le biais de l'inversion d'un des noyaux pyrène vers un rotamère de géométrie dépliée (*E,Z*). La di-2-pyrénylurée existe sous la forme d'une seule conformation repliée qui est en équilibre avec un rotamère déplié (*E,Z*) moins stable. Les spectres d'absorption et de fluorescence des dipyrénylurées à 77 K, dans un verre rigide, sont semblables à ceux des composés modèles de la famille des monopyrénylurées. Toutefois, en solution fluide, les dipyrénylurées présentent une fluorescence d'excimère et une très faible fluorescence de monomère qui ont des temps de dégénérescence identiques. On attribue ce comportement à un rapide équilibre rotationnel entre les rotamères repliés qui présentent de la fluorescence d'excimère et les rotamères dépliés qui présente de la fluorescence de monomère. On compare le comportement des dipyrénylurées avec celui des diarylurées et d'autres systèmes qui forment des excimères pyrènes intramoléculaires.

**Mots clés :** rotamères à l'état excité, dipyrénylurées, excimères de pyrène, uréeaphane.

[Traduit par la Rédaction]

## Introduction

Pyrene excimer fluorescence is among the most widely used probes of molecular conformation and structure (1). The calculated optimum excimer geometry for two independent pyrene molecules is a slightly slipped sandwich structure (2). Molecules possessing two pyrene chromophores that can adopt sandwich structures display large monomer–excimer spectral shifts. Examples include the 1,3-dipyrenylpropanes (**1** and **2**) (3–6) and [*n,n*](2,7)pyrenophanes (*n* = 2, 3, or 4) (3–5) (7). Conversely, molecules in which only partial overlap of the two pyrenes is possible dis-

play either monomer fluorescence or excimer fluorescence with small monomer–excimer spectral shifts. Examples include 1,2-di(1-pyrenyl)ethane (3), which cannot adopt a parallel sandwich structure, and [2.2](1,3)pyrenophane (**6**) (8) and [2.2](1,8)pyrenophane (**7**) (9), which have extended and splayed ground state structures, respectively. A particularly instructive example of the effect of overlap on pyrene fluorescence is provided by the 1,8-dipyrenyl-naphthalenes (**8**–**10**) investigated by Staab and co-workers (10). Both the di-2-pyrenylnaphthalene (**10**) and the syn rotamer of the di-1-pyrenylnaphthalene (**8**) have extensive overlap between pyrenes and display excimer fluorescence, whereas the anti-

Received 6 February 2003. Published on the NRC Research Press Web site at <http://canjchem.nrc.ca> on 24 June 2003.

This paper is dedicated to Donald R. Arnold in recognition of his contributions to the study of radical ions in photochemistry.

**F.D. Lewis<sup>1</sup>** and **T.L. Kurth**, Department of Chemistry, Northwestern University, Evanston, IL 60208-3113, U.S.A.

<sup>1</sup>Corresponding author (e-mail: [lewis@chem.northwestern.edu](mailto:lewis@chem.northwestern.edu)).



**Fig. 1.** HF/6-31G\*\* optimized rotamers (a) *syn-E,E,N,N'*-dimethyl-*N,N'*-di-1-pyrenylurea, (b) low energy *anti-E,E,N,N'*-dimethyl-*N,N'*-di-1-pyrenylurea, and (c) high energy *anti-E,E,N,N'*-dimethyl-*N,N'*-di-1-pyrenylurea. Each structure is depicted with the urea unit in the Y-Z plane.

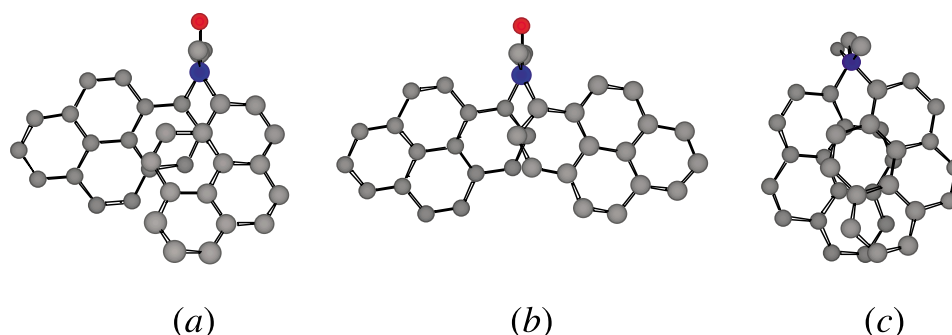
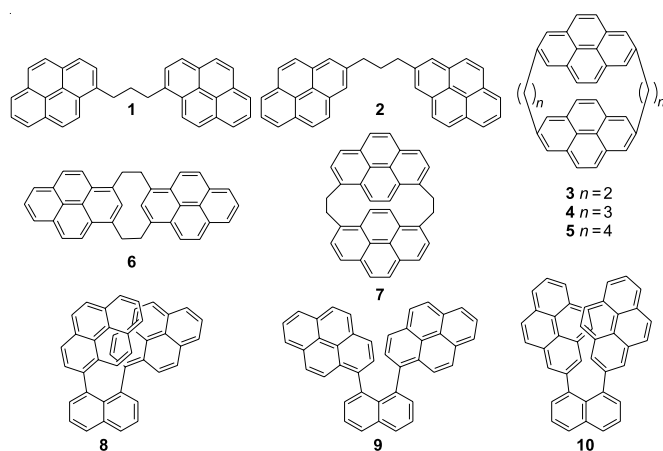


**Chart 1.**

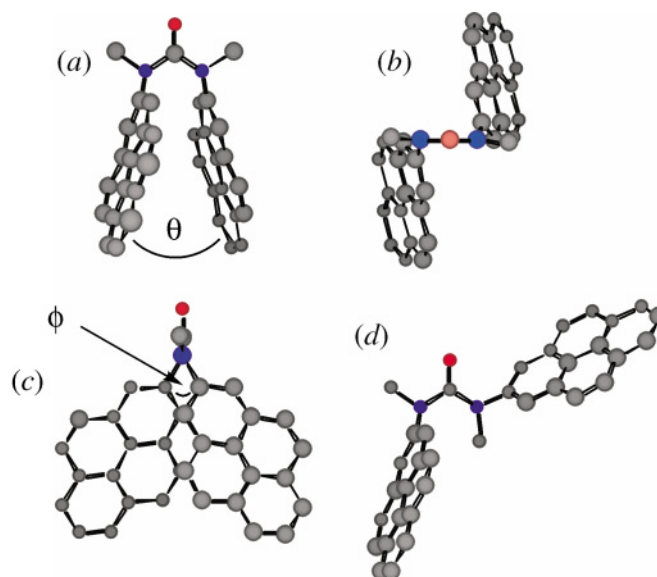


rotamer of the di-1-pyrenyl-naphthalene (**9**) has minimal overlap and displays monomer fluorescence. Vögtle refers to systems in which two aryl groups are constrained to a face-to-face geometry by a single linker as “protophanes”, to distinguish them from cyclophanes in which aryl groups are connected by two or more linkers (11). Structures of **1–10** are shown in Chart 1.

Several *N,N'*-dimethyl-*N,N'*-diarylureas adopt folded (*E,E*) structures, both in the solid state and in solution, in which the two aryl groups are face-to-face (e.g., Fig. 1) (**12**). Computational studies of the ground state conformational energy surface of *N,N'*-dimethyl-*N,N'*-di-1-naphthylurea indicate that the folded (*E,E*) rotamers are more stable than the (*E,Z*) isomers by 2 to 3 kcal/mol.<sup>2</sup> The tertiary diarylureas are unique among conformationally mobile, singly linked diaryl systems in their preferential formation of face-to-face conformers.

We have previously observed that several diarylureas display excimer fluorescence in solution and monomer fluorescence in rigid glasses at 77 K (13). Evidently, large amplitude geometric relaxation of the locally excited, Franck–Condon singlet state of the folded (*E,E*) rotamers is necessary for the formation of a fluorescent excimer. Reported here are the syntheses, calculated structures, and fluorescence spectra of *N,N'*-dimethyl-*N,N'*-di-1-pyrenylurea

**Fig. 2.** Folded and extended conformations of *N,N'*-dimethyl-*N,N'*-di-2-pyrenylurea (**12**) (a) depiction with urea in the X-Y plane, (b) urea in the X-Z plane, (c) urea in the Y-Z plane, and (d) extended conformation with urea in the X-Y plane.



(**11**) (Fig. 1), *N,N'*-dimethyl-*N,N'*-di-2-pyrenylurea (**12**) (Fig. 2), and their monoaryl analogs *N,N,N'*-trimethyl-*N'*-1-pyrenylurea (**11m**) and *N,N,N'*-trimethyl-*N'*-2-pyrenylurea (**12m**). The dipyrenylureas exhibit both monomer and excimer fluorescence, which are attributed to the major folded rotamer (excimer) and a minor extended rotamer (monomer), respectively, (e.g., Fig. 2d). The monomer–excimer spectral shifts are dependent upon the strength of the intramolecular pyrene–pyrene interaction in the relaxed excited state.

## Results and discussion

### Molecular structures

HF/6-31G\*\* geometry optimizations (14) confirm that, as in the case of other tertiary diarylureas, conformers in which the Py-N-C=O geometry is E are of lower energy than their Z isomers (12, 13, 15). The *E,E*-di-1-pyrenylurea **11** is pre-

<sup>2</sup>Manuscript in preparation.



dicted to exist as a mixture of syn- and anti-rotamers, the former being more stable by ca. 1.0 kcal/mol (see Figs. 1a and 1b). The more symmetric *E,E*-di-2-pyrenylurea **12** exists in a single conformation (Fig. 2a–2c). For **11** and **12**, the calculated energy of the *E,E*-rotamer is lower than that of the *E,Z* by ca. 1.5–2.5 kcal/mol. The minimized structures shown in Figs. 1 and 2 illustrate that the tertiary dipyrenylureas have large angles between the pyrene planes. While the short axes of the pyrenyl planes are approximately parallel, the rotational ( $\theta$ ) and splay ( $\phi$ ) angles are roughly 50° and 60°, respectively, (see Figs. 2a and 2c). These geometries presumably result from alleviation of the repulsive aryl–aryl interactions, causing a slight perturbation of the loosely constrained urea linker. A slightly higher energy minimum (+0.72 kcal/mol), corresponding to inversion of the nitrogen centers and having more extensive pyrene–pyrene interaction, exists for *anti*-**11** (Fig. 1c). The barrier to urea nitrogen inversion is very low (16), thus, creating a broad potential energy minimum in which urea linker strain is balanced against the repulsive through space aryl–aryl interactions. Although symmetry prevents the observation of similar multiple conformations for *syn*-**11** and **12**, their potential energy surfaces are undoubtedly similar.

The ab initio optimized *E,E* geometries of **11** and **12** are consistent with crystal structures of several tertiary diarylureas that adopt folded geometries (12). Further evidence for protophane structures of **11** and **12** is provided by their  $^1\text{H}$  NMR spectra (Fig. 3). Comparison of the spectra of the mono- and dipyrenylureas show that the aryl protons of the latter lie up-field of the former, as expected for folded conformations with face-to-face aromatic groups (17). In the case of **11**, exchange broadening is observed in the room temperature  $^1\text{H}$  NMR spectrum, in accord with the restricted interconversion of the syn- and anti-*E,E*-rotamers. Having only a single *E,E* conformation, no such broadening is observed in the spectrum of **12**.

### Absorption and fluorescence spectra

The long-wavelength portions of the absorption spectra of the mono- and dipyrenylureas in methyltetrahydrofuran (MTHF) are shown in Fig. 4. They all have long-wavelength maxima near that of pyrene (see Table 1) and weaker tails at longer wavelengths. The absorption spectra of **11** and **11m** appear to be broadened and display increased intensity at longer wavelengths when compared to the spectra of **12** and **12m**. This is as expected due to the greater electronic interaction of the pyrene frontier orbitals with substituents at the 1- vs. 2-position (18). ZINDO calculations (19) for the mono-arylureas also correctly predict a small red shift for the first maximum and a stronger long-wavelength tail in the spectrum of **11m** relative to that of **12m**. Vibrational structure similar to that of pyrene is observed in the tails of the absorption spectra of **11m** and **12m**. The band shifts and broadening in the UV spectra of **11** and **12** prevent the observation of such long-wavelength structure. We previously suggested that the broader spectrum of **11** vs. **11m** might be a consequence of weak exciton coupling between the two pyrenes (13). This may also be the case in the spectra of **12** with respect to **12m**.

The fluorescence excitation and emission spectra of the mono- and dipyrenylureas at 77 and 298 K in MTHF are

**Fig. 3.** Low-field  $^1\text{H}$  NMR spectra (298 K,  $\text{CDCl}_3$ ) of the tertiary mono- (**11m** and **12m**) and dipyrenylureas (**11** and **12**).

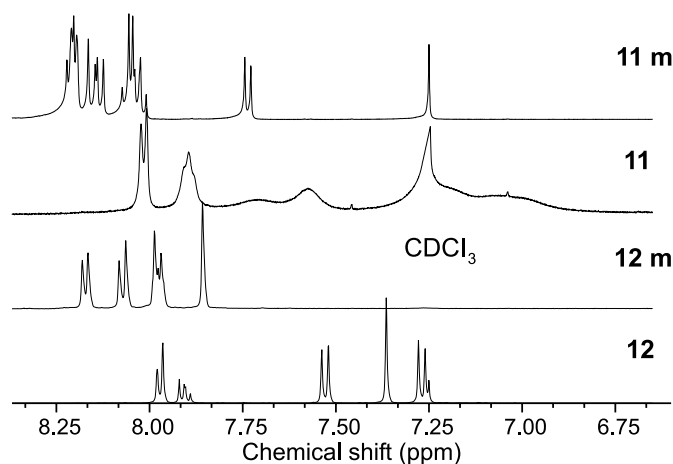
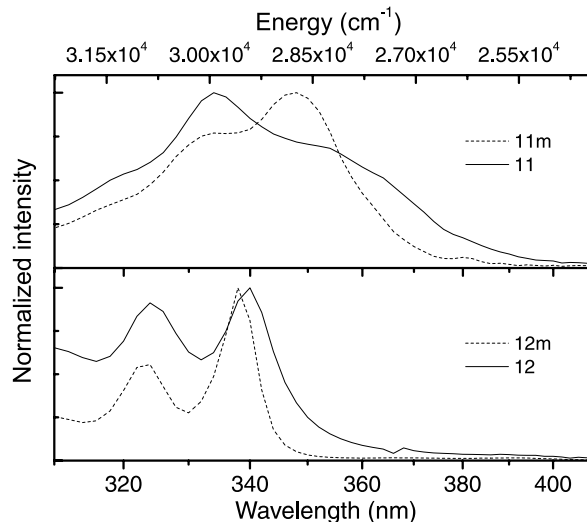


**Fig. 4.** Absorption spectra in MTHF of the mono- (**11m** and **12m**) (dashed lines) and dipyrenylureas (**11** and **12**) (solid lines).



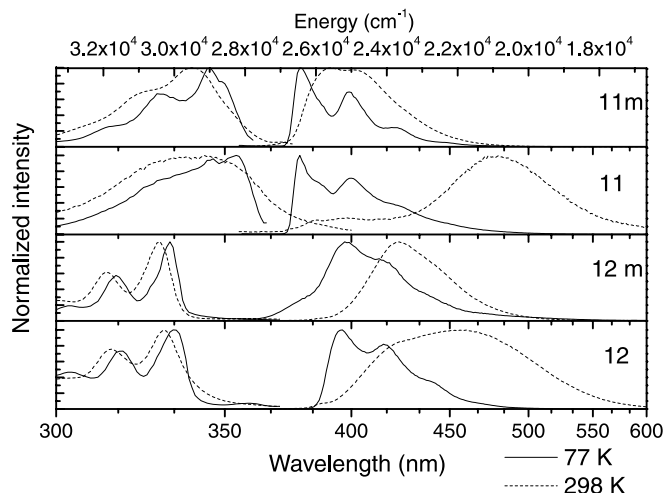
shown in Fig. 5. The excitation spectra are independent of the wavelength of emission monitored. The 298 K excitation spectra are similar in appearance to the absorption spectra (Fig. 4). The fluorescence maxima of the 1-pyrenylureas are at shorter wavelengths than those of the 2-pyrenylureas. The deceptive Stokes shifts in the spectra of **12m** and **12** are a consequence of the long-wavelength absorption bands having very low oscillator strength. Well-resolved vibronic structure is observed in the emission spectra of all four pyrenylureas at 77 K. The spectra of **11** and **12** are similar to those of their monoarylurea analogs **11m** and **12m**. No phosphorescence is observed for any of the pyrenylureas.

The fluorescence maxima, quantum yields, and decay times for pyrene and the pyrenylureas are reported in Table 1. The 77 K fluorescence decays of all the ureas are best fit by dual exponentials. The multiple exponential decays are most likely a consequence of an array of closely related conformations that are frozen in the solvent matrix, the behavior of which can be effectively fit with either distributed or the



**Table 1.** Absorption and fluorescence spectral data for pyrene and the ureaphanes.

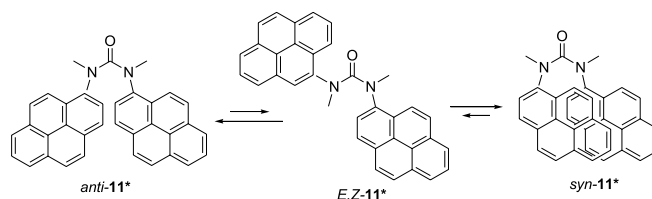
	<i>T</i> (K)	$\lambda_{\text{abs}}$ (nm)	$\lambda_{\text{fl}}$ (nm)	$\Phi_{\text{fl}}$	$\tau_1$ (ns) <sup>a</sup>	$\tau_2$ (ns) <sup>a</sup>
Pyrene <sup>b</sup>	298	334	385	0.32	450	
<b>11m</b>	77		378	0.37	61 (6.9)	16 (7.5)
	298	348	390	0.31	21	
<b>11</b>	77		378	0.19	54 (3.6)	14 (8.8)
	298	334	400	0.0008	21	
	298	334	480	0.01	21	
<b>12m</b>	77		395	0.10	65 (4.1)	10 (3.4)
	298	338	422	0.03	36	
<b>12</b>	77		395	0.21	60 (8.4)	9 (2.0)
	298	340	417 <sup>c</sup>	0.002	36	
	298	340	455, 460 <sup>c</sup>	0.02	36	

<sup>a</sup>Preexponentials in parenthesis.<sup>b</sup>Data from ref. (2).<sup>c</sup>Deconvolution results.**Fig. 5.** Excitation and emission spectra in MTHF of the mono- (**11m** and **12m**) and dipyrrenylureas (**11** and **12**). Solid lines represent 77 K data. Dashed lines represent 298 K data.

multiple component kinetics. In the case of **11**, different decay times might be expected for the syn- and anti-rotamers,<sup>3</sup> whereas **12** is expected to exist predominantly as a single rotamer.

The 298 K fluorescence emission spectra of **11m** and **12m** are broadened and red-shifted when compared to their 77 K spectra. These changes reflect the occurrence of geometric relaxation prior to emission in fluid solution and may be attributed to increased molecular planarity in the singlet state. The calculated (HF/6-31G\*\*) (14) dihedral angles between the pyrene and urea planes are 69° and 118° in the ground states of **11m** and **12m**, respectively. Upon excitation, planarization and thus, an increase in the pyrene—N bond order would result in more effective conjugation leading to a decrease in the HOMO—LUMO gap and a bathochromic shift in the fluorescence spectrum.

Large red shifts are observed for the fluorescence of **11** and **12** at 298 vs. 77 K, the red shift for **11** being larger than

**Scheme 1.**

that for **12**. These shifts are attributed to the formation of intramolecular pyrene excimers. The appearance of excimer fluorescence at 298 K but not 77 K indicates that geometric relaxation of the Franck–Condon singlet state occurs in fluid solution, presumably resulting in contraction of both the splay and rotational angles of the dipyrrenylureas. Weak short-wavelength shoulders are observed in the 298 K fluorescence spectra of both **11** and **12**. The positions of these shoulders are similar to the maxima of the monoarylureas **11m** and **12m**, respectively (see Table 1). Deconvolution of the spectrum of **12** results in slightly shifted monomer and excimer maxima. The monomer and excimer emission have identical excitation spectra.

The decay times for both the excimer fluorescence and the weak monomer fluorescence from **11** and **12** at 298 K are the same, indicative of rapid equilibrium between the species responsible for excimer and monomer fluorescence. We attribute these emissions to the folded (*E,E*) and extended (*E,Z*) ground state rotamers, respectively. In the case of **11** both the syn- and anti-(*E,E*)-rotamers must be in equilibrium with the *E,Z* rotamer (Scheme 1). A similar kinetic scheme was proposed by Zachariasse et al. (4) to account for the observation of a single decay time for the extended and twofolded excited state rotamers of **1** in toluene at temperatures above 20°C. The very weak monomer emission observed for **11** and **12** is indicative of a low population of the extended (*E,Z*) rotamer in the excited state as well as in the ground state. The decay times for **11** and **12** are identical to those of the monopyrrenylureas **11m** and **12m** (Table 1). This agreement may simply be fortuitous, as the *E,Z* rotamers of

<sup>3</sup> Variable low-temperature fluorescence decay analyses led to the resolution of lifetimes corresponding to those of the syn and anti rotamers of *N,N'*-dimethyl-*N,N'*-di-1-naphthylurea. Manuscript submitted.



**11** and **12** possess two nonequivalent pyrenes, whereas **11m** and **12m** possess a single pyrene.

Equilibrium between excited state rotamers requires that the rate of equilibration be faster than the decay time of the shortest-lived conformer (ca.  $3\text{--}5 \times 10^7 \text{ s}^{-1}$  for **11** and **12**). Assuming that the conversion of *E,E* to *E,Z* conformers is isoentropic, a barrier of 5 to 6 kcal/mol would result in a rate constant of  $\sim 1 \times 10^9 \text{ s}^{-1}$ . The line broadening observed in the NMR spectrum of **11** is consistent with a ground state barrier of this magnitude. Rotational barriers of ca. 10–28 kcal/mol have been determined for protophane systems (20). Linker geometry and repulsive polar and steric interactions between the opposing aryl groups can lower this barrier.

### Comparison with other intramolecular excimer-forming molecules

The excimer fluorescence maxima and monomer–excimer spectral shifts for **11** and **12** and those of several other dipyrrenyl systems are summarized in Table 2. The 1,3-dipyrrenylpropanes **1** and **2** have nonfolded structures in the ground state, and they display monomer fluorescence at 77 K and excimer fluorescence at 298 K. They can readily adopt unstrained face-to-face sandwich excimer geometries and have large values of  $\Delta\nu$ , which are similar for the 1,1-, 2,2-, and 1,2-pyrenyl isomers (5). The [*n,n*](2,7)pyrenophanes **3–5** have parallel sandwich-like structures in the ground state and display excimer fluorescence both in a 1.3 K glass and at room temperature (7).<sup>4</sup> Their  $\Delta\nu$  values decrease as the length of the alkyl tethers increases, presumably because of decreased electronic interaction between the two pyrenes. The [2.2](1,3)pyrenophane **6** has an extended ground state structure and displays pyrene monomer fluorescence in non-polar solvents, both at 77 and 298 K (8). In polar solvents, it displays overlapping monomer and excimer fluorescence. The observation of excimer fluorescence in polar solvents is attributed to a “harpooning” mechanism in which photo-induced charge transfer triggers folding. The value of  $\Delta\nu$  in polar solvents is smaller than that for either **1** or **3**, suggesting that it does not adopt a fully overlapping structure. The [2.2](1,8)pyrenophane **7** has a splayed structure and displays a smaller value of  $\Delta\nu$  than those for the other cyclophanes (9).

The crystal structures of the 1,8-di-1-pyrenylnaphthalenes display nearly parallel pyrene rings, with splay angles  $<3^\circ$  and rotational angles of  $<15^\circ$  (10). The two pyrene rings of **8** and **10** have slightly slipped sandwich geometries, where **9** has only partial pyrene–pyrene overlap. The barrier for thermal isomerization of **9** to **8** is 28 kcal/mol, much higher than the value obtained for the interconversion of *syn*- and *anti*-*E,E*-*N,N'*-dimethyl-*N,N'*-di-1-naphthylurea, ca. 12 kcal/mol (calculated via <sup>1</sup>H NMR exchange simulations).<sup>2</sup> The values of  $\Delta\nu$  for **8–10** in a 1.3 K MTHF glass reflect their structural differences. The smallest value is observed for **9**, which has the least extensive overlap in the ground state, and **8**, with maximal overlap, has the greatest.

The calculated ground state structures of **11** and **12** have rather poor pyrene–pyrene overlap and a large splay angle, similar to that of **7**. Thus, it is not surprising that they do not

**Table 2.** Comparison of dipyrrenyl fluorescence data in MTHF.

	Ground state structure	$\lambda_{\text{fl}}$ (nm) <sup>a</sup>	$\Delta\nu$ (cm <sup>−1</sup> ) <sup>b</sup>
<b>1</b> <sup>c</sup>	Extended	498	6500
<b>2</b> <sup>c</sup>	Extended	487	6250
<b>3</b> <sup>d</sup>	Parallel cyclophane	555 <sup>c</sup>	7850
<b>4</b> <sup>d</sup>	Parallel cyclophane	515 <sup>c</sup>	6450
<b>5</b> <sup>d</sup>	Parallel cyclophane	469 <sup>c</sup>	4450
<b>6</b> <sup>e</sup>	Extended cyclophane	385, <sup>f</sup> 475	0, <sup>f</sup> 3800
<b>7</b> <sup>g</sup>	Splayed cyclophane	410	1500
<b>8</b> <sup>h</sup>	Sandwich (extensive overlap)		5800
<b>9</b> <sup>h</sup>	Sandwich (minimal overlap)		1000
<b>10</b> <sup>h</sup>	Sandwich (extensive overlap)		4000
<b>11</b> <sup>i</sup>	Splayed (partial overlap)	417, <sup>f</sup> 460	0, <sup>f</sup> 5620
<b>12</b> <sup>i</sup>	Splayed (partial overlap)	400, <sup>f</sup> 480	0, <sup>f</sup> 3340

<sup>a</sup>Fluorescence maxima at 298 K. Multiple entries indicate deconvoluted components.

<sup>b</sup>Difference between the monomer and excimer band maxima at room temperature.

<sup>c</sup>Data from ref. (5).

<sup>d</sup>Data from ref. (7).

<sup>e</sup>Data from ref. (8).

<sup>f</sup>Monomer fluorescence.

<sup>g</sup>Data from ref. (8).

<sup>h</sup>Data from ref. (9).

<sup>i</sup>Data from the present study.

display excimer fluorescence in a 77 K glass. The formation of a fluorescent excimer at 298 K presumably requires a decrease in the average pyrene–pyrene separation, which would result in increased strain in the urea linkage. Thus, the difference in energy between folded *E,E* and extended *E,Z* conformations may actually be smaller in the excited state than in the ground state. The value of  $\Delta\nu$  for **11**, which exists predominantly as the *syn* conformer, is similar to that for *syn*-1,8-di-1-pyrenylnaphthalene (**8**). The value of  $\Delta\nu$  for **12** is similar to that for 1,8-di-2-pyrenylnaphthalene (**10**). Thus, we might expect that the relaxed pyrene excimer geometries of **11** and **12** are similar to those of **8** and **10**, respectively.

The behavior of the dipyrrenylureas is qualitatively similar to that of several other diarylureas that we have studied. Tertiary di-2-naphthylurea and di-2-anthrylurea also display monomer fluorescence at 77 K and broadened, red-shifted emission in solution. The values of  $\Delta\nu$  for these tertiary ureas are 2200 and 2900 cm<sup>−1</sup>, respectively, significantly smaller than the values for **11** and **12**. As a consequence of these small spectral shifts, it is not possible to resolve monomer and excimer fluorescence. The fluorescence decays of the dinaphthyl- and dianthrylureas are also single exponentials, indicative of either emission from a single rotamer or rapid equilibration between rotamers.

### Concluding remarks

The fluorescence properties of excimer-forming dipyrrenyl systems are highly dependent upon the nature of the linker connecting the two pyrene chromophores. Systems such as the pyrenophanes **3–5** and the 1,8-dipyrrenylnaphthalenes in which the two pyrenes are parallel and strongly overlapping display excimer fluorescence both in low temperature

<sup>4</sup>F. Diederich. Personal communication, 2002.



glasses and in room temperature solutions. Systems with poor overlap and rigid linkers such as the pyrenophanes **6** and **7** and the 1,8-dipyrenylnaphthalene **9** display monomer fluorescence both in glasses and in solution. Systems with highly flexible linkers such as the 1,3-dipyrenylpropanes **1** and **2** display monomer fluorescence in rigid glasses and excimer fluorescence in solution.

The protophanes **11** and **12** possess a linker which restricts ground state conformational mobility, resulting in weak electronic interactions between poorly stacked pyrenes. As a consequence, **11** and **12** display monomer fluorescence in a rigid glass, unlike the 1,8-dipyrenylnaphthalenes **8** and **10** which display excimer emission at 1.3 K. In fluid solution the locally excited states of **11** and **12** can undergo geometric relaxation to form excimers with monomer–excimer spectral shifts similar to those of **8** and **10** (Table 2). The unique conformational properties of the tertiary diarylureas, as well as their ease of synthesis, make them well suited for the study of intramolecular excimer and exciplex behavior in “ureaphane” systems with two or more arene layers.

## Experimental

### General

<sup>1</sup>H NMR spectra were measured on an Inova 500 spectrometer. UV–vis spectra were measured on a Hewlett-Packard 8452A diode array spectrometer using a 1 cm path length quartz cell. Total emission spectra were measured on a SPEX Fluoromax spectrometer. Low-temperature spectra were measured in a Suprasil quartz “EPR” tube (id = 3.3 mm) using a quartz liquid nitrogen cold finger dewar at 77 K. Total emission quantum yields were measured by comparing the integrated area under the total emission curve at an equal absorbance and the same excitation wavelength as an external standard (9-methylanthracene) ( $\Phi_f = 0.35$  at 298 K in cyclohexane) (21). Emission spectra are uncorrected and the estimated error for the quantum yields is  $\pm 10\%$ . Fluorescence decays were measured using a Photon Technologies International (PTI) stroboscopic detection instrument with a hydrogen or nitrogen lamp using a scattering solution to profile the instrument response function. Nonlinear least-squares fitting of the decay curves employed the Levenburg–Marquardt algorithm as described by James et al. (22) and implemented by the PTI Timemaster software (23). Goodness-of-fit was determined by simultaneously judging the  $\chi^2$  ( $< 1.2$  in all cases), the residuals, the Durbin–Watson parameter ( $> 1.5$  in all cases), and the Runs Test ( $> 1.9$  in all cases). Multiple wavelength detection and global analyses were applied in relevant cases. All solutions were either purged with nitrogen for 30 min or degassed under vacuum ( $< 0.1$  torr (1 torr = 133.322 Pa)) through five freeze–pump–thaw cycles.

### Materials

All reagents are commercially available and were used as received. Anhydrous MTHF containing 200 ppm 2,6-di-*tert*-butyl-4-methylphenol (BHT, Aldrich) was distilled from potassium hydroxide under a nitrogen atmosphere immediately prior to use.

### 2-Aminopyrene

2-Aminopyrene was synthesized via the method of Streitwieser et al. (24). This method consists of a potassium metal reduction of liquid ammonia, forming a potassium amide solution, to which 1-bromopyrene is added. The resulting mixture of 1- and 2-aminopyrene is purified by HCl extraction. The isomers are then separated by crystallization and multiple column and preparative TLC. Our yields were less than those reported by Streitwieser ( $< 10\%$ ). <sup>1</sup>H NMR (CDCl<sub>3</sub>, 500 MHz)  $\delta$ : 4.13 (s, 2H), 7.46 (s, 2H), 7.86 (t, <sup>3</sup>*J* = 8 Hz, 1H), 7.87 (d, *J* = 9 Hz, 2H), 7.98 (d, *J* = 9 Hz, 2H), 8.09 (d, *J* = 8 Hz, 2H). MS *m/z*: 217 (M<sup>+</sup>).

### N,N'-Diarylureas

To a solution of amine (10 mmol) in dichloromethane (20 mL), was added 2.2 equiv of triethylamine, followed by 1.6 mmol of triphosgene. After the mixture had been stirred for 10 min, the solvent was removed using a rotary evaporator. The solid residue was washed with water and recrystallized from DMF–water (10:1). The resulting crystalline amide was washed with water and dried under vacuum. *N,N'*-Di-1-pyrenylurea was characterized and reported previously (13). Due to its insolubility, NMR data was not obtainable for *N,N'*-di-2-pyrenylurea.

#### *N,N*-Dimethyl-*N'*-2-pyrenylurea:

<sup>1</sup>H NMR (DMSO-*d*<sub>6</sub>, 500 MHz)  $\delta$ : 3.08 (s, 6H), 8.01 (t, *J* = 7.5 Hz, 2H), 8.09 (d, *J* = 9 Hz, 2H), 8.16 (d, *J* = 9 Hz, 2H), 8.27 (d, *J* = 7 Hz, 1H), 8.45 (s, 2H), 8.90 (s, 1H).

#### *N,N'*-Dimethyl-*N,N'*-diarylureas

To a solution of *N,N'*-diarylurea (10 mmol) in 20 mL DMF was added drop-wise 1.5 equiv of NaH in 10 mL DMF, followed by 1.5 equiv of MeI. The mixture was stirred at room temperature until the starting material was consumed (ca. 2 to 3 h), and was then mixed with water, and extracted with CH<sub>2</sub>Cl<sub>2</sub>. The organic layer was washed with water and dried with anhydrous potassium carbonate. After the solvent was removed, the residue was purified by column chromatography using mixed solvent (acetone and hexane). The *N,N'*-dimethyl-*N,N'*-di-1-pyrenylurea (**11**) was characterized and reported previously (13).

#### *N,N'*-Dimethyl-*N,N'*-di-2-pyrenylurea (**12**):

<sup>1</sup>H NMR (CDCl<sub>3</sub>, 500 MHz)  $\delta$ : 3.46 (s, 6H), 7.26 (d, *J* = 9 Hz, 2H), 7.36 (s, 2H), 7.52 (d, *J* = 9 Hz, 2H), 7.90 (t, *J* = 7.7 Hz, 1H), 7.97 (d, *J* = 7.7 Hz, 2H).

### *N,N,N'*-Trimethyl-*N'*-arylureas

To a solution of aminopyrene (0.66 g, 3 mmol) in dichloromethane (20 mL) was added 1.4 mL triethylamine (10 mmol), followed by 0.3 g triphosgene (1 mmol). After the mixture had been stirring for 30 min, a mixture of 0.6 g dimethylamine hydrochloride (7 mmol), 1.4 mL triethylamine (10 mmol), and 20 mL CH<sub>2</sub>Cl<sub>2</sub> was added. The mixture was refluxed for 10 min, the solvent was then removed using a rotary evaporator. The solid residue was washed with water and recrystallized from acetone–hexane (1:1) to give the relevant *N,N*-dimethyl-*N'*-pyrenyl urea. The *N,N*-dimethyl-*N'*-1-pyrenylurea was characterized and reported previously (13).



*N,N*-Dimethyl-*N'*-2-pyrenylurea:

$^1\text{H}$  NMR (DMSO- $d_6$ , 500 MHz)  $\delta$ : 3.08 (s, 6H), 8.01 (t,  $J = 7.5$  Hz, 2H), 8.09 (d,  $J = 9$  Hz, 2H), 8.16 (d,  $J = 9$  Hz, 2H), 8.27 (d,  $J = 7$  Hz, 1H), 8.45 (s, 2H), 8.90 (s, 1H). This was methylated with MeI–NaH as described above. The crude *N,N,N'*-trimethyl-*N'*-pyrenylureas were purified by column chromatography. *N,N,N'*-Trimethyl-*N'*-1-pyrenylurea (**11m**) was characterized and reported previously (13).

*N,N,N'*-Trimethyl-*N'*-2-dipyrenylurea (**12m**):

$^1\text{H}$  NMR (CDCl<sub>3</sub>, 500 MHz)  $\delta$ : 2.71 (s, 6H), 3.46 (s, 3H), 7.85 (s, 2H), 7.97 (t,  $^3J = 7.4$  Hz, 1H), 7.971 (d,  $J = 9$  Hz, 2H), 8.06 (d,  $J = 9$  Hz, 2H), 8.16 (d,  $J = 9$  Hz, 2H).

## Acknowledgements

Funding for this project was provided by NSF grant CHE-0100596.

## References

1. F.M. Winnik. *Chem. Rev.* **93**, 587 (1993).
2. (a) J.B. Birks. *Photophysics of aromatic molecules*. Wiley, London, 1970; (b) E.J.P. Malar and A.K. Chandra. *Indian J. Chem., Sect. A: Inorg. Phys. Theor. Anal.* **19A**, 283 (1980).
3. K.A. Zachariasse and W. Kühnle. *Z. Phys. Chem. N.F.* **101**, 267 (1976).
4. K.A. Zachariasse, G. Duveneck, and R. Busse. *J. Am. Chem. Soc.* **106**, 1045 (1984).
5. (a) K.A. Zachariasse, G. Duveneck, and W. Kühnle. *Chem. Phys. Lett.* **113**, 337 (1985); (b) A. Tsuchida, T. Ikawa, T. Tomie, and M. Yamamoto. *J. Phys. Chem.* **99**, 8196 (1995).
6. K.A. Zachariasse, R. Busse, G. Duveneck, and W. Kühnle. *J. Photochem.* **28**, 237 (1985).
7. H.A. Staab, N. Riegler, F. Diederich, C. Krieger, and D. Schweitzer. *Chem. Ber.* **117**, 246 (1984).
8. (a) T. Hayashi, T. Suzuki, N. Mataga, Y. Sakata, and S. Misumi. *J. Phys. Chem.* **81**, 420 (1977); (b) T. Hayashi, N. Mataga, Y. Sakata, and S. Misumi. *Chem. Phys. Lett.* **41**, 325 (1976).
9. T. Kawashima, T. Otsubo, Y. Sakata, and S. Misumi. *Tetrahedron Lett.* 5115, (1978).
10. P. Wahl, C. Krieger, D. Schweitzer, and H.A. Staab. *Chem. Ber.* **117**, 260 (1984).
11. F. Vögtle. *Cyclophane chemistry*. John Wiley and Sons, New York, 1993. Chap. 9.
12. (a) G. Lepore, S. Migdal, D.E. Blagdon, and M. Goodman. *J. Org. Chem.* **38**, 2590 (1973); (b) K. Yamaguchi, G. Matsumura, H. Kagechika, I. Azumaya, Y. Ito, A. Itai, and K. Shudo. *J. Am. Chem. Soc.* **113**, 5474 (1991).
13. F.D. Lewis, T.L. Kurth, and W. Liu. *Photochem. Photobiol. Sci.* **1**, 30 (2002).
14. Jaguar Version 4.1. Schrodinger Inc., Portland, Oregon. 1991–2000.
15. T.L. Kurth, F.D. Lewis, C.M. Hattan, R.C. Reiter, and C.D. Stevenson. *J. Am. Chem. Soc.* **125**, 1460 (2003).
16. E.L. Eliel, S.H. Wilen, and L.N. Mander. *Stereochemistry of organic compounds*. Wiley-Interscience, New York, 1994. p. 57.
17. P. Reynnders, W. Kuehnle, and K.A. Zachariasse. *J. Phys. Chem.* **94**, 4073 (1990).
18. B.-C. Wang, J.-C. Chang, H.-C. Tso, and C.-Y. Cheng. *Huaxue*, **59**, 545 (2001).
19. CAChe Version 4.4. Fujitsu Ltd., Campbell, California 95008. 2000.
20. (a) W. Cross, G.W. Hawkes, R.T. Kroemer, K.R. Liedl, T. Loerting, R. Nasser, R.G. Pritchard, M. Steele, M. Watkinson, and A. Whiting. *J. Chem. Soc., Perkin Trans. 2*, 1261 (2001); (b) J.A. Zoltewicz, N.M. Maier, S. Lavieri, I. Ghiviriga, K.A. Abboud, and W.M.F. Fabian. *Tetrahedron*, **53**, 5379 (1997); (c) F. Cozzi and J.S. Siegel. *Pure Appl. Chem.* **67**, 683 (1995).
21. I.B. Berlman. *Handbook of fluorescence spectra of aromatic molecules*. 2nd ed. Academic Press, New York, 1971. p. 358.
22. D.R. James, A. Siemiarzczuk, and W.R. Ware. *Rev. Sci. Instrum.* **63**, 1710 (1992).
23. Timemaster Version 1.2x. Photon Technologies Inc., Monmouth Junction, New Jersey 08852. 1998.
24. A. Streitwieser, Jr., R.G. Lawler, and D. Schwaab. *J. Org. Chem.* **30**, 1470 (1965).



# Aminosilanes as two-electron donors: A technological application of radical cation chemistry

Ian R. Gould, Stephen A. Godleski, Paul A. Zielinski, and Samir Farid

**Abstract:** Aminosilanes possess the appropriate structural features for use as two-electron sensitizers in silver halide photography. Here, we describe studies of the nucleophile-assisted cleavage reactions of the C—Si bonds in their radical cations. Water is identified as a useful nucleophile. It is found that the kinetics of these reactions are best described by taking into account a radical cation – water complex. The cleavage reactions are also controlled by steric effects at silicon and by the proximity of a carboxylate group that can modify the nucleophilicity of the water. Cleavage forms an  $\alpha$ -amino radical that can donate a second electron to 9,10-dicyanoanthracene as a solution-phase electron acceptor.

**Key words:** silane, radical cation, two-electron sensitization, fragmentation, steric effects.

**Résumé :** Les aminosilanes possèdent les caractéristiques structurales appropriées qui permettent de les utiliser comme sensibilisateurs à deux électrons dans la photographie à l'halogénure d'argent. Nous décrivons les études portant sur les réactions de clivage, avec assistance nucléophile, de la liaison C—Si dans leurs cations radicalaires. L'eau est identifiée comme un nucléophile utile. On a trouvé que les cinétiques de ces réactions sont mieux décrites en tenant compte d'un complexe cation radicalaire – eau. Les réactions de clivage sont contrôlées également par les effets stériques du silicium, et par la proximité du groupe carboxylate qui peut modifier la nucléophilicité de l'eau. Le clivage conduit à un radical  $\alpha$ -amino qui peut donner un second électron au 9,10-dicyanoanthracène en tant qu'accepteur d'électron dans la phase en solution.

**Mots clés :** silane, cation radicalaire, sensibilisation à deux électrons, fragmentation, effets stériques.

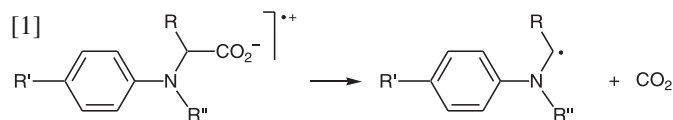
[Traduit par la Rédaction]

## Introduction

Fragmentation reactions of radical cations yield interesting and useful catalytic species, such as radicals, protons, and electrophiles (1). Pioneering work on these reactions by Arnold and co-workers explored their scope and defined their thermodynamics (2), and qualitative and quantitative studies on a wide variety of radical cation fragmentation reactions have now been reported (1, 2). Recently, a technological application for radical cation fragmentation was discovered in silver halide photography (3, 4). The primary event in the photographic process is excitation of a sensitizing dye that results in one-electron injection from the excited dye into the silver halide (5). Trapping of the resultant oxidized dye by electron transfer from an organic amine forms the amine radical cation. Fragmentation of this radical cation forms an  $\alpha$ -amino radical that is capable of injecting a

second electron into the silver halide, potentially doubling the efficiency of the photographic system (3, 4). This application of radical cation chemistry is termed two-electron sensitization (TES) of silver halide, and the amine precursor to the radical cation is a two-electron sensitizer (3, 4).

For proper operation, a two-electron sensitizer must meet several criteria. One of these is that the radical cation should fragment on the microsecond timescale, preferably with a rate constant,  $k_{fr}$ , that is controllable (3). The fragmentation reactions of the TES compounds described to date are decarboxylation reactions of amine carboxylates, as shown schematically in eq. [1]. The rate constants for fragmentation,  $k_{fr}$ , of several of these radical cations were reported (3).



They exhibit a strong dependence on the oxidation potential of the amine. A useful method of controlling the fragmentation rate constant that does not depend upon oxidation potential or, even better, that could compensate for the effect of oxidation potential, would provide a greater degree of control in the application of these compounds. The development of structures that provide such control is the subject of the present paper, which describes fragmentation reactions of aminosilane radical cations. These reactions are subject to control by steric factors and respond to the medium in a

Received 16 January 2003. Published on the NRC Research Press Web site at <http://canjchem.nrc.ca> on 25 June 2003.

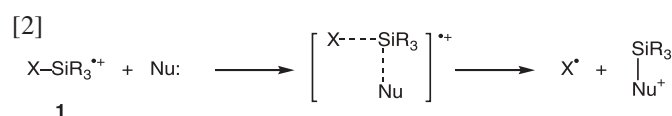
*Dedicated to Donald R. Arnold, a pioneer in the chemistry of radical cations.*

**I.R. Gould,<sup>1</sup>** Department of Chemistry and Biochemistry, Arizona State University, Tempe, AZ 85287-1604, U.S.A.  
**S.A. Godleski, P.A. Zielinski, and S. Farid.** Research Laboratories, Eastman Kodak Company, Rochester, NY 14650-2109, U.S.A.

<sup>1</sup>Corresponding author (e-mail: [igould@asu.edu](mailto:igould@asu.edu)).

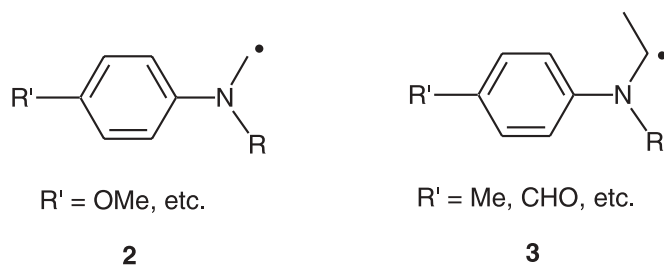


different way than do the decarboxylation reactions. Fragmentation reactions of aminosilane radical cations have been described previously by Mariano and co-workers, and kinetic measurements of these reactions were reported (6). Here, we describe more detailed kinetic studies; we further explore the factors that control the rate constants for fragmentation of these radical cations; and we provide solution-phase evidence that aminosilanes can act as TES reagents. Fragmentation of the C—Si bond in silane radical cations is usually not a unimolecular reaction for many systems but occurs via a nucleophilic-assisted mechanism, as indicated in eq. [2], where  $X\text{---SiR}_3^{++}$  represents a generic silane radical cation (6, 7). One consequence of this is that the bimolecular rate constants for the desilylation reactions have been found to be sensitive to steric effects, particularly with respect to substitution at silicon (7).



For example, the reactivity of triethyl derivatives (**1**,  $R_3 = \text{Et}_3$ ) was observed to be almost an order of magnitude lower than the corresponding trimethyl analogues ( $R_3 = \text{Me}_3$ ) (7). The reactivity of the derivative  $R_3 = \text{Me}_2\text{-}i\text{-Bu}$  was still lower, and the  $R_3 = i\text{-Pr}_3$  compound was dramatically less reactive than the triethylsilane compound,  $R_3 = \text{Et}_3$ . Because the substituents on silicon have only a small influence on the oxidation potential of the compound, these donors offer an obvious way to change,  $k_{\text{fr}}$ , without changing the oxidation potential of the radical cation precursor.

In the TES scheme, the radical  $X^\bullet$  should be reducing enough to inject an electron into the conduction band of silver halide, i.e., it should have an oxidation potential that is equal to, or more negative than, ca.  $-0.9 \text{ V}$  vs. SCE (3). From previous work on the carboxylate TES donors, a set of structural features to meet this requirement for  $X^\bullet$  have been identified (3). Specifically, a radical site that is  $\alpha$  to nitrogen in a dialkylaniline (Structure **2**) is sufficiently reducing — even when the radical is primary — so long as the aniline is substituted with a strong electron-donating group, e.g., 4-methoxy. However, with weakly electron-donating groups or with electron-withdrawing groups in the 4 position, such a radical must have secondary substitution (Structure **3**) to be sufficiently reducing.



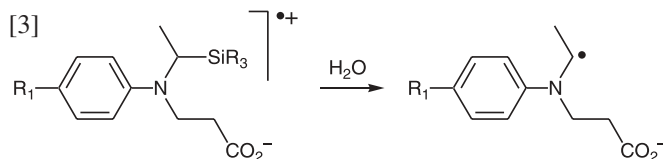
To generate such radicals via desilylation reactions, trialkylsilicon groups should be placed at the  $\alpha$  positions of dialkylanilines. In addition, to be useful for photographic purposes, such compounds require a water-solubilizing

substituent. Here, we describe a series of useful TES donors, based on desilylation chemistry, which satisfy these various requirements.

## Results and discussion

### Structural features and synthetic approach

The basic structure that has the important required features is shown in eq. [3].



Cleavage of the C—Si bond generates the desired  $\alpha$ -amino radical. The  $\beta$ -propionate group serves as a water-solubilizing functionality. Decarboxylation, as in eq. [1], does not occur because this would generate a primary, unstabilized alkyl radical.

The synthetic route employed is outlined in Scheme 1. The *tert*-butyl ester of aniline  $\beta$ -propionate, prepared via Michael addition of *tert*-butyl acrylate to aniline, was reacted with the appropriate trialkylsilane triflates (see experimental section) to provide the *tert*-butyl ester silyl aniline derivatives **4E** and **5E**. The *tert*-butyl group was removed with trifluoroacetic acid, and the sodium carboxylate salt **4S** was obtained using sodium methoxide or sodium hydroxide. The 4-formyl *tert*-butyl ester derivatives **6E** and **7E** were obtained from **4E** and **5E** via a Vilsmeier reaction. Removal of the *tert*-butyl group as before gave the carboxylate **6S**. The structures of the compounds are summarized in Table 1.

### Solution phase studies on the radical cations

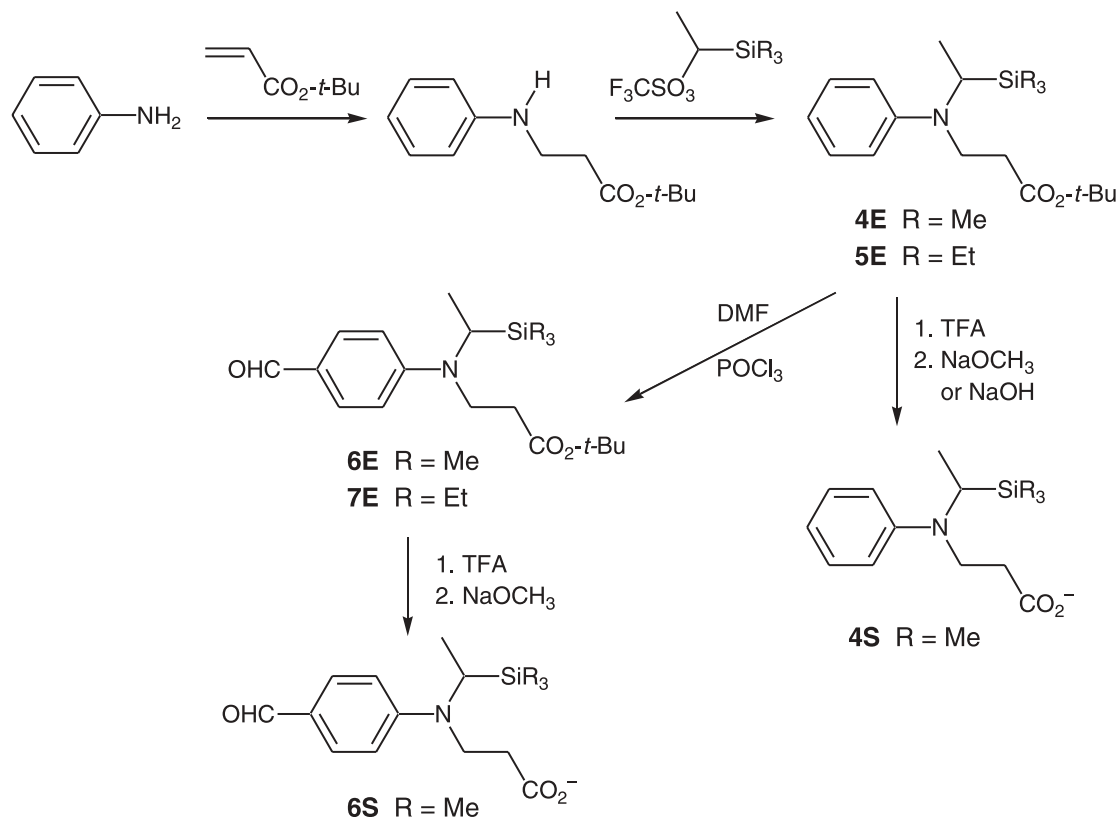
#### Experimental approach

The rate constants for fragmentation of the radical cations were obtained using transient absorption spectroscopy, using 9,10-dicyanoanthracene (DCA) as the excited-state electron acceptor. The radical cations of the donor molecules,  $X\text{---SiR}_3^{++}$ , were formed by oxidation of the donor using a biphenyl radical cation ( $C^{++}$ ) in a cosensitization scheme (Scheme 2) (8).

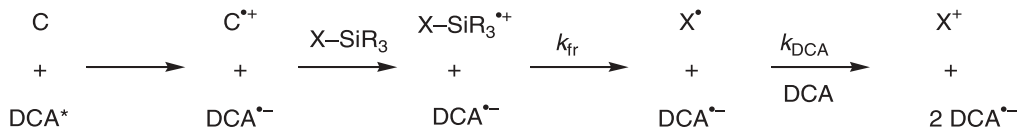
Fragmentation of  $X\text{---SiR}_3^{++}$  leads to the formation of the radical,  $X^\bullet$ . If  $X^\bullet$  is sufficiently reducing, it can donate an electron to another DCA molecule so that *two* reduced acceptors are formed for *one* absorbed photon in an exact solution phase analogue of the TES scheme (3). Formation of this second-reduced DCA can easily be observed in a time-resolved absorption experiment when  $k_{\text{fr}}$  is not so small that its formation is significantly slower than the processes that remove the  $\text{DCA}^{\bullet-}$ . Indeed, observation of two DCA reduction processes represents a convenient method for confirmation of fragmentation of the radical cations, because it provides evidence for formation of the ( $X^\bullet$ ) radical cleavage product. In general, reduction of two DCA molecules is observed for all of the silane radical cations studied here, when  $k_{\text{fr}}$  is greater than ca.  $10^6 \text{ s}^{-1}$  (see for example, Fig. 1 below). As discussed further below, in some cases the  $X^\bullet$  radicals could be directly observed. When evidence of radical forma-



Scheme 1.



Scheme 2.



tion was obtained in this way, the rate constant for fragmentation of the radical cation,  $k_{\text{fr}}$ , was simply equated to the observed rate constant for its pseudo-first-order decay.

The decay kinetics of the donor radical cation can be monitored in different ways, depending on the system under investigation. One problem is that there is no analyzing wavelength where only the radical cation absorbs, i.e., contributions from the DCA radical anion ( $\text{DCA}^{\bullet-}$ ) to the overall absorption decay kinetics are always observed. The simplest way to deal with this is to saturate the solution with oxygen, which scavenges  $\text{DCA}^{\bullet-}$  to form the nonabsorbing superoxide ( $\text{O}_2^{\bullet-}$ ). Under these conditions, a fast-absorption decay is observed, owing to the reaction of  $\text{DCA}^{\bullet-}$ , with a pseudo-first-order rate constant,  $k_{\text{O}_2}$ , which is usually ca.  $7 \times 10^6 \text{ s}^{-1}$  in aqueous acetonitrile. This is followed by a slower pseudo-first-order decay as a result of the reaction of the donor radical cation. This method is easily implemented when the  $\text{X-SiR}_3^{\bullet+}$  fragmentation rate is much slower than the rate of reaction of the  $\text{DCA}^{\bullet-}$  with oxygen. As  $k_{\text{fr}}$  increases to ca.  $2\text{--}3 \times 10^6 \text{ s}^{-1}$ , it becomes necessary to analyze the observed absorption decay as a sum of two exponentials.

In principle, the fragmentation rate can also be determined from the rate of growth of the radical product,  $\text{X}^{\bullet}$  (Scheme 2). The radical products derived from **4** and **5** cannot be readily observed in the visible region of the spectrum.

With the 4-formyl derivatives **6** and **7**, however, the radicals can be observed at long wavelengths ( $>730 \text{ nm}$ ). In this wavelength region, the radical cation and radical anion absorb only weakly, and grow-in of  $\text{X}^{\bullet}$  can be observed as a result of fragmentation of the  $\text{X-SiR}_3^{\bullet+}$ . As discussed above, however, the radicals also react with the DCA sensitizer to form  $\text{DCA}^{\bullet-}$ , so that the exponential grow-in is followed by an exponential absorption decay with a pseudo-first-order rate,  $k_{\text{DCA}}$ , that depends upon the DCA concentration, (Scheme 2). One interesting feature of such a double exponential kinetic scheme is that the rates can become "reversed" (9). This is the case if the rate of decay of the radical caused by the reaction with DCA,  $k_{\text{DCA}}$ , is faster than the rate at which it is formed owing to the fragmentation reaction,  $k_{\text{fr}}$ . Under these conditions, the rate of *growth* of the absorption signal is equal to  $k_{\text{DCA}}$  (i.e., the process that *removes* the  $\text{X}^{\bullet}$ ) and the rate of the *decay* of the absorption signal is equal to  $k_{\text{fr}}$  (i.e., the process that *forms* the  $\text{X}^{\bullet}$ ) (9). The two processes can be distinguished, and the fragmentation rate correctly identified, by changing the concentration of DCA, which affects only the pseudo-first-order  $k_{\text{DCA}}$  and not  $k_{\text{fr}}$ .

Finally, under certain conditions, an estimate for  $k_{\text{fr}}$  can be obtained from analysis of the growth of the second  $\text{DCA}^{\bullet-}$  signal because of the reaction of  $\text{X}^{\bullet}$  with DCA. When  $k_{\text{fr}}$  and



**Table 1.** Kinetic parameters for fragmentation of aminosilane radical cations in acetonitrile, using water as a nucleophile, at room temperature.<sup>a</sup>

Structure	Compound number	$K_{\text{eq}}^b$ ( $\text{M}^{-1}$ )	$k_{\text{Nu}}^c$ ( $\text{s}^{-1}$ )	$K_{\text{eq}}k_{\text{Nu}}^d$ ( $\text{M}^{-1} \text{s}^{-1}$ )	$k_0^e$ ( $\text{s}^{-1}$ )
	<b>4S</b>	0.1	$1.4 \times 10^6$	$1.4 \times 10^5$	$\sim 1 \times 10^5$
	<b>4E</b>	0.08	$5.1 \times 10^6$	$4.1 \times 10^5$	$\sim 5 \times 10^4$
	<b>5E</b>	0.15	$4.3 \times 10^5$	$6.5 \times 10^4$	$\sim 5 \times 10^4$
	<b>6S</b>	0.1	$1.4 \times 10^7$	$1.4 \times 10^6$	$\sim 4 \times 10^5$
	<b>6E</b>	0.1	$3.6 \times 10^7$	$3.6 \times 10^6$	$\sim 5 \times 10^5$
	<b>7E</b>	0.1	$5.4 \times 10^6$	$5.4 \times 10^5$	$\sim 4 \times 10^5$

<sup>a</sup>The parameters are obtained from fitting the data according to eq. [7]; see text for details and a discussion of errors.

<sup>b</sup>Equilibrium constant for complex formation between radical cation and water,  $k_c/k_c$ .

<sup>c</sup>Unimolecular rate constant for nucleophile-assisted cleavage of radical cation in water complex.

<sup>d</sup>The effective bimolecular rate constant for water-assisted fragmentation of the radical cation.

<sup>e</sup>First-order rate constant for decay of the radical cation in acetonitrile.

$k_{\text{DCA}}$  are of similar magnitude, a double exponential analysis of the data can be used to estimate both rate constants, as illustrated in Fig. 1, below.

In the present study, we have used all three techniques as  $k_{\text{fr}}$  varied as a function of the concentration of the nucleophile (usually water, see below). The absorbance as a function of time, in each case, is analyzed according to a specific type of double exponential analysis. Shown in Fig. 2 are representative transient absorption spectra observed upon excitation of a solution of DCA–biphenyl in the presence of the aminosilanes, in this case silane **4S**. According to Scheme 2, after oxidation of the silane by the biphenyl radical cation and before its fragmentation, equal concentrations of the silane radical cation and the DCA radical anion are present. From the previously determined extinction coefficient of the DCA radical anion (8), the extinction coefficient of the silane radical cations can thus be obtained by comparing the signal sizes due to the radical anion and radical cation. The optimum wavelength for observing the silane radical cations

is clearly around 530 nm (Fig. 2 and ref. 6), and wavelengths in this region were chosen for direct observation of these species.

Shown in Fig. 3 is a transient absorption decay at 530 nm for excitation of DCA–biphenyl in the presence of aminosilane **6E**. A fast-absorbance decay caused by reaction of  $\text{DCA}^{\bullet-}$  with oxygen is observed, followed by a slower decay as a result of fragmentation of the silyl radical cation,  $\text{6E}^{\bullet+}$ . The total absorbance,  $A$ , is fitted to an equation of the form shown in eq. [4], where  $t$  is time and  $A_1$  and  $A_2$  represent the

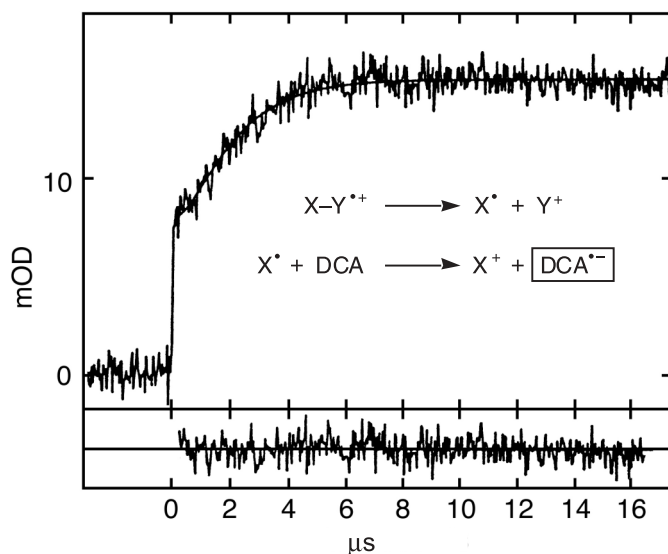
$$[4] \quad A = A_1 e^{-k_1 t} + A_2 e^{-k_2 t} + A_3$$

absorbances owing to  $\text{DCA}^{\bullet-}$  and  $\text{6E}^{\bullet+}$ , respectively, and  $A_3$  represents small amounts of residual absorbance at infinite time. In this case,  $k_1$  corresponds to  $k_{\text{O}_2}$  and  $k_2$  corresponds to  $k_{\text{fr}}$ .

Figure 4 shows the formation and decay of the radical,  $\text{X}^{\bullet}$ , formed from fragmentation of the radical cation of the 4-formyl-substituted silylaniline **7E**. The absorbance is fitted



**Fig. 1.** Optical density (in units of  $10^{-3}$ , mOD) at 705 nm, as a function of time,  $t$ , observed upon excitation of DCA–biphenyl and **4S** in argon-purged acetonitrile containing 9.3 M water, showing two-electron reduction of DCA. The absorbance at this wavelength is mainly due to the radical anion  $\text{DCA}^{\bullet-}$ . The jump in optical density at zero time initial is owing to absorbance by  $\text{4S}^{*+}$  and  $\text{DCA}^{\bullet-}$ . The growth in absorbance is owing to reduction of a second DCA after fragmentation of the  $\text{4S}^{*+}$ . The change in absorbance with time is described by a consecutive  $a \rightarrow b \rightarrow c$  process in which  $c$  is monitored. The smooth curve represents the best fit to the data according to  $15.3 - 12.2 \exp(-6.1 \times 10^5 t) + 5.0 \exp(-1.5 \times 10^6 t)$ . The slower component corresponds to the  $\text{4S}^{*+}$  reaction,  $k_{\text{fr}}$  under the present conditions, and the faster component to reduction of the second DCA.



to an equation of the form shown in eq. [5], where  $A_1$  represents the absorbance of  $X^*$  at the concentration of the  $X\text{--SiR}_3^{*+}$  precursor extrapolated to zero time and  $A_2$  represents

$$[5] \quad A = (A_1 k_1)/(k_2 - k_1) (e^{-k_1 t} - e^{-k_2 t}) + A_2$$

the residual absorbance at infinite time. In this case, the “normal” situation applies, i.e.,  $k_1$  corresponds to  $k_{\text{fr}}$ , and  $k_2$  corresponds to  $k_{\text{DCA}}$ . Figure 1 shows the growth in absorption caused by the formation of the second  $\text{DCA}^{\bullet-}$ , as a result of reaction of  $X^*$  with DCA, for excitation of DCA–biphenyl with silane **4S**. The absorbance is fitted according to eq. [6], where  $A_1$  represents the absorbance of the second  $\text{DCA}^{\bullet-}$  at infinite time,  $A_2$  represents the absorbance of the first  $\text{DCA}^{\bullet-}$  that appears at essentially zero time, and  $k_1$  corresponds to  $k_{\text{fr}}$  and  $k_2$  to  $k_{\text{DCA}}$ .

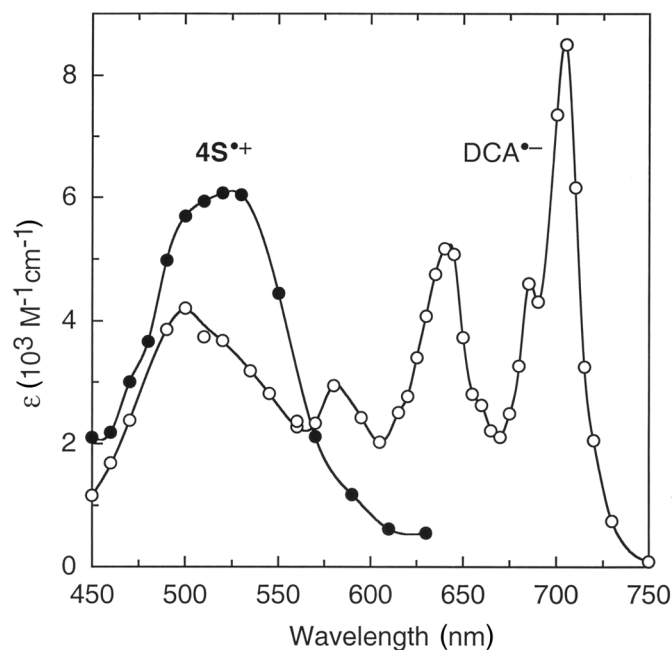
$$[6] \quad A = A_1[1 + (k_2 e^{-k_1 t} - k_1 e^{-k_2 t})/(k_2 - k_1)] + A_2$$

#### Fragmentation rate constants

Experiments were performed in acetonitrile at a varying concentrations of water because, in a photographic dispersion, water is the likely nucleophile to assist the fragmentation process. In all cases, the rate of fragmentation of the radical cations increased with increasing water concentration (6, 7). Typical data are shown in Fig. 5 for the radical cations of silanes **6E** and **4E**.

As observed previously (6), the dependence on added water as a nucleophile is somewhat nonlinear, with the reaction

**Fig. 2.** Transient absorption spectra of (open circles) the radical anion of 9,10-dicyanoanthracene ( $\text{DCA}^{\bullet-}$ ) in acetonitrile solvent and (closed circles) the radical cation of a representative aminosilane **4S** ( $\text{4S}^{*+}$ ) in acetonitrile in the presence of 20% water, showing overlap of the spectra. The spectrum of  $\text{4S}^{*+}$  in acetonitrile in the presence of less water is somewhat broader. The figure indicates that the optimum wavelength for direct observation of the aminosilane radical cations is around 530 nm.



rate becoming less dependent at higher water concentrations. The kinetics of reactions involving high concentrations of hydroxylic quenchers, such as water, often exhibit nonlinear behavior that has been subject to a variety of explanations (6, 10). For example, with increasing water concentration, the character of the solvent gradually changes from polar aprotic to polar protic, which would be expected to decrease the nucleophilicity of the water (11). However, the radical cations are strong Lewis acids, and an alternate explanation of the behavior, in this case, may be due to reversible formation of a complex. Previously, Mariano and co-workers suggested a similar explanation for the nonlinear dependence of this reaction on water concentration, in terms of a covalent complex between the oxygen of the nucleophile and the silicon on the radical cation (6). Such a complex, whatever its structure, can be characterized by a second-order rate constant for formation,  $k_{\text{C}}$ , and a first-order rate constant for separation,  $k_{-\text{C}}$ , Scheme 3. The ratio of these rate constants,  $k_{\text{C}}/k_{-\text{C}}$ , defines an overall equilibrium constant,  $K_{\text{eq}}$ . Nucleophile-assisted fragmentation can occur within the complex, with a first-order rate constant,  $k_{\text{Nu}}$ , Scheme 3. In this scheme,  $k_0$  is the pseudo-first-order decay rate constant of the radical cation in the absence of added nucleophile. Based on Scheme 3, the decay of the radical cation and the growth of the radical  $X^*$  are properly described by two exponential components. However, when  $k_{-\text{C}}$  is much larger than  $k_{\text{Nu}}$ , the time constant for one of these components is much larger than the other, and this fast component also has a small amplitude. Under these conditions, only the larger and slower component is actually observed. The time constant



Scheme 3.

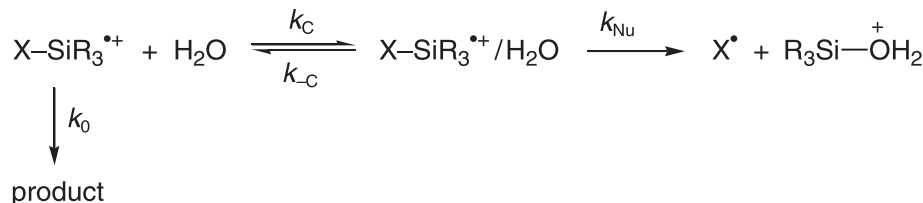
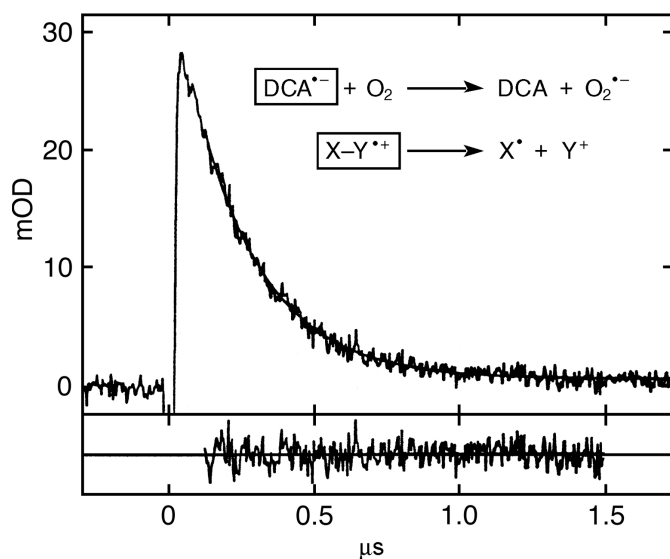


**Fig. 3.** Optical density (in units of  $10^{-3}$ , mOD) at 530 nm, as a function of time,  $t$ , observed upon excitation of DCA-biphenyl and **6E** in oxygen-purged acetonitrile containing 1.1 M water. Both the radical anion of DCA ( $\text{DCA}^{\bullet-}$ ) and the radical cation  $\text{6E}^{\bullet+}$  contribute to the total absorbance, and the decay is thus a sum of two independent pseudo-first-order exponentials. The smooth curve represents the best fit to the data and is given by:  $5.1 \exp(-8.1 \times 10^6 t) + 32.3 \exp(-4.0 \times 10^6 t) + 0.6$ . The faster decay corresponds to reaction of  $\text{DCA}^{\bullet-}$  with oxygen and the slower decay to reaction of  $\text{6E}^{\bullet+}$  with water, i.e.,  $k_{\text{fr}}$  under the present conditions.

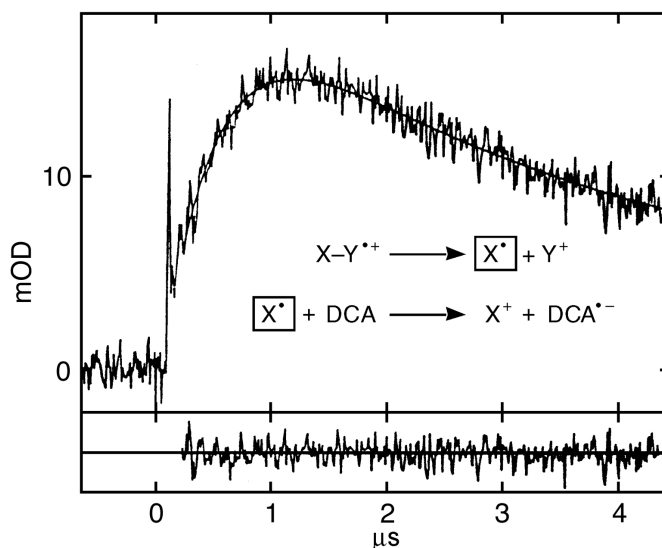


for this component is given by eq. [7] and is equated to  $k_{\text{fr}}$ .<sup>2</sup> Using eq. [7], values for  $K_{\text{eq}}$  and  $k_{\text{Nu}}$  that reproduce the observed dependence of  $k_{\text{fr}}$  on water concentration can be obtained.<sup>3</sup>

$$\begin{aligned}
 [7] \quad k_{\text{fr}} = & 0.5 \{k_C [\text{H}_2\text{O}] + k_0 + k_{-C} + k_{\text{Nu}}\} \\
 & - 0.5 \{(k_C [\text{H}_2\text{O}] + k_0 - k_{-C} - k_{\text{Nu}})^2 \\
 & + 4k_C [\text{H}_2\text{O}]k_{-C}\}^{0.5}
 \end{aligned}$$

The data are summarized in Table 1. The values for  $K_{\text{eq}}$  are roughly the same for all of the reactions studied here and are small, ca.  $0.1 \text{ M}^{-1}$ . In contrast to  $K_{\text{eq}}$ , however,  $k_{\text{Nu}}$  depends quite strongly upon the substituents on the radical cat-

**Fig. 4.** Optical density (in units of  $10^{-3}$ , mOD) at 740 nm, as a function of time,  $t$ , observed upon excitation of DCA-biphenyl and **7E** in argon-purged acetonitrile containing 2.1 M water. The absorbance at this wavelength is mainly owing to the radical resulting from fragmentation of the radical cation,  $\text{7E}^{\bullet+}$ . The absorbance is described by a consecutive  $a \rightarrow b \rightarrow c$  process in which the intermediate  $b$  is monitored. The smooth curve represents the best fit to the data and is given by:  $-21.05 \exp(-2.1 \times 10^6 t) + 19.1 \exp(-3.4 \times 10^5 t) + 3.9$ .<sup>4</sup> The negative component corresponds to radical growth,  $k_{\text{fr}}$  under the present conditions, and the positive component to radical decay caused by reduction of DCA. The spike at early time is owing to the biphenyl (cosensitizer) radical cation (see text), which reacts very rapidly with **7E**.



ion (Table 1). Although Table 1 summarizes the best values for the parameters, we find that reasonable fits to the data can actually be obtained using both slightly higher and lower values for  $K_{\text{eq}}$  (by ca. 30%) than those given in Table 1, with corresponding changes in  $k_{\text{Nu}}$  in the opposite direction. Although there is some uncertainty associated with absolute values of  $K_{\text{eq}}$  and  $k_{\text{Nu}}$ , the product  $K_{\text{eq}}k_{\text{Nu}}$  is determined quite accurately and represents a good measure of the relative reactivities of the different compounds, Table 1.  $K_{\text{eq}}k_{\text{Nu}}$  has dimensions of  $\text{M}^{-1} \text{ s}^{-1}$ , is equivalent to the initial slope of the observed rate constant vs. water concentration,

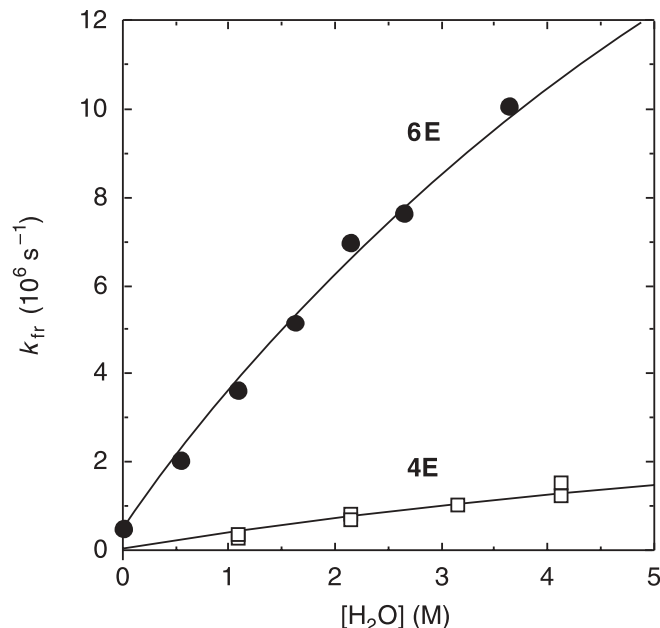
<sup>2</sup>Equation [7] gives the time constant of the slower observed component as a difference between two functions. The time constant of the faster component is given by the sum of the same two functions, which is too large ( $>10^8 \text{ s}^{-1}$ ) to be resolved under the experimental conditions.

<sup>3</sup>In principle, fitting of the dependence of  $k_{\text{fr}}$  on  $[\text{H}_2\text{O}]$  using eq. [7] allows determination of values for both  $k_C$  and  $k_{-C}$ . However, the  $k_{\text{fr}}$  calculated using eq. [7] are insensitive to the absolute values of  $k_C$  and  $k_{-C}$  when  $k_C$  is  $\sim 10^8 \text{ M}^{-1} \text{ s}^{-1}$  or larger.

<sup>4</sup>The form of this equation is not identical to that of eq. [5] due to a small absorption at this wavelength of  $\text{DCA}^{\bullet-}$ , the kinetics of which are superimposed and are described by eq. [6].



**Fig. 5.** Observed rate constants for pseudo-first-order decay of the radical cations  $6E^{+}$  and  $4E^{+}$ ,  $k_{fr}$ , as a function of water concentration, in acetonitrile at room temperature, illustrating the effect of the oxidation potential of the precursor. The curves are calculated as described in the text, with values for effective bimolecular rate constants,  $K_{eq}k_{Nu}$ , of  $3.6 \times 10^6 \text{ M}^{-1} \text{ s}^{-1}$  for  $6E^{+}$  and  $4.1 \times 10^5 \text{ M}^{-1} \text{ s}^{-1}$  for  $4E^{+}$ .

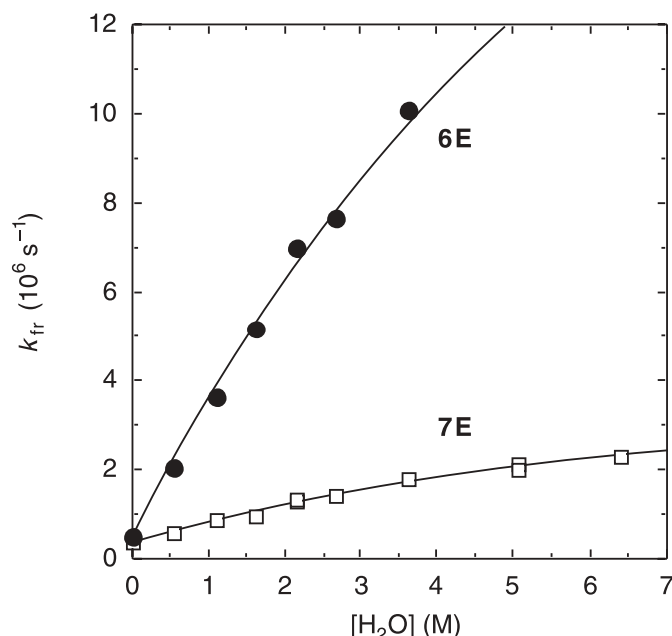


and represents the “effective” bimolecular rate constant. This value can thus be compared to the bimolecular rate constants reported for nucleophile-assisted fragmentation of silane radical cations reported elsewhere (6, 7). Importantly, the use of  $K_{eq}k_{Nu}$  allows for the nonlinear dependence on water concentration to be properly accounted for.

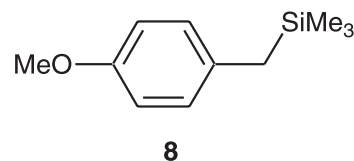
The effect of a 4-formyl substituent is to significantly enhance the reactivity toward water as a nucleophile. This is expected based upon previous work on silane and other radical cations (1, 2, 6, 7) and is easily explained using the thermodynamic cycle approach to understanding radical cation reactivity, pioneered by Arnold and co-workers (12). Using such cycles, it can easily be shown that when all other factors are equal, the thermodynamics of a radical cation reaction should become more favorable with increasing oxidation potential of the precursor, leading to a faster reaction (12). In the present case, the electron-withdrawing formyl group increases the oxidation potential of the aminosilane and faster reaction results, as observed in the comparison between  $6E$  and  $4E$  in Fig. 5. The data of Table 1 (see also  $6S$  vs.  $4S$  and  $7E$  vs.  $5E$ ) indicate that the effect of the 4-formyl substituent is to increase  $K_{eq}k_{Nu}$  by approximately one order of magnitude, as compared with the corresponding unsubstituted compound. Comparable increases in rate constant for cleavage using methanol as the nucleophile were observed previously by Mariano and co-workers for similar silane radical cations with electron-withdrawing groups on nitrogen (6).

The aminosilanes are considerably easier to oxidize than the aryltrialkylsilanes studied previously (7), yet the reactivities of their radical cations towards water as a nucleophile are almost as high. This may be a consequence of the fact

**Fig. 6.** Observed rate constants for pseudo-first-order decay of the radical cations  $6E^{+}$  and  $7E^{+}$ ,  $k_{fr}$ , as a function of water concentration, in acetonitrile at room temperature, illustrating the effect of steric hindrance at silicon. The curves are calculated as described in the text, with values for effective bimolecular rate constants,  $K_{eq}k_{Nu}$ , of  $3.6 \times 10^6 \text{ M}^{-1} \text{ s}^{-1}$  for  $6E^{+}$  and  $5.4 \times 10^5 \text{ M}^{-1} \text{ s}^{-1}$  for  $7E^{+}$ .



that the positive charge is likely to be more localized on the nitrogen in the aminosilane radical cations, i.e., close to the site of nucleophilic attack. In the anisyl silane, **8**, the positive charge may be located more on the oxygen, i.e., away from the site of nucleophilic attack.

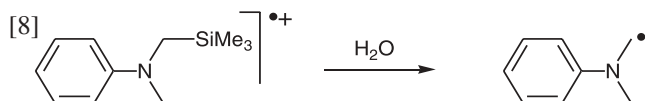


In addition to oxidation potential, the silanes offer a means to control the rate of fragmentation via steric effects, as illustrated in Fig. 6, where the dependence on water concentration is shown for trimethylsilyl **6E** and triethylsilyl **7E**. The  $K_{eq}k_{Nu}$  for the triethylsilanes are smaller than those of the trimethyl analogues by a factor of  $ca. 6 \pm 1$  for both the unsubstituted and the 4-formyl anilines (Table 1, see **5E** vs. **4E** and **7E** vs. **6E**). Steric effects of similar magnitude were observed in corresponding reactions of the radical cations of benzyltrialkylsilanes (7). Interestingly, a comparison of the *tert*-butyl esters and the corresponding carboxylate salts shows that the carboxylates react with water more slowly by a factor of  $ca. 3$  (Fig. 7 and Table 1, see **4S** vs. **4E** and **6S** vs. **6E**). A definitive explanation of this effect cannot be given, but it may be attributed to hydration of the carboxylate group, which will decrease the nucleophilicity of the water in the microenvironment of the C—Si bond (11).

The literature experiment that most closely relates to the present work is the water-assisted radical cation fragmenta-



tion reaction shown in eq. [8], studied by Mariano and co-workers (6c). As mentioned above, a nonlinear dependence on water concentration was also observed in this previous work, and a rate constant was estimated at low water concentrations to be  $1.3 \times 10^6$ .



This value is somewhat higher than the ( $K_{eq}k_{Nu}$ ) for either of the *p*-H-substituted trimethylsilyl-radical cations included in the present study (Table 1). The reasons for this small effect is not exactly clear. It may further illustrate the subtle effects that substituents on nitrogen can have on the micropolarity and, thus, the nucleophilicity of the water. Alternatively, it may reflect the somewhat different methods of kinetic analysis used in the two studies.

The nature of the decay process of the radical cation in the absence of added water,  $k_0$ , has not been established. These values are either measured directly in the absence of water or are obtained as part of the fitting procedure described below. Pseudo-first-order rate constants less than ca.  $10^6 \text{ s}^{-1}$  are often difficult to measure accurately in experiments such as these because of competing second-order recombination reactions. They are also the least accurately determined parameters obtained from the fitting procedure. Nevertheless, it is clear that the decay constants of the unsubstituted, aminosilane radical cations **4E** and **5E**, in the absence of water, are in the range of  $\sim 5 \times 10^4 \text{ s}^{-1}$ , whereas those of the 4-formyl analogues **6E** and **7E** are nearly an order of magnitude larger,  $\sim 4\text{--}5 \times 10^5 \text{ s}^{-1}$ . The higher reactivity of the 4-formyl derivatives, relative to the unsubstituted analogues, is understandable based on the thermodynamic arguments given above. It is not possible to confirm fragmentation by the observation of two-electron reduction under these conditions, because the  $k_{fr}$  would be too small. It is possible that the decays under these conditions may be due to deprotonation (6) or perhaps to reaction with impurities.

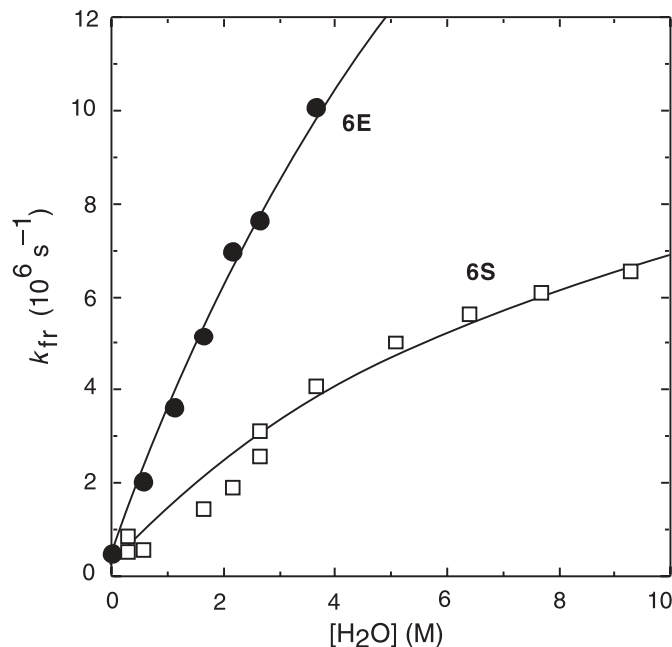
## Conclusions

The properties of a series of aminosilanes have been investigated as potential two-electron donors for silver halide photography. Solution-phase studies have been performed that confirm the radical cations of the donors fragment to give appropriately reducing radicals in the presence of an appropriate nucleophile. By varying the steric bulk of the substituents on the silicon, the rate of fragmentation of the radical cations can be varied substantially with minimal changes in the oxidation potential of the donor. Pseudo-first-order rate constants for fragmentation varying over ca. 2 orders of magnitude have been measured by varying the silane oxidation potential, the size of the substituents at silicon, and the concentration of water as an external nucleophile.

## Experimental

The solvents were spectrograde and used as received. 9,10-Dicyanoanthracene and biphenyl were available from previous studies (3). The laser flash photolysis experiments

**Fig. 7.** Observed rate constants for pseudo-first-order decay of the radical cations **6E**<sup>•+</sup> and **6S**<sup>•+</sup> as a function of water concentration, in acetonitrile at room temperature, illustrating the effect of a proximal carboxylate group. The curves are calculated as described in the text, with values for effective bimolecular rate constants,  $K_{eq}k_{Nu}$ , of  $3.6 \times 10^6 \text{ M}^{-1} \text{ s}^{-1}$  for **6E**<sup>•+</sup> and  $1.4 \times 10^6 \text{ M}^{-1} \text{ s}^{-1}$  for **6S**<sup>•+</sup>.



were performed using a nanosecond pulsed excimer (Questek model 2620, 308 nm, ca. 20 ns, ca. 100 mJ) pumped dye laser (Lambda Physik model FL 3002). The laser dye was DPS in dioxane (410 nm, ca. 20 ns, ca. 10 mJ). The analyzing light source was a pulsed 150W xenon arc lamp (Osram XBO 150/W). The arc lamp power supply was a PRA model 302, and the pulser was a PRA model M-306. The pulser increased the light output by ca. 100-fold for a time period of ca. 2–3 ms. The analyzing light was focused through a small aperture (ca. 1.5 mm) in a cell holder designed to hold 1 cm<sup>2</sup> cuvettes. The laser and analyzing beams irradiated the cell from opposite directions and crossed at a narrow angle (ca. 15°). After leaving the cell, the analyzing light was collimated and focused onto the slit (1 mm, 4 nm bandpass) of an ISA H-20 monochromator. The light was detected using a Hamamatsu model R446 photomultiplier. The output of the photomultiplier tube was terminated into 50 ohm and captured using a Tektronix DSA-602 digital oscilloscope. The experiments were performed in 1 cm<sup>2</sup> cuvettes, equipped with arms for degassing. The DCA and biphenyl concentrations in all of the time-resolved experiments were ca.  $10^{-4}$  and ca. 0.1 M, respectively. The concentrations of the aminosilanes was typically ca.  $2\text{--}4 \times 10^{-3} \text{ M}$ .

NMR spectra were run on a Varian 300 MHz spectrometer, generally at a concentration of ca. 100 mg mL<sup>-1</sup>. For selected examples, additional NMR data obtained from measurements at concentrations of 10–20 mg mL<sup>-1</sup>, including coupling constants, are given in Table 2. Preparation of the materials was performed as follows:



**Table 2.** Detailed NMR data of representative compounds.

R	Me	Et	Me	Me
R'	H	H	CHO	CHO
R''	CO <sub>2</sub> <sup>-</sup>	CO <sub>2</sub> - <i>t</i> -Bu	CO <sub>2</sub> <sup>-</sup>	CO <sub>2</sub> - <i>t</i> -Bu
Compound (solvent)	<b>4S</b> (D <sub>2</sub> O)	<b>5E</b> (CDCl <sub>3</sub> )	<b>6S</b> (CD <sub>3</sub> OD)	<b>6E</b> (CDCl <sub>3</sub> )
H <sub>a</sub>	3.49	3.63	3.75	3.73
H <sub>b</sub>	3.38	3.47	3.57	3.54
H <sub>c</sub>	2.41	2.59	2.57	2.62
H <sub>d</sub>	2.31	2.41	2.37	2.43
H <sub>e</sub>	3.34	3.51	3.62	3.49
H <sub>f</sub>	1.14	1.24	1.36	1.31
<i>o</i> -H	6.83	6.73	6.84	6.72
<i>m</i> -H	7.20	7.20	7.67	7.69
<i>p</i> -H	6.65	6.65	—	—
CHO	—	—	9.52	9.7
<i>t</i> -Bu	—	1.47	—	1.46
Si(CH <sub>3</sub> ) <sub>3</sub>	-0.01	—	0.09	0.1
Si(CH <sub>2</sub> CH <sub>3</sub> ) <sub>3</sub>	—	0.65	—	—
Si(CH <sub>2</sub> CH <sub>3</sub> ) <sub>3</sub>	—	0.97	—	—
<b><i>J</i> values</b>				
<i>J</i> <sub>ab</sub>	15.0	15.5	14.8	15.1
<i>J</i> <sub>ac</sub>	5.2	5.2	4.8	5.2
<i>J</i> <sub>ad</sub>	10.2	10.4	11.0	10.5
<i>J</i> <sub>bc</sub>	9.7	9.7	11.1	10.2
<i>J</i> <sub>bd</sub>	5.8	5.8	5.5	5.8
<i>J</i> <sub>cd</sub>	14.9	14.9	14.8	15.7
<i>J</i> <sub>ef</sub>	7.4	7.4	7.3	7.4

***tert*-Butyl 3-(*N*-phenylamino)propionate**

Aniline (126.7 g, 1.36 mol), *tert*-butyl acrylate (174.5 g, 1.36 mol), and methanesulfonic acid catalyst (4 mL) were combined and stirred at gentle reflux (135°C) for 4 h. The mixture was cooled and petroleum ether (1 L) was added. The resulting precipitated salt was removed by filtration and discarded. The filtrate was concentrated in vacuo at 90°C to an oil (232 g). The desired pure ester was obtained by vacuum distillation (138 g, 46%, 115–125°C at 0.3–0.5 mmHg (1 mmHg = 133.322 Pa)).

<sup>1</sup>H NMR (300 MHz, CDCl<sub>3</sub>) δ: 1.45 (s, 9H, -C(CH<sub>3</sub>)<sub>3</sub>), 2.50 (t, 2H, -CH<sub>2</sub>CH<sub>2</sub>CO-), 3.40 (t, 2H, -NHCH<sub>2</sub>CH<sub>2</sub>CO-), 4.20 (s, 1H, -NH-), 6.60 (d, 2H, *o*-H), 6.70 (t, 1H, *p*-H), 7.30 (t, 2H, *m*-H).

<sup>13</sup>C NMR (75 MHz, CDCl<sub>3</sub>) δ: 8.11 (-CH<sub>3</sub>), 35.16 (-CH<sub>2</sub>CH<sub>2</sub>CO-), 39.69 (-NHCH<sub>2</sub>CH<sub>2</sub>-), 80.82 (-O-C(CH<sub>3</sub>)<sub>3</sub>), 113.06 (2,6-aromatic C), 117.60 (4-aromatic C), 129.25 (3,5-aromatic C), 147.80 (1-aromatic C), 171.69 (-COO-).

**1-Trimethylsilylethyl trifluoromethanesulfonate**

Pyridine (6.7 g, 84.6 mmol) and dichloromethane (200 mL) were cooled to -25°C. Trifluoromethanesulfonic

anhydride (23.9 g, 84.6 mmol) was added over 2 min. A thick slurry resulted. 1-Trimethylsilylethanol (10.0 g, 84.6 mmol) was added and the mixture stirred for 1 h while the temperature was allowed to rise to 25°C. The resulting pyridine trifluoromethanesulfonate was removed by filtration. The filtrate was concentrated in vacuo at 25°C to give 18.2 g (86 %) of the sulfonate.

<sup>1</sup>H NMR (300 MHz, CDCl<sub>3</sub>) δ: 0.12 (s, 9H, -Si(CH<sub>3</sub>)<sub>3</sub>), 1.55 (d, 3H, CH<sub>3</sub>CH-), 4.92 (q, 1H, -SiCHOTfCH<sub>3</sub>).

<sup>13</sup>C NMR (75 MHz, CDCl<sub>3</sub>) δ: -4.47 (-Si(CH<sub>3</sub>)<sub>3</sub>), 17.38 (CH<sub>3</sub>CH-), 85.36 (CH<sub>3</sub>CH-), 118.0 (q, -SO<sub>2</sub>CF<sub>3</sub>).

**1-Triethylsilylethanol**

Borane–tetrahydrofuran complex (1.0 M solution in tetrahydrofuran, 290 mL, 0.29 mol) was cooled to 0°C. Triethylvinylsilane (41.2 g, 0.29 mol) was added over 10 min, keeping the reaction temperature between 0 and 10°C. The mixture was stirred for 1 h, and the temperature was allowed to rise to 25°C. Water (10 mL) was cautiously added dropwise, followed by 3 M aqueous sodium hydroxide (97 mL, 0.29 mol) over 10 min. Hydrogen peroxide (30%, 99 mL, 0.96 mol) was added over 10 min, keeping the reac-



tion temperature at ca. 30°C. The mixture was refluxed for 1 h. Cooling to 25°C gave three liquid phases. The addition of anhydrous potassium carbonate (150 g, 1.09 mol) produced two clear liquid phases. The top organic phase was dried over magnesium sulfate and concentrated in vacuo at 25°C to give a ca. 1:1 mixture (53.6 g) of the desired 1-triethylsilylethanol and the unwanted isomer 2-triethylsilylethanol. The crude mixture was distilled, and the fraction boiling at 90–100°C, 12 mmHg, was collected (26.8 g). This material was distilled again, and the fraction boiling at 87–90°C, 12 mmHg, was the desired pure isomer (10.0 g, 22%).

$^1\text{H}$  (300 MHz,  $\text{CDCl}_3$ )  $\delta$ : 0.60 (q, 6H,  $-\text{Si}(\text{CH}_2\text{CH}_3)_3$ ), 0.90 (t, 9H,  $-\text{Si}(\text{CH}_2\text{CH}_3)_3$ ), 1.25 (s, 1H,  $-\text{OH}$ ), 1.30 (d, 3H,  $\text{CH}_3\text{CH}-$ ), 3.62 (q, 1H,  $\text{CH}_3\text{CH}-$ ).

$^{13}\text{C}$  (75 MHz,  $\text{CDCl}_3$ )  $\delta$ : 1.46 ( $-\text{Si}(\text{CH}_2\text{CH}_3)_3$ ), 7.42 ( $-\text{Si}(\text{CH}_2\text{CH}_3)_3$ ), 20.21 ( $-\text{CHCH}_3$ ), 60.07 ( $-\text{CHCH}_3$ ).

### 1-Triethylsilylethyl trifluoromethanesulfonate

A mixture of pyridine (4.9 g, 62 mmol) and dichloromethane (150 mL) was cooled to  $-25^\circ\text{C}$ . Trifluoromethanesulfonic acid anhydride (17.5 g, 62 mmol) in dichloromethane (25 mL) was added, resulting in a thick slurry. A solution of 1-triethylsilylethanol (9.96 g, 62 mmol) and dichloromethane (25 mL) was added and the reaction mixture stirred for 1 h while the temperature was allowed to rise to 25°C. Most of the solid had dissolved. Additional pyridine (ca. 1.5 mL) was added to raise the pH of the reaction mixture from ca. 3 to 5, resulting again in a thick slurry. The salt (14.7 g) was removed by filtration and the filtrate concentrated in vacuo at 25°C to a semi-solid (20 g). Petroleum ether (200 mL) was added, and more resulting salt was removed by filtration. The filtrate was treated with decolorizing carbon and concentrated in vacuo at 25°C to an oil (13.12 g). The oil was determined by  $^1\text{H}$  NMR to be a 70:30 mixture of the desired triflate – starting 1-triethylsilylethanol and was used without further purification.

$^1\text{H}$  NMR (300 MHz,  $\text{CDCl}_3$ )  $\delta$ : 0.50–0.72 (m,  $-\text{Si}(\text{CH}_2\text{CH}_3)_3$ ), 0.90–1.05 (m,  $-\text{Si}(\text{CH}_2\text{CH}_3)_3$ ), 1.30 (d,  $-\text{CH}(\text{OH})\text{CH}_3$ ), 1.60 (d,  $-\text{CH}(\text{OTf})\text{CH}_3$ ), 3.65 (q,  $-\text{CH}(\text{OH})\text{CH}_3$ ), 5.08 (q,  $-\text{CH}(\text{OTf})\text{CH}_3$ ).

$^{13}\text{C}$  NMR (75 MHz,  $\text{CDCl}_3$ )  $\delta$ : 1.17 ( $-\text{CHOTfSi}(\text{CH}_2\text{CH}_3)_3$ ), 1.47 ( $-\text{CHOHSi}(\text{CH}_2\text{CH}_3)_3$ ), 6.92 ( $-\text{CHOTfSi}(\text{CH}_2\text{CH}_3)_3$ ), 7.42 ( $-\text{CHOHSi}(\text{CH}_2\text{CH}_3)_3$ ), 17.96 ( $-\text{CHOTfCH}_3$ ), 20.17 ( $-\text{CHOHCH}_3$ ), 60.07 ( $-\text{CHOHCH}_3$ ), 83.97 ( $-\text{CHOTfCH}_3$ ), 118.0 (q,  $-\text{SO}_2\text{CF}_3$ ).

### Compound 4E

A mixture of 1-trimethylsilylethyl trifluoromethanesulfonate (6.38 g, 25.5 mmol), *tert*-butyl 3-anilinopropionate (5.64 g, 25.5 mmol), potassium carbonate (3.52 g, 25.5 mmol), and butyronitrile (25 mL) was stirred at reflux for 16 h. The mixture was filtered to remove salt, and the filtrate was concentrated in vacuo at 50°C to give 6.9 g of a yellow oil. The desired product was the first eluting material (3.7 g, 45%) obtained via flash chromatography (silica gel, 9 parts petroleum ether : 1 part ethyl acetate).

$^1\text{H}$  NMR (300 MHz,  $\text{CDCl}_3$ )  $\delta$ : 0.12 (s, 9H,  $-\text{Si}(\text{CH}_3)_3$ ), 1.25 (d, 3H,  $\text{CH}_3\text{CH}-$ ), 1.48 (s, 9H,  $-\text{C}(\text{CH}_3)_3$ ), 2.40–2.65 (m, 2H,  $-\text{CH}_2\text{CH}_2\text{CO}-$ ), 3.35 (q, 1H,  $\text{CH}_3\text{CH}-$ ), 3.45–3.7 (m,

2H,  $-\text{NCH}_2\text{CH}_2-$ ), 6.65 (t, 1H, *p*-CH), 6.75 (d, 2H, *o*-CH), 7.20 (m, 2H, *m*-CH).

$^{13}\text{C}$  NMR (75 MHz,  $\text{CDCl}_3$ )  $\delta$ :  $-1.89$  ( $-\text{Si}(\text{CH}_3)_3$ ), 13.61 ( $\text{CH}_3\text{CH}-$ ), 28.13 ( $-\text{C}(\text{CH}_3)_3$ ), 34.87 ( $-\text{CH}_2\text{CH}_2\text{CO}-$ ), 44.47 ( $-\text{NCH}_2\text{CH}_2-$ ), 47.05 ( $\text{CH}_3\text{CH}-$ ), 80.50 ( $-\text{C}(\text{CH}_3)_3$ ), 112.89 (*o*-CH), 115.98 (*p*-CH), 129.12 (*m*-CH), 148.63 (aromatic C-N), 171.47 ( $-\text{CO}-$ ).

### Compound 4S

The *tert*-butyl ester **4E** (3.70 g, 11.5 mmol) and trifluoroacetic acid (10 mL, ca. 130 mmol) were stirred at 25°C for 16 h. The reaction mixture was concentrated in vacuo at 25°C. The oil was dissolved in ethyl ether (100 mL) and washed with water ( $2 \times 25$  mL). The ether layer was washed with aqueous sodium bicarbonate (3.5 g, 42 mmol, 25 mL water). The bottom aqueous layer (pH ca. 7) was discarded and the top ether layer treated with anhydrous sodium bicarbonate – magnesium sulfate. The dried organic extract was concentrated in vacuo at 25°C to give the free acid as a golden oil (2.7 g, 88%). The acid (2.50 g, 9.4 mmol) was stirred with a mixture of diethyl ether (50 mL), water (50 mL), and sodium hydroxide (0.37 g, 9.3 mmol). The top ether layer was discarded. The bottom aqueous layer (pH 10) was washed with fresh ether and the ether layer again discarded. The bottom aqueous layer was treated with decolorizing carbon and silica gel, resulting in a pH ca. 9. A few drops of acetic acid were added to bring the pH to ca. 7–8. The solution was concentrated in vacuo at 25°C to give a brown oil (2 g, 74%). The oil was dissolved in acetonitrile and treated with anhydrous sodium sulfate and decolorizing carbon. The solvent was removed at 25°C to give **4S** as a hygroscopic gum.

$^1\text{H}$  NMR (300 MHz,  $\text{D}_2\text{O}$ )  $\delta$ : 0.00 (s, 9H,  $-\text{Si}(\text{CH}_3)_3$ ), 1.23 (bs, 3H,  $\text{CH}_3\text{CH}-$ ), 2.20–2.60 (bm, 2H,  $-\text{NCH}_2\text{CH}_2\text{CO}-$ ), 3.30 (m, 1H,  $\text{CH}_3\text{CH}-$ ), 3.40–3.80 (bd, 2H,  $-\text{NCH}_2\text{CH}_2-$ ), 4.80 (s, HOD), 6.65 (bm, 1H, *p*-CH), 6.77 (bs, 2H, *o*-CH), 7.07 (bm, 2H, *m*-CH). See also Table 2.

$^{13}\text{C}$  NMR (75 MHz,  $\text{D}_2\text{O}$ )  $\delta$ : 0.00 ( $-\text{Si}(\text{CH}_3)_3$ ), 15.12 ( $\text{CH}_3\text{CH}-$ ), 36.84 ( $-\text{CH}_2\text{CH}_2\text{CO}-$ ), 50.23 ( $-\text{NCH}_2\text{CH}_2-$ ), 52.11 ( $\text{CH}_3\text{CH}-$ ), 118.69 (*o*-CH), 122.55 (*p*-CH), 132.40 (*m*-CH), 148.80 (aromatic C-N), 182.38 ( $-\text{COO}-$ ).

### Compound 5E

*tert*-Butyl 3-(*N*-phenylamino)propionate (9.96 g, 45 mmol), diisopropylethylamine (5.80 g, 45 mmol), and acetonitrile (25 mL) were combined. 1-Triethylsilylethyl triflate (13.12 g, 45 mmol, ca. 70% pure, the remainder being the parent alcohol) was added, followed by additional acetonitrile (25 mL). The mixture was stirred for 2 h at 25°C, then at reflux for 3 h. The mixture was concentrated in vacuo at 40°C to give an oil. Petroleum ether (100 mL) was added and the resulting salt filtered and discarded. The filtrate was concentrated in vacuo at 40°C to give an oil (13.5 g). Flash chromatography (silica gel, 9 parts petroleum ether : 1 part ethyl acetate) gave the crude product, **5E** (4.6 g) with trace silyl impurities. A second flash chromatographic operation gave the pure desired product (3.0 g, 18%).

$^1\text{H}$  NMR (300 MHz,  $\text{CDCl}_3$ )  $\delta$ : 0.65 (q, 6H,  $-\text{Si}(\text{CH}_2\text{CH}_3)_3$ ), 1.00 (t, 9H,  $-\text{Si}(\text{CH}_2\text{CH}_3)_3$ ), 1.28 (d, 3H,  $-\text{CHCH}_3$ ), 1.50 (s, 9H,  $-\text{C}(\text{CH}_3)_3$ ), 2.40–2.50 and 2.55–2.70 (m, m, 1H, 1H,



-CH<sub>2</sub>CH<sub>2</sub>CO-), 3.45–3.70 (m, 3H, -NCH<sub>2</sub>CH<sub>2</sub>- and -NCHCH<sub>3</sub>), 6.65 (t, 1H, *p*-H), 6.75 (d, 2H, *o*-H), 7.20 (m, 2H, *m*-H). See also Table 2.

<sup>13</sup>C NMR (75 MHz, CDCl<sub>3</sub>) δ: 3.75 (-Si(CH<sub>2</sub>CH<sub>3</sub>)<sub>3</sub>), 7.62 (-Si(CH<sub>2</sub>CH<sub>3</sub>)<sub>3</sub>), 12.79 (-CHCH<sub>3</sub>), 28.13 (-C(CH<sub>3</sub>)<sub>3</sub>), 34.86 (-CH<sub>2</sub>CH<sub>2</sub>CO-), 44.85 (-NCH<sub>2</sub>CH<sub>2</sub>-), 45.47 (-CHCH<sub>3</sub>), 80.49 (-O-C(CH<sub>3</sub>)<sub>3</sub>), 113.63 (*o*-CH), 115.98 (*p*-CH), 129.15 (*m*-CH), 148.42 (aromatic C-N), 171.52 (-CO-).

### Compound 6E

Dimethylformamide (DMF, 50 mL) was chilled to -10°C. Phosphorous oxychloride (3.20 g, 21 mmol) was added. A solution of *tert*-butyl 3-(*N*-phenylamino)propionate (3.36 g, 10.4 mmol) and DMF (15 mL) was added and the mixture stirred at 25°C for 16 h. The reaction mixture was added to a solution of sodium acetate (17.22 g, 220 mmol) and water (230 mL) and allowed to stir for 2 h. The product was extracted with petroleum ether (3 × 50 mL). The petroleum ether extracts were dried over magnesium sulfate and treated with carbon. The treated extracts were concentrated in vacuo at 25°C to give 3.4 g of oil. The pure **6E**, 3.04 g (84%), was obtained via flash chromatography (silica gel, 9 parts petroleum ether : 1 part ethyl acetate).

<sup>1</sup>H NMR (300 MHz, CDCl<sub>3</sub>) δ: 0.10 (s, 9H, -Si(CH<sub>3</sub>)<sub>3</sub>), 1.32 (d, 3H, CH<sub>3</sub>CH), 1.45 (s, 9H, -C(CH<sub>3</sub>)<sub>3</sub>), 2.40–2.70 (m, 2H, -NCH<sub>2</sub>CH<sub>2</sub>CO-), 3.50 (q, 1H, CH<sub>3</sub>CH-), 3.55–3.80 (m, 2H, -NCH<sub>2</sub>CH<sub>2</sub>-), 6.70 (d, 2H, *o*-CH), 7.70 (d, 2H, *m*-CH), 9.70 (s, 1H, -CHO). See also Table 2.

<sup>13</sup>C NMR (75 MHz, CDCl<sub>3</sub>) δ: -2.03 (-Si(CH<sub>3</sub>)<sub>3</sub>), 14.12 (CH<sub>3</sub>CH-), 28.03 (-C(CH<sub>3</sub>)<sub>3</sub>), 34.40 (-CH<sub>2</sub>CH<sub>2</sub>CO-), 44.68 (-NCH<sub>2</sub>CH<sub>2</sub>-), 47.10 (CH<sub>3</sub>CH-), 81.04 (-C(CH<sub>3</sub>)<sub>3</sub>), 111.61 (*o*-CH), 125.01 (*p*-C-CHO), 132.01 (*m*-CH), 152.84 (aromatic C-N), 170.63 (-COO-), 189.69 (-CHO).

### Compound 6S

The 4-formyl *tert*-butyl ester **6E** (3.04 g, 8.7 mmol) was cooled to -25°C, trifluoroacetic acid (10 mL, ca. 130 mmol) was added, and the solution was stirred at 25°C for 16 h. The reaction mixture was concentrated in vacuo at 25°C to a dark oil (9.23 g). The oil was partitioned between ethyl ether (100 mL) and aqueous sodium bicarbonate (4.92 g, 58.6 mmol, 100 mL water). The bottom aqueous layer had a pH ca. 7–8. The top organic layer was treated with magnesium sulfate and decolorizing carbon and concentrated in vacuo at 25°C to an oil (1.9 g). Pure free carboxylic acid (1.46 g, 57%) was obtained via flash chromatography (silica gel: 9 parts dichloromethane : 1 part methanol). The free acid (1.46 g, ca. 5 mmol) was combined with methanolic sodium methoxide (0.5 M, 9.5 mL, 4.75 mmol) to give a pH of ca. 8. Acetic acid was added to lower the pH to ca. 7. The solution was concentrated in vacuo at 25°C to give an oil (1.96 g). The oil was triturated with acetonitrile (3 × 5 mL) and the solvent again removed in vacuo at 25°C to give **6S** as a hygroscopic gum (0.83 g).

<sup>1</sup>H NMR (300 MHz, D<sub>2</sub>O) δ: 0.12 (bs, 9H, -Si(CH<sub>3</sub>)<sub>3</sub>), 1.38 (bd, 3H, CH<sub>3</sub>CH-), 2.0 (bs, acetonitrile), 2.15 (bs, acetic acid), 2.40–2.70 (bm, 2H, -CH<sub>2</sub>CH<sub>2</sub>CO-), 3.55–3.85 (bq and bm, 3H, CH<sub>3</sub>CH-, NCH<sub>2</sub>CH<sub>2</sub>-), 6.90 (bd, 2H, *o*-CH), 7.75 (bd, 2H, *m*-CH), 9.45 (bs, 1H, -CHO). See also Table 2.

<sup>13</sup>C NMR (75 MHz, D<sub>2</sub>O) δ: 0.02 (-Si(CH<sub>3</sub>)<sub>3</sub>), 16.48 (CH<sub>3</sub>CH-), 39.02 (-CH<sub>2</sub>CH<sub>2</sub>CO-), 48.62 (-NCH<sub>2</sub>CH<sub>2</sub>-), 49.76 (CH<sub>3</sub>CH-), 114.59 (*o*-CH), 125.37 (*p*-C-CHO), 135.93 (*m*-CH), 157.02 (aromatic C-N), 183.03 (-COO-), 195.47 (-CHO).

### Compound 7E

DMF (40 mL) was cooled to -10°C. Phosphorous oxychloride (2.11 g, 13.7 mmol) was added, followed by the *tert*-butyl ester **5E**. The mixture was allowed to warm to 25°C and stirred for 16 h. The yellow solution was added to a solution of sodium acetate (11.2 g, 137 mmol) and water (150 mL) and the resulting mixture stirred for 1 h. The product was extracted with petroleum ether (3 × 50 mL), the extracts treated with magnesium sulfate and decolorizing carbon and concentrated in vacuo at 35°C to an oil (2.9 g). Flash chromatography (silica gel: 9 parts petroleum ether : 1 part ethyl acetate) gave the purified 4-formyl *tert*-butyl ester, **7E** (2.3 g, 85%).

<sup>1</sup>H NMR (300 MHz, CDCl<sub>3</sub>) δ: 0.65 (q, 6H, -Si(CH<sub>2</sub>CH<sub>3</sub>)<sub>3</sub>), 0.90 (t, 9H, -Si(CH<sub>2</sub>CH<sub>3</sub>)<sub>3</sub>), 1.30 (d, 3H, -CHCH<sub>3</sub>), 1.45 (s, 9H, -C(CH<sub>3</sub>)<sub>3</sub>), 2.35–2.50 and 2.60–2.75 (m, m, 1H, 1H, -CH<sub>2</sub>CH<sub>2</sub>CO-), 3.45–3.60, 3.65, and 3.70–3.80 (m, q, m, 1H, 1H, 1H, -NCH<sub>2</sub>CH<sub>2</sub>-, -CHCH<sub>3</sub>), 6.73 (d, 2H, *o*-H), 6.80 (d, 2H, *m*-H), 9.70 (s, 1H, -CHO).

<sup>13</sup>C NMR (75 MHz, CDCl<sub>3</sub>) δ: 3.25 (-Si(CH<sub>2</sub>CH<sub>3</sub>)<sub>3</sub>), 7.47 (-Si(CH<sub>2</sub>CH<sub>3</sub>)<sub>3</sub>), 15.12 (-CHCH<sub>3</sub>), 28.06 (-C(CH<sub>3</sub>)<sub>3</sub>), 34.45 (-CH<sub>2</sub>CH<sub>2</sub>CO-), 45.13 (DEPT confirmed, -NCH<sub>2</sub>CH<sub>2</sub>- and -NCHCH<sub>3</sub>), 81.07 (-O-C(CH<sub>3</sub>)<sub>3</sub>), 111.61 (*o*-CH), 125.06 (*p*-C-CHO), 131.80 (*m*-CH), 152.64 (aromatic C-N), 170.68 (-COO-), 189.72 (-CHO).

### Acknowledgments

The authors would like to thank Jerome Lenhard and Annabel Muentner (Eastman Kodak Company) for valuable discussions.

### References

- (a) E. Baciocchi, M. Bietti, and O. Lanzalunga. *Acc. Chem. Res.* **33**, 243 (2000); (b) E.R. Gaillard and D.G. Whitten. *Acc. Chem. Res.* **29**, 292 (1996); (c) A. Albini, E. Fasani, and M. Freccero. *Adv. Electron Transfer Chem.* **5**, 103 (1996); (d) J.-M. Saveant. *Adv. Electron Transfer Chem.* **4**, 53 (1994); (e) P. Maslak. *Top. Curr. Chem.* **168**, 1 (1993); (f) R. Popielarz and D.R. Arnold. *J. Am. Chem. Soc.* **112**, 3068 (1990); (g) S.L. Mattes and S. Farid. *Org. Photochem.* **6**, 233 (1983).
- (a) D. Mangion and D.R. Arnold. *Can. J. Chem.* **77**, 1655 (1999); (b) L.A. Eriksson, C.M. Jansson, D.R. Arnold, and R.J. Boyd. *Can. J. Chem.* **76**, 1817 (1998); (c) X. Du, D.R. Arnold, R.J. Boyd, and Z. Shi. *Can. J. Chem.* **69**, 1365 (1991); (d) R. Popielarz and D.R. Arnold. *J. Am. Chem. Soc.* **112**, 3068 (1990); (e) D.R. Arnold and L.J. Lamont. *Can. J. Chem.* **67**, 2119 (1989); (f) A. Okamoto, M.S. Snow, and D.R. Arnold. *Tetrahedron*, **42**, 6175 (1986); (g) A. Okamoto and D.R. Arnold. *Can. J. Chem.* **63**, 2340 (1985).
- (a) I.R. Gould, J.R. Lenhard, A.A. Muentner, S.A. Godleski, and S. Farid. *J. Am. Chem. Soc.* **122**, 11 934 (2000); (b) I.R. Gould, J.R. Lenhard, A.A. Muentner, S.A. Godleski, and S. Farid. *Pure Appl. Chem.* **73**, 455 (2001).



4. (a) S.Y. Farid, J.R. Lenhard, C.H. Chen, A.A. Muentner, I.R. Gould, S.A. Godleski, and P.A. Zielinski. U.S. Patent 5 747 235, May 5, 1998; (b) S.Y. Farid, J.R. Lenhard, C.H. Chen, A.A. Muentner, I.R. Gould, S.A. Godleski, P.A. Zielinski, and C.H. Weidner. U.S. Patent 5 747 236, May 5, 1998; (c) I.R. Gould, S. Farid, S.A. Godleski, J.R. Lenhard, A.A. Muentner, and P.A. Zielinski. U.S. Patent 5 994 051, Nov. 30, 1999; (d) S.Y. Farid, J.R. Lenhard, C.H. Chen, A.A. Muentner, I.R. Gould, S.A. Godleski, P.A. Zielinski, and C.H. Weidner. U.S. Patent 6 010 841, Jan. 4, 2000; (e) A. Adin, J.J. Looker, S.Y. Farid, I.R. Gould, S.A. Godleski, J.F. Lenhard, A.A. Muentner, L.C. Vishwakarma, and P.A. Zielinski. U.S. Patent 6 054 260, Apr. 25, 2000; (f) S.Y. Farid, I.R. Gould, S.A. Godleski, J.R. Lenhard, A.A. Muentner, P.A. Zielinski, and C.H. Weidner. U.S. Patent 6 153 371, Nov. 28, 2000; (g) A. Adin, J.J. Looker, S.Y. Farid, I.R. Gould, S.A. Godleski, J.R. Lenhard, A.A. Muentner, L.C. Vishwakarma, and P.A. Zielinski. U.S. Patent 6 306 570, Oct. 23, 2001.
5. J.R. Fyson, P.J. Twist, and I.R. Gould. Electron transfer processes in silver halide photography. In *Electron transfer in chemistry*. Vol. 5. Edited by V. Balzani. Wiley-VCH, New York. 2001. p. 285.
6. (a) Z. Su, D.E. Falvey, U.C. Yoon, and P.S. Mariano. *J. Am. Chem. Soc.* **119**, 5261 (1997); (b) Z. Su, P.S. Mariano, D.E. Falvey, U.C. Yoon, and S.W. Oh. *J. Am. Chem. Soc.* **120**, 10 676, (1998); (c) X. Zhang, S.-R. Yeh, S. Hong, M. Freccero, A. Albini, D.E. Falvey, and P.S. Mariano. *J. Am. Chem. Soc.* **116**, 4211 (1994).
7. (a) H.J.P. de Lijser, D.W. Snelgrove, J.P. Dinnocenzo. *J. Am. Chem. Soc.* **123**, 9698 (2001); (b) J.P. Dinnocenzo, S. Farid, J.L. Goodman, I.R. Gould, W.P. Todd, and S.L. Mattes. *J. Am. Chem. Soc.* **111**, 8973 (1989); (c) J.P. Dinnocenzo, S. Farid, J.L. Goodman, I.R. Gould, and W.P. Todd. *Mol. Cryst. Liq. Cryst.* **194**, 151 (1991); (d) W.P. Todd, J.P. Dinnocenzo, S. Farid, J.L. Goodman, and I.R. Gould. *J. Am. Chem. Soc.* **113**, 3601 (1991); (e) W.P. Todd, J.P. Dinnocenzo, S. Farid, J.L. Goodman, and I.R. Gould. *Tetrahedron Lett.* **34**, 2863 (1993); (f) K.P. Dockery, J.P. Dinnocenzo, S. Farid, J.L. Goodman, I.R. Gould, and W.P. Todd. *J. Am. Chem. Soc.* **119**, 1876 (1997).
8. I.R. Gould, D. Ege, J.E. Moser, and S. Farid. *J. Am. Chem. Soc.* **112**, 4290 (1990).
9. J.W. Moore and R.G. Pearson. *Kinetics and mechanism*. 3rd ed. Wiley-Interscience, New York. 1981. p. 290.
10. See, for example (a) L.M. Tolbert and J.E. Haubrich. *J. Am. Chem. Soc.* (1994) **116**, 10 593; (b) G.W. Robinson. *J. Phys. Chem.* **95**, 10 386 (1991).
11. N. Isaacs. *Physical organic chemistry*. 2nd ed. Longman, England. 1987.
12. (a) R. Popielarz and D.R. Arnold. *J. Am. Chem. Soc.* **112**, 3068 (1990); (b) P. Maslak, T.M. Vallombroso, W.H. Chapman, Jr., and J.N. Narvaez. *Angew. Chem. Int. Ed. Engl.* **33**, 73 (1994).



# Photochemistry of rhodamine dye salts involving intra-ion-pair electron transfer

Guilford Jones II, Xiaochun Wang, and Jingqiu Hu

**Abstract:** The electron-transfer photochemistry of rhodamine 6G thiocyanate ion pairs has been investigated. For dye in a low polarity solvent, such as ethyl acetate, the emission of rhodamine 6G is significantly quenched by thiocyanate counterions. Laser photolysis of rhodamine 6G and thiocyanate in ethyl acetate was studied in detail with the identification of the reduced rhodamine 6G radical species ( $\lambda_{\text{max}} = 410$  nm). The growth and decay of the R6G radical could be accounted for in part by a mechanism involving initial formation of dye triplet followed by electron transfer which provides a triplet radical-pair state on a  $\mu\text{s}$  timescale.

**Key words:** electron transfer, ion pair, rhodamine 6G, triplet state.

**Résumé :** On a étudié la photochimie par transfert d'électron de la paire d'ions rhodamine 6G/thiocyanate. Pour les colorants dans des solvants de faible polarité, comme l'acétate d'éthyle, l'émission de rhodamine 6G est désactivée de façon significative par le contre-ion thiocyanate. On a étudié soigneusement la photolyse au laser de la rhodamine 6G et du thiocyanate dans l'acétate d'éthyle en identifiant l'espèce radicalaire rhodamine 6G réduite ( $\lambda_{\text{max}} = 410$  nm). On peut, en partie, attribuer la croissance et la décroissance du radical de R6G à un mécanisme impliquant la formation initiale d'un triplet colorant suivie d'un transfert d'électron qui conduit à l'état triplet de la paire de radicaux dans une échelle de temps de l'ordre de la  $\mu\text{s}$ .

**Mots clés :** transfert d'électron, paire d'ions, rhodamine 6G, état triplet.

[Traduit par la Rédaction]

## Introduction

A large variety of organic dyes that are used in dye lasers, printing, and photography are ionic, including members of the rhodamine, triarylmethane, and cyanine families. The likelihood that dyes of this type will be paired or complexed with cationic or anionic partners has often been neglected in the examination of dye properties. The phenomenon of ion pairing is well-established as a mechanistic feature for numerous organic systems that incorporate species of opposite charge in media of moderate polarity (1). Although incompletely understood, there are a number of potential effects on the photochemical and photophysical properties of dyes that are ion paired, which will depend on the nature of the counterions that accompany dye salts and other medium conditions. For media less polar than water, including solid hosts such as organic polymers, it is indeed probable that electrostatic complexes will be important, if not dominant. Under these circumstances, dye species are more properly understood to exist as "tight" or "contact" ion pairs (1–3).

Several recent reports, including the work of Schuster and co-workers (4), Armitage and O'Brien (5), and Neckers and co-workers (6), have documented the spectroscopic or photochemical effects of ion pairing on cyanine and other

chromophores and borate anions in organic solvents and other media such as aqueous liposomes. The photochemistry that results from visible photolysis, which appears to have practical utility in photoinduced radical polymerization (4, 6), involves a general mechanism of intra-ion-pair electron transfer, followed by the fragmentation of initial radical pair species to give free radical intermediates.

Ion-pairing or charge-type effects have been observed in photochemical studies of dyes that are commonly used in dye lasers. For example, charge and counterion effects on the laser output and other parameters for pyridiniumoxazoles have been reported (7). The quenching of emission of rhodamine-6G (R6G) (Scheme 1) by ferrocyanide has been investigated through phototransient studies that revealed interactions involving both ion diffusion and ion pairing (8). Other recent reports document the roles of counterions and ion pairing in the alteration of spectra, photobleaching, and the distribution of geometric isomers for cyanine and triarylmethane dyes (9).

We became interested in the effects of ion pairing on the photochemistry of cationic dyes on the basis that electrostatic attraction and tight ion pairing by counterions would introduce a special type of medium effect (10) based on electrostatic charge for laser dyes. Depending on the nature

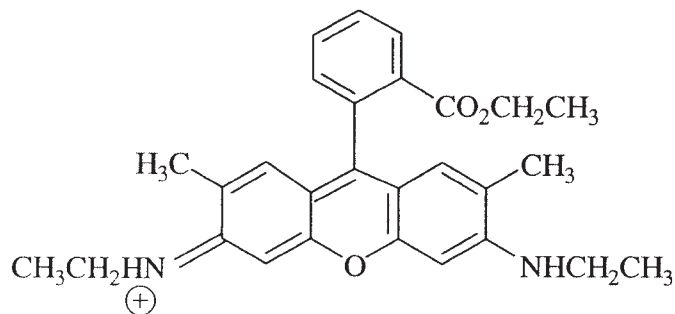
Received 3 February 2003. Published on the NRC Research Press Web site at <http://canjchem.nrc.ca> on 27 June 2003.

*Dedicated to Professor Don R. Arnold for his significant contributions to chemistry.*

**G. Jones, II,<sup>1</sup> X. Wang, and J. Hu.** Department of Chemistry and the Center for Photonics, Boston University, Boston MA 02215, U.S.A.

<sup>1</sup>Corresponding author (e-mail: [jones@chem.bu.edu](mailto:jones@chem.bu.edu)).



Scheme 1. Structure of the R6G<sup>+</sup> cation.

of the counterion, it seemed likely that most photophysical properties such as fluorescence yield and lifetime, as well as dye photostability, could be altered to some degree in comparison with the behavior of “free” dye in fluid medium, where the principal interaction with solvent overshadows the interaction with a neighboring charged species. Also of interest was the previous observation (11) that the triaryl methane dye, crystal violet (CV<sup>+</sup>), on UV or visible photolysis with excess polyacrylate as counterion in water led to efficient dye photobleaching. The photobleaching of dye for CV<sup>+</sup>X<sup>-</sup> salts in a solvent of moderate polarity (e.g., 2-propanol) is also counterion dependent with the observed trend in rate of bleaching (Cl<sup>-</sup> > Br<sup>-</sup> > I<sup>-</sup>) (12).

The most widely studied rhodamine dye, rhodamine-6G (R6G<sup>+</sup> cation, Scheme 1) features outstanding photophysical and photochemical properties for use in dye lasers (10). Its fluorescence yield is high for many solvents suitable for lasing applications (e.g.,  $\phi_f = 0.88$ , methanol solvent) (13). The general insensitivity of the emission yield to excitation wavelength and medium makes it a popular fluorescence yield standard. The dominance of radiative decay is also reflected in the low value that has been obtained for the quantum yield of intersystem crossing for R6GCl; for ethanol solutions  $\phi_T = 0.0021$  and a triplet decay time ( $\tau_T = 3.5 \mu\text{s}$ ) have been recorded (14). Accounts have been published previously of the investigation of rhodamine and other dyes under conditions in which they form electrostatic complexes with anionic polyelectrolytes in water (11, 15, 16).

In the present study, we have focused on ion-pair effects on the photochemistry of rhodamine-6G under circumstances in which salts of the cationic dye are dissolved in organic solvents of low to intermediate polarity. The role of ion pairing with several different counterions for R6G<sup>+</sup> could be confirmed through observation of alteration in dye spectra and dye fluorescence quenching. Ion pairing with the thiocyanate anion (SCN<sup>-</sup>) was particularly effective. Along with the finding of significant emission quenching, laser flash photolysis experiments showed that free radicals are generated on ion pair photolysis. From the phototransient data, it was possible to determine radical yields and the relative rate constants associated with the competition between return electron transfer and cage escape. A mechanism in which electron transfer proceeds via the formation of dye triplets (i.e., an alternate mechanism of intersystem crossing for a rhodamine) was established. From the results, some insight is provided regarding the participation and consequences of intra-ion-pair electron transfer for dyes that have affinity for oppositely charged sites in self-assembled systems.

## Experimental methods

### Materials

Rhodamine 6G chloride (Aldrich) was recrystallized from ethanol three times. Its purity was confirmed by NMR and by TLC (alumina, ethanol solvent). Tetrabutylammonium thiocyanate (TBASCN), tetrabutylammonium acetate (TBAOAc), and tetrabutylammonium iodide (TBAI) (Aldrich) were recrystallized from ethyl acetate before use. All solvents used for spectroscopic measurements were either spectrograde or HPLC quality and used as received.

### Instrumentation

Absorption measurements were conducted using a Beckman model DU-7 spectrophotometer with wavelength resolution of 0.5 nm. For some measurements which accompanied spontaneous dye photodegradation (mostly with I<sup>-</sup> in nonpolar solvents), spectra were measured immediately after the solution was prepared (within 5 s, and the measurement completed within about 20 s). Emission measurements were conducted using an SLM 48000 fluorimeter.

Absolute fluorescence quantum yields ( $\phi_{f(s)}$ ) were measured by comparing the spectrally corrected emission intensity (F) of the sample to that of a fluorescence standard using the following equation.

$$[1] \quad \phi_{f(s)} = \phi_{f(r)} \left( \frac{\int F_s(\lambda) d\lambda}{\int F_r(\lambda) d\lambda} \right) \left( \frac{A_r}{A_s} \right) \left( \frac{n_s^2}{n_r^2} \right)$$

where  $\int F_s(\lambda) d\lambda$  and  $\int F_r(\lambda) d\lambda$  are the integrated emission intensities for the sample (s) and the reference (r),  $A_r/A_s$  is the ratio of light intensities absorbed by the two solutions at the excitation wavelength, and  $n$  is the refractive index of the solvents. The fluorescence standard chosen for this study (10-methylacridinium hexafluorophosphate) has a known fluorescence quantum yield of 1.0 in water. The excitation wavelength was selected toward the blue side of the  $S_0 \rightarrow S_1$  absorption of rhodamine dye (500 nm); absorbance at the excitation wavelength was less than 0.2.

Laser flash photolysis measurements were conducted using a nanosecond laser flash photolysis system (16) that is based on a Quantel YG-581 Nd:YAG laser, whose second (532 nm) or third (355 nm) harmonic were used as excitation sources. The system included a Lecroy TR8818 transient recorder, a Kinetic Systems CAMAC dataway, and a 150 W Xe lamp. The Xe lamp was synchronously fired with the laser and used as a monitoring light for the transient signals. A monochromator and PMT were used to obtain transient spectra with a spectral resolution of 1 nm. Solution samples were prepared in either 1 × 2 cm and 1 × 1 cm pyrex cells (0.1–10  $\mu\text{M}$  in dye) and were purged 20 min with argon gas prior to the initiation of experiments. Rate constants were calculated based on the rise and decay profiles.

Quantum yields of phototransient formation were measured by monitoring the signal associated with the R6G<sup>+</sup> transient at 410 nm and using the triplet absorption at 520 nm ( $\epsilon = 6500 \text{ M}^{-1} \text{ cm}^{-1}$ ) (17) of benzophenone (0.5 mM in acetonitrile) as a standard. The ratio of the time-zero transient ODs was multiplied by the inverse ratio of both absorbances at the excitation wavelength (355 and 532 nm)



**Table 1.** Photophysical properties of R6GCl with and without added salts in three solvents.

Solvents	Ethanol ( $\epsilon$ 24.6)	THF ( $\epsilon$ 7.58)	Ethyl acetate ( $\epsilon$ 6.02)
<b>R6GCl</b>			
$\lambda_{\max}$ (nm)	529	536	538
$\epsilon$ ( $\times 10^4$ M $^{-1}$ cm $^{-1}$ )	9.4	7.5	7.5
$\lambda_f$ (nm)	557	561	567
$\phi_f$	0.88 <sup>a</sup>	0.43	0.38
$\tau_0$ (ns)	4.2 <sup>b</sup>	3.8	2.8
$E_{00}$ (nm) <sup>c</sup>	543	549	552
<b>(R6GCl + 0.29 M TBASCN)</b>			
$\lambda_{\max}$ (nm)	530	535	537
$\epsilon$ ( $\times 10^4$ M $^{-1}$ cm $^{-1}$ )	9.3	1.06	8.8
$\lambda_f$ (nm)	559	566	568
$\phi_f$	0.33	0.049	0.041
$\phi_f^{\text{ipd}}$	—	0.043	0.038
<b>(R6GCl + 25 mM TBAPF<sub>6</sub>)</b>			
$\lambda_{\max}$ (nm)	528		526
$\epsilon$ ( $\times 10^4$ M $^{-1}$ cm $^{-1}$ )	9.5		8.9
$\lambda_f$ (nm)	557		556
$\phi_f$	0.87		0.93

<sup>a</sup>Reported  $\phi_f = 0.88 \pm 0.02$  (ethanol) (13).<sup>b</sup> $\tau_0 = 3.8$  ns (methanol) and 3.4 ns (ethanol) (19).<sup>c</sup>From the intersection of absorption and emission spectra.<sup>d</sup>Ion pair limiting fluorescence quantum yield.

and the extinction coefficients of R6GX and the standard. The following equation was utilized:

$$[2] \quad \phi_{\text{R6G}\cdot} = \phi_{\text{BP}} \left( \frac{P_{355}}{P_{532}} \right) \left( \frac{\epsilon_{\text{BP}}^{520}}{\epsilon_{\text{R6G}\cdot}^{520}} \right) \left( \frac{A_{\text{BP}}^{355}}{A_{\text{R6G}}^{355}} \right) \left( \frac{\text{OD}_{\text{R6G}\cdot}^{410}}{\text{OD}_{\text{BP}}^{520}} \right)$$

where  $P_{532}$  and  $P_{355}$  are the respective photon fluxes for the laser pulses for the YAG second and third harmonic wavelengths. The latter were obtained by measurement of pulse energies for 532 and 355 nm beams with a calorimeter (e.g., 70 and 28 mJ/pulse, respectively). Thus, a photon flux ratio could be calculated (e.g.,  $70/28 \times 532/355 = 3.75$ ). The ratio of R6G ground state absorbances at 532 and 355 nm was 9.5. Also used in the application of eq. [2] are the values  $\epsilon_{\text{R6G}\cdot}^{410} = 43\,000$  M $^{-1}$  cm $^{-1}$  and  $\epsilon_{\text{BP}}^{520} = 6500$  M $^{-1}$  cm $^{-1}$  (17) for the radical and benzophenone triplet transients, respectively.

Cyclic voltammetry was carried out using an EG&G PAR 273 potentiostat/galvanostat controlled by the EG&G M270A (version 4.0) software package (scan rates: 1 mV/s – 5 V/s), or an EG&G PARC model 175 Universal Programmer function generator equipped with a Tektronix TD 320 two-channel oscilloscope (scan rate: 1 mV/s – 10 000 V/s) and using Tektronix Docuwave software. The three-electrode system consisted of a glass carbon (GC) working electrode, an aqueous Ag/AgCl, KCl (satd.) reference electrode ( $E^\circ$  vs. NHE =  $E^\circ$  vs. Ag/AgCl + 0.197), and a Pt counter-electrode. The reference electrode potential was checked against the ferrocene–ferrocenium couple and the electrochemical cell was thermostated at 20°C. Experiments were performed on argon-purged methylene chloride solutions containing 5 mM R6GCl and 0.1 M tetrabutylammonium hexafluorophosphate (TBAPF<sub>6</sub>, Aldrich) at scan rates ranging from 50 to 1000 mV/s.

## Results and discussion

### Photophysical properties of R6G in the presence of excess salts in different solvents

Ethanol ( $\epsilon = 24.6$ ) has served as a solvent of choice for rhodamine dyes in dye lasers and other spectroscopic applications (10). In the present study, ethanol served as a reference solvent in the sense that its polarity is sufficiently high that the formation of ion pairs was expected to be suppressed for moderate concentrations of rhodamine dye and added salts. Ethyl acetate ( $\epsilon = 6.02$ ) was selected for investigation to represent a typical nonpolar solvent which is capable of dissolving the salts of relatively hydrophobic dye cations. Additional data were obtained for THF ( $\epsilon = 7.58$ ), a complementary solvent of intermediate polarity. Three anions, thiocyanate (SCN $^-$ ), iodide (I $^-$ ), and acetate (OAc $^-$ ), as their tetrabutylammonium (TBA) salts were used as additives to R6GCl solutions for inspection of ion-pairing effects in the aforementioned solvents. A low dye concentration of 10  $\mu$ M was employed to minimize complicating features associated with dye aggregation (18) (but note discussion below).

The data regarding absorption and emission properties for R6G $^+$  with chloride as counterion (10  $\mu$ M) and for the dye with excess SCN $^-$  or with hexafluorophosphate (PF<sub>6</sub> $^-$ ) in three solvents are shown in Table 1. For the more polar solvent, ethanol, absorption and emission maxima and spectral shapes were perturbed only slightly on addition of excess salts (Fig. 1). Absorption was characterized for all media by the familiar (10) low energy visible band ( $S_0 \rightarrow S_1$ , 528–530 nm) or the weaker transition in the UV ( $S_0 \rightarrow S_2$ , 347 nm), up to the concentration limit for added salt ( $\sim 0.3$  M). Fluorescence spectra were also almost identical in shape and  $\lambda_{\max}$  for ethanol solutions with the various addi-



**Fig. 1.** (a) Absorption and (b) emission spectra of 10  $\mu\text{M}$  R6GCl in the presence of added TBASCN in ethanol ( $\lambda_{\text{ex}} = 532 \text{ nm}$ ).

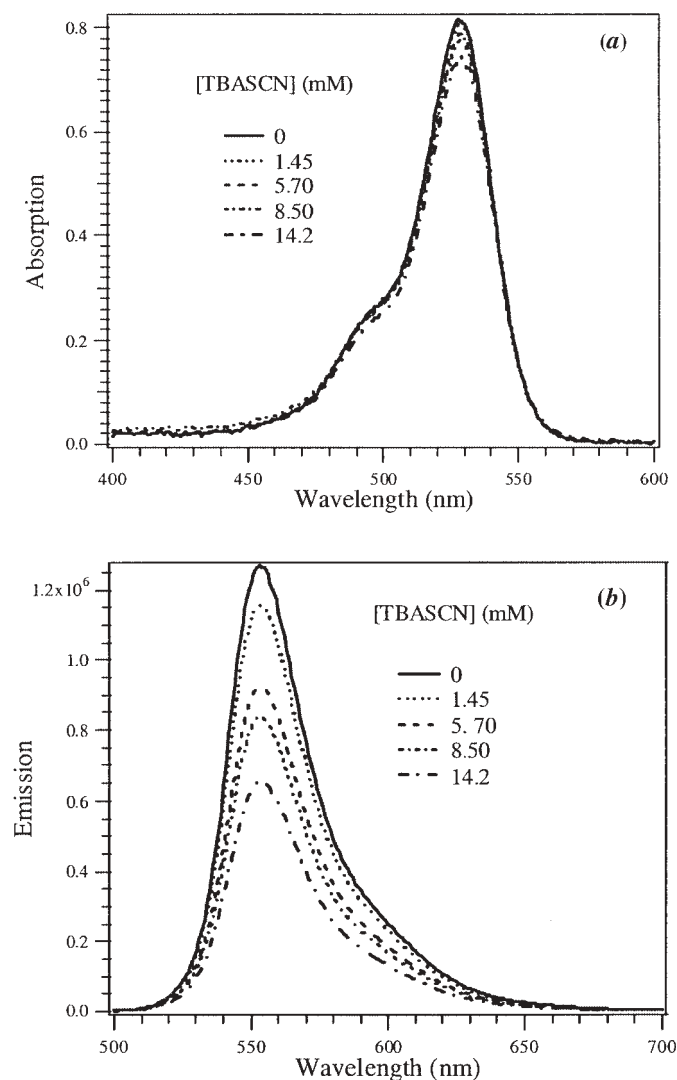
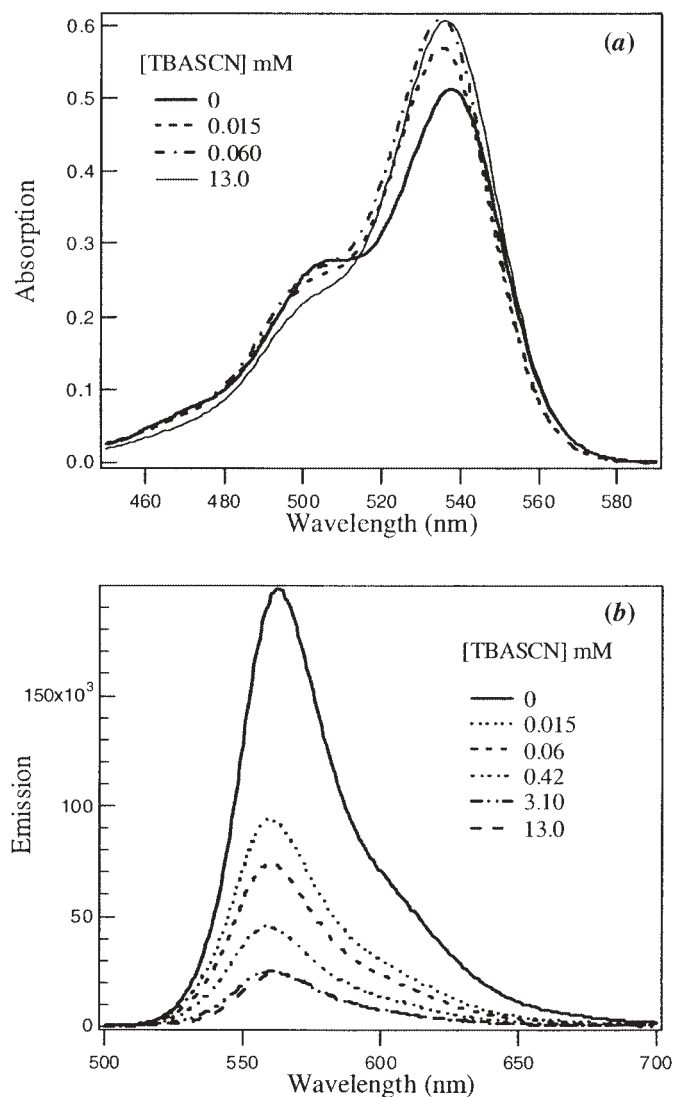


**Fig. 2.** Absorption (a) and emission (b) spectra of 10  $\mu\text{M}$  R6GCl in the presence of added TBASCN in ethyl acetate ( $\lambda_{\text{ex}} = 532 \text{ nm}$ ).



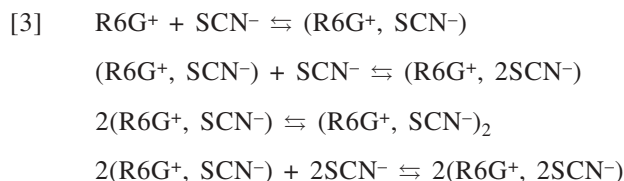
tives. For the less polar media (THF and ethyl acetate) alterations in spectra were more pronounced. The noticeable trends included a shift to the red (5–12 nm) of the  $\lambda_{\text{max}}$  for visible absorption bands as well as emission bands. This effect was observed for solutions in which the counterion was simply chloride or for added excess  $\text{SCN}^-$ , but not for the case of  $\text{PF}_6^-$ . Extinction coefficients were also moderately perturbed (generally, a 10–20% reduction, Table 1) for salts in the less polar THF and ethyl acetate. Modest perturbations associated with the alteration of transition moments and oscillator strengths on binding of polarizable counterions (e.g., for  $\text{SCN}^-$  or  $\text{Cl}^-$  but not  $\text{PF}_6^-$ ) have been reported (18).

Aggregation effects are common for organic dyes in a variety of media (11, 15, 16, 18, 20–22), and several subtle spectral clues suggest that dye–dye interaction may play a role for the rhodamine salts. For R6GCl in ethyl acetate (Fig. 2a), a noticeable shoulder appears with  $\lambda_{\text{max}} \sim 500 \text{ nm}$ , a feature that is diminished on addition of excess  $\text{SCN}^-$ . The broad spectral features that appear as blue shifts of the prin-

cipal absorption bands, consistent with the formation of dye dimers, are also observed on addition of other excess salts. Addition of both acetate and iodide results in strong perturbation of the visible band. A new band of this type assigned to the dye aggregate ( $\lambda_{\text{max}} \sim 500 \text{ nm}$ ) has been identified for  $\text{R6G}^+$  (e.g., for more concentrated dye–alcohol solutions) (13, 18). As reference points, the equilibrium constants for dimerization of R6GCl in ethanol and water are  $K_D = 0.27 \text{ M}^{-1}$  (22) and  $6.2 \times 10^3 \text{ M}^{-1}$  (18), respectively. For a 10  $\mu\text{M}$  solution of R6GCl in ethanol, the ratio of dimer to monomer at equilibrium is computed from the  $K_D$  value to be  $2.7 \times 10^{-6}$ .

The “deaggregation” of R6GCl by  $\text{SCN}^-$  in ethyl acetate displayed novel behavior. As shown in Fig. 2a, the maximum in the visible is shifted slightly to the blue and then back to the red on progressive addition of TBASCN. This subtle effect could be associated with an alteration in the stoichiometry of ion pairing as shown with the following equilibria.





In this model the dimer aggregate that is formed in a modest amount on dissolution of salt in ethyl acetate is shifted via the second equilibrium to a complex of 2:1 stoichiometry which favors the counterion and relieves dye-dye interaction on addition of excess  $\text{X}^-$ . This model is reminiscent of that proposed by Armitage and O'Brien (5) which dealt with the 2:1 stoichiometry of complexation of two positively charged dyes and a bulky counterion triphenylbenzyl borate ( $\text{R6G}^+:\text{Ph}_3\text{BnB}^- = 2:1$ ). For the present case of  $\text{R6GSCN}$ , the 1:2 cluster might adopt a sandwich structure in which two  $\text{SCN}^-$  ions lie on opposite sides of the xanthene ring. Another case of deaggregation has been reported (15) in which  $\text{R6G}^+$  at moderate concentration in water ( $>1 \times 10^{-5} \text{ M}$ ) is relieved of dye-dye interaction on addition of the domain-forming polyelectrolyte, poly (methacrylic acid). Depending on the pH of solutions, dye is either bound to spaced charges on the polyelectrolyte chain or sequestered as individual dye cations in folded polymer interior (hydrophobic) spaces (15).

The most pronounced influence of non-polar solvents on the photophysics of rhodamine salts is observed in the quenching of fluorescence (Fig. 2b). As shown in Fig. 3, the quantum yield of emission that peaks at about 565 nm is diminished substantially with added TBASCN for ethyl acetate solvent. An important part of the trend is that the chloride counterion results in about a twofold quenching, whereas the effect is nearly an order of magnitude larger for the  $\text{SCN}^-$  counterion (ethyl acetate vs. ethanol). The series of Stern-Volmer plots (Fig. 4) shows different profiles of emission quenching, depending on the selected excess salt. For the more polar solvent (ethanol) the amount of excess counterion required for complete or nearly complete fluorescence quenching was much higher (e.g., 0.29 M TBASCN), whereas lower concentrations of added salts resulted in substantial quenching for ethyl acetate solutions ( $<5 \text{ mM}$ ). Notably, the addition of acetate was markedly less effective than addition of  $\text{SCN}^-$  or  $\text{I}^-$ .

#### The fluorescence quenching mechanism — ion pairing

The results of the fluorescence measurements in which various salts were employed as quenchers (counterions, acetate vs. iodide vs. thiocyanate) for  $\text{R6G}^+$  in ethanol are shown in Fig. 4. Notably, all of the Stern-Volmer plots showed downward curvature. Furthermore, if the approximately linear portions of the plots are used to obtain nominal slopes, with values  $25 \text{ M}^{-1}$  and  $1.7 \times 10^4 \text{ M}^{-1}$  for quenching by  $\text{SCN}^-$  in ethanol and ethyl acetate, respectively, quenching constants are obtained ( $k_q = 5.9 \times 10^9$  and  $6.1 \times 10^{12} \text{ M}^{-1} \text{ s}^{-1}$ ) that are quite different. The latter value (ethyl acetate samples) is much larger than that allowed by a diffusion-limited mechanism (23), whereas, for ethanol solutions, the quenching constant observed is quite close to that predicted for bimolecular diffusion ( $k_{\text{diff}} = 6.1 \times 10^9 \text{ M}^{-1} \text{ s}^{-1}$  at  $25^\circ\text{C}$ ) (24). For this analysis, fluorescence lifetimes for dye solutions with no added salt ( $\tau_f = 4.2$  and  $2.8 \text{ ns}$ ) for

**Fig. 3.** Stern-Volmer plot of fluorescence quenching data for  $10 \mu\text{M}$   $\text{R6GCl}$  with added TBASCN in aerated ethyl acetate ( $\lambda_{\text{ex}} = 500 \text{ nm}$ ). Insert: Benesi-Hildebrand plot.

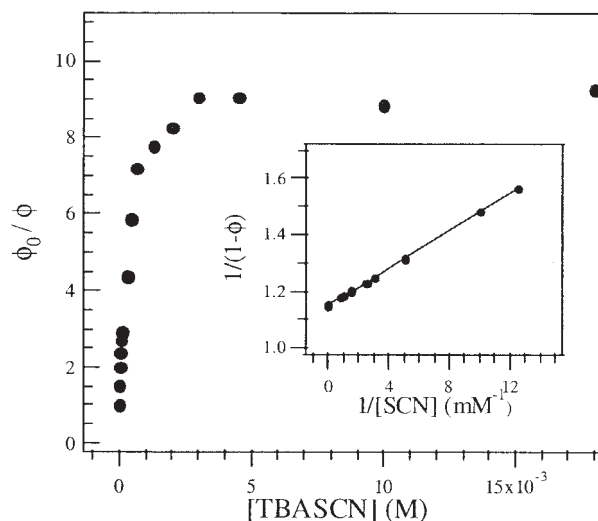
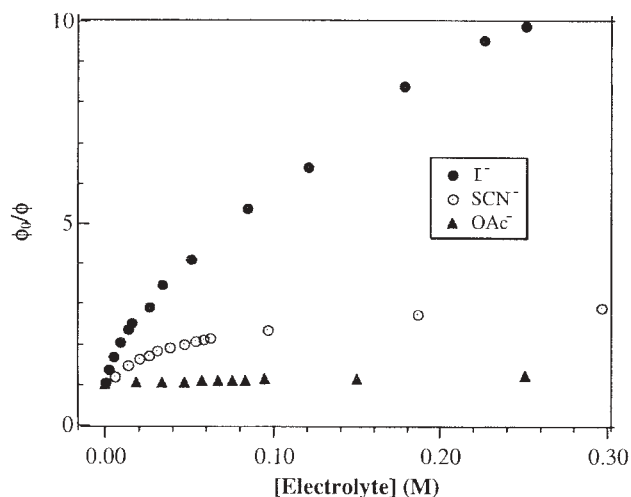
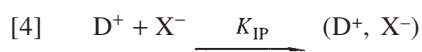


**Fig. 4.** Stern-Volmer plot of fluorescence quenching data for  $10 \mu\text{M}$   $\text{R6GCl}$  with added TBASCN, TBAI, and TBAOAc in aerated ethanol ( $\lambda_{\text{ex}} = 500 \text{ nm}$ ).



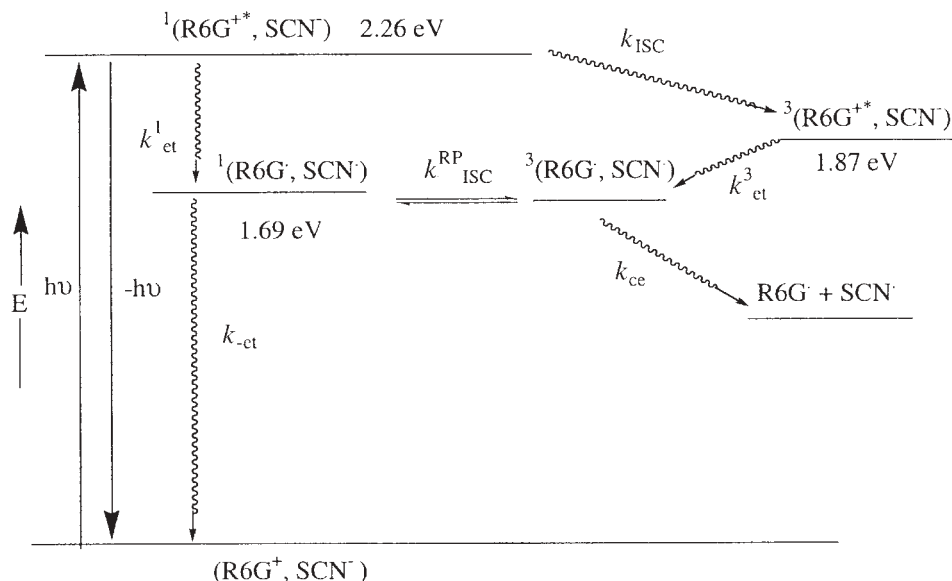
$10 \mu\text{M}$   $\text{R6GCl}$  in ethanol and ethyl acetate, respectively, were obtained by phase-shift fluorimetry.

The conclusion from the fluorescence quenching measurements is that, for the ethyl acetate medium, quenching takes place by a static mechanism involving complexation of dye and counterion. For ethanol solutions a dynamic quenching mechanism is most likely, or a small contribution by ion pairing may be important (vide infra). The quenching results thus provided, for the less polar medium, an opportunity to examine dye-counterion complexation in terms of an ion pair equilibrium:



If a 1:1 ion-pairing stoichiometry is assumed, and the unquenched emission yield is taken as that value obtained for  $\text{R6GCl}$  fluorescence ( $\phi_0$ ), the relationship eq. [5] can be



**Scheme 2.** State energy diagram for the photochemistry of the R6G<sup>+</sup>SCN<sup>-</sup> ion pair.

used to obtain an ion pairing constant ( $K_{IP}$ ). The Benesi-Hildebrand procedure (25) and eq. [5] utilize values recorded for  $\phi$ , the total emission yield for complexed and uncomplexed species and  $\Delta$ , the difference between yields of complexed and uncomplexed species, as a function of quencher concentration ( $D_0$ ).

$$[5] \quad \frac{1}{\phi_0 - \phi} = \frac{1}{\Delta} + \frac{1}{K_{IP} \Delta D_0}$$

Linear plots were obtained from the fluorescence quenching data for the R6G<sup>+</sup>–SCN<sup>-</sup> system for the three solvents ethyl acetate (Fig. 3, insert plot), THF, and (for completeness) ethanol. These plots were used to calculate  $K_{IP}$  values ( $K_{IP} = 71$ ,  $9.3 \times 10^3$ , and  $3.1 \times 10^4$  M<sup>-1</sup> for dye complexation in ethanol, THF, and ethyl acetate, respectively). Not unexpectedly, as solvent polarity decreases,  $K_{IP}$  increases; i.e., a lower polarity medium facilitates ion pairing, consistent with numerous studies of the ion-pairing phenomenon (1–3). Also, for the completely complexed dye cations, quenching by thiocyanate reduces the yield of emission to <10% of its value for uncomplexed R6G<sup>+</sup> (Fig. 3).

#### Electrochemistry of R6G<sup>+</sup> and the driving force for ion pair electron transfer

Redox potentials were required to evaluate the energetics of a hypothetical electron transfer that could occur for dye ion pairs. Reversible waves associated with R6G<sup>+</sup> reduction were obtained with an assembly that employed an Ag working electrode and with scan rates of 200 mV/s for dye in methylene chloride ( $\epsilon = 8.90$ ) with supporting electrolyte. From these data the half-wave potential ( $E_{1/2}$  (R6G<sup>+</sup>/R6G·)) = -0.92 V vs. SCE in CH<sub>2</sub>Cl<sub>2</sub>) was obtained. Using this value and a reported value ( $E_{1/2}$  (SCN<sup>-</sup>/SCN·)) = +0.77 V vs. SCE) (26) for (reversible) thiocyanate oxidation in water, the radical pair energy (relative to the ground state for R6GSCN) was obtained:  $\Delta G_0 = E^\circ$  (SCN/SCN·) –  $E^\circ$  (R6G<sup>+</sup>/R6G·) = 1.69 eV. This estimated value for the radical pair energy is well below that for the dye singlet state (ca. 0.5 eV) and

close to but below the energy of the dye triplet. The relationships among the energies of the various states are depicted in Scheme 2.

#### Flash photolysis of rhodamine ion pairs: free radical transients and photokinetics

Since R6G<sup>+</sup> has a dominant fluorescence that occurs in the ns regime ( $\tau_f = 3$  to 4 ns, Table 1), and since non-radiative decay is inefficient, the dye fails to generate appreciable phototransients in the 100 ns to 1 ms time domain in laser pump–probe experiments (e.g., the triplet yield = 0.0021 for R6G<sup>+</sup> in ethanol) (14). However, our preliminary results showed that ion pairing of the dye with the counterion SCN<sup>-</sup> (also I<sup>-</sup>) led to a significant yield of phototransients on laser photolysis. Investigation of R6G<sup>+</sup> with other anions in non-polar solvents was included for comparison.

On pulsed photolysis of an ethyl acetate solution of 10 mM R6GCl with a Nd/YAG laser (532 nm, 60 mJ/pulse), the transient spectrum that was observed consisted of weak bands broadly absorbing at ca. 400 and 600 nm, along with a dominant dye bleach centered at 540 nm. The assignments are consistent with the appearance of the rhodamine triplet state (<sup>3</sup>R6G<sup>+</sup>\* with  $\lambda_{max} = 620$  nm and  $\epsilon = 16\,000$  M<sup>-1</sup> cm<sup>-1</sup>) (27) and the semireduced dye species, the R6G· radical ( $\lambda_{max} = 410$  nm) (28). These transients were also recorded for solutions that contained TBASCN with levels of salt concentration that corresponded to 75–97% ion pairing (0.1–1.0 mM), >99% ion pairing (3.0 mM, Fig. 5), and a level at which clustering of ions (vide supra) is important (20 mM, and up to the saturation limit of 30 mM). The transient bleach is associated with ground state depletion for which  $\epsilon^{540} = 67\,000$  M<sup>-1</sup> cm<sup>-1</sup>.

On addition of excess SCN<sup>-</sup> the radical signal at 410 nm increased in intensity, with a fast onset (<30 ns) and a slower rise that could be followed accurately (~1  $\mu$ s) (Fig. 6). The fraction of the fast process increased until [SCN<sup>-</sup>] reached 1.0 mM (where ion pairing is complete). The slow rise appeared with [SCN<sup>-</sup>] = 1.0 mM and became increasingly important (up to 20 mM TBASCN). Notably, the fast rise



**Fig. 5.** Transient spectra of 10  $\mu\text{M}$  R6GCl with 3.0 mM TBASCN in Ar-purged ethyl acetate ( $\lambda_{\text{ex}} = 532 \text{ nm}$ ).

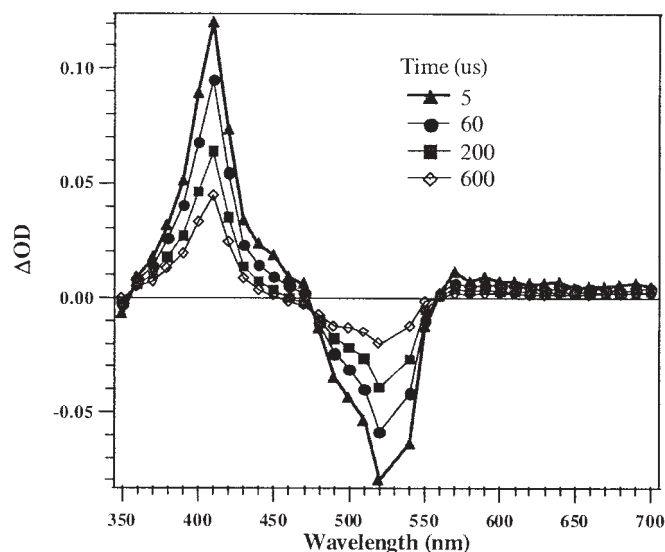
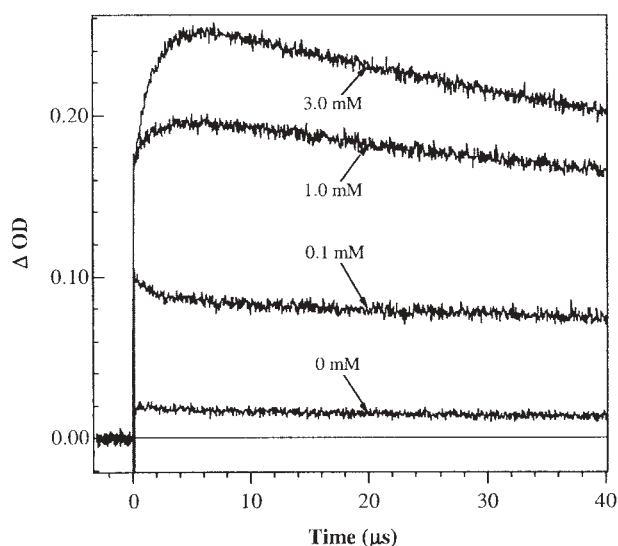


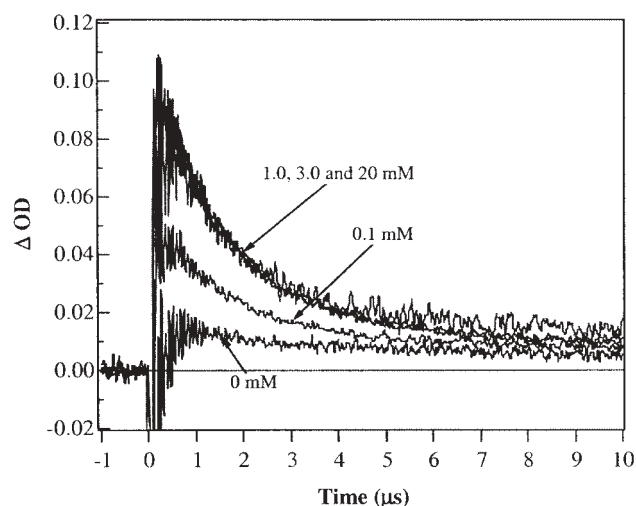
**Fig. 6.** Growth and decay profiles for the radical transient ( $\lambda_{\text{max}} = 410 \text{ nm}$ ) for 10  $\mu\text{M}$  R6GCl as a function of added TBASCN in Ar-purged ethyl acetate ( $\lambda_{\text{ex}} = 532 \text{ nm}$ ).



time recorded at 410 nm was constant for this range of  $[\text{SCN}^-]$ . The decay of the R6G $\cdot$  radical occurred on the 100 ms timescale by a process that could be evaluated as second order or the sum of two exponentials; for example, a half-life of the dye-derived radical of 150  $\mu\text{s}$  was recorded for a solution having 10  $\mu\text{M}$  R6G $^+$  and 3.0 mM  $\text{SCN}^-$  (Fig. 5).

The signal associated with the dye triplet species ( $^3\text{R6G}^{+*}$ ) at 620 nm grew in intensity on addition of thiocyanate up to about 1.0 mM  $[\text{SCN}^-]$ . Notably also, its decay accelerated with added excess salt, reaching a rate corresponding to a decay time of  $\sim 1 \mu\text{s}$  (Fig. 7). Transient depletion of the absorption because of the R6G $^+$  ground state at 540 nm and its recovery were observed in all samples. For R6GCl without added salt, the recovery was comprised of two components, a dominant fast process ( $< 50 \text{ ns}$ ),

**Fig. 7.** Decay profiles for the triplet transient (620 nm) for 10  $\mu\text{M}$  R6GCl with TBASCN in Ar-purged ethyl acetate ( $\lambda_{\text{ex}} = 532 \text{ nm}$ ).



accompanied by a small contribution from a slow recovery ( $\sim 200 \mu\text{s}$ ). With the addition of excess  $\text{SCN}^-$ , the proportion due to the slow recovery was greatly enhanced and an intermediate recovery time developed ( $\sim 1 \mu\text{s}$ ).

Another finding in parallel with the evidence involving excess  $\text{SCN}^-$  came on flash photolysis of 10 mM R6G $^+$  with 1.0 mM  $\text{I}^-$ , excited at 532 nm in ethyl acetate. These results were also consistent with a mechanism in which the decay of the observed R6G radical and the recovery of ground state dye are coupled, for long time regimes ( $> 10 \mu\text{s}$ ). This recovery mechanism is most readily related to a return electron transfer that occurs involving R6G radical and oxidized species through bimolecular encounter (vide infra).

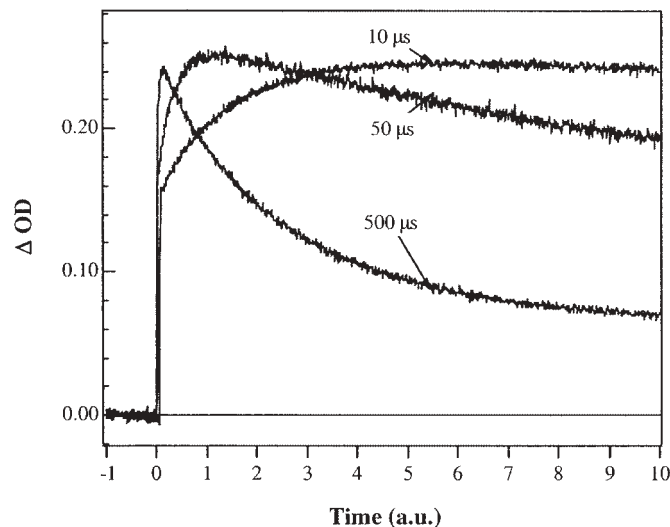
#### Rise time for the R6G radical transient: mechanisms of intra-ion-pair electron transfer

The profile of growth and decay for the 410 nm signal vs.  $[\text{SCN}^-]$  is shown in Fig. 8. The findings include observation of a fast rise that occurs essentially with the laser pulse, followed by a slower process of transient formation in about 1  $\mu\text{s}$ . The evolution of species is recorded in Fig. 9 for samples (3.0 mM in TBASCN) in terms of the growth of R6G radicals (410 nm), the decay of triplets (620 nm), and the recovery of dye bleaching (540 nm). The first-order rise and (or) decay times obtained from these plots are 1.4, 1.7, and 1.9  $\mu\text{s}$ , respectively.

Proceeding on the assumption that dye photoreduction occurred via ion-pair electron transfer, we sought to establish further the respective roles of dye singlet and triplet states. Most noticeable was the finding that about 1  $\mu\text{s}$  was required in order for the 410 nm transient to reach its maximum absorbance; in other words, there is a slow rise on the  $\mu\text{s}$  timescale that follows a more prompt mechanism for radical formation. This feature requires either (i) that a slower process of radical formation involving a diffusive encounter of the dye excited singlet state is important, or (ii) that another intermediate precedes the semireduced dye transient. Since, under the optimum conditions for radical formation (3.0 mM  $\text{SCN}^-$ , corresponding to virtually complete association of



**Fig. 8.** Growth and decay profiles for the radical transient (R6G, 410 nm) for 10  $\mu\text{M}$  R6GCl with 3.0 mM TBASCN in Ar-purged ethyl acetate ( $\lambda_{\text{ex}} = 532$  nm), shown with regard to three timescales (10, 50, and 500  $\mu\text{s}$  full scale).

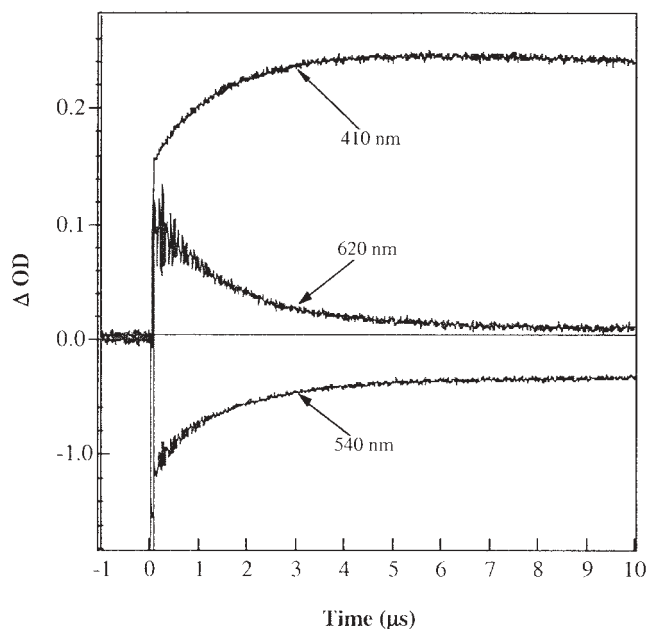


R6G<sup>+</sup> and SCN<sup>-</sup> and quenching of rhodamine fluorescence (Fig. 3)), the probability of a diffusional step that would compete with dye singlet decay is eliminated. More telling is the observation that the decay of the 620 nm dye triplet transient matches substantially the growth of the 410 nm species (Fig. 9). Although the data are limited to inspection of only about two 1/e times, estimates can be made from these curves for radical growth and triplet decay ( $k_r = 7 \times 10^5 \text{ s}^{-1}$  and  $k_d = 6 \times 10^5 \text{ s}^{-1}$ , respectively) based on reasonable fits of the data to a first-order rate law.

A compelling feature of the phototransient data had to do with the relative yields of triplet and radical intermediates, as a function of the concentration of excess SCN<sup>-</sup>. As noted in Fig. 7, the yield of the triplet (600 nm transient) is not enhanced for [SCN<sup>-</sup>] > 1.0 mM (i.e., after ion pairing is substantially complete). In contrast, on further addition of excess salt, the proportion of the signal at 410 nm grows (in the interval of 1.0 to 20.0 mM SCN<sup>-</sup>). Thus, an increase in yield of radical is not the result of a further increase in triplet yield, but has to do with a more competitive rate or yield for the electron transfer that occurs via the dye triplet ion pair. The key may lie in the 1:2 clustering of rhodamine with excess SCN<sup>-</sup> which could be responsible for a reduced rate of the back electron transfer that competes with the release of caged radicals (see below for the potential involvement of the oxidized species ((SCN)<sub>2</sub><sup>-</sup>)).

A mechanism that includes two possible pathways for formation of radical transients for R6GSCN can be understood in terms of the energy diagram of Scheme 2. Intra-ion-pair electron transfer may originate from singlet states on a relatively fast timescale and correspond to the appearance of the radical transient within the time of the laser pulse in ns measurements. A slower process follows intersystem crossing of ion-paired rhodamine dye and intra-pair electron transfer of dye triplet species. The latter sequence, which is apparently slowed in comparison to the singlet mechanism by two orders of magnitude ( $1 \times 10^6$  vs.  $1 \times 10^8 \text{ s}^{-1}$ ), proceeds with a

**Fig. 9.** Growth and decay profiles for the radical (410 nm) and triplet (620 nm) transients and ground state bleach (540 nm) observed on laser photolysis of 10  $\mu\text{M}$  R6GCl with 3.0 mM TBASCN in Ar-purged ethyl acetate ( $\lambda_{\text{ex}} = 532$  nm).



driving force that is diminished by 0.39 eV (the difference in  $S_1$  and  $T_1$  excitation energies (Scheme 2)).

An effort was made to characterize the formation of a thiocyanate-derived radical species. The product of one-electron oxidation of thiocyanate that is well-characterized is the pseudodimeric species ((SCN)<sub>2</sub><sup>-</sup>) a radical that could result in the present case from diffusion of radicals SCN<sup>•</sup> into bulk solution and trapping by SCN<sup>-</sup> (or by in-cage capture in the case of a 2:1 ion-pair stoichiometry). Although its visible absorption is weak, the (SCN)<sub>2</sub><sup>-</sup> radical has been observed on flash photolysis or pulse radiolysis in a variety of settings (for water solutions  $\lambda_{\text{max}} = 480$  nm,  $\epsilon^{480} = 7800 \text{ M}^{-1}$ ) (26). Unfortunately, this spectral region is congested by strong local dye absorption ( $\epsilon^{540} = 67\,000 \text{ M}^{-1} \text{ cm}^{-1}$  and for the shoulder  $\epsilon^{472} = 12\,200 \text{ M}^{-1} \text{ cm}^{-1}$ ).

Further comparison can be made with spectra obtained on flash photolysis of ethyl acetate solutions having excess iodide. What appears in the case of iodide is a feature also associated with a trapped (secondary) radical product, a contribution at 380 nm which is convoluted with the R6G transient absorption at 405 nm. The iodide derived radical ( $\text{I}_2^{\cdot-}$ ) is also a well-established intermediate ( $\epsilon^{380} = 15\,600 \text{ M}^{-1} \text{ cm}^{-1}$ ) (29) whose observation provides further confirmation of an overall electron transfer mechanism.

#### Estimate of dye triplet and R6G free radical yields

Based on the calculated  $\epsilon^{410}$  for the R6G radical ( $43\,000 \text{ M}^{-1} \text{ cm}^{-1}$ , vide supra) and the absence of any excitation wavelength dependence on the photochemistry, an estimate of R6G radical yield on pulsed photolysis for several conditions of ion pairing was made (Table 2). The method required the recording of transient ODs that were extrapolated to zero time from decay data recorded on the 0–1  $\mu\text{s}$  timescale. Samples of rhodamine dye with added salts were



**Table 2.** Radical and triplet quantum yield<sup>a</sup> for R6GSCN in ethyl acetate on laser flash photolysis ( $\lambda_{\text{ex}} = 532$  nm).

[SCN] (mM)	0	0.1	1.0	3.0	20	30
$\Phi_{\text{R6G}\cdot}$	0.001	0.005	0.011	0.014	0.024	0.022
$\Phi_{\text{T}}$	0.003	0.008	0.016	0.016	0.016	0.016

<sup>a</sup>Quantum yields of transient formation (R6G $\cdot$  (410 nm) and R6G $^+$  triplet state (620 nm)) based on benzophenone triplet (520 nm,  $\Phi = 1.0$ ).

photolyzed at 532 nm, whereas the actinometric standard based on the observation of the triplet state transient for benzophenone ( $\lambda_{\text{max}} = 520$  nm,  $\epsilon = 6500$  M $^{-1}$  cm $^{-1}$ ) (17) required use of the 355 nm laser wavelength with correction factors applied as described in the *Experimental* section. Estimation of the yield of long-lived rhodamine triplets for the ion pairs was more difficult, since decay times are relatively short for this weaker transient and the data comparatively noisy at early times following the laser pulse.

What is confirmed again is that SCN $^-$  ion pairing for R6G $^+$  results in an elevated transient yield, well above the reported triplet yield for dye in ethanol (0.002) (14). There are at least two scenarios involving ion-pair effects that could account for enhanced triplet formation and therefore allow an appreciable yield of electron transfer product via dye triplets. The counterion itself could play a special role as part of the dye "medium", namely, introducing spin orbit interactions not present for the free dye (including a heavy atom effect involving the S center). Not to be ruled out also is the possibility that dye aggregates are important (even for SCN $^-$  complexes which show little spectral perturbation); dye dimers and higher order species are known to give higher yields of triplets (28). Some insight regarding these possibilities is provided in the finding that the quenching of R6G $^+$  in the presence of I $^-$  in ethyl acetate results in a significantly lower residual fluorescence for the complexed ion pair. Increased yields of triplets on iodide complexation have been rationalized previously in terms of the halide counterion providing enhanced spin orbit coupling (30).

## Conclusions

The addition of excess salts that include the counterions SCN $^-$ , OAc $^-$ , and I $^-$  result in moderate alteration of the absorption spectra for the rhodamine dye R6G $^+$ . The counterions SCN $^-$  and I $^-$  are especially effective in that they lead to significant quenching of rhodamine dye fluorescence. The iodide and thiocyanate counterions are distinguished particularly in having relatively low ionization energies as reflected in their potentials for oxidation in solution. The data are consistent with the formation of ion-pair complexes of cationic dyes and counterions, with the photochemical outcome dictated by the counterion oxidation potential. The quenching of rhodamine dye fluorescence on addition of thiocyanate was used to determine equilibrium constants for ion pairing; complexation with counterions is much suppressed for R6G $^+$  in ethanol.

A mechanism for excited-state quenching was established using laser flash photolysis methods. Phototransients associated with intra-ion-pair electron transfer were identified (for the rhodamine radical transient  $\lambda_{\text{max}} = 410$  nm). The growth and decay of the R6G radical could be accounted for in part

by a mechanism involving initial formation of a dye triplet followed by electron transfer which provides a triplet radical pair on a  $\mu$ s timescale. The enhancement of the yield of triplets observed for rhodamine ion pairs in ethyl acetate solvent may be due to enhanced spin orbit coupling involving counterion orbitals or the subtle alteration of the triplet radical pair energy gaps brought about by ion pairing. In summary, the data provide some insight to the competition kinetics that dictate the yield of long-lived free radical phototransients for an important class of cationic (rhodamine) dyes that are capable of ion pair formation in lower polarity media.

## Acknowledgement

Support of this research by the Office of Basic Energy Sciences, U.S. Department of Energy, is gratefully acknowledged.

## References

1. M. Szwarc. *In* Ions and ion pairs in organic reactions. Wiley, New York. 1973. Chap. 1.
2. T.H. Lowry and K.S. Richardson. *In* Mechanism and theory in organic chemistry. Harper and Row, New York. 1987. Chap. 2.
3. T.E. Hogen-Esch and J. Smid. *J. Am. Chem. Soc.* **87**, 669 (1965); T.E. Hogen-Esch and J. Smid. *J. Am. Chem. Soc.* **88**, 307 (1966); *J. Am. Chem. Soc.* **88**, 318 (1966).
4. (a) D.J. Owen, D. VanDerveer, and G.B. Schuster. *J. Am. Chem. Soc.* **120**, 1705 (1998); (b) D.J. Owen and G.B. Schuster. *J. Am. Chem. Soc.* **118**, 259 (1996).
5. B. Armitage and D.F. O'Brien. *J. Am. Chem. Soc.* **114**, 7396 (1992); B. Armitage and D.F. O'Brien. *J. Am. Chem. Soc.* **113**, 9678 (1991).
6. K. Ren, J.H. Maplert, H. Li, H. Gu, and D.C. Neckers. *Macromolecules*, **35**, 1632 (2002).
7. J.M. Kaufmann and J.H. Bentley. *Laser Chem.* **8**, 49 (1988).
8. D.D. Eads, B.G. Dismar, and G.R. Fleming. *J. Chem. Phys.* **93**, 1136 (1990).
9. (a) A.A. Ishchenko. *Russ. Chem. Rev.* **60**, 865 (1991); (b) A.S. Tatikolov, Kh.S. Dzhulibekov, L.A. Shvedova, V.A. Kuzmin, and A.A. Ishchenko. *J. Phys. Chem.* **99**, 6525 (1995).
10. G. Jones, II. *In* Dye lasers: Principles with applications. Edited by F.J. Duarte and L.W. Hillman. Academic Press, New York. 1990. Chap. 7.
11. (a) G. Jones, II, K. Goswami, and A.M. Halpern. *Nouv. J. Chim.* **9**, 647 (1985); (b) G. Jones, II, C. Oh, and K.J. Goswami. *J. Photochem. Photobiol. A*, **57**, 65 (1991).
12. G. Jones, II and K. Goswami. *J. Phys. Chem.* **90**, 5414 (1986).
13. J. Olmsted. *J. Phys. Chem.* **83**, 2581 (1979).
14. D.N. Dempster, T. Morrow, and M.F. Quinn. *J. Photochem.* **2**, 343 (1974).
15. G. Jones, II and M.A. Rahman. *Opt. Commun.* **97**, 140 (1993).
16. G. Jones, II and C. Oh. *J. Phys. Chem.* **98**, 2367 (1994).
17. R. Bensasson and J. Gramain. *J. Chem. Soc., Faraday Trans. 1*, **76**, 1801 (1980).
18. (a) T.L. Arbeloa, I.L. Arbeloa, and I. Garcia-Moreno. *Chem. Phys. Lett.* **299**, 315 (1999); (b) I.L. Arbeloa and P.R. Ojeda. *J. Photochem. Photobiol. A*, **45**, 313 (1988).
19. E.M. Kosower. *Tetrahedron Lett.* **50**, 4481 (1965).
20. N.J. Turro. *In* Modern molecular photochemistry. Benjamin/Cummings Pub. Co., Menlo Park, California. 1978. Chap. 7.



21. J. Georges. *Spectrochim. Acta*, **51A**, 985 (1995).
22. O. Valdes-Aguilera and D.C. Neckers. *Acc. Chem. Res.* **22**, 171 (1989).
23. N.J. Turro. *In* Modern molecular photochemistry. Benjamin/Cummings Pub. Co. Menlo Park, California. 1978. Chap. 6.
24. S.L. Murov, I. Carmichael, and G.L. Hug. *In* Handbook of photochemistry. M. Dekker Inc., New York. 1993. Chap. 7.
25. H.A. Benesi and J.H. Hildebrand. *J. Am. Chem. Soc.* **70**, 3978 (1948); H.A. Benesi and J.H. Hildebrand. *J. Am. Chem. Soc.* **71**, 2703 (1949).
26. (a) R.B. Draper and M.A. Fox. *J. Phys. Chem.* **94**, 4628 (1990); (b) R.C. Weast and M.J. Astle (*Editors*). *In* CRC handbook of chemistry and physics. CRC Press Inc., Boca Raton, Florida. 1982.
27. I. Carmichael, W.P. Helman, and G.L. Hug. *J. Phys. Chem. Ref. Data*, **16**, 239 (1987).
28. A.K. Chibisov and T.D. Slavnova. *J. Photochem.* **8**, 285 (1978).
29. E.T. Kaiser and L. Kevan. *In* Radical ions. Interscience, New York. 1968.
30. (a) H.E. Lessing. *J. Mol. Struct.* **84**, 281 (1982); (b) G. Porter. *Chem. Phys. Lett.* **49**, 416 (1977).



# Generation and reactivity of the radical cations of coniferyl alcohol and isoeugenol in solution

N.P. Schepp and Y. Rodríguez-Evora

**Abstract:** Nanosecond laser flash photolysis of coniferyl alcohol and isoeugenol in acetonitrile leads to the formation of transient species that are identified as the corresponding radical cations. These radical cations decay with rate constants of ca.  $1 \times 10^6 \text{ s}^{-1}$  in dry acetonitrile. Both radical cations react rapidly with hydroxylic solvents like water and alcohols to give 4-vinylphenoxy radicals, indicating that these reagents behave as bases rather than nucleophiles. In addition, anionic reagents (acetate, cyanide, and chloride) react rapidly with the radical cations with second-order rate constants that are close to diffusion controlled. The main products generated in the presence of the anionic reagents are again the 4-vinylphenoxy radicals, suggesting that these reagents also behave as bases. The lifetime of the radical cations in acidic acetonitrile was found to increase dramatically due to a shift in the radical cation – vinyl phenoxy radical acid–base equilibrium to the side of the radical cation. An estimate of the  $\text{p}K_{\text{a}}$  of the radical cation in acetonitrile of 4.0 was obtained from the data.

**Key words:** radical cations, laser flash photolysis, lignan, vinylphenols.

**Résumé :** La photolyse éclair au laser, avec des impulsions de l'ordre de la nanoseconde, de l'alcool du coniféryle et de l'isoeugénol dans l'acétonitrile conduit à la formation d'espèces intermédiaires qui sont en fait les cations radicalaires correspondants. Ces cations radicalaires se désintègrent avec une constante de vitesse de l'ordre de  $1 \times 10^6 \text{ s}^{-1}$  dans l'acétonitrile. Les deux cations radicalaires réagissent rapidement avec les solvants hydroxylés tels que l'eau et les alcools pour donner des radicaux 4-vinylphénoxyles, indiquant ainsi que ces réactifs se comportent plutôt comme des bases que comme des nucléophiles. De plus, les réactifs anioniques (acétate, cyanure et chlorure) réagissent rapidement avec les cations radicalaires avec des constantes de vitesse d'ordre deux qui sont très proches de celles d'une diffusion contrôlée. Les produits majoritaires générés en présence des réactifs anioniques sont encore des radicaux 4-vinylphénoxyles, ces résultats suggèrent que ces réactifs se comportent également comme des bases. On a trouvé que le temps vie de ces cations radicalaires, dans l'acétonitrile en milieu acide, augmente dramatiquement à cause d'un déplacement de l'équilibre acide–base, cation radicalaire – radical vinylphénoxyle, du côté du cation radicalaire. À partir des données on a pu évaluer à 4,0 le  $\text{p}K_{\text{a}}$  du cation radicalaire dans l'acétonitrile.

**Mots clés :** cations radicalaires, photolyse éclair au laser, lignan, vinylphénols.

[Traduit par la Rédaction]

## Introduction

Naturally occurring compounds (including 4-hydroxycinnamates like syringic acid and 1-(4-hydroxyphenyl)propen-3-ols like coniferyl alcohol) that contain a 4-vinylphenol moiety are important materials in a number of biological systems. In particular, these kinds of organic molecules are building blocks for the biosynthesis of natural products such as plant lignans (1), which often have important medicinal properties, and lignin, a major constituent of

wood. While specific details concerning the biosynthesis of these compounds are not well understood, it is generally accepted that initial oxidation induced by an oxidizing enzyme such as a peroxidase or a laccase to give a resonance-stabilized 4-vinylphenoxy radical is a key step. Enzyme-mediated dimerization of these 4-vinylphenoxy radicals then leads to production of the lignan-type materials (2, 3).

One pathway for the formation of the 4-vinylphenoxy radicals involves enzyme-induced, one-electron oxidation of the 4-vinylphenol substrate to its corresponding radical cation which then undergoes rapid deprotonation, Scheme 1.

While the chemistry of 4-vinylphenoxy radicals has been studied using several methods, including direct detection methods such as flash photolysis and ESR spectroscopy (4–6), the radical cations of the 4-vinylphenol substrates have not yet been investigated. In the present work, we focus on the chemistry of two 4-vinylphenol radical cations, namely the coniferyl alcohol and isoeugenol radical cations, Scheme 2.

Our principle goals were to obtain rate constants for the reactions of these radical cations, both with solvent and with

Received 17 February 2003. Published on the NRC Research Press Web site at <http://canjchem.nrc.ca> on 30 June 2003.

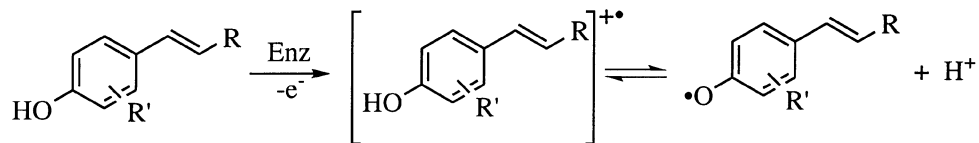
*This paper is dedicated to Professor Don Arnold in appreciation of his many contributions to radical ion chemistry.*

N.P. Schepp<sup>1</sup> and Y. Rodríguez-Evora. Department of Chemistry, Dalhousie University, Halifax, NS B3H 4J3, Canada.

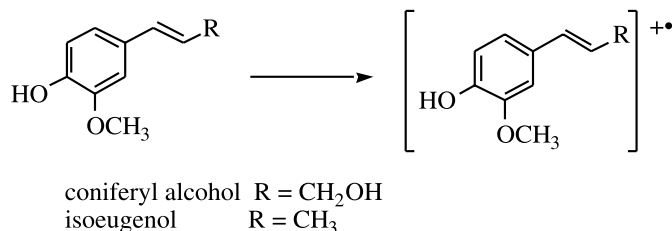
<sup>1</sup>Corresponding author (e-mail: [norman.schepp@dal.ca](mailto:norman.schepp@dal.ca)).



Scheme 1.



Scheme 2.



added bases and nucleophiles, and to examine the effect of acidity on their reactivity. We were also interested in determining if these radical cations are sufficiently long-lived to participate in bimolecular reactions. If so, it may be possible that such species play a more significant role in the biosynthesis of lignans by participating directly in the dimerization process.

## Experimental

### Materials

Coniferyl alcohol and isoeugenol were purchased (Aldrich) and used as received. Acetonitrile was spectroscopic grade (Omnisolve, BDH). All other materials were the best available commercial grades and used without further purification.

### Laser flash photolysis

The nanosecond laser flash photolysis system at Dalhousie University has been described previously (7). A Lambda Physik excimer laser (308 nm, XeCl, 10 ns/pulse, <100 mJ/pulse) was used as the excitation source for most experiments. In experiments using chloranil or di-*tert*-butylperoxide, a Continuum Nd:YAG NY-61 laser (355 nm; 8 ns/pulse; <35 mJ/pulse) was used as the excitation source.

Solutions for kinetics experiments were prepared by addition of small aliquots (ca. 10  $\mu\text{L}$ ) of stock solutions of coniferyl alcohol or isoeugenol to 2.0 or 3.0 mL of acetonitrile in  $7 \times 7 \text{ mm}^2$  laser cells made out of Suprasil quartz tubing. The absorption of the 4-vinylphenols in the laser cells was approximately 0.4 at 308 nm, corresponding to concentrations of ca. 0.1 mM. Most laser experiments were carried out using aerated samples. When oxygen-free solutions were required, the samples were bubbled with a slow stream of dry nitrogen 20 min prior to laser irradiation. Measurements of quenching rate constants were made by adding small amounts (1–20  $\mu\text{L}$ ) of a stock solution with a known concentration of the quencher (*n*-Bu<sub>4</sub>NCl, *n*-Bu<sub>4</sub>NCN, or *n*-Bu<sub>4</sub>NO<sub>2</sub>CCH<sub>3</sub>) dissolved in acetonitrile. Solutions for the experiments carried out under acidic conditions were prepared by making a 0.010 M HClO<sub>4</sub> stock solution in acetonitrile and then making appropriate dilu-

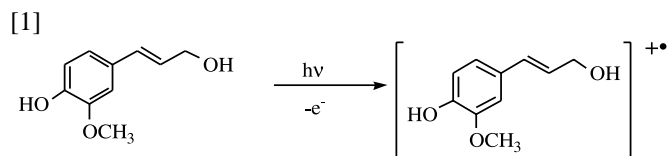
tions of this solution using acetonitrile. To minimize the possibility of acid-catalyzed decomposition of coniferyl alcohol or isoeugenol, these materials were added to the acidic sample solutions just prior to performing the laser experiments. All kinetics experiments were carried out at room temperature ( $22 \pm 1^\circ\text{C}$ ). For measurement of absorption spectra, a flow cell system was used to ensure that only fresh solution was subjected to each laser pulse.

## Results and discussion

### Laser irradiation in acetonitrile

Laser irradiation of coniferyl alcohol in dry acetonitrile leads to the formation of distinct absorption bands at 380 and 580 nm, Fig. 1. These two bands are formed promptly within the laser pulse, and both decay in a first-order manner with identical rate constants of  $8 \times 10^5 \text{ s}^{-1}$  (Fig. 1, inset). The similar kinetic behaviour of these two bands indicates that both bands belong to a single transient species.

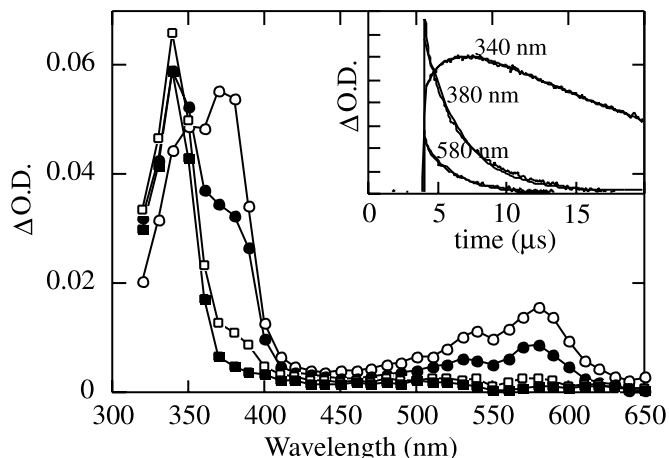
The absorption spectrum is very similar to the known spectra of substituted styrene radical cations that have two strong bands near 360 and 580 nm (8). In addition, the decay of the transient is insensitive to oxygen, but is greatly accelerated in the presence of hydroxylic solvents like water and methanol and in the presence of anionic reagents like bromide and chloride. These observations provide strong evidence for the identification of the transient species as the radical cation of coniferyl alcohol produced by laser-induced photoionization of coniferyl alcohol, eq. [1].



Evidence to support this assignment comes from results obtained under photoinduced electron-transfer conditions. Selective laser irradiation (355 nm) of chloranil in the presence of 1.0 mM coniferyl alcohol in acetonitrile leads initially to the formation of the triplet of chloranil with an absorption maximum at 500 nm (9). This band decays rapidly in the presence of coniferyl alcohol, Fig. 2 (inset), and leads to the formation of absorption bands at 380 and 580 nm, Fig. 2, that are closely similar to those produced upon direct laser irradiation of coniferyl alcohol. Absorption due to the presence of the chloranil radical anion at 450 nm (9) is also observed, with the rate constant for the growth of this band being identical to that for the decay of the triplet and for the growth of the bands at 380 and 580 nm. These results are consistent with initial formation of the chloranil triplet with absorption at 500 nm, which then undergoes an electron-transfer reaction with coniferyl alcohol to produce

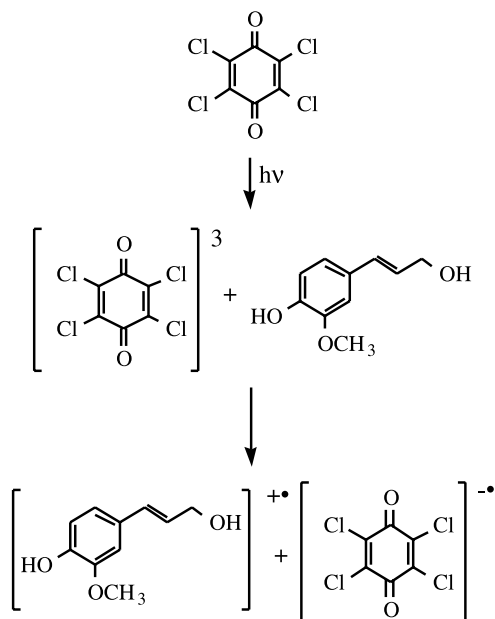


**Fig. 1.** Transient absorption spectra generated (○) 200 ns, (●) 920 ns, (□) 3.2 μs, and (■) 6.4 μs after 308 nm laser irradiation of coniferyl alcohol in air-saturated acetonitrile. Inset shows time-resolved changes in optical density at 380, 580, and 340 nm upon 308 nm irradiation of coniferyl alcohol in air-saturated acetonitrile.



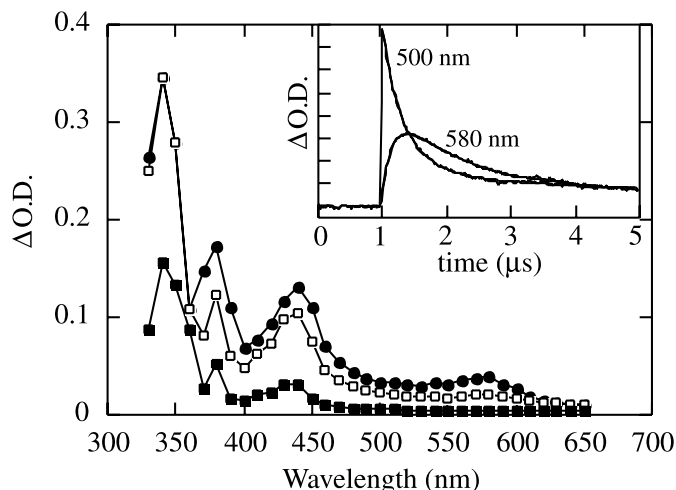
the 4-vinylphenol radical cation and the radical anion of chloranil, eq. [2].

[2]



As shown in Fig. 1, a strong absorption band centered at 340 nm is observed upon 308 nm irradiation of coniferyl alcohol in addition to the radical cation absorption at 380 and 580 nm. However, unlike the radical cation absorption, which appears promptly after the laser pulse, the 340 nm band grows in as a function of time. The observed rate constant of  $8 \times 10^5 \text{ s}^{-1}$  for the formation of this band is identical to that for the decay of the 380 and 580 nm bands, Fig. 1 (inset), indicating the transient responsible for the absorption at 340 nm is a product of the reaction of the radical cation. The decay of the 340 nm transient is not affected by the

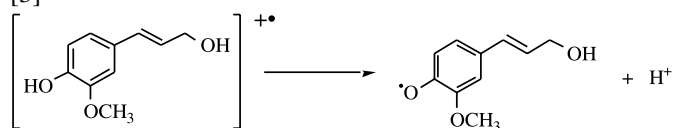
**Fig. 2.** Transient absorption spectra generated (●) 1 μs, (□) 2 μs, and (■) 7 μs after 355 nm laser irradiation of chloranil in air-saturated acetonitrile with 0.001 M coniferyl alcohol. Inset shows time-resolved changes in optical density at 500 and 580 nm upon 355 nm laser irradiation of chloranil in air-saturated acetonitrile with 0.001 M coniferyl alcohol.



presence or absence of oxygen, nor is its decay influenced by the addition of protic reagents like water or methanol or anionic reagents like chloride or cyanide.

As observed for methoxy-substituted phenol radical cations, which rapidly deprotonate to give simple phenoxyl radicals (10), the main reaction of the 4-vinylphenol radical cation is likely to be deprotonation to give in this case a 4-vinylphenoxyl radical, eq. [3].

[3]

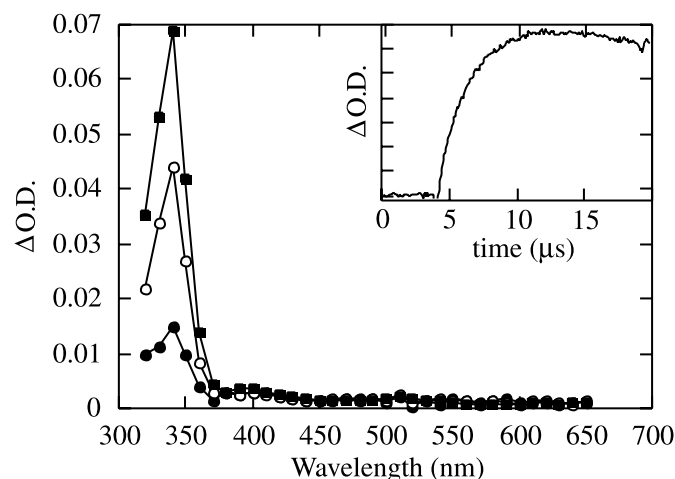


It is therefore reasonable to suggest that the 340 nm absorption band generated upon decay of the coniferyl alcohol radical cation is the 2-methoxy-4-(3-hydroxy-1-propenyl) phenoxyl radical. Evidence supporting this suggestion was obtained upon 355 nm laser irradiation of a solution of di-*tert*-butylperoxide in the presence of small amounts of coniferyl alcohol. This is expected to lead to the formation of the phenoxyl radical by initial photochemical formation of the *tert*-butoxy radical, followed by rapid hydrogen abstraction from the phenol hydroxy group of the coniferyl alcohol. As shown in Fig. 3, a transient with an absorption maximum at 340 nm identical to that produced upon reaction of the coniferyl alcohol radical cation is observed. These results therefore provide good evidence that the main reaction of the radical cation is indeed deprotonation to the 4-vinylphenoxyl radical, eq. [3].

A long-lived species with an absorption maximum at 350 nm has been observed previously upon irradiation of coniferyl alcohol in aqueous or alcoholic solvents (6, 11, 12). This transient has been assigned as the quinone methide generated by a mechanism that is thought to involve

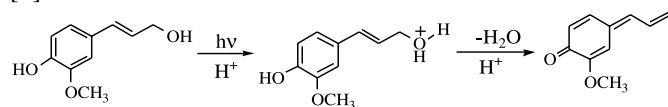


**Fig. 3.** Transient absorption spectra generated (●) 480 ns, (○) 1.9  $\mu$ s, and (■) 13  $\mu$ s after 355 nm laser irradiation of di-*tert*-butylperoxide in air-saturated acetonitrile with 0.001 M conferyl alcohol. Inset shows time-resolved changes in optical density at 340 nm.



photoinduced protonation of the  $\beta$ -OH group, followed by elimination of water and deprotonation (6) (12), eq. [4].

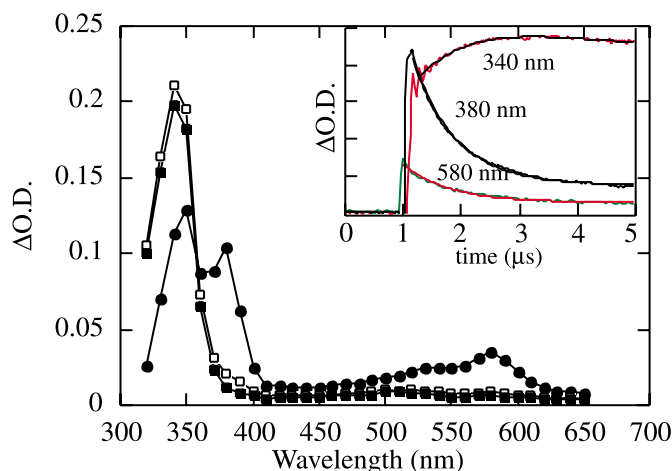
[4]



However, the absorption band at 340 nm generated in our experiments decays completely within 1 ms after the laser pulse, which is consistent with the reactivity of other phenoxyl radicals (13). This reactivity is considerably different from that observed for the quinone methide in aqueous solution at room temperature, where its lifetime is several minutes (12). Furthermore, our results clearly show that the 340 nm transient is a product of the reaction of the radical cation; it is difficult to assign a reasonable mechanism for the conversion of the radical cation to the quinone methide, while conversion to the phenoxyl radical by deprotonation is a sensible reaction pathway.

Similar results to those described above were observed upon direct 308 nm irradiation of isoeugenol in acetonitrile, Fig. 4, and upon 355 nm irradiation of chloranil in the presence of isoeugenol. In both cases, the isoeugenol radical cation was observed with absorption bands at 380 and 580 nm. The radical cation decayed in a first-order manner in dry acetonitrile with a rate constant of  $9 \times 10^5 \text{ s}^{-1}$ . As the radical cation decayed, a new absorption band at 340 nm was observed. This new absorption band is assigned to the corresponding 4-vinylphenoxyl radical on the basis of its similarity to the absorption band observed upon 355 nm irradiation of di-*tert*-butylperoxide in the presence of isoeugenol.

**Fig. 4.** Transient absorption spectra generated (●) 400 ns, (□) 1.8  $\mu$ s, and (■) 3.0  $\mu$ s after 308 nm laser irradiation of isoeugenol in air-saturated acetonitrile. Inset shows time-resolved changes in optical density at 380, 580, and 340 nm observed upon 308 nm irradiation of isoeugenol in air-saturated acetonitrile.



#### Effect of water and alcohols on decay of conferyl alcohol radical cation in acetonitrile

Throughout the course of our experiments into the reactivity of the conferyl alcohol and isoeugenol radical cations in neat acetonitrile, rate constants measured for the decay of the radical cations varied somewhat between  $7 \times 10^5$  and  $1 \times 10^6 \text{ s}^{-1}$ . This variability depended mainly on the quality of the acetonitrile used: in acetonitrile from a freshly opened bottle, the radical cation was longer-lived, while the radical cation in acetonitrile that had previously been exposed to air was somewhat shorter-lived. The most likely source of this variability was the presence or absence of water in the acetonitrile, with acetonitrile from a freshly opened bottle having a lower water content compared with that from an already opened bottle. The rate constants of  $7 \times 10^5$  and  $9 \times 10^5 \text{ s}^{-1}$  were the slowest rate constants measured for the conferyl alcohol and the isoeugenol radical cations, respectively, in acetonitrile dried with activated molecular sieves.

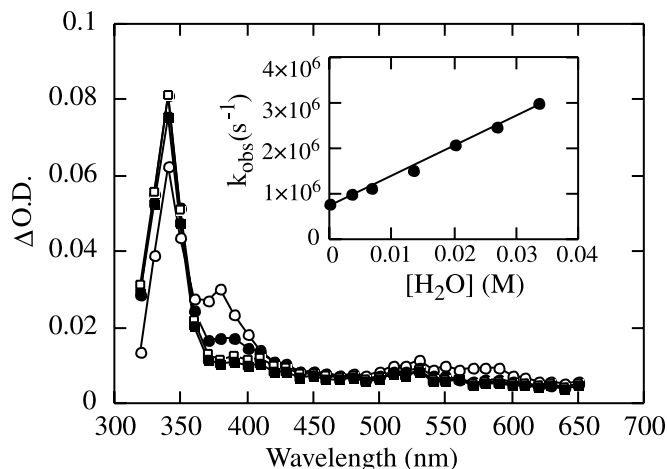
To quantitatively determine the influence of water content, the decay of the radical cation was measured as a function of water concentration in acetonitrile. As shown in Fig. 5 (inset), even small quantities of water greatly accelerate the rate constant for the decay, such that in the presence of 0.034 M water, the rate constant more than triples from  $0.8 \times 10^6$  to  $3.0 \times 10^6 \text{ s}^{-1}$ . The relationship between the observed rate constants<sup>2</sup> for the decay of the conferyl alcohol radical cation and water concentration is linear. Least-squares analysis leads to the second-order rate constant for the reaction with water of  $6.5 \times 10^7 \text{ M}^{-1} \text{ s}^{-1}$ .

The decay of the conferyl alcohol radical cation also increased rapidly with increasing concentrations of methanol, ethanol, 2-propanol, and *tert*-butyl alcohol. In each case, a linear relationship was obtained between the observed rate constants and alcohol concentration. Least-squares analysis

<sup>2</sup>Tables of rate data (Tables S1-S10) have been deposited and may be purchased from the Depository of Unpublished Data, Document Delivery, CISTI, National Research Council Canada, Ottawa, ON K1A 0S2, Canada ([http://www.nrc.ca/cisti/irm/unpub\\_e.shtml](http://www.nrc.ca/cisti/irm/unpub_e.shtml) for information on ordering electronically).

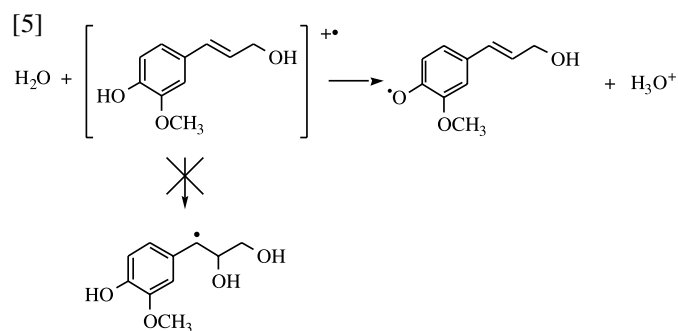


**Fig. 5.** Transient absorption spectra generated (○) 90 ns, (●) 460 ns, (□) 1.8 μs, and (■) 3.2 μs after 308 nm laser irradiation of isoeugenol in air-saturated acetonitrile with 0.03 M water. Inset shows the relationship between the observed rate constants for the decay of the coniferyl alcohol radical and the concentration of added water in acetonitrile.



gave second-order rate constants that were similar for each alcohol, ranging from  $2 \times 10^7$  to  $4 \times 10^7 \text{ M}^{-1} \text{ s}^{-1}$ . These rate constants are summarized in Table 1.

In the presence of added water or alcohols, the accelerated decay of the radical cation continued to lead to the formation of the 340 nm band assigned to the substituted 4-vinylphenoxy radical, Fig. 5, and the rate constants for the growth of the radical continued to match the rate constants for the radical cation decay. No evidence was found for the presence of an oxygen-sensitive phenethyl radical that would have been formed upon nucleophilic addition of water or alcohol to the radical. Thus, water and the alcohols appear to act as bases rather than nucleophiles in their reaction with the radical cation, eq. [5].



In addition, little variation is observed in the second-order rate constants for the reaction of the radical cation with the four alcohols, Table 1. Such a lack of sensitivity to the steric bulk of the alcohols is expected for a situation in which the alcohols, which have similar basicities but different nucleophilicities, act as bases rather than nucleophiles. Furthermore, the rate constants given in Table 1 are considerably larger than the rate constant of  $3 \times 10^4 \text{ M}^{-1} \text{ s}^{-1}$  for the reaction of methanol with the 1-(4-methoxyphenyl)propene radical cation (8). This radical cation is analogous to the 4-

**Table 1.** Second-order rate constants for the reaction of the coniferyl alcohol radical cation with water and alcohols in acetonitrile ( $22 \pm 1^\circ \text{C}$ ).

Water or alcohol	Coniferyl alcohol $k_{\text{Nuc}} (\text{M}^{-1} \text{ s}^{-1})$
H <sub>2</sub> O	$(6.5 \pm 0.5) \times 10^7$
CH <sub>3</sub> OH	$(3.1 \pm 0.1) \times 10^7$
CH <sub>3</sub> CH <sub>2</sub> OH	$(2.0 \pm 0.1) \times 10^7$
(CH <sub>3</sub> ) <sub>2</sub> CHOH	$(4.7 \pm 0.2) \times 10^7$
(CH <sub>3</sub> ) <sub>3</sub> COH	$(4.9 \pm 0.2) \times 10^7$

vinylphenol radical cations, with the hydroxy group on the aromatic ring being replaced by a methoxy group. The 1-(4-methoxyphenyl)propene radical cation thus has no strongly acidic proton, and the low value for the rate constant for its reaction with water and alcohols indicates a relatively slow nucleophilic addition reaction. Rate constants for nucleophilic addition to the coniferyl alcohol radical cation should be similar; the fact that the measured rate constants are greater is consistent with the availability of a more rapid deprotonation reaction.

The rate constants for deprotonation from the coniferyl alcohol radical cation are of the same order of magnitude for the deprotonation from methoxy-substituted phenols in acetonitrile. For example, deprotonation of 3,5-dimethoxyphenol radical cation by water and methanol in acetonitrile takes place with rate constants of  $2.5 \times 10^8$  and  $8.2 \times 10^7 \text{ M}^{-1} \text{ s}^{-1}$  (10), respectively, which are about three-fold greater than the rate constants for the deprotonation of coniferyl alcohol.

#### Effect of anions on decay of coniferyl alcohol and isoeugenol radical cations in acetonitrile

In acetonitrile, styrene radical cations react with anionic reagents like halide, cyanide, and acetate ions at diffusion-controlled rate constants of approximately  $10^{10} \text{ M}^{-1} \text{ s}^{-1}$ , with the primary reaction being nucleophilic addition to generate substituted phenethyl radicals (8). In the present work, the reactivity of the coniferyl alcohol and isoeugenol radical cations in the presence of these anions in acetonitrile was also measured. In each case, the decay of the radical cations did increase rapidly as a function of increasing concentration of the anions. The relationships between the observed rate constant for the decay of the radical cations and the concentrations of the anions were all linear. Least-squares analysis gave second-order rate constants in the  $1\text{--}2 \times 10^{10} \text{ M}^{-1} \text{ s}^{-1}$  range for reaction of acetate and cyanide ions, Table 2, indicating that these two anions react with the radical cations at the diffusion-controlled limit. The second-order rate constant for the reaction of the chloride ion with the two radical cations was similar at about  $2 \times 10^{10} \text{ M}^{-1} \text{ s}^{-1}$ .

Figure 6 shows the absorption spectrum generated upon quenching of the coniferyl alcohol radical cation in the presence of 0.1 mM chloride. At this concentration of chloride, the bands at 380 and 580 nm associated with the radical cation are almost completely quenched, and in their place is an absorption band with a maximum at 340 nm. This absorption band, which is also formed upon reaction of the radical cation with acetate and cyanide ions, is identical to that of the 4-vinylphenoxy radical produced by deprotonation of



**Fig. 6.** Absorption spectra generated (●) 900 ns, (□) 3.6  $\mu$ s, and (■) 6.4  $\mu$ s after 308 nm irradiation of coniferyl alcohol in acetonitrile with 0.10 mM  $n$ -Bu<sub>4</sub>NCl.

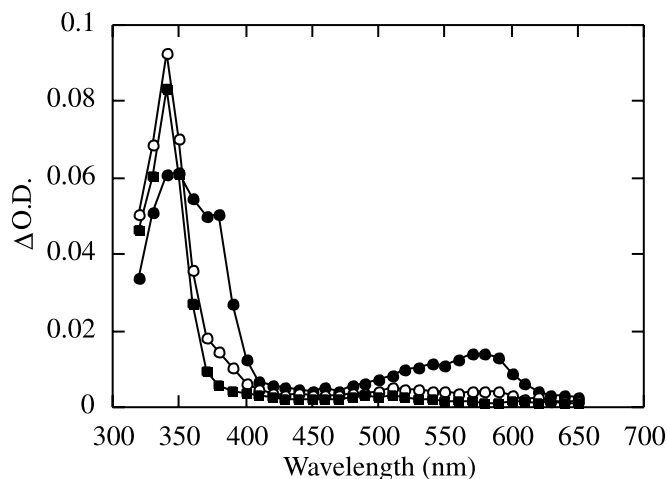


**Table 2.** Second-order rate constants for the reaction of the coniferyl alcohol and isoeugenol radical cations with anionic reagents ( $22 \pm 1^\circ\text{C}$ ).

Anion	Coniferyl alcohol <sup>++</sup> $k_{\text{Nuc}}$ ( $\text{M}^{-1} \text{s}^{-1}$ )	Isoeugenol <sup>++</sup> $k_{\text{Nuc}}$ ( $\text{M}^{-1} \text{s}^{-1}$ )
$\text{CH}_3\text{CO}_2^-$	$(1.9 \pm 0.2) \times 10^{10}$	$(1.0 \pm 0.1) \times 10^{10}$
$\text{CN}^-$	$(2.0 \pm 0.2) \times 10^{10}$	$(1.4 \pm 0.2) \times 10^{10}$
$\text{Cl}^-$	$(2.5 \pm 0.4) \times 10^{10}$	$(1.9 \pm 0.3) \times 10^{10}$

the coniferyl alcohol radical cation in neat acetonitrile or in acetonitrile containing water. The 340 nm band is also unaffected by the presence of oxygen.

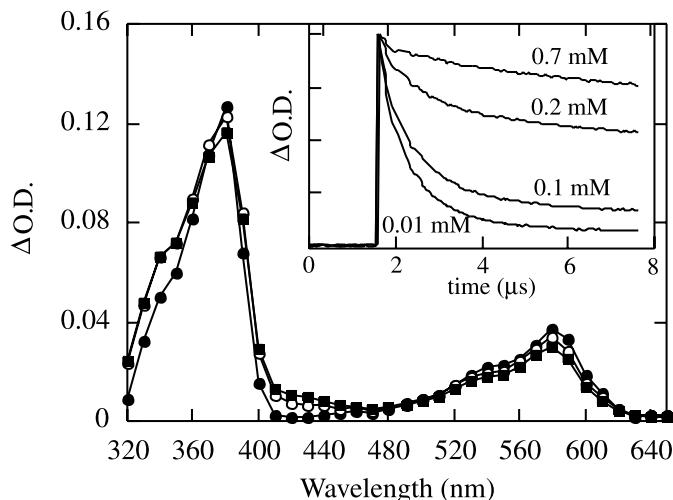
These observations indicate that the 4-vinylphenoxy radical observed in neat acetonitrile and in acetonitrile containing hydroxylic additives is still generated upon reaction of the radical cations with anionic nucleophiles. Thus, despite the demonstrated ability of acetate, cyanide, and chloride to react rapidly with styrene radical cations by nucleophilic addition, deprotonation continues to be an important reaction pathway in the case of the coniferyl radical cation, due to the presence of its acidic proton.

We considered the possibility that the vinylphenoxy radicals are generated as secondary products, with the nucleophile adding to the radical cation to generate a substituted phenethyl radical that then undergoes a hydrogen atom abstraction reaction with the pool of unreacted coniferyl alcohol. However, bimolecular rate constants for hydrogen atom transfer from phenols to alkyl radicals are typically slow (14), and such a reaction at the low concentration of coniferyl alcohol (ca. 0.15 mM) used in the present study is unlikely. Thus, the most likely explanation for the observation that reaction of the radical cation with anionic nucleophiles leads to 4-vinylphenoxy formation is that the anionic reagents like chloride and cyanide are acting as bases rather than nucleophiles.

#### Acidity of isoeugenol radical cation in acetonitrile

Figure 7 shows the transient absorption spectra generated upon 308 nm irradiation of isoeugenol in acetonitrile con-

**Fig. 7.** Transient absorption spectra generated (●) 480 ns, (○) 3  $\mu$ s, and (■) 6  $\mu$ s after 308 nm laser irradiation of isoeugenol in air-saturated acetonitrile with 0.7 mM  $\text{HClO}_4$ . Inset shows time-resolved changes in absorption at 580 nm because of the decay of the isoeugenol radical cation in acetonitrile at different concentrations of  $\text{HClO}_4$ .



taining 0.7 mM  $\text{HClO}_4$ . Clearly, the radical cation is still generated under these conditions in the same manner as observed for experiments in acetonitrile without added acid. However, unlike the situation in neat acetonitrile where the radical cation decayed rapidly, absorption due to the presence of the radical cation remains essentially unchanged over the 10  $\mu$ s time range of the experiment. Thus, the lifetime of the radical cation is dramatically increased in the presence of low concentrations of the strong acid.

This situation is more clearly illustrated in Fig. 7 (inset), which shows the effect of perchloric acid concentration on the lifetime of the radical cation in acetonitrile. In very dilute acidic acetonitrile,  $[\text{HClO}_4] = 0.01 \text{ mM}$ , absorption due to the radical cation at 580 nm decays in a first-order manner to almost zero absorbance with a rate constant of approximately  $10^6 \text{ s}^{-1}$ . In the presence of 0.1 mM perchloric acid, the radical cation no longer decays via simple first-order kinetics. Instead, the radical cation now decays via two sequential first-order processes. The fast process occurs with a rate constant of ca.  $10^6 \text{ s}^{-1}$ , while the second component is considerably slower, taking place with a rate constant of approximately  $2 \times 10^4 \text{ s}^{-1}$ . As the acid content increases, the significance of the faster component continues to decrease, while the second component becomes more dominant. By the time the acid concentration reaches 0.7 mM perchloric acid, the fast component is no longer visible, and the radical cation now decays with a single slow component having a rate constant of ca.  $2 \times 10^4 \text{ s}^{-1}$ .

These results indicate that, at increasing acid concentrations, the radical cation is no longer completely converted to its conjugate base, the 4-vinylphenoxy radical. Instead, the radical cation decays until an equilibrium state consisting of significant amounts of both the radical and the radical cation is reached. The equilibrium state then decays more slowly either by reaction of the 4-vinylphenoxy radical or by nucleophilic addition of solvent or residual water to the radical cation.



By measuring the fraction of radical cation present after the equilibrium state is reached as a function of acid concentration, an estimate of the  $pK_a$  of the radical cation in acetonitrile can be determined. According to eq. [6], the ratio of the absorption of the radical cation at 580 nm after the equilibrium state is reached,  $Abs_{eq}^{580nm}$ , to the initial absorption of the radical cation at 580 nm immediately after the laser pulse,  $Abs_{initial}^{580nm}$ , will change as a function of acid concentration.

$$[6] \quad \frac{Abs_{eq}^{580nm}}{Abs_{initial}^{580nm}} = \frac{[H^+]}{[H^+] + K_a}$$

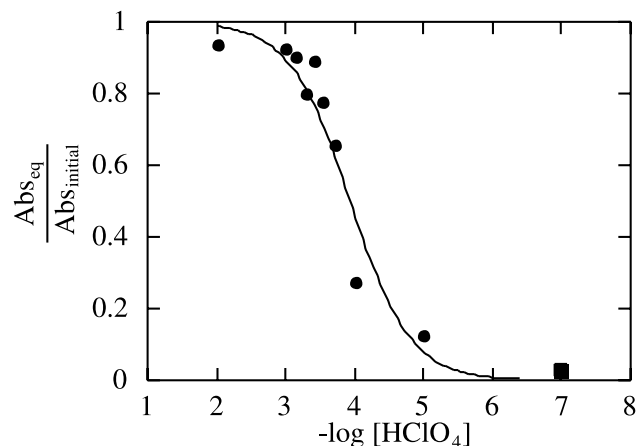
The ratio is plotted as a function of  $H^+$  concentration in Fig. 8. As can be seen, the ratio is small at low acid concentrations because of the 4-vinylphenoxy radical being the dominant species. As the concentration of acid increases, the ratio increases as the equilibrium is shifted to the side of the radical cation. At acid concentrations greater than 0.5 mM, the ratio reaches a maximum value near one, and no further increase is observed. Fitting of these data to eq. [6] then leads to a value for  $K_a = 1.1 \times 10^{-4}$  M, indicating that the radical cation has a  $pK_a \approx 4$  in acetonitrile. Since cationic acids are typically 7 to 8 orders of magnitude less acidic in acetonitrile than in water (15), we can estimate a  $pK_a \approx -3$  to  $-4$  for the acidity of the isoeugenol radical cation in aqueous solution. This value is consistent with  $pK_a$  values near  $-5$  estimated for other methoxy-substituted phenol radical cations in aqueous solution (16).

## Conclusions

The results presented here demonstrate that the radical cations of 4-vinylphenols in a dry polar solvent are short-lived species, with deprotonation to the corresponding 4-vinylphenoxy radical being the major reaction pathway. However, in an acidic environment, the lifetimes of the radical cations are dramatically enhanced. Under these conditions, the radical cations should be sufficiently long-lived to participate in an addition reaction with their neutral counterpart to give lignan-like dimers in a manner similar to that previously demonstrated for 4-methoxystyrene radical cations (8, 17–19). The enhanced lifetime also raises the possibility that the biosynthesis of lignans could, at least in principle, proceed via a radical-cation-mediated dimerization process instead of via vinylphenoxy radical coupling, especially if the enzyme active site provides a dry, acidic environment.

It is worth noting that no quenching of the coniferyl alcohol or isoeugenol radical cations by their neutral precursor was observed in our experiments even under acidic conditions where the radical cations are long-lived. However, this inability to detect coupling by time-resolved techniques does not necessarily indicate that radical-cation-mediated dimerization cannot take place. For example, the decay of 4-methoxystyrene derivatives such as the 1-(4-methoxyphenyl)-propene radical cation with a methyl group attached to the  $\beta$ -position of the carbon-carbon double bond shows no dependence on precursor concentration in time-resolved experiments (20), while product studies clearly demonstrate radical-cation-mediated dimerization does indeed occur (21). Further experiments using potentially more reactive species

**Fig. 8.** Fraction long-lived isoeugenol radical cation measured from the absorption at 580 nm after equilibration ( $Abs_{eq}$ ) and immediately after the laser pulse ( $Abs_{initial}$ ) as a function of acid content in acetonitrile. The data point (■), corresponding to  $-\log [HClO_4] = 7$ , is for the ratio measured in neat acetonitrile and was not included in determining the line-of-best-fit.



such as the 2-methoxy-4-vinylphenol radical cation are currently under way to determine if 4-vinylphenol radical cations lacking a  $\beta$ -alkyl group are capable of undergoing coupling reactions in competition with deprotonation.

## Acknowledgements

We are grateful to the Natural Sciences and Engineering Research Council of Canada (NSERC) for financial support of this research. We also thank Prof. Fran Cozens for helpful discussions.

## References

1. M.J. Kato, A. Chu, L.B. Davin, and N.G. Lewis. *Phytochemistry*, **47**, 583 (1998).
2. D.C. Ayres and J.D. Loike. *Lignans. Chemical, biological and clinical properties*. Cambridge University Press, Cambridge, U.K. 1990.
3. L.B. Davin, H.B. Wang, A.L. Crowell, D.L. Bedgar, D.M. Martin, S. Sarkanen, and N.G. Lewis. *Science* (Washington, D.C.), **275**, 362 (1997).
4. G.J. Smith and I.J. Miller. *Aust. J. Chem.* **28**, 193 (1975).
5. I.J. Miller and G.J. Smith. *Tetrahedron Lett.* 2277 (1973).
6. G. Leary. *J. Chem. Soc. Perkins Trans. 2*, 640 (1972).
7. F.L. Cozens, M. O'Neill, R. Bogdanova, and N.P. Schepp. *J. Am. Chem. Soc.* **119**, 10 652 (1997).
8. L.J. Johnston and N.P. Schepp. *J. Am. Chem. Soc.* **115**, 6564 (1993).
9. J.J. Andre and G. Weill. *Mol. Phys.* **15**, 97 (1968).
10. T.A. Gadosy, D. Shukla, and L.J. Johnston. *J. Phys. Chem. A*, **103**, 8834 (1999).
11. G. Leary. *J. Chem. Soc. Chem. Comm.* 688 (1971).
12. K. Radotic, J. Zakrezevska, D. Sladic, and M. Jeremic. *Photochem. Photobiol.* **65**, 284 (1997).
13. E.J. Land and G. Porter. *Trans. Faraday Soc.* **59**, 2016 (1963).
14. C. Evans, J.C. Scaiano, and K.U. Ingold. *J. Am. Chem. Soc.* **114**, 4589 (1992).
15. D. Augustin-Nowacka, M. Makowski, and L. Chmurzynski. *Anal. Chim. Acta*, **418**, 233 (2000).



16. F.G. Bordwell and J.-P. Cheng. *J. Am. Chem. Soc.* **113**, 1736 (1991).
17. S. Kadota, K. Tsubono, K. Makino, M. Takeshita, and T. Kikuchi. *Tetrahedron Lett.* **28**, 2857 (1987).
18. R.M. Wilson, J.G. Dietz, T.A. Shepherd, D.M. Ho, K.A. Schnapp, R.C. Elder, J.W. Watkins, L.S. Geraci, and C.F. Campana. *J. Am. Chem. Soc.* **111**, 1749 (1989).
19. N.P. Schepp and L.J. Johnston. *J. Am. Chem. Soc.* **116**, 10 330 (1994).
20. N.P. Schepp and L.J. Johnston. *J. Am. Chem. Soc.* **118**, 2872 (1996).
21. F.D. Lewis and M. Kojima. *J. Am. Chem. Soc.* **110**, 8664 (1988).



# Photolabile calixarene-based rosette

Zaiguo Li, Huy Chiu, and Andrei G. Kutateladze

**Abstract:** A model calix[4]arene-based rosette carrying two alternating photocleavable dithianyl-hydroxy-methyl moieties and two benzophenonecarboxylates was synthesized and shown to be capable of photoinduced fragmentation, with efficiency comparable to that of the externally sensitized parent dithiane–benzaldehyde adducts.

**Key words:** photoinduced electron transfer, photofragmentation, calixarene, dithiane–carbonyl adducts.

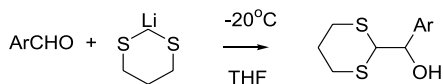
**Résumé :** On a effectué la synthèse d'une rosette modèle à base de calix[4]arène portant deux portions alternées de dithianyl-hydroxy-méthyle photoclivables et de deux benzophénonecarboxylates; on a démontré qu'il est possible d'en provoquer une fragmentation photoinduite avec une efficacité comparable à celle des adduits parents dithiane–benzaldéhyde sensibilisés d'une façon externe.

**Mots clés :** transfert d'électron photoinduit, photofragmentation, calixarène, adduits dithiane–carbonyle.

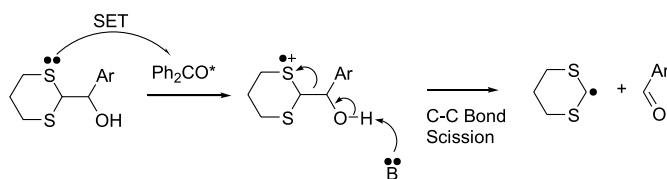
[Traduit par la Rédaction]

## Introduction

Calixarenes modified at their upper or lower rim are often used as scaffolds for modular assembly of complex macromolecules. The relative rigidity of the calixarenic macrocycle makes it a spacer of choice for positioning various substituents and (or) molecular blocks in a daisy-wheel-like fashion. Specific examples range from ion-selective chelators and ionophores (1) to tethered polypeptides capable of protein surface recognition (2) to recognition-based sensing of other peptides (3), etc. We suggest that an attractive functional feature for such modular designs would be to assemble them by interconnecting the core scaffold and the auxiliary peripheral modules via photolabile tethers. This in essence is the approach that we have been developing based on the recently discovered photofragmentation reaction of  $\alpha$ -hydroxyalkyl dithianes and related compounds in the presence of an electron transfer sensitizer, such as benzophenone (4). These compounds are readily available through nearly quantitative lithiodithiane additions to carbonyl compounds — a reaction that was developed three decades ago by Corey and Seebach (5), and that over the years has been implemented in numerous successful synthetic procedures.

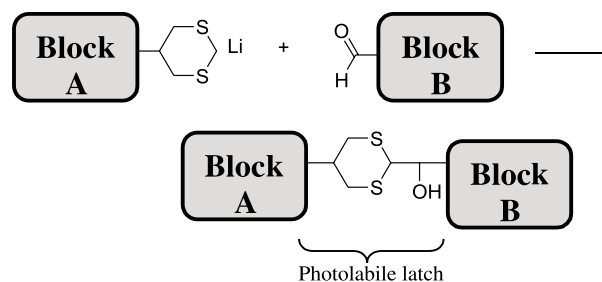


The photofragmentation is initiated by photoinduced electron transfer from the dithiane moiety to the excited triplet benzophenone, followed by mesolytic cleavage in the generated cation–radical (4).



Mechanistic aspects of similar fragmentations in cation–radicals containing other heteroatoms were studied by Arnold, Whitten, Maslak, and co-workers (6).

We use such dithiane–carbonyl adducts as photolabile “latches” that can hold together various molecular blocks, and are capable of releasing them upon photoirradiation (7).



In this communication, we report the synthesis of a model calixarene-based photocleavable rosette outfitted with an internal sensitizer, and its photoinduced fragmentation. Unsubstituted dithiane is used as a simple “model” of a macromolecular block that potentially can be attached to the calixarenic scaffold via dithianes substituted at position 5, for example 5-carboxy- or 5-hydroxymethyldithiane.

Received 10 January 2003. Published on the NRC Research Press Web site at <http://canjchem.nrc.ca> on 30 June 2003.

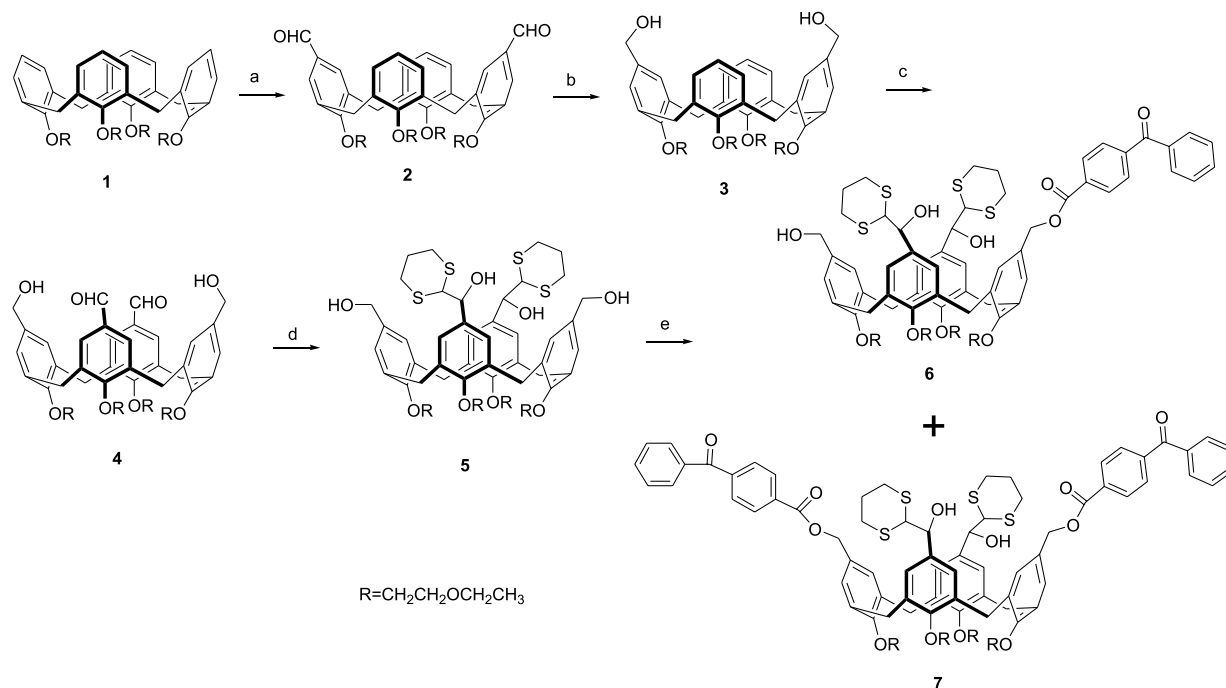
This paper is dedicated to Professor Don Arnold.

**Z. Li, H. Chiu, and A.G. Kutateladze.**<sup>1</sup> Department of Chemistry and Biochemistry, University of Denver, Denver, CO 80208-2436, U.S.A.

<sup>1</sup>Corresponding author (e-mail: [akutatel@du.edu](mailto:akutatel@du.edu)).



**Scheme 1.** (a)  $\text{CHCl}_2\text{OCH}_3\text{--SnCl}_4\text{--CHCl}_3$ , 46%; (b)  $\text{NaBH}_4\text{--EtOH}$  86%; (c)  $\text{CHCl}_2\text{OCH}_3\text{--TiCl}_4\text{--CHCl}_3$ , 41%; (d) excess lithiated dithiane, THF,  $-78^\circ\text{C}$  to r.t., 42%; (e)  $\text{PhC(O)PhCOCl}$ ,  $\text{Et}_3\text{N}$ ,  $\text{CH}_2\text{Cl}_2$ , 20 h (see text).



The overall synthetic scheme is presented below (Scheme 1). Commercially available calix[4]arene was tetraalkylated with 2-ethoxyethylbromide to give **1** and then bis-formylated according to the procedure by Arduini et al. (8) yielding **2**. The dialdehyde **2** was reduced with sodium borohydride and the formylation was repeated. The  $\text{C}_2$ -symmetric dialdehyde-diol **4** was reacted with excess lithiated dithiane to furnish bis-adduct **5** (42%).

Addition of dithianyl anion to dialdehyde **4** was expected to produce a pair of diastereomers. Given the large spatial separation of the chiral centers, we did not expect any diastereoselectivity and the NMR spectrum of bis-adduct **5** seems to corroborate this conclusion. As is shown in Fig. 1, the proton signal for the primary benzylic alcohols, which is a singlet in **4**, is represented by two separate peaks in **5** (4.17 and 4.15 ppm). Also, the calixarenic methylenes,  $\text{Ar-CH}_2\text{-Ar}$  (both sets of four “in” and four “out”), which are doublets in

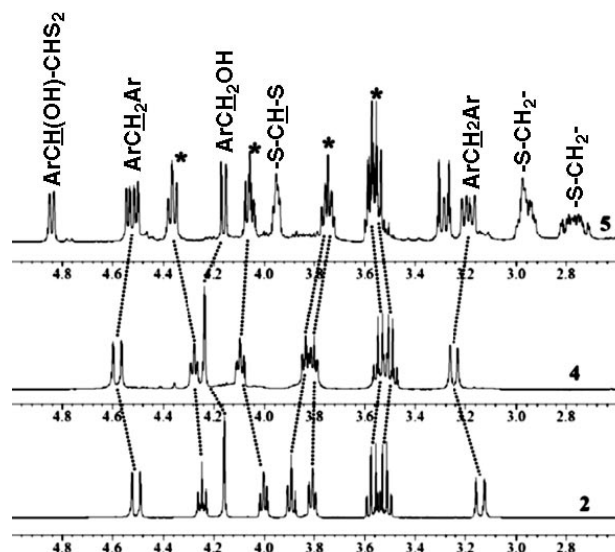
**1–4**, are represented by two sets of doublets each in the compound **5** (and **7**).<sup>2</sup>

An alternative rationale for the observed doubling of the benzylic peaks is that **5** is a single diastereomer, but the crowded steric environment in it prevents free rotation of the dithianyl groups and they are caught in an unsymmetrical conformation, resulting in magnetically nonequivalent protons. Formation of only one diastereomer is, however, unlikely. We heated the sample of **5** in deuterated chloroform to  $55^\circ\text{C}$  and did not observe any coalescence of the benzylic signals in NMR. We, therefore, interpret the observed NMR spectrum as a 1:1 mixture of diastereomers. Both diastereomers are suitable for the assembly of the target photolabile rosettes. In this study we employed benzophenone-4-carboxylic acid as a tethered internal sensitizer. It was first converted into *p*-benzoylbenzoyl chloride via reaction with oxalyl chloride in dichloromethane and then cou-

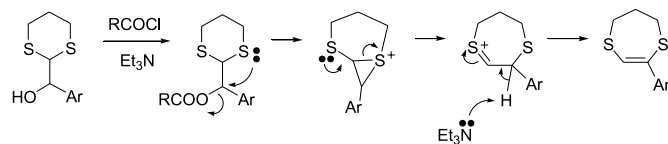
<sup>2</sup> 5,17-Dihydroxymethyl-25, 26, 27, 28-tetrakis(2-ethoxyethoxy)calix[4]arene (**3**):  $^1\text{H}$  NMR data (400MHz,  $\text{CDCl}_3$ ): 6.89 (d,  $J = 8.0$  Hz, 4H), 6.76 (t,  $J = 8.0$  Hz, 2H), 6.40 (s, 4H), 4.51 (d,  $J = 13.2$  Hz, 4H), 4.24 (t,  $J = 6.4$  Hz, 4H), 4.16 (s, 4H), 4.00 (t,  $J = 5.6$  Hz, 4H), 3.89 (t,  $J = 6.4$  Hz, 4H), 3.81 (t,  $J = 5.6$  Hz, 4H), 3.59–3.49 (m, 8H), 3.14 (d,  $J = 13.6$  Hz, 4H), 1.98 (s, 2H), 1.24–1.16 (m, 12H). 5,17-Diformyl-11,23-dihydroxymethyl-25,26,27,28-tetrakis(2-ethoxyethoxy)calix[4]arene (**4**): 9.66 (s, 2H), 7.24 (s, 4H), 6.61 (s, 4H), 4.57 (d,  $J = 13.6$  Hz, 4H), 4.27 (t,  $J = 6.4$  Hz, 4H), 4.24 (s, 4H), 4.09 (t,  $J = 6.4$  Hz, 4H), 3.83–3.77 (m, 8H), 3.56–3.46 (m, 8H), 3.24 (d,  $J = 13.6$  Hz, 4H), 1.22–1.14 (m, 12H). Bis-adduct **5**: 7.23 (s, 2H), 7.15 (s, 2H), 6.66–6.62 (m, 4H), 4.84 (d,  $J = 7.3$  Hz, 2H), 4.54 and 4.51 (2d,  $J = 12.4$  Hz, 4H), 4.36 (t,  $J = 6.8$  Hz, 4H), 4.16 (d,  $J = 7.3$  Hz, 2H), 4.06 (t,  $J = 6.6$  Hz, 4H), 3.97–3.92 (m, 4H), 3.77–3.72 (m, 4H), 3.61–3.50 (m, 8H), 3.31–3.27 (m, 4H), 3.21 and 3.17 (2d,  $J = 12.4$  Hz, 4H), 3.00–2.71 (m, 8H), 2.13–1.90 (m, 4H), 1.22 (m, 12H). Monobenzoylated compound **6**: 8.21 (d,  $J = 8.1$  Hz, 2H), 7.84 (d,  $J = 8.8$  Hz, 2H), 7.77 (d,  $J = 8.8$  Hz, 2H), 7.65 (t,  $J = 7.3$  Hz, 1H), 7.52 (t,  $J = 7.3$  Hz, 2H), 7.35 (d,  $J = 2.2$  Hz, 1H), 7.29 (d,  $J = 2.2$  Hz, 1H), 7.20 (d,  $J = 2.2$  Hz, 1H), 7.06 (d,  $J = 2.2$  Hz, 1H), 6.39–6.28 (m, 4H), 6.18 (d,  $J = 8.1$  Hz, 1H), 4.76–4.70 (m, 2H), 4.50–4.43 (m, 4H), 4.36 (d,  $J = 7.3$  Hz, 1H), 4.27–4.20 (m, 4H), 3.92–3.70 (m, 16H), 3.56–3.46 (m, 8H), 3.18–3.09 (m, 4H), 3.01–2.77 (m, 8H), 1.82–1.72 (m, 2H), 1.18–1.04 (m, 12H). Bis-benzoylated compound **7**: 8.24 (d,  $J = 8.8$  Hz, 4H), 7.87 (d,  $J = 8.8$  Hz, 4H), 7.8 (d,  $J = 8.8$  Hz, 4H), 7.67 (t,  $J = 7.3$  Hz, 2H), 7.54 (t,  $J = 7.3$  Hz, 4H), 7.38 (d,  $J = 2.2$  Hz, 2H), 7.32 (d,  $J = 2.2$  Hz, 2H), 6.37 (d,  $J = 2.2$  Hz, 2H), 6.27 (d,  $J = 2.2$  Hz, 2H), 6.21 (d,  $J = 8.1$  Hz, 2H), 4.74 (d,  $J = 8.1$  Hz, 2H), 4.48 and 4.44 (2d,  $J = 13.2$  Hz, 4H), 4.27 (m, 4H), 3.89–3.70 (m, 16H), 3.53 (m, 8H), 3.18 (d,  $J = 13.2$  Hz, 4H), 3.05–2.81 (m, 8H), 1.80–1.75 (m, 2H), 1.18 (t,  $J = 7.3$  Hz, 6H), 1.10 (t,  $J = 7.3$  Hz, 6H). MS ( $m/z$ ): 1485.5 ( $\text{MH}^+$ ), 1433.1, 1402.5, 1297.6, 1189.6, 1123.7, 1069.5, 1015.7, 967.6, 951.4, 897.7, 977.7, 209.0, 119.0.



**Fig. 1.** Comparison of  $^1\text{H}$  NMR spectra ( $\text{CDCl}_3$ ) for **2**, **4**, and **5**; signals of the protons belonging to ethoxyethoxy tails ( $\text{CH}_3\text{CH}_2\text{OCH}_2\text{CH}_2\text{O}-$ ) are marked by asterisks.



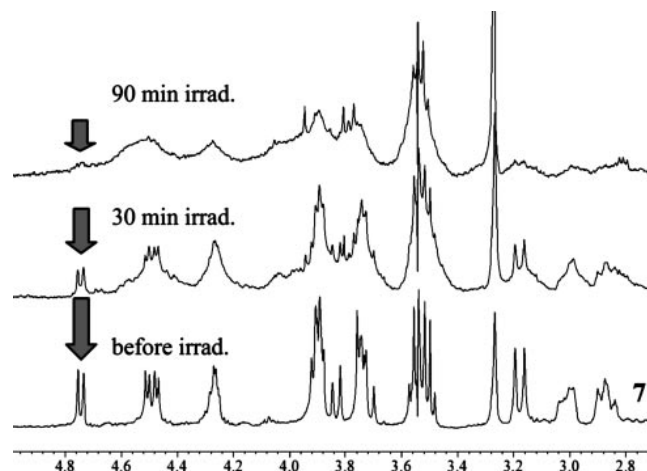
pled with alcohol **5** in the presence of triethylamine. We expected that the difference in reactivity between the primary benzylic and the more hindered secondary benzylic alcohols will ensure chemoselectivity. It appeared, however, that the difference in reactivities was not sufficient to completely shut off acylation of the latter. Judging by  $^1\text{H}$  NMR, benzoylation produced several products. We speculate that acylation of the secondary alcohol groups may have triggered dehydrative ring expansion producing seven-membered dithielines (**9**) and lowering the yield of the target rosette **7**.



Direct dicyclohexylcarbodiimide-mediated coupling of **5** with benzoylbenzoic acid did not improve the yield of the bis-adduct **7**. The presence of the carbonyl group in the sensitizer moiety precluded an alternative route to **7** via benzoylation of the diol **4** with the subsequent addition of dithianyl anion. Our attempt to implement this route produced a mixture of dithiane addition products to both formyl groups and also to benzophenone carbonyls. Successful synthesis of **7** was achieved via the acylation of **5** with *p*-benzoylbenzoyl chloride under partial (45%) conversion conditions. HPLC separation of the reaction mixture on a C-18 reversed phase column ( $\text{MeCN}-\text{H}_2\text{O}$ , 1:1) produced diester **7** (18% based on reacted **5**) and monobenzoylated adduct **6** (25%).

Having isolated the diastereomers **7**, we then proceeded with photochemical studies. Irradiation of **7** in acetonitrile

**Fig. 2.** Irradiation of **7** in  $\text{CD}_3\text{CN}$ .



with a medium pressure mercury lamp and Pyrex filter (300 nm cutoff) was monitored by  $^1\text{H}$  NMR by following the disappearance of the benzylic dithianyl-CH-OH doublet. As shown in Fig. 2, the relative intensity of the doublet decreases with irradiation. In our previous work, we also followed the photofragmentation by NMR monitoring of the release of aromatic aldehydes (**4**). In the present study, while we see formyl singlets appearing in the NMR spectrum of the irradiated **7**, the aldehydes do not accumulate significantly upon extended photolysis. Our rationale is that the photoexcited benzophenone, being tethered in close proximity, oxidizes the liberated aldehyde. The overall efficiency of the self-sensitized photofragmentation of rosette **7** is comparable to that of a simple parent adduct of benzaldehyde and dithiane (quantum yield of about 0.12).

To rule out the involvement of calixarenic framework in sensitization of the dithiane-carbonyl fragmentation, we carried out a control experiment by irradiating tetra-alcohol **5**, which lacks the benzophenone-based sensitizing units. Irradiation of **5** under similar conditions (medium pressure mercury lamp, Pyrex filter) for 1 h produced no changes in the  $^1\text{H}$  NMR spectrum of **5**, ruling out self-sensitization by the calixarene itself.

In summary, we have synthesized a model calixarene-based photolabile rosette capable of self-sensitized photofragmentation. Work is in progress in our laboratory to assemble functional rosettes with 5-substituted dithianes carrying macromolecular modules, for example, modules equipped with hydrogen bond-based elements of molecular recognition.<sup>3</sup>

## Acknowledgments

Support of this research by the NIH (GM62773) is gratefully acknowledged.

## References

1. A. Casnati, S. Barbosa, H. Rouquette, M.-J. Schwing-Weill, F. Arnaud-Neu, J.-F. Dozol, and R. Ungaro. *J. Am. Chem. Soc.* **123**, 12 182 (2001).

<sup>3</sup>Supplementary data may be purchased from the Depository of Unpublished Data, Document Delivery, CISTI, National Research Council Canada, Ottawa, ON K1A 0S2, Canada ([http://www.nrc.ca/cisti/irm/unpub\\_e.shtml](http://www.nrc.ca/cisti/irm/unpub_e.shtml) for information on ordering electronically).



2. H.S. Park, Q. Lin, and A.D. Hamilton. *J. Am. Chem. Soc.* **121**, 8 (1999).
3. H. Hioki, M. Kubo, H. Yoshida, M. Bando, Y. Ohnishi, and M. Kodama. *Tetrahedron Lett.* **43**, 7949 (2002).
4. (a) W.A. McHale and A. Kutateladze. *J. Org. Chem.* **63**, 9924 (1998); (b) P. Vath, D.E. Falvey, L.A. Barnhurst, and A.G. Kutateladze. *J. Org. Chem.* **66**, 2886 (2002).
5. For a review see: B.-T. Gröbel and D. Seebach. *Synthesis*, 357 (1977).
6. (a) A. Okamoto, M.S. Snow, and D.R. Arnold. *Tetrahedron*, **42**, 6175 (1986); (b) D.R. Arnold and L.J. Lamont. *Can. J. Chem.* **67**, 2119 (1989); (c) R. Popielarz and D.R. Arnold. *J. Am. Chem. Soc.* **112**, 3068 (1990); (d) T.M. Bockman, S.M. Hubig, and J.K. Kochi. *J. Am. Chem. Soc.* **120**, 6542 (1998); (e) S. Sankararaman, S. Perrier, and J.K. Kochi. *J. Am. Chem. Soc.* **111**, 6448 (1989); (f) D.S. Han and H.J. Shine. *J. Org. Chem.* **61**, 3977 (1996); (g) J.H. Penn and J.H. Duncan. *J. Org. Chem.* **58**, 2003 (1993); (h) J.H. Penn and Z. Lin. *J. Org. Chem.* **55**, 1554 (1990); (i) J.H. Penn, D.L. Deng, and S.K. Aleshire. *J. Org. Chem.* **53**, 3572 (1988); (j) E.R. Gaillard and D.G. Whitten. *Acc. Chem. Res.* **29**, 292 (1996); (k) H. Gan, U. Leinhos, I.R. Gould, and D.G. Whitten. *J. Phys. Chem.* **99**, 3566 (1995); (l) M.A. Kellett and D.G. Whitten. *Res. Chem. Intermed.* **21**, 587 (1995); (m) J.W. Leon and D.G. Whitten. *J. Am. Chem. Soc.* **117**, 2226 (1995); (n) D.G. Whitten, M.A. Kellett, J. Leon, H. Gan, and Z.W. Tian. *Photochem. Photoelectrochem. Convers. Storage Sol. Energy, Proc. Int. Conf.*, 9th, 1992. 1993. p. 257; (o) M.A. Kellett and D.G. Whitten. *Mol. Cryst. Liq. Cryst.* **194**, 275 (1991); (p) X. Ci and D.G. Whitten. *J. Am. Chem. Soc.* **111**, 3459 (1989); (q) X. Ci, D.G. Whitten, M.A. Fox, and M. Chanon. *Photoinduced Electron Transfer. Part C*, 553 (1988); (r) L.Y.C. Lee, X. Ci, C. Giannotti, and D.G. Whitten. *J. Am. Chem. Soc.* **108**, 175 (1986); (s) P. Maslak and W.H. Chapman, Jr. *J. Org. Chem.* **61**, 2647 (1996); (t) P. Maslak, W.H. Chapman, Jr., T.M. Vallombroso, and B.A. Watson. *J. Am. Chem. Soc.* **117**, 12 380 (1995); (u) P. Maslak. *Top. Curr. Chem.* **168**, 1 (1993); (v) Y. Wang, L.A. Lucia, and K.S. Schanze. *J. Phys. Chem.* **99**, 1961 (1995); (w) R.D. Burton, M.D. Bartberger, Y. Zhang, J.R. Eyler, and K.S. Schanze. *J. Am. Chem. Soc.* **118**, 5655 (1996).
7. (a) Y. Wan, O. Mitkin, L. Barnhurst, A. Kurchan, and A. Kutateladze. *Org. Lett.* **2**, 3817 (2000); (b) O.D. Mitkin, A.N. Kurchan, Y. Wan, B.F. Schiwal, and A.G. Kutateladze. *Org. Lett.* **3**, 1841 (2001); (c) O. Mitkin, Y. Wan, A. Kurchan, and A. Kutateladze. *Synthesis*, 1133 (2001); (d) L.A. Barnhurst and A.G. Kutateladze. *Org. Lett.* **3**, 2633 (2001); (e) Y. Wan, J.K. Angleson, and A.G. Kutateladze. *J. Am. Chem. Soc.* **124**, 5610 (2002).
8. A. Arduini, S. Fanni, G. Manfredi, A. Pochini, R. Ungaro, A.R. Sicuri, and F. Ugozzoli. *J. Org. Chem.* **60**, 1448 (1995).
9. (a) C.A.M. Afonso, M.T. Barros, L.S. Godinho, and C.D. Maycock. *Synthesis*, **7**, 575 (1991); (b) Y. Wan, A.N. Kurchan, and A.G. Kutateladze. *J. Org. Chem.* **66**, 1894 (2001).



---

This special issue is dedicated to

Professor Donald R. Arnold

to honour his outstanding contributions to organic photochemistry and free radical chemistry.

*Associate Editor:* James Pincock

Ce numéro spécial est dédié au

Professeur Donald R. Arnold

pour saluer ses précieuses contributions aux domaines de la photochimie et de la chimie des radicaux libres.

*Directeur scientifiques associé :* James Pincock

---





Professor Donald R. Arnold



## TRIBUTE / HOMMAGE

### Professor Donald R. Arnold

Professor Arnold was born and raised in Buffalo, New York, and graduated from Amherst High School in 1953. His undergraduate years were spent at Bethany College in Bethany, West Virginia, from which he graduated in 1957 with a B.S. degree in mathematics and chemistry. While at Bethany, Don married Janet Price whom he had met in high school. He graduated with a Ph.D. from the University of Rochester, New York, in 1961. His thesis *Part I: Attempted Synthesis of Some Nonbenzenoid Aromatic Compounds; Part II: Cleavage of vic-Primary Amines* was directed by Professor Marshall Gates, a distinguished natural products chemist and long-time editor of the *Journal of the American Chemical Society*. Professor Gates instilled in his students a regimen of careful experimental work, attention to detail, and precise writing, qualities that Don has encouraged his own students to acquire throughout his professional career.

In 1960, Don accepted a position at the Union Carbide Research Institute in White Plains, New York, where he pioneered applied research in organic photochemistry. After a decade at Union Carbide, Don was lured into an academic career by the late Professor Paul de Mayo who persuaded him to join the Photochemistry Unit at the University of Western Ontario in London, Ontario. This unit was one of a number of specialized research centres set up with funding from the National Research Council of Canada to foster collaborative research on specific themes. Led by Paul de Mayo, the unit at its peak boasted seven internationally recognized faculty members, all of whom were also members of the Department of Chemistry at UWO.

In 1979, Don was attracted to move to Nova Scotia by Dalhousie University's offer of an Izaak Walton Killam Research Professorship. He proceeded to build an impressive research group, while also serving as the nucleus of an active cadre of physical organic chemists at Dalhousie, raising the levels of research and teaching in the department. For these contributions he was named to the Alexander McLeod Chair of Chemistry in 1991. In the process, he determined that the first incumbent of the Chair was appointed in 1884 and he encouraged historian Michael Haines to document the history behind the endowing of the Chair. This documentation was included in Don's inaugural lecture on October 16, 1992.

Don is an internationally recognized leader in the field of organic photochemistry. His astute use of a broad range of techniques to study organic photochemical problems has enabled him to bridge organic and physical photochemistry, thus, contributing to the virtual disappearance of this division. These techniques include electrochemistry, electron spin resonance spectroscopy, flash photolysis, single-photon counting fluorescence lifetime measurements, chemically induced dynamic nuclear polarization, quantum yields,  $pK_a$  measurements, and mass spectrometry as well as molecular orbital and molecular mechanics calculations.

While Don's fundamental studies as one of the pioneers of modern organic photochemistry are well-known, his research in free radical chemistry is equally distinguished. Among other seminal contributions, he developed a comprehensive scale of substituent constants for benzylic free radicals based on the  $\alpha$ -hyper fine coupling constants of ring-

### Professeur Donald R. Arnold

Le professeur Arnold naît et grandit à Buffalo (New York) et il termine ses études secondaires à l'école Amherst en 1953. Il suit des études de premier cycle au Collège Bethany, à Bethany (Virginie-Occidentale), d'où il décroche un baccalauréat en mathématiques et en chimie en 1957. Pendant ses études, Don épouse Janet Price, une amie qu'il avait connue à l'école secondaire. En 1961, il obtient un doctorat de l'Université de Rochester (New York). Sa thèse, qui est divisée en deux parties : (I) *Attempted Synthesis of Some Nonbenzenoid Aromatic Compounds*; (II) *Cleavage of vic-Primary Amines*, est menée sous la direction du professeur Marshall Gates, éminent chimiste spécialiste des produits naturels et rédacteur de longue date du *Journal of the American Chemical Society*. Le professeur Gates a su inculquer à ses étudiants le souci du détail et le goût du travail expérimental minutieux et de la rédaction précise, qualités que Don a incité ses propres étudiants à acquérir pendant sa carrière professionnelle.

En 1960, Don accepte un poste à l'Institut de recherches d'Union Carbide, à White Plains (New York) où il amorce des recherches appliquées en photochimie organique. Après dix ans chez Union Carbide, Don est attiré dans une carrière universitaire par le défunt professeur Paul de Mayo, qui le persuade de se joindre à l'unité de photochimie de l'Université Western Ontario, à London (Ontario). Cette unité était l'un des nombreux centres de recherches spécialisés subventionnés par le Conseil national de recherches du Canada afin de favoriser la recherche concertée sur des thèmes particuliers. Sous la direction de Paul de Mayo, l'unité de recherche, à ses plus belles heures, a mis en valeur sept professeurs de réputation internationale qui étaient aussi tous membres du Département de chimie de l'UWO.

En 1979, Don est attiré par un professorat de recherche Izaak Walton Killam que lui offre l'Université Dalhousie de Nouvelle-Écosse. Il constitue alors un impressionnant groupe de chercheurs qui deviennent aussi le noyau d'un cadre actif de chimistes en physique organique à Dalhousie, qui permet d'élever les niveaux de la recherche et de l'enseignement au département. Pour souligner ses contributions, on le nomme à la chaire de chimie Alexander McLeod en 1991. Il détermine alors que le premier titulaire de la chaire a été nommé en 1884 et il incite l'historien Michael Haines à documenter l'historique de cette chaire. Cette documentation fait partie de la première conférence de Don livrée le 16 octobre 1992.

Don est un chef de file de réputation internationale dans le domaine de la photochimie organique. Son utilisation avisée d'une vaste gamme de techniques d'étude des problèmes en photochimie organique lui permet de faire le pont entre la photochimie organique et physique et ainsi d'éliminer presque complètement la division entre les deux branches. Les techniques qu'il utilise comprennent l'électrochimie, la spectroscopie par résonance paramagnétique électronique, la photolyse éclair, des mesures de la durée de vie de la fluorescence par comptage de photons uniques, la polarisation nucléaire dynamique par voie chimique, les rendements quantiques, les mesures  $pK_a$ , la spectrométrie de masse



substituted benzyl radicals. This scale provides an accurate measure of substituent effects on the thermodynamic stabilities of benzylic free radicals. He showed remarkable foresight when he initiated his research on photo-induced electron-transfer reactions. He has written several classic papers to a field on which the majority of the published literature in photochemistry is now based. Part I of this series is summarized in this issue of the Journal. Although he is not considered to be a synthetic organic chemist, the quest for new, synthetically useful reactions has been the common thread of his distinguished research career which has resulted in more than 120 publications.

He has received numerous awards and honours including an Alfred P. Sloan Research Fellowship (1971–73), a John Simon Guggenheim Memorial Fellowship (1980–81), and the Alfred Bader Award in Organic Chemistry (1995). In April of 2001 he was honoured by his alma mater, Bethany College, with an "Alumni Distinction Award". He has served on the editorial boards of several journals and on a number of NSERC committees, including the Chemistry Grant Selection Committee (1978–81) and Grant and Scholarship Committee (1983–86). He has held important positions in many organizations, including President of the Inter-American Photochemical Society and Director of Organic Chemistry of the Canadian Society for Chemistry. In addition, his participation in conferences, whether as an organizer, an invited lecturer, a contributor of a talk or poster, or as one taking part in the questions, answers, and comments following a talk, he always raised the scientific level for all who attended.

Dalhousie University requires that all its staff retire in the year after their 65th birthday. Don was again honoured, this time with the title of Professor Emeritus and he continues to be an active presence in the life of the Department. He does, however, have more time to indulge in his long-held interests of enjoying and preserving the outdoors, in reading, especially Arthur Conan Doyle, and in taking pride in his children and grandchildren. He is delighted that one of his children, Bradley (Department of Chemistry and Biochemistry, University of Maryland, Baltimore County) has followed his footsteps in an academic career including research in physical organic photochemistry.

This issue of the Canadian Journal of Chemistry honours Don's contribution to chemistry. This dedication is especially appropriate in view of Don's unflagging support over the years as a member of the Editorial Advisory Board and especially for choosing to publish his work almost exclusively in this journal.

James A. Pincock

ainsi que les calculs des orbitales moléculaires et de la mécanique moléculaire.

Même ses études fondamentales font partie des grandes innovations dans le domaine de la photochimie organique moderne, ses recherches dans la chimie des radicaux libres sont également dignes de mention. Parmi ses autres contributions de taille, il a mis au point une échelle globale des constantes substituantes pour les radicaux libres benzyl-iques reposant sur les constantes de couplage  $\alpha$ -hyperfin des radicaux benzyliques de substitution. Cette échelle permet de mesurer avec précision les effets des substituants sur la stabilité thermodynamique des radicaux libres benzyl-iques. Il a fait preuve d'une remarquable perspicacité dans ses recherches sur les réactions de transfert d'électron photo-induit. Il a rédigé dans ce domaine plusieurs communications classiques sur lesquelles repose dorénavant la plus grande partie des documents publiés en photochimie. Le présent numéro de cette Revue résume la partie I de cette série. Même s'il n'est pas considéré comme un chimiste spécialiste de la chimie organique synthétique, la recherche de nouvelles réactions synthétiquement utiles est le fil conducteur de sa brillante carrière de chercheur qui débouche sur plus de 120 publications.

Il a reçu un grand nombre de distinctions et de prix, notamment une bourse de recherche Alfred P. Sloan (1971–1973), une bourse John Simon Guggenheim Memorial (1980–1981) et le prix Alfred Bader en chimie organique (1995). En avril 2001, son alma mater, le Collège Bethany, lui rend hommage en lui décernant un « Prix de distinction de classe ». Il a siégé au comité de rédaction de plusieurs journaux ainsi qu'à de nombreux comités du CRSNG, notamment le comité de sélection des subventions en chimie (1978–1981) et le comité des subventions et des bourses (1983–1986). Il a occupé des postes importants dans de nombreux organismes, notamment celui de président de l'Inter-American Photochemical Society et de directeur de la chimie organique de la Société canadienne de chimie. De plus, sa participation à des conférences, que ce soit à titre d'organisateur, de conférencier invité, de collaborateur à un exposé ou à une affiche ou encore de participant pendant les périodes de questions, réponses et commentaires à la suite d'un exposé, a toujours élevé le niveau scientifique de tous les autres participants.

L'Université Dalhousie exige que tous les membres de son personnel se retirent de la vie active dans l'année qui suit leur 65<sup>e</sup> anniversaire. Don a reçu un autre hommage, soit le titre de professeur émérite, et il continue de jouer un rôle actif dans la vie du département. Il a cependant plus de temps à consacrer à ses activités de longue date, par exemple, profiter du grand air et préserver la nature, lire, surtout les romans d'Arthur Conan Doyle, et s'enorgueillir de ses enfants et petits-enfants. Il est ravi que l'un de ses enfants, Bradley (Département de chimie et de biochimie, Université du Maryland, comté de Baltimore), chercheur en photochimie organique et physique, ait suivi ses traces dans une carrière universitaire.

Le présent numéro de la *Revue canadienne de chimie* souligne la contribution de Don à la chimie. Cet hommage est tout particulièrement approprié compte tenu du soutien indéfectible dont Don a fait preuve au fil des ans à titre de membre du comité consultatif de rédaction et surtout du fait qu'il ait choisi de publier le fruit de ses recherches presque exclusivement dans cette Revue.

James A. Pincock



## AWARD LECTURE / CONFÉRENCE D'HONNEUR

Synthetic studies related to CP-225,917<sup>1</sup>

Derrick L.J. Clive, Paulo W.M. Sgarbi, Xiao He, Shaoyi Sun, Junhu Zhang, and Ligong Ou

**Abstract:** Synthetic studies related to CP-225,917 are described, including the preparation of the fully oxygenated tetracyclic central core **3**.

**Key words:** CP-225,917, siloxy-Cope rearrangement, Cope rearrangement, strain-assisted rearrangement, furan, ruthenium dioxide, bridgehead olefin.

**Résumé :** On décrit des études synthétiques reliées au CP-225,917 comprenant la préparation du noyau central tétracyclique complètement oxygéné **3**.

**Mots clés :** CP-225,917, réarrangement siloxy-Cope, réarrangement de Cope, réarrangement assisté par la tension, furane, dioxyde de ruthénium, oléfine pontée.

[Traduit par la Rédaction]

## Introduction

I am going to describe synthetic work related to the natural product CP-225,917 (**1**) (**1**, **2**).<sup>3</sup> The compound is an inhibitor of *ras* farnesyl transferase, and this fact means that it might serve as a lead structure for the design of anticancer drugs (**1**). It also has another significant biological property — it inhibits squalene synthase (**1**) — but the real attraction to an organic chemist is the structural complexity of the molecule, and a great deal of synthetic work has now been published in this area.<sup>4</sup> The unnatural enantiomer of CP-225,917 has been made by the Nicolaou group (**3**) and racemic material by the Danishefsky group (**4**). Two syntheses of the related compound CP-263,114 (**2**) have also been reported (**5**). This compound can be generated from **1** by treatment with methane sulfonic acid (**1**), and the reverse transformation — conversion of **2** into **1** — has been achieved under controlled basic conditions (**3**).

My own research has led to the synthesis of the fully oxygenated core structure **3**, which is a crystalline substance whose dimensions were obtained by single crystal X-ray analysis (Scheme 1).

CP-225,917 is an unusual molecule in which the bridgehead double bond is embedded within a framework that can fairly easily accommodate such a bond without violating

Bredt's rule. This accommodation is possible mainly because the double bond is in a nine-membered ring.

When we began work in this area no synthesis had yet been published, but there was some background information available in the literature. CP-225,917 is really a hemiacetal of the structural type **4**, and the two related substances **6** and **7** had been prepared many years ago (**6**) as a mixture, but the method used to make them — acid catalyzed dehydration of alcohols **5** — did not seem to be well-suited to the task of synthesizing the natural product, mainly because there was little control over the final position of the double bond. In fact, the bridgehead olefin **7** was the minor product (Scheme 2).

There are a good many ways in which the synthesis of ketones of type **4** might be attempted, and after some exploratory experiments, we decided to look at the possibility of using an oxy-Cope rearrangement (**7**).

We had noticed a potential relationship between the CP-225,917 bridgehead olefinic core and the [2.2.1] bicyclic structure **8** (Scheme 3).

If **8** is subjected to conditions for an anionic oxy-Cope rearrangement, then enolate **9** would be formed, and we hoped it could be trapped by a suitable electrophile, such as Mander's reagent, so as to generate a keto ester (**9** → **10**). When the keto ester is redrawn as **11**, its resemblance to the

Received 18 February 2003. Published on the NRC Research Press Web site at <http://canjchem.nrc.ca> on 4 July 2003.

**D.L.J. Clive,<sup>2</sup> P.W.M. Sgarbi, X. He, S. Sun, J. Zhang, and L. Ou.** Department of Chemistry, University of Alberta, Edmonton, AB T6G 2G2, Canada.

<sup>1</sup>2002 Alfred Bader Award Lecture. Presented at C.S.C. meeting, Vancouver, 3 June 2002.

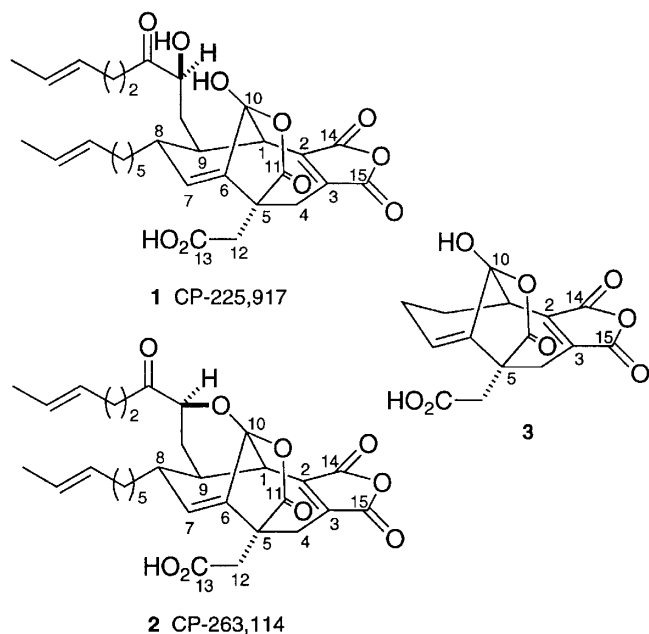
<sup>2</sup>Corresponding author (e-mail: [derrick.clive@ualberta.ca](mailto:derrick.clive@ualberta.ca)).

<sup>3</sup>Non-systematic numbering is used in diagram **1**, and the corresponding numbers are used for all other structures.

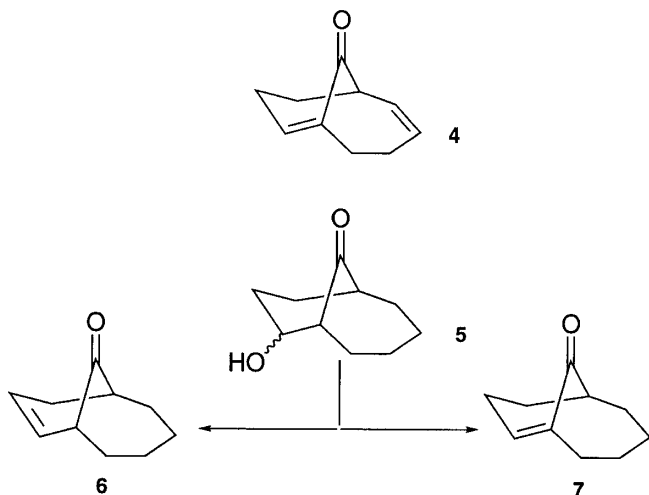
<sup>4</sup>For references to the many model studies, see ref. 2f.



Scheme 1.



Scheme 2.



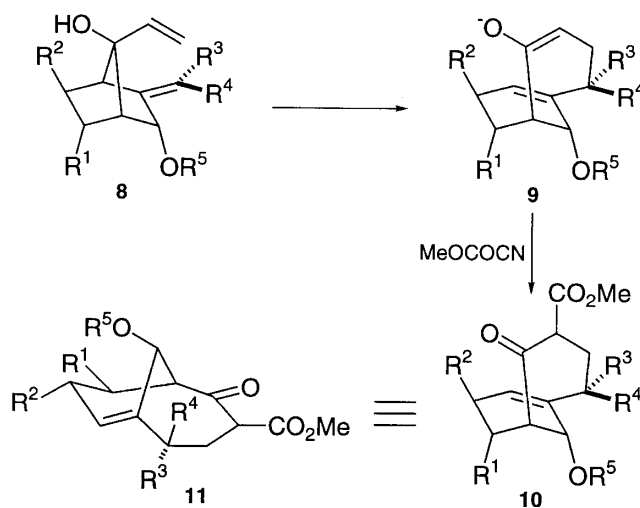
core of CP-225,917 is obvious. Structures **8–11** include several generic groups,  $R^1$ – $R^5$ , in order to show that this approach should accommodate the early introduction of some of the substituents that are present in the natural product.

To test our plan, we carried out a model study in which most of these generic substituents were absent.

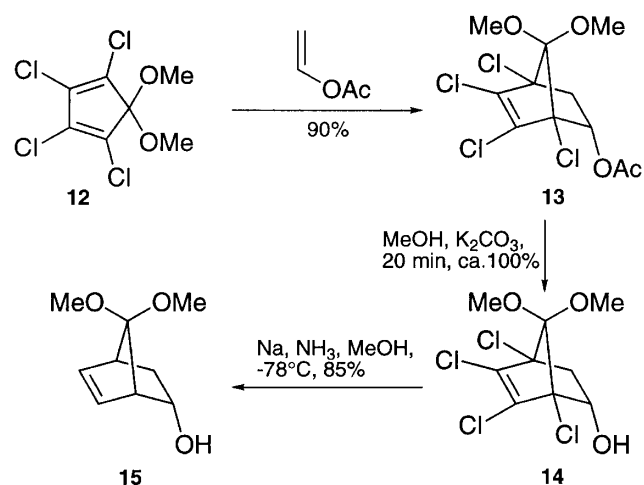
The short sequence shown in Scheme 4, which is reported in the literature (8), was repeated: a Diels–Alder reaction between tetrachlorocyclopentadienone dimethyl acetal (**12**) and vinyl acetate, followed by acetate hydrolysis (**13** → **14**), and dechlorination (**14** → **15**) gave us the basic [2.2.1] bicyclic skeleton. The yields are good, but the starting material **12** is expensive.

The double bond in **15** was then hydrogenated, and the hydroxyl was protected as its benzoyl ester (Scheme 5). We later found that this hydrogenation is unnecessary because, if

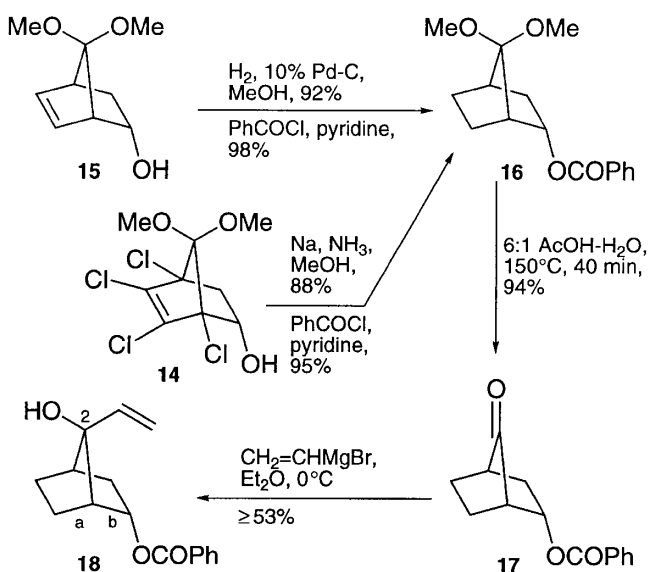
Scheme 3.



Scheme 4.

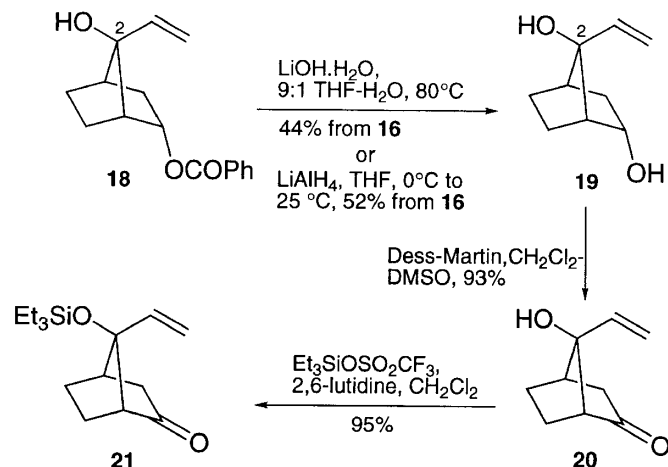


Scheme 5.

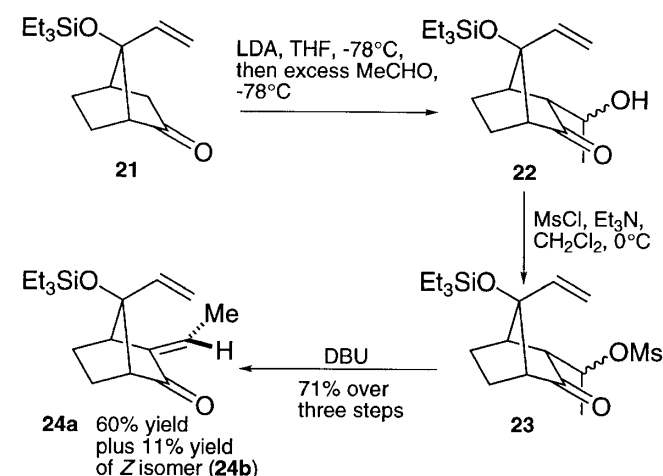




Scheme 6.



Scheme 7.



an excess of sodium is used in the dechlorination step, as well as a longer reaction time (1 h instead of 5 min), then the double bond is also reduced and in better overall yield. Finally, acid hydrolysis of the acetal released the parent ketone (16  $\rightarrow$  17). When we tried to hydrolyze the acetal without protecting the hydroxyl, extensive decomposition occurred, presumably, by a retroaldol process.

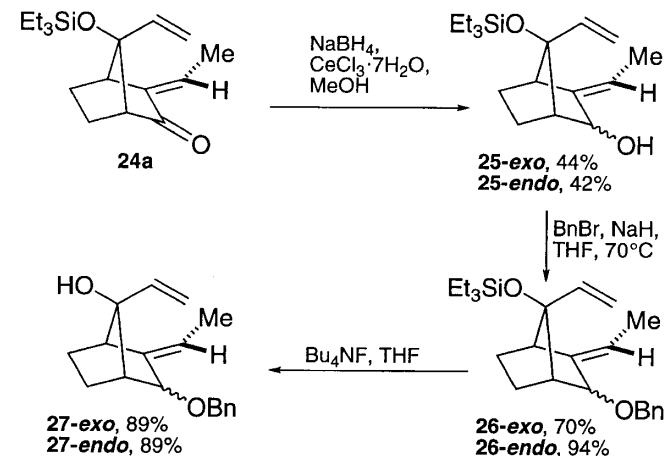
Ketone 17 reacted with vinylmagnesium bromide to give mainly alcohol 18. We did not separate the C(2) isomer at this stage, but the yield of isomer 18 is at least 53%.

The facial selectivity is presumably because of the fact that, of the two single bonds "a" and "b" (see 18), the former is more electron-rich and interacts preferentially with the developing sigma star orbital at C(2) (9) if the organo-metallic attacks from the right.

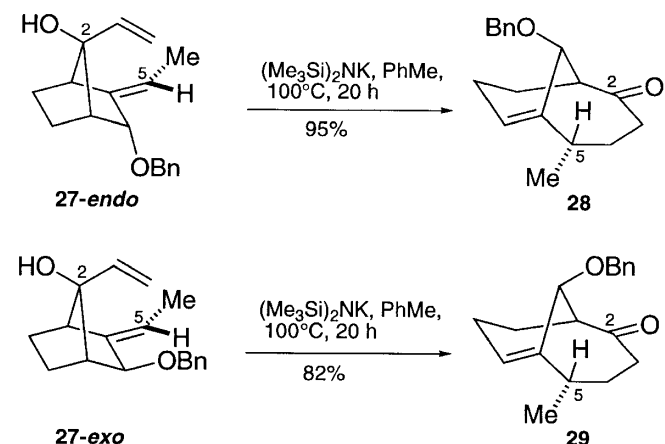
The mixture of hydroxy vinyl benzoates resulting from the Grignard addition was then hydrolyzed (Scheme 6). Initially, the hydrolysis was done with lithium hydroxide, but later, the process of removing the benzoyl group was improved by using  $\text{LiAlH}_4$ . The diol 19 was easy to purify, and at this point the C(2) epimers were separated.

The secondary hydroxyl of 19 was now oxidized with the Dess–Martin reagent, and then the tertiary hydroxyl was protected by silylation. This was done in order to hinder the

Scheme 8.



Scheme 9.



possibility of fragmentation by a retroaldol mechanism. We tried to make the *tert*-butyldimethylsilyl ether or a *p*-methoxybenzyl ether, but those experiments were not successful.

At this point, to set the stage for an anionic oxy-Cope rearrangement, we had to introduce an exocyclic double bond at the  $\text{CH}_2$  group adjacent to the carbonyl. Formation of the double bond was accomplished by a short sequence (Scheme 7) starting with an aldol condensation with acetaldehyde (21  $\rightarrow$  22).

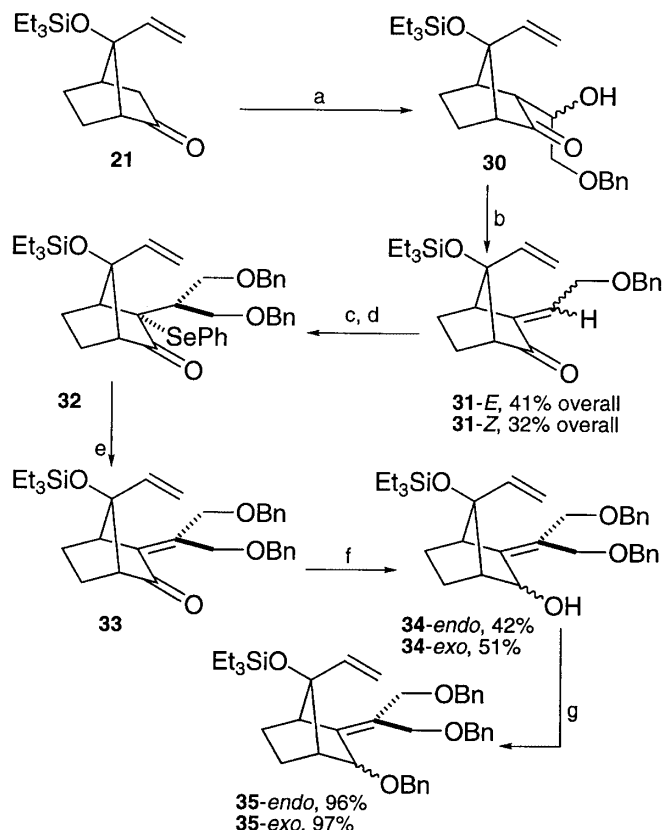
The aldol mixture was treated with mesyl chloride and then with DBU. Those operations gave ketone 24a in reasonable yield, plus a small amount of the Z isomer (24b). The compounds are easy to separate, and we continued our experiments using only the major isomer — the *E* olefin.

Sodium borohydride reduction in the presence of cerium chloride gave a 1:1 mixture of *exo* and *endo* alcohols (Scheme 8, 25-*exo*, 25-*endo*). Each of these was separately benzylated under standard conditions and then desilylated (25  $\rightarrow$  26  $\rightarrow$  27), and we were then ready to test the anionic oxy-Cope rearrangement.

When the alcohols 27-*endo* and 27-*exo* were individually heated in toluene in the presence of potassium hexamethyldisilazide, they were slowly converted into the desired enolates, and workup gave ketones 28 and 29, respectively, in good yield (Scheme 9). When we tried the reaction in



**Scheme 10.** (a) LDA, THF,  $-78^{\circ}\text{C}$ , then excess  $\text{BnOCH}_2\text{CHO}$ ,  $-78^{\circ}\text{C}$ ; (b)  $\text{MsCl}$ ,  $\text{Et}_3\text{N}$ ; DBU; (c)  $\text{BnOCH}_2\text{SnBu}_3$ ,  $\text{BuLi}$ ,  $i\text{-PrMgCl}$ ,  $\text{CuBr}\cdot\text{SMe}_2$ ,  $\text{BF}_3\cdot\text{Et}_2\text{O}$ ,  $-78^{\circ}\text{C}$ ; (d)  $\text{BF}_3\cdot\text{OEt}_2$ ,  $-45^{\circ}\text{C}$ ;  $\text{PhSeCl}$ , HMPA,  $-45$  to  $0^{\circ}\text{C}$ ; 66% for *E*, 65% for *Z*-isomer; (e)  $\text{H}_2\text{O}_2$ , pyridine,  $\text{CH}_2\text{Cl}_2$ ,  $30\text{--}35^{\circ}\text{C}$ ; 84%; (f)  $\text{LiBH}_4$ ,  $\text{CeCl}_3\cdot 7\text{H}_2\text{O}$ ,  $\text{MeOH}$ ,  $0^{\circ}\text{C}$ ; (g)  $\text{BnBr}$ ,  $\text{NaH}$ , THF, reflux.

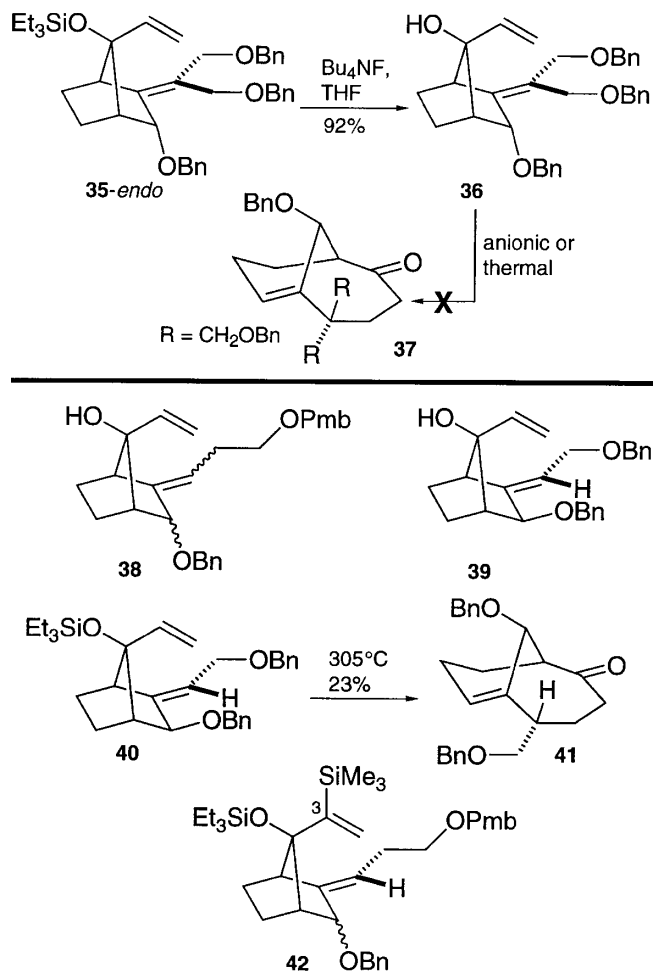


refluxing THF the process was slower, and addition of 18-crown-6 did not accelerate the reaction. Although these anionic oxy-Cope rearrangements are slow, the experiments served the purpose of showing that bridgehead olefins structurally related to CP-225,917 could be generated from [2.2.1] bicyclic systems.

What we had to do next was to repeat the sequence with an additional carbon at C(5) in place of the hydrogen (see structures **27**), so that the required C(5) quaternary center would be generated in the rearrangement.

To that end, ketone **21** was condensed with benzyloxyacetaldehyde (Scheme 10), and the hydroxyl in the products was eliminated by mesylation and base treatment to afford enones **31**. These underwent conjugate addition with [(benzyloxy)methyl]cuprate in the presence of boron trifluoride and isopropylmagnesium chloride. The latter scavenges traces of copper(II) that would otherwise cause dimerization of the cuprate reagent. The purpose of the borontrifluoride is simply to activate the enone to conjugate addition. The resulting enolate reacted with benzeneselenenyl chloride. We found that if the enolate from the conjugate addition is quenched to afford the ketone, then we could not introduce the selenium by deprotonation with LDA and reaction with benzeneselenenyl chloride. Evidently, the selenation is dependent on the precise nature of the enolate; we also found

**Scheme 11.**



that the presence of HMPA is essential. Finally, selenoxide elimination (**32**  $\rightarrow$  **33**) proceeded without incident, bringing us to ketone **33**. Reduction with lithium borohydride in the presence of ceric chloride gave the corresponding alcohol as a separable mixture of *endo* and *exo* isomers.

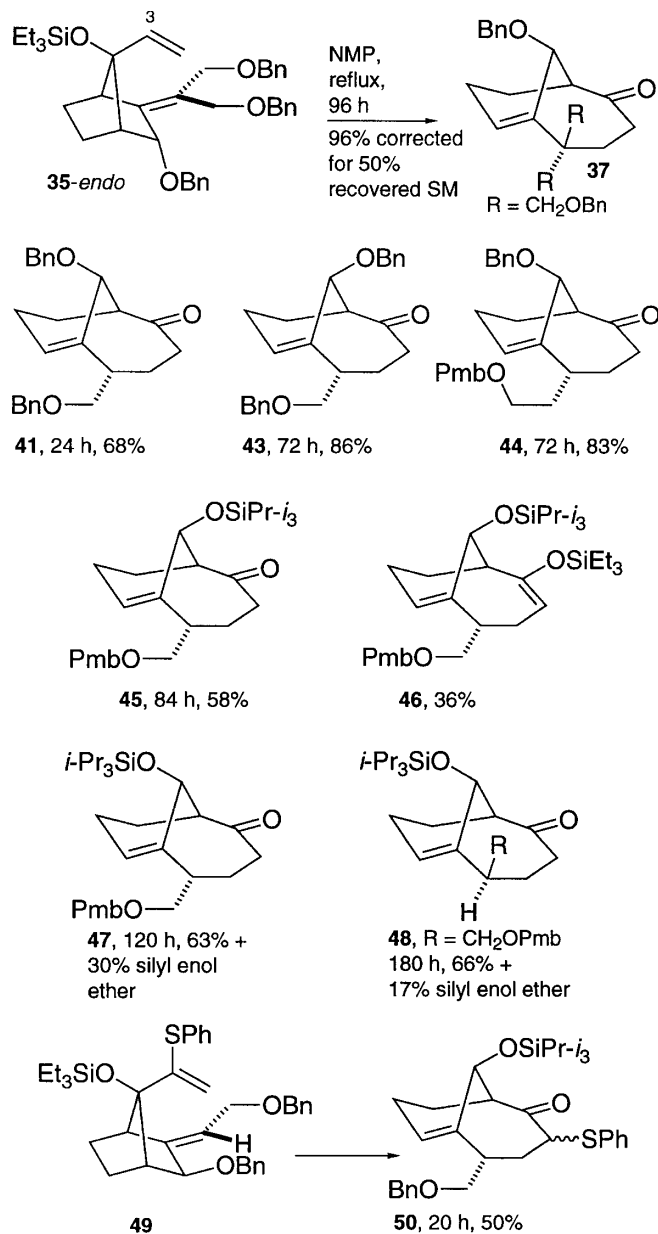
The hydroxyl was protected by benzylation (**34**  $\rightarrow$  **35**), and we then removed the silyl group by treatment with tetrabutylammonium fluoride in the usual way (Scheme 11).

With **36** (and the corresponding *exo*-isomer) in hand, we were ready to test the oxy-Cope rearrangement. Surprisingly, this reaction did not work. We tried a variety of conditions and, besides an anionic process, we also examined purely thermal reactions, as well as potential catalysis by palladium or mercuric ion. Scheme 11 shows our observations with an *endo* *O*-benzyl group (see **36**), but the *exo* isomer behaved in the same way. We also heated the silyl ether **35-endo** neat at  $230^{\circ}\text{C}$ . Again no rearrangement occurred.

The fact that our first model, in which the exocyclic double bond is only trisubstituted (see Scheme 9), did rearrange prompted us to make compounds **38** (Scheme 11) in the hope that the trisubstituted nature of the double bond would permit oxy-Cope rearrangement. However, even these compounds did not rearrange under anionic conditions or in the presence of a palladium catalyst.



Scheme 12.

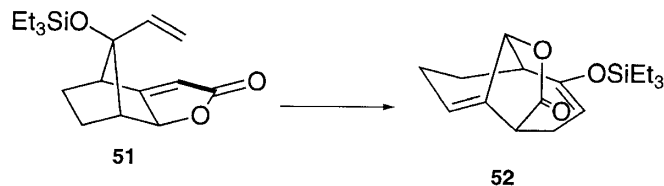


It was clear that the number as well as the length of the substituents on the exocyclic double bond are critical factors that determine the ease of rearrangement, and so we studied the two truncated models **39** and **40**. Again we tried a number of conditions: anionic for alcohol **39** and catalyzed and purely thermal for the silyl ether **40**. However, only simple heating of the silyl ether as a neat oil gave the desired product **41**, although the yield was poor (23%).

In the compounds we had examined so far the C(2) vinyl group was free to adopt a conformation in which it points away from the exocyclic double bond, and so we decided to try to bias the conformational preference by placing a bulky substituent on the vinyl group. To this end we prepared compounds **42**, but even they did not rearrange when heated to 300°C.

The modest conversion of **40** into **41** caused us to examine thermal processes more closely, and we soon found that

Scheme 13.



1-methyl-2-pyrrolidinone (NMP) is an excellent solvent that facilitates the desired rearrangement (Scheme 12).

Heating compound **35-endo** for a very long time gave ketone **37** in high yield, if correction is made for recovered starting material. The initial product is, of course, a silyl enol ether, but the silyl group is probably transferred to the solvent, so that on workup we get the corresponding ketone.

We have carried out a number of related reactions in which we vary the substitution pattern on the exocyclic double bond, the orientation (*exo* or *endo*) of the oxygen function on the [2.2.1] bicycle, as well as the nature of the protecting groups. In all cases, we observe rearrangement (see Scheme 12, compounds **41**, **43–48**, and **50**). Sometimes, as in the formation of **45** and **46**, which both arise from the same starting material, some of the silyl enol ether is actually isolated. The same is true in the case of **47** and **48**.

When the phenylthio substrate **49** was heated it gave **50**, as expected. The reaction is faster than the other cases, although the yield is not very good.

1-Methyl-2-pyrrolidinone has been reported before (10, 11) as a solvent for oxy-Cope rearrangement, but only for alcohols, where it can become involved in hydrogen bonding; its use for silyl ethers has not been recognized. All of our rearrangements are very clean if degassed 1-methyl-2-pyrrolidinone is used, and so we now had a method for making the simplified bridgehead olefin substructure of CP-225,917.

While these studies were going on, another member of my group examined an alternative way of speeding up the siloxy-Cope rearrangement.

We had noticed from inspection of models that incorporation of the exocyclic double bond into a lactone ring, as in structure **51** (Scheme 13), generates some strain in the [2.2.1] bicyclic system; this should provide a driving force for rearrangement, and in the event, that is exactly what was observed. Lactone **51** was prepared as shown in Schemes 14 and 15.

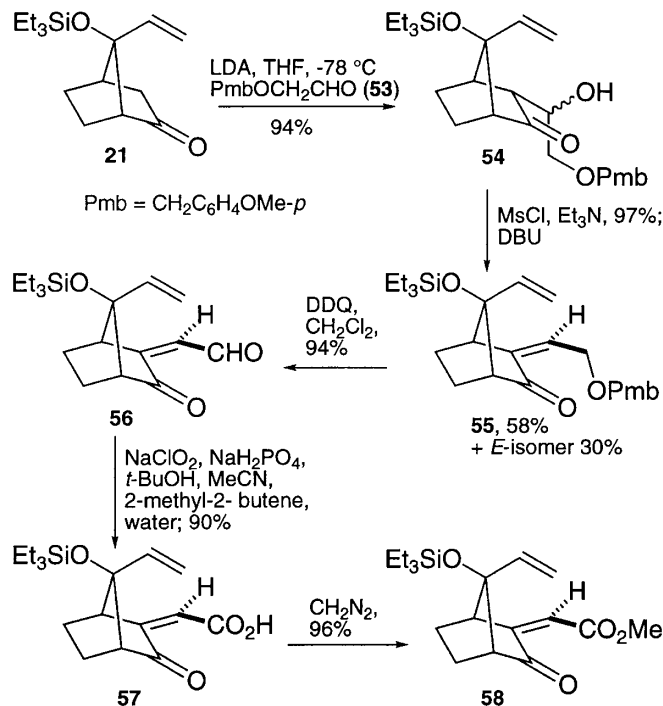
Aldol condensation of ketone **21** with (*p*-methoxybenzyl-oxy)acetaldehyde (**53**) worked very well, and the aldols were mesylated and treated with DBU. Those experiments allowed us to isolate the desired *Z* olefin **55** in just under 60% yield. The *p*-methoxybenzyl group was removed by the action of DDQ, and with this reagent an aldehyde (**56**) was obtained directly. Oxidation in the standard manner gave the corresponding acid, and that was trapped as its methyl ester (**56**  $\rightarrow$  **57**  $\rightarrow$  **58**).

Reduction of **58** with sodium borohydride in the presence of ceric chloride gave largely the desired *exo* alcohol **59** (Scheme 15). The *endo* isomer was isolated in a little under 20% yield, but we did not try to recycle the material by oxidation and reduction.

Ester hydrolysis now gave the hydroxy acid **60**, and the material was cyclized to lactone **51** using *N*-methyl-2-



Scheme 14.



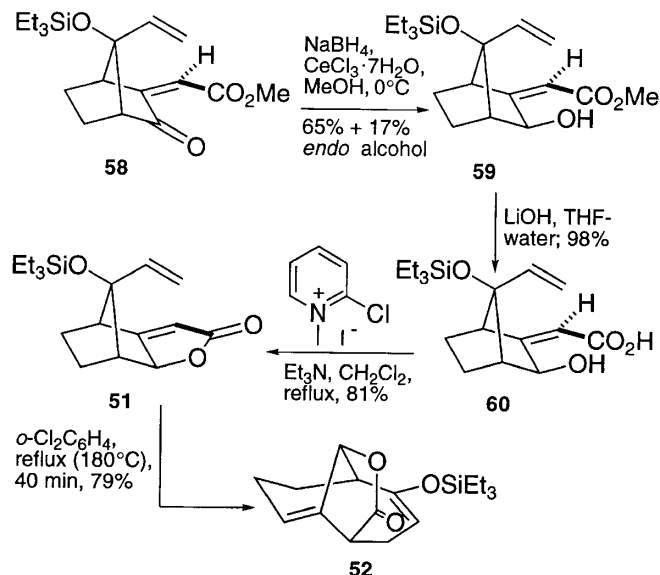
chloropyridinium iodide. When the lactone was heated in *o*-dichlorobenzene it rearranged smoothly in the required manner, and we could isolate the product in almost 80% yield. We later found that these conditions are harsher than they need to be, but it was clear that the additional strain associated with the lactone unit does indeed facilitate the oxy-Cope process. It is also very fortunate that the additional strain is not so large as to hinder formation of the lactone or to make it very sensitive to hydrolysis. The use of a strained lactone has also been investigated independently by Bio and Leighton, who have priority of publication (2b, 12).

At this point in our research we had two methods for converting [2.2.1] bicyclic systems into bridgehead olefins that resemble CP-225,917, but we decided to use only the strained lactone approach for further work, and we dealt first of all with the problem of generating the quaternary center.

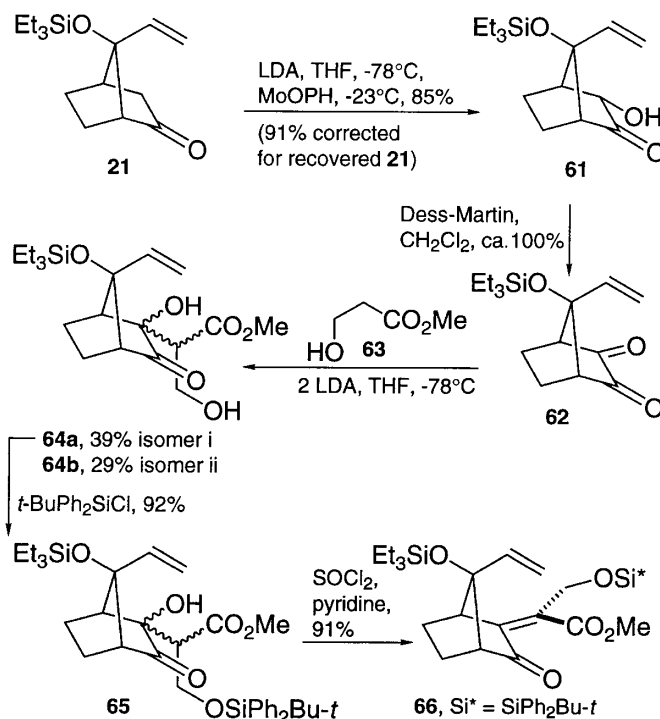
Ketone **21** was hydroxylated under standard conditions (Scheme 16), and then oxidation by the Dess–Martin procedure afforded the corresponding  $\alpha$ -diketone **62**. This was condensed with the dianion derived from methyl 3-hydroxypropanoate (**63**). That experiment afforded a mixture of two isomers, which were easily separated, but the stereochemistry was not determined. The primary hydroxyl of the major isomer was silylated (*t*-BuPh<sub>2</sub>SiCl), and dehydration with thionyl chloride and pyridine served to generate the *Z* enone **66**. The yields in this sequence are good, but there is no stereocontrol in the aldol condensation; that is a factor that still has to be dealt with.

Reduction of ketone **66** with the sodium borohydride – ceric chloride combination gave mainly the *exo* alcohol **67** (Scheme 17), and again we did not try to recycle the *endo* isomer. Demethylation of the ester was accomplished this time with the lithium salt of propanethiol, and then cyclization, as before, generated the strained lactone **68**. When this was heated in *o*-dichlorobenzene for 10 min it seemed to

Scheme 15.



Scheme 16.



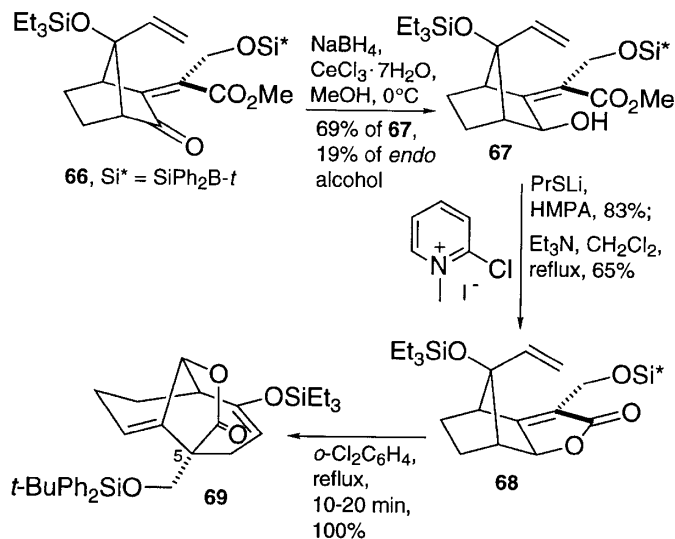
have rearranged completely, and after a further 10 min we could isolate the siloxy-Cope rearrangement product **69** in quantitative yield.

That experiment showed that we now had a procedure for dealing with the C(5) quaternary center, and the next thing to do was to find out how to construct the anhydride and how to make the exocyclic double bond of **66** in a stereocontrolled manner. We dealt first of all with the stereochemical problem.

In our earlier work we had used the dianion derived from hydroxy ester **63**; we now (Scheme 18) used an ester with a protected hydroxyl (**70**), and we found that the isomer ratio



Scheme 17.



was improved from 4:3 for **64a:64b** to 10:1 for **71a:71b**. It is not clear why this happens, but it was certainly a very welcome fact.

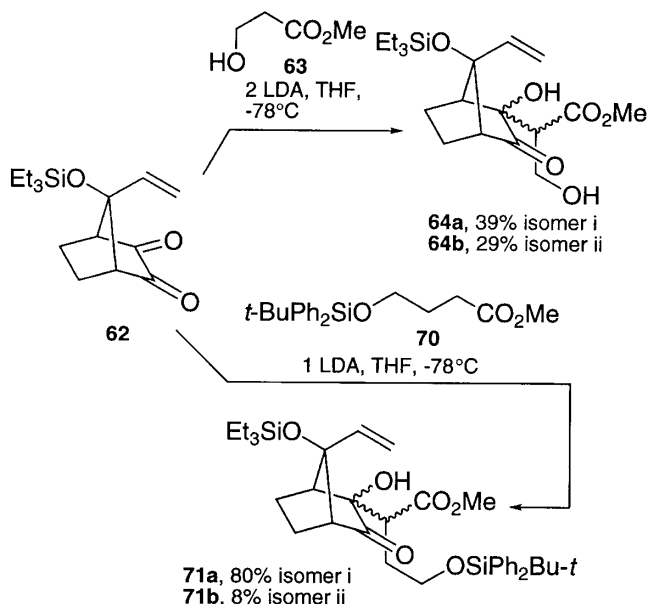
When the major isomer (**71a**) was dehydrated with thionyl chloride and pyridine (Scheme 19), we were very pleased to obtain the desired *Z* olefin **72** (Scheme 19). Reduction of the ketone carbonyl with sodium borohydride showed only a 3:1 selectivity in favor of the required *exo* alcohol, but the *endo* isomer was easily reconverted into the starting ketone (**73-endo**  $\rightarrow$  **72**). Once again, the ester was demethylated with the lithium salt of propanethiol, and the resulting hydroxy acid was cyclized to the lactone (**73-exo**  $\rightarrow$  **74**). Finally, thermal rearrangement gave us a product (**75**) with the quaternary center and the correct chain length at C(5).

At this point we needed to develop a method for making the anhydride unit that is characteristic of CP-225,917.

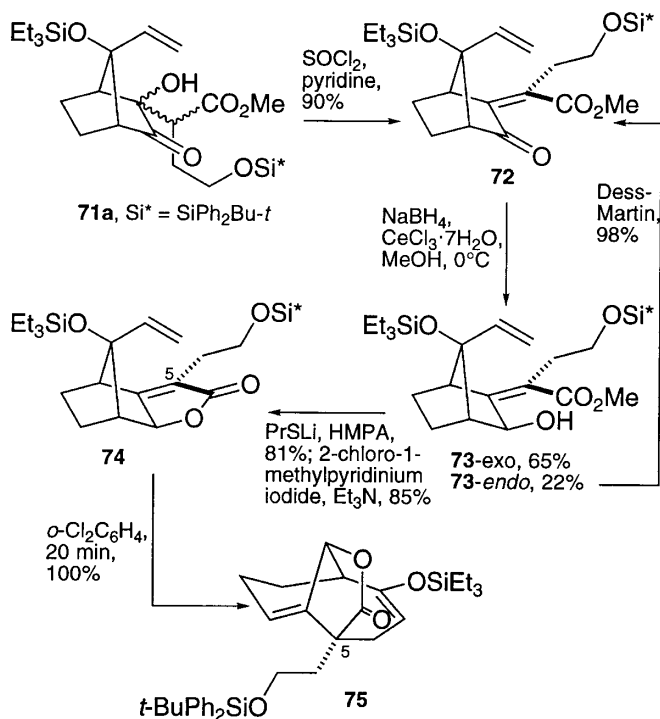
Our initial experiments (Scheme 20) were done with **45** and some related compounds, which were all obtained by the method using thermolysis in 1-methyl-2-pyrrolidinone. We discovered that these compounds have a tendency to enolize towards the bridgehead, and so, in order to introduce C(15) (which is needed for the eventual anhydride), we had to block the bridgehead position. That can be done, as shown in Scheme 20, but such a route is cumbersome, and so we modified our approach in such a way that C(15) is introduced at a very early stage — in fact, before oxy-Cope rearrangement.

Our route (Scheme 21) follows along the lines of our previous experiments, except that we treat ketone **17** with isopropenylmagnesium bromide instead of vinylmagnesium bromide. Alcohol **78** is formed in acceptable yield, and we then oxidized what I call C(15), using *tert*-butylhydroperoxide in the presence of a catalytic amount of selenium dioxide. This allylic oxidation is quite slow — it takes 3 days at room temperature. The desired alcohol **79** can be isolated in 60% yield, but almost 30% of the corresponding aldehyde **80** is also formed. Fortunately, the two compounds are easy to separate, and the aldehyde can be reduced efficiently to the alcohol, so that the overall transformation to **79** is quite efficient (81%).

Scheme 18.



Scheme 19.

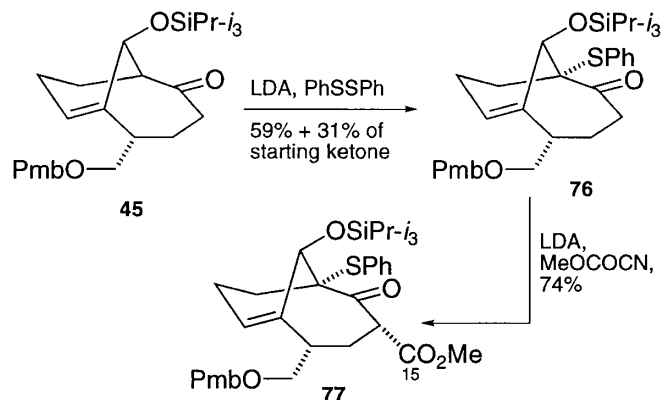


Next, the primary hydroxyl at C(15) was protected as its *p*-anisoyloxymethyl (AOM) ether, under phase-transfer conditions (**79**  $\rightarrow$  **81**, 69%). The selectivity is not as high as I would have wished, and 16% of the doubly etherified material is also formed, but that product can be hydrolyzed in over 80% yield back to the starting diol **79**, and so, after one recycling, the mono-protected compound **81** can be obtained in 82% yield.

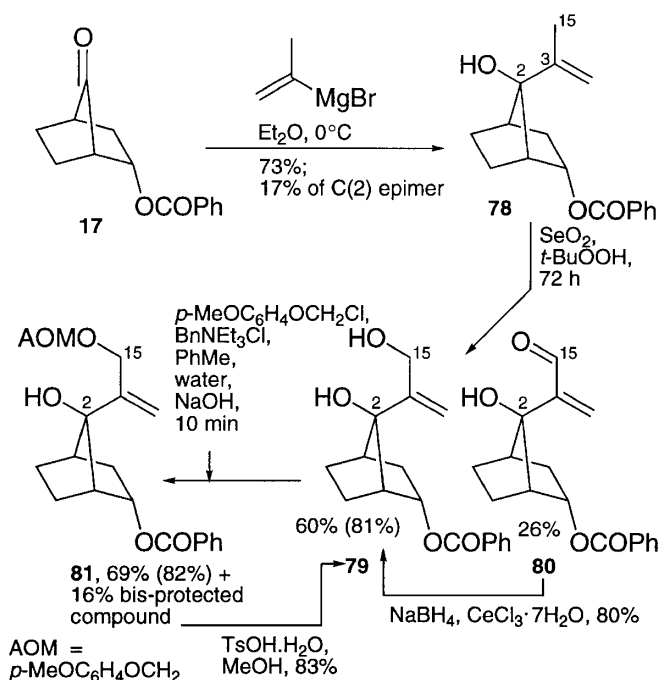
The remaining tertiary hydroxyl (at C(2)) was then silylated (Scheme 22, **81**  $\rightarrow$  **82**); the benzoate group was removed by treatment with lithium aluminum hydride, and the



Scheme 20.



Scheme 21.

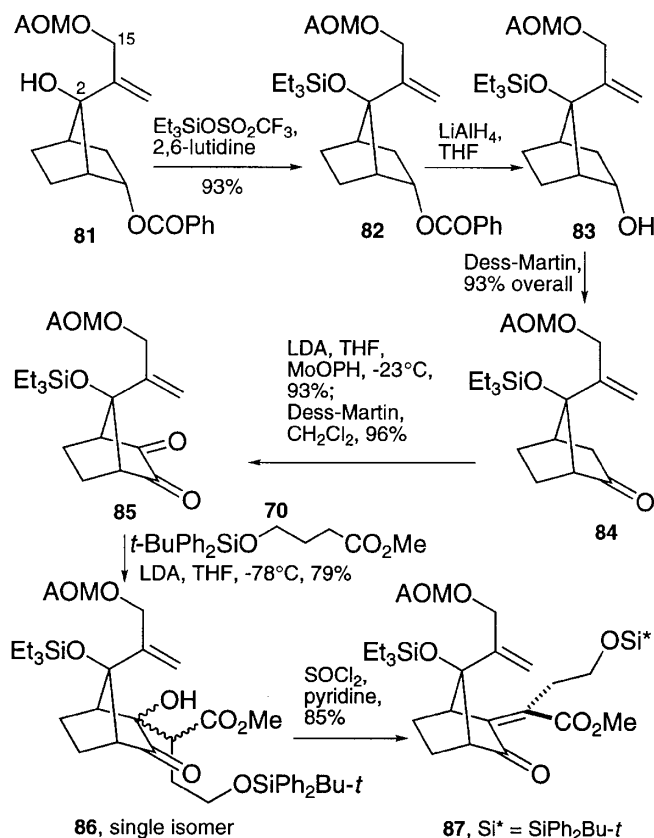


alcohol released in that experiment was oxidized with the Dess–Martin reagent (**82**  $\rightarrow$  **83**  $\rightarrow$  **84**). The resulting ketone was subjected to  $\alpha$ -hydroxylation and then to oxidation, again with the Dess–Martin reagent, so as to generate diketone **85**. All these experiments are very simple, and the yields are good. We condensed the diketone with our silylated ester (**70**) and obtained the condensation product **86** as a single isomer in nearly 80% yield. We did not look for other isomers in the reaction mixture. Dehydration with thionyl chloride generated the required *Z* double bond in high yield (**86**  $\rightarrow$  **87**), and once again we were at a stage where we needed to form a strained lactone and then carry out the thermal rearrangement.

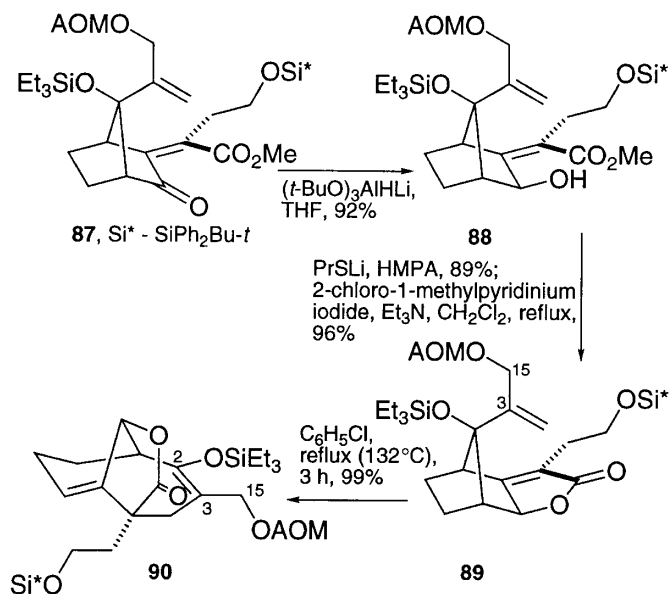
All those transformations were achieved by the methods that had served us well in the simpler models, although we did make some improvements.

The reduction of ketone **87** was done with a very hindered hydride (Scheme 23). The reaction was quite slow — it took

Scheme 22.



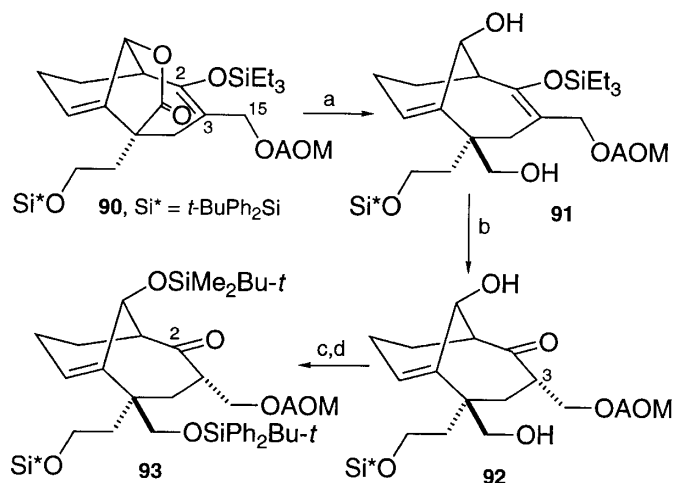
Scheme 23.



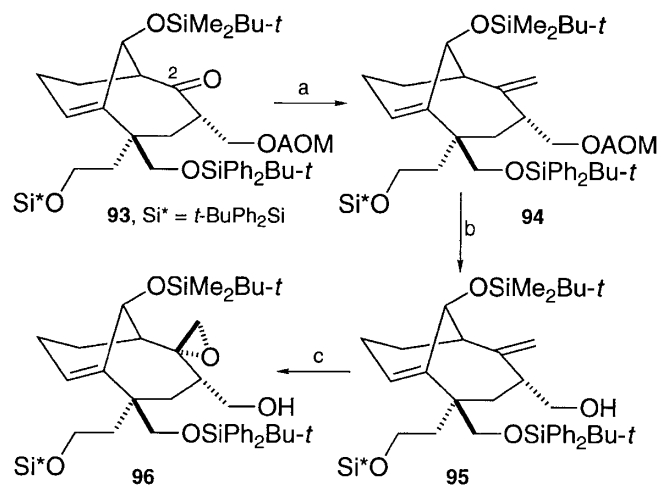
6 h at room temperature — but the stereoselectivity was good. The ester was demethylated in the usual way, and lactonization was again achieved in high yield with the pyridinium reagent (**87**  $\rightarrow$  **88**  $\rightarrow$  **89**). When we did the siloxy-Cope rearrangement (**89**  $\rightarrow$  **90**), we used chlorobenzene instead of *o*-dichlorobenzene. Its boiling point is 55°C lower, and so the reaction takes longer, but the yield is al-



**Scheme 24.** (a)  $\text{LiBH}_4$ , THF, 93%; (b)  $\text{CF}_3\text{CO}_2\text{H}$ , THF, water, 67%; (c)  $t\text{-BuPh}_2\text{SiCl}$ ,  $\text{Et}_3\text{N}$ , DMAP,  $\text{CH}_2\text{Cl}_2$ , 99%; (d)  $t\text{-BuMe}_2\text{SiOSO}_2\text{CF}_3$ , 2,6-lutidine,  $\text{CH}_2\text{Cl}_2$ , 95%.



**Scheme 25.** (a) Tebbe reagent, THF, 77%; (b) bromocatecholborane,  $\text{CH}_2\text{Cl}_2$ ,  $-78^\circ\text{C}$ , 84%; (c)  $\text{VO}(\text{acac})_2$ ,  $t\text{-BuOOH}$ , PhH, 70%.



most the same, and we felt it was advisable to practice with milder conditions, with a view to eventually using more delicate substrates.

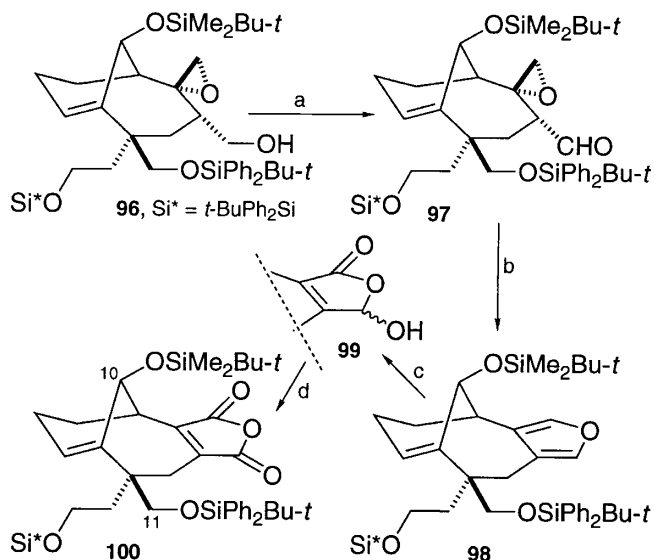
In order to construct the anhydride unit, we need to add one carbon at C(2) (see **90**, Scheme 24), and so we had to first liberate the potential carbonyl at C(2) and protect the lactone carbonyl.

The lactone ring was opened by reduction with lithium borohydride (**90**  $\rightarrow$  **91**), and then the silyl enol ether was hydrolyzed (**91**  $\rightarrow$  **92**) to set the stage for introduction of C(14) of the anhydride unit.

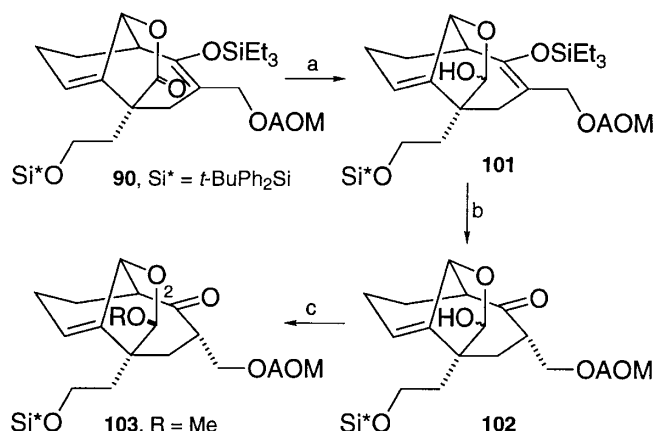
The primary hydroxyl of **92** was selectively protected as its *tert*-butyldiphenylsilyl ether, after which the secondary hydroxyl was silylated with *tert*-butyldimethylsilyl triflate. Both protection steps go in good yield, and the next task was to introduce a carbon at C(2).

In some earlier studies we had found that ketones of similar structure to **93** did not behave properly with Wittig or Peterson reagents, but that they did react with the Tebbe reagent, and in the present case (Scheme 25), treatment of

**Scheme 26.** (a) Dess–Martin oxidation,  $\text{CH}_2\text{Cl}_2$ , 89%; (b) DBU, THF, then HCl, 5 min, 97%; (c) Rose Bengal, tungsten light, DBU,  $\text{O}_2$ ,  $-78^\circ\text{C}$ , then  $0^\circ\text{C}$ ; (d)  $\text{Pr}_4\text{NRuO}_4$ , *N*-methylmorpholine *N*-oxide, 86% overall.



**Scheme 27.** (a) DIBAL-H,  $\text{CH}_2\text{Cl}_2$ ,  $-78^\circ\text{C}$ , 95%; (b)  $\text{CF}_3\text{CO}_2\text{H}$ –THF–water, 90%; (c)  $\text{CH}(\text{OMe})_3$ , TsOH–pyridine, 96%.



**93** with 2 equiv of the Tebbe reagent gave the desired olefin **94** in acceptable yield (77%).

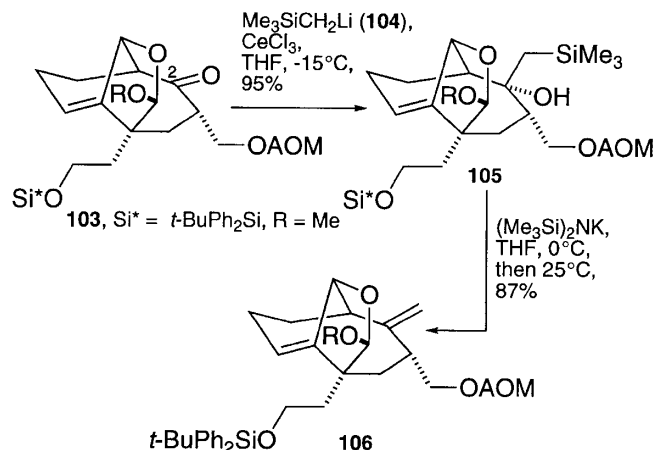
Removal of the AOM group (**94**  $\rightarrow$  **95**) was carried out with bromocatechol borane. With a number of related substrates we had found that ceric ammonium nitrate, magnesium bromide, bromodimethylborane, or *N*-bromosuccinimide did not work, but bromocatecholborane was satisfactory.

The homoallylic alcohol **95** was amenable to epoxidation, which brought the sequence to compound **96**, from which point we could finish construction of the anhydride, as shown in Scheme 26.

The free hydroxyl group of **96** was oxidized to the corresponding aldehyde with the Dess–Martin reagent. In this case, the Swern procedure gave a complex mixture. Treatment of the epoxy aldehyde first with DBU to open the epoxide by deprotonation  $\alpha$  to the aldehyde group, followed by brief treatment with acid to effect dehydration, gave the



Scheme 28.



expected furan **98**. This was then converted by photo-oxygenation to a mixture of hydroxybutenolides **99** (and the regioisomers with the OH and C=O interchanged), which were oxidized with TPAP. Those experiments all work in good yield, and they afforded anhydride **100**.

Having reached a model with the quaternary center and the anhydride, the next step was to generate the lactone unit that spans C(10) and C(11).

Our attempts to do that, starting from **100** or its furan precursor **98**, were not at all promising, and so we returned to the product of the siloxy-Cope rearrangement (**90**) and elaborated it in a different way.

Previously, we had reduced the lactone **90** down to the diol stage (see Scheme 24); this time we took the lactone only to the lactol oxidation level (Scheme 27, **90** → **101**). The lactols were then treated with acid in order to hydrolyze the silyl enol ether. That experiment gave a single lactol (**102**) whose stereochemistry was not established. Another isomer was isolated in 7% yield. The major product (**102**) was converted into lactol methyl ether **103**, which has the stereochemistry shown.

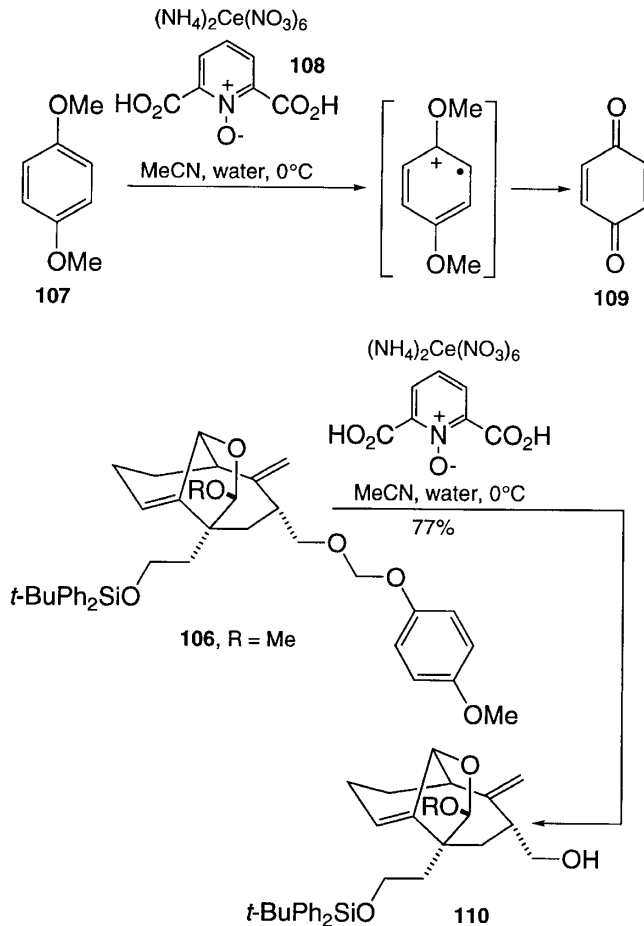
The next task was to introduce a carbon at C(2) (see **103**). Use of the Tebbe reagent gave a very low yield, but we eventually found that a modified Peterson reaction (13) worked very well.

The lithium salt **104** was added to ceric chloride to generate a reagent that gave alcohol **105** very efficiently (Scheme 28).

The alcohol is crystalline, and its structure was assigned by X-ray analysis. Deprotonation of the alcohol with potassium hexamethyldisilazide gave the desired olefin **106**. When we then tried to remove the AOM group, we found the reaction very troublesome. In fact, treatment with ceric ammonium nitrate under standard conditions simply did not work — the AOM group is inert, to our surprise. We tried a variety of methods and almost abandoned this protecting group, but, fortunately, we recognized something about the deprotection that proved to be very helpful.

We realized that the mechanism for deprotection should be similar to that for converting *p*-dimethoxybenzene (**107**) into *p*-benzoquinone (**109**) (Scheme 29), and so we examined the literature for that transformation and found that the pyridinedicarboxylic acid *N*-oxide **108** facilitates reaction

Scheme 29.



when ceric ammonium nitrate is used as the oxidant (14). Scheme 29 shows compound **106** drawn in such a way as to emphasize the structural similarity between an AOM group and *p*-dimethoxybenzene. We found that, although ceric ammonium nitrate itself causes no reaction with **106**, in the presence of the pyridine oxide diacid we can get almost 80% yield of the parent alcohol **110**. The beneficial effect of the catalyst appears to be a general one for removal of AOM groups.

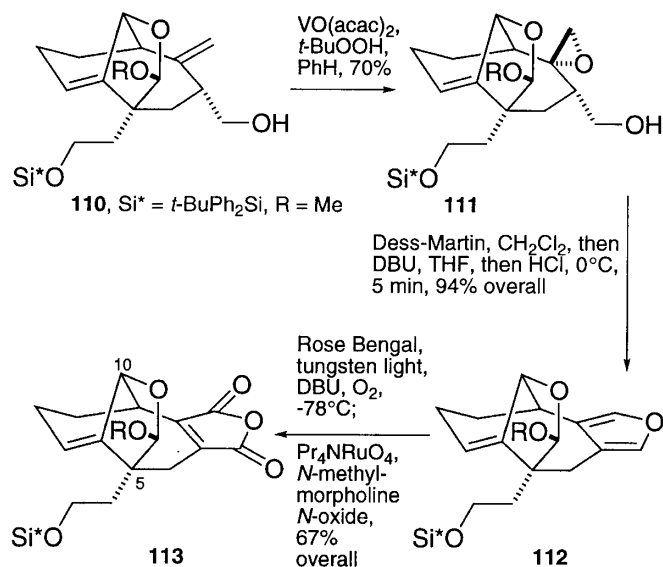
Epoxidation under standard conditions (Scheme 30) took us to **111**, and the corresponding aldehyde was made by Dess–Martin oxidation. Treatment with base served to open the epoxide, and then brief treatment with hydrochloric acid completed assembly of the furan (**111** → **112**). Once again, photo-oxygenation and TPAP oxidation converted the furan into the anhydride (**112** → **113**).

At this point the remaining transformations were oxidation of the side chain on the quaternary center and introduction of oxygen at C(10).

We decided to approach these tasks by regenerating the lactone unit that spans C(5) and C(10). We would then open the lactone by basic hydrolysis so as to expose the C(10) oxygen as an alcohol, which we would oxidize in the basic medium to the corresponding ketone. The ketone, in turn, should spontaneously form the desired hemiacetal on acidification.



Scheme 30.



To regenerate the lactone, we needed to replace the methoxy group of the lactol ether **113** by an OH group. Acid hydrolysis and trimethylsilyl iodide were unsuitable, but boron trichloride – dimethyl sulfide complex performed well (Scheme 31) and gave the desired lactols **114** as a mixture of two isomers, together with some of the corresponding chloride. Treatment with aqueous silver nitrate converted the chlorine byproduct into the lactols, so that the overall yield is high. Finally, Dess–Martin oxidation regenerated the lactone subunit (**114** → **115**). Most of our Dess–Martin oxidations are done at room temperature; this one required rather more vigorous conditions but was still efficient. Lactone **115** is crystalline, and X-ray analysis confirmed the structure.

With the lactone in place, we now had to oxidize the side chain, and to prepare for that the silicon group was removed by prolonged exposure — some 50 h — to aqueous trifluoroacetic acid.

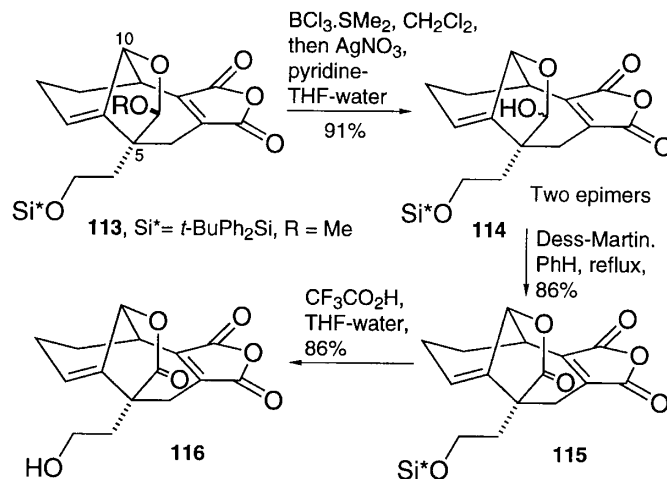
The resulting primary alcohol (**116**) was oxidized first to the aldehyde and then to the carboxylic acid (Scheme 32), so as to obtain compound **117**. This substance does not have very convenient chromatographic behavior and was, therefore, used crude.

The material was stored for 12 h in 1 M aqueous sodium hydroxide with the intention of opening both the lactone and the anhydride. The resulting salt was oxidized by addition of ruthenium dioxide (15) to the basic solution, which was kept at 70–80°C for 12 h. After acidification, we were able to isolate the complete tetracyclic core of CP-225,917 (**3**) in 40% yield from alcohol **116**.

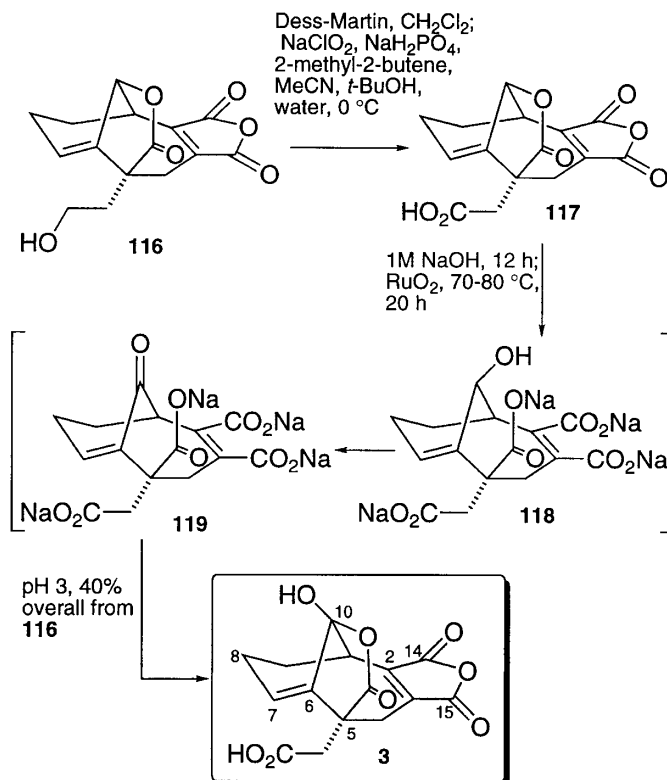
The core is crystalline, and X-ray analysis gave us the dimensions of the molecule. A noticeable feature of the structure is the shape of the bridgehead double bond. The four atoms C(8), C(7), C(6), and C(10) are in a plane — the deviation is less than 1° — but C(5) is 19° out of that plane. The other dimensions of the molecule are not unusual, although the lactone carbonyl angle is on the small side — 110°.

During this work we had encountered a large number of unexpected difficulties, and so we took the precaution of devising an alternative route to the core. This route, which

Scheme 31.



Scheme 32.

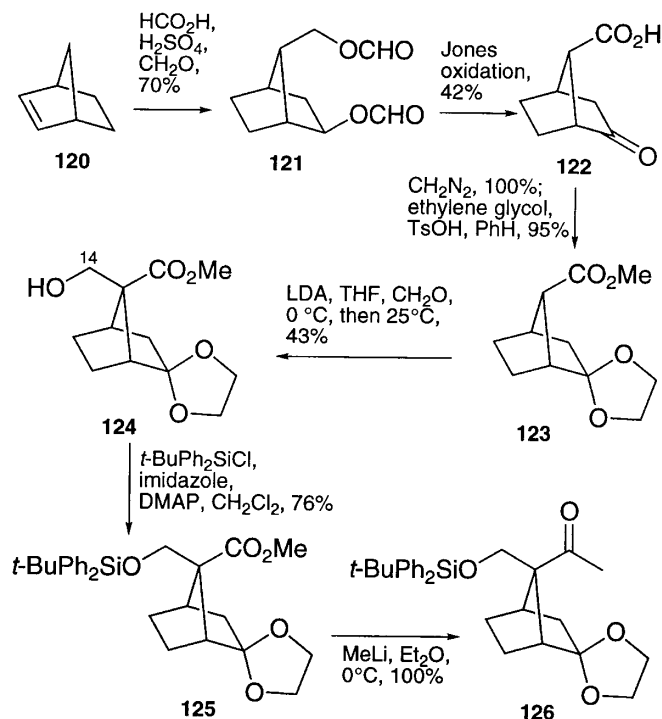


turned out to be shorter, involves a strain-assisted Cope rearrangement as opposed to oxy-Cope or siloxy-Cope rearrangement, and we also used a different method for making the anhydride.

The starting point is norbornene (**120**), which was converted in four simple steps into ester acetal **123** (Scheme 33). These steps are all reported in the literature (16). A Prins reaction converts norbornene into the bisformate **121**; Jones oxidation gives the corresponding keto acid **122**, and methylation with diazomethane, followed by ketalization, provides **123**. Although the yield in the oxidation step is low, the experiments are simple, and the ketal ester is easily made on a 20-g scale.



Scheme 33.



Deprotonation with  $\text{LDA}$  and condensation with paraformaldehyde affords a mixture of alcohols, and the major isomer (**124**) can be isolated in 43% yield. The carbon of the hydroxymethyl group was destined to become one of the carbonyl carbons of the anhydride, and it has been introduced very early, thereby bypassing some of the difficulties we had experienced in the first route.

After protection of the hydroxyl, the ester was treated with methyllithium. That experiment gave ketone **126**.

The next task was to introduce the second carbonyl carbon of the anhydride. To that end, our ketone was first converted into an enol phosphate.

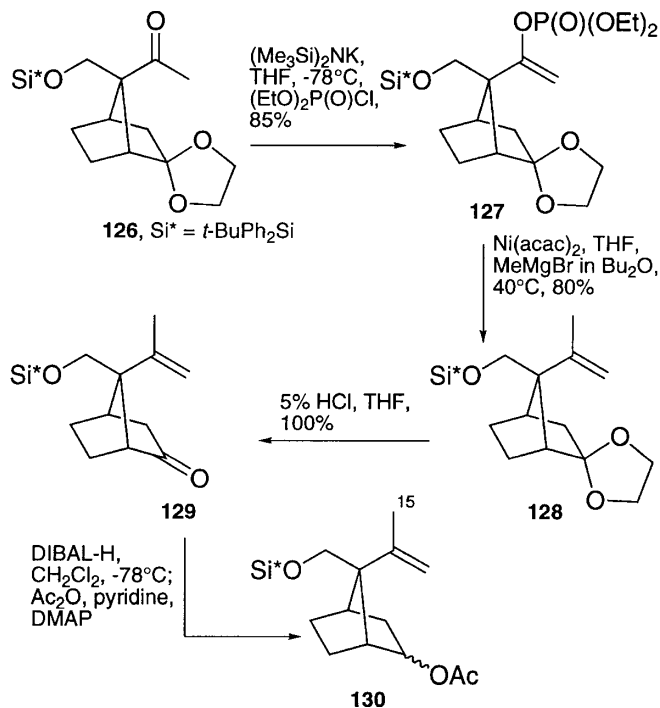
That was accomplished (Scheme 34) in the usual way, by deprotonation and treatment with diethyl chlorophosphate (**126**  $\rightarrow$  **127**). The product was treated with methylmagnesium bromide in the presence of nickel acetylacetonate (**17**) in warm dibutyl ether, and the result was introduction of a methyl group that was destined to become one of the carbonyl carbons of the anhydride.

Next the ketal was hydrolyzed, and the resulting ketone (**129**) was reduced with  $\text{DIBAL}$  and acetylated to give a mixture of epimeric acetates (**130**).

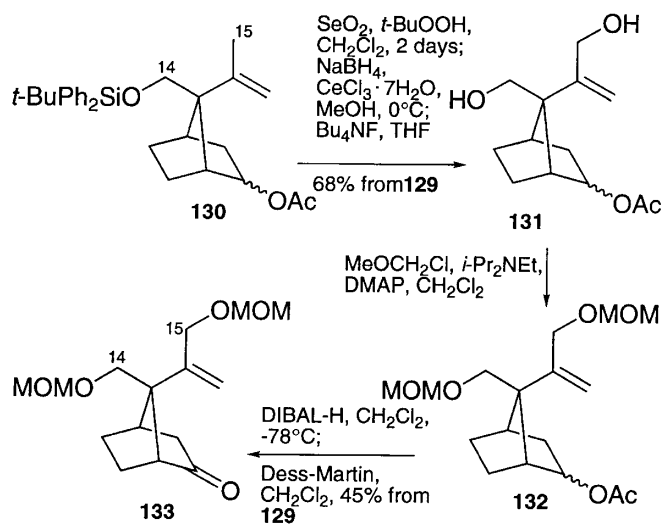
To place an oxygen at C(15), the acetates were treated with a catalytic amount of selenium dioxide in the presence of *tert*-butyl hydroperoxide (Scheme 35). The reaction was very slow and there was some overoxidation to the aldehyde, but treatment with sodium borohydride in the presence of ceric chloride served to make the necessary adjustment, and desilylation in the usual way gave diols **131** in a little under 70% from ketone **129**.

The free hydroxyls were protected as MOM ethers (**131**  $\rightarrow$  **132**), and we removed the acetyl group with  $\text{DIBAL}$ . Finally, Dess–Martin oxidation gave the expected ketone **133** — as a single compound, of course. During the last

Scheme 34.



Scheme 35.



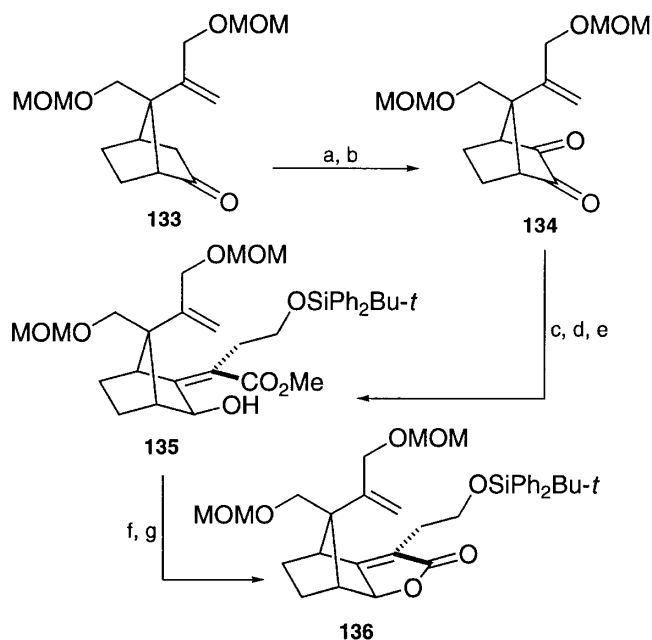
seven steps we had been working with mixtures of epimeric acetates, and that is why the Schemes do not indicate individual yields. The overall transformation can be done in 45% yield from ketone **129**, representing an average of 89% per step.

With ketone **133** in hand we were now in familiar territory. Both carbons for the anhydride carbonyls were in place, and we now had to build up the strained lactone system.

We used almost the same reactions that had served us well in the previous experiments. Ketone **133** was hydroxylated (Scheme 36) by treating the derived enolate with  $\text{MoOPH}$  (oxodiperoxymolybdenum(pyridine)(hexamethylphosphorotriamide)), and then oxidation gave the symmetrical diketone



**Scheme 36.** (a)  $(\text{Me}_3\text{Si})_3\text{NK}$ , THF, MoOPH,  $-23^\circ\text{C}$ , 72%; (b) Dess–Martin oxidation,  $\text{CH}_2\text{Cl}_2$ , 77%; (c) ester **70**, LDA, THF,  $-78^\circ\text{C}$ ; (d)  $\text{SOCl}_2$ , pyridine; (e)  $\text{NaBH}_4$ ,  $\text{CeCl}_3 \cdot 7\text{H}_2\text{O}$ , 55% from **134**; (f)  $\text{PrSLi}$ , HMPA, 83%; (g) 2-chloro-1-methylpyridinium iodide,  $\text{CH}_2\text{Cl}_2$ , reflux, 77%.



**134.** That was condensed with the enolate derived from the protected ester **70**, and the resulting alcohols were dehydrated with the thionyl chloride – pyridine combination. Finally, reduction with sodium borohydride afforded alcohol **135** (**134**  $\rightarrow$  **135**). In retrospect, we should have tried a very hindered reducing agent because it ought to have given better stereoselectivity, but nonetheless, the overall yield for the three steps used to convert **134** into **135** was acceptable.

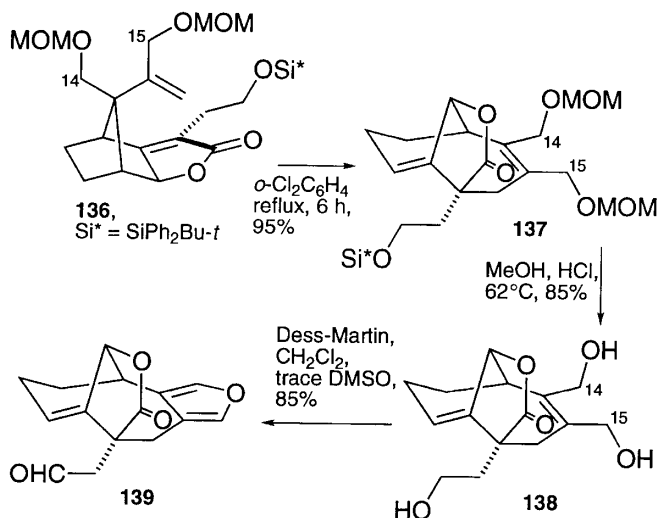
Demethylation of the ester with lithium propanethiolate and lactonization brought us to the intended substrate for the Cope rearrangement (**135**  $\rightarrow$  **136**). That process does not benefit from the factors that make the oxy-Cope rearrangement especially favorable, and so we wondered if the strain in the lactone would be sufficient to allow reaction under reasonably mild conditions.

We heated the lactone in *o*-dichlorobenzene and were very pleased to find that rearrangement does indeed occur (Scheme 37, **136**  $\rightarrow$  **137**) and in good yield, although the rate is lower than for the corresponding siloxy process.

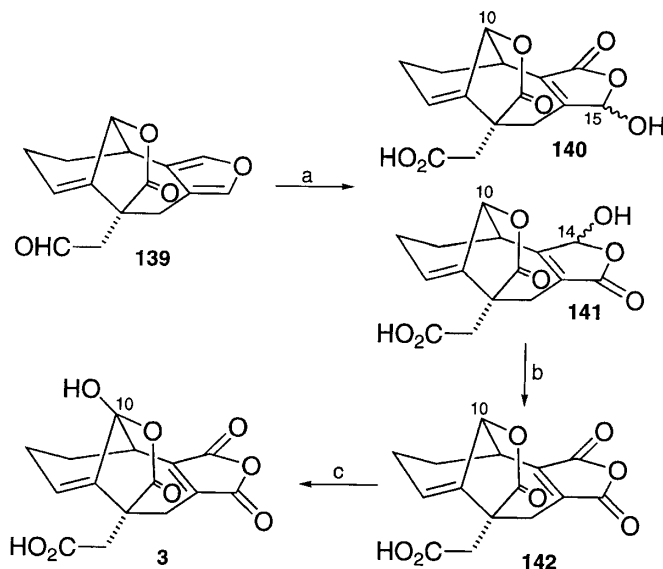
Global deprotection with hydrochloric acid gave triol **138**, and that was subjected to Dess–Martin oxidation to afford furan aldehyde **139**. There are several reactions involved here, of course. We assume that each of the hydroxyls at C(14) and C(15) is independently converted into an aldehyde, and the remaining hydroxyl — either C(15) or C(14) — forms a lactol, which, in turn, is dehydrated.

Next, we oxidized the aldehyde function to the corresponding acid, using standard conditions (Scheme 38), and we were very pleased to find that at the same time the furan was converted into the isomeric hydroxybutenolides **140** and **141**, each of which is equally suitable for the next step. That involves oxidation to the anhydride. The conversion of a

**Scheme 37.**



**Scheme 38.** (a)  $\text{NaClO}_2$ ,  $\text{NaH}_2\text{PO}_4$ , 2-methyl-2-butene, *t*-BuOH, water, 12 h; (b)  $\text{Pr}_4\text{NRuO}_4$ , *N*-methylmorpholine *N*-oxide, 50% from **139**; (c) 1 N NaOH, *t*-BuOH,  $70^\circ\text{C}$ , 12 h; catalytic  $\text{RuO}_2 \cdot x\text{H}_2\text{O}$ , stoichiometric  $\text{NaIO}_4$ ; pH 3,  $\geq 40\%$ .



$\beta,\beta'$ -disubstituted furan into an hydroxybutenolide under these conditions seems to be general. Finally, we dissolve anhydride **142** in aqueous sodium hydroxide, as before. The base opens up the lactone function to expose an hydroxyl group at C(10). That hydroxyl was converted into a ketone, and, after acidic workup, we were able to isolate once more the complete core of CP-225,917.

## Conclusion

In summary, we have developed two routes to the fully oxygenated core of CP-225,917. One route is based on a siloxy-Cope rearrangement and the other on a Cope rearrangement. Both processes are driven by release of strain in the [2.2.1] bicyclic starting materials. The core of CP-225,917 is crystalline, and X-ray analysis has provided



structural details of this unusual system. Further work is being directed to the task of repeating one or both of our approaches with suitable substituents that can be elaborated into the C<sub>8</sub> side chains of the natural product.

## Acknowledgments

We acknowledge financial support from the Natural Sciences and Engineering Research Council of Canada (NSERC) and Merck Frosst, and we thank Dr. V. Gagliardini for the experiments with compounds **49** and **50**.

## References

1. T.T. Dabrah, T. Kaneko, W. Massefski, Jr., and E.B. Whipple. *J. Am. Chem. Soc.* **119**, 1594 (1997).
2. (a) P.W.M. Sgarbi and D.L.J. Clive. *J. Chem. Soc. Chem. Commun.* 2157 (1997); (b) D.L.J. Clive, S. Sun, X. He, J. Zhang, and V. Gagliardini. *Tetrahedron Lett.* **40**, 4605 (1999); (c) D.L.J. Clive and J. Zhang. *Tetrahedron* **55**, 12 059 (1999); (d) D.L.J. Clive, S. Sun, V. Gagliardini, and M.K. Sano. *Tetrahedron Lett.* **41**, 6259 (2000); (e) D.L.J. Clive and S. Sun. *Tetrahedron Lett.* **42**, 6267 (2001); (f) D.L.J. Clive and L. Ou. *Tetrahedron Lett.* **43**, 4559 (2002).
3. (a) K.C. Nicolaou, P.S. Baran, Y.-L. Zhong, H.-S. Choi, W.H. Yoon, Y. He, and K.C. Fong. *Angew. Chem. Int. Ed. Engl.* **38**, 1669 (1999); (b) K.C. Nicolaou, P.S. Baran, Y.-L. Zhong, K.C. Fong, Y. He, W.H. Yoon, and H.-S. Choi. *Angew. Chem. Int. Ed. Engl.* **38**, 1676 (1999); (c) K.C. Nicolaou, J.-K. Jung, W.H. Yoon, Y. He, Y.-L. Zhong, and P.S. Baran. *Angew. Chem. Int. Ed. Engl.* **39**, 1829 (2000); (d) K.C. Nicolaou, Y.-L. Zhong, P.S. Baran, J. Jung, H.-S. Choi, and W.H. Yoon. *J. Am. Chem. Soc.* **124**, 2202 (2002).
4. Q. Tan and S.J. Danishefsky. *Angew. Chem. Int. Ed. Engl.* **39**, 4509 (2000).
5. Synthesis of CP-263,114: ref. 3 and (a) N. Waizumi, T. Itoh, and T. Fukuyama. *J. Am. Chem. Soc.* **122**, 7825 (2000); (b) C. Chen, M.E. Layton, S.M. Sheehan, and M.D. Shair. *J. Am. Chem. Soc.* **122**, 7424 (2000); (c) Synthesis of naturally occurring isomers of CP-molecules: D. Meng, Q. Tan, and S.J. Danishefsky. *Angew. Chem. Int. Ed. Engl.* **38**, 3197 (1999).
6. B.G. Cordiner, M.R. Vegar, and R.J. Wells. *Tetrahedron Lett.* **38**, 2285 (1970).
7. For a recent review, see L.A. Paquette. *Tetrahedron* **53**, 13 971 (1997).
8. L.A. Paquette, K.S. Learn, J.L. Romine, and H.-S. Lin. *J. Am. Chem. Soc.* **110**, 879 (1988).
9. Cf. (a) A.S. Cieplak. *J. Am. Chem. Soc.* **103**, 4540 (1981); (b) A.S. Cieplak, B.D. Tait, and C.R. Johnson. *J. Am. Chem. Soc.* **111**, 8447 (1989); (c) C.K. Cheung, L.T. Tseng, M.-H. Lin, S. Srivastava, and W.J. le Noble. *J. Am. Chem. Soc.* **108**, 1598 (1986); (d) G. Mehta and F.A. Khan. *J. Am. Chem. Soc.* **112**, 6140 (1990); (e) G. Mehta, F.A. Khan, B. Ganguly, and J. Chandrasekhar. *J. Chem. Soc. Perkin Trans. 2*, 2275 (1994); (f) Y.-D. Wu, J.A. Tucker, and K.N. Houk. *J. Am. Chem. Soc.* **113**, 5018 (1991).
10. (a) T. Onishi, Y. Fujita, and T. Nishida. *Synthesis*, 651 (1980) and references therein; (b) Y. Fujita, T. Onishi, and T. Nishida. *Synthesis*, 934 (1978); (c) M.A. Battiste, J.R. Rocca, and R.L. Wydra. *Tetrahedron Lett.* **29**, 6565 (1988); (d) A. Utogawa, H. Hirota, S. Ohno, and T. Takahashi. *Bull. Chem. Soc. Jpn.* **61**, 1207 (1988).
11. Use of DMF with *O*-methyl ethers: D. Backhaus and L.A. Paquette. *Tetrahedron Lett.* **8**, 29 (1997).
12. M.M. Bio and J.L. Leighton. *J. Am. Chem. Soc.* **121**, 890 (1999).
13. C.R. Johnson and B.D. Tait. *J. Org. Chem.* **52**, 281 (1987).
14. L. Syper, K. Kloc, J. Mlochowski, and Z. Szulc. *Synthesis*, 521 (1979).
15. (a) G. Green, W.P. Griffith, D.M. Hollinshead, S.V. Ley, and M. Schröder. *J. Chem. Soc. Perkin Trans. 1*, 681 (1984); (b) M. Masakatsu and N. Watanabe. *J. Org. Chem.* **49**, 3435 (1984).
16. (a) P. Flury and C.A. Grob. *Helv. Chim. Acta* **66**, 1981 (1983); (b) P. Kramp, G. Helmchen, and A.B. Holmes. *J. Chem. Soc. Chem. Commun.* 551 (1993).
17. (a) T. Hayashi, T. Fujiwa, Y. Okamoto, Y. Katsuro, and M. Kumada. *Synthesis*, 1001 (1981); (b) A.S.E. Karlström, K. Itami, and J.-E. Bäckvall. *J. Org. Chem.* **64**, 1745 (1999). Karlström, K. Itami, and J.-E. Bäckvall. *J. Org. Chem.* **64**, 1745 (1999).



# Synthesis and characterization of a linked, $\pi$ - $\pi$ stacked organotin compound of 2-mercapto-6-nitrobenzothiazolyl diphenyltin chloride with 2-ethoxyl-6-nitrobenzothiazole

Chunlin Ma, Qin Jiang, and Rufen Zhang

**Abstract:** The new organotin compound,  $\text{Ph}_2\text{Sn}(\text{Cl})[\text{S}(\text{C}_7\text{H}_3\text{N}_2\text{O}_2\text{S})]\cdot[(\text{C}_7\text{H}_3\text{N}_2\text{O}_2\text{S})\text{OEt}]$ , assembled by an intermolecular aromatic benzothiazole–benzothiazole  $\pi$ - $\pi$  stacking interaction, has been synthesized by the reaction of diphenyltin dichloride with 2-mercapto-6-nitrobenzothiazole. The title compound was characterized by elemental, IR,  $^1\text{H}$  NMR, and X-ray crystallography analyses. Single-crystal X-ray diffraction data reveals that the title compound has two different molecular components. The component  $\text{Ph}_2\text{Sn}(\text{Cl})[\text{S}(\text{C}_7\text{H}_3\text{N}_2\text{O}_2\text{S})]$  has a pentacoordinate tin, which further forms an infinite one-dimensional chain by intermolecular non-bonded  $\text{Cl}\cdots\text{S}$  interactions, resulting in an intercalation lattice that holds  $(\text{C}_7\text{H}_3\text{N}_2\text{O}_2\text{S})\text{OEt}$  molecules. The formation of the molecule  $(\text{C}_7\text{H}_3\text{N}_2\text{O}_2\text{S})\text{OEt}$  as well as its intercalated mechanism has also been discussed.

**Key words:** organotin, assemble,  $\pi$ - $\pi$  stacking interaction, 2-mercapto-6-nitrobenzothiazole, non-bonded interaction, crystal structure.

**Résumé :** Le nouveau composé organostannique  $\text{Ph}_2\text{Sn}(\text{Cl})[\text{S}(\text{C}_7\text{H}_3\text{N}_2\text{O}_2\text{S})]\cdot[(\text{C}_7\text{H}_3\text{N}_2\text{O}_2\text{S})\text{OEt}]$ , assemblé par interaction aromatique intermoléculaire d'empilement  $\pi$ - $\pi$  benzothiazole–benzothiazole, a été synthétisé par la réaction du dichlorure de diphenylétain avec le 2-mercapto-6-nitrobenzothiazole. Le composé mentionné dans le titre a été caractérisé par des analyses élémentaires, IR, de RMN  $^1\text{H}$  et par diffraction des rayons X sur un cristal unique qui révèle qu'il est formé de deux composantes moléculaires différentes. Le composant  $\text{Ph}_2\text{Sn}(\text{Cl})[\text{S}(\text{C}_7\text{H}_3\text{N}_2\text{O}_2\text{S})]$  comporte un atome d'étain pentacoordonné qui forme une chaîne infinie monodimensionnelle par le biais d'interactions intermoléculaires non liées  $\text{Cl}\cdots\text{S}$  qui sert de réseau d'intercalation pour retenir des molécules de  $(\text{C}_7\text{H}_3\text{N}_2\text{O}_2\text{S})\text{OEt}$ . On discute aussi de la formation de la molécule de  $(\text{C}_7\text{H}_3\text{N}_2\text{O}_2\text{S})\text{OEt}$  ainsi que du mécanisme d'intercalation.

**Mots clés :** organostannique, assemblage, interaction d'empilement  $\pi$ - $\pi$ , 2-mercapto-6-nitrobenzothiazole, interaction non liée, structure cristalline.

[Traduit par la Rédaction]

## Introduction

The coordination chemistry of tin is extensive with various geometries and coordination numbers known for both inorganic and organometallic complexes (1). Higher coordination numbers can be generated either by inter- and (or) intramolecular interaction, especially in complexes where tin bonds to electronegative atoms, such as oxygen, nitrogen, and sulfur. Studies of adducts of organotin halides continue to provide fundamental information about both the Lewis acid–base model and the reactivity of organotin species (2).

While tin is generally classified as a hard acid, many organotin–sulfur bonded complexes are known. To date only a few papers have been published on the X-ray structures of organotin(IV) complexes formed with thiol S and heterocyclic N (3). To investigate these kinds of complex structures, we used the reaction of diphenyltin dichloride with 2-mercapto-6-nitrobenzothiazole, and we wished to gain a one- or two-dimensional complex by the coordination of sulfur and nitrogen atoms with tin. To our surprise, we obtained an infinite one-dimensional linked compound assembled by aromatic benzothiazole–benzothiazole  $\pi$ - $\pi$  stacking interactions.  $\pi$ - $\pi$  stacking interaction has been extensively studied in recent years (4–6), including that of phenyl–phenyl (7), imidazole–imidazole (8), and so on. It has been proved that this strong attractive interaction can stabilize the packing of aromatic molecules in crystals (9) and play an important part in the field of host–guest chemistry (10). Through in-depth investigation into the intermolecular interactions, new light may be thrown on supramolecular architecture of organotin complexes possessing a particular structure and property. In this paper, we characterized the

Received 3 January 2003. Published on the NRC Research Press Web site at <http://canjchem.nrc.ca> on 10 June 2003.

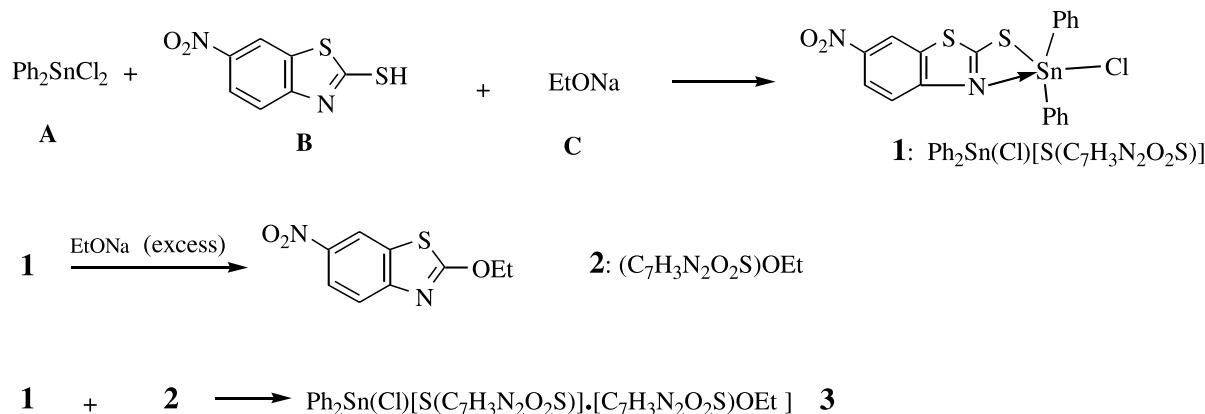
C. Ma,<sup>1,2</sup> Q. Jiang, and R. Zhang. Department of Chemistry, Liaocheng University, Liaocheng 252059, P.R. China.

<sup>1</sup>Present address: Department of Chemistry, Taishan University, Taian 271021, P.R. China.

<sup>2</sup>Corresponding author (e-mail: [macl@lctu.edu.cn](mailto:macl@lctu.edu.cn)).



Scheme 1.



title compound by elemental, IR,  $^1\text{H}$  NMR, and X-ray diffraction analyses and give a discussion on its reactive mechanism and structure. The procedure is described in Scheme 1.

## Experimental

### Materials and measurements

Diphenyltin dichloride and 2-mercapto-6-nitrobenzothiazole were commercially available, and they were used without further purification. The melting points were obtained with Kofler micro melting point apparatus and are uncorrected. Infrared spectra were recorded on a Nicolet-460 spectrophotometer using KBr discs and sodium chloride optics.  $^1\text{H}$  NMR spectra were obtained on a JEOL-FX-90Q NMR spectrometer; chemical shifts were given in ppm relative to  $\text{Me}_4\text{Si}$  in  $\text{CDCl}_3$  solvent. Elemental analyses were performed with a PE-2400II apparatus.

### Synthesis

The reaction was carried out under nitrogen atmosphere. The 2-mercapto-6-nitrobenzothiazole (0.212 g, 1.0 mmol) and sodium ethoxide (0.102 g, 1.5 mmol) were added to a solution of benzene (20 mL) in a Schlenk flask and stirred for 0.5 h. After the diphenyltin dichloride (0.343 g, 1.0 mmol) was added to the reactor, the reaction mixture was stirred for 12 h at  $40^\circ\text{C}$  and then filtrated. The filtrate was gradually removed by vaporization under vacuum until solid product was obtained. The solid was then recrystallized from ether–dichloromethane. There were two colored crystal compounds formed. One is yellow while the other is orange. Total yield: 0.462 g.

The compound **3** (orange crystal): mp  $88\text{--}90^\circ\text{C}$ . IR (KBr) ( $\text{cm}^{-1}$ ):  $\nu_{\text{as}}(\text{Sn-C})$ , 275;  $\nu_{\text{s}}(\text{Sn-C})$ , 229;  $\nu(\text{Sn-Cl})$ , 260;  $\nu(\text{Sn-S})$ , 290;  $\nu(\text{Sn-N})$ , 453;  $\nu(\text{C-S})$ , 746;  $\nu(\text{C=N})$ , 1637, 1598;  $\nu_{\text{s}}(\text{C-O})$  1065.  $^1\text{H}$  NMR ( $\text{CDCl}_3$ , ppm): 6.81–7.86 (m, 16H), 2.50–2.62 (q, 2H), 0.90–1.10 (t, 3H). Anal. calcd. for  $\text{C}_{28}\text{H}_{21}\text{ClN}_4\text{O}_5\text{S}_3\text{Sn}$ : C 45.20, H 2.85, N 7.53, S 12.91; found: C 45.51, H 2.93, N 7.44, S 12.87.

The complex **1** (yellow crystal): mp  $149\text{--}151^\circ\text{C}$ . IR (KBr):  $\nu_{\text{s}}(\text{Sn-C})$ , 278;  $\nu_{\text{as}}(\text{Sn-C})$ , 232;  $\nu(\text{Sn-Cl})$ , 266;  $\nu(\text{Sn-S})$ , 290;  $\nu(\text{Sn-N})$ , 448;  $\nu(\text{C-S})$ , 748;  $\nu(\text{C=N})$ , 1599.  $^1\text{H}$  NMR ( $\text{CDCl}_3$ , ppm): 7.46–7.79 (m, 13H). Anal. calcd. for  $\text{C}_{19}\text{H}_{13}\text{ClN}_2\text{O}_2\text{S}_2\text{Sn}$ : C 43.91, H 2.52, N 5.39, S 12.32; found: C 43.86, H 2.52, N 5.29, S 12.31.

### X-ray structure determination

All X-ray crystallographic studies were done using a Bruker Smart 1000 diffractometer fitted with graphite-monochromated Mo  $\text{K}\alpha$  radiation ( $\lambda = 0.71073 \text{ \AA}$ ). The  $\omega/2\theta$  scan technique was employed. Corrections were applied for Lorentz and polarization effects but not for absorption, satisfying  $I \geq 2\sigma(I)$ . Criterion of observability was used for the solution and refinement. The structure was solved using direct methods and refined by a full-matrix least squares procedure based on  $F^2$ , using the SHELXL-97 program system. All non-H atoms were included in the model at their calculated positions. All data were collected at a temperature of 298(2) K. For complex **1** and compound **3**, the crystal structures and unit cells are shown in Figs. 1–4, respectively. Selected bond distances and angles are listed in Table 1.

Crystal data for compound **3**: formula  $\text{C}_{28}\text{H}_{21}\text{ClN}_4\text{O}_5\text{S}_3\text{Sn}$ ,  $M = 743.81$ , monoclinic, space group  $P2_1/c$ ,  $a = 15.041(6)$ ,  $b = 16.647(6)$ ,  $c = 12.742(5)$ ,  $\beta = 109.973(6)^\circ$ ,  $V = 2999(2) \text{ \AA}^3$ ,  $Z = 4$ ,  $D_{\text{calcd}} = 1.648 \text{ g cm}^{-3}$ ,  $\mu = 1.195 \text{ mm}^{-1}$ ,  $F(000) = 1488$ ,  $\text{GoF} = 0.886$ , 16 278 reflections collected ( $\theta = 1.44^\circ$  to  $26.47^\circ$ ), 5821 of which were used in the refinement to give the final  $R_1 = 0.0658$  and  $wR_2 = 0.1238$ . Residual electron density: 0.567 and  $-0.883 \text{ e \AA}^{-3}$ .

Crystal data for complex **1**: formula  $\text{C}_{19}\text{H}_{13}\text{ClN}_2\text{O}_2\text{S}_2\text{Sn}$ ,  $M = 519.57$ , triclinic, space group  $P\bar{1}$ ,  $a = 12.961(6)$ ,  $b = 13.835(7)$ ,  $c = 16.412(8) \text{ \AA}$ ,  $\alpha = 69.184(8)^\circ$ ,  $\beta = 89.862(9)^\circ$ ,  $\gamma = 62.579(8)^\circ$ ,  $V = 2395(2) \text{ \AA}^3$ ,  $Z = 4$ ,  $D_{\text{calcd}} = 1.441 \text{ g cm}^{-3}$ ,  $\mu = 1.367 \text{ mm}^{-1}$ ,  $F(000) = 1024$ .  $\text{GoF} = 0.748$ , 13 476 reflections collected ( $\theta = 1.80^\circ$  to  $26.63^\circ$ ), 9316 of which were used in the refinement to give the final  $R_1 = 0.0591$  and  $wR_2 = 0.0828$ . Residual electron density: 0.605 and  $-0.642 \text{ e \AA}^{-3}$ .

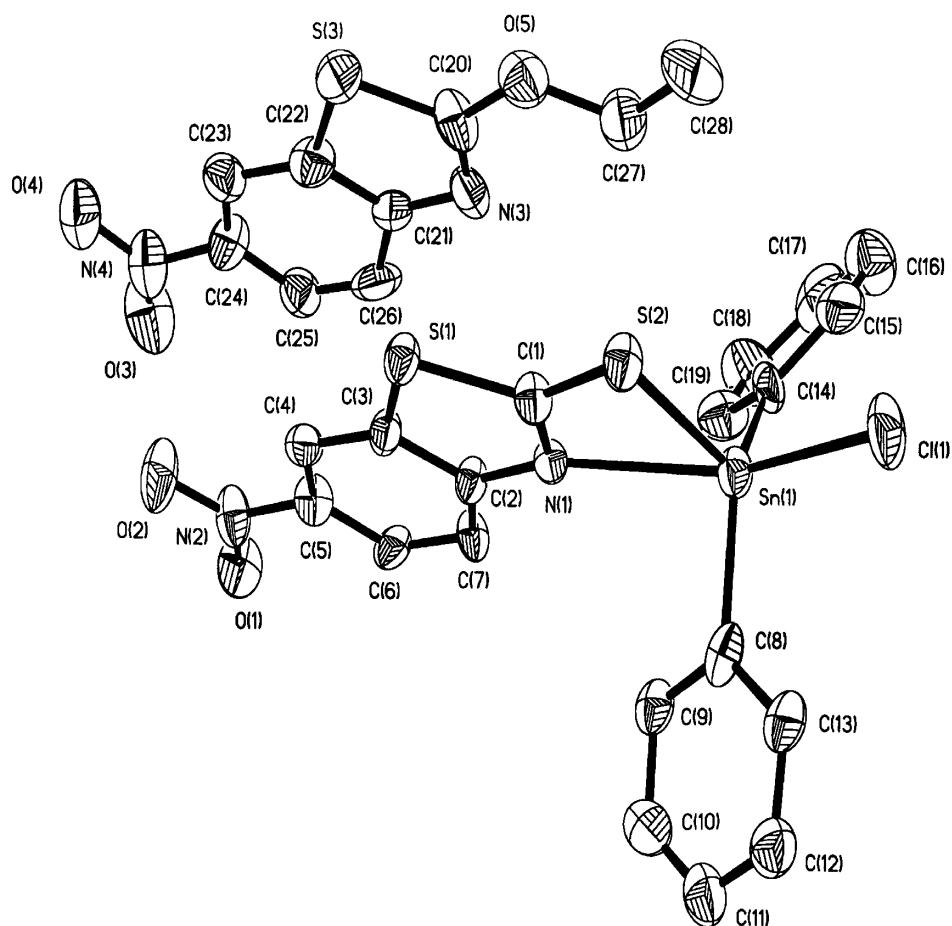
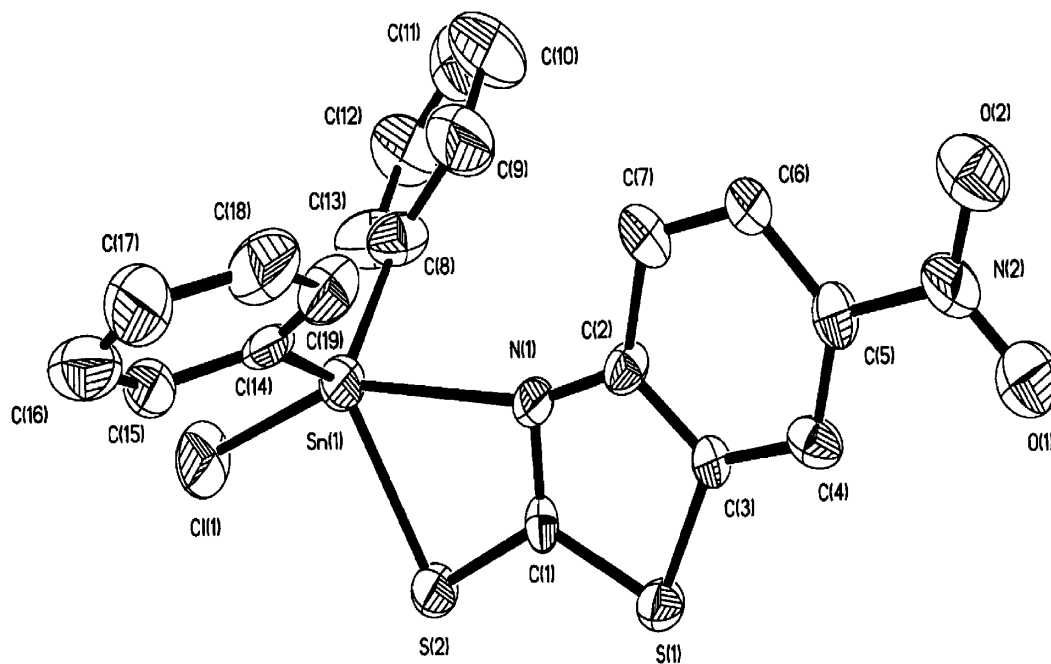
## Results and discussion

### Syntheses aspects

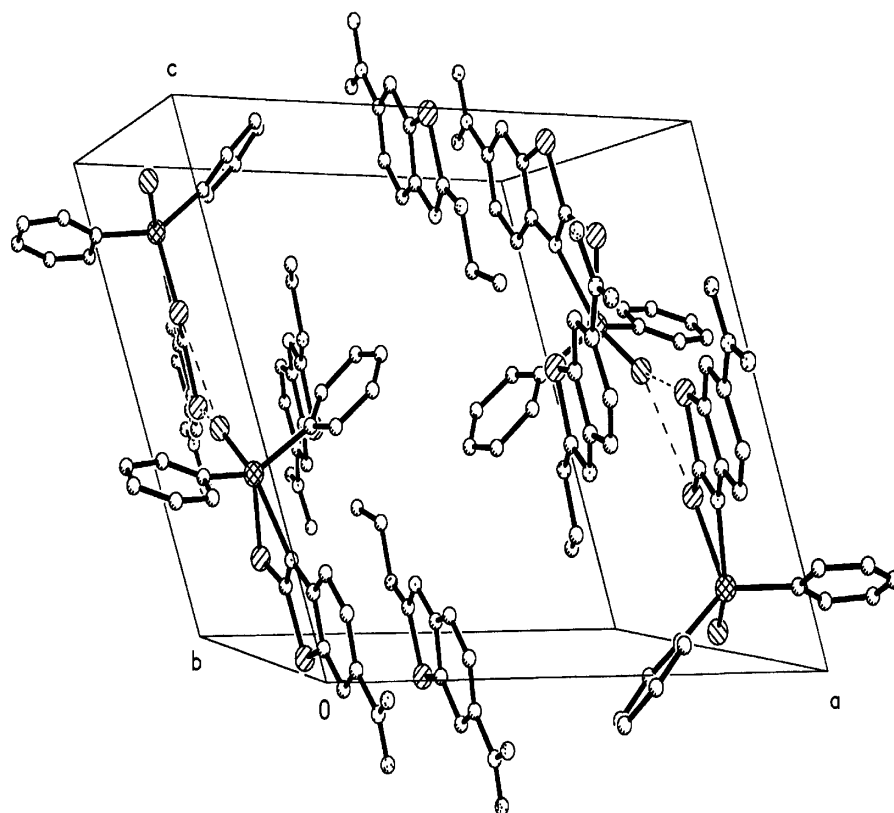
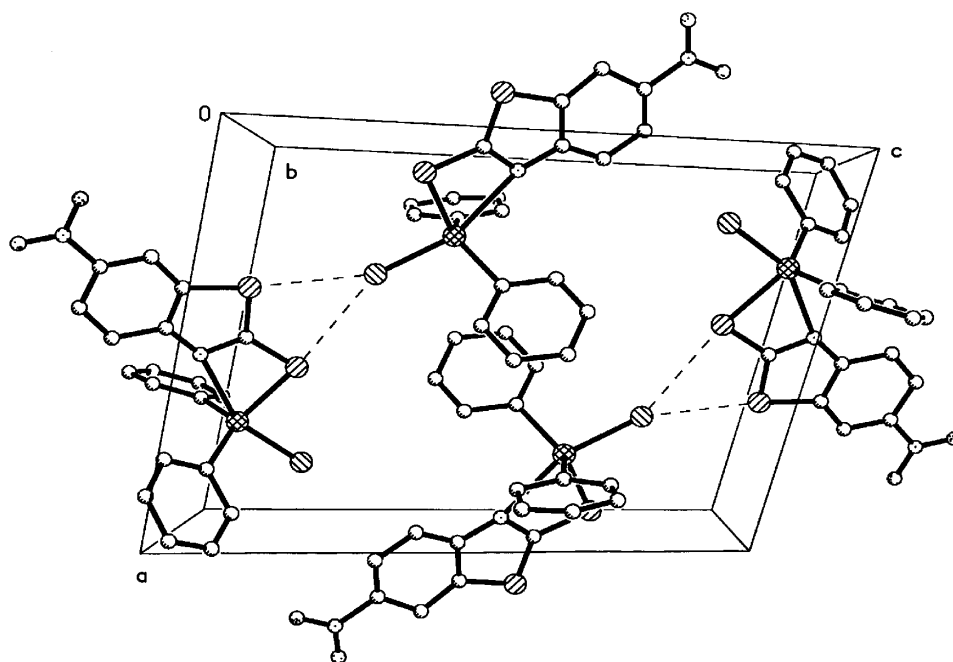
It was surprising that we obtained an infinite one-dimensional linked compound **3** assembled by aromatic benzothiazole–benzothiazole  $\pi\text{--}\pi$  stacking interactions. To investigate the synthetical mechanism of the reaction, we carried out a series of further experiments (with the same approach as that for compound **3**), as shown in Table 2.

According to experiments (a), (b), and (c), we can conclude that the possible synthetical mechanism of **3** is a three-step process, as follows: First, the 2-mercapto-6-nitrobenzo-



**Fig. 1.** Molecular structure of the compound **3**.**Fig. 2.** Molecular structure of the complex **1**.



**Fig. 3.** Unit cell of the compound **3**.**Fig. 4.** Unit cell of the complex **1**.

thiazole (**B**) reacts with sodium ethoxide (**C**) to form its sodium salt, which then reacts with the diphenyltin dichloride to form **1**. Second, **1** continues to react with excess **C** to form **2**. Finally, through the benzothiazole–

benzothiazole  $\pi$ - $\pi$  stacking interaction, **1** and **2** constitute the linked compound **3**.

The formation of substitutional product **2** is owed to the existence of **1** and excess **C**. Because of the interaction of



**Table 1.** Selected bond distances (Å) and angles (°) for compound **3** and complex **1**.

Compound (3)		Complex (1)	
Bond distances (Å)			
Sn(1)—C(14)	2.103(13)	Sn(1)—C(14)	2.066(10)
Sn(1)—C(8)	2.110(11)	Sn(1)—C(8)	2.102(12)
Sn(1)—Cl(1)	2.384(3)	Sn(1)—Cl(1)	2.367(3)
Sn(1)—S(2)	2.448(3)	Sn(1)—S(2)	2.444(2)
Sn(1)—N(1)	2.582(7)	Sn(1)—N(1)	2.595(7)
S(2)—C(1)	1.672(9)	N(1)—C(1)	1.316(8)
N(1)—C(1)	1.302(10)	S(2)—C(1)	1.730(8)
S(1)—C(1)	1.800(9)	Sn(2)—C(33)	2.026(12)
S(3)—C(22)	1.715(11)	Sn(2)—C(27)	2.084(11)
N(3)—C(21)	1.335(12)	Sn(2)—Cl(2)	2.373(2)
O(5)—C(27)	1.502(13)	Sn(2)—S(4)	2.446(3)
O(5)—C(20)	1.298(12)	Sn(2)—N(3)	2.580(6)
N(3)—C(20)	1.319(13)	N(3)—C(20)	1.332(10)
S(3)—C(20)	1.732(13)	S(4)—C(20)	1.727(8)
S(1)—C(3)	1.756(10)	Cl(2)···S(1)	3.415
N(1)—C(2)	1.401(10)	Cl(2)···S(2)	3.511
Cl(2)···S(1)	3.45	Cl(2)···S(3)	3.44
Cl(2)···S(2)	3.48	Cl(2)···S(4)	3.57
Bond angles (°)			
C(14)—Sn(1)—C(8)	124.6(4)	C(14)—Sn(1)—C(8)	123.6(4)
S(2)—Sn(1)—N(1)	63.02(17)	S(2)—Sn(1)—N(1)	62.90(16)
C(14)—Sn(1)—Cl(1)	101.4(3)	C(14)—Sn(1)—Cl(1)	101.4(3)
C(8)—Sn(1)—N(1)	90.0(3)	C(8)—Sn(1)—N(1)	90.0(3)
C(14)—Sn(1)—N(1)	90.5(3)	C(14)—Sn(1)—N(1)	90.5(3)
Cl(1)—Sn(1)—N(1)	153.97(18)	Cl(1)—Sn(1)—N(1)	153.96(16)
C(14)—Sn(1)—S(2)	115.0(3)	C(14)—Sn(1)—S(2)	116.1(2)
Cl(1)—Sn(1)—S(2)	90.95(10)	Cl(1)—Sn(1)—S(2)	91.08(9)
C(8)—Sn(1)—S(2)	114.2(2)	C(8)—Sn(1)—S(2)	113.9(3)
N(1)—C(1)—S(2)	124.0(7)	C(8)—Sn(1)—Cl(1)	100.6(3)
C(8)—Sn(1)—Cl(1)	101.7(3)	C(33)—Sn(2)—C(27)	123.5(4)
C(1)—N(1)—Sn(1)	87.8(5)	S(4)—Sn(2)—N(3)	63.06(17)
C(1)—S(2)—Sn(1)	85.2(3)	C(33)—Sn(2)—Cl(2)	102.2(3)
O(5)—C(20)—S(3)	118.6(9)	C(27)—Sn(2)—N(3)	91.2(3)
O(5)—C(20)—N(3)	125.2(11)	C(33)—Sn(2)—N(3)	88.3(3)
N(3)—C(20)—S(3)	116.2(8)	Cl(2)—Sn(2)—N(3)	154.78(18)
C(20)—N(3)—C(21)	110.6(9)	C(33)—Sn(2)—S(4)	113.1(3)
C(22)—S(3)—C(20)	88.3(6)	Cl(2)—Sn(2)—S(4)	91.72(10)
C(20)—O(5)—C(27)	115.6(10)	C(27)—Sn(2)—S(4)	116.6(2)

the S—Sn, the sulfur—carbon (Sn—S—C) bond strength in **1** becomes weaker and the carbon atom [C=N(S)(S)] becomes more electropositive than those of **B**, respectively, which makes the carbon—sulfur bond much easier to cleave. So, the group EtO<sup>−</sup> can substitute for the <sup>−</sup>S—SnPh<sub>2</sub>(Cl) group and form **2**. Here, Ph<sub>2</sub>SnCl<sub>2</sub> functions as a Lewis-acid catalyst in the replacement reaction. This point of view is well support by the results of experiments (a), (b), and (c). There were several mechanisms of carbon—sulfur bond cleavage put forward before (11), but the conditions of all those reactions were rigid, catalysts were needed, and the reaction was often accompanied with oxidation. Our results may provide a new way to these kinds of reactions.

It is worthy to note that despite using a 1:2:2 molar ratio of **A**:**B**:**C**, we didn't obtain the product with two chlorides

replaced in Ph<sub>2</sub>SnCl<sub>2</sub>; see experiment (d). The result suggested that the spatial resistance from two phenyl groups is strong enough to prevent another ligand chelating to the central tin atom. The conclusion coincides well with the case of Ph<sub>2</sub>SnCl(MBT) reported in the literature (12).

### IR data

The explicit feature in the infrared spectra of the title compound is the absence of the band in the region 2600–2550 cm<sup>−1</sup>, which appears in the free ligand as the ν(S—H) vibration, thus indicating metal—ligand bond formation through this site. In the far-infrared spectra, strong absorption at 290 cm<sup>−1</sup> (for both compound **3** and complex **1**), which is absent in the spectrum of the ligand, is assigned to the Sn—S stretching mode of vibration, and all the values are consistent with that detected for a number of organotin(IV)—sulfur derivatives (3). Medium-intensity bands at 275 and 229 cm<sup>−1</sup> for compound **3** and 278 and 232 cm<sup>−1</sup> for complex **1** can be assigned to ν<sub>as</sub>(Sn—C) and ν<sub>s</sub>(Sn—C). The ν(C=N) band, occurring at 1599 cm<sup>−1</sup> for **1**, is shifted considerably towards a lower frequency with respect to that of the free ligand, confirming the coordination of the heterocyclic N to the tin. The stretching frequency is lowered due to the displacement of electron density from the N to the Sn atom, thus resulting in the weakening of the C=N bond, as reported in the literature (13). Therefore, the weak- or medium-intensity band at 448 cm<sup>−1</sup> (for complex **1**) can be assigned to Sn—N stretching vibrations, while in the title compound **3**, there occur two bands that can be attributed to the ν(C=N). The band at 1598 cm<sup>−1</sup> is similar to the ν(C=N) band of complex **1**, and the band at about 1637 cm<sup>−1</sup> is near to the ν(C=N) value of the free ligand. Together with the band at 1065 cm<sup>−1</sup>, recognized as ν<sub>s</sub>(C—O), these messages provide evidence for the existence of the molecule (C<sub>7</sub>H<sub>3</sub>N<sub>2</sub>O<sub>2</sub>S)OEt.

### <sup>1</sup>H NMR data

<sup>1</sup>H NMR data showed that the signal of the <sup>−</sup>SH proton, present in the spectrum of the ligand, is absent in the title compound **3** and the complex **1**, indicating the removal of the SH proton and the formation of Sn—S bonds. The information accords well with what the IR data revealed. As anticipated, the spectrum consists of the phenyl hydrogen resonance at 7.32–7.86 ppm for complex **1** and the phenyl hydrogen resonance at 6.81–7.86 ppm for the mixture of **1** and **2** in compound **3**. In addition, there is a resonance due to the ethoxyl hydrogen in compound **3** at 2.50–2.62 ppm (q, 2h) and 0.90–1.10 ppm (t, 3H), which also proves the presence of the molecule (C<sub>7</sub>H<sub>3</sub>N<sub>2</sub>O<sub>2</sub>S)OEt **2**.

### Molecular structures

For compound **3**, single crystal X-ray diffraction data reveal that it has two different molecular components. The component Ph<sub>2</sub>Sn(Cl)[S(C<sub>7</sub>H<sub>3</sub>N<sub>2</sub>O<sub>2</sub>S)] has a pentacoordinated tin. The four primary bonds to the centered tin atom are two to the phenyl groups and one each to sulfur and chloride atoms. In addition, there exists interaction between tin and nitrogen atoms. The Sn(1)—N(1) bond length (2.582(7) Å) coincides with those of the type “SnCl<sub>2</sub>N<sub>2</sub>C<sub>2</sub>” recorded in the Cambridge Crystallographic Database (14), ranging from



**Table 2.** A series of further experiments.

	A (mmol)	B (mmol)	C (mmol)	Solution	Temperature (°C)	Products
a	1.0	1.0	1.5	Benzene (20 ml)	40	Complex <b>1</b> and compound <b>3</b>
b	1.0	1.0	1.0	Benzene (20 ml)	40	Complex <b>1</b>
c	0.0	1.0	1.0	Benzene (20 ml)	40	Complex <b>2</b>
d	1.0	2.0	2.0	Benzene (20 ml)	40	Complex <b>1</b>

2.27 to 2.58 Å; equal to that of [2-(Me<sub>2</sub>NCH<sub>2</sub>)C<sub>6</sub>H<sub>4</sub>]SnPh<sub>2</sub>Cl (2.52 Å) (15); and longer than that of Ph<sub>2</sub>SnCl(MBT) (2.41 Å) (12), but much shorter than the sum of the van der Waals radii of Sn and N, 3.74 Å (16), thus providing a 4-membered chelate ring with a bite angle, N(1)–Sn(1)–S(2), of 63.02(17)°. If the tin–nitrogen interaction is included, the geometry at Sn then becomes a distorted *cis*-trigonal bipyramidal with Cl(1) and N(1) in axial sites (Cl(1)–Sn(1)–N(1) = 153.97(18)°) and C(8), C(14), and S(2) occupying the equatorial plane (C(14)–Sn(1)–C(8) = 124.6(4)°). The sum of the angles subtended at the tin atom in the trigonal plane is 358.3°, so the tin atom shows no significant deviation from the equatorial plane. The Sn(1)–Cl(1) bond length (2.384(3) Å) lies in the range of the covalent radii (2.37–2.60 Å) (15). The Sn(1)–S(2) bond length (2.448(3) Å) is well within the range — from 2.41 to 2.48 Å — that is reported for triphenyltin heteroareneithiolates (3), slightly shorter than that of Ph<sub>2</sub>SnCl(MBT) (2.49 Å) (12), and almost equal to that of Ar<sub>3</sub>Sn[S(C<sub>5</sub>H<sub>4</sub>N)] (17). Finally, the Sn–C bond lengths are approximately equal (Sn(1)–C(8) = 2.110(11) and Sn(1)–C(14) = 2.103(13) Å) and are similar to the average value, 2.13 Å (14).

Besides, in the represented crystalline structure, a relatively close contact between the Cl atom of Ph<sub>2</sub>Sn(Cl)–[S(C<sub>7</sub>H<sub>3</sub>N<sub>2</sub>O<sub>2</sub>S)] and the two S atoms of its adjacent molecule (Cl(2)···S(1), 3.45 Å and Cl(2)···S(2), 3.45 Å) was recognized, which coincided well with that reported in (PhCH<sub>2</sub>)<sub>2</sub>SnClS<sub>2</sub>CNC<sub>4</sub>H<sub>8</sub>O (3.49 Å) (18) but was much shorter than the sum of the van der Waals radii (3.97 Å) for these atoms (19). And it is the intermolecular, non-bonded Cl···S interaction that favored the regular self-assembly of Ph<sub>2</sub>Sn(Cl)[S(C<sub>7</sub>H<sub>3</sub>N<sub>2</sub>O<sub>2</sub>S)] and further made it an infinite 1D chain. Intermolecular, non-bonded S···X (X = O, S, N, etc.) interactions have been investigated for characterization of the molecular structures of a large number of organosulfur compounds (20). But we have seen few discussions about the Cl···S interaction up to now. So, we can regard it as another new type of close contact.

Quite unexpectedly, the two different molecular components Ph<sub>2</sub>Sn(Cl)[S(C<sub>7</sub>H<sub>3</sub>N<sub>2</sub>O<sub>2</sub>S)] and (C<sub>7</sub>H<sub>3</sub>N<sub>2</sub>O<sub>2</sub>S)OEt are accommodated in parallel layers. The layers of Ph<sub>2</sub>Sn(Cl)–[S(C<sub>7</sub>H<sub>3</sub>N<sub>2</sub>O<sub>2</sub>S)] result in an intercalation lattice that holds (C<sub>7</sub>H<sub>3</sub>N<sub>2</sub>O<sub>2</sub>S)OEt molecules. All those atoms on the benzothiazole ring in Ph<sub>2</sub>Sn(Cl)[S(C<sub>7</sub>H<sub>3</sub>N<sub>2</sub>O<sub>2</sub>S)] are in the same plane, with only a negligible tilt (dihedral angle between the phenyl ring (C(2)–C(7)) and the heterocyclic ring (C(1)–C(3), N(1), S(1)), 0.6°), while two benzothiazole–benzothiazole ring planes, C(1)–C(7) in Ph<sub>2</sub>Sn(Cl)[S(C<sub>7</sub>H<sub>3</sub>N<sub>2</sub>O<sub>2</sub>S)] and C(20)–C(26) in (C<sub>7</sub>H<sub>3</sub>N<sub>2</sub>O<sub>2</sub>S)OEt, are almost parallel to each other, and the dihedral angle is 4.1°. The shortest distance of C(25) to C(1)–C(7) is 3.30 Å and the average distance is 3.42 Å, which is terribly consistent with that of a benzene polymer in theoretical studies (3.4 Å) (21) and ap-

proaches that of imidazole–imidazole (3.29 Å) (6). It implies that there exists a strong face-to-face  $\pi$ – $\pi$  stacking interaction between the two benzothiazole–benzothiazole ring planes. In virtue of the significant interlayer interaction, the gaps between netlike layers of Ph<sub>2</sub>Sn(Cl)[S(C<sub>7</sub>H<sub>3</sub>N<sub>2</sub>O<sub>2</sub>S)] are filled by the molecule [C<sub>7</sub>H<sub>3</sub>N<sub>2</sub>O<sub>2</sub>S]OEt. The molar ratio of (C<sub>7</sub>H<sub>3</sub>N<sub>2</sub>O<sub>2</sub>S)OEt:Ph<sub>2</sub>Sn(Cl)[S(C<sub>7</sub>H<sub>3</sub>N<sub>2</sub>O<sub>2</sub>S)] is 1:1, so that the molecular formula can be written in brief as Ph<sub>2</sub>Sn(Cl)–[S(C<sub>7</sub>H<sub>3</sub>N<sub>2</sub>O<sub>2</sub>S)]·[(C<sub>7</sub>H<sub>3</sub>N<sub>2</sub>O<sub>2</sub>S)OEt].

For the complex **1**, as far as bond lengths, bond angles, and intermolecular Cl···S non-bonded interactions are concerned, its structure is very similar to that of the title compound **3**, and it is a one-dimensional chain, too. However, there exists no molecule in its crystal grids and no intermolecular  $\pi$ – $\pi$  stacking interaction. The Cl···S distance ranges from 3.42 Å to 3.57 Å. For detailed data see Table 1.

## Acknowledgments

We thank the National Natural Foundation, P.R. China (20271025), the Key Teachers Foundation from the State Education Ministry of China, and the National Natural Foundation of Shandong Province, P.R. China for financial support of this work.

## References

1. P.J. Smith (*Editor*). Chemistry of tin. 2nd ed. Blackie, London, 1998.
2. C.H. Yoder, L.A. Margolis, and J.M. Horne. *J. Organomet. Chem.* **633**, 33 (2001).
3. (a) C.V.R. Moura, A.P.G. Sousa, R.M. Silva, A. Abras, M. Horner, A.J. Bortoluzzi, C.A.L. Filgueiras, and J.L. Wardell. *Polyhedron*, **18**, 2961 (1999); (b) R. Schmiedgen, F. Huber, H. Preut, G. Ruisi, and R. Barbieri. *Appl. Organomet. Chem.* **8**, 397 (1994).
4. C.A. Hunter and J.K.M. Sanders. *J. Am. Chem. Soc.* **112**, 5525 (1990).
5. C. Janiak. *J. Chem. Soc. Dalton Trans.* 3885 (2000).
6. N.W. Alcock, P.R. Barker, J.M. Haider, M.J. Hannon, C.L. Painting, Z. Pikramenou, E.A. Plummer, K. Rissanen, and P. Saarenketo. *J. Chem. Soc. Dalton Trans.* 1447 (2000).
7. D.Z. Zhu, X.M. Song, J.M. Dou, Y. Liu, D.Q. Wang. *J. Chin. Chem.* **20**, 424 (2002).
8. M. Du, Z.L. Shang, X.B. Leng, and X.H. Bu. *Polyhedron*, **20**, 3065 (2001).
9. G.R. Desiraju and A.J. Gavezzotti. *J. Am. Chem. Soc. Chem. Commun.* 621 (1989).
10. D.B. Smithrud and F.J. Diederich. *J. Am. Chem. Soc.* **112**, 339 (1990).
11. (a) A. Touthkine and E.L. Clennan. *J. Am. Chem. Soc.* **122**, 1834 (2000); (b) U. Riaz, O.J. Curnow, and M.D. Curtis. *J. Am. Chem. Soc.* **116**, 4357 (1994).



12. A.P.G. de Sousa, R.M. Silva, A. Cesar, J.L. Wardell, J.C. Huffman, and A. Abras. *J. Organomet. Chem.* **605**, 82 (2000).
13. C. Pettinari, F. Marchetti, R. Pettinari, D. Martini, A. Drozdov, and S. Troyanov. *Inorg. Chim. Acta*, **103**, 325 (2001), and refs. therein.
14. F.H. Allen, S.A. Bellard, M.D. Brice, B.A. Cartwright, A. Doubleday, H. Higgs, T. Hummelink, B.G. Hummelink-Peters, O. Kennard, W.D.S. Motherwell, J.R. Rogers, and D.G. Watson. *Acta Crystallogr.* **B35**, 2331 (1979).
15. R.A. Narga, M. Schuermann, and C. Silvestru. *J. Organomet. Chem.* **623**, 161 (2001).
16. A. Bondi. *J. Phys. Chem.* **68**, 441 (1964).
17. J.E. Huheey, E.A. Keiter, and R.L. Keiter. *Principles and applications of inorganic chemistry*. 4th ed. Harper Collins, New York. 1993.
18. H.D. Yin, C.H. Wang, C.L. Ma, and Y. Wang. *Chin. J. Chem.* **20**, 913 (2002).
19. R.T. Boere, K.H. Mok, and M.Z. Parvez. *Anorg. Allg. Chem.* **620**, 1589 (1994).
20. Y. Nagao, H. Nishijima, H. Iimori, H. Ushiroguchi, S. Sano, and M. Shiro. *J. Organomet. Chem.* **611**, 172 (2000).
21. R.L. Jaffe and G.D. Smith. *J. Chem. Phys.* **105**, 2780 (1996).



# Dediazoniation of *p*-hydroxy and *p*-nitrobenzenediazonium ions in an aqueous medium: Interference by the chelating agent diethylenetriaminepentaacetic acid

B. Quintero, M.C. Cabeza, M.I. Martínez, P. Gutiérrez, and P.J. Martínez

**Abstract:** We have made a comparative study of the dediazonation of *p*-hydroxy and *p*-nitrobenzenediazonium ions. The electron-withdrawing and donating properties of the -NO<sub>2</sub> and -OH groups strongly determine the reactivity of both compounds, thus exerting different influences upon the dediazonation reaction. We describe here how the decomposition of *p*-hydroxy and *p*-nitrobenzenediazonium ions in a neutral aqueous medium follows a different pattern in the presence of the metal-chelator diethylenetriaminepentaacetic acid (DTPA). The decomposition rate of *p*-hydroxybenzenediazonium decreases whilst the decomposition of the *p*-nitrobenzenediazonium ion is enhanced. The experimental data are discussed with reference to a common scheme of interference for both benzenediazonium ions in the light of the radical-scavenging capacity of DTPA.

**Key words:** *p*-hydroxybenzenediazonium ion, *p*-nitrobenzenediazonium ion, di-ethylenetriaminepentaacetic acid, dediazonation, radical scavenging, artifacts.

**Résumé :** On a réalisé une étude comparative des réactions de dédiazotation des ions *p*-hydroxy et *p*-nitrobenzènediazonium. Les propriétés électroaffinitaires et électrorépluses des groupes -NO<sub>2</sub> et -OH influencent fortement la réactivité de ces deux composés et exercent donc des influences différentes sur leur réaction de dédiazotation. La décomposition des ions *p*-hydroxy- et *p*-nitrobenzènediazonium dans un milieu aqueux neutre, en présence de l'acide diéthylènetriaminépentaacétique (DTPA) qui agit comme chélatant de métaux se produit selon des voies différentes. La vitesse de décomposition de l'ion *p*-nitrobenzènediazonium diminue alors que celle de l'ion *p*-hydroxynitrobenzènediazonium augmente. On discute des données expérimentales en fonction d'un schéma commun d'interférence pour les deux ions benzènediazonium et en tenant compte de la capacité du DTPA à piéger les radicaux.

**Mots clés :** ion *p*-hydroxybenzènediazonium, ion *p*-nitrobenzènediazonium, acide diéthylènetriaminépentaacétique, dédiazotation, piège de radicaux, artefacts.

[Traduit par la Rédaction]

## Introduction

Arenediazonium ions are widely used in chemical synthesis. Apart from diazo-coupling reactions (1–3), these ions can undergo either thermal or photochemical heterolytic dediazonation, yielding the aryl cation (1, 4, 5). Arenediazonium ions can also be dediazoniated in a homolytic process via one-electron reduction, thus generating aryl radicals. Arenediazonium ions and their precursors, arylhydrazides and arylhydrazines, are believed to be genotoxic (6, 7). Although most arenediazonium ions are recognised as being oxidants, such structural characteristics as the electron-donating and withdrawing properties of the substituents in the aromatic ring, together with interference from solvent

interactions, other reducing and (or) oxidizing compounds, light, or the conditions of the reaction medium may substantially modify their reactivity, giving rise to different patterns of decomposition and resulting in different biological effects. In this context heterolytic dediazonation has been reported to occur with methylbenzenediazonium and *p*-nitrobenzenediazonium (pNO) ions in an aqueous medium (8, 9), whilst other authors have interpreted their results as showing evidence of heterolytic and homolytic processes during the thermal and photochemical dediazonation of several arenediazonium ions in trifluoroethanol and ethanol (10, 11). Furthermore, in certain cases the reducing capacity of water has been sufficient to reduce arenediazonium to the aryl radical (12). It is obvious therefore that reaction conditions need to be chosen carefully when trying to establish the mechanisms involved in the decomposition of such versatile compounds as arenediazonium ions. We have studied the dediazonation of the *p*-hydroxybenzenediazonium ion (PDQ) in a neutral aqueous medium (13) and have observed that in the presence of DTPA the rate of dediazonation decreases together with the intensity of the signal produced by the aryl radical adduct as measured in EPR, using the spin

Received 10 January 2003. Published on the NRC Research Press Web site at <http://canjchem.nrc.ca> on 13 June 2003.

B. Quintero,<sup>1</sup> M.C. Cabeza, M.I. Martínez, P. Gutiérrez, and P.J. Martínez. Dpt. of Physical Chemistry, Faculty of Pharmacy, University of Granada, Spain.

<sup>1</sup>Corresponding author (e-mail: bqosso@ugr.es).



trap DMPO (5,5-dimethyl-1-pyrroline-*N*-oxide). The use of DTPA as metal chelator has been recommended in the literature to avoid interference from the redox activity of any contaminating metal ions present in solution (14–17). We report here on a comparative study carried out with pNO and PDQ, the dediazonation rates of which are influenced differently by the chelating agent DTPA.

## Experimental

Chemicals of the highest available purity (Merck and Aldrich) were used. Chelex 100 resin (50–100 dry mesh, sodium form), nitrobenzene, *p*-nitrophenol, and pNO tetrafluoroborate were bought from Sigma and used as received. PDQ tetrafluoroborate was synthesized following the procedure described by Danêk et al. (18) with slight modifications. Sodium tetrafluoroborate (2.24 g) in distilled water (6 mL) was treated with perchloric acid (70%, 1.7 mL) and used to dissolve *p*-aminophenol (1.09 g) (Solution 1). Another solution was made by dissolving sodium nitrite (0.71 g) in distilled water (2.5 mL) (Solution 2). Solution 2 was added gradually to Solution 1, while stirring continuously and keeping the reaction in darkness within a temperature range of 0–5°C. The resulting mixture was kept at –10°C for 24 h. A solid was separated by filtration and washed first with cold ethanol and then with diethyl ether. Crystallization was made by precipitation from the solution obtained, dissolving the solid in ethanol at 70°C. A second crystallization was carried out by adding diethyl ether to an acetone solution of the solid. Re-crystallized PDQ tetrafluoroborate is a yellowish crystalline solid that melts between 135 and 140°C accompanied by a noticeable change in colour and the production of a gas. Elemental analysis revealed C 42.8%, H 2.76%, and N 17.05%, which agrees very well with the formation of the tetrafluoroborate of the PDQ dimer. IR: 2189 cm<sup>–1</sup> (N≡N stretching) and 1591 cm<sup>–1</sup> (aromatic group). Both benzenediazonium salts were stored below –18°C in darkness.

A Huco Erlöss Cintra 10 spectrophotometer was used for spectrophotometric analysis. HPLC was done with a Merck L-6220 biocompatible pump and a Merck L-4500 diode array detector (Merck-Hitachi). Aqueous media were filtered through Millipore HA filters with a pore size of about 0.45 µm. The column was a Spherisorb ODS-2 (4.6 mm × 200 mm) with a particle size of 5 µm. Mobile phase acetonitrile–methanol–acetic acid (1%) (30:30:40) with a flow of 0.7 mL·min<sup>–1</sup> was routinely used. Samples were dissolved in phosphate buffer (0.1 M, pH 7.2) previously treated with Chelex 100 resin by the column method. A Radiometer pH M64 potentiometer with a GK2401C mixed electrode was used whenever called for. The calibrations were carried out with Crison buffer references (pH 4 and pH 7). pH values were checked throughout the kinetic measurements, and no significant changes were observed. An oxygraph equipped with a Clark-type electrode was used to measure oxygen consumption. Twice-distilled water was obtained by the Milli Q system and used in all experiments. Oxygen for deaerated samples was purged by bubbling with argon for at least 10 min.

We checked for any effects on PDQ and pNO decomposition that might be caused by either environmental laboratory

light or apparatus light sources. The results were taken into account when designing the methods for spectrophotometric measurement. In the case of PDQ, measurements were routinely made with aliquots taken from a stock solution kept in darkness. Neither environmental nor instrumental light interference was observed in the case of pNO.

Kinetic analyses were made by incubating 0.4 mM PDQ solutions kept in darkness at 37°C either in the presence or absence of DTPA. Aliquots were taken from these solutions to make PDQ 0.01 mM solutions, which were then used for spectrophotometric measurements. Kinetic measurements were made with pNO in the presence or absence of DTPA either by incubating 1.33 mM pNO solutions and then taking aliquots to make 3.26 × 10<sup>–5</sup> M pNO solutions or by placing the sample (0.11 mM) directly into the spectrophotometric cell.

## Results and discussion

### Dediazoniation of PDQ and pNO in the absence of DTPA

The absorption spectrum of PDQ in a phosphate-buffered aqueous medium (pH 7.2) presented a band with its maximum at 350 nm ( $\epsilon$ : 41 990 L·mol<sup>–1</sup>·cm<sup>–1</sup>) and a less intense band at 250 nm ( $\epsilon$ : 3010 L·mol<sup>–1</sup>·cm<sup>–1</sup>), whereas the absorption spectrum of pNO obtained in an identical medium showed a band with its maximum at 259 nm ( $\epsilon$ : 15 590 L·mol<sup>–1</sup>·cm<sup>–1</sup>) and a minor absorption at 314 nm ( $\epsilon$ : 2234 L·mol<sup>–1</sup>·cm<sup>–1</sup>).

We have reported previously (13) that, under experimental conditions controlled to prevent photochemical and (or) heterolytic side reactions, the dediazonation of PDQ in a neutral aqueous medium (37°C in phosphate buffer, pH 7.2) occurs via three pathways (Scheme 1): Pathway **1** represents dediazonation induced by a hydroxyl ion, a slow process at neutral pH and even slower with deaerated samples. In pathway **2** the formation of a semiquinone radical via the reaction of an aryl radical with oxygen is considered to justify the increase in the dediazonation rate in the presence of oxygen. Finally, in pathway **3**, hydroquinone, produced by semiquinone dismutation, may act as an additional reducing agent. PDQ dediazonation was characterized by a gradual decrease in absorbance at 350 nm. pNO dediazonation, on the other hand, using a sample concentration of 1.33 mM, led to a decrease at 259 nm followed by the simultaneous appearance of an absorption band at 350 nm, which increased with time. No band was recorded beyond 370 nm (Fig. 1). As the concentration of pNO fell (0.11 mM), the picture changed, with a new band appearing at about 390 nm, as well as the absorption at 350 nm (Fig. 2). A chromatographic analysis of these samples containing a low concentration of pNO was made using acetonitrile–methanol–acetic acid 0.2 M (30:30:40) as the mobile phase. The chromatograms showed three main peaks with retention times of 3.05, 4.01, and 7.26 min, respectively, and a minor peak at 10.41 min, which, by comparing the associated UV spectra with those of the authentic products, were assigned to pNO, PDQ, *p*-nitrophenol (pNP), and nitrobenzene (NB), respectively. The unexpected presence of NB led us to repeat the HPLC analysis using fresh samples of pNO in 1 × 10<sup>–4</sup> M HCl at 25°C, which should be very stable according to the



Scheme 1.

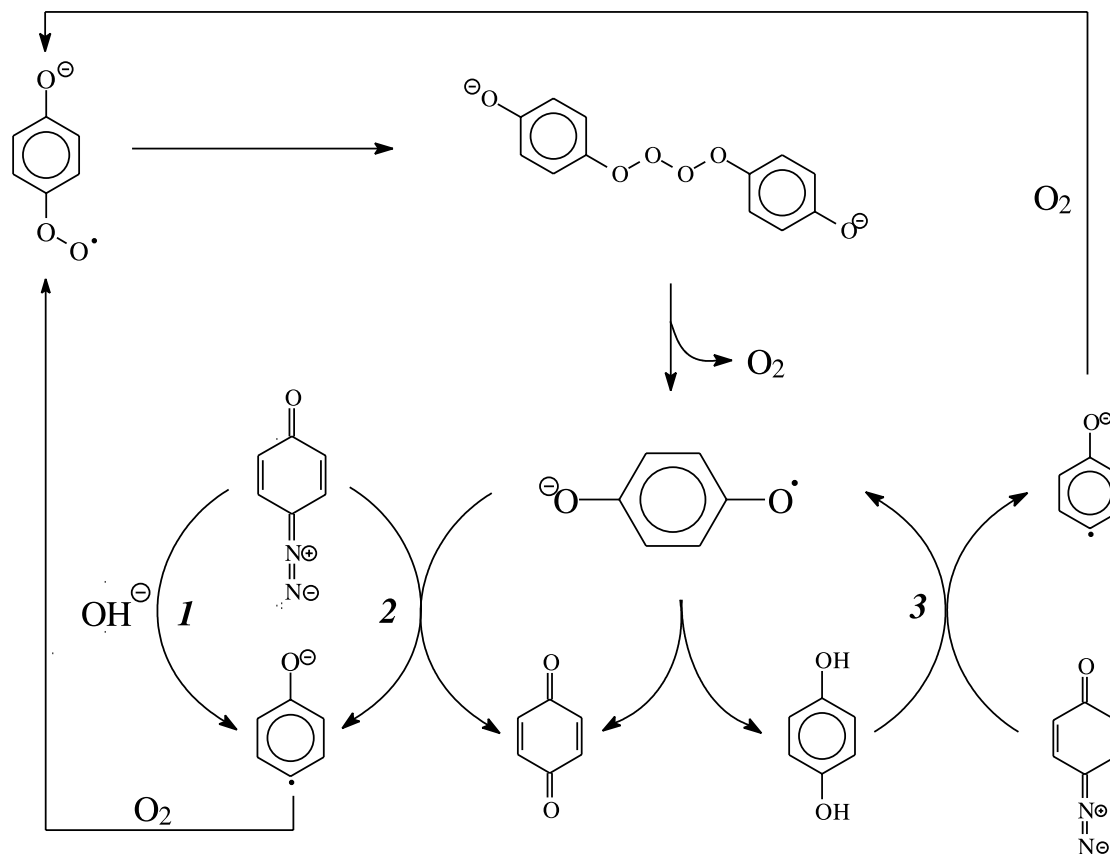
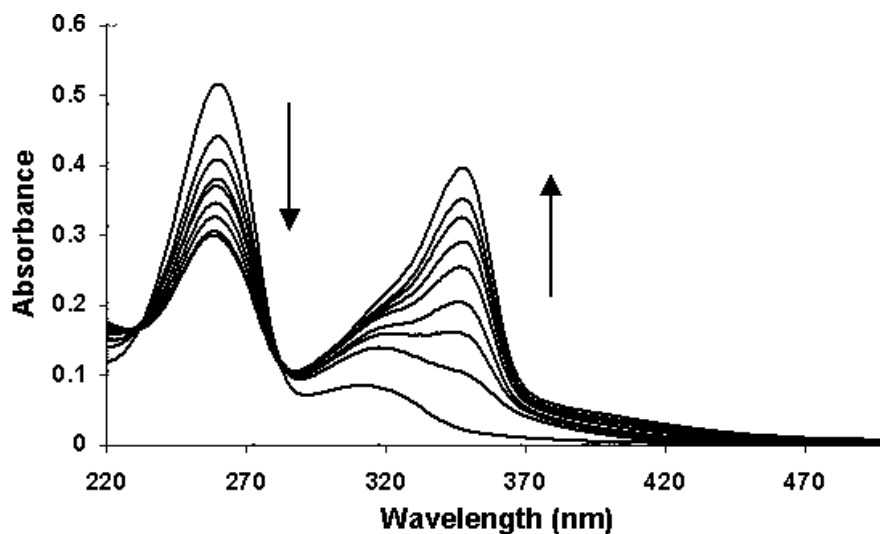


**Fig. 1.** Absorption spectra measured at different times (total time: 2 h) with  $3.26 \times 10^{-5}$  M aliquots taken from 1.36 mM pNO buffered solutions (phosphate buffer, pH 7.2, 0.1 M, treated with Chelex 100) kept in darkness at 37°C.



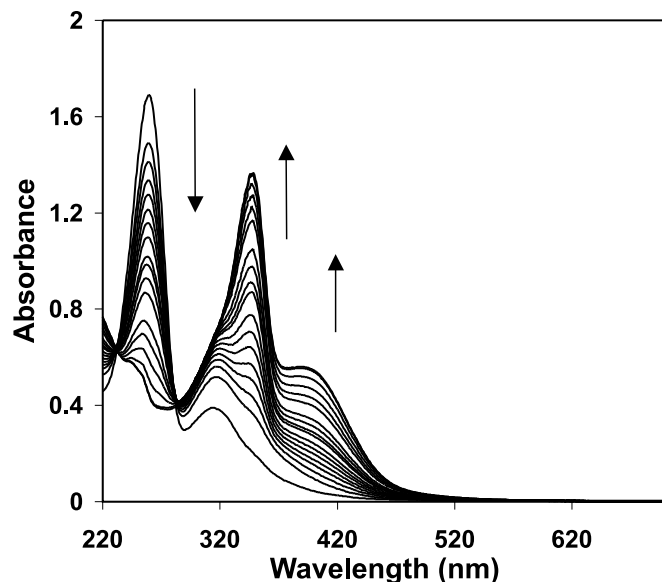
data published in the literature (9–11), and once again we found an NB peak. Since no hydrogen-atom donor could be present under our experimental conditions we are currently investigating the possible interference of an instrumental artifact.

The lack of reactivity of pNO to thermal solvolytic decomposition and the subsequent formation of the aryl ion has been reported elsewhere (11), where it has been put

down to the propensity of the nitro substituent to destabilize the aryl cation more than it does the arenediazonium ion (11, 19). In addition to this we checked the photochemical stability of pNO during our experiments by comparing the spectrum of a sample irradiated in a quartz UV spectrophotometer cuvette under the experimental conditions routinely used throughout the spectrophotometric analysis with that of an aliquot kept in darkness at the same temperature. These data



**Fig. 2.** Absorption spectra measured at different times (total time: 4 h 40 min) with a 0.11 mM pNO buffered solution (phosphate buffer, pH 7.2, 0.1 M, treated with Chelex 100) kept at 37°C.



led us to conclude that the formation of an aryl cation from the thermal and (or) photochemical heterolytic decomposition of pNO should not be expected. Therefore, we have initially considered that the decomposition of both benzenediazonium ions can be described according to Scheme 2.

In this scheme it is accepted, according to the well known Gomberg–Bachman reaction and the mechanism described by Rüchardt and Merz (20), that in the absence of any other reductant the dediazonation process for both benzenediazonium ions has a common starting point, the attack of the hydroxide anion (reaction **a**) to form a covalently bound intermediate, diazohydroxide, in equilibrium with its dissociated form, diazotate (reaction **b**).

In principle, two parallel pathways (Scheme 2), both mediated by the diazotate anion, would explain the products derived from the dediazonation of PDQ and pNO. Thus,  $-\text{OArN}_2^+$  might be formed via aromatic nucleophilic displacement. Clearly, this process would only be detectable with pNO since with PDQ the reactant ( $\text{RArN}_2^+$ , where  $\text{R} = ^-\text{O}$  at the pH of the medium) and reaction product ( $-\text{OArN}_2^+$ ) are identical. Whilst a hydroxide ion may act as the nucleophile to displace the nitrite ion from the initial arenediazonium ion, Kuplet-skaya and Kazitsyna (21) have also described such a substitution involving the diazotate ion as the nucleophile. Here an attack by  $\text{O}_2\text{NArN} = \text{N}-\text{O}^-$  on pNO followed by the displacement of  $\text{NO}_2^-$  would give a diazotate ether,  $\text{O}_2\text{NArN} = \text{N}-\text{O}-\text{ArN}_2^+$ ; heterolytic dissociation of this ether regenerates pNO and gives the  $-\text{OArN}_2^+$  product. Thus we checked whether a kinetic analysis could confirm this bimolecular process. The nucleophilic attack by the diazotate anion can be expressed by the following set of equations:

$$[1] \quad \frac{-d[\text{pNO}]}{dt} = \frac{d[\text{PDQ}]}{dt} = k[\text{diazotate}][\text{pNO}]$$

$$K_b = \frac{[\text{diazotate}][\text{H}^+]}{[\text{diazohydroxide}]} \quad K_a = \frac{[\text{diazohydroxide}]}{[\text{pNO}][\text{OH}^-]}$$

$$[2] \quad \frac{-d[\text{pNO}]}{dt} = kK_aK_b \frac{[\text{OH}^-]}{[\text{H}^+]} [\text{pNO}]^2 = k_g [\text{pNO}]^2$$

in which the rate of PDQ formation is equal to the pNO decomposition rate (eq. [1]), in accordance with the spectroscopic results shown in Fig. 1, where it is apparent that very little interference from pNP should be expected. We tested the final equation (eq. [2]) with the absorbance values measured at 350 nm and thus obtained a plot with a value of  $88.9 \text{ M}^{-1}\cdot\text{min}^{-1}$  for the global constant  $k_g$  (Fig. 3). This value, which is significantly lower than that obtained for the reduction of pNO with hydroquinone (22), suggests the absence of any reductant capable of directly reducing pNO by a “non-bonded” outer-sphere mechanism. Besides this, the kinetic results support a bimolecular reaction, involving diazotate anion as a nucleophile, since no better fitting of the experimental data was obtained by considering a first-order reaction, which might be expected as a result of a nucleophilic substitution by  $\text{OH}^-$ .

The other product ( $\text{RArOH}$ ) formed from the dediazonation of PDQ and pNO might be the result of a reaction between the diazotate anion and the diazonium ion to give diazoanhydride, which then breaks down homolytically to produce the diazenyl radical, from whence is formed the aryl radical, and a further reaction with molecular oxygen leads to a substituted phenol, as indicated for PDQ in Scheme 1. Nevertheless, such a mechanism is not supported by the concentration dependence observed in the proportion of the major products (PDQ and pNP) derived from the decomposition of pNO. If pNP and PDQ were the products that occurred as a result of a parallel reaction during pNO decomposition, an increase in the concentration of pNO would not justify an increase in PDQ concomitant with a decrease in pNP, as can be observed by comparing Figs. 1 and 2. Furthermore, the formation of hydroquinone from PDQ occurs as a result of a homolytic pathway that involves molecular oxygen (Scheme 1), whereas pNP appears when either aerated or deaerated samples of pNO are incubated. An alternative pathway for pNP formation can be formulated on the basis of the homolytic breakdown of diazohydroxide, which leads to the appearance of the aryl and hydroxyl radicals. In fact it has been pointed out (16) that pNO is particularly reactive in neutral buffers, giving EPR signals corresponding to adducts of  $\bullet\text{OH}$  and aryl radicals even without any added electron donors. A few years ago some discussion arose as to whether a hydroxyl radical might not be involved in the dediazonation of benzenediazonium ions. Thus  $\bullet\text{OH}$  adducts detected by EPR have been considered to be artifacts resulting from the fragmentation of a transient hydroxylamine (16). On the other hand, the results obtained by Lawson, Gannett, and co-workers (23, 24) under conditions where no reducing agent was present appear to be consistent with the homolytic fragmentation of a diazohydroxide intermediate. In the light of this latter experimental evidence, therefore, we believe that the recombination of aryl and hydroxyl radicals would provide a simple explanation for the appearance of pNP.

Thus, on the basis of the experimental results obtained, a tentative general mechanism can be proposed, as described in Scheme 3.



Scheme 2.

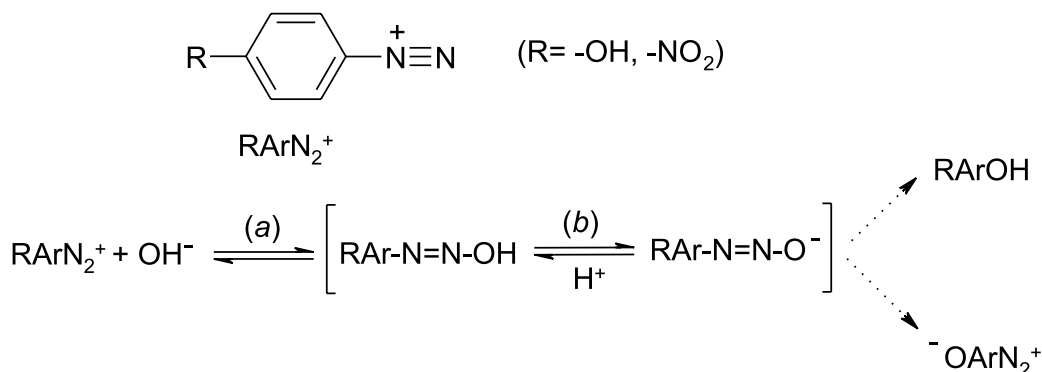
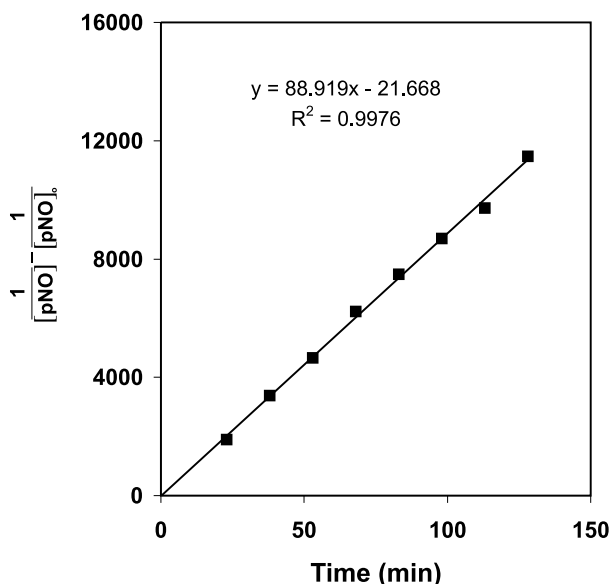


**Fig. 3.** Kinetic analyses of the data obtained from the absorbance measured at 350 nm in the spectra shown in Fig. 1.



It is clear that under our experimental conditions PDQ dediazonation occurs mainly via the reaction sequence (a) → (b) → (f) → (h) → (i), wherein reaction i encompasses the processes detailed in Scheme 1, producing hydroquinone–quinone as stable products of the reaction and secondary reductant (hydroquinone), whereas pNO decomposition might occur either via (a) → (b) → (e) → (g), which generates PDQ, or the homolytic path (a) → (c) → (d), which produces pNP.

The differences observed in the dediazonation mechanisms for PDQ and pNO might be put down to the different chemical natures of the aromatic substituents in the compounds analysed. The electron-withdrawing and donating properties of the  $-\text{NO}_2$  and  $-\text{OH}$  groups strongly determine the reactivity of either compound and consequently exert different influences upon the dediazonation reaction, as observed experimentally.

#### DTPA interference into PDQ and pNO dediazonation

PDQ dediazonation in a neutral aqueous medium was clearly affected by the presence of DTPA either using a phosphate buffer treated with Chelex resin or an untreated phosphate buffer. No change in the spectrum shape was no-

ticeable following the addition of DTPA, suggesting that any interaction between DTPA and PDQ to block the reduction of this latter compound might be ruled out. Apart from this, the introduction of DTPA led to a period of about 2 h during which the reaction seemed to cease. After this period decomposition continued at a rate very close to that observed for the reaction in the absence of DTPA (Fig. 4). Moreover, the presence of DTPA appears to be associated with a decrease in oxygen consumption, as shown in Fig. 5.

On the other hand, the dediazonation of pNO behaved differently in the presence of DTPA, its dediazonation rate increasing (Table 1). Likewise, DTPA brought about an increase in the proportion of pNP in relation to PDQ (cf. Table 1 and Fig. 6). Furthermore, pNO underwent complete and immediate decomposition when the initial DTPA:pNO ratio was 5 or higher. In this case only two absorption bands were recorded, with maxima at 270 nm and 369–370 nm. Similar results (Fig. 7) were obtained by adding ethanol (4%) to the buffered solutions of pNO (maxima at 268 and 388–390 nm).

If we exclude any association between the arenediazonium ions and DTPA or chelating effects upon any residual metal ions present in the buffer, an additional pathway must be considered to justify the observed increase in the decomposition rate, wherein DTPA would promote the homolysis of pNO. As a matter of fact, on using a higher concentration of DTPA (6.6 mM) this additional pathway plays a more important part, as indicated by the appearance of an absorption band with a maximum at about 270 nm. This band also appears when pNO decomposes in the presence of ethanol (4%), which may scavenge aryl radicals by donating a hydrogen atom (11). These spectrophotometric results are consistent with HPLC analyses, which showed, together with the peaks corresponding to PDQ and pNP, the competitive formation of an appreciable quantity of NB, resulting in the almost complete conversion of pNO into NB when the ethanol concentration was increased to 50%.

Bearing in mind the fast rate of dediazonation in the presence of a relatively high concentration of DTPA and also the appearance of NB under such conditions, it is reasonable to suppose that DTPA triggers the homolytic decomposition of pNO. Some experimental evidence is reported in the literature concerning the scavenging capacity of DTPA to react with  $\bullet\text{OH}$  and  $\text{CO}_3^{\bullet-}$  when used in relatively high concentrations ( $>100 \mu\text{M}$ ) (25). The data obtained during pNO dediazonation suggest the possible formation of a DTPA



**Scheme 3.**

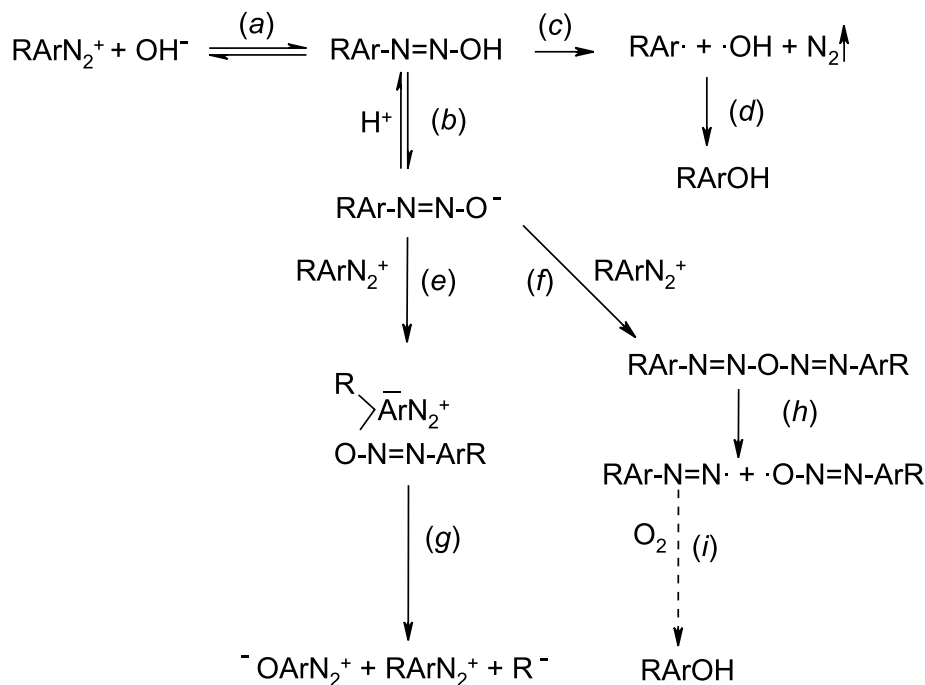


**Fig. 4.** Plot of the absorbance measured at 348 nm vs. time obtained with 1:40 diluted aliquots taken from 0.4 mM PDQ buffered solutions (phosphate buffer pH 7.2; 0.1 M) kept in darkness at 37°C. Influence of the DTPA concentration: (a) without DTPA; (b) in the presence of 1 mM DTPA; and (c) in the presence of 1.5 mM DTPA.

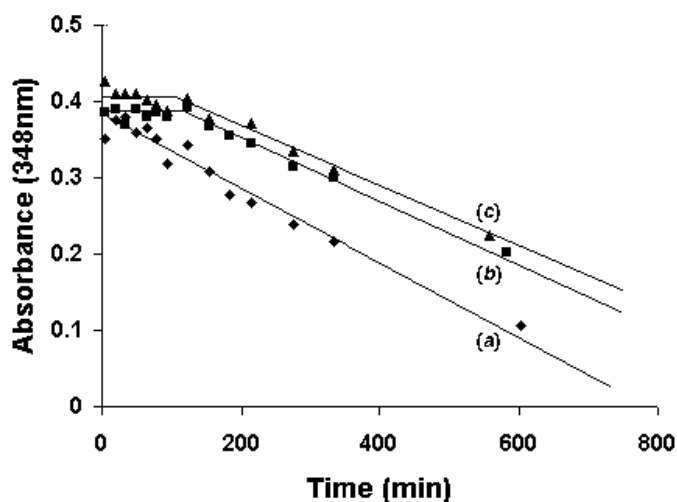
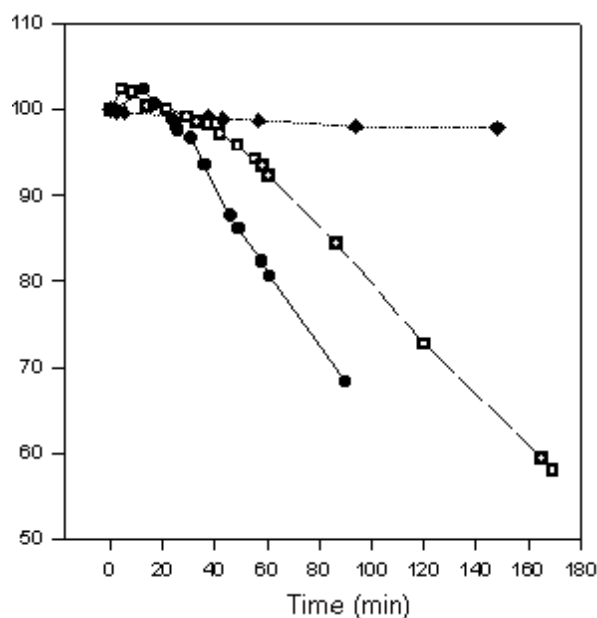
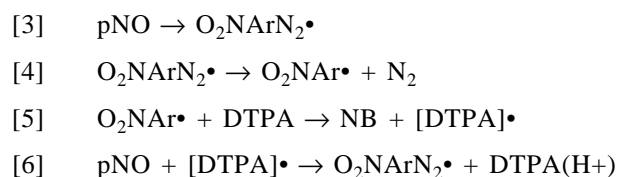


**Fig 5.** Plot of oxygen consumption vs. time for samples containing distilled water (◆), 10 mM PDQ in the presence of 0.5 mM DTPA in phosphate buffer pH 7 (□), and 10 mM PDQ solution in phosphate buffer pH 7 (●).  $T = 37^{\circ}\text{C}$ .



radical that interacts with pNO, thus increasing the decomposition rate according to the following general scheme:



wherein reaction [3] summarizes pathways **(a)**  $\rightarrow$  **(b)**  $\rightarrow$  **(f)**  $\rightarrow$  **(h)** whilst reactions [3] and [4] are equivalent to the pathway

**(a)  $\rightarrow$  (c).** In any case the occurrence of the aryl radical  $\text{O}_2\text{NAr}\cdot$ , derived from pNO (11), allows the interfering DTPA scavenging aryl radical to produce NB (reaction [5]), and also leads to the subsequent attack on pNO (reaction [6]), which could go on to give pNP via pathway **(i)**.

It is apparent that these reactions do not work in the case of PDQ because an increase in the concentration of DTPA is not followed by a concomitant increase in the decomposition of PDQ, as observed for pNO. Nevertheless, a similar reac-



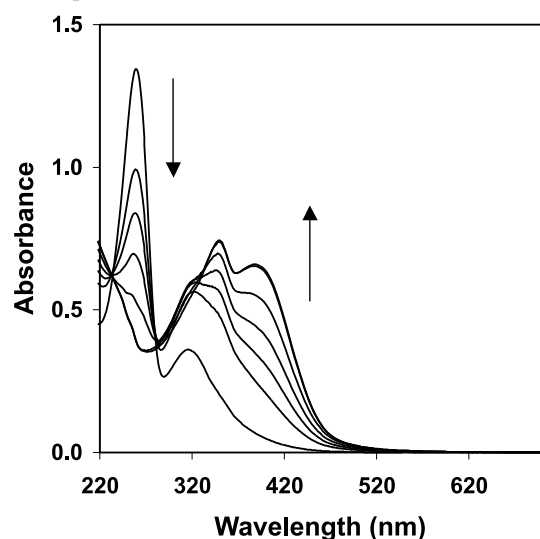
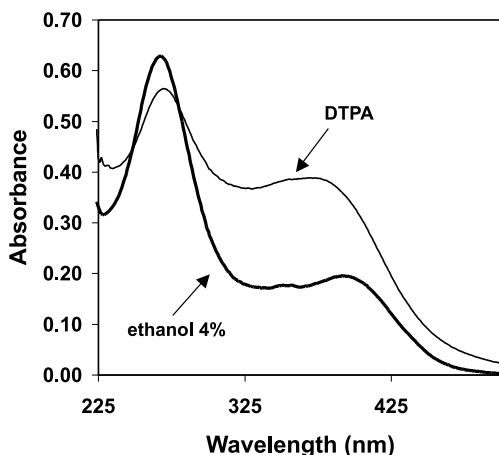
**Table 1.** Influence of DTPA upon pNO (0.11 mM) decomposition rate at 37°C in phosphate buffer (pH = 7.2).<sup>a</sup>

[DTPA] (mol·L <sup>-1</sup> )	Total time (min)	[PDQ] (mol·L <sup>-1</sup> (%))	[pNP] <sub>T</sub> <sup>b</sup> (mol·L <sup>-1</sup> (%))	[pNO] <sup>c</sup> (mol·L <sup>-1</sup> (%))
0	280	$2.5 \times 10^{-5}$ (23)	$6.7 \times 10^{-5}$ (62)	$1.6 \times 10^{-5}$ (15)
$1 \times 10^{-4}$	99	$0.9 \times 10^{-5}$ (9)	$7.8 \times 10^{-5}$ (77)	$1.4 \times 10^{-5}$ (14)
$2 \times 10^{-4}$	45	$0.6 \times 10^{-5}$ (6)	$8.3 \times 10^{-5}$ (81)	$1.3 \times 10^{-5}$ (13)

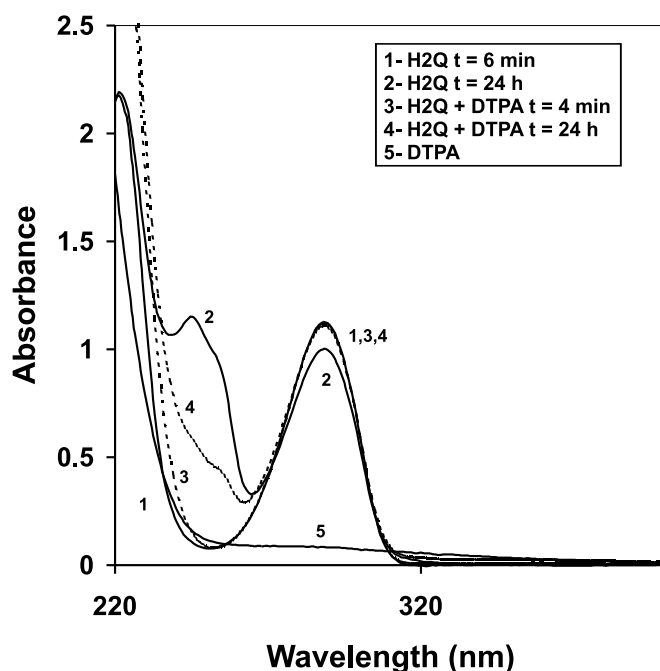
<sup>a</sup>Analyses carried out by monitoring absorbance at 259, 350, and 400 nm and using the following  $\epsilon$  (L·mol<sup>-1</sup>·cm<sup>-1</sup>) values: 2500 (dissociated pNP, 259 nm); 1320 (undissociated pNP, 259 nm); 5230 (dissociated pNP, 350 nm); 3950 (undissociated pNP, 350 nm); 15 480 (dissociated pNP, 400 nm); 70 (undissociated pNP, 400 nm); 3050 (PDQ, 259 nm); 41 990 (PDQ, 350 nm); 15 590 (pNO, 259 nm); 325 (pNO, 350 nm).  $pK_a = 7.15$  for pNP at 25°C was taken from ref. 26.

<sup>b</sup>[pNP]<sub>T</sub> = total concentration of *p*-nitrophenol.

<sup>c</sup>pNP and PDQ are taken to be the main products derived from the decomposition of pNO.

**Fig. 6.** Absorption spectra measured at different times (total time: 1 h 39 min) with a 0.11 mM pNO buffered solution (phosphate buffer, pH 7.2, 0.1 M, treated with Chelex 100) kept at 37°C in the presence of 0.1 mM DTPA.**Fig. 7.** Absorption spectra measured at 5 min with 1:10 diluted aliquots taken from 1.33 mM pNO buffered solutions (phosphate buffer, pH 7.2, 0.1 M, treated with Chelex 100) kept at 37°C in the presence of (a) 6.65 mM DTPA; (b) ethanol 4% (v/v).

tion pattern might occur with PDQ in the presence of DTPA, although not affecting PDQ directly. In fact we have observed that the absorption spectrum of a 0.44 mM hydroquinone (H2Q) solution in phosphate buffer at pH 7 changes

**Fig. 8.** Absorption spectra measured at different times with 0.44 mM hydroquinone (H2Q) buffered solutions (phosphate buffer pH 7) both in the presence and absence of DTPA (2.8 mM).  $T = 37^\circ\text{C}$ . See legends in the inset to identify the spectra.

24 h after the solution is prepared. The band located at 288 nm decreases (approx. 11%), and a new band appears centred at 245 nm. In the presence of DTPA (2.8 mM) the band at 288 nm remains practically constant, and the band at 245 nm is significantly less intense (Fig. 8). These results indicate that a relatively high concentration of DTPA can lead to an interference that affects the intermediate semiquinone radical in hydroquinone auto-oxidation. Bearing this in mind, the decrease observed in the PDQ decomposition rate would be justified since PDQ reduction by the semiquinone scavenger radical would be partially interrupted, thus giving rise to a concomitant decrease in oxygen consumption.

## Conclusion

In summary, we have found that the chelating agent DTPA interferes with the dediazotization of *p*-hydroxybenzenediazonium and *p*-nitrobenzenediazonium ions. Although the different pattern of decomposition observed for both ions,



either in the absence or presence of DTPA, suggests the existence of different mechanisms for each, most of our observations strongly support the idea that this interference may be because of a common mechanism based on the scavenging activity of DTPA. Therefore any possible interference by DTPA should be thoroughly investigated when it is used as a chelator in biochemical and biological systems in which radical reactions occur.

## Acknowledgments

This work was supported in part by the Junta de Andalucía and Universidad de Granada. The authors thank A.L. Tate for revising the English text.

## References

1. H. Zollinger. *In* Diazo chemistry. Vol. 1. Aromatic and hetero-aromatic compound. VCH Publishers, Inc., Weinheim. 1994.
2. J. Griffiths and R. Cox. *Dyes Pigm.* **47**, 65 (2000).
3. Y.-T. Kong, S. Imabayashi, and T. Kakiuchi. *J. Am. Chem. Soc.* **122**, 8215 (2000).
4. H.B. Ambroz, T.J. Kemp, and G.K. Przybytniak. *J. Photochem. Photobiol. A*, **108**, 149 (1997).
5. J. Keiper, L.S. Romsted, J. Yao, and V. Soldi. *Colloids Surf. A*, **176**, 53 (2001).
6. B. Toth, K. Patil, J. Erickson, and P. Gannett. *In Vivo*, **13**, 125 (1999).
7. B. Toth. *In Vivo*, **14**, 299 (2000).
8. C. Bravo-Díaz, L.S. Romsted, M. Harbowy, M.E. Romero-Nieto, and E. González-Romero. *J. Phys. Org. Chem.* **12**, 130 (1999).
9. R. Pazo Llorente, M.J. Sarabia Rodríguez, C. Bravo Díaz, and E. González Romero. *Int. J. Chem. Kinet.* **31**, 73 (1999).
10. P.S.J. Canning, K. McCrudden, H. Maskill, and B. Sexton. *Chem. Commun.* 1971 (1998).
11. P.S.J. Canning, K. McCrudden, H. Maskill, and B. Sexton. *J. Chem. Soc. Perkin Trans. 2*, 2735 (1999).
12. P.M. Gannett, J.H. Powell, R. Rao, X. Shi, T. Lawson, C. Kolar, and B. Toth. *Chem. Res. Toxicol.* **12**, 297 (1999).
13. B. Quintero, J.J. Morales, M. Quirós, M.C. Cabeza, and M.I. Martínez-Puente. *Free Radical Biol. Med.* **29**, 464 (2000).
14. K. Hiramoto, T. Kato, and K. Kikugawa. *Mutat. Res.* **306**, 153 (1994).
15. K.J. Reszka and C.F. Chignell. *Photochem. Photobiol.* **61**, 269 (1995).
16. K.J. Reszka and C.F. Chignell. *Chem. Biol. Interact.* **96**, 223 (1995).
17. R. Munday. *Free Radical Biol. Med.* **26**, 1475 (1999).
18. O. Daněk, D. Snobl, I. Knišek, and S. Nouzová. *Collect. Czech. Chem. Commun.* **32**, 1642 (1967).
19. R. Glaser, C.J. Horan, M. Lewis, and Z.H. Zollinger. *J. Org. Chem.* **64**, 902 (1999).
20. C. Rüchardt, and E. Merz. *Tetrahedron Lett.* **21**, 2431 (1964).
21. N.B. Kuplet-skaya and L.A. Kazitsyna. *Russ. J. Org. Chem.* **22**, 1114 (1986) (translated from *Zh. Org. Khim.* **22**, 1237 (1986)).
22. K.C. Brown and M.P. Doyle. *J. Org. Chem.* **53**, 3255 (1988).
23. T. Lawson, P.M. Gannett, W.-M. Yau, N.S. Dalal, and B. Toth. *J. Agric. Food Chem.* **43**, 2627 (1995).
24. P.M. Gannett, T. Lawson, M. Miller, D.D. Thakkar, J.W. Lord, W.-M. Yau, and B. Toth. *Chem. Biol. Interact.* **101**, 149 (1996).
25. R. Radi, G. Peluffo, M.N. Alvarez, M. Naviliatand, and A. Cayota. *Free Radical Biol. Med.* **30**, 463 (2001).
26. CRC handbook of chemistry and physics. 3rd ed. (electronic). Press LLC, Boca Raton. 2000; L.D. Pettit and H.K.J. Powell. 1992–2000. IUPAC stability constants database and ITS associated software [computer program]. Academic Software, Otley, Yorkshire, U.K. and references cited therein.



# Pressure and temperature dependence of the excess thermodynamic properties of binary dimethyl carbonate + *n*-octane mixtures

Luis Lugo, María J.P. Comuñas, Enriqueta R. López, Josefa García, and Josefa Fernández

**Abstract:** In this work we report several excess thermodynamic properties for the dimethyl carbonate + *n*-octane system in an effort to better understand their behavior over wide temperature and pressure ranges. From previous experimental  $pVTx$  data for this system, the changes in the excess molar Gibbs energies, in the excess molar entropies, and in the excess molar enthalpies due to pressure have been determined over a wide temperature range and for pressures up to 25 MPa. A correlation of the excess volume as a function of pressure was used for each composition and temperature, together with a new, recently proposed equation for the excess molar volume as a function of temperature, pressure, and composition. Excess molar enthalpies and excess molar Gibbs energies at 298.15 K and for pressures up to 25 MPa were calculated using literature data at atmospheric pressure. Furthermore, the excess isothermal compressibility, the excess isobaric expansivity, and the excess internal pressure were calculated. The expression for the internal pressure of an ideal mixture suggested recently by Marczak has been used.

**Key words:** excess thermodynamic properties, dimethyl carbonate, *n*-octane, high pressure.

**Résumé :** Dans ce travail nous donnons les valeurs de plusieurs propriétés thermodynamiques d'excès pour le système binaire carbonate de diméthyle + *n*-octane avec l'objectif de comprendre le comportement de ces grandeurs d'excès dans un large domaine de températures et de pressions. Nous avons déterminé à partir des valeurs  $pVTx$  de ce système, l'évolution avec la pression des énergies de Gibbs d'excès, des entropies molaire d'excès et des enthalpies molaires d'excès dans un large domaine de températures et jusqu'à 25 MPa. Une corrélation du volume d'excès fonction de la pression, à chaque température et composition a été utilisée, et aussi une nouvelle expression proposée dans un article précédent, pour faire le lissage du volume d'excès en fonction du triplet, température, pression et composition. La compressibilité isotherme d'excès, l'expansivité isobare d'excès et la pression interne d'excès, ont été aussi déterminées. L'expression pour la pression interne d'un mélange idéal proposée par Marczak a été utilisée.

**Mots clés :** propriétés thermodynamiques d'excès, carbonate de diméthyle, *n*-octane, haute pression.

## Introduction

In recent years, the number of patents and papers on dimethyl carbonate (DMC) has increased because DMC is environmentally benign, biodegradable, made by a clean chemical process, and is a prototype of a green reagent because it is nontoxic (1). DMC has been proposed as a gasoline additive and as a paint solvent (2). Furthermore, several lubricants containing dimethyl carbonate and other organic carbonates have been patented or proposed (3, 4) and are used in automobile air-conditioning apparatus. Concerning the thermophysical properties of dimethyl carbonate and diethyl carbonate, Comuñas et al. (5) recently published the densities, isothermal compressibilities, and internal pressures from 283.15 to 353.15 K and for pressures up to 60 MPa, to-

gether with the viscosities, and both temperature and pressure viscosity coefficients up to 100 MPa.

The physical properties of DMC + octane mixtures are important in establishing DMC as a potential fuel additive. Also, to develop models that are able to predict properties of pure and mixed lubricants of the carbonate type, experimental properties of carbonate + alkane systems are needed.

For systems containing alkyl carbonate (6–10), a substantial body of thermodynamic data exists, mainly at atmospheric pressure. The work reported here is a study of DMC + *n*-octane mixtures. García et al. (11) and Cocero et al. (12) have measured, respectively, the excess enthalpies and the VLE of this mixture at 298.15 K and atmospheric pressure. The excess volumes at the same temperature and pressure are also available (13). Recently, we measured densities of

Received 12 December 2002. Published on the NRC Research Press Web site at <http://canjchem.nrc.ca> on 10 July 2003.

**L. Lugo, M.J.P. Comuñas, E.R. López, J. García,<sup>1</sup> and J. Fernández.<sup>2</sup>** Laboratorio de Propiedades Termofísicas, Facultad de Física, Universidad de Santiago de Compostela, E-15782 Santiago de Compostela, Spain.

<sup>1</sup>Present address: Dpto. de Física Aplicada, Facultad de Ciencias, Universidade de Vigo, E-36200 Vigo, Spain.

<sup>2</sup>Corresponding author (e-mail: [fajferna@usc.es](mailto:fajferna@usc.es)).



liquid DMC + *n*-octane mixtures (14) at temperatures from 278.15 to 353.15 K and for pressures up to 25 MPa or up to the appearance of liquid–liquid equilibrium (LLE). From these data, excess volumes were determined and correlated with a new  $V_m^E(T, p, x)$  function (15).

In the present work we report several excess thermodynamic properties at high pressures calculated from these experimental  $pVTx$  data. For this purpose the Maxwell relations are very useful (16) in order to relate different thermodynamic properties. Particularly, the change of the excess molar Gibbs energy,  $\Delta G_m^E(T, p, x)$ , of the excess molar entropy,  $\Delta S_m^E(T, p, x)$ , and of the excess molar enthalpy,  $\Delta H_m^E(T, p, x)$  due to pressure were determined over wide ranges of pressure and temperature. Taking into account the excess Gibbs energies reported by Cocero et al. (12) and the excess enthalpies reported by García et al. (11) at 298.15 K and atmospheric pressure, the excess molar Gibbs energy,  $G_m^E(298.15 \text{ K}, p, x)$ , and the excess molar enthalpy,  $H_m^E(298.15 \text{ K}, p, x)$ , were determined up to 25 MPa. Moreover, we have evaluated the excess isothermal compressibilities,  $\kappa_T^E$ , the excess isobaric expansivities,  $\alpha_p^E$ , and the excess internal pressures,  $\pi^E$ . The aim of this work is to analyze how the pressure and the temperature affect these thermodynamic properties, thereby providing information on the intermolecular interactions and on packing and ordering effects for this type of mixture.

## Derived properties

The database for the DMC + *n*-octane system used in this work consists of 717 experimental density values at nine pressures (from 0.1 to 25 MPa) and nine temperatures (from 278.15 to 353.15 K) and nine mole fractions of DMC between 0.10449 and 0.90164. We have also utilized 162 experimental density values for pure octane and pure DMC in the same pressure and temperature ranges. These experimental density values have been published in a previous paper (14). Using this database we have determined the excess molar volumes,  $V_m^E$ , of the DMC + *n*-octane system over the complete composition range (15). To obtain the derived thermodynamic properties, we have correlated the  $V_m^E$  data in two ways: as a rational polynomial function of pressure,  $V_m^E(p) = 1/(a + bp)$ , for each composition and each temperature and as a function of temperature, pressure, and DMC mole fraction,  $V_m^E(T, p, x)$ , using the new correlation

$$[1] \quad V_m^E(T, p, x) = (1/(a + bp))x(1 - x) \times \sum_{i=1}^3 \sum_{j=1}^3 B_{ij}(2x - 1)^{i-1}(T - T_0)^{j-1}$$

proposed previously (15). The reference temperature was  $T_0 = 273.15 \text{ K}$ . This last equation involves 11 parameters and correlates the 717  $V_m^E$  experimental data points for the DMC + *n*-octane system with a standard deviation of  $0.02 \text{ cm}^3 \cdot \text{mol}^{-1}$ , which is only marginally higher than the experimental accuracy. These results and the parameter values were reported in a previous work (15).

## Excess molar Gibbs energy, $G_m^E$

The effect of pressure on the excess molar Gibbs energy can be calculated using the relation

$$[2] \quad \Delta G_m^E(T, p, x) = G_m^E(T, p, x) - G_m^E(T, p_0, x) = \int_{p_0}^p V_m^E(T, p, x) dp$$

where  $p_0$  is the reference pressure. In this work we use  $p_0 = 0.1 \text{ MPa}$ .

The two-parameter rational polynomial function,  $V_m^E(p) = 1/(a + bp)$ , has been fitted to the values of the excess molar volumes at fixed  $T$  and  $x$ . This function has been used to evaluate the integral in eq. [2], thereby obtaining values of  $\Delta G_m^E$  for each temperature–composition pair at different pressures. This method has been used before by several authors for different mixtures (17–20). Taking into account the uncertainties in the temperature ( $\pm 0.01 \text{ K}$ ), pressure ( $\pm 0.001 \text{ MPa}$ ), mole fraction ( $\pm 5 \times 10^{-5}$ ), and excess molar volumes ( $\pm 5 \times 10^{-3} \text{ cm}^3 \cdot \text{mol}^{-1}$ ), this procedure provides values for  $\Delta G_m^E$  with an estimated error of  $\pm 1 \text{ J} \cdot \text{mol}^{-1}$ . The results for  $\Delta G_m^E$  are reported in Table 1. We have also determined  $\Delta G_m^E$  using eqs. [1] and [2]. The absolute average deviation (AAD) between both sets of  $\Delta G_m^E$  values is 2%.

In Fig. 1a,  $\Delta G_m^E$  at 323.15 K is plotted against the mole fraction of DMC, whereas in Fig. 1b the variation of  $\Delta G_m^E$  with the temperature for  $x = 0.50160$  is presented. At a given temperature and composition,  $\Delta G_m^E$  becomes more positive as the pressure increases. When  $\Delta G_m^E$  increases it is possible to reach the conditions in which  $G_m^E(x)$  becomes convex for a composition range, i.e., immiscibility occurs. In fact, we have detected this immiscibility through the large fluctuations in the oscillation period of the densimeter for the highest pressures and the lowest temperature for the following DMC mole fractions:  $x = 0.50160$ ,  $x = 0.60227$ , and  $x = 0.69048$ . Consequently, we do not report thermodynamic property values for these  $Tpx$  conditions. We must point out that González et al. (21) have determined LLE experimental data at atmospheric pressure for DMC + (*n*-decane, *n*-dodecane, *n*-tetradecane, or *n*-hexadecane). From these values we estimate that the upper critical solution temperature (UCST) for the DMC + octane system is about 273 K at atmospheric pressure.

Taking into account the Redlich-Kister correlation made by Cocero et al. (12) for the excess molar Gibbs energy of DMC + *n*-octane at 298.15 K and 0.1 MPa, we have calculated the values of  $G_m^E$  at 298.15 K and at different pressures up to 25 MPa using the equation

$$[3] \quad G_m^E(298.15 \text{ K}, p, x) = G_m^E(298.15 \text{ K}, 0.1 \text{ MPa}, x) + \int_{0.1}^p V_m^E(298.15 \text{ K}, 0.1 \text{ MPa}, x) dp$$

At each isobar and each mole fraction, a polynomial temperature function has been fitted to the  $V_m^E$  values to determine the integral of eq. [3]. The values of the excess molar Gibbs energy obtained in this manner are reported in Table 2 at 298.15 K for several pressures. We have also determined



**Fig. 1.** Change in excess molar Gibbs energy due to pressure for  $x$  DMC +  $(1 - x)$   $n$ -octane, (a) vs. composition at  $T = 323.15$  K and (b) vs. temperature at  $x = 0.50160$ ; ■ 1 MPa; □ 2.5 MPa; ▲ 5 MPa; △ 7.5 MPa; ◆ 10 MPa; ◇ 15 MPa; ● 20 MPa; ○ 25MPa.

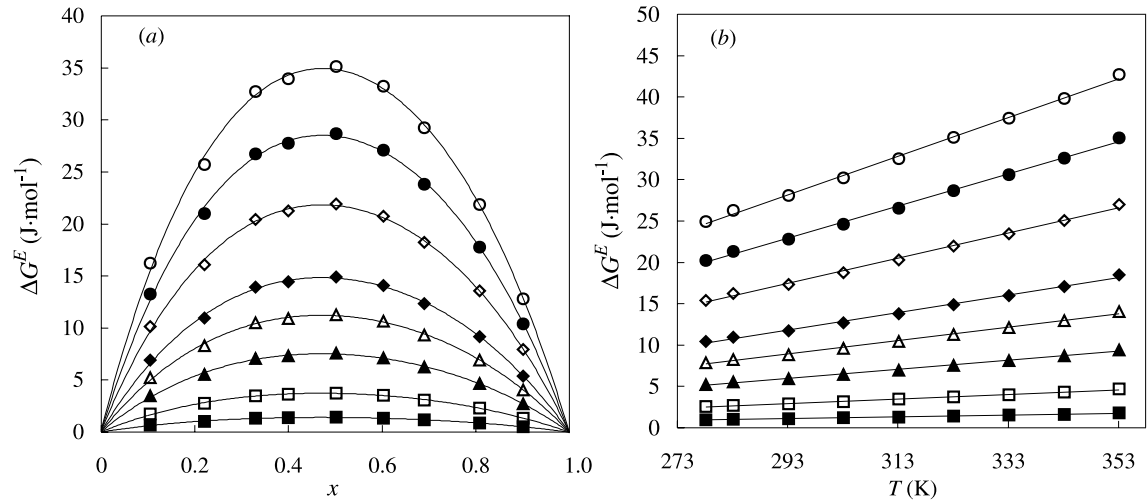


**Table 1.** Change in excess molar Gibbs energy,  $\Delta G_m^E$  (J·mol<sup>-1</sup>), for  $x$ DMC +  $(1 - x)$   $n$ -octane mixtures.

$T$ (K)						$T$ (K)					
$x$	$p$ (MPa)	293.15	313.15	333.15	353.15	$x$	$p$ (MPa)	293.15	313.15	333.15	353.15
0.10449	1.000	0.5	0.6	0.7	0.8	0.60277	1.000	1.0	1.2	1.4	1.7
	5.000	2.8	3.2	3.6	4.2		5.000	5.6	6.6	7.6	8.9
	10.000	5.6	6.4	7.2	8.2		10.000	11.2	13.0	15.1	17.4
	15.000	8.3	9.4	10.6	12.0		15.000	16.5	19.2	22.2	25.5
	20.000	10.9	12.3	13.8	15.6		20.000	21.7	25.2	29.0	33.2
0.22037	25.000	13.5	15.0	16.9	19.0		25.000	26.7	30.9	35.5	40.4
	1.000	0.8	1.0	1.1	1.3	0.69048	1.000	0.9	1.1	1.3	1.5
	5.000	4.5	5.2	6.0	6.9		5.000	5.0	5.8	6.7	7.8
	10.000	9.0	10.2	11.7	13.4		10.000	9.9	11.5	13.2	15.3
	15.000	13.3	15.1	17.2	19.6		15.000	14.6	17.0	19.5	22.4
	20.000	17.4	19.7	22.4	25.4		20.000	19.3	22.3	25.5	29.2
0.32926	25.000	21.4	24.1	27.4	30.9		25.000	23.7	27.4	31.2	35.6
	1.000	1.1	1.2	1.4	1.6	0.80821	1.000	0.7	0.8	0.9	1.1
	5.000	5.7	6.6	7.5	8.7		5.000	3.8	4.3	5.0	5.7
	10.000	11.2	13.0	14.9	17.0		10.000	7.5	8.6	9.8	11.2
	15.000	16.6	19.2	21.8	24.8		15.000	11.2	12.7	14.5	16.5
	20.000	21.8	25.1	28.4	32.1		20.000	14.7	16.7	18.9	21.5
0.39960	25.000	26.8	30.7	34.8	39.1		25.000	18.2	20.6	23.2	26.3
	1.000	1.1	1.3	1.5	1.7	0.90164	1.000	0.4	0.5	0.5	0.6
	5.000	5.8	6.8	7.9	9.1		5.000	2.2	2.5	2.9	3.3
	10.000	11.5	13.4	15.5	17.9		10.000	4.5	5.1	5.7	6.5
	15.000	17.0	19.7	22.7	26.1		15.000	6.7	7.5	8.4	9.5
	20.000	22.3	25.7	29.7	33.9		20.000	8.8	9.9	11.1	12.5
0.50160	25.000	27.5	31.5	36.3	41.3		25.000	10.9	12.2	13.6	15.3
	1.000	1.1	1.3	1.5	1.8						
	5.000	5.9	7.0	8.1	9.4						
	10.000	11.7	13.8	16.0	18.5						
	15.000	17.4	20.3	23.4	27.0						
	20.000	22.8	26.6	30.6	35.1						
	25.000	28.1	32.6	37.4	42.7						

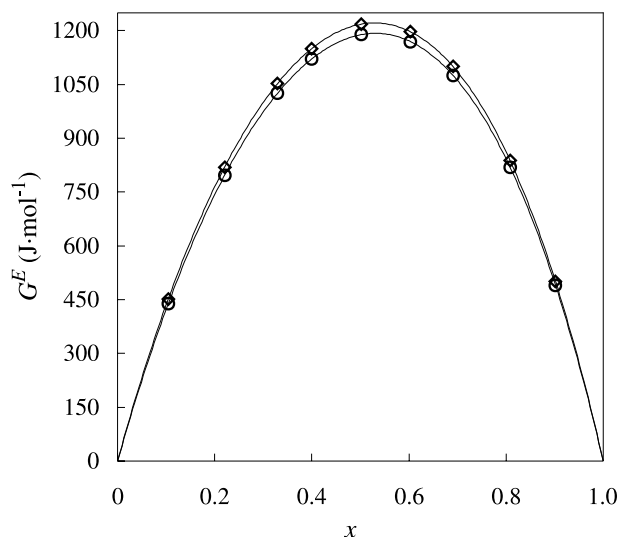
$G_m^E(298.15 \text{ K}, p, x)$  using eqs. [1] and [3], wherein we obtained an average absolute deviation of 0.03% and a bias of 0.003% between both sets of values.

The values of the excess molar Gibbs energy are all positive, as illustrated in Table 2. Also,  $G_m^E$  increases with pressure in the range  $0.1 \text{ MPa} \leq p \leq 25 \text{ MPa}$ , at fixed mole



**Table 2.** Excess molar Gibbs energy,  $G_m^E$  (J·mol<sup>-1</sup>), for  $x$ DMC +  $(1 - x)$   $n$ -octane mixtures at 298.15 K.

$x$	$p$ (MPa)						
	0.100	1.000	5.000	10.000	15.000	20.000	25.000
0.10449	439 <sup>a</sup>	439	442	445	447	450	452
0.22037	797 <sup>a</sup>	798	801	806	811	815	819
0.32926	1025 <sup>a</sup>	1026	1031	1037	1042	1047	1052
0.39960	1121 <sup>a</sup>	1122	1127	1133	1139	1144	1150
0.50160	1189 <sup>a</sup>	1190	1195	1201	1207	1213	1218
0.60277	1170 <sup>a</sup>	1171	1175	1181	1187	1192	1197
0.69048	1076 <sup>a</sup>	1077	1081	1086	1091	1096	1101
0.80821	819 <sup>a</sup>	820	823	827	831	835	838
0.90164	491 <sup>a</sup>	491	493	495	497	500	502

<sup>a</sup>Cocero et al. (12).**Fig. 2.** Excess molar Gibbs energy for  $x$  DMC +  $(1 - x)$   $n$ -octane at  $T = 298.15$  K against the mole fraction. ○ 0.1 MPa [12]; ◇ 25 MPa.

fraction, and at 298.15 K.  $\Delta G_m^E/G_m^E(T, 0.1 \text{ MPa}, x)$  rises linearly with pressure for all mole fractions, ranging from 0.1% at 1 MPa to 2.5% at 25 MPa. In Fig. 2 we show the mole fraction dependence of the excess Gibbs energy for the DMC +  $n$ -octane system. This figure shows that there are no changes in the symmetry of the  $G_m^E(x)$  curve with pressure.

#### Change in the excess molar entropy, $\Delta S_m^E$

The change in the excess molar entropy,  $\Delta S_m^E$ , due to pressure can be calculated from the following thermodynamic relations

$$[4] \quad \Delta S_m^E(T, p, x) = S_m^E(T, p, x) - S_m^E(T, 0.1 \text{ MPa}, x) \\ = - \left( \frac{\partial \Delta G_m^E}{\partial T} \right)_{p, x}$$

$(\partial \Delta G_m^E / \partial T)_{p, x}$  has been evaluated for each pressure,  $p$ , and for each mole fraction,  $x$ , using a quadratic temperature fit of  $\Delta G_m^E$ . In Table 3 the values of the entropic contribution,  $T\Delta S_m^E$ , obtained from the Gibbs energy, are reported, with an estimated error close to 3%. We have also determined  $T\Delta S_m^E$  by using the overall correlation,  $V_m^E(T, p, x)$ , given by eq. [1],

and by using eqs. [2] and [4], but in this case no additional correlations are needed. The absolute average deviation between both sets of values is 5%. As can be seen in Table 3, the values of  $T\Delta S_m^E$  are negative over the entire temperature and pressure ranges, and they become more negative when the pressure and the temperature increase. This is because of the fact that when the mixture is compressed, the molecules become more ordered. From the Maxwell relation for the Gibbs function, it is easy to show that if the excess volume increases with the temperature (as occurs in the DMC +  $n$ -octane system), then the excess entropy must decrease with the pressure.

#### Excess molar enthalpy, $H_m^E$

The excess molar enthalpy due to changes in pressure can be obtained from the following expression

$$[5] \quad \Delta H_m^E(T, p, x) = H_m^E(T, p, x) - H_m^E(T, 0.1 \text{ MPa}, x) \\ = \int_{p_0}^p \left[ V_m^E(T, p, x) - T \left( \frac{\partial V_m^E}{\partial T} \right)_{p, x} \right] dp$$

Moreover, since we have obtained the values of  $\Delta G_m^E$  and  $\Delta S_m^E$ , we can also get the values of  $\Delta H_m^E$  from the thermodynamic relation

$$[6] \quad \Delta H_m^E(T, p, x) = \Delta G_m^E(T, p, x) + T\Delta S_m^E(T, p, x)$$

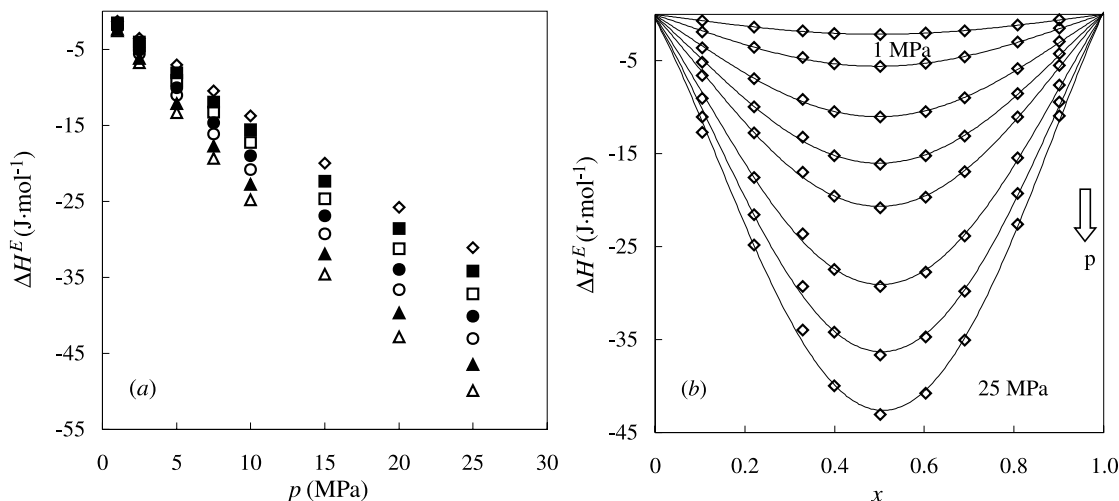
We have calculated  $\Delta H_m^E$  by using both procedures, and the two sets of values are in agreement within 4%. The observed discrepancy includes errors introduced by the approximate numerical procedures (integration and differentiation). Nevertheless, by using eq. [6], additional errors in the calculation of the derivative  $(\partial V_m^E / \partial T)_{p, x}$  are avoided. The values of  $\Delta H_m^E$  at  $x = 0.50160$  and at different temperatures are plotted against the pressure in Fig. 3a.  $\Delta H_m^E$  becomes more negative when the pressure and the temperature increase. In Fig. 3b it can be seen that the  $\Delta H_m^E(x)$  curve is symmetric over the entire pressure interval.

For the DMC +  $n$ -octane system, both the excess molar Gibbs energy and the excess molar enthalpy at 298.15 K and atmospheric pressure are available in the literature (11), so we can calculate  $H_m^E$  for this system over the entire pressure range at this temperature using the following:



**Table 3.** Change in excess molar entropy,  $T\Delta S_m^E$  ( $\text{J}\cdot\text{mol}^{-1}$ ), for  $x\text{DMC} + (1-x)$   $n$ -octane mixtures.

$x$	$p$ (MPa)	$T$ (K)				$x$	$p$ (MPa)	$T$ (K)			
		293.15	313.15	333.15	343.15			293.15	313.15	333.15	343.15
0.10449	1.000	-0.7	-1.1	-1.6	-1.8	0.60277	1.000	-2.6	-3.1	-3.6	-3.9
	5.000	-3.9	-5.9	-8.3	-9.5		5.000	-14.1	-16.4	-18.8	-20.1
	10.000	-7.4	-11.3	-15.7	-18.1		10.000	-27.9	-31.7	-35.9	-38.0
	15.000	-10.4	-16.1	-22.5	-25.9		15.000	-40.8	-45.9	-51.2	-53.9
	20.000	-13.2	-20.4	-28.5	-32.8		20.000	-53.2	-58.9	-64.8	-67.9
0.22037	25.000	-15.6	-24.3	-33.9	-39.0	0.69048	25.000	-64.9	-70.9	-77.2	-80.4
	1.000	-1.6	-2.1	-2.7	-3.0		1.000	-2.1	-2.7	-3.2	-3.5
	5.000	-8.5	-11.1	-13.9	-15.5		5.000	-11.4	-13.9	-16.7	-18.1
	10.000	-16.4	-21.2	-26.4	-29.2		10.000	-22.3	-26.9	-31.8	-34.4
	15.000	-23.8	-30.2	-37.3	-41.0		15.000	-32.8	-38.9	-45.4	-48.9
0.32926	20.000	-30.5	-38.4	-46.9	-51.5	0.80821	20.000	-42.7	-49.9	-57.6	-61.6
	25.000	-36.8	-45.8	-55.5	-60.7		25.000	-52.2	-60.1	-68.6	-73.0
	1.000	-2.4	-2.9	-3.4	-3.7		1.000	-1.6	-1.9	-2.2	-2.3
	5.000	-12.4	-14.9	-17.5	-18.9		5.000	-8.1	-9.7	-11.4	-12.3
	10.000	-24.2	-28.6	-33.3	-35.8		10.000	-15.7	-18.7	-21.8	-23.5
0.39960	15.000	-35.1	-41.0	-47.3	-50.6	0.90164	15.000	-22.6	-26.8	-31.3	-33.7
	20.000	-45.3	-52.3	-59.8	-63.8		20.000	-29.0	-34.3	-40.0	-43.0
	25.000	-54.8	-62.6	-70.9	-75.3		25.000	-34.9	-41.1	-47.9	-51.4
	1.000	-2.5	-3.1	-3.8	-4.1		1.000	-1.9	-1.0	-1.3	-1.4
	5.000	-13.1	-16.2	-19.5	-21.2		5.000	-3.9	-5.0	-6.3	-6.9
0.50160	10.000	-25.5	-31.1	-37.1	-40.3		10.000	-7.5	-9.7	-12.1	-13.3
	15.000	-37.0	-44.6	-52.9	-57.2		15.000	-10.9	-13.9	-17.2	-19.0
	20.000	-47.7	-57.0	-67.1	-72.4		20.000	-14.1	-17.8	-21.9	-24.1
	25.000	-57.7	-68.3	-79.8	-85.8		25.000	-17.1	-21.4	-26.1	-28.7
	1.000	-2.6	-3.2	-3.9	-4.3						
	5.000	-14.0	-17.0	-20.3	-22.0						
	10.000	-27.3	-32.8	-38.7	-41.9						
	15.000	-39.7	-47.3	-55.4	-59.7						
	20.000	-51.4	-60.5	-70.3	-75.5						
	25.000	-62.3	-72.7	-83.9	-89.8						

**Fig. 3.** Change in the excess molar enthalpy for  $x$  DMC +  $(1-x)$   $n$ -octane due to pressure (a) vs. pressure at  $x = 0.50160$  for several temperatures:  $\diamond$  283.15 K;  $\blacksquare$  293.15 K;  $\square$  303.15 K;  $\bullet$  313.15 K;  $\circ$  323.15 K;  $\blacktriangle$  333.15 K;  $\triangle$  343.15 K; (b) vs. the mole fraction at  $T = 323.15$  K for several pressures.

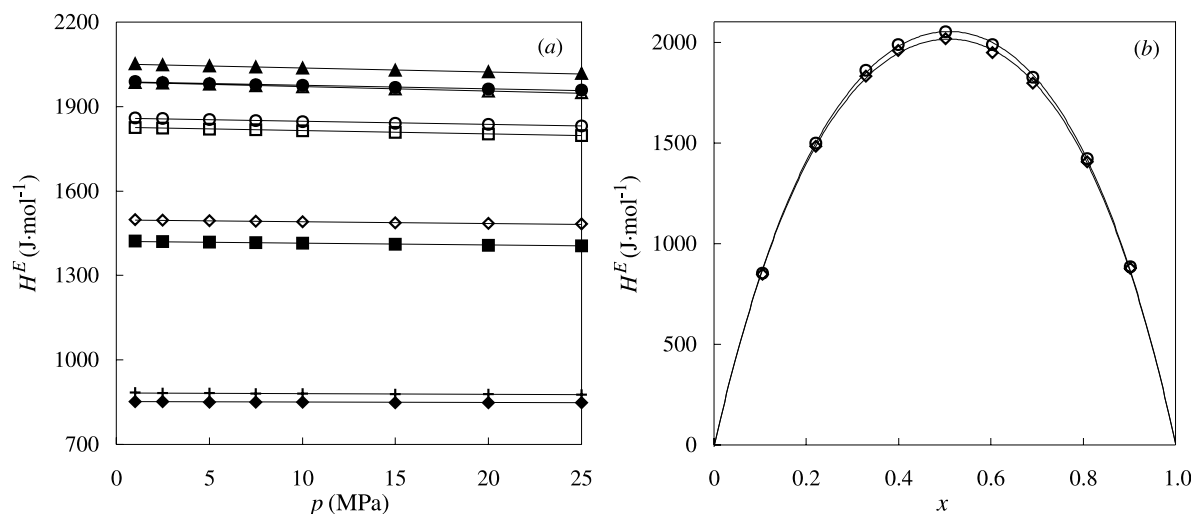
$$[7] \quad H_m^E(298.15 \text{ K}, p, x) = \Delta G_m^E(298.15 \text{ K}, p, x) + T\Delta S_m^E(298.15 \text{ K}, p, x) + H_m^E(298.15 \text{ K}, 0.1 \text{ MPa}, x)$$

We have calculated the values of  $H_m^E$  at 0.1 MPa and at 298.15 K for the nine mole fractions analyzed here by taking into account the Redlich-Kister fit of



**Table 4.** Excess molar enthalpy,  $H_m^E$  (J·mol<sup>-1</sup>), for  $x$ DMC +  $(1 - x)$   $n$ -octane mixtures at 298.15 K.

$x$	$p$ (MPa)						
	0.1000	1.000	5.000	10.000	15.000	20.000	25.000
0.10449	852 <sup>a</sup>	852	851	849	849	848	848
0.22037	1499 <sup>a</sup>	1498	1495	1491	1488	1485	1483
0.32926	1861 <sup>a</sup>	1860	1854	1847	1842	1836	1832
0.39960	1990 <sup>a</sup>	1988	1982	1975	1969	1963	1958
0.50160	2053 <sup>a</sup>	2051	2044	2036	2029	2023	2017
0.60277	1988 <sup>a</sup>	1986	1979	1970	1963	1955	1949
0.69048	1827 <sup>a</sup>	1826	1820	1814	1808	1803	1798
0.80821	1423 <sup>a</sup>	1422	1419	1415	1411	1408	1405
0.90164	884 <sup>a</sup>	884	882	881	879	878	877

<sup>a</sup>García et al. (11).**Fig. 4.** Excess molar enthalpy for  $x$  DMC +  $(1 - x)$   $n$ -octane at  $T = 298.15$  K, (a) against pressure for different  $x$ :  $\blacklozenge$  0.10449;  $\diamond$  0.22037;  $\circ$  0.32926;  $\bullet$  0.39960;  $\blacktriangle$  0.50160;  $\triangle$  0.60277;  $\square$  0.69048;  $\blacksquare$  0.80821;  $+$ , 0.90164; (b) vs. the composition,  $\circ$  0.1 MPa (11);  $\diamond$  25 MPa.

$H_m^E(298.15 \text{ K}, 0.1 \text{ MPa}, x)$  published by García et al. (11) with a standard deviation of  $10 \text{ J·mol}^{-1}$ . The values of  $\Delta G_m^E(p, x)$  at  $T_0 = 298.15 \text{ K}$  have been obtained from the data in Table 2 and  $\Delta S_m^E(298.15 \text{ K}, 0.1 \text{ MPa}, x)$  from eq. [4].

The values of  $H_m^E(p, x)$  obtained using eq. [7] over the pressure range 0.1–25 MPa at 298.15 K are presented in Table 4. We have also calculated  $H_m^E(298.15 \text{ K}, p, x)$  using eqs. [1] and [7]; an absolute average deviation of 0.04% and a bias of  $-0.002\%$  between both sets of data were found. The pressure dependence of the excess molar enthalpy for all the analyzed mole fractions is shown in Fig 4a. It can be observed in this Figure that  $H_m^E$  is positive in all the cases (diminishing slightly throughout isopleths for a given temperature), ranging from 0.5% for  $x = 0.10449$  to 2% at the equimolecular composition. The curves for  $H_m^E(298.15 \text{ K}, p, x)$  along two isobars (0.1 MPa (11) and 25 MPa) are plotted in Fig 4b, which shows that both curves have approximately the same symmetry. For DMC +  $n$ -octane mixtures, the excess volumes are positive and increase as the temperature increases, so there is a compensation between the two terms in eq. [5]. For this reason the pressure dependence of the enthalpy is very weak. For this system, the absolute values of  $T(\partial V_m^E / \partial T)_{p, x}$  are greater than

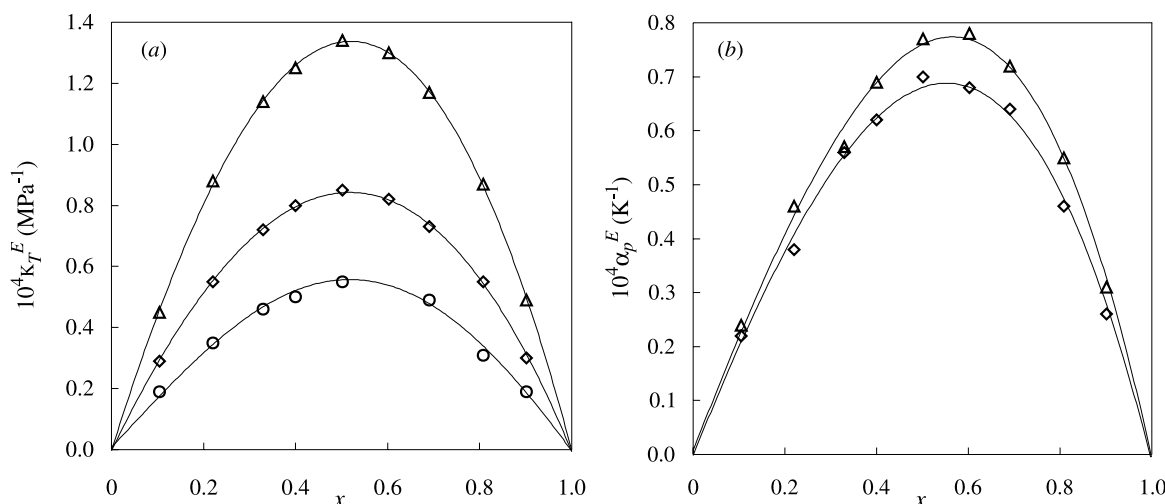
the  $V_m^E$  values over the entire temperature and pressure range. Concerning the temperature dependence of excess enthalpy for this type of system, it is interesting to point out that Lohmann et al. (22) have recently published experimental excess enthalpies for DMC +  $n$ -heptane mixtures. These authors find that  $H_m^E$  increases very slightly as the temperature increases.

We have shown above that the excess enthalpies are positive at 298.15 K up to 25 MPa. Taking into account our  $V_m^E(298.15 \text{ K}, p, x)$  data, it can be concluded that the excess internal energy is also positive over the pressure range. This means that during the mixing process the overall molecular interaction energy diminishes in absolute terms. Furthermore, from the  $H_m^E(298.15 \text{ K}, p, x)$  and  $G_m^E(298.15 \text{ K}, p, x)$  values, it can be concluded that the excess molar entropy at 298.15 K is positive, which means that dimethyl carbonate +  $n$ -octane mixtures are less ordered than the ideal mixture. This is because of the destruction of both the dipolar order of the carbonate and the orientational order of the alkane during the mixing process.

Analyzing the energetic and entropic terms involved in the excess Gibbs energy using eq. [6], it turns out that both  $\Delta H_m^E$  and  $T\Delta S_m^E$  are negative, whereas  $\Delta G_m^E$  is positive for the



**Fig. 5.** (a) Excess isothermal compressibilities,  $\kappa_T^E$ , and (b) excess isobaric expansivities,  $\alpha_p^E$ , for  $x$  DMC +  $(1 - x)$   $n$ -octane vs. the composition at  $p = 5$  MPa for several temperatures:  $\circ$  283.15 K;  $\diamond$  313.15 K;  $\triangle$  343.15 K.



DMC +  $n$ -octane system. This means that when the pressure changes, the entropic contribution to the Gibbs energy dominates, being about twice as large as the enthalpic contribution.

Several authors (17, 20) have found similar variations in  $\Delta G_m^E$ ,  $\Delta H_m^E$ , and  $\Delta S_m^E$  with pressure and temperature for binary systems containing a polar compound and an alkane (2-butanone + 2,2,4-trimethylpentane and 1,2-dichloroethane + 2,2,4-trimethylpentane).

#### Excess quantities for the derived properties $\alpha_p$ and $\kappa_T$

The excess isobaric expansivity and the excess isothermal compressibility, denoted by  $\alpha_p^E$  and  $\kappa_T^E$ , were calculated using the following expressions

$$[8] \quad \alpha_p^E = \alpha_{pm} - \alpha_p^{\text{id}} = \alpha_{pm} - \sum_{i=1}^2 \phi_i \alpha_{pi}^*$$

$$[9] \quad \kappa_T^E = \kappa_{Tm} - \kappa_T^{\text{id}} = \kappa_{Tm} - \sum_{i=1}^2 \phi_i \kappa_{Ti}^*$$

where the superscript \* denotes the properties for pure liquids, which have been reported in a previous paper (14), and  $\phi_i$  is the volume fraction calculated by

$$[10] \quad \phi_i = \frac{x_i V_{m,i}^*}{\sum_{i=1}^2 x_i V_{m,i}^*}$$

Taking into account the temperature, pressure, and mole fraction uncertainties and the accuracy of the derived properties and the molar volumes of pure compounds, the estimated uncertainties for  $\alpha_p^E$  and  $\kappa_T^E$  are  $\pm 1.4 \times 10^{-5} \text{ K}^{-1}$  and  $\pm 3.9 \times 10^{-6} \text{ MPa}^{-1}$ , respectively. As shown in Fig. 5a, the excess isothermal compressibilities are positive over the entire temperature and pressure ranges and are symmetric around the equimolar composition, increasing with temperature and decreasing with pressure along isopleths. The posi-

tive values of  $\kappa_T^E$  and  $V_m^E$  indicate that the mixture is more compressible and less compact than the pure components.

In Fig. 5b we present the excess isobaric expansivities, which are positive and slightly asymmetric with respect to the equimolar composition, with a maximum in the DMC-rich region. As in the case of  $\kappa_T^E$ , the excess isobaric expansivities increase with temperature and decrease with pressure at constant composition. Pardo and co-workers (7, 23, 24) have also found that  $\alpha_p^E$  and  $\kappa_T^E$  are positive at atmospheric pressure for other dialkyl carbonate + alkane systems. The positive values of  $\alpha_p^E$  indicate that the mixture is more expansible than the pure compounds and that its structure is less rigid. These properties are in agreement with the sign of  $V_m^E$ ,  $\kappa_T^E$ , and  $H_m^E$ .

The DMC +  $n$ -octane system shows positive values of  $V_m^E$ ,  $H_m^E$ ,  $G_m^E$ ,  $\alpha_p^E$ , and  $\kappa_T^E$ . The analysis of these properties for dialkyl carbonate + alkane systems in terms of interaction energies, packing effects, and order creation was carried out previously by García and co-workers (11, 13, 25) and by Pardo and co-workers (7, 23, 24). In the mixture process, the rupture of strong dipole-dipole interactions between the DMC molecules is predominant; this causes expansion and endothermicity. This interpretation agrees with the result reported in a previous paper (8) in which we had determined, in the framework of the Nitta-Chao model, the diminution of the number of contacts between the carbonate groups during the mixing process.

Furthermore, the DMC +  $n$ -octane system gives a W-shape for the excess molar capacities (26) from 288.15 to 308.15 K. The interpretation of the properties of systems containing a polar component and an alkane has been subject of controversy. First, Grolier et al. (27) and Wilhelm (28) explained the excess properties for this class of systems in terms of the conformational and molecular orientation changes in the mixing process. Later, Saint-Victor and Patterson (29) proposed a semi-quantitative model that involves two contributions, one random and the other non-random. Their model can explain the appearance of the W-shape in the  $C_{p,m}^E$  curves in the region close to the upper critical solution temperature (UCST).



**Table 5.** Internal pressure,  $\pi^M$  (MPa), for  $x$  DMC +  $(1 - x)$   $n$ -octane mixtures.

$x$	$p$ (MPa)	$T$ (K)				$x$	$p$ (MPa)	$T$ (K)			
		283.15	313.15	333.15	343.15			283.15	313.15	333.15	343.15
0.00000	1.000	283	259	245	238	0.60277	1.000	338	304	285	277
	5.000	284	261	247	241		5.000	340	307	289	280
	10.000	286	263	251	245		10.000	343	310	292	285
	15.000	287	266	254	249		15.000	345	313	296	289
	20.000	289	268	257	253		20.000	348	316	299	293
0.10449	1.000	284	264	249	242	0.69048	1.000	349	318	298	288
	5.000	285	266	252	245		5.000	351	320	301	292
	10.000	286	268	255	248		10.000	353	323	305	296
	15.000	288	270	258	252		15.000	356	326	309	301
	20.000	289	272	261	255		20.000	358	329	312	305
0.22037	1.000	294	270	254	246	0.80821	1.000	376	338	317	308
	5.000	295	271	256	249		5.000	378	340	321	312
	10.000	296	274	260	253		10.000	379	343	324	317
	15.000	298	276	263	257		15.000	381	346	328	321
	20.000	299	278	265	260		20.000	383	348	332	326
0.32926	1.000	305	278	260	251	0.90164	1.000	396	362	341	331
	5.000	306	280	263	255		5.000	398	364	344	334
	10.000	308	282	266	259		10.000	400	367	348	339
	15.000	309	285	270	263		15.000	402	370	351	343
	20.000	311	287	273	266		20.000	403	372	354	347
0.39960	1.000	311	283	265	257	1.00000	1.000	433	396	374	364
	5.000	313	285	268	261		5.000	434	398	377	367
	10.000	315	288	272	265		10.000	436	400	380	370
	15.000	317	291	276	269		15.000	437	402	383	374
	20.000	318	293	279	273		20.000	439	404	385	377
0.50160	1.000	322	293	274	265						
	5.000	324	295	278	269						
	10.000	326	298	281	274						
	15.000	328	301	285	278						
	20.000	330	304	288	282						

**Excess internal pressure,  $\pi^E$** 

In recent years several studies concerning the expressions for the properties of ideal mixtures (30–33), such as isentropic expansivity, speed of sound, or internal pressure, have been published. Marczak (32) has suggested that the correct expression for the internal pressure of a thermodynamically ideal mixture is given by

$$[11] \quad \pi^{\text{id}} = \sum_i \psi_i \pi_i(T, p)$$

where  $\pi_i(T, p)$  is the internal pressure of the component  $i$  in the mixture and  $\psi_i$  is the compression fraction given by

$$[12] \quad \psi_i = \frac{x_i V_{mi} \kappa_{Ti}}{\sum_j x_j V_{mj} \kappa_{Tj}}$$

This suggests that the excess internal pressure should be calculated using the following expression

$$[13] \quad \pi^E(T, p, x) = \pi^M(T, p, x) - \psi_1 \pi_1(T, p) - \psi_2 \pi_2(T, p)$$

where  $\pi^M(T, p, x)$  is the internal pressure of the mixture. The same equation can be obtained using the ideal mixing law proposed by Douheret and Viallard (33) for the isochoric

pressure coefficient,  $\gamma_V = (\partial p / \partial T)_V$ , using the relation  $\pi = T(\partial p / \partial T)_V - p$ . The estimated uncertainty of  $\pi^E$  is  $\pm 1.4$  MPa.

The internal pressure of an ideal mixture is usually considered to be the mole-fraction-weighted average of the internal pressure of the pure compounds. Several authors (34–37) have erroneously used this definition to determine the excess internal pressure. We will define the deviation of internal pressure, following Aminabhavi et al. (38), using the following expression

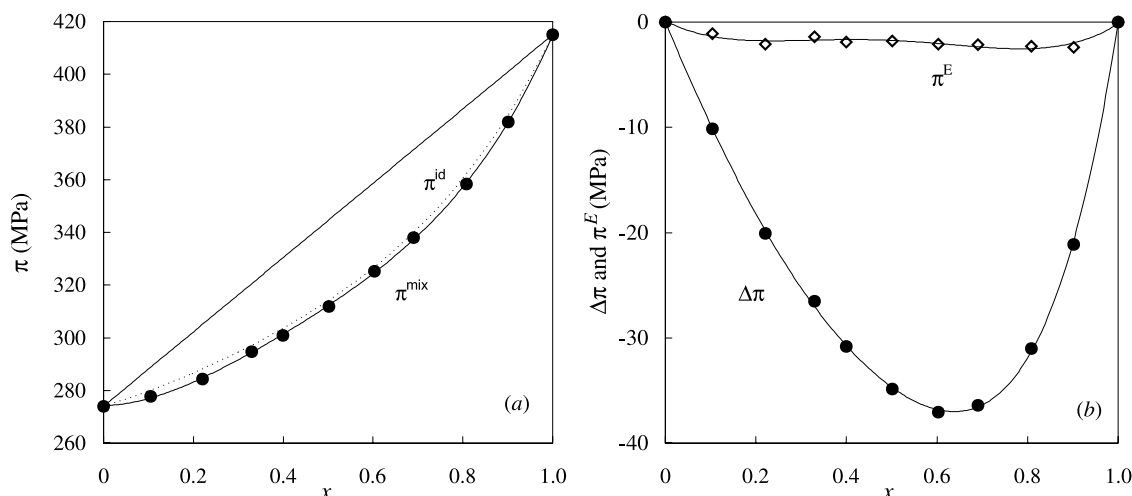
$$[14] \quad \Delta\pi(T, p, x) = \pi^M(T, p, x) - x_1 \pi_1(T, p) - x_2 \pi_2(T, p)$$

We have evaluated both  $\Delta\pi$  and  $\pi^E$  using the internal pressures of the mixtures reported in Table 5. Figure 6a illustrates the dependence on composition of the internal pressure of the mixture  $\pi^M$  and of the ideal mixture  $\pi^{\text{id}}$ . For the DMC +  $n$ -octane mixtures at the indicated  $p$  and  $T$  conditions,  $\pi^M$  and  $\pi^{\text{id}}$  are very similar in magnitude. This means that the variation of the internal energy during expansion for this system is almost identical to that of an ideal mixture.

Figure 6b illustrates the significant differences between the excess internal pressure  $\pi^E$  and the deviation of the internal pressure  $\Delta\pi$ . Examining all the pressure and temperature intervals, we have found that  $\pi^E$  ranges from  $-10$  to  $6$  MPa,



**Fig. 6.** (a) Internal pressure for  $x$  DMC +  $(1 - x)$   $n$ -octane mixture at 303.15 K and at 20 MPa: —,  $x_1\pi_1(T,p) + x_2\pi_2(T,p)$ ; - - -, correct ideal internal pressure, eq. [11] and (●) internal pressure of the mixture; (b) Excess internal pressure for  $x$  DMC +  $(1 - x)$   $n$ -octane mixture at 1 MPa: (◇) calculated with eq. [13] and (●) deviation in the internal pressure taking into account eq. [14].



whereas  $\Delta\pi$  is always negative, reaching a minimum value of  $-40$  MPa. The large differences between  $\pi^E$  and  $\Delta\pi$  are owing to the fact that the compressibilities and the molar volumes are much higher for pure  $n$ -octane than for pure dimethyl carbonate. Marczak (32) has calculated both  $\Delta\pi$  and  $\pi^E$  for methanol + 1-propanol mixtures, obtaining a sigmoidal shape for the  $\Delta\pi(x)$  curve with a maximum value around 0.3 MPa and a minimum value near  $-0.2$  MPa, whereas the  $\pi^E(x)$  curve is parabolic with a minimum near  $-1.1$  MPa.

In a previous paper (14) we used  $pVTx$  data to determine the values of the attractive and repulsive contributions to the internal pressure for DMC +  $n$ -octane mixtures using Mie's potential and the Tait equation. Applying eq. [13] to these previous values, it is easy to obtain the attractive and repulsive contributions to the excess internal pressures. We have shown that the first contribution of  $\pi^E$  is negative and decreases when the temperature and the pressure increase reaches a minimum value of  $-15$  MPa, whereas the second contribution is positive and increases when the pressure rises and when the temperature decreases. Over the entire pressure and temperature range the more important contribution to the total excess internal pressure comes from the attractive excess internal pressure.

## Conclusions

$pVT$  data have been used to calculate the changes with pressure of several thermodynamic excess properties —  $\Delta G_m^E$ ,  $\Delta S_m^E$ ,  $\Delta H_m^E$ ,  $\pi^E$ ,  $\alpha_p^E$ , and  $\kappa_T^E$  — for DMC +  $n$ -octane mixtures over wide temperature and pressure ranges. The results obtained using two different correlations of  $V_m^E$  (as a function of  $p$  at fixed temperature and mole fraction and as function of temperature, pressure, and mole fraction) were very similar, though the first equation involves two parameters for each mole fraction and each temperature, and only 11 parameters are needed for the second correlation. The changes with pressure in the excess Gibbs energy are positive, whereas the enthalpic,  $\Delta H_m^E$ , and entropic,  $T\Delta S_m^E$ , terms are negative. The absolute values of  $G_m^E$  and  $H_m^E$  at 298.15 K

and at several pressures up to 25 MPa have also been obtained and show that  $G_m^E$  increases whereas  $H_m^E$  decreases with pressure.

This system shows very large positive  $H_m^E$  values, positive  $V_m^E$ ,  $U_m^E$ , and  $S_m^E$  values, and the W-shaped  $C_{p,m}^E$  curve is a typical example of the so-called non-randomness proposed by Saint-Victor and Patterson (29). According to the positive values of  $V_m^E$ ,  $\kappa_T^E$ , and  $\alpha_p^E$ , DMC +  $n$ -octane mixtures are less compact, more compressible, and less expansible than the pure compounds.

## Acknowledgements

This work was carried out under research project QUI98-1071-C02-01 and PPQ2001-3022 MCYT-Spain. We thank S.X.I.D. Xunta de Galicia for equipment funding.

## References

1. P. Tundo. *Pure Appl. Chem.* **73**, 1117 (2001).
2. M.A. Pacheco and C.L. Marshall. *Energy & Fuels*, **11**, 2 (1997).
3. L.R. Rudnick and R.L. Shubkin. *Synthetic lubricants and high-performance functional fluids*. 2nd ed. Marcel Dekker, New York, 1999.
4. T. Hayashi, M. Tanaka, K. Takeuchi, K. Takahata, and N. Sakamoto. *Proceedings of the 1996 International Refrigeration Conference at Purdue*, Purdue University, W. Lafayette, Indiana, U.S.A. 285-290. 1996.
5. M.J.P. Comuñas, A. Baylaucq, C. Boned, and J. Fernández. *Int. J. Thermophys.* **22**, 749 (2001).
6. H.-P. Luo, W.-D. Xiao, and K.-H. Zhu. *Fluid Phase Equilib.* **175**, 91 (2000).
7. J.M. Pardo, C.A. Tovar, C.A. Cerdeiría, E. Carballo, and L. Román. *J. Chem. Thermodyn.* **31**, 787 (1999).
8. E.R. López, L. Lugo, M.J.P. Comuñas, J. García, and J. Fernández. *J. Chem. Thermodyn.* **32**, 743 (2000).
9. R. Francesconi, F. Comelli, and S. Ottani. *Thermochim. Acta*, **277**, 121 (1996).
10. J. Lohmann and J. Gmehling. *J. Chem. Eng. Jpn.* **34**, 43 (2001).



11. I. García, J.C. Cobos, J.A. González, C. Casanova, and M.J. Cocero. *J. Chem. Eng. Data*, **33**, 423 (1988).
12. M.J. Cocero, I. García, J.A. González, and J.C. Cobos. *Fluid Phase Equilib.* **68**, 151 (1991).
13. J. García, L. Lugo, M.J.P. Comuñas, E.R. López, and J. Fernández. *J. Chem. Soc. Faraday Trans.* **94**, 1707 (1998).
14. L. Lugo, M.J.P. Comuñas, E.R. López, and J. Fernández. *Fluid Phase Equilib.* **186**, 235 (2001).
15. L. Lugo, M.J.P. Comuñas, E.R. López, and J. Fernández. *Fluid Phase Equilib.* **199**, 135 (2002).
16. J.M. Prausnitz, R.N. Lichtenthaler, and E.G. Azevedo. *Molecular thermodynamics of fluid-phase equilibria*. Prentice Hall, New Jersey, 1999.
17. R. Malhotra and L.A. Woolf. *J. Chem. Thermodyn.* **28**, 701 (1996).
18. J. Kulka and G.M. Schneider. *J. Chem. Thermodyn.* **19**, 205 (1987).
19. A. Compostizo, A.C. Colin, M.R. Vigil, R.G. Rubio, and M.D. Peña. *J. Phys. Chem.* **95**, 319 (1991).
20. R. Malhotra and L.A. Woolf. *Fluid Phase Equilib.* **94**, 253 (1994).
21. J.A. González, I. García, J.C. Cobos, and C. Casanova. *J. Chem. Eng. Data*, **36**, 162 (1991).
22. J. Lohmann, R. Boelts, and J. Gmehling. *J. Chem. Eng. Data*, **46**, 208 (2001).
23. J. M. Pardo, C.A. Tovar, D. González, E. Carballo, and L. Romaní. *J. Chem. Eng. Data*, **46**, 212 (2001).
24. J.M. Pardo, D. González-Salgado, C.A. Tovar, C.A. Cerdeiriña, E. Carballo, and L. Romaní. *Can. J. Chem.* **80**, 370 (2002).
25. I. García, J.A. González, J.C. Cobos, and C. Casanova. *J. Solution Chem.* **24**, 827 (1995).
26. J.M. Pardo. Ph.D. Thesis, University of Vigo, Spain. 1999.
27. J.-P.E. Grolier, A. Inglese, A.H. Roux, and E. Wilhelm. *Induced conformational changes in mixtures containing n-alkanes. Chemical engineering thermodynamics. Edited by S.A. Newman*. Ann Arbor Science, Michigan. 1983.
28. E. Wilhelm. *Thermochim. Acta*, **94**, 47 (1985).
29. M.E. Saint-Victor and D. Patterson. *Fluid Phase Equilib.* **35**, 237 (1987).
30. G. Douhéret, M.I. Davis, J.C.R. Reis, and M.J. Blandamer. *Chem. Phys. Chem.* **2**, 148 (2001).
31. J.C.R. Reis, M.J. Blandamer, M.I. Davis, and G. Douhéret. *Phys. Chem. Chem. Phys.* **3**, 1465 (2001).
32. W. Marczak. *Phys. Chem. Chem. Phys.* **4**, 1889 (2002).
33. G. Douhéret and A. Viillard. *J. Chim. Phys.* **80**, 809 (1983).
34. J.D. Pandey, N. Pant, and B.R. Chaturvedi. *Chemica Scripta*, **18**, 224 (1981).
35. L. Acevedo, G.C. Pedrosa, and M. Katz. *J. Solution Chem.* **19**, 911 (1990).
36. M.I. Aralaguppi, T.M. Aminabhavi, R.H. Balundgi, and S.S. Joshi. *J. Phys. Chem.* **95**, 5299 (1991).
37. V. Rajendran. *J. Pure Appl. Phys.* **31**, 812 (1993).
38. T.M. Aminabhavi, V.B. Patil, K. Banerjee, and R.H. Balundgi. *Bull. Chem. Soc. Jpn.* **72**, 1187 (1999).

## List of symbols

$a$	coefficient in eq. [1]
AAD	absolute average deviation
$b$	coefficient in eq. [1]
bias	average deviation
$B_{ij}$	coefficient in eq. [1]
$C_p$	isobaric capacity
$G_m^E$	excess molar Gibbs energy
$H_m^E$	excess molar enthalpy
$p$	pressure
$p_0$	reference pressure
$S_m^E$	excess molar entropy
$T$	temperature
$T_0$	reference temperature
$U$	internal energy
$U_m^E$	excess molar internal energy
$V$	volume
$V_m$	molar volume
$V_m^E$	excess molar volume
$x$	mole fraction of DMC

## Greek symbols

$\alpha_p$	isobaric thermal expansivity
$\alpha_p^E$	excess isobaric thermal expansivity
$\Delta G_m^E$	change in the excess molar Gibbs energy
$\Delta H_m^E$	change in the excess molar enthalpy
$\Delta S_m^E$	change in the excess molar entropy
$\phi$	volume fraction of DMC
$\kappa_T$	isothermal compressibility
$\kappa_T^E$	excess isothermal compressibility
$\pi_i$	internal pressure of component $i$
$\pi^{id}$	internal pressure of an ideal mixture
$\pi^M$	internal pressure of the mixture
$\pi^E$	excess internal pressure
$\rho$	density
$\psi$	compression fraction



# The dissolution of organic solvents from Amerlock 400 epoxy paint

J.M. Ball, J.C. Wren, and J.R. Mitchell

**Abstract:** The dissolution of organic solvents from containment coatings into the sump water is expected to be a key rate-controlling process, influencing the pH, the steady-state water radiolysis product concentration, and the formation of organic iodides in containment following a postulated reactor accident. The dissolution process is therefore an important component in modelling iodine behaviour in post-accident containment. The rate of release of ethyl benzene and *m*- and *o*-xylene from Amerlock 400 epoxy paint in contact with water has been measured. The release rate was found to be comparable to the release rate of methyl isobutyl ketone from various polyurethane, vinyl, and epoxy paints. The pseudo-first-order rate constant for dissolution of the solvents from these containment coatings is dependent only upon paint thickness and temperature, whereas the total amount of solvent released depends upon paint thickness. The solvent-release process is governed by the rate of uptake of water by the coupons, a Fickian diffusion-controlled process.

*Key words:* dissolution, kinetics, organic solvents, paint.

**Résumé :** On s'attend à ce que la dissolution des solvants organiques, provenant des couches protectrices, dans les puits soit l'étape déterminante des processus qui influencent le pH, la concentration des produits de radiolyse de l'eau à l'état stationnaire, et la formation d'iodures organiques dans la couche protectrice à la suite d'un accident impliquant un réacteur. Le processus de dissolution est alors une composante importante dans la modélisation du comportement de l'iode à la suite d'un accident dans la couche protectrice. On a mesuré la vitesse de dégagement de l'éthyl benzène, du *m*-xylène et du *o*-xylène à partir de la peinture époxy Amerlock-400 au contact de l'eau. On a trouvé que la vitesse de dégagement est comparable à celle de la méthyl isobutyl cétone produite par divers polyuréthanes et par des peintures à base de vinyle et à base d'époxy. Le pseudo ordre 1 de la constante de vitesse de dissolution des solvants provenant de ces couches protectrices dépend uniquement de la consistance de la peinture et de la température, tandis que la quantité totale de solvant dégagée dépend de la consistance de la peinture. Le processus de dégagement du solvant est régi par la vitesse d'absorption d'eau par les échantillons, un processus de diffusion contrôlée de Fickian.

*Mots clés :* dissolution, cinétique, solvants organiques, peinture.

[Traduit par la Rédaction]

## Introduction

The behaviour of iodine under postulated nuclear reactor accident conditions has been the subject of extensive studies by the nuclear industry for many years. Iodine species are important in the assessment of the radiological consequences of a nuclear reactor accident because the radiologically toxic  $^{131}\text{I}$  is one of the most abundant fission products that would be released from fuel. Iodine has the potential to form numerous volatile species, which, once airborne in nuclear re-

actor containments, could be released to the atmosphere through containment leakage or during controlled venting.

It has been established that the pH and the steady-state concentration of water radiolysis<sup>2</sup> products in the containment sump water will determine the overall rate of production of volatile iodine species in containment (1, 2). These factors control the rate of interconversion between the non-volatile  $\text{I}^-$  initially dissolved in the sump water and volatile  $\text{I}_2$  (1, 2).<sup>3</sup> Organic impurities in the sump water would have a profound influence on both factors. Furthermore, organic

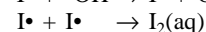
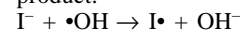
Received 21 January 2003. Published on the NRC Research Press Web site at <http://canjchem.nrc.ca> on 11 July 2003.

J.M. Ball,<sup>1</sup> J.C. Wren, and J.R. Mitchell. AECL, Chalk River Laboratories, Containment and Thermalhydraulics Analysis Branch, Chalk River, ON K0J 1J0, Canada.

<sup>1</sup>Corresponding author (e-mail: [ballj@aecl.ca](mailto:ballj@aecl.ca)).

<sup>2</sup> $4.1 \text{ H}_2\text{O} = 2.6 \text{ e}_{\text{aq}}^- + 0.6 \cdot\text{H} + 2.7 \cdot\text{OH} + 0.7 \text{ H}_2\text{O}_2 + 2.6 \text{ H}^+ + 0.45 \text{ H}_2$ . Coefficients in this equation are the G-values for  $\gamma$ -radiolysis products of water (units of molecules produced per 100 eV absorbed dose).

<sup>3</sup>In the presence of a radiation field,  $\text{I}_2$  is formed from aqueous solutions containing  $\text{I}^-$  by reaction with  $\cdot\text{OH}$ , a water radiolysis product:



and reduced to  $\text{I}^-$  by reaction with water,  $\text{O}_2^-$ , and  $\text{H}_2\text{O}_2$ . The reduction reactions are strongly dependent upon aqueous pH.



**Table 1.** Constituents of Amerlock 400 epoxy paint.

Component	Organic compound	% by weight
Part A (Amerlock 400 White Resin)	Aromatic hydrocarbons	5–10
	Epoxy resin	30–60
	Fatty amine carboxylate	1–5
	Furfuryl alcohol	1–5
	Methanol	1–5
Part B (Amerlock 400FD Cure)	Nonyl phenol	10–30
	Polyamide resin	5–10
	Polyoxyalkyleneamine	1–5
	Tri(dimethylaminomethyl) phenol	1–5
	Xylene	10–30
Amercoat 65 Thinner	Ethylbenzene	10–30
	Xylenes	60–100

**Note:** As reported in Material Safety Data Sheets provided by manufacturer. Only hazardous materials are listed in the table.

impurities in sump water would lead to the formation of organic iodides, some of which are volatile, and could contribute directly to the gaseous iodine fraction.

The dissolution of organic solvents from containment coatings into the sump water is expected to be a key rate-controlling process influencing the pH, the steady-state water radiolysis product concentration, and the formation of organic iodides in containment following an accident (1, 2). The dissolution process is therefore an important component in modelling iodine behaviour in post-accident containment.

Previous studies, on coupons coated with prototypical epoxy, polyurethane, and vinyl containment paints, established that these paints released organic solvents when immersed in water. The rate constant for release of organic solvents from these surfaces was observed to be dependent on temperature but relatively independent of paint or solvent type (3). Dissolution rate constants were also found to be unaffected by radiation. The total amount of organic solvent released was found to be a function of paint ageing, indicating that evaporative losses of solvents from paints did occur over time.

The present study was undertaken to examine the effect of coating thickness, wetted surface area : volume ratio, and absorption of water on the dissolution kinetics of solvents from painted surfaces. The paint used in the studies was Amerlock 400, an epoxy resin based paint. Limited measurements were also performed with Ripolin epoxy paint.

## Experimental

Painted coupons were made from cylindrical slabs of carbon steel with a surface area of approximately 5.7 cm<sup>2</sup>. Each coupon was sandblasted and then within 2 h was painted with Amerlock 400 paint. Subsequently, additional layers of coating were applied, each after the underlying layer had been dried for the recommended curing time. Amerlock 400 epoxy paint consists of two separate components, a resin and a curing agent. A thinner was used to reduce the viscosity of the paint for application to the coupons. The main constituents for each of the Amerlock 400 epoxy paint components are listed in Table 1. Amerlock painted coupons were stored for a period of 4–7 months in a ventilated area at room temperature (i.e., under conditions that did not inhibit solvent release by evaporation).

Ripolin painted coupons were prepared in a similar manner, with four coats of paint applied to give an approximate coating thickness of 0.03 cm. Ripolin paint uses only water as a thinner; however, the epoxy polyamide resin contains an unspecified quantity of ketones and xylenes. Ripolin painted coupons were stored for 6 years prior to being used.

The average thickness of successive layers of Amerlock 400 coating was determined by performing 30 paint-thickness measurements on 6 coupons. Each coupon was measured prior to painting and then measured after the application of 5 successive coatings of paint. The measurements, average thickness, and standard deviations are given in Table 2.

Glass vessels with total volumes ranging from 385 to 455 cm<sup>3</sup> were used for the experiments. Prior to each test the vessels were baked at 500°C to remove any trace organic compounds. One or two painted coupons were placed inside a glass vessel, a known amount of distilled and deionized water was added, and then the vessel was sealed and kept at a constant temperature for a set period of time. The pH was not controlled and did not change appreciably throughout the experiment. The amount of water used in each vessel was varied to maintain a gas–liquid volume ratio of approximately 6:1.

Dissolution studies were done at 25, 40, and 90°C. The temperature was controlled by the use of a circulating water bath for the 25 and 40°C tests. For the 90°C tests it was controlled by the use of a heating tape, a variac power regulator, and an insulated aluminum cylinder block. Each vessel was fitted with an internal thermo-well that allowed temperature monitoring of the liquid phase by thermocouples.

During the experiments, samples were taken at regular intervals and analyzed using a Hewlett-Packard model 5890 gas chromatograph fitted with an O/I Analytical photoionization detector. The gas chromatography instrument was regularly calibrated using gas mixtures of known composition.

Vessels were sealed with a screw-on cap using a Teflon seal and a Mininert push button valve with a replaceable septum. The valve system allowed each vessel to remain sealed while taking a gas sample. All gas samples were taken using a Hamilton gas-tight syringe. At the conclusion of some of the dissolution experiments at 90°C, coupons with 1 and 2 coats of paint had formed blisters on the bot-



**Table 2.** Measured coating thickness (in cm).

Coupon	Coating thickness				
	1 coat	2 coats	3 coats	4 coats	5 coats
1	0.0051	0.010	0.015	0.020	0.028
2	0.010	0.013	0.020	0.023	0.036
3	0.0076	0.015	0.020	0.025	0.038
4	0.0076	0.013	0.020	0.025	0.036
5	0.0051	0.013	0.018	0.020	0.030
6	0.0051	0.010	0.015	0.020	0.028
<b>Average</b>	0.0068	0.012	0.018	0.022	0.033
<b>Standard deviation</b>	0.0029	0.0019	0.0023	0.0023	0.0043

tom surface of the coupon (the portion of the surface in contact with the glass vessel). In dissolution experiments performed on coupons containing only 1 coat of paint at 90°C, the coupons had rust spots showing through the painted surface. It was also noticed that there was sometimes a decrease in the concentration of organic solvents measured in the gas phase during the latter stages of some of the 90°C experiments. The concentration decrease suggests that there were small leaks in the system. These leaks would be expected to have a larger impact on the gas phase concentrations measured at higher temperatures, because a larger portion of the inventory of the organic compound is in the gas phase at higher temperatures.

Water absorption measurements were performed at various temperatures between 25 and 60°C by placing a known quantity of distilled, deionized water into a glass vessel along with one Amerlock 400 epoxy painted coupon. Limited measurements were also performed on coupons painted with Ripolin epoxy paint. The glass vessel with water and coupon was sealed and heated to the desired test temperature. At specified time intervals, the glass vessel was opened and the coupon was removed, surface dried, and weighed. Following the weighing, the coupon was placed back into the glass vessel with fresh distilled, deionized water, sealed, and heated. The duration of each test varied depending upon the test temperature and number of coats of the Amerlock 400 epoxy paint on each coupon. Tests were performed on coupons containing paint of varying thickness. Attempts were made to measure water absorption at 90°C, but at this temperature the paint became detached from the underlying coupon structure. At this temperature the coupons underwent an initial weight loss (greater than that expected, owing to release of solvents) and became bubbled and cracked. The overall weight change as a result of water absorption was also lower for the coupons at 90°C than those at 25 and 60°C.

Measurements of the amount of organic solvent released from the immersed coupons were performed by monitoring gas-phase concentrations; therefore, partitioning of the solvents between the gas and aqueous phase had to be accounted for. The solvent-release kinetics were obtained by assuming instantaneous equilibrium partitioning of the organic compounds between the gas and aqueous phase. Previous experimental studies have established that partitioning is fast with respect to the dissolution process (3). Partition coefficients of 3.67, 3.91, and 6.11 (4) were assumed for ethyl benzene, *m*-xylene, and *o*-xylene, respectively, at room tem-

perature. The partition coefficients at 40 and 90°C were calculated from the reported values of  $\Delta H/R$  (4) according to

$$[1] \quad k_{\text{HT}} = k_{\text{H298}} \exp \left[ \frac{\Delta H}{R} \left( \frac{1}{T} - \frac{1}{298\text{K}} \right) \right]$$

where  $k_{\text{HT}}$  and  $k_{\text{H298}}$  are the dimensionless Henry's law constants (dimensionless ratio between the aqueous phase concentration and the gas phase concentration) at temperatures  $T$  and 298 K, respectively;  $R$  is the gas constant ( $\text{J}\cdot\text{K}^{-1}\cdot\text{mole}^{-1}$ ); and  $\Delta H$  is the enthalpy of solution.

## Results and discussion

### Water uptake

Measurements were performed to determine the rate of the uptake of water by painted coupons at several temperatures, to compare the rate of absorption of water into the polymer with the rate of dissolution of solvents out of the polymer. The fractional uptake of water at various temperatures is shown in Fig. 1. Water absorption by both Amerlock and Ripolin painted coupons displays classical Fickian diffusion behaviour (5). When the concentration of a sorbent at the surface is kept constant, absorption into a membrane containing an initial uniform concentration of the sorbent can be represented by (5)

$$[2] \quad k_{\text{HT}} = k_{\text{H298}} \exp \left[ \frac{\Delta H}{R} \left( \frac{1}{T} - \frac{1}{298\text{K}} \right) \right]$$

where  $M_t$  is the mass of sorbent in the film at time  $t$ ,  $M_\infty$  is the equilibrium mass,  $D$  is the diffusion coefficient,  $t$  is the time, and  $\ell$  is the film or paint thickness.

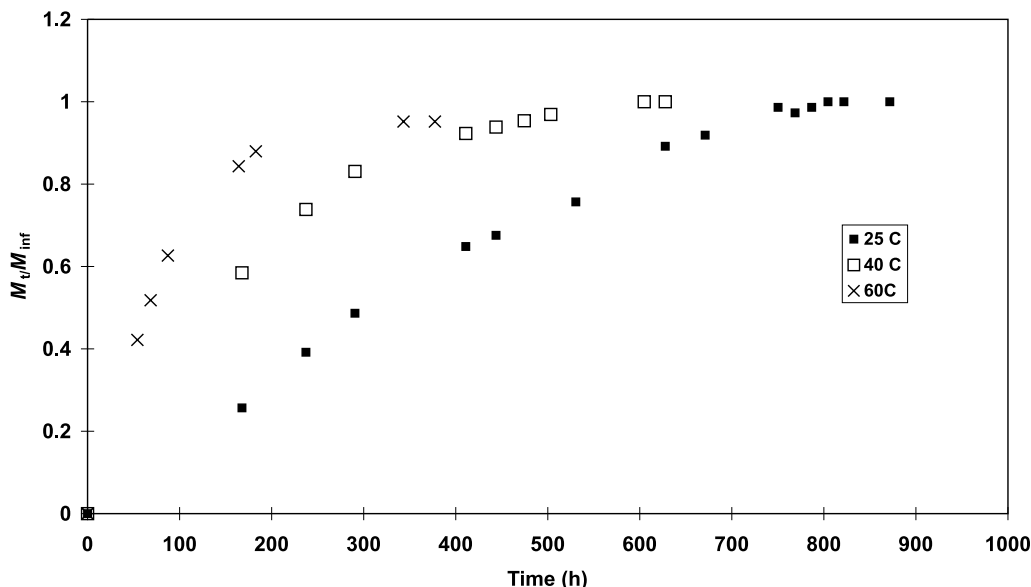
The solution can be approximated by

$$[3] \quad \frac{M_t}{M_\infty} = 2(Dt/\ell^2\pi)^{1/2} \text{ at small values of } t (\text{i.e., } \frac{M_t}{M_\infty} \leq 0.5)$$

$$[4] \quad \frac{M_t}{M_\infty} = 1 - \frac{8}{\pi^2} e^{-\pi^2 Dt/4\ell^2} \text{ at large values of } t (\text{i.e., } \frac{M_t}{M_\infty} \geq 0.5)$$



**Fig. 1.** Fractional uptake of water by Amerlock 400 (epoxy) coupons (coating thickness 0.033 cm) at 25, 40, and 60°C.



From eq. [3], it can be seen that the slope of a plot of  $M_t/M_\infty$  vs.  $2t^{1/2}/\pi^{1/2}\ell$  for values of  $M_t/M_\infty$  up to 0.5 can be used to estimate the diffusion coefficient  $D$ . Plots of the fractional uptake of water ( $M_t/M_\infty$ ) as a function of  $2t^{1/2}/\pi^{1/2}\ell$  at various temperatures and paint thickness are shown in Fig. 2, and the estimates for the diffusion coefficients obtained from taking an average of several measurements at each temperature are listed in Table 3. Note that at a given temperature, the curves for coatings of different thickness are, within experimental error, superimposable on one another.

An Arrhenius plot of the temperature dependence of the diffusion coefficient is shown in Fig. 3. An activation energy of  $51 \pm 7 \text{ kJ}\cdot\text{mol}^{-1}$  was estimated from the plot. Note that an additional uncertainty in the value for  $D$  exists, owing to the uncertainty in the coating thickness  $\ell$ , which varies by about 30% from coupon to coupon (see Table 2).

### Solvent release

Previous solvent-release experiments performed on painted coupons established that solvent evaporation from paints was very slow under dry conditions and that significant quantities of solvents (millimolar, based on paint volume) were retained in painted coupons aged for several years (2, 3). In the presence of water, however, it was observed that solvent was released relatively rapidly, indicating that diffusion of the solvent out of the paint matrix was en-

hanced in the presence of water (2, 3). The dissolution of methyl isobutyl ketone (MIBK) and other solvents from polyurethane, vinyl, and epoxy paints was found to obey simple first-order kinetics, with the total amount of solvent released into the aqueous phase as a function of time expressed as<sup>4</sup>

$$[5] \quad [\text{ORG}(\text{aq})_t] = [\text{ORG}(\text{aq})_\infty] \cdot (1 - \exp(-kt))$$

where  $[\text{ORG}(\text{aq})_t]$  is the amount of solvent in the water at time  $t$ ;  $[\text{ORG}(\text{aq})_\infty]$  is the amount of solvent released in total at the end of the test (i.e., after dissolution is complete) and is related to the amount of solvent initially in the paint;<sup>5</sup> and  $k$  is the pseudo-first-order rate constant for solvent release.

The current study has found that the dissolution of ethyl benzene, *m*-xylene, and *o*-xylene from Amerlock 400 paint immersed in water also obeys the same first-order kinetic behaviour. Table 3 summarizes the rate constants  $k$  obtained from non-linear regression analysis of experimental data using eq. [5]. It also shows the total amount of solvent  $\text{ORG}(\text{p})_\infty$  calculated<sup>6</sup> to have been released at test end. Figure 4 shows typical fits to the data using eq. [5] and the values of  $[\text{ORG}(\text{aq})_\infty]$  presented in Table 3. For a given set of conditions, values determined for the rate constants ( $k$ ) for release of ethyl benzene, *m*-xylene, and *o*-xylene were statistically indistinguishable. Consequently, an average value of

<sup>4</sup>Note that the release kinetics can also be expressed in terms of the amount of solvent in the gas phase.

<sup>5</sup>The sum of the amounts of organic compound in the gas ( $\text{ORG}(\text{g})_\infty$ ) and aqueous ( $\text{ORG}(\text{aq})_\infty$ ) phases at test end will be equal to the amount in the paint ( $\text{ORG}(\text{p})_0$ ) at the start of the test ( $\text{ORG}(\text{aq})_\infty + \text{ORG}(\text{g})_\infty = \text{ORG}(\text{p})_0$ ). The amount in each phase can be calculated from the concentrations by multiplying the concentration by the volume (e.g.,  $\text{ORG}(\text{g})_\infty = [\text{ORG}(\text{g})_\infty] \times V_g$  where  $V_g$  is the volume of the gas phase). Using  $[\text{ORG}(\text{g})_\infty] = [\text{ORG}(\text{aq})_\infty]/H$ , where  $H$  is the partition coefficient, and solving the mass balance equation, one obtains

$$[\text{ORG}(\text{aq})_\infty] = \frac{[\text{ORG}(\text{p})_0] \cdot V_p}{V_g/H + V_{\text{aq}}}$$

<sup>6</sup> $\text{ORG}(\text{p})$  is the total amount of solvent released. This was obtained by summing the total amount in the gas and aqueous phase at test end. The amount in the gas phase at test end was calculated using non-linear least squares regression analysis of the data. The amount of solvent in the aqueous phase was calculated from the final gas phase concentration by using the partition coefficient at the appropriate temperature.



**Fig. 2.** Plots of the fractional uptake of water ( $M_t/M_\infty$ ) as a function of  $2t^{1/2}/\pi^{1/2}l$  at various temperatures and paint thicknesses. Lines show a fit to the data using eq. [2].

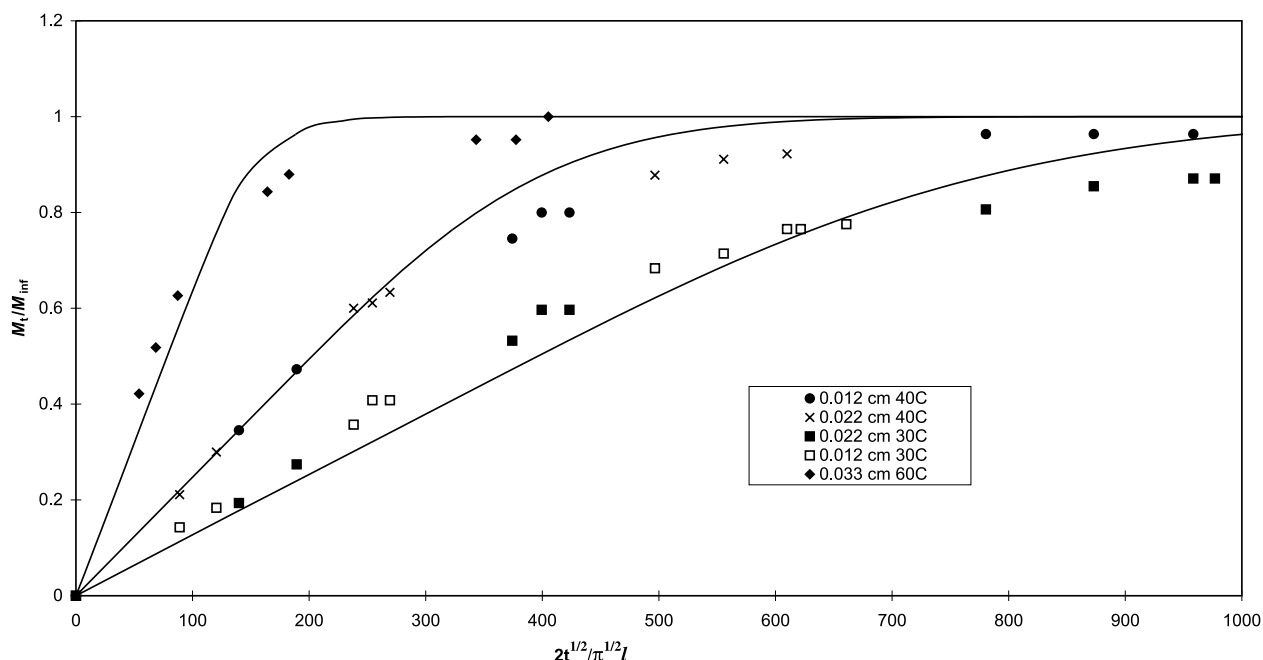


**Table 3.** Summary of solvent-release data for immersed Amerlock 400 painted coupons.<sup>a</sup>

Sample No.	No. of coupons	No. of coats	Coating thickness ( $\mu\text{m}$ )	$T$ ( $^{\circ}\text{C}$ )	$k^b$ ( $\text{h}^{-1}$ )	e-benz(p) $_{\infty}^a$ ( $\mu\text{mol}$ )	m-xyl(p) $_{\infty}^a$ ( $\mu\text{mol}$ )	o-xyl(p) $_{\infty}^{a,c}$ ( $\mu\text{mol}$ )	$L$	$D$ ( $10^{-6}\text{cm}^2\cdot\text{h}^{-1}$ )
1	1	1	$68 \pm 29$	25	0.01	0.030	0.17	0.18	0.2	2.2
2	1	2	$120 \pm 19$	25	0.005	0.084	0.42	0.42	0.2	2.2
3	1	2	$120 \pm 19$	25	0.004	0.10	0.61	0.52	0.2	2.2
4	1	4	$220 \pm 23$	25	0.003	0.12	0.72	0.6	1.5	2.2
5	1	1	$68 \pm 29$	40	0.027	0.07	0.48	0.48	0.15	6
6	1	2	$120 \pm 19$	40	0.012	0.08	0.54	0.53	0.4	6
7	1	2	$120 \pm 19$	40	0.012	0.05	0.37	0.33	0.4	6
8	1	4	$220 \pm 23$	40	0.01	0.18	1.45	1.05	1.5	6
9	1	1	$68 \pm 29$	90	0.22	0.14	0.83	0.86	0.15	$9^d$
10	1	2	$120 \pm 19$	90	0.15	0.12	0.84	0.75	0.4	$9^d$
11	2	1	$68 \pm 29$	90	0.35	0.12	0.73	0.73	0.15	$9^d$
12	2	2	$120 \pm 22$	90	0.20	0.16	0.94	0.88	0.4	$9^d$
13	1	4	$220 \pm 23$	90	0.10	0.30	1.7	1.4	0.9	$9^d$

<sup>a</sup>e-benz = ethyl benzene, o-xyl = o-xylene, m-xyl = m-xylene.

<sup>b</sup> $k$  is an average value for ethyl benzene, o-xylene, and m-xylene.

<sup>c</sup>o-xyl(p) $_{\infty}$  is the total amount of o-xylene released. This was obtained by summing the total amount in the gaseous and aqueous phases at test end. The amount in the gas phase at test end was calculated using non-linear least squares regression analysis of the data. The amount of solvent in the aqueous phase was calculated from the final gas phase concentration by using the partition coefficient at the appropriate temperature.

<sup>d</sup>Estimated from Arrhenius plots of diffusion coefficients obtained from 20 to 65°C.

$k$  is listed in Table 3 and was used to generate the data fits shown in Fig. 4.

From Table 3, it is apparent that the rate constant,  $k$ , does not depend upon surface area; i.e., within the error limits of the coating thickness, the rate constant for solvent release from one coupon with two coats of paint was the same as from two coupons with two coats of paint. Intuitively, the value of ORG(p) $_{\infty}$  should increase with increasing paint thickness, since one would expect that a larger volume of paint would lead to a greater amount of solvent being released. This general trend was observed in some instances,

with coupons containing four coats of paint releasing more solvent than those containing only one coat of paint. However, in two cases, the amount of solvent released from coupons containing only 1 coat of paint was similar or higher than the amount released from coupons painted with 2 coats of paint. Likewise, for a given paint thickness, the value of ORG(p) $_{\infty}$  (total amount of solvent released at test end) should increase with increasing surface area; therefore, the overall amount of solvent released from two coupons with one coat of paint each should be higher than from one coupon with one coat of paint. This is not borne out by the data,



Fig. 3. Arrhenius plot for the diffusion coefficient of water in Amerlock 400 painted coupons.

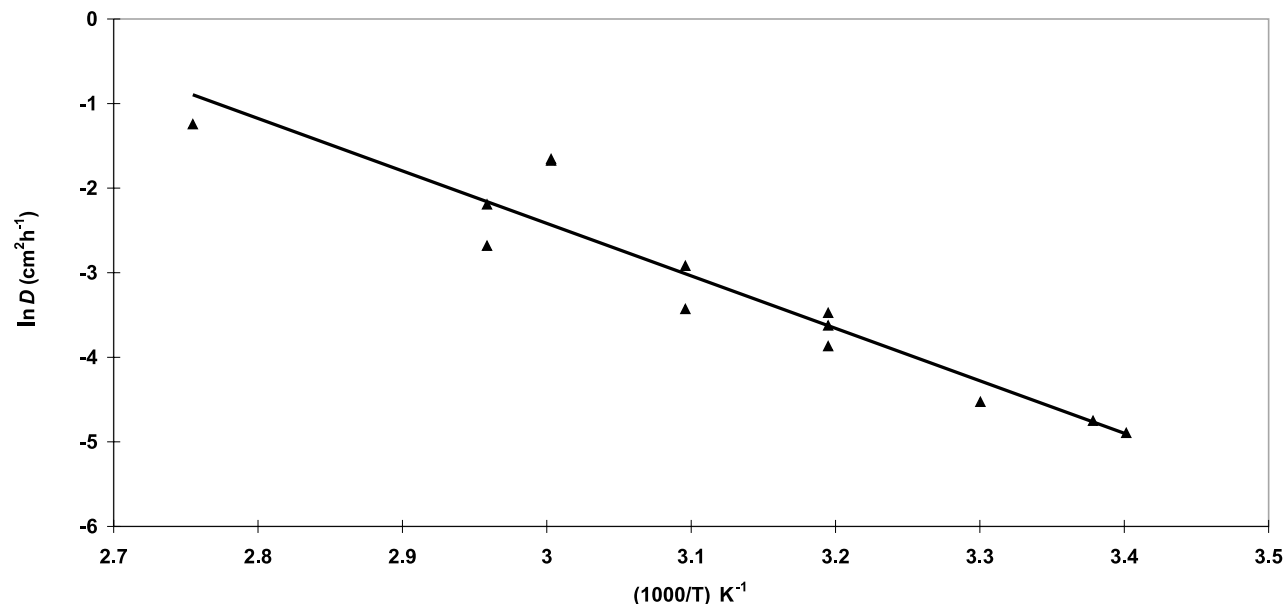
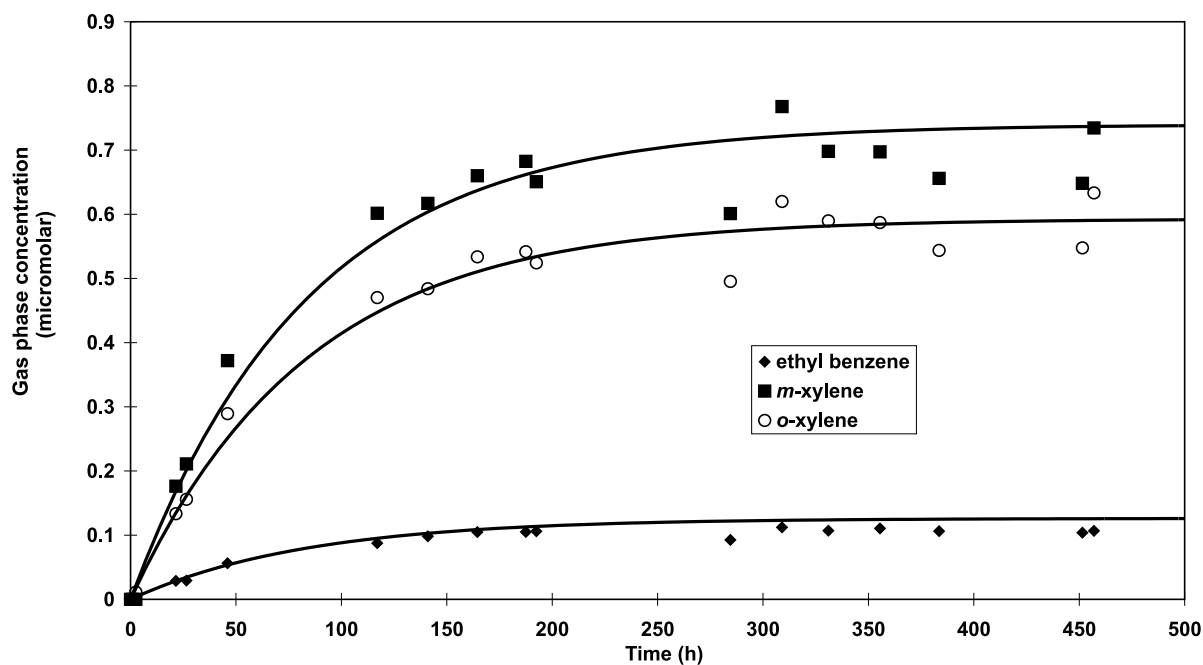


Fig. 4. Gas-phase concentrations of ethyl-benzene, *m*-xylene, and *o*-xylene from an Amerlock 400 painted coupon (coating thickness 0.022 cm) immersed in water at 25°C. The lines drawn through the data are those calculated using eq. [5].



however. In previous studies it was observed that there was a wide variation in the amount of solvent released from coupons covered with nominally uniform thickness of polyurethane, epoxy, and vinyl paints (3). This was attributed to differences in the ageing of individual coupons, and the same phenomena could be responsible for the fact that in these studies, an increased immersed paint volume does not necessarily lead to more solvent being released from the paint.

The pseudo-first-order rate constant  $k$ , used to obtain a fit of the data to eq. [5], was found to be inversely dependent upon the coating thickness, with  $k$  increasing as coating

thickness decreased (Table 3). An inverse relationship between coating thickness and rate of uptake or evaporation from the coating is indicative of a diffusion-controlled process (5). Note that the magnitude of the values for the first-order rate constant  $k$  measured in these experiments was similar to those measured for MIBK release from coupons coated with various paints but with similar paint thickness (Table 4).

The effect of temperature on the pseudo-first-order rate constant  $k$  for release of *m*-xylene from coupons having three different coating thickness is shown in the Arrhenius plot in Fig. 5. The average of the slopes of the three plots,

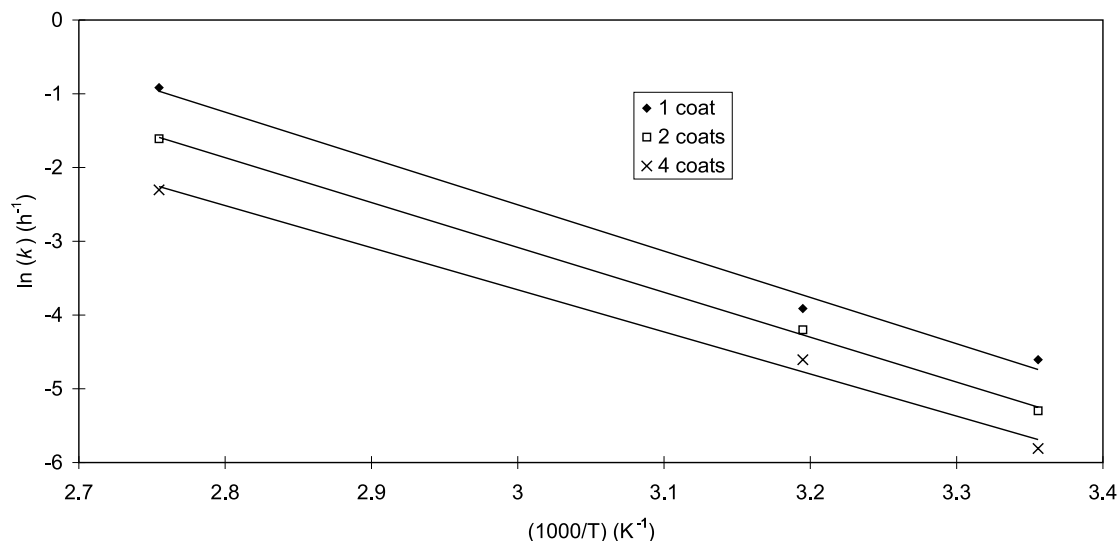


**Table 4.** Comparison of rate constants for solvent release from various painted surfaces of similar thickness.<sup>a,b</sup>

<i>T</i> (°C)	Amerlock <sup>a</sup> (epoxy) <i>k</i> (h <sup>-1</sup> )	Amercoat 66 <sup>b</sup> (epoxy) <i>k</i> (h <sup>-1</sup> )	Intravinyx <sup>b</sup> (vinyl, vinyl- acetate) <i>k</i> (h <sup>-1</sup> )	Normac <sup>b</sup> (polyurethane) <i>k</i> (h <sup>-1</sup> )
25	0.004	0.001	0.003	0.001
40	0.01	0.004	0.008	0.008
90	0.1	0.3	0.77	0.28

<sup>a</sup>Coupon thickness  $0.022 \pm 0.002$  cm. *k* is the first-order rate constant used to obtain best fit (eq. [5]) to the data for release of ethylbenzene, *m*-, and *o*-xylene.

<sup>b</sup>Coupon thickness  $\approx 0.03$  cm. *k* is the first-order rate constant used to obtain best fit (eq. [5]) to the data for release of methyl isobutyl ketone. The first-order rate constant *k* for release of other organic compounds was similar.

**Fig. 5.** Arrhenius plot of the dissolution rate constants observed for the release of *o*-xylene from Amerlock 400 painted coupons.

$\ln k$  vs.  $(1/T)$ , provides an activation energy,  $E_a$ , of  $50 \pm 4$  kJ·mol<sup>-1</sup> for the dissolution process. This value is slightly smaller than the average value of  $65 \pm 4$  kJ·mol<sup>-1</sup> reported for *m*-xylene release from polyurethane, epoxy, and vinyl painted surfaces (3). It was previously reported that, for a given ageing time, the temperature-dependent dissolution rate constant is nearly independent of the type of organic solvent and the type of paint. The smaller activation energy obtained from these experiments in comparison to previous experiments would suggest otherwise; however they are based on a considerably smaller sample size, and there were some experimental difficulties associated with obtaining measurements at 90°C. It is worth noting that the activation energy estimated only from data at 25 and 40°C is  $57 \pm 5$  kJ·mol<sup>-1</sup>. The small differences observed in the slopes of the plots for coupons containing different numbers of coats are not significant in view of the uncertainty in the width of each coating layer (see Table 2).

A comparison of the rate of water uptake and solvent release is shown in Fig. 6. For a given thickness of paint, solvent release is slower than water absorption. There is also a delay between the onset of water absorption and solvent release, indicating that solvent diffusion out of the paint polymer occurs only after water is adsorbed. These findings, coupled with previous observations that significant quantities of solvent are retained for several years in painted cou-

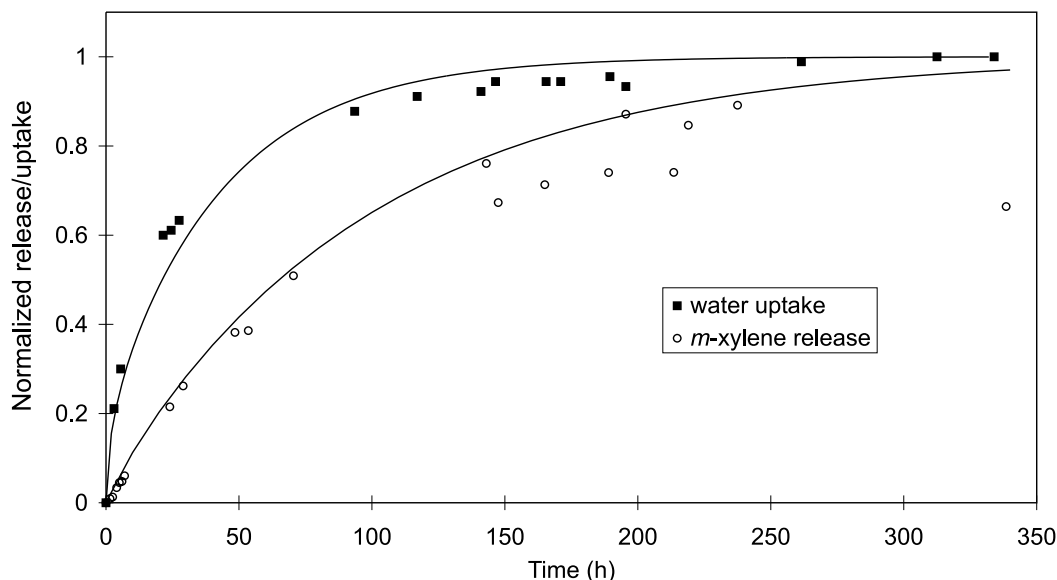
pons not exposed to water (3), suggest that solvent release is dependent upon the presence of water in the paint matrix.

Diffusion of water through various paints is expected to have an activation energy ranging between 50 and 100 kJ·mol<sup>-1</sup> (6) whereas the activation energy for diffusion of organic compounds in water is lower (10–20 kJ·mol<sup>-1</sup> (7)). The activation energy of 50 kJ·mol<sup>-1</sup> for solvent release measured in these studies suggests that the rate-determining step for the process is transport of water by diffusion into the paint matrix and not transport of the solvents through a diffusional boundary layer in the water outside of the paint. Similar observations have been made for the release of ethyno-diol from silicone polymers in the presence of polyethylene glycol (8) and for the release of various pharmaceuticals from cross-linked polymer systems immersed in water (9). It should also be noted that the average activation energy of 50 kJ·mol<sup>-1</sup> estimated for solvent release from these experiments is, within experimental error, very close in value to the estimated activation energy (51 kJ·mol<sup>-1</sup>) for diffusion of water through the paint.

The kinetics for solvent release shown in Fig. 4 can be rationalized by viewing the process as being analogous to solvent evaporation from a membrane (5) in which the driving force for transport of the solvent from inside the membrane to the gas phase is the difference between the solvent concentration inside the membrane and the concentration on the



**Fig. 6.** Fractional uptake of water and release of *m*-xylene from Amerlock 400 painted (0.013 cm thick) coupons. The lines drawn through the data are those calculated using eqs. [2] and [5].



membrane exterior. In the case of immersed paint, the medium is water rather than air, and the dissolution is dependent upon the rate of diffusion of the water-solvent mixture through the polymer. The driving force for water adsorption is the water concentration differential between the interior and exterior of the membrane. For solvent evaporation, the diffusion equations for the rate of loss from the surface of a membrane can be represented by

$$[6] \quad -D \frac{\partial C}{\partial x} = \alpha(C_{eq} - C_s)$$

$$[7] \quad \frac{\partial C}{\partial t} = D \frac{\partial^2 C}{\partial x^2}$$

where  $C_s$  is the solvent concentration inside the membrane;  $C_{eq}$  is the solvent concentration required to maintain equilibrium with the surrounding medium; and  $\alpha$  is a constant of proportionality<sup>7</sup> (5).

Solving for the concentration of solvent at the water-paint interface ( $x = 0$ ) as a function of time leads to an expression for the total amount of solvent leaving the interface as a fraction of the corresponding quantity after infinite time

$$[8] \quad \frac{M_t}{M_\infty} = 1 - \sum_{n=1}^{\infty} \frac{2L^2 \exp(-\beta_n^2 D t / \ell^2)}{\beta_n^2 (\beta_n^2 + L^2 + L)}$$

where the  $\beta_n$ s are the positive roots of  $\beta \tan(\beta) = L$ ;  $L = \ell \alpha / D$ ;  $M_t$  is the mass (or concentration) of a species in solution at time  $t$ ;  $M_\infty$  is the final mass (or concentration) of the species in solution;  $D$  is the diffusion coefficient of water inside the polymer;  $t$  is the time;  $n$  is a positive integer; and  $\ell$  is the film or paint thickness. That is,  $M_t$  is equivalent to

$$- \int_0^x C_s dx$$

where  $x$  is changing with time, owing to water diffusion into the paint.

The solvent-release kinetics observed in Fig. 4 can be modeled very accurately, using eq. [8] and assuming that the diffusion coefficient for the solvent through the water polymer mixture is the same as the diffusion coefficient obtained from measurements of the uptake of water at the appropriate temperature. Figure 7 shows a typical example of solvent-release data and a comparison of the fit obtained using eq. [8] to that obtained using the simple exponential fit in eq. [5]. The models predict very similar time-release behaviour, and the subtle differences are well within the error in the experimental measurements.

The exponential form of eq. [8] explains the observation that solvent release from all of the paints we have studied follows simple first-order kinetics. In fact, for the conditions in our experiments, eq. [8] is approximately

$$[9] \quad \frac{M_t}{M_\infty} = 1 = \exp(-\beta^2 D t / \ell^2)$$

Equation [9] is identical to eq. [5], with  $k$  replaced by  $\beta^2 D / \ell^2$ .

The relationship between the value  $k$ , the diffusion coefficient  $D$ , and the coupon thickness is not immediately obvious from eqs. [5] and [8]. However, within the error limits of the data, an empirical relationship between the values for  $k$  and  $D$  can be derived from the expression<sup>8</sup>

$$[10] \quad k = 25 \text{ cm}^{-1} D / \ell$$

<sup>7</sup>The proportionality constant  $\alpha$  can be viewed as being a mass transfer coefficient  $D/\delta x$  where  $\delta x$  is a diffusional boundary layer.  $\alpha$  has the units length  $\times$  time<sup>-1</sup>.

<sup>8</sup>Using  $k = \beta^2 D / \ell$  and the approximation  $\beta^2 = L$ , which holds for values of  $L$  up to 1, the relationship  $k = LD/\ell$  or  $k = \alpha/\ell$  can be derived. The relationship in eq. [10] is therefore equivalent to stating that  $\alpha = (25 \text{ cm}^{-1}) D$ .



**Fig. 7.** Fractional release of solvents from an immersed coupon painted with two layers of Amerlock 400 paint at 25°C. Lines show the fit of the data using eqs. [5] and [8].

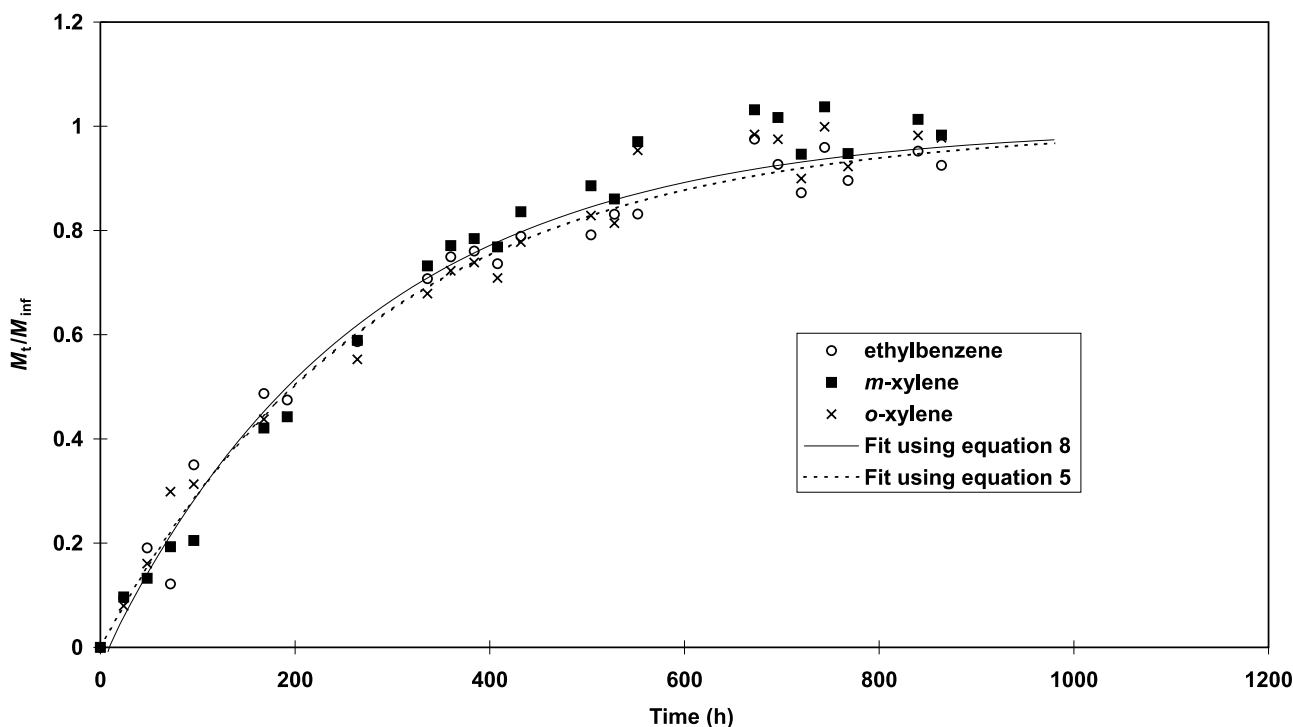


**Table 5.** Comparison of values for first-order rate constant  $k$ .

Sample No.	Paint type	Thickness ( $\mu\text{m}$ )	$T$ ( $^{\circ}\text{C}$ )	$D$ ( $10^{-6}\text{cm}^2\text{h}^{-1}$ )	$k_{\text{calcd}}^a$ ( $\text{h}^{-1}$ )	$k_{\text{fit}}^b$ ( $\text{h}^{-1}$ )
1	Amerlock	68	25	2.4	0.0088	0.010
2, 3	Amerlock	120	25	2.4	0.005	0.005
4	Amerlock	220	25	2.4	0.0027	0.003
5	Amerlock	68	40	6	0.022	0.03
6, 7	Amerlock	120	40	6	0.013	0.012
8	Amerlock	220	40	6	0.007	0.010
9, 11	Amerlock	68	90	9	0.33	0.22, 0.35 <sup>c</sup>
10, 12	Amerlock	120	90	9	0.19	0.20
13	Amerlock	220	90	9	0.1	0.10
14	Ripolin	33	40	6	0.045	0.040

<sup>a</sup>Calculated from eq. [10] and the measured diffusion coefficient of water in the polymer.

<sup>b</sup> $k$  used in eq. [5] to fit the solvent-release data (methyl isobutyl ketone in the case of Ripolin paint; *m*-, *o*-xylene, and ethylbenzene in the case of Amerlock 400 paint) from immersed surfaces.

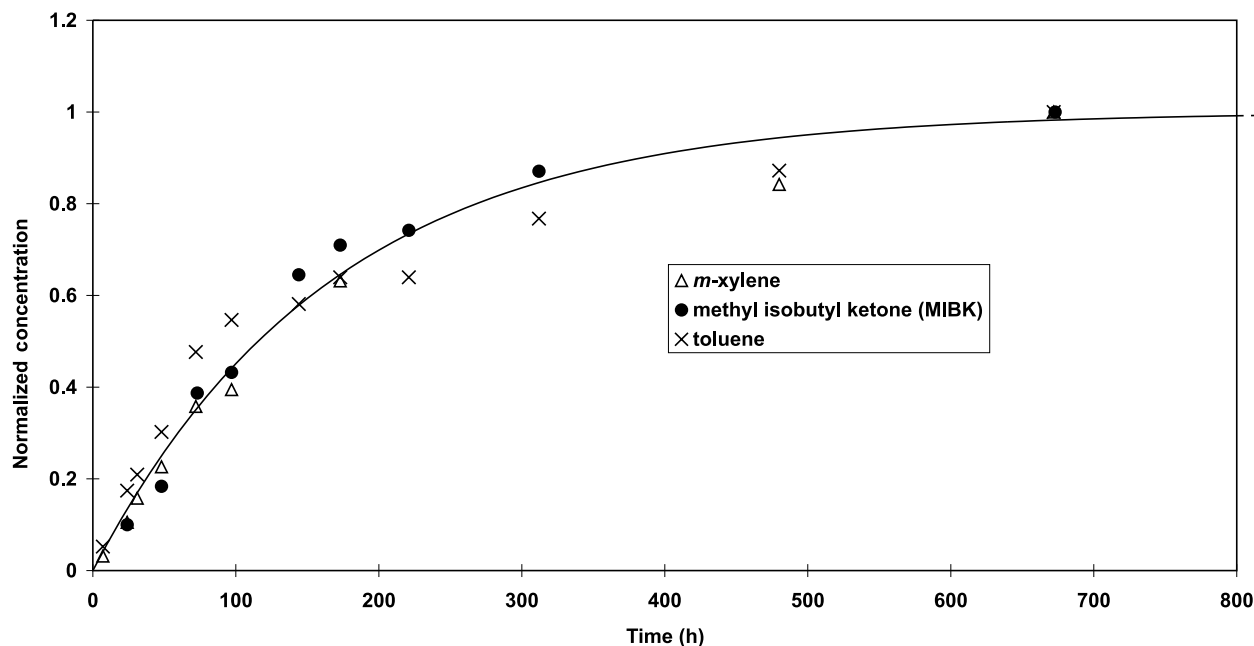
<sup>c</sup>Two samples gave slightly different values.

Values calculated for  $k$ , as compared with those obtained from a best fit to the data, are listed in Table 5. The values are in very good agreement for every experiment. The applicability of eq. [10] to deriving the first-order rate constants for solvent release from other paints, or paint aged for different time periods, has not been established. However, for measurements performed on the uptake of water by and release of methyl isobutyl ketone from Ripolin (epoxy) paint, the relationship appears to hold (see Table 5). The correlation between the value for  $k$  and the diffusion coefficient for water uptake also supports the argument that solvent release is dependent upon the rate of water uptake.

The observed difference between the rates of water uptake and solvent release (Fig. 6) can be explained by the difference in the concentrations of the species at the interface between the paint and the water. For water absorption, the concentration of the sorbent (i.e., water) at the paint-solution interfacial boundary is constant. The water concentration within the diffusional boundary layer (i.e., inside the paint) is also constant, although the length of the boundary layer changes with time. The net driving force for water diffusion is therefore always large; water is always diffusing from an area of constant concentration into an area of zero concentration. In the case of solvent release, the concentra-



**Fig. 8.** Normalized release rate of *m*-xylene, MIBK, and toluene from vinyl painted zinc-primed coupons immersed in water at 25°C and at pH 10. The lines drawn through the data are those calculated using eq. [5].



tion gradient of the solvent decreases as time proceeds, because the solvent concentration in solution (and therefore at the water paint interface) continually increases. This decrease in the concentration gradient reduces the driving force for the net diffusion of the solvent out of the paint. As a result, diffusion of solvent out of the paint matrix is always slower than diffusion of water into the matrix.

A number of mechanisms have been proposed for solvent release from, or solute uptake into, immersed surfaces. Pseudo-first-order kinetic behaviour has been observed for the release or uptake of dyes into natural and synthetic polymers (9) and the release of drugs from various gels (8). Models for the kinetic behaviour vary, however. Some models incorporate moving boundary layer analysis, in which a diffusional boundary layer exists between a water front advancing into a membrane and the edge of the membrane (8). Other analyses incorporate an assumption that there is a thick skin on the membrane that inhibits diffusion (9), and still others assume that there is a diffusional boundary layer on the outside of the membrane (9). What the models all have in common is that release or uptake of a water-soluble substrate by a given material is primarily dependent upon the rate of diffusion of the solvent–water mix in the material. The dependence on the rate of diffusion of water is believed to arise because the movement of materials through the polymer requires that the polymer segments are mobile. Absorption of water is believed to significantly enhance polymer segment mobility and, therefore, transport of materials through the polymer by relaxing and swelling the paint matrix (7–9).

In transport of dyes or drugs through polymers, the uptake or release of a substrate dissolved in solvent has been observed to be somewhat dependent also upon other factors besides the rate of diffusion of water in the polymer (7–9). These factors are: (a) the diffusion coefficient of the sub-

strate in water; (b) the size of the substrate; and (c) the size exclusion characteristics of the polymer.

None of these factors have been examined in detail in the present study. However, the solvent-release rate constants for ethyl benzene and *o*- and *m*-xylene from Amerlock 400 were very similar, and previous studies (3) on polyurethane, epoxy, and vinyl containment paints established that solvent-release rate constants for a very wide range of solvent types (e.g., chlorinated hydrocarbons, aldehydes, ketones, and aromatic hydrocarbons) were relatively independent of the nature of the solvent (see Figs. 8 and 9). The independence of the solvent-release rate constant on the nature of the solvents from all of these experiments is not surprising given that the diffusion coefficients of small organic molecules in water span a very narrow range (10).

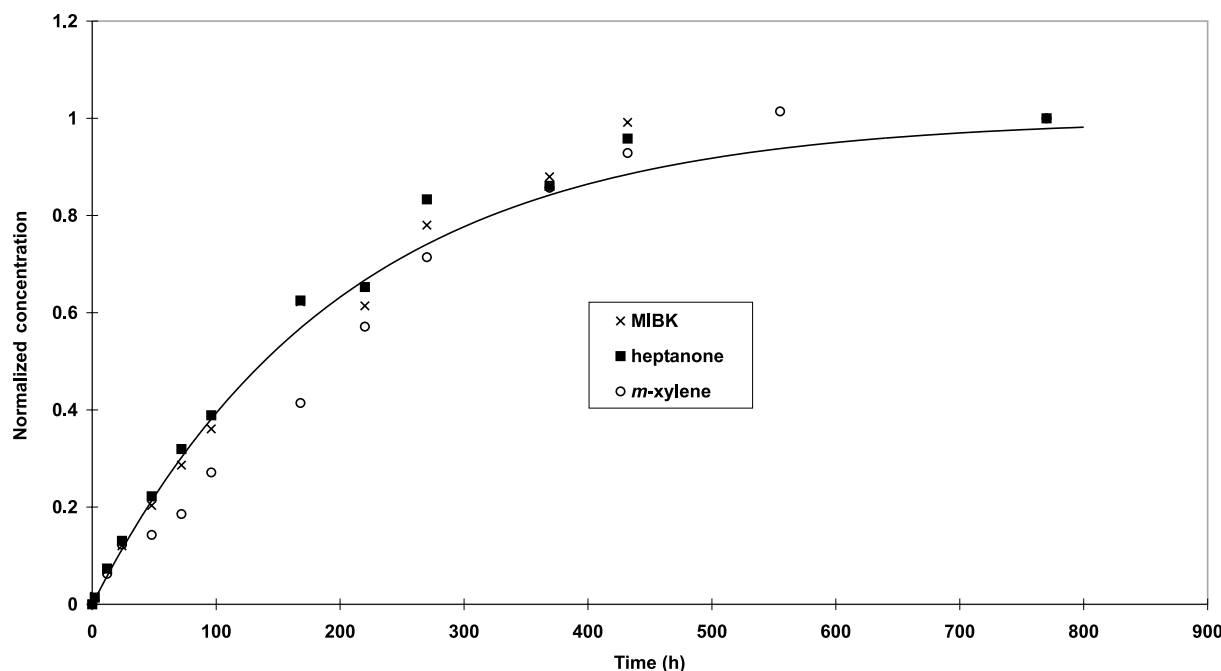
In all of the studies performed to date on the release of solvents from containment paints, the rate constant ( $k$ ) appears to be relatively independent of paint type. If, as the current studies indicate, the rate constant is dependent upon the diffusion coefficient of water in the polymers, the independence of the rate constant on paint type implies that the diffusion coefficient of water in all of the paints is similar. The independence of solvent release on paint type also implies that, under the conditions of our experiments (and those expected in containment), the solvent-release rate is independent of the size exclusion characteristics of the polymer.

## Conclusions

The release of solvents from Amerlock 400 painted coupons exhibits the same pseudo-first-order behaviour as the rate of release of other solvents from polyurethane, vinyl, and epoxy paints. The release rate is dependent upon the rate of water uptake by the coupons and can be modelled by as-



**Fig. 9.** Normalized release rate of methyl isobutyl ketone (MIBK), heptanone, and *m*-xylene from epoxy painted zinc-primed coupons immersed in water at 40°C and at pH 5. The lines drawn through the data are those calculated using eq. [5].



suming Fickian diffusion kinetics (5). The pseudo-first-order rate constant ( $k$ ) was found to be inversely proportional to the coating thickness. A value for  $k$  for the coupons used in this study can be estimated from the relationship  $k = (25 \text{ cm}^{-1}) D/\ell$ , where  $D$  is the diffusion coefficient of water in the paint and  $\ell$  is the paint thickness. The activation energy for solvent release does not appear to depend upon the coating thickness (Fig. 5).

Values of  $k$  for solvent release from immersed Amerlock 400 paint are similar to those determined for release of methyl isobutyl ketone from polyurethane, vinyl, and epoxy containment paints, implying that the diffusion coefficient for water in these paints is very similar to that in Amerlock 400. The insensitivity of the solvent-release kinetics to solvent type or paint type suggests that it might be possible to construct a model for dissolution of solvents from containment paints that will be applicable to all containment paints. This study, in agreement with previous studies, indicates that the rate for solvent release can be described by eq. [5] and

$$[11] \quad D_T = D_{298} \exp \left[ \frac{-\Delta E}{T} \left( \frac{1}{T} - \frac{1}{298 \text{ K}} \right) \right]$$

where  $D_T$  and  $D_{298}$  are the diffusion coefficients of water in the paint at temperatures  $T$  and 298 K, respectively.

A comprehensive study on the activation energy ( $\Delta E$ ) for water absorption by paint and the amount of solvent initially in the paint, as a function of paint ageing, is currently being performed.

## Acknowledgements

The authors would like to acknowledge P. Taylor at Institute de Radioprotection et de Sûreté Nucléaire (IRSN) for many helpful discussions. This work was funded by the COG (CANDU Owners Group) R&D Program, Working Party 06, Containment Behaviour under the joint participation of Ontario Power Generation, Hydro Quebec, New Brunswick Power, and Atomic Energy of Canada Limited (AECL).

## References

1. J.C. Wren, J.M. Ball, and G.A. Glowa. Nucl. Technol. **125**, 337 (1999).
2. J.C. Wren, J.M. Ball, and G.A. Glowa. Nucl. Technol. **129**, 297 (2000).
3. J.C. Wren, D.J. Jobe, G.G. Sanipelli, and J.M. Ball. Can. J. Chem. **78**, 464 (2000).
4. J. Dewulf, D. Drijvers, and H. van Langenhove. Atmos. Environ. **29**, 323 (1995).
5. J. Crank. In The mathematics of diffusion. 2nd ed. Clarendon Press, Oxford. 1975.
6. E.H. Oelkers. Geochim. Cosmochim. Acta, **55**, 3515 (1991).
7. T. Skoulikidis and A. Ragoussis. Corrosion (Houston), **88**, 666 (1992).
8. N.E. Cooke. J. Polym. Sci. Part B Polym. Phys. **29**, 1633 (1991).
9. C.S. Brazel and N.A. Peppas. Polymer, **40**, 3383 (1999).
10. J. Crank and G.S. Park (Editors). In Diffusion in polymers. Academic Press, New York. 1968.



# 2-Thiophen-2-ylbenzothiazole, -benzoxazole, and -benzimidazole platinum complexes

Xiao-Feng He, Christopher M. Vogels, Andreas Decken, and Stephen A. Westcott

**Abstract:** Oxidative cyclization of 2-aminothiophenol, 2-aminophenol, and 1,2-phenylenediamine with 2-thiophenecarboxaldehyde affords the corresponding 2-thiophen-2-ylbenzothiazole, -benzoxazole, and -benzimidazole compounds. Addition of these ligands (L) to  $[\text{PtCl}_2(\text{coe})]_2$  (coe = *cis*-cyclooctene) gives complexes of the type *trans*- $\text{PtCl}_2\text{L}(\text{coe})$  in moderate yields. Crystals of the benzothiazole derivative (**1**) were monoclinic, space group  $P2(1)/c$ ,  $a = 11.561(4)$  Å,  $b = 15.335(15)$  Å,  $c = 11.769(4)$  Å,  $\beta = 105.182(5)^\circ$ ,  $Z = 4$ .

**Key words:** platinum, imine, benzothiazole, benzoxazole, benzimidazole.

**Résumé :** La cyclisation oxydante du 2-aminothiophénol, du 2-aminophénol et de la 1,2-phénylènediamine avec le 2-thiophèncarboxaldéhyde fournit les composés correspondants : le 2-thiophène-2-ylbenzothiazole, le benzoxazole et le benzimidazole. L'addition de ces ligands (L) sur le  $[\text{PtCl}_2(\text{coe})]_2$  (coe = cyclooctene *cis*) donne des complexes du type  $\text{PtCl}_2\text{L}(\text{coe})$  *trans* avec des rendements modérés. Les cristaux du dérivé du benzothiazole (**1**) sont monocliniques et appartiennent au groupe d'espace  $P2(1)/c$ , avec  $a = 11,561(4)$  Å,  $b = 15,335(15)$  Å,  $c = 11,769(4)$  Å,  $\beta = 105,182(5)^\circ$ ,  $Z = 4$ .

**Mots clés :** platine, imine, benzothiazole, benzoxazole, benzimidazole.

[Traduit par la Rédaction]

## Introduction

Since the discovery that cisplatin (*cis*- $[\text{PtCl}_2(\text{NH}_3)_2]$ ) can be used as an effective treatment against testicular, ovarian, and head and neck carcinomas, considerable research has focussed on designing new platinum-based drugs with improved therapeutic regimes (1–10). The generation of most platinum complexes for this application was based on an early structure–activity relationship which stated that potentially active complexes should be neutral and contain two inert amine ligands (with at least one N—H bond) in the *cis* orientation and two semilabile leaving groups (11). More recent work, however, has shown that derivatives of transplatin (*trans*- $[\text{PtCl}_2(\text{NH}_3)_2]$ ) also show significant cytotoxicities, paving the way for future studies on *trans*-Pt complexes (12–17). Our interest in making platinum complexes containing biologically active ligands (18), along with the discovery that  $[\text{PtCl}_2(\text{coe})]_2$  (coe = *cis*-cyclooctene) can be used as an organic soluble starting material to generate both *cis*-bidentate and *trans*-monodentate amine dichloroplatinum complexes, prompted us to investigate its reactivity with 2-

thiophen-2-ylbenzothiazole, -benzoxazole, and -benzimidazoles. The results of which are presented within.

## Experimental

Reagents and solvents used were obtained from Aldrich Chemicals. Platinum salts were obtained from Precious Metals Online Ltd.  $[\text{PtCl}_2(\text{coe})]_2$  was prepared by established procedures (19). NMR spectra were recorded on a JEOL JNM-GSX270 FT NMR spectrometer.  $^1\text{H}$  NMR chemical shifts are reported in ppm and referenced to residual protons in deuterated solvent at 270 MHz.  $^{13}\text{C}$  NMR chemical shifts are referenced to solvent carbon resonances as internal standards at 68 MHz. Multiplicities are reported as singlet (s), doublet (d), triplet (t), quartet (q), multiplet (m), broad (br), and overlapping (ov). Infrared spectra were obtained using a Mattson Genesis II FT IR spectrometer and reported in  $\text{cm}^{-1}$ . Melting points were measured uncorrected with a Mel-Temp apparatus. Microanalyses for C, H, and N were carried out at Chemisar Laboratories Inc. (Guelph, Ontario). All reactions were carried out in the air and products are stable indefinitely under such conditions.

### General procedure for the preparation of complexes 1–3

The starting benzothiazole (20), benzoxazole (20), and the benzimidazole (21) compounds were prepared by established procedures.

### Complex 1

2-Thiophen-2-ylbenzothiazole (62 mg, 0.29 mmol) in 10 mL of  $\text{CH}_2\text{Cl}_2$  was added dropwise to a stirred solution of  $[\text{PtCl}_2(\text{coe})]_2$  (100 mg, 0.13 mmol) in 10 mL of  $\text{CH}_2\text{Cl}_2$ .

Received 10 March 2003. Published on the NRC Research Press Web site at <http://canjchem.nrc.ca> on 11 July 2003.

X.-F. He, C.M. Vogels, and S.A. Westcott,<sup>1</sup> Department of Chemistry, Mount Allison University, Sackville, NB E4L 1G8, Canada.

A. Decken,<sup>2</sup> Department of Chemistry, University of New Brunswick, Fredericton, NB E3B 5A3, Canada.

<sup>1</sup>Corresponding author (e-mail: [swestcott@mta.ca](mailto:swestcott@mta.ca)).

<sup>2</sup>Corresponding author (crystallography) (e-mail: [adecken@unb.ca](mailto:adecken@unb.ca)).



The reaction mixture was heated at reflux for 7 h, at which point the solvent was removed under vacuum to afford a yellow solid. Ethanol ( $2 \times 3$  mL) was used to wash the solid. Yield: 97 mg (63%); mp  $165^\circ\text{C}$  (decomposition). IR (Nujol): 2964 (s), 2935 (s), 2902 (s), 2872 (s), 1527 (m), 1456 (s), 1412 (s), 1377 (s), 1319 (m), 1277 (m), 1230 (m), 1159 (w), 1126 (w), 1065 (w), 943 (m), 831 (m), 760 (s), 719 (s), 609 (w), 569 (w), 528 (m).  $^1\text{H}$  NMR ( $\text{CDCl}_3$ )  $\delta$ : 9.02 (d,  $J = 8$  Hz, 1H), 8.06 (dd,  $J = 4, 2$  Hz, 1H), 7.83–7.79 (ov m, 2H), 7.66 (ov dt,  $J = 8, 2$  Hz, 1H), 7.50 (ov dt,  $J = 8, 2$  Hz, 1H), 7.21 (t,  $J = 8$  Hz, 1H), 5.74 (m,  $J_{\text{H-Pt}} = 62$  Hz, 2H,  $-\text{CH}=\text{CH}-$ ), 2.65 (br m, 2H), 2.52 (br m, 2H), 1.92 (br m, 2H), 1.49 (br m, 6H).  $^{13}\text{C}$  NMR ( $\text{CDCl}_3$ )  $\delta$ : 164.0, 149.7, 133.6, 133.1, 132.8, 131.1, 128.1, 127.8, 127.0, 123.6, 121.7, 95.4 ( $-\text{CH}=\text{CH}-$ ), 29.3, 28.3, 26.3. Anal. calcd. for  $\text{PtCl}_2\text{C}_{19}\text{H}_{21}\text{NS}_2$ : C 38.45, H 3.57, N 2.36; found: C 38.64, H 3.58, N 2.33.

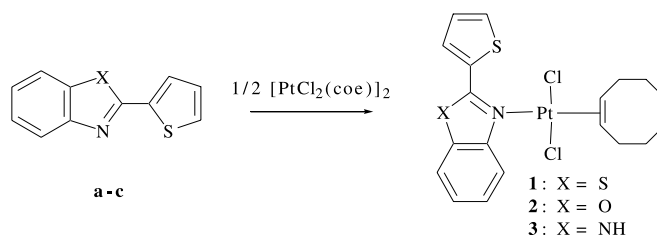
### Complex 2

2-Thiophen-2-ylbenzoxazole (30 mg, 0.15 mmol) in 10 mL of  $\text{CH}_2\text{Cl}_2$  was added dropwise to a stirred solution of  $[\text{PtCl}_2(\text{coe})]_2$  (59 mg, 0.08 mmol) in 10 mL of  $\text{CH}_2\text{Cl}_2$ . The reaction mixture was heated at reflux for 7 h, at which point the solvent was removed under vacuum to afford a red solid. Ethanol ( $2 \times 3$  mL) was used to wash the solid. Yield: 38 mg (42%); mp  $170^\circ\text{C}$  (decomposition). IR (Nujol): 3064 (w), 2947 (s), 2906 (s), 2868 (s), 1605 (m), 1574 (s), 1468 (s), 1454 (s), 1416 (m), 1379 (m), 1356 (m), 1298 (w), 1254 (m), 1232 (m), 1171 (m), 1078 (m), 1041 (m), 997 (w), 955 (w), 924 (w), 852 (m), 796 (m), 764 (s), 658 (w), 604 (w), 567 (w), 528 (m).  $^1\text{H}$  NMR ( $\text{CDCl}_3$ )  $\delta$ : 8.51 (d,  $J = 4$  Hz, 1H), 8.29 (d,  $J = 8$  Hz, 1H), 7.87 (d,  $J = 4$  Hz, 1H), 7.63–7.49 (ov m, 3H), 7.30 (d,  $J = 4$  Hz, 1H), 5.80 (m,  $J_{\text{H-Pt}} = 64$  Hz, 2H,  $-\text{CH}=\text{CH}-$ ), 2.73 (br m, 2H), 2.56 (br m, 2H), 1.92 (br m, 2H), 1.53 (br m, 6H).  $^{13}\text{C}$  NMR  $\delta$ : 159.1, 149.0, 137.9, 134.9, 134.6, 128.4, 127.2, 126.3, 125.4, 119.6, 111.2, 96.0 ( $-\text{CH}=\text{CH}-$ ), 29.3, 28.3, 26.3. Anal. calcd. for  $\text{PtCl}_2\text{C}_{19}\text{H}_{21}\text{NSO}$ : C 39.52, H 3.67, N 2.43; found: C 39.60, H 3.74, N 2.45.

### Complex 3

2-Thiophen-2-ylbenzimidazole (27 mg, 0.13 mmol) in 10 mL of  $\text{CH}_2\text{Cl}_2$  was added dropwise to a stirred solution of  $[\text{PtCl}_2(\text{coe})]_2$  (50 mg, 0.07 mmol) in 10 mL of  $\text{CH}_2\text{Cl}_2$ . The reaction mixture was heated at reflux for 7 h, at which point the solvent was removed under vacuum to afford a yellow solid. Ethanol ( $2 \times 3$  mL) was used to wash the solid. Yield: 32 mg (40%); mp  $210^\circ\text{C}$  (decomposition). IR (Nujol): 3199 (m), 3180 (m), 2920 (s), 2860 (s), 1566 (m), 1498 (w), 1458 (s), 1377 (s), 1319 (m), 1286 (m), 1234 (m), 1173 (w), 1151 (w), 1117 (w), 1005 (w), 958 (w), 926 (w), 843 (m), 820 (w), 798 (w), 756 (s), 739 (s), 700 (s), 669 (w), 636 (w), 609 (w), 569 (w), 528 (w).  $^1\text{H}$  NMR ( $\text{CDCl}_3$ )  $\delta$ : 10.51 (s, 1H), 8.22 (d,  $J = 8$  Hz, 1H), 7.43–7.39 (ov m, 2H), 7.22 (t,  $J = 8$  Hz, 1H), 6.98–6.87 (ov m, 2H), 6.68 (t,  $J = 8$  Hz, 1H), 5.75 (m,  $J_{\text{H-Pt}} = 62$  Hz, 2H,  $-\text{CH}=\text{CH}-$ ), 2.68 (br m, 2H), 2.60 (br m, 2H), 1.92 (br m, 2H), 1.54 (br m, 6H).  $^{13}\text{C}$  NMR ( $\text{CDCl}_3$ )  $\delta$ : 145.6, 139.4, 131.8, 130.6, 130.4, 127.8, 127.6, 125.2, 123.9, 118.0, 111.5, 95.7 ( $-\text{CH}=\text{CH}-$ ), 29.4, 28.2, 26.4. Anal. calcd. for  $\text{PtCl}_2\text{C}_{19}\text{H}_{22}\text{N}_2\text{S}$ : C 39.56, H 3.85, N 4.86; found: C 39.70, H 3.88, N 4.78.

**Scheme 1.** Synthesis of organometallic platinum 2-thiophen-2-ylbenzothiazole derivatives **1–3**.



### X-ray crystallography

Crystals of **1** were grown from a saturated acetone solution at  $5^\circ\text{C}$ . Single crystals were coated with Paratone-N oil, mounted using a glass fibre, and frozen in the cold stream of the goniometer. A hemisphere of data were collected on a Bruker AXS P4/SMART 1000 diffractometer using  $\omega$  and  $\theta$  scans with a scan width of  $0.3^\circ$  and 10 s exposure times. The detector distance was 5 cm. The data were reduced (22) and corrected for absorption (23). The structure was solved by direct methods and refined by full-matrix least-squares on  $F^2$  (24). All non-hydrogen atoms were refined anisotropically. Hydrogen atoms were located in Fourier difference maps and refined isotropically.

### Results and discussion

2-Arylbenzothiazole derivatives are an important class of biologically active compounds (25–30). For instance, the unusual antitumor activity associated with 2-(4-amino-phenyl)benzothiazole was originally discovered in a program designed for screening tyrosine kinase inhibitors (31). Analogues possessing superior growth inhibitory properties have since been synthesized and their biological profiles are unlike that of any known anticancer agent (32). Analysis of the structure–activity relationship identified the benzothiazole unit as being essential for potent activity.

Our interest in generating platinum compounds with biologically active carrier ligands prompted us to make complexes containing arylbenzothiazole, and related benzoxazole and benzimidazole groups. Our initial efforts in this area focussed on thiophene derivatives **a–c** as compounds containing a thiophene group have also shown remarkable biological activities (33, 34) and can act as ligands by binding through the sulfur atom (35). Compounds **a–c** were prepared by the oxidative cyclization of the appropriate Schiff bases (20, 21).

Addition of benzothiazole **a** to a solution of  $[\text{PtCl}_2(\text{coe})]_2$  in  $\text{CH}_2\text{Cl}_2$  gave the novel organometallic complex *trans*- $\text{PtCl}_2(\text{coe})(\text{a})$  (**1**) in moderate yields (63%, Scheme 1). NMR spectroscopic data confirmed the presence of a bound coe group. For instance,  $^1\text{H}$  NMR data showed a broad peak at  $\delta$  5.74 ppm attributed to the olefinic C—H bonds and platinum coupling ( $J_{\text{H-Pt}} = 62$  Hz) suggests that the cyclooctene unit is still coordinated to the metal centre. Similarly, the coordinated alkene shows up at  $\delta$  95.4 ppm in the  $^{13}\text{C}$  NMR spectra.

Although NMR data can be used to confirm the coordination of the cyclooctene group, it cannot unambiguously show how the thiophene benzothiazole unit is bound to the metal



**Fig. 1.** Molecular structure of **1** showing the atomic labeling scheme and 30% probability displacement ellipsoids with hydrogen atoms omitted for clarity.

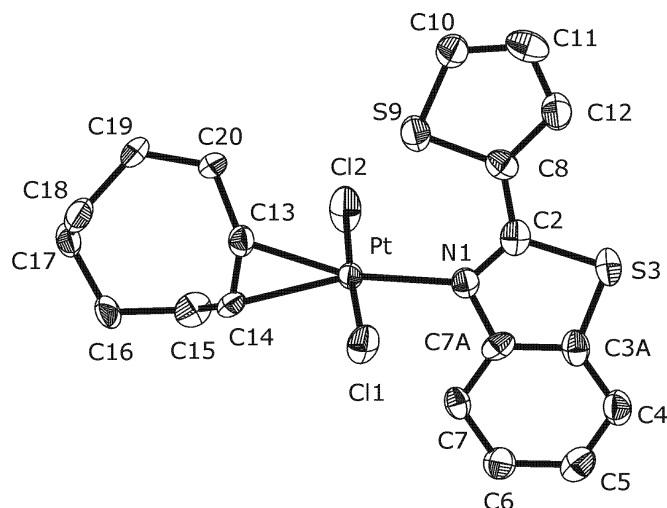


**Table 1.** Crystallographic data collection parameters for **1**.

Complex	<b>1</b>
Formula	C <sub>19</sub> H <sub>21</sub> Cl <sub>2</sub> NPtS <sub>2</sub>
fw	593.48
Crystal system	Monoclinic
Space group	<i>P</i> 2(1)/ <i>c</i>
<i>a</i> (Å)	11.561(4)
<i>b</i> (Å)	15.335(15)
<i>c</i> (Å)	11.769(4)
β (°)	105.182(5)
<i>V</i> (Å <sup>3</sup> )	2013.6(11)
<i>Z</i>	4
ρ <sub>calcd</sub> (mg m <sup>-3</sup> )	1.958
Crystal size (mm <sup>3</sup> )	0.275 × 0.35 × 0.525
Temperature (K)	198(1)
Radiation	MoKα (λ = 0.71073)
μ (mm <sup>-1</sup> )	7.444
Total reflections	9026
Total unique reflections	3384
No. of variables	226
<i>R</i> <sub>int</sub>	0.0810
θ range (°)	1.83 to 24.99
Largest difference peak/hole (e Å <sup>-3</sup> )	2.436/−1.762
<i>S</i> (GoF) on <i>F</i> <sup>2</sup>	1.142
<i>R</i> 1 <sup>a</sup> ( <i>I</i> > 2σ( <i>I</i> ))	0.0398
<i>wR</i> 2 <sup>b</sup> (All data)	0.1086

$$^a R1 = \sum(|F_o| - |F_c|) / \sum|F_o|$$

$$^b wR2 = (\sum[w(F_o^2 - F_c^2)^2] / \sum[wF_o^4])^{1/2}, \text{ where } w = 1/[\sigma^2(F_o^2) + (0.0285P)^2 + (14.809P)], \text{ where } P = (\max(F_o^2, 0) + 2F_c^2)/3.$$

centre. We therefore conducted an X-ray diffraction study on **1** (Fig. 1). Crystallographic data are given in Table 1<sup>3</sup>

**Table 2.** Selected bond lengths (Å) and angles (°) for **1**.

Bond lengths (Å)	
Pt—N(1)	2.064(7)
Pt—C(13)	2.159(8)
Pt—C(14)	2.179(8)
Pt—Cl(2)	2.300(2)
Pt—Cl(1)	2.303(2)
N(1)—C(2)	1.298(11)
C(2)—S(3)	1.746(9)
C(3A)—S(3)	1.747(9)
C(8)—S(9)	1.710(9)
S(9)—C(10)	1.696(9)
C(2)—C(8)	1.459(12)
C(10)—C(11)	1.349(14)
C(11)—C(12)	1.409(14)
C(13)—C(14)	1.367(11)
Bond angles (°)	
N(1)—Pt—C(13)	161.4(3)
N(1)—Pt—C(14)	161.3(3)
C(13)—Pt—C(14)	36.7(3)
N(1)—Pt—Cl(2)	88.05(19)
C(13)—Pt—Cl(2)	95.7(2)
C(14)—Pt—Cl(2)	94.1(2)
N(1)—Pt—Cl(1)	88.60(19)
C(13)—Pt—Cl(1)	87.7(2)
C(14)—Pt—Cl(1)	88.9(2)
Cl(2)—Pt—Cl(1)	176.60(8)
C(2)—N(1)—C(7A)	112.0(7)
C(2)—N(1)—Pt	126.4(6)
C(7A)—N(1)—Pt	121.1(6)
N(1)—C(2)—C(8)	127.2(8)
N(1)—C(2)—S(3)	114.6(7)
C(8)—C(2)—S(3)	118.2(6)
C(7A)—C(3A)—C(4)	121.8(8)
C(7A)—C(3A)—S(3)	110.0(6)
C(4)—C(3A)—S(3)	128.2(7)
C(2)—S(3)—C(3A)	89.3(4)
C(3A)—C(7A)—N(1)	114.1(8)
C(7)—C(7A)—N(1)	123.4(8)
C(12)—C(8)—S(9)	110.1(7)
C(2)—C(8)—S(9)	124.4(6)
C(10)—S(9)—C(8)	92.1(4)
C(11)—C(10)—S(9)	112.9(7)

and selected bond distances and angles shown in Table 2. The benzothiazole ligand is bound to the metal through the imine nitrogen with a nitrogen–platinum bond distance of 2.064(7) Å, similar to those reported in other platinum–imine complexes (14, 36, 37). Slightly longer Pt–N bond distances have been observed in related five-coordinate [PtMe(cod)(N–N)]BF<sub>4</sub> (cod = 1,5-cyclooctadiene, N–N = diimine) complexes (38). The structure confirms the pres-

<sup>3</sup>Supplementary material may be purchased from the Depository of Unpublished Data, Document Delivery, CISTI, National Research Council Canada, Ottawa, ON K1A 0S2, Canada ([http://www.nrc.ca/cisti/irm/unpub\\_e.shtml](http://www.nrc.ca/cisti/irm/unpub_e.shtml) for information on ordering electronically). Crystallographic information has also been deposited with the Cambridge Crystallographic Data Centre (CCDC 205641). Copies of the data can be obtained free of charge via [www.ccdc.cam.ac.uk/conts/retrieving.html](http://www.ccdc.cam.ac.uk/conts/retrieving.html) (or from the Cambridge Crystallographic Data Centre, 12 Union Road, Cambridge CB2 1EZ, U.K.; fax: +44 1223 336033; or deposit@ccdc.cam.ac.uk).



ence of the *trans* cyclooctene group, showing a typical Pt—C bond distance of 2.169(8) Å (19). The carbon—carbon bond distance of 1.367(11) Å shows a slight weakening because of  $\pi$ -backbonding from the metal to the empty  $\pi^*$  orbital of the alkene (39). A Pt-S(9) distance of 3.110(3) Å precludes any significant interaction of the metal with the thiophene group.

Complex **1** was heated at reflux in toluene in the presence of excess ligand for prolonged periods of time in an effort to remove the bound cyclooctene group and generate *cis*-PtCl<sub>2</sub>(2-thiophen-2-ylbenzothiazole). No changes were observed by <sup>1</sup>H NMR spectroscopy, however, and attempts to generate this latter complex by addition of 2-thiophen-2-ylbenzothiazole to aqueous solutions of K<sub>2</sub>PtCl<sub>4</sub> also proved unsuccessful and resulted in the generation of several new products. Similar decomposition products arising from a ring opening of the benzothiazole have been reported previously (40, 41).

Platinum complexes **2** and **3** were prepared as described for **1**, and displayed similar spectroscopic characteristics. For instance, a significant chemical shift is observed for the alkene peaks in the <sup>1</sup>H NMR when the imine is *trans* to the cyclooctene group (5.80 ppm for **2** and 5.75 ppm for **3**; cf. 5.62 ppm for free *coe*). The olefinic carbons are observed at 96.0 ppm (**2**) and 95.7 ppm (**3**) in the <sup>13</sup>C NMR spectra, compared to 130 ppm for free *coe*.

Interestingly, recent studies have shown that certain *trans* imine complexes display cytotoxicities against both cisplatin-sensitive and cisplatin-resistant cell lines (42–44). With this in mind, we will examine complexes **1–3** for their potential anticancer activities, the results of which will be published in due course.

## Acknowledgements

Thanks are gratefully extended to the Research Corporation (Cottrell College Science Award), the Canada Research Chairs program/Canadian Foundation for Innovation/Atlantic Innovation Fund, Natural Sciences and Engineering Research Council of Canada (NSERC), and Mount Allison University for financial support. We also thank Dan E.C.S. Durant (MAU) and Michael P. Shaver (UBC) for expert technical assistance.

## References

1. E. Wong and C.M. Giandomenico. *Chem. Rev.* **99**, 2451 (1999).
2. R. Jamieson and S.J. Lippard. *Chem. Rev.* **99**, 2467 (1999).
3. P.J. Ferguson. *J. Otolaryng.* **24**, 242 (1995).
4. J. Reedijk. *Chem. Rev.* **99**, 2499 (1999).
5. H. Rauter, R.D. Domencio, E. Menta, A. Oliva, Y. Qu, and N. Farrell. *Inorg. Chem.* **36**, 3919 (1997).
6. B. Lippert. In *Cisplatin*. Wiley-VCH, Zürich. 1999.
7. J. Reedijk. *Chem. Commun.* 801 (1996).
8. T.W. Hambley. *J. Chem. Soc., Dalton Trans.* 2711 (2001).
9. T. Okada, I.M. El-Mehasseb, M. Kodaka, T. Tomohiro, K. Okamoto, and H. Okuno. *J. Med. Chem.* **44**, 4661 (2001).
10. S.T. Sullivan, J.S. Saad, F.P. Fanizzi, and L.G. Marzilli. *Inorg. Chem.* **124**, 1558 (2002).
11. M.J. Cleare and J.D. Hoeschele. *Bioinorg. Chem.* **2**, 187 (1973).
12. Y. Qu, J.A. Fitzgerald, H. Rauter, and N. Farrell. *Inorg. Chem.* **40**, 6324 (2001).
13. N. Farrell, T.T. Ha, J.P. Souchard, F.L. Wimmer, S. Cross, and N.P. Johnson. *J. Med. Chem.* **32**, 2240 (1989).
14. M. Coluccia, A. Nassi, F. Loseto, A. Boccarelli, M.A. Mariggio, G. Giordano, F.P. Intini, P. Caputo, and G.A. Natile. *J. Med. Chem.* **36**, 510 (1993).
15. Y. Najajreh, J.M. Perez, C. Navarro-Ranninger, and D. Gibson. *J. Med. Chem.* **45**, 5189 (2002).
16. E. Khazanov, Y. Barenholz, D. Gibson, and Y. Najajreh. *J. Med. Chem.* **45**, 5196 (2002).
17. E.T. Martins, H. Baruah, J. Kramarczyk, G. Saluta, C.S. Day, G.L. Kucera, and U. Bierbach. *J. Med. Chem.* **44**, 4492 (2001), and refs. therein.
18. C.M. Vogels, H.L. Wellwood, T.L. Hennigar, K. Biradha, M.J. Zaworotko, and S.A. Westcott. *Can. J. Chem.* **77**, 1196 (1999).
19. M.P. Shaver, C.M. Vogels, A.I. Wallbank, T.L. Hennigar, K. Biradha, M.J. Zaworotko, and S.A. Westcott. *Can. J. Chem.* **78**, 568 (2000).
20. J. Chang, K. Zhaob, and S. Pana. *Tetrahedron Lett.* **43**, 951 (2002).
21. K.J. Duffy, A.T. Price, E. Delorme, S.B. Dillon, C. Duquenne, C. Erickson-Miller, L. Giampa, Y. Huang, R.M. Keenan, P. Lamb, N. Liu, S.G. Miller, J. Rosen, A.N. Shaw, H. Smith, K.J. Wiggall, L. Zhang, and J.I. Luengo. *J. Med. Chem.* **45**, 3576 (2002).
22. SAINT 6.02. Bruker AXS Inc., Madison, Wisconsin. 1997–1999.
23. G.M. Sheldrick. SADABS. Bruker AXS Inc., Madison, Wisconsin. 1999.
24. G.M. Sheldrick. SHELXTL 5.1. Bruker AXS Inc., Madison, Wisconsin. 1997.
25. I. Hutchinson, M.-S. Chua, H.L. Browne, V. Trapani, T.D. Bradshaw, A.D. Westwell, and M.F.G. Stevens. *J. Med. Chem.* **44**, 1446 (2001).
26. I. Hutchinson, S.A. Jennings, B.R. Vishnuvajjala, A.D. Westwell, and M.F.G. Stevens. *J. Med. Chem.* **45**, 744 (2002).
27. R.H. Tale. *Org. Lett.* **4**, 1641 (2002).
28. M.L. López-Rodríguez, M. Murcia, B. Benhamb, A. Viso, M. Campillo, and L. Pardo. *J. Med. Chem.* **45**, 4806 (2002).
29. S. Sato, T. Kajiura, M. Noguchi, K. Takehana, T. Kobayashi, and T. Tsuji. *J. Antibiot.* **54**, 102 (2001).
30. Y. Lee, E. Shepard, J. Smith, D.M. Dooley, and L.M. Sayre. *Biochemistry*, **40**, 822 (2001).
31. D.-F. Shi, T.D. Bradshaw, S. Wrigley, C.J. McCall, P. Lelieveld, I. Fichtner, and M.F.G. Stevens. *J. Med. Chem.* **39**, 3375 (1996).
32. T.D. Bradshaw, S. Wrigley, D.-F. Shi, R.J. Schultz, K.D. Paull, and M.F.G. Stevens. *Br. J. Cancer*, **77**, 745 (1998).
33. C. Wu, E.R. Decker, N. Blok, J. Li, A.R. Bourgoyne, H. Bui, K.M. Keller, V. Knowles, W. Li, F.D. Stavros, G.W. Holland, T.A. Brock, and R.A.F. Dixon. *J. Med. Chem.* **44**, 1211 (2001).
34. C.E. Tranberg, A. Zickgraf, B.N. Giunta, H. Luetjens, H. Figler, L.J. Murphree, R. Falke, H. Fleischer, J. Linden, P.J. Scammells, and R.A. Olsson. *J. Med. Chem.* **45**, 382 (2002).
35. C. Bianchini and A. Meli. *Acc. Chem. Res.* **31**, 109 (1998).
36. A.M. Gonzalez, R. Cini, F.P. Intini, C. Pacifico, and G. Natile. *Inorg. Chem.* **41**, 470 (2002).
37. J.G. Hinman, C.R. Baar, M.C. Jennings, and R.J. Puddephatt. *Organometallics*, **19**, 563 (2000).
38. F. Di Bianca, G. Bandoli, A. Dolmella, S. Antonaroli, and B. Crociani. *J. Chem. Soc., Dalton Trans.* 212 (2002).
39. F.R. Hartley. *The chemistry of platinum and palladium*. John Wiley and Sons, New York. 1973.



40. L.F. Lindoy and S.E. Livingstone. *Inorg. Chim. Acta*, **1**, 365 (1967).
41. A. Garg and J.P. Tandon. *Transition Met. Chem.* **12**, 42 (1987).
42. A.R. Khokhar, S. Al-Baker, S. Shamsuddin, and Z.H. Siddik. *J. Med. Chem.* **40**, 112 (1997).
43. J.M. Pérez, E.I. Montero, A.M. González, X. Solans, M. Font-Bardia, M.A. Fuertes, C. Alonso, and C. Navarro-Ranninger. *J. Med. Chem.* **43**, 2411 (2000).
44. Y. Liu, C. Pacifico, G. Natile, and E. Sletten. *Angew. Chem. Int. Ed.* **40**, 1226 (2001).



# Determination of potential energy functions of argon, krypton, and xenon via the inversion of reduced-viscosity collision integrals at zero pressure<sup>1</sup>

Elaheh K. Goharshadi, Mina JamiAlahmadi, and Bijan Najafi

**Abstract:** The pair potential energy functions of argon, krypton, and xenon have been determined via the inversion of reduced-viscosity collision integrals at zero pressure. A comparison of the potentials with the previously determined potentials are included. The viscosity and thermal conductivity of argon, krypton, and xenon at different temperatures and pressures have been calculated and compared with experimental values. The present potentials for argon, krypton, and xenon provide a good overall account of the experimental properties of these compounds, considering the stated uncertainty in the measurements.

*Key words:* potential energy function, collision integral, viscosity, thermal conductivity.

**Résumé :** On a déterminé la paire de fonctions d'énergie potentielle de l'argon, du krypton et du xénon en utilisant l'inversion des intégrales de collision à viscosité réduite et à pression nulle. On inclut une comparaison des potentiels avec ceux déterminés antérieurement. On a calculé la viscosité et la conductivité thermique de l'argon, du krypton et du xénon à différentes températures et à différentes pressions et on les a comparées aux valeurs expérimentales. Les potentiels actuels de l'argon, du krypton et du xénon fournissent une bonne analyse des propriétés expérimentales de ces composés en tenant compte de l'incertitude reconnue de ces mesures.

*Mots clés :* fonction d'énergie potentielle, intégrale de collision, viscosité, conductivité thermique.

[Traduit par la Rédaction]

## Introduction

Molecular interactions are the key to understanding the structure and properties of liquids and solids and the properties of gases.

There are two fundamental methods for obtaining the potential energy functions, theoretical calculations and experimental measurements of macroscopic and microscopic properties of matter such as gas imperfection, spectroscopic methods, molecular beam scattering measurements, and transport properties.

There exists two ways for extracting the potential energy function from experimental data. One is a fitting procedure and the other is an inversion method. A potential model with a few adjustable parameters is assumed in fitting procedures. The parameters of the potential model are varied so as to obtain the optimum agreement between experiment and theory. The potentials from this method do not appear to be unique. Specific information about a potential energy function can be extracted by the inversion of experimental data. In particular, direct inversion techniques for the determination of po-

tential from data on molecular transport properties and second virial coefficients that do not require any explicit assumption to be made about the functional form of the potential have been developed (1–4).

Knowledge of pair potentials in addition to three-body interactions is sufficient to reproduce the thermodynamic properties of argon, krypton, and xenon through a wide range of temperatures and pressures (5–7). For example, Anta et al. (5) have showed that the combination of an accurate pair potential plus three-body interactions reproduces the gas–liquid coexistence curve of argon. These authors also indicated that, when an inaccurate pair potential such as Lennard-Jones is combined with the three-body interactions, the calculated curve deviates appreciably from the experimental data.

The main purpose of the present paper is to determine accurate pair potential energy functions of argon, krypton, and xenon by inversion of the reduced-viscosity collision integrals at zero pressure.

The second objective of the work is to present the tables of collision integrals at zero pressure that are needed in eval-

Received 4 February 2003. Published on the NRC Research Press Web site at <http://canjchem.nrc.ca> on 11 July 2003.

**E.K. Goharshadi<sup>2</sup> and M.J. Alahmadi.** Department of Chemistry, Ferdowsi University, Mashhad 91779, Iran.

**B. Najafi.** Department of Chemistry, Isfahan University of Technology, Isfahan 84154, Iran.

<sup>1</sup>Presented at the 14th Canadian Symposium on Theoretical Chemistry, CSTC 2001, Ottawa, Canada, August 4–9, 2001.

<sup>2</sup>Corresponding author (e-mail: [gohari@ferdowsi.um.ac.ir](mailto:gohari@ferdowsi.um.ac.ir)).



uating the transport coefficients of argon, krypton, and xenon at any pressure.

Finally, we have calculated the viscosity and thermal conductivity for argon, krypton, and xenon at different temperatures and pressures.

## Theory

### Inversion procedure from viscosity data

The macroscopic properties of gases can be explained in terms of the motion and interaction of molecules. Enskog and Chapman developed this theory for transport properties of monatomic dilute gases (8, 9). The most significant feature of their theory is that each transport coefficient of the gas or gas mixture can be expressed in terms of a series of collision integrals, namely  $\Omega^{(l,s)}(T)$  (characterized by the values of  $l$  and  $s$ ), over the intermolecular potential for each of the possible binary encounters in the system. For example, viscosity of a pure monatomic gas is related to  $\Omega^{(2,2)}$ , and the binary diffusion depends on  $\Omega^{(1,1)}$ . The collision integrals are determined by the dynamics of binary collisions between molecules and hence depend upon the intermolecular potential itself. All of the information about the intermolecular potential from transport coefficients is therefore contained in the collision integrals. Of the transport coefficients, the viscosity has proved the easiest to measure accurately.

The kinetic theory expression for the coefficient of viscosity of a pure dilute monatomic gas of molecular mass  $m$  at a temperature  $T$  is

$$[1] \quad \eta = \frac{5}{16} \frac{\sqrt{m\pi kT}}{\Omega^{(2,2)}(T)} f_\eta$$

where  $k$  is the Boltzmann constant and  $f_\eta$  represents the higher-order correction to the first order kinetic theory approximation (8).

The temperature-dependent collision integral  $\Omega^{(2,2)}$  for monatomic gases is explicitly related to  $V(r)$  through the following classical mechanical expressions (9):

$$[2] \quad \Omega^{(2,2)}(T) = \frac{1}{6(kT)^4} \int_0^\infty Q^{(2)}(E) e^{-E/kT} E^3 dE$$

$$[3] \quad Q^{(2)}(E) = 3\pi \int_0^\infty b(1 - \cos^2 \chi) db$$

and

$$[4] \quad \chi(b, E) = \pi - 2b \int_{r_0}^\infty \left( 1 - \frac{b^2}{r^2} - \frac{V(r)}{E} \right)^{-1/2} \frac{dr}{r^2}$$

where  $E$  is the relative kinetic energy of a pair of colliding molecules,  $Q^{(2)}(E)$  is a transport cross section,  $b$  is the impact parameter,  $\chi$  is the scattering angle, and  $r_0$  is the classical distance of closest approach in a collision.

It is convenient to define reduced collision integrals  $\Omega^{(2,2)*}(T^*)$  by

$$[5] \quad \Omega^{(2,2)*}(T^*) = \Omega^{(2,2)}(T) / \Omega_{rs}^{(2,2)}(T)$$

where  $\Omega_{rs}^{(2,2)}(T)$  is the collision integral for rigid spheres of diameter  $\sigma$ ,

$$[6] \quad \Omega_{rs}^{(2,2)}(T) = \pi \sigma^2$$

and the reduced temperature,  $T^*$ , is defined by  $T^* = kT/\epsilon$ , where  $\epsilon$  is the potential well depth.

The direct inversion procedure for the viscosity is based on the idea that at a given temperature the values of  $\Omega^{(2,2)*}$  are determined by the potential over only a small range of separation distance around a value  $r_0$  (1, 2). For a given potential it is always possible to make this idea exact by defining a function  $G_\eta$  such that

$$[7] \quad \Omega^{(2,2)*} = \pi r_0^2$$

and

$$[8] \quad V(r_0) = G_\eta T^*$$

The parameter  $G_\eta$  depends almost entirely on the single variable  $T^*$  and is only weakly dependent on other features of the potential (1). Finding  $V(r)$  from  $\Omega^{(2,2)*}$  is straightforward when  $\epsilon$  is unity. A reasonable potential model is chosen to start the iteration, from which trial values of  $V(r_0)$  are calculated, and so on until convergence is obtained and the  $\Omega^{(2,2)*}$  calculated from the potential agrees with the correlated values within some predicted limit over the available temperature range. An initial estimate of  $G_\eta$  is calculated from Table 1 of ref. 10. Convergence is usually obtained after only two iterations.

The inversion method based on viscosity collision integrals usually utilizes the principle of corresponding states (11, 12) for obtaining the interaction potential. It has been proved that these principles are capable of correlating the equilibrium and transport properties of noble gases, some polyatomic gases, and multi-component mixtures over a very wide temperature range with an accuracy comparable to the best measurements (11, 12).

### The initial density dependence of transport properties

The physical properties of moderately dense gases may be expanded in powers of the density  $\rho$  by expressions of the form:

$$[9] \quad X(P, T) = X_0(T) [1 + B_X(T)\rho + \dots]$$

where  $X_0(T)$  is the zero-density physical property.

For example, the pressure  $P$  and the viscosity  $\eta$  are expanded as

$$[10] \quad P = \rho kT (1 + B\rho + \dots)$$

$$[11] \quad \eta = \eta_0 (1 + B_\eta \rho + \dots)$$

where  $B$  is the second pressure virial coefficient.  $\eta_0$  represents the zero-density viscosity coefficient.  $B_\eta$  is the second viscosity virial coefficient.

According to the theory of Rainwater and Friend (13, 14), the second transport virial coefficient,  $B_x$  ( $x$  can be viscosity ( $\eta$ ), thermal conductivity ( $\lambda$ ), etc.), consists of three contributions:

$$[12] \quad B_x = B_x^{(2)} + B_x^{(3)} + B_x^{(M-D)}$$

where  $B_x^{(2)}$  is the contribution of two free monomers,  $B_x^{(3)}$  represents the effect of three monomers contribution, and  $B_x^{(M-D)}$  is the contribution from monomer-dimer collisions.



Najafi and his colleagues (15) have calculated the second viscosity virial coefficient of the noble gases based on the Rainwater–Friend theory. Their results implied that there may be a universal function for the calculation of  $B_\eta$  for all noble gases at moderate densities over a wide temperature range. According to this correlation, the reduced second viscosity virial coefficient,  $B_\eta^*$  ( $B_\eta^* \equiv B_\eta/\sigma^3$ ), is the universal function of  $(T^*)^{-i}$  in the form of a sixth order polynomial:

$$[13] \quad B_\eta^* = \sum_{i=1}^6 b_i (T^*)^{-i}$$

where  $b_i$  is the coefficient of the universal correlation function. The values of  $b_i$  for the noble gases were given in ref. 15. The viscosity of moderately dense gases at a specified temperature and density can be calculated via the equation:

$$[14] \quad \eta = \eta_0 (1 + N_A \sigma^3 B_\eta^* \rho)$$

where  $N_A$  is Avogadro's number,  $\sigma$  is the collision diameter, and  $\rho$  is the density.

Najafi et al. (16) have extended eq. [17] to a very high density range (up to 40 mol dm<sup>-3</sup> and 900 MPa) by the following equation:

$$[15] \quad \eta = \eta_0 (1 + N_A \sigma^3 B_\eta^* \rho) + (1 + aT)^2 \left( \frac{b_1 \rho + b_2 \rho^2}{1 + c_1 \rho + c_2 \rho^2} \right)$$

where the values of parameters  $a$ ,  $b_1$ ,  $b_2$ ,  $c_1$ , and  $c_2$  have been given in ref. 15.

The thermal conductivity of moderately dense gases (up to 2 mol dm<sup>-3</sup>) at a specified temperature and density can be calculated via the following equation (17):

$$[16] \quad \lambda = \lambda_0 (1 + N_A \sigma^3 B_\lambda^* \rho)$$

where  $B_\lambda^*$  is the reduced second thermal conductivity virial coefficient. Najafi et al. (17) have shown that there exists a corresponding states behavior for  $B_\lambda^*$  for all noble gases:

$$[17] \quad B_\lambda^* = a_0 + a_1/T^*$$

The values of parameters  $a_0$  and  $a_1$  have been given in ref. 17.

The thermal conductivity of gases at high density, up to 40 mol dm<sup>-3</sup>, at a specified temperature and pressure can be calculated via the following equation (17):

$$[18] \quad \lambda = \lambda_0 (1 + N_A \sigma^3 B_\lambda^* \rho) + D_\lambda$$

where  $D_\lambda$  is a function of the fluid density (17) and is represented by

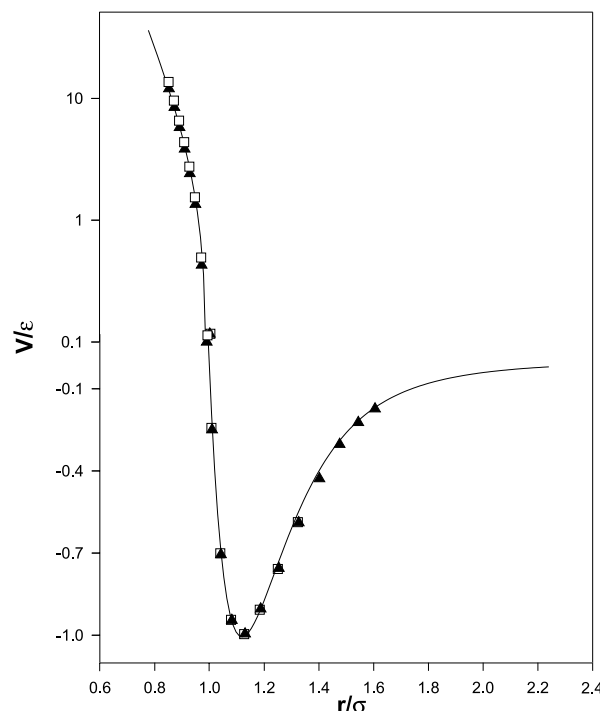
$$[19] \quad \frac{D_\lambda}{\lambda^*} = \sum_{j=2,4,5,8} d_j (\rho/\rho^*)^j$$

where the expansion coefficients,  $d_j$ , and the coefficients  $\lambda^*$  and  $\rho^*$  have been given in ref. 17.

#### Determination of interatomic potentials via the inversion of reduced-viscosity collision integrals at zero pressure

In the previous inversion algorithms for direct determination of interaction potentials from the extended principle of corresponding states, it has been assumed that the influence

**Fig. 1.** Reduced potential energy function of argon by inversion of corresponding states reduced-viscosity collision integrals ( $\blacktriangle$ ) (21) and by inversion of reduced-viscosity collision integrals at zero pressure ( $\square$ ). The solid curve is the Aziz and Slaman potential (19).



of the initial density dependence of transport properties is small and negligible in comparison with the uncertainties associated with the experimental methods (1–4, 18). In other words, the framework of the law of corresponding states (11, 12) is based on experimental values at relatively low densities, since values at zero density are not accessible to direct measurements. In principle, such an assumption cannot be accepted because the difference between the zero density and the atmospheric viscosity data is not always negligible, especially at low temperatures.

The reduced-viscosity collision integral at zero pressure,  $\Omega_o^{(2,2)*}$ , can be obtained by inserting eq. [1] into eq. [14]:

$$[20] \quad \frac{1}{\sigma_{cs}^2 \Omega_{cs}^{(2,2)*}} = \frac{[1 + N_A \sigma^3 B_\eta^* \rho]}{\sigma_o^2 \Omega_o^{(2,2)*}}$$

where  $\sigma_{cs}$  and  $\Omega_{cs}^{(2,2)*}$  have their usual meanings and are taken from a corresponding states correlation (11).  $\sigma_o$  is the corresponding value of an accurate potential (19, 20).

The  $\Omega_o^{(2,2)*}$  can be used to determine the interaction potential by an inversion procedure as described above. One of the peculiar features of the inversion procedure is that it identifies a point on the experimental  $\Omega^{(2,2)}$  vs.  $T$  curve with a single point on the  $V(r)$  vs.  $r$  curve. The inversion method based on viscosity collision integrals usually utilizes the principle of corresponding states for obtaining the interaction potential. In this work, we have used the extended principle of corresponding states (12) to obtain the viscosity collision integrals,  $\Omega_{cs}^{(2,2)*}$ , and then using eq. [20] the collision integrals at zero pressure,  $\Omega_o^{(2,2)*}$ , can be obtained.



**Fig. 2.** Reduced potential energy function of krypton by inversion of corresponding states reduced-viscosity collision integrals ( $\blacktriangle$ ) (22) and by inversion of reduced-viscosity collision integrals at zero pressure ( $\square$ ). The solid curve is the Aziz and Slaman potential (19).

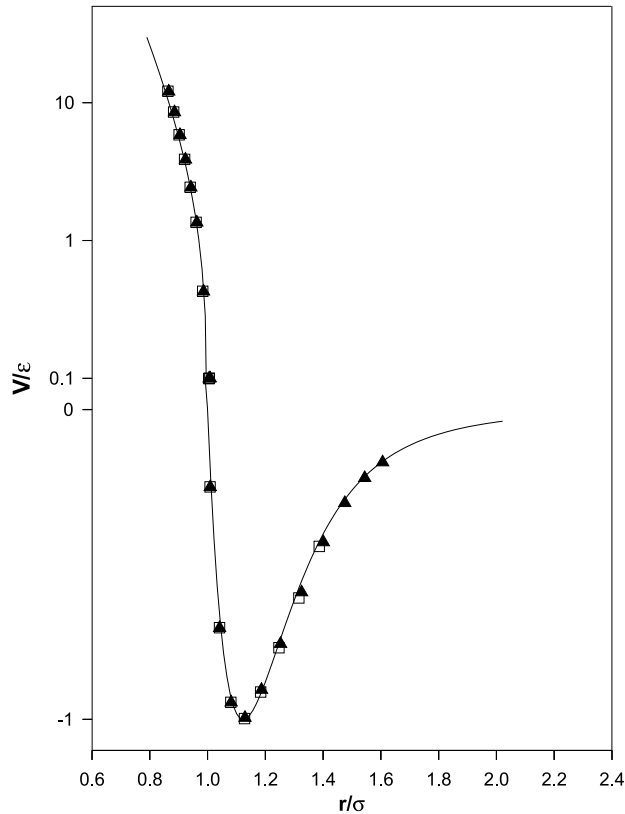
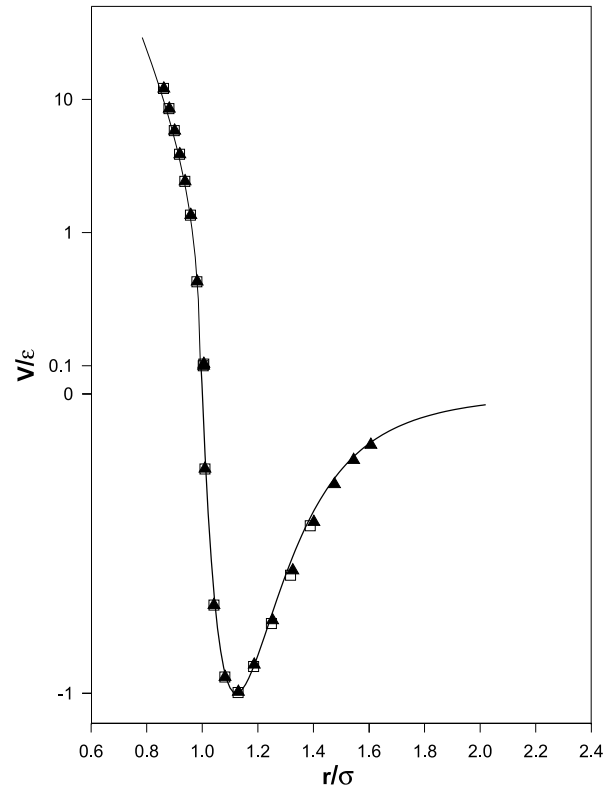


**Fig. 3.** Reduced potential energy function of xenon by inversion of corresponding states reduced-viscosity collision integrals ( $\blacktriangle$ ) (22) and by inversion of reduced-viscosity collision integrals at zero pressure ( $\square$ ). The solid curve is the Dham et al. potential (20).



**Results**

The potential energy functions of argon, krypton, and xenon have been obtained using the inversion of the reduced-viscosity collision integrals at zero pressure. A comparison of these potentials with the previously determined potentials (19–23) are included (Figs. 1–3). These accurate potentials can be used to obtain the kinetic-theory collision integrals needed to calculate transport properties other than viscosity. The most commonly needed collision integrals and their ratios for argon, krypton, and xenon at zero pressure are given in Tables 1–3.

The accurate tables of the viscosity and thermal conductivity for argon, krypton, and xenon have been generated in the temperature range from the normal boiling point of the relevant gas up to 5000 K for zero density and for different pressures. The results are summarized in Tables 4 and 5, including the pressure range,  $P_{\min}$ – $P_{\max}$ , and the temperature range,  $T_{\min}$ – $T_{\max}$ , along with the minimum and maximum percent deviation of the calculated values from their corresponding literature values.

**Concluding remarks**

As Figs. 1 to 3 show, there exists a good agreement between the potentials calculated by the inversion of corre-

**Table 1.** Dimensionless collision integrals  $\Omega^{(l,s)*} = \Omega^{(l,s)}/\pi\sigma^2$  and the related ratios for argon at 0 atm (1 atm = 101.325 kPa).

$\log_{10} T^*$	$\Omega^{*(1,1)}$	$\Omega^{*(1,2)}$	$\Omega^{*(2,2)}$	$\Omega^{*(1,3)}$	$B^*$	$C^*$
–0.1	1.5740	1.3179	1.7539	1.1638	1.2288	0.8373
0.0	1.4095	1.1899	1.5659	1.0656	1.1970	0.8442
0.1	1.2705	1.0875	1.4051	0.9886	1.1673	0.8559
0.2	1.1558	1.0061	1.2730	0.9273	1.1430	0.8705
0.3	1.0624	0.9409	1.1672	0.8773	1.1251	0.8856
0.4	0.9866	0.8876	1.0835	0.8349	1.1134	0.8997
0.5	0.9245	0.8428	1.0170	0.7977	1.1070	0.9117
0.6	0.8727	0.8037	0.9635	0.7636	1.1047	0.9210
0.7	0.8283	0.7685	0.9191	0.7318	1.1049	0.9277
0.8	0.7893	0.7358	0.8806	0.7016	1.1059	0.9323
0.9	0.7540	0.7053	0.8454	0.6732	1.1053	0.9353
1.0	0.7217	0.6769	0.8115	0.6475	1.1011	0.9379
1.1	0.6921	0.6513	0.7776	0.6252	1.0917	0.9410
1.2	0.6654	0.6291	0.7435	0.6072	1.0772	0.9454
1.3	0.6421	0.6110	0.7099	0.5937	1.0594	0.9516
1.4	0.6226	0.5972	0.6783	0.5845	1.0409	0.9593
1.5	0.6067	0.5873	0.6499	0.5788	1.0238	0.9679
1.6	0.5954	0.5812	0.6275	0.5761	1.0109	0.9761
1.7	0.5873	0.5772	0.6096	0.5751	1.0014	0.9837
1.8	0.5820	0.5762	0.5968	0.5754	0.9954	0.9900
1.9	0.5790	0.5761	0.5882	0.5765	0.9923	0.9949
2.0	0.5777	0.5768	0.5830	0.5778	0.9911	0.9983

**Note:**  $B^* = [5\Omega^{(1,2)*} - 4\Omega^{(1,3)*}] / \Omega^{(1,1)}$  and  $C^* = \Omega^{(1,2)*} / \Omega^{(1,1)*}$ .



**Table 2.** Dimensionless collision integrals  $\Omega^{(l,s)*} = \Omega^{(l,s)}/\pi\sigma^2$  and the related ratios for krypton at 0 atm.

$\log_{10} T^*$	$\Omega^{*(1,1)}$	$\Omega^{*(1,2)}$	$\Omega^{*(2,2)}$	$\Omega^{*(1,3)}$	$B^*$	$C^*$
-0.1	1.5483	1.3127	1.7334	1.1649	1.2299	0.8479
0.0	1.3953	1.1888	1.5567	1.0672	1.2004	0.8520
0.1	1.2634	1.0880	1.4023	0.9901	1.1711	0.8612
0.2	1.1527	1.0071	1.2732	0.9286	1.1463	0.8737
0.3	1.0614	0.9419	1.1686	0.8782	1.1277	0.8875
0.4	0.9865	0.8885	1.0852	0.8355	1.1154	0.9006
0.5	0.9248	0.8433	1.0187	0.7979	1.1086	0.9120
0.6	0.8730	0.8040	0.9650	0.7636	1.1060	0.9209
0.7	0.8285	0.7684	0.9203	0.7314	1.1060	0.9274
0.8	0.7893	0.7356	0.8815	0.7011	1.1066	0.9320
0.9	0.7539	0.7048	0.8459	0.6727	1.1057	0.9350
1.0	0.7214	0.6764	0.8116	0.6469	1.1012	0.9376
1.1	0.6917	0.6507	0.7774	0.6247	1.0916	0.9408
1.2	0.6649	0.6286	0.7430	0.6068	1.0769	0.9454
1.3	0.6416	0.6106	0.7092	0.5934	1.0589	0.9516
1.4	0.6222	0.5969	0.6777	0.5843	1.0404	0.9594
1.5	0.6067	0.5873	0.6499	0.5788	1.0238	0.9679
1.6	0.5952	0.5811	0.6269	0.5760	1.0105	0.9763
1.7	0.5871	0.5776	0.6093	0.5751	1.0011	0.9839
1.8	0.5819	0.5762	0.5965	0.5754	0.9953	0.9902
1.9	0.5790	0.5761	0.5881	0.5765	0.9922	0.9950
2.0	0.5777	0.5768	0.5829	0.5778	0.9911	0.9984

**Table 3.** Dimensionless collision integrals  $\Omega^{(l,s)*}$  and the related ratios for xenon at 0 atm.

$\log_{10} T^*$	$\Omega^{(1,1)*}$	$\Omega^{(1,2)*}$	$\Omega^{(2,2)*}$	$\Omega^{(1,3)*}$	$B^*$	$C^*$
-0.1	1.5464	1.3109	1.7336	1.1629	1.2306	0.8477
0.0	1.3934	1.1869	1.5562	1.0654	1.2007	0.8518
0.1	1.2615	1.0862	1.4011	0.9883	1.1713	0.8610
0.2	1.1508	1.0053	1.2716	0.9268	1.1464	0.8736
0.3	1.0596	0.9402	1.1668	0.8765	1.1277	0.8873
0.4	0.9848	0.8868	1.0833	0.8339	1.1153	0.9005
0.5	0.9231	0.8418	1.0167	0.7965	1.1084	0.9119
0.6	0.8714	0.8025	0.9631	0.7623	1.1057	0.9209
0.7	0.8271	0.7671	0.9184	0.7303	1.1057	0.9275
0.8	0.7880	0.7344	0.8797	0.7001	1.1063	0.9320
0.9	0.7527	0.7038	0.8443	0.6718	1.1055	0.9351
1.0	0.7203	0.6755	0.8101	0.6461	1.1009	0.9378
1.1	0.6907	0.6500	0.7760	0.6240	1.0911	0.9410
1.2	0.6641	0.6280	0.7417	0.6063	1.0763	0.9456
1.3	0.6409	0.6101	0.7080	0.5931	1.0583	0.9519
1.4	0.6216	0.5966	0.6766	0.5841	1.0399	0.9597
1.5	0.6063	0.5870	0.6490	0.5787	1.0233	0.9682
1.6	0.5949	0.5809	0.6262	0.5759	1.0102	0.9766
1.7	0.5869	0.5776	0.6087	0.5751	1.0009	0.9841
1.8	0.5818	0.5762	0.5962	0.5755	0.9951	0.9904
1.9	0.5789	0.5761	0.5878	0.5765	0.9921	0.9951
2.0	0.5777	0.5768	0.5828	0.5779	0.9910	0.9985

sponding states reduced-viscosity collision integrals (20–23) and by the inversion of the reduced-viscosity collision integrals at zero pressure with the accurate potentials (19, 20). The potentials obtained by the inversion of the corresponding states reduced-viscosity collision integral show little deviation at long range, where the attractive forces

**Table 4.** The pressure and temperature ranges of calculated viscosity.

Fluid	$P_{\min}-P_{\max}$ (MPa)	$T_{\min}-T_{\max}$ (K)	$100(\eta_{\text{calcd}} - \eta_{\text{expt}})/\eta_{\text{expt}}$ (min–max)
Ar <sup>a</sup>	0.101–90	87.28–5000	0.08–1.49
Kr <sup>b</sup>	0.101–10.11	119.78–5000	0.07–1.22
Xe <sup>c</sup>	0.101–80	165.03–1250	0.06–0.78

<sup>a</sup>References 24–28.<sup>b</sup>References 24, 29.<sup>c</sup>References 24, 30.**Table 5.** The pressure and temperature range of calculated thermal conductivity.

Fluid	$P_{\min}-P_{\max}$ (MPa)	$T_{\min}-T_{\max}$ (K)	$100(\lambda_{\text{calcd}} - \lambda_{\text{expt}})/\lambda_{\text{expt}}$ (min–max)
Ar <sup>a</sup>	0.101–400	87.28–600	0.80–2.40
Kr <sup>b</sup>	0.101–100	119.78–600	0.52–1.20
Xe <sup>b</sup>	0.101–100	165.03–600	0.6–1.00

<sup>a</sup>References 24, 31–33.<sup>b</sup>Reference 31.

dominate, since the density dependence of viscosity is very significant at low temperatures. Therefore, the potentials obtained in this work are superior representations to those provided by the inversion of the corresponding states reduced-viscosity collision integrals (21–23).

The results show that the density dependence of the viscosity is much weaker at higher temperature. This is due to the diminishing of the monomer–dimer contribution and the near cancellation of the two-monomer and three-monomer contributions at high temperatures (15).

From the present results, we can draw some important conclusions:

1. The remarkable feature of the inversion method employed in this work is that the specific information about potential energy function is obtained using experimental data directly without assuming a functional form for the potential.

The present potentials for argon, krypton, and xenon provide a good overall account of the experimental properties of these compounds, considering the stated uncertainty in their measurements.

2. The present paper provides the collision integrals and their ratios for argon, krypton, and xenon at zero density, for which one would need to calculate the transport coefficients of these compounds in the moderate and high densities ranges, at any temperature, in a predictive mode, within experimental errors.

4. This work results in much greater confidence in the precision and (or) accuracy of transport coefficients in the moderately and highly dense regions of argon, krypton, and xenon than those found in previous, similar works (21–23).

## References

1. D.W. Gough, G.C. Maitland, and E.B. Smith. *Mol. Phys.* **24**, 151 (1972).
2. A. Boushehri, L.A. Viehland, and E.A. Mason. *Chem. Phys.* **28**, 313 (1977).



3. E.K. Goharshadi. *Int. J. Thermophys.* **19**, 227 (1998).
4. E.K. Goharshadi, Z. MirAfzali, and Z. Tavangar. *J. Phys. Soc. Jpn.* **67**, 4296 (1998).
5. J.A. Anta, E. Lomba, and M. Lombardero. *Phys. Rev.* **55**, 2707 (1997).
6. G. Marcelli and R.J. Sadus. *J. Chem. Phys.* **111**, 1533 (1999).
7. R. Bukowski and K. Szalewicz. *J. Chem. Phys.* **114**, 9518 (2001).
8. J.O. Hirschfelder, C.F. Curtiss, and R.B. Bird. *Molecular theory of gases and liquids*. 4th ed. John Wiley and Sons Inc., New York. 1954.
9. S. Chapman and T.G. Cowling. *The mathematical theory of non-uniform gases*. 3rd ed. Cambridge University Press, New York. 1970.
10. D.W. Gough, G.P. Matthews, E.B. Smith, and G.C. Maitland. *Mol. Phys.* **29**, 1759 (1975).
11. B. Najafi, E.A. Mason, and J. Kestin. *Physica*, **119A**, 387 (1983).
12. A. Boushehri, J. Bzowski, J. Kestin, and E.A. Mason. *J. Phys. Chem. Ref. Data*, **16**, 445 (1987).
13. D.G. Friend and J.C. Rainwater. *Chem. Phys. Lett.* **107**, 590 (1984).
14. D.G. Friend and J.C. Rainwater. *Phys. Rev.* **36A**, 4062 (1987).
15. B. Najafi, Y. Ghayeb, J.C. Rainwater, S. Alavi, and R.F. Sinder. *Physica*, **260A**, 31 (1998).
16. B. Najafi, Y. Ghayeb, and G.A. Parsafar. *Int. J. Thermophys.* **21**, 1011 (2000).
17. B. Najafi, R. Araghi, J.C. Rainwater, S. Alavi, and R.F. Sinder. *Physica*, **275A**, 48 (2000).
18. E.K. Goharshadi and A. Boushehri. *Bull. Chem. Soc. Jpn.* **68**, 1859 (1995).
19. R.A. Aziz and M.J. Slaman. *Mol. Phys.* **58**, 679 (1986).
20. A.K. Dham, W.J. Meath, A.R. Allnatt, R.A. Aziz, and M.J. Slaman. *Chem. Phys.* **142**, 173 (1990).
21. A. Boushehri and A. Maghari. *J. Phys. Soc. Jpn.* **59**, 4302 (1990).
22. A. Boushehri and J.M. Absardi. *Bull. Chem. Soc. Jpn.* **62**, 1313 (1989).
23. A. Boushehri and M.H. Mousazadeh. *J. Phys. Soc. Jpn.* **64**, 331 (1995).
24. E. Bich, J. Millat, and E. Vogel. *Phys. Chem. Ref. Data*, **19**, 1289 (1990).
25. J. Slaman and R.A. Aziz. *Int. J. Thermophys.* **12**, 837 (1991).
26. R.A. Dawe and E.B. Smith. *J. Chem. Phys.* **52**, 693 (1970).
27. B.A. Younglove and H.J.M. Hanley. *J. Phys. Chem. Ref. Data*, **15**, 1323 (1986).
28. N.J. Trappeniers, P.S. van der Gulik, and H. van den Hooff. *Chem. Phys. Lett.* **70**, 438 (1980).
29. N.J. Trappeniers, A. Botzen, J. van Oosten, and H.R. van den Berg. *Physica*, **31**, 945 (1965).
30. N.B. Vargaftic. *Handbook of physical properties of liquids and gases*. 2nd ed. Hemisphere, New York. 1983.
31. J. Kestin, R. Paul, A. Clifford, and W.A. Wakeham. *Physica*, **100A**, 349 (1980).
32. B.W. Tiesinga, E.P. Sakonidou, H.R. van den Berg, J. Luethmann-Strathmann, and J.V. Sengers. *J. Chem. Phys.* **101**, 6944 (1994).
33. R.A. Perkins, D.G. Friend, H.M. Roder, and C.A. Nieto de Castro. *Int. J. Thermophys.* **12**, 965 (1991).



# Synthesis, characterization, and molecular structures of nitrosyl nitrito complexes of osmium porphyrins: Disproportionation of nitric oxide in its reaction with Os(P)(CO) (P = porphyrinato dianion)

Felipe A. Leal, Ivan M. Lorkovic, Peter C. Ford, Jonghyuk Lee, Li Chen, Lindsey Torres, Masood A. Khan, and George B. Richter-Addo

**Abstract:** The Os(P)(NO)(ONO) compounds (P = TTP, TMP, OEP, TmTP; TTP = 5,10,15,20-tetra-*p*-tolylporphyrinato dianion, TMP = 5,10,15,20-tetramesitylporphyrinato dianion, OEP = octaethylporphyrinato dianion, TmTP = tetra(*m*-tolyl)porphyrinato dianion) have been prepared from the reaction of the precursor carbonyl complexes Os(P)(CO) with excess nitric oxide. Nitrous oxide was detected as a by-product of the reaction. The IR spectra of the Os(P)(NO)(ONO) compounds (as KBr pellets) reveal bands in the 1790–1804 cm<sup>-1</sup> range that are assigned to  $\nu_{\text{NO}}$ . The IR spectra also reveal two new bands for each complex in the 1495–1531 and 913–962 cm<sup>-1</sup> ranges indicative of O-bound nitrito ligands. The linearity of the bound NO groups and the O-binding of the *trans* nitrito ligands in the Os(P)(NO)(ONO) complexes are evident in the single-crystal X-ray crystal structures of the TTP and TMP derivatives. The kinetics of the reaction were studied by stopped-flow mixing techniques. Spectroscopic analysis of rapidly mixed solutions of Os(P)CO and NO in toluene showed a biphasic approach to the Os(P)(NO)(ONO) and N<sub>2</sub>O products, owing to the starting material Os(P)CO scavenging CO formed during the reaction to give Os(P)(CO)<sub>2</sub> ( $K_{\text{CO}} = 10^6 \text{ M}^{-1}$ ). The dicarbonyl was the only transient species observed. It is proposed that the rate-determining step of the reaction leading to Os(P)(NO)(ONO) is NO displacement of CO from Os(P)(CO) via initial formation of an unstable 19 electron Os(P)(NO)(CO) intermediate.

**Key words:** osmium, nitric oxide, X-ray, nitrosyl, porphyrin, kinetics.

**Résumé :** Les composés du type Os(P)(NO)(ONO), où P = TTP, TMP, OEP, TmTP; TTP= le dianion 5,10,15,20-tétra-*p*-tolylporphyrinato, TMP = le dianion 5,10,15,20-tétramésitylporphyrinato, OEP = le dianion octaéthylporphyrinato, TmTP = le dianion tétra(*m*-tolyl)porphyrinato, ont été préparés à partir de la réaction des complexes carbonylés précurseurs OS(P)(CO) en présence d'un excès d'oxyde nitrique. On a détecté l'oxyde nitreux comme produit secondaire de la réaction. Les spectres IR des composés Os(P)(NO)(ONO) (sous forme de pastilles de KBr) révèlent des bandes dans la région de 1790–1804 cm<sup>-1</sup> que l'on attribue à la vibration  $\nu_{\text{NO}}$ . Les spectres IR révèlent également, pour chaque complexe, deux nouvelles bandes dans les régions : 1495–1531 et 913–962 cm<sup>-1</sup> caractéristiques des ligands nitrito liés par l'oxygène. La linéarité des liens des groupes NO et le lien impliquant l'oxygène des ligands nitrito *trans* dans les complexes Os(P)(NO)(ONO) apparaissent clairement dans les structures des dérivés TTP et TMP déterminées par cristallographie de rayons X sur un monocristal. On a étudié la cinétique de la réaction par les techniques de mélange à flux stoppé. L'analyse spectroscopique des solutions OS(P)CO et de NO rapidement mélangées dans le toluène montrent une approche biphasique aux produits Os(P)(NO)(ONO) et N<sub>2</sub>O à cause du produit de départ OS(P)CO qui piège le CO formé au cours de la réaction pour donner le OS(P)(CO)<sub>2</sub> ( $K_{\text{CO}} = 10^6 \text{ M}^{-1}$ ). Le composé dicarbonylé est la seule espèce transitoire observée. On suggère que l'étape déterminante de la réaction conduisant au Os(P)(NO)(ONO) est le déplacement du CO par NO à partir du OS(P)(CO) via la formation initiale d'un intermédiaire instable Os(P)(NO)(CO) à 19 électrons.

**Mots clés :** osmium, oxyde nitrique, rayons X, nitrosyle, porphyrine, cinétique.

[Traduit par la Rédaction]

Received 14 November 2002. Published on the NRC Research Press Web site at <http://canjchem.nrc.ca> on 14 July 2003.

**F.A. Leal, I.M. Lorkovic, and P.C. Ford.**<sup>1</sup> Department of Chemistry and Biochemistry, University of California, Santa Barbara, California 93106, U.S.A.

**J. Lee, L. Chen, L. Torres, M.A. Khan, and G.B. Richter-Addo.**<sup>2</sup> Department of Chemistry and Biochemistry, University of Oklahoma, 620 Parrington Oval, Norman, Oklahoma 73019, U.S.A.

<sup>1</sup>Corresponding author (e-mail: [ford@chem.ucsb.edu](mailto:ford@chem.ucsb.edu)).

<sup>2</sup>Corresponding author (e-mail: [grichteraddo@ou.edu](mailto:grichteraddo@ou.edu)).



## Introduction

Metalloporphyrin-induced  $\text{NO} \rightarrow \text{N}_2\text{O}$  conversions are very important biologically in the global nitrogen cycle (1). For example, nitric oxide reductase cytochrome P450<sub>nor</sub> from the fungus *Fusarium oxysporum* reduces NO to  $\text{N}_2\text{O}$ , and the enzyme contains heme at the active site (2, 3). The bacterial nitric oxide reductase from *Paracoccus denitrificans* also contains heme at the dinuclear active site and catalyzes the reduction of NO to  $\text{N}_2\text{O}$  (4, 5). The subject of biological NO reduction has been recently reviewed (1).

Heme-dependent NO oxidations are gaining widespread recognition in the chemistry of NO. For example, some flavohemoglobins have recently been described as NO dioxygenases (6, 7). Metal-assisted  $\text{NO} \rightarrow \text{NO}_2$  conversions are also important in the biological and urban environment. In particular, knowledge of the efficiency of metal-assisted conversions of  $\text{NO} \rightarrow \text{N}_x\text{O}_y$  is an essential component in the design of catalytic converters for automobile engines (8). While the mechanisms of such conversions are not known with certainty, synthetic metal complexes that catalyze the formation of  $\text{NO}_2$  (bound or free) from NO and vice versa, as well as the structures of metal- $\text{NO}_2$  coordination complexes, are of interest in this regard. In some instances, the addition of oxygen (or air) to the metal-NO precursor is necessary for the production of the metal- $\text{NO}_2$  complex. We recently demonstrated such a metal-NO to metal- $\text{NO}_2$  conversion using an iron nitrosyl porphyrin (9). Other metalloporphyrin-NO complexes of Co and Rh have been shown to behave similarly (10, 11).

There are many examples of non-heme transition metal complexes that promote NO disproportionation to give metal nitrite derivatives and  $\text{N}_2\text{O}$  (12). However, we have found that ferrous porphyrins do *not* promote NO disproportionation in the absence of oxygen; they react with NO to produce only mononitrosyl or weakly bound dinitrosyl complexes (13). The apparently contradictory results concerning the ability of iron porphyrins to promote the disproportionation of NO (in the presence or absence of trace air) are discussed in ref. 14. Iron porphyrin nitrite complexes containing the N-bound nitrite ligand are known, and their solid-state structures have been reviewed (15). We reported that ruthenium porphyrins react with NO *in the absence of oxygen* to produce the nitrosyl nitrito complexes  $\text{Ru(P)(NO)(ONO)}$  and  $\text{N}_2\text{O}$  (16–18), and we spectroscopically characterized a *trans*-dinitrosyl intermediate  $\text{Ru(P)(NO)}_2$  during this NO disproportionation reaction (19, 20). The occurrence of NO disproportionation with ruthenium, but not with iron, led us to extend these studies to the osmium porphyrin congeners.

In this paper, we show that osmium porphyrins react with NO to give nitrosyl nitrito products with the release of  $\text{N}_2\text{O}$ . Solid-state molecular structures for two of these nitrosyl nitrito products have been obtained and, to the best of our knowledge, represent the first published osmium nitrito X-ray crystal structures to be reported. While the products are analogous to those found for the reaction of NO with similar ruthenium porphyrins  $\text{Ru(P)(CO)}$  (19, 20), unlike the ruthenium analogues, reactions of NO with  $\text{Os(P)(CO)}$  proceed without the generation of observable nitrosyl-containing intermediates. Instead, the CO released from reaction of NO

with  $\text{Os(P)(CO)}$  is scavenged by the remaining  $\text{Os(P)(CO)}$  to give the dicarbonyl complex  $\text{Os(P)(CO)}_2$  in a “dead-end” equilibrium. The latter eventually is also converted to  $\text{Os(P)(NO)(ONO)}$ .

## Experimental section

All reactions were performed under an atmosphere of prepurified nitrogen using standard Schlenk glassware and (or) in an Innovative Technology Labmaster 100 Dry Box. Solutions for spectral studies were also prepared under a nitrogen atmosphere. Solvents were distilled from appropriate drying agents under nitrogen just prior to use: benzene (Na), toluene (Na or  $\text{CaH}_2$ ), hexane, chloroform, and cyclohexane ( $\text{CaH}_2$ ).

### Chemicals

The  $\text{Os(P)(CO)}$  compounds were prepared by literature methods (P = TTP, TMP, OEP, TmTP; TTP = 5,10,15,20-tetra-*p*-tolylporphyrinato dianion, TMP = 5,10,15,20-tetramesitylporphyrinato dianion, OEP = octaethylporphyrinato dianion, TmTP = tetra(*m*-tolyl)porphyrinato dianion) (21).  $\text{Os(OEP)(CO)}$  was also purchased from Midcentury Chemicals. Chloroform-*d* (99.8%) was obtained from Cambridge Isotope Laboratories. Nitric oxide (98%, Matheson Gas) for the synthesis work was passed through KOH pellets and two cold traps (dry ice–acetone,  $-78^\circ\text{C}$ ) to remove higher nitrogen oxides. For experiments involving detection of evolved  $\text{N}_2\text{O}$ , NO was purified as described elsewhere (14).

### Instrumentation

Infrared spectra were recorded on a Bio-Rad FT-155 FT-IR spectrometer.  $^1\text{H}$  NMR spectra were obtained on Varian 300 MHz or 400 MHz spectrometers and the signals referenced to the residual signal of the solvent employed. All coupling constants are in Hz. FAB mass spectra were obtained on a VG-ZAB-E mass spectrometer.

### Preparation of $\text{Os(TTP)(NO)(ONO)}$

A Schlenk flask was charged with  $\text{Os(TTP)(CO)}$  (0.055 g, 0.062 mmol) and benzene (30 mL). The mixture was stirred to generate an orange-red solution, and NO gas was then bubbled through the solution for ~15 min. The solvent was removed in vacuo, and the residue was redissolved in benzene (10 mL) and filtered through a neutral alumina column ( $1.5 \times 15$  cm). The red band was collected and dried in vacuo. The product was further purified by crystallization from a toluene–hexane mixture at  $-20^\circ\text{C}$  to give  $\text{Os(TTP)(NO)(ONO)}$  (0.025 g, 0.027 mmol, 43% isolated yield). IR (KBr) ( $\text{cm}^{-1}$ ):  $\nu_{\text{NO}}$  = 1804 (s),  $\nu_{\text{ONO}}$  = 1528 (m), 921 (m).  $^1\text{H}$  NMR ( $\text{CDCl}_3$ )  $\delta$ : 9.00 (s, 8H, pyrrole-H of TTP), 8.15 (d,  $J$  = 8 Hz, 4H, *o*-H of TTP), 8.05 (d,  $J$  = 8 Hz, 4H, *o'*-H of TTP), 7.56 (app t (overlapping d's), 8H, *m/m'*-H of TTP), 2.70 (s, 12H,  $\text{CH}_3$  of TTP). Low-resolution FAB-MS  $m/z$  (%): 906 ( $[\text{Os(TTP)(ONO)}]^+$ , 15%), 890 ( $[\text{Os(TTP)(NO)}]^+$ , 100%), 860 ( $[\text{Os(TTP)}]^+$ , 18%). This compound was prepared previously in low yield from the reaction of  $\text{Os(TTP)(NO)(S-}i\text{-C}_5\text{H}_{11})$  with excess NO (22).



### Preparation of Os(TMP)(NO)(ONO)

A Schlenk flask was charged with Os(TMP)(CO) (0.082 g, 0.082 mmol) and benzene (30 mL). The mixture was stirred to generate a dark orange-red solution, and NO gas was then bubbled through the solution for 30 min. During this time, the color of the reaction mixture turned bright red. The solvent was removed in vacuo, and the residue was redissolved in benzene (15 mL) and filtered through a neutral alumina column (2 × 20 cm). The red band was collected, and the filtrate was dried in vacuo to give Os(TMP)(NO)(ONO) (0.077 g, 0.073 mmol, 90% isolated yield). IR (KBr) (cm<sup>-1</sup>):  $\nu_{\text{NO}}$  = 1799 (s),  $\nu_{\text{ONO}}$  = 1531 (m), 919 (m). <sup>1</sup>H NMR (CDCl<sub>3</sub>)  $\delta$ : 8.77 (s, 8H, *pyrrole*-H of TMP), 7.29 (s, 4H, *m*-H of TMP), 7.26 (s, 4H, *m'*-H of TMP), 2.62 (s, 12H, *p*-CH<sub>3</sub> of TMP), 1.95 (s, 12H, *o*-CH<sub>3</sub> of TMP), 1.69 (s, 12H, *o'*-CH<sub>3</sub> of TMP). Low-resolution FAB-MS *m/z* (%): 1048 ([Os(TMP)(NO)(ONO)]<sup>+</sup>, 6%), 1019 ([Os(TMP)(ONO) + H]<sup>+</sup>, 43%), 1002 ([Os(TMP)(NO)]<sup>+</sup>, 100%), 972 ([Os(TMP)]<sup>+</sup>, 13%).

The following two compounds were also prepared similarly.

### Os(OEP)(NO)(ONO)

43% isolated yield. IR (KBr) (cm<sup>-1</sup>):  $\nu_{\text{NO}}$  = 1790 (s),  $\nu_{\text{ONO}}$  = 1495 (m), 962 (s br (overlap with porphyrin band)). <sup>1</sup>H NMR (CDCl<sub>3</sub>)  $\delta$ : 10.41 (s, 4H, *meso*-H of OEP), 4.16 (q, *J* = 8 Hz, 16H, CH<sub>2</sub>CH<sub>3</sub> of OEP), 2.00 (t, *J* = 8 Hz, 24H, CH<sub>2</sub>CH<sub>3</sub> of OEP). This compound has similar spectral properties to a compound formulated as Os(OEP)(NO)<sub>2</sub> (23).

### Os(TmTP)(NO)(ONO)

This compound was obtained in 95% yield (by <sup>1</sup>H NMR spectroscopy) when the reaction was performed in dry toluene or methylcyclohexane and in 25% yield (by <sup>1</sup>H NMR spectroscopy) when performed in CH<sub>2</sub>Cl<sub>2</sub>. The compound was further purified by chromatography over silica gel using a pentane–CH<sub>2</sub>Cl<sub>2</sub> (2:1) solvent mixture. IR (KBr) (cm<sup>-1</sup>):  $\nu_{\text{NO}}$  = 1803 (s),  $\nu_{\text{ONO}}$  = 1528 (m), 913 (m). IR (cyclohexane) (cm<sup>-1</sup>):  $\nu_{\text{NO}}$  = 1805 (s),  $\nu_{\text{ONO}}$  = 1540 (m). <sup>1</sup>H NMR (CDCl<sub>3</sub>)  $\delta$ : 9.02 (s, 8H, *pyrrole*-H of TmTP), 8.10 (m, 4H, *o*-H of TmTP), 7.99 (m, 4H, *o'*-H of TmTP), 7.50–7.60 (m, 8H, *m/p*-H of TmTP), 2.66 (s, 6H, CH<sub>3</sub> of TmTP), 2.62 (s, 6H, CH<sub>3</sub> of TmTP).

### Kinetics experiments

NO was plumbed via stainless steel lines through a stainless steel column of Ascarite (Thomas Scientific) to scrub out NO<sub>2</sub> and (or) N<sub>2</sub>O<sub>3</sub>. When desired, the N<sub>2</sub>O impurity was removed by passage of NO through a cold (–78°C) activated silica column (6' × 1/4" i.d. stainless steel, Alltech). NO was quantified manometrically using known solubilities in toluene and cyclohexane (24) and transferred cryogenically to desired reaction flasks of known total volume and solution volume fitted with Teflon high vacuum stopcocks. Infrared solution spectra were recorded in amalgam-sealed cells with CaF<sub>2</sub> windows (ICL) on a Bio-Rad FTS-60 FT-IR

instrument. Stopped-flow mixing experiments were performed on an Applied Photophysics SX17-MV instrument with custom made tonometers (20) for NO solution preparation and transfer to drive syringes. Flow IR experiments were performed with a home-built, manually actuated stopped-flow mixing apparatus utilizing gas tight syringes (Hamilton 5 mL) and PEEK tubing, valves, and fittings (Upchurch), connected after mixing to a standard amalgam-sealed CaF<sub>2</sub> cell inserted into the FT-IR instrument. To avoid back-pressure-induced IR cell rupture, the stop syringe was disconnected and the output directed to a waste container. FT-IR spectra showing intermediate species in the reaction of Os(P)(CO) with NO were obtained by a single interferometric scan during constant flow of freshly mixed (aging time ~0.2 s) solutions through the cell.

### CO binding equilibrium constant measurements

Carbon monoxide (Praxair, 99.5%) was added by gas-tight syringe to toluene solutions (~5 mL) of Os(OEP)(CO) and Os(TmTP)(CO) (~8  $\mu$ M) under Ar (*P*<sub>T</sub> = 760 torr (1 torr = 133.322 Pa)) within special cuvette cells (~70 mL total volume) at 21 ± 1°C. [CO] was calculated from the known solubility of CO in toluene (25) and the known volume of solution and headspace. Under these conditions the [CO] may be less than [Os] within the solution, but the total amount of CO within the closed system of the cell is always at least ten times greater than the amount of Os in the solution, and therefore [CO] may be considered to be constant, independent of the extent of reaction.

### Structural determinations by X-ray crystallography

Crystal data were collected on a Siemens (Bruker) P4 diffractometer using monochromated Mo K $\alpha$  radiation ( $\lambda$  = 0.71073 Å).<sup>3</sup> The data were corrected for Lorentz and polarization effects, and empirical absorption corrections based on  $\psi$ -scans were applied (26). The structures were solved by the heavy atom method using the SHELXTL 5.03 (Bruker) system and refined by full-matrix least squares on *F*<sup>2</sup> using all reflections (SHELXL-93). The thermal ellipsoids in Figs. 1 and 2 are drawn at the 35% probability level. Details of the crystal data and refinement are given in Table 1.

### Os(TTP)(NO)(ONO):toluene

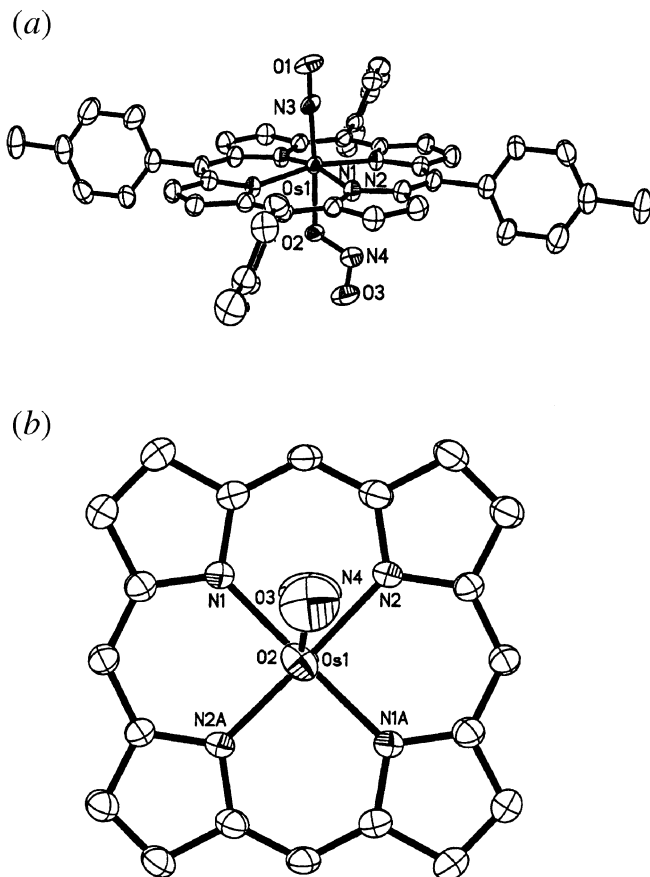
A suitable crystal for structure determination was grown by recrystallization of the compound from toluene–hexane at –20°C. All the non-hydrogen atoms were refined anisotropically except the atoms (C25–C33) belonging to the disordered toluene molecules, which were refined isotropically. Hydrogen atoms were included in the refinement with idealized parameters; the hydrogen atoms for the disordered solvent molecules were not included.

Considerable difficulty was encountered during the refinement because of the disorder of the Os atom and the atoms belonging to the axial groups and the solvent molecules. The structure was solved initially in the non-centric space group *Cc* and gave very poor refinement with unreasonable N—O

<sup>3</sup>Supplementary data (drawings and tables of crystallographic data for Os(TTP)(NO)(ONO) and Os(TMP)(NO)(ONO)) may be purchased from the Depository of Unpublished Data, Document Delivery, CISTI, National Research Council Canada, Ottawa, ON K1A 0S2, Canada ([http://www.nrc.ca/cisti/irm/unpub\\_e.shtml](http://www.nrc.ca/cisti/irm/unpub_e.shtml) for information on ordering electronically). CCDC 214514 and 214515 contain the supplementary data for this paper. These data can be obtained, free of charge, via [www.ccdc.cam.ac.uk/conts/retrieving.html](http://www.ccdc.cam.ac.uk/conts/retrieving.html) (or from the Cambridge Crystallographic Data Centre, 12 Union Road, Cambridge, U.K.; fax +44 1223 336033; or [deposit@ccdc.cam.ac.uk](mailto:deposit@ccdc.cam.ac.uk)).

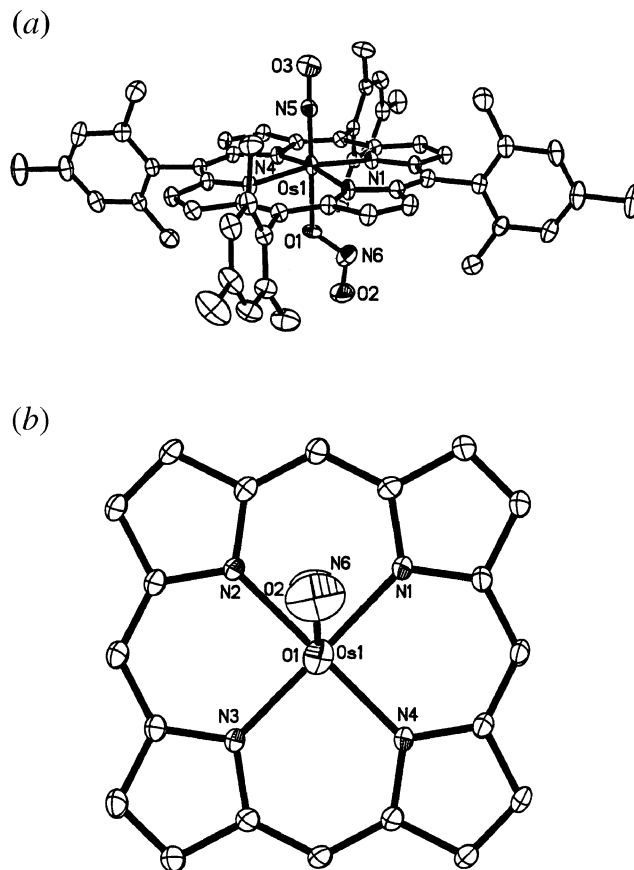


**Fig. 1.** (a) Molecular structure of Os(TTP)(NO)(ONO). Hydrogen atoms have been omitted for clarity. Only one of the two disordered positions of the Os atom and the NO and ONO groups is shown; (b) View of the orientation of the nitrito ligand relative to the porphyrin skeleton. The porphyrin tolyl substituents and the *trans* NO ligand have been omitted for clarity.



and O—N—O bond lengths and several non-positive definite temperature factors. The structure was then solved and refined in the centric space group  $C2/c$ , where the molecule lies on the inversion center and only half of the molecule is unique. Thus, the axial NO and ONO groups are disordered over both sides of the porphyrin plane. The initial refinement used a model in which the Os atom was placed on a special position at the inversion center. This model gave elongated thermal ellipsoids for the Os atom, and the Os—N3 and Os—O2 distances were unreasonable. Finally, the Os atom was allowed to refine out of the porphyrin plane towards the NO ligand (0.241(3) Å out of the 24-atom mean porphyrin plane). In the final model, the Os atom and the NO and ONO groups are completely disordered over two sites. In addition to the disorder of the molecule, the crystal lattice contains two sites with partially disordered toluene solvent molecules. One of these toluene solvent sites is 50% populated, and the other site is also 50% populated; disorder at these sites results in the two sites having only 25% occupancy. The toluene solvent molecules were refined isotropically because of this disorder, and hydrogen atoms for these molecules were not included in the refinement. SHELXTL restraints (ISOR, DELU, SIMU, and DFIX) were needed to stabilize the refinement. The final values of  $R_1 =$

**Fig. 2.** (a) Molecular structure of Os(TMP)(NO)(ONO). Hydrogen atoms have been omitted for clarity. Only one of the two disordered positions of the Os atom and the NO and ONO groups is shown; (b) View of the orientation of the nitrito ligand relative to the porphyrin skeleton. The porphyrin mesityl substituents and the *trans* NO ligand have been omitted for clarity.



0.0583 for 3651 “observed reflections” [ $I > 2\sigma(I)$ ] and  $wR_2 = 0.1665$  for all reflections (4421 unique data) were obtained.

#### *Os(TMP)(NO)(ONO)·3(benzene)*

Suitable crystals for X-ray crystallography were grown by slow evaporation of a benzene solution of the compound at room temperature under inert atmosphere. All the non-hydrogen atoms were refined anisotropically, and the hydrogen atoms were included in the refinement with idealized parameters. The asymmetric unit contains one molecule of Os(TMP)(NO)(ONO) and three molecules of benzene. The Os atom and the NO and ONO groups are disordered over two sites along the axial direction. In addition, one of the benzene solvent molecules is disordered over two sites. Attempts to refine the two fragments did not yield a stable refinement. Thus, the geometry of the two fragments was idealized in the final cycles of refinement, and the thermal parameters were fixed at the values obtained from the earlier refinement cycles. The final values of  $R_1 = 0.0374$  for 8660 “observed reflections” [ $I > 2\sigma(I)$ ] and  $wR_2 = 0.1036$  for all reflections (10 961 unique data) were obtained.

#### *Os(OEP)(NO)(ONO)*

Both laboratories have independently crystallized this compound. Although we have not been able to grow high-



**Table 1.** Crystal data and structure refinement.

Compound	Os(TTP)(NO)(ONO)-toluene	Os(TMP)(NO)(ONO)-3(C <sub>6</sub> H <sub>6</sub> )
Formula (fw)	C <sub>55</sub> H <sub>44</sub> N <sub>6</sub> O <sub>3</sub> Os (1027.16)	C <sub>74</sub> H <sub>70</sub> N <sub>6</sub> O <sub>3</sub> Os (1281.56)
<i>T</i> (K)	153(2)	173(2)
Crystal system	Monoclinic	Triclinic
Space group	<i>C</i> 2/ <i>c</i>	<i>P</i> $\bar{1}$
Unit cell dimensions		
<i>a</i> (Å), $\alpha$ (°)	26.861(5), 90	12.1823(12), 81.362(9)
<i>b</i> (Å), $\beta$ (°)	9.947(2), 119.19(3)	13.031(2), 80.014(10)
<i>c</i> (Å), $\gamma$ (°)	21.933(4), 90	20.732(3), 76.857(10)
<i>V</i> (Å <sup>3</sup> ), <i>Z</i>	5116.1(18), 4	3135.2(7), 2
<i>D</i> <sub>calcd</sub> (g cm <sup>-3</sup> )	1.334	1.358
Absorption coefficient (mm <sup>-1</sup> )	2.539	2.087
<i>F</i> (000)	2064	1312
Crystal size (mm)	0.48 × 0.36 × 0.28	0.38 × 0.36 × 0.26
$\theta$ range for data collection (°)	2.13–24.99	1.80–25.00
Index ranges	0 ≤ <i>h</i> ≤ 31, 0 ≤ <i>k</i> ≤ 11, −26 ≤ <i>l</i> ≤ 22	−13 ≤ <i>h</i> ≤ 14, −14 ≤ <i>k</i> ≤ 15, −24 ≤ <i>l</i> ≤ 24
Reflections collected	4522	11 526
Independent reflections	4421 ( <i>R</i> <sub>int</sub> = 0.0649)	10 966 ( <i>R</i> <sub>int</sub> = 0.0337)
Absorption correction	Empirical	Semi-empirical
Max. and min. transmission	0.8876 and 0.5998	0.4872 and 0.3951
Data/restraints/parameters	4421/14/327	10 961/6/841
Goodness-of-fit on <i>F</i> <sup>2</sup>	1.172	1.068
Final <i>R</i> indices [ <i>I</i> > 2σ( <i>I</i> )]	<i>R</i> <sub>1</sub> = 0.0583, <i>wR</i> <sub>2</sub> = 0.1553	<i>R</i> <sub>1</sub> = 0.0374, <i>wR</i> <sub>2</sub> = 0.0858
<i>R</i> indices (all data)	<i>R</i> <sub>1</sub> = 0.0732, <i>wR</i> <sub>2</sub> = 0.1665	<i>R</i> <sub>1</sub> = 0.0568, <i>wR</i> <sub>2</sub> = 0.1036
Largest diff. peak and hole (e Å <sup>-3</sup> )	1.573 and −0.706	0.794 and −1.357

quality, good-sized crystals, the results of separate preliminary X-ray crystallographic analyses (by both laboratories) on the crystals obtained to date unambiguously confirm the nitrosyl nitrito Os(OEP)(NO)(ONO) formulation.

## Results and discussion

We reported that the Ru(P)(CO) compounds (P = OEP, TTP, TmTP) react with NO in solution to give the nitrosyl nitrito complexes Ru(P)(NO)(ONO) and N<sub>2</sub>O as the final products (16, 17, 19, 20). Using similar methodologies, we have prepared the nitrosyl nitrito complexes of osmium porphyrins. Thus, the reaction of Os(TTP)(CO) with NO in benzene at ambient temperature for ~15 min gives, after workup, the nitrosyl nitrito product Os(TTP)(NO)(ONO) in 43% isolated yield. The product is soluble in dichloromethane, benzene, and toluene, but is insoluble in hexane. The IR spectrum of Os(TTP)(NO)(ONO) (as a KBr pellet) reveals a band at 1804 cm<sup>-1</sup> assigned to  $\nu_{\text{NO}}$ . This  $\nu_{\text{NO}}$  band is of higher frequency than the corresponding bands for the alkoxide complex Os(TTP)(NO)(O-*i*-C<sub>5</sub>H<sub>11</sub>) (1770 cm<sup>-1</sup>) (22), the thiolate derivative Os(TTP)(NO)(S-*i*-C<sub>5</sub>H<sub>11</sub>) (1760 cm<sup>-1</sup>) (22), and the organometallic compound Os(TTP)(NO)Me (1732 cm<sup>-1</sup>) (27). In addition, the IR spectrum indicates new bands at 1528 and 921 cm<sup>-1</sup> due to the O-bound nitrito ligand (28).

The <sup>1</sup>H NMR spectrum of Os(TTP)(NO)(ONO) (in CDCl<sub>3</sub>) reveals peaks due to the pyrrole protons of the porphyrin macrocycle (at  $\delta$  9.00) and the tolyl substituents. The inequivalence of the *ortho* protons of the tolyl substituents suggests restricted rotation of the tolyl groups in this unsymmetrical Os(P)(NO)X compound; such a feature of restricted rotation is not uncommon for *p*-substituted tetraphenyl-

porphyrin complexes of the form M(P)(X)(Y) (29, 30). The FAB mass spectrum of Os(TTP)(NO)(ONO) reveals peaks due to loss of the NO and (or) ONO ligands.

We were also able to prepare other nitrosyl nitrito complexes of the type Os(P)(NO)(ONO), where P = TMP, OEP, and TmTP. The IR spectra of the complexes (as KBr pellets) reveal their nitrosyl  $\nu_{\text{NO}}$  bands at 1803 cm<sup>-1</sup> (TmTP), 1799 cm<sup>-1</sup> (TMP), and 1790 cm<sup>-1</sup> (OEP), reflecting the increasing electron donor properties of the porphyrin macrocycles along the series TTP  $\cong$  TmTP < TMP < OEP, as expected. The TMP, OEP, and TmTP derivatives also show medium intensity bands assignable to nitrito  $\nu_{\text{N-O}}$ . The N<sub>2</sub>O gaseous by-product formed during the reaction was identified by IR spectroscopy as described previously (19).

## Solid-state molecular structures

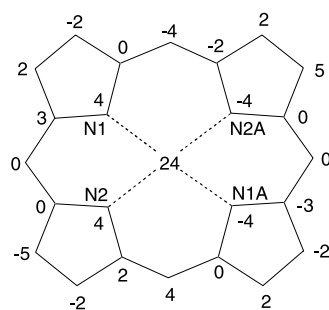
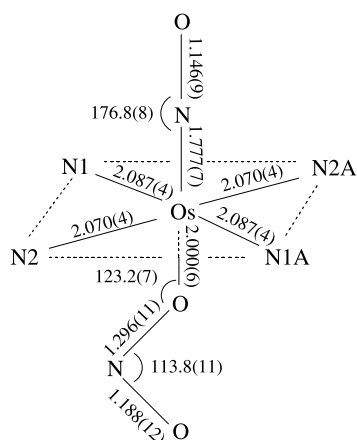
As mentioned in the Introduction, no X-ray crystal structures of osmium nitrito complexes had been reported prior to our study. Interestingly, there is only a single report of an osmium nitro (i.e.,  $\eta^1$ -N bound) structure in the literature, namely that for Os(H<sub>2</sub>L)(PPh<sub>3</sub>)<sub>2</sub>(CO)( $\eta^1$ -NO<sub>2</sub>)-H<sub>2</sub>O (L = 3-ethyliminio-5-methyl-2-oxidophenyl-C<sup>1</sup>,O) (31), although some bridging nitro moieties [Os-N(O)O-Os] have been characterized by crystallography (32–34).

We were successful in obtaining suitable crystals of two of the Os(P)(NO)(ONO) compounds for single-crystal X-ray diffraction studies. The solid-state molecular structure of Os(TTP)(NO)(ONO) is shown in Fig. 1a, and the axial nitrito ligand conformation is shown in Fig. 1b. As is evident in Fig. 1, the ONO group is bound to the Os center through an O-atom, and the ONO group essentially bisects adjacent porphyrin nitrogen atoms, with an N2-Os-O2-N4 torsion angle of 33° (Fig. 1b). The molecular structure of the related

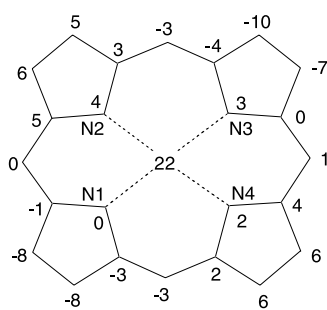
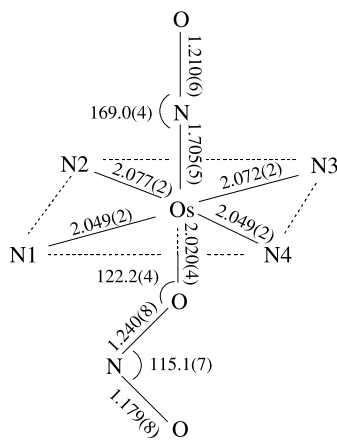


**Fig. 3.** Structural data for Os(TTP)(NO)(ONO) and Os(TMP)(NO)(ONO). Selected bond lengths and angles are shown in the top sketches. Perpendicular atom displacements from the 24-atom porphyrin planes (in 0.01 Å units) are shown in the bottom sketches.

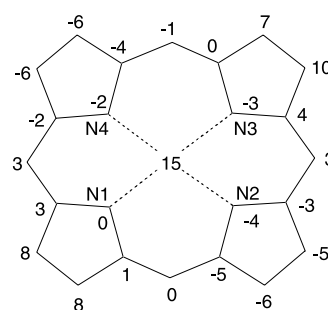
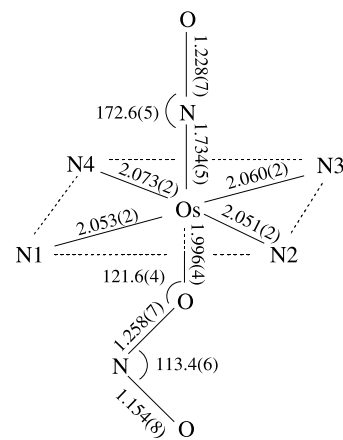
(a) Os(TTP)(NO)(ONO)



axial N-Os-O = 175.0(3)°

(b) Os(TMP)(NO)(ONO)  
1st disordered component

axial N-Os-O = 178.5(2)°

(c) Os(TMP)(NO)(ONO)  
2nd disordered component

axial N-Os-O = 178.7(2)°

Os(TMP)(NO)(ONO) is shown in Fig. 2. In this compound, the nitrito ligand is also bound to osmium through an O-atom, and the ONO ligand essentially bisects adjacent porphyrin nitrogens, with an N1-Os-O1-N6 torsion angle of 46°. Selected bond lengths and angles for both compounds and atom displacements from the 24-atom mean porphyrin planes are displayed in Fig. 3.

There are several features to note from these solid-state structures. First, the nitrosyl Os-NO groups are essentially linear. Second, the Os atoms are displaced from the 24-atom mean porphyrin plane *towards* the axial NO ligand; 0.24 Å for the TTP compound and 0.22 Å (or 0.15 Å for the second disordered component) for the TMP compound. Third, the bond lengths within the nitrito ligand are consistent with the Os-O-N=O formulation; thus, the O—N bond lengths are longer than the nitrito N=O bond lengths. Surprisingly, this is not always the case for metal nitrito crystallographic data. Selected structural data for M(NO)(ONO)-containing complexes reported to date are collected in Table 2. However, there is little consistency in the reported bond lengths involving the ONO ligand, and this may be partly because of the fact that many of these structures suffer from ligand disorder problems.

### Proposed reaction pathway for the formation of nitrosyl nitrito species

UV-vis spectroscopic monitoring of the reaction of a dilute solution of Os(OEP)(CO) in toluene with NO (Fig. 4, top) reveals an apparent clean conversion of Os(OEP)(CO) to Os(OEP)(NO)(ONO). Stopped-flow experiments monitored at several single-wavelengths suggest that the reaction is biphasic, involving the formation of a transient species with spectral features similar but not identical to that of Os(OEP)(CO) (Fig. 4, bottom and inset). Within a few seconds, this intermediate spectrum gives way to that of the final Os(OEP)(NO)(ONO) product. Isosbestic points for the slower and faster processes are observed at 536 and 553 nm and therefore the faster and slower processes may be individually followed at these monitoring wavelengths. Under these conditions, the reactions appeared to be first order with the respective rate constants  $k_{\text{obs}}(536) = 7 \pm 1 \text{ s}^{-1}$  (fast) and  $k_{\text{obs}}(553) = 0.7 \pm 0.1 \text{ s}^{-1}$  (slow). Analogous UV-vis spectral features are observed for the TmTP derivative as well.

To gain further insight into these processes, stopped-flow mixing experiments coupled with FT-IR spectroscopic detection were performed on the more soluble TmTP and OEP derivatives. The FT-IR difference spectrum of the solution



**Table 2.** Selected structural data for metal nitrosyl nitrito complexes.

Compound	<i>cis-trans</i> <sup>a</sup>	M—ONO (Å)	MO—NO (Å)	MON—O (Å)	M-O-NO (°)	MO-N-O (°)	Reference
CpCr(NO) <sub>2</sub> (ONO)	<i>cis</i>	1.982(4)	1.292(8)	1.182(9)	125(1)	115(2)	39
[Ni(NO)(ONO)dpppe] <sub>2</sub> <sup>b</sup>	<i>cis</i>	2.123(12)	1.097(14)	1.192(13)	109.0(12)	127.4(17)	40
[Fe(L)(NO)(ONO)(NO <sub>2</sub> )]ClO <sub>4</sub> <sup>c</sup>	<i>cis</i>	1.914(3)	1.322(5)	1.216(6)	125.1(3)	116.3(4)	41
		[1.935(3)]	[1.305(5)]	[1.213(6)]	[125.7(3)]	[116.1(4)]	
Cr(py) <sub>3</sub> (NO)(ONO) <sub>2</sub> py	<i>cis</i>	1.96(1)	1.34(1)	1.13(1)	115.0(7)	112(1)	42
[Ru(NO)(ONO)(2,2'-bpy) <sub>2</sub> ](PF <sub>6</sub> ) <sub>2</sub>	<i>cis</i>	2.030(8)	1.24(1)	1.17(1)	125.6 <sup>d</sup>	118(1)	43
[Ru(NO)(ONO)(2,2'-bpy)(py) <sub>2</sub> ](PF <sub>6</sub> ) <sub>2</sub>	<i>cis</i>	2.033(4)	1.324(6)	1.227(7)	124.0 <sup>d</sup>	116.3(6)	43
Mn(NO) <sub>2</sub> (ONO)(PEt <sub>3</sub> ) <sub>2</sub>	<i>cis</i>	2.08	1.19	<sup>e</sup>	123	118	44
Ru(sal <sub>2</sub> en)(NO)(ONO) <sup>f</sup>	<i>trans</i>	2.011 avg.	<sup>e</sup>	<sup>e</sup>	<sup>e</sup>	116.5 avg.	37
[Mn(Pc)(NO)(ONO)](PNP) <sup>g</sup>	<i>trans</i>	1.953(8)	1.189(7)	1.165(7)	117.9(6)	108.2(8)	35
[Fe(TpivPP)(NO)(ONO)] <sup>h</sup>	<i>trans</i>	2.080(8)	1.188(14)	1.28(2)	124.1(8)	112.2(14)	36
Ru(TPP)(NO)(ONO) <sup>i</sup>	<i>trans</i>	2.00(2)	0.94(5)	1.33(4)	137(3)	109(5)	16
Ru(TPP)(NO)(ONO) <sup>i</sup>	<i>trans</i>	1.90(2)	1.16(2)	1.23(2)	137.3(18)	108.0(30)	17
Ru(OEP)(NO)(ONO)	<i>trans</i>	1.984(6)	1.214(10)	1.188(9)	122.0(6)	117.3(9)	17
Ru(TTP)(NO)(ONO) <sup>j,k</sup>	<i>trans</i>	1.998(6)	1.148(18)	1.126(25)	124.0(11)	110.9(20)	38
			[1.136(35)]	[1.447(39)]	[128.0(18)]	[92.2(24)]	
Os(TTP)(NO)(ONO) <sup>i</sup>	<i>trans</i>	2.000(6)	1.296(11)	1.188(12)	123.2(7)	113.8(11)	This work
Os(TMP)(NO)(ONO) <sup>i</sup>	<i>trans</i>	2.020(4)	1.240(8)	1.179(8)	122.2(4)	115.1(7)	This work
		[1.996(4)]	[1.258(7)]	[1.154(8)]	[121.6(4)]	[113.4(6)]	

<sup>a</sup>*Cis* or *trans* with respect to NO and ONO.<sup>b</sup>dpppe = Ph<sub>2</sub>PCH<sub>2</sub>CH<sub>2</sub>PPh<sub>2</sub>.<sup>c</sup>Two molecules in the unit cell. The values for the second molecule are in brackets. L = 1,4,7-triazacyclononane.<sup>d</sup>Data obtained from the Cambridge Structural Database.<sup>e</sup>Metrical data not reported.<sup>f</sup>sal<sub>2</sub>en = *N,N'*-ethylenebis(salicylideneiminato). There are two molecules in the unit cell.<sup>g</sup>PNP = (Ph<sub>3</sub>P)<sub>2</sub>N<sup>+</sup>.<sup>h</sup>TpivPP =  $\alpha,\alpha,\alpha,\alpha$ -tetrakis(*o*-pivalamidophenyl)porphyrinato dianion. The ONO group is present as a linkage isomer together with the N-bound NO<sub>2</sub> group in the same molecule.<sup>i</sup>The axial NO and ONO ligands are disordered over the two porphyrin faces.<sup>j</sup>The ONO ligand is disordered. The values for the second disordered component are in brackets.<sup>k</sup>Two molecules in the unit cell, and only the values for molecule A are shown.

obtained from the reaction of Os(TmTP)(CO) in cyclohexane with NO (Fig. 5, top) revealed, in addition to Os(TmTP)(CO) ( $\nu_{\text{CO}}$  1924 cm<sup>-1</sup>) and the final product Os(TmTP)(NO)(ONO) ( $\nu_{\text{NO}}$  1805 cm<sup>-1</sup>;  $\nu_{\text{ONO}}$  1540 cm<sup>-1</sup>), a new species displaying a strong band at 1974 cm<sup>-1</sup>.

Since the independent reaction of Os(TmTP)(CO) with added CO gave a new species displaying a  $\nu_{\text{CO}}$  band at 1974 cm<sup>-1</sup> twice as intense as that of Os(TmTP)(CO) (Fig. 5, bottom), we assign this band to the *trans* dicarbonyl complex Os(TmTP)(CO)<sub>2</sub>. Therefore, its appearance as a transient in the reaction of NO with Os(TmTP)(CO) can be attributed to the Os(TmTP)(CO) scavenging the CO released during the reaction.

Formation of the dicarbonyl complexes Os(P)(CO)<sub>2</sub> (eq. [1]) was studied independently in toluene by probing optical spectrum changes upon addition of CO to toluene solutions of Os(P)(CO) (e.g., Fig. 6). In this manner the equilibrium constants  $K_2 = 0.9 \pm 0.2 \times 10^6$  and  $1.0 \pm 0.2 \times 10^6$  M<sup>-1</sup> were determined for P = TmTP and OEP, respectively. The latter value is  $\sim 10^2$  larger than that observed for the corresponding Ru(OEP)(CO) complex ( $1.1 \times 10^4$  M<sup>-1</sup>) (20).



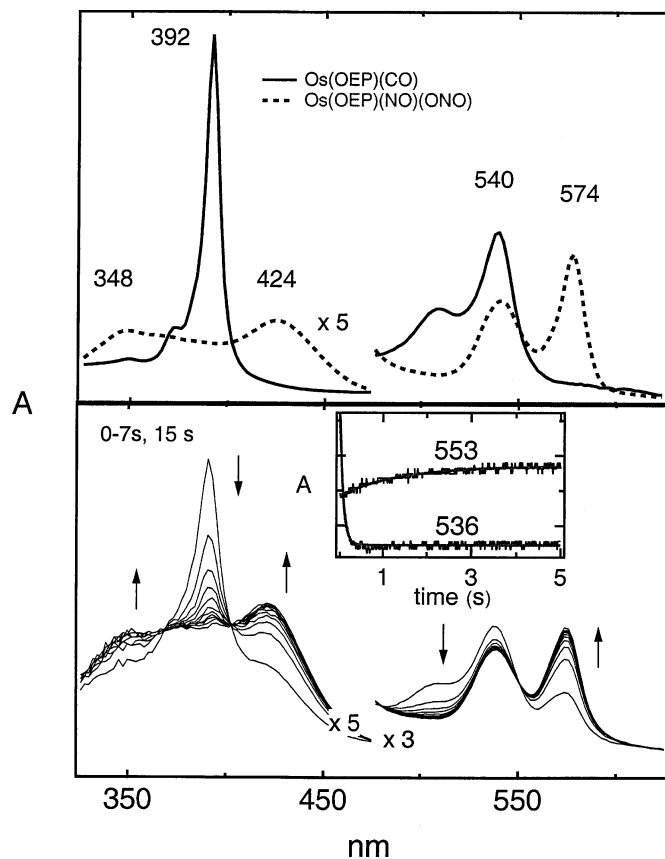
The high affinity of Os(P)(CO) for CO explains the detection of Os(P)(CO)<sub>2</sub> as a transient in the stopped-flow experi-

ment described above. No other species with distinctive IR spectral signatures, such as expected for Os–nitrosyl intermediates, were detected during the stopped-flow study of the reaction of Os(P)(CO) with NO. This is in sharp contrast to the analogous reaction of Ru(P)(CO) with NO where the dinitrosyl complex Ru(P)(NO)<sub>2</sub> was a spectroscopically observable intermediate (20). Given that under the reaction conditions [NO] is always much greater than [CO], detecting Os(P)(CO)<sub>2</sub> as the only transient suggests that  $K_2$  for CO binding to Os(P)(CO) is at least four orders of magnitude larger than the equilibrium constant for analogous binding of NO.

Scheme 1 is a proposed explanation for these kinetics and spectral observations during the formation of Os(P)(NO)(ONO) from Os(P)(CO) and NO. This is based largely on the behavior of the ruthenium analogues for which the dinitrosyl intermediate Ru(P)(NO)<sub>2</sub> was observed (19, 20). The initial step is very likely the reversible and endergonic formation of the 19-electron complex Os(P)(CO)(NO). Upon rate-limiting CO dissociation from Os(P)(CO)(NO), a rapid sequence of steps would lead to the disproportionation products. However, CO is also a product, and it will be rapidly scavenged by Os(P)(CO) to give the much less reactive Os(P)(CO)<sub>2</sub> in a dead-end equilibrium. Thus, the reaction slows, owing to the lower effective concentration of Os(P)(CO). Since no other transient species



**Fig. 4.** *Top:* UV-vis spectra of the reactant Os(OEP)(CO) in toluene and the product of its reaction with nitric oxide, Os(OEP)(NO)(ONO). *Bottom:* Spectral changes upon stopped-flow mixing of a solution of Os(OEP)(CO) (10  $\mu\text{M}$  in toluene after mix) with nitric oxide (5 mM after mix). The stacked plot shows no obvious intermediate, but single wavelength observation shows evidence for a fast ( $7\text{ s}^{-1}$ ) and a slow ( $0.7\text{ s}^{-1}$ ) process in this reaction. However, the two stages in the kinetics suggest the formation of an intermediate in solution whose spectrum is very similar to that of the starting solution.



**Scheme 1.**

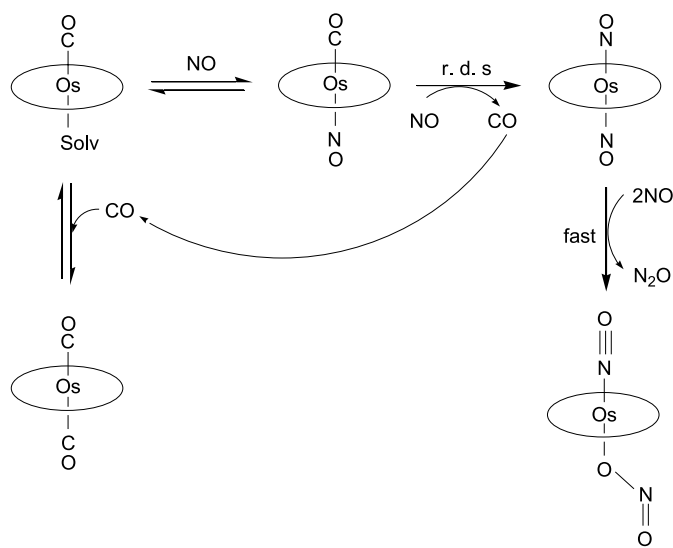
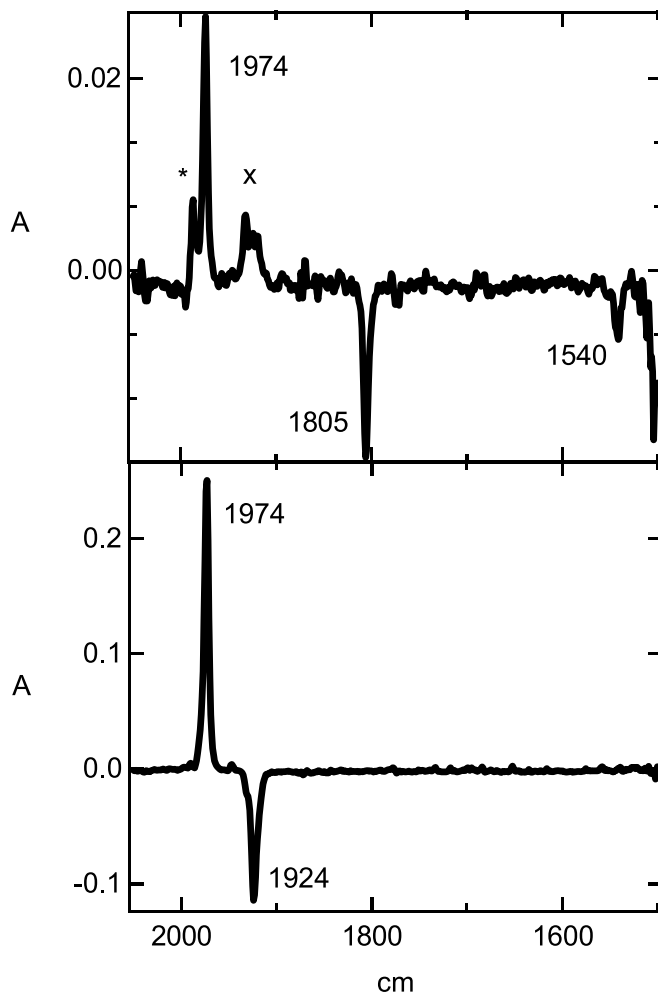


**Fig. 5.** *Top:* Difference FT-IR spectrum of the solution obtained by mixing solutions of Os(TmTP)(CO) ( $\sim 100\text{ }\mu\text{M}$  in cyclohexane after mix) with NO ( $\sim 4\text{ mM}$  in cyclohexane after mix). The difference spectra shown are the result of subtracting the spectrum of the final product solution. Therefore, the  $\nu_{\text{NO}}$  at  $1805\text{ cm}^{-1}$  and  $\nu_{\text{ONO}}$  at  $1540\text{ cm}^{-1}$  for the product Os(TmTP)(NO)(ONO) are seen as negative peaks. The only observable new species in this reaction is the dicarbonyl Os(TmTP)(CO)<sub>2</sub> identified by its peak at  $1974\text{ cm}^{-1}$  (see below). The peak marked with an asterisk is a cyclohexane subtraction artifact and that marked "x" is suspended insoluble Os(TmPP)(CO). *Bottom:* Difference infrared spectrum of Os(TmTP)(CO)<sub>2</sub> in cyclohexane after CO addition to a solution of Os(TmTP)(CO), minus the spectrum observed prior to CO addition. The new species shows a single carbonyl band at  $1974\text{ cm}^{-1}$  that is twice as intense as that for the monocarbonyl (at  $1924\text{ cm}^{-1}$ ), consistent with a *trans*-dicarbonyl structure.

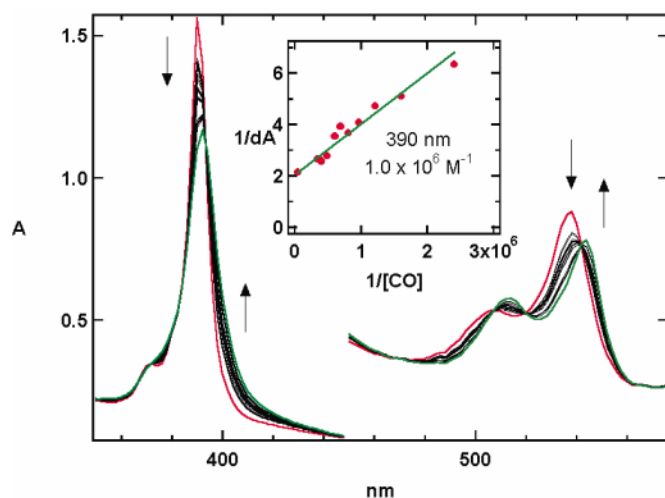


were observed in the stopped-flow IR experiments, we conclude that likely intermediates along the productive pathway — for example, the dinitrosyl Os(P)(NO)<sub>2</sub> — are too reactive to build to detectable steady-state concentrations.

This scheme would explain the observation of the two-stage kinetics observed under a large excess of NO. Initially all the osmium carbonyl is in the monocarbonyl form, and the reaction proceeds rapidly. Since the fast reaction was monitored near the Os(P)(CO)–Os(P)(CO)<sub>2</sub> isosbestic point (Fig. 6), this will show (pseudo) first order kinetics for the



**Fig. 6.** Measurement of the equilibrium constant for the reaction of CO with Os(OEP)(CO) in toluene. The inset shows a Lineweaver–Burke fit for the spectral change induced by addition of CO aliquots to a dry toluene solution of Os(OEP)(CO) ( $\sim 10 \mu\text{M}$ ). The total amount of CO (most of which is contained in the headspace but in equilibrium with that in solution) available for the equilibrium reaction is much greater than the total amount of Os in the solution. Thus,  $[\text{CO}]$  in solution can be approximated as being constant, although it is much lower than  $[\text{Os}]$ . The measured equilibrium constant is  $1.0 \pm 0.2 \times 10^6 \text{ M}^{-1}$ .



absorbance changes due to reaction along the productive pathway to give Os(P)(NO)(ONO) (reaction of Os(P)(CO) with the released CO is not observed owing to the isosbestic behavior at that wavelength). Once most of the remaining osmium carbonyl is sequestered as the dicarbonyl, further reaction will be slower, owing to the low steady-state concentration of the monocarbonyl. Consistent with this interpretation is the qualitative observation that the overall reaction is dramatically slowed in the presence of excess added CO. The slow second stage observed in the absence of added CO also appeared to follow first order kinetics; however, this may result from a fortuitous combination of conditions, since the continued production of CO should make the reaction auto-inhibitory.

## Conclusion

We have successfully prepared several nitrosyl nitrito complexes of the form Os(P)(NO)(ONO) from the reaction of the precursor carbonyl complexes Os(P)(CO) with nitric oxide. Single-crystal X-ray crystallographic studies of two of these compounds confirm the O-binding modes of the nitrito ligands. To the best of our knowledge, these are the first X-ray crystal structures of osmium nitrito moieties to be reported.

Results from stopped-flow kinetics studies of the reactions suggest a mechanism in which initial adduct formation between Os(P)(CO) and NO is followed by a rate-determining replacement of CO by a second NO molecule. Subsequent reaction with more NO leads to an effective NO disproportionation to give the final nitrosyl nitrito product Os(P)(NO)(ONO) and nitrous oxide. The behavior of the osmium complexes is in marked contrast to the failure of

Fe(P)(NO) analogs to promote such disproportionation in rigorously dried and deaerated solvents (14). A greater parallel can be drawn to the Ru(P)(CO) analogues (20); however, the likely osmium nitrosyl intermediates suggested by this analogy are apparently too reactive to build to detectable concentrations.

## Acknowledgments

GBRA acknowledges National Science Foundation (CHE-0076640) for funding. Studies at the University of California, Santa Barbara (UCSB) were supported by grants from the National Science Foundation (CHE-0095144) and the ACS Petroleum Research Fund for support of this research to PCF. FAL thanks the University of California CAMP program for a research fellowship.

## References

1. I.M. Wasser, S. de Vries, P. Moenne-Loccoz, I. Schroder, and K.D. Karlin. *Chem. Rev.* **102**, 1201 (2002).
2. H. Shimizu, S.-Y. Park, Y. Shiro, and S.-i. Adachi. *Acta Crystallogr.* **D58**, 81 (2002).
3. D.L. Harris. *Int. J. Quantum Chem.* **88**, 183 (2002).
4. S.J. Field, L. Prior, M.D. Roldan, M.R. Cheesman, A.J. Thomson, S. Spiro, J.N. Butt, N.J. Watmough, and D.J. Richardson. *J. Biol. Chem.* **277**, 20 146 (2002).
5. E. Pinakoulaki, S. Gemeinhardt, M. Saraste, and C. Varotsis. *J. Biol. Chem.* **277**, 23 407 (2002).
6. P.R. Gardner, A.M. Gardner, L.A. Martin, and A.L. Salzman. *Proc. Natl. Acad. Sci. U.S.A.* **95**, 10 378 (1998).
7. A.M. Gardner and P.R. Gardner. *J. Biol. Chem.* **277**, 8166 (2002).
8. R.L. Klimisch and J.G. Larson. *In The catalytic chemistry of nitrogen oxides*. Plenum Press, New York. 1975.
9. L. Cheng, D.R. Powell, M.A. Khan, and G.B. Richter-Addo. *Chem. Commun.* 2301 (2000).
10. T.S. Kurtikyan. *Russ. J. Inorg. Chem.* **25**, 28 (1999).
11. B.B. Wayland and A.R. Newman. *Inorg. Chem.* **20**, 3093 (1981).
12. P.C. Ford and I.M. Lorkovic. *Chem. Rev.* **102**, 993 (2002).
13. I. Lorkovic and P.C. Ford. *J. Am. Chem. Soc.* **122**, 6516 (2000).
14. M.D. Lim, I.M. Lorkovic, K. Wedeking, A.W. Zanella, C.F. Works, S.M. Massick, and P.C. Ford. *J. Am. Chem. Soc.* **124**, 9737 (2002); T.S. Kurtikyan, G.G. Martirosyan, I.M. Lorkovic, and P.C. Ford. *J. Am. Chem. Soc.* **124**, 10 124 (2002).
15. G.R.A. Wyllie and W.R. Scheidt. *Chem. Rev.* **102**, 1067 (2002).
16. K.M. Kadish, V.A. Adamian, E.V. Caemelbecke, Z. Tan, P. Tagliatesta, P. Bianco, T. Boschi, G.-B. Yi, M.A. Khan, and G.B. Richter-Addo. *Inorg. Chem.* **35**, 1343 (1996).
17. K.M. Miranda, X. Bu, I. Lorkovic, and P.C. Ford. *Inorg. Chem.* **36**, 4838 (1997).
18. I.M. Lorkovic, K.M. Miranda, B. Lee, S. Bernhard, J.R. Schoonover, and P.C. Ford. *J. Am. Chem. Soc.* **120**, 11 674 (1998).
19. I.M. Lorkovic and P.C. Ford. *Chem. Commun.* 1225 (1999).
20. I.M. Lorkovic and P.C. Ford. *Inorg. Chem.* **38**, 1467 (1999).
21. C.-M. Che, C.-K. Poon, W.-C. Chung, and H.B. Gray. *Inorg. Chem.* **24**, 1277 (1985).
22. G.-B. Yi, L. Chen, M.A. Khan, and G.B. Richter-Addo. *Inorg. Chem.* **36**, 3876 (1997).
23. J. Buchler and P.D. Smith. *Chem. Ber.* **109**, 1465 (1976).



24. C.L. Young. Oxides of nitrogen. *In* IUPAC solubility data series. Vol. 8. Pergamon Press, Oxford. 1981.
25. R.W. Cargill. Carbon monoxide. *In* IUPAC solubility data series. Vol. 43. Pergamon Press, Oxford. 1990.
26. A.T.C. North, D.C. Philips, and F.S. Mathews. *Acta Crystallogr.* **A24**, 351 (1968).
27. L. Cheng, L. Chen, H.-S. Chung, M.A. Khan, G.B. Richter-Addo, and V.G. Young, Jr. *Organometallics*, **17**, 3853 (1998).
28. K. Nakamoto. Infrared and Raman spectra of inorganic and coordination compounds. Part B: applications in coordination, organometallic, and bioinorganic chemistry. John Wiley and Sons, New York. 1997. pp 50–51.
29. S.S. Eaton and G.R. Eaton. *J. Am. Chem. Soc.* **97**, 3660 (1975).
30. S.S. Eaton and G.R. Eaton. *J. Am. Chem. Soc.* **99**, 6594 (1977).
31. K. Pramanik, P. Ghosh, and A. Chakravorty. *J. Chem. Soc. Dalton Trans.* 3553 (1997).
32. B.K.-M. Hui and W.-T. Wong. *J. Chem. Soc. Dalton Trans.* 447 (1998).
33. B.K.-M. Hui and W.-T. Wong. *J. Chem. Soc. Dalton Trans.* 3977 (1998).
34. B.K.-M. Hui and W.-T. Wong. *J. Chem. Soc. Dalton Trans.* 2177 (1996).
35. M. Goldner, B. Geniffke, A. Franken, K.S. Murray, and H. Homborg. *Z. Anorg. Allg. Chem.* **627**, 935 (2001).
36. H. Nasri, M.K. Ellison, S. Chen, B.H. Huynh, and W.R. Scheidt. *J. Am. Chem. Soc.* **119**, 6274 (1997).
37. M.A.A.F.C.T. Carrondo, P.R. Rudolf, A.C. Skapski, J.R. Thornback, and G. Wilkinson. *Inorg. Chim. Acta*, **24**, L95 (1977).
38. D.S. Bohle, C.-H. Hung, and B.D. Smith. *Inorg. Chem.* **37**, 5798 (1998).
39. I.L. Eremenko, A.A. Pasynskii, V.T. Kalinnikov, Y.T. Struchkov, and G.G. Aleksandrov. *Inorg. Chim. Acta*, **52**, 107 (1981).
40. J. Kriege-Simonsen and R.D. Feltham. *Inorg. Chim. Acta*, **71**, 185 (1983).
41. C. Hauser, T. Glaser, E. Bill, T. Weyhermuller, and K. Wieghardt. *J. Am. Chem. Soc.* **122**, 4352 (2000).
42. C.M. Lukehart and J.M. Troup. *Inorg. Chim. Acta*, **22**, 81 (1977).
43. D. Ooyama, N. Nagao, H. Nagao, Y. Miura, A. Hasegawa, K. Ando, F.S. Howell, M. Mukaida, and K. Tanaka. *Inorg. Chem.* **34**, 6024 (1995).
44. R.D. Wilson and R. Bau. *J. Organomet. Chem.* **191**, 123 (1980).



# A new class of bolaforms bearing sulfobetaine and cationic heads: Synthesis and aggregation properties

Souad Souirti and Michel Baboulene

**Abstract:** We describe here a convenient route to a new family of bolaforms bearing sulfobetaine and cationic heads, which could be scaled up for industrial applications. Their aggregation modes were studied by measurement of surface tension and by dynamic light scattering and transmission electronic microscopy methods. Grafting a hydrophobic chain onto the cationic head modifies both the surface properties and aggregation. Compared to conventional bolaforms, the relationship between the length of the spacer and the side-chain and the resultant hydrophobic interactions are at the origin of these novel properties. Various models of these molecular associations were proposed.

**Key words:** dissymmetric bolaform, sulfobetaine, cationic amphiphile, aggregation.

**Résumé :** Nous décrivons une nouvelle famille de bolaformes comportant une tête sulfobétaine et une tête cationique. Les synthèses proposées sont aisément transposables à l'échelle industrielle. Le mode d'agrégation de ces bolaformes a été étudié par diverses techniques: tensiométrie, diffusion de la lumière et microscopie électronique à transmission. Il en résulte que le greffage d'une chaîne hydrophobe sur la tête cationique modifie les propriétés de surface et d'agrégation comparativement aux conventionnels bolaformes. Une relation entre la longueur de l'espaceur et celle de la chaîne carbonée additive est mise en évidence en fonction des interactions hydrophobes propres à la structure chimique de ces nouveaux bolaformes. Différents modèles d'association moléculaire sont dès lors proposés.

**Mots clés :** bolaforme dissymétrique, sulfobétaine, amphiphile cationique, agrégation.

## Introduction

There is growing interest in the properties of difunctional surfactants such as bolaforms. Surfactants of this category, characterized by two hydrophilic heads linked by a hydrophobic chain, are attractive models for biological membranes (1–3) and can display various properties (4, 5). The potential applications suggested by these properties have led to a renewed interest in bolaforms by the industrial community (6, 7). However, from an academic standpoint, the molecular self-association of these molecules still leaves various questions unanswered. To further our understanding of these systems, it therefore appears necessary to make available a large range of these compounds with varied chemical structures. But the synthesis of bolaforms with non-identical head-groups presents certain technical difficulties, which explains the rather limited number of studies reported to date. Recently, we proposed a simple, efficient, and industrially realistic route to obtain bolaforms either with two betaine heads (carboxybetaine and (or) sulfobetaine) (8) or with at least one sulfobetaine head (9) (Fig. 1). These molecules have also shown interesting

surfactant properties that depend on the structure of the polar head as well as on the length of the spacer that links them (10).

Pursuing this line of research, the reaction scheme we developed was used to graft a second long hydrophobic chain onto one of the nitrogen atoms. This generated original compounds **1** with a structure intermediate between that of conventional bolaforms and of gemini surfactants (Fig. 2). Longer than the rather rigid C6 spacer but shorter than the very flexible C16 spacer, the dodecyl spacer appeared to be the most suitable for our research aims. Owing to the molecular organisation properties of these novel compounds, we were able to study the influence of chain–chain interactions in relation with the different structures of the polar heads. It is in this perspective that we report a new extended range of hybrid molecules **1** and the study of their aggregation properties.

## Results and discussion

### Synthesis

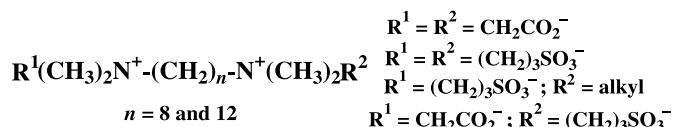
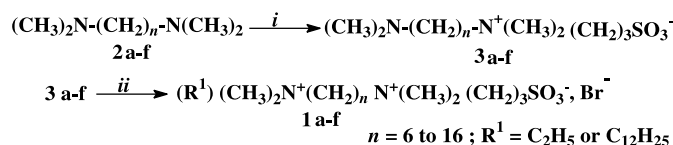
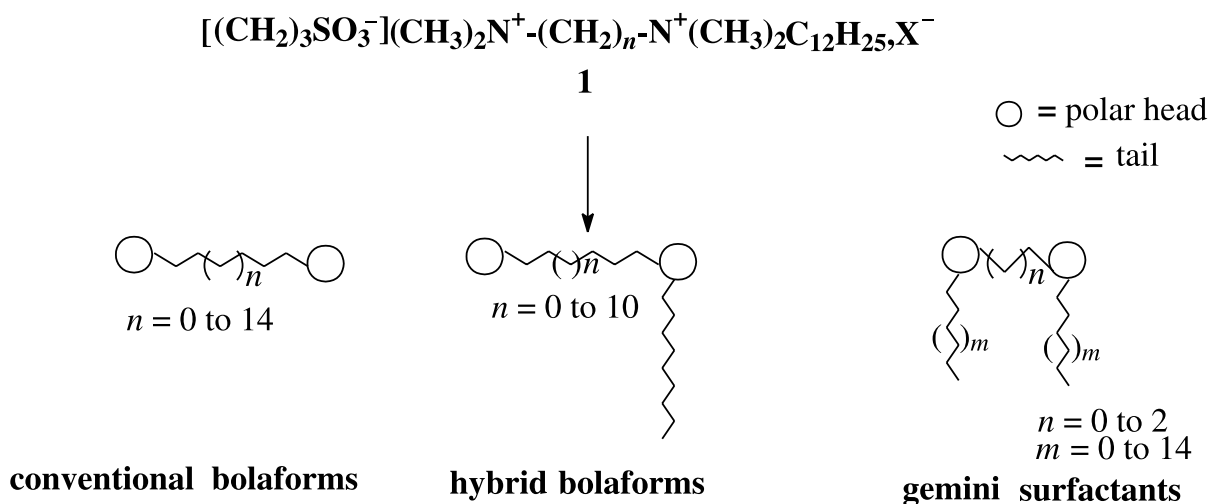
The synthetic approach used is based on previous studies (9) into the preparation of sulfobetaine bolaforms. From the monosulfobetaine intermediate **3**, formation of a quaternary nitrogen by reaction with dodecyl bromide led quantitatively to the required bolaforms **1** (Scheme 1). Table 1 reports the various bolaforms **1** synthesized.

Received 15 February 2003. Published on the NRC Research Press Web site at <http://canjchem.nrc.ca> on 18 July 2003.

**S. Souirti and M. Baboulene.**<sup>1</sup> IMRCP Laboratory, Paul Sabatier University, UMR(CNRS) 5623, 118 route de Narbonne, 31062 Toulouse CEDEX, France.

<sup>1</sup>Corresponding author (e-mail: [mbab@chimie.ups-tlse.fr](mailto:mbab@chimie.ups-tlse.fr)).



**Fig. 1.** Various structures of the betaine bolaforms.**Scheme 1.** Synthesis of the hybrid bolaforms **1**; (i) 1,3-propane sultone, acetone, 15–20°C; (ii) R<sup>1</sup>X, methanol, reflux.**Fig. 2.** Structure of the hybrid bolaforms **1**.

### Surface properties

The surfactant properties of these hybrid bolaforms **1** were studied by measuring interfacial tension in water and calculating the surface property parameters using the Gibbs' equation (11). The data are illustrated in Fig. 3 and listed in Table 2.

All compounds tested led to a marked reduction in interfacial tension at the air–water interface (29–36 mN·m<sup>−1</sup>). In the interfacial tension vs. concentration plots, we noted that the values of the critical micellar concentration (cmc) (2.4–8.2 mmol<sup>−1</sup>) were strongly decreased in comparison with those of conventional bolaforms, which is promising for industrial applications. This was attributed to increased hydrophobicity on addition of the second alkyl chain (comparison between **1a**, **1c**, **1e**, and **1f**) and is in agreement with the values reported in the literature. However, an “anomaly” was observed with compound **1e** ( $n = 16$ ), as shown in the curve of Fig. 3 where the linear decrease in the value of the cmc vs. increasing spacer length shows that the cmc of **1e** ( $n = 16$ ; cmc = 3.1 mmol<sup>−1</sup>) is greater than that of **1d** ( $n = 12$ ; cmc = 2.4 mmol<sup>−1</sup>).

This result is difficult to explain, but it can be proposed that differences in chain–chain interactions are responsible. This hypothesis is supported by the analysis of the curve in Fig. 4, which reveals differences in the conformations of the various bolaforms at the air–water interface. Compounds **1a**, **1b**, and **1c** present total areas for the polar heads of 280, 275, and 284 Å<sup>2</sup>, respectively, which is much greater than the sum of the head areas taken individually (135 Å<sup>2</sup>). This suggests that a “straight” conformation is taken up by the bolaforms, leaving the hydrophobic side chain as far from the interface as possible (Fig. 5a). This arrangement could

be favoured because the chain (C12) is longer than the spacer (C6–C10). This hypothesis is supported by data from the literature, which attribute strong rigidity to bolaforms with a spacer of 10 carbon atoms or fewer (12, 13). A spacer with 12 carbons is known to make the molecule take up a looped (“wicket-like”) conformation, bringing about a total polar surface area equivalent to the sum of the areas of the two polar heads. This is what was observed for compound **1d** ( $n = 12$ , total area 188 Å<sup>2</sup> (Fig. 4)), as illustrated by Fig. 5b. Moreover, it should be noted that this value is close to the total polar head area (167 Å<sup>2</sup>) found for a similar compound **1f** ( $n = 12$ ) in which the side-chain only has two carbon atoms (R = C<sub>2</sub>H<sub>5</sub>).

Taking into account the margins of error inherent in the measurements, it could also be proposed that the slightly higher value for the total area of bolaform **1d** with respect to **1f** indicates the beginnings of chain–chain interactions, impeding the flexibility of the spacer and not allowing complete folding (Fig. 5b). But there is once more a spread-out conformation for bolaform **1e** ( $n = 16$ , total area 254 Å<sup>2</sup>), as illustrated in Fig. 5c. However, the chain–chain interactions (side-chain shorter than the spacer) reduce the flexibility of the spacer, making these structures act similarly to bicatenar bolaforms. Overall, from these results, it appears that the term of critical aggregation concentration (cac) would be more appropriate for this type of compound.

### Dynamic light scattering

With the exception of compound **1e** ( $n = 16$ ), none of the bolaforms synthesized here underwent spontaneous molecular aggregation without sonication. After 15 min sonication all the bolaforms generated various objects. Typical results,

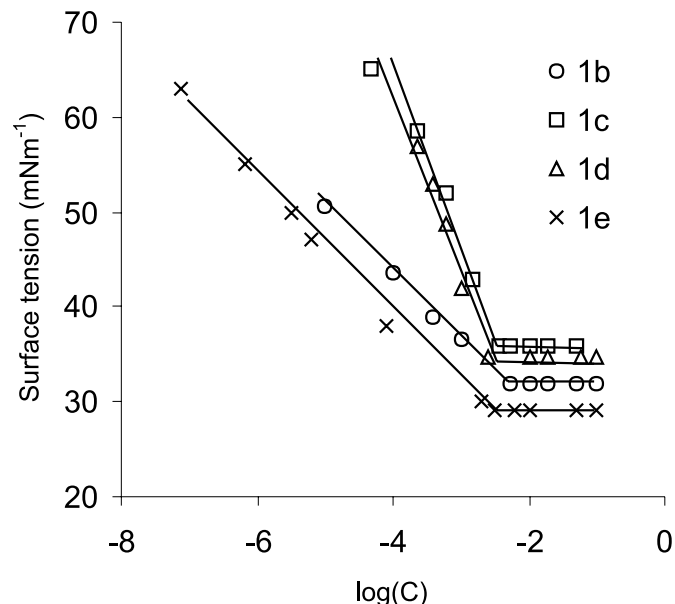


**Table 1.** Yield of the synthesized hybrid bolaforms **1**.

<i>n</i>	Compound <b>2</b>		Compound <b>3</b>		<i>R</i> <sup>1</sup>	Compound <b>1</b>	
	No.	Yield (%)	No.	Yield (%)		No.	Yield (%)
6	<b>2a</b>	98	<b>3a</b>	98	C <sub>12</sub> H <sub>25</sub>	<b>1a</b>	90
8	<b>2b</b>	98	<b>3b</b>	96	C <sub>12</sub> H <sub>25</sub>	<b>1b</b>	87
10	<b>2c</b>	92	<b>3c</b>	97	C <sub>12</sub> H <sub>25</sub>	<b>1c</b>	92
12	<b>2d</b>	98	<b>3d</b>	95	C <sub>12</sub> H <sub>25</sub>	<b>1d</b>	85
16	<b>2e</b>	75	<b>3e</b>	75	C <sub>12</sub> H <sub>25</sub>	<b>1e</b>	85
12					C <sub>2</sub> H <sub>5</sub>	<b>1f</b>	90

**Table 2.** Surface parameters of the hybrid bolaforms **1** at 25°C in water.

Compound No.	<i>n</i>	$\gamma^a$ (mN·m <sup>-1</sup> )	cmc <sup>b</sup> (mM)	$\Gamma^c$ (mol·m <sup>-2</sup> )	<i>A</i> <sup>d</sup> (Å <sup>2</sup> )	Light scattering	
						Ø (nm)	%
<b>1a</b>	6	35	8.2	$5.7 \times 10^{-7}$	280	—	—
<b>1b</b>	8	32	5	$6.02 \times 10^{-7}$	275	286	80
<b>1c</b>	10	36	3.6	$5.85 \times 10^{-7}$	284	399	15
<b>1d</b>	12	35	2.4	$8.83 \times 10^{-7}$	188	281	56
<b>1e</b>	16	29	3.1	$6.53 \times 10^{-7}$	254	180	30
<b>1f</b>	12	33	70	$10 \times 10^{-7}$	167	—	—

<sup>a</sup> $\gamma$  = surface tension.<sup>b</sup>cmc = critical micellar concentration.<sup>c</sup> $\Gamma$  = superficial excess.<sup>d</sup>*A* = total area of the polar heads.**Fig. 3.** Plots of the surface tension vs. log[bolaform] at 25°C in water.

from an average of 10–15 trials for each determination of the diameter, are reported in Table 2. In general, for 10 carbons or more, the distribution of the objects was found to follow a dispersion with a fairly low percentage. The diameter of the objects, which was closely linked to the spacer length, decreased as the number of carbon atoms increased. However, for 8 carbons, polydispersion occurred, but the size of the main objects remained close to that obtained for molecules with spacers 10 or more carbons long.

### Transmission electronic microscopy (TEM)

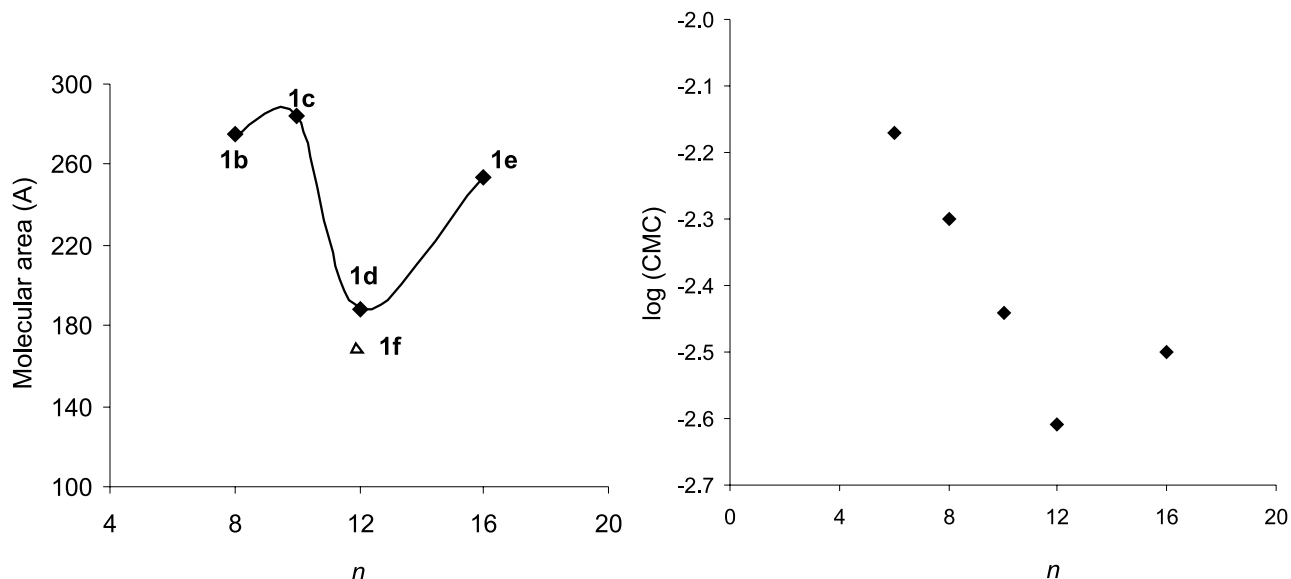
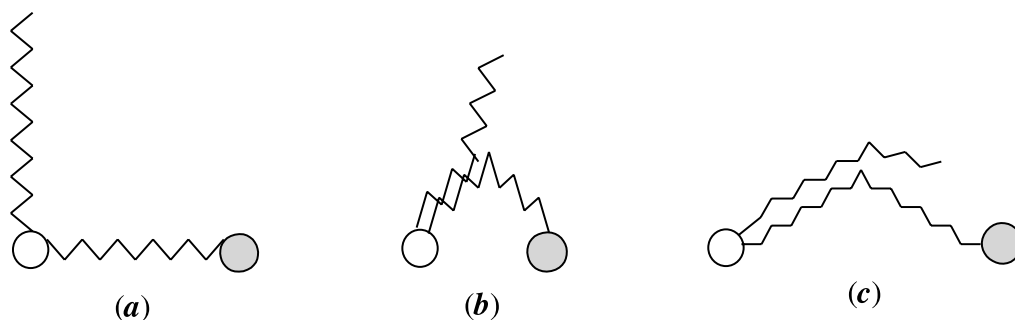
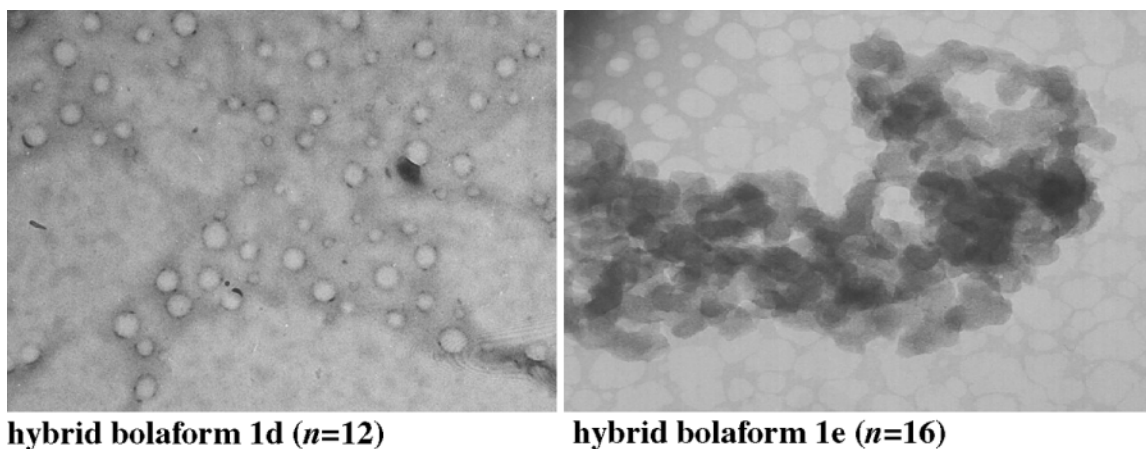
The sonicated aqueous solutions prepared for TEM observation remained optically translucent for several weeks. As mentioned, without sonication only compound **1e** spontaneously formed aggregates. This self-organisation was not modified by sonication. This result illustrates the influence of spacer length (only parameter modified) and thus the role played by variations in the hydrophobic interactions allowed by the structure of the hybrid molecules studied here. The analogy with 2-chain bolaforms is again possible in that the latter are known to spontaneously form vesicles when the spacer is over 8 carbons long (14). It should however be noted that whereas sonication gave rise to vesicles for compounds with from C10 to C16 spacers (examples **1d** and **1e** given in Fig. 6), no aggregates were found for compound **1a** (*n* = 6). These results call for comments.

Based on previous results and on the “straight” molecular organisation that bicatenaar bolaforms tend to adopt (15), we propose that compound **1e** (*n* = 16) is organised in a monolayer. However, the possibility for the spacer in compound **1d** (*n* = 12) to fold suggests bilayer aggregation similar to that proposed for cationic (16) and gemini (17, 18) bolaforms. These types of molecular association present an interesting advantage, owing to the difficulties of the synthesis of the bicatenaar and gemini bolaforms with two different heads.

### Conclusion

During this study, we have shown that the synthesis route we recently proposed for bolaforms with sulphobetain heads can be easily generalized to obtain high yields of cationic sulphobetain hybrid bolaforms. Grafting a hydrophobic



**Fig. 4.** Molecular area and cmc values in function of the length of the spacer of the hybrid bolaforms **1**.**Fig. 5.** Schematic proposition for the conformation of the hybrid bolaforms **1**.**Fig. 6.** Representative micrographs of aggregates by TEM method obtained from sonicated solutions ( $5 \times 10^{-3}$  M) of **1d** (1 cm = 660 nm) and **1e** (1 cm = 350 nm).

chain onto the cationic head modifies both the surface properties and aggregation in aqueous medium. Compared to conventional bolaforms, the relationship between the length of the spacer and of the side-chain and the resulting hydrophobic interactions are at the origin of these novel proper-

ties. Favouring a given molecular association can therefore be envisaged by modulating these interactions by adjusting the chemical structure of the two chains. Access to new molecules should be possible using the reaction scheme proposed here. Work along these lines is in progress.



## Experimental

### General

Reagents were of commercial quality and were used without purification. Anhydrous acetone and methanol were of extra dry quality (Acros Organics France). IR spectra ( $\nu$ ,  $\text{cm}^{-1}$ ) were recorded on a PerkinElmer 683 spectrophotometer.  $^1\text{H}$  and  $^{13}\text{C}$  NMR spectra ( $\delta$ , ppm;  $J$ , hertz) were obtained on Bruker AC 80 or Bruker AC 200 instruments.

### Aggregation mode

Parameters of the surface-active properties were calculated using Gibbs' equation (11) with the data obtained from measurements carried out on a Prolabo n°3 tensiometer using the stirrup detachment method. The size of aggregates was determined by light scattering using a Malvern Zetasizer 3000 instrument. An EM-301 Philips transmission electron microscope was used for TEM studies. Vesicles were prepared by sonication (Sonics instrument: 600 W) at 110 W for 15–20 min. Dust was removed by centrifugation (3000 rpm for 10 min) and filtration through a millipore 0.45  $\mu$  filter. One drop of the above dispersion was placed onto a carbon-coated grid (400 mesh). Filter paper was employed to wick away the excess water. One drop of 2% uranyl acetate solution was added.

It was then kept under mechanical vacuum for approximately 1 h. Micrographs were then recorded.

### Typical procedure for the synthesis of compounds 2

A solution of dimethylamine (33% of ethanol) ( $3 \times 10^{-2}$  mol) and dibromoalkane ( $10^{-2}$  mol) were added with sodium carbonate ( $2 \times 10^{-2}$  mol) into 60 mL of ethanol and 15 mL of water. The reaction mixture was refluxed and stirred for 24 h. Then the resulting compound was isolated by evaporation of the solvent under reduced pressure. The crude product, washed with 10 mL of water, was extracted with  $\text{EtO}_2$ . The organic phase was dried on anhydrous  $\text{Na}_2\text{SO}_4$  and evaporated in vacuo. The crude oil was purified by distillation.

#### 1,6 Bis (N,N-dimethylamino)hexane, 2a

Yield: 98%. Colourless oil, bp =  $68^\circ\text{C}$  at 1 mmHg (1 mmHg = 133.322 Pa).  $^1\text{H}$  NMR (200 MHz,  $\text{CDCl}_3$ )  $\delta$ : 1.10 (m, 8H,  $(\text{CH}_2)_4$ ), 1.92 (s, 12H,  $2 \times \text{N}(\text{CH}_3)_2$ ), 2.31 (t,  $J = 6.4$ , 4H,  $2 \times \text{NCH}_2$ ).  $^{13}\text{C}$  NMR (200 MHz,  $\text{CDCl}_3$ )  $\delta$ : 27.23–28.30 ( $(\text{CH}_2)_4$ ), 45.20 ( $\text{NCH}_3$ ), 59.66 ( $\text{NCH}_2$ ). Anal. calcd. (%) for  $\text{C}_{10}\text{H}_{24}\text{N}_2$  (172.30): C 69.70, H 14.04, N 16.25; found: C 69.82, H 14.24, N 16.02.

#### 1,8 Bis (N,N-dimethylamino)octane, 2b

Yield: 98%. Colourless oil, bp =  $60^\circ\text{C}$  at 0.06 mmHg.  $^1\text{H}$  NMR (200 MHz,  $\text{CDCl}_3$ )  $\delta$ : 1.12 (m, 12H,  $(\text{CH}_2)_6$ ), 1.92 (s, 12H,  $2 \times \text{N}(\text{CH}_3)_2$ ), 2.31 (t,  $J = 6.5$ , 4H,  $2 \times \text{NCH}_2$ ).  $^{13}\text{C}$  NMR (200 MHz,  $\text{CDCl}_3$ )  $\delta$ : 27.23–28.30 ( $(\text{CH}_2)_6$ ), 45.20 ( $\text{NCH}_3$ ), 59.66 ( $\text{NCH}_2$ ). Anal. calcd. (%) for  $\text{C}_{12}\text{H}_{28}\text{N}_2$  (200.37): C 71.86, H 13.97, N 13.97; found: C 71.66, H 14.15, N 14.13.

#### 1,10 Bis (N,N-dimethylamino)decane, 2c

Yield: 92%. Colourless oil, bp =  $62^\circ\text{C}$  at 0.05 mmHg.  $^1\text{H}$  NMR (200 MHz,  $\text{CDCl}_3$ )  $\delta$ : 1.09 (m, 12H,  $(\text{CH}_2)_6$ ), 1.24 (m, 4H,  $2 \times \text{CH}_2\text{-C-N}$ ), 1.92 (s, 12H,  $2 \times \text{N}(\text{CH}_3)_2$ ), 2.03 (t,  $J =$

6.3, 4H,  $2 \times \text{CH}_2\text{N}$ ).  $^{13}\text{C}$  NMR (200 MHz,  $\text{CDCl}_3$ )  $\delta$ : 27.4–28.51 ( $(\text{CH}_2)_8$ ), 45.42 ( $\text{NCH}_3$ ), 59.87 ( $\text{NCH}_2$ ). Anal. calcd. (%) for  $\text{C}_{14}\text{H}_{32}\text{N}_2$  (228.40): C 73.61, H 14.12, N 12.26; found: C 74.08, H 13.96, N 12.62.

#### 1,12 Bis (N,N-dimethylamino)dodecane, 2d

Yield: 98%. Colourless oil, bp =  $80\text{--}82^\circ\text{C}$  at 0.05 mmHg.  $^1\text{H}$  NMR (200 MHz,  $\text{CDCl}_3$ )  $\delta$ : 1.12 (m, 20H,  $(\text{CH}_2)_{10}$ ), 1.91 (s, 12H,  $2 \times \text{N}(\text{CH}_3)_2$ ), 2.12 (t,  $J = 6.3$ , 4H,  $2 \times \text{NCH}_2$ ).  $^{13}\text{C}$  NMR (200 MHz,  $\text{CDCl}_3$ )  $\delta$ : 27.43–28.53 ( $(\text{CH}_2)_{10}$ ), 45.42 ( $\text{NCH}_3$ ), 59.87 ( $\text{NCH}_2$ ). Anal. calcd. (%) for  $\text{C}_{16}\text{H}_{36}\text{N}_2$  (256.47): C 74.86, H 14.03, N 10.92; found: C 74.73, H 13.90, N 11.62.

#### 1,16 Bis (N,N-dimethylamino)hexadecane, 2e

Yield: 75%. Colourless oil, decomposition during the distillation.  $^1\text{H}$  NMR (200 MHz,  $\text{CDCl}_3$ )  $\delta$ : 1.19 (m, 24H,  $(\text{CH}_2)_{12}$ ), 1.23 (m, 4H,  $2 \times \text{CH}_2\text{CN}$ ), 2.16 (s, 12H,  $2 \times \text{N}(\text{CH}_3)_2$ ), 2.25 (t,  $J = 6.4$ , 4H,  $2 \times \text{NCH}_2$ ).  $^{13}\text{C}$  NMR (200 MHz,  $\text{CDCl}_3$ )  $\delta$ : 27.43–28.53 ( $(\text{CH}_2)_{14}$ ), 45.42 ( $\text{NCH}_3$ ), 59.87 ( $\text{NCH}_2$ ). Anal. calcd. (%) for  $\text{C}_{20}\text{H}_{44}\text{N}_2$  (312.56): C 76.85, H 14.19, N 8.96; found: C 76.73, H 13.92, N 8.62.

### Typical procedure for the synthesis of compounds 3

Sulfobetaine **3** was prepared by the addition of  $\alpha,\omega$ -bis(*N,N*-dimethylamino) alkane **2** ( $10^{-2}$  mol) to a stirred solution of 1,3-propane sultone ( $7 \times 10^{-3}$  mol) in 50 mL of anhydrous acetone. The reaction mixture was stirred at room temperature for 3 h, cooled, and filtered. The amphiphilic product was purified by recrystallization from methanol-ether (1:9) and dried in vacuo over phosphorus pentoxide.

#### 1-(N,N-Dimethylammonio,N-propyl-1-sulfonate)-8-(N',N'-dimethylamino) octane, 3b

Yield: 96%. White powder, mp =  $198\text{--}200^\circ\text{C}$ . IR (KBr)  $\nu$ : 1480 ( $\text{C-N}^+$ ), 1040 ( $\text{S=O}$ ).  $^1\text{H}$  NMR (80 MHz,  $\text{D}_2\text{O}$ )  $\delta$ : 1.25 (m, 12H,  $(\text{CH}_2)_6$ ), 1.99–2.18 (m, 10H,  $\text{NCH}_2$ ,  $\text{N}(\text{CH}_3)_2$ ,  $\text{CH}_2\text{-C-SO}_3^-$ ), 2.72–3.21 (m, 12H,  $\text{N}^+(\text{CH}_3)_2$ ,  $\text{N}^+\text{CH}_2$ ,  $\text{CH}_2\text{SO}_3^-$ ).  $^{13}\text{C}$  NMR (200 MHz,  $\text{D}_2\text{O}$ )  $\delta$ : 20.73–31.66 ( $(\text{CH}_2)_6$ ), 46.52 ( $\text{NCH}_3$ ), 49.81 ( $\text{CH}_2\text{-C-SO}_3^-$ ), 53.16 ( $\text{N}^+\text{CH}_3$ ), 61.43 ( $\text{NCH}_2$ ), 64.54 ( $\text{N}^+\text{CH}_2$ ), 66.71 ( $\text{CH}_2\text{SO}_3^-$ ). Anal. calcd. (%) for  $\text{C}_{15}\text{H}_{34}\text{N}_2\text{SO}_3$  (322.5): C 55.86, H 10.63, N 8.69, S 9.94; found: C 55.50, H 10.46, N 8.46, S 9.62.

#### 1-(N,N-Dimethylammonio,N-propyl-1-sulfonate)-10-(N',N'-dimethylamino) decane, 3c

Yield: 97%. White powder, mp =  $218^\circ\text{C}$ . IR (KBr)  $\nu$ : 1480 ( $\text{C-N}^+$ ), 1040 ( $\text{S=O}$ ).  $^1\text{H}$  NMR (80 MHz,  $\text{D}_2\text{O}$ )  $\delta$ : 1.27 (m, 16H,  $(\text{CH}_2)_8$ ), 1.82–2.16 (m, 8H,  $\text{NCH}_2$ ,  $\text{N}(\text{CH}_3)_2$ ), 2.33 (t,  $J = 6.6$ , 2H,  $\text{NCH}_2$ ), 2.65 (t,  $J = 8.1$ , 2H,  $\text{CH}_2\text{SO}_3^-$ ), 3 (s, 6H,  $\text{N}(\text{CH}_3)_2$ ).  $^{13}\text{C}$  NMR (200 MHz,  $\text{D}_2\text{O}$ )  $\delta$ : 20.72–31.65 ( $(\text{CH}_2)_{10}$ ), 46.52 ( $\text{NCH}_3$ ), 49.84 ( $\text{CH}_2\text{-C-SO}_3^-$ ), 53.16 ( $\text{N}^+\text{CH}_3$ ), 61.44 ( $\text{NCH}_2$ ), 64.52 ( $\text{N}^+\text{CH}_2$ ), 66.71 ( $\text{CH}_2\text{SO}_3^-$ ). Anal. calcd. (%) for  $\text{C}_{17}\text{H}_{38}\text{N}_2\text{SO}_3$  (350): C 58.09, H 10.52, N 4.7, S 5.34; found: C 57.80, H 10.57, N 4.3, S 5.27.

#### 1-(N,N-Dimethylammonio,N-propyl-1-sulfonate)-12-(N',N'-dimethylamino) dodecane, 3d

Yield: 95%. White powder, mp =  $230^\circ\text{C}$ . IR (KBr)  $\nu$ : 1480 ( $\text{C-N}^+$ ), 1040 ( $\text{S=O}$ ).  $^1\text{H}$  NMR (80 MHz,  $\text{D}_2\text{O}$ )  $\delta$ : 1.22 (m, 20H,  $(\text{CH}_2)_{10}$ ), 1.91–2.15 (m, 10H,  $\text{NCH}_2$ ,  $\text{N}(\text{CH}_3)_2$ ,



$\text{CH}_2\text{-C-SO}_3^-$ ), 2.91–3.25 (m, 12H,  $\text{N}^+(\text{CH}_3)_2$ ,  $\text{N}^+\text{CH}_2$ ,  $\text{CH}_2\text{-CH}_2\text{SO}_3^-$ ).  $^{13}\text{C}$  NMR (200 MHz,  $\text{D}_2\text{O}$ )  $\delta$ : 20.75–31.65 ( $(\text{CH}_2)_{10}$ ), 46.52 ( $\text{NCH}_3$ ), 49.84 ( $\text{CH}_2\text{-C-SO}_3^-$ ), 53.16 ( $\text{N}^+\text{CH}_3$ ), 61.44 ( $\text{NCH}_2$ ), 64.52 ( $\text{N}^+\text{CH}_2$ ), 66.72 ( $\text{CH}_2\text{SO}_3^-$ ). Anal. calcd. (%) for  $\text{C}_{19}\text{H}_{42}\text{N}_2\text{SO}_3$  (378.6): C 60.27, H 11.18, N 7.40, S 8.47; found: C 59.93, H 11.02, N 7.07, S 8.54.

**1-(N,N-Dimethylammonio,N-propyl-1-sulfonate)-12-(N',N'-dimethylamino) hexadecane, 3e**

Yield: 75%. White powder, mp = 238°C. IR (KBr) v: 1480 ( $\text{C-N}^+$ ), 1040 ( $\text{S} = \text{O}$ ).  $^1\text{H}$  NMR (80 MHz,  $\text{D}_2\text{O}$ )  $\delta$ : 1.22 (m, 28H,  $(\text{CH}_2)_{14}$ ), 1.72 (m, 2H,  $\text{NCCCH}_2$ ), 2.13–2.55 (m, 8H,  $\text{N}(\text{CH}_3)_2$ ,  $\text{NCH}_2$ ), 2.84 (m, 2H,  $\text{CH}_2\text{-CSO}_3^-$ ), 3.18 (m, 8H,  $\text{N}^+(\text{CH}_3)_2$ ,  $\text{N}^+\text{CH}_2$ ), 3.45 (t,  $J = 7.9$ , 2H,  $\text{SO}_3\text{CH}_2$ ).  $^{13}\text{C}$  NMR (200 MHz,  $\text{D}_2\text{O}$ )  $\delta$ : 19.51–29.6 ( $(\text{CH}_2)_{14}$ ), 45.54 ( $\text{NCH}_3$ ), 47.63 ( $\text{CH}_2\text{-C-SO}_3^-$ ), 50.61 ( $\text{N}^+\text{CH}_3$ ), 60.40 ( $\text{N}^+\text{CH}_2$ ), 63.52 ( $\text{N}^+\text{CH}_2$ ), 63.42 ( $\text{N}^+\text{CH}_2$ ), 64.54 ( $\text{CH}_2\text{SO}_3^-$ ). Anal. calcd. (%) for  $\text{C}_{23}\text{H}_{50}\text{N}_2\text{SO}_3$  (434.4): C 63.59, H 11.52, N 6.44, S 7.37; found: C 62.93, H 11.22, N 7.01, S 7.54.

**Typical procedure for the synthesis of compounds 1**

A mixture of sulfobetaine **3** ( $10^{-2}$  mol) and of haloalkane ( $1.2 \times 10^{-2}$  mol) in 50 mL of absolute MeOH was heated at reflux for 4 h. After removing the solvent in vacuo, the residual oil was precipitated by trituration with anhydrous ether. After filtration, the solid was washed by  $3 \times 20$  mL of anhydrous ether and dried in vacuo over phosphorus pentoxide.

**1-(N,N-Dimethylammonio,N-propyl-1-sulfonate)-8-(N',N'-dimethyl,N'-dodecylammonium bromide) octane, 1b**

Yield: 87%. White powder, mp = 120°C. IR (KBr) v: 1480 ( $\text{C-N}^+$ ), 1040 ( $\text{S} = \text{O}$ ).  $^1\text{H}$  NMR (80 MHz,  $\text{D}_2\text{O}$ )  $\delta$ : 0.85 (t,  $J = 7.3$ , 3H,  $\text{CH}_3\text{-C}_{11}$ ), 1.26 (m, 32H,  $(\text{CH}_2)_{10}$ ,  $(\text{CH}_2)_6$ ), 2.09 (m, 2H,  $\text{CH}_2\text{-C-SO}_3^-$ ), 2.64–3.33 (m, 22H,  $2 \times \text{N}(\text{CH}_3)_2$ ,  $4 \times \text{NCH}_2$ ,  $\text{CH}_2\text{SO}_3^-$ ).  $^{13}\text{C}$  NMR (200 MHz,  $\text{D}_2\text{O}$ )  $\delta$ : 16.61 ( $\text{C-CH}_3$ ), 20.75–34.61 ( $(\text{CH}_2)_6$ ,  $(\text{CH}_2)_{10}$ ), 49.90 ( $\text{CH}_2\text{-C-SO}_3^-$ ), 53.51 and 54.45 ( $\text{NCH}_3$ ), 64.46 and 66.32 ( $\text{NCH}_2$ ), 66.69 ( $\text{CH}_2\text{SO}_3^-$ ), 69.35 ( $\text{N}^+\text{CH}_2$ ). Anal. calcd. (%) for  $\text{C}_{27}\text{H}_{59}\text{N}_2\text{SO}_3\text{Br}$  (574.77): C 56.61, H 10.38, N 4.89, S 5.59; found: C 56.95, H 10.95, N 4.80, S 6.00.

**1-(N,N-Dimethylammonio,N-propyl-1-sulfonate)-10-(N',N'-dimethyl,N'-dodecylammonium bromide) decane, 1c**

Yield: 92%. White powder, mp = 115°C. IR (KBr) v: 1480 ( $\text{C-N}^+$ ), 1040 ( $\text{S} = \text{O}$ ).  $^1\text{H}$  NMR (80 MHz,  $\text{D}_2\text{O}$ )  $\delta$ : 0.85 (t,  $J = 7.1$ , 3H,  $\text{CH}_3\text{-C}$ ), 1.23 (m, 36H,  $(\text{CH}_2)_{10}$ ,  $(\text{CH}_2)_8$ ), 1.72–2.15 (m, 10H,  $\text{CH}_2\text{CN}$ ,  $\text{CH}_2\text{-C-SO}_3^-$ ), 2.84–3.05 (m, 12H,  $2 \times \text{N}(\text{CH}_3)_2$ ), 3.35 (m, 2H,  $\text{CH}_2\text{SO}_3^-$ ).  $^{13}\text{C}$  NMR (200 MHz,  $\text{D}_2\text{O}$ )  $\delta$ : 16.63 ( $\text{C-CH}_3$ ), 20.75–34.59 ( $(\text{CH}_2)_8$ ,  $(\text{CH}_2)_{10}$ ), 49.96 ( $\text{CH}_2\text{-C-SO}_3^-$ ), 53.25 and 53.63 ( $\text{NCH}_3$ ), 64.33 and 66.96 ( $\text{NCH}_2$ ), 66.48 ( $\text{CH}_2\text{SO}_3^-$ ), 69.76 ( $\text{N}^+\text{CH}_2$ ). Anal. calcd. (%) for  $\text{C}_{29}\text{H}_{63}\text{N}_2\text{SO}_3\text{Br}$  (599.86): C 57.96, H 10.57, N 4.66, S 5.33; found: C 58.79, H 10.05, N 4.42, S 5.55.

**1-(N,N-Dimethylammonio,N-propyl-1-sulfonate)-12-(N',N'-dimethyl,N'-dodecylammonium bromide) dodecane, 1d**

Yield: 85%. White powder, mp = 105°C. IR (KBr) v: 1480 ( $\text{C-N}^+$ ), 1040 ( $\text{S} = \text{O}$ ).  $^1\text{H}$  NMR (80 MHz,  $\text{D}_2\text{O}$ )  $\delta$ : 0.85 (t,  $J = 7.2$ , 3H,  $\text{CH}_3\text{-C}_{11}$ ), 1.27 (m, 40H,  $2 \times (\text{CH}_2)_{10}$ ), 2.09 (m, 2H,  $\text{CH}_2\text{-C-SO}_3^-$ ), 3.07–3.33 (m, 22H,  $2 \times \text{N}(\text{CH}_3)_2$ ,  $4 \times \text{NCH}_2$ ,  $\text{CH}_2\text{SO}_3^-$ ).  $^{13}\text{C}$  NMR (200 MHz,  $\text{D}_2\text{O}$ )  $\delta$ : 16.61

( $\text{C-CH}_3$ ), 20.63–34.40 ( $(\text{CH}_2)_{10}$ ), 49.90 ( $\text{CH}_2\text{-C-SO}_3^-$ ), 53.52 and 54.36 ( $\text{NCH}_3$ ), 64.21 and 66.06 ( $\text{NCH}_2$ ), 66.34 ( $\text{CH}_2\text{SO}_3^-$ ). Anal. calcd. (%) for  $\text{C}_{31}\text{H}_{67}\text{N}_2\text{SO}_3\text{Br}$  (627.87): C 59.20, H 10.74, N 4.45, S 5.09; found: C 59.79, H 10.35, N 4.42, S 5.55.

**1-(N,N-Dimethylammonio,N-propyl-1-sulfonate)-16-(N',N'-dimethyl,N'-dodecylammonium bromide) hexadecane, 1e**

Yield: 85%. White powder, mp = 135°C. IR (KBr) v: 1485 ( $\text{C-N}^+$ ), 1040 ( $\text{S} = \text{O}$ ).  $^1\text{H}$  NMR (80 MHz,  $\text{D}_2\text{O}$ )  $\delta$ : 0.87 (t,  $J = 7.3$ , 3H,  $\text{CH}_3$ ), 1.24–1.35 (m, 48H,  $(\text{CH}_2)_{14}$ ,  $(\text{CH}_2)_{10}$ ), 2.13 (m, 2H,  $\text{CH}_2\text{-C-S}$ ), 2.91–3.13 (m, 14H,  $2 \times \text{N}(\text{CH}_3)_2$ ,  $\text{CH}_2\text{SO}_3^-$ ), 3.35 (m, 8H,  $4 \times \text{N}^+\text{CH}_2$ ).  $^{13}\text{C}$  NMR (200 MHz,  $\text{D}_2\text{O}$ )  $\delta$ : 18.13 ( $\text{CH}_3$ ), 21.10–35.12 ( $(\text{CH}_2)_{14}$ ,  $(\text{CH}_2)_{10}$ ), 48.98 ( $\text{CH}_2\text{-C-S}$ ), 50.40 and 52.2 ( $\text{NCH}_3$ ), 60.62, 64.75, and 65.81 ( $\text{N}^+\text{CH}_2$ ), 66.75 ( $\text{CH}_2\text{S}$ ). Anal. calcd. (%) for  $\text{C}_{35}\text{H}_{75}\text{N}_2\text{SO}_3\text{Br}$  (683.98): C 61.36, H 11.03, N 4.09, S 4.68; found: C 61.82, H 10.35, N 4.98, S 4.35.

**1-(N,N-Dimethylammonio,N-propyl-1-sulfonate)-12-(N',N'-dimethyl,N'-ethylammonium bromide) dodecane, 1f**

Yield: 90%. White powder, mp = 125°C.  $^1\text{H}$  NMR (80 MHz,  $\text{D}_2\text{O}$ )  $\delta$ : 1.13 (t,  $J = 7.2$ , 3H,  $\text{CH}_3$ ), 1.34 (m, 16H,  $(\text{CH}_2)_8$ ), 2.25 (m, 2H,  $\text{CH}_2\text{-C-SO}_3^-$ ), 2.94–3.25 (m, 14H,  $2 \times \text{N}(\text{CH}_3)_2$ ,  $\text{CH}_2\text{SO}_3^-$ ), 3.31 (m, 8H,  $4 \times \text{NCH}_2$ ), 3.52 (t,  $J = 7.2$ , 2H,  $\text{NCH}_2\text{-C-C-S}$ ).  $^{13}\text{C}$  NMR (200 MHz,  $\text{D}_2\text{O}$ )  $\delta$ : 10.03 ( $\text{CH}_3$ ), 20.73–31.12 ( $(\text{CH}_2)_8$ ), 49.81 ( $\text{CH}_2\text{-C-S}$ ), 52.43 ( $\text{NCH}_3$ ), 53.21 ( $\text{CH}_3\text{N-S}$ ), 62.0, 64.48, and 65.75 ( $\text{NCH}_2$ ), 66.6 ( $\text{CH}_2\text{S}$ ). Anal. calcd. (%) for  $\text{C}_{21}\text{H}_{47}\text{N}_2\text{SO}_3\text{Br}$  (487.62): C 49.88, H 9.77, N 5.54, S 4.08; found: C 50.12, H 10.02, N 5.38, S 4.32.

**References**

1. P.K. Eggers, T.M. Fyles, K.D.D. Mitchell, and T. Sutherland. *J. Org. Chem.* **68**, 1050 (2003).
2. L.M. Cameron, T.M. Fyles, and C. Hu. *J. Org. Chem.* **67**, 1548 (2002).
3. J.H. Fuhrhop and D. Fritsch. *Acc. Chem. Res.* **19**, 130 (1986).
4. Y. Yan, J. Huang, Z. Li, F. Han, and J. Ma. *Langmuir*, **19**, 972 (2003).
5. N. Aydogan and N.L. Abbott. *J. Colloid Interface Sci.* **242**, 411 (2001).
6. Y. Chevalier. *Curr. Opin. Colloid Interface Sci.* **7**, 3 (2002).
7. R.C. Advincula, C. Xia, J. Locklin, and X. Fan. *Polymer Preprints (Am. Chem. Soc.)*, **43**, 345 (2002).
8. S. Souirti and M. Baboulène. *Synth. Commun.* **31**, 9 (2001).
9. S. Souirti and M. Baboulène. *Can. J. Chem.* **79**, 1153 (2001).
10. S. Souirti. Ph.D thesis, Toulouse University, France, 2002.
11. J.W. Gibbs. The collected works of J.W. Gibbs. Longmans and Green, London. 1928. Vol. 1. p. 119.
12. S. Franceschi, N. De Viguerie, E. Perez, M. Rivière, and A. Lattes. *J. Dispersion Sci. Technol.* **20**, 1523 (1999).
13. F. Brisset, R. Garelli-Calvet, J. Azema, C. Chebli, A. Moissant, and I. Rico-Lattes. *New. J. Chem.* **20**, 95 (1996).
14. J.H. Fuhrhop, H.H. David, J. Mathieu, U. Liman, H.J. Winter, and E. Boekema. *J. Am. Chem. Soc.* **108**, 1785 (1986).
15. J.H. Fuhrhop and R. Bach. *Supramol. Chem.* **2**, 25 (1992).
16. Y. Okahata and T. Kunitake. *J. Am. Chem. Soc.* **101**, 5231 (1979).
17. S. Bhattacharya and S. De. *Langmuir*, **15**, 3400 (1999).
18. S. Bhattacharya, S. De, and S.K. George. *Chem. Commun.* **23**, 2287 (1997).



# Voltammetric studies and assay of the anti-inflammatory drug ketoprofen in pharmaceutical formulation and human plasma at a mercury electrode

M.M. Ghoneim and A. Tawfik

**Abstract:** The electrochemical reduction of the anti-inflammatory drug ketoprofen was studied in a Britton-Robinson (B-R.) buffer series of pH 2–11 using dc-polarography, cyclic voltammetry, and coulometry techniques. The electrode reaction pathway of the drug at the dropping mercury electrode was proposed and discussed. A new adsorptive cathodic stripping square-wave voltammetric procedure was optimized for the assay of bulk drug in a B-R. buffer of pH 2.0. The peak current was linear with the drug concentration over the ranges  $2 \times 10^{-9}$  to  $2 \times 10^{-7}$  M of the bulk drug, using a 60 s accumulation time period at  $-0.6$  V (vs. Ag/AgCl/KCl<sub>s</sub>). The percentage recovery of the bulk drug was  $99.57 \pm 0.54$  and a detection limit of  $0.10$  ng mL<sup>-1</sup> was achieved. The proposed procedure was successfully applied for the assay of ketoprofen in pharmaceutical formulation (Ketofan®) and human plasma. The percentage recoveries were  $99.66 \pm 0.47$  and  $101.76 \pm 0.64$  in pharmaceutical formulation and human plasma, respectively. A detection limit of  $0.14$  ng mL<sup>-1</sup> plasma was achieved which was below that reported in literature using the different analytical techniques.

**Key words:** ketoprofen (Ketofan®) determination, polarography, cyclic voltammetry, adsorptive cathodic stripping square-wave voltammetry, human plasma.

**Résumé :** On a étudié la réduction électrochimique de la drogue anti-inflammatoire le cétoprofpène, dans une série de tampons de Britton-Robinson (B-R.) dont les pH varient de 2 à 11, en faisant appel à des techniques de polarographie dc, de voltamétrie cyclique et de coulométrie. On propose en détail un schéma réactionnel pour la réaction à l'électrode de la drogue au niveau de l'électrode à goutte de mercure. On a optimisé un nouveau procédé de voltamétrie à impulsion carrée avec accumulation à la surface de la cathode, pour un essai avec la drogue encombrée dans le B-R. à un pH de 2,0. L'intensité des courants de pic est proportionnelle la concentration de la drogue encombrée pour des concentrations supérieures à l'intervalle de  $2 \times 10^{-9}$  à  $2 \times 10^{-7}$  en utilisant des période de temps d'accumulation de 60 s à 0,6 V (vs. Ag/AgCl/KCl<sub>s</sub>). Le pourcentage de récupération de la drogue encombrée est de  $99,57 \pm 0,54$  avec une limite de détection de  $0,10$  ng mL<sup>-1</sup>. On a utilisé avec succès la méthode proposée lors d'un essai du cétoprofpène en formule pharmaceutique (Ketofan®) et dans le plasma humain. Les pourcentages de récupération sont de  $99,66 \pm 0,47$  et de  $101,76 \pm 0,64$  respectivement. On a atteint une limite de détection de  $0,14$  ng mL<sup>-1</sup> de plasma, cette limite est inférieure à celles reportées dans la littérature pour des techniques analytiques différentes.

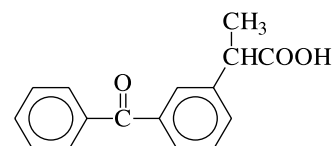
**Mots clés :** cétoprofpène (Ketofan®) détermination, polarographie, voltamétrie cyclique voltamétrie à impulsion carrée avec accumulation à la surface de la cathode, plasma humain.

[Traduit par la Rédaction]

## Introduction

Ketoprofen (I):  $\alpha$ -(3-benzoylphenyl) propionic acid, is a nonsteroidal anti-inflammatory agent with pronounced analgesic properties (1). Ketoprofen is used for anti-inflammatory and analgesic effects in the symptomatic treatment of acute and chronic rheumatoid arthritis and osteoarthritis. Ketoprofen is also used to relieve mild to moderate pain and

for the management of primary dysmenorrhea (2). It is formulated as a 50 mg capsule or a 100 mg suppository.



(I)

Ketoprofen is absorbed rapidly regardless of the route of administration. It reaches a peak maximum in the first hour of administration if taken by the oral and 6 h if taken by the subcutaneous route (3).

Received 11 February 2002. Published on the NRC Research Press Web site at <http://canjchem.nrc.ca> on 21 July 2003.

M.M. Ghoneim<sup>1</sup> and A. Tawfik. Chemistry Department, Faculty of Science, Tanta University, 31527 Tanta, Egypt.

<sup>1</sup>Corresponding author (e-mail: mmghoneim@hotmail.com).



The metabolism of ketoprofen undergoes through two major processes a hydroxylation process and glucuronide conjugation. The glucuronide conjugation pathway is predominant in the rabbit and in man but in man the hydroxylation is not totally absent (4, 5).

It is generally assumed that the nonsteroidal anti-inflammatory drugs diffuse back to plasma and that the metabolism of the drug within the joint does not occur (4). Ketoprofen and *p*-hydroxy ketoprofen are the major drug-related components in human plasma and the concentration of the metabolite (*p*-hydroxy ketoprofen) is very low (5, 6).

Various methods of determination of ketoprofen in pharmaceutical formulations and biological fluids have been reported. These mainly include: NMR spectroscopy (7), UV spectrophotometry (8–10), Fourier transform IR spectrometry (11, 12), capillary electrophoresis (13, 14), chromatography (15, 16), HPLC (17–42), GC–MS (43–47), and electrochemistry (9, 48). The electrochemical reduction of ketoprofen and its assay in pharmaceutical formulations were studied by differential-pulse polarography in a buffer of pH 6 (48), in which a single peak was observed at  $E_p = -1.15$  V vs. SCE. The peak current varied linearly with the concentration of the drug over the range  $1 \times 10^{-5}$  to  $5 \times 10^{-4}$  M. This procedure was sensitive to about  $2.5 \mu\text{g mL}^{-1}$ . Also, the assay of ketoprofen in capsules was studied in 0.1 M perchlorate (pH 3.8) using direct current stripping voltammetry (9). The peak current varied linearly with the drug concentration over the range  $1 \times 10^{-8}$  to  $1 \times 10^{-6}$  M with a detection limit of  $0.50 \text{ ng mL}^{-1}$ . In general, the detection limit of the reported procedures varied from  $10 \mu\text{g mL}^{-1}$  to  $0.5 \text{ ng mL}^{-1}$  depending on the applied analytical technique (7–48).

The aim of the present work was to clarify the polarographic behavior of ketoprofen in a Britton-Robinson (B-R.) buffer series (pH 2–11) and to shed light on its electrode reaction pathway at the dropping mercury electrode. Also, an adsorptive stripping square-wave voltammetry procedure was optimized for determination of the drug in bulk, pharmaceutical formulation, and human plasma with detection limits lower than those reported in literature (7–48).

## Experimental

### Materials

Bulk ketoprofen was kindly supplied by Squibb Company Cairo, Egypt and Ketofan<sup>®</sup> capsules (Amriya Pharm. Ind., Egypt) were purchased from the Egyptian local market. Human plasma samples were kindly supplied by the Tanta City Blood Bank.

### Reagents and solutions

A standard stock solution of  $1 \times 10^{-3}$  M bulk ketoprofen was prepared in ethanol (Merck) and stored in the dark at  $4^\circ\text{C}$ . More dilute solutions ( $1 \times 10^{-6}$  to  $1 \times 10^{-4}$  M) were prepared daily by accurate dilution with ethanol just before use. The ketoprofen solutions were stable and their concentrations did not change with time. A series of B-R. buffers of pH 2–11 was prepared (49).

Human plasma spiked with ketoprofen and a solution of ketoprofen extracted from Ketofan<sup>®</sup> capsules were prepared according to the procedure described previously (50).

A Mettler balance (Toledo AB104) was used for weighing the solid materials. Deionized water was obtained from an AquaMatic bi-distillation water system connected to a Purite Still Plus HP deionizer.

### Instrumentation

A Polarograph model 4001 (Sargent-Welch) was used for study of the polarographic behaviour of ketoprofen. A polarographic cell, with a dropping mercury electrode (DME) as a working electrode (mass of mercury flowing from the capillary per second  $m = 1.03 \text{ mg s}^{-1}$ ,  $t = 3.3 \text{ s}$  at mercury height = 60 cm) and a saturated calomel electrode (SCE) as a reference electrode, was used.

The Potentiostat/Galvanostat model 173 supplied with a digital Coulometer model 179 (PAR) was used for the controlled-potential coulometry measurements. A coulometric microcell, incorporated with a platinum wire sealed through the cell bottom for contact with a mercury pool as a working electrode, a SCE as a reference electrode, and a platinum gauze immersed in a bridge tube as a counter electrode, was used.

The cyclic and square-wave voltammograms were recorded using a Potentiostat/Galvanostat model 273A-PAR interfaced with a PC loaded with the software package 270/250 (PAR). The electrode assembly 303A (PAR), with a dark microelectrolysis cell incorporated with a hanging mercury drop electrode (HMDE) as a working electrode, Ag/AgCl/KCl<sub>s</sub> as a reference electrode, and a platinum wire as a counter electrode, was used.

### Analysis procedure

A known volume of ketoprofen solution was pipetted into a 10 mL-calibrated flask and made up to the mark with a B-R. buffer of pH 2.0. The solution was then transferred into the electrolysis cell and deoxygenated with pure nitrogen for 15 min. The accumulation potential ( $E_{\text{acc}} = -0.6$  V vs. Ag/AgCl/KCl<sub>s</sub>) was applied to the working electrode for a selected accumulation time period ( $t_{\text{acc}} = 60 \text{ s}$ ) while the solution was stirred. At the end of the accumulation period, the stirrer was stopped and 10 s were allowed for the solution to become quiescent. Stripping voltammograms were then recorded by scanning the potential towards the negative direction using the square-wave waveform. A calibration graph was constructed under the optimized conditions of the assay.

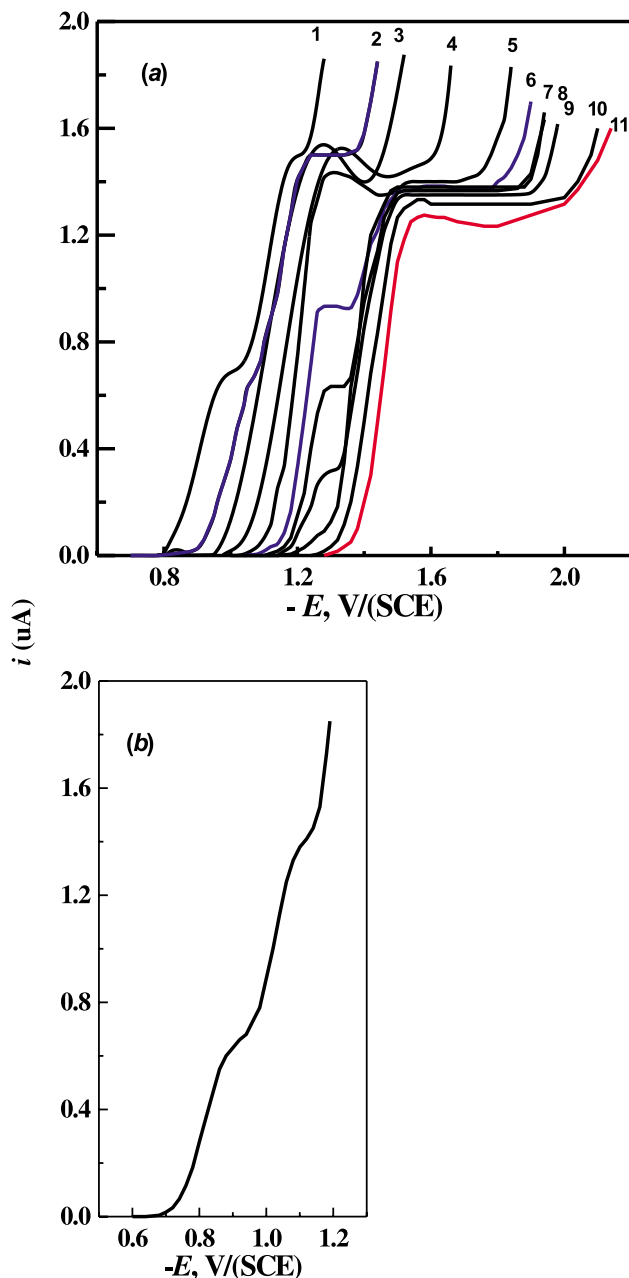
## Results and discussion

### dc-Polarography

The dc-polarograms for the  $2.6 \times 10^{-4}$  M bulk ketoprofen drug in the B-R. buffers of pH values  $\leq 3.0$  showed two one-electron irreversible waves of equal heights, both intermingled into a single two-electron irreversible wave in solutions of  $4 < \text{pH} < 6$ . On the increase of pH of the medium, the single wave started to split again into two waves, the height of the second wave increased at the expense of the first one until the latter disappeared completely in solutions of pH  $> 9$  (Fig. 1a). In solutions of pH  $> 9$ , a single two-electron wave was observed at more negative potentials. The total limiting current ( $i_l$ ) was pH independent throughout the entire pH range of 2–11 (Fig. 2a). The  $i_l$ -pH curves for the first wave (pH  $< 9$ ) and the second wave or the single wave (pH  $> 6$ )



**Fig. 1.** dc-Polarograms for  $2.6 \times 10^{-4}$  M ketoprofen in: (a) B-R. buffers of different pH values (1) pH 2.0, (2) pH 3.0, (3) pH 4.0, (4) pH 5.0, (5) pH 6.0, (6) pH 7.0, (7) pH 7.8, (8) pH 8.2, (9) pH 9.1, (10) pH 9.9, (11) pH 11.0; and (b) 0.1 M HCl.

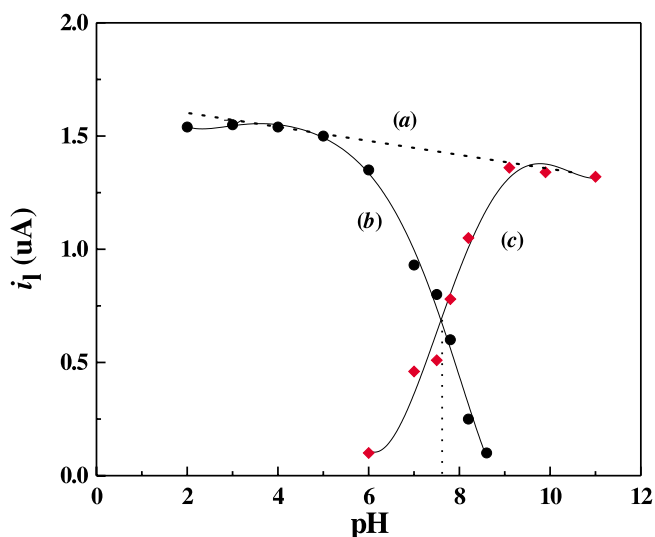


recalled dissociation and association curves, respectively (Fig. 2b, 2c) which may be attributed to the presence of the ketoprofen molecules in an acid-base equilibrium (51).

Controlled-potential coulometry studies revealed that the number of electrons involved in the reduction process of ketoprofen was two electrons/reactant molecule over the entire pH range of 2–11, which corresponded to the reduction of the carbonyl group site of the ketoprofen molecule.

The half-wave potentials ( $E_{1/2}$ ) of the ketoprofen reduction waves recorded in solutions of pH < 6.0, and that of the first wave recorded in solutions of pH values 6–9 shifted toward more negative values with the increase of pH of the

**Fig. 2.**  $i_p$ -pH plots for  $2.6 \times 10^{-4}$  M ketoprofen. (a) Total current; (b) first wave; (c) second wave.



medium. This behaviour indicated the involvement of protons in the rate-determining step and that the proton transfer precedes the electron transfer reaction (51). On the other hand, the  $E_{1/2}$  of both the second wave (pH 6–9) and the single wave (pH > 9) were practically pH independent.

The  $E_{1/2}$ -pH plot for the single wave (pH < 6) was a straight line (Fig. 3a) with a slope value ( $\delta E_{1/2}/\delta \text{pH} = S_1$ ) reported in Table 1 ( $S_1 = [0.0591/\alpha n_a] \cdot Z_H^+$ , where  $Z_H^+$  and  $n_a$  are the number of hydrogen ions and number of electrons, respectively, participating in the rate-determining step and  $\alpha$  is the transfer coefficient). Also the  $E_{1/2}$ -pH plots for the first wave (Fig. 3b) and for the second wave (pH 6–9) or the single wave (pH > 9) (Fig. 3c) were straight lines. These plots indicated that the  $E_{1/2}$  of the first wave (pH 6–9) was pH dependent while those of the second wave (pH 6–9) and the single wave (pH > 9) were practically pH independent. The pH value at the point of intersection of curves a and c (Fig. 3) was approximately equal to the  $\text{pK}_a'$  value of ketoprofen (pH =  $\text{pK}_a' \approx 7.5$ ) (52).

The ketoprofen reduction waves at the DME were analysed using the fundamental equation for the irreversible polarographic waves (53):

$$E_{\text{d.e.}} = E_{1/2} - (0.0591/\alpha n_a) \log (i/i_d - i)$$

The plots of the potential of the dropping mercury electrode ( $E_{\text{d.e.}}$ ) against  $\log (i/i_d - i)$  at different pH values were straight lines with the slope values  $S_2$  reported in Table 1 ( $S_2 = 0.0591/\alpha n_a$ ).

The number of hydrogen ions ( $Z_H^+$ ) participating in the rate-determining step (pH < 6) were determined by applying the relationship (53, 54):

$$\delta E_{1/2}/\delta \text{pH} = (0.0591/\alpha n_a) \cdot Z_H^+$$

$$\text{(i.e., } Z_H^+ = (\delta E_{1/2}/\delta \text{pH})/(0.0591/\alpha n_a) = S_1/S_2)$$

The data reported in Table 1 indicated that, in acidic media (pH < 6), the rate-determining step involved the consumption of one proton ( $Z_H^+ = 1$ ) and one electron ( $n_a = 1$ ), while in solutions of pH > 9,  $n_a = 2$ . Accordingly, the reduc-

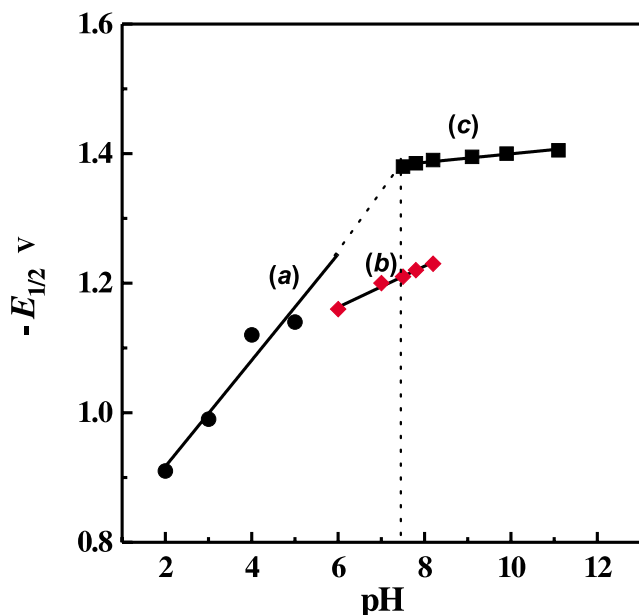


**Table 1.** Data obtained from dc-polarographic measurements for  $2.6 \times 10^{-4}$  M ketoprofen in B-R buffers of different pH values at 25°C.

pH	$-E_{1/2}$ (V) vs. SCE	$S_1$ (mV)	$S_2$ (mV)	$\alpha n_a$ ( $n_a = 1$ )	$\alpha$ ( $n_a = 2$ )	$Z_H^+$ ( $S_1/S_2$ )
In acidic media						
2.0	0.91	77.0	81.83	0.72	0.36	0.94
3.0	0.99		80.84	0.73	0.37	0.95
5.0	1.13		74.90	0.79	0.39	1.03
In alkaline media						
9.1	1.37	*	59.95	0.98	0.49	—
9.9	1.39	*	58.21	1.01	0.51	—
11.1	1.42	*	56.45	1.04	0.52	—

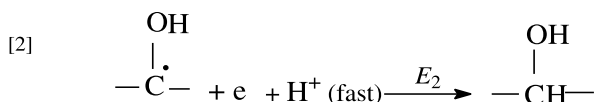
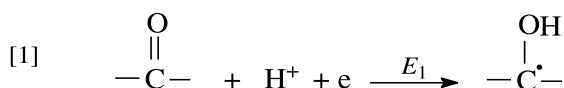
\* $E_{1/2}$  was practically pH independent in solutions of pH > 9.

**Fig. 3.**  $E_{1/2}$ -pH plots for  $2.6 \times 10^{-4}$  M ketoprofen in B-R buffers: (a) single wave (pH < 6); (b) first wave (pH 6–9); and (c) second wave (pH 6–9) and single wave (pH > 9).



tion reaction pathway of the carbonyl group of the ketoprofen molecule at the DME surface can be expressed as follows:

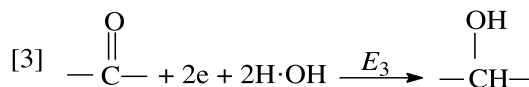
(i) In acidic solutions (pH < 6.0): the sequence of the electrode reaction was proton, electron, electron, proton ( $H^+$ , e, e,  $H^+$ ) (51).



In solutions of pH < 4,  $E_1 \neq E_2$ , thus, the reduction of the carbonyl group took place via two one-electron irreversible waves of equal heights (rxns. [1] and [2] represent the first and second waves, respectively). In 0.1 M HCl (pH 1), two one-electron irreversible waves of equal heights were also

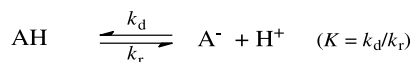
observed (Fig. 1b). At higher pH values ( $4 < \text{pH} < 6$ ),  $E_1 = E_2 = E_{1/2}$ , thus, a single two-electron irreversible wave was recorded (sum of rxns. [1] + [2]), while the total limiting current ( $i_l$ ) was still practically pH independent over the entire pH range.

(ii) In alkaline solutions (pH > 9): the sequence of the electrode reaction was electron, electron, proton, proton (e, e,  $H^+$ ,  $H^+$ ) (51). The protons required were supplied from the water molecules.



Over this pH range, the reduction of the carbonyl group took place at more negative potentials ( $E_3 > E_1$  and  $E_2$ ) via a single two-electron irreversible wave (rxn.[3]).

(iii) In solutions of intermediate pH values 6–9: over this pH range, the ketoprofen molecule was expected to be present in an acid–base equilibrium ( $\text{p}K_a \approx 7.5$ ) (52), both the acidic (AH) and basic ( $A^-$ ) forms were electroactive.



Thus, the reduction of the drug within the pH range 6–9 took place via two steps, and the height of the second step (because of the reduction of the basic form) increased at the expense of the first one (due to the reduction of the acidic form) on the increase of pH of the medium until the latter one disappeared completely at pH values >9 (Figs. 1 and 2). Thus, the electrode reaction of ketoprofen over the pH range (6–9) was considered to consist of mixed processes (rxns. [1], [2], and [3]). As the pH of the medium was increased, rxn. [3] became the dominant one.

According to Zuman (51), the existence of an electroactive compound in an acid–base equilibrium leads to the variation of the reduction current with the change of hydrogen ion concentration  $[H^+]$  as governed by the equation (55):

$$\frac{i_{\text{AH}}}{i_l} = \frac{0.886 \left\{ \left( \frac{k_r t_l}{K} \right) [H^+] \right\}^{1/2}}{1 + 0.886 \left\{ \left( \frac{k_r t_l}{K} \right) [H^+] \right\}^{1/2}}$$



which was modified to the following forms (51, 56):

$$\text{pH} = \log 0.886 \left( \frac{k_r t_1}{K} \right)^{1/2} + \log \left( \frac{i_l - i_{\text{AH}}}{i_{\text{AH}}} \right)$$

$$\text{pH} = \log 0.886 \left( \frac{k_r t_1}{K} \right)^{1/2} + \log \left( \frac{i_l - i_{\text{A}^-}}{i_{\text{A}^-}} \right)$$

( $i_{\text{AH}}$  and  $i_{\text{A}^-}$  are the reduction currents of acidic and basic forms, respectively).

The plots of  $[\log (i_l - i_{\text{AH}})/i_{\text{AH}}]$  or  $[\log (i_l - i_{\text{A}^-})/i_{\text{A}^-}]$  vs. the pH values 6–9, respectively, for the first and second waves, yielded straight lines (Fig. 4) which indicated the validity of the previous equations and consequently confirmed the presence of ketoprofen molecules in an acid–base equilibrium within the pH range 6–9. The pH value corresponded to the intersection point of the two curves (Fig. 4a, 4b) equaled to the  $\text{p}K_{\text{a}}'$  value of ketoprofen ( $\text{pH} = \text{p}K_{\text{a}}' \approx 7.5$ ) (52).

### Cyclic voltammetry

The cyclic voltammograms of ketoprofen in B-R. buffers of  $\text{pH} < 6$  and  $\text{pH} > 9$  showed a single cathodic peak, while two cathodic peaks were observed in solutions of  $\text{pH} 6$ – $9$ . No anodic peaks were observed in the reverse scan, which confirmed the irreversible nature of the ketoprofen electrode reaction. These results agree well with that of the polarographic studies of the drug over the pH range 2–11. The irreversible nature of the reduction process was also confirmed by the shift of the peak potential ( $E_{\text{p}}$ ) to more negative values with the increase of the scan rate  $\nu$  from 20 to 500  $\text{mV s}^{-1}$  (57). On plotting  $\log i_{\text{p}}$  vs.  $\log \nu$ , a linear correlation was obtained with a slope value close to the theoretical expected value of 1.0 for an ideal reaction of surface species (58). So in this case the process appears to have an important adsorptive component. The electrode surface coverage can be calculated from the amount of charge consumed by the surface process as calculated by the integration of the area under the peak of the cyclic voltammogram corrected to residual current (59). According to the equation:  $\Gamma = Q/nFA$ , the surface coverage  $\Gamma$  ( $\text{mol cm}^{-2}$ ) was calculated, where  $n$  is the overall number of electrons consumed in the reduction process ( $n = 2$ ),  $F$  is Faraday's constant (96 487 C) and  $A$  is the electrode surface area ( $0.026 \text{ cm}^2$ ). On dividing the number of coulombs transferred ( $1.267 \mu\text{C}$ ) by the conversion factor ( $nFA$ ), a monolayer surface coverage of  $2.525 \times 10^{-10} \text{ mol cm}^{-2}$  was obtained. Each adsorbed ketoprofen molecule therefore occupies an area of  $6.5748 \text{ nm}^2$ .

### Adsorptive stripping square-wave voltammetry

The adsorptive preconcentration of ketoprofen at the HMDE surface and the application of a subsequent scan in the negative direction using the square-wave waveform gave rise to a single reduction peak in B-R. buffers of different pH values. A well-developed and sharper peak was observed in a B-R. buffer of  $\text{pH} 2.0$ . Figure 5 shows a large response for  $2 \times 10^{-7} \text{ M}$  ketoprofen after preconcentration for 60 s. On the contrary, the direct response ( $t_{\text{acc}} = 0$ ) showed a smaller reduction peak current. This indicates that ketopro-

**Fig. 4.** Plots of  $\log [(i_l - i_{\text{HA}})/i_{\text{HA}}]$  and  $\log [(i_l - i_{\text{A}^-})/i_{\text{A}^-}]$  vs. pH for  $2.6 \times 10^{-4} \text{ M}$  ketoprofen in B-R. buffers of different pH values. (a) First wave; (b) second wave recorded in solutions of pH 6–9.

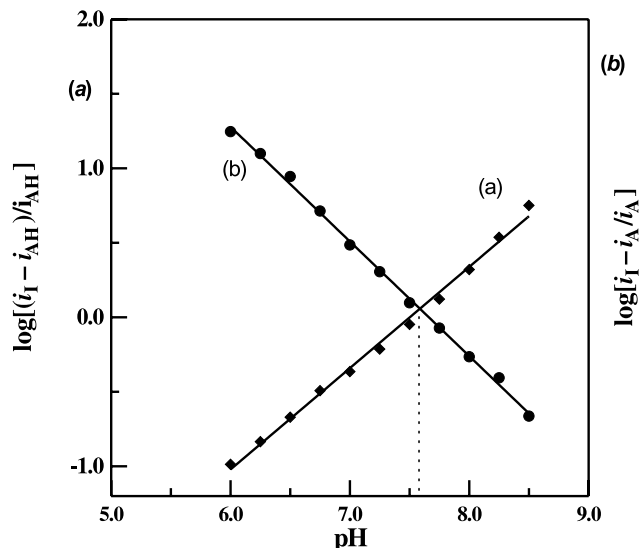
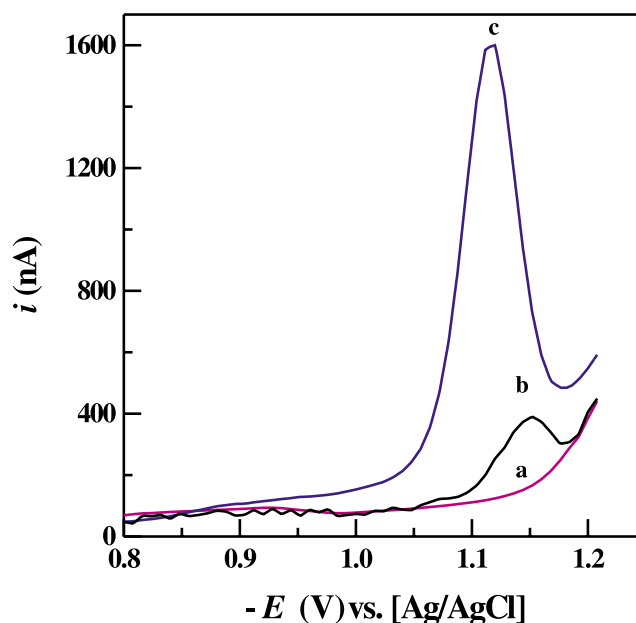


**Fig. 5.** Square-wave voltammograms for  $2 \times 10^{-7} \text{ M}$  ketoprofen in a B-R. buffer of  $\text{pH} 2$ : (a) background; (b) without preconcentration ( $t_{\text{acc}} = 0$ ); and (c) after preconcentration for 60 s.  $E_{\text{acc}} = -0.6 \text{ V}$ , frequency = 120 Hz, scan increment = 8 mV, pulse amplitude = 25 mV, and rest period = 10 s.

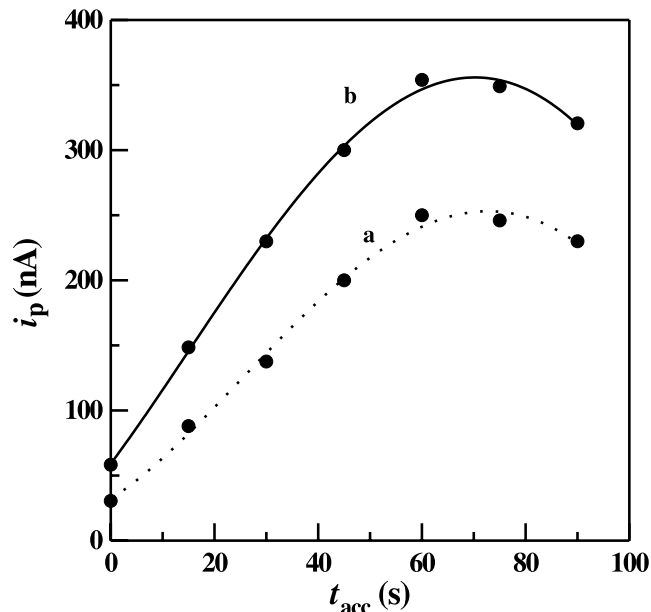


fen can be preconcentrated at the HMDE surface by adsorption.

Considering the large response obtained by adsorptive stripping square-wave (AdSSW) voltammetry compared to that of direct square-wave stripping (SWS) voltammetry, it was possible to determine trace levels of ketoprofen using AdSSW voltammetry. Experiments were made to optimize the conditions for the adsorption of the drug onto the HMDE surface. Several stripping voltammograms were recorded at



**Fig. 6.** Influence of the accumulation time on the peak current of AdSSW voltammograms for: (a)  $2 \times 10^{-8}$  M ketoprofen; and (b)  $2 \times 10^{-7}$  M ketoprofen. Other conditions as illustrated in Fig. 5.



different accumulation potentials,  $E_{acc}$ , (0 to  $-1.0$  V), pulse amplitudes (10–70 mV), scan increments (2–10 mV), and frequencies (20–120 Hz). Finally, the effect of the accumulation time ( $t_{acc}$ ) was studied for two concentrations ( $2 \times 10^{-8}$  M and  $2 \times 10^{-7}$  M) of ketoprofen under the optimized conditions:  $E_{acc} = -0.6$  V, pulse amplitude = 25 mV, scan increment = 8 mV, frequency = 120 Hz, rest period = 10 s, and drop size =  $0.026 \text{ cm}^2$ . The resultant peak current showed a linear relationship with the accumulation time up to 60 s for both concentrations studied (Fig. 6).

The applicability of the AdSSW voltammetry technique as an analytical method for the determination of bulk ketoprofen was tested as a function of its concentration (Fig. 7). Linear response was obtained over the concentration ranges  $2 \times 10^{-9}$  to  $2 \times 10^{-7}$  M ( $t_{acc} = 60$  s) or  $1 \times 10^{-8}$  to  $3 \times 10^{-7}$  M of ketoprofen ( $t_{acc} = 30$  s). The variations of peak current ( $i_p$ ) with ketoprofen concentration ( $C$ ) after preconcentration for 60 s and 30 s were represented by the following straight line equations:

$$i_p(\text{nA}) = 10.4024C(\text{nM}) + 42.75,$$

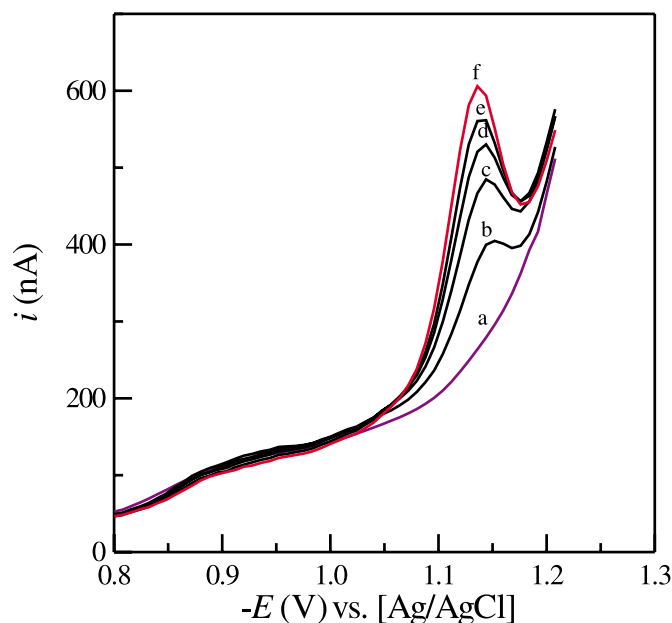
correlation coefficient  $r = 0.998$  ( $n = 14$ ),  
 $t_{acc} = 60$  s and,

$$i_p(\text{nA}) = 7.2896C(\text{nM}) + 18.22,$$

$r = 0.995$  ( $n = 14$ ),  $t_{acc} = 30$  s

The percentage recovery of the drug was  $99.57 \pm 0.54$ . The drug detection limit was calculated using the equation  $dl = 3sd/a$  (60) where  $sd$  is the standard deviation of the blank and  $a$  is the slope of the calibration curve. A detection limit of  $0.10 \text{ ng mL}^{-1}$  of the bulk drug was achieved.

**Fig. 7.** AdSSW voltammograms for different concentrations of ketoprofen spiked to human plasma: (a) background; (b)  $2 \times 10^{-9}$  M ketoprofen; (c)  $6 \times 10^{-9}$  M ketoprofen; (d)  $1 \times 10^{-8}$  M ketoprofen; (e)  $1.4 \times 10^{-8}$  M ketoprofen; and (f)  $1.8 \times 10^{-8}$  M ketoprofen ( $t_{acc} = 60$  s, other conditions as illustrated in Fig. 5).



### Interference studies

Selectivity of the optimized procedure for the assay of  $3 \times 10^{-8}$  M ketoprofen was examined in the presence of some common excipients in the same ratios usually used in pharmaceutical preparations (e.g., starch, gelatin, lactose, talc, and magnesium stearate). The mean percentage recovery of  $98.56 \pm 0.61$  showed no significant interference from excipients, thus, the procedure was able to assay ketoprofen in the presence of excipients and hence, it can be considered selective.

### Applications

#### Analysis of Ketofan® capsules

The proposed procedure was successfully applied for the assay of ketoprofen in pharmaceutical formulation (Ketofan® capsules). The percentage recovery of ketoprofen based on the average of four replicate experiments was found to equal  $99.66 \pm 0.47$ . The results were favorably compared with those obtained by assay of the same capsules using a reported HPLC method (20).

#### Analysis of spiked human plasma

The present optimized AdSSW voltammetry procedure was also successfully applied for the determination of ketoprofen in protein-free spiked human plasma (Fig. 7). The variation of peak current ( $i_p$ ) vs. ketoprofen concentration ( $C$ ) was represented by a straight-line equation:  $i_p(\text{nA}) = 9.28151C(\text{nM}) + 45.3146$ ,  $r = 0.997$  ( $n = 14$ ). The linear concentration range was  $5 \times 10^{-9}$  to  $2 \times 10^{-7}$  M ketoprofen. The percentage recovery of ketoprofen based on the average of four replicate experiments was found to equal  $101.76 \pm$



0.64, which compared well with that obtained by a reported HPLC method (20). A drug detection limit of 0.14 ng mL<sup>-1</sup> plasma was achieved.

## Conclusions

In this work, the reduction reaction pathway of ketoprofen at the mercury electrode surface in B-R. buffers of pH 2–11 was clearly elucidated and discussed. Also, a simple, fast, accurate, highly sensitive and a less cost adsorptive cathodic stripping square-wave voltammetric procedure was optimized and successfully applied for the determination of ketoprofen in bulk, pharmaceutical formulation, and human plasma. The reached detection limits of the drug were below those reported in the literature when applying the different analytical techniques (7–48). The optimized procedure did not require sample pretreatment or any time-consuming extraction steps other than centrifugal separation of the precipitated proteins from plasma samples prior to the drug assay. The proposed procedure could possibly be adopted for the pharmacokinetic as well as quality control laboratories.

## References

1. F.D. Hart. Rheumatic disorders. *In* Drug treatment: principles and practice of clinical pharmacology and therapeutics. Vol. 88. 2nd ed. Edited by G.S. Avery. ADIS Press, Sydney. 1980. p. 846.
2. G.K. Mcevoy. AHFS Drug Information. American Society of Hospital Pharmacists. Inc., Bethesda, Md. 1990. p. 1034.
3. F. Klaus. Analytical profiles of drug substances. Vol. 10. Academic Press, New York. 1981.
4. O.D. Richard, J.M. Andrew, G.G. Garry, and M.W. Kenneth. *Clin. Pharmacokinet.* **36**, 196 (1999).
5. P. Courpron, V.L. Brazier, P. Meunier, B. Ribon, and A. Bannier. *Lyon Med.* **239**, 477 (1978).
6. P. Populaire, B. Terlain, S. Pascal, B. Decouvelaere, A. Renard, and J.P. Thomas. *Ann. Pharm. Fr.* **31**, 735 (1973).
7. K. Akira and Y. Shinohara. *Anal. Chim. Acta*, **334**, 67 (1996).
8. M. Blanco, J. Coello, H. Iturriaga, S. Maspoch, and S. Alaoui-Ismaili. *Fresenius J. Anal. Chem.* **357**, 967 (1997).
9. K.M. Emara, A.M.M. Ali, and N.A.E. Maali. *Talanta*, **41**, 639 (1994).
10. M. El-Sadek, S. Eladl, M. Aboukull, and S.M. Sakr. *Talanta*, **40**, 585 (1993).
11. A. Van Overbeke, W. Baeyens, and W. Van den Bossche. *Vib. Spectrosc.* **9**, 121 (1995).
12. M.J. Sanchez-Dasi, S. Garrigues, M.L. Cervera, and M. de la Guardia. *Anal. Chim. Acta*, **361**, 253 (1998).
13. M. Blanco, J. Coello, H. Iturriaga, S. Maspoch, and C. Perez-Maseda. *J. Chromatogr. A*, **799**, 301 (1998).
14. M. Friedberg and Z.K. Shihabi. *J. Chromatogr. B: Biomed. Sci. Appl.* **695**, 193 (1999).
15. M.G. Donato, W. Baeyens, W. Van den Bossche, and P. Sandra. *J. Pharm. Biomed. Anal.* **12**, 21 (1994).
16. F. Leclerc, D. Deruaz, A. Bannier, and J.L. Brazier. *Anal. Lett.* **27**, 1325 (1994).
17. J. Haginaka, C. Seyama, and N. Kanasugi. *Anal. Chem.* **67**, 2359 (1995).
18. M.T.J. Garcia, T.M. Marchetti, and M.V.L.B. Bentley. *Anal. Lett.* **34**, 1865 (2001).
19. E. Ameyibor and J.T. Stewart. *J. Pharm. Biomed. Anal.* **17**, 83 (1998).
20. N.G. Grubb, D.W. Rudy, and S.D. Hall. *J. Chromatogr. B: Biomed. Sci. Appl.* **678**, 237 (1996).
21. R. Lovlin, M. Vakily, and F. Jamali. *J. Chromatogr. B: Biomed. Sci. Appl.* **679**, 19 (1996).
22. R.A. Carr, G. Caillé, A.H. Ngoc, and R.T. Foster. *J. Chromatogr. B: Biomed. Sci. Appl.* **668**, 175 (1995).
23. R. Harraez-Hernandez, N.C. van de Merbel, and U.A.Th. Brinkman. *J. Chromatogr. B: Biomed. Sci. Appl.* **666**, 127 (1995).
24. M.R. Wright and F. Jamali. *J. Chromatogr.* **616**, 59 (1993).
25. A. Shibukawa, A. Terakita, J.Y. He, and T. Nakagawa. *J. Pharm. Sci.* **81**, 710 (1992).
26. C. Mannucci, J. Bertini, A. Cocchini, A. Perico, F. Salvagnini, and A. Triolo. *J. Liq. Chromatogr.* **15**, 327 (1992).
27. Y. Oda, N. Asakawa, S. Abe, Y. Yoshida, and T. Sato. *J. Chromatogr. Biomed. Appl.* **572**, 133 (1991).
28. E.L. Palylyk and F. Jamali. *J. Chromatogr. Biomed. Appl.* **568**, 187 (1991).
29. M.H. Abdel-Hamid and M.A. Etman. *Alexandria J. Pharm. Sci.* **4**, 32 (1990).
30. M. Yagi, A. Shibukawa, and T. Nakagawa. *Chem. Pharm. Bull.* **38**, 2513 (1990).
31. J.H. Satterwhite and F.D. Boudinot. *J. Chromatogr. Biomed. Appl.* **431**, 444 (1988).
32. R.T. Foster and F. Jamali. *J. Chromatogr. Biomed. Appl.* **416**, 388 (1987).
33. B.C. Sallustio, A. Abas, P.J. Hayball, Y.J. Purdie, and P.J. Meffin. *J. Chromatogr. Biomed. Appl.* **374**, 329 (1986).
34. A. Bannier, J.L. Brazier, B. Ribon, and C. Quincy. *J. Pharm. Sci.* **69**, 763 (1980).
35. S. Wanwimolruk, S.Z. Wanwimolruk, and A.R. Zoest. *J. Liq. Chromatogr.* **14**, 3685 (1991).
36. P.J. Hayball, R.L. Nation, F. Bochner, and R.K. Leleu. *J. Chromatogr. Biomed. Appl.* **570**, 446 (1991).
37. C.Y. Wong, M.K. Yeh, and D.P. Wang. *J. Liq. Chromatogr.* **15**, 1215 (1992).
38. Y. Oda, N. Asakawa, Y. Yoshida, and T. Sato. *J. Pharm. Biomed. Anal.* **10**, 81 (1992).
39. E.L. Palylyk and F. Jamali. *J. Chromatogr. Biomed. Appl.* **568**, 187 (1991).
40. G. Tamai, M. Edani, and H. Imai. *Anal. Sci.* **7**, 29 (1991).
41. S. Bjorkman. *J. Chromatogr. Biomed. Appl.* **414**, 465 (1987).
42. N. Rifai, M. Lafi, M. Sakamoto, and T. Law. *Ther. Drug Monit.* **19**, 175 (1997).
43. D.S. Jack, R.H. Rumble, N.W. Davies, and H.W. Francis. *J. Chromatogr. Biomed. Appl.* **584**, 189 (1992).
44. E. Benoit, P. Jaussaud, S. Besse, B. Videmann, D. Courtot, O. Delatour, and Y. Bonnaire. *J. Chromatogr. Biomed. Appl.* **583**, 167 (1992).
45. E.G. De-Jong, J. Kiffers, and R.A.A. Maes. *J. Pharm. Biomed. Anal.* **7**, 1617 (1989).
46. J. De-Graeve, C. Frankinet, and J.E. Gielen. *Biomed. Mass Spectrom.* **6**, 249 (1979).
47. H.J. Leis, M. Leis, and W. Windischhofer. *J. Mass Spectrom.* **31**, 486 (1996).
48. L. Amankwa and L.G. Chatten. *Analyst (Cambridge, U.K.)*, **109**, 57 (1984).
49. H.T.S. Britton. *Hydrogen ions*. 4th ed. Chapman and Hall, London. 1952.
50. M.M. Ghoneim, M.M. Mabrouk, A.M. Hassanein, and A. Tawfik. *J. Pharm. Biomed. Anal.* **25**, 933 (2001).



51. P. Zuman. The elucidation of organic electrode processes. Academic Press, New York. 1969. pp. 20–51.
52. A. Tawfik. Ph.D. thesis, Chemistry Department, Faculty of Science, Tanta University, Tanta, Egypt, 1999.
53. L. Meits. Polarographic techniques. 2nd ed. Interscience Publishers, New York. 1965. pp. 232–248.
54. M.M. Ghoneim and M.A. Ashy. *Can. J. Chem.* **57**, 1249 (1979).
55. J. Koutecky. *Coll. Czech. Chem. Commun.* **18**, 587 (1953).
56. T.M. Salem, R.M. Issa, and A.M. Hindawey. *Ann. Chim. (Rome)*, **64**, 735 (1974).
57. P. Delahay. New instrumental methods in electrochemistry. Interscience, New York. 1966. Chap. 6.
58. E. Laviron. *J. Electroanal. Chem.* **112**, 1 (1980).
59. A. Webber, M. Shah, and J. Osteryoung. *Anal. Chim. Acta*, **157**, 17 (1984).
60. M.R. Smyth and J.G. Osteryoung. *Anal. Chem.* **50**, 1632 (1978).



# Phase behaviour and structure of amphiphilic poly(ethylene oxide)–poly(propylene oxide) triblock copolymers ((EO)<sub>4</sub>(PO)<sub>59</sub>(EO)<sub>4</sub> and (EO)<sub>17</sub>(PO)<sub>59</sub>(EO)<sub>17</sub>) in ternary mixtures with water and xylene

Pius Kipkemboi, Ali Khan, Björn Lindman, and Viveka Alfredsson

**Abstract:** The isothermal ternary phase behaviour and structure of amphiphilic copolymer–water–xylene systems was investigated for two poly(ethylene oxide)–poly(propylene oxide) (PEO–PPO) triblock copolymers, (EO)<sub>4</sub>(PO)<sub>59</sub>(EO)<sub>4</sub> and (EO)<sub>17</sub>(PO)<sub>59</sub>(EO)<sub>17</sub>, at 25°C. The phase boundaries were identified using <sup>2</sup>H NMR and inspection under polarized light. The microstructure and structural length scales in the lyotropic liquid crystalline phases were determined and characterized by small-angle X-ray scattering. The amounts and relative proportions of the selective solvents can modulate the resulting microstructures, although the phase sequence observed depends on the relative PEO–PPO block ratio. A variety of lyotropic liquid crystalline (LLC) phases are thermodynamically stable in the system with copolymer (EO)<sub>17</sub>(PO)<sub>59</sub>(EO)<sub>17</sub>, both of the normal (“oil-in-water”) and of the reverse (“water-in-oil”) morphology. The high hydrophobic content of copolymer (EO)<sub>4</sub>(PO)<sub>59</sub>(EO)<sub>4</sub>, however, favours reverse LLC structures with low interfacial curvature. No normal LLC phases are formed by this system.

**Key words:** amphiphilic, triblock copolymers, poly(ethylene oxide), poly(propylene oxide), ternary mixtures, phase behaviour, lyotropic liquid crystals, SAXS, <sup>2</sup>H NMR.

**Résumé :** Opérant à 25 °C, on a étudié le comportement de la phase ternaire isotherme et de la structure des systèmes copolymère–eau–xylène amphiphiles de deux copolymères à trois blocs de poly(oxyde d'éthylène)–poly(oxyde de propylène) (PEO–PPO), (EO)<sub>4</sub>(PO)<sub>59</sub>(EO)<sub>4</sub> et (EO)<sub>17</sub>(PO)<sub>59</sub>(EO)<sub>17</sub>. On a identifié les barrières des phases par RMN du <sup>2</sup>H et par inspection sous de la lumière polarisée. On a déterminé la microstructure et les échelles de longueur dans des phases de cristaux liquides lyotropes et on les a caractérisées par diffraction des rayons X à angle faible. Les quantités et les proportions relatives de solvants choisis peuvent moduler les microstructures qui en résultent, même si la séquence de phase qui est observée dépend du rapport relatif des blocs PEO–PPO. Une variété de phases de cristaux liquides lyotropes (LLC) sont thermodynamiquement stables dans le système avec le copolymère (EO)<sub>17</sub>(PO)<sub>59</sub>(EO)<sub>17</sub> de morphologie tant normale (huile dans l'eau) qu'inversée (eau dans l'huile). Toutefois, le contenu hydrophobe élevé du copolymère (EO)<sub>4</sub>(PO)<sub>59</sub>(EO)<sub>4</sub> favorise les structures LLC inversées avec de faibles courbures interfaciales. Il n'y a pas de phases LLC normales qui se forment dans ce système.

**Mots clés :** amphiphile, copolymères à trois blocs, poly(oxyde de propylène), poly(oxyde de propylène), comportement de phase, cristaux liquides lyotropes, SAXS, RMN du <sup>2</sup>H.

[Traduit par la Rédaction]

## Introduction

Amphiphilic molecules can self-assemble in solution, forming thermodynamically stable aggregates. The amphiphilic molecules can be low molecular weight synthetic surfactants, natural lipids, or large molecules such as block copolymers. Block copolymers are an interesting class of amphiphiles. Amphiphilic triblock copolymers consisting of

a relatively hydrophobic poly(propylene oxide) (PPO) middle block and two hydrophilic poly(ethylene oxide) (PEO) end blocks are commercially available as Poloxamers or Pluronics in a large variety of molecular weights and PEO–PPO ratios (1, 2). The interest in the self-assembly of poly(ethylene oxide)–poly(propylene oxide)–poly(ethylene oxide) (PEO–PPO–PEO) block copolymers has grown considerably over the past decade (1–4). Self-assembly of these polymers is facilitated, as in the case of common low-molecular-weight surfactants, by the presence of the two different but covalently bonded parts. In the presence of a solvent selective for the hydrophilic PEO blocks such as water and a solvent selective for the hydrophobic PPO block such as xylene (“oil”), PEO–PPO–PEO block copolymers self-organize into a whole spectrum of self-assembled structures, from micellar solutions to lyotropic liquid crystalline phases with lamellar, hexagonal, and micellar or bi-

Received 22 May 2002. Published on the NRC Research Press Web site at <http://canjchem.nrc.ca> on 26 July 2003.

**P. Kipkemboi.**<sup>1</sup> Department of Chemistry, Moi University, P.O. Box 1125, Eldoret, Kenya.

**A. Khan, B. Lindman, and V. Alfredsson.** Physical Chemistry 1, Center for Chemistry and Chemical Engineering, Lund University, P.O. Box 124, S-221 00 Lund, Sweden.

<sup>1</sup>Corresponding author (e-mail: [keronei@yahoo.com](mailto:keronei@yahoo.com)).



continuous cubic microstructures (3). The micellar solutions possess only short-range order (at the micelle level). The lyotropic liquid crystals exhibit long-range order beyond the level of the structural element (i.e., spherical, cylindrical, or planar block copolymer micelles). Both normal (oil-in-water) and reverse (water-in-oil) morphologies can be formed at constant temperature, depending on the ternary composition (4, 5). A notable feature that distinguishes the self-assembling behaviour of the PEO-PPO-PEO block copolymers from that of the low-molecular-weight surfactants (6) is the ability of the block copolymer to exhibit much richer structural polymorphism and to form a great variety of both normal and reverse liquid crystalline microstructures, as demonstrated in recent reports (3, 5, 7–10). Such an ability to form many normal and reverse structures at the same temperature has never before been observed in ternary systems of common surfactants with water and oil. The presence of oil enables the formation of reverse phases, where the oil is the continuous phase, in addition to the normal ones, where water is the continuous one. The concentration range over which the different phases form depend on the block copolymer molecular weight, the block PEO-PPO ratio, and the solvent quantity and quality. PEO-PPO-PEO block copolymers thus allow for great flexibility in attaining the desired structure under different conditions and can be viewed as model self-assembled systems (5).

For a PEO-PPO block copolymer of a given composition and molecular weight, the type of structures obtained in the presence of selective solvents appears to be a function of the volume fraction of the polar (water-like) – apolar (oil-like) components; this is attributed to the ability of the macromolecular blocks to swell to a different extent (based on the amount of solvent available) with the respective solvents and to thus modulate the interfacial “curvature” and resulting structure (11). The initial interfacial curvature can be readily modified by the ability of the copolymer blocks to swell to different extents with selective solvents. Thus the proper solvent selection allows for a large diversity in the microstructure of the final product and its corresponding properties. The quality of the solvent and its ability to swell the different blocks will of course affect the phase behaviour and structure, as a recent study suggests (8). Owing to the great potential for modification of their phase behaviour and to the variety of their physico-chemical properties, numerous industrial applications are found for Polaxamers (12). This class of materials is a rather new field of research, and ternary phase diagrams of many different systems have been reported recently (3, 5, 8–11, 13–22).

The phase behaviour and microstructure in ternary systems composed of amphiphilic copolymers, an aqueous solvent (“water”), and an organic solvent (“oil”) are the subjects of an ongoing investigation by our research group (3, 5, 7–11, 16–18, 20–22). The work described here focuses on the isothermal phase behaviour and microstructure of ternary systems based on  $(\text{EO})_4(\text{PO})_{59}(\text{EO})_4$  and  $(\text{EO})_{17}(\text{PO})_{59}(\text{EO})_{17}$ , triblock copolymers containing water and *p*-xylene as selective solvents for PEO and PPO, respectively. The two triblock copolymers studied have the same hydrophobic PPO block length, but the size of the PEO blocks differ and allow us to examine the effects of hydrophilic block size on the phase behaviour. Visual observation under polarized light

and  $^2\text{H}$  NMR quadrupolar splittings have been used to delineate the phase boundaries, and small-angle X-ray scattering (SAXS) was used to characterize the structures.

## Experimental section

### Materials and sample preparation

The poly(ethylene oxide)–poly(propylene oxide)–poly(ethylene oxide) copolymers with the trade names Pluronic L101 and P103 were obtained as a gift from BASF Corp., New Jersey, U.S.A. and were used as received. The polymers have nominal molecular weights of 3800 (10% PEO content) and 4950 (30% PEO content)  $\text{g mol}^{-1}$ , respectively. The resulting compositions are as follows: L101 —  $(\text{EO})_4(\text{PO})_{59}(\text{EO})_4$  and P103 —  $(\text{EO})_{17}(\text{PO})_{59}(\text{EO})_{17}$ . Deuterated water (99.80 atom %  $^2\text{H}$ ) was purchased from Dr. Glaser AG, Basel, Switzerland. *p*-Xylene (1,4-dimethylbenzene) of purity >99.0% was obtained from Aldrich. The bulk density of the two copolymers is approximately 1.03 and 1.05  $\text{g mL}^{-1}$ , respectively. The bulk densities of *p*-xylene and deuterated water at 25°C are 0.861 and 1.105  $\text{g mL}^{-1}$ , respectively. The above stated densities were used in calculating volume fractions from weight fractions. The samples were prepared individually by weighing appropriate amounts in 8 mm (i.d.) glass tubes, which were flame-sealed immediately. The samples were centrifuged repeatedly in alternating directions at regular intervals over a few days to facilitate proper mixing. After this treatment the samples were left to stand in a 25°C temperature-controlled room for at least one month for homogenization and to reach equilibration.

### Delineation of phase boundaries

The equilibrated samples were examined by visual inspection in normal light and between crossed polarizers to check for phase separation, homogeneity, and birefringency. One-phase samples are clear and macroscopically homogeneous. Anisotropic phases can be recognized from their optical birefringence. Micellar solutions and cubic liquid crystals are optically isotropic and nonbirefringent. Whether a certain sample consisted of a single homogeneous phase or of two or three phases was also established from  $^2\text{H}$  NMR measurements (carried out at a resonance frequency of 15.37 MHz on a Bruker MSL 100 superconducting spectrometer working in the Fourier transform mode). The sample temperature was controlled by passing air of  $25 \pm 0.5^\circ\text{C}$  through the sample holder. The method uses the fact that the spectrum of an isotropic phase consists of a sharp singlet whereas anisotropic phases (hexagonal and lamellar) give rise to a doublet of broad peaks (a so-called quadrupolar splitting), and significant differences in magnitude are often observed (7). Mixtures of phases then display superposition of the known spectra of the individual phases, whereby the phase equilibrium can be determined.

### Structural characterization using small-angle X-ray scattering (SAXS)

SAXS measurements were performed on a kratky compact small-angle system equipped with a position-sensitive detector (OED 50M from MBraun, Austria), containing 1024 channels of width 53.6  $\mu\text{m}$ . Cu  $\text{K}\alpha$  radiation of wavelength 1.542 Å was provided by a Seifert ID-300 X-ray gen-



erator, operating at 50 kV and 40 mA. The obtained Bragg peaks were relatively sharp, in which case the peak positions were evaluated from the slit-smeared SAXS data (3, 7). The sample-to-detector distance was 277 mm. The volume between the sample and the detector was kept under vacuum during the measurements to minimize scattering from the air. The samples were filled into a 0.5-mm quartz capillary using a syringe; samples whose consistencies were very stiff were filled into a paste sample holder with thin mica windows. The temperature was controlled by a Peltier element with an accuracy of  $\pm 0.1^\circ\text{C}$ . All SAXS measurements were performed at  $25^\circ\text{C}$ .

The structure of the lyotropic liquid crystalline phases was determined from the relative positions of the SAXS diffraction peaks. For the lamellar (smectic) and hexagonal (cylindrical assemblies crystallized in a two-dimensional hexagonal lattice) structures, the scattering pattern consists of a  $\gamma$ -function at each reciprocal-lattice vector, i.e., Bragg peaks whose positions are in the ratio 1:2:3:4... and 1: $\sqrt{3}$ :2: $\sqrt{7}$ :3..., respectively. The lattice parameters  $d$  (lamellar periodicity) and  $\alpha$  (distance between the centers of adjacent cylinders) of the lamellar and hexagonal structures, respectively, were obtained from the position ( $q^*$ ) of the first and most intense diffraction peak according to

$$[1] \quad \text{lamellar: } q^* = \frac{2\pi}{d}, \quad \text{hexagonal: } q^* = \frac{4\pi}{\alpha\sqrt{3}}$$

For the calculations involved in the SAXS analysis of the liquid-crystalline phases identified in the ternary system, the system is assumed to contain only two types of components, apolar and polar, separated by a sharp interface. The assumption made above concerning the components that constitute the polar and apolar domains is equivalent to strong segregation. The apolar component is the PPO part of the copolymer and the  $p$ -xylene, and the polar component is the PEO of the copolymer and the water. The volume fraction of the apolar domain,  $f$ , is defined as (3):

$$[2] \quad f = x\Phi_p + \Phi_{\text{oil}}$$

where  $x$  is the volume fraction of PPO in the copolymer and  $\Phi_p$  is the total volume fraction of the copolymer. The thickness of the apolar domains,  $\delta$ , in the lamellar structure and the radius of the apolar domains,  $R$ , in the normal hexagonal structure were calculated from the lattice parameters and the volume fraction,  $f$ , of the apolar components for a ternary system (3, 7):

$$[3] \quad \text{lamellar: } \delta = df \quad \text{hexagonal: } R = \alpha \sqrt{\left(\frac{\sqrt{3}}{2\pi} f\right)}$$

The interfacial area per PEO block,  $a_p$ , or the area that a PEO block of the PEO-PPO-PEO block copolymer occupies at the interface between polar and apolar domains is another characteristic parameter of the microstructure, providing valuable information on the packing of the macromolecules. In the lamellar structure, the effective area per PEO block at the interface between polar and apolar domains can be determined from the lattice parameters without any assumptions concerning the degree of segregation or the local structure of the copolymer film (3, 7). The calculation

of  $a_p$  in the normal hexagonal structure also involved the copolymer and apolar volume fractions. The interfacial area can be calculated from

$$[4] \quad \text{lamellar: } a_p = \frac{v_p}{d\Phi_p}$$

$$\text{hexagonal: } a_p = \frac{v_p}{\alpha\Phi_p} \sqrt{\left(\frac{2\pi}{\sqrt{3}} f\right)}$$

where  $v_p$  is the volume of one block-copolymer molecule ( $\sim 6126 \text{ \AA}^3$  for  $\text{EO}_4\text{PO}_{59}\text{EO}_4$  and  $\sim 7828 \text{ \AA}^3$  for  $\text{EO}_{17}\text{PO}_{59}\text{EO}_{17}$ , calculated from their bulk densities).

## Results

### Overview of the ternary phase behavior and structure of the $(\text{EO})_{17}(\text{PO})_{59}(\text{EO})_{17}$ -D<sub>2</sub>O- $p$ -xylene system

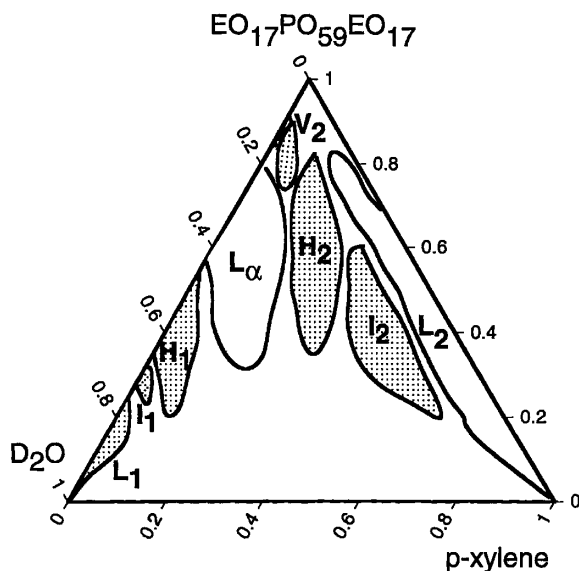
The isothermal phase diagram of the  $(\text{EO})_{17}(\text{PO})_{59}(\text{EO})_{17}$ -D<sub>2</sub>O- $p$ -xylene ternary system at  $25^\circ\text{C}$  is presented in Fig. 1. Solid lines indicate the boundaries of the one-phase regions. The samples whose compositions fall outside the one-phase regions are dispersions of two or three (depending on the location in the phase diagram (3, 5, 7)). This system is remarkable in that six different lyotropic liquid crystalline phases have been identified: a lamellar ( $L_\alpha$ ), normal ( $H_1$ ) and reverse hexagonal ( $H_2$ ) phases; a reverse bicontinuous cubic ( $V_2$ ) phase; normal ( $I_1$ ) and reverse micellar cubic ( $I_2$ ) phases; as well as two isotropic solution phases, one (normal micellar) rich in water ( $L_1$ ) and one with a high xylene-to-water ratio ( $L_2$ ). The relative location of the various phases in the block copolymer – water – oil phase diagram follows the sequence  $L_1 \rightarrow I_1 \rightarrow H_1 \rightarrow L_\alpha \rightarrow V_2 \rightarrow H_2 \rightarrow I_2 \rightarrow L_2$  (clockwise, starting from the water-rich corner of the ternary phase diagram Fig.1). This structural phase sequence is consistent with a decreasing interfacial mean curvature ( $H$ ) from left ( $H > 0$ ) to the right ( $H < 0$ ), with  $H = 0$  in the lamellar phase (23). This modulation of the interfacial curvature (and the resulting structure) has been attributed to the ability of the macromolecular blocks to swell with solvent to a varying extent depending on the amounts of solvent available. The interfacial curvature decreases because of a decreased swelling (solvation) of the PEO blocks with increasing solvent content. For the liquid crystalline phases the structures were ascertained based on the characteristic X-ray scattering patterns. The  $L_\alpha$ ,  $H_2$ ,  $I_2$ , and  $L_2$  phases dominate the triangular diagram, whereas the  $L_1$ ,  $I_1$ ,  $H_1$ , and  $V_2$  phases have more limited stability ranges. The  $L_1$ ,  $I_1$ ,  $H_1$ , and  $L_\alpha$  structures are all formed along the copolymer–water axis and can swell to a varying extent with the oil. The ordered lyotropic liquid crystalline phases accommodate xylene to different degrees. The amount of xylene it is possible to accommodate increases from the  $I_1$  phase to the  $I_2$  phase. A presentation of the different phases and their structures follows.

### Normal and reverse hexagonal phases, $H_1$ and $H_2$

The samples in the hexagonal regions are relatively stiff, transparent, and optically birefringent (anisotropic) and exhibit a splitting in the  $^2\text{H}$  NMR spectrum. The structure in hexagonal phases consists of long parallel cylindrical aggregates arranged on a two-dimensional hexagonal lattice in the



**Fig. 1.** Phase diagram of the (EO)<sub>17</sub>(PO)<sub>59</sub>(EO)<sub>17</sub>-D<sub>2</sub>O-*p*-xylene system at 25°C.



plane perpendicular to the cylinder axis. In the  $H_1$  phase the cylinders have an apolar interior (oil and PPO) while in the  $H_2$  phase the interior is polar (water and PEO). The  $H_1$  region is stable in the 25–55 wt % copolymer range along the binary water-(EO)<sub>17</sub>(PO)<sub>59</sub>(EO)<sub>17</sub> axis and swells with up to 6 wt % xylene. Typical scattering diffraction patterns of samples belonging to the  $H_1$  domains are reported in Fig. 2a. The relative positions of the Bragg reflections,  $1:\sqrt{3}:\sqrt{4}:\sqrt{7}$ , are consistent with the two-dimensional hexagonal order. Characteristic structural parameters for samples in the  $H_1$  region are given in Table 1. The nearest neighbour (cylinder) distance decreased with increasing (EO)<sub>17</sub>(PO)<sub>59</sub>(EO)<sub>17</sub> copolymer content from 194 to 127 Å, consistent with a denser packing of the cylinders as their number increased. The interfacial area per PEO block was found to be in the range 133–147 Å<sup>2</sup>.

The reverse  $H_2$  phase in the (EO)<sub>17</sub>(PO)<sub>59</sub>(EO)<sub>17</sub>-D<sub>2</sub>O-*p*-xylene system appears between about 40 and 81 wt % of copolymer with a maximum water content of about 25 wt %. SAXS diffraction pattern from an  $H_2$  sample ternary system of (EO)<sub>17</sub>(PO)<sub>59</sub>(EO)<sub>17</sub>-D<sub>2</sub>O-*p*-xylene is presented in Fig. 2b; the  $1:\sqrt{3}:2:\sqrt{7}$  relative position of the four Bragg peaks observed confirmed the two-dimensional hexagonal structure. The reverse (water-in-oil) morphology was ascertained from the location of the  $H_2$  region in the ternary phase diagram between the  $L_\alpha$  and  $I_2$  phases. Characteristic structural parameters for samples spanning the reverse hexagonal region are summarized in Table 1. The distance between the centers of two adjacent cylinders decreased (from 153 to 112 Å) with increasing copolymer concentration; the polar (PEO + water) cylinder radius,  $R$ , also decreased (from 45 to 33 Å). The interfacial area per PEO block decreased in the range 127–103 Å<sup>2</sup> with increasing copolymer concentration.

### The lamellar phase ( $L_\alpha$ )

The samples in the  $L_\alpha$  regions have the simplest, one-dimensional microstructure, consisting of lamellae (planar

**Table 1.** Characteristic parameters in the  $H_1$ ,  $H_2$ , and  $L_\alpha$  phases of the (EO)<sub>17</sub>(PO)<sub>59</sub>(EO)<sub>17</sub>-D<sub>2</sub>O-*p*-xylene system.

Phase	Volume fractions				$d, \alpha^b$ (Å)	$R, \delta^c$ (Å)	$a_p^d$ (Å <sup>2</sup> )
	$\Phi_P$	$\Phi_{D_2O}$	$\Phi_{oil}$	$f^a$			
$H_1$	0.41	0.59	0	0.3	145	42	136
$H_1$	0.46	0.54	0	0.33	137	41	136
$H_1$	0.52	0.48	0	0.37	131	42	135
$H_1$	0.56	0.44	0	0.4	127	43	133
$H_1$	0.31	0.63	0.06	0.28	194	54	133
$H_1$	0.36	0.58	0.06	0.32	163	48	142
$H_1$	0.41	0.53	0.07	0.36	150	47	147
$H_2$	0.47	0.18	0.36	0.69	153	45	116
$H_2$	0.47	0.28	0.24	0.58	122	41	127
$H_2$	0.67	0.15	0.15	0.64	121	38	111
$H_2$	0.73	0.11	0.15	0.68	112	33	103
$L_\alpha$	0.59	0.41	0	0.43	109	46	122
$L_\alpha$	0.66	0.34	0	0.48	106	50	112
$L_\alpha$	0.72	0.28	0	0.52	103	54	105
$L_\alpha$	0.76	0.24	0	0.55	98	54	105
$L_\alpha$	0.81	0.19	0	0.58	101	59	96
$L_\alpha$	0.45	0.45	0.1	0.42	144	61	121
$L_\alpha$	0.5	0.38	0.12	0.48	132	63	120
$L_\alpha$	0.55	0.3	0.15	0.54	126	68	113
$L_\alpha$	0.58	0.27	0.15	0.57	120	68	112
$L_\alpha$	0.64	0.23	0.13	0.59	110	65	111
$L_\alpha$	0.68	0.2	0.12	0.61	98	60	117
$L_\alpha$	0.68	0.09	0.23	0.72	97	70	119
$L_\alpha$	0.74	0.15	0.12	0.65	112	73	95
$L_\alpha$	0.77	0.08	0.15	0.71	89	63	114
$L_\alpha$	0.79	0.09	0.12	0.69	90	62	110

<sup>a</sup> $f$  is the apolar volume fraction.

<sup>b</sup> $d$  and  $\alpha$  are the lattice parameters.

<sup>c</sup> $R$  is the hexagonal cylinder radius and  $\delta$  is the lamellar thickness.

<sup>d</sup> $a_p$  is the interfacial area per PEO block.

micelles). Macroscopically the samples in the  $L_\alpha$  regions are transparent, optically birefringent and less stiff compared with the samples in the  $H_1$  and  $H_2$  phases. They exhibit a splitting in the <sup>2</sup>H NMR spectrum with a higher value than the splitting in the  $H_1$  and  $H_2$  phases. The  $L_\alpha$  phase is formed on the binary water-(EO)<sub>17</sub>(PO)<sub>59</sub>(EO)<sub>17</sub> axis at copolymer concentrations greater than 38 wt % and continues up to about 81% copolymer (Fig. 1).  $L_\alpha$  is the most extensive of the one-phase regions; it can accommodate up to 21 wt % xylene and allows a high degree of swelling with oil.

The one-dimensional structure of the samples in the  $L_\alpha$  region was established by SAXS measurements that gave diffraction patterns with second- and even third-order Bragg peaks. The relative positions of the peaks follow the expected sequence for a lamellar structure: 1:2:3: ... (see Fig. 3a). Values for the lamellar lattice periodicity (spacing),  $d$ , the apolar (PPO + xylene) thickness,  $\delta$ , and the interfacial area per block,  $a_p$ , determined in the  $L_\alpha$  regions of the (EO)<sub>17</sub>(PO)<sub>59</sub>(EO)<sub>17</sub>-D<sub>2</sub>O-*p*-xylene system are given in Table 1. The lamellae domain lengths vary according to varia-



**Fig. 2.** SAXS diffraction patterns from representative samples in the (a) normal hexagonal phase,  $H_1$ , and (b) reverse hexagonal phase,  $H_2$ , of the  $(EO)_{17}(PO)_{59}(EO)_{17}$ -D<sub>2</sub>O-xylene system at 25°C. The sample compositions are 35.7:59.7:4.6 and 49.3:19.7:30.9 wt % copolymer:water:oil, respectively. The Bragg peaks are marked with arrows and the Miller indices.

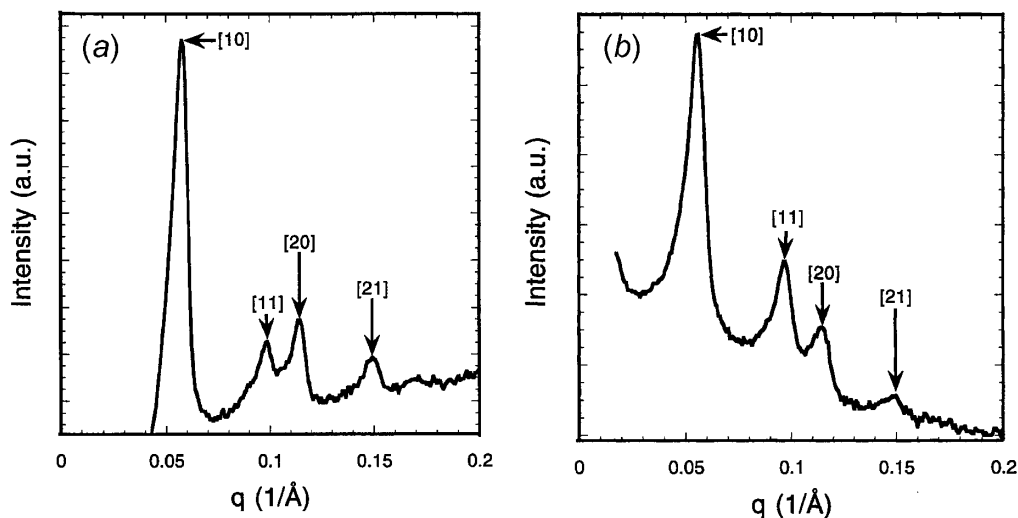
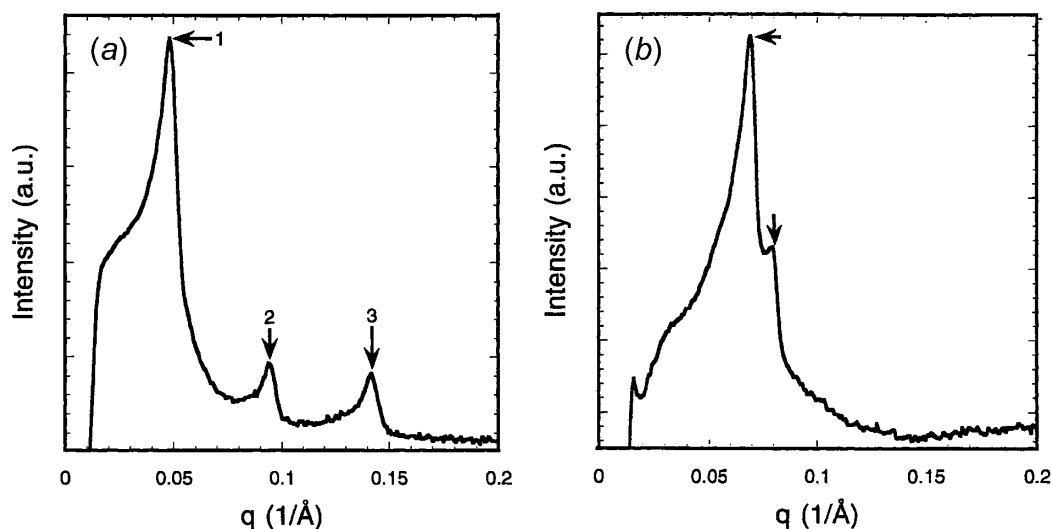


**Fig. 3.** SAXS diffraction patterns from representative samples in the (a) Lamellar phase,  $L_\alpha$ , and (b) reverse bicontinuous cubic,  $V_2$ , of the  $(EO)_{17}(PO)_{59}(EO)_{17}$ -D<sub>2</sub>O-*p*-xylene system at 25°C. The sample compositions are 50.5:34.6:14.9 and 84.5:5.6:9.9 wt % copolymer:water:oil, respectively. The arrows mark the positions of the observed reflections.



tions in volume fractions, i.e., increased copolymer concentration leads to decreased  $d$  values at constant oil concentration. The interfacial area per PEO block is found to be in the range 95–122 Å<sup>2</sup>. The  $\delta$  values are in the range 46–73 Å.

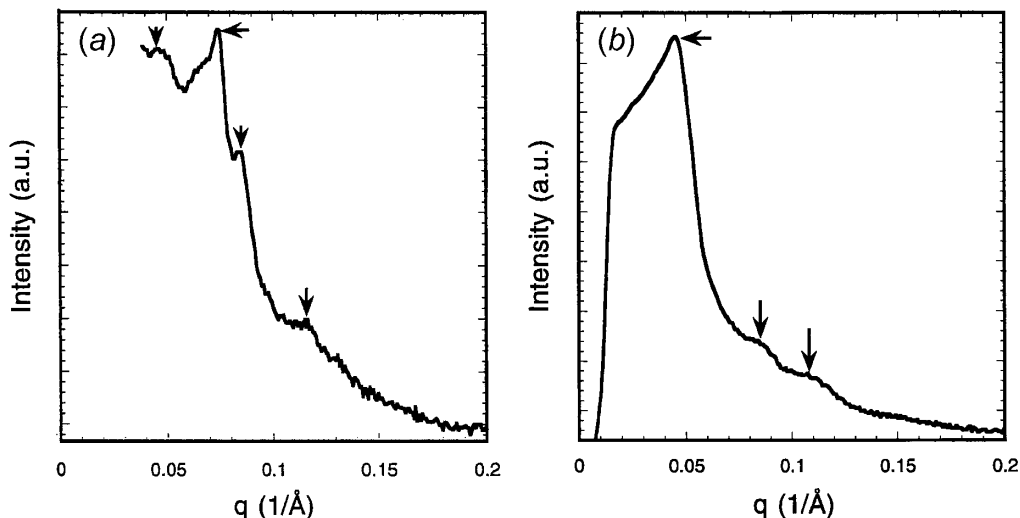
#### Reverse bicontinuous cubic liquid crystalline phase ( $V_2$ )

The  $V_2$  region is observed in the  $(EO)_{17}(PO)_{59}(EO)_{17}$ -water-xylene system as a small region at high (75–82 wt %) copolymer concentration. The relative position of this cubic phase in the phase diagram (between the  $L_\alpha$  and  $H_2$  phases) indicates that its structure is bicontinuous with the curvature of the polar-apolar interface toward water (23). The corresponding  $V_1$  phase was not observed. The homogeneous samples in this region are clear, optically isotropic, and very stiff and exhibit a sharp singlet in the <sup>2</sup>H NMR spectrum,

features characteristic of a cubic structure. A typical SAXS diffraction pattern is shown in Fig. 3b. Scattering data from lyotropic cubic liquid crystalline phases generally contain only a small number of reflections, which makes a proper indexation and space group determination essentially difficult. As seen in Fig. 3b, the present system is no exception in this respect. The scattering function is dominated by a strong correlation peak at  $q = 0.035$ , while another reflection is observed at  $q = 0.057$  Å<sup>-1</sup>. The most commonly observed crystallographic space group for the bicontinuous cubic phases of surfactants and lipids (23, 24), as well as in amphiphilic block copolymer systems (3, 5, 9, 11, 16), is  $Im3d$  ( $Q^{230}$ ). This space group allows the Bragg reflections  $hkl = 211, 220, 321, 400, \dots$ , which give peaks in the relative (scattering vector) positions  $\sqrt{6}, \sqrt{8}, \sqrt{14}, \sqrt{16}, \dots$ . Recent structure factor calculations (25) have shown the first reflec-



**Fig. 4.** SAXS diffraction patterns from representative samples in the (a) normal micellar cubic phase,  $I_1$ , and (b) reverse micellar cubic phase,  $I_2$ , of the  $(EO)_{17}(PO)_{59}(EO)_{17}$ -D<sub>2</sub>O-*p*-xylene system at 25°C. The sample compositions are 30.2:69.8:0 and 34.6:10.1:55.4 wt % copolymer:water:oil, respectively. The scattering positions are marked with arrows and the Miller indices.



tion, corresponding to  $hkl = 211$ , to be the most intense. The two reflections in the present cubic phase are  $\sqrt{6}$  and  $\sqrt{8}$ , which are consistent with the first two reflections of the  $Ia3d$  space group. The first two Bragg peaks in the diffraction pattern shown in Fig. 3b are indexed as 211 and 220. Therefore, although the reflections are very few, the two peaks of the cubic lattice matches only, and is assigned to, the  $Ia3d$  crystallographic space group. The cubic lattice of the  $Ia3d$  space group is consistent with that afforded by the Gyroid minimal surface (23, 26).

#### Micellar cubic structures (normal, $I_1$ , and reverse, $I_2$ )

Macroscopically the samples in the homogeneously one-phase  $I_1$  and  $I_2$  regions are very stiff with a clear glassy appearance, and they are optically isotropic (nonbirefringent) gels. They exhibit a sharp singlet in the  $H^2$  NMR spectrum, characteristic of an isotropic structure. The  $L_1$ - $I_1$  and  $L_2$ - $I_2$  phase transitions are easy to detect with the eye, since the cubic phases are significantly more viscous. The micellar cubic lyotropic liquid crystalline structural elements (micelles) can be arranged in a large number of cubic lattices belonging to different crystallographic space groups (23, 26). The positions of the Bragg diffraction peaks obey different relationships for the different space groups. However, all space groups can be classified in three main families of cubic lattices (26): primitive (P), body-centered (I), and face-centered (F). A small homogenous one-phase  $I_1$  region is found in the  $(EO)_{17}(PO)_{59}(EO)_{17}$ -D<sub>2</sub>O-xylene system along the copolymer-water binary axis between the isotropic micellar solution  $L_1$  and the hexagonal  $H_1$  phase. The cubic structure forms over a more limited copolymer concentration range (25–35 wt %) at 25°C. The location of this cubic phase in the ternary phase diagram suggests (23) that it is composed of normal micelles that have crystallized into a cubic lattice. A SAXS diffraction pattern, typical of samples in the  $I_1$  region for the  $(EO)_{17}(PO)_{59}(EO)_{17}$ -D<sub>2</sub>O-xylene system, is presented in Fig. 4a. A total of four Bragg peaks are identified, which can be indexed as the  $hkl = 111$ , 220, 311, and 422 reflections of a face-centered space group,

$Fd3m$  ( $Q^{227}$ ), characterized by Bragg reflections whose reciprocal  $d$  spacings follow the relationship  $\sqrt{3}$ ,  $\sqrt{8}$ ,  $\sqrt{11}$ ,  $\sqrt{24}$ . The four reflections in the present cubic phase are hence consistent with the first, second, third, and sixth reflections in the  $Fd3m$  space group. The  $Fd3m$  face-centered micellar cubic structure has also been found in other similar copolymer-water-oil systems (5, 11). A proposed structural model for the  $Fd3m$  cubic phases involves a total of 24 spherical micelles per unit cell, with a bimodal size distribution composed of 8 larger and 16 smaller micelles (27).

A large isotropic liquid crystalline  $I_2$  region is observed between the isotropic reverse micellar solution  $L_2$  and the reverse hexagonal  $H_2$  phase. The cubic  $I_2$  structure is stable over a wide copolymer concentration range of about 20–60 wt % at 25°C. The location of this cubic phase in the ternary phase diagram suggests (11, 23) that its microstructure consists of reverse micelles that have crystallized into a cubic lattice. A SAXS diffraction pattern obtained from an  $I_2$  sample is presented in Fig. 4b. Only three Bragg peaks can be identified in the diffraction pattern as the higher order peaks have very low intensities. The relative intensity of the observed peaks and the inability to discern higher-order reflections follow the trend expected from structures of cubic aspect 8 and, more specifically, from the centrosymmetric  $Im3m$  ( $Q^{229}$ ) space group (26). The first strong correlation peak and other weaker reflections have been indexed according to a body-centered structure (bcc, space group  $Im3m$ ) that allows the Bragg reflections  $hkl = 110$ , 200, 211, 220, 310, 222, 321, 400, 441, and so forth, which give peaks in the relative (scattering vector  $q$ ) positions  $\sqrt{2}$ ,  $\sqrt{4}$ ,  $\sqrt{6}$ ,  $\sqrt{8}$ ,  $\sqrt{10}$ ,  $\sqrt{12}$ ,  $\sqrt{14}$ ,  $\sqrt{16}$ , and so forth. The three reflections in the present cubic phase are hence consistent with the first, fourth, and sixth reflections in the  $Im3m$  space group.

#### Water-rich and water-lean solution (normal micellar, $I_1$ , and reverse micellar, $I_2$ )

In addition to the phases of liquid crystalline microstructure that occupy the major part of the  $(EO)_{17}(PO)_{59}(EO)_{17}$ -D<sub>2</sub>O-*p*-xylene phase diagram (above 25 wt %



copolymer), two isotropic solution regions,  $L_1$  and  $L_2$ , are present in the water-rich corner and the water-lean side, respectively, of the phase diagram. In the  $L_1$  phase, micelles can form without the presence of oil, while in the  $L_2$  phase, micelle formation appears to require a small amount of water (28–31). In this respect the polyoxyalkylene block copolymers are similar to nonionic surfactants of the alkyl-oligoethylene oxide type (32). An isotropic (as judged from optical inspection as well as the single sharp peak in the deuterium NMR spectra) water-rich solution region ( $L_1$ ) is found along the copolymer–water axis, up to 25 wt %  $(EO)_{17}(PO)_{59}(EO)_{17}$  copolymer, and can solubilize no more than 2 wt % xylene. The  $L_2$  phase in the  $(EO)_{17}(PO)_{59}(EO)_{17}$ – $D_2O$ – $p$ -xylene ternary system is more extensive, extending up to about 80 wt % copolymer. The reverse micelles can solubilize a maximum of 7 wt % water before phase separation occurs. The  $L_1$  and  $L_2$  micellar solution phases are isotropic, optically transparent, and fluid, but they progressively become more viscous as the copolymer increases.

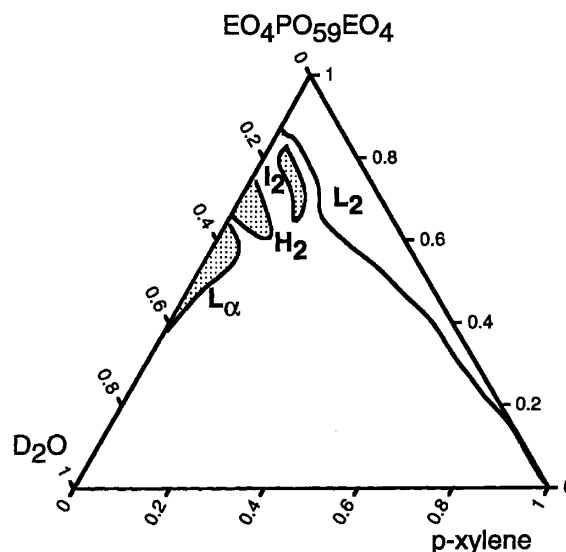
### Overview of the ternary phase behavior and structure of the $(EO)_4(PO)_{59}(EO)_4$ – $D_2O$ – $p$ -xylene system

The  $(EO)_4(PO)_{59}(EO)_4$  triblock copolymer is a cloudy liquid at 25°C. The copolymer is very hydrophobic and asymmetric in PEO–PPO composition (contains 10 wt % PEO and 90 wt % PPO). Owing to the low PEO block molecular weight, the PEO does not crystallize at low temperatures. Hence, the copolymer is disordered in the dry state at ambient temperatures. The isothermal phase diagram of the  $(EO)_4(PO)_{59}(EO)_4$ – $D_2O$ – $p$ -xylene ternary system at 25°C is presented in Fig. 5. The phase boundaries of the one-phase regions are shown by solid lines. The homogeneous one-phase regions observed, when starting on the water axis and progressing clockwise over to the oil corner, are the following: lamellar  $L_\alpha$  phase, reverse hexagonal  $H_2$  phase, reverse micellar cubic phase  $I_2$ , reverse micellar  $L_2$  phase. The  $L_2$  phase dominates the triangular diagram, whereas  $L_\alpha$ ,  $H_2$ , and  $I_2$  phases have more limited stability ranges. The high PPO (hydrophobic) content of  $(EO)_4(PO)_{59}(EO)_4$  favors reverse (water-in-oil) phases with low interfacial curvature. No phase of normal (oil-in-water) morphology has been found for any composition at 25°C in this system. The copolymer is completely miscible with  $p$ -xylene. An abrupt increase in water solubilization is observed in the  $L_2$  phase at copolymer concentrations above 40 wt %. This is characteristic for micelle formation (33). Increased water content at high copolymer concentrations increases interactions between the micelles and a reverse micellar cubic phase is formed (34). The samples in the  $I_2$  phase are stiff and isotropic. Upon even higher water concentrations, the curvature of the formed aggregates changes and an anisotropic liquid crystalline hexagonal  $H_2$  phase is formed. A narrow anisotropic lamellar liquid crystalline  $L_\alpha$  phase with zero interfacial curvature is found on the binary copolymer–water axis. A presentation of the different phases and their structures follows.

#### The lamellar phases ( $L_\alpha$ )

The samples in the  $L_\alpha$  regions have the simplest, one-dimensional microstructure consisting of lamellae (planar micelles). The samples in the  $L_\alpha$  regions are soft, optically birefringent with a cloudy appearance and exhibit splittings

**Fig. 5.** Phase diagram of the  $(EO)_4(PO)_{59}(EO)_4$ – $p$ -xylene system at 25°C.



in the  $^2H$  NMR spectrum with a higher value than the splittings in the  $H_2$  phases. The  $L_\alpha$  region is stable in the 40–65 wt % copolymer range along the binary water– $(EO)_4(PO)_{59}(EO)_4$  axis and swells with up to 5 wt % xylene (Fig. 5). The  $L_\alpha$  phase contains quite a lot of water.

The one-dimensional lamellar structure was established by SAXS measurements. The scattering profiles of the samples proved the lamellar structure by showing diffraction peaks in the relative position 1:2:3 (see Fig. 6a). In each sample, two to three peaks following this sequence are usually registered, confirming the lamellar microstructure. The lattice parameter,  $d$ , was obtained directly from the position of the first peak of the SAXS spectra using eq. [1]. The results for the lattice parameter, including the apolar thickness,  $\delta$ , and the interfacial area per PEO block, are summarized in Table 2. The  $d$  values decreased from 145 to 85 Å with increasing copolymer volume fraction from 0.4 to 0.6. The apolar thickness indeed remained almost constant (at 51–58 Å<sup>2</sup>) throughout the wide composition range examined, whereas the interfacial area increased to a limited extent with increasing copolymer concentration.

#### Reverse hexagonal lyotropic liquid crystalline phases ( $H_2$ )

In the reverse hexagonal phase water is inside and the oil is outside the cylinders. The samples in the  $H_2$  region are clear, relatively stiff, and optically anisotropic and exhibit a splitting in the  $^2H$  NMR spectrum. The two-dimensional hexagonal structure (hexagonally packed array of cylindrical micelles) was established by SAXS experiments, while the reversed morphology was ascertained from the location of the hexagonal region,  $H_2$ , in the ternary phase diagram.

The reverse hexagonal phase,  $H_2$ , is formed between the  $L_\alpha$  and  $I_2$  phases. The  $H_2$  region extends in the 60–75 wt % copolymer range. The polar domain of the  $H_2$  phase can swell with a large amount of water, up to a maximum content of about 34 wt %. A SAXS diffraction pattern, typical of samples in the  $H_2$  region, is presented in Fig. 6b. The 1:



**Fig. 6.** SAXS diffraction patterns from representative samples in the (a) lamellar phase,  $L_\alpha$ ; (b) reverse hexagonal phase,  $H_2$ ; and (c) reverse micellar cubic phase,  $I_2$ , of the  $(EO)_4(PO)_{59}(EO)_4$ - $D_2O$ - $p$ -xylene system at 25°C. The sample compositions are 49.7:50.3:0, 69.6:25.2:5.2, and 79.4:15.2:5.4 wt % copolymer:water:oil, respectively. The Bragg peaks are marked with arrows and the Miller indices.

**Table 2.** Characteristic parameters in the  $H_2$  and  $L_\alpha$  phases of the  $(EO)_4(PO)_{59}(EO)_4$ - $D_2O$ - $p$ -xylene system.

Phase	Volume fractions			$f^a$	$d, \alpha^b$ (Å)	$R, \delta^c$ (Å)	$a_p^d$ (Å <sup>2</sup> )
	$\Phi_P$	$\Phi_{D_2O}$	$\Phi_{oil}$				
$H_2$	0.69	0.31	0	0.64	127	40	80
$H_2$	0.7	0.3	0	0.65	145	45	67
$H_2$	0.75	0.25	0	0.7	126	36	67
$H_2$	0.66	0.28	0.06	0.61	166	54	66
$H_2$	0.7	0.24	0.06	0.71	152	43	58
$H_2$	0.71	0.26	0.03	0.69	150	44	61
$H_2$	0.8	0.17	0.03	0.78	122	30	49
$L_\alpha$	0.41	0.59	0	0.38	145	52	104
$L_\alpha$	0.45	0.55	0	0.41	123	51	111
$L_\alpha$	0.51	0.49	0	0.48	122	58	98
$L_\alpha$	0.6	0.4	0	0.56	101	56	101
$L_\alpha$	0.61	0.36	0.03	0.6	85	51	117

<sup>a</sup> $f$  is the apolar volume fraction.

<sup>b</sup> $d$  and  $\alpha$  are the lattice parameters.

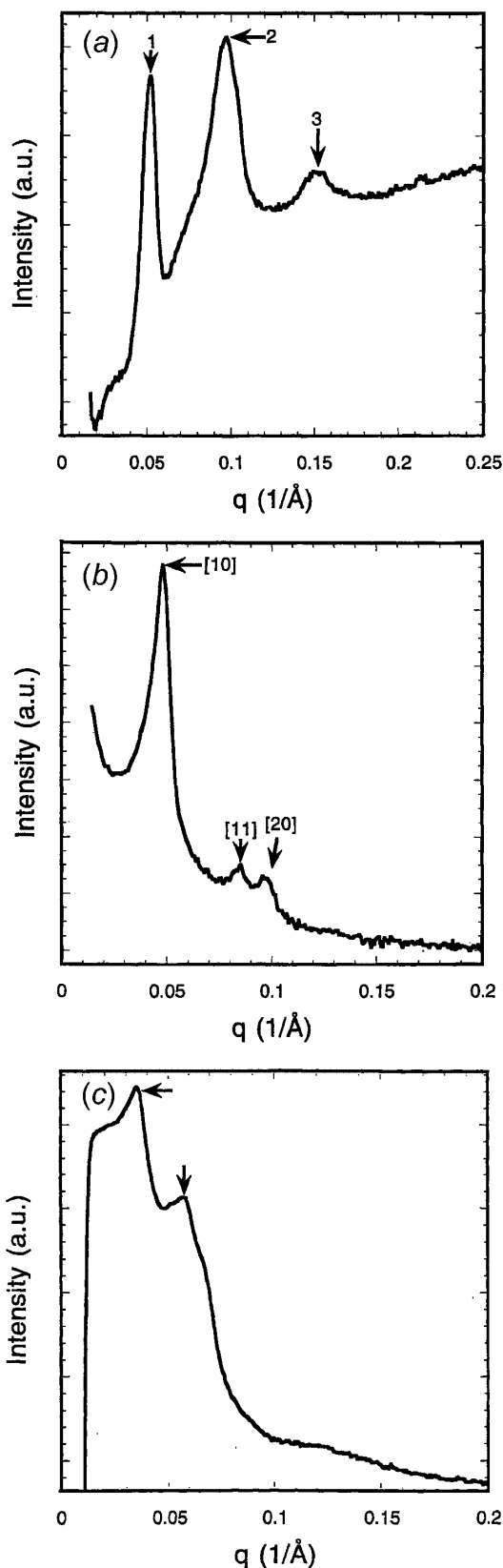
<sup>c</sup> $R$  is the hexagonal cylinder radius and  $\delta$  is the lamellar thickness.

<sup>d</sup> $a_p$  is the interfacial area per PEO block.

$\sqrt{3}:2:\sqrt{7}$  relative position of the Bragg peaks (with respect to that of the first and most intense peak) confirms the two-dimensional hexagonal structure. Characteristic structural parameters for some representative samples in the  $H_2$  region are given in Table 2. The distance between the centers of two adjacent cylinders decreased (from 166 to 122 Å) with increasing copolymer volume fraction (from 0.66 to 0.80). The polar (PEO +  $D_2O$ ) cylinder radius,  $R$ , is found in the range 30–54 Å, while the interfacial area per PEO copolymer block decreased to a limited extent with increasing copolymer concentration.

### Reverse micellar cubic lyotropic liquid crystalline phase ( $I_2$ )

The homogeneous reverse  $I_2$  phase is found in a rather narrow and restricted region but stretching inside the ternary phase diagram between the  $H_2$  and  $L_2$  phases at fairly higher copolymer concentration. The one-phase  $I_2$  region exists only when xylene is present in the system. The samples in the  $I_2$  region are very stiff, clear, optically isotropic (nonbirefringent), and exhibit a sharp singlet in their  $^2H$  NMR spectra, all characteristic of the cubic structure. The cubic structure forms over a more limited copolymer concentration range (25–35 wt %) at 25°C. The location of this cubic phase in the ternary phase diagram suggests (23) that it is composed of reverse micelles that have crystallized into a cubic lattice. A SAXS diffraction pattern, typical of sam-



ples in the  $I_2$  region for the  $(EO)_4(PO)_{59}(EO)_4$ -water-xylene system, is presented in Fig. 6c. Samples in the  $I_2$  region display two fairly strong Bragg peaks at low  $q$  for all compositions, indicating long-range order of micelles with a



relatively large unit cell characteristic of an ordered structure, but the scattering peaks at higher  $q$  are badly resolved. As the reflections are too few, indexation to a cubic space group is very uncertain.

### Reverse (oil-rich) micellar solution phase, $L_2$

The  $L_2$  phase occupies a large area in the diagram of Fig. 5.  $(EO)_4(PO)_{59}(EO)_4$  is miscible with  $p$ -xylene in all proportions, and the  $L_2$  phase extends along the whole water-lean side of the phase diagram. Water can be solubilized in the  $p$ -xylene- $(EO)_4(PO)_{59}(EO)_4$  solution; the amount of solubilized water increases with increasing copolymer concentration (see Fig. 5). These binary solutions can dissolve up to a maximum of about 13 wt %, producing an isotropic  $L_2$  phase.

### Deuterium NMR in liquid crystalline phases for both systems

The NMR spectrum from the deuterated water is dominated by the interaction of the deuteron-quadrupole moment with the electric-field gradients in the nucleus. In anisotropic lyotropic liquid-crystalline (LLC) samples the quadrupole interaction generates an NMR spectrum with two peaks of equal intensity, while for an isotropic LLC or solution a single sharp peak will be the result because of the rapid and isotropic molecular motion, which averages the interaction to zero (35, 36). The magnitude of the deuterium-quadrupole splitting also contains information on the hydration of the amphiphilic copolymers and additional evidence of the structural identification can be obtained from  $^2H$  NMR experiments. The observed quadrupole splittings in LLC phases can be further analyzed by the conventional two-site model (35), which assumes that water is either "free" or "bound", with a fast exchange between the free and bound water within the NMR time scale and the ordering of free water molecules being negligible:

$$[5] \quad \Delta(^2H) = n\nu_Q S(X_p/X_w)$$

where  $\nu_Q$  is the quadrupole splitting constant,  $S$  the order parameter of bound water molecules,  $n$  is the hydration number, and  $(X_p/X_w)$  is the molar ratio between polymer and water.

Representative  $^2H$  NMR spectra are presented in Fig. 7. The presence of an isotropic phase is directly noted from the presence of a sharp singlet (Fig. 7a) and that of an anisotropic phase from a doublet of peaks. The hexagonal phase is characterized by a pair of sharp peaks (Fig. 7b). The lamellar phase exhibits a broader doublet with a larger quadrupole splitting than for the hexagonal phase (Fig. 7c). Deuterium quadrupole splitting values ( $\Delta^2H$ ) for some typical samples in the liquid crystalline phases of the  $(EO)_{17}(PO)_{59}(EO)_{17}$ -D<sub>2</sub>O- $p$ -xylene and  $(EO)_4(PO)_{59}(EO)_4$ -D<sub>2</sub>O- $p$ -xylene systems at 25°C are shown in Tables 3 and 4, respectively.  $\Delta^2H$  values observed in the lamellar phase region are much larger than those in the hexagonal phase region for both systems. The magnitude of the  $\Delta^2H$  values is found to depend not only on copolymer-to-water molar ratio but also on the xylene content. Samples with high water content give rather small  $\Delta^2H$  values, while those with low water contents give rise to  $\Delta^2H$  values of larger magnitude. However,  $\Delta^2H$

values recorded for the  $(EO)_{17}(PO)_{59}(EO)_{17}$ -D<sub>2</sub>O- $p$ -xylene system are larger than those measured for  $(EO)_4(PO)_{59}(EO)_4$ -D<sub>2</sub>O- $p$ -xylene system in both hexagonal and lamellar phase regions. Tables 3 and 4 show that, for samples with fairly constant xylene content, the values of  $\Delta^2H$  increase with increasing copolymer-water molar ratio for both liquid crystalline phases. Further analysis of the  $\Delta^2H$  values shows no linear increase with increasing molar ratio of copolymer-water. Deviations from the two-site model with constant hydration number and order parameter as expected from eq. [5] may be due to the non-ideal swelling of liquid crystals (35).

### Discussion

The isothermal phase diagrams of the  $(EO)_{17}(PO)_{59}(EO)_{17}$ -D<sub>2</sub>O- $p$ -xylene and the  $(EO)_4(PO)_{59}(EO)_4$ -D<sub>2</sub>O- $p$ -xylene ternary systems at 25°C are presented in Figs. 1 and 5, respectively. The difference in the phase behavior in water-xylene of the two copolymers  $(EO)_{17}(PO)_{59}(EO)_{17}$  and  $(EO)_4(PO)_{59}(EO)_4$  with similar hydrophobic middle block is striking. The  $(EO)_{17}(PO)_{59}(EO)_{17}$ -D<sub>2</sub>O- $p$ -xylene system exhibited a nearly identical phase diagram to the  $(EO)_{27}(PO)_{61}(EO)_{27}$ -D<sub>2</sub>O- $p$ -xylene system (9), whereas the  $(EO)_4(PO)_{59}(EO)_4$ -D<sub>2</sub>O- $p$ -xylene system displayed a phase diagram similar to that of the  $(EO)_5(PO)_{68}(EO)_5$ -D<sub>2</sub>O- $p$ -xylene system (22). As is seen in Figs. 1 and 5, the two phase diagrams are quite different. The major difference between the two systems concerns the observed phase sequence. The fairly symmetric copolymer  $(EO)_{17}(PO)_{59}(EO)_{17}$  exhibits a ternary phase behaviour, which is almost symmetric with respect to the interchange of water and oil volume fractions.  $(EO)_{17}(PO)_{59}(EO)_{17}$  allows a greater variation in the phase behavior both along the copolymer-water axis and when "oil" is present. A full phase sequence from  $L_1$  to  $L_2$  is observed, i.e.,  $L_1 \rightarrow I_1 \rightarrow H_1 \rightarrow L_\alpha \rightarrow V_2 \rightarrow H_2 \rightarrow I_2 \rightarrow L_2$ . Thus the ternary-phase diagram of  $(EO)_{17}(PO)_{59}(EO)_{17}$ -D<sub>2</sub>O- $p$ -xylene, as presented here, is very rich with a record number of eight different phases. The sequence of microstructures formed by  $(EO)_{17}(PO)_{59}(EO)_{17}$  in water-oil mixtures is similar to that encountered in solvent-free block copolymers at temperatures below the order-disorder transition (ODT) (37, 38). However, copolymers of different relative block composition are needed to attain the different structures in the solvent-free case (38). On the other hand, with the highly hydrophobic and asymmetric copolymer  $(EO)_4(PO)_{59}(EO)_4$ , the sequence is "truncated" and gives preferably reverse structures. It is worth noting here that a truncated phase sequence is normally observed in ternary surfactant-water-oil systems (39). The phase of surfactants is influence-limited by a "preferred" interfacial curvature (originating from the surfactant geometry) so that a ternary isothermal surfactant-water-oil phase diagram exhibits either normal (oil-in-water) or reverse (water-in-oil) phases, but usually not both (6, 22, 40). The high hydrophobic PPO content of  $(EO)_4(PO)_{59}(EO)_4$  results in an interfacial curvature that is biased towards water-in-oil structures. Thus the similarity of the  $(EO)_4(PO)_{59}(EO)_4$  and surfactant phase diagrams is striking. Similar observations have been obtained for the  $(EO)_5(PO)_{68}(EO)_5$ -D<sub>2</sub>O- $p$ -xylene system (22).



**Fig. 7.** Typical  $^2\text{H}$  NMR spectra for various samples of the  $(\text{EO})_{17}(\text{PO})_{59}(\text{EO})_{17}$ - $\text{D}_2\text{O}$ - $p$ -xylene system at  $25^\circ\text{C}$ : (a) sharp singlet indicative of an isotropic phase (line width at half-maximum height  $\approx 13$  Hz); (b) one splitting from a hexagonal phase ( $\Delta^2\text{H} = 88$  Hz); (c) one splitting from a lamellar phase ( $\Delta^2\text{H} = 234$  Hz); (d) a two-phase region consisting of isotropic and anisotropic mixtures; (e) a two-phase region containing a mixture of hexagonal and lamellar phases. The sample compositions are 38.6:15.6:45.8, 30.0:65.1:4.9, 64.7:24.7:10.6, 81.2:17.1:1.7, and 42.3:34.8:22.9 wt % copolymer:water:oil, respectively.

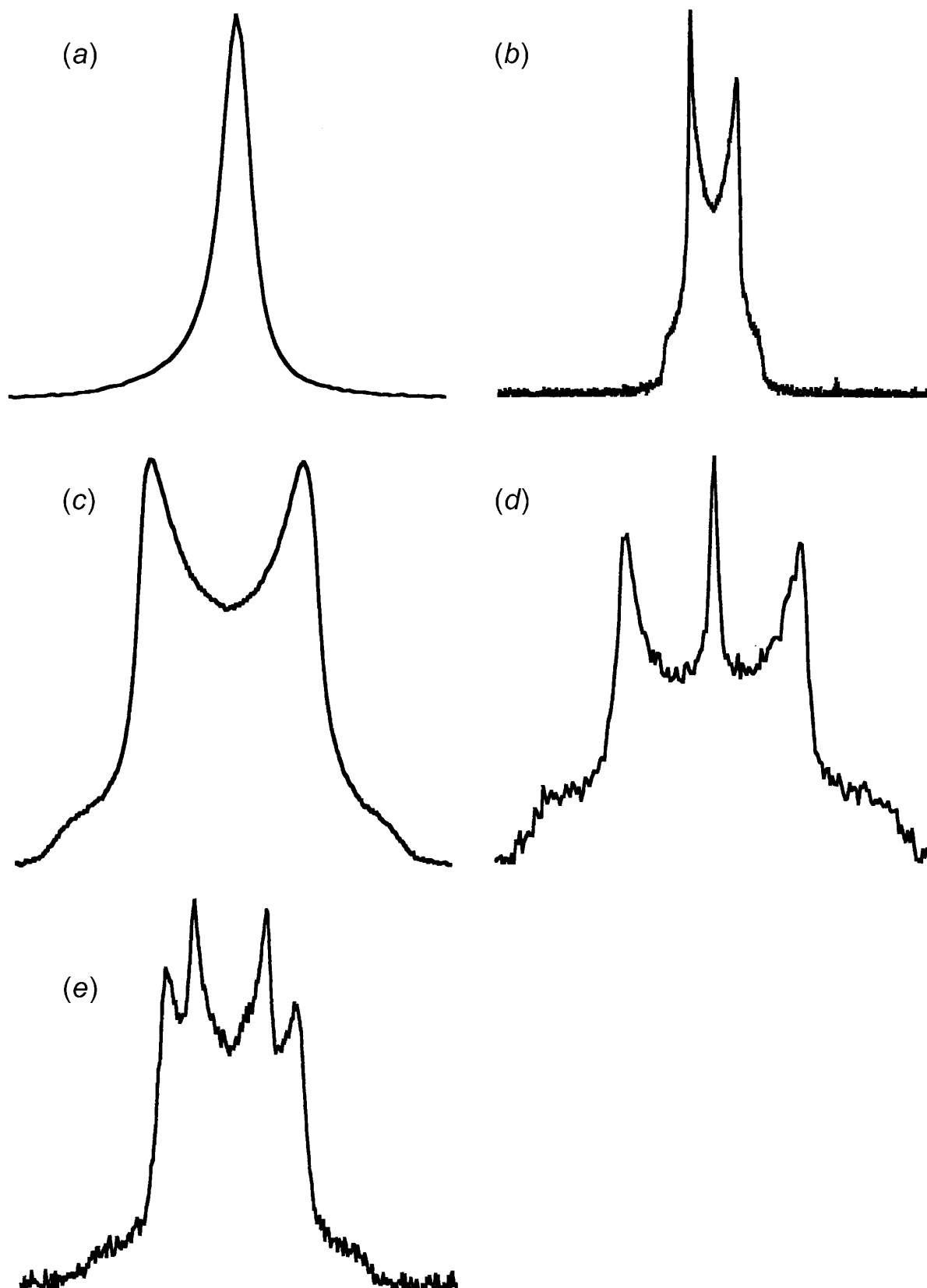




**Table 3.** Deuterium quadrupole splitting values ( $\Delta^2H$  in Hz) for some selected samples in the  $H_1$ ,  $H_2$ , and  $L_\alpha$  phases of the  $(EO)_{17}(PO)_{59}(EO)_{17}$ -D<sub>2</sub>O-*p*-xylene system at 25°C.

Composition (% , w/w)			Polymer:D <sub>2</sub> O molar ratio	Phase	$\Delta$ (Hz)
Polymer	D <sub>2</sub> O	<i>p</i> -Xylene			
39.9	60.1	0	0.0024	H <sub>1</sub>	94
54.95	45.05	0	0.0049	H <sub>1</sub>	98
29.98	65.14	4.88	0.0019	H <sub>1</sub>	88
35.69	59.7	4.61	0.0024	H <sub>1</sub>	96
39.96	54.69	5.35	0.003	H <sub>1</sub>	97
49.33	19.74	30.93	0.0101	H <sub>2</sub>	126
48.62	30.87	20.51	0.0064	H <sub>2</sub>	121
68.79	16.17	15.04	0.0172	H <sub>2</sub>	138
74.82	12.26	12.92	0.0247	H <sub>2</sub>	135
65.03	34.97	0	0.0075	L <sub><math>\alpha</math></sub>	231
74.81	25.19	0	0.012	L <sub><math>\alpha</math></sub>	244
44.76	47.23	8	0.0038	L <sub><math>\alpha</math></sub>	173
49.62	40.42	9.97	0.005	L <sub><math>\alpha</math></sub>	185
54.56	35.23	10.21	0.0063	L <sub><math>\alpha</math></sub>	193
64.69	24.74	10.57	0.0106	L <sub><math>\alpha</math></sub>	234
68.77	21.14	10.09	0.0132	L <sub><math>\alpha</math></sub>	237
74.8	15.05	10.15	0.0201	L <sub><math>\alpha</math></sub>	235

**Table 4.** Deuterium quadrupole splitting values ( $\Delta^2H$  in Hz) for some selected samples in the  $H_2$  and  $L_\alpha$  phases of the  $(EO)_5(PO)_{59}(EO)_5$ -D<sub>2</sub>O-*p*-xylene system at 25°C.

Composition (% , w/w)			Polymer:D <sub>2</sub> O molar ratio	Phase	$\Delta$ (Hz)
Polymer	D <sub>2</sub> O	<i>p</i> -Xylene			
67.33	32.67	0	0.0109	H <sub>2</sub>	92
74.05	25.95	0	0.015	H <sub>2</sub>	101
65.39	29.64	4.97	0.0116	H <sub>2</sub>	109
69.87	27.64	2.62	0.0133	H <sub>2</sub>	128
79.44	17.74	2.82	0.0236	H <sub>2</sub>	142
38.73	61.27	0	0.0033	L <sub><math>\alpha</math></sub>	162
42.94	57.06	0	0.004	L <sub><math>\alpha</math></sub>	165
49.7	50.3	0	0.0052	L <sub><math>\alpha</math></sub>	169
58.5	41.5	0	0.0074	L <sub><math>\alpha</math></sub>	178
60.09	37.44	2.47	0.0085	L <sub><math>\alpha</math></sub>	182

In the ternary block copolymer systems, the structural sequence is driven as a function of the related composition parameter (11), which has been defined as  $f$  (see eq. [4]). The phase sequence for the  $(EO)_{17}(PO)_{59}(EO)_{17}$  copolymer is symmetric around  $f = 0.5$  with lamellar stability in the range  $0.4 < f < 0.7$ , and the normal and reverse hexagonal phases in the range  $0.3 < f < 0.4$  and  $0.6 < f < 0.7$ , respectively. For the system with short PEO blocks ( $(EO)_4(PO)_{59}(EO)_4$ -D<sub>2</sub>O-*p*-xylene system), the lamellar phase is shifted towards higher  $f$ . Thus the PEO-PPO block ratio determines the stability range of the various phases in any copolymer-water-oil system. The results of the present study corroborate the observations and findings reported by Svensson et al. (22),

as could be expected, since phase behaviour depends more on the PEO-PPO ratio than on molecular weight, which was fixed for their copolymers. Reference is therefore made to their work (see ref. 22) for further discussion concerning our present study.

## Conclusion

The complete ternary phase diagrams for the two systems  $(EO)_{17}(PO)_{59}(EO)_{17}$ -D<sub>2</sub>O-*p*-xylene and  $(EO)_4(PO)_{59}(EO)_4$ -D<sub>2</sub>O-*p*-xylene have been determined at 25°C. The two copolymers have the same size middle-block (PPO) but different size end-blocks (PEO) and asymmetry. The  $(EO)_{17}(PO)_{59}(EO)_{17}$ -D<sub>2</sub>O-*p*-xylene system exhibits a record eight different phases, all thermodynamically stable at the same temperature: normal micellar cubic ( $I_1$ ), normal hexagonal ( $H_1$ ), lamellar ( $L_\alpha$ ), reverse bicontinuous cubic ( $V_2$ ), reverse hexagonal ( $H_2$ ), and reverse micellar cubic ( $I_2$ ) lyotropic liquid crystalline phases, as well as water-rich ( $L_1$ ) and water-lean micellar ( $L_2$ ) solutions. In the  $(EO)_4(PO)_{59}(EO)_4$ -D<sub>2</sub>O-*p*-xylene system the  $L_1$ ,  $I_1$ ,  $H_1$ , and  $V_2$  structures are absent. An extensive  $L_2$  region is observed. The highly asymmetric and hydrophobic  $(EO)_4(PO)_{59}(EO)_4$  copolymer shows a truncated phase sequence, which is a consequence of early solvent water saturation of the short PEO blocks (22). The self-assembly mode of the  $(EO)_4(PO)_{59}(EO)_4$  copolymer in water + oil is strikingly similar to the self-assembly of  $(EO)_5(PO)_{68}(EO)_5$  as well as surfactants in solutions (22). Normally, the surfactant phase diagrams are less rich than the ones observed with most polyoxyalkene block copolymers. The surfactants, and in particular the nonionic surfactants, can often be described as having a preferred or spontaneous mean curvature of the polar-apolar interface, which limits the range of stable structures and reduces the richness of the phase diagram (22, 40). The high hydrophobic (PPO) content of the  $(EO)_4(PO)_{59}(EO)_4$  copolymer results in an interfacial curvature that is biased towards water-in-oil structures. No normal (oil-in-water) phases were observed in  $(EO)_4(PO)_{59}(EO)_4$ -D<sub>2</sub>O-*p*-xylene system at 25°C.

## Acknowledgments

P.K.K. is grateful to Professor Bjorn Lindman and his group at Physical Chemistry 1, Chemical Center, Lund University, Sweden for their warm hospitality during his sabbatical stay in Lund. The stay in Lund of P.K.K. was supported by the Swedish Institute Guest Research Fellowship. The acquisition of the SAXS apparatus was funded by the Swedish Council for planning and Coordination of Research (FRN). BASF is thanked for providing the block copolymers. Helpful referee comments are gratefully acknowledged.

## References

1. P. Alexandridis and T.A. Hatton. *Colloid Surf. A*, **96**, 1 (1995).
2. P. Alexandridis. *Curr. Opin. Colloid Interface Sci.* **2**, 478 (1997).
3. P. Alexandridis, U. Olsson, and B. Lindman. *Macromolecules*, **28**, 7700 (1995).
4. B. Chu, Z. Zhou. *In Nonionic surfactants: Polyoxyalkylene block copolymers. Edited by V.M. Nace. Surfactant Science Series. Vol. 60. Marcel Dekker, New York. 1996.*



5. P. Alexandridis, U. Olsson, and B. Lindman. *Langmuir*, **14**, 2627 (1998).
6. D.F. Evans and H. Wennerström. *The colloidal domain*. 2nd ed. Wiley-VCH, New York. 1999.
7. P. Alexandridis, D. Zhou, and A. Khan. *Langmuir*, **12**, 2690 (1996).
8. P. Holmqvist, P. Alexandridis, and B. Lindman. *Macromolecules*, **30**, 6788 (1997).
9. B. Svensson, P. Alexandridis, and U. Olsson. *J. Phys. Chem. B*, **102**, 7541 (1998).
10. M. Svensson, P. Alexandridis, and P. Linse. *Macromolecules*, **32**, 5435 (1999).
11. P. Alexandridis, U. Olsson, and B. Lindman. *Langmuir*, **13**, 23 (1997).
12. P. Alexandridis. *Curr. Opin. Colloid Interface Sci.* **1**, 490 (1996).
13. H. Altinok, G.E. Yu, K. Nixon, P.A. Gorry, D. Attwood, and C. Booth. *Langmuir*, **13**, 5837 (1997).
14. C. Booth, G.E. Yu, and V.M. Nace. *In* *Amphiphilic block copolymers. Self-assembly and applications*. Edited by P. Alexandridis and B. Lindman. Elsevier, Amsterdam. 2000.
15. P. Alexandridis, U. Olsson, and B. Lindman. *J. Phys. Chem.* **100**, 280 (1996).
16. P. Alexandridis, P. Holmqvist, and B. Lindman. *Colloids Surf. A*, **129–130**, 3 (1997).
17. P. Holmqvist, P. Alexandridis, and B. Lindman. *J. Phys. Chem. B*, **102**, 1149 (1998).
18. A. Caragheorgheopol and S. Schlick. *Macromolecules*, **31**, 7736 (1998).
19. A. Caragheorgheopol, J. Pilar, and S. Schlick. *Macromolecules*, **30**, 2923 (1997).
20. P. Alexandridis, R. Ivanova, and B. Lindman. *Langmuir*, **16**, 3660 (2000).
21. R. Ivanova, B. Lindman, and P. Alexandridis. *Langmuir*, **16**, 3676 (2000).
22. B. Svensson, U. Olsson, and P. Alexandridis. *Langmuir*, **16**, 6839 (2000).
23. K. Fontell. *Colloid Polym. Sci.* **268**, 264 (1990).
24. G. Lindblom and L. Rilfors. *Biochim. Biophys. Acta*, **988**, 221 (1989).
25. M. Clerc and E. Dubois-Violette. *J. Phys. II*, **4**, 275 (1994).
26. P. Mariani, V. Luzzati, and H. Delacroix. *J. Mol. Biol.* **204**, 165 (1988).
27. V. Luzzati, R. Vargas, A. Gulik, P. Mariani, J.M. Seddon, and E. Rivas. *Biochemistry*, **31**, 279 (1992).
28. B. Chu and G. Wu. *Macromol. Symp.* **90**, 251 (1995).
29. G. Wu, B. Chu, and D.K. Schneider. *J. Phys. Chem.* **98**, 12 018 (1994).
30. G. Wu, L. Liu, V.B. Buu, B. Chu, and D.K. Schneider. *Physica A*, **231**, 73 (1996).
31. S. Zhou, J. Su, and B. Chu. *J. Polym. Phys.* **36**, 889 (1998).
32. U. Olsson, M. Jonströmer, K. Nagai, O. Söderman, H. Wennerström, and G. Klose. *Prog. Colloid. Polym. Sci.* **76**, 75 (1988).
33. P. Alexandridis and K. Andersson. *J. Phys. Chem. B*, **101**, 8103 (1997).
34. I.R. Schmolka. *J. Am. Oil Chem. Soc.* **68**, 206 (1991).
35. H. Wennerström, B. Lindman, and G. Lindblom. *Chem. Scr.* **6**, 97 (1974).
36. B. Halle and H. Wennerström. *J. Chem. Phys.* **75**, 1928 (1981).
37. F.S. Bates. *Science*, **251**, 898 (1991).
38. F.S. Bates, M.F. Schulz, A.K. Khandpur, S. Förster, J.H. Rose-dale, K. Almdal, and K. Mortensen. *Faraday Discuss.* **98**, 7 (1994).
39. P. Ekvall, L. Mandell, and K. Fontell. *Mol. Cryst. Liq. Cryst.* **8**, 157 (1969).
40. U. Olsson and H. Wennerström. *Adv. Colloid Interface Sci.* **49**, 113 (1994).



# The activity of 3- and 7-hydroxyflavones as scavengers of superoxide radical anion generated from photo-excited riboflavin

Paulina Montaña, Nora Pappano, Nora Debattista, Vicente Ávila, Ariana Posadaz, Sonia G. Bertolotti, and Norman A. García

**Abstract:** The visible-light irradiation of the system Riboflavin plus 3-hydroxyflavone or plus 7-hydroxyflavone, under aerobic conditions, produces a series of competitive processes that depend on the relative concentrations of the pigment and the flavones. The picture comprises photochemical mechanisms that potentially operate in nature. They mainly include the quenching of Rf singlet ( $^1\text{Rf}^*$ ) and triplet ( $^3\text{Rf}^*$ ) excited states (with bimolecular rate constants in the order of  $10^9 \text{ M}^{-1} \text{ s}^{-1}$ ) and superoxide radical anion-mediated reactions. The participation of the oxidative species singlet molecular oxygen was not detected. The overall result shows chemical transformations in both Rf and 3-hydroxyflavone. No experimental evidence was found indicating any chemical reaction involving 7-hydroxyflavone. The fate of the pigment also depends on the amount of the dissolved flavonoid. At 50 mM concentrations of these compounds or higher, practically no photochemistry occurs, owing to the extensive quenching of  $^1\text{Rf}^*$ . When the concentration of the flavones is in the mM range or lower,  $^3\text{Rf}^*$  is photogenerated. Then, the excited triplet species can be quenched mainly by the flavones through an electron-transfer process, yielding the semireduced pigment. The latter interacts with dissolved oxygen producing  $\text{O}_2^{\bullet-}$ , which reacts with both the pigment and 3-hydroxyflavone. In summary, 3-hydroxyflavone and 7-hydroxyflavone participate in the generation of superoxide ion in an Rf-sensitized process, and simultaneously 3-hydroxyflavone constitutes a degradable quencher of the oxidative species.

**Key words:** flavones, riboflavin, sensitization, singlet molecular oxygen, superoxide radical anion.

**Résumé :** L'irradiation en lumière visible du système Riboflavine plus 3-hydroxyflavone ou plus 7-hydroxyflavone, dans des conditions aérobiques, produit une série de processus compétitifs qui dépendent des concentrations relatives du pigment et des flavones. L'étude englobe les mécanismes photochimiques qui potentiellement se produisent dans la nature. Ils comprennent principalement la désactivation des états excités singulet Rf ( $^1\text{Rf}^*$ ) et triplet ( $^3\text{Rf}^*$ ) (avec des constantes de vitesse bimoléculaire de l'ordre de  $10^9 \text{ M}^{-1} \text{ s}^{-1}$ ) et des réactions du radical superoxyde induites par un anion. On n'a pas mis en évidence la participation de l'espèce oxydante : l'oxygène moléculaire singulet. Le résultat global montre les transformations chimiques à la fois dans les états excités Rf et dans la 3-hydroxyflavone. On n'a pas trouvé de preuves expérimentales d'une réaction chimique impliquant la 7-hydroxyflavone. Le sort du pigment dépend également de la quantité de flavonoïde dissoute. A des concentrations en flavonoïdes de l'ordre de 50 mM ou plus, il ne se produit pratiquement pas de photochimie à cause de la désactivation importante de l'état singulet excité  $^1\text{Rf}^*$ . Quand la concentration en flavones est de l'ordre du mM ou moins, l'état triplet  $^3\text{Rf}^*$  est photogénéré. Dans ces conditions l'espèce à l'état triplet peut-être désactivée principalement par les flavones, via un processus impliquant un transfert d'électrons, conduisant alors au pigment semi réduit. Ce dernier interagit avec l'oxygène dissous produisant  $\text{O}_2^{\bullet-}$ , qui réagit à la fois avec le pigment et avec la 3-hydroxyflavone. En résumé, la 3-hydroxyflavone et la 7-hydroxyflavone participent à la génération de l'ion superoxyde dans un processus sensibilisé par l'état excité Rf, et simultanément la 3-hydroxyflavone constitue un désactivateur dégradable des espèces oxydantes.

**Mots clés :** flavones, riboflavine, sensibilisation, oxygène moléculaire singulet, anion radicalaire superoxyde.

[Traduit par la Rédaction]

## Introduction

A considerable number of articles have been published, specially in the last decade, on the isolation (1), synthesis

(2), and properties (3–5) of natural and artificial flavonoids. The interest is mainly because of the antioxidative properties (6–8) of this family of compounds, widely distributed in nature, whose applications, among others, include the signifi-

Received 31 March 2003. Published on the NRC Research Press Web site at <http://canjchem.nrc.ca> on 7 August 2003.

P. Montaña, N. Pappano, and N. Debattista. Área de Química Física, Universidad Nacional de San Luis, 5700 San Luis, Argentina. V. Ávila, A. Posadaz, S.G. Bertolotti, and N.A. García.<sup>1</sup> Dto. de Química, Universidad Nacional de Río Cuarto 5800 Río Cuarto, Argentina.

<sup>1</sup>Corresponding author (e-mail: [ngarcia@exa.unrc.edu.ar](mailto:ngarcia@exa.unrc.edu.ar)).



cant protective effect against fat deterioration (9–11), antibacterial activities (1), and potential inhibitory action against cancer initiation (2, 5). These processes take place by different mechanisms, including the scavenging or trapping of activated electrophilic forms of carcinogenics: oxygen radicals such as peroxy radicals, singlet molecular oxygen [ $O_2(^1\Delta_g)$ ], superoxide anion ( $O_2^{\cdot-}$ ), or hydroxyl radicals. Nevertheless, the antioxidant properties of certain flavonoids have been the subject of contradictory interpretations, and even promotion of oxidizing activity has been suggested (12–14).

In recent years we have studied the ability of different flavonoids to act as quenchers of  $O_2(^1\Delta_g)$  photochemically generated from Rose Bengal (RB), the synthetic xanthene dye most frequently used as an  $O_2(^1\Delta_g)$  sensitizer (15). The whole process is depicted by steps [11], [12], and [13], as shown in Scheme 1 (see Results section). In the scheme, S is a dye sensitizer responsible for the visible light absorption (RB), whereas  $^1S^*$  and  $^3S^*$  are the respective singlet and triplet-excited states of S and  $O_2(^3\Sigma_g^-)$  is the ground state molecular oxygen.  $O_2(^1\Delta_g)$  is the singlet molecular oxygen generated by energy transfer from  $^3S^*$  to  $O_2(^3\Sigma_g^-)$ .  $O_2(^1\Delta_g)$  can be physically deactivated by collision with solvent molecules (process [13]) or with the flavonoid and (or) the sensitizer (process [11]), or it can react with the latter compounds, giving rise to oxidation products (step [12]). Results from other authors (14) and from ourselves (9–11) indicate that the effectiveness of flavones as  $O_2(^1\Delta_g)$  quenchers mainly depends on structural effects and particularly on the number and position of the OH groups in the flavonoid skeleton.

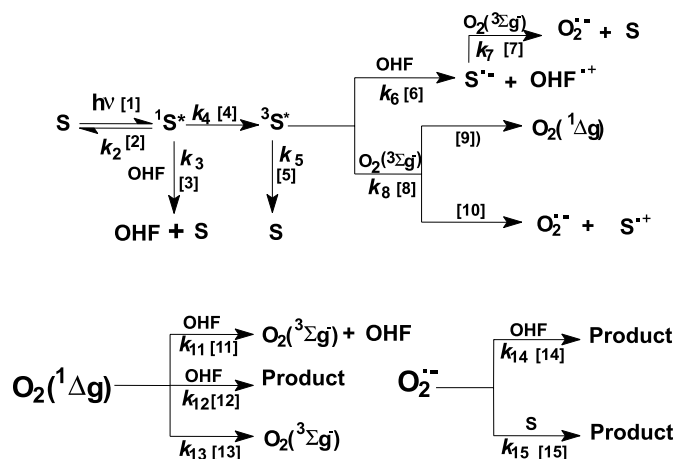
Regarding the involvement of flavonoids in the generation and quenching of oxidative species, a satisfactory approach to the actual situation in living environments can be the study of photoprocesses occurring in the presence of natural dye-sensitizers. A pigment of particular interest is vitamin B2 or Riboflavin (Rf) (Fig. 1), which has been postulated as a possible sensitizer for the photooxidative degradation of a number of relevant natural substrates present in different classes of foods and living organisms (16). Nevertheless, the potential properties of Rf as a redox intermediary of the visible-light-transparent flavones in its presence (as a visible-light-sensitizer) has not been investigated, according to our knowledge. This is the aim of the present kinetic and mechanistic study, employing 3-hydroxyflavone (3-OHF) and 7-hydroxyflavone (7-OHF) (Fig. 1). Since both Rf and the hydroxyflavones (OHF) can occupy common locations in diverse biological assemblies, all information about the behaviour of the visible-light-promoted interactions between the flavones and the relevant pigment Rf will help increase the knowledge of the behaviour of activated oxidative species in nature.

## Experimental

### Materials

3-Hydroxyflavone, 7-hydroxyflavone, Riboflavin (all from Sigma), and sodium azide ( $NaN_3$ ) (Aldrich) were employed as received. The solvent was MeOH, HPLC grade from Sintorga (Argentina).

**Scheme 1.** Possible photoprocesses upon visible light irradiation of the system Rf–OHF in MeOH; S = Riboflavin and OHF = 3- or 7-hydroxyflavone.



### Methods

Aerobic photolysis of methanolic solutions containing OHF (0.4–0.5 mM for the observation of changes in the UV spectra) and Rf (ca. 0.02 mM) were carried out in a PTI unit provided with a high-pass monochromator and 150 W Xe lamp, irradiating the Rf solutions with  $440 \pm 10$  nm and ensuring that the light was only absorbed by the sensitizer. The rates of Rf photodecomposition in nitrogen-saturated solutions, either in the presence or in the absence of the OHF, were evaluated by monitoring the absorbance decrease at 445 nm as a function of irradiation time.

The Rf-sensitized photooxygenation rates of the flavones were determined from the initial slopes of oxygen consumption vs. irradiation time, employing a specific oxygen electrode (Orion 97–08).

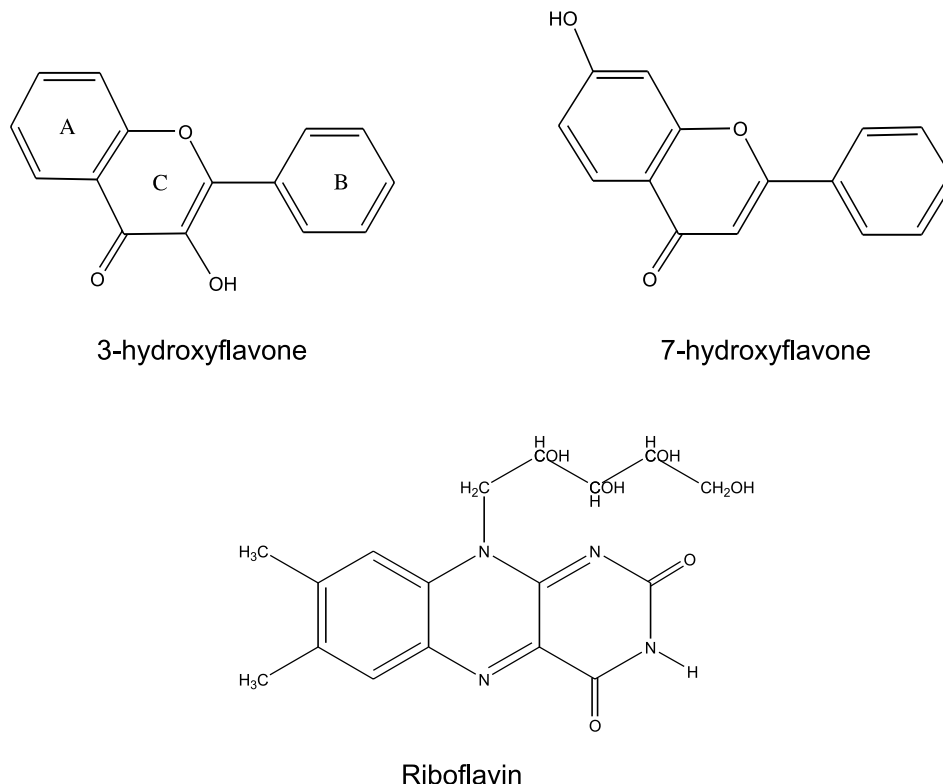
The steady-state quenching of the Rf fluorescence (absorbance at 445 nm  $\approx 0.1$ ) was studied with an RF 5301-PC Shimadzu spectrofluorimeter at  $25 \pm 1^\circ\text{C}$  in air-equilibrated solutions. Fluorescence lifetimes were measured by the time-correlated single photon counting technique on an Edinburgh FL-9000CD instrument. In both cases excitation and emission wavelengths were 445 and 515 nm, respectively. Ground-state absorption spectra were registered in a Hewlett-Packard 8452A diode array spectrophotometer.

$N_2$ -saturated aqueous solutions of Rf (0.01 mM) were photolysed using a flash photolysis apparatus. A nanosecond Nd:YAG laser system (Spectron) at 355 nm was the excitation source, employing a 150 W xenon lamp as the analysing light. The detection system comprised a PTI monochromator and a red-extended photomultiplier (Hamamatsu R666). The signal, acquired and averaged by a digital oscilloscope (Hewlett-Packard 54504A), was transferred to a PC via an HPIB parallel interface, where it was analysed and stored.

### Results

It is known that many aromatic compounds form relatively stable ground-state complexes with Rf (17–19). Nevertheless, no ground state interactions could be detected by



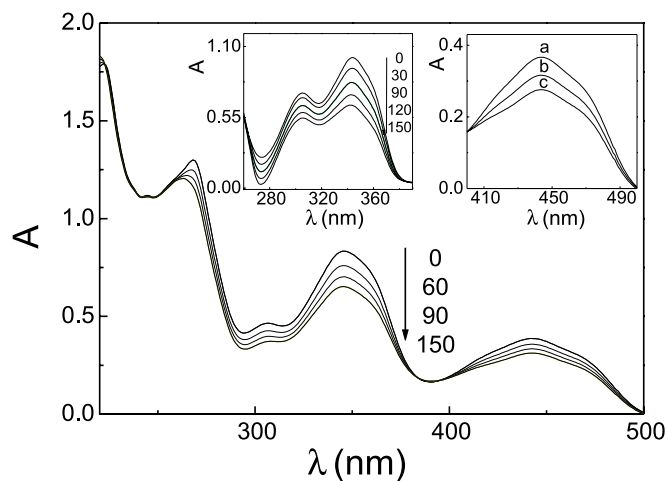
**Fig. 1.** Chemical structures of Riboflavin and the flavonoids, 3-hydroxyflavone and 7-hydroxyflavone.

absorption spectroscopy in the cases of the systems 3-OHF – Rf and 7-OHF – Rf.

The Rf-sensitized photoirradiation of air-equilibrated methanolic solutions of 3-OHF (ca. 0.5 mM) produces different changes in the whole absorption spectrum of the mixture, which reflect the addition of chemical changes in both the OHF and the Rf itself (Fig. 2). No spectral changes in the absorption of the flavonoid moiety were observed when 7-OHF was irradiated under identical experimental conditions, even when employing irradiation times ca. 10-fold higher. The spectral changes in the 3-OHF – Rf system were qualitatively similar, although slightly reduced in magnitude when similar irradiation doses were delivered to the described solutions in the presence of NaN<sub>3</sub> (20 mM). The salt is a known physical quencher of O<sub>2</sub>(<sup>1</sup>Δ<sub>g</sub>) with a rate constant (20) in MeOH of  $2.3 \times 10^8 \text{ M}^{-1} \text{ s}^{-1}$  for process [11]. Under these experimental conditions the lifetime of O<sub>2</sub>(<sup>1</sup>Δ<sub>g</sub>) in MeOH (20) is reduced from 10 μs to approximately 0.2 μs, owing to the presence of NaN<sub>3</sub>, making negligible, in practice, any O<sub>2</sub>(<sup>1</sup>Δ<sub>g</sub>)-mediated reaction.

Photoirradiation of diluted individual methanolic solutions of Rf (0.02 mM) + 3-OHF (0.5 mM) gave rise to measurable oxygen consumption (approximately 0.1 ppm O<sub>2</sub> min<sup>-1</sup>). No oxygen consumption was detected when 3-OHF was replaced by 7-OHF.

It is known that anaerobic photodegradation of Rf under visible light irradiation predominantly proceeds through the triplet state (21), and the rate of the process can be estimated by absorption spectroscopy. Comparative irradiations of N<sub>2</sub>-saturated methanolic solutions of Rf in the absence and in the presence of ca. 0.05 mM 3-OHF and 7-OHF showed that this rate is decreased in the presence of the flavones (Fig. 2,

**Fig. 2.** Spectral evolution of the mixture Rf (ca. 0.015 mM) plus 3-hydroxyflavone (0.5 mM) in MeOH vs. MeOH. Numbers on the spectra represent irradiation time in seconds. Left inset: time evolution of the difference spectra Rf (ca. 0.015 mM) plus 3-hydroxyflavone (0.5 mM) vs. Rf (ca. 0.015 mM). Numbers on the spectra represent irradiation time in seconds. Right inset: decrease in the 445 nm absorption band of Rf (ca. 0.015 mM) upon irradiation in argon-saturated solutions: (a) without irradiation; (b) irradiated 2 min in the presence of 7-OHF (0.2 mM); (c) irradiated 2 min. In all cases, irradiation at 450 ± 10 nm at room temperature (RT).

right inset), suggesting a quenching process of electronic excited states of Rf.

Most of the above-mentioned experimental evidence strongly indicates the occurrence of specific interactions of



the OHF with the singlet- and triplet-excited states of the pigment under aerobic and anaerobic conditions. To elucidate the reaction mechanism, the following kinetic scheme was employed in the interpretation and discussion of the experimental results (Scheme 1).

Rf represents the sensitizer S, i.e., a species that absorbs radiation in a wavelength range, typically that of visible light where the OHF are transparent. The absorption of incident light promotes Rf to the electronically excited singlet (reaction [1]) and triplet (reaction [4]) states. Both states can be quenched, through reactions [3], and [6] and [8], respectively. The excited triplet state can react (process [8]) with ground-state-triplet molecular oxygen  $O_2(^3\Sigma_g^-)$  dissolved in the medium, generating  $O_2(^1\Delta_g)$  [9] and (or)  $O_2^{\cdot-}$  [10]. By means of the electron-transfer reaction [6], the respective semireduced and semioxidized Rf and OHF forms can be produced. The first one, by means of reaction [7], generates  $O_2^{\cdot-}$ , which can react with OHF and (or) with the pigment (reactions [14] and [15], respectively).

#### Quenching of the excited singlet state of Rf by OHF

The emissive properties of Rf are well known. The pigment has an intense fluorescence emission band, centred at 515 nm, with a reported quantum yield of 0.25 (16). The steady-state fluorescence, the intensity, and the excited singlet lifetime were decreased in the presence of OHF > 1 mM. Through the classical Stern–Volmer treatment ( $1/\tau = (1/\tau_0) + k_3 [OHF]$ ), the rate constant values,  $k_3$  (process [3]), were graphically determined for 3-OHF and 7-OHF, respectively (Table 1, Fig. 3). The intercept gave a value of the fluorescence lifetime for Rf ( $\tau_0$ ) of 5.75 ns, in excellent agreement with previous published data (22).

#### Quenching of the excited triplet state of Rf by OHF

The disappearance of the Rf triplet state ( $^3Rf^*$ ) in MeOH, generated by a 355 nm laser pulse, was monitored from the first-order decay of the absorbance at 670 nm, a region where the interference from other possible species is negligible. The triplet decay was measured at low Rf concentration (typically 0.02 mM) and at low enough laser energy to avoid undesired effects such as self quenching and triplet–triplet annihilation, respectively. In this way, it was observed that the lifetime of  $^3Rf^*$  decreases appreciably in the presence of OHF in the mM concentration range. Analysis of the triplet quenching (Fig. 4), using the expression  $1/\tau = (1/\tau_0) + k_6 [OHF]$  (where  $^3\tau_0$  and  $^3\tau$  are the experimentally determined triplet lifetimes of Rf in the absence and in the presence of OHF, respectively), yielded the bimolecular rate constant value for the quenching of  $^3Rf$  by OHF shown in Table 1.

In Fig. 5, the transient absorption spectrum of Rf immediately after the laser pulse is shown. This spectrum is similar to the one reported for the Rf neutral triplet state in MeOH (23). The lower trace in Fig. 5, recorded at 20  $\mu$ s after the laser pulse under identical experimental conditions as described above but in the presence of 0.5 mM OHF (either 3-OHF or 7-OHF), possesses a similar shape to those that have been assigned to the presence of the well known Rf radical anion (24, 25). This experimental evidence could indicate that the triplet quenching by OHF is due to an electron-transfer process from OHF to the pigment, with the concomitant production of the semireduced pigment ( $Rf^{\cdot-}$ , reaction

**Table 1.** Rate constants for the quenching of singlet-excited ( $^1Rf^*$ ) and triplet-excited ( $^3Rf^*$ ) riboflavin,  $k_3$  and  $k_6$ , respectively, by 3-hydroxyflavone (3-OHF) and 7-hydroxyflavone (7-OHF) in MeOH at room temperature.

Compound	$k_3$ ( $10^{-9} \text{ M}^{-1} \text{ s}^{-1}$ )	$k_6$ ( $10^{-9} \text{ M}^{-1} \text{ s}^{-1}$ )
3-OHF	3.5	2.3
7-OHF	3.0	0.53

**Fig. 3.** Stern–Volmer plot for the quenching of singlet-excited Rf by (○) 3-hydroxyflavone; (●) 7-hydroxyflavone in MeOH at RT.

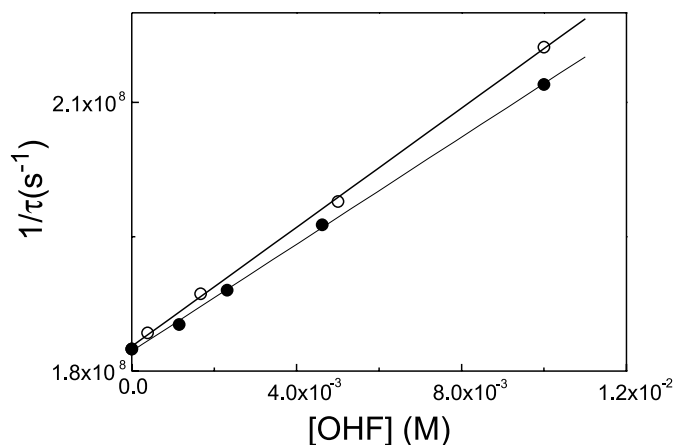
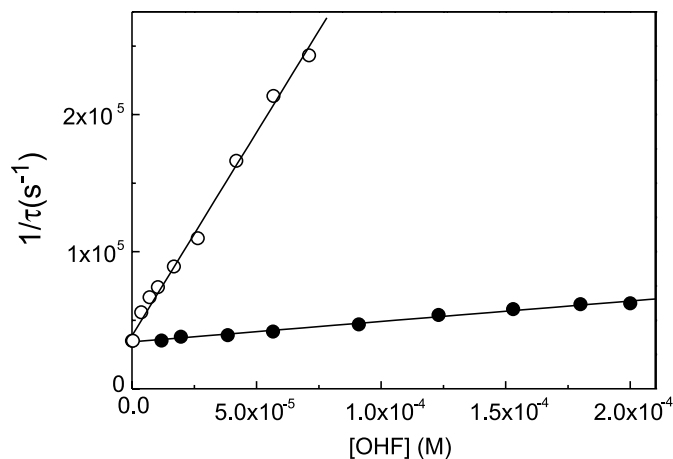


**Fig. 4.** Stern–Volmer plot for the quenching of triplet-excited Rf by (○) 3-hydroxyflavone; (●) 7-hydroxyflavone in MeOH at RT.



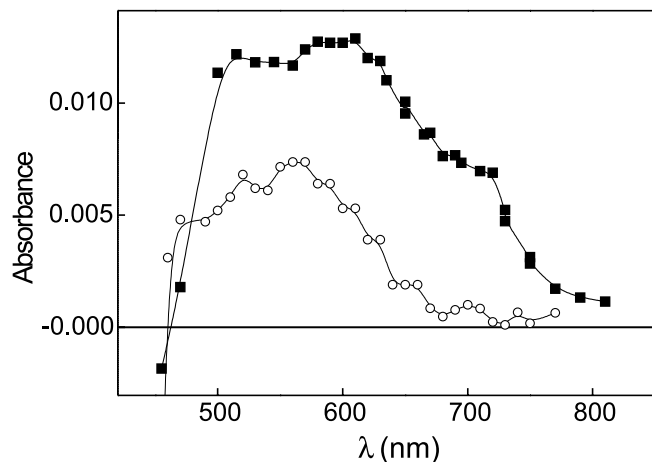
[6] from Scheme 1). This reaction has already been described for other hydroxyaromatic derivatives, including chlorophenols (26), hydroxypyridines (27), and indoles (17).

## Discussion

Reactions [5], [6], and [8], in Scheme 1, are competitive. The predominance of a given process will depend on the competition between  $O_2$  and OHF for the quenching of  $^3Rf^*$ . It is known (28) that the quenching of  $^3Rf^*$  by  $O_2$  occurs with a rate constant,  $k_8$ , in water of  $9 \times 10^8 \text{ M}^{-1} \text{ s}^{-1}$ . Nevertheless, in kinetic terms, and taking into account that the reported quantum yield value for the generation of  $O_2(^1\Delta_g)$



**Fig. 5.** Transient absorption spectra of Rf (0.02 mM) in argon-saturated methanolic solution (■) 2  $\mu$ s after the laser pulse and in the presence (○) of 3-OHF (0.5 mM) at 20  $\mu$ s after the laser pulse.



(process [9], with  $S = \text{Rf}$ ) and of  $\text{O}_2^{\cdot-}$  (process [10]) from  $^3\text{Rf}^*$  are 0.5 and 0.009, respectively (29), the direct generation of  $\text{O}_2^{\cdot-}$  by electron transfer from  $^3\text{Rf}^*$  to  $\text{O}_2$  can be considered insignificant.

In a previous paper (10), we studied the interaction of 3-OHF and 7-OHF with  $\text{O}_2(^1\Delta_g)$  in MeOH- $\text{CHCl}_3$  3:1 (v/v), employing Rose Bengal as a dye-sensitizer. The 7-OH derivative was a mere physical quencher of  $\text{O}_2(^1\Delta_g)$  with a rate constant,  $k_{11}$ , of  $2.3 \times 10^8 \text{ M}^{-1} \text{ s}^{-1}$ , whereas 3-OHF reacted chemically with the oxidative species with a rate constant,  $k_{12}$ , of  $1.7 \times 10^6 \text{ M}^{-1} \text{ s}^{-1}$ . Nevertheless our present results show an aerobic phototransformation of 3-OHF even in the presence of  $\text{NaN}_3$  (20 mM), with a slightly diminished rate as compared with that in the absence of the salt. This observation indicates that there is no significant contribution of an  $\text{O}_2(^1\Delta_g)$ -mediated degradation of 3-OHF. The small inhibitory effect in the rate of 3-OHF decomposition observed in the irradiation of the 3-OHF – Rf –  $\text{O}_2(\text{air})$  –  $\text{NaN}_3$  system possibly conforms to the known quenching of  $^3\text{Rf}^*$  by the azide anion, for which a rate constant,  $k_6$ , of  $6 \times 10^7 \text{ M}^{-1} \text{ s}^{-1}$  has been reported (20) (process [6] with OHF being replaced by  $\text{NaN}_3$  in Scheme 1). According to the rate constants reported in Table 1, the excited singlet state of Rf is effectively unquenched by the OHF at concentrations in the range 0.1–0.5 mM, concentrations similar to those employed in the experiments shown in the spectra (Fig. 2). The data in Table 1 also indicates that the triplet-excited Rf can be effectively quenched by both 3-OHF and 7-OHF in the range of concentrations used, with the subsequent production of the semireduced form of Rf (step [6]). According to flash photolysis results, process [6] with  $[\text{OHF}] = 5\text{--}10 \text{ mM}$  could compete with the generation of  $\text{O}_2(^1\Delta_g)$  (process [9]). Consequently, under air-saturated conditions, i.e., with a concentration of dissolved oxygen approximately equals to 2.1 mM (30), the species  $\text{Rf}^{\cdot-}$  could be formed by electron transfer from OHF (process [6]). In the presence of dissolved oxygen, superoxide ion can be generated through an electron-transfer process (step [7]). A rate constant value of  $1.4 \times 10^8 \text{ M}^{-1} \text{ s}^{-1}$  has been recently reported (29) for this process, a reaction that at the same time regenerates ground state Rf.

The Rf-sensitized photooxidation, mediated by superoxide ion, has been postulated to account for a series of hydroxy-aromatic compounds belonging to biologically relevant families (11, 17). El-Sukkary and Speier (31) reported, in 1981, the oxidation of 3-hydroxyflavone in tetrahydrofuran by thermally generated  $\text{O}_2^{\cdot-}$ . According to our experimental evidence (spectral changes and oxygen uptake measurements), in the present case superoxide ion effectively reacts with 3-OHF and Rf (steps [14] and [15], respectively).

As already reported by Tournaire et al. for polyhydroxy-flavonoids (14) and later confirmed by ourselves for monohydroxyflavones (9, 10), the activation of the double bond on ring C by the presence of the hydroxyl group (the case of 3-OHF, see Fig. 1) is the main factor that determines the reactivity towards the oxidative species. It should also be considered that 3-OHF might be more reactive than 7-OHF because of the intramolecular H-bonding in the 3-hydroxy compound, which results in a conjugated enolate system. This case could be similar to that reported for the perinaphthenone-sensitized photooxidation of methyl salicylate, methyl-3-hydroxy benzoate, and methyl-4-hydroxy benzoate, in which the higher photooxidation efficiency was reached by the H-bonded compound methyl salicylate (32).

In summary, we conclude that the kinetic results indicate the participation of ground state 3-OHF and 7-OHF in the visible-light-mediated photogeneration of superoxide ion in MeOH, sensitized by Rf. The process involves triplet-excited Rf and also dissolved atmospheric oxygen. At concentrations of the flavones in the order of mM or lower, only the excited triplet state of Rf is quenched by these compounds. Electron-transfer processes produce the superoxide ion and the subsequent photodecomposition of the pigment and 3-OHF. Nevertheless this flavonoid simultaneously acts as a sacrificial scavenger of superoxide ion, provided that it is consumed in the quenching process. There is no evidence for the reactive quenching of the superoxide ion by 7-OHF. By successive increases of the OHF concentration, starting from the mM range, the partial, and subsequently the substantial, quenching of singlet-excited Rf is achieved. As a result, superoxide ion is not generated and the photodecomposition of both 3-OHF and the pigment is prevented.

## Acknowledgements

Thanks are given to CONICET, ANPCyT, SECyT UNRC, and UNSL (all from Argentina) for financial support.

## References

1. M. Sato, S. Fujiwara, H. Tsuchiya, T. Fujii, M. Inuma, H. Fosa, and Y. Ohkawa. *J. Ethnopharmacol.* **54**, 171 (1996).
2. K. Gulasci, G. Litkei, S. Antus, T.E. Gunda, G. Gershauser, D. Lantuit, R.C. Moon, R.M. Moritarty, and J.M. Pezzuto. *Tetrahedron*, **54**, 13 867 (1998).
3. L.L. Song, J.W. Kosmeder, and S.K. Lee. *Cancer Res.* **59**, 578 (1999).
4. D. Barron and R.K. Ibrahim. *Phytochemistry*, **43**, 921 (1996).
5. H.A. Chung, L.Ch. Chang, S.K. Lee, and L.A. Snhamon. *J. Agric. Food Chem.* **47**, 36 (1999).
6. T. Yokosawa, E. Dong, Z.W. Lui, and M. Shimizu. *Phytother. Res.* **11**, 446 (1997).



7. N. Cotellet, J.L. Bernier, J.P. Catteau, J. Pommery, J.C. Wallet, and E.M. Gaydou. *Free Radical Biol. Med.* **20**, 35 (1996).
8. J. Gabrielska, J. Oszmiansky, R. Zylka, and M. Komorowska. *Z. Naturforsch.* **52**, 817 (1997).
9. S. Criado, S.G. Bertolotti, A.T. Soltermann, V. Avila, and N.A. García. *Fat Sci. Technol.* **97**, 265 (1995).
10. S. Criado, M.I. Gutiérrez, V. Avila, S.G. Bertolotti, and N.A. García. *Fett/Lipid*, **98**, 172 (1996).
11. V. Ávila, S.G. Bertolotti, N. Pappano, N. Debattista, and N.A. García. *Int. J. Food Sci. Technol.* **36**, 25 (2001).
12. M.J. Laughton, B. Hallivel, P.J. Evans, and J.R.B. Hoult. *Biochem. Pharmacol.* **38**, 2859 (1989).
13. S. Ahmad and R.S. Pardini. *Photochem. Photobiol.* **51**, 303 (1990).
14. C. Tournaire, S. Croux, M.T. Maurette, I. Beck, M. Ockquoux, A.M. Braun, and E. Oliiveros. *J. Photochem. Photobiol. B*, **19**, 295 (1993).
15. D.C. Neckers. *J. Photochem. Photobiol. A*, **47**, 1 (1989).
16. P.F. Heelis. *Chem. Soc. Rev.* **11**, 15 (1982).
17. S. Miskoski and N.A. García. *Coll. Czech. Chem. Commun.* **56**, 1838 (1991).
18. G.R. Penzer and G.K. Radda. *Q. Rev. Chem. Soc.* **21**, 43 (1966).
19. M.A. Slifkin. *Charge transfer interactions of biomolecules*. Academic Press, London. 1971.
20. F. Wilkinson, W.P. Helman, and A. Ross. *J. Phys. Chem. Ref. Data*, **24**, 663 (1995).
21. B.J. Fritz, K. Matsui, S. Kasai, and A. Yoshimura. *Photochem. Photobiol.* **45**, 539 (1987).
22. S.G. Bertolotti, C.M. Previtali, A.M. Rufs, and M.V. Encinas. *Macromolecules*, **32**, 2920 (1999).
23. S.G. Bertolotti, C.M. Previtali, A.M. Rufs, and M.V. Encinas. *Macromolecules*, **32**, 2920 (1999).
24. J.N. Chacón, J. McLearnie, and R.S. Sinclair. *Photochem. Photobiol.* **47**, 647 (1988).
25. C. El Hanine-Lmoumene and L. Lindqvist. *Photochem. Photobiol.* **66**, 591 (1997).
26. S. Miskoski and N.A. García. *J. Toxicol. Environ. Chem.* **25**, 33 (1989).
27. A. Pajares, J. Gianotti, G. Stettler, S. Bertolotti, S. Criado, A. Posadaz, F. Amat-Guerri, and N.A. García. *J. Photochem. Photobiol. A*, **139**, 199 (2001).
28. C. Lu, W. Lin, W. Wang, Z. Han, S. Yao, and N. Lin. *Phys. Chem. Chem. Phys.* **2**, 239 (2000).
29. C.M. Krishna, S. Uppuluri, P. Riesz, J.S. Zigler, and D. Balasubramanian. *Photochem. Photobiol.* **54**, 51 (1991).
30. S.L. Murov. *Handbook of photochemistry*. M. Decker, New York. 1993.
31. M.M.A. El-Sukkary and G. Speier. *J. Chem. Soc. Chem. Commun.* 745 (1981).
32. A.T. Soltermann, D. De la Peña, S. Nonell, F. Amat-Guerri, and N.A. García. *Polym. Degrad. Stab.* **49**, 371 (1995).



# 5-Hydroxy[1,2]oxazinan-3-ones as potential carbapenem and D-ala-D-ala surrogates

Saul Wolfe, Christiana Akuche, Stephen Ro, Marie-Claire Wilson, Chan-Kyung Kim, and Zheng Shi

**Abstract:** The title compounds are amino acids whose nitrogen atom is enclosed in a six-membered cyclic hydroxamate bearing a C5-hydroxyl group. They belong to a proposed new family of antibacterial agents targeted to the penicillin receptor. The glycine and alanine members of the family have been synthesized, as racemates, in seven steps from the four-carbon synthon diketene and the *tert*-butyl esters of *N*-hydroxyglycine and *N*-hydroxyalanine. Numerous alternatives to diketene have also been examined, but these lead mainly to five-membered cyclic hydroxamates. The theoretical considerations that have led to this synthetic programme are discussed in some detail. They include analysis of the structures of natural and unnatural penicillin surrogates, analysis of the penicillin pharmacophore, and a treatment of the chemical reaction with which penicillin blocks bacterial cell wall synthesis. The glycine derivative exhibits marginal but real activity vs. *Micrococcus luteus*. The alanine derivative, which more closely resembles D-ala-D-ala, is fifty times more active. Two five-membered structural isomers of the glycine derivative are inactive.

**Key words:** cyclocanaline, cycloserine, lactivicin, oxamazins, peptidoglycan, penicillin-binding proteins.

**Résumé :** Les composés mentionnés dans le titre sont des acides aminés dont l'atome d'azote est compris dans un hydroxamate cyclique à six chaînons portant un groupe hydroxyle en position 5. Ils font partie de ce qui est proposé comme une nouvelle famille d'agents antibactériens orientés vers les récepteurs de la pénicilline. On a synthétisé les membres glycine et alanine de la famille, sous la forme de racémiques, en sept étapes à partir du dicétène, un synthon à quatre atomes de carbone, et des esters *t*-butyliques de la *N*-hydroxyglycine et de la *N*-hydroxyalanine. On a examiné la possibilité d'utiliser plusieurs autres composés à la place du dicétène, mais dans chacun des cas ces dérivés de remplacement ont conduit principalement à la formation d'hydroxamates cycliques à cinq chaînons. On discute en détail des considérations théoriques qui ont conduit à ce programme de synthèse. Elles comprennent l'analyse des structures de substituts naturels et non naturels à la pénicilline, l'analyse du pharmacophore de la pénicilline et à un traitement de la réaction chimique par laquelle la pénicilline bloque la synthèse de la membrane de la cellule des bactéries. Le dérivé de la glycine présente une activité faible, mais réelle vis-à-vis du *Micrococcus luteus*. Le dérivé de l'alanine, qui ressemble plus au D-ala-D-ala, est cinquante fois plus actif. Deux isomères de structure à cinq chaînons du dérivé de la glycine sont inactifs.

**Mots clés :** cyclocanaline, cyclosérine, lactivicine, oxamazines, peptidoglycane, protéines se liant à la pénicilline.

[Traduit par la Rédaction]

## Introduction

Cycloserine (Oxamycin, Seromycin, **1**), produced by *Streptomyces orchidaceus* (**1**), and lactivicin (**2**), isolated from culture filtrates of *Empedobacter lactagenus* YK-258 and *Lysobacter albus* YK-422 (**2**), are antibiotics whose action is directed against the biosynthesis of the bacterial cell wall peptidoglycan. Although both antibiotics contain an

isoxazolidinone ring (a cyclic hydroxamate), they have different configurations at C4 and they operate at different stages of cell wall synthesis. D-Cycloserine, a cyclic analog of D-alanine (**3**), is a competitive inhibitor of both alanine racemase (**3**) and D-alanyl-D-alanine synthetase (**4**). Lactivicin has the L-configuration at C4 and a 2-oxoglutarate appendage attached to the ring nitrogen. Because it exhibits affinity to penicillin-binding proteins and susceptibility to  $\beta$ -

Received 19 November 2002. Published on the NRC Research Press Web site at <http://canjchem.nrc.ca> on 15 August 2003.

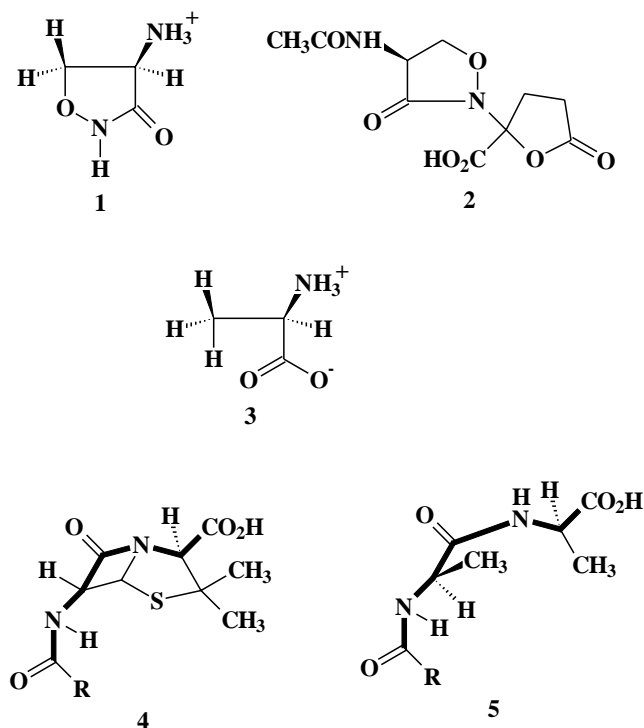
*This paper is dedicated to the memory of Raymond Lemieux (1920–2000), lifelong mentor and friend. ... "wherefore I say that your chief aim in the building up of Man is not to give him learning, which serves no end if he be but a walking book, but to lift his eyes and point him to those higher levels on which there are no more things-in-themselves, but only aspects of that divine bond which binds things together" (Saint-Exupéry).*

S. Wolfe,<sup>1</sup> C. Akuche, S. Ro, M.-C. Wilson, C.-K. Kim, and Z. Shi. Department of Chemistry, Simon Fraser University, Burnaby, BC V5A 1S6, Canada.

<sup>1</sup>Corresponding author (e-mail: [swolfe@sfu.ca](mailto:swolfe@sfu.ca)).



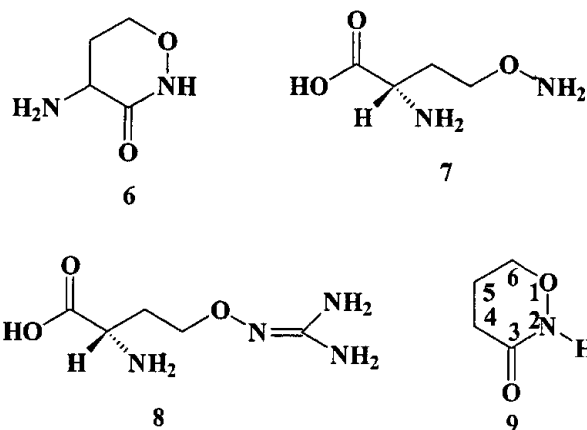
lactamases (2, 5), lactivicin can be regarded as a structural analog of penicillin (4), which is, in turn, a structural analog of the *N*-acyl-D-ala-D-ala terminus (5) of the growing peptidoglycan (6). The isoxazolidin-3-one ring of lactivicin thus appears to function as a  $\beta$ -lactam surrogate, and the 5-oxo-tetrahydrofuran-2-carboxylic acid substituent appears to function as a D-alanine surrogate.



The 6-membered homolog of cycloserine is cyclocaniline (6), the cyclodehydration product of caniline (7). L-Caniline, the 5-oxa isostere of ornithine, is the only naturally occurring amino acid that possesses an aminooxy moiety. The compound is found in leguminous plants and is derived from L-canavanine (8), the 5-oxa isostere of L-arginine, by arginase-mediated hydrolysis (7). Canavanine is an important metabolite of higher plants, as it has a dual function in chemical defense against herbivores and in nitrogen storage, where it can account for 90% or more of the seed nitrogen allocated to free amino acids (8). The free aminooxy group of L-caniline forms Schiff base adducts with  $\alpha$ -keto acids (9) and with the pyridoxal phosphate ( $B_6$ ) cofactor of many  $B_6$ -dependent enzymes (10). These properties endow caniline with antimetabolite (11), anticancer (11), and antimalarial activities (12).

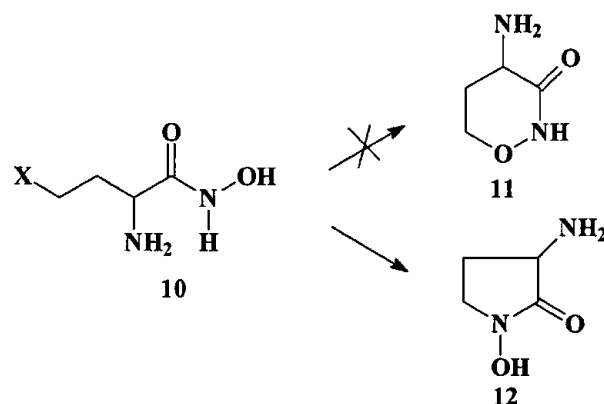
The first syntheses of [1,2]oxazinan-3-one (9) and cyclocaniline were accomplished by cyclization of 4-aminooxybutyric esters under forcing basic or acidic conditions, i.e., N2—C3 bond formation (13).

Attempts to secure these compounds by O1—C6 cyclization of halohydroxamic acids (10→11) were frustrated by competing N2—C6 bond formation (10→12) (14). The introduction of the aminooxy substituent into caniline has been achieved using ethyl *N*-hydroxyacetimidate (15), acetone oxime (13a), hydroxyurethane (16), or *N*-benzoylhy-



droxylamine (17) on appropriately protected and activated homoserine synthons.

Khomutov and co-workers have reported that DL-



cyclocaniline has activity against *Mycobacterium tuberculosis* (18, 19).

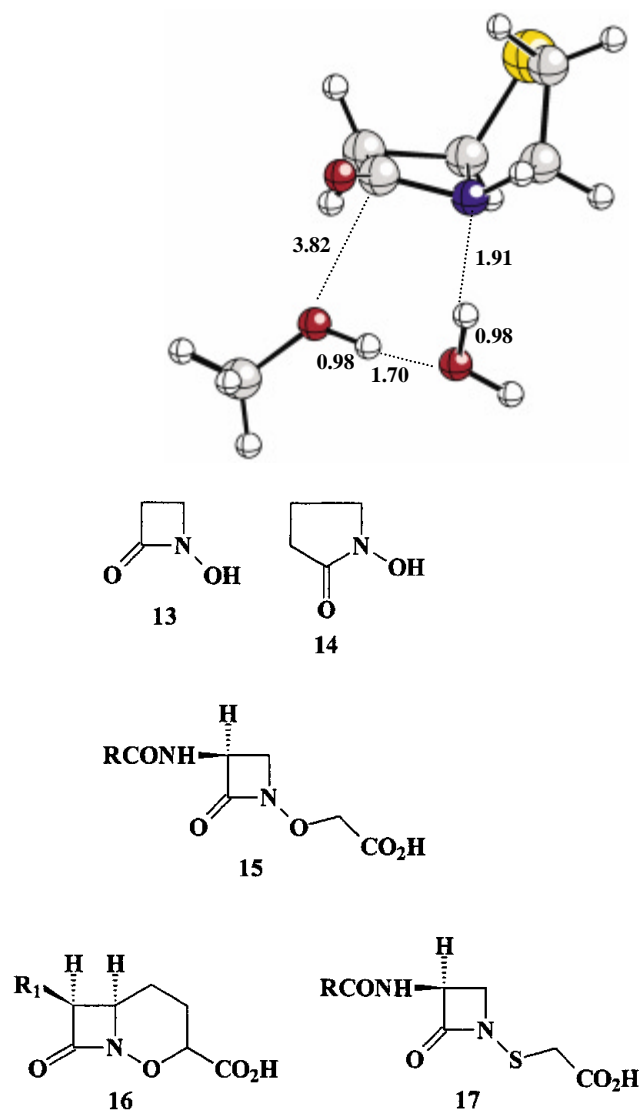
The parent 5-membered and 6-membered cyclic hydroxamates are structural isomers of the *N*-hydroxylactams 13 and 14, and rearrangement of an *N*-hydroxy-2-azetidinone into a 5-membered cyclic hydroxamate has been observed by Hirose et al. (20a) and by Miller and co-workers (20b), who have published extensively on oxamazins (15), heteroatom-activated  $\beta$ -lactams (21). Monocyclic oxamazins exhibit significant antibacterial activity vs. Gram negative bacteria. Their mechanism of action has not been established with certainty,<sup>2</sup> but it is noteworthy that the carboxyl group of 15 is one carbon further removed from the  $\beta$ -lactam nitrogen than in  $\beta$ -lactam antibiotics. In the case of the bicyclic [4.2.0] oxamazins 16, both diastereomers at the point of attachment of the carboxyl group are claimed to have good antibacterial activity (22). In contrast, thiamazins (17) are inactive (23).

Boyd, Miller, and co-workers (24) have discussed the difference in the activities of oxamazins and thiamazins in terms of their putative three-dimensional relationship to the penicillin nucleus, i.e., their ability to "fit" into the active sites of the serine peptidase receptors of  $\beta$ -lactam antibiotics. The chemical reaction that follows — namely, acylation of the serine hydroxyl group by the  $\beta$ -lactam ring — has been

<sup>2</sup>Personal communication from Professor M.J. Miller.



**Fig. 1.** Methanolysis of penam, with catalysis by one water molecule. Left: 3–21G\* reactant complex. Right: 3–21G\* transition structure. Graphics performed using Xmol.



the subject of extensive theoretical research (25). In our laboratory (26) the relative “reactivities” of different substrates are calculated, as shown in Fig. 1, for penam, the penicillin nucleus. The reaction is modeled theoretically as a one-step, cooperative process (27), in which  $\text{O}=\text{C}\cdots\text{O}$  bond formation by methanol and  $\text{N}\cdots\text{H}$  bond formation by a catalytic water molecule are concerted with the cleavage of the  $\beta$ -lactam bond. The structure on the left of Fig. 1 is the reactant complex, optimized at the 3–21G\* level (28); the optimized transition structure is shown on the right. The barrier, based on single-point MP2/6–31G\* calculations, is 29.36 kcal/mol. This number is shown in Table 1, together with the barriers calculated similarly for the water-assisted methanolyses of penem, *N*-methylazetidinone, and mono- and bicyclic oxamazins and thiamazins. In the latter two systems, there is more than one conformation of the 6-membered ring; based on a recent quantitative treatment of the Curtin–Hammett principle (29), the number shown in the table refers to the energy difference between the most stable reactant complex and the most stable transition structure.

**Table 1.** Calculated “barriers”<sup>a</sup> and nitrogen pyramidalities<sup>b</sup> in various azetidinones.

Azetidinone	“Barrier” (kcal/mol) <sup>a</sup>	Pyramidalities <sup>b</sup>
Penam	29.4	336.1
Penem	28.0	333.9
<i>N</i> -methylazetidinone	30.7	360.0
<i>N</i> -methoxyazetidinone	29.6	337.5
<i>N</i> -methylthioazetidinone	34.2	357.0
Bicyclic oxamazin	32.5	348.6
Bicyclic thiamazin	34.2	352.4

<sup>a</sup>See text for definition of “barrier”.

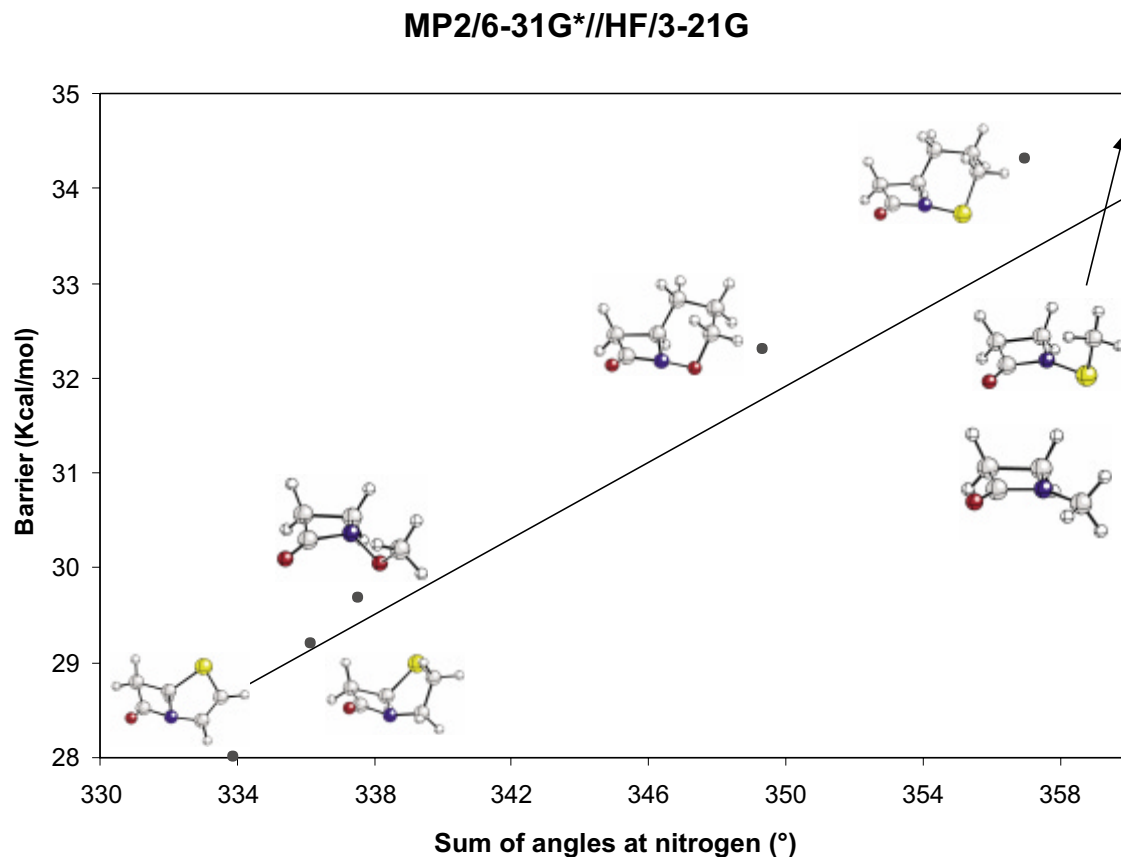
<sup>b</sup>Sum of the angles at nitrogen (3–21G or 3–21G\* calculations; the 3–21G\* basis set is used with sulfur-containing compounds).

It can be seen that *N*-methoxyazetidinone is comparable in “reactivity” to the bicyclic penam and is substantially more “reactive” than *N*-methylthioazetidinone. In addition, unlike compounds in which carbon or sulfur is attached to the  $\beta$ -lactam nitrogen, the monocyclic *N*-methoxyazetidinone is substantially more “reactive” than the bicyclic structure.

These trends can be understood by consideration of the pyramidalities of the  $\beta$ -lactam nitrogen, as given by the sum of the angles at this center. This sum is included in Table 1. The geometry at nitrogen has received continuous attention (30) since Woodward first proposed (31) that the  $\text{O}=\text{C}-\text{N}\leftrightarrow(-)\text{O}-\text{C}=\text{N}(+)$  amide resonance, which contributes to the stability and planarity of an amide linkage, is suppressed in a four-membered ring and cannot be achieved within the bicyclic penam structure. An equivalent, molecular orbital interpretation (32) is that  $n_p-\pi_{\text{CO}}^*$  charge transfer in an amide is most effective when the nitrogen *p*-orbital can conjugate with the  $\pi$ -system, i.e., when the nitrogen is planar. This is not possible when the  $\beta$ -lactam nitrogen is at a bridgehead position. In *N*-methoxy- and *N*-methylthioazetidinone, minimization of lone-pair – lone-pair repulsion between the *p*-orbital on nitrogen and the *p*-orbital on oxygen or sulfur (33) causes the methyl group to be perpendicular to the ring, so that the nitrogen *p*-orbital and the X–C bond are eclipsed. If the resulting  $n_p-\sigma_{\text{XC}}^*$  interaction competes with the  $n_p-\pi_{\text{CO}}^*$  interaction, the combined effects will produce nonplanarity at nitrogen, as is seen in *N*-methoxyazetidinone.



**Fig. 2.** A plot of the MP2/6-31G\*//3-21G(G\*) “barriers” vs. the sum of the angles at nitrogen of some  $\beta$ -lactam compounds (from Table 1).



The magnitude of the  $n_p-\sigma_{XC}^*$  interaction depends inversely upon the energy difference between  $n_p$  and  $\sigma_{XC}^*$  and also upon the square of the overlap between the interacting orbitals (34). Although the sulfur  $\sigma^*$  acceptor orbital is lower-lying than the oxygen  $\sigma^*$  acceptor orbital, the  $n_p-\sigma_{SC}^*$  interaction is not effective because of the longer nitrogen—sulfur bond (33). Consequently, the monocyclic and bicyclic thiazins exhibit similar “barriers” and near planarity at nitrogen. In the case of the oxamazins, closing the second ring increases the dihedral angle between  $n_p$  and  $\sigma_{OC}^*$  and decreases the contribution of the  $n_p-\sigma_{OC}^*$  interaction, resulting in increased planarity at nitrogen and an increased “barrier”.

As seen in Fig. 2, there is a rough linear relationship ( $R^2 = 0.81$ ) between the calculated sum of the angles at nitrogen and the calculated “barriers”.

#### Cyclic hydroxamates as $\beta$ -lactam surrogates

The foregoing considerations suggested that the cyclic hydroxamate 2-methyl-isoxazolidin-3-one (**18**), identified earlier as a  $\beta$ -lactam surrogate from its presence in lactivicin, would exhibit somewhat greater planarity at nitrogen and a somewhat higher “barrier” than its isomer *N*-methoxyazetidinone. The calculations on **18** and its homolog 2-methyl-[1,2]-oxazinan-3-one (**19**), which are summarized in Fig. 3, are consistent with this prediction. Nonetheless, both **18** and **19** are found to have significant “reactivity”, intermediate between penam and *N*-methylazetidinone, so that 2-substituted 4-acylamino-cycloserines and cyclocanelines such as

**20–22** might be expected to behave as penicillin–lactivicin–*N*-acyl-D-ala-D-ala analogs and exhibit antibacterial activity.

This proposal is not new. Phenylacetylation of L- and D-cycloserine, followed by coupling to *tert*-butyl (DL)-2-bromopropionate, separation of isomers, and deprotection,

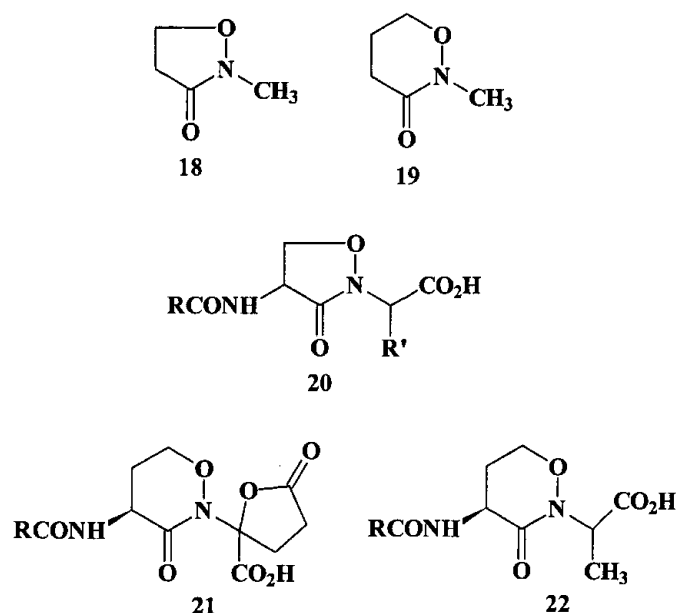
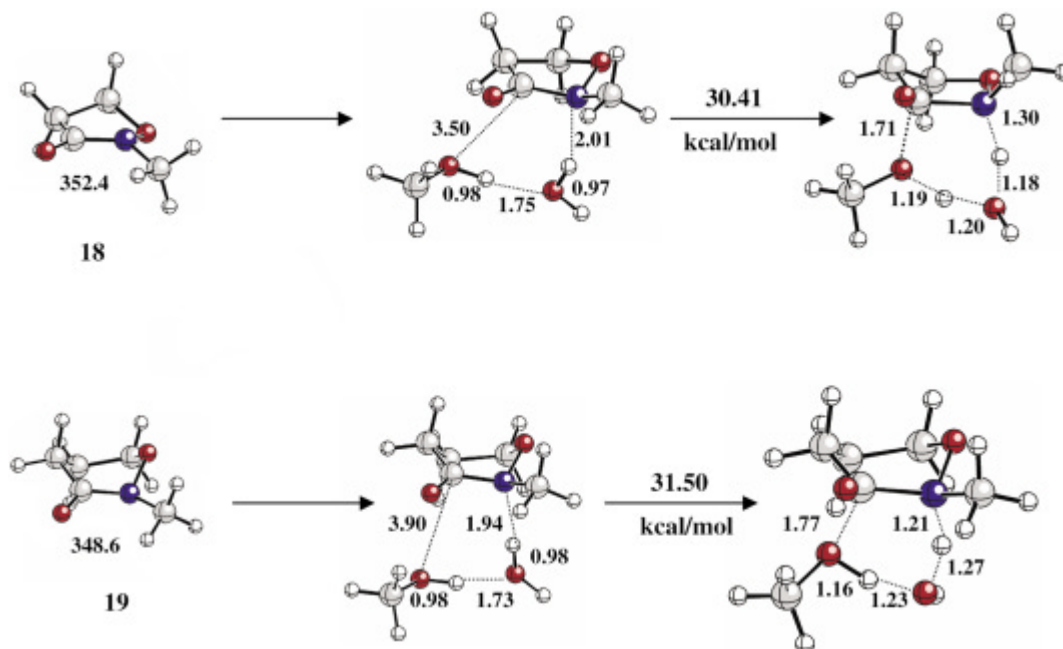




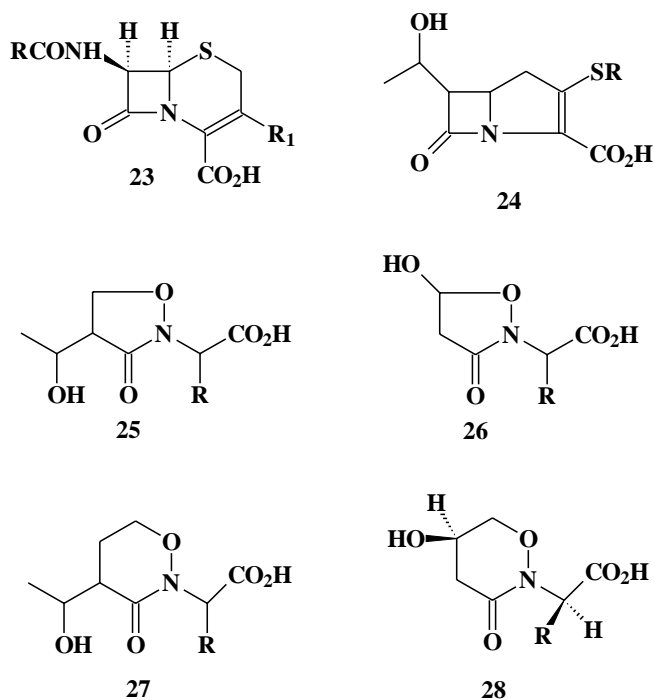
**Fig. 3.** Left: 3–21G optimized structures and the sum of the angles at nitrogen in **18** and **19**. Centre: 3–21G reactant complexes for the methanolyse of **18** and **19**, with catalysis by one water molecule. Right: 3–21G transition structures. The “barriers” are based on single point MP2/6–31G\* calculations.



afforded all four stereoisomers of **20** (R = phenylacetyl, R' = Me) (35). However, none of these compounds exhibited activity vs. *Staphylococcus aureus* or *Escherichia coli*. Likewise, phenoxyacetylation of L-cycloserine, followed by coupling to allyl 2-chloro-2-ethoxyacetate, deprotection, and separation of isomers yielded **20** (R = phenoxyacetyl, R' = OEt) (36), which were inactive against *S. aureus* and *E. coli* at concentrations up to 1000 µg/mL. Although **21** has been claimed to have antibacterial activity (37), this claim cannot be confirmed (38); **22** is also inactive (38).

The penicillin pharmacophore consists of a reactive  $\beta$ -lactam ring with an ionizable acidic group located near the azetidinone nitrogen (24, 39, 40) and, unless the  $\beta$ -lactam ring is exceptionally reactive (41), a hydrogen-bond donor located near the azetidinone carbonyl group (42). In penicillins and cephalosporins (**23**), the hydrogen-bond donor is the N–H of the acylamino side chain, geminal to the carbonyl carbon. In the carbapenems (**24**) (43), the hydrogen-bond donor is the exocyclic hydroxyl group of the side chain, two atoms removed from the carbonyl carbon. A possible five-membered cyclic hydroxamate surrogate of a carbapenem could have an exocyclic beta hydroxyl group, as in **25**, or an endocyclic beta hydroxyl group, as in the hemiacetal **26**. The corresponding six-membered cyclic hydroxamates are **27** and **28**.

Figure 4 shows the PM3-optimized (44) global minimum of penicillin G and a PM3-optimized conformation of the  $\beta$ -lactam and carbapenem surrogate 2R-(5R-hydroxy-3-oxo-[1,2]oxazinan-2-yl)-propionic acid (**29**, R = Me). This compound is an amino acid (D-alanine) whose nitrogen atom is enclosed in the [1,2]oxazinan-3-one ring. Despite the (as yet unexplained) absence of activity in **16–18**, we decided to pursue syntheses related to **29**. This paper reports non-stereospecific routes to **29**, R = H (glycine) and R = Me



(alanine), and evidence of antibacterial activity in these compounds, with significantly greater activity in the alanine derivative.

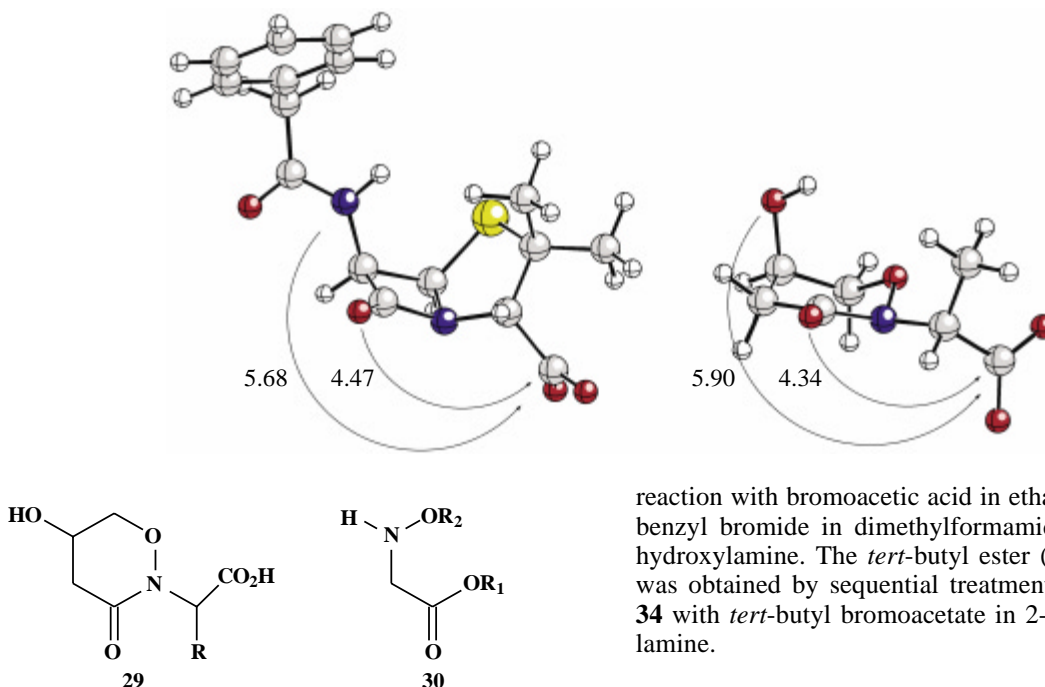
## Results and discussion

### Syntheses in the glycine series

The O-benzyl ethyl ester of N-hydroxyglycine (**30**, R<sub>1</sub> = Et, R<sub>2</sub> = Bn) was synthesized by reaction of O-benzylhy-

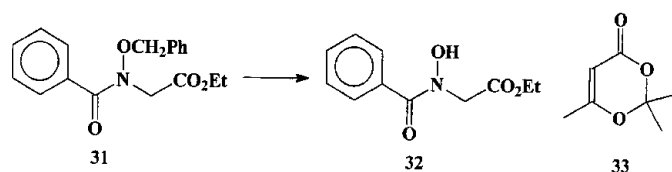


**Fig. 4.** Left: Carboxyl carbon to side chain nitrogen and carboxyl carbon to  $\beta$ -lactam oxygen distances in PM3-optimized penicillin G. Right: Carboxyl carbon to side chain oxygen and carboxyl carbon to C3 carbonyl oxygen distances in one of the conformations of 2*R*-(5*R*-hydroxy-3-oxo-[1,2]oxazinan-2-yl)-propionic acid.



droxylamine hydrochloride with glyoxylic acid in refluxing ethanol (45) and reduction of the oxime with pyridine-borane (46).

Benzoylation yielded **31**, which was debenzylated with aluminium chloride and anisole in nitromethane (47). Since the same compound (**32**) was obtained by direct benzoylation of *N*-hydroxyglycine ethyl ester (**30**,  $R_1 = \text{Et}$ ,  $R_2 = \text{H}$ ), it was concluded that this ester undergoes *N*- and not *O*-acylation. This permitted an approach to **29**,  $R = \text{H}$ , based on *N*-hydroxyglycine or one of its esters and a four-carbon synthon. A large number of these were examined, including vinylacetic acid, cyclic anhydrides, 3,4-dihydroxybutanoic acid,  $\gamma$ -butyrolactone, diketene, and the diketene-acetone adduct 2,2,6-trimethyl-4*H*-1,3-dioxin-4-one (**33**).



Scheme 1 (48–50) summarizes the syntheses of the ethyl, benzyl, and *tert*-butyl esters of *N*-hydroxyglycine (**30**,  $R_1 = \text{Et}$ ,  $\text{Bn}$ , *t*-Bu,  $R_2 = \text{H}$ ). *E*-Benzaldoxime was isomerized to the *Z*-isomer **34** with hydrogen chloride in refluxing toluene. Reaction of the sodium salt with ethyl bromoacetate in ethanol afforded *N*-benzylideneglycine *N*-oxide ethyl ester **35**, and **30** ( $R_1 = \text{Et}$ ,  $R_2 = \text{H}$ ) was obtained in 80% yield when **35** was treated with hydroxylamine. The benzyl ester (**30**,  $R_1 = \text{Bn}$ ,  $R_2 = \text{H}$ ) was synthesized from the sodium salt of **34** by

reaction with bromoacetic acid in ethanol, esterification with benzyl bromide in dimethylformamide, and treatment with hydroxylamine. The *tert*-butyl ester (**30**,  $R_1 = t\text{-Bu}$ ,  $R_2 = \text{H}$ ) was obtained by sequential treatment of the sodium salt of **34** with *tert*-butyl bromoacetate in 2-propanol and hydroxylamine.

#### Vinylacetic acid as a synthon

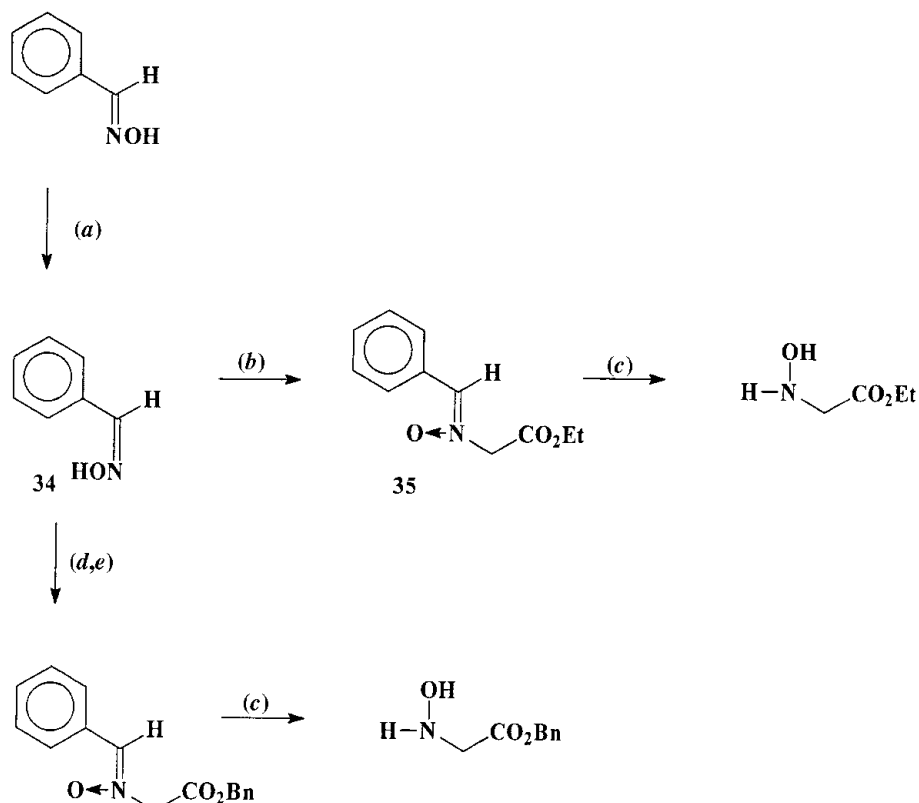
Dicyclohexylcarbodiimide coupling of vinylacetic acid with **30** ( $R_1 = \text{Et}$ ,  $R_2 = \text{H}$ ) gave **36**, which, like **32**, exhibited infrared absorption at  $1625\text{ cm}^{-1}$ . Bromination of **36** in chloroform at room temperature afforded a dibromide, which, upon exposure to sodium bicarbonate, yielded a colourless oil whose elemental analysis and mass, infrared, and proton NMR spectra were consistent with the isoxazolidinone structure **37**,  $X = \text{Br}$ . The infrared absorptions at  $1710$  and  $1755\text{ cm}^{-1}$  were assigned to the carbonyl groups of the ester and isoxazolidinone ring. The proton NMR spectrum showed a downfield shift of the tertiary hydrogen from  $4.55\text{ ppm}$  in the dibromide to  $4.80\text{ ppm}$  in **37**. The EI mass spectrum exhibited peaks at  $m/z$  85, 93, and 95, which were assigned to **38** and the bromomethyl side chain of **37**. The presence of a peak at  $m/z$  85 was used subsequently to recognize the presence of a 5-substituted isoxazolidinone ring.

The bromide **37** ( $X = \text{Br}$ ) was stable to the action of silver acetate in refluxing acetic acid, sodium formate in dimethylformamide (51), potassium phthalimide in refluxing toluene (52), sodium azide and tetrabutylammonium bromide in refluxing benzene (53), and triethylamine and formic acid in acetonitrile (54). The preference for cyclization to a five-membered ring (55) and the stability of the  $\text{Br-C-C-ON}$  moiety to nucleophilic displacement (56) suggested a synthesis of **39**, a structural isomer of the target compound **29** ( $R = \text{H}$ ). Coupling of **30**,  $R_1 = \text{Bn}$ ,  $R_2 = \text{H}$ , with vinylacetic acid and iodination with iodine and sodium bicarbonate in acetonitrile (57) gave **37** ( $X = \text{I}$ ) as the benzyl ester. Peracid oxidation (58), followed by hydrogenolysis, yielded **39**.

Reaction of the alkene **36** with *N*-bromosuccinimide or *N*-bromoacetamide in methanol, followed by a bicarbonate wash, afforded three products, the bromide **37** and a 1:1 mixture of **40** and **41**. The GC-MS of this mixture exhibited



**Scheme 1.** Reagents and conditions: (a) HCl, toluene; then NaOH, NH<sub>4</sub>Cl, Et<sub>2</sub>O; (b) ROH, Na; then BrCH<sub>2</sub>CO<sub>2</sub>Et; (c) NH<sub>2</sub>OH; (d) BrCH<sub>2</sub>CO<sub>2</sub>H; (e) BnBr, Et<sub>3</sub>N, DMF.



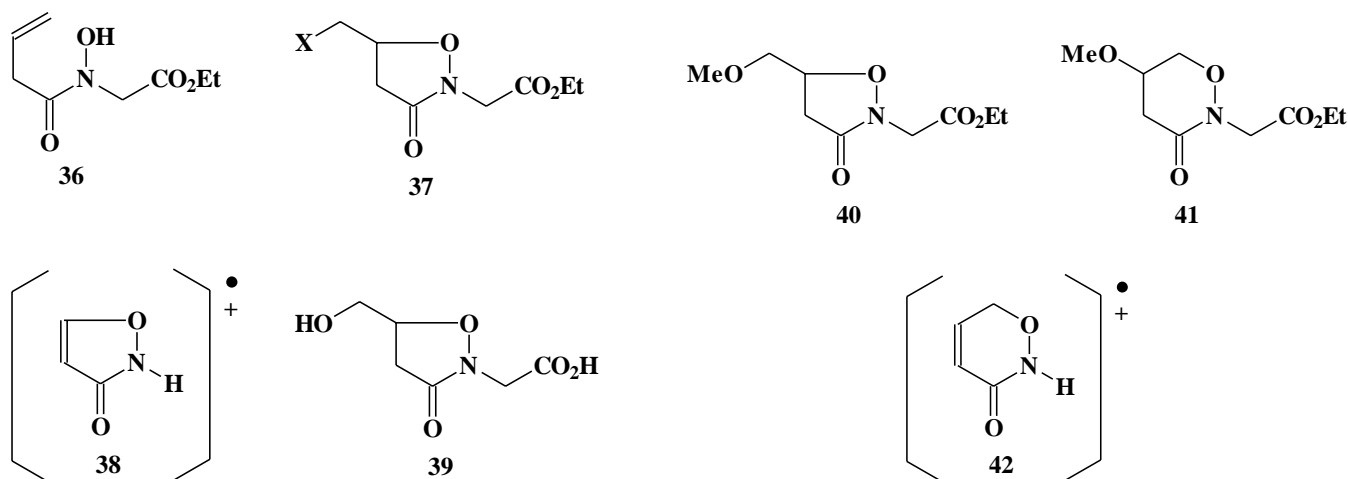
peaks at 8.07 min, with an EI-MS fragmentation at  $m/z$  99, assigned to **42**, and at 8.43 min, with the EI-MS fragmentation at  $m/z$  85 previously assigned to **38**. The <sup>1</sup>H NMR spectra of **40** and **41** and related compounds are summarized in Tables 2 and 3.

#### Cyclic anhydrides as synthons

Following Procter et al. (59), reaction of the benzyl ester **30** (R<sub>1</sub> = Bn, R<sub>2</sub> = H) with a cyclic anhydride, followed by cyclization with carbodiimide, afforded the 3,6-diones **43–45** from, respectively, succinic anhydride, acetoxy succinic anhydride, and maleic anhydride.

#### 3,4-Dihydroxybutanoic acid as a synthon

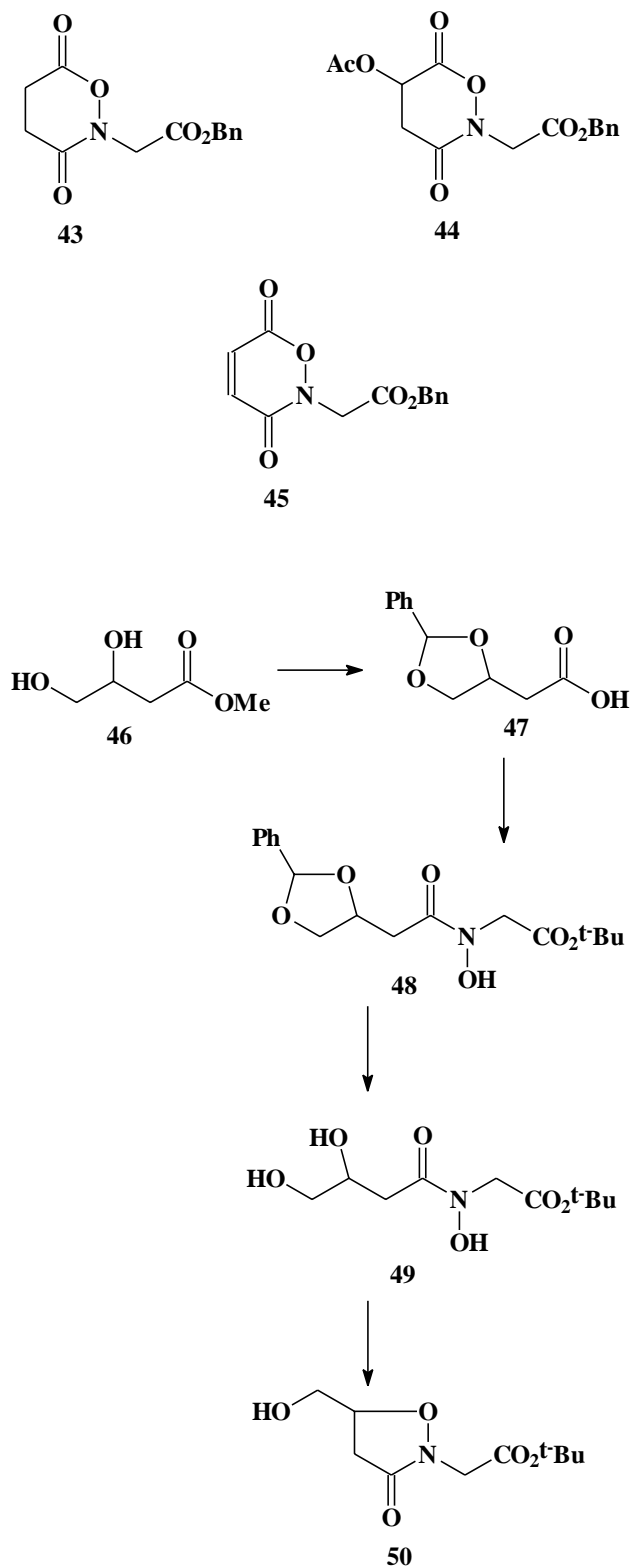
Reaction of methyl 3,4-dihydroxybutanoate (**46**) (60, 61) with benzaldehyde dimethyl acetal and a catalytic amount of *p*-toluenesulfonic acid monohydrate in dimethylformamide (62), followed by alkaline hydrolysis, yielded the acid **47**. This was coupled to the *tert*-butyl ester of *N*-hydroxyglycine to give **48**, and hydrogenolysis yielded **49**. The reaction of **49** with triphenylphosphine and diethyl azodicarboxylate in refluxing tetrahydrofuran (63) gave the isoxazolidinone **50**. Deprotection with trifluoroacetic acid produced the hydroxyacid **39**. Alternative cyclization – Mitsunobu conditions (63) did not give promising results.





**Table 2.**  $^1\text{H}$  NMR spectra of isoxazolidin-3-ones with a  $\text{CH}_2\text{X}$  substituent at C5.

	R = Me <sup>d</sup> ; X = Br		R = Et <sup>d</sup> ; X = I		R = Et <sup>d</sup> ; X = Br		R = Et <sup>d</sup> ; X = I		R = Et <sup>d</sup> ; X = Br		R = Et <sup>d</sup> ; X = I		R = Et <sup>d</sup> ; X = Br		R = Et <sup>d</sup> ; X = I		R = Et <sup>d</sup> ; X = Br		R = Et <sup>d</sup> ; X = I		R = Me <sup>d</sup> ; X = OMe		R = Et <sup>d</sup> ; X = OMe		R = <i>t</i> -Bu <sup>d</sup> ; X = OMe	
	$\delta$	$J$	$\delta$	$J$	$\delta$	$J$	$\delta$	$J$	$\delta$	$J$	$\delta$	$J$	$\delta$	$J$	$\delta$	$J$	$\delta$	$J$	$\delta$	$J$	$\delta$	$J$	$\delta$	$J$	$\delta$	$J$
	(ppm)	(Hz)	(ppm)	(Hz)	(ppm)	(Hz)	(ppm)	(Hz)	(ppm)	(Hz)	(ppm)	(Hz)	(ppm)	(Hz)	(ppm)	(Hz)	(ppm)	(Hz)	(ppm)	(Hz)	(ppm)	(Hz)	(ppm)	(Hz)	(ppm)	(Hz)
H <sub>a</sub>	4.78		4.78		4.67		4.67		4.78		4.67		4.78		4.67		4.78		4.67		4.74		4.74		4.73	
H <sub>b</sub>	4.29	17.0	4.29	17.0	4.26	17.0	4.26	17.0	4.29	17.0	4.26	17.0	4.29	17.0	4.26	17.0	4.29	17.0	4.26	17.0	4.28	17.8	4.28	17.8	4.20	17.7
H <sub>c</sub>	4.28	17.0	4.28	17.0	4.24	17.0	4.24	17.0	4.28	17.0	4.24	17.0	4.28	17.0	4.24	17.0	4.28	17.0	4.24	17.0	4.22	17.8	4.22	17.8	4.12	17.7
H <sub>d</sub>	3.58	10.8	3.58	10.8	3.39	10.4	3.39	10.4	3.58	10.8	3.39	10.4	3.58	10.8	3.39	10.4	3.58	10.8	3.39	10.4	3.62	10.9	3.62	10.9	3.63	10.9
	5.5		5.5		5.5		5.5		5.5		5.5		5.5		5.5		5.5		5.5		6.2		6.2		6.2	
H <sub>e</sub>	3.53	10.8	3.53	10.8	3.35	10.4	3.35	10.4	3.53	10.8	3.35	10.4	3.53	10.8	3.35	10.4	3.53	10.8	3.35	10.4	3.54	10.9	3.54	10.9	3.55	10.9
	6.7		6.8		6.8		6.8		6.7		6.8		6.7		6.8		6.7		6.8		3.6		3.6		3.6	
H <sub>f</sub>	3.01	16.8	3.01	16.8	3.00	16.8	3.00	16.8	3.01	16.8	3.00	16.8	3.01	16.8	3.00	16.8	3.01	16.8	3.00	16.8	2.81	16.6	2.81	16.6	2.81	16.6
	8.2		8.2		8.2		8.2		8.2		8.2		8.2		8.2		8.2		8.2		8.2		8.2		8.2	
H <sub>g</sub>	2.83	16.8	2.83	16.8	2.76	16.8	2.76	16.8	2.83	16.8	2.76	16.8	2.83	16.8	2.76	16.8	2.83	16.8	2.76	16.8	2.75	16.6	2.75	16.6	2.74	16.6
	7.0		7.0		7.2		7.2		7.0		7.2		7.0		7.2		7.0		7.2		8.8		8.8		8.8	

<sup>a</sup>In CDCl<sub>3</sub>.  
<sup>b</sup>In D<sub>2</sub>O.**Butyrolactone as a synthon**

Attempts to prepare compounds of type **51** by a direct reaction of *N*-hydroxyglycine esters with butyrolactone, using trimethylaluminium (**64**) or aluminium trichloride (**65**) as catalysts, were not successful. Therefore, using the method of Larcheveque and Henrot (**66**), butyrolactone was converted to the iodo acid **51**, X = I, with trimethylsilyl iodide

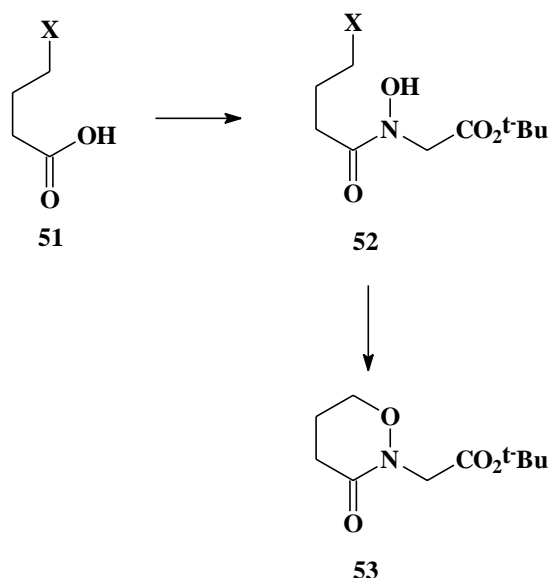


**Table 3.**  $^1\text{H}$  NMR spectra of 1,2-oxazin-3-ones.

	R = OMe <sup>a</sup> ; R' = Me		R = OMe <sup>a</sup> ; R' = Et		R = OMe <sup>a</sup> ; R' = <i>t</i> -Bu		R = OH <sup>b</sup> ; R' = Na	
	$\delta$ (ppm)	<i>J</i> (Hz)	$\delta$ (ppm)	<i>J</i> (Hz)	$\delta$ (ppm)	<i>J</i> (Hz)	$\delta$ (ppm)	<i>J</i> (Hz)
H <sub>a</sub>	3.99		3.99		4.01		4.49	
H <sub>b</sub>	4.51	17.8	4.51	17.8	4.43	17.7	4.28	17.4
H <sub>c</sub>	4.22	17.8	4.23	17.8	4.13	17.7	4.09	17.4
H <sub>d</sub>	4.32	11.9	4.33	11.9	4.34	11.9	4.29	12.0
		6.0		6.0		6.0		4.6
H <sub>e</sub>	4.07	11.9	4.07	11.9	4.07	11.9	4.02	12.0
		3.2		3.2		3.6		3.2
H <sub>f</sub>	2.79	16.0	2.80	16.0	2.90	15.6	2.92	16.8
		5.8		5.8		5.9		5.9
H <sub>g</sub>	2.67	16.0	2.68	16.0	2.75	15.6	2.52	16.8
		4.7		4.7		4.8		3.2

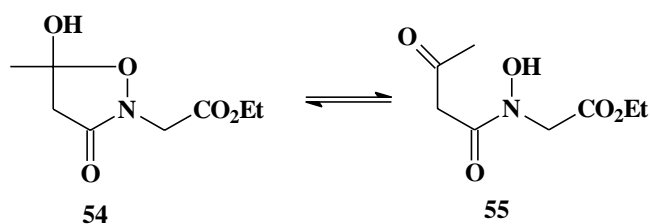
<sup>a</sup>In CDCl<sub>3</sub>.<sup>b</sup>In D<sub>2</sub>O.

in refluxing dichloromethane, and this acid was coupled to the *tert*-butyl ester of *N*-hydroxyglycine to give **52**. Cyclization to **53** was accomplished using 1,8-diazabicyclo[5.4.0]undec-7-ene (DBU).



#### 2,2,6-Trimethyl-4H-1,3-dioxin-4-one and diketene as synthons

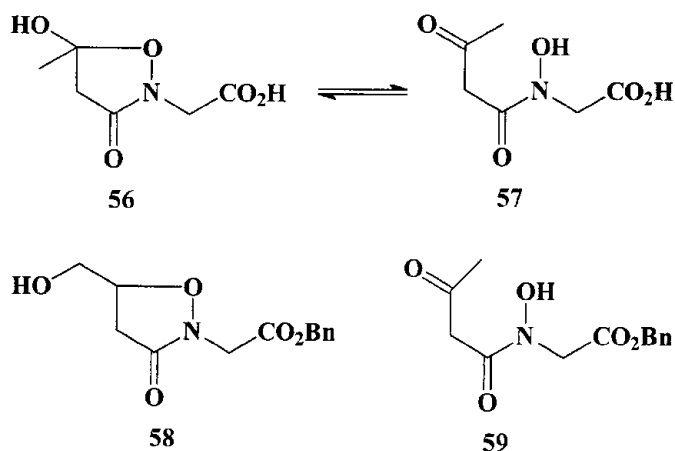
The reaction of the O-benzyl ethyl ester **30** (R<sub>1</sub> = Et, R<sub>2</sub> = Bn) with the diketene–acetone adduct **33** in refluxing toluene (**67**), followed by hydrogenolysis, yielded the hemiketal **54**, which, in chloroform-*d*, exists as an 85:15 tautomeric mixture of esters **54** and **55**.

**Table 4.**  $^1\text{H}$  NMR spectra of 5-hydroxy-5-methylisoxazolidinones.

	<b>56</b> , R = H <sup>a</sup>		<b>54</b> , R = Et <sup>b</sup>		<b>58</b> , R = Bn <sup>b</sup>	
	$\delta$ (ppm)	<i>J</i> (Hz)	$\delta$ (ppm)	<i>J</i> (Hz)	$\delta$ (ppm)	<i>J</i> (Hz)
H <sub>b</sub>	4.39	17.7	4.51	18.2	4.53	18.1
H <sub>c</sub>	4.20	17.7	4.12	18.2	4.19	18.1
H <sub>d</sub>	3.17	17.2	3.02	16.8	3.00	16.8
H <sub>e</sub>	2.77	17.2	2.76	16.8	2.76	16.8

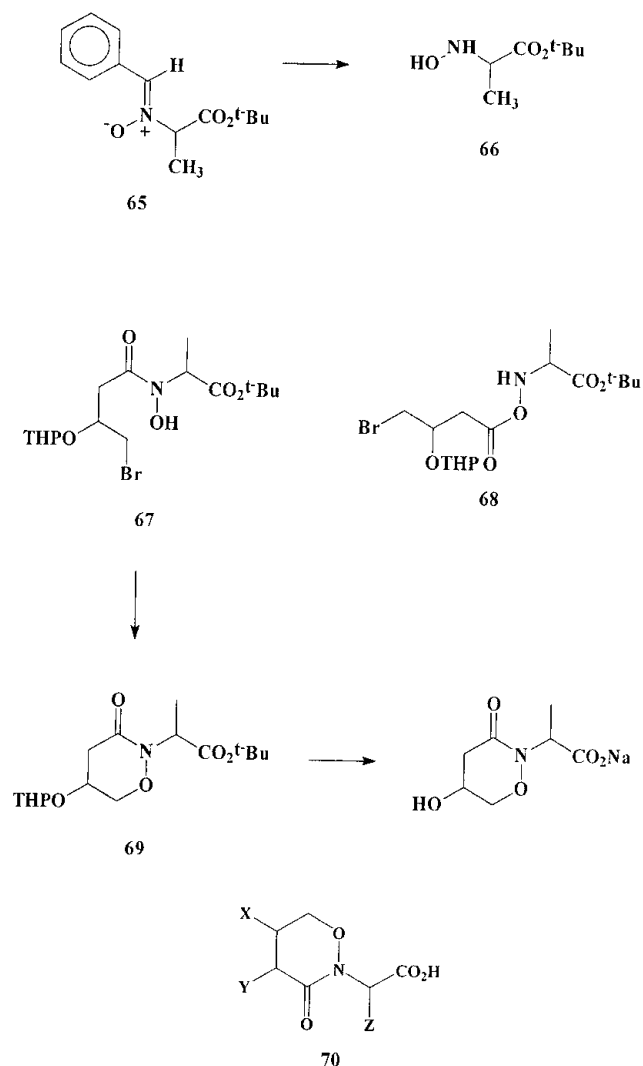
<sup>a</sup>In D<sub>2</sub>O.<sup>b</sup>In CDCl<sub>3</sub>.

The preparation of the acid **56** (which, like **39**, is a structural isomer of the target compound **29**, R = H) was accomplished using diketene in place of the diketene–acetone adduct (**68**). Reaction with the benzyl ester of *N*-hydroxyglycine afforded a product, which, in chloroform-*d*, exists as an 83:17 tautomeric mixture of benzyl esters **58** and **59**. Hydrogenolysis produced **56** and **57** as a 2:1 tautomeric mixture in water solvent. Table 4 summarizes the  $^1\text{H}$  NMR spectra of **54**, **56**, and **58**.



The synthesis of **29**, R = H, is summarized in Scheme 2. Bromination of diketene at  $-25^\circ\text{C}$  in the presence of benzyl alcohol afforded benzyl bromoacetoacetate **60** in quantitative yield via the acyl bromide. Reduction with sodium boro-





hydride in tetrahydrofuran–methanol produced the bromohydrin ester **61** in 80% yield. Protection of the hydroxyl group with dihydropyran and one crystal of para-toluenesulfonic acid in dichloromethane (69) yielded the tetrahydropyranyl derivative **62** as a mixture of diastereomers in an overall yield of 64% from diketene. The benzyl ester **62** was deprotected by hydrogenolysis to give **63**, and this was coupled to the *tert*-butyl ester of *N*-hydroxyglycine. Cyclization with 1,8-diazabicyclo[5.4.0]undec-7-ene (DBU) and removal of both protecting groups with trifluoroacetic acid produced the target compound.

The sodium salt, which is chemically stable, was isolated by successive treatment of **64** with trifluoroacetic acid and sodium bicarbonate. The  $^1\text{H}$  NMR spectrum is summarized in Table 3.

#### Synthesis of **29**, $R = \text{Me}$

For the synthesis of *N*-hydroxy-α-alanine, the nitron **65** was prepared in 40% yield by the reaction of the sodium salt of **34** with *tert*-butyl α-bromopropionate in isopropanol. Hydrolysis with hydroxylamine hydrochloride in the presence of sodium methoxide then gave the racemic *N*-hydroxyalanine ester **66** in 71% yield. Coupling of **66** to **63** using dicyclohexylcarbodiimide produced a mixture of *N*-acylated

diastereomers **67** in 54% yield and also, in contrast to the observations made previously with *N*-hydroxyglycine esters, the *O*-acylated compounds **68**. Cyclization of **67** using DBU yielded the oxazinone **69** in 65% yield. Deprotection with trifluoroacetic acid or formic acid, followed by extraction with sodium bicarbonate and lyophilization produced the sodium salt as a mixture of diastereomers.

#### Bioassay results

Bioassays were performed on agar plates seeded with *M. luteus* (see Experimental). Figure 5 shows the zones of inhibition obtained with **29**,  $R = \text{H}$ , and its two structural isomers **39** and **56** compared with the results for penicillin G and desacetoxycephalosporin G. It can be seen that the racemate **29** exhibits some activity but **39** and **56** are inactive at 1000 μg. Table 5 summarizes semiquantitative test data relative to penicillin G and desacetoxycephalosporin G, expressed as (diameter of the zone in mm)/(μM of test material) for **29**,  $R = \text{H}$ , and **29**,  $R = \text{Me}$ . Although both compounds are only weakly active, the alanine surrogate, as a mixture of stereoisomers, is ca. 50 times more active than the glycine surrogate. These findings have encouraged us to continue with this programme and to attempt to devise stereospecific routes to compounds having the general structure **70**. These studies are reported elsewhere (38).

#### Experimental

All solvents were dried and distilled before use according to standard literature procedures (70). Except where indicated, chemicals were of the highest available purity from Aldrich. All reactions were performed under dry nitrogen using oven-dried (140 °C, 24 h) glassware. The glassware was allowed to cool in a desiccator under vacuum and assembled cold, capped with rubber septa, and evacuated with dry nitrogen gas. Both  $^1\text{H}$  and  $^{13}\text{C}$  nuclear magnetic resonance (NMR) spectra were recorded on a Bruker Model AMX 400 Spectrometer operating at 400.1 and 100.6 MHz, respectively. Chemical shifts ( $\delta$ ) are reported in parts per million (ppm) relative to tetramethylsilane (TMS) in an appropriate deuterated solvent.  $^1\text{H}$  NMR data are reported in the following manner: chemical shift, integration, peak multiplicity, coupling constants, and identification. The peak multiplicities are abbreviated as s (singlet), d (doublet), t (triplet), q (quartet), dd (doublet of doublets), ddd (doublet of doublets of doublets), m (multiplet), etc.  $^{13}\text{C}$ MR data are reported as  $\delta$  values in ppm downfield from tetramethylsilane. Infrared (IR) spectra were recorded on a Bomen–Hartmann–Braun spectrometer (1% KBr or 1% solution). High-resolution mass spectra refer to either direct inlet electron impact (EI) measurements or chemical ionization (CI) measurements, using isobutane, and were provided by Dr. G. Eigendorf at the University of British Columbia. Low-resolution mass spectra refer to direct inlet EI measurements or CI measurements, using isobutane, or fast-atom bombardment (FAB), employing xenon gas, on a Kratos MS50 Spectrometer operated at 70 eV by G. Owens at Simon Fraser University. Melting points (mp) were determined on a Fisher–Johns apparatus and are uncorrected. Analytical thin-layer chromatography was carried out on precoated Merck Silica Gel 60 F-254 plates with aluminium backing. Spots



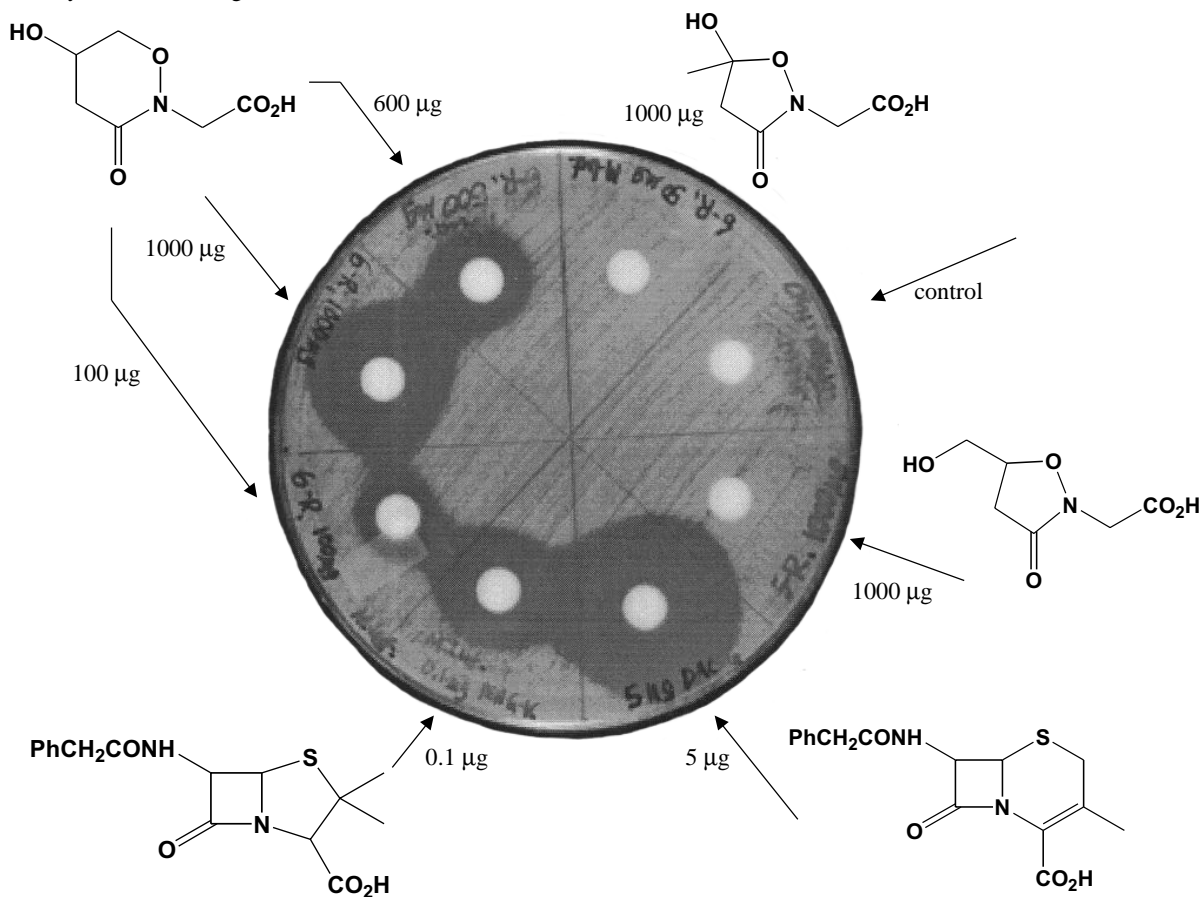
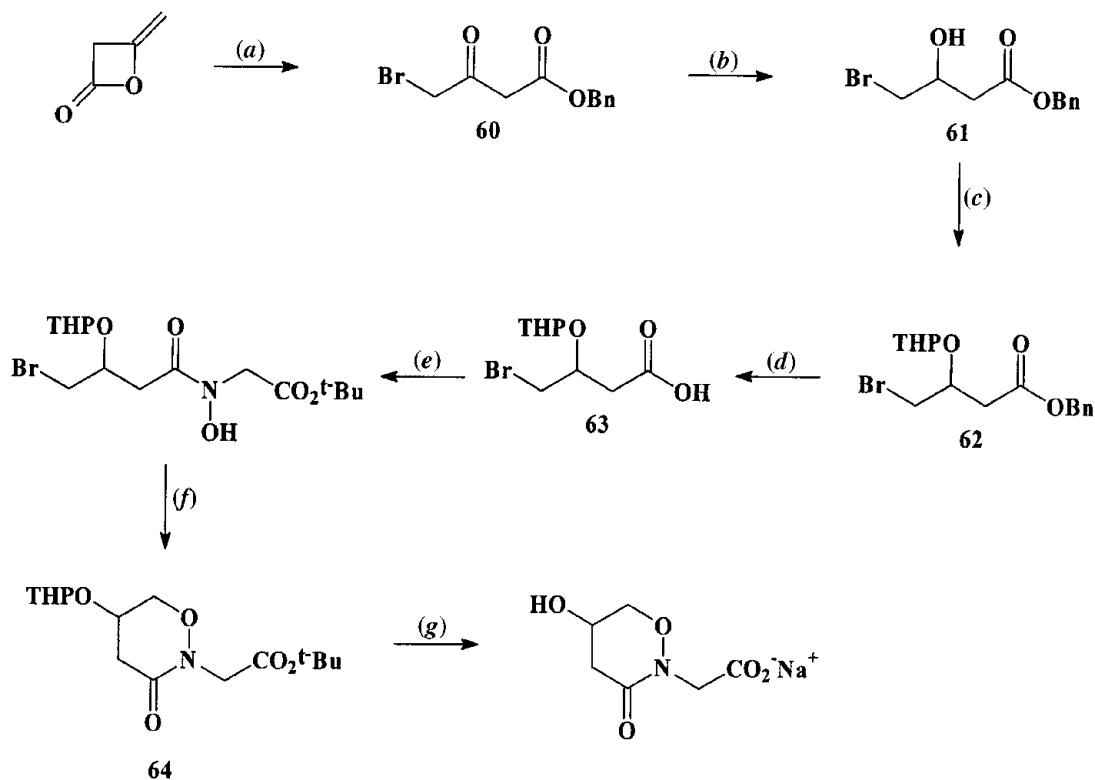




**Table 5.** Zones of inhibition vs. *M. luteus*.

Compound	Weight (µg)	Moles (µM)	Zone size (mm)	Ratio (mm/µM)
Pen G <sup>a</sup>	0.1	$2.99 \times 10^{-4}$	25	83 600
DACG <sup>b</sup>	5	$1.51 \times 10^{-2}$	38	2 520
<b>29</b> (R = H)	600	3.05	21	7
<b>29</b> (R = Me)	12	0.0569	20	350

<sup>a</sup>Penicillin G (**4**, R = benzyl).<sup>b</sup>Desacetoxycephalosporin G (**23**, R = benzyl, R' = Me).

were observed under short-wavelength ultraviolet light or were visualized with iodine vapour, ninhydrin, or ceric sulfate. Flash column chromatography was carried out on Merck Silica Gel 60 (230–400 Mesh), according to the method of Still et al. (71) unless stated otherwise, using only distilled solvents under dry nitrogen gas. Elemental analyses were performed by M.K. Yang on a Carlo Erba model 1106 elemental analyzer at Simon Fraser University.

### Z-Benzaldoxime

Benzaldehyde (5.3 g, 0.05 mol) (Fisher) and hydroxylamine hydrochloride (3.6 g, 0.052 mol) (Mallinckrodt) were added successively at room temperature to a stirred solution of sodium hydroxide (5 g, 0.125 mol). Stirring was continued until a clear solution was obtained and the temperature had increased to 70 °C. The reaction mixture was cooled to 35 °C, and carbon dioxide was passed in until the pH had decreased from 14 to 10. The two layers were then separated. The aqueous layer was extracted with toluene (4 × 25 mL), and the combined organic phase was dried over anhydrous magnesium sulfate, filtered, and poured into a 250 mL three-necked flask equipped with a large-bore gas inlet tube, stirrer, thermometer, and condenser. The flask was heated on an oil bath, and 20 mL of toluene was removed by distillation. The remaining solution was reheated to boiling, the oil bath was removed, and a strong flow of anhydrous hydrogen chloride was sparged through the vigorously stirred solution. Addition of the gas was continued until the oil that first separated had solidified and the temperature had fallen to 50 °C. The resulting white slurry was cooled to 10 °C in an ice-water bath and filtered. The white crystalline solid was washed with toluene (2 × 25 mL) and hexane and stored in a desiccator over potassium hydroxide pellets. Diethyl ether (50 mL) was added to a stirred solution of sodium hydroxide (4 g, 0.1 mol) in water (40 mL). The mixture was cooled to 10 °C and the crude Z-benzaldoxime hydrochloride was added rapidly with stirring until all of the solid had dissolved. A solution of ammonium chloride (10 g, 0.187 mol) (Fisher) in water (40 mL) was added, and the mixture was stirred until a clear solution was obtained (1 min). The two layers were separated, and the aqueous layer was extracted with ether (2 × 25 mL). The combined ethereal extracts were dried over anhydrous magnesium sulfate and concentrated. Hexane (40 mL) was added to the white slurry and the mixture concentrated again. Another 40 mL of hexane were added, the mixture was filtered, and the solid was air dried until a constant weight was obtained. The Z-benzaldoxime was obtained as white needles (4.26 g, 70%); mp 131 °C (lit. (45) mp 130 °C). <sup>1</sup>H NMR (CDCl<sub>3</sub>) δ: 8.19 (1H, s, CH=N), 7.60 (2H, m, ArH), 7.45 (3H, m, ArH).

4.71 (2H, s), 4.26 (2H, q) 1.29 (3H, t). EI-MS (*m/z*): 121 ([M]<sup>+</sup>). Anal. calcd. for C<sub>7</sub>H<sub>7</sub>NO: C 69.42, H 5.79, N 11.57; found: C 69.44, H 5.96, N 10.99.

### N-Benzylideneglycine N-oxide ethyl ester (35)

Ethyl bromoacetate (0.244 mL, 0.367 g, 2.2 mmol) was added to a stirred solution of sodium (0.46 g, 0.02 g-atom) and Z-benzaldoxime (0.242 g, 2.0 mmol) in ethanol (15 mL). Stirring was continued until a wet pH 7 was reached. The reaction mixture was poured into water (20 mL), extracted with ether (2 × 20 mL), dried, and concentrated under reduced pressure. The golden yellow oil was purified by flash chromatography on silica gel (4.5 g) (40% ethyl acetate – hexane) and subsequently crystallized from ethyl acetate – hexane. The pale yellow crystals weighed 0.298 g (73%); mp 53 °C. IR (film, cm<sup>-1</sup>): 1743 (C=O), 1584 (C=N). <sup>1</sup>H NMR (CDCl<sub>3</sub>) δ: 8.19 (1H, s, (CH=N), 7.60 (2H, m, ArH), 7.45 (3H, m, ArH), 4.71 (2H, s), 4.26 (2H, q), 1.29 (3H, t). EI-MS (*m/z*): 207 ([M]<sup>+</sup>). Anal. calcd. for C<sub>11</sub>H<sub>13</sub>NO<sub>3</sub>: C 63.76, H 6.32, N 6.76; found: C 64.04, H 6.41, N 6.60.

### N-Hydroxyglycine ethyl ester

#### Method A

The nitron **35** (180 mg, 0.87 mmol) was added to a stirred suspension of sodium methoxide (64.8 mg, 1.2 mmol) (Anachemia) and hydroxylamine hydrochloride (83.4 mg, 1.2 mmol) (Mallinckrodt) in methanol (3 mL). The reaction mixture was heated on a water bath (40 °C) with stirring until the wet pH was slightly acidic (2 min) and then concentrated under reduced pressure. The residue was triturated with toluene (2 × 10 mL), concentrated, and purified by flash chromatography (5 g silica gel and 40% ethyl acetate – hexane) to give a pale yellow oil (82.7 mg, 80%). IR (film, cm<sup>-1</sup>): 3319 (O-H, br), 3267 (N-H, m), 1735 (C=O). <sup>1</sup>H NMR (CDCl<sub>3</sub>) δ: 5.89 (2H, br, NH-OH), 4.23 (2H, q, OCH<sub>2</sub>CH<sub>3</sub>), 3.67 (2H, s), 1.29 (3H, t, OCH<sub>2</sub>CH<sub>3</sub>).

#### Method B

A mixture of glyoxylic acid (1.094 g, 0.014 mol) (Eastman), hydroxylamine hydrochloride (1.00 g, 14 mmol) (Mallinckrodt), and *p*-toluenesulfonic acid (0.273 g, 1 mmol) (Fisher) in dry ethanol (8 mL) was heated under reflux for 5 h with removal of water using a Dean-Stark trap. The reaction mixture was concentrated, ether (100 mL) and saturated sodium bicarbonate (100 mL) were added, and the mixture was stirred until the phases became clear. The organic layer was separated, washed with saturated ammonium chloride, dried over anhydrous magnesium sulfate, and concentrated under reduced pressure to yield ethyl glyoxylate oxime (1.11 g, 66%). IR (film, cm<sup>-1</sup>): 3347 (OH, br), 1725 (C=O, s), 1623 (C=N, m). <sup>1</sup>H NMR (CDCl<sub>3</sub>) δ: 9.55 (1H, b, =NOH), 7.56 (1H, s, HC=NOH), 4.31 (2H, q, CO<sub>2</sub>CH<sub>2</sub>CH<sub>3</sub>), 1.33 (3H, t, CO<sub>2</sub>CH<sub>2</sub>CH<sub>3</sub>). CI-MS (*m/z*): 118 ([M + 1]). Anal. calcd. for C<sub>4</sub>H<sub>7</sub>NO<sub>3</sub>: C 41.03, H 5.98, N 11.96; found: C 41.41, H 6.12, N 11.43.

Ethanollic hydrogen chloride (6.76 mL of a 7 N solution prepared by diluting 30 mL of 36% HCl to 50 mL with ethanol) was added to a stirred solution of the oxime ethyl ester (1.0 g, 8.5 mmol), and pyridine–borane complex (2.16 mL



of 8 mol/L, 17.28 mmol) in ethanol (10 mL) was added at such a rate that the reaction temperature remained below 40 °C. Stirring was continued for 8 h, while the reaction was monitored by thin layer chromatography (TLC). The reaction mixture was then concentrated, and the pale yellow syrupy residue was dissolved in dichloromethane (50 mL). Sodium carbonate (4 g) was added, and the mixture was stirred at room temperature for 30 h, filtered, and the filtrate concentrated under reduced pressure. The crude oil was purified by flash chromatography (60% ethyl acetate – hexane) to give a pale yellow oil (0.673 g, 67%). CI-MS ( $m/z$ ): 120 ( $[M + 1]$ ). Anal. calcd. for  $C_4H_6NO_3$ : C 40.34, H 7.56, N 11.76; found: C 40.21, H 7.55, N 11.54.

### ***N*-Benzyloxyoxime of ethyl glyoxylate**

A mixture of glyoxylic acid (0.476 g, 6.26 mmol) (Eastman), *O*-benzylhydroxylamine hydrochloride (1.00 g, 6.26 mmol), and *p*-toluenesulfonic acid (0.12 g, 0.626 mmol) (Fisher) in dry ethanol (8 mL) was refluxed for 6 h with removal of water using a Dean-Stark trap. The reaction mixture was concentrated and dichloromethane (50 mL) was added to the yellow oily residue. The solution was washed successively with water (30 mL), saturated sodium bicarbonate (30 mL), and saturated sodium chloride (30 mL), dried over anhydrous magnesium sulfate, and concentrated under reduced pressure to give a pale yellow oil (1.08 g, 83%). IR ( $CDCl_3$ ,  $cm^{-1}$ ): 1727 (C=O), 1600 (C=N).  $^1H$  NMR ( $CDCl_3$ )  $\delta$ : 7.57 (1H, s, N=CH), 7.39 (5H, s,  $OCH_2Ph$ ), 5.32 (2H, s,  $OCH_2Ph$ ), 4.33 (2H, q,  $OCH_2CH_3$ ), 1.36 (3H, t,  $OCH_2CH_3$ ). CI-MS ( $m/z$ ): 208 ( $[M + 1]$ ). Anal. calcd. for  $C_{11}H_{13}NO_3$ : C 63.77, H 6.28, N 6.76; found: C 63.06, H 6.33, N 7.34.

### ***N*-Benzyloxyglycine ethyl ester (30, $R_1 = Et$ , $R_2 = Bn$ )**

Ethanolic hydrogen chloride (6.76 mL of a 7 N solution prepared by diluting 30 mL of 36% HCl to 50 mL with ethanol) was added to a stirred solution of the oxime (3.5 g, 16.91 mmol), and pyridine–borane (8.54 mL of 8 mol/L, 68.32 mmol) in ethanol (10 mL) was added at such a rate that the reaction temperature did not exceed 40 °C. Stirring was continued for 13.5 h with monitoring by TLC, and the solvent was then removed. The pale yellow syrup was dissolved in dichloromethane (50 mL), and the solution was washed with *N*-sodium hydroxide, dried over anhydrous sodium sulfate, and concentrated under reduced pressure. The crude oil was purified by flash chromatography using 2% ethanol in dichloromethane as the eluent. The pale yellow oil thereby obtained weighed 3.0 g (85%). IR ( $CDCl_3$ ,  $cm^{-1}$ ): 3273 (N-H, w), 1739 (C=O, s).  $^1H$  NMR ( $CDCl_3$ )  $\delta$ : 7.36 (5H, s,  $OCH_2Ph$ ), 6.13 (1H, t, N-H), 4.75 (2H, s,  $OCH_2Ph$ ), 4.24 (2H, q,  $OCH_2CH_3$ ), 3.62 (2H, d,  $NCH_2C(O)$ ), 1.30 (3H, t,  $OCH_2CH_3$ ). CI-MS ( $m/z$ ): 210 ( $[M + 1]$ ). Anal. calcd. for  $C_{11}H_{15}NO_3$ : C 63.16, H 7.18, N 6.70; found: C 63.37, H 7.01, N 7.50.

### ***N*-Benzylidene glycine *N*-oxide**

Sodium (0.46 g, 0.02 g-atom) and *Z*-benzaldoxime (1.21 g, 10 mmol) in ethanol (40 mL) were stirred until the sodium dissolved. Then bromoacetic acid (1.53 g, 11 mmol) (Lancaster) was added in one portion, with stirring. Stirring was continued for 1 h at 70 °C, and the solvent was re-

moved. A suspension of the residue in water (10 mL) was cooled, acidified with 0.1 N hydrochloric acid (9.5 mL), and filtered. The white crystals were collected and dried at 1 torr (1 torr = 133.322 Pa) to give 1.21 g (66%) of product; mp 175–177 °C (lit. (47) mp 178–179 °C). IR (KBr,  $cm^{-1}$ ): 3069, 1724, 1617. EI-MS ( $m/z$ ): 179 ( $[M]^+$ ).

### ***N*-Benzylidene-glycine *N*-oxide benzyl ester**

To a cloudy solution of *N*-benzylideneglycine *N*-oxide (0.181 g, 1.01 mmol) in dimethylformamide (2 mL) was added triethylamine (0.141 mL, 103 mg, 1.01 mmol), followed by dropwise addition of benzyl bromide (0.120 mL, 0.173 g, 1.01 mmol) (Sigma). The reaction mixture was stirred for 13 h, poured into water (10 mL), and extracted with chloroform (2  $\times$  10 mL). The chloroform extract was dried over anhydrous sodium sulfate, concentrated, and the residue was purified by column chromatography (60% ethyl acetate – hexanes) to give 0.191 g (70%) of product. IR ( $CH_2Cl_2$ ,  $cm^{-1}$ ): 3054, 1753, 1587.  $^1H$  NMR ( $CDCl_3$ )  $\delta$ : 8.25 (2H, m, Ar + =CH), 7.45–7.34 (9H, m, Ar), 5.27 (2H, s,  $CH_2Ph$ ), 4.76 (2H, s,  $CH_2$ ). EI-MS ( $m/z$ ): 269 ( $[M]^+$ ). Anal. calcd. for  $C_{16}H_{15}NO_3$ : C 71.37, H 5.58, N 5.20; found: C 71.13, H 5.80, N 5.40.

### ***N*-Hydroxyglycine benzyl ester**

A suspension of *N*-benzylideneglycine *N*-oxide benzyl ester (1.35 g, 5.02 mmol) and hydroxylamine hydrochloride (352 mg, 5.02 mmol) (Mallinckrodt) in ethanol (10 mL) was brought into solution by heating. The solution was concentrated, and the residue was taken up in ether (50 mL) and washed with saturated sodium bicarbonate (20 mL). The ether layer was separated, dried over anhydrous magnesium sulfate, and the solvent was removed under reduced pressure. The product was purified by flash chromatography (60% ethyl acetate – hexanes) to give 772 mg (85%) of white solid. IR ( $CH_2Cl_2$ ,  $cm^{-1}$ ): 3290, 3055, 1741.  $^1H$  NMR ( $CDCl_3$ )  $\delta$ : 7.36 (5H, s, Ar), 5.22 (2H, s,  $PhCH_2$ ), 3.73 (2H, s,  $NCH_2$ ). EI-MS ( $m/z$ ): 181 ( $[M]^+$ ). Anal. calcd. for  $C_8H_{11}NO_3$ : C 59.67, H 6.08, N 7.73; found: C 59.74, H 6.07, N 7.11.

### ***tert*-Butyl bromoacetate**

A solution of oxalyl chloride (6.18 mL, 8.99 g, 0.071 mol) in dichloromethane (10 mL) was added to a cooled (0 °C) solution of bromoacetic acid (8.21 g, 0.059 mol) (Lancaster) and dimethylformamide (3 drops) in dichloromethane (40 mL). The pale yellow solution was stirred for 1 h at 0 °C, then at room temperature for 3 h, concentrated to about 10 mL, and slowly added to a cooled solution of *tert*-butanol (5.255 g, 0.071 mol) and triethylamine (10.71 mL, 7.78 g, 0.077 mol) in dichloromethane (45 mL). The dark brown suspension was stirred for 45 min at 0 °C, then for 3 h at room temperature, and poured into water (60 mL). The organic layer was separated and the aqueous layer extracted with dichloromethane (2  $\times$  15 mL). The organic extract was washed with saturated sodium bicarbonate (50 mL), dried over anhydrous magnesium sulfate, and concentrated to give 4.48 g (39%) of product.  $^1H$  NMR ( $CDCl_3$ )  $\delta$ : 3.74 (2H, s), 1.47 (9H, s). CI-MS ( $m/z$ ): 197:195 (1:1).



***N*-Benzylidene glycine *N*-oxide *tert*-butyl ester**

Z-Benzaldoxime (5.64 g, 46.61 mmol) and *tert*-butyl bromoacetate (7.58 mL, 10 g, 51.27 mmol) were added successively to a solution prepared by dissolving 1.07 g (0.047 g-atom) of sodium metal in 2-propanol (120 mL). The dark brown suspension was stirred for 2 h at room temperature, poured into water (100 mL), and extracted with dichloromethane (5 × 20 mL). The combined organic extracts were dried over anhydrous magnesium sulfate and concentrated. The crude product was purified by flash chromatography (60% ethyl acetate – hexanes) to give 8.74 g (80%) of an oil. IR (CH<sub>2</sub>Cl<sub>2</sub>, cm<sup>-1</sup>): 3054, 1746, 1580, 1260. <sup>1</sup>H NMR (CDCl<sub>3</sub>) δ: 8.24 (2H, m, Ar + =CH), 7.42 (4H, m, Ar), 4.62 (2H, s, CH<sub>2</sub>), 1.51 (9H, s, *t*-Bu). CI-MS (*m/z*): 236 ([M + 1]). Anal. calcd. for C<sub>13</sub>H<sub>17</sub>NO<sub>3</sub>: C 66.38, H 7.23, N 5.96; found: C 66.78, H 7.10, N 6.01.

***N*-Hydroxyglycine *tert*-butyl ester**

The nitron (1.3 g, 5.53 mmol) was added to a stirred suspension of sodium methoxide (0.418 g, 7.74 mmol) (Anachemia) and hydroxylamine hydrochloride (0.538 g, 7.74 mmol) (Mallinckrodt) in methanol (6 mL). The reaction mixture was placed in a water bath (50 °C), stirred until all of the nitron had dissolved, and was then concentrated. The residue was dissolved in dichloromethane (50 mL), filtered, and concentrated. The resultant oil was purified by flash chromatography (60% ethyl acetate – hexanes) to give 0.650 g (80%) of the product. IR (film, cm<sup>-1</sup>): 3279, 1735. <sup>1</sup>H NMR (CDCl<sub>3</sub>) δ: 5.46 (2H, br, HNOH), 3.62 (2H, s, CH<sub>2</sub>), 1.49 (9H, s, *t*-Bu). CI-MS (*m/z*): 148 ([M + 1]). Anal. calcd. for C<sub>6</sub>H<sub>13</sub>NO<sub>3</sub>: C 48.98, H 8.84, N 9.52; found: C 49.13, H 8.65, N 9.44.

***tert*-Butyl 2-bromopropionate**

Isobutylene (2.4 g, 42.8 mmol) was condensed into a pressure bottle at -15 °C. Dioxane (6 mL) and 2-bromopropionic acid (3.5 mL, 38.9 mmol) were added, and the mixture was stirred for 5 min, warmed to -10 °C, and concentrated sulfuric acid (250 µL) was added. The bottle was sealed, the reaction mixture was stirred overnight at room temperature, and the bottle was then opened and the contents poured into dichloromethane (50 mL). The solution was washed with 20% potassium carbonate (50 mL) and water (50 mL), dried over anhydrous magnesium sulfate, and evaporated to give *tert*-butyl bromopropionate (2.17 g, 27%). <sup>1</sup>H NMR (CDCl<sub>3</sub>) δ: 4.31 (1H, q, 7.1 Hz), 1.81 (3H, d, 7.1 Hz), 1.52 (9H, s).

***tert*-Butyl *N*-benzylidenealanine *N*-oxide**

Z-Benzaldoxime (580 mg, 4.79 mmol) and *tert*-butyl 2-bromopropionate (980 mg, 4.69 mmol) were added successively to a solution of sodium hydride (200 mg of a 60% dispersion in mineral oil, 5.00 mmol) in 2-propanol (20 mL). The suspension was stirred at room temperature for 3 h, then poured into water, and extracted with ethyl acetate (2 × 20 mL). The organic extract was dried over anhydrous magnesium sulfate and evaporated to give a white solid. Trituration with anhydrous ether (8 mL) afforded the nitron (464 mg, 40%); mp 115–117 °C. IR (KBr, cm<sup>-1</sup>): 1736, 1582. <sup>1</sup>H NMR (CDCl<sub>3</sub>) δ: 8.26–8.23 (2H, m, Ar + HC=N<sup>+</sup>), 7.43–7.41 (4H, m, Ar), 4.65 (1H, q, 7.0 Hz, α-CH), 1.73 (3H, d, 7.0 Hz, CH<sub>3</sub>), 1.47 (9H, s, CO<sub>2</sub>C(CH<sub>3</sub>)<sub>3</sub>). CI-MS

(*m/z*): 250 ([M + 1]). Anal. calcd. for C<sub>14</sub>H<sub>19</sub>NO<sub>3</sub>: C 67.45, H 7.68, N 5.62; found: C 67.10, H 7.59, N 5.90.

***tert*-Butyl *N*-hydroxyalanine**

The *N*-oxide (460 mg, 185 mmol) was added to a stirred suspension of sodium methoxide (141 mg, 2.61 mmol) and hydroxylamine hydrochloride (182 mg, 2.62 mmol) in dry methanol (5.5 mL). This mixture was stirred at 40 °C until the solid dissolved, and the solution was then concentrated. The residue was shaken with ethyl acetate (10 mL), filtered, and the filtrate was concentrated. The residue was chromatographed on silica gel. Elution with ethyl acetate – hexanes (2:3) afforded 211 mg (71%) of *N*-hydroxyalanine *tert*-butyl ester; mp 73–74 °C. IR (KBr, cm<sup>-1</sup>): 3158, 1746. <sup>1</sup>H NMR (CDCl<sub>3</sub>) δ: 5.61 (2H, br s, NH + OH), 3.60 (1H, q, 7.1 Hz, α-CH), 1.48 (9H, s, CO<sub>2</sub>C(CH<sub>3</sub>)<sub>3</sub>), 1.22 (3H, d, 7.1 Hz, CH<sub>3</sub>). <sup>13</sup>C NMR (CDCl<sub>3</sub>) δ: 173.37 (ester C=O), 81.54 (CO<sub>2</sub>C(CH<sub>3</sub>)<sub>3</sub>), 60.97 (α-CH), 28.06 (CO<sub>2</sub>C(CH<sub>3</sub>)<sub>3</sub>), 14.65 (CH<sub>3</sub>). CI-MS (*m/z*): 162 ([M + 1]). Anal. calcd. for C<sub>7</sub>H<sub>15</sub>NO<sub>3</sub>: C 52.16, H 9.38, N 8.69; found: C 51.98, H 9.30, N 8.55.

***N*-Benzoyl, *N*-benzyloxyglycine ethyl ester (31)**

Benzoyl chloride (0.028 mL, 0.034 g, 0.23 mmol) (Fluka) was added dropwise to a cooled (0 °C) solution of *N*-benzyloxyglycine ethyl ester (48 mg, 0.23 mmol) and triethylamine (0.032 mL, 0.023 g, 0.023 mmol) in dichloromethane (0.5 mL). The cloudy solution was stirred for 20 min, diluted with dichloromethane (25 mL), and washed successively with saturated sodium bicarbonate (10 mL) and saturated sodium chloride (10 mL), dried over anhydrous magnesium sulfate, and concentrated to a pale yellow oil (70.7 mg, 98%). IR (film, cm<sup>-1</sup>): 1746 (C=O, s), 1626. <sup>1</sup>H NMR (CDCl<sub>3</sub>) δ: 7.71–7.07 (10H, m, Ar), 4.71 (2H, s, OCH<sub>2</sub>Ar), 4.42 (2H, s, CH<sub>2</sub>), 4.24 (2H, q, CO<sub>2</sub>CH<sub>2</sub>CH<sub>3</sub>), 1.29 (3H, t, CO<sub>2</sub>CH<sub>2</sub>CH<sub>3</sub>). CI-MS (*m/z*): 314 ([M + 1]).

**Synthesis of 32****Method A**

A solution of **31** (38.2 mg, 0.12 mmol) and anisole (0.053 mL, 0.49 mmol) (BDH) in dichloromethane (1 mL) was added dropwise at 0 °C to a solution of aluminium trichloride (48.8 mg, 0.37 mmol) (Anachemia) in nitromethane (1 mL). The resultant pink solution was stirred at 0 °C for 90 min and then at room temperature for 10 min. The reaction mixture was diluted with ethyl acetate (30 mL) and washed successively with *N*-hydrochloric acid (10 mL) and 4% sodium bicarbonate (40 mL). The organic layer was dried over anhydrous magnesium sulfate and concentrated to give a bright orange oil, which was purified by preparative layer chromatography (PLC) (40% ethyl acetate – hexane). The product (12.5 mg, 45%) was identical to that obtained from Method B.

**Method B**

Benzoyl chloride (0.016 mL, 0.019 g, 0.14 mmol) (Fluka) was added dropwise to a cooled (0 °C) solution of *N*-hydroxyglycine ethyl ester (16.4 mg, 0.14 mmol) and triethylamine (0.019 mL, 0.014 g, 0.014 mmol) in dichloromethane (0.5 mL). The suspension was stirred for 1 h, and



the solvent was then removed. The residue was redissolved in ether (10 mL), filtered, and the filtrate was concentrated. The oil was subjected to PLC (60% ethyl acetate – hexanes) to give 14.8 mg (41%) of the product. IR (film,  $\text{cm}^{-1}$ ): 1743 ( $\text{C}=\text{O}$ , s), 1672.  $^1\text{H}$  NMR ( $\text{CDCl}_3$ )  $\delta$ : 7.72 (5H, m, Ar), 4.47 (2H, s), 4.25 (2H, q), 1.30 (3H, t). CI-MS ( $m/z$ ): 224 ( $[\text{M} + 1]$ ).

### Vinylacetamido *N*-hydroxyglycine ethyl ester (36)

To a stirred solution of *N*-hydroxyglycine ethyl ester (117 mg, 0.98 mmol) in dichloromethane (2 mL) was added vinylacetic acid (0.088 mL, 0.089 g, 1.03 mmol) in one portion. The solution was cooled to 0 °C, and a solution of dicyclohexylcarbodiimide (213 mg, 1.03 mmol) (BDH) in dichloromethane (2 mL) was added dropwise during 10 min. Stirring was continued for 11 h while the mixture warmed to room temperature. The mixture was then concentrated under reduced pressure, and the residue was extracted with ether (2  $\times$  10 mL). The combined organic extracts were dried, concentrated, and the crude product was purified by flash chromatography (30 g silica gel and 40% ethyl acetate – hexane) to give a pale yellow oil (94 mg, 51%). IR (film,  $\text{cm}^{-1}$ ): 3318 (O-H, br), 3083 ( $\text{C}=\text{C}$ , w), 1742 ( $\text{C}=\text{O}$ , s), 1625 (N-C(O), s).  $^1\text{H}$  NMR ( $\text{CDCl}_3$ )  $\delta$ : 5.98–5.91 (1H, m,  $\text{CH}=\text{CH}_2$ ), 5.21–5.18 (2H, d,  $\text{CH}=\text{CH}_2$ ), 4.48 (2H, s), 4.22 (2H, q), 3.36 (2H, d), 1.29 (3H, t). EI-MS ( $m/z$ ): 187 ( $[\text{M}]^+$ ).

### Bromination of 36

A solution of bromine (0.041 mL, 0.128 g, 0.80 mmol) (Fisher) in chloroform (1 mL) was added dropwise, under nitrogen, at room temperature, to a stirred solution of vinylacetamido *N*-hydroxyglycine ethyl ester (0.125 g, 0.66 mmol) in chloroform (0.6 mL). Stirring was continued for 2 h, and the solvent was then removed to give a deep orange oil (0.148 g, 100%). IR (film,  $\text{cm}^{-1}$ ): 3211 (OH, br), 1745 ( $\text{C}=\text{O}$ ), 1650 (N-C(O)).  $^1\text{H}$  NMR ( $\text{CDCl}_3$ )  $\delta$ : 7.87 (1H, OH, br), 4.55 (1H, m), 4.50 (2H, s), 4.33 (2H, q), 3.86 (2H, dd), 3.38 (2H, dd), 1.30 (3H, t). EI-MS ( $m/z$ ): 345 : 347 : 349 (1:2:1). The oil was dissolved in dichloromethane (2 mL), and saturated sodium bicarbonate (3 mL) was added. The mixture was stirred for 2 h, washed with saturated sodium chloride (5 mL), dried, and concentrated. The crude product was purified by PLC (60% ethyl acetate – hexane) to give a colourless oil (0.077 g, 50%). IR (film,  $\text{cm}^{-1}$ ): 1718–1750 ( $\text{C}=\text{O}$ ).  $^1\text{H}$  NMR ( $\text{CDCl}_3$ )  $\delta$ : 4.80–4.75 (1H, m), 4.29 (1H, d,  $\text{CHH}$ , 17 Hz), 4.28 (1H, d,  $\text{CHH}$ , 17 Hz), 3.58 (1H, dd, 10.78, 5.52 Hz), 3.53 (1H, dd, 10.78, 6.76 Hz), 3.02 (1H, dd, 16.84, 8.24 Hz), 2.83 (1H, dd, 16.84, 7.04 Hz), 4.23 (2H, q,  $\text{CO}_2\text{CH}_2\text{CH}_3$ ), 1.29 (3H, t,  $\text{CO}_2\text{CH}_2\text{CH}_3$ ). EI-MS ( $m/z$ ) (relative intensity): 267 (12.1), 265 (12.6), 194 (78.4), 192 (68.3), 149 (58.2), 147 (57.4), 95 (7.4), 93 (8.7), 85 (17.8). Anal. calcd. for  $\text{C}_8\text{H}_{12}\text{NO}_4\text{Br}$ : C 36.11, H 4.55, N 5.26; found: C 35.75, H 4.58, N 5.25.

### Iodination of 36

Iodine (0.41 g, 1.60 mmol) and sodium bicarbonate (0.27 g, 3.21 mmol) were added to a solution of **36** (0.20 g, 1.07 mmol) in acetonitrile (5 mL). The solution was stirred for 7 h at 0 °C and then diluted with ether (50 mL) and washed successively with saturated sodium thiosulfate (30 mL), water (30 mL), and saturated sodium chloride

(30 mL), dried over anhydrous magnesium sulfate, and evaporated under reduced pressure. The product was purified by flash chromatography (60% ethyl acetate – hexanes) to give an oil 93 mg (28%). IR (film,  $\text{cm}^{-1}$ ): 1718, 1750 ( $\text{C}=\text{O}$ ).  $^1\text{H}$  NMR ( $\text{CDCl}_3$ )  $\delta$ : 4.70–4.63 (1H, m), 4.26 (1H, d,  $\text{CHH}$ , 17.88 Hz), 4.24 (1H, d,  $\text{CHH}$ , 17.88 Hz), 4.22 (2H, q), 3.39 (1H, dd, 10.40, 5.52 Hz), 3.35 (1H, dd, 10.40, 7.44 Hz), 3.0 (1H, dd, 16.78, 8.0 Hz), 2.76 (1H, dd, 16.78, 7.24 Hz), 1.28 (3H, t).

### Oxidation of 37, X = I

*m*-Chloroperbenzoic acid (45 mg of 85%, 0.22 mmol) was added to a solution of the iodide (46 mg, 0.15 mmol) in dichloromethane (2 mL). The purple solution was stirred for 5 h, then diluted with dichloromethane (10 mL), washed with saturated sodium thiosulfate (10 mL), and dried over anhydrous magnesium sulfate. The residue was purified by PLC (80% ethyl acetate – hexanes) to give 8 mg of product (25%). IR ( $\text{CHCl}_3$ ,  $\text{cm}^{-1}$ ): 1747, 1703 ( $\text{C}=\text{O}$ ).  $^1\text{H}$  NMR ( $\text{CDCl}_3$ )  $\delta$ : 4.69–4.63 (1H, m), 4.57 (1H, d,  $\text{CHH}$ , 18 Hz), 4.24 (2H, q), 4.06 (1H, d,  $\text{CHH}$ , 18 Hz), 3.91 (1H, dd, 12.80, 2.40 Hz), 3.67 (1H, dd, 12.80, 4.0 Hz), 2.96 (1H, dd, 16.60, 8.70 Hz), 2.90 (1H, dd, 16.60, 6.20 Hz), 1.30 (3H, t). CI-MS ( $m/z$ ): 204 ( $[\text{M} + 1]$ ). EI-MS ( $m/z$ ): 203 ( $[\text{M}]^+$ ).

### Coupling of *N*-hydroxyglycine benzyl ester and vinylacetic acid

Dicyclohexylcarbodiimide (1.38 g, 6.68 mmol) (BDH) was added to a cooled solution of *N*-hydroxyglycine benzyl ester (1.15 g, 6.36 mmol) and vinylacetic acid (0.57 mL, 575 mg, 6.68 mmol) in dichloromethane (30 mL). The cloudy mixture was stirred for 0.5 h at 0 °C and then for 3.5 h at room temperature, filtered, and concentrated. The resulting oil was purified by flash chromatography (60% ethyl acetate – hexane) to give 912 mg (58%) of the product. IR (film,  $\text{cm}^{-1}$ ): 3200 (OH, s), 1749 ( $\text{C}=\text{O}$ , s), 1633 ( $\text{C}=\text{O}$ , amide, s).  $^1\text{H}$  NMR ( $\text{CDCl}_3$ )  $\delta$ : 7.38–7.33 (5H, m, Ar), 6.02–5.89 (1H, m), 5.21–5.17 (2H, m,  $=\text{CH}_2$ ), 5.19 (2H, s,  $\text{CH}_2\text{Ph}$ ), 4.52 (2H, s), 3.34 (2H, d,  $\text{CH}_2\text{C}(\text{O})$ ). CI-MS ( $m/z$ ): 250 ( $[\text{M} + 1]$ ). Anal. calcd. for  $\text{C}_{13}\text{H}_{15}\text{NO}_4$ : C 62.65, H 6.02; N, 5.62; found: C 62.88, H 6.22, N 6.00.

### Iodocyclization of the benzyl ester

Iodine (1.23 g, 4.83 mmol) and sodium bicarbonate (0.41 g, 8.83 mmol) were added to a solution of the benzyl ester (0.40 g, 1.61 mmol) in acetonitrile (10 mL). The solution was stirred for 3 h at 0 °C and then diluted with ether (20 mL) and washed successively with saturated sodium thiosulfate (20 mL) and saturated sodium chloride (20 mL), dried over anhydrous magnesium sulfate, and evaporated under reduced pressure. The product was purified by flash chromatography (60% ethyl acetate – hexanes) to give an oil 0.345 g (57%). IR (film,  $\text{cm}^{-1}$ ): 1718, 1750 ( $\text{C}=\text{O}$ ).  $^1\text{H}$  NMR ( $\text{CDCl}_3$ )  $\delta$ : 7.38–7.33 (5H, m, Ar), 5.21 (1H, d,  $\text{CHHPh}$ , 12.08 Hz), 5.19 (1H, d,  $\text{CHHPh}$ , 12.08 Hz), 4.61–4.58 (1H, m), 4.33 (1H, d,  $\text{CHH}$ , 17.84 Hz), 4.30 (1H, d,  $\text{CHH}$ , 17.84 Hz), 3.33 (1H, dd, 10.36, 5.52 Hz), 3.28 (1H, dd, 10.36, 7.56 Hz), 2.98 (1H, dd, 16.80, 8.04 Hz), 2.73 (1H, dd, 16.80, 7.24 Hz). EI-MS ( $m/z$ ): 375 ( $[\text{M}]^+$ ).



### Oxidation of the iodomethyl benzyl ester

*m*-Chloroperbenzoic acid (68%) (351 mg, 1.38 mmol) was added to a solution of the ester (345 mg, 0.92 mmol) in dichloromethane (6 mL). The purple solution was stirred for 24 h, then diluted with ether (50 mL), washed with saturated sodium thiosulfate (10 mL), and dried over anhydrous magnesium sulfate. The residue was purified by PLC (80% ethyl acetate – hexanes) to give 66 mg of product (27%). IR ( $\text{CHCl}_3$ ,  $\text{cm}^{-1}$ ): 1718, 1750 ( $\text{C}=\text{O}$ ).  $^1\text{H}$  NMR ( $\text{CDCl}_3$ )  $\delta$ : 7.38–7.33 (5H, m, Ar), 5.21 (1H, d,  $\text{CHHPh}$ , 12.08 Hz), 5.19 (1H, d,  $\text{CHHPh}$ , 12.08 Hz), 4.66–4.60 (1 H, m), 4.57 (1H, d,  $\text{CHH}$ , 18 Hz), 4.13 (1H, d,  $\text{CHH}$ , 18 Hz), 3.87 (1H, dd, 12.80, 2.48 Hz), 3.66 (1H, dd, 12.80, 4.24 Hz), 2.92 (1H, dd, 16.66, 8.56 Hz), 2.87 (1H, dd, 16.66, 6.68 Hz). CI-MS ( $m/z$ ): 266 ( $[\text{M} + 1]$ ).

### Synthesis of 39

Palladium (10% on carbon) (250 mg) was added to a solution of the benzyl ester (190.5 mg, 0.72 mmol) in ethanol (10 mL). The resulting suspension was fitted with a balloon, flushed thrice with hydrogen, and then stirred under hydrogen for 1 h at room temperature. After filtration through Celite and evaporation of the filtrate, the oil was redissolved in water (10 mL), filtered, and the filtrate was lyophilized to give a pale green viscous oil 120 mg (95%).  $^1\text{H}$  NMR ( $\text{D}_2\text{O}$ )  $\delta$ : 4.74 (1H, m), 4.36 (1H, d, 18.16 Hz), 4.34 (1H, d, 18.16 Hz), 3.78 (1H, dd, 12.88, 3.2 Hz), 3.74 (1H, dd, 12.88, 5.64 Hz), 3.02 (1H, dd, 17.04, 8.76 Hz), 2.79 (1H, dd, 17.04, 7.68 Hz). CI-MS ( $m/z$ ): 176 ( $[\text{M} + 1]$ ).

### Reaction of 36 with *N*-bromosuccinimide in methanol

A solution of **36** (100 mg, 0.53 mmol) in dry methanol (5 mL) was cooled in an ice-water bath, and *N*-bromosuccinimide (95 mg, 0.53 mmol) (BDH) was added in one portion. Stirring was continued at 0 °C for 15 min and then at room temperature for 45 min. The reaction mixture was concentrated, and the residue was subjected to flash chromatography (60% ethyl acetate – hexanes). Two products were obtained. These were dissolved in dichloromethane (3 mL), washed with saturated sodium bicarbonate (2 mL), dried over anhydrous sodium sulfate, and concentrated to give **37** (**X** = **Br**) (9.6 mg) and a mixture of **40** and **41** (25 mg). IR (film,  $\text{cm}^{-1}$ ): 1793, 1751, 1700.  $^1\text{H}$  NMR ( $\text{CDCl}_3$ )  $\delta$ : **41**: 4.51 (1H, d, 17.8 Hz,  $\text{CHH}$ ), 4.23 (1H, d, 17.8 Hz,  $\text{CHH}$ ), 4.33 (1H, dd, 11.9, 6.0 Hz,  $\text{CHH}$ ), 4.23 (2H, q,  $\text{OCH}_2\text{CH}_3$ ), 4.07 (1H, dd, 11.9, 3.6 Hz,  $\text{CHH}$ ), 4.02–3.98 (1H, m, CH), 2.80 (1H, dd, 16.0 Hz, 5.8 Hz,  $\text{CHH}$ ), 2.68 (1H, dd, 16.0 Hz, 4.7 Hz,  $\text{CHH}$ ), 1.30 (3H, t,  $\text{OCH}_2\text{CH}_3$ ). **40**: 4.75–4.73 (1H, m, CH), 4.28 (1H, d, 17.8 Hz,  $\text{CHH}$ ), 4.23 (2H, q,  $\text{OCH}_2\text{CH}_3$ ), 4.22 (1H, d, 17.8 Hz,  $\text{CHH}$ ), 3.62 (1H, dd, 10.9, 6.2 Hz,  $\text{CHH}$ ), 3.54 (H, dd, 10.9, 3.6 Hz,  $\text{CHH}$ ), 2.81 (1H, dd, 16.6, 8.2 Hz,  $\text{CHH}$ ), 2.75 (1H, dd, 16.6, 8.8 Hz,  $\text{CHH}$ ), 1.30 (3H, t,  $\text{OCH}_2\text{CH}_3$ ). EI-MS ( $m/z$ ): 217 ( $[\text{M}]^+$ ), 144, 112, 99, 85. CI-MS ( $m/z$ ): 218 ( $[\text{M} + 1]$ ). GC-CI-MS ( $m/z$ ): 218 ( $[\text{M} + 1]$ ), 99 (RT = 9.4 min), 218 ( $[\text{M} + 1]$ ), 85 (RT = 9.7 min).

### Synthesis of 43

Succinic anhydride (100 mg, 1 mmol) was suspended in dichloromethane (0.5 mL), and a solution of *N*-hydroxyglycine benzyl ester (181 mg, 1 mmol) in dichloromethane

(0.5 mL) was added with stirring. Stirring was continued for 16 h. The suspension was then filtered, and the white solid was dried at 1 torr to give 183 mg (65%) of the product.  $^1\text{H}$  NMR ( $(\text{CD}_3)_2\text{CO}$ )  $\delta$ : 7.41–7.33 (5H, m, Ar), 5.17 (2H, s,  $\text{CH}_2\text{Ph}$ ), 4.41 (2H, s), 2.82–2.55 (4H, m,  $(\text{CH}_2)_2$ ). The hydroxysuccinamic acid (175.6 mg, 0.62 mmol) was suspended in dichloromethane (0.65 mL) under nitrogen at 0 °C, and dicyclohexylcarbodiimide (128 mg, 0.62 mmol) was added in one portion. Stirring was continued for 4 h at 0 °C. The mixture was then filtered through Celite and the filtrate concentrated under reduced pressure to afford an oily residue. Purification by PLC (40% ethyl acetate – hexanes) gave 105 mg (64%) of the product as an oil.  $^1\text{H}$  NMR ( $\text{CDCl}_3$ )  $\delta$ : 7.41–7.33 (5H, m, Ar), 5.21 (2H, s,  $\text{CH}_2\text{Ph}$ ), 4.49 (2H, s), 2.91–2.87 (2H, m), 2.77–2.74 (2H, m). CI-MS ( $m/z$ ): 264 ( $[\text{M} + 1]$ ).

### 5-Acetoxy-tetrahydro-1,2-oxazin-3,6-dione (44)

*N*-Hydroxyglycine benzyl ester (362 mg, 2 mmol) in dichloromethane (1 mL) was added with stirring to a solution of acetoxy succinic anhydride (4.11 mg, 2.6 mmol) in dichloromethane (1 mL). Stirring was continued for 16 h. The suspension was then filtered, and the white solid was collected and dried at 1 torr to give 518.2 mg (80%) of the product.  $^1\text{H}$  NMR ( $(\text{CD}_3)_2\text{CO}$ )  $\delta$ : 7.41–7.33 (5H, m, Ar), 5.87 (1H, dd, 2.68, 2.76 Hz), 5.20 (2H, s,  $\text{CH}_2\text{Ph}$ ), 4.66 (1H, d, 17.6 Hz), 4.18 (1H, d, 17.6 Hz), 3.10 (1H, dd, 17, 2.72 Hz), 2.59 (1H, dd, 17.10 Hz). CI-MS ( $m/z$ ): 340 ( $[\text{M} + 1]$ ). This product (500 mg, 1.55 mmol) was suspended under nitrogen in dichloromethane (1.5 mL), the suspension was cooled to 0 °C, and dicyclohexylcarbodiimide (319 mg, 1.55 mmol) was added in one portion. Stirring was continued at 0 °C for 4 h, and the slurry was then filtered through Celite and the filtrate concentrated under reduced pressure. The oily residue was purified by PLC (40% ethyl acetate – hexanes) to give 417.3 mg (88%) of the product as an oil.  $^1\text{H}$  NMR ( $\text{CDCl}_3$ )  $\delta$ : 7.41–7.32 (5H, m, Ar), 5.61 (1H, dd, 5.28, 11.16 Hz), 5.20 (2H, s,  $\text{CH}_2\text{Ph}$ ), 4.58 (1H, d, 18.12 Hz), 4.49 (1H, d, 18.12 Hz), 3.22 (1H, dd, 16.72, 11.16 Hz), 3.34 (1H, dd, 16.72, 5.28 Hz). CI-MS ( $m/z$ ): 322 ( $[\text{M} + 1]$ ).

### Synthesis of 45

Maleic anhydride (98 mg, 1 mmol) was suspended in dichloromethane (0.5 mL), and a solution of *N*-hydroxyglycine benzyl ester (181 mg, 1 mmol) in dichloromethane (0.5 mL) was added with stirring. Stirring was continued for 16 h. The suspension was then filtered, and the white solid was dried at 1 torr to give 178 mg (64%) of a solid.  $^1\text{H}$  NMR ( $\text{CDCl}_3$ )  $\delta$ : 7.41–7.32 (5H, m, Ar), 7.11 (1H, d, 12.88 Hz), 6.35 (1H, d, 12.88 Hz), 5.22 (2H, s,  $\text{CH}_2\text{Ph}$ ), 4.59 (2H, s). The solid (171 mg, 0.61 mmol) was suspended in dichloromethane (1 mL) under nitrogen; the suspension was cooled 0 °C, and dicyclohexylcarbodiimide (126.5 mg, 0.61 mmol) was added in one portion. Stirring was continued at 0 °C for 4 h. The slurry was then filtered through Celite and the filtrate concentrated under reduced pressure to afford an oily residue. Purification by PLC (40% ethyl acetate – hexanes) gave 154 mg (96%) of the product as a yellow solid.  $^1\text{H}$  NMR ( $\text{CDCl}_3$ )  $\delta$ : 7.39–7.32 (5H, m, Ar), 7.01 (1H, d, 10.2 Hz), 6.78 (1H, d, 10.2 Hz), 5.20 (2H, s,  $\text{CH}_2\text{Ph}$ ), 4.66 (2H, s). CI-MS ( $m/z$ ): 262 ( $[\text{M} + 1]$ ).



### Methyl 3,4-dihydroxybutanoate

DL-Malic acid (20 g, 0.15 mol) was dissolved in a solution prepared by addition of acetyl chloride (6.7 mL) (Fisher) to methanol (134 mL). The solution was stirred at room temperature for 13 h and then concentrated. The product was purified by flash chromatography (60% ethyl acetate – hexanes) to give a colourless oil (18.5 g, 77%). IR (film,  $\text{cm}^{-1}$ ): 3470, 1732.  $^1\text{H}$  NMR ( $\text{CDCl}_3$ )  $\delta$ : 4.44 (1H, br), 3.75 (3H, s), 3.65 (3H, s), 3.18 (1H, br), 2.81 (1H, dd, 16.48, 4.36 Hz), 2.74 (1H, dd, 16.48, 6.12 Hz). CI-MS ( $m/z$ ): 163 ( $[\text{M} + 1]$ ). Anal. calcd. for  $\text{C}_6\text{H}_{10}\text{O}_5$ : C 44.44, H 6.17; found: C 44.20, H 6.13.

Borane–dimethylsulfide (11 mL of 10 mol/L, 0.11 mol) was added dropwise to a solution of dimethylmalate (17.80 g, 0.11 mol) in tetrahydrofuran (220 mL). The solution was stirred at 20 °C for 30 min, and sodium borohydride (0.208 g, 5.5 mmol) (BDH) was added in one portion. Stirring was continued for 30 min, methanol (70 mL) was added dropwise, and after an additional 30 min the solvent was removed under reduced pressure. The product was purified by flash chromatography (60% ethyl acetate – hexanes) to give a colourless viscous oil (12.27 g, 83%). IR (film,  $\text{cm}^{-1}$ ): 3414, 1738.  $^1\text{H}$  NMR ( $\text{CDCl}_3$ )  $\delta$ : 4.07 (1H, m), 3.66 (3H, s), 3.61 (1H, dd, 11.36, 3.52 Hz), 3.46 (1H, dd, 11.36, 6.2 Hz), 2.80 (2H, br), 2.50 (1H, dd, 16.64, 8.52 Hz), 2.44 (1H, dd, 16.64, 4.16 Hz). CI-MS ( $m/z$ ): 135 ( $[\text{M} + 1]$ ). Anal. calcd. for  $\text{C}_5\text{H}_{10}\text{O}_4$ : C 44.78, H 7.46; found: C 44.12, H 7.55.

### Benzylidene derivative of methyl 3,4-dihydroxybutanoate

A solution of methyl 3,4-dihydroxybutanoate (11.44 g, 85.36 mmol), benzaldehyde dimethyl acetal (11 mL, 11.15 g, 3.16 mmol), and *p*-toluenesulfonic acid monohydrate (812 mg, 4.27 mmol) (Fisher) in dimethylformamide (20 mL) was stirred at room temperature for 24 h and then poured into ice-water (50 mL) and extracted with ethyl acetate (5  $\times$  40 mL). The organic extract was washed with saturated sodium chloride (30 mL), dried over anhydrous sodium sulfate, and concentrated. Purification by column chromatography (60% ethyl acetate – hexanes) gave 18.5 g (77%) of a colourless oil. IR (film,  $\text{cm}^{-1}$ ): 3034, 1737 (C=O).  $^1\text{H}$  NMR ( $\text{CDCl}_3$ )  $\delta$ : 7.49–7.35 (5H, m, Ar), 5.96 (1H, s), 5.86 (1H, s), 4.68–4.60 (1H, m), 4.21 (1H, dd, 8.28, 6.72 Hz), 4.12 (1H, dd, 8.44, 6.16 Hz), 3.98 (1H, dd, 8.44, 6.60 Hz), 3.86 (1H, dd, 8.28, 5.68 Hz), 2.85 (1H, dd, 16.06, 6.36 Hz), 2.82 (1H, dd, 16.06, 6.36 Hz), 2.66 (1H, dd, 16.06, 7.20 Hz), 2.65 (1H, dd, 16.06, 7.32 Hz). CI-MS ( $m/z$ ): 223 ( $[\text{M} + 1]$ ).

### Preparation of 47

Sodium hydroxide (25 mL of 1 mol/L, 25 mmol) was added to a solution of the benzylidene methyl ester (5.75 g, 25.9 mmol) in methanol (40 mL). The reaction mixture was stirred for 30 min, and the solvent was then removed. The residue was dissolved in ethyl acetate (50 mL) and water (30 mL). The aqueous phase was acidified with *N*-hydrochloric acid and extracted with dichloromethane (4  $\times$  30 mL). This extract was dried over anhydrous sodium sulfate and concentrated to give 3.16 g (59%) of product. IR (film,  $\text{cm}^{-1}$ ): 3037, 1713 (C=O).  $^1\text{H}$  NMR ( $\text{CDCl}_3$ )  $\delta$ : 7.49–7.36 (5H, m, Ar), 5.96 (1H, s), 5.82 (1H, s), 4.68–4.60 (1H, m), 4.37 (1H, dd, 8.50, 6.20 Hz), 4.11 (1H, dd, 8.32,

6.72 Hz), 3.99 (1H, dd, 8.32, 5.48 Hz), 3.75 (1H, dd, 8.50, 6.60 Hz), 2.88 (1H, dd, 16.36, 6.60 Hz), 2.71 (1H, dd, 16.36, 6.96 Hz), 2.68 (1H, dd, 16.36, 6.80 Hz). CI-MS ( $m/z$ ): 209 ( $[\text{M} + 1]$ ).

### Coupling of 47 and *N*-hydroxyglycine *tert*-butyl ester

Dicyclohexylcarbodiimide (0.859 g, 4.16 mmol) (BDH) was added to a cooled solution of 47 (0.87 g, 4.16 mmol) and *N*-hydroxyglycine *tert*-butyl ester (0.60 g, 4.09 mmol) in dichloromethane (20 mL). The cloudy mixture was stirred at 0 °C for 0.5 h and at room temperature for 4 h and then filtered and the filtrate concentrated. Purification of the oil by flash chromatography (60% ethyl acetate – hexane) gave 0.650 g (47%) of the product 48. IR (film,  $\text{cm}^{-1}$ ): 3249, 1739, 1641.  $^1\text{H}$  NMR ( $\text{CDCl}_3$ )  $\delta$ : 7.49–7.35 (5H, m, Ar), 5.96 (1H, s), 5.86 (1H, s), 4.59–4.62 (1H, m), 4.45 (1H, d, 17.72 Hz), 4.39 (1H, dd, 8.56, 6.08 Hz), 4.38 (1H, d, 17.76 Hz), 4.31 (1H, d, 17.76 Hz), 4.29 (1H, d, 17.72 Hz), 4.25 (1H, dd, 8.20, 6.80 Hz), 3.89 (1H, dd, 8.20, 5.84 Hz), 3.79 (1H, dd, 8.56, 7.12 Hz), 3.20 (1H, dd, 15.92, 6.12 Hz), 3.02 (1H, dd, 15.54, 5.60 Hz), 2.92 (1H, dd, 15.54, 7 Hz), 2.81 (1H, dd, 15.92, 7.16 Hz), 1.48 (9H, s, *tert*-butyl). CI-MS ( $m/z$ ): 338 ( $[\text{M} + 1]$ ). Anal. calcd. for  $\text{C}_{17}\text{H}_{23}\text{NO}_6$ : C 60.53, H 6.82, N 4.15; found: C 60.84, H 7.07, N 4.36.

### Hydrogenolysis of 48

Palladium on carbon (10%) (0.400 g) was added to a solution of 48 (0.400 g, 1.19 mmol) in tetrahydrofuran (15 mL). The suspension was flushed thrice with hydrogen, then stirred under hydrogen for 3 h, filtered through Celite, and the filtrate concentrated. The residue was purified by PLC (80% ethyl acetate – hexanes) to give 49 as a viscous golden oil (0.150 g, 51%). IR (film,  $\text{cm}^{-1}$ ): 3362, 1737, 1635.  $^1\text{H}$  NMR ( $\text{D}_2\text{O}$ )  $\delta$ : 4.37 (1H, d, 17.72 Hz), 4.30 (1H, d, 17.72 Hz), 4.13 (1H, m), 3.62 (1H, dd, 11.76, 4 Hz), 3.53 (1H, dd, 11.76, 6.88 Hz), 2.78 (1H, dd, 15.15, 8.24 Hz), 2.71 (1H, dd, 15.15, 4.96 Hz), 1.49 (9H, s). CI-MS ( $m/z$ ): 250 ( $[\text{M} + 1]$ ). Anal. calcd. for  $\text{C}_{10}\text{H}_{19}\text{NO}_6 \cdot 1.5\text{H}_2\text{O}$ : C 43.47, H 7.37, N 5.07; found: C 43.45, H 7.29, N 5.26.

### Cyclization of 49

A mixture of the diol 49 (68.8 mg, 0.28 mmol), triphenylphosphine (78.3 mg, 0.30 mmol), and diethylazodicarboxylate (65  $\mu\text{L}$ , 72 mg, 0.41 mmol) in tetrahydrofuran (9 mL) was stirred for 24 h at room temperature and then concentrated under reduced pressure. The residue was purified by PLC (60% ethyl acetate – hexanes) to give 50 (68 mg). IR (film,  $\text{cm}^{-1}$ ): 3279, 1735.  $^1\text{H}$  NMR ( $\text{CDCl}_3$ )  $\delta$ : 4.64–4.59 (1H, m), 4.37 (1H, d, 17.84 Hz), 3.98 (1H, d, 17.84 Hz), 3.86 (1H, dd, 12.64, 2.68 Hz), 3.65 (1H, dd, 12.64, 4.16 Hz), 2.89 (1H, dd, 16.56, 8.52 Hz), 2.85 (1H, dd, 16.56, 6.64 Hz), 1.47 (9H, s). EI-MS ( $m/z$ ): 231 ( $[\text{M}]^+$ ). CI-MS ( $m/z$ ): 232. This compound was dissolved in trifluoroacetic acid (0.5 mL) and stirred under a nitrogen atmosphere for 1.5 h. The solution was then freeze-dried to give 28 mg (57%) of 39.  $^1\text{H}$  NMR ( $\text{D}_2\text{O}$ )  $\delta$ : 4.74 (1H, m), 4.36 (1H, d, 18.16 Hz), 4.34 (1H, d, 18.16 Hz), 3.78 (1H, dd, 12.88, 3.2 Hz), 3.74 (1H, dd, 12.88, 5.64 Hz), 3.02 (1H, dd, 17.0, 8.76 Hz), 2.79 (1H, dd, 17.0, 7.68 Hz). CI-MS ( $m/z$ ): 176 ( $[\text{M} + 1]$ ).



#### 4-Iodobutanoic acid

Trimethylsilyl chloride (5.0 mL, 4.28 g, 33.4 mmol) was added dropwise under nitrogen to a suspension of sodium iodide (5.84 g, 34.0 mmol) in dichloromethane (60 mL). The mixture was stirred for 15 min, and  $\gamma$ -butyrolactone (2.0 mL, 2.24 g, 26.0 mmol) was then added dropwise (15 min). Stirring was continued at room temperature for 1.5 h and then at reflux for 42 h. Water (50 mL) and ether (100 mL) were added, and the organic layer was separated, washed with 10% sodium thiosulfate (50 mL), and then extracted with sodium bicarbonate (50 mL). The bicarbonate extract was acidified to pH 2–3 with 1 mol/L hydrochloric acid and extracted with ether (2  $\times$  25 mL). The ether extract was washed with saturated sodium chloride (50 mL), dried over anhydrous sodium sulfate, and evaporated under reduced pressure to give 814 mg (15%) of a colourless oil.  $^1\text{H}$  NMR ( $\text{CDCl}_3$ )  $\delta$ : 3.25 (2H, t, 6.72 Hz), 2.52 (2H, t, 7.28 Hz), 2.13 (2H, q).

#### Reaction of 4-iodobutanoic acid with *N*-hydroxyglycine *tert*-butyl ester

Dicyclohexylcarbodiimide (51 mg, 0.25 mmol) (BDH) was added under nitrogen to a cooled (0 °C) solution of the acid (65 mg, 0.30 mmol) in dichloromethane (2 mL), and a solution of *N*-hydroxyglycine *tert*-butyl ester (34 mg, 0.23 mmol) in dichloromethane (2 mL) was added dropwise, with stirring. The cloudy mixture was stirred for 12 h at 0 °C – room temperature and was then filtered. The filtrate was evaporated, and the residue was purified by flash chromatography (40% ethyl acetate – hexane) to give 16.8 mg (21%) of **52** as a yellow oil.

#### Preparation of *tert*-butyl 3-oxo-[1,2]oxazinan-2-yl-acetate

The oil **52** (4 mg, 0.012 mmol) was dissolved in dichloromethane (5 mL); triethylamine (13  $\mu\text{L}$ , 9.44 mg, 0.093 mmol) was added, and the solution was stirred for 3 h. Then DBU (4  $\mu\text{L}$ , 4.1 mg, 0.027 mmol) was added, and stirring was continued for 3.5 h. The solvent was then removed. The residue was dissolved in ethyl acetate (5 mL), washed with saturated sodium chloride, dried over anhydrous sodium sulfate, and concentrated to give 3 mg of **53**.  $^1\text{H}$  NMR ( $\text{CDCl}_3$ )  $\delta$ : 4.28 (2H, s,  $\text{CH}_2$ ), 4.16 (2H, t, 6.84 Hz,  $\text{OCH}_2$ ), 2.55 (2H, t, 7.2 Hz,  $\text{CH}_2\text{CO}$ ), 2.14 (2H, m), 1.47 (9H, s).

#### Acetoacetamido *N*-benzyloxyglycine ethyl ester

A solution of *N*-benzyloxyglycine ethyl ester (0.159 g, 0.76 mmol) and 2,2,6-trimethyl-4*H*-1,3-dioxin-4-one (0.1 mL, 0.76 mmol) in toluene (0.76 mL) was immersed in a preheated (110 °C) oil bath and stirred vigorously for 4 h and monitored by TLC. The reaction mixture was then concentrated under reduced pressure and further dried at 1 torr for 2 h to give a viscous orange oil (0.222 g, 100%). IR ( $\text{CDCl}_3$ ,  $\text{cm}^{-1}$ ): 1749 (C=O, s), 1670 (NC(O)).  $^1\text{H}$  NMR ( $\text{CDCl}_3$ )  $\delta$ : 7.40 (5H, s,  $\text{OCH}_2\text{Ph}$ ), 4.88 (2H, s,  $\text{OCH}_2\text{Ph}$ ), 4.32 (2H, s, (O) $\text{CCH}_2\text{C}(\text{O})$ ), 4.22 (2H, q,  $\text{OCH}_2\text{CH}_3$ ), 3.55 (2H, s,  $\text{NCH}_2\text{CO}_2\text{Et}$ ), 2.25 (3H, s,  $\text{CH}_3\text{C}(\text{O})$ ), 1.29 (3H, t,  $\text{OCH}_2\text{CH}_3$ ). CI-MS ( $m/z$ ): 294 ( $[\text{M} + 1]$ ). Anal. calcd. for  $\text{C}_{15}\text{H}_{19}\text{NO}_5$ : C 61.43, H 6.48, N 4.78; found: C 61.21, H 6.74, N 5.14.

#### Hydrogenolysis of acetoacetamido *N*-benzyloxyglycine ethyl ester

Palladium on carbon (10%) (97 mg) was added to a solution of acetoacetamido *N*-benzyloxyglycine ethyl ester (104 mg, 0.35 mmol) in ethanol (2 mL). The resulting suspension was fitted with a balloon, flushed thrice with hydrogen, and then stirred under hydrogen for 1 h at room temperature. After filtration through Celite and evaporation of the filtrate, the oil was purified by chromatography through a short column of silica gel using 60% ethyl acetate–hexanes. The colourless oil (65.2 mg, 91%) was identified as an 85:15 mixture of **54** and **55**. IR (film,  $\text{cm}^{-1}$ ): 3390, 1746, 1687.  $^1\text{H}$  NMR ( $\text{CDCl}_3$ )  $\delta$ : **54**: 4.52 (1H, d, 18.16 Hz), 4.24 (2H, q), 4.12 (1H, d, 18.16 Hz), 3.03 (1H, d, 16.76 Hz), 2.75 (1H, d, 16.76 Hz), 1.60 (3H, s), 1.29 (3H, t); **55**: 4.54 (2H, s), 4.24 (2H, q), 3.75 (2H, s), 2.29 (3H, s), 1.29 (3H, s). CI-MS ( $m/z$ ): 204 ( $[\text{M} + 1]$ ). Anal. calcd. for  $\text{C}_8\text{H}_{13}\text{NO}_5$ : C 47.29, H 6.70, N 6.20; found: C 47.57, H 6.40, N 6.90.

#### Synthesis of **56**

Diketene (0.13 mL, 0.12 g, 1.67 mmol) was added to a solution of *N*-hydroxyglycine benzyl ester (0.303 g, 1.67 mmol) in chloroform (3 mL). The solution was stirred for 3 h at room temperature, concentrated under reduced pressure, and purified by PLC (60% EtOAc–hexanes). The product was a yellow solid (0.16 g, 36%).  $^1\text{H}$  NMR ( $\text{CDCl}_3$ )  $\delta$ : 7.37–7.32 (5H, m, Ar), 5.18 (2H, s,  $\text{CH}_2\text{Ph}$ ), 4.53 (1H, d, 18.12 Hz), 4.19 (1H, d, 18.12 Hz), 3 (1H, d, 16.84 Hz), 2.76 (1H, d, 16.84 Hz), 1.60 (3H, s,  $\text{CH}_3$ ). CI-MS ( $m/z$ ): 266 ( $[\text{M} + 1]$ ). The solid (150 mg, 0.57 mmol) was dissolved in ethanol, and palladium on carbon (150 mg, 10%) was added. The suspension was fitted with a balloon, flushed thrice with hydrogen, and then stirred under hydrogen for 1 h at room temperature, filtered through Celite, and evaporated. The oil was redissolved in water (10 mL), filtered, and the filtrate was lyophilized to give a brown solid (0 mg, 81%) identified as a 2:1 mixture of **56** and **57**.  $^1\text{H}$  NMR ( $\text{D}_2\text{O}$ )  $\delta$ : **56**: 4.39 (1H, d, 17.72 Hz), 4.20 (1H, d, 17.72 Hz), 3.17 (1H, d, 17.16 Hz), 2.77 (1H, d, 17.16 Hz), 1.60 (3H, s); **57**: 4.38 (2H, s), 3.38 (2H, s), 2.29 (3H, s). CI-MS ( $m/z$ ): 176 ( $[\text{M} + 1]$ ).

#### Benzyl- $\gamma$ -bromoacetoacetate

Diketene (500  $\mu\text{L}$ , 545 mg, 6.5 mmol) was dissolved in dichloromethane (2 mL), and the solution was cooled to –25 °C and treated dropwise with a solution of bromine (333  $\mu\text{L}$ , 1.02 g, 6.5 mmol) in dichloromethane (2 mL). After the addition was complete, the solution was stirred at –25 °C for 15 min, and benzyl alcohol (700  $\mu\text{L}$ , 732 mg, 6.8 mmol) was added dropwise. Stirring was continued for 15 min, and the solution was warmed to room temperature and evaporated. The residue was dissolved in diethyl ether (20 mL), washed successively with saturated sodium bicarbonate (2  $\times$  20 mL), water (20 mL), and saturated sodium chloride (20 mL), dried over anhydrous magnesium sulfate, and evaporated to give benzyl  $\gamma$ -bromoacetoacetate as a pale yellow oil (1.70 g, 97%). IR (neat,  $\text{cm}^{-1}$ ): 3033, 1734, 1654.  $^1\text{H}$  NMR ( $\text{CDCl}_3$ )  $\delta$ : 7.36 (5H, m), 5.19 (2H, s), 4.02 (2H, s), 3.75 (2H, s). CI-MS ( $m/z$ ): 271, 273 ( $[\text{M} + 1]$ ,  $[\text{M} +$



3]). Anal. calcd. for  $C_{11}H_{11}BrO_3$ : C 48.69, H 4.05; found: C 48.55, H 3.94.

### Benzyl-3-hydroxy-4-bromobutanoate

Benzyl bromoacetate (500 mg, 1.84 mmol) was dissolved in a mixture of tetrahydrofuran (9 mL) and methanol (1 mL), the solution was cooled in an ice-bath, and sodium borohydride (72 mg, 1.90 mmol) was added in one portion. Stirring was continued in the ice-bath for 15 min and ethyl acetate (50 mL) and 1 mol/L hydrochloric acid (1.5 mL) were added. The aqueous layer was separated, extracted with ethyl acetate (20 mL), and the combined organic layers were washed with saturated sodium bicarbonate (40 mL), dried over anhydrous magnesium sulfate, and evaporated to give benzyl 3-hydroxy-4-bromobutanoate 433 mg, 86%). IR (neat,  $cm^{-1}$ ): 3443, 3064, 1731, 1624.  $^1H$  NMR ( $CDCl_3$ )  $\delta$ : 7.36 (5H, s), 5.17 (2H, s), 4.26 (1H, m), 3.50 (1H, dd, 5.0, 10.5 Hz), 3.47 (1H, dd, 5.6, 10.5 Hz), 3.06 (1H, d, 5.1 Hz), 2.72 (1H, dd, 5.0, 16.6 Hz), 2.69 (1H, dd, 7.3, 16.6 Hz). CI-MS ( $m/z$ ): 273, 275 ( $[M + 1]$ ,  $[M + 3]$ ). Anal. calcd. for  $C_{11}H_{13}BrO_3 \cdot 0.5H_2O$ : C 53.75, H 5.88; found: C 53.65, H 5.60.

### Benzyl 3-[2-tetrahydropyranyloxy]-4-bromobutanoate

The bromohydrin (845 mg, 3.09 mmol) was dissolved in dichloromethane (10 mL), and dihydropyran (300  $\mu$ L, 277 mg, 3.29 mmol) and *p*-toluenesulfonic acid monohydrate (3 crystals) were added. The solution was stirred at room temperature for 1.5 h. Diethyl ether (40 mL) was then added, and the solution was washed with saturated sodium bicarbonate ( $2 \times 40$  mL), dried over anhydrous sodium sulfate, and evaporated. Purification by column chromatography using ethyl acetate – hexanes (3:7) gave the product **62** (1.07 g, 97%) as a 1:1 mixture of diastereomers. IR (neat,  $cm^{-1}$ ): 3033, 1737. CI-MS ( $m/z$ ): 357, 359 ( $[M + 1]$ ,  $[M + 3]$ ). Calcd. for  $C_{16}H_{21}BrO_4$ : C 53.75, H 5.88; found: C 53.65, H 5.60.

### 3-[2-Tetrahydropyranyloxy]-4-bromobutanoic acid

The protected bromohydrin **62** (73 mg, 0.20 mmol) was dissolved in tetrahydrofuran (3 mL) and 10% palladium on charcoal (65 mg) was added. The mixture was flushed thrice with nitrogen, thrice with hydrogen, and then stirred under hydrogen for 45 min. The mixture was filtered through Celite, the Celite was rinsed with ethyl acetate (10 mL), and the combined filtrates were evaporated to give the product **63** as a colourless oil, 54 mg (98%). IR (neat,  $cm^{-1}$ ): 1715. CI-MS ( $m/z$ ): 267, 269 ( $[M + 1]$ ,  $[M + 3]$ ).

### Coupling of **63** with *tert*-butyl *N*-hydroxyglycine

The acid **63** (85 mg, 0.32 mmol) was dissolved in methylene chloride (3 mL), the solution was cooled in an ice-bath, stirred, and dicyclohexylcarbodiimide (70 mg, 0.34 mmol) was added, followed by a solution of the *tert*-butyl ester (46.8 mg, 0.32 mmol) in methylene chloride (3 mL). The cloudy mixture was stirred, initially at 0 °C, and allowed to warm to room temperature. After 12 h, ether (20 mL) was added, the mixture was filtered, and the filtrate was evaporated. The product was purified by chromatography on silica

gel. Elution with 30:70 ethyl acetate:hexane gave 81 mg (64%) of a viscous oil.

### Protected 2-carboxymethyl-5-hydroxy-1,2-oxazine-3-one

A portion of the above oil (37 mg, 0.093 mmol) was dissolved in methylene chloride (2 mL), and triethylamine (14  $\mu$ L, 10.2 mg, 0.10 mmol) was added. The solution was left under nitrogen for 1 h, and DBU (7.0  $\mu$ L, 0.047 mmol) was added, followed after 2.5 h by an additional 5.0  $\mu$ L (0.33 mmol) of DBU. Stirring was continued under nitrogen for 3.2 h, and the reaction mixture was then diluted with methylene chloride (10 mL), washed with water (10 mL), dried over anhydrous sodium sulfate, and evaporated. Chromatography on silica gel and elution with 45:55 ethyl acetate:hexane gave the protected oxazinone as a semisolid and as a 1:1 mixture of diastereomers.  $^1H$  NMR ( $CDCl_3$ )  $\delta$ : 4.66 (1H, m, THP proton, one isomer), 4.41 (1H, m, THP proton, second isomer), 4.32–4.45 (2H, m, both isomers), 3.83 (1H, m, 5-H of one isomer), 2.94–2.62 (2H, both isomers, two ddd), 1.8 (2H, m), 1.7 (2H, m), 1.55 (2H, m), 1.47 (9H, s).

### 5-Hydroxy-3-oxo-[1,2]oxazinan-2-yl-acetic acid

The protected oxazinone (11 mg, 0.35 mmol) was dissolved in methylene chloride (1 mL), cooled in an ice-bath, and trifluoroacetic acid (500  $\mu$ L) was added. Additional trifluoroacetic acid (3  $\mu$ L) was added after 15 min, after an additional 20 min (500  $\mu$ L), and after an additional 30 min (300  $\mu$ L). After an additional 55 min, the solvent was removed. The residue was redissolved in trifluoroacetic acid (500  $\mu$ L), evaporated after 30 min, and the residue shaken with ethyl acetate (2 mL), water (1 mL), and sodium bicarbonate (3 mg). The aqueous phase was separated, washed with ethyl acetate, and lyophilized to give **29**, R = H, as the sodium salt.  $^1H$  NMR ( $D_2O$ )  $\delta$ : 4.49 (1H, m), 4.29 (1H, dd, 12.1, 4.6 Hz), 4.28 (1H, d, 18.2 Hz), 4.15 (1H, d, 18.2 Hz), 4.02 (1H, ddd, 12.1, 3.24, 0.8 Hz), 2.92 (1H, dd, 16.8, 5.9 Hz), 2.52 (1H, ddd, 16.8, 3.16 Hz).

### Coupling of **63** to the *tert*-butyl ester of *N*-hydroxyalanine

The acid **63** (54 mg, 0.20 mmol) was dissolved in dichloromethane (3 mL), the solution was cooled in an ice-bath, stirred, and dicyclohexylcarbodiimide (41 mg, 0.20 mmol) was added, followed by a solution of the *tert*-butyl ester in dichloromethane (2 mL). The mixture was stirred in the ice-bath for 5 min; the ice-bath was then removed, and stirring was continued for 3 h. The mixture was filtered, and the filtrate was evaporated. The residue was chromatographed on silica gel. Elution with ethyl acetate – hexanes (2:3) gave **67** (74 mg, 54%) and products of O-acylation. IR ( $CH_2Cl_2$ ,  $cm^{-1}$ ): 3432, 1736, 1657. CI-MS ( $m/z$ ): 410, 412 ( $[M + 1]$ ,  $[M + 3]$ ).

### Cyclization of **67**

The *N*-acylated compound **67** (36 mg, 0.088 mmol) was dissolved in dichloromethane (10 mL), cooled in an ice-bath, and 1,8-diazabicyclo[5.4.0]undec-7-ene (15  $\mu$ L, 0.1 mmol) was added. The solvent was removed after 1 h. The residue was dissolved in ethyl acetate (25 mL), and the solution was washed with water ( $2 \times 25$  mL), dried over anhydrous mag-



nesium sulfate, and evaporated to give the protected oxazinone **69** (25 mg, 85%). IR ( $\text{CH}_2\text{Cl}_2$ ,  $\text{cm}^{-1}$ ): 1736, 1678. CI-MS ( $m/z$ ): 330 ( $[\text{M} + 1]$ ). HR-MS-CI calcd. for  $\text{C}_{16}\text{H}_{27}\text{NO}_6$ : 330.1917 ( $[\text{M} + 1]$ ); found: 330.1916.

## 2-(5-Hydroxy-3-oxo-[1,2]oxazinan-2-yl)-propionic acid (**29**, $\text{R} = \text{Me}$ )

The protected oxazinone **69** (10.1 mg, 0.031 mmol) was dissolved in dichloromethane; the solution was cooled in an ice-bath, and trifluoroacetic acid (1 mL, 13.0 mmol) was added. The solution was stirred for 30 min, and the solvent was then removed. The residue was dissolved in trifluoroacetic acid (500  $\mu\text{L}$ ), and the solution was stirred at room temperature for 15 min and evaporated. The residue was shaken with ethyl acetate (3 mL) and a solution of sodium bicarbonate (2.8 mg) in water (2 mL). The aqueous phase was lyophilized to give the sodium salt of **29**,  $\text{R} = \text{Me}$  as an approximately 1:1 mixture of *RR*-*SS* and *RS*-*SR* diastereomers.  $^1\text{H}$  NMR ( $\text{D}_2\text{O}$ )  $\delta$ : 4.89 (1H, q, 7.3 Hz,  $\alpha\text{-CH}$ , one isomer), 4.88 (1H, q, 7.3 Hz,  $\alpha\text{-CH}$ , second isomer), 4.72–4.69 (2H, m, H5, both isomers), 4.54 (1H, d, 10.5 Hz, H6, one isomer), 4.53 (1H, d, 10.5 Hz, H6, second isomer), 4.35 (2H, d, 10.5 Hz, H6, both isomers), 2.97 (1H, d, 18.3 Hz, H4, one isomer), 2.95 (1H, d, 18.3 Hz, H4, second isomer), 2.51 (2H, m, 18.3 Hz, H4, both isomers), 1.45 (3H, d, 7.3 Hz,  $\text{CH}_3$ , one isomer), 1.42 (3H, d, 7.3 Hz,  $\text{CH}_3$ , second isomer). CI-MS ( $m/z$ , for the acid): 190 ( $[\text{M} + 1]$ ), 172 ( $[\text{M} + 1 - \text{H}_2\text{O}]$ ). HR-MS-CI calcd. for  $\text{C}_7\text{H}_{12}\text{NO}_5$ : 190.0716 ( $[\text{M} + 1]$ ); found: 190.0712.

## Bioassays

### Materials

#### Agar medium (1% w/v)

Yeast extract (1.5 g), peptone (2.5 g), glucose (0.5 g), and agar (5.0 g) were dissolved in deionized water; the volume was diluted to 500 mL, and the solution was sterilized by autoclaving at 121 °C for 20 min.

#### Preparation of agar plates

Under sterile conditions, the agar medium (150 mL) was heated to 100 °C, cooled to 50 °C, and distributed into ten petri dishes. Once the medium had hardened, the plates were inverted and stored at 4 °C.

#### Liquid medium

Yeast extract (0.3 g), peptone (0.5 g), and glucose (0.1 g) were dissolved in deionized water; the volume was diluted to 100 mL, and the solution was sterilized by autoclaving at 121 °C for 20 min.

### Methods

Step 1: Under sterile conditions, freeze-dried *M. luteus* was dissolved in liquid medium (10 mL) and incubated at 250 rpm for 12 h at 30 °C.

Step 2: Liquid bacterial culture from step 1 (0.5 mL) and 40% glycerol in deionized water (0.5 mL) were vortexed under sterile conditions in a tube fitted with a screw cap and an air-tight gasket. The resulting 20% glycerol bacterial stock solution was stored at –80 °C.

Step 3: An inoculating needle was dipped into 20% glycerol bacterial stock solution from Step 2 and, under sterile conditions, streaked onto the surface of an agar plate. The inverted plate was incubated at 30 °C for 12 h and then stored at 4 °C.

Step 4: Under sterile conditions, a bacterial colony of *M. luteus* was lifted from the surface of the agar plate from Step 3 using a toothpick, added to liquid medium (10 mL), and incubated at 250 rpm for 12 h at 30 °C.

Step 5: Under sterile conditions, the agar medium (150 mL) was heated to 100 °C, cooled to 50 °C; liquid bacterial culture from Step 4 (4 mL) was added with swirling, and the medium was distributed into ten petri dishes. Once the medium had hardened, the plates were inverted and stored at 4 °C.

Step 6: A sterile filter disc was treated with an aliquot of a known concentration of the test compound, and the solvent was removed by air drying under sterile conditions. This disc, a solvent control disc, and a disc containing a known weight of a penicillin or cephalosporin were placed on an agar plate seeded with *M. luteus* from Step 5. The plate was inverted and incubated for 12 h at 30 °C.

## Acknowledgement

This research was supported financially by an Individual Operating Grant from the Natural Sciences and Engineering Research Council of Canada (NSERC).

## References

1. C.H. Stammer, A.N. Wilson, F.W. Holly, and K. Folkers. *J. Am. Chem. Soc.* **77**, 2346 (1955).
2. S. Harada, S. Tsubotani, T. Hida, H. Ono, and H. Okazaki. *Tetrahedron Lett.* **27**, 6229 (1986); Y. Nozaki, N. Katayama, H. Ono, S. Tsubotani, T. Harada, H. Okazaki, and Y. Nakao. *Nature (London)*, **325**, 179 (1987).
3. D. Peisach, D.M. Chipman, P.W. Van Ophem, J.M. Manning, and D. Ringe. *J. Am. Chem. Soc.* **120**, 2268 (1998).
4. F.C. Neuhaus and J.L. Lynch. *Biochemistry*, **3**, 471 (1964); B. Badet and C.T. Walsh. *Biochemistry*, **24**, 1333 (1985).
5. S. Harada, S. Tsubotani, T. Hida, K. Koyama, M. Kondo, and H. Ono. *Tetrahedron*, **44**, 6589 (1988); Y. Nakao. *Spec. Publ. R. Soc. Chem.* **70**, 119 (1989); Y. Nozaki, N. Katayama, S. Harada, H. Ono, and H. Okazaki. *J. Antibiot.* **42**, 84 (1989).
6. D.J. Tipper and J.L. Strominger. *Proc. Natl. Acad. Sci. U.S.A.* **54**, 1133 (1965).
7. M. Kitagawa and T. Tomiyama. *J. Biochem. (Tokyo)*, **11**, 265 (1929); M. Kitagawa and H. Yamada. *J. Biochem. (Tokyo)*, **16**, 339 (1932); M. Kitagawa and K.-I. Monobe. *J. Biochem. (Tokyo)*, **18**, 333 (1933); M. Kitagawa and A. Takani. *J. Biochem. (Tokyo)*, **23**, 181 (1936); M. Kitagawa. *J. Biochem. (Tokyo)*, **24**, 197 (1936); **25**, 23 (1937).
8. G.A. Rosenthal. *Biochem. Syst. Ecol.* **5**, 219 (1977).
9. A.J.L. Cooper. *Arch. Biochem. Biophys.* **233**, 603 (1984).
10. E.-L. Rahiala, M. Kekomaki, J. Janne, A. Raina, and N.C.R. Raiha. *Biochim. Biophys. Acta*, **227**, 337 (1971); E.-L. Rahiala. *Acta. Chem. Scand.* **27**, 3861 (1973).
11. G.A. Rosenthal. *Life Sci.* **60**, 1635 (1997).
12. B.J. Berger. *Antimicrob. Agents Chemother.* **44**, 2540 (2000).
13. (a) R.M. Khomutov, M.Ya. Karpeiskii, and E.S. Severin. *Izv. Akad. Nauk. SSSR Ser. Khim.* 1074 (1962); (b) M. Frankel, Y.



- Knobler, E. Bonni, S. Bittner, and G. Zvilichovsky. *J. Chem. Soc. C*, 1746 (1969).
14. J. Smrt, J. Beranek, and M. Horak. *Coll. Czech. Chem. Commun.* **24**, 1672 (1959); N.K. Kotchetkov, R.M. Khomutov, E.S. Severin, M.Ya. Karpeiskii, E.I. Budovskii, and V.I. Erashko. *Zh. Obsch. Khim.* **29**, 3417 (1959).
15. M.Ya. Karpeiskii, R.M. Khomutov, and S. Severin. *Zh. Obsch. Khim.* **32**, 1357 (1962).
16. D.D. Nyberg and B.E. Christensen. *J. Am. Chem. Soc.* **79**, 1222 (1957).
17. A.J. Ozinskas and G.A. Rosenthal. *J. Org. Chem.* **51**, 5047 (1986).
18. R.M. Khomutov, M. Karpeiskii, M.A. Breger, and E.S. Severin. *Vopr. Med. Khim.* **8**, 389 (1962).
19. R.M. Khomutov, M.Y. Karpeiskii, M.A. Breger, and E.S. Severin. *Fed. Proc.* **22**, 637 (1963).
20. (a) T. Hirose, K. Chiba, S. Mishio, J. Nakano, and H. Uno. *Heterocycles*, **19**, 1019 (1982); (b) C.K. Zercher and M.J. Miller. *Tetrahedron Lett.* **30**, 7009 (1989); (c) A. Biswas, M.J. Miller, M.A. Crook, and S.R. Woulfe. *Spec. Publ. R. Soc. Chem.* **52**, 305 (1985).
21. S.R. Woulfe and M.J. Miller. *Tetrahedron Lett.* **25**, 3293 (1984); S.R. Woulfe and M.J. Miller. *J. Med. Chem.* **28**, 1447 (1985); M.J. Miller. *Acc. Chem. Res.* **19**, 49 (1986).
22. D. Kroenthal, P. Kuester, and W.H. Koster. *Intl. Congr. Heterocycl. Chem.* 10th, Abstract G3-25, 1985.
23. S.R. Woulfe, H. Iwagami, and M.J. Miller. *Tetrahedron Lett.* **26**, 3891 (1985); S.R. Woulfe and M.J. Miller. *J. Org. Chem.* **51**, 3133 (1986).
24. D.B. Boyd, C. Eigenbrot, J.M. Indelicato, M.J. Miller, C.E. Pasini, and S.R. Woulfe. *J. Med. Chem.* **30**, 528 (1987).
25. D.B. Boyd. *In Amide linkage. Edited by A. Greenberg, C.M. Breneman, and J.F. Liebman.* John Wiley, New York, 2000. p. 337; J. Frau, J. Donosa, F. Munoz, and F.G. Blanco. *Helv. Chim. Acta*, **77**, 1557 (1994); G. Dive, D. Dehareng, and D. Peeters. *Int. J. Quantum Chem.* **58**, 85 (1996); J. Frau, J. Donoso, F. Munoz, and F. Garcia-Blanco. *Helv. Chim. Acta*, **79**, 353 (1996); J. Pitarch, M.F. Ruiz-Lopez, J.-L. Pascual-Ahuir, E. Silla, and I. Tunon. *J. Phys. Chem. B*, **101**, 3581 (1997); J. Frau, J. Donoso, F. Munoz, B. Vilanova, and F. Garcia-Blanco. *Helv. Chim. Acta*, **80**, 739 (1997); M. Coll, J. Frau, J. Donoso, and F. Munoz. *THEOCHEM.* **426**, 323 (1998); J. Frau, J. Donoso, F. Munoz, B. Vilanova, and F. Garcia-Blanco. *THEOCHEM.* **426**, 313 (1998); J. Pitarch, M.F. Ruiz-Lopez, E. Silla, J.-L. Pascual-Ahuir, and I. Tunon. *J. Am. Chem. Soc.* **120**, 2146 (1998); N. Diaz, D. Suarez, and T.L. Sordo. *Chem. Eur. J.* **5**, 1045 (1999); N. Diaz, D. Suarez, and T.L. Sordo. *J. Org. Chem.* **64**, 3281 (1999); I. Massova and P.A. Kollman. *J. Phys. Chem. B*, **103**, 8628 (1999); G. Dive and D. Dehareng. *Int. J. Quantum Chem.* **73**, 161 (1999); J. Pitarch, J.-L. Pascal-Ahuir, E. Silla, I. Tunon, and M.F. Ruiz-Lopez. *J. Comput. Chem.* **20**, 1401 (1999); J. Pitarch, J.-L. Pascual-Ahuir, E. Silla, I. Tunon, and V. Moliner. *J. Am. Chem. Soc. Perkin Trans. 2*, 1351 (1999); J. Pitarch, J.-L. Pascual-Ahuir, E. Silla, I. Tunon, M.F. Ruiz-Lopez, C. Millot, and J. Bertran. *Theor. Chem. Acc.* **101**, 336 (1999); R. Lopez, M.I. Menendez, N. Diaz, D. Suarez, P. Campomanes, and T.L. Sordo. *Rec. Res. Dev. in Phys. Chem.* **4**, 157 (2000); J. Pitarch, J.-L. Pascual-Ahuir, E. Silla, and I. Tunon. *Perkin 2*, 761 (2000); N. Diaz, D. Suarez, T.L. Sordo, and K.M. Merz, Jr. *J. Phys. Chem. B*, **105**, 11302 (2001); N. Diaz, D. Suarez, T.L. Sordo, I. Tunon, and E. Silla. *Chem. Eur. J.* **8**, 859 (2002); N. Diaz, T.L. Sordo, K.M. Merz, Jr., and D. Suarez. *J. Am. Chem. Soc.* **125**, 672 (2003).
26. S. Wolfe. *Can. J. Chem.* **72**, 1014 (1994); S. Wolfe, C.-K. Kim, and K. Yang. *Can. J. Chem.* **72**, 1033 (1994).
27. S. Wolfe, C.-K. Kim, K. Yang, N. Weinberg, and Z. Shi. *J. Am. Chem. Soc.* **117**, 4240 (1995); S. Wolfe, Z. Shi, K. Yang, S. Ro, N. Weinberg, and C.-K. Kim. *Can. J. Chem.* **76**, 114 (1998).
28. W.J. Hehre, L. Radom, P. von R. Schleyer, and J.A. Pople. *Ab initio molecular orbital theory.* Wiley-Interscience, New York, 1986.
29. S. Wolfe, A.V. Buckley, and N. Weinberg. *Can. J. Chem.* **79**, 1284 (2001).
30. R.M. Sweet and L.F. Dahl. *J. Am. Chem. Soc.* **92**, 5489 (1970).
31. R.B. Woodward. *In The chemistry of penicillin. Edited by H.T. Clarke, J.R. Johnson, and R. Robinson.* Princeton University Press, Princeton, N.J. 1949. p. 440.
32. A. Rauk. *Orbital interaction theory of organic chemistry.* John Wiley, New York, N.Y. 1994.
33. T.A. Albright, J.K. Burdett, and M.-H. Whangbo. *Orbital interactions in chemistry.* John Wiley, New York, N.Y. 1985.
34. S. Wolfe and Z. Shi. *Isr. J. Chem.* **40**, 343 (2000).
35. A. Tsuji, T. Yamana, S. Matsutani, and N. Tsuji. *Heterocycles*, **8**, 153 (1977). See also footnote 18 of J. Marchand-Bryner and L. Ghosez. *Recent Prog. Chem. Synth. Antibiot.* 727 (1990).
36. J.E. Baldwin, C. Lowe, and C.J. Schofield. *Tetrahedron Lett.* **31**, 2211 (1990).
37. K. Yoshioka and T. Miwa. *Jpn Kokai Tokkyo Koho JP 62215585.* Sept 22, 1987. *Chem. Abstr.* **108**, P186753z (1988).
38. S. Wolfe, M.-C. Wilson, M.-H. Cheng, G.V. Shustov, and C.I. Akuche. *Can. J. Chem.* This issue.
39. J. Lamotte, G. Dive, and J.-M. Ghuysen. *Eur. J. Med. Chem.* **26**, 43 (1991).
40. N.C. Cohen. *J. Med. Chem.* **26**, 259 (1983).
41. H.R. Pfaendler, J. Gosteli, R.B. Woodward, and G. Rihs. *J. Am. Chem. Soc.* **103**, 4526 (1981).
42. S. Wolfe, K. Yang, and M. Khalil. *Can. J. Chem.* **66**, 2733 (1988).
43. T.N. Salzmann, R.W. Ratcliffe, B.G. Christensen, and F.A. Bouffard. *J. Am. Chem. Soc.* **102**, 6161 (1980).
44. J.J.P. Stewart. *J. Comput. Chem.* **10**, 209 (1989).
45. E.F. Schoenewaldt, R.B. Kinnel, and P. Davis. *J. Org. Chem.* **33**, 4270 (1968).
46. T. Polinski and A. Chimiak. *J. Org. Chem.* **41**, 2092 (1976).
47. E. Buehler and G.B. Brown. *J. Org. Chem.* **32**, 265 (1967).
48. J.D.M. Herscheid and H.C.J. Ottenheijm. *Tetrahedron Lett.* **51**, 5143 (1978).
49. M.W. Tjihuis, J.D.M. Herscheid, and H.C.J. Ottenheijm. *Synthesis*, 890 (1980).
50. T. Tsuji, T. Kataoka, M. Yoshioka, Y. Sendo, S. Hirai, T. Maeda, and W. Nagata. *Tetrahedron Lett.* **30**, 2793 (1979).
51. M. Sato, J. Sakaki, K. Takayama, S. Kobayashi, M. Suzuki, and C. Kaneko. *Chem. Pharm. Bull.* **38**, 94 (1990).
52. J. Zhu, S. Robin, N. Goasdoue, A. Loupy, and H. Galons. *Synlett*, 97 (1995).
53. A. Koziara, K. Osowska-Pacewicz, S. Zawadzki, and A. Zwierzak. *Synthesis*, 202 (1985).
54. J. Alexander, M.L. Renyer, and H. Veerapanane. *Synth. Commun.* **25**, 3875 (1995).
55. J.E. Baldwin. *J. Chem. Soc. Chem. Commun.* 734 (1976).
56. A. Streitwieser, Jr. *Chem. Rev.* **56**, 571 (1956).
57. G. Cardillo and M. Orena. *Tetrahedron*, **46**, 3321 (1990); J.M. Barks and D.W. Knight. *Tetrahedron Lett.* **35**, 7259 (1994).
58. H.J. Reich and S.L. Peake. *J. Am. Chem. Soc.* **100**, 4888 (1978).



59. G. Procter, J. Nally, and N.H.R. Ordsmith. *Tetrahedron*, **51**, 12 837 (1995).
60. T. Takigawa and T. Matsuo. *Tetrahedron*, **35**, 933 (1979).
61. S. Saito, T. Hasegawa, M. Inaba, R. Nishida, T. Fujii, S. Nomizu, and T. Moriwake. *Chem. Lett.* 1389 (1984).
62. C. Brockway, P. Kocienski, and C. Pant. *J. Chem. Soc. Perkin Trans. 1*, 875 (1984).
63. D.I. Hughes. *Org. React. (New York)*, **42**, 335 (1992).
64. M.F. Lipton, A. Basha, and S.A. Weinreb. *Org. Synth.* **59**, 49 (1979).
65. D.C. Harrowven and R.F. Dainty. *Tetrahedron Lett.* **36**, 6739 (1995).
66. M. Larcheveque and S. Henrot. *Tetrahedron*, **46**, 4277 (1990).
67. R.J. Clemens and J.A. Hyatt. *J. Org. Chem.* **50**, 2431 (1985).
68. R.J. Clemens. *Chem. Rev.* **86**, 241 (1986).
69. K.F. Bernady, M.B. Floyd, J.F. Poletto, and M.J. Weiss. *J. Org.Chem.* **44**, 1438 (1979).
70. D.D. Perrin and W.L.F. Armarego. *In Purification of laboratory chemicals*. 3rd ed. Pergamon. 1988.
71. W.C. Still, M. Kahn, and A. Mitra. *J. Org. Chem.* **43**, 2923 (1978).



# Cyclic hydroxamates, especially multiply substituted [1,2]oxazinan-3-ones

Saul Wolfe, Marie-Claire Wilson, Ming-Huei Cheng, Gennady V. Shustov, and Christiana I. Akuche

**Abstract:** Routes to putative *N*-acyl-D-ala-D-ala surrogates, beginning with the conversion of 4-, 5-, and 6-membered lactones into 5-, 6-, and 7-membered cyclic hydroxamates, are reported. The key step of the synthesis is trimethylaluminium-promoted cyclization of an  $\omega$ -aminoxyester. The 7-membered cyclic hydroxamate crystallizes in a chair conformation. Extension of the reaction sequence to homoserine or homoserine lactone leads to cyclocanaline and *N*-acylated cyclocanalines. The 4-phenylacetamido derivative of cyclocanaline crystallizes in a boat conformation. The attachment of a 2-carboxypropyl substituent to the ring nitrogen of a 4-acylaminocyclocanaline has been effected, prior to cyclization, by coupling of the acyclic aminoxyester precursor to the triflate of benzyl lactate or, after cyclization, by coupling to *tert*-butyl  $\alpha$ -bromopropionate in the presence of potassium fluoride – alumina, followed by removal of the protecting group in each case. A six-membered homolog of the antibiotic lactivicin has been synthesized by the reaction of 4-phenylacetamidocyclocanaline with benzyl 2-oxoglutarate in the presence of carbodiimide, followed by hydrogenolysis. Starting with methyl 2,4-dibromo-2,4-dideoxy-L-erythronate, which is available in two steps from L-ascorbic acid, these reaction sequences have been applied to the stereospecific synthesis of a D-alanine derivative whose nitrogen atom is enclosed within a 3,4-disubstituted [1,2]oxazinan-3-one.

**Key words:** D-ala-D-ala surrogate, cyclocanaline, homolactivicin, peptidoglycan, trimethylaluminium.

**Résumé :** On a développé des nouvelles voies permettant de préparer des produits de substitutions potentiels de la *N*-acyl-D-ala-D-ala; elles débutent par la conversion des lactones à 4-, 5- et 6-chaînon en hydroxamates cycliques à 5-, 6- et 7-chaînon. L'étape clé de la synthèse est une cyclisation catalysée par le triméthylaluminium d'un  $\omega$ -aminoxyester. L'hydroxamate cyclique à sept chaînon cristallise dans une conformation chaise. L'extension de la séquence de réaction à l'homosérine ou à la lactone de l'homosérine conduit à la formation de la cyclocanaline et à des cyclocanalines *N*-acétylées. Le dérivé 4-phénylacétamido de la cyclocanaline cristallise dans la conformation bateau. On a effectué la fixation d'un substituant 2-carboxycyclopropyle sur l'azote du cycle d'une 4-acylaminocyclocanaline avant la cyclisation, par le couplage du précurseur aminoxyester acyclique au triflate du lactate de benzyle, ou après la cyclisation, par couplage à l' $\alpha$ -bromopropionate de *t*-butyle en présence de fluorure de potassium et d'alumine, suivi dans chaque cas de l'enlèvement du groupe protecteur. On a réalisé la synthèse d'un homologue à six chaînon de l'antibiotique lactivicine par réaction de la 4-phénylacétamidocyclocanaline avec du 2-oxoglutarate de benzyle en présence de carbodiimide, suivie d'une hydrogénolyse. Utilisant comme produit de départ le 2,4-dibromo-2,4-didésoxy-L-érythronate de méthyle qui est disponible en deux étapes à partir de l'acide L-ascorbique, on a appliqué cette séquence de réactions à la synthèse stéréospécifique d'un dérivé D-alanine dont l'atome d'azote est inclus dans une [1,2]oxazinan-3-one disubstituée dans les positions 3 et 4.

**Mots clés :** substitut de D-ala-D-ala, cyclocanaline, homolactivicine, peptidoglycane, triméthylaluminium.

[Traduit par la Rédaction]

## Introduction

We have recently given theoretical and experimental reasons for our belief that the six-membered cyclic hydroxamate **1** can function as a  $\beta$ -lactam surrogate (1). Since penicillin (2), the quintessential  $\beta$ -lactam compound, is itself a conformationally constrained surrogate of *N*-acyl-D-ala-D-ala (3) (the peptide terminus of the growing bacterial cell wall peptidoglycan (2)), the introduction of an acylamino group at

C4 of **1** and the attachment of a 2-carboxypropyl substituent onto the ring nitrogen of the resulting cyclocanaline derivative **4** (3) would lead to **5**, a novel but conformationally flexible surrogate of **3**.

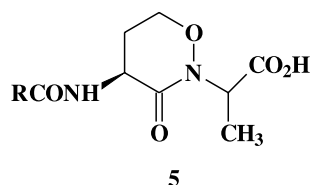
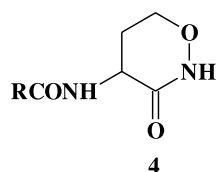
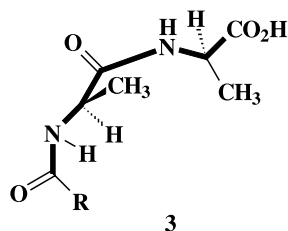
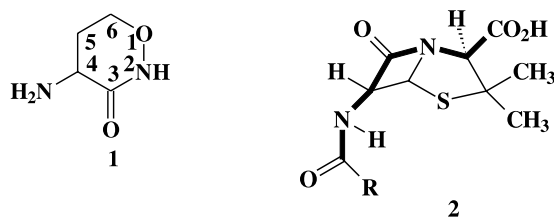
There is precedent for the proposal of **5** as a synthetic target in the structure of the natural product lactivicin (6), which exhibits affinity to penicillin-recognizing enzymes (4), and in the claim that homolactivicins (7) have antibacterial activity (5). However, as a caveat, it was known at the

Received 19 November 2002. Published on the NRC Research Press Web site at <http://canjchem.nrc.ca> on 15 August 2003.

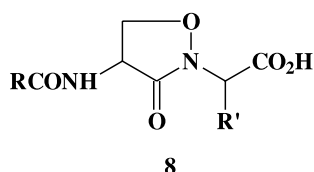
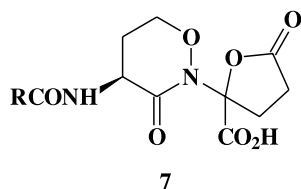
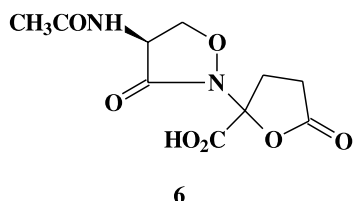
S. Wolfe,<sup>1</sup> M.-C. Wilson, M.-H. Cheng, G.V. Shustov, and C.I. Akuche. Department of Chemistry, Simon Fraser University, Burnaby, BC V5A 1S6, Canada.

<sup>1</sup>Corresponding author (e-mail: [swolfe@sfu.ca](mailto:swolfe@sfu.ca)).



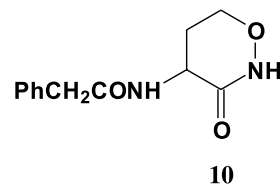
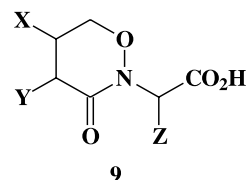


beginning of the present work that cycloserine derivatives such as **8** are inactive (6).



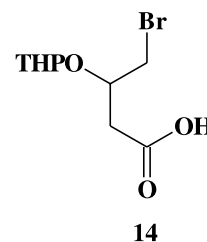
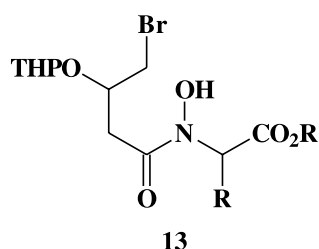
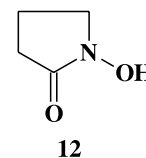
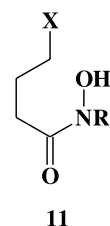
In this paper we describe a reaction sequence leading from lactone precursors to cyclic hydroxamates and the application of this sequence to the synthesis of biologically inactive D-cyclocaniline, to non-stereospecific syntheses of biologically inactive **5** and **7**, and to a stereospecific approach to the more general structure **9**.

Crystal structures of the parent 7-membered cyclic hydroxamate [1,2]oxazepan-3-one and phenylacetylcyclocaniline **10** are also reported.



## Results and discussion

Although earlier workers (7) had found cyclization of unsubstituted  $\gamma$ -halohydroxamic acids (**11**, R = H, X = halogen) to lead mainly to the 5-membered 1-hydroxypyrrolidin-2-one (**12**) and not to the 6-membered **1**, we observed that only the 6-membered ring is produced in the cyclization of **13**, R = H or Me (**1**). However, in the latter case (R = Me), the N-acylated product **13**, formed by coupling of the *tert*-butyl ester of N-hydroxyalanine to **14**, was accompanied by the O-acylated product.



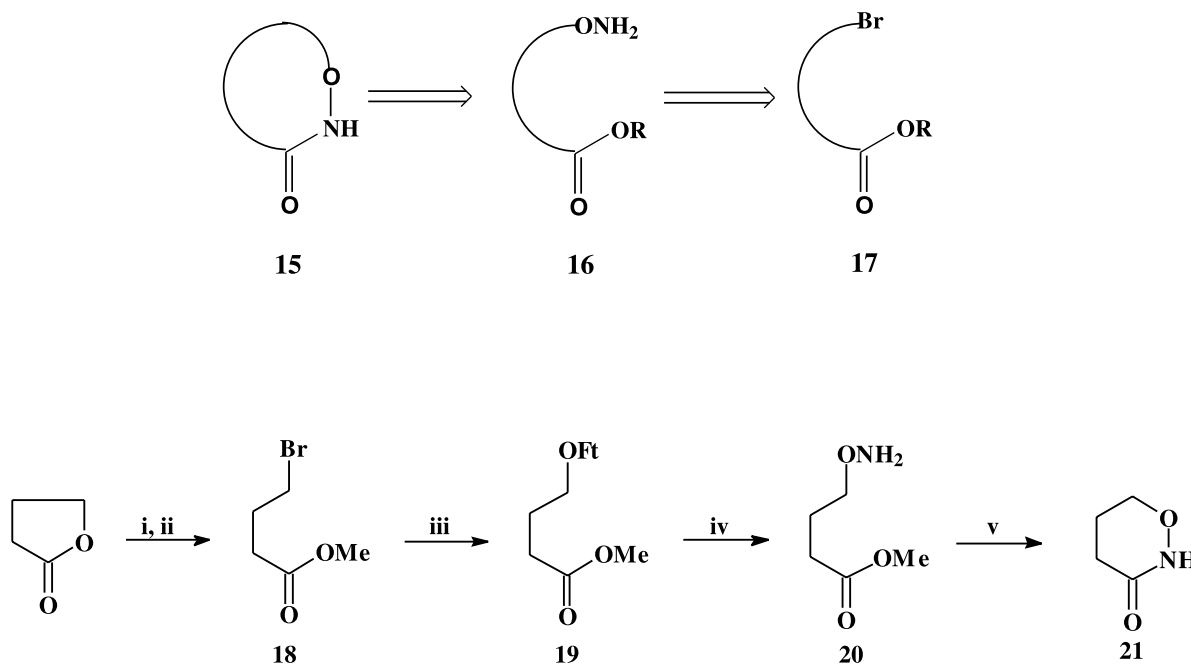
To avoid this problem in the general case Z  $\neq$  H, we examined the sequence **15**  $\rightarrow$  **16**  $\rightarrow$  **17**, in which ring closure proceeds by N2—C3 bond formation. Previous workers had reported (8) that this strategy produces cyclocaniline in 35% yield by the action of ethanolic KOH on caniline ethyl ester and N-benzoyl cyclocaniline in 75% yield upon treatment of N-benzoyl caniline ethyl ester with methanolic NaOH. We have now found trimethylaluminium (9) cyclization of aminoxy esters to be a general reaction for the production of cyclic hydroxamates of increasing complexity. The work proceeded in five stages.

## 5-, 6-, 7-, And 8-membered cyclic hydroxamates from 4-, 5-, 6-, and 7-membered lactone precursors

In the first stage, with  $\gamma$ -butyrolactone as the prototype



**Scheme 1.** Reagents and conditions: (i) 45% HBr–HOAc, 75 °C; (ii) MeOH; (iii) FtOH, Et<sub>3</sub>N, MeCN, reflux; (iv) MeNHNH<sub>2</sub>, CH<sub>2</sub>Cl<sub>2</sub>; (v) AlMe<sub>3</sub>, THF.



(Scheme 1), a four-step synthesis of the parent 5-, 6-, 7-, and 8-membered cyclic hydroxamates from 4-, 5-, 6-, and 7-membered lactones was developed, consisting of conversion to  $\omega$ -bromo methyl esters, displacement of bromine with *N*-hydroxyphthalimide, removal of the phthalimido (Ft) protecting group with methylhydrazine, and cyclization.

Heating of butyrolactone at 75 °C with a 45% solution of hydrogen bromide in acetic acid, followed by addition of methanol, gave methyl  $\gamma$ -bromobutyrate (**18**) in 86% yield (10). A protected aminooxy group was introduced by displacement of bromine with *N*-hydroxysuccinimide (11) or *N*-hydroxyphthalimide (12). Both products were crystalline, with mp 69–71.5 and 79–81 °C, respectively, but the yield of methyl  $\gamma$ -phthalimidooxybutyrate (**20**) was 78%, and the yield of methyl  $\gamma$ -succinimidooxybutyrate could not be increased above 28%. Removal of the succinimido protecting group required a 12 h treatment with 4 equiv of hydrazine hydrate in methanol at room temperature to give **20** in 45% yield (12). In contrast, **19** gave a quantitative yield of **20** with 1.5 equiv of methylhydrazine in dichloromethane for 1.5 h at –10 to 0 °C (13). The methyl ester was stable to these conditions. The cyclization of **20** was achieved initially using the basic conditions reported by Khomutov et al. (8). Refluxing with potassium hydroxide in methanol for 2 h, followed by stirring at room temperature overnight, produced **21** in 24% yield. The <sup>1</sup>H NMR spectrum showed peaks at 8.89 (1H, br s, NH), 4.03 (2H, t, 6.5 Hz, CH<sub>2</sub>O), 2.52 (2H, t, 7.2 Hz, COCH<sub>2</sub>), and 2.10 (2H, quintet, 6.9 Hz, COCH<sub>2</sub>CH<sub>2</sub>) ppm. The <sup>13</sup>C NMR spectrum showed peaks at 172.93, 69.04, 27.42, and 21.55 ppm. Infrared absorptions at 3403 and 1667 cm<sup>–1</sup> were assigned to the N–H and carbonyl groups. The CI mass spectrum showed an [M + 1] peak at *m/z* 102. The EI mass spectrum showed, in addition to the molecular ion, a peak at [M – 32], corresponding to loss of H<sub>2</sub>NO (**22**). Trimethylaluminum gave better results. With

2 equiv in tetrahydrofuran or toluene and at room temperature or reflux temperature, the yield of **21** was 65–79%.

Following these exploratory experiments, the 5-, 7-, and 8-membered cyclic hydroxamates were prepared, as summarized in Table 1. The EI mass spectra all showed, in addition to the molecular ion, the peak at [M – 32]. In the case of the 8-membered ring, [1,2]oxazocan-3-one, after numerous unsuccessful experiments, cyclization of the aminooxy ester was performed by dropwise treatment of 4 equiv of a 0.18 mol/L solution of trimethylaluminum in heptane (4.96 mL) and toluene (50 mL) with 50 mL of a 0.4% solution of the ester in toluene, followed by stirring at room temperature for six days. After addition of water and concentration to near dryness, the gelatinous residue was dissolved in 1:4 dichloromethane:tetrahydrofuran, filtered through Celite, and evaporated. Preparative layer chromatography yielded three bands, one of which contained 84 mg of material. The GC of this material contained several peaks, one of which, comprising 2% of the total, gave an EI-MS with peaks at *m/z* 129, corresponding to the molecular ion, and 97, corresponding to loss of H<sub>2</sub>NO. In Yamamoto's trimethylaluminum-promoted lactam synthesis (14), the 8-membered ring was obtained in 7% yield, which was increased to 43% using triethylgallium.

The 7-membered ring [1,2]oxazepan-3-one crystallized as colourless plates, mp 84.5–85.8 °C, and its crystal structure was determined. The compound crystallizes in the *P*2<sub>1</sub>/*a* space group and is centrosymmetric with four molecules, consisting of two hydrogen-bonded dimers, in the unit cell. Figure 1 shows several views of the crystal structure. As seen in the centre of this figure, the dimer is held together by linear NH...O=C hydrogen bonds; this causes the two monomeric units to be offset with respect to each other, unlike the structure drawn at the bottom. The monomeric structure is a chair.



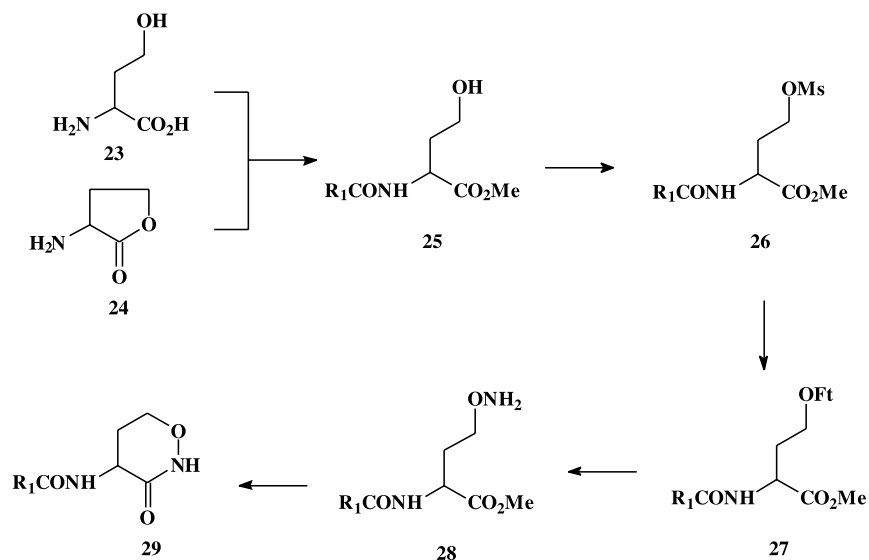
**Table 1.** Conversion of lactones into cyclic hydroxamates.

<i>n</i>	Yield (%)	Yield (%)	Yield (%)	Yield (%)	Yield (%)
1	56	21 <sup>a</sup>	50	45	
2	86	78	quantitative	79	
3	87	74	97	82 <sup>b</sup>	
4	95	99	98	trace <sup>c</sup>	

<sup>a</sup>This reaction was found to proceed via methyl acrylate. The compound was therefore prepared more conveniently by addition of *N*-hydroxyphthalimide to methyl acrylate in refluxing methanol containing triethylamine.

<sup>b</sup>The 7-membered ring ([1,2]oxazepan-3-one) crystallized as colourless plates; mp 84.5–85.8 °C, and its X-ray structure was determined.

<sup>c</sup>See text.

**Scheme 2.**

### Cyclocanaline and *N*-acylcyclocanalines

In the second stage, with trimethylaluminium-promoted cyclization of an  $\omega$ -aminooxyester established as a viable reaction, syntheses of cyclocanaline and *N*-acylated cyclocanalines from homoserine (**23**) or homoserine lactone (**24**) were undertaken, as shown in Scheme 2, via **26**, the mesylate of the *N*-acylated methyl ester **25**. The conversion of **26** to **27** proceeded in 64% yield with  $R_1 = \textit{tert}$ -butoxy, using *N*-hydroxyphthalimide and DBU in dimethylformamide, and in 84% yield with  $R_1 = \text{benzyl}$ , using *N*-hydroxyphthalimide and triethylamine in acetonitrile. In both cases the removal of the phthalimido group and the subsequent cyclization of **28** to **29** proceeded without incident. Deprotection of **29**,  $R_1 = \textit{t}$ -BuO, to the trifluoroacetic acid salt of cyclocanaline took place in 98% yield, and this salt was converted to **29**,  $R_1 = \text{PhOCH}_2$ .

The phenylacetyl derivative **10** crystallized as colourless plates, mp 164–165 °C, of acceptable quality for an X-ray structure determination. The compound crystallizes in the *P2<sub>1</sub>/a* space group and is centrosymmetric with four molecules (two enantiomeric pairs) in the unit cell. Figure 2 shows one of these pairs. The oxazinone ring has a boat con-

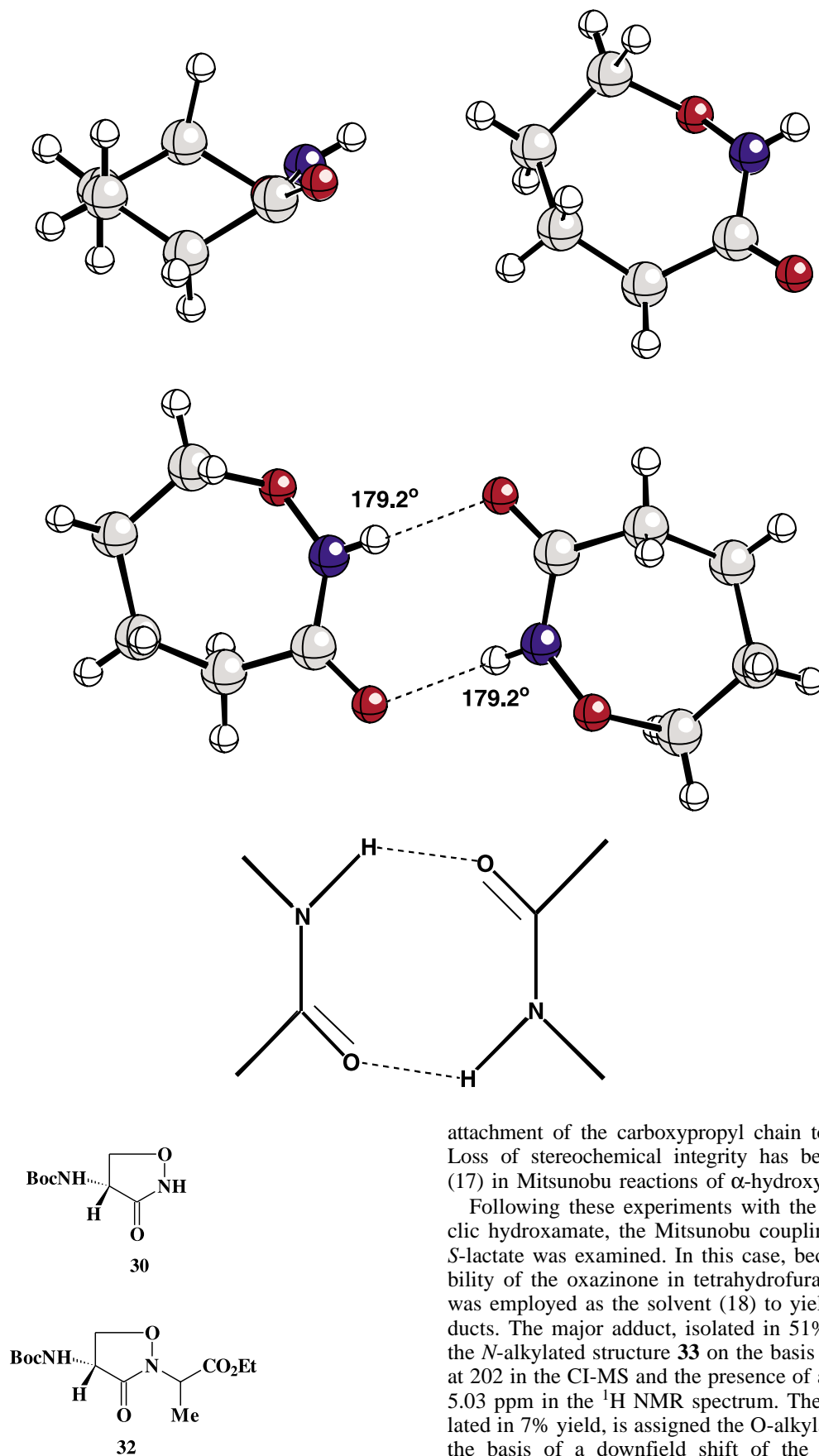
formation with O1 and C4 at the apices and an equatorial acylamino substituent.

The reaction sequences just described were carried out from racemic homoserine, from commercially available *S*-homoserine lactone, and from *R*-methionine, which is readily converted to *R*-homoserine lactone (**15**). D-Cyclocanaline was inactive at a concentration of 125  $\mu\text{g/mL}$  against a panel of gram-positive, gram-negative, and  $\beta$ -lactam-producing organisms.

### N2-alkylation of cyclic hydroxamates

In the third stage we examined the attachment of a substituent to the ring nitrogen of a cyclic hydroxamate. The initial experiments were performed under Mitsunobu conditions (**16**), using *tert*-butoxycarbonyl-protected *R*-cycloserine (**30**) and ethyl *S*-lactate (**31**). With tetrahydrofuran as the solvent, these experiments yielded a mixture of two products whose <sup>1</sup>H NMR spectra featured methyl doublets at 1.53 and 1.58 ppm and methine quartets at 4.80 and 4.96 ppm. The CI mass spectrum showed an  $[M + 1]$  peak at  $m/z$  303 and a prominent peak at 247 corresponding to loss of  $\text{C}_4\text{H}_8$ . The mixture is assigned structure **32**, formed by nonstereospecific

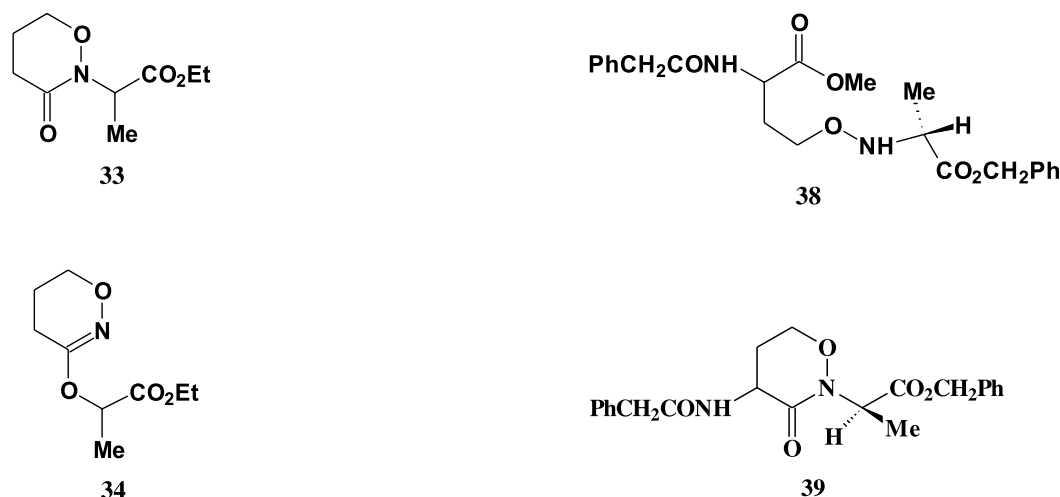


**Fig. 1.** Crystal structure of [1,2]oxazepan-3-one.

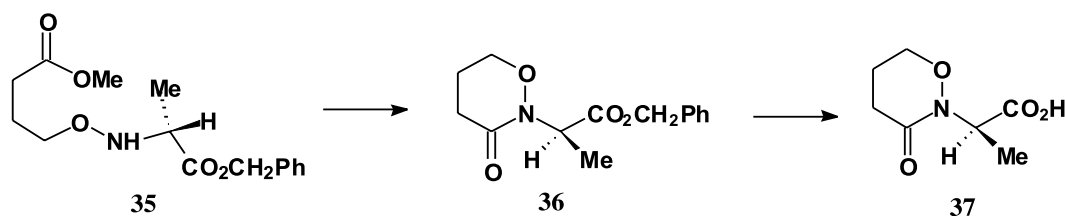
attachment of the carboxypropyl chain to the ring nitrogen. Loss of stereochemical integrity has been seen previously (17) in Mitsunobu reactions of  $\alpha$ -hydroxyesters.

Following these experiments with the five-membered cyclic hydroxamate, the Mitsunobu coupling of **21** with ethyl *S*-lactate was examined. In this case, because of the insolubility of the oxazinone in tetrahydrofuran, dichloromethane was employed as the solvent (18) to yield two isomeric adducts. The major adduct, isolated in 51% yield, is assigned the *N*-alkylated structure **33** on the basis of an  $[M + 1]$  peak at 202 in the CI-MS and the presence of a methine quartet at 5.03 ppm in the  $^1\text{H}$  NMR spectrum. The minor adduct, isolated in 7% yield, is assigned the *O*-alkylated structure **34** on the basis of a downfield shift of the methine quartet to





Scheme 3.



5.20 ppm. O-Alkylation is a known reaction of *N*-acylated hydroxylamines (19).

The loss of stereochemical integrity in the attachment of the carboxypropyl moiety to the ring nitrogen in the case of *tert*-butoxycarbonyl *R*-cycloserine and the competing O-alkylation in the reaction of the oxazinone suggested that the introduction of a carboxypropyl substituent be performed prior to cyclization, i.e., **20** → **35**. However, **20** was unreactive under Mitsunobu conditions.

It was then discovered (Scheme 3) that **35** could be synthesized in 74% yield by alkylation of the amino group of **20** with the triflate of benzyl *S*-lactate. This alkylation reaction is reported to proceed with inversion of configuration (20), a finding confirmed in the present work (*vide infra*).

The cyclization of **35** using trimethylaluminium proceeded in 84% yield to give the benzyl ester **36**, which was successfully deprotected by hydrogenolysis to the acid **37**.

#### N2- and N'-functionalized [1,2]oxazinan-3-ones

Alkylation of **28**,  $R_1 = \text{PhCH}_2$ ,  $R_2 = \text{Me}$ , with the triflate of benzyl *S*-lactate afforded **38** in 29% yield as a 1:1 mixture of diastereomers. Cyclization with trimethylaluminium produced one of the isomers of **39** in 36% yield.

More effectively in this case (Scheme 4), treatment of **10** with *tert*-butyl *S*- $\alpha$ -bromopropionate in the presence of potassium fluoride – alumina produced the diastereomeric products **40a** (26%) and **40b** (31%). Deprotection with trifluoroacetic acid gave **5a**, mp 58–60 °C, from **40a** and **5b**, mp 189–190 °C, from **40b**. The  $^1\text{H}$  NMR spectra of these compounds, *neither of which was active at a concentration of 32  $\mu\text{g/mL}$  against a panel of Gram-positive, Gram-*

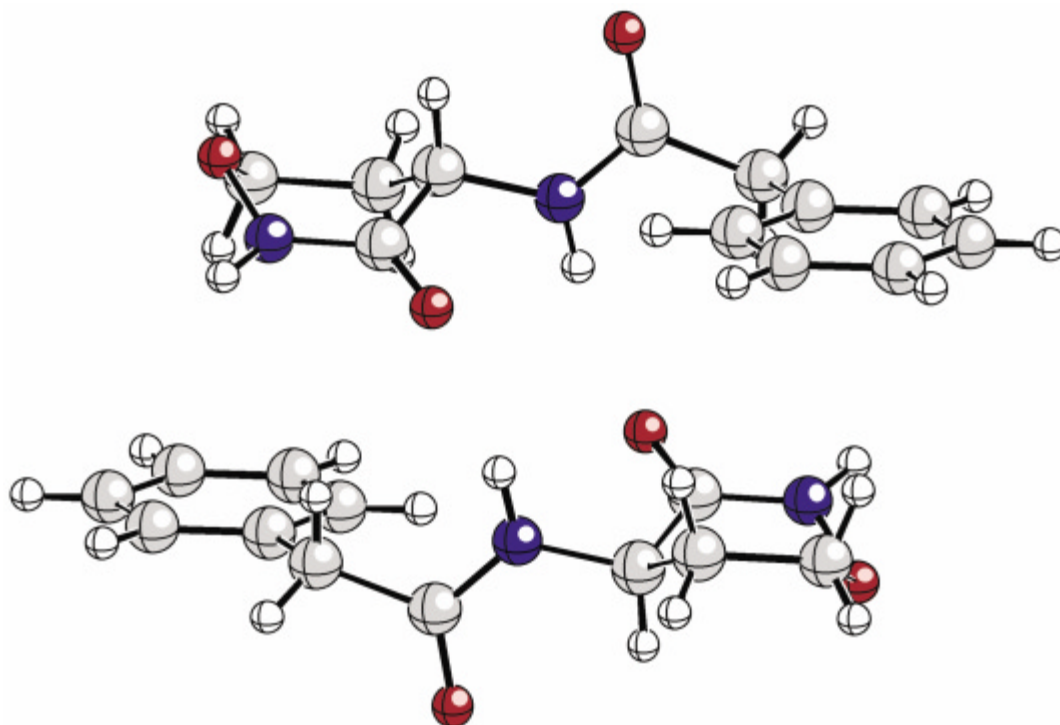
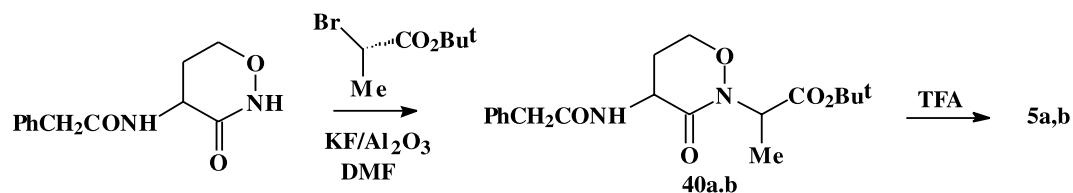
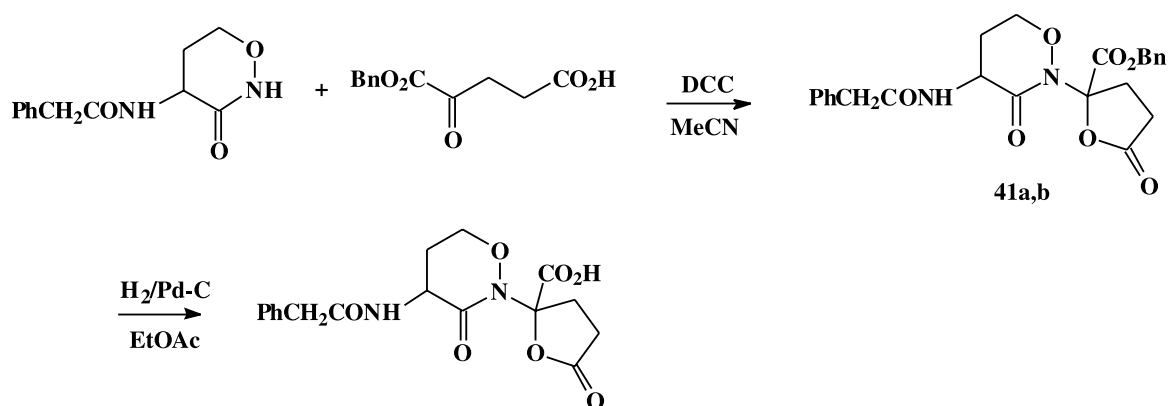
*negative, and  $\beta$ -lactam-producing organisms, are shown in Figs. 3 and 4.*

For the synthesis of homolactivicin (**7**,  $R = \text{PhCH}_2$ ) (Scheme 5), racemic **10**, benzyl 2-oxoglutarate, and dicyclohexylcarbodiimide were stirred for three days in acetonitrile to give the diastereomeric products **41a** (31%) and **41b** (21%). Hydrogenolysis of a 1:1 mixture of **41a** and **41b** gave a homolactivicin, mp 150–152 °C, as a mixture of isomers, which was inactive at a concentration of 32  $\mu\text{g/mL}$  against a panel of Gram-positive, Gram-negative, and  $\beta$ -lactam-producing organisms.

#### Stage 5: Chiral synthesis of 2,4,5-trisubstituted [1,2]oxazinan-3-ones

As summarized in Scheme 6, calcium L-threonate (**42**), prepared in 95% yield by hydrogen peroxide oxidation of L-ascorbic acid (21), was converted in 90% yield to methyl 2,4-dibromo-2,4-dideoxy-L-erythronate (**43**) by the procedure of Bock et al. (22). Methoxymethylation using dimethoxymethane and boron trifluoride, followed by reaction with sodium azide in dimethylformamide, gave the protected azido threonate **44** in 68% yield over the two steps. Hydrogenolysis in the presence of di-*tert*-butyl carbonate yielded the protected threonate methyl ester **45** (74%), and the introduction of the aminooxy function by an *N*-hydroxyphthalimide-methylhydrazine sequence produced **46** in 46% yield from **45**. Reaction of **46** with the triflate of benzyl L-lactate gave a single *N*-hydroxyalanine product, assigned the *R*-configuration **47**, in 66% yield. The cyclizations of **46** and **47** to **48** and **49** were achieved in 90% and 63% yield, respectively.



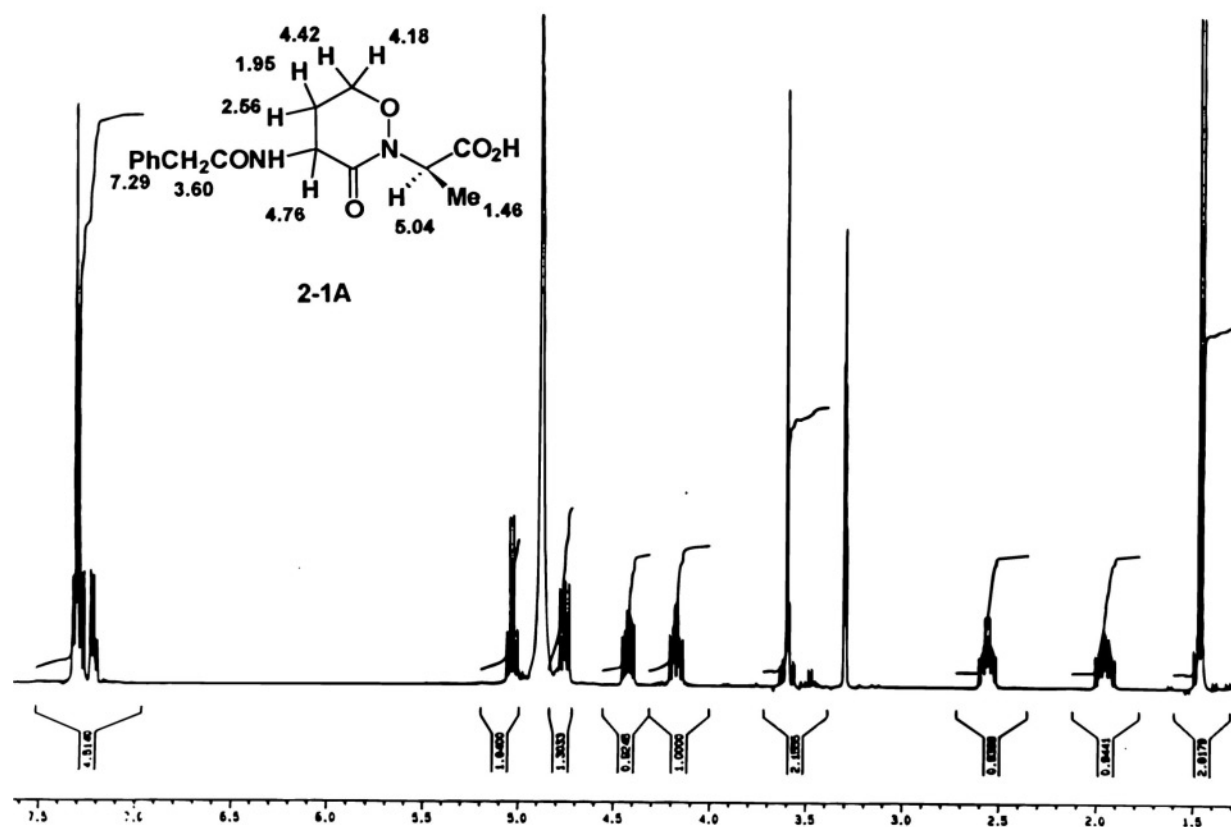
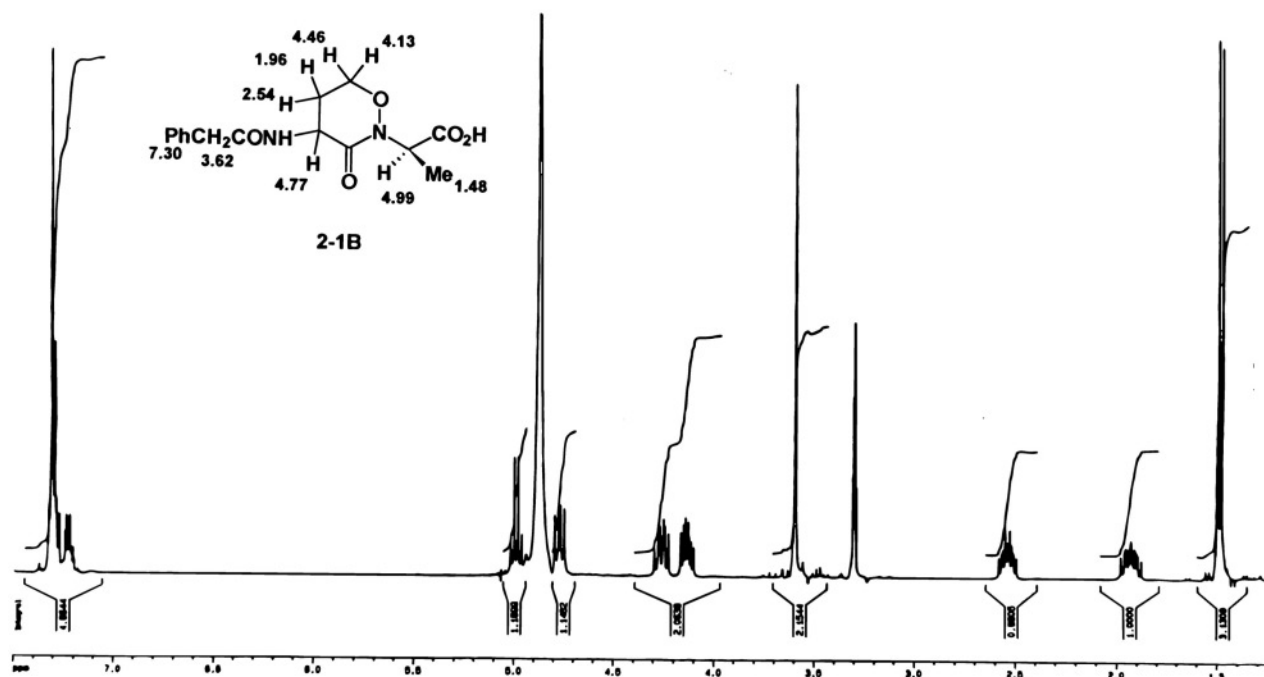
**Fig. 2.** Crystal structure of phenylacetylcyclocanaline.**Scheme 4.****Scheme 5.**

## Experimental

Scheme 7 summarizes the conversion of **49** to **52**, which has the *R*-configuration in the alanine side chain, the *R*-configuration at C4, and the *S*-configuration at C5. This compound exhibited weak activity vs. *Micrococcus luteus* (Table 2).

Nuclear magnetic resonance spectra were recorded on Bruker 100SY ( $^1\text{H}$  at 100 MHz) and Bruker AMX-400 ( $^1\text{H}$  at 400 MHz and  $^{13}\text{C}$  at 100 MHz) spectrometers. Chemical shifts are denoted in  $\delta$  units (ppm) relative to the solvent and converted to the TMS scale using  $\delta(\text{CHCl}_3) = 7.27$  ppm for



Fig. 3.  $^1\text{H}$  NMR spectrum of **5a** in  $\text{CD}_3\text{OD}$ .Fig. 4.  $^1\text{H}$  NMR spectrum of **5b** in  $\text{CD}_3\text{OD}$ .

the  $^1\text{H}$  spectra and  $\delta (\text{CDCl}_3) = 77.23$  ppm for the  $^{13}\text{C}$  spectra. Infrared spectra were recorded on a PerkinElmer 599B spectrometer. Low-resolution mass spectra, determined as

direct inlet electron impact (EI) measurements or chemical ionization (CI) measurements, were recorded on a Hewlett-Packard 5985 GC-MS-IS system. Elemental analyses were



**Scheme 6.** Reagents and conditions: (i) 50%  $\text{H}_2\text{O}_2$ ,  $\text{CaCO}_3$ ; (ii) 30%  $\text{HBr-HOAc}$ , room temperature (RT), then MeOH, reflux; (iii)  $\text{CH}_2(\text{OMe})_2$ ,  $\text{BF}_3\cdot\text{Et}_2\text{O}$ ; (iv)  $\text{NaN}_3$ , DMF; (v)  $\text{H}_2$ , Pd-C,  $(\text{BOC})_2\text{O}$ , EtOAc; (vi) FtOH, DBU, DMF; (vii)  $\text{MeNHNH}_2$ ,  $\text{CH}_2\text{Cl}_2$ ; (viii)  $S\text{-CF}_3\text{SO}_2\text{OCHMeCO}_2\text{Bn}$ , 2,6-lutidine,  $\text{CH}_2\text{Cl}_2$ .

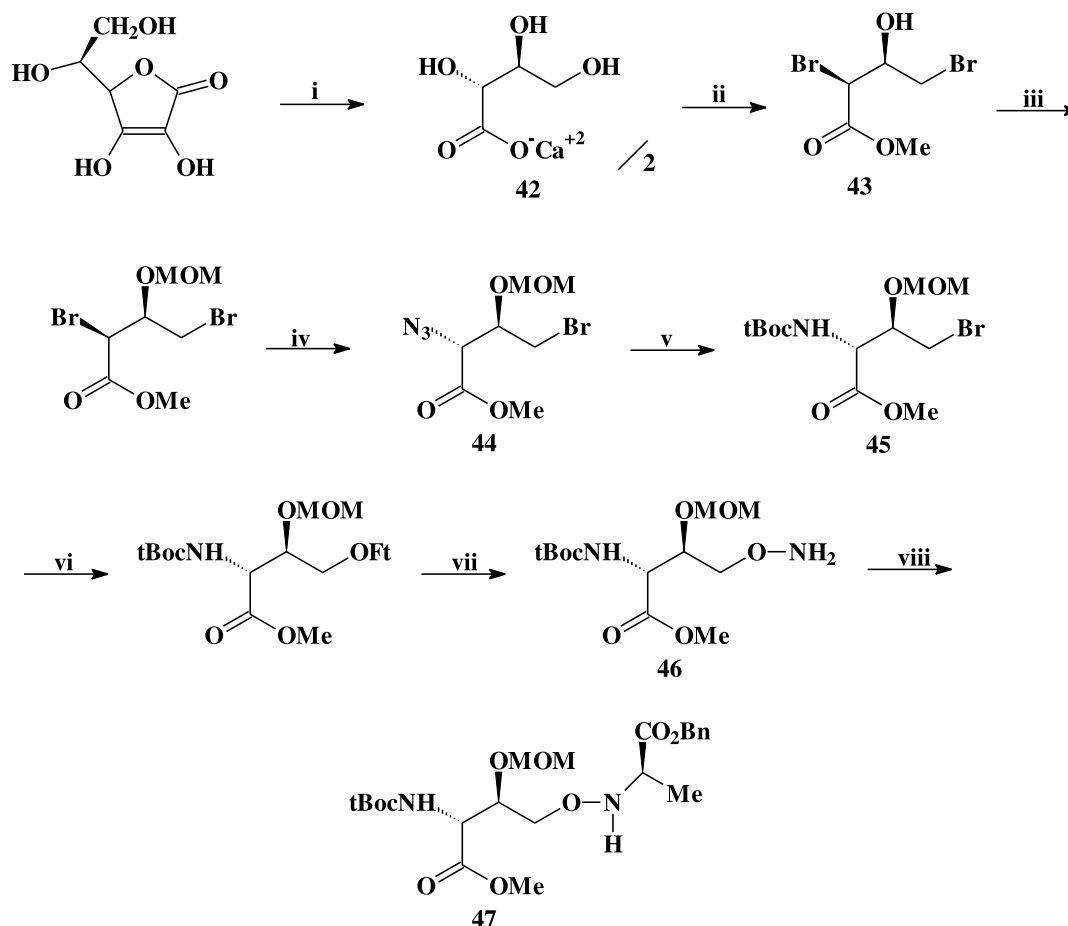


**Table 2.** Zones of inhibition vs. *M. luteus*.

Compound	Weight ( $\mu\text{g}$ )	Moles ( $\mu\text{M}$ )	Zone size (mm)	Ratio (mm/ $\mu\text{M}$ )
DACG <sup>a</sup>	10	$3.01 \times 10^{-2}$	39	1300
DL-cyclocaniline	600	3.05	58	11
DL-cyclocaniline	400	3.44	48	14
<b>37</b>	400	2.31	23	10
<b>52</b>	600	1.86	38	20
<b>52</b>	400	1.24	32	26

<sup>a</sup>Desacetoxycephalosporin G.

performed on a Carlo Erba model 1106 elemental analyzer. Melting points (mp) were obtained on a Fisher-Johns apparatus and are uncorrected. Preparative layer chromatography (PLC) was carried out on precoated Merck Silica Gel 60 F-254 plates with aluminium backing. Spots were observed under short-wavelength ultraviolet light and were visualized with a solution of 1% ceric sulfate or 2% molybdc acid in 10% sulfuric acid. Flash column chromatography was carried out on Merck Silica Gel 60 (230–400 Mesh).

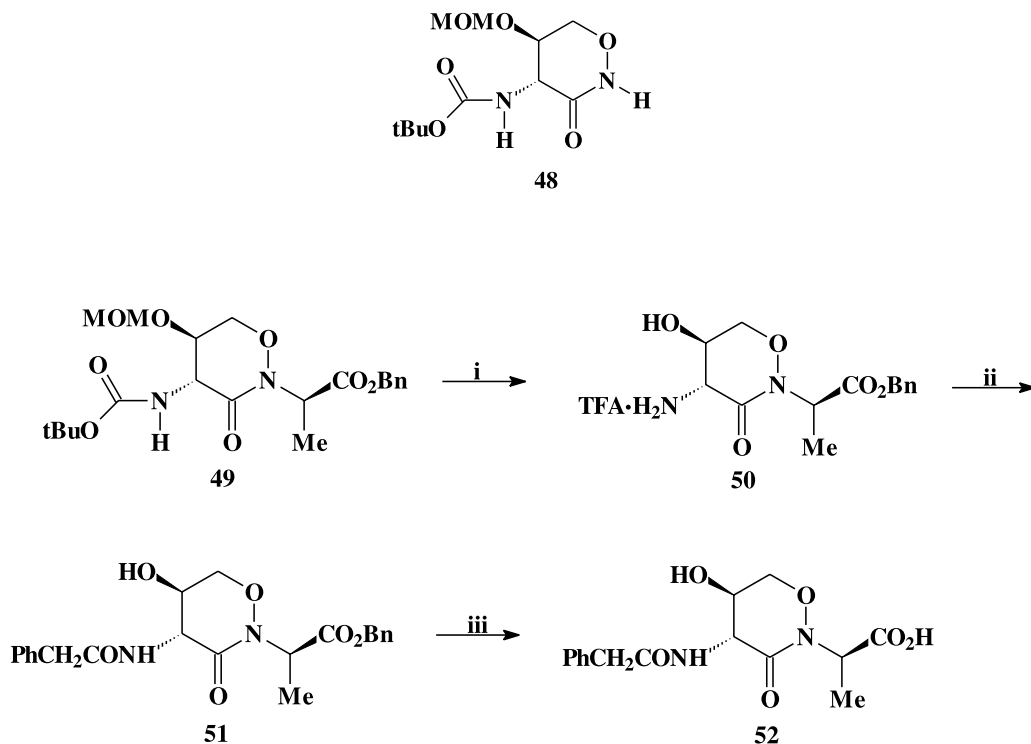
#### Methyl $\gamma$ -bromobutyrate (18)

A solution of  $\gamma$ -butyrolactone (25 mL, 28.0 g, 0.325 mol) in a 45% solution of hydrogen bromide in acetic acid

(75 mL) was heated for 4 h at 75 °C, cooled to room temperature, treated with methanol (150 mL), and stirred overnight. Evaporation of the solvent gave a dark oil, which was dissolved in ethyl acetate (150 mL) and washed successively with saturated sodium bicarbonate ( $2 \times 150$  mL) and saturated sodium chloride (150 mL), dried over anhydrous magnesium sulfate, and evaporated to yield a clear oil (48.8 g, 86%). IR (neat) ( $\text{cm}^{-1}$ ): 1738.  $^1\text{H}$  NMR ( $\text{CDCl}_3$ )  $\delta$ : 3.68 (3H, s,  $\text{OCH}_3$ ), 3.44 (2H, t, 6.4 Hz,  $\text{CH}_2\gamma$ ), 2.51 (2H, t, 7.2 Hz,  $\text{CH}_2\alpha$ ), 2.17 (2H, quintet, 6.8 Hz,  $\text{CH}_2\beta$ ).  $^{13}\text{C}$  NMR ( $\text{CDCl}_3$ )  $\delta$ : 172.96, 51.70, 32.66, 32.19, 27.70. CI-MS ( $m/z$ ): 181 ( $[\text{M} + 1]$ ), 183 ( $[\text{M} + 3]$ ). Calcd. for  $\text{C}_5\text{H}_9\text{O}_2\text{Br}$ : C 33.17, H 5.02; found: C 32.62, H 4.85.



**Scheme 7.** Reagents and conditions: (i) TFA, anisole; (ii)  $\text{PhCH}_2\text{COCl}$ ,  $\text{Et}_3\text{N}$ ,  $\text{CH}_2\text{Cl}_2$ ; (iii)  $\text{H}_2$ , 5% Pd-C, EtOAc.



### Methyl $\gamma$ -succinimidooxybutyrate

#### Method A

Methyl  $\gamma$ -bromobutyrate (0.5 g, 2.9 mmol) was added dropwise to a solution of *N*-hydroxysuccinimide (0.308 g, 2.6 mmol) and triethylamine (0.38 mL, 0.276 g, 2.6 mmol) in tetrahydrofuran (20 mL). The reaction mixture was stirred for 4 h at room temperature and then filtered. The filtrate was evaporated under reduced pressure to give crystals (47 mg, 10%); mp 69–71.5 °C. IR (KBr) ( $\text{cm}^{-1}$ ): 1727, 1710.  $^1\text{H}$  NMR ( $\text{CDCl}_3$ )  $\delta$ : 4.15 (2H, t, 6.1 Hz,  $\text{CH}_2\gamma$ ), 3.69 (3H, s,  $\text{OCH}_3$ ), 2.70 (4H, s, succinimido ring), 2.60 (2H, t, 7.3 Hz,  $\text{CH}_2\alpha$ ), 2.03 (2H, t, 7.3 Hz, 6.8 Hz,  $\text{CH}_2\beta$ ).  $^{13}\text{C}$  NMR ( $\text{CDCl}_3$ )  $\delta$ : 173.35, 171.10, 76.18, 51.67, 29.87, 25.44, 23.41. CI-MS ( $m/z$ ): 216 ( $[\text{M} + 1]$ ). Calcd. for  $\text{C}_9\text{H}_{13}\text{NO}_5$ : C 50.22, H 6.10, N 6.51; found: C 50.24, H 6.14, N 6.52.

#### Method B

A solution of methyl  $\gamma$ -bromobutyrate (1.01 g, 5.5 mmol), *N*-hydroxysuccinimide (0.576 g, 5.5 mmol), and sodium methoxide (0.282 g, 5.5 mmol) in dimethylformamide (11 mL) was heated at 100 °C for 6 h. The solvent was then removed under reduced pressure, and the residue was dissolved in ethyl acetate (100 mL) and washed successively with water (2  $\times$  100 mL) and saturated sodium chloride (100 mL), dried over anhydrous magnesium sulfate, and evaporated to give a solid, which was crystallized from ethanol to yield 0.331 g (28%) of product, identical to the product of Method A.

#### Method C

A solution of methyl  $\gamma$ -bromobutyrate (1.01 g, 5.5 mmol), *N*-hydroxysuccinimide (0.587 g, 5.5 mmol), and triethylamine (1.54 mL, 1.12 g, 11.1 mmol) in acetonitrile (10 mL)

was refluxed for 3 h, then cooled and filtered. The precipitate was washed with water and recrystallized from ethanol to give 0.180 g (15%) of the product, identical to the product of Method A.

#### Method D

A solution of methyl  $\gamma$ -bromobutyrate (1.01 g, 5.5 mmol), *N*-hydroxysuccinimide (0.584 g, 5.5 mmol), and triethylamine (0.77 mL, 0.559 g, 5.5 mmol) in dimethylformamide (11 mL) was stirred at room temperature for 24 h, then poured into water (80 mL) and extracted with ethyl acetate (2  $\times$  60 mL). This extract was washed successively with water (2  $\times$  100 mL) and saturated sodium chloride (100 mL), dried over anhydrous magnesium sulfate, and evaporated to give a solid, which was crystallized from ethanol to yield 0.175 g (15%) of the product, identical to the product of Method A.

### Methyl $\gamma$ -phthalimidooxybutyrate (19)

A mixture of methyl  $\gamma$ -bromobutyrate (14.7 g, 81.5 mmol), *N*-hydroxyphthalimide (13.3 g, 81.5 mmol), and triethylamine (22.7 mL, 16.5 g, 0.163 mol) in acetonitrile (110 mL) was refluxed for 3 h. The insoluble solid was removed by filtration, and the filtrate was evaporated. The residue was diluted with ethyl acetate (100 mL), and this solution was washed successively with water (3  $\times$  100 mL) and saturated sodium chloride (100 mL), dried over anhydrous magnesium sulfate, and evaporated. The solid was recrystallized from hot ethanol to give 16.8 g (78%); mp 79–81 °C. IR (KBr) ( $\text{cm}^{-1}$ ): 1735, 1727.  $^1\text{H}$  NMR ( $\text{CDCl}_3$ )  $\delta$ : 7.79 (4H, m, phthalimido ring), 4.26 (2H, t, 6.1 Hz,  $\text{CH}_2\gamma$ ), 3.70 (3H, s,  $\text{OCH}_3$ ), 2.66 (2H, t, 7.3 Hz,  $\text{CH}_2\alpha$ ), 2.09 (2H, quintet, 6.7 Hz,  $\text{CH}_2\beta$ ).  $^{13}\text{C}$  NMR ( $\text{CDCl}_3$ )  $\delta$ : 174.50, 163.63, 134.43, 128.94, 123.48, 78.20, 51.50, 33.85, 25.14.



CI-MS ( $m/z$ ): 264 ( $[M + 1]$ ). Calcd. for  $C_{13}H_{13}NO_5$ : C 59.30, H 4.99, N 5.32; found: C 59.17, H 4.97, N 5.49.

### Methyl $\gamma$ -aminooxybutyrate (20)

#### Method A

A solution of methyl  $\gamma$ -phthalimidooxybutyrate (2.75 g, 10.45 mmol) in dichloromethane (50 mL) was cooled to  $-10^\circ\text{C}$  and treated dropwise, with stirring, with methylhydrazine (0.83 mL, 0.72 g, 15.7 mmol). Stirring was continued for 1.5 h at  $-10$  to  $0^\circ\text{C}$ , and the mixture was then filtered. The filtrate was concentrated, and the residue, in ethyl acetate (50 mL), was washed with 1:1 saturated sodium chloride:saturated sodium bicarbonate (22 mL). The aqueous layer was washed with ethyl acetate (50 mL), and the combined organic extracts were dried over anhydrous magnesium sulfate and evaporated to give a yellow oil (1.39 g, 100%). IR (neat) ( $\text{cm}^{-1}$ ): 3322, 1734.  $^1\text{H}$  NMR ( $\text{CDCl}_3$ )  $\delta$ : 5.25 (2H, br s,  $\text{NH}_2$ ), 3.68 (2H, t, 6.2 Hz,  $\text{CH}_2\gamma$ ), 3.68 (3H, s,  $\text{OCH}_3$ ), 2.38 (2H, t, 7.3 Hz,  $\text{CH}_2\alpha$ ), 1.92 (2H, quintet, 6.7 Hz,  $\text{CH}_2\beta$ ).  $^{13}\text{C}$  NMR ( $\text{CDCl}_3$ )  $\delta$ : 173.95, 74.78, 51.58, 30.71, 23.65. CI-MS ( $m/z$ ): 134 ( $[M + 1]$ ). Calcd. for  $C_5H_{11}NO_3$ : C 45.09, H 8.34, N 10.52; found: C 45.02, H 8.36, N 10.49.

#### Method B

Hydrazine hydrate (0.07 mL, 74.6 mg, 1.49 mmol) was added, with stirring, to a solution of methyl  $\gamma$ -succinimidooxybutyrate (80 mg, 0.37 mmol) in methanol (3 mL). Stirring was continued at room temperature for 12 h, and the solvent was then removed. The solid residue was triturated with ethyl acetate ( $2 \times 8$  mL,  $1 \times 4$  mL), and the ethyl acetate was evaporated to give the product as an oil (22.3 mg, 45%), identical with the product of Method A.

### [1,2]Oxazinan-3-one (21)

#### Method A

A solution of methyl  $\gamma$ -aminooxybutyrate (0.51 g, 3.75 mmol) in toluene (37.5 mL) was treated with a 2.0 mol/L solution of trimethylaluminium in hexanes (3.75 mL, 7.5 mmol). The resulting mixture was refluxed for 2 h, cooled to room temperature, and poured onto a mixture of 5% hydrochloric acid and ice. The aqueous layer was extracted with chloroform and the organic layer was evaporated to dryness. The residue was purified by flash chromatography on silica gel, using 7:1 ethyl acetate:hexanes as the eluent, to yield a colourless oil (0.30 g, 79%). IR ( $\text{CH}_2\text{Cl}_2$ ) ( $\text{cm}^{-1}$ ): 3403, 1667.  $^1\text{H}$  NMR ( $\text{CDCl}_3$ )  $\delta$ : 8.89 (1H, br s,  $\text{NH}$ ), 4.03 (2H, t, 6.5 Hz,  $\text{CH}_2\text{O}$ ), 2.52 (2H, t, 7.2 Hz,  $\text{COCH}_2$ ), 2.10 (2H, quintet, 6.9 Hz,  $\text{COCH}_2\text{CH}_2$ ).  $^{13}\text{C}$  NMR ( $\text{CDCl}_3$ )  $\delta$ : 172.93, 69.04, 27.42, 21.55. CI-MS ( $m/z$ ): 102 ( $[M + 1]$ ). Anal. calcd. for  $C_4H_7\text{NO}_2 \cdot 0.1\text{H}_2\text{O}$ : C 46.68, H 6.97, N 13.61; found: C 46.73, H 7.01, N 13.21.

#### Method B

Potassium hydroxide (0.042 g, 0.75 mmol) in methanol (4 mL) was added to a solution of methyl  $\gamma$ -aminooxybutyrate (0.10 g, 0.75 mmol) in methanol (10 mL), and the mixture was refluxed for 2 h, cooled to room temperature, stirred overnight, neutralized with 5% hydrochloric acid, and evaporated. The residue was purified by preparative layer

chromatography on silica gel using ethyl acetate as the eluent to yield an oil (18 mg, 24%), identical to the product of Method A.

#### Method C

A solution of methyl  $\gamma$ -aminooxybutyrate (3.03 g, 22.8 mmol) in tetrahydrofuran (40 mL) was cooled to  $0^\circ\text{C}$ , and a 2.0 mol/L solution of trimethylaluminium in hexanes (22.8 mL, 45.6 mmol) was added in portions. The reaction mixture was allowed to warm to room temperature with stirring during 2 h and quenched with acetone (15 mL) with stirring for 30 min and then by slow addition of water (50 mL). Most of the solvent was removed under reduced pressure, and 1:4 dichloromethane:tetrahydrofuran (300 mL) was added. Filtration through Celite and evaporation of the filtrate gave an oil (1.51 g, 65%), identical to the product of Method A.

### Methyl $\beta$ -bromopropionate

A solution of  $\beta$ -propiolactone (2 mL, 2.29 g, 30.8 mmol) in 30% hydrogen bromide in acetic acid (10 mL) was stirred at room temperature for 20 h. Then methanol (20 mL) was added, and stirring was continued for an additional 15 h. Evaporation of the solvent gave a dark oil, which was dissolved in ethyl acetate (50 mL) and washed successively with saturated sodium bicarbonate ( $2 \times 50$  mL) and saturated sodium chloride (50 mL), dried over anhydrous magnesium sulfate, and evaporated to yield a clear oil (2.88 g, 56%). IR (neat) ( $\text{cm}^{-1}$ ): 1742.  $^1\text{H}$  NMR ( $\text{CDCl}_3$ )  $\delta$ : 3.77 (3H, s,  $\text{OCH}_3$ ), 3.62 (2H, t, 6.8 Hz,  $\text{CH}_2\beta$ ), 2.96 (2H, t, 6.8 Hz,  $\text{CH}_2\alpha$ ). CI-MS ( $m/z$ ): 167 ( $[M + 1]$ ), 169 ( $[M + 3]$ ).

### Methyl $\beta$ -phthalimidooxypropionate

#### Method A

A solution of *N*-hydroxyphthalimide (18.1 g, 0.111 mol) and triethylamine (15.5 mL, 11.3 g, 0.111 mol) in methanol (100 mL) was stirred at room temperature for 10 min. Methyl acrylate (10 mL, 9.56 g, 0.111 mol) was added dropwise, and the solution was heated to reflux for 18 h and then cooled to room temperature. The solvent was removed under reduced pressure and the residue was dissolved in ethyl acetate (150 mL) and washed successively with water (50 mL), saturated sodium bicarbonate ( $5 \times 50$  mL), water (50 mL), 5% citric acid (50 mL), water (50 mL), and saturated sodium chloride (50 mL), dried over anhydrous magnesium sulfate, and evaporated. The solid residue was recrystallized from hot ethanol to give white crystals, 5.88 g (21%). IR (KBr) ( $\text{cm}^{-1}$ ): 1745, 1727, 1657.  $^1\text{H}$  NMR ( $\text{CDCl}_3$ )  $\delta$ : 7.81 (4H, m, phthalimido ring), 4.51 (2H, t, 6.5 Hz,  $\text{CH}_2\beta$ ), 3.71 (3H, s,  $\text{OCH}_3$ ), 2.85 (2H, t, 6.5 Hz,  $\text{CH}_2\alpha$ ).  $^{13}\text{C}$  NMR ( $\text{CDCl}_3$ )  $\delta$ : 170.58, 163.44, 134.53, 128.90, 123.58, 73.40, 51.95, 33.65. CI-MS ( $m/z$ ): 250 ( $[M + 1]$ ). Calcd. for  $C_{12}H_{11}N_1O_5$ : C 57.82, H 4.46, N 5.62; found: C 57.70, H 4.50, N 5.46.

#### Method B

A mixture of methyl  $\beta$ -bromopropionate (0.50 g, 2.99 mmol), *N*-hydroxyphthalimide (0.49 g, 2.99 mmol), and triethylamine (0.64 mL, 0.45 g, 4.49 mmol) in acetonitrile (7 mL) was refluxed for 3 h, cooled, and filtered. The



filtrate was evaporated under reduced pressure, and the residue was dissolved in ethyl acetate (20 mL). This solution was washed successively with water (3 × 20 mL) and saturated sodium chloride (20 mL), dried over anhydrous magnesium sulfate, and evaporated. Recrystallization from hot ethanol gave 48.9 mg (6%) of white crystals, identical to the product of Method A.

#### Methyl β-aminooxypropionate

A solution of methyl β-phthalimidooxypropionate (1.5 g, 6.02 mmol) in dichloromethane (50 mL) was cooled to −10 °C and methylhydrazine (0.5 mL, 0.433 g, 9.03 mmol) was added dropwise with stirring. Stirring was continued for 1.5 h at −10 to 0 °C. The mixture was then filtered, and the filtrate was concentrated. The residue was dissolved in ethyl acetate (30 mL), and this solution was washed with 1:1 saturated sodium chloride:saturated sodium bicarbonate (8 mL). The aqueous layer was washed with ethyl acetate (30 mL), and the combined organic layers were dried over anhydrous magnesium sulfate and evaporated. Purification by short column chromatography on silica gel, using a gradient solvent system (hexanes to ethyl acetate) gave 0.359 g (50%) of an oil. <sup>1</sup>H NMR (CDCl<sub>3</sub>) δ: 5.85 (2H, s, NH<sub>2</sub>), 3.73 (3H, s, CH<sub>3</sub>), 3.26 (2H, t, 6.2 Hz, CH<sub>2</sub>β), 2.67 (2H, t, 6.2 Hz, CH<sub>2</sub>α). CI-MS (*m/z*): 120 ([M + 1]).

#### Isoxazolidin-3-one

A solution of methyl β-aminooxypropionate (0.251 g, 2.10 mmol) in tetrahydrofuran (25 mL) was cooled to 0 °C and a 2.0 mol/L solution of trimethylaluminum in hexanes (2.1 mL, 4.20 mmol) was added in portions. The reaction mixture was allowed to warm to room temperature with stirring during 4 h and then by slow addition of water (2 mL) with stirring for 30 min. Most of the solvent was removed under reduced pressure, and chloroform (300 mL) was added. Filtration through Celite and evaporation of the filtrate gave a colourless oil (83.0 mg, 45%). <sup>1</sup>H NMR (CDCl<sub>3</sub>) δ: 9.21 (1H, br s, NH), 4.41 (2H, t, 8.2 Hz, CH<sub>2</sub>β), 2.79 (2H, t, 8.2 Hz, CH<sub>2</sub>α). CI-MS (*m/z*): 88 ([M + 1]). Calcd. for C<sub>3</sub>H<sub>5</sub>NO<sub>2</sub>: C 41.38, H 5.79, N 16.09; found: C 40.89, H 5.84, N 15.55.

#### Methyl δ-bromopentanoate

A solution of δ-valerolactone (5.0 mL, 5.39 g, 53.8 mmol) in 30% hydrogen bromide in acetic acid (15 mL) was heated at 75 °C for 5 h, cooled to room temperature, and methanol (20 mL) was added. The mixture was stirred overnight, and the solvent was evaporated to give a dark oil, which was dissolved in ethyl acetate (50 mL) and washed successively with saturated sodium bicarbonate (2 × 50 mL) and saturated sodium chloride (50 mL), dried over anhydrous magnesium sulfate, and evaporated to yield a clear oil (9.16 g, 87%). IR (neat) (cm<sup>−1</sup>): 1737. <sup>1</sup>H NMR (CDCl<sub>3</sub>) δ: 3.67 (3H, s, OCH<sub>3</sub>), 3.41 (2H, t, 6.4 Hz, CH<sub>2</sub>δ), 2.35 (2H, t, 7.3 Hz, CH<sub>2</sub>α), 1.90 (2H, m, CH<sub>2</sub>γ), 1.79 (2H, m, CH<sub>2</sub>β). <sup>13</sup>C NMR (CDCl<sub>3</sub>) δ: 173.55, 51.58, 33.00, 31.97, 23.47. CI-MS (*m/z*): 195 ([M + 1]), 197 ([M + 3]).

#### Methyl δ-phthalimidooxypentanoate

A mixture of methyl δ-bromopentanoate (6.01 g, 30.8 mmol), *N*-hydroxyphthalimide (5.03 g, 30.8 mmol),

and triethylamine (8.6 mL, 6.24 g, 61.5 mmol) in acetonitrile (40 mL) was refluxed for 3 h, cooled, and filtered. The filtrate was evaporated under reduced pressure, and the residue was dissolved in ethyl acetate (75 mL). This solution was washed successively with water (3 × 75 mL) and saturated sodium chloride (75 mL), dried over anhydrous magnesium sulfate, and evaporated. Recrystallization from hot ethanol gave 6.33 g (74%) of product. IR (KBr) (cm<sup>−1</sup>): 1727, 1710. <sup>1</sup>H NMR (CDCl<sub>3</sub>) δ: 7.81 (4H, m, phthalimido ring), 4.21 (2H, t, 6.1 Hz, CH<sub>2</sub>δ), 3.68 (3H, s, OCH<sub>3</sub>), 2.43 (2H, t, 7.1 Hz, CH<sub>2</sub>α), 1.86 (4H, m, CH<sub>2</sub>βCH<sub>2</sub>γ). <sup>13</sup>C NMR (CDCl<sub>3</sub>) δ: 173.74, 163.60, 134.45, 128.93, 123.49, 77.88, 51.55, 33.45, 27.51, 21.11. CI-MS (*m/z*): 278 ([M + 1]). Calcd. for C<sub>14</sub>H<sub>15</sub>NO<sub>5</sub>: C 60.63, H 5.46, N 5.05; found: C 60.54, H 5.43, N 5.06.

#### Methyl δ-aminooxypentanoate

A solution of methyl δ-phthalimidooxypentanoate (2.01 g, 72.4 mmol) in dichloromethane (50 mL) was cooled to −10 °C, and methylhydrazine (0.58 mL, 0.50 g, 10.8 mmol) was added dropwise with stirring. Stirring was continued for 1.5 h, and the mixture was then filtered and the filtrate evaporated. The residue was dissolved in ethyl acetate (50 mL), and this solution was washed with 1:1 saturated sodium chloride:saturated sodium bicarbonate (30 mL). The aqueous layer was extracted with ethyl acetate (50 mL), and the combined organic layers were dried over anhydrous magnesium sulfate and evaporated to give an oil (1.03 g, 97%). IR (neat) (cm<sup>−1</sup>): 3320, 1732. <sup>1</sup>H NMR (CDCl<sub>3</sub>) δ: 4.50 (2H, br s, NH<sub>2</sub>), 3.67 (3H, s, OCH<sub>3</sub>), 3.66 (2H, t, 6.2 Hz, CH<sub>2</sub>δ), 2.34 (2H, t, 7.0 Hz, CH<sub>2</sub>α), 1.66 (4H, m, CH<sub>2</sub>βCH<sub>2</sub>γ). <sup>13</sup>C NMR (CDCl<sub>3</sub>) δ: 173.97, 75.37, 51.50, 33.76, 27.43, 21.49. CI-MS (*m/z*): 148 ([M + 1]).

#### [1,2]Oxazepin-3-one

A solution of methyl δ-aminooxypentanoate (96.6 mg, 0.656 mmol) in tetrahydrofuran (3 mL) was cooled to 0 °C, and a 2.0 mol/L solution of trimethylaluminum in hexanes (0.68 mL, 1.36 mmol) was added dropwise. The resulting solution was allowed to warm to room temperature and was stirred for 5.5 h. Acetone (0.8 mL) was added, and after 20 min, water (2 mL) was added dropwise. Most of the solvent was removed under reduced pressure; 1:4 dichloromethane:tetrahydrofuran (50 mL) was added, and the mixture was filtered through Celite. Evaporation of the filtrate gave a white solid, which was recrystallized from hot ethyl acetate (61.7 mg, 82%); mp 84.5–85.8 °C. IR (KBr) (cm<sup>−1</sup>): 3419, 1642. <sup>1</sup>H NMR (CDCl<sub>3</sub>) δ: 8.27 (1H, br s, NH), 4.07 (2H, m, CH<sub>2</sub>δ), 2.63 (2H, m, CH<sub>2</sub>α), 1.91 (2H, m, CH<sub>2</sub>γ), 1.81 (2H, m, CH<sub>2</sub>β). <sup>13</sup>C NMR (CDCl<sub>3</sub>) δ: 179.36, 78.37, 35.79, 30.94, 21.85. CI-MS (*m/z*): 116 ([M + 1]). Calcd. for C<sub>5</sub>H<sub>9</sub>NO<sub>2</sub>: C 52.15, H 7.89, N 12.17; found: C 52.12, H 7.91, N 12.18.

#### Methyl ε-bromohexanoate

A solution of ε-caprolactone (5.2 mL, 5.36 g, 46.9 mmol) in 30% hydrogen bromide in acetic acid (12.5 mL) was heated for 6 h at 75 °C, cooled to room temperature, treated with methanol (20 mL), and stirred overnight. Evaporation of the solvent gave a dark oil, which was dissolved in ethyl acetate (50 mL) and washed successively with saturated so-



dium bicarbonate (2 × 50 mL) and saturated sodium chloride (50 mL), dried over anhydrous magnesium sulfate, and evaporated to yield a clear oil (9.31 g, 95%). <sup>1</sup>H NMR (CDCl<sub>3</sub>) δ: 3.67 (3H, s, OCH<sub>3</sub>), 3.40 (2H, t, 6.8 Hz, CH<sub>2</sub>ε), 2.33 (2H, t, 7.5 Hz, CH<sub>2</sub>α), 1.87 (2H, m, CH<sub>2</sub>δ), 1.66 (2H, m, CH<sub>2</sub>β), 1.47 (2H, m, CH<sub>2</sub>γ). CI-MS (*m/z*): 209 ([M + 1]), 211 ([M + 3]).

#### Methyl ε-phthalimidooxyhexanoate

A mixture of methyl ε-bromohexanoate (6.44 g, 30.8 mmol), *N*-hydroxyphthalimide (5.02 g, 30.8 mmol), and triethylamine (8.6 mL, 6.24 g, 61.5 mmol) in acetonitrile (40 mL) was refluxed for 3 h, cooled, and filtered. The filtrate was concentrated and the residue diluted with ethyl acetate (50 mL). This solution was washed successively with water (3 × 50 mL) and saturated sodium chloride (50 mL), dried over anhydrous magnesium sulfate, and evaporated. Recrystallization from hot ethanol gave 8.89 g (99%). IR (KBr) (cm<sup>-1</sup>): 1787, 1731. <sup>1</sup>H NMR (CDCl<sub>3</sub>) δ: 7.80 (4H, m, phthalimido ring), 4.20 (2H, t, 6.6 Hz, CH<sub>2</sub>ε), 3.67 (3H, s, OCH<sub>3</sub>), 2.35 (2H, t, 7.4 Hz, CH<sub>2</sub>α), 1.80 (2H, m, CH<sub>2</sub>δ), 1.72 (2H, m, CH<sub>2</sub>β), 1.55 (2H, m, CH<sub>2</sub>γ). <sup>13</sup>C NMR (CDCl<sub>3</sub>) δ: 173.06, 163.58, 134.49, 128.90, 123.53, 77.28, 51.68, 29.96, 23.52. CI-MS (*m/z*): 292 ([M + 1]). Calcd. for C<sub>15</sub>H<sub>17</sub>NO<sub>5</sub>: C 61.84, H 5.89, N 4.81; found: C 61.49, H 5.92, N 4.75.

#### Methyl ε-aminooxyhexanoate

A solution of methyl ε-phthalimidooxyhexanoate (1.05 g, 3.60 mmol) in dichloromethane (19 mL) was cooled to -10 °C; methylhydrazine (0.29 mL, 0.251 g, 5.4 mmol) was added dropwise with stirring, and stirring was continued for 1.5 h at -10 to 0 °C. The mixture was then filtered, and the filtrate was evaporated. The residue was dissolved in ethyl acetate (50 mL) and washed with 1:1 saturated sodium chloride:saturated sodium bicarbonate (30 mL). The aqueous extract was washed with ethyl acetate (50 mL), and the combined organic layers were dried over anhydrous magnesium sulfate and evaporated to give an oil (0.567 g, 98%). <sup>1</sup>H NMR (CDCl<sub>3</sub>) δ: 5.10 (2H, br s, NH<sub>2</sub>), 3.66 (3H, s, OCH<sub>3</sub>), 3.64 (2H, t, 6.6 Hz, CH<sub>2</sub>ε), 2.30 (2H, t, 7.4 Hz, CH<sub>2</sub>α), 1.64 (2H, m, CH<sub>2</sub>δ), 1.58 (2H, m, CH<sub>2</sub>β), 1.35 (2H, m, CH<sub>2</sub>γ).

#### [1,2]Oxazocan-3-one

A 2.0 mol/L solution of trimethylaluminum in heptane (4.96 mL, 9.92 mmol) was added to toluene (50 mL), cooled to 0 °C, and a solution of methyl-ε-aminooxyhexanoate (0.400 g, 2.48 mmol) in toluene (50 mL) was added dropwise. The resulting solution was allowed to warm to room temperature and was stirred for 6 days. Water (20 mL) was added dropwise, and the mixture was stirred for 30 min. Most of the solvent was removed under reduced pressure, and 1:4 dichloromethane:tetrahydrofuran (50 mL) was added. Filtration through Celite and evaporation of the filtrate gave a trace amount of product. CI-MS (*m/z*): 130 ([M + 1]).

#### α-Amino-γ-butyrolactone hydrobromide

A solution of DL-homoserine (0.31 g, 2.6 mmol) in 2.4 mol/L hydrobromic acid (5 mL, 12 mmol, 4.6 equiv) was refluxed for 3 h and then stirred overnight. Removal of the solvent afforded a white solid, which was dissolved in ethanol and cooled to give a solid, which was collected by

filtration and washed with cold ethanol to yield 0.384 g (81%); mp 117–119 °C. CI-MS (*m/z*): 102 ([M + 1]). Calcd. for C<sub>4</sub>H<sub>8</sub>NO<sub>2</sub>Br: C 26.40, H 4.44, N 7.70; found: C 26.35, H 4.25, N 7.51.

#### α-Amino-γ-bromobutyric acid hydrobromide

A suspension of α-amino-γ-butyrolactone hydrobromide (97 mg, 0.53 mmol) in 45% hydrogen bromide in acetic acid (3 mL) was stirred for 4 h at 75 °C, cooled to room temperature, and concentrated under reduced pressure to give a white solid (140 mg, 100%), which was used in the next step without further purification. IR (KBr) (cm<sup>-1</sup>): 3451, 1720. <sup>1</sup>H NMR (D<sub>2</sub>O) δ: 4.10 (1H, t, 6.8 Hz, CHα), 3.59 (2H, t, 7.0 Hz, CH<sub>2</sub>γ), 2.50 (1H, m, CHβ), 2.38 (1H, m, CHβ).

#### BOC-α-amino-γ-bromobutyric acid

α-Amino-γ-bromobutyric acid hydrobromide (130 mg, 0.50 mmol) was dissolved in 50% aqueous acetone (1.8 mL), triethylamine (0.14 mL, 0.102 g, 1.0 mmol) and BOC-ON (141 mg, 0.55 mmol) were added, and the solution was stirred for 3 h at room temperature. The solvent was then removed under reduced pressure, and the residue was dissolved in water (3 mL), washed with ethyl acetate (3 mL), acidified to pH 3 with 5% citric acid, and again extracted with ethyl acetate (3 × 3 mL). The latter extracts were combined, washed successively with water (2 × 3 mL) and saturated sodium chloride (3 mL), dried over anhydrous magnesium sulfate, and evaporated to give 29.5 mg (21%) of the product. <sup>1</sup>H NMR (CDCl<sub>3</sub>) δ: 5.56 (1H, br s, NH), 4.50 (1H, m, CHα), 3.82 (2H, m, CH<sub>2</sub>γ), 2.18 (1H, m, CHβ), 1.78 (1H, m, CHβ), 1.48 (9H, s, C(CH<sub>3</sub>)<sub>3</sub>).

#### BOC-α-amino-γ-butyrolactone

A solution of triethylamine (7.75 mL, 5.63 g, 56.0 mmol) in dichloromethane (10 mL) was added slowly to a suspension of DL-α-amino-γ-butyrolactone hydrobromide (10 g, 55.0 mmol) in dichloromethane (100 mL). The mixture was cooled to 0 °C, and a solution of BOC anhydride (13.19 g, 60.4 mmol) in dichloromethane (25 mL) was added during 5 min. The resulting suspension was allowed to warm to room temperature, stirred for 96 h, and then washed successively with 5% citric acid (50 mL), water (50 mL), and saturated sodium chloride (50 mL), dried over anhydrous magnesium sulfate, and evaporated to give a white solid. This was recrystallized from toluene to yield 9.93 g (90%); mp 124–126 °C. IR (KBr) (cm<sup>-1</sup>): 3359, 1787, 1684, 1528. <sup>1</sup>H NMR (CDCl<sub>3</sub>) δ: 5.05 (1H, br s, NH), 4.44 (1H, m, CHγ), 4.34 (1H, m, CHα), 4.24 (1H, m, CHγ), 2.76 (1H, m, CHβ), 2.18 (1H, m, CHβ), 1.47 (9H, s, C(CH<sub>3</sub>)<sub>3</sub>). <sup>13</sup>C NMR (CDCl<sub>3</sub>) δ: 175.68, 155.72, 80.55, 65.83, 50.21, 30.34, 28.30. CI-MS (*m/z*): 202 ([M + 1]). Calcd. for C<sub>9</sub>H<sub>15</sub>NO<sub>4</sub>: C 53.71, H 7.53, N 6.96; found: C 53.98, H 7.58, N 7.19.

#### BOC-homoserine

##### Method A

To a solution of DL-homoserine (5.00 g, 42.0 mmol) in 50% aqueous acetone (50 mL) were added, with stirring, triethylamine (8.8 mL, 6.34 g, 63.0 mmol) and BOC anhydride (10.1 g, 46.2 mmol). After 14 h, the solvent was removed under reduced pressure, and the residue was



dissolved in water (30 mL). This solution was acidified to pH 3–4 with 5% citric acid (130 mL) and extracted with ethyl acetate (3 × 50 mL). The combined organic extracts were washed with saturated sodium chloride (50 mL), dried over anhydrous magnesium sulfate, and evaporated to give a yellow oil (6.79 g, 74%). <sup>1</sup>H NMR (CDCl<sub>3</sub>) δ: 5.49 (1H, br s, NH), 4.50 (1H, m, CHα), 3.79 (2H, m, CH<sub>2</sub>γ), 2.21 (1H, m, CHβ), 1.77 (1H, m, CHβ), 1.41 (9H, s, C(CH<sub>3</sub>)<sub>3</sub>). <sup>13</sup>C NMR (CDCl<sub>3</sub>) δ: 176.82, 156.40, 80.14, 58.33, 51.50, 35.14, 28.30. CI-MS (*m/z*): 220 ([M + 1]). Calcd. for C<sub>9</sub>H<sub>17</sub>NO<sub>5</sub>: C 49.30, H 7.83, N 6.39; found: C 48.72, H 7.67, N 6.04.

### Method B

To a solution of BOC-α-amino-γ-butyrolactone (7.00 g, 34.8 mmol) in dry methanol (80 mL) was added in portions a solution of potassium hydroxide (3.44 g, 52.2 mmol) in methanol (20 mL). The mixture was stirred at room temperature for 24 h, and Amberlyst 15 (H<sup>+</sup>) (14.0 g, 62.6 mmol), presoaked in methanol, was added. The resin was then removed by filtration, and the solution was evaporated under reduced pressure to an oil (7.39 g, 97%), identical with the product of Method A.

### Benzhydryl ester of BOC-homoserine

A solution of BOC-homoserine (0.803 g, 3.66 mmol) in a mixture of dichloromethane (20 mL) and acetonitrile (20 mL) was treated dropwise, with stirring, with a solution of diphenyldiazomethane (0.713 g, 3.66 mmol) in dichloromethane (3 mL). Stirring was continued for 2 h after the addition was complete, and the solvent was then removed under reduced pressure to give a yellow oil. This was dissolved in ethyl acetate (50 mL) and washed successively with water (2 × 50 mL) and saturated sodium chloride (50 mL), dried over anhydrous magnesium sulfate, and evaporated. Purification by flash chromatography on silica gel, using ethyl acetate – hexanes (1:1) as the eluent, gave the product as an oil (0.992 g, 70%). IR (neat) (cm<sup>-1</sup>): 3499, 3321, 1736, 1688. <sup>1</sup>H NMR (CDCl<sub>3</sub>) δ: 7.31 (10H, m, Ar), 6.90 (1H, s, CHO), 5.38 (1H, br d, 7.9 Hz, NH), 4.62 (1H, m, CHα), 3.65 (2H, m, CH<sub>2</sub>γ), 3.80 (1H, br s, OH), 2.24 (1H, m, CHβ), 1.58 (1H, m, CHβ), 1.44 (9H, s, C(CH<sub>3</sub>)<sub>3</sub>). CI-MS (*m/z*): 386 ([M + 1]). Calcd. for C<sub>22</sub>H<sub>27</sub>NO<sub>5</sub>: C 68.54, H 7.04, N 3.63; found: C 68.68, H 7.14, N 3.61.

### Benzhydryl ester of BOC-α-amino-γ-succinimidoxy-butyric acid

A solution of the benzhydryl ester (1.01 g, 2.62 mmol) and *N*-hydroxysuccinimide (0.313 g, 2.72 mmol) in tetrahydrofuran (12 mL) was cooled to 15 °C, and triphenylphosphine (0.702 g, 2.67 mmol) and diethyl azodicarboxylate (0.45 mL, 0.498 g, 2.86 mmol) were added successively. The reaction mixture was allowed to warm to room temperature, stirred overnight, and the solvent was then removed under reduced pressure. Purification by flash chromatography on silica gel using 3:1 hexanes:ethyl acetate as the eluent gave a white solid (0.589 g, 47%). <sup>1</sup>H NMR (CDCl<sub>3</sub>) δ: 7.33 (10H, m, Ar), 6.92 (1H, s, CHO), 5.81 (1H, br d, 8.2 Hz, NH), 4.62 (1H, m, CHα), 4.13 (2H, m, CH<sub>2</sub>γ), 2.65 (4H, s, succinimido ring), 2.27 (2H, m, CH<sub>2</sub>β), 1.44 (9H, s, C(CH<sub>3</sub>)<sub>3</sub>). CI-MS (*m/z*): 383 ([M + 1 – BOC]). Calcd. for C<sub>26</sub>H<sub>30</sub>N<sub>2</sub>O<sub>7</sub>H<sub>2</sub>O: C 62.38, H 6.46; found: C 62.38, H 6.60.

### Methyl α-amino-γ-bromobutyrate hydrochloride

Hydrogen chloride was bubbled for 2 h into a suspension of α-amino-γ-bromobutyrate hydrobromide (0.165 g, 0.586 mmol) in methanol (5 mL) at such a rate that the temperature did not exceed 40 °C. The solvent was then removed under reduced pressure, the residue was dissolved in methanol, and the solution was reevaporated. This procedure was repeated once more, and the residual oil was dried in vacuo in a desiccator over sodium hydroxide pellets. The resulting crystals were triturated with ether, collected, and washed with ether to give 89 mg (65%); mp 96–98 °C. <sup>1</sup>H NMR (D<sub>2</sub>O) δ: 4.33 (1H, t, 6.67 Hz, CHα), 3.83 (3H, s, OCH<sub>3</sub>), 3.59 (2H, m, CH<sub>2</sub>γ), 2.56 (1H, m, CHβ), 2.39 (1H, m, CHβ). CI-MS (*m/z*): 196 ([M + 1]), 198 ([M + 3]).

### Methyl ester of BOC-α-amino-γ-bromobutyric acid

To a solution of methyl α-amino-γ-bromobutyrate hydrochloride (29.7 mg, 0.129 mmol) in 50% aqueous acetone (1 mL) were added, with stirring, triethylamine (0.039 mL, 28.3 mg, 0.258 mmol) and BOC anhydride (30.1 mg, 0.142 mmol). Stirring was continued at room temperature for 3 h, and the solvent was then removed under reduced pressure. The residue was purified by preparative layer chromatography on silica gel, using 2:1 hexanes:ethyl acetate as the eluent, to give 28.4 mg (75%) of the product. <sup>1</sup>H NMR (CDCl<sub>3</sub>) δ: 5.05 (1H, br d, 7.5 Hz, NH), 4.41 (1H, m, CHα), 3.73 (3H, s, OCH<sub>3</sub>), 3.40 (2H, t, 6.8 Hz, CH<sub>2</sub>γ), 2.37 (2H, m, CH<sub>2</sub>β), 1.42 (9H, s, C(CH<sub>3</sub>)<sub>3</sub>).

### Methyl ester of BOC-homoserine

A solution of homoserine (5.00 g, 42.0 mmol) in 50% aqueous acetone (50 mL) was treated with triethylamine (8.8 mL, 6.39 g, 63.0 mmol) and BOC anhydride (10.1 g, 46.2 mmol) and stirred overnight at room temperature. Removal of the solvent gave the triethylamine salt of BOC-homoserine (13.5 g, 100%). IR (CH<sub>2</sub>Cl<sub>2</sub>) (cm<sup>-1</sup>): 3413, 1709, 1693. <sup>1</sup>H NMR (D<sub>2</sub>O) δ: 4.02 (1H, m, CHα), 3.64 (2H, m, CH<sub>2</sub>γ), 3.18 (2H, q, 7.3 Hz, CH<sub>2</sub>CH<sub>3</sub>), 1.98 (1H, m, CHβ), 1.82 (1H, m, CHβ), 1.41 (9H, s, C(CH<sub>3</sub>)<sub>3</sub>), 1.26 (3H, t, 7.3 Hz, CH<sub>3</sub>). <sup>13</sup>C NMR (D<sub>2</sub>O) δ: 181.68, 160.33, 83.76, 61.09, 55.48, 49.30, 36.57, 30.28, 10.85. CI-MS (*m/z*): 164 ([M + 1 – BOC]).

A solution of the salt (7.49 g, 23.4 mmol) in dimethylformamide (50 mL) was cooled to 0–10 °C and stirred; iodomethane (1.6 mL, 3.65 g, 25.7 mmol) was added; the cooling bath was removed, and stirring was continued overnight. Most of the solvent was removed under reduced pressure, and the residue was diluted with ethyl acetate (80 mL) and washed with water (20 mL). The aqueous extract was washed with ethyl acetate (2 × 25 mL), and the combined organic extracts were washed successively with 5% citric acid (2 × 15 mL), water (15 mL), saturated sodium sulfite (15 mL), saturated sodium bicarbonate (2 × 15 mL), and saturated sodium chloride (2 × 15 mL), dried over anhydrous magnesium sulfate, and evaporated to give a colourless oil (5.15 g, 94%). <sup>1</sup>H NMR (CDCl<sub>3</sub>) δ: 5.43 (1H, br s, NH), 4.52 (1H, m, CHα), 3.80 (3H, s, CH<sub>3</sub>O), 3.73 (2H, m, CH<sub>2</sub>γ), 3.26 (1H, br s, OH), 2.11 (1H, m, CHβ), 1.64 (1H, m, CHβ), 1.49 (9H, s, C(CH<sub>3</sub>)<sub>3</sub>). <sup>13</sup>C NMR (CDCl<sub>3</sub>) δ: 173.62, 156.80, 80.16, 58.65, 52.50, 51.04, 36.18, 28.66. CI-MS (*m/z*): 234 ([M + 1]).



### Mesylation of the BOC methyl ester (**26**, $R_1 = t\text{-BuO}$ , $R_2 = \text{Me}$ )

Methanesulfonyl chloride (2.14 mL, 3.16 g, 27.6 mmol) was added dropwise at  $-15$  to  $-10$  °C to a solution of the methyl ester of BOC-homoserine (5.6 g, 24.0 mmol) and triethylamine (4.0 mL, 2.90 g, 28.8 mmol) in dichloromethane (80 mL). The reaction mixture was allowed to warm to 0 °C and was stirred at that temperature for 1 h. Cold 10% potassium bisulfate (25 mL) was added, and the aqueous layer was separated and washed with dichloromethane (2 × 25 mL). The combined organic layers were washed with sodium bicarbonate (2 × 35 mL), dried over anhydrous magnesium sulfate, and evaporated to give a pale yellow oil (7.25 g, 97%).  $^1\text{H}$  NMR ( $\text{CDCl}_3$ )  $\delta$ : 5.25 (1H, br s,  $\text{NH}$ ), 4.75 (1H, m,  $\text{CH}\alpha$ ), 4.35 (2H, m,  $\text{CH}_2\gamma$ ), 3.82 (3H, s,  $\text{CH}_3\text{O}$ ), 3.07 (3H, s,  $\text{SO}_2\text{CH}_3$ ), 2.36 (1H, m,  $\text{CH}\beta$ ), 2.15 (1H, m,  $\text{CH}\beta$ ), 1.49 (9H, s,  $\text{C}(\text{CH}_3)_3$ ).

### $\alpha$ -Phenylacetamido- $\gamma$ -butyrolactone

Triethylamine (7.7 mL, 5.6 g, 55.0 mmol) was added slowly to a suspension of  $\alpha$ -amino- $\gamma$ -butyrolactone hydrobromide (5.0 g, 27.5 mmol) in dichloromethane (50 mL). The mixture was stirred for 10 min, cooled to  $-5$  °C, and treated, during 30 min, with a solution of phenylacetyl chloride (3.3 mL, 3.83 g, 24.8 mmol) in dichloromethane (20 mL). The mixture was allowed to warm to room temperature, stirred for 3 h, and then washed successively with water (25 mL), 1 N hydrochloric acid (15 mL), water (15 mL), and 1:1 water:saturated sodium bicarbonate (20 mL), dried over anhydrous magnesium sulfate, and evaporated to give a white solid (5.14 g, 95%); mp  $124\text{--}126$  °C. IR (KBr) ( $\text{cm}^{-1}$ ): 3305, 1779, 1652.  $^1\text{H}$  NMR ( $\text{CDCl}_3$ )  $\delta$ : 7.33 (5H, m, Ar), 5.97 (1H, br s,  $\text{NH}$ ), 4.50 (1H, m,  $\text{CH}\gamma$ ), 4.43 (1H, t, 9.1 Hz,  $\text{CH}\alpha$ ), 4.25 (1H, m,  $\text{CH}\gamma$ ), 3.63 (2H, s,  $\text{PhCH}_2$ ), 2.79 (1H, m,  $\text{CH}\beta$ ), 2.08 (1H, m,  $\text{CH}\beta$ ).  $^{13}\text{C}$  NMR ( $\text{CDCl}_3$ )  $\delta$ : 174.98, 171.49, 134.06, 129.39, 129.13, 127.59, 65.95, 49.37, 43.31, 30.32. CI-MS ( $m/z$ ): 220 ( $[\text{M} + 1]$ ). Calcd. for  $\text{C}_{12}\text{H}_{13}\text{NO}_3$ : C 65.73, H 5.99, N 6.39; found: C 65.69, H 5.97, N 6.12.

### Phenylacetamido homoserine

A solution of potassium hydroxide (4.51 g, 68.8 mmol) in methanol (20 mL) was added in portions to a suspension of  $\alpha$ -phenylacetamido- $\gamma$ -butyrolactone (10.1 g, 45.9 mmol) in dry methanol (100 mL). The mixture was stirred at room temperature for 24 h, and Amberlyst 15 ( $\text{H}^+$ ) (18.5 g, 82.5 mmol), presoaked in methanol, was added. The mixture was filtered, and the filtrate was evaporated to an oil (10.9 g, 96%), which was used directly in the next step.

### Methyl ester of phenylacetamidom homoserine (**25**, $R_1 = \text{PhCH}_2$ , $R_2 = \text{Me}$ )

A solution of phenylacetamidom homoserine (3.19 g, 13.5 mmol) in dimethylformamide (30 mL) was treated dropwise with a solution of triethylamine (1.88 mL, 1.36 g, 13.5 mmol) in dimethylformamide (10 mL). Then iodomethane (1.68 mL, 3.82 g, 26.9 mmol) was added in one portion, and stirring was continued overnight. Most of the solvent was removed under reduced pressure, and the residue was diluted with ethyl acetate (100 mL) and water (20 mL). The aqueous layer was washed with ethyl acetate

(2 × 25 mL), and the combined organic layers were washed successively with 5% citric acid (2 × 15 mL), water (15 mL), saturated sodium sulfite (15 mL), saturated sodium bicarbonate (2 × 15 mL), and saturated sodium chloride (2 × 15 mL), dried over anhydrous magnesium sulfate, and evaporated to give a pale yellow oil (2.02 g, 60%). IR ( $\text{CH}_2\text{Cl}_2$ ) ( $\text{cm}^{-1}$ ): 3297, 1743, 1658.  $^1\text{H}$  NMR ( $\text{CDCl}_3$ )  $\delta$ : 7.32 (5H, m, Ar), 6.38 (1H, br d, 6.8 Hz,  $\text{NH}$ ), 4.73 (1H, m,  $\text{CH}\alpha$ ), 3.73 (3H, s,  $\text{CH}_3$ ), 3.64 (1H, m,  $\text{CH}\gamma$ ), 3.63 (2H, s,  $\text{PhCH}_2$ ), 3.49 (1H, m,  $\text{CH}\gamma$ ), 2.33 (1H, br s,  $\text{OH}$ ), 2.13 (1H, m,  $\text{CH}\beta$ ), 1.56 (1H, m,  $\text{CH}\beta$ ).  $^{13}\text{C}$  NMR ( $\text{CDCl}_3$ )  $\delta$ : 172.94, 172.15, 134.21, 129.32, 129.09, 127.56, 58.09, 52.64, 49.66, 43.45, 35.63. CI-MS ( $m/z$ ): 252 ( $[\text{M} + 1]$ ).

### Mesylation of the methyl ester of phenylacetamidom homoserine (**26**, $R_1 = \text{PhCH}_2$ , $R_2 = \text{Me}$ )

A solution of the methyl ester (1.90 g, 7.56 mmol) and triethylamine (1.26 mL, 0.91 g, 9.07 mmol) in dichloromethane (30 mL) was cooled to  $-15$  to  $-10$  °C and methanesulfonyl chloride (0.67 mL, 1.00 g, 8.70 mmol) was added dropwise. The mixture was allowed to warm to 0 °C and was stirred at that temperature for 1 h. Cold 10% potassium bisulfate (15 mL) was added, and the aqueous layer was separated and washed with dichloromethane (2 × 15 mL). The combined organic layers were washed with sodium bicarbonate (2 × 25 mL), dried over anhydrous magnesium sulfate, and evaporated to give a yellow oil (2.23 g, 90%).  $^1\text{H}$  NMR ( $\text{CDCl}_3$ )  $\delta$ : 7.38 (5H, m, Ar), 6.19 (1H, br d, 7.1 Hz,  $\text{NH}$ ), 4.70 (1H, m,  $\text{CH}\alpha$ ), 4.17 (2H, t, 6.2 Hz,  $\text{CH}_2\gamma$ ), 3.76 (3H, s,  $\text{COCH}_3$ ), 3.64 (2H, s,  $\text{PhCH}_2$ ), 2.90 (3H, s,  $\text{SO}_2\text{CH}_3$ ), 2.34 (1H, m,  $\text{CH}\beta$ ), 2.12 (1H, m,  $\text{CH}\beta$ ).  $^{13}\text{C}$  NMR ( $\text{CDCl}_3$ )  $\delta$ : 171.73, 171.02, 134.36, 129.34, 129.12, 127.55, 65.68, 52.77, 49.34, 43.63, 37.16, 31.46. CI-MS ( $m/z$ ): 330 ( $[\text{M} + 1]$ ).

### Synthesis of **27** ( $R_1 = t\text{-BuO}$ , $R_2 = \text{Me}$ )

1,8-Diazabicyclo[5.4.0]undec-7-ene (3.2 mL, 3.18 g, 20.9 mmol) was added dropwise to a solution of *N*-hydroxyphthalimide (3.40 g, 20.9 mmol) in dimethylformamide (30 mL). The solution was stirred for 30 min, cooled to  $10\text{--}15$  °C, and a solution of **26** ( $R_1 = t\text{-BuO}$ ,  $R_2 = \text{Me}$ ) (6.5 g, 20.9 mmol) in dimethylformamide (10 mL) was added dropwise. The mixture was then allowed to warm to room temperature and stirred for 48 h. Approximately 30 mL of solvent was removed under reduced pressure, and ethyl acetate (100 mL) and water (30 mL) were added. The layers were separated, and the aqueous layer was washed with ethyl acetate (2 × 50 mL). The combined organic layers were washed successively with saturated sodium bicarbonate (5 × 30 mL), water (30 mL), 5% citric acid (30 mL), water (30 mL), and saturated sodium chloride (30 mL), dried over anhydrous magnesium sulfate, and evaporated to yield 8.58 g of a solid. Recrystallization from hot ethanol gave white crystals, 5.07 g (64%); mp  $135\text{--}136$  °C. IR (KBr) ( $\text{cm}^{-1}$ ): 3365, 1746, 1725, 1680.  $^1\text{H}$  NMR ( $\text{CDCl}_3$ )  $\delta$ : 7.81 (4H, m, phthalimido ring), 5.68 (1H, d, 7.6 Hz,  $\text{NH}$ ), 4.55 (1H, m,  $\text{CH}\alpha$ ), 4.31 (2H, t, 6.1 Hz,  $\text{CH}_2\gamma$ ), 3.76 (3H, s,  $\text{CH}_3$ ), 2.30 (2H, m,  $\text{CH}_2\beta$ ), 1.45 (9H, s,  $\text{C}(\text{CH}_3)_3$ ). CI-MS ( $m/z$ ): 379 ( $[\text{M} + 1]$ ). Calcd. for  $\text{C}_{18}\text{H}_{22}\text{N}_2\text{O}_7$ : C 57.13, H 5.87, N 7.40; found: C 57.21, H 5.93, N 7.33.



**Methyl BOC- $\alpha$ -amino- $\gamma$ -aminooxybutyrate (28,  $R_1 = t$ -BuO,  $R_2 = \text{Me}$ )**

A solution of **27**,  $R_1 = t$ -BuO,  $R_2 = \text{Me}$  (0.50 g, 1.32 mmol), in dichloromethane (20 mL) was cooled to  $-10^\circ\text{C}$  and methylhydrazine (0.10 mL, 91.1 mg, 1.98 mmol) was added dropwise with stirring. Stirring was continued for 2 h at  $-10^\circ\text{C}$ , and the mixture was then filtered. The filtrate was concentrated and the residue, in ethyl acetate (15 mL), was washed with 1:1 saturated sodium chloride:saturated sodium bicarbonate (10 mL). The aqueous layer was washed with ethyl acetate (15 mL), and the combined organic layers were dried over anhydrous magnesium sulfate and evaporated to give a white solid (0.325 g, 100%). IR (KBr) ( $\text{cm}^{-1}$ ): 3336, 1738, 1698.  $^1\text{H}$  NMR ( $\text{CDCl}_3$ )  $\delta$ : 5.62 (2H, br s,  $\text{ONH}_2$ ), 5.29 (1H, d, 6.0 Hz,  $\text{NH}$ ), 4.41 (1H, m,  $\text{CH}\alpha$ ), 3.75 (3H, s,  $\text{CH}_3$ ), 3.75 (2H, t, 6.2 Hz,  $\text{CH}_2\gamma$ ), 2.07 (2H, m,  $\text{CH}_2\beta$ ), 1.45 (9H, s,  $\text{C}(\text{CH}_3)_3$ ). CI-MS ( $m/z$ ): 249 ( $[\text{M} + 1]$ ). Calcd. for  $\text{C}_{10}\text{H}_{20}\text{N}_2\text{O}_5$ : C 48.37, H 8.13, N 11.28; found: C 48.77, H 7.96, N 11.36.

**4-tert-Butoxycarbonylamino-[1,2]oxazinan-3-one (29,  $R = t$ -BuO)**

A solution of **28** ( $R_1 = t$ -BuO,  $R_2 = \text{Me}$ ) (0.150 g, 0.607 mmol) in tetrahydrofuran (15 mL) was cooled to  $0^\circ\text{C}$  and a 2.0 mol/L solution of trimethylaluminum in heptane (0.60 mL, 1.21 mmol) was added dropwise. The reaction mixture was allowed to warm to room temperature and was stirred for 4 h. Water (2 mL) was added dropwise, and after 15 min, the solution was concentrated to near dryness, diluted with 1:4 dichloromethane:tetrahydrofuran (50 mL), and filtered through Celite. The filtrate was concentrated to give a white solid (128 mg, 98%); mp  $119$ – $120^\circ\text{C}$ . IR (KBr) ( $\text{cm}^{-1}$ ): 3364, 1696, 1679, 1528.  $^1\text{H}$  NMR ( $\text{CDCl}_3$ )  $\delta$ : 8.65 (1H, br s,  $\text{ONH}$ ), 5.43 (1H, br s,  $\text{NH}$ ), 4.54 (1H, m,  $\text{CH}\alpha$ ), 4.21 (1H, m,  $\text{CH}\gamma$ ), 4.08 (1H, m,  $\text{CH}\gamma$ ), 2.88 (1H, m,  $\text{CH}\beta$ ), 1.74 (1H, m,  $\text{CH}\beta$ ), 1.46 (9H, s,  $\text{C}(\text{CH}_3)_3$ ).  $^{13}\text{C}$  NMR ( $\text{CDCl}_3$ )  $\delta$ : 174.11, 155.35, 80.03, 69.77, 47.78, 29.74, 28.09. CI-MS ( $m/z$ ): 217 ( $[\text{M} + 1]$ ). Calcd. for  $\text{C}_9\text{H}_{16}\text{N}_2\text{O}_4$ : C 49.98, H 7.47, N 12.96; found: C 50.17, H 7.47, N 12.74.

**Methyl  $\alpha$ -phenylacetamido- $\gamma$ -phthalimidooxybutyrate (27,  $R_1 = \text{PhCH}_2$ ,  $R_2 = \text{Me}$ )**

Triethylamine (0.95 mL, 6.78 mmol) was added slowly to a solution of *N*-hydroxyphthalimide (1.11 g, 6.78 mmol) in acetonitrile (15 mL). The solution was stirred for 20 min, cooled to  $10$ – $15^\circ\text{C}$ , and a solution of **26** ( $R_1 = \text{PhCH}_2$ ,  $R_2 = \text{Me}$ ) (2.23 g, 6.78 mmol) in acetonitrile (5 mL) was added dropwise. The reaction mixture was allowed to warm to room temperature, and stirring was continued for 24 h. The solvent was removed, and the residue was dissolved in ethyl acetate (50 mL). This solution was washed successively with water ( $2 \times 15$  mL), saturated sodium bicarbonate ( $8 \times 15$  mL), water (15 mL), 5% citric acid (15 mL), water (15 mL), and saturated sodium chloride (15 mL), dried over anhydrous magnesium sulfate, and evaporated. The resulting solid was recrystallized from hot ethanol to give 2.25 g (84%); mp  $138$ – $139^\circ\text{C}$ . IR (KBr) ( $\text{cm}^{-1}$ ): 3348, 1792, 1735, 1664.  $^1\text{H}$  NMR ( $\text{CDCl}_3$ )  $\delta$ : 7.81 (4H, m, phthalimido ring), 7.24 (5H, m, *Ph*), 6.15 (1H, br s,  $\text{NH}$ ), 4.87 (1H, m,  $\text{CH}\alpha$ ), 4.21 (2H, t, 5.8 Hz,  $\text{CH}_2\gamma$ ), 3.73 (3H, s,

$\text{CH}_3$ ), 3.67 (2H, s,  $\text{PhCH}_2$ ), 2.30 (2H, m,  $\text{CH}_2\beta$ ). CI-MS ( $m/z$ ): 397 ( $[\text{M} + 1]$ ). Calcd. for  $\text{C}_{21}\text{H}_{20}\text{N}_2\text{O}_6$ : C 63.62, H 5.10, N 7.07; found: C 63.97, H 5.19, N 7.12.

**Methyl 2-phenylacetamido-4-aminooxybutyrate (28,  $R_1 = \text{PhCH}_2$ ,  $R_2 = \text{Me}$ )**

Methylhydrazine (0.20 mL, 0.174 g, 3.78 mmol) was added dropwise at  $-10^\circ\text{C}$  to a solution of **27**,  $R_1 = \text{PhCH}_2$ ,  $R_2 = \text{Me}$  (1.0 g, 2.52 mmol), in dichloromethane (40 mL). The cooling bath was removed, and stirring was continued for 3 h. The mixture was then filtered, and the filtrate was evaporated. The residue, in ethyl acetate (30 mL), was washed with 1:1 saturated sodium chloride:saturated sodium bicarbonate (6 mL). The aqueous layer was extracted with ethyl acetate (30 mL), and the combined organic extract was dried over anhydrous magnesium sulfate and evaporated to give a pale yellow oil (0.664 g, 99%).  $^1\text{H}$  NMR ( $\text{CDCl}_3$ )  $\delta$ : 7.35 (5H, m, *Ph*), 6.50 (1H, br s,  $\text{NH}$ ), 4.68 (1H, m,  $\text{CH}\alpha$ ), 3.75 (3H, s,  $\text{COCH}_3$ ), 3.65 (2H, t, 5.8 Hz,  $\text{CH}_2\gamma$ ), 3.65 (2H, s,  $\text{PhCH}_2$ ), 2.03 (2H, m,  $\text{CH}_2\beta$ ). CI-MS ( $m/z$ ): 267 ( $[\text{M} + 1]$ ).

**4-Phenylacetamido-[1,2]oxazinan-3-one (10)**

A 2.0 mol/L solution of trimethylaluminum in hexanes (1.13 mL, 2.25 mmol) was added dropwise at  $0^\circ\text{C}$  to a solution of **28**,  $R_1 = \text{PhCH}_2$ ,  $R_2 = \text{Me}$  (0.300 g, 1.13 mmol), in toluene (20 mL). The ice bath was removed, and stirring was continued for 4 h. The reaction mixture was then treated dropwise with water (1 mL). After an additional 15 min, the solvent was removed under reduced pressure to near-dryness; 1:4 dichloromethane:tetrahydrofuran (150 mL) was added, and the mixture was filtered through Celite. The filtrate was concentrated, and the residue was purified by short column chromatography on silica gel with a gradient solvent system (hexanes to ethyl acetate) to give a white solid (91.2 mg, 35%); mp  $164$ – $165^\circ\text{C}$ . IR (KBr) ( $\text{cm}^{-1}$ ): 3307, 1694, 1660.  $^1\text{H}$  NMR ( $\text{CDCl}_3$ )  $\delta$ : 8.17 (1H, br s,  $\text{ONH}$ ), 7.32 (5H, m, *Ar*), 6.41 (1H, br s,  $\text{NH}$ ), 4.72 (1H, m,  $\text{CH}\alpha$ ), 4.23 (1H, m,  $\text{CH}\gamma$ ), 4.04 (1H, m,  $\text{CH}\gamma$ ), 3.63 (2H, s,  $\text{PhCH}_2$ ), 2.98 (1H, m,  $\text{CH}\beta$ ), 1.63 (1H, m,  $\text{CH}\beta$ ).  $^{13}\text{C}$  NMR ( $\text{CDCl}_3$ )  $\delta$ : 173.52, 171.08, 134.45, 129.30, 128.96, 127.37, 69.84, 47.02, 43.56, 28.99. CI-MS ( $m/z$ ): 235 ( $[\text{M} + 1]$ ). Calcd. for  $\text{C}_{12}\text{H}_{14}\text{N}_2\text{O}_3$ : C 61.52, H 6.04, N 11.96; found: C 61.32, H 6.04, N 11.92.

**TFA salt of cyclocanaline**

The BOC derivative **27**,  $R = t$ -BuO (50.9 mg, 0.235 mmol), was added, with stirring, to a cooled ( $0$  to  $-5^\circ\text{C}$ ) solution of trifluoroacetic acid (0.75 mL). The mixture was allowed to warm to room temperature and was stirred for 1 h. The solvent was then removed under reduced pressure, and the residue was triturated with ether to give a white solid (53.0 mg, 98%).  $^1\text{H}$  NMR ( $\text{D}_2\text{O}$ )  $\delta$ : 4.29 (1H, m,  $\text{CH}\gamma$ ), 4.09 (1H, m,  $\text{CH}\gamma$ ), 4.08 (1H, m,  $\text{CH}\alpha$ ), 2.77 (1H, m,  $\text{CH}\beta$ ), 2.06 (1H, m,  $\text{CH}\beta$ ).

**4-Phenoxyacetamido-[1,2]oxazinan-3-one**

Triethylamine (0.2 mL, 1.43 mmol) was added slowly to a suspension of the trifluoroacetic acid salt of cyclocanaline (0.150 g, 0.63 mmol) in dichloromethane



(5 mL); the mixture was cooled to  $-10\text{ }^{\circ}\text{C}$ , and a solution of phenoxyacetyl chloride (0.079 mL, 97.2 mg, 0.57 mmol) in dichloromethane (2 mL) was added dropwise. The reaction mixture was allowed to warm to room temperature and was stirred overnight and then washed successively with water (2 mL), 5% citric acid (2 mL), water (2 mL), and 1:1 saturated sodium chloride:saturated sodium bicarbonate (2 mL), dried over anhydrous magnesium sulfate, and evaporated. The residue was purified by short column chromatography on silica gel, using hexanes to ethyl acetate gradient solvent system, to give a white solid (29.8 mg, 38%). IR (KBr) ( $\text{cm}^{-1}$ ): 3314, 1686, 1655.  $^1\text{H}$  NMR ( $\text{CDCl}_3$ )  $\delta$ : 7.53 (1H, br s, NH), 7.15 (5H, m, Ar), 4.84 (1H, m,  $\text{CH}\alpha$ ), 4.55 (2H, s,  $\text{PhOCH}_2$ ), 4.28 (1H, m,  $\text{CH}\gamma$ ), 4.11 (1H, m,  $\text{CH}\gamma$ ), 3.03 (1H, m,  $\text{CH}\beta$ ), 1.78 (1H, m,  $\text{CH}\beta$ ).  $^{13}\text{C}$  NMR ( $\text{CDCl}_3$ )  $\delta$ : 173.06, 168.47, 157.20, 129.75, 122.17, 114.79, 69.89, 67.29, 46.66, 28.94. CI-MS ( $m/z$ ): 251 ( $[\text{M} + 1]$ ).

### Carbobenzoxy D-methionine

D-Methionine (29.4 g, 0.20 mol) was added to a solution of 2 N sodium bicarbonate (500 mL). The mixture was cooled in an ice bath, and benzyl chloroformate (37 mL, 0.26 mol) was added dropwise. After the addition, the mixture was allowed to warm to room temperature and was stirred for 22 h. The unreacted benzyl chloroformate was then removed by extraction with ether ( $4 \times 300\text{ mL}$ ). The pH of the aqueous solution was adjusted to 2–3 using 6 N HCl (a whitish precipitate formed), and the mixture was extracted with ethyl acetate ( $5 \times 200\text{ mL}$ ). These extracts were dried over anhydrous sodium sulfate, and the solvent was removed to give 41.72 g (74%) of a light yellow oil.  $^1\text{H}$  NMR (100 MHz,  $\text{CDCl}_3$ ): 2.10 (s, 3H,  $-\text{SCH}_3$ ), 2.15 (t, 2H,  $\text{NHCHCH}_2$ ), 2.60 (t, 2H,  $\text{NHCHCH}_2\text{CH}_2$ ), 4.60 (m, 1H,  $\text{NHCH}$ ), 5.20 (s, 2H,  $\text{CH}_2\text{Ph}$ ), 5.50 (d, 1H, NH), 7.40 (s, 5H, ArH).

### Carbobenzoxy R- $\alpha$ -amino- $\gamma$ -butyrolactone

Carbobenzoxy D-methionine (41.72 g, 0.1474 mol) was dissolved in a mixture of glacial acetic acid (44.5 mL) and 80% HF (89 mL); iodomethane (16.7 mL, 0.268 mol) was added, and the mixture was left in the dark for 15 h, producing a clear, orange solution. This solution was concentrated in vacuo below  $40\text{ }^{\circ}\text{C}$ , and the resulting oily residue was triturated with dry ether ( $3 \times 20\text{ mL}$ ). The ether-insoluble orange oil was dissolved in 1 N sodium hydroxide (180 mL). The white crystals that appeared after cooling to  $0\text{ }^{\circ}\text{C}$  were collected, washed well with water, and maintained at 1 torr (1 torr = 133.322 Pa) for 5 h. The mother liquor from the washings was then acidified to pH 2 with concentrated hydrochloric acid, allowed to stand at room temperature for 1 h, and extracted with ethyl acetate ( $3 \times 200\text{ mL}$ ). The combined extracts were washed with 4% sodium bicarbonate ( $2 \times 100\text{ mL}$ ), brine ( $2 \times 100\text{ mL}$ ), and dried over anhydrous magnesium sulfate. Removal of the solvent afforded a yellow precipitate, which was crystallized from isopropyl alcohol. The total yield of product was 6.62 g (20%).  $^1\text{H}$  NMR (100 MHz,  $\text{CDCl}_3$ ): 2.30 (m, 1H,  $\text{NHCHCHH}$ ), 2.80 (m, 1H,  $\text{NHCHCHH}$ ), 4.20 (m, 3H,  $\text{NHCH}$  and  $\text{NHCHCH}_2\text{CH}_2$ ), 5.20 (s, 2H,  $\text{CH}_2\text{Ph}$ ), 5.40 (br. s, 1H, NH), 7.40 (s, 5H, ArH).

### Methyl ester of R-carbobenzoxyhomoserine

A solution of potassium hydroxide (0.716 g, 12.77 mmol) in methanol (8 mL) was added dropwise to a stirred suspension of the carbobenzoxy lactone (2.00 g, 8.51 mmol) in methanol (12 mL). The resulting solution was stirred at room temperature for 18 h, and the reaction was then quenched with a stream of carbon dioxide. Evaporation of the solvent produced a white crystalline solid. This solid was dissolved in dimethylformamide (10 mL), and iodomethane (1.72 mL, 0.028 mmol) was added. The reaction mixture was stirred at room temperature for 66 h, and the solvent was evaporated. The residue was shaken with ethyl acetate (40 mL) and water (10 mL). The aqueous phase was extracted with ethyl acetate ( $2 \times 10\text{ mL}$ ), and the combined organic extracts were washed successively with water (10 mL), saturated sodium thiosulfate (10 mL), saturated sodium bicarbonate (10 mL), brine (10 mL), and dried over anhydrous magnesium sulfate. Removal of the solvent afforded 1.73 g (76%) of the product as a pale yellow oil.  $^1\text{H}$  NMR (100 MHz,  $\text{CDCl}_3$ ): 1.60 (m, 1H,  $\text{NHCHCHH}$ ), 2.40 (m, 1H,  $\text{NHCHCHH}$ ), 3.60–3.90 (m, 5H,  $\text{NHCHCH}_2\text{CH}_2$  and  $\text{CO}_2\text{CH}_3$ ), 4.40–4.70 (m, 1H,  $\text{NHCH}$ ), 5.20 (s, 2H,  $\text{CH}_2\text{Ph}$ ), 5.70 (br. s, 1H, NH), 7.40 (s, 5H, ArH).

### Mesylation of the methyl ester of R-carbobenzoxyhomoserine

The carbobenzoxy methyl ester (1.71 g, 6.40 mmol) was dissolved in methylene chloride (30 mL), and triethylamine (1.2 mL, 8.499 mmol) was added in one portion. After 5 min of stirring, the reaction mixture was cooled ( $-5$  to  $-10\text{ }^{\circ}\text{C}$ ), and methanesulfonyl chloride (0.63 mL, 8.206 mmol) was added dropwise. The reaction mixture was stirred at  $0\text{ }^{\circ}\text{C}$  for 2 h, diluted with methylene chloride (20 mL), and washed successively with water ( $2 \times 10\text{ mL}$ ), 1 N hydrochloric acid (10 mL), water (10 mL), saturated sodium bicarbonate (10 mL + 10 mL of water), and dried over anhydrous magnesium sulfate. Removal of the solvent afforded 2.10 g (100%) of the mesylate as a yellow oil.  $^1\text{H}$  NMR (100 MHz,  $\text{CDCl}_3$ ): 2.30 (m, 2H,  $\text{NHCHCH}_2$ ), 3.02 (s, 3H,  $\text{SO}_2\text{CH}_3$ ), 3.82 (s, 3H,  $\text{CO}_2\text{CH}_3$ ), 4.25–4.55 (m, 3H,  $\text{NHCH}$  and  $\text{NHCHCH}_2\text{CH}_2$ ), 5.18 (s, 2H,  $\text{CH}_2\text{Ph}$ ), 5.55 (br. d, 1H, NH), 7.45 (d, 5H, ArH).

### Methyl ester of R-2-carbobenzoxyamido-4-phthalimidoxybutyric acid

1,8-Diazabicyclo[5.4.0]undec-7-ene (1.74 mL, 11.62 mmol) was added portionwise, with stirring, to a solution of *N*-hydroxyphthalimide (2.08 g, 12.75 mmol) in dimethylformamide (12 mL). After 20 min, the dark red reaction mixture was cooled to  $10$ – $15\text{ }^{\circ}\text{C}$ , and a solution of the mesylate (2.10 g, 6.68 mmol) in dimethylformamide (10 mL) was added dropwise with stirring. The reaction mixture was stirred at room temperature for 24 h and then diluted with ethyl acetate (80 mL) and washed with water ( $6 \times 15\text{ mL}$ ) until a pale yellow aqueous phase was obtained. The organic layer was washed with saturated sodium bicarbonate ( $9 \times 12\text{ mL}$ ) and saturated brine ( $2 \times 12\text{ mL}$ ), dried over anhydrous magnesium sulfate, and evaporated. The resulting pale yellow solid (2.32 g) was recrystallized from 85% ethanol to yield 1.81 g (66%) of the mesylate as a white powder; mp



102–104 °C.  $^1\text{H}$  NMR (100 MHz,  $\text{CDCl}_3$ ): 2.30 (q, 2H,  $\text{NHCHCH}_2$ ), 3.80 (s, 3H,  $\text{CO}_2\text{CH}_3$ ), 4.38 (t, 2H,  $\text{NHCHCH}_2\text{CH}_2$ ), 4.70 (m, 1H,  $\text{NHCH}$ ), 5.20 (s, 2H,  $\text{CH}_2\text{Ph}$ ), 6.20 (br. d, 1H,  $\text{NH}$ ), 7.40 (s, 5H,  $\text{ArH}$ ), 7.85 (m, 4H,  $\text{ArH}$  from *N*-hydroxyphthalimide).

#### Methyl ester of *R*-2-carbobenzoxyamido-4-aminooxy-butyric acid

A solution of methylhydrazine (0.34 mL, 6.305 mmol) in tetrahydrofuran (2 mL) was added dropwise, with cooling at 5 °C and stirring, to a solution of the phthalimidooxy compound (2.00 g, 4.85 mmol) in tetrahydrofuran (15 mL). The reaction mixture was allowed to warm to room temperature, and stirring was continued for 24 h. A white precipitate was then removed by filtration, and the filtrate was evaporated to dryness. The residue was then dissolved in methylene chloride (10 mL) and filtered through a plug of Silica Gel 60H for TLC, with elution by methylene chloride (35 mL). Evaporation of the solvent afforded 1.18 g (86%) of the product as a pale yellow oil.  $^1\text{H}$  NMR (100 MHz,  $\text{CDCl}_3$ ): 2.10 (m, 2H,  $\text{NHCHCH}_2$ ), 3.75 (m, 5H,  $\text{NHCHCH}_2\text{CH}_2$  and  $\text{CO}_2\text{CH}_3$ ), 4.55 (m, 1H,  $\text{NHCH}$ ), 4.15 (s, 2H,  $\text{CH}_2\text{Ph}$ ), 5.65 (br. d, 1H,  $\text{NH}$ ), 7.40 (s, 5H,  $\text{ArH}$ ).

#### Carbobenzoxy *R*-cyclocanaline

A solution of the carbobenzoxy methyl ester (1.15 g, 4.08 mmol) in tetrahydrofuran (65 mL) was treated dropwise at 0–5 °C with trimethylaluminum (2.45 mL of a 2 mol/L solution in hexane, 4.89 mmol). Stirring of the colourless reaction mixture was continued for 1 h, and the cooling bath was then removed while stirring continued for another 2 h. The slightly yellowish reaction mixture was then cooled to 0 °C, water (7 mL) was added dropwise, and stirring was continued for 1 h. Removal of the solvent afforded a white solid, which was triturated with ethyl acetate (100 mL) and filtered through a plug of Silica Gel 60H for TLC. Elution with ethyl acetate (100 mL) and evaporation of the solvent yielded 1.17 g of a pale yellow semi-solid, which was further purified by column chromatography on silica gel (30% ethyl acetate – hexanes to 60% ethyl acetate – hexanes) to give 456 mg (44%) of carbobenzoxy *D*-cyclocanaline as a white solid (mp 126–127 °C).  $^1\text{H}$  NMR (100 MHz,  $\text{CD}_3\text{CN}$ ): 1.60–2.10 (m, 1H,  $\text{NHCHCH}$ ), 2.40–2.80 (m, 1H,  $\text{NHCHCHH}$ ), 3.90–4.70 (m, 3H,  $\text{NHCH}$  and  $\text{NHCHCH}_2\text{CH}_2$ ), 5.80–6.20 (br. d, 1H,  $\text{NHCH}$ ), 7.30–7.50 (s, 5H,  $\text{ArH}$ ), 8.60–9.00 (br. s, 1H,  $\text{ONH}$ ). CI-MS (isobutane)  $m/z$ : 251 ( $[\text{M}^+ + 1]$ ). Calcd. for  $\text{C}_{12}\text{H}_{14}\text{N}_2\text{O}_4$ : C 57.65, H 5.64, N 11.20; found: C 57.89, H 5.71, N 11.34.

#### *R*-Cyclocanaline

The carbobenzoxy compound (268 mg, 1.071 mmol) was treated in one portion with 30% hydrogen bromide in acetic acid (0.80 mL) in a flask protected with a calcium chloride drying tube. A gas was produced immediately. The mixture was allowed to stand at room temperature for 1 h with occasional shaking, and ether (5 mL) was then added. The supernatant was decanted, and the precipitated solid was triturated with ether, maintained at 1 torr for 2 h, and then dissolved in methanol and treated, with shaking for 5 min, with an ion-exchange resin (CGA-540,  $\text{OH}^-$  form, 1.15 g). The resin was filtered, rinsed with methanol (10 mL), and

the combined filtrates were evaporated to yield 77.1 mg (62%) of yellow crystals.  $^1\text{H}$  NMR (100 MHz,  $\text{D}_2\text{O}$ ): 1.20–2.00 (m, 2H,  $\text{NH}_2\text{CHCH}_2$ ), 3.00–3.30 (m, 1H,  $\text{NH}_2\text{CH}$ ), 3.40 (t, 2H,  $\text{NH}_2\text{CHCH}_2\text{CH}_2$ ).

#### BOC-*R*-cycloserine (30)

To a suspension of *R*-cycloserine (2.00 g, 19.6 mmol) in 50% aqueous acetone (25 mL) were added triethylamine (4.1 mL, 2.98 g, 29.4 mmol) and BOC-ON (5.31 g, 21.5 mmol). The reaction mixture was stirred overnight at room temperature; most of the solvent was removed under reduced pressure, and ethyl acetate (70 mL) was added. The aqueous layer was separated, acidified to pH 3–4 with 5% citric acid (75 mL), and extracted with ethyl acetate (90 mL). The latter extract was washed successively with water (3  $\times$  90 mL) and saturated sodium chloride (90 mL), dried over anhydrous magnesium sulfate, and evaporated. Purification by flash chromatography on silica gel, using ethyl acetate – hexanes (2:1) as the eluent, gave 2.41 g (61%) of the product; mp 140–142 °C. IR ( $\text{CH}_2\text{Cl}_2$ ) ( $\text{cm}^{-1}$ ): 1711, 1689.  $^1\text{H}$  NMR ( $\text{CDCl}_3$ )  $\delta$ : 9.88 (1H, br s,  $\text{NH}$ ), 5.50 (1H, br s,  $\text{BOCNH}$ ), 4.79 (1H, m,  $\text{CH}\beta$ ), 4.58 (1H, m,  $\text{CH}\alpha$ ), 4.10 (1H, m,  $\text{CH}\beta$ ), 1.45 (9H, s,  $\text{C}(\text{CH}_3)_3$ ).  $^{13}\text{C}$  NMR ( $\text{CDCl}_3$ )  $\delta$ : 170.81, 155.73, 80.78, 74.80, 52.77, 28.24. CI-MS ( $m/z$ ): 203 ( $[\text{M} + 1]$ ). Calcd. for  $\text{C}_8\text{H}_{14}\text{N}_2\text{O}_4$ : C 47.52, H 6.98, N 13.85; found: C 47.67, H 7.07, N 13.10.

#### Mitsunobu reaction of 30 with ethyl *S*-lactate

Diethyl azodicarboxylate (0.058 mL, 64.1 mg, 0.371 mmol) was added to a solution of triphenylphosphine (0.103 g, 0.393 mmol) in tetrahydrofuran (3.2 mL) and cooled to –56 to –50 °C. The solution was stirred for 10 min; ethyl *S*-lactate (0.031 mL, 32.3 mg, 0.272 mmol) was added, and stirring was continued for an additional 10 min at –50 °C, at which time BOC-*R*-cycloserine (50.0 mg, 0.247 mmol) was added. Stirring was continued while the resulting mixture was allowed to warm to room temperature during 2.5 h. The solvent was then removed under reduced pressure. Purification of the residue by flash chromatography on silica gel, using 2:1 hexanes:ethyl acetate as the eluent, yielded a 1:1 mixture of diastereomeric products (64.7 mg, 87%).  $^1\text{H}$  NMR ( $\text{CDCl}_3$ )  $\delta$ : 5.25 (1H, br s,  $\text{BOCNH}$ , both isomers), 4.96 (1H, q, 6.9 Hz,  $\text{CHCH}_3$ , one isomer), 4.80 (1H, q, 7.5 Hz,  $\text{CHCH}_3$ , second isomer), 4.71 (1H, m,  $\text{CH}\beta$ , both isomers), 4.57 (1H, m,  $\text{CH}\alpha$ , both isomers), 4.22 (2H, q, 7.1 Hz,  $\text{CH}_2\text{CH}_3$ , one isomer), 4.21 (2H, q, 7.1 Hz,  $\text{CH}_2\text{CH}_3$ , second isomer), 4.21 (1H, m,  $\text{CH}\beta$ , both isomers), 1.58 (3H, d, 6.7 Hz,  $\text{CHCH}_3$ , one isomer), 1.53 (3H, d, 7.4 Hz,  $\text{CHCH}_3$ , second isomer), 1.45 (9H, s,  $\text{C}(\text{CH}_3)_3$ , one isomer), 1.44 (9H, s,  $\text{C}(\text{CH}_3)_3$ , second isomer), 1.29 (3H, t, 7.1 Hz,  $\text{CH}_2\text{CH}_3$ , one isomer), 1.28 (3H, t, 7.1 Hz,  $\text{CH}_2\text{CH}_3$ , second isomer). CI-MS ( $m/z$ ): 303 ( $[\text{M} + 1]$ ) (both isomers).

#### Mitsunobu reaction of 21 with ethyl *S*-lactate

Ethyl *S*-lactate (0.062 mL, 64.6 mg, 0.544 mmol) was added at room temperature to a stirred solution of [1,2]oxazinan-3-one (**21**) (45.4 mg, 0.449 mmol) in dichloromethane (2.8 mL). Triphenylphosphine (0.157 g, 0.597 mmol) was added; stirring was continued for 10 min at room temperature; the reaction mixture was cooled in an ice bath, and diethyl azodicarboxylate (0.093 mL, 0.103 g,



0.593 mmol) was added dropwise. The solution was allowed to warm to room temperature overnight, with stirring. The solvent was removed under reduced pressure, and the residue was purified by preparative layer chromatography on silica gel, using 7:4 hexanes:ethyl acetate as the eluent, to give 46.4 mg (51%) of the *N*-alkylated adduct **33** and 6.7 mg (7%) of the *O*-alkylated adduct **34**. *N*-Alkylated adduct:  $^1\text{H}$  NMR ( $\text{CDCl}_3$ )  $\delta$ : 5.03 (1H, q, 6.9 Hz, *CH*), 4.23 (2H, q, 7.1 Hz,  $\text{CH}_2\text{CH}_3$ ), 3.87 (2H, m,  $\text{CH}_2\gamma$ ), 2.34 (2H, m,  $\text{CH}_2\alpha$ ), 2.03 (2H, m,  $\text{CH}_2\beta$ ), 1.51 (3H, d, 7.0 Hz,  $\text{CHCH}_3$ ), 1.31 (3H, t, 7.1 Hz,  $\text{CH}_2\text{CH}_3$ ). *O*-Alkylated adduct:  $^1\text{H}$  NMR ( $\text{CDCl}_3$ )  $\delta$ : 5.20 (1H, q, 7.3 Hz, *CH*), 4.24 (2H, q, 7.1 Hz,  $\text{CH}_2\text{CH}_3$ ), 4.17 (2H, m,  $\text{CH}_2\gamma$ ), 2.56 (2H, m,  $\text{CH}_2\alpha$ ), 2.14 (2H, m,  $\text{CH}_2\beta$ ), 1.50 (3H, d, 7.3 Hz,  $\text{CHCH}_3$ ), 1.29 (3H, t, 7.2 Hz,  $\text{CH}_2\text{CH}_3$ ).

### Benzyl (*S*)-lactate

1,8-Diazabicyclo[5.4.0]undec-7-ene (18 mL, 18.3 g, 0.12 mol) was added slowly, with stirring, to a solution of 85% *S*-lactic acid (12.7 g, 0.12 mol) in methanol (50 mL). The solvent was removed under reduced pressure at 70–80 °C, and the resulting oil, in dimethylformamide (50 mL), was cooled to 15 °C. Benzyl bromide (11.9 mL, 17.1 g, 0.10 mol) was added dropwise, and the reaction mixture was stirred at room temperature for 30 h. After removal of approximately 40 mL of solvent by vacuum distillation, ethyl acetate (100 mL) was added, followed by water (30 mL). The aqueous layer was washed with ethyl acetate (2  $\times$  30 mL), and the combined organic extracts were washed successively with water (30 mL), 5% citric acid (30 mL), water (30 mL), saturated sodium bicarbonate (3  $\times$  30 mL), and saturated sodium chloride (2  $\times$  30 mL), dried over anhydrous magnesium sulfate, and evaporated. The crude product was distilled, to give a colourless oil (13.8 g, 76%); bp 119–123 °C at 1 torr. IR (neat) ( $\text{cm}^{-1}$ ): 3483, 1738.  $^1\text{H}$  NMR ( $\text{CDCl}_3$ )  $\delta$ : 7.37 (5H, m, Ar), 5.21 (2H, s,  $\text{PhCH}_2$ ), 4.32 (1H, q, 6.9 Hz, *CH*), 2.38 (1H, br s, OH), 1.43 (3H, d, 6.9 Hz,  $\text{CH}_3$ ).  $^{13}\text{C}$  NMR ( $\text{CDCl}_3$ )  $\delta$ : 175.52, 135.23, 128.66, 128.54, 128.22, 67.31, 66.84, 20.37. CI-MS ( $m/z$ ): 181 ( $[\text{M} + 1]$ ). Calcd. for  $\text{C}_{10}\text{H}_{12}\text{O}_3$ : C 66.64, H 6.73; found: C 66.30, H 6.75.

### Coupling of **20** with the triflate of benzyl *S*-lactate

A solution of 2,6-lutidine (0.35 mL, 0.32 g, 3.0 mmol) in dichloromethane (3 mL) was added at –78 °C to a solution of benzyl *S*-lactate (0.271 g, 1.5 mmol) in dichloromethane (15 mL). The solution was stirred for 10 min, trifluoromethanesulfonic anhydride (0.25 mL, 0.42 g, 1.5 mmol) was added dropwise, and stirring was continued for 30 min at –78 to –50 °C. A solution of methyl  $\gamma$ -aminooxybutyrate (0.170 g, 1.28 mmol) and 2,6-lutidine (0.175 mL, 0.16 g, 1.5 mmol) in dichloromethane (6 mL) was then added dropwise at –78 °C. The reaction mixture was allowed to warm to room temperature, stirred for 18 h, and then washed with water (2  $\times$  10 mL). The organic phase was further washed with saturated sodium chloride (10 mL), dried over anhydrous magnesium sulfate, and evaporated. Purification by flash chromatography on silica gel using a gradient system, hexanes to ethyl acetate, gave 1.63 g (74%) of **35**. IR (neat) ( $\text{cm}^{-1}$ ): 3264, 1741, 1736.  $^1\text{H}$  NMR ( $\text{CDCl}_3$ )  $\delta$ : 7.34 (5H, m, Ar), 5.19 (2H, s,  $\text{PhCH}_2$ ), 5.14 (1H, br d, ONH),

3.75 (1H, q, 7.0 Hz, *CH*), 3.69 (2H, t, 6.3 Hz,  $\text{CH}_2\gamma$ ), 3.65 (3H, s,  $\text{OCH}_3$ ), 2.33 (2H, t, 7.4 Hz,  $\text{CH}_2\alpha$ ), 1.87 (2H, m,  $\text{CH}_2\beta$ ), 1.23 (3H, d, 7.0 Hz,  $\text{CHCH}_3$ ).  $^{13}\text{C}$  NMR ( $\text{CDCl}_3$ )  $\delta$ : 174.11, 173.89, 135.67, 128.55, 128.28, 128.11, 73.01, 66.55, 58.88, 51.54, 30.68, 23.91, 14.75. CI-MS ( $m/z$ ): 296 ( $[\text{M} + 1]$ ).

### Cyclization of **35**

A solution of **35** (1.63 g, 5.5 mmol) in toluene (80 mL) was cooled to 0 °C and a 2.0 mol/L solution of trimethylaluminum in toluene (5.4 mL, 10.8 mmol) was added dropwise. The reaction mixture was allowed to warm to room temperature, stirred overnight, and then cooled to 0 °C, treated dropwise with methanol (16 mL), and stirred for 20 min. Water (10 mL) was added; the ice bath was removed, and stirring was continued for another 15 min. The solution was then concentrated to near-dryness, 1:4 dichloromethane:tetrahydrofuran (200 mL) was added, and the mixture was filtered through Celite. The filtrate was evaporated to give the crude product, 1.19 g, together with some unreacted starting material. Purification by flash chromatography on silica gel using an ethyl acetate – hexanes gradient solvent system, 10–40%, gave a clear oil (0.99 g, 84%). IR (neat) ( $\text{cm}^{-1}$ ): 1744, 1660.  $^1\text{H}$  NMR ( $\text{CDCl}_3$ )  $\delta$ : 7.35 (5H, m, Ar), 5.24 (1H, q, 7.3 Hz, *CH*), 5.20 (1H, d, 13.0 Hz,  $\text{PhCH}$ ), 5.14 (1H, d, 13.0 Hz,  $\text{PhCH}$ ), 4.14 (1H, m,  $\text{CH}\gamma$ ), 3.98 (1H, m,  $\text{CH}\gamma$ ), 2.51 (2H, m,  $\text{CH}_2\alpha$ ), 2.08 (2H, m,  $\text{CH}_2\beta$ ), 1.50 (3H, d, 7.3 Hz,  $\text{CHCH}_3$ ).  $^{13}\text{C}$  NMR ( $\text{CDCl}_3$ )  $\delta$ : 170.90, 170.13, 135.45, 128.53, 128.30, 128.07, 69.32, 67.09, 53.17, 28.32, 22.11, 13.76. CI-MS ( $m/z$ ): 264 ( $[\text{M} + 1]$ ).

### Hydrogenolysis of **36**

To ethyl acetate (15 mL) was added 10% palladium on activated carbon (83.0 mg, 0.078 mmol), and the suspension was stirred in an atmosphere of hydrogen for 1 h. The benzyl ester **36** (0.206 g, 0.78 mmol) in ethyl acetate (15 mL) was then added, and stirring was continued for 24 h. The mixture was filtered through Celite, which was washed with ethyl acetate (2  $\times$  4 mL), and the combined filtrates were evaporated to give **37** as a white solid (0.13 g, 99%). IR (KBr) ( $\text{cm}^{-1}$ ): 1744, 1621.  $^1\text{H}$  NMR ( $\text{CDCl}_3$ )  $\delta$ : 5.22 (1H, q, 7.3 Hz, *CH*), 4.23 (1H, m,  $\text{CH}\gamma$ ), 4.05 (1H, m,  $\text{CH}\gamma$ ), 2.56 (2H, m,  $\text{CH}_2\alpha$ ), 2.13 (2H, m,  $\text{CH}_2\beta$ ), 1.52 (3H, d, 7.3 Hz,  $\text{CHCH}_3$ ).  $^{13}\text{C}$  NMR ( $\text{CDCl}_3$ )  $\delta$ : 173.78, 171.18, 69.61, 53.19, 28.26, 22.09, 13.58. CI-MS ( $m/z$ ): 174 ( $[\text{M} + 1]$ ). Calcd. for  $\text{C}_7\text{H}_{11}\text{NO}_4$ : C 49.54, H 6.61, N 8.09; found: C 49.36, H 6.52, N 7.86.

### Alkylation of **28**, $\text{R}_1 = \text{PhCH}_2$ , $\text{R}_2 = \text{Me}$ , with the triflate of benzyl *S*-lactate

A solution of 2,6-lutidine (0.60 mL, 0.54 g, 5.0 mmol) in dichloromethane (3 mL) was added, with stirring, to a cooled (–78 °C) solution of benzyl *S*-lactate (0.450 g, 2.5 mmol) in dichloromethane (15 mL). After 10 min, trifluoromethanesulfonic anhydride (0.42 mL, 0.71 g, 2.5 mmol) was added dropwise, and stirring was continued at –78 to –50 °C for an additional 30 min. A solution of methyl 2-phenylacetamido-4-aminooxybutyrate (**28**) (0.678 g, 2.5 mmol) and 2,6-lutidine (0.30 mL, 0.27 g, 2.5 mmol) in dichloromethane (15 mL) was then added dropwise. When the addition was complete, the reaction mixture was allowed to warm to room



temperature and stirred for 18 h. Water ( $2 \times 10$  mL) was added, and the separated organic phase was washed with saturated sodium chloride (10 mL), dried over anhydrous magnesium sulfate, and evaporated. The residue was purified by flash chromatography on silica gel using a gradient system, hexanes to ethyl acetate, to give an oil (0.304 g, 29%). 4-Phenylacetamido-[1,2]oxazinan-3-one (**10**) was also found as a side product (0.136 g, 23%). IR ( $\text{CH}_2\text{Cl}_2$ ) ( $\text{cm}^{-1}$ ): 3286, 1742, 1660.  $^1\text{H}$  NMR of **38** ( $\text{CDCl}_3$ )  $\delta$ : 7.34 (10H, m,  $\text{PhCH}_2\text{CO}$ ,  $\text{PhCH}_2\text{O}$ , both isomers), 6.35 (1H, d, 7.9 Hz,  $\text{CONH}$ , one isomer, exchanges in  $\text{CD}_3\text{OD}$ ), 6.32 (1H, d, 7.5 Hz,  $\text{CONH}$ , second isomer, exchanges in  $\text{CD}_3\text{OD}$ ), 5.77 (1H, d, 9.5 Hz,  $\text{ONH}$ , one isomer, exchanges in  $\text{CD}_3\text{OD}$ ), 5.74 (1H, d, 8.9 Hz,  $\text{ONH}$ , second isomer, exchanges in  $\text{CD}_3\text{OD}$ ), 5.16 (2H, d, 4.12 Hz,  $\text{PhCH}_2\text{O}$ , one isomer), 5.15 (2H, d, 4.12 Hz,  $\text{PhCH}_2\text{O}$ , second isomer), 4.62 (1H, m,  $\text{CH}$   $\alpha$ , both isomers), 3.69 (2H, t, 6.3 Hz,  $\text{CH}_2\gamma$ , both isomers), 3.68 (3H, s,  $\text{OCH}_3$ , one isomer), 3.67 (3H, s,  $\text{OCH}_3$ , second isomer), 3.68–3.66 (1H, m,  $\text{CHCH}_3$ , both isomers), 3.59 (2H, m,  $\text{PhCH}_2\text{CO}$ , both isomers), 2.01 (2H, m,  $\text{CH}_2\beta$ , both isomers), 1.19 (3H, d, 7.2 Hz,  $\text{CHCH}_3$ , one isomer) 1.18 (3H, d, 7.2 Hz,  $\text{CHCH}_3$ , second isomer).  $^{13}\text{C}$  NMR ( $\text{CDCl}_3$ )  $\delta$ : 173.56, 172.32, 170.82, 135.55, 134.74, 129.37, 128.90, 128.87, 128.59, 128.21, 127.25, 70.30 ( $\text{PhCH}_2\text{O}$ , one isomer), 70.09 ( $\text{PhCH}_2\text{O}$ , second isomer), 66.76 ( $\text{CH}_2\gamma$ , both isomers), 58.63 ( $\text{CHCH}_3$ , one isomer), 58.57 ( $\text{CHCH}_3$ , second isomer), 52.36 ( $\text{PhCH}_2\text{CO}$ , both isomers), 50.23 ( $\text{OCH}_3$ , both isomers), 43.50 ( $\text{CH}\alpha$ , both isomers), 30.45 ( $\text{CH}_2\beta$ , both isomers), 14.72 ( $\text{CHCH}_3$ , one isomer), 14.62 ( $\text{CHCH}_3$ , second isomer). CI-MS ( $m/z$ ): 429 ( $[\text{M} + 1]$ ). Calcd. for  $\text{C}_{23}\text{H}_{28}\text{N}_2\text{O}_6 \cdot 0.75\text{H}_2\text{O}$ : C 62.51, H 6.68, N 6.34; found: C 62.36, H 6.35, N 6.38.

### Cyclization of **38**

A 2.0 mol/L solution of trimethylaluminum in hexanes (0.20 mL, 0.4 mmol) was added dropwise, at 0 °C, to a solution of **38** (42 mg, 0.10 mmol) in toluene (10 mL). The cooling bath was removed, and the reaction mixture was stirred overnight. Water (1 mL) was then added slowly, and stirring was continued for 15 min. The solvent was evaporated to near-dryness under reduced pressure; 1:4 dichloromethane:tetrahydrofuran (100 mL) was added, and the mixture was filtered through Celite. The filtrate was evaporated to give an oil (18 mg). Purification by short column chromatography, using a hexanes to ethyl acetate gradient solvent system, gave 3.9 mg of one isomer as a white solid; mp 106–107 °C.  $^1\text{H}$  NMR ( $\text{CD}_3\text{OD}$ ): 7.31 (10H, m,  $\text{PhCH}_2\text{CO}$ ,  $\text{PhCH}_2\text{O}$ ), 6.44 (1H, d, 5.6 Hz,  $\text{CONH}$ ), 5.14 (2H, q, 8.8 Hz,  $\text{PhCH}_2\text{O}$ ), 5.10 (1H, q, 7.2 Hz,  $\text{CHCH}_3$ ), 4.66 (1H, m,  $\text{CH}\alpha$ ), 4.22 (1H, m,  $\text{CH}$   $\gamma$ ), 4.06 (1H, m,  $\text{CH}$   $\gamma$ ), 3.61 (2H, s,  $\text{PhCH}_2$ ), 2.85 (1H, m,  $\text{CH}\beta$ ), 1.60 (1H, m,  $\text{CH}\beta$ ), 1.48 (3H, d, 7.3 Hz,  $\text{CH}_3$ ).  $^{13}\text{C}$  NMR ( $\text{CD}_3\text{OD}$ ): 170.88, 170.42, 170.03, 135.03, 134.46, 129.35, 129.00, 128.66, 128.30, 127.41, 69.01, 67.43, 53.67, 47.51, 43.68, 29.15.

### Synthesis of the *tert*-butyl esters **40a** and **40b**

To a stirred solution of 4-phenylacetamido-[1,2]oxazinan-3-one (**10**) (0.447 g, 1.91 mmol) and *tert*-butyl *S*- $\alpha$ -bromopropionate (0.398 g, 1.91 mmol) in dry dimethylformamide (15 mL) was added  $\text{KF} \cdot \text{Al}_2\text{O}_3$  (40 wt %, 1.94 g) in one portion. Stirring was continued at room temperature for 63 h.

The reaction mixture was then diluted with ethyl acetate (40 mL) and filtered through a pad of Silica Gel 60H (for TLC), which was washed with ethyl acetate (30 mL). The filtrate was washed with water ( $4 \times 30$  mL), 10% potassium bisulfate (15 mL), saturated sodium bicarbonate (15 mL), and brine (30 mL), and dried over anhydrous magnesium sulfate. Removal of the solvent provided 0.621 g of a yellowish oil, which was purified by flash chromatography (Silica Gel 60, 15% ethyl acetate – hexanes  $\rightarrow$  70% ethyl acetate – hexanes) to afford **40a** (0.183 g, 26%) and **40b** (0.215 g, 31%) as colourless oils.

#### **40a**

IR (film) ( $\text{cm}^{-1}$ ): 3319, 2988, 1737, 1658, 1537, 1370.  $^1\text{H}$  NMR (400 MHz,  $\text{CDCl}_3$ ): 1.42 (3H, d,  $^3J = 7.4$ , a-*Me*), 1.44 (9H,  $\text{CMe}_3$ ), 1.69 (1H, m,  $^2J = -12.1$ ,  $^3J = 10.0$ , 12.0, C5-*HI*), 2.91 (1H, m,  $^2J = -12.1$ ,  $^3J = 4.8$ , 6.9, 7.0, C5-*H2*), 3.60 (2H,  $\text{CH}_2\text{Ph}$ ), 4.14 (1H, m,  $^2J = -10.1$ ,  $^3J = 7.0$ , 10.0, C6-*H4*), 4.40 (1H, m,  $^2J = -10.1$ ,  $^3J = 4.8$ , 10.0, C6-*H3*), 4.67 (1H, m,  $^3J = 6.8$ , 6.9, 12.0, C4-*H5*), 4.95 (1H, q,  $^3J = 7.4$ , a-*CH*), 6.49 (1H, br. d,  $^3J = 6.8$ , *NH*), 7.26–7.37 (5H, m, *Ph*).  $^{13}\text{C}$  NMR (100 MHz,  $\text{CDCl}_3$ ): 14.06, 27.93, 29.24, 47.51, 54.33, 69.00, 82.30, 127.34, 128.94, 129.32, 134.51, 169.21, 170.28, 170.86. CI-MS (isobutane)  $m/z$ : 363 ( $[\text{M}^+ + 1]$ ).

#### **40b**

IR (film) ( $\text{cm}^{-1}$ ): 3311, 2981, 1739, 1657, 1539, 1370.  $^1\text{H}$  NMR (400 MHz,  $\text{CDCl}_3$ ): 1.42 (9H,  $\text{CMe}_3$ ), 1.44 (3H, d,  $^3J = 7.3$ , a-*Me*), 1.61 (1H, m,  $^2J = -12.4$ , C5-*HI*), 2.95 (1H, m,  $^2J = -12.4$ ,  $^3J = 4.9$ , 7.2, 10.1, C5-*H2*), 3.62 (2H,  $\text{CH}_2\text{Ph}$ ), 4.02 (1H, m,  $^2J = -10.2$ ,  $^3J = 4.9$ , 10.1, C6-*H4*), 4.24 (1H, m,  $^2J = -10.2$ ,  $^3J = 6.9$ , 10.3, C6-*H3*), 4.71 (1H, m,  $^3J = 5.6$ , 7.2, 11.7, C4-*H5*), 4.87 (1H, q,  $^3J = 7.3$ , a-*CH*), 6.48 (1H, br. d,  $^3J = 5.6$ , *NH*), 7.24–7.37 (5H, m, *Ph*).  $^{13}\text{C}$  NMR ( $\text{CDCl}_3$ ): 13.40, 27.90, 28.94, 43.67, 47.77, 54.86, 69.15, 82.38, 127.36, 128.96, 129.35, 134.52, 168.27, 170.87, 171.94. CI-MS (isobutane)  $m/z$ : 363 ( $[\text{M} + 1]$ ).

### Deprotection of **40a**

Ice-cold trifluoroacetic acid (1.5 mL) was added dropwise to **40a** (0.149 g, 0.41 mmol), with cooling (0 to –5 °C) and stirring. The reaction mixture was stirred for 1 h at room temperature and evaporated to dryness under reduced pressure. The semisolid residue was triturated with dry ether and dried in vacuo to afford 0.075 g (60%) of the acid **5a** as a white solid; mp 58–60 °C. IR (KBr) ( $\text{cm}^{-1}$ ): 3280, 2950, 1735, 1654, 1544, 1454.  $^1\text{H}$  NMR (400 MHz,  $\text{CD}_3\text{OD}$ ): 1.46 (3H, d,  $^3J = 7.3$ , a-*Me*), 1.96 (1H, m,  $^2J = -12.5$ ,  $^3J = 6.5$ , 9.5, C5-*HI*), 2.56 (1H, m,  $^2J = -12.5$ ,  $^3J = 5.4$ , 7.4, 9.5, C5-*H2*), 3.61 (2H,  $\text{CH}_2\text{Ph}$ ), 4.18 (1H, m,  $^2J = -10.3$ ,  $^3J = 6.5$ , 10.3, C6-*H4*), 4.43 (1H, m,  $^2J = -10.3$ ,  $^3J = 5.4$ , 9.5, C6-*H3*), 4.76 (1H, dd,  $^3J = 7.4$ , 10.5, C4-*H5*), 5.04 (1H, q,  $^3J = 7.3$ , a-*CH*), 7.21–7.38 (5H, m, *Ph*).  $^{13}\text{C}$  NMR ( $\text{CD}_3\text{OD}$ ): 14.23, 30.05, 43.61, 48.36, 55.01, 70.19, 127.90, 129.55, 130.23, 136.70, 171.89, 173.26, 174.20. CI-MS (isobutane),  $m/z$ : 307 ( $[\text{M} + 1]$ ).

### Deprotection of **40b**

Repetition of the above experiment with **40b** afforded the acid **5b** in 58% yield as a white solid; mp 189–190 °C. IR



(KBr) ( $\text{cm}^{-1}$ ): 3284, 2935, 1712, 1671, 1645, 1541, 1438.  $^1\text{H}$  NMR (400 MHz,  $\text{CD}_3\text{OD}$ ): 1.49 (3H, d,  $^3J = 7.3$ , a-Me), 1.93 (1H, m,  $^2J = -12.7$ ,  $^3J = 6.9$ , 9.0, 11.6, C5-H1), 2.54 (1H, m,  $^2J = -12.7$ ,  $^3J = 5.3$ , 7.5, 9.0, C5-H2), 3.60 (2H,  $\text{CH}_2\text{Ph}$ ), 4.14 (1H, m,  $^2J = -10.9$ ,  $^3J = 5.3$ , 9.0, C6-H4), 4.26 (1H, m,  $^2J = -10.9$ ,  $^3J = 6.9$ , 9.0, C6-H3), 4.77 (1H, dd,  $^3J = 7.5$ , 11.6, C4-H5), 4.99 (1H, q,  $^3J = 7.3$ , a-CH), 7.19–7.40 (5H, m, Ph).  $^{13}\text{C}$  NMR ( $\text{CD}_3\text{OD}$ ): 13.80, 29.98, 43.63, 48.36, 55.42, 70.44, 127.91, 129.57, 130.23, 136.66, 172.74, 172.81, 174.01. CI-MS (isobutane),  $m/z$ : 307 ( $[\text{M} + 1]$ ).

### Benzyl ester of homolactivicin

A solution of dicyclohexylcarbodiimide (0.357 g, 1.73 mmol) in acetonitrile (10 mL) was added dropwise to a stirred solution of the oxazinone **10** (0.311 g, 1.33 mmol) and benzyl 2-oxoglutarate (0.408 g, 1.73 mmol) in acetonitrile (20 mL). After three days of stirring, a white precipitate was collected by filtration and washed with methylene chloride. The filtrate was evaporated under reduced pressure to give 0.85 g of a dark semi-solid, which was purified by flash column chromatography (Silica Gel 60, ethyl acetate) to afford diastereomers **41a** (0.189 g) and **41b** (0.126 g) (52% total yield) as white solids.

### Homolactivicin

To a 1:1 mixture of **41a** and **41b** (0.217 g, 0.48 mmol) in ethyl acetate (30 mL) was added 5% Pd–C (0.106 g) in one portion. The mixture was stirred at room temperature, under hydrogen, for 7.5 h. The catalyst was then removed by filtration through a pad of Silica Gel 60H (for TLC), followed by washing with ethyl acetate (50 mL) and tetrahydrofuran (50 mL). The combined filtrates were evaporated under reduced pressure, and the white solid residue was triturated with dry ether ( $3 \times 5$  mL) and dried in vacuo to afford 0.0945 g (54%) of racemic homolactivicin (a mixture of diastereoisomers) as a white powder; mp 150–152 °C (decomposition temperature (dec)). IR (KBr) ( $\text{cm}^{-1}$ ): 3348, 2942, 1804, 1713, 1542, 1185, 1032.  $^1\text{H}$  NMR (400 MHz,  $\text{CD}_3\text{CN}$ ): 1.85 (1H, br.m), 2.45 (1H, br.m), 2.56 (2H, br.m), 2.72 (1H, br.m), 2.90 (2H, br.m), 3.52 (2H,  $\text{CH}_2\text{Ph}$ ), 4.13 (1H, br.m), 4.26 (2H, br.m), 4.71 (1H, br.m), 6.71 (br.s, NH), 7.2–7.4 (5H, m, Ph). Calcd for  $\text{C}_{17}\text{H}_{18}\text{N}_2\text{O}_7$ : C 56.35, H 5.01, N 7.73; found: C 56.31, H 5.11, N 7.69.

### Calcium L-threonate

Calcium carbonate (60.06 g, 0.6 mol) was added to a solution of L-ascorbic acid (52.8 g, 0.3 mol) in water (410 mL). The slurry was cooled to 0–5 °C and hydrogen peroxide (50% w/w, 61.2 mL, 0.9 mol) was added dropwise during 1 h at 5–20 °C. Stirring was continued at room temperature for 16 h, and the reaction mixture was then heated at 70–75 °C for 1 h until gas was no longer evolved. The suspension was filtered hot, and the filter cake was washed with 50–60 °C hot water ( $2 \times 30$  mL). The combined filtrates were concentrated to about 120 mL under reduced pressure at 55 °C. Methanol (250 mL) was added dropwise to the warm concentrate (50 °C) until the solution became cloudy, and the mixture was then stirred at room temperature for 12 h, filtered, and the precipitate was washed with methanol ( $3 \times 30$  mL). The solid was dried to a constant weight at 60 °C (3 h) to give 45.2 g (94.6%) of **42**. IR (KBr) ( $\text{cm}^{-1}$ ):

1600 (s).  $^1\text{H}$  NMR ( $\text{D}_2\text{O}$ , 400 MHz): 4.02 (d, 1H,  $\text{H}_c$ ,  $J_{bc} = 2.3$  Hz), 3.94 (ddd, 1H,  $\text{H}_b$ ,  $J_{ab} = 7.7$  Hz,  $J_{ab'} = 5.2$  Hz,  $J_{bc} = 2.2$  Hz), 3.65 (ABX, 1H,  $\text{H}_a'$ ,  $J_{aa'} = 11.6$  Hz,  $J_{ab} = 5.2$  Hz), 3.58 (ABX, 1H,  $\text{H}_a$ ,  $J_{aa'} = 11.6$  Hz,  $J_{ab} = 7.7$  Hz).

### Methyl 2,4-dibromo-2,4-dideoxy-L-erythronate (**43**)

Calcium L-threonate (34.98 g, 0.11 mol) was stirred for 24 h with 30% w/w hydrogen bromide – acetic acid solution (210 mL, 1.05 mol), and methanol (420 mL) was then added. The solution was stirred at room temperature for an additional 12 h, and the mixture was then refluxed for 2 h. The solvent was evaporated under reduced pressure to give an oil, which was dissolved in ethyl acetate (250 mL). This solution was washed with brine (100 mL), dried over sodium sulfate, and evaporated to give **43** (27.38 g, 90.2%) as an oil. IR (film) ( $\text{cm}^{-1}$ ): 3340 (m), 1745 (s).  $^1\text{H}$  NMR ( $\text{CDCl}_3$ , 400 MHz): 4.32 (d, 1H,  $\text{H}_c$ ,  $J_{bc} = 8.8$  Hz), 4.24 (m, 1H,  $\text{H}_b$ ), 3.81 (s, 3H,  $\text{CO}_2\text{Me}$ ), 3.80 (AB, 2H,  $\text{H}_a\text{H}_a'$ ). CI-MS ( $m/z$ ): 277 ( $[\text{M} + 1]$ ).

### Methoxymethylation of **43**

Boron trifluoride etherate (9.35 mL, 74 mmol) was added dropwise under nitrogen during 10 min at 0–5 °C to a solution of **43** (16.55 g, 60 mmol) in dichloromethane (70 mL) and dimethoxymethane (33 mL). The reaction mixture was stirred at room temperature for 10–12 h, cooled to 0–5 °C, and quenched by dropwise addition of water (50 mL) during 15 min. Dichloromethane (80 mL) was added, and the organic layer was washed with saturated sodium bicarbonate ( $2 \times 50$  mL) and brine (100 mL), dried over anhydrous sodium sulfate, and evaporated under reduced pressure to give a pale yellow oil (18.10 g, 92%). IR (film) ( $\text{cm}^{-1}$ ): 1747 (s).  $^1\text{H}$  NMR ( $\text{CDCl}_3$ , 400 MHz): 4.71 (AB, 2H,  $\text{H}_d$ ,  $\text{MeOCH}_2\text{O}$ ), 4.43 (d, 1H,  $\text{H}_c$ ,  $J_{bc} = 9.1$  Hz), 4.16 (dt, 1H,  $\text{H}_b$ ,  $J_{ab} \sim J_{ab'} = 2.9$  Hz,  $J_{bc} = 9.1$  Hz), 3.86 (ABX, 2H,  $\text{H}_a\text{H}_a'$ ,  $J_{aa'} = 11.5$  Hz,  $J_{ab} = 2.8$  Hz,  $J_{ab'} = 3.1$  Hz), 3.79 (s, 3H,  $\text{CO}_2\text{Me}$ ), 3.41 (s, 3H,  $\text{MeOCH}_2\text{O}$ ).

### Methyl 2-azido-4-bromo-2,4-dideoxy-3-methoxymethoxy-L-threonate (**44**)

Sodium azide (2.18 g, 33.5 mmol) was added in one portion at 10–15 °C to a solution of the MOM derivative (10.23 g, 32.0 mmol) in dimethylformamide (40 mL). The mixture was stirred at 10 °C to room temperature for 12 h. Water (35 mL) was then added at 0–5 °C, and the mixture was extracted with ethyl acetate ( $2 \times 80$  mL). The combined extracts were washed with water ( $3 \times 20$  mL) and brine (20 mL), dried over anhydrous sodium sulfate, and evaporated under reduced pressure to give an oil. Purification by flash chromatography using 5% ethyl acetate as eluent yielded 6.40 g (71%) of **44**. IR (film) ( $\text{cm}^{-1}$ ): 2115 (s), 1744 (s).  $^1\text{H}$  NMR ( $\text{CDCl}_3$ , 400 MHz): 4.67 (AB, 2H,  $\text{MeOCH}_2\text{O}$ ), 4.33 (ddd, 1H,  $\text{H}_b$ ,  $J_{ab} = 9.0$  Hz,  $J_{ab'} = 5.0$  Hz,  $J_{bc} = 2.5$  Hz), 4.29 (d, 1H,  $\text{H}_c$ ,  $J_{bc} = 2.5$  Hz), 3.85 (s, 3H,  $\text{CO}_2\text{Me}$ ), 3.58 (ABX, 1H,  $\text{H}_a'$ ,  $J_{aa'} = 10.2$  Hz,  $J_{ab} = 5.0$  Hz), 3.53 (ABX, 1H,  $\text{H}_a$ ,  $J_{aa'} = 10.2$  Hz,  $J_{ab} = 5.0$  Hz), 3.36 (s, 3H,  $\text{MeOCH}_2\text{O}$ ). CI-MS ( $m/z$ ): 282 ( $[\text{M} + 1]$ ), 284 ( $[\text{M} + 3]$ ), along with 0.40 g (5.2%) of the diazide-compound. IR (film) ( $\text{cm}^{-1}$ ): 2109 (vs), 1751 (s).  $^1\text{H}$  NMR ( $\text{CDCl}_3$ , 400 MHz): 4.68 (AB, 2H,  $\text{MeOCH}_2\text{O}$ ), 4.18 (ddd, 1H,  $\text{H}_b$ ,  $J_{ab} = 7.3$  Hz,  $J_{ab'} = 6.1$  Hz,  $J_{bc} = 2.9$  Hz), 3.95 (d, 1H,  $\text{H}_c$ ,  $J_{bc} = 2.9$  Hz),



3.84 (s, 3H,  $\text{CO}_2\text{Me}$ ), 3.62 (ABX, 1H,  $\text{H}_a$ ,  $J_{aa'} = 12.4$  Hz,  $J_{ab} = 6.1$  Hz), 3.49 (ABX, 1H,  $\text{H}_a$ ,  $J_{aa'} = 12.4$  Hz,  $J_{ab} = 7.3$  Hz), 3.36 (s, 3H,  $\text{MeOCH}_2\text{O}$ ). CI-MS ( $m/z$ ) 245 ( $[\text{M} + 1]$ ).

#### Reduction of 44 and protection as the BOC derivative 45

A 5% Pd-C suspension (0.60 g) in ethyl acetate (55 mL) was stirred for 2 h in a hydrogen atmosphere, and a solution of **44** (4.30 g, 15.0 mmol) and di-*tert*-butyl dicarbonate (4.00 g, 18.0 mmol) in ethyl acetate (25 mL) was added. The mixture was stirred under hydrogen until the starting material had disappeared (48 h) and then filtered through Celite. The Celite pad was washed with ethyl acetate ( $3 \times 10$  mL), and the filtrate was concentrated under reduced pressure. The crude product was purified by flash chromatography (12% ethyl acetate in hexane) to give 4.03 g (74%) of **45** as a colourless oil. IR (film) ( $\text{cm}^{-1}$ ): 1754 (s), 1721 (s).  $^1\text{H}$  NMR ( $\text{CDCl}_3$ , 400 MHz): 5.19 (d, 1H, NH,  $J_{\text{NHHC}} = 10.3$  Hz), 4.64 (AB, 2H,  $\text{MeOCH}_2\text{O}$ ), 4.36 (t, 1H,  $\text{H}_b$ ,  $J_{ab} = 6.4$  Hz), 3.77 (s, 3H,  $\text{CO}_2\text{Me}$ ), 3.43 (ABX, 2H,  $\text{H}_a$ ,  $J_{ab} = 6.4$  Hz), 3.31 (s, 3H,  $\text{MeOCH}_2\text{O}$ ), 1.48 (s, 9H,  $-\text{CO}_2\text{CMe}_3$ ). CI-MS ( $m/z$ ): 356 ( $[\text{M} + 1]$ ), 358 ( $[\text{M} + 3]$ ).

#### Conversion of 45 to the phthalimidoxy compound

A solution of *N*-hydroxyphthalimide (2.40 g, 14.8 mmol) and DBU (2.20 g, 14.4 mmol) in dimethylformamide (25 mL) was added dropwise with stirring at 10–15 °C to a solution of **45** (4.40 g, 12.4 mmol) in dimethylformamide (10 mL). The mixture was stirred for 60 h and allowed to warm to room temperature. Ethyl acetate (120 mL) was then added, and the organic layer was washed with saturated sodium bicarbonate ( $5 \times 15$  mL) and brine (20 mL), dried over anhydrous sodium sulfate, and evaporated to give an oil. Purification by flash chromatography using 30% ethyl acetate in hexane as eluent afforded 2.93 g (54.0%) of the phthalimidoxy compound as a colourless oil. IR (film) ( $\text{cm}^{-1}$ ): 1739 (s), 1732 (s), 1719 (s).  $^1\text{H}$  NMR ( $\text{CDCl}_3$ , 400 MHz): 7.80 (AB, 4H), 5.28 (d, 1H, NH,  $J_{\text{NHHC}} = 9.8$  Hz), 4.76 (AB, 2H,  $\text{MeOCH}_2\text{O}$ ), 4.65 (d, 1H,  $\text{H}_c$ ,  $J_{\text{NHHC}} = 9.8$  Hz), 4.58 (m, 1H,  $\text{H}_b$ ,  $J_{ab} = 7.0$  Hz,  $J_{ab'} = 4.8$  Hz,  $J_{bc} = 1.5$  Hz), 4.36 (ABX, 1H,  $\text{H}_a$ ,  $J_{aa'} = 10.6$  Hz,  $J_{ab} = 4.8$  Hz), 4.28 (ABX, 1H,  $\text{H}_a$ ,  $J_{aa'} = 10.6$  Hz,  $J_{ab} = 7.0$  Hz), 3.79 (s, 3H,  $\text{CO}_2\text{Me}$ ), 3.31 (s, 3H,  $\text{MeOCH}_2\text{O}$ ), 1.43 (s, 9H,  $-\text{CO}_2\text{CMe}_3$ ). CI-MS ( $m/z$ ): 439 ( $[\text{M} + 1]$ ).

#### Formation of the aminoxy compound 46

A solution of the phthalimidoxy compound (2.40 g, 5.48 mmol) in dichloromethane (25 mL) was treated, with stirring at –15 °C, with a solution of methylhydrazine (0.38 g, 8.26 mmol) in dichloromethane (2 mL). The cooling bath was then removed, and stirring was continued for 4 h. The solvent and excess methylhydrazine were evaporated under reduced pressure, and the residue was triturated with ethyl acetate ( $6 \times 3$  mL) and filtered through a short silica gel plug. The filtrate was evaporated to give 1.44 g (85.3%) of **46** as a colourless oil. IR (film) ( $\text{cm}^{-1}$ ): 3451 (b), 3323 (m), 1745 (s), 1714 (s).  $^1\text{H}$  NMR ( $\text{CDCl}_3$ , 400 MHz): 5.54 (b, 2H,  $-\text{ONH}_2$ ), 5.25 (d, 1H, NH,  $J_{\text{NHHC}} = 9.6$  Hz), 4.61 (AB, 2H,  $\text{MeOCH}_2\text{O}$ ), 4.47 (dd, 1H,  $\text{H}_c$ ,  $J_{bc} = 1.6$  Hz,  $J_{\text{NHHC}} = 9.8$  Hz), 4.40 (td, 1H,  $\text{H}_b$ ,  $J_{ab} \sim J_{ab'} = 6.2$  Hz,  $J_{bc} = 1.6$  Hz), 3.76 (s, 3H,  $\text{CO}_2\text{Me}$ ), 3.73 (ABX, 2H,  $\text{H}_{aa'}$ ,  $J_{aa'} =$

11.2 Hz,  $J_{ab} = J_{ab'} = 6.2$  Hz), 3.31 (s, 3H,  $\text{MeOCH}_2\text{O}$ ), 1.47 (s, 9H,  $-\text{CO}_2\text{CMe}_3$ ). CI-MS ( $m/z$ ): 309 ( $[\text{M} + 1]$ ).

#### Reaction of 46 with the triflate of benzyl L-lactate

Trifluoromethanesulfonic anhydride (0.79 mL, 4.69 mmol) was added dropwise, with stirring at –78 °C, to a solution of benzyl L-lactate (0.84 g, 4.66 mmol) and 2,6-lutidine (0.70 g, 6.53 mmol) in dichloromethane (35 mL). After 20 min a solution of **46** (1.30 g, 4.22 mmol) and 2,6-lutidine (0.46 g, 4.29 mmol) in dichloromethane (20 mL) was added dropwise at –78 to –60 °C. Stirring was continued at –78 to –50 °C for 1 h, and the cooling bath was then removed. After an additional 10 h of stirring the reaction mixture was washed with cold water ( $2 \times 5$  mL), dried over anhydrous sodium sulfate, and evaporated to give an oil. Purification by flash chromatography using 25% ethyl acetate in hexane as eluent yielded 1.31 g (66%) of **47**. IR (film) ( $\text{cm}^{-1}$ ): 3445 (b), 3367 (m), 1744 (s), 1719 (s).  $^1\text{H}$  NMR ( $\text{CDCl}_3$ , 400 MHz): 7.37 (m, 5H,  $\text{PhCH}_2$ ), 6.07 (d, 1H, ONH,  $J_{\text{ONHd}} = 8.8$  Hz), 5.23 (d, 1H, NH,  $J_{\text{NHHC}} = 9.9$  Hz), 5.18 (AB, 2H,  $\text{PhCH}_2$ ), 4.56 (AB, 2H,  $\text{MeOCH}_2\text{O}$ ), 4.43 (d, 1H,  $\text{H}_c$ ,  $J_{\text{NHHC}} = 9.9$  Hz), 4.32 (t, 1H,  $\text{H}_b$ ,  $J_{ab} = 6.0$  Hz), 3.80 (m, 1H,  $\text{H}_d$ ,  $J_{de} = 7.2$  Hz,  $J_{\text{ONHd}} = 8.8$  Hz), 3.77 (d, 2H,  $\text{H}_a$ ,  $J_{ab} = 6.4$  Hz), 3.75 (s, 3H,  $\text{CO}_2\text{Me}$ ), 3.27 (s, 3H,  $\text{MeOCH}_2\text{O}$ ), 1.45 (s, 9H,  $-\text{CO}_2\text{CMe}_3$ ), 1.24 (d, 3H,  $\text{H}_e$ ,  $J_{de} = 7.2$  Hz). CI-MS ( $m/z$ ): 471 ( $[\text{M} + 1]$ ).

#### Cyclization of 46

A 2.0 mol/L solution of trimethylaluminium in hexane (1.68 mL, 3.36 mmol) was added dropwise, with stirring at 0–5 °C, to a solution of **46** (0.86 g, 2.80 mmol) in dry tetrahydrofuran (70 mL). Stirring was continued for 40 min after addition was complete, and for 3.5 h after the cooling bath was removed. Ice-cold water (1 mL) was added, and after 20 min, the solvent was removed under reduced pressure. The residue was triturated with tetrahydrofuran ( $6 \times 5$  mL) and dichloromethane ( $4 \times 5$  mL) and filtered through a short silica gel – Celite pad. The filtrate was evaporated to give **48**, 0.70 g (90%), as an oil. IR (film) ( $\text{cm}^{-1}$ ): 3342 (m), 3232 (m), 1698 (vs).  $^1\text{H}$  NMR ( $\text{CDCl}_3$ , 400 MHz): 8.80 (s, 1H,  $\text{NH}_2$ ), 5.19 (d, 1H,  $\text{NH}_d$ ,  $J_{\text{NHdHc}} = 7.0$  Hz), 4.69 (AB, 2H,  $\text{MeOCH}_2\text{O}$ ,  $J = 7.0$  Hz), 4.57 (dd, 1H,  $\text{H}_c$ ,  $J_{\text{NHdHc}} = 7.1$  Hz,  $J_{bc} = 7.1$  Hz), 4.26 (ABM, 1H,  $\text{H}_a$ ,  $J_{aa'} = 12.2$  Hz,  $J_{ab} = 5.9$  Hz), 4.14 (ABM, 1H,  $\text{H}_a$ ,  $J_{aa'} = 12.2$  Hz,  $J_{ab} = 3.3$  Hz), 3.99 (ddd, 1H,  $\text{H}_b$ ,  $J_{ab} = 3.3$  Hz,  $J_{ab'} = 5.9$  Hz,  $J_{bc} = 7.8$  Hz), 3.37 (s, 3H,  $\text{MeOCH}_2\text{O}$ ), 1.45 (s, 9H,  $-\text{CO}_2\text{CMe}_3$ ). CI-MS ( $m/z$ ): 277 ( $[\text{M} + 1]$ ).

#### Cyclization of 47

A 2.0 mol/L solution of trimethylaluminium in hexane (3.40 mL, 6.82 mmol) was added dropwise, with stirring at 0–5 °C, to a solution of **47** (0.76 g, 1.62 mmol) in dry toluene (70 mL). Stirring was continued for 40 min at 0–5 °C and then for 4 h after removal of the cooling bath. Ice-cold water (1 mL) was added, the mixture was stirred for 20 min, and the solvent was then removed under reduced pressure. The residue was triturated with tetrahydrofuran ( $8 \times 6$  mL) and dichloromethane ( $3 \times 6$  mL) and filtered through a short silica gel – Celite pad. Evaporation of the filtrate gave an oil, which was purified by flash chromatography (using ethyl acetate:hexane (20:80) as eluent); this eluted to yield 0.45 g



(62.6%) of **49**. IR (film) ( $\text{cm}^{-1}$ ): 3351 (w), 1745 (s), 1719 (s), 1687 (s).  $^1\text{H}$  NMR ( $\text{CDCl}_3$ , 400 MHz): 7.37 (m, 5H,  $\text{PhCH}_2$ -), 5.16 (AB, 2H,  $\text{PhCH}_2$ -), 5.13 (q, 1H,  $\text{H}_d$ ,  $J_{de} = 7.3$  Hz), 4.71 (m, 1H,  $\text{H}_c$ ), 4.64 (AB, 2H,  $\text{MeOCH}_2\text{O}$ ), 4.54 (ABM, 1H,  $\text{H}_{a'}$ ,  $J_{aa'} = 11.9$  Hz,  $J_{ab} = 6.6$  Hz), 4.00 (ABX, 1H,  $\text{H}_a$ ,  $J_{aa'} = 11.9$  Hz,  $J_{ab} = 3.1$  Hz), 3.86 (ddd, 1H,  $\text{H}_b$ ,  $J_{ab} = 3.1$  Hz,  $J_{a'b} = 6.6$  Hz,  $J_{bc} = 8.5$  Hz), 3.34 (s, 3H,  $\text{MeOCH}_2\text{O}$ -), 1.50 (d, 3H,  $J_{de} = 7.3$  Hz), 1.45 (s, 9H,  $-\text{CO}_2\text{CMe}_3$ ). CI-MS ( $m/z$ ): 439 ( $[\text{M} + 1]$ ).

### Removal of the BOC and MOM groups of **49**

Trifluoroacetic acid (1.25 mL, 16.30 mmol) was added dropwise with stirring at 0–5 °C to a solution of **49** (0.25 g, 0.57 mmol) in dichloromethane (1.0 mL) and anisole (0.5 mL). After removal of the cooling bath, stirring was continued for 10 h. The solvent was then removed under reduced pressure, and the residue was washed with ether (2  $\times$  3 mL) to give a solid. The solid that resulted was dried in vacuo to 70 mg (30%) of **50** as an off-white powder. IR (KBr) ( $\text{cm}^{-1}$ ): 3459 (b), 3217 (m), 1731 (s), 1683 (vs).  $^1\text{H}$  NMR ( $\text{CD}_3\text{OD}$ , 400 MHz): 7.36 (m, 5H,  $\text{Ph}$ -), 5.18 (q, 1H,  $\text{H}_d$ ,  $J_{de} = 7.3$  Hz), 5.17 (AB, 2H,  $\text{PhCH}_2\text{OCO}$ -), 4.70 (ddd, 1H,  $\text{H}_b$ ,  $J_{ab} = 2.6$  Hz,  $J_{a'b} = 7.1$  Hz,  $J_{bc} = 4.3$  Hz), 4.58 (ABM, 1H,  $\text{H}_{a'}$ ,  $J_{aa'} = 11.8$  Hz,  $J_{a'b} = 7.1$  Hz), 4.27 (d, 1H,  $\text{H}_c$ ,  $J_{bc} = 4.3$  Hz), 3.98 (ABX, 1H,  $\text{H}_a$ ,  $J_{aa'} = 11.8$  Hz,  $J_{ab} = 2.6$  Hz), 1.54 (d, 3H,  $\text{H}_e$ ,  $J_{de} = 7.3$  Hz). CI-MS ( $m/z$ ): 295 ( $[\text{M}]^+$ ).

### Phenylacetylation of **50**

To a solution of the trifluoroacetic acid salt (70 mg, 0.17 mmol) in dichloromethane (6.0 mL) were added dropwise, with stirring at –20 to –10 °C, triethylamine (52.0 mg, 0.51 mmol), followed by a solution of phenylacetyl chloride (31.7 mg, 0.20 mmol) in dichloromethane (1.0 mL). The cooling bath was removed and stirring was continued for 6 h. Dichloromethane (10 mL) was then added, and the reaction mixture was washed successively with 5 °C water (1.5 mL), saturated sodium bicarbonate (3  $\times$  1.5 mL), and brine (1.5 mL), dried over anhydrous sodium sulfate, and evaporated to give an oil. Purification by flash chromatography using ethyl acetate as eluent afforded 37.8 mg (54%) of **49** as an off-white powder. IR (KBr) ( $\text{cm}^{-1}$ ): 3464 (b), 3304 (m), 1736 (s), 1681 (s), 1644 (vs).  $^1\text{H}$  NMR ( $\text{CD}_3\text{CN}$ , 400 MHz): 7.37 (m, 10H,  $\text{Ph}$ -), 6.71 (d, 1H,  $\text{NH}$ ,  $J_{\text{NHHC}} = 7.4$  Hz), 5.11 (AB, 2H,  $\text{PhCH}_2\text{O}$ ), 5.07 (q, 1H,  $\text{H}_d$ ,  $J_{de} = 7.2$  Hz), 4.67 (dd, 1H,  $\text{H}_c$ ,  $J_{bc} = 3.8$  Hz,  $J_{\text{NHHC}} = 7.4$  Hz), 4.55 (m, 1H,  $\text{H}_b$ ), 4.48 (ABM, 1H,  $\text{H}_{a'}$ ,  $J_{aa'} = 11.6$  Hz,  $J_{a'b} = 7.4$  Hz), 3.86 (ABX, 1H,  $\text{H}_a$ ,  $J_{aa'} = 11.6$  Hz,  $J_{ab} = 2.4$  Hz), 3.65 (d, 1H,  $\text{OH}$ ,  $J_{\text{OHHC}} = 4.4$  Hz), 3.61 (AB, 2H,  $\text{PhCH}_2\text{CONH}$ -), 1.45 (d, 3H,  $\text{H}_e$ ,  $J_{de} = 7.2$  Hz). CI-MS ( $m/z$ ): 413 ( $[\text{M} + 1]$ ).

### Hydrogenolysis of **51**

A suspension of 5% Pd–C (0.035 g) in ethyl acetate (6 mL) was activated in a hydrogen atmosphere for 2 h. A solution of the benzyl ester **51** (35 mg, 0.085 mmol) in ethyl acetate (10 mL) was added, and the mixture was stirred in a hydrogen atmosphere until the starting material had disappeared (4 h). The mixture was filtered through Celite; the Celite pad was washed with methanol (4  $\times$  5 mL), and the filtrate was evaporated under reduced pressure to give **52**

(25 mg 92%) as a white powder. IR (KBr) ( $\text{cm}^{-1}$ ): 3459 (b), 3283 (w), 1727 (w), 1666 (s), 1644 (vs).  $^1\text{H}$  NMR ( $\text{CD}_3\text{OD}$ , 400 MHz): 7.30 (m, 5H,  $\text{Ph}$ -), 4.97 (q, 1H,  $\text{H}_d$ ,  $J_{de} = 7.3$  Hz), 4.80 (m, 1H,  $\text{H}_c$ ), 4.57 (m, 1H,  $\text{H}_b$ ,  $J_{ab} = 1.8$  Hz,  $J_{a'b} = 7.4$  Hz,  $J_{bc} = 3.7$  Hz), 4.52 (ABM, 1H,  $\text{H}_{a'}$ ,  $J_{aa'} = 10.9$  Hz,  $J_{a'b} = 7.4$  Hz), 3.92 (ABX, 1H,  $\text{H}_a$ ,  $J_{aa'} = 10.9$  Hz,  $J_{ab} = 1.8$  Hz), 3.68 (AB, 2H,  $\text{PhCH}_2\text{CONH}$ -), 1.50 (d, 3H,  $\text{H}_e$ ,  $J_{de} = 7.3$  Hz). CI-MS ( $m/z$ ): 323 ( $[\text{M} + 1]$ ).

### Bioassays

The data of Table 2 were obtained using seeded agar plates, prepared as described in ref 1. MIC (minimum inhibitory concentration) data were provided by the Health Sciences Centre, Winnipeg, and by NAEJA Pharmaceuticals, Edmonton.

### Acknowledgements

This research was supported financially by an Individual Operating Grant from the Natural Sciences and Engineering Research Council of Canada (NSERC) and by the Western Technology Seed Investment Fund. The authors thank Dr. Raymond Batchelor for the crystal structures and Sarah Chinapoo for technical assistance.

### References

1. S. Wolfe, C.I. Akuche, S. Ro, M.-C. Wilson, C.-K. Kim, and Z. Shi. *Can. J. Chem.* This issue.
2. D.J. Tipper and J.L. Strominger. *Proc. Natl. Acad. Sci. U.S.A.* **54**, 1133 (1965).
3. M. Kitagawa and T. Tomiyama. *J. Biochem. (Tokyo)*, **11**, 265 (1929); M. Kitagawa and H. Yamada. *J. Biochem. (Tokyo)*, **16**, 339 (1932); M. Kitagawa and K.-I. Monobe. *J. Biochem. (Tokyo)*, **18**, 333 (1933); M. Kitagawa and A. Takani. *J. Biochem. (Tokyo)*, **23**, 181 (1936); M. Kitagawa. *J. Biochem. (Tokyo)*, **24**, 197 (1936); **25**, 23 (1937).
4. S. Harada, S. Tsubotani, T. Hida, H. Ono, and H. Okazaki. *Tetrahedron Lett.* **27**, 6229 (1986); Y. Nozaki, N. Katayama, H. Ono, S. Tsubotani, T. Harada, H. Okazaki, and Y. Nakao. *Nature*, **325**, 179 (1987); S. Harada, S. Tsubotani, T. Hida, K. Koyama, M. Kondo, and H. Ono. *Tetrahedron*, **44**, 6589 (1988); Y. Nakao. *Spec. Publ. R. Soc. Chem.* **70**, 119 (1989); Y. Nozaki, N. Katayama, S. Harada, H. Ono, and H. Okazaki. *J. Antibiot.* **42**, 84 (1989).
5. K. Yoshioka and T. Miwa. *Jpn Kokai Tokkyo Koho JP 62215585*. Sept 22, 1987. *Chem. Abstr.* **108**, P186753z (1988).
6. A. Tsuji, T. Yamana, S. Matsutani, and N. Tsuji. *Heterocycles*, **8**, 153 (1977); J.E. Baldwin, C. Lowe, and C.J. Schofield. *Tetrahedron Lett.* **31**, 2211 (1990); see also footnote 18 of J. Marchand-Bryner and L. Ghosez. *Recent Progr. Chem. Synth. Antibiot.* 727 (1990).
7. J. Smrt, J. Beranek, and M. Horak. *Coll. Czech. Chem. Commun.* **24**, 1672 (1959); N.K. Kochetkov, R.M. Khomutov, E.S. Severin, M.Ya. Karpeiskii, E.I. Budovskii, and V.I. Erashko. *Zh. Obsch. Khimii*, **29**, 3417 (1959); I.A. Motorina, F.W. Fowler, and D.S. Grierson. *J. Org. Chem.* **62**, 2098 (1997).
8. R.M. Khomutov, M. Ya. Karpeiskii, and E.S. Severin. *Bull. Acad. Sci. USSR Div. Chem. Sci. Engl. Transl.* 2068 (1962); M. Frankel, Y. Knobler, E. Bonni, S. Bittner, and G. Zvilichovsky. *J. Chem. Soc. C*, 1746 (1969).



9. J.I. Levin, E. Turos, and S.M. Weinreb. *Synth. Commun.* **12**, 989 (1982); M.C. Pirrung and J.H.-L. Chau. *J. Org. Chem.* **60**, 8084 (1995).
10. K. Jost and J. Rudinger. *Coll. Czech. Chem. Commun.* **32**, 2485 (1967); P.S. Manchand, K.-C. Luk, P.S. Belica, S.C. Choudhry, and C.C. Wei. *J. Org. Chem.* **53**, 5507 (1988).
11. I.O. Edafiogho, K.R. Scott, J.A. Moore, V.A. Farrar, and J.M. Nicholson. *J. Med. Chem.* **34**, 387 (1991); B.J. Ludwig, D.B. Reisner, M. Meyer, L.S. Powell, L. Simet, and F.J. Steifel. *J. Med. Chem.* **13**, 60 (1970); L. Bauer and B.K. Ghosh. *J. Org. Chem.* **30**, 4298 (1965).
12. G.H. Hamor and F. Rubessa. *J. Med. Chem.* **15**, 472 (1972).
13. B. Bhat, E.E. Swayze, P. Wheeler, S. Dimock, M. Perbost, and Y.S. Sanghvi. *J. Org. Chem.* **61**, 8186 (1996).
14. Y. Yamamoto and T. Furuta. *Chem. Lett.* 797 (1989).
15. A.J. Ozinskas and G.A. Rosenthal. *J. Org. Chem.* **51**, 5047 (1986).
16. D.I. Hughes. *Org. React.* **42**, 335 (1992).
17. R. Pellagata, I. Dosi, M. Villa, G. Lesma, and G. Palmisano. *Tetrahedron*, **41**, 5607 (1985).
18. B. Smith III, K.J. Hale, and R.A. Rivero. *Tetrahedron Lett.* **27**, 5813 (1986).
19. P.J. Maurer and M.J. Miller, *J. Am. Chem. Soc.* **104**, 3096 (1982); B.H. Lee and M.J. Miller. *J. Org. Chem.* **48**, 24 (1983); A.O. Stewart and D.W. Brooks. *J. Org. Chem.* **57**, 5020 (1992).
20. T.P. Kogan and T.E. Rawson. *Tetrahedron Lett.* **33**, 7089 (1992).
21. C.C. Wei, S. DeBernardo, J.P. Teng, J. Borgese, and M. Weigle. *J. Org. Chem.* **50**, 3462 (1985).
22. K. Bock, I. Lundt, and C. Pedersen. *Acta Chem. Scand. Ser. B*, **37**, 341 (1983).



# Geometrical and vibrational DFT studies of $\text{HOBr} \cdot (\text{H}_2\text{O})_n$ clusters ( $n = 1-4$ )

Cristina Maria P. Santos, Roberto B. Faria, Wagner B. De Almeida, Juan O. Machuca-Herrera, and Sérgio P. Machado

**Abstract:** The geometrical structures and the vibrational spectra of the  $\text{HOBr} \cdot (\text{H}_2\text{O})_n$  clusters ( $n = 1-4$ ) have been calculated at the DFT level of theory, using the pBP method and the DN\* and DN\*\* numerical basis sets. The results showed that the interaction involving the H of the HOBr and the O of the water molecule represent the preferred arrangements for these hydrated compounds. Both  $\text{HOBr} \cdot \text{H}_2\text{O}$  and  $\text{HOBr} \cdot (\text{H}_2\text{O})_2$  clusters presented stable structures with *syn* and *anti* conformations, the *syn* being the most stable. The  $\text{HOBr} \cdot (\text{H}_2\text{O})_3$  and the  $\text{HOBr} \cdot (\text{H}_2\text{O})_4$  clusters have presented stable cyclic structures. In the  $\text{HOBr} \cdot \text{H}_2\text{O}$  and  $\text{HOBr} \cdot (\text{H}_2\text{O})_2$  clusters, low-frequency stretching values could be assigned to hydrogen bonds, but the same could not be done so clearly for the  $\text{HOBr} \cdot (\text{H}_2\text{O})_3$  and the  $\text{HOBr} \cdot (\text{H}_2\text{O})_4$  cyclic clusters. The binding energies were also determined for these HOBr hydrated clusters, showing that the addition of a water molecule to the  $\text{HOBr} \cdot \text{H}_2\text{O}$  and  $\text{HOBr} \cdot (\text{H}_2\text{O})_2$  clusters increases the binding energy by approximately 4 kcal mol<sup>-1</sup>, while the addition of a water molecule to the  $\text{HOBr} \cdot (\text{H}_2\text{O})_3$  cluster decreases this value by 4 kcal mol<sup>-1</sup>.

**Key words:** DFT, numerical basis,  $\text{HOBr} \cdot (\text{H}_2\text{O})_n$ , clusters.

**Résumé :** On a calculé, théoriquement au niveau DFT, les structures géométriques et les spectres de vibration des agrégats de  $\text{HOBr} \cdot (\text{H}_2\text{O})_n$  ( $n = 1-4$ ) en utilisant la méthode pBP et les ensembles de base DN\* et DN\*\*. Les résultats montrent que l'interaction impliquant le H du HOBr et le O de la molécule d'eau représente les arrangements privilégiés de ces composé hydratés. Les deux agrégats de  $\text{HOBr} \cdot \text{H}_2\text{O}$  et de  $\text{HOBr} \cdot (\text{H}_2\text{O})_2$  ont des structures stables avec des conformations *syn* et *anti*, la conformation *syn* étant la plus stable. Les agrégats de  $\text{HOBr} \cdot (\text{H}_2\text{O})_3$  et de  $\text{HOBr} \cdot (\text{H}_2\text{O})_4$  ont des structures cycliques stables. Dans les agrégats de  $\text{HOBr} \cdot \text{H}_2\text{O}$  et de  $\text{HOBr} \cdot (\text{H}_2\text{O})_2$  on peut attribuer les elongations de faible fréquence aux liaisons hydrogènes mais cette attribution ne peut être faite aussi clairement dans le cas des agrégats de  $\text{HOBr} \cdot (\text{H}_2\text{O})_3$  de  $\text{HOBr} \cdot (\text{H}_2\text{O})_4$  et des agrégats cycliques. On a également déterminé les énergies de liaison de ces agrégats de HOBr hydratés, en montrant que l'addition d'une molécule d'eau aux  $\text{HOBr} \cdot \text{H}_2\text{O}$  et  $\text{HOBr} \cdot (\text{H}_2\text{O})_2$  augmente approximativement l'énergie de liaison de 4 kcal mol<sup>-1</sup>, tandis que l'addition d'une molécule d'eau au  $\text{HOBr} \cdot (\text{H}_2\text{O})_3$  diminue cette valeur de 4 kcal mol<sup>-1</sup>.

**Mots clés :** DFT, base numérique,  $\text{HOBr} \cdot (\text{H}_2\text{O})_n$ , agrégats.

[Traduit par la Rédaction]

## Introduction

The water solvation process involving compounds associated with catalytic reactions related to the ozone depletion in the stratosphere (1–3) has been receiving great attention in the past few years. The importance of this process is justified by the higher water concentration in the Earth's atmosphere and the tendency of water to form hydrogen bonds, making possible the association between two or more water molecules (4–7) and between different water clusters and other species present in the atmosphere (8). Among these associations, we have been interested in the HOBr hydrated complexes once the bromine species are directly involved in reactions converting ozone to oxygen, and there is a discus-

sion about the origin of an unexpected higher bromine radical concentration observed on ice surfaces present on the stratospheric clouds and on the Arctic snow pack (9). The questioned participation of the ice surfaces in the catalytic reactions and the hydrogen bonds involved in the hydrated clusters have been considered important for the understanding of the properties of weakly bound molecular complexes, for the determination of the hydrated cluster concentration on the troposphere and stratosphere, and for the prediction of catalytic reactions responsible for the chemical atmospheric changes.

In this context, we present theoretical results of equilibrium geometries and vibrational frequencies related to the structures generated by the association of HOBr and water

Received 2 November 2002. Published on the NRC Research Press Web site at <http://canjchem.nrc.ca> on 12 August 2003.

**C.M.P. Santos, R.B. Faria,<sup>1</sup> J.O. Machuca-Herrera, and S.P. Machado.** Departamento de Química Inorgânica, Instituto de Química, Universidade Federal do Rio de Janeiro, Caixa Postal 68563, Rio de Janeiro, RJ, 21945-970, Brazil.

**W.B. De Almeida.** LQC-MM: Laboratório de Química Computacional e Modelagem Molecular, Departamento de Química, ICEx, Universidade Federal de Minas Gerais, Campus Pampulha, CEP 31270-901, Belo Horizonte, MG, Brazil.

<sup>1</sup>Corresponding author (e-mail: [faria@iq.ufjf.br](mailto:faria@iq.ufjf.br)).



molecules. These results are compared with other halogen hydrate complexes involving interactions of HOCl with 1–4 water molecules (10–12) and of HOBr with only one water molecule (13).

## Methods

DFT equilibrium geometries and vibrational frequencies were performed using PC SPARTAN PRO (Wavefunction Inc., Irvine, CA) and a nonlocal perturbative Becke–Perdew (14, 15) model with a potential comprising a local part and a gradient correction. In this perturbative model the gradient correction is introduced only after the convergence, based on the local potential, has been achieved and not at each self-consistent field interaction, which represent a time calculation reduction. The DN\* and DN\*\* numerical basis sets employed describe the inner shell of each atomic orbital by a single function and the valence shell by a pair of functions, together with a set of five *d*-type polarization functions. The difference between DN\*\* and DN\* is that the first includes *p*-type polarization functions for hydrogen atoms. The calculations were done on Pentium III, 233 MHz, with 10 GB of disk space and 128 MB RAM.

The pBP method, with numerical basis sets, was employed in our previous study involving the equilibrium geometries of  $\text{HBrO}_x$  ( $x = 1\text{--}3$ ) isomers (16) with good results.

The calculated pBP binding energy values are presented without basis set superposition error (BSSE) corrections. This procedure was based on the fact that DFT methods, using basis sets of quality, give low BSSE values.

## Results

Three different associations between the HOBr and the  $\text{H}_2\text{O}$  molecules have been studied based on interactions involving the Br and the O of the water molecule, the O of the HOBr and one H of the water molecule, and the H of HOBr and the O of the water molecule. The results pointed to the structures obtained by the last interaction as the most stable configurations.

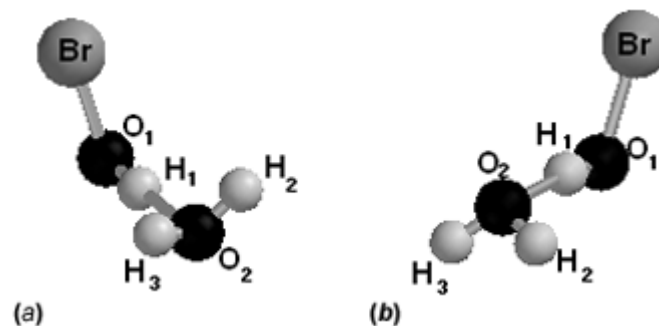
The atomic charge distribution was obtained from the electrostatic potential, giving qualitative information about the electronic density on the atoms of the hydrated complexes. For all clusters, this charge distribution has presented the bromine atom with a low positive charge and the hydrogen and the oxygen atoms with positive and negative density charges, respectively.

The details for each association of water molecules with HOBr are given below.

### $\text{HOBr}\cdot\text{H}_2\text{O}$

Two  $C_s$  structures, with the water molecule oriented in *syn* (dihedral angle of  $0.0^\circ$ ) and in *anti* (dihedral angle of  $180.0^\circ$ ) positions with respect to the bromine, were submitted to geometry optimization. The optimized *syn* and *anti* conformers have  $C_s$  and  $C_1$  symmetry, respectively, and both present a nearly linear hydrogen bond. The  $\text{HOBr}\cdot\text{H}_2\text{O}$  optimized structures are presented in Fig. 1, and the corresponding geometrical parameters are listed in Table 1, together with the Ying and Zhao B3LYP/6-311++G(d,p) results (13).

Fig. 1.  $\text{HOBr}\cdot(\text{H}_2\text{O})$  structures: (a) symmetric; (b) antisymmetric.



As the results obtained using DN\* and DN\*\* basis sets have not presented significant geometrical differences, each optimized geometry was submitted to an analytical second derivatives calculation using only the more polarized DN\*\* basis set. The pBP/DN\*\* vibrational frequencies obtained are listed in Table 2, together with the B3LYP/6-311++G(d,p) values (13).

### $\text{HOBr}\cdot(\text{H}_2\text{O})_2$

The second water molecule was added to the *syn* and *anti*  $\text{HOBr}\cdot\text{H}_2\text{O}$  optimized structures, with the hydrogen of the first water molecule interacting with the oxygen of the second water molecule, giving a *syn* and an *anti*  $\text{HOBr}\cdot(\text{H}_2\text{O})_2$  conformation. These *syn* and *anti* references are also based on the orientation of the first water molecule with respect to the bromine. The *syn* and *anti*  $\text{HOBr}\cdot(\text{H}_2\text{O})_2$  clusters, which were obtained by a previous conformer search process, were submitted to a geometry optimization, including vibrational frequency determination, and the optimized structures have presented nonlinear hydrogen bonds. These clusters are presented in Fig. 2, and their geometrical parameters can be found in Table 3.

The *anti* and *syn* pBP/DN\*\*  $\text{HOBr}\cdot(\text{H}_2\text{O})_2$  vibrational frequency values are listed in Table 4. As many vibrational modes have appeared conjugated, it was difficult to assign all of them.

The charge distribution on the  $\text{HOBr}\cdot(\text{H}_2\text{O})_2$  clusters showed that the proximity between the  $\text{H}_5$  and  $\text{O}_1$  atoms on the *anti* conformer ( $\text{H}_5\cdots\text{O}_1 = 1.928 \text{ \AA}$ ) did not represent a charge transfer from  $\text{O}_1$  to the  $\text{H}_5$  atom.

### $\text{HOBr}\cdot(\text{H}_2\text{O})_3$

The most stable structure of this cluster was found considering two initial possibilities. The first was the association of the second and third water molecules to the different hydrogen atoms of the water molecule in the  $\text{HOBr}\cdot\text{H}_2\text{O}$  structures presented in Fig. 1. The second possibility was a consecutive association of the water molecules, as considered on water clusters where the free hydrogens are oriented above and below the ring.

In the first case, the optimized geometry conformers and the vibrational frequency results have suggested noncorrespondence to a minimum energy on all tested structures; this possibility was thus refused.

For the second case, the association of the third water molecule was based on *syn* and *anti*  $\text{HOBr}\cdot(\text{H}_2\text{O})_2$  clusters. All the *anti*  $\text{HOBr}\cdot(\text{H}_2\text{O})_3$  clusters obtained presented geometrical

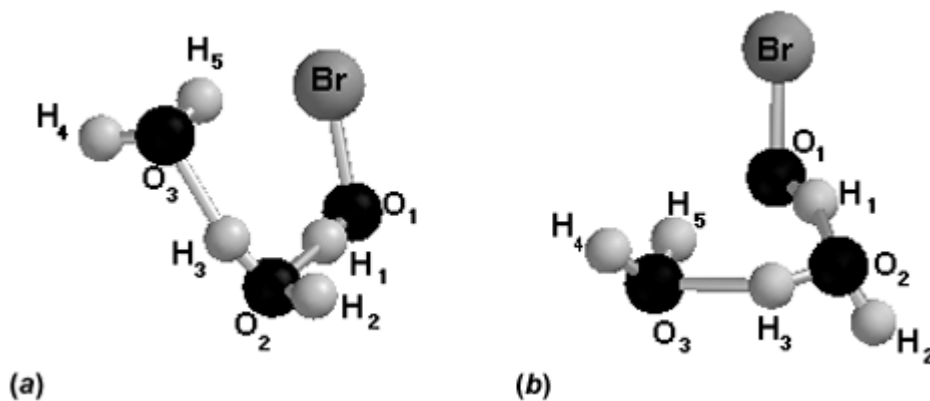


**Table 1.** Calculated geometry parameters of *syn* and *anti* HOBr·H<sub>2</sub>O structures.

	<i>syn</i>			<i>anti</i>		
	pBP/DN*	pBP/DN**	B3LYP <sup>a</sup>	pBP/DN*	pBP/DN**	B3LYP <sup>a</sup>
<b>Bond lengths (Å)</b>						
Br—O <sub>1</sub>	1.882	1.883	1.865	1.881	1.882	1.865
O <sub>1</sub> —H <sub>1</sub>	1.014	1.007	0.980	1.012	1.005	0.980
H <sub>1</sub> ···O <sub>2</sub>	1.758	1.763	1.820	1.757	1.752	1.815
O <sub>2</sub> —H <sub>2</sub>	0.986	0.977	0.963	0.984	0.976	0.963
O <sub>2</sub> —H <sub>3</sub>	0.986	0.977	0.963	0.985	0.977	0.963
<b>Bond angles (°)</b>						
BrO <sub>1</sub> H <sub>1</sub>	100.91	100.96	103.2	102.34	102.31	103.8
O <sub>1</sub> H <sub>1</sub> ···O <sub>2</sub>	174.85	174.93	179.5	173.02	172.90	173.1
H <sub>1</sub> ···O <sub>2</sub> H <sub>2</sub>	109.94	107.77	—	113.25	113.22	—
H <sub>1</sub> ···O <sub>2</sub> H <sub>3</sub>	109.94	107.77	—	112.40	112.31	—
H <sub>2</sub> O <sub>2</sub> H <sub>3</sub>	105.34	105.31	106.2	105.77	105.87	106.1
BrO <sub>1</sub> H <sub>1</sub> ···O <sub>2</sub>	0.00	0.00	0.00	−177.95	−178.92	180.0
O <sub>1</sub> H <sub>1</sub> ···O <sub>2</sub> H <sub>2</sub>	−57.76	−56.60	−67.4	73.64	76.87	64.7
O <sub>1</sub> H <sub>1</sub> ···O <sub>2</sub> H <sub>3</sub>	57.76	56.60	67.4	−46.17	−42.98	−64.7
<b>Symmetry</b>	C <sub>s</sub>	C <sub>s</sub>	C <sub>s</sub>	C <sub>1</sub>	C <sub>1</sub>	C <sub>s</sub>
<b>E<sub>T</sub><sup>b</sup></b>	−2726.782	−2726.801	−2726.42	−2726.79	−2726.799	−2726.415

<sup>a</sup>6-311++G(*d,p*) basis set (13).<sup>b</sup>Values in hartree (energies without ZPE corrections).**Table 2.** Vibrational frequencies (cm<sup>−1</sup>) of *syn* and *anti* HOBr·H<sub>2</sub>O conformers.

Attributions	<i>syn</i>		<i>anti</i>	
	B3LYP <sup>a</sup>	pBP/DN**	B3LYP <sup>a</sup>	pBP/DN**
HOH wag	10 (A'')	72	61 (A'')	79
Rock of molecule	75 (A')	117	68 (A')	123
H <sub>1</sub> O <sub>2</sub> stretch	216 (A')	240	204 (A')	221
BrO <sub>1</sub> H <sub>1</sub> O <sub>2</sub> torsion	226 (A'')	258	222 (A'')	279
Rock H <sub>2</sub> O <sub>2</sub> H <sub>3</sub>	227 (A')	339	269 (A')	308
BrO <sub>1</sub> stretch	619 (A')	598	616 (A')	601
H bond wag	727 (A'')	829	735 (A'')	778
BrO <sub>1</sub> H <sub>1</sub> bend	1280 (A')	1314	1281 (A')	1279
H <sub>2</sub> O <sub>2</sub> H <sub>3</sub> bend	1619 (A')	1676	1620 (A')	1570
O <sub>1</sub> H <sub>1</sub> stretch	3549 (A')	3208	3550 (A')	3239
O <sub>2</sub> H <sub>2,3</sub> symmetric stretch	3817 (A')	3781	3813 (A')	3661
O <sub>2</sub> H <sub>2,3</sub> asymmetric stretch	3918 (A'')	3801	3914 (A'')	3781

<sup>a</sup>6-311++G(*d,p*) basis set (13).**Fig. 2.** HOBr·(H<sub>2</sub>O)<sub>2</sub> clusters: (a) symmetric; (b) antisymmetric.



**Table 3.** Calculated geometry parameters of *syn* and *anti* HOBr·(H<sub>2</sub>O)<sub>2</sub> clusters (pBP/DN\*\* method).

Parameters	<i>syn</i>	<i>anti</i>
<b>Bond lengths (Å)</b>		
Br—O <sub>1</sub>	1.874	1.885
O <sub>1</sub> —H <sub>1</sub>	1.026	1.024
H <sub>1</sub> ...O <sub>2</sub>	1.641	1.659
O <sub>2</sub> —H <sub>2</sub>	0.976	0.977
O <sub>2</sub> —H <sub>3</sub>	1.004	1.005
H <sub>3</sub> ...O <sub>3</sub>	1.742	1.795
O <sub>3</sub> —H <sub>4</sub>	0.977	0.976
O <sub>3</sub> —H <sub>5</sub>	0.989	0.995
<b>Bond angles (°)</b>		
BrO <sub>1</sub> H <sub>1</sub>	102.61	103.75
O <sub>1</sub> H <sub>1</sub> ...O <sub>2</sub>	176.25	156.17
H <sub>1</sub> ...O <sub>2</sub> H <sub>2</sub>	112.79	114.88
H <sub>1</sub> ...O <sub>2</sub> H <sub>3</sub>	103.88	90.55
H <sub>2</sub> O <sub>2</sub> H <sub>3</sub>	105.91	106.49
O <sub>2</sub> H <sub>3</sub> ...O <sub>3</sub>	163.39	151.44
H <sub>3</sub> ...O <sub>3</sub> H <sub>4</sub>	115.07	117.86
H <sub>3</sub> ...O <sub>3</sub> H <sub>5</sub>	96.57	89.64
H <sub>4</sub> O <sub>3</sub> H <sub>5</sub>	105.66	105.83
BrO <sub>1</sub> H <sub>1</sub> O <sub>2</sub>	80.68	126.21
O <sub>1</sub> H <sub>1</sub> ...O <sub>2</sub> H <sub>2</sub>	-173.00	98.18
O <sub>1</sub> H <sub>1</sub> ...O <sub>2</sub> H <sub>3</sub>	-58.78	-10.32
H <sub>1</sub> ...O <sub>2</sub> H <sub>3</sub> ...O <sub>3</sub>	-9.79	0.73
H <sub>2</sub> O <sub>2</sub> H <sub>3</sub> ...O <sub>3</sub>	109.25	-115.47
O <sub>2</sub> H <sub>3</sub> ...O <sub>3</sub> H <sub>4</sub>	112.87	-109.33
O <sub>2</sub> H <sub>3</sub> ...O <sub>3</sub> H <sub>5</sub>	2.14	-1.55
<b>Energy<sup>a</sup></b>	-2803.2852	-2803.2856

<sup>a</sup>Values in hartree (energies without ZPE corrections).

and vibrational results with a noncorrespondence to a minimum energy. In this way, based only on the *syn* HOBr·(H<sub>2</sub>O)<sub>2</sub> cluster, three HOBr·(H<sub>2</sub>O)<sub>3</sub> structures were obtained. The less stable optimized structure corresponded to a noncyclic configuration with an energy value of -2879.7652 hartree (1 hartree = 4.359748 × 10<sup>-18</sup> J). The other two cyclic structures were optimized and the more stable provided a minimum energy of -2879.7772 hartree, corresponding to a closed cyclic chain. This structure is presented in Fig. 3, and the geometrical parameters and vibrational frequencies are listed in Tables 5 and 6, respectively.

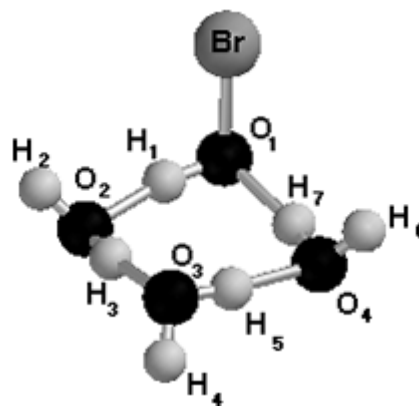
The atomic charge distribution shows H<sub>7</sub> with a charge lower than the charges of the other hydrogens involved in hydrogen bonding but higher than the atomic charges on the free hydrogens (H<sub>2</sub> and H<sub>6</sub>). The H<sub>4</sub> atom, placed in the opposite way to the bromine atom, presents an atomic charge higher than the charges on the other free hydrogen atoms. The vibrational frequency values related to the BrO<sub>1</sub> and O<sub>1</sub>H<sub>1</sub> stretch and H<sub>1</sub>O<sub>2</sub>H<sub>3</sub> bend do not present significant differences when compared with the previous HOBr·(H<sub>2</sub>O)<sub>2</sub> structures, but the OH stretch frequencies related to the water molecules were observed in a characteristic region (above 2900 cm<sup>-1</sup>), being all conjugated.

**Table 4.** Vibrational frequencies (cm<sup>-1</sup>) of *anti* and *syn* HOBr·(H<sub>2</sub>O)<sub>2</sub> conformers.

<i>anti</i>	<i>syn</i>
36; 95 – molecule torsions	38; 115 – molecule torsions
155 – H <sub>1</sub> O <sub>2</sub> H <sub>3</sub> bend	122 – H <sub>1</sub> O <sub>2</sub> H <sub>3</sub> bend
232 – H <sub>3</sub> O <sub>3</sub> stretch	230 – rock H <sub>4</sub> O <sub>3</sub> H <sub>5</sub>
274 – H <sub>1</sub> O <sub>2</sub> stretch	249 – H <sub>3</sub> O <sub>3</sub> stretch
283 – O <sub>2</sub> H <sub>3</sub> O <sub>3</sub> H <sub>4</sub> torsion	275 – rock H <sub>2</sub> O <sub>2</sub> H <sub>3</sub>
368 – H <sub>2</sub> O <sub>2</sub> H <sub>3</sub> O <sub>3</sub> torsion	298 – H <sub>1</sub> O <sub>2</sub> stretch
397 – rock HOH molecules	361 – O <sub>2</sub> H <sub>3</sub> O <sub>3</sub> H <sub>4</sub> and H <sub>2</sub> O <sub>2</sub> H <sub>3</sub> O <sub>3</sub> torsion
491 – rock HOH molecules	474 – rock HOH molecules
601 – BrO <sub>1</sub> stretch	539 – O <sub>2</sub> H <sub>3</sub> O <sub>3</sub> H <sub>5</sub> torsion
657 – H <sub>5</sub> wag	602 – BrO <sub>1</sub> stretch
798 – rock H <sub>1</sub> O <sub>2</sub> H <sub>3</sub>	882 – rock H <sub>1</sub> O <sub>2</sub> H <sub>3</sub>
1080 – H <sub>1</sub> O <sub>2</sub> H <sub>3</sub> and H <sub>3</sub> O <sub>3</sub> H <sub>5</sub> bend	949 – H <sub>3</sub> O <sub>3</sub> H <sub>5</sub> and H <sub>1</sub> O <sub>2</sub> H <sub>3</sub> bend
1320 – H <sub>1</sub> O <sub>1</sub> Br bend	1394 – H <sub>1</sub> O <sub>1</sub> Br bend
1590 – asym. <sup>a</sup> H <sub>2</sub> O <sub>2</sub> H <sub>3</sub> and H <sub>4</sub> O <sub>3</sub> H <sub>5</sub> bend	1562 – H <sub>4</sub> O <sub>3</sub> H <sub>5</sub> bend
1597 – sym. <sup>b</sup> H <sub>2</sub> O <sub>2</sub> H <sub>3</sub> and H <sub>4</sub> O <sub>3</sub> H <sub>5</sub> bend	1605 – H <sub>2</sub> O <sub>2</sub> H <sub>3</sub> bend
2915 – O <sub>1</sub> H <sub>1</sub> stretch	2890 – O <sub>1</sub> H <sub>1</sub> stretch
3223 – O <sub>2</sub> H <sub>3</sub> stretch	3223 – O <sub>2</sub> H <sub>3</sub> stretch
3389 – O <sub>3</sub> H <sub>5</sub> stretch	3488 – O <sub>3</sub> H <sub>5</sub> stretch
3722 – O <sub>2</sub> H <sub>2</sub> stretch	3724 – O <sub>3</sub> H <sub>4</sub> stretch
3730 – O <sub>3</sub> H <sub>4</sub> stretch	3731 – O <sub>2</sub> H <sub>2</sub> stretch

<sup>a</sup>asym. = asymmetric.

<sup>b</sup>sym. = symmetric.

**Fig. 3.** HOBr·(H<sub>2</sub>O)<sub>3</sub> cluster.

### HOBr·(H<sub>2</sub>O)<sub>4</sub>

In the HOBr·(H<sub>2</sub>O)<sub>4</sub> cluster, one stable cyclic structure has been found, with OH bonds placed above and below the ring made up of five oxygen atoms. This structure can be observed in Fig. 4, and the geometrical parameters are listed in Table 7.

The atomic charge distribution on the HOBr·(H<sub>2</sub>O)<sub>4</sub> cluster was very close to the distribution observed for the HOBr·(H<sub>2</sub>O)<sub>3</sub> cluster, which can be considered as a typical







**Table 7.** Calculated geometry parameters of the HOBr·(H<sub>2</sub>O)<sub>4</sub> cluster (pBP/DN\*\* method).

Distances (Å)		Angles (°)		Dihedral angles (°)	
Br—O <sub>1</sub>	1.882	BrO <sub>1</sub> H <sub>1</sub>	102.66	BrO <sub>1</sub> H <sub>1</sub> ...O <sub>2</sub>	136.25
O <sub>1</sub> —H <sub>1</sub>	1.056	O <sub>1</sub> H <sub>1</sub> ...O <sub>2</sub>	176.67	O <sub>1</sub> H <sub>1</sub> ...O <sub>2</sub> H <sub>2</sub>	−167.10
H <sub>1</sub> ...O <sub>2</sub>	1.51	H <sub>1</sub> ...O <sub>2</sub> H <sub>2</sub>	112.07	O <sub>1</sub> H <sub>1</sub> ...O <sub>2</sub> H <sub>3</sub>	−48.27
O <sub>2</sub> —H <sub>2</sub>	0.976	H <sub>1</sub> ...O <sub>2</sub> H <sub>3</sub>	111.0	H <sub>1</sub> ...O <sub>2</sub> H <sub>3</sub> ...O <sub>3</sub>	−15.73
O <sub>2</sub> —H <sub>3</sub>	1.029	H <sub>2</sub> O <sub>2</sub> H <sub>3</sub>	106.4	H <sub>2</sub> O <sub>2</sub> H <sub>3</sub> ...O <sub>3</sub>	106.45
H <sub>3</sub> ...O <sub>3</sub>	1.594	O <sub>2</sub> H <sub>3</sub> ...O <sub>3</sub>	177.09	O <sub>2</sub> H <sub>3</sub> ...O <sub>3</sub> H <sub>4</sub>	141.49
O <sub>3</sub> —H <sub>4</sub>	0.976	H <sub>3</sub> ...O <sub>3</sub> H <sub>4</sub>	113.48	O <sub>2</sub> H <sub>3</sub> ...O <sub>3</sub> H <sub>5</sub>	23.47
O <sub>3</sub> —H <sub>5</sub>	1.022	H <sub>3</sub> ...O <sub>3</sub> H <sub>5</sub>	109.61	H <sub>3</sub> ...O <sub>3</sub> H <sub>5</sub> ...O <sub>4</sub>	−20.29
H <sub>5</sub> ...O <sub>4</sub>	1.631	H <sub>4</sub> O <sub>3</sub> H <sub>5</sub>	105.8	H <sub>4</sub> O <sub>3</sub> H <sub>5</sub> ...O <sub>4</sub>	−143.00
O <sub>4</sub> —H <sub>6</sub>	0.976	O <sub>3</sub> H <sub>5</sub> ...O <sub>4</sub>	178.7	O <sub>3</sub> H <sub>5</sub> ...O <sub>4</sub> H <sub>6</sub>	−81.81
O <sub>4</sub> —H <sub>7</sub>	1.015	H <sub>5</sub> ...O <sub>4</sub> H <sub>6</sub>	110.2	O <sub>3</sub> H <sub>5</sub> ...O <sub>4</sub> H <sub>7</sub>	34.43
H <sub>7</sub> ...O <sub>5</sub>	1.655	H <sub>5</sub> ...O <sub>4</sub> H <sub>7</sub>	109.14	H <sub>5</sub> ...O <sub>4</sub> H <sub>7</sub> ...O <sub>5</sub>	12.89
O <sub>5</sub> —H <sub>8</sub>	0.975	H <sub>6</sub> O <sub>4</sub> H <sub>7</sub>	106.16	H <sub>6</sub> O <sub>4</sub> H <sub>7</sub> ...O <sub>5</sub>	131.71
O <sub>5</sub> —H <sub>9</sub>	1.007	O <sub>4</sub> H <sub>7</sub> ...O <sub>5</sub>	172.0	O <sub>4</sub> H <sub>7</sub> ...O <sub>5</sub> H <sub>8</sub>	−172.07
H <sub>9</sub> ...O <sub>1</sub>	1.72	H <sub>7</sub> ...O <sub>5</sub> H <sub>8</sub>	121.91	O <sub>4</sub> H <sub>7</sub> ...O <sub>5</sub> H <sub>9</sub>	−45.79
		H <sub>7</sub> ...O <sub>5</sub> H <sub>9</sub>	110.48	H <sub>7</sub> ...O <sub>5</sub> H <sub>9</sub> ...O <sub>1</sub>	20.82
		H <sub>8</sub> O <sub>5</sub> H <sub>9</sub>	106.6	O <sub>5</sub> H <sub>9</sub> ...O <sub>1</sub> Br	−93.92
		O <sub>5</sub> H <sub>9</sub> ...O <sub>1</sub>	173.34	O <sub>5</sub> H <sub>9</sub> ...O <sub>1</sub> H <sub>1</sub>	16.21
		H <sub>9</sub> ...O <sub>1</sub> Br	107.83	H <sub>8</sub> O <sub>5</sub> H <sub>9</sub> ...O <sub>1</sub>	155.26
		H <sub>9</sub> ...O <sub>1</sub> H <sub>1</sub>	107.67	H <sub>9</sub> ...O <sub>1</sub> H <sub>1</sub> ...O <sub>2</sub>	22.61

**Note:** HOBr·(H<sub>2</sub>O)<sub>4</sub>: *E* = −2956.26299 hartree; dipole = 2.199 D. Energy value without ZPE correction.

**Table 8.** Vibrational frequencies for the HOBr·(H<sub>2</sub>O)<sub>4</sub> cluster.

Wavenumber (cm <sup>−1</sup> )	Vibrational modes
29.9; 54.1; 56.8; 87.1; 95.6; 122.2	—
197.8	Molecule breazing
242.6; 270.6; 277.9	Torsion between water molecules
300.3; 332.7; 359.0; 395.7; 414.2	Hydrogen wag
486.9; 523.7; 572.2; 583.1	Rock involving water molecules
617.6	BrO <sub>1</sub> stretch
781.4; 917.6; 988.4	Rock involving water molecules
1080.0; 1193.3	H <sub>1</sub> O <sub>2</sub> H <sub>3</sub> , and H <sub>5</sub> O <sub>4</sub> H <sub>7</sub> bend
1438	BrO <sub>1</sub> H <sub>1</sub> bend
1588.1; 1604.9; 1631.0; 1648.0	Water molecule bends
2431.1	OH stretch (HOBr molecule)
2800.7; 2941.8; 3058.3; 3180.2; 3714.3; 3722.3; 3726.6; 3738.8	OH stretch (HOH molecules)

be considered a method reliable for the reproduction of hydrogen bonds in small clusters.

### Binding energies

The binding energies could be calculated using the pBP/DN\*\* energy values of −2650.3070 hartree — with zero-point vibrational energy correction included — obtained for the isolated HOBr molecule in our previous study (16) and the pBP/DN\*\* energy values of the HOH molecule and the water clusters calculated in this study. The energies of the water monomer, water clusters, HOBr·(H<sub>2</sub>O)<sub>*n*</sub> clusters (*n* = 1–4), and the binding energies are presented in Table 10, all including the zero-point vibrational energy correction.

Considering the pBP/DN\*\* energy values for the *syn* and *anti* HOBr·H<sub>2</sub>O conformers of −2726.7640 hartree and −2726.7631 hartree and including the zero-point vibrational

energy corrections, the *syn* and *anti* binding energy values were 0.0069 hartree (4.3 kcal mol<sup>−1</sup>) and 0.0056 hartree (3.5 kcal mol<sup>−1</sup>), respectively. The binding energy values obtained by Ying and Zhao (13) for the *syn* and *anti* conformers were higher than ours, being 5.6 kcal mol<sup>−1</sup> and 5.5 kcal mol<sup>−1</sup>, respectively, for B3LYP/6-311++G(*d,p*) calculations. The difference of 0.8 kcal mol<sup>−1</sup> observed between the *syn* and *anti* binding energy values, which was higher than the difference of 0.1 kcal mol<sup>−1</sup> observed by Ying and Zhao (13), are probably an effect of the *C<sub>s</sub>* and *C<sub>1</sub>* symmetries obtained for the *syn* and *anti* pBP/DN\*\* conformers, respectively. Dibble and Francisco (10), using the MP2/6-311++G(*d,p*) method, calculated the binding energy difference between the *syn* and *anti* HOCl·H<sub>2</sub>O conformers (both with *C<sub>s</sub>* symmetry) to be 0.1 kcal mol<sup>−1</sup>.

Each water molecule addition in a cluster increases the binding energies by approximately 4 kcal mol<sup>−1</sup>, except



**Table 9.** Calculated geometry parameters of the H<sub>2</sub>O molecule and (H<sub>2</sub>O)<sub>n</sub> clusters (pBP/DN\*\* method).

Parameters	H <sub>2</sub> O	(H <sub>2</sub> O) <sub>2</sub>	(H <sub>2</sub> O) <sub>3</sub>	(H <sub>2</sub> O) <sub>4</sub>
H <sub>f</sub> —O <sub>wa</sub> (Å)	0.975	0.974	0.975	0.976
O <sub>wa</sub> —H <sub>b</sub> (Å)		0.988	1.004	1.019
H <sub>f</sub> O <sub>wa</sub> H <sub>b</sub> (°)	104.69	104.54	106.43	105.42
H <sub>b</sub> ...O <sub>wb</sub> (Å)		1.874	1.792	1.649
O <sub>wa</sub> H <sub>b</sub> ...O <sub>wb</sub> (°)		175.45	151.70	169.83
H <sub>f</sub> —O <sub>wb</sub> (Å)		0.976	0.975	0.976
O <sub>wb</sub> —H <sub>b</sub> (Å)			1.004	1.019
H <sub>f</sub> O <sub>wb</sub> H <sub>b</sub> (°)		105.40	105.64	106.21
H <sub>b</sub> ...O <sub>wc</sub> (Å)			1.792	1.653
O <sub>wb</sub> H <sub>b</sub> ...O <sub>wc</sub> (°)			153.28	167.99
H <sub>f</sub> —O <sub>wc</sub> (Å)			0.976	0.976
O <sub>wc</sub> —H <sub>b</sub> (Å)			1.004	1.018
H <sub>f</sub> O <sub>wc</sub> H <sub>b</sub> (°)			105.84	105.67
H <sub>b</sub> ...O <sub>wa</sub> (Å)			1.803	1.646
O <sub>wc</sub> H <sub>b</sub> ...O <sub>wa</sub> (°)			152.36	
O <sub>wd</sub> H <sub>b</sub> ...O <sub>wa</sub> (°)				168.12
H <sub>b</sub> ...O <sub>wd</sub> (Å)				1.659
O <sub>wc</sub> H <sub>b</sub> ...O <sub>wd</sub> (°)				168.50
H <sub>f</sub> —O <sub>wd</sub> (Å)				0.976
O <sub>wd</sub> —H <sub>b</sub> (Å)				1.019
H <sub>f</sub> O <sub>wd</sub> H <sub>b</sub> (°)				106.21
Energy <sup>a</sup>	-76.470700	-152.948683	-229.436684	-305.928417

**Note:** H<sub>f</sub> = hydrogen free; H<sub>b</sub> = hydrogen bonded; O<sub>wa</sub>, O<sub>wb</sub>, O<sub>wc</sub>, O<sub>wd</sub> = oxygen of a, b, c, and d water molecules, respectively.

<sup>a</sup>Optimized energies, without ZPE corrections; values in hartree.

**Table 10.** Optimized energy (with zero-point vibrational energy correction) and binding energy values for HOBr·(H<sub>2</sub>O)<sub>n</sub> and water clusters.

HOBr·(H <sub>2</sub> O) <sub>n</sub> energies <sup>a</sup>	(H <sub>2</sub> O) <sub>n</sub> energies <sup>a</sup>	Binding energies <sup>b</sup>
HOBr·H <sub>2</sub> O <i>syn</i>	-2726.7640	H <sub>2</sub> O -76.4501 0.0069 (4.33)
HOBr·(H <sub>2</sub> O) <sub>2</sub> <i>syn</i>	-2803.22425	(H <sub>2</sub> O) <sub>2</sub> -152.90348 0.0137 (8.60)
HOBr·(H <sub>2</sub> O) <sub>3</sub>	-2879.69162	(H <sub>2</sub> O) <sub>3</sub> -229.36508 0.0195 (12.24)
HOBr·(H <sub>2</sub> O) <sub>4</sub>	-2956.15317	(H <sub>2</sub> O) <sub>4</sub> -305.83215 0.0140 (8.79)

**Note:** E<sub>HOBr</sub> = -2650.3070 hartree (with ZPE correction).

<sup>a</sup>Energy in hartree.

<sup>b</sup>Values in parenthesis in kcal mol<sup>-1</sup>.

when the HOBr·(H<sub>2</sub>O)<sub>4</sub> cluster is generated. This cluster presents almost the same stability as the HOBr·(H<sub>2</sub>O)<sub>2</sub> cluster; the HOBr·(H<sub>2</sub>O)<sub>3</sub> is the more energetically favorable cluster among the studied clusters. This change in the binding energy tendency can be attributed to a contribution of the nuclear repulsion energy, which was greater for HOBr·(H<sub>2</sub>O)<sub>4</sub> than in the other HOBr species. Ortiz-Repiso et al. (12) have studied the HOCl·(H<sub>2</sub>O)<sub>n</sub> clusters (*n* = 1–4) and found an increase in the binding energy when each water molecule is added to the previous species; HOCl·(H<sub>2</sub>O)<sub>4</sub> is thus the more energetically favorable cluster. This different behavior can be attributed to the different size of the bromine and chlorine atoms, which affects the repulsion energies.

## Discussion

### HOBr·H<sub>2</sub>O

The pBP/DN\*\* energy values pointed to the *syn* structure as slightly more stable than the *anti* structure, as obtained by

Ying and Zhao (13). Our *syn* conformer was 0.5 kcal mol<sup>-1</sup> more stable than the *anti* conformer, while the difference observed by Ying and Zhao (13), using the B3LYP/6-311++G(*d,p*) method, was only 0.2 kcal mol<sup>-1</sup>. Generally, the *syn* and *anti* conformers did not present significant bond lengths changes; the *syn* bond length values were slightly longer than the *anti*. The BrO<sub>1</sub>H<sub>1</sub>, O<sub>1</sub>H<sub>1</sub>...O<sub>2</sub>, and H<sub>2</sub>O<sub>2</sub>H<sub>3</sub> angles presented differences of 1.3, 2.0, and 0.5° between the *syn* and *anti* conformers, respectively.

The comparison between the pBP/DN\*\* and B3LYP/6-311++G(*d,p*) (13) results showed that the pBP bond lengths were 1% longer, with the exception of H<sub>1</sub>...O<sub>2</sub>, which was approximately 3% shorter. The *syn* pBP/DN\*\* O<sub>1</sub>H<sub>1</sub>...O<sub>2</sub> angle was 4.5° lower than that obtained by the B3LYP/6-311++G(*d,p*) method, while the *anti* one was practically coincident. The *syn* and *anti* pBP/DN\*\* BrO<sub>1</sub>H<sub>1</sub> angles were, respectively, 2.2° and 1.5° lower than the corresponding B3LYP/6-311++G(*d,p*) values, while the *syn* and *anti* pBP/DN\*\* H<sub>2</sub>O<sub>2</sub>H<sub>3</sub> angles did not present significant changes.



The comparison with the corresponding chlorine hydrated complex showed that our *syn* and *anti*  $\text{H}_1\cdots\text{O}_2$  hydrogen bonds were shorter than the equivalent bonds obtained by Dibble and Francisco (10) and Ortiz-Repiso et al. (12) for the  $\text{HOCl}\cdot\text{H}_2\text{O}$  complex (using the MP2/6-311++G(*d,p*) method), which were, respectively, 1.809 Å and 1.811 Å for the *syn* structure and 1.807 Å and 1.806 Å for the *anti* structure. This would suggest that the hydrogen bond between HOBr and  $\text{H}_2\text{O}$  is stronger than HOCl and  $\text{H}_2\text{O}$ , but, as we are comparing values calculated by different methods, we cannot be sure about this conclusion.

The comparison between the hydrated complexes and the HOBr and  $\text{H}_2\text{O}$  monomers showed that the addition of a water molecule to HOBr decreased the  $\text{BrO}_1$  bond length by 0.5% and increased the  $\text{O}_1\text{H}_1$  bond length by 2%, while the  $\text{O}_2\text{H}_{2,3}$  bond lengths remained the same. Changes in angles were all less than  $0.7^\circ$ . The orientation of the hydrogens of the water molecule related to the bromine on the *syn* conformer has closed the  $\text{BrO}_1\text{H}_1$  angle.

The vibrational frequency values listed in Table 2 for the *syn* and *anti* conformers showed that, in general, our results did not present any significant discrepancy when compared with the B3LYP/6-311++G(*d,p*) results (13).

For the *syn* and *anti* conformers, the comparison between pBP/DN\*\* and B3LYP/6-311++G(*d,p*) vibrational frequencies showed that the pBP/DN\*\*  $\text{O}_1\text{H}_1$  stretches were 10% and 9% lower than the B3LYP/6-311++G(*d,p*) values, respectively, while the  $\text{H}_1\text{O}_2$  stretches were 10% and 8% higher. For the *syn* conformer, our pBP/DN\*\* HOBr and HOH bends were 3% higher than the values obtained by Ying and Zhao (13). For the *anti* conformer, the symmetric and asymmetric pBP/DN\*\* vibrational modes related to the water molecule showed lower frequencies than the values obtained by the B3LYP/6-311++G(*d,p*) method.

The HOBr- $\text{H}_2\text{O}$  stretch and bend vibrational modes, when compared with the correspondent HOBr values, showed that the *syn* and *anti* structures gave  $\text{BrO}_1$  stretch values that increased by 1.2% and 1.6%, respectively. Both conformers presented HOBr bend frequencies higher than the isolated species; the values for the *syn* and *anti* structures were 14% and 12% higher, respectively. The  $\text{O}_1\text{H}_1$  stretches were 11% lower than the values observed for the HOBr molecule, suggesting that the hydrogen bond with the water molecule weakens this bond. The HOBr- $\text{H}_2\text{O}$  modes, when compared with the corresponding values on the  $\text{H}_2\text{O}$ -isolated molecule, showed that the HOH bend and the symmetric  $\text{O}_2\text{H}_{2,3}$  stretch were 6% and 3% higher for the *syn* conformer and only 0.2% and 0.7% lower for the *anti* conformer, respectively. As the *syn* conformer is the most stable, it shows that the *syn* HOBr- $\text{H}_2\text{O}$  formation disturbs the water molecule more than in the case of the *anti* conformer, as expected.

Table 2 shows that the *syn* and *anti* HOBr- $\text{H}_2\text{O}$  conformers present the *syn*  $\text{H}_2\text{O}_2\text{H}_3$  bend value 6% higher than the *anti*. For the  $\text{O}_2\text{H}_{2,3}$  symmetric stretch, the *syn* conformer value was 3% higher than the value for the *anti* conformer. These differences were not observed in the B3LYP/6-311++G(*d,p*) results, probably because of the same  $C_s$  symmetry found on *syn* and *anti* structures.

The electrostatic potential surface and the calculated pBP/DN\*\* atomic charge distribution pointed to a difference between the  $\text{H}_2$  and  $\text{H}_3$  atoms in the *anti* conformer as a nat-

ural consequence of the  $C_1$  symmetry obtained for this conformer. The electrostatic potential surface showed a high electronic density located on the atoms of the HOBr molecule, suggesting an electronic-density transfer from the  $\text{H}_2\text{O}$  molecule to the HOBr molecule when the hydrated complex is formed.

### HOBr-( $\text{H}_2\text{O}$ )<sub>2</sub>

As compared with the  $\text{HOCl}\cdot(\text{H}_2\text{O})_2$  cluster (12) that presented only one structure with the chlorine atom placed off the planar ring made up of three oxygen, our calculations pointed to two stable structures with a small energy difference for the HOBr-( $\text{H}_2\text{O}$ )<sub>2</sub> cluster. The geometrical parameters listed in Table 3 make some interesting comparisons possible.

For the *anti* conformer, the  $\text{O}_1\text{—H}_1$  bond length was augmented by 4% and 2%, respectively, when compared with the isolated HOBr and with the HOBr- $\text{H}_2\text{O}$ , while the  $\text{Br—O}_1$  length was still practically the same. The  $\text{H}_1\text{O}_1\text{Br}$  angle was  $2^\circ$  and  $1.5^\circ$  higher than the values obtained for the isolated HOBr molecule and for the HOBr- $\text{H}_2\text{O}$  complex, respectively, showing that this angle increases as more water molecules are added. The  $\text{O}_2\text{—H}_3$  bond length was longer than the other free  $\text{O}_2\text{—H}_2$ ,  $\text{O}_3\text{—H}_4$ , and  $\text{O}_3\text{—H}_5$  bond lengths as a consequence of the interaction of the  $\text{H}_3$  atom with the oxygen of the second water molecule. The *anti*  $\text{O}_3\text{—H}_5$  bond length was larger than the other free  $\text{O—H}$  bonds and than the *syn*  $\text{O}_3\text{—H}_5$  bond (see, in Fig. 2, the proximity between the  $\text{H}_5$  and  $\text{O}_1$  atoms). The  $\text{H}_2\text{O}_2\text{H}_3$  angle was slightly higher than that obtained for isolated HOH and for HOBr- $\text{H}_2\text{O}$ , while the  $\text{H}_4\text{O}_3\text{H}_5$  angle was very close to the  $\text{H}_2\text{O}_2\text{H}_3$  terminal angle in HOBr with one water molecule. The introduction of the second water molecule closed the  $\text{H}_1\cdots\text{O}_2\text{H}_3$  angle by 19%, approximately, showing a first tendency for a cyclic structure formation.

With respect to the *syn* structure, the  $\text{Br—O}_1$  bond length was 0.8% and 0.5% lower than the values obtained for the isolated HOBr molecule and for HOBr with one water molecule, respectively, while the  $\text{O}_1\text{—H}_1$  bond length was increased by 4% and 2%, respectively, as occurred on the *anti* structure. The  $\text{H}_1\text{O}_1\text{Br}$  angle was increased  $1^\circ$  and  $1.7^\circ$  when compared with the isolated HOBr molecule and the HOBr- $\text{H}_2\text{O}$  molecule, respectively. The  $\text{O}_2\text{—H}_2$ ,  $\text{O}_2\text{—H}_3$ ,  $\text{O}_3\text{—H}_4$ , and  $\text{O}_3\text{—H}_5$  bond lengths were practically the same as the *anti* conformer.

The *syn* and *anti*  $\text{H}_1\cdots\text{O}_2$  hydrogen bonds between the HOBr and the first water molecule have shown values shorter than those found for the monohydrated HOBr complex. The  $\text{H}_3\cdots\text{O}_3$  hydrogen bond between the first and second water molecule presented a value close to the  $\text{H}_1\cdots\text{O}_2$  value observed in the HOBr- $\text{H}_2\text{O}$  complex, being smaller than the experimental hydrogen bond (2.03 Å) determined by Dyke et al. (4) for the water dimer. For the stable  $\text{HOCl}\cdot(\text{H}_2\text{O})_2$  cluster, Ortiz-Repiso et al. (12), using the MP2/6-311++G(*d,p*) method, calculated the corresponding  $\text{H}_1\cdots\text{O}_2$  hydrogen bond as 1.933 Å and the  $\text{H}_3\cdots\text{O}_3$  hydrogen bond as 1.765 Å, just the opposite of our results, with the first hydrogen bond being longer than the second. The  $\text{H}_3\cdots\text{O}_3$  hydrogen bond values were shorter than the calculated  $\text{H}\cdots\text{O}$  distance obtained for the water dimer: our pBP/DN\*\*  $\text{H}\cdots\text{O}$  distance was 1.874 Å, while the MP2 cal-



culations made by Xantheas and Dunning (5) and Ortiz-Repiso et al. (12) pointed to this distance as 1.95 Å, using aug-cc-pVDZ and 6-311++G(*d,p*) basis sets. Our *syn* and *anti* O<sub>2</sub>...O<sub>3</sub> distances of 2.74 Å and 2.79 Å were, respectively, close to the experimental value of 2.976 Å obtained for the water dimer (5).

The geometrical differences mentioned above for both conformers have shown bond length- and angle-specific behaviors when the atoms are placed in terminal position or in the middle of the molecule chain.

The vibrational frequencies presented in Table 4 show that the BrO<sub>1</sub> and O<sub>1</sub>H<sub>1</sub> stretch values are very close for the *anti* and *syn* structures, but 2% higher and 20% lower, respectively, than the values obtained for the isolated HOBr molecule. The comparison of the *anti* and *syn* H<sub>1</sub>O<sub>1</sub>Br bending values with the corresponding values for the isolated HOBr molecule showed an increase of 15% and 20%, respectively. These differences are in concordance with the geometrical HOBr changes observed when the HOBr is associated with the water molecule. Comparing with the isolated water molecule, the O<sub>2</sub>H<sub>3</sub> and O<sub>3</sub>H<sub>5</sub> stretch values were close to the symmetric modes, while the O<sub>2</sub>H<sub>2</sub> and O<sub>3</sub>H<sub>4</sub> stretch values were close to the asymmetric modes, in both *syn* and *anti* conformers. The O...H bond between different water molecules could be verified by the presence of H<sub>1</sub>O<sub>2</sub> and H<sub>3</sub>O<sub>3</sub> stretch frequencies with low values, being very far from the O—H stretch characteristic region in pure water.

### HOBr·(H<sub>2</sub>O)<sub>3</sub> and HOBr·(H<sub>2</sub>O)<sub>4</sub>

For the HOBr·(H<sub>2</sub>O)<sub>3</sub> and HOBr·(H<sub>2</sub>O)<sub>4</sub> clusters, only O—H bonds are located in the ring, contrasting with the Ortiz-Repiso et al. (12) results that have also presented stable structures with O—Cl bonds in the ring. This difference can be attributed to the different sizes between the bromine and the chlorine atoms.

The calculated OH...O angles show that the HOBr·(H<sub>2</sub>O)<sub>3</sub> cluster is less planar than the HOBr·(H<sub>2</sub>O)<sub>4</sub> cluster, although the ring that has four water molecules is more distorted than the ring with three water molecules. The O<sub>4</sub>—H<sub>7</sub> and the O<sub>5</sub>—H<sub>9</sub> bond lengths are shorter than the other O—H distances on the water cluster, indicating a lower interaction between the H<sub>7</sub> and H<sub>9</sub> atoms and the O<sub>1</sub> atom on the respective clusters.

In the HOBr·(H<sub>2</sub>O)<sub>3</sub> cluster, the O...H hydrogen bonds were approximately 1.6 Å. This value is shorter than the pBP and MP2 (5, 12) hydrogen bond values of 1.79 Å and 1.9 Å obtained, respectively, for the water trimer. The hydrogen bond of 1.653 Å calculated by Ortiz-Repiso et al. (12) for the HOCl·(H<sub>2</sub>O)<sub>3</sub> cluster was longer than our H<sub>1</sub>...O<sub>2</sub> value of 1.560 Å obtained for the HOBr·(H<sub>2</sub>O)<sub>3</sub> cluster, which is probably a consequence of the planarity obtained for the cyclic HOCl·(H<sub>2</sub>O)<sub>3</sub> cluster.

In the HOBr·(H<sub>2</sub>O)<sub>4</sub> cluster, the O...H hydrogen bonds were practically the same as the corresponding values obtained for the HOBr·(H<sub>2</sub>O)<sub>3</sub> cluster, with the H<sub>9</sub>...O<sub>1</sub> slightly shorter than the H<sub>7</sub>...O<sub>1</sub>. These H<sub>9</sub>...O<sub>1</sub> and H<sub>7</sub>...O<sub>1</sub> distances of 1.720 Å and 1.765 Å, respectively, which were longer than the other H...O distances, can justify the atomic charges calculated for the H<sub>9</sub> and H<sub>7</sub> atoms, which were lower than the other hydrogen charges verified on the hydrogen bonds.

The HOBr·(H<sub>2</sub>O)<sub>3</sub> and HOBr·(H<sub>2</sub>O)<sub>4</sub> vibrational frequencies did not present significant value differences, making possible the identification of specific ranges for the BrO and OH stretch and BrOH bend frequencies corresponding to the HOBr molecule and the OH stretch regions characteristic to the water molecules. For these clusters we could not identify one specific stretch frequency related to the OH hydrogen bond, as observed on the other small clusters.

## Conclusion

In considering several different interactions between HOBr and H<sub>2</sub>O molecules, the calculations using the pBP method and DN\*\* basis set showed that the interaction involving the H of the HOBr and the O of the water molecule represents the preferred arrangement for the HOBr·(H<sub>2</sub>O)<sub>*n*</sub> clusters (*n* = 1–4). These pBP/DN\*\* calculations have predicted the existence of the *syn* and *anti* stable conformers for the HOBr·(H<sub>2</sub>O) and HOBr·(H<sub>2</sub>O)<sub>2</sub> clusters. Related to the HOBr·(H<sub>2</sub>O) complex, our energy values pointed to the *syn* structure as being slightly more stable than the *anti* one, as obtained by Ying and Zhao (13). The pBP/DN\*\* results have also predicted the formation of two cyclic stable structures corresponding to the HOBr·(H<sub>2</sub>O)<sub>3</sub> and HOBr·(H<sub>2</sub>O)<sub>4</sub> clusters. A non-linear hydrogen bond was first observed in the HOBr·(H<sub>2</sub>O)<sub>2</sub> cluster, showing a tendency to cyclic arrangement, which was satisfied in the cluster with three and four water molecules.

In the HOBr·(H<sub>2</sub>O)<sub>*n*</sub> clusters, all free O—H bonds have presented with practically the same bond values that they had in the water molecule, while the other hydrogen bonds that have contributed to the formation and stability of these clusters have presented with their length increased. The H...O distances calculated for the different clusters were shorter than the calculated H...O distances obtained for the water dimer, trimer, and tetramer.

The addition of a water molecule to the HOBr·H<sub>2</sub>O and HOBr·(H<sub>2</sub>O)<sub>2</sub> clusters increases the binding energy by approximately 4 kcal mol<sup>−1</sup>, while the addition of a water molecule to the HOBr·(H<sub>2</sub>O)<sub>3</sub> cluster decreases this value by 4 kcal mol<sup>−1</sup>, the HOBr·(H<sub>2</sub>O)<sub>3</sub> cluster being the more energetically favorable among the studied clusters.

Looking for the vibrational frequencies, we could observe that the O—H stretches corresponding to the hydrogen bond in the HOBr·(H<sub>2</sub>O) and HOBr·(H<sub>2</sub>O)<sub>2</sub> conformers were in a low frequency region, being very far from the usual O—H bond. The cyclic HOBr·(H<sub>2</sub>O)<sub>3</sub> and HOBr·(H<sub>2</sub>O)<sub>4</sub> clusters presented conjugated O—H stretch vibrations that did not permit a specific O—H stretch assignment corresponding to a hydrogen bond. In general, the vibrational frequencies calculated for the HOBr·(H<sub>2</sub>O)<sub>*n*</sub> clusters have reflected the geometrical HOBr and HOH changes observed when the hydrated HOBr clusters and the water clusters are generated.

Finally, as a general behavior, we notice that the calculated dipole values decreased with the increasing number of water molecules associated with the HOBr compound, with the higher difference occurring between the HOBr·H<sub>2</sub>O and the HOBr·(H<sub>2</sub>O)<sub>2</sub> clusters.



## Acknowledgments

This work was supported by the Fundação de Amparo à Pesquisa do Estado do Rio de Janeiro (FAPERJ), Fundação José Bonifácio (FUJB), Coordenação de Aperfeiçoamento de Pessoal de Nível Superior (CAPES), and Conselho Nacional de Desenvolvimento Científico e Tecnológico (CNPq).

## References

1. G.P. Brasseur, J.J. Orlando, and G.S. Tyndall. Atmospheric chemistry and global change. Oxford University Press, New York. 1999.
2. M.J. Molina and F.S. Rowland. *Nature* (London), **249**, 810 (1974).
3. S.C. Wofsy, M.B. McElroy, and Y.L. Yung. *Geophys. Res. Lett.* **2**, 215 (1975).
4. T.R. Dyke, K.M. Mack, and J.S. Muentner. *J. Chem. Phys.* **66**, 498 (1977).
5. S.S. Xantheas and T.H. Dunning, Jr. *J. Chem. Phys.* **99**, 8774 (1993).
6. K. Liu, J.D. Cruzan, and R.J. Saykally. *Science* (Washington, D.C.), **271**, 929 (1996).
7. I.M.B. Nielsen, E.T. Seidl, and C.L. Janssen. *J. Chem. Phys.* **110**, 9435 (1999).
8. V. Vaida and J.E. Headrick. *J. Phys. Chem. A*, **104**, 5401 (2000).
9. C.T. McElroy, C.A. McLinden, and J.C. McConnell. *Nature* (London), **397**, 338 (1999).
10. T.S. Dibble and J.S. Francisco. *J. Phys. Chem.* **99**, 1919 (1995).
11. F.M. Geiger, J.M. Hicks, and A.C. de Dios. *J. Phys. Chem. A*, **102**, 1514 (1998).
12. M. Ortiz-Repiso, R. Escribano, and P.C. Gómez. *J. Phys. Chem. A*, **104**, 600 (2000).
13. L.M. Ying and X.S. Zhao. *J. Phys. Chem. A*, **101**, 3569 (1997).
14. A.D. Becke. *Phys. Rev. A At. Mol. Opt. Phys.* **38**, 3089 (1988).
15. J.P. Perdew. *Phys. Rev. B Condens. Matter*, **33**, 8822 (1986).
16. C.M.P. Santos, R.B. Faria, J.O. Machuca-Herrera, and S. de P. Machado. *Can. J. Chem.* **79**, 1135 (2001).



# Determination of phenyl-*N*-methycarbamates and their hydrolysis products in water, using solid-phase extraction and reversed-phase liquid chromatography with UV and electrospray mass spectrometric detection<sup>1</sup>

Latifa Latrous El Atrache and Sadok Sabbah

**Abstract:** In this study, eight phenyl-*N*-methycarbamates (PNMCs) were considered. Reversed-phase LC was set up for UV and mass spectrometry (MS) detection mode. Gradient elution was used, and the mobile phase was composed of acetonitrile and water. UV-vis was performed at 220 nm. The method was tested with different reversed-phase columns. Comparison between chromatographic parameters: retention time ( $t_R$ ), resolution ( $R_S$ ), and selectivity ( $\alpha$ ) was established. Hydrolysis kinetics of three of the PNMCs were reported. The major hydrolysis products were determined by LC-UV, and the effect of pH on hydrolysis was also studied. Also, chromatographic separation of a mixture of PNMCs and four of their hydrolysis products was carried out. The preconcentration of 12 studied solutes was realized by solid-phase extraction. C18 extraction cartridges of 1 g were used to extract solutes from a 100 mL volume of tap and surface water spiked at 10 µg/L. The recoveries were, respectively, between 68–86% and 62–83% with relative a standard deviation of less than 11%. Limits of detection (LODs) and limits of quantitation (LOQs) ranged, respectively, from 1–4 µg/L and from 4–10 µg/L. Since standard UV detection does not provide adequate selectivity for water samples, an electrospray (ES)-MS instrument equipped with a triple quadrupole mass filter was used. MS data acquisition was performed by a time-scheduled, selected-ion monitoring (SIM) program. Limits of quantitation gave values between 0.1–0.5 µg/L.

**Key words:** phenyl-*N*-methycarbamates, water analysis, solid-phase extraction, LC-UV-vis, LC-ES-MS.

**Résumé :** Cette étude concerne le développement d'une méthode d'analyse permettant la détermination à l'état de traces de 8 phényl-*N*-méthycarbamates (PNMCS) dans les eaux potables et les eaux de surface. Les conditions d'analyse ont été déterminées par chromatographie liquide à polarité de phases inversée, en terme de séparation : choix de la colonne et optimisation de la phase mobile et de détection : spectrométrie d'absorption UV et spectrométrie de masse. Avec un gradient de phase mobile eau-acétonitrile et une colonne octadécyle type XTerra on obtient une séparation convenable. En ce qui concerne la détection le choix de la longueur d'onde  $\lambda = 220$  nm est un compromis acceptable pour lequel on obtient des réponses voisines pour l'ensemble des composés examinés. L'étude cinétique de trois PNMCs est reportée. La mise en évidence des produits d'hydrolyse est effectuée par LC-UV et les constantes de vitesses sont déterminées en fonction du pH. Par ailleurs, nous avons déterminé les conditions de séparation chromatographique des 8 PNMCs associés à 4 de leurs produits d'hydrolyse. L'étude de l'efficacité de concentration des 12 solutés examinés est réalisée par extraction liquide solide au moyen de silice greffée alkyle. Les préconcentrations ont été menées sur des cartouches de masse 1 g remplies de silice greffée octadécyle sur lesquelles sont percolés 100 mL d'échantillon d'eau de robinet et de surface dopés à 10 µg/L les taux de récupération varient respectivement entre 68–86 % et 62–83 % avec une déviation standard relative inférieure à 11 %. Les limites de détection et de quantification varient respectivement entre 1–4 µg/L et 4–10 µg/L; afin d'améliorer la sensibilité les 12 composés ont été analysés par couplage LC-MS assistée par ionization electrospray en mode positif. En appliquant la méthode de scrutation d'ion spécifique (SIM), nous obtenons des limites de quantification comprises entre 0,1 et 0,5 µg/L.

**Mots clés :** phenyl-*N*-methycarbamates, analyse de l'eau, extraction en phase solide, LC-UV-vis, LC-ES-MS.

Received 4 June 2002. Published on the NRC Research Press Web site at <http://canjchem.nrc.ca> on 12 August 2003.

**L.L. El Atrache and S. Sabbah.**<sup>2</sup> Laboratoire de Chimie Analytique et Electrochimie, Département de Chimie, Faculté des Sciences de Tunis, Campus Universitaire, 1060 Tunis.

<sup>1</sup>This article has been published without the benefit of author's corrections.

<sup>2</sup>Corresponding author (e-mail: [Sadok.Sabbah@fst.rnu.tn](mailto:Sadok.Sabbah@fst.rnu.tn)).



## Introduction

Phenyl-*N*-methylcarbamate (PNMCs) insecticides are aryl esters of phenyl-*N*-methyl-substituted carbamic acids (1). As shown in Fig. 1, the substituents on the phenyl ring can change the characteristic nature of the parent compound in hydrophobic, electronic, and hydrogen bonding and can thus affect the ability of complexation with acetylcholinesterase, a determining factor for its cholinesterase inhibition activity (2).

PNMCs constitute a class of pesticides of growing importance, widely used as substitutes for organochlorine pesticides because of their greater biodegradation ability.

Most PNMCs are degraded into their metabolites shortly after application. In alkaline media PNMCs can be easily hydrolyzed to form methylamine and substituted phenols. For example, carbofuranphenol was the major product from carbofuran in water, whereas 3-hydroxy and 3-keto derivatives were identified as the corresponding degradation products in soil (3). Some papers have dealt with the half-life of carbamates in an aquatic environment with a range of between 4 and 12 weeks (4).

Because of the proven or suspected toxicity of many of these pesticides, it is necessary to monitor them from both a regulatory and a consumer point of view; for example, 0.1–0.5 µg/L of carbofuran was found in ground water from Almeria (Spain) (5).

A large number of analytical methods have been published regarding methods of determination of carbamates, such as supercritical fluid chromatography (SFC) with capillary (6–7) and packed columns (8), thin layer chromatography (TLC) (9), and capillary electrophoresis (10–11), but most analytical methods until now apply to gas chromatography (GC) (12–13) and high pressure liquid chromatography (HPLC) (14–15). In general, carbamates and their transformation products are often quoted as being polar and thermally labile; these properties limit the use of GC, which exhibits derivatization prior to analysis. So LC is an obvious choice for the simultaneous determination of PNMCs.

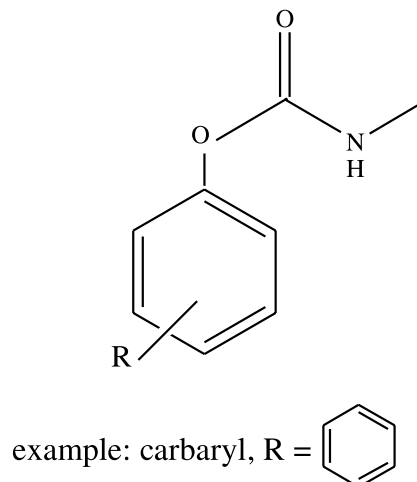
As regards detection, UV detection is the most widely applied in LC analysis (16).

Fluorescence detection also has good sensitivity, achieved by post-column derivatization; the functional group of the carbamates, with subsequent conversion of methylamine formed with *o*-phthaldehyde (OPA), yields a highly fluorescent isoinolide (17); however, it needs many intermediate steps.

MS detection is very attractive because it offers the possibility of achieving high sensitivity with a high degree of selectivity (18). Several reviews and articles on the different types of interfaces used, including transport systems, direct liquid introduction, thermospray, atmospheric pressure ionization, electrospray, and particle beam, have been published (19–23). During the last few years, atmospheric pressure ionization (API) techniques, high-flow pneumatically assisted electrospray ionization (ESI), and atmospheric pressure chemical ionization (APCI) have become the most popular interface techniques. The main limitation of APCI is that pesticides can undergo thermal degradation (24–26) in comparison with ESI where the sample is ionized directly in the liquid phase at quasi-ambient temperature, thus leaving intact fragile pesticides (27–28).

When carbamate pesticides were correctly applied, their residues could be found in the soil itself and in run-offs from

Fig. 1. Phenyl-*N*-methylcarbamate.



the soil, as well as in food, crops, and water. The importance of the presence of the target carbamates and their degradation products in water also must be considered. Degradation leads to compounds more toxic than the parent pesticides; therefore it is of vital importance to be able to determine these pesticides in aquatic media.

The most common preconcentration technique is solid-phase extraction (SPE). The use of SPE and LC techniques to analyze carbamate pesticides and their derivative products in water — focusing on off-line and on-line SPE with different kinds of sorbents — was reviewed (29).

Analytical methods for the determination of a mixture of oxime carbamates and PNMCs are relatively well established in water matrices (30), but simultaneous determination only of PNMC residues and the study of some of their degradation products in water with hydrolysis are not considerably extended.

The purpose of this study was, firstly, to optimize the separation of PNMCs in terms of selectivity, efficiency, and time analysis (for that, various columns were tested using the HPLC–UV–vis method) and, secondly, to determine the kinetics of the hydrolysis of carbaryl, carbofuran, and landrin. The identification of the major hydrolysis products was realized by LC. The rate constants were measured in various buffer solutions ranging from pH 8 to 12.

Therefore, we developed a method for analyzing, simultaneously, PNMCs and their hydrolytic degradation products in water samples. This method is based on combining SPE of water samples with HPLC–UV. The optimization of different parameters affecting the chromatographic separation and the SPE procedures was carried out.

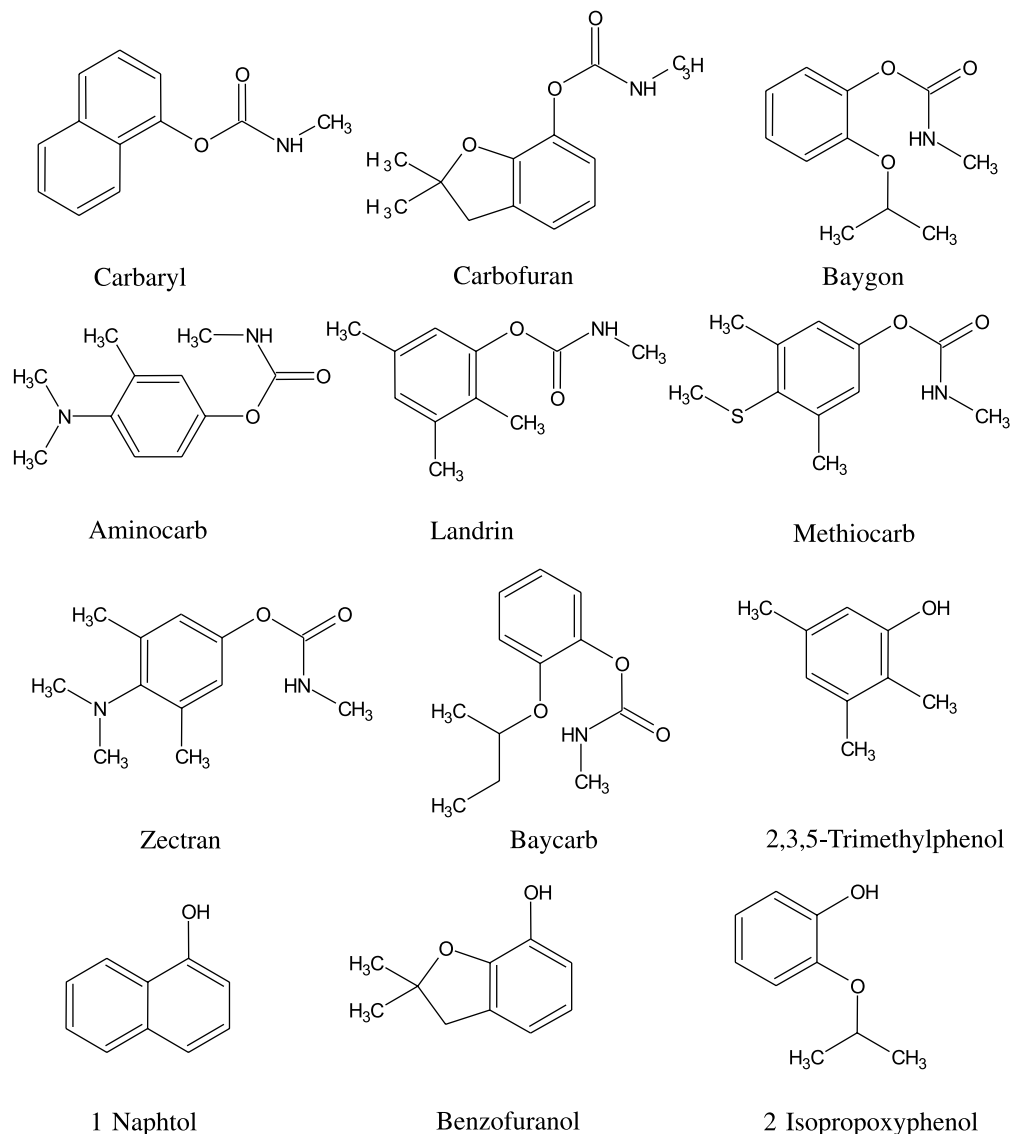
To increase sensitivity and to obtain low detection limits, the LC–ES–MS method was used.

## Experimental

### Chemicals and materials

PNMCs (aminocarb, baygon, carbofuran, carbaryl, methiocarb, baycarb, landrin, and zectran) and degradation products (2,2-dimethyl-2-dihydrobenzofuran-7-ol,  $\alpha$ -naphthol, 2-isopropoxyphenol, 2,3,5-trimethylphenol) were obtained from Supelco.



**Fig. 2.** Structures and common names of compound used.

The chemical structures of all studied compounds are shown in Fig. 2.

Standard stock solutions were prepared in methanol, which contained each compound at concentrations of 1000 µg/mL, and were stored in glass bottle at 4°C. Standard working solutions of various concentrations were prepared daily by appropriate dilution of aliquots of the stock in the methanol.

The methanol and acetonitrile used are HPLC grade from LAB SCAN (Ireland). HPLC grade water was obtained by purification of demineralized water in a Milli-Q system (Millipore, Elix). Mobile phases were degassed with helium before use.

Silica-based sorbents with octadecyl functional group bond Elut Jr. C18 were acquired from Varian.

### Chromatographic conditions

#### LC-UV analysis

The system consists of a gradient Model 127 LC pump from Beckman, a rehodyne six-port injection valve (Model

7125) with a 20 µL loop. A Model 166 wavelength UV-vis detector from Beckman. Recording of chromatograms and quantitative measurements of peak areas were performed with an HP 3395.

The mobile phases were set at a flow rate of 1 mL/min. Measurement wavelength was 220 nm; in fact, the most common wavelengths are of 210 and 220 nm (31). The solvent employed for the mobile phase was acetonitrile and water, using two gradients. The gradient (a) was 30% acetonitrile isocratic, which was increased linearly to 100% over 20 min and held at 100% for 5 min. A return to the initial conditions was carried out over 10 min. The gradient (b) was 20% acetonitrile, which was increased to 100% over 40 min and held at 100% for 10 min. The return to the initial conditions was carried out in 10 min. The separation was performed using the following different analytical columns:

- (i) LC8, 150 × 4.6 mm i.d., 5 µm particulate size
- (ii) Waters SYMMETRY C18, 150 × 3.9 mm i.d., 5 µm particulate size
- (iii) XTerra, 250 × 4.6 mm i.d., 5 µm particulate size



**Table 1.** Retention time of PNMCS obtained for different LC columns.

Peak No.	PNMCS	Retention time (min) RSD <sup>a</sup> (%)			
		C8	C18		
		Supelcosil	Symmetry	XTerra <sup>b</sup>	XTerra <sup>b</sup>
1	Aminocarb	7.59 (0.04)	10.47 (0.23)	11.96 (0.10)	13.99 (0.41)
2	Baygon	7.84 (0.04)	1078 (0.47)	12.51 (0.23)	14.82 (0.46)
3	Carbofuran	7.84 (0.04)	11.09 (0.47)	12.83 (0.48)	15.18 (0.91)
4	Carbaryl	8.60 (0.10)	12.05 (0.35)	14.32 (0.60)	17.48 (0.35)
5	Landrin	9.47 (0.08)	13.24 (0.41)	14.95 (0.59)	18.40 (0.48)
6	Baycarb	10.98 (0.08)	14.32 (0.46)	16.04 (1.00)	20.73 (0.18)
7	Methiocarb	19.04 (0.04)	15.65 (0.48)	16.47 (0.91)	21.39 (0.60)
8	Zectran	19.04 (0.04)	15.65 (0.48)	16.86 (0.35)	22.02 (0.23)

Note:  $\lambda = 220$  nm.

<sup>a</sup>Five replicate.

<sup>b</sup>Elution programme.

### LC-MS analysis

The system LC-ES-MS consists of PE Sciex API 2000 with an analyst station for recording chromatograms. A gradient model 200 pump from PerkinElmer and a rehodyne injection valve (model 7125) with a 20  $\mu$ L loop was used. Separation was performed on a 100  $\times$  3 mm i.d. SYMMETRY column packed with C18 bonded silica phase.

The gradient selected for LC-ES-MS, at the flow rate of 0.25 mL/min, was 50% methanol, which was increased linearly to 75% over 5 min. A return to the initial conditions was carried out in 5 min. The MS was operated in the positive-ion mode by application of a voltage of 5000 V to the capillary. The source temperature was maintained at 325°C. Ions were generated using highly pure nitrogen as the drying gas at a flow rate of 10 L/min and nebulizing gas at a pressure of 40 psig.

Full scan LC-MS chromatograms were obtained by scanning for  $m/z$  50 to 500. LC-MS chromatograms were obtained by operating, in the time scheduled, one selected ion monitoring (SIM) acquisition mode.

### Sample preparations

Solid-phase extraction was used to preconcentrate selected compound from water. Each sample (100 mL) was extracted onto SPE cartridges packed with 1 g of C18 bonded silica. The solid phase was first conditioned with 6 mL of methanol, then with 7 mL of deionized water. Following sample extraction, the solutes were eluted with 5 mL of methanol. The eluent was collected in a graduated tube and concentrated, under a stream of nitrogen with Kuderna-Danish, to 1 mL.

## Results and discussion

### Optimization of HPLC-UV parameters

Various workers (17, 32–34) have shown that a multi-pesticide mixture of nine to 12 oxime carbamates and PNMCS can be separated using a binary gradient of water with methanol or acetonitrile.

Thus, for the separation of eight PNMCS, we have used an acetonitrile–water gradient.

In this present work, three columns were tested at 220 nm. Comparison between the columns was made at the same

**Table 2.** Resolution and selectivity of eight PNMCS using Xterra column and acetonitrile–water gradient.

PNMCS	Elution program			
	(a)		(b)	
	$R_s$	$\alpha$	$R_s$	$\alpha$
Aminocarb–baygon	1.35	1.05	1.05	1.05
Baygon–carbofuran	0.75	1.03	1.25	1.04
Carbofuran–carbaryl	3.75	1.13	5.50	1.16
Carbaryl–landrin	1.50	1.05	2.50	1.06
Landrin–baycarb	2.75	1.08	6.00	1.014
Baycarb–methiocarb	1.00	1.03	1.75	1.04
Methiocarb–zectran	1.00	1.03	1.75	1.03

chromatographic conditions (solvent programme *a*). The relative retention times and retention factors of all analytes are presented in Table 1.

Two pairs of PNMCS remain unresolved on LC8; on the SYMMETRY C18 we picked up one co-elution as (methiocarb and zectran). But on the XTerra column we obtained good separation and peak resolution with an analysis time shorter than 20 min. So, the XTerra column was the best column for the separation of PNMCS. In Fig. 3, a chromatogram of a standard mixture of PNMCS is shown.

To study the effect of the mobile phase composition on separation, a gradient elution programme (*b*) was tested. According to the chromatogram obtained (in Fig. 4) and the results presented in Table 2, the best separation parameters were given with the latter programme.

Operating conditions of analyses by LC-UV-vis were determined, and our objective in what follows is to separate a mixture of the eight mentioned PNMCS and four of their hydrolytic degradation products, so a kinetic study of three PNMCS such as carbaryl, carbofuran, and landrin was given.

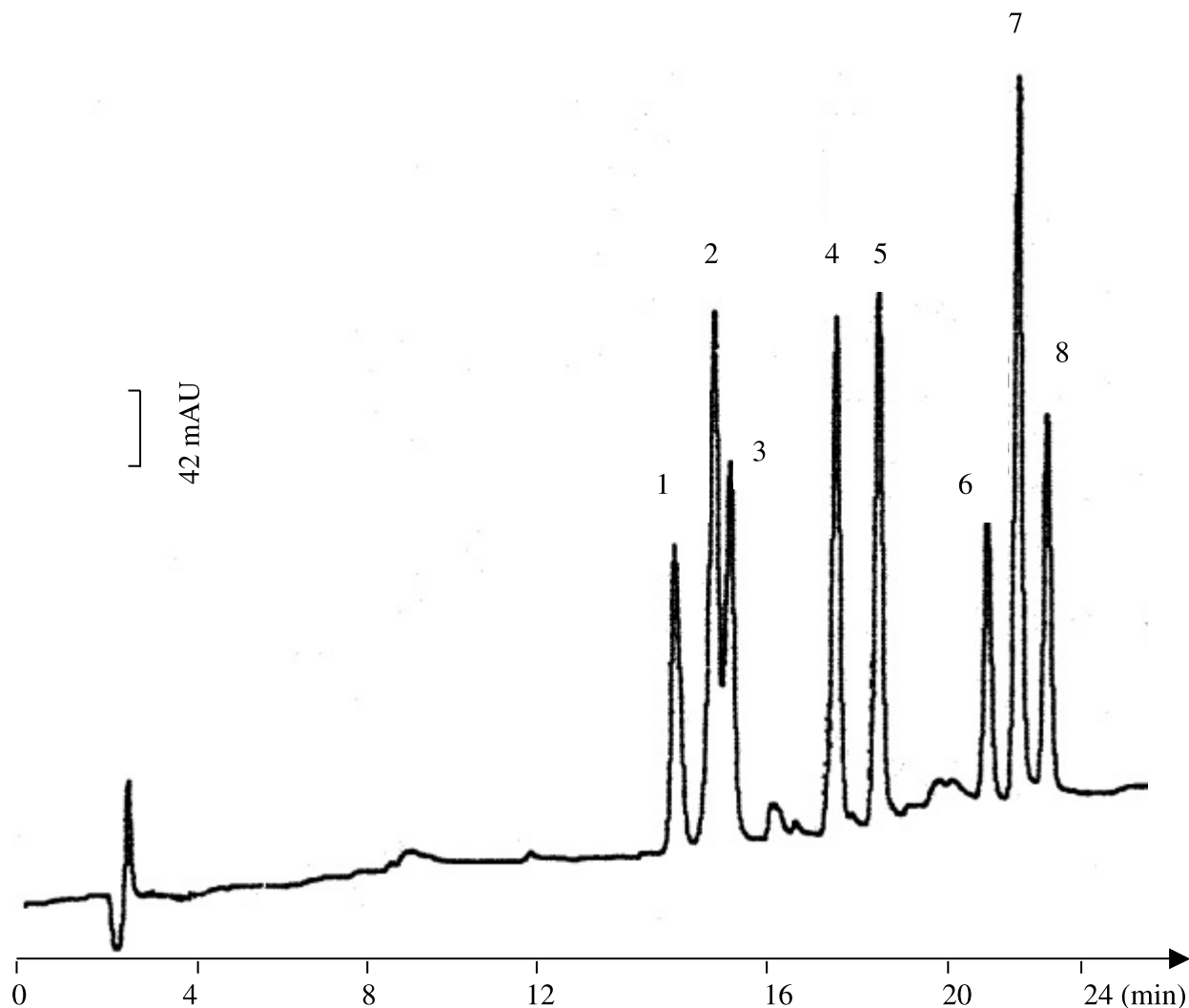
### Hydrolysis kinetics of PNMCS

#### Product analysis of the hydrolysis reaction

An aliquot of each PNMCS hydrolysis reaction in a buffer solution (carbamates 20  $\mu$ g/L) at pH 8.8 was analyzed using high-pressure liquid chromatography, with a reversed phase, in an acetonitrile–water mixture.



**Fig. 3.** HPLC of a standard solution containing 1 mg/L of carbaryl, 20 mg/L of baycarb, 10 mg/L of aminocarb, baygon, landrin, methiocarb, and zectran, using XTerra in LC-grade water (a) registered at  $\lambda = 220$  nm. Peak numbers correspond to those in Table 1.



The hydrolysis products were identified by comparing their retention times to standard solution ones.

#### Effect of pH

Carbaryl, landrin, and carbofuran hydrolysis exhibited pseudo-first-order kinetics in aqueous media, and the rate constants were measured in various buffer solutions, varying from pH 8 to 12. The ultraviolet spectra plotted as a function of time show two isosbestic points, indicating no accumulation of intermediates. Table 3 gives the half-life times of carbaryl, carbofuran, and landrin at different pH values. pH has an important effect on the hydrolysis rate of such PNMCS. Shorter hydrolysis half-lives were obtained for higher pH values. At pH 12, half-lives of carbaryl, carbofuran, and landrin were, respectively, 0.18, 0.83, and 866.30 min. Furthermore, it can be pointed out that the order of degradation is carbaryl, carbofuran, and landrin.

We have also determined the half-lives of such PNMCS round about pH 7. It was noted that carbofuran and landrin were practically stable, and the carbaryl half-life time was 15 days.

**Table 3.** Effect of pH on Hydrolysis.

	Half-life (min)					
	pH					
PNMCs	8.8	9.5	9.8	10.3	11	12
Carbaryl	277.20	700.00	22.30	9.30	1.51	0.18
Carbofuran	1386.00	301.30	—	27.39	8.15	0.83
Landrin	—	—	—	—	—	866.30 <sup>a</sup>

<sup>a</sup>pH = 12.2.

Because of the hydrolytic degradation of the studied PNMCS, we were induced to study a mixture of 12 compounds, including PNMCS and their hydrolysis products.

#### Separation of PNMCS and their hydrolysis products

According to the kinetic study given above, we must consider the presence of PNMCS as well as their hydrolysis products. A mixture of 12 compounds, including  $\alpha$ -naphthol, 2,3,5-trimethylphenol, 2-isopropoxyphenol, and benzofuranol, was examined.



**Fig. 4.** HPLC separation of PNMCs in LC-grade water (*b*). Experimental conditions as in Fig. 3. Peak numbers correspond to those in Table 1.

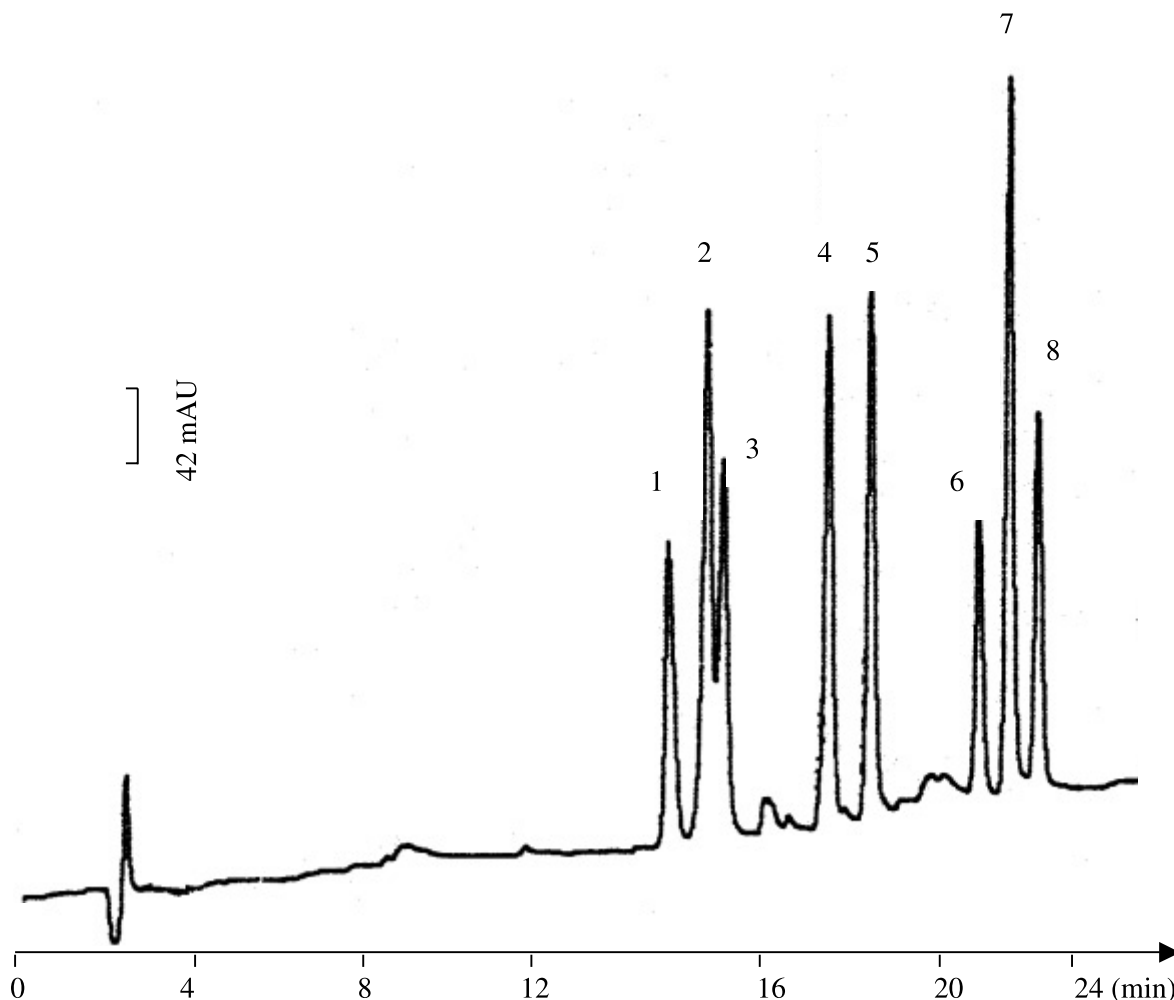


**Table 4.** Retention time of eight carbamates and four degradation products using an XTerra column and acetonitrile water gradient.

Peak No.	Carbamates and (or) degradation products	Retention time (RSD%) <sup>a</sup>
1	Aminocarb	13.83 (0.10)
2	Baygon	14.92 (0.15)
3	Carbofuran	15.29 (0.24)
4	Benzofuranol	15.81 (0.24)
5	2-Isopropoxyphenol	17.19 (0.47)
6	Carbaryl	17.61 (0.48)
7	Landrin	18.51 (0.49)
8	2,3,5-Trimethylphenol	20.43 (0.91)
9	$\alpha$ -Naphthol	20.43 (0.91)
10	Baycarb	20.86 (0.28)
11	Methiocarb	21.55 (0.72)
12	Zectran	22.06 (0.62)

<sup>a</sup>Five replicate.

In Fig. 5, the chromatogram of a standard mixture of 12 solutes is shown; the separation is less than 25 min. Despite the short analysis time, one pair of studied compounds remains unresolved ( $\alpha$ -naphthol, 2,3,5-trimethylphenol). The retention times and relative standard deviation of all analytes

are presented in Table 4. Detection limits calculated for a signal-to-noise ratio of 3:1 are, on average, 1–4  $\mu\text{g/L}$ .

#### Solid-phase extraction

Liquid-chromatographic determination of PNMCs and their hydrolytic products was examined, and our aim in what follows was to present a method for preconcentrating the mixture of 12 solutes. SPE is presently the most extended method for preconcentrating solutes. Two SPE procedures are used, such as off-line and on-line.

In the present work, we investigated off-line SPE because of its operational flexibility and simplicity. It has been used for the preconcentration of carbaryl (35), carbofuran (36), and their respective metabolites. In addition, this procedure offers the opportunity to apply on-site field sampling and conservation of the analytes on the solid-phase material; this helps in stabilizing the labile carbamates. In fact, complete recovery for desethylatrazine and fenamiphos was observed in precolumns kept at  $-20^{\circ}\text{C}$  for 1 month when preconcentrating 2 mL of ground water spiked at 10  $\mu\text{g/L}$ . Degradation of fenamiphos and fenitrothion occurred in precolumns stored at  $4^{\circ}\text{C}$  and at room temperature after 1 month (37).

Furthermore, the stability of carbaryl and carbofuran stored on C18 cartridges at three different temperatures



**Fig. 5.** LC–UV chromatogram of a standard mixture containing 1 mg/L of carbaryl, 20 mg/L of baycarb, 10 mg/L of aminocarb, baygon, landrin, methiocarb, zectran, 2,3,5-trimethylphenol,  $\alpha$ -naphthol, 2-isopropoxyphenol, and benzofuranol in LC-grade water (b) registered at 220 nm. Peak numbers correspond to those in Table 4.

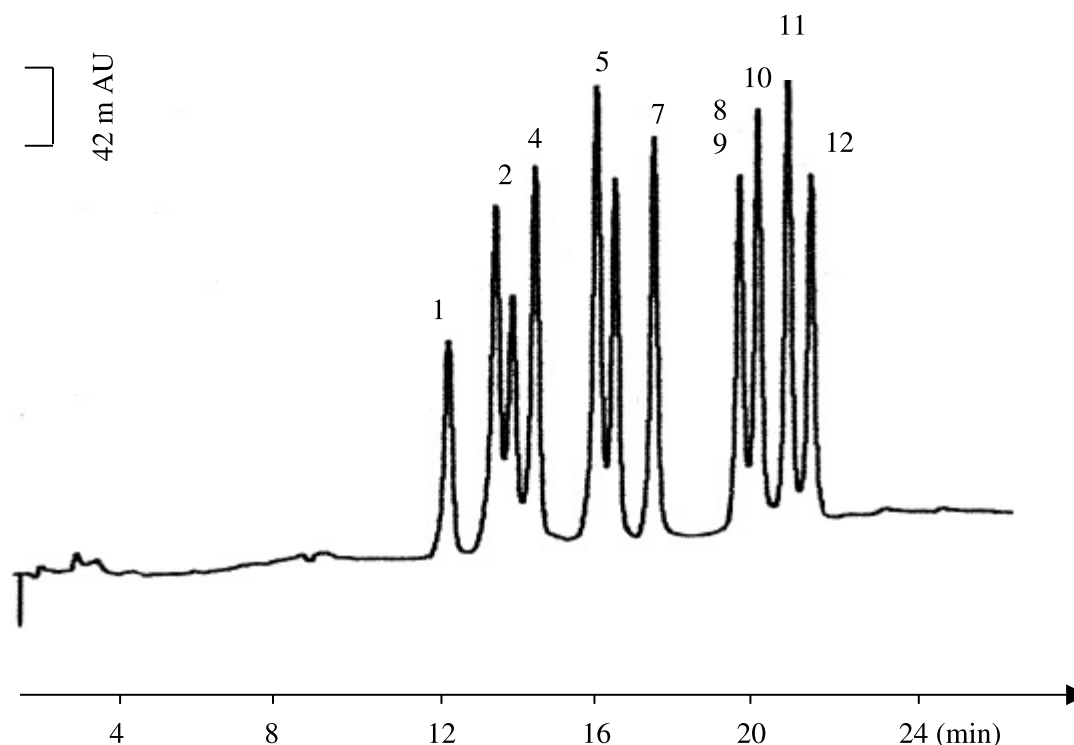


**Table 5.** Recoveries of carbamates and their degradation products in Milli-Q water at different sample volumes.

Carbamates and (or) degradation products	Recovery (RSD) <sup>a</sup> (%)			
	Volume (mL)			
	100	250	500	1000
Aminocarb	82 (5)	74 (6)	62 (6)	30 (7)
Baygon	86 (4)	80 (6)	70 (5)	44 (8)
Carbofuran	75 (5)	71 (8)	69 (6)	45 (10)
Benzofuranol	69 (6)	62 (7)	59 (6)	28 (5)
2,3,5-Trimethylphenol	75 (4)	69 (7)	57 (4)	46 (7)
$\alpha$ -Naphthol	78 (4)	70 (6)	59 (7)	30 (6)
Carbaryl	83 (7)	80 (6)	74 (7)	45 (10)
Landrin	80 (8)	74 (9)	68 (5)	37 (8)
2-Isopropoxyphenol	85 (6)	79 (8)	74 (6)	29 (7)
Methiocarb	90 (7)	82 (8)	77 (4)	45 (8)
Baycarb	78 (8)	73 (7)	65 (5)	38 (7)
Zectran	80 (5)	72 (6)	63 (4)	35 (6)

<sup>a</sup>Three replicate.

(–10, 4, and 20°C) during periods of 1 week to 1 month was examined. At 4°C and after 1 month recoveries were 67.33 and 72.24%, respectively, for carbaryl and carbofuran.

To determine the optimum conditions of the extraction process, several variables were optimized. The first parameter studied was the extraction solvent for the elution of the compounds retained in the C18 cartridges. A 100 mL volume of Milli-Q water spiked with standard pesticides at a level of 2  $\mu$ g/mL was passed through the cartridges. The cartridges were eluted with different volumes of acetonitrile or methanol. The best recovery was obtained with the second solvent for a volume of 5 mL.

Extraction was done with a blank of cartridges, to check for the presence of interferences, but none were found.

The next parameter was the sample volume preconcentrated onto the cartridges; the extraction process was carried out with 100, 250, 500, and 1000 mL of Milli-Q water spiked at 1  $\mu$ g/mL. The results of recovery against sample volume are given in Table 5.

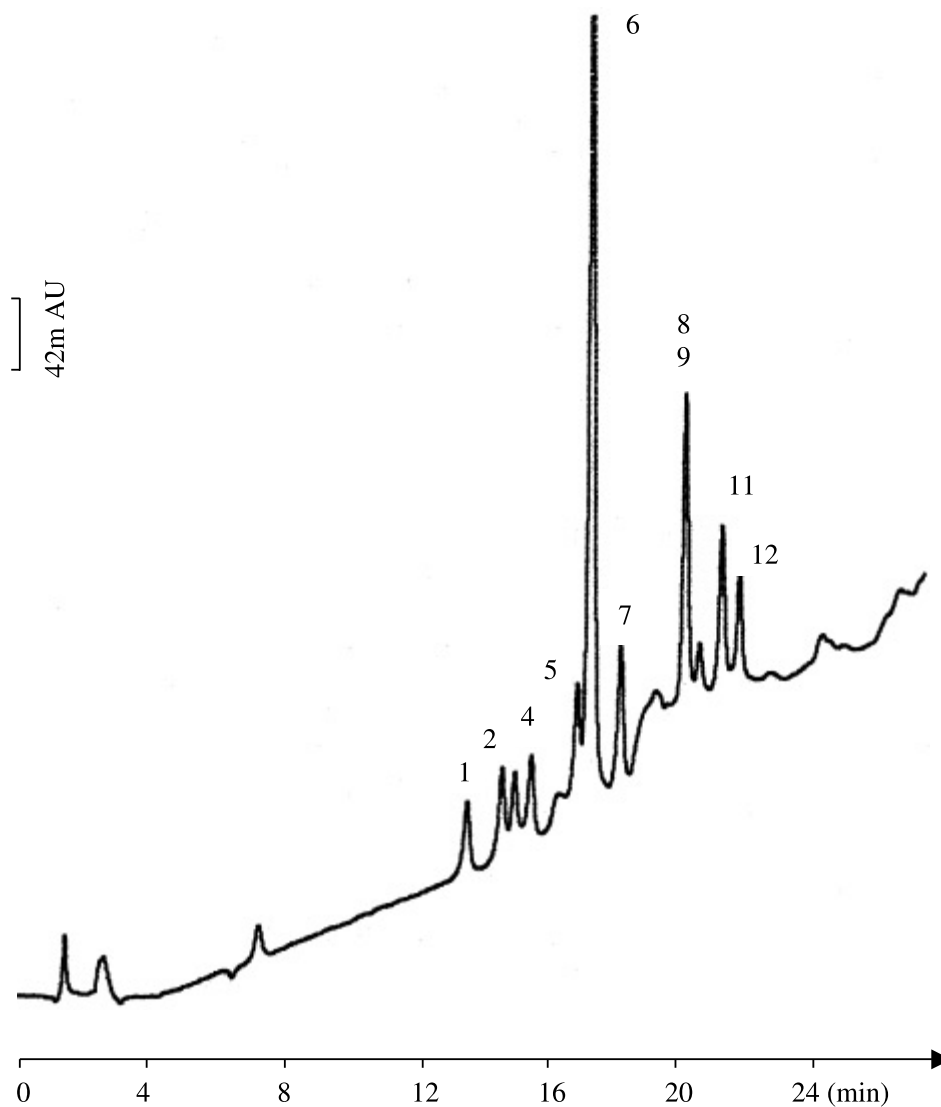
There was a significant decrease in the recovery of studied solutes when the sample volume passed from 100 to 1000 mL. So, 100 mL was chosen as the optimum volume.

The performance of the method for real samples was tested in tap and surface water samples; the results obtained



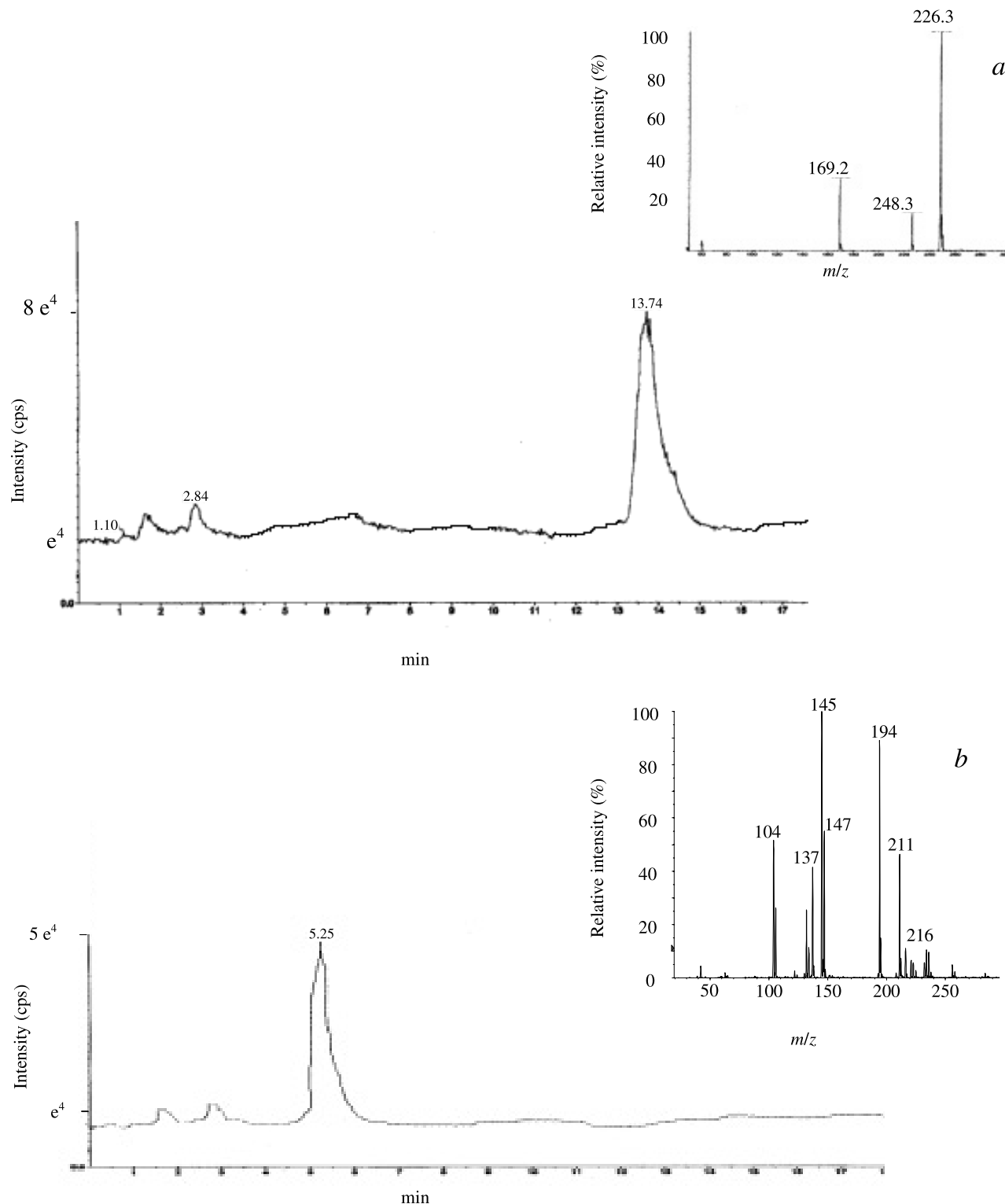
**Table 6.** Recoveries of carbamates and their degradation products added at two concentration levels to different water samples.

Carbamates and (or) degradation products	Recovery (RSD) <sup>a</sup> (%)		
	Drinking water <sup>b</sup>	River water <sup>b</sup>	River water <sup>c</sup>
Aminocarb	80 (4)	77 (7)	81 (9)
Baygon	82 (6)	79 (5)	83 (7)
Carbofuran	78 (2)	74 (8)	79 (8)
Benzofuranol	68 (3)	62 (3)	65 (4)
2,3,5-Trimethylphenol	75 (5)	71 (4)	74 (5)
$\alpha$ -Naphthol	77 (7)	72 (5)	73 (10)
Carbaryl	83 (8)	80 (6)	86 (5)
Landrin	84 (7)	79 (11)	85 (6)
2-Isopropoxyphenol	86 (2)	83 (3)	82 (8)
Methiocarb	79 (4)	76 (4)	84 (7)
Baycarb	77 (5)	74 (9)	80 (11)
Zectran	81 (3)	75 (3)	79 (3)

<sup>a</sup>Five replicate.<sup>b</sup>Spiking level 10  $\mu\text{g/L}$ .<sup>c</sup>Spiking level 5  $\mu\text{g/L}$ .**Fig. 6.** HPLC of surface water samples after 100 mL of a water sample fortified with eight PNMCs and four hydrolytic degradation products at 10  $\mu\text{g/L}$  on 1 g C18 cartridges. Peak numbers correspond to those in Table 4.



**Fig. 7.** SIM chromatograms and mass spectra of surface sample at 1 µg/L of methiocarb (a)  $m/z$  248; carbaryl (b)  $m/z$  224, in LC-ES-MS.



are given in Table 6. The samples were fortified with a standard mixture of eight PNMCS and four hydrolysis products at a fortification level of 10 µg/L. When a sample volume of 100 mL was passed through the SPE cartridges, the recoveries for tap water and surface water were, respectively, in the range of 68–86% (RSD 2–8%) and 62–83% (RSD 3–11%).

We should note that the highest recoveries for all compounds were obtained in tap water. A reduction in the extraction efficacy, as well as the formation of a solute–humic substance complex, can be owed to the presence of humic substances in surface water. The latter formation cannot be retained by adsorption on the solid phase considered.



**Table 7.** List of compound, molecular weights, and quantitation ions for SIM conditions.

Compound	Molecular weight	Quantitation ion ( <i>m/z</i> )
Aminocarb	208	231.2
Baygon	209	232.3
Carbofuran	221	244.2
Carbaryl	201	224.2
Landrin	193	216.2
Methiocarb	225	248.3
Baycarb	207	230.2
Zectran	222	223.2

Further experiments carried out with 100 mL samples spiked at 5 and 10 µg/L levels show essentially constant recovery and satisfactory RSD (3–11%).

A chromatogram of a 100 mL surface water sample at pH 7.4, fortified with eight parent PNMCS and four hydrolysis products at a concentration of 10 µg/L and extracted on 1 g C18 bonded silica cartridges, is shown in Fig. 6. The chromatogram is remarkably free from interfering peaks. With the optimized procedure, for the entire listed compound, minimum detectable concentrations (signal-to-noise ratio = 3:1) were in the range of 4–10 µg/L.

#### Analyses by LC–ES–MS

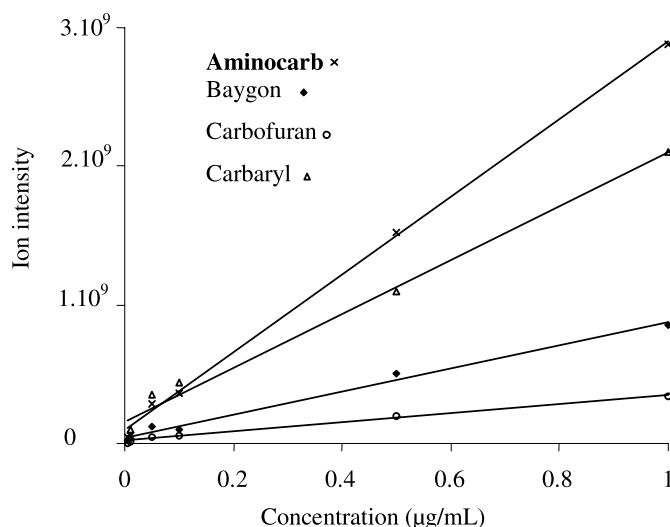
To improve sensitivity, the results obtained by LC–ES–MS (equipped with a triple quadrupole mass filter) were involved. MS data acquisition was performed by a time-scheduled, selected-ion monitoring (SIM) program. The quantitation ions chosen for SIM are listed in Table 7. Under the experimental conditions described in the Experimental section (Chromatographic conditions), no thermal degradation for target compounds was observed. The ion signals for the analytes considered were obtained when LC–ES–MS instrumentation was operated with a mobile phase described in the Experimental section. The LC–ES–MS spectrum of carbaryl and methiocarb in the experimental conditions proposed can be observed in Fig. 7. At 30 V of fragmentor voltage, ES in the positive mode produces three main ions corresponding to  $[M + Na]^+$ ,  $[M + H]^+$ , and  $[M + CH_3NCO]^+$ , e.g., for carbaryl, ES in the positive mode produces  $[M + Na]^+ = 224$ ,  $[M + H]^+ = 202$ , and  $[M + CH_3NCO]^+ = 145$ , then it can be deduced the soft ionization offered by the electrospray.

Calibrations graphs were obtained for different concentrations of analytes. The regression coefficients were >0.999 in all cases. The values found for the calibration in the graph show good linearity for all PNMCS (Fig. 8). The detection limits calculated for each pesticide range between 0.1 and 0.3 µg/L.

The same analysis was carried out for river water samples, and good linearity was also obtained for the same range. The limit of quantitation for the analytes ranged between 0.1 and 0.5 µg/L injected into the LC column from the extracts of the water river matrices.

#### Conclusion

A mixture of eight PNMCS and four of their hydrolysis products was studied by LC–UV and LC–ES–MS. Hydroly-

**Fig. 8.** Calibration graphs of carbaryl (Δ), carbofuran (○), aminocarb (×), and baygon (◆) obtained from standard solutions using time-scheduled SIM LC–ES–MS.

sis affects the degradation of PNMCS, so hydrolysis kinetics were investigated. In SPE–LC–UV, the analytes were enriched with 100 mL surface water samples on C18 cartridges eluted with methanol and separated by gradient LC on C18 analytical columns and detected by UV. Satisfactory recovery values (62–83%) were given. The quantitation limits of 12 compounds were 4–10 µg/L. LC–MS is highly sensitive (0.1–0.5 µg/L) and specific. Detection limits can be further enhanced using ES–MS–MS.

#### Acknowledgments

We would like to thank Doctor Jean Pierre Morizur (University Evry Val d'Essonne Paris) and his group for use of the LC–MS spectrometer and their laboratory assistance.

#### References

1. N.L. Wolfe, R.G. Zeep, and D.F. Paris. *Water Res.* **12**, 565 (1987).
2. J.R. Corbett, K. Wright, and A.C. Baillie. *The biochemical mode of action of pesticides*. 2nd ed. Academic Press, New York. 1984.
3. J. Jayaraman, L.P. Celino, K.H. Lee, R.B. Mohamed, J. Sun, N. Tayaputch, and Z. Zhang. *Water Air Soil Pollut.* **45**, 371 (1989).
4. N. Aharonson. *Pure Appl. Chem.* **59**, 1419 (1987).
5. S. Chiron and D. Barceló. *J. Chromatogr.* **645**, 125 (1993).
6. H.T. Kalinoski, B.W. Wright, and R.D. Smith. *Biomed. Environ. Mass Spectrom.* **13**, 33 (1986).
7. J.L. Bernal, J.J. Jiménez, J.M. Rivera, L. Toribo, and M.J. del Nozal. *J. Chromatogr. A*, **754**, 145 (1996).
8. A.J. Berry, D.E. Games, I.C. Mylchreest, J.R. Perkins, and S. Pleasances. *Biomed. Environ. Mass Spectrom.* **15**, 105 (1988).
9. S.C. Mc Ginnis and J. Sherma. *J. Liq. Chromatogr. Relat. Technol.* **17**, 151 (1994).
10. H. Susse and H. Muller. *Fresenius' J. Anal. Chem.* **352**, 470 (1995).
11. A. Farran, S. Ruiz, C. Serra, and M. Aguilar. *J. Chromatogr. A*, **737**, 109 (1996).



12. H. Kobayashi, K. Ohyama, N. Tomiyama, Y. Jimbo, O. Matano, and S. Soto. *J. Chromatogr. A*, **643**, 197 (1993).
13. A. Tanabe, H. Mitobe, K. Kawata, and M. Sakai. *J. Chromatogr. A*, **754**, 159 (1996).
14. I. Liska and J. Slobodnik. *J. Chromatogr. A*, **733**, 235 (1996).
15. S.S. Yang, A.I. Goldsmith, and I. Smetena. *J. Chromatogr. A*, **754**, 3 (1996).
16. R.A. Hoodless, J.A. Sidwell, J.C. Kinner, and R.D. Treble. *J. Chromatogr. A*, **166**, 279 (1978).
17. A. de Kok, M. Hiemstra, and U.A.Th. Brinkman. *J. Chromatogr. A*, **623**, 265 (1992).
18. B. Mc Garvey. *J. Chromatogr. A*, **642**, 89 (1993).
19. A.P. Bruins. *Trends Anal. Chem.* **13**, 37 (1994).
20. A.P. Bruins. *Trends Anal. Chem.* **13**, 81 (1994).
21. D. Barceló and M.C. Henion. *Anal. Chim. Acta*, **318**, 1 (1995).
22. D. Barceló. *Anal. Chim. Acta*, **263**, 1 (1992).
23. J. Slobodnik, B.L.K.M. Van Baar, and U.A.Th. Brinkman. *J. Chromatogr. A*, **703**, 81 (1995).
24. A. Di Corcia, A. Crescenzi, A. Lagana, and E. Sebastiani. *J. Agric. Food Chem.* **44**, 1930 (1996).
25. L. Lacassie, M.D. Dreyfuss, J.L. Daguet, M. Vignaud, D. Marquet, and G. Lachatre. *J. Chromatogr. A*, **830**, 135 (1999).
26. C. Aguilar, I. Ferrer, F. Borrull, R.M. Marcé, and D. Barceló. *J. Chromatogr. A*, **794**, 147 (1998).
27. H. Itoh, S. Kawasaki, and J. Tadano. *J. Chromatogr. A*, **754**, 61 (1996).
28. H. Subik and R. Jeannot. *J. Chromatogr. A*, **818**, 197 (1998).
29. J.M. Soriano, B. Jiménez, G. Font, and J.C. Moltó. *Crit. Rev. Anal. Chem.* **31**, 19 (2001).
30. U.S. E.P.A. Method 531, EPA-600/4-85/054. United States Environmental Protection Agency, Washington, D.C. 1985.
31. S. Guenu and M.C. Henion. *J. Chromatogr. A*, **725**, 57 (1996).
32. K.M. Hill, R.H. Hollowel, and Dal Cortivo. *Anal. Chem.* **56**, 2465 (1984).
33. M.W. Dong, F.L. Vandemark, W.M. Reuter, and M.V. Pickering. *Am. Environ. Lab.* **2**, 14 (1990).
34. K.W. Edgell, L.A. Biederman, and J.E. Ionbottom. *J. Assoc. Off. Anal. Chem.* **39**, 309 (1991).
35. J.R. Strait, G.C. Thornwall, and M. Ehrich. *J. Agric. Food Chem.* **72**, 845 (1989).
36. K.W. Beauchamp, Jr., D.D.W. Liu, and E.J. Kikta, Jr. *J. Assoc. Off. Anal. Chem.* **72**, 845 (1989).
37. I. Ferrer and D. Barceló. *J. Chromatogr. A*, **778**, 161 (1997).



# Cyclic voltammetric studies of tris(alkylisocyanide)-bis(triarylphosphine)cobalt(II) and tris-(alkylisocyanide)bis(triarylphosphine)cobalt(I) complexes exhibiting synthetic interconvertability

Jamil Ahmad, Florence Bothata-Nareetsile, and Clifford A.L. Becker

**Abstract:** Nine pairs of corresponding  $[\text{Co}^{\text{I}}(\text{CNR})_3(\text{PR}'_3)_2]\text{X}$ ,  $[\text{Co}^{\text{II}}(\text{CNR})_3(\text{PR}'_3)_2]\text{X}_2$  complexes — where  $\text{X} = \text{ClO}_4$ ,  $\text{BF}_4$ ;  $\text{CNR} = \text{CNCMe}_3$ ,  $\text{CNCHMe}_2$ ,  $\text{CNC}_6\text{H}_{11}$ ,  $\text{CNCH}_2\text{Ph}$ ;  $\text{PR}'_3 = \text{PPh}_3$ ,  $\text{P}(\text{C}_6\text{H}_4\text{Me-}p)_3$ ,  $\text{P}(\text{C}_6\text{H}_4\text{OMe-}p)_3$  — have been studied using cyclic voltammetry in  $\text{CH}_3\text{CN}$  solutions. All cycles are reversible, and  $E_{1/2}$  for the  $\text{Co}(\text{I})$  complexes, initially oxidized, are within experimental error identical to  $E_{1/2}$  values for the corresponding  $\text{Co}(\text{II})$  complexes, initially reduced.  $E_{1/2}$  values are strongly dependent on the triarylphosphine ligand, decreasing in the order  $\text{PPh}_3 > > \text{P}(\text{C}_6\text{H}_4\text{Me-}p)_3 > \text{P}(\text{C}_6\text{H}_4\text{OMe-}p)_3$ , and weakly dependent on the alkylisocyanide ligand, decreasing in the order  $\text{CNCH}_2\text{Ph} > \text{CNCMe}_3 > \text{CNC}_6\text{H}_{11} \geq \text{CNCHMe}_2$ . Solution  $\nu(\text{N}\equiv\text{C})$  IR patterns reveal that the  $[\text{Co}^{\text{I}}(\text{CNR})_3(\text{PR}'_3)_2]\text{X}$  complexes do not have regular trigonal bipyramidal coordination, their structure being determined by the particular CNR ligand, while the  $[\text{Co}^{\text{II}}(\text{CNR})_3(\text{PR}'_3)_2]\text{X}_2$  complexes, specifically in  $\text{CF}_3\text{CH}_2\text{OH}$ , appear to have regular trigonal bipyramidal coordination.

**Key words:** cyclic voltammetry, cobalt(I) complexes, cobalt(II) complexes, alkylisocyanide ligands, triarylphosphine ligands.

**Résumé :** Utilisant la voltamétrie cyclique on a étudié neuf paires de complexes de  $[\text{Co}^{\text{I}}(\text{CNR})_3(\text{PR}'_3)_2]\text{X}$ , et de  $[\text{Co}^{\text{II}}(\text{CNR})_3(\text{PR}'_3)_2]\text{X}_2$  dans lesquels  $\text{X} = \text{ClO}_4$ ,  $\text{BF}_4$ ;  $\text{CNR} = \text{CNCMe}_3$ ,  $\text{CNCHMe}_2$ ,  $\text{CNC}_6\text{H}_{11}$ ,  $\text{CNCH}_2\text{Ph}$ ;  $\text{PR}'_3 = \text{PPh}_3$ ,  $\text{P}(\text{C}_6\text{H}_4\text{Me-}p)_3$ ,  $\text{P}(\text{C}_6\text{H}_4\text{OMe-}p)_3$ . Tous les cycles sont réversibles et les valeurs de  $E_{1/2}$  pour les complexes de  $\text{Co}^{\text{I}}$ , préalablement oxydés sont, à l'intérieur des erreurs expérimentales, identiques aux valeurs de  $E_{1/2}$  des complexes correspondant de  $\text{Co}^{\text{II}}$  préalablement réduits. Les valeurs de  $E_{1/2}$  dépendent fortement du ligand triarylphosphine et décroissent dans l'ordre :  $\text{PPh}_3 > > \text{P}(\text{C}_6\text{H}_4\text{Me-}p)_3 > \text{P}(\text{C}_6\text{H}_4\text{OMe-}p)_3$ ; ces valeurs également dépendent faiblement du ligand alkylisocyanure et décroissent dans l'ordre :  $\text{CNCH}_2\text{Ph} > \text{CNCMe}_3 > \text{CNC}_6\text{H}_{11} \geq \text{CNCHMe}_2$ . L'allure des spectres IR  $\nu(\text{N}\equiv\text{C})$  révèle que les complexes  $[\text{Co}^{\text{I}}(\text{CNR})_3(\text{PR}'_3)_2]\text{X}$  n'ont pas une coordination bipyramidale trigonale régulière, la structure étant déterminée par le ligand particulier CNR, tandis que les complexes  $[\text{Co}^{\text{II}}(\text{CNR})_3(\text{PR}'_3)_2]\text{X}_2$  spécifiquement dans le  $\text{CF}_3\text{CH}_2\text{OH}$  semblent avoir une coordination bipyramidale trigonale régulière.

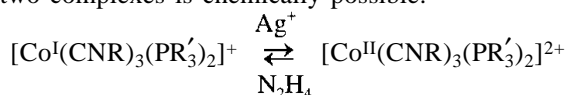
**Mots clés :** voltamétrie cyclique, complexes de cobalt (I), complexes de cobalt (II), ligands alkylisocyanures, ligands triarylphosphines.

[Traduit par la Rédaction]

## Introduction

Reactions of triarylphosphines with cobalt(II)-alkylisocyanide complexes have been characterized by reduction – ligand-substitution, producing disubstituted  $\text{Co}(\text{I})$  complexes,  $[\text{Co}^{\text{I}}(\text{CNR})_3(\text{PR}'_3)_2]\text{X}$  ( $\text{X} = \text{ClO}_4$ ,  $\text{BF}_4$ ) in good yields (1–5). Cyclic voltammograms of some tris(alkylisocyanide)bis(triarylphosphine)cobalt(I) complexes showed quasi-reversible behavior for oxidative cycles (5), suggesting the existence of stable  $[\text{Co}^{\text{II}}(\text{CNR})_3(\text{PR}'_3)_2]^{2+}$  species, however, and a number

of tris(alkylisocyanide)bis(triarylphosphine)cobalt(II) complexes have since been synthesized (6). The pairs of corresponding  $\text{Co}(\text{I})$  and  $\text{Co}(\text{II})$  complexes,  $[\text{Co}^{\text{I}}(\text{CNR})_3(\text{PR}'_3)_2]\text{X}$  and  $[\text{Co}^{\text{II}}(\text{CNR})_3(\text{PR}'_3)_2]\text{X}_2$ , having the same alkylisocyanide (CNR) and triarylphosphine ( $\text{PR}'_3$ ) ligands show what may be termed “regular behavior” in that mutual interconversion of the two complexes is chemically possible:



This is opposed to “irregular behavior” for cases where only the  $\text{Co}(\text{I})$  or only the  $\text{Co}(\text{II})$  complex has been synthesized and where it has not been possible to isolate the corresponding  $\text{Co}(\text{II})$  or  $\text{Co}(\text{I})$  complex, respectively.  $\text{Co}(\text{I})$  complexes showing clearly irreversible cyclic voltammograms, for example, cannot be oxidized to the corresponding  $\text{Co}(\text{II})$  complexes with  $\text{AgClO}_4$  or  $\text{AgBF}_4$  (6).

In this paper, corresponding pairs of  $\text{Co}(\text{I})$  and  $\text{Co}(\text{II})$  complexes are investigated using cyclic voltammetry; cycles

Received 20 November 2002. Published on the NRC Research Press Web site at <http://canjchem.nrc.ca> on 12 August 2003.

J. Ahmad, F. Bothata-Nareetsile, and C.A.L. Becker.<sup>1</sup>  
Department of Chemistry, University of Botswana,  
P/Bag 0022, Gaborone, Botswana.

<sup>1</sup>Corresponding author (e-mail: [Beckerca@mopipi.ub.bw](mailto:Beckerca@mopipi.ub.bw)).



for the Co(I) complexes were initially scanned oxidatively, and cycles for the Co(II) complexes were initially scanned reductively. If results of these two scans are equivalent, within experimental error, this should confirm that the Co(II) species observed in the voltammograms of the Co(I) species are indeed the recently synthesized  $[\text{Co}^{\text{II}}(\text{CNR})_3(\text{PR}'_3)_2]\text{X}_2$  complexes. Since there are a limited number of known series of transition metal complexes, differing only in the oxidation state of the metal, this should be a worthwhile study.

## Results

The equilibrium cyclic voltammetric data for the  $[\text{Co}^{\text{I}}(\text{CNR})_3(\text{PR}'_3)_2]\text{X}$ ,  $[\text{Co}^{\text{II}}(\text{CNR})_3(\text{PR}'_3)_2]\text{X}_2$  corresponding pairs of complexes are summarized in Table 1. The equilibrium scans are quite similar in shape to the respective first scans and have quite close  $E$  values. A characteristic set of cyclic voltammograms (for  $[\text{Co}^{\text{I}}(\text{CNC}_6\text{H}_{11})_3(\text{PPh}_3)_2]\text{ClO}_4$ ) at various scan rates is pictured in Fig. 1. The dependence of the peak currents from these voltammograms on the scan rate is shown in Fig. 2. This dependence was used as a diagnostic tool to decide if the electrochemical processes were reversible. The  $\nu(\text{N}\equiv\text{C})$  IR values for the five-coordinate Co(I) and Co(II) complexes in  $\text{CF}_3\text{CH}_2\text{OH}$ ,  $\text{CH}_3\text{NO}_2$ , and  $\text{CH}_2\text{Cl}_2$  are tabulated in Table 2, and the four distinct patterns for the  $[\text{Co}^{\text{I}}(\text{CNR})_3(\text{PR}'_3)_2]\text{X}$  complexes are pictured in Fig. 3.

### Interpretation of the voltammograms

The plots of the peak current vs. the square root of the scan rate are linear for all of the complexes (see Fig. 2 for compound (cpd) 9). The peak potentials also do not change significantly with the scan rate. According to these criteria, the electrode processes are reversible (7–9). This system has a high solution resistance between the working and the reference electrode because of the non-aqueous nature of the solvent and the low concentration (0.05 M) of the background electrolyte, which is necessitated by its low solubility in  $\text{CH}_3\text{CN}$ . The measured potential is increased by an amount equal to this ohmic ( $iR$ ) drop. The net result is an increase in the peak separation between the anodic and cathodic peak potential values (8). This “ohmic distortion” contributes to the apparent nonconformity of the system to a third criterion of reversibility, namely the requirement that the peak separation be around 57 mV.

Another source of this discrepancy for high  $\Delta E$  values is the junction potential created across the ion bridge between the reference electrode and the sample solution. This is caused by the difference in the diffusion coefficients of the cations and the anions of the supporting electrolyte (10). Measurements made on ferrocene–ferrocenium, which is a known reversible couple, under conditions identical to those reported herein gave a peak separation of 110 mV at a  $0.1 \text{ V s}^{-1}$  scan rate, thereby confirming that the observed peak separation is inherent in the experimental conditions and not characteristic of the redox couple.

### Interpretation of the $E_{1/2}$ values

Experimental error of  $\pm 10 \text{ mV}$  in measurement of the  $E_{1/2}$  values was estimated by repetitive scans of the same samples. Within this margin of error, the  $E_{1/2}$  values measured

for the Co(I) complexes, initially oxidized, and the  $E_{1/2}$  values measured for the Co(II) complexes, initially reduced, are essentially identical (see Table 1). This experimental fact, observed for nine pairs of corresponding Co(I), Co(II) complexes, would seem to confirm that the recently synthesized  $[\text{Co}^{\text{II}}(\text{CNR})_3(\text{PR}'_3)_2]\text{X}_2$  complexes are indeed the same Co(II) species observed in cyclic voltammetric oxidation of the previously known  $[\text{Co}^{\text{I}}(\text{CNR})_3(\text{PR}'_3)_2]\text{X}$  complexes.

Alternately, these Co(II) complexes are reduced by cyclic voltammetry to the same Co(I) complexes that are obtained by chemical reduction with hydrazine or that served as starting materials for synthesis of the Co(II) complexes. Generation of the same chemical species electrolytically and by  $\text{N}_2\text{H}_4$  reduction –  $\text{Ag}^+$  oxidation is thus confirmed.

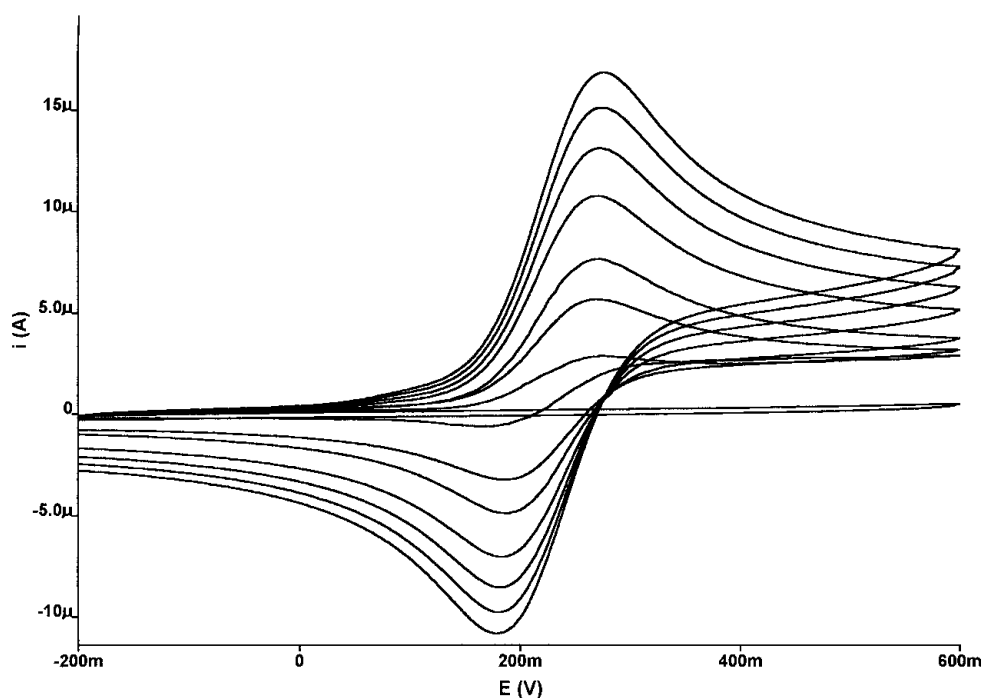
The  $E_{1/2}$  dependence on variation of the  $\text{PR}'_3$  ligand with respect to constant CNR ligands for both Co(I) and Co(II) complexes is very pronounced, with the definite trend in decreasing  $E_{1/2}$  values,  $\text{PPh}_3 \gg \text{P}(\text{C}_6\text{H}_4\text{Me-}p)_3 > \text{P}(\text{C}_6\text{H}_4\text{OMe-}p)_3$ . This is expected since *para*-substituents with increasing electron-donating ability should make the phosphines both stronger  $\sigma$ -donating and less  $\pi^*$ -accepting, favoring stabilization of Co(II) over Co(I). This trend also correlates with the ease or difficulty of synthesizing the Co(II) complexes as opposed to isolating only Co(I). Decreasing Co(II) and (or) increasing Co(I) stability for the species  $[\text{Co}(\text{CNR})_3(\text{PR}'_3)_2]^{n+}$  has been observed to be favored by  $\text{P}(\text{C}_6\text{H}_4\text{NMe}_2-p)_3 > \text{P}(\text{C}_6\text{H}_4\text{OMe-}p)_3 > \text{P}(\text{C}_6\text{H}_4\text{Me-}p)_3 > \text{PPh}_3 > \text{P}(\text{C}_6\text{H}_4\text{F-}p)_3 \approx \text{P}(\text{C}_6\text{H}_4\text{Cl-}p)_3 > \text{P}(\text{C}_6\text{H}_4\text{CF}_3-p)_3$  (6, 11), this trend running to both extremes.  $[\text{Co}^{\text{I}}(\text{CNCMe}_3)_3\{\text{P}(\text{C}_6\text{H}_4\text{NMe}_2-p)_3\}_2]\text{ClO}_4$ , prepared by  $\text{N}_2\text{H}_4$  reduction in  $\text{CH}_2\text{Cl}_2$  of the initially isolated  $[\text{Co}^{\text{II}}(\text{CNCMe}_3)_3\{\text{P}(\text{C}_6\text{H}_4\text{NMe}_2-p)_3\}_2](\text{ClO}_4)_2$ , for example, spontaneously oxidizes back to the Co(II) complex in  $\text{CF}_3\text{CH}_2\text{OH}$  solution (11), while  $[\text{Co}^{\text{I}}(\text{CNCMe}_3)_3(\text{PR}'_3)_2]\text{ClO}_4$  complexes with  $\text{PR}'_3 = \text{P}(\text{C}_6\text{H}_4\text{F-}p)_3$ ,  $\text{P}(\text{C}_6\text{H}_4\text{Cl-}p)_3$ , and  $\text{P}(\text{C}_6\text{H}_4\text{CF}_3-p)_3$  are not oxidized by  $\text{AgClO}_4$  (6). These latter Co(I) complexes show irreversible voltammograms under oxidation (5). No substantial difference in ease of synthesis for  $[\text{Co}^{\text{II}}(\text{CNR})_3(\text{PPh}_3)_2]\text{X}_2$  vs.  $[\text{Co}^{\text{II}}(\text{CNR})_3\{\text{P}(\text{C}_6\text{H}_4\text{Me-}p)_3\}_2]\text{X}_2$  complexes sufficient to justify these  $E_{1/2}$  values has been observed, but the Hammett  $\sigma$  constants do indicate a much larger difference between reactivity involving a  $-\text{C}_6\text{H}_5$  group and the  $-\text{C}_6\text{H}_4\text{Me-}p$  group than between  $-\text{C}_6\text{H}_4\text{Me-}p$  and  $-\text{C}_6\text{H}_4\text{OMe-}p$  groups (12), so this may be reflected in the  $E_{1/2}$  values.

The  $E_{1/2}$  dependence on variation of the CNR ligand with respect to constant  $\text{PR}'_3$  ligands is relatively small but seems to follow the trend in decreasing  $E_{1/2}$  values,  $\text{CNCH}_2\text{Ph} > \text{CNCMe}_3 > \text{CNC}_6\text{H}_{11} > \text{CNCHMe}_2$ . This trend parallels the decreasing ability of the alkylisocyanide substituent to stabilize a  $\delta^+$  charge on the C atom adjacent to the isocyanide functional group. Analogous variation of  $E_{1/2}$  values with alkylisocyanide ligands was reported by Dart et al. (2) for  $[\text{Co}(\text{CNR})_3(\text{PPh}_3)_2]\text{PF}_6$  complexes (measured in  $\text{CH}_2\text{Cl}_2$  solution), with  $E_{1/2}$  values decreasing in the order  $\text{R} = t\text{-Bu}$  (0.29 V)  $> i\text{-Pr}$  (0.20 V)  $> \text{Me}$  (0.12 V).  $E_{1/2}$  values reported for  $[\text{M}(\text{CO})_4\text{L}_2]$  complexes (where  $\text{M} = \text{Cr}, \text{Mo}, \text{W}$ ;  $\text{L} = \text{CNCHMe}_2, \text{CNCMe}_3$ ), however, show very little difference (13). Previous work from this laboratory (5) indicated a narrow range of  $E_{1/2}$  values for variation in CNR ligands (i.e., 0.20–0.25 V), but the trend of  $\text{CNCMe}_3 > \text{CNCHMe}_2$  values was detected. For  $[\text{PtL}_2(\text{CNR})\text{Me}]^+$  ( $\text{L} = \text{PMePh}_2, \text{PMe}_2\text{Ph}$ )



**Table 1.** Cyclic voltammetric results for corresponding pairs of tris(alkylisocyanide)bis(triarylphosphine)cobalt(I) and tris(alkylisocyanide)bis(triarylphosphine)cobalt(II) complexes in acetonitrile solution at 0.1 V s<sup>-1</sup> scan rate.

	Compound	$E_{\text{oxidation}}$ (mV vs. Ag–AgCl)	$E_{\text{reduction}}$ (mV)	$E_{1/2}$	$\Delta E$
1	[Co <sup>I</sup> (CNCHMe <sub>2</sub> ) <sub>3</sub> {P(C <sub>6</sub> H <sub>4</sub> OMe- <i>p</i> ) <sub>3</sub> } <sub>2</sub> ][ClO <sub>4</sub> ]	155	70	113	85
2	[Co <sup>II</sup> (CNCHMe <sub>2</sub> ) <sub>3</sub> {P(C <sub>6</sub> H <sub>4</sub> OMe- <i>p</i> ) <sub>3</sub> } <sub>2</sub> ](ClO <sub>4</sub> ) <sub>2</sub>	163	96	130	67
3	[Co <sup>I</sup> (CNC <sub>6</sub> H <sub>11</sub> ) <sub>3</sub> {P(C <sub>6</sub> H <sub>4</sub> OMe- <i>p</i> ) <sub>3</sub> } <sub>2</sub> ][ClO <sub>4</sub> ]	179	116	148	63
4	[Co <sup>II</sup> (CNC <sub>6</sub> H <sub>11</sub> ) <sub>3</sub> {P(C <sub>6</sub> H <sub>4</sub> OMe- <i>p</i> ) <sub>3</sub> } <sub>2</sub> ](ClO <sub>4</sub> ) <sub>2</sub>	179	109	144	70
5	[Co <sup>I</sup> (CNCMe <sub>3</sub> ) <sub>3</sub> {P(C <sub>6</sub> H <sub>4</sub> OMe- <i>p</i> ) <sub>3</sub> } <sub>2</sub> ][ClO <sub>4</sub> ]	193	126	160	67
6	[Co <sup>II</sup> (CNCMe <sub>3</sub> ) <sub>3</sub> {P(C <sub>6</sub> H <sub>4</sub> OMe- <i>p</i> ) <sub>3</sub> } <sub>2</sub> ](ClO <sub>4</sub> ) <sub>2</sub>	207	137	172	70
7	[Co <sup>I</sup> (CNCHMe <sub>2</sub> ) <sub>3</sub> (PPh <sub>3</sub> ) <sub>2</sub> ][ClO <sub>4</sub> ]	246	183	215	63
8	[Co <sup>II</sup> (CNCHMe <sub>2</sub> ) <sub>3</sub> (PPh <sub>3</sub> ) <sub>2</sub> ](ClO <sub>4</sub> ) <sub>2</sub>	253	175	214	78
9	[Co <sup>I</sup> (CNC <sub>6</sub> H <sub>11</sub> ) <sub>3</sub> (PPh <sub>3</sub> ) <sub>2</sub> ][ClO <sub>4</sub> ]	267	190	229	77
10	[Co <sup>II</sup> (CNC <sub>6</sub> H <sub>11</sub> ) <sub>3</sub> (PPh <sub>3</sub> ) <sub>2</sub> ](ClO <sub>4</sub> ) <sub>2</sub>	270	193	232	77
11	[Co <sup>I</sup> (CNCMe <sub>3</sub> ) <sub>3</sub> (PPh <sub>3</sub> ) <sub>2</sub> ][ClO <sub>4</sub> ]	295	218	257	77
12	[Co <sup>II</sup> (CNCMe <sub>3</sub> ) <sub>3</sub> (PPh <sub>3</sub> ) <sub>2</sub> ](ClO <sub>4</sub> ) <sub>2</sub>	284	200	242	84
13	[Co <sup>I</sup> (CNCH <sub>2</sub> Ph) <sub>3</sub> (PPh <sub>3</sub> ) <sub>2</sub> ][BF <sub>4</sub> ]	298	235	267	63
14	[Co <sup>II</sup> (CNCH <sub>2</sub> Ph) <sub>3</sub> (PPh <sub>3</sub> ) <sub>2</sub> ](BF <sub>4</sub> ) <sub>2</sub>	312	231	272	81
15	[Co <sup>I</sup> (CNCHMe <sub>2</sub> ) <sub>3</sub> {P(C <sub>6</sub> H <sub>4</sub> Me- <i>p</i> ) <sub>3</sub> } <sub>2</sub> ][ClO <sub>4</sub> ]	204	105	155	99
16	[Co <sup>II</sup> (CNCHMe <sub>2</sub> ) <sub>3</sub> {P(C <sub>6</sub> H <sub>4</sub> Me- <i>p</i> ) <sub>3</sub> } <sub>2</sub> ](ClO <sub>4</sub> ) <sub>2</sub>	207	109	158	98
17	[Co <sup>I</sup> (CNC <sub>6</sub> H <sub>11</sub> ) <sub>3</sub> {P(C <sub>6</sub> H <sub>4</sub> Me- <i>p</i> ) <sub>3</sub> } <sub>2</sub> ][ClO <sub>4</sub> ]	225	112	169	113
18	[Co <sup>II</sup> (CNC <sub>6</sub> H <sub>11</sub> ) <sub>3</sub> {P(C <sub>6</sub> H <sub>4</sub> Me- <i>p</i> ) <sub>3</sub> } <sub>2</sub> ](ClO <sub>4</sub> ) <sub>2</sub>	227	133	180	94

**Fig. 1.** Cyclic voltammograms of [Co<sup>I</sup>(CNC<sub>6</sub>H<sub>11</sub>)<sub>3</sub>(PPh<sub>3</sub>)<sub>2</sub>][ClO<sub>4</sub>], cpd 9 (1 mM in CH<sub>3</sub>CN), with 0.05 M tetrabutylammonium hexafluorophosphate background electrolyte. The flat (innermost) trace is for the background electrolyte only, at a scan rate of 0.1 V s<sup>-1</sup>. The other curves are, in order, for scan rates of 0.01, 0.05, 0.1, 0.2, 0.3, 0.4, and 0.5 V s<sup>-1</sup>.

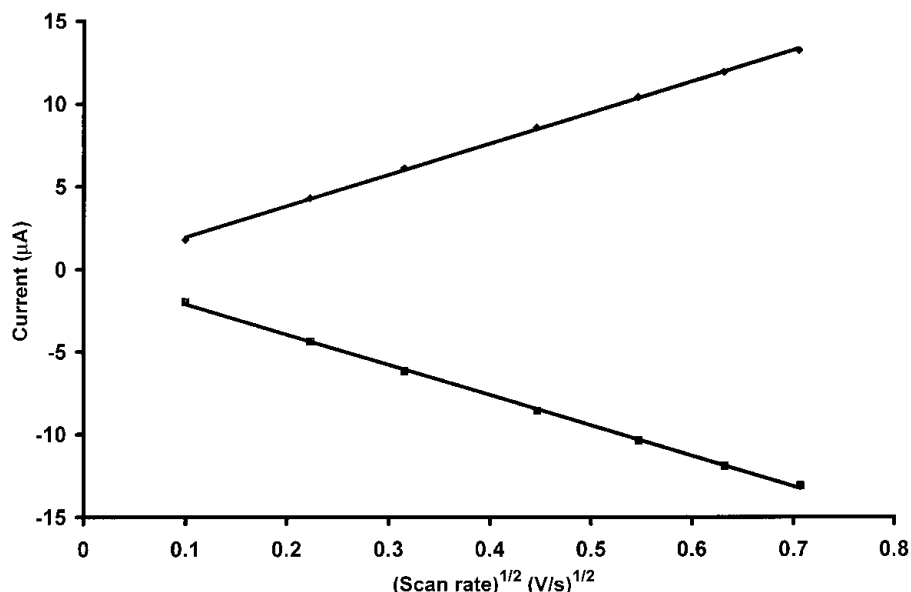
it is suggested that the  $\sigma$ -donor strength of CNR is essentially independent of the inductive properties of R, making variation in  $E_{1/2}$  dependent only on the relatively slight differences in  $\pi^*$ -accepting ability of the CNR (14).

Strong  $E_{1/2}$  dependence on the triarylphosphine ligands, with relatively little sensitivity to the alkylisocyanide ligands, has been attributed to effective  $\sigma$ -donation from the

phosphines in axial positions and ineffective  $\sigma$ -donation by the alkylisocyanides in equatorial positions of trigonal bipyramidal coordination in the Co(I) complexes (5). For diamagnetic  $d^8$  Co(I) complexes in trigonal bipyramidal coordination, the electronic configuration of  $(d_{xz})^2(d_{yz})^2(d_{xy})^2(d_{x^2-y^2})^2$  should hinder  $\sigma$ -donation from the equatorial ligands (i.e., the alkylisocyanides) while allowing effective  $\sigma$ -donation



**Fig. 2.** Plots of anodic and cathodic currents vs. square root of scan rate for cpd 9 (i.e.,  $[\text{Co}^{\text{I}}(\text{CNC}_6\text{H}_{11})_3(\text{PPh}_3)_2]\text{ClO}_4$ ) from the voltammograms in Fig. 1.



from the axial ligands (i.e., the triarylphosphines) by electron donation into the empty  $3d_{2z^2-x^2-y^2}$  orbital on the Co(I) (5). Possibly spectral data can provide insight into this question.

#### Interpretation of solution $\nu(\text{N}\equiv\text{C})$ IR patterns

In previous cyclic voltammetric studies of five-coordinate Co(I) complexes, when quasi-reversible behavior was assigned on the basis of  $\Delta E$  values exceeding 57 mV, two alternate explanations were offered for quasi-reversibility. One explanation was that Co(I) in a regular trigonal bipyramidal (TBP) coordination is oxidized to Co(II) in a regular TBP structure that rapidly undergoes chemical change to a square pyramidal (SP) solution structure of  $C_{2v}$  symmetry (15). The other explanation was that Co(I) in a distorted TBP coordination is oxidized to Co(II) in a regular TBP structure (5). The  $\nu(\text{N}\equiv\text{C})$  IR patterns in the solid state (i.e., Nujol mull) are significantly different for the Co(I) (3–5) and Co(II) (6, 16) complexes, but solution structures are more relevant in this study. Solution structures for  $[\text{Co}^{\text{I}}(\text{CNR})_3(\text{PR}'_3)_2]^+$  species in general have been considered only approximately TBP, the strongest evidence for deviation from rigorous ( $D_{3h}$ ) TBP coordination coming from combined IR and Raman data for the arylisocyanide complexes (17). Spectral data for the Co(I) complexes in this paper were measured over a period of years on different spectrophotometers, so solution IR measurements have now been repeated on superior instrumentation under identical conditions. These data, in Table 2, reveal trends in the  $\nu(\text{N}\equiv\text{C})$  IR patterns hitherto unrecognized.

The shape of the  $\nu(\text{N}\equiv\text{C})$  IR patterns for these  $[\text{Co}^{\text{I}}(\text{CNR})_3(\text{PR}'_3)_2]\text{X}$  complexes in solution is unique for each alkylisocyanide, but independent of the particular triarylphosphine and solvent used. Figure 3 illustrates these four distinct patterns, corresponding to Co(I) complexes with the  $\text{CNC}_6\text{H}_{11}$ ,  $\text{CNCH}_2\text{Ph}$ ,  $\text{CNCHMe}_2$ , and  $\text{CNCMe}_3$  ligands, respectively (top to bottom). The patterns for  $\text{CNCMe}_3$  (seen for cpd 5, 11) and  $\text{CNCHMe}_2$  (cpd 1, 7, 15) are clearly in-

compatible with  $D_{3h}$  symmetry (one,  $E'$ , allowed band), and even  $\text{CNC}_6\text{H}_{11}$  (cpd 3, 9, 17) suggests some distortion in the solution state. Only  $\text{CNCH}_2\text{Ph}$  (represented by one complex, 13) could be assigned  $D_{3h}$  symmetry and only if the weak, albeit persistent, higher energy shoulder is ignored. Solution structures of the  $[\text{Co}^{\text{I}}(\text{CNR})_3(\text{PR}'_3)_2]\text{X}$  complexes cannot be assumed to be regular TBP.

The shapes of the  $\nu(\text{N}\equiv\text{C})$  IR patterns for the  $[\text{Co}^{\text{II}}(\text{CNR})_3(\text{PR}'_3)_2]\text{X}_2$  complexes in solution are distinctly different from those for the Co(I) complexes and seem to vary mostly depending on solvent. In  $\text{CF}_3\text{CH}_2\text{OH}$  almost all spectra exhibit a lone strong band, expected for  $D_{3h}$  (regular) TBP structure (see Table 2). Cpds 12 and 14 in  $\text{CF}_3\text{CH}_2\text{OH}$  and many Co(II) complexes in  $\text{CH}_2\text{Cl}_2$  and especially in  $\text{CH}_3\text{NO}_2$ , however, exhibit additional shoulders and (or) weak bands in the energy region appropriate for Co(II). These additional bands are normally accompanied by weak to medium bands attributed to the corresponding  $[\text{Co}^{\text{I}}(\text{CNR})_3(\text{PR}'_3)_2]\text{X}$  complex (produced by reduction in solution), except for cpd 14 where reduction is extensive. These data could indicate that a non-TBP structure for Co(II) is more prone to reduction than TBP coordination. These data also suggest that the  $[\text{Co}^{\text{II}}(\text{CNR})_3(\text{PR}'_3)_2]\text{X}_2$  complexes in  $\text{CF}_3\text{CH}_2\text{OH}$  at least tend to be TBP.

Now that the Co(I)–Co(II) couples have been recognized as being reversible, a difference in the solution coordination structures for the two oxidation states is interesting. This would imply that identical coordination structures for oxidized and reduced species is not a requirement for reversibility.

#### Experimental

Commercially available alkylisocyanides — i.e.,  $\text{CNCMe}_3$ ,  $\text{CNCHMe}_2$ ,  $\text{CNC}_6\text{H}_{11}$ , and  $\text{CNCH}_2\text{Ph}$  (Fluka, Strem, Fluka, and Aldrich Chemicals, respectively) — were used without redistillation. Commercially available triarylphosphines —

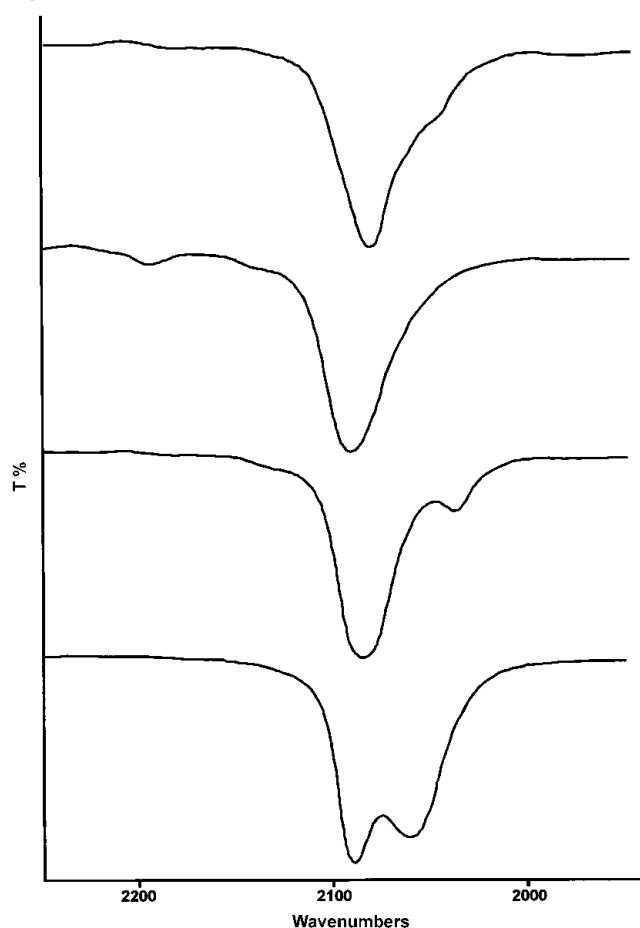


**Table 2.** Solution  $\nu(-N\equiv C)$  IR patterns for the  $[\text{Co}^{\text{I}}(\text{CNR})_3(\text{PR}'_3)_2]\text{X}$  and  $\text{Co}^{\text{II}}(\text{CNR})_3(\text{PR}'_3)_2\text{X}_2$  complexes.

Compound <sup>a</sup>	$\nu(-N\equiv C)$ IR pattern <sup>b</sup>		
	$\text{CF}_3\text{CH}_2\text{OH}$	$\text{CH}_3\text{NO}_2$	$\text{CH}_2\text{Cl}_2$
1	~2132 w(sh) 2085 vs 2039 m	~2131 w(sh) 2082 vs 2038 m	~2130 w(sh) 2079 vs 2036 m
2	2186 vs	~2211 vw(sh) 2189 vs ~2086 m <sup>c</sup> ~2035 vw <sup>c</sup>	2189 vs
3	2083 vs ~2050 w(sh)	2081 vs ~2047 w(sh)	2079 vs ~2048 w(sh)
4	2183 vs	2186 vs ~2081 m <sup>c</sup>	2186 vs ~2153 vw(sh) ~2079 vw <sup>c</sup>
5	2091 s 2062 s	2089 s 2061 s	2088 s 2059 s
6	2175 vs	~2202 vw(sh) 2177 vs ~2144 vw(sh) ~2090m <sup>c</sup> ~2060m <sup>c</sup>	~2201 vw(sh) 2177 vs ~2144 vw(sh)
7	~2132 w(sh) 2091 vs 2038 m	~2135 w(sh) 2090 vs 2037 m	~2133 w(sh) 2088 vs 2036 m
8	2189 vs	~2212 vw(sh) 2193 vs 2091 m <sup>c</sup> 2037 vw <sup>c</sup>	~2214 vw(sh) 2194 vs 2157 w 2088 m <sup>c</sup> ~2034 vw <sup>c</sup>
9	2087 vs ~2049 w(sh)	2086 vs ~2048 w(sh)	2085 vs ~2046 w(sh)
10	2187 vs	2190 vs 2086 s <sup>c</sup>	2192 vs ~2155 vw(sh) ~2085 w <sup>c</sup>
11	2093 vs 2066 s	2092 vs 2064 s	2090 vs 2063 s
12	~2200 w(sh) 2179 vs	2204 m 2181 vs 2092 m <sup>c</sup> ~2064 m <sup>c</sup>	2204 w 2182 vs 2149 m 2091 m <sup>c</sup> ~2060 w <sup>c</sup>
13	~2142 w(sh) 2092 vs	~2142 w(sh) 2093 vs	~2140 w(sh) 2090 vs
14	~2220 vw(sh) 2197 vs 2094 m <sup>c</sup>	2196 m ~2144 w(sh) 2095 vs	2192 w ~2142 w(sh) 2091 vs
15	2188 m <sup>d</sup> ~2134 w(sh) 2087 vs 2039 m	2134 w(sh) 2085 vs 2037 m	~2132 w(sh) 2082 vs 2037 m
16	2188 vs	~2213 w(sh) 2191 vs ~2088 m <sup>c</sup> ~2035 vw <sup>c</sup>	~2214 vw(sh) 2191 vs 2155 w 2082 w <sup>c</sup>
17	2083 vs ~2050 w(sh)	2083 vs ~2048 w(sh)	2081 vs ~2047 w(sh)

**Table 2 (concluded).**

Compound <sup>a</sup>	$\nu(-N\equiv C)$ IR pattern <sup>b</sup>		
	$\text{CF}_3\text{CH}_2\text{OH}$	$\text{CH}_3\text{NO}_2$	$\text{CH}_2\text{Cl}_2$
18	2185 vs	~2210 w(sh) 2188 vs 2083 m <sup>c</sup>	2189 vs 2080 vw <sup>c</sup>

<sup>a</sup>Complexes listed in the same order as in Table 1.<sup>b</sup>The  $\nu(-N\equiv C)$  in  $\text{cm}^{-1}$ ; w = weak, m = medium, s = strong, v = very, sh = shoulder.<sup>c</sup>Bands due to the corresponding  $[\text{Co}^{\text{I}}(\text{CNR})_3(\text{PR}'_3)_2]\text{X}$  complex formed in solution.<sup>d</sup>Bands due to the corresponding  $[\text{Co}^{\text{II}}(\text{CNR})_3(\text{PR}'_3)_2]\text{X}_2$  complex formed in solution.**Fig. 3.** The  $\nu(-N\equiv C)$  IR patterns for  $[\text{Co}^{\text{I}}(\text{CNR})_3(\text{PR}'_3)_2]\text{X}$  complexes. Top to bottom:  $[\text{Co}(\text{CNC}_6\text{H}_{11})_3\{\text{P}(\text{C}_6\text{H}_4\text{Me-}p)_3\}_2]\text{ClO}_4$ ,  $[\text{Co}(\text{CNCH}_2\text{Ph})_3(\text{PPh}_3)_2]\text{BF}_4$ ,  $[\text{Co}(\text{CNCHMe}_2)_3\{\text{P}(\text{C}_6\text{H}_4\text{OMe-}p)_3\}_2]\text{ClO}_4$ , and  $[\text{Co}(\text{CNCMe}_3)_3\{\text{P}(\text{C}_6\text{H}_4\text{Me-}p)_3\}_2]\text{ClO}_4$  all in  $\text{CF}_3\text{CH}_2\text{OH}$  solution.

i.e.,  $\text{PPh}_3$ ,  $\text{P}(\text{C}_6\text{H}_4\text{Me-}p)_3$ , and  $\text{P}(\text{C}_6\text{H}_4\text{OMe-}p)_3$  (Aldrich Chemicals) — were used without recrystallization. Anhydrous  $\text{AgClO}_4$  and  $\text{AgBF}_4$  were supplied by Strem Chemicals, Inc. 2,2,2-Trifluoroethanol (puriss grade) from Fluka was used for IR spectra. Anhydrous diethyl ether was filtered through an alumina column immediately before use. The  $[\text{Co}^{\text{I}}(\text{CNR})_3(\text{PR}'_3)_2]\text{X}$  and  $[\text{Co}^{\text{II}}(\text{CNR})_3(\text{PR}'_3)_2]\text{X}_2$  ( $\text{X} = \text{ClO}_4$ ,  $\text{BF}_4$ ) complexes were synthesized as previously re-



ported (3–6). Ferrocene, which was used to test the experimental setup, was prepared by standard procedure (18).

For cyclic voltammetry, 1 mM solutions of the compounds were freshly prepared in chromatographic-grade acetonitrile containing 0.05 M tetrabutylammonium hexafluorophosphate (TBAH) as the supporting electrolyte. Cyclic voltammetry measurements were performed using a Metrohm 757 VA Computerace system with a three-electrode compartment cell. The working and auxiliary electrodes were both made of glassy carbon. The reference electrode was a double junction Ag–AgCl system. The voltammograms were recorded in the potential range,  $-0.2$  to  $+0.6$  V vs. Ag–AgCl, at various scan rates ranging from  $0.01$  V  $s^{-1}$  to  $0.5$  V  $s^{-1}$ . Nitrogen gas was bubbled through each solution for 500 s prior to the run. IR spectra were recorded on a PerkinElmer 2000 FT-IR spectrophotometer in spectro-grade  $CH_2Cl_2$ ,  $CH_3NO_2$ , and  $CF_3CH_2OH$ .

## Acknowledgements

The authors wish to thank the Faculty of Science Research and Publications Committee of the University of Botswana for a grant supporting this research.

## References

1. R.B. King and M.S. Saran. *Inorg. Chem.* **11**, 2112 (1972).
2. J.W. Dart, M.K. Lloyd, R. Mason, J.A. McCleverty, and J. Williams. *J. Chem. Soc. Dalton Trans.* 1747 (1973).
3. C.A.L. Becker, A. Anisi, G. Myer, and J.D. Wright. *Inorg. Chim. Acta*, **111**, 11 (1986).
4. C.A.L. Becker, S.A. Al-Qallaf, and J.C. Cooper. *Inorg. Chim. Acta*, **188**, 99 (1991).
5. C.A.L. Becker and K.R. Barqawi. *J. Coord. Chem.* **34**, 273 (1995).
6. C.A.L. Becker. *J. Coord. Chem.* **50**, 89 (2000).
7. R. Nicholson and I. Shain. *Anal. Chem.* **36**, 706 (1964).
8. W.E. Geiger. *Laboratory techniques in electrochemistry. Edited by P.T. Kissinger and W.R. Heineman.* Marcel Dekker, New York. 1996. pp. 683–717.
9. J.J. Van Benschoten, J.Y. Lewis, W.R. Heineman, D.A. Roston, and P.T. Kissinger. *J. Chem. Educ.* **60**, 773 (1983).
10. G.A. Mabbott. *J. Chem. Educ.* **60**, 699 (1983).
11. C.A.L. Becker and O. Al-Jowder. 208th National Meeting of the American Chemical Society, Washington, DC, August 1994. Abstract No. 511 (Inorg. Div.).
12. N.S. Issacs. *Physical organic chemistry.* Longman Scientific & Technical, New York. 1987. Chap 4.
13. M.K. Lloyd, J.A. McCleverty, D.G. Orchard, J.A. Connor, M.B. Hall, I.H. Hillier, E.M. Jones, and G.K. McEwen. *J. Chem. Soc. Dalton Trans.* 1743 (1973).
14. H.C. Clark, W.J. Cherwinski, and L.E. Manzer. *Inorg. Chem.* **11**, 1511 (1972).
15. J. Hanzlik, G. Albertin, E. Bordignon, and A.A. Orio. *Inorg. Chem.* **38**, 207 (1980).
16. C.A.L. Becker. *Synth. React. Inorg. Met.-Org. Chem.* **22**, 99 (1992).
17. C.A.L. Becker and G.C. Papavassiliou. 180th National Meeting of the American Chemical Society, August 1980, Abstract No. 295 (Inorg. Div.).
18. W.L. Jolly. *Inorg. Synth.* **11**, 120 (1968).



# 3,3'-Dipyrrolyl sulfides, useful building blocks for the syntheses of macrocycles containing dipyrromethene units

Qingqi Chen and David Dolphin

**Abstract:** 5,5'-Dicarboxy-3,3'-dipyrrolyl sulfide was condensed with 5,5'-diformyl-3,3'-dipyrrolyl sulfide or 5,5'-diformyldipyrromethane under acidic conditions to produce, in high yields, macrocycles containing four dipyrromethene units.

**Key words:** 3,3-dipyrrolyl sulfide, cyclopolypyrrole, dipyrromethene, macrocycle.

**Résumé :** On a condensé le sulfure de 5,5'-dicarboxy-3,3'-dipyrroyle avec le sulfure de 5,5'-diformyl-3,3'-dipyrroyle ou avec le 5,5'-diformyldipyrrométhane en milieu acide pour former, avec des rendements élevés, des macrocycles contenant 4 unités dipyrrométhène.

**Mots clés :** sulfure de 3,3'-dipyrroyle, cyclopolypyrrole, dipyrrométhène, macrocycle.

[Traduit par la Rédaction]

## Introduction

In recent years expanded porphyrins and macrocycles related to porphyrins have been receiving increasing attention (1–4), and they are being utilized in fields such as photo-dynamic therapy (PDT), neutral substrate binding, and anion recognition.

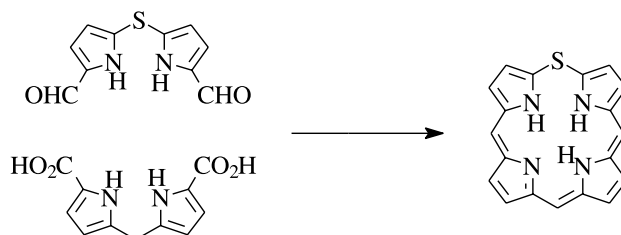
Macrocycles containing six (3), eight (4, 5), ten (6), and twelve (7) pyrrolic rings have been reported, and recently *meso*-aryl-substituted expanded porphyrins containing up to 12 pyrrolic rings have been described (8). We report here a new type of macrocycle, which contains dipyrromethene units linked by sulfur atoms prepared via a McDonald synthesis.

## Results and discussion

5,5'-Diformyl-2,2'-dipyrrolyl sulfides have been known for many years as intermediates in the synthesis of thiaporphyrins (Scheme 1) (9, 10). We attempted to condense a 5,5'-diformyl-3,3'-dipyrrolyl sulfide **6** with a 5,5'-dicarboxy-3,3'-dipyrrolyl sulfide **3** under acidic conditions and were surprised to find that the product was not the expected compound **7**, but the macrocyclic product **8**, which contained eight pyrrole rings (Schemes 2 and 3) where the dipyrromethene units were linked by sulfur atoms.

The precursor 5,5'-dicarboxy-3,3'-dipyrrolyl sulfide **3** was prepared from 2-ethoxycarbonyl-3,5-dimethylpyrrole **1** via two steps: reacting **1** with sulfur dichloride (11), followed by

Scheme 1.



treatment with sodium hydroxide to give the diacid **3**. Another important intermediate **6** was synthesized from **1** in 3 steps. Thus compound **1** was saponified and decarboxylated under basic condition (sodium hydroxide) at 180 °C using ethylene glycol as solvent to yield 2,4-dimethylpyrrole (**4**), which was converted to 2-formyl-3,5-dimethylpyrrole (**5**) under Vilsmeier formylation conditions. Coupling **5** with sulfur dichloride gave the key intermediate compound **6** in high yield (11).

Compound **8** is formally a dimer of **7** (Scheme 3), which was formed in a [2 + 2 + 2 + 2] condensation from 2 equiv each of **3** and **6**.

To extend our work, we tried to condense **3** with **9** and **6** with **10** under similar acidic conditions. Once again, these reactions did not provide the [2 + 2] product **11**, but the [2 + 2 + 2 + 2] condensation product **12** (Scheme 4). Similar [2 + 2 + 2 + 2] condensations have previously been observed by Sessler, Vogel, and their co-workers (2, 4, 5, 12). In general these reactions occurred with yields usually below 20%, lower than those reported here, which range from 80 to 90%.

The composition of the new macrocycle **8** was established by combustion analysis, UV-vis, and FAB mass spectrometry. As expected, **8** does not possess macrocyclic aromaticity

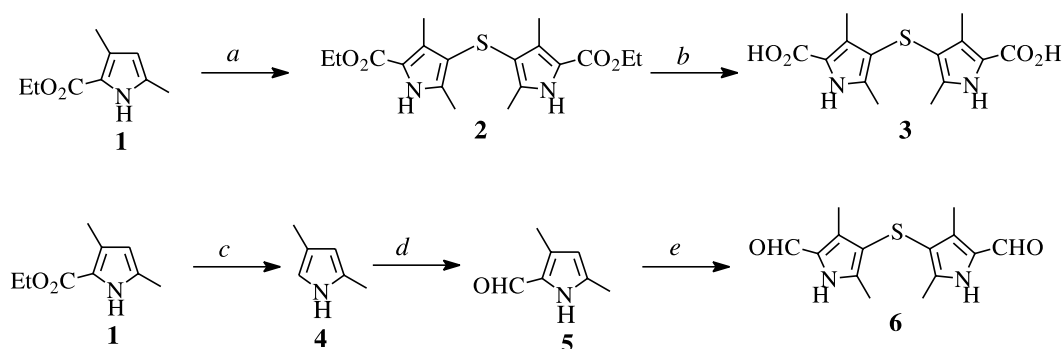
Received 13 August 2002. Published on the NRC Research Press Web site at <http://canjchem.nrc.ca> on 15 August 2003.

**Q. Chen and D. Dolphin.**<sup>1</sup> Department of Chemistry, University of British Columbia, 2036 Main Mall, Vancouver, BC V6T 1Z1, Canada.

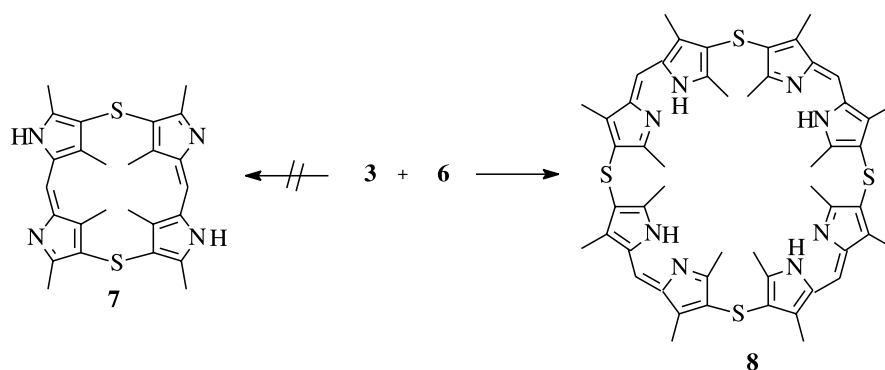
<sup>1</sup>Corresponding author (email: [ddolphin@qtlinc.com](mailto:ddolphin@qtlinc.com)).



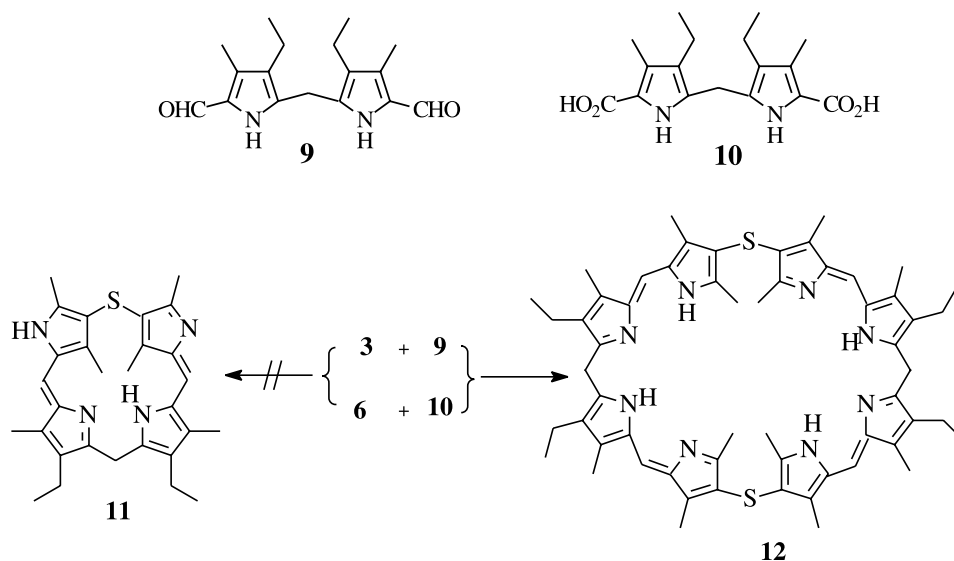
**Scheme 2.** Reagents and condition: (a)  $\text{SCl}_2\text{-CH}_2\text{Cl}_2$ ,  $-50\text{ }^\circ\text{C}$ ; (b)  $\text{NaOH-EtOH}$ , reflux 3 h, then  $\text{HOAc}$ ,  $\text{pH} = 4$ ; (c)  $\text{NaOH-glycol}$ ,  $180\text{ }^\circ\text{C}$ ; (d)  $\text{POCl}_3\text{-DMF}$ , then  $\text{NaOH}$ ; (e)  $\text{SCl}_2\text{-CH}_2\text{Cl}_2$ ,  $-60\text{ }^\circ\text{C}$ .



**Scheme 3.**



**Scheme 4.**



since the conjugated system is interrupted by the sulfur bridges. The molecule has high symmetry, which is consistent with its  $^1\text{H}$  and  $^{13}\text{C}$  NMR spectra; there are two types of  $\text{CH}_3$  signals, one for  $\alpha\text{-CH}_3$  and the other for  $\beta\text{-CH}_3$  groups, and one  $\text{-CH=}$  signal at 7.00 ppm. Moreover, the  $^{13}\text{C}$  NMR of **8** in  $\text{TFA-d}$  showed 5  $sp^2$  signals, which correspond to one  $\text{-CH=}$  and four carbons in each pyrrole ring. Compound **8** has very low solubility in most common solvents such as

dichloromethane, chloroform, methanol, acetone, DMF, DMSO, acetic acid, acetonitrile, THF, dioxane, and pyridine. However, it is soluble in trifluoroacetic acid, in which it displays a beautiful purple color. In other solvents **8** can have a red to yellow color depending on its degree of protonation. Macrocycle **12** was characterized as above, and its optical properties are similar to those of macrocycle **8**; **12** is more soluble than **8** in most solvents.



## Experimental section

### General

All reagents and solvents were purchased and used as received. Melting points were determined on a Thomas hot stage or Buchi apparatus and are uncorrected.  $^1\text{H}$  and  $^{13}\text{C}$  NMR spectra were recorded on a Bruker AC-200 or AMX-300 instrument. The high- and low-resolution mass spectra were obtained by the departmental mass spectroscopy service laboratory. Combustion analyses were performed by the departmental microanalytical laboratory. Optical spectra were recorded on an HP8452A Photo diode array spectrophotometer (instrumental precision  $\pm 2$  nm).

Bis(5-ethoxycarbonyl-2,4-dimethylpyrrole-3-yl)sulfide **2** and bis(5-formyl-2,4-dimethyl pyrrole-3-yl)sulfide (**6**) were prepared according to literature procedures (11).

### Bis(5-carboxy-2,4-dimethylpyrrol-3-yl) sulfide (**3**)

Bis(5-ethoxycarbonyl-2,4-dimethylpyrrol-3-yl) sulfide (20 g, 55 mmol) was suspended in ethanol (180 mL). The mixture was stirred, and a solution of sodium hydroxide (8.8 g in 20 mL water) was added all at once. The suspension was then stirred under reflux for 3 h, and the solvent was then removed under vacuum. The residue was stirred with brine (100 mL) at  $-10^\circ\text{C}$ ; then acetic acid was added dropwise until pH 4. The precipitate was collected by suction filtration and by washing with cold water. After drying under vacuum, the desired product was obtained as a pink solid (16.2 g, 96%).

mp  $220^\circ\text{C}$  (decomposition (dec)).  $^1\text{H}$  NMR (200 MHz,  $\text{DMSO}-d_6$ ) (ppm)  $\delta$ : 2.20 (s, 12H, 4 $\text{CH}_3$ ), 11.20 (s, 2H, 2NH), 12.00 (s, 2H, COOH).  $^{13}\text{C}$  NMR (75 MHz,  $\text{DMSO}-d_6$ ) (ppm)  $\delta$ : 11.26, 11.72, 111.57, 119.53, 127.35, 133.68, 163.77 (COOH).  $\text{C}_{14}\text{H}_{16}\text{N}_2\text{O}_4\text{S}$  required: C 54.54, H 5.19, N 9.09; found: C 54.06, H 5.54, N 8.86.

### Synthesis of 8·2TFA

5,5'-Dicarboxy-3,3'-dipyrrolyl sulfide **3** (200 mg, 0.66 mmol) was suspended in trifluoroacetic acid (10 mL) and stirred at  $40^\circ\text{C}$  until all the solid had dissolved. The red mixture was cooled to room temperature. To this solution was added 5,5'-diformyl-3,3'-dipyrrolyl sulfide (**6**) (181 mg, 0.66 mmol) under continuous stirring. After 10 min, a mixture of dichloromethane (20 mL), methanol (20 mL), and hydrogen bromide (3 mL, 48% in acetic acid) was added. The red mixture was allowed to stir overnight at room temperature. Anhydrous ether (100 mL) was added. The suspension was allowed to stir for another 2 h. The red solid was collected by suction filtration and washed with anhydrous ether to give **8** (378 mg, 92%). An analytic sample was prepared by repeating the following procedure four times: the crude product was dissolved in a minimum amount of TFA and precipitated by methanol – anhydrous ether (40:60, v/v). The solid was collected by suction filtration and washed with methanol.

mp  $320^\circ\text{C}$  (dec.). UV-vis ( $\text{CH}_2\text{Cl}_2$  + TFA),  $\lambda_{\text{max}}$  (nm) ( $\epsilon$ ): 520 (136 400). FAB-MS  $m/e$ : 921 ( $[\text{M} + 1]^+$ ).  $^1\text{H}$  NMR (TFA- $d$ , 400 MHz) (ppm)  $\delta$ : 2.51 (s, 24H, 8 $\text{CH}_3$ ), 2.57 (s, 24H, 8 $\text{CH}_3$ ), 7.50 (s, 4H, 4  $-\text{CH}=\text{}$ ), 11.50 (bs, obscured by TFA signal, NH).  $^{13}\text{C}$  NMR (TFA- $d$ , 75 MHz) (ppm)  $\delta$ : 12.09, 14.54, 122.91, 124.55, 129.69, 152.14, 160.39. HR-

MS (LSIMS, thioglycerol), calcd. for  $([\text{C}_{52}\text{H}_{56}\text{N}_8\text{S}_4 + 1])$ , required: 921.35890; found: 921.35874.  $\text{C}_{52}\text{H}_{56}\text{N}_8\text{S}_4 \cdot 2\text{TFA} \cdot 2\text{H}_2\text{O}$ , required (%): C 56.74, H 5.27, N 9.45; found: C 56.34, H 4.94, N 8.96.

### Synthesis of 12·2TFA

#### Method A, from **3** and **9**

5,5'-Dicarboxy-3,3'-dipyrrolyl sulfide (**3**) (200 mg, 0.66 mmol) was suspended in trifluoroacetic acid (10 mL) and stirred at  $40^\circ\text{C}$  until all the solid had dissolved. The red mixture was cooled to room temperature. To this solution was added the 5,5'-diformyldipyrromethane **9** (188 mg, 0.66 mmol) under continuous stirring. After 10 min, a mixture of dichloromethane (20 mL), methanol (20 mL), and hydrogen bromide (3 mL, 48% in acetic acid) was added. The red mixture was allowed to stir overnight at room temperature. Anhydrous ether (100 mL) was added. The suspension was allowed to stir for another 2 h. The red solid was collected by suction filtration and washed by anhydrous ether to give **12** (375 mg, 90%).

#### Method B, from **6** and **10**

The 5,5'-diformyl-3,3'-dipyrrolyl sulfide (**6**) (200 mg, 0.72 mmol) was suspended in trifluoroacetic acid (10 mL) and stirred at  $40^\circ\text{C}$  until all the solid had dissolved. The red mixture was cooled to room temperature. To this solution was added the 5,5'-dicarboxydipyrromethane **10** (230 mg, 0.72 mmol) under continuous stirring. After 10 min, a mixture of dichloromethane (20 mL), methanol (20 mL), and hydrogen bromide (3 mL, 48% in acetic acid) was added. The red mixture was allowed to stir overnight at room temperature. Anhydrous ether (100 mL) was added. The suspension was allowed to stir for another 2 h. The red solid was collected by suction filtration and washed with anhydrous ether to give the product (391 mg) in an 86% yield. An analytic sample was prepared by repeating the following procedure four times: the crude product was dissolved in a minimum amount of TFA and precipitated by methanol – anhydrous ether (40:60, v/v). The solid was collected by suction filtration and washed with methanol.

mp  $295^\circ\text{C}$  (dec).  $^1\text{H}$  NMR ( $\text{CDCl}_3$ , 200 MHz) (ppm)  $\delta$ : 0.85 (t,  $J = 7.32$  Hz, 12H, 4 $\text{CH}_2\text{CH}_3$ ), 2.15 (s, 12H, 4 $\text{CH}_3$ ), 2.21 (s, 12H, 4 $\text{CH}_3$ ), 2.31 (s, 12H, 4 $\text{CH}_3$ ), 2.50 (q,  $J = 7.32$  Hz, 8H, 4 $\text{CH}_2$ ), 5.00 (s, 4H, 2 $\text{CH}_2$ ), 7.12 (s, 4H, 4 $-\text{CH}=\text{}$ ), 14.10 (s, 4H, 4NH), 14.35 (s, 4H, 4NH).  $^{13}\text{C}$  NMR (TFA- $d$ , 75 MHz) (ppm)  $\delta$ : 10.05, 11.01, 13.91, 14.42, 17.50, 23.59, 118.25, 121.97, 126.97, 128.39, 132.32, 146.31, 149.11, 150.09, 157.40. UV-vis ( $\text{CH}_2\text{Cl}_2$  + TFA)  $\lambda_{\text{max}}$  (nm) ( $\epsilon$ ): 450 (109 600), 520 (96 000). FAB-MS  $m/e$ : 941 ( $[\text{M} + 1]^+$ ). HR-MS (LSIMS, thioglycerol), calcd. for  $([\text{C}_{58}\text{H}_{69}\text{N}_8\text{S}_2]^+)$ , required: 941.50866; found: 941.50744.  $\text{C}_{58}\text{H}_{69}\text{N}_8\text{S}_2 \cdot 2\text{TFA} \cdot \text{H}_2\text{O}$ , required (%): C 62.71, H 6.11, N 9.44; found: C 63.07, H 6.46, N 9.50.

## Conclusion

Vogel (12) has noted that the equimolar MacDonald-type condensation of a diformyl bipyrrrole with a dipyrrole dicarboxylic acid gives, in most cases, octaphyrins as the sole products. The present study extends these observations and



shows that related octapyrroles can be produced, in high yield, from 3,3'-dipyrrolyl sulfides via a [2 + 2 + 2 + 2] MacDonald synthesis. Further work on the application of the present method for the synthesis of cyclooctapyrroles and cyclopolypyrroles using 3,3'-dipyrromethanes is in progress.

## Acknowledgment

This work was supported by the Natural Sciences and Engineering Council of Canada (NSERC).

## References

1. A. Jasat and D. Dolphin. *Chem. Rev.* **97**, 2267 (1997).
2. J.L. Sessler and S.T. Weghorn. Expanded, contracted & isomeric porphyrin. Pergamon, N.Y. 1997.
3. (a) M.G.P.M.S. Neves, R.M. Martin, A.C. Tome, A.J.D. Silvestre, A.M.S. Silva, V. Felix, M.G.B. Drew, and J.A.S. Cavaleiro. *Chem. Commun.* 385 (1999); (b) C. Bruckner, E.D. Sternberg, R.W. Boyle, and D. Dolphin. *Chem. Commun.* 1689 (1997); (c) S.J. Narayanan, B. Sridevi, T.K. Chandrashekar, A. Vij, and R. Roy. *Angew. Chem. Int. Ed. Engl.* **37**, 3394 (1998).
4. E. Vogel, M. Broring, J. Fink, D. Rosen, H. Schmickler, J. Lex, K.W.K. Chan, Y.-D. Wu, D.A. Plattner, M. Nendel, and K.N. Houk. *Angew. Chem. Int. Ed. Engl.* **34**, 2511 (1995).
5. M. Broring, J. Jendry, L. Zander, H. Schmickler, J. Lex, Y.-D. Wu, M. Nendel, J. Chen, D.A. Plattner, K.N. Houk, and E. Vogel. *Angew. Chem. Int. Ed. Engl.* **34**, 2515 (1995).
6. J.L. Sessler, S.J. Weghorn, V. Lynch, and M.R. Johnson. *Angew. Chem. Int. Ed. Engl.* **33**, 1509 (1994).
7. J.A. Wytke, M. Michels, L. Zander, J. Lex, H. Schmickler, and E. Vogel. *J. Org. Chem.* **65**, 8709 (2000).
8. J.-Y. Shin, H. Furata, K. Yoza, S. Igarashi, and A. Osuka. *J. Am. Chem. Soc.* **123**, 7191 (2001).
9. (a) G.M. Badger, R.L.N. Harris, and R.A. Jones. *Aust. J. Chem.* **17**, 1022 (1964); (b) R.L.N. Harris. *Tetrahedron Lett.* 3689 (1969); (c) M.J. Broadhurst, R. Grigg, and A.W. Johnson. *J. Chem. Soc. Chem. Commun.* 807 (1970); (d) M.J. Broadhurst, R. Grigg, and A.W. Johnson. *J. Chem. Soc. Perkin Trans. I*, 1124 (1972); (e) H. Falk and H. Flodl. *Monatsh. Chem.* **120**, 45 (1989).
10. A. Treibs, L. Schulze, F.-H. Kreuzer, and H.-G. Kolm. *Liebigs Ann. Chem.* 207 (1973).
11. Q. Chen and D. Dolphin. *Synthesis*, **1**, 40 (2001).
12. E. Vogel. *Heterocycles*, **37**, 6168 (1994).



# The extended hyper-Wiener index

X.H. Li

**Abstract:** According to the definition of molecular connectivity and the definition of a hyper-Wiener index, a novel set of hyper-Wiener indexes ( $R_n$ ,  ${}^mR_n$ ) are defined and are named the extended hyper-Wiener indexes. Where  $n = 1, 2, 3, 4, \dots$  represents the type of subgraph units and is the number of endmost atoms of the subgraph unit,  $m$  is the number of atoms of the subgraph unit. Here  $n = 1$  means the subgraph unit is an atom,  $n = 2$  means the subgraph units are straight-line combinations of  $m$  atoms ( $m = 2, 3, 4, 5, 6, \dots$ ), and  $n = 3$  means the subgraph units are Y types of combinations of  $m$  atoms ( $m = 4, 5, 6, 7, 8, \dots$ ), and so on. The potential usefulness of the extended hyper-Wiener index in QSAR and (or) QSPR is evaluated by its correlation with a number of  $C_3$ – $C_8$  alkanes and by a favorable comparison with models based on the molecular connectivity index and the overall Wiener index. To verify the robustness and the predictive ability of the models, a cross-validation procedure, leave-one-out, and a random test were also performed. The results show that the extended hyper-Wiener indexes examined demonstrate a good potential for QSAR and QSPR studies. Considerably better statistics are obtained when extending the hyper-Wiener index to the extended hyper-Wiener index. The extended hyper-Wiener indexes provided statistical results as good as the molecular connectivity indexes and the overall Wiener index in all models, and the standard deviations provided by these three sets of indexes are rather close. Moreover, this method may provide a better way to apply the Wiener number and the hyper-Wiener index to the system of unsaturated hydrocarbons and organic compounds, including heteroatoms, according to the method of the molecular connectivity index. This can extend the usefulness of the Wiener number and hyper-Wiener index and can make them a kind of widely used topological index in practice.

**Key words:** hyper-Wiener index ( $R$ ), extended hyper-Wiener index, molecular connectivity index.

**Résumé :** En se basant sur la définition de la connectivité moléculaire et de l'indice hyper-Wiener, on définit de nouveaux indices hyper-Wiener ( $R_n$ ,  ${}^mR_n$ ) appelés indices hyper-Wiener élargis. Quand  $n = 1, 2, 3, 4, \dots$ , représente le type d'unités du sous-graphe et qu'il correspond au nombre d'atomes d'atomes terminaux de l'unité du sous-graphe,  $m$  correspond au nombre d'atomes de l'unité du sous-graphe. Dans ce cas,  $n = 1$  signifie que l'unité du sous-graphe est un atome,  $n = 2$  signifie que les unités du sous-graphe sont des combinaisons linéaires de  $m$  atomes ( $m = 2, 3, 4, 5, 6, \dots$ ) et  $n = 3$  signifie que les unités du sous-graphe sont des combinaisons de type Y de  $m$  atomes ( $m = 4, 5, 6, 7, 8, \dots$ ) et ainsi de suite. On a évalué l'utilité potentielle de l'indice hyper-Wiener élargi dans des études QSAR–QSPR par sa corrélation avec un certain nombre d'alcane comportant de 3 à 8 atomes de carbones et par une comparaison favorable avec des modèles basés sur l'indice de connectivité et sur l'indice Wiener global. Dans le but de vérifier la solidité des modèles et leur habilité à faire des prédictions, on a aussi effectué un test au hasard ainsi qu'une procédure de validation croisée en ne tenant pas compte d'un atome. Les résultats démontrent que les indices hyper-Wiener étendus examinés présentent un bon potentiel pour des études QSAR et QSPR. On obtient de bien meilleures statistiques en passant de l'indice hyper-Wiener à l'indice hyper-Wiener étendu. Les indices hyper-Wiener étendus conduisent à des résultats statistiques comme les indices de connectivité moléculaire et l'indice Wiener global dans tous les modèles et les déviations standards fournis pas ces trois ensembles d'indices sont assez près. De plus, il peut conduire à une meilleure façon d'appliquer le nombre de Wiener et l'indice hyper-Wiener au système d'hydrocarbures insaturés et de composés organiques comportant des hétéroatomes suivant la méthode de l'indice de connectivité moléculaire. Ceci pourrait étendre l'utilité du nombre de Wiener et de l'indice hyper-Wiener qui pourrait les faire passer au rang d'indice topologique largement utilisé dans la pratique.

**Mots clés :** indice hyper-Wiener ( $R$ ), indice hyper-Wiener élargi, indice de connectivité moléculaire.

[Traduit par la Rédaction]

## Introduction

The hyper-Wiener index  $R(G)$  was proposed by Randić et al. (1); he generalized the Wiener index ( $W$ ) to the hyper-Wiener index by the much-studied  $W$  graph invariant (2–4).

Wiener defined  $W$  as the sum of the distances between pairs of vertices of the graph under study (5). For trees, the main difference between  $W$  and  $R$  is that Randić considered paths  $p$  instead of edges  $e$  in the Wiener index. In his definition,  $R$  is the sum of contributions  $K_{ij}$ ; here subscripts  $i$  and  $j$  repre-

Received 23 October 2002. Published on the NRC Research Press Web site at <http://canjchem.nrc.ca> on 15 August 2003.

**X.H. Li.** Department of Chemistry, Wenzhou Normal College, Wenzhou, Zhejiang 325027, P.R.China. (e-mail: [lixinhua01@263.net](mailto:lixinhua01@263.net)).



sent a pair of vertices.  $K_{ij}$  can be obtained (6, 7) using the following two-step algorithm: (i) Remove the path (for trees there is only one path) between vertices  $i$  and  $j$ ; two nonconnected subgraphs will be obtained. (ii) Multiply the number of vertices of the first subgraph by the number of vertices of the second one.  $R$  may be obtained by adding  $K_{ij}$  for all pairs of vertices  $i$  and  $j$ . There are  $N(N-1)/2$  terms altogether, where  $N$  denotes the number of vertices (i.e., the number of carbons in H-suppressed graphs).

Klein et al. and Hosoya (8, 9) found that the hyper-Wiener index is equal to half of the Wiener index plus half of the sum of squared distances between pairs of vertices:

$$[1] \quad R = \frac{1}{2} \left[ \sum_{i < j} d_{ij}^2 + \sum_{i < j} d_{ij} \right] = \frac{1}{2} \sum_{i < j} d_{ij}^2 + \frac{1}{2} W$$

There have been many studies on the hyper-Wiener index in recent years (10, 11), especially by Tratch and his co-workers, who earlier introduced their index, similar to the hyper-Wiener index (12), and also made the suggestion to extend the Wiener number to sequences of number invariants (13, 14).

But the usefulness of the hyper-Wiener number is not as popular as the molecular connectivity index. Some limits prevent the usefulness of this number; for example, it can only be used for saturated hydrocarbons. There should be a further factor that is not accounted for by the hyper-Wiener number.

Randić introduced the concept of a connectivity (branching) index in 1975 (15). The concept has been further developed and applied extensively by Randić, Kier, Hall, and their co-workers (16, 17). The molecular connectivity index was proved to be one of the most successful and widely used indexes.

According to the definition of molecular connectivity, the first-order connectivity index  ${}^1\chi$  is the sum over all bonds  $i-j$  (eq. [2]), where  $\delta_i$  is the valence of carbon atom  $i$  in the carbon skeleton of a hydrocarbon.

$$[2] \quad {}^1\chi = \sum_{\text{bonds}} \left( \frac{1}{\delta_i \times \delta_j} \right)^{\frac{1}{2}}$$

And the second-order molecular index  ${}^2\chi$  is a sum over 2-bond paths  $i-j-k$  of terms  $1/(\delta_i\delta_j\delta_k)^{1/2}$ . A hierarchy of additional indexes  ${}^m\chi_t$  of order  $m$  and type  $t$  can be obtained by summing analogous terms over substructural units involving path ( $t = p$ ), cluster ( $t = c$ ), path-cluster ( $t = pc$ ), or chain ( $t = ch$ ) combinations of  $m$  bonds.

### The extended hyper-Wiener index

According to the definition of molecular connectivity and the definition of the hyper-Wiener index, we can define the extended hyper-Wiener index for tree graphs ( $R_n$ ,  ${}^mR_n$ ,  $n \leq m$ ) as follows.

First,  $n = 1, 2, 3, 4, \dots$  represents the type of subgraph units and is the number of endmost atoms of the subgraph unit. Second,  $m$  is the number of atoms of the subgraph unit. Here  $n = 1$  means the subgraph unit is an atom,  $n = 2$  means the subgraph units are straight-line combinations of  $m$  atoms ( $m = 2, 3, 4, 5, 6, \dots$ ), and  $n = 3$  means the subgraph units are

$Y$  types of combinations of  $m$  atoms ( $m = 4, 5, 6, 7, 8, \dots$ ), and so on.

#### Definition 1

The 1-type extended hyper-Wiener index  $R_1$  is defined as the sum over all atoms  $i$ . Here  $n_i$  denotes the number of vertices in a tree graph if all the edges and internal vertices of a path are not deleted from the parent graph.

$$[3] \quad R_1 = \sum_{\text{atoms}} n_i$$

#### Definition 2

The 2-type extended hyper-Wiener index  $R_2$  is the sum of contributions  $K_{ij}$ , where subscripts  $i$  and  $j$  denote a pair of vertices.  $K_{ij}$  may be obtained by using the following two-step algorithm: (i) Remove the path (for trees there is only one path) between vertices  $i$  and  $j$  (linear subgraph units); two nonconnected subgraphs will be obtained. (ii) Multiply the number of vertices of the first subgraph  $n_i$  by the number of vertices of the second one  $n_j$ .  $R_2$  may be obtained by adding  $K_{ij}$  for all pairs of vertices  $i$  and  $j$ .

$$[4] \quad R_2 = \sum_{\text{all paths}} n_i \times n_j$$

From the definition we can see that the 2-type extended hyper-Wiener index  $R_2$  is equal to the Wiener number.

#### Definition 3

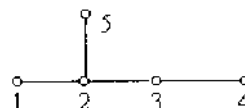
The  $m$ th-order ( $m \geq 2$ ) extended hyper-Wiener index of 2-type  ${}^mR_2$  is the sum of contributions  $K_{ij}$ , where subscripts  $i$  and  $j$  denote a pair of vertices.  $K_{ij}$  may be obtained by using the following two-step algorithm: (i) Remove the path between vertices  $i$  and  $j$  (linear subgraph unit combinations of  $m$  atoms); two nonconnected subgraphs will be obtained. (ii) Multiply the number of vertices of the first subgraph by the number of vertices of the second one.  ${}^mR_2$  may be obtained by adding  $K_{ij}$  for all linear subgraph unit combinations of  $m$  atoms.

From definition 2 and definition 3 we can see that  $R_2$  is the sum of  ${}^mR_2$ , where  $m = 2, 3, 4, \dots$

A hierarchy of additional indexes of type  $n$  ( $R_n$ ) can be obtained by summing analogous terms over substructural units involving 3 types, 4 types, 5 types, 6 types, ..., just like definition 2.

A hierarchy of additional indexes of order  $m$  and type  $n$  ( ${}^mR_n$ ) can be obtained by summing analogous terms over substructural units involving 3 types, 4 types, 5 types, ..., combinations of  $m$  atoms, just like definition 3.

Example: for 2-methylbutane, the extended hyper-Wiener indexes  ${}^mR_n$  can be calculated as follows:



$$n = 1: 1, 2, 3, 4, 5; R_1 = 1 + 1 + 1 + 1 + 1 = 5$$

$$n = 2: 1-2, 2-3, 3-4, 2-5, 1-5, 1-3, 3-5, 2-4, 1-4, 4-5;$$

$$R_2 = 4 \times 1 + 3 \times 2 + 4 \times 1 + 4 \times 1 + 1 \times 1 + 1 \times 2 + 2 \times 1 + 3 \times 1 + 1 \times 1 + 1 \times 1 = 28$$

$$m = 2, n = 2: 1-2, 2-3, 3-4, 2-5; {}^2R_2 = 4 \times 1 + 3 \times 2 + 4 \times 1 + 4 \times 1 = 18$$

$$m = 3, n = 2: 1-5, 1-3, 3-5, 2-4; {}^3R_2 = 1 \times 1 + 1 \times 2 + 2 \times 1 + 3 \times 1 = 8$$



**Table 1.** Experimental values for the physical properties of the 38 alkanes.

No.	Molecule <sup>a</sup>	bp (°C)	<i>T</i> (°C)	<i>P</i> (atm) <sup>b</sup>	ST (0.1 μN/cm)
1	C3	-42.070	96.80	42.01	
2	nC4	-0.500	152.01	37.47	
3	2MC3	-11.730	134.98	36.00	
4	nC5	36.074	196.62	33.31	16.00
5	2MC4	27.852	187.80	32.90	15.00
6	22MMC3	9.503	160.60	31.57	
7	nC6	68.740	234.70	29.92	18.42
8	2MC5	60.271	224.90	29.95	17.38
9	3MC5	63.282	231.20	30.83	18.12
10	23MMC4	57.988	227.10	30.99	17.37
11	22MMC4	49.741	216.20	30.67	16.30
12	nC7	98.427	267.01	27.01	20.26
13	2MC6	90.052	257.90	27.20	19.29
14	3MC6	91.850	262.40	28.10	19.79
15	3EC5	93.475	267.60	28.60	20.44
16	24MMC5	80.500	247.10	27.40	18.15
17	23MMC5	89.784	264.60	29.20	19.96
18	22MMC5	79.197	247.70	28.40	18.02
19	33MMC5	86.064	263.00	30.00	19.59
20	223MMMC4	80.882	258.30	29.75	18.76
21	nC8	125.665	296.20	24.64	21.76
22	2MC7	117.647	288.00	24.80	20.60
23	3MC7	188.925	292.00	25.60	21.17
24	4MC7	117.709	290.00	25.60	21.17
25	3EC6	118.534	292.00	25.74	21.51
26	25MMC6	109.103	279.00	25.00	19.73
27	24MMC6	109.429	282.00	25.80	20.05
28	22MMC6	106.840	279.00	25.60	19.60
29	23MMC6	115.607	293.00	26.60	20.99
30	34MMC6	117.725	298.00	27.40	21.64
31	2M3EC5	115.650	295.00	27.40	21.52
32	33MMC6	111.969	290.84	27.20	20.63
33	3M3EC5	118.259	305.00	28.90	21.99
34	224MMMC5	99.238	271.15	25.50	18.77
35	234MMMC5	113.467	295.00	27.60	21.14
36	223MMMC5	109.841	294.00	28.20	20.67
37	233MMMC5	114.760	303.00	29.00	21.56
38	2233MMMMC4	106.470	270.87	24.50	

<sup>a</sup>M and E stand for methyl and ethyl, respectively; the numbers denote the position of the methyl and ethyl branches.<sup>b</sup>1 std. atm = 101.325 kPa.

$$\begin{aligned}
 m = 4, n = 2: & \text{1-4, 4-5; } {}^4R_2 = 1 \times 1 + 1 \times 1 = 2 \\
 n = 3: & \text{1-3-5, 1-4-5; } R_3 = 1 \times 1 \times 2 + 1 \times 1 \times 1 = 3 \\
 m = 4, n = 3: & \text{1-3-5; } {}^4R_3 = 1 \times 1 \times 2 = 2 \\
 m = 5, n = 3: & \text{1-4-5; } {}^5R_3 = 1 \times 1 \times 1 = 1
 \end{aligned}$$

### Quantitative structure–property relationships with the extended hyper-Wiener index

The potential of the extended hyper-Wiener for structure–property and structure–activity studies can be evaluated by performing comparative modeling of ref. 18 against the molecular connectivity index, the most widely used molecular descriptors in QSAR and (or) QSPR. In this study, we apply multiple regression analysis (MRA) in a QSPR modeling of four physical properties of C<sub>3</sub>–C<sub>8</sub> alkanes. The properties are boiling point, bp, in °C; critical temperature, *T*, in °C; critical pressures, *P*, in atm; and surface tension, ST, in 0.1 μN/cm (Table 1) (19). The models of molecular connec-

tivity are taken from Bonchev (18); the best models have been selected by the computer program.

The extended hyper-Wiener indexes of the 38 molecules are shown in Table 2, and their physical properties are shown in Table 1. Table 3 summarizes the statistics (correlation coefficient *r*, standard deviation *s*, and the Fischer ration *F*) of the molecular connectivity and the overall Wiener index of the C<sub>3</sub>–C<sub>8</sub> alkanes derived with five variables (18).

The best five-parameter, extended hyper-Wiener models obtained for the four examined alkane properties are given below.

$$\begin{aligned}
 [5] \quad \text{bp} = & -128.57725 + 47.67585 {}^2R_2 \\
 & - 103.72337 {}^3R_2 + 64.42522 {}^4R_2 \\
 & - 12.5043 {}^5R_2 + 5.3353 {}^6R_2 \\
 n = 38, s = 1.70, F = 4394, r = 0.9996
 \end{aligned}$$



**Table 2.** The extended hyper-Wiener index of the 38 alkanes.

No.	Molecule <sup>a</sup>	$R_1$	$R_2(^2R_2, ^3R_2, ^4R_2, ^5R_2, ^6R_2)$	$R_3(^4R_3, ^5R_3, ^6R_3)$	$R_4(^5R_4, ^6R_4)$	$R_5(^7R_5)$	$R_6$
1	C3	3	5(4, 1, 0, 0, 0)				
2	nC4	4	15(10, 4, 1, 0, 0)				
3	2MC3	4	12(9, 3, 0, 0, 0)	1(1, 0, 0)			
4	nC5	5	35(20, 10, 4, 1, 0)				
5	2MC4	5	28(18, 8, 2, 0, 0)	3(2, 1, 0)			
6	22MMC3	5	22(16, 6, 0, 0, 0)	4(4, 0, 0)	1(1, 0)		
7	nC6	6	70(35, 20, 10, 4, 1)				
8	2MC5	6	58(32, 17, 7, 2, 0)	6(3, 2, 1)			
9	3MC5	6	54(31, 16, 6, 1, 0)	9(4, 4, 1)			
10	23MMC4	6	47(29, 14, 4, 0, 0)	10(6, 4, 0)	1(0, 1)		
11	22MMC4	6	44(28, 13, 3, 0, 0)	10(7, 3, 0)	3(2, 1)		
12	nC7	7	126(56, 35, 20, 10, 4)				
13	2MC6	7	108(52, 31, 16, 7, 2)	10(4, 3, 2)			
14	3MC6	7	99(50, 29, 14.5, 1)	16(6, 7, 4)			
15	3EC5	7	90(48, 27, 12, 3, 0)	27(8, 12, 6)			
16	24MMC5	7	91(48, 27, 12, 4, 0)	18(8, 6, 4)	1(0, 0)		
17	23MMC5	7	83(46, 25, 10, 2, 0)	23(10, 10, 3)	3(0, 2)		
18	22MMC5	7	84(46, 25, 10, 3, 0)	19(10, 6, 3)	6(3, 2)		
19	33MMC5	7	76(44, 23, 8, 1, 0)	24(12, 10, 2)	9(4, 4)		
20	223MMMC4	7	69(42, 21, 6, 0, 0)	23(14, 9, 0)	8(3, 5)	1(1)	
21	nC8	8	210(84, 56, 35, 20, 10)				
22	2MC7	8	185(79, 51, 30, 16, 7)	15(5, 4, 3)			
23	3MC7	8	170(76, 48, 27, 13, 5)	30(8, 10, 7)			
24	4MC7	8	165(75, 47, 26, 12, 4)	36(9, 12, 10)			
25	3EC6	8	150(72, 44, 23, 9, 2)	54(12, 20, 15)			
26	25MMC6	8	161(74, 46, 25, 12, 4)	28(10, 8, 6)	1(0,0)		
27	24MMC6	8	147(71, 43, 22, 9, 2)	40(13, 14, 10)	3(0,0)		
28	22MMC6	8	149(71, 43, 22, 10, 3)	32(13, 9, 6)	10(4, 3)		
29	23MMC6	8	143(70, 42, 21, 8, 2)	42(14, 16, 9)	6(0,3)		
30	34MMC6	8	134(68, 40, 19, 6, 1)	48(16, 20, 10)	9(0,4)		
31	2M3EC5	8	129(67, 39, 18, 5, 0)	56(17, 24, 13)	9(0,4)		
32	33MMC6	8	131(67, 39, 18, 6, 1)	45(17, 17, 9)	18(6, 7)		
33	3M3EC5	8	118(64, 36, 15, 3, 0)	54(20, 24, 9)	27(8, 12)		
34	224MMMC5	8	127(66, 38, 17, 6, 0)	40(18, 13, 9)	12(4, 3)	1(0)	
35	234MMMC5	8	122(65, 37, 16, 4, 0)	45(19, 20, 6)	11(0, 6)	1(0)	
36	223MMMC5	8	115(63, 35, 14, 3, 0)	43(18, 19, 6)	17(4, 9)	3(2)	
37	233MMMC5	8	111(62, 34, 13, 2, 0)	48(22, 21, 5)	21(6, 11)	3(2)	
38	2233MMMMC4	8	97(58, 30, 9, 0, 0)	44(26, 18, 0)	23(8, 15)	6(6)	1

<sup>a</sup>M and E stand for methyl and ethyl, respectively; the numbers denote the position of the methyl and ethyl branches.

**Table 3.** Comparison of multilinear regression statistics (correlation coefficient, standard deviation, and the Fischer ratio) for the C3–C8 alkane property models with 5 parameters produced by the set of topological indexes  $\chi/OW(ext)$  (overall Wiener index =  $OW(ext)$ ).

Properties	Molecular connectivity index $\chi$				Overall Wiener index $OW(ext)$			
	$n$	$r$	$s$	$F$	$n$	$r$	$s$	$F$
Boiling point	38	0.9972	3.31	1151	38	0.9993	1.70	4393
Critical temperature	38	0.9962	4.76	831	38	0.9983	3.23	1790
Critical pressure	38	0.9920	0.50	397	38	0.9950	0.40	638
Surface tension	33	0.9938	0.22	432	33	0.9958	0.18	641

[6]

$$T = 86.00246 + 6.03808 \text{ } ^2R_2 - 20.1607 \text{ } ^5R_2$$

$$+ 10.69308 \text{ } ^6R_2 - 5.43957 \text{ } ^4R_3 - 3.80837 \text{ } ^7R_5$$

$$n = 38, s = 4.70, F = 853, r = 0.9963$$

[7]

$$P = 61.83744 - 7.34938 \text{ } R_1 + 0.46271 \text{ } ^2R_2$$

$$- 1.31561 \text{ } ^5R_2 + 0.90337 \text{ } ^6R_2 - 5.37976 \text{ } R_6$$

$$n = 38, s = 0.33, F = 9.14, r = 0.9965$$



**Table 4.** The results of cross-validation.

Properties	$s_{\min}$	$r_{\min}$	$s_{\max}$	$r_{\max}$	$s_{\text{mean}}$	$r_{\text{mean}}$
Boiling point	1.58	0.9990	1.72	0.9994	1.70	0.9993
Critical temperature	3.77	0.9956	4.77	0.9968	4.69	0.9963
Critical pressure	0.29	0.9952	0.34	0.9974	0.33	0.9965
Surface tension	0.20	0.9934	0.21	0.9951	0.21	0.9944

**Table 5.** The statistical results of random validation.

Properties	Training set		Test set	
	$r_{\text{mean}}$	$s_{\text{mean}}$	$r_{\text{mean}}$	$s_{\text{mean}}$
Boiling point	0.9994	1.50	0.9983	2.02
Critical temperature	0.9967	4.51	0.9905	4.64
Critical pressure	0.9967	0.33	0.9922	0.31
Surface tension	0.9946	0.19	0.9866	0.22

$$[8] \quad \text{ST} = 1.95062 + 4.36731 {}^2R_2 - 9.8391 {}^3R_2 \\ + 6.696 {}^4R_2 - 1.94851 {}^5R_2 + 0.84374 {}^6R_2 \\ n = 33, s = 0.21, F = 471, r = 0.9943$$

## Discussion

A comparison of the statistical results in Table 3 shows that the extended hyper-Wiener indexes give good statistics for each of the properties, and the standard deviations provided by these three sets of indexes are rather close.

To verify the robustness of the models, a cross-validation procedure, leave-one-out, was performed, and the results are listed in Table 4.

From Table 4 we can see that the maximum, minimum, and mean values of the correlation coefficient  $r$  and the standard deviation  $s$  are rather close; this indicates that the four five-parameter models are more stable.

A random test was also performed to verify the predictive ability of the four five-parameter models. Five times the tests were performed altogether, each time one third (for the surface tension model, 8 samples were removed, while 13 samples were removed for the other models) of the samples were randomly removed as a test set with the 25 remaining samples as the training set. The statistical results of the training set and test set are listed in Table 5.

The mean values of the correlation coefficient  $r$  and standard deviation  $s$  of the training sets and test sets are rather close; this also indicates that the four five-parameter models have good predictive ability.

## Results and conclusion

Upon summarizing the results, one may conclude that the extended hyper-Wiener indexes examined show a good potential for use in QSAR and QSPR studies. The results show that considerably better statistics are obtained when extending the hyper-Wiener index to the extended Hyper-Wiener Index. The extended hyper-Wiener indexes provided statistical results as the molecular connectivity index and the overall Wiener index in all models, and the standard deviations provided by these three sets of indexes are rather close. Moreover, it may provide a better way to apply the Wiener number and the hyper-Wiener index to the system of unsatu-

rated hydrocarbons and organic compounds, including heteroatoms, according to the method of molecular connectivity index. This can extend the usefulness of the Wiener number and the hyper-Wiener index and can make them a kind of widely used topological index in practice.

It needs to be mentioned that this conclusion is drawn for linear-regression models; the comparison of nonlinear models remains open for later studies.

## Acknowledgments

The authors acknowledge the financing of this research by the "551" Distinguished Person Foundation of Wenzhou and the Wenzhou science and technology developmental plan (the first group of 2003).

## References

1. M. Randić, X. Gou, T. Oxley, and H. Krishnapriyan. *J. Chem. Inf. Comput. Sci.* **33**, 709 (1993).
2. H. Wiener. *J. Am. Chem. Soc.* **69**, 2636 (1947).
3. H. Wiener. *J. Am. Chem. Soc.* **69**, 17 (1947).
4. S. Nikolic and Z. Trinajstić. *Croat. Chem. Acta*, **68**, 105 (1995).
5. A. Roberto, H. Pierre, and M. Federico. *J. Chem. Inf. Comput. Sci.* **41**, 958 (2001).
6. M. Randić. *Chem. Phys. Lett.* **211**, 478 (1993).
7. M. Randić, X. Gou, T. Oxley, H. Krishnapriyan, and L. Naylor. *J. Chem. Inf. Comput. Sci.* **34**, 361 (1994).
8. D.J. Klein, I. Lukovits, and I. Gutman. *J. Chem. Inf. Comput. Sci.* **35**, 50 (1995).
9. H. Hosoya. *Bull. Chem. Soc. Jpn.* **44**, 2332 (1971).
10. A.T. Balaban. *In From chemical topology to three dimensional geometry. Vol. 1. Edited by Plenum Publishing Corporation, New York. 1997. pp. 15–21.*
11. J. Devillers and A.T. Balaban. *In Topological indices and related descriptors in QSAR and QSPR. Vol. 1. Edited by Gordon and Breach, The Netherlands. 1999. pp. 31–35.*
12. S.S. Tratch, M.I. Stankevich, and N.S. Zefirov. *J. Chem. Inf. Comput. Sci.* **11**, 899 (1990).
13. D.J. Klein and I. Gutman. *J. Chem. Inf. Comput. Sci.* **39**, 534 (1999).
14. H.Y. Zhu, D.J. Klein, and I. Lukovits. *J. Chem. Inf. Comput. Sci.* **36**, 420 (1996).
15. M. Randić. *J. Am. Chem. Soc.* **97**, 6609 (1975).
16. L.B. Kier and L.H. Hall. *In Molecular connectivity and drug research. Vol. 1. Edited by Academic Press, New York. 1976. pp. 10–20.*
17. L.B. Kier and L.H. Hall. *In Molecular connectivity in structure-activity analysis. Edited by Wiley, New York. 1986. pp. 45–48.*
18. D. Bonchev. *J. Chem. Inf. Comput. Sci.* **41**, 582 (2001).
19. E.N. Diane, I.C. Wei, and P.G. Seybold. *J. Am. Chem. Soc.* **110**, 4186 (1988).



# Preparation of benzocyclobutenols by low temperature reaction of ketone enolates with benzyne

Sasmita Tripathy, Ranga Reddy, and Tony Durst

**Abstract:** The reaction of benzyne, generated from halobenzenes with lithium tetramethylpiperide (LTMP) at  $-40$  to  $-78$  °C, with ketone enolates affords benzocyclobutenols in fair to good yields.

**Key words:** benzyne, ketone enolates, anthracenes, benzocyclobutenol, alkoxides.

**Résumé :** Les benzyne, obtenues à partir des halobenzènes avec le tétraméthylpipéridure de lithium (LTMP) dans un intervalle de température de  $-40$  à  $-78$  °C, réagissent avec des énoles de cétone pour conduire à des benzocyclobuténols avec des rendements allant de assez bons à bons.

**Mots clés :** benzyne, énoles de cétone, anthracènes, benzocyclobuténol, alcoolates.

[Traduit par la Rédaction]

## Introduction

Benzocyclobutanols have considerable utility as precursors to *ortho*-quinodimethanes (**1**) and hence, for the preparation of a variety of polycyclic targets (**2**), including natural products (**3**). A number of routes exist for the preparation of these intermediates. These include: (i) photolysis of *o*-substituted phenyl alkyl ketones (**4**); (ii) reduction of or addition of organometallic reagents to benzocyclobutenones (**5**); (iii) cyclization of *ortho*- or iodo-substituted benzyl alkyl ketones (**5**); (iv) 2 + 2 cycloaddition of ketene equivalents to benzyne (**6**); and (v) trapping of benzyne with ketone enolates (**7**).

The latter reaction has been investigated extensively by the Caubere group (**7**) over a number of years using  $\text{NaNH}_2/t\text{-BuOK}$  in THF above room temperature to generate both the benzyne and the enolate. Under these conditions only a relatively small group of ketone enolates combine with benzyne to give isolable quantities of benzocyclobutenols. The most successful results were obtained with the enolates of five- to seven-membered ring ketones. We surmise that the explanation for the divergent behaviour is due to the difference in stability of the intermediate alkoxy-benzocyclobutenes under the reaction conditions. Typically, the alkali metal alkoxides of benzocyclobutenols such as **1** are unstable at temperatures as low as  $-78$  °C; they open, either by a cycloreversion to an *ortho*-quinodimethane **2** or revert to an aryllithium **3** (**8**). In the case of **1a**, the initial product of the cycloaddition of the enolate of cyclopentanone or cyclohexanone to benzyne, the concerted conrotatory cycloreversion pathway is very difficult since it results in the

generation of a highly strained trans double bond in a seven- or eight-membered ring, respectively, i.e., **4** (Scheme 1).

The tendency for cycloreversion of benzocyclobutene alkoxides has been exploited synthetically (**9**). Olofson and co-workers (**10**) described the reaction of benzyne with the enolate of acetaldehyde followed by ring opening of the resultant intermediate **1** ( $\text{R} = \text{R}_1 = \text{H}$ ) to **5**. This step is followed by a second trapping reaction with benzyne thereby yielding a series of symmetrical anthracenes. Unsymmetrical anthracenes were formed starting with the benzocyclobutanol **6**, LTMP, and a halobenzene (**10**) (Scheme 2).

Choy and Yang (**8**) showed that the lithium salt of *trans*-2-phenylbenzocyclobutenol undergoes cycloreversion at  $-78$  °C. Trapping of this intermediate with dimethyl maleate or dimethyl fumarate gave the expected tetrahydronaphthalenes mainly with retention of the alkene configuration.

## Results and discussion

We have reported that benzyne generation can be carried out at  $-40$  °C to  $-78$  °C with LTMP starting with iodo- and bromobenzene, respectively. When benzyne generation is carried out at these temperatures in the presence of a variety of ketone or enolates, the expected benzocyclobutenols can be isolated, generally in at least fair yield (eq. [1]). Typically, 10–40% of the starting ketone was recovered when equimolar amounts of the ketone enolate and bromobenzene were used (Table 1). The use of chlorobenzene as the benzyne precursor compared with bromo- or iodobenzene improved the yield of the benzocyclobutanol **7a** ( $\text{R}_1 = \text{Ph}$ ,  $\text{R}_2 = \text{H}$ ) with yields being 35, 28, and 15%, respectively. In each instance about 40% of the starting ketone was recov-

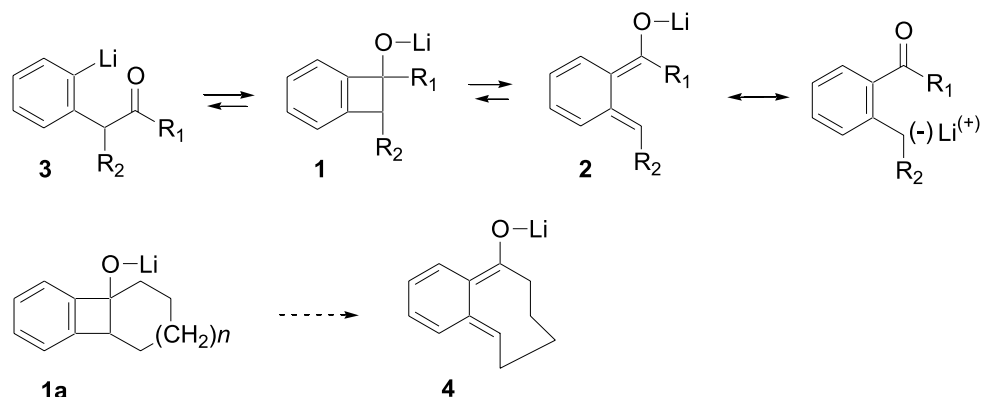
Received 28 January 2003. Published on the NRC Research Press Web site at <http://canjchem.nrc.ca> on 14 August 2003.

S. Tripathy, R. Reddy, and T. Durst.<sup>1</sup> Department of Chemistry, University of Ottawa, Ottawa, ON K1N 6N5, Canada.

<sup>1</sup>Corresponding author (tdurst@science.uottawa.ca).



Scheme 1.



Scheme 2.

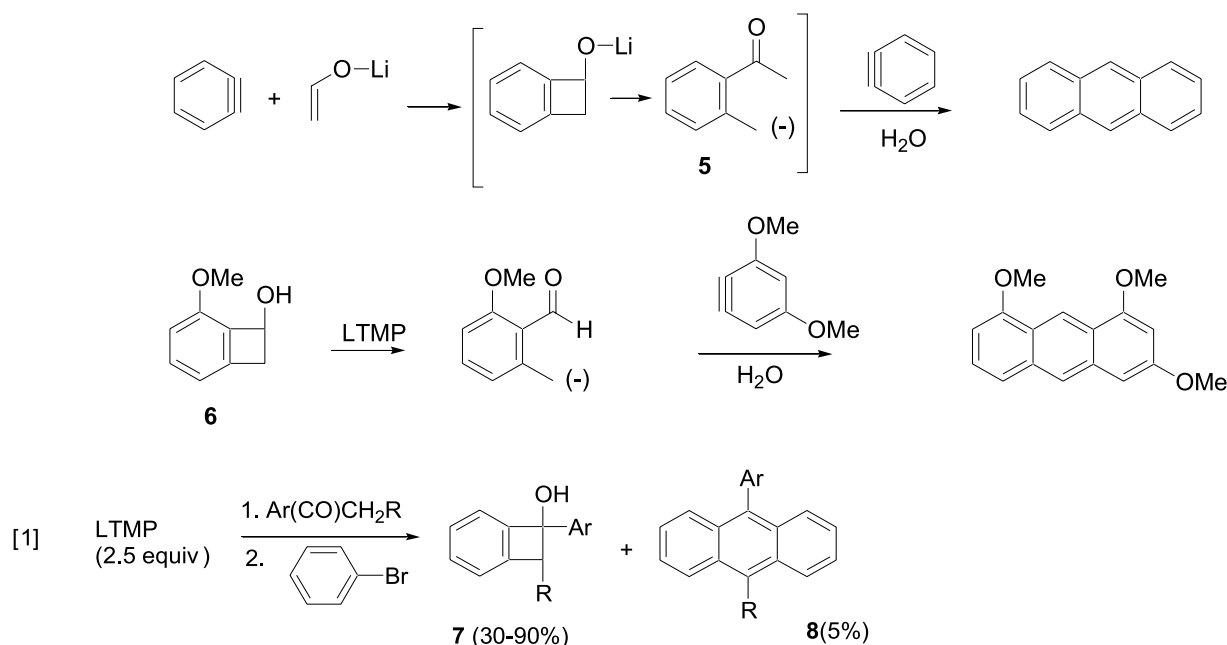
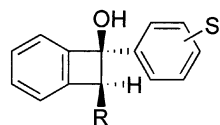


Table 1. Synthesis of 1-arylbenzocyclobutenols.



Entry	R	S	Yield (%)	Recovered ketone (%)
7a	H	H	35	39
7b	CH <sub>3</sub>	H	57	40
7c	C <sub>2</sub> H <sub>5</sub>	H	36	16
7d	Ph	H	52	12
7e	H	4-OCH <sub>3</sub>	41	14
7f	H	3,4-OCH <sub>3</sub>	42	12

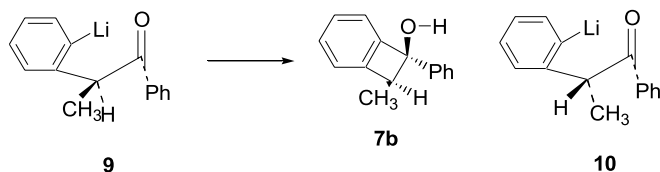
ered. An increase in the benzyne precursor (chlorobenzene) to enolate ratio from 1:1 to 2:1 improved the yield of **7a** from 38 to 55%. In addition to the benzocyclobutenols **7** and some recovered ketones, approximately 5% of the 9-

phenylanthracenes could also be isolated. These compounds ( $R_1 = \text{H}, \text{CH}_3, \text{C}_2\text{H}_5$ ) are formed via the same mechanism as is shown for the anthracenes in Scheme 2.

The stereochemistry of the benzocyclobutenol **7b** was assigned as shown on the basis of nOe experiments. Irradiation of the quartet at  $\delta = 3.8$  due to the remaining benzylic hydrogen showed enhancement of the signal for the methyl group at  $\delta = 1.5$ , but had no effect on the O-H group at  $\delta = 2.9$ . An nOe effect on the nearby aromatic signals was observed. In contrast, irradiation of the methyl signal augmented significantly those of the O-H, the benzylic methine, and the nearby aromatic hydrogens. Finally, irradiation of the O-H peak caused a strong enhancement on the methyl signal but had almost no effect on the benzylic methine hydrogen. The observed stereochemistry is reasonable on mechanistic grounds since the transition state from the intermediate **9** leading to **7b** should be preferred for steric reasons over the alternate possibility commencing with **10**. The stereochemistry of the other benzocyclobutenols carrying two ad-



ditional substituents on the cyclobutene ring is assumed to be the same as **7b** with the non-hydrogen substituent at C-2 being cis to the hydroxyl group.



1-Phenylbenzocyclobutenols, predictably substituted in either or both aromatic rings, were also prepared. Thus, compounds **11a** and **11b** were obtained using 2-methoxybromobenzene as the benzyne precursor, together with the appropriate enolate.

Not surprisingly, the yields of the tricyclic benzocyclobutenols **12a–12c**, obtained from the trapping of benzynes with the enolates of cyclic ketones, were better than those observed in the above described examples. The best result, an 82% isolated yield of **12c**, was obtained with the enolate of cycloheptanone. The cyclobutenols **12a** and **12b** were obtained in 65 and 55% yield, respectively. In the latter cases, the monosubstitution products **13a** and **13b** were also isolated.

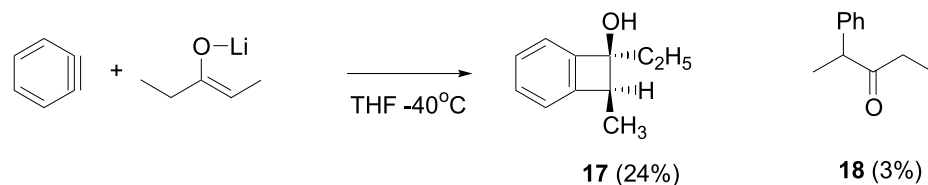
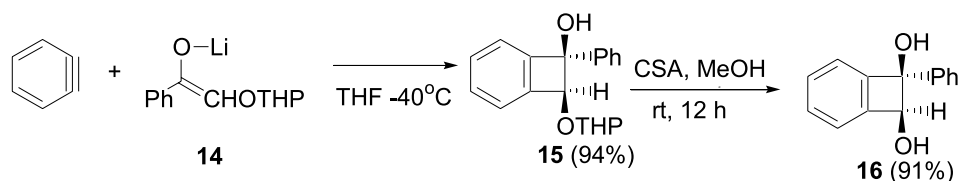
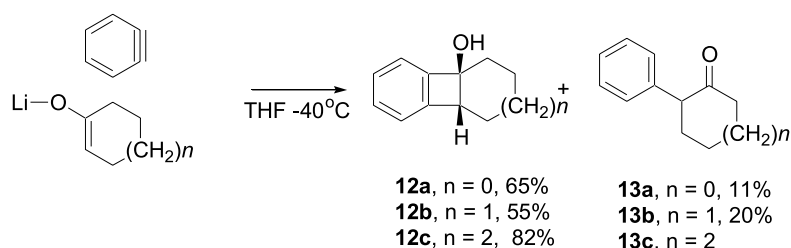
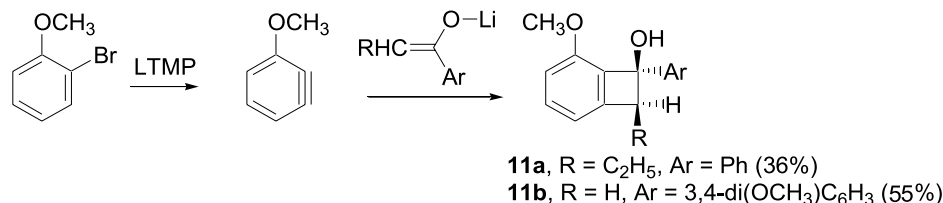
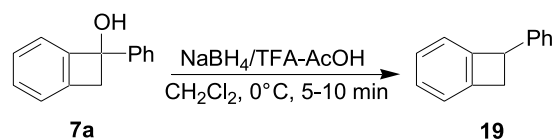
Trapping of benzyne with the enolate **14**, obtained from THP-protected 2-hydroxyacetophenone gave the expected benzocyclobutenol **15** in 94% yield based on 14% recovered starting material; acid-catalyzed hydrolysis afforded the cis

diol **16**. In contrast, the enolates of noncyclic aliphatic ketones such as 3-pentanone gave only 24% yield of the desired product **17**, the minor product being 2-phenyl-3-pentanone **18**, the result of arylation of the enolate.

We were disappointed that the aldehyde enolates reacted much less cleanly with benzynes under our reaction conditions. Examination of the crude products obtained with aldehydes such as hexanal and cyclohexanecarboxaldehyde showed the formation of numerous products (NMR peaks in the spectrum of the crude products possibly representing the desired product indicated a yield of less than 15%). These mixtures were not further investigated.

## Summary

The method described in this paper constitutes a simple route to benzocyclobutenols, in particular 1-arylbenzocyclobutenols and the tricyclic derivatives **12**. Since treatment of **7a** with  $\text{NaBH}_4/\text{TFA}-\text{AcOH}$  afforded cleanly the benzocyclobutene **19** in 59% yield, the reaction of benzynes with the enolates of aryl alkyl ketones can also lead to 1-arylbenzocyclobutenes.





## Experimental

### General procedure for the generation of benzynes in the presence of ketone and aldehyde enolates

*t*-BuLi in hexane (7.95 mmol) was added dropwise to a stirred solution of tetramethylpiperidine (7.95 mmol) in anhyd THF (10 mL) under nitrogen at  $-40^{\circ}\text{C}$ . The mixture was stirred for 10 min and a solution of ketone (3.18 mmol) in THF (5 mL) was added. This was followed by the addition of solution of halobenzene (3.18 mmol) in THF (5 mL). The reaction mixture was stirred at  $-40^{\circ}\text{C}$  for 5 h. An aqueous ammonium chloride solution was added and the resulting solution was extracted with ethyl acetate. The combined organic extracts were washed with brine, dried over  $\text{Na}_2\text{SO}_4$ , and concentrated under reduced pressure. The residue was purified by chromatography on silica gel with EtOAc–hexanes to give the benzocyclobutenol.

#### 1-Phenylbenzocyclobutenol (7a) (11)

Yield: 32%.  $^1\text{H}$  NMR ( $\text{CDCl}_3$ , 200 MHz)  $\delta$ : 3.38 (s, 1H), 3.60 (ABq, 2H), 7.20–7.58 (m, 9H).  $^{13}\text{C}$  NMR ( $\text{CDCl}_3$ , 50 MHz)  $\delta$ : 50.4, 82.1, 122.3, 124.8, 126.3, 128.1, 128.3, 128.9, 130.3, 134.4, 142.7, 144.1, 149.7. HR-MS calcd. for  $\text{C}_{14}\text{H}_{12}\text{O}$   $m/z$ : 196.0888; found: 196.0861.

#### cis-2-Methyl-1-phenylbenzocyclobutenol (7b)

Yield: 35%.  $^1\text{H}$  NMR ( $\text{CDCl}_3$ , 200 MHz)  $\delta$ : 1.51 (d,  $J = 8.0$  Hz, 3H), 2.61 (s, 1H), 3.81 (q,  $J = 8.0$  Hz, 1H), 7.21–7.45 (m, 9H).  $^{13}\text{C}$  NMR ( $\text{CDCl}_3$ , 50 MHz)  $\delta$ : 15.2, 54.1, 82.9, 122.8, 123.5, 126.9, 127.9, 128.0, 128.1, 128.6, 129.2, 130.3, 144.8, 149.0, 149.1. HR-MS calcd. for  $\text{C}_{15}\text{H}_{14}\text{O}$   $m/z$ : 210.1045; found: 210.1035.

#### cis-2-Ethyl-1-phenylbenzocyclobutenol (7c)

Yield: 36%.  $^1\text{H}$  NMR ( $\text{CDCl}_3$ , 200 MHz)  $\delta$ : 1.18 (t,  $J = 7.3$  Hz, 3H), 1.73–1.98 (m, 2H), 2.57 (s, 1H), 3.59 (t,  $J = 7.7$  Hz, 1H), 7.21–7.46 (m, 9H).  $^{13}\text{C}$  NMR ( $\text{CDCl}_3$ , 50 MHz)  $\delta$ : 13.0, 24.1, 61.4, 83.2, 122.7, 124.0, 126.1, 127.8, 128.9, 130.2. HR-MS calcd. for  $\text{C}_{16}\text{H}_{16}\text{O}$   $m/z$ : 224.1201; found: 224.1191.

#### cis-1,2-Diphenylbenzocyclobutenol (7d)

Yield: 52%, mp  $144\text{--}146^{\circ}\text{C}$ .  $^1\text{H}$  NMR ( $\text{CDCl}_3$ , 200 MHz)  $\delta$ : 2.70 (s, 1H), 5.41 (s, 1H), 6.96–7.37 (m, 12H), 7.71 (m, 2H).  $^{13}\text{C}$  NMR ( $\text{CDCl}_3$ , 50 MHz)  $\delta$ : 49.7, 75.9, 126.7, 127.3, 127.5, 127.7, 127.9, 128.2, 128.3, 128.5, 128.8, 129.5, 129.7, 137.8, 142.2, 144.7, 147.3. HR-MS calcd. for  $\text{C}_{20}\text{H}_{16}\text{O}$   $m/z$ : 272.1201; found: 272.1101.

#### 4-Methoxyphenylbenzocyclobutenol (7e) (11)

Yield: 41%.  $^1\text{H}$  NMR ( $\text{CDCl}_3$ , 200 MHz)  $\delta$ : 2.71 (brs, 1H), 3.58 (ABq, 2H), 3.77 (s, 3H), 6.86 (d,  $J = 8.8$  Hz, 2H), 7.21–7.49 (m, 6H).  $^{13}\text{C}$  NMR ( $\text{CDCl}_3$ , 50 MHz)  $\delta$ : 50.2, 55.9, 81.8, 114.2, 122.3, 124.8, 127.7, 128.2, 130.2, 136.4, 142.7, 149.8, 159.5. HR-MS calcd. for  $\text{C}_{15}\text{H}_{14}\text{O}_2$   $m/z$ : 226.0994; found: 226.0983.

#### 3,4-Dimethoxyphenylbenzocyclobutenol (7f) (11)

Yield: 42%.  $^1\text{H}$  NMR ( $\text{CDCl}_3$ , 200 MHz)  $\delta$ : 2.88 (brs, 1H), 3.57 (ABq, 2H), 3.82 and 3.83 (2s, 6H), 6.73 (d,  $J = 8.3$  Hz, 1H), 6.88 (dd,  $J = 8.3$ , 1.3 Hz, 1H), 7.09 (d,  $J = 8.3$  Hz, 1H), 7.32 (m, 4H).  $^{13}\text{C}$  NMR ( $\text{CDCl}_3$ , 50 MHz)  $\delta$ :

50.4, 58.4, 58.5, 81.8, 108.7, 111.2, 118.2, 118.8, 122.1, 124.8, 128.2, 130.2, 138.8, 142.7, 148.4, 148.7, 148.8. HR-MS calcd. for  $\text{C}_{16}\text{H}_{16}\text{O}_3$   $m/z$ : 256.10998; found: 256.10887.

#### 6-Methoxy-cis-2-ethyl-1-phenylbenzocyclobutenol (11a)

Yield: 36%.  $^1\text{H}$  NMR ( $\text{CDCl}_3$ , 200 MHz)  $\delta$ : 1.13 (t,  $J = 7.4$  Hz, 3H), 1.61–1.99 (m, 2H), 2.65 (s, 1H), 3.45 (t,  $J = 8.0$  Hz, 1H), 3.71 (s, 3H), 6.80 (t,  $J = 8.4$  Hz, 1H), 7.21–7.49 (m, 6H).  $^{13}\text{C}$  NMR ( $\text{CDCl}_3$ , 50 MHz)  $\delta$ : 13.5, 24.1, 58.2, 60.1, 83.5, 115.5, 116.2, 126.1, 128.2, 128.4, 132.2, 146.1, 150.1, 152.1, 156.2. HR-MS calcd. for  $\text{C}_{17}\text{H}_{18}\text{O}_2$   $m/z$ : 254.13074; found: 254.13061.

#### 6-Methoxy-1-(3,4-dimethoxyphenyl)benzocyclobutenol (11b)

Yield: 55%.  $^1\text{H}$  NMR ( $\text{CDCl}_3$ , 200 MHz)  $\delta$ : 3.40 (s, 1H), 3.42 (s, 2H), 3.63 (s, 3H), 3.80 (s, 6H), 6.75 (m, 3H), 6.90 (d,  $J = 8.8$  Hz, 1H), 7.08 (s, 1H), 7.22 (t,  $J = 8.8$  Hz, 1H).  $^{13}\text{C}$  NMR ( $\text{CDCl}_3$ , 50 MHz)  $\delta$ : 50.1, 55.7, 56.6, 80.9, 108.9, 110.6, 113.0, 116.2, 117.6, 131.2, 133.2, 137.1, 143.6, 148.0, 148.6, 157.3. HR-MS calcd. for  $\text{C}_{17}\text{H}_{18}\text{O}_4$   $m/z$ : 286.1205; found: 286.1190.

#### Tricyclo (4,3,0,0) hydroxy-1-nonadecatriene-2,4,6 (12a) (12d)

Yield: 65%, mp  $56$  to  $57^{\circ}\text{C}$ .  $^1\text{H}$  NMR ( $\text{CDCl}_3$ , 200 MHz)  $\delta$ : 1.01–1.29 (m, 1H), 1.56–1.89 (m, 4H), 2.10 (m, 1H), 1.65 (brs, 1H), 3.51 (t,  $J = 1.6$  Hz, 1H), 7.11–7.39 (m, 4H).  $^{13}\text{C}$  NMR ( $\text{CDCl}_3$ , 50 MHz)  $\delta$ : 25.1, 29.1, 36.3, 57.6, 89.8, 121.4, 123.6, 128.5, 130.2, 144.4, 148.3.

#### 2-Phenylcyclopentanone (13a) (12e)

$^1\text{H}$  NMR ( $\text{CDCl}_3$ , 200 MHz)  $\delta$ : 1.81–2.61 (m, 6H), 3.51 (t,  $J = 8.0$  Hz, 1H), 7.21–7.49 (m, 5H).  $^{13}\text{C}$  NMR ( $\text{CDCl}_3$ , 50 MHz)  $\delta$ : 22.1, 32.1, 38.5, 56.1, 128.1, 129.4, 129.9, 140.1.

#### Tricyclo (4,4,0,0) hydroxy-1-dodecatriene-2,4,6 (12b) (12a–12c)

Yield: 55%, mp  $106\text{--}108^{\circ}\text{C}$ .  $^1\text{H}$  NMR ( $\text{CDCl}_3$ , 200 MHz)  $\delta$ : 1.11–2.11 (m, 8H), 2.29 (brs, 1H), 3.39 (t,  $J = 7.6$  Hz, 1H), 7.10–7.35 (m, 4H).  $^{13}\text{C}$  NMR ( $\text{CDCl}_3$ , 50 MHz)  $\delta$ : 18.0, 18.4, 24.3, 32.1, 54.2, 79.6, 121.6, 123.7, 128.1, 129.7, 146.1, 149.9. HR-MS calcd. for  $\text{C}_{12}\text{H}_{14}\text{O}$   $m/z$ : 174.1045; found: 174.1071.

#### 2-Phenylcyclohexanone (13b) (12e)

Yield: 20%.  $^1\text{H}$  NMR ( $\text{CDCl}_3$ , 200 MHz)  $\delta$ : 1.71–2.61 (m, 8H), 3.61 (dd,  $J = 8.0$ , 16.0 Hz, 1H), 7.11–7.49 (m, 5H).  $^{13}\text{C}$  NMR ( $\text{CDCl}_3$ , 50 MHz)  $\delta$ : 25.9, 28.4, 35.7, 42.8, 58.0, 127.5, 128.9, 129.1, 139.3, 210.0. HR-MS calcd. for  $\text{C}_{12}\text{H}_{14}\text{O}$   $m/z$ : 174.1045; found: 174.1057.

#### Tricyclo (4,5,0,0) hydroxy-1-tridecatriene-2,4,6 (12c) (12a–12c)

Yield: 82%.  $^1\text{H}$  NMR ( $\text{CDCl}_3$ , 200 MHz)  $\delta$ : 1.31–2.21 (m, 10H), 2.70 (s, 1H), 3.41 (dd,  $J = 4.5$ , 10.0 Hz, 1H), 7.10–7.31 (m, 4H).  $^{13}\text{C}$  NMR ( $\text{CDCl}_3$ , 50 MHz)  $\delta$ : 24.8, 28.1, 31.4, 32.6, 36.8, 60.8, 84.2, 121.4, 123.5, 128.0, 129.7, 146.3, 149.8.



### Compound 15

*t*-BuLi in hexane (4.68 mL, 7.96 mmol) was added dropwise to a stirred solution of tetramethylpiperidine (1.34 mL, 7.96 mmol) in anhyd THF (10 mL) under nitrogen at  $-40^{\circ}\text{C}$ . The mixture was stirred for 10 min and a solution of 2-*O*-tetrahydropyranyloxy acetophenone (0.70 g, 3.18 mmol) in THF (5 mL) was added. This was followed by the addition of a solution of bromobenzene (0.50 g, 3.18 mmol) in THF (5 mL). After being stirred for 5 h at  $-40^{\circ}\text{C}$ , the reaction mixture was quenched by the addition of  $\text{NH}_4\text{Cl}$  solution and the mixture was allowed to warm to room temperature. The resulting solution was extracted with ethyl acetate, and the combined organic solutions were washed with brine, dried over  $\text{Na}_2\text{SO}_4$ , and evaporated. The residue was purified by chromatography on silica gel with 8% EtOAc–hexanes to afford **15** in 94% yield.  $^1\text{H}$  NMR ( $\text{CDCl}_3$ , 200 MHz)  $\delta$ : 1.5–2.0 (m, 6H), 3.52 (m, 1H), 4.0 (m, 1H), 4.55 (s, 1H), 4.70 and 4.90 (2m, 1H), 5.12 and 5.28 (2s, 1H), 7.10–7.50 (m, 9H).

### 1-Phenyl-cis-benzocyclobuten-1,2-diol (16)

To a stirred solution of **15** (0.27 g, 0.94 mmol) in 5 mL of methanol was added CSA (30 mg) and the reaction mixture was stirred for 30 min. Methanol was evaporated and the residue was extracted with ethyl acetate, washed with satd.  $\text{NaHCO}_3$  solution, dried over  $\text{Na}_2\text{SO}_4$ , and evaporated. The residue was purified by chromatography on silica gel with 40% EtOAc–hexanes to afford **16** in 91% yield, mp 128–130  $^{\circ}\text{C}$ .  $^1\text{H}$  NMR ( $\text{CDCl}_3$ , 200 MHz)  $\delta$ : 3.12, 3.40 (2bs, OH), 5.20 (s, 1H), 7.20–7.40 (m, 9H).  $^{13}\text{C}$  NMR ( $\text{CDCl}_3$ , 50 MHz)  $\delta$ : 80.8, 83.7, 123.5, 124.7, 126.1, 128.2, 128.9, 130.7, 131.1, 142.8, 146.7, 148.9. HR-MS calcd. for  $\text{C}_{14}\text{H}_{12}\text{O}_2$   $m/z$ : 212.08376; found: 212.8368.

### cis-2-Ethyl-1-methylbenzocyclobutenol (17)

Yield: 24%.  $^1\text{H}$  NMR ( $\text{CDCl}_3$ , 200 MHz)  $\delta$ : 1.15 (t,  $J$  = 7.36 Hz, 3H), 1.30 (d,  $J$  = 7.22 Hz, 3H), 1.62–1.82 (m, 2H), 2.20 (brs, 1H), 3.44 (q,  $J$  = 7.19 Hz, 1H), 7.13–7.28 (m, 4H).  $^{13}\text{C}$  NMR ( $\text{CDCl}_3$ , 50 MHz)  $\delta$ : 8.4, 13.8, 27.6, 53.4, 82.7, 121.5, 122.6, 127.2, 129.2, 146.7, 148.7. HR-MS calcd. for  $\text{C}_{11}\text{H}_{14}\text{O}$   $m/z$ : 162.1045; found: 162.1036.

### 1-Phenylbenzocyclobutene (19) (13)

To a solution of glacial acetic acid (6 mL) and trifluoroacetic acid (6 mL) at  $0^{\circ}\text{C}$  was added sodium borohydride (0.59 g, 10 equiv). The benzocyclobutanol **7a** (0.31 g, 1.58 mmol) in  $\text{CH}_2\text{Cl}_2$  (10 mL) was immediately added and stirred for 2 min followed by the rapid addition of sodium borohydride (0.30 g, 5 equiv). The solution was stirred for 5–10 min and diluted with  $\text{H}_2\text{O}$  (40 mL) and extracted with  $\text{CH}_2\text{Cl}_2$  (3  $\times$  25 mL), dried over  $\text{Na}_2\text{SO}_4$ , and evaporated. The residue was purified by chromatography on silica gel with 3% EtOAc–hexanes to afford **19** in 59% yield.  $^1\text{H}$  NMR ( $\text{CDCl}_3$ , 200 MHz)  $\delta$ : 3.28 (dd,  $J$  = 2.85, 13.78 Hz, 1H), 3.90 (dd,  $J$  = 5.37, 13.78 Hz, 1H), 4.87 (dd,  $J$  = 2.85, 5.37 Hz, 1H), 7.32–7.54 (m, 9H).  $^{13}\text{C}$  NMR ( $\text{CDCl}_3$ , 50 MHz)  $\delta$ : 40.1, 47.6, 122.9, 123.4, 126.6, 127.1, 127.3, 127.8, 128.6, 142.9, 144.2, 147.8. HR-MS calcd. for  $\text{C}_{14}\text{H}_{12}$   $m/z$ : 180.0939; found: 180.0928.

### Acknowledgments

The continued support of the Natural Sciences and Engineering Research Council of Canada (NSERC) of the TD group's basic research program, including this project, is gratefully acknowledged.

### References

- (a) G. Coll, A. Costa, P.M. Deya, F. Flexas, C. Rotger, and J.M. Saa. *J. Org. Chem.* **57**, 6222 (1992); (b) H. Tomioka, M. Ichihashi, and K. Yamamoto. *Tetrahedron Lett.* **36**, 5371 (1995); (c) X. Zhang and C.S. Foote. *J. Org. Chem.* **59**, 5235 (1994); (d) J.L. Charlton, K. Koh, and G.L. Plourde. *Tetrahedron Lett.* **30**, 3279 (1989).
- (a) J.L. Segura and N. Martin. *Chem. Rev.* **99**, 3199 (1999), and refs. cited therein; (b) S. Christophe, C.K. Caubere, P. Renard, B. Pfeiffer, and P. Caubere. *Tetrahedron Lett.* **39**, 9431 (1998); (c) M.A. Zouaoui, A. Mouaddib, B.J. Gregoire, S. Ianneli, M. Nardelli, and P. Caubere. *J. Org. Chem.* **56**, 4078 (1991); (d) P. Geoffroy, A. Mouaddib, M.C. Carre, and P. Caubere. *Tetrahedron Lett.* **29**, 1385 (1988); (e) J.L. Charlton, D. Bogucki, and P. Guo. *Can. J. Chem.* **73**, 1463 (1995); (f) J.L. Charlton, G.L. Plourde, K. Koh, and A.S. Secco. *Can. J. Chem.* **68**, 2022 (1990).
- (a) H. Nemoto and K. Fukumoto. *Tetrahedron*, **54**, 5425 (1998); (b) D.I. Macdonald and T. Durst. *J. Org. Chem.* **53**, 3663 (1998); (c) K. Kobayashi, M. Itoh, and H. Sugimoto. *Tetrahedron Lett.* **28**, 3369 (1987); (d) K. Kobayashi, M. Itoh, A. Sasaki, and H. Sugimoto. *Tetrahedron*, **47**, 5437 (1991); (e) S. Shimada, K. Osoada, and K. Narsaka. *Bull. Chem. Soc. Jpn.* **66**, 1254 (1993); (f) D.M. Coltart and J.L. Charlton. *Can. J. Chem.* **74**, 88 (1996).
- (a) P.G. Sammes. *Tetrahedron*, **32**, 405 (1976); (b) P.J. Wagner, M. Sobczak, and B.-S. Park. *J. Am. Chem. Soc.* **120**, 2488 (1998); (c) Y. Ito, G. Kano, and N. Nakamura. *J. Org. Chem.* **63**, 5643 (1998); (d) P.J. Wagner, D. Subramanyam, and B.-S. Park. *J. Am. Chem. Soc.* **113**, 709 (1991); (e) M. Yoshioka, K. Iida, E. Kawata, K. Maeda, S. Kumakura, and T. Hasegawa. *J. Org. Chem.* **62**, 2655 (1997); (f) M.-C. Carre, M.-L.V. Villame, and P. Caubere. *J. Chem. Soc., Perkin Trans. 1*, **10**, 2542 (1979).
- (a) J.E. Almlof, M.W. Feyereisen, T.H. Jozefiak, and L.L. Miller. *J. Am. Chem. Soc.* **112**, 1206 (1990); (b) M.A. Ardakani and T.W. Wallace. *Tetrahedron Lett.* **24**, 1829 (1983); (c) D.N. Hickman, T.W. Wallace, and J.M. Wardleworth. *Tetrahedron Lett.* **32**, 819 (1991); (d) K. Kobayashi, Y. Kanno, S. Seko, and H. Sugimoto. *Chem. Commun.* 780 (1992); (e) I.S. Aidhen and N.S. Narasimhan. *Tetrahedron Lett.* **32**, 2171 (1991).
- (a) T.W. Wallace and A. Ardakani. *Tetrahedron*, **44**, 5939 (1988); (b) R.V. Stevens and G.S. Bisacchi. *J. Org. Chem.* **47**, 2393 (1982).
- (a) B. Gregoire, M.-C. Carre, and P. Caubere. *J. Org. Chem.* **51**, 1419 (1986); (b) M.-C. Carre, B. Gregoire, and P. Caubere. *J. Org. Chem.* **49**, 2050 (1984); (c) P. Caubere. *Acc. Chem. Res.* **7**, 301 (1974).
- W. Choy and H. Yang. *J. Org. Chem.* **53**, 5796 (1988).
- (a) J.J. Fitzgerald, N.E. Drysdale, and R.A. Olofson. *Synth. Commun.* **22**, 1807 (1992); (b) I. Fleming and T. Mah. *J. Chem. Soc., Perkin Trans. 1*, 964 (1975).
- J.J. Fitzgerald, N.E. Drysdale, and R.A. Olofson. *J. Org. Chem.* **57**, 7122 (1992).



11. K. Kobayashi, Y. Kanno, S. Seko, and H. Suginome. *J. Chem. Soc., Perkin Trans. 1*, 3111 (1992).
12. (a) P. Caubere, G. Guillaumet, and M.S. Mourad. *Tetrahedron*, **29**, 1843 (1973); (b) P. Caubere, G. Guillaumet, and M.S. Mourad. *Tetrahedron Lett.* **48**, 4673 (1971); (c) G. Adam, J. Andrieux, and M. Plat. *Tetrahedron*, **41**, 399 (1985); (d) P. Caubere, N. Derozier, and B. Loubinoux. *Bull. Soc. Chim. Fr.* 302 (1971); (e) M.W. Rathke and D. Vogiazoglou. *J. Org. Chem.* **52**, 3697 (1987).
13. (a) A. Padwa, D. Dehm, T. Oine, and G.A. Lee. *J. Am. Chem. Soc.* **97**, 1837 (1975); (b) L. Horner, P.V. Subramaniam, and K. Eiben. *Liebigs Ann. Chem.* **714**, 91 (1968).



# Novel synthesis of a highly functionalized cyclopropane derivative

Stéphane Trudeau and Pierre Deslongchamps

**Abstract:** A model study was carried out to explore the feasibility of synthesizing fused tricyclic ring structures containing a C<sub>7</sub>—C<sub>8</sub> double bond juncture (steroid numbering) by employing an S<sub>N</sub>2' cyclization of a silyl enol ether to displace an allylic acetate as the key step. Instead of the anticipated product, highly functionalized cyclopropanes were obtained. These novel cyclopropane structures are the result of the concomitant 1,2-migration of a dithiane thioether moiety and the eventual displacement of the acetate group, followed by the cyclization of the silyl enol ether.

**Key words:** tricycles, S<sub>N</sub>2' cyclization, inductive effect, cyclopropane.

**Résumé :** Une étude modèle a été réalisée pour vérifier la possibilité de produire des tricycles possédant une double liaison entre les carbones C<sub>7</sub> et C<sub>8</sub> (numérotation des stéroïdes) par une réaction de cyclisation S<sub>N</sub>2' entre un éther d'énol silylé et un acétate allylique comme étape clé. Or, une réaction inattendue s'est produite pour conduire à la synthèse de cyclopropanes hautement fonctionnalisés au lieu du produit attendu. Cela étant le résultat d'une cyclisation entre un éther d'énol silylé sur un groupement dithiane où l'un des thioéthers a subi une migration-1,2 tout en déplaçant le groupement acétate partant.

**Mots clés :** tricycles, cyclisation S<sub>N</sub>2', effet inductif, cyclopropane.

## Introduction

More than 25 years ago, Nozaki and co-workers (1) studied cationic cyclization of allylic acetates via nucleophilic participation of silyl enol ether. In light of this study, we recently conducted a model study to investigate the possibility of using an S<sub>N</sub>2'-type cyclization of a silyl enol ether to displace an allylic acetate to generate C<sub>7</sub>—C<sub>8</sub> (steroid numbering) unsaturated fused tricyclic ring structures (cf. **1**, Fig. 1). In model structures containing a sulfone moiety (X = SO<sub>2</sub>Ph, Y = H) or a methylene group (X = Y = H) next to the acetate leaving group no cyclization occurred. In contrast, when the model compound was decorated with a dithiane functionality (X, Y = S-(CH<sub>2</sub>)<sub>3</sub>-S) adjacent to the acetate leaving group, instead of obtaining the anticipated product **1** (Fig. 1), the unexpected formation of a highly functionalized cyclopropane was observed (cf. **2**, Fig. 1). The details of this investigation are disclosed herein.

## Results and discussion

The use of a sulfone connector for the coupling of rings A and C was explored initially. The intermediate **7** was synthesized starting from the commercially available (R)-(-)-

carvone. Thus, Michael addition of phenylthiomethyl phenyl sulfone (**2**, **3**) and trapping of the attendant enolate with *tert*-butyldimethylsilyl trifluoromethanesulfonate furnished thioether **4** (Scheme 1). It is noteworthy that the presence of the thioether moiety in the nucleophile was necessary to achieve exclusive 1,4-addition. Thioether **4** was then subjected to *n*-Bu<sub>3</sub>SnH–AIBN reduction in refluxing benzene to obtain sulfone **5**. Deprotonation of sulfone **5** with *n*-BuLi, followed by alkylation with the commercially available reagent, 1-cyclohexene-1-carboxaldehyde, afforded the alcohol **6**. The latter product was then acylated with acetic anhydride and catalytic DMAP in pyridine to yield the acetate **7**. All attempts to procure the ABC-fused tricyclic structure, **8**, using the acetate **7** were in vain. For instance, in protic acidic medium, Lewis acid medium, or under anionic conditions, only deprotection of the silyl enol ether was observed. Even with palladium, the formation of the π-allyl palladium species was not observed, and only starting material was recovered instead. It may therefore be concluded that the inductive effect of the sulfonyl group prohibits the solvolysis of the acetate, thus precluding the formation of the π-allyl cation that would have been trapped by the silyl enol ether.

To circumvent the obstacle encountered with the sulfonyl group, alcohol **6** was oxidized with TPAP–NMO in dichloromethane in the presence of 4 Å molecular sieves to produce the ketosulfone **9** (Scheme 2). Subsequent desulfurization with *n*-Bu<sub>3</sub>SnH–AIBN in refluxing toluene yielded ketone **10** (**4**), which was immediately converted to the corresponding alcohol using Luche reduction conditions (NaBH<sub>4</sub>–CeCl<sub>3</sub> in methanol). The alcohol thus obtained was then acylated with acetic anhydride – DMAP (catalytic) in pyridine to obtain the acetate **11**. To our dismay, all efforts directed at effecting cyclization of the precursor acetate **11** to form **12**

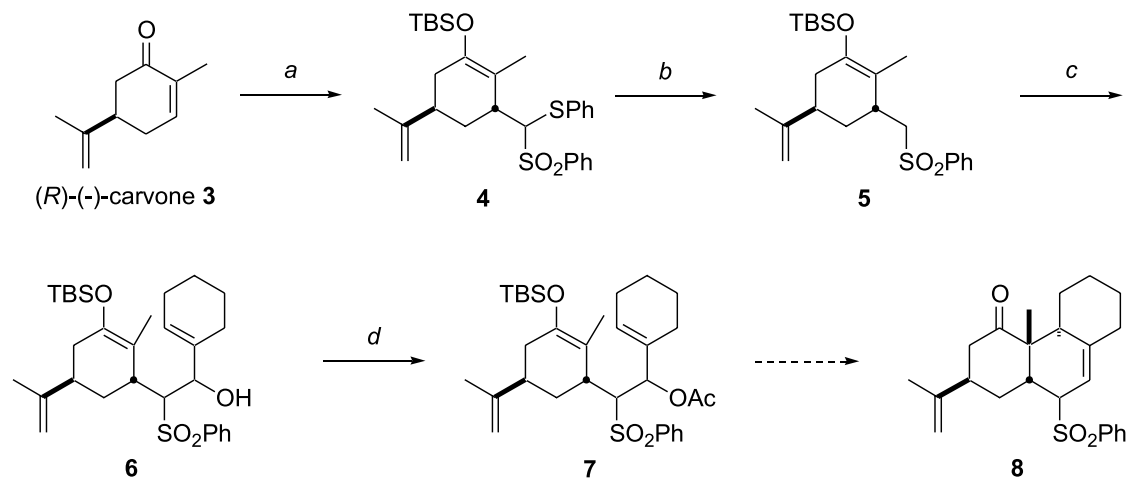
Received 28 February 2003. Published on the NRC Research Press Web site at <http://canjchem.nrc.ca> on 29 August 2003.

**S. Trudeau and P. Deslongchamps.**<sup>1</sup> Laboratoire de synthèse organique, Département de Chimie, Institut de Pharmacologie de Sherbrooke, Université de Sherbrooke, 3001, 12<sup>e</sup> Avenue nord, Sherbrooke, QC J1H 5N4, Canada.

<sup>1</sup>Corresponding author (e-mail: pierre.deslongchamps@usherbrooke.ca).



**Scheme 1.** (a) *i.* Phenylsulfonylphenylthiomethane, *n*-BuLi, THF; *ii.* (*R*)-(-)-carvone; *iii.* TBS-OTf, Et<sub>3</sub>N (quant.); (b) *n*-Bu<sub>3</sub>SnH, AIBN, PhH (87%); (c) *i.* *n*-BuLi, THF; *ii.* 1-cyclohexene-1-carboxaldehyde (61%); (d) Ac<sub>2</sub>O, DMAP, pyridine (92%).



**Scheme 2.** (a) TPAP, NMO, MS 4A, CH<sub>2</sub>Cl<sub>2</sub> (60%); (b) *n*-Bu<sub>3</sub>SnH, AIBN, toluene (quant.); (c) NaBH<sub>4</sub>, CeCl<sub>3</sub>, MeOH (79%); (d) Ac<sub>2</sub>O, DMAP, pyridine (86%).

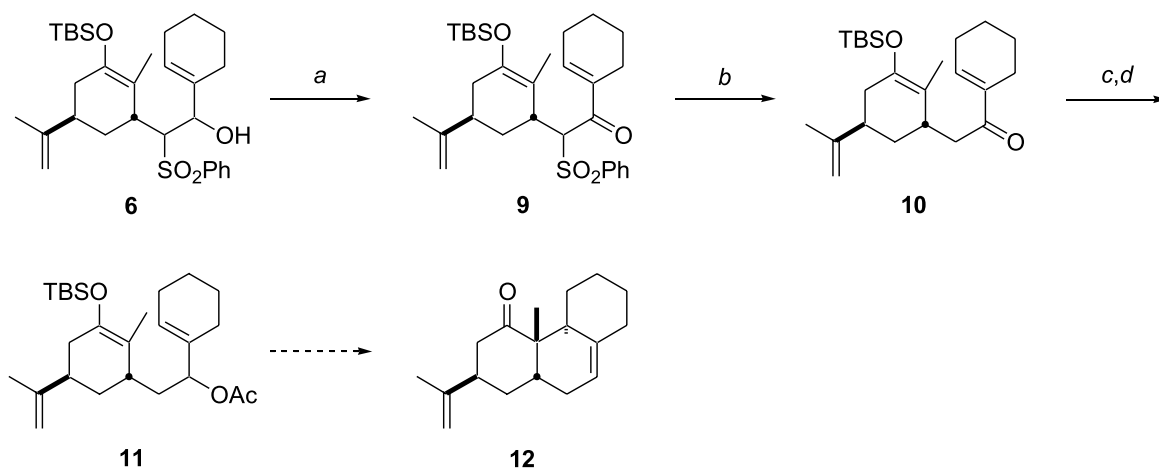
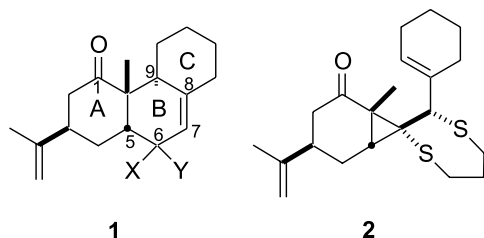


**Fig. 1.** Target structures.



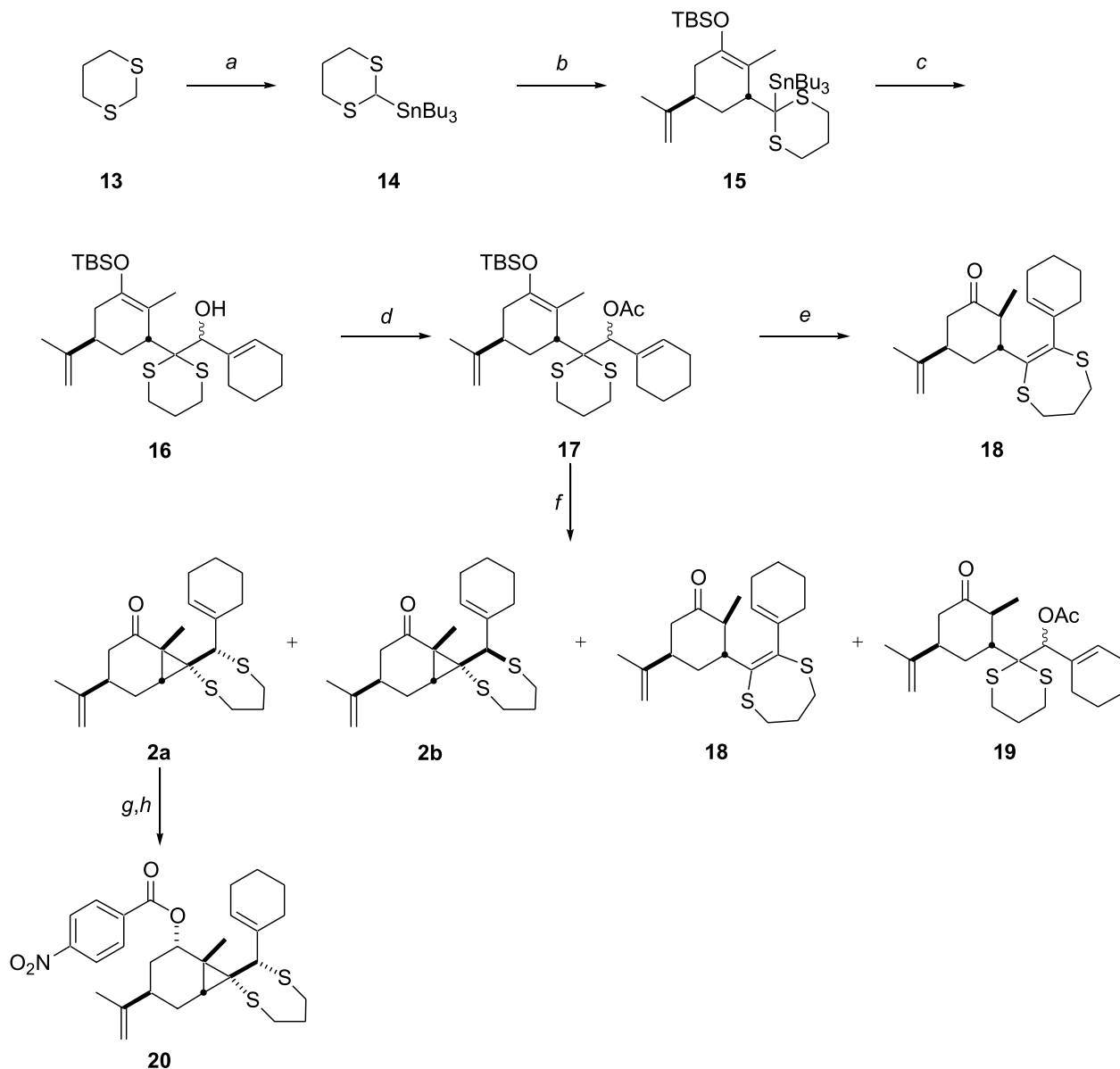
were unsuccessful. Exclusive deprotection of the silyl enol ether occurred in most cases (acidic medium as well as anionic conditions). With palladium species, only starting material was recovered. On the basis of the above studies, it can be concluded that even in absence of the inductive effect of the sulfonyl group, the acetate group is reluctant to leave and thereby induce cyclization.

Recently, Saigo and co-workers (5) reported that allylic acetates with a thioether as a neighboring group can undergo

S<sub>N</sub>2' coupling with silyl enol ether in the presence of a Lewis acid. Keeping this in mind, the synthesis of acetate **17** was then undertaken, starting from the commercially available 1,3-dithiane **13** (Scheme 3). Deprotonation of the latter with LDA and trapping of the attendant anion with *n*-Bu<sub>3</sub>SnCl furnished stannane **14** in quantitative yield (6). Deprotonation of intermediate **14** with LDA followed by a 1,4-Michael addition with (*R*)-(-)-carvone and trapping of the resultant enolate with *tert*-butyldimethylsilyl trifluoromethanesulfonate in the presence of triethylamine yielded compound **15**. Transmetalation of the stannyl moiety in **15** with *n*-BuLi, followed by alkylation with 1-cyclohexene-1-carboxaldehyde, afforded alcohol **16** in a 3:1 diastereomeric ratio. The alcohol **16** was then acylated with acetic anhydride – DMAP (catalytic) in pyridine to provide the acetate **17** (3:1 diastereomeric mixture). With acetate **17** in hand, a preliminary attempt was made to induce the S<sub>N</sub>2' cyclization using *p*-TSA in benzene. The neighboring group participation induced by the dithiane helped the departure of the acetate group, furnishing compound **18** in 64% yield. Thus,



**Scheme 3.** (a) *i.* LDA, THF; *ii.*  $n\text{-Bu}_3\text{SnCl}$  (quant.); (b) *i.* LDA, THF; *ii.* (*R*)-(-)-carvone, HMPA; *iii.* TBS-OTf,  $\text{Et}_3\text{N}$  (88%); (c) *i.*  $n\text{-BuLi}$ , THF *ii.* 1-cyclohexene-1-carboxaldehyde (75%) (ratio of diastereoisomers = 3:1); (d)  $\text{Ac}_2\text{O}$ , DMAP, pyridine (79%); (e) *p*-TSA, PhH (64%); (f) TMS-OTf,  $\text{CH}_2\text{Cl}_2$  (77%) (ratio **2a:2b:18:19** = 3:1:1.2:1.5); (g)  $\text{LiAlH}_4$ , THF (71%) (ratio of diastereoisomers = 7.5:1); (h) 4-nitrobenzoyl chloride, DMAP, pyridine,  $\text{CH}_2\text{Cl}_2$  (40%).

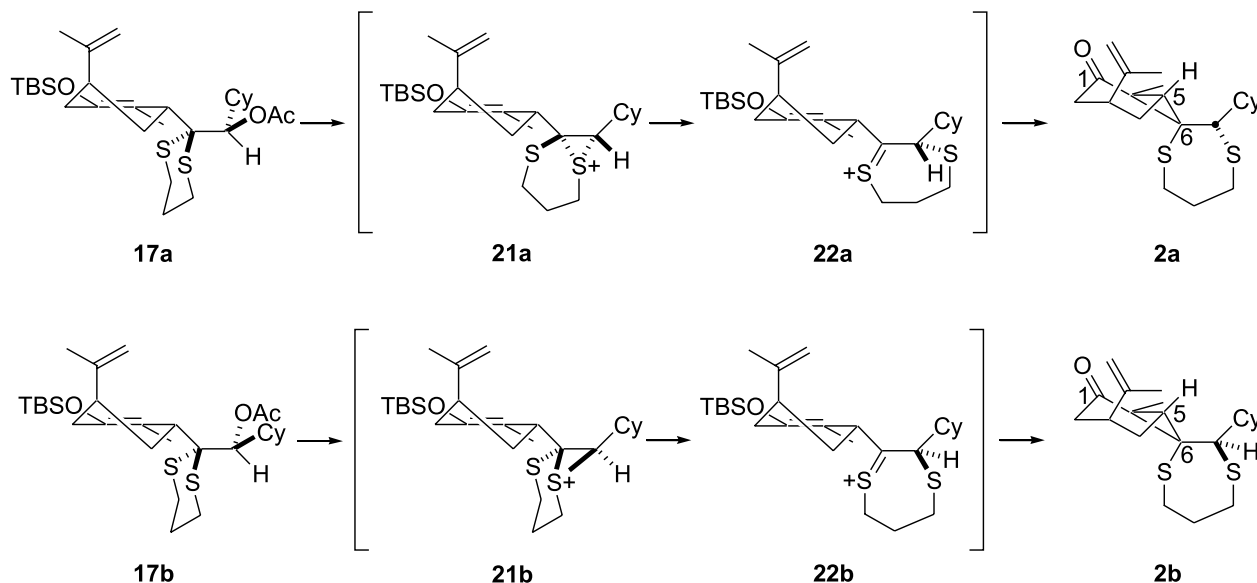


hydrogen abstraction and formation of a double bond induced a net 1,2-migration of a thioether. The structure of compound **18** was assigned by spectral analysis, including DEPT NMR studies. A similar 1,2-migration of a thioether has also been recently reported by Kutateladze and co-workers (7).

We next explored the possibility of effecting the  $\text{S}_{\text{N}}2'$  cyclization under Lewis acid conditions. To our great surprise, however, when acetate **17** was treated with trimethylsilyl trifluoromethanesulfonate in dichloromethane at  $-78^\circ\text{C}$ , cyclopropane **2** was obtained in 46% yield as a separable 3:1 mixture of two diastereoisomers. Compounds **18** and **19** were also isolated from the reaction mixture (14% and 17%

yield, respectively). Again, it can be surmised that the dithiane facilitated the departure of the acetate group in compounds **17a** and **17b** to form intermediate **21a** and **21b** as sulfonium cations (Fig. 2). These sulfonium cations could then rearrange to intermediates **22a** and **22b** and, thereby, induce a net 1,2-migration of a thioether moiety. Thus, the silyl enol ether participates in a C—C bond formation at  $\text{C}_6$  in a Mukaiyama thio-aldol fashion instead of promoting cyclization at  $\text{C}_9$  in an  $\text{S}_{\text{N}}2'$  manner, contrary to our initial expectations. Moreover, it can be presumed that the Mukaiyama thio-aldol process was stereoselective, as the diastereoisomeric composition in cyclopropane products was identical to that in the acetate starting material. The structure



**Fig. 2.** Proposed mechanism for formation of cyclopropanes **2a** and **2b**.

of the major diastereoisomer **2a** was assigned by single-crystal X-ray diffraction crystallography of the benzoate **20** (Fig. 3).<sup>2</sup> This product was prepared from compound **2a**, which was reduced with  $\text{LiAlH}_4$  in THF to give two diastereoisomers (7.5:1) that were readily separable by flash chromatography on silica gel. The major diastereoisomer was subsequently acylated, using 4-nitrobenzoyl chloride – DMAP (catalytic) – pyridine in dichloromethane, to provide **20**.

## Experimental

### General

All reactions were performed under  $\text{N}_2$  atmosphere with flame-dried glassware. Solvents were distilled and dried according to standard procedures. Analytical TLC were performed on precoated glass plates (0.25 mm) with silica gel 60F-250 (Merck). Flash-chromatography was performed with 230–400 mesh gel 60 (Merck).  $^1\text{H}$  and  $^{13}\text{C}$  NMR spectra were recorded on a Bruker AC-300 and are referenced with respect to the residual signals of the solvent; they are described using standard abbreviations. IR spectra were recorded on a PerkinElmer 1600 FT-IR. Mass spectra were recorded on a ZAB-1F micromass spectrometer.

### Thioether (4)

To a solution of phenylthiomethyl phenyl sulfone (**2**, 4) (0.55 g, 2.1 mmol) in THF (27.0 mL) cooled to  $-78^\circ\text{C}$  was added *n*-butyllithium ( $1.24\text{ mol}\cdot\text{L}^{-1}$  in hexane) (1.7 mL, 2.1 mmol). The solution was stirred for 1 h at  $-78^\circ\text{C}$ , then (*R*)-(-)-carvone (0.26 g, 1.7 mmol) in THF (6.0 mL) was added. The mixture was stirred for 2 h at  $-78^\circ\text{C}$  before *tert*-butyldimethylsilyl trifluoromethanesulfonate (1.2 mL, 5.2 mmol) was added. The mixture was stirred for another

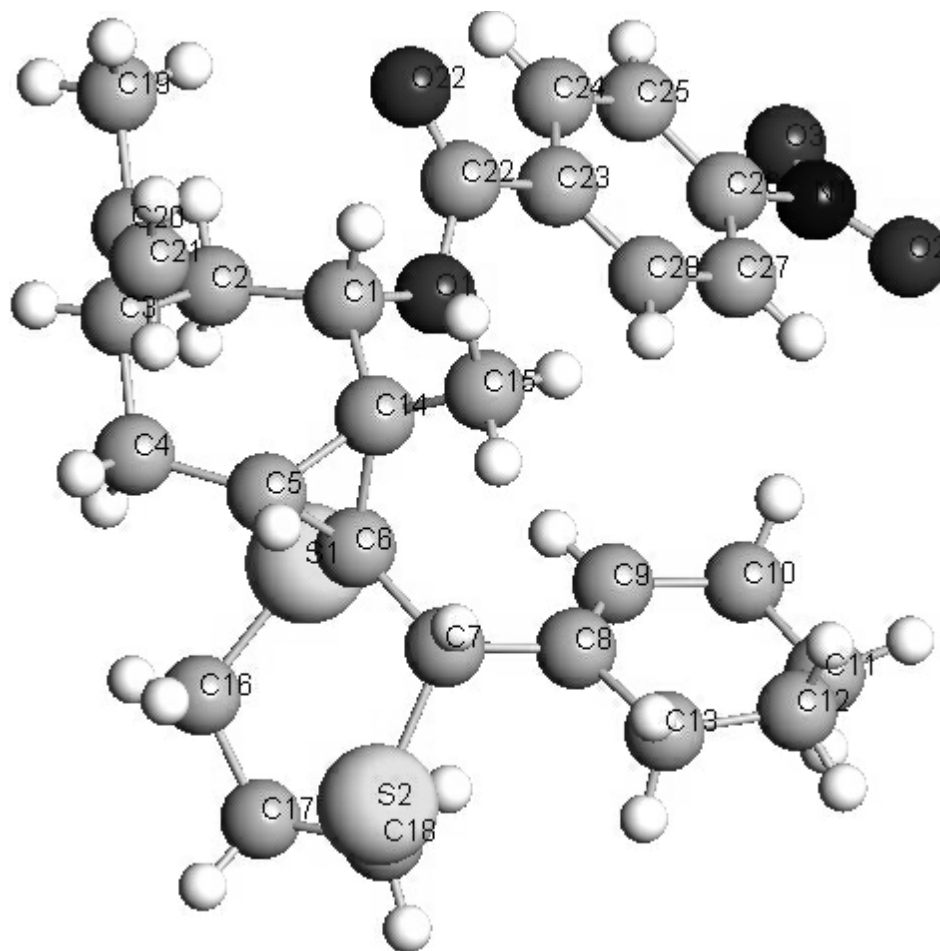
0.75 h, and then triethylamine (1.2 mL, 8.7 mmol) was added. The mixture was warmed to room temperature, stirred for 0.15 h, poured into a saturated aqueous solution of  $\text{NaHCO}_3$  (30 mL), and extracted with ether ( $3 \times 30\text{ mL}$ ). The combined organic phases were washed with brine (100 mL), dried with  $\text{MgSO}_4$ , filtered, and concentrated under reduced pressure. The crude product was purified by flash chromatography (hexane–ether 8:2) to give the thioether **4** (0.97 g, quantitative) as a pale yellow oil (mixture of diastereoisomers).  $[\alpha]_{\text{D}} = +63.51^\circ$  ( $c\ 1.71$ ,  $\text{CHCl}_3$ ). IR (film,  $\text{cm}^{-1}$ ): 3476, 3063, 2955, 2857, 1710, 1583, 1472, 1448, 1307, 1255, 1148, 1083, 836, 741, 688.  $^1\text{H}$  NMR (300 MHz,  $\text{CDCl}_3$ , ppm)  $\delta$ : 7.92 (2H, m, *H* arom. ortho to  $\text{SO}_2\text{R}$ ), 7.58 (1H, m, *H* arom. para to  $\text{SO}_2\text{R}$ ), 7.46 (2H, m, *H* arom. meta to  $\text{SO}_2\text{R}$ ), 7.14 (2H, m, *H* arom. ortho to SR), 7.07 (2H, m, *H* arom. meta to SR), 6.96 (1H, m, *H* arom. para to SR), 4.73 and 4.64 (2H, 2d,  $J = 17.9$  and  $35.5\text{ Hz}$ ,  $(\text{CH}_3)\text{C}=\text{CH}_2$ ), 4.30 (1H, dd,  $J = 37.0$  and  $2.0\text{ Hz}$ ,  $\text{PhSO}_2\text{-CH-SPh}$ ), 3.29 (1H, m), 3.00 (1H, m), 2.38–1.78 (4H, m), 1.77 and 1.63 (3H, 2s,  $(\text{CH}_3)\text{C}=\text{CH}_2$ ), 1.60 and 1.42 (3H, 2s, TBSO-C=C-CH<sub>3</sub>), 0.95 (9H, m,  $(\text{CH}_3)_3\text{-C-Si}$ ), 0.13 (6H, m,  $(\text{CH}_3)_2\text{-Si}$ ).  $^{13}\text{C}$  NMR (75 MHz,  $\text{CDCl}_3$ , ppm)  $\delta$ : 148.1, 147.9, 147.1, 138.4, 137.7, 134.3, 133.7, 133.6, 132.3, 131.8, 129.8, 129.4, 129.1, 129.0, 128.8, 127.9, 112.8, 111.0, 109.5, 109.3, 107.8, 105.2, 80.2, 76.4, 39.9, 38.2, 37.8, 37.7, 36.2, 35.4, 34.4, 28.7, 27.2, 26.0, 25.8, 25.8, 25.6, 22.6, 21.2, 20.2, 18.2, 18.0, 16.6, 14.2,  $-3.5$ ,  $-3.6$ . EI-MS: 528 ( $[\text{M}]^+$ ). HR-MS ( $[\text{M}]^+$ ) calcd. for  $\text{C}_{29}\text{H}_{40}\text{O}_3\text{S}_2\text{Si}$ : 528.2188; found: 528.2184.

### Sulfone (5)

To a solution of thioether **4** (1.1 g, 2.0 mmol) in benzene (52.0 mL) was added tributyltin hydride (1.1 mL, 4.3 mmol) and AIBN (0.033 g, 0.20 mmol).  $\text{N}_2$  was bubbled for 0.1 h

<sup>2</sup>Crystallographic data (excluding structure factors) for the structures in this paper have been deposited. Supplementary data may be purchased from the Depository of Unpublished Data, Document Delivery, CISTI, National Research Council Canada, Ottawa, ON K1A 0S2, Canada ([http://www.nrc.ca/cisti/irm/unpub\\_e.shtml](http://www.nrc.ca/cisti/irm/unpub_e.shtml) for information on ordering electronically). CCDC 200815 contain the supplementary data for this paper. These data can be obtained, free of charge, via [www.ccdc.cam.ac.uk/conts/retrieving.html](http://www.ccdc.cam.ac.uk/conts/retrieving.html) (or from the Cambridge Crystallographic Data Centre, 12 Union Road, Cambridge, U.K.; fax +44 1223 336033; or [deposit@ccdc.cam.ac.uk](mailto:deposit@ccdc.cam.ac.uk)).



**Fig. 3.** Single-crystal X-ray structure of cyclopropane **20**.

into the solution to exclude  $O_2$ . The solution was then heated at reflux for 2 h, cooled to room temperature, and concentrated under reduced pressure. The crude product was purified by flash chromatography (hexane–ether 9:1) to give the sulfone **5** (0.69 g, 87%) as a clear oil.  $[\alpha]_D^{25} = +26.56^\circ$  (*c* 1.51,  $CHCl_3$ ). IR (film,  $cm^{-1}$ ): 2930, 2858, 1683, 1472, 1447, 1306, 1253, 1197, 1150, 1087, 1064, 929, 837.  $^1H$  NMR (300 MHz,  $CDCl_3$ , ppm)  $\delta$ : 7.93 (2H, m, *H* arom. ortho to  $SO_2R$ ), 7.61 (3H, *H* arom. meta and para to  $SO_2R$ ), 4.71 (3H, d,  $J = 17.0$  Hz,  $(CH_3)C=CH_2$ ), 3.10 (2H, m,  $-CH_2-SO_2Ph$ ), 2.64 (1H, s), 2.21 (1H, m), 2.00 (3H, m), 1.69 (3H, s,  $(CH_3)C=CH_2$ ), 1.49 (1H, td,  $J = 13.0$  and 5.0 Hz), 1.40 (3H, s, TBSO-C=C- $CH_3$ ), 0.91 (9H, s,  $(CH_3)_3C-Si$ ), 0.08 (6H, s,  $(CH_3)_2Si$ ).  $^{13}C$  NMR (75 MHz,  $CDCl_3$ , ppm)  $\delta$ : 147.9, 145.7, 139.6, 133.6, 129.3, 128.0, 110.9, 109.7, 105.2, 58.1, 37.0, 35.3, 34.7, 31.3, 25.7, 20.8, 18.2, 14.2, -3.7, -3.8. EI-MS: 420 ( $[M]^+$ ). HR-MS ( $[M]^+$ ) calcd. for  $C_{23}H_{36}O_3SSi$ : 420.2154; found: 420.2151.

#### Alcohol (**6**)

To a solution of sulfone **5** (0.14 g, 0.32 mmol) in THF (2.0 mL) at  $-78^\circ C$  was added *n*-butyllithium (1.24 mol·L $^{-1}$  in hexane) (0.26 mL, 0.32 mmol). The solution was stirred for 1 h at  $-78^\circ C$  and then 1-cyclohexene-1-carboxaldehyde (0.033 mL, 0.29 mmol) was added. The mixture was stirred for 2.5 h and was slowly warmed to  $-50^\circ C$ . It was then poured into a saturated aqueous solution of  $NH_4Cl$  (4 mL)

and extracted with ether ( $3 \times 5$  mL). The combined organic phases were washed with brine (15 mL), dried with  $MgSO_4$ , filtered, and concentrated under reduced pressure. The crude product was purified by flash chromatography (hexane–ether 9:1 to 7:3) to give the alcohol **6** (0.095 g, 61%) as a pale yellow oil (mixture of diastereoisomers).  $[\alpha]_D^{25} = +34.76^\circ$  (*c* 1.03,  $CHCl_3$ ). IR (film,  $cm^{-1}$ ): 3491, 2931, 2858, 1682, 1447, 1302, 1176, 1140, 1083, 1056, 913, 834, 731.  $^1H$  NMR (300 MHz,  $CDCl_3$ , ppm)  $\delta$ : 7.89 (2H, m, *H* arom. ortho to  $SO_2R$ ), 7.53 (3H, m, *H* arom. meta and para to  $SO_2R$ ), 5.77 (1H, s,  $HC=C-CH-OH$ ), 4.71 (2H, d,  $J = 33.5$  Hz,  $(CH_3)C=CH_2$ ), 4.66 (1H, d,  $J = 12.5$  Hz,  $CH-OH$ ), 3.70 (1H, dd,  $J = 8.5$  and 3.0 Hz,  $CH-SO_2Ph$ ), 3.00 (1H, d,  $J = 4.5$  Hz,  $CH-OH$ ), 2.56 (2H, s), 2.26 (2H, m), 2.00 (4H, m,  $CH_2-CH=C-CH_2$ ), 1.78 (1H, qu,  $J = 6.5$  Hz), 1.71 (3H, s,  $(CH_3)C=CH_2$ ), 1.63 (1H, m), 1.55 (3H, s, TBSO-C=C- $CH_3$ ), 1.46 (4H, m,  $CH_2-CH_2-CH=C-CH_2-CH_2$ ), 0.94 (9H, s,  $(CH_3)_3C-Si$ ), 0.15 (6H, d,  $J = 10$  Hz,  $(CH_3)_2Si$ ).  $^{13}C$  NMR (75 MHz,  $CDCl_3$ , ppm)  $\delta$ : 147.2, 144.5, 142.9, 136.3, 133.0, 128.6, 128.1, 127.7, 109.6, 109.4, 75.9, 67.9, 37.7, 37.7, 34.2, 28.0, 25.8, 25.1, 22.9, 22.2, 22.1, 21.7, 18.1, 14.5, -3.6. EI-MS: 530 ( $[M]^+$ ). HR-MS ( $[M]^+$ ) calcd. for  $C_{30}H_{46}O_4SSi$ : 530.2886; found: 530.2894.

#### Acetate (**7**)

Acetic anhydride (0.068 mL, 0.72 mmol) and DMAP (0.012 g, 0.10 mmol) were added to a solution of the alcohol



**6** (0.26 g, 0.48 mmol) in pyridine (5.0 mL). The solution was stirred for 2 h at room temperature, neutralized with HCl 1 N (5 mL) at 0 °C, and extracted with ethyl acetate (3 × 5 mL). The organic phase was washed with brine (20 mL), dried with MgSO<sub>4</sub>, filtered, and concentrated under reduced pressure. The crude product was purified by flash chromatography (hexane–ether 8:2 to 7:3) to yield acetate **7** (0.25 g, 92%) as a clear oil (mixture of diastereoisomers).  $[\alpha]_D^{25} = +13.98^\circ$  (*c* 1.18, CHCl<sub>3</sub>). IR (film, cm<sup>-1</sup>)  $\nu$ : 2930, 2858, 1747, 1682, 1447, 1306, 1229, 1177, 1144, 913, 832, 730. <sup>1</sup>H NMR (300 MHz, CDCl<sub>3</sub>, ppm)  $\delta$ : 7.80 (2H, dd, *J* = 8.0 and 1.2 Hz, *H* arom. ortho to SO<sub>2</sub>R), 7.52 (3 H, m, *H* arom. meta and para to SO<sub>2</sub>R), 5.91 (1H, s, CH=C(C=O)), 5.74 (1H, d, *J* = 10.1 Hz, CH-OAc), 4.72 (2H, d, *J* = 30.5 Hz, (CH<sub>3</sub>)C=CH<sub>2</sub>), 4.00 (1H, dd, *J* = 10.1 and 2.2 Hz, CH-SO<sub>2</sub>Ph), 2.64 (1H, m), 2.57 (1H, m), 2.42–2.24 (2H, m), 2.00 (4H, m, CH<sub>2</sub>-CH<sub>2</sub>-CH=C-CH<sub>2</sub>-CH<sub>2</sub>), 1.85 (1H, m), 1.80 (3H, s, CH-O(C=O)-CH<sub>3</sub>), 1.74 (1H, m), 1.71 (3H, s, (CH<sub>3</sub>)C=CH<sub>2</sub>), 1.50 (4H, m, CH<sub>2</sub>-CH=C-CH<sub>2</sub>), 1.43 (3H, s, TBSO-C=C-CH<sub>3</sub>), 0.95 (9H, m, (CH<sub>3</sub>)<sub>3</sub>C-Si), 0.17 (6H, d, *J* = 10.0 Hz, (CH<sub>3</sub>)<sub>2</sub>Si). <sup>13</sup>C NMR (75 MHz, CDCl<sub>3</sub>, ppm)  $\delta$ : 168.6, 147.2, 144.0, 143.8, 132.7, 132.1, 131.5, 128.9, 126.9, 109.9, 109.4, 77.8, 64.1, 37.6, 37.1, 34.4, 26.9, 25.9, 25.1, 22.8, 22.1, 21.9, 20.8, 18.1, 14.2, -3.7, -3.8. EI-MS: 572 ([M]<sup>+</sup>). HR-MS ([M]<sup>+</sup>) calcd. for C<sub>32</sub>H<sub>48</sub>O<sub>5</sub>SSi: 572.2992; found: 572.3000.

#### Ketosulfone (9)

To a solution of alcohol **6** (0.49 g, 0.92 mmol) in dichloromethane (9.2 mL) was added 4 Å molecular sieves (0.92 g), 4-methylmorpholine *N*-oxide (0.22 g, 1.9 mmol), and tetrapropylammonium perruthenate (0.032 g, 0.090 mmol). The mixture was stirred for 0.5 h at room temperature, and the solvent was then concentrated under reduced pressure. Ether (10 mL) was added, and the mixture was filtered through a silica gel pad. The pad was rinsed with ether (10 mL), and the combined filtrates were concentrated under reduced pressure. The crude product was purified by flash chromatography (hexane–ether 9:1 to 7:3) to give the ketosulfone **9** (0.30 g, 60%) as a pale yellow oil.  $[\alpha]_D^{25} = +78.64^\circ$  (*c* 1.03, CHCl<sub>3</sub>). IR (film, cm<sup>-1</sup>)  $\nu$ : 2931, 2859, 1663, 1633, 1448, 1321, 1255, 1196, 1146, 1083, 921, 840. <sup>1</sup>H NMR (300 MHz, CDCl<sub>3</sub>, ppm)  $\delta$ : 7.89 (2H, m, *H* arom. ortho to SO<sub>2</sub>R), 7.57 (1H, m, *H* arom. para to SO<sub>2</sub>R), 7.47 (2H, m, *H* arom. meta to SO<sub>2</sub>R), 6.70 (1H, t, *J* = 4.0 Hz, CH=C(C=O)), 4.96 (1H, d, *J* = 10.1 Hz, CH-SO<sub>2</sub>Ph), 4.79 (2H, m, (CH<sub>3</sub>)C=CH<sub>2</sub>), 3.11 (1H, m), 2.69 (1H, m), 2.61 (1H, d, *J* = 13.6 Hz), 2.12 (6H, m), 1.79 (3H, s, (CH<sub>3</sub>)C=CH<sub>2</sub>), 1.58 (1H, td, *J* = 13.0 and 4.4 Hz), 1.42 (4H, m, CH<sub>2</sub>-CH=C-CH<sub>2</sub>), 1.25 (3H, s, TBSO-C=C-CH<sub>3</sub>), 0.88 (9H, s, (CH<sub>3</sub>)<sub>3</sub>C-Si), 0.04 (6H, d, *J* = 12.6 Hz, (CH<sub>3</sub>)<sub>2</sub>Si). <sup>13</sup>C NMR (75 MHz, CDCl<sub>3</sub>, ppm)  $\delta$ : 193.2, 148.2, 147.5, 142.6, 140.5, 138.7, 133.6, 129.9, 128.6, 111.6, 109.6, 70.7, 41.2, 37.0, 35.1, 31.1, 26.3, 25.7, 23.2, 21.5, 21.1, 20.5, 18.1, 17.4, -3.7, -3.8. EI-MS: 528 ([M]<sup>+</sup>). HR-MS ([M]<sup>+</sup>) calcd. for C<sub>30</sub>H<sub>44</sub>O<sub>4</sub>SSi: 528.2729; found: 528.2722.

#### Ketone (10)

To a solution of ketosulfone **9** (0.29 g, 0.54 mmol) in toluene (5.4 mL) was added tributyltin hydride (0.58 mL,

2.16 mmol). N<sub>2</sub> was bubbled for 5 min into the solution to exclude O<sub>2</sub>. The solution was then heated at reflux, and AIBN (0.060 g, 0.37 mmol) was added. The solution was heated at reflux 5 min, and then a second portion of AIBN (0.037 g, 0.12 mmol) was added. The solution was heated at reflux another 10 min, cooled to room temperature, and concentrated under reduced pressure. The crude product was purified by flash chromatography (hexane–ether 10:0 to 8:2) to give the enone **10** (0.23 g, quantitative) as a clear liquid.  $[\alpha]_D^{25} = +19.46^\circ$  (*c* 1.12, CHCl<sub>3</sub>). IR (film, cm<sup>-1</sup>)  $\nu$ : 2929, 2858, 1661, 1463, 1378, 1252, 1174, 1072, 926, 837. <sup>1</sup>H NMR (300 MHz, CDCl<sub>3</sub>, ppm)  $\delta$ : 6.89 (1H, m, CH=C(C=O)), 4.71 (2H, m, (CH<sub>3</sub>)C=CH<sub>2</sub>), 2.69 (2H, s, CH<sub>2</sub>-C=O), 2.32 (1H, m), 2.24 (4H, m), 2.03 (1H, m), 1.70 (3H, s, (CH<sub>3</sub>)C=CH<sub>2</sub>), 1.76–1.24 (8H, m), 1.50 (3H, s, TBSO-C=C-CH<sub>3</sub>), 0.95 (9H, m, (CH<sub>3</sub>)<sub>3</sub>C-Si), 0.13 (6H, s, (CH<sub>3</sub>)<sub>2</sub>Si). <sup>13</sup>C NMR (75 MHz, CDCl<sub>3</sub>, ppm)  $\delta$ : 201.2, 148.9, 143.9, 139.7, 113.7, 109.0, 40.0, 37.4, 35.8, 35.6, 31.9, 27.8, 26.8, 26.1, 25.8, 23.2, 22.0, 21.5, 17.5, 13.6, -3.7, -3.9. EI-MS: 388 ([M]<sup>+</sup>). HR-MS ([M]<sup>+</sup>) calcd. for C<sub>24</sub>H<sub>40</sub>O<sub>2</sub>Si: 388.2797; found: 388.2801.

#### Acetate (11)

Sodium borohydride (0.012 g, 0.32 mmol) was dissolved in methanol (0.50 mL), and the mixture was cooled to 0 °C. To this mixture was added dropwise a solution of cerium (III) chloride heptahydrate (0.12 g, 0.32 mmol) and ketone **10** (0.11 g, 0.29 mmol) in methanol (0.94 mL). The mixture was stirred for 0.5 h at 0 °C and 0.5 h at room temperature. It was cooled back to 0 °C, and a saturated aqueous solution of NH<sub>4</sub>Cl (2 mL) was added. The mixture was extracted with dichloromethane (3 × 3 mL). The combined organic phases were washed with brine (10 mL), dried with MgSO<sub>4</sub>, filtered, and concentrated under reduced pressure. The crude product was purified by flash chromatography (hexane–ether 95:5 to 9:1) to give the alcohol (0.089 g, 79%) as a colorless liquid (mixture of diastereoisomers).  $[\alpha]_D^{25} = +14.22^\circ$  (*c* 1.16, CHCl<sub>3</sub>). IR (film, cm<sup>-1</sup>)  $\nu$ : 3350, 2929, 2858, 1682, 1645, 1448, 1256, 1178, 922, 889, 837, 779, 735. <sup>1</sup>H NMR (300 MHz, CDCl<sub>3</sub>, ppm)  $\delta$ : 5.65 (1H, d, *J* = 3.5 Hz, CH=C(C=O)), 4.72 (2H, d, *J* = 0.45 Hz, (CH<sub>3</sub>)C=CH<sub>2</sub>), 4.08–3.97 (1H, m, CH-OH), 2.40–1.35 (16H, m), 1.74 (3H, s, (CH<sub>3</sub>)C=CH<sub>2</sub>), 1.59 (3H, s, TBSO-C=C-CH<sub>3</sub>), 0.93 (9H, s, (CH<sub>3</sub>)<sub>3</sub>C-Si), 0.10 (6H, d, *J* = 1.1 Hz, (CH<sub>3</sub>)<sub>2</sub>Si). <sup>13</sup>C NMR (75 MHz, CDCl<sub>3</sub>, ppm)  $\delta$ : 149.2, 143.3, 143.1, 140.7, 139.2, 124.8, 122.1, 114.8, 114.4, 108.9, 108.8, 76.3, 74.5, 38.1, 37.3, 37.2, 36.9, 36.2, 35.7, 35.7, 35.5, 31.6, 31.4, 30.9, 25.9, 25.1, 24.9, 24.0, 22.6, 22.5, 20.7, 18.2, 15.1, 14.9, -3.7, -3.8, -3.8, -3.9. EI-MS: 390 ([M]<sup>+</sup>). HR-MS ([M]<sup>+</sup>) calcd. for C<sub>24</sub>H<sub>42</sub>O<sub>2</sub>Si: 390.2954; found: 390.2951.

Acetic anhydride (0.032 mL, 0.34 mmol) and DMAP (5.5 mg, 0.050 mmol) were added to a solution of the alcohol (0.088 g, 0.23 mmol) of the preceding reaction in pyridine (2.3 mL). The solution was stirred for 3 h at room temperature, neutralized with an aqueous solution of HCl 1 N (5 mL), and extracted with ethyl acetate (3 × 5 mL). The organic phase was washed with brine (15 mL), dried with MgSO<sub>4</sub>, filtered, and concentrated under reduced pressure. The crude product was purified by flash chromatography (hexane–ether 97:3) to yield acetate **11** (0.083 g, 86%) as a colorless liquid (mixture of diastereoisomers).  $[\alpha]_D^{25} =$



+10.10° (*c* 1.00, CHCl<sub>3</sub>). IR (film, cm<sup>-1</sup>)  $\nu$ : 2927, 1738, 1682, 1645, 1448, 1371, 1236, 1180, 1017, 922, 838, 780, 734. <sup>1</sup>H NMR (300 MHz, CDCl<sub>3</sub>, ppm)  $\delta$ : 5.69 (1H, d, *J* = 13.7 Hz, CH=C-CH-OAc), 5.15 (1H, m, CH-OAc), 4.72 (2H, s, (CH<sub>3</sub>)C=CH<sub>2</sub>), 2.38–2.28 (1H, m), 2.02 (3H, d, *J* = 11.2 Hz, CH-O-(C=O)-CH<sub>3</sub>), 1.99–1.34 (15H, m), 1.73 (3H, d, *J* = 5.9 Hz, (CH<sub>3</sub>)C=CH<sub>2</sub>), 1.58 (3H, d, *J* = 5.5 Hz, TBSO-C=C-CH<sub>3</sub>), 0.93 (9H, m, (CH<sub>3</sub>)<sub>3</sub>C-Si), 0.10 (6H, m, (CH<sub>3</sub>)<sub>2</sub>Si). <sup>13</sup>C NMR (75 MHz, CDCl<sub>3</sub>, ppm)  $\delta$ : 170.5, 170.3, 149.0, 148.9, 143.5, 143.4, 136.4, 135.1, 126.5, 125.9, 124.3, 123.8, 114.2, 114.0, 110.5, 110.4, 109.0, 108.9, 105.2, 78.2, 76.3, 40.0, 39.4, 38.9, 37.3, 37.2, 36.4, 36.1, 35.9, 35.6, 35.6, 34.4, 31.1, 30.9, 25.8, 25.0, 24.9, 24.8, 23.3, 22.4, 21.4, 21.3, 20.8, 20.7, 18.2, 15.0, 14.8, -3.7, -3.9. EI-MS: 432 ([M]<sup>+</sup>). HR-MS ([M]<sup>+</sup>) calcd. for C<sub>26</sub>H<sub>44</sub>O<sub>3</sub>Si: 432.3060; found: 432.3063.

### Stannane (15)

Tributyl-[1,3]dithian-2-yl-stannane **14** (1.2 g, 2.9 mmol) was dried via azeotropic removal of water with benzene (3 × 3 mL) and was then dissolved in THF (2.5 mL) and cooled to -30 °C. In another flask, diisopropylamine (0.40 mL, 2.9 mmol) was dissolved in THF (2.5 mL), cooled to 0 °C, and a solution of *n*-butyllithium (1.35 mol·L<sup>-1</sup> in hexane) (2.0 mL, 2.7 mmol) was added dropwise. The solution was stirred for 0.25 h at 0 °C, cooled down to -30 °C, and transferred via canula to the first solution containing the stannane. The mixture was stirred for 3 h at -30 °C and cooled to -78 °C; HMPA (1.0 mL, 5.7 mmol) was added, and the mixture was stirred for another 0.5 h. A solution of (*R*)-(-)-carvone (0.20 g, 1.3 mmol) in THF (1.5 mL) pre-cooled to -78 °C was transferred via canula to the mixture, which was stirred for 1.25 h at -78 °C before *tert*-butyldimethylsilyl trifluoromethanesulfonate (0.60 mL, 2.6 mmol) was added. The mixture was stirred for 0.25 h at -78 °C, triethylamine (0.55 mL, 3.9 mmol) was added, and the mixture was warmed at room temperature and stirred for 0.5 h. Water (10 mL) was added, and the mixture was extracted with ether (3 × 10 mL). The combined organic phases were washed with brine (25 mL), dried with MgSO<sub>4</sub>, filtered, and concentrated under reduced pressure. The crude product was purified by flash chromatography (hexane) to give the stannane **15** (0.78 g, 88%) as a colorless oil. [ $\alpha$ ]<sub>D</sub> = +28.14° (*c* 1.13, CHCl<sub>3</sub>). IR (film, cm<sup>-1</sup>)  $\nu$ : 2956, 2856, 1667, 1463, 1252, 1194, 931, 837. <sup>1</sup>H NMR (300 MHz, CDCl<sub>3</sub>, ppm)  $\delta$ : 4.74 (2H, s, (CH<sub>3</sub>)C=CH<sub>2</sub>), 3.19 (1H, m), 3.13 (1H, m), 2.90 (1H, m), 2.69 (1H, m), 2.35–1.97 (8H, m), 1.94 (3H, s, TBSO-C=C-CH<sub>3</sub>), 1.76 (3H, s, (CH<sub>3</sub>)C=CH<sub>2</sub>), 1.52 (6H, m, Sn-(CH<sub>2</sub>-CH<sub>2</sub>-CH<sub>2</sub>-CH<sub>3</sub>)<sub>3</sub>), 1.33 (6H, m, Sn-(CH<sub>2</sub>-CH<sub>2</sub>-CH<sub>2</sub>-CH<sub>3</sub>)<sub>3</sub>), 1.06 (6H, m, Sn-(CH<sub>2</sub>-CH<sub>2</sub>-CH<sub>2</sub>-CH<sub>3</sub>)<sub>3</sub>), 0.91 (18H, m, (CH<sub>3</sub>)<sub>3</sub>C-Si and Sn-(CH<sub>2</sub>-CH<sub>2</sub>-CH<sub>2</sub>-CH<sub>3</sub>)<sub>3</sub>), 0.14 (6H, s, (CH<sub>3</sub>)<sub>2</sub>Si). <sup>13</sup>C NMR (75 MHz, CDCl<sub>3</sub>, ppm)  $\delta$ : 149.3, 145.4, 114.9, 108.7, 46.8, 36.6, 35.5, 34.0, 29.2, 27.6, 26.5, 25.9, 25.1, 25.0, 20.6, 18.7, 13.7, 10.1, -3.1, -3.3. EI-MS: 617 ([M - C<sub>4</sub>H<sub>9</sub>]<sup>+</sup>). HR-MS ([M - C<sub>4</sub>H<sub>9</sub>]<sup>+</sup>) calcd. for C<sub>28</sub>H<sub>53</sub>O<sub>2</sub>SiSn: 617.2329; found: 617.2322.

### Alcohol (16)

Stannane **15** (0.61 g, 0.91 mmol) was dried via azeotropic removal of water with benzene (3 × 10 mL); it was then dissolved in THF (10.0 mL), cooled to -100 °C, and a solution

of *n*-butyllithium (1.35 mol·L<sup>-1</sup> in hexane) (1.3 mL, 1.8 mmol) was added dropwise. The solution was stirred for 0.5 h at -100 °C, and a solution of 1-cyclohexene-1-carboxaldehyde (0.33 mL, 2.9 mmol) in THF (15.0 mL) was added via canula. The solution was stirred for 1.25 h at -100 °C, brought to 0 °C, neutralized with a saturated aqueous solution of NH<sub>4</sub>Cl (20 mL), and extracted with ether (3 × 25 mL). The combined organic phases were washed with brine (50 mL), dried with MgSO<sub>4</sub>, filtered, and concentrated under reduced pressure. The crude product was purified by flash chromatography (hexane-ether 100:0 to 95:5) to give alcohol **16** (0.33 g, 75%) as a clear oil (mixture of diastereoisomers, ratio = 3:1). [ $\alpha$ ]<sub>D</sub> = +10.50° (*c* 1.14, CHCl<sub>3</sub>). IR (film, cm<sup>-1</sup>)  $\nu$ : 3444, 2929, 2857, 1667, 1644, 1252, 1192, 927, 837, 780, 734. <sup>1</sup>H NMR (300 MHz, CDCl<sub>3</sub>, ppm)  $\delta$ : 6.00 (1H, s, CH=C-CH-OH), 4.73 (2H, m, (CH<sub>3</sub>)C=CH<sub>2</sub>), 4.51 (1H, m, CH-OH), 3.29–1.34 (15H, m), 1.80 (3H, d, *J* = 9.3 Hz, TBSO-C=C-CH<sub>3</sub>), 1.75 (3H, d, *J* = 4.3 Hz, (CH<sub>3</sub>)C=CH<sub>2</sub>), 1.61 (4H, m), 1.40 (1H, tt, *J* = 13.1 and 4.8 Hz), 0.95 (9H, d, *J* = 1.7 Hz, (CH<sub>3</sub>)<sub>3</sub>C-Si), 0.16 (6H, s, (CH<sub>3</sub>)<sub>2</sub>Si). <sup>13</sup>C NMR (75 MHz, CDCl<sub>3</sub>, ppm)  $\delta$ : 149.4, 149.3, 148.8, 136.8, 136.4, 127.4, 127.1, 111.9, 111.5, 108.8, 108.7, 78.1, 76.4, 62.1, 61.9, 45.1, 43.0, 38.2, 37.4, 35.3, 35.1, 31.9, 31.8, 28.8, 28.5, 28.5, 27.8, 27.4, 27.2, 25.9, 25.9, 25.5, 24.4, 24.1, 23.1, 23.1, 22.4, 22.1, 20.5, 20.4, 19.5, 18.9, -3.2, -3.3, -3.4. EI-MS: 476 ([M - H<sub>2</sub>O]<sup>+</sup>); 437 ([M - C<sub>4</sub>H<sub>9</sub>]<sup>+</sup>). HR-MS ([M - H<sub>2</sub>O]<sup>+</sup>) calcd. for C<sub>27</sub>H<sub>44</sub>O<sub>2</sub>Si: 476.2603; found: 476.2596.

### Acetate (17)

Acetic anhydride (0.27 mL, 2.9 mmol) and DMAP (71.0 mg, 0.58 mmol) were added to a solution of the alcohol **16** (0.79 g, 0.58 mmol) in pyridine (5.8 mL). The solution was stirred for 4 h at room temperature, neutralized with HCl 1 N (5 mL), and extracted with ethyl acetate (3 × 10 mL). The organic phase was washed with brine (15 mL), dried with MgSO<sub>4</sub>, filtered, and concentrated under reduced pressure. The crude product was purified by flash chromatography (hexane-ether 95:5) to give acetate **17** (0.24 g, 79%) as a colorless oil (mixture of diastereoisomers, ratio = 3:1). [ $\alpha$ ]<sub>D</sub> = +9.56° (*c* 1.13, CHCl<sub>3</sub>). IR (film, cm<sup>-1</sup>)  $\nu$ : 2929, 2857, 1742, 1667, 1438, 1368, 1230, 1170, 1019, 926, 837, 780, 733. <sup>1</sup>H NMR (300 MHz, CDCl<sub>3</sub>, ppm)  $\delta$ : 5.94 (1H, s, CH=C-CH-OAc), 5.76 (1H, d, *J* = 19.2 Hz, CH-OAc), 4.74 (2H, m, (CH<sub>3</sub>)C=CH<sub>2</sub>), 3.30–3.09 (2H, m), 2.98 (1H, m), 2.76 (1H, m), 2.64–2.46 (1H, m), 2.33–2.12 (3H, m), 2.08 (3H, d, *J* = 2.7 Hz, CH-O-(C=O)-CH<sub>3</sub>), 2.03–1.89 (1H, m), 1.84 (3H, d, *J* = 10.5 Hz, TBSO-C=C-CH<sub>3</sub>), 1.75 (3H, d, *J* = 3.8 Hz, (CH<sub>3</sub>)C=CH<sub>2</sub>), 1.26 (6H, m), 0.95 (9H, d, *J* = 1.0 Hz, (CH<sub>3</sub>)<sub>3</sub>C-Si), 0.16 (6H, t, *J* = 4.5 Hz, (CH<sub>3</sub>)<sub>2</sub>Si). <sup>13</sup>C NMR (75 MHz, CDCl<sub>3</sub>, ppm)  $\delta$ : 169.5, 149.5, 149.4, 148.4, 134.9, 134.6, 129.5, 128.5, 111.7, 111.2, 108.8, 108.6, 82.4, 78.5, 59.7, 59.3, 45.7, 43.5, 37.7, 35.3, 35.1, 31.8, 31.7, 31.6, 28.8, 28.0, 27.7, 27.5, 27.4, 25.9, 25.4, 24.3, 24.2, 22.9, 22.6, 22.0, 22.0, 21.4, 20.5, 20.4, 19.8, 19.2, 18.2, 14.1, -3.3, -3.4. CI-MS: 537 ([MH]<sup>+</sup>). HR-MS ([MH]<sup>+</sup>) calcd. for C<sub>29</sub>H<sub>49</sub>O<sub>3</sub>S<sub>2</sub>Si: 537.2892; found: 537.2887.

### Ketone (18)

Acetate **17** (0.026 g, 0.048 mmol) was dried via azeotropic removal of water with benzene (3 × 1 mL) and



then dissolved in benzene (1.0 mL), and *p*-toluenesulfonic acid monohydrate (2.0 mg, 0.010 mmol) was added. The solution was heated at reflux for 16 h, cooled to room temperature, neutralized with a saturated aqueous solution of  $\text{NaHCO}_3$  (3 mL), and extracted with ether ( $3 \times 5$  mL). The organic phase was dried with  $\text{MgSO}_4$ , filtered, and concentrated under reduced pressure. The crude product was purified by flash chromatography (hexane–ether 95:5) to give ketone **18** (8.1 mg, 46%) as a yellow oil.  $[\alpha]_D = -72.35^\circ$  (*c* 1.15,  $\text{CHCl}_3$ ). IR (film,  $\text{cm}^{-1}$ ): 2929, 1708, 1448, 904, 733.  $^1\text{H}$  NMR (300 MHz,  $\text{CDCl}_3$ , ppm): 5.39 (1H, m,  $\text{CH}=\text{C}$ ), 4.84 and 4.61 (2H, 2s,  $(\text{CH}_3)\text{C}=\text{CH}_2$ ), 3.08–2.51 (9H, m), 2.18 (4H, m), 1.97 (2H, m), 1.77 (1H, dd,  $J = 13.7$  and 2.7 Hz), 1.70 (3H, d,  $J = 0.6$  Hz,  $(\text{CH}_3)\text{C}=\text{CH}_2$ ), 1.63–1.47 (5H, m), 0.94 (3H, d,  $J = 6.5$  Hz,  $(\text{C}=\text{O})-\text{C}-\text{CH}_3$ ).  $^{13}\text{C}$  NMR (75 MHz,  $\text{CDCl}_3$ , ppm): 212.6, 146.9, 141.0, 138.1, 137.9, 125.9, 112.4, 47.8, 45.9, 44.6, 41.0, 33.0, 32.4, 31.8, 31.4, 28.3, 25.1, 22.6, 22.5, 21.7, 12.5. EI-MS: 362 ( $[\text{M}]^+$ ). HR-MS ( $[\text{M}]^+$ ) calcd. for  $\text{C}_{21}\text{H}_{30}\text{OS}_2$ : 362.1738; found: 362.1729.

### Cyclopropanes (**2a** and **2b**)

Acetate **17** (0.35 g, 0.65 mmol) was dried via azeotropic removal of water with benzene ( $3 \times 10$  mL) and then dissolved in dichloromethane (33.0 mL) and cooled to  $-78^\circ\text{C}$ . Trimethylsilyl trifluoromethanesulfonate (0.12 mL, 0.65 mmol) was added slowly, and the solution was stirred for 5 min before a saturated aqueous solution of  $\text{NaHCO}_3$  (25 mL) was added. The mixture was extracted with ether ( $3 \times 25$  mL). The combined organic phases were washed with brine (50 mL), dried with  $\text{MgSO}_4$ , filtered, and concentrated under reduced pressure. The crude product was purified by flash chromatography (hexane–ether 95:5) to give compound **19** (0.041 g, 17%), compound **18** (0.033 g, 14%), and the cyclopropane **2** (0.11 g, 46%) as a mixture of two diastereoisomers, which were separated by preparative TLC (eluted 2 times with toluene) to give the major product **2a** (0.033 g) and the minor product **2b** (0.011 g). Major product **2a**:  $[\alpha]_D = -361.07^\circ$  (*c* 1.40,  $\text{CHCl}_3$ ). IR (film,  $\text{cm}^{-1}$ ): 2923, 1693, 1438, 1407, 1376, 1301, 1103, 894, 755.  $^1\text{H}$  NMR (300 MHz,  $\text{CDCl}_3$ , ppm): 6.19 (1H, s,  $\text{C}=\text{CH}$ ), 4.86 and 4.59 (2H, 2s,  $(\text{CH}_3)\text{C}=\text{CH}_2$ ), 3.25 (1H, m), 3.05 (1H, m), 2.81 (2H, m), 2.63 (3H, m), 2.38 (3H, m), 2.12 (3H, m), 1.95 (2H, m), 1.79 (3H, s,  $(\text{CH}_3)\text{C}=\text{CH}_2$ ), 1.62 (5H, m), 1.27 (1H, dd,  $J = 8.1$  and 4.0 Hz), 1.17 (3H, s,  $(\text{C}=\text{O})-\text{C}-\text{CH}_3$ ).  $^{13}\text{C}$  NMR (75 MHz,  $\text{CDCl}_3$ , ppm): 208.9, 147.4, 132.2, 128.1, 111.1, 59.9, 45.0, 43.7, 40.4, 39.5, 35.4, 31.5, 30.7, 28.3, 25.8, 25.1, 24.2, 23.2, 22.5, 21.7, 18.2. EI-MS: 362 ( $[\text{M}]^+$ ). HR-MS ( $[\text{M}]^+$ ) calcd. for  $\text{C}_{21}\text{H}_{30}\text{OS}_2$ : 362.1738; found: 362.1743. Minor product **2b**:  $[\alpha]_D = -96.25^\circ$  (*c* 0.40,  $\text{CHCl}_3$ ). IR (film,  $\text{cm}^{-1}$ ): 2925, 1692, 1448, 1409, 1305, 1101, 894, 730.  $^1\text{H}$  NMR (300 MHz,  $\text{CDCl}_3$ , ppm): 5.91 (1H, s,  $\text{C}=\text{CH}$ ), 4.85 and 4.62 (2H, 2s,  $(\text{CH}_3)\text{C}=\text{CH}_2$ ), 3.30 (1H, m), 3.26 (1H, m), 2.90 (3H, m), 2.76 (1H, dd,  $J = 16.7$  and 4.9 Hz), 2.63 (3H, m), 2.46–2.18 (3H, m), 2.12 (3H, m), 1.88 (3H, m), 1.77 (3H, s,  $(\text{CH}_3)\text{C}=\text{CH}_2$ ), 1.66 (3H, m), 1.35 (3H, s,  $(\text{C}=\text{O})-\text{C}-\text{CH}_3$ ), 1.27 (1H, m).  $^{13}\text{C}$  NMR (75 MHz,  $\text{CDCl}_3$ , ppm): 210.2, 147.5, 133.1, 128.3, 126.7, 111.0, 56.7, 44.2, 40.4, 35.9, 31.6, 30.6, 28.2, 25.8, 25.7, 24.0, 23.1, 22.4, 21.6, 17.4, 14.1. EI-MS: 362 ( $[\text{M}]^+$ ). HR-MS ( $[\text{M}]^+$ ) calcd. for

$\text{C}_{21}\text{H}_{30}\text{OS}_2$ : 362.1738; found: 362.1743. Compound **19**:  $[\alpha]_D = -41.06^\circ$  (*c* 2.63,  $\text{CHCl}_3$ ). IR (film,  $\text{cm}^{-1}$ ): 2929, 1708, 1438, 1414, 892, 754.  $^1\text{H}$  NMR (300 MHz,  $\text{CDCl}_3$ , ppm): 5.45 (1H, m,  $\text{CH}=\text{C}$ ), 4.74 (2H, d,  $J = 12.3$  Hz,  $\text{C}(\text{CH}_3)=\text{CH}_2$ ), 3.55 (1H, m), 3.17 (2H, m), 2.92 (1H, m), 2.85 (1H, m), 2.77 (1H, m), 2.60 (1H, dd,  $J = 15.0$  and 4.4 Hz), 2.36 (1H, qu,  $J = 6.5$  Hz), 2.18 (3H, m), 2.05 (4H, m), 1.90 (2H, m), 1.72 (3H, s,  $(\text{CH}_3)\text{C}=\text{CH}_2$ ), 1.71–1.54 (4H, m), 1.06 (3H, d,  $J = 6.8$  Hz,  $\text{CH}_3-\text{CH}$ ).  $^{13}\text{C}$  NMR (75 MHz,  $\text{CDCl}_3$ , ppm): 211.8, 147.9, 138.6, 128.3, 125.4, 112.4, 109.8, 47.2, 47.0, 45.3, 41.1, 36.6, 33.3, 32.5, 31.3, 28.4, 25.1, 22.7, 21.8, 20.6, 12.7. EI-MS: 362 ( $[\text{M}]^+$ ). HR-MS ( $[\text{M}]^+$ ) calcd. for  $\text{C}_{21}\text{H}_{30}\text{OS}_2$ : 362.1738; found: 362.1729.

### Nitrobenzoate (**20**)

To a solution of cyclopropane **2a** (0.024 g, 0.066 mmol) in THF (1.3 mL) was added lithium aluminum hydride (3.7 mg, 0.099 mmol). The solution was stirred for 15 min at room temperature, neutralized with a dropwise addition of a saturated aqueous solution of  $\text{NH}_4\text{Cl}$  (5 mL), and extracted with ether ( $3 \times 5$  mL). The organic phase was dried with  $\text{MgSO}_4$ , filtered, and concentrated under reduced pressure. The crude product was purified by flash chromatography (hexane–ether 100:0 to 98:2) to give the alcohol as the major diastereoisomer (0.015 g, 63%) and the minor diastereoisomer (2.0 mg, 8%). Major diastereoisomer:  $[\alpha]_D = -173.82^\circ$  (*c* 1.10,  $\text{CHCl}_3$ ). IR (film,  $\text{cm}^{-1}$ ): 3788, 3492, 2921, 1641, 1446, 1403, 1013, 885.  $^1\text{H}$  NMR (300 MHz,  $\text{CDCl}_3$ , ppm): 6.46 (1H, s,  $\text{CH}=\text{C}$ ), 4.79 (2H, d,  $J = 24.2$  Hz,  $(\text{CH}_3)\text{C}=\text{CH}_2$ ), 3.75 (1H, t,  $J = 9.2$  Hz,  $\text{CH}-\text{OH}$ ), 3.25 (1H, m), 3.10 (1H, m), 2.87 (1H, m), 2.63 (2H, m), 2.40 (2H, m), 2.36–2.11 (3H, m), 2.07 (2H, m), 1.92 (2H, m), 1.78 (1H, m), 1.74 (3H, s,  $(\text{CH}_3)\text{C}=\text{CH}_2$ ), 1.61 (5H, m), 1.14 (3H, s,  $(\text{C}=\text{O})-\text{C}-\text{CH}_3$ ), 1.11 (1H, m).  $^{13}\text{C}$  NMR (75 MHz,  $\text{CDCl}_3$ , ppm): 147.4, 133.5, 127.3, 110.2, 73.9, 61.5, 46.0, 39.7, 36.9, 34.8, 34.7, 31.7, 30.6, 28.5, 25.8, 25.3, 23.8, 23.3, 23.0, 22.6, 22.3. EI-MS: 364 ( $[\text{M}]^+$ ). HR-MS ( $[\text{M}]^+$ ) calcd. for  $\text{C}_{21}\text{H}_{32}\text{OS}_2$ : 364.1894; found: 364.1888.

The major diastereoisomer of the preceding alcohol (4.5 mg, 0.012 mmol) was dissolved in dichloromethane (0.35 mL) and pyridine (0.35 mL). 4-Nitrobenzoyl chloride (0.023 g, 0.12 mmol) and DMAP (0.7 mg, 6.0  $\mu\text{mol}$ ) were added, and the solution was stirred for 16 h at room temperature and concentrated under reduced pressure, and the crude product was purified by flash chromatography (hexane–ether 95:5) to give nitrobenzoate **20** (2.5 mg, 40%) as a yellow solid. IR (film,  $\text{cm}^{-1}$ ): 2928, 1720, 1608, 1529, 1148, 1409, 1348, 1321, 1272, 1117, 1104, 755, 719.  $^1\text{H}$  NMR (300 MHz,  $\text{CDCl}_3$ , ppm): 8.32 (4H, m, *H* arom.), 6.46 (1H, s,  $\text{C}=\text{CH}$ ), 5.35 (1H, dd,  $J = 7.7$  and 10.9 Hz,  $\text{CH}-\text{OAc}$ ), 4.91 (2H, d,  $J = 24.3$  Hz,  $(\text{CH}_3)\text{C}=\text{CH}_2$ ), 3.26 (1H, m), 3.13 (1H, m), 2.91 (1H, dt,  $J = 13.9$  and 3.1 Hz), 2.67 (2H, m), 2.45 (1H, m), 2.37 (3H, m), 2.25 (1H, m), 1.98 (2H, m), 1.87 (1H, m), 1.83 (3H, s,  $(\text{CH}_3)\text{C}=\text{CH}_2$ ), 1.65–1.46 (7H, m), 1.26 (1H, m), 1.14 (3H, s,  $-\text{CO}_2-\text{C}-\text{CH}_3$ ).  $^{13}\text{C}$  NMR (75 MHz,  $\text{CDCl}_3$ , ppm): 164.5, 146.7, 134.1, 130.8, 126.6, 123.5, 110.8, 85.0, 78.0, 61.0, 46.9, 46.6, 39.8, 37.1, 32.0, 31.2, 30.5, 30.5, 28.3, 25.3, 25.2, 23.3, 23.2, 22.9, 22.4, 22.4. EI-MS: 513 ( $[\text{M}]^+$ ). HR-MS ( $[\text{M}]^+$ ) calcd. for  $\text{C}_{28}\text{H}_{35}\text{NO}_4\text{S}_2$ : 513.2007; found: 513.1997.



## Conclusion

We have studied the plausibility of an  $S_N2'$  cyclization using a silyl enol ether onto an allylic acetate by varying the functional groups adjacent to the acetate leaving group. Clearly, the inductive effect of the neighboring group plays a significant role in the departure of the leaving group, as the results with the dithiane neighboring group revealed. Several other alternatives were pursued but without success. Unfortunately, the model studies discussed herein proved that this strategy cannot be employed to access the  $C_7$ – $C_8$  unsaturated tricyclic structures. However, in the case of the substrates containing a dithiane next to the allylic acetate, the synthesis of novel highly functionalized cyclopropanes was observed instead of the desired  $S_N2'$  cyclization. This cyclopropanation is due to the cyclization of the silyl enol ether with concomitant 1,2-migration of a thioether and displacement of the acetate.

## Acknowledgments

A research chair from Merck Frosst is gratefully acknowledged, as well as the Natural Sciences and Engineering Re-

search Council of Canada (NSERC) and Le fonds québécois de la recherche sur la nature et les technologies (FQRNT). We wish to thank Mr. Andreas Decken (University of New Brunswick) for X-ray analysis, as well as Mr. Gaston Boulay for MS analyses and Dr. Hamid Hoveyda for the preparation of the manuscript.

## References

1. S. Hashimoto, A. Itoh, Y. Kitawaga, H. Yamamoto, and H. Nozaki. *J. Am. Chem. Soc.* **99**, 4192 (1977).
2. F.G. Bordwell and B.B. Jarvis. *J. Org. Chem.* **33**, 1182 (1968).
3. N. Toyooka, M. Okumura, H. Takahata, and H. Nemoto. *Tetrahedron*, **55**, 10 673 (1999).
4. A.B. Smith III, K.J. Hale, and J.P. McCauley, Jr. *Tetrahedron Lett.* **30**, 5579 (1989).
5. K. Kudo, Y. Hashimoto, H. Houchigai, M. Hasegawa, and K. Saigo. *Bull. Chem. Soc. Jpn.* **66**, 848 (1993).
6. D. Seebach, I. Willert, A.K. Beck, and B-T. Gröbel. *Helv. Chim. Acta*, **61**, 2510 (1978).
7. Y. Wan, A. Kurchan, and A. Kutateladze. *J. Org. Chem.* **66**, 1894 (2001).



# Alkyl substituent effect on the polarity of phenols-tri-*n*-alkylamine complexes

Zbigniew Pawełka and Therese Zeegers-Huyskens

**Abstract:** The formation constants and the dipole moments of the H-bonded adducts of 1:1 and 2:1 stoichiometries formed between three different phenols (phenol, 2,4,6-trichlorophenol, and 2,4-dinitrophenol) and different tri-*n*-alkylamines are determined in solvents of weak polarity. The polarity of the 1:1 complexes of 2,4,6-trichlorophenol with tri-*n*-alkylamines markedly increases with increasing degree of amine alkylation, in contrast with the complexes involving the two other phenols. The influence of the basicity and steric hindrance of the tri-*n*-alkylamines on the proton-transfer constant is discussed and quantitative correlations are deduced.

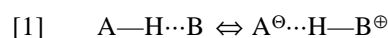
**Key words:** phenols, tri-*n*-alkylamines, H-bonded complexes, proton transfer, polarity, steric effect.

**Résumé :** Les constantes de formation et les moments dipolaires de complexes à liaison hydrogène formés entre trois différents phénols (phénol, 2,4,6-trichlorophénol et 2,4-dinitrophénol) et différentes tri-*n*-alkylamines sont déterminés dans des solvants de faible polarité. La polarité des complexes de 1:1 stoechiométrie formés entre le 2,4,6-trichlorophénol et les tri-*n*-alkylamines augmente avec le degré d'alkylation, contrairement aux complexes des deux autres phénols. L'effet de la basicité et de l'encombrement stérique des tri-*n*-alkylamines sur la constante de transfert de proton est discuté et des corrélations quantitatives sont présentées.

**Mots clés :** phénols, tri-*n*-alkylamines, complexes à liaison hydrogène, transfert de proton, polarité, effet stérique.

## Introduction

One of the most spectacular manifestations of hydrogen bond (H-bond or HB) interactions (AH...B) is the enhancement of the dipole moment  $\mu_{\text{AHB}}$  in comparison with the vectorial sum of the dipole moments of the isolated molecules,  $\bar{\mu}_{\text{AH}}$  and  $\bar{\mu}_{\text{B}}$ . The dependence of the H-bond polarity  $\Delta\bar{\mu}$  ( $= \bar{\mu}_{\text{AHB}} - \bar{\mu}_{\text{AH}} - \bar{\mu}_{\text{B}}$ ) on the aqueous  $\Delta pK_{\text{a}}$  ( $= pK_{\text{BH}^+} - pK_{\text{AH}}$ ) of the interacting species AH and B is very characteristic (1–5). For homologous series of complexes, e.g., phenols–triethylamine (1), the  $\Delta\bar{\mu}$  vs.  $\Delta pK_{\text{a}}$  curve presents a sigmoidal shape with a strong increase of  $\Delta\bar{\mu}$  in the inversion region. The  $\Delta\bar{\mu}/\Delta pK_{\text{a}}$  gradient in that region is so high that an increase of  $\Delta pK_{\text{a}}$  by two units can lead to a new protonic state of the complex, i.e., to hydrogen-bonded ion pair  $\text{A}^{\ominus}\cdots\text{HB}^{\oplus}$ . The polarity of the adducts in the inversion region can be explained in terms of the protomeric equilibrium (1–7)



governed by the proton transfer (PT) constant  $K_{\text{PT}}$ . Such H-bonded systems are very sensitive to the intrinsic basicity or acidity of the two partners and also to environmental effects (8–17). Moreover, these complexes show anomalous spectroscopic phenomena, e.g., low isotopic ratio, large shift of the  $\nu_{\text{AH}}$  vibration frequencies, highly downfield proton chemical

shift, etc. Low-barrier, strong hydrogen bonds (LBHBs) were proposed to explain the above particularities (18–20). The H-bonds formed by groups with similar  $pK_{\text{a}}$ s possess some partial covalent character, as they are the result of orbital overlapping between the matched energy states of AH and B. This covalent character contributes to the strength of the H bond, in addition to the pure electrostatic forces. The dependence of the strength and polarity of the AH...B system on  $\Delta pK_{\text{a}}$  can be demonstrated by changing the H-bond donating ability of AH in the families of phenols or carboxylic acids complexed with triethylamine or pyridines (1–5, 21–23).

The alkyl substitution effect on the basicity of amines has been discussed for a long time (24–40). There is much less information about this effect on the polarity of the molecular complexes. The sensitivity to N-alkylation is manifested in charge transfer complexes (41–46). For instance, the dipole moment of the triethylamine– $\text{I}_2$  complex is higher by about 0.5 D than that of trimethylamine adduct, irrespective of the solvent (45, 46).

To discuss the influence of N-alkylation on the proton acceptor abilities of tri-*n*-alkylamines, we have determined in the present work the dipole moments of hydrogen-bond complexes involving phenols and aliphatic tertiary amines characterized by different degrees of substitution. The studied phenols are unsubstituted phenol, 2,4,6-trichlorophenol,

Received 6 February 2003. Published on the NRC Research Press Web site at <http://canjchem.nrc.ca> on 1 September 2003.

**Z. Pawełka.**<sup>1</sup> Faculty of Chemistry, University of Wrocław, 14 Joliot-Curie, 50-385 Wrocław, Poland.

**Th. Zeegers-Huyskens.** Department of Chemistry, University of Leuven, 200F Celestijnenlaan, B-3001 Heverlee, Belgium.

<sup>1</sup>Corresponding author (e-mail: [zp@wchuwr.chem.uni.wroc.pl](mailto:zp@wchuwr.chem.uni.wroc.pl)).



**Table 1.** Parameters of eq. [10] and dipole moments of 2,4,6-trichlorophenol and tri-*n*-alkylamines in tetrachloroethylene (or carbon tetrachloride).

Compound	Range of $x_2$	$\alpha\epsilon_1$	$\beta$	$\gamma n_1^2$	$P$ (cm <sup>3</sup> )	$\mu$ (D)
2,4,6-Trichlorophenol	0.008–0.017	2.533	–0.0232	0.3859	36.7	1.33
Diethylmethylaniline (DMA)	0.012–0.086	1.072	–0.6391	–0.3682	24.7	1.09
Triethylamine (TEA)	0.022–0.071	0.407	–0.7385	–0.4133	14.4	0.83
Tri- <i>n</i> -propylamine (TPrA)	0.008–0.059	0.157	–0.9702	–0.4695	11.0	0.73
Tri- <i>n</i> -butylamine <sup>a</sup> (TBA)	0.019–0.040	0.070	–1.1681	–0.4440	9.7	0.69
Tri- <i>n</i> -pentylamine (TPeA)	0.012–0.086	0.087	–1.3615	–0.4322	9.6	0.68
Tri- <i>n</i> -octylamine (TOA)	0.011–0.063	0.214	–2.0315	–0.7064	9.9	0.69
	0.009–0.0033	0.292	–2.0882	–0.0774	13.3	0.80 <sup>b</sup>
Tri- <i>n</i> -dodecylamine (TDA)	0.031–0.079	–0.475	–2.8441	–0.9228	9.9	0.69
	0.016–0.046	0.237	–2.9172	–0.0373	14.8	0.85 <sup>b</sup>

<sup>a</sup>From ref. (15).<sup>b</sup>In carbon tetrachloride.

and 2,4-dinitrophenol, and the tertiary aliphatic amines are diethylmethyl-, triethyl-, tri-*n*-propyl-, tri-*n*-butyl-, tri-*n*-pentyl-, tri-*n*-octyl-, and tri-*n*-dodecylamine. These systems were chosen to cover a broad  $\Delta pK_a$  range.

It is well recognized that in nonpolar solvents (used in our dielectric measurements), the tertiary amines form both 1:1 (AHB) and 2:1 [(AH)<sub>2</sub>B] adducts (15, 16, 47, 48). Thus the starting point of the dielectric investigations was the determination of the  $K_{\text{AHB}}$  and  $K_{(\text{AH})_2\text{B}}$  formation constants by IR spectrometry. Knowledge of both stability constants allowed us to attribute the dielectric polarization to adducts of a given stoichiometry. In the present work we focused our attention on the H-bond polarities and on the proton transfer degrees in the 1:1 and 2:1 complexes formed between 2,4,6-trichlorophenol and various trialkylamines.

## Results and discussion

### Dipole moments of the components

The dipole moments of amines and 2,4,6-trichlorophenol in tetrachloroethylene (or carbon tetrachloride) are reported in Table 1. The values obtained for amines are of the expected magnitudes (see values in other solvents (49)) and will not be discussed hereafter. The increase of the dipole moments in CCl<sub>4</sub> as compared with tetrachloroethylene may be accounted for by a charge-transfer interaction  $\equiv\text{N}\cdots\text{Cl}-\text{C}\equiv$  (50, 51). In the case of amines with a lower degree of substitution, their photochemical reaction with CCl<sub>4</sub> leads, after some time, to a turbidity of the solution. This was the reason for which — in the time-consuming dielectric measurements — CCl<sub>4</sub> was replaced by tetrachloroethylene. In the next section, the dielectric polarizations of amines are employed in the calculation of dielectric polarizations of the 1:1 and 2:1 complexes. The dipole moments of amines and 2,4,6-trichlorophenol are also necessary for assessing the dipole moments of the molecular HB ( $\mu_{\text{HB}}$ ) and ion pair PT ( $\mu_{\text{PT}}$ ) forms of the further discussed 1:1 complexes of 2,4,6-trichlorophenol with trialkylamines.

### Dielectric polarizations and dipole moments of the complexes

The formation constants  $K_{\text{AHB}}$  and  $K_{(\text{AH})_2\text{B}}$  of the 2,4,6-trichlorophenol–trialkylamine complexes in a given solvent were estimated simultaneously by the method of the appar-

ent constant ( $K_{\text{app}}$ ), based on a model of 1:1 stoichiometry (47)

$$[2] \quad \frac{1}{2C_{\text{AH}} + K_{\text{app}}C_{\text{AH}}^2} = \frac{1}{K_{\text{AHB}}} \left( \frac{K_{\text{app}}}{2C_{\text{AH}} + K_{\text{app}}C_{\text{AH}}^2} \right) - K_{(\text{AH})_2\text{B}}$$

The intensity of the  $\nu(\text{OH})$  absorption at ca. 3600 cm<sup>–1</sup> was used in the determination of the concentration of the nonbonded phenol derivative. It is worth mentioning that this method gives the total concentration of complexes in their neutral (OH $\cdots$ N), as well in their ionic (O<sup>–</sup> $\cdots$ HN<sup>+</sup>), forms. At the low concentrations used in this work, secondary interactions such as stacking effects are unlikely to occur.

The equilibrium constants are indicated in Table 2. It may be seen that the formation constants  $K_{(\text{AH})_2\text{B}}$  are larger than  $K_{\text{AHB}}$ , which indicates a strong tendency to form 2:1 species.

Both equilibrium constants are used for the simultaneous estimation of the dielectric polarizations of the 1:1 ( $P_{\text{AHB}}$ ) and 1:2 ( $P_{(\text{AH})_2\text{B}}$ ) species. It is worth noticing that the  $K$  values reported in Table 2 indicate that in an excess of amine larger than 5, the 1:1 complex dominates in the solution. These conditions were therefore taken for the determination of the dipole moment of the 1:1 complexes. In excess of amine the following relation is valid:

$$[3] \quad \frac{P - P_1x_1}{x_B} = P_B + P_{\text{AHB}} \frac{x_{\text{AH}}^\circ}{x_B}$$

where  $P$ ,  $P_1$ ,  $P_B$ , and  $P_{\text{AHB}}$  are the dielectric polarizations of solution, solvent, amine, and the 1:1 complex, respectively, and  $x_B$  ( $x_B = x_B^\circ - x_{\text{AH}}^\circ$ ) and  $x_{\text{AH}}^\circ$  are the molar fractions of the amine and 2,4,6-trichlorophenol; the superscript  $^\circ$  indicates the initial molar fractions.

Figure 1 shows the plot of  $(P - P_1x_1)/x_B$  against  $x_{\text{AH}}^\circ/x_B$  for selected complexes. Similar linear relationships were also observed for other systems. The molar dielectric polarizations and dipole moments obtained in this way are collected in Table 3.

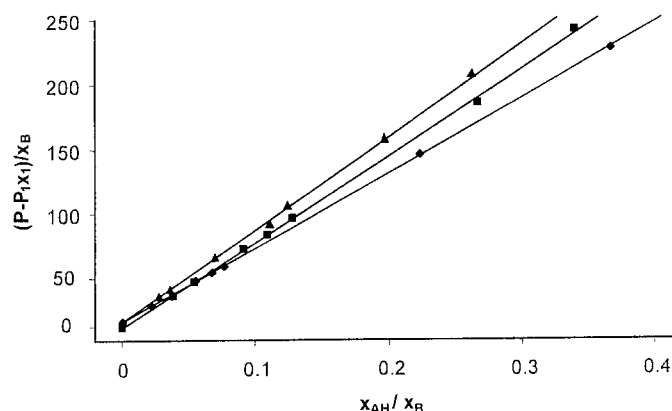
One should note the very good coincidence of the  $P_B$  values found from the linear equation, eq. [3] (Fig. 1), and from



**Table 2.** Formation constants of 1:1 ( $K_{\text{AHB}}$ ) and 2:1 ( $K_{(\text{AH})_2\text{B}}$ ) complexes between 2,4,6-trichlorophenol and tri-*n*-alkylamines in carbon tetrachloride.

Amine	$K_{\text{AHB}}$ ( $\text{dm}^3 \text{ mol}^{-1}$ )	$K_{(\text{AH})_2\text{B}}$ ( $\text{dm}^3 \text{ mol}^{-1}$ )
Triethylamine	55	54
Tri- <i>n</i> -propylamine	20.5	44
Tri- <i>n</i> -butylamine	23	57
Tri- <i>n</i> -pentylamine	28.5	84.5
Tri- <i>n</i> -octylamine	36.5	77
Tri- <i>n</i> -dodecylamine	45	64

**Fig. 1.** Dielectric polarization ( $P - P_1x_1$ )/ $x_B$  as a function of the  $x_{\text{AH}}/x_B$  ratio (eq. [3]). Complexes of 2,4,6-trichlorophenol with ▲ tri-*n*-dodecylamine ( $\text{CCl}_4$ ), ■ tri-*n*-butylamine, and ◆ triethylamine.



independent measurements in binary solutions (indicated in parentheses). The data reported in Table 3 reveal that the dipole moment markedly increases on going from diethylmethyl- to tri-*n*-butylamine and that only smooth changes are observed for longer alkyl chains. This effect was compared with analogous results for much weaker (phenol-trialkylamines) and much stronger (2,4-dinitrophenol-trialkylamines) interactions. The unsubstituted phenol-trialkylamine complex belongs to the typical molecular hydrogen-bonded form  $\text{OH}\cdots\text{N}$ , in which the polarity enhancement of the order of 0.7–1 D is caused by induction and charge transfer effects. In contrast, the 2,4-dinitrophenol-trialkylamine adduct is the hydrogen-bonded ion pair  $\text{O}^\ominus\cdots\text{HN}^\oplus$ , in which the proton is transferred to the nitrogen atom of the amine. The results obtained from eq. [3] are summarized in Table 4.

A rough inspection of the data in Table 4 shows a moderate increase in the dipole moment when the triethyl group is replaced by the tri-*n*-dodecyl one. Our measurements were carried out at low concentration of phenols. Nevertheless, in the case of 2,4,6-trichlorophenol complexed with long chain amines, one could admit association of the following type: monomer  $\rightleftharpoons$  dimer  $\rightleftharpoons$  *n*-mer. As a final step, an inverted micelle may be formed with the polar O-H $\cdots$ N group in its interior and the lipophilic alkyl chains directed towards the nonpolar solvent. In principle such an aggregation should enlarge the effective dipole moment resulting from specific dipole orientation. To establish the effect of the proton donor

concentration on  $\mu_{\text{AHB}}$ , we carried out additional measurements in an excess of tri-*n*-dodecylamine ((concentration = *c*)  $c_{\text{B}}/c_{\text{AH}} \approx 10$ ) at concentrations of 2,4,6-trichlorophenol ranging from  $0.4 \times 10^{-3}$  to  $1 \times 10^{-2} \text{ mol dm}^{-3}$ . The dipole moments at  $x_{\text{AHB}} = 4.23 \times 10^{-4}$  and  $1.06 \times 10^{-2}$  are equal to 6.08 and 6.01 D, respectively. Moreover, the mean deviation from the average value of  $\mu_{\text{AHB}}$  for the whole concentration range is only  $\pm 0.04$  D, which indicates the lack of self-association of the complex.

Finally, to estimate the alkylation effect on the polarity of the  $(\text{AH})_2\text{B}$  complex, we have compared the dipole moments of the 2:1 adduct of 2,4,6-trichlorophenol with triethylamine and tri-*n*-dodecylamine. The equilibrium concentrations of all species in the solution were evaluated using the formation constants  $K_{\text{AHB}}$  and  $K_{(\text{AH})_2\text{B}}$ . In the next step, the dielectric polarizations  $P_{\text{AHB}}$  and  $P_{(\text{AH})_2\text{B}}$  were estimated according to the linear equation

$$[4] \quad P^* = \frac{P - P_1x_1 - P_{\text{AH}}x_{\text{AH}} - P_{\text{B}}x_{\text{B}}}{x_{\text{AHB}}} \\ = P_{\text{AHB}} + P_{(\text{AH})_2\text{B}} \frac{x_{(\text{AH})_2\text{B}}}{x_{\text{AHB}}}$$

To allow the 1:1 or 2:1 species to be in excess, the measurements were carried out within a wide range of initial  $x_{\text{AH}}/x_{\text{B}}$  ratios. For these ratios, the corresponding  $x_{(\text{AH})_2\text{B}}/x_{\text{AHB}}$  values comprise between 0.02 and 2.45.

The  $\mu_{\text{AHB}}$  and  $\mu_{(\text{AH})_2\text{B}}$  values of the 2,4,6-trichlorophenol-TEA adduct in tetrachloroethylene were obtained by us earlier (16). Equation [4], applied to all investigated complexes of 2,4,6-trichlorophenol, can be expressed as:

$$[4.1] \quad P^*(\text{TEA}, \text{C}_2\text{Cl}_4) \\ = 610 + 1830 (x_{(\text{AH})_2\text{B}}/x_{\text{AHB}}) \begin{pmatrix} N = 7 \\ R = 1 \end{pmatrix}$$

$$[4.2] \quad P^*(\text{TEA}, \text{CCl}_4) \\ = 610 + 1740 (x_{(\text{AH})_2\text{B}}/x_{\text{AHB}}) \begin{pmatrix} N = 6 \\ R = 0.99 \end{pmatrix}$$

$$[4.3] \quad P^*(\text{TDA}, \text{C}_2\text{Cl}_4) \\ = 770 + 1820 (x_{(\text{AH})_2\text{B}}/x_{\text{AHB}}) \begin{pmatrix} N = 10 \\ R = 0.99 \end{pmatrix}$$

The corresponding dipole moments of the triethylamine adducts are  $\mu_{\text{AHB}} = 5.42 \pm 0.02$  D and  $\mu_{(\text{AH})_2\text{B}} = 9.42 \pm 0.05$  D in tetrachloroethylene, and  $\mu_{\text{AHB}} = 5.43 \pm 0.07$  D and  $\mu_{(\text{AH})_2\text{B}} = 9.17 \pm 0.14$  D in  $\text{CCl}_4$ . Equation [4.3] gives values of  $\mu_{\text{AHB}} = 6.10 \pm 0.06$  D and  $\mu_{(\text{AH})_2\text{B}} = 9.38 \pm 0.14$  D for the tri-*n*-dodecylamine adduct. The good agreement between the  $\mu_{\text{AHB}}$  value determined in excess of amine (see Table 3) and that resulting from eq. [4] is worth noticing. Earlier data based on infrared spectrometry or dipole measurements (15–17, 48) have demonstrated that the adducts of 2:1 stoichiometry between trihalogenophenols and tributylamine are hydrogen-bonded ion pairs. The similar value of the dipole moment of the tridodecylamine complexes indicate that this conclusion can be extended to more hindered amines. The 2:1 complexes are characterized by the struc-



**Table 3.** Dielectric polarizations and dipole moments of the 1:1 complexes formed between 2,4,6-trichlorophenol and tri-*n*-alkylamines in tetrachloroethylene (or carbon tetrachloride).

Amine	Range of $x_{\text{AH}}/x_{\text{B}}$	$P_{\text{AHB}}(\text{cm}^3)$	$P_{\text{B}}^a(\text{cm}^3)$	$\mu_{\text{AHB}}(\text{D})$
Diethylmethylaniline	0.022–0.158	475	24.5 (24.7)	4.79±0.07
Triethylamine	0.021–0.338	580	24.7	5.28±0.04 <sup>b</sup>
	0.023–0.215	600	14.9 (14.4)	5.40±0.02
Tri- <i>n</i> -propylamine	0.030–0.108	600	11.7 (11.0)	5.38±0.06
Tri- <i>n</i> -butylamine	0.037–0.327	700	9.5 (9.7)	5.81±0.03
Tri- <i>n</i> -pentylamine	0.019–0.271	680	9.6 (9.6)	5.74±0.05
Tri- <i>n</i> -octylamine	0.024–0.226	745	13.3 (13.3)	6.00±0.05 <sup>b</sup>
	0.054–0.233	765	9.6 (9.8)	6.08±0.04
Tri- <i>n</i> -dodecylamine	0.026–0.118	750	14.9 (14.8)	6.02±0.08 <sup>b</sup>

<sup>a</sup>Values in parentheses are determined in a binary solution.<sup>b</sup>In carbon tetrachloride.**Table 4.** Dielectric polarizations and dipole moments of the 1:1 H-bonded complexes formed between some phenols and trialkylamines in tetrachloroethylene.

System	Range of $x_{\text{AH}}/x_{\text{B}}$	$P_{\text{B}}^a(\text{cm}^3)$	$P_{\text{AHB}}(\text{cm}^3)$	$\mu_{\text{AHB}}(\text{D})$
Phenol–triethylamine	0.007–0.242	14.5 (14.9)	190	3.04±0.02
Phenol–tri- <i>n</i> -dodecylamine	0.059–0.206	9.9 (9.8)	210	3.18±0.05
2,4-Dinitrophenol–triethylamine	0.027–0.263	14.8 (14.9)	2640	11.29±0.03
2,4-Dinitrophenol–tri- <i>n</i> -dodecylamine	0.051–0.318	9.5 (9.8)	2720	11.46±0.02

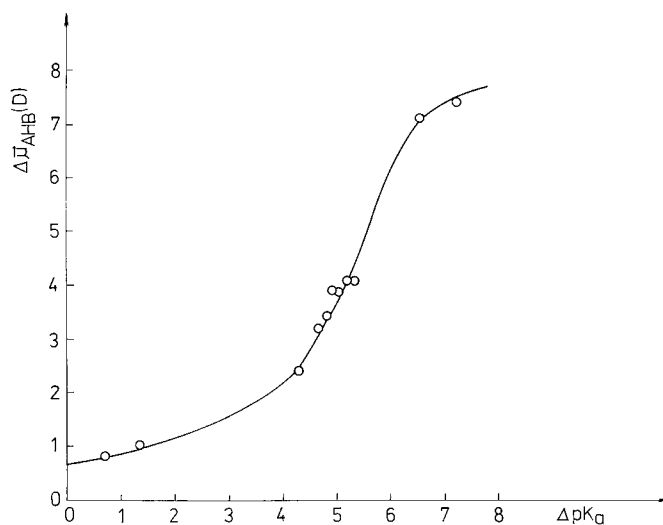
<sup>a</sup>Values in parentheses are determined in a binary solution.

ture  $\text{OH}\cdots\text{O}^-\cdots\text{HN}^+$ . In this structure, both  $\text{OH}\cdots\text{O}^-$  and  $\text{O}^-\cdots\text{HN}^+$  hydrogen bonds become stronger than the  $\text{OH}\cdots\text{O}$  and  $\text{OH}\cdots\text{N}$  hydrogen bonds in the corresponding phenol dimer and in the 1:1 complex. This  $\sigma$ -bond cooperative effect results in a large charge redistribution and proton transfer in the  $\text{O}-\text{H}\cdots\text{N}$  bridge. Despite a relatively large error ( $\pm 0.15$  D) in the determination of  $\mu_{(\text{AH})_2\text{B}}$ , the very low sensitivity to the lengthening of the alkyl groups in the amine moiety is worth mentioning. This behaviour is apparently analogous to that found in the 1:1 complexes of 2,4-dinitrophenol with the same tri-*n*-alkylamines (see Table 4).

These results indicate that the effect of N-alkyl substitution on the polarity is weak in complexes characterized by normal  $\text{OH}\cdots\text{N}$  hydrogen bonds and in proton-transfer complexes characterized by  $\text{O}^-\cdots\text{HN}^+$  hydrogen bonds. For both types of complexes, only a very small increase in  $\Delta\mu_{\text{AHB}}$  with  $\Delta\text{p}K_{\text{a}}$  is observed. This feature is displayed in Fig. 2, which also illustrates the sigmoidal shape found for other systems (1–5).

### Proton transfer constant in the 1:1 complexes between 2,4,6-trichlorophenol and tri-*n*-alkylamines

As discussed in the previous section, the polarity of the of 2,4,6-trichlorophenol–trialkylamine complexes increases with increasing extent of alkylation of the amine. This complex lies in the inversion region of the  $\Delta\mu_{\text{AHB}}$  vs.  $\Delta\text{p}K_{\text{a}}$  curve (Fig. 2). The polarity of such systems can be discussed in terms of the protomeric equilibrium (1). To discuss the alkylation effect more quantitatively, we calculated the H-bond polarity  $\Delta\bar{\mu}$ , defined as  $\Delta\bar{\mu} = \bar{\mu}_{\text{AHB}} - (\bar{\mu}_{\text{AH}} + \bar{\mu}_{\text{B}})$ , as well as the proton transfer constant  $K_{\text{PT}}$ . For the calculation of  $\Delta\bar{\mu}$ , the vectorial scheme proposed in ref. (2) was applied. The degree of proton transfer,  $x_{\text{PT}}$ , was calculated from the relation

**Fig. 2.** Dipole moment increment of the 1:1 complexes between phenol, 2,4,6-trichlorophenol, and 2,4-dinitrophenol with tri-*n*-alkylamines as a function of  $\Delta\text{p}K_{\text{a}}$ . The dipole moments of phenol and 2,4-dinitrophenol in carbon tetrachloride are 1.45 and 3.31 D, respectively; their  $\text{p}K_{\text{a}}$  are 9.95 and 4.10.

$$[5] \quad x_{\text{PT}} = \frac{\mu_{\text{AHB}}^2 - \mu_{\text{HB}}^2}{\mu_{\text{PT}}^2 - \mu_{\text{HB}}^2}$$

The proton transfer constant  $K_{\text{PT}}$  was taken as the ratio  $x_{\text{PT}}/x_{\text{HB}}$ .

The dipole moments of the molecular  $\text{AH}\cdots\text{B}$  ( $\mu_{\text{HB}}$ ) and proton-transferred  $\text{A}^{\ominus}\cdots\text{HB}^{\oplus}$  ( $\mu_{\text{PT}}$ ) forms were estimated assuming  $\Delta\bar{\mu} = 0.8$  D (3) in the former and  $\Delta\bar{\mu} = 9.3$  D (1) in the latter one. These data are summarized in Table 5.



**Table 5.** The  $pK_a$  and molar volumes of the tri-*n*-alkylamines, polarity of the hydrogen bond ( $\Delta\mu$ ), proton transfer degree (% PT), and  $\log K_{PT}$  in the 2,4,6-trichlorophenol–tri-*n*-alkylamines complexes.

Amine	$pK_a$	$V$ (dm <sup>3</sup> mol <sup>-1</sup> )	$\Delta\mu$ (D)	% PT	$-\log K_{PT}$
Diethylmethylaniline	10.29	0.120	2.46	10.5	0.931
Triethylamine	10.65	0.139	3.21 <sup>a</sup>	16.2 <sup>a</sup>	0.714 <sup>a</sup>
			3.34	17.3	0.679
Tri- <i>n</i> -propylamine	10.65	0.192	3.42	17.8	0.664
Tri- <i>n</i> -butylamine	10.89	0.242	3.89	22.2	0.545
Tri- <i>n</i> -pentylamine	11.00	0.292	3.83	21.5	0.562
Tri- <i>n</i> -octylamine	11.19	0.462	4.08 <sup>a</sup>	21.5 <sup>a</sup>	0.498 <sup>a</sup>
			4.16	24.9	0.479
Tri- <i>n</i> -dodecylamine	11.3 <sup>b</sup>	0.697	4.10	24.3	0.498

<sup>a</sup>In carbon tetrachloride.<sup>b</sup>Obtained from extrapolation of the  $pK_a$  values as a function of the number of CH<sub>2</sub> groups in the aliphatic chain.

The increase in  $\Delta\mu$  or  $K_{PT}$  may be rationalized in terms of the increasing proton-accepting abilities of amine. The proton affinity is a direct measure of the intrinsic basicity, unaffected by solvation effects. Unfortunately, the proton affinities are known only for the aliphatic tertiary amines characterized by a low degree of substitution, and they increase from 232.3 to 234.8 kcal mol<sup>-1</sup> on going from triethylamine to tri-*n*-butylamine (52). Therefore, we decided to correlate the  $K_{PT}$  values with the basic properties of amines in water (24, 27) (see Table 5). The classical relation

$$[6] \quad \log K_{PT} = \xi \Delta pK_a + C$$

takes for the present complexes the following form:

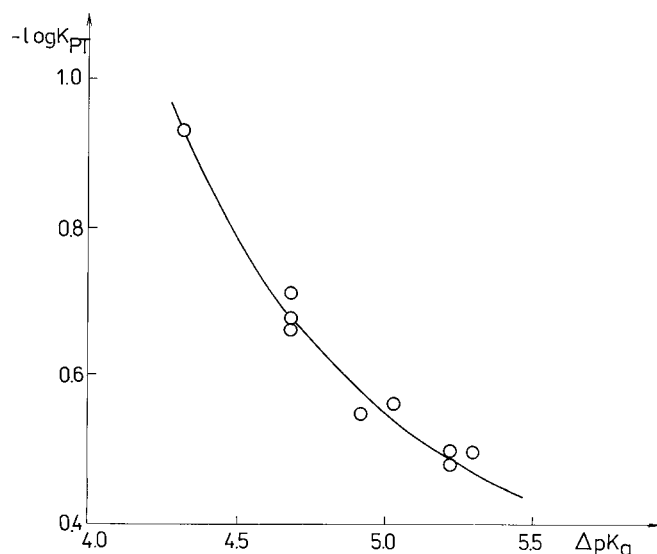
$$[7] \quad \log K_{PT} = -2.67 + 0.42 \Delta pK_a \left( \begin{array}{l} N = 7 \\ R = 0.944 \end{array} \right)$$

As illustrated in Fig. 3, marked deviations from this linear correlation are observed for tri-*n*-pentyl-, tri-*n*-octyl-, and tri-*n*-dodecylamine, where the bulky substituents restrict the approach of the proton. This steric hindrance must be larger in the 2,4,6-trichlorophenol complexes than in monohydrate B<sup>⊕</sup>H<sup>⊖</sup>·OH<sub>2</sub>. This comparison is justified since it appears that steric hindrance to ion solvation in bulk water is comparable in magnitude to steric hindrance of solvation by only one H<sub>2</sub>O molecule (36). To estimate quantitatively the effect of steric hindrances on  $K_{PT}$ , we have added to eq. [6] a term dependent on the molar volume of the amine in tetrachloroethylene ( $V$  in dm<sup>3</sup> mol<sup>-1</sup>, see Table 5). The two-parameter linear regression now gives the following relation:

$$[8] \quad \log K_{PT} = -3.24 - 0.55 \Delta pK_a + 0.03(\log V)^{-1} \left( \begin{array}{l} N = 7 \\ R = 0.989 \end{array} \right)$$

characterized by a better correlation coefficient than that of eq. [7]. It may be concluded that both the  $C$  and  $\xi$  parameters in eq. [6] are to some degree connected with the steric effects.

A last remark concerns the influence of steric hindrance on the formation constants of the 1:1 complexes. For complexes between phenols and aliphatic tertiary amines characterized by normal OH···N hydrogen bonds, the formation constants have been shown to depend on the polar and steric parameters of Taft (27). Similar correlations could not be de-

**Fig. 3.**  $\log K_{PT}$  as a function of  $\Delta pK_a$  for the 1:1 complexes between 2,4,6-trichlorophenol and trialkylamine.

duced for the present complexes because, as discussed in this section, both OH···N and O<sup>-</sup>···HN<sup>+</sup> species are present in solution. The O(H)···N distance is considerably shorter (2.50–2.55 Å) than the O<sup>-</sup>···HN<sup>+</sup> one (2.75–2.85 Å) (27), and as a consequence, the normal OH···N hydrogen bonds are expected to be more sensitive to steric interactions than the ionic O<sup>-</sup>···HN<sup>+</sup> ones.

#### Comparison with the crystal structures

In the solids, the inflection point, where 50% PT is formally reached, occurs with the weaker bases. This is in agreement with expectations since the crystal lattice favors the polar PT state (53). When 2,4-dinitrophenol forms complexes with diamines or tertiary amines, in all the published structures where the hydrogen atoms have been located, the phenol completely transfers the proton to the amine (54–59).

The structure of the (phenol)<sub>2</sub>-1,4-diazabicyclo[2,2,2]octane (DABCO) complex, determined at -130°, is worth mentioning. In this complex, the hydrogen atoms stay firmly attached to the phenol oxygen atoms. Strong hydrogen bonds are formed, the two O···N distances being 2.694 and 2.681 Å, respectively, and the corresponding OH···N angles



167° and 165°. No PT structure is observed in this case. This may result from the fact that DABCO is less basic than triethylamine; its  $pK_a$  is indeed equal to 8.8. A second factor that plays a determinant role is the anticooperativity in the hydrogen bond. The formation of the OH...N hydrogen bond on one of the N atom of DABCO decreases the proton-acceptor ability of the second N atom (60).

## Experimental

The dielectric permittivity ( $\epsilon$ ) was measured on a Dipolemeter DM01 (WTW) at 2 MHz. The dielectric capacity was determined with an accuracy of  $\Delta C/C \leq 1 \times 10^{-4}$ . The density ( $d$ ) was determined picnometrically with an accuracy of  $\pm 1 \times 10^{-4} \text{ g cm}^{-3}$ , and the refractive index ( $n$ ) for the D sodium line was measured using an Abbé refractometer with an accuracy of  $\pm 1 \times 10^{-4}$ . All the measurements were performed at  $25 \pm 0.02 \text{ }^\circ\text{C}$ .

The dipole molar polarization ( $P$ ) of the liquid was calculated according to the Onsager equation (61)

$$[9] \quad P = \frac{(\epsilon - n^2)(2\epsilon + n^2)}{\epsilon(n^2 + 2)^2} V$$

where  $V$  is the molar volume of liquid.

The dipole moments of phenols and amines in binary solution were calculated using the Hedestrand extrapolation procedure (62), in which  $\epsilon$ ,  $d$ , and  $n^2$  were plotted against the molar fraction  $x_2$  of the solute. From the slopes, denoted by  $\alpha$ ,  $\beta$ , and  $\gamma$  (see Table 1), the molar dipole polarization  $P_2$  of the solute at infinite dilution was obtained by eq. [9], which takes the following form (63):

$$[10] \quad P_2 = \frac{(\epsilon_1 - n_1^2)(2\epsilon_1 + n_1^2)}{\epsilon_1(n_1^2 + 2)^2} \times V_1 \left( \frac{\alpha\epsilon_1 - \gamma n_1^2}{\epsilon_1 - n_1^2} + \frac{2\alpha\alpha_1 + \gamma n_1^2}{2\epsilon_1 + n_1^2} - \frac{2\gamma n_1^2}{n_1^2 + 2} - \alpha - \beta + \frac{M_2}{M_1} \right)$$

where  $M$  is the molar mass and the subscripts 1 and 2 refer to the solvent and the solute, respectively. Finally, the  $\mu$  value of the solute has been obtained from the relation  $\mu = [(9kT/4\pi N) \times P_2]^{1/2}$ .

The formation constants of the 1:1 ( $K_{\text{AHB}}$ ) and 2:1 ( $K_{(\text{AH})_2\text{B}}$ ) complexes between 2,4,6-trichlorophenol and trialkylamines in  $\text{CCl}_4$  at  $25 \text{ }^\circ\text{C}$  were determined from the absorbance of the  $\nu(\text{OH})$  stretching vibration of the free phenol. In this determination the infrared spectra were recorded on a PerkinElmer 883 instrument equipped with thermostatic KBr cells with variable path length.

The phenols were crystallized from petroleum ether and the trialkylamines were fractionally distilled and dried over sodium or  $4 \text{ \AA}$  molecular sieves. Carbon tetrachloride and tetrachloroethylene were purified by standard methods (64) and dried over molecular sieves.

## Acknowledgements

This work was done in the framework of the cooperation between the Catholic University of Leuven and the University of Wrocław. The authors thank the anonymous referee who provided the structure of the (phenol)<sub>2</sub>-DABCO complex. Z.P. thanks the University of Leuven for a post-doctoral fellowship.

## References

1. H. Ratajczak and L. Sobczyk. *Bull. Acad. Pol. Sci. Ser. Sci. Chim.* **29**, 93 (1970).
2. R. Nouwen and P. Huyskens. *J. Mol. Struct.* **16**, 459 (1973).
3. J. Hawranek, J. Oszust, and L. Sobczyk. *J. Phys. Chem.* **76**, 2112 (1972).
4. L. Sobczyk and Z. Pawełka. *J. Chem. Soc. Faraday Trans.* **70**, 832 (1974).
5. L. Sobczyk. *Pure Appl. Chem.* **51**, 1659 (1979).
6. P. Huyskens and Th. Zeegers-Huyskens. *J. Chim. Phys. Phys. Chim. Biol.* **61**, 81 (1964).
7. J. Kraft, S. Walker, and M.D. Magee. *J. Phys. Chem.* **79**, 881 (1975).
8. H. Baba, A. Matsuyama, and H. Kokubun. *Spectrochim. Acta*, **A25**, 1709 (1969).
9. J. Jadżyn and J. Małecki. *Acta Phys. Pol.* **A41**, 599 (1972).
10. D. Eustace and E. Grunwald. *J. Am. Chem. Soc.* **96**, 7171 (1974).
11. R. Scott, D. De. Palma, and S. Vinogradov. *J. Phys. Chem.* **72**, 3192 (1968); **73**, 1890 (1969).
12. J. Fritsch and G. Zundel. *J. Phys. Chem.* **85**, 556 (1981).
13. R. Krämer and G. Zundel. *J. Chem. Soc. Faraday Trans.* **86**, 301 (1990).
14. R. Krämer, G. Zundel, B. Brzeziński, and J. Olejnik. *J. Chem. Soc. Faraday Trans.* **88**, 1659 (1992).
15. T. Kuc, Z. Pawełka, and L. Sobczyk. *Phys. Chem. Chem. Phys.* **2**, 211 (2000).
16. T. Kuc, Th. Zeegers-Huyskens, and Z. Pawełka. *J. Mol. Liq.* **89**, 147 (2000).
17. T. Kuc and Z. Pawełka. *J. Solution Chem.* **30**, 375 (2001).
18. W.W. Cleand and M.M. Kreevoy. *Science*, **264**, 1887 (1994).
19. P.A. Frey, S.A. Whitt, and J.B. Tobin. *Science*, **264**, 1927 (1994).
20. S. Shan, S. Loh, and D. Herschlag. *Science*, **272**, 97 (1996).
21. Th. Zeegers-Huyskens and P. Huyskens. *In Molecular interactions. Vol. 2. Edited by H. Ratajczak and W.J. Orville-Thomas.* John Wiley and Sons, Chichester. 1981.
22. Th. Zeegers-Huyskens. *J. Mol. Struct.* **135**, 93 (1986).
23. P.L. Huyskens, Th. Zeegers-Huyskens, and Z. Pawełka. *J. Solution Chem.* **28**, 915 (1999).
24. H.K. Hall. *J. Am. Chem. Soc.* **79**, 5441 (1957).
25. H.A. Staab. *Einführung in die Theoretische Organische Chemie.* Verlag Chemie, Weinheim/Bergstr. 1959.
26. M.S.B. Munson. *J. Am. Chem. Soc.* **87**, 2332 (1965).
27. D. Clotman and Th. Zeegers-Huyskens. *Spectrochim. Acta*, **23A**, 1627 (1967).
28. J.I. Brauman and L.K. Blair. *J. Am. Chem. Soc.* **91**, 2126 (1969).
29. J.I. Brauman, J.M. Riveros, and L.K. Blair. *J. Am. Chem. Soc.* **93**, 3914 (1971).
30. W.J.Le. Noble and T. Asano. *J. Org. Chem.* **40**, 1179 (1975).

<sup>2</sup>Referee of the present work. Personal communication.



31. H. Umeyama and K. Morokuma. *J. Am. Chem. Soc.* **98**, 4400 (1976).
32. D.H. Aue, H.M. Webb, and M.T. Bowers. *J. Am. Chem. Soc.* **98**, 311 (1976).
33. E.M. Arnett, B. Chawla, L. Bell, M. Taagepera, W.J. Hehre, and R.W. Taft. *J. Am. Chem. Soc.* **99**, 5729 (1977).
34. H.P. Hopkins, C.J. Alexander, and S.Z. All. *J. Phys. Chem.* **82**, 1268 (1978).
35. M. Meot-Ner (Mautner) and L.W. Sieck. *J. Am. Chem. Soc.* **105**, 2956 (1983).
36. M. Meot-Ner (Mautner). *J. Am. Chem. Soc.* **106**, 1257 (1984).
37. P. Burk, I.A. Koppel, I. Koppel, I. Leito, and O. Travnikova. *Chem. Phys. Lett.* **323**, 482 (2000).
38. Z.B. Maksic and R. Vianello. *J. Phys. Chem.* **A106**, 419 (2002).
39. R. Schwesinger, J. Willaredt, H. Schlemper, M. Keller, D. Schmitt, and H. Fritz. *Chem. Ber.* **127**, 2435 (1994).
40. J.E. Douglas and P.A. Kollman. *J. Am. Chem. Soc.* **100**, 5226 (1978).
41. J.J. Oh, K.W. Hillig II, and R.L. Kuczkowski. *J. Am. Chem. Soc.* **113**, 7480 (1991).
42. H. Yada, J. Tanaka, and S. Nagakura. *Bull. Chem. Soc. Jpn.* **33**, 1660 (1960).
43. S. Nagakura. *J. Am. Chem. Soc.* **80**, 520 (1958).
44. H. Mihono and K. Toyada. *Bull. Chem. Soc. Jpn.* **44**, 272 (1971).
45. A.J. Hamilton and L.E. Sutton. *Chem. Commun.* **460** (1968).
46. A. Funatsu and K. Toyada. *Bull. Chem. Soc. Jpn.* **43**, 279 (1970).
47. D. Clotman, D. Van Lerberghe, and Th. Zeegers-Huyskens. *Spectrochim. Acta*, **A26**, 1625 (1970).
48. Z. Pawełka and Th. Zeegers-Huyskens. *Bull. Soc. Chim. Belg.* **106**, 481 (1997).
49. A.L. McClellan. *Tables of experimental dipole moments*. Vol. 1. Freeman and Company, San Francisco. 1963; Vol. 2. Rahara Enterprises, El Cerrito. 1974.
50. D.P. Stevenson and G.M. Coppinger. *J. Am. Chem. Soc.* **84**, 149 (1962).
51. J. Lautenberger, E.N. Jones, and J.G. Miller. *J. Am. Chem. Soc.* **90**, 1110 (1968).
52. S.G. Lias, J.E. Bartmess, J.E. Liebman, J.L. Holmes, R.D. Levin, and W.G. Mallard. *J. Phys. Chem. Ref. Data*, **17** (1988).
53. Z. Malarski, M. Rospenk, L. Sobczyk, and E. Grech. *J. Phys. Chem.* **86**, 401 (1982).
54. S.J. Grabowski. *Pol. J. Chem.* **68**, 473 (1994).
55. I. Majerz, T. Glowiak, and A. Koll. *J. Mol. Struct.* **374**, 339 (1996).
56. A. Usman, S. Chantrapomma, and H.-K. Fun. *Acta Crystallogr. Sect. C Cryst. Struct. Commun.* **57**, 1443 (2001).
57. A. Usman, S. Chantrapomma, H.-K. Fun, B.-L. Poh, and C. Karalai. *Acta Crystallogr. Sect. C Cryst. Struct. Commun.* **58**, 136 (2002).
58. S. Chantrapomma, A. Usman, H.-K. Fun, B.-L. Poh, and C. Karalai. *Acta Crystallogr. Sect. E*, **58**, 102 (2002).
59. S. Chantrapomma, A. Usman, H.-K. Fun, B.-L. Poh, and C. Karalai. *Acta Crystallogr. Sect. E*, **58**, 108 (2002).
60. P.L. Huyskens. *J. Am. Chem. Soc.* **99**, 2578 (1977).
61. L. Onsager. *J. Am. Chem. Soc.* **58**, 1486 (1936).
62. G. Hedestrand. *Z. Phys. Chem. Abt. B*, **2**, 428 (1929).
63. Z. Pawełka. *J. Chem. Soc. Faraday Trans. 2*, **84**, 1683 (1988).
64. L.A. Weissberger and E.S. Proskauer. *Technique of organic chemistry, organic solvents*. Vol. VII. Interscience, New York. 1955.



# Synthesis and molecular recognition of the uridine-containing derivative of *p*-tert-butylcalix[4]arene

Jian Liang, Haiying Fu, Yu Liu, Li Wang, Zhifeng Ye, and Xianfa Shi

**Abstract:** The new uridine-containing derivative of *p*-tert-butylcalix[4]arene — 5,11,17,23-tetra-*tert*-butyl-25,26,27-trihydroxyl-28-oxyuridinecalix[4]arene (CU) — was synthesized and characterized by  $^1\text{H}$  NMR,  $^{13}\text{C}$  NMR, IR, EI-MS, and ESI-MS spectra. By the aid of UV-vis spectra, the molecular recognition of CU was studied. The hypochromic effect in UV-vis spectra showed the obvious molecular recognition of CU to ATP. This recognition is actually the hydrogen bond interaction between the uracil group of CU and the base radical of ATP. The association constant between CU and adenine was determined by UV titration at low concentrations.

**Key words:** calixarene, uridine, molecular recognition, UV-vis spectra.

**Résumé :** On a réalisé la synthèse d'un nouveau dérivé du *p*-tert-butylcalix[4]arène contenant de l'uridine, le 5,11,17,23-tétra-*tert*-butyl-25,26,27-trihydroxyl-28-oxyuridinecalixa[4]arène (CU), et on l'a caractérisé grâce à la spectroscopie IR, RMN du  $^1\text{H}$  et du  $^{13}\text{C}$  et à la spectroscopie de masse « EI-MS » et « ESI-MS ». On a étudié les spectres UV-visible comme méthode de reconnaissance moléculaire du CU. L'effet hypochrome dans le spectre UV-visible présente la méthode évidente de reconnaissance du CU avec l'ATP. Cette méthode de reconnaissance correspond à une interaction de liaison hydrogène entre le groupe uracile du CU et le radical de base de l'ATP. La constante d'association entre le CU et l'adénine a été déterminée par titrage UV à faibles concentrations.

**Mots clés :** calixarène, uridine, reconnaissance moléculaire, spectre UV-visible.

[Traduit par la Rédaction]

## Introduction

Calixarenes are cavity-containing macrocyclic compounds made up of substituted phenols with aldehydes (1), which can be used as a basic skeleton in the design of new receptors (2).

We have studied the supramolecular catalysis in the hydrolysis of ATP facilitated by calix[4]arene-5,11,17,23-tetrasulfonate and proved the molecular recognition between calix[4]arene-5,11,17,23-tetrasulfonate and ATP using laser photolysis and pulse radiolysis (3). We also investigated the transport of ATP in an  $\text{H}_2\text{O}-\text{CH}_2\text{Cl}_2$  :  $\text{CCl}_4-\text{H}_2\text{O}$  liquid membrane system with *p*-tert-butylcalix[4]arene as a carrier (4). The studies showed that *p*-tert-butylcalix[4]arene or calix[4]arene-5,11,17,23-tetrasulfonate could recognize ATP by hydrogen bonds between the phenol hydroxyl group in calixarene and the phosphate group in ATP. But this is not the only kind of molecular recognition model for a nucleotide.

Considering that in the life process, the self-replication of DNA is primarily based on the principle of recognition and pairing of nucleotide bases (A to T, C to G), we want to introduce a nucleoside group (uridine in this paper) into a calixarene molecule as a "recognition factor" or "sensor" for a certain nucleotide (such as ATP) or specific nucleoside. Furthermore, we can develop some applications for these kinds of new calixarene derivatives in recognition of the order of nucleic acid, specific-site cleavage, selective separation, membrane transport, and mimicry of enzymatic catalysis to nucleic acid, etc.

This paper reports the synthesis and characterization of 5,11,17,23-tetra-*tert*-butyl-25,26,27-trihydroxyl-28-oxyuridinecalix[4]arene (CU). The molecular recognition of CU to nucleotide, nucleoside, and base radical was investigated using UV-vis electronic spectroscopy. Furthermore, the association constant between CU and adenine was calculated too.

## Experimental

### Materials and method

$^1\text{H}$  NMR and  $^{13}\text{C}$  NMR were recorded at 500 MHz using an AM500 spectrometer in  $\text{CDCl}_3$ . IR spectra were recorded on a Nicolet FT-IR 170SX spectrometer. UV-vis spectra were obtained using a PerkinElmer Lambda Bio40 spectrometer. An LCQ electrospray ionization mass spectrometer (ES-MS Finnigan) was employed for molecular mass determination.

Received 14 January 2003. Published on the NRC Research Press Web site at <http://canjchem.nrc.ca> on 9 September 2003.

**J. Liang, H. Fu, Y. Liu, L. Wang, and Z. Ye.** Department of Chemistry, Tongji University, Shanghai 200092, P.R. China.

**X. Shi.**<sup>1</sup> State Key Laboratory of Coordination Chemistry, Nanjing University, Nanjing, Jiangsu 210093, P. R. China.

<sup>1</sup>Corresponding author (e-mail : [xfshi@mail.tongji.edu.cn](mailto:xfshi@mail.tongji.edu.cn)).



Uridine, adenine, ATP, and GMP were obtained as biochemicals and used without further purification. THF was distilled over sodium pellets. Water used here was deionized (with a conductivity of  $1 \times 10^{-6} \text{ s}^{-1} \sim 1 \times 10^{-7} \text{ s}$ ). All the other chemicals were of AR grade and were used without further purification.

### Synthesis and characterization of CU

The preparation of the compound CU is depicted in Scheme 1. *p*-*tert*-Butylcalix[4]arene **I**, 2',3'-*o*-isopropylidene-uridine **II**, and 5'-(2',3'-*o*-isopropylidene-uridine)-*p*-methylphenyl-sulfonate **III** were synthesized according to the literature (5, 6) and characterized by  $^1\text{H}$  NMR, IR spectroscopy, EI and ESI mass spectroscopy, and elemental analysis.

A mixture of 1.51 g *p*-*tert*-butylcalix[4]arene **I** (2.33 mmol), 0.47 g 5'-(2',3'-*o*-isopropylidene-uridine)-*p*-methylphenylsulfonate **III** (1.08 mmol), and 0.71 g potassium carbonate (5.17 mmol) in dry THF (40 mL) was stirred under an atmosphere of  $\text{N}_2$  at 27 °C for 72 h. The resulting solution was filtered to remove potassium carbonate, and the filtrate was concentrated and purified by column chromatography. Then the crude product was recrystallized from methanol to give 0.2 g (21%) as a white powder.

Characterization: mp 146.8–148.8 °C. IR (KBr) ( $\text{cm}^{-1}$ ): 3436 (N-H), 3179 (O-H), 2960 ( $\text{CH}_3$ ), 1745 (C=O).  $^1\text{H}$  NMR (ppm)  $\delta$ : 1.22 (10H,  $\text{C}(\text{CH}_3)_3$ ), 1.34 (6H,  $\text{C}(\text{CH}_3)_3$ ), 1.56 (6H,  $\text{C}(\text{CH}_3)_3$ ), 2.19 (2H,  $\text{C}(\text{CH}_3)_3$ ), 2.46 (12H,  $\text{C}(\text{CH}_3)_3$ ), 3.45–3.50, 4.26–4.38 (10H, Ar- $\text{CH}_2$ -Ar and - $\text{CH}_2$ -in uridine), 4.79–4.81 (2H, in sugar, uridine), 4.92–4.94 (2H, C-OH in sugar, uridine), 5.67 (2H, in sugar, uridine), 5.73–5.75 (1H, uracil), 7.06 (2H, ArH, calixarene), 7.34–7.36 (4H, ArH, calixarene), 7.78–7.79 (2H, ArH, calixarene), 7.78–7.79 (1H, uracil), 10.36 (1H, NH, uracil).  $^{13}\text{C}$  NMR (ppm)  $\delta$ : 25.23 (Ar- $\text{CH}_2$ -Ar), 27.05 (Ar- $\text{CH}_2$ -Ar), 31.38 ( $\text{C}(\text{CH}_3)_3$ ), 32.63 ( $\text{C}(\text{CH}_3)_3$ ), 69.25 (5'-C, uridine), 76.69 (3'-C, uridine), 77.33 (2'-C, uridine), 84.97 (4'-C, uridine), 94.79 (1'-C, uridine), 102.74 (5-C, uridine), 114.70 (ArC- $\text{CH}_2$ -Ar), 125.94 (Ar-CH), 127.96 (Ar-CH), 129.90 (ArC- $\text{C}(\text{CH}_3)_3$ ), 132.82 (ArC- $\text{C}(\text{CH}_3)_3$ ), 142.12 (6-C, uridine), 145.23 (ArC-OH), 146.80 (ArC-O-uridine), 149.98 (2-C, uridine), 163.04 (4-C, uridine). EI-MS  $m/z$  (%): 648 (M-Uridine (calix[4]arene (Cal)), 31), 592 (Cal -  $\text{C}(\text{CH}_3)_3$ , 10), 536 (Cal -  $2\text{C}(\text{CH}_3)_3$ , 7), 480 (Cal -  $3\text{C}(\text{CH}_3)_3$ , 4), 423 (Cal -  $4\text{C}(\text{CH}_3)_3$ , 22), 91 ( $\text{C}_7\text{H}_7^+$ , 100). ESI-MS  $m/z$  (%): 898([M + Na] $^+$ , 100), 461([M + 2Na] $^{2+}$ , 53).

### Study on the molecular recognition between CU and ATP, GMP, adenine, and $\text{KH}_2\text{PO}_4$

A series of standard solutions of varying concentrations ( $1 \times 10^{-3} \sim 1 \times 10^{-6} \text{ mol}\cdot\text{L}^{-1}$ ) of CU was prepared. The absorbance of the standard solutions was determined at 260 nm, and the UV standard curve of CU was taken. The UV standard curves of ATP (260 nm), GMP (252.7 nm and 260 nm), and adenine (260 nm) were determined using the same method. The absorption of  $\text{KH}_2\text{PO}_4$  was zero at the UV wave band.

A series of mixed solution samples of CU and ATP were prepared, to maintain the total concentration of the two components constant — about  $5 \times 10^{-5} \text{ mol}\cdot\text{L}^{-1}$  — but varying the concentration ratio of CU and ATP as follows: 5:0,

4.5:0.5, 3.5:1.5, 2.5:2.5, 1.5:3.5, 0.5:4.5, 0:5. Their absorbances were measured at 260 nm, which was the experimental value of absorbance of the sample. For every sample solution, the single absorbance of each component can be calculated by use of their own standard curves, according to the actual concentration in the sample; thus the two single calculated absorbances of the two component were added together, and we got the calculated value of absorbance of the sample. If there is no interaction between the two components in the sample solution, the calculated absorbance value should be the same as its experimental value. So, by comparing the absorbance experimental value to its calculated value, we could find out the information that would enable us to ensure whether there was any interaction between the two components.

A GMP solution, about  $1 \times 10^{-4} \text{ mol}\cdot\text{L}^{-1}$ , was prepared, and its concentration was determined using its standard curve taken at 252.7 nm. But, in the sample solutions, the individual absorbance was calculated using its standard curve taken at 260 nm. The total concentration and the concentration ratio of the two components were the same as in the experiment of the interaction between CU and ATP.

An adenine solution, about  $1 \times 10^{-4} \text{ mol}\cdot\text{L}^{-1}$ , was prepared, and its concentration was determined using its standard curve taken at 260 nm. The total concentration and the concentration ratio of the two components were the same as in the experiment of the interaction between CU and ATP.

A solution of  $1.645 \times 10^{-4} \text{ mol}\cdot\text{L}^{-1} \text{ KH}_2\text{PO}_4$  was prepared, and the total concentration and the concentration ratio of the two components were the same as in the experiment of the interaction between CU and ATP.

### Determination of the association constant of the supermolecule formed between CU and adenine by UV titration

UV titration has been extensively employed to determine binding constants (7–9). The quantitative determination of the formation constant is based on the absorbance variation of the receptor in the presence of a substrate with certain concentration. Difference absorption spectra were recorded on an Agilent 8453 UV-vis spectrometer. All spectra were obtained in 10 mm cells at  $25 \pm 1$  °C. The added substrate was dissolved in the solution-containing receptor, while the total concentration of the receptor remained constant throughout the titration. The experiments were performed in a concentration range wherein the absorbance of every sample obeyed Beer's law.

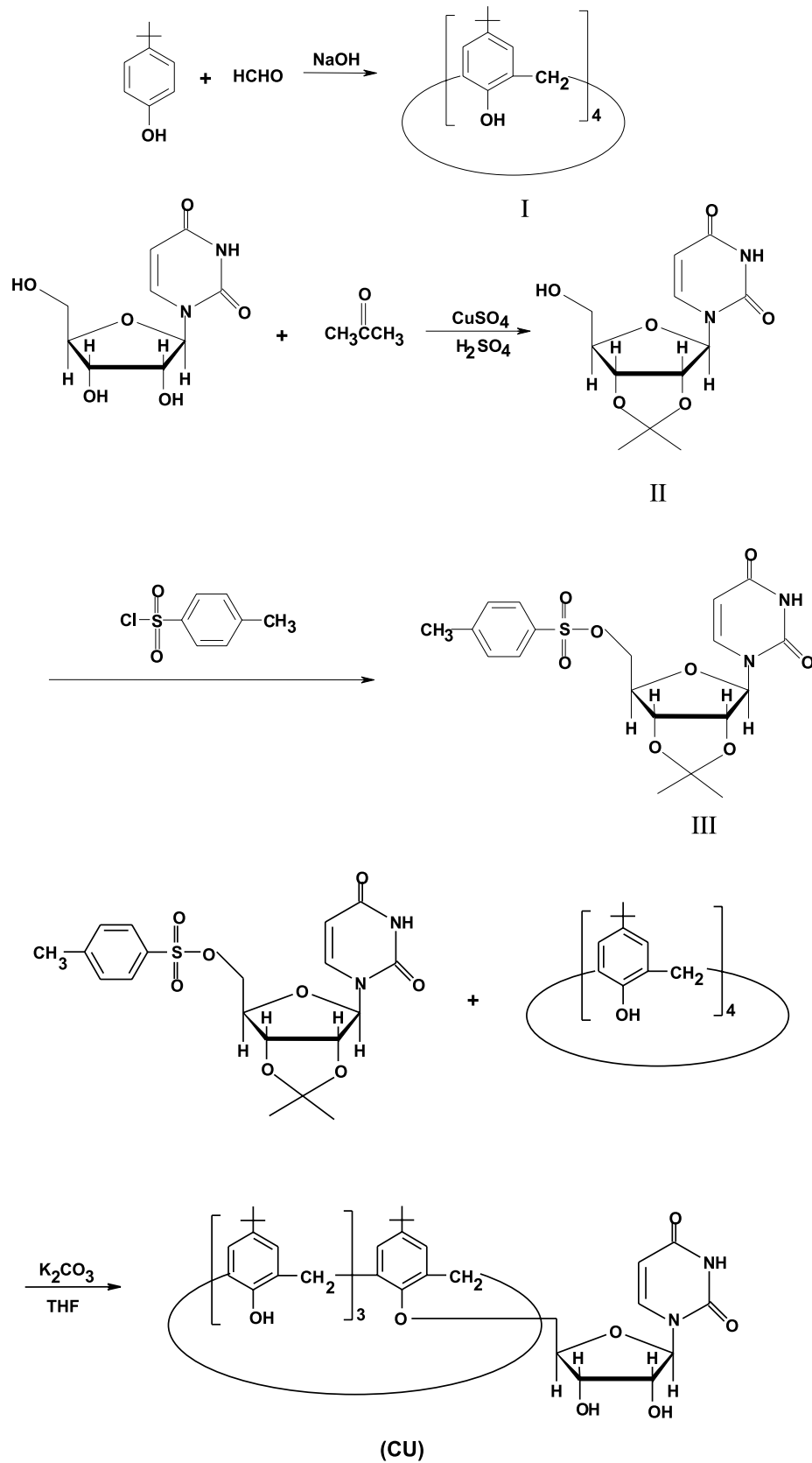
The experimental results of the UV titration showed that the association between CU and adenine leads to the formation of only a 1:1 supramolecular complex that has an association constant,  $K$ , according to the following equation:

$$\text{R} + \text{S} \rightleftharpoons \text{C}$$

$$[1] \quad K = \frac{[\text{C}]}{[\text{R}][\text{S}]} = \frac{[\text{C}]}{([\text{R}]_0 - [\text{C}])([\text{S}]_0 - [\text{C}])}$$

where R, S, and C represent the receptor, the substrate, and the formed supermolecule, respectively, while [R], [S], and [C] are the equilibrium concentration of R, S, and C, respectively;  $[\text{R}]_0$  and  $[\text{S}]_0$  are the total concentration of R and S.



**Scheme 1.** Synthesis of 5,11,17,23-tetra-*tert*-butyl-25,26,27-trihydroxyl-28-oxyuridinecalix[4]arene (CU).



The absorbance,  $A$ , measured at a certain wavelength is expressed as:

$$A = l([R]\epsilon_R + [S]\epsilon_S + [C]\epsilon_C)$$

where  $\epsilon_R$ ,  $\epsilon_S$ , and  $\epsilon_C$  are the molar extinction coefficients of R, S, and C, respectively, and  $l$  is the width of the absorption cell, while the absorbance in the reference cell,  $A_r$ , is expressed as:

$$A_r = l[R]_0\epsilon_R$$

Therefore, the difference in the absorbance,  $\Delta A$ , is expressed as:

$$[2] \quad \Delta A = A - A_r = l([C](\epsilon_C - \epsilon_R - \epsilon_S) + [S]_0\epsilon_S)$$

Using eqs. [1] and [2], the association constant  $K$  can be calculated.

## Results and discussion

### Synthesis and characterization of CU

CU is a new compound whose synthesis, characterization, and properties have not been reported. This paper reports the synthesis and characterization of CU. The characterization methods included IR,  $^1\text{H}$  NMR,  $^{13}\text{C}$  NMR, EI-MS, and ESI-MS — especially the ESI-MS spectrum, which showed, clearly, a strong peak for the molecular ion ( $m/z = 898$  ( $[\text{M} + \text{Na}]^+$ )) and a strong bivalent ion peak ( $m/z = 461$  ( $[\text{M} + 2\text{Na}]^{2+}$ )). The characteristic peaks for either calixarene or uridine were found in the  $^1\text{H}$  NMR and  $^{13}\text{C}$  NMR spectra of the synthesized compound CU. The analogous phenomena were observed in the IR or UV spectra of CU too. All these results indicate that the compound synthesized can be identified as the target compound.

### UV-vis spectroscopy study of CU

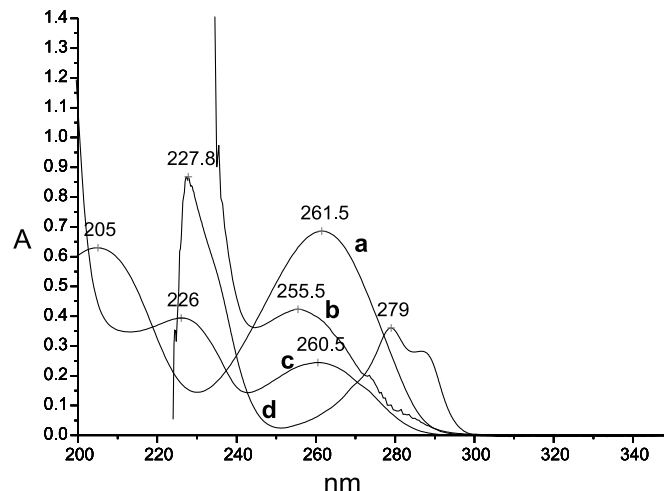
Figure 1 displays the absorption spectra of uridine, 5'-(2',3'-*o*-isopropylidene-uridine)-*p*-methyl-phenylsulfonate **III**, CU, and *p*-*tert*-butylcalix[4]arene **I**. As illustrated in Fig. 1, CU has two obvious absorbance peaks at 260.5 and 226 nm. The two peaks correspond, respectively, to the characteristic absorbance peak of uracil at 261.5 nm (Fig. 1a) (10) and that of *p*-alkylphenol in the calixarene structure at 227.8 nm (Fig. 1d) (11). This shows that the compound CU is composed of calix[4]arene and uridine.

Using the standard curve of CU taken at 260 nm, the value of the molar absorptivity,  $\epsilon_{\text{CU}260}$ , can be determined as  $1.7955 \times 10^4$ . For uridine, the value of the molar absorptivity,  $\epsilon_{\text{uridine}260}$ , can also be determined as  $1.028 \times 10^4$  ( $1.01 \times 10^4$  in the literature (10)), using the same method. The absorption of *p*-*tert*-butylcalix[4]arene **I** is low at around 260 nm, so the corresponding molar absorptivity,  $\epsilon_{\text{cal}260}$ , is very small. The experimental results showed that CU is a new compound, different from calix[4]arene and uridine.

### Molecular recognition study between CU and ATP, GMP, adenine, and $\text{KH}_2\text{PO}_4$

CU, ATP, GMP, and adenine all have the characteristic absorbance peak of a nucleotide base group near 260 nm (10). So there is no obvious shift to be found for the charac-

**Fig. 1.** UV-vis spectra of (a)  $1 \times 10^{-5}$  mol·L $^{-1}$  uridine in water; (b)  $1 \times 10^{-5}$  mol·L $^{-1}$  5'-(2',3'-*o*-isopropylidene-uridine)-*p*-methyl-phenylsulfonate **III** in THF; (c)  $1 \times 10^{-5}$  mol·L $^{-1}$  CU in water; (d)  $1 \times 10^{-5}$  mol·L $^{-1}$  *p*-*tert*-butylcalix[4]arene **I** in  $\text{CH}_2\text{Cl}_2$ .



teristic absorbance peak of every component in the mixed system of CU and ATP, GMP, or adenine,  $\text{KH}_2\text{PO}_4$ , no matter whether they react with each other or not. But an obvious hypochromic effect was indeed found at 260 nm for the mixed system, which shows that there was an interaction between the components in the system.

### Interaction between CU and ATP

The experimental data are plotted in Fig. 2a. When there was only CU or ATP in the sample solution, the experimental value was equivalent to the calculated value. For the mixed solutions, the experimental values were always smaller than the corresponding calculated values. Especially when the concentration ratio was 1:1, the difference between the experimental value and the calculated value reached a maximum. This hypochromic effect implies that there is molecular recognition between CU and ATP. Indeed, the molar absorptivity of the formed supermolecule by CU with ATP,  $\epsilon_{\text{CU-ATP}}$ , can be calculated as  $3.1862 \times 10^4$  when the component concentration ratio is 1:1.

### Interaction between CU and GMP

The experimental data were plotted in Fig. 2b. As illustrated in the figure, the experimental values were almost equivalent to the corresponding calculated values. This did not show a hypochromism or a hyperchromism. This result implies that there is no significant interaction between CU and GMP. The studies reveal that CU can recognize ATP, but not GMP.

### Interaction between CU and adenine

The experimental data were plotted in Fig. 2c. As illustrated in the figure, when there was only CU or adenine in the solution, the experimental value was equivalent to the calculated value. For the mixed solutions, the experimental values were always obviously smaller than the corresponding calculated values. Especially when the concentration ratio was 1:1, the difference between the experimental value and the corresponding calculated value reached a maximum.



**Fig. 2.** The absorbance of the sample solutions mixed by CU with ATP (a); GMP (b); adenine (c);  $\text{KH}_2\text{PO}_4$  (d). Solid line stands for the experimental value; dotted line stands for the calculated value.

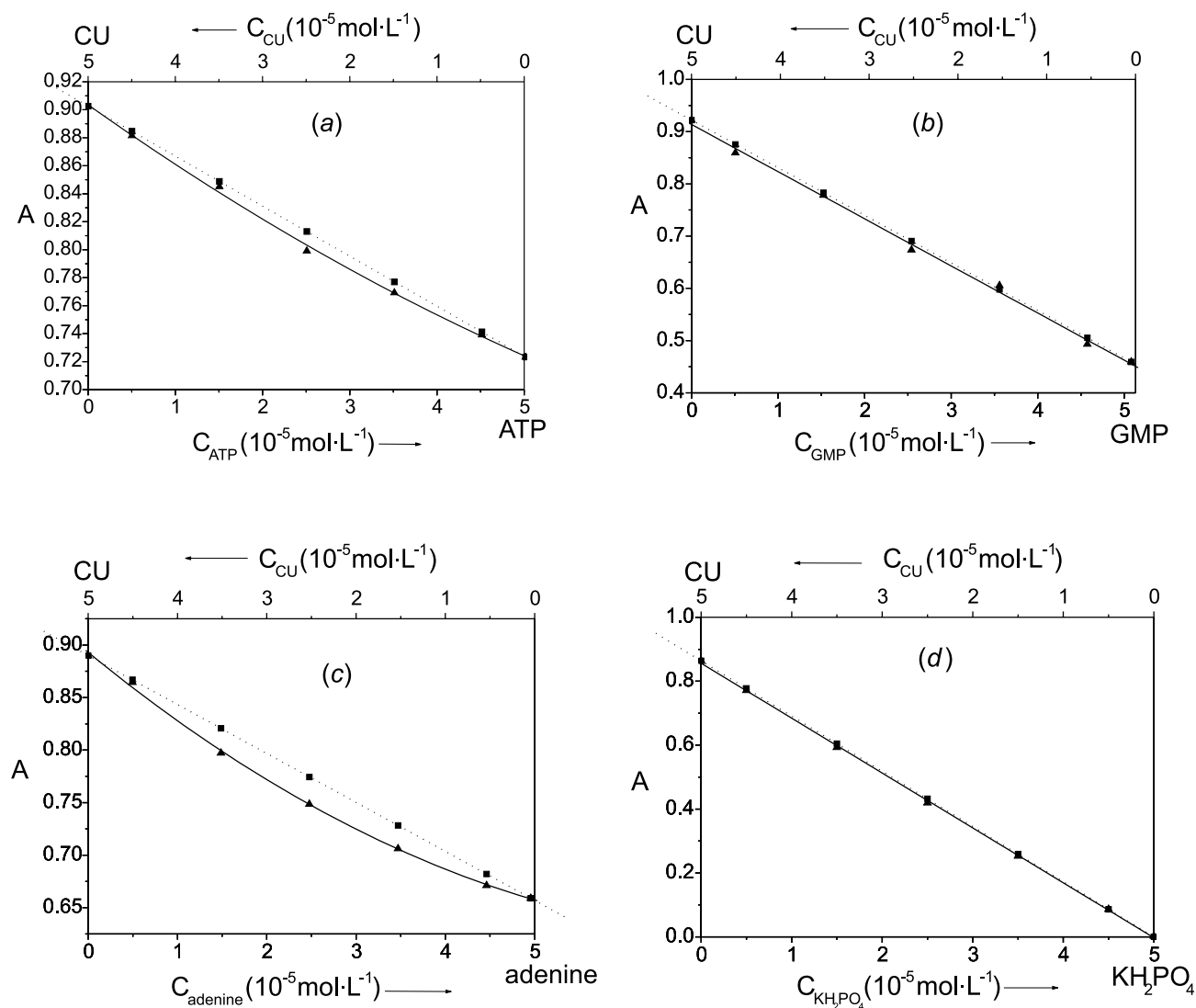
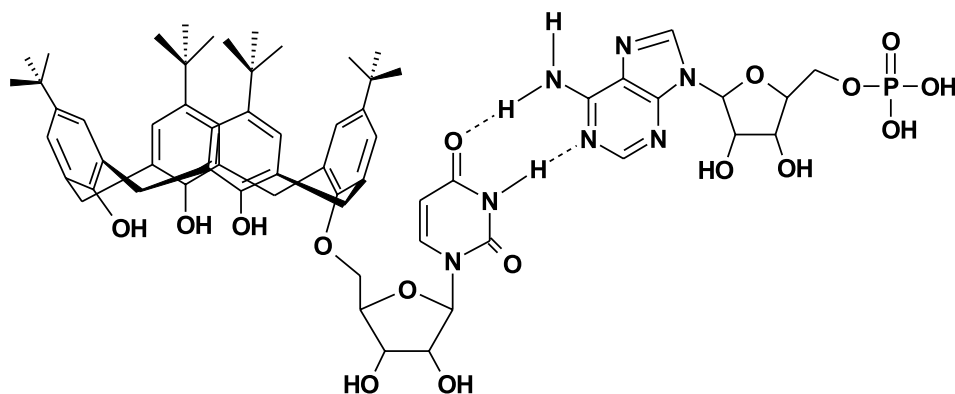


**Fig. 3.** The molecular recognition of CU to adenosine and the formed supermolecule.



This significant hypochromic effect implies that there is obvious molecular recognition between CU and adenine, similar to that between CU and ATP. The base of this molecular

recognition may be interpreted as the structural complementarity and hydrogen bonding between the uracil of CU and the adenine in ATP or adenosine.



### Interaction between CU and $\text{KH}_2\text{PO}_4$

The interaction between CU and  $\text{KH}_2\text{PO}_4$  was investigated too. The experimental data were plotted in Fig. 2d. As illustrated in the figure, the experimental values were almost equivalent to the corresponding calculated values. There is neither a hypochromism nor a hyperchromism. This result shows that CU cannot recognize  $\text{KH}_2\text{PO}_4$  and implies that the recognition site between CU and ATP is not a phosphate group of ATP.

All the studies suggest that CU can recognize adenosine in the ATP (See Fig. 3), but not the phosphate group. We have studied the molecular recognition between calix[4]arene-5,11,17,23-tetrakisulfonate and ATP and found that the basis of recognition was hydrogen bonds formed between hydroxyl group in calix[4]arene-5,11,17,23-tetrakisulfonate and the phosphate group in ATP (3). That shows that the recognition mechanisms in these two cases are different.

### Determination of the association constant between CU and adenine

In the process of calculation of the association constant between CU and adenine, the self-association of adenine was neglected. The dimerization of CU was not taken into account, as was also the case with adenine. These factors simplify the calculation.

The wavelength of interest was 227 nm, because the difference between the molar extinction coefficients of CU and adenine reaches a maximum at 227 nm.

By using this method, the association constant between CU and adenine was calculated as  $2 \times 10^4 \text{ mol}^{-1}\cdot\text{L}$ .

### Conclusion

The experimental results show that the molecular recognition of CU to ATP is based on the recognition of the uridine group in CU to the adenine group in ATP. This recognition function is the same as the one in the process of formation of DNA and RNA, i.e., the base pairing (T to A or U to A).

The experimental result, that CU cannot recognize GMP, also confirms the above recognition function based on U–A pairing. Therefore, according to the idea of molecular design and assembling, by introducing the uridine group (in fact, the uracil group), the target receptor CU can actually work as a “recognition factor” that has the molecular recognition ability for some specific nucleotide, nucleoside, or base (such as ATP, adenosine, or adenine). With this method we can design and synthesize a series of receptors that can have specific molecular recognition ability for given specific nucleotides.

### Acknowledgement

This work was supported by the National Natural Science Foundation of China (No. 29 971 023).

### References

1. C.D. Gutsche. *In* Calixarenes, monographs in supramolecular chemistry. Vol. 1. Edited by the Royal Society of Chemistry, Cambridge. 1989.
2. S. Shinkai. *Pure Appl. Chem.* **58**, 1523 (1986).
3. T.M. Yao, Z.F. Ye, L. Wang, J.Y. Gu, S.D. Yao, and X.F. Shi. *Spectrochim. Acta A*, **58**, 3033 (2002).
4. Y. Liu, Y.Q. Tao, Y.Y. Cao, J. Liang, J.Y. Gu, and X.F. Shi. *Huaxue Xuebao*, **60** (6), 1111 (2002).
5. C.D. Gutsche, M. Iqbal, and D. Stewart. *J. Org. Chem.* **51**, 742 (1986).
6. P.A. Levene and R.S. Tipson. *J. Biol. Chem.* **106**, 113 (1934).
7. D. Landy, S. Fourmentin, M. Salome, and G. Surpateanu. *J. Inclusion Phenom. Macrocyclic Chem.* **38**, 187 (2000).
8. D. Tsiourvas, Z. Sideratou, A.A. Haralabakopoulos, G. Pistolis, and C.M. Paleos. *J. Phys. Chem.* **100**, 14 087 (1996).
9. W.M. Scovell and T. O'Connor. *J. Am. Chem. Soc.* **99**(1), 120 (1977).
10. J. Sambrook, E.F. Fritsch, and T. Maniatis. *In* Molecular cloning a laboratory manual. 2nd ed. Edited by Cold Spring Harbor Laboratory Press, New York. 1989.
11. L. Huang and D.Q. Yu. *In* Application of UV spectrum in organic chemistry. Edited by Science Publisher, Beijing. 1988.



# Reactions of dimethoxycarbene with thiocarbonyl compounds

Malgorzata Dawid, Grzegorz Mloston, Darren L. Reid, and John Warkentin

**Abstract:** A diverse sample of thiocarbonyl compounds were examined to determine what the ultimate stable products are of their reactions with dimethoxycarbene. Those ultimate products can be significantly different for an oxyphosphinyl dithioformate, methyl dithiobenzoate, *O*-methyl thiobenzoate, and dimethyl xanthate.

**Key words:** dimethoxycarbene, thiocarbonyl compounds, 2,5-dihydro-2,2-dimethoxy-5,5-dimethyl-1,3,4-oxadiazole.

**Résumé :** On a étudié un large échantillonnage de composés thiocarbonylés pour déterminer la nature de leurs produits ultimes et stables de leurs réactions avec le diméthoxycarbène. Ces produits ultimes varient beaucoup suivant la nature du produit de départ, dithioformate d'oxyphosphinyle, dithiobenzoate de méthyle, thiobenzoate de *O*-méthyle ou xanthate de diméthyle.

**Mots clés :** diméthoxycarbène, composés thiocarbonylés, 2,5-dihydro-2,2-diméthoxy-5,5-diméthyl-1,3,4-oxadiazole.

[Traduit par la Rédaction]

## Introduction

Carbenes bearing heteroatom substituents (NR<sub>2</sub>, OR, SR) are nucleophilic, attacking preferentially alkenes with electron-withdrawing substituents. Dimethoxycarbene does not react with cyclohexene (1), but it does add to maleates and fumarates, for example (2). Nucleophilic carbenes react also with carbonyl and thiocarbonyl compounds (3), as do electrophilic carbenes, but the former probably make one bond initially to the electrophilic center (4) or else add in a concerted but asynchronous manner. The latter bond to the carbonyl oxygen (or to thiocarbonyl sulfur) to form ylide intermediates (5). Some of these reactions are illustrated in Scheme 1.

We have examined a diverse sample of thiocarbonyl compounds to determine what the ultimate stable products are, of their reactions with dimethoxycarbene. Surprisingly, those ultimate products can be significantly different for different thiocarbonyl compounds, including *S*-methyl-bis(1-methylethoxy)phosphinecarbothioate-1-oxide (4) (also known as *S*-methyl-diisopropoxyphosphinyl-dithioformate), *S*-methyl benzenecarbothioate (or methyl dithiobenzoate) (8), *O*-methyl benzenecarbothioate (or *O*-methyl thiobenzoate) (17), and *O,S*-dimethyl dithiocarbonate (or dimethyl xanthate) (22).

The carbene was generated from 2,2-dimethoxy-5,5-dimethyl-Δ<sup>3</sup>-1,3,4-oxadiazoline (1, also known as 2,5-dihydro-2,2-dimethoxy-5,5-dimethyl-1,3,4-oxadiazole) at 110 °C in a benzene solution containing the thiocarbonyl compound in a sealed tube (Scheme 2). The sequence by which the oxadiazoline undergoes thermolysis is well established (6). The

first step is 1,3-dipolar cycloreversion to N<sub>2</sub> and a carbonyl ylide (2). The latter is short lived, losing acetone to afford dimethoxycarbene (DMC, 3).

## Results and discussion

Treatment of 4 with DMC gave, in 50% isolated yield, product 7. It is presumably formed by cycloaddition of DMC to the thiocarbonyl group to generate 5, which then undergoes desulfurization (typical of such thiiranes) (7) to ketene acetal 6. Hydrolysis of the sensitive ketene acetal leads to 7, Scheme 3. The structure of 7 was established by means of spectroscopy and mass spectrometry.

Under similar conditions, dithiobenzoate 8 gave products 11 (not isolable), 12, 13 (22%), and 16 (28%). The presumed intermediates, 10, 14, and 15, also could not be isolated, and spectroscopic evidence for 12 was based on <sup>1</sup>H and <sup>13</sup>C NMR spectroscopy only. We assume that 8 reacted with DMC to afford 10, either via intermediate 9 or directly, by a concerted process, and that thiirane 10 was desulfurized (7) to give ketene acetal 12. Ketene acetal 12, like most other ketene acetals, is expected to hydrolyse during workup and to give 13 as the stable end product, Scheme 4. Formation of compound 11 (the probable source of 14) can be understood in terms of a 1,2-migration of the thiomethyl group in an intermediate like 9, Scheme 4.

A possible mechanism to 16 is more complicated because it requires two carbene units. The thiocarbonyl group of 11 is expected to be quite reactive toward DMC, and addition would afford 14. Desulfurization of 14 (7) and hydrolysis, in

Received 7 May 2003. Published on the NRC Research Press Web site at <http://canjchem.nrc.ca> on 5 September 2003.

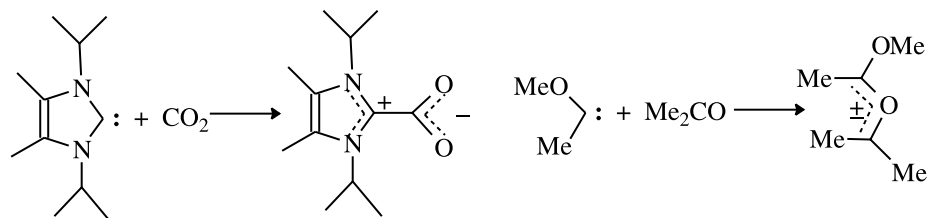
**M. Dawid, D.L. Reid, and J. Warkentin.**<sup>1</sup> Department of Chemistry, McMaster University, 1280 Main Street West, Hamilton, ON L8S 4M1, Canada.

**G. Mloston.** Department of Organic and Applied Chemistry, University of Łódź, Łódź, Poland.

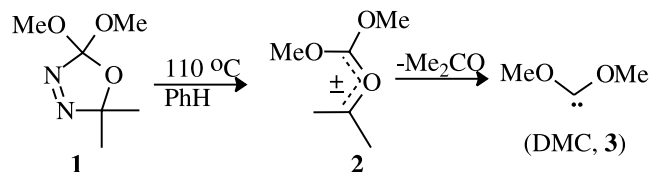
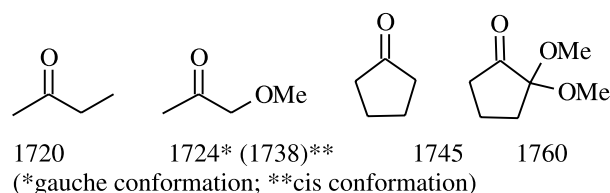
<sup>1</sup>Corresponding author (e-mail: [warkent@mcmaster.ca](mailto:warkent@mcmaster.ca)).



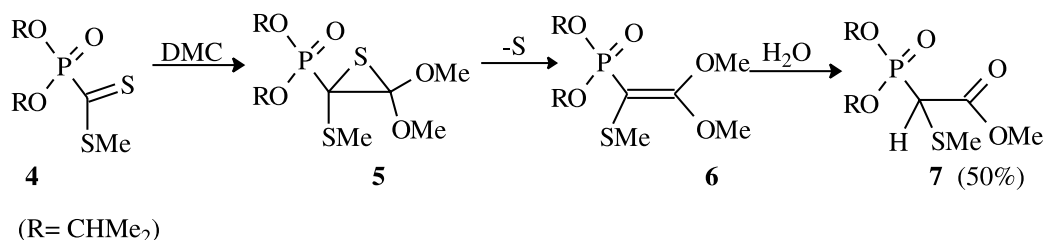
Scheme 1.



Scheme 2.

Fig. 1. Carbonyl stretching frequencies ( $\text{cm}^{-1}$ ) of ketones and methoxy ketones.

Scheme 3.



either order, would furnish another ketene acetal (**15**) that would hydrolyze during workup to the end product **16**.

A similar product was formed by reaction of **17** with DMC. Two equivalents of DMC were incorporated, and in this case we were able to identify **21** by means of  $^1\text{H}$  and  $^{13}\text{C}$  NMR spectroscopy, although it too was desulfurized and hydrolyzed to dimethyl phenyl malonate (**16**, 84%). The partial identification of **21** strengthens the analogous mechanism in Scheme 4. Although **19** was not found, it is likely that the first adduct (something like zwitterion **18**) underwent methoxy migration to generate thione **19**, which must be more reactive towards DMC than **17**. We propose, tentatively, that the trimethoxymethyl group of **19** enhances the reactivity of the thiocarbonyl group toward DMC. It might do this by participation of the methoxyl oxygens at the transition state for addition of DMC (**20**) if that transition state were dipolar, as depicted in Scheme 5. A similar suggestion for interaction by a methoxy group was made earlier (3c). Alternatively, the reactivity of the thiocarbonyl group might be enhanced by the polar effect of the trimethoxymethyl group. A steric effect, operating in the other direction, would have to be smaller than the polar effect. To support the existence of the polar effect, we compared published values (8, 9) of the IR carbonyl stretching frequencies of the  $\alpha$ -methoxyketones (below) with those of corresponding ketones, Fig. 1. It is clear that an  $\alpha$ -methoxy group raises the  $\text{C}=\text{O}$  frequency and that the inductive effect of three such groups at a carbon alpha to a carbonyl group could raise its reactivity significantly, although not to the level of acyl

chlorides, which have  $\text{C}=\text{O}$  stretching frequencies near  $1800\text{ cm}^{-1}$ .

Compound **22** reacted fairly cleanly with DMC to afford **25** as the major product (40%, isolated). Scheme 6 depicts a possible mechanism for the formation of **25**. In intermediate **24** there is the option of migration of either the methoxy or the methylthio group. The greater polarizability of S and the weaker  $\text{C}-\text{S}$  bond (relative to O and the  $\text{C}-\text{O}$  bond) readily account for the preferential migration of the SMe group.

## Experimental

### Preparation of starting materials

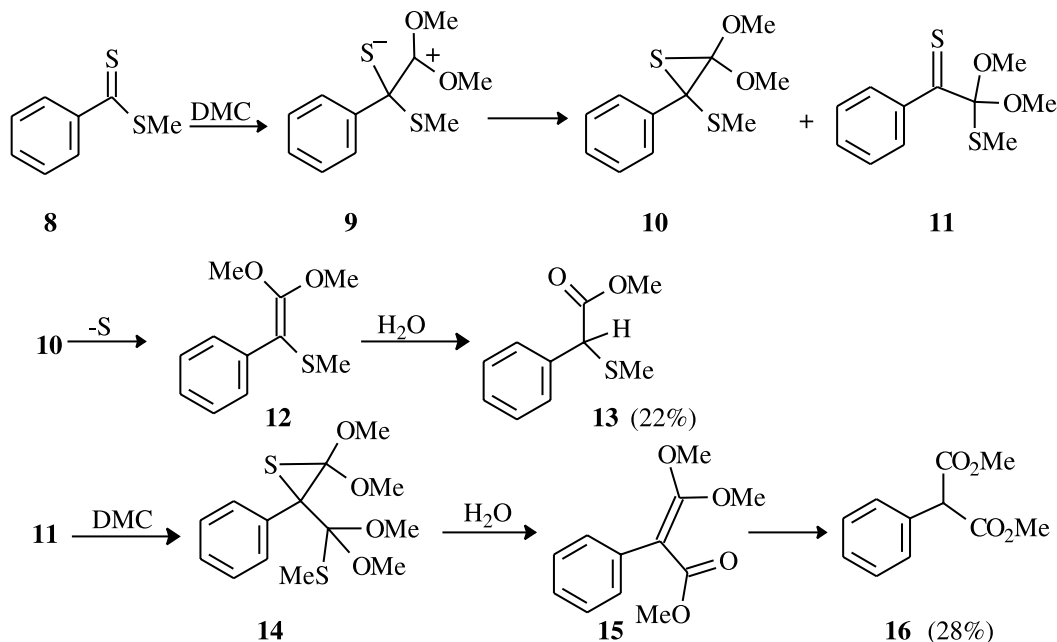
Compound **1** was prepared according to a published procedure (10); **4** was prepared according to the protocol by D.W. Grisley, Jr. (11); **8** was synthesized by thionation of benzoic acid with the Davy reagent (12); **17** was prepared from methyl benzoate and Lawesson's reagent (13), and **22** was available from methoxide, carbon disulfide, and dimethyl sulfate or methyl iodide (14).

### Thermolysis of **1** in the presence of **4**

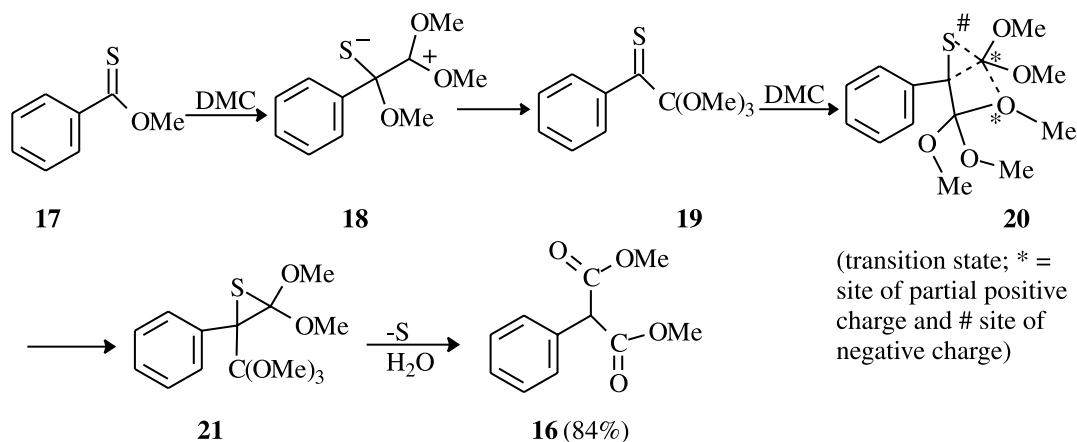
The following thermolysis procedure is typical. A solution of **4** (0.128 g, 0.50 mmol) and **1** (0.080 g, 0.50 mmol) in dry benzene (5 mL) in a thermolysis tube was degassed by means of three freeze-pump-thaw cycles before the tube was sealed under vacuum. It was then placed into an oil bath ( $110^\circ\text{C}$ ) for a 24 h period. In the case of **4**, evaporation of



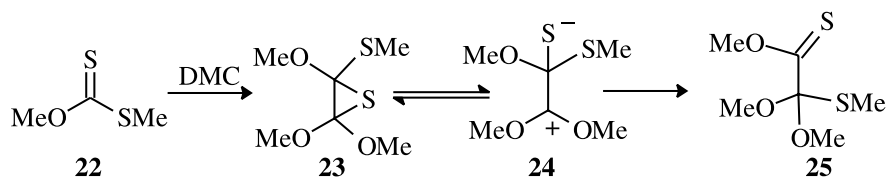
Scheme 4.



Scheme 5.



Scheme 6.



the solvent and the volatile components left a residue that was purified by chromatography on silica (Chromatotron, 1 mm plate, 10% EtOAc in hexane) to afford **7** (50% yield) as a final, stable product.

7

Colourless oil.  $^1H$  NMR (200 MHz,  $CDCl_3$ )  $\delta$ : 1.37–1.32 (overlapping d, 12H), 2.29 (s) and 2.30 (s) (together 3H), 3.54 (d,  $^1J_{P-H}$  = 19.6 Hz, 1H), 3.77 (s, 3H), 4.79 (m, 2H).  $^{13}C$  NMR (75 MHz,  $CDCl_3$ )  $\delta$ : 23.8, 24.3, 44.7, 47.5, 53.0,

72.7, 72.8, 128.4, 168.0. EI-MS  $m/z$  (%): 284 ( $[M]^+$ , 2), 238 (15), 197 (22), 155 (40), 154 (40), 123 (15), 86 (30), 84 (55), 49 (100). CI-MS  $m/z$  (%): 302 ( $[M + NH_4]^+$ , 3), 285 ( $[M + 1]^+$ , 100).

#### Thermolysis of **1** in the presence of **8**

The standard thermolysis procedure gave, from **8** (0.084 g, 0.50 mmol) and **1** (0.080 g, 0.50 mmol), a residue that was chromatographed on silica (Chromatotron plate, 1 mm, 5% EtOAc in hexane (50 mL) and 10% EtOAc in



hexane (100 mL)) to afford **13** (22%) and **16** (28%) as final, stable products. Small amounts of unstable products **12** and **15** were also isolated.

## 12

Colourless oil.  $^1\text{H}$  NMR (300 MHz,  $\text{CDCl}_3$ )  $\delta$ : 1.98 (s, 3H), 3.52 (s, 3H), 3.77 (s, 3H), 7.18–7.47 (m, 5H).  $^{13}\text{C}$  NMR (125 MHz,  $\text{CDCl}_3$ )  $\delta$ : 17.0, 57.5, 97.5, 126.4, 128.1, 129.7, 136.9, 159.2 (from 2d NMR, two of the aromatic carbon signals are coincident). EI-MS  $m/z$  (%): 210 ( $[\text{M}]^+$ , 70), 195 (100), 167 (32), 135 (15), 121 (85), 105 (58), 91 (12), 77 (55). Compound **12** hydrolyzed spontaneously to **13**.

## 13

Colourless oil (15).  $^1\text{H}$  NMR (300 MHz,  $\text{CDCl}_3$ )  $\delta$ : 2.08 (s, 3H), 3.74 (s, 3H), 4.52 (s, 1H), 7.26–7.46 (m, 5H).  $^{13}\text{C}$  NMR (125 MHz,  $\text{CDCl}_3$ )  $\delta$ : 14.9, 52.6, 53.4, 128.1, 128.4, 128.6, 135.7, 171.1. HR-MS  $m/z$ : calcd.: 196.0558, found: 196.0545.

## 15

Colourless oil.  $^1\text{H}$  NMR (300 MHz,  $\text{CDCl}_3$ )  $\delta$ : 3.55 (s, 3H), 3.75 (s, 3H), 3.93 (s, 3H), 7.34–7.20 (m, 5H).  $^{13}\text{C}$  NMR (125 MHz,  $\text{CDCl}_3$ )  $\delta$ : 51.6, 57.0, 59.2, 126.7, 127.5, 130.7, 135.2, 166.8, 168.1. Compound **15** hydrolyzed spontaneously to **16**.

## 16

(16). IR (neat) ( $\text{cm}^{-1}$ ): 2921, 2841, 1740, 1622, 1229, 1152, 1985, 1066, 699. EI-MS  $m/z$  (%): 208 ( $[\text{M}]^+$ , 58), 164 (29), 149 (45), 121 (100), 118 (25), 105 (30), 90 (28), 77 (25). The  $^1\text{H}$  and  $^{13}\text{C}$  NMR spectra were in agreement with those of Yang et al. (16) but not with those of Mueller and Tohill (17), which appear to be incorrect.

## Thermolysis of 1 in the presence of 17

The standard thermolysis procedure gave, from **17** (0.078 g, 0.52 mmol) and **1** (0.080 g, 0.50 mmol), a residue that was chromatographed on silica (Chromatotron plate, 1 mm, 10% EtOAc in hexane (50 mL), 20% EtOAc in hexane (50 mL), and 40% EtOAc in hexane (100 mL)) to afford **21** (84%).

## 21

Colourless solid, mp about room temperature.  $^1\text{H}$  NMR (300 MHz,  $\text{CDCl}_3$ )  $\delta$ : 3.23 (s, 3H), 3.34 (s, 9H), 3.68 (s, 3H), 7.26–7.32 (m, 3H), 7.53–7.57 (m, 2H).  $^{13}\text{C}$  NMR (125 MHz,  $\text{CDCl}_3$ )  $\delta$ : 51.4 ( $\text{C}(\text{OMe})_3$ ), 56.0, 57.9, 108.1, 113.1, 127.1, 127.4, 128.8, 130.6, 137.0. EI-MS  $m/z$  (%): 269 ( $[\text{M} - \text{S} + \text{H}]^+$ , 29), 223 (21), 209 (10), 149 (9), 105 (100).

## Thermolysis of 1 in the presence of 22

A thermolysis tube (50 mL) was charged with a solution of **22** (3.064 g, 25.1 mmol,  $1.0 \text{ mol}\cdot\text{L}^{-1}$ ), and **1** (0.401 g, 2.50 mmol,  $0.10 \text{ mol}\cdot\text{L}^{-1}$ ) in dry benzene. Following three freeze–pump–thaw cycles, the thermolysis tube was sealed and placed in a thermolysis bath at  $110 \pm 0.1^\circ\text{C}$  for 24 h at which point it was cooled and opened. GC–MS and  $^1\text{H}$  NMR of the crude indicated that a fairly clean reaction had occurred to give only one product derived from **22**. The product (**25**, 40% isolated yield) was obtained by removing

~90% of the excess **22** by means of bulb-to-bulb distillation ( $80\text{--}90^\circ\text{C}$  bath temp, 14 mmHg (1 mmHg = 133.322 Pa)) and by centrifugal chromatography of the residue on a 2 mm silica plate with hexanes to elute the remaining **22**, followed by 5% ethyl acetate in hexanes to elute **25**. IR (neat,  $\nu_{\text{max}}$ ) ( $\text{cm}^{-1}$ ): 2976, 2942, 2835, 1442, 1266, 1225, 1101, 1067, 1005, 955.  $^1\text{H}$  NMR (200 MHz,  $\text{C}_6\text{D}_6$ )  $\delta$ : 1.87 (s, 3H, SMe), 3.15 (s, 6H, OMe), 3.69 (s, 3H,  $\text{CO}_2\text{Me}$ ).  $^{13}\text{C}$  NMR (50.3 MHz,  $\text{C}_6\text{D}_6$ )  $\delta$ : 13.4 (SMe), 50.9 (OMe), 58.8 ( $\text{C}(\text{OMe})_2\text{SMe}$ ), 111.5 ( $\text{C}(\text{OMe})_2\text{SMe}$ ), 211.6 ( $\text{C}=\text{S}$ ). GC–MS (ei)  $m/z$  (relative intensity): 165 ( $[\text{M} - 15]^+$ , 4), 149 (62), 121 (74), 75 (100), 59 (42), 47 (30).

## Acknowledgements

M.D., D.L.R., and J.W. are grateful for the financial support of the Natural Sciences and Engineering Research Council of Canada (NSERC). G.M. acknowledges support by the Polish State Committee for Scientific Research (grant No. 4 T09A 046 25).

## References

1. R.W. Hoffmann, K. Steinbach, and B. Dittrich. *Chem. Ber.* **106**, 2174 (1973).
2. R.W. Hoffmann, W. Lilienblum, and B. Dittrich. *Chem. Ber.* **107**, 3395 (1974).
3. (a) P.C. Venneri and J. Warkentin. *Can. J. Chem.* **78**, 1194 (2000); (b) V. Nair, S. Bindu, and L. Balagopal. *Tetrahedron Lett.* **42**, 2043 (2001); (c) M. Dawid, G. Mloston, and J. Warkentin. *Chem. Eur. J.* **8**, 2184 (2002).
4. (a) N. Kuhn, H. Bohnen, and G.N. Henkel. *Z. Naturforsch.* **49b**, 1473 (1994); (b) N. Kuhn, M. Steimann, and G.Z. Weyers. *Z. Naturforsch.* **54b**, 427 (1999).
5. M. Békhaizi and J. Warkentin. *J. Am. Chem. Soc.* **105**, 1289 (1983).
6. (a) P. Couture, M. El-Saidi, and J. Warkentin. *Can. J. Chem.* **75**, 326 (1997); (b) P.K. Sharma and J. Warkentin. *Tetrahedron Lett.* **36**, 7591 (1995); (c) M. Dawid and J. Warkentin. *Can. J. Chem.* **81**, 598 (2003).
7. (a) Y. Hata, M. Watanabe, S. Inove, and S. Oae. *J. Am. Chem. Soc.* **97**, 2557 (1975); (b) G. Mloston and H. Heimgartner. *Helv. Chim. Acta*, **79**, 1785 (1996); (c) G. Mloston and H. Heimgartner. *In The chemistry of heterocyclic compounds*. Vol. 59. Edited by A. Padwa and W.H. Pearson. Wiley, New York. 2002. Chap. 5.
8. R.T. Conley. *Infrared spectroscopy*. Allyn and Bacon, Inc, Boston. 1966.
9. C. Kowalski, X. Creary, A.J. Rollin, and M.C. Burke. *J. Org. Chem.* **43**, 2601 (1978).
10. A. de Meijere, S.I. Kozhushkov, D.S. Yufit, R. Boese, T. Haumann, D.L. Pole, P.K. Sharma, and J. Warkentin. *Liebigs Ann. Chem.* 601 (1996).
11. D.W. Grisley, Jr. *J. Org. Chem.* **26**, 2544 (1961).
12. H. Davy. *J. Chem. Soc. Chem. Commun.* 457 (1982).
13. B.S. Pedersen, S. Scheibye, K. Clausen, and S.-O. Lawesson. *Bull. Soc. Chim. Belg.* **87**, 293 (1978).
14. A.I. Vogel. *Practical organic chemistry*. 3rd ed. Longman, London. 1957. Chap. 3. p 499.
15. K. Nishihata and M. Nishio. *Tetrahedron Lett.* 1695 (1976).
16. M. Yang, P.R. Webb, and P. Livant. *J. Org. Chem.* **66**, 4945 (2001).
17. P. Mueller and S. Tohill. *Tetrahedron*, **56**, 1725 (2000).



# Macroscopically chiral system of three independent orientational effects as a condition for absolute asymmetric synthesis

Roman Bielski and Michal Tencer

**Abstract:** The paper introduces the concept of using three independent, macroscopic factors affecting mutual orientation of the reactant molecules to accomplish absolute asymmetric synthesis. Unlike with other methodologies of asymmetric synthesis in physical fields, none of the utilized factors is chiral in itself (as, e.g., circularly polarized light would be), but the combination of the three constitutes a macroscopically chiral influence. Examples of applicable directional factors are time-even vector fields (e.g., electric field and the directional effects of surfaces and interfaces) and the time-odd directional transport with encounter control. The directional factors employed may act simultaneously or, if their effect can be preserved, consecutively, thus allowing, e.g., a repeat use of the electric field. The electric field strength needed to achieve a practically useful degree of molecular orientation was estimated to be ca. 3 MV/cm, which is now commonly achieved with organic materials in the area of nonlinear optics. Practical implications are discussed, as well as the implications for the origins of natural homochirality.

**Key words:** macroscopic chirality, absolute asymmetric synthesis, homochirality, physical fields.

**Résumé :** Dans ce travail, on propose l'utilisation de trois facteurs macroscopiques indépendants qui affectent l'orientation mutuelle des molécules de réactifs pour faire des synthèses asymétriques absolues. Contrairement aux autres méthodes de synthèses asymétriques dans des champs physiques, aucun des facteurs utilisés n'est chiral en lui-même (comme le serait la lumière polarisée de façon circulaire); toutefois, l'application d'une combinaison des trois constitue une influence chirale macroscopique. Comme exemples de facteurs directionnels applicables, on peut signaler les champs vectoriels appariés en fonction du temps (par exemple, le champ électrique et les effets directionnels de surfaces et d'interfaces) et le transport directionnel non apparié en fonction du temps, mais soumis à un contrôle de rencontre. Les facteurs directionnels utilisés peuvent agir simultanément ou, si leur effet peut être conservé, consécutivement; ce qui permet, par exemple, d'utiliser le champ électrique une autre fois. On a évalué à environ 3 MV/cm la force du champ électrique nécessaire à l'obtention d'un degré d'orientation moléculaire utile d'un point de vue pratique, valeur maintenant fréquemment atteinte dans le domaine de l'optique non linéaire grâce à l'utilisation de composés organiques. Les implications pratiques sont discutées ainsi que les implications pour les origines de l'homochiralité naturelle.

**Mots clés :** chiralité macroscopique, synthèse asymétrique absolue, homochiralité, champs physiques.

[Traduit par la Rédaction]

## Introduction

Absolute asymmetric synthesis has been the object of scientific fascination for several decades; not so much for practical reasons as because of the implications in the important discussion concerning the origin of optically pure compounds in the universe and thus the origin of life itself. The proposed explanations of homochirality derive from two very different directions. One option can be considered a

“random mechanism” and includes such phenomena as preferential enantiomorphic crystallization and stereoselective adsorption on quartz, although the latter mechanism has been disputed (1). The other option, “determinate mechanisms”, advocates interaction of non-chiral or racemic chemical systems with chiral physical phenomena (2, 3). However, none of the proposed answers is quite satisfactory (3–5). A recent paper (6) critically reviewed various attempts at asymmetric synthesis in external fields, mostly from the viewpoint of theoretical symmetry considerations of different field types. Also, in the last decade, it was disputed whether or not a very minute but calculable energy difference between enantiomers — caused by the fundamental dissymmetry of weak interactions at the subatomic level — could be responsible for the observed homochirality of the animate world (7, 8).

This paper discusses the possibility of simultaneously using three cooperative macroscopic external factors (such as physical fields) to impart spatial directionality on reacting

Received 21 April 2003. Published on the NRC Research Press Web site at <http://canjchem.nrc.ca> on 12 September 2003.

**R. Bielski.**<sup>1</sup> Value Recovery Inc., 510 Heron Drive, Suite 301, Bridgeport, NJ 08014, U.S.A.

**M. Tencer.**<sup>2</sup> Nortel Networks, P.O. Box 3511, Station C, Ottawa, ON K1Y 4H7, Canada.

<sup>1</sup>Corresponding author (e-mail: [bielski@ptcvalue.com](mailto:bielski@ptcvalue.com)).

<sup>2</sup>Corresponding author (e-mail: [mtencer@nortelnetworks.com](mailto:mtencer@nortelnetworks.com)).



molecules, thus creating conditions of macroscopic chirality. In reactions in which a chiral compound is created from either non-chiral or racemic precursors, such macroscopic chirality should result in formation of, preferentially, one enantiomer, provided that the external directional factors are sufficiently strong to give the reacting molecules a predominant orientation. Thus, each of the directional factors confers, onto molecules, orientation along one of three orthogonal directions, which, for simplicity, we shall deem to be identical with the Cartesian axes. While none of these factors is chiral by itself, such a system, as it will be shown below, is chiral. Here, we are interested in the ability of a given field or some other macroscopic factors to hold molecules in a desirable orientation; we do not delve into the theory and intrinsic symmetry properties of individual factors, although those of magnetic fields deserve some comments (see further in the text).

All the methods of enantioselective synthesis and (or) resolution of racemic mixture boil down to formation of a diastereomeric interaction at some stage. For example, enzymes, using this type of interaction, provide spatial directionality on a micro scale, molecule by molecule. We would like to achieve the same effect on a macro scale, directionality being imparted "remotely" on all the reacting pairs at the same time. The question is how to position reacting molecules along the Cartesian axes in such a way that a specific direction of collisions is enforced. If it can be accomplished, a reaction in which a chiral center is formed from non-chiral precursors (or in which the reaction takes place at a chiral center of a racemic compound) will produce a non-racemic mixture. Moreover, based on the relative directions of reacting molecules, one should be able to predict the enantiomer formed in excess. The proposed approach should be valid for reactions at both  $sp^2$  and  $sp^3$  centers.

Let us consider two non-chiral compounds — one of them being prochiral — that react to form a product with one center of chirality. Let the structure of the prochiral compound include functionalities that enable one to define alignment of the molecules with regard to two Cartesian axes using two different physical phenomena. Now, if it were possible to use another physical phenomenon to position the molecules of the other reactant with regard to the prochiral molecules, then optically active products would be formed without introduction of any chiral molecules into the reaction mixture.<sup>3</sup> Of course, by no means are we escaping, here, chirality as the cause of the asymmetry of the product. The novelty of this approach lies in the fact that chirality in this case is macroscopic in nature and is defined by us by the choice of the relative directionality of the three physical phenomena vs. each other. It is different from the proposal by Pierre Curie (see 6 for reference) to introduce asymmetry with electric and magnetic fields, in that Curie's approach proposes two parallel rather than three orthogonal fields and aims to utilize inherent symmetry properties of the fields in what is now considered a false chiral system (6), while we are interested in the orienting effect of the fields. It is also different from the application of magnetochiral dichroism, where unpolarized

light parallel to a magnetic field forms a real chiral influence, leading to a small but measurable enantiomeric excess (9).

In reactions performed in the presence of weaker directional factors the resulting enantiomeric excess should depend on the degree of achieved orientation, but even a limited degree of spatial orientation of reacting molecules would be of interest here, since any enrichment of an original non-racemic mixture could shed light on the possible origin of homochirality in nature.

## Introducing macroscopic chirality

As an example leading to a further generalization let us have a hypothetical prochiral molecule P (a compound with a carbonyl group attached to substituents M and S, Fig. 1a) with functionalities that enable its unequivocal orientation vs. a plane. Such two functionalities may be, for example, a group enabling covalent or non-covalent attachment to a smooth flat surface and a polar group that confers a dipole moment onto the molecule. In the compound P the carbonyl group is the site of prochirality of the molecule. It may also act as a polar group that imparts a non-zero dipole moment onto the molecule. If the flat surface lies in the  $xz$  plane and we turn on electric field **E** along the  $x$  direction, the  $sp^2$  prochiral center will be defined within the  $xy$  plane (Fig. 1a). The molecule P is reacted with the other reactant, e.g., a nucleophile N. The only reactive site of the reactant N is represented by a group B. Now, if another, yet undefined, directing influence **F** can orient N in the  $z$  direction as shown then a specific, predictable, absolute configuration of the reaction product will result.

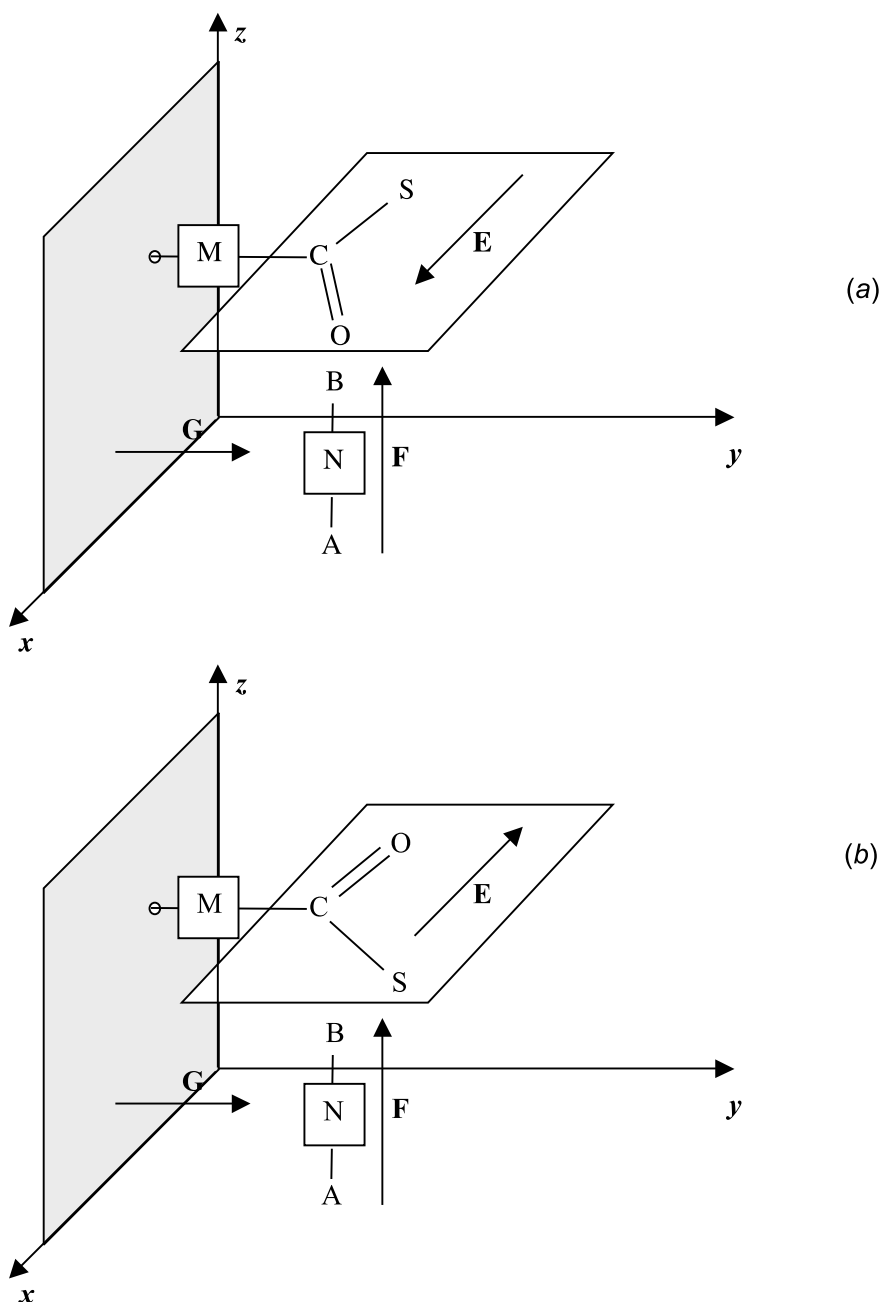
Since directionality of a flat surface is defined by a vector **G** normal to it, for the situation in Fig. 1a the relationship between the three directional orthogonal vectors **G**, **E**, and **F** is given through cross products,  $\mathbf{G} \times \mathbf{E} = k\mathbf{F}$ , where  $k$  is any scalar proportionality constant. Reversal of the direction of any one vector leads to the formation of a group of vectors that is not identical (i.e., not superimposable) with the original one,  $\mathbf{G} \times \mathbf{E} = -k\mathbf{F}$ , and a subsequent reversal (reflection) of any of the three vectors leads back to the original cross-product relationship. (However, for limitations operating here, vide infra.)

Considering the stereogenic center of the structure shown in Fig. 1a, let the bond formed by the entering nucleophile in the final product be of the lowest priority (in the Cahn–Ingold–Prelog sense). Let the carbon–oxygen bond be of the highest priority, substituent M be ranked second (medium), and substituent S be ranked third (small). Then the absolute configuration of the formed chiral center will be *R*. Reflecting this situation in a mirror parallel to the  $yz$  plane (which is equivalent to reversing the direction of the electric field **E**) will produce the opposite enantiomer, *S* (Fig. 1b). Similarly, replacing the flat surface by its mirror image (equivalent to turning the reaction vessel by 180° around the  $z$  axis) or reversing the direction of **F** would result in the formation of the *S* enantiomer. Two such changes would lead, again, to the *R* product.

<sup>3</sup>A similar argument could be made for a racemic mixture reacting at the chiral center. In the presence of macroscopic chirality due to three directional effects, one of the enantiomers would be formed preferentially, provided that the reactants contain appropriate functionalities.



**Fig. 1.** Macroscopic chirality in the three directional vector system: (a) leading to the *R* enantiomer, (b) its mirror image leading to the *S* enantiomer.





to a mirror reflection. Unfortunately for our purpose, a paramagnetic molecule does not have a per se defined directionality in terms of the north (N), south (S) poles, and thus, even though in the presence of a strong spin-orbit coupling it can be aligned along the field lines, no directional sense will be preferred. In this sense a paramagnetic molecule is different from a piece of a (ferro) magnet whose orientation in the **B** field can be, in fact, considered an effect of *two* consecutively acting magnetic fields, the first of which was needed to magnetize the material. Perhaps, in the future, progress in molecular magnet research (10) may change our evaluation of the usefulness of magnetic fields as directional physical phenomena.

Thus, since the set of three orthogonal vectors has been shown to be chiral, to achieve an optically active product three such directional effects should be employed, either at the same time or consecutively, although not all of the above factors are compatible with each other. Two of these factors should orient one reactant and the third factor must affect the other reactant. The three vectors should be time-even, polar for thermodynamic control of the reaction, but under kinetic conditions one of them may be time-odd.

## Imparting directionality

The proposed macroscopic system can be looked upon from two different points of view. Firstly, it would be of major importance to show experimentally that the application of orienting macroscopic phenomena to an appropriately designed system of reagents can produce a non-negligible enantiomeric excess (ee). It could open a possibility of synthesizing certain optically active compounds without introducing chiral molecules into reaction mixtures. Secondly, it may provide another possible mechanism with which to explain the origin of homochirality.

With the former viewpoint, the directional influences used should be strong enough to lead to a convincing and reproducible ee. Of course, an ee leading to a practical enantioselective synthesis would certainly be convincing. With the latter viewpoint, the formation of even relatively low enantiomeric excesses can be of great interest. A "one-time" event of macrochirality followed by amplification could have eventually led to the L-amino acids and D-sugars we encounter today. Philosophically, this would not differ from other one-time events.

## Electric field

Molecules in an external field are subject to two opposing effects: the organizing effect of the field and the randomizing effect of thermal motion. A significant degree of directionality can be achieved if the energy of interaction  $\epsilon$  of the molecule with the field is greater than  $k_B T$  ( $k_B$ , the Boltzmann constant;  $T$ , temperature) amounting to ca. 0.025 eV ( $4 \times 10^{-21}$  J) at the ambient temperature of 300 K or, in molar terms,  $RT$  (ca. 2.5 kJ/mole). The proper merit number showing the effectiveness of the field is, here, the ratio  $u \equiv \epsilon/k_B T$ . On top of it, a racemic mixture is entropically preferred by a numerically similar value of free en-

ergy,  $k_B T \ln 2$  ( $RT \ln 2$  or 1.7 kJ/mole). Thus, to be effective, fields have to supply at least several  $k_B T$  worth of energy of interaction per molecule, as will be shown in more detail below.

If the reacting center is separate from the site of the directing center (e.g., dipole moment), the two moieties should be connected with some kind of rigid structure. This condition of rigidity does not exist if these two centers are one and the same, as in Fig. 1, where the carbonyl is both the site of prochirality and of the dipole moment.

## "Convincing" *E* fields

The energy of interaction of the electric field **E** with a molecule having a dipole moment  $\mu$  is  $\epsilon = \mu E$ . Thus,  $u = \mu E/k_B T$ . For the **E** fields typically encountered in the laboratory (e.g., with dielectric measurements), the degree of orientation<sup>4</sup> is quite small and can be given by the Debye approximation (11) as  $\langle \cos \theta \rangle = u/3$ . Such a small degree of orientation would have no noticeable chemical effect, and any attempt to utilize it in asymmetric synthesis would be futile. To achieve a significant orientation, a much stronger **E** field has to be applied. The average degree of orientation is then given (11) by the Langevin function [1]

$$[1] \quad \langle \cos \theta \rangle = \frac{\mu_i}{\mu} = \coth(u) - \frac{1}{u}$$

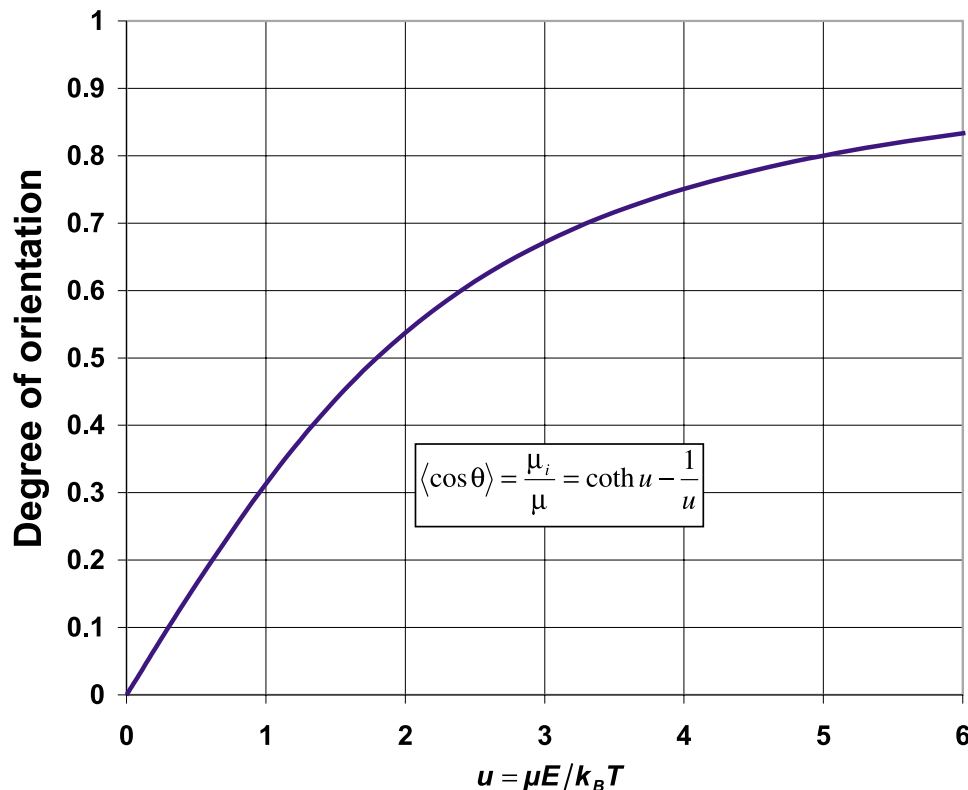
The effect of **E** on the degree of orientation, as calculated from this function, is shown in Fig. 2. We can see that, to achieve a "convincing" degree of orientation — say 60% — the value of  $u$  should amount to 2.5 or more. Strongly conjugated organic molecules can have dipole moment as high as 30 D (12). Assuming a more moderate dipole moment of 10 D ( $3.34 \times 10^{-29}$  C·m), we arrive at the field value of  $E = 3 \times 10^8$  V/m or 3 MV/cm. This kind of electric field strength is typically close to dielectric breakdown conditions. One way of overcoming dielectric breakdown is to use a large series resistance to prevent any breakdown current. A common way to introduce such resistance is the corona-poling technique in which air is one of the electrodes. It is commonly used in the area of nonlinear optical organic materials (13). Even without resorting to corona poling, a field of 3.7 MV/cm has been achieved before breakdown, and stable reproducible poling was achieved at fields in excess of 3.0 MV/cm (14). Hence, while it is not yet a routine task, it will be possible to orient many organic molecules in an electric field to a significant degree.

## Soft matter

Some organized forms of matter, where even moderate field strengths have a strong orienting effect, can decrease the field requirements even further. For example, liquid crystals (LCs) can be easily aligned in electric (and magnetic) fields, owing to the fact that the molecules of a liquid crystal have no choice but to move in unison (15). Therefore, energy of interaction with the field must be multiplied by a value on the order of the Avogadro number (ca.  $10^{22}$ ). The orienting property of LCs has been used in the study of or-

<sup>4</sup>In dielectric theory, the degree of orientation is defined as the ratio of the effective dipole moment,  $\mu_i$ , in the direction of the field to the dipole moment of the molecule. It is also the average cosine of the angle between the dipole moment and **E**,  $\langle \cos \theta \rangle$ .



**Fig. 2.** Degree of orientation of a dipolar molecule as a function of the applied electric field.

ganic reaction mechanisms (16). Liquid crystals are so easy to orient that even container walls can impart directionality on them (15, 17).

#### Effect of temperature

The directional effect of a field can be greatly enhanced by lowering the temperature, as the value of  $u = \epsilon/k_B T$  becomes very large as  $T$  approaches 0 K. However, the penalty here would be the kinetics of the process. Since values of  $\epsilon$  attainable in relatively weak fields are close to  $k_B T$  (2.5 kJ/mole) and activation enthalpies for organic reactions are typically 80–100 kJ/mole, by lowering the temperature we lose much more on reactivity than we gain on selectivity. This is true even for diffusion-controlled reactions, as the activation energy may amount to 20 kJ/mole or more. On the other hand, as far as the origin of natural chirality is concerned, Nature has plenty of time to work at very low temperatures, and thus even moderate fields could have imparted enough directionality to preferentially form one enantiomer over another in the given circumstances.

#### Freezing of orientation

If the solvent can be either polymerized or cooled below the glass-transition temperature while the **E** field operates, the resulting molecular orientation can be frozen in place. The field will not be needed anymore and thus can be removed before another orienting factor is applied. This would make the system easier experimentally but again, at the expense of reaction kinetics. Another option is to covalently attach molecules equipped with appropriate functionalities to a flat surface (see below), while subjected to the electric

field. After the reaction is completed the **E** field may be removed, its effect being fixed in space. Thus, the **F** field of Fig. 1 could be another **E** field, acting later in time.

#### Surfaces and interfaces

Directionality of chemical functional groups in a molecule can be accomplished by attaching these molecules to a surface that is genuinely flat and smooth on the molecular level. The attached molecules can then attain directionality in a manner similar to being in the presence of an external field. Availability of appropriate surfaces is limited. Gold, silicon, or cleaved mica (18) may serve as examples. However, gold and other conductive surfaces may be incompatible with the **E** field. Organic monolayers can be prepared at either solid–vacuum (gas), liquid–air, or solid–liquid interfaces (19). Liquid–air interfaces can provide precisely controlled molecular orientation when the Langmuir technique is used to prepare organic films. The films can then be transferred onto solid substrates, forming Langmuir–Blodgett films (20). Monolayers can also be formed directly on solid surfaces in a self-assembly process (21). Of these, the most studied systems are silane compounds on silica (22) and thiols on gold surfaces. Both chemisorbed and physisorbed monolayers can be employed, as long as they are stable in the reaction conditions. It should be possible to detach the molecule from the surface after the reaction without damaging the active center. For rigid molecules, there should be no limitation on the distance of the functional groups from the surface. With flexible molecules (e.g., attached through an alkane chain), the orientation effect may decrease with distance from the surface because of bond rotation, folding, etc. (one can, per-



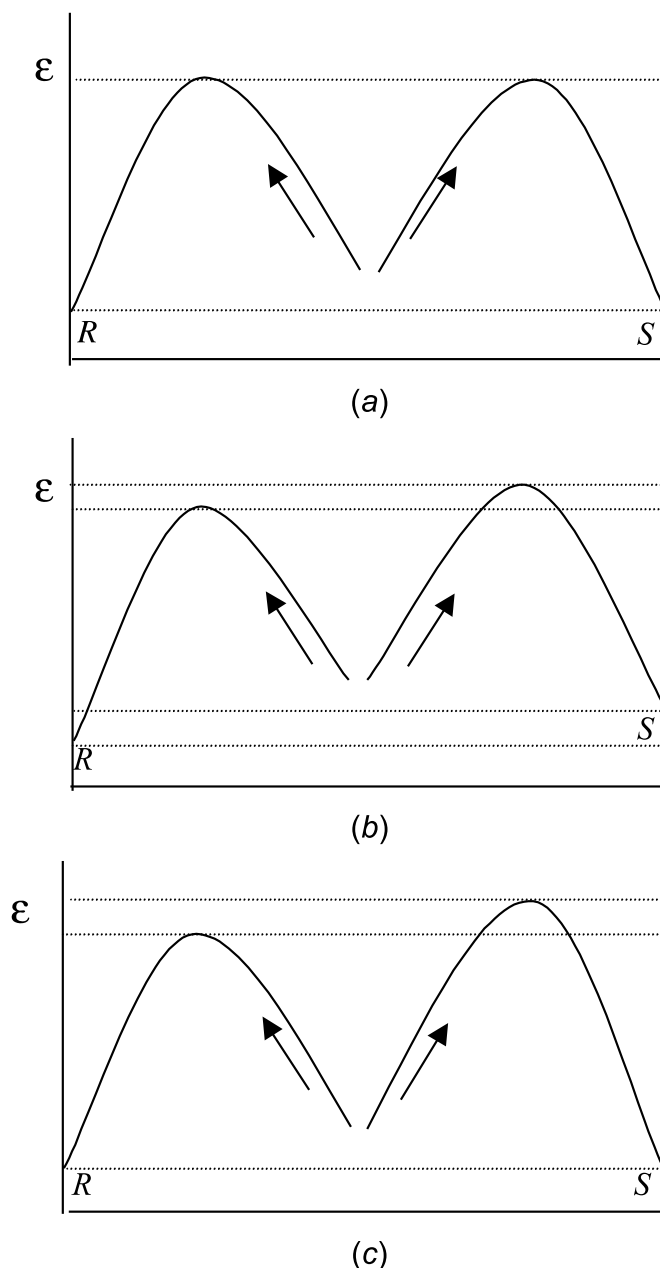
haps, talk here about a certain “correlation distance” dependent on the structure).

The oil–water (or water–air) interfaces at which an amphiphilic reagent is oriented perpendicularly to the phase border are in many respects similar to monolayers. The energy of the thus imparted orientation is similar to that of a hydrogen bond. In a system employing both the oil–water interface and a monolayer attached to a flat surface, the solid surface must be vertical, as the liquid interface is horizontal. The fact that only molecules at the surface react reduces the amount of available product by a factor of  $10^7$  when compared with bulk. Ways to partially overcome this difficulty are proposed further in the text.

### Directionality of transport — encounter control

Let us imagine molecules of a nucleophile migrating in the  $z$  direction and reacting with a prochiral carbonyl compound that has been oriented vs. the  $x$  and  $y$  directions. Such directionality could be achieved if the source of the nucleophile is in a different phase. If kinetic conditions typical of most organic reactions operate, all sense of directionality will be lost. Let us assume that the reaction in solution between the prochiral molecule  $P$  and the nucleophile  $N$  consists of two steps: the diffusion-controlled formation of the encounter pair  $PN$ , followed by formation of the chiral molecule,  $C$  (23). For typical organic reactions, the second step is orders of magnitude slower than the first one. It means that  $P$  and  $N$  will collide many times within the solvent cage before they react, and when it finally happens, the reaction can proceed from either side with equal probability. The situation that would interest us is when the first step is slower, i.e., when the rate is controlled by diffusion and the reaction takes place on the first encounter. This can happen when the chemical step of the reaction is very fast ( $>10^9$  L/mol·s). Unfortunately, this case is limited to ion neutralization, electron transfer, and certain photochemical processes (e.g., fluorescence quenching), all of which are of limited utility in asymmetric synthesis, with the possible exception of electrochemical reduction of carbonyl, which, it has been claimed, leads to asymmetric synthesis in the presence of a magnetic field (24). At the other extreme, if the viscosity of the solvent was very high (which could be achieved by polymerization), one can imagine that the nucleophile would not be free to move around after collisions and would maintain the sense of directionality. Even if this could be achieved, the distance between the source of the nucleophile and the reactive center should be relatively small because the diffusion process has a “random-walk” character, and the probability of the nucleophile entering the solvent cage from the wrong side increases with distance. Also, the obvious drawback here would be the time penalty we would have to pay — the reaction could be too slow to be of practical value. It may be beneficial for our cause, however, that in supercooled liquids the inverse relationship between translational motion and viscosity breaks down whereas that between rotational motion and viscosity holds. It is found that near glass-transition temperature, molecules translate faster by as much as two orders of magnitude than expected based on their viscosity. In other words, when the temperature is lowered, molecules translate progressively more for every rotation they undergo (25).

**Fig. 3.** Free energy profiles for formation of  $R$  and  $S$  enantiomers (a) in the presence of 0 to 2 fields, (b) in the presence of 3 fields, and (c) in the presence of 2 fields and directional transport with encounter control.



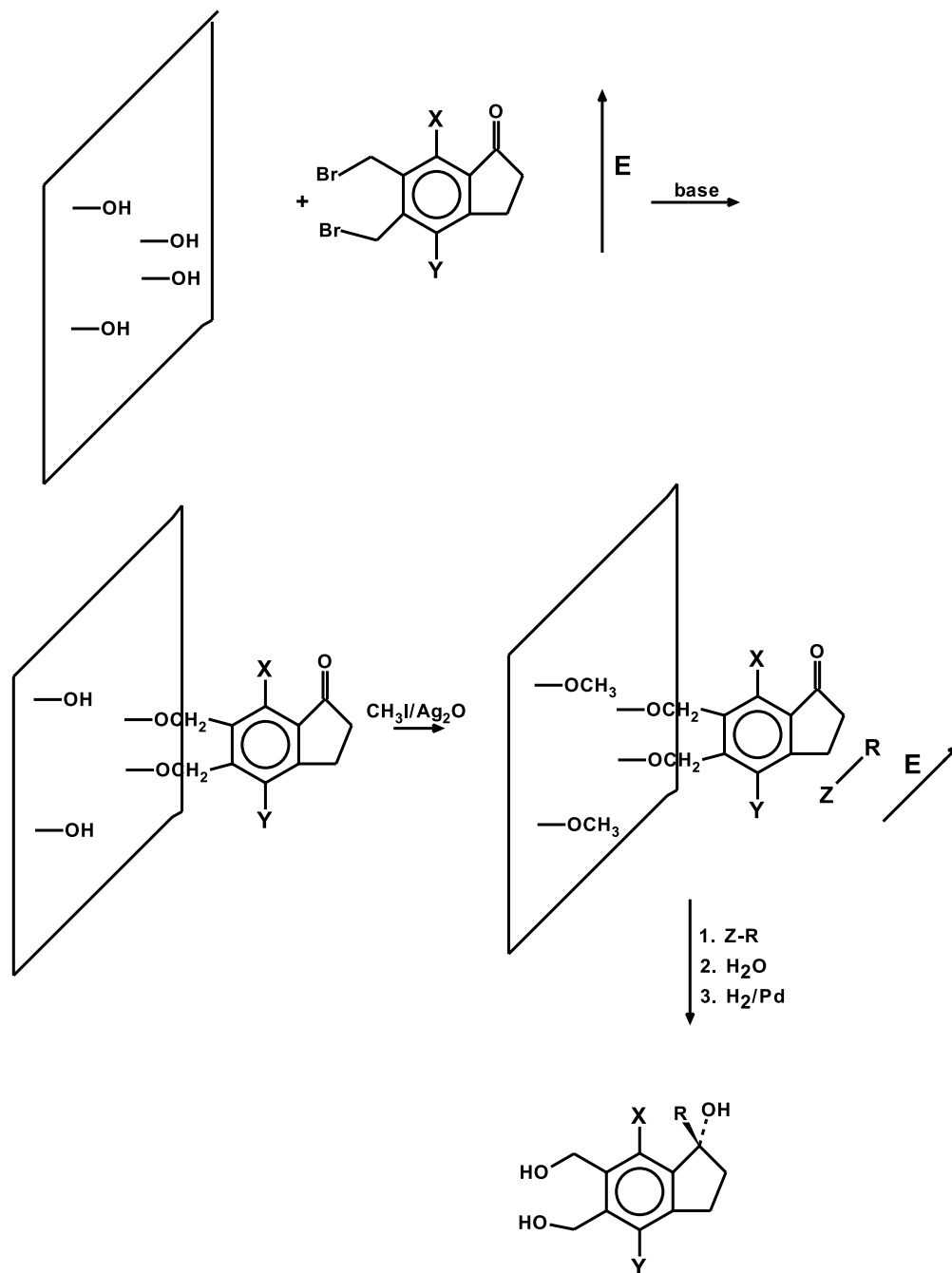
In the gas phase, directionality could be maintained with molecular beams of the nucleophile. In this case molecules in the beam with enough energy would react on first encounter; other ones would be scattered away (26).

### Thermodynamic vs. kinetic control

The simultaneous or consecutive presence of three physical fields, e.g., two consecutive electric fields and a flat surface that can be represented by the three vectors,  $\mathbf{E}$ ,  $\mathbf{F}$ , and  $\mathbf{G}$  in Fig. 1, provides real macroscopic chirality and, as such, can affect the free energy of the chiral products, as well as that of the transition states vs. reactants (6). Thus, the out-



**Fig. 4.** A possible route to asymmetric synthesis using a surface reaction and two consecutive electric fields, both parallel to the surface and orthogonal to each other. X: electron acceptor or negatively charged substituent, Y: electron donor or positively charged substituent, R-Z: a polar reagent (e.g., alkyllithium or Grignard reagent).



come of a reaction under these conditions can be both thermodynamically and kinetically controlled (see Figs. 3a and 3b). The thermodynamic preference of one enantiomer over the other will disappear when the fields are turned off; thus, we have to be careful that the subsequent work-up of the reaction mixture does not lead to racemization.

If one of the orienting influences is directional transport with encounter control (represented by the velocity vector  $\mathbf{v}$ ), *R* and *S* products are not differentiated by free energy.

Such a reaction would not lead to an enantiomeric excess if carried out to thermodynamic equilibrium. However, enantiomeric excess can be achieved here through kinetic control (Fig. 3c).<sup>5</sup>

As a relevant example of kinetic control, let us consider nucleophilic substitution at a chiral center. Let us assume here for the sake of simplicity that all three directional effects are very strong and render 100% orientation in each direction. If the reaction goes through the planar transition

<sup>5</sup>This could be considered a situation of Barron's "false" chiral conditions, as the vector system  $\mathbf{E}$ ,  $\mathbf{G}$ ,  $\mathbf{v}$  can be converted into its mirror image  $\mathbf{E}$ ,  $\mathbf{G}$ ,  $-\mathbf{v}$  by the time reversal; see (6) for references.



state ( $S_N1$ ), the structure of the product is independent of the configuration of the starting material; both the racemate and the pure enantiomer will produce a single enantiomer. Its configuration depends only on the direction of the effects orienting the nucleophile and the carbocation vs. each other.

The outcome would be different for the  $S_N2$  mechanism, where the attack of the nucleophile takes place from the side opposite to the leaving group. Since only one direction of attack is allowed in the presence of the fields, only one enantiomer of a racemic starting material would enter into reaction, leading to a single enantiomer of the product. Surprisingly, an enantiomeric starting material would produce either the inversed product or would not react at all. Of course, in a real system, 100% alignment would never happen, and we would have enantiomeric enrichment rather than a pure enantiomer.

## Practical considerations

Finally, let us look briefly at criteria that should be considered when selecting potential directional factors, potential reactants, and reaction conditions. The choice of the three directional factors from the ones described above depends on their accessibility, the required ee, and the acceptable minimum amount of reaction product. It would be elegant if we were able to take advantage of a simultaneous use of three different (orthogonal) fields, but this does not seem practical at this point. As the high electric field is relatively easy to effectively apply (13, 14), it seems reasonable to employ it twice, if possible. An example of such application is shown in Fig. 4. In this example, a prochiral molecule A with a high dipole moment (due to the electronegative and electropositive substituents X and Y) is reacted with reactive groups on a flat surface (e.g., mica) in the presence of the **E** field. A variety of plausible surface chemistries were described recently (27). Upon completion of this reaction the field can be removed because the orientation of A is frozen. At least two bonds have to be involved for the A attachment to achieve this effect. Next, after unreacted functional groups on the surface are blocked, an electric field perpendicular to the one previously applied is turned on, and a strongly polar reactant B (for example, a metalloorganic compound R-Z; Z represents a metal atom such as lithium) is introduced and allowed to react with the prochiral center of the previously fixed A. After the work-up, an optically active compound will be produced. If R is a methyl group, then the absolute configuration of the product shown in Fig. 4 will be R. Possible candidates for this approach include, i.e., nucleophilic ( $S_N1$ ) substitution (racemate as a starting material), nucleophilic reactions at the carbonyl group or its derivatives, Michael addition, and concerted reactions such as Diels-Alder and the ene syntheses.

As mentioned before, a reaction involving interaction with a surface will lead inevitably to rather miniscule amounts of optically active product, which is the main drawback of the approach. To increase the reacting quantities, one can introduce a large number of parallel sheets of flat surfaces into the reaction vessel, all facing the same direction. Alternatively, it is conceivable to use a constantly moving, closed-loop tape with one reactive side to which a reagent would be attached before entering the consecutive reactors, followed

by removal of the product in the post-vessel. Upon continuous operation, the concentration of the chiral product in the post-vessel would increase gradually until it reaches a usable level. In this connection, with a properly designed system, even small yields of an optically active material can potentially be turned into a very significant ee through autocatalysis, as was convincingly shown recently (28).

## Acknowledgment

The authors would like to thank Dr. Florian Dufey (Department of Theoretical Physics, Technische Universität München) for a very helpful discussion of magnetic field effects.

## References

1. (a) W. Bonner. *Top. Stereochem.* **18**, 1 (1988); (b) M. Quack. *Angew. Chem. Int. Ed.* **41**, 4618 (2002); (c) E. Klabunovskii and W. Thieman. *Origins Life Evol. Biosphere*, **30**, 431 (2000).
2. W.A. Bonner. *Chem. Ind. (London)*, 640 (1992).
3. B.L. Feringa and R.A. van Delden. *Angew. Chem. Int. Ed.* **38**, 3418 (1999).
4. M.-Ch. Maurel and J.-L. Décourt. *Tetrahedron*, **55**, 3141 (1999).
5. R.E. Hegstrom and D.K. Kondepudi. *Sci. Am.* **262**, 108 (1990).
6. M. Avalos, R. Babiano, P. Cintas, J.L. Jiménez, J.C. Palacios, and L.D. Barron. *Chem. Rev.* **98**, 2391 (1998) and references cited therein.
7. H. Buschmann, R. Thede, and D. Heller. *Angew. Chem. Int. Ed.* **39**, 4033 (2000).
8. (a) M. Avalos, R. Babiano, P. Cintas, J.L. Jiménez, and J.C. Palacios. *Tetrahedron Asymmetry*, **11**, 2845 (2000); (b) P. Cintas. *ChemPhysChem*, **2**, 409 (2001).
9. G.L.J.A. Rikken and E. Raupach. *Nature (London)*, **405**, 932 (2000).
10. (a) L. Thomas, F. Lioni, R. Ballou, D. Gatteschi, R. Sessoli, and B. Barbara. *Nature (London)*, **383**, 145 (1996); (b) W. Wernsdorfer, R. Sessoli, A. Caneschi, D. Gatteschi, and A. Cornia. *Europhys. Lett.* **50**, 552 (2000).
11. P. Debye. *Polar molecules*. Chemical Catalog Co., Reinhold Publishing Co. 1929.
12. M. Szablewski, P.R. Thomas, A. Thornton, D. Bloor, G.H. Cross, J.M. Cole, J.A.K. Howard, M. Malagoli, F. Meyers, J.-L. Brédas, W. Wenseleers, and E. Goovaerts. *J. Am. Chem. Soc.* **119**, 3144 (1997).
13. K.D. Singer and J.H. Andrews. *In Molecular nonlinear optics — materials, physics, and devices*. Edited by J. Zyss. Academic Press, Boston. 1994.
14. A. Otomo, G.I. Stegeman, W.H.G. Horsthuis, and G.R. Möhlmann. *Appl. Phys. Lett.* **65**, 2389 (1994).
15. P.G. de Gennes. *The physics of liquid crystals*. Clarendon Press, Oxford. 1974.
16. R.G. Weiss. *Tetrahedron*, **44**, 3413 (1988).
17. J. van Haaren. *Nature (London)*, **411**, 29 (2001).
18. D.K. Schwartz, S. Steinberg, J. Israelachvili, and J.A.N. Zasadzinski. *Phys. Rev. Lett.* **69**, 3354 (1992).
19. N.J. Tao. *In Frontiers of electrochemistry*. Vol. 5. Edited by J. Lipkowski and P.N. Ross. Wiley-VCH, Inc., New York. 1999. p. 211.



20. G. Roberts. Langmuir-Blodgett Films. Plenum Press, New York. 1990.
21. A. Ulman. Chem. Rev. **96**, 1533 (1996).
22. E.E.P. Pluedeman. Silane coupling agents. Plenum, New York. 1982.
23. S.A. Rice. Diffusion-limited reactions, chemical kinetics. Vol. 25. *Edited by* C.H. Bamford, C.F.H Tipper, and R.G. Compton. Elsevier, Amsterdam. 1985.
24. F. Takahashi, K. Tomii, and H. Takahashi. Electrochim. Acta, **31**, 127 (1986).
25. P.G. Debenedetti and F.H. Stillinger. Nature (London), **410**, 259 (2001) and references cited therein.
26. P.W. Atkins. Physical chemistry. 2nd ed. W.H. Freeman and Co, San Francisco. 1982.
27. G. Ashkenazy, D. Cahen, R. Cohen, A. Shanzer, and A. Vilan. Acc. Chem. Res. **35**, 121 (2002).
28. K. Soai, I Sato, and T. Shibata. The Chemical Record, **1**, 321 (2001).



# The adsorption of cyclohexanone on aluminum oxide – hydroxide powders in relation to its electrocatalytic hydrogenation

François Laplante, Nicolas-Alexandre Bouchard, Patrick Dubé, Hugues Ménard, and Louis Brossard

**Abstract:** Henry's law constants were determined for cyclohexanone adsorption onto aluminium oxide – hydroxide powders by dynamic isotherm measurements using the HPLC method. The key parameters that control cyclohexanone adsorption were established. Further, it is suggested that the amount of cyclohexanone adsorbed onto aluminium oxide – hydroxide compounds (AOHC) is of paramount importance for its electrocatalytic hydrogenation in the presence of composite nickel–AOHC powders.

**Key words:** adsorption isotherm, electrocatalytic hydrogenation (ECH), cyclohexanone, aluminum oxide – hydroxide powders.

**Résumé :** En se basant sur des mesures d'isothermes dynamiques effectuées par le biais de la méthode de la chromatographie liquide à haute performance, on a déterminé les constantes de la loi de Henry pour l'adsorption de la cyclohexanone sur des poudres d'oxyde – hydroxyde d'aluminium. On a établi la nature des paramètres clés qui contrôlent l'adsorption de la cyclohexanone. De plus, il est suggéré que la quantité de cyclohexanone adsorbée sur des composés à base d'oxyde – hydroxyde d'aluminium (COHA) est de prime importance pour son hydrogénation électrocatalytique en présence de poudres composites de nickel–COHA.

**Mots clés :** isotherme d'adsorption, hydrogénation électrocatalytique (HEC), cyclohexanone, poudres d'oxyde – hydroxyde d'aluminium.

[Traduit par la Rédaction]

## Introduction

The electrocatalytic hydrogenation (ECH) of cyclohexanone to cyclohexanol was recently carried out in the presence of composite powder particles suspended in aqueous solution under vigorous stirring conditions (1, 2). The brief contact of the composite powder particles with a porous carbon cathode was sufficient to form adsorbed hydrogen on the metallic nanoaggregates during water electrolysis to initiate the ECH. The yield of the ECH reaction was closely dependent on both the nature of the metallic nanoaggregates deposited on the non-conductive powder (e.g., alumina and activated carbon) and the nature of the latter. Using a very strong adsorbent matrix material, such as activated carbon, for organic molecules is preferable to using a moderate adsorbent, such as  $\gamma$ -alumina, the latter being more active than

$\text{Al}(\text{OH})_3$  and  $\text{AlO}(\text{OH})$ . Consequently, the key role of the adsorption–desorption of the organic compounds involved in the ECH reaction was deduced. The same general deduction is also applicable to the ECH of phenol to cyclohexanol, the composite powders being trapped in a reticulated vitreous carbon matrix cathode (3). In both situations, however, the exact nature of the adsorption–desorption processes of the organic molecules on the adsorbent matrix remains unclear, and further investigation is required.

The present study pertains mainly to the adsorption of cyclohexanone under the experimental conditions previously reported (1), using  $\gamma\text{-Al}_2\text{O}_3$ ,  $\text{AlO}(\text{OH})$ , and  $\text{Al}(\text{OH})_3$  adsorbent matrices. The adsorption isotherms, through dynamic measurements, allow the determination of Henry's law constants ( $k_H$ ) for the adsorption of cyclohexanone on the matrix. It is shown that the ECH yield of cyclohexanone is linked to the Henry's law constant value.

## Theory

As previously described (4–6), the technique used to calculate the Henry constant ( $k_H$ ) can be defined as follows:

$$[1] \quad Q_e = k_H C_e$$

where  $Q_e$  is the adsorption capacity at equilibrium, and  $C_e$  is the equilibrium concentration of cyclohexanone in the mobile phase.

Received 9 June 2003. Published on the NRC Research Press Web site at <http://canjchem.nrc.ca> on 12 September 2003.

F. Laplante, N.-A. Bouchard, P. Dubé, H. Ménard,<sup>1</sup> and L. Brossard.<sup>2</sup> Centre de recherche en électrochimie et électrocatalyse, Département de chimie, Université de Sherbrooke, 2500 boul. Université, Sherbrooke, QC J1K 2R1, Canada.

<sup>1</sup>Current address: Institut de recherche d'Hydro-Québec (IREQ), 1800 boul. Lionel-Boulet, Varennes, QC J3X 1S1, Canada.

<sup>2</sup>Corresponding author (e-mail: [brossard.louis@ireq.ca](mailto:brossard.louis@ireq.ca)).



From the elution profile, based on the chromatogram,  $Q_e$  corresponds to:

$$[2] \quad Q_e = \frac{n_i I_1}{m I_2}$$

and  $C_e$  is expressed by

$$[3] \quad C_e = \frac{n_i h}{I_2}$$

where  $n_i$  is the amount (in moles) of cyclohexanone injected into the chromatographic column,  $m$  is the mass (in grams) of adsorbent packed in the column, and  $h$  is the peak height (arbitrary units).

The  $I_1$  and  $I_2$  parameters are determined from the elution profile of the chromatograms, as shown in Fig. 1. The integral  $I_1$  is given by the area of the prism ABCD. Line CD links the peak maxima.  $I_1$  is expressed by

$$[4] \quad I_1 = \int_0^h (\tau_r - \tau_0) dh$$

where  $\tau_r$  and  $\tau_0$  are, respectively, the retention time of cyclohexanone and the dead time (in minutes), with the latter corresponding to the appearance of a non-retained compound.  $I_2$  represents the amount of the compound injected into the column and is proportional to the area under the elution profile.  $I_2$  is given by

$$[5] \quad I_2 = \int_{\tau_1}^{\tau_2} h d\tau$$

where  $\tau_1$  and  $\tau_2$  are the times delimiting the beginning and the end of the chromatographic peak. From different amounts of cyclohexanone injected in the column, the distribution factor of cyclohexanone between the adsorbed state ( $Q_e$ ) and the mobile phase ( $C_e$ ) allows the determination of  $k_H$ .

## Experimental

The different  $\text{Al}(\text{OH})_3$  powders with specific BET surfaces of 0.23 and  $35 \text{ m}^2 \text{ g}^{-1}$  were supplied by Alcan International. All the powders were sifted to provide particles with a narrow distribution of diameters. The powder with a BET surface of  $0.23 \text{ m}^2 \text{ g}^{-1}$  was further heated at  $350^\circ\text{C}$  or  $800^\circ\text{C}$  for 24 h to induce changes in the chemical nature of the compound, namely,  $\text{AlO}(\text{OH})$  at  $350^\circ\text{C}$  and  $\gamma\text{-Al}_2\text{O}_3$  at  $800^\circ\text{C}$ . The average particle size remained close to a given value between 17 and  $52 \mu\text{m}$ , depending on the set of the experiments carried out. Each powder was individually packed in the chromatographic column for further characterization.

HPLC-grade water (Caledon) was used for the solution preparation. The mobile phase contained  $\text{KH}_2\text{PO}_4$  ( $0.05 \text{ mol L}^{-1}$ , Fluka  $\geq 99.5\%$ ) and  $\text{NaOH}$  ( $0.05 \text{ mol L}^{-1}$ , Aldrich 99.99%). The pH was adjusted to 7.0 by adding  $\text{NaOH}$ . The buffer was filtered under vacuum with Millipore filters ( $0.22 \mu\text{m}$ ) prior to the HPLC measurements.

The columns (Supelco, stainless steel column blanks,  $4.6 \text{ mm i.d.} \times 6.35 \text{ mm o.d.} \times 100 \text{ mm long}$ ) and the injector nozzle were filled with an aluminium oxide – hydroxide

**Fig. 1.** Elution profile obtained by HPLC measurements for the determination of  $k_H$ .

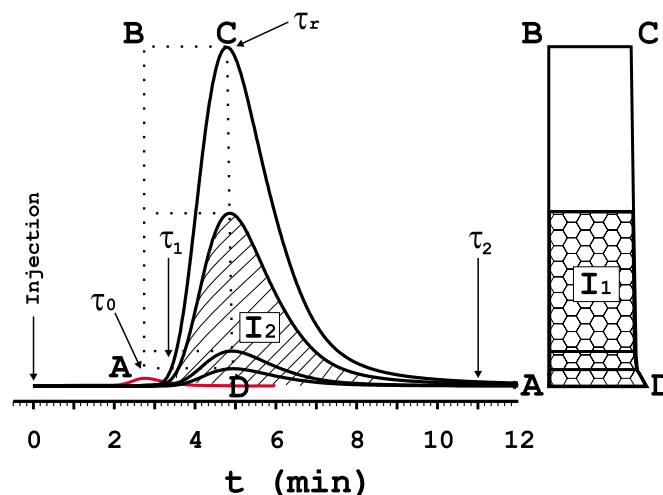


**Table 1.** Characteristics of sifted  $\text{Al}(\text{OH})_3$  powders used to establish the effect of BET surface on the  $k_H$  value.

Entry	Specific surface (BET) ( $\text{m}^2 \text{ g}^{-1}$ )	Average particle diameter ( $\mu\text{m}$ )	Geometric surface <sup>a</sup> ( $\text{m}^2 \text{ g}^{-1}$ )
A	0.95	17.1	$0.145^b$
B	35	16.9	$0.146^b$

<sup>a</sup> $\text{Al}(\text{OH})_3$  density:  $2.42 \text{ g cm}^{-3}$ .

<sup>b</sup>A single particle is assimilated to a perfect sphere.

powder, according to the slurry packing method in water. Afterwards, to condition the column, a phosphate buffer ( $\text{KH}_2\text{PO}_4$ ,  $1 \text{ mol L}^{-1}$  and  $\text{NaOH}$ ,  $1 \text{ mol L}^{-1}$ , adjusted to pH 7.0) was pumped (Beckman, model 100A) through the column for 2 h at a flow rate of  $0.15 \text{ mL min}^{-1}$ . Martin and Giochon (7) reported a complete review on the packing techniques for the HPLC columns.

Solutions of cyclohexanone were prepared from a  $0.5 \text{ mol L}^{-1}$  stock solution. Solution ( $5 \mu\text{L}$ ) containing from 25 to  $2500 \text{ nmol}$  of cyclohexanone was injected into an HPLC system (Agilent, HPLC 1100 series) equipped with a diode array detector (Agilent, DAD module 1100 series) operating at a wavelength of  $278 \text{ nm}$ . The temperature was maintained at  $25^\circ\text{C}$  by using a thermostat module (Agilent, 1100 series thermostated column compartment). The buffer ( $0.05 \text{ mol L}^{-1}$ ) flow rate was set to  $0.5 \text{ mL min}^{-1}$ . The determination of the column dead time was made by injecting  $5 \mu\text{L}$  of deuterium oxide into the column. The passage of eluted  $\text{D}_2\text{O}$  through the diode array module induced a slight variation of the base line indicating the column void volume (or the dead time,  $\tau_0$ ).

## Results

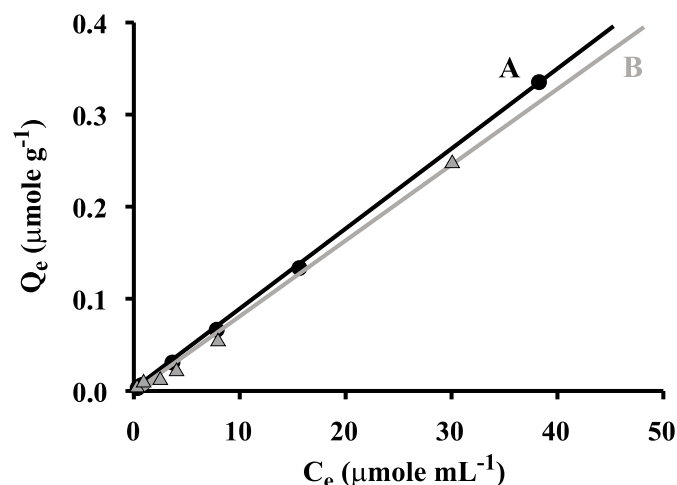
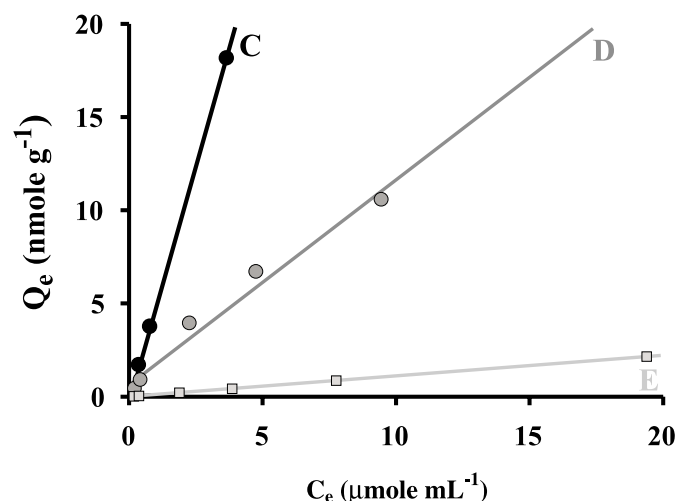
### Adsorption vs. specific surface

$\text{Al}(\text{OH})_3$  powders with two different specific surface areas ( $0.95 \text{ m}^2 \text{ g}^{-1}$  and  $35 \text{ m}^2 \text{ g}^{-1}$ ) were used to determine the adsorption of cyclohexanone under dynamic isotherm conditions. Table 1 summarizes the characteristics of the powders. Despite the large variation of the BET surface, the value of



**Table 2.** Characteristics of sifted powders collected from  $\text{Al}(\text{OH})_3$  ( $0.23 \text{ m}^2 \text{ g}^{-1}$ )<sup>a</sup> used to demonstrate the effect of particle size.

Entry	Mesh size ( $\mu\text{m}$ )	Specific surface <sup>b</sup> (BET) ( $\text{m}^2 \text{ g}^{-1}$ )	Average particles diameter ( $\mu\text{m}$ )	Geometric surface ( $\text{m}^2 \text{ g}^{-1}$ )
C	$x < 45$	0.94	22.7	$0.109^c$
D	$45 < x < 53$	0.80	46.6	$0.053^c$
E	$x > 63$	0.21	52.0	$0.048^c$

<sup>a</sup>Prior to sifting.<sup>b</sup>After sifting.<sup>c</sup>See footnote *b* in Table 1.**Fig. 2.** Adsorption isotherm for two different BET surfaces.  $\text{Al}(\text{OH})_3$  powders in Table 1. Powder A,  $k_H = 8.7 \times 10^{-3} \text{ mL g}^{-1}$ ; powder B,  $k_H = 8.3 \times 10^{-3} \text{ mL g}^{-1}$ .**Fig. 3.** Adsorption isotherms for three different average particle diameters. Powders in Table 2. Powder C,  $k_H = 5.30 \times 10^{-3} \text{ mL g}^{-1}$ ; powder D,  $k_H = 1.08 \times 10^{-3} \text{ mL g}^{-1}$ ; powder E,  $k_H = 0.11 \times 10^{-3} \text{ mL g}^{-1}$ .**Table 3.** Characteristics of the aluminium oxide – hydroxide powders used to correlate  $k_H$  with the type of support.

Entry	Support	Specific surface (BET) ( $\text{m}^2 \text{ g}^{-1}$ )	Particles diameter ( $\mu\text{m}$ )	Geometric surface ( $\text{m}^2 \text{ g}^{-1}$ )
F	$\gamma\text{-Al}_2\text{O}_3$	203	28.5	$0.087^a$
G	$\text{Al}(\text{OH})_3$	0.36	30.6	$0.081^a$
H	$\text{AlO}(\text{OH})$	67.6	29.2	$0.085^a$

<sup>a</sup>See footnote *b* in Table 1.

$k_H$  is practically the same (Fig. 2), indicating that the adsorption of cyclohexanone is independent of the BET surface.

#### Adsorption vs. particle diameter

To establish the relationship between particle diameter and adsorption,  $\text{Al}(\text{OH})_3$  powder with a specific surface of  $0.23 \text{ m}^2 \text{ g}^{-1}$  was sifted and separated into three fractions (Table 2). Since the effect of the BET surface area on cyclohexanone adsorption is marginal and the variation of the BET surface area with particle diameter is small, it was deduced that the smaller the particle diameter, the larger the adsorption (Fig. 3).

#### Adsorption vs. type of support

The aluminum hydroxide calcinations were carried out according to ref. 1, to obtain  $\text{AlO}(\text{OH})$  and  $\gamma\text{-Al}_2\text{O}_3$ . Each

powdered aluminum compound, including  $\text{Al}(\text{OH})_3$ , was sifted in such a way that the fraction with a mean particle diameter of  $29.4 \pm 1.1 \mu\text{m}$  was collected (Table 3). The adsorption of cyclohexanone was seen to increase in the following order:  $\text{AlO}(\text{OH}) < \text{Al}(\text{OH})_3 < \gamma\text{-Al}_2\text{O}_3$  (Fig. 4). The constant  $k_H$  is 400 times lower for  $\text{AlO}(\text{OH})$  compared with  $\gamma\text{-Al}_2\text{O}_3$ .

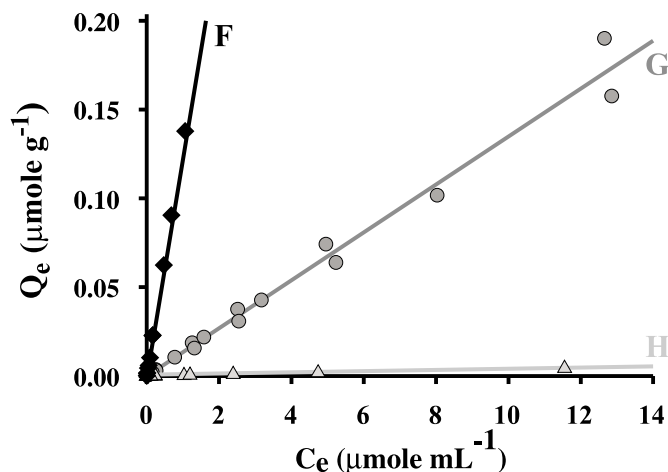
## Discussion

### Cyclohexanone adsorption

As far as the adsorption of cyclohexanone is concerned, it was deduced from Fig. 2 that the adsorption is located near the particle surface and is negligible at depth. The adsorption of cyclohexanone at depth is negligible because the solution does not penetrate inside the pores to reach the core



**Fig. 4.**  $Q_e$  against  $C_e$  of cyclohexanone for three different aluminum compounds. Powders in Table 3. Powder F,  $k_H = 120 \times 10^{-3} \text{ mL g}^{-1}$ ; powder G,  $k_H = 13 \times 10^{-3} \text{ mL g}^{-1}$ ; powder H,  $k_H = 0.3 \times 10^{-3} \text{ mL g}^{-1}$ .



of the particles. On the other hand, the gas used for the BET measurements may easily penetrate the particle to the core. Consequently, as reported in Fig. 2, there is no correlation between the BET surface area and the  $k_H$  value. Values of  $k_H$  should be related to the characteristics of the “skin” of the particles, as the geometric surface ( $\text{m}^2 \text{g}^{-1}$ ) available and the nature of the compound in the particle surface region (8). As observed, the greater the geometric surface or the smaller the particle diameter, the greater the adsorption (Fig. 3). Moreover, the amount of cyclohexanone adsorbed (ACAD) on the particle surface is largely dependent on the chemical nature of the particles (Fig. 4), with the ACAD being greatest in the presence of  $\gamma\text{-Al}_2\text{O}_3$ . The features reported in Fig. 4 for cyclohexanone adsorption are consistent with the views of Madsen and Blokhust (9) concerning the adsorption of benzoic acid on  $\alpha$ -alumina and boehmite. In addition, it may be pointed out from the latter reference that the finer the particle powder, the greater the adsorption capacity.

It is perhaps relevant to point out that cyclohexanone adsorption is weak on the three aluminum compounds considered in the present paper. This may be ascribed to the hydrophilic character of the aluminum oxide – hydroxide compound under consideration (10, 11). Since water is a polar solvent, the adsorption sites tend to be taken up by water molecules, and few sites remain available for cyclohexanone adsorption. The fact that water comes in contact with the particles prior to the cyclohexanone injection most likely contributes to lowering the cyclohexanone adsorption capacity.

#### Adsorption vs. ECH yield

For composite materials, such as a metal deposited onto an oxide, the different steps involved in the ECH of an organic compound through water electrolysis are

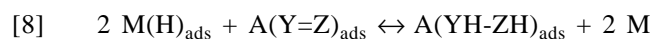
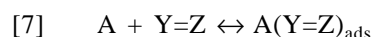
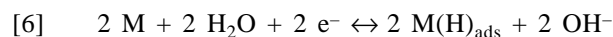
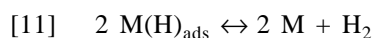
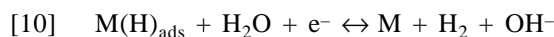
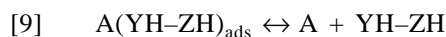


**Table 4.** ECH yield<sup>a</sup> of cyclohexanone on composite aluminium oxide – hydroxide – nickel powders reported in ref. 1.

Support	Particle diameter ( $\mu\text{m}$ )	Nickel loading (% w/w)	ECH yield (%)
$\text{Al(OH)}_3$	25.3	1.10	56
$\text{Al(OH)}_3$	20.3	1.10	66
$\text{Al(OH)}_3$	5.4	0.70	86
$\text{AlO(OH)}$	25.4	0.15	31
$\text{Al(OH)}_3$	25.3	0.37	38
$\gamma\text{-Al}_2\text{O}_3$	26.4	0.20	69

<sup>a</sup>For a total charge consumption of 1400 C.



The first step, eq. [6], consists of the formation of chemisorbed hydrogen on the metallic sites (M) by the reduction of water, with the chemisorbed hydrogen represented by  $\text{M(H)}_{\text{ads}}$ . The adsorption of the organic compound proceeds onto the adsorption sites (A) (step 2, eq. [7]). The adsorption sites are located on the oxide. Two pathways are possible for the adsorbed atomic hydrogen: it may be involved in the ECH reaction (step 3, eq. [8]) or lost through steps 6 or 7 (eqs. [10] and [11]) (12). The greater the fraction of atomic hydrogen involved in eq. [8], the higher the ECH yield. Step 3 (eq. [8]) occurs at the adlineation point, where the metal nanoaggregates (M), the adsorbent (A), and the solution come in contact (2, 3, 13). Consequently, since the rate-determining step of the ECH is a surface reaction, it may be deduced that the greater the number of adsorption sites filled by the reactant (the reactant being the organic compound under consideration, such as cyclohexanone), the easier the pathway for the ECH process (eqs. [8] and [9]). In other words, the greater the adsorption capacity of cyclohexanone at the adsorption sites (A), the higher the ECH yield. In the present study, the smaller the particle diameter, the larger the adsorption capacity (Fig. 3), with the latter increasing in the following order:  $\text{AlO(OH)} < \text{Al(OH)}_3 < \gamma\text{-Al}_2\text{O}_3$ . If the adsorption of cyclohexanone is rate-determining, the ECH yield should increase as the particle diameter decreases and from  $\text{AlO(OH)}$  to  $\gamma\text{-Al}_2\text{O}_3$  as the adsorption materials. This is fully consistent with the ECH yields recently reported, regarding the ECH of cyclohexanone on composite aluminum oxide – hydroxide powders with a small amount of nickel deposited on the particle surfaces (Table 4).

The nature of the adsorption sites of aluminum oxide – hydroxide powders remains to be further investigated. The acid–base properties of the compounds under consideration are of paramount importance for the adsorption capacity of organic molecules and are intimately linked to the crystallization nature of the material, which is hydration-dependent (14). Since orthophosphate is present in the solution and the affinity of phosphate species is considerable for aluminum oxide – hydroxide compounds (15–18), phosphate complexes and (or) aluminum phosphate may be present at the solution-support interface, and the cyclohexanone adsorption may be affected. The theoretical approach (19, 20) developed by



other groups may be useful in shedding light on the adsorption process.

## Conclusion

The amount of cyclohexanone adsorbed on aluminum oxide – hydroxide powders increases as the powder particles become smaller, in the following order:  $\text{AlO}(\text{OH}) < \text{Al}(\text{OH})_3 < \text{Al}_2\text{O}_3$ , and regardless of the BET surface area. Furthermore, when the cyclohexanone ECH is carried out on the same adsorbent compounds with a small loading of nickel nano-aggregates on the particle surfaces; the larger the amount of cyclohexanone adsorbed onto the aluminum oxide – hydroxide compounds, the higher the ECH yield.

## Acknowledgements

The authors would like to thank the Natural Sciences and Engineering Research Council of Canada (NSERC) and le Fonds Québécois de la recherche sur la nature et les technologies (FQRNT) for their financial support.

## References

1. P. Dubé, L. Brossard, and H. Ménard. *Can. J. Chem.* **80**, 345 (2002).
2. P. Dubé, F. Kerdouss, F. Laplanche, P. Proulx, L. Brossard, and H. Ménard. *J. Appl. Electrochem.* **33**, 541 (2003).
3. F. Laplanche, H. Ménard, and L. Brossard. *Can. J. Chem.* **81**, 258 (2003).
4. N.A. Chuduk, Y.A. Eltekov, and A.V. Kiselev. *J. Colloid Interface Sci.* **84**, 149 (1981).
5. L. Noel and H. Ménard. *J. Chromatogr.* **436**, 391 (1988).
6. J.F.K. Hubert and R.G. Gerritse. *J. Chromatogr.* **58**, 137 (1971).
7. M. Martin and G. Guiochon. *Chromatographia*, **10**, 194 (1977).
8. E.B. Maxted and J.S. Elkins. *J. Chem. Soc.* 5086 (1961).
9. L. Madsen and A.M. Blokhust. *J. Colloid Interface Sci.* **166**, 259 (1994).
10. Y. Men, H. Gnaser, and C. Ziegler. *Anal. Bioanal. Chem.* **375**, 912 (2003).
11. B.A. Hendriksen, D.R. Pearce, and R. Rudham. *J. Catal.* **24**, 82 (1972).
12. J.M. Chapuzet, A. Lasia, and J. Lessard. *In Electrocatalysis frontiers of electrochemistry series. Edited by J. Lipkowski and P.N. Ross. VCH Publishers Inc., New York.* 1998. pp. 155–196.
13. E.B. Maxted and H.C. Evans. *J. Chem. Soc.* 2071 (1938).
14. J.T. Richardson. *In Principles of catalyst development, fundamental and applied catalysis.* Plenum Press, New York. 1992.
15. E. Laiti, P. Persson, and L.-O. Öhman. *Langmuir*, **12**, 2969 (1996).
16. P. Persson, E. Laiti, and L.-O. Öhman. *J. Colloid Interface Sci.* **190**, 341 (1997).
17. W.H. Van Riemsdijk and J. Lyklema. *J. Colloid Interface Sci.* **76**, 55 (1980).
18. A.K.H. Nohman, G.A.H. Mekhemer, N.E. Fouad, and H.A. Khalaf. *Adsorpt. Sci. Technol.* **17**, 665 (1999).
19. O. Maresca, A. Allouche, J.P. Aycard, M. Rajzmann, S. Clemendot, and F. Hutschka. *J. Mol. Struct. THEOCHEM*, **505**, 81 (2000).
20. J.B. Peri. *J. Phys. Chem.* **69**, 220 (1965).



# A study of the decomposition behaviour of 12-tungstophosphate heteropolyacid in solution

Zhirong Zhu, Ruan Tain, and Colin Rhodes

**Abstract:** In this paper, the decomposition of  $\text{H}_3\text{PW}_{12}\text{O}_{40}$  in aqueous solution or in mixed solutions of water–ethanol or water–acetone is investigated by potentiometric titration and  $^{31}\text{P}$  NMR. Identification of the products from  $\text{H}_3\text{PW}_{12}\text{O}_{40}$  decomposition over a pH range of 1–12 was achieved using preparation high performance liquid chromatography (Pre-HPLC) combined with IR, UV–vis spectroscopy, and inductively coupled plasma atomic emission spectroscopy (ICP). It is found that  $\text{H}_3\text{PW}_{12}\text{O}_{40}$  in aqueous solution decomposes in a stepwise fashion with increasing pH, with the following solution compositions:  $[\text{PW}_{12}\text{O}_{40}]^{3-}$  (at pH  $\sim 1$ )  $\rightarrow [\text{PW}_{12}\text{O}_{40}]^{3-} + [\text{P}_2\text{W}_{21}\text{O}_{71}]^{6-} + [\text{PW}_{11}\text{O}_{39}]^{7-}$  (at pH 2.2)  $\rightarrow [\text{PW}_{12}\text{O}_{40}]^{3-} + [\text{P}_2\text{W}_{21}\text{O}_{71}]^{6-} + [\text{PW}_{11}\text{O}_{39}]^{7-} + [\text{P}_2\text{W}_{18}\text{O}_{62}]^{6-} + [\text{P}_2\text{W}_{19}\text{O}_{67}]^{10-}$  (at pH 3.5)  $\rightarrow [\text{P}_2\text{W}_{21}\text{O}_{71}]^{6-} + [\text{PW}_{11}\text{O}_{39}]^{7-} + [\text{P}_2\text{W}_{18}\text{O}_{62}]^{6-}$  (at pH 5.4)  $\rightarrow [\text{PW}_9\text{O}_{34}]^{9-}$  (at pH 7.3)  $\rightarrow \text{PO}_4^{3-} + \text{WO}_4^{2-}$  (pH  $> 8.3$ ). In the first stages at pH  $< 8$ ,  $\text{H}_3\text{PW}_{12}\text{O}_{40}$  decomposes partially with removal of W=O units. In the second stage at pH  $> 8$ , tungstophosphoric completely decomposes to  $\text{PO}_4^{3-}$ . In contrast, the decomposition of  $\text{H}_3\text{PW}_{12}\text{O}_{40}$  is reduced, or the stability of the  $[\text{PW}_{12}\text{O}_{40}]^{3-}$  anion is enhanced, in ethanol–water or acetone solution at pH  $< 8$ .

**Key words:** 12-tungstophosphate heteropolyacid, decomposition behaviour, potentiometric titration,  $^{31}\text{P}$  NMR, preparation high performance liquid chromatography.

**Résumé :** Faisant appel à des titrages potentiométriques et à la RMN du  $^{31}\text{P}$ , on a étudié la décomposition du  $\text{H}_3\text{PW}_{12}\text{O}_{40}$  en solution aqueuse, dans des solutions mixtes d'eau et d'éthanol ou d'eau et d'acétone. L'identification des produits résultants de la décomposition du  $\text{H}_3\text{PW}_{12}\text{O}_{40}$  à des pH allant de 1 à 12 a été effectuée par chromatographie liquide à haute performance au niveau préparatif (CLHP-Pré) combinée aux méthodes spectroscopiques IR, UV–visible et d'émission atomique des plasmas à couplage inductif (ICP). On a observé que, en solution aqueuse, le  $\text{H}_3\text{PW}_{12}\text{O}_{40}$  se décompose par étape avec une augmentation du pH; la composition de la solution passe de  $[\text{PW}_{12}\text{O}_{40}]^{3-}$  (à un pH d'environ 1)  $\rightarrow [\text{PW}_{12}\text{O}_{40}]^{3-} + [\text{P}_2\text{W}_{21}\text{O}_{71}]^{6-} + [\text{PW}_{11}\text{O}_{39}]^{7-}$  (à un pH de 2,2)  $\rightarrow [\text{PW}_{12}\text{O}_{40}]^{3-} + [\text{P}_2\text{W}_{21}\text{O}_{71}]^{6-} + [\text{PW}_{11}\text{O}_{39}]^{7-} + [\text{P}_2\text{W}_{18}\text{O}_{62}]^{6-} + [\text{P}_2\text{W}_{19}\text{O}_{67}]^{10-}$  (à un pH de 3,5)  $\rightarrow [\text{P}_2\text{W}_{21}\text{O}_{71}]^{6-} + [\text{PW}_{11}\text{O}_{39}]^{7-} + [\text{P}_2\text{W}_{18}\text{O}_{62}]^{6-}$  (à un pH de 5,4)  $\rightarrow [\text{PW}_9\text{O}_{34}]^{9-}$  (à un pH de 7,3)  $\rightarrow \text{PO}_4^{3-} + \text{WO}_4^{2-}$  (à un pH supérieur à 8,3). Dans les premiers stades, à des pH inférieurs à 8, le  $\text{H}_3\text{PW}_{12}\text{O}_{40}$  se décompose partiellement avec l'élimination d'unités W=O. Dans un deuxième stade, à un pH supérieur à 8, l'entité tungstophosphorique se décompose complètement en  $\text{PO}_4^{3-}$ . Par ailleurs, en solution dans un mélange éthanol–eau ou acétone–eau, à des pH inférieurs à 8,0, le  $\text{H}_3\text{PW}_{12}\text{O}_{40}$  est réduit ou la stabilité de l'anion  $[\text{PW}_{12}\text{O}_{40}]^{3-}$  augmentée.

**Mots clés :** hétéropolyacide du 12-tungstophosphate, comportement de décomposition, titrage potentiométrique, RMN du  $^{31}\text{P}$ , chromatographie liquide à haute performance préparative.

[Traduit par la Rédaction]

## Introduction

The study of polyoxometalates, which are unmatched in terms of molecular and electronic structural versatility, is an increasingly important field, having wide applications in analytical and clinical chemistry, biochemistry, catalysis, medicine, and materials science (1). The synthesis of hundreds of polyoxometalate compounds has been described since the first heteropolytungstate compound was discovered by

Marignac in 1862 (2). Most polyoxometalates are synthesized in aqueous solution, and consequently the processes involved in the assembly of polyoxometalates are important in understanding the fundamental processes that give rise to the final compound (3, 4). Recently, Raman spectroscopy,  $^{17}\text{O}$  magic angle spin - nuclear magnetic resonance (MAS-NMR), and fast atomic bombardment mass spectroscopy (FAB) have been used to discern the important relationships that exist between structures in aqueous solution and the nature of the resulting solid (5–7). The behaviour of heteropolymolybdates in aqueous solution has been studied in detail using potentiometric titration combined with  $^{31}\text{P}$  NMR (8, 9). As a result, the formation of Keggin species was observed in solution at pH  $< 2$ , and other polyoxo-species were obtained from decomposition of the Keggin species with increasing pH of solution.

The chemical structure of the heteropolyacid  $\text{H}_3\text{PW}_{12}\text{O}_{40}$  was identified by Keggin in 1933 as being a compact, edge-

Received 5 November 2002. Published on the NRC Research Press Web site at <http://canjchem.nrc.ca> on 16 September 2003.

**Z. Zhu<sup>1</sup> and R. Tain.** Shanghai Research Institute of Petrochemical Technology, Pudong Beilu 1658, Shanghai 201208, China.

**C. Rhodes.** Department of Chemistry, University of Cardiff, Wales, PO Box 912, CF10 3TB, U.K.

<sup>1</sup>Corresponding author (e-mail: [zhuzhirong@yahoo.com](mailto:zhuzhirong@yahoo.com)).



shared polyhedral arrangement (10). Of the Keggin structures,  $\text{H}_3\text{PW}_{12}\text{O}_{40}$  is considered to be the most stable and the most acidic of the heteropolyacids and is used as an acid catalyst (11, 12). In the solid form, often, the catalysts are supported to improve surface area. Upon support materials, heteropoly acids are known to exhibit reduced acidic character and are known to undergo varying degrees of decomposition. For example, the decomposition of Keggin  $\text{H}_3\text{PW}_{12}\text{O}_{40}$  has been observed to occur when  $\text{H}_3\text{PW}_{12}\text{O}_{40}$  is supported on the surface of basic materials, such as  $\text{Al}_2\text{O}_3$  and  $\text{MgO}$  (13). However, in such cases the compounds formed by  $\text{H}_3\text{PW}_{12}\text{O}_{40}$  decomposition were not identified, although  $[\text{PW}_{11}\text{O}_{39}]^{7-}$  of the lacunary Keggin structure was presumed to exist. It is known that in dilute solutions (1 wt%) with pH ca.2,  $\text{H}_3\text{PW}_{12}\text{O}_{40}$  may decompose to form the lacunary  $[\text{PW}_{11}\text{O}_{39}]^{7-}$  anion (14). Similarly, it has been shown that under appropriate conditions, other tungstophosphate anions, such as  $[\text{PW}_9\text{O}_{34}]^{9-}$ ,  $[\text{P}_2\text{W}_{18}\text{O}_{62}]^{6-}$ , and  $[\text{P}_2\text{W}_{21}\text{O}_{71}]^{6-}$ , may be formed (15, 16). It was reported that  $\text{H}_3\text{PW}_{12}\text{O}_{40}$  decomposed to  $\text{PO}_4^{3-}$  and  $\text{WO}_4^{2-}$  with the addition of NaOH through several intermediates, i.e.,  $\text{H}_3\text{PW}_{12}\text{O}_{40} + \text{OH}^- \rightarrow [\text{P}_2\text{W}_{21}\text{O}_{71}]^{6-} + \text{OH}^- \rightarrow [\text{PW}_{11}\text{O}_{39}]^{7-} + \text{OH}^- \rightarrow [\text{P}_2\text{W}_{19}\text{O}_{67}]^{10-} + \text{OH}^- \rightarrow [\text{PW}_9\text{O}_{34}]^{9-} + \text{OH}^- \rightarrow \text{PO}_4^{3-}$  (17). During the decomposition of polyoxometalates, the mechanism of decomposition between  $\text{H}_3\text{PW}_{12}\text{O}_{40}$  and  $\text{H}_4\text{SiW}_{12}\text{O}_{40}$  was similar, i.e.,  $\text{H}_3\text{PW}_{12}\text{O}_{40}$  ( $\text{H}_4\text{SiW}_{12}\text{O}_{40}$ ) +  $\text{OH}^- \rightarrow [\text{PW}_{11}\text{O}_{39}]^{7-}$  ( $[\text{SiW}_{11}\text{O}_{39}]^{8-}$ ) +  $\text{OH}^- \rightarrow [\text{PW}_9\text{O}_{34}]^{9-}$  ( $[\text{SiW}_9\text{O}_{34}]^{10-}$ ) +  $\text{OH}^- \rightarrow \text{PO}_4^{3-}$  ( $\text{SiO}_4^{4-}$ ), but this was not investigated over a wide pH range of 1 ~ 12, owing to the difficulty in identifying products (18, 19). Detusheva et al. (20) studied the reaction of  $\text{H}_3\text{PW}_{12}\text{O}_{40}$  with NaOH in aqueous solution (neutralized to pH < 7.8) using  $^{31}\text{P}$  NMR, IR, and Raman spectroscopy. The products formed during decomposition of  $\text{H}_3\text{PW}_{12}\text{O}_{40}$  were identified as  $[\text{P}_2\text{W}_{21}\text{O}_{71}]^{6-}$ ,  $[\text{PW}_{11}\text{O}_{39}]^{7-}$ ,  $[\text{PW}_9\text{O}_{34}]^{9-}$ ,  $[\text{PW}_{12}\text{O}_{42}]^{12-}$ , and  $\text{WO}_4^{2-}$ , and a Raman spectroscopic method was developed to analyze some components from the decomposition of  $\text{H}_3\text{PW}_{12}\text{O}_{40}$ , but only with a very limited range for determination. Maksimovskaya (21) investigated the titration of  $\text{H}_3\text{PW}_{12}\text{O}_{40}$  (0.002 ~ 0.1 mol·L<sup>-1</sup>) with MOH (M = Li, Na, K),  $\text{Li}_2\text{CO}_3$ , and  $\text{MgCO}_3$  or  $\text{CaCO}_3$  at pH 1.5 ~ 9 in aqueous solution, using  $^{31}\text{P}$  NMR. At the first stage, the  $\text{H}_3\text{PW}_{12}\text{O}_{40}$  converted into  $[\text{PW}_{11}\text{O}_{39}]^{7-}$  through some intermediates, and this conversion is reversible at pH 1.5 ~ 4. At the second stage (pH > 7),  $[\text{PW}_{11}\text{O}_{39}]^{7-}$  decomposed to  $\text{PO}_4^{3-}$  and  $\text{WO}_4^{2-}$  directly (with Na, Li) or indirectly (with K, Mg) through the intermediates of monomeric heteropoly acids ( $\text{PW}_x$ ) with W/P < 11. However, the products formed during decomposition of  $\text{H}_3\text{PW}_{12}\text{O}_{40}$  were identified only by NMR, with the result that the identification of some intermediates appears vague.

Therefore, accurate identification of the formed products (i.e., analysis of the components of the  $\text{H}_3\text{PW}_{12}\text{O}_{40}$  solution) is a key in the study of the mechanism of  $\text{H}_3\text{PW}_{12}\text{O}_{40}$  decomposition, and the combination of multiple methods, especially the method for the separation of mixed heteropoly acids, is an ideal way to solve this problem. On the other hand, heteropoly acids have been widely used in organic-water systems, but the mechanism of  $\text{H}_3\text{PW}_{12}\text{O}_{40}$  decomposition has not been studied in detail. Moreover, to identify all the components resulting from the decomposition of solid  $\text{H}_3\text{PW}_{12}\text{O}_{40}$  is extremely difficult, and the initial step to un-

derstanding the properties of the solid phase is to understand, first, the steps of decomposition in solution.

In this paper, the behaviour of  $\text{H}_3\text{PW}_{12}\text{O}_{40}$  decomposition is investigated by potentiometric titration and  $^{31}\text{P}$  NMR in aqueous solution, in a mixed solution of water-ethanol, and in water-acetone. The components of the  $\text{H}_3\text{PW}_{12}\text{O}_{40}$  solution were separated by preparative high pressure liquid chromatography (Pre-HPLC). Characterization of the components of products from  $\text{H}_3\text{PW}_{12}\text{O}_{40}$  decomposition was achieved using IR, UV-vis spectroscopy, and inductively coupled plasma atomic emission spectroscopy (ICP).

## Experimental section

Hydrated 12-tungstophosphoric acid ( $\text{H}_3\text{PW}_{12}\text{O}_{40}$ ) (supplied by Aldrich, > 99%) was dried at 393 K for 8 h to obtain  $\text{H}_3\text{PW}_{12}\text{O}_{40} \cdot 6\text{H}_2\text{O}$  (22, 23). Subsequently, the hexahydrate was used to prepare 0.1 mol·L<sup>-1</sup>  $\text{H}_3\text{PW}_{12}\text{O}_{40}$  in water, 0.1 mol·L<sup>-1</sup>  $\text{H}_3\text{PW}_{12}\text{O}_{40}$  solution in water-ethanol (volume fraction 50/50), and 0.1 mol·L<sup>-1</sup>  $\text{H}_3\text{PW}_{12}\text{O}_{40}$  in water-acetone (volume fraction 50/50).

### Potentiometric titration

Potentiometric titration was carried out by adding 0.2 N NaOH standard aqueous solution into each of the  $\text{H}_3\text{PW}_{12}\text{O}_{40}$  solutions (20 mL, 0.1 mol·L<sup>-1</sup>) at a rate of 2 drops per second at room temperature, using Fisherbrand AR10 pH equipment with a glass hydrogen electrode that was calibrated before and after every titration. Water was boiled just before being used, and the titration container was isolated from air with the flow of helium.

### Component identification

The above samples, obtained with the titration of NaOH and after ageing for 1 day, were analyzed using  $^{31}\text{P}$  NMR and HPLC at the same time, and the pH of the solution was determined again.  $^{31}\text{P}$  NMR spectra were measured (161.97 MHz) using a Bruker MSL-400 instrument at 298 K, using 5  $\mu\text{s}$  pulses and a relaxation time of 10 s and the resolution of 3.052 Hz per point. Exponential multiplication with 3 Hz line-broadening was applied prior to Fourier transformation. Phosphoric acid (85% in  $\text{D}_2\text{O}$ ) was used as an external reference.

The solid material formed from tungstophosphate in water-ethanol or water-acetone was recovered by filtration. A PerkinElmer 2000 FT-IR spectrometer was used to characterize the solids produced, which were combined with KBr to form self-supporting discs.

The components of products from  $\text{H}_3\text{PW}_{12}\text{O}_{40}$  decomposition in aqueous solution were separated using a Waters 4000 Pre-HPLC instrument fitted with a reverse-phase C18 preparation column and a photodiode array UV detector (254 nm). HPLC grade  $\text{H}_2\text{O}$  and 90% (volume fraction) methanol solution, both containing 60 mM  $\text{BuNH}_3$  and 20 mM citrate, were used for the linear gradient elution, according to the following program (time in minutes ( $\text{H}_2\text{O}$  – 90% methanol ~ (volume fraction))): 0 (90/10), 10 (80/20), 10 (50/50), 10 (15/85). The separated components were collected in a flask and recovered by evaporation under vacuum. The P/W elemental ratio of the components obtained above was determined using a BRUKER PS-6 ICP instrument.



## Results and discussion

### Behaviour of $\text{H}_3\text{PW}_{12}\text{O}_{40}$ decomposition with increasing pH in aqueous solution

Potentiometric titration has been widely used to study the decomposition of 12-tungstophosphate heteropolyacid as the pH of the solution changes (23, 24). Figure 1 shows how the pH of an  $\text{H}_3\text{PW}_{12}\text{O}_{40}$  solution changes from pH 1.1 to 12.0 with addition of 0.2 N NaOH solution. As is expected, the pH value of the original solution, pH  $\sim 1$ , indicates that  $\text{H}_3\text{PW}_{12}\text{O}_{40}$  is more acidic than ordinary mineral acids or the corresponding oxoacids arising from any combination of its constituent elements.

Initially, the pH changes slowly — from pH  $\sim 1$  to pH  $\sim 4.5$  — as NaOH is added. Continued addition of NaOH leads to a rapid increase in the rate of pH change between pH  $\sim 4.5$ –8. An indistinct endpoint emerges at pH  $\sim 8$ , which indicates that the potentiometric curve for pH  $< 8$  is consistent with the presence of more than one acidic species or single polyprotic species, with narrowly spaced  $\text{pK}$  values.

At pH  $\sim 8$  further addition of NaOH does not lead to a significant increase in the overall pH of the solution. Rapid addition of NaOH causes only a temporary rise in the measured pH, but after standing, or by reducing the velocity at which NaOH is introduced to the mixture, the pH returns to ca. 8. This effect becomes more pronounced as more NaOH is added. Clearly the ability of the polyoxometalate to maintain the pH of the solution to within 0.5 pH units indicates that tungstophosphoric acid has high buffering capacity. Further addition of NaOH ultimately produces a very obvious endpoint when the molar ratio of  $\text{OH}^-:\text{H}_3\text{PW}_{12}\text{O}_{40}$  is 27. This feature is similar to those observed for normal acid–base titrations, and a sharp rise in pH from 8.5 to 11.5 is seen to take place.

$^{31}\text{P}$  NMR spectra of the solutions produced during the titration of  $\text{H}_3\text{PW}_{12}\text{O}_{40}$  with NaOH are shown in Fig. 2. At the pH of the original solution, ca. 1.1, the singlet at  $-14.7$  ppm, characteristic of the P heteroatom of the Keggin 12-series tungstophosphate, is clear. As NaOH is added to the  $\text{H}_3\text{PW}_{12}\text{O}_{40}$  solution, however, the spectra become increasingly complex up to pH = 3.5, after which further addition of NaOH leads to the spectra becoming increasingly simpler. At pH = 7.3, a singlet at  $-8$  ppm is visible. When the pH of the solution exceeds 8 an additional peak at 0 ppm, attributable to  $\text{PO}_4^{3-}$ , can be observed, the intensity of which increases as further NaOH is added. Upon complete decomposition of the heteropolyacid at pH = 12, only the peak attributable to  $\text{PO}_4^{3-}$  is visible.

In conclusion, the whole process of  $\text{H}_3\text{PW}_{12}\text{O}_{40}$  titration with NaOH may be divided into two stages. In the first stage, where the pH of the solution is  $< 8$ , the behaviour of  $\text{H}_3\text{PW}_{12}\text{O}_{40}$  is similar to a mixture of acids or a polyprotic acid. In the second stage, tungstophosphoric acid behaves as the acid salt of a normal weak acid, such as  $\text{NaHCO}_3$  or  $\text{Na}_2\text{HPO}_4$ .

### Determination of the composition of tungstophosphate solution

Identification of the products from  $\text{H}_3\text{PW}_{12}\text{O}_{40}$  decomposition has been investigated using HPLC. A few scattered re-

**Fig. 1.** The pH titration curve of  $0.1 \text{ mol}\cdot\text{L}^{-1} \text{H}_3\text{PW}_{12}\text{O}_{40}$  with  $0.2 \text{ N NaOH}$  in aqueous solution.

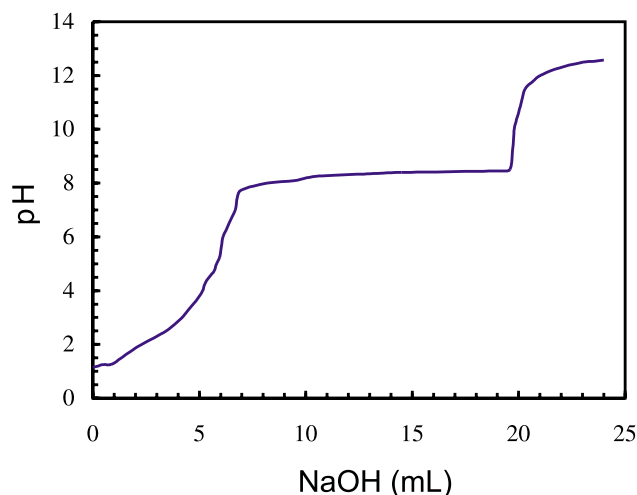
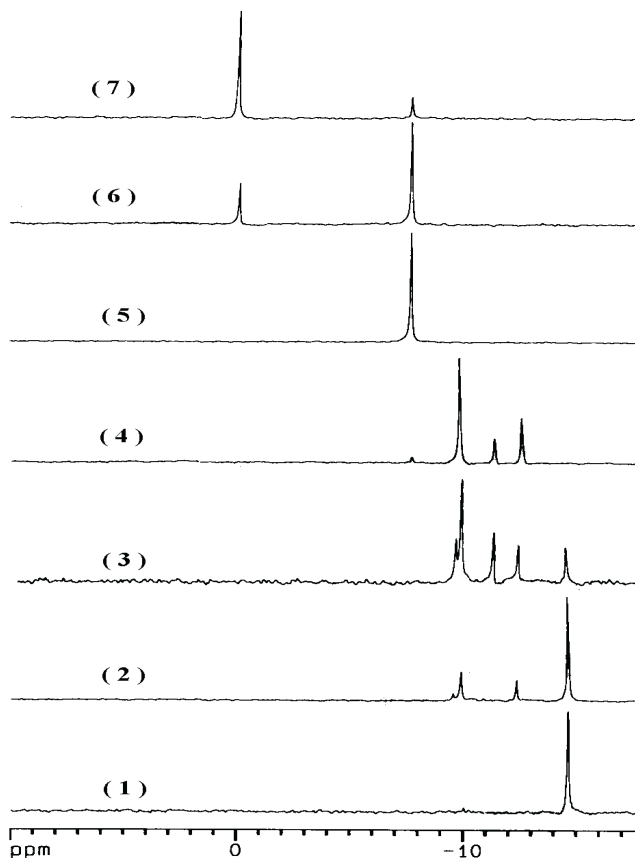


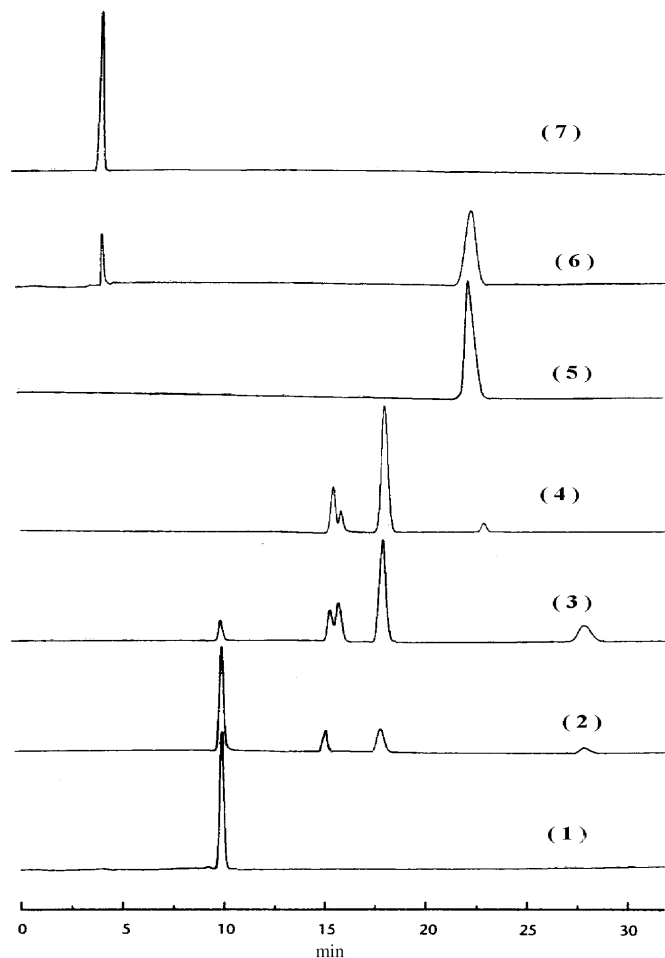
**Fig. 2.**  $^{31}\text{P}$  NMR spectra of aqueous tungstophosphate solution formed during the titration of  $0.2 \text{ N NaOH}$ : (1) original  $\text{H}_3\text{PW}_{12}\text{O}_{40}$ , (2) pH = 2.2, (3) pH = 3.5, (4) pH = 5.4, (5) pH = 7.3, (6) pH = 8.3, (7) pH = 12.1.



ports of chromatography for certain subclasses of polyoxometalates have appeared (25–27). The reversed-phase HPLC with a methanol–water gradient, using ion-interaction reagents to promote retention and a citrate ion as the competing ion, resulted in excellent and rapid separations of mixed



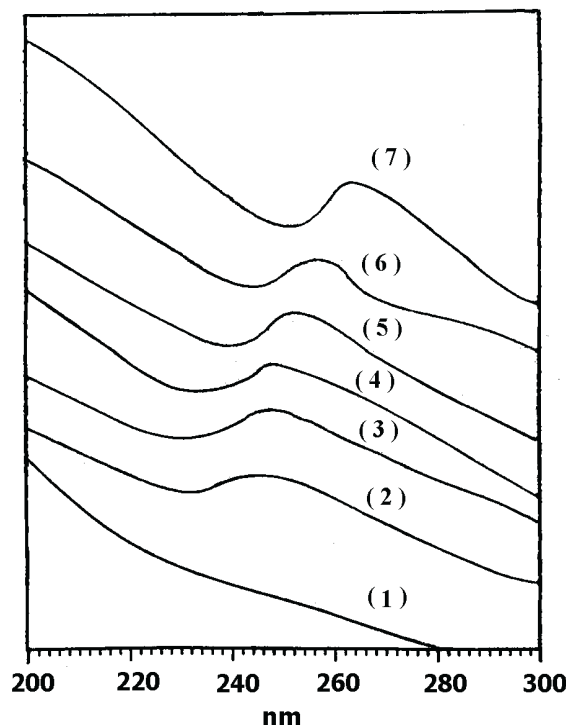
**Fig. 3.** HPLC chromatograms of the decomposition products produced from the addition of 0.2 N NaOH to 12-tungstophosphate solution: (1) original  $\text{H}_3\text{PW}_{12}\text{O}_{40}$ , (2) pH = 2.2, (3) pH = 3.5, (4) pH = 5.4, (5) pH = 7.3, (6) pH = 8.3, (7) pH = 12.1.



polyoxometalates, such as  $[\text{PW}_{11}\text{VO}_{40}]^{5-}$ ,  $[\text{PW}_{10}\text{V}_2\text{O}_{40}]^{5-}$ , and  $[\text{PW}_9\text{V}_3\text{O}_{40}]^{6-}$  (28). Recently, some reversed-phase HPLC methods using ion-interaction reagents and competing ions have also been developed, including separation of tungstophosphate anions (29, 30). Figure 3 presents the chromatograms resulting from the decomposition experiments of  $\text{H}_3\text{PW}_{12}\text{O}_{40}$ . The chromatograms correlate well with the NMR data in the number of species present in solution as the pH is varied from pH ~ 1 to pH ~ 12.

As each component was eluted from the HPLC instrument, a UV spectrum was collected by the detector, which was fitted with an automatic scanning function. The data collected are presented in Fig. 4. With the aid of a preparation-scale HPLC column, the individual fractions (components) of products from the tungstophosphate decomposition process were collected for further identification. The W/P ratio of the components, corresponding to chromatographic peaks, was determined by ICP analysis, and combined with  $^{31}\text{P}$  NMR and UV-vis spectra reported previously (15, 17, 31, 32), each component may be identified accurately (shown in Table 1). In addition, each of the fractions collected was re-injected for HPLC analysis, and

**Fig. 4.** UV spectra of the decomposition products separated using HPLC. Peaks with the following retention time (min): (1) 4.2, (2) 17.8, (3) 22.1, (4) 15.5, (5) 26.3, (6) 15.0, (7) 9.9.



only one peak was observed, which shows that every component is stable under HPLC separation conditions. It is observed in the UV spectrum in Fig. 4 that the wavelength of maximum UV absorption of tungstophosphate anions decreases with decreasing W/P. This results from the fact that the increase of charge density in tungstophosphate anions leads to enhancement in P—O  $\pi$ -bonding as the tungsten-oxygen units surrounding the heteroatom are removed (31).

#### Effect of organic solvent on the behaviour of $\text{H}_3\text{PW}_{12}\text{O}_{40}$ decomposition

It is seen clearly in Figs. 5 and 6 that the pH-titration curve of  $\text{H}_3\text{PW}_{12}\text{O}_{40}$  in water-ethanol is almost the same as that in water-acetone, both of which are different from that in aqueous solution. The apparent pH value of the  $\text{H}_3\text{PW}_{12}\text{O}_{40}$  solution (the value indicated by pH equipment) is higher (near 1.7) in water-ethanol or water-acetone solutions than in aqueous solution, which indicates that the acidity of  $\text{H}_3\text{PW}_{12}\text{O}_{40}$  solution is decreased by the addition of organic solvents.

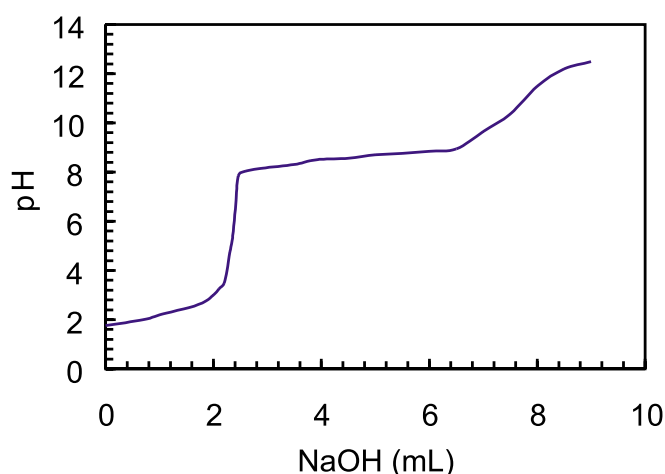
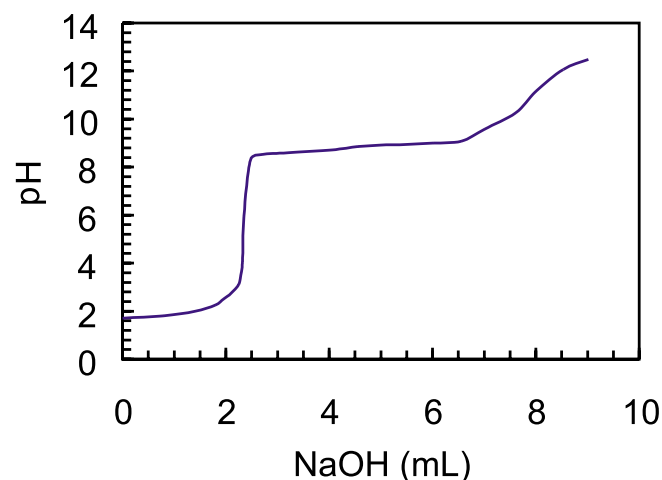
As is expected, the endpoint of the acid-base titration emerges at an exact 3  $\text{OH}^-$ : $\text{H}_3\text{PW}_{12}\text{O}_{40}$ , which indicates that the  $\text{H}_3\text{PW}_{12}\text{O}_{40}$  anion is stable at pH < 8 when in a water-ethanol or water-acetone solution. As observed for the aqueous solution, the pH remains 8.5–9.0 when NaOH continues to be added. Eventually a precipitate is formed in solution with further addition of NaOH, and meanwhile, the pH of solution increases rapidly.

If the addition of NaOH is stopped at this stage, the solution pH will fall to about 9 in several minutes, and the precipitate will redissolve. Continued addition of NaOH

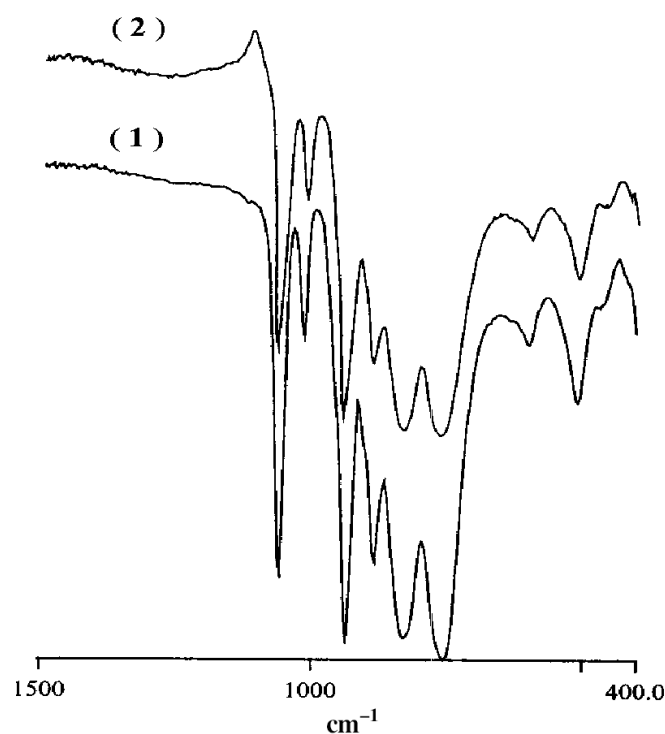


**Table 1.** Characterization data of components of tungstophosphate solution.

Compound	Chemical shift of $^{31}\text{P}$ NMR (min)	Retention time of HPLC (min)	Wavelength at maximum absorption (nm)	W/P ratio by ICP
$[\text{PW}_{12}\text{O}_{40}]^{3-}$	-14.7	9.9	264	12.08
$[\text{P}_2\text{W}_{21}\text{O}_{71}]^{6-}$	-12.6	15.0	257	10.59
$[\text{P}_2\text{W}_{19}\text{O}_{67}]^{10-}$	-9.4	26.3	253	9.64
$[\text{P}_2\text{W}_{18}\text{O}_{62}]^{6-}$	-11.2	15.5	250	8.93
$[\text{PW}_{11}\text{O}_{39}]^{7-}$	-9.8	17.8	244	10.95
$[\text{PW}_9\text{O}_{34}]^{9-}$	-7.6	22.1	249	9.02
$\text{PO}_4^{3-}$	0.1	4.2	<200	

**Fig. 5.** The pH titration curve of  $\text{H}_3\text{PW}_{12}\text{O}_{40}$  with NaOH in water-ethanol.**Fig. 6.** The pH titration curve of  $\text{H}_3\text{PW}_{12}\text{O}_{40}$  with NaOH in water-acetone.

produces a precipitate that will not redissolve readily. IR spectra of the precipitate produced from water-ethanol and water-acetone solutions are presented in Fig. 7, and the solid is positively identified as  $[\text{PW}_9\text{O}_{34}]^{9-}$ , according to the report (33). At pH ~12, all the deposit is dissolved, but a period of several hours or days is needed, depending on solution temperature.

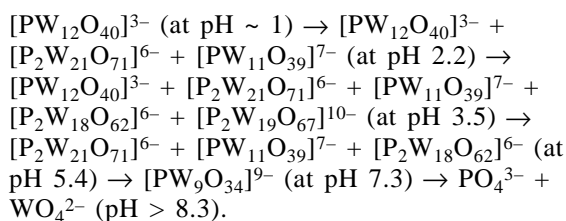
**Fig. 7.** IR spectra of the deposit formed during titration in water-ethanol or water-acetone at pH > 9.0: (1) in water-ethanol, (2) in water-acetone.

$^{31}\text{P}$  NMR clearly shows (in Fig. 8) that the decomposition pathway of tungstophosphate upon addition of NaOH is much simpler in water-ethanol and water-acetone than in aqueous solution. The  $\text{H}_3\text{PW}_{12}\text{O}_{40}$  anion remains intact in solution to pH ~8 with no peaks due to  $[\text{P}_2\text{W}_{19}\text{O}_{67}]^{10-}$  or  $[\text{P}_2\text{W}_{18}\text{O}_{62}]^{6-}$  being visible in the  $^{31}\text{P}$  NMR spectra. At pH = 8.6, decomposition of the anion is observable with a small amount of precipitate produced, which redissolves readily. At pH = 9.4, all the  $[\text{PW}_{12}\text{O}_{40}]^{3-}$  and  $[\text{P}_2\text{W}_{21}\text{O}_{71}]^{6-}$  anions have decomposed to form  $[\text{PW}_{11}\text{O}_{39}]^{7-}$  and  $[\text{PW}_9\text{O}_{34}]^{9-}$ , and eventually, when pH = 11.7, only  $\text{PO}_4^{3-}$  remains.

#### Mechanism of tungstophosphate variation with increasing pH

Based on the above experimental results, it may be considered that  $\text{H}_3\text{PW}_{12}\text{O}_{40}$  in aqueous solution decomposes with the following solution compositions in increasing pH:





The above mode for  $\text{H}_3\text{PW}_{12}\text{O}_{40}$  decomposition is similar to that proposed previously (17). However, our study clearly shows that although the lacunary  $[\text{PW}_{11}\text{O}_{39}]^{7-}$  anion is the main product of  $\text{H}_3\text{PW}_{12}\text{O}_{40}$  decomposition, it exists simultaneously with dimeric anions of tungstophosphate, i.e.,  $[\text{P}_2\text{W}_{21}\text{O}_{71}]^{6-}$ ,  $[\text{P}_2\text{W}_{18}\text{O}_{62}]^{6-}$ , and  $[\text{P}_2\text{W}_{19}\text{O}_{67}]^{10-}$ , in the region of pH 2–6. The relationship between  $[\text{PW}_{11}\text{O}_{39}]^{7-}$  and  $[\text{P}_2\text{W}_{21}\text{O}_{71}]^{6-}$  is not easy to observe or explain because the conversion from  $\text{H}_3\text{PW}_{12}\text{O}_{40}$  to  $[\text{PW}_{11}\text{O}_{39}]^{7-}$  and  $[\text{P}_2\text{W}_{21}\text{O}_{71}]^{6-}$  anions is too rapid to be studied in detail.

It has been considered in previous reports that  $[\text{P}_2\text{W}_{21}\text{O}_{71}]^{6-}$  was directly produced from  $[\text{PW}_{12}\text{O}_{40}]^{3-}$  decomposition. For example, the solute–support interaction between  $\text{H}_3\text{PW}_{12}\text{O}_{40}$  with  $\text{SiO}_2$  or  $\text{TiO}_2$  lead to partial transformation in  $[\text{P}_2\text{W}_{21}\text{O}_{71}]^{6-}$ , and contact of  $\text{H}_3\text{PW}_{12}\text{O}_{40}$  in ethanol–water solution with  $\text{Al}_2\text{O}_3$  gave rise to the  $[\text{P}_2\text{W}_{21}\text{O}_{71}]^{6-}$  species (15). During preparation of supported  $\text{H}_3\text{PW}_{12}\text{O}_{40}$  on  $\text{Al}_2\text{O}_3$ , the appearance of the dimeric species of  $[\text{P}_2\text{W}_{21}\text{O}_{71}]^{6-}$  was revealed by  $^{31}\text{P}$  NMR after a tungstophosphoric acid solution had contacted with basic  $\text{Al}_2\text{O}_3$ , which produced a substantial change of solution pH, from 1.1 to 4.0 (16).

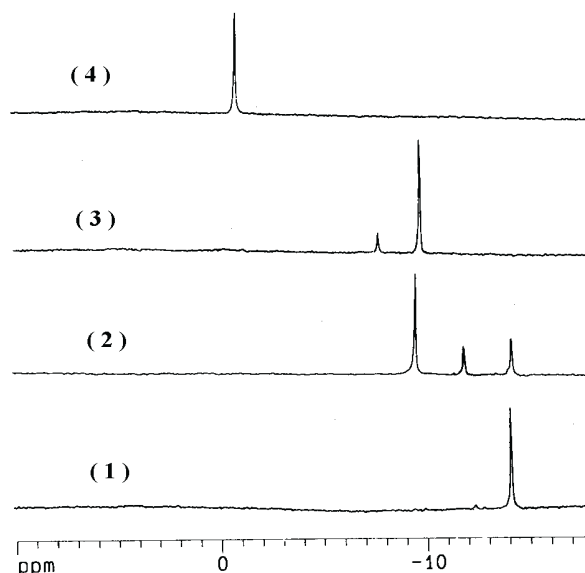
However, in the previous study of  $\text{H}_3\text{PW}_{12}\text{O}_{40}$  solution, it was found that  $\text{H}_3\text{PW}_{12}\text{O}_{40}$  decomposed initially to  $[\text{PW}_{11}\text{O}_{39}]^{7-}$  at diffusion-controlled rates at pH > 1.5 (21). It was also reported that  $\text{H}_3\text{PW}_{12}\text{O}_{40}$  decomposed to  $[\text{P}_2\text{W}_{21}\text{O}_{71}]^{6-}$ , and there was equilibrium between  $\text{H}_3\text{PW}_{12}\text{O}_{40}$  and  $[\text{P}_2\text{W}_{21}\text{O}_{71}]^{6-}$  at pH 1.3 ~ 2.3 (34). Besides, a very dilute solution of 1 wt%  $\text{H}_3\text{PW}_{12}\text{O}_{40}$  at pH ca. 2 decomposed to form the lacunary  $[\text{PW}_{11}\text{O}_{39}]^{7-}$  anion (14). It was reported that  $[\text{P}_2\text{W}_{18}\text{O}_{62}]^{6-}$  and  $[\text{P}_2\text{W}_{21}\text{O}_{71}]^{6-}$  were formed from  $[\text{PW}_{11}\text{O}_{39}]^{7-}$  decomposition during contact of  $[\text{PW}_{11}\text{O}_{39}]^{7-}$  with  $\text{TiO}_2$ , as well (15). Therefore, it is possible that a series of equilibria exists between  $[\text{PW}_{11}\text{O}_{39}]^{7-}$  and dimers in the tungstophosphate solution in the region of pH 2–6. It was reported that a similar equilibrium in the molybdophosphate system depended on solution pH (8), and that the cation in solution affected the rate of tungstophosphate decomposition (19). It may be considered that the ratio of  $[\text{PW}_{11}\text{O}_{39}]^{7-}$ : $[\text{P}_2\text{W}_{21}\text{O}_{71}]^{6-}$  in this equilibrium depends on both the pH and other ions in solution. As a result, many different results were obtained for a variety of tungstophosphate solutions. Therefore, during the conversion of the solution components described in the beginning of this paragraph, it may be considered that there are certain equilibria between these components, as follows:

(a) An equilibrium between  $[\text{PW}_{12}\text{O}_{40}]^{3-}$  and  $[\text{P}_2\text{W}_{21}\text{O}_{71}]^{6-}$  and  $[\text{PW}_{11}\text{O}_{39}]^{7-}$  at pH 2.2 ~ 3.5.

(b) An equilibrium between  $[\text{P}_2\text{W}_{21}\text{O}_{71}]^{6-}$  and  $[\text{PW}_{11}\text{O}_{39}]^{7-}$  at pH 2.2 ~ 5.4.

(c) An equilibrium between  $[\text{PW}_{11}\text{O}_{39}]^{7-}$  and  $[\text{P}_2\text{W}_{18}\text{O}_{62}]^{6-}$  at pH 3.5 ~ 5.4.

**Fig. 8.**  $^{31}\text{P}$  NMR spectra of tungstophosphate solution (water–acetone) formed during titration: (1) original  $\text{H}_3\text{PW}_{12}\text{O}_{40}$ , (2) pH = 8.6, (3) pH = 9.4, (4) pH = 11.7.



(d) An equilibrium between  $[\text{P}_2\text{W}_{19}\text{O}_{67}]^{10-}$  and  $[\text{P}_2\text{W}_{18}\text{O}_{62}]^{6-}$  at about pH 3.5.

The previous study has shown that the conversion of  $[\text{PW}_{12}\text{O}_{40}]^{3-}$  to  $[\text{PW}_{11}\text{O}_{39}]^{7-}$  takes only milliseconds, with  $[\text{PW}_{11}\text{O}_{39}]^{7-}$  to  $[\text{PW}_9\text{O}_{34}]^{9-}$  taking several seconds (18, 23). This conversion from  $[\text{PW}_{11}\text{O}_{39}]^{7-}$  and the dimeric species to  $[\text{PW}_9\text{O}_{34}]^{9-}$  is very rapid, and only a little NaOH leads to a rapid increase of solution pH and completion of the conversion. It was seen from the HPLC chromatogram (Fig. 3) and  $^{31}\text{P}$  NMR spectra (Fig. 2) that the  $[\text{PW}_9\text{O}_{34}]^{9-}$  anion alone is formed at about pH 6.8. This is in agreement with the previous investigation of tungstophosphate, which found that in weakly alkaline solutions of pH 7–9, the  $[\text{PW}_{11}\text{O}_{39}]^{7-}$  degradation into  $[\text{PW}_9\text{O}_{34}]^{9-}$  anion takes place rapidly, but the period for the total decomposition to  $\text{PO}_4^{3-}$  varies from minutes to hours, depending on temperature and pH (23). It is observed in this study that the decomposition of  $[\text{PW}_9\text{O}_{34}]^{9-}$  to  $\text{PO}_4^{3-}$  is relatively slow, and the velocity of  $[\text{PW}_9\text{O}_{34}]^{9-}$  decomposition increases with increasing pH and temperature. It is easy to understand that the complete destruction of the lacunary Keggin structure needs higher activation energy than the removal of  $\text{W}=\text{O}$  units from the lacunary Keggin structure.

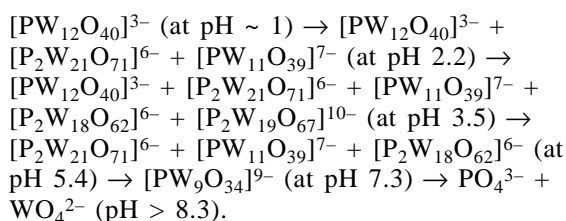
It has been suggested previously that this enhanced stability results from protons being only partially removed by organic solvents. It was found that  $\text{H}_3\text{PW}_{12}\text{O}_{40}$  was completely deprotonated in aqueous solution and partially deprotonated in polar organic solvent (35, 36) and that protons may stabilize tungstophosphate anions by decreasing the intramolecular repulsion in the interior structure of the Keggin unit. It is well established that organic molecules in solution can reduce the dissociation of protons from a conjugate base. As a result, the proton activity of  $\text{H}_3\text{PW}_{12}\text{O}_{40}$  acid decreases and the stability of the acid increases in organic solvents. On the other hand, the action of water molecules on tungstophosphate anions is weakened by absorption of organic mole-



cules, with the hydration number of tungstophosphoric acids decreasing. Anion repulsion also plays a role with anion–anion repulsion being more intense than that corresponding to aqueous or acidified-with-HCl solutions (37).

## Conclusion

$\text{H}_3\text{PW}_{12}\text{O}_{40}$  decomposition with NaOH addition in aqueous solution may be divided into two stages. In the first stages at  $\text{pH} < 8$ ,  $\text{H}_3\text{PW}_{12}\text{O}_{40}$  decomposes partially with removal of  $\text{W=O}$  units. In the second stage at  $\text{pH} > 8$ , tungstophosphoric acid completely decomposes to  $\text{PO}_4^{3-}$ . As well, a series of equilibria exists between  $[\text{PW}_{11}\text{O}_{39}]^{7-}$  and tungstophosphate dimers in solution at  $\text{pH}$  2–6, depending on the  $\text{pH}$  and the other ions in solution. It may be considered that  $\text{H}_3\text{PW}_{12}\text{O}_{40}$  in aqueous solution decomposes in increasing  $\text{pH}$  with the following solution compositions:



A normal endpoint of acid–base titration may be observed at an exact ratio of 3  $\text{OH}^-$ : $\text{H}_3\text{PW}_{12}\text{O}_{40}$ , which indicates that the  $\text{H}_3\text{PW}_{12}\text{O}_{40}$  anion is stable in  $\text{pH} < 8$  water–ethanol or acetone solution. The proton activity of  $\text{H}_3\text{PW}_{12}\text{O}_{40}$  acid decreases and the stability of the acid increases in the presence of organic solvents. On the other hand, the action of water molecules on tungstophosphate anions is weakened by absorption of organic molecules.

## References

1. M.T. Pope and A. Muller. *Polyoxometalate chemistry*. Kluwer, New York. 2001.
2. M.T. Pope and A. Muller. *Angew. Chem. Int. Ed. Eng.* **30**, 34 (1991).
3. C.L. Hill. *Chem. Rev.* **98**, 1 (1998).
4. K.H. Tytko and O. Glemser. *Inorg. Synth.* **27**, 71 (1990).
5. W. Turek, E.S. Pomarzenska, A. Pron, and J. Haber. *J. Catal.* **189**, 297 (2000).
6. I.V. Kozhevnikov, A. Sinnema, R.J.J. Jansen, and H. Van Bekkum. *Catal. Lett.* **27**, 187 (1994).
7. K.S. Suslick, J.C. Cook, B. Rapko, M.W. Droege, and R.G. Finke. *Inorg. Chem.* **25**, 241 (1986).
8. L. Pettersson, I. Andersson, and L.O. Ohman. *Inorg. Chem.* **25**, 4726 (1986).
9. J.A. Veen, O. Sudmeijer, C. Emeis, and H. Dewit. *J. Chem. Soc. Dalton Trans.* 1825 (1986).
10. K.C. Kim, M.T. Pope, G.J. Gama, and M.H. Dickman. *J. Am. Chem. Soc.* **121**, 11 164 (1999).
11. M. Misono, N. Mizuno, K. Katamurn, K. Ksai, Y. Sakata, T. Okuhara, and Y. Yoneda. *Bull. Chem. Soc. Jpn.* **55**, 400 (1982).
12. I.V. Kozhevnikov and K.I. Matveev. *Appl. Catal. A*, **5**, 135 (1983).
13. N. Nowinska, R. Fiedorov, and J. Adamiec. *J. Chem. Soc. Faraday Trans.* **87**, 749 (1991).
14. I.V. Kozhevnikov. *Catal. Lett.* **27**, 187 (1994).
15. L.R. Pizzio, C.V. Caceres, and M.N. Blanco. *Appl. Surf. Sci.* **151**, 99 (1999).
16. L.R. Pizzio, C.V. Caceres, and M.N. Blanco. *Appl. Catal.* **167**, 283 (1998).
17. M.T. Pope. *Heteropoly and isopolyoxometalates*. Springer, New York. 1983.
18. D.L. Kepert and J.H. Kyle. *J. Chem. Soc. Dalton Trans.* 137 (1978).
19. D.L. Kepert and J.H. Kyle. *J. Chem. Soc. Dalton Trans.* 1781 (1978).
20. L.G. Detusheva, E.N. Yurchenko, S.T. Khankhasaeva, I.V. Kozhevnikov, T.P. Lazarenko, and R.I. Maksimovskaya. *Koord. Khim.* **16**, 619 (1990).
21. R.I. Maksimovskaya. *Neorg. Khim. (Itogi Nauki Tekh.)*, **43**, 1960 (1998).
22. F. Marme, G. Condurier, and J.C. Vedrine. *Microporous Mesoporous Mater.* **22**, 151 (1998).
23. J.H. Kyle. *J. Chem. Soc. Dalton Trans.* 2609 (1983).
24. G.P. Vazquez, M.N. Blanco, and C.V. Caceres. *Catal. Lett.* **60**, 205 (1999).
25. Z. Zhu, Z. Xie, Y. Chen, E. Wang and Y. Yao. *React. Kinet. Catal. Lett.* **70**, 379 (2000).
26. N. Sakurai, K. Kadohata, N. Ichinose, and Z. Fresenius. *Anal. Chem.* **314**, 634 (1983).
27. M. Braungart and H. Russel. *Chromatographia*, **19**, 185 (1984).
28. A.D. Kirk, W. Riske, D.K. Lyon, B. Rapko, and R.G. Finke. *Inorg. Chem.* **28**, 792 (1989).
29. Y. Ying and M. Zhu. *Acta Chem. Soc. Chin.* **51**, 386 (1993).
30. M.H. Zhu and Y.P. Wang. *Chin. J. Chromatogr.* **10**, 320 (1997).
31. K. Nomiya, Y. Sugie, K. Amimoto, and M. Miwa. *Polyhedron*, **6**, 519 (1987).
32. R. Massart, R. Contant, J. Fruchart, J. Ciabrini, and M. Fournier. *Inorg. Chem.* **16**, 2916 (1977).
33. W.H. Knoch, P.J. Domallie, and R.D. Farlee. *Organometallics*, **4**, 62 (1985).
34. L.R. Pizzio, C.V. Caceres, and M.N. Blanco. *J. Colloid Interface Sci.* **190**, 318 (1997).
35. I.V. Kozhevnikov. *Russ. Chem. Rev.* **56**, 811 (1987); **62**, 473 (1993).
36. Y. Izumi, K. Urabe, and M. Onaka. *Zeolite, clay and heteropoly acid in organic reaction*. Kodansha/VCH, Tokyo. 1992.
37. M. Castillo, P. Vazquez, C. Caceres, and M. Blanco. *J. Chem. Soc. Faraday Trans.* **92**, 2997 (1996).



# Supercritical argon as a mobile phase for the flame photometric detection of sulfur

Kevin B. Thurbide and Brad W. Cooke

**Abstract:** The background emission properties of supercritical argon and supercritical carbon dioxide mobile phases in packed column supercritical fluid chromatography (pSFC) with flame photometric detection (FPD) were compared. As column flow rates were increased toward common values used in pSFC, the carbon dioxide background emission grew enormously. The resulting emission spectrum displayed dominant features at wavelengths between 325 and 525 nm, consisting of a complex series of overlapping molecular emission band systems partly attributed to CO\* and CH\*. By comparison, when using the same flow rates with a supercritical argon mobile phase, the background emission was identical to that of the FPD flame without column effluent. In terms of intensity, when using a column flow rate of 2 mL/min, supercritical carbon dioxide contributes a background emission in the FPD that is about  $3 \times 10^5$  times larger than that produced by supercritical argon. This difference leads to an improvement of two orders of magnitude in the pSFC-FPD signal-to-noise ratio for sulfur when a supercritical argon mobile phase is used. Results indicate that supercritical argon could also be advantageous for the pSFC-FPD analysis of other elements.

**Key words:** supercritical fluid chromatography, packed column, flame photometric detection, supercritical argon.

**Résumé :** On a comparé les propriétés de l'émission ambiante des phases mobiles de l'argon et du dioxyde de carbone supracritiques en chromatographie à fluide supracritique dans une colonne à remplissage (CFSr) avec détection photométrique à flamme (DPF). L'émission ambiante du dioxyde de carbone croît énormément lorsque l'on augmente la vitesse d'écoulement de la colonne vers les valeurs couramment utilisées en CFSr. Le spectre d'émission résultant révèle des caractéristiques importantes à des longueurs d'onde comprises entre 325 et 525 nm, consistant en une série complexes due au recouvrement des systèmes de bandes d'émission moléculaire que l'on attribue partiellement au CO\* et au CH\*. En comparaison lorsqu'on utilise la même vitesse d'écoulement pour la phase mobile de l'argon supracritique l'émission ambiante est identique à celle de la flamme DPF sans l'effluent de la colonne. En termes d'intensité, lorsque l'on utilise une vitesse d'écoulement de 2 mL/min, la contribution du dioxyde de carbone supracritique à l'émission ambiante dans le DPF est d'environ  $3 \times 10^5$  fois plus élevée que celle due l'argon supracritique. Cette différence conduit à une amélioration de deux ordres de grandeur du rapport signal : bruit pour le soufre lorsque l'on utilise une phase mobile d'argon supracritique. Les résultats indiquent que l'argon supracritique peut aussi être avantageux pour l'analyse par CFSr-DPF d'autres éléments.

**Mots clés :** chromatographie à fluide supracritique, colonne à remplissage, détection photométrique à flamme, argon supracritique.

[Traduit par la Rédaction]

## Introduction

Packed column supercritical fluid chromatography (pSFC) is being used in an increasing number of applications and provides a complimentary separation method to conventional high performance liquid chromatography (HPLC) and gas chromatography (GC) (1, 2). This is mainly attributed to the increased speed and selectivity that pSFC can offer, compared with HPLC, and the wider range of compounds that can be analyzed by pSFC relative to GC (3, 4). Carbon diox-

ide is the most common mobile phase in pSFC, and since it decompresses to a gas after leaving the separation column, pSFC can also greatly facilitate the union of HPLC-type separations with conventional gas-phase GC detectors. While numerous applications of this method using the universal flame ionization detector have been reported (1, 2, 5), specific GC sensors such as the electron capture and thermionic detectors have also been used in pSFC (6). One of the most common selective GC detectors used for the specific analysis of sulfur is the well-known flame photometric detector (FPD), which is based on chemiluminescence emanating from a low-temperature, fuel-rich, hydrogen-air flame (7).

Previously, a thorough optimization of the use of FPD to monitor sulfur in capillary column supercritical fluid chromatography (cSFC) has been reported (8, 9). The authors achieved very good detection limits for sulfur and demonstrated that cSFC-FPD yields a performance that is similar

Received 9 April 2003. Published on the NRC Research Press Web site at <http://canjchem.nrc.ca> on 19 September 2003.

**K.B. Thurbide<sup>1</sup> and B.W. Cooke.** Department of Chemistry, University of Calgary, 2500 University Drive, NW, Calgary, AB T2N 1N4, Canada.

<sup>1</sup>Corresponding author (e-mail: [thurbide@ucalgary.ca](mailto:thurbide@ucalgary.ca)).



to conventional GC-FPD in many respects. A major obstacle noted in that work and others in this area is the large background emission that is observed in the FPD flame when carbon dioxide is used as the mobile phase (8–10). This can interfere with the detection of sulfur emission in the FPD and leads to baseline variations when the column flow is changed. As such, the need to reduce this background emission was cited as being extremely important in regards to the performance of the detector.

In addition to independent control of flow and pressure, modern pSFC instruments also use much larger columns and mobile phase volumes compared with cSFC (6). For instance, the typical column flow rate of 40  $\mu\text{L}/\text{min}$  used in previous cSFC-FPD studies generated about 14 mL/min of carbon dioxide gas directed into the FPD. In contrast to this, pSFC commonly uses column flow rates of about 2–3 mL/min, which translates into over 1000 mL/min of carbon dioxide gas upon decompression. As such, the background emission of a typical FPD can be expected to increase dramatically and cause much greater interference with the use of pSFC as compared with cSFC. In relation to this, the FPD literature in this area is dominated by cSFC applications (8–11). While it is possible to operate pSFC-FPD in the split mode, where only a portion of the column effluent and analyte are directed into the detector, this option is often less desirable because of the variable split ratio and detailed design considerations associated with such pSFC interfaces (6, 12, 13).

An interesting, alternative mobile phase used in recent years is supercritical argon (critical point: 48 atm (1 atm = 101.325 kPa) and  $-122\text{ }^{\circ}\text{C}$ ), which can be readily produced by conventional pumping instrumentation and has been shown to provide similar performance to that of supercritical carbon dioxide (critical point: 72 atm and  $31\text{ }^{\circ}\text{C}$ ) (14). In addition to its low cost, inertness, and available purity, other significant advantages of using supercritical argon as a mobile phase include its optical transparency in infrared analyses and its compatibility with the determination of nonmetals by inductively coupled plasma atomic emission spectroscopy (15). Whereas, in this method, supercritical carbon dioxide can create a very large background signal, the use of supercritical argon eliminates this problem since argon is also the plasma reagent gas. Further, while supercritical xenon can offer some similar benefits, it is much more expensive, and other inert gases such as nitrogen and helium are much less efficient as supercritical mobile phases when compared with carbon dioxide (14, 16). Thus it would be interesting to examine the improvements that might be offered by using this approach in pSFC-FPD. However, no reports comparing the use of supercritical argon and supercritical carbon dioxide as mobile phases in this detector have appeared.

Considering the lack of available information and the potential difficulties regarding the operation of a splitless pSFC-FPD system, it would be useful to acquire more knowledge of the interference presented by high flows of carbon dioxide in the FPD. Particularly beneficial would be more insight into the spectral distribution of the carbon dioxide background emission and how it impacts the performance of this widely used detector (17–19). Such information would be helpful since more than twenty other elements besides sulfur are known to provide useful analyti-

cal emission in the visible wavelength range of the FPD (20). Finally, since it could provide potential improvements in this area, it would be interesting to evaluate how the FPD performance when using supercritical argon compares with that obtained when using supercritical carbon dioxide. This paper presents a comparison of the spectral distribution and relative intensity of the FPD background emission obtained from using a supercritical carbon dioxide and a supercritical argon mobile phase under typical pSFC conditions. To gauge the effects of any differences observed, the performance of the FPD in the detection of sulfur, using each of these mobile phases under optimized conditions, will also be compared.

## Experimental

The pSFC system used was a Gilson series SF3 (Gilson, Villiers-le-Bel, France) comprised of a dual reciprocating pump – solvent delivery system (model 308 and 306), a column oven (model 831), a back pressure regulator (model 821), and an evaporative light scattering detector (ELSD; Sedere, CEDEX, France). This system is designed to facilitate delivery of the mobile phase by continually cooling the pump heads with chilled water (typically  $-5$  to  $5\text{ }^{\circ}\text{C}$ ) from a refrigerated circulating bath. A 250 mm  $\times$  4.6 mm i.d. Lichrosorb Diol column (10  $\mu\text{m}$  particles; Alltech, Deerfield, IL, U.S.A.) was used for separations. The GC-FPD system used for adaptation to the pSFC instrument was a Shimadzu model GC-8A (Shimadzu, Kyoto, Japan). Flame emissions were monitored using an R-1104 photomultiplier tube (PMT) (wavelength range of 185–850 nm; Hamamatsu, Bridgewater, NJ). Spectra were acquired using a 1/4 m Jarrell-Ash monochromator (1180 lines/mm grating, 3 nm/mm bandpass). Instrument-grade carbon dioxide and high purity hydrogen, air, and argon were obtained from Praxair (Praxair, Calgary, AB, Canada). Tetrahydrothiophene (99%) and carbon disulfide (99.9%) were used as obtained from Aldrich (Aldrich, Oakville, ON, Canada).

The FPD is connected downstream from the back pressure regulator, where the ELSD is normally attached via a splitless interface (6). With the ELSD disconnected, a 4 foot (1 foot = 0.3048 m) length of 1/16" (1" = 25.4 mm)  $\times$  0.01" i.d. stainless steel tubing (Alltech) is instead used to guide the effluent from the pSFC into the GC oven through a side port. Using a stainless steel zero dead volume union (Alltech), this tubing is connected to a 20 cm length of 0.10 mm i.d. deactivated, fused-silica restrictor tubing (Alltech), which extends into the base of the FPD burner. In this way, the pSFC effluent combines with the hydrogen and flows concentrically around the central tube, delivering air to the flame. The restrictor position within this arrangement was not found to critically affect the flame stability or response. However, optimal conditions for this transfer line were realized when the GC oven was maintained above  $60\text{ }^{\circ}\text{C}$  and the FPD detector base was maintained at  $250\text{ }^{\circ}\text{C}$ . The pSFC oven was normally operated at  $60\text{ }^{\circ}\text{C}$ , and the typical FPD flame gas-flow rates used were 300 mL/min of hydrogen and 90 mL/min of air. Variations on these conditions are outlined in the text.

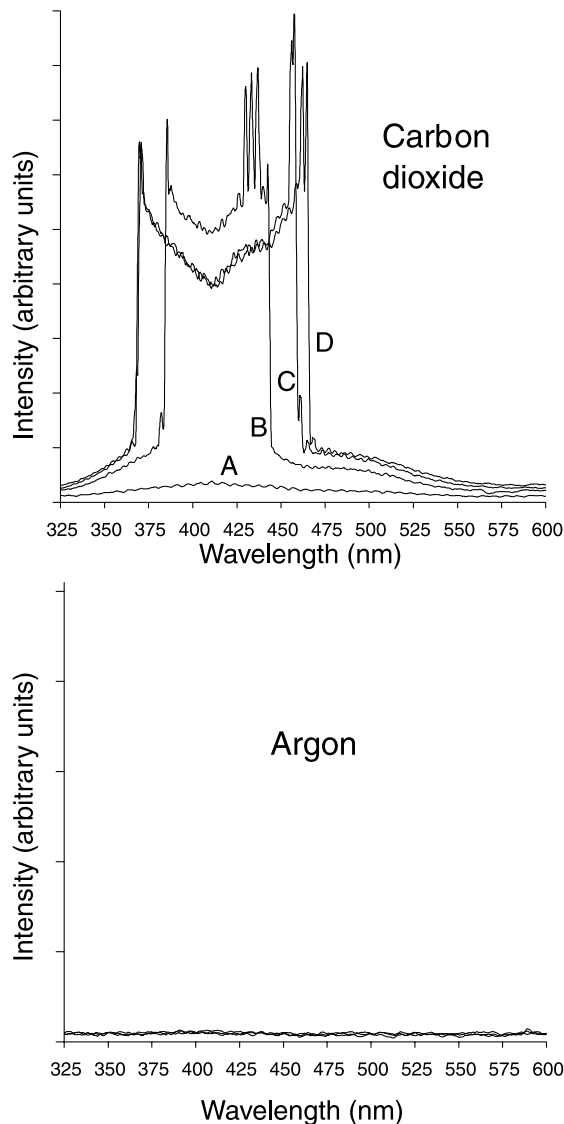


## Results and discussion

Given the much larger flow rates in pSFC compared with cSFC, it might be anticipated that flame instability in the FPD could be a problem. However, this was not found to be the case, and the flame remained very stable over a wide range of column flow rates tested — up to 5 mL/min — with no visible signs of flicker or lift off from the burner. The steady interface between the mobile phase and the flame is certainly facilitated by the smooth transition of supercritical carbon dioxide into a gas upon decompression. More importantly, however, this stability in the presence of several liters per minute of carbon dioxide gas flow is a result of the burner configuration, which has the hydrogen and the column effluent enter concentrically about the central tube delivering air to the flame, as is common in GC-FPD (7). Since the FPD flame relies upon a very hydrogen-rich stoichiometry to deliver response, this arrangement prevents solvent peaks and, in this case, large flows of carbon dioxide from diluting and starving the flame of oxygen, causing it to extinguish. Similar attempts to introduce the column effluent through the central air tube caused the flame to extinguish at pSFC flow rates of less than 0.5 mL/min.

Although the flame remained stable at large column flow rates, it was visually clear that, as the flow of carbon dioxide increased in the detector, the flame luminescence grew from barely observable to an intense blue emission. To examine the features of this background emission and how it might be affected by varying amounts of carbon dioxide, spectra of the FPD flame were acquired using several pSFC column flow rates. Figure 1 displays these spectra and indicates that the emission from carbon dioxide in the FPD is predominantly situated between 325 and 525 nm. At a low column flow rate of 0.5 mL/min (trace A), the blue flame emission stems from a distribution of narrowly spaced bands that appear to reside upon an underlying continuum. Although no flame spectra under pSFC-FPD conditions have been reported, this spectrum does agree very well with the “carbon monoxide flame bands” of CO<sub>2</sub> (21), which were also speculated earlier as the background emission source in cSFC-FPD (8). Therefore, at this low pSFC flow rate (which is about ten times larger than those used in cSFC), the FPD background emission features still appear similar for the two methods. However, as the flow rates are increased to more common pSFC values of 1 mL/min and greater, the background emission becomes enormous and assumes a very complex appearance. Gaydon details several molecular emission band systems obtained from excited CO (21) that could possibly be ascribed to the luminescence observed for carbon dioxide in the FPD flame. Owing to the overlapping wavelengths of many of the systems described, an exact identification of some of the spectral features presented in Fig. 1 could not be firmly established; however, certain interesting correlations can be noted. For instance, the bands superimposed on the spectrum obtained at a flow rate of 1 mL/min (trace B) match very well with those assigned for excited CH, which is also commonly found for carbon emission in GC-FPD (20, 21). As the flow rate increases to 1.5 and 2 mL/min (traces C and D, respectively), the spectra broaden and resemble the distribution features of Emeléus’s cool-flame formaldehyde spectrum and also those noted for the comet-tail system of excited CO emission (21). Also in-

**Fig. 1.** Upper trace: the emission spectrum of carbon dioxide in the FPD at pSFC column flow rates of 0.5 (A), 1.0 (B), 1.5 (C), and 2.0 (D) mL/min and a pressure of 15 MPa. Lower trace: the emission spectrum of argon in the FPD at pSFC flow rates of 2.0, 3.0, and 4.0 mL/min (superimposed) and a pressure of 27 MPa. Flame gas flow rates are 300 mL/min of hydrogen and 100 mL/min of air. The bandpass is 1.5 nm.



teresting is that, despite the large flow of carbon as CO<sub>2</sub> in the FPD flame, no evidence of excited C<sub>2</sub> emission was observed, which is another common feature in GC-FPD carbon spectra (20).

The most significant feature realized from the spectra in Fig. 1 is that the carbon dioxide background emission is distributed over exactly the same wavelength range as that produced by sulfur emission in the FPD, which is used for analytical purposes to measure quadratic S<sub>2</sub>\* response (7). While some methods add a sulfur compound to the mobile phase in attempts to linearize this response, the same sulfur emission spectrum is produced (7). Therefore, serious interference from this carbon dioxide background emission should be anticipated in the pSFC-FPD analysis of sulfur and other elements that are monitored in this wavelength



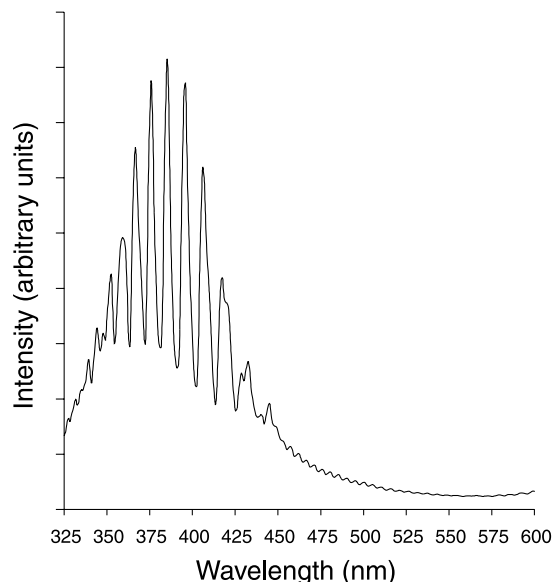
range (e.g., manganese atomic lines and tin quartz surface emission) (7, 20). By comparison, other elements emitting outside of this range should be less affected. For example, earlier cSFC-FPD studies in which analyte emissions of phosphorus at 530 nm and of tin (gas-phase emission) at 610 nm (which are more remote to the carbon dioxide emission spectrum shown in Fig. 1) were monitored, less interference from baseline variations was observed when the column flow rate was changed (10, 11). This is understandable considering that the carbon dioxide emission shown in Fig. 1 is reduced by a factor of about ten between the 400 and 530 nm wavelength regions where sulfur and phosphorus are, respectively, monitored.

In this context, it is interesting to note that "pulsed" FPD methods can temporally resolve sulfur and carbon emissions to yield less interference and greater selectivity (22). However, it is unknown if such benefits could be extended to pSFC-FPD since it greatly depends on the emission spectrum of carbon dioxide in that detector and its time dependence relative to other analytical emissions under typical pSFC conditions. Thus, although such investigations are beyond the scope of the current study, this approach could be potentially useful.

Also presented in Fig. 1 is the FPD background emission, generated when a supercritical argon mobile phase is introduced at pSFC flow rates equal to or greater than those examined for supercritical carbon dioxide. As can be seen, even when using substantial flows of 4 mL/min of supercritical argon, no spectral features are observed and the background emission remains steady. In fact, for all of the flows investigated, supercritical argon produced the same spectra and emission intensities as that of the FPD flame without any column effluent. This lack of variation implies that argon provides little or no emission in the FPD and is consistent with visual observations of the flame under these conditions, which showed no change when supercritical argon was introduced into it. This finding, while somewhat expected, agrees with the conditions of the relatively cool, small FPD flame compared with the larger, high-temperature flames and plasmas used as excitation sources in conventional spectroscopy (20). For example, in contrast to the thermal luminescence produced in those methods, emission in the FPD is generated by chemiluminescence, which is favored by cooler flame conditions (7). Further, it has been estimated that the FPD yields a maximum excitation energy of 3.6 eV, which is far lower than the excitation potentials associated with argon emission lines (20, 23). While traces of a molecular emission system due to excited ArO is also known to occur near 558 nm (21), no evidence of this exists in Fig. 1, also possibly as a result of the low-temperature, hydrogen-rich conditions under which the FPD is operated.

The essentially unobstructed background spectrum obtained with supercritical argon in the FPD makes it potentially much more suitable than supercritical carbon dioxide for monitoring the emission of sulfur and other elements by pSFC-FPD. Figure 2 illustrates this with the spectrum of sulfur emission in the FPD using a supercritical argon mobile phase. This spectrum clearly displays the characteristic  $S_2^*$  emission bands of sulfur chemiluminescence in the FPD and, compared with Fig. 1, demonstrates that the emissions

**Fig. 2.** The emission spectrum of sulfur (as carbon disulfide) in the FPD using 2.0 mL/min of supercritical argon as the pSFC mobile phase. Other conditions as for supercritical argon in Fig. 1.



of sulfur and carbon dioxide severely overlap in this detector under pSFC conditions.

To better gauge the relative background emission that each mobile phase generates in the FPD, the flame intensity was monitored at various column flow rates with the two supercritical fluids. Figure 3 shows the background emission of the FPD as a function of supercritical carbon dioxide column flow rates tested up to 4 mL/min. As seen in the figure, even at modest flow rates of supercritical carbon dioxide, the background increases by about 5 orders of magnitude. In comparison to this, similar flows of supercritical argon produce no increase in the observed background emission of the FPD flame. Given the considerable difference between the two, supercritical argon should generate much less interference than supercritical carbon dioxide when emission in the FPD is monitored, particularly for elements such as sulfur that emit in the 400 nm wavelength region.

Figure 4 demonstrates this with the sulfur response obtained for a series of tetrahydrothiophene standard solutions monitored in the FPD under the same optimum flame conditions for both a supercritical argon and a supercritical carbon dioxide mobile phase. The response is measured as the sulfur signal-to-noise (i.e., peak-to-peak fluctuations of the baseline) ratio, and as seen in the figure, it greatly differs between the two mobile phases. When using supercritical carbon dioxide, the sulfur response increases over two orders of magnitude to an upper mass flow limit of about 0.1  $\mu$ g of sulfur per second. In terms of detectivity (i.e., corresponding to a signal-to-noise ratio of two), the response yields a mass flow detection limit of almost 1 ng of sulfur per second. This value is about 25 times larger than the average value of the sulfur detection limits reported for cSFC-FPD (8), which is reasonable, considering the much greater column flow rate used in the current pSFC experiments. It should be noted that the data in Fig. 4 were obtained in the open



**Fig. 3.** A comparison of the relative background emission intensity generated in the pSFC-FPD system using a supercritical argon (■) and a supercritical carbon dioxide (●) mobile phase at various column flow rates. Conditions as in Fig. 1.

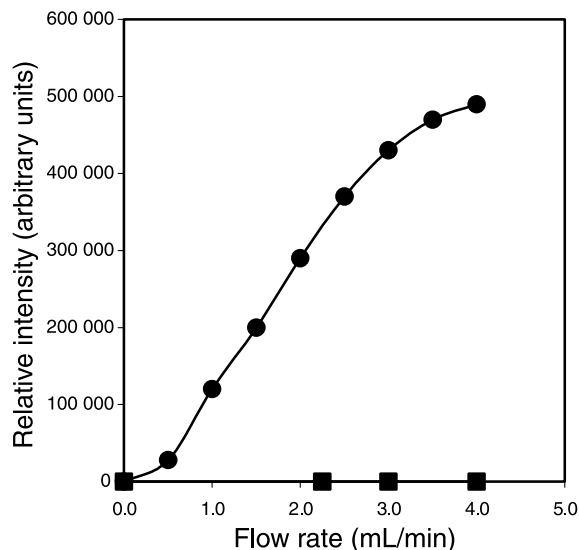
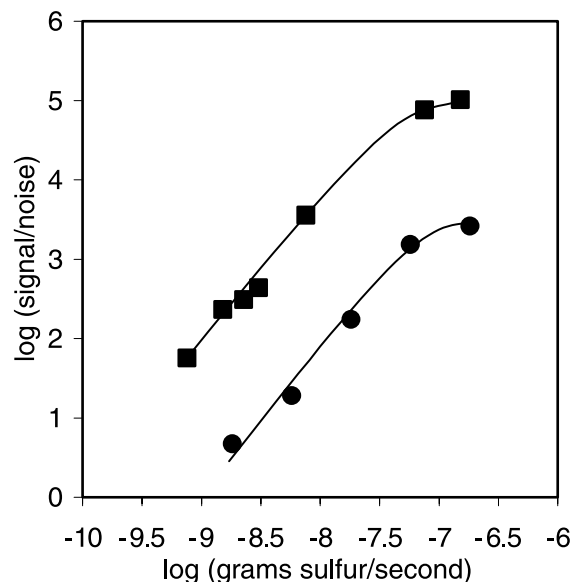


**Fig. 4.** The pSFC-FPD system response toward varying amounts of sulfur (as tetrahydrothiophene) using a supercritical argon (■) mobile phase at 2.5 mL/min and 28 MPa and a supercritical carbon dioxide (●) mobile phase at 2.0 mL/min and 15 MPa. Flame gas flow rates are 300 mL/min of hydrogen and 90 mL/min of air.



nonwavelength dispersive mode, which is often employed in GC-FPD to increase sensitivity by monitoring a greater fraction of the analyte emission bands. While narrow-band interference filters can also be employed to increase the selectivity of sulfur response over other flame emissions, this is usually accompanied by a decrease in sensitivity (20). Not surprisingly then, owing to the direct overlap of the sulfur and the carbon dioxide emission bands in the FPD, the

use of such filters in these experiments did not improve the discrimination between the two and only further reduced sensitivity.

By comparison, in Fig. 4, the sulfur response over the same concentration range is much improved when a supercritical argon mobile phase is used. As expected, the resulting curve yields the same slope and upper calibration limit; however, the response is increased by nearly two orders of magnitude. Since the flame conditions were not varied, this finding can be directly attributed to the large decrease in background emission obtained when using supercritical argon in the FPD. Previous GC-FPD studies have verified that the peak-to-peak baseline noise increases as a square-root function of the background emission intensity if the noise is random and increases proportionally if the noise becomes correlated with the signal at higher levels (24). As observed, the difference in the background emission intensity of Fig. 3 (i.e., about  $1 \times 10^5$ ) and the corresponding difference in the signal-to-noise ratio of Fig. 4 (i.e., about  $1 \times 10^2$ ) is related by greater than a square-root function. This suggests that the high level of carbon dioxide in pSFC-FPD also generates flame noise that is not entirely random in nature, which differs from earlier studies using supercritical carbon dioxide that showed cSFC-FPD to be shot-noise limited (9). In the absence of carbon dioxide, as a result of the nearly quadratic sulfur response in the FPD, the improved signal-to-noise ratio when supercritical argon is used translates into a minimum detectable flow of about 100 pg of sulfur per second. In contrast to the above, this value, obtained from the pSFC-FPD system, compares quite well to those reported for cSFC-FPD (8). Thus, relative to a conventional supercritical carbon dioxide mobile phase, supercritical argon can provide improved sulfur detection limits in pSFC-FPD by greatly reducing the background emission to levels on the same order as the FPD flame itself. This also indicates that supercritical argon may be advantageous for the pSFC-FPD analysis of other elements.

## Acknowledgements

An operating grant in support of this work was provided by the Natural Sciences and Engineering Research Council of Canada (NSERC).

## References

1. T.L. Chester, J.D. Pinkston, and D.E. Raynie. *Anal. Chem.* **70**, 301R (1998).
2. T.L. Chester and J.D. Pinkston. *Anal. Chem.* **74**, 2801 (2002).
3. M.C. Ventura, W.P. Farrell, C.M. Aurigemma, and M.J. Greig. *Anal. Chem.* **71**, 2410 (1999).
4. M.C. Ventura, W.P. Farrell, C.M. Aurigemma, and M.J. Greig. *Anal. Chem.* **71**, 4223 (1999).
5. D.R.P. Thiébaud and E.C. Robert. *Analysis*, **27**, 681 (1999).
6. T.A. Berger. In *Supercritical fluid chromatography with packed columns: Techniques and applications*. Edited by K. Anton and C. Berger. Marcel Dekker, New York, 1998. Chap 2; F. Véron and K. Coleman. In *Supercritical fluid chromatography with packed columns: Techniques and applications*. Edited by K. Anton and C. Berger. Marcel Dekker, New York, 1998. Chap 3.



7. M. Dressler. *In* Selective gas chromatographic detectors, journal of chromatography library. Vol. 36. Elsevier, Amsterdam. 1986. Chap 7.
8. S.V. Olesik, L.A. Pekay, and E.A. Paliwoda. *Anal. Chem.* **61**, 58 (1989).
9. L.A. Pekay and S.V. Olesik. *Anal. Chem.* **61**, 2616 (1989).
10. K.E. Markides, E.D. Lee, R. Bolick, and M.L. Lee. *Anal. Chem.* **58**, 740 (1986).
11. J. Dachs and J.M. Bayona. *J. Chromatogr.* **636**, 277 (1993).
12. H. Koizumi and Y. Suzuki. *Anal. Sci.* **7**, 241 (1991).
13. T.A. Berger and B.S. Todd. *Chromatographia*, **54**, 777 (2001).
14. S. Liang and D.C. Tilotta. *Anal. Chem.* **70**, 616 (1998).
15. S. Liang and D.C. Tilotta. *Anal. Chem.* **70**, 4487 (1998).
16. J.W. King and Z. Zhang. *Anal. Chem.* **70**, 1431 (1998).
17. C.H. Wang, S.S. Lin, W.U. Hwang, and H.S. Weng. *Ind. Eng. Chem. Res.* **41**, 666 (2002).
18. A. Macone, M. Nardini, A. Antonucci, A. Maggio, and R.M. Matarese. *J. Agric. Food Chem.* **50**, 2169 (2002).
19. S. Otsuki, T. Nonaka, N. Takashima, W. Qian, A. Ishihara, T. Imai, and T. Kabe. *Energy Fuels*, **14**, 1232 (2000).
20. X-Y. Sun, B. Millier, and W.A. Aue. *Can. J. Chem.* **70**, 1129 (1992).
21. R.W.P. Pearse and A.G. Gaydon. *The identification of molecular spectra*. 4th ed. Chapman and Hall, London. 1976.
22. S. Cheskis, E. Atar, and A. Amirav. *Anal. Chem.* **65**, 539 (1993).
23. A.N. Zaidel', V.K. Prokof'ev, S.M. Raiskii, V.A. Slavnyi, and E.Ya. Shreider. *Tables of spectral lines*. 3rd ed. Plenum, New York. 1970.
24. W.A. Aue, H. Singh, and X-Y. Sun. *J. Chromatogr.* **687**, 283 (1994).



# An ionic liquid mediated Friedel–Crafts addition of arenes to isothiocyanates

Prashant U. Naik, Susheel J. Nara, Jitendra R. Harjani, and  
Manikrao M. Salunkhe

**Abstract:** A new protocol is developed for the synthesis of *N*-substituted thioamides, employing arenes and isothiocyanates in 1-butyl-3-methylimidazolium chloroaluminate ionic liquid, [bmim]Cl·2AlCl<sub>3</sub>, as a homogenous Lewis acid catalyst and solvent. The effect of Lewis acidity and the stoichiometry of the ionic liquid on the extent of product formation is studied. Studies reveal that a progressive increase in yields was observed with increasing Lewis acidity, and two equivalents of [bmim]Cl·2AlCl<sub>3</sub> was the optimal amount for the reaction. A distinct *para* selectivity for the incoming thioamido group on activated arenes was observed under ambient conditions.

**Key words:** arenes, isothiocyanates, Friedel–Crafts, ionic liquids, thioamides.

**Résumé :** On a développé un nouveau protocole pour la synthèse de thioamides *N*-substitués qui fait appel à l'utilisation d'arènes et d'isothiocyanates dans du chloroaluminate de 1-butyl-3-méthylimidazolium, [bmim]Cl·2AlCl<sub>3</sub>, un liquide ionique qui agit comme catalyseur acide de Lewis homogène et comme solvant. On a étudié l'effet de l'acidité de Lewis et la stoechiométrie du liquide ionique sur le niveau de formation du produit. Les études révèlent qu'une augmentation progressive des rendements peut être observée avec une augmentation de l'acidité de Lewis et que deux équivalents de [bmim]Cl·2AlCl<sub>3</sub> correspond à la quantité optimale pour la réaction. Dans les conditions ambiantes, on a observé une sélectivité *para* pour le groupe thioamido qui s'insère sur les arènes activés.

**Mots clés :** arènes, isothiocyanates, Friedel–Crafts, liquides ioniques, thioamides.

[Traduit par la Rédaction]

## Introduction

Room temperature ionic liquids have attracted considerable attention as novel reaction media, offering cleaner and environmentally benign protocols to a number of chemical processes (1). An appropriate amalgamation of properties possessed by these liquids, such as high thermal stability, reusability, nonvolatility, and excellent solvating ability has undoubtedly made them the most protean and promising solvents of the future (2). The most interesting feature of ionic liquids is the extensive flexibility they offer in terms of alteration of properties such as density, viscosity, Lewis acidity, hydrophobicity, hydrophilicity, etc. (3). This feature of ionic liquids has enabled chemists to design and engineer them so that a proper equilibrium of properties is attained, making them the most suitable and compatible solvents for several chemical processes (4–8).

The significance of thioamides and their polyfunctional

derivatives as useful building blocks in organic syntheses has been recently reviewed (9). Thioamides are a class of compounds that comprise a variety of derivatives that possess diverse physiological properties such as antigastric, antiulcer, antidiabetic, antitubercular, fungistatic, etc. (10). Besides, they have been technically applied in a number of commercial applications as vulcanisation promoters, antioxidants, corrosion inhibitors, etc. (10). Activated arenes are known to undergo Lewis acid mediated amidation (11, 12) and thioamidation (13, 14) with isocyanates and isothiocyanates, respectively. In contrast to the Lewis acid mediated amidation of arenes with isocyanates, thioamidation with isothiocyanates has been particularly attractive, as the former procedure often suffers from the disadvantage of low yields of products. The isothiocyanato group is one of the excellent acceptors of nucleophiles, and its reactivity has been aptly utilized in various synthetic procedures (15). With Lewis acids, the isothiocyanato group is known to

Received 25 May 2003. Published on the NRC Research Press Web site at <http://canjchem.nrc.ca> on 22 September 2003.

P.U. Naik, S.J. Nara, J.R. Harjani, and M.M. Salunkhe.<sup>1</sup> Department of Chemistry, The Institute of Science, 15 Madam Cama Road, Mumbai 400 032, India.

<sup>1</sup>Corresponding author (e-mail: [mmsalunkhe@hotmail.com](mailto:mmsalunkhe@hotmail.com)).



form a charged complex containing electrophilic carbon (16), which is believed to be involved as an intermediate in its reaction with arenes.

## Results and discussion

Over the last two years, our group has developed considerable interest in investigating the Friedel–Crafts (17–19) and condensation (20, 21) reactions in the Lewis acidic chloroaluminate ionic liquids. As a part of our ongoing venture to exploit chloroaluminate ionic liquids for newer reactions, we present herein an account of the execution of 1-butyl-3-methylimidazolium chloroaluminate, [bmim]Cl·AlCl<sub>3</sub> ( $0.67 \geq N > 0.50$ ;  $N$  is the apparent mole fraction of AlCl<sub>3</sub> in the ionic liquid) mediated addition of activated arenes to isothiocyanates (Scheme 1).

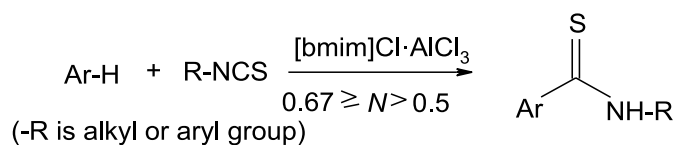
We anticipated an exhortive result in the case of activated arenes such as phenols, and they were therefore an obvious choice for the preliminary investigations. A reaction performed in [bmim]Cl did not fetch any product. The encouraging results obtained in the subsequent investigations carried out in [bmim]Cl·AlCl<sub>3</sub>,  $N = 0.67$ , prompted us to plan a systematic study aimed at the optimization of Lewis acidity and stoichiometry of the ionic liquid and time of reaction, to develop an ambient protocol for thioamidation. 2,5-Xylenol, being sufficiently reactive, was preferred as a model substrate for these optimizations.

To study the effect of the Lewis acidity of [bmim]Cl·AlCl<sub>3</sub> ( $0.67 \geq N \geq 0.50$ ) on the extent of product formation, a series of ionic liquids with varying Lewis acidities were prepared. The molar proportion of 2,5-xylenol, phenyl isothiocyanate, and ionic liquid was maintained at 1:1:1 at room temperature for 24 h, and the extent of conversion in terms of the percentage yield of the product obtained in each case was compared. The results reflected that an increase in the Lewis acidity resulted in an increase in the percentage yield of product formed, but in all the cases the yields were too low to be quantitative. The yield increased from 0% to 30% as  $N$  increased from 0.50 to 0.63, progressively, and only 64% yield was realized for [bmim]Cl·AlCl<sub>3</sub>,  $N = 0.67$ .

The [bmim]Cl·AlCl<sub>3</sub>,  $N = 0.67$ , was an obvious choice for all further investigations. With a view to obtain an optimal yield of the product, we further planned to study the effect of stoichiometry of [bmim]Cl·AlCl<sub>3</sub>,  $N = 0.67$ , on the extent of product formation. A series of experiments were planned in which the molar proportion of 2,5-xylenol and phenyl isothiocyanate was fixed at 1:1 and varying amounts of [bmim]Cl·AlCl<sub>3</sub>,  $N = 0.67$ , ranging from 1 to 2.5 mole equivalents, was added. The reaction time was 24 h at room temperature. The results indicated that the optimal product formation calls for the use of at least 2 mole equivalents of [bmim]Cl·AlCl<sub>3</sub>,  $N = 0.67$ . No significant increase in yields was observed with a further increase in stoichiometry of the ionic liquid.

To optimize the time for the thioamidation procedure, a series of experiments were planned in which the molar proportion of 2,5-xylenol, phenyl isothiocyanate, and [bmim]Cl·AlCl<sub>3</sub> ( $N = 0.67$ ) was maintained at 1:1:2 at room temperature for different time periods (ranging from 2–12 h). The yields of the product formed at different time in-

**Scheme 1.** The [bmim]Cl·AlCl<sub>3</sub> ( $0.67 = N > 0.50$ ) catalyzed addition of arenes to isothiocyanates.



tervals were compared. The results indicated that the optimal time for the reaction is 8 h, beyond which no substantial increase in yield was observed. No improvement in yield was realized, even after a prolonged reaction time of 30 h.

To generalize the procedure and to study the effect of substituents on product formation, a variety of arenes were screened under optimized conditions. The results obtained are indicative of successful thioamidation of activated arenes (Table 1). The reaction of phenyl isothiocyanate did not occur with benzene, but with *m*-xylene 83% yield of the product was obtained. In terms of yields and selectivity, the method is comparable to a nitromethane–AlCl<sub>3</sub> system (13). In general, aryl isothiocyanates fetched better yields than alkyl isothiocyanates. In contrast to a number of classical carbonylation procedures, an exquisite *para*-selectivity was observed in reaction even with the arene that has both *ortho* positions unblocked (entry 5). In the case of substrates with the *para* position blocked, such as *p*-xylene and *p*-cresol, no reaction was observed.

The present methodology can be easily extended to *ortho* carbonylation of benzoic acids, i.e., conversion of benzoic acids to phthalic acids and also for conversion of phthalic acids to homophthalic acids, which are synthetically versatile intermediates (22, 23). In addition, the method can serve as an advantageous alternative to the synthesis of certain benzoic acids and benzyl amines, which cannot be synthesized by other methods.

## Conclusion

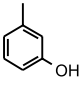
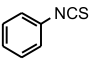
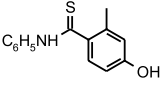
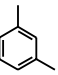
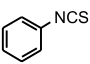
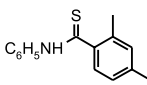
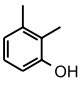
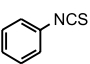
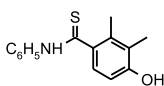
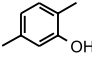
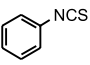
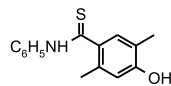
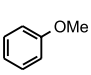
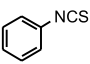
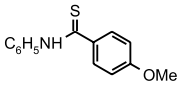
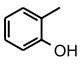
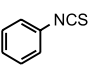
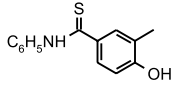
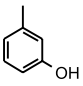
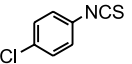
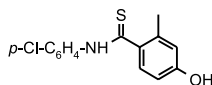
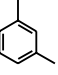
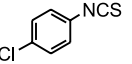
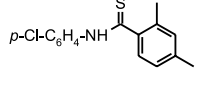
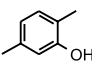
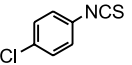
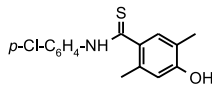
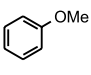
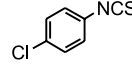
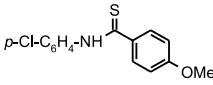
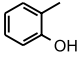
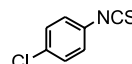
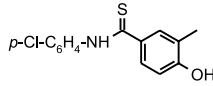
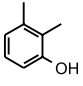
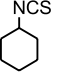
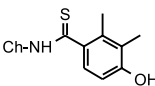
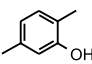
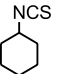
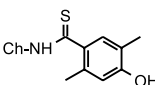
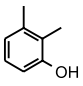
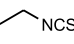
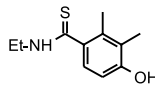
In effect, we found 1-butyl-3-methylimidazolium chloroaluminate, [bmim]Cl·AlCl<sub>3</sub> ( $N = 0.67$ ), to be a homogenous Lewis acidic medium for Friedel–Crafts type addition of activated arenes to isothiocyanates, thus eliminating the use of conventional obnoxious or volatile solvents such as halogenated hydrocarbons, nitromethane, and carbon disulphide. Homogenous catalysis, reduced reaction times, ambient conditions, and exquisite *para*-selectivity are some of distinctively notable advantages offered by the novel procedure.

## Experimental

The ionic liquids used in the present study were prepared as per the procedures reported earlier (24, 25). In a typical experimental procedure for thioamidation of arene, to the weighed quantity of the arene (5 mmol) and isothiocyanate (5 mmol), the ionic liquid [bmim]Cl·AlCl<sub>3</sub> ( $N = 0.50$ – $0.67$ , 5–15 mmol (as specified in the text)) was added, and the reaction mixture was stirred for a specified time at room temperature. All additions were carried out under a nitrogen atmosphere glove box. The reactions were quenched with 6 mol L<sup>-1</sup> HCl under cold conditions. The resultant solution



**Table 1.** The [bmim]Cl·AlCl<sub>3</sub> (*N* = 0.67) mediated addition of arenes to isothiocyanates.

Entry	Arene	Isothiocyanate	Thioamide	% Yield <sup>a</sup>
1				80
2				83
3				85
4				92
5				81
6				79
7				82
8				88
9				82
10				88
11				92
12				72
13				69
14				66

**Note:** Reactions carried out at room temperature for 8 h.<sup>a</sup>Indicates isolated yields.

was extracted using ethyl acetate (3 × 10 mL). The combined organic extracts were dried using anhydrous Na<sub>2</sub>SO<sub>4</sub> and evaporated under reduced pressure to obtain the crude

product. The crude products were chromatographed using silica gel column chromatography to yield pure thioamides, which were characterized by physical constants, IR, and



NMR. The analytical and spectral data was consistent with that reported in the literature (13).

## References

1. See special issue on "ionic liquids". *Green Chem.* **4**, 73 (2002).
2. J. Dupont, R.F. de Souza, and P.A.Z. Suarez. *Chem. Rev.* **102**, 3667 (2002).
3. P. Wasserscheid and W. Keim. *Angew. Chem., Int. Ed. Engl.* **39**, 3772 (2000).
4. A.C. Cole, J.L. Jensen, I. Ntai, K.L.T. Tran, K.J. Weaver, D.C. Forbes, and J.H. Davis Jr. *J. Am. Chem. Soc.* **124**, 5962 (2002).
5. C. Wheeler, K.N. West, C.L. Liotta, and C.A. Eckert. *Chem. Commun.* 887 (2001).
6. Y. Ishida, H. Miyauchi, and K. Saigo. *Chem. Commun.* 2240 (2002).
7. P. Wasserscheid, A. Bösmann, and C. Bolm. *Chem. Commun.* 200 (2002).
8. J. van den Broeke, F. Winter, B.-J. Deelan, and G. van Koten. *Org. Lett.* **4**, 3851 (2002).
9. T. Jagodziński. *Chem. Rev.* **103**, 197 (2003) and references therein.
10. J. Zabicky. *In The chemistry of amides. Edited by S. Patai.* Wiley, New York. 1970. pp. 461–463.
11. G. Balduzzi, F. Bigi, G. Casiraghi, G. Casnati, and G. Sartori. *Synthesis*, 879 (1982).
12. O. Piccolo, L. Filippini, L. Tinucci, E. Valoti, and A. Citterio. *Tetrahedron*, **42**, 885 (1986).
13. T. Jagodziński. *Synthesis*, 717 (1988) and references therein.
14. E.P. Papadopoulos. *J. Org. Chem.* **41**, 962 (1976).
15. Ľ. Drobica, P. Kristián, and J. Augustín. *In The chemistry of cyanates and their thio derivatives. Part 2. Edited by S. Patai.* Wiley, New York. 1977. pp. 1003–1221.
16. T. Jagodziński, E. Jagodzińska, and Z. Jabłoński. *Tetrahedron*, **42**, 3683 (1986).
17. J.R. Harjani, S.J. Nara, and M.M. Salunkhe. *Tetrahedron Lett.* **42**, 1979 (2001).
18. S.J. Nara, J.R. Harjani, and M.M. Salunkhe. *J. Org. Chem.* **66**, 8616 (2001).
19. S.S. Mohile, M.K. Potdar, and M.M. Salunkhe. *Tetrahedron Lett.* **44**, 1255 (2003).
20. M.K. Potdar, S.S. Mohile, and M.M. Salunkhe. *Tetrahedron Lett.* **42**, 9285 (2001).
21. J.R. Harjani, S.J. Nara, and M.M. Salunkhe. *Tetrahedron Lett.* **43**, 1127 (2002).
22. P.A.S. Smith and R.O. Kan. *J. Am. Chem. Soc.* **82**, 4753 (1960).
23. P.A.S. Smith and R.O. Kan. *J. Org. Chem.* **29**, 2261 (1964).
24. J.S. Wilkes, J.A. Levisky, R.A. Wilson, and C.L. Hussey. *Inorg. Chem.* **21**, 1263 (1982).
25. A.K. Abdul-Sada, A.M. Greenway, K.R. Seddon, and T. Welton. *Org. Mass Spectrom.* **28**, 759 (1993).



# Comparison of supported liquid membranes and solid-phase extraction for quantitative removal of lead from aqueous solutions

Emily R. Yourd and Julian F. Tyson

**Abstract:** The selective transport of a target metal ion across a membrane from a donor to an acceptor solution is an attractive concept for preconcentration or separation in a flow injection (FI) system. However, we found that the transport of lead across a supported liquid membrane consisting of dicyclohexano-18-crown-6 in decanol embedded in Celgard 2400 was too slow to be practical for an FI atomic spectrometry system. On the other hand, the same chemistry in an on-line, solid-phase reactor (a mini-column containing Pb-Spec resin) gave a satisfactory performance. In an attempt to understand the kinetics of the system, we have calculated the rate of transport across the membrane. As flux is proportional to concentration on the donor side — which decreases with time — we performed a series of numerical simulations involving fixed time intervals of decreasing values. These calculations show that for the sizes of membranes in a typical FI system, transport is very slow compared with the adsorption of lead by the Pb-Spec resin: it takes about 100 min for the concentration in a 0.06 mL donor solution to decrease by a factor of 1000. The time required for the same decrease in concentration for a membrane having the same surface area and ligand concentration as the Pb-Spec column was calculated as approximately 9 s.

**Key words:** supported liquid membrane, solid-phase extraction, flow-injection, lead.

**Résumé :** Le transport sélectif d'un ion métallique cible à travers une membrane à partir d'un donneur vers une solution accepteuse est un concept attrayant pour la préconcentration ou la séparation dans un système à injection continue (IC). Cependant, nous avons trouvé que le transport du plomb à travers une membrane liquide incrustée dans un support, cette membrane est constituée de dicyclohexano-18-couronne-6 dans le décanol incorporé dans du Celgard 2400, est trop lent pour être pratique dans un système de spectrométrie atomique à injection continue (IC). Par ailleurs la même chimie en continu dans un réacteur en phase solide (une mini colonne contenant une résine Pb-Spec), a donné une performance satisfaisante. Dans une tentative pour comprendre la cinétique du système, nous avons calculé la vitesse de transport à travers la membrane. Comme le flux est proportionnel à la concentration du côté du donneur, laquelle diminue avec le temps, nous avons réalisé une série de simulations numériques impliquant des intervalles de temps fixes de valeurs décroissantes. Ces calculs montrent que, compte tenu des dimensions des membranes dans un système typique à injection continue, le transport est très lent comparativement à l'adsorption du plomb par la résine Pb-Spec; il faut environ 100 minutes pour que la concentration dans 0,06 mL d'une solution donneuse décroisse d'un facteur de 1000. Le temps requis pour la même diminution de concentration dans le cas d'une membrane ayant la même superficie et la même concentration de ligand dans une colonne de Pb-Spec est selon les calculs approximativement de 9 s.

**Mots clés :** membrane liquide supportée, extraction en phase solide, injection continue, plomb.

[Traduit par la Rédaction]

## Introduction

Analytical method development often involves sample pretreatment so that a potentially interfering component of the sample matrix, which may be present in relatively high concentration compared with that of the analyte, is removed. Another common problem is that the analyte concentration is below the detection limit, and thus preconcentration is needed. For example, the determination of trace elements in

forensic bullet samples by inductively coupled plasma mass spectrometry (ICP-MS) is inhibited by the presence of the lead matrix, which causes analyte signal suppression. The removal of this element prior to introduction to the instrument is therefore required. On the other hand, the determination of lead in drinking water by flame atomic absorption spectrometry (FAAS) requires preconcentration. Flow injection (FI) analysis is a versatile sample pretreatment technique that can be useful for the automated removal of a

Received 6 April 2002. Published on the NRC Research Press Web site at <http://canjchem.nrc.ca> on 25 September 2003.

**E.R. Yourd and J.F. Tyson.**<sup>1</sup> Department of Chemistry, University of Massachusetts, 710 N. Pleasant Street, Amherst, MA 01003–9306, U.S.A.

<sup>1</sup>Corresponding author (e-mail address: [tyson@chem.umass.edu](mailto:tyson@chem.umass.edu)).



sample matrix or the preconcentration of a sample component (1–3). FI manifolds can be tailored to specific applications by incorporating the appropriate on-line components, such as a packed column for solid-phase extraction (SPE) or a membrane cell.

In developing a method for the analysis of bullets by ICP-MS, we initially chose FI-SPE to remove the lead (4). Most of the previous work on the use of solid-phase reactors in FI systems for the separation of analytes from matrices has been based on a protocol whose primary goal is preconcentration. The analytes are retained from a relatively large volume of solution, while the unwanted matrix components are discarded to waste. Following removal of any unretained matrix materials from the reactor, the analytes are eluted in the direction opposite to that in which the species were loaded and are transported to the detector.

Several design features of such a reactor are desirable. There should be rapid transport from the bulk liquid in the interstices between the solid particles to the surface of the particles. The binding of the analytes to the particle surface should also be rapid, while the reverse reaction should be slow (i.e., the reaction between the analyte and the surface-immobilized reagent should have a high “equilibrium” or binding constant). The surface density of the binding sites should be such that the reactor has sufficient capacity to retain all of the analyte species. As is well known from HPLC theory, important factors include particle size, column dimensions, and flow rate; to get high efficiency (in the chromatographic sense of minimum band broadening) when using HPLC, the particle size should be small: 5  $\mu\text{m}$  or less. Even for the miniature columns that are typically used in FI-SPE applications, the back-pressure generated by using small particles is often sufficiently high that it is difficult to obtain useful flow rates from peristaltic pump delivery.

In the typical FI-SPE preconcentration procedure, such considerations are not of prime importance, as the first part of the experiment is performed under conditions such that the capacity factor is very large (the analyte is retained on the column). All that is necessary is that during the passage of any given solute through the column, there is a high probability that the species will interact with the reagent immobilized at the particle surface and will be retained. For the second part of the experiment, broadening processes are relevant, as the goal is to elute the retained analyte in as small a zone of fluid as possible. This maximizes the instrument response peak height and minimizes the time required for this portion of the experiment. Guidelines, based on these considerations, have been developed by Fang (2) and can be summarized as the optimum conditions for FI-SPE preconcentration for trace element determination by atomic spectrometry. These guidelines involve column volumes between 20 and 250  $\mu\text{L}$  with aspect ratios (5) of 10–15, containing particles of 150–200  $\mu\text{m}$ , and sample loading at 8–9  $\text{mL min}^{-1}$ . Elution flow rates depend on the detection mode, as the eluent is delivered directly to the spectrometer.

When FI-SPE is to be used for matrix removal by retention of the matrix and direct determination of the analytes, the guidelines described above no longer apply. Now there are two important considerations: (a) there must be sufficient retention of the matrix element to reduce its concentration to below that which causes problems with the

subsequent analyte determinations, and (b) there should be minimum peak broadening of the unretained analytes. The first consideration means that the columns are significantly larger than those typically used for trace element preconcentration and, thus, may be capable of substantial peak broadening. In addition to the purely “chromatographic” features of the experiment, the flow rate is constrained to values at which the detector has suitable signal-to-noise ratio, and factors affecting the throughput have to be considered. Both of these considerations have implications for the sample volume injected, which, as always in flow injection experiments, cannot simultaneously maximize signal and minimize throughput. In addition, the elution characteristics of the system are still relevant, as the retained matrix component must be removed at frequent intervals by a suitable eluent.

It is clear, though, from basic HPLC theory that from the viewpoint of both retaining a matrix component and minimizing the broadening of non-retained components, the particle size should be decreased. A number of beneficial features would be realized by working with particle sizes of 10  $\mu\text{m}$  or less. For these values, not only is the peak broadening very much less than for larger particle sizes, but the broadening is also essentially independent of flow rate, and relatively high flow rates could be used to load samples rapidly. Unfortunately, there is a practical limitation related to the high back-pressure generated by columns of useful dimensions filled with particles of this size, which far exceeds the capabilities of the peristaltic pumps used for fluid handling in such experiments. Because of the additional costs and complexities associated with high-pressure pumping in multi-line manifolds, this option is not considered viable. As the performance of a method based on SPE is clearly limited, we considered other options.

While there are a number of such procedures that might be considered for implementation in an FI format, selective transport across a flat membrane is attractive. The procedure may be implemented in a device with minimum back-pressure and thus, when fluid is delivered by peristaltic pump, could accept much higher fluid flows than can a packed bed solid-phase reactor. The device also allows the facile separation of phases associated with interaction between a liquid sample and an immobilized “reagent”; this is not realized when phase transfer into another mobile phase (either liquid or gas) forms the basis of the separation.

There are numerous recent reports of chemical separations by supported liquid membranes (SLM) (6–13). The pores of a microporous solid support are impregnated with a hydrophobic liquid, forming the membrane that separates the sample (donor) and receiver solutions. The analyte, if it is soluble in the membrane liquid, diffuses from the sample solution, through the membrane, and into the receiver solution. The mass-transport efficiency can be significantly enhanced when the membrane incorporates a carrier molecule that complexes with the analyte and facilitates its transit through the membrane to the receiver solution, where the complex dissociates. The carrier remains within the membrane.

The affinity of macrocyclic crown ethers for specific cations is well known (14–17). Those cations with ionic radii most closely matching the dimensions of the cavity of the macrocycle will be selectively complexed. Cations that are



significantly smaller than the cavity will be too far from the lone pairs of the oxygen to form an appreciable bond, while larger cations will not fit inside the cavity. The selectivity of crown ethers can be used to separate certain cations from a mixture, both for preconcentration purposes and for matrix removal.

We have investigated the feasibility of using an SLM in the flat-sheet configuration with the goal of removing lead from a matrix, as part of the sample pretreatment in the analysis of high-lead materials such as bullets. The membrane was impregnated with the crown ether dicyclohexano-18-crown-6 (DC18C6), which has a cavity size selective for lead (9, 17, 18). The lead-containing solution was introduced to the donor compartment of the membrane cell, and the receiver side was monitored for the appearance of transported lead. The transport process was also modeled mathematically. The experimental results were compared with the behavior predicted on the basis of the calculations. The model was also applied to a rapid FI-SPE procedure (4) based on the almost identical extraction chemistry (0.75 mol L<sup>-1</sup> di-*tert*-butyldicyclohexano-18-crown-6 in decanol immobilized on Amberchrom CG-71 (19)), to understand why this process is kinetically favorable to FI applications while the SLM procedure is not.

## Experimental

### Reagents and standards

Celgard 2400 polypropylene membranes (thickness 25 µm, porosity 35%, pore sizes 0.041 µm × 0.12 µm; Celgard Inc., Charlotte, NC) and Pb-Spec (100–150 µm diameter, Eichrom, Inc., Darien, IL) were used as received. Dicyclohexano-18-crown-6, phenylhexane, and decanol (Sigma-Aldrich, Milwaukee, WI) were also used as received. Ten millilitre solutions of 0.05 and 0.10 mol L<sup>-1</sup> crown ether in decanol and 0.05 mol L<sup>-1</sup> crown ether in phenylhexane were prepared. A stock solution of 1000 mg L<sup>-1</sup> Pb was prepared by dissolving the appropriate amount of lead nitrate (Certified ACS grade, Fisher Scientific) in 2% (volume fraction) nitric acid (Mallinckrodt). Solutions of 50 and 250 µg L<sup>-1</sup> Pb and 20 mg L<sup>-1</sup> Pb, all in 2% HNO<sub>3</sub>, were prepared through the dilution of a 1000 mg L<sup>-1</sup> atomic absorption standard (Sigma-Aldrich, Milwaukee, WI). Solutions of 3% HNO<sub>3</sub> and 0.1 mol L<sup>-1</sup> ammonium citrate (Certified ACS grade, Fisher Scientific, pH 5.23) were prepared for use in the membrane cell. A dilute solution of alkaline phenolphthalein (Certified ACS grade, Fisher Scientific) was made by dissolving a sufficient amount of the indicator along with some sodium hydroxide (Mallinckrodt) in water to produce a strongly colored solution. All solutions were prepared using deionized water with a resistivity of 18.0 MΩ (E-Pure, Barnstead) and were stored in acid-washed polyethylene (Nalgene) bottles.

### Apparatus

A flame atomic absorption spectrometer model 1100B (PerkinElmer, Shelton, CT, U.S.A.) with deuterium background correction was used. The instrument was operated with a lead hollow cathode lamp according to the manufacturer's recommended conditions. The 10 cm air-acetylene burner head position was optimized in three dimensions

while aspirating a 20 mg L<sup>-1</sup> solution of Pb in 2% HNO<sub>3</sub>. The position of the nebulizer capillary in the venturi throat was adjusted such that the nebulizer suction was zero. This positioning ensured that the flow rate of the solution reaching the nebulizer was controlled solely by the peristaltic pump of the flow injection manifold.

A graphite furnace atomic absorption spectrometer model 4100ZL (PerkinElmer, Shelton, CT, U.S.A.) with Zeeman background correction and a lead hollow cathode lamp was operated in accordance with the manufacturer's recommended conditions. An AS-71 autosampler transferred 20 µL of solution to the furnace, and the standard program for lead without matrix modification was used. The autosampler probe was rinsed with deionized water between injections. Peak area was measured.

An Olympus BH-2 transmission microscope was used to visually inspect the Pb-Spec resin. The 40× objective was used with a 10× eyepiece for a total magnification of 400×. A small amount of resin was placed on a glass slide and suspended in a few drops of water. A coverslip was placed over the beads to hold them in place.

The flow injection manifold consisted of one peristaltic pump (Ismatec), one 6-port rotary valve, and a membrane cell. The manifold is shown schematically in Fig. 1.

The cell was constructed from two nylon blocks (8 cm × 3 cm × 2 cm), each with a central groove (4 cm × 2 mm × 0.2 mm for receiver, 0.75 mm for donor). The sample volume of 130 µL was propelled through a 20 cm length of tubing into the top block of the cell with a flow rate of 1.3 mL min<sup>-1</sup>. The receiver solution was pumped in the opposite direction from the donor, creating a counter-current flow. The Celgard 2400 polymeric membrane was soaked in a solution of dicyclohexano-18-crown-6 and either decanol or phenylhexane for a minimum of 15 min, then placed between the blocks, physically separating the two channels. The entire cell was clamped between two aluminum plates. The pump tubing was Tygon 1.52 mm i.d. three-stop tubing (blue-yellow); manifold components were connected via 0.8 mm i.d. PTFE tubing.

The SPE manifold, which provides the basis for the comparison, has been described previously (4). To summarize, a 130 µL sample was injected into a nitric acid carrier that moved the sample through a glass column (5 cm × 4 mm i.d.) packed with 105 mg of Pb-Spec resin. The now lead-free sample passed directly into the ICP-mass spectrometer for the determination of the diagnostic elements in bullets: Ag, As, Bi, Cd, Cu, Sb, and Sn. The resin was rinsed with 0.1 mol L<sup>-1</sup> ammonium citrate after every third sample injection to remove the accumulated lead.

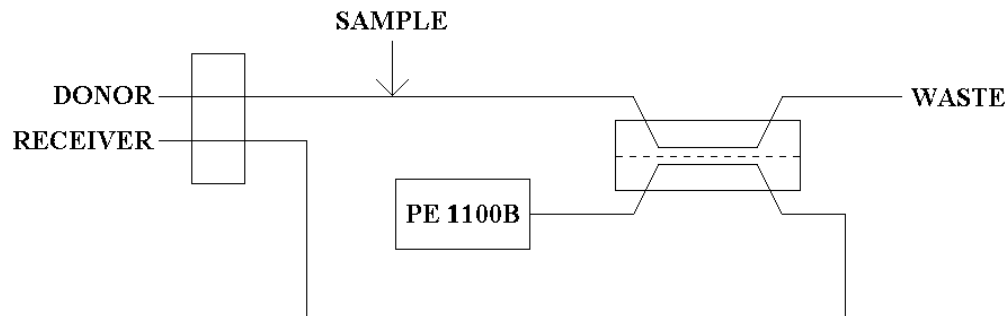
### Characterization of transport

To determine when the injected sample solution completely filled the donor channel, the time required for the sample to travel from the injection valve to the membrane cell was measured. A basic solution of phenolphthalein was injected into a water carrier so that this transport time could be evaluated visually.

Different compositions of receiver solution were investigated. The acceptor stream was 3% HNO<sub>3</sub> or 0.1 mol L<sup>-1</sup> ammonium citrate. The amount of Pb transported to the re-



**Fig. 1.** Flow injection manifold for the SLM experiment. The dashed line indicates the position of the membrane.



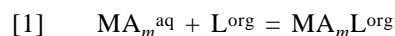
ceiver was observed for each solution after various stop times.

The contact time between the sample and the membrane was an important experimental parameter. The time required for lead to travel from the donor solution to the receiver was determined through a series of stopped-flow experiments with crown ether concentrations of 0.05 and 0.1 mol L<sup>-1</sup> in decanol and 0.05 mol L<sup>-1</sup> in phenylhexane. The 1000 mg L<sup>-1</sup> Pb sample was injected into the 3% HNO<sub>3</sub> carrier stream and transported into the donor channel of the membrane cell. The pump controlling the two streams was stopped for a measured period of time (0, 5, 15, 30, 60, 120, and 1320 min) and then restarted. The absorbance due to lead in the ammonium citrate receiver solution was monitored by FAAS, and the height of the resulting lead peak was recorded.

The number of moles of lead transported across the SLM was quantified by electrothermal atomization atomic absorption spectrometry (ETAAS). The 1000 mg L<sup>-1</sup> Pb sample solution was placed in contact with the SLM containing 0.1 mol L<sup>-1</sup> DC18C6 in decanol for a stop time of 15 min. At the end of the stop time, the receiver solution was pumped into a 25 mL volumetric flask and approximately 2 mL were collected. The solution was made to volume with 2% HNO<sub>3</sub>. This sample was measured ( $n = 10$ ) along with standards of 0, 50, and 250 µg L<sup>-1</sup> Pb in 2% HNO<sub>3</sub>. Each standard was measured five times.

### Mechanism of transport and calculations

A theory of transport of divalent cations through a crown-ether-containing SLM has been developed (17, 20, 21). The cation flux is strongly dependent on the equilibrium constant ( $K_{\text{ex}}$ ) for the following reaction (20):



In this equation, M represents the metal cation, and A is a counterion present in the stoichiometric quantity  $m$ . L represents ligand. The superscripts in the equation refer to the aqueous (donor) and organic (membrane) phases. This reaction is the pertinent one, rather than the expected  $\text{M}^{m+} + n\text{L} = \text{M}^{m+}\text{L}_n$ , because the transport of a cation by a neutral macrocycle requires the simultaneous transport of an anion to maintain electroneutrality. The transported moiety is therefore equivalent to  $\text{MA}_m$ , a neutral species. Additionally, it is known that the rate-determining step in the mechanism is the diffusion of the complex through the membrane. A more accurate model would also account for the loss of macrocycle from the membrane, since carrier leaching

would diminish the concentration of macrocycle available to move the cation.

The cation flux,  $J$ , can be calculated from a single equation containing terms whose values can either be measured or calculated readily (20):

$$[2] \quad J = \frac{DK_{\text{ex}}[\text{L}_{\text{total}}^{\text{org}}][\text{MA}_m^{\text{aq}}]}{l(1 + K_{\text{ex}}[\text{MA}_m^{\text{aq}}])}$$

The variables are defined as follows:  $D$  is the diffusion coefficient of the neutral solute species,  $\text{MA}_m\text{L}^{\text{org}}$ , through the membrane solvent;  $[\text{L}_{\text{total}}^{\text{org}}]$  is the total concentration of crown ether in the organic solvent;  $[\text{MA}_m^{\text{aq}}]$  is the concentration of neutral solute species in the source phase; and  $l$  is the membrane diffusion path length. The value of  $D/l$  is generally calculated, because the  $l$  value is difficult to obtain alone, owing to the need to include a term to account for membrane porosity and tortuosity. These values are calculated for each solvent-membrane system, so the value for Celgard 2400 with phenylhexane is used. The  $K_{\text{ex}}$  value can be measured experimentally, and the concentration of ligand is known from the membrane solutions. The units of  $J$  are mol s<sup>-1</sup> m<sup>-2</sup>, incorporating time, area, and amount of substance.

This equation was used to predict the permeation behavior of Pb through a Celgard 2400 membrane soaked with DC18C6 in decanol or phenylhexane under stopped-flow conditions. The time required for the Pb concentration to change from 1000 to 1 mg L<sup>-1</sup> in the donor solution was desired. This corresponded to the removal of a specific quantity of Pb matrix from a sample, which provided a value for the number of moles transported. The area of the SLM in contact with the donor in the flow injection experiments was calculated from measurements of the channel dimensions. These values, when combined with the calculated flux, allowed for the calculation of the transport time. To a first approximation, it was assumed that the behavior of the system with decanol was similar to that with phenylhexane, so the equilibrium constants and other variables for phenylhexane were used.

Before it is possible to calculate the flux of Pb across the membrane, however, the concentration of the neutral species available for transport must be obtained. The remaining variables in the flux equation are known:  $D/l$  for the Celgard 2400-phenylhexane system ( $3.19 \times 10^{-4}$  L s<sup>-1</sup> m<sup>-2</sup>) (20),  $K_{\text{ex}}$  for the complexation of Pb(NO<sub>3</sub>)<sub>2</sub> with DC18C6 (398.11) (20), and the concentration of DC18C6 in the membrane soaking solution. The only unknown, then, is the concentra-



tion of  $\text{Pb}(\text{NO}_3)_2$  in the donor. This value depends on the initial amount of Pb in the sample ( $1000 \text{ mg L}^{-1}$ ) and the concentration of  $\text{HNO}_3$  (volume fraction 0.02).

To calculate the amount of Pb in the sample present as  $\text{Pb}(\text{NO}_3)_2$ , an iterative approach to the systematic treatment of equilibrium was taken. Using the  $\beta$  (log stepwise formation constant) values (18) for the formation of  $\text{PbNO}_3^+$  and  $\text{Pb}(\text{NO}_3)_2$  (2.14 and 2.15, respectively) and the sample concentration of  $1000 \text{ mg L}^{-1}$  for the total amount of Pb, it was possible to compute  $[\text{Pb}^{2+}]$  from the mass balance equation for lead. This value for  $[\text{Pb}^{2+}]$  was used, along with the appropriate  $\beta$  value and the concentration of unbound  $\text{NO}_3^-$  in solution, to obtain the concentration of  $\text{Pb}(\text{NO}_3)_2$ . The total amount of nitrate anion bound up in all of the complexes was calculated and subtracted from the initial value. This adjusted initial value was used as the starting condition for the next iteration of the calculation, yielding a new  $[\text{Pb}(\text{NO}_3)_2]$  and  $[\text{unbound NO}_3^-]$ . This iterative process was performed five times, at which point the calculated concentrations of  $\text{Pb}(\text{NO}_3)_2$  and  $\text{NO}_3^-$  had each converged. The concentration of the neutral species was substituted into the flux equation, and the flux was calculated, yielding the quantity of Pb that could be transported.

The flux equation only describes an instantaneous condition. Immediately after the transport of Pb begins, the total concentration of Pb on the donor side decreases. This produces a new concentration for the neutral species and, hence, a different value for the flux. To account for this, the flux was assumed to be constant over a specific period of time, after which the concentration of Pb remaining in the donor solution was calculated and a new flux computed. The initial Pb concentration in the sample was  $1000 \text{ mg L}^{-1}$  and the desired final concentration was  $1 \text{ mg L}^{-1}$ , which produced a defined end for the process. Time increments of 600, 300, 60, 15, and 1 s were used.

In earlier work (4) we devised an FI-SPE procedure based on Pb-Spec ( $0.75 \text{ mol L}^{-1}$  di-*tert*-butyldicyclohexano-18-crown-6 in decanol immobilized on Amberchrom CG-71 (19)), which successfully removed the lead from digested bullet samples, allowing for accurate analyte determinations by ICP-MS. Although the overall analysis time was rather long for routine use, the rate of the lead removal was compatible with a flow rate of approximately  $1 \text{ mL min}^{-1}$ . To compare the performance of a column of Pb-Spec with that of the SLM, Pb-Spec was considered to consist of a thin coating of crown ether solution on the surfaces of impermeable spherical particles. Thus, each particle was imagined to function as a miniature, single-sided liquid membrane.

Physical characteristics of the Pb-Spec resin were calculated from information provided by the manufacturer, Eichrom, Inc. The resin bead size ranged from 100 to  $150 \mu\text{m}$ , so for spherical beads the surface area ranged from  $0.0314$  to  $0.0707 \text{ mm}^2$  per bead. Visual inspection through a transmission light microscope showed that the particles appeared uniformly spherical. It was therefore concluded that the surface area calculated on the basis of spherical resin beads was sufficient for use in subsequent calculations. From the dimensions of the resin bed ( $2.3 \text{ cm} \times 4 \text{ mm i.d.}$ ) within the glass column, the volume of resin was  $0.289 \text{ mL}$ . The resin has a free column volume of  $0.65 \text{ mL}$  per  $\text{mL}$  resin bed (19), or  $0.188 \text{ mL}$  in this specific column. Thus the

volume occupied by the resin was  $0.101 \text{ mL}$ . By considering the volume of spheres with diameters of 100 and  $150 \mu\text{m}$ , the total number of beads in a volume of  $0.101 \text{ mL}$  was computed:  $1.93 \times 10^5$  beads if they are all  $100 \mu\text{m}$  and  $5.71 \times 10^4$  if  $150 \mu\text{m}$ . Factoring in the surface area of an individual bead, the total surface area in a column containing 105 mg of  $100 \mu\text{m}$  beads is  $0.00605 \text{ m}^2$  and  $0.00403 \text{ m}^2$  for a column of  $150 \mu\text{m}$  beads.

As the flux is calculated per unit area, the effect of membrane surface area is one of direct proportion. Different surface areas were considered. The contact area of the flat sheet membrane in the nylon cell,  $8 \times 10^{-5} \text{ m}^2$ , was included, as well as the Pb-Spec column areas of  $0.00403$  and  $0.00605 \text{ m}^2$ .

The effect of crown ether concentration on rate of transport was examined. Values of  $0.05 \text{ mol L}^{-1}$  DC18C6 (SLM) and  $0.75 \text{ mol L}^{-1}$  (Pb-Spec) were substituted into eq. [2].

## Results and discussion

### Experimental

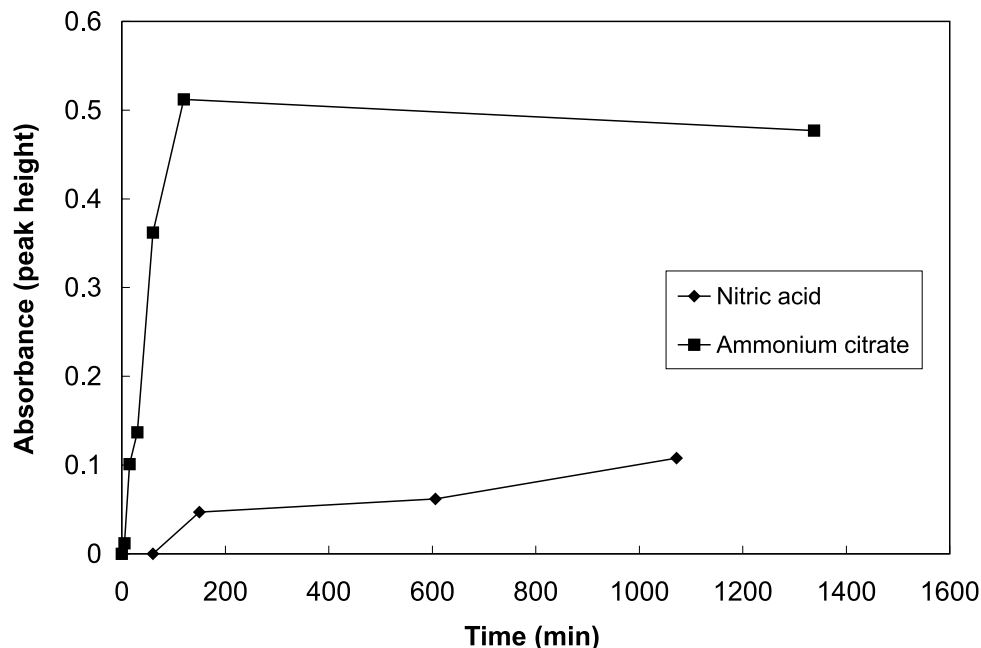
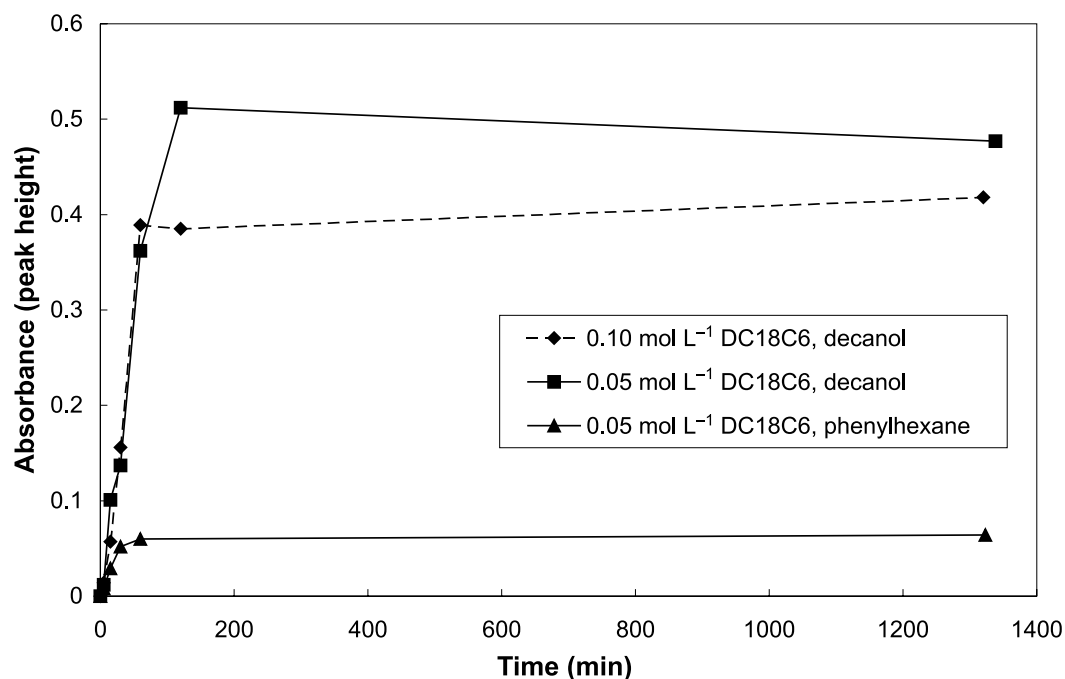
The membrane polymeric support consisted of a sheet of Celgard 2400 with approximate dimensions  $4.5 \text{ cm} \times 3.5 \text{ cm}$ . This effectively covered the faces of the membrane cell blocks. The white membrane, made from  $25 \mu\text{m}$  thick polypropylene, was hydrophobic and shed water as droplets. After the membrane was soaked in an organic solvent, however, it was completely wetted and became transparent. Because the membrane was then placed in contact with aqueous donor and receiver solutions, it was vital that the organic solvent be immiscible in water. A comparison (18) of water solubilities of common membrane solvents (chloroform:  $7950 \text{ mg L}^{-1}$ ; toluene:  $526 \text{ mg L}^{-1}$ ; 1,2-dichlorobenzene:  $156 \text{ mg L}^{-1}$ ; decanol (22):  $3.70 \text{ mg L}^{-1}$ ; phenylhexane:  $0.902 \text{ mg L}^{-1}$ ) indicates that phenylhexane is the solvent with the lowest water solubility, followed by decanol.

The time required for the phenolphthalein slug to arrive at the membrane cell and fill the donor channel was 12 s. The dye experiment revealed that the  $130 \mu\text{L}$  sample slug underwent noticeable dispersion, allowing only a relatively small portion of the sample volume to be in contact with the membrane during the stop time.

The better receiver solution was  $0.1 \text{ mol L}^{-1}$  ammonium citrate. This result, displayed in Fig. 2, was anticipated. The transport of Pb through the membrane was expected to be enhanced when the Pb was actively stripped from the membrane. The acid receiver was more passive, allowing the Pb to diffuse into it from the membrane. The ammonium citrate solution, however, allowed for the formation of a strong lead citrate complex, which provided an additional driving force for the Pb transport.

Figure 3 shows the results for the stopped-flow experiments using the two crown ether concentrations. The concentration of lead in the receiver solution increased with time until a constant value was obtained, which indicated that an equilibrium was reached. That is, the rates of transport of lead across the membrane in each direction were then equal. The results indicate that the membrane that contained  $0.05 \text{ mol L}^{-1}$  DC18C6 allowed more permeation of Pb than the other membranes. These findings contradict the results



**Fig. 2.** The effect of different receiver solutions on Pb transport.**Fig. 3.** Results for stopped-flow experiments. Each point represents a single measurement.

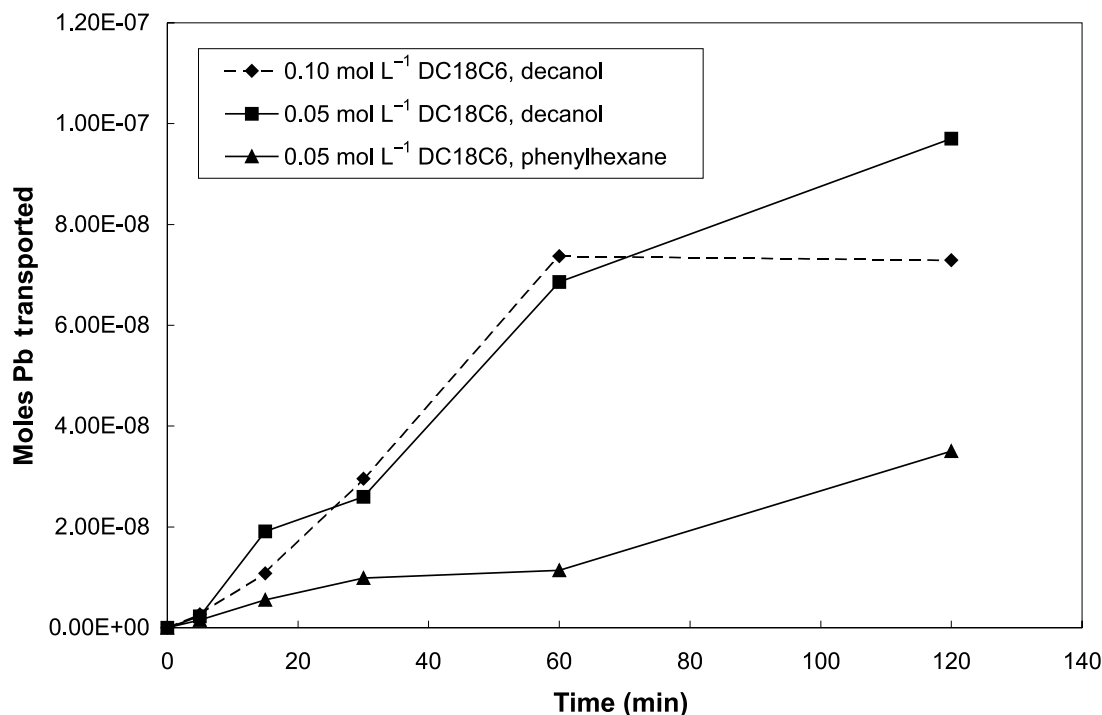
expected on the basis of eq. [2], from which it would be expected that the presence of more carrier molecules in the membrane would cause more Pb to be transferred. However, the higher concentration of crown ether may decrease the diffusion coefficient term in the numerator of eq. [2], which could account for the slower-than-expected rate of transport. Further investigation of this possibility was considered beyond the scope of the present study.

The Pb content of the 15 min stop flow point (0.1 mol L<sup>-1</sup> DC18C6 membrane) was measured off-line by ETAAS. The

least-squares calibration equation produced by three standard solutions was  $y = 0.0016x - 0.0058$ , where  $y$  is the absorbance and  $x$  the Pb concentration in  $\mu\text{g L}^{-1}$ . The correlation coefficient  $r$  was 0.9996. The concentration of Pb in the sample was  $89.4 \mu\text{g L}^{-1}$ , corresponding to  $1.1 \times 10^{-8}$  moles Pb in the 25 mL flask. This amount of Pb was transported across the membrane in 15 min. Assuming a linear relation between absorbance and concentration, the FAAS absorbances for each of the other stop times were calculated from this point, as shown in Fig. 4. The 0.05 mol L<sup>-1</sup>



**Fig. 4.** The number of moles transported across the membrane at each stopped-flow time. The 15 min point for the 0.1 mol L<sup>-1</sup> DC18C6 membrane was quantified by ETAAS, from which all other y-values are calculated.



DC18C6 membrane absorbances were also calculated from this value.

It is clear from Figs. 3 and 4 that the kinetics of transport for the flat sheet SLM are too slow for the process to be implemented in a flow injection mode. The transfer mechanism relies on the diffusion of the Pb – crown ether complex through the membrane, for which the concentration gradient of Pb is a driving force. Thus, if the receiver solution is not stagnant, this diffusion would continue, and eventually the desired amount of lead could be transported across the membrane. However, in this mode of operation, the transport processes would not produce any preconcentration.

The Pb transport rate is also proportional to the membrane area. As the dispersion of the sample slug allowed only a small portion of the initial volume to be in contact with the membrane during the stop time, the rate of transport was less than would be obtained with either a larger surface area or a smaller sample volume. Although, the additional dispersion incurred with a smaller sample volume would probably offset this benefit, owing to the decreased concentration in the donor phase.

#### Model calculations

The calculated number of moles of Pb remaining in the donor solution is plotted as a function of the elapsed time in Fig. 5. As the time increments decreased, the system was described more accurately, since chemical processes are rapid. Also, the new plots became more and more similar until they converged. It was therefore assumed that further reducing the increments would not substantially alter the predicted transport time.

The line for the calculations using 5 s increments overlapped that for the 1 min increments so that they are indis-

tinguishable on the figure. Both lines showed a total transport time of 105 min; the 5 s trace was subsequently omitted from the plot for clarity.

In addition to calculating the number of moles of Pb remaining in the donor solution vs. elapsed time, the number of moles appearing in the receiver could be derived. A comparison between the calculated transport and the experimental values for the two membranes containing 0.05 mol L<sup>-1</sup> crown ether may be made from the plots in Fig. 6. One reason for the low experimental rate compared with the calculated rate may be the leaching of macrocycle from the membrane. Izatt et al. (20) calculated that for a similar crown ether and phenylhexane in Celgard 2400, about 90% of the macrocycle was lost. It should be noted, however, that their calculations modeled transport under conditions in which both the donor and acceptor solutions were constantly stirred.

When the total surface area of the Pb-Spec resin was inserted into the flux equation, the time for the lead concentration to reach 1 mg L<sup>-1</sup> was significantly diminished for a membrane containing 0.05 mol L<sup>-1</sup> ligand. For an area of 0.00605 m<sup>2</sup> (100 µm resin), the transport time is 2.5 min for 10 s increments. The time is 4.1 min when the area is 0.00403 m<sup>2</sup> (150 µm resin) for the same increments.

Increasing the ligand concentration in the SLM had a significant effect on the transport time. With 0.75 mol L<sup>-1</sup> ligand and the membrane area held at the experimental value of 8 × 10<sup>-5</sup> m<sup>2</sup>, the time was 6.7 min with 10 s increments of constant flux. When the area of the 100 µm resin is combined with the increased ligand concentration, the transfer time calculated from 1 s increments is diminished to 8.7 s. The value obtained for the 150 µm resin corresponds to 15.3 s.



**Fig. 5.** Calculated number of moles remaining in the sample as a function of time for different time increments used in the flux calculations. Inset is an enlargement of the region where the calculated concentrations go below  $1 \text{ mg L}^{-1} \text{ Pb}$ .

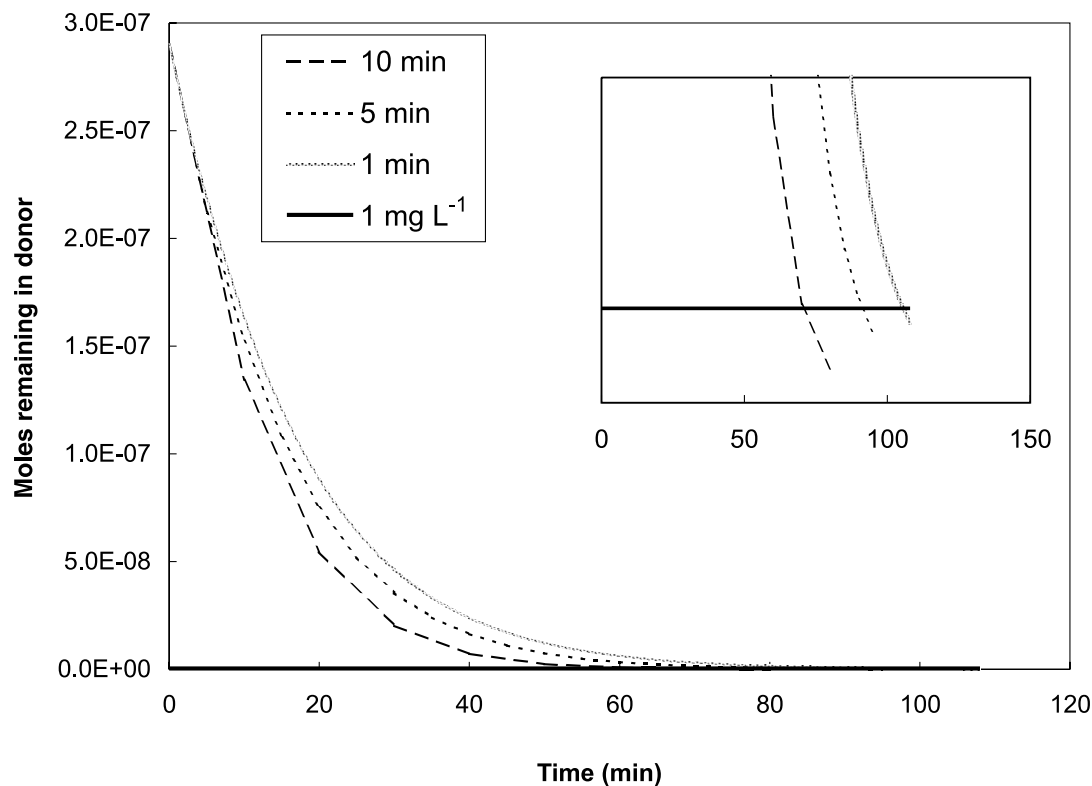
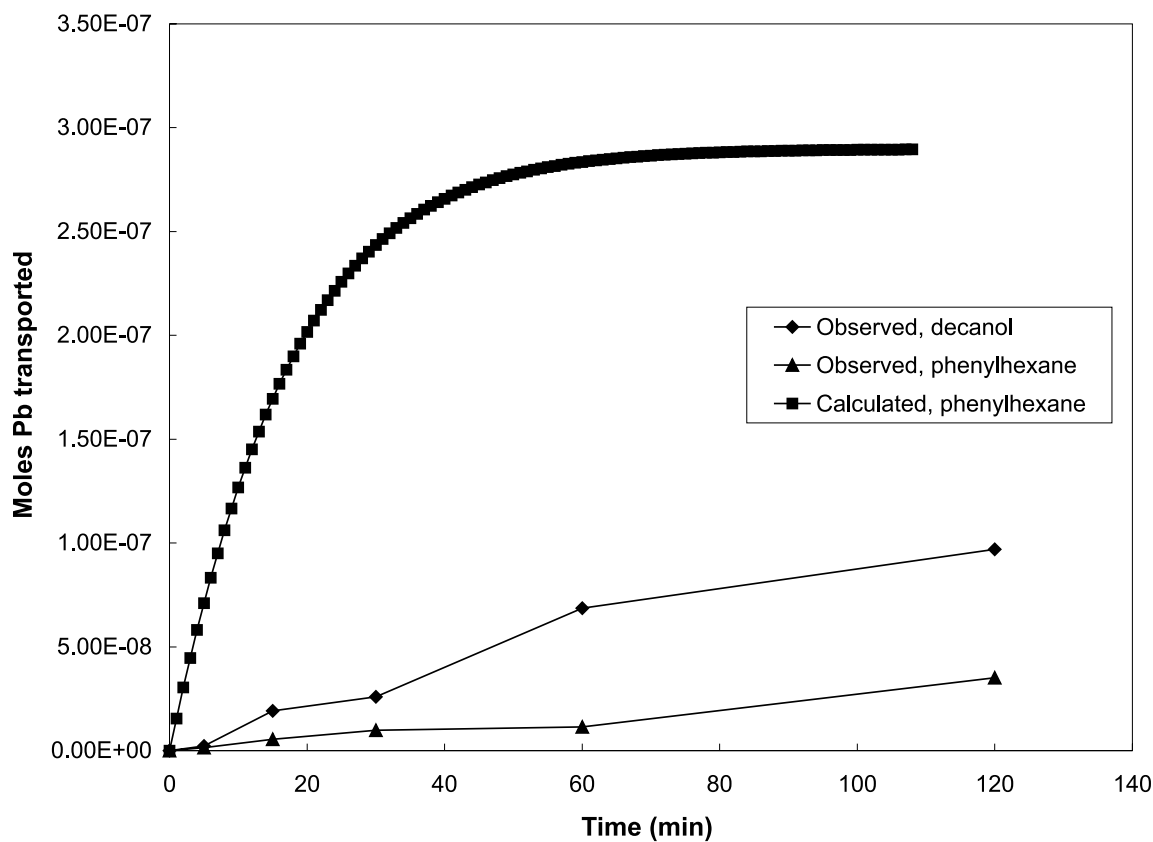


**Fig. 6.** Comparison of calculated and observed transport of Pb across the  $0.05 \text{ mol L}^{-1} \text{ DC18C6}$  membranes. Calculated results based on 1 min increments.





As can be seen from Figs. 3, 4, and 6, decanol is to be preferred over phenylhexane as an SLM solvent, though the reasons for this are not immediately obvious. Decanol has higher viscosity and water solubility than phenylhexane, though information regarding the diffusion coefficients of DC18C6 in these solvents is not immediately available. However, the results confirm that decanol is an appropriate choice for the formulation of the Pb-Spec SPE material.

## Conclusions

Separations by SLM systems are not feasible for on-line, dynamic, flow injection applications. Although the advantages of SLMs (i.e., the lack of back-pressure and sample dispersion, as well as the single-step analysis procedure) make these devices attractive for this type of analysis, both experimental results and model calculations indicate that the transport processes are too slow for typical FI systems. On the other hand, the same chemistry conducted in thin films coated on spherical beads is compatible with FI time scales. It is concluded that this is due largely to the increased surface area of the "membrane". This raises the question, to what extent could the SLM performance be improved by using a bundle of hollow fibers instead of a flat sheet? For example, a bundle of 140 Celgard X-30 240 fibers (i.d. 240  $\mu\text{m}$ , o.d. 300  $\mu\text{m}$ ) packed into a 5 cm column has a total internal surface area of approximately 0.0045  $\text{m}^2$ . This value is comparable to that obtained for the 100  $\mu\text{m}$  Pb-Spec beads, implying that such a bundle might have a feasible rate of transport for use in a flow injection manifold.

## Acknowledgements

Financial support for E.Y. from The Schering-Plough Research Institute is gratefully acknowledged. We also thank Celgard, Inc. for the gift of Celgard 2400 and Eichrom, Inc., for the donation of Pb-Spec. This material is based on work supported by the National Science Foundation under grant No. 0094568.

## References

1. Z. Fang. Flow injection atomic absorption spectrometry. John Wiley & Sons, New York. 1995.
2. Z.-L. Fang. Flow injection separation and preconcentration. VCH Publishers, Inc., New York. 1993.
3. A. Sanz-Medel (*Editor*). Flow analysis with atomic spectrometric detectors. Elsevier Science, Amsterdam. 1999.
4. E.R. Yourd, J.F. Tyson, and R.D. Koons. Spectrochim. Acta B, **56**, 1731 (2001).
5. M.A. Marshall and H.A. Mottola. Anal. Chem. **57**, 729 (1985).
6. J. de Gyves and E.R. de San Miguel. Ind. Eng. Chem. Res. **38**, 2182 (1999).
7. J.A. Jonsson and L. Mathiasson. Trends Anal. Chem. **18**, 325 (1999).
8. K.K. Sirkar, P.V. Shanbhag, and A.S. Kovvali. Ind. Eng. Chem. Res. **38**, 3715 (1999).
9. J.D. Lamb, R.M. Izatt, D.G. Garrick, J.S. Bradshaw, and J.J. Christensen. J. Membr. Sci. **9**, 83 (1981).
10. N. Parthasarathy and J. Buffle. Anal. Chim. Acta, **284**, 649 (1994).
11. A. El-Bachiri, A. Hagege, and M. Burgard. J. Membr. Sci. **121**, 159 (1996).
12. M. Akhond and M. Shamsipur. Sep. Sci. Technol. **32**, 1223 (1997).
13. N.K. Djane, K. Ndungu, F. Malcus, G. Johansson, and L. Mathiasson. Fresenius J. Anal. Chem. **358**, 822 (1997).
14. J.D. Lamb and M.D. Christenson. J. Incl. Phenom. Mol. Recogn. Chem. **32**, 107 (1998).
15. J.S. Bradshaw and R.M. Izatt. Acc. Chem. Res. **30**, 338 (1997).
16. J.D. Lamb, R.M. Izatt, P.A. Robertson, and J.J. Christensen. J. Am. Chem. Soc. **102**, 2452 (1980).
17. S. Dernini, A. Scrugli, S. Palmas, and A.M. Polcaro. J. Chem. Eng. Data **41**, 1388 (1996).
18. J.D. Lamb, R.L. Bruening, R.M. Izatt, Y. Hirashima, P.K. Tse, and J.J. Christensen. J. Membr. Sci. **37**, 13 (1988).
19. E.P. Horwitz, M.L. Dietz, S. Rhoads, C. Felinto, N.H. Gale, and J. Houghton. Anal. Chim. Acta, **292**, 263 (1994).
20. R.M. Izatt, R.L. Bruening, M.L. Bruening, G.C. Lindh, and J.J. Christensen. Anal. Chem. **61**, 1140 (1989).
21. G. Audunsson. Anal. Chem. **58**, 2714 (1986).
22. P.H. Howard and W.M. Meylan (*Editors*). Handbook of physical properties of organic chemicals. CRC Press, Inc., Boca Raton, Fla, U.S.A. 1997.



# Syntheses, characterization, and X-ray crystal structures of diorganotin(IV) derivatives of 2-pyridinethiolato-*N*-oxide

Chunlin Ma, Junhong Zhang, and Rufen Zhang

**Abstract:** The diorganotin(IV) dichloride reacts with sodium 2-pyridinethiolato-*N*-oxide in a 1:1 ratio to produce [Me<sub>2</sub>SnCl(2-SpyO)] (**1**), [Et<sub>2</sub>SnCl(2-SpyO)] (**2**), [Bu<sub>2</sub>SnCl(2-SpyO)] (**3**), [Ph<sub>2</sub>SnCl(2-SpyO)] (**4**), and [(PhCH<sub>2</sub>)<sub>2</sub>SnCl(2-SpyO)] (**5**). The new complexes have been characterized by elemental analysis and IR and NMR (<sup>1</sup>H, <sup>119</sup>Sn, and <sup>13</sup>C) spectroscopy. On the basis of <sup>119</sup>Sn NMR data the effective coordination number in solution is five. The structures **1** and **4** have been confirmed by X-ray crystallography. Crystals of **1** are triclinic with space group *P* $\bar{1}$  and those of **4** are monoclinic, *P*2<sub>1</sub>/*n*. The tin environment is a distorted trigonal bipyramid with the Cl and oxygen atoms in apical positions. Both complexes exhibit strong  $\pi$ - $\pi$  stacking interactions.

**Key words:** diorganotin,  $\pi$ - $\pi$  stacking interaction, 2-pyridinethiolato-*N*-oxide, crystal structure.

**Résumé :** Le dichlorure de diorganoétain(IV) réagit avec le 2-pyridinethiolato-*N*-oxyde de sodium dans un rapport de 1:1 pour donner: [Me<sub>2</sub>SnCl(2-SpyO)] (**1**), [Et<sub>2</sub>SnCl(2-SpyO)] (**2**), [Bu<sub>2</sub>SnCl(2-SpyO)] (**3**), [Ph<sub>2</sub>SnCl(2-SpyO)] (**4**) et [(PhCH<sub>2</sub>)<sub>2</sub>SnCl(2-SpyO)] (**5**). On a caractérisé les nouveaux complexes par l'analyse élémentaire, par la spectroscopie IR et RMN (<sup>1</sup>H, <sup>119</sup>Sn, <sup>13</sup>C). Les données de la RMN du <sup>119</sup>Sn révèlent un indice effectif de coordination de 5 en solution. Les structures **1** et **4** ont été confirmées par cristallographie de rayons X. Les cristaux du composé **1** sont tricliniques et appartiennent au groupe d'espace *P* $\bar{1}$  et ceux du composé **4** sont monocliniques et appartiennent au groupe d'espace *P*2<sub>1</sub>/*n*. L'environnement de l'atome d'étain est une bipyramide trigonale déformée avec les atomes de Cl et d'oxygène en positions apicales. Les deux complexes exhibent de fortes interactions d'empilement  $\pi$ - $\pi$ .

**Mots clés :** diorganoétain, interaction d'empilement  $\pi$ - $\pi$ , 2-pyridinethiolato-*N*-oxyde, structure cristalline.

[Traduit par la Rédaction]

## Introduction

The synthesis and characterization of organotin(IV) complexes have been a continuing subject of study in recent years (1–6). Organotin(IV) compounds containing electro-negative atoms, such as halogen atoms, show Lewis acid character, and the tin atom increases its coordination number from four to five, six, or seven upon addition of neutral, organic donor ligands (7, 8). There have been numerous studies on adduct formation by organotin(IV) halides with a variety of O-, S-, and N-containing ligands (9–11). Owing to widespread applications of organotin (IV) complexes, they have played an important role in medicine, agriculture, and industry. A variety of organotin(IV) complexes are now known to show antitumor activity (12), and some others are well established for use as fungicides, biocides, and pesticides (13–15).

In the past few years, studies on organotin complexes with 2-pyridylthiolato (2-Spy), essentially concerning diorganotin derivatives of the type R<sub>2</sub>Sn(2-Spy)<sub>2</sub> or R<sub>2</sub>SnCl(2-Spy), have been reported (16–19). Evidence was obtained for tin chelation by thiol sulfur and one heterocyclic nitrogen atom. In our previous work, we have reported some novel macro-cycle organotin complexes with sulfur, nitrogen, and oxygen donor ligands (20–22). To continue our research in the field, we herein describe the synthesis and characterization of five diorganotin(IV) complexes R<sub>2</sub>SnCl(2-SpyO) (R = Mt, Et, *N*-Bu, Ph, or PhCH<sub>2</sub>), along with the X-ray crystal structures of Me<sub>2</sub>SnCl(2-SpyO) **1** and Ph<sub>2</sub>SnCl(2-SpyO) **4**. The reaction equation may be found in Scheme 1.

## Experimental

### Materials and measurements

Dimethyltin dichloride, diethyltin dichloride, *N*-dibutyltin dichloride, diphenyltin dichloride, and sodium 2-pyridinethiolato-*N*-oxide were purchased from Aldrich Company, and they were used without further purification. Dibenzyltin dichloride was prepared by a standard method reported in the literature (23). The melting points were obtained with a Kofler micro melting point apparatus and were uncorrected. Infrared spectra were recorded on a Nicolet-460 spectrophotometer using KBr discs and sodium chloride optics. <sup>1</sup>H, <sup>13</sup>C, and <sup>119</sup>Sn NMR spectra were recorded on a Bruker AMX-300 spectrometer operating at 300, 75.3, and

Received 23 May 2003. Published on the NRC Research Press Web site at <http://canjchem.nrc.ca> on 25 September 2003.

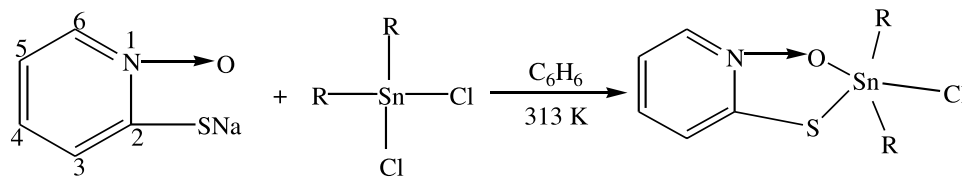
C. Ma,<sup>1,2</sup> J. Zhang, and R. Zhang, Department of Chemistry, Liaocheng University, 252059 Liaocheng, P.R. China.

<sup>1</sup>Corresponding author (e-mail: [macl@lctu.edu.cn](mailto:macl@lctu.edu.cn)).

<sup>2</sup>Present address: Taishan University, 271021 Taian, P.R. China.



Scheme 1.



Where: R = Me (**1**) ; Et (**2**); Bu (**3**); Ph (**4**); PhCH<sub>2</sub> (**5**)

111.9 MHz, respectively. The spectra were acquired at room temperature (298 K) unless otherwise specified; <sup>13</sup>C spectra are broadband proton decoupled. The chemical shifts were reported in ppm with respect to the references and were stated relative to external tetramethylsilane (TMS) for <sup>1</sup>H and <sup>13</sup>C NMR and to neat tetramethyltin for <sup>119</sup>Sn NMR. Elemental analyses were performed with a PE-2400II apparatus.

## Syntheses

### [Me<sub>2</sub>SnCl(2-SpyO)] **1**

The reaction was carried out under nitrogen atmosphere. The sodium 2-pyridinethiolato-*N*-oxide (0.149 g, 1.0 mmol) was added to a solution of benzene (20 mL) in a Schlenk flask and stirred; then dimethyltin dichloride (0.219 g, 1.0 mmol) was added to the reactor. The reaction mixture was stirred for 12 h at 40 °C and then was filtrated. The filtrate was gradually removed by evaporation under vacuum until a solid product was obtained. The solid was then recrystallized from dichloromethane–hexane. Colorless crystals were formed. Complex **1**: Yield 88%. mp 108–110 °C. IR (KBr, cm<sup>-1</sup>): 1596 (C = N), 1460 (C-N), 1207 (N-O), 750 (C-S), 350 (Sn-O), 305, 270 ν<sub>as</sub>, ν<sub>s</sub>(Sn-C), 301 (Sn-S), 238 (Sn-Cl). <sup>1</sup>H NMR (CDCl<sub>3</sub>) δ: 1.02 (s, 6H, Sn-CH<sub>3</sub>, <sup>2</sup>J<sub>SnH</sub> = 78.1 Hz), 7.35 (1H, 3-CH), 7.65 (1H, 4-CH), 7.05 (1H, 5-CH), 8.15 (1H, 6-CH). <sup>13</sup>C NMR (ppm) δ: 7.2 (s, Sn-CH<sub>3</sub>, <sup>1</sup>J<sub>SnC</sub> = 578 Hz); δ (C<sub>5</sub>H<sub>4</sub>NS): 118.8, 128.6, 129.1, 137.1, 157.2. <sup>119</sup>Sn NMR (CDCl<sub>3</sub>) (ppm): -52.6. Anal. calcd. for C<sub>7</sub>H<sub>10</sub>NCIOSSn (%): C 27.09, H 3.25, N 4.51, S 10.33; found: C 27.00, H 3.23, N 4.48, S 10.29.

### [Et<sub>2</sub>SnCl(2-SpyO)] **2**

Complex **2** was prepared similarly to **1** by using sodium 2-pyridinethiolato-*N*-oxide (1.0 mmol), benzene (25 mL), and Et<sub>2</sub>SnCl<sub>2</sub> (1.0 mmol). It was recrystallized from ether–hexane. Yield 76%. mp 118–120 °C. IR (KBr, cm<sup>-1</sup>): 1594 (C = N), 1462 (C-N), 1209 (N-O), 743 (C-S), 356 (Sn-O), 315, 280 ν<sub>as</sub>, ν<sub>s</sub>(Sn-C), 308 (Sn-S), 235 (Sn-Cl). <sup>1</sup>H NMR (CDCl<sub>3</sub>, 293 K) δ: 1.37 (t, 6H, -CH<sub>3</sub>), 1.62 (q, 4H, -CH<sub>2</sub>, <sup>2</sup>J<sub>SnH</sub> = 76.5 Hz), 7.34 (1H, 3-CH), 7.48 (1H, 4-CH), 6.96 (1H, 5-CH), 8.19 (1H, 6-CH). <sup>13</sup>C NMR (ppm) δ: 10.3, 18.7 (<sup>1</sup>J<sub>SnC</sub> = 548 Hz); δ (C<sub>5</sub>H<sub>4</sub>NS): 119.6, 128.3, 129.7, 138.3, 156.5. <sup>119</sup>Sn NMR (CDCl<sub>3</sub>) (ppm): -69.2. Anal. calcd. for C<sub>9</sub>H<sub>14</sub>NCIOSSn (%): C 32.14, H 4.19, N 4.17, S 9.53; found: C 32.08, H 4.12, N 4.13, S 9.56.

### [Bu<sub>2</sub>SnCl(2-SpyO)] **3**

Complex **3** was prepared similarly to **1** by using sodium 2-pyridinethiolato-*N*-oxide (1.0 mmol), benzene (30 mL), and Bu<sub>2</sub>SnCl<sub>2</sub> (1.0 mmol). It was recrystallized from di-

chloromethane–hexane. Yield 79%. mp 123–125 °C. IR (KBr, cm<sup>-1</sup>): 1604 (C = N), 1467 (C-N), 1215 (N-O), 746 (C-S), 366 (Sn-O), 323, 282 ν<sub>as</sub>, ν<sub>s</sub>(Sn-C), 306 (Sn-S), 237 (Sn-Cl). <sup>1</sup>H NMR (CDCl<sub>3</sub>) δ: 0.88 (t, 6H, -CH<sub>3</sub>), 1.28–1.70 (mbr, 12H, -CH<sub>2</sub>), 7.30 (1H, 3-CH), 7.43 (1H, 4-CH), 6.93 (1H, 5-CH), 8.12 (1H, 6-CH). <sup>13</sup>C NMR (ppm) δ: 13.81, 26.02, 27.0, 28.6 (<sup>n</sup>Bu, <sup>1</sup>J<sub>SnC</sub> = 494 Hz, <sup>2</sup>J<sub>SnC</sub> = 36.6 Hz, <sup>3</sup>J<sub>SnC</sub> = 101.7 Hz); δ (C<sub>5</sub>H<sub>4</sub>NS): 118.3, 129.5, 129.9, 138.8, 156.7. <sup>119</sup>Sn NMR (CDCl<sub>3</sub>) (ppm): -78.6. Anal. calcd. for C<sub>13</sub>H<sub>22</sub>NCIOSSn (%): C 39.79, H 5.07, N 3.57, S 8.15; found: C 39.73, H 5.11, N 3.51, S 8.11.

### [Ph<sub>2</sub>SnCl(2-SpyO)] **4**

Complex **4** was prepared similarly to **1** by using sodium 2-pyridinethiolato-*N*-oxide (1.0 mmol), benzene (30 mL), and Ph<sub>2</sub>SnCl<sub>2</sub> (1.0 mmol). The solid was then recrystallized from ether–dichloromethane. Colorless crystals were formed. Complex **4**: Yield 80%. mp 154–156 °C. IR (KBr, cm<sup>-1</sup>): 1606 (C = N), 1470 (C-N), 1215 (N-O), 745 (C-S), 368 (Sn-O), 328, 289 ν<sub>as</sub>, ν<sub>s</sub>(Sn-C), 310 (Sn-S), 245 (Sn-Cl). <sup>1</sup>H NMR (CDCl<sub>3</sub>) δ: 7.17–7.65 (mbr, 10H, ph-H, <sup>3</sup>J<sub>SnH</sub> = 89 Hz), 7.35–7.40 (m, 1H, 3-CH), 7.37–7.41 (m, 1H, 4-CH), 6.80 (1H, 5-CH), 8.11 (1H, 6-CH). <sup>13</sup>C NMR (ppm) δ: (C<sub>6</sub>H<sub>5</sub>) 124.7 (<sup>3</sup>J<sub>SnC</sub> = 50 Hz, *m*-C), 129.6 (<sup>4</sup>J<sub>SnC</sub> = 12 Hz, *p*-C), 136.9 (<sup>2</sup>J<sub>SnC</sub> = 36 Hz, *p*-C), 146.5 (<sup>1</sup>J<sub>SnC</sub> = 597 Hz, *i*-C); δ (C<sub>5</sub>H<sub>4</sub>NS): 119.7, 128.1, 128.5, 137.0, 154.1. <sup>119</sup>Sn NMR (CDCl<sub>3</sub>) (ppm): -177.6. Anal. calcd. for C<sub>17</sub>H<sub>14</sub>NCIOSSn (%): C 47.00, H 4.11, N 3.22, S 7.36; found: C 46.96, H 4.08, N 3.27, S 7.39.

### [(PhCH<sub>2</sub>)<sub>2</sub>SnCl(2-SpyO)] **5**

Complex **5** was prepared similarly to **1** using sodium 2-pyridinethiolato-*N*-oxide (1.0 mmol), benzene (30 mL), and (PhCH<sub>2</sub>)<sub>2</sub>SnCl<sub>2</sub> (1.0 mmol). It was recrystallized from dichloromethane–hexane. Yield 85%. mp 168–170 °C. IR (KBr, cm<sup>-1</sup>): 1608 (C = N), 1467 (C-N), 1215 (N-O), 747 (C-S), 370 (Sn-O), 325, 281 ν<sub>as</sub>, ν<sub>s</sub>(Sn-C), 309 (Sn-S), 250 (Sn-Cl). <sup>1</sup>H NMR (CDCl<sub>3</sub>) δ: 7.26–7.65 (mbr, 10H, -Ph), 3.26 (4H, CH<sub>2</sub>-Ph), 7.35 (d, 1H, 3-CH), 7.40 (1H, 4-CH), 6.89 (1H, 5-CH), 8.09 (1H, 6-CH). <sup>13</sup>C NMR (CDCl<sub>3</sub>) (ppm) δ: 38.5 (CH<sub>2</sub>-Ph, <sup>1</sup>J<sub>SnC</sub> = 546 Hz), 125.4 (<sup>4</sup>J<sub>SnC</sub> = 30 Hz, *m*-C), 127.0 (<sup>5</sup>J<sub>SnC</sub> = 26 Hz, *p*-C), 130.5 (<sup>3</sup>J<sub>SnC</sub> = 44 Hz, *o*-C), 139.0 (<sup>2</sup>J<sub>SnC</sub> = 36 Hz, *i*-C); δ (C<sub>5</sub>H<sub>4</sub>NS): 119.9, 128.5, 136.6, 141.5, 153.8. <sup>119</sup>Sn NMR (CDCl<sub>3</sub>) (ppm): -178.9. Anal. calcd. for C<sub>19</sub>H<sub>18</sub>NCIOSSn (%): C 49.34, H 3.89, N 3.03, S 6.92; found: C 49.29, H 3.83, N 3.07, S 6.88.

## X-ray structure determination

X-ray crystallographic studies of complexes **1** and **4** were done using a Bruker Smart 1000 diffractometer fitted with



graphite-monochromated Mo K $\alpha$  radiation ( $\lambda = 0.71073 \text{ \AA}$ ).<sup>3</sup> The  $\omega/2\theta$  scan technique was employed. Corrections were applied for Lorentz and polarization effects but not for absorption, satisfying  $I \geq 2\sigma(I)$ . Criterion of observability was used for the solution and refinement. The structures were solved using direct methods and refined by a full-matrix least-squares procedure based on  $F^2$  using the SHELXL-97 program system. All non-H atoms were included in the model at their calculated positions.

### In vitro antitumour activity tests of complexes 1, 2, 3, 4, and 5

The in vitro antitumour activity tests of complexes 1–5 against the cell lines were performed according to the PIT method described previously (24).

## Results and discussion

### IR data

In the IR spectra of 1–5 we have assigned some bonds in the range 350–370  $\text{cm}^{-1}$  to Sn–O, which in our series seems to be little influenced by the type of halogen that is bonded to tin. In the far IR region complexes 1–5 show a strong absorption in the 301–310  $\text{cm}^{-1}$  range, due to the Sn–S stretching mode of vibration. The Sn–C and Sn–Cl stretching vibrations agree well with the trends previously observed in similar complexes containing N-donor chelating ligands (9). In the spectra of alkyl derivatives 1, 2, and 3, the Sn–Cl stretching bands are observed between 235 and 238  $\text{cm}^{-1}$ , while in 4 and 5 these bonds fall in the region 245–250  $\text{cm}^{-1}$ , being shifted to lower frequencies with respect to those reported for corresponding  $\text{Ph}_2\text{SnCl}(\text{Ma})$  (25).

### NMR data

The chemical shift values of the ligand protons in complexes 1–5 are in the region 6.80–8.19 ppm. The  $^2J(^{119}\text{Sn}-^1\text{H})$  of dimethyltin derivative 1 has a value of 78.1 Hz, typical of five-coordinated tin species. On the basis of Lockart's equation (26), the Me–Sn–Me angle is estimated to be approximately 128°, which agrees with that found in the crystal structure. Moreover, the  $^1\text{H}$  NMR spectra of complex 4 shows two multiplets attributable to the H(2,6) and H(3,4,5) of the phenyl protons. The resonance of H(2,6) has tin satellites with  $^3J_{\text{SnH}}$  (89 Hz) greater than in uncomplexed  $\text{Ph}_2\text{SnCl}_2$  (81.3 Hz) (27). The increase in the coupling constant indicates the higher coordination number of tin.

The  $^{119}\text{Sn}$  NMR chemical shifts of 1–5 are in accordance with those of five-coordinate diorganotin(IV) halide complexes involving halide or phosphine ligands (28), as well as chelating S-donor and O-donor complexes (29, 30). Five-coordinate  $\text{ClPh}_2\text{SnXY}$  compounds (X and Y = electronegative groups) in solution have  $^{119}\text{Sn}$  NMR values in the region –140 to –180 ppm, depending on the groups present (31, 32). The  $^{119}\text{Sn}$  value for 4 at –177.6 ppm in solution suggests that the Sn–O interaction probably survives in solution and that a five-coordinate species is maintained.

**Table 1.** ID<sub>50</sub> values in ng mL<sup>–1</sup> against two human tumour cells, MCF-7 and WiDr, of the complexes and reference compounds.

Complexes	MCF-7	WiDr
1	276	894
2	288	1185
3	96	295
4	295	1143
5	292	1182
CPT	699	967
ETO	2594	150
5FU	18	<3

The  $^{13}\text{C}$  NMR spectra show a significant downfield shift of all carbon resonances. The shift is a consequence of an electron density transfer from the ligand to the acceptor. The  $^nJ(^{119}\text{Sn}-^{13}\text{C})$  coupling constants were detected in the case of sufficiently soluble derivatives. In complexes 1–5, the order of magnitude of the coupling constants is the same as those previously reported for analogous five-coordinate derivatives (33, 34). By using the simple linear relationship between  $^1J_{\text{SnC}}$  and the C–Sn–C bond angles derived by Lockart and Manders (26) and Howard et al. (27) for the dimethyltin species, a value has been found for complex 1 in the range 126–132°, which agrees well with the angles of 125° and 129° found in the crystal structure.

### Biologic activity measurement

The in vitro activities of all complexes 1–5, expressed as ID<sub>50</sub> values against two human tumour cells, MCF-7 and WiDr, are given in Table 1. They are compared with the ID<sub>50</sub> values obtained for some reference compounds (12). All the activities are rather poor. Complex 3 exhibited the highest activity, slightly better than *cis*-platin (CPT) and comparable or slightly better than etoposide (ETO) against MCF-7 but less than 5-fluorouracil (5FU) against MCF-7 and WiDr (12).

### Molecular structures

The crystal data and refinement details of complexes 1 and 4 are given in Table 2. Selected bond distances and angles are shown in Tables 3 and 4. The crystal structures and unit cell packing figures are shown in Figs. 1–4, respectively.

For complex 1, the molecular structure and the atom numbering scheme is shown in Fig. 1. The asymmetric unit cell contains two crystallographically independent molecules **A** and **B**. Conformations of the two independent molecules are almost the same, with only little differences in bond lengths and bond angles (see Table 3). The coordination geometry about Sn(IV) is a distorted trigonal bipyramid in which the two methyl groups and a sulfur atom form the equatorial plane, while the halogen and the ligand oxygen occupy the apical positions. In this way the ligand behaves as a

<sup>3</sup>Supplementary crystallographic data (excluding structure factors) for the structure analysis of complexes 1 and 4 may be purchased from the Depository of Unpublished Data, Document Delivery, CISTI, National Research Council Canada, Ottawa, ON K1A 0S2, Canada ([http://www.nrc.ca/cisti/irm/unpub\\_e.shtml](http://www.nrc.ca/cisti/irm/unpub_e.shtml) for information on ordering electronically). CCDC 207124 and 192505 contain the supplementary data for this paper. These data can be obtained, free of charge, via [www.ccdc.cam.ac.uk/conts/retrieving.html](http://www.ccdc.cam.ac.uk/conts/retrieving.html) (or from the Cambridge Crystallographic Data Centre, 12 Union Road, Cambridge, U.K.; fax +44 1223 336033; or [deposit@ccdc.cam.ac.uk](mailto:deposit@ccdc.cam.ac.uk)).



**Table 2.** Crystal data and refinement details for complexes **1** and **4**.

Complexes	<b>1</b>	<b>4</b>
Chemical formula	C <sub>7</sub> H <sub>10</sub> NCIOSSn	C <sub>17</sub> H <sub>14</sub> NCIOSSn
Formula weight	310.36	434.49
Temperature (K)	298(2)	298(2)
Crystal system	Triclinic	Monoclinic
Space group	<i>P</i> $\bar{1}$	<i>P</i> 2 <sub>1</sub> / <i>n</i>
<i>a</i> (Å)	9.281(13)	8.667(3)
<i>b</i> (Å)	9.462(13)	15.541(5)
<i>c</i> (Å)	13.512(18)	13.025(4)
$\alpha$ (°)	75.15(2)	90
$\beta$ (°)	84.88(2)	103.162(4)
$\gamma$ (°)	76.198(19)	90
<i>V</i> (Å <sup>3</sup> )	1108(3)	1708.4(9)
<i>D<sub>c</sub></i> (g cm <sup>-3</sup> )	1.860	1.689
<i>Z</i>	4	4
<i>F</i> (000)	600	856
Crystal size (mm)	0.43 × 0.15 × 0.20	0.40 × 0.30 × 0.10
Crystal colour	Colourless	Colourless
$\theta$ range (°)	1.57–26.37	2.07–23.31
Absorption (mm <sup>-1</sup> )	2.692	1.774
Reflections (collected/unique)	5223/4115	7314/2464
	[ <i>R</i> <sub>int</sub> = 0.027]	[ <i>R</i> <sub>int</sub> = 0.0299]
Goodness-of-fit on <i>F</i> <sup>2</sup>	0.896	1.008
<i>R</i> indices (all data)	<i>R</i> <sub>1</sub> = 0.0877, <i>wR</i> <sub>2</sub> = 0.1167	<i>R</i> <sub>1</sub> = 0.0408, <i>wR</i> <sub>2</sub> = 0.0525
Largest diff. peak and hole (e Å <sup>-3</sup> )	0.746 and -0.682	0.636 and -0.317

**Table 3.** Selected bond distances (Å) and angles (°) for [Me<sub>2</sub>SnCl(2-SpyO)] (**1**).

Molecule A		Molecule B	
<b>Bond distances (Å)</b>			
Sn(2)—C(8)	2.075(8)	Sn(1)—C(2)	2.084(8)
Sn(2)—C(9)	2.091(8)	Sn(1)—C(1)	2.120(8)
Sn(2)—Cl(2)	2.467(4)	Sn(1)—Cl(1)	2.465(4)
Sn(2)—S(2)	2.449(4)	Sn(1)—S(2)	2.459(4)
Sn(2)—O(2)	2.212(6)	Sn(1)—O(1)	2.223(6)
O(2)—N(2)	1.328(8)	O(1)—N(1)	1.334(8)
C(10)—N(2)	1.338(9)	C(7)—N(1)	1.342(9)
C(14)—N(2)	1.349(10)	C(3)—N(1)	1.351(9)
S(2)—C(10)	1.727(9)	S(1)—C(3)	1.717(8)
<b>Bond angles (°)</b>			
O(2)—Sn(2)—Cl(2)	162.21(17)	Cl(1)—Sn(1)—O(1)	160.41(16)
C(8)—Sn(2)—C(9)	125.9(4)	C(2)—Sn(1)—C(1)	129.1(4)
C(8)—Sn(2)—O(2)	92.1(3)	O(1)—Sn(1)—C(2)	90.6(3)
C(9)—Sn(2)—O(2)	89.2(3)	O(1)—Sn(1)—C(1)	92.3(3)
C(8)—Sn(2)—S(2)	112.3(3)	S(1)—Sn(1)—C(2)	117.9(3)
C(9)—Sn(2)—S(2)	120.8(3)	S(1)—Sn(1)—C(1)	112.2(3)
O(2)—Sn(2)—S(2)	78.01(15)	S(1)—Sn(1)—O(1)	76.85(16)
C(8)—Sn(2)—Cl(2)	98.4(3)	Cl(1)—Sn(1)—C(2)	96.6(3)
C(9)—Sn(2)—Cl(2)	96.2(3)	Cl(1)—Sn(1)—C(1)	97.1(3)
Cl(2)—Sn(2)—S(2)	84.71(10)	Cl(1)—Sn(1)—S(1)	83.69(8)

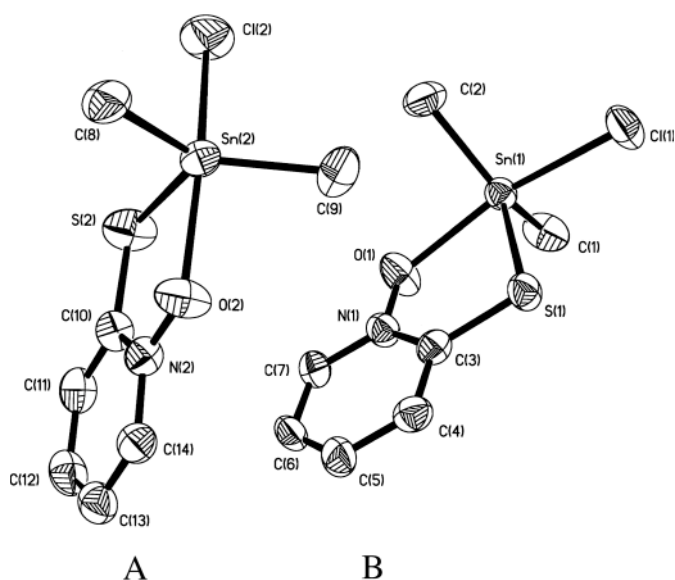
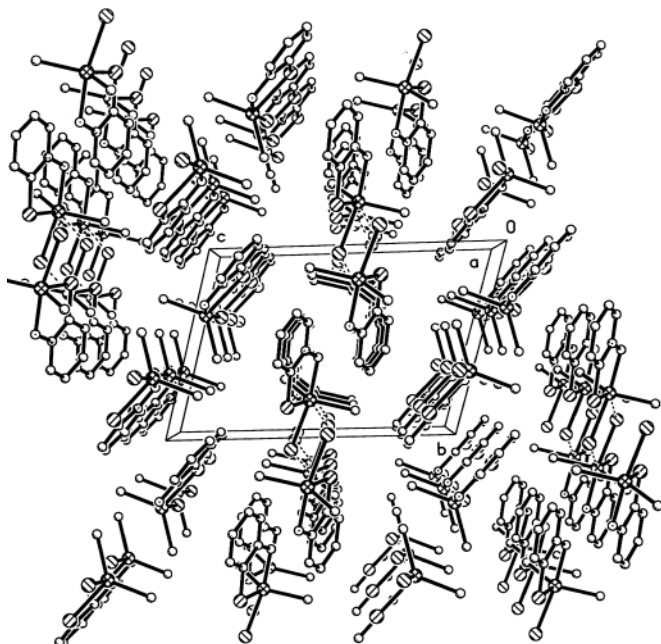
bidentate species and chelates the tin atom by means of the oxygen and the thiolato sulfur. The consequence is formation of a five-membered ring with an S—Sn—O bite angle (76.85(16)° for Sn(1), 78.01(15)° for Sn(2)), which is a little

**Table 4.** Selected bond distances (Å) and angles (°) for [Ph<sub>2</sub>SnCl(2-SpyO)] (**4**).

<b>Bond distances (Å)</b>			
Sn(1)—C(12)	2.123(4)	Sn(1)—O(1)	2.188(3)
Sn(1)—C(6)	2.132(4)	N(1)—O(1)	1.331(4)
Sn(1)—Cl(1)	2.4710(11)	N(1)—C(1)	1.359(5)
Sn(1)—S(1)	2.4402(14)	S(1)—C(1)	1.722(4)
<b>Bond angles (°)</b>			
O(1)—Sn(1)—Cl(1)	165.75(8)	C(12)—Sn(1)—C(6)	126.65(14)
O(1)—Sn(1)—C(12)	90.74(13)	C(12)—Sn(2)—Cl(1)	95.61(11)
O(1)—Sn(1)—C(6)	92.12(13)	C(6)—Sn(1)—Cl(1)	94.27(10)
S(1)—Sn(1)—C(12)	119.76(11)	O(1)—Sn(2)—S(1)	78.57(8)
S(1)—Sn(1)—C(6)	112.98(11)	S(1)—Sn(1)—Cl(1)	87.21(4)

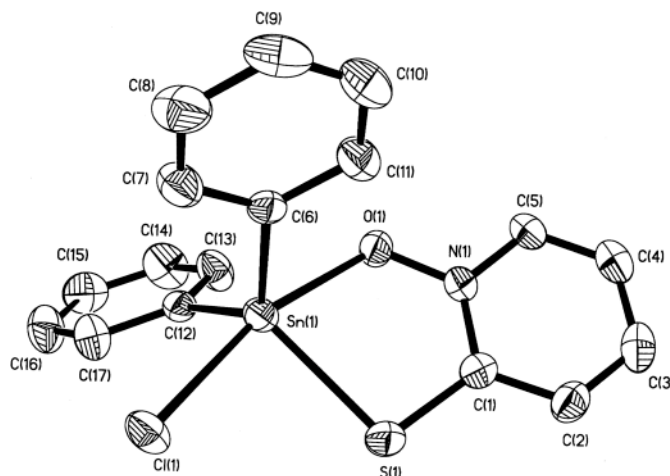
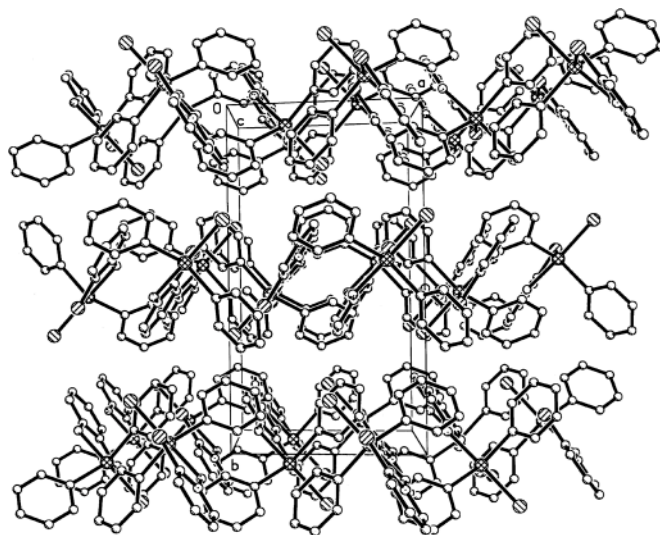
bigger than those found in [Me<sub>2</sub>Sn(2-SpyO)<sub>2</sub>] (72.0(1)° and 73.5(1)°) (33, 35). The Sn—C distances (2.075(8)–2.120(8) Å) and the Sn—S distances (2.459(4) and 2.449(4) Å) are similar to those found in [Me<sub>2</sub>SnCl(TNEE)] (2.110(6) and 2.473(2) Å, respectively) (36), but shorter than those found in other trialkyltin(chelate) systems (37). The Sn—O distances (Sn(1)—O(1) = 2.223(6) Å and Sn(2)—O(2) = 2.212(6) Å) are well within the range observed for pyridine-*N*-oxide adducts of organotin(II) (38). The S—C bond distances (1.717(8) and 1.727(9) Å) are shorter than those found in [R<sub>2</sub>Sn(Spy)<sub>2</sub>] (1.751(7) Å) (19) and are consistent with single-bond character. These values suggest that the ability of HSpy to transform its thione to the thiol is higher when compared with HSpyO. The Sn—Cl bond length (Sn(1)—Cl(1), 2.465(4) Å and Sn(2)—Cl(2), 2.467(4) Å),



**Fig. 1.** Molecular structure of complex **1**.**Fig. 2.** Crystal packing of complex **1**.

lies in the range of the normal covalent radii, 2.37–2.60 Å (39). In molecule **B**, as seen in Fig. 2, the closest intermolecular Sn(1)···Cl(1)<sup>#</sup> distance is 3.974 Å, which is just comparable to the sum of the van der Waals radii of Sn and Cl (4.0 Å) (40). It is apparent that the presence or absence of the additional intermolecular Sn···Cl interaction has only a small effect on the molecular geometry of the R<sub>2</sub>SnCl(2-SpyO) complexes.

For complex **4**, which is similar to complex **1**, the geometry at Sn is also a distorted *cis*-trigonal bipyramidal with Cl and O atoms in axial sites (Cl(1)–Sn(1)–O(1) 165.75(8)°) and one S and two phenyl C atoms occupying the equatorial plane (C(12)–Sn(1)–C(6) 126.65(14)°, C(12)–Sn(1)–S(1)

**Fig. 3.** Molecular structure of complex **4**.**Fig. 4.** Crystal packing of complex **4**.

119.76(11)°, C(6)–Sn(1)–S(1) 112.98(13)°. The Sn–S bond length (Sn(1)–S(2), 2.4402(14) Å) lies in the range of that reported for triphenyltin heteroareneithiolates (2.41 to 2.48 Å) (41) and is shorter than that of Ph<sub>2</sub>SnCl(MBT) (2.485(22) Å) (24). Finally, the Sn–C bond lengths are approximately equal (2.123(4) and 2.132(4) Å) and similar to the average value, 2.13 Å (41).

Both of the crystal structures of complexes **1** and **4** show ring-stacking interactions; each SpyO group is arranged face-to-face at a distance of 3.588 Å for molecule **A** and 3.625 Å for molecule **B** in complex **1**, and 3.557 Å in complex **4**, which shows significant  $\pi$ – $\pi$  stacking interactions (42, 43).

## Acknowledgements

This work was supported by the National Nature Science Foundation of Shandong Province, P.R. China and the National Natural Foundation, P.R. China (20271025).



## References

1. T.S. Basu Baul, S. Dhar, E. Rivarola, F.E. Smith, R. Butcher, X.Q. Song, M. McCain, and G. Eng. *Appl. Organometal. Chem.* **17**, 261 (2003).
2. M. Nath, R. Yadav, G. Eng, and P. Musingarimi. *J. Chem. Res.* S409 (1998).
3. M. Gielen. *Coord. Chem. Rev.* **151**, 41 (1996).
4. S.P. Gupta. *Chem. Rev.* **94**, 1507 (1994).
5. P.J. Smith. *Chemistry of tin*. Blackie Academic & Professional, London, U.K. 1998.
6. A.G. Davies. *Organotin chemistry*. VCH, Weinheim, Germany. 1997.
7. A.G. Davies and P. Smith. In *Comprehensive organometallic chemistry*. Vol. 2. Edited by G. Wilkinson, F.G.A. Stone, and E.W. Abel. Pergamon Press, New York. 1982. p. 519.
8. F. Huber, R. Schmiedgen, M. Schürmann, R. Barbieri, G. Ruisi, and A. Silvestri. *Appl. Organometal. Chem.* **11**, 869 (1997).
9. P. Tavridou, U. Russo, D. Marton, G. Valle, and D. Kovala-Demertzi. *Inorg. Chim. Acta*, **231**, 139 (1995).
10. D. Kovala-Demertzi, P. Tavridou, U. Russo, and M. Gielen. *Inorg. Chim. Acta*, **239**, 177 (1995).
11. C. López, A. Sanchez Gonzalez, M.E. Garcia, J.S. Casas, and J. Sordo. *J. Organomet. Chem.* **434**, 261 (1992).
12. M. Gielen. *Appl. Organomet. Chem.* **16**, 481 (2002).
13. M.F. Mahon, K.C. Molly, and P.C. Waterfield. *J. Organomet. Chem.* **361**, C5 (1989).
14. C.J. Evans and S. Karpel. *J. Organomet. Chem.* **16**, 1 (1985).
15. A.K. Saxena. *Appl. Organomet. Chem.* **1**, 39 (1987).
16. M.V. Castaño, A. Macias, A. Castiñeiras, A.S. González, E.G. Martinez, J.S. Casas, J. Sordo, W. Hiller, and E.E. Catellano. *J. Chem. Soc. Dalton Trans.* 1001 (1990).
17. M. Bouâlam, J. Meunier-Piret, M. Biesemans, R. Willem, and M. Gielen. *Inorg. Chim. Acta* **198**, 249 (1992).
18. R. Schmiedgen, F. Huber, and H. Preut. *Acta Crystallogr. Sect. C Cryst. Struct. Commun.* **49**, 1735 (1993).
19. R. Schmiedgen, F. Huber, H. Preut, G. Ruisi, and R. Barbieri. *Appl. Organomet. Chem.* **8**, 397 (1994).
20. C.L. Ma, F. Li, D.Q. Wang, and H.D. Yin. *J. Organomet. Chem.* **667**, 5 (2003).
21. C.L. Ma, Q. Jiang, R.F. Zhang, and D.Q. Wang. *J. Chem. Soc. Dalton Trans.* **15**, 2975 (2003).
22. C.L. Ma, Q. Jiang, and R.F. Zhang. *J. Organomet. Chem.* **678**, 148 (2003).
23. K.A. Koreschkow. *Chem. Ber.* **66**, 1961 (1935).
24. R. Van Lambalgen and P. Lelieveld. *Investig. New Drugs*, **5**, 161 (1987).
25. D. Fregona, Z. Guo, G. Faraglia, and S. Sitran. *J. Coord. Chem.* **28**, 73 (1993).
26. T.P. Lockhart and W.F. Manders. *Inorg. Chem.* **25**, 892 (1986).
27. W.F. Howard, Jr., R.W. Crecely, and W.H. Nelson. *Inorg. Chem.* **24**, 2204 (1985).
28. A. Tarassoli, T. Sedaghat, B. Neumüller, and M. Ghassemzadeh. *Inorg. Chim. Acta*, **318**, 15 (2001).
29. R. Colton and D. Dakternieks. *Inorg. Chim. Acta*, **148**, 31 (1988).
30. K. Handlř, A. Lyčka, J. Holeček, M. Nádvorník, V. Pejchal, and A. Sebal. *Collect. Czech. Chem. Commun.* **59**, 885 (1994).
31. C. Pettinari, F. Marchetti, A. Gregori, A. Cingolani, J. Tanski, M. Rossi, and F. Caruso. *Inorg. Chim. Acta*, **257**, 37 (1997).
32. Z.H. Chohan, R.A. Howie, and J.L. Wardell. *J. Organomet. Chem.* **577**, 140 (1999).
33. C. Pettinari, M. Pellei, C. Santini, I. Natali, F. Accorroni, and A. Lorenzotti. *Polyhedron*, **17**, 4487 (1998).
34. B. Wrackmeyer. *Annu. Rep. NMR Spectrosc.* **16**, 73 (1985).
35. S.W. Ng, C. Wei, V.G. Komar Das, and T.C.W. Mak. *J. Organomet. Chem.* **334**, 295 (1987).
36. M.D. Couce, G. Faraglia, U. Russo, L. Sindellari, and G. Valle. *J. Organomet. Chem.* **513**, 77 (1996).
37. S.W. Ng, C. Wei, V.G. Kumar Das, and T.C.W. Mak. *J. Organomet. Chem.* **326**, 61 (1987).
38. A.L. Rheingold, S.W. Ng, and J.J. Zuckerman. *Organometallics*, **3**, 233 (1984).
39. F.H. Allen, S.A. Bellard, M.D. Brice, B.A. Cartwright, A. Doubleday, H. Higgs, T. Hummelink, B.G. Hummelink-Peters, O. Kennard, W.D.S. Motherwell, J.R. Rogers, and D.G. Watson. *Acta Crystallogr.* **B35**, 2331 (1979).
40. A. Bondi. *J. Phys. Chem.* **68**, 441 (1964).
41. J.E. Huheey, E.A. Keiter, and R.L. Keiter. *Principles and applications of inorganic chemistry*. 4th ed. Harper Collins, New York. 1993. p. 292.
42. T. Steiner, B. Lutz, J. van der Maas, A.M.M. Kroon, and M. Tamm. *Chem. Commun.* 171 (1998).
43. B.H. Ye, X.M. Chen, G.Q. Xue, and L.N. Ji. *J. Chem. Soc. Dalton Trans.* 2827 (1998).



# Synthesis, characterization, and optical properties of a novel azo-dye bearing an oligo(ethylene glycol) methyl ether side chain in solution and in the solid state

Ernesto Rivera, Michel Belletête, Almeria Natansohn, and Gilles Durocher

**Abstract:** A novel azobenzene compound bearing a short poly(ethylene glycol) methyl ether side chain, *N*-methyl-*N*-{4-[(*E*)-(4-nitrophenyl)diazényl]phényl}-*N*-(3,6,9,12,15,18,21,24-octaoxapentacos-1-yl)amine (RED-PEGM-8) was synthesized and characterized. RED-PEGM-8 exhibits a thermal behavior similar to that of Disperse Red-1; however, its thermal stability, as well as its  $T_g$  and  $T_m$  values, are lower because of the presence of the PEGM segment. The optical properties of this compound in solution and in the solid state were studied by UV-vis spectroscopy. The appearance of a blue-shifted band in aqueous solutions at high concentrations of the chromophore reveals the existence of H-type aggregates, resulting from  $\pi$ - $\pi$  intermolecular interactions between the azobenzene units. Strong intermolecular interactions were also confirmed by  $^1\text{H}$  NMR measurements. Optical properties of RED-PEGM-8 in the solid state (thin film) also suggest the presence of H aggregates. However, a tail is also detected in the red region of the absorption spectrum, which could be because of the formation of J-type aggregates in the thin film.

**Key words:** aggregation, azo-dye, poly(ethylene glycol) methyl ether.

**Résumé :** Un nouveau dérivé de type azobenzène, ayant une courte chaîne poly(éthylène)glycol méthyl éther, soit le *N*-méthyl-*N*-{4-[(*E*)-(4-nitrophényl)diazényl]phényl}-*N*-(3,6,9,12,15,18,21,24-octaoxapentacos-1-yl)amine (RED-PEGM-8), a été synthétisé et caractérisé. RED-PEGM-8 montre un comportement thermique similaire à celui du Disperse Red-1. Cependant, sa stabilité thermique de même que les valeurs de  $T_g$  et  $T_m$  sont inférieures à celles du Disperse Red-1 à cause de la présence du segment PEGM. Les propriétés optiques de ce composé en solution et à l'état solide (film mince) ont été étudiées à l'aide de la spectroscopie UV-visible. En solution aqueuse, à hautes concentrations, ce composé montre l'apparition d'une bande d'absorption dans la région bleue du spectre. Ces résultats révèlent la présence d'aggrégats de type H provenant d'interactions intermoléculaires  $\pi$ - $\pi$  entre unités azobenzène. L'étude des spectres RMN protoniques a confirmé la présence d'interactions intermoléculaires fortes. Finalement, les propriétés optiques du RED-PEGM-8 à l'état solide (film mince) suggèrent également la présence d'aggrégats de type-H. Cependant, le spectre d'absorption du film mince montre aussi l'apparition d'une queue aux grandes longueurs d'onde, qui pourrait être due à la formation d'aggrégats de type J dans le film.

**Mots clés :** aggrégation, colorant azo, poly(éthylène)glycol méthyl éther.

## Introduction

Poly(ethylene glycol) (PEG) has been widely studied because of its interesting and useful properties, such as solvent-selective combination, owing to its water solubility. These properties make it attractive for the synthesis of new amphiphilic compounds (1a). PEG has been widely used for the preparation of nonionic surfactants, which can act as

demulsifiers, dispersing agents, and emulsion stabilizers. For instance, polyhydroxystearic acid – PEG copolymers are used in emulsion polymerization, and PEG-alkyd resins are used for producing water-emulsifiable gloss paints and industrial degreaser concentrates (1b). Besides, PEG has been often used in the synthesis of ionic conducting materials (2) because of its ability to complex cations and forms charge-transfer complexes (CT) (3). In a recent study, an end-

Received 12 May 2003. Published on the NRC Research Press Web site at <http://canjchem.nrc.ca> on 26 September 2003.

*In memoriam: dedicated to Almeria with all our respect and admiration. Thanks for everything I received from you. ER*

**E. Rivera<sup>1</sup> and A. Natansohn.** Department of Chemistry, Queen's University, Chernoff Hall, Kingston, ON K7L 3N6, Canada.  
**M. Belletête and G. Durocher.<sup>2</sup>** Département de Chimie, Université de Montréal, C.P. 6128, Succursale Centre-ville, Montréal, QC H3C 3J7, Canada.

<sup>1</sup>Present address: Instituto de Investigaciones en Materiales UNAM, Circuito Exterior Ciudad Universitaria, C.P. 04510 México, D.F. México.

<sup>2</sup>Corresponding author (e-mail: [gilles.durocher@umontreal.ca](mailto:gilles.durocher@umontreal.ca)).



capped sample, oligo(ethylene glycol) methyl ether 3,5-dinitrobenzoate (DNB), has been synthesized, and the formation of an intramolecular CT in a water solution has been reported, resulting from the coiling of the highly hydrophilic oligo(ethylene glycol) methyl ether (PEGM) chain around the hydrophobic DNB unit (4).

On the other hand, azobenzenes are very versatile chromophores for incorporation in novel materials, owing to the *trans*–*cis* photoisomerization of the azobenzene groups. For instance, photoinduced motions at different levels occur when azopolymers are irradiated with laser polarized light (5). Several reviews covering most of the implications of azobenzene photoisomerization in polymer structures have been published (6–10). In the last few years, Natansohn and co-workers have synthesized and characterized various polymers bearing amino-nitro substituted azobenzene units (11–13). In general, they exhibit absorption wavelength maxima close to those observed for similar push–pull azo compounds (14). Some azopolymers have also been studied in Langmuir–Blodgett films (15–17). In these materials, both J- and H-type aggregation have been observed.

Since azopolymers are highly versatile materials and PEG provides water solubility and other interesting properties, we have decided to link a PEGM oligomer chain to donor–acceptor azobenzene chromophores, thus forming new amphiphilic dyes. We believe that these azo-dyes can provide valuable information about optical properties of self-assemblies, Langmuir–Blodgett films, and mono and multi-layer systems. In this paper, we report on the synthesis, characterization, and optical properties of *N*-methyl-*N*-[4-[(*E*)-(4-nitrophenyl)diazanyl]phenyl]-*N*-(3,6,9,12,15,18,21,24-octaoxapentacos-1-yl)amine (RED-PEGM-8) in organic and aqueous solutions, as well as in the solid state (casted film). The appearance of new absorption bands in the blue region were found in aqueous solutions and in the solid state and were interpreted in terms of aggregate formation.

## Experimental section

All the solvents and reagents employed in the synthesis were purchased from Aldrich and used as received. *N*-methylaniline was freshly distilled under reduced pressure prior to use. Materials were dissolved in spectral quality solvents, purchased from Aldrich, for UV–vis spectroscopy. The  $^1\text{H}$  and  $^{13}\text{C}$  NMR spectra of the compounds were recorded in solution on a Bruker ARX-400 spectrometer. Thermal properties of the compounds such as stability, glass transition temperature ( $T_g$ ), and melting point ( $T_m$ ) were determined by thermogravimetric analysis (TGA) from 20 to 800 °C and differential scanning calorimetry (DSC) from –150 to 300 °C. Absorption spectra of RED-PEGM-8 were recorded on a Varian Cary 1 Bio UV–vis (model 8452A) spectrophotometer using 1 cm quartz cells.

### Synthesis of RED-PEGM-8

#### PEGM-Ts (1)

To an ice–salt cooled mixture of poly(ethylene glycol) methyl ether (PEGM), bearing an  $M_w$  of 350 (52.5 g, 150 mmol) in 170 mL of pyridine, tosyl chloride (29.6 g, 155 mmol) was added. The mixture was vigorously stirred

until tosyl chloride was completely solubilized. The mixture was put in the refrigerator overnight, then poured into 500 mL of HCl 50%, and extracted with chloroform. The combined organic extracts were washed with a saturated solution of  $\text{Na}_2\text{CO}_3$  and then with water. The organic phase was dried with  $\text{Na}_2\text{SO}_4$  and concentrated under vacuum. PEGM-Ts was obtained as a transparent liquid (72.8 g, 135 mmol). Yield 90%.

#### PEGM-I (2)

To a solution of **1** (43.8 g, 81.2 mmol) in 98 mL of acetone, NaI (26 g, 173 mmol) was added and heated to reflux for 24 h. The solution was filtered to remove the TsONa generated during the reaction and the filtrates concentrated under reduced pressure. PEGM-I crude product (37.9 g, 79.6 mmol) was obtained as a yellowish, viscous oil and used immediately in the next step. Yield 85%.

#### *N*-PEGM-*N*-methylaniline (3)

To a solution of *N*-methylaniline (8.5 g, 79.5 mmol) and  $\text{Na}_2\text{CO}_3$  (8.6 g, 81 mmol) in DMF (120 mL), **2** (37.9 g, 79.6 mmol) dissolved in 20 mL of DMF was added, and the mixture was heated with vigorous stirring at 70 °C for 24 h. The reaction mixture was poured into water and extracted with chloroform. The organic phase was dried with  $\text{Na}_2\text{SO}_4$  and concentrated under vacuum. The crude product was purified by flash column chromatography, first eluting with ethyl acetate 100% to remove the remaining starting material and then with a mixture of  $\text{CHCl}_3$ –MeOH, 10:1. *N*-PEGM-*N*-methylaniline **3** (see Scheme 1) was obtained as an orange liquid (20.9 g, 47.7 mmol). Yield 60%. IR (film) ( $\text{cm}^{-1}$ ): 3092 (s, aromatic C–H), 2873 (s,  $\text{CH}_2$  and  $\text{CH}_3$ ), 1600, 1507, 1451 (s, aromatic ring C=C), 1350 (s, C–N), 1111 (s, O– $\text{CH}_2$ ), 750, 694 (out of plane, aromatic =C–H).  $^1\text{H}$  NMR ( $\text{CDCl}_3$ , 300 MHz) (ppm)  $\delta$ : 7.17 (t, 2H,  $\text{H}^2$ ), 6.67 (m, 3H,  $\text{H}^1$  and  $\text{H}^3$ ), 3.61–3.33 (m, 28.6H, all  $-\text{CH}_2-$ ), 3.34 (s, 3H,  $-\text{OCH}_3$ ), 2.93 (s, 3H,  $\text{CH}_3$ –N).  $^{13}\text{C}$  NMR ( $\text{CDCl}_3$ , 75MHz) (ppm)  $\delta$ : 149.81 ( $\text{C}^a$ ), 129.76 (2C,  $\text{C}^c$ ), 116.82 (1C,  $\text{C}^d$ ), 112.71 (2C,  $\text{C}^b$ ), 72.56, 71.32, 71.27, 71.21, 71.13, 69.18 (15C, all O– $\text{CH}_2$ ), 59.62 (1C, O– $\text{CH}_3$ ), 52.96 (1C, N– $\text{CH}_2$ –), 39.52 (1C,  $\text{CH}_3$ –N).

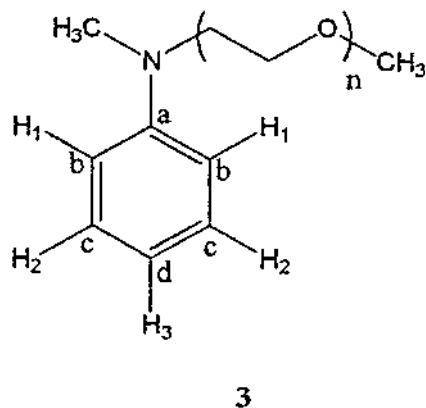
#### RED-PEGM (4)

To a suspension of *p*-nitrobenzenediazonium tetrafluoroborate (0.85 g, 3.58 mmol) in acetic acid 50% (13 mL), a solution of **3** (1.5 g, 3.41 mmol) in acetic acid 50% (2.5 mL) was added slowly, dropwise, keeping the temperature around 0 °C. After the addition was completed, the reaction mixture was stirred vigorously for 1 h at this temperature and then at room temperature for 4 h. Further, it was neutralized with a saturated solution of  $\text{Na}_2\text{CO}_3$  and extracted with chloroform. The chloroform extracts were combined and the organic phase was washed with water, dried with  $\text{Na}_2\text{SO}_4$ , and concentrated under reduced pressure. The crude product RED-PEGM was obtained as a dark red viscous liquid (1.74 g, 2.88 mmol). Yield 80%.

Since the crude product is a mixture of compounds with a variety of oligo(ethylene glycol) methyl ether chains with different values of  $n$ , all these compounds were separated by column chromatography in silica gel using a mixture of hexane–acetone, 1:1, as eluant. RED-PEGM with  $n = 8$  or



Scheme 1.



*N*-methyl-*N*-{4-[(*E*)-(4-nitrophenyl)diazenyl]phenyl}-*N*-(3,6,9,12,15,18,21,24-octaoxapentacos-1-yl)amine (named here RED-PEGM-8) was isolated and further purified by flash column chromatography in silica gel, using a mixture of hexane–acetone, 1:4, as eluant.

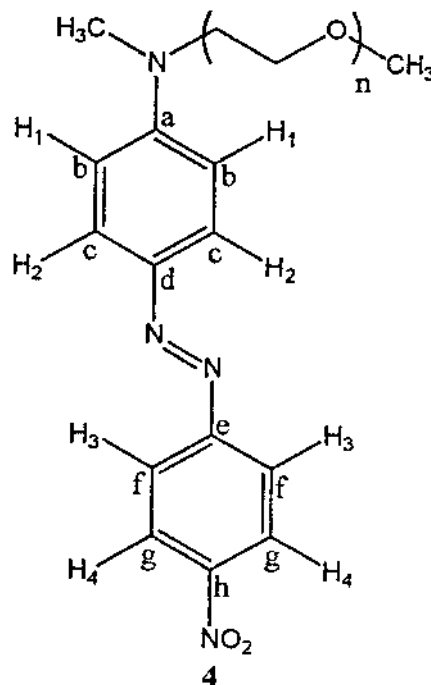
For RED-PEGM-8 (see Scheme 2): IR (KBr) ( $\text{cm}^{-1}$ ): 3102 (s, aromatic C-H), 2923 (s,  $\text{CH}_2$  and  $\text{CH}_3$ ), 1606, 1509 (s,  $\text{NO}_2$ ), 1465 (s, aromatic C=C), 1430 (s, N=N), 1383, 1341, 1115 (s, O- $\text{CH}_2$ ), 958, 827 (out of plane, aromatic C=C-H).  $^1\text{H}$  NMR ( $\text{CDCl}_3$ , 300 MHz) (ppm)  $\delta$ : 8.34 (d,  $J = 8.7$  Hz, 2H,  $\text{H}^4$ ), 7.95 (d,  $J = 6.9$  Hz, 2H,  $\text{H}^3$ ), 7.94 (d, 2H,  $J = 3.6$  Hz,  $\text{H}^2$ ), 6.81 (d, 2H,  $J = 9.3$  Hz,  $\text{H}^1$ ), 3.73–3.55 (m, 32H, all  $\text{CH}_2$ ), 3.39 (s, 3H,  $\text{OCH}_3$ ) and 3.17 (s, 3H,  $\text{CH}_3\text{-N}$ ).  $^{13}\text{C}$  NMR ( $\text{CDCl}_3$ , 75 MHz) (ppm)  $\delta$ : 157.40 (1C,  $\text{C}^e$ ), 153.22 (1C,  $\text{C}^a$ ), 147.92 (1C,  $\text{C}^h$ ), 144.34 (1C,  $\text{C}^d$ ), 126.77 (2C,  $\text{C}^c$ ), 125.28 (2C,  $\text{C}^g$ ), 123.22 (2C,  $\text{C}^f$ ), 112.14 (2C,  $\text{C}^b$ ), 72.56, 71.47, 71.28, 71.13, 69.18 (all  $\text{OCH}_2$ ), 59.65 (1C,  $\text{OCH}_3$ ), 52.84 (1C,  $\text{N-CH}_2$ ), 40.02 (1C,  $\text{CH}_3\text{-N}$ ). Elemental analysis ( $\text{C}_{30}\text{H}_{46}\text{N}_4\text{O}_{10}$ ) $_n$  (622) $_n$  calcd.: C 57.86, H 7.44, N 8.99; found: C 57.84, H 7.41, N 9.00.

## Results and discussion

### Synthesis of RED-PEGM-8

RED-PEGM was prepared from *N*-methylaniline according to the synthetic sequence shown in Fig. 1. Poly(ethylene glycol) methyl ether (with  $M_w \approx 350$  g  $\text{mol}^{-1}$  and  $n$  values from 2 to 11) was reacted in the presence of tosyl chloride and pyridine to give the corresponding tosylate PEGM-Ts (1). This compound was treated with NaI to give the alkylating agent PEGM-I (2) with an overall yield of 76%. Compound 2 was further reacted with *N*-methylaniline in the presence of  $\text{Na}_2\text{CO}_3$  to give the *N*-PEGM-*N*-methylaniline (3) with 60% yield. A comparison between the  $^1\text{H}$  NMR spectrum of the PEGM used as the starting material and that of 3 showed that both compounds possessed the same average number of methylenes. Finally, 3 was coupled, according to a procedure described in the literature (18), with *p*-nitrobenzenediazonium tetrafluoroborate at 0 °C, using acetic acid 50% as solvent, to give RED-PEGM (4) with 90% yield. Compound 4 contains a distribution of products each having a different number of methylenes (from 2 to 11). The crude RED-PEGM was purified, first by column chromatography using a mixture of  $\text{MeOH-CHCl}_3$ , 9:1, as eluant. The  $^1\text{H}$  NMR spectrum shows that 4 is a mixture of *para* and

Scheme 2.

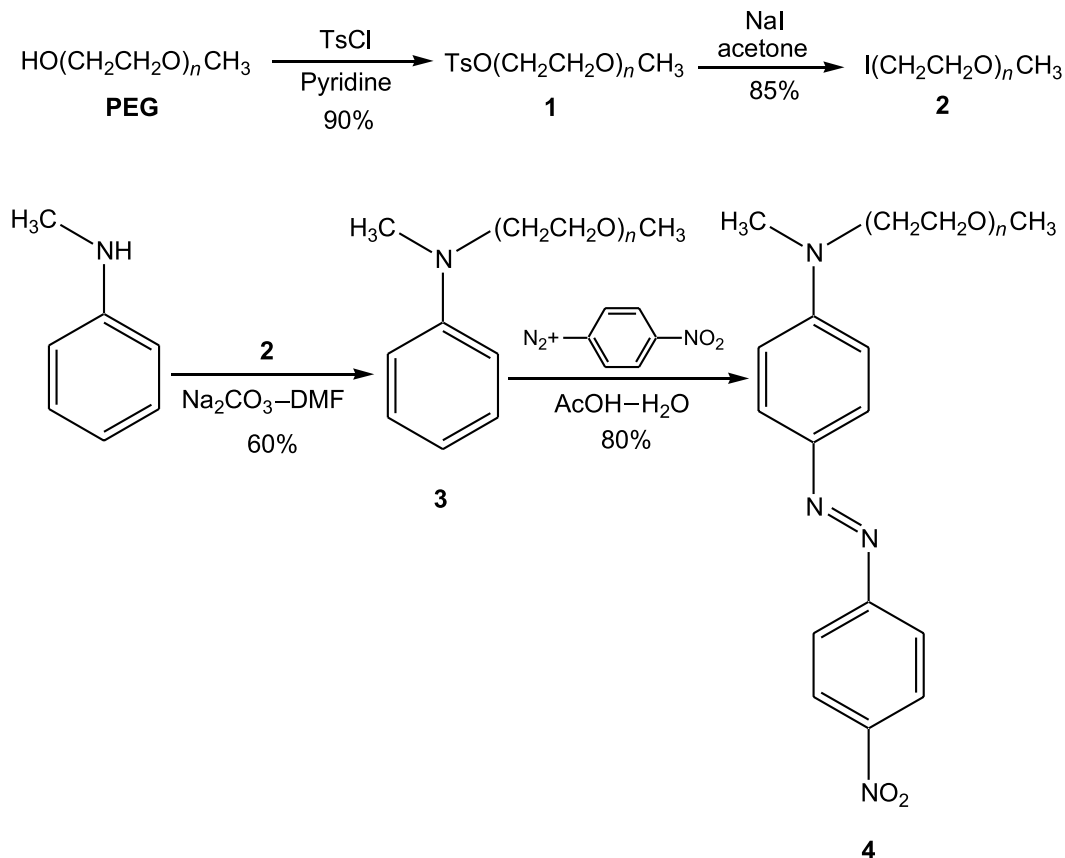


*ortho* isomers for each  $n$  value of the distribution. This was also confirmed by thin layer chromatography (TLC). A well-defined alternated distribution of *para* and *ortho* isomers (with  $n$  values from 2 to 11) was observed when a mixture of hexane–acetone, 1:1, was used as eluant. Since it was not possible to get the whole distribution of products containing only the desired *para* isomers, only one *para*-compound bearing an exact number of methylenes in the PEGM chain ( $n = 8$ ) was isolated for our study. In a first step, the different products of the distribution were separated by column chromatography, using a mixture of hexane–acetone, 1:1, as eluant. In a second step, the *para* isomer of RED-PEGM with  $n = 8$  (RED-PEGM-8) was isolated from the *ortho* by-product by column chromatography, eluting with a mixture of hexane–acetone, 1:4.

### Characterization of RED-PEGM-8

$^1\text{H}$  NMR spectrum of RED-PEGM-8 in  $\text{CDCl}_3$  solution (Fig. 2A) shows two doublets at 8.43 and 7.95 ppm, belonging to protons  $\text{H}^4$  and  $\text{H}^3$  present in the nitro-substituted aromatic ring (see Scheme 2), as well as two additional doublets at 7.94 and 6.81 ppm, belonging to protons  $\text{H}^2$  and  $\text{H}^1$  present in the *N*-PEGM-*N*-methylaniline-substituted one. A multiplet at 3.73–3.55 ppm, integrating for 32 protons and two singlets at 3.39 and 3.17 ppm, belonging to methylene groups, methoxy group, and the *N*-methyl group, respectively, were also observed. The  $^{13}\text{C}$  NMR spectrum of RED-PEGM-8 displayed 8 signals between 157.4–112.14 ppm, belonging to the aromatic carbons, followed by five signals at 72.56–69.18 ppm, which can be attributed to all the  $\text{OCH}_2$  groups present in the PEGM side chain and three signals at 59.65, 52.84, and 40 ppm, belonging to the  $\text{OCH}_3$ ,  $\text{N-CH}_2$ , and  $\text{CH}_3\text{-N}$ , respectively, present in the molecule. The purity of this compound was confirmed by elemental analysis.



**Fig. 1.** Synthesis of RED-PEGM.

RED-PEGM-8 is an azo-dye totally soluble in chloroform, acetone, ethyl acetate, methanol, and fairly soluble in water. It is very well known that the azobenzene group is hydrophobic while the PEGM chain is highly hydrophilic. The ground state dipole moment of RED-PEGM-8, estimated by AM1 (Austin model 1) semi-empirical calculations (19), is very high (9.63 D) because of the presence of strong donor and acceptor groups in the *para* positions of the azobenzene chromophore.

#### Thermal properties of RED-PEGM-8

According to TGA measurements recorded from 20 to 800 °C (Fig. 3), RED-PEGM-8 displays a good thermal stability with a  $T_{10}$  (10% weight loss temperature) at 268 °C. This thermal stability is lower than that measured for a similar compound, [(4-nitrophenylazo)-*N*-ethyl-phenylamino] ethanol or Disperse Red-1 ( $T_{10} = 273$  °C), and much higher than that measured for the corresponding oligo(ethylene glycol) methyl ether used in the synthesis ( $T_{10} = 179$  °C). Moreover, this compound exhibits a fast degradation around 300 °C, reaching 90% of weight loss at 500 °C. Disperse Red-1 behaves similarly and shows, also, fast degradation around this temperature, but for this dye degradation takes place in two steps, reaching 90% of weight loss at 749 °C. On the other hand, PEGM degrades rapidly between 200–300 °C, reaching 90% of weight loss at 300 °C and having 1.5% remaining at 400 °C. Consequently, we can affirm that the presence of the PEGM segment decreases the stability of the dye towards decomposition.

On the other hand, DSC measurements were recorded from –150 to 300 °C (Fig. 4), and in this range of temperatures, RED-PEGM-8 displayed a  $T_g$  at –18 °C, much lower than that of Disperse Red-1 (142 °C) and higher than that of the corresponding PEGM used as starting material (–87 °C). RED-PEGM-8 also displayed a crystallization temperature,  $T_c$ , at 10 °C. A melting point  $T_m$  at 45 °C was found, which is much lower than that of Disperse Red-1 ( $T_m = 168$  °C) but remarkably higher than that of PEGM (–3.4 °C followed by two additional weaker endothermic  $T_m$ s at –28 and –47 °C). Thus, as expected, RED-PEGM-8 possesses a thermal behaviour typical of a liquid crystalline structure. The presence of crystallization can be attributed to the packing of the PEGM oligomer within the azobenzene unit, and the low glass transition temperature and melting point indicate the influence of the PEGM segment over the thermal properties because the presence of the oligomer decreases significantly the  $T_g$  and  $T_m$  values of this dye compared with our reference dye (Disperse Red-1). Along these lines, it is worth pointing out that PEGM itself and non-end-capped poly(ethylene glycol)s possess low  $T_g$  and  $T_m$  values (20).

#### Optical properties of RED-PEGM-8

The azobenzene molecule is characterized spectroscopically by a low-intensity  $n \rightarrow \pi^*$  band in the visible region of the spectrum and a high-intensity  $\pi \rightarrow \pi^*$  band in the UV. Substitution by a pull and a push substituent like in 4-dimethylamino-4'-nitroazobenzene increases the charge-transfer character (CT) of the  $\pi \rightarrow \pi^*$  transition along the



**Fig. 2.** (A)  $^1\text{H}$  NMR 400 MHz in solution of RED-PEGM-8: (a) in  $\text{CDCl}_3$ , (b) in  $\text{D}_2\text{O}$ ; (B)  $^1\text{H}$  NMR 400 MHz in solution of RED-PEG-8 with amplification of the aromatic region: (a) in  $\text{CDCl}_3$ , (b) in  $\text{D}_2\text{O}$ .

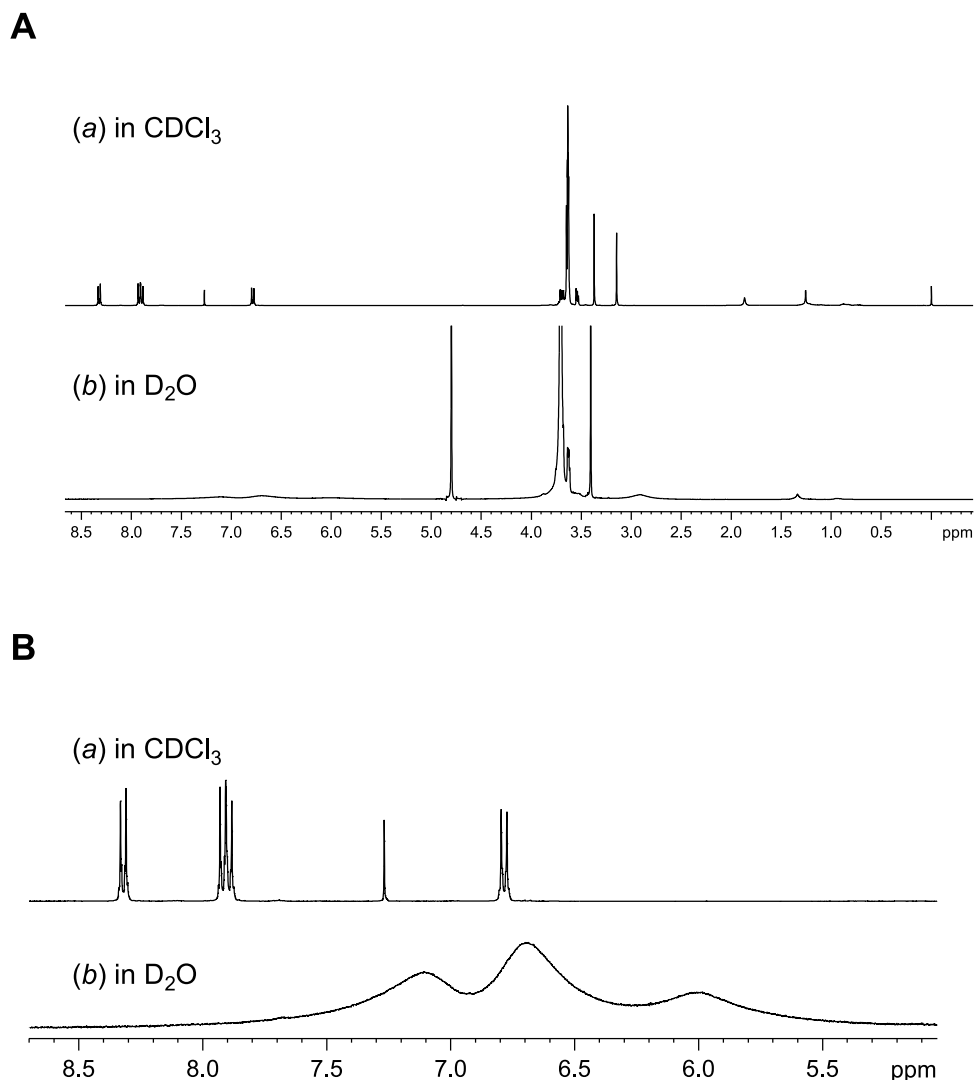
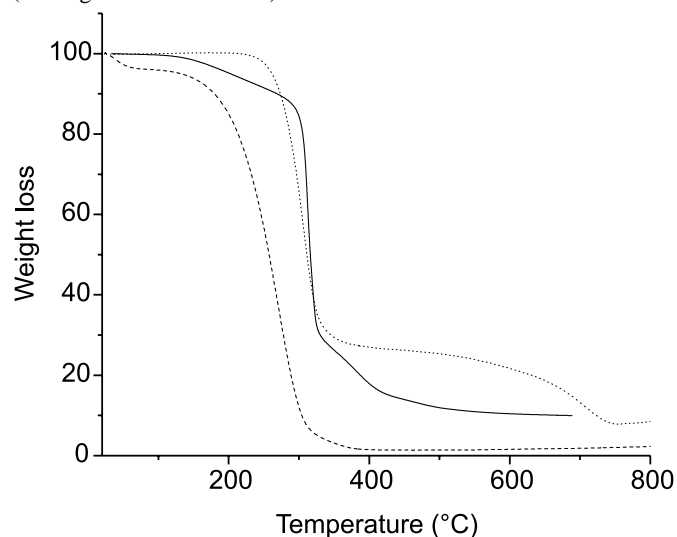


**Fig. 3.** TGA measurements of RED-PEGM-8 (—), Disperse Red-1 (.....), and PEGM (- - -) recorded from 20 to 800  $^{\circ}\text{C}$  (heating rate 10  $^{\circ}\text{C min}^{-1}$ ).



long molecular axis and shifts the corresponding band far to the red, thus overlapping the weak  $n \rightarrow \pi^*$  band (14). The CT character of the band causes a strong dependence of the band position on the solvent polarity (21).

The absorption spectrum of RED-PEGM-8 has been recorded in chloroform for various concentrations of the chromophore (Fig. 5). The long wavelength absorption band of this molecule appears around 477 nm. We have measured the same absorption wavelength for RED-PEGM-8 dissolved in tetrahydrofuran (THF). In a previous work, Whitten and co-workers have recorded an absorption peak at 489 nm for 4-diethylamino-4'-nitroazobenzene in THF (21). This clearly indicates that the oligo(ethylene glycol) methyl ether chain reduces the donor effect of the dimethylamino substituent, thus causing a blue shift of the absorption band. No changes in the shape of the absorption spectra is observed by increasing the concentration of the chromophore in chloroform. This shows that this azo-dye is well solubilized in this organic solvent, avoiding significant intermolecular interactions.

Figure 6 shows the absorption spectra of RED-PEGM-8 in water at various concentrations. These spectra exhibit a



**Fig. 4.** DSC measurements of (A) RED-PEGM-8 and (B) PEGM recorded from  $-150$  to  $200$  °C (heating rate  $10$  °C  $\text{min}^{-1}$ ).

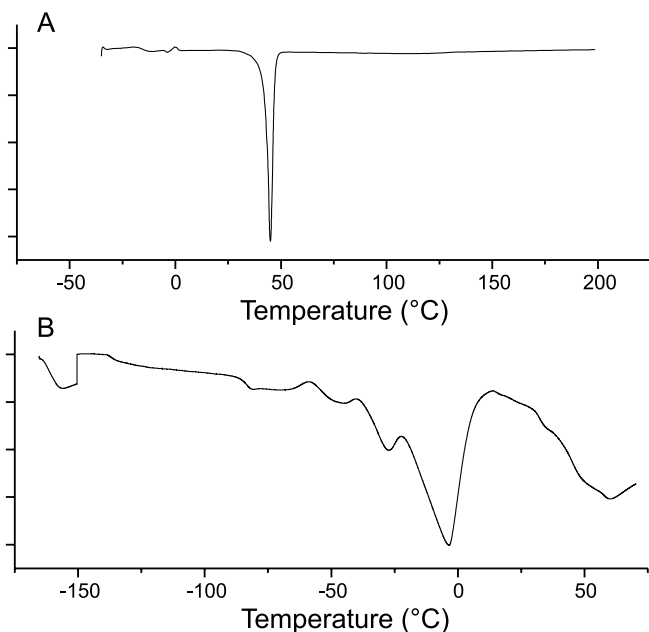
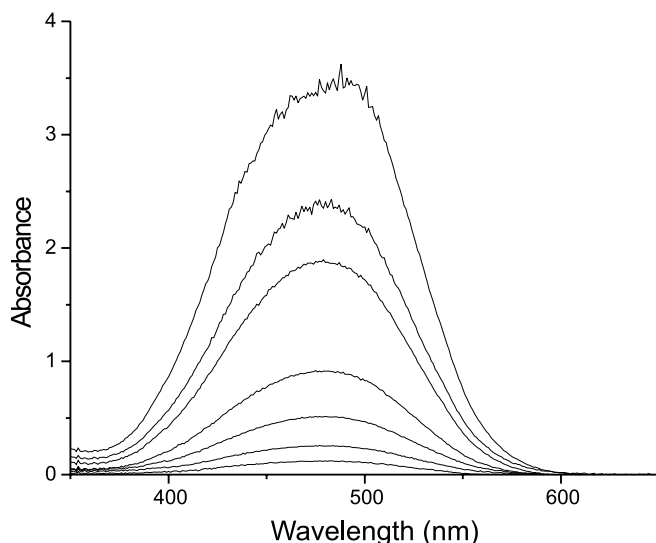
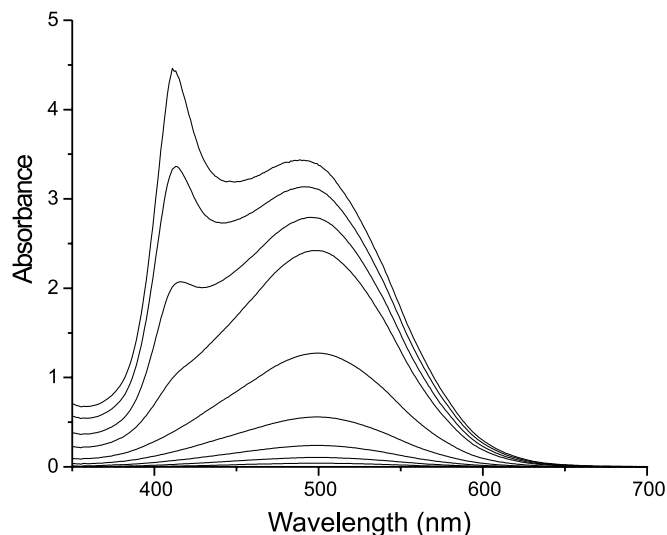


**Fig. 5.** Absorption spectra of RED-PEGM-8 in  $\text{CHCl}_3$  at different concentrations of the chromophore (from the top to the bottom: (a)  $1.25 \times 10^{-4}$  mol  $\text{L}^{-1}$ , (b)  $1 \times 10^{-4}$  mol  $\text{L}^{-1}$ , (c)  $7.5 \times 10^{-5}$  mol  $\text{L}^{-1}$ , (d)  $3.75 \times 10^{-5}$  mol  $\text{L}^{-1}$ , (e)  $1.87 \times 10^{-5}$  mol  $\text{L}^{-1}$ , (f)  $9.3 \times 10^{-6}$  mol  $\text{L}^{-1}$ , (g)  $4.6 \times 10^{-6}$  mol  $\text{L}^{-1}$ ).



broad band around  $500$  nm, which is red-shifted by about  $23$  nm compared with the one measured in chloroform. This solvatochromic shift is surely due to the increase in the solvent polarity going from chloroform to water, as mentioned above for push-pull azobenzenes. By increasing the concentration of the chromophore in water, a new band around  $415$  nm is observed. We believe that this spectral behavior involves an excitonic coupling effect, which causes a band-splitting (22). Thus, the absorption band in the blue region would involve face-to-face molecular arrangements (H-

**Fig. 6.** Absorption spectra of RED-PEGM-8 in water at different concentrations of the chromophore (from the top to the bottom: (a)  $3.12 \times 10^{-4}$  mol  $\text{L}^{-1}$ , (b)  $2.5 \times 10^{-4}$  mol  $\text{L}^{-1}$ , (c)  $1.25 \times 10^{-4}$  mol  $\text{L}^{-1}$ , (d)  $1 \times 10^{-4}$  mol  $\text{L}^{-1}$ , (e)  $7.5 \times 10^{-5}$  mol  $\text{L}^{-1}$ , (f)  $3.75 \times 10^{-5}$  mol  $\text{L}^{-1}$ , (g)  $1.87 \times 10^{-5}$  mol  $\text{L}^{-1}$ , (h)  $9.3 \times 10^{-6}$  mol  $\text{L}^{-1}$ , (i)  $4.6 \times 10^{-6}$  mol  $\text{L}^{-1}$ ).



aggregates) whereas head-to-tail molecular arrangements (J-aggregates) are not detected in the RED-PEGM-8 – water system. Recently, azo-dye aggregates have also been observed on dendrimer surfaces (23) and incorporated in surfactants (24).

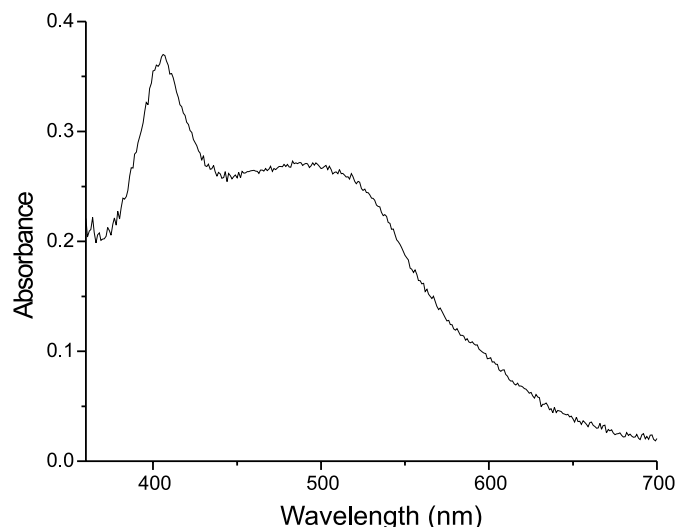
The absorption spectrum of RED-PEGM-8 in the solid state (thin film), casted from a chloroform solution at room temperature, is shown in Fig. 7. One can see that this spectrum is similar to the one recorded at high concentrations of the chromophore in water ( $\lambda_{\text{max}} = 500$  nm). This could imply that H-aggregates are also formed in the thin film of this compound. Moreover, compared with the spectrum obtained in chloroform solution ( $\lambda_{\text{max}} = 477$  nm), the solid state absorption spectrum is red-shifted and shows a tail in the red region. These spectral observations might be because of the formation of J-aggregates in the thin film, indicating a higher molecular alignment in the solid state. However, physical aggregation could also take place in the solid state and be responsible of this behavior. Since RED-PEGM-8 is a non-emissive dye, we were not able to monitor the aggregation phenomenon via steady-state and time-resolved fluorescence studies.

#### NMR spectra of RED-PEGM-8

$^1\text{H}$  NMR spectrum of RED-PEGM-8 in a  $\text{CDCl}_3$  solution (Fig. 2A) shows well-defined signals at  $8.43$ ,  $7.95$ ,  $7.94$ , and  $6.81$ , belonging to aromatic protons and at  $3.73$ – $3.55$ ,  $3.39$ , and  $3.17$ , belonging to methylene groups, which were previously assigned in the characterization section. The  $^1\text{H}$  NMR spectrum of the same compound in  $\text{D}_2\text{O}$  (Figs. 2A and 2B) shows three broad signals at  $7.11$  ( $\text{H}^4$ ),  $6.69$  (protons  $\text{H}^2$  and  $\text{H}^3$ ), and  $6.0$  ppm ( $\text{H}^1$ ) followed by three signals centered at  $3.69$ ,  $3.63$  (all  $\text{CH}_2$ ), and  $3.47$  ( $\text{OCH}_3$ ). Besides, the signal corresponding to  $\text{CH}_3\text{-N}$  appears at  $4.82$  ppm, which is downfield shifted compared with that observed in  $\text{CDCl}_3$ .



**Fig. 7.** Absorption spectrum of RED-PEGM-8 in the solid state (thin film) casted from a chloroform solution at room temperature.



(2.93 ppm). This is due to the formation of H-bonds between  $D_2O$  and the amino group, which decreases the electron density of the nitrogen atom. By contrast, no significant difference in shift was observed for the methylene signals of the PEGM oligomer segment in both solvents. On the other hand, one can observe a remarkable broadening of the aromatic signals, which are also upfield shifted by 1.21 ppm in  $D_2O$ . These results reveal the existence of strong intermolecular interactions (aggregation) in  $D_2O$ , which are in agreement with the results obtained by UV-vis spectroscopy. We are currently studying the NMR and optical properties for a series of similar azo-dyes having different donor-acceptor substituents and varied chain length of the PEGM segment. These results should provide valuable information about the aggregation process occurring in these types of oligomers.

## Summary

A novel azobenzene compound bearing a short poly(ethylene glycol) methyl ether side chain (RED-PEGM-8) has been synthesized and characterized. RED-PEGM-8 is well solubilized in chloroform and THF, avoiding any significant intermolecular interactions. On the other hand, aqueous solutions of this compound show the appearance of blue-shifted bands at high concentrations, which are interpreted in terms of the formation of H-aggregates.  $^1H$  NMR spectra measured in  $D_2O$  also reveal the existence of strong intermolecular interactions (aggregation), which confirm the optical properties measured in water. It is also suggested that H-aggregates are formed for RED-PEGM-8 in the solid state (thin film). Moreover, the observation of a tail in the red region of the solid-state absorption spectrum could imply the formation of J-type aggregates. However, physical aggregation could also explain this spectroscopic behavior.

## Acknowledgments

We thank the Natural Sciences and Engineering Research Council of Canada (NSERC) for financial support. We are also grateful to Miguel Angel Canseco for his help with the TGA and DSC measurements and Gerardo Cedillo for his assistance recording  $^1H$  NMR (400 MHz) spectra.

## References

1. (a) B. Jonsson, B. Lindman, K. Homberg, and B. Kronberg. *Surfactants and polymers in aqueous solution*. Edited by John Wiley & Sons, Chichester. 1998; (b) Th. F. Tadros. *Surfactants*. Academic Press Inc., London. 1984. p. 309.
2. T.A. Skotheim, R.L. Elsenbaumer, and J.F. Reynolds. *In Handbook of conducting polymers*. 2nd ed. Edited by Marcel Dekker, New York. 1998.
3. R. Foster. *Organic charge-transfer complexes*. Academic Press, London. 1969.
4. G. Cojocariu and A. Natansohn. *Macromolecules*, **34**, 3827 (2001).
5. T. Todorov, L. Nikalova, and N. Tomova. *Appl. Opt.* **23**, 4309 (1984).
6. S. Xie, A. Natansohn, and P. Rochon. *Chem. Mater.* **5**, 403 (1993).
7. N.K. Viswanathan, D.Y. Kim, S. Bian, J. Williams, W. Liu, L. Li, L. Samuelson, J. Kumar, and S. Tripathy. *J. Mater. Chem.* **9**, 1941 (1999).
8. K. Ichimura. *Chem. Rev.* **100**, 1847 (2000).
9. J.A. Delaire and K. Nakatani. *Chem. Rev.* **100**, 1817 (2000).
10. A. Natansohn and P. Rochon. *Chem. Rev.* **102**, 4139 (2002).
11. M.S. Ho, A. Natansohn, and P. Rochon. *Can. J. Chem.* **73**, 1773 (1995).
12. X. Meng, A. Natansohn, P. Rochon, and C. Barrett. *Macromolecules*, **29**, 946 (1996).
13. A. Natansohn, S. Xie, and P. Rochon. *Macromolecules*, **25**, 5531 (1992).
14. Rau H. *Photochemistry and photophysics*. Vol II. Edited by J.K. Rabek. Boca Raton, CRC Press, Florida. 1990.
15. A. Dhanabalan, D.S. Dos Santos, Jr., C.R. Mendonça, L. Misoguti, D.T. Balogh, J.A. Giacometti, S.C. Zilio, and O.N. Oliveira. *Langmuir*, **15**, 4560 (1999).
16. D.S. Dos Santos, Jr., C.R. Mendonça, D.T. Balogh, A. Dhanabalan, J.A. Giacometti, S.C. Zilio, and O.N. Oliveira, Jr. *Polymer*, **43**, 4385 (2002).
17. D.S. Dos Santos, Jr., C.R. Mendonça, D.T. Balogh, A. Dhanabalan, J.A. Giacometti, S.C. Zilio, and O.N. Oliveira, Jr. *Synth. Met.* **121**, 1479 (2001).
18. L. Yu, W. Chan, and Z. Bao. *Macromolecules*, **25**, 5609 (1992).
19. M.J.S. Dewar and K. Dieter. *J. Am. Chem. Soc.* **108**, 8075 (1986).
20. J. Brandrup, E.H. Immergut, and E.A. Grulke. *Polymer handbook*. 4th ed. Edited by John Wiley and Sons, New York. 1999.
21. D.M. Shin, K.S. Schanze, and D.G. Whitten. *J. Am. Chem. Soc.* **111**, 8494 (1989).
22. M. Kasha. *Radiat. Res.* **20**, 55 (1963).
23. K.K. Karukstis, L.A. Perelman, and W.K. Wong. *Langmuir*, **18**, 10 363 (2002).
24. R.T. Buwalda, J.M. Jonker, and J.N.F.N. Engberts. *Langmuir*, **15**, 1083 (1999).



# The photochemistry of indenyl alcohols and esters: Substituent effects on the competition between ion- and radical-derived products

J.A. Pincock and I.S. Young

**Abstract:** The photochemistry of the indenyl acetates **1** and pivalates **2**, substituted with X = H, 5-CH<sub>3</sub>O, and 6-CH<sub>3</sub>O, have been examined in both methanol and cyclohexane. The precursor alcohols **3** were also found to be photoreactive. Although only radical-derived products were obtained in cyclohexane, both ion- and radical-derived products were formed in methanol. The absence of significant fluorescence emission from any of the substrates **1**, **2**, and **3** indicates that the excited singlet states are highly reactive. A mechanism is proposed for the ion-derived products that proceeds through direct heterolytic cleavage to give an indenyl cation – carboxylate anion pair. The indenyl cations generated are anti-aromatic in the ground state and their efficient generation by this photochemical solvolysis is in sharp contrast to the very low reactivity of related ground-state substrates. For the pivalate esters **2**, an excited-state migratory decarboxylation is proposed for the formation of *tert*-butyl derived products.

**Key words:** ester photochemistry, indenyl cations, indenyl radicals.

**Résumé :** La photochimie des acétates **1** et des pivalates **2** d'indényle, substitués avec X = H, 5-CH<sub>3</sub>O et 6-CH<sub>3</sub>O a été étudiée dans le méthanol et dans le cyclohexane. On a trouvé que les alcools précurseurs **3** sont également photo-réactifs. Dans le cas du cyclohexane on n'obtient que des produits d'origine radicalaire, par contre dans le cas du méthanol on obtient des produits d'origine ionique et d'origine radicalaire. L'absence d'émission de fluorescence significative à partir des substrats **1**, **2** et **3** indique que les états singulets excités sont hautement réactifs. On propose un mécanisme qui explique la formation des produits d'origine ionique via le clivage hétérolytique direct pour donner une paire cation indényle – anion carboxylate. Les cations indényles générés sont anti aromatiques dans l'état fondamental et leur production efficace par cette solvolysé photochimique est en nette opposition avec la très faible réactivité des substances apparentées à l'état fondamental. Pour les esters pivalates **2**, on propose une décarboxylation migratoire de l'état excité pour expliquer la formation des produits dérivés du *t*-butyle.

**Mots clés :** photochimie des esters, cations indényles, radicaux indényles.

[Traduit par la Rédaction]

## Introduction

The photochemistry of arylmethyl esters (ArCH<sub>2</sub>O-(CO)-R) in nucleophilic solvents (1) and arylmethyl compounds with leaving groups in general (ArCH<sub>2</sub>-LG) (2) has recently attracted considerable interest. As outlined in the mechanism in Scheme 1, products are derived from both radical pair and ion pair (photosolvolysis) intermediates and, for esters at least, only from the excited singlet state. Apart from a fundamental interest in the factors (substituents, solvent, leaving group, excited-state multiplicity) that control the partitioning between these two pathways, the potential of applying this process to the design of photolabile protecting groups or phototriggers has been explored (3, 4).

On the basis of extensive studies on a range of functionalized arylmethyl esters, we have proposed a mecha-

nism where the major pathway for reactivity is homolytic cleavage ( $k_{\text{hom}}$ ) of the carbon—oxygen bond to give a radical pair (1, 2). Competition between electron transfer ( $k_{\text{et}}$ ) to form an ion pair and decarboxylation ( $k_{\text{CO}_2}$ ) of the acyloxy radical then controls product distribution. This latter process serves as a radical clock with the rate constant differing by many orders of magnitude, depending on the stability of the radical formed. Values range from  $\sim 10^6 \text{ s}^{-1}$  for ArCO<sub>2</sub>• (5) to  $\sim 10^9 \text{ s}^{-1}$  for RCO<sub>2</sub>• with primary alkyl groups (6). For cases that form highly stabilized radicals, such as Ar<sub>2</sub>C(OH)CO<sub>2</sub>•, the decarboxylation occurs within a few picoseconds; the rate constants approach those for barrier-free unimolecular reactions (7). The rate of electron transfer also ranges over several orders of magnitude and follows Marcus theory in both the normal and the inverted region (8, 9). On the basis of high-level MO calculations, this mechanism has been questioned in favor of one involving direct heterolytic cleavage ( $k_{\text{het}}$ ) from S<sub>1</sub>, particularly for substrates with *meta*-methoxy substituents (10, 11).

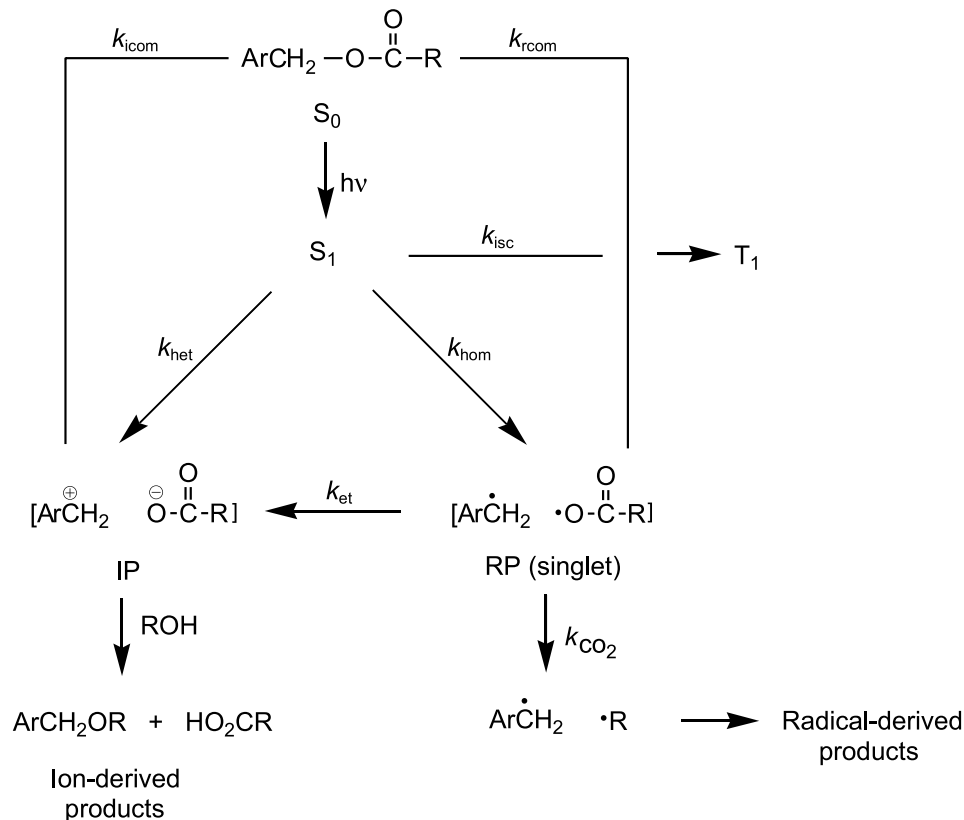
The high reactivity and the high yield of ion-derived products for the photochemistry of 9-fluorenol in mixed organic–aqueous media has been interpreted as resulting from the formation of a cyclically conjugated  $4n \pi$  cation (12, 13).

Received 9 June 2003. Published on the NRC Research Press Web site at <http://canjchem.nrc.ca> on 26 September 2003.

J.A. Pincock<sup>1</sup> and I.S. Young, Department of Chemistry, Dalhousie University, Halifax, NS B3H 4J3, Canada.

<sup>1</sup>Corresponding author (e-mail: james.pincock@dal.ca).



**Scheme 1.** General mechanistic scheme for the photolysis of benzylic substrates.

Recent picosecond laser flash photolysis (LFP) experiments (14) have shown that in fact 9-fluorenyl reacts to form the 9-fluorenyl cation very rapidly (<10 ps) in solvents (water, TFE, HFIP) of high polarity ( $E_T^N$ ). The antiaromatic character of the 9-fluorenyl cation has been discussed in a recent review (15) with the conclusion that it will be attenuated relative to that for cyclopentadienyl and indenyl cations. In fact, on the basis of recent calculations, the fluorenyl cation has been described as nonaromatic by some criteria and antiaromatic by others (16). The possible photochemical generation of indenyl cations, which, from experiment and calculation, have more antiaromatic character than fluorenyl cations, is therefore of interest.

We now report on the photochemistry of six indenyl esters **1a–c** and **2a–c** and three indenyl alcohols **3a–c** in the solvents methanol and cyclohexane. The photochemistry of the alcohols was examined to allow a more direct comparison with the photochemistry of 9-fluorenyl. The choice of examining acetate esters **1** vs. pivalates **2** was made because the rate constants of decarboxylation of their corresponding acyloxy radicals differ by an order of magnitude ( $\sim 10^9 \text{ s}^{-1}$  for  $\text{CH}_3\text{CO}_2^\bullet$  vs.  $1.1 \times 10^{10} \text{ s}^{-1}$  for  $(\text{CH}_3)_3\text{CCO}_2^\bullet$ ) (6), and these radicals are good probes for radical pair chemistry. The choice of 5-methoxy vs. 6-methoxy was made in order to examine the effect of the change in position of the electron-donating group from *para* (5-methoxy) in **1b**, **2b**, and **3b** to *meta* (6-methoxy) in **1c**, **2c**, and **3c** relative to the arylmethyl center with the leaving group. The results will also be compared with those obtained previously for the corresponding indenyl derivatives (17).

## Results and discussion

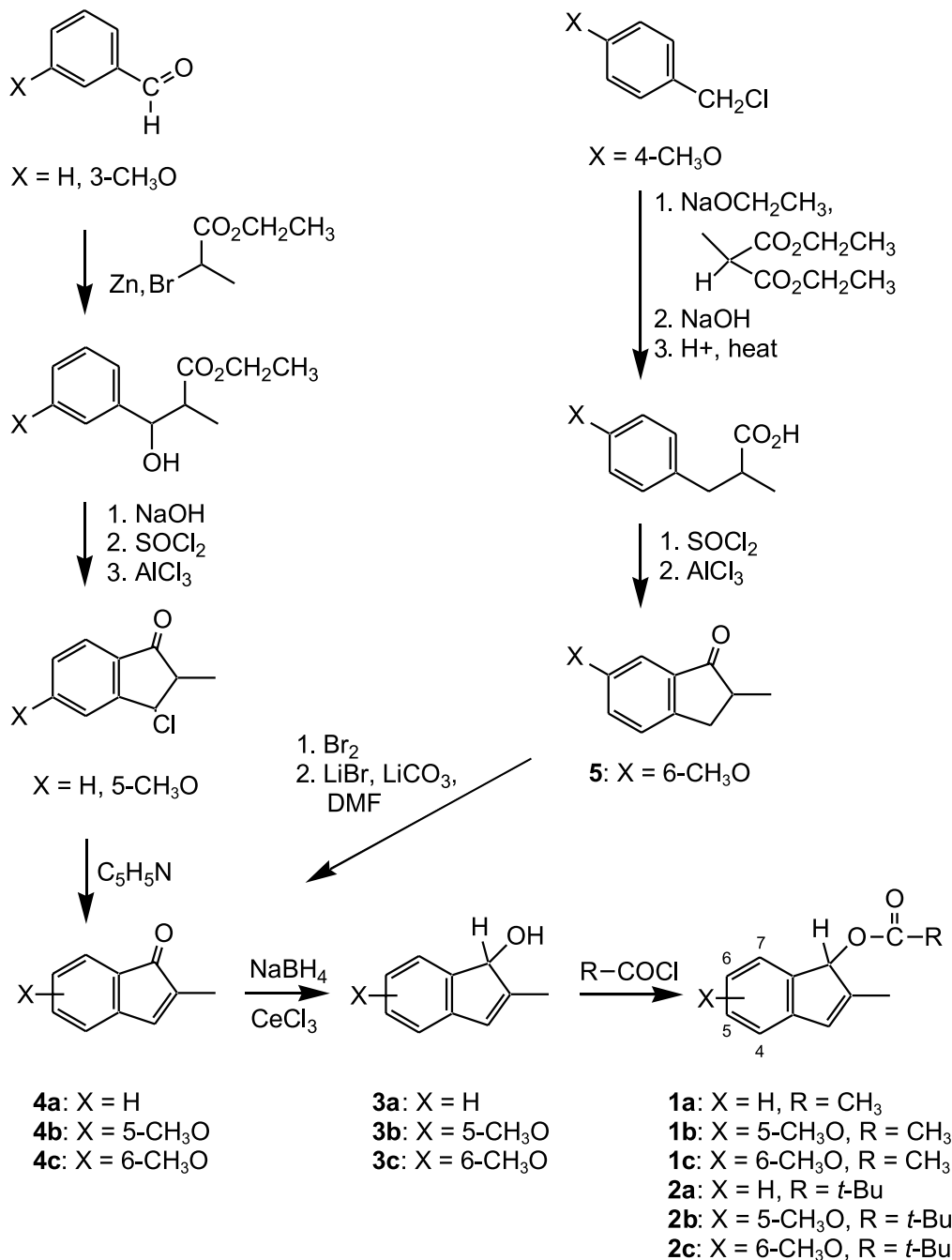
### Synthesis of alcohols and esters

The esters were synthesized from the corresponding alcohols **3** by reaction with the appropriate acid chloride in benzene–pyridine, Scheme 2. The alcohols were obtained by reduction of the ketones **4** with  $\text{NaBH}_4$  with added  $\text{CeCl}_3$ . In the absence of the  $\text{CeCl}_3$ , considerable reduction of the indenone double bond occurred (18). Two of the indenones (**4a**:  $\text{X} = \text{H}$  and **4b**:  $\text{X} = 5\text{-CH}_3\text{O}$ ) were prepared by a procedure developed by Floyd and Allen (19) and used in our laboratory previously (20). The indanone **5** ( $\text{X} = 6\text{-CH}_3\text{O}$ ) could not be prepared by this method because the Friedel–Crafts cyclization was not successful. Instead, the method of Sam and Plampin (21) was used. The indenone **4c** ( $\text{X} = 6\text{-CH}_3\text{O}$ ) was then prepared from **5** by a bromination–dehydrobromination sequence.

### Absorption and emission spectra of the esters and alcohols in methanol

In general, indene derivatives have UV absorption spectra with two bands, a weak one ( $\epsilon \sim 10^2 (\text{mol L}^{-1})^{-1} \text{ cm}^{-1}$ ) between 280 and 300 nm, corresponding to the symmetry-forbidden  $^1\text{L}_b$  band in benzene, usually partially overlapped by a stronger one ( $\epsilon \sim 10^4 (\text{mol L}^{-1})^{-1} \text{ cm}^{-1}$ ) around 260 nm, corresponding to the symmetry-allowed  $^1\text{L}_a$  band in benzene (22). In methanol, the unsubstituted indenyl ester **1a** has two similar bands ( $\lambda_{\text{max}} = 266 \text{ nm}$ ,  $\epsilon = 7130 (\text{mol L}^{-1})^{-1} \text{ cm}^{-1}$  and  $306 \text{ nm}$ ,  $391 \text{ kJ mol}^{-1}$  (the longest wavelength maximum in the long wavelength band),  $\epsilon = 950 (\text{mol L}^{-1})^{-1} \text{ cm}^{-1}$ ), but



**Scheme 2.** Synthesis of the esters **1a–c** and **2a–c** and the alcohols **3a–c**.

these are shifted to somewhat longer wavelength than that for 2-methylindene (**22**) in cyclohexane ( $\lambda_{\text{max}} = 257 \text{ nm}$ ,  $\epsilon = 11\,700 \text{ (mol L}^{-1})^{-1} \text{ cm}^{-1}$  and  $295 \text{ nm}$ ,  $\epsilon \sim 500 \text{ (mol L}^{-1})^{-1} \text{ cm}^{-1}$ ) or *cis*-phenylpropene (**23**) in hexane ( $\lambda_{\text{max}} = 256$  and  $288 \text{ nm}$ ). The long wavelength band has a series of obvious, but broad, vibrational bands in contrast to the shorter wavelength band, which does not. The methoxy-substituted esters **1b** and **1c** have similar absorption bands (see Experimental section), although the long wavelength band lacks vibrational structure and moves to even lower energy ( $320 \text{ nm}$ ,  $373 \text{ kJ mol}^{-1}$ ) for the 6-methoxy isomer **1c**, as expected when compared with a similar shift to longer wavelength for

*trans*-1-(4-methoxyphenyl)propene ( $\lambda_{\text{max}} = 298 \text{ nm}$ ) relative to *trans*-1-phenylpropene itself ( $\lambda_{\text{max}} = 284 \text{ nm}$ ) (**23**).

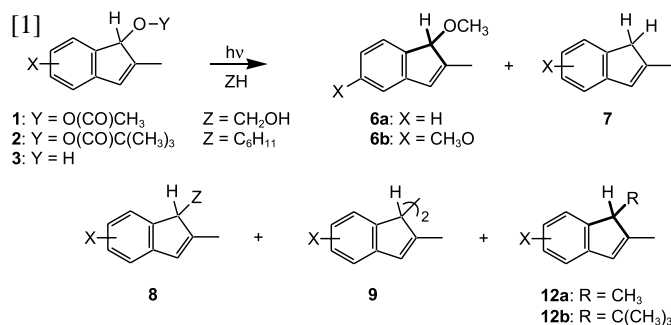
Fluorescence spectra for the three indenyl esters **1** in methanol revealed only extremely weak, if any, emission. The quantum yields of emission were estimated to be less than 0.001 when compared with that for naphthalene (0.21). The alcohols **3**, precursors for the esters, also did not fluoresce significantly. In contrast, 3-methylindene, which is photochemically unreactive in hexane, has a quantum yield of fluorescence of 0.077 and excited singlet state lifetimes of  $13.9 \text{ ns}$  (**22**); the major process competing with fluorescence from the excited singlet state is likely intersystem crossing.



The very inefficient fluorescence for the indenyl compounds studied here strongly suggests that they are undergoing rapid ( $k > 10^9 \text{ s}^{-1}$ ) excited-state cleavage of the indenyl C1 to oxygen bond. The absence of measurable fluorescence unfortunately prevents the determination of excited-state lifetimes and rate constants for excited-state processes.

### Photochemistry of the alcohols **3** in methanol and cyclohexane

The photolysis of the indenyl alcohols in either methanol or cyclohexane gave the products expected from arylmethyl photochemistry, as shown, in a general way, in eq. [1].<sup>2</sup>

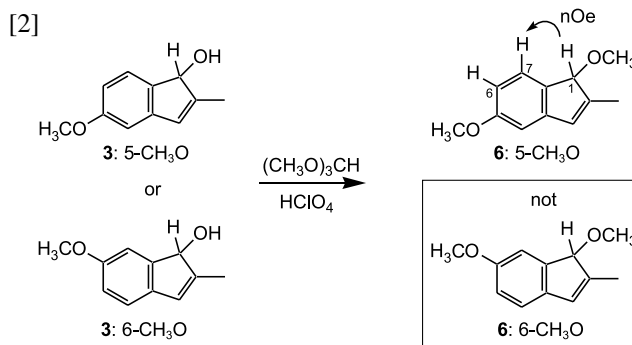


The methyl ethers **6**, formed only in methanol, are of particular interest because they are clearly derived from indenyl cations. The hydrocarbon products **7–9** are radical derived. The reactions are relatively efficient; irradiation of 60 mg of **3a** (X = H) in 100 mL of methanol with 254 nm lamps in a Rayonet reactor resulted in 72% conversion in 15 min. The difficulties in completely characterizing the photoproducts of these reactions can be exemplified by this case. At this extent of conversion, the mass balance (GC peak areas) was only 60%. This is characteristic of the photochemistry of indene derivatives where quantum yields for disappearance of starting material are often considerably higher than those for appearance of volatile products (24), presumably as a consequence of oligomerization processes. Moreover, complete separation by flash or radial chromatography of the non-polar hydrocarbon products was not possible. GC–MS analysis of mixtures of variable composition was invaluable for preliminary structural assignment. For the unsubstituted substrate, **3a**, the hydrocarbons **7** (X = H) (commercial sample, Aldrich) and the dimers **9** (X = H) (*meso* and *dl* diastereomers) are known (25, 26), and literature <sup>1</sup>H NMR spectra were helpful in identifying components in the mixtures obtained by chromatography.

The methyl ethers **6** were synthesized from the indenols **3** using trimethyl orthoformate under acidic conditions (aqueous HClO<sub>4</sub>) (27). An attempt to alkylate **3a** (X = H) using NaH–DMSO followed by CH<sub>3</sub>I resulted in 2,2-dimethylindanone, confirming that the indenyl hydrogen at C1 is more acidic ( $\text{p}K_{\text{a}} = 20$ ) than an alcohol ( $\text{p}K_{\text{a}}$  [CH<sub>3</sub>OH] = 29) in DMSO (28). Using the trimethyl orthoformate procedure for the indenols **3b** (X = 5-OCH<sub>3</sub>) and **3c** (X = 6-OCH<sub>3</sub>) resulted in the isolation of only one ether in-

dependent of which alcohol was used as the starting material, eq. [2].

The compound obtained was shown to be the 5-methoxy



isomer, **6b**, by NOE difference spectra: irradiation of H1 ( $\delta = 4.82$  ppm) gave a strong enhancement for H7, which is assigned by its higher chemical shift ( $\delta = 7.30$  ppm) relative to that of H6 ( $\delta = 6.64$  ppm) for the two aromatic protons, which are *ortho* to each other and therefore have a coupling constant of 8.0 Hz. This acid-catalyzed reaction, which presumably proceeds through the indenyl cation, raises an interesting point for reactions that generate indenyl cations or radicals at C1 of the 5-methoxy and 6-methoxy substrates. Because of delocalization through C1, C2, and C3 of these intermediates, both substrates will generate the same intermediate for either the cation **10** or the radical **11**, Fig. 1.

This observation prompted us to examine the charge and spin distribution in these species by PM3 calculations.<sup>3</sup> As shown in Fig. 1a, nine resonance forms can be drawn for an indenyl cation with a positive charge on each one of the nine carbons. From the calculations for the indenyl cation ( $C_{2v}$  symmetry), the positive charge is mainly on C1 and C3 (+0.34 for each, 0.68 total, with hydrogen charges summed into the carbons), as indicated by the first two resonance forms. This suggests that, to a first approximation, the indenyl cation can be viewed as an allyl cation fused to a benzene ring. For 5-substituted indenyl cations, the  $C_{2v}$  symmetry is no longer present. For these preliminary calculations, as shown in Fig. 1b, we chose the substituent as OH to model the OCH<sub>3</sub> group in order to minimize conformational complications. For the radical, the spin population at C1 (0.89) and C3 (0.72) is similar and delocalization results in a structure with similar bond lengths in the upper and lower part, i.e., the OH group only slightly perturbs the plane passing through C2 and bisecting the C5–C6 bond. In contrast, the calculations of the atomic charge density for the cation reveal a much higher positive charge at C1 (+0.21) than C3 (–0.03); values for C1 (+0.44) and C3 (+0.25) are obtained with hydrogen charges summed into the carbons. In addition, the bond lengths indicate that the indenyl ring system can be pictured as almost two independent  $\pi$ -systems. The first, a 5-hydroxy pentadienyl cation for the string of carbons from C1 through the ring fusion to C7, C6, and C5, with almost equal bond lengths ( $1.41 \pm 0.02 \text{ \AA}$ ) and the sec-

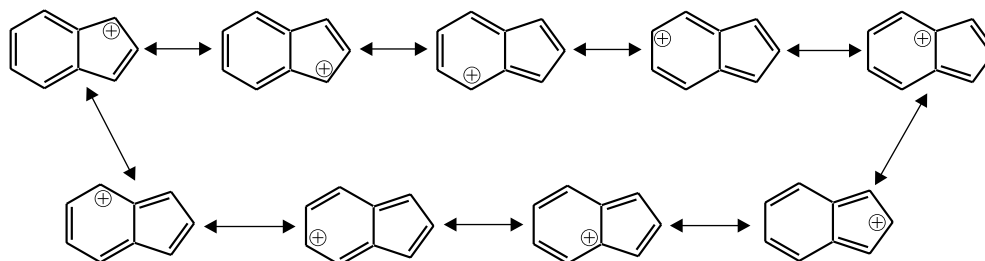
<sup>2</sup>The products **12** in eq. [1] cannot be formed from the alcohols **3** but only from the esters **1** and **2**, as will be discussed later.

<sup>3</sup>We thank Dr. F. Ban, Dalhousie University, Department of Chemistry, Halifax, Nova Scotia, for these calculations.

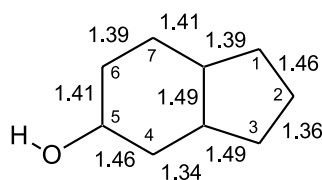


**Fig. 1.** (a) Resonance structures for the indenyl cation and (b) bond lengths (Å), atomic charges, and spin densities for the 5-hydroxy-1-indenyl cation and radical. Values in brackets for the cation have the charge for the hydrogen atom summed into the value for the carbon.

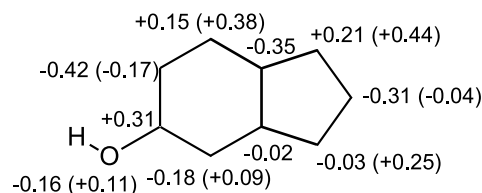
1a



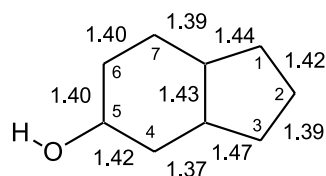
1b



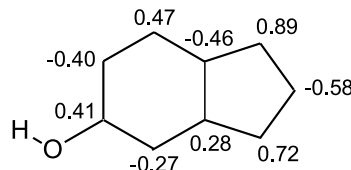
10 (cation): bond lengths



10 (cation): charges



11 (radical): bond lengths



11 (radical): spin densities

ond, an isolated butadiene fragment from C2 to C4 with alternating short (~1.35 Å) and long (1.49 Å) bond lengths; i.e., the OH group severely perturbs the structure on either side of the same plane (defined above) for the radical. The high positive charge density at C1 of the cation, which was obtained from these calculations, rationalizes nicely why both indenols **3** (X = 5-OCH<sub>3</sub> and X = 6-OCH<sub>3</sub>) give the same ether **6** (X = 5-OCH<sub>3</sub>) in the synthesis, eq. [2], and in the photochemistry, eq. [1]. The calculations for the hydroxyindenyl radical **10** will also be relevant to the photolysis results described below. Higher level MO calculations on the charge and spin distribution in substituted indenyl cations and radicals are in progress.

Another issue in the photolysis experiments was that of

secondary photochemistry of several kinds. First, alkyl indenenes are well known to photoisomerize (24). For instance, 2-methylindene **7** (X = H) isomerizes to both 1- and 3-methylindene ( $\Phi = 0.13$ ) on photolysis in hexane and even isomerizes to 2-methyleneindane under acidic conditions (29). Similarly, 1,2-dimethylindene **12a** (X = H, R = CH<sub>3</sub>) isomerizes to the 2,3-isomer (24). We have confirmed these previous observations by the photolysis of 2-methylindene in methanol, which gave three isomers (GC-MS) along with 2-methoxy-2-methylindane by *anti*-Markovnikov addition of methanol, also as reported previously (30). In agreement with these observations, at higher conversions, the initially formed products decreased in yield as the other isomers appeared (GC-MS). Second, photolysis in methanol of the



**Table 1.** Product yields for the photolysis of the alcohols **3** in cyclohexane and methanol.

	X	Solvent	% Con ( <i>t</i> ) <sup>a</sup>	<b>6</b>	<b>7</b> <sup>b</sup>	<b>8</b> <sup>b</sup>	<b>9</b> <sup>c</sup>
<b>3a</b>	H	CH <sub>3</sub> OH	27 (5)	7	7	35	50 (1:1.2)
<b>3a</b>	H	C <sub>6</sub> H <sub>12</sub>	30 (5)	—	15	60	25 (1:1.2)
<b>3b</b>	5-CH <sub>3</sub> O	CH <sub>3</sub> OH	21 (2)	80	20 (1:1.2)	—	—
<b>3b</b>	5-CH <sub>3</sub> O	C <sub>6</sub> H <sub>12</sub>	58 (5)	—	10 (1:1.6)	90 (1:1.3)	—
<b>3c</b>	6-CH <sub>3</sub> O	CH <sub>3</sub> OH	12 (2) <sup>d</sup>	80	20 (1:1.5)	—	—
<b>3c</b>	6-CH <sub>3</sub> O	C <sub>6</sub> H <sub>12</sub>	18 (5) <sup>e</sup>	—	10 (1:1.4)	90 (1:1.1)	—

**Note:** Yields are normalized to 100%. Estimated error  $\pm 5\%$ .

<sup>a</sup>Percent conversion (photolysis time) for  $\sim 50$  mg of substrate in 100 mL of solvent.

<sup>b</sup>Numbers in brackets refer to the ratio of the two possible regioisomers.

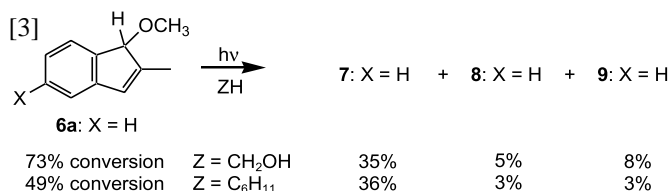
<sup>c</sup>Numbers in brackets refer to the ratio of the two possible diastereomers.

<sup>d</sup>Ratio of **3c**:**3b** = 12:1 at this percent conversion.

<sup>e</sup>Ratio of **3c**:**3b** = 7.8:1 at this percent conversion.

ether **6a** (X = H), the ion-derived product, resulted in formation of the radical-derived products **7**, **8**, and **9**, eq. [3].

The major product in this photolysis, 2-methylindene **7** (X = H), is probably derived by disproportionation of the indenyl-methoxy radical pair, as proposed previously for the photolysis of 9-methoxyfluorene derivatives (12, 13). Third, as indicated in Table 1, the 6-methoxy alcohol **3c** converts photochemically to the 5-methoxy isomer **3b**. For instance, at 14% conversion in cyclohexane, the ratio of **3c**:**3b** was 7.8:1. As a consequence of these various secondary photochemistries, only product yields obtained at low conversions (<5%) give values that are useful for mechanistic consideration. These values are given in Table 1. Because the percentage conversion is too small to reliably determine the mass balance, the yields are normalized to 100%.

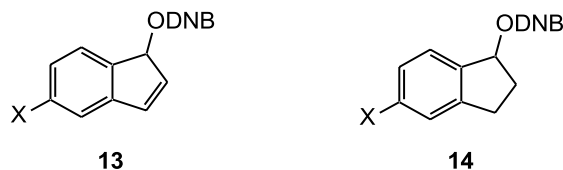


The products shown in eq. [1] and Table 1 for the photolysis of the alcohols **3** are easily explained by formation of indenyl radical and cation intermediates. A mechanism is outlined in Scheme 3, a specific example of the general Scheme 1. The most interesting observation is the very high yield in methanol of the ion-derived product, the methyl ester **6**, particularly from the methoxy-substituted substrates **3b** and **3c** (82%). Also, the same product yields are obtained for both substrates **3b** and **3c**, indicating that both the indenyl radical and cation lose, as expected, the memory of the substrate from which they originated. The radical-derived products **7** and **8** from **3b** and **3c** are mixtures (ratio  $\sim 1.3:1$ ) of two regioisomers, as expected for the unequal spin distribution at C1 and C3 for the methoxy-substituted indenyl radical. The formation of these products is rationalized (Scheme 3) by exothermic hydrogen abstraction (31) by the hydroxyl radical from the solvents methanol (bond dissociation energy (BDE) = 393 kJ mol<sup>-1</sup>) and cyclohexane (BDE = 401 kJ mol<sup>-1</sup>) to give water (BDE = 497 kJ mol<sup>-1</sup>) and the hydroxymethyl and cyclohexyl radical, respectively. The indenyl radical will not abstract a hydrogen atom from these

solvents because the process would not be exothermic (BDE = 351 kJ mol<sup>-1</sup> for the C1—H bond in indene). Reaction of the two radicals by disproportionation then gives **7**, whereas coupling gives **8**, in a ratio of 1:9 in cyclohexane. In methanol, only disproportionation was observed. The other major products that are radical derived are the two indenyl dimers, **9** (X = H), now diastereomers (*dl* and *meso*) because regioisomers are not possible. For reasons that are not obvious, similar dimers were not observed for the methoxy-substituted substrates.

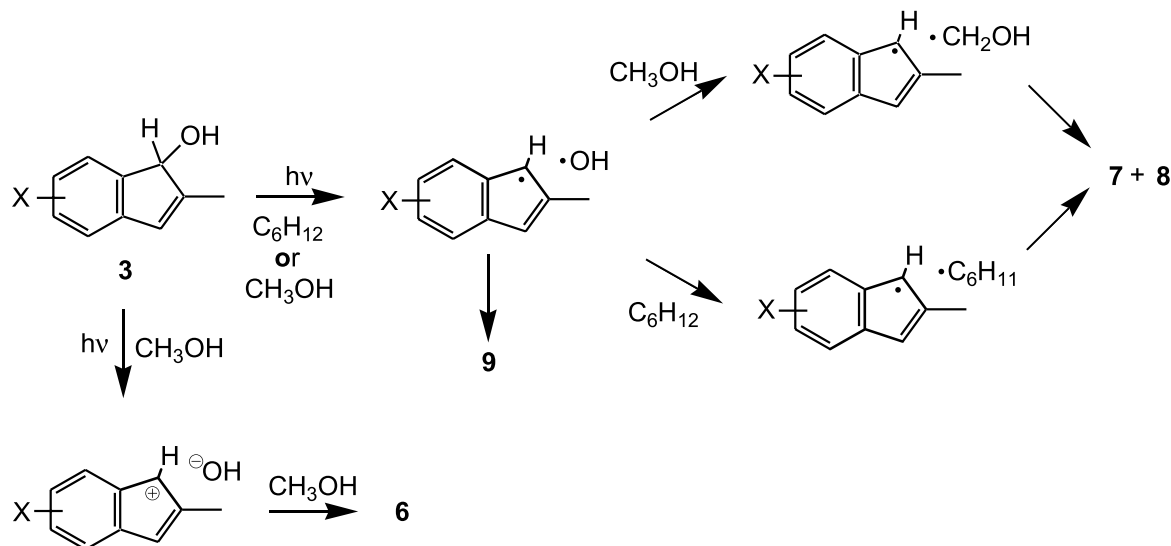
The major conclusion from these results is that indenyl cations are efficiently formed in the photochemistry of indenyl alcohols. Similar cations have been generated by ground-state solvolysis of the indenyl compounds **13**, and rate retardations of approximately 10<sup>-5</sup> have been measured relative to the corresponding indanes **14** in 80% aqueous acetone, reflecting the antiaromatic destabilization of the cation derived by solvolysis of **13** (32).

Product studies indicated that two regioisomeric alcohols are formed from both **13** (X = CH<sub>3</sub>) and **13** (X = CH<sub>3</sub>O), although the experimental evidence for the latter compound is not conclusive. Moreover, these solvolysis reactions were carried out at high temperature (100 °C for 22 days), conditions where 5- and 6-substituted indene derivatives may be equilibrating thermally by 1,5-hydrogen migrations involving isoindene derivatives (33). The question as to whether



the ion pair is generated by direct heterolytic cleavage ( $k_{\text{het}}$ , Scheme 1) or by electron transfer from an initially formed radical pair ( $k_{\text{et}}$ ) cannot be answered from these results. However, the clear evidence from LFP experiments for direct heterolytic cleavage to the ion pair for 9-fluorenol in polar protic solvents (14) suggests that the first pathway is possible. Moreover, the very high oxidation potential expected for the indenyl radical makes the latter seem unlikely. Therefore, the efficient photochemical formation of the indenyl cations (Scheme 3) would seem to be another exam-



**Scheme 3.** Mechanistic pathways for the photolysis of the alcohols **3a–c** in methanol and cyclohexane.

ple of the generation of a  $4n \pi$  cation, first proposed by Wan and co-workers for the photodehydroxylation of fluorenol (12, 13).

#### Photochemistry of the esters **1** and **2** in methanol and cyclohexane

The photolysis of the indenyl esters **1** and **2** in either methanol or cyclohexane again gave the products expected from arylmethyl photochemistry, also shown in eq. [1]. Again, the reactions are relatively efficient; irradiation of 100 mg of **1a** ( $X = H$ ,  $R = CH_3$ ) in 100 mL of methanol with 254 nm lamps in a Rayonet reactor resulted in 50% conversion in 15 min. The same difficulties as for the alcohols **3** (lack of separation of non-polar products and secondary photochemistry) were encountered in completely characterizing the photoproducts for the esters. Moreover, an additional secondary photochemical process was revealed, involving the coupling products **12b** ( $R = C(CH_3)_3$ ). The ratio of these two *tert*-butyl products derived from the 5- and 6-methoxy pivalate esters changed with the percent conversion. Parallel to this process, the yield of the two isomeric 5- and 6-methoxy-2-methylindene derivatives **7** increased. For instance, the yield of **7** for photolysis of the pivalates **2b** and **2c** in methanol was essentially zero at very low conversion (<5%) but reached 20–25% at high conversion (>80%). Finally, the 6-methoxy esters **1c** and **2c** were converted to the corresponding 5-methoxy substrate **1b** and **2b** (see footnotes in Tables 2 and 3). This observation is expected on the basis of the internal return processes ( $k_{i\text{com}}$  and  $k_{r\text{com}}$ , Scheme 1) previously observed for the intermediates in ester photochemistry (34–36). Again as a consequence of these competing processes, only product yields obtained at very low conversions (<5%) are useful for mechanistic consideration. These values are given in Table 2 for reactions in cyclohexane and in Table 3 for those in methanol. Because the percentage conversion is too small to determine reliably, the yields are normalized to 100%.

The photolysis products obtained for the esters **1** and **2** in cyclohexane are easily explained by the radical pair mecha-

**Table 2.** Product yields for the photolysis of the esters **1** and **2** in cyclohexane.

	X	R	<b>7</b> <sup>a</sup>	<b>9</b> <sup>a</sup>	<b>12</b> <sup>b</sup>
<b>1a</b> <sup>c</sup>	H	CH <sub>3</sub>	—	15 (1:1.3)	80
<b>2a</b>	H	(CH <sub>3</sub> ) <sub>3</sub> C	20	15 (1:1.3)	65
<b>1b</b>	5-CH <sub>3</sub> O	CH <sub>3</sub>	—	—	100 (1:2.3)
<b>2b</b>	5-CH <sub>3</sub> O	(CH <sub>3</sub> ) <sub>3</sub> C	15 (1:1.1)	—	85 (1:2.5)
<b>1c</b> <sup>d</sup>	6-CH <sub>3</sub> O	CH <sub>3</sub>	—	—	100 (1:1.5)
<b>2c</b> <sup>e</sup>	6-CH <sub>3</sub> O	(CH <sub>3</sub> ) <sub>3</sub> C	25 (1:1.1)	—	75 (1:2.1)

**Note:** Yields are for low conversion (<10%) and normalized to 100%. Estimated error  $\pm 5\%$ .

<sup>a</sup>Numbers in brackets refer to the ratio of the two possible diastereomers.

<sup>b</sup>Numbers in brackets refer to the ratio of the two possible regioisomers.

<sup>c</sup>For **1a**, 8% of the material was 1-cyclohexyl-2-methylindene **8**, a product not detected for the other five compounds.

<sup>d</sup>Ratio of **1c**:**1b** = 5.8:1 at 41% conversion.

<sup>e</sup>Ratio of **2c**:**2b** = 3.9:1 at 75% conversion.

nism in Scheme 4, where the radical paired with the indenyl one is now an acyloxy, rather than hydroxyl as it was for the indenols in Scheme 3. For the acetates **1** ( $R = CH_3$ ), decarboxylation gives the methyl radical leading to the coupling product **12a** ( $R = CH_3$ ) (two regioisomers for  $X = 5\text{-CH}_3\text{O}$  and  $6\text{-CH}_3\text{O}$ ). For the pivalates **2** ( $R = C(CH_3)_3$ ), decarboxylation now gives the *tert*-butyl radical, leading to the coupling product **12b** ( $R = C(CH_3)_3$ ) and disproportionation to 2-methylindene **7** (again, two regioisomers for  $X = 5\text{-}$  and  $6\text{-CH}_3\text{O}$  for both **7** and **12b**). As in the photolysis of the indenols **3** (Table 1), the out-of-cage dimers were only obtained for the unsubstituted esters **1a** and **1b**. The very similar yields of **7** and **12** obtained for both the 5- and 6-methoxy substrates, independent of which one is the starting material, indicates that the indenyl radical again loses the memory of its precursor.

The products obtained for the photolysis of the indenyl esters in methanol are given in Table 3. Particularly striking is the very high yield of the ion-derived product, the methyl ether **6**, particularly from the 5- and 6-methoxy acetates, **1b**



**Table 3.** Product yields for the photolysis of the esters **1** and **2** in methanol.

	X	R	<b>6</b>	<b>7</b>	<b>9</b> <sup>a</sup>	<b>12</b> <sup>b</sup>	Ion:radical <sup>c</sup>	Ion:radical <sup>d</sup>
<b>1a</b>	H	CH <sub>3</sub>	15	—	25 (1:1.4)	60	0.18:1	1.4:1
<b>2a</b>	H	(CH <sub>3</sub> ) <sub>3</sub> C	—	10	20 (1:1.2)	70	<0.02:1	0.21:1
<b>1b</b>	5-CH <sub>3</sub> O	CH <sub>3</sub>	75	—	—	25 (1:2.1)	3.0:1	0.10:1
<b>2b</b>	5-CH <sub>3</sub> O	(CH <sub>3</sub> ) <sub>3</sub> C	20	—	—	80 (1:1.6)	0.25:1	<0.02:1
<b>1c</b> <sup>e</sup>	6-CH <sub>3</sub> O	CH <sub>3</sub>	100	—	—	—	>50:1	2.3:1
<b>2c</b> <sup>f</sup>	6-CH <sub>3</sub> O	(CH <sub>3</sub> ) <sub>3</sub> C	30	—	—	70 (1:1.2)	0.33:1	0.25:1

**Note:** Yields are for low conversion (<5%) and normalized to 100%. Estimated error  $\pm 5\%$ .

<sup>a</sup>Numbers in brackets refer to the ratio of the two diastereomers.

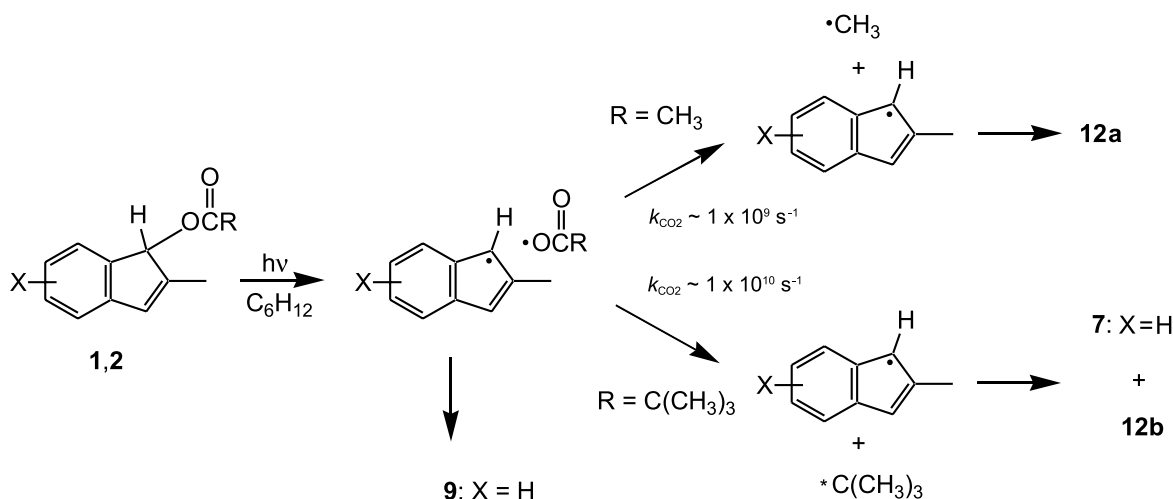
<sup>b</sup>Numbers in brackets refer to the ratio of the two possible regioisomers.

<sup>c</sup>Ratio of ion- to radical-derived products for the indenyl esters **1** and **2**.

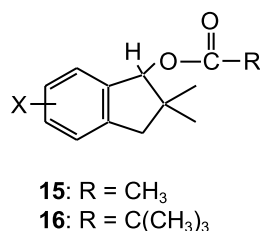
<sup>d</sup>Ratio of ion- to radical-derived products for the analogous indanyl esters, **15** and **16**, ref. 17.

<sup>e</sup>Ratio of **1c**:**1b** = 8.7:1 at 48% conversion.

<sup>f</sup>Ratio of **2c**:**2b** = 40:1 at 32% conversion.

**Scheme 4.** Mechanistic pathways for the photolysis of the esters **1a–c** and **2a–c** in cyclohexane.

and **1c**. The ratio of ion- to radical-derived product is significantly larger for the methoxy-substituted substrates than the corresponding indanyl (Table 3) derivatives **15** and **16** (17). In fact, the ion-derived ether **6b** (X = 5-CH<sub>3</sub>O) is the only product observed (at low conversion) for the acetate **1c** (X = 6-CH<sub>3</sub>O). The change in product distribution for the change in substrate from acetate esters **1** to pivalate esters **2** has been used effectively in the past by us (1) and others (37) to test for the intervention of acyloxy radicals. Their very different rates of decarboxylation serve as radical clocks for other possible processes of the radical, in particular, the electron transfer process ( $k_{et}$ , Scheme 1) that converts the radical pair to the ion pair.

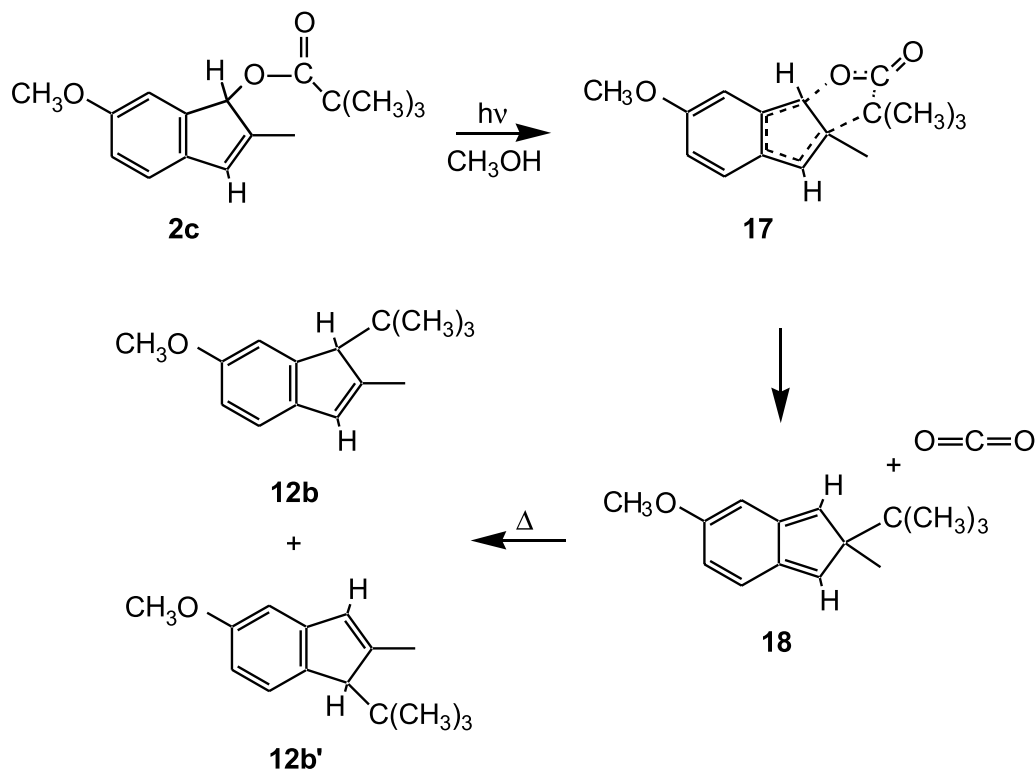


However, the surprising observation of the absence of the disproportionation products **7** in the photolysis of the 5- and

6-methoxy pivalate esters **2b** and **2c** at low conversion in methanol suggests that free *tert*-butyl radicals are not formed. This observation emphasizes why product yields at low conversion are essential for understanding the photochemistry involved. As mentioned above, the yield of **7** increases with the extent of conversion by a process of secondary photochemistry involving **12b** (X = C(CH<sub>3</sub>)<sub>3</sub>). The parallel change in the ratio of the two regioisomeric coupling products **12** indicates that this secondary photochemistry is homolytic carbon—carbon bond cleavage to generate the indenyl-*tert*-butyl radical pair, allowing for both disproportionation and regioisomeric equilibration to occur.

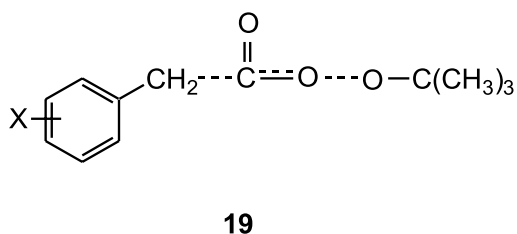
The question then arises as to the mechanism of formation of the *tert*-butyl coupling products if *tert*-butyl radicals are not involved in the primary photochemistry of the methoxy pivalate esters in methanol. A tentative proposal is an excited-state migratory (from C1 to C2) decarboxylation of the *tert*-butyl group via a five-membered transition state **17** (shown in Scheme 5 for the 6-methoxypivalate **2c**) to form an isoindene derivative **18**. Excited state migrations from C1 to C2 are well known for phenyl-substituted indenenes (38). The resulting isoindenenes would be thermally unstable and revert to indene. On the basis of migratory aptitudes (CH<sub>3</sub> <



**Scheme 5.** Proposed mechanism for the formation of the coupling products **12** and **12'** for the photolysis of the ester **2c** in methanol.

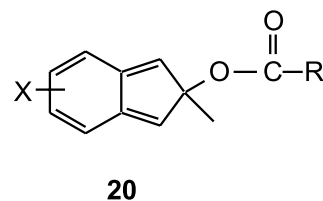
$\text{CH}_2\text{CH}_3 < \text{CH}(\text{CH}_3)_2$ ) previously determined (33) for the thermal reversion of isoindenes to indenes, the *tert*-butyl group in **18** will migrate in preference to methyl, giving the two observed regioisomeric products, **12b** and **12b'**. The process described by transition state **17** is not observed and not possible for other benzylic substrates, which lack the required indenyl type conjugation. In those cases, disproportionation always accompanies coupling of *tert*-butyl radicals, as expected (39).

This process is reminiscent of that proposed for the thermal decomposition of peresters, which are concerted (40, 41), where the potential acyloxy radical will fragment very rapidly because of the stability of the radical generated, **19**. These reactions have negative  $\rho$  values (approximately  $-1.1$ ), indicating that the transition states have some positive character on carbon and negative on oxygen (42). The photochemical migration suggested by structure **17** in Scheme 5 might also have a substituent effect, which could potentially explain why the yield of the isomers **12** are slightly different for the 5-methoxy **2b** (80%) vs. the 6-methoxy (70%) pivalate ester **3b**. The substituent effect could also rationalize why the unsubstituted substrate **2a** seems to undergo normal homolytic bond cleavage and give both coupling (**12**) and disproportionation (**7**) products.



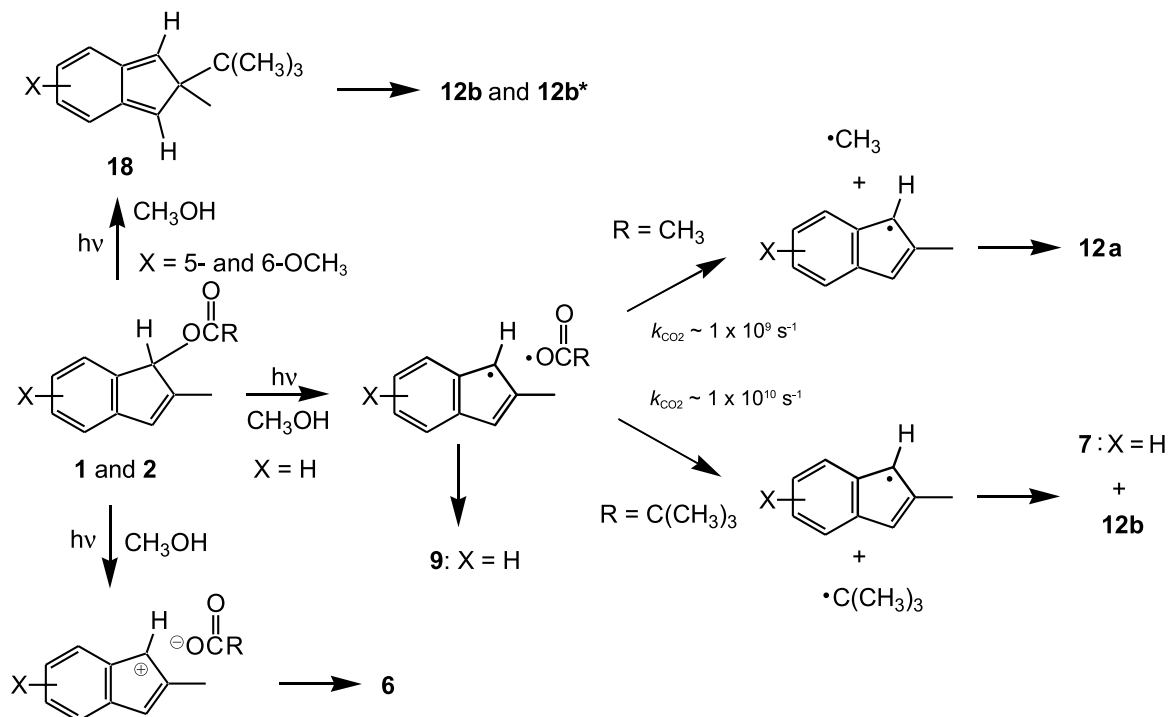
The mechanistic proposals for the indenyl esters can then be summarized as follows: In cyclohexane, all three esters react by homolytic cleavage to give radical-derived products as shown in Scheme 4. In methanol, as outlined in Scheme 6, the unsubstituted esters **1a** and **2a** react by the same mechanism for the radical-derived products, but now formation of the ion pair leads to low yields (15%) of the methoxy ether **6** for the acetate **1a**. The decrease in the yield of **6**, as a consequence of the change from acetate **1a** to pivalate **2a**, suggests that the radical clock method is operative and that the ion pair is formed (at least partially) from the radical pair by redox electron transfer ( $k_{\text{et}}$ , Scheme 1) in competition with the rate of decarboxylation, which is faster by an order of magnitude for the  $(\text{CH}_3)_3\text{CCO}_2$  radical.

Two other potential photochemically generated intermediates that have not yet been discussed should be mentioned as possible precursors for the ion-derived ether product in methanol. The first, **20**, an isoindene, would result from migration of the acyloxy group from C1 to C2 of the indene.

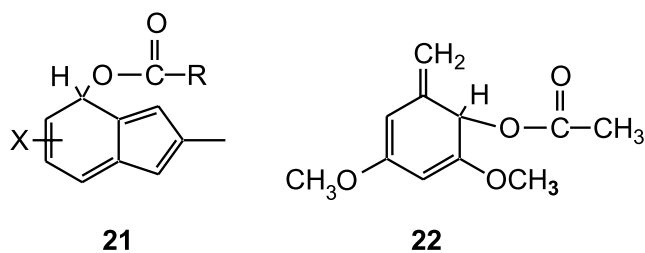


The second, **21**, analogous to the intermediate **22** observed in the photolysis of 3,5-dimethoxybenzyl acetate in methanol and other alcohol solvents (43), would be formed by acyloxy migration from C1 to C7. A similar intermediate has been reported for the photolysis of 9-fluorenone in methanol.



**Scheme 6.** Mechanistic pathways for the photolysis of the esters **1a–c** and **2a–c** in methanol.

nol (44) and non-acidic zeolites (45). Either of these could be very reactive (thermally or photochemically) in methanol as solvent. For instance, the half life for ground-state solvolysis of **22** in methanol is approximately 2 min. We are currently conducting nanosecond laser flash photolysis experiments to examine the reactive intermediates for the photochemistry described above.



## Conclusions

For the 5- and 6-methoxy-substituted esters in methanol, the proposed mechanism is that direct heterolytic cleavage from the excited state to form an ion pair (Scheme 6) competes with migratory decarboxylation of the ester to give the isoidene derivative **18** (as shown in Scheme 5). This latter process is less important for the acetates **1b** and **1c** than the pivalates **2b** and **2c**, and therefore, the acetates give very high yields of the ion-derived ether **6**, reaching 100% for the 6-methoxy acetate **1c**! This substrate has the activating group *meta* to the reactive benzylic centre. The photochemical “*meta* effect”, as originally proposed by Zimmerman and co-workers (46) for methoxy-substituted benzylic acetates and supported by studies of methoxy-substituted benzylic alcohols by Wan and co-workers (47), predicts enhanced efficiency for heterolytic cleavage reactions for leaving groups

*meta* (and *ortho*) to electron-donating substituents. It seems to be playing an important role in the photochemistry of these indenyl esters. This suggestion is in marked contrast to our proposal for all previously studied ester substrates where homolytic cleavage followed by electron transfer is considered to be the dominant mechanistic pathway for the formation of ion-derived products. Although the limited data available make these mechanistic conclusions somewhat speculative, the fact that products derived from indenyl cations are formed in these photoreactions is certain. This may well be a consequence of the antiaromatic character of these  $4n$   $\pi$  cations, in agreement with Wan and co-workers’ proposal for 9-fluorenyl derivatives (12, 13).

## Experimental section

### General procedures

Proton ( $^1\text{H}$ ) and carbon ( $^{13}\text{C}$ ) nuclear magnetic resonance (NMR) spectra were obtained in  $\text{CDCl}_3$  on an AC 250 F NMR spectrometer in automation mode. Ultraviolet (UV) spectra were obtained in 1 cm quartz cuvettes on a Varian-Cary Bio 100 spectrometer. Fluorescence measurements were done in methanol, with non-degassed samples, using a PTI spectrometer at 25 °C. Corrected spectra were obtained. GC–MS analyses were performed on a PerkinElmer Autosystem XL instrument with a mass selective detector. The column used was a Supelco 30 m  $\times$  0.25 mm MDN-5S 5% phenyl methylsiloxane, film thickness 0.50  $\mu\text{m}$ , temperature programmed: 60 °C for 1 min; 20 °C increase per min to 240 °C; 240 °C for 10 min. GC–FID analyses were done in a similar way except on a Supelco DB200 column. Mass spectral data are reported in units of mass over charge ( $m/z$ ) for all values between 50 and the molecular ion if greater



than 10% of the base peak. Intensities are reported as a percent of the base peak.

### Indenone synthesis

#### 2-Methyl-1-indenone 4a and 5-methoxy-2-methyl-1-indenone 4b

These indenones were prepared using the procedure of Floyd and Allen ( ), outlined in Scheme 2.

#### 6-Methoxy-2-methyl-1-indenone 4c

The precursor to this indenone, 6-methoxy-2-methyl-1-indanone **5** ( $X = 6\text{-CH}_3\text{O}$ ), was prepared using the procedure of Sam and Plampin ( ), outlined in Scheme 2. To a solution of 13.9 g (79 mmol) of **5** ( $X = 6\text{-CH}_3\text{O}$ ) in 170 mL of  $\text{CCl}_4$  was added 14.4 g (90 mmol) of bromine in 70 mL of  $\text{CCl}_4$ . After the addition was complete, the mixture was stirred at room temperature for 2 h. The solvent and excess bromine were removed under reduced pressure and 20.5 g (79 mmol, 100%) of the crude bromide, as a brown solid, resulted.  $^1\text{H}$  NMR ( $\text{CDCl}_3$ )  $\delta$ : 7.22–7.32 (m, 3H), 3.85 (s, 3H), 3.72 (d, 1H,  $J = 18$  Hz), 3.41 (d, 1H,  $J = 18$  Hz), 1.95 (s, 3H).  $^{13}\text{C}$  NMR ( $\text{CDCl}_3$ )  $\delta$ : 200.4, 160.0, 141.8, 133.8, 127.1, 125.3, 106.7, 60.3, 55.7, 45.8, 27.0. GC–MS: 256 (19), 254 (18), 176 (58), 175 (100), 174 (22), 161 (96), 148 (20), 147 (41), 146 (10), 133 (29), 132 (23), 131 (41), 117 (16), 115 (32), 105 (10), 104 (11), 103 (42), 102 (14), 91 (36), 89 (14), 79 (19), 78 (29), 77 (77), 76 (18), 75 (17), 74 (20), 65 (13), 64 (10), 63 (45), 62 (15), 51 (34), 50 (13). HR–MS calcd. for  $\text{C}_{11}\text{H}_{11}\text{O}_2\text{Br}$ : 253.9942; found: 253.9934. A mixture of 20.5 g (79 mmol) of crude bromoindanone, 12.1 g (139 mmol) LiBr, and 10.4 g (140 mmol)  $\text{Li}_2\text{CO}_3$  in 175 mL of DMF was heated between 135–140 °C for 3 h under a nitrogen atmosphere. After cooling, the mixture was poured into 300 mL of water and extracted three times with ether. The combined ether layers were washed twice with water and dried with  $\text{MgSO}_4$ . Evaporation of the ether produced 10.4 g of thick red oil that contained crystals. This material was purified by flash chromatography on silica gel producing 3.60 g (21 mmol, 26%) of bright orange needles: mp 82–84 °C.  $^1\text{H}$  NMR ( $\text{CDCl}_3$ )  $\delta$ : 7.06 (q, 1H,  $J = 1.8$  Hz), 6.97 (d, 1H,  $J = 2.4$  Hz), 6.78 (d, 1H,  $J = 7.9$ ), 6.67 (dd, 1H,  $J_1 = 2.4$ ,  $J_2 = 7.9$  Hz), 3.77 (s, 3H), 1.81 (d, 3H,  $J = 1.8$  Hz).  $^{13}\text{C}$  NMR ( $\text{CDCl}_3$ )  $\delta$ : 198.6, 160.1, 144.1, 136.6, 134.9, 132.7, 121.6, 116.1, 110.9, 55.6, 10.0. GC–MS: 175 (12), 174 (100), 159 (40), 131 (92), 115 (10), 103 (74), 102 (21), 77 (64), 76 (21), 75 (20), 63 (25), 62 (12), 51 (18). HR–MS calcd. for  $\text{C}_{11}\text{H}_{10}\text{O}_2$ : 174.0681; found: 174.0675.

### Indenol syntheses

Indenols **3** were prepared from the corresponding indenones using Luche's reagent (18). The yields were 60–95%.

#### 2-Methyl-1-indenol 3a

mp 84–86 °C.  $^1\text{H}$  NMR ( $\text{CDCl}_3$ )  $\delta$ : 7.09–7.50 (m, 4H), 6.33 (broad s, 1H), 4.84 (broad s, 1H), 2.07 (broad s, 3H), 1.66 (broad s, 1H).  $^{13}\text{C}$  NMR ( $\text{CDCl}_3$ )  $\delta$ : 148.3, 145.2, 143.0, 128.5, 127.0, 124.9, 123.3, 120.1, 78.9, 13.8. GC–MS: 146 (86), 145 (38), 132 (10), 131 (100), 129 (13), 128 (22), 127 (14), 117 (15), 116 (11), 115 (46), 103 (31), 91

(14), 89 (10), 77 (21), 63 (16), 51 (15). HR–MS calcd. for  $\text{C}_{10}\text{H}_{10}\text{O}$ : 146.0731; found: 146.0741.

#### 5-Methoxy-2-methyl-1-indenol 3b

mp 77–78 °C.  $^1\text{H}$  NMR ( $\text{CDCl}_3$ )  $\delta$ : 7.32 (d, 1H,  $J = 7.9$  Hz), 6.68 (d, 1H,  $J = 2.3$  Hz), 6.61 (dd, 1H,  $J_1 = 7.9$ ,  $J_2 = 2.3$  Hz), 6.27 (s, 1H), 4.78 (broad s, 1H), 3.79 (s, 3H), 2.05 (broad s, 3H), 1.64 (broad s, 1H).  $^{13}\text{C}$  NMR ( $\text{CDCl}_3$ )  $\delta$ : 160.3, 149.9, 144.74, 137.3, 126.6, 123.9, 109.1, 106.9, 78.2, 55.4, 13.9. GC–MS: 176 (70), 175 (27), 174 (13), 162 (11), 161 (100), 160 (22), 159 (11), 146 (19), 145 (30), 133 (19), 132 (10), 131 (20), 118 (13), 116 (12), 115 (35), 105 (11), 103 (24), 102 (11), 91 (12), 89 (13), 79 (12), 78 (10), 77 (34), 75 (10), 63 (20), 51 (13). HR–MS calcd. for  $\text{C}_{11}\text{H}_{12}\text{O}_2$ : 176.0837; found: 176.0835.

#### 6-Methoxy-2-methyl-1-indenol 3c

mp 103–105 °C.  $^1\text{H}$  NMR ( $\text{CDCl}_3$ )  $\delta$ : 7.08 (d, 1H,  $J = 2.4$  Hz), 7.01 (d, 1H,  $J = 8.0$  Hz), 6.74 (dd, 1H,  $J_1 = 8.0$ ,  $J_2 = 2.4$  Hz), 6.27 (s, 1H), 4.81 (d, 1H,  $J = 8.9$  Hz), 3.80 (s, 3H), 2.04 (broad s, 3H), 1.49 (d, 1H,  $J = 8.9$  Hz).  $^{13}\text{C}$  NMR ( $\text{CDCl}_3$ )  $\delta$ : 158.0, 147.1, 146.1, 135.7, 126.5, 120.4, 113.1, 110.7, 79.0, 55.6, 13.7. GC–MS: 177 (10), 176 (87), 175 (18), 162 (11), 161 (100), 160 (33), 159 (18), 146 (15), 145 (40), 133 (23), 131 (12), 118 (17), 117 (16), 116 (19), 115 (60), 105 (13), 103 (20), 102 (11), 91 (13), 79 (11), 77 (24), 63 (17), 51 (16). HR–MS calcd. for  $\text{C}_{11}\text{H}_{12}\text{O}_2$ : 176.0837; found: 176.0841.

### General method for the preparation of esters 1a–c and 2a–c

The corresponding acid chloride (4 mmol) in 5 mL of dry benzene was added to a solution of the corresponding indenol (2 mmol) and pyridine (4 mmol) in 10 mL of dry benzene. The solution was stirred overnight at room temperature, then 50 mL of water was added, and the two layers were separated. The benzene layer was washed twice with 10% aqueous HCl and once with saturated aqueous sodium bicarbonate and finally with water. The esters were purified by column chromatography on silica gel. The yields were 50–75%. Solid samples were recrystallized and oils were bulb-to-bulb distilled.

#### 2-Methyl-1-indenyl acetate, 1a

bp 87–91 °C at 2–3 mmHg (1 mmHg = 133.322 Pa). UV (methanol)  $\lambda_{\text{max}}$  (nm) ( $\epsilon$  ((mol L<sup>−1</sup>)<sup>−1</sup> cm<sup>−1</sup>)): 266 (7130), 306 (952).  $^1\text{H}$  NMR ( $\text{CDCl}_3$ )  $\delta$ : 7.04–7.36 (m, 4H), 6.40 (s, 1H), 6.13 (s, 1H), 2.16 (s, 3H), 1.97 (s, 3H).  $^{13}\text{C}$  NMR ( $\text{CDCl}_3$ )  $\delta$ : 171.4, 144.4, 143.7, 142.1, 129.3, 128.8, 125.1, 124.2, 120.3, 78.4, 21.0, 14.0. GC–MS: 188 (15), 147 (11), 146 (100), 145 (29), 131 (68), 129 (21), 128 (74), 127 (16), 117 (10), 115 (31). HR–MS calcd. for  $\text{C}_{12}\text{H}_{12}\text{O}_2$ : 188.0837; found: 188.0843.

#### 5-Methoxy-2-methyl-1-indenyl acetate, 1b

UV (methanol)  $\lambda_{\text{max}}$  (nm) ( $\epsilon$  ((mol L<sup>−1</sup>)<sup>−1</sup> cm<sup>−1</sup>)): 279 (2880), 306 (1560).  $^1\text{H}$  NMR ( $\text{CDCl}_3$ )  $\delta$ : 7.27 (d, 1H,  $J = 7.9$  Hz), 6.71 (d, 1H,  $J = 2.4$  Hz), 6.59 (dd, 1H,  $J_1 = 2.4$ ,  $J_2 = 7.9$  Hz), 6.38 (broad s, 1H), 6.07 (broad s, 1H), 3.79 (s, 3H), 2.17 (s, 3H), 1.98 (broad s, 3H).  $^{13}\text{C}$  NMR ( $\text{CDCl}_3$ )  $\delta$ : 171.6, 160.7, 145.5, 134.1, 129.1, 125, 109.4, 107.2, 78.1,



55.4, 21.1, 14.2. GC-MS: 218 (23), 177 (12), 176 (100), 175 (24), 161 (65), 160 (19), 159 (26), 158 (24), 145 (22), 144 (11), 117 (10), 116 (26), 115 (66), 91 (12). HR-MS calcd. for  $C_{12}H_{14}O_3$ : 218.0943; found: 218.0931.

#### 6-Methoxy-2-methyl-1-indenyl acetate, 1c

bp 100–102 °C at 2 mmHg. UV (methanol)  $\lambda_{\max}$  (nm) ( $\epsilon$  ((mol L<sup>-1</sup>)<sup>-1</sup> cm<sup>-1</sup>)): 273 (8850), 320 (1190). <sup>1</sup>H NMR (CDCl<sub>3</sub>)  $\delta$ : 7.02 (d, 1 H,  $J$  = 8.0 Hz), 6.99 (d, 1H,  $J$  = 2.3 Hz), 6.75 (dd, 1H,  $J_1$  = 2.3,  $J_2$  = 8.0 Hz), 6.37 (broad s, 1H), 6.10 (broad s, 1H), 3.78 (s, 3H), 2.18 (s, 3H), 1.95 (broad s, 3H). <sup>13</sup>C NMR (CDCl<sub>3</sub>)  $\delta$ : 171.5, 158.1, 143.9, 142.2, 136.5, 128.9, 120.6, 114.0, 111.7, 78.5, 55.6, 21.1, 14.0. GC-MS: 218 (26), 177 (11), 176 (100), 175 (19), 161 (58), 159 (19), 158 (25), 145 (15), 116 (19), 115 (48). HR-MS calcd. for  $C_{12}H_{14}O_3$ : 218.0943; found: 218.0935.

#### 2-Methyl-1-indenyl pivalate, 2a

<sup>1</sup>H NMR (CDCl<sub>3</sub>)  $\delta$ : 7.05–7.31 (m, 4 H), 6.43 (broad s, 1H), 6.14 (broad s, 1H), 1.97 (s, 3H), 1.26 (s, 9H). <sup>13</sup>C NMR (CDCl<sub>3</sub>)  $\delta$ : 179.0, 144.9, 143.8, 142.4, 129.0, 128.7, 125.1, 123.9, 120.3, 78.2, 39.1, 27.3, 14.0. GC-MS: 230 (15), 146 (66), 145 (14), 131 (25), 129 (42), 128 (100), 127 (21), 115 (19), 57 (75). HR-MS calcd. for  $C_{15}H_{18}O_2$ : 230.1307; found: 230.1314.

#### 5-Methoxy-2-methyl-1-indenyl pivalate, 2b

mp 63–64 °C. <sup>1</sup>H NMR (CDCl<sub>3</sub>)  $\delta$ : 7.21 (d, 1H,  $J$  = 8.1 Hz), 6.71 (d, 1H,  $J$  = 2.3 Hz), 6.59 (dd, 1H,  $J_1$  = 8.1 Hz,  $J_2$  = 2.3 Hz), 6.37 (broad s, 1H), 6.07 (broad s, 1H), 3.78 (s, 3H), 1.96 (broad s, 3H), 1.25 (s, 9H). <sup>13</sup>C NMR (CDCl<sub>3</sub>)  $\delta$ : 179.0, 160.6, 146.3, 145.5, 134.4, 128.8, 124.6, 109.3, 107.2, 77.8, 55.4, 39.0, 27.2, 14.1. GC-MS: 260 (11), 176 (47), 175 (21), 161 (17), 160 (11), 159 (36), 158 (29), 116 (20), 115 (40), 57 (100). HR-MS calcd. for  $C_{16}H_{20}O_3$ : 260.1412; found: 260.1403.

#### 6-Methoxy-2-methyl-1-indenyl pivalate, 2c

mp 54–56 °C. <sup>1</sup>H NMR (CDCl<sub>3</sub>)  $\delta$ : 7.03 (d, 1H,  $J$  = 8.1 Hz), 6.92 (d, 1H,  $J$  = 2.3 Hz), 6.76 (dd, 1H,  $J_1$  = 8.1 Hz,  $J_2$  = 2.3 Hz), 6.37 (broad s, 1H), 6.10 (broad s, 1H), 3.78 (s, 3H), 1.94 (broad s, 3H), 1.26 (s, 9H). <sup>13</sup>C NMR (CDCl<sub>3</sub>)  $\delta$ : 179.0, 158.0, 144.2, 142.7, 136.5, 128.5, 120.5, 113.0, 111.6, 78.2, 55.6, 39.0, 27.2, 13.9. GC-MS: 260 (11), 176 (51), 175 (21), 161 (20), 159 (34), 158 (34), 116 (21), 115 (39), 57 (100). HR-MS calcd. for  $C_{16}H_{20}O_3$ : 260.1412; found: 260.1408.

#### Preparation of ethers, 3

The ethers were prepared from the corresponding indenols using the procedure of Freidrich and Taggart (48) and were purified by chromatography on silica gel. The yields of these reactions were not high (<20%), particularly for the methoxy-substituted cases, and the <sup>1</sup>H NMR of the crude indicated the appropriate peaks for the ethers superimposed on broad, featureless bands (oligomers?). Only one ether **9** (X = 5-OCH<sub>3</sub>) was obtained when starting with either 5- or 6-methoxy-2-methyl-1-indenol, although GC analysis indicated that the isomer was formed (<5%). <sup>1</sup>H NOE difference spectra demonstrated that this ether was 1-methoxy-5-methoxy-2-methylindene. This ether **3** (X = 5-CH<sub>3</sub>O) was

also isolated from photolysis of 6-methoxy-2-methyl-1-indenol in methanol.

#### 1-Methoxy-2-methylindene

<sup>1</sup>H NMR (CDCl<sub>3</sub>)  $\delta$ : 7.02–7.42 (m, 4H), 6.42 (broad s, 1H), 4.84 (broad s, 1H), 3.02 (s, 3H), 2.02 (broad s, 3H). <sup>13</sup>C NMR (CDCl<sub>3</sub>)  $\delta$ : 145.9, 143.9, 141.9, 128.7, 128.4, 124.7, 123.8, 120.2, 84.9, 51.8, 14.1. GC-MS: 160 (82), 159 (11), 145 (100), 130 (14), 129 (23), 128 (45), 127 (20), 117 (40), 116 (12), 115 (60), 102 (17), 91 (22), 77 (12), 63 (18), 51 (16). HR-MS calcd. for  $C_{11}H_{12}O$ : 160.0888; found: 160.0887.

#### 1-Methoxy-5-methoxy-2-methylindene

<sup>1</sup>H NMR (CDCl<sub>3</sub>)  $\delta$ : 7.30 (d, 1H,  $J$  = 8.0 Hz), 6.72 (d, 1H,  $J$  = 2.3 Hz), 6.64 (dd, 1H,  $J_1$  = 8.0 Hz,  $J_2$  = 2.3 Hz), 6.39 (broad s, 1H), 4.82 (broad s, 1H), 3.81 (s, 3H), 3.02 (s, 3H), 2.03 (broad s, 3H). <sup>13</sup>C NMR (CDCl<sub>3</sub>)  $\delta$ : 160.3, 147.3, 145.5, 133.6, 128.4, 124.3, 109.1, 106.9, 84.2, 55.4, 52.6, 14.2. GC-MS: 191 (11), 190 (88), 189 (15), 176 (11), 175 (100), 160 (25), 159 (32), 147 (28), 144 (16), 132 (13), 116 (23), 115 (55), 103 (12), 91 (18), 89 (13), 77 (14), 63 (15), 51 (10).

#### Quantitative photolyses

A solution of ~100 mg of the appropriate ester **1** and **2** in 100 mL methanol or cyclohexane was purged with nitrogen and then irradiated in a Rayonet photochemical reactor using 4 lamps (75 W, 254 nm). The temperature was controlled at 25 °C by circulating water in an immersion tube. Reaction progress was monitored by GC, and the reaction stopped when the ester was less than 5% consumed. For the alcohols **3** and the ether **6** (X = H), ~50 mg in 100 mL of the appropriate solvent (methanol or cyclohexane) was used.

#### Acknowledgements

We thank the Natural Sciences and Engineering Research Council of Canada (NSERC) for financial support; Sepracor Canada Ltd., Windsor, Nova Scotia, for the donation of chemicals; and Dr. M. Lumsden, ARMRC, Department of Chemistry, Dalhousie University, Halifax, Nova Scotia, for the NOE NMR experiments. I.S.Y. also thanks NSERC for a Student Research Award.

#### References

1. J.A. Pincock. Acc. Chem. Res. **30**, 43 (1997).
2. S.A. Fleming and J.A. Pincock. Organic molecular photochemistry. Vol. 3. Marcel Dekker, New York. 1999. p. 211.
3. C.G. Bochet. J. Chem. Soc. Perkin Trans. 1, 125 (2002).
4. A.P. Pelliccioli and J. Wirz. Photochem. Photobiol. Sci. **1**, 441 (2002).
5. J. Chateaufneuf, J. Luszyk, and K.U. Ingold. J. Am. Chem. Soc. **110**, 2877 (1988).
6. J.W. Hilborn and J.A. Pincock. J. Am. Chem. Soc. **113**, 2683 (1991).
7. T.M. Bockman, S.M. Hubig, and J. K. Kochi. J. Org. Chem. **62**, 2210 (1997).
8. D.P. DeCosta and J.A. Pincock. J. Am. Chem. Soc. **115**, 2180 (1993).



9. W. Hilborn, E. MacKnight, J.A. Pincock, and P.J. Wedge. *J. Am. Chem. Soc.* **116**, 3337 (1994).
10. H.E. Zimmerman. *J. Am. Chem. Soc.* **117**, 8988 (1995).
11. H.E. Zimmerman. *J. Phys. Chem. A*, **102**, 5616 (1998).
12. P. Wan and E. Krogh. *J. Am. Chem. Soc.* **111**, 4887 (1989).
13. A. Blazek, M. Pungente, E. Krough, and P. Wan. *J. Photochem. Photobiol. A Chem.* **64**, 315 (1992).
14. G.G. Gurzadyan and S. Steenken. *Chem. Eur. J.* **7**, 1808 (2001).
15. A.D. Allen and T.T. Tidwell. *Chem. Rev.* **101**, 1333 (2001).
16. H. Jiao, P. von R. Schleyer, Y. Mo, M.A. McAllister, and T.T. Tidwell. *J. Am. Chem. Soc.* **119**, 7075 (1997).
17. J.A. Pincock and P.J. Wedge. *J. Org. Chem.* **60**, 4067 (1995).
18. J.-L. Luche. *J. Am. Chem. Soc.* **100**, 2226 (1978).
19. M.B. Floyd and G.R. Allen. *J. Org. Chem.* **35**, 2647 (1970).
20. S. Kapur, N.C. Mathur, K. McManus, A.L. Pincock, and J.A. Pincock. *Can. J. Chem.* **66**, 2888 (1988).
21. J. Sam and P. Plampin. *J. Am. Chem. Soc.* **82**, 5205 (1960).
22. T. Waugh and H. Morrison. *J. Am. Chem. Soc.* **121**, 3083 (1999).
23. F.D. Lewis, D. M. Bassani, R.A. Caldwell, and D.J. Unett. *J. Am. Chem. Soc.* **116**, 10 477 (1994).
24. H. Morrison, D. Giacherio, and F. J. Palensky. *J. Org. Chem.* **47**, 1051 (1982).
25. N.E. Heimer, M. Hojjatie, and C. A. Panetta. *J. Org. Chem.* **47**, 2593 (1982).
26. P. Nicolet, J.-Y. Sanchez, A. Benaboura, and M.J.M. Abadie. *Synthesis*, 202 (1987).
27. E.C. Friedrich and D.B. Taggart. *J. Org. Chem.* **40**, 720 (1975).
28. F.G. Bordwell. *Acc. Chem. Res.* **21**, 456 (1988).
29. H. Morrison and D. Giacherio. *J. Org. Chem.* **47**, 1058 (1982).
30. H. Morrison, D. Giacherio, and G. Pandey. *Tetrahedron Lett.* **23**, 3427 (1982).
31. D.F. McMillen and D.M. Golden. *Ann. Rev. Phys. Chem.* **33**, 493 (1982).
32. E.C. Friedrich and D.B. Taggart. *J. Org. Chem.* **43**, 805 (1978).
33. W.R. Dolbier, K.E. Anapolle, L. McCullaugh, K. Matsui, J.M. Reimann, and D. Rolison. *J. Org. Chem.* **44**, 2845 (1979).
34. J.M. Kim and J.A. Pincock. *Can. J. Chem.* **73**, 885 (1995).
35. R.S. Givens, B. Matuszewski, N. Levi, and D. Leung. *J. Am. Chem. Soc.* **99**, 1896 (1977).
36. D.A. Jaeger and G.H. Angelos. *Tetrahedron Lett.* **22**, 803 (1981).
37. Y. Shi, J.E.T. Corrie, and P. Wan. *J. Org. Chem.* **62**, 8278 (1997).
38. J.J. McCullough. *Acc. Chem. Res.* **13**, 270 (1980).
39. M.T. Gibian and R.G. Corley. *Chem. Rev.* **73**, 441 (1973).
40. P.D. Bartlett and R.R. Hiatt. *J. Am. Chem. Soc.* **80**, 1398 (1958).
41. S.S. Kim, I.S. Baek, A. Tuchkin, and K.M. Go. *J. Org. Chem.* **66**, 4006 (2001).
42. P.D. Bartlett and C. Ruchardt. *J. Am. Chem. Soc.* **82**, 1756 (1960).
43. (a) D.P. DeCosta, N. Howell, A.L. Pincock, J.A. Pincock, and S. Rifai. *J. Org. Chem.* **65**, 4698 (2000); (b) F.L. Cozens, A.L. Pincock, J.A. Pincock, and R. Smith. *J. Org. Chem.* **63**, 434 (1998).
44. E. Gaillard, M.A. Fox, and P. Wan. *J. Am. Chem. Soc.* **111**, 2180 (1989).
45. M.A. O'Neill, F.L. Cozens, and N.P. Schepp. *Tetrahedron*, **56**, 6969 (2000).
46. (a) H.E. Zimmerman and V.R. Sandel. *J. Am. Chem. Soc.* **85**, 915 (1963); (b) H.E. Zimmerman and S. Somasekhara. *J. Am. Chem. Soc.* **85**, 922 (1963).
47. (a) P. Wan and B. Hall. *J. Photochem and Photobiol. A*, **56**, 35 (1991); (b) P. Wan, B. Chak, and E. Krough. *J. Photochem and Photobiol. A*, **46**, 49 (1989); (c) P. Wan and B. Chak. *J. Chem. Soc. Perkin Trans. 2*, 1751 (1986); (d) P.J. Wan. *J. Org. Chem.* **50**, 2583 (1985).
48. E.C. Friedrich and D.B. Taggart. *J. Org. Chem.* **40**, 720 (1975).



# CuO – activated carbon catalysts for methanol decomposition to hydrogen and carbon monoxide

Tanya Tsoncheva, Radostin Nickolov, Svetoslava Vankova, and  
Dimitar Mehandjiev

**Abstract:** A comparison of the abilities of CuO – activated carbon catalysts, prepared by different copper precursors and preparation techniques, in the methanol decomposition reaction to carbon monoxide and hydrogen, was undertaken. Higher catalytic activity and stability are found for the catalysts obtained from an ammonia solution of copper carbonate. The nature of the catalytic active complex in the samples is also discussed.

**Key words:** methanol decomposition, CuO – activated carbon catalysts, catalytic active complex.

**Résumé :** On a réalisé une comparaison de la réaction de décomposition du méthanol en monoxyde de carbone et en hydrogènes sous l'action de divers catalyseurs de CuO sur des charbons activés, préparés à partir différents précurseurs de cuivre et par diverses techniques. On a observé que l'activité catalytique et la stabilité des catalyseurs étaient plus élevées pour les catalyseurs obtenus à partir de solutions ammoniacales de carbonate de cuivre. On discute aussi de la nature du complexe catalytique actif dans les échantillons.

**Mots clés :** décomposition du méthanol, catalyseurs de CuO sur du charbon activé, complexe catalytique actif.

[Traduit par la Rédaction]

## Introduction

In view of the application of methanol as an alternative ecological fuel (1–4), its catalytic decomposition to CO and hydrogen is a process of considerable interest. Some copper-containing materials appear to be promising catalysts (5–7) for this purpose. In our previous investigations we considered the favorable effect of activated carbon used as a support for the preparation of efficient catalysts for methanol decomposition (8–13). The role of the copper precursor in the catalytic activity and selectivity of these materials has been also reported (10, 12, 13). In this aspect, we would like to draw attention to some peculiarities in methanol decomposition on copper-oxide-supported catalysts obtained by different preparation techniques and to look for a correlation with the nature of the catalytic active complex (CAC) in them (14).

## Experimental

### Materials

This investigation encompasses three copper-containing catalysts supported on activated carbon, a commercial product (15). The specific surface area of the support is  $1060 \text{ m}^2 \text{ g}^{-1}$ ; the pore volume is  $0.91 \text{ cm}^3 \text{ g}^{-1}$ . The catalysts were prepared by an incipient wetness method as follows:

### Sample Cu-AC-N

The active phase was deposited by four-fold spraying of the support with an aqueous solution of  $\text{Cu}(\text{NO}_3)_2$ .

### Sample Cu-AC-A1

The active phase was deposited by four-fold spraying of the support with 2.4 wt% basic copper carbonate in ammonia water and ammonium carbonate, pH = 9.9.

### Sample Cu-AC-A2

The active phase was deposited by single spraying of the support with 2.4 wt% basic copper carbonate in ammonia water and ammonium carbonate, pH = 9.9.

After each deposition, the samples were kept for 24 h in a closed volume and subjected to drying for 1 h under vacuum at 298 K and then for 1 h in air at 313 K. The samples were decomposed at 480 K in air for 1 h.

### Methods and apparatus

Copper content in the samples was determined by atomic absorption spectrometry (Pye Unicam SP 90B spectrometer). X-ray diffraction powder patterns were obtained on a Philips APD-15 diffractometer equipped with a  $\text{Cu K}\alpha$  radiation source and graphite monochromator. XP and Auger spectra were registered using an ESCA LAB Mk II (VG Scientific). The ESR spectra were obtained in an ERS-220

Received 29 March 2002. Published on the NRC Research Press Web site at <http://canjchem.nrc.ca> on 30 September 2003.

**T. Tsoncheva.**<sup>1</sup> Institute of Organic Chemistry, Bulgarian Academy of Sciences, Sofia 1113, Bulgaria.

**R. Nickolov and D. Mehandjiev.** Institute of General and Inorganic Chemistry, Bulgarian Academy of Sciences, Sofia 1113, Bulgaria.

**S. Vankova.** Department of Chemistry, "St. Kl. Ohridski", Sofia 1000, Bulgaria.

<sup>1</sup>Corresponding author (e-mail: [ormm@orgchm.bas.bg](mailto:ormm@orgchm.bas.bg)).



spectrometer (Germany) at 298 K. The magnetic measurements were performed with a Faraday-type magnetic balance in a temperature range of 298–473 K.

The catalytic experiments were carried out in a flow reactor with partial pressure of methanol at 1.57 kPa and WHSV at 1.5 h<sup>-1</sup> in a thermo-programmed regime with a heating rate of 1 K min<sup>-1</sup>. A standard catalytic test with time on stream (about 200 min) at selected temperatures was also performed. The on-line gas chromatographic analysis was performed.

## Results and discussion

In Table 1 data of the copper content and specific surface area for the initial copper-oxide-supported materials are presented. The magnetic susceptibility of the active phase, calculated as CuO at 298 K, is also given. An essential decrease in the BET surface area for all copper-loaded samples in comparison with the parent activated carbon is observed. Therefore, a highly dispersed copper species, located mainly within the pores of the support, seems to be formed.

In Fig. 1 the temperature dependencies of methanol conversion for the copper oxide – activated carbon samples, obtained by different techniques, are presented. The main registered products are CO and H<sub>2</sub>. Methyl formate (MF) is also found at lower temperatures. A well-defined tendency for increased conversion with increasing temperatures is registered for Cu-AC-A1. In this case the conversion remains unchanged (about 100%) above 530 K. On the contrary, a maximum in the conversion curve at 510 K for Cu-AC-N is observed. Further increase in methanol conversion above 600 K is also found. The catalytic activity for Cu-AC-N is lower compared with that for Cu-AC-A1 in the whole temperature interval that was investigated. The conversion curve for Cu-AC-A2 is close to that for Cu-AC-A1, up to 600 K, but a sharp decrease above this temperature is registered. So, a favourable effect of active phase deposition from ammonia solution is concluded. However, the preparation technique that includes a four-fold spraying of the support with copper solution facilitates the formation of more stable catalysts.

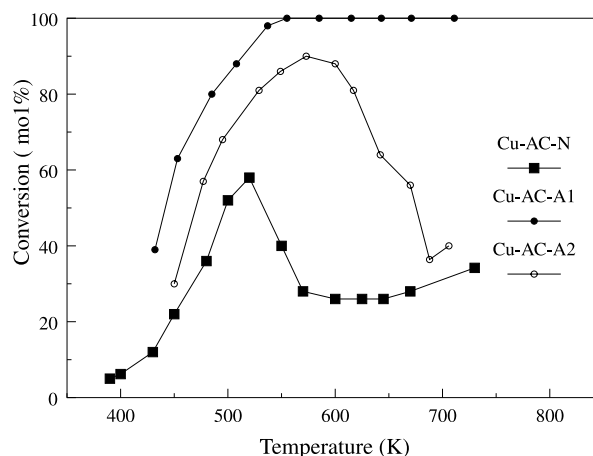
As far as the fact that the activated carbon does not exhibit a catalytic activity in methanol decomposition on its own (not shown), some significant differences in the copper state for the initial catalysts could be assumed. Further changes in the copper state during the catalytic process could also be expected.

To describe the peculiarities of the active-phase state on the investigated catalysts, a complex study by different methods was performed. The XRD spectra for the initial samples are identical, and CuO is the only phase observed (Fig. 2, curve 1). However, two ESR signals are also found in all investigated samples (Fig. 3), in spite of the fact that CuO does not register on ESR spectra. This is also in accordance with the results in ref. 16. A sharp ESR signal, typical of single Cu<sup>2+</sup> ions, is registered. The presence of Cu<sup>2+</sup> ions interacting with each other (Cu<sup>2+</sup>–Cu<sup>2+</sup>) and characterized with a broader ESR signal are found as well. So, despite the nature of the used copper precursor, the CAC in the initial sample contains predominantly Cu<sup>2+</sup> ions, differing in coordination and type of interaction. This conclusion is proved by the magnetic measurements as well. The calculated mag-

**Table 1.** Copper content, specific surface area, and magnetic susceptibility of the initial samples obtained by different preparation techniques.

Samples	Cu content (wt%)	BET (m <sup>2</sup> g <sup>-1</sup> )	χ <sub>g</sub> (g ions × 10 <sup>6</sup> )
AC	0.0	1060	–0.6
Cu-AC-N	4.0	960	19.0
Cu-AC-A1	5.0	958	7.5
Cu-AC-A2	5.0	657	18.4

**Fig. 1.** Total conversion vs. temperature on various copper-loaded samples.



netic susceptibilities, per g mol Cu<sup>2+</sup> ions in the initial samples, are rather different (Table 1). The lower magnetic susceptibility for Cu-AC-A1 could be an indication of the presence of copper species in a lower oxidative state in this sample, since their effective magnetic susceptibility is zero (17). Indeed, only in the case of the initial Cu-AC-A1 does XPS analysis show the presence of Cu<sup>1+</sup> ions (Table 2). So, the participation of copper species in different oxidative states (Cu<sup>2+</sup>, Cu<sup>2+</sup>–Cu<sup>2+</sup>, and Cu<sup>1+</sup>) in the CAC Cu-AC-A1 could be assumed. On the contrary, Cu<sup>2+</sup> and Cu<sup>2+</sup>–Cu<sup>2+</sup> ions are exclusively present in the CAC of the initial Cu-AC-N. In this relation, the observed higher activity for Cu-AC-A1 (Fig. 1) could be ascribed to the presence of Cu<sup>1+</sup> ions in the initial CAC. The favourable role of the ammonia copper precursor for these types of CAC formations in the process of catalyst preparation is considered. This assumption is also proved by the higher turnover frequencies (TOF), calculated on the basis of the initial conversion at different temperatures, for Cu-AC-A1 in comparison with Cu-AC-N (Fig. 4). However, the similarities of TOF values for both samples above 530 K could be evidence for some essential changes in CAC for Cu-AC-N during the reaction. This conclusion is confirmed by the XPS spectra for Cu-AC-N, where Cu<sup>0</sup>, together with Cu<sup>2+</sup> and Cu<sup>1+</sup>, is found (Table 2). Intensive signals, typical of Cu<sup>0</sup>, are also observed in the XRD spectrum for this sample (Fig. 2, curve 2). On the contrary, no Cu<sup>0</sup> is found for the used Cu-AC-A1. Hence, a more stable CAC in Cu-AC-A1 with respect to the reaction medium influence is most probably formed.

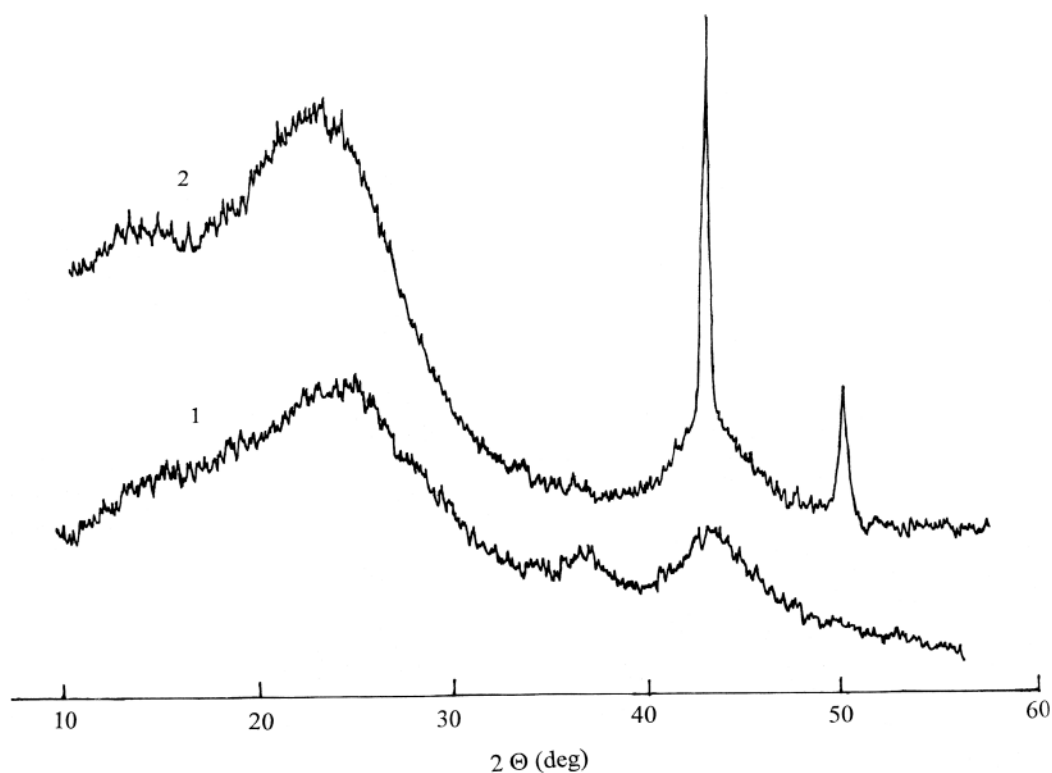
The higher stability of CAC in the ammonia-obtained sample compared with that in Cu-AC-N could also be



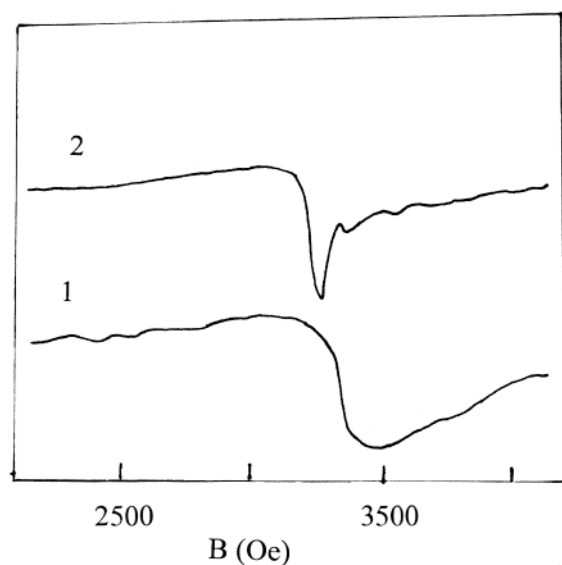
**Table 2.** Binding energies of Cu  $2p_{3/2}$  and O  $1s$  and the kinetic energy of the Cu  $L_3M_{4,5}M_{4,5}$  peak (eV) of the initial (I) samples and those used in the catalytic test at 700 K (T).

Samples	Cu $2p_{3/2}$			Cu LMM Auger			O $1s$		
	CuO	Cu <sub>2</sub> O	Cu	CuO	Cu <sub>2</sub> O	Cu	CuO	Cu <sub>2</sub> O	Cu(OH) <sub>2</sub>
Cu-AC-N (I)	934.1	—	—	917.9	—	—	529.8	—	531.6
Cu-AC-A1 (I)	934.0	933.6	—	917.8	917.2	—	530.0	530.3	531.9
Cu-AC-N (T)	933.6	932.5	932.0	917.9	917.1	919.0	530.4	530.9	531.7

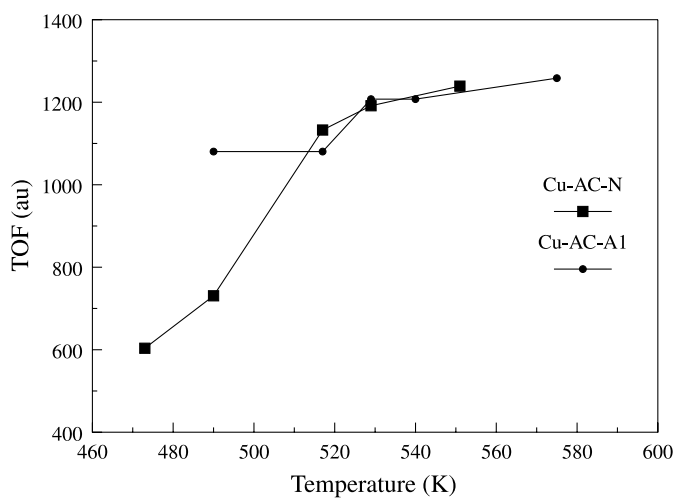
**Fig. 2.** XRD patterns of the initial Cu-AC-N (curve 1) and that used in the catalytic test at 700 K (curve 2).



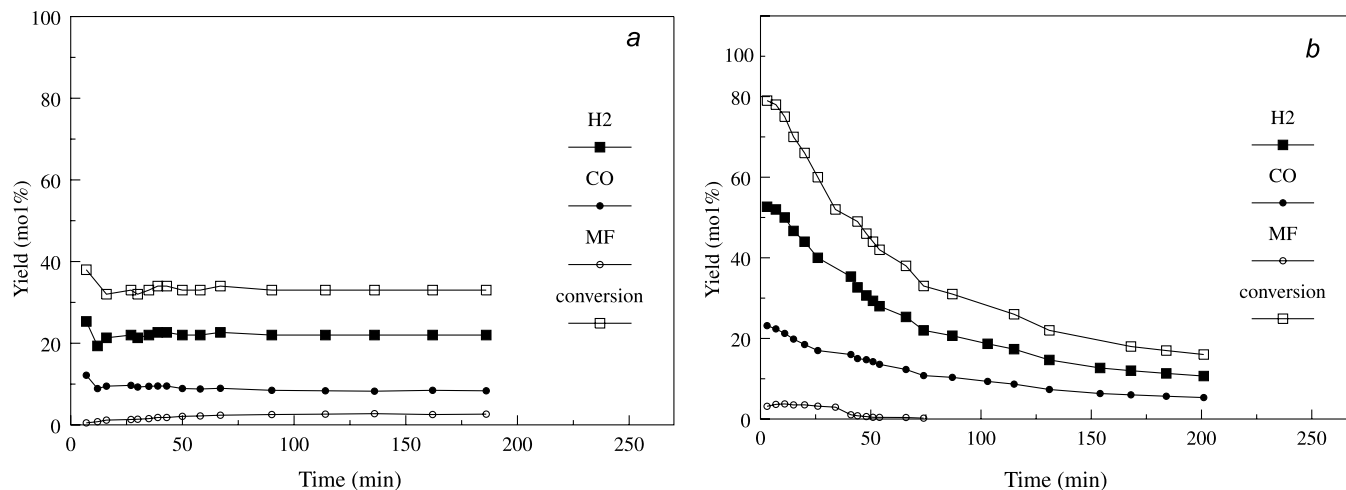
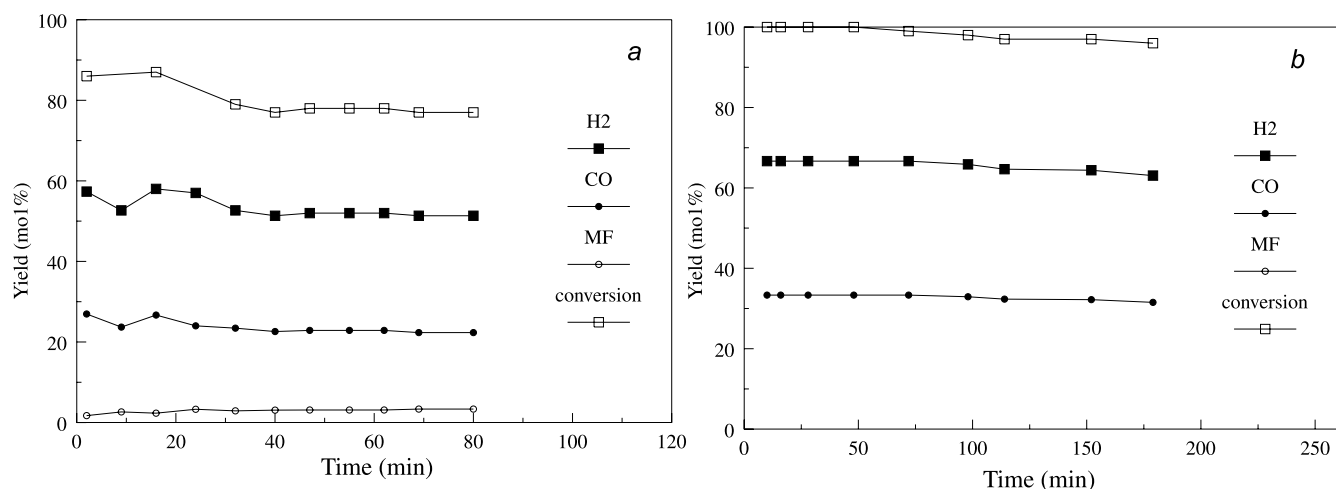
**Fig. 3.** ESR spectra of activated carbon (curve 1) and the initial Cu-AC-N (curve 2).



**Fig. 4.** Temperature dependences of TOF for Cu-AC-A1 and Cu-AC-N.





**Fig. 5.** Evolution of the conversion and product distribution with time on stream on Cu-AC-N at 473 K (a) and 551 K (b).**Fig. 6.** Evolution of the conversion and product distribution with time on stream on Cu-AC-A1 at 490 K (a) and 575 K (b).

proved by the catalytic experiments in isothermal conditions (Figs. 5 and 6). For Cu-AC-N, the conversion remains unchanged only at lower temperatures (Fig. 5a). However, it gradually decreases at 550 K (Fig. 5b), and the catalyst practically loses its catalytic activity after about 5 h. On the contrary, no essential changes with time on stream are registered for Cu-AC-A1 even at 575 K (Fig. 6).

## Conclusions

In comparison with the nitrate-obtained, copper-loaded activated carbon materials, the catalysts prepared from the ammonia precursor exhibit higher catalytic activity during methanol decomposition to CO and hydrogen. In this case, the preparation technique that includes four-fold spraying of the support with the precursor is favoured as producing the catalyst with the best stability in this reaction. It results in easier formation and better stabilization of the CAC, containing  $\text{Cu}^{1+}$  ions on the support in the process of catalyst preparation. Indeed, the nature of the CAC is only one aspect of the complex problem of optimization of catalysts. Higher catalytic activity, selectivity, and stability at low

temperatures are needed. In relation to this, further investigations are in progress.

## References

1. L. Pettersson and K. Sjöström. *Combust. Sci. and Tech.* **80**, 265 (1991).
2. À. Yildiz and K. Pekmez. *In Hydrogen energy system*. NATO ASI Series. Ser. E. Vol. 295. Edited by Y. Yürüm. Kluwer Academic Publishers, Netherlands. 1995. p. 195.
3. W.H. Cheng and H.H. Kung (*Editors*). *In Methanol production and use*. Marcel Dekker, New York. 1994. Chap 1.
4. W.H. Cheng. *Acc. Chem. Res.* **32**, 685 (1999).
5. M. Clement, Y. Zhang, D.S. Brands, E.K. Poels, and A. Blik. *Stud. Surf. Sci. Catal.* **130**, 2123 (2000).
6. A. Fisher and A.T. Bell. *J. Catal.* **184**, 357 (1999).
7. D.B. Clarke, D.-K. Lee, M.J. Sandoval, and A.T. Bell. *J. Catal.* **150**, 81 (1994).
8. T. Tsoncheva, R. Nickolov, Ya. Neinska, Chr. Minchev, and D. Mehandjiev. *Bulg. Chem. Commun.* **32**, 218 (2000).
9. R. Nickolov, T. Tsoncheva, and D. Mehandjiev. *Fuel*, **81**, 203 (2002).
10. T. Tsoncheva, R. Nickolov, and D. Mehandjiev. *React. Kinet. Catal. Lett.* **72**, 383 (2001).



11. T. Tsoncheva, R. Nickolov, and D. Mehandjiev. *In Proceedings of the 9th International Symposium of Heterogeneous Catalysis, Edited by L. Petrov, Ch. Bonev, and G. Kadinov. Bulgaria. 2000. p. 755.*
12. T. Tsoncheva. *C. R. Acad. Bulg. Sci.* **54**, 59 (2001).
13. T. Tsoncheva. *C. R. Acad. Bulg. Sci.* **54**, 65 (2001).
14. D. Mehandjiev. *In Proceedings of the 9th International Symposium of Heterogeneous Catalysis. Edited by L. Petrov, Ch. Bonev, and G. Kadinov. Bulgaria. 2000. p. 19.*
15. V. Minkova, M. Razvigorova, M. Goranova, L. Ljutzakanov, and G. Angelova. *Fuel*, **70**, 713 (1991).
16. N. Stankova, M. Khristova, and D. Mehandjiev. *J. Colloid Interface Sci.* **241**, 439 (2001).
17. D. Mehandjiev and S. Angelov. *In Magnetochemistry of the solid state. Nauka I Izkustvo, Sofia, Bulgaria. 1979. p. 134.*



# A theoretical analysis of the conformational behaviour of substituted methylenecyclohexanes

Robert C. Mawhinney, Heidi M. Muchall, and Jean Lessard

**Abstract:** The use of the PBE0 hybrid density functional theory method in conjunction with the COSMO solvation model allowed us to reproduce, both qualitatively and quantitatively, the experimentally observed conformational compositions of 2-substituted and 2,7-disubstituted methylenecyclohexanes. An analysis revealed several different interactions that influence the overall equilibrium. It was found that the endo (general) anomeric effect plays a significant role in the equilibrium and that the “unsaturation effect” possibly comprises two effects.

**Key words:** conformational analysis, methylenecyclohexanes, anomeric effect, unsaturation effect.

**Résumé :** L'utilisation de la méthode théorique fonctionnelle de densité hybride PBE0 de concert avec le modèle de solvation COSMO nous permet de reproduire qualitativement et quantitativement, les compositions conformationnelles, observées expérimentalement, des méthylèncyclohexanes substitués en position 2 et disubstitués en positions 2 et 7. Une analyse révèle plusieurs interactions différentes qui influencent l'équilibre global. On a trouvé que l'effet anomère endo (général) joue un rôle important dans l'équilibre et que l'effet d'insaturation comporte probablement deux effets.

**Mots clés :** analyse conformationnelle, méthylèncyclohexanes, effet anomère, effet d'insaturation.

[Traduit par la Rédaction]

## Introduction

The anomeric effect is invoked to explain the unusual stability of the more sterically unfavoured synclinal (*gauche*) conformer over the sterically favoured antiperiplanar (*anti*) conformer (1). A number of theories have been hypothesized to explain these findings (2). To test these theories, Lessard and co-workers (3–6) assessed the equilibrium composition of a number of systems using  $^{13}\text{C}$  NMR spectroscopy, including substituted methylenecyclohexanes.

The first article in the series (3) revealed that the dipole–dipole – dipole–quadrupole and rabbit-ear (or  $n$ – $n$  interaction) theories for the anomeric effect were negligible (the latter because the chosen system did not have any endocyclic atoms with electron lone pairs), leaving only the double bond – no bond resonance or  $\pi_{\text{C}=\text{C}}-\sigma_{\text{C}-\text{O}}^*$  orbital overlap as the main interaction. This appeared to explain the finding that the introduction of a methoxy substituent to the methylene group (position 7) in 2-methoxymethylenecyclohexane led to a stabilization of the axial conformer to such an extent that the equatorial conformer was not observed.

In the second paper (4) this was explored further by changing the 2-substituent. It was found that the introduction of a  $\pi$  system had the unexpected result of switching the

conformer preference from axial to equatorial, with the proportion of equatorial orientation on going from methoxy (OMe) to vinyloxy (OVi) to acetoxy (OAc) increasing from 41% to 61% to 80% at 0 °C. Based on double bond – no bond resonance, the increase in anion stability of the 2-substituent along this series should produce the opposite effect. Similarly, the  $\pi_{\text{C}=\text{C}}-\sigma_{\text{C}-\text{O}}^*$  interaction should become more pronounced, since the  $\sigma_{\text{C}-\text{O}}^*$  orbital energy should decrease along the series. This counter observation was termed the “unsaturation effect”.

Instead of invoking a double bond – no bond resonance or  $\pi_{\text{C}=\text{C}}-\sigma_{\text{C}-\text{O}}^*$  stabilizing interaction, a number of these results could also have been explained through an  $n_{\text{O}}-\pi_{\text{C}=\text{C}}^*$  stabilizing interaction. To examine the effect of the  $n_{\text{O}}-\pi_{\text{C}=\text{C}}^*$  interaction, Lessard et al. (5) examined a series of 7-substituted 2-methoxymethylenecyclohexanes. The substituent on the methylene carbon was changed from hydrogen to methoxy (OMe), phenyl (Ph), and cyano (CN), and the observed proportion of equatorial orientation changed from 41% (0 °C) to <5% (–113 °C), 12% (–113 °C), and 88% (–60 °C), respectively. These results showed that  $n_{\text{O}}-\pi_{\text{C}=\text{C}}^*$  orbital interactions are not the dominant factor for determining the equilibrium composition.

In the last paper of this series (6), the authors brought together all previous results, as well as those for several similar systems, and concluded that the generalized anomeric effect is operating in these systems along with a contribution from electrostatic (dipole–quadrupole) interactions. Most important, however, is the as yet unexplained “unsaturation effect”, which appears to override the generalized anomeric effect in a number of cases.

To understand the “unsaturation effect”, we started a computational study of the axial preference for the 2-substituted

Received 23 June 2003. Published on the NRC Research Press Web site at <http://canjchem.nrc.ca> on 2 October 2003.

**R.C. Mawhinney and H.M. Muchall.**<sup>1</sup> Department of Chemistry and Biochemistry, Concordia University, Montreal, QC H4B 1R6, Canada.

**J. Lessard.** Département de Chimie, Université de Sherbrooke, Sherbrooke, QC J1K 2R1, Canada.

<sup>1</sup>Corresponding author (e-mail: [muchall@alcor.concordia.ca](mailto:muchall@alcor.concordia.ca)).



methylenecyclohexanes (7). The experimentally observed trend was reproduced qualitatively. While the equilibria for the methoxy- and vinyloxy-substituted compounds were best obtained at single point solvated levels of theory, the large equatorial preference for the acetoxy species could only be reproduced when solvent-optimized geometries and energies were employed. Even then the equilibrium composition could only be estimated, since a minimum for one of the conformers was not located.

In this paper we have undertaken a reexamination of the 2-substituted equilibrium compositions. We report that the use of the COSMO solvation model (8–10) in conjunction with the empirical-parameter-free PBE0 hybrid density functional method (11, 12) not only correctly predicts the compositional preferences in the 2-substituted methylenecyclohexanes but also those seen for the 2,7-disubstituted systems (Scheme 1). This combination of theory and solvation model has recently been shown to give reliable results for examining the role of stereoelectronic effects in the collagen dipeptide (13).

## Computational details

The Gaussian 98 suite of programs was used in all calculations (14). The minimum energy conformations were optimized using the empirical-parameter-free hybrid density functional PBE0 (11, 12) and the Pople split valence 6-31G(d) basis set (15–19), starting from the previously optimized gas phase HF/6-31G(d) structures (7). The COSMO polarizable continuum solvent model (8–10) was used, with dichloromethane as solvent, in all optimizations. All minima were confirmed by harmonic vibrational frequency analyses. Since all relative energies are based on rotational conformers, there is negligible dependence on entropy, and we report zero-point corrected, as opposed to free energy, values.

## Results and discussion

As in the previous work (7), rotational isomers for both the axial and equatorial conformers were explored. In all cases, two rotamers are obtained within a 2.5 kcal/mol cut-off criterion. In Fig. 1 the structures for **2-OMe** are given. As one can see, the O—R<sup>1</sup> bond is aligned antiperiplanar with one of two possible C—C bonds, either C—C<sub>sp<sup>3</sup></sub> or C—C<sub>sp<sup>2</sup></sub>. This general feature is the same in all systems. All species will from here on be labelled by their conformations, axial (a) or equatorial (e), antiperiplanar to C<sub>sp<sup>3</sup></sub> or C<sub>sp<sup>2</sup></sub> (i.e., a(sp<sup>3</sup>), a(sp<sup>2</sup>), e(sp<sup>3</sup>), e(sp<sup>2</sup>)), as shown in Fig. 1. In the case of the vinyloxy-substituted system there are twice as many conformers because of the *cis* and *trans* orientations in the C—O—CH=CH<sub>2</sub> fragment. While also possible for the acetoxy substituent, it was found earlier (7) that the *cis* species lie around 8 kcal/mol higher in energy and therefore are not a factor in the equilibrium composition. Unlike the previous study, we have now been able to locate solvent-optimized minima for all four conformers in the acetoxy system and can therefore concentrate on understanding the causes of the effects that lead to the observed equilibria.

### Compositional analysis

The experimentally observed axial:equatorial equilibrium composition for the 2-substituted methylenecyclohexanes is

Scheme 1.

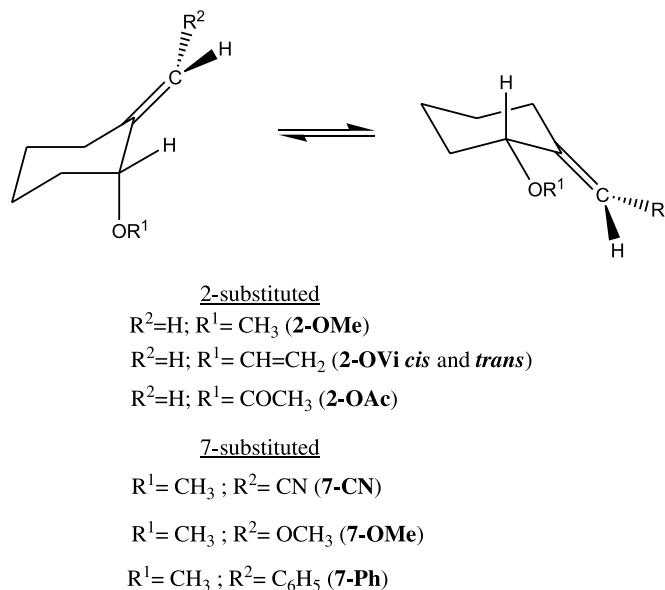
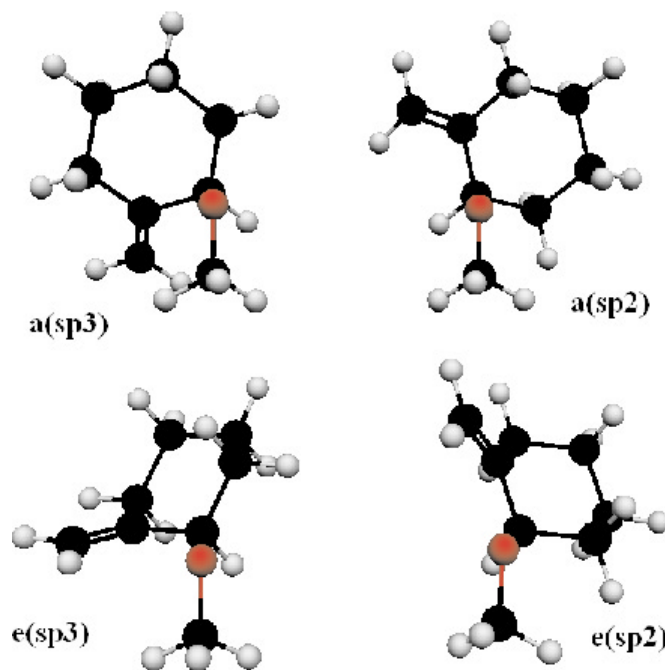


Fig. 1. Representation and labelling scheme of the two rotamers of each anomer (for **2-OMe**, but all other systems exhibit the same general feature).



59:41 (**2-OMe**), 39:61 (**2-OVi**), and 20:80 (**2-OAc**) (4) and for the 7-substituted 2-methoxymethylenecyclohexane systems is 12:88 (**7-CN**), >95:<5 (**7-OMe**), and 88:12 (**7-Ph**) (5). The relative energy differences for each of the species that make up the equilibrium are given in Table 1. The equilibrium composition is derived from these energy differences by combining the Boltzmann distribution relationship with the molar fractions distribution relationship (20, 21). As shown in Table 1, our results are both qualitatively and quantitatively in good agreement with the experimental values. The largest differences are observed for **2-OVi** ( $\Delta = -12\%$ ) and **7-Ph** ( $\Delta = +16\%$ ). All other results are within at



**Table 1.** Relative energies<sup>a</sup> and equilibrium compositions (evaluated at experimental temperatures).

	<b>2-OMe<sup>b</sup></b>	<b>2-OVi (trans)<sup>b</sup></b>	<b>2-OVi (cis)<sup>b</sup></b>	<b>2-OAc<sup>b</sup></b>	<b>7-CN<sup>c</sup></b>	<b>7-OMe<sup>c</sup></b>	<b>7-Ph<sup>d</sup></b>
<b>ΔE (kcal/mol)</b>							
a(sp <sup>3</sup> )	0.00 <sup>e</sup>	0.60	0.49	0.69	0.75	0.00 <sup>e</sup>	0.00 <sup>e</sup>
a(sp <sup>2</sup> )	2.03	1.03	1.63	0.95	2.20	1.71	1.55
e(sp <sup>3</sup> )	0.35	0.00 <sup>e</sup>	0.12	0.13	0.00 <sup>e</sup>	1.69	0.57
e(sp <sup>2</sup> )	0.91	0.53	0.65	0.00 <sup>e</sup>	0.03	1.51	0.85
<b>Equilibrium composition (%)</b>							
a(sp <sup>3</sup> )	57.5	9.7 (17.7) <sup>f</sup>	11.9 (26.1) <sup>f</sup>	12.5	4.7	98.2	70.3
a(sp <sup>2</sup> )	1.4	4.4 (8.1) <sup>f</sup>	1.5 (3.2) <sup>f</sup>	7.7	0.1	0.5	1.8
e(sp <sup>3</sup> )	30.3	29.3 (53.9) <sup>f</sup>	23.5 (51.5) <sup>f</sup>	35.3	49.9	0.5	18.4
e(sp <sup>2</sup> )	10.8	11.0 (20.3) <sup>f</sup>	8.8 (19.3) <sup>f</sup>	44.5	45.4	0.9	9.4
<b>Axial composition of equilibrium (%)</b>							
calcd.	59		27 (26; 29) <sup>f</sup>	20	5 (12) <sup>b</sup>	99 (91) <sup>b</sup>	72 (65) <sup>b</sup>
exptl.	59		39	20	12	>95	88

<sup>a</sup>Relative energies include zero-point vibrational corrections.<sup>b</sup>Equilibrium composition evaluated at 0 °C.<sup>c</sup>Equilibrium composition evaluated at -113 °C.<sup>d</sup>Equilibrium composition evaluated at -60 °C.<sup>e</sup>Total energies (in hartree (1 hartree = 4.3597482 × 10<sup>-18</sup> J) for the lowest energy conformers: -387.813339 (**2-OMe**), -425.849143 (**2-OVi**), -501.049114 (**2-OAc**), -479.96288 (**7-CN**), -502.179296 (**7-OMe**), -618.517203 (**7-Ph**).<sup>f</sup>cis and trans components separated.

least 7%, and for three systems (**2-OMe**, **2-OAc**, and **7-OMe**) there is no appreciable error.

In the 2-substituted systems, the major change in equilibrium composition on going from methoxy (**2-OMe**) to vinyloxy (**2-OVi**) is a decrease in a(sp<sup>3</sup>) (from 57.5 to 21.6% (9.7(trans) + 11.9(cis))) and a concomitant increase in e(sp<sup>3</sup>) (from 30.3 to 52.8%). In **2-OAc**, the decrease in a(sp<sup>3</sup>) is accompanied by an additional major increase in e(sp<sup>2</sup>) (from 10.8 to 44.5%). In the 7-substituted series, the introduction of the cyano group (**7-CN**) has a similar effect to that of the acetoxy group (**2-OAc**) in the 2-substituted series. The exchange of the hydrogen atom in **2-OMe** for a phenyl ring (**7-Ph**) in the 7-position has only a small effect on the energy differences, stabilizing a(sp<sup>2</sup>) and destabilizing e(sp<sup>3</sup>), thereby shifting the equilibrium composition further towards axial. The 7-methoxy substitution (**7-OMe**) dramatically destabilizes both equatorial species so that a(sp<sup>3</sup>) now makes up ~98% of the equilibrium.

### Geometric evidence

The anomeric effect, aside from energetic considerations, is typically accompanied by certain geometric changes that form the basic reasoning behind a number of its explanations (1). In particular, the C—X bond in the anomeric position is usually observed to be elongated in the axial conformer with respect to the equatorial conformer. This is also the case here, as shown for the C—O bond distances given in Table 2. In all 2-methoxy systems (**2-OMe**, **7-CN**, **7-OMe**, and **7-Ph**) the difference between the axial and equatorial C—O distance is ca. 0.012 Å. This difference increases as the electronegativity of the 2-substituent increases, as expected

for an anomeric effect. This is demonstrated by a difference of 0.015 Å in **2-OVi** and a difference of 0.018 Å in **2-OAc**. These results are consistent with the conclusions of Lessard and co-workers that the generalized anomeric effect is operating in these systems (6).

The C—O bond distances in both axial and equatorial conformers increase as the electronegativity of the 2-substituent increases. This in itself is not surprising. What is surprising is that the C—O bond distance is affected by 7-substitution. For example, the addition of the electron-withdrawing cyano group (**7-CN**) shortens r<sub>C-O</sub> with respect to the unsubstituted system (**2-OMe**). The addition of an electron-donating group (**7-OMe**) is accompanied by an increase in r<sub>C-O</sub>, and conjugation (**7-Ph**) elicits no change. An examination of the r<sub>C-O</sub> differences between axial and equatorial species also shows this trend. The difference of 0.012 Å (as assessed using the raw bond distances from which Table 2 was created) in the unsubstituted **2-OMe** decreases to 0.011 Å with the addition of an electron-withdrawing group (**7-CN**), increases to 0.013 Å with an electron-donating group (**7-OMe**), and is unchanged (0.012 Å) by conjugation (**7-Ph**). This remote effect implies that the methylene π system has an effect on both anomers and is probably part of the reason behind the “unsaturation effect”.

The operation of another effect, the exo-anomeric effect, is revealed by the r<sub>C-C</sub> entries in Table 2. When O—R<sup>1</sup> is antiperiplanar to C<sub>sp<sup>3</sup></sub> (left hand structures in Fig. 1), the overlap between an oxygen lone pair (n<sub>O</sub>) and σ<sub>C-C<sub>sp<sup>2</sup></sub></sub><sup>\*</sup> is maximized. Consequently, r<sub>C-C<sub>sp<sup>2</sup></sub></sub> is found to be longer in a(sp<sup>3</sup>) and e(sp<sup>3</sup>) than in a(sp<sup>2</sup>) and e(sp<sup>2</sup>) (Table 2). Simi-



**Table 2.** Selected bond lengths (Å).

	<b>2-OMe</b>	<b>2-OVi</b> ( <i>trans</i> )	<b>2-OVi</b> ( <i>cis</i> )	<b>2-OAc</b>	<b>7-CN</b>	<b>7-OMe</b>	<b>7-Ph</b>
<b><math>r_{C-O}</math></b>							
a( $sp^3$ )	1.423	1.432	1.436	1.451	1.415	1.426	1.421
a( $sp^2$ )	1.423	1.435	1.436	1.452	1.419	1.427	1.422
e( $sp^3$ )	1.409	1.420	1.420	1.433	1.406	1.413	1.409
e( $sp^2$ )	1.411	1.420	1.421	1.434	1.406	1.414	1.410
<b><math>r_{C-C_{sp^2}}</math></b>							
a( $sp^3$ )	1.512	1.510	1.509	1.507	1.512	1.505	1.514
a( $sp^2$ )	1.508	1.507	1.506	1.505	1.507	1.502	1.510
e( $sp^3$ )	1.512	1.510	1.509	1.506	1.509	1.510	1.515
e( $sp^2$ )	1.508	1.507	1.505	1.504	1.504	1.506	1.510
<b><math>r_{C-C_{sp^3}}</math></b>							
a( $sp^3$ )	1.526	1.526	1.524	1.522	1.527	1.526	1.528
a( $sp^2$ )	1.533	1.531	1.529	1.527	1.534	1.533	1.534
e( $sp^3$ )	1.528	1.528	1.526	1.526	1.531	1.527	1.530
e( $sp^2$ )	1.534	1.531	1.530	1.528	1.536	1.533	1.536
<b><math>r_{C=C}</math></b>							
a( $sp^3$ )	1.333	1.332	1.333	1.332	1.345	1.337	1.343
a( $sp^2$ )	1.332	1.332	1.332	1.332	1.344	1.336	1.343
e( $sp^3$ )	1.332	1.331	1.332	1.331	1.344	1.335	1.342
e( $sp^2$ )	1.332	1.332	1.332	1.332	1.344	1.335	1.342

larly, when O–R<sup>1</sup> is antiperiplanar to C<sub>sp<sup>2</sup></sub> (right hand structures in Fig. 1), the  $n_O-\sigma_{C-C_{sp^3}}^*$  interaction is maximized and  $r_{C-C_{sp^3}}$  is longer in these species. These results also demonstrate that the effect on distance is larger in C–C<sub>sp<sup>3</sup></sub> than in C–C<sub>sp<sup>2</sup></sub>. For example, in the **2-OMe** case the former changes by 0.006–0.007 Å and the latter by 0.004 Å. This is a reflection of the differing strengths of the C<sub>sp<sup>3</sup></sub>–C<sub>sp<sup>3</sup></sub> and C<sub>sp<sup>3</sup></sub>–C<sub>sp<sup>2</sup></sub> bonds, as shown by the shorter overall C<sub>sp<sup>3</sup></sub>–C<sub>sp<sup>2</sup></sub> distances.

As expected, this effect diminishes as O–R<sup>1</sup> becomes more electronegative. The average  $r_{C-C_{sp^2}}$  bond difference decreases from 0.004 Å (**2-OMe**) to 0.003 Å (**2-OVi**) and to 0.002 Å (**2-OAc**). Similarly, the average  $r_{C-C_{sp^3}}$  bond difference decreases from 0.007 Å (**2-OMe**) to ~0.004 Å (**2-OVi**) and ~0.003 Å (**2-OAc**). In the  $r_{C-C_{sp^2}}$  case, there is virtually no variation in the axial and equatorial differences. The  $r_{C-C_{sp^3}}$  case, on the other hand, exhibits some variation between the axial and equatorial differences, which also increases along the series **2-OMe**, **2-OVi**, and **2-OAc**. The effect of 7-substitution is rather small, if present at all, and no discernable pattern can be ascertained in the  $r_{C-C_{sp^3}}$  case. The  $r_{C-C_{sp^2}}$  bond distances reveal that the addition of an electron withdrawing group increases the  $sp^3-sp^2$  difference in both anomers (**7-CN**), an electron-donating group decreases it in the axial anomer (**7-OMe**), and conjugation increases it in the equatorial anomer (**7-Ph**).

Aside from the changes due to 7-substitution, the C=C distance is fairly insensitive, owing to the stiffness of the bond (even more so than for the C<sub>sp<sup>3</sup></sub>–C<sub>sp<sup>2</sup></sub> bond). This is expected, and the lack of any appreciable change in C=C distance on its own does not imply that  $\pi_{C=C}-\sigma_{C-O}^*$  and  $n_O-\pi_{C=C}^*$  interactions do not play a significant role in these systems, as has been concluded earlier (3, 5). In fact, the ex-

pected small lengthening of the C=C bond in the axial species can be seen most clearly in **7-OMe** and **7-Ph**.

### Decomposition of energy differences

The equilibrium composition depends on the energy differences between the different species, as described earlier. As well, the Edward–Lemieux effect (which incorporates both the endo- and exo-anomeric effects, similar to our case) can be “energetically quantified by the energy difference between the sum of the endo- and exo-anomeric effects for one of the anomers and the sum for the other anomer” (22). Within this context, we have plotted the energy relationships between the different conformers (the *cis* and *trans* components of vinyloxy have been separated) as a function of the % axial composition (all calculated at 0 °C). The overall results, along with the linear trend lines and corresponding correlation coefficients, are presented in Fig. 2.

In most cases there does not seem to be any direct relationship between energy difference and equilibrium composition. The one exception is the e( $sp^3$ ) – a( $sp^3$ ) energy difference, where there is a strong correlation ( $r^2 = 0.97$ ). This relationship corresponds to the endo- (generalized) anomeric effect, as Lessard and co-workers have concluded (6). However, our results do not show a second overall effect offsetting it; perhaps there are two effects within the subsets that are masking each other on a global scale. To explore this further, we have separated out the two systems, **2-OMe**, **2-OVi(cis)**, **2-OVi(trans)**, and **2-OAc** (“2-substituted”) and **2-OMe**, **7-CN**, **7-OMe**, and **7-Ph** (“7-substituted”) and again plotted the energy differences between the different conformers as a function of the % axial composition. These are given in Figs. 3 and 4, respectively.



**Fig. 2.** The overall relationship between energy differences (kcal/mol) and % axial composition:  $\blacktriangle E_{a(sp^2)} - E_{a(sp^3)}$ ;  $\blacklozenge E_{e(sp^2)} - E_{e(sp^3)}$ ;  $\times E_{e(sp^3)} - E_{a(sp^3)}$ ;  $\blacksquare E_{e(sp^2)} - E_{a(sp^2)}$ .

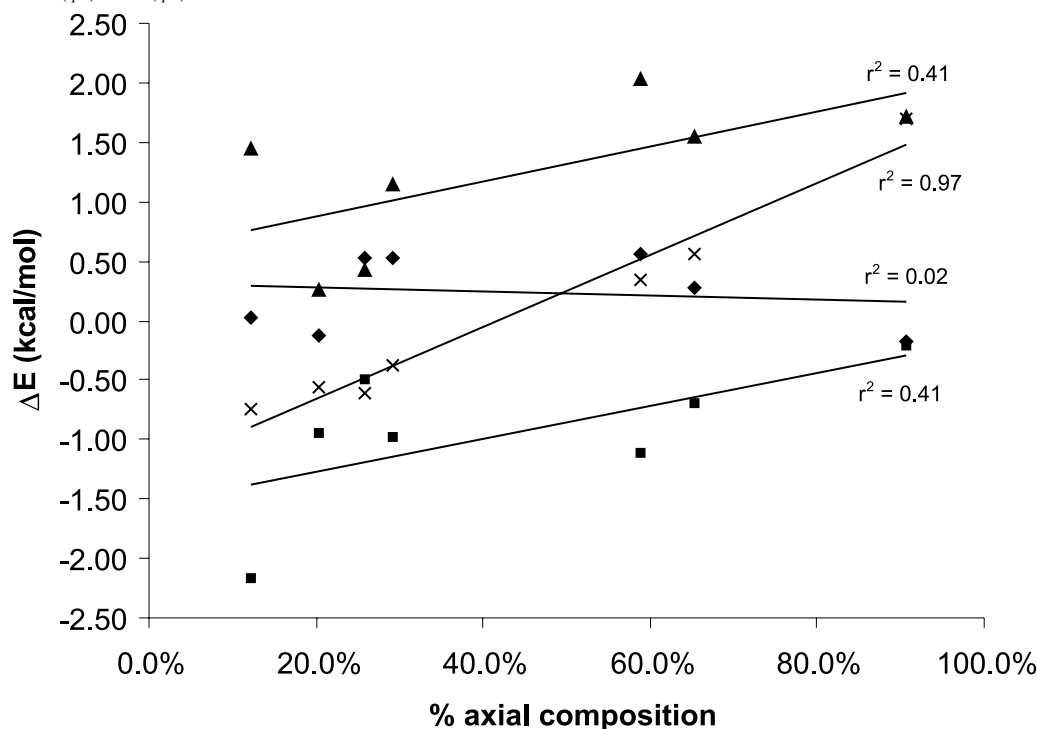
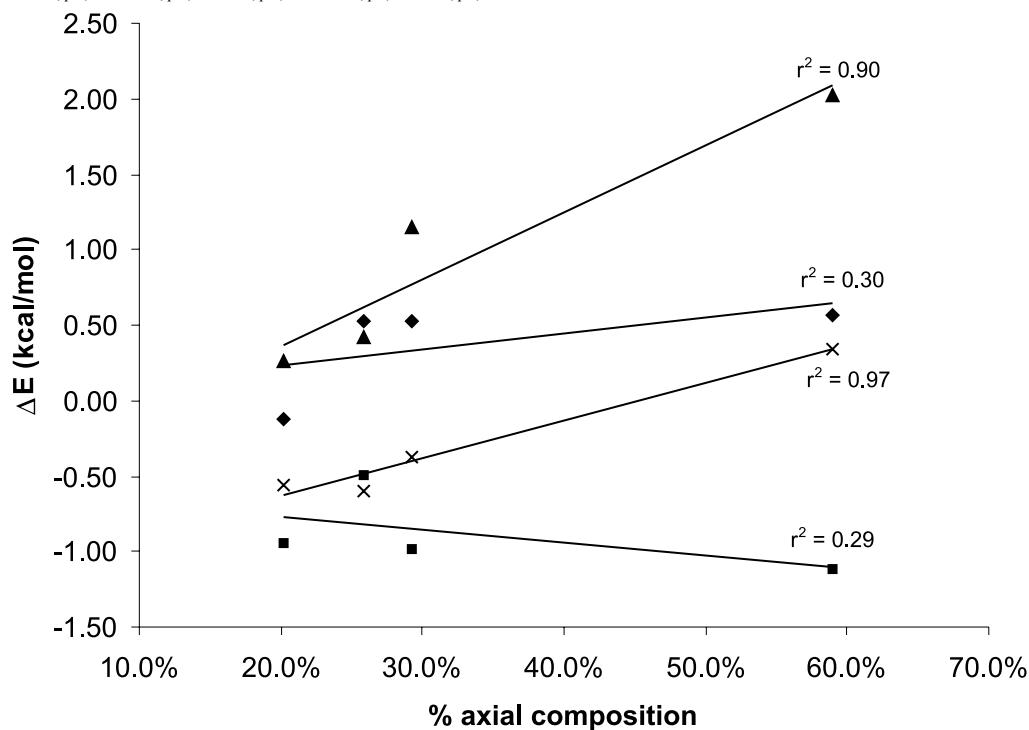


**Fig. 3.** The relationship between energy differences (kcal/mol) and % axial composition in the 2-substituted systems:  $\blacktriangle E_{a(sp^2)} - E_{a(sp^3)}$ ;  $\blacklozenge E_{e(sp^2)} - E_{e(sp^3)}$ ;  $\times E_{e(sp^3)} - E_{a(sp^3)}$ ;  $\blacksquare E_{e(sp^2)} - E_{a(sp^2)}$ .

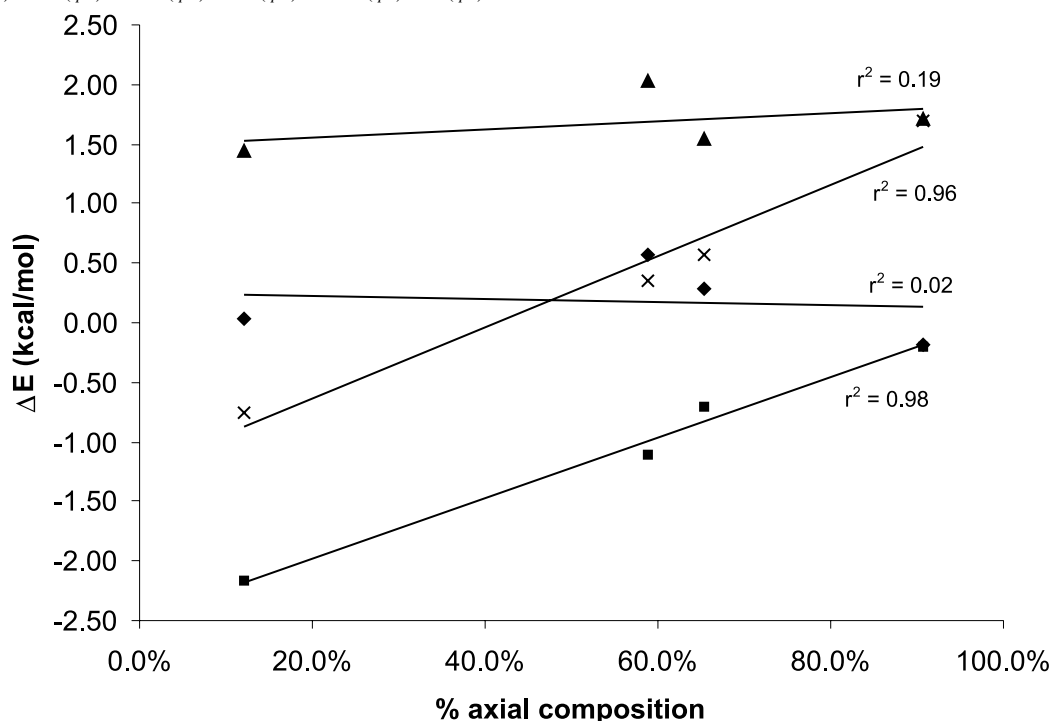


The  $e(sp^3) - a(sp^3)$  energy difference shows the same strong correlation ( $r^2 = 0.97$  and  $0.96$ ) in both 2- and 7-substituted systems. In the 2-substituted systems there is

also a considerable correlation ( $r^2 = 0.90$ ) with the exo-anomeric effect in the axial conformers,  $a(sp^2) - a(sp^3)$ , as seen in Fig. 3. The 7-substituted systems, where the



**Fig. 4.** The relationship between energy differences (kcal/mol) and % axial composition in the 7-substituted systems:  $\blacktriangle$   $E_{a(sp^2)} - E_{a(sp^3)}$ ;  $\blacklozenge$   $E_{e(sp^2)} - E_{e(sp^3)}$ ;  $\times$   $E_{e(sp^2)} - E_{a(sp^3)}$ ;  $\blacksquare$   $E_{e(sp^2)} - E_{a(sp^2)}$ .



substituent effect is removed from the exo portion of the ring, do not show any correlation ( $r^2 = 0.19$ ) with the  $a(sp^2) - a(sp^3)$  energy difference. They do, however, exhibit a strong correlation ( $r^2 = 0.98$ ) with the other endo-anomeric effect,  $e(sp^2) - a(sp^2)$  (Fig. 4).

The fact that there are two main trends to each series and only one of them in common suggests that the “unsaturation effect” is a combined effect. There is no straightforward explanation, and since within each conformer there are three common energy components (steric, electrostatic, and electronic) (23), a full understanding will only come from a complete analysis of all energetic contributions. Also, one must realize that most of the data points in the figures are essentially clustered at one end, as intermediate experimental data are not available at this moment. Further studies, both experimental and computational, are planned to remedy this situation.

## Conclusions

In this work we have shown that the combination of PBE0 and COSMO reliably predicts the experimentally observed axial:equatorial equilibrium compositions in 2-substituted and 2,7-disubstituted methylenecyclohexanes. We have analyzed the compositions with respect to both the endo- and exo-anomeric effects, jointly known as the Edward–Lemieux effect.

The geometries of the species that make up the equilibrium composition revealed evidence of three different effects. The  $r_{C-O}$  distances exhibit the generalized anomeric effect. The exo-anomeric effect reveals itself as an increase in C—C bond lengths due to  $n_O - \sigma_{C-C}^*$  interactions. The rigidity of the C=C bond limits its use as a detector of

$\pi_{C=C} - \sigma_{C-O}^*$  and  $n_O - \pi_{C=C}^*$  interactions. However, 7-substitution has an effect on  $r_{C-O}$  in both anomers, unlike typical anomeric systems, which implies that the methylene  $\pi$  system might be the source of the “unsaturation effect”. This is supported by an analysis of energy differences and their relationship to the observed equilibrium composition in that an overall endo- (generalized) anomeric effect for one of the rotamers ( $e(sp^3) - a(sp^3)$ ) is accompanied by two more correlations within the subsets of 2- and 7-substituted systems.

Studies are now underway to examine this further. These include an AIM analysis (24) of the electron density, as has been done previously (25–27); an NBO analysis (28) to examine the role of the suspected orbital interactions (29–34); and a bond energy analysis (35–37), which, to our knowledge, has never been used for the examination of the anomeric effect but should reveal results about steric, electrostatic, and electronic effects similar to other energy decomposition methods (38–40). As well, experiments are underway to examine all possible permutations within the two subsets.

## Acknowledgments

Calculations were performed at the Center for Research in Molecular Modeling (CERMM), which was established with the financial support of the Concordia University Faculty of Arts and Science, the Ministère de l'Éducation du Québec (MEQ), and the Canada Foundation for Innovation (CFI). This work was supported by a research grant from the Natural Sciences and Engineering Research Council of Canada (NSERC).



## References

1. A.J. Kirby. Stereoelectronic effects. Oxford University Press, New York. 1996.
2. A.J. Kirby and N.H. Williams. In Anomeric effect and associated stereoelectronic effects. *Edited by* G.R.J. Thatcher. ACS Symposium Series 539. American Chemical Society, Washington, D.C. 1993. pp. 55–69.
3. J. Lessard, M.T.P. Viet, R. Martino, and J.K. Saunders. *Can. J. Chem.* **55**, 1015 (1977).
4. M.T.P. Viet, J. Lessard, and J.K. Saunders. *Tetrahedron Lett.* **4**, 317 (1979).
5. J. Lessard, J.K. Saunders, and M.T.P. Viet. *Tetrahedron Lett.* **23**, 2059 (1982).
6. A. Ouedraogo, T.P.V. Minh, J.K. Saunders, and J. Lessard. *Can. J. Chem.* **65**, 1761 (1987).
7. H.M. Muchall, P.R.N. Kanya, and J. Lessard. *Can. J. Chem.* **81**, 689 (2003).
8. V. Barone, M. Cossi, and J. Tomasi. *J. Comput. Chem.* **19**, 404 (1998).
9. V. Barone, M. Cossi, and J. Tomasi. *J. Chem. Phys.* **107**, 3210 (1997).
10. M. Cossi, V. Barone, R. Cammi, and J. Tomasi. *Chem. Phys. Lett.* **255**, 327 (1996).
11. J.P. Perdew, M. Ernzerhof, and K. Burke. *J. Chem. Phys.* **105**, 9982 (1996).
12. C. Adamo and V. Barone. *J. Chem. Phys.* **110**, 6158 (1999).
13. R. Improta, C. Benzi, and V. Barone. *J. Am. Chem. Soc.* **123**, 12 568 (2001).
14. M.J. Frisch, G.W. Trucks, H.B. Schlegel, G.E. Scuseria, M.A. Robb, J.R. Cheeseman, V.G. Zakrzewski, J.J.A. Montgomery, R.E. Stratmann, J.C. Burant, S. Dapprich, J.M. Millam, A.D. Daniels, K.N. Kudin, M.C. Strain, O. Farkas, J. Tomasi, V. Barone, M. Cossi, R. Cammi, B. Mennucci, C. Pomelli, C. Adamo, S. Clifford, J. Ochterski, G.A. Petersson, P.Y. Ayala, Q. Cui, K. Morokuma, N. Rega, P. Salvador, J.J. Dannenberg, D.K. Malick, A.D. Rabuck, K. Raghavachari, J.B. Foresman, J. Cioslowski, J.V. Ortiz, A.G. Baboul, B.B. Stefanov, G. Liu, A. Liashenko, P. Piskorz, I. Komaromi, R. Gomperts, R.L. Martin, D.J. Fox, T. Keith, M.A. Al-Laham, C.Y. Peng, A. Nanayakkara, M. Challacombe, P.M.W. Gill, B. Johnson, W. Chen, M.W. Wong, J.L. Andres, C. Gonzalez, M. Head-Gordon, E.S. Replogle, and J.A. Pople. Gaussian 98 [computer program]. Revision A.11.4. Gaussian, Inc., Pittsburgh, PA. 2002.
15. P.C. Hariharan and J.A. Pople. *Theor. Chim. Acta*, **28**, 213 (1973).
16. P.C. Hariharan and J.A. Pople. *Mol. Phys.* **27**, 209 (1974).
17. W.J. Hehre, R. Ditchfield, and J.A. Pople. *J. Chem. Phys.* **56**, 2257 (1972).
18. M.S. Gordon. *Chem. Phys. Lett.* **76**, 163 (1980).
19. R. Ditchfield, W.J. Hehre, and J.A. Pople. *J. Chem. Phys.* **54**, 724 (1971).
20. L.G. Sillen. In *Coordination chemistry*. Vol. 1. *Edited by* A.E. Martell. Van Nostrand Reinhold, New York. 1971. pp. 481–541.
21. C.F. Baes and R.E. Mesmer. The hydrolysis of cations. Wiley, New York. 1976.
22. G.R.J. Thatcher. In Anomeric effect and associated stereoelectronic effects. *Edited by* G.R.J. Thatcher. ACS Symposium Series 539. American Chemical Society, Washington, D.C. 1993. pp. 6–25.
23. B.M. Pinto and R.Y.N. Leung. In Anomeric effect and associated stereoelectronic effects. *Edited by* G.R.J. Thatcher. ACS Symposium Series 539. American Chemical Society, Washington, D.C. 1993. pp. 126–155.
24. R.F.W. Bader. *Acc. Chem. Res.* **18**, 9 (1985).
25. N.H. Werstiuk, K.E. Laidig, and J. Ma. In Anomeric effect and associated stereoelectronic effects. *Edited by* G.R.J. Thatcher. ACS Symposium Series 539. American Chemical Society, Washington, D.C. 1993. pp. 176–204.
26. G. Madrid, A. Rochin, E. Juaristi, and G. Cuevas. *J. Org. Chem.* **66**, 2925 (2001).
27. A. Vila and R.A. Mosquera. *J. Phys. Chem. A*, **104**, 12 006 (2000).
28. A.E. Reed, L.A. Curtiss, and F. Weinhold. *Chem. Rev.* **88**, 899 (1988).
29. F. Cortes, J. Tenorio, O. Collera, and G. Cuevas. *J. Org. Chem.* **66**, 2918 (2001).
30. L. Carballeira and I. Perez-Juste. *J. Comput. Chem.* **21**, 462 (2000).
31. U. Salzner and P.v.R. Schleyer. *J. Am. Chem. Soc.* **115**, 10 231 (1993).
32. A.E. Reed and F. Weinhold. *Israel J. Chem.* **31**, 277 (1991).
33. A.E. Reed and P.v.R. Schleyer. *J. Am. Chem. Soc.* **109**, 7362 (1987).
34. A.E. Reed and P.v.R. Schleyer. *Inorg. Chem.* **27**, 3969 (1988).
35. G.T. Velde, F.M. Bickelhaupt, E.J. Baerends, C.F. Guerra, S.J.A. Van Gisbergen, J.G. Snijders, and T. Ziegler. *J. Comput. Chem.* **22**, 931 (2001).
36. F.M. Bickelhaupt and E.J. Baerends. In *Reviews in computational chemistry*. Vol. 15. *Edited by* K.B. Lipkowitz and D.B. Boyd. Wiley-VCH, New York. 2000. pp. 1–86.
37. G. Frenking, K. Wichmann, N. Frohlich, C. Loschen, M. Lein, J. Frunzke, and V.M. Rayon. *Coord. Chem. Rev.* **238–239**, 55 (2003).
38. F. Grein and P. Deslongchamps. *Can. J. Chem.* **70**, 1562 (1992).
39. F. Grein. In Anomeric effect and associated stereoelectronic effects. *Edited by* G.R.J. Thatcher. ACS Symposium Series 539. American Chemical Society, Washington, D.C. 1993. pp. 205–226.
40. F. Grein. *J. Mol. Struct. (Theochem)*, **536**, 87 (2001).



# Electroreduction of 1-methyl 5-nitroindole, 5-nitrobenzofurane, and 5-nitrobenzothiophene in acidic and basic hydroorganic media: Generation and trapping of iminoquinone-type intermediates and electrosynthesis of ring-substituted amino derivatives

Luc Bouchard, Ian Marcotte, Jean Marc Chapuzet, and Jean Lessard

**Abstract:** Preparative electrolysis of 1-methyl-5-nitroindole (**1b**, X = NCH<sub>3</sub>), 5-nitrobenzofurane (**1c**, X = O), and 5-nitrobenzothiophene (**1d**, X = S) at Hg, in acidic hydromethanolic media, leads to the formation of the corresponding 4-substituted amino derivatives **5**, which result from the 100% regioselective addition to iminoquinone-type intermediate **4** of methanol or of any other good nucleophile present in the electrolytic solution. In acidic medium, the iminoquinonium intermediates **4b** and **4c** were trapped in a cycloaddition reaction with cyclopentadiene added to the electrolysis medium. The regiochemistry of the nucleophilic addition is discussed in light of AM1 calculations.

**Key words:** 1-methyl-5-nitroindole, 5-nitrobenzofurane, 5-nitrobenzothiophene, iminoquinone, electrosynthesis.

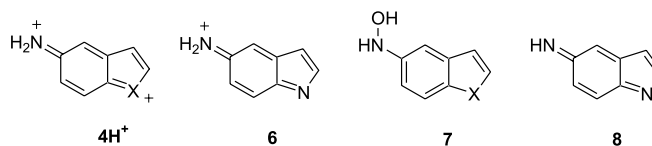
**Résumé :** L'électrolyse préparative du 1-méthyl-5-nitroindole (**1b**, X = NCH<sub>3</sub>), du 5-nitrobenzofurane (**1c**, X = O) et du 5-nitrobenzothiophène (**1d**, X = S), sur Hg et en milieu hydrométhanolique, mène à la formation des amines correspondantes **5** substituées en position 4, lesquelles proviennent de l'addition, aux intermédiaires de type iminoquinonique **4**, du méthanol ou d'autres bons nucléophiles présents au sein de la solution électrolytique. L'addition du nucléophile est 100% régiosélective. En milieu acide, les intermédiaires diiminoquinonium **4b** et **4c** ont été piégés par une réaction péricyclique avec le cyclopentadiène ajouté à la solution électrolytique. La régiochimie de l'addition du nucléophile est discutée à la lumière des résultats de calculs AM1.

**Mots clés :** 1-méthyl-5-nitroindole, 5-nitrobenzofurane, 5-nitrobenzothiophène, iminoquinone, électrosynthèse.

## Introduction

Recently, we reported the electroreduction at a mercury cathode of 5-nitroindole (**1a**) in acidic, neutral, and basic hydroorganic media (1, 2). As shown in Scheme 1, preparative electrolysis of 5-nitroindole (**1a**) in acidic or basic methanolic solutions gives 4-substituted-5-aminoindoles **5a**. In acidic medium, the latter are formed through dehydration of the protonated hydroxylamine **2a** to the diiminoquinonium intermediate **4a** followed by the regioselective addition of methanol and (or) of any other good nucleophile present in the electrolytic solution. In such acidic medium (0.15 mol L<sup>-1</sup> in acid, pH = 0.3), two monoprotonated diiminoquinones **4a**

and **6** are potential intermediates, and one could consider the possibility of a diprotonated intermediate **4aH<sup>+</sup>**, depending on the basicity of the imino nitrogen of **4a** and of the ring nitrogen of **6**. In basic medium, the hydroxylamine and the diiminoquinone are not protonated (see **7a** and **8**, respectively). In the presence of a good nucleophile, such as bromide ion in acidic medium or thiophenolate anion in basic medium, substituted aminoindole **5a** is the sole compound isolated in yields of 71%–86% and 59%, respectively (2).



a: X = NH; b: X = NCH<sub>3</sub>; c: X = O; d: X = S

Received 25 June 2003. Published on the NRC Research Press Web site at <http://canjchem.nrc.ca> on 7 October 2003.

L. Bouchard, I. Marcotte, J.M. Chapuzet, and J. Lessard.<sup>1</sup>

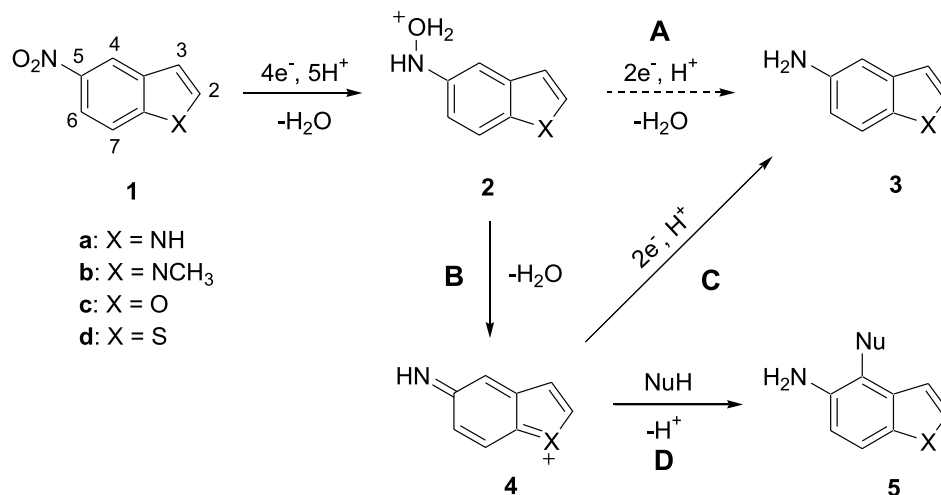
Laboratoire de chimie et électrochimie organiques, Département de chimie, Université de Sherbrooke, Sherbrooke, QC J1K 2R1, Canada.

<sup>1</sup>Corresponding author (e-mail: Jean.Lessard@USherbrooke.ca).

We studied the electroreduction of 1-methyl-5-nitroindole (**1b**), 5-nitrobenzofurane (**1c**), and 5-nitrobenzothiophene (**1d**) at a mercury cathode, in the same acidic (pH = 0.3) and basic (pH = 13.5) aqueous methanolic solutions (MeOH–H<sub>2</sub>O 95:5 (volume fraction)) as those used for the electro-



Scheme 1.



reduction of **1a** (**2**). The aim was to get a better understanding of the nature and reactivity towards nucleophiles of cationic iminoquinone intermediates **4** and (or) **4H<sup>+</sup>** (neutral diiminoquinones are not possible intermediates in these cases) and to see if substituted 5-amino derivatives **5** could also be obtained in good yield and high regioselectivity from this family of nitro compounds.

### Voltammetric measurements

Cyclic voltammetry was used to determine the reduction potential of 1-methyl-5-nitroindole (**1b**), 5-nitrobenzofurane (**1c**), and 5-nitrobenzothiophene (**1d**) in acidic and basic aqueous methanolic solutions. The data are summarized in Table 1. An increase of the scan rate from 100 to 500 mV s<sup>-1</sup> caused the expected increase of current for the diffusion controlled processes. In acidic medium (entries 2–4 and 6–8), the cyclic voltammograms of the three nitro compounds are similar to that of 5-nitroindole (**1a**) (entries 1 and 5) (**2**) and show only one peak, corresponding to a six-electron reduction to the amine. 5-Nitrobenzofurane (**1c**) has the most negative reduction potential, –0.58 and –0.51 V vs. ECS (entries 3 and 7, respectively), followed by 5-nitrobenzothiophene (**1d**), –0.51 and –0.47 V (entries 4 and 8), then by 1-methyl-5-nitroindole (**1b**), –0.47 and –0.44 V (entries 2 and 6), and finally by 5-nitroindole (**1a**), –0.34 V (entry 1) and –0.35 V (entry 5). In basic medium, the cyclic voltammograms of 1-methyl-5-nitroindole (**1b**) (entry 10: (*E*<sub>pc</sub>)<sub>1</sub> = –1.03 V and (*E*<sub>pc</sub>)<sub>2</sub> = –1.25 V) and of 5-nitrobenzofurane (**1c**) (entry 11: (*E*<sub>pc</sub>)<sub>1</sub> = –1.03 V and (*E*<sub>pc</sub>)<sub>2</sub> = –1.25 V) are also similar to that of 5-nitroindole (**1a**) (entry 9: (*E*<sub>pc</sub>)<sub>1</sub> = –1.06 V and (*E*<sub>pc</sub>)<sub>2</sub> = –1.28 V) (**2**) in showing two reduction peaks (*i*<sub>1</sub> + *i*<sub>2</sub>/*i*<sub>1</sub> of about 2), corresponding, respectively, to the reversible monoelectronic reduction to the radical anion and to the irreversible three-electron reduction of the radical anion to the hydroxylamine. However, the cyclic voltammogram of 5-nitrobenzothiophene (**1d**) shows only one four-electron reduction peak (entry 12: (*E*<sub>pc</sub>)<sub>1</sub> = –1.09 V). The cyclic voltammograms of all four nitro derivatives show the presence, on the second and third half-cycles at a less negative potential, of the hydroxylamine–nitroso reversible redox couple (see peaks (*E*<sub>pc</sub>)<sub>3</sub> and *E*<sub>pa</sub> in entries 9 to 12). Thus,

the voltammetric behaviour of these nitro derivatives in basic medium is similar to the well-known voltammetric behaviour of nitroaryl groups (**3**). The decreasing order of ease of reduction in basic medium (**1c** > **1b** > **1a** > **1d**) differs from that in acidic medium (**1a** > **1b** > **1d** > **1c**), so there seems to be no straightforward relationship between the structure (for instance, the electronegativity of X and its electron-withdrawing or electron-donating ability) and the reduction potential.

### Preparative electrolyses of 1-methyl-5-nitroindole (**1b**)

The results of preparative electroreduction of 1-methyl-5-nitroindole (**1b**) at Hg, in methanol–water (95:5 volume fraction) solutions and under controlled potential conditions (*E*<sub>W</sub> ~ (*E*<sub>pc</sub>)<sub>1</sub> – 100 mV in acidic medium, *E*<sub>W</sub> ~ (*E*<sub>pc</sub>)<sub>1</sub> – 300 mV in basic medium), are presented in Table 2.

In acidic medium (entries 1 to 3), the results are very similar to those reported previously for the electroreduction of the parent 5-nitroindole (**1a**) in the same media (**2**). With HBr as acid and supporting electrolyte (0.15 mol L<sup>-1</sup>, pH = 0.3) (entry 1), the electroreduction of **1b** consumed 4.6 F mol<sup>-1</sup> (1 F = 96 488 C) and led to 1-methyl-4-bromo-5-aminoindole (**5b**, Nu = Br) as the unique product in 57% yield. With H<sub>2</sub>SO<sub>4</sub> as acid and supporting electrolyte (0.15 mol L<sup>-1</sup>) (entry 2), the electrolysis of **1b** gave a 0.7 ratio of **3b** and **5b** (Nu = MeO) and consumed also 4.6 F mol<sup>-1</sup>. The mechanistic hypothesis for the formation of **3b** and **5b** (Scheme 1) is the same as that proposed previously for the electroreduction of 5-nitroindole (**1a**) in an acidic medium (**2**). First, **1b** is reduced to the protonated hydroxylamine **2b** through four successive electron and proton transfers. Then, there could be a competition between path A, the two-electron reduction of **2b** to aminoindole **3b** (protonated in the medium), and path B, acid-catalyzed elimination of water from **2b** to give a diiminoquinonium intermediate (**4b** and (or) **4bH<sup>+</sup>**). Since **3b** was not detected in the products of the electrolysis in the HBr medium (Table 2, entry 1), it is reasonable to assume that reaction A is slower than reaction B and thus may be neglected as proposed for the electroreduction of **1a** (**2**). 1-Methyl-5-aminoindole (**3b**) would



**Table 1.** Cyclic voltammetric data of 1-methyl-5-nitroindole (**1b**), 5-nitrobenzofurane (**1c**), and 5-nitrobenzothiophene (**1d**) at Hg in methanol–water (95:5 volume fraction).

Entry	Electrolyte <sup>a</sup>	Substrate <sup>b</sup>	( $E_{pc}$ ) <sub>1</sub> (V)	( $i_{pc}$ ) <sub>1</sub> (μA)	( $E_{pc}$ ) <sub>2</sub> (V)	( $i_{pc}$ ) <sub>t</sub> <sup>c</sup> (μA)	$E_{pa}$ (V)	$i_{pa}$ (μA)	( $E_{pc}$ ) <sub>3</sub> (V)	( $i_{pc}$ ) <sub>3</sub> (μA)
1	HBr	<b>1a</b>	−0.34	−7.05						
2		<b>1b</b>	−0.47	−5.36						
3		<b>1c</b>	−0.58	−2.55						
4		<b>1d</b>	−0.51	−4.54						
5 <sup>d</sup>	H <sub>2</sub> SO <sub>4</sub>	<b>1a</b>	−0.35	−6.95						
6		<b>1b</b>	−0.44	−4.91						
7		<b>1c</b>	−0.51	−3.18						
8		<b>1d</b>	−0.47	−4.05						
9 <sup>d</sup>	KOH	<b>1a</b>	−1.06	−2.70	−1.28	−5.07	−0.58	0.41	−0.61	−0.17
10		<b>1b</b>	−1.03	−1.56	−1.25	−2.24	−0.56	0.56	−0.68	−0.48
11		<b>1c</b>	−0.95	−0.91	−1.42	−2.10	−0.50	0.46	−0.57	−0.20
12		<b>1d</b>	−1.09	−3.48			−0.46	0.63	−0.52	−0.30

**Note:**  $T = 25 \pm 2$  °C; glassy carbon as auxiliary electrode; Ag/AgCl/(Cl)<sub>dil</sub> as reference electrode;  $\nu = 100$  mV s<sup>−1</sup>. Variations in peak current are due in part to variations of the surface of the mercury hanging drop electrode.

<sup>a</sup>Electrolytes: 0.15 mol L<sup>−1</sup> HBr; 0.15 mol L<sup>−1</sup> H<sub>2</sub>SO<sub>4</sub>; 0.15 mol L<sup>−1</sup> KOH.

<sup>b</sup>Substrate concentration:  $2.5 \times 10^{-4}$  mol L<sup>−1</sup>.

<sup>c</sup> $i_t$  represents the sum  $i_1 + i_2$  where  $i_1$  is the current of the first peak and  $i_2$  the current of the second peak.

<sup>d</sup>Taken from ref. 2.

**Table 2.** Controlled potential electroreduction of 1-methyl-5-nitroindole (**1b**) ( $6 \times 10^{-3}$  mol L<sup>−1</sup> solution) at Hg in MeOH–H<sub>2</sub>O (95:5 volume fraction).

Entry	Supporting electrolyte <sup>b</sup>	Added nucleophile <sup>c</sup>	$E_W^d$ (V)	Charge (F mol <sup>−1</sup> )	Yield of products (%) <sup>a</sup>	
					<b>3b</b>	<b>5b</b>
1	HBr	—	−0.54	4.6	—	57 (Nu = Br)
2	H <sub>2</sub> SO <sub>4</sub>	—	−0.56	4.6	13 <sup>e</sup>	19 (Nu = MeO) <sup>e</sup>
3	H <sub>2</sub> SO <sub>4</sub>	PhSH	−0.56	3.8	5 <sup>e</sup>	9 (Nu = MeO) <sup>e</sup> 20 (Nu = PhS) <sup>e,f</sup>
4	KOH	—	−1.31	8.5	2 <sup>e,g</sup>	7 (Nu = MeO) <sup>e</sup>

<sup>a</sup>Yield of product(s) isolated by flash chromatography on silica gel (unless stated otherwise) and based on two to three electrolyses (range given when variations were larger than  $\pm 4\%$ ).

<sup>b</sup>Supporting electrolyte concentration; see footnote *b* of Table 1.

<sup>c</sup>Added nucleophile concentration:  $1.2 \times 10^{-2}$  mol L<sup>−1</sup>.

<sup>d</sup>Working potential vs. SCE.

<sup>e</sup>Determined by vapor-phase chromatography.

<sup>f</sup>A third substitution product, 5-amino-1-methyl-3-thiophenoxyindole (**9b**), was isolated in 20% yield.

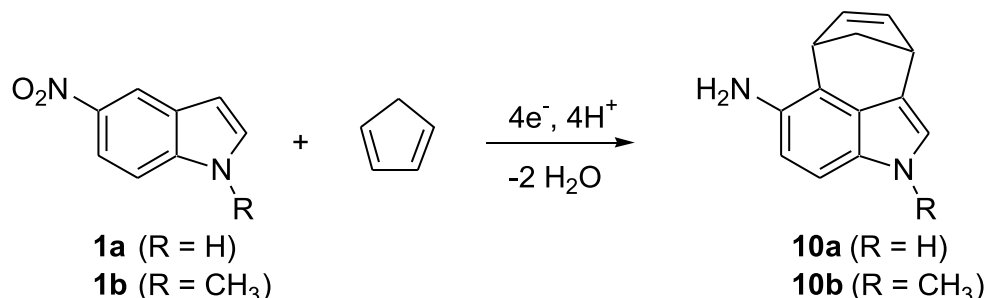
<sup>g</sup>The 5,5'-azo derivative **11b** was isolated in 27% yield.

then be formed by a two-electron reduction of the diiminoquinonium intermediates **4b** and (or) **4bH**<sup>+</sup> (path C), and 4-bromo-5-aminoindole (**5b**, Nu = Br) would result from the addition of a bromide ion to these intermediates (path D). The fact that 4-bromo-5-amino-1-methylindole (**5b**, Nu = Br) was the sole product isolated shows that the addition of Br<sup>−</sup> to **4b** and (or) **4bH**<sup>+</sup> (path D) is faster than their reduction to **3b** (path C). In the absence of bromide ions — methanol being a weaker nucleophile than Br<sup>−</sup> in such protic medium (hydrogen bonds to Br<sup>−</sup> are weak) — the reduction of **4b** and (or) **4bH**<sup>+</sup> to **5b** (path C) now competes effectively with the addition of methanol to these intermediates (path D), the rate of the two reactions being similar (rate of reaction D : rate of reaction C  $\sim 1.5$ , entry 2). In the presence of thiophenol (entry 3), the electroreduction of 1-methyl-5-nitroindole (**1b**) gave 1-methyl-5-aminoindole (**3b**) (5%), 1-methyl-4-methoxy-5-aminoindole (**5b**, Nu = MeO) (9%), and two substituted 5-amino indoles in equimolar amounts: the 4-thiophenoxy derivative **5b** (Nu = PhS) (20%) and the 3-thiophenoxy derivative **9b** (20%). These results

are again similar to those obtained with 5-nitroindole (**1a**) under the same conditions (formation of **9a** in 14% yield) (2). It is reasonable to assume that both isomers **5b** (Nu = SPh) and **9b** come from the addition of thiophenol to **4b** and (or) **4bH**<sup>+</sup>. The larger proportion of thiophenoxyindoles (**5b** (Nu = SPh) + **9b**: 40%) over 4-methoxy-5-aminoindole (**5b**, Nu = OMe: 9%) shows that thiophenol is a better nucleophile than methanol in the electrolysis medium (protic medium), which is in agreement with the fact that hydrogen bonding to sulphur is weaker than hydrogen bonding to oxygen. That thiophenol is a better nucleophile than methanol in such protic medium is seen also in the relative proportion of substituted-1-methyl-5-aminoindoles (**5b** + **9b**) and 1-methyl-5-aminoindole (**3b**) (proportional to the ratio of the rate of reaction D over the rate of reaction C, Scheme 1), which is larger in the presence of thiophenol ( $(\mathbf{5b}(\%) + \mathbf{9b}(\%))/\mathbf{3b}(\%) \sim 10$ , entry 3) than in its absence ( $\mathbf{5b}(\%)/\mathbf{3b}(\%) \sim 1.5$ , entry 2). The material balance based on the weight of crude product after work-up was nearly quantitative for all electrolyses in acidic medium (entries 1 to 3),

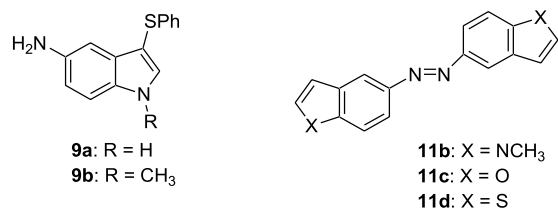


Scheme 2.



and both **3b** and **5b** were shown to be stable in the electrolysis medium, as well as during the work-up and chromatographic separation. So (i) the low material balances (32% in entry 2, 54% in entry 3, and 57% in entry 1) after chromatographic separation and (ii) the fact that the higher the material balance, the better the nucleophile suggests processes giving molecules that are retained on silica gel must be competing with path D and, to a lesser extent, path C (Scheme 1). One probable hypothesis is polymerization and (or) oligomerization of the diiminoquinonic intermediate **4b** (polymerization and (or) oligomerization of the diprotonated form **4bH<sup>+</sup>** appears less likely). The polymers and (or) oligomers formed would be strongly adsorbed on silica gel, and this would explain why all attempts to isolate any polymeric and (or) oligomeric material failed. In the presence of a good nucleophile ( $\text{Br}^-$  or  $\text{PhSH}$ , entries 1 and 2), polymerization and (or) oligomerization would account for about 40% of the products, and in methanol only (entry 2), it would be the main reaction (about 70% of the products).

The formation of **4b** and (or) **4bH<sup>+</sup>** was confirmed beyond any doubt by the isolation of the tetracyclic compound **10b** ( $\text{R} = \text{CH}_3$ ) in 31% yield (Scheme 2) when electrolysis of **1b** in acidic medium ( $\text{H}_2\text{SO}_4$   $0.15 \text{ mol L}^{-1}$ ) was carried out in the presence of cyclopentadiene in excess (8 equiv). The formation of **10a** has been previously reported for the electrolysis of **1a** under the same conditions (2). Adducts **10** most probably result from a  $[\pi^6s + \pi^4s]$  cycloaddition reaction between the fulvene part of the diiminoquinonic intermediate(s) and cyclopentadiene, as has already been suggested (2). Fulvenes are known to undergo  $[\pi^6s + \pi^4s]$  cycloadditions with cyclic 1,3-dienes (4, 5).



In basic medium (Table 2, entry 4), the electroreduction of 1-methyl-5-nitroindole (**1b**) gave 2% of 1-methyl-5-aminoindole **3b**, 7% of 4-methoxy-5-aminoindole (**5b**,  $\text{Nu} = \text{MeO}$ ), and 27% of the 5,5'-azo derivative **11b**. The formation of **3b** and **5b** ( $\text{Nu} = \text{MeO}$ ) is again explained by the mechanistic hypothesis of Scheme 1 with the following difference: the intermediate hydroxylamine is not protonated (see structure **7b**). Therefore, (i) path A does not occur at all since unprotonated arylhydroxylamines are not reducible (3)

and (ii) the dehydration of unprotonated hydroxylamine **7b** to the diiminoquinonium cation **4b** occurs by elimination of  $\text{OH}^-$ . Such elimination would be expected to be slower than in acidic medium (acid-catalyzed elimination of  $\text{H}_2\text{O}$  from **2b** (see path B in Scheme 1)). Assuming that the low material balance after chromatographic separation (36%) is due to polymerization and (or) oligomerization of the diiminoquinonium cation **4b**, which occurs also in basic medium (the crude material balance is again close to 100%), the elimination of  $\text{OH}^-$  from hydroxylamine **7b** would be faster than the condensation between **7b** and its nitroso precursor (structure not shown), a well-documented reaction in the electroreduction of aryl nitro groups (3) in basic medium; rate of elimination : rate of condensation  $\sim 73:27$ . The hydroxylamine–nitroso coupling gives the azoxy derivative first, which is reduced to the azo compound **11b** at the electrolysis potential (3). Azo compounds are more easily reducible than azoxy compounds (3), and **11b** is immediately reduced to the hydrazo derivative during the electrolysis. The latter is rapidly oxidized back to the azo compound **11b** in the presence of oxygen during the basic work-up (3), and the azo derivative **11b** was isolated in 27% yield. The hydroxylamine–nitroso condensation is much slower in acidic medium (3) and did not occur during the electroreduction of **1b** under acidic conditions discussed above. It was not observed either during the electroreduction of 5-nitroindole (**1a**) in basic medium (2) because the dehydration of the unprotonated hydroxylamine **7a**, being base catalyzed (abstraction of the proton at position 1 by  $\text{OH}^-$ ), is much faster than the nitroso–hydroxylamine coupling reaction. Finally, the low yield of 1-methyl-5-aminoindole (**3b**) and of 1-methyl-4-methoxy-5-aminoindole (**5b**) shows that polymerization and (or) oligomerization of the diiminoquinonium cation **4b** (about 64% of the reaction products) is faster than its reaction with nucleophiles (path D of Scheme 1) and its reduction (path C) (9% of reaction products).

### Preparative electrolyses of 5-nitrobenzofurane (**1c**)

The results of preparative electroreduction of 5-nitrobenzofurane (**1c**) at Hg, in  $\text{MeOH-H}_2\text{O}$  (95:5 volume fraction) solutions, are presented in Table 3. In acidic medium (entries 1 to 3), the electrochemical reduction of 5-nitrobenzofurane (**1c**) gives 4-substituted-5-aminobenzofuranes (**5c**:  $\text{Nu} = \text{Br}$ ,  $\text{OCH}_3$ ,  $\text{SPh}$ ) as the major products (Scheme 1). They represent 70%–100% of the isolated products. The other products isolated are 5-aminobenzofurane



**Table 3.** Electroreduction of 5-nitrobenzofurane (**1c**) ( $6 \times 10^{-3}$  mol L $^{-1}$  solution) at Hg in MeOH–H $_2$ O (95:5 volume fraction).

Entry	Supporting electrolyte <sup>b</sup>	Added nucleophile <sup>c</sup>	$E_W$ (V) <sup>d</sup>	Charge (F mol $^{-1}$ )	Yield of products (%) <sup>a</sup>	
					<b>3c</b>	<b>5c</b>
1	HBr	—	–0.67	4.1	6	63–69 (Nu = Br) 11 (Nu = MeO) <sup>e</sup>
2	H $_2$ SO $_4$	—	–0.61	4.0	—	66–79 (Nu = MeO) <sup>f</sup>
3	H $_2$ SO $_4$	PhSH	–0.61	3.8	18–27	46–55 (Nu = MeO) 4 (Nu = PhS)
4	KOH	—	–1.40	8.4	10	— <sup>g</sup>

<sup>a</sup>Yield of product isolated by flash chromatography on silica gel after *N*-acetylation (see the Experimental section) unless stated otherwise and based on two to three electrolyses (range given when variations were larger than  $\pm 4\%$ ); see Scheme 1 for structures of **3c** and **5c**.

<sup>b</sup>Supporting electrolyte concentration; see footnote *b* of Table 1.

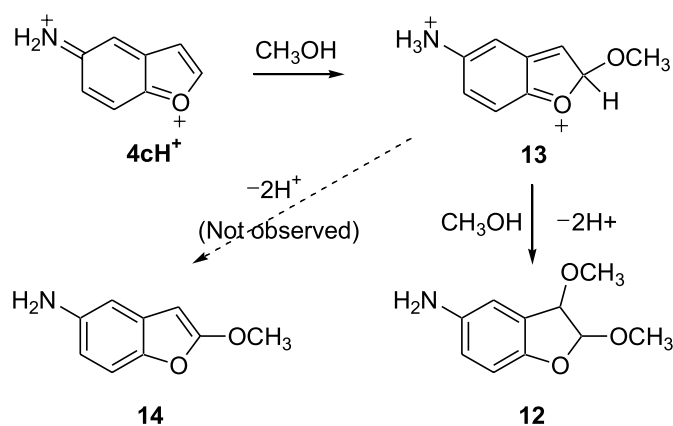
<sup>c</sup>Added nucleophile concentration:  $1.2 \times 10^{-2}$  mol L $^{-1}$ .

<sup>d</sup>Working potential vs. SCE.

<sup>e</sup>Trace amounts of *trans*-5-amino-2,3-dihydro-2,3-dimethoxybenzofurane (**12**).

<sup>f</sup>5-Amino-2,3-dihydro-2,3-dimethoxybenzofurane (**12**) was also isolated in an 11%–18% yield (ratio *trans*:*cis* = 1.5).

<sup>g</sup>Azo derivative **11c** was isolated in a 69% yield.

**Scheme 3.**

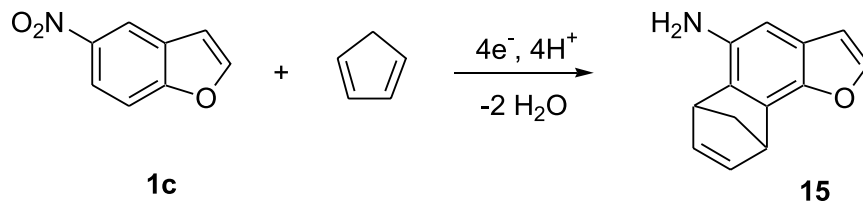
(**3c**) (6% in entry 1, 18%–27% in entry 3) and *cis*- and *trans*-2,3-dihydro-2,3-dimethoxy-5-aminobenzofurane (see **12** in Scheme 3) (trace amounts of *trans* isomer in entry 2 and 11%–18% of a mixture of *cis* and *trans* isomers (*cis*:*trans* = 0.66) in entry 3). The aminofuranes **3c** and **5c** must be formed through the same mechanistic pathways (Scheme 1, X = O) as those discussed above for the electroreduction of 5-nitroindole (**1a**) (2) and 1-methyl-5-nitroindole (**1b**) (Scheme 1, X = NH and NCH $_3$ , respectively). The dimethoxy derivatives **12** could have been formed as described in Scheme 3 — addition of a first molecule of methanol to the dication **4cH** $^{+}$ , followed by the addition of a second methanol molecule on the resulting dication **13** — which would be faster than deprotonation of **13** since 3-methoxy-5-aminobenzofurane (**14**) was not detected. The charge of about 4 F mol $^{-1}$  in the first three entries of Table 2 correlates very well with the fact that the main products isolated are 4-substituted-5-aminobenzofuranes (**5c**), the formation of which involves four electrons (Scheme 1, paths B and D). These results also show that the acid-catalyzed dehydration of the protonated hydroxylamine **2c** (path B) is faster than its reduction to **3c** (path A), as for the electroreduction of **1a** and **1b**. The material balance, after chromatographic separation, is higher with 5-nitrobenzofurane (**1c**) (Table 3: 83%, 79%, and 78% in entries 1, 2, and 3, respectively) than with 1-methyl-5-nitroindole (**1b**) (Table 2:

57%, 32%, and 53% in entries 1, 2, and 3, respectively) (the material balance before separation was 100%, as in the electroreduction of **1b**). This difference in material balance strongly suggests that the cationic intermediate **4c** has a lesser tendency to polymerize and (or) oligomerize and (or) is more reactive towards nucleophiles (paths D of Scheme 1) than the cationic intermediate **4b**. The diprotonated intermediate **4cH** $^{+}$  would also be more reactive towards nucleophiles than the diprotonated intermediate **4bH** $^{+}$ . Moreover, when a nucleophile other than methanol is also present in the reaction medium (is competing with methanol), the relative amount of methoxy derivative (Nu = OCH $_3$ ) in the 4-substituted-5-amino derivatives **5** is higher in the benzofurane series **c** (17% (MeOH vs. Br $^{-}$ ) in entry 1 of Table 3, 96% (MeOH vs. PhSH) in entry 3) than in the indole series **b** (0% (MeOH vs. Br $^{-}$ ) in entry 1 of Table 2, 23% (MeOH vs. PhSH) in entry 3). This can be readily explained by the fact that the cation **4c** and dication **4cH** $^{+}$  would be harder electrophiles than cation **4b** and dication **4bH** $^{+}$ , oxygen being more electronegative than nitrogen and MeOH being a harder nucleophile than Br $^{-}$  and PhSH for electronegativity reasons as well. When the electrolysis of 5-nitrobenzofurane (**1c**) was carried out in acidic medium in the presence of cyclopentadiene in excess (8 equiv), the cycloadduct **15** was isolated in a low yield of 7% (Scheme 4). As seen above, the yield of cycloadduct **10a** was 32% for the electrolysis of 1-methyl-5-nitroindole (**1b**) carried out under the same conditions (Scheme 2). This difference in yield of cycloaddition is readily explained again by the greater reactivity of cationic electrophiles **4c** and (or) **4cH** $^{+}$  towards the hard nucleophile methanol when compared with the reactivity of the softer cationic electrophiles **4b** and (or) **4bH** $^{+}$ . Cyclopentadiene is a much softer nucleophile than methanol. It must be noted that cations **4c** and (or) **4cH** $^{+}$  act as dienophiles (2-electron partner) at the 5,6 positions in a Diels–Alder reaction ( $\pi^4s + \pi^2s$ ) cycloaddition) with cyclopentadiene (Scheme 4), whereas cations **4b** and (or) **4bH** $^{+}$  act as the 6-electron component (fulvene moiety) in a  $[\pi^6s + \pi^4s]$  cycloaddition, as already seen (Scheme 2).

In basic medium (Table 3, entry 4), the electroreduction of 5-nitrobenzofurane (**1c**) gave the azo derivative **11c** as the main product (69%) and some 5-aminobenzofurane (**3c**) (10%). Since unprotonated arylhydroxylamines are not re-



Scheme 4.



ducible in protic medium, as already mentioned (3), 5-aminobenzofuran (**3c**) must have been formed by reduction of the cationic intermediate **4c** (path C of Scheme 1). No methoxy derivative such as **5c** ( $Nu = OCH_3$ ), resulting from the addition of a methoxide anion to **4c** (path D), was observed. This shows that, in basic medium, the reduction of **4c** is faster than its reaction with methoxide ions and (or) methanol. Moreover, elimination of  $OH^-$  from hydroxylamine **7c** to give the cationic intermediate **4c** is slower than the hydroxylamine–nitroso coupling reaction, leading ultimately to the isolation of azo derivative **11c**. In the case of hydroxylamine **7b**, the elimination of  $OH^-$  to form **4b** was faster than the coupling reaction, as seen above. This difference in reactivity between **7c** and **7b** can be ascribed to the fact that oxygen is more electronegative than nitrogen, the cationic intermediate **4c** being more difficult to form (having a higher enthalpy) than intermediate **4b**.

### Preparative electrolyses of 5-nitrobenzothiophene (**1d**)

The results of preparative electroreduction of 5-nitrobenzothiophene (**1d**) under the same conditions as those used for the electroreduction of the two other nitro compounds, **1b** and **1c**, are presented in Table 4. Those results are similar to those reported in Table 3 for the electroreduction of 5-nitrobenzofuran (**1c**) for both acidic and basic media (charge passed, yields, and relative proportion of 5-amino product **3** and of 4-substituted-5-amino derivative **5**), except that no dimethoxy derivative analogous to **12** was detected in the products of electroreduction of 5-nitrobenzothiophene (**1d**) in acidic medium (compare entries 2 and 3 in Table 4 with entries 2 and 3, respectively, in Table 3). Another slight difference in reactivity was noted when the electroreduction of 5-nitrobenzothiophene (**1d**) in acidic medium was carried out in the presence of cyclopentadiene under the same conditions as those used with 5-nitrobenzofuran (**1c**). No cycloadduct analogous to **15** (or any other possible adduct) was detected (**15** was isolated in a low 7% yield from the electroreduction of **1c**). So the mechanisms must be the same for the three nitro compounds (see Scheme 1), and the reactivities of the various intermediates (**2d**, **4d** and **4dH<sup>+</sup>**, **7d**) must be comparable to those of the related intermediates involved in the reduction of 5-nitrobenzofuran (**1c**). This close similarity seems surprising since sulphur is less electronegative and is a third-row element.

### Regioselectivity of ring substitution

A very interesting aspect of the electroreduction of 5-nitroindoles **1a** and **1b** and of the related 5-nitrobenzofuran

(**1c**) and 5-nitrobenzothiophene (**1d**) is the high regioselectivity of the addition of nucleophiles (*i*) to cationic intermediates **4a–4aH<sup>+</sup>** (2), **4b–4bH<sup>+</sup>**, **4c–4cH<sup>+</sup>**, and **4d–4dH<sup>+</sup>** (this work) in acidic medium and (*ii*) to neutral intermediate **8** (2), as well as to cationic intermediates **4b**, **4c**, and **4d** in basic medium (this work). The addition occurs exclusively at carbon 4 and not at the other electrophilic positions (positions 2, 3, 6, and 7) except (*i*) for the addition of methanol to **4c** and (or) **4cH<sup>+</sup>** (Table 3, entry 2) in acidic medium with a regioselectivity of about 83%, some addition taking place at carbon 2 of **4cH<sup>+</sup>** (see Scheme 3) and (*ii*) for the addition of PhSH to cationic intermediates **4a** and (or) **4aH<sup>+</sup>** with a regioselectivity of 62% (38% of 3-thiophenoxy derivative **5a**) (2) and to intermediates **4b** and (or) **4bH<sup>+</sup>** with a regioselectivity of 50% (50% of 3-thiophenoxy derivative **5b**) (Table 2, entry 3).

According to frontier molecular orbital theory, the most important frontier orbital interaction in a reaction between an electrophile and a nucleophile (5, 6) is that between the LUMO of the electrophile and the HOMO of the nucleophile. In the case of the addition of a nucleophile to a multivalent electrophile, the reaction would be the fastest at the carbon where the coefficient of the LUMO is the largest (5, 6). The results of theoretical calculations using the AM1 method (7, 8) on intermediates **4** (Scheme 1) and their conjugate acids **4H<sup>+</sup>** are gathered in Table 5. They show that the LUMO of unprotonated intermediates **4** and protonated **4H<sup>+</sup>** have the largest coefficient on carbon 4, which agrees entirely with the experimental results: the regioselective formation of 4-substituted-5-amino derivatives **5** in acidic media. However, the largest coefficient of the LUMO of the protonated intermediate **6** (reduction of 5-nitroindole (**1a**)) is on carbon 6 (2). Although calculations give a slightly higher gas-phase enthalpy of formation for cationic intermediate **4a** (257.6 kcal mol<sup>-1</sup>) than for cationic intermediate **6** (255.4 kcal mol<sup>-1</sup>) (2), the similarity of the experimental results obtained with 5-nitroindole (**1a**) (2) and 1-methyl-5-nitroindole (**1b**) (the cationic intermediate **4b** is the sole possible) and the calculated largest coefficient on carbon 4 strongly suggest the participation of intermediate **4a** and (or) **4aH<sup>+</sup>** instead of intermediate **6** in the electroreduction of **1a**. As for the low regioselectivity of substitution observed in the electroreduction of 5-nitroindole (**1a**) (62%) and 1-methyl-5-nitroindole (**1b**) (50%) in acidic medium in the presence of thiophenol, it would be surprising that it would be because of the fact that the addition of thiophenol to **4a–4aH<sup>+</sup>** and **4b–4bH<sup>+</sup>** would be much less regioselective than the addition of the other nucleophiles (bromide ion and methanol). One possibility is that the addition of thiophenol would occur regioselectively at position 4 of **4a–4aH<sup>+</sup>** and **4b–4bH<sup>+</sup>**. Then there would be a competition between deprotonation of the initial adduct **16** to give the 4-thio-



**Table 4.** Electroreduction of 5-nitrobenzothiophene (**1d**) ( $6 \times 10^{-3}$  mol L $^{-1}$ ) at Hg in MeOH–H $_2$ O (95:5 volume fraction).

Entry	Supporting electrolyte <sup>b</sup>	Added nucleophile <sup>c</sup>	<i>E</i> (V) <sup>d</sup>	Charge (F mol $^{-1}$ )	Yield of products (%) <sup>a</sup>	
					<b>3d</b>	<b>5d</b>
1	HBr	—	–0.61	4.2	—	47 (Nu = Br) 12–22 (Nu = MeO)
2	H $_2$ SO $_4$	—	–0.57	4.1	—	70–80 (Nu = MeO)
3	H $_2$ SO $_4$	PhSH	–0.57	4.9	34–40	46–52 (Nu = MeO) 7 (Nu = PhS)
4	KOH	—	–1.19	8.5	—	— <sup>e</sup>

<sup>a</sup>Yield of product isolated by flash chromatography on silica gel (unless stated otherwise) and based on two to three electrolyses (range given when variations were larger than  $\pm 4\%$ ).

<sup>b</sup>Supporting electrolyte concentration; see footnote *b* of Table 1.

<sup>c</sup>Added nucleophile concentration:  $1.2 \times 10^{-2}$  mol L $^{-1}$  for PhSH.

<sup>d</sup>Working potential vs. SCE.

<sup>e</sup>Azo derivative **11d** was isolated in a 78% yield.

**Table 5.** Heats of formation, coefficient of the LUMO, and Mulliken charges of intermediates **4** and **4H** $^+$ .

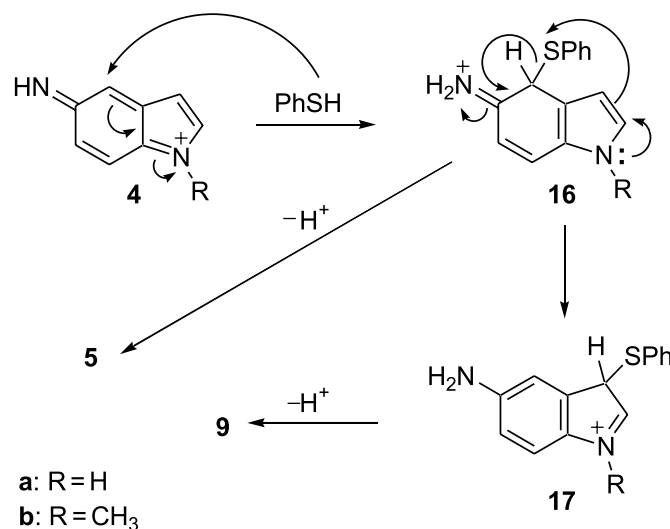
Intermediate	$\Delta H_f$ (kCal mol $^{-1}$ )	Coefficient of the LUMO (charge) <sup>a</sup>				
		C $_2$	C $_3$	C $_4$	C $_6$	C $_7$
<b>4b</b> (X = NCH $_3$ )	259.5	0.01 (–0.09)	–0.24 (–0.09)	0.49 (–0.06)	0.35 (–0.06)	–0.13 (–0.14)
<b>4bH</b> $^+$	496.9	–0.13 (–0.06)	0.21 (–0.07)	0.34 (–0.05)	–0.23 (–0.15)	0.27 (–0.01)
<b>4c</b> (X = O)	237.8	0.10 (–0.08)	–0.16 (–0.20)	0.49 (–0.02)	0.41 (–0.00)	–0.05 (–0.24)
<b>4cH</b> $^+$	491.3	–0.11 (–0.04)	0.13 (–0.19)	–0.36 (–0.08)	–0.30 (–0.16)	0.22 (–0.11)
<b>4d</b> (X = S)	252.3	0.08 (–0.48)	–0.25 (–0.02)	0.50 (0.15)	0.32 (–0.08)	–0.07 (–0.11)
<b>4dH</b> $^+$	490.6	0.03 (–0.55)	–0.30 (0.06)	0.39 (0.01)	0.18 (–0.18)	–0.22 (0.04)

<sup>a</sup>C $_2$ , C $_3$ , etc. correspond to the numbering of carbons of indole, benzofurane, and benzothiophene (see **1**, Scheme 1).

phenoxy derivative **5** (Nu = SPh) and rearrangement of **16** into adduct **17** as shown in Scheme 5 for the monocationic intermediates **4**. Deprotonation of **17** would give the 3-thiophenoxy derivatives **9**. Interestingly, the electroreduction of 5-nitroindole (**1a**) in the presence of thiophenol in basic medium was reported to give 59% of 4-thiophenoxy-5-aminoindole (**9a**) as the sole substitution product (2), which then means that the addition of a thiophenolate anion to diiminoquinone **8** is 100% regioselective, as with the other nucleophiles, and occurs solely at position 4. The AM1 calculations once more agree with this result; the LUMO of the neutral diiminoquinone **8** has the largest coefficient on carbon 4 (2).

## Conclusion

In this paper, we have shown that the electroreduction of 1-methyl-5-nitroindole (**1b**), 5-nitrobenzofurane (**1c**), and 5-nitrobenzothiophene (**1d**) at Hg, in acidic hydromethanolic media, gives the corresponding 4-substituted amino derivatives **5b**, **5c**, and **5d** in good yields and high regioselectivity. The proposed mechanism (Scheme 1) involves first the electroreduction of the nitro substrate **1** to the corresponding protonated hydroxylamine **2**, which is quickly dehydrated to an electrophilic quinonic intermediate **4–4H** $^+$  (step B). The latter reacts with nucleophiles present in the medium (step D) faster than it is reduced to the corresponding amino compound **3** (step C). The mechanism was confirmed by unequivocal trapping of the intermediates diiminoquinonium cation **4b–4bH** $^+$  and iminoquinonium cation **4c–4cH** $^+$ , via a

**Scheme 5.**

pericyclic reaction with cyclopentadiene in the electrolysis of 1-methyl-5-nitroindole (**1b**) (Scheme 2), and 5-nitrobenzofurane (**1c**) (Scheme 4) in acidic medium. The material balance was always lower than 100% after chromatographic separation. This has been attributed to a competition between, on the one hand, reduction of the intermediate quinonium species **4** and its reaction with nucleophiles (steps C and D) and, on the other hand, their polymerization and (or) oligomerization. The electro-



reduction of all of the nitro compounds **1** in basic medium gives the corresponding azo derivative **11** as the major product. In the case of 5-nitrobenzofurane (**1c**) and 5-nitrobenzothiophene (**1d**), the hydroxylamine–nitroso coupling reaction is faster than dehydration of the hydroxylamine in basic medium. It is slower in the case of 1-methyl-5-nitroindole (**1b**), and the main process in basic medium is polymerization and (or) oligomerization of **4b**.

## Experimental

### General information

All commercially available chemicals were purchased from Aldrich and BDH, and all the solvents were distilled before use. Infrared spectra were recorded in chloroform on a PerkinElmer 1600 FT-IR spectrometer, and nuclear magnetic resonance spectra were recorded in deuteriochloroform or deuterioacetone on a Bruker AC-300 spectrometer using the signal from chloroform or acetone as reference (s = singlet, d = doublet, t = triplet, q = quartet, dd = doublet of doublets, m = multiplet). Vapor phase chromatography was performed on a Hewlett-Packard (HP) 5710A chromatograph with an FID detector, an HP 3390A integrator, and a DB-5 fused silica capillary column (30 m). High resolution mass spectra were recorded on a ZAB-2F model VG apparatus. Flash chromatography was carried out on Silicycle Inc. silica gel (70–230 mesh). Solutions for all electrochemical experiments were deoxygenated by bubbling dry argon through them for 15 min, and an argon atmosphere was maintained throughout the experiments. The cyclic voltammetry (CV) experiments were performed using a Princeton Applied Research PAR 273 potentiostat in a single compartment cell with 7 mL of 0.25 mmol L<sup>-1</sup> solutions of the substrate in methanol–water (95:5 volume fraction) containing the supporting electrolyte (see Table 1). No correction was applied to compensate for the solution resistance. The voltammograms were recorded and processed using EG&G software M270. The working electrode was a mercury hanging drop Metrohm, model E410. A glassy carbon rod was used as the counter electrode and an Ag/AgCl/(Cl<sup>-</sup>)<sub>sat</sub> electrode, the potential of which was adjusted to that of an SCE, served as the reference. The controlled potential electrolyses were carried out on a mercury pool, in a vertical glass cell with two concentric compartments separated by a fritted glass, using an ElectroSynthesis Company (ESC) 410 potentiostat with an ESC 640 coulometer and an ammeter connected in series within the auxiliary circuit. The volume of the cathodic compartment was 45 mL and that of the anodic compartment 10 mL. The same reference electrode as the one described above was used, and a platinum grid was used as the counter electrode. The other conditions are given in Tables 2–4.

### Computational procedure

All calculations were performed at the RHF level using the AM1 method (7, 8). The first input files for MOPAC 6.00 were created by means of SYBIL 6.01 (Tripos Associates, Inc., St-Louis, Mo.) for IBM RS/6000 computers. The gradients of the norm of these draft structures were then fully optimized using the EF subroutine. The AM1 method

was considered more adequate than the PM3 method for calculations on cationic species.

### Substrate and authentic sample synthesis

All prepared compounds had spectral and physical characteristics identical to those reported in the literature.

1-Methyl-5-nitroindole (**1b**) was prepared by alkylation of commercially available 5-nitroindole (**1a**) with iodomethane (9). 5-Nitrobenzofurane (**1c**) was synthesized by nitration (10) and decarboxylation (11) of coumarillic acid, previously prepared by the method of Suzuki et al. (12). 5-Nitrobenzothiophene (**1d**) was prepared by the method of Zambias and Hammond (13).

1-Methyl-5-aminoindole (**3b**) was synthesized by reduction of 1-methyl-5-nitroindole (**1b**) by NaBH<sub>2</sub>S<sub>3</sub> (14) and was used as an authentic sample. To a suspension of freshly prepared NaBH<sub>2</sub>S<sub>3</sub> (15) (300 mg, 2.28 mmol) in THF (70 mL), a solution of 1-methyl-5-nitroindole (**1b**) (200 mg, 1.14 mmol) in anhydrous THF was slowly added. The mixture was refluxed for 24 h. The solvent was removed at room temperature under reduced pressure, and a solid residue was obtained. The crude material was hydrolyzed with HCl (1 mol L<sup>-1</sup>) in the presence of diethyl ether. The solids were filtered and rinsed with diethyl ether. The filtrate was basified to pH 11 with NaOH (1 mol L<sup>-1</sup>). The aqueous phase was extracted with diethyl ether. The organic phase was washed with brine, and the organic phases were combined, dried (Na<sub>2</sub>SO<sub>4</sub>), and filtrated. The solvent was evaporated under vacuum, and a dark oil was obtained. After flash chromatography on silica gel, 67 mg of 1-methyl-5-aminoindole (**3b**) were obtained (40% yield) as a dark oil (lit. (15) mp = 100–101 °C). IR (CHCl<sub>3</sub>) (cm<sup>-1</sup>): 3005 (CH aro), 2930 (CH ali), 1630 (C=C), 1497 (C=C), 1455 (CH<sub>3</sub>), 1250 (C-N). <sup>1</sup>H NMR (300 MHz, CDCl<sub>3</sub>) (ppm) δ: 7.17 (1H, d, *J* = 8.6, H7), 7.14 (1H, d, *J* = 2.2, H4), 7.00 (1H, d, *J* = 3.0, H2), 6.86 (1H, dd, *J* = 2.2, *J* = 8.6, H6), 6.34 (1H, d, *J* = 3.0, H3), 3.73 (3H, s, CH<sub>3</sub>). <sup>13</sup>C NMR (75 MHz, CDCl<sub>3</sub>) (ppm) δ: 139.1, 131.8, 129.1, 128.0, 112.5, 109.7, 105.7, 99.5, 32.8. HR-MS, *m/z*: calcd. for C<sub>9</sub>H<sub>10</sub>N<sub>2</sub>: 146.0844; found: 146.0849.

### Typical electrolysis procedure

Electroreduction of 1-methyl-5-nitroindole (**1b**) in acidic HBr medium (entry 1, Table 2). Argon was bubbled through the cathodic compartment containing the electrolyte for 1 h, and an argon atmosphere was maintained throughout the electrolysis. A pre-electrolysis was performed at -0.54 V vs. SCE until the current was 0.1 mA or less. The circuit was opened, then **1b** (48.9 mg, 0.27 mmol) was added to the catholyte. The potential was applied, and the electrolysis was stopped when the current had dropped to 0.1 mA or less. The electrolysis solution was transferred to a round-bottomed flask, the cell was washed with methanol and water, and methanol was removed on a rotatory evaporator. The pH of the resulting solution was brought to 12 with aqueous NaOH (1 mol L<sup>-1</sup>); the solution was saturated with NaCl and extracted with ether (4 × 50 mL). The organic phase was washed with brine, dried (Na<sub>2</sub>SO<sub>4</sub>), and the solvent removed under vacuum. The crude material was purified by flash chromatography on silica gel (elution with 20% volume



fraction AcOEt–hexanes) to give 35.4 mg of **5b** (Nu = Br) (57% yield).

The crude product from the electroreduction of 5-nitrobenzofurane (**1c**) was acetylated by acetic anhydride in ethyl acetate before chromatographic separation, and the amino compounds were isolated as their *N*-acetyl derivative. The acetylation was quantitative.

### Characterization of electrolysis products

#### 5-Acetamidobenzofurane (acetylated **3c**)

Dark oil. IR (CHCl<sub>3</sub>) (cm<sup>-1</sup>): 3438 (NH), 3011 (CH aro.), 1684 (C=O), 1524 (C=C), 1215 (C-N). <sup>1</sup>H NMR (300 MHz, CDCl<sub>3</sub>) (ppm) δ: 7.89 (1H, d, *J* = 2.1, H4), 7.63 (1H, m, NH), 7.59 (1H, d, *J* = 1.9, H2), 7.40 (1H, d, *J* = 8.8, H7), 7.21 (1H, dd, *J* = 2.3, *J* = 6.6, H6), 6.70 (1H, d, *J* = 2.1, H3), 2.03 (3H, s, CH<sub>3</sub>). <sup>13</sup>C NMR (75 MHz, CDCl<sub>3</sub>) (ppm) δ: 168.6, 145.8, 117.7, 113.2, 111.3, 106.8, 152.0, 133.0, 127.8, 24.4. HR-MS, *m/z*: calcd. for C<sub>10</sub>H<sub>9</sub>NO<sub>2</sub>: 175.0633; found: 175.0636.

#### 5-Aminobenzothiophene (**3d**)

Dark oil. IR (acetone) (cm<sup>-1</sup>): 3369 (NH), 3075 (CH aro.), 1667 (C=C), 1608 (C=C), 1491 (C=C). <sup>1</sup>H NMR (300 MHz, CD<sub>3</sub>OD) (ppm) δ: 7.58 (1H, d, *J* = 8.5, H7), 7.41 (1H, d, *J* = 5.4, H2), 7.15 (1H, d, *J* = 2.2, H4), 7.12 (1H, d, *J* = 5.5, H3), 6.83 (1H, dd, *J* = 2.2, *J* = 8.5, H6). <sup>13</sup>C NMR (75 MHz, CD<sub>3</sub>OD) (ppm) δ: 145.6, 142.4, 131.6, 127.7, 124.1, 123.5, 116.5, 109.8. HR-MS, *m/z*: calcd. for C<sub>8</sub>H<sub>7</sub>NS: 149.0299; found: 149.0294.

#### 1-Methyl-4-bromo-5-aminoindole (**5b**, Nu = Br)

Yellow oil. IR (CHCl<sub>3</sub>) (cm<sup>-1</sup>): 3007 (CH aro.), 2947 (CH ali.), 1495 (C=C), 1440 (CH<sub>3</sub>), 1254 (C-N). <sup>1</sup>H NMR (300 MHz, CDCl<sub>3</sub>) (ppm) δ: 7.10 (1H, d, *J* = 8.5, H7), 7.01 (1H, d, *J* = 3.0, H2), 6.75 (1H, d, *J* = 8.5, H6), 6.37 (1H, d, *J* = 3.0, H3), 3.73 (3H, s, CH<sub>3</sub>). <sup>13</sup>C NMR (75 MHz, CDCl<sub>3</sub>) (ppm) δ: 136.8, 131.3, 129.6, 129.3, 112.2, 109.1, 100.2, 99.9, 33.0. HR-MS, *m/z*: calcd. for C<sub>9</sub>H<sub>9</sub>N<sub>2</sub>Br: 223.9949; found: 223.9945.

#### 1-Methyl-4-methoxy-5-aminoindole (**5b**, Nu = MeO)

Dark oil. IR (CHCl<sub>3</sub>) (cm<sup>-1</sup>): 2930 (CH ali.), 1501 (C=C), 1446 (CH<sub>3</sub>), 1265 (C-N). <sup>1</sup>H NMR (300 MHz, CDCl<sub>3</sub>) (ppm) δ: 6.94 (1H, d, *J* = 3.1, H2), 6.90 (1H, d, *J* = 8.4, H7 or H6), 6.76 (1H, d, *J* = 8.4, H6 or H7), 6.45 (1H, d, *J* = 3.1, H3), 4.02 (3H, s, O-CH<sub>3</sub>), 3.72 (3H, s, N-CH<sub>3</sub>). <sup>13</sup>C NMR (75 MHz, CDCl<sub>3</sub>) (ppm) δ: 135.7, 133.3, 129.9, 128.4, 113.3, 112.1, 104.8, 96.8, 58.5, 33.0. HR-MS, *m/z*: calcd. for C<sub>10</sub>H<sub>12</sub>N<sub>2</sub>O: 176.0950; found: 176.0953.

#### 1-Methyl-4-thiophenoxy-5-aminoindole (**5b**, Nu = PhS)

Dark oil. IR (CHCl<sub>3</sub>) (cm<sup>-1</sup>): 3001 (CH aro.), 2946 (CH ali.), 1613 (C=C), 1505 (C=C), 1253 (C-N). <sup>1</sup>H NMR (300 MHz, CDCl<sub>3</sub>) (ppm) δ: 7.25 (1H, d, *J* = 8.6, H6), 7.18–7.14 (2H, m, H phenyl), 7.07–7.03 (3H, m, H phenyl), 6.98 (1H, d, *J* = 3.0, H2), 6.82 (1H, d, *J* = 8.6, H7), 6.44 (1H, d, *J* = 3.0, H3), 3.76 (3H, s, CH<sub>3</sub>). <sup>13</sup>C NMR (75 MHz, CDCl<sub>3</sub>) (ppm) δ: 142.8, 137.1, 129.6, 128.8, 128.5, 127.9, 127.3, 126.0, 124.8, 112.2, 111.9, 100.0, 33.0 (CH<sub>3</sub>). HR-MS, *m/z*: calcd. for C<sub>15</sub>H<sub>14</sub>N<sub>2</sub>S: 254.0878; found: 254.0884.

#### 4-Bromo-5-acetamidobenzofurane (acetylated **5c**, Nu = Br)

Beige solid. mp = 160–161 °C. IR (CHCl<sub>3</sub>) (cm<sup>-1</sup>): 3416 (NH), 3010 (CH aro.), 1693 (C=O), 1518 (NH), 1432 (CH<sub>3</sub>), 1252 (C-O), 1211 (C-N). <sup>1</sup>H NMR (300 MHz, acetone-d<sub>6</sub>) (ppm) δ: 8.66 (1H, m, NH), 7.94 (1H, d, *J* = 2.2, H2), 7.81 (1H, d, *J* = 8.8, H4), 7.52 (1H, d, *J* = 8.8, H6), 6.87 (1H, d, *J* = 2.2, H3), 2.08 (3H, s, CH<sub>3</sub>). <sup>13</sup>C NMR (acetone-d<sub>6</sub>) (ppm) δ: 168.4 (C=O), 146.1, 119.4, 110.8, 107.2, 151.2, 131.1, 129.0, 105.6, 24.6. HR-MS, *m/z*: calcd. for C<sub>10</sub>H<sub>8</sub>NO<sub>2</sub>Br: 252.9738; found: 252.9743.

#### 4-Methoxy-5-acetamidobenzofurane (acetylated **5c**, Nu = MeO)

Dark oil. IR (CHCl<sub>3</sub>) (cm<sup>-1</sup>): 3426 (NH), 3320 (NH), 3006 (CH aro.), 2947 (CH ali.), 2838 (CH<sub>2</sub>), 1677 (C=O), 1597 (C=C), 1544 (NH), 1254 (C-O). <sup>1</sup>H NMR (300 MHz, CDCl<sub>3</sub>) (ppm) δ: 8.20 (1H, d, *J* = 8.9, H7), 7.75 (1H, m, NH), 7.52 (1H, d, *J* = 2.3, H2), 7.15 (1H, d, *J* = 8.9, H6), 6.87 (1H, d, *J* = 2.3, H3), 4.08 (3H, s, O-CH<sub>3</sub>), 2.08 (3H, s, CH<sub>3</sub>). <sup>13</sup>C NMR (75 MHz, CDCl<sub>3</sub>) (ppm) δ: 168.2, 144.4, 118.0, 115.3, 103.4, 153.0, 141.8, 123.7, 117.1, 59.9, 24.6. HR-MS, *m/z*: calcd. for C<sub>11</sub>H<sub>11</sub>NO<sub>3</sub>: 205.0739; found: 205.0742.

#### 4-Thiophenoxy-5-acetamidobenzofurane (acetylated **5c**, Nu = PhS)

Dark oil. IR (CHCl<sub>3</sub>) (cm<sup>-1</sup>): 3476 (R<sub>2</sub>N-H), 3367 (R<sub>2</sub>N-H), 3009 (C-H arom.), 1679 (C=O amide), 1613, 1582 (C=C), 1215 (C-N). <sup>1</sup>H NMR (300 MHz, CDCl<sub>3</sub>) (ppm) δ: 8.56 (1H, m, NH), 8.24 (1H, d, *J* = 8.6 Hz, H<sub>7</sub>), 7.45 (1H, d, *J* = 8.8 Hz, H<sub>6</sub>), 7.20 (1H, m, H<sub>2</sub>), 7.16 (2H, d, *J* = 7.7 Hz, H phenyl), 7.05 (3H, m, H phenyl), 6.58 (1H, m, H<sub>3</sub>), 2.09 (3H, s, CH<sub>3</sub>). <sup>13</sup>C NMR (75 MHz, CDCl<sub>3</sub>) (ppm) δ: 168.4, 136.0, 133.9, 132.7, 131.6, 129.1, 126.6, 126.0, 125.6, 116.2, 113.2, 102.7, 24.7. HR-MS, *m/z*: calcd. for C<sub>16</sub>H<sub>13</sub>NO<sub>2</sub>S: 282.0827; found: 282.0833.

#### 4-Bromo-5-aminobenzothiophene (**5d**, Nu = Br)

Dark oil. IR (acetone) (cm<sup>-1</sup>): 3464 (NH), 3001 (CH aro.), 1623 (C=C), 1502 (C=C). <sup>1</sup>H NMR (300 MHz, CD<sub>3</sub>OD) (ppm) δ: 7.57 (1H, d, *J* = 8.7, H7), 7.54 (1H, d, *J* = 5.7, H2), 7.27 (1H, d, *J* = 5.5, H3), 6.92 (1H, d, *J* = 8.6, H6). <sup>13</sup>C NMR (75 MHz, CD<sub>3</sub>OD) (ppm) δ: 143.5, 141.5, 131.0, 128.8, 124.4, 122.8, 116.2, 102.6. HR-MS, *m/z*: calcd. for C<sub>8</sub>H<sub>6</sub>NSBr: 226.9404; found: 226.9409.

#### 4-Methoxy-5-aminobenzothiophene (**5d**, Nu = MeO)

Dark oil. IR (acetone) (cm<sup>-1</sup>): 3459 (NH), 3005 (CH aro.), 2937 (CH ali.), 1620 (C=C), 1509 (C=C), 1454 (CH<sub>3</sub>). <sup>1</sup>H NMR (300 MHz, CD<sub>3</sub>OD) (ppm) δ: 7.44 (1H, d, *J* = 5.5, H2), 7.39 (1H, d, *J* = 8.5, H7), 7.31 (1H, d, *J* = 5.5, H3), 6.92 (1H, d, *J* = 8.6, H6), 4.91 (3H, s, CH<sub>3</sub>). <sup>13</sup>C NMR (75 MHz, CD<sub>3</sub>OD) (ppm) δ: 143.0, 137.0, 135.5, 132.9, 127.5, 120.4, 119.2, 117.4, 60.8. HR-MS, *m/z*: calcd. for C<sub>9</sub>H<sub>9</sub>NOS: 179.0405; found: 179.0399.

#### 4-Thiophenoxy-5-aminobenzothiophene (**5d**, Nu = PhS)

Dark oil. IR (acetone) (cm<sup>-1</sup>): 3494 (NH), 3004 (CH aro.), 1616 (C=C). <sup>1</sup>H NMR (300 MHz, CD<sub>3</sub>OD) (ppm) δ: 7.71 (1H, d, *J* = 8.6, H7), 7.46 (1H, d, *J* = 5.5, H2), 7.34 (1H, d, *J* = 5.5, H3), 7.17–7.12 (2H, m, H phenyl), 7.07–6.95



(4H, m, H6 and H phenyl).  $^{13}\text{C}$  NMR (75 MHz,  $\text{CD}_3\text{OD}$ ) (ppm)  $\delta$ : 149.4, 145.9, 138.2, 130.8, 129.9, 128.8, 127.2, 126.2, 125.8, 124.3, 115.8, 106.9. HR-MS,  $m/z$ : calcd. for  $\text{C}_{14}\text{H}_{11}\text{NS}_2$ : 257.0333; found: 257.0339.

#### 1-Methyl-3-thiophenoxy-5-aminoindole (9b)

Dark oil. IR ( $\text{CHCl}_3$ ) ( $\text{cm}^{-1}$ ): 3004 (CH aro.), 2974 (CH ali.), 1627 (C=C), 1493 ( $\text{CH}_3$ ), 1241 (C-N).  $^1\text{H}$  NMR (300 MHz,  $\text{CDCl}_3$ ) (ppm)  $\delta$ : 7.24 (1H, s, H2), 7.19 (1H, d,  $J = 8.6$ , H7), 7.15–7.09 (2H, m, H phenyl), 7.07–7.03 (3H, m, H phenyl), 6.93 (1H, d,  $J = 2.2$ , H4), 6.78 (1H, dd,  $J = 2.2$ ,  $J = 8.6$ , H6), 3.78 (3H, s,  $\text{CH}_3$ ).  $^{13}\text{C}$  NMR (75 MHz,  $\text{CDCl}_3$ ) (ppm)  $\delta$ : 140.5, 139.9, 135.4, 132.4, 131.0, 128.6, 125.4, 124.5, 113.2, 110.4, 104.3, 98.5. HR-MS,  $m/z$ : calcd. for  $\text{C}_{15}\text{H}_{14}\text{N}_2\text{S}$ : 254.0878; found: 254.0884.

#### Compound 10b (cyclopentadiene cycloadduct)

Dark oil. IR ( $\text{CHCl}_3$ ) ( $\text{cm}^{-1}$ ): 3431 (NH), 3359 (NH), 3001 (CH aro.), 2946 (CH ali.), 1506 (C=C), 1456 ( $\text{CH}_3$ ), 1256 (C-N).  $^1\text{H}$  NMR (300 MHz,  $\text{CDCl}_3$ ) (ppm)  $\delta$ : 6.92 (1H, d,  $J = 8.4$ , H7), 6.66 (1H, s, H2), 6.63 (1H, d,  $J = 8.4$ , H6), 5.95–5.92 (2H, m, H9 and H10), 3.81–3.77 (1H, m, H11 or H8), 3.71–3.69 (1H, m, H8 or H11), 3.65 (3H, s,  $\text{CH}_3$ ), 2.48–2.41 (1H, m, H12b), 1.99 (1H, d,  $J = 9.8$ , H12a).  $^{13}\text{C}$  NMR (75 MHz,  $\text{CDCl}_3$ ) (ppm)  $\delta$ : 130.8, 132.3, 130.5, 124.8, 121.1, 117.1, 113.9, 112.7, 108.2, 39.4, 38.7, 44.1, 32.7. HR-MS,  $m/z$ : calcd. for  $\text{C}_{14}\text{H}_{14}\text{N}_2$ : 210.1157; found: 210.1299.

#### Azo compound 11b

Yellow solid. mp = 196–198 °C. IR ( $\text{CHCl}_3$ ) ( $\text{cm}^{-1}$ ): 3007 (CH aro), 2946 (CH ali), 1613 (C=C), 1490 (C=C), 1449 ( $\text{CH}_3$ ), 1237 (C-N).  $^1\text{H}$  NMR (300 MHz,  $\text{CDCl}_3$ ) (ppm)  $\delta$ : 8.25 (2H, d,  $J = 1.7$ , H4 and H4'), 7.94 (2H, dd,  $J = 8.3$ ,  $J = 1.7$ , H6 and H6'), 7.40 (2H, d,  $J = 8.8$ , H7 and H7'), 7.11 (2H, d,  $J = 3.1$ , H2 and H2'), 6.64 (2H, d,  $J = 3.1$ , H3 and H3'), 3.85 (6H, s,  $\text{CH}_3$ ).  $^{13}\text{C}$  NMR (75 MHz,  $\text{CDCl}_3$ ) (ppm)  $\delta$ : 130.0, 118.3, 115.3, 109.5, 102.9, 147.1, 137.9, 128.5, 33.2. HR-MS,  $m/z$ : calcd. for  $\text{C}_{18}\text{H}_{16}\text{N}_4$ : 288.1375; found: 288.1371.

#### Azo compound 11c

Orange solid. mp = 160–162 °C. IR ( $\text{CHCl}_3$ ) ( $\text{cm}^{-1}$ ): 3020 (CH aro), 1454 (C=C), 1269 (C-O), 1095 (C-O).  $^1\text{H}$  NMR (300 MHz,  $\text{CDCl}_3$ ) (ppm)  $\delta$ : 8.09–7.93 (6H, m, H2, H2', H4, H4', H7 and H7'), 7.71 (2H, d,  $J = 8.8$ , H6 and H6'), 7.09 (2H, d,  $J = 2.2$ , H3 and H3').  $^{13}\text{C}$  NMR (75 MHz,  $\text{CDCl}_3$ ) (ppm)  $\delta$ : 146.9, 119.3, 117.2, 112.1, 107.8, 156.7, 149.4, 128.4. HR-MS,  $m/z$ : calcd. for  $\text{C}_{16}\text{H}_{10}\text{N}_2\text{O}_2$ : 262.0742; found: 262.0747.

#### Azo compound 11d

Orange solid. mp = 165–166 °C. IR ( $\text{CHCl}_3$ ) ( $\text{cm}^{-1}$ ): 3018 (CH aro), 1463 (C=C).  $^1\text{H}$  NMR (300 MHz,  $\text{CDCl}_3$ ) (ppm)  $\delta$ : 8.42 (2H, s, H4 and H4'), 8.10–7.95 (4H, m, H2, H2', H7 and H7'), 7.58–7.49 (4H, m, H3, H3', H6 and H6').  $^{13}\text{C}$  NMR (75 MHz,  $\text{CDCl}_3$ ) (ppm)  $\delta$ : 150.2, 140.2, 131.8, 129.7, 124.9, 123.0, 120.3, 117.4. HR-MS,  $m/z$ : calcd. for  $\text{C}_{16}\text{H}_{10}\text{N}_2\text{S}_2$ : 294.0285; found: 294.0290.

#### trans-2,3-Dimethoxy-2,3-dihydro-5-acetamidobenzofurane (trans 12)

Dark oil. IR ( $\text{CHCl}_3$ ) ( $\text{cm}^{-1}$ ): 3437 (NH), 3011 (CH aro.), 1684 (C=O), 1490 (C=C), 1230 (C-N), 1194 (C-O).  $^1\text{H}$  NMR (300 MHz,  $\text{CDCl}_3$ ) (ppm)  $\delta$ : 7.67 (1H, d,  $J = 2.3$ , H4), 7.25 (1H, dd,  $J = 2.3$ ,  $J = 8.6$ , H6), 7.08 (1H, broad peak, NH), 6.83 (1H, d,  $J = 8.6$ , H7), 5.41 (1H, s, H2), 4.64 (1H, s, H3), 3.54 (3H, s,  $\text{OCH}_3$ ), 3.43 (3H, s,  $\text{OCH}_3$ ), 2.15 (3H, s,  $\text{CH}_3$ ).  $^{13}\text{C}$  NMR (75 MHz,  $\text{CDCl}_3$ ) (ppm)  $\delta$ : 168.3, 156.5, 144.8, 131.5, 123.3, 119.2, 111.2, 110.8, 85.1, 56.4, 56.2, 24.4. HR-MS,  $m/z$ : calcd. for  $\text{C}_{12}\text{H}_{15}\text{NO}_4$ : 237.1001; found: 237.1005.

#### cis-2,3-Dimethoxy-2,3-dihydro-5-acetamidobenzofurane (cis 12)

Dark oil. IR ( $\text{CHCl}_3$ ) ( $\text{cm}^{-1}$ ): 3437 (NH), 3009 (CH aro.), 1685 (C=O), 1490 (C=C), 1210 (C-N), 1202 (C-O).  $^1\text{H}$  NMR (300 MHz,  $\text{CDCl}_3$ ) (ppm)  $\delta$ : 7.55 (1H, d,  $J = 2.2$ , H4), 7.00 (1H, dd,  $J = 2.2$ ,  $J = 8.5$ , H6), 7.12 (1H, broad peak, NH), 6.77 (1H, d,  $J = 8.5$ , H7), 5.48 (1H, d,  $J = 5.2$ , H2), 4.87 (1H, d,  $J = 5.2$ , H3), 3.63 (3H, s,  $\text{OCH}_3$ ), 3.52 (3H, s,  $\text{OCH}_3$ ), 2.14 (3H, s,  $\text{CH}_3$ ).  $^{13}\text{C}$  NMR (75 MHz,  $\text{CDCl}_3$ ) (ppm)  $\delta$ : 168.2, 154.1, 131.5, 126.0, 123.1, 118.9, 110.5, 106.8, 79.9, 58.2, 57.2, 29.7. HR-MS,  $m/z$ : calcd. for  $\text{C}_{12}\text{H}_{15}\text{NO}_4$ : 237.1001; found: 237.1003.

#### Acetylated compound 15 (acetylated cycloaddition product)

Dark oil. IR ( $\text{CHCl}_3$ ) ( $\text{cm}^{-1}$ ): 3001 (CH aro.), 1654 (C=O), 1468 ( $\text{CH}_2$ ), 1437 ( $\text{CH}_3$ ).  $^1\text{H}$  NMR (300 MHz,  $\text{CDCl}_3$ ) (ppm)  $\delta$ : 8.25 (1H, m, NH), 7.59 (1H, d,  $J = 2.3$ , H2), 7.30 (1H, d,  $J = 9.3$ , H4), 6.82 (1H, d,  $J = 2.3$ , H3), 5.82 (1H, dd,  $J = 2.4$ ,  $J = 5.5$ , H6), 5.16 (1H, m, H7), 3.79 (2H, m, H5 and H8), 2.45 (3H, s,  $\text{CH}_3$ ), 2.30 (2H, m, H9).  $^{13}\text{C}$  NMR (75 MHz,  $\text{CDCl}_3$ ) (ppm)  $\delta$ : 170.3, 150.7, 130.5, 125.2, 124.3, 116.1, 145.2, 139.3, 120.6, 108.9, 104.8, 60.2, 41.0, 37.3, 25.3. HR-MS,  $m/z$ : calcd. for  $\text{C}_{15}\text{H}_{13}\text{NO}_2$ : 239.0946; found: 239.0951.

## Acknowledgements

Financial support from the Natural Sciences and Engineering Research Council of Canada (NSERC) and the Fonds FCAR du Québec is gratefully acknowledged.

## References

1. J.M. Chapuzet, R. Labrecque, M. Lavoie, E. Martel, and J. Lessard. *J. Chim. Phys.* **93**, 601 (1996).
2. I. Marcotte, M. Lavoie, Y. Dory, J.M. Chapuzet, and J. Lessard. *Acta Chem. Scand.* **53**, 849 (1999).
3. H. Lund and M.M. Baizer. *In Organic electrochemistry: An introduction and a guide. Edited by M.M. Baizer and H. Lund.* Marcel Dekker, New York. 1990. pp. 412–419.
4. K.N. Houk and L.J. Luskus. *J. Org. Chem.* **38**, 3836 (1972).
5. I. Flemming. *Frontier orbitals and organic chemical reactions.* Wiley, London. 1976.
6. N. Trong Anh. *Orbitales frontières: Manuel pratique.* InterEditions and CNRS Éditions, Paris. 1995.
7. M.J.S. Dewar, E.G. Zoebish, E.F. Healy, and J.J.P. Stewart. *J. Am. Chem. Soc.* **107**, 3902 (1985).
8. J.J.P. Stewart. *J. Comput. Chem.* **10**, 209 (1989); **10**, 221 (1989).



9. G. Bartoli, M. Bosco, R. Dalpozzo, and P.E. Todesco. *J. Org. Chem.* **51**, 3694 (1986).
10. G. Lamotte, P. Demerseman, and R. Royer. *J. Heterocyclic Chem.* **15**, 1373 (1978).
11. F.G. Bordwell and C.J. Albisetti. *J. Am. Chem. Soc.* **70**, 1948 (1955).
12. T. Suzuki, T. Horayuchi, and T. Shimizu. *Bull. Chem. Soc. Jpn.* **56**, 2726 (1983).
13. R.A. Zambias and M.L. Hammond. *Synth. Comm.* **21**, 959 (1991).
14. J.M. Lalancette and J.R Brindle. *Can. J. Chem.* **49**, 2990 (1971).
15. J.M. Lalancette, A. Frêche, and R. Monteux. *Can. J. Chem.* **46**, 2754 (1968).



# Orthogonene: A computational study of a strongly twisted alkene

E. Lewars

**Abstract:** The strongly twisted (calculated dihedral angle  $84^\circ$ ) alkene orthogonene (tetracyclo[8,2,2,0<sup>2,7</sup>,0<sup>3,10</sup>]tetradecene-2(3)) was studied at the DFT (B3LYP/6-31G\*) and ab initio (HF/6-31G\* and MP2(fc)/6-31G\*) levels with a view to exploring the question of how realistic a synthetic objective it is, particularly in view of the fact that an attempt was made to synthesize it. Orthogonene is a relative minimum on the potential energy surface at the B3LYP/6-31G\* and MP2(fc)/6-31G\* levels, but is predicted to have a very low barrier ( $1.2 \text{ kJ mol}^{-1}$  from the B3LYP calculations) to rearrangement by a 1,2-carbon shift to a carbene, which in turn isomerizes to a cyclopropane and (or) an alkene (the carbene is perhaps not a stationary point on the potential energy surface). Thus, very likely orthogonene could be observed only at temperatures approaching absolute zero, if at all.

**Key words:** orthogonene, tetracyclo[8,2,2,0<sup>2,7</sup>,0<sup>3,10</sup>]tetradecene-2(3), twisted double bond, orthogonal double bond, carbene-strained alkene isomerization, ab initio, DFT.

**Résumé :** Faisant appel à des calculs théoriques aux niveaux DFT (B3LYP/6-31G\*) et ab initio (HF/6-31G\* et MP2(fc)/6-31G\*), on a étudié l'alcène orthogonène {tétracyclo[8.2.2.0<sup>2,7</sup>,0<sup>3,10</sup>]tétradéc-2(3)-ène} qui est fortement déformé dans le but d'évaluer s'il est réaliste d'espérer réaliser la synthèse de ce composé, surtout en tenant compte du fait qu'un tel essai a déjà été tenté. L'orthogonène est un minimum relatif sur la surface d'énergie potentielle aux niveaux DFT (B3LYP/6-31G\*) et MP2(fc)/6-31G\*, mais les calculs B3LYP prédisent que la barrière est très faible ( $1,2 \text{ kJ mol}^{-1}$ ) pour son réarrangement en carbène (par le biais d'un déplacement 1,2 de carbone) qui subit une isomérisation ultérieure en cyclopropane et/ou en un alcène (le carbène n'est peut-être pas un point stationnaire sur la surface d'énergie potentielle). Sur cette base, on peut en conclure que si cela peut se faire, l'orthogonène ne pourrait vraisemblablement être observé qu'à des températures s'approchant du zéro absolu.

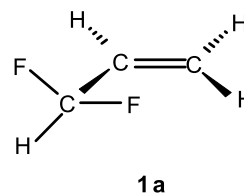
**Mots clés :** orthogonène, tétracyclo[8.2.2.0<sup>2,7</sup>,0<sup>3,10</sup>]tétradéc-2(3)-ène, double liaison déformée, double liaison orthogonale, isomérisation carbène-alcène tendu, ab initio, DFT.

[Traduit par la Rédaction]

## Introduction

One cornerstone of the structural theory of organic chemistry is that "the carbon—carbon double bond is flat", i.e., that the two carbons and the four attached groups lie in, or nearly in, a plane. Of course, when the molecule as a whole lacks a symmetry plane strict planarity is not expected. In  $\text{CHF}_2\text{—CH=CH}_2$ , for instance, in conformer **1a**, an H vs. an F breaks the symmetry of the two faces of the double bond; the calculated (B3LYP/6-31G\*) double bond H—C=C—H dihedral angle is  $0.4^\circ$ . More interesting are cases in which nonplanarity, although not dictated by lack of symmetry nor imposed by steric conflict (1), is nonetheless found. Wagner et al. (2) showed, with ab initio calculations, that some strained alkenes, like bicyclo-1(3)butene, should be nonplanar (we find from B3LYP/6-31G\* calculations an angle of  $44^\circ$  between the two CCC planes). This nonplanarity was

discussed in terms of orbital overlap (2) and was analyzed in detail by Spangett-Larson and Gleiter (3). Pyramidalization of double bond carbons, which is what nonplanarity in bicyclic alkene systems amounts to, is a well-recognized phenomenon (4–7).



Particularly fascinating would be a molecule designed to impose on a carbon—carbon double bond a twist of  $90^\circ$ ; in the context of the  $\sigma/\pi$  model, this represents loss of  $p/p$  atomic orbital overlap (the  $\sigma/\pi$  model is not correct in any absolute sense, but it will be convenient to employ it here (8, 9)). Such a molecule was conceived almost two decades ago: orthogonene, **1** (Scheme 1), was explored both experimentally (10) and with semiempirical calculations (11) by Jeffrey and Maier (the synthesis failed some steps short of its goal). Concurring with these workers that this is an "exciting molecule" (11), I report here the results of a reasonably high-level ab initio and DFT study.

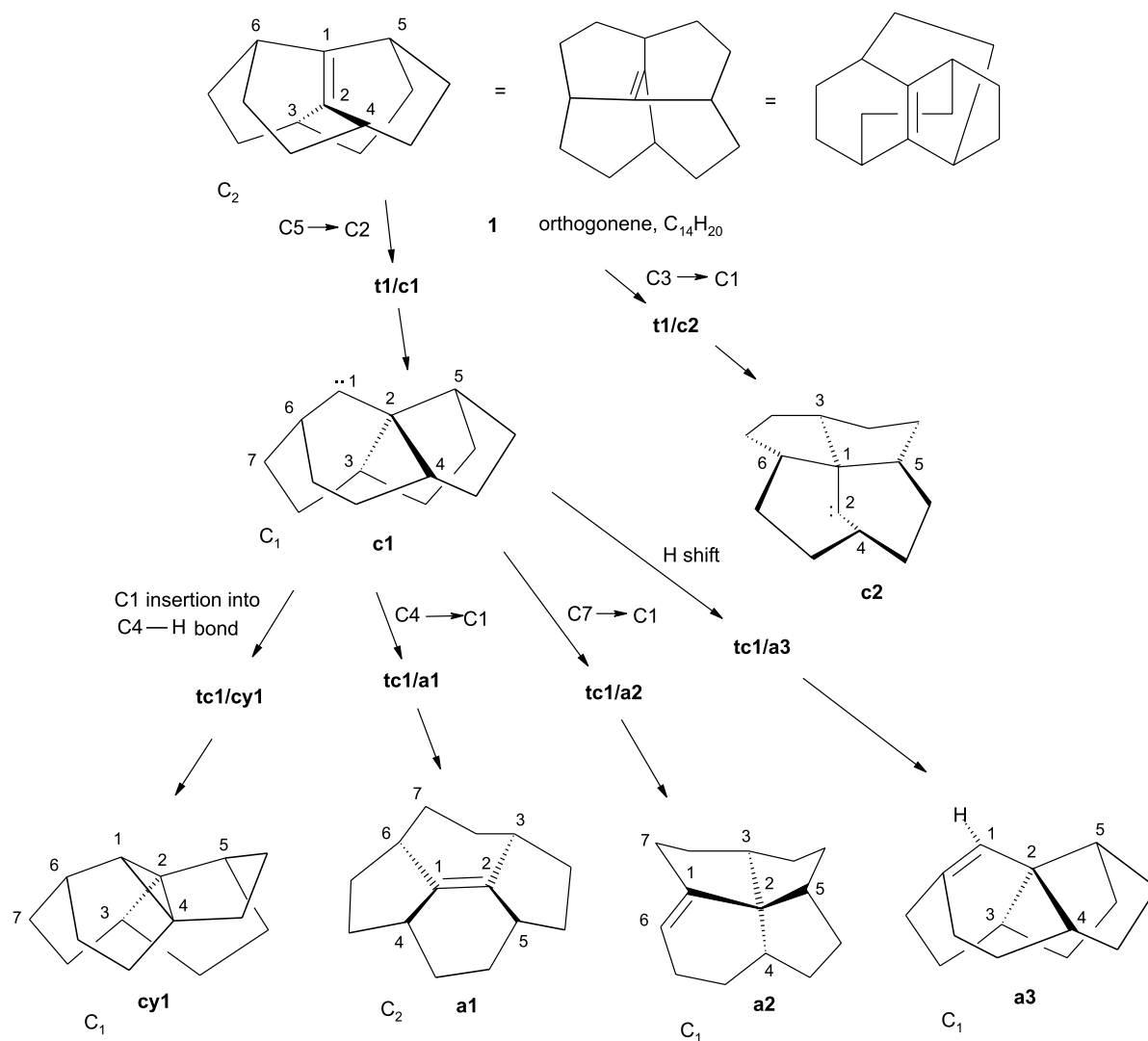
Received 8 May 2003. Published on the NRC Research Press Web site at <http://canjchem.nrc.ca> on 9 October 2003.

**E. Lewars.**<sup>1</sup> Department of Chemistry, Trent University, Peterborough, ON K9J 7B8, Canada. (e-mail: [elewars@trentu.ca](mailto:elewars@trentu.ca)).

<sup>1</sup>Adjunct Professor, Department of Chemistry, Queen's University, Kingston, ON K7L 3N6, Canada.



**Scheme 1.** Rearrangement pathways of orthogonene, **1**. The symmetry of species that were stationary points at the B3LYP/6-31G\* and MP2(fc)/6-31G\* levels ( $C_2$  and  $C_1$ ) is shown; the transition states had  $C_1$  symmetry (at the HF/6-31G\* level **1** was a TS with  $C_2$  symmetry).



## Computational methods

Calculations were done with Gaussian 98 for Windows (G98W) (12) and visualized with GaussView 2.1 for Windows (13) on a 933 MHz Pentium 3 or a 1.5 GHz Pentium 4 computer equipped with Microsoft Windows NT 4.00, 1 GB of memory, and 15 360 MB of scratch space. Ab initio (14) HF and DFT (15) B3LYP calculations were full geometry optimizations followed by frequency calculations (16), except for the calculation of vertical ionization energies, where a single-point calculation on the radical cation at the geometry of the neutral was done and zero-point energies (ZPEs) were not used. For calculating relative MP2 energies, energies from MP2(fc)/6-31G\* optimizations were corrected with B3LYP/6-31G\* frequencies because of the long times needed for calculating MP2/6-31G\* frequencies on molecules of this size; the similarity of the MP2 and B3LYP ge-

ometries left little doubt that the former structures were relative minima (no attempt was made to locate transition states at the MP2 level). For orthogonene, MP2(fc)/6-31G\* frequencies were calculated to confirm the curvature of the MP2(fc)/6-31G\* potential energy surface at that stationary point (indeed a relative minimum). ZPEs from the frequency jobs were multiplied by the appropriate correction factors (0.9135 for HF/6-31G\* and 0.9806 for B3LYP/6-31G\*) recommended by Scott and Radom (17) and were added to the raw energies to give the ZPE-corrected energies. The two species connected by a transition state (a stationary point with one imaginary frequency) were identified by animation of the imaginary frequency with GaussView or, in ambiguous cases, by following the intrinsic reaction coordinate (IRC) well toward reactant and product (18). Absolute total energies, ZPEs, and ZPE-corrected energies are given in the supplementary material.<sup>2</sup>

<sup>2</sup>Supplementary data may be purchased from the Depository of Unpublished Data, Document Delivery, CISTI, National Research Council Canada, Ottawa, ON K1A 0S2, Canada ([http://www.nrc.ca/cisti/irm/unpub\\_e.shtml](http://www.nrc.ca/cisti/irm/unpub_e.shtml) for information on ordering electronically).



**Table 1.** Relative energies (kJ mol<sup>-1</sup>) of species in Scheme 1.

Species	HF/6-31G*	B3LYP/6-31G*	MP2(fc)/6-31G*
<b>1</b>	0	0	0
<b>c1</b>	-796.5	-602.3	Not a stationary point at this level: goes toward <b>cy1</b>
<b>c2</b>	-602.6	Not a stationary point at this level: goes toward <b>a1</b>	Not a stationary point at this level: goes toward <b>cy1</b>
<b>cy1</b>	-1057.7	-885.1	-883.4
<b>a1</b>	-1127.7	-953.2	-925.9
<b>a2</b>	-854.2	-713.5	-695.4
<b>a3</b>	-797.2	-676.1	-666.4
<b>t1-c1</b>	0 ( <b>1</b> is a TS connecting two <b>c1</b> enantiomers)	+1.23	
<b>t1-c2</b>	<b>1</b> is a TS connecting two <b>c1</b> enantiomers	<b>c2</b> is not a stationary point at this level ( <b>c2</b> goes toward <b>a1</b> )	
<b>tc1-cy1</b>	-757.4	-601.4	
<b>tc1-a1</b>	-738.6	-584.5	
<b>tc1-a2</b>	-645.2	-509.6	
<b>tc1-a3</b>	-489.3	-387.8	

Note: The location of transition states at the MP2(fc)/6-31G\* level was not attempted.

**Table 2.** Activation energies (kJ mol<sup>-1</sup>) for reactions of orthogonene **1** and the carbene **c1** (Scheme 1) based on relative energies in Table 1.

Reaction	HF/6-31G*	B3LYP/6-31G*	MP2(fc)/6-31G*
<b>1</b> → <b>c1</b>	0 ( <b>1</b> is a TS connecting two <b>c1</b> enantiomers)	1.2	<b>c1</b> is not a stationary point at this level: goes toward <b>cy1</b>
<b>1</b> → <b>c2</b>	<b>1</b> is a TS, not a relative minimum, at this level	<b>c2</b> is not a stationary point at this level: goes toward <b>a1</b>	<b>c2</b> is not a stationary point at this level: goes toward <b>a1</b>
<b>c1</b> → <b>cy1</b>	39.1	1.6	
<b>c1</b> → <b>a1</b>	57.9	17.8	
<b>c1</b> → <b>a2</b>	151.3	92.7	
<b>c1</b> → <b>a3</b>	307.2	214.5	

Note: The location of transition states at the MP2(fc)/6-31G\* level was not attempted.

## Results and discussion

### Preliminary survey

Intuitively (or from a general knowledge of the chemistry of strained alkenes), one suspects that the likeliest reactions of orthogonene will be isomerization to a carbene. In **1**, shift (migration) of a β-C — C5 moving to C2 (Scheme 1; the numbering pattern here is for convenience and does not reflect a systematic name) — would give the carbene **c1**, and the shift of C3 to C1 would give the carbene **c2**. Such interconversion of carbenes and strained alkenes is well-established (4, 5, 19) and should of course proceed in the direction that releases strain, a consideration that clearly points to conversion of **1** to carbenes. As a heuristic, at least, such alkene → carbene reactions can be viewed as migration of a carbon to the positive end of a double bond with <sup>+</sup>C—C<sup>-</sup> character (C<sup>+</sup> and C<sup>-</sup> singly-bonded). We return later to the question of polarization of the orthogonene formal double bond.

Focusing on the fate of **c1**, which calculations indicate (below) is much more likely than **c2** to be the favored proximate product from **1**, one envisages the following four possibilities:

(1) Insertion of the carbene carbon into a β-C C—H bond (this can also be viewed as an H atom shift) forming a cyclopropane; **c1** lacks a symmetry plane (it belongs to the C<sub>1</sub> symmetry group) and C4 represents the closest β-C and has the closest C—H bond (C1—C4 = 2.185 Å, C1—H = 2.051 Å). These two atoms are thus within bonding distance of C1. The intramolecular insertion of a carbene into a C—H bond on a β-C has long been known (20). This reaction would generate the cyclopropane **cy1**.

(2) Shift of C4 to C1, giving the alkene **a1**. This is a carbene–alkene interconversion of the kind relating **1** and **c1** (and **1** and **c2**).

(3) Shift of C7 to C1 giving the alkene **a2**. This is another carbene–alkene interconversion.

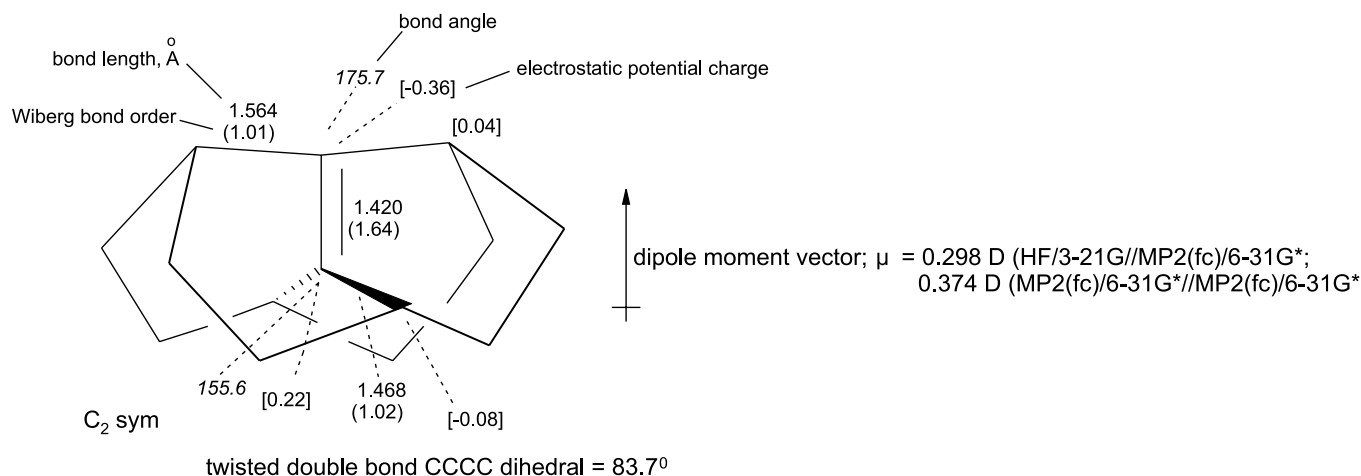
(4) A 1,2-H shift giving the alkene **a3**. Such shifts are the best known and normally the most facile kind of intramolecular reaction of carbenes (21).

### Orthogonene to carbenes **c1** and **c2**

The relative energies, where available, of **1**, **c1**, **c2**, **cy1**, **a1**, **a2**, **a3**, and the transition states (TS) (**t1-c1**, etc.) connecting various species are given in Table 1, and the activation energies based on these relative energies are given in Table 2. The most salient indication from these calculations is that orthogonene is restrained from isomerization by a



**Fig. 1.** Selected parameters of MP2(fc)/6-31G\* geometry, electrostatic potential charges (HF/3-21G//MP2(fc)/6-31G\*), and Wiberg bond orders (HF/3-21G//MP2(fc)/6-31G\*).



barrier that is either nonexistent (at the HF/6-31G\* level it is a transition state linking enantiomeric **c1** molecules) or tiny (at the B3LYP/6-31G\* level the barrier to isomerization to **c1** is a mere 1.2 kJ mol<sup>-1</sup>). The carbene **c1** is itself calculated to readily suffer insertion into the proximate C—H bond (see above), forming the cyclopropane **cy1**, the HF and B3LYP activation energies for this process being 39.1 and 1.6 kJ mol<sup>-1</sup>, respectively. The likely situation is either (1) **1** is a real molecule with a very low barrier to isomerization to carbene **c1** or perhaps directly to the cyclopropane **cy1** (higher-level calculations may indicate that **c1** is not a stationary point), or (2) **1** is a TS linking enantiomeric **c1** molecules or perhaps linking enantiomeric **cy1** molecules.

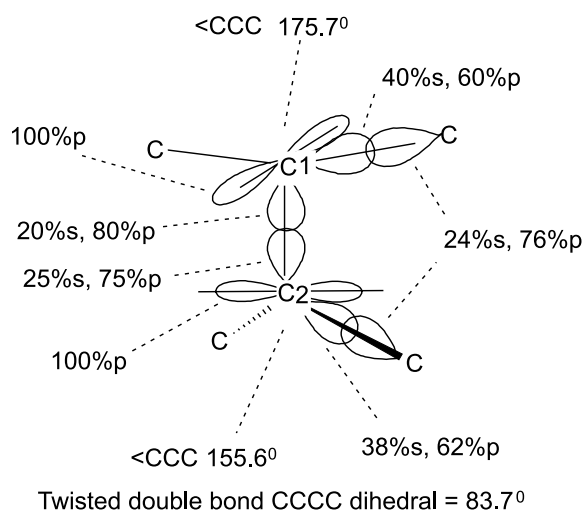
Concerning the carbene **c2**, the product of the alternative carbon shift in **1** (C3 → C1 instead of C5 → C2) on the HF/6-31G\* potential energy surface **1** is merely a transition state leading to **c1** enantiomers, while on the B3LYP/6-31G\* surface, the **1** → **c1** barrier is exceedingly low (1.2 kJ mol<sup>-1</sup>) and **c2** is not a stationary point: attempts to optimize it from lower-level geometries lead to the alkene **a1**.

Besides the cyclopropane **cy1**, the alkenes **a1**, **a2**, and **a3** can reasonably be postulated as products of the carbene **c1**. From the data in Table 2, the only product from **c1** that might compete with **cy1** is the alkene **a1** (barriers to **a1**, **a2**, **a3**, HF/B3LYP: 57.9/17.8; 151.3/92.7; 307.2/214.5 kJ mol<sup>-1</sup>). Note the good agreement between relative energies calculated at the B3LYP and MP2 levels for **1**, the cyclopropane, and the three alkenes (Table 1). It is known that correlated-level barriers are lower than those calculated at the HF level and closer to experimental values, although the trends predicted by HF-level calculations are usually reliable (22). From these energetic relationships and the curvature of the potential energy surface (viz., minima, transition states, and non-stationary points) indicated by these calculations we may conclude that attempts to synthesize orthogonene will lead to the formation of the cyclopropane **cy1** and possibly the alkene **a1**, but the possibility of detection of **1** and (or) **c1** under matrix-isolation (23) conditions cannot be ruled out.

### Structure and electronic properties of orthogonene

Tacitly assuming **1** is actually a relative minimum on the potential energy surface (i.e., that it is a real molecule), a

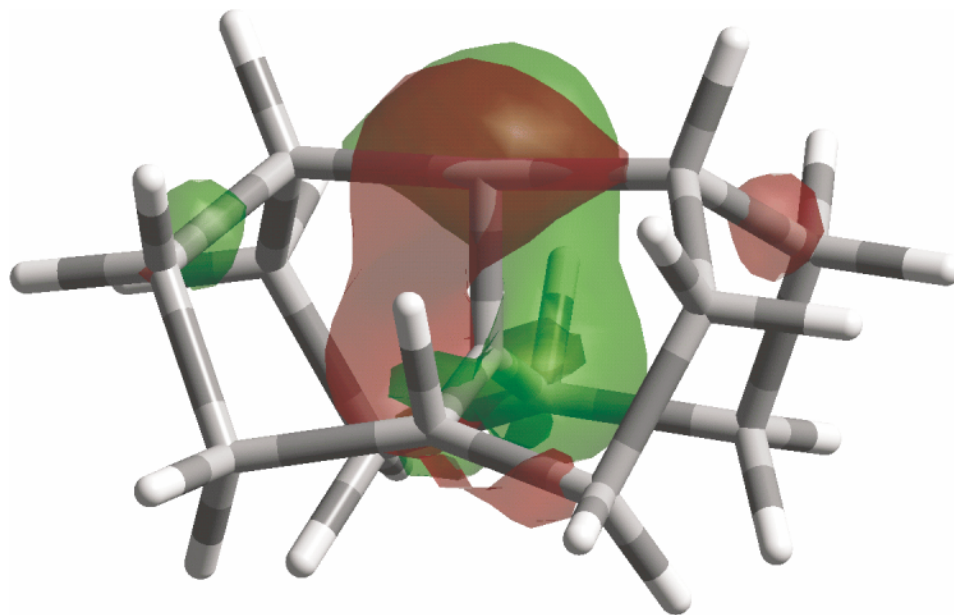
**Fig. 2.** Orbital hybridizations associated with the orthogonene double bond, from Weinhold natural population analysis (STO-3G//MP2(fc)/6-31G\*).



brief look at its “static” properties is warranted. Selected values for geometry, bond orders, and electrostatic potential atomic charges (24) and the dipole moment are shown in Fig. 1. The length (MP2(fc)/6-31G\*) of the formal double bond (1.420 Å) is close to the average of the standard C—C single and double bond lengths: 1/2 (1.54 + 1.33) Å = 1.435 Å. Its Wiberg bond order of 1.64 (from a Weinhold natural population analysis (NPA) (25)) is only a little more than the value (1.5) one would intuitively assign to a “one-and-a-half” bond. In comparison, tetramethylethene at the same computational levels has a C=C double bond length of 1.352 Å and a bond order of 1.85 (this molecule has a calculated C-C-C-C dihedral angle of 2.6°). A dramatic indication of the weakness of the double bond of **1** is its calculated stretching frequency: 1348 cm<sup>-1</sup>, cf. 1765 cm<sup>-1</sup> for tetramethylethene. These are MP2(fc)/6-31G\* uncorrected frequencies; the frequency- (not the ZPE-) correction factor of Scott and Radom (17), 0.9434, predicts experimental frequencies of 1272 and 1665 cm<sup>-1</sup>. The calculated formal double bond C=C frequency of **1** is actually somewhat closer to



**Fig. 3.** The HOMO and LUMO (the two are visually indistinguishable) of orthogonene (HF/3-21G//MP2(fc)/6-31G\*).



a calculated C—C *single* bond stretch (e.g.,  $1050\text{ cm}^{-1}$  for  $\text{CH}_3\text{—CH}_3$ , MP2(fc)/6-31G\*) than to a normal double bond stretch like that in tetramethylethene. This stretch in **1** has a calculated relative intensity (the strongest vibration is a CH stretch) of 8%, but the corresponding vibration in tetramethylethene is undetectable in the IR (26) because of symmetry. The electrostatic potential charges indicate a modest polarization of this bond, in keeping with its modest IR intensity.

Figure 2 shows the NPA hybridization for the bonding orbitals associated with the twisted double bond. C1 and C2 both utilize ca. 40% *s* : 60% *p* hybrid orbitals to bond to their adjacent carbons, which overlap these with normal  $sp^3$  orbitals (ca. 25% *s* : 75% *p*). The  $\sigma$  bond of the formal C=C double bond is approximately  $sp^3\text{—}sp^3$  (20% *s* : 80% *p* — 25% *s* : 75% *p*) and the (presumably weak)  $\pi$  bond results from twisted *p*:*p* overlap. The very wide ( $155.6^\circ$ ) and extraordinarily wide ( $175.7^\circ$ ) C—C—C angles at the ends of the double bond can be rationalized in terms of the high *s* character of the *sp* hybrids (ca. 40% *s* : 60% *p*, approaching the 50% *s* : 50% *p* character of the linearly disposed *sp* hybrids of alkynes) used to bond to the neighboring carbons, but it is unclear why one angle is so much bigger than the other; a referee suggested that the dissimilar angles may indicate it is energetically favorable to distort one carbon more to reduce strain at the other.

As a C=C double bond is twisted toward  $90^\circ$ , the HOMO and LUMO should tend to become degenerate atomic *p* orbitals, and the closed-shell molecule should approach singlet diradical status (this kind of twisting has been analyzed in detail for ethene and its C—Si and Si—Si analogues (27)). Since the single-determinant molecular orbital wavefunction usually used for normal closed-shell molecules is based on filling molecular orbitals pairwise (28), this approach may not be valid for strongly twisted double bonds (ref. 27 used the GVB method). One test of the validity of normal DFT calculations on such systems is to compare the results of unrestricted and restricted DFT calculations (4, 29). Restricted

and unrestricted B3LYP/6-31G\* optimizations + frequencies on **1** gave identical results, and the spin contamination parameter  $\langle S^2 \rangle$  before and after spin annihilation was 0.0000. The appearance of the HOMO and LUMO, visualized with GaussView (HF/3-21G wavefunction from the MP2 geometry), was identical (Fig. 3); these orbitals look as one would expect from twisting a normal alkene HOMO. The HOMO : LUMO energies (MP2/6-31G\*/MP2/6-31G\*) are  $-4.80 : 3.13\text{ eV}$ , giving a frontier orbital gap of  $7.93\text{ eV}$ . From Koopmans' theorem (30) the HOMO gives an approximate vertical ionization energy (IE) for **1** of  $4.80\text{ eV}$ . The energy difference between neutral **1** and the radical cation at the geometry of the neutral (no ZPEs used) gives a vertical IE of  $5.36\text{ eV}$  (MP2(fc)/6-31G\*/MP2/6-31G\*). For tetramethylethene the HOMO : LUMO energies are  $-8.56 : 5.18\text{ eV}$ , giving a frontier orbital gap of  $13.74\text{ eV}$ , much bigger than for **1**, as expected. For tetramethylethene the Koopmans and energy-difference IEs are  $8.56$  and  $8.24\text{ eV}$ ; experimental values of ca.  $8.3\text{--}8.8\text{ eV}$  are typical of alkenes (31). Normally, Koopmans' theorem values are about  $1.0\text{--}1.5\text{ eV}$  too high, and MP2/6-31G\*  $\Delta E$  values tend to be within ca.  $0.4\text{ eV}$  (32). For the exotic **1** the Koopmans IE is, however, lower than the energy-difference one. Nevertheless, we can be confident that the IE of **1** (assuming it to be a "real molecule") is ca.  $5\text{ eV}$ . This is a remarkably low IE for an alkene; it is essentially the same as the value of  $4.6\text{ eV}$  calculated by Radom and Rasmussen for the hypothetical dimethanospiro-octaplane, a cycloalkane predicted to have a planar carbon atom, and as these workers point out for their molecule, possibly lower than the IEs of lithium and sodium ( $5.39$  and  $5.14\text{ eV}$ ) (33). In both hydrocarbons this anomaly arises, of course, from the decoupling of normally bonding orbitals: the HOMO of dimethanospiro-octaplane is essentially a carbon *p* orbital, and that of orthogonene has high *p* orbital character by virtue of the weak interaction between the nearly orthogonal carbon *p* orbitals (Figs. 2 and 3).

These calculations apply to the singlet energy surface; our main purpose here was to investigate the stability and fate of



**1** understood as a twisted singlet alkene. However, the unusual double bond of **1** raises the possibility that the normal situation is reversed, and the triplet is the lower-energy state. Comparing the energies (ZPE-corrected) of fully-optimized geometries at different levels we find the following:  $E(\text{triplet}) - E(\text{singlet}) = +221.9 \text{ kJ mol}^{-1}$  (HF/6-31G\*),  $-72.1 \text{ kJ mol}^{-1}$  (UB3LYP/6-31G\*),  $-4.8 \text{ kJ mol}^{-1}$  (UMP2(fc)/6-31G\*). Thus at the noncorrelated level the triplet is much the higher-energy state, but with UB3LYP the triplet is moderately lower, and with UMP2 it is very marginally lower than the singlet. These results suggest only that the two states may not differ widely in energy; they leave open the possibility that attempts to synthesize **1** by some route involving entry to the singlet potential energy surface will lead to triplet **1** by intersystem crossing.

## Conclusions

Orthogonene was calculated to be at best highly unstable toward isomerization to a carbene, the HF/6-31G\* barrier being zero and the B3LYP/6-31G\* barrier  $1.2 \text{ kJ mol}^{-1}$ . The carbene itself may in fact not be a stationary point and orthogonene may go directly to a cyclopropane and (or) to an alkene (these latter two arise, formally at least, by carbene insertion into a nearby C—H bond or by 1,2-carbon shift). We note a referee's suggestion that it may be possible to find substituents to stabilize orthogonene.

## References

- (a) Y. Yang, J.L. Petersen, and K.K. Wang. *J. Org. Chem.* **68**, 5832 (2003); (b) E. Mollins, C. Miravittalles, E. Espinosa, and M. Ballester. *J. Org. Chem.* **67**, 7175 (2002); (c) T. Okazaki, K. Ogawa, T. Kitagawa, and K. Takeuchi. *J. Org. Chem.* **67**, 5981 (2002); (d) T.W. Bell, V.J. Catalano, M.G.B. Drew, and D.J. Phillips. *Chem. Eur. J.* **8**, 5001 (2002); (e) K. Beck, R. Gompper, K. Polborn, and H.-U. Wagner. *Angew. Chem. Int. Ed. Engl.* **32**, 1352 (1993).
- H.-U. Wagner, G. Szeimies, J. Chandrasekhar, P.v.R. Schleyer, J.A. Pople, and J.S. Binkley. *J. Am. Chem. Soc.* **100**, 1210 (1978).
- J. Spangett-Larsen and R. Gleiter. *Tetrahedron*, **39**, 3345 (1983).
- T. Ströter and G. Szeimies. *J. Am. Chem. Soc.* **121**, 7476 (1999).
- T. Ströter, O. Jarosch, and G. Szeimies. *Chem. Eur. J.* **5**, 1422 (1999).
- S. Glück-Walther, O. Jarosch, and G. Szeimies. *Eur. J. Org. Chem.* 493 (1998).
- G. Szeimies. *J. Prakt. Chem.* **340**, 11 (1998).
- P.B. Karadakov, J. Gerratt, D.L. Cooper, and M. Raimondi. *J. Am. Chem. Soc.* **115**, 6863 (1993).
- P.A. Schultz and R.P. Messmer. *J. Am. Chem. Soc.* **115**, 10 925 (1993).
- D.A. Jeffrey. I. Synthetic approaches toward orthogonene. II. Computational studies of simple fulvenes and fulvalenes. Ph.D. dissertation. University of California, Berkeley, 1985. Univ. Microfilms Int., order No. DA8524999. Diss. Abstr. Int. B, 3054, **46**(9) (1986).
- D.A. Jeffrey and W.F. Maier. *Tetrahedron*, **40**, 2799 (1984).
- R.E. Stratman, J.C. Burant, S. Dapprich, J.M. Millam, A.D. Daniels, K.N. Kudin, M.C. Strain, O. Farkas, J. Tomasi, V. Barone, M. Cossi, R. Cammi, B. Mennucci, C. Pomelli, C. Adamo, S. Clifford, J. Ochterski, G.A. Petersson, P.Y. Ayala, Q. Cui, K. Morokuma, D.K. Malick, A.D. Rabuck, K. Raghavachari, J.B. Foresman, J. Cioslowski, J.V. Ortiz, A.G. Baboul, B.B. Stefanov, G.Liu, A. Liashenko, P. Piskorz, I. Komaromi, R. Gomperts, R.L. Martin, D.J. Fox, T. Keith, M.A. Al-Laham, B. Johnson, W. Chen, M.W. Wong, J.L. Andres, C. Gonzalez, M. Head-Gordon, E.S. Replogle, and J.A. Pople. Gaussian 98 [computer program]. Revision a.9. Gaussian, Inc., Pittsburgh, PA. 1998.
- GaussView 2.1 [computer program]. Gaussian Inc., Carnegie Office Park, Bldg. 6, Pittsburgh, PA 15106, U.S.A. 2000.
- (a) W.J. Hehre, L. Radom, P.v.R. Schleyer and J.A. Pople. *Ab initio molecular orbital theory*. Wiley-Interscience, New York. 1986; (b) J.B. Foresman and A. Frisch. *Exploring chemistry with electronic structure methods*. 2nd ed. Gaussian Inc., Pittsburgh, U.S.A. 1996.
- (a) G.N. Merrill, S. Gronert, and S.R. Kass. *J. Phys. Chem. A*, **101**, 208 (1997); (b) W. Kohn, A.D. Becke, and R.G. Parr. *J. Phys. Chem.* **100**, 12 974 (1996); (c) L.J. Bartolotti and K. Flurchick. *Rev. Comput. Chem.* **7**, 187 (1996); (d) A. St-Amant. *Rev. Comput. Chem.* **7**, 217 (1996).
- J.B. Foresman and A. Frisch. *Exploring chemistry with electronic structure methods*. 2nd ed. Gaussian Inc., Pittsburgh, U.S.A. 1996. Chap 4.
- A.P. Scott and L. Radom. *J. Phys. Chem.* **100**, 16 502 (1996).
- J.B. Foresman and A. Frisch. *Exploring chemistry with electronic structure methods*. 2nd ed. Gaussian Inc., Pittsburgh, U.S.A. 1996. Chap 8.
- L. Friedman and L. Shechter. *J. Am. Chem. Soc.* **82**, 1002 (1960).
- (a) A. Padwa and A.E. Krumpe. *Tetrahedron*, **48**, 5385 (1992); (b) S.D. Burke and P.A. Grieco. *Org. React.* **26**, 361 (1979); (c) L. Friedman and J.G. Berger. *J. Am. Chem. Soc.* **83**, 492 500 (1961); (d) W. Kirmse and W. von E. Doering. *Tetrahedron*, **11**, 266 (1960).
- (a) J.A. LaVilla and J.L. Goodman. *J. Am. Chem. Soc.* **111**, 6877 (1989); (b) G. Ho, K. Jespersion, R.A. Moss, S. Shen, R.S. Sheridan, and R. Subramanian. *J. Am. Chem. Soc.* **111**, 6875 (1989); (c) J.E. Jackson, N. Soundararajan, W. White, M.T.H. Liu, R. Bonneau, and M.S. Platz. *J. Am. Chem. Soc.* **111**, 6874 (1989).
- I.N. Levine. *Quantum chemistry*. 5th ed. Prentice Hall, Upper Saddle River, New Jersey. 2000. pp. 702, 703.
- I.R. Dunkin. *Matrix-isolation techniques: a practical approach*. Oxford University Press, Oxford. 1998.
- C.M. Breneman and K.B. Wiberg. *J. Comp. Chem.* **11**, 431 (1990).
- (a) E.D. Glendening, A.E. Reed, J.E. Carpenter, and F. Weinhold. Gaussian NBO [computer program]. Version 3.1. As implemented in Gaussian 98, revision A9. 1998; (b) A.E. Reed, L.A. Curtis, and F. Weinhold. *Chem. Rev.* **88**, 899 (1988); (c) F. Weinhold and J.E. Carpenter. *Plenum*. 227 (1988); (d) J.E. Carpenter and F. Weinhold. *J. Mol. Struct. Theochem*, **169**, 41 (1988); (e) A.E. Reed, R.B. Weinstock, and F. Weinhold. *J. Chem. Phys.* **83**, 735 (1985); (f) A.E. Reed and F. Weinhold. *J. Chem. Phys.* **78**, 1736 (1983); **78**, 735 (1983); (g) J.P. Foster and F. Weinhold. *J. Am. Chem. Soc.* **102**, 7211 (1980).
- R.M. Silverstein, G.C. Bassler, and T.C. Morrill. *Spectrometric identification of organic compounds*. Wiley, New York. 1981. p. 108.
- Y. Wang and R.A. Poirier. *Can. J. Chem.* **76**, 477 (1998) and references therein.
- E. Lewars. *Computational chemistry*. Kluwer Academic Publishers, Boston. 2003. Chap 5.



29. (a) E. Goldstein, B. Benoit, and K.N. Houk. J. Am. Chem. Soc. **118**, 6036 (1996). (b) D.A. Hrovat, J.A. Duncan, and W.T. Borden. J. Am. Chem. Soc. **121**, 169 (1999).
30. I.N. Levine. Quantum chemistry. 5th ed. Prentice Hall, Upper Saddle River, New Jersey. 2000. pp. 504, 505.
31. S.G. Lias, J.E. Bartmess, J.F. Liebman, J.L. Holmes, R.D. Levin, and W.G. Mallard. J. Phys. Chem. Ref. Data Suppl. **17**(S1) (1988). pp. 315, 316, 360, 361.
32. E. Lewars. Computational chemistry. Kluwer Academic Publishers, Boston. 2003. pp. 315, 316.
33. L. Radom and D.R. Rasmussen. Pure and Appl. Chem. **70**, 1977 (1998).



## Additions and corrections: Synthesis and molecular recognition of the uridine-containing derivative of *p*-tert-butylcalix[4]arene

Jian Liang, Haiying Fu, Yu Liu, Li Wang, Zhifeng Ye, and Xianfa Shi

Ref: Can. J. Chem. 81(9): 1019–1024 (2003).

The author would like the reader to know that Dr. X. Shi is affiliated with both Tongji University and Nanjing University. In addition, the author would like to acknowledge that their work was supported by the State Key Laboratory of Coordination Chemistry, Nanjing University, Nanjing, P.R. China.

Received 19 September 2003. Published on the NRC Research Press Web site at <http://canjchem.nrc.ca> on 9 October 2003.

**J. Liang, H. Fu, Y. Liu, L. Wang, Z. Ye, and X. Shi.**<sup>1</sup> Department of Chemistry, Tongji University, Shanghai 200092, P.R. China.

**X. Shi.** State Key Laboratory of Coordination Chemistry, Nanjing University, Nanjing, Jiangsu 210093, P.R. China.

<sup>1</sup>Corresponding author (e-mail: [xfshi@mail.tongji.edu.cn](mailto:xfshi@mail.tongji.edu.cn)).



# Synthesis and study of platinum silylene complexes of the type $(R_3P)_2Pt=SiMes_2$ (Mes = 2,4,6-trimethylphenyl)<sup>1</sup>

Jay D. Feldman, Gregory P. Mitchell, Jörn-Oliver Nolte, and T. Don Tilley

**Abstract:** The synthesis and characterization of neutral platinum silylene complexes  $(R_3P)_2Pt=SiMes_2$  ( $R = i\text{-Pr}$  (**1**) or cyclohexyl (**2**), Mes = 2,4,6-trimethylphenyl) is reported. The dimethylsilylene ligand in **2** is displaced by a number of ligands including phosphines, alkenes, alkynes, and  $O_2$ . Complex **2** reacts with ROH substrates ( $R = H, Me, Et$ ) to give  $(Cy_3P)_2Pt$  and  $Mes_2Si(OR)(H)$  and with  $H_2$  to give  $trans\text{-}(Cy_3P)_2Pt(H)SiHMe_2$  (**3**). Reaction of  $H_2SiMes_2$  with  $(Cy_3P)_2Pt$  gave  $cis\text{-}(Cy_3P)_2Pt(H)SiHMe_2$  (**4**). EXSY NMR experiments of **4** reveal that exchange of silicon and platinum hydrides occurs via reductive elimination – oxidative addition and not via a silylene intermediate.

**Key words:** silylene, EXSY, platinum, hydride.

**Résumé :** On a effectué la synthèse et la caractérisation de complexes neutres de silylène de platine,  $(R_3P)_2Pt=SiMes_2$  ( $R = \text{isopropyle}$  (**1**) ou cyclohexyle (**2**); Mes = 2,4,6-triméthylphényle). Le ligand diméthylsilylène du composé **2** est déplacé par un grand nombre de ligands, dont les phosphines, les alcènes, les alcynes et le dioxygène. Le complexe **2** réagit avec des substrats de formule ROH ( $R = H, Me, Et$ ) pour conduire à la formation de  $(Cy_3P)_2Pt$  et de  $Mes_2Si(OR)(H)$ ; il réagit aussi avec  $H_2$  pour donner le  $trans\text{-}(Cy_3P)_2Pt(H)SiHMe_2$  (**3**). La réaction du  $H_2SiMes_2$  avec le  $(Cy_3P)_2Pt$  conduit à la formation du  $cis\text{-}(Cy_3P)_2Pt(H)SiHMe_2$  (**4**). Des expériences de RMN de type « EXSY » effectuées sur le composé **4** révèlent qu'il se produit un échange des hydrides de silicium et de platine par le biais d'une réaction d'élimination réductrice – addition oxydante et non pas par le biais d'un intermédiaire silylène.

**Mots clés :** silylène, « EXSY », platine, hydruure.

[Traduit par la Rédaction]

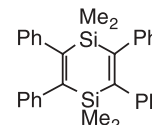
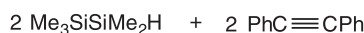
## Introduction

Platinum complexes play an important role as catalysts in transformations of organosilanes. These metal species are used to effect olefin hydrosilylation (1), dehydrogenative coupling of silanes to produce oligomers (2), and redistribution of substituents on silicon (3, 4). The latter two transformations occur extensively with low-valent platinum catalysts and are usually observed concurrently. Because these processes occur together it is likely that they involve a common intermediate. One possible mechanism for this redistribution–oligomerization reaction involves an intermediate silylene complex ( $L_nPt=SiR_2$ ) and migration chemistry (Scheme 1), although a mechanism involving reductive elimination – oxidative addition (Scheme 2) is preferred by some (4). While many of the proposed steps for redistribution via

the latter mechanism have precedent (e.g., Si–H oxidative addition and reductive elimination), there is little evidence to support the direct addition of an Si–C bond to platinum.

In 1971 Kumada and co-workers discovered the first hydrosilane oligomerization and redistribution reactions catalyzed by a platinum complex (3b, 5). In the presence of  $trans\text{-}(Et_3P)_2PtCl_2$  as a precatalyst,  $Me_3SiSiMe_2H$  was transformed into  $Me_3SiH$  (redistribution product) and  $Me\text{-}(SiMe_2)_nH$  ( $n = 3\text{--}6$ , oligomerization products). The investigators subsequently found that introducing diphenylacetylene into the reaction resulted in formation of a disilacyclohexadiene (eq. [1]), which was proposed to result from the trapping of dimethylsilylene (5).

[1]



More recently, Tanaka suggested that the formation of a platina-sila-cyclohexadiene, by the addition of phenylacetylene to a similar oligomerization–redistribution system, resulted from the trapping of a  $Pt^0$  silylene complex (6) (eq. [2]). Although these results suggested a mechanism involving intermediate platinum silylene species, the goal of isolating and probing the reactivity of such a complex still remained. Additionally, given the utility of carbene com-

Received 6 May 2002. Published on the NRC Research Press Web site at <http://canjchem.nrc.ca> on 23 May 2003.

This paper is dedicated to John Harrod, in recognition of his many contributions to homogeneous catalysis and metal–silicon chemistry.

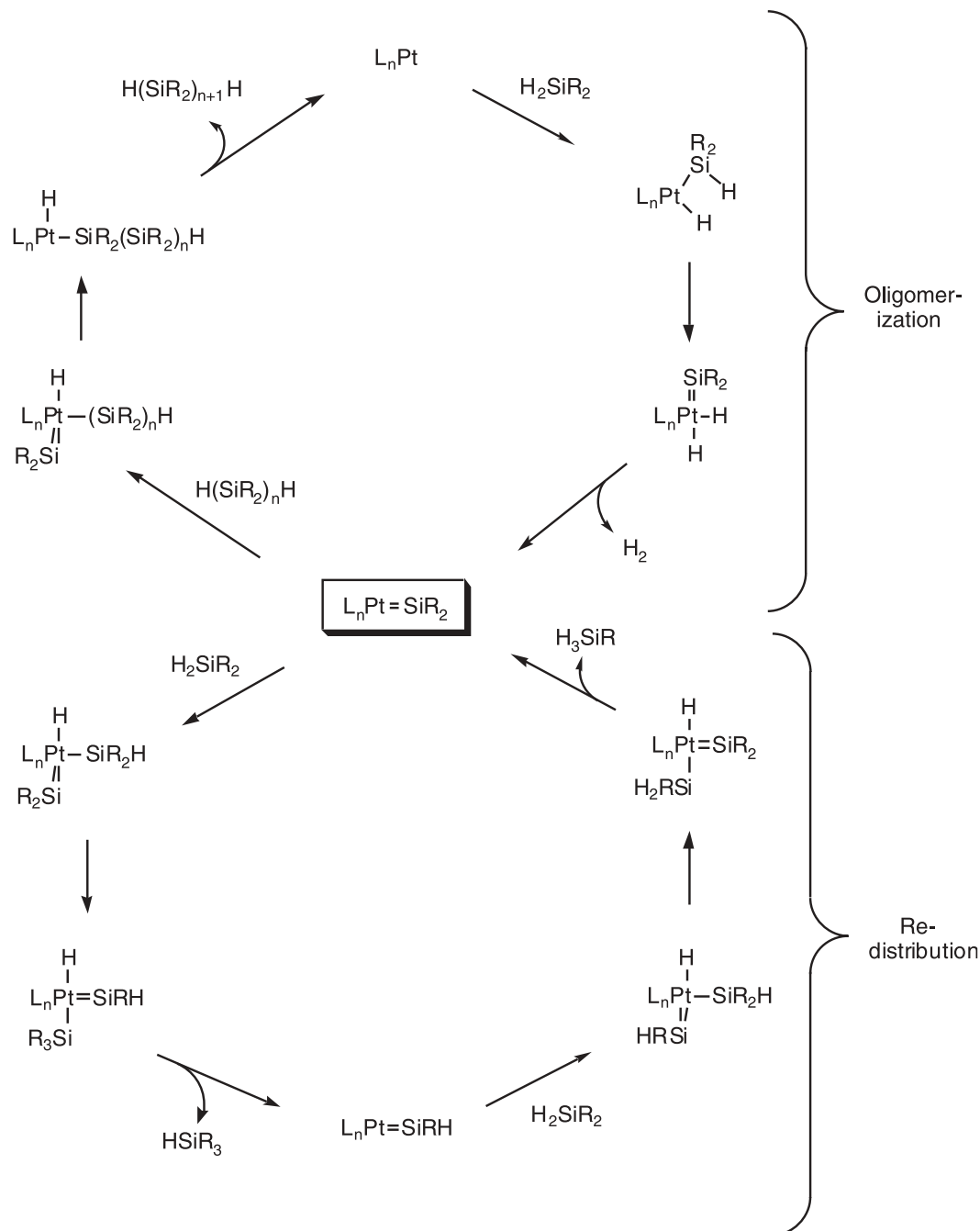
J.D. Feldman, G.P. Mitchell, J.-O. Nolte, and T.D. Tilley.<sup>2</sup>  
Department of Chemistry, University of California at Berkeley, Berkeley, CA 94720–1460, U.S.A.

<sup>1</sup>This article is part of a Special Issue dedicated to Professor John Harrod.

<sup>2</sup>Corresponding author (email: [tdtilley@socrates.berkeley.edu](mailto:tdtilley@socrates.berkeley.edu)).

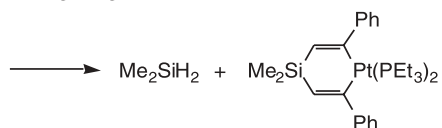
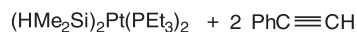


Scheme 1.



plexes as catalysts and synthons in organic and polymer chemistry (7), it is likely that development of silylene chemistry will lead to similar advancements in organosilicon chemistry.

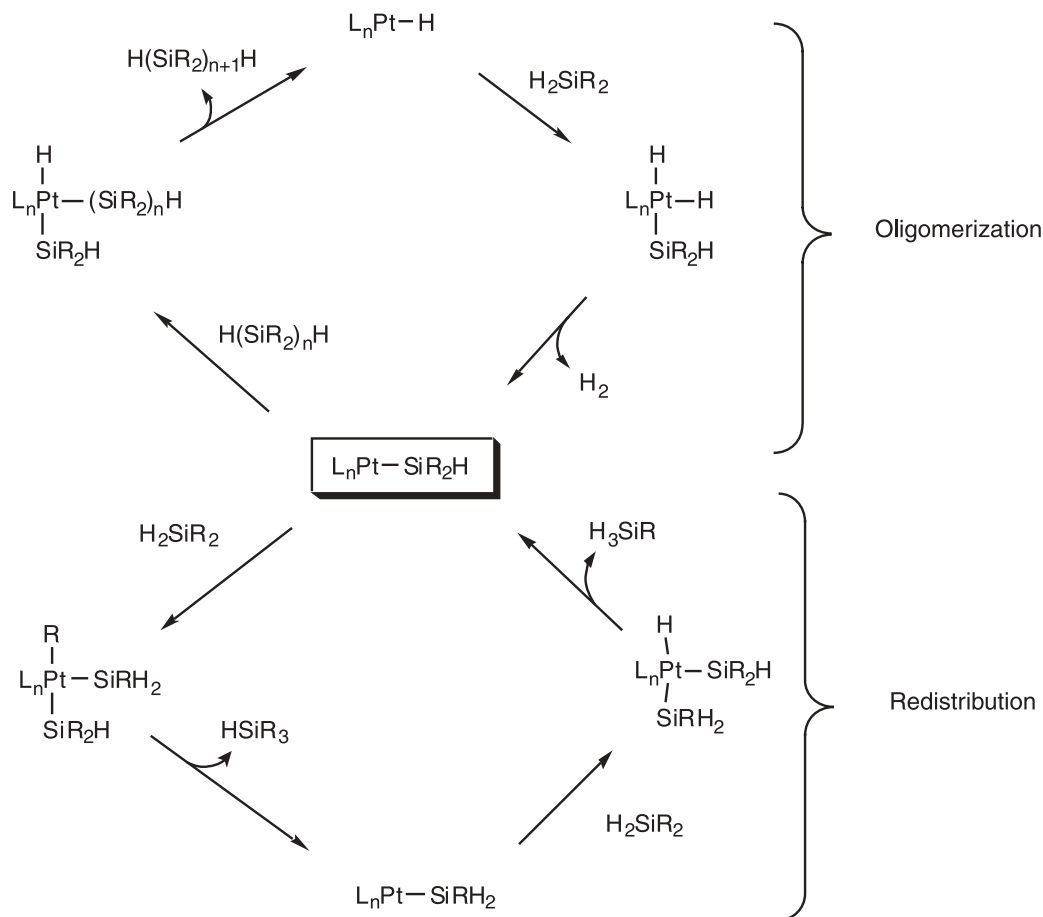
[2]



Many synthetic efforts have targeted the isolation of complexes featuring silylene ligands. In recent years, these efforts have culminated in the syntheses of a number of transition metal compounds containing  $sp^2$ -hybridized silicon (8). For the most part, these compounds are cationic, having been obtained via an “anion-abstraction” method (8a–e). However, some neutral silylene complexes have been prepared via coordination of a stable free diamidosilylene (of which there are very few) to a transition metal (8k–o). The free silylenes are conjugated, five-membered rings in which the Si atoms are stabilized via heteroatom coordination to nitrogen.



Scheme 2.



Only two platinum silylene complexes have been previously reported,  $[trans-(Cy_3P)_2(H)Pt=Si(SET)_2][BPh_4]$  (8c) and  $[(i-Pr_2PCH_2CH_2P-i-Pr_2)(H)Pt=SiMes_2][MeB(C_6F_5)_3]$  (8f). Neither of these cationic compounds is a good model for silylenes of the type  $(R_3P)_2Pt=SiR_2$ , which have been the primary focus of speculation regarding catalytic silylene intermediates (9). In an effort to prepare neutral platinum(0) silylene complexes, we have explored reactions of metastable silylenes generated in situ with zero-valent platinum compounds. Some of this work has been communicated (10).

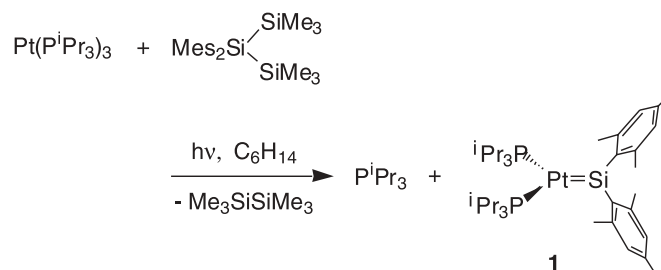
## Results and discussion

### Survey of reactions and observation of $(i-Pr_3P)_2Pt=SiMes_2$

Silylenes were generated photolytically from linear or cyclic trisilanes, including  $Mes_2Si$ : ( $Mes$  = mesityl) from  $Mes_2Si(SiMe_3)_2$  (11) or  $(Mes_2Si)_3$  (12),  $Ph_2Si$ : (13) from  $Ph_2Si(SiMe_3)_2$ , and  $Me_2Si$ : from  $(Me_2Si)_6$  (14). The photolyses were carried out using a quartz tube and in hexanes with a 1:1 stoichiometry of silylene precursor to platinum substrate. The first reactions surveyed involved the generation of  $Mes_2Si$ : from  $(Mes_2Si)_3$  in the presence of  $Pt(PEt_3)_3$  (15),  $(C_2H_4)Pt(PPh_3)_2$  (15),  $Pt(P-i-Pr_3)_3$  (15),  $Pt(PCy_3)_2$  (15), or  $Pd(PCy_3)_2$  (16). While no reaction was observed with  $Pt(PEt_3)_3$ ,  $(C_2H_4)Pt(PPh_3)_2$ , or  $Pd(PCy_3)_2$ ,

small amounts (<10%) of new products were observed (by  $^{31}P$  NMR spectroscopy) with  $Pt(P-i-Pr_3)_3$  and  $Pt(PCy_3)_2$ . It is notable that in these two cases the reacting platinum species is 2-coordinate, since  $Pt(P-i-Pr_3)_3$ , unlike  $Pt(PEt_3)_3$ , readily dissociates one of its phosphines in solution to give  $Pt(P-i-Pr_3)_2$  and an equivalent of free phosphine. Thus, further experiments concentrated on the use of these 2-coordinate species. The generation of  $Me_2Si$ : or  $Ph_2Si$ : in the presence of  $Pt(P-i-Pr_3)_2$  (+ free phosphine) or  $Pt(PCy_3)_2$  gave no new complexes (by  $^{31}P$  NMR spectroscopy). However,  $Mes_2Si$ : generated from  $Mes_2Si(SiMe_3)_2$  gave >85% of a new, blood-red complex (**1**) as observed by  $^{31}P$  NMR spectroscopy (eq. [3]). Furthermore, use of a slight excess of  $Mes_2Si(SiMe_3)_2$  (1.2 equiv) gave **1** as the only platinum phosphine species observed.

[3]





Although there are many examples of silylene-bridged, dimeric bis(phosphine) platinum complexes (dimeric analogs of **1**) (17), the observation of only a single resonance with  $^{195}\text{Pt}$  satellites in the  $^{31}\text{P}$  NMR spectrum ( $\delta$ : 82.2  $^1J_{\text{PtP}} = 3119$  Hz) is consistent with a monomeric structure for **1**. Apparently, the steric protection provided by the Mes and *i*-Pr substituents is sufficient to prevent the formation of a more thermodynamically stable 4-coordinate silicon species via dimerization. The  $^{29}\text{Si}$  NMR data for **1** are also consistent with the characterization of this complex as monomeric, with an  $sp^2$ -hybridized silicon atom. Silylene complexes exhibit characteristically large downfield chemical shifts, typically in the range of 250 to 340 ppm (8). Significantly, the resonance for **1** (Fig. 1) was observed at  $\delta$ : 367 ( $^2J_{\text{SiP}} = 107$  Hz;  $^1J_{\text{SiPt}} = 2973$  Hz). For comparison, the only other platinum silylene complexes to be reported have  $^{29}\text{Si}$  resonances at  $\delta$ : 309 for  $[\text{trans}-(\text{Cy}_3\text{P})_2(\text{H})\text{Pt}=\text{Si}(\text{SEt})_2][\text{BPh}_4]$  (8c) and  $\delta$ : 338 for  $[(i\text{-Pr})_2\text{PCH}_2\text{CH}_2\text{P}(i\text{-Pr})_2(\text{H})\text{Pt}=\text{SiMe}_2][\text{MeB}(\text{C}_6\text{F}_5)_3]$  (8f). Complexes related to **1** include several dimeric analogs of the type  $[(\text{R}_3\text{P})_2\text{Pt}(\mu\text{-SiR}_2)]_2$ , which were prepared from reactions of secondary silanes with  $\text{Pt}(\text{PR}_3)_n$  complexes (17), as well as the trimer  $[\text{Pt}(\mu\text{-SiPh}_2)(\text{PMe}_3)]_3$ , which was derived from loss of  $\text{Ph}_2\text{SiH}_2$  and  $\text{PMe}_3$  from  $\text{cis}-(\text{Me}_3\text{P})_2\text{Pt}(\text{SiHPh}_2)$  (18). While the  $[(\text{R}_3\text{P})_2\text{Pt}(\mu\text{-SiR}_2)]_2$  complexes exhibit  $^{29}\text{Si}$  NMR shifts that are over 400 ppm upfield of that for **1** (in the range of  $\delta$ : -65 to -95),  $[\text{Pt}(\mu\text{-SiPh}_2)(\text{PMe}_3)]_3$  has a  $^{29}\text{Si}$  chemical shift of 279 ppm, which is uncharacteristically downfield for a 4-coordinate silicon species.

Repeated attempts to isolate **1** were unsuccessful. Removal of the solvent afforded  $\text{Pt}(\text{P-}i\text{-Pr}_3)_3$ , along with a variety of unidentified silicon-containing products. When  $\text{Pt}(\text{P-}i\text{-Pr}_3)_2$  (19) (without a third equivalent of  $\text{P-}i\text{-Pr}_3$  present) was employed as a trapping reagent, the only platinum product observed upon photolysis was  $\text{trans-H}_2\text{Pt}(\text{P-}i\text{-Pr}_3)_2$  (20) (by  $^1\text{H}$  and  $^{31}\text{P}$  NMR spectroscopy) presumably resulting from C-H activation of the hexanes solvent. When the photolysis reaction was performed in benzene- $d_6$ , neither solvent activation nor efficient formation of **1** were observed.

### Synthesis and structure of $(\text{Cy}_3\text{P})_2\text{Pt}=\text{SiMe}_2$ (**2**)

Photolysis of a mixture of  $\text{Me}_2\text{Si}(\text{SiMe}_3)_2$  and  $\text{Pt}(\text{PCy}_3)_2$  in hexanes gave a green, supersaturated solution of  $\text{Me}_3\text{SiSiMe}_3$  (by  $^1\text{H}$  and  $^{29}\text{Si}$  NMR spectroscopy) and the silylene complex  $(\text{Cy}_3\text{P})_2\text{Pt}=\text{SiMe}_2$  (**2**). Cooling the solution to  $0^\circ\text{C}$ , concentrating the solution in vacuo, or allowing the solution to stand for a few hours facilitated precipitation of microcrystalline **2** (54% isolated yield). Complex **2** is completely insoluble in alkane solvents, dichloromethane, fluorobenzene, and tetrahydrofuran (THF) and is only slightly soluble in toluene or benzene. The  $^1\text{H}$  NMR spectrum of **2** in benzene- $d_6$  consists of resonances for each of the three types of Mes protons (*o*-Me, *p*-Me, ArH) as well as a group of multiplets for the cyclohexyl protons. Likewise, the  $^{31}\text{P}$  NMR spectrum contains a single peak with  $^{195}\text{Pt}$  satellites ( $\delta$ : 71.7,  $^1J_{\text{PtP}} = 3068$ ). Because of its low solubility, a long accumulation time was required to observe the  $^{29}\text{Si}$  NMR resonance for **2** at  $\delta$ : 358 ( $^2J_{\text{SiP}} = 112$  Hz). This large

Fig. 1.  $^{29}\text{Si}$  spectrum of **1**.

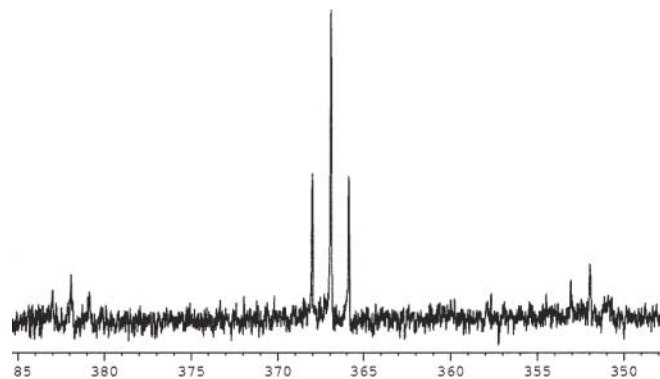
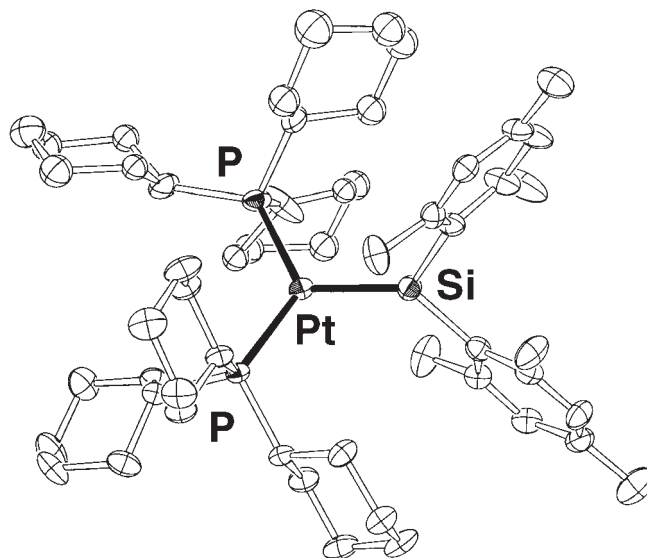


Fig. 2. ORTEP diagram of **2**.



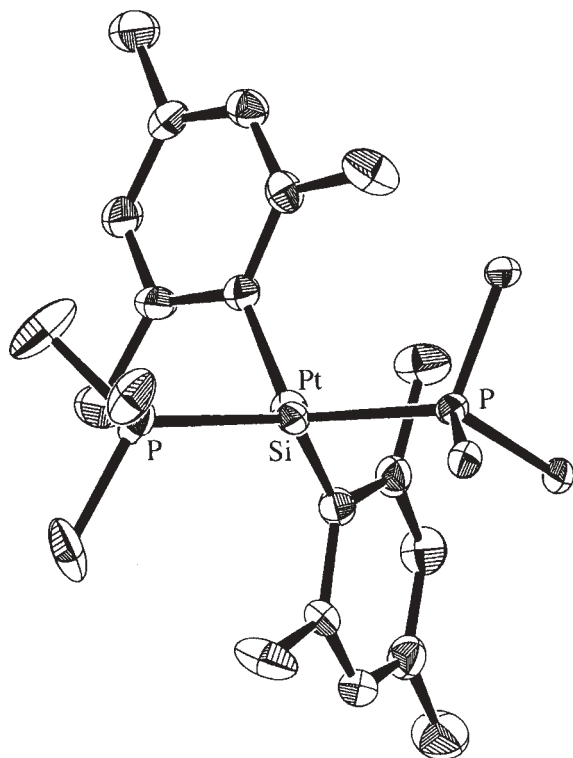
downfield chemical shift is evidence for the presence of an  $sp^2$ -hybridized silicon atom, confirming the assignment of **2** as a silylene complex.

X-ray quality crystals of **2** were grown from dilute ( $<0.04$  M) reaction solutions over a 3–4 h period.<sup>3</sup> An ORTEP diagram of **2** is shown in Fig. 2. The Pt—Si bond distance of 2.210(2) Å is the shortest yet reported and is about 6% shorter than typical Pt—Si single bonds (2.30–2.40 Å) (1, 21). For comparison, the Pt—Si distance in  $[\text{trans}-(\text{Cy}_3\text{P})_2(\text{H})\text{PtSi}(\text{SEt})_2][\text{BPh}_4]$  is 2.270(2) Å, but note that the latter complex was characterized as being somewhat Fischer-like, with both Si—S and Pt—Si  $\pi$ -bonding (8c, 22). The summation of angles about Si,  $359.8(6)^\circ$ , confirms the presence of a planar,  $sp^2$ -hybridized silicon atom, and the angles about platinum also sum within experimental error to  $360^\circ$ . The least-squares plane of the silylene ligand (including Pt, Si, and the two *ipso* carbons) and the coordination plane of platinum (Si, Pt, P, P) intersect at a dihedral angle of  $68.6^\circ$  (see Fig. 3), which is not optimal for Pt-to-Si  $\pi$ -donation. The ideal dihedral angle for overlap between the HOMO of the  $\text{L}_2\text{Pt}$  fragment and the empty *p*-orbital on silicon is  $90^\circ$ , which is the

<sup>3</sup>Supplementary data may be purchased from the Depository of Unpublished Data, Document Delivery, CISTI, National Research Council Canada, Ottawa, ON K1A 0S2, Canada ([http://www.nrc.ca/cisti/irm/unpub\\_e.shtml](http://www.nrc.ca/cisti/irm/unpub_e.shtml) for information on ordering electronically).



**Fig. 3.** ORTEP view of **2** in which most of the cyclohexyl carbon atoms have been removed for clarity. The dihedral angle between the silicon coordination plane and platinum coordination plane is 68.6°.



observed angle of the related germylene and stannylene complexes ( $(\text{Et}_3\text{P})_2\text{PtGe}[\text{N}(\text{SiMe}_3)_2]_2$  (**23**) and  $(i\text{-Pr}_2\text{PCH}_2\text{CH}_2\text{P-}i\text{-Pr}_2)\text{PdSn}[\text{CH}(\text{SiMe}_3)_2]_2$  (**24**), respectively. The deviation from 90° for **2** appears to result from steric interactions between the Mes and Cy substituents.

It is interesting that although complexes of the type  $(\text{R}_3\text{P})_2\text{PtER}'_2$  are known for tin, germanium, and now silicon, no such analogs are known with carbon. The complexes with germanium (**23**) and tin (**24**) were prepared by reacting a stable, free germylene or stannylene with a platinum complex of the type  $(\text{R}_3\text{P})_2\text{PtL}$ , where *L* is a leaving group such as an alkene, alkyne, or oxalate (which forms 2 equiv of  $\text{CO}_2$ ). It is noteworthy that while  $(\text{Et}_3\text{P})_2\text{PtGe}[\text{N}(\text{SiMe}_3)_2]_2$  decomposes in ambient laboratory light (**25**), silylene complexes **1** and **2** are generated under intense UV-vis irradiation. Also, no mention has been made of the sensitivity of stannylene complexes to light.

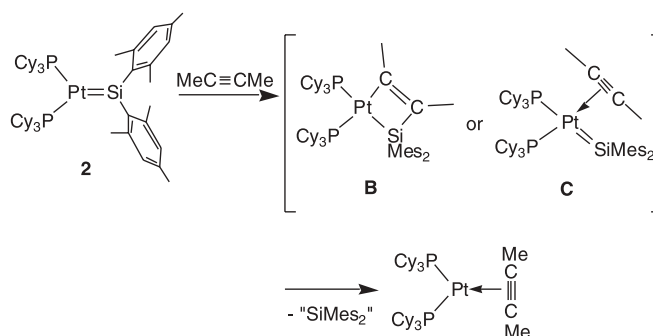
### Reactivity of **2**

Given that **2** is a member of the  $(\text{R}'_3\text{P})_2\text{Pt=SiR}_2$  class of compounds proposed as intermediates in hydrosilane oligomerization and redistribution, we have searched for similarities between the reactivity of **2** and that of the proposed intermediate species. Alkyne coupling with extruded silylenes is the primary evidence supporting such an intermediate species (vide supra); thus we have examined reactions of **2** with substrates containing unsaturated C—C

bonds. Given the high steric congestion surrounding the Pt=Si bond, small substrates, including 2-butyne, propyne, and ethylene, were employed.

Addition of 2-butyne to a benzene-*d*<sub>6</sub> solution of **2** initially resulted in the formation of an unsymmetrical complex with inequivalent resonances in the  $^{31}\text{P}$  NMR spectrum. This is consistent with a complex derived from either alkyne addition across the Pt=Si double bond (eq. [4], structure **B**) or coordination of the alkyne to the silylene complex (structure **C**).

[4]



This species appears to be an intermediate and is only observed in very small concentrations (<5% by  $^{31}\text{P}$  NMR spectroscopy), as the silylene complex is converted into the alkyne complex  $(\text{Cy}_3\text{P})_2\text{Pt}(\eta^2\text{-MeCCMe})$ .<sup>4</sup> The  $^{31}\text{P}$  NMR spectrum of the intermediate consists of two doublets with  $^{195}\text{Pt}$  satellites ( $\delta$ : 41.6,  $d^2J_{\text{PP}} = 34$  Hz,  $^1J_{\text{PPt}} = 3483$  Hz;  $\delta$ : 33.3,  $d^1J_{\text{PPt}} = 2899$  Hz). An analogous process is observed when propyne or ethylene (1 atm (1 atm = 101.325 kPa)) is used as the reactant in place of 2-butyne. In this ligand-displacement reaction the dimesitylsilylene is lost as multiple uncharacterized silicon-containing products. The apparent low stability of the intermediate species is likely due to the steric congestion associated with **2** and its derivatives.

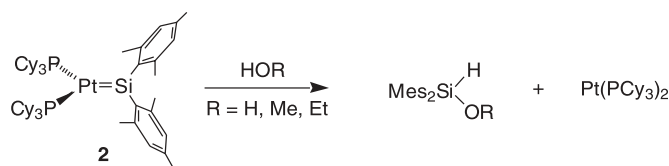
Hydrosilanes do not react cleanly with **2**; however, NMR tube reactions indicate that redistribution and, to a small extent, oligomerization processes take place. For example, addition of  $\text{PhSiH}_3$  (4 equiv) to a green benzene-*d*<sub>6</sub> solution of **2** resulted in bleaching of the color and formation of  $\text{Me}_2\text{SiH}_2$  as the only mesityl-containing product. Redistribution products  $\text{Ph}_2\text{SiH}_2$ ,  $\text{SiH}_4$ , and other Si-H containing products, as well as trace amounts of  $\text{H}_2$  (presumably from dehydrocoupling), were also observed (by  $^1\text{H}$  NMR spectroscopy). The platinum-containing product from this reaction has equivalent phosphines, as well as a hydride ligand (by NMR spectroscopy). These data are consistent with its formulation as *trans*- $(\text{Cy}_3\text{P})_2\text{Pt}(\text{H})(\text{SiHPh}_2)$ , although this could not be confirmed as it was not isolated. Furthermore, the symmetrical complex *trans*- $(\text{Cy}_3\text{P})_2\text{PtH}_2$  (**20**) (also consistent with the NMR data) could be ruled out based on comparison of NMR data to an authentic sample.

Complex **2** quantitatively transfers its silylene group to water and alcohols, giving O—H bond insertion products (eq. [5]).

<sup>4</sup>The alkyne complex,  $(\text{Cy}_3\text{P})_2\text{Pt}(\eta^2\text{-MeCCMe})$ , was generated via the addition of 2-butyne to  $(\text{Cy}_3\text{P})_2\text{Pt}$  in order to compare its  $^{31}\text{P}$  spectrum with the product mentioned here.  $(\text{Cy}_3\text{P})_2\text{Pt}(\text{2-butyne})$   $^{31}\text{P}$  NMR ( $\text{C}_6\text{D}_6$ )  $\delta$ : 36.8,  $^1J_{\text{PPt}} = 3302$  Hz.



[5]



Thus, addition of ROH ( $R = \text{H, Me, Et}$ ) to **2** resulted in the clean formation of  $\text{Pt}(\text{PCy}_3)_2$  and the corresponding siloxane  $\text{Mes}_2\text{Si}(\text{OR})\text{H}$ . No intermediates were observed in the reaction of **1** with ethanol at  $-60^\circ\text{C}$  (by  $^1\text{H}$  and  $^{31}\text{P}$  NMR spectroscopy in toluene- $d_8$ ). Related reactivity was previously reported for the base-stabilized silylene complex  $[\text{Cp}^*(\text{Me}_3\text{P})_2\text{RuSiPh}_2(\text{NCMe})]^+$ , which was presumed to dissociate acetonitrile prior to reaction with an alcohol (26). This reactivity contrasts with what has been observed for (*i*-Pr) $_2\text{PCH}_2\text{CH}_2\text{P}$ -*i*-Pr $_2$   $\text{PdSn}[\text{CH}(\text{SiMe}_3)_2]_2$ , which reversibly adds  $\text{H}_2\text{O}$  across the Pd—Sn bond to form a palladium hydride species (27).

Many reactions of **2** result in loss of the silylene ligand. For example,  $\text{O}_2$  reacts with **2** to give  $\text{Pt}(\text{PCy}_3)_2(\eta^2\text{-O}_2)$  (**28**), and the displaced silylene ligand is observed to decompose to a number of species (but not to significant amounts of the silylene dimerization product,  $\text{Mes}_2\text{Si}=\text{SiMes}_2$ ). This reactivity is unlike that of the related germylene complex,  $(\text{Et}_3\text{P})_2\text{-PtGe}[\text{N}(\text{SiMe}_3)_2]_2$ , which cleanly adds  $\text{O}_2$  across its double bond (29). Reactions of **2** in benzene- $d_6$  with an excess amount of *i*-Pr $_2\text{PCH}_2\text{CH}_2\text{P}$ -*i*-Pr $_2$ ,  $\text{Ph}_2\text{PCH}_2\text{CH}_2\text{PPh}_2$ , and  $\text{PMe}_3$  led to  $\text{PCy}_3$  and  $\text{Mes}_2\text{Si}$ : displacement, with quantitative formation of the corresponding  $\text{PtL}_4$  (**30**) complex (by  $^{31}\text{P}$  NMR spectroscopy). Addition of 1 equiv of phosphine resulted in partial conversion to  $\text{PtL}_4$ , and no other products were observed. These results suggest that the dimethylsilylene ligand in **2** is rather labile. However, attempts to trap the silylene by reacting **2** with 2 equiv of 2,3-dimethylbutadiene (which is known to react with free dimethylsilylene) (**31**) in benzene- $d_6$  over 3 days at room temperature failed to give the expected cycloaddition product,  $\text{Mes}_2\text{Si}(\text{CH}_2\text{CMe}_2\text{CH}_2)$ . Instead, several unidentified mesityl-containing species were observed by  $^1\text{H}$  NMR spectroscopy. This suggests that complex decomposition pathways are operative in silylene displacement reactions. Unlike cationic silylene complexes, **2** is stable in the presence of 1 equiv of the nitrogen bases *para*-dimethylaminopyridine and acetonitrile and does not form a base-stabilized silylene complex (**32**). Formation of the four-coordinate adduct may be disfavored due to the significant steric protection of the electrophilic,  $sp^2$ -hybridized silylene.

#### Formation of *trans*-( $\text{Cy}_3\text{P}$ ) $_2\text{Pt}(\text{H})(\text{SiHMe}_2)$ (**3**) from **2** and $\text{H}_2$

Hydrogen (1 atm) reacted with a benzene solution of **2** over 2 days to form *trans*-( $\text{Cy}_3\text{P}$ ) $_2\text{Pt}(\text{H})(\text{SiHMe}_2)$  (**3**, Scheme 3). With this slow conversion there was competing decomposition of **2** via loss of the silylene ligand to produce

*trans*-( $\text{Cy}_3\text{P}$ ) $_2\text{PtH}_2$  (**20**) (ca. 50%; without formation of  $\text{Mes}_2\text{SiH}_2$ ). At higher temperatures (refluxing benzene- $d_6$ ), **3** was hydrogenated to give *trans*-( $\text{Cy}_3\text{P}$ ) $_2\text{PtH}_2$  and  $\text{Mes}_2\text{SiH}_2$ . In contrast to the germylene complex  $(\text{Et}_3\text{P})_2\text{PtGe}[\text{N}(\text{SiMe}_3)_2]_2$  (**33**), the addition of hydrogen to **2** is irreversible.

Complex **3** is fluxional in solution, as observed by variable-temperature  $^{31}\text{P}$  NMR spectroscopy. At  $-29^\circ\text{C}$ , two doublets ( $\delta$ : 26.9,  $d\ ^1J_{\text{PtP}} = 2632\text{ Hz}$ ,  $^2J_{\text{PP}} = 346\text{ Hz}$ ;  $\delta$ : 33.6,  $d\ ^1J_{\text{PtP}} = 2715\text{ Hz}$ ) are observed, which, upon heating, broaden and coalesce to a singlet ( $\delta$ : 28.9,  $^1J_{\text{PtP}} = 2707\text{ Hz}$ ) at  $91^\circ\text{C}$ . This behavior is consistent with restricted rotation about the sterically congested Pt—Si bond; the rotational barrier ( $\Delta G^\ddagger_{\text{rot}}$ ) was calculated to be  $15.8 \pm 0.4\text{ kcal mol}^{-1}$ . The mechanism of hydrogen addition to **2** could involve oxidative addition to the platinum center followed by migration of hydride to the silylene ligand, or direct addition of hydrogen to the Pt=Si double bond. At this point the mechanism is unknown, but it is interesting to note that whereas the *trans* silyl hydride is formed by this reaction, the oxidative addition of  $\text{Mes}_2\text{SiH}_2$  to  $\text{Pt}(\text{PCy}_3)_2$  exclusively gives *cis*-( $\text{Cy}_3\text{P}$ ) $_2\text{-Pt}(\text{H})(\text{SiHMe}_2)$  (vide infra).

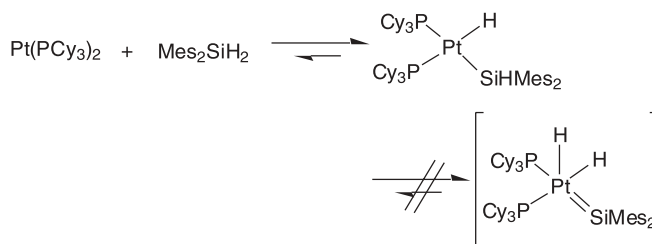
#### Synthesis and EXSY NMR Studies of *cis*-( $\text{Cy}_3\text{P}$ ) $_2\text{Pt}(\text{H})(\text{SiHMe}_2)$ (**4**)

The *cis* isomer of **3** is obtained via the addition of  $\text{Mes}_2\text{SiH}_2$  to  $\text{Pt}(\text{PCy}_3)_2$  in 48% isolated yield. Competing *cis*–*trans* isomerization and decomposition took place upon thermolysis ( $80^\circ\text{C}$ , 6 h) or photolysis (2.5 h) of a benzene solution of **4**.

The Pt–H and Si–H resonances of **4** are broad at room temperature, suggesting that exchange of these protons takes place. Cooling the sample to  $-70^\circ\text{C}$  (toluene- $d_8$ ) only partially resolved the broad peaks. The cyclohexyl resonances prevent observation of the Pt–H–Si–H proton coalescence at high temperatures, and thus exchange NMR spectroscopy (EXSY) was used to study this process. The  $^1\text{H}$  EXSY experiment confirms the exchange of the platinum and silicon hydrides. The rate constant for exchange was determined to be  $23 \pm 4\text{ Hz}$  ( $27^\circ\text{C}$ ).<sup>5</sup>

Given the stability of silylene ligands in this system, it seemed possible that this exchange could occur via an  $\alpha$ -H migration process to give a 5-coordinate intermediate (eq. [6]).

[6]



However, a reductive elimination – oxidative addition couple could also account for this observation. An intermolecular mechanism was suggested upon close examina-

<sup>5</sup> EXSY NMR experiments (phase sensitive NOESY) were performed at two different mixing times of 12 and 25 ms, and exchange rate constants were determined using the program D2DNMR.



Scheme 3.

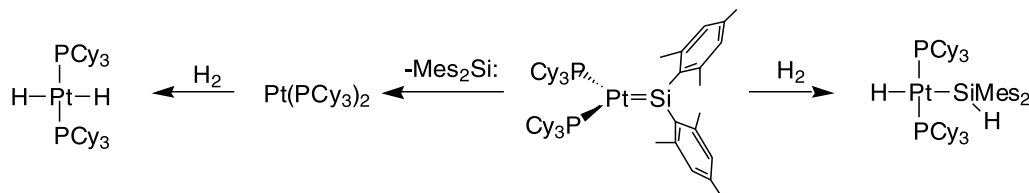
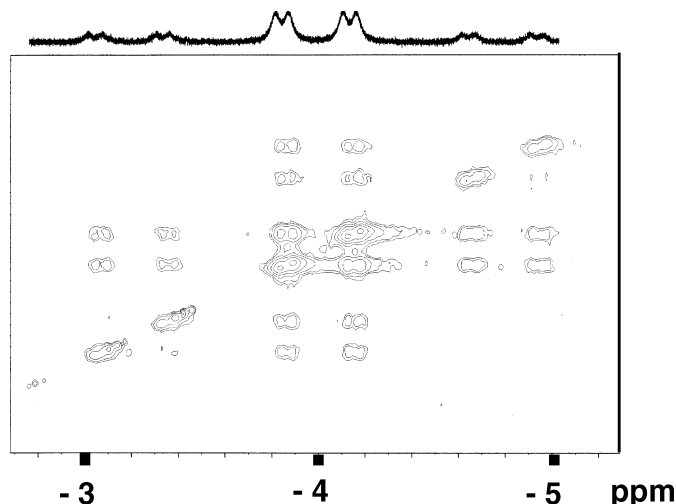


Fig. 4. Pt-H region of  $^1\text{H}$  EXSY NMR spectrum of **4** showing exchange cross peaks between different Pt isotopes.

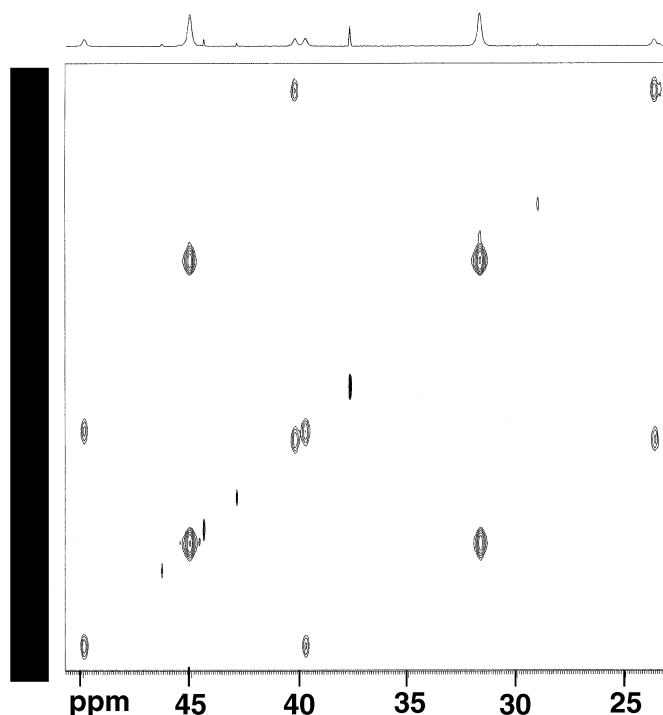


tion of the Pt-H region of the EXSY spectrum, Fig. 4, which contains cross-peaks corresponding to the exchange of  $^{195}\text{Pt}$ -H hydrides with molecules of complex **4** containing other Pt isotopes. More significantly, EXSY experiments revealed the exchange of Pt-H hydrides with the Si-H hydrides of *free*  $\text{H}_2\text{SiMe}_2$  (25 equiv) with a rate constant of  $23 \pm 4$  Hz ( $27^\circ\text{C}$ ). Also, addition of  $\text{D}_2\text{SiMe}_2$  to **4** resulted in concurrent incorporation of deuterium into the Pt-H and Si-H positions of **4**. In addition,  $^{31}\text{P}$  EXSY NMR experiments provided a similar rate constant ( $27 \pm 4$  Hz) for phosphine exchange. This process was shown to be intramolecular, based on the absence of cross peaks between  $^{195}\text{Pt}$ -P phosphines with those bound to other isotopes of platinum (Fig. 5), as well as the lack of exchange with free phosphine (5 equiv). Coalescence of the phosphorus resonances of **4** into a broad singlet occurred at  $135^\circ\text{C}$  (toluene- $d_8$ ), yielding an energy of activation of  $16.1 \pm 0.5$  kcal mol $^{-1}$ . Thus, hydrogen exchange in *cis*-( $\text{Cy}_3\text{P}$ ) $_2\text{Pt}(\text{H})(\text{SiHMe}_2)$  occurs via the rate-determining reductive elimination of dimesitylsilane, which does not require prior phosphine dissociation. These results are consistent with the recent observation that hydrogen appears not to migrate to platinum in 4-coordinate (*i*-Pr $_2\text{PCH}_2\text{CH}_2\text{P-}i$ -Pr $_2$ )Pt(Me)SiHMe $_2$ , whereas the 3-coordinate cation [*i*-Pr $_2\text{PCH}_2\text{CH}_2\text{P-}i$ -Pr $_2$ )PtSiHMe $_2$ ] $^+$  rapidly converts to [*i*-Pr $_2\text{PCH}_2\text{CH}_2\text{P-}i$ -Pr $_2$ )(H)Pt=SiMe $_2$ ] $^+$  (8f).

## Conclusion

The first examples of neutral, platinum(0) silylene complexes have been synthesized and characterized by  $^{29}\text{Si}$

Fig. 5.  $^{31}\text{P}$  EXSY NMR spectrum of **4**.



NMR spectroscopy (**1** and **2**) as well as by X-ray crystallography and UV-vis, IR, and Raman spectroscopies (**2**). Their preparation was achieved via a novel route: trapping of a metastable silylene with electron-rich bis(phosphine)platinum compounds. These are the first silylene complexes to closely resemble proposed catalytic intermediates, in that the  $\text{L}_2\text{Pt}=\text{SiR}_2$  compounds (**1** and **2**) resemble species proposed in the redistribution and oligomerization of hydrosilanes by platinum catalysts. Steric protection of the reactive Pt=Si double bond not only stabilizes **1** and **2**, thus allowing for their isolation, but apparently also limits their reactivity. Dihydrogen is the only reactant to yield a product with an intact Si-Pt bond (**3**). Other substrates either displace the silylene ligand or fail to react with **2**. Although no direct analogies can be drawn between the reactivity of the isolated and proposed intermediate silylenes, the very existence of **1** and **2** lends some credence to mechanisms which invoke this class of compounds. Studies of the closely related and dynamic molecule *cis*-( $\text{Cy}_3\text{P}$ ) $_2\text{Pt}(\text{H})\text{SiMe}_2\text{H}$  (**4**) point to a Pt-H-Si-H exchange mechanism that does not involve a silylene intermediate, but rather a reductive elimination-oxidative addition couple. This observation is consistent with the notion that a metal center must be unsaturated for



silylene complex formation by  $\alpha$ -migration to be favorable (see ref. 8f).

## Experimental

### General information

Unless otherwise noted, all manipulations were performed under an atmosphere of nitrogen using standard Schlenk techniques and (or) in a glovebox. Dry, oxygen-free solvents were employed throughout. Diethyl ether ( $\text{Et}_2\text{O}$ ), pentane, hexane, and toluene were distilled from sodium benzophenone ketyl and stored under  $\text{N}_2$  prior to use. Benzene- $d_6$  and toluene- $d_8$  were purified by vacuum distillation from Na-K alloy. Unless otherwise specified, all reagents were purchased from commercial suppliers and used without further purification. Pyridine was distilled from sodium and stored under  $\text{N}_2$ .  $\text{Pt}(\text{P-}i\text{-Pr}_3)_3$  (15),  $\text{Pt}(\text{PCy}_3)_2$  (15),  $\text{Mes}_2\text{Si}(\text{SiMe}_3)_2$  (11), and  $\text{Mes}_2\text{SiH}_2$  (34) were prepared by literature methods. Lithium aluminum hydride was recrystallized from  $\text{Et}_2\text{O}$  and dried in vacuo prior to use. Ethylene (99.9%) was obtained from Airgas, and 2-butyne (Aldrich) was vac-transferred and stored over molecular sieves prior to use. Photolysis reactions were carried out in a Rayonet RPR-100 Hg lamp reactor.

NMR spectra were recorded with a Bruker AMX-400 at 400.1 MHz ( $^1\text{H}$ ) and 162.0 MHz ( $^{31}\text{P}$ ) or a DRX-500 at 125.8 MHz ( $^{13}\text{C}$ ) instrument and at room temperature and in benzene- $d_6$  unless otherwise noted.  $^{29}\text{Si}$  NMR spectra were obtained with the Bruker DRX-500 instrument at 99.4 MHz using 10 mg of  $\text{Cr}(\text{acac})_3$  as a relaxation agent. EXSY NMR experiments (phase sensitive NOESY) were performed at two different mixing times of 12 and 25 ms, and exchange rate constants were determined using the program D2DNMR (35). Melting points were taken under  $\text{N}_2$  in sealed capillaries and are uncorrected. Elemental analyses were performed by the UCB Microanalytical Laboratory. Infrared (IR) spectra were obtained on a Mattson Galaxy 3000 FT-IR spectrometer, and all absorptions are reported in  $\text{cm}^{-1}$ . The UV-vis spectrum of **2** in toluene were recorded on a Hewlett Packard 8452A Diode Array spectrophotometer, respectively.

### $\text{Pt}(\text{P-}i\text{-Pr}_3)_2$

A previous report described the low-yield conversion of  $\text{Pt}(\text{P-}i\text{-Pr}_3)_3$  to  $\text{Pt}(\text{P-}i\text{-Pr}_3)_2$  in vacuo (19). An improved synthesis is reported here. In a PTFE-sealed vessel,  $(i\text{-Pr}_3\text{P})_2\text{PtCl}_2$  (1.94 g, 3.30 mmol) was dissolved in 25 mL of THF, and 1% sodium amalgam (55 g, 30 equiv Na) was added. The pale yellow solution turned red over the reaction time of 3 days. The solution was transferred away from the remaining amalgam-NaCl mixture via cannula. The amalgam was washed with  $2 \times 5$  mL pentane, and the washings were combined with the original supernatant. All solvent was removed in vacuo to give a viscous red oil. To this, 30 mL of pentane were added, giving a red solution and purple precipitate. The solution was filtered and concentrated to dryness to give red crystals of  $\text{Pt}(\text{P-}i\text{-Pr}_3)_3$  (1.62 g, 96%).  $^1\text{H}$  NMR  $\delta$ : 1.99 (m, 1H, CH), 1.31 (virtual q  $^2J_{\text{HP}} = ^1J_{\text{HH}} = 7$  Hz, 3H,  $\text{CH}_3$ ).  $^{31}\text{P}$  NMR  $\delta$ : 72.2 (s with  $^{195}\text{Pt}$  satellites,  $^1J_{\text{PPt}} = 4179$  Hz).

### $(i\text{-Pr}_3\text{P})_2\text{Pt}=\text{SiMes}_2$ (**1**)

Complex **1** was prepared by the same method employed for **2** (vide infra), using  $\text{Pt}(\text{P-}i\text{-Pr}_3)_3$ . This red compound was observed in solution but was not isolated.  $^{31}\text{P}$  NMR  $\delta$ : 82.2 (s with  $^{195}\text{Pt}$  satellites,  $^1J_{\text{PPt}} = 3119$  Hz).  $^{29}\text{Si}$  NMR  $\delta$ : 367 (t with  $^{195}\text{Pt}$  satellites,  $^2J_{\text{PSi}} = 107$  Hz,  $^1J_{\text{SiPt}} = 2973$  Hz).

### $(\text{Cy}_3\text{P})_2\text{Pt}=\text{SiMes}_2$ (**2**)

A fused silica Schlenk tube containing a magnetic stir bar was charged with  $\text{Pt}(\text{PCy}_3)_2$  (314 mg, 0.415 mmol),  $\text{Mes}_2\text{Si}(\text{SiMe}_3)_2$  (212 mg, 0.499 mmol), and 12 mL of hexane. The resulting mixture was stirred rapidly until all solids dissolved (10 min). Within minutes of beginning photolysis, the color of the solution changed from colorless to green. This color persisted and darkened over the photolysis period of 120 min at which time a green precipitate was observed on the sides of the tube. The hexane and hexamethyldisilane byproduct were removed under vacuum. The resulting mixture was washed with  $2 \times 5$  mL of hexane to remove tetramethyldisilene (the silylene dimerization byproduct) as well as unreacted  $\text{Pt}(\text{PCy}_3)_2$ . The remaining green solid was dried in vacuo to give analytically pure **2** (mp  $104^\circ\text{C}$  decomposition (dec)). Yield: 231 mg (54%). X-ray quality crystals of **2** were grown from dilute ( $<0.04$  M) reaction solutions over a 3–4 h period during photolysis. UV-vis ( $\epsilon$  ( $\text{M}^{-1} \text{cm}^{-1}$ )): 282 (14 000), 316 (14 000), 392 (2900). IR: 3033 (w), 1601 (w), 1448 (s), 1265 (w), 1173 (w), 1046 (w), 1002 (w), 850 (m), 738 (w), 723 (w), 613 (w), 512 (w), 464 (m).  $^1\text{H}$  NMR  $\delta$ : 6.83 (s, 4H, ArH), 2.72 (s, 12H, *ortho*-Me), 2.19 (s, 6H, *para*-Me), 0.8–2.1 (br m, Cy).  $^{31}\text{P}$  NMR  $\delta$ : 71.7 (s with  $^{195}\text{Pt}$  satellites,  $^1J_{\text{PPt}} = 3068$  Hz).  $^{29}\text{Si}$  NMR  $\delta$ : 358 (t,  $^2J_{\text{PSi}} = 112$  Hz). Anal. calcd for  $\text{C}_{54}\text{H}_{88}\text{P}_2\text{PtSi}$ : C 63.44, H 8.68; found: C 63.35, H 8.87.

### Reaction of **2** with 2-butyne

In an NMR tube, **2** (11 mg, 0.01 mmol), 2-butyne (1  $\mu\text{L}$ , 0.01 mmol), and benzene- $d_6$  were combined, and the tube was inverted several times to mix the reactants. The reaction was monitored by  $^{31}\text{P}$  NMR spectroscopy and produced  $(\text{Cy}_3\text{P})_2\text{Pt}(\eta^2\text{-MeCCMe})$  via an unsymmetrical intermediate over several hours.<sup>4</sup> The  $^{31}\text{P}$  NMR spectrum of the intermediate consists of two doublets with  $^{195}\text{Pt}$  satellites ( $\delta$ : 41.6, d  $^2J_{\text{PP}} = 34$  Hz,  $^1J_{\text{PPt}} = 3483$  Hz;  $\delta$ : 33.3, d  $^1J_{\text{PPt}} = 2899$  Hz).

### Reaction of **2** with ethylene

A sealable PTFE-capped NMR tube containing **2** (10 mg, 0.01 mmol) and benzene- $d_6$  was degassed via three freeze-pump-thaw cycles, and 1 atm of ethylene was introduced. The reaction was monitored by  $^{31}\text{P}$  NMR spectroscopy as it was converted to  $(\text{Cy}_3\text{P})_2\text{Pt}(\eta^2\text{-C}_2\text{H}_4)$  via an unsymmetrical intermediate over several hours.

### Reaction of **2** with $\text{PhSiH}_3$

Compound **2** (11 mg, 0.01 mmol),  $\text{PhSiH}_3$  (5  $\mu\text{L}$ , 0.04 mmol), and benzene- $d_6$  were combined in an NMR tube, which was then inverted several times to mix the reactants. The green color of **2** was rapidly bleached, and  $^1\text{H}$  NMR spectroscopy revealed the presence of  $\text{Mes}_2\text{SiH}_2$ ,  $\text{Ph}_2\text{SiH}_2$ ,  $\text{SiH}_4$ , and trace  $\text{H}_2$ .



### Formation of *trans*-(Cy<sub>3</sub>P)<sub>2</sub>Pt(H)SiMes<sub>2</sub>H (**3**) from **2** and H<sub>2</sub>

A sealable PTFE-capped NMR tube containing a solution of **2** (7 mg, 6 μmol) and benzene-*d*<sub>6</sub> was degassed via two freeze-pump-thaw cycles, and 1 atm of H<sub>2</sub> was introduced. (Cy<sub>3</sub>P)<sub>2</sub>Pt=SiMes<sub>2</sub> dissolved slowly over the reaction period of 2 days. During this time, the solution changed color from green to pale yellow. The formation of **3** and (Cy<sub>3</sub>P)<sub>2</sub>PtH<sub>2</sub> (ca. 1:1) was observed by NMR spectroscopy. <sup>1</sup>H NMR (for **3**) δ: 6.66 (s, 4H, ArH), 5.76 (m with <sup>195</sup>Pt satellites, <sup>2</sup>J<sub>HPt</sub> = 319 Hz, 1H, SiH), 2.43 (s, 12H, *ortho*-Me), 2.25 (s, 6H, *para*-Me), 1.0–2.5 (br m, Cy), –3.12 (t with <sup>195</sup>Pt satellites, <sup>2</sup>J<sub>HP</sub> = 17.6 Hz, <sup>1</sup>J<sub>HPt</sub> = 629 Hz, 1H, PtH). <sup>31</sup>P NMR (–29°C, toluene-*d*<sub>8</sub>) δ: 33.58 (d, <sup>2</sup>J<sub>PP</sub> = 346 Hz, <sup>1</sup>J<sub>PPt</sub> = 2715 Hz), 26.94 (d with <sup>195</sup>Pt satellites, <sup>2</sup>J<sub>PP</sub> = 346 Hz, <sup>1</sup>J<sub>PPt</sub> = 2632).

### *cis*-(Cy<sub>3</sub>P)<sub>2</sub>Pt(H)SiMes<sub>2</sub>H (**4**)

A Schlenk tube containing Pt(PCy<sub>3</sub>)<sub>2</sub> (228 mg, 0.302 mmol), a magnetic stir bar, and 25 mL of hexane was stirred and cooled to 0°C. Simultaneously, another tube containing Mes<sub>2</sub>SiH<sub>2</sub> (81 mg, 0.302 mmol) and 10 mL of hexane was likewise cooled and stirred. The dimesitylsilane solution was added to the first vessel dropwise via cannula over 12 min. Stirring at 0°C was continued for another 10 min, and then the solution was allowed to warm to room temperature. After 1.5 h the solvent was removed in vacuo. Recrystallization from diethyl ether afforded 147 mg (48%) of **4** (mp 159°C dec). IR (KBr): 3014 (m), 2932 (m), 2660 (w), 2150 (w), 2064 (m), 1596 (m), 1546 (w), 1446 (s), 1410 (w), 1328 (w), 1260 (m), 1173 (m), 1105 (m), 1011 (m), 928 (w), 887 (m), 846 (s), 737 (m), 710 (w), 599 (w), 519 (m), 496 (m), 432 (w). <sup>1</sup>H NMR δ: 6.89 (s, 4H, ArH), 5.86 (br, 1H, SiH), 2.85 (s, 12H, *ortho*-Me), 2.23 (s, 6H, *para*-Me), 1–2.2 (br m, Cy), –3.98 (br dd with <sup>195</sup>Pt satellites, <sup>2</sup>J<sub>HPcis</sub> = 37 Hz, <sup>2</sup>J<sub>HPtrans</sub> = 183 Hz, <sup>2</sup>J<sub>HPt</sub> = 1050 Hz, PtH). <sup>31</sup>P NMR δ: 45.1 (s with <sup>195</sup>Pt satellites, <sup>1</sup>J<sub>PPt</sub> = 1580 Hz), 31.6 (s with <sup>195</sup>Pt satellites, <sup>1</sup>J<sub>PPt</sub> = 2740 Hz). <sup>13</sup>C NMR δ: 144.2 (br, *ortho*-C), 143.1 (br, *ipso*-C), 136.0 (br, *para*-C), 129.3 (s, *meta*-C), 39.6, 37.1, 31.1, 28.6, 28.2, 27.4, 27.2 (br, Cy), 25.4 (br, *ortho*-Me), 21.6 (s, *para*-Me). Anal. calcd for C<sub>54</sub>H<sub>90</sub>P<sub>2</sub>PtSi: C 63.31, H 8.85; found: C 63.84, H 9.28.

### Reactions of **1** with ROH (*R* = H, Me, Et)

In three separate reactions, water (ca. 0.2 μL, 0.01 mmol), methanol (0.3 μL, 0.01 mmol), or ethanol (0.6 μL, 0.01 mmol) was injected into a septum-capped NMR tube containing **1** (10 mg, 0.01 mmol) and benzene-*d*<sub>6</sub>. The tube was then inverted several times to assure mixing. The resulting colorless solutions were then analyzed by <sup>1</sup>H and <sup>31</sup>P NMR spectroscopy, which revealed quantitative formation of Pt(PCy<sub>3</sub>)<sub>2</sub> and Mes<sub>2</sub>Si(OR)H, which were identified by comparison with independently prepared siloxanes (*R* = H (36), Me (37), Et (38)).

### Acknowledgment

Acknowledgment is made to the National Science Foundation for their generous support of this work.

### References

- (a) I. Ojima. The chemistry of organic silicon compounds. Edited by S. Patai and Z. Rappoport. Wiley, New York. 1989. Chap 25, p 1479; (b) S.B. Choe, H. Sanai, and J. Klabunde. J. Am. Chem. Soc. **111**, 2875 (1989).
- (a) F. Gauvin, J.F. Harrod, and H.G. Woo. Adv. Organomet. Chem. **42**, 363 (1998); (b) T.D. Tilley. Accounts Chem. Res. **26**, 22 (1993); (c) J.Y. Corey. Advances in silicon chemistry. Vol. 1. JAI Press, Greenwich. 1991. p. 327
- (a) T. Kobayashi, T. Hayahi, H. Yamahita, and M. Tanaka. Chem. Lett. 1411 (1988); (b) K. Yamamoto, H. Okinoshima, and M. Kumada. J. Organomet. Chem. **27**, C31 (1971).
- M.D. Curtis and P.S. Epstein. Adv. Organomet. Chem. **19**, 213 (1981).
- K. Yamamoto, H. Okinoshima, and M. Kumada. J. Organomet. Chem. **23**, C70 (1970).
- H. Yamashita, M. Tanaka, and M. Goto. Organometallics, **11**, 3227 (1992).
- (a) M.P. Doyle and D.C. Forbes. Chem. Rev. **98**, 911 (1998); (b) D.F. Harvey and D.M. Sigano. Chem. Rev. **96**, 271 (1996).
- Silylene complexes with *sp*<sup>2</sup> silicon atoms: (a) D.A. Straus, S.D. Grumbine, and T.D. Tilley. J. Am. Chem. Soc. **112**, 7801 (1990); (b) S.D. Grumbine, T.D. Tilley, and A.L. Rheingold. J. Am. Chem. Soc. **115**, 358 (1993); (c) S.D. Grumbine, T.D. Tilley, F.P. Arnold, and A.L. Rheingold. J. Am. Chem. Soc. **115**, 7884 (1993); (d) S.D. Grumbine, T.D. Tilley, F.P. Arnold, and A.L. Rheingold. J. Am. Chem. Soc. **116**, 5495 (1994); (e) S.D. Grumbine, D.A. Straus, T.D. Tilley, and A.L. Rheingold. Polyhedron, **14**, 127 (1995); (f) G.P. Mitchell and T.D. Tilley. Angew. Chem. Int. Ed. **37**, 2524 (1995); (g) P.W. Wanandi, P.B. Glaser, and T.D. Tilley. J. Am. Chem. Soc. **122**, 972 (2000); (h) B.V. Mork, and T.D. Tilley. J. Am. Chem. Soc. **123**, 9702 (2001); (i) S.R. Klei, T.D. Tilley, and R.G. Bergman. Organometallics, **20**, 3220 (2001); (j) K. Ueno, S. Asami, N. Watanabe, and H. Ogino. Organometallics, **21**, 1326 (2002); (k) M. Denk, R.K. Hayashi, and R. West. Chem. Commun. 33 (1994); (l) B. Gehrhus, P.B. Hitchcock, M.F. Lappert, and H. Maciejewski. Organometallics, **17**, 5599 (1998); (m) S.H.A. Petri, D. Eikenberg, B. Neumann, H.-G. Stammler, and P. Jutzi. Organometallics, **18**, 2615 (1999); (n) X. Cai, B. Gehrhus, P.B. Hitchcock, and M.F. Lappert. Can. J. Chem. **78**, 1484 (2000); (o) D. Amoroso, M. Haaf, G.P.A. Yap, R. West, and D.E. Fogg. Organometallics, **21**, 534 (2002); (p) W.A. Herrmann, P. Härter, C.W.K. Gstöttmayr, F. Bielert, N. Seeboth, and P. Sirsch. J. Organomet. Chem. **649**, 141 (2002).
- L*<sub>2</sub>M=SiR<sub>2</sub> intermediates (*M* = Pd, Pt): (a) Reference 3b; (b) H. Yamashita, M. Tanaka, and M. Goto, Organometallics, **11**, 3227 (1992); (c) D. Seyferth, M.L. Shannon, S.C. Vick, and T.F.O. Lim. Organometallics, **4**, 57 (1985); (d) Y. Tanaka, H. Yamashita, and M. Tanaka. Organometallics, **14**, 530 (1995); (e) K. Tamao, G.-R. Sun and A. Kawachi. J. Am. Chem. Soc. **117**, 8043 (1995); (f) W.S. Palmer and K.A. Woerpel. Organometallics, **16**, 4824 (1997).
- J.D. Feldman, G.P. Mitchell, J.O. Nolte, and T.D. Tilley. J. Am. Chem. Soc. **120**, 11 184 (1998).
- M.J. Fink, M.J. Michalczyk, K.J. Haller, R. West, and J. Michl. Organometallics, **3**, 793 (1984).
- (a) S. Masamune, S. Muradami, J.T. Snow, H. Tobita, and D.J. Williams. Organometallics, **3**, 3330 (1984); (b) S. Murakami, S. Collins, and S. Masamune. Tetrahedron Lett. **25**, 2131 (1984).
- R.A. Jackson and C.J. Rhodes. J. Organomet. Chem. **336**, 45 (1987).



14. (a) H. Gilman and R.A. Tomasi. *J. Org. Chem.* **28**, 1651 (1963); (b) T.J. Drahnak, J. Michl, and R. West. *J. Am. Chem. Soc.* **101**, 5427 (1979); (c) H. Vancik, G. Raabe, M.J. Michalczyk, R. West, and J. Michl. *J. Am. Chem. Soc.* **107**, 4097 (1985), and refs. therein.
15. (a) T. Yoshida and S. Otsuka. *Inorg. Synth.* **28**, 116, 120 (1990).
16. V.V. Grushin, C. Bensimon, and H. Alper. *Inorg. Chem.* **33**, 4804 (1994).
17. (a) E.A. Zarate, C.A. Tessier-Youngs, and W.J. Youngs. *J. Am. Chem. Soc.* **110**, 4068 (1988); (b) E.A. Zarate, C.A. Tessier-Youngs, and W.J. Youngs. *Chem. Commun.* 587 (1989). (c) A.B. Anderson, P. Shiller, E.A. Zarate, C.A. Tessier-Youngs, and W.J. Youngs. *Organometallics*, **8**, 2320 (1989); (d) R.H. Heyn and T.D. Tilley. *J. Am. Chem. Soc.* **112**, 1917 (1992); (e) L.M. Sanow, M.H. Chai, D.B. McConville, K.J. Galat, R.S. Simons, P.L. Rinaldi, W.J. Youngs, and C.A. Tessier. *Organometallics*, **19**, 192 (2000).
18. K. Osakada, M. Tanabe, and T. Tanase. *Angew. Chem. Int. Ed.* **39**, 4053 (2000).
19. Pt(P-*i*-Pr<sub>3</sub>)<sub>2</sub> was previously reported; however, an improved synthesis is presented in the experimental section; for the original prep, see S. Otsuka, T. Yoshida, M. Matsumoto, and K. Nakatsu. *J. Am. Chem. Soc.* **98**, 5850 (1976).
20. (a) P.G. Leviston and M. G. H. Wallbridge. *J. Organomet. Chem.* **110**, 271 (1976); (b) H.C. Clark, A.B. Goel, and C.S. Wong. *J. Organomet. Chem.* **152**, C45 (1978).
21. J.Y. Corey and J. Braddock-Wilking. *Chem. Rev.* **99**, 175 (1999).
22. F.P. Arnold. *J. Organomet. Chem.* **617–618**, 647 (2001).
23. K.E. Litz, K. Henderson, R.W. Gourley, and M.M. Banaszak Holl. *Organometallics*, **14**, 5008 (1995).
24. J. Krause, K.-J. Haack, K.-R. Pörschke, B. Gabor, R. Goddard, C. Pluta, and K. Seevogel. *J. Am. Chem. Soc.* **118**, 804 (1996).
25. K.E. Litz, J.E. Bender, R.D. Sweeder, M.M. Banaszak Holl, and J.W. Kampf. *Organometallics*, **19**, 1186 (2000).
26. C. Zhang, S.D. Grumbine, and T.D. Tilley. *Polyhedron*, **10**, 1173 (1991).
27. F. Schager, K. Seevogel, K.-R. Pörschke, M. Kessler, and C. Krüger. *J. Am. Chem. Soc.* **118**, 13 075 (1996).
28. A.B. Goel and S. Goel. *Inorg. Chim. Acta.* **77**, L5 (1983).
29. K.E. Litz, M.M.B. Holl, J.W. Kampf, and G.B. Carpenter. *Inorg. Chem.* **37**, 6461 (1998).
30. B.E. Mann and A. Musco. *J. Chem. Soc. Dalton Trans.* **5**, 776 (1980).
31. R.T. Conlin, J.C. Netto-Ferreira, S. Zhang, and J.C. Scaiano. *Organometallics*, **9**, 1332 (1990).
32. (a) D.A. Straus, T.D. Tilley, A.L. Rheingold, and S.J. Geib, *J. Am. Chem. Soc.* **109**, 5872 (1987); (b) D.A. Straus, C. Zhang, G.E. Quimbata, S.D. Grumbine, R.H. Heyn, T.D. Tilley, A.L. Rheingold, and S.J. Geib. *J. Am. Chem. Soc.* **112**, 2673 (1990); (c) S.D. Grumbine, D.A. Straus, T.D. Tilley, and A.L. Rheingold. *Polyhedron*, **14**, 2673 (1995); (d) J.M. Dysard and T.D. Tilley. *Organometallics*, **19**, 4726 (2000).
33. K.E. Litz, J.E. Bender IV, J.W. Kampf, and M.M. Banaszak Holl. *Angew. Chem. Int. Ed. Engl.* **36**, 496 (1997).
34. J. Braddock-Wilking, M. Schieser, L. Brammer, J. Huhmann, and R. Shaltout. *J. Organomet. Chem.* **499**, 89 (1995).
35. E.W. Abel, T.P.J. Coston, K.G. Orell, V. Sik, and D. Stephenson. *J. Mag. Res.* **70**, 34 (1986).
36. (a) M.J. Michalczyk, M.J. Fink, K.J. Haller, R. West, and J. Michl. *Organometallics*, **5**, 531 (1986); (b) M.J. Fink, D.J. De Young, R. West, and J. Michl. *J. Am. Chem. Soc.* **105**, 1070 (1983); M.J. Fink, K.J. Haller, R. West, and J. Michl. *J. Am. Chem. Soc.* **106**, 822 (1984).
37. (a) M. Ishikawa, K. Nishimura, H. Sugisawa, and M. Kumada. *J. Organomet. Chem.* **194**, 147 (1980).
38. (a) W. Ando, Y. Hamada, and A. Sekiguchi. *Tetrahedron Lett.* **25**, 5057 (1984); (b) G.R. Gillette, G.H. Noren, and R. West. *Organometallics*, **6**, 2617 (1987).



# Isocyanide insertion reactions into the Ta—C bonds of cationic and zwitterionic tantalocenes<sup>1</sup>

Kevin S. Cook, Warren E. Piers, Brian O. Patrick, and Robert McDonald

**Abstract:** The insertion of isonitriles  $R'NC$  ( $R' = t\text{-Bu}$ ,  $C_6H_{11}$ ,  $CH_2C_6H_5$ ) occurs exclusively into the Ta—CH<sub>2</sub> bonds of the zwitterionic compounds  $(C_5H_4R)_2Ta[CH_2B(C_6F_5)_3]CH_3$  ( $R = H$ , **1a**;  $R = CH_3$ , **1b**) at relatively slow rates at room temperature to form *N-out* isomers as the sole kinetic products. By comparison, insertion of the same isonitrile substrates into a Ta—CH<sub>3</sub> bond of the non-zwitterionic analogs  $[(C_5H_4R)_2Ta(CH_3)_2][A]$  ( $R = H$ ,  $A = B(C_6F_5)_4$ , **3a**;  $R = CH_3$ ,  $A = BF_4$ , **3b**) occurs much more rapidly, again to form *N-out* isomers exclusively under kinetic conditions. The difference in rate is attributed to the presence of a ground state  $\alpha$ -agostic interaction in the zwitterionic compounds, which is not featured in the dimethyl ion pairs. All of the *N-out* isomers formed undergo thermal and irreversible conversion to the corresponding *N-in* isomers at rates that are conveniently followed by <sup>1</sup>H NMR spectroscopy. The rates were studied at different temperatures to obtain activation parameters for each transformation. The rate and activation trends for this isomerization were analyzed as a function of the structural changes in the compounds. It was found that the rate decreased as the steric bulk of the isonitrile substituent  $R'$  increased and that the rates were faster for the series that incorporated the more electron-donating  $C_5H_4CH_3$  ancillary ligand. Furthermore, isomerization rates for the zwitterionic *N-out* compounds were faster than those found in the non-zwitterionic series. This study represents one of the more extensive kinetic analyses of the rate of *N-out* to *N-in* isomerization as a function of structural changes. The observations are consistent with the mechanistic picture that has been developed for this process, involving dissociation of the  $\eta^2$  iminoacyl ligand, rotation about the M—C<sub>iminoacyl</sub> bond and recoordination to the inside site of the metallocene wedge.

**Key words:** cationic metallocenes, isocyanide insertion, agostic interactions, tantalum.

**Résumé :** À la température ambiante, l'insertion d'isonitriles,  $R'NC$  ( $R' = t\text{-Bu}$ ,  $C_6H_{11}$ ,  $CH_2C_6H_5$ ) se produit à des vitesses relativement faibles et uniquement dans les liaisons Ta—CH<sub>2</sub> des composés zwitterioniques  $(C_5H_4R)_2Ta[CH_2B(C_6F_5)_3]CH_3$  ( $R = H$ , **1a**;  $R = CH_3$ , **1b**) pour conduire à la formation d'isomères *N-out* comme seuls produits cinétiques. Par comparaison, l'insertion des mêmes substrats isonitriles dans une liaison Ta—CH<sub>3</sub> des analogues non zwitterioniques  $[(C_5H_4R)_2Ta(CH_3)_2][A]$  ( $R = H$ ,  $A = B(C_6F_5)_4$ , **3a**;  $R = CH_3$ ,  $A = BF_4$ , **3b**) se produit beaucoup plus rapidement, mais dans des conditions cinétiques il ne se forme encore une fois que les isomères *N-out*. La différence de vitesse est attribuée à la présence, dans l'état fondamental des composés zwitterioniques, d'une interaction  $\alpha$ -agostique qu'on n'existe pas dans les paires d'ions diméthylées. Tous les composés *N-out* qui se forment subissent une conversion thermique et irréversible vers les isomères correspondants *N-in*, à des vitesses qui peuvent être facilement suivies par spectroscopie RMN du <sup>1</sup>H. On a étudié les vitesses à différentes températures pour déterminer les paramètres d'activation de chacune des transformations. On a analysé les tendances dans les vitesses et les activations en fonction des changements structuraux dans les composés. On a trouvé que la vitesse diminue avec une augmentation de l'encombrement stérique du substituant  $R'$  des isonitriles et que les vitesses augmentent pour les séries qui incorporent le ligand ancillaire électrodonneur  $C_5H_4CH_3$ . De plus, les vitesses d'isomérisation des composés *N-out* zwitterioniques sont plus rapides que celles des séries non zwitterioniques. Cette étude représente l'une des analyses cinétiques les plus extensives de la vitesse d'isomérisation *N-out* en *N-in* en fonction de changements structuraux. Les observations sont en accord avec les idées mécanistiques qui ont été développées pour ce processus et qui impliquent une dissociation du ligand  $\eta^2$ -iminacyle, une rotation autour de la liaison M—C<sub>iminoacyl</sub> et une recoordination vers le site intérieur de l'extrémité du métallocène.

**Mots clés :** métallocènes cationiques, insertion d'isocyanure, interactions agostiques, tantale.

Received 14 January 2003. Published on the NRC Research Press Web site at <http://canjchem.nrc.ca> on 28 May 2003.

*Dedicated to Prof. John Harrod for his outstanding contributions to organometallic chemistry.*

**Kevin S. Cook and Warren E. Piers.**<sup>2</sup> Department of Chemistry, University of Calgary, 2500 University Drive N. W., Calgary, AB T2N 1N4, Canada.

**Brian O. Patrick.** Department of Chemistry, University of British Columbia, 2036 Main Mall, Vancouver, BC V6T 1Z1, Canada.

**Robert McDonald.** X-Ray Structure Laboratory, Department of Chemistry, University of Alberta, Edmonton, AB T6G 2G2, Canada.

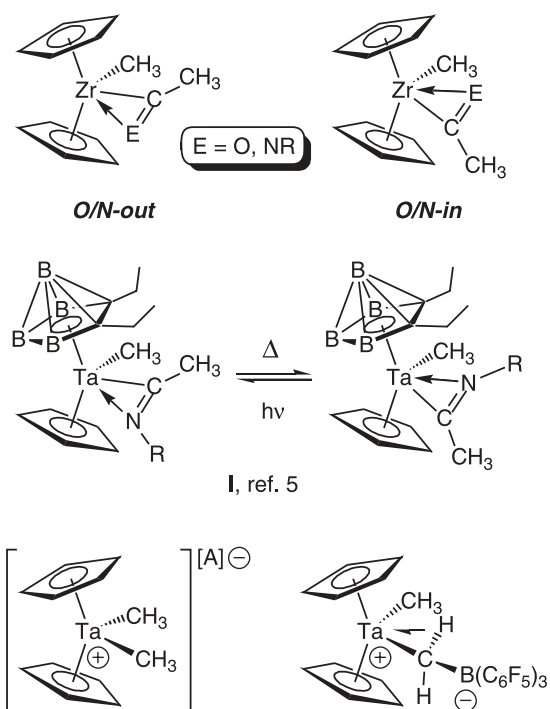
<sup>1</sup>This article is part of a Special Issue dedicated to Professor John Harrod.

<sup>2</sup>Corresponding author (e-mail: [wpiers@ucalgary.ca](mailto:wpiers@ucalgary.ca)).



## Introduction

The migratory insertion of CO or CNR into metal—carbon bonds is a key C—C bond-forming reaction in organometallic chemistry (1). Its mechanism has been investigated in several classic studies (1), and stoichiometric insertions into the metal—carbon bonds of early transition metal, bent metallocenes such as  $\text{Cp}_2\text{ZrMe}_2$  have figured prominently in this body of research (2). For these electrophilic organometallic substrates, the resulting acyl or iminoacyl products adopt an  $\eta^2$  bonding mode where an O or N lone pair also contributes electron density to the Lewis acidic metal center. Consequently, the  $\eta^2$  acyl or iminoacyl complexes can exist as “*O/N-out*” or “*O/N-in*” isomers (Chart 1), and the latter has been shown to be the thermodynamically favored isomer, while the former is the kinetically preferred product. Better orbital overlap between the acyl-iminoacyl ligand frontier orbitals with the available metallocene orbitals in the *N-in* isomer accounts for the greater overall stability of this isomer (3).



The *O/N-out* to *O/N-in* isomerization is often quite rapid, and the *O/N-out* isomers are for the most part only fleetingly observed, making detailed study of this process difficult. However, based on both experimental (2) and computational (3, 4) studies, it is accepted that the isomerization probably takes place via dissociation of O or N to form an  $\eta^1$  acyl-iminoacyl complex that can undergo rotation about the  $\text{M}-\text{C}_{\text{acyl-iminoacyl}}$  bond. Much qualitative experimental evidence in support of this picture exists, but few studies have reported quantitative kinetic and thermodynamic data as a function of systematic structural variation to delineate the factors influencing this isomerization process.

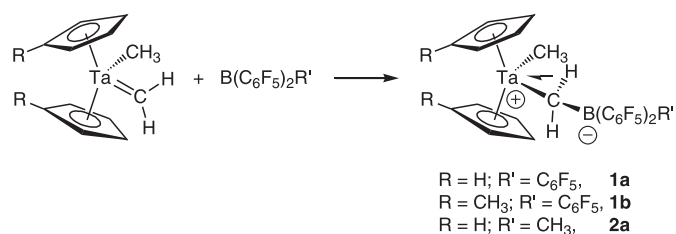
While group 4 metal-based metallocenes have played a crucial role in the development of this chemistry, recently the reactions of tantalocene mimics containing dianionic

carborane (5), borollide (6), or imide (7) donors (which are isoelectronic to, for example,  $\text{Cp}_2\text{ZrMe}_2$ ) with various isonitriles have also been studied and shown to undergo similar chemistry. In one of these systems — the tantalum(V) carborane system **I** shown in Chart 1 and reported by Finn, Grimes, and co-workers (5) — the *N-out* isomers formed with a variety of isocyanides were observed to be somewhat more stable than those of the group 4 metallocenes, allowing for the direct observation of the interconversion of these isomers. The *N-out* structure thermally converts to the *N-in* isomer, which can in turn be driven back to the *N-out* species photochemically. While no kinetic data were reported, both *N-out* and *N-in* isomers of one particular compound were structurally characterized for direct comparison.

By virtue of their dianionic Cp mimics, these Ta(V) dialkyls are similar to the group 4 dialkyls in that they are neutral. Another family of Ta(V) dialkyls isoelectronic to  $\text{Cp}_2\text{ZrMe}_2$  are the cationic compounds  $[\text{Cp}_2\text{TaMe}_2]^+[\text{A}]^-$ , formed readily by abstraction of methide anion from the neutral trimethyl precursor  $\text{Cp}_2\text{TaMe}_3$  (8). A subgroup of this series are the zwitterionic analogs of these ion pairs, prepared by the reaction of Schrock's methyldene methyl complex  $\text{Cp}_2\text{Ta}(\text{=CH}_2)\text{CH}_3$  with the highly electrophilic borane  $\text{B}(\text{C}_6\text{F}_5)_3$  (9). We found that the zwitterions react slowly with *tert*-butyl isonitrile to form an *N-out* iminoacyl complex, resulting from regioselective insertion into the  $\text{Ta}-\text{CH}_2\text{B}(\text{C}_6\text{F}_5)_3$  bond. Surprisingly, isonitrile insertions involving ion pairs  $[\text{Cp}_2\text{TaMe}_2]^+[\text{A}]^-$  have not been reported, so to compare the characteristics of these reactions with those observed for zwitterions, we have prepared examples of compounds  $[\text{Cp}_2\text{TaMe}_2]^+[\text{A}]^-$  and evaluated their reactivity with  $\text{RNC}$  ( $\text{R} = t\text{-Bu}$ ,  $\text{C}_6\text{H}_{11}$ , and  $\text{CH}_2\text{C}_6\text{H}_5$ ). In all cases we find the kinetic *N-out* isomers to be isolable and stable towards isomerization under ambient conditions. All, however, undergo clean conversion to their thermodynamic *N-in* isomers under controlled conditions, allowing for determination of the kinetic and thermodynamic parameters of this isomerization for a variety of related compounds.

## Results and discussion

As shown in eq. [1], the methyldene methyl tantalocene compounds  $\text{Cp}_2\text{Ta}(\text{=CH}_2)\text{CH}_3$  and  $\text{Cp}'_2\text{Ta}(\text{=CH}_2)\text{CH}_3$  ( $\text{Cp} = \text{C}_5\text{H}_5$ ;  $\text{Cp}' = \text{C}_5\text{H}_4\text{Me}$ ) react rapidly with the perfluoroaryl borane Lewis acids  $\text{B}(\text{C}_6\text{F}_5)_3$  (10) and  $\text{H}_3\text{CB}(\text{C}_6\text{F}_5)_2$  (11) via electrophilic attack on the nucleophilic carbene ligand. [1]



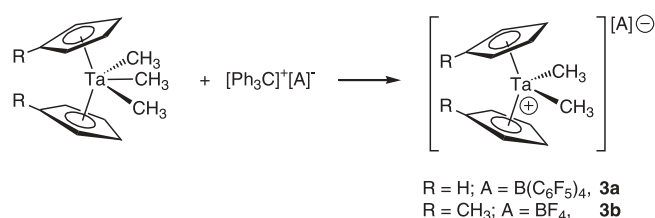
The products, as detailed in our earlier communication (9), are the zwitterionic tantalum dialkyl compounds **1a–b** and **2a** and are characterized by a strong ground state  $\alpha$  agostic interaction involving one of the C—H bonds of the borate-substituted alkyl ligand. Strong evidence for this



interaction is found in the solid state structure of compound **1a**, and it persists in solution, as evidenced by the low average  $^1J_{\text{C-H}}$  values of 82–100 Hz found for the  $\text{CH}_2$  group. In all three compounds, the anionic charge associated with the borate moiety is largely localized on the methylene carbon, rendering the C—H bonds quite electron rich and capable of strong donation to the cationic metal center. In so doing, the agostic interaction utilizes the last available metallocene orbital and perhaps stabilizes the complex with respect to a neutralizing  $-\text{C}_6\text{F}_5$  transfer from boron to tantalum, a process that is apparently quite facile in related, titanium-based zwitterions formed upon elimination of methane from ion pairs of the general formula  $[\text{Cp}(\text{L})\text{TiCH}_3]^+[\text{H}_3\text{CB}(\text{C}_6\text{F}_5)_3]^-$  (12).

Non-zwitterionic dialkyl tantalocene ion pairs **3a–b** are trivially synthesized via methide abstraction from  $\text{Cp}_2\text{TaMe}_3$  and  $\text{Cp}_2'\text{TaMe}_3$  using trityl salts (eq. [2]).

[2]



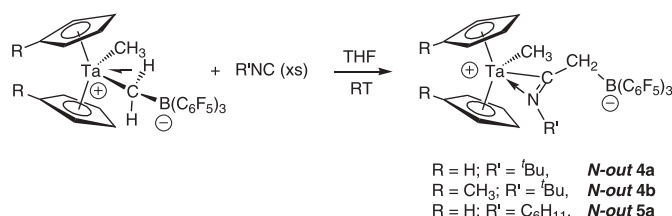
This reaction has been known for some time and is a key step in the synthesis of  $\text{Cp}_2\text{Ta}(\text{=CH}_2)\text{CH}_3$  (8). Note that the counteranions in compounds **3** are different; in **3a**, the counteranion is the tetrakis-perfluoroarylborate  $[\text{B}(\text{C}_6\text{F}_5)_4]^-$ , while for the  $\text{C}_5\text{H}_4\text{Me}$ -stabilized metallocene cation **3b**, the  $[\text{BF}_4]^-$  counteranion is used. The reasons for this discrepancy have to do with the solubility properties of the various ion pairs and the requirements for the kinetic studies described below. The  $\text{C}_5\text{H}_5\text{—BF}_4$  combination gave an ion pair that was sparingly soluble even in donor solvents, while the compound  $[(\text{C}_5\text{H}_4\text{Me})_2\text{TaMe}_2][\text{B}(\text{C}_6\text{F}_5)_4]$  was too soluble, even in non-donor solvents, for us to isolate in purity sufficient to carry out reliable kinetic studies. The  $\text{C}_5\text{H}_5\text{—B}(\text{C}_6\text{F}_5)_4$  and  $\text{C}_5\text{H}_4\text{Me—BF}_4$  combinations, however, had ideal solubility properties. Since the  $[\text{Cp}_2\text{TaMe}_2]^+$  cation has been shown to be very weakly coordinating towards perfluoroaryl borate counteranions (13), and since even the relatively more coordinating triflate anion shows little interaction with the related  $[(\text{C}_5\text{Me}_5)\text{CpTaMe}_2]^+$  cation (14), we feel that any effects due to the change in anion can be largely ignored in the interpretation of the data presented below. Nevertheless, this is an assumption and must be acknowledged as such.

While compound **3b** has been reported previously (8), **3a**, with the  $[\text{B}(\text{C}_6\text{F}_5)_4]^-$  counteranion, is a new ion pair. The  $^1\text{H}$  NMR spectrum of the cation is identical to that reported for the  $[\text{BF}_4]^-$  salt, lending credence to the above assumption that the anion has little effect on the properties of the cation. The  $^{19}\text{F}$  NMR data for the  $[\text{B}(\text{C}_6\text{F}_5)_4]^-$  anion is typical for this species (15). Analytically pure samples of **3a** were pre-

pared in order to carry out the kinetic studies described below. Unlike the zwitterionic compounds, neither **3a** nor **3b** exhibits any evidence for  $\alpha$  agostic interactions in the ground state. No low-frequency IR C—H stretches are observed in the IR spectra, and  $^1J_{\text{C-H}}$  coupling constants for the Ta— $\text{CH}_3$  groups are normal, although admittedly perturbation in this value would not be expected to be large given the six C—H bonds over which the agostic interaction would be averaged.

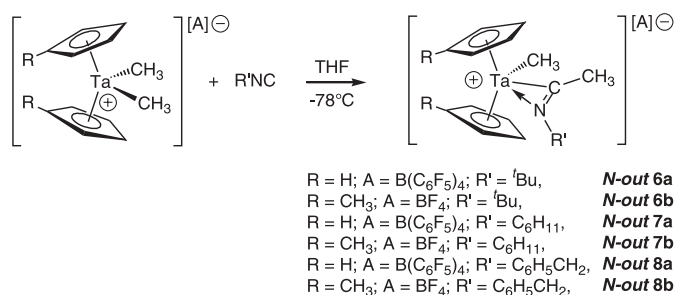
The zwitterions **1** react slowly with isocyanides to form new *N-out* iminoacyl zwitterions via selective insertion of the isocyanide reagent into the Ta— $\text{CH}_2$  bond; no products resulting from insertion into the Ta— $\text{CH}_3$  bond are observed (eq. [3]) (16).

[3]



In order for the reaction to proceed cleanly, an excess of the isocyanide reagent is required; with only 1 equiv, the reactions are very slow. Under pseudo-first-order conditions, the reactions are clean and conveniently followed by NMR spectroscopy. The products **4a–b** and **5a** are assigned<sup>3</sup> as the  $\eta^2$  *N-out* iminoacyl isomers on the basis of  $^{13}\text{C}$  NMR spectroscopy,  $^1\text{H}$  ROESY experiments, and the X-ray structure for *N-out* **4b**, which has been discussed in detail elsewhere (9). In sharp contrast to the sluggish pace of the reactions of eq. [3], reaction of ion pairs **3a** and **3b** with 1 equiv of RNC at  $-78^\circ\text{C}$  results in a rapid reaction and provides the iminoacyl compounds **6a–b** (*t*-BuNC), **7a–b** ( $\text{C}_6\text{H}_{11}\text{NC}$ ), and **8a–b** ( $\text{C}_6\text{H}_5\text{CH}_2\text{NC}$ ) as one isomer (eq. [4]).

[4]

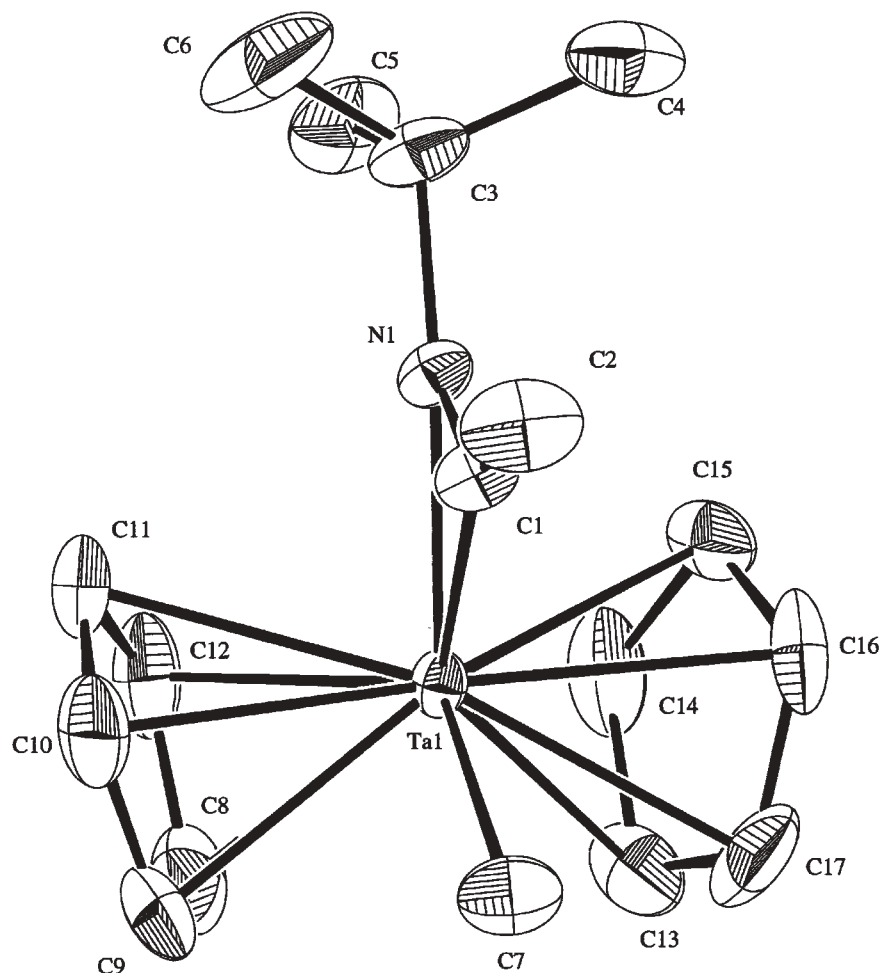


These reactions are essentially complete upon mixing and are quantitative by  $^1\text{H}$  NMR spectroscopy, as indicated in particular by a downfield shift of one of the Ta— $\text{CH}_3$  groups by about 2 ppm upon iminoacyl group formation. The  $^{13}\text{C}$  NMR chemical shifts for the iminoacyl carbon all appear

<sup>3</sup> Although IR spectroscopy is a valuable analytical tool for iminoacyl compounds because of the C=N chromophore, the stretching frequency does not correlate well with the nature of the bonding, i.e.  $\eta^1$  vs.  $\eta^2$  or *N-out* vs. *N-in*. Therefore, since the iminoacyl compounds reported herein have been well characterized by NMR spectroscopy and X-ray crystallography, we have not acquired IR data for the new compounds.



**Fig. 1.** ORTEP diagram of the cation in **N-out 6a**; the anion has been omitted for clarity. Selected bond distances (Å): Ta(1)—N(1), 2.143(2); Ta(1)—C(1), 2.147(3); Ta(1)—C(7), 2.267(3); C(1)—N(1), 1.259(4); C(1)—C(2), 1.472(4); N(1)—C(3), 1.500(4). Selected bond angles (°): C(7)—Ta(1)—C(1), 78.7(1); C(1)—Ta(1)—N(1), 34.1(1); N(1)—Ta(1)—C(7), 112.9(1); C(2)—C(1)—N(1), 134.4(3); Ta(1)—C(1)—C(2), 152.8(2).



within the narrow range of 210.1–211.7 ppm and are characteristic of  $\eta^2$ -iminoacyl ligands (2a).

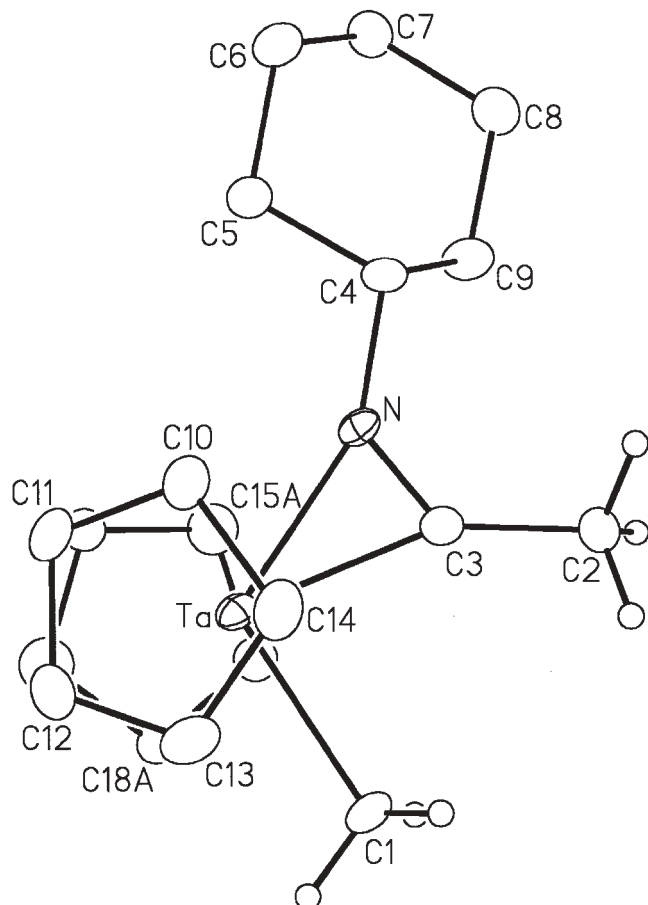
As in the reactions involving the zwitterions, the *N-out* isomers were formed exclusively under these conditions and were stable enough to isolate and fully characterize. The X-ray structures of *N-out 6a* and *N-out 7a* were carried out to demonstrate this conclusively; ORTEP diagrams of the cations for these compounds are given in Figs. 1 and 2 along with selected bond distances and angles. Full details on these structure determinations are available in the supporting information.<sup>4</sup> Given the similarity in the <sup>13</sup>C NMR data, the other compounds were also assigned to the *N-out* geometry. As can be seen in the figures, the nitrogen of the iminoacyl ligand is coordinated to the Ta center on the outside of the metallocene wedge in both cases. For transition metal iminoacyl complexes, the parameter  $\Delta$  is defined as  $d(\text{M}—\text{N}) - d(\text{M}—\text{C})$  and correlates at least qualitatively with the

electrophilicity of the metal center (2a). That is, the more electrophilic the metal center, the stronger is the dative M—N bond and the lower is the value observed for  $\Delta$ . For *N-out 6a* and *7a*, the values of  $\Delta$  are 0.004 Å and 0.000 Å, respectively, which are similar to the value of –0.002 Å reported for the carborane *N-out I* isomer of Chart 1 (5). Given the cationic nature of the Ta centers in *N-out 6a* and *7a*, one might expect a larger difference in  $\Delta$  compared with the neutral (and relatively electron-rich) dicarbollide complex. It should be noted, however, that the values of  $\Delta$  for  $\eta^2$  iminoacyl complexes have been, for the most part, determined only for *N-in* isomers. Since the *N-out* isomers are thermodynamically less stable than the *N-in* isomers, owing to poorer overlap of the nitrogen lone pair with metallocene orbitals in this geometry (3, 4),  $\Delta$  is likely less affected by electronic changes at the metal center and more prone to steric effects in the *N-out* isomer. Consistent with this

<sup>4</sup>Supplementary data may be purchased from the Depository of Unpublished Data, Document Delivery, CISTI, National Research Council Canada, Ottawa, ON K1A 0S2, Canada ([http://www.nrc.ca/cisti/irm/unpub\\_e.shtml](http://www.nrc.ca/cisti/irm/unpub_e.shtml) for information on ordering electronically). CCDC 210457 (**6a**) and 210458 (**7a**) contain the supplementary data for this paper. These data can be obtained, free of charge, via [www.ccdc.cam.ac.uk/conts/retrieving.html](http://www.ccdc.cam.ac.uk/conts/retrieving.html) (or from the Cambridge Crystallographic Data Centre, 12 Union Road, Cambridge, U.K.; fax +44 1223 336033; or [deposit@ccdc.cam.ac.uk](mailto:deposit@ccdc.cam.ac.uk)).



**Fig. 2.** ORTEP diagram of the cation in *N-out* **7a**; the anion has been omitted for clarity. Selected bond distances (Å): Ta—N(1), 2.130(6); Ta—C(3), 2.130(7); Ta—C(1), 2.287(7); C(3)—N(1), 1.245(8); C(2)—C(3), 1.496(10); N(1)—C(4), 1.508(9). Selected bond angles (°): C(1)—Ta—C(3), 79.0(3); C(3)—Ta—N(1), 34.0(12); N(1)—Ta—C(1), 112.6(3); C(2)—C(3)—N(1), 132.0(7); Ta—C(3)—C(2), 154.7(6).

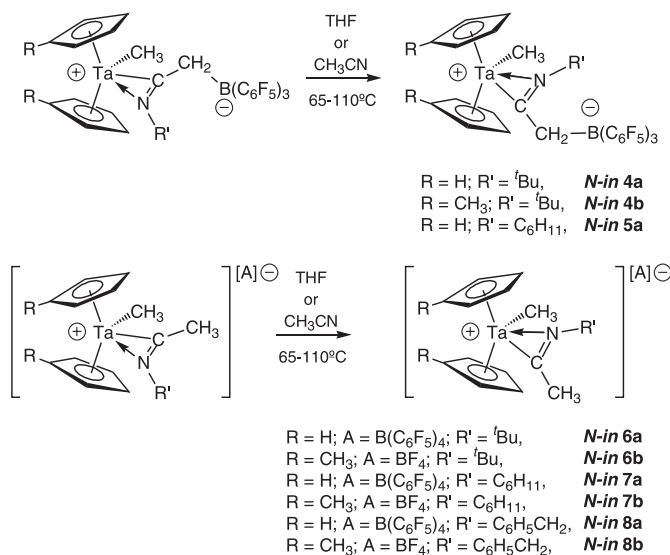


notion is the larger value of  $\Delta$  of 0.088 Å observed for the *N-in* isomer of **I**, which is more in line with expectations for a neutral and relatively electron-rich  $d^0$  complex (17).

The reason for the marked difference in reaction rates for the insertion of RNC, involving zwitterions **1** vs. ion pairs **3**, has its roots in the different ground-state structures for these compounds. Kinetic studies on the reaction of *t*-BuNC with **1a** under pseudo-first-order conditions pointed to a mechanism for insertion that involves dissociation of the  $\alpha$  agostic interaction prior to isocyanide coordination and insertion (9). Most telling was the substantial inverse  $k_H/k_D$  of 0.84(4) at 30°C, observed when comparing the rates of insertion for **1a** and **d<sub>5</sub>-1a** (prepared from  $\text{Cp}_2\text{Ta}(\text{=CD}_2)\text{CD}_3$  and  $\text{B}(\text{C}_6\text{F}_5)_3$ ). In the deuterated compound, the equilibrium between agostic and non-agostic structures will be perturbed towards the latter, allowing for faster rates of isocyanide coordination (and therefore insertion) in the labeled compound. In comparison to the ion pairs **3**, the necessity for dissociation of the  $\alpha$  agostic C—H bond in zwitterions **1**, with its itinerant charge separation, slows the overall rate of the reaction considerably. Since the compounds **3** do not exhibit this interaction, they have an orbital available to accept the isocyanide

donor, allowing for rapid insertion chemistry. The lower steric demands of the dimethyl compounds probably also contribute to the dramatic rate difference observed.

[5]



Iminoacyl compounds *N-out* **4–8** are unusual in that they are essentially immune to isomerization to *N-in* isomers under ambient conditions. All of them do, however, undergo clean conversion to the thermodynamic *N-in* isomers under thermal duress (60–110°C, eq. [5]).

The isomerization is signaled in the  $^1\text{H}$  NMR spectrum by a slight upfield shift in the cyclopentadienyl resonances and a downfield shift in the Ta—CH<sub>3</sub> and iminoacyl CH<sub>*n*</sub> protons ( $n = 2$  for **4** and **5**;  $n = 3$  for **6**, **7**, and **8**). In addition, the  $^{13}\text{C}$  chemical shift for the iminoacyl carbon shifts downfield 8–9 ppm into the ranges of 221.7–223.6 ppm for the zwitterions and 217.7–220.2 ppm for compounds **6–8**. Thus, the two isomers are easily distinguishable on the basis of their  $^{13}\text{C}$  NMR spectra.

Baseline separation in the signals for the two isomers in the  $^1\text{H}$  NMR spectra allows for convenient monitoring of the isomerization and determination of first-order rate constants for the various compounds in the study; this data, along with the thermodynamic activation parameters obtained from Eyring plots, is collected in Table 1. The reactions were all found to be first order in the *N-out* isomer for greater than 3 half lives, and the rate constants given are an average of two separately determined values.

There are few studies measuring the activation parameters for the *N-out* to *N-in* isomerization process and no studies employing a wide range of derivatives. Bullock and co-workers have investigated the isomerization of the zirconocene system prepared through reaction of  $\text{Cp}(\text{PMe}_2)_2\text{RuCH=CHZrClCp}_2$  with *t*-BuNC, the first system studied that showed irreversible rearrangement to the *N-in* isomer (18). Activation parameters reported for this zirconocene system were  $\Delta H^\ddagger = 19.9(6)$  kcal mol<sup>−1</sup>,  $\Delta S^\ddagger = -3.4(22)$  eu, with a  $\Delta G^\ddagger_{298} = 20.9$  kcal mol<sup>−1</sup>. Measurement of the barrier to *N-out*/*N-in* interconversion in fluxional systems has also been reported. For example, Adams and Chodosh (19) have investigated the molybdenum system



**Table 1.** Rate constants and activation parameters for *N-out* to *N-in* isomerization of  $\eta^2$ -iminoacyl complexes.

Compound <sup>a</sup>	<i>T</i> (K)	$10^{-4} k$ (s <sup>-1</sup> )	$\Delta H^\ddagger$ (kcal mol <sup>-1</sup> )	$\Delta S^\ddagger$ (eu)	$\Delta G^\ddagger_{298}$ (kcal mol <sup>-1</sup> )
<i>N-out</i> <b>4b</b>	356	4.49(7)	26.9(7)	1(2)	26.5(7)
<i>N-out</i> <b>4b</b>	346	1.30(1)			
<i>N-out</i> <b>4b</b>	334	0.35(2)			
<i>N-out</i> <b>5a</b>	356	16.9(4)	25.5(3)	0(1)	25.5(3)
<i>N-out</i> <b>5a</b>	345	6.10(9)			
<i>N-out</i> <b>5a</b>	336	2.09(2)			
<i>N-out</i> <b>5a</b>	324	0.45(1)	34.5(8)	14(3)	30.2(8)
<i>N-out</i> <b>6a</b>	391	5.4(1)			
<i>N-out</i> <b>6a</b>	380	1.80(2)			
<i>N-out</i> <b>6a</b>	372	0.436(7)	26.9(1)	-2.0(4)	27.5(1)
<i>N-out</i> <b>6a</b>	360	0.121(3)			
<i>N-out</i> <b>6b</b>	358	1.05(1)			
<i>N-out</i> <b>6b</b>	347	0.320(9)	26.8(9)	0(3)	27.1(9)
<i>N-out</i> <b>6b</b>	335	0.068(3)			
<i>N-out</i> <b>7a</b>	359	2.15(4)			
<i>N-out</i> <b>7a</b>	348	0.795(7)	21(2)	-15(6)	26(2)
<i>N-out</i> <b>7a</b>	338	0.205(3)			
<i>N-out</i> <b>7b</b>	355	2.95(4)			
<i>N-out</i> <b>7b</b>	343	1.75(2)	26.2(4)	-3(2)	27.0(4)
<i>N-out</i> <b>7b</b>	333	0.507(4)			
<i>N-out</i> <b>7b</b>	323	0.147(3)			
<i>N-out</i> <b>8a</b>	369	5.65(9)	26.4(1)	0.3(4)	26.3(1)
<i>N-out</i> <b>8a</b>	358	1.91(3)			
<i>N-out</i> <b>8a</b>	346	0.498(3)			
<i>N-out</i> <b>8a</b>	335	0.15(6)	26.4(1)	0.3(4)	26.3(1)
<i>N-out</i> <b>8b</b>	357	6.04(3)			
<i>N-out</i> <b>8b</b>	345	1.70(2)			
<i>N-out</i> <b>8b</b>	334	0.461(7)	26.4(1)	0.3(4)	26.3(1)
<i>N-out</i> <b>8b</b>	323	0.108(6)			

<sup>a</sup>Reliable kinetic data for compound *N-out* **4a** could not be obtained because of the long reaction times required to effect isomerization. Higher temperatures also gave poor data owing to undesired side reactions.

<sup>b</sup>The range observed in  $\Delta S^\ddagger$  (e.g., **6a** and **7b**) likely is a reflection of the narrow temperature ranges we were restricted to experimentally.

$\text{Cp}(\text{CO})_2\text{Mo}[\eta^2\text{-C(=NMe)Me}]$  and found activation parameters of  $\Delta H^\ddagger = 14.7(5)$  kcal mol<sup>-1</sup>,  $\Delta S^\ddagger = -1.7(15)$  eu, and  $\Delta G^\ddagger_{298} = 20.9$  kcal mol<sup>-1</sup>. Rothwell and co-workers (20) have reported a Gibbs free energy of activation of  $\Delta G^\ddagger_{233} = 11.4(5)$  kcal mol<sup>-1</sup> for the observed rotation in  $(\text{ArO})_2\text{Zr}[\eta^2\text{-C(=N(2,6-Me}_2\text{C}_6\text{H}_3))\text{CH}_2\text{Ph}]_2$  (Ar = 2,6-C<sub>6</sub>-*t*-Bu<sub>2</sub>H<sub>3</sub>). The less bulky derivative (Ar = 2,6-C<sub>6</sub>Ph<sub>2</sub>H<sub>3</sub>) gave a result of  $\Delta G^\ddagger_{208} = 10.3(5)$  kcal mol<sup>-1</sup>. Lappert et al. have also observed the interconversion of the two isomers of  $\text{Cp}_2\text{Zr}(\text{Cl})[\eta^2\text{-C(=N}(p\text{-C}_6\text{H}_4\text{CH}_3))\text{CH}(\text{SiMe}_3)_2]$  (**16b**). While our values for  $\Delta S^\ddagger$  are comparable to those found in other systems — the magnitudes consistent with an intramolecular process, as can be seen in Table 1 — the  $\Delta H^\ddagger$  and  $\Delta G^\ddagger_{298}$  values are generally substantially larger in the present cationic tantalocene systems than these previously reported examples. This can be attributed to the stronger metal—ligand bonds for third row transition metal complexes, as well as the increased electrophilicity of the cationic tantalum center. Assuming the mechanism of isomerization involves slippage of the  $\eta^2$ -iminoacyl to an  $\eta^1$ -bound species, a stronger tantalum—nitrogen dative bond must be dissociated to form an  $\eta^1$ -iminoacyl ligand.

A trend is apparent in the rate of isomerization based on the steric bulk of the iminoacyl substituent on the nitrogen atom. The C<sub>5</sub>H<sub>5</sub> cationic complexes, *N-out* **6a**, *N-out* **7a**,

and *N-out* **8a**, exhibit isomerization rate constants that increase as the alkyl group on the nitrogen atom changes from *t*-Bu ( $k_{360} = 1.21 \times 10^{-5}$  s<sup>-1</sup>) to C<sub>6</sub>H<sub>11</sub> ( $k_{358} = 2.15 \times 10^{-4}$  s<sup>-1</sup>), which is similar to that found for the C<sub>6</sub>H<sub>5</sub>CH<sub>2</sub> isomerization ( $k_{358} = 1.96 \times 10^{-4}$  s<sup>-1</sup>). The  $\Delta G^\ddagger$  values parallel the trend in rate constants, and a similar phenomenon is observed for the C<sub>5</sub>H<sub>4</sub>Me cations. The origin of this effect likely resides in steric interactions between the N-iminoacyl substituent and the Cp rings upon rotation about the Ta—C<sub>iminoacyl</sub> bond in the  $\eta^1$  structure.

Comparison of the isomerization rates of the unsubstituted cyclopentadienyl cations *N-out* **6a–8a** with those of the methylcyclopentadienyl compounds *N-out* **6b–8b** provides further insight. In each cation pair the isomerization of the methylcyclopentadienyl derivative proceeds at an elevated rate compared with the Cp derivative. For example, the *t*-BuNC insertion product *N-out* **6a** isomerizes with a rate constant of  $k_{360} = 1.21 \times 10^{-5}$  s<sup>-1</sup>, nearly an order of magnitude slower than *N-out* **6b** ( $k_{358} = 1.05 \times 10^{-4}$  s<sup>-1</sup>). The presence of more electron-donating cyclopentadienyl rings for the C<sub>5</sub>H<sub>4</sub>Me derivatives facilitates the slippage of the iminoacyl from  $\eta^2$  bonded to the  $\eta^1$  intermediate.

Interestingly, a comparison of the rates of isomerization between analogous zwitterions and ion pairs (*N-out* **4b** vs. *N-out* **6b** and *N-out* **5a** vs. *N-out* **7a**) reveals that the zwitterion



terions undergo more rapid isomerization at comparable temperatures. This seems counterintuitive given that, in the ground state of the *N-out* isomers whose structures have been determined, the bond distances from Ta to the iminoacyl nitrogen are comparable for *N-out* **4b** (2.121(5) Å) to those for the ion pairs *N-out* **6a** (2.143(2) Å) and *N-out* **7a** (2.130(6) Å). Indeed, the  $\Delta$  parameter for the zwitterion is smaller (−0.061 Å), suggesting a more electrophilic metal center in the zwitterions. It might also be expected that more steric hindrance would exist in the iminoacyl rotation necessary for isomerization in the zwitterionic species. Nevertheless, the rates for zwitterions isomerization are about an order of magnitude higher than the non-zwitterionic counterpart, suggesting that differences in ion pairing in the zwitterionic vs. the non-zwitterionic ion pairs may be important in the transition state.

## Conclusions

The results reported herein add to the body of research on the mechanistic aspects of isonitrile insertion into M—C bonds, providing corroborative evidence for the general mechanistic picture of the insertion step and the isomerization of *N-out* isomers to *N-in* structures. In particular, we have shown how ground state  $\alpha$  agostic interactions can hamper coordination of the isonitrile substrate, leading to overall lower rates of insertion in comparison to non-agostic reactions. These results also show that kinetic *N-out* isomers are stabilized in highly electrophilic species, and that the barriers to conversion to the thermodynamic *N-in* isomers are influenced by a variety of factors, including the steric bulk of the isonitrile substituent and the electron-donating ability of the Cp ligands on the metallocene. Finally, the rate of isomerization in the zwitterionic *N-out* compounds is somewhat faster than the non-zwitterionic reactions, although the origin of this phenomenon is less clear.

## Experimental section

### General procedures

General procedures have been described in detail elsewhere (21).

### Synthesis of $\text{Cp}_2\text{Ta}[\text{CH}_2\text{B}(\text{C}_6\text{F}_5)_3]\text{CH}_3$ , **1a**

Toluene (15 mL) was condensed into an evacuated flask containing  $\text{B}(\text{C}_6\text{F}_5)_3$  (214 mg, 0.418 mmol) and a slight excess of  $\text{Cp}_2\text{Ta}(\text{=CH}_2)\text{CH}_3$  (156 mg, 0.458 mmol) at  $-78^\circ\text{C}$ . The solution was warmed to  $25^\circ\text{C}$  and stirred for 30 min. The toluene was removed under reduced pressure to leave a yellow residue. Hexane (15 mL) was condensed into the vessel, and the light yellow precipitate was isolated by filtration. The precipitate was washed by back distillation of hexane, and the solvent was removed under reduced pressure. Yield of **1a**: 324 mg, 0.380 mmol, 91%. X-ray quality crystals were grown by cooling a saturated 1,2-dichloroethane solution to  $-25^\circ\text{C}$ .  $^1\text{H}$  NMR ( $\text{C}_6\text{D}_6$ ): 5.93 (s, 10H,  $\text{C}_5\text{H}_5$ ), 2.13 (br., 2H,  $\text{CH}_2$ ), 0.56 (s, 3H,  $\text{CH}_3$ ).  $^{13}\text{C}$  NMR ( $\text{C}_6\text{D}_6$ ): 150.3 ( $\text{CH}_2$ ,  $^1J_{\text{CH}} = 98.7$  Hz), 108.4 ( $\text{C}_5\text{H}_5$ ), 21.4 ( $\text{CH}_3$ ,  $^1J_{\text{CH}} = 129.1$  Hz).  $^{11}\text{B}$  NMR ( $\text{C}_6\text{D}_6$ ): −9.4.  $^{19}\text{F}$  NMR ( $\text{C}_6\text{D}_6$ ): −132.0 (2F, *o*-F), −159.7 (1F, *p*-F), −164.4 (2F, *m*-F).

Anal. calcd. for  $\text{C}_{30}\text{H}_{15}\text{BF}_{15}\text{Ta}$ : C 42.28, H 1.77; found: C 42.42, H 1.50.

### Synthesis of $\text{Cp}'_2\text{Ta}[\text{CH}_2\text{B}(\text{C}_6\text{F}_5)_3]\text{CH}_3$ , **1b**

A procedure analogous to the synthesis of **1a**, using  $(\text{C}_5\text{H}_4\text{Me})_2\text{Ta}(\text{=CH}_2)(\text{CH}_3)$ , was employed. The product was isolated with 0.5 equiv of toluene by  $^1\text{H}$  NMR after extended exposure to vacuum. Reagent amounts:  $\text{B}(\text{C}_6\text{F}_5)_3$  (690 mg, 1.35 mmol),  $(\text{C}_5\text{H}_4\text{Me})_2\text{Ta}(\text{=CH}_2)(\text{CH}_3)$  (500 mg, 1.36 mmol). Yield of **1b**, accounting for toluene: 1.183 g, 1.28 mmol, 95%.  $^1\text{H}$  NMR ( $\text{THF}-d_8$ ): 6.05 (m, 2H,  $\text{C}_5\text{H}_4$ ), 5.83 (m, 2H,  $\text{C}_5\text{H}_4$ ), 5.62 (m, 2H,  $\text{C}_5\text{H}_4$ ), 5.57 (m, 2H,  $\text{C}_5\text{H}_4$ ), 2.24 (s, 6H,  $\text{C}_5\text{H}_4\text{-CH}_3$ ), 1.91 (br, 2H,  $\text{CH}_2$ ), 0.43 (s, 3H,  $\text{CH}_3$ ).  $^{13}\text{C}$  NMR ( $\text{THF}-d_8$ ): 139.9 ( $\text{CH}_2$ ,  $^1J_{\text{CH}} = 100.1$  Hz), 126.2 ( $\text{C}_5\text{H}_4\text{-CH}_3$ ), 114.2 ( $\text{C}_5\text{H}_4$ ), 109.1 ( $\text{C}_5\text{H}_4$ ), 109.0 ( $\text{C}_5\text{H}_4$ ), 102.9 ( $\text{C}_5\text{H}_4$ ), 27.7 ( $\text{Ta-CH}_3$ ,  $^1J_{\text{CH}} = 124.9$  Hz), 14.8 ( $\text{C}_5\text{H}_4\text{-CH}_3$ ).  $^{11}\text{B}$  NMR ( $\text{THF}-d_8$ ) = −4.4.  $^{19}\text{F}$  NMR ( $\text{THF}-d_8$ ): −130.9 (2F, *o*-F), −161.2 (1F, *p*-F), −164.8 (2F, *m*-F). Anal. calcd. for  $\text{C}_{32}\text{H}_{19}\text{BF}_{15}\text{Ta}$ : C 46.03, H 2.50; found: C 45.98, H, 2.42.

### $\text{Cp}_2\text{Ta}[\text{CH}_2\text{B}(\text{C}_6\text{F}_5)_2\text{CH}_3]\text{CH}_3$ , **2a**

In a dry box, benzene (10 mL) was added to a flask containing  $\text{H}_3\text{CB}(\text{C}_6\text{F}_5)_2$  (122 mg, 0.338 mmol) and  $\text{Cp}_2\text{Ta}(\text{=CH}_2)\text{CH}_3$  (113 mg, 0.332 mmol). The solution was stirred at  $25^\circ\text{C}$  for 1 h, and the light yellow precipitate was isolated by filtration. The precipitate was washed with benzene through back distillation, and the solvent was removed under reduced pressure. Yield of **2a**: 183 mg, 0.261 mmol, 79%.  $^1\text{H}$  NMR ( $\text{CD}_2\text{Cl}_2$ ): 6.07 (s, 10H,  $\text{C}_5\text{H}_5$ ), 2.46 (br. s, 2H,  $\text{CH}_2$ ), 0.42 (s, 3H,  $\text{Ta-CH}_3$ ), 0.36 (br. s, 3H,  $\text{B-CH}_3$ ).  $^{13}\text{C}$  NMR ( $\text{CD}_2\text{Cl}_2$ ): 159.6 ( $\text{C}_5\text{H}_5$ ), 108.0 ( $\text{CH}_2$ ,  $^1J_{\text{CH}} = 82.7$  Hz), 20.6 ( $\text{Ta-CH}_3$ ,  $^1J_{\text{CH}} = 112.3$  Hz), 14 ( $\text{B-CH}_3$ ).  $^{11}\text{B}$  NMR ( $\text{CD}_2\text{Cl}_2$ ): −7.0.  $^{19}\text{F}$  NMR ( $\text{CD}_2\text{Cl}_2$ ): −133.7 (2F), −163.5 (1F), −166.0 (2F). Anal. calcd. for  $\text{C}_{25}\text{H}_{18}\text{BF}_{10}\text{Ta}$ : C 42.89, H 2.59; found: C 42.59, H 2.20.

### Synthesis of $[\text{Cp}_2\text{TaMe}_2]^+[\text{B}(\text{C}_6\text{F}_5)_4]^-$ , **3a**

$\text{CH}_2\text{Cl}_2$  (10 mL) was condensed into an evacuated flask containing  $\text{Cp}_2\text{TaMe}_3$  (1.513 g, 4.25 mmol). In separate flask,  $\text{CH}_2\text{Cl}_2$  (40 mL) was condensed over  $[\text{Ph}_3\text{C}]^+[\text{B}(\text{C}_6\text{F}_5)_4]^-$  (3.918 g, 4.25 mmol). The solution of trityl salt was added to the  $\text{Cp}_2\text{TaMe}_3$  solution by cannula at  $25^\circ\text{C}$  with rapid stirring. An immediate light yellow precipitate formed, and the solution was stirred for an additional 15 min. The precipitate was isolated by filtration and washed once by back distillation of  $\text{CH}_2\text{Cl}_2$ . The solvent was then removed under reduced pressure. Yield of **3a**: 3.917 g, 3.84 mmol, 90%.  $^1\text{H}$  NMR resonances are identical to those previously reported for the cation (9, 13).  $^{13}\text{C}$  NMR ( $\text{THF}-d_8$ ): 114.1 ( $\text{C}_5\text{H}_5$ ), 55.6 ( $\text{Ta-CH}_3$ ,  $^1J_{\text{CH}} = 125.6$  Hz).  $^{11}\text{B}$  NMR ( $\text{THF}-d_8$ ): −13.6.  $^{19}\text{F}$  NMR ( $\text{THF}-d_8$ ): −130.9 (2F, *o*-F), −163.0 (1F, *p*-F), −166.5 (2F, *m*-F). Anal. calcd. for  $\text{C}_{26}\text{H}_{16}\text{BF}_{20}\text{Ta}$ : C 42.38, H 1.58; found: C 41.94, H 1.48.

### Reaction of **1a** with *t*-BuNC: Synthesis of *N-out* **4a**

THF (10 mL) was condensed into an evacuated flask containing **1a** (315 mg, 0.370 mmol) at  $-78^\circ\text{C}$ . Under a flow of argon, an excess of *tert*-butylisocyanide (400 mL, 3.83 mmol) was syringed into the flask. The solution was warmed to  $25^\circ\text{C}$  and stirred for 75 min. THF was removed



under reduced pressure to leave a white residue, which was filtered after suspension in hexane (10 mL). The precipitate was washed by back distillation using hexane, and the solvent was removed under reduced pressure. Yield of **N-out 4a**: 288 mg, 0.308 mmol, 83%.  $^1\text{H}$  NMR (THF- $d_8$ ): 5.67 (s, 10 H,  $\text{C}_5\text{H}_5$ ), 3.75 (br., 2H,  $\text{CH}_2$ ), 1.35 (s, 9H,  $\text{C}(\text{CH}_3)_3$ ), 0.39 (s, 3H,  $\text{CH}_3$ ).  $^{13}\text{C}$  NMR (THF- $d_8$ ): 219.8 ( $\text{C}=\text{N}-t\text{-Bu}$ ), 107.4 ( $\text{C}_5\text{H}_5$ ), 62.9 ( $\text{C}(\text{CH}_3)_3$ ), 34.5 ( $\text{CH}_2$ ), 29.2 ( $\text{C}(\text{CH}_3)_3$ ), 5.0 ( $\text{CH}_3$ ).  $^{11}\text{B}$  NMR (THF- $d_8$ ): -10.9.  $^{19}\text{F}$  NMR: -129.4 (2F, *o*-F), -162.2 (1F, *p*-F), -165.7 (2F, *m*-F). Anal. calcd. for  $\text{C}_{35}\text{H}_{24}\text{NBF}_{15}\text{Ta}$ : C 44.95, H 2.59, N 1.50; found: C 44.69, H 2.39, N 1.57.

#### Isomerization of **N-out 4a** to **N-in 4a**

**N-out 4a** (170 mg, 0.18 mmol) was placed into a 25 mL glass bomb and THF (10 mL) was condensed in. The bomb was heated at 70°C for 10 days. The colourless solution was cannula-transferred into a 25 mL round bottom flask with filtering frit. The THF was removed to leave a sticky, colourless residue. Hexanes (10 mL) were condensed in at -78°C, and the residue sonicated to produce a white powder. The product was filtered off, washed with hexanes by distillation (3 × 5 mL), and volatiles were removed in vacuo. Yield of **N-in 4a**: 152 mg, 0.16 mmol, 89%.  $^1\text{H}$  NMR (THF- $d_8$ ): 5.46 (s, 10 H,  $\text{C}_5\text{H}_5$ ), 3.85 (br, 2H,  $\text{CH}_2$ ), 1.41 (s, 9H,  $\text{C}(\text{CH}_3)_3$ ), 0.78 (s, 3H,  $\text{CH}_3$ ).  $^{13}\text{C}$  NMR (THF- $d_8$ ): 221.7 ( $\text{C}=\text{N}-t\text{-Bu}$ ), 106.0 ( $\text{C}_5\text{H}_5$ ), 66.1 ( $\text{C}(\text{CH}_3)_3$ ), 35.0 ( $\text{CH}_2$ ), 30.0 ( $\text{C}(\text{CH}_3)_3$ ), 3.9 ( $\text{CH}_3$ ).  $^{11}\text{B}$  NMR (THF- $d_8$ ): -10.0.  $^{19}\text{F}$  NMR: -130.0 (2F, *o*-F), -160.3 (1F, *p*-F), -164.6 (2F, *m*-F).

#### Reaction of **1b** with *t*-BuNC: Synthesis of **N-out 4b**

THF (10 mL) was condensed into an evacuated flask containing **1b** (325 mg, 0.35 mmol) at -78°C. Under a flow of argon, an excess of *tert*-butylisocyanide (400 mL, 3.83 mmol) was syringed into the flask. The solution was warmed to 25°C and stirred for 2 h. THF was removed under reduced pressure to leave a white residue, which was filtered from hexane (10 mL). The precipitate was washed by back distillation with hexane, and the solvent was removed under reduced pressure. Yield of **N-out 4b**: 283 mg, 0.29 mmol, 84%. X-ray quality crystals were grown by layering a saturated  $\text{CH}_2\text{Cl}_2$  solution with hexanes.  $^1\text{H}$  NMR (THF- $d_8$ ): 5.75 (m, 2H,  $\text{C}_5\text{H}_4$ ), 5.61 (m, 2H,  $\text{C}_5\text{H}_4$ ), 5.35 (m, 2H,  $\text{C}_5\text{H}_4$ ), 5.01 (m, 2H,  $\text{C}_5\text{H}_4$ ), 3.76 (br, 2H,  $\text{CH}_2$ ), 2.01 (s, 6H,  $\text{C}_5\text{H}_4(\text{CH}_3)$ ), 1.35 (s, 9H,  $\text{C}(\text{CH}_3)_3$ ), 0.22 (s, 3H,  $\text{CH}_3$ ).  $^{13}\text{C}$  NMR (THF- $d_8$ ): 220.7 ( $\text{C}=\text{N}-t\text{-Bu}$ ), 121.4 ( $\text{C}_5\text{H}_4-\text{CH}_3$ ), 110.0 ( $\text{C}_5\text{H}_4$ ), 109.7 ( $\text{C}_5\text{H}_4$ ), 108.2 ( $\text{C}_5\text{H}_4$ ), 94.4 ( $\text{C}_5\text{H}_4$ ), 62.9 ( $\text{C}(\text{CH}_3)_3$ ), 33.1 ( $\text{CH}_2$ ), 29.4 ( $\text{C}(\text{CH}_3)_3$ ), 14.2 ( $\text{C}_5\text{H}_4-\text{CH}_3$ ), 9.4 ( $\text{Ta}-\text{CH}_3$ ).  $^{11}\text{B}$  (THF- $d_8$ ): -9.0.  $^{19}\text{F}$  NMR (THF- $d_8$ ): -129.3 (2F, *o*-F), -162.3 (1F, *p*-F), -165.7 (2F, *m*-F). Anal. calcd. for  $\text{C}_{37}\text{H}_{28}\text{NBF}_{15}\text{Ta}\cdot\text{CH}_2\text{Cl}_2$ : C 43.54, H 2.88, N 1.34; found: C 43.63, H 2.78, N 1.34.

#### Isomerization of **N-out 4b** to **N-in 4b**

**N-out 4b** (350 mg, 0.360 mmol) was placed into a 25 mL glass bomb and THF (10 mL) was condensed into the vessel. The bomb was heated at 70°C for 2 days. The colourless solution was cannula-transferred into a 25 mL round bottom flask with filtering frit. The THF was removed to leave a colourless, waxy residue. Hexanes (10 mL) were condensed

in at -78°C, and the suspension was sonicated to produce a white powder. The product was isolated by filtration, washed with hexanes by distillation (3 × 5 mL), and dried in vacuo. Yield of **N-in 4b**: 250 mg, 0.257 mmol, 71%.  $^1\text{H}$  NMR (THF- $d_8$ ): 5.34 (m, 2H,  $\text{C}_5\text{H}_4$ ), 5.10 (m, 2H,  $\text{C}_5\text{H}_4$ ), 5.06 (m, 2H,  $\text{C}_5\text{H}_4$ ), 5.02 (m, 2H,  $\text{C}_5\text{H}_4$ ), 3.85 (br, 2H,  $\text{CH}_2$ ), 1.99 (s, 6H,  $\text{C}_5\text{H}_4(\text{CH}_3)$ ), 1.38 (s, 9H,  $\text{C}(\text{CH}_3)_3$ ), 0.55 (s, 3H,  $\text{CH}_3$ ).  $^{13}\text{C}$  NMR (THF- $d_8$ ): 223.3 ( $\text{C}=\text{N}-t\text{-Bu}$ ), 125.5 ( $\text{C}_5\text{H}_4-\text{CH}_3$ ), 108.1 ( $\text{C}_5\text{H}_4$ ), 103.9 ( $\text{C}_5\text{H}_4$ ), 103.6 ( $\text{C}_5\text{H}_4$ ), 98.4 ( $\text{C}_5\text{H}_4$ ), 66.0 ( $\text{C}(\text{CH}_3)_3$ ), 35.2 ( $\text{CH}_2$ ), 30.3 ( $\text{C}(\text{CH}_3)_3$ ), 14.6 ( $\text{C}_5\text{H}_4-\text{CH}_3$ ), 11.1 ( $\text{Ta}-\text{CH}_3$ ).  $^{11}\text{B}$  NMR (THF- $d_8$ ): -9.9.  $^{19}\text{F}$  NMR: -129.8 (2F, *o*-F), -160.6 (1F, *p*-F), -164.7 (2F, *m*-F).

#### Reaction of **1a** with $\text{C}_6\text{H}_{11}\text{NC}$ : Synthesis of **N-out 5a**

A procedure analogous to that employed for the synthesis of **N-out 4a** was used to prepare this compound. Reagent amounts: **1a** (300 mg, 0.352 mmol), cyclohexyl isocyanide (500 mL, 4.02 mmol). Yield of **N-out 5a**: 247 mg, 0.256 mmol, 76%.  $^1\text{H}$  NMR (THF- $d_8$ ): 5.66 (s, 10 H,  $\text{C}_5\text{H}_5$ ), 3.60 (br. s, 3H,  $\text{CH}_2$  and  $\text{CH}$ ,  $\text{C}_6\text{H}_{11}$ ), 1.05–1.95 (m, 10H,  $\text{C}_6\text{H}_{11}$ ) 0.53 (s, 3H,  $\text{CH}_3$ ).  $^{11}\text{B}$  NMR (THF- $d_8$ ): -9.3.  $^{19}\text{F}$  NMR: -129.5 (2F, *o*-F), -161.7 (1F, *p*-F), -165.5 (2F, *m*-F). Anal. calcd. for  $\text{C}_{37}\text{H}_{26}\text{NBF}_{15}\text{Ta}\cdot\text{C}_7\text{H}_8$ : C 50.16, H 3.25, N 1.33; found: C 50.36, H 3.07, N 1.39.

#### Isomerization of **N-out 5a** to **N-in 5a**

**N-out 5a** (221 mg, 0.230 mmol) was placed in a 25 mL glass bomb and THF (15 mL) was condensed in at -78°C. The bomb was sealed and placed in an oil bath at 65°C for 24 h. The light yellow solution was then cannula-transferred to a 25 mL round bottom flask equipped with a filtering frit. The THF was removed under reduced pressure to leave a yellow oil. Hexanes (10 mL) were condensed onto the oil at -78°C and the solution sonicated to produce light yellow powder. The powder was filtered off, washed with hexanes (3 × 5 mL) by back distillation, and dried in vacuo. Yield of **N-in 5a**: 153 mg, 0.159, 61%.  $^1\text{H}$  NMR (THF- $d_8$ ): 5.63 (s, 10 H,  $\text{C}_5\text{H}_5$ ), 3.85 (br. s, 2H,  $\text{CH}_2$  and *ipso*- $\text{CH}$ ,  $\text{C}_6\text{H}_{11}$ ), 1.05–1.95 (m, 10H,  $\text{C}_6\text{H}_{11}$ ) 0.75 (s, 3H,  $\text{CH}_3$ ).  $^{13}\text{C}$  NMR (THF- $d_8$ ): 223.6 ( $\text{C}=\text{N}$ ), 105.9 ( $\text{C}_5\text{H}_5$ ), 60.4 (*ipso*- $\text{C}$ ,  $\text{C}_6\text{H}_{11}$ ), 32.3 ( $\text{CH}_2$ ), 31.6 ( $\text{C}_6\text{H}_{11}$ ), 26.4 ( $\text{C}_6\text{H}_{11}$ ), 25.9 ( $\text{C}_6\text{H}_{11}$ ), 3.2 ( $\text{Ta}-\text{CH}_3$ ).  $^{11}\text{B}$  NMR (THF- $d_8$ ): -11.2.  $^{19}\text{F}$  NMR: -129.7 (2F, *o*-F), -160.7 (1F, *p*-F), -164.6 (2F, *m*-F).

#### Reaction of **3a** with *t*-BuNC: Synthesis of **N-out 6a**

THF (20 mL) was condensed into an evacuated flask containing **3a** (454 mg, 0.45 mmol) at -78°C. Under a flow of argon, an excess of *tert*-butylisocyanide (300 mL, 2.87 mmol) was syringed into the flask at -78°C. An immediate colour change from yellow to colourless was noted and the solution was warmed to 25°C. THF was removed under reduced pressure and the white residue filtered after suspension in hexanes. The solid was washed once with hexanes and dried under reduced pressure. Yield of **N-out 6a**: 450 mg, 0.41 mmol, 92%. X-ray quality crystals were grown by cooling a saturated  $\text{CH}_2\text{Cl}_2$  solution to -35°C.  $^1\text{H}$  NMR (THF- $d_8$ ): 5.87 (s, 10H,  $\text{C}_5\text{H}_5$ ), 2.80 (s, 3H,  $\text{C}(\text{N}-t\text{-Bu})\text{CH}_3$ ), 1.49 (s, 9H,  $\text{C}(\text{CH}_3)_3$ ), 0.76 (s, 3H,  $\text{Ta}-\text{CH}_3$ ).  $^{13}\text{C}$  NMR (THF- $d_8$ ): 211.1 ( $\text{C}=\text{N}-t\text{-Bu}$ ), 107.3 ( $\text{C}_5\text{H}_5$ ), 62.9 ( $\text{C}(\text{CH}_3)_3$ ), 28.7 ( $\text{C}(\text{CH}_3)_3$ ), 15.3 ( $\text{C}(\text{N}-t\text{-Bu})\text{CH}_3$ ), 5.6 ( $\text{Ta}-$



CH<sub>3</sub>). <sup>11</sup>B NMR (THF-*d*<sub>8</sub>): −13.6. <sup>19</sup>F NMR (THF-*d*<sub>8</sub>): −130.9 (2F, *o*-F), −163.1 (1F, *p*-F), −166.6 (2F, *m*-F). Anal. calcd. for C<sub>41</sub>H<sub>25</sub>NBF<sub>20</sub>Ta: C 44.63, H 2.28, N 1.27; found: C 44.28, H 2.26, N 1.25.

#### Isomerization of *N*-out 6a to *N*-in 6a

*N*-out 6a (250 mg, 0.226 mmol) was placed into a 25 mL glass bomb and THF (15 mL) was condensed in at −78°C. The vessel was backfilled with argon and placed in a 110°C oil bath for 24 h. The solution was cooled and then cannula-transferred to a 25 mL round bottom flask with a filtering frit. The THF was removed in vacuo to leave a sticky colourless oil. The oil was broken into a precipitate through sonication with hexanes (15 mL). The hexanes were then removed under reduced pressure to give a white powder. More hexanes (10 mL) were condensed in to make a slurry, from which the precipitate was filtered. The product was washed with hexanes (2 × 5 mL) by back distillation and the volatiles removed in vacuo. Yield of *N*-in 6a: 228 mg, 0.206 mmol, 91%. <sup>1</sup>H NMR (THF-*d*<sub>8</sub>): 5.85 (s, 10H, C<sub>5</sub>H<sub>5</sub>), 3.20 (s, 3H, C(=N-*t*-Bu)CH<sub>3</sub>), 1.37 (s, 9H, C(CH<sub>3</sub>)<sub>3</sub>), 0.82 (s, 3H, Ta-CH<sub>3</sub>). <sup>13</sup>C NMR (THF-*d*<sub>8</sub>): 217.7 (C=N-*t*-Bu), 106.6 (C<sub>5</sub>H<sub>5</sub>), 65.2 (C(CH<sub>3</sub>)<sub>3</sub>), 29.2 (C(CH<sub>3</sub>)<sub>3</sub>), 23.1 (C(=N-*t*-Bu)CH<sub>3</sub>), 3.8 (Ta-CH<sub>3</sub>). <sup>11</sup>B NMR (THF-*d*<sub>8</sub>): −13.6. <sup>19</sup>F NMR (THF-*d*<sub>8</sub>): −130.9 (2F, *o*-F), −163.1 (1F, *p*-F), −166.6 (2F, *m*-F). Anal. calcd. for C<sub>41</sub>H<sub>25</sub>NBF<sub>20</sub>Ta: C 44.63, H 2.28, N 1.27; found: C 44.52, H 2.36, N 1.56.

#### Reaction of 3b with *t*-BuNC: Synthesis of *N*-out 6b

[Cp<sub>2</sub>TaMe<sub>2</sub>]<sup>+</sup>[BF<sub>4</sub>]<sup>−</sup>, 3b (295 mg, 0.647 mmol), was weighed into a 25 mL two-necked, round bottomed flask with septum, and CH<sub>2</sub>Cl<sub>2</sub> (10 mL) was condensed in at −78°C to dissolve the solid. *tert*-Butylisocyanide (75 mL, 0.663 mmol) was syringed into the solution at −78°C and resulted in an immediate colour change from yellow to colourless. The solution was stirred for 30 min at 25°C and the CH<sub>2</sub>Cl<sub>2</sub> was removed in vacuo to give a colourless oil. Hexane (10 mL) was condensed into the vessel and the solution sonicated to generate a white powder. The hexane was removed under reduced pressure, and a second quantity of hexane (10 mL) was condensed into the flask. The vessel was sonicated to free the white powder from the wall, the powder filtered, and volatiles removed in vacuo. Yield of *N*-out 6b: 299 mg, 0.555 mmol, 86%. <sup>1</sup>H NMR (CD<sub>2</sub>Cl<sub>2</sub>): 5.92 (m, 2H, C<sub>5</sub>H<sub>4</sub>), 5.70 (m, 2H, C<sub>5</sub>H<sub>4</sub>), 5.66 (m, 2H, C<sub>5</sub>H<sub>4</sub>), 5.24 (m, 2H, C<sub>5</sub>H<sub>4</sub>), 2.73 (s, 3H, C(=NC(CH<sub>3</sub>)<sub>3</sub>)CH<sub>3</sub>), 2.04 (s, 6H, C<sub>5</sub>H<sub>4</sub>CH<sub>3</sub>), 1.49 (s, 9H, C(CH<sub>3</sub>)<sub>3</sub>), 0.62 (s, 3H, Ta-CH<sub>3</sub>). <sup>13</sup>C NMR (CD<sub>3</sub>CN): 211.7 (C=N), 118.3 (C-Me, C<sub>5</sub>H<sub>4</sub>Me, under solvent resonance), 113.1 (C<sub>5</sub>H<sub>4</sub>Me), 111.1 (C<sub>5</sub>H<sub>4</sub>Me), 103.9 (C<sub>5</sub>H<sub>4</sub>Me), 100.7 (C<sub>5</sub>H<sub>4</sub>Me), 62.7 (C(CH<sub>3</sub>)<sub>3</sub>), 29.0 (C(CH<sub>3</sub>)<sub>3</sub>), 13.8 (C<sub>5</sub>H<sub>4</sub>-CH<sub>3</sub>), 13.6 (NC-CH<sub>3</sub>), 7.6 (Ta-CH<sub>3</sub>). <sup>11</sup>B NMR (CD<sub>2</sub>Cl<sub>2</sub>): −1.0. <sup>19</sup>F NMR (CD<sub>2</sub>Cl<sub>2</sub>): −152.2 (4F). Anal. calcd. for C<sub>19</sub>H<sub>29</sub>NBF<sub>4</sub>Ta: C 42.32, H 5.42, N 2.60; found: C 41.76, H 5.44, N 2.53.

#### Isomerization of *N*-out 6b to *N*-in 6b

*N*-out 6b (32 mg, 0.060 mmol) was weighed into a J. Young NMR tube, and an NMR amount of CD<sub>3</sub>CN was added by Pasteur pipette. The tube was placed in a 110°C oil bath for 16 h. <sup>1</sup>H NMR (CD<sub>3</sub>CN): 5.64 (m, 2H, C<sub>5</sub>H<sub>4</sub>), 5.58

(m, 2H, C<sub>5</sub>H<sub>4</sub>), 5.43 (m, 2H, C<sub>5</sub>H<sub>4</sub>), 5.33 (m, 2H, C<sub>5</sub>H<sub>4</sub>), 3.11 (s, 3H, C(=NC(CH<sub>3</sub>)<sub>3</sub>)CH<sub>3</sub>), 2.02 (s, 6H, C<sub>5</sub>H<sub>4</sub>CH<sub>3</sub>), 1.33 (s, 9H, C(CH<sub>3</sub>)<sub>3</sub>), 0.62 (s, 3H, Ta-CH<sub>3</sub>). <sup>13</sup>C NMR (CD<sub>3</sub>CN): 219.6 (C=N), 118.3 (C-Me, C<sub>5</sub>H<sub>4</sub>Me, under solvent resonance), 107.6 (C<sub>5</sub>H<sub>4</sub>Me), 107.2 (C<sub>5</sub>H<sub>4</sub>Me), 106.1 (C<sub>5</sub>H<sub>4</sub>Me), 101.6 (C<sub>5</sub>H<sub>4</sub>Me), 65.4 (C(CH<sub>3</sub>)<sub>3</sub>), 29.9 (C(CH<sub>3</sub>)<sub>3</sub>), 23.7 (NC-CH<sub>3</sub>), 14.7 (C<sub>5</sub>H<sub>4</sub>-CH<sub>3</sub>), 8.8 (Ta-CH<sub>3</sub>). <sup>11</sup>B NMR (CD<sub>2</sub>Cl<sub>2</sub>): −1.0. <sup>19</sup>F NMR (CD<sub>2</sub>Cl<sub>2</sub>): −152.2 (4F).

#### Reaction of 3a with C<sub>6</sub>H<sub>11</sub>NC: Synthesis of *N*-out 7a

A procedure analogous to that used to prepare *N*-out 6a was used to prepare this compound. Reagent amounts: 3a (366 mg, 0.359 mmol), cyclohexyl isocyanide (60 mL, 0.483 mmol). Yield of *N*-out 7a: 295 mg, 0.261 mmol, 73%. <sup>1</sup>H NMR (THF-*d*<sub>8</sub>): 5.88 (s, 10H, C<sub>5</sub>H<sub>5</sub>), 4.03 (m, 1H, CH, C<sub>6</sub>H<sub>11</sub>), 2.70 (s, 3H, C(=NC<sub>6</sub>H<sub>11</sub>)CH<sub>3</sub>), 2.01 (m, 4H, C<sub>6</sub>H<sub>11</sub>), 1.58–1.30 (m, 6H, C<sub>6</sub>H<sub>11</sub>), 0.78 (s, 3H, Ta-CH<sub>3</sub>). <sup>13</sup>C NMR (THF-*d*<sub>8</sub>): 210.5 (C=N), 107.5 (C<sub>5</sub>H<sub>5</sub>), 63.5 (CH, C<sub>6</sub>H<sub>11</sub>), 32.5 (C<sub>6</sub>H<sub>11</sub>), 26.0 (C<sub>6</sub>H<sub>11</sub>), 25.8 (C<sub>6</sub>H<sub>11</sub>), 14.9 (NC-CH<sub>3</sub>), 5.3 (Ta-CH<sub>3</sub>). <sup>11</sup>B NMR (THF-*d*<sub>8</sub>): −13.6. <sup>19</sup>F NMR (THF-*d*<sub>8</sub>): −130.9 (2F, *o*-F), −163.1 (1F, *p*-F), −166.6 (2F, *m*-F).

#### Isomerization of *N*-out 7a to *N*-in 7a

Prepared in the same manner as *N*-in 6a. Reagent amounts: *N*-out 7a (276 mg, 0.244 mmol). Yield of *N*-in 7a: 240 mg, 0.212, 87%. <sup>1</sup>H NMR (CD<sub>3</sub>CN): 5.71 (s, 10H, C<sub>5</sub>H<sub>5</sub>), 4.01 (m, 1H, CH, C<sub>6</sub>H<sub>11</sub>), 2.94 (s, 3H, C(=NC<sub>6</sub>H<sub>11</sub>)CH<sub>3</sub>), 1.80–1.10 (m, 10H, C<sub>6</sub>H<sub>11</sub>), 0.76 (s, 3H, Ta-CH<sub>3</sub>). <sup>13</sup>C NMR (CD<sub>3</sub>CN): 217.8 (C=N), 106.0 (C<sub>5</sub>H<sub>5</sub>), 68.4 (*ipso*-C, C<sub>6</sub>H<sub>11</sub>), 31.9 (C<sub>6</sub>H<sub>11</sub>), 26.1 (C<sub>6</sub>H<sub>11</sub>), 25.8 (C<sub>6</sub>H<sub>11</sub>), 21.0 (NC-CH<sub>3</sub>), 3.7 (Ta-CH<sub>3</sub>). <sup>11</sup>B NMR (THF-*d*<sub>8</sub>): −13.6. <sup>19</sup>F NMR (THF-*d*<sub>8</sub>): −130.9 (2F, *o*-F), −163.1 (1F, *p*-F), −166.6 (2F, *m*-F). Anal. calcd. for C<sub>43</sub>H<sub>27</sub>NBF<sub>20</sub>Ta: C 45.73, H 2.41, N 1.24; found: C 45.47, H 2.45, N 1.37.

#### Reaction of 3b with C<sub>6</sub>H<sub>11</sub>NC: Synthesis of *N*-out 7b

A procedure analogous to the synthesis of *N*-out 6b was used to prepare this compound. Reagent amounts: 3b (298 mg, 0.653 mmol), cyclohexyl isocyanide (82 mL, 0.659 mmol). Yield of *N*-out 7b: 332 mg, 0.587 mmol, 89%. <sup>1</sup>H NMR (CD<sub>2</sub>Cl<sub>2</sub>): 5.91 (m, 2H, C<sub>5</sub>H<sub>4</sub>), 5.68 (m, 4H, C<sub>5</sub>H<sub>4</sub>), 5.34 (m, 2H, C<sub>5</sub>H<sub>4</sub>), 4.05 (m, 1H, *ipso*-CH, C<sub>6</sub>H<sub>11</sub>), 2.62 (s, 3H, C(=NC<sub>6</sub>H<sub>11</sub>)CH<sub>3</sub>), 1.96 (s, 6H, C<sub>5</sub>H<sub>4</sub>CH<sub>3</sub>), 1.96 (m, 3H, C<sub>6</sub>H<sub>11</sub>), 1.51 (m, 7H, C<sub>6</sub>H<sub>11</sub>), 0.62 (s, 3H, Ta-CH<sub>3</sub>). <sup>13</sup>C NMR (CD<sub>2</sub>Cl<sub>2</sub>): 211.0 (C=N), 119.6 (C-CH<sub>3</sub>, C<sub>5</sub>H<sub>4</sub>CH<sub>3</sub>), 112.9 (C<sub>5</sub>H<sub>4</sub>), 110.3 (C<sub>5</sub>H<sub>4</sub>), 103.9 (C<sub>5</sub>H<sub>4</sub>), 100.4 (C<sub>5</sub>H<sub>4</sub>), 63.3 (*ipso*-CH, C<sub>6</sub>H<sub>11</sub>), 32.4 (C<sub>6</sub>H<sub>11</sub>), 25.6 (C<sub>6</sub>H<sub>11</sub>), 25.6 (C<sub>6</sub>H<sub>11</sub>), 14.0 (C<sub>5</sub>H<sub>4</sub>CH<sub>3</sub>), 13.5 (C(=NC<sub>6</sub>H<sub>11</sub>)CH<sub>3</sub>), 7.3 (Ta-CH<sub>3</sub>). <sup>11</sup>B NMR (THF-*d*<sub>8</sub>): −1.0. <sup>19</sup>F NMR (CD<sub>2</sub>Cl<sub>2</sub>): −152.2 (4F). Anal. calcd. for C<sub>21</sub>H<sub>30</sub>NBF<sub>4</sub>Ta: C 44.70, H 5.36, N 2.48; found: C 44.14, H 5.85, N 2.46.

#### Isomerization of *N*-out 7b to *N*-in 7b

*N*-out 7b (30 mg, 0.052 mmol) was weighed into a J. Young NMR tube, and an NMR amount of CD<sub>3</sub>CN was added by Pasteur pipette. The tube was placed in a 100°C oil bath for 16 h. <sup>1</sup>H NMR (CD<sub>3</sub>CN): 5.62 (m, 2H, C<sub>5</sub>H<sub>4</sub>), 5.60 (m, 2H, C<sub>5</sub>H<sub>4</sub>), 5.45 (m, 2H, C<sub>5</sub>H<sub>4</sub>), 5.35 (m, 2H, C<sub>5</sub>H<sub>4</sub>), 4.05 (m, 1H, *ipso*-CH, C<sub>6</sub>H<sub>11</sub>), 2.97 (s, 3H, C(=NC<sub>6</sub>H<sub>11</sub>)CH<sub>3</sub>), 1.99 (s, 6H, C<sub>5</sub>H<sub>4</sub>CH<sub>3</sub>), 1.81 (m, 2H,



$C_6H_{11}$ ), 1.65 (m, 3H,  $C_6H_{11}$ ), 1.51 (m, 2H,  $C_6H_{11}$ ), 1.12–1.40 (m, 3H,  $C_6H_{11}$ ), 0.62 (s, 3H, Ta-CH<sub>3</sub>). <sup>13</sup>C NMR (CD<sub>3</sub>CN): 219.1 (C=N), 122.1 (C-CH<sub>3</sub>, C<sub>5</sub>H<sub>4</sub>CH<sub>3</sub>), 108.7 (C<sub>5</sub>H<sub>4</sub>), 106.6 (C<sub>5</sub>H<sub>4</sub>), 105.0 (C<sub>5</sub>H<sub>4</sub>), 101.7 (C<sub>5</sub>H<sub>4</sub>), 59.3 (*ipso*-CH,  $C_6H_{11}$ ), 32.5 (C<sub>6</sub>H<sub>11</sub>), 26.0 (C<sub>6</sub>H<sub>11</sub>), 25.9 (C<sub>6</sub>H<sub>11</sub>), 21.0 (C(=NC<sub>6</sub>H<sub>11</sub>)CH<sub>3</sub>), 14.5 (C<sub>5</sub>H<sub>4</sub>CH<sub>3</sub>), 8.2 (Ta-CH<sub>3</sub>). <sup>11</sup>B NMR (CD<sub>3</sub>CN): –1.0. <sup>19</sup>F NMR (CD<sub>3</sub>CN): –152.2 (4F).

#### Reaction of 3a with C<sub>6</sub>H<sub>5</sub>CH<sub>2</sub>NC: Synthesis of *N-out* 8a

Compound **3a** (312 mg, 0.306 mmol) was weighed into a two-necked, round bottom flask fitted with a filtering frit and rubber septum. THF (10 mL) was condensed in at –78°C to produce a yellow solution, and benzyl isocyanide (37 mL, 0.306 mmol) was syringed in under a flow of argon. The resulting white slurry was stirred for 45 min while warming to room temperature and THF removed under reduced pressure to give a clear residue. Hexanes (20 mL) were condensed into the flask and the solution sonicated to break down the residue into a white powder. Solvent was removed in vacuo, and to leave a fine white powder, a second portion of hexanes (10 mL) was added, the resulting white slurry filtered, and solvent removed in vacuo. Yield of *N-out* **8a**: 300 mg, 0.263 mmol, 86%. <sup>1</sup>H NMR (THF-*d*<sub>8</sub>): 7.49 (m, 5H, C<sub>6</sub>H<sub>5</sub>), 5.70 (s, 10H, C<sub>5</sub>H<sub>5</sub>), 5.05 (s, 2H, CH<sub>2</sub>), 2.64 (s, 3H, C(=NCH<sub>2</sub>C<sub>6</sub>H<sub>5</sub>)CH<sub>3</sub>), 0.75 (s, 3H, Ta-CH<sub>3</sub>). <sup>13</sup>C NMR (THF-*d*<sub>8</sub>): 210.1 (C(=NCH<sub>2</sub>C<sub>6</sub>H<sub>5</sub>)), 134.7 (*ipso*-C, C<sub>6</sub>H<sub>5</sub>), 130.9 (C<sub>6</sub>H<sub>5</sub>), 130.6 (C<sub>6</sub>H<sub>5</sub>), 107.5 (C<sub>5</sub>H<sub>5</sub>), 57.1 (CH<sub>2</sub>), 14.2 (C(=NCH<sub>2</sub>C<sub>6</sub>H<sub>5</sub>)CH<sub>3</sub>), 5.4 (TaCH<sub>3</sub>). <sup>11</sup>B NMR (THF-*d*<sub>8</sub>): –13.6. <sup>19</sup>F NMR (THF-*d*<sub>8</sub>): –130.9 (2F, *o*-F), –163.1 (1F, *p*-F), –166.6 (2F, *m*-F). Anal. calcd. for C<sub>44</sub>H<sub>23</sub>NBF<sub>20</sub>Ta: C 46.46, H 2.04, N 1.23; found: C 46.25, H 2.00, N 1.27.

#### Isomerization of *N-out* 8a to *N-in* 8a

*N-out* **8a** (30 mg, 0.052 mmol) was weighed into a J. Young NMR tube, and an NMR amount of THF-*d*<sub>8</sub> was added by Pasteur pipette. The tube was placed in an 80°C oil bath for 16 h. <sup>1</sup>H NMR (THF-*d*<sub>8</sub>): 7.36 (m, 3H, C<sub>6</sub>H<sub>5</sub>), 7.24 (m, 2H, C<sub>6</sub>H<sub>5</sub>), 5.69 (s, 10H, C<sub>5</sub>H<sub>5</sub>), 4.82 (s, 2H, CH<sub>2</sub>), 3.06 (s, 3H, C(=NCH<sub>2</sub>C<sub>6</sub>H<sub>5</sub>)CH<sub>3</sub>), 0.73 (s, 3H, Ta-CH<sub>3</sub>). <sup>13</sup>C NMR (THF-*d*<sub>8</sub>): 218.9 (C(=NCH<sub>2</sub>C<sub>6</sub>H<sub>5</sub>)), 134.9 (*ipso*-C, C<sub>6</sub>H<sub>5</sub>), 130.6 (C<sub>6</sub>H<sub>5</sub>), 130.1 (C<sub>6</sub>H<sub>5</sub>), 129.7 (C<sub>6</sub>H<sub>5</sub>), 106.3 (C<sub>5</sub>H<sub>5</sub>), 49.4 (CH<sub>2</sub>), 20.7 (C(=NCH<sub>2</sub>C<sub>6</sub>H<sub>5</sub>)CH<sub>3</sub>), 5.1 (Ta-CH<sub>3</sub>). <sup>11</sup>B NMR (THF-*d*<sub>8</sub>): –13.6. <sup>19</sup>F NMR (THF-*d*<sub>8</sub>): –130.9 (2F, *o*-F), –163.1 (1F, *p*-F), –166.6 (2F, *m*-F).

#### Reaction of 3b with C<sub>6</sub>H<sub>5</sub>CH<sub>2</sub>NC: Synthesis of *N-out* 8b

An analogous procedure to that employed for the synthesis of *N-out* **6b** was employed, except that pentane was used in the isolation of the product rather than hexane. Reagent amounts: **3b** (310 mg, 0.680 mmol); benzylisocyanide (83 mL, 0.681 mmol). Yield of *N-out* **8b**: 306 mg, 0.534 mmol, 79%. <sup>1</sup>H NMR (CD<sub>2</sub>Cl<sub>2</sub>): 7.45 (m, 5H, C<sub>6</sub>H<sub>5</sub>), 5.70 (m, 2H, C<sub>5</sub>H<sub>4</sub>), 5.53 (m, 2H, C<sub>5</sub>H<sub>4</sub>), 5.47 (m, 2H, C<sub>5</sub>H<sub>4</sub>), 5.12 (m, 2H, C<sub>5</sub>H<sub>4</sub>), 5.03 (s, CH<sub>2</sub>), 2.55 (s, 3H, C(=NCH<sub>2</sub>C<sub>6</sub>H<sub>5</sub>)CH<sub>3</sub>), 1.86 (s, 6H, C<sub>5</sub>H<sub>4</sub>CH<sub>3</sub>), 0.58 (s, 3H, Ta-CH<sub>3</sub>). <sup>13</sup>C NMR (CD<sub>2</sub>Cl<sub>2</sub>): 211.1 (C=N), 133.8 (*ipso*-C, C<sub>6</sub>H<sub>5</sub>), 130.7 (C<sub>6</sub>H<sub>5</sub>), 130.2 (C<sub>6</sub>H<sub>5</sub>), 129.9 (C<sub>6</sub>H<sub>5</sub>), 118.8 (C-CH<sub>3</sub>, C<sub>5</sub>H<sub>4</sub>CH<sub>3</sub>), 112.9 (C<sub>5</sub>H<sub>4</sub>), 109.2 (C<sub>5</sub>H<sub>4</sub>), 104.3 (C<sub>5</sub>H<sub>4</sub>), 100.5 (C<sub>5</sub>H<sub>4</sub>), 57.3 (CH<sub>2</sub>), 14.0 (C<sub>5</sub>H<sub>4</sub>CH<sub>3</sub>), 13.0 (C(=NCH<sub>2</sub>C<sub>6</sub>H<sub>5</sub>)CH<sub>3</sub>), 7.5 (Ta-CH<sub>3</sub>). <sup>11</sup>B NMR (THF-*d*<sub>8</sub>): –1.0. <sup>19</sup>F NMR (CD<sub>2</sub>Cl<sub>2</sub>): –152.2 (4F). Anal. calcd. for

C<sub>22</sub>H<sub>27</sub>NBF<sub>4</sub>Ta: C 46.10, H 4.75, N 2.44; found: C 45.71, H 4.97, N 2.41.

#### Isomerization of *N-out* 8b to *N-in* 8b

*N-out* **8b** (30 mg, 0.052 mmol) was weighed into a J. Young NMR tube, and an NMR amount of CD<sub>3</sub>CN was added by Pasteur pipette. The tube was placed in an 80°C oil bath for 16 h. <sup>1</sup>H NMR (CD<sub>3</sub>CN): 7.38 (m, 3H, C<sub>6</sub>H<sub>5</sub>), 7.27 (m, 2H, C<sub>6</sub>H<sub>5</sub>), 5.66 (m, 2H, C<sub>5</sub>H<sub>4</sub>), 5.56 (m, 2H, C<sub>5</sub>H<sub>4</sub>), 5.49 (m, 2H, C<sub>5</sub>H<sub>4</sub>), 5.22 (m, 2H, C<sub>5</sub>H<sub>4</sub>), 4.83 (s, CH<sub>2</sub>), 2.98 (s, 3H, C(=NCH<sub>2</sub>C<sub>6</sub>H<sub>5</sub>)CH<sub>3</sub>), 1.80 (s, 6H, C<sub>5</sub>H<sub>4</sub>CH<sub>3</sub>), 0.52 (s, 3H, Ta-CH<sub>3</sub>). <sup>13</sup>C NMR (CD<sub>2</sub>Cl<sub>2</sub>): 220.2 (C=N), 135.4 (*ipso*-C, C<sub>6</sub>H<sub>5</sub>), 131.5 (C<sub>6</sub>H<sub>5</sub>), 131.2 (C<sub>6</sub>H<sub>5</sub>), 129.6 (C<sub>6</sub>H<sub>5</sub>), 121.6 (C-CH<sub>3</sub>, C<sub>5</sub>H<sub>4</sub>CH<sub>3</sub>), 110.8 (C<sub>5</sub>H<sub>4</sub>), 106.1 (C<sub>5</sub>H<sub>4</sub>), 103.6 (C<sub>5</sub>H<sub>4</sub>), 101.1 (C<sub>5</sub>H<sub>4</sub>), 48.6 (CH<sub>2</sub>), 21.0 (C(=NCH<sub>2</sub>C<sub>6</sub>H<sub>5</sub>)CH<sub>3</sub>), 13.9 (C<sub>5</sub>H<sub>4</sub>CH<sub>3</sub>), 7.7 (Ta-CH<sub>3</sub>). <sup>11</sup>B NMR (THF-*d*<sub>8</sub>): –1.0. <sup>19</sup>F NMR (CD<sub>2</sub>Cl<sub>2</sub>): –152.2 (4F).

#### Kinetic measurements for isocyanide insertion into the Ta—CH<sub>2</sub> bond of zwitterions 1

In a glove box, a known amount of zwitterions **1a** or **1b** was dissolved into an NMR amount of THF-*d*<sub>8</sub> and the NMR tube fitted with a rubber septum. Using a vacuum line in a vented fumehood, dry isocyanide reagent (~10 equiv) was syringed out of the glass bomb under a flow of argon. The isocyanide was added to the zwitterion solution at –78°C through the rubber septum, and the NMR sample was then placed into the NMR probe equilibrated to the desired temperature. Prior to each analysis the temperature of the NMR probe was checked against a standard of methanol. Kinetic data was collected by following the disappearance of the cyclopentadienyl proton resonance for **1a** or the methyl signal in **1b**, as compared with an internal standard of ferrocene. <sup>1</sup>H NMR spectra were generated with eight pulses (90°) with a 5 s relaxation delay. At higher temperatures, the reaction remains first order in [1] for greater than 3 half-lives, while the reaction remained linear throughout the experiment time for lower temperatures. Typical reagent amounts: **1a** (23 mg, 0.027 mmol), ferrocene (5 mg, 0.027 mmol), THF-*d*<sub>8</sub> (0.63 mL), and cyclohexyl isocyanide (40 mL, 0.322 mmol).

#### Kinetic measurements for *N-out* to *N-in* isomerization of η<sup>2</sup>-iminoacyl complexes

In a glove box, the *N-out* isomer was weighed into an NMR tube with a sealable Pyrex neck and secured to a vacuum line with a 180° needle valve. A known amount of CD<sub>3</sub>CN or THF-*d*<sub>8</sub> was vacuum-transferred into the tube. The sample was kept at –78°C and sealed under ~0.9 atm of argon. The NMR tube was placed in the NMR probe and equilibrated to the analysis temperature, which was checked using an ethylene glycol standard. Kinetic data were collected by following the disappearance of the cyclopentadienyl proton resonance or the Ta-CH<sub>3</sub> signal in the <sup>1</sup>H NMR spectrum. For *t*-BuNC and benzylisocyanide derivatives, ferrocene was used as an internal standard and weighed directly into the NMR tube with analyte. For cyclohexyl derivatives, an internal standard, toluene, was used by spiking CD<sub>3</sub>CN (61 mg of toluene in 6.223 g of CD<sub>3</sub>CN). <sup>1</sup>H NMR spectra were generated with four pulses (90°) with a 5 s delay. At higher temperatures, the reaction



**Table 2.** Summary of data collection and structure refinement details for *N-out 6a* and *N-out 7a*.

	<i>N-out 6a</i> <sup>a</sup>	<i>N-out 7a</i> <sup>b</sup>
Formula	C <sub>41</sub> H <sub>25</sub> NF <sub>20</sub> BTa	C <sub>43</sub> H <sub>27</sub> BF <sub>20</sub> NTa·CH <sub>2</sub> Cl <sub>2</sub>
FW	1103.38	1214.34
Temperature (K)	173(1)	193(1)
Crystal size (mm <sup>3</sup> )	0.30 × 0.25 × 0.20	0.42 × 0.09 × 0.08
λ (Å)	0.71069	0.71073
Crystal system	Monoclinic	Orthorhombic
Space group	<i>P</i> 2 <sub>1</sub> / <i>n</i>	<i>Pbca</i>
<i>a</i> (Å)	13.8132(5)	16.5684(14)
<i>b</i> (Å)	19.1799(6)	22.7930(19)
<i>c</i> (Å)	14.5419(5)	23.0095(19)
β (°)	92.836(3)	
<i>V</i> (Å <sup>3</sup> )	3848.0(2)	8689.4(13)
<i>Z</i>	4	8
<i>D</i> <sub>calcd</sub> (mg m <sup>−3</sup> )	1.904	1.856
μ (mm <sup>−1</sup> )	2.984	2.775
<i>F</i> (000)	2144.00	4736
Max, min transmission	1.000, 0.7608	0.8085, 0.3887
2θ <sub>max</sub> (°)	55.7	52.86
Reflections	32 197	37 899
Unique reflections	7922	8917
No. of variables	577	601
Restraints	0	0
<i>R</i> <sub>1</sub>	0.022	0.054
<i>wR</i> <sub>2</sub>	0.065	0.127
GoF	0.95	1.019
Residual density (min, max) (e Å <sup>−3</sup> )	−1.67, 1.23	−1.119, 1.689

<sup>a</sup>*R*<sub>1</sub> (calcd on *F*, *I* > 3σ(*I*)) = Σ ||*F*<sub>o</sub>|| − ||*F*<sub>c</sub>|| / Σ ||*F*<sub>o</sub>||.

<sup>b</sup>*R*<sub>1</sub> (calcd on *F*, *I* > 2σ(*I*)) = Σ ||*F*<sub>o</sub>|| − ||*F*<sub>c</sub>|| / Σ ||*F*<sub>o</sub>||; *wR*<sub>2</sub> (calcd on *F*<sup>2</sup>, all data) = [Σ (*w*(*F*<sub>o</sub><sup>2</sup> − *F*<sub>c</sub><sup>2</sup>)) / Σ (*w*(*F*<sub>o</sub><sup>2</sup>))]<sup>1/2</sup>.

remains first order in the *N-out* isomer for greater than 3 half-lives, while the reaction remained linear throughout the experiment time for lower temperatures. Typical reagent amounts: *N-out 6a* (24 mg, 0.021 mmol), ferrocene (5 mg, 0.027 mmol), and THF-*d*<sub>8</sub> or CD<sub>3</sub>CN (0.599 g). Reaction rates in THF-*d*<sub>8</sub> and CD<sub>3</sub>CN were identical within experimental error.

## X-ray crystallography

### *N-out 6a*

See supporting information<sup>4</sup> and Table 2 for full experimental details.

### *N-out 7a*

Data were collected on a Bruker P4/RA/SMART 1000 CCD diffractometer using Mo Kα radiation at −80°C. Unit cell parameters were obtained from a least-squares refinement of the setting angles of the number of reflections from the data collection. An empirical absorption correction was applied to the data through use of the SADABS procedure. The structures were solved using the direct-methods program SHELXS-86 (22) and full-matrix least-squares refinement on *F*<sup>2</sup> was completed using the program SHELXL-93 (23). Hydrogen atoms were assigned positions based on the geometries of their attached carbon atoms and were given isotropic thermal parameters 20% greater than the equivalent isotropic displacement parameters of the attached carbons.

## Acknowledgments

Funding for this work came from the Natural Sciences and Engineering Research Council of Canada (NSERC) in the form of a Discovery Grant (to WEP), an E.W.R. Steacie Fellowship (2001–2003) (to WEP) and Scholarship support (PGSA and PGSB) to KSC. KSC also thanks the Alberta Heritage Scholarship Fund for a Ralph Steinhauer Award of Distinction Scholarship (2000–2001).

## References

1. J.P. Collman, L.S. Hegedus, J.R. Norton, and R.G. Finke. Principles and applications of organotransition metal chemistry. University Science Books, Mill Valley, CA. 1987.
2. (a) G. Erker. Acc. Chem. Res. **17**, 103 (1984); (b) L.D. Durfee and I.P. Rothwell. Chem. Rev. **88**, 1059 (1988); (c) G. Gachinetti, C. Floriani, F. Marchetti, and S. Merlino. J. Chem. Soc. Chem. Commun. 522 (1976); (d) G. Fachinetti, G. Fochi, and C. Floriani. J. Chem. Soc. Dalton Trans. 1946 (1977).
3. K. Tatsumi, A. Nakamura, P. Hofmann, P. Stauffert, and R. Hoffmann. J. Am. Chem. Soc. **107**, 4440 (1985).
4. (a) P. Hofmann, P. Stauffert, and N.E. Schore. Chem. Ber. **115**, 2153 (1982); (b) F. De Angelis, S. Sgamellotti, and N. Re. Organometallics, **19**, 4904 (2000); (c) F. De Angelis, S. Sgamellotti, and N. Re. J. Chem. Soc. Dalton Trans. 1023 (2001).
5. E. Boring, M. Sabat, M.G. Finn, and R.N. Grimes. Organometallics, **16**, 3993 (1997).



6. G.C. Bazan, S.J. Donnelly, and G. Rodriguez. *J. Am. Chem. Soc.* **117**, 2671 (1995).
7. F. Amor, J. Sanchez-Nieves, P. Royo, H. Jacobsen, O. Blaque, H. Berke, M. Lanfranchi, M.A. Pellinghelli, and A. Tiripicchio. *Eur. J. Inorg. Chem.* 2810 (2002).
8. R.R. Schrock and P.R. Sharp. *J. Am. Chem. Soc.* **100**, 2389 (1978).
9. K.S. Cook, W.E. Piers, S.J. Rettig, and R. MacDonald. *Organometallics*, **19**, 2243 (2000).
10. A.G. Massey and A.J. Park. *J. Organomet. Chem.* **2**, 245 (1964).
11. R.E. v H. Spence, W.E. Piers, Y. Sun, M. Parvez, L.R. MacGillivray, and M.J. Zaworotko. *Organometallics*, **17**, 2459 (1998).
12. (a) J.D. Scollard, D.H. McConville, and S.J. Rettig. *Organometallics*, **16**, 1810 (1997); (b) M.G. Thorn, J.S. Vilardo, P.E. Fanwick, and I.P. Rothwell. *Chem. Commun.* 2427 (1998); S. Zhang, W.E. Piers, X. Gao, and M. Parvez. *J. Am. Chem. Soc.* **122**, 5499 (2000).
13. E.Y.-X. Chen and D.A. Abboud. *Organometallics*, **19**, 5541 (2000).
14. W.P. Schaefer, R.W. Quan, and J.E. Bercaw. *Acta Cryst. Ser. C*, **48**, 1610 (1992).
15. E.Y.-X. Chen and T.J. Marks. *Chem. Rev.* **100**, 1391 (2000).
16. (a) J. Jeffery, M.F. Lappert, N.T. Luong-thi, M. Webb, J.L. Atwood, and W.E. Hunter. *J. Chem. Soc. Dalton Trans.* 1593 (1981); (b) M.F. Lappert, N.T. Luong-Thi, and C.R.C. Milne. *J. Organomet. Chem.* **174**, C35 (1979).
17. (a) C. Floriani, K. Schenk, A. Chiesi-Villa, and C. Rizzoli. *Organometallics*, **15**, 337 (1996); (b) R. Fandos, M. Lanfranchi, A. Otero, M.A. Pellinghelli, M.J. Ruiz, and P. Terreros. *Organometallics*, **15**, 4725 (1996).
18. F.R. Lemke, D.J. Szalda, and R.M. Bullock. *Organometallics*, **11**, 876 (1992).
19. R.D. Adams and D.F. Chodosh. *Inorg. Chem.* **17**, 41 (1978).
20. L.R. Chamberlain, L.D. Durfee, P.E. Fanwick, L. Kobringer, S.L. Latesky, A.K. McMullen, I.P. Rothwell, K. Folting, J.C. Huffman, W.E. Streib, and R. Wang. *J. Am. Chem. Soc.* **109**, 390 (1987).
21. (a) K.S. Cook, W.E. Piers, T.K. Woo, S.J. Rettig, and R. MacDonald. *Organometallics*, **20**, 3937 (2001); (b) K.S. Cook, W.E. Piers, P.G. Hayes, and M. Parvez. *Organometallics*, **21**, 2422 (2002).
22. G.M. Sheldrick. *Acta Crystallogr.* **A46**, 467 (1990).
23. G.M. Sheldrick. 1993. SHELXL-93: Program for crystal structure determination [computer program]. University of Göttingen, Germany.



# The formation of mixed metal aminophosphinidene clusters via reactions of terminal chloroaminophosphido complexes with $\text{Co}_2(\text{CO})_8$ <sup>1</sup>

Javier Sánchez-Nieves, Brian T. Sterenberg, Konstantin A. Udachin, and Arthur J. Carty

**Abstract:** Reactions of terminal chloroaminophosphido complexes with  $\text{Co}_2(\text{CO})_8$  have been examined. The ruthenium phosphido complexes  $[\text{Cp}^*\text{Ru}(\text{CO})_2\{\text{P}(\text{Cl})\text{TMP}\}]$  (**1a**) and  $[\text{CpRu}(\text{CO})_2\{\text{P}(\text{Cl})\text{TMP}\}]$  (**1b**) (TMP = 2,2,6,6-tetramethylpiperidinyl) react with  $\text{Co}_2(\text{CO})_8$  to form the cobalt cluster  $[\text{Co}_4(\text{CO})_7(\mu\text{-CO})_3(\mu_3\text{-P}(\text{TMP}))]$  (**2**) with complete transfer of the phosphinidene unit to cobalt. In contrast, the phosphido complex  $[\text{Cp}^*\text{Ru}(\text{CO})_2\{\text{P}(\text{Cl})\text{N-}i\text{-Pr}_2\}]$  (**1c**) affords the spiked-triangular cluster  $[\text{Cp}^*\text{RuCo}_3(\text{CO})_8(\mu\text{-CO})_2(\mu_3\text{-PN-}i\text{-Pr}_2)]$  (**3**), which retains the  $\text{Cp}^*\text{Ru}$  unit upon reaction with  $\text{Co}_2(\text{CO})_8$ . The molybdenum phosphido complex  $[\text{CpMo}(\text{CO})_2\{\text{P}(\text{Cl})\text{TMP}\}]$  (**4**) reacts with  $\text{Co}_2(\text{CO})_8$  to form cluster **2**, while  $[\text{Cp}^*\text{Mo}(\text{CO})_3\{\text{P}(\text{Cl})\text{N-}i\text{-Pr}_2\}]$  (**5**) generates the mixed metal tetrahedral cluster  $[\text{Cp}^*\text{MoCo}_3(\text{CO})_5(\mu\text{-CO})_4(\mu_3\text{-PN-}i\text{-Pr}_2)]$  (**6**).

**Key words:** phosphido, phosphinidene, cobalt, ruthenium, molybdenum, cluster.

**Résumé :** On a étudié les réactions de complexes du  $\text{Co}_2(\text{CO})_8$  comportant des groupes chloroaminophosphido terminaux. Les complexes phosphido du ruthénium  $[\text{Cp}^*\text{Ru}(\text{CO})_2\{\text{P}(\text{Cl})\text{TMP}\}]$  (**1a**) et  $[\text{CpRu}(\text{CO})_2\{\text{P}(\text{Cl})\text{TMP}\}]$  (**1b**) (TMP = 2,2,6,6-tétrapiéridinyl) réagissent avec le  $\text{Co}_2(\text{CO})_8$  avec formation de l'agrégat de cobalt  $[\text{Co}_4(\text{CO})_7(\mu\text{-CO})_3(\mu_3\text{-P}(\text{TMP}))]$  (**2**) et un transfert complet de l'unité phosphinidène au cobalt. Par ailleurs, le complexe phosphido  $[\text{Cp}^*\text{Ru}(\text{CO})_2\{\text{P}(\text{Cl})\text{N-}i\text{-Pr}_2\}]$  (**1c**) fournit l'agrégat à triangle en aiguille  $[\text{Cp}^*\text{RuCo}_3(\text{CO})_8(\mu\text{-CO})_2(\mu_3\text{-PN-}i\text{-Pr}_2)]$  (**3**) qui retient l'unité  $\text{Cp}^*\text{Ru}$  lors de la réaction avec le  $\text{Co}_2(\text{CO})_8$ . Le complexe phosphido du molybdène  $[\text{CpMo}(\text{CO})_2\{\text{P}(\text{Cl})\text{TMP}\}]$  (**4**) réagit avec le  $\text{Co}_2(\text{CO})_8$  avec formation de l'agrégat **2** alors que le complexe  $[\text{Cp}^*\text{Mo}(\text{CO})_3\{\text{P}(\text{Cl})\text{N-}i\text{-Pr}_2\}]$  (**5**) génère l'agrégat tétraédrique à métal mixte  $[\text{Cp}^*\text{MoCo}_3(\text{CO})_5(\mu\text{-CO})_4(\mu_3\text{-PN-}i\text{-Pr}_2)]$  (**6**).

**Mots clés :** phosphido, phosphinidène, cobalt, ruthénium, molybdène, agrégat.

[Traduit par la Rédaction]

## Introduction

Phosphido ( $\text{PR}_2$ ) and phosphinidene (PR) groups are important and versatile ligands in organometallic chemistry (1, 2). As a terminal ligand, the phosphido group is analogous to an alkyl fragment, acting as a one-electron donor; however, the phosphorus lone pair also allows it to act as a three-electron donor (3). Terminal phosphinidene complexes are analogous to carbene complexes and show similar reactivity, ranging from nucleophilic to electrophilic behaviour (4). In some cases, the phosphinidene lone pair can also form a do-

nor interaction with the metal, resulting in a net four-electron donor (5).

In cluster chemistry, both phosphido and phosphinidene ligands have been used extensively to enhance structural integrity and stability (6). In bimetallic and cluster complexes, the phosphido fragment generally acts as a doubly bridging ligand and a net three-electron donor (2), although examples of co-ordination to more than two metals are known (7, 8). The phosphinidene fragment commonly co-ordinates as a  $\mu_2$ ,  $\mu_3$ , or  $\mu_4$  ligand and rarely as a  $\mu_5$  ligand (8, 9) and contributes two or four electrons.

Over the past several years we have developed an extensive chemistry based on the transformation of functionalized phosphido and phosphinidene ligands. For example, we have used chloroaminophosphido complexes as precursors to terminal, electrophilic phosphinidene complexes, enabling the isolation and characterization of these elusive compounds for the first time (10–12). We have also exploited the propensity of cluster-bound aminophosphinidene complexes to undergo P—N bond cleavage and substitution at the phosphinidene phosphorus atom, to develop a versatile route to co-ordinated phosphorus monoxide clusters (13) and a variety of functionalized phosphinidenes (14, 15).

Received 3 February 2003. Published on the NRC Research Press Web site at <http://canjchem.nrc.ca> on 12 August 2003.

J. Sánchez-Nieves, B.T. Sterenberg, K.A. Udachin, and A.J. Carty.<sup>2</sup> Steacie Institute for Molecular Sciences, National Research Council Canada, 100 Sussex Drive, Ottawa, ON K1A 0R6, Canada and the Ottawa-Carleton Chemistry Research Institute, Department of Chemistry, University of Ottawa, Ottawa, ON K1N 6N5, Canada.

<sup>1</sup>This article is part of a Special Issue dedicated to Professor John Harrod.

<sup>2</sup>Corresponding author (e-mail: [arthur.carty@nrc.ca](mailto:arthur.carty@nrc.ca)).



In a previous paper (16), we described the syntheses of several bimetallic  $\mu_2$ -aminophosphinidene complexes via reactions of terminal molybdenum chloroaminophosphido complexes with  $\text{Co}_2(\text{CO})_8$  (see Scheme 1). In this paper, we describe similar reactions of ruthenium and molybdenum phosphido complexes with  $\text{Co}_2(\text{CO})_8$  that lead to homo- and heterometallic clusters containing  $\mu_3$ -aminophosphinidene ligands.

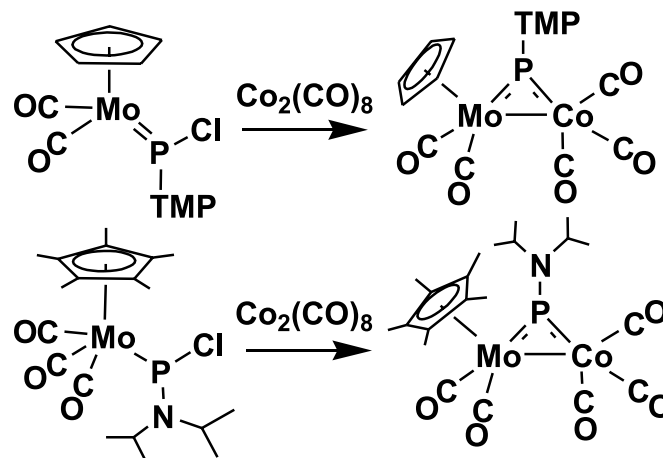
## Results and discussion

Although a number of complexes of the type  $\text{CpM}(\text{CO})_2\text{PR}_2$  ( $\text{M} = \text{Fe}, \text{Ru}$ ) containing terminal phosphido groups are known (17), the compounds  $[\text{Cp}^*\text{Ru}(\text{CO})_2\{\text{P}(\text{Cl})\text{TMP}\}]$  (**1a**) and  $[\text{CpRu}(\text{CO})_2\{\text{P}(\text{Cl})\text{TMP}\}]$  (**1b**) are new, and with  $[\text{Cp}^*\text{Ru}(\text{CO})_2\{\text{P}(\text{Cl})\text{N-}i\text{-Pr}_2\}]$  (**1c**), briefly described earlier (10), represent the first terminal chloroaminophosphido complexes of the fragments  $\text{Cp}^*\text{Ru}(\text{CO})_2$  and  $\text{CpRu}(\text{CO})_2$ . They were synthesized in good yield (65–68%) via the reaction of the potassium salts of the respective ruthenium anions with the dichloroaminophosphine  $\text{Cl}_2\text{P}(\text{TMP})$  in THF. Both **1a** and **1b** exhibit two  $\nu(\text{CO})$  bands in the infrared, indicating that only one conformation of the phosphido ligand is present, likely the conformer in which the bulky TMP ligand points away from the Cp or  $\text{Cp}^*$  ring. This conformation was confirmed in the previously reported X-ray crystal structure of **1c** (10). The  $^{31}\text{P}\{^1\text{H}\}$  NMR spectrum shows singlet resonances at  $\delta$  251.3 (**1a**) and  $\delta$  303.5 (**1b**), typical of terminal  $\text{P}(\text{Cl})\text{NR}_2$  ligands (10, 11, 18).

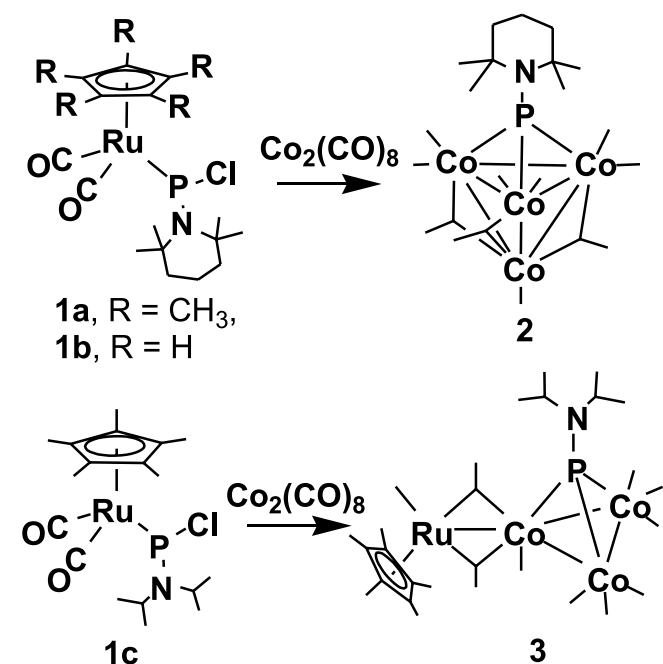
Reaction of the ruthenium phosphido complexes  $[\text{Cp}^*\text{Ru}(\text{CO})_2\{\text{P}(\text{Cl})\text{TMP}\}]$  (**1a**) and  $[\text{CpRu}(\text{CO})_2\{\text{P}(\text{Cl})\text{TMP}\}]$  (**1b**) with  $\text{Co}_2(\text{CO})_8$  led to the tetracobalt cluster  $[\text{Co}_4(\text{CO})_7(\mu\text{-CO})_3\{\mu_3\text{-P}(\text{TMP})\}]$  (**2**) as the major isolable product (Scheme 2). In these reactions, the aminophosphinidene unit has been transferred completely to cobalt and the Cp or  $\text{Cp}^*$  ruthenium fragment is eliminated. In contrast to the related Mo system, no RuCo bimetallic complexes could be isolated or detected in the reaction, regardless of stoichiometry and reaction conditions. Attempts to isolate or identify ruthenium-containing fragments from the reaction mixture were unsuccessful. Infrared spectroscopy of the mother solution after crystallization of **2** showed a complex mixture of carbonyl complexes.

The cluster **2** has been structurally characterized. An ORTEP diagram is shown in Fig. 1 and selected distances and angles are shown in Table 1. The structure consists of a tetrahedral core of four cobalt centres with one trigonal face capped by the aminophosphinidene ligand, resulting in a trigonal bipyramidal arrangement of the core  $\text{Co}_4\text{P}$  atoms. Each cobalt atom of the phosphinidene-capped face also has two terminal carbonyl ligands. The fourth cobalt centre bears one terminal carbonyl. A carbonyl ligand bridges each of the metal–metal bonds between the equatorial cobalt atoms and the axial cobalt. The cobalt–phosphorus distances of 2.144(1), 2.156(1), and 2.172(1) Å are similar to those of previous cobalt  $\mu_3$ -phosphinidene complexes (19–23). The cluster electron count is 60, consistent with a tetrahedral  $\text{M}_4$  structure if only the metal atoms are considered part of the skeleton. Alternatively, with 6 skeletal electron pairs, **2** has a closo trigonal bipyramidal  $\text{Co}_4\text{P}$  framework. Surprisingly, **2** appears to be the first simple diamagnetic  $\mu_3$ -phosphinidene

Scheme 1.



Scheme 2.



cobalt carbonyl cluster, although several paramagnetic complexes of the type  $[\text{Co}_3(\text{CO})_9(\mu_3\text{-PR})]$  have been described (20, 22, 24), as have  $\text{Co}_3$  phosphinidene–phosphido (23) and phosphinidene–boride clusters (21). Also of note are the tetracobalt clusters  $[\text{Co}_4(\mu_3\text{-PPh})_4(\text{PPh}_3)_4]$  and  $[\text{Co}_4(\mu_3\text{-PPh})_4(\text{PPh}_3)_4]^+$ , which consist of a tetrahedron of cobalt atoms surrounded by four  $\mu_3$ -phosphinidene ligands (19), and  $[\text{Co}_4(\text{CO})_{10}(\text{P-}i\text{-Pr})_3]$ , in which two  $\text{Co}_2$  units are bridged by three  $\mu_3\text{-PR}$  units (25). Cobalt clusters containing  $\mu_4$ -phosphinidene ligands are, on the other hand, relatively common (20, 26).

The  $^{31}\text{P}$  NMR spectrum of **2** shows a peak for the phosphinidene phosphorus atom at  $\delta$  503.5, which is in the typical range for  $\mu_3$ -phosphinidene ligands. In all of the cobalt clusters described, the phosphorus resonances are broad as a result of quadrupolar coupling to  $^{59}\text{Co}$  and  $^{14}\text{N}$ . The  $^1\text{H}$  NMR spectrum shows the expected peaks for the TMP



**Fig. 1.** ORTEP diagram of the X-ray crystal structure of  $[\text{Co}_4(\text{CO})_7(\mu\text{-CO})_3\{\mu_3\text{-P}(\text{TMP})\}]$  (**2**). Thermal ellipsoids are shown at the 50% level, and hydrogen atoms have been omitted for clarity.

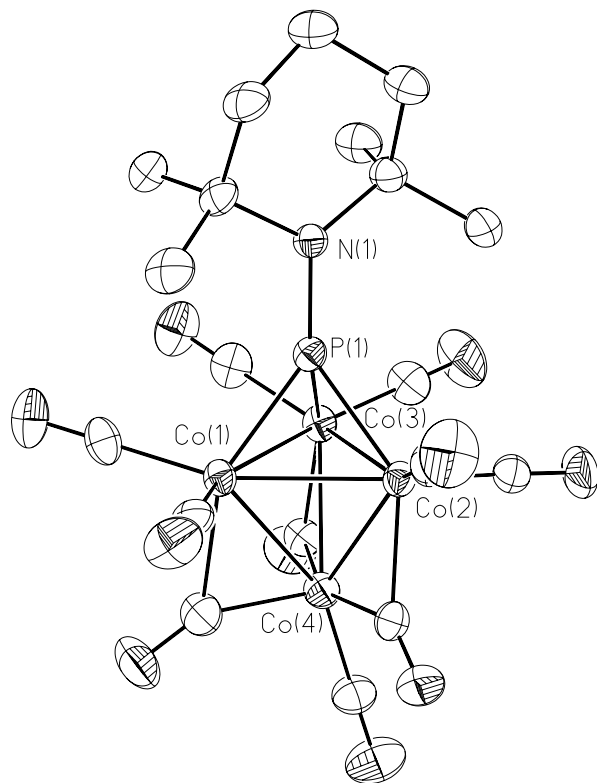


**Table 1.** Selected bond distances and angles for  $[\text{Co}_4(\text{CO})_7(\mu\text{-CO})_3\{\mu_3\text{-P}(\text{TMP})\}]$  (**2**).

Bond distances (Å)			
Co(1)—P(1)	2.144(1)	Co(2)—Co(4)	2.4599(6)
Co(1)—Co(3)	2.5128(6)	Co(2)—Co(3)	2.5457(6)
Co(1)—Co(2)	2.5242(6)	Co(3)—P(1)	2.172(1)
Co(1)—Co(4)	2.5278(7)	Co(3)—Co(4)	2.5077(7)
Co(2)—P(1)	2.156(1)	P(1)—N(1)	1.656(3)
Bond angles (°)			
Co(3)—Co(1)—Co(2)	60.72(2)	Co(1)—Co(3)—Co(2)	59.86(2)
Co(3)—Co(1)—Co(4)	59.67(2)	Co(2)—Co(4)—Co(3)	61.65(2)
Co(2)—Co(1)—Co(4)	58.28(2)	Co(2)—Co(4)—Co(1)	60.79(2)
Co(4)—Co(2)—Co(1)	60.93(2)	Co(3)—Co(4)—Co(1)	59.87(2)
Co(4)—Co(2)—Co(3)	60.10(2)	N(1)—P(1)—Co(1)	139.0(1)
Co(1)—Co(2)—Co(3)	59.42(2)	N(1)—P(1)—Co(2)	135.3(1)
Co(4)—Co(3)—Co(1)	60.46(2)	N(1)—P(1)—Co(3)	138.0(1)
Co(4)—Co(3)—Co(2)	58.25(2)		

group. The IR spectrum shows terminal carbonyl stretching bands at 2038, 2028, and 1906  $\text{cm}^{-1}$  and a bridging carbonyl stretch at 1862  $\text{cm}^{-1}$ .

In contrast, reaction of the phosphido complex  $[\text{Cp}^*\text{Ru}(\text{CO})_2\{\text{P}(\text{Cl})\text{N-}i\text{-Pr}_2\}]$  (**1c**), which has a less sterically demanding di-isopropylamino group on the phosphido ligand, led to the cluster  $[\text{Cp}^*\text{RuCo}_3(\text{CO})_8(\mu\text{-CO})_2(\mu_3\text{-PN-}i\text{-Pr}_2)]$  (**3**). An ORTEP diagram of **3** is shown in Fig. 2 and selected distances and angles are shown in Table 2. The molecule consists of a triangle of cobalt atoms

**Fig. 2.** ORTEP diagram of the X-ray crystal structure of  $[\text{Cp}^*\text{RuCo}_3(\text{CO})_8(\mu\text{-CO})_2(\mu_3\text{-PN-}i\text{-Pr}_2)]$  (**3**). Thermal ellipsoids are shown at the 50% level, and hydrogen atoms have been omitted for clarity.

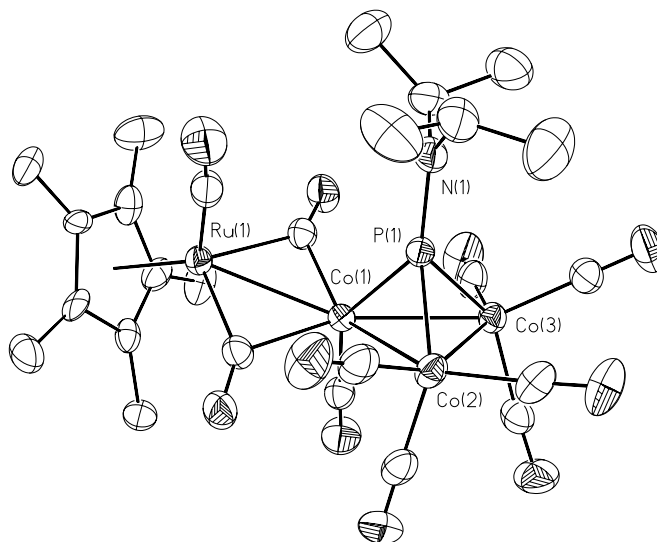


**Table 2.** Selected bond distances and angles for  $[\text{Cp}^*\text{RuCo}_3(\text{CO})_8(\mu\text{-CO})_2(\mu_3\text{-PN-}i\text{-Pr}_2)]$  (**3**).

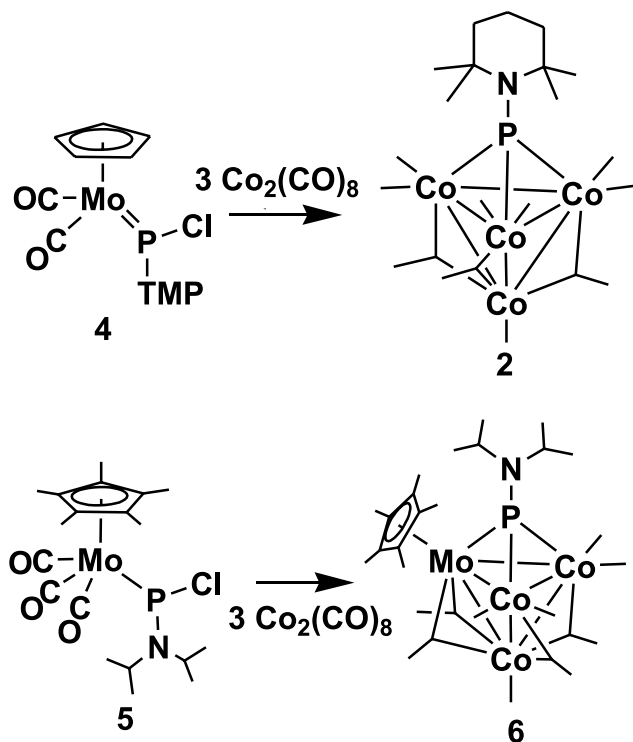
Bond distances (Å)			
Co(1)—P(1)	2.1345(9)	Co(3)—Co(2)	2.6150(6)
Co(1)—Co(3)	2.5944(6)	Co(2)—P(1)	2.1228(9)
Co(1)—Co(2)	2.7114(6)	P(1)—N(1)	1.659(3)
Co(3)—P(1)	2.1584(9)		
Bond angles (°)			
Co(3)—Co(1)—Ru(1)	157.86(2)	N(1)—P(1)—Co(2)	136.9(1)
Co(3)—Co(1)—Co(2)	59.01(2)	N(1)—P(1)—Co(1)	136.8(1)
Ru(1)—Co(1)—Co(2)	128.72(2)	Ru(1)—C(2)—Co(1)	82.8(1)
Co(1)—Co(3)—Co(2)	62.78(2)	Co(1)—C(3)—Ru(1)	84.1(1)
Co(3)—Co(2)—Co(1)	58.26(2)		

capped by a  $\mu_3$ -phosphinidene ligand with the  $\text{Cp}^*$  ruthenium fragment bound to one of the cobalt atoms, resulting in a spiked-triangular arrangement of the metals. The two cobalt atoms that are not bound to ruthenium each have three terminal carbonyl ligands. The ruthenium-bound cobalt atom has one terminal carbonyl ligand and two carbonyls bridge the cobalt—ruthenium bond. In addition to the bridging carbonyls, the ruthenium atom is attached to the  $\text{Cp}^*$  ligand and one terminal carbonyl. The overall cluster electron count is 64, consistent with the presence of only four metal—metal bonds. The ruthenium atom in **3** is not coplanar with the  $\text{Co}_3$  triangle but deviates from the plane by 0.8879 Å on the same side of the plane as the phosphinidene ligand. Compound **3** appears to be a unique example of a ruthenium spiked cobalt triangle, although spiked triangular clusters involving other transition metals are well known (27).

The phosphorus—nitrogen distance of 1.659(3) Å is intermediate between P—N single and P=N double bonds, which is typical of bridging aminophosphinidene ligands in clusters and consistent with partial P—N multiple bonding (15, 28). The geometry at nitrogen is nearly planar.



Scheme 3.



The phosphinidene phosphorus atom of **3** appears at  $\delta$  461.4 in the  $^{31}\text{P}$  NMR spectrum. The  $^1\text{H}$  NMR spectrum exhibits one set of peaks for the isopropyl groups and the  $\text{Cp}^*$  methyl groups, indicating that there is free rotation about the P—N bond and suggesting that the  $\text{Np}\pi\text{---Pp}\pi$  bonding is weak. Terminal carbonyl stretching bands are observed at 2069, 2031, 2012, 2000, 1985, and 1969  $\text{cm}^{-1}$  and the bridging carbonyl stretch appears at 1797  $\text{cm}^{-1}$ .

Given the facility of cluster formation by ruthenium phosphido complexes with  $\text{Co}_2(\text{CO})_8$  and our inability to isolate any RuCo bimetallic complexes, we re-examined the reactions with the Mo phosphido complexes. In our previous paper, conditions were optimized for the formation of bimetallic complexes. However, by reacting the bimetallic MoCo complexes with further  $\text{Co}_2(\text{CO})_8$  or by reacting the starting phosphido complexes with excess  $\text{Co}_2(\text{CO})_8$  we anticipated favouring the formation of phosphinidene clusters.

Thus the reaction of  $[\text{CpMo}(\text{CO})_2\{\text{P}(\text{Cl})\text{TMP}\}]$  (**4**) with excess  $\text{Co}_2(\text{CO})_8$  led to the formation of  $[\text{Co}_4(\text{CO})_7(\mu\text{-CO})_3\{\mu_3\text{-P}(\text{TMP})\}]$  (**2**), the same product that was observed in the reaction with  $[\text{Cp}^*\text{Ru}(\text{CO})_2\{\text{P}(\text{Cl})\text{TMP}\}]$  (**1a**) and  $[\text{CpRu}(\text{CO})_2\{\text{P}(\text{Cl})\text{TMP}\}]$  (**1b**). Again, we observed a complete transfer of the phosphinidene unit from Mo to Co and loss of the Mo fragment (Scheme 3).

However, in sharp contrast, the reaction of  $[\text{Cp}^*\text{Mo}(\text{CO})_3\{\text{P}(\text{Cl})\text{N-}i\text{-Pr}_2\}]$  (**5**) with excess  $\text{Co}_2(\text{CO})_8$  did not result in a complete transfer of the phosphinidene unit and instead led to the formation of the heterometallic cluster  $[\text{Cp}^*\text{MoCo}_3(\text{CO})_5(\mu\text{-CO})_4(\mu_3\text{-PN-}i\text{-Pr}_2)]$  (**6**). An ORTEP diagram of **6** is shown in Fig. 3 and selected distances and angles are shown in Table 3. The core structure is similar to that of **2** with a trigonal bipyramidal arrangement of the four metals and the phosphorus atom. The molybdenum atom occupies one of the equatorial positions and is bound to the

**Fig. 3.** ORTEP diagram of the X-ray crystal structure of  $[\text{Cp}^*\text{MoCo}_3(\text{CO})_5(\mu\text{-CO})_4(\mu_3\text{-PN-}i\text{-Pr}_2)]$  (**6**). Thermal ellipsoids are shown at the 50% level, and hydrogen atoms have been omitted for clarity.

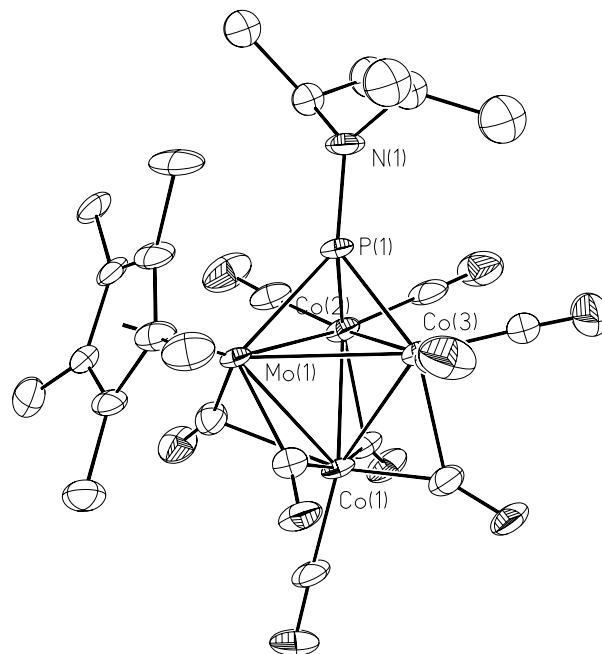


**Table 3.** Selected bond distances and angles for  $[\text{Cp}^*\text{MoCo}_3(\text{CO})_5(\mu\text{-CO})_4(\mu_3\text{-PN-}i\text{-Pr}_2)]$  (**6**).

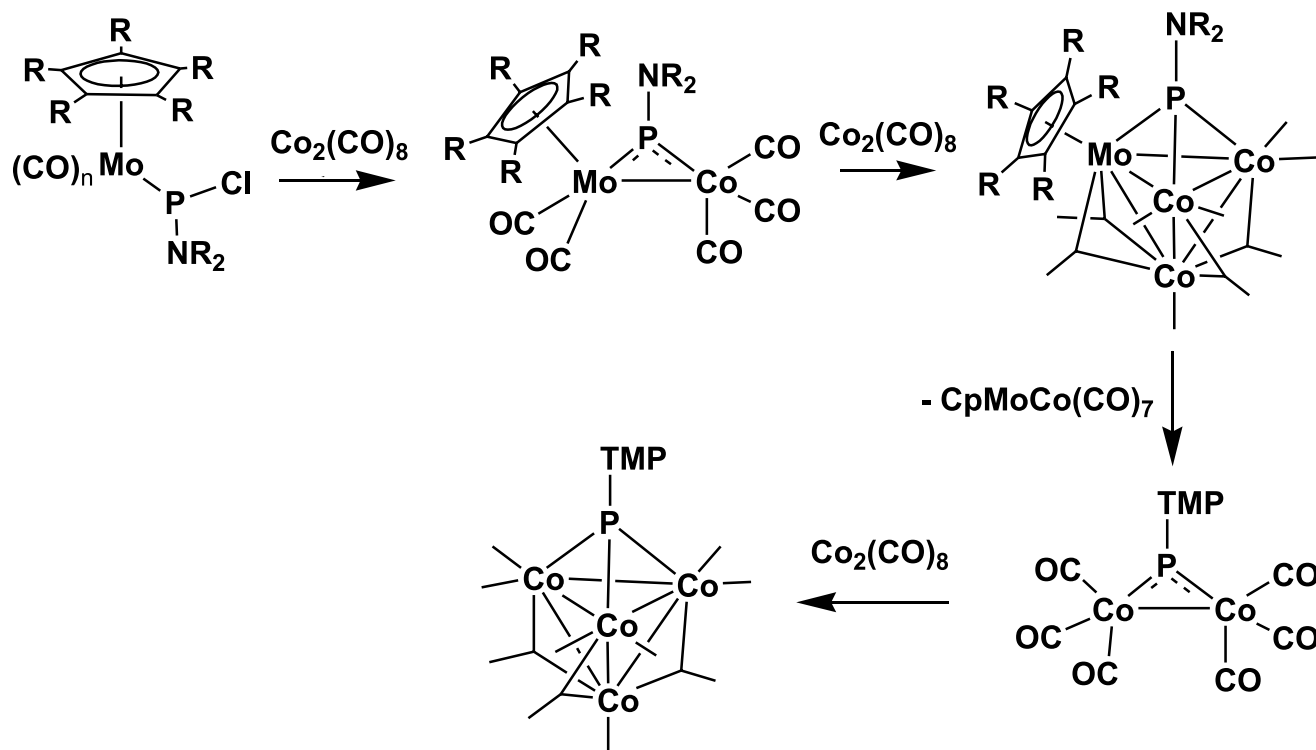
Bond distances (Å)			
Mo(1)—P(1)	2.390(1)	Co(1)—Co(3)	2.506(1)
Mo(1)—Co(1)	2.6492(9)	Co(2)—P(1)	2.157(2)
Mo(1)—Co(2)	2.823(1)	Co(2)—Co(3)	2.554(1)
Mo(1)—Co(3)	2.848(1)	Co(3)—P(1)	2.142(2)
Co(1)—Co(2)	2.496(1)	P(1)—N(1)	1.653(6)
Bond angles (°)			
P(1)—Mo(1)—Co(1)	89.97(4)	Co(1)—Co(2)—Co(3)	59.48(3)
P(1)—Mo(1)—Co(2)	48.00(4)	Co(1)—Co(2)—Mo(1)	59.37(3)
Co(1)—Mo(1)—Co(2)	54.15(3)	Co(3)—Co(2)—Mo(1)	63.72(3)
P(1)—Mo(1)—Co(3)	47.28(4)	Co(1)—Co(3)—Co(2)	59.09(3)
Co(1)—Mo(1)—Co(3)	54.10(3)	Co(1)—Co(3)—Mo(1)	58.91(3)
Co(2)—Mo(1)—Co(3)	53.55(3)	Co(2)—Co(3)—Mo(1)	62.73(3)
Co(2)—Co(1)—Co(3)	61.43(3)	N(1)—P(1)—Co(3)	135.8(2)
Co(2)—Co(1)—Mo(1)	66.48(3)	N(1)—P(1)—Co(2)	127.6(2)
Co(3)—Co(1)—Mo(1)	67.00(3)	N(1)—P(1)—Mo(1)	139.8(2)

phosphinidene phosphorus atom and the  $\text{Cp}^*$  ring, as well as to two carbonyl ligands that bridge the molybdenum and the axial cobalt centre. Each equatorial cobalt atom is bound to phosphorus and to two terminal carbonyls. In addition, there is a carbonyl bridge between each of the equatorial cobalt centres and the axial cobalt centre. The axial cobalt is bound to only one terminal carbonyl ligand in addition to the four bridging carbonyl ligands mentioned.

Bonding to the  $\mu_3$ -phosphinidene ligand is significantly unsymmetrical, as expected given the smaller atomic radius of Co compared with Mo. The P—Co distances are 2.158(2) and 2.142(2) Å and the Mo—P distance is 2.391(1) Å. Also



Scheme 4.



of note is the distortion of the phosphinidene ligand away from the pseudo threefold axis that would pass through P, N, and the centroid of the three equatorial metal atoms. In most  $\mu_3$ -phosphinidene complexes, the P—X bond is essentially perpendicular to the metal plane. In complex **6**, the P—N bond forms an angle of 80.5° to the Co<sub>2</sub>Mo plane. This deviation may be attributed to the steric interaction between the Cp\* and di-isopropyl amine groups. Unfortunately, we were unable to synthesize the Cp analogue for comparison. However, it is clear that an analogous complex to **6** containing the bulkier TMP group on the phosphinidene would suffer from severe steric congestion.

The <sup>31</sup>P NMR spectrum of complex **6** shows a peak at  $\delta$  514.4, which corresponds to the  $\mu_3$ -phosphinidene ligand. The <sup>1</sup>H NMR spectrum shows peaks for two equivalent isopropyl groups and the Cp\* methyl groups.

One side product was also isolated from this reaction, which was identified as [Cp\*MoCo(CO)<sub>7</sub>] (**7**). It is somewhat surprising that this compound was observed only for this reaction, since the main product still contains the Cp\*Mo unit. However, the yield of the main product is moderate, and there are clearly other reactions occurring. While we were unable to identify side products for any of the other reactions, we can speculate on the mechanism of the reactions (Scheme 4). For the molybdenum complexes, the initial products are the bimetallic complexes [(C<sub>5</sub>R<sub>5</sub>)MoCo(CO)<sub>7</sub>(μ-PNR<sub>2</sub>)]. The other product of this initial reaction is presumably an unstable cobalt carbonyl chloride. The second step of the reaction is the addition of a second equivalent of Co<sub>2</sub>(CO)<sub>8</sub> across the Mo—Co bond, leading to a cluster with the formulation [(C<sub>5</sub>R<sub>5</sub>)MoCo<sub>3</sub>(CO)<sub>9</sub>(μ<sub>3</sub>-PNR<sub>2</sub>)]. With the phosphinidene PN-*i*-Pr<sub>2</sub>, this is the final stable product. With the bulkier phosphinidene ligand P(TMP),

steric congestion probably induces the elimination of [Cp\*MoCo(CO)<sub>7</sub>], leading to a phosphinidene-bridged dicobalt cluster, which adds Co<sub>2</sub>(CO)<sub>8</sub>, leading to the final product [Co<sub>4</sub>(CO)<sub>7</sub>(μ-CO)<sub>3</sub>{μ<sub>3</sub>-P(TMP)}] (**2**). The mechanism of the reactions with the ruthenium phosphido complexes is more difficult to discern. Formation of compound **2** may occur by an analogous mechanism to that above. However, bimetallic CoRu complexes could not be isolated, and the spiked tetrahedral structure [Cp\*RuCo<sub>3</sub>(CO)<sub>8</sub>(μ-CO)<sub>2</sub>(μ<sub>3</sub>-PN-*i*-Pr<sub>2</sub>)] (**3**) clearly does not fit into such a reaction scheme.

In reactions of both the Mo phosphido complexes and the Ru phosphido complexes, the TMP substituent encourages transfer of the phosphinidene ligand and elimination of the metal fragment containing the Cp or Cp\* ligand. This reactivity is likely a result of steric interactions between the very bulky TMP group and the other ligands. Thus, some degree of steric control over the reactivity of the terminal phosphido complexes can be achieved. With the bulkier TMP ligand, the phosphido complex acts as a source of phosphinidene (PR). With the smaller di-isopropylamino group, the entire phosphido complex is incorporated into the cluster.

In summary, the results in this paper confirm that readily accessible terminal chloroaminophosphido complexes serve as useful precursors for the synthesis of new phosphinidene-based homo- and heteronuclear clusters.

## Experimental section

All procedures were carried out under a nitrogen atmosphere using standard Schlenk techniques or a glovebox. The compounds [Cp\*Ru(CO)<sub>2</sub>{P(Cl)N-*i*-Pr<sub>2</sub>}] (**10**), [CpMo(CO)<sub>2</sub>{P(Cl)TMP}] (**29**), and [Cp\*Mo(CO)<sub>3</sub>{P(Cl)N-*i*-Pr<sub>2</sub>}] (**18**)



were prepared according to published procedures. All NMR spectra were recorded in  $\text{CDCl}_3$ , and infrared spectra were recorded in hexane solution.

### Preparation of compounds

#### $[\text{Cp}^*\text{Ru}(\text{CO})_2\{\text{P}(\text{Cl})\text{TMP}\}]$ (**1a**)

$[\text{Cp}^*\text{Ru}(\text{CO})_2]_2$  (100 mg, 0.17 mmol) and  $\text{KC}_8$  (56 mg, 0.41 mmol) were stirred in THF (15 mL) for 12 h. The resulting solution was filtered and added dropwise to a solution of  $\text{Cl}_2\text{P}(\text{TMP})$  (83 mg, 0.34 mmol) in THF (10 mL), resulting in the formation of a pale yellow solution. The solvent was removed in vacuo, and the residue was extracted into hexane (5 mL), filtered, and cooled to  $-25^\circ\text{C}$ , resulting in the formation of pale yellow crystals of  $[\text{Cp}^*\text{Ru}(\text{CO})_2\{\text{P}(\text{Cl})\text{TMP}\}]$  (**1a**). Yield 110 mg, 65%. IR ( $\nu(\text{CO})$ ,  $\text{cm}^{-1}$ ): 2007 (s), 1952 (s).  $^1\text{H}$  NMR  $\delta$ : 1.87 (s, 5H,  $\text{C}_5(\text{CH}_3)_5$ ), 1.53 (b, 18H,  $\text{CH}_3$  and  $\text{CH}_2$ ).  $^{31}\text{P}\{^1\text{H}\}$  NMR  $\delta$ : 303.5. Anal. calcd. for  $\text{C}_{21}\text{H}_{33}\text{NO}_2\text{PClRu}$ : C 50.55, H 6.67, N 2.81; found: C 50.33, H 6.98, N 2.77.

#### $[\text{CpRu}(\text{CO})_2\{\text{P}(\text{Cl})\text{TMP}\}]$ (**1b**)

$[\text{CpRu}(\text{CO})_2]_2$  (190 mg, 0.43 mmol) and  $\text{KC}_8$  (140 mg, 1.0 mmol) were stirred in THF (15 mL) for 12 h. The resulting solution was filtered and added dropwise to a solution of  $\text{Cl}_2\text{P}(\text{TMP})$  (208 mg, 0.86 mmol) in THF (10 mL), resulting in the formation of a pale yellow solution. The solvent was removed in vacuo, and the residue was extracted into hexane (5 mL), filtered, and cooled to  $-25^\circ\text{C}$ , resulting in the formation of pale yellow crystals of  $[\text{CpRu}(\text{CO})_2\{\text{P}(\text{Cl})\text{TMP}\}]$  (**1b**). Yield 250 mg, 68%. IR ( $\nu(\text{CO})$ ,  $\text{cm}^{-1}$ ): 2027 (s), 1976 (s).  $^1\text{H}$  NMR  $\delta$ : 5.35 (s, 5H,  $\text{C}_5\text{H}_5$ ), 1.64 (b, 12H,  $\text{CH}_3$ ), 1.51 (b, 6H,  $\text{CH}_2$ ).  $^{31}\text{P}\{^1\text{H}\}$  NMR  $\delta$ : 251.3. Anal. calcd. for  $\text{C}_{16}\text{H}_{23}\text{NO}_2\text{PClRu}$ : C 44.81, H 5.41, N 3.27; found: C 44.75, H 5.70, N 3.15.

#### Reaction of $[\text{Cp}^*\text{Ru}(\text{CO})_2\{\text{P}(\text{Cl})\text{TMP}\}]$ (**1a**) with $\text{Co}_2(\text{CO})_8$

A solution of  $[\text{Cp}^*\text{Ru}(\text{CO})_2\{\text{P}(\text{Cl})\text{TMP}\}]$  (**1a**, 100 mg, 0.200 mmol) and  $\text{Co}_2(\text{CO})_8$  (220 mg, 0.643 mmol) in hexane (10 mL) was stirred for 2 h and then filtered. The solvent volume was reduced to approximately 3 mL, and the resulting solution was cooled to  $-25^\circ\text{C}$ , resulting in the gradual formation of black crystals of  $[\text{Co}_4(\text{CO})_7(\mu\text{-CO})_3\{\mu_3\text{-P}(\text{TMP})\}]$  (**2**). Yield, 75 mg, 47%. IR ( $\nu(\text{CO})$ ,  $\text{cm}^{-1}$ ): 2038 (s), 2028 (m), 1906 (w), 1862 (w).  $^1\text{H}$  NMR  $\delta$ : 1.89 (6H,  $\text{CH}_2$ ), 1.83 (12 H,  $\text{CH}_3$ ).  $^{31}\text{P}\{^1\text{H}\}$  NMR  $\delta$ : 503.5 (bs). Anal. calcd. for  $\text{C}_{19}\text{H}_{18}\text{NO}_{10}\text{PCo}_4$ : C 33.22, H 2.64, N 2.04; found: C 33.34, H 2.47, N 2.08.

#### Reaction of $[\text{CpRu}(\text{CO})_2\{\text{P}(\text{Cl})\text{TMP}\}]$ (**1b**) with $\text{Co}_2(\text{CO})_8$

Using the procedure described above,  $[\text{CpRu}(\text{CO})_2\{\text{P}(\text{Cl})\text{TMP}\}]$  (**1b**, 100 mg, 0.20 mmol) was reacted with  $\text{Co}_2(\text{CO})_8$  (240 mg, 0.70 mmol) to form  $[\text{Co}_4(\text{CO})_7(\mu\text{-CO})_3\{\mu_3\text{-P}(\text{TMP})\}]$  (**2**). Yield: 0.068 mg, 50%.

#### Reaction of $[\text{Cp}^*\text{Ru}(\text{CO})_2\{\text{P}(\text{Cl})\text{N-}i\text{-Pr}_2\}]$ (**1c**) with $\text{Co}_2(\text{CO})_8$

A solution of  $[\text{Cp}^*\text{Ru}(\text{CO})_2\{\text{P}(\text{Cl})\text{N-}i\text{-Pr}_2\}]$  (**1c**, 200 mg, 0.44 mmol) and  $\text{Co}_2(\text{CO})_8$  (300 mg, 0.88 mmol) in hexane

(15 mL) was stirred for 2 h and then filtered. The solvent volume was reduced to approximately 5 mL, and the solution was cooled to  $-25^\circ\text{C}$ , resulting in the formation of black crystals of  $[\text{Cp}^*\text{RuCo}_3(\text{CO})_8(\mu\text{-CO})_2\{\mu_3\text{-PN-}i\text{-Pr}_2\}]$  (**3**). Yield: 180 mg, 51%. IR ( $\nu(\text{CO})$ ,  $\text{cm}^{-1}$ ): 2069 (s), 2031 (s), 2012 (s), 2000 (m), 1985 (w), 1969 (m), 1797 (w).  $^1\text{H}$  NMR  $\delta$ : 4.03 (septet,  $^3J(\text{HH}) = 6.8$  Hz, 2H,  $\text{CH}(\text{CH}_3)_2$ ), 1.92 (s, 15H,  $\text{C}_5(\text{CH}_3)_5$ ), 1.34 (d,  $^2J(\text{HH}) = 6.8$  Hz, 12H,  $\text{CH}(\text{CH}_3)_2$ ).  $^{31}\text{P}\{^1\text{H}\}$  NMR  $\delta$ : 461.4. Anal. calcd. for  $\text{C}_{26}\text{H}_{29}\text{NO}_{10}\text{PCo}_3\text{Ru}$ : C 37.88, H 3.55, N 1.70; found: C 37.46, H 3.52, N 1.90.

#### Reaction of $[\text{CpMo}(\text{CO})_2\{\text{P}(\text{Cl})\text{TMP}\}]$ (**4**) with $\text{Co}_2(\text{CO})_8$

A solution of  $[\text{CpMo}(\text{CO})_2\{\text{P}(\text{Cl})\text{TMP}\}]$  (**4**, 100 mg, 0.24 mmol) and  $\text{Co}_2(\text{CO})_8$  (270 mg, 0.80 mmol) in hexane (10 mL) was stirred for 2 h and then filtered. The solvent volume was reduced to approximately 3 mL, and the resulting solution was cooled to  $-25^\circ\text{C}$ , resulting in the gradual formation of black crystals of  $[\text{Co}_4(\text{CO})_7(\mu\text{-CO})_3\{\mu_3\text{-P}(\text{TMP})\}]$  (**2**). Yield, 160 mg, 53%.

#### Reaction of $[\text{Cp}^*\text{Mo}(\text{CO})_3\{\text{P}(\text{Cl})\text{N-}i\text{-Pr}_2\}]$ (**5**) with $\text{Co}_2(\text{CO})_8$

A solution of  $[\text{Cp}^*\text{Mo}(\text{CO})_3\{\text{P}(\text{Cl})\text{N-}i\text{-Pr}_2\}]$  (**5**, 100 mg, 0.21 mmol) and  $\text{Co}_2(\text{CO})_8$  (220 mg, 0.64 mmol) in hexane (10 mL) was stirred for 2 h and then filtered. The volume of the filtrate was reduced to approximately 3 mL. The solution was then cooled to  $-25^\circ\text{C}$ , resulting in the gradual formation of a mixture of black crystals of  $[\text{Cp}^*\text{MoCo}_3(\text{CO})_5(\mu\text{-CO})_4\{\mu_3\text{-PN-}i\text{-Pr}_2\}]$  (**6**) and red crystals that were identified as  $[\text{Cp}^*\text{MoCo}(\text{CO})_7]$  by infrared spectroscopy and X-ray crystallography. Spectral data for **6**:  $^1\text{H}$  NMR  $\delta$ : 4.37 (septet, 2H,  $\text{CH}(\text{CH}_3)_2$ ,  $^3J(\text{HH}) = 6.8$  Hz), 2.04 (s, 15H,  $\text{C}_5(\text{CH}_3)_5$ ), 1.60 (d, 12H,  $\text{CH}(\text{CH}_3)_2$ ,  $^3J(\text{HH}) = 6.8$  Hz).  $^{31}\text{P}\{^1\text{H}\}$  NMR  $\delta$ : 514.4 (bs). Accurate elemental analysis for **6** could not be obtained because samples could not be completely separated from  $[\text{Cp}^*\text{MoCo}(\text{CO})_7]$ .

### X-ray structure determination

Crystals of compounds **2**, **3**, and **6** were mounted on glass fibres. Intensity data were collected on a Siemens SMART CCD diffractometer using graphite-monochromated Mo  $\text{K}\alpha$  radiation at 173(2) K. Unit cells were determined from randomly selected reflections obtained using the SMART CCD automatic search, centre, index, and least-squares routines. Integration was carried out using SAINT and empirical absorption corrections were applied using SADABS. Structure solution was carried out using the SHELXTL 5.1 suite of programs. Initial solutions were obtained by direct methods and refined by successive least-squares cycles. Full matrix least-squares refinements minimized the function  $\sum_{hkl} w(|F_o| - |F_c|)^2$ , where  $w = 1/(\sigma(F_o)^2)$ ,  $\sigma(F_o) = \sigma(F_o)/2F_o$ , and  $\sigma(F_o)^2 = [\sigma(I_{\text{raw}})^2 + (0.02I_{\text{net}})^2]^{1/2}/Lp$ . Crystal data and collection parameters are listed in Table 4. For compound **3**, the  $\text{Cp}^*$  ring was disordered over three positions with occupancies of 0.8, 0.2, and 0.2. The major disordered ring was refined with anisotropic thermal parameters, while the minor disordered rings were refined isotropically. For compound **6**, the isopropyl groups were disordered over two positions, and the carbon atoms of that group were refined isotropically.



**Table 4.** Crystal data and structure refinement.

	<b>2</b>	<b>3</b>	<b>6</b>
Empirical formula	C <sub>19</sub> H <sub>18</sub> NO <sub>10</sub> PCo <sub>4</sub>	C <sub>26</sub> H <sub>29</sub> NO <sub>10</sub> PCo <sub>3</sub> Ru	C <sub>25</sub> H <sub>29</sub> NO <sub>9</sub> PCo <sub>3</sub> Mo
Formula weight	687.03	824.33	791.19
Crystal system	Orthorhombic	Monoclinic	Orthorhombic
Space group	<i>Pbca</i>	<i>P2<sub>1</sub>/c</i>	<i>P2<sub>1</sub>2<sub>1</sub>2<sub>1</sub></i>
Unit cell dimensions			
<i>a</i> (Å)	16.4177(8)	12.5239(8)	11.2142(9)
<i>b</i> (Å)	16.4664(8)	15.2065(9)	14.4148(11)
<i>c</i> (Å)	18.4705(9)	17.344(1)	18.0412(14)
$\beta$ (°)		103.985(1)	
Volume (Å <sup>3</sup> )	4993.3(4)	3205.2(3)	2916.4(4)
<i>Z</i>	8	4	4
<i>D</i> <sub>calcd</sub> (Mg m <sup>-3</sup> )	1.828	1.708	1.802
Absorption coefficient (mm <sup>-1</sup> )	2.728	2.089	2.202
<i>F</i> (000)	2736	1648	1584
Theta range (°)	2.07–28.73	1.68–28.75	1.81–28.79
Index ranges	–22 ≤ <i>h</i> ≤ 22 –22 ≤ <i>k</i> ≤ 22 –24 ≤ <i>l</i> ≤ 24	–16 ≤ <i>h</i> ≤ 16 –20 ≤ <i>k</i> ≤ 20 –23 ≤ <i>l</i> ≤ 23	–15 ≤ <i>h</i> ≤ 15 –17 ≤ <i>k</i> ≤ 19 –24 ≤ <i>l</i> ≤ 24
Reflections collected	56 956	37 652	28 380
Independent reflections	6471	8306	7569
<i>R</i> (int)	0.1145	0.0770	0.0881
Completeness to theta	99.9	99.7	99.7
Data/restraints/parameters	6471/0/316	8306/0/441	7569/6/396
Goodness-of-fit on <i>F</i> <sup>2</sup>	0.918	0.948	1.040
<i>R</i> <sub>1</sub> [ <i>I</i> > 2σ( <i>I</i> )]	0.0445	0.0400	0.0599
<i>wR</i> <sub>2</sub>	0.0900	0.0864	0.1455
<i>R</i> <sub>1</sub> (all data)	0.0840	0.0650	0.0768
<i>wR</i> <sub>2</sub> (all data)	0.1020	0.0950	0.1565
Largest diff. peak (e Å <sup>-3</sup> )	0.747	0.809	2.470
Largest diff. hole (e Å <sup>-3</sup> )	–0.650	–0.808	–2.608

## Acknowledgements

We are grateful to the Natural Sciences and Engineering Research Council of Canada (NSERC) and the National Research Council Canada (NRC) for financial support of this work.

## References

1. P. Braunstein. Perspectives in coordination chemistry. VCH, Basel. 1992; T.P. Fehlner. Inorganometallic chemistry. Plenum Press, New York. 1992; A.J. Carty, S.A. MacLaughlin, and D. Nucciarone. In Phosphorus-31 NMR spectroscopy in stereochemical analysis. Chap 16: Stereochemistry of metal complexes: phosphido bridging ligands. Edited by J.G. Verkade and L.D. Quinn. VCH, Deerfield Beach. 1987.
2. A.J. Carty. Adv. Chem. Ser. **196**, 163 (1982).
3. A.M. Arif, A.H. Cowley, M. Pakulski, and M.-A. Pearsall. J. Chem. Soc. Dalton Trans. 2713 (1988).
4. A.H. Cowley. Acc. Chem. Res. **30**, 445 (1997); K.B. Dillon, F. Mathey, and J.F. Nixon. Phosphorus: the carbon copy. John Wiley & Sons, Ltd., Chichester. 1998.
5. A.H. Cowley and B. Pellerin. J. Am. Chem. Soc. **112**, 6734 (1990); C.C. Cummins, R.R. Schrock, and W.M. Davis. Angew. Chem. Int. Ed. Engl. **32**, 756 (1993).
6. G. Huttner and K. Knoll. Angew. Chem. Int. Ed. Engl. **26**, 743 (1987).
7. E. Alonso, J. Forniés, C. Fortuño, and A. Martín. Chem. Commun. 231 (1996); D.J. Brauer, G. Hessler, P.C. Knüppel, and O. Stelzer. Inorg. Chem. **29**, 2370 (1990); R. Bender, P. Braunstein, A. Dedieu, and Y. Dusaosoy. Angew. Chem. Int. Ed. **28**, 923 (1989); J.F. Corrigan, S. Doherty, N.J. Taylor, and A.J. Carty. J. Am. Chem. Soc. **114**, 7557 (1992); E. Alonso, J. Forniés, C. Fortuño, A. Martín, and A.G. Orpen. Organometallics, **19**, 2690 (2000); H. Jungbluth and G. Süss-Fink. Organometallics, **9**, 1670 (1990).
8. A. Eichhöfer, D. Fenske, and W. Holstein. Angew. Chem. Int. Ed. **32**, 242 (1993).
9. D.F. Rieck, J.A. Gavney, R.L. Norman, R.K. Hayashi, and L.F. Dahl. J. Am. Chem. Soc. **114**, 10 369 (1992); D. Fenske and S. Falk. Angew. Chem. Int. Ed. **36**, 230 (1997).
10. B.T. Sterenberg, K.A. Udachin, and A.J. Carty. Organometallics, **20**, 2657 (2001).
11. J. Sánchez-Nieves, B.T. Sterenberg, K.A. Udachin, and A.J. Carty. J. Am. Chem. Soc. **125**, 2404 (2003).
12. B.T. Sterenberg, K.A. Udachin, and A.J. Carty. Organometallics. In press.
13. J.F. Corrigan, S. Doherty, N.J. Taylor, and A.J. Carty. J. Am. Chem. Soc. **116**, 9799 (1994); W. Wang, J.F. Corrigan, S. Doherty, G.D. Enright, N.J. Taylor, and A.J. Carty. Organometallics, **15**, 2770 (1996); W. Wang and A.J. Carty.



- New J. Chem. **21**, 773 (1997); J.H. Yamamoto, K.A. Udachin, G.D. Enright, and A.J. Carty. Chem. Commun. 2259 (1998).
14. W. Wang, G.D. Enright, and A.J. Carty. J. Am. Chem. Soc. **119**, 12 370 (1997); W. Wang, G.D. Enright, J. Driediger, and A.J. Carty. J. Organomet. Chem. **541**, 461 (1997); L. Scoles, J.H. Yamamoto, L. Brissieux, B.T. Sterenberg, K.A. Udachin, and A.J. Carty. Inorg. Chem. **40**, 6731 (2001).
15. J.H. Yamamoto, L. Scoles, K.A. Udachin, G.D. Enright, and A.J. Carty. J. Organomet. Chem. **600**, 84 (2000).
16. J. Sánchez-Nieves, B.T. Sterenberg, K.A. Udachin, and A.J. Carty. Inorg. Chim. Acta, **350**, 486 (2003).
17. L. Weber, K. Reizig, and R. Boese. Organometallics, **4**, 1890 (1985); M. Driess, H. Pritzkow, and U. Winkler. J. Organomet. Chem. **529**, 313 (1997); M.J. Barrow and G.A. Sim. J. Chem. Soc. Dalton Trans. 291 (1975); W. Malish, W. Angerer, A.H. Cowley, and N.C. Norman. J. Chem. Soc. Chem. Commun. 1811 (1985); L. Weber, K. Reizig, and R. Boese. Chem. Ber. **118**, 1193 (1985).
18. B.T. Sterenberg and A.J. Carty. J. Organomet. Chem. **617–618**, 696 (2001).
19. D. Fenske, R. Basoglu, J. Hachgenei, and F. Rogel. Angew. Chem. Int. Ed. **23**, 160 (1984).
20. A.M. Arif, A.H. Cowley, M. Pakulski, M.B. Hursthouse, and A. Karauloz. Organometallics, **4**, 2227 (1985).
21. J. Feilong, T.P. Fehlner, and A.L. Rheingold. Angew. Chem. Int. Ed. **27**, 424 (1988).
22. H. Beurich, T. Madach, F. Richter, and H. Vahrenkamp. Angew. Chem. Int. Ed. **18**, 690 (1979).
23. S. Onaka, H. Muto, Y. Katsukawa, and S. Takagi. J. Organomet. Chem. **543**, 241 (1997).
24. R.B. King, W.-K. Fu, and E.M. Holt. J. Chem. Soc. Chem. Commun. 1439 (1984); R.B. King, W.-K. Fu, and E.M. Holt. Inorg. Chem. **25**, 2390 (1986).
25. J. Queisser, H. Oesen, D. Fenske, and B. Lehari. Z. Anorg. Allg. Chem. **620**, 1821 (1994).
26. M.G. Richmond and J.K. Kochi. Inorg. Chem. **25**, 1334 (1986); R.C. Ryan, C.U. Pittman, J.P. O'Connor, and L.F. Dahl. J. Organomet. Chem. **193**, 247 (1980); M.G. Richmond and J.K. Kochi. Organometallics, **6**, 254 (1987); M.G. Richmond and J.K. Kochi. Organometallics, **6**, 777 (1987); E. Lindner, G.A. Weiss, W. Hiller, and R. Fawzi. J. Organomet. Chem. **312**, 365 (1986); J. Feilong, T.P. Fehlner, and A.L. Rheingold. J. Chem. Soc. Chem. Commun. 1395 (1987); R.C. Ryan and L.F. Dahl. J. Am. Chem. Soc. **97**, 6904 (1975); M.G. Richmond and J.K. Kochi. Inorg. Chim. Acta, **126**, 83 (1987).
27. A.J. Arce, A. Karam, Y.D. Sanctis, R. Machado, M.V. Capparelli, and J. Manzur. Inorg. Chim. Acta, **254**, 119 (1997); C.-W. Shiu, Y. Chi, A.J. Carty, S.-M. Peng, and G.-H. Lee. Organometallics, **16**, 5368 (1997); M. Bergamo, T. Beringhelli, G. D'Alfonso, G. Ciani, M. Moret, and A. Sironi. Organometallics, **15**, 1637 (1996); T. Beringhelli, G. D'Alfonso, and M. Zarini. J. Chem. Soc. Dalton Trans. 2407 (1995).
28. S. Kahlal, K.A. Udachin, L. Scoles, A.J. Carty, and J.-Y. Saillard. Organometallics, **19**, 2251 (2000).
29. A.H. Cowley, D.M. Giolando, C.M. Nunn, M. Pakulski, D. Westmoreland, and N.C. Norman. J. Chem. Soc. Dalton Trans. 2127 (1988).



# Band-gap tuning by solid-state intercalations of Mg, Ni, and Cu into $\text{Mo}_3\text{Sb}_7$ <sup>1</sup>

N. Soheilnia, E. Dashjav, and H. Kleinke

**Abstract:**  $\text{Mo}_3\text{Sb}_7$  was synthesized by heating the elements in the stoichiometric ratio in a sealed silica tube at 700 °C. The title compounds  $A_8\text{Mo}_3\text{Sb}_7$  ( $A = \text{Mg}, \text{Ni}, \text{Cu}$ ) were prepared by annealing prereacted  $\text{Mo}_3\text{Sb}_7$  with different amounts of  $A$  in powder form between 500 and 750 °C. According to our single-crystal structure studies, the  $A$  atoms can be intercalated in small amounts into the cubic voids of the  $\text{Mo}_3\text{Sb}_7$  structure without noticeable symmetry changes (space group  $\text{Im}\bar{3}\text{m}$ ). The different cations cause different band-gap decreases that depend on the element as well as its concentration.

**Key words:** thermoelectrics, band-gap tuning, intercalation, antimonide, electronic structure.

**Résumé :** On a réalisé la préparation du  $\text{Mo}_3\text{Sb}_7$  en chauffant les éléments à 700 °C, dans un rapport stoechiométrique, dans un tube de silice scellé. Les composés mentionnés dans le titre,  $A_8\text{Mo}_3\text{Sb}_7$  ( $A = \text{Mg}, \text{Ni}, \text{Cu}$ ) ont été préparés par recuisson à des températures allant de 500 à 750 °C, du  $\text{Mo}_3\text{Sb}_7$  obtenu antérieurement avec diverses quantités de l'élément  $A$  sous la forme de poudre. D'après les études de diffraction des rayons X effectuées sur des mono cristaux, les atomes de l'élément  $A$  peuvent s'intercaler dans les vides cubiques de la structure de  $\text{Mo}_3\text{Sb}_7$  sans changement notable de symétrie (groupe d'espace  $\text{Im}\bar{3}\text{m}$ ). Les différents cations provoquent des diminutions de la largeur de bande interdite qui dépendent de la nature de l'élément ainsi que de sa concentration.

**Mots clés :** thermoélectrique, ajustement de la largeur de bande interdite, intercalation, antimoine, structure électronique.

[Traduit par la Rédaction]

## Introduction

Our motivation to chemically modify  $\text{Mo}_3\text{Sb}_7$  (1) stems from our research interests in thermoelectric materials. Thermoelectrics are used to convert electricity into a temperature gradient (e.g., for Peltier cooling) or vice versa (for power generation) (2). The materials commercially used are usually narrow band-gap semiconductors comprising heavy elements. Several new materials are currently under investigation because of their promising thermoelectric properties (3). Among them are bismuth chalcogenides (4–8), germanium- and tin-based clathrates (9–12), and tin- and antimony-based half-Heusler compounds (13–17). In particular, many researchers from different countries concentrate on the filled skutterudites (18–26). The general formula of the filled skutterudites is  $\text{Ln}_8\text{M}_4\text{Sb}_{12}$  with  $0 \leq \delta \leq 1$ , with  $\text{Ln}$  being a lanthanoid and  $M$  a late transition element such as Fe, Co, and Ni. While the parent compound,  $\text{LaFe}_4\text{Sb}_{12}$ , is metallic,  $\text{LaFe}_3\text{CoSb}_{12}$  exhibits outstanding thermoelectric properties, for its high thermopower and electrical conduc-

tivity are combined with an extraordinarily low thermal conductivity. The latter stems from the high vibrations of the La atom situated in a large “cage” of Sb atoms, a phenomenon usually referred to as *rattling*. Thus, the filled skutterudites may serve as an ideal for a phonon-glass, electron-crystal material (27, 28).

$\text{Mo}_3\text{Sb}_7$ , albeit a metallic material, is another interesting candidate for the thermoelectric energy conversion, as we have recently demonstrated that it becomes semiconducting by a partial Sb–Te exchange. The highest Seebeck coefficient in the series  $\text{Mo}_3\text{Sb}_{7-y}\text{Te}_y$  is found at  $y = 2.2$  (29). Furthermore, its crystal structure ( $\text{Ir}_3\text{Ge}_7$  type) comprises large cubic voids, which may be filled with small cations to create the rattling effect discussed above. This article deals with the successful intercalation of Mg, Ni, and Cu, as confirmed via single-crystal X-ray studies and EDS investigations, and its consequences for the electronic structure and, thus, the physical properties.

## Experimental

### Synthesis

All starting materials were used as acquired in powder form from ALFA AESAR and ALDRICH, with purities of at least 99.5%.  $\text{Mo}_3\text{Sb}_7$  was prepared first by annealing the elements Mo and Sb in the stoichiometric 3:7 ratio in an evacuated fused silica tube at 700 °C for at least 72 h. In attempts to investigate the possibility of filling the cubic void of the  $\text{Mo}_3\text{Sb}_7$  structure, the elements  $A = \text{Mg}, \text{Ni}, \text{and Cu}$  were added in three different amounts each to  $\text{Mo}_3\text{Sb}_7$ , resulting

Received 25 February 2003. Published on the NRC Research Press Web site at <http://canjchem.nrc.ca> on 12 August 2003.

*Dedicated to Professor John Harrod.*

N. Soheilnia, E. Dashjav, and H. Kleinke.<sup>2</sup> Department of Chemistry, University of Waterloo, Waterloo, ON N2L 3G1, Canada.

<sup>1</sup>This article is part of a Special Issue dedicated to Professor John Harrod.

<sup>2</sup>Corresponding author (e-mail: [kleinke@uwaterloo.ca](mailto:kleinke@uwaterloo.ca)).



in nine different reactions, aiming for the product  $A_\delta\text{Mo}_3\text{Sb}_7$  with  $\delta = 0.1, 0.25$ , and  $0.5$ . The number of  $A$  atoms per  $\text{Mo}_3\text{Sb}_7$  unit required to fill all cubic voids of the structure is  $0.5$ .

These mixtures were annealed at different temperatures between  $500$  and  $750^\circ\text{C}$ . The most homogeneous samples were obtained at  $600^\circ\text{C}$ . Subsequent attempts, starting from the elements, yielded the same X-ray powder diffractograms, i.e., most likely the same products. As only the reactions with  $\delta = 0.1$  gave (seemingly) single phase powder diagrams of  $A_\delta\text{Mo}_3\text{Sb}_7$ , it is concluded that less than  $0.25$   $A$  cations may be intercalated into  $\text{Mo}_3\text{Sb}_7$ .

### Analysis

EDS investigations (LEO 1530, with integrated EDAX Pegasus 1200) on selected crystals of the products of the nominal composition " $\text{Cu}_{0.10}\text{Mo}_3\text{Sb}_7$ " revealed that no impurities were present. While the peak of the Cu-K line was very small in each case, its presence was obvious, supporting the incorporation of Cu atoms in these crystals. Averaging the integrations over all peaks obtained from the four crystals resulted in a Cu:Mo:Sb ratio of 1:28:71 atomic %. Since the Cu concentration was not a function of the acceleration voltage, it is not a surface effect.

### Structure determination

Three different block- to cubic-like single crystals of the nominal composition " $A_{0.25}\text{Mo}_3\text{Sb}_7$ " with  $A = \text{Mg}, \text{Ni}$ , and  $\text{Cu}$  were selected under an optical microscope and then mounted on glass fibers. This composition was chosen to ensure that the upper limit of the  $A$  intercalation was determined. Single-crystal X-ray diffraction data were collected with the use of graphite-monochromatized  $\text{Mo K}\alpha$  radiation ( $\lambda = 0.71073 \text{ \AA}$ ) at  $298(2) \text{ K}$  on a Bruker Smart APEX CCD diffractometer. The crystal-to-detector distance was  $4.550 \text{ cm}$ . Data were collected by a scan of  $0.3^\circ$  in  $\omega$  in groups of 606 frames. The data were corrected for Lorentz and polarization effects. Absorption corrections were based on fitting a function to the empirical transmission surface, as sampled by multiple equivalent measurements using SADABS (30). Diffraction peaks obtained from all frames of the reciprocal space images were used to determine the unit cell parameters, which were slightly, yet significantly, enlarged, e.g., from  $a = 9.559(3) \text{ \AA}$  ( $\text{Mo}_3\text{Sb}_7$ ) to  $a = 9.5829(9) \text{ \AA}$  ( $\text{Cu}_{0.041(6)}\text{Mo}_3\text{Sb}_7$ ).

First refinements using SHELXTL (31) were done for  $A = \text{Cu}$ , with the space group and the atomic positions taken from our earlier refinements on  $\text{Mo}_3\text{Sb}_7$  (29). This resulted in small residual factors (e.g.,  $R(F) = 0.0236$ ), but a high rest electron density of  $10.5 \text{ e/\AA}^3$  at  $(0, 0, 0)$ , the location of the cubic void. The other remaining peaks in the difference-Fourier map were below  $2.5 \text{ e/\AA}^3$ . Refining this site, then, as a Cu atom with free occupancy lowered the residual factor to  $0.0219$  (by changing the data:parameter ratio from 164:10 to 164:12) and resulted in an occupancy factor of 8%. No hints towards ordering of the Cu atoms by a symmetry reduction (formation of an ordered superstructure) were found. Repeating this procedure for  $A = \text{Mg}$  and  $\text{Ni}$  yielded similar occupancy factors. The final refined formulas are  $\text{Mg}_{0.07(2)}\text{Mo}_3\text{Sb}_7$  and  $\text{Ni}_{0.04(1)}\text{Mo}_3\text{Sb}_7$  and  $\text{Cu}_{0.041(6)}\text{Mo}_3\text{Sb}_7$ ,

respectively. Details of the structure determinations are given in the Table 1.

### Electronic structure calculations

The self-consistent, tight-binding *first principles* LMTO (LMTO = linear muffin tin orbitals) approach (32, 33) was used for all band structure calculations. In the LMTO approach, the density-functional theory is used with the local density approximation (LDA) (34). The integrations in  $k$  space were performed by an improved tetrahedron method (35) on grids of more than 200 independent  $k$  points of the first Brillouin zone, depending on its size and symmetry. Several structure models were calculated, namely  $\text{Mo}_3\text{Sb}_7$  as taken from our single crystal data, hypothetical " $A_{0.125}\text{Mo}_3\text{Sb}_7$ " (with  $A = \text{Mg}, \text{Ni}, \text{Cu}$ ), and " $\text{Mg}_{0.25}\text{Mo}_3\text{Sb}_7$ " and " $\text{Mg}_{0.5}\text{Mo}_3\text{Sb}_7$ " using the structure parameters of  $\text{Mo}_3\text{Sb}_7$ . For the last case, the  $(0, 0, 0)$  position was filled completely with Mg atoms, retaining the space group. For the other two, the cell had to be enlarged, as it originally contains only one  $A$  atom in the primitive unit cell. Then, one  $A$  atom out of two and one  $A$  atom out of four were filled per cell causing symmetry reduction, modeling " $\text{Mg}_{0.25}\text{Mo}_3\text{Sb}_7$ " and " $A_{0.125}\text{Mo}_3\text{Sb}_7$ ", respectively. Modeling structures with smaller  $A$  content (e.g., corresponding to " $A_{0.0625}\text{Mo}_3\text{Sb}_7$ ") was not possible, since that unit cell would become too large, containing too many valence orbitals for our computational facilities.

## Results and discussion

### Crystal structure

$\text{Mo}_3\text{Sb}_7$  was confirmed to crystallize in the cubic  $\text{Ir}_3\text{Ge}_7$  type. Its structure comprises pairs of face-condensed (distorted)  $\text{MoSb}_8$  square antiprisms, which are interconnected to form infinite chains by Sb—Sb bonds between neighboring pairs. This connection occurs with the formation of an empty  $\text{Sb}_8$  cube, which we were able to partly fill with the cations Mg, Ni, and Cu. As all six faces of each cube are part of a face of an  $\text{MoSb}_8$  square antiprism, three chains orthogonal to each other are interpenetrating at the  $\text{Sb}_8$  cube, thus forming a three-dimensional network of interwoven chains. Parallel chains are interconnected via a short Sb—Sb bond from one cube of one chain to one of the next. Figure 1 shows the whole crystal structure of  $A_\delta\text{Mo}_3\text{Sb}_7$  in a projection onto the  $a, b$  plane on the left and two parallel chains on the right.

While there is only one Mo site as well as one  $A$  site in this structure, two symmetrically independent Sb atoms are present. The Sb(1) atoms form the face in the center of the pair of  $\text{MoSb}_8$  square antiprisms, with Sb—Sb distances of  $3.38 \text{ \AA}$  within the face (dashed lines in Fig. 1). On the other hand, the Sb(2) atoms form the cube, with shorter Sb—Sb distances of  $3.10 \text{ \AA}$  within the cube and the shortest Sb—Sb bond of this structure ( $2.91 \text{ \AA}$ ) between the Sb(2) atoms of the cubes of two parallel chains. The  $2.91 \text{ \AA}$  bond length compares well to the length of Sb—Sb single bonds, as in the Zintl compound  $\text{KSb}$  ( $2.83$  and  $2.85 \text{ \AA}$ ) (36). On the other hand, Sb—Sb bonds around  $3.10 \text{ \AA}$  (the longer Sb(2)—Sb(2) distance) are usually described as half bonds

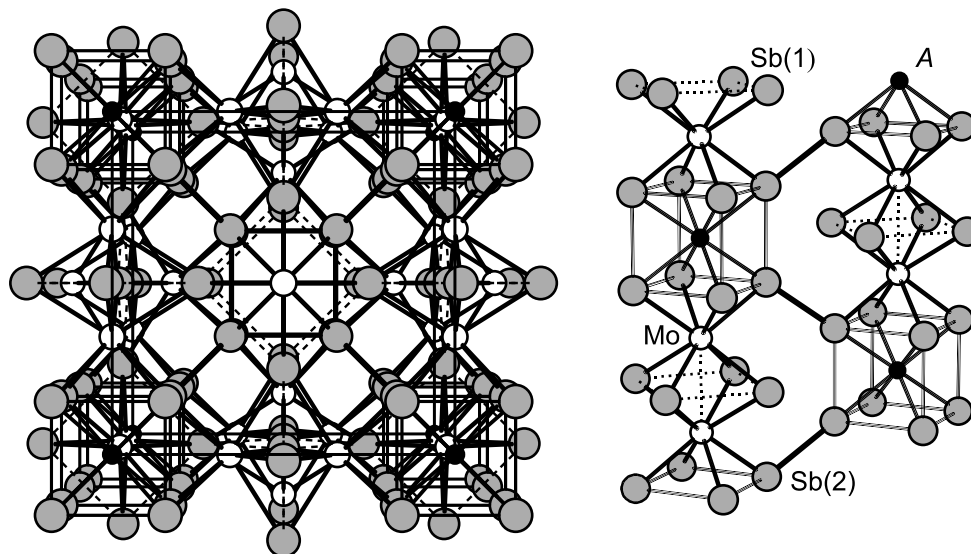


**Table 1.** Crystallographic data for  $A_8\text{Mo}_3\text{Sb}_7$ .

Empirical formula	$\text{Mg}_{0.07(2)}\text{Mo}_3\text{Sb}_7$	$\text{Ni}_{0.04(1)}\text{Mo}_3\text{Sb}_7$	$\text{Cu}_{0.041(6)}\text{Mo}_3\text{Sb}_7$
Formula weight (g/mol)	1141.71	1142.42	1145.15
Diffractometer used	Smart Apex CCD	Smart Apex CCD	Smart Apex CCD
Temperature (K)	298(2)	298(2)	298(2)
Wavelength (Å)	0.71073	0.71073	0.71073
Space group	$\text{Im}\bar{3}\text{m}$ (No. 229)	$\text{Im}\bar{3}\text{m}$ (No. 229)	$\text{Im}\bar{3}\text{m}$ (No. 229)
Unit cell dimensions, $a$ (Å)	9.5740(7)	9.5734(6)	9.5829(9)
$V$ (Å <sup>3</sup> )	877.6(1)	877.4(1)	880.0(1)
$Z$	4	4	4
Calculated density (mg/m <sup>3</sup> )	8.641	8.648	8.643
Absorption coefficient (1/mm)	25.229	25.312	25.342
$F(000)$	1935	1936	1941
Crystal size (μm)	$25 \times 25 \times 20$	$34 \times 20 \times 10$	$32 \times 31 \times 25$
Theta range for data collection (°)	3.01–33.06	3.01–29.87	3.01–34.90
Reflections collected	2213	1625	1193
Independent reflections ( $R_{\text{int}}$ )	198 (0.047)	155 (0.085)	219 (0.036)
Absorption correction	SADABS	SADABS	SADABS
Max. and min. transmission	1.00 and 0.79	1.00 and 0.43	1.00 and 0.78
Goodness-of-fit on $F^2$	1.06	1.14	0.95
$R(F)^a$ , $R_w(F^2)^b$ ( $I > 2\sigma(I)$ )	0.023, 0.049	0.033, 0.063	0.022, 0.030
Extinction coefficient	0.00076(9)	0.0006(1)	0.00035(3)
Largest diff. peak and hole (e/Å <sup>3</sup> )	1.32 and –1.64	2.37 and –1.78	1.01 and –1.24

$$^a R(F_o) = \Sigma ||F_o| - |F_c|| / \Sigma |F_o|.$$

$$^b R_w(F_o^2) = [\Sigma [w(F_o^2 - F_c^2)^2] / \Sigma [w(F_o^2)^2]]^{1/2}.$$

**Fig. 1.** Crystal structure of  $A_8\text{Mo}_3\text{Sb}_7$  (left) and chains of face-condensed  $\text{MoSb}_8$  square antiprisms and  $\text{ASb}_8$  cubes (right). Small, black circles: A atoms; medium, white: Mo; large, gray: Sb.

(37–40). Weakly bonding interactions of 3.2–3.4 Å occur quite often in transition-metal antimonides (41–43).

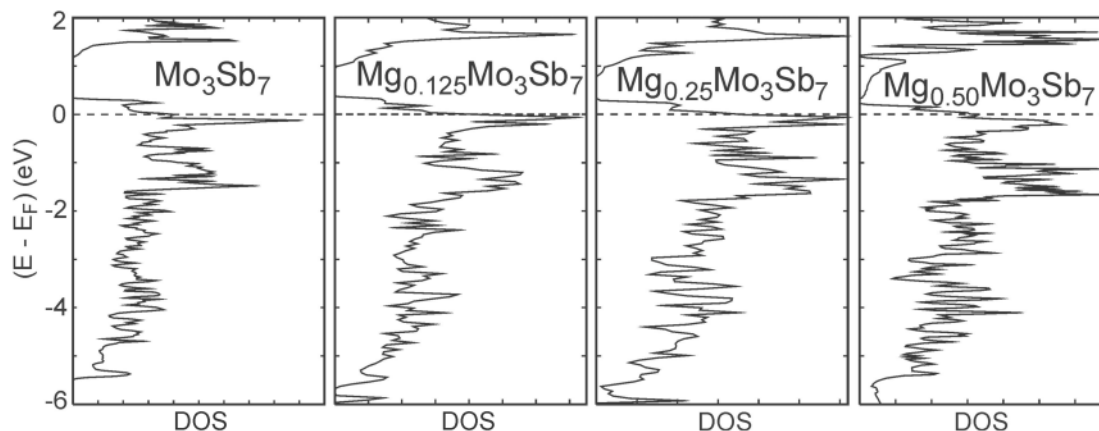
As well, the Mo—Sb distances are different for both Sb atoms: 2.82 Å for the four Mo—Sb(1) bonds vs. 2.79 Å for the four Mo—Sb(2) bonds per Mo atom. The Mo—Sb bonds of  $\text{Mo}_3\text{Sb}_7$ , the only known binary Mo antimonide, compare well to those of the recently published Mo antimonide-chalcogenides, namely  $\text{Mo}_2\text{Sb}_2\text{S}_2$  (shortest Mo—Sb bond: 2.83 Å) (44),  $\text{MoSb}_2\text{S}$  (2.82 Å) (45), and  $\text{MoSb}_2\text{Se}$  (2.80 Å) (46). These distances are all longer than the sums of the sin-

gle bond radii, e.g., after Pauling:  $r_{\text{Mo}} + r_{\text{Sb}} = 1.29 \text{ Å} + 1.39 \text{ Å} = 2.68 \text{ Å}$  (47).

The  $\text{MoSb}_8$  antiprisms are face-condensed; an Mo—Mo contact of 3.00 Å is present across the shared face. As we have reported before (29), all these distances have bonding character, albeit of different strength.

In the binary  $\text{Mo}_3\text{Sb}_7$ , the distance between each corner of the  $\text{Sb}_8$  cube (i.e., the cubic void) and its center is 2.69 Å, which corresponds to a reasonable A—Sb bond: the shortest Mg—Sb bond in  $\text{Mg}_3\text{Sb}_2$  is 2.82 Å (48); the Ni—Sb bond in



**Fig. 2.** Densities of states of  $\text{Mo}_3\text{Sb}_7$  (left) and “ $\text{Mg}_\delta\text{Mo}_3\text{Sb}_7$ ” (with increasing  $\delta$  from left to right).

$\text{NiSb}_2$  is 2.44 Å (49); and the Cu—Sb bond in  $\text{Cu}_2\text{Sb}$  is 2.62 Å (50). Thus, a rattling effect would best be achieved using Ni atoms or, better yet, even smaller ones.

The next nearest neighbors would be six Mo atoms that form A—Mo contacts of 3.28 Å through the centers of the  $\text{Sb}_8$  cube. It is thus not surprising that intercalating Mg, Ni, or Cu atoms into the cubic voids leads only to small structural changes, the most obvious being a slight enlargement of the unit cell. Other changes are slight shifts in the atomic positions. Both the A atom (located on (0, 0, 0)) and the Sb(1) atom (on (1/4, 0, 1/2)) are on fixed positions, while the Mo atom (on (x, 0, 0)) and the Sb(2) atom (on (x, x, x)) both have one free parameter each. A list of the different lattice dimensions, occupancies, and positional parameters may be found in Table 2. In all the four cases studied, the x parameter of the Mo atom remains the same within its standard deviation, while the x parameter of Sb(2) is constant among the ternary representatives (again within its standard deviation, i.e., between 0.16235(9) and 0.16239(4)) but somewhat smaller in  $\text{Mo}_3\text{Sb}_7$  (0.16220(8)).

Along with these partly significant variations in the lattice dimensions and atomic positions come differences in the interatomic distances, which are listed in Table 3. As expected based on the comparable atomic positions and lattice parameters between  $\text{Mg}_{0.07}\text{Mo}_3\text{Sb}_7$  and  $\text{Ni}_{0.04}\text{Mo}_3\text{Sb}_7$ , all distances of these two structures are equivalent within their standard deviations. While the fractional coordinates of the third ternary antimonide,  $\text{Cu}_{0.04}\text{Mo}_3\text{Sb}_7$ , are not significantly different, its lattice parameter is significantly larger at 9.5829(9) Å, compared with 9.5740(7) and 9.5734(6) Å for A = Mg and Ni, respectively. Thus, all interatomic distances are largest in the case of A = Cu, with differences of a few hundredth of an Å.

Because of the smaller volume of  $\text{Mo}_3\text{Sb}_7$ , its interatomic distances between the atoms on fixed positions are some hundredth of an Å shorter than in the ternary compounds. However, the shifts of the Mo and the Sb(2) site occur with equivalent Mo—Mo distances (3.00 Å for  $\text{Mo}_3\text{Sb}_7$  and  $\text{Mg}_{0.07}\text{Mo}_3\text{Sb}_7$ ) and equivalent short Sb(2)—Sb(2) distances (2.91 Å in all cases studied).

### Electronic structure

Since the electronic structure of  $\text{Mo}_3\text{Sb}_7$  was published before (29), we concentrate here on the differences resulting

**Table 2.** Atomic positions<sup>a</sup> and occupancy factors of  $\text{A}_\delta\text{Mo}_3\text{Sb}_7$ .

A	Occupancy (A)	a (Å)	x (Mo)	x (Sb(2))
— <sup>b</sup>	0	9.559(3)	0.3432(2)	0.16220(8)
Mg	14(4)%	9.5740(7)	0.3433(1)	0.16237(5)
Ni	8(2)%	9.5734(6)	0.3432(2)	0.16235(9)
Cu	8(1)%	9.5829(9)	0.3431(1)	0.16239(4)

<sup>a</sup>A on Wyckoff site 2a: (0, 0, 0); Mo on 12c: (x, 0, 0); Sb(1) on 12d: (1/4, 0, 1/2); Sb(2) on 16f: (x, x, x).

<sup>b</sup>Data from single crystal analysis of the binary  $\text{Mo}_3\text{Sb}_7$  (29).

from the additions of the A atoms. The densities of states (DOS) of  $\text{Mo}_3\text{Sb}_7$  and of the three models for hypothetical “ $\text{Mg}_\delta\text{Mo}_3\text{Sb}_7$ ” (with  $\delta = 0.125, 0.25$ , and  $0.5$ ) are shown in Fig. 2. In all cases, a band gap is present slightly above the Fermi level, albeit of different sizes, which would be reached with 55 valence electrons per formula unit ( $\text{Mo}_3\text{Sb}_7$ : 53; “ $\text{Mg}_{0.5}\text{Mo}_3\text{Sb}_7$ ”: 54). Therefore, adding only Mg atoms to  $\text{Mo}_3\text{Sb}_7$  is not sufficient to yield semiconducting properties, as required for thermoelectric materials, for one Mg atom adds two valence electrons and each Sb—Te substitution adds one more; 55 valence electrons are obtained with the general formula “ $\text{Mg}_\delta\text{Mo}_3\text{Sb}_5 + 2\delta\text{Te}_2 - 2\delta$ ”.

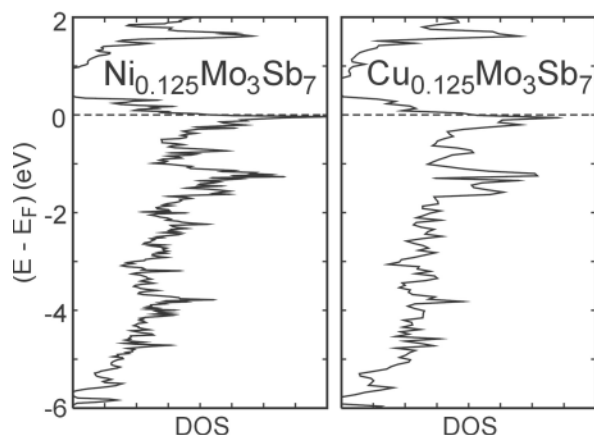
Increasing the Mg content not only adds valence electrons and thus fills more electronic states, it also leads to a decrease in the size of the band gap, i.e., from 0.9 eV in  $\text{Mo}_3\text{Sb}_7$ , to 0.5 eV in “ $\text{Mg}_{0.125}\text{Mo}_3\text{Sb}_7$ ”, to less than 0.1 eV in “ $\text{Mg}_{0.5}\text{Mo}_3\text{Sb}_7$ ”. A band-gap decrease from 0.9 eV is advantageous when considering thermoelectric applications, as theory dictates an ideal band gap size of 0.1–0.6 eV (which is temperature dependent) (51). Such a decrease, to 0.5 eV, was already obtained by going from  $\text{Mo}_3\text{Sb}_7$  to  $\text{Mo}_3\text{Sb}_5\text{Te}_2$  (29), and the trend to decreasing band gap size will continue while adding Mg atoms. It should be noted that all ternary structure models calculated have more Mg than the maximum Mg content obtain experimentally (0.07(2)). Owing to physical computation limits, we could not calculate the more realistic model “ $\text{Mg}_{0.0625}\text{Mo}_3\text{Sb}_7$ ”, as this requires an unreasonably large unit cell with one out of 16 Mg sites filled and, thus, with  $16 \times 6 = 96$  Mo atoms and 224 Sb atoms.

Using Ni and Cu atoms as the A atoms in the model “ $\text{A}_{0.125}\text{Mo}_3\text{Sb}_7$ ” also occurs with a band-gap decrease compared with  $\text{Mo}_3\text{Sb}_7$  (Fig. 3). Adding Ni instead of Mg to



**Table 3.** Selected interatomic distances  $d$  (Å) of  $A_8\text{Mo}_3\text{Sb}_7$  and –ICOHP values (eV per bond) of selected bonds in  $\text{Mo}_3\text{Sb}_7$  and hypothetical  $\text{Mg}_{0.5}\text{Mo}_3\text{Sb}_7$ .

Bond	No.	$d$ (no A)	$d$ (0.07 Mg)	$d$ (0.04 Ni)	$d$ (0.04 Cu)	–ICOHP (no A)	–ICOHP (0.5 Mg)
Mo—Mo	1	2.998(4)	3.001(3)	3.002(4)	3.007(2)	1.01	1.21
Mo—Sb(1)	4	2.821(1)	2.8250(7)	2.825(1)	2.8284(6)	1.62	1.70
Mo—Sb(2)	4	2.793(2)	2.7986(9)	2.798(2)	2.8005(8)	2.03	1.91
Sb(1)—Sb(1)	2	3.380(1)	3.385(1)	3.385(1)	3.3881(6)	0.10	0.09
Sb(2)—Sb(2)	1	2.907(3)	2.906(2)	2.907(3)	2.908(2)	0.79	0.77
Sb(2)—Sb(2)	3	3.101(2)	3.109(1)	3.109(2)	3.1124(9)	0.40	0.35
A—Mo	2	—	3.286(1)	3.286(1)	3.2879(6)	—	0.35
A—Sb(2)	8	—	2.6925(9)	2.692(1)	2.6954(8)	—	1.20

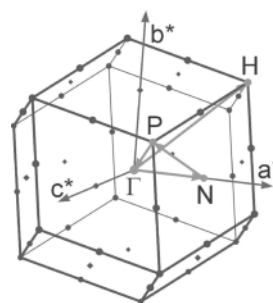
**Fig. 3.** Densities of states of “ $\text{Ni}_{0.125}\text{Mo}_3\text{Sb}_7$ ” (left) and “ $\text{Cu}_{0.125}\text{Mo}_3\text{Sb}_7$ ” (right).

$\text{Mo}_3\text{Sb}_7$  leads to a very comparable band gap, while the Cu addition yields a significantly narrower band gap of about 0.4 eV.

To answer the question of why the band gap decreases upon A intercalation, we compare the band structures of  $\text{Mo}_3\text{Sb}_7$  and “ $\text{Mg}_{0.5}\text{Mo}_3\text{Sb}_7$ ” using the notations suggested by Bradley and Cracknell for the cubic body-centered Bravais lattice (52), as indicated in a plot of the first Brillouin zone (Fig. 4) (53).

We used the *fat band* representation (54) to emphasize the Mo  $d_{z^2}$  contributions for the  $\text{Mo}_3\text{Sb}_7$  band structure (left part of Fig. 5). In the “ $\text{Mg}_{0.5}\text{Mo}_3\text{Sb}_7$ ” model, the Mg  $s$  contributions are highlighted (right part of Fig. 5). It is evident that the band-gap decrease stems exclusively from lowering the lowest unoccupied band at both the N and H point, for the energies of the highest-filled bands remain virtually unchanged upon Mg intercalation. More important in this context is the band at the H point, as this is where the smallest direct gap occurs. This band has mainly Mo  $d_{z^2}$  character, which gets stabilized (i.e., its energy gets lowered) by interacting with the Mg  $s$  orbital.

To investigate possible changes in the bonding character of the different interactions arising from the Mg addition, we turn our attention to the crystal orbital Hamilton population (COHP) curves of the model “ $\text{Mg}_{0.5}\text{Mo}_3\text{Sb}_7$ ”. The COHP formalism differentiates the states into bonding and antibonding contributions (55), which gives results comparable to the longer-established crystal orbital overlap populations (COOP) (56) used to weigh the DOS obtained via extended Hückel calculations (57, 58). Bonding contribu-

**Fig. 4.** First Brillouin zone for cubic body-centered lattices.

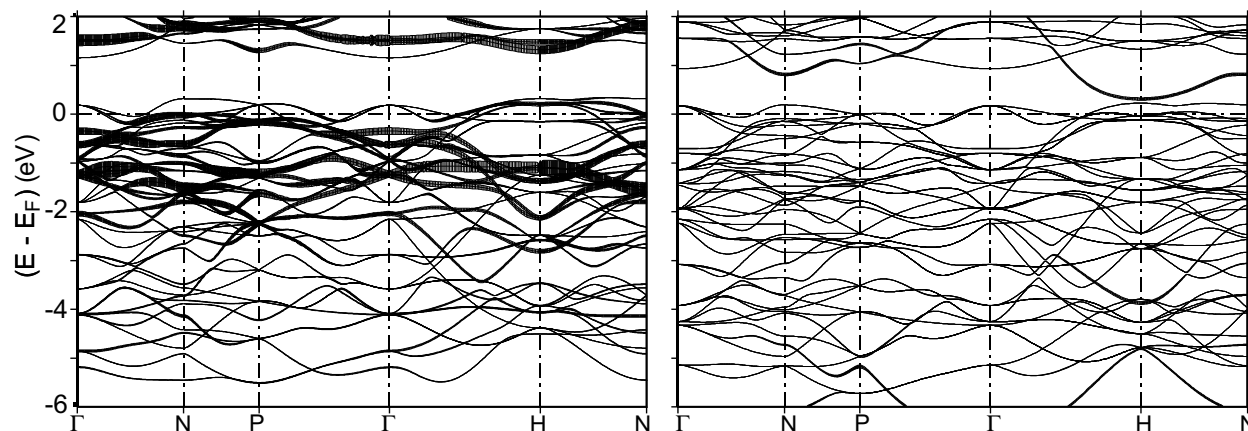
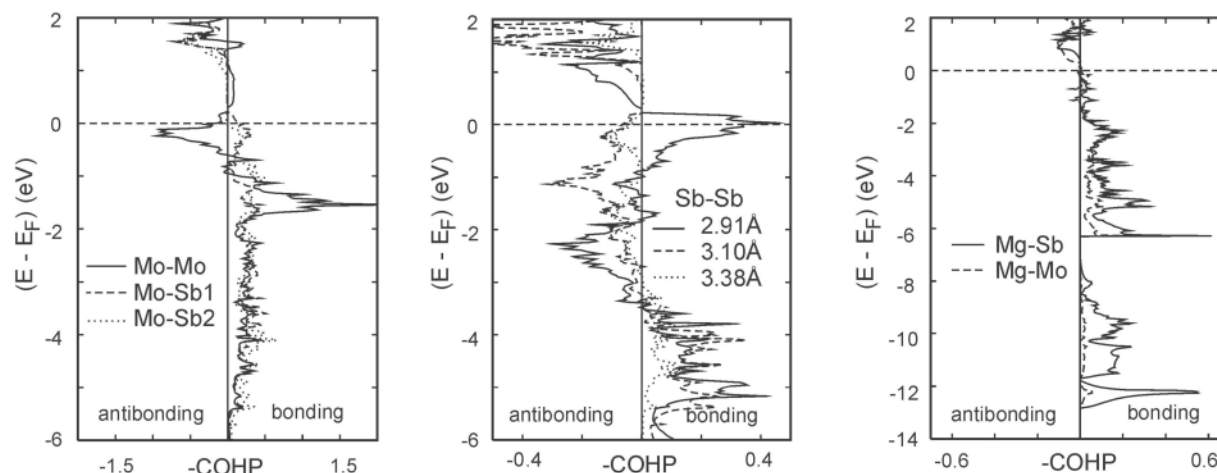
tions are reflected in negative COHPs but positive COOPs. We plotted –COHP vs. energy in order to have the COHP diagrams resemble the COOPs from earlier publications on related topics, i.e., with the bonding part on the right side. Figure 6 shows all interatomic interactions shorter than 3.5 Å, not weighted according to their multiplicity in the unit cell — i.e., simply depicted per bond.

Overall, all of these interactions have bonding character, although in some cases significant amounts of antibonding states are filled as well. The latter is true for all homonuclear interactions, i.e., the Mo—Mo bond, as well as the three different Sb—Sb interactions. On the other hand, almost exclusively bonding states are filled in the cases of the heteronuclear Mg—Mo, Mg—Sb, Mo—Sb(1), and Mo—Sb(2) interactions. The last one shows a few antibonding states that are starting to become filled just under the Fermi level.

It is obvious that adding Mg atoms to  $\text{Mo}_3\text{Sb}_7$  leads to the formation of bonding Mg—Sb and Mg—Mo bonds. How far the other bonds are influenced must be analyzed in more detail. A suitable procedure is to integrate over all filled states, which results in ICOHP values, in analogy to the Mulliken overlap populations (MOP) (59) obtained from COOP curves. ICOHP values differ from MOP values in their sign (i.e., negative values indicate bonding character) and units (eV per bond vs. electrons per bond). As demonstrated before (60), the absolute ICOHP values are typically higher than the corresponding MOP values (ignoring the different units).

For a detailed investigation, we added two columns of –ICOHP values (i.e., ICOHP multiplied with (–1)) to Table 3, one for  $\text{Mo}_3\text{Sb}_7$  and one for “ $\text{Mg}_{0.5}\text{Mo}_3\text{Sb}_7$ ”. Two interactions are stronger in “ $\text{Mg}_{0.5}\text{Mo}_3\text{Sb}_7$ ”, namely the Mo—Mo (–1.21 vs. 1.01 eV/bond) and the Mo—Sb(1) bond (–1.70 vs. 1.62 eV/bond). Reasons for this bond strengthen-



**Fig. 5.** Band structures of  $\text{Mo}_3\text{Sb}_7$  (left) and “ $\text{Mg}_{0.5}\text{Mo}_3\text{Sb}_7$ ” (right).**Fig. 6.** Selected COHP curves for “ $\text{Mg}_{0.5}\text{Mo}_3\text{Sb}_7$ ”.

ing are the increase in the number of valence electrons, thus filling more bonding states, and covalent mixing with the added Mg states. All the other bonds decrease in strength on going from  $\text{Mo}_3\text{Sb}_7$  to “ $\text{Mg}_{0.5}\text{Mo}_3\text{Sb}_7$ ”, in most cases because more antibonding states become filled by adding Mg atoms to  $\text{Mo}_3\text{Sb}_7$  (with the exception of the short Sb(2)—Sb(2) bond of 2.91 Å).

## Summary

This contribution describes the successful intercalation of small cations into  $\text{Mo}_3\text{Sb}_7$ , which was motivated by attempts to create the rattling effect and to tune the band gap, both strategies to enhance the thermoelectric properties. The cubic void of  $\text{Mo}_3\text{Sb}_7$  may be filled with up to 14% Mg, 8% Ni, or 8% Cu without detectable long-range order. This leads to a small increase of the unit cell, the formation of bonding Mg—Sb and Mg—Mo interactions, and a decrease of the band gap.

The mixed occupancies will likely help in lowering the thermal conductivity, and the decrease of the band gap leads to a narrow gap, as desired for thermoelectrics. To reach the band gap, the Sb atoms have in part to be replaced by Te atoms, as described before for the unfilled  $\text{Mo}_3\text{Sb}_7$ . As 55 valence electrons are necessary to fill all bands below the gap,

the ideal formula for the Mg-containing material is “ $\text{Mg}_8\text{Mo}_3\text{Sb}_5 + 28\text{Te}_2 - 28$ ”. The thermoelectric properties of these quaternary materials are currently under investigation. In particular, we are investigating the possibility of intercalating smaller A cations to create the rattling effect.

## Acknowledgment

Financial support from Materials and Manufacturing Ontario, the Natural Sciences and Engineering Research Council of Canada (NSERC), Canadian Foundation for Innovation, Ontario Innovation Trust (Ontario Distinguished Researcher Award for H.K.), the province of Ontario (Premier’s Research Excellence Award for H.K.), and the Canada Research Chair program (CRC for H.K.) is appreciated.

## References

1. A. Brown. *Nature (London)*, **206**, 502 (1965).
2. D.M. Rowe. *CRC handbook of thermoelectrics*. CRC Press, Boca Raton, Fla. 1995.
3. D.J. Singh. *Semicond. Semimet.* **70**, 125 (2001).
4. M.G. Kanatzidis, T.J. McCarthy, T.A. Tanzer, L.-H. Chen, L. Iordanidis, T. Hogan, C.R. Kannewurf, C. Uher, and B. Chen. *Chem. Mater.* **8**, 1465 (1996).



5. D.-Y. Chung, T. Hogan, P. Brazis, M. Rocci-Lane, C. Kannewurf, M. Bastea, C. Uher, and M.G. Kanatzidis. *Science* (Washington, D.C.), **287**, 1024 (2000).
6. K.-F. Hsu, D.-Y. Chung, S. Lal, A. Mrotzek, T. Kyratsi, T. Hogan, and M.G. Kanatzidis. *J. Am. Chem. Soc.* **124**, 2410 (2002).
7. T. Kyratsi, J.S. Dyck, W. Chen, D.-Y. Chung, C. Uher, K.M. Paraskevopoulos, and M.G. Kanatzidis. *J. Appl. Phys.* **92**, 965 (2002).
8. D.-Y. Chung, S. Jovic, T. Hogan, C.R. Kannewurf, R. Brec, J. Rouxel, and M.G. Kanatzidis. *J. Am. Chem. Soc.* **119**, 2505 (1997).
9. N.P. Blake, L. Mollnitz, G. Kresse, and H. Metiu. *J. Chem. Phys.* **111**, 3133 (1999).
10. F. Chen, K.L. Stokes, and G.S. Nolas. *J. Phys. Chem. Solids*, **63**, 827 (2002).
11. A. Bientien, B.B. Iversen, J.D. Bryan, G.D. Stucky, A.E.C. Palmqvist, A.J. Schultz, and R.W. Henning. *J. Appl. Phys.* **91**, 5694 (2002).
12. J. Kitagawa, T. Sakakawa, T. Suemitsu, T. Takabatake, and M. Ishikawa. *J. Phys. Soc. Jpn.* **71**, 1222 (2002).
13. D.P. Young, P. Khalifah, R.J. Cava, and A.P. Ramirez. *J. Appl. Phys.* **87**, 317 (2000).
14. Y. Xia, S. Bhattacharya, V. Ponnambalam, A.L. Pope, S.J. Poon, and T.M. Tritt. *J. Appl. Phys.* **88**, 1952 (2000).
15. S. Bhattacharya, A.L. Pope, R.T.I. Littleton, T.M. Tritt, V. Ponnambalam, Y. Xia, and S.J. Poon. *Appl. Phys. Lett.* **77**, 2476 (2000).
16. Q. Shen, L. Zhang, L. Chen, T. Goto, and T. Hirai. *J. Mater. Science Lett.* **20**, 2197 (2001).
17. Q. Shen, L. Chen, T. Goto, T. Hirai, J. Yang, G.P. Meisner, and C. Uher. *Appl. Phys. Lett.* **79**, 4165 (2001).
18. B.C. Sales, D. Mandrus, and R.K. Williams. *Science* (Washington, D.C.), **272**, 1325 (1996).
19. S. Katsuyama, Y. Shichijo, M. Ito, K. Majima, and H. Nagai. *J. Appl. Phys.* **84**, 6708 (1998).
20. M. Fornari and D.J. Singh. *Phys. Rev. B*, **59**, 9722 (1999).
21. G.S. Nolas, D.T. Morelli, and T.M. Tritt. *Annu. Rev. Mater. Sci.* **29**, 89 (1999).
22. N.R. Dilley, E.D. Bauer, M.B. Maple, S. Dordevic, D.N. Basov, F. Freibert, T.W. Darling, A. Migliori, B.C. Chakoumakos, and B.C. Sales. *Phys. Rev. B*, **61**, 4608 (2000).
23. H. Kitagawa, M. Hasaka, T. Morimura, H. Nakashima, and S.I. Kondo. *Mater. Res. Bull.* **35**, 185 (2000).
24. H. Takizawa, M. Ito, K. Uheda, and T. Endo. *J. Ceram. Soc. Jpn.* **108**, 530 (2000).
25. N.R. Dilley, E.D. Bauer, M.B. Maple, and B.C. Sales. *J. Appl. Phys.* **88**, 1948 (2000).
26. J.S. Dyck, W. Chen, C. Uher, L. Chen, X. Tang, and T. Hirai. *J. Appl. Phys.* **91**, 3698 (2002).
27. G.A. Slack. In *CRC handbook of thermoelectrics*. Edited by D.M. Rowe. CRC Press, Boca Raton, Fla. 1995. p. 407.
28. G.A. Slack. *Mater. Res. Soc. Symp. Proc.* **478**, 47 (1997).
29. E. Dashjav, A. Szczepienowska, and H. Kleinke. *J. Mater. Chem.* **12**, 345 (2002).
30. Siemens Analytical X-ray Instruments Inc. SAINT [computer program]. Version 4. Siemens Analytical X-ray Instruments Inc., Madison, Wis. 1995.
31. G.M. Sheldrick. SHELXTL [computer program]. Version 5.12. Reference manual, Siemens Analytical X-Ray Systems, Inc, Madison, Wis. 1995; Madison, Wis., 1996.
32. O.K. Andersen. *Phys. Rev. B*, **12**, 3060 (1975).
33. H.L. Skriver. *The LMTO method*. Springer, Berlin. 1984.
34. L. Hedin and B.I. Lundqvist. *J. Phys. C*, **4**, 2064 (1971).
35. P.E. Blöchl, O. Jepsen, and O.K. Andersen. *Phys. Rev. B*, **49**, 16223 (1994).
36. W. Hönle and H.-G. von Schnering. *Z. Kristallogr.* **155**, 307 (1981).
37. G. Bolloré, M.J. Ferguson, R.W. Hushagen, and A. Mar. *Chem. Mater.* **7**, 2229 (1995).
38. H. Kleinke. *Eur. J. Inorg. Chem.* 1369 (1998).
39. G.A. Papoian and R. Hoffmann. *Angew. Chem. Int. Ed. Engl.* **39**, 2408 (2000).
40. H. Kleinke. *J. Am. Chem. Soc.* **122**, 853 (2000).
41. H. Kleinke. *J. Mater. Chem.* **9**, 2703 (1999).
42. H. Kleinke. *Inorg. Chem.* **38**, 2931 (1999).
43. H. Kleinke. *Chem. Soc. Rev.* **29**, 411 (2000).
44. C.-S. Lee, A. Safa-Sefat, J.E. Greedan, and H. Kleinke. *Chem. Mater.* **15**, 780 (2003).
45. C.-S. Lee and H. Kleinke. *Eur. J. Inorg. Chem.* 591 (2002).
46. H. Kleinke. *Chem. Commun. (Cambridge)*, 1941 (2000).
47. L. Pauling. *The nature of the chemical bond*. Cornell University Press, Ithaca, N.Y. 1948.
48. M. Martinez-Ripoll, A. Haase, and G. Brauer. *Acta Crystallogr.* **30B**, 2006 (1974).
49. A. Kjekshus, P.G. Peterzens, T. Rakke, and A.F. Andresen. *Acta Chem Scand.* **33A**, 469 (1979).
50. W.B. Pearson. *Z. Kristallogr.* **171**, 23 (1985).
51. J.O. Sofo and G.D. Mahan. *Phys. Rev. B*, **49**, 4565 (1994).
52. C.J. Bradley and A.P. Cracknell. *The mathematical theory of symmetry in solids*. Clarendon Press, Oxford. 1972.
53. A. Kokalj. *J. Mol. Graphics Modell.* **17**, 176 (1999).
54. O. Jepsen and O.K. Andersen. *Z. Phys.* **97**, 25 (1995).
55. R. Dronskowski and P.E. Blöchl. *J. Phys. Chem.* **97**, 8617 (1993).
56. T. Hughbanks and R. Hoffmann. *J. Am. Chem. Soc.* **105**, 3528 (1983).
57. R. Hoffmann. *J. Chem. Phys.* **39**, 1397 (1963).
58. M.-H. Whangbo and R. Hoffmann. *J. Am. Chem. Soc.* **100**, 6093 (1978).
59. R.S. Mulliken. *J. Chem. Phys.* **23**, 2343 (1955).
60. I. Elder, C.-S. Lee, and H. Kleinke. *Inorg. Chem.* **41**, 538 (2002).



# Insertion reactions of nitrosobenzene and ketenes into silaaziridines<sup>1</sup>

Adrian G. Brook and Abraha Habtemariam

**Abstract:** Nitrosobenzene, trimethylsilyl ketene, and diphenylketene insert into the ring of silaaziridines to yield relatively unstable 5-membered heterocyclic ring systems. The new compounds, which have been characterized by <sup>1</sup>H, <sup>13</sup>C, and <sup>29</sup>Si NMR spectroscopy, arise from two different modes of insertion into the ring Si—N bond, leading to compounds with an exocyclic C=N bond (from nitrosobenzene) or two exocyclic C=C bonds (from the ketenes).

**Key words:** silaaziridines, ring insertion, nitrosobenzene, ketenes, heterocyclic rings.

**Résumé :** Le nitrosobenzène, le triméthylsilylcétène et le diphenylcétène s'insèrent dans le cycle des silaaziridines pour conduire à des systèmes cycliques hétérocycliques à cinq chaînons instables. Les nouveaux composés, qui ont été caractérisés par spectroscopie RMN du <sup>1</sup>H, du <sup>13</sup>C et du <sup>29</sup>Si, découlent de deux modes différents d'insertion dans la liaison Si—N du cycle conduisant à des composés avec une liaison C=N exocyclique ou deux liaisons C=C exocycliques (à partir des cétènes).

**Mots clés :** silaaziridines, insertion dans un cycle, nitrosobenzène, cétènes, noyaux hétérocycliques.

[Traduit par la Rédaction]

## Introduction

Previously we have described the insertion reactions of aldehydes and isocyanates (1) into the ring of silaaziridines (2) that yielded 5-membered ring heterocycles **4** and **5**, respectively (see Scheme 1).

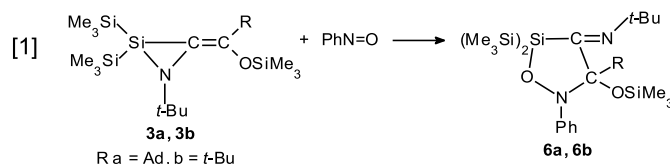
Also, the insertion of some isocyanides into the silaaziridine ring leading to 4-membered ring heterocycles has been reported (3). It seemed probable that other reagents would also insert into the silaaziridine ring, and this note describes reactions with nitrosobenzene, trimethylsilylketene, and diphenylketene, each of which led to novel heterocyclic compounds.

## Results and discussion

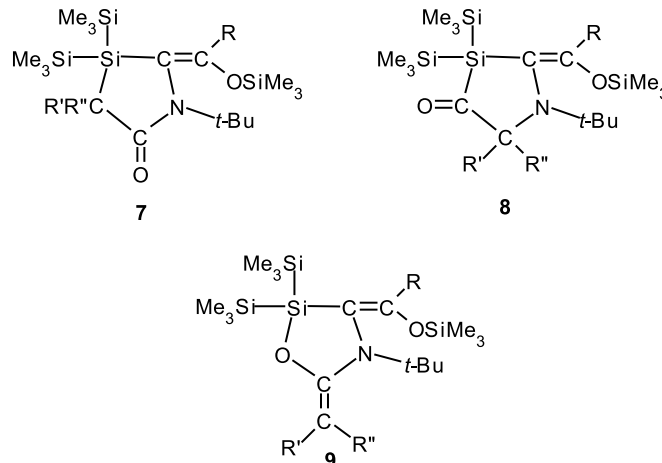
By virtue of their similar polarization it seemed probable that silaaziridines would react with nitrosobenzene in the same manner as with an aromatic aldehyde, yielding analogs of **4**. This was found to be the case since the unstable heterocycles **6a** and **6b** were the major products of reaction of nitrosobenzene with the silaaziridines derived from either the adamantylsilene **2a** or the *tert*-butylsilene **2b** in the dark at room temperature (see eq. [1]). Each of these products

(**6a**, **6b**) is characterized by a prominent <sup>13</sup>C NMR absorption at 184 ppm, as observed in **4**.

On the other hand, benzonitrile, a much less polar molecule, failed to react over several days with silaaziridines.



In contrast to the behavior of the silaaziridines with aldehydes or nitrosobenzene, their reactions with ketenes gave rise to unstable compounds which did **not** contain C=N groups, based on the <sup>13</sup>C NMR data. Instead we believe that the original C=C double bond of the silaaziridine survives as a double bond exocyclic to a five-membered ring, based again on the <sup>13</sup>C NMR data for the C=C carbon atoms. Three possible structures, **7**, **8**, and **9** must be considered as discussed below.



Received 17 September 2002. Published on the NRC Research Press Web site at <http://canjchem.nrc.ca> on 15 August 2003.

Dedicated to Professor John Harrod for his many important contributions to Organosilicon Chemistry.

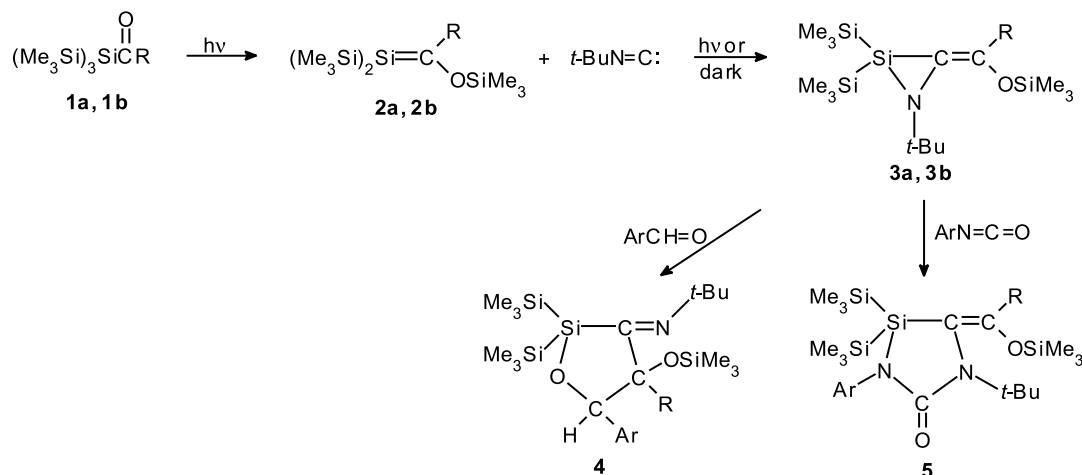
**A.G. Brook<sup>2</sup> and A. Habtemariam.** Lash Miller Chemical Laboratories, University of Toronto, Toronto, ON M5S 3H6, Canada.

<sup>1</sup>This article is part of a Special Issue dedicated to Professor John Harrod.

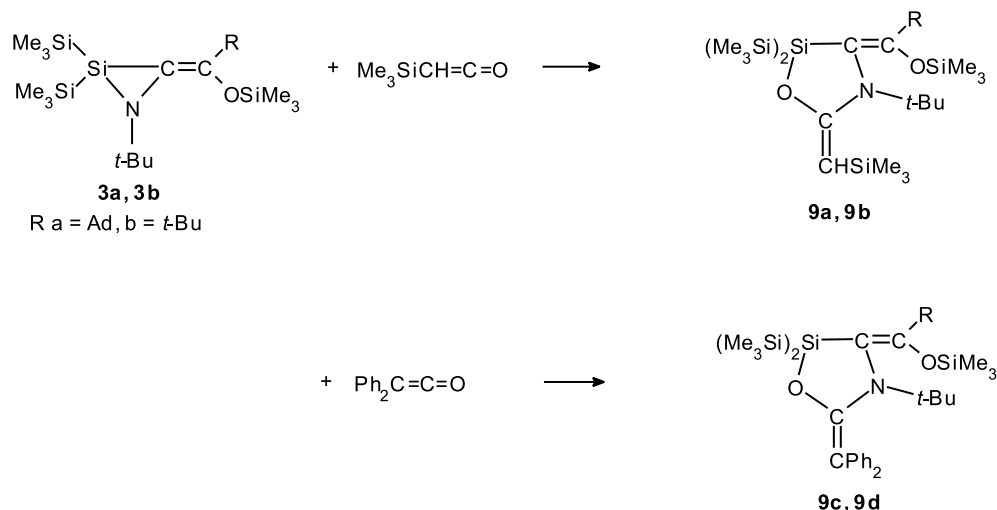
<sup>2</sup>Corresponding author (e-mail: [abrook@chem.utoronto.ca](mailto:abrook@chem.utoronto.ca)).



Scheme 1.



Scheme 2.



The structure **7**, which could be formed analogously to the reaction of silaaziridines with isocyanates (**1**) (nominal addition of the Si—N bond of the silaaziridine across the ends of the C=C bond of the ketene), seems unlikely, especially for the trimethylsilylketene adduct where  $\text{R}' = \text{H}$ ,  $\text{R}'' = \text{Me}_3\text{Si}$ , since the position of the ring CH in the  $^1\text{H}$  NMR spectrum, observed at approximately 4.1 ppm, is not reasonable for a hydrogen on a carbon attached to two  $\text{Me}_3\text{Si}$  groups (expected 1–2 ppm). Also, the IR frequency for an amide C=O in such a structure is expected in the region of  $1700\text{ cm}^{-1}$  rather than the observed  $1612\text{ cm}^{-1}$ . This data appears to rule out **7** as an appropriate structure.

An isomeric structure<sup>3</sup> — **8**, a cyclic acylsilane — could arise from nominal addition of the Si—N bond of the silaaziridine across the ends of the C=C bond in the ketenes with the alternative regiochemistry. This structure would be expected to have C=O IR absorption in the range  $1636\text{--}1650\text{ cm}^{-1}$ , as observed for previously described acylsilanes (**4**), and not at  $1612\text{ cm}^{-1}$ , as observed. Also the  $^{13}\text{C}$  NMR absorption of the carbon atom of the C=O group would be expected to occur in the range  $230\text{--}260\text{ ppm}$  (**5**), whereas we

observed  $158\text{--}165\text{ ppm}$ . Based on the distinctive differences from expectation we rule this structure out also.

Finally, considering structure **9**, in principle this could arise by addition of the Si—N bond of the silaaziridine across the ends of the C=O group (see Scheme 2). We assign the IR absorption at  $1612\text{--}1625$  to the C=C groups of all four adducts characterized. For the pair of trimethylsilylketene adducts, the signal in the  $^1\text{H}$  NMR spectrum at about 4.1 ppm for the  $\text{Me}_3\text{SiCH}=\text{C}=\text{O}$  hydrogen seems reasonable. There are four signals in the  $^{13}\text{C}$  NMR spectra of each compound that can be assigned to the two double bonds, two at about 115 ppm and two at about 161 ppm, due to the carbon atoms of the C=C that bear the  $\text{OSiMe}_3$  group, and for the trimethylsilylketene adducts **9a** and **9b**, two signals at about 86 ppm and 165 ppm for the residual double bond of the original ketene. The  $^{29}\text{Si}$  NMR signals due to the ring silicon atom, found in all compounds in the region  $-2$  to  $-6\text{ ppm}$ , are completely consistent with a silicon atom bearing two trimethylsilyl groups, a carbon atom, and an oxygen atom (**1**). For the diphenylketene products **9c** and **9d** the other signals appear at about 120 and 154 ppm. We believe that this

<sup>3</sup>We are indebted to one of the referees for suggesting that this structure should be considered.



structure, of all considered, best fits the experimental data. It is regrettable that we could not get stable crystals for an X-ray crystal structure, which would have established the structures unambiguously.

A mechanism related to that proposed earlier (1) for the reaction of benzaldehyde with the silaaziridines, which involves dipolar intermediates derived from ring opening and rearrangement, appears to account adequately for the current results with nitrosobenzene. Thus nucleophilic attack on the ring silicon atom of the silaaziridine ring **3** by nitrosobenzene would result in breaking the ring Si—N bond, leading to the dipolar species **10**, which closes via attack by the resonance carbanion contributor **10'** onto the nitrogen atom, leading to the observed product **6**, as summarized in Scheme 3.

A mechanism accounting for the formation of the products derived from the reactions of the silaaziridines with the two ketenes is shown in Scheme 4. Silaphilic attack by the oxygen of the ketene on the silicon atom of the silaaziridine would result in ring opening and the formation of the intermediate dipolar species **11**, which on ring closure would yield the adducts **9**.

In summary, it is clear that a variety of polar reagents having either simple polar functional groups (e.g., C=O or N=O) or more complex functionality (C=C=O or N=C=O) will insert under very mild conditions into the Si—N ring bond of silaaziridines, yielding in each case 5-membered ring heterocycles. However, the adducts described in this paper were, in general, rather unstable, which precluded further investigation of their behavior.

## Experimental

All NMR spectra were run either on a Varian XL400 or Varian XL200 spectrometer in C<sub>6</sub>D<sub>6</sub> unless otherwise noted, using TMS as reference. Where appropriate APT (6) or DEPT (7) NMR pulse sequences were employed for <sup>13</sup>C NMR spectra. <sup>29</sup>Si NMR spectra were run in the DEPT mode or were run NOE suppressed.

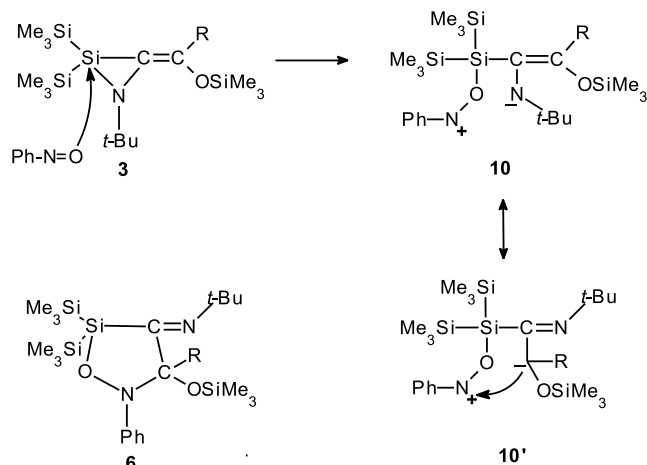
Solutions in sealed NMR tubes were photolyzed inside a water-cooled Dewar flask maintained at 10 °C, using three external 100-watt Par 38 mercury spot lamps (BLAK RAY long wavelength ultraviolet lamps, Ultraviolet Products Inc.), having wavelengths ≥ 360 nm.

### Reaction of silaaziridine **3a** with nitrosobenzene:

#### Formation of **6a**

Silaaziridine **3a** was prepared by photolysis of a solution of the adamantylacetylsilane **1a** (0.21 g, 0.5 mmol) in 2 mL C<sub>6</sub>D<sub>6</sub> with 0.08 mL (4.4 mmol) of *t*-BuN=C: for 58 h according to the published procedure (1, 2). To the silaaziridine solution was added 0.06 g (0.56 mmol) of nitrosobenzene (**8**) and the solution was left in the dark overnight. The <sup>1</sup>H NMR spectrum showed that all the silaaziridine had been converted to the new product **6a**. The volatiles were removed under reduced pressure, and the NMR spectra were taken of the residue. Attempts to purify the material by chromatography on silica gel led to serious decomposition. <sup>1</sup>H NMR δ: 0.20, 0.33, 0.50 (each 9 H, s, Me<sub>3</sub>Si), 1.25 (9 H, s, Me<sub>3</sub>C), 1.6–2.1 (15 H, m, Ad), 6.8–7.3, 7.8–8.3 (5 H, m,

Scheme 3.



Ph). <sup>13</sup>C NMR δ: 0.45, 0.63, 4.78 (Me<sub>3</sub>Si), 29.20 (CH Ad), 30.15 (Me<sub>3</sub>C), 37.28, 37.41 (CH<sub>2</sub> Ad), 40.55 (C quat Ad), 59.48 (Me<sub>3</sub>C), 100.32 (ring C *sp*<sup>3</sup>), 117.59, 120.84, 128.21 (CH *sp*<sup>2</sup> Ph), 150.41 (quat C *sp*<sup>2</sup> Ph), 184.22 (C=N). <sup>29</sup>Si NMR δ: -14.62, -12.98 (Me<sub>3</sub>Si), -5.12 (ring Si), 7.88 (OSiMe<sub>3</sub>).

### Reaction of silaaziridine **3b** with nitrosobenzene **6b**

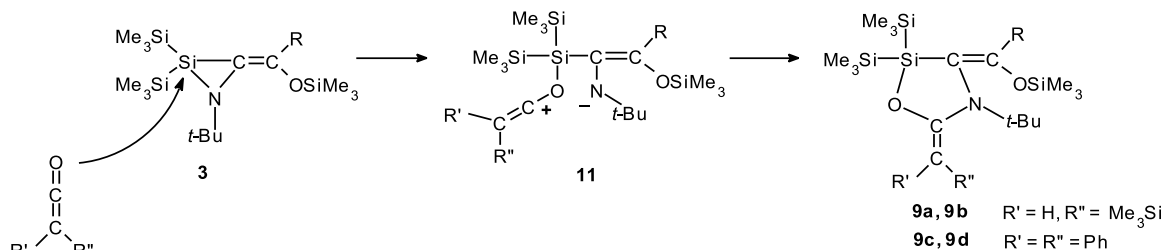
Following the above procedure but using acetylsilane **1b**, the volatiles were removed under reduced pressure and flash chromatography on silica gel eluting with hexane – ethyl acetate (9:1) gave a fraction that contained relatively pure **6b**, based on the NMR spectra. <sup>1</sup>H NMR δ: 0.17, 0.26, 0.45 (each 9 H, s, Me<sub>3</sub>Si), 1.10 (9 H, Me<sub>3</sub>C), 1.19 (9 H, Me<sub>3</sub>C-N), 6.8–7.3, 7.7–8.4 (5 H, m, Ph). <sup>13</sup>C NMR δ: 0.42, 0.60, 4.70 (Me<sub>3</sub>Si), 28.81, 30.06 (Me<sub>3</sub>C), 44.78 (Me<sub>3</sub>C-C), 59.34 (Me<sub>3</sub>C-N), 100.92 (ring C *sp*<sup>3</sup>), 118.52, 121.55, 128.16 (CH *sp*<sup>2</sup> Ph), 150.13 (quat C *sp*<sup>2</sup>), 184.28 (C=N). <sup>29</sup>Si NMR δ: -14.91, -13.00 (Me<sub>3</sub>Si), -4.74 (ring Si), 7.65 (OSiMe<sub>3</sub>).

### Reaction of silaaziridine **3a** with trimethylsilylketene **9a**

To the silaaziridine **3a** prepared from 0.41 g (1.0 mmol) of the adamantylacetylsilane **1a** in 4 mL C<sub>6</sub>D<sub>6</sub> was added 0.19 g (1.1 mmol) of trimethylsilylketene (**9**) with vigorous shaking, and the solution was then left in the dark at room temperature. The <sup>1</sup>H NMR spectrum indicated that the silaaziridine was 40% converted to a single product after 30 min and completely converted after 24 h. The volatile material was removed under reduced pressure, and the residue was redissolved in C<sub>6</sub>D<sub>6</sub>. Attempts to further purify the material by chromatography on alumina, eluting with hexane – ethyl acetate 9:1, led to much decomposition. **9a**: IR (film) (cm<sup>-1</sup>): 1612 (C=C). <sup>1</sup>H NMR δ: 0.27 (9 H, s, Me<sub>3</sub>Si), 0.32 (18 H, s, two Me<sub>3</sub>Si), 0.33 (9 H, s, Me<sub>3</sub>Si), 1.34 (9 H, Me<sub>3</sub>C), 1.6–2.1 (Ad), 4.08 (1 H, s, ring CH). <sup>13</sup>C NMR δ: 0.34, 0.55, 0.66, 2.10 (Me<sub>3</sub>Si), 28.79 (CH Ad), 29.19 (Me<sub>3</sub>C), 37.00, 40.47 (CH<sub>2</sub> Ad), 39.87 (quat C Ad), 61.38 (Me<sub>3</sub>C), 86.81, 117.92, 161.44, 165.11 (C=C). <sup>29</sup>Si NMR δ: -16.48, -13.27, -10.24 (Me<sub>3</sub>Si), -2.19 (ring Si), 15.13 (OSiMe<sub>3</sub>).



Scheme 4.



#### Reaction of silaaziridine 3b with trimethylsilylketene 9b

After following the above procedure using acylsilane **1b**, the volatiles were pumped off under reduced pressure, and the residue was dissolved in  $\text{C}_6\text{D}_6$ . **9b**: IR (film) ( $\text{cm}^{-1}$ ): 1614 ( $\text{C}=\text{C}$ ).  $^1\text{H}$  NMR  $\delta$ : 0.26 (9 H, s,  $\text{Me}_3\text{Si}$ ), 0.31 (18 H, s, two  $\text{Me}_3\text{Si}$ ), 0.34 (9 H, s,  $\text{Me}_3\text{Si}$ ), 1.12 (9 H,  $\text{Me}_3\text{C}-\text{C}$ ), 1.34 (9 H,  $\text{Me}_3\text{C}-\text{N}$ ), 4.07 (1 H, s, ring CH).  $^{13}\text{C}$  NMR  $\delta$ : 0.26, 0.33, 0.64, 1.91 ( $\text{Me}_3\text{Si}$ ), 29.10 ( $\text{Me}_3\text{C}-\text{C}$  and  $\text{Me}_3\text{C}-\text{N}$  overlapped), 37.44 ( $\text{Me}_3\text{C}-\text{C}$ ), 61.11 ( $\text{Me}_3\text{C}-\text{N}$ ), 86.74, 117.47, 160.85, 165.17 ( $\text{C}=\text{C}$ ).  $^{29}\text{Si}$  NMR  $\delta$ : -16.72, -14.13 ( $\text{Me}_3\text{Si}-\text{Si}$ ), -10.26 ( $\text{Me}_3\text{Si}-\text{C}$ ), -2.58 (ring Si), 15.24 ( $\text{OSiMe}_3$ ).

#### Reaction of silaaziridine 3a with diphenylketene 9c

To the silaaziridine **3a** prepared from 0.21 g (0.5 mmol) of the adamantylacylsilane **1a** and  $t\text{-BuN}=\text{C}$ : (0.085 mL, 0.7 mmol) in 2 mL  $\text{C}_6\text{D}_6$  was added 0.11 g (0.6 mmol) of diphenylketene (**10**). The very slow reaction was monitored by  $^1\text{H}$  NMR spectroscopy for 10 days, by which time the ratio of the adduct **9c** to the silaaziridine **3a** was 3:1. The material remaining after removal of the volatiles was chromatographed on silica gel, being eluted with hexane – ethyl acetate 30:1 to give a relatively pure oily solid **12c**. IR (film) ( $\text{cm}^{-1}$ ): 1625 ( $\text{C}=\text{C}$ ).  $^1\text{H}$  NMR  $\delta$ : 0.08, 0.29, 0.42 (each 9 H, s,  $\text{Me}_3\text{Si}$ ), 1.28 (9 H, s,  $\text{Me}_3\text{C}$ ), 1.6–2.1 (15 H, m, Ad), 7.14–7.21, 7.50–7.59 (10 H, m, Ph).  $^{13}\text{C}$  NMR  $\delta$ : -0.83, -0.35, 2.42 ( $\text{Me}_3\text{Si}$ ), 28.57 (CH Ad), 29.55 ( $\text{Me}_3\text{C}$ ), 36.57, 40.26 ( $\text{CH}_2$  Ad), 40.11 (quat C Ad), 65.11 ( $\text{Me}_3\text{C}$ ), 112.48, 120.02 ( $\text{C}=\text{C}$ ) 125.26, 125.41, 128.12, 128.28, 131.41, 132.10 (CH  $sp^2$  Ph), 143.70, 143.79 (quat C  $sp^2$  Ph), 154.25, 159.63 ( $\text{C}=\text{C}$ ).  $^{29}\text{Si}$  NMR  $\delta$ : 14.93, -13.78 ( $\text{Me}_3\text{Si}$ ), -6.11 (ring Si), 11.68 ( $\text{OSiMe}_3$ ).

#### Reaction of silaaziridine 3b with diphenylketene 9d

To the silaaziridine prepared in the usual way from 0.5 g (1.5 mmol) of the *tert*-butylacylsilane **1b** and 0.2 mL (2.4 mmol) of  $t\text{-BuN}=\text{C}$ : in 4 mL  $\text{C}_6\text{D}_6$  was added 0.3 g (1.5 mmol) of diphenylketene. No reaction was observed overnight so the solution was photolyzed for 5 h, after which

time a new compound was observed in a 1:2 ratio with unconsumed silaaziridine. After 21 h further photolysis NMR spectroscopy indicated that all the silaaziridine **3b** had been converted to the product **9d**. Chromatography on silica gel, with elution using hexane – ethyl acetate 9:1 gave purer material. IR (film) ( $\text{cm}^{-1}$ ): 1623 ( $\text{C}=\text{C}$ ).  $^1\text{H}$  NMR  $\delta$ : 0.08, 0.26, 0.41 (each 9 H, s,  $\text{Me}_3\text{Si}$ ), 1.15 (9 H, s,  $\text{Me}_3\text{C}-\text{C}$ ), 1.27 (9 H, s,  $\text{Me}_3\text{C}-\text{N}$ ), 6.95–7.60 (10 H, m, Ph).  $^{13}\text{C}$  NMR  $\delta$ : -0.50, 0.03, 2.71 ( $\text{Me}_3\text{Si}$ ), 29.54, 29.88 ( $\text{Me}_3\text{C}$ ), 38.03 ( $\text{Me}_3\text{C}-\text{C}$ ), 65.26 ( $\text{Me}_3\text{CN}$ ), 112.47 (ring  $\text{C}=\text{C}$ ), 120.00 ( $\text{C}=\text{C}$ ), 125.22, 125.41, 126.21, 127.52, 131.37, 131.94 (CH  $sp^2$  Ph), 143.52, 143.70 (quat C  $sp^2$  Ph), 154.17 ( $\text{C}=\text{C}$ ), 158.66 ( $\text{C}=\text{C}$ ).  $^{29}\text{Si}$  NMR  $\delta$ : -15.25, -14.35 ( $\text{Me}_3\text{Si}$ ), -6.28 (ring Si), 11.92 ( $\text{OSiMe}_3$ ).

#### Acknowledgment

This research was supported by the Natural Sciences and Engineering Research Council of Canada (NSERC).

#### References

1. A.G. Brook, D. Azarian, A. Baumegeger, S.S. Hu, and A.J. Lough. *Organometallics*, **12**, 529 (1993).
2. A.G. Brook, Y.K. Kong, A.K. Saxena, and J.F. Sawyer. *Organometallics*, **7**, 2245 (1988).
3. A.G. Brook, A.K. Saxena, and J.F. Sawyer. *Organometallics*, **8**, 850 (1989).
4. See Table III, A.G. Brook, *Adv. Organomet. Chem.* **7**, 108 (1968).
5. A.G. Brook, F. Abdesaken, G. Gutekunst, and N. Plavac. *Organometallics*, **1**, 994 (1982).
6. S.L. Pitt and T.N. Shoolery. *J. Mag. Res.* **46**, 535 (1982).
7. D.T. Pegg, D.M. Doddrell, and M.R. Bendall. *J. Chem. Phys.* **77**, 2745 (1982).
8. Vogel's textbook of practical organic chemistry. 5th ed. Longmans, Harlow, Essex. 1989. p. 956.
9. W.T. Brady and K. Saidi, *J. Org. Chem.* **44**, 733 (1979).
10. L.I. Smith and H.H. Hoehn. *Org. Synth.* **52**, 36 (1972).



# Crystal structures, magnetic properties, and absorption spectra of nickel(II) thiocyanato complexes: a comparison of different coordination geometries<sup>1</sup>

Bruno Larue, Lan-Tâm Tran, Dominique Luneau, and Christian Reber

**Abstract:** Thiocyanatonickel(II) compounds with composition  $\{(\text{AsPh}_4)_2[\text{Ni}(\text{NCS})_4]\}$  **1**,  $\{(\text{Cat})[\text{Ni}(\text{NCS})_4]\}$  **2**,  $\{(\text{AsPh}_4)_4[\text{Ni}_2(\text{NCS})_8]\}$  **3**,  $\{(\text{Cat})_2[\text{Ni}_2(\text{NCS})_8] \cdot 2\text{CH}_3\text{NO}_2\}$  **4**, and  $\{(\text{Et}_4\text{N})_4[\text{Ni}(\text{NCS})_6]\}$  **5** ( $\text{Cat}^{2+} = (p\text{-xylylenebis(triphenylphosphonium)})^{2+}$ ) were prepared. The crystal structures of compounds **1**, **3**, and **4** were determined. Compound **1** crystallizes in the monoclinic  $C2/c$  space group with  $a = 22.761(2)$  Å,  $b = 15.055(1)$  Å,  $c = 15.054(1)$  Å,  $\beta = 108.915(1)^\circ$ ,  $V = 4879.9(6)$  Å<sup>3</sup>, and  $Z = 4$ . Compound **3** crystallizes in the triclinic  $P\bar{1}$  space group with  $a = 11.2183(6)$  Å,  $b = 14.2551(8)$  Å,  $c = 16.629(1)$  Å,  $\alpha = 79.326(1)^\circ$ ,  $\beta = 73.605(1)^\circ$ ,  $\gamma = 75.496(1)^\circ$ ,  $V = 2451.0(2)$  Å<sup>3</sup>,  $Z = 2$ . Compound **4** crystallizes in the monoclinic  $P2_1/n$  space group with  $a = 13.1148(9)$  Å,  $b = 27.128(2)$  Å,  $c = 14.882(1)$  Å,  $\beta = 114.056(2)^\circ$ ,  $V = 4834.8(6)$  Å<sup>3</sup>,  $Z = 4$ . The magnetic properties of compounds **1–4** were studied over the 2–300 K temperature range. Compounds **1** and **2** with monometallic  $[\text{Ni}(\text{NCS})_4]^{2-}$  complex units have similar magnetic properties, in agreement with nickel(II) ions in pseudo-tetrahedral environments. Compounds **3** and **4** with bimetallic  $[\text{Ni}_2(\text{NCS})_8]^{4-}$  complex units exhibit magnetic properties, which are indicative of Ni(II)–Ni(II) ferromagnetic interactions with zero-field splitting effects caused by the pseudo-square-pyramidal or pseudo-trigonal-bipyramidal coordination environments of the nickel(II) ion in compounds **3** and **4**, respectively. The structures and magnetic results for all compounds are correlated with NIR–UV–vis absorption spectra.

**Key words:** nickel(II) thiocyanato complexes, crystal structures, paramagnetism, molecular magnetism, exchange coupling, absorption spectroscopy.

**Résumé :** Les composés à base de complexes thiocyanate de nickel(II) de composition  $\{(\text{AsPh}_4)_2[\text{Ni}(\text{NCS})_4]\}$  **1**,  $\{(\text{Cat})[\text{Ni}(\text{NCS})_4]\}$  **2**,  $\{(\text{AsPh}_4)_4[\text{Ni}_2(\text{NCS})_8]\}$  **3**,  $\{(\text{Cat})_2[\text{Ni}_2(\text{NCS})_8] \cdot 2\text{CH}_3\text{NO}_2\}$  **4** et  $\{(\text{Et}_4\text{N})_4[\text{Ni}(\text{NCS})_6]\}$  **5** [ $\text{Cat}^{2+} = (p\text{-xylylènebis(triphenylphosphonium)})^{2+}$ ] ont été synthétisés. Les structures cristallines des composés **1**, **3** et **4** ont été déterminées. Le composé **1** cristallise dans le groupe d'espace monoclinique  $C2/c$  avec  $a = 22.761(2)$  Å,  $b = 15.055(1)$  Å,  $c = 15.054(1)$  Å,  $\beta = 108.915(1)^\circ$ ,  $V = 4879.9(6)$  Å<sup>3</sup>,  $Z = 4$ . Le composé **3** cristallise dans le groupe d'espace triclinique  $P\bar{1}$  avec  $a = 11.2183(6)$  Å,  $b = 14.2551(8)$  Å,  $c = 16.629(1)$  Å,  $\alpha = 79.326(1)^\circ$ ,  $\beta = 73.605(1)^\circ$ ,  $\gamma = 75.496(1)^\circ$ ,  $V = 2451.0(2)$  Å<sup>3</sup>,  $Z = 2$ . Le composé **4** cristallise dans le groupe d'espace monoclinique  $P2_1/n$  avec  $a = 13.1148(9)$  Å,  $b = 27.128(2)$  Å,  $c = 14.882(1)$  Å,  $\beta = 114.056(2)^\circ$ ,  $V = 4834.8(6)$  Å<sup>3</sup>,  $Z = 4$ . Les propriétés magnétiques des composés **1–4** ont été étudiées dans le domaine de température 2–300 K. Les composés **1** et **2** contiennent l'entité complexe mononucléaire  $[\text{Ni}(\text{NCS})_4]^{2-}$  et ont des comportements magnétiques identiques caractéristiques d'un ion nickel(II) dans un environnement pseudo tétraédrique. Les composés **3** et **4** contiennent l'entité complexe dinucléaire  $[\text{Ni}_2(\text{NCS})_8]^{4-}$  et ont des comportements magnétiques qui indiquent l'existence d'interactions ferromagnétiques Ni(II)–Ni(II) associées aux effets de levée de dégénérescence en champ nul dus au nickel(II) dans un environnement pseudo pyramide à base carrée (composé **3**) ou pseudo bipyramide trigonale (composé **4**). Les structures et résultats des mesures magnétiques pour tous les composés sont mis en rapport aux spectres d'absorption.

**Mots clés :** complexes thiocyanato du nickel(II), structures cristallines, paramagnétisme, aimants moléculaires, interaction d'échange, spectroscopie d'absorption.

Received 12 April 2003. Published on the NRC Research Press Web site at <http://canjchem.nrc.ca> on 26 August 2003.

Dedicated to Professor John F. Harrod.

**B. Larue, L.-T. Tran, and C. Reber.**<sup>2</sup> Département de Chimie, Université de Montréal, Montréal, QC H3C 3J7, Canada.

**D. Luneau.**<sup>3</sup> Laboratoire de Chimie Inorganique et Biologique (UMR 5046), DRFMC, CEA-Grenoble, 17 rue des Martyrs, 38054 Grenoble CEDEX 09, France.

<sup>1</sup>This article is part of a Special Issue dedicated to Professor John Harrod.

<sup>2</sup>Corresponding author (e-mail: [reber@chimie.umontreal.ca](mailto:reber@chimie.umontreal.ca)).

<sup>3</sup>Current address: Université Claude Bernard Lyon 1, Bât. 305 – 43 avenue du 11 novembre 1918, 69622 Villeurbanne CEDEX, France.



## Introduction

The magnetic properties of coordination compounds have received renewed interest in view of the recent discoveries of molecular magnetic materials (1–4). In some cases, understanding their magnetism still poses a challenge even when simple molecular building blocks, such as the title compounds, are involved. In the vast majority of the published work, the temperature dependence of the magnetic properties is given and explained based on only the crystal structure of the material. It is sometimes difficult, however, to understand even fundamental magnetic properties, such as deviations from spin-only behavior for chemically related compounds, if only structural data is used. More detailed information on the electronic structure and precise energies of electronic states are then needed. In this report we use absorption spectroscopy to provide such information.

The thiocyanato and other isoelectronic bridging ligands have attracted interest from a crystal engineering perspective, as they lead to many different of molecular and extended structures, and a variety of nickel(II) thiocyanato complexes have been reported (5–7). In the following, we reexamine a previously characterized set of nickel(II) complexes with thiocyanato ligands (5). Room-temperature solid-state reflectance spectra and the magnetic susceptibility of the title compounds — also mainly at room temperature — were measured, but neither the absorption spectroscopy nor the magnetic properties have been explored in detail. In the following, we present temperature-dependent magnetic measurements, single-crystal absorption spectra, and crystal structures. Octahedral, distorted tetrahedral, square-pyramidal, and trigonal-bipyramidal coordination geometries are investigated. The absorption spectra obtained from crystals at low temperature depend strongly on the coordination geometry. They are analyzed with a quantitative ligand-field model based on the experimental metal–ligand angular geometry. The ground-state properties obtained from this analysis are then compared with the observed  $\chi T$  values (the product of the molar magnetic susceptibility with temperature) at room temperature. We also show that for bimetallic compounds, complementary information on magnetic exchange interactions can be obtained from temperature-dependent absorption spectra, even if the exchange coupling is relatively weak and the bands are not highly resolved. The combination of experimental techniques and quantitative empirical models gives detailed insight that is valid for high-symmetry complexes with a single nickel(II) center and for bimetallic complexes with lower symmetry. The approach is based on absorption spectra without highly resolved structure and appears to be applicable to larger clusters and higher-dimensional systems with a variety of bridging ligands.

## Experimental

### Synthesis

All reagents were purchased from commercial sources and used without further purification. Compounds (AsPh<sub>4</sub>)<sub>2</sub>[Ni(NCS)<sub>4</sub>] **1**, (Cat)[Ni(NCS)<sub>4</sub>] **2**, (AsPh<sub>4</sub>)<sub>4</sub>[Ni<sub>2</sub>(NCS)<sub>8</sub>] **3**, (Cat)<sub>2</sub>[Ni<sub>2</sub>(NCS)<sub>8</sub>]·2CH<sub>3</sub>NO<sub>2</sub> **4**, and (Et<sub>4</sub>N)<sub>4</sub>[Ni(NCS)<sub>6</sub>] **5** (Cat<sup>2+</sup> = (*p*-xylylenebis(triphenylphosphonium))<sup>2+</sup>) were synthesized according to literature methods (5).

### Crystallography

Single crystal diffraction data were collected at room temperature (298 K) with a Bruker SMART CCD diffractometer equipped with a normal monochromatized focus X-ray tube having a molybdenum target. The data were processed through the SAINT reduction software (8a). Empirical absorption corrections were carried out by SADABS (G.B. Sheldricks, 1994) (8b). The structures were solved and refined on  $F^2$  using the SHELXTL software (8c). Scattering factors were taken from the International tables for crystallography (9). All non-hydrogen atoms were refined with anisotropic thermal parameters. The hydrogen atoms were included in the final refinement in calculated positions with isotropic thermal parameters. Crystal structure and refinement data are summarized in Table 1. Weighting functions used were  $w = 1/[\sigma^2(F_o^2) + (0.0894P)^2]$  for compound **1** and  $w = 1/[\sigma^2(F_o^2) + (0.1000P)^2]$  with  $P = (F_o^2 + 2 F_c^2)/3$  for compounds **3** and **4**.

### Magnetic susceptibility measurements

The temperature dependence of the magnetic susceptibility was measured on the bulk material between 6 and 300 K with an SHE superconducting SQUID magnetometer operating at a field strength of 0.5 T. The data were corrected for diamagnetism of the constituent atoms using Pascal constants.

### Spectroscopy

Absorption spectra were measured with a Varian Cary 5E spectrometer using the photomultiplier tube and the PbS detector for the visible and near-infrared wavelength ranges, respectively. The sample crystals were cooled in an He gas flow cryostat (Oxford Instruments CF-1204), and the temperature was monitored with an RhFe resistor connected to an electronic controller (Oxford Instruments ITC4) to stabilize the temperature to better than  $\pm 1$  K, by adjusting both a heater for the He gas cooling the sample and the gas flow valve from the He storage Dewar to the cryostat. All spectra presented in the following are unpolarized. Raman spectra of solid samples at low temperature were measured using a Renishaw System 3000 Raman microscope, using 782 or 514.5 nm excitation wavelengths. Selected spectra and frequencies are given in the supplementary material.<sup>4</sup> No evidence for electronic Raman transitions was observed.

<sup>4</sup>Temperature dependence of  $\chi T$  for **2**, selected Raman spectra, powder diffraction diagrams for **3**, calculated energies of triplet electronic states as a function of  $\tau$ , complete output for all ligand-field (Angular overlap model) calculations summarized in Table 4. Supplementary data may be purchased from the Depository of Unpublished Data, Document Delivery, CISTI, National Research Council Canada, Ottawa, ON K1A 0S2, Canada ([http://www.nrc.ca/cisti/irm/unpub\\_e.shtml](http://www.nrc.ca/cisti/irm/unpub_e.shtml) for information on ordering electronically). CCDC 207620–207622 contain the supplementary data for this paper. These data can be obtained, free of charge, via [www.ccdc.cam.ac.uk/conts/retrieving.html](http://www.ccdc.cam.ac.uk/conts/retrieving.html) (or from the Cambridge Crystallographic Data Centre, 12 Union Road, Cambridge, U.K.; fax +44 1223 336033; or [deposit@ccdc.cam.ac.uk](mailto:deposit@ccdc.cam.ac.uk)).



**Table 1.** Summary of data collection and refinement for compounds **1**, **3**, and **4**.

Compound	<b>1</b>	<b>3</b>	<b>4</b>
Formula	C <sub>52</sub> H <sub>40</sub> As <sub>2</sub> N <sub>4</sub> NiS <sub>4</sub>	C <sub>104</sub> H <sub>80</sub> As <sub>4</sub> N <sub>8</sub> Ni <sub>2</sub> S <sub>8</sub>	C <sub>98</sub> H <sub>78</sub> N <sub>10</sub> Ni <sub>2</sub> O <sub>4</sub> P <sub>4</sub> S <sub>8</sub>
fw	1057.67	2115.34	1957.48
Color	Blue	Green	Yellow
Crystal size (mm)	0.07 × 0.07 × 0.15	0.5 × 0.5 × 0.5	0.2 × 0.2 × 0.2
<i>T</i> (K)	298(2)	298(2)	298(2)
$\lambda$ (Å)	0.71073	0.71073	0.71073
Crystal system	Monoclinic	Triclinic	Monoclinic
Space group	<i>C2/c</i>	<i>P</i> $\bar{1}$	<i>P2</i> <sub>1</sub> / <i>c</i>
<i>a</i> (Å)	22.761(2)	11.2183(6)	13.1148(9)
<i>b</i> (Å)	15.055 (1)	14.2551(8)	27.128(2)
<i>c</i> (Å)	15.054(1)	16.629(1)	14.882(1)
$\alpha$ (°)	90	79.326(1)	90
$\beta$ (°)	108.915(1)	73.605(1)	114.056(2)
$\gamma$ (°)	90	75.496(1)	90
<i>V</i> (Å <sup>3</sup> )	4879.9(6)	2451.0(2)	4834.8(6)
<i>Z</i>	4	2	4
<i>D</i> (g cm <sup>-3</sup> )	1.440	1.433	1.345
$\mu$ (mm <sup>-1</sup> )	1.954	1.945	0.684
Crystallization solvent	None	None	Nitromethane
<i>F</i> (000)	2152	1076	2024
$\theta$ range (°)	1.65–28.87	2.57–29.01	1.70–29.57
Index ranges	<i>h</i> = −24 → 27 <i>k</i> = −20 → 10 <i>l</i> = −18 → 20	<i>h</i> = −14 → 6 <i>k</i> = −19 → 19 <i>l</i> = −21 → 19	<i>h</i> = −16 → 12 <i>k</i> = −35 → 33 <i>l</i> = −20 → 7
Measured reflections	9703	15 972	19 801
Independent reflections	5229	11 237	9381
GOF	0.970	0.833	0.725
<i>R</i> ( <i>F</i> ) <sup>a</sup>	0.0478	0.0424	0.0476
<i>wR</i> ( <i>F</i> <sup>2</sup> ) <sup>b</sup>	0.1395	0.1241	0.1568

<sup>a</sup>*I* > 2 $\sigma$ (*I*), *R*(*F*) =  $\Sigma ||F_o| - |F_c|| / \Sigma |F_o|$ .<sup>b</sup>All data, *wR*(*F*<sup>2</sup>) = [ $\Sigma w(F_o^2 - F_c^2)^2 / \Sigma w(F_o^2)^2$ ]<sup>1/2</sup>.

## Results

### Crystal structures

#### (AsPh<sub>4</sub>)<sub>2</sub>[Ni(NCS)<sub>4</sub>] **1**

The crystal structure consists of the anionic [Ni(NCS)<sub>4</sub>]<sup>2−</sup> monometallic complex units shown on Fig. 1 with AsPh<sub>4</sub><sup>+</sup> cations. Selected bond lengths and angles are given in Tables 2 and 3. In each complex unit, the nickel(II) ion is located on a *C*<sub>2</sub> axis and has a pseudo-tetrahedral ligand environment. The Ni—N bond lengths are similar (1.929(4) and 1.921(4) Å). The structural features for the [Ni(NCS)<sub>4</sub>]<sup>2−</sup> complex unit in compound **1** show slight differences from those previously determined for the same complex unit in Cat[Ni(NCS)<sub>4</sub>] **2** (10). In compound **2**, three of the Ni—N bonds are shorter (1.906(6)–1.908(7) Å) and one is longer (1.937(7) Å) than in compound **1**. However, the mean values (1.92 Å) are identical for both compounds **1** and **2**, as shown in Table 2. Owing to the (AsPh<sub>4</sub>)<sup>+</sup> cations, the [Ni(NCS)<sub>4</sub>]<sup>2−</sup> complex units are well separated from each other. The shortest intermolecular distances in compound **1** are found between the S(thiocyanato) atoms (5.777(3) Å), while the shortest intermolecular distance between two nickel(II) ions is 8.1260(6) Å.

**Fig. 1.** View of the complex unit [Ni(NCS)<sub>4</sub>]<sup>2−</sup> for (AsPh<sub>4</sub>)<sub>2</sub>[Ni(NCS)<sub>4</sub>] **1**. Ellipsoids are drawn at the 30% probability level. The letter A denotes symmetry related atoms (−*x*, *y*, −*z* + 3/2).

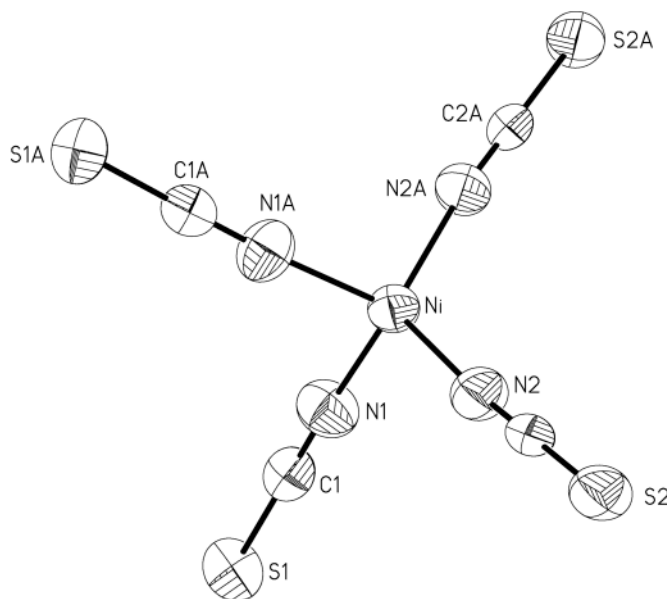




**Table 2.** Selected bond lengths (Å) for compounds **1–4**.

	<b>1</b>	<b>2</b>	<b>3</b>	<b>4</b>
Ni—N1	1.919(4)	1.906(6)	1.994(3)	2.039(4)
Ni—N2	1.921(4)	1.908(7)	1.990(3)	2.016(5)
Ni—N3		1.908(7)	2.025(3)	1.997(4)
Ni—N4		1.937(7)	1.983(3)	1.997(5)
Ni—S1A			2.5319(9)	2.485(1)
Ni...Ni			5.6745(6)	5.715(1)
C1—S1	1.613(5)	1.612(8)	1.650(3)	1.651(6)
C2—S2	1.612(5)	1.594(9)	1.615(3)	1.612(6)
C3—S3		1.611(8)	1.627(3)	1.634(5)
C4—S4		1.600(8)	1.622(3)	1.626(6)
C1—N1	1.150(6)	1.15(1)	1.145(3)	1.157(6)
C2—N2	1.139(6)	1.15(1)	1.148(3)	1.170(6)
C3—N3		1.14(1)	1.149(4)	1.142(5)
C4—N4		1.17(1)	1.141(4)	1.154(6)

**Note:** Data for compound **2** are extracted from ref. 10. Letter A denotes the symmetry related atoms ( $-x, y, -z + 3/2$ ) for **1** and ( $-x, -y, -z$ ) for **3** and **4**.

### (AsPh<sub>4</sub>)<sub>4</sub>[Ni<sub>2</sub>(NCS)<sub>8</sub>]**3**

The crystal structure consists of the anionic [Ni<sub>2</sub>(NCS)<sub>8</sub>]<sup>4-</sup> bimetallic complex units, shown in Fig. 2, with AsPh<sub>4</sub><sup>+</sup> cations. Selected bond lengths and angles are given in Tables 2 and 3. The bimetallic complex units [Ni<sub>2</sub>(NCS)<sub>8</sub>]<sup>2-</sup> are centrosymmetrical and are built from two [Ni(NCS)<sub>4</sub>]<sup>2-</sup> moieties, which are double-bridged by two NCS<sup>-</sup> ligands in the end-to-end fashion (Ni—S1A = 2.5319(9) Å). The two nickel(II) ions and the two thiocyanato bridges are coplanar with a maximum out-of-plane deviation of 0.03 Å. The Ni...Ni separation in the bimetallic unit is 5.6745(6) Å. The nickel(II) ions are in a pseudo-square-pyramidal environment (Tables 2 and 3) (11). The atoms N1, N2, N3, and S1A, forming the base of the pyramid, are coplanar (Fig. 2) with a maximum out-of-plane deviation of 0.08 Å. The nickel(II) ion is located 0.3 Å above this plane. To measure the degree of distortion of the square pyramidal polyhedron we calculated the geometric parameter,  $\tau$ , defined by Addison et al. (12) to systematize five-coordinate coordination geometries intermediate between the idealized square-pyramidal and trigonal-bipyramidal structures. The parameter  $\tau$  is defined as  $\tau = (\beta - \alpha)/60$ , with  $\beta$  and  $\alpha$  the largest ligand-metal-ligand bond angles and  $\beta > \alpha$ . These angles are schematically illustrated in Fig. S5 of the supporting information.<sup>4</sup> The parameter  $\tau$  is equal to zero for perfectly square pyramidal structures and is unity for perfectly trigonal-bipyramidal coordination geometries. Table 3 shows that for compound **3** the angle  $\beta$  corresponds to the N1-Ni-N2 bond angle (165.5°) and  $\alpha$  is the N3-Ni-S1A angle (160.1°). These angles lead to a  $\tau$  parameter of 0.09, which is close to the value for a perfect square-pyramidal structure. The NiNCS atoms (N coordination) are found to be almost collinear (Ni-N-C: 165–172°), but for the NiSCN fragment (S coordination), the Ni-S1A-C1A bond angle is 104.36° (Table 2). These values are comparable to those previously found in di- $\mu$ -thiocyanato-bridged nickel(II) complexes (7, 13). The four Ni—N bond lengths are similar (1.983(3) and 2.025(3) Å) but longer than those in the pseudo-tetrahedral

**Table 3.** Selected bond angles (°) for compounds **1–4**.

	<b>1</b>	<b>2</b>	<b>3</b>	<b>4</b>
N1-Ni-N2	108.9(2)	104.1(3)	165.5(1)	169.8(2)
N1-Ni-N1A	102.4(3)			
N2-Ni-N1A	107.6(2)			
N2-Ni-N2A	120.0(3)			
N1-Ni-N3		101.4(2)	92.1(1)	89.9(2)
N1-Ni-N4		115.6(3)	97.1(1)	91.8(2)
N2-Ni-N3		126.3(3)	91.51	92.2(2)
N2-Ni-N4		105.1(3)	96.2(1)	96.8(2)
N3-Ni-N4		105.1(3)	99.2(1)	110.4(2)
N1-Ni-S1A			90.78(7)	90.7(1)
N2-Ni-S1A			81.2(8)	81.0(1)
N3-Ni-S1A			160.1(9)	136.9(1)
N4-Ni-S1A			99.9(9)	112.7(1)
C1-N1-Ni	175.6(4)	173.5(7)	165.9	165.4(4)
C2-N2-Ni	173.1(4)	175.0(7)	162.7	169.5(4)
C3-N3-Ni		171.4(6)	173.7	164.1(4)
C4-N4-Ni		171.0(6)	172.1	169.1(4)
C1-S1-Ni			104.4(1)	105.3(2)
N1-C1-S1	179.8(4)	177.6(7)	178.6(3)	178.3
N2-C2-S2	179.1(5)	177.5(8)	179.3(3)	179.4(5)
N3-C3-S3		179.2(8)	179.2(3)	179.6(5)
N4-C4-S4		178.5(7)	178.6(3)	177.5(5)

**Note:** Data for compound **2** are extracted from ref. 10. Letter A denotes the symmetry related atoms ( $-x, y, -z + 3/2$ ) for **1** and ( $-x, -y, -z$ ) for **3** and **4**.

[Ni(NCS)<sub>4</sub>]<sup>2-</sup> complex unit with either AsPh<sub>4</sub><sup>+</sup> **1** or Cat<sup>2+</sup> **2** counterions (Table 2). The Ni—S1A bond length is 2.5319(9) Å. The [Ni<sub>2</sub>(NCS)<sub>8</sub>]<sup>2-</sup> bimetallic units are well separated by the (AsPh<sub>4</sub>)<sup>+</sup> cations. The shortest intermolecular distance between two complex units is found between the S atoms (4.332(3) Å) while the shortest intermolecular distances between two nickel(II) ions is 11.2183(6) Å.

### (Cat)<sub>2</sub>[Ni<sub>2</sub>(NCS)<sub>8</sub>]**2**·2CH<sub>3</sub>NO<sub>2</sub> **4**

The crystal structure consists of the anionic [Ni<sub>2</sub>(NCS)<sub>8</sub>]<sup>4-</sup> bimetallic complex units, shown in Fig. 3, with Cat<sup>2+</sup> cations and nitromethane as the crystallization solvent. Selected bond lengths and angles are given in Tables 2 and 3. As for **3**, the bimetallic complex units [Ni<sub>2</sub>(NCS)<sub>8</sub>]<sup>2-</sup> are centrosymmetrical and are built from two [Ni(NCS)<sub>4</sub>]<sup>2-</sup> moieties bridged by two NCS<sup>-</sup> ligands in the end-to-end fashion. The two nickel(II) ions and the two thiocyanato bridges are again coplanar with a maximum out-of-plane deviation of 0.01 Å. The Ni...Ni distance is 5.715(1) Å. In compound **4**, the nickel(II) ions of the [Ni<sub>2</sub>(NCS)<sub>8</sub>]<sup>2-</sup> bimetallic units are in a pseudo-trigonal-bipyramidal environment (11). Atoms N3, N4, and S1A (Fig. 3) define the base of the bipyramid and the nickel(II) ion is only 0.03 Å out of this plane. As for compound **3**, we calculated the parameter  $\tau$  (12) to determine the distortion from an ideal trigonal-bipyramidal coordination geometry. Table 3 shows that for compound **4** the angle  $\beta$  again corresponds to the N1-Ni-N2 bond angle (169.8°) and the angle  $\alpha$  is again N3-Ni-S1A (136.9°). The  $\tau$  parameter equals 0.55, a value halfway between the perfectly square-pyramidal and trigonal-bipyramidal coordination geometries. The NiNCS (N coordination) atoms are



**Fig. 2.** View of the complex unit  $[\text{Ni}_2(\text{NCS})_8]^{4-}$  for  $(\text{AsPh}_4)_4[\text{Ni}_2(\text{NCS})_8]$  **3**. Ellipsoids are drawn at the 30% probability level. The letter A denotes symmetry related atoms ( $-x, -y, -z$ ).

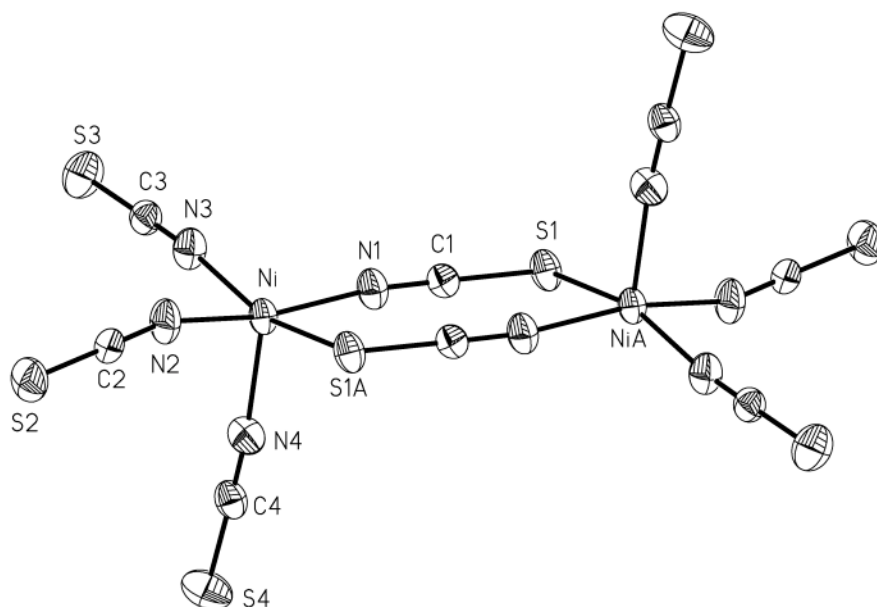
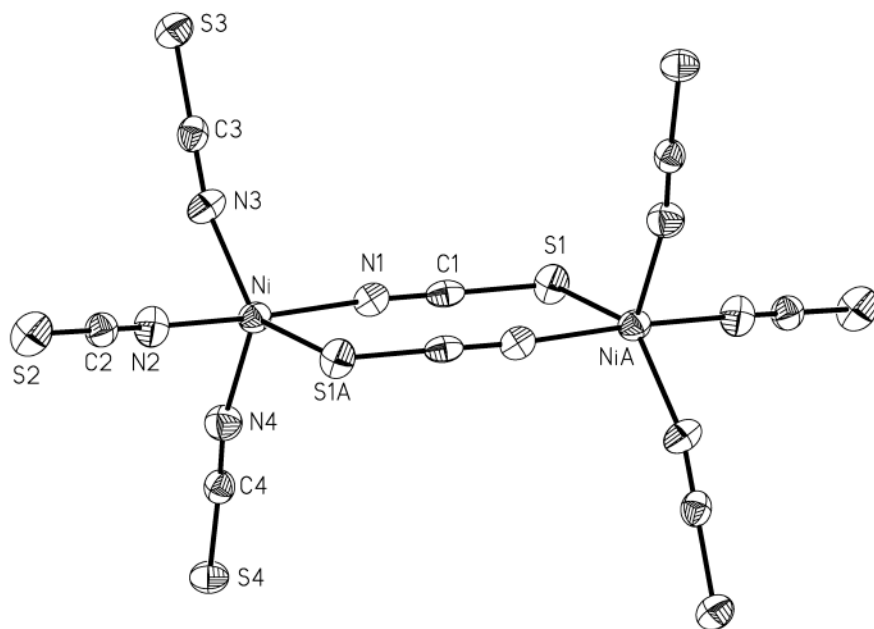


**Fig. 3.** View of the complex unit  $[\text{Ni}_2(\text{NCS})_8]^{4-}$  for  $(\text{Cat})_2[\text{Ni}_2(\text{NCS})_8]$  **4** ( $\text{Cat}^{2+} = (p\text{-xylylenebis(triphenylphosphonium)})^{2+}$ ). Ellipsoids are drawn at the 30% probability level. The letter A denotes symmetry related atoms ( $-x, -y, -z$ ).



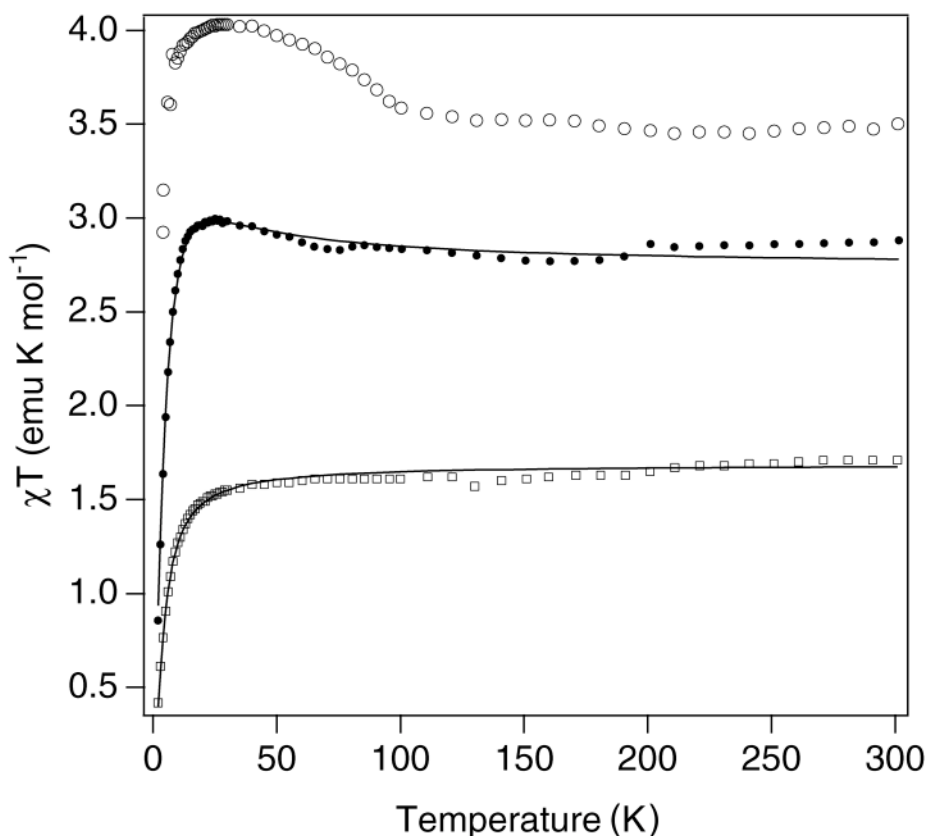
found to be almost collinear ( $\text{Ni-N-C}$ :  $164\text{--}170^\circ$ ), but for the  $\text{NiSCN}$  fragment ( $\text{S}$  coordination), the  $\text{Ni-S1A-C1A}$  bond angle is  $105.3(2)^\circ$ . These structural features are similar to those found in compound **3** and in previous di- $\mu$ -thiocyanato-bridged nickel(II) complexes (7, 13). The  $\text{Ni-N}$  bond distances are comparable to those found for compound **3** ( $1.997(4)$  and  $2.039(5)$  Å) and are again longer than for the monometallic complex  $[\text{Ni}(\text{NCS})_4]^{2-}$  either with  $\text{AsPh}_4^+$  or with  $\text{Cat}^{2+}$  (10) cations, as summarized in Table 2. The  $\text{Ni-S1A}$  bond length is  $2.485(1)$  Å. Owing to the

$\text{Cat}^{2+}$  cations, the  $[\text{Ni}_2(\text{NCS})_8]^{4-}$  units are again well separated. The shortest intermolecular distance between two complex units is found between the  $\text{S}(\text{thiocyanato})$  atoms ( $3.516(3)$  Å), and the shortest intermolecular distances between two nickel(II) ions is  $11.036(1)$  Å.

Compounds **3** and **4** both undergo an irreversible color change from olive-green and brown-orange to blue at temperatures above  $100^\circ\text{C}$ , as reported in the literature (5, 14). Powder X-ray diffraction patterns and Raman spectra shown in the supporting material indicate that the blue high-



**Fig. 4.** Temperature dependence of  $\chi T$ . From top to bottom:  $(\text{Cat})_2[\text{Ni}_2(\text{NCS})_8]$  **4**, open circles;  $(\text{AsPh}_4)_4[\text{Ni}_2(\text{NCS})_8]$  **3**, solid circles;  $(\text{AsPh}_4)_2[\text{Ni}(\text{NCS})_4]$  **1**, open squares. Solid lines denote fits as described in the text.



temperature product contains pseudo-tetrahedral  $[\text{Ni}(\text{NCS})_4]^{2-}$  chromophores, as expected from the color, which corresponds to that of the distorted tetrahedral chromophores in **1** and **2**.

### Magnetic properties

The magnetic properties of compounds **1**, **3**, and **4** in relation to the temperature dependence of  $\chi T$ , the product of the molar magnetic susceptibility with temperature, are shown in Fig. 4. Magnetic measurements for compound **2** are in good agreement with literature values reported between room temperature and 95 K (5), as shown in the supplementary material.<sup>4</sup>

#### $(\text{AsPh}_4)_2[\text{Ni}(\text{NCS})_4]$ **1** and $\text{Cat}_2[\text{Ni}(\text{NCS})_4]$ **2**

The two monometallic compounds exhibit similar magnetic properties, illustrated for compound **1** by the bottom trace in Fig. 4. At room temperature,  $\chi T$  is 1.71  $\text{emu K mol}^{-1}$  for **1** and 1.56  $\text{emu K mol}^{-1}$  for **2**.  $\chi T$  decreases slowly with temperature down to 50 K, where it reaches 1.59  $\text{emu K mol}^{-1}$  for **1** and 1.38  $\text{emu K mol}^{-1}$  for **2**. At lower temperatures,  $\chi T$  falls abruptly. The large deviation of  $\chi T$  at room temperature from the spin-only value ( $S = 1$ ,  $\chi T = 1 \text{ emu K mol}^{-1}$ ) is due to significant angular momentum contributions, as expected for nickel(II) ions in a tetrahedral environment with a  $^3T_1$  ground state (6, 15, 16). The deviation from the Curie law behavior at low temperature can be attributed to zero-field splittings. The crystal structure shows that the  $[\text{Ni}(\text{NCS})_4]^{2-}$  units are well separated

from each other and therefore only extremely weak intermolecular antiferromagnetic interactions are expected. Their contribution to the decrease of  $\chi T$  at low temperature is negligible.

We tentatively tried to fit the magnetic behavior using the expression of the magnetic susceptibility derived by Ginsberg et al. (13), taking into account a single-ion zero-field splitting parameter ( $D$ ) and assuming  $g$  to be isotropic. The experimental behavior is well reproduced with  $g = 2.3$  and  $D = -8.9 \text{ cm}^{-1}$  for compound **1**, as shown in Fig. 4a, and with  $g = 2.2$  and  $D = -2.9 \text{ cm}^{-1}$  for compound **2**, as shown in the supplementary material.<sup>4</sup>

#### $(\text{AsPh}_4)_4[\text{Ni}_2(\text{NCS})_8]$ **3**

At room temperature,  $\chi T$  is 2.87  $\text{emu K mol}^{-1}$  per bimetallic molecular unit, and it increases upon cooling to reach the value of 3.00  $\text{emu K mol}^{-1}$  at 50 K. At lower temperatures,  $\chi T$  decreases abruptly. As for **1** and **2**, the large deviation from the spin-only value at room temperature has to be ascribed to the ground-state angular momentum in the pseudo-square-pyramidal coordination environment. The value at room temperature is 1.43  $\text{emu K mol}^{-1}$  per nickel(II) ion, lower than the value measured for **1** and in agreement with previous reports, which show that generally  $\chi T$  values for square-pyramidal nickel(II) complexes deviate less from the spin-only value than those of tetrahedral or trigonal-bipyramidal nickel(II) complexes (6).

The increase of  $\chi T$  upon cooling below 50 K is the signature of ferromagnetic interactions between the two nickel(II)



ions within the  $[\text{Ni}_2(\text{NCS})_8]^{4-}$  unit. The zero-field splitting cannot account for such an increase in  $\chi T$ , as is confirmed by comparison with compounds **1** and **2**, which show a clear decrease of  $\chi T$  at the lowest temperatures. In addition, the  $[\text{Ni}_2(\text{NCS})_8]^{4-}$  units are well separated by the  $(\text{AsPh}_4)^+$  cations, and intermolecular interactions are unlikely to account for the ferromagnetic behavior. The increase of  $\chi T$  is therefore due to intramolecular Ni–Ni ferromagnetic interactions operating through the  $[\text{Ni}_2(\text{NCS})_2]$  bridge, as is generally found for end-to-end di- $\mu$ -thiocyanato-bridged nickel(II) compounds (7, 13, 17, 18). We simulate the magnetic behavior using the expression of the magnetic susceptibility derived by Ginsberg et al. (13) and taking into account the zero-field splitting parameter ( $D$ ), an isotropic  $g$  factor, and a ferromagnetic intramolecular interaction ( $H_{\text{ex}} = -2JS_1S_2$ ). The experimental behavior is well reproduced with  $g = 2.06$ ,  $J = 4.5 \text{ cm}^{-1}$ , and  $D = -3.9 \text{ cm}^{-1}$ .

#### *(Cat)*<sub>2</sub>[Ni<sub>2</sub>(NCS)<sub>8</sub>]·2CH<sub>3</sub>NO<sub>2</sub> **4**

At room temperature,  $\chi T$  is  $3.50 \text{ emu K mol}^{-1}$  per bimetallic molecular unit. Its value increases slightly upon cooling to reach a maximum of  $4.03 \text{ emu K mol}^{-1}$  at 50 K. At lower temperatures, it falls abruptly. As for compounds **1** to **3**, the large deviation from spin-only behavior at room temperature is due to the significant contribution of orbital angular momentum in the pseudo-trigonal-bipyramidal environment shown in Fig. 3. The value of  $1.71 \text{ emu K mol}^{-1}$  per nickel(II) ion at room temperature is comparable to the value for **1** but higher than the value for the bimetallic compound **3**. This is in qualitative agreement with previous reports showing that trigonal-bipyramidal nickel(II) complexes exhibit deviations from spin-only behavior that are intermediate between those for tetrahedral and square-pyramidal nickel(II) complexes (6). As for compound **3**, the increase of  $\chi T$  upon cooling is the signature of ferromagnetic interactions coupling the two nickel(II) ions within the  $[\text{Ni}_2(\text{NCS})_8]^{2-}$  units. Our attempts to simulate the magnetic behavior using the same approach as for compounds **1** and **3** were unsuccessful, but the qualitative comparison with the results for compound **3** indicates a ferromagnetic intramolecular coupling of comparable magnitude.

#### Absorption spectroscopy

Figure 5 shows a comparison of the low-temperature solid-state absorption spectra of nickel(II) complexes with tetrahedral (**1**), octahedral (**5**), square-pyramidal (**3**), and trigonal-bipyramidal (**4**) coordination geometries. The complexes in compounds **1** and **5** have a single nickel(II) center with tetrahedral and octahedral coordination geometries, respectively. They show the expected three spin-allowed ligand-field bands, as illustrated by the two lowest traces in Fig. 5. All band maxima from low-temperature solid-state absorption spectra are numbered in Fig. 5, and their energies are given in Table 4. The two lowest-energy bands correspond to transitions between states arising from the  $^3F$  free ion term. Their maxima are lower (by approximately  $4000 \text{ cm}^{-1}$ ) for the tetrahedral complex **1** than for the octahedral complex **5**, indicating the expected weaker ligand-field strength in **1**. A room-temperature reflectance spectrum in the literature (5) shows similar energies, shapes, and relative intensities as given for bands 1, 2, and 4 of **1** in the bot-

tom spectrum of Fig. 5. The weak band 3 is not observed in the literature spectrum. The bimetallic complexes show distinct differences from the compounds with only one nickel(II) center. Their lowest-energy broad absorption band maxima are at intermediate energies between those of tetrahedral and octahedral complexes, as qualitatively expected from ligand-field arguments. A quantitative model based on the crystal structures is essential to assign their bands, as discussed in section 4.1.

Figure 6 shows a detailed view of the band maxima of two spin-allowed absorption bands with resolved vibronic structure at 5 K: band 3 (Fig. 5) for the octahedral complex **5** and band 4 (Fig. 5) for the square-bipyramidal complex **3**. The average energy difference between maxima forming the progression is  $204 \pm 20 \text{ cm}^{-1}$ , an interval in the range expected for metal–ligand stretching modes in the title complexes. This progression interval is similar for the two compounds, indicating that no large differences in bond strength are caused by the change of coordination geometry or by the influence of one sulfur ligand atom. Raman spectra of these compounds are given in the supplementary material<sup>4</sup> and show transitions attributed to ground-state Ni–NCS stretching modes at  $211 \text{ cm}^{-1}$  and at 201, 224, and  $260 \text{ cm}^{-1}$  for **5** and **3**, respectively, indicating that offsets along these normal coordinates lead to the vibronic progressions in Fig. 6.

Several weak features are observed in addition to the broad spin-allowed bands. A first peak or shoulder occurs between  $12\,000$  and  $14\,000 \text{ cm}^{-1}$  in all compounds. This is the lowest-energy spin-flip transition to a singlet excited state, and it has been observed and interpreted for many different octahedral complexes of nickel(II) (19). For the octahedral compound **5**, the band is weaker than usual for coordination to six nitrogen ligand atoms because the closest spin-allowed bands are relatively far in energy. In most complexes with nitrogen donor ligands, the lowest-energy spin-allowed band occurs in the same energy range as the transition to the first singlet excited state (19), leading to a strong intensity enhancement of the spin-forbidden transition and a characteristic interference dip observed even in unresolved spectra (20–22). This observation confirms that  $\text{NCS}^-$  is a relatively weak ligand compared with other nitrogen donors (19). Additional transitions to higher energy singlet states are observed for the two bimetallic complexes at approximately  $17\,600 \text{ cm}^{-1}$  for **3** and  $17\,950 \text{ cm}^{-1}$  for **4**. All energies of singlet bands determined from absorption spectra are given in Table 4.

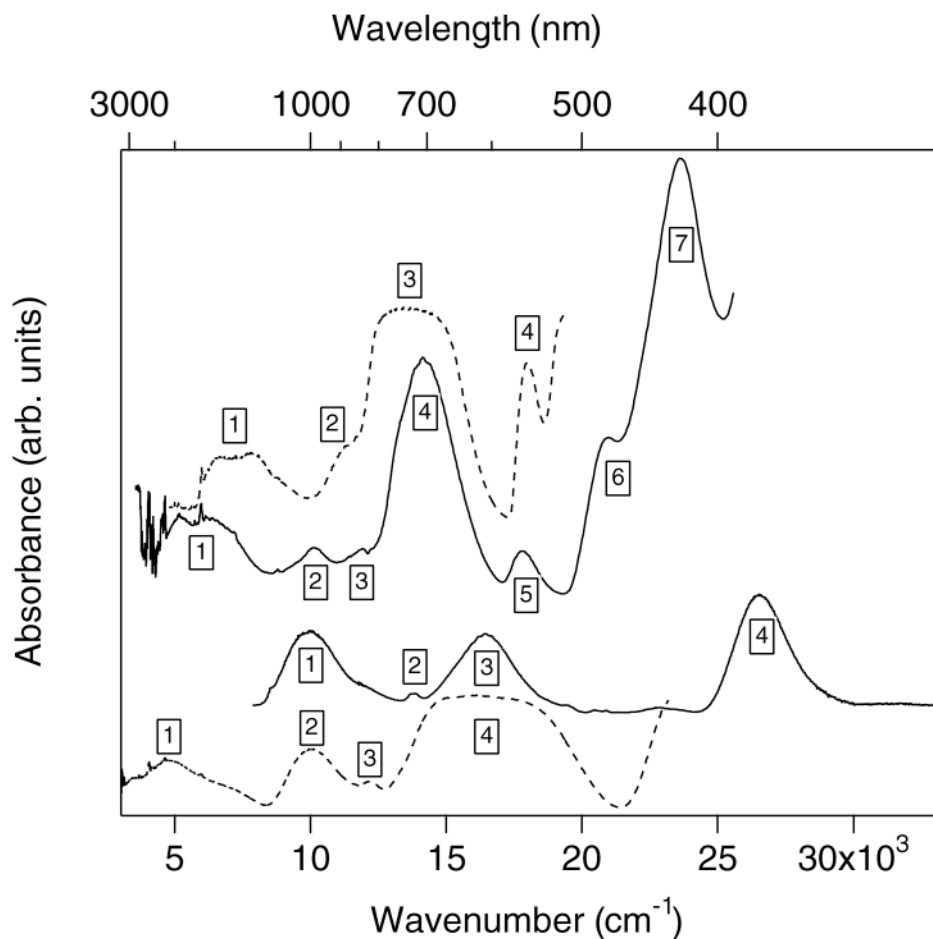
## Discussion

### Assignment of absorption bands

A quantitative analysis of the observed absorption spectra, summarized in Fig. 5, is based on the angular overlap model (AOM), a modern implementation of ligand-field theory. The title complexes have only thiocyanato ligands, an attractive situation for this analysis because a single set of AOM parameters can be used for all compounds. We base our calculations (23) on the crystal structures of the anionic complexes shown in Figs. 1–3. The first calculations are carried out for the four- and six-coordinate complexes with a single nickel(II) center shown as the bottom two traces in Fig. 5.



**Fig. 5.** Overview absorption spectra recorded on single crystals at 5 K. Bottom to top:  $(\text{AsPh}_4)_2[\text{Ni}(\text{NCS})_4]$  **1** (pseudo-tetrahedral coordination geometry, dashed line);  $(\text{Et}_4\text{N})_4[\text{Ni}(\text{NCS})_6]$  **5** (octahedral coordination geometry, solid line);  $(\text{AsPh}_4)_4[\text{Ni}_2(\text{NCS})_8]$  **3** (pseudo-square-pyramidal coordination geometry, solid line);  $(\text{Cat})_2[\text{Ni}_2(\text{NCS})_8]$  **4** (pseudo-trigonal-bipyramidal coordination geometry, dashed line).



These spectra show three spin-allowed bands, as expected in idealized  $T_d$  and  $O_h$  point-group symmetries, and the final states of the transitions are easily assigned from literature Tanabe–Sugano diagrams. The traditional ligand-field parameters  $B$ ,  $C$ ,  $\Delta_{\text{oct}}$ , and  $\Delta_{\text{tet}}$  can be determined from the band maxima. This analysis reproduces the observed band maxima well, leading to a  $B$  value of  $825 \text{ cm}^{-1}$  (76% of the free-ion value) and a ratio  $C/B$  of 4.6, values in the range determined in the literature for a large number of nickel(II) complexes (19). The angular-overlap approach replaces the parameters  $\Delta_{\text{oct}}$  and  $\Delta_{\text{tet}}$  with the point-group symmetry independent parameters  $e_\sigma$  and  $e_\pi$ , assumed to be identical for each  $\text{NCS}^-$  ligand. The six spin-allowed bands of the two bottom traces in Fig. 5 allow these parameters to be fitted and values of  $4720$  and  $1000 \text{ cm}^{-1}$  are obtained for  $e_\sigma$  and  $e_\pi$ , respectively. The resolution of the spectra used to determine these parameter values is not sufficient to reveal spin-orbit splittings, and the spin-orbit coupling constant  $\zeta$  is set to zero for all calculations described in the following.

The parameter set obtained from the two bottom spectra can be used to calculate absorption band maxima for compounds **1**, **3**, and **4** using the polar coordinates of the ligands determined from the structural data reported in Tables 2 and 3. These  $\theta$  and  $\phi$  angles are given in Table 4. The calculations

assume identical  $e_\sigma$  and  $e_\pi$  values for all ligands, thereby neglecting the variations of Ni–N bond lengths and the different nature of the S ligand atom for one metal–ligand bond in **3** and **4**. These assumptions allow us to calculate energies for all compounds without introducing additional adjustable parameters and lead to a good overall agreement of calculated and observed band maxima, as documented in Table 4.

The calculated splittings of degenerate excited triplet states for **1** due to deviations from perfect tetrahedral coordination geometry are less than  $1000 \text{ cm}^{-1}$ , as given in Table 4, and cannot be determined from the broad, unresolved bands of the experimental spectrum, shown as the bottom trace in Fig. 5. The lowest-energy singlet state is observed lower (by  $800 \text{ cm}^{-1}$ ) than calculated, a discrepancy most likely because of our choice of  $C/B$  ratio and indicating that both independently fitted Racah parameters and a nonzero spin-orbit coupling constant would be needed for a perfect agreement. The band positions for octahedral compound **5** are very well reproduced by the parameters chosen for our calculations.

In contrast to complexes **1** and **5**, the absorption spectra of bimetallic complexes **3** and **4** cannot be analyzed in an idealized high-symmetry point group. The crystal structures and



**Table 4.** Observed and calculated absorption band maxima determined from the spectra shown in Fig. 5.

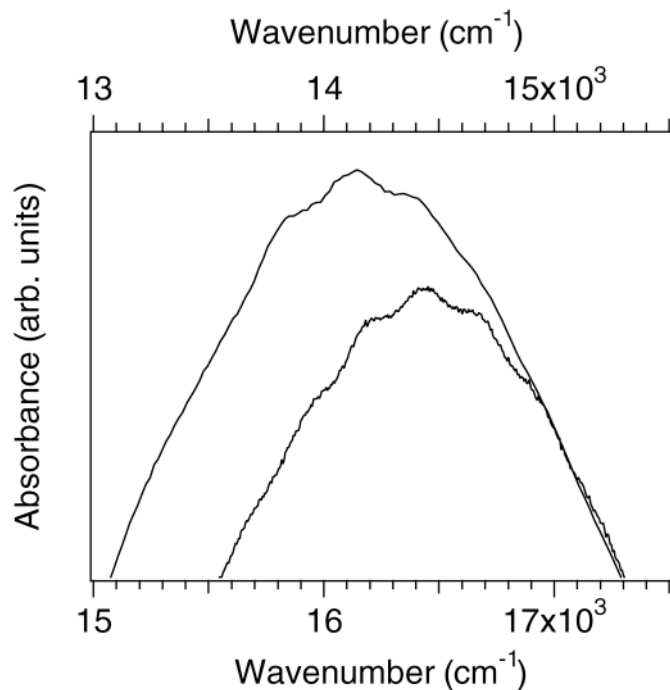
AOM angle	(AsPh <sub>4</sub> ) <sub>2</sub> [Ni(NCS) <sub>4</sub> ] <b>1</b>	(Et <sub>4</sub> N) <sub>4</sub> [Ni(NCS) <sub>6</sub> ] <b>5</b>	(AsPh <sub>4</sub> ) <sub>4</sub> [Ni <sub>2</sub> (NCS) <sub>8</sub> ] <b>3</b>	(Cat) <sub>2</sub> [Ni <sub>2</sub> (NCS) <sub>8</sub> ] <b>4</b>
$\theta_1, \phi_1$ (°)	108.9, 0	0, 0	0, 0	0, 0
$\theta_2, \phi_2$ (°)	107.6, -131.6	90, 0	99.2, 175.2	89.9, -90.9
$\theta_3, \phi_3$ (°)	102.4, 114.1	90, 90	96.2, 82.3	92.2, 79.16
$\theta_4, \phi_4$ (°)	0, 0	90, 180	97.1, -92.3	110.4, 180
$\theta_5, \phi_5$ (°)		90, -90	99.9, 0	136.9, 0
$\theta_6, \phi_6$ (°)		180, 0		
Band No.	Observed (cm <sup>-1</sup> )	Calculated (cm <sup>-1</sup> )	Observed (cm <sup>-1</sup> )	Calculated (cm <sup>-1</sup> )
1	4 700	0, 1 370, 1 800 <sup>a</sup>		0, 2 800 <sup>a</sup>
2	9 900	4 500, 4 940, 5 290	6 000	6 180, 6 670
3	12 200	9 120	10 100	9 550
4	16 300	13 030 s, 13 300 s	11 900	12 040 s
5		16 320, 16 460, 17 050	14 100	13 350, 13 800
6			17 600	19 430 s
7			20 900	21 860
			23 600	23 040, 23 830

**Note:** The following ligand-field parameters were used for all calculations:  $e_g(N) = 4720 \text{ cm}^{-1}$ ,  $e_g(N) = 1000 \text{ cm}^{-1}$ ,  $B = 825 \text{ cm}^{-1}$ ,  $C = 3795 \text{ cm}^{-1}$  ( $C/B = 4.6$ ). For the bimetallic complexes,  $e_g(S) = e_g(N)$  and  $e_g(S) = e_g(N)$  were used. The angles  $\theta$  and  $\phi$  are determined from the crystal structures. The N4—Ni and N3—Ni bonds were set to  $\theta = 0$  for compounds **3** and **4**, respectively. The Ni—S1A bonds were set to  $\phi = 0$  in the plane perpendicular to the bond defining  $\theta$  for both **3** and **4**. The angle  $\psi$  and the spin-orbit coupling constant  $\zeta$  were set to zero for all calculations. All calculated triplet states and selected singlet states, denoted as s, are given.

<sup>a</sup>Calculated ground-state splittings, not observed in the absorption spectra.



**Fig. 6.** Resolved vibronic structure for octahedral  $[\text{Ni}(\text{NCS})_6]^{4-}$  molecular units in  $(\text{Et}_4\text{N})_4[\text{Ni}(\text{NCS})_6]$  **5**, bottom trace and bottom wavenumber scale, and pseudo-square-pyramidal  $[\text{Ni}(\text{NCS})_4(\text{SCN})]^{3-}$  molecular units in  $(\text{AsPh}_4)_4[\text{Ni}_2(\text{NCS})_8]$  **3**, top trace and top wavenumber scale. The bands enlarged here are labeled in Fig. 5 as bands 3 and 4 of the lower and upper solid traces, respectively.



AOM parameter set determined above allow us to calculate absorption maxima without adjusting any parameters. The overall agreement between calculated and observed energies is good, as documented in Table 4. The correct number and energies of spin-allowed transitions are obtained from the calculations. As was the case for **1**, the energies of the singlet states are less reliably reproduced, again most likely a consequence of the  $C/B$  ratio that was not treated as an adjustable parameter. Nevertheless, a good interpretation of the absorption spectra is obtained and we conclude that band energies are strongly influenced by the single-ion coordination geometry, with no clear-cut effects of the exchange interaction between the two nickel(II) centers evident in the 5 K spectra of compounds **3** and **4** in Fig. 5. The analysis of exchange effects requires detailed temperature-dependent measurements, as discussed in section 4.2. It is interesting to note that the exact coordination geometries of the nickel(II) centers in **3** and **4** are required for the analysis of the spectrum. This is illustrated by the lowest-energy absorption bands shown in Fig. 5 (labeled 1 on the top two traces). The band maximum for the distorted square-pyramidal complex **3** is lower in energy by approximately  $800\text{ cm}^{-1}$  than for the pseudo-trigonal-bipyramidal complex **4**, an energetic order correctly reproduced by our AOM analysis based on the crystal structures. In contrast, AOM calculations for perfect square-pyramidal and trigonal-bipyramidal structures with the parameter values used above lead to band maxima of  $7200$  and  $6200\text{ cm}^{-1}$ , respectively, not only in worse agreement with the experimental maxima but also in the wrong

energetic order. The observed variation of spin-allowed absorption band maxima is quantitatively rationalized by a comparison of the calculated energies for all triplet states as a function of  $\tau$ , the parameter used to classify the five-coordinate coordination geometries of **3** and **4** in the Results: Crystal structures section. These calculated energies are shown in Fig. S5 of the supporting information.<sup>4</sup> The deviations from idealized symmetry in **3** and **4** have, therefore, a significant effect on the observed absorption bands, and care should be taken when analyzing absorption spectra in an idealized coordination geometry, as was done in a recent study of nickel(II) thiocyanato complexes (7).

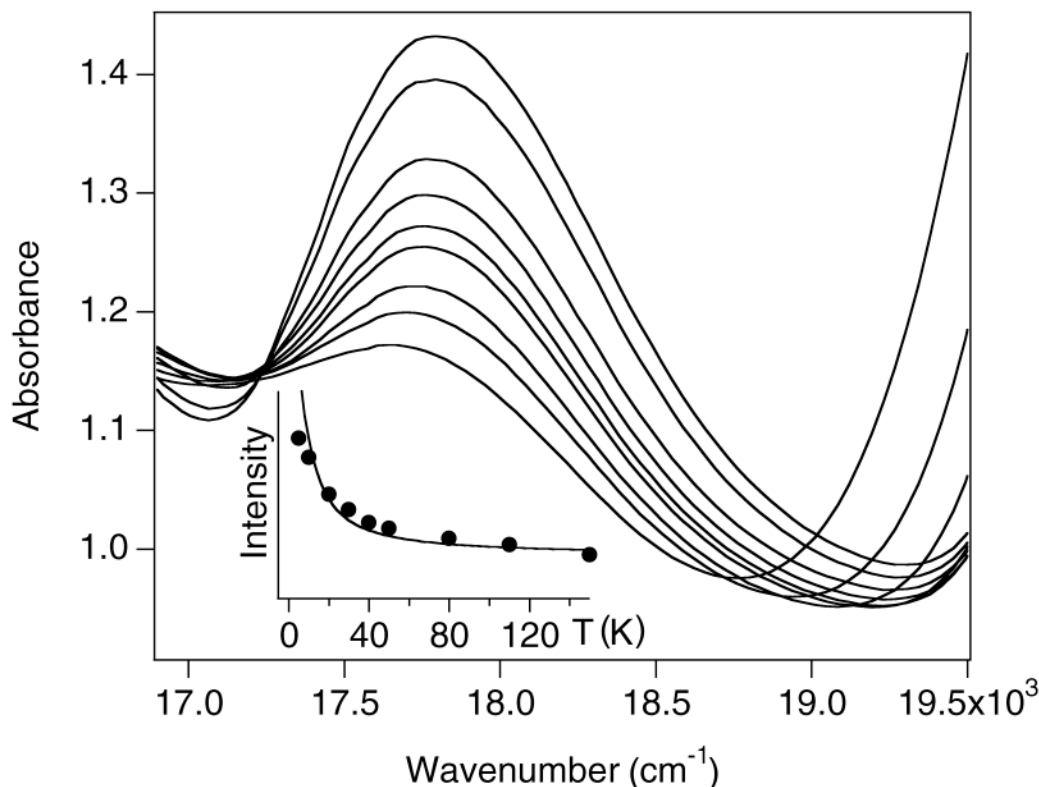
The calculated energy differences between the lowest triplet states for **1**, **3**, and **4** (given in Table 4) can be qualitatively related to the  $\chi T$  values measured at room temperature. Compound **1** has the smallest splitting with levels at  $0$ ,  $1370$ , and  $1800\text{ cm}^{-1}$ , and its  $\chi T$  value per nickel(II) ion is  $1.71\text{ emu K mol}^{-1}$ , higher than the value of  $1.56\text{ emu K mol}^{-1}$  measured for compound **2**. The same order of  $\chi T$  values at  $290\text{ K}$  is reported in the literature (5):  $1.68$  and  $1.64\text{ emu K mol}^{-1}$  for compounds **1** and **2**, respectively. The calculated splitting for **2** indicates levels at  $1300$  and  $2600\text{ cm}^{-1}$  — larger energy differences than for compound **1** — and therefore the lower  $\chi T$  value is justified. The correlation between AOM calculations and  $\chi T$  values remains qualitative because the effects of spin-orbit coupling are neglected, and identical  $e_\sigma$  and  $e_\pi$  values are used for each metal—ligand bond. The latter assumption is justified for compound **1**, where all four nickel(II)—N bond lengths are comparable, but less so for compound **2**, where one bond is longer by  $0.3\text{ \AA}$  than the other three. This bond-length difference further increases the ground-state splitting of **2** and reduces the  $\chi T$  value; thus, the large difference between compounds **1** and **2** is rationalized. The bimetallic compound **4** has a  $\chi T$  value of  $1.75\text{ emu K mol}^{-1}$  per nickel(II) ion, corresponding to a relatively small calculated splitting of  $2800\text{ cm}^{-1}$ . The calculated energy difference between the two lowest-energy triplet states for compound **3** is larger than  $6000\text{ cm}^{-1}$ , and the strongest quenching of the orbital angular momentum is therefore expected for this compound, in agreement with the smallest room-temperature  $\chi T$  value of  $1.43\text{ emu K mol}^{-1}$  per nickel(II) center, as observed in Fig. 4, very similar to the literature value of  $1.39\text{ emu K mol}^{-1}$  (5). The AOM analysis of the absorption spectra allows us to qualitatively understand the magnetic properties at high temperature and indicates that the parameter values obtained with a minimum number of adjustable quantities are reasonable.

#### Exchange interaction in $(\text{AsPh}_4)_4[\text{Ni}_2(\text{NCS})_8]$ and $(\text{Cat})_2[\text{Ni}_2(\text{NCS})_8]$

The magnetic measurements for bimetallic compounds **3** and **4** in Fig. 4 show a ferromagnetic coupling between the nickel(II) centers. The coupling constant,  $J$ , of  $4.5\text{ cm}^{-1}$  determined for **3** is well within the range of  $2.5$ – $6.3\text{ cm}^{-1}$  observed for other thiocyanato-bridged bimetallic complexes and linear chains containing nickel(II) ions, as summarized in Table 3 of ref. 7. Complementary information on exchange interactions is often obtained from temperature-dependent absorption intensities and is used to determine ground-state exchange splittings (24, 25). Figure 7 shows a detailed view of the spin-forbidden band of  $(\text{AsPh}_4)_4$ -



**Fig. 7.** Temperature dependence of the spin-forbidden, ligand-field transition of  $(\text{AsPh}_4)_4[\text{Ni}_2(\text{NCS})_8]$  **3**, labeled as band 5 on the upper solid line in Fig. 5. Traces are given for temperatures of 5, 10, 20, 30, 40, 50, 80, 110, and 150 K (top to bottom). The inset shows the integrated intensities of this band as a function of temperature. The solid line was obtained with the parameters determined from the fit to the magnetic measurements shown as solid circles in Fig. 4.



$[\text{Ni}_2(\text{NCS})_8]$  **3**, labeled 5 in Fig. 5. This weak band has been assigned as a spin-forbidden transition from the AOM analysis in Table 4. Its intensity shows a strong decrease with increasing temperature from 5 to 150 K. In this temperature range, the thermal population of the ground-state levels, split by both the exchange interactions and coordination geometry of each nickel(II) center, changes significantly. The ferromagnetic coupling determined from the magnetic measurements indicates that the lowest energy state of the bimetallic complex has a total spin  $S_{\text{total}} = 2$ , with the  $S_{\text{total}} = 1$  and  $S_{\text{total}} = 0$  levels higher in energy. The final state of the transition in Fig. 7 has  $S_{\text{total}}^* = 1$ . The observation of an absorption band with decreasing intensity at higher temperature indicates that the single-ion intensity mechanism (26, 27) dominates the observed band, as its spin selection rule is  $\Delta S_{\text{total}} = 0 \pm 1$ , and a transition from the lowest-energy level is possible. In contrast, the pair mechanism (28, 29) has a strict  $\Delta S_{\text{total}} = 0$  selection rule, and an intensity increase with temperature, corresponding to the thermal population of the  $S_{\text{total}} = 1$  ground-state level, would be expected. This mechanism can therefore be excluded for compound **3**. We apply the model derived to fit the magnetic data in Fig. 4 (middle trace, solid line) and calculate the Boltzmann population of the lowest energy level over the temperature range for which absorption spectra are shown in Fig. 7. These populations are then scaled and compared with the temperature-dependent experimental absorption intensities, whose estimated error is on the order of 10% from uncertainties of the

baseline. The inset to Fig. 7 illustrates the good agreement obtained by adjusting only a scaling factor, confirming the validity of our analysis of the magnetic data and showing that the distinct character of absorption transitions can reveal information on exchange coupling, in this case on the magnitude of the ground-state exchange coupling in compound **3**. The band in Fig. 7 is larger by several orders of magnitude than the ground-state splitting caused by the exchange interaction. It is therefore not possible to resolve transitions arising from each ground-state level or to determine exchange splittings in the excited state, as has been reported for other bimetallic complexes with weak exchange coupling (25, 30). The intensity variation of this absorption band supports the assignment of the increase in  $\chi T$  to an intramolecular ferromagnetic coupling, as  $d-d$  band intensities are not expected to depend strongly on intermolecular exchange effects. No corresponding temperature effect is observed for the bimetallic compound **4**, possibly because of the higher energy of the corresponding singlet band, which is in closer proximity to the intense transitions at higher energy and therefore more likely to borrow intensity from these allowed transitions. This intensity borrowing can easily mask an intensity change, as illustrated in Fig. 7. Complexes **1**, **2**, and **5** have only a single metal center and do not show any intensity changes comparable to Fig. 7, again indicating that this temperature-dependent absorption band does involve exchange coupling between nickel(II) ions bridged by thiocyanato ligands.



The structural, magnetic, and spectroscopic study of the title compounds shows the influence of coordination geometries on electronic states and energies of absorption maxima in the near-infrared and visible spectral regions. The exact experimental structures have to be used for a quantitative understanding of the spectra and the magnitude of  $\chi T$  at room temperature. Magnetic measurements reveal a ferromagnetic coupling in the bimetallic compounds, confirmed by temperature-dependent absorption spectra.

## Acknowledgements

Financial support from the Natural Sciences and Engineering Research Council of Canada (NSERC), the Centre Jacques Cartier, and the Commission Permanente de Coopération Franco-Québécoise is gratefully acknowledged.

## References

1. M. Verdaguer, A. Bleuzen, V. Marvaud, J. Vaissermann, M. Seuleman, C. Desplanches, A. Scullier, C. Train, R. Garde, G. Gelly, C. Lomenech, I. Rosenman, P. Veillet, C. Cartier, and F. Villain. *Coord. Chem. Rev.* **190–192**, 1023 (1999).
2. D. Luneau. *Curr. Opin. Solid State Mater. Sci.* **5**, 123 (2001).
3. V.I. Ovcharenko and R.Z. Sagdeev. *Russ. Chem. Rev.* **68**, 345 (1999).
4. C. Benelli and D. Gatteschi. *Chem. Rev.* **102**, 2369 (2002).
5. D. Forster and D.M.L. Goodgame. *Inorg. Chem.* **4**, 823 (1965).
6. L. Sacconi, F. Mani, and A. Bencini. *Comprehensive coordination chemistry*. Vol. 5. Edited by G. Wilkinson. Pergamon Press, Oxford. 1985. pp. 1.
7. B. Zurewska, J. Mrozinski, M. Julve, F. Lloret, A. Maslejova, and W. Sawka-Dobrowolska. *Inorg. Chem.* **41**, 1771 (2002).
8. (a) Bruker Analytical X-ray Instruments, Inc. SAINT [computer program]. Bruker Analytical X-ray Instruments, Inc., Madison, Wis. 1998; (b) G.M. Sheldrick. SADABS [computer program]. University of Göttingen, Germany. 1994; (c) Bruker Analytical X-ray Instruments, Inc. SHELXTL [computer program]. Bruker Analytical X-ray Instruments, Inc., Madison, Wis. 1998.
9. A.J.C. Wilson (*Editor*). *International tables for crystallography*. Vol. C. Mathematical, physical, and chemical tables. Kluwer Academic Publishers, Dordrecht, Boston, London. 1995.
10. D. Reinen, R. Allmann, G. Baum, B. Jakob, U. Kaschuba, W. Massa, and G.J. Miller. *Z. Anorg. Allg. Chem.* **548**, 7 (1987).
11. E.L. Muetterties and L.J. Guggenberger. *J. Am. Chem. Soc.* **96**, 1748 (1974).
12. A.W. Addison, T.N. Rao, J. Reedijk, and G.C. Verschoor. *J. Chem. Soc. Dalton Trans.* 1349 (1984).
13. A.P. Ginsberg, R.L. Martin, R.W. Brookes, and R.C. Sherwood. *Inorg. Chem.* **11**, 2884 (1972).
14. D.R. Bloomquist and R.D. Willett. *Coord. Chem. Rev.* **47**, 125 (1982).
15. R.L. Carlin and A.J. van Duyneveldt. *Magnetic properties of transition metal compounds*. Springer-Verlag, New York. 1977.
16. O. Kahn. *Molecular magnetism*. VCH Publishers, New York. 1993.
17. D.M. Duggan and D.N. Hendrickson. *Inorg. Chem.* **13**, 2929 (1974).
18. T. Rojo, R. Cortes, L. Lezama, J.L. Mesa, and G. Villeneuve. *Inorg. Chim. Acta*, **162**, 11 (1989).
19. J. Reedijk, P.W.N.M. Van Leeuwen, and W.L. Groeneveld. *Recl. Trav. Chim. Pays-Bas*, **87**, 129 (1968).
20. G. Bussière and C. Reber. *J. Am. Chem. Soc.* **120**, 6306 (1998).
21. G. Bussière, C. Reber, D.A. Walter, D. Neuhauser, and J.I. Zink. *J. Phys. Chem. A*, **107**, 1258 (2003).
22. M.-C. Nolet, R. Beaulac, A.-M. Boulanger and C. Reber. *Struct. Bonding*, accepted for publication.
23. H. Adamsky. AOMX – an angular overlap program [computer program]. Institut für Theoretische Chemie, Heinrich-Heine-Universität Düsseldorf, Düsseldorf, Germany. 1995. Available at <http://www.theochem.uni-duesseldorf.de/users/heribert/aomx> [cited 9 August, 2003].
24. Y. Pelletier and C. Reber. *Can. J. Chem.* **73**, 249 (1995).
25. R. Schenker, S. Heer, H.U. Güdel, and H. Weihe. *Inorg. Chem.* **40**, 1482 (2001).
26. M. Naito. *J. Phys. Soc. Jpn.* **34**, 1491 (1973).
27. S. Decurtins and H.U. Güdel. *Inorg. Chem.* **21**, 3598 (1982).
28. Y. Tanabe, T. Moriya, and S. Sugano. *Phys. Rev. Lett.* **15**, 1023 (1965).
29. J. Ferguson, H.J. Guggenheim, and Y. Tanabe. *J. Phys. Soc. Jpn.* **21**, 692 (1966).
30. C. Reber and H.U. Güdel. *Inorg. Chem.* **26**, 3186 (1987).



# Ferrocenyl-penta-( $\beta$ -naphthyl)benzene — Synthesis, structure, and dynamic behaviour<sup>1</sup>

Laura E. Harrington, James F. Britten, and Michael J. McGlinchey

**Abstract:** 3-Ferrocenyl-2,4,5-tri-( $\beta$ -naphthyl)cyclopentadienone undergoes a Diels–Alder reaction with di-( $\beta$ -naphthyl)acetylene to yield, after elimination of carbon monoxide, ferrocenyl-penta-( $\beta$ -naphthyl)benzene (**4**). <sup>1</sup>H and <sup>13</sup>C variable-temperature NMR studies on **4** reveal the existence of multiple diastereoisomers at low temperature. These data are interpreted in terms of slowed rotation of the naphthyl groups, and are supported by the X-ray crystal structure of **4**, which exhibits disorder at three of the naphthyl sites.

**Key words:** sterically crowded molecules, hindered rotations, crystallography, NMR.

**Résumé :** La 3-ferrocényl-2,4,5-tri-( $\beta$ -naphtyl)cyclopentadiénone donne une réaction de Diels–Alder avec le di-( $\beta$ -naphtyl)acétylène pour donner, après élimination de monoxyde de carbone, au ferrocényl-penta-( $\beta$ -naphtyl)benzène (**4**). Des études RMN du <sup>1</sup>H et du <sup>13</sup>C du composé **4** à températures variables démontrent l'existence de nombreux diastéréoisomères à basse température. On interprète ces données en fonction d'un ralentissement de la rotation des groupes naphtyles et ces conclusions sont appuyées par les études de diffraction des rayons X du composé **4** qui montrent l'existence d'un désordre à trois des sites naphtyles.

**Mots clés :** molécules stériquement encombrées, empêchement à la rotation, cristallographie, RMN.

[Traduit par la Rédaction]

## Introduction

The pioneering work of Gust and Mislow (1) on sterically hindered organic molecules, especially hexa-substituted arenes, prompted a number of subsequent studies on molecular paddle-wheels and propellers (2). Recognition of the novelty and utility of a system that could exhibit correlated rotation of crowded substituents about a central ring (3) stimulated a variety of investigations directed towards their potential application as molecular machines (4).

On the NMR time-scale, the pendant groups in hexaarylbenzenes are perpendicular to the central ring, and substitution is required to invoke observable barriers to rotation. Ortho-substituted derivatives exhibit significantly higher barriers to peripheral ring rotation (~33 kcal mol<sup>-1</sup>), than do their meta-substituted analogues. In the latter cases, the barriers (~17 kcal mol<sup>-1</sup>) are more reflective of the buttressing effects of the ortho-hydrogens (5). These  $\Delta G^\ddagger$  values have been ascribed to diastereomeric interconversions via the independent rotation of one ring at a time through approximately  $\pi$  radians (5, 6). Ultimately, these successive rotations provide the most favourable pathway for inversion of the propeller helicity; enantiomerization requires the rotation of *all* substituted peripheral rings, and the synchronous,

correlated rotation of six rings is entropically and energetically disfavored.

The necessity for increased steric bulk and the presence of a probe to detect restricted rotation has led to the development of organometallic derivatives of hexaarylbenzenes ((C<sub>n</sub>Ar<sub>n</sub>)ML<sub>x</sub>) where  $n = 5, 6$ , or  $7$ ; progress in this area has recently been reviewed (2). Whereas Gust elegantly labeled the peripheral substituents by “painting the edges different colours” (5), our focus has been to “paint the faces” of the rings differently (7).

Towards this goal, we have reported the synthesis and fluxional behaviour of hexaphenylbenzene chromium tricarbonyl (**1**), in which the metal moiety is bonded to one of the peripheral phenyl rings (8). As depicted in Scheme 1, under conditions of rapid rotation of all six peripheral rings, the molecule exhibits time-averaged C<sub>2v</sub> symmetry, which is lowered to C<sub>s</sub> when rotation of the chromium-complexed ring is slowed on the NMR time-scale at -100 °C. Unfortunately, X-ray crystallographic data are not available for **1**, but it is a reasonable assumption that the peripheral phenyls are not all arranged perpendicular to the central ring. The NMR-derived barrier towards rotation of the chromium-complexed ring was 12.2 ± 0.2 kcal mol<sup>-1</sup>. Although this work represented an advance in the development of

Received 8 February 2003. Published on the NRC Research Press Web site at <http://canjchem.nrc.ca> on 26 August 2003.

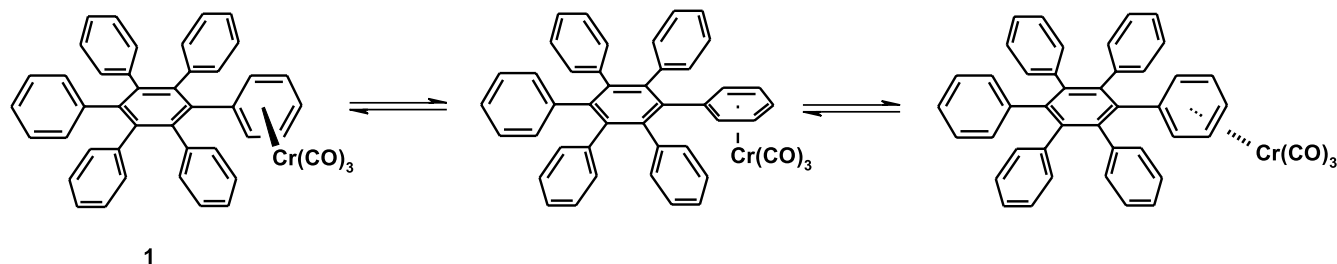
*This paper is dedicated to Professor John Harrod, a friend, a scholar and a gentleman, in recognition of his major contributions to inorganic and organometallic chemistry.*

**L.E. Harrington and J.F. Britten.** Department of Chemistry, McMaster University, Hamilton, ON L8S 4M1, Canada.  
**M.J. McGlinchey.**<sup>2</sup> Department of Chemistry, University College Dublin, Belfield, Dublin 4, Ireland.

<sup>1</sup>This article is part of a Special Issue dedicated to Professor John Harrod.

<sup>2</sup>Corresponding author (e-mail: [michael.mcglinchey@ucd.ie](mailto:michael.mcglinchey@ucd.ie)).



**Scheme 1.** Fluxional behaviour of  $(C_6Ph_6)Cr(CO)_3$ .

sterically encumbered organometallic derivatives based on molecular propellers, the barrier observed was lower than those observed for Gust's *ortho*- or *meta*-substituted hexaarylbenzenes. This could be interpreted either as lowering the barrier towards peripheral ring rotation, or a consequence of raising the energy of the ground state. Clearly, an increase in the steric bulk of the metal moiety, or an enhancement of its interaction with neighbouring substituents must be achieved.

This concept was further developed by the replacement of a peripheral phenyl ring by a ferrocenyl group, and led to intriguing results, including the possibility of correlated rotation (9). In the solid state,  $C_6Ph_5Fc$  (**2**) does not adopt a propeller conformation, but rather exhibits an incremental progression of dihedral angles ( $51^\circ$  to  $120^\circ$ ) as discussed in more detail below. It is tempting to invoke a "domino effect" (10) such that rotation of the ferrocenyl group would proceed with correlated rotation of the phenyl rings. However, since variable-temperature  $^1H$  and  $^{13}C$  NMR studies on **2** gave no indication of restricted ferrocenyl or phenyl ring rotation on the NMR time-scale, no definitive conclusions could be drawn (9).

With the aim of augmenting the interactions between the organometallic fragment and the peripheral aryl groups, our attention turned toward naphthyl derivatives, which act as phenyl groups with a labelled edge and a greater "wing-span". We have recently reported the syntheses, structures, and dynamic behaviour of several naphthyl-substituted (cyclopentadienone)rhodium acetylacetonate complexes (**3a**, **3b**) for which restricted rotation of the naphthyl groups was clearly detectable via splitting of the  $^{31}P$  NMR signals of the

triphenylphosphine substituent. The barriers to naphthyl rotation were evaluated as  $8.2 \pm 0.5$  kcal mol $^{-1}$  (11).

Although a number of purely organic naphthyl-substituted benzenes have been described (12), and several naphthyl rotation barriers have been determined (13), we are unaware of any analogous organometallic derivatives apart from Rausch's naphthyl-cyclobutadiene cobalt systems (14). With the goal of investigating the dynamic behaviour of an arene possessing both ferrocenyl and naphthyl substituents, we now report the synthesis, structure, and variable-temperature NMR spectra of ferrocenyl-penta-( $\beta$ -naphthyl)benzene (**4**).

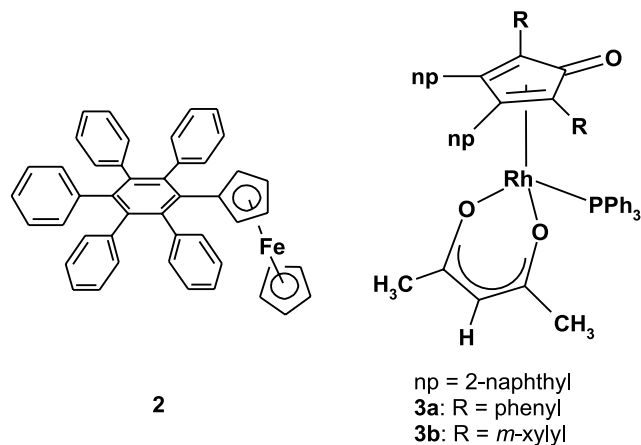
## Results and discussion

### Synthesis

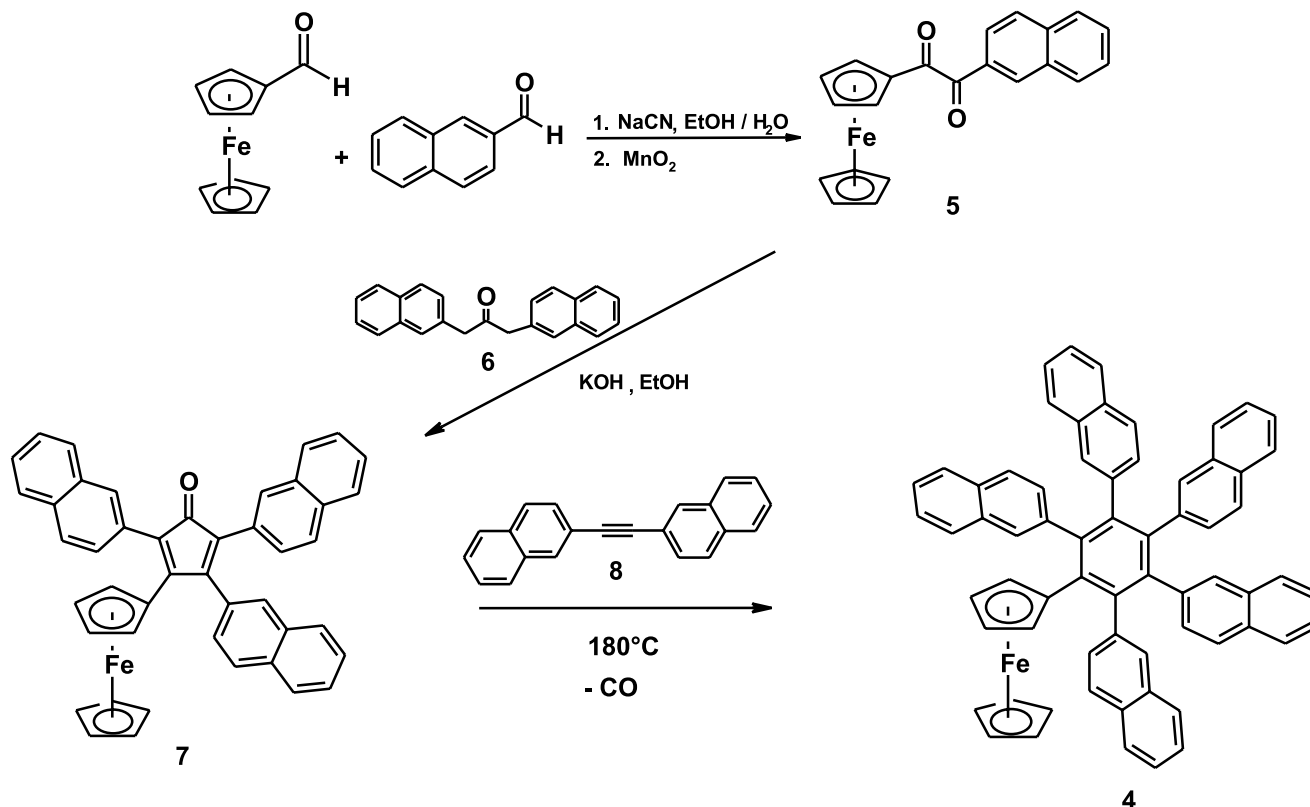
The synthesis of **4** was achieved by a method similar to that previously reported (9) for  $C_6Ph_5Fc$  (**2**) and is summarized in Scheme 2. The sodium-cyanide-catalyzed reaction of ferrocene carboxaldehyde with  $\beta$ -naphthaldehyde, followed by manganese dioxide oxidation yielded the diketone **5**. Base-catalyzed aldol condensation of **5** with 1,3-di-( $\beta$ -naphthyl)propanone (**6**) furnished 3-ferrocenyl-2,4,5-tri-( $\beta$ -naphthyl)cyclopentadienone (**7**), which underwent a Diels-Alder addition with di-( $\beta$ -naphthyl)acetylene (**8**) at  $180^\circ C$  and, after loss of carbon monoxide, afforded the desired product (**4**).

### NMR spectroscopic results

As indicated above, the 500 MHz  $^1H$  and 125 MHz  $^{13}C$  NMR spectra of ferrocenylpentaphenylbenzene (**2**) remained essentially unchanged to temperatures as low as 188 K, thus, offering no evidence for the restricted rotation of the ferrocenyl group or peripheral phenyl substituents. In contrast, although at room temperature the 500 MHz  $^1H$  NMR spectrum of the naphthyl analogue (**4**) exhibits the expected well-resolved aromatic signals attributable to the naphthyl and ferrocenyl protons, as the temperature is decreased, there is marked broadening of all of the signals in the ferrocenyl region. Moreover, the singlet at 3.73 ppm, assigned to the  $\alpha$ -CH protons in the  $C_5H_4$  ring, splits into at least three peaks (3.58, 3.66, and 3.69 ppm at 203 K; Fig. 1a). These findings are mirrored in the 125 MHz  $^{13}C$  NMR spectra, in which the corresponding peak for the ferrocenyl  $\alpha$ -carbon gradually splits into three peaks as the temperature is reduced (72.5, 73.1, and 73.3 ppm at 203 K; Fig. 1b). The peaks for the other ferrocenyl carbon and hydrogen atoms appear to broaden, but do not cleanly decoalesce at low temperature. There is similar broadening and decoalescence behaviour in the aromatic region, but severe overlap of the naphthyl signals in both the proton and

**Chart 1.** Ferrocenylpentaphenylbenzene (**2**) and naphthyl-substituted cyclopentadienone rhodium acetylacetonate complexes (**3**).



**Scheme 2.** Synthetic route to ferrocenyl-penta-( $\beta$ -naphthyl)benzene (**4**).

carbon regimes at low temperature renders these peak assignments ambiguous, even at 11.74 T.

If the ferrocenyl and naphthyl ring rotations have slowed on the NMR time-scale, and the molecule has adopted a single favoured conformation, one would expect to see four equal intensity <sup>1</sup>H and <sup>13</sup>C NMR resonances attributable to the C<sub>5</sub>H<sub>4</sub> moiety. However, since decoalescence gives rise to three signals of unequal intensity for the ferrocenyl  $\alpha$ -carbon, it is unlikely that restricted ferrocenyl rotation is the single explanation for the observed behaviour. An alternative rationale is that restricted rotation of the naphthyl groups gives rise to a number of diastereomers and, as a result, each ferrocenyl environment gives rise to distinct peaks, the intensities of which correspond to the relative stability of each of the rotamers.

Another possibility, but one that would require extensive labelling of the naphthyls (such as by incorporation of <sup>19</sup>F nuclei as independent probes) to verify, is that of residual stereoisomerism, a phenomenon originally recognized in maximally labelled Ar<sub>3</sub>Z and Ar<sub>3</sub>ZX moieties (**1b**, **3b**). In those cases, correlated ring rotation gave rise to closed subsets of interconverting isomers separated by substantial barriers. Thus, the interdependent motion of all three rings imposes a constraint on the relationship between torsional angles, and so blocks a number of interconversion pathways among the full set of conformers. If such a phenomenon were to be viable for **4**, it would imply that, on a given time-scale, ferrocenyl rotation is correlated with naphthyl rotation, but that individual naphthyl rings could not undergo independent rotation through  $\pi$  radians.

Such speculation assumes that the naphthyl rings in **4** can adopt a variety of up and (or) down combinations, thus, generating several diastereomers that interconvert slowly on the NMR time-scale at low temperatures. To test this hypothesis, an X-ray crystallographic study on ferrocenyl-penta-( $\beta$ -naphthyl)benzene (**4**) was initiated.

#### X-ray crystallographic results

Numerous attempts to grow single crystals of **4** suitable for an X-ray crystallographic study were thwarted, either by the slow decomposition of the sample, or rapid conversion to powder. Finally, slow evaporation of a CH<sub>2</sub>Cl<sub>2</sub> solution furnished crystals that were uniformly small and thin, and by no means ideal candidates for a crystallographic investigation. Nevertheless, it was possible to acquire a data set from which one could establish the atom connectivity and unequivocally characterize the molecule. Although the structure could, eventually, be refined to an *R* value of 18%, we clearly cannot claim high accuracy for the bond lengths and angles.

Figure 2 displays the structure of **4**, and the unit cell parameters are summarized in Table 1. The molecule exhibits several interesting features, notably the up and (or) down orientations of the naphthyl substituents. The possibility of two orientations for each naphthyl group often leads to disorder in crystal structures (cf. ref. 11), and in this instance, three of the naphthyl groups exhibit a disorder in which both orientations are represented. In particular, this phenomenon is seen for the naphthyl substituents at central ring carbons C(2) and C(6) (i.e., those adjacent to the ferrocenyl



**Fig. 1.** Variable-temperature NMR spectra of **4**, showing the decoalescence behaviour of (a) the ferrocenyl  $^1\text{H}$  environments at 500 MHz, and (b) the corresponding  $^{13}\text{C}$  resonances at 125 MHz.

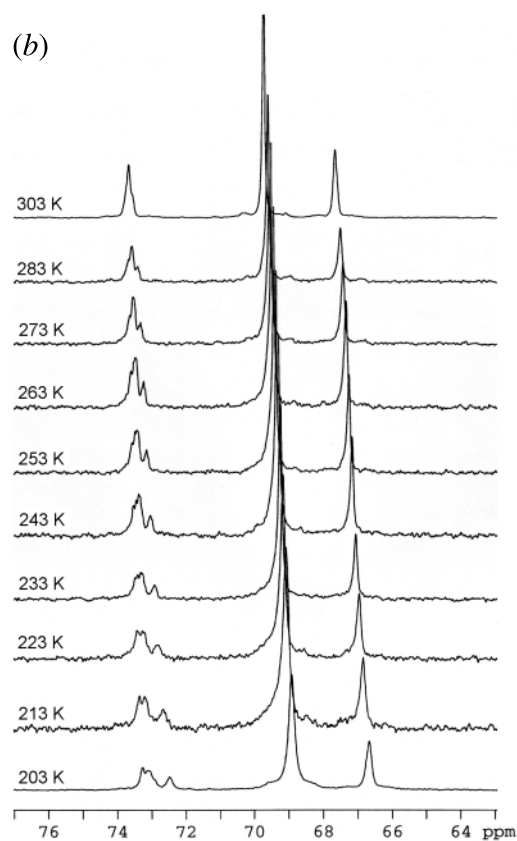
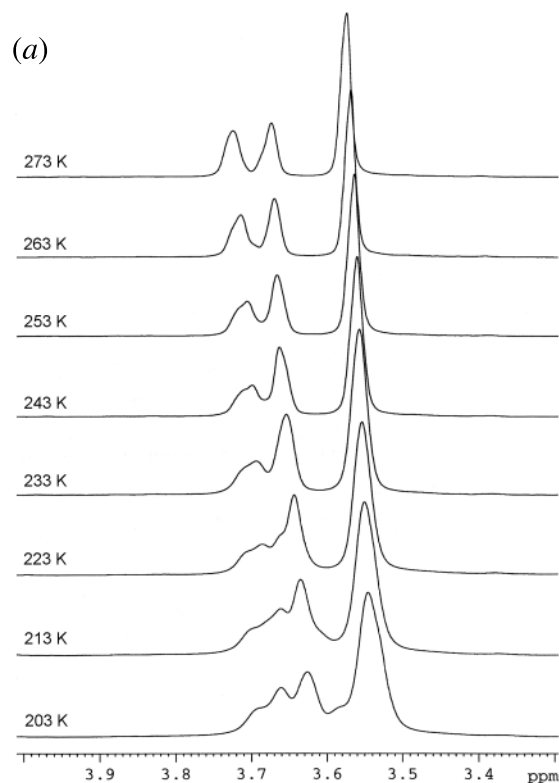
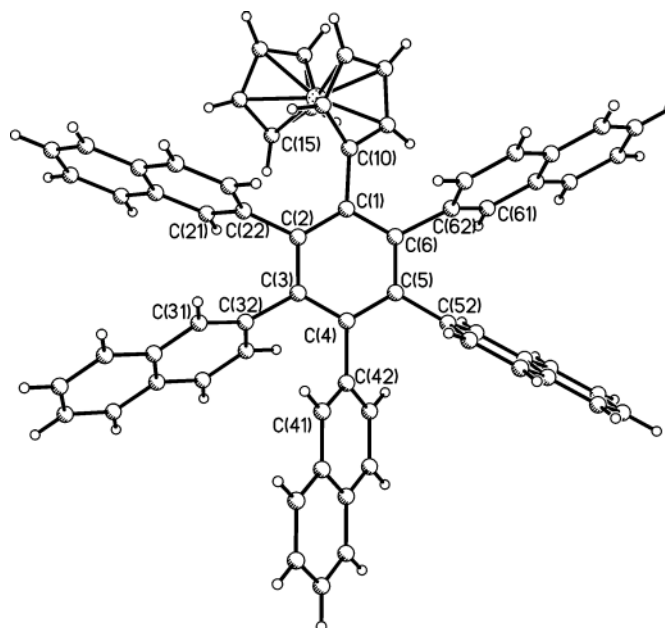


**Fig. 2.** X-ray crystal structure of **4** showing the atom numbering scheme.



substituent), as well as for the naphthyl ring bonded to C(3). It is tempting to draw a parallel between the solid state structure, in which these diastereomers are clearly similar in energy, and the solution state dynamic behaviour, in which several naphthyl groups apparently exhibit restricted rotation, and give rise to more than one conformer.

It is also informative to examine the dihedral angles of the peripheral substituents with respect to the central ring. As noted previously, in the crystal structure of **2** (see Fig. 3a) there is an incremental progression of angles from  $51^\circ$  to  $120^\circ$ , thus suggesting a “domino effect” that may offer insight into the mechanism for propeller interconversion (9, 10). This may be contrasted with the propeller conformation of the phenyl groups in hexaphenylbenzene, which all adopt interplanar angles of  $75^\circ$  with respect to the central ring (15). In **4** (see Fig. 3b), there is a progression of angles similar to that expressed by **2** (esd  $\sim 1^\circ$ ):  $134^\circ$  for the ferrocenyl substituent, followed by  $106^\circ$ ,  $81^\circ$ ,  $62^\circ$ ,  $65^\circ$ , and  $73^\circ$  for the naphthyls bonded to central ring carbons C(6) through C(2). The interesting contrast to **2** is that the naphthyl groups bonded to carbons C(2) through C(4) show a decrease in dihedral angle rather than an increase; thus, the angles do not display a clear incremental progression leading to propeller interconversion. This phenomenon is not limited to the groups adjacent to the bulky ferrocenyl group; there is evidently significant interaction among the naphthyl substituents themselves, leading to the expression of more dramatic dihedral angles than in the phenyl analogue. The interplanar angles displayed are not influenced by the disorder in the up and (or) down orientation of the naphthyl groups since these conformations are coplanar.

Although the X-ray crystal structure data are not of sufficient quality to permit the evaluation of bond lengths and angles with very high precision, they do allow a realistic assessment of the relative orientations of the peripheral substituents. In particular, one can draw viable comparisons



**Table 1.** Crystallographic collection and refinement parameters for **4**.

Empirical formula	C <sub>66</sub> H <sub>44</sub> Fe
Molecular weight	892.27
Size (mm <sup>3</sup> )	0.08 × 0.07 × 0.06
Temperature (K)	173(2)
Crystal system	Triclinic
Space group	<i>P</i> (-1)
<i>a</i> (Å)	10.858(2)
<i>b</i> (Å)	14.299(3)
<i>c</i> (Å)	16.777(3)
α (°)	112.147(5)
β (°)	90.700(6)
γ (°)	104.116(5)
<i>V</i> (Å <sup>3</sup> )	2324.1(7)
<i>Z</i>	2
Calculated density (g cm <sup>-3</sup> )	1.250
Scan mode	φ- and ω-scans
<i>F</i> (000)	913
Absorption coefficient (m <sup>-1</sup> )	2.912
θ range (°)	2.86 to 40.29
Index ranges	-8 ≤ <i>h</i> ≤ 9, -11 ≤ <i>k</i> ≤ 11, -14 ≤ <i>l</i> ≤ 13
Reflections collected	7545
Independent reflections	2833 ( <i>R</i> (int) = 0.3317)
Data/restraints/parameters	2833 / 0 / 129
GOF on <i>F</i> <sup>2</sup> (all)	1.195
Final <i>R</i> ( <i>I</i> > 2σ( <i>I</i> ))	<i>R</i> <sub>1</sub> = 0.1784, <i>wR</i> <sub>2</sub> = 0.3987
<i>R</i> indices (all data)	<i>R</i> <sub>1</sub> = 0.3155, <i>wR</i> <sub>2</sub> = 0.4714
Transmission (ratio of max to min)	1.0552
Largest diff peak (e Å <sup>-3</sup> )	0.874
Largest diff hole (e Å <sup>-3</sup> )	-0.585

with the dihedral angles formed by the peripheral substituents relative to the central ring in ferrocenyl-pentaphenylbenzene (**2**) ferrocenyl-penta-(β-naphthyl)benzene (**4**), and hexaphenylbenzene.

## Conclusions

The juxtaposition of ferrocenyl and five β-naphthyl substituents within a benzene ring results in the generation of at least three diastereomers arising from different up and (or) down combinations of naphthyl rings. In the solid state, this is reflected in disorder at three peripheral ring sites; correspondingly, variable-temperature <sup>1</sup>H and <sup>13</sup>C NMR spectra in solution indicate the presence of multiple rotamers. These observations may be compared with the analogous data for ferrocenylpentaphenylbenzene (**2**), which adopts a similar "non-propeller type" structure in the solid state, but which does not exhibit restricted rotation of the peripheral rings. This manifestation of the enhanced steric requirements of naphthyl substituents suggest that it may be possible to construct a six-bladed molecular propeller exhibiting correlated motion. Future reports will describe the use of other substituents, such as anthracenyl or fluorenyl, which have even larger wingspans.

## Experimental section

All reactions were carried out under an atmosphere of dry nitrogen employing conventional benchtop and glovebag techniques. Silica gel (particle size 20–45 μm) was employed for flash column chromatography. <sup>1</sup>H and <sup>13</sup>C NMR spectra were obtained on a Bruker DRX 500 spectrometer operating at 500.13 MHz and 125.76 MHz, respectively, and were referenced to the residual proton or <sup>13</sup>C signal of the solvent. Assignments were based on standard <sup>1</sup>H-<sup>1</sup>H and <sup>1</sup>H-<sup>13</sup>C two-dimensional techniques. Mass spectra were determined using a Finnigan 4500 spectrometer by direct electron impact (DEI) or direct chemical ionization (DCI) with NH<sub>3</sub> or on a Micromass GCT TOF instrument, as well as electrospray (ESI). Infrared spectra were recorded on a Bio-Rad FTS-40 spectrometer. Melting points (uncorrected) were determined on a Fisher-Johns melting point apparatus.

Ferrocene carboxaldehyde, β-naphthaldehyde, and benzophenone were obtained from Aldrich Chemical Co. and used as received. Di-(β-naphthylmethyl)ketone (**6**) was synthesized by using the phase-transfer method outlined in ref. (16). Di-β-naphthylacetylene (**8**) was synthesized following the methodology described in ref. (17); however, the oxidation was performed using silver oxide rather than mercuric oxide, as in ref. (18).

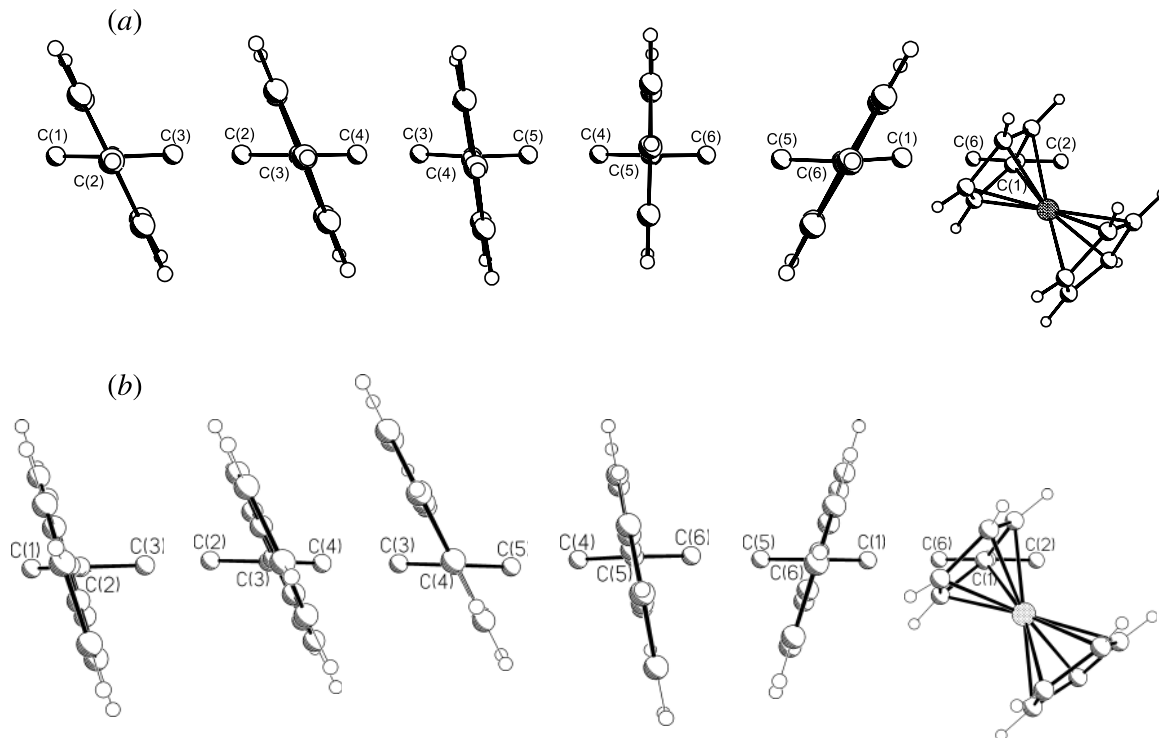
### Preparation of 2-ferrocenyl-2-hydroxy-1-naphthylethanone

Ferrocene carboxaldehyde (7.135 g, 0.03 mol), β-naphthaldehyde (5.83 g, 0.04 mol), and NaCN (1.16 g, 0.02 mol) were dissolved in 20 mL H<sub>2</sub>O and 40 mL ethanol, then refluxed for 1 h. The solution was cooled, resulting in the formation of a red precipitate, which was collected by suction filtration to give the desired product (9.05 g, 0.02 mol, 73%), mp 142–145 °C (dec). IR (KBr) (cm<sup>-1</sup>): 3364 (OH), 1656 (CO). <sup>1</sup>H NMR (500 MHz, CD<sub>2</sub>Cl<sub>2</sub>) δ: 7.90 (1H, s, naphthyl-H<sub>1</sub>), 7.88 (1H, d, *J*<sub>HH</sub> = 8.9 Hz, naphthyl-H<sub>8</sub>), 7.86 (1H, d, *J*<sub>HH</sub> = 8.5 Hz, naphthyl-H<sub>4</sub>), 7.84 (1H, dd, *J*<sub>HH</sub> = 7.9 Hz, 1.7 Hz, naphthyl-H<sub>5</sub>), 7.52 (1H, ddd, naphthyl-H<sub>6</sub>), 7.50 (1H, ddd, naphthyl-H<sub>7</sub>), 7.43 (1H, dd, *J*<sub>HH</sub> = 8.5, 1.6 Hz, naphthyl-H<sub>3</sub>), 5.67 (1H, d, *J*<sub>HH</sub> = 6.0 Hz, CH), 4.89 (1H, dd, *J*<sub>HH</sub> = 1.3 Hz, 1.3 Hz, ferrocenyl-H<sub>2</sub>), 4.69 (1H, dd, *J*<sub>HH</sub> = 1.3, 1.3 Hz, ferrocenyl-H<sub>5</sub>), 4.65 (1H, d, *J*<sub>HH</sub> = 6.0 Hz, OH), 4.56 (1H, ddd, *J*<sub>HH</sub> = 2.4, 2.4, 1.2 Hz, ferrocenyl-H<sub>3</sub>), 4.47 (1H, ddd, *J*<sub>HH</sub> = 2.4, 2.2 Hz, 1.3 Hz, ferrocenyl-H<sub>4</sub>), 4.08 (5H, s, ferrocenyl-C<sub>5</sub>H<sub>5</sub>). <sup>13</sup>C NMR (125 MHz, CD<sub>2</sub>Cl<sub>2</sub>) δ: 203.6 (CO), 133.8 (naphthyl-C<sub>4a</sub>), 133.7 (naphthyl-C<sub>8a</sub>), 129.3 (naphthyl-C<sub>4</sub>), 128.5 (naphthyl-C<sub>8</sub>), 128.2 (naphthyl-C<sub>2</sub>), 128.2 (naphthyl-C<sub>5</sub>), 127.8 (naphthyl-C<sub>1</sub>), 127.0 (naphthyl-C<sub>6</sub>), 127.0 (naphthyl-C<sub>7</sub>), 125.4 (naphthyl-C<sub>3</sub>), 77.5 (ferrocenyl-*ipso*-C), 75.4 (C-OH), 73.6 (ferrocenyl-C<sub>3</sub>), 73.6 (ferrocenyl-C<sub>4</sub>), 70.8 (ferrocenyl-C<sub>5</sub>), 70.7 (ferrocenyl-C<sub>5</sub>H<sub>5</sub>), 70.4 (ferrocenyl-C<sub>2</sub>). MS (DEI, *m/z* (%)): 370 (M<sup>+</sup>, 96), 353 (M-OH, 17), 213 (C<sub>5</sub>H<sub>5</sub>-Fe-C<sub>5</sub>H<sub>4</sub>-CO, 100), 185 (C<sub>5</sub>H<sub>5</sub>-Fe-C<sub>5</sub>H<sub>4</sub>, 39), 129 (74), 121 (35), 81 (17). MS (DCI, *m/z* (%)): 372 (M + 2H, 30), 371 (M + H, 100), 370 (M<sup>+</sup>, 30), 353 (M-OH, 30), 213 (C<sub>5</sub>H<sub>5</sub>-Fe-C<sub>5</sub>H<sub>4</sub>-CO, 30), 129 (18). HR-MS (EI) calcd. for C<sub>22</sub>H<sub>18</sub>O<sub>2</sub>Fe: 370.0656; found: 370.0647.

### Preparation of 1-ferrocenyl-2-naphthylethanedione (**5**)

2-Ferrocenyl-2-hydroxy-1-naphthylethanone (6.51 g, 0.02 mol) was dissolved in 150 mL CHCl<sub>3</sub> and heated to



**Fig. 3.** Progression of dihedral angles in (a) ferrocenyl-pentaphenylbenzene (**2**), and in (b) ferrocenyl-penta-( $\beta$ -naphthyl)benzene **4**.

reflux. In small portions, freshly prepared  $\text{MnO}_2$  was added (2.26 g, 0.02 mol) and the mixture was stirred under reflux for 24 h. After cooling to room temperature, the solution was filtered and the solvent was removed by rotary evaporation to give **5** (5.66 g, 0.015 mol, 88%) as a red solid, mp 98–100 °C (dec). Pure **5** was obtained by column chromatography under nitrogen (50:50,  $\text{CH}_2\text{Cl}_2$ :hexanes). IR (KBr) ( $\text{cm}^{-1}$ ): 1669 (CO), 1650 (CO).  $^1\text{H}$  NMR (500 MHz,  $\text{CD}_2\text{Cl}_2$ )  $\delta$ : 8.60 (1H, s, naphthyl- $\text{H}_1$ ), 8.12 (1H, dd,  $J_{\text{HH}} = 8.6, 1.7$  Hz, naphthyl- $\text{H}_3$ ), 8.00 (1H, d,  $J_{\text{HH}} = 8.6$  Hz, naphthyl- $\text{H}_4$ ), 8.00 (1H, d, naphthyl- $\text{H}_8$ ), 7.93 (1H, dd, naphthyl- $\text{H}_5$ ), 7.66 (1H, dd,  $J_{\text{HH}} = 7.5, 6.9, 1.2$  Hz, naphthyl- $\text{H}_6$ ), 7.59 (1H, ddd,  $J_{\text{HH}} = 8.2, 7.5, 1.1$  Hz, naphthyl- $\text{H}_7$ ), 4.90 (2H, dd,  $J_{\text{HH}} = 1.95, 1.92$  Hz, ferrocenyl- $\text{H}_{2,5}$ ), 4.71 (2H, dd,  $J_{\text{HH}} = 2.0, 2.0$  Hz, ferrocenyl- $\text{H}_{3,4}$ ), 4.28 (5H, s, ferrocenyl- $\text{C}_5\text{H}_5$ ).  $^{13}\text{C}$  NMR (125 MHz,  $\text{CD}_2\text{Cl}_2$ )  $\delta$ : 199.3 (naphthyl-C=O), 193.5 (ferrocenyl-C=O), 136.8 (naphthyl- $\text{C}_2$ ), 133.6 (naphthyl- $\text{C}_1$ ), 133.1 (naphthyl- $\text{C}_{4a}$ ), 131.0 (naphthyl- $\text{C}_{8a}$ ), 130.5 (naphthyl- $\text{C}_8$ ), 129.9 (naphthyl- $\text{C}_6$ ), 129.5 (naphthyl- $\text{C}_4$ ), 128.5 (naphthyl- $\text{C}_5$ ), 127.7 (naphthyl- $\text{C}_7$ ), 124.7 (naphthyl- $\text{C}_3$ ), 75.4 (ferrocenyl-*ipso*-C), 74.6 (ferrocenyl- $\text{C}_{3,4}$ ), 71.1 (ferrocenyl- $\text{C}_{2,5}$ ), 71.1 (ferrocenyl- $\text{C}_5\text{H}_5$ ). MS (DEI,  $m/z$  (%)): 368 ( $\text{M}^+$ , 100), 213 ( $\text{C}_5\text{H}_5\text{-Fe-C}_5\text{H}_4\text{-CO}$ , 75), 185 ( $\text{C}_5\text{H}_5\text{-Fe-C}_5\text{H}_4$ , 15), 155 ( $\text{C}_{10}\text{H}_7\text{-CH}_2\text{O}$ , 10), 129 (40), 127 ( $\text{C}_{10}\text{H}_7$ , 20), 84 (25). MS (DCI,  $m/z$  (%)): 369 ( $\text{M} + \text{H}$ , 100), 213 ( $\text{C}_5\text{H}_5\text{-Fe-C}_5\text{H}_4\text{-CO}$ , 29), 155 ( $\text{C}_{10}\text{H}_7\text{-CH}_2\text{O}$ , 14), 129 (14). HR-MS (EI) calcd. for  $\text{C}_{22}\text{H}_{16}\text{O}_2\text{Fe}$ : 368.0465; found: 368.0500

#### Preparation of 2,4,5-trinaphthyl-3-ferrocenylcyclopentadienone (**7**)

1-Ferrocenyl-2-naphthylethanedione (**5**, 0.77 g, 2.1 mmol) and KOH (0.2 g, 3.6 mmol) were dissolved in 50 mL etha-

nol and heated to reflux. A solution of di-( $\beta$ -naphthylmethyl)ketone (**6**, 0.68 g, 2.2 mmol) was dissolved in 50 mL ethanol and added dropwise, the mixture was then stirred under reflux for 2 h. The solution was cooled to room temperature, then in ice, and filtered with suction to give **7** as a dark blue powder (0.69 g, 1.1 mmol, 49%), mp 247–250 °C (dec). The powder was purified by column chromatography under nitrogen (50:50,  $\text{CH}_2\text{Cl}_2$ :hexanes) before further use. The sample is indefinitely stable as a solid, however, it decomposes in a wide variety of solvents over time.  $^1\text{H}$  NMR (500 MHz,  $\text{CD}_2\text{Cl}_2$ )  $\delta$ : 7.94 (9H, m, naphthyl-H), 7.61 (9H, m, naphthyl-H), 7.39 (2H, m, naphthyl-H), 7.18 (1H, m, naphthyl-H), 4.25 (2H, s, ferrocenyl- $\text{H}_{2,5}$ ), 4.05 (5H, s, ferrocenyl- $\text{C}_5\text{H}_5$ ), 3.98 (2H, s, ferrocenyl- $\text{H}_{3,4}$ ).  $^{13}\text{C}$  NMR (125 MHz,  $\text{CD}_2\text{Cl}_2$ )  $\delta$ : 200.27 (CO), 157.6, 154.0 (cyclopentadienone-C), 134.2, 134.0, 133.8, 133.7, 133.6, 133.4, 133.0, 132.2 (naphthyl-Cs), 130.5, 129.9 (naphthyl-CHs), 129.3 (naphthyl-C), 128.9, 128.8, 128.7, 128.6, 128.5, 128.3, 128.0, 127.8, 127.6, 127.3, 126.8, 126.5 (naphthyl-CHs), 123.8 (cyclopentadienone-C), 77.7 (ferrocenyl-*ipso*-C), 72.1 (ferrocenyl- $\text{C}_{2,5}$ ), 72.0 (ferrocenyl- $\text{C}_{3,4}$ ), 71.0 ( $\text{C}_5\text{H}_5$ ). IR (KBr) ( $\text{cm}^{-1}$ ): 1689 (CO). HR-MS (EI) calcd. for  $\text{C}_{45}\text{H}_{30}\text{OFe}$ : 642.1646; found: 642.1635.

#### Preparation of ferrocenyl-penta-( $\beta$ -naphthyl)benzene (**4**)

Benzophenone (5 g) was melted by heating to 120 °C in a 100 mL round bottom flask. The temperature of the oil bath was increased to 150 °C, then di( $\beta$ -naphthyl)acetylene (**8**, 0.42 g, 1.50 mmol) and 2,4,5-tri( $\beta$ -naphthyl)-3-ferrocenylcyclopentadienone (**7**, 0.96 g, 1.49 mmol) were added. The mixture was stirred and heated at 180–190 °C for 52 h with a reflux condenser (to prevent loss of benzophenone). The flask was cooled almost to room temperature and benzene



(5 mL) was added to prevent solidification of the benzophenone. The resulting mixture was purified by column chromatography under nitrogen (75:25, CH<sub>2</sub>Cl<sub>2</sub>:hexanes) to give **4** as a yellow-orange powder (0.30 g, 0.33 mmol, 22%), mp 260 °C (dec). <sup>1</sup>H NMR (500 MHz, CD<sub>2</sub>Cl<sub>2</sub>) δ: 7.81–7.00 (35H, m, naphthyl-H), 3.75 (2H, s, ferrocenyl-H<sub>2,5</sub>), 3.69 (2H, s, ferrocenyl-H<sub>3,4</sub>), 3.59 (5H, s, C<sub>5</sub>H<sub>5</sub>). <sup>13</sup>C NMR (125 MHz, CD<sub>2</sub>Cl<sub>2</sub>) δ: 142.6–125.7 (naphthyl-CH, C, cyclopentadienone-C), 87.5 (C<sub>5</sub>H<sub>4</sub>-C), 73.6 (ferrocenyl-C<sub>2,5</sub>), 69.6 (C<sub>5</sub>H<sub>5</sub>), 67.5 (ferrocenyl-C<sub>3,4</sub>). MS (ESI): 892.4 (M<sup>+</sup>, 100). HR-MS (EI) calcd. for C<sub>66</sub>H<sub>44</sub>Fe: 892.2792; found: 892.2721.

### Crystallographic data for **4**

X-ray crystallographic data for **4** were collected on a P4 Bruker diffractometer equipped with a Bruker SMART 1K CCD area detector (employing the program SMART) (19) and a rotating anode utilizing graphite-monochromated Mo Kα radiation (λ = 0.710 73 Å). Data processing was carried out by use of the program SAINT (20), while the program SADABS (21) was utilized for the scaling of diffraction data, the application of a decay correction and an empirical absorption correction based on redundant reflections. Structures were solved by using the direct-methods procedure in the Bruker SHELXTL (22) program library and refined by full-matrix least-squares methods on F<sup>2</sup>. As a result of the size of the crystal and the absence of diffraction data beyond 1.2 Å, we were unable to refine anisotropically on the carbon atoms. Hydrogen atoms were added as fixed contributors at calculated positions, with isotropic thermal parameters based on the carbon atom to which they are bonded. Three disordered naphthyl groups were located in the course of the refinement process for **4**, which complicated the analysis; rigid naphthyl groups were imposed.

### Acknowledgements

Financial support from the Natural Sciences and Engineering Research Council of Canada (NSERC) and from McMaster University is gratefully acknowledged. LEH thanks NSERC for a postgraduate scholarship. Mass spectra were obtained courtesy of Dr. Kirk Green of the McMaster Regional Centre for Mass Spectrometry.

### References

- (a) D. Gust and K. Mislow. *J. Am. Chem. Soc.* **95**, 1535 (1973); (b) K. Mislow. *Acc. Chem. Res.* **9**, 26 (1976).
- S. Brydges, L.E. Harrington, and M.J. McGlinchey. *Coord. Chem. Rev.* **233–234**, 75 (2002), and refs. therein.

- (a) J.M. Chance, J.H. Geiger, and K. Mislow. *J. Am. Chem. Soc.* **111**, 2326 (1989); (b) P. Finocchiaro, D. Gust, and K. Mislow. *J. Am. Chem. Soc.* **96**, 3198 (1974).
- (a) K. Mislow. *Chemtracts: Org. Chem.* **2**, 151 (1989); (b) H. Iwamura and K. Mislow. *Acc. Chem. Res.* **21**, 175 (1988); (c) A.M. Rouhi. *Chem. Eng. News*, **76**, 57 (1998).
- D. Gust and A. Patton. *J. Am. Chem. Soc.* **100**, 8175 (1978).
- D. Gust. *J. Am. Chem. Soc.* **99**, 6980 (1977).
- B. Mailvaganam, B.E. McCarry, B.G. Sayer, R.E. Perrier, R. Faggiani, and M.J. McGlinchey. *J. Organomet. Chem.* **335**, 213 (1987).
- B. Mailvaganam, B.G. Sayer, and M.J. McGlinchey. *J. Organomet. Chem.* **395**, 177 (1990).
- H.K. Gupta, S. Brydges, and M.J. McGlinchey. *Organometallics*, **18**, 115 (1999).
- S. Brydges and M.J. McGlinchey. *J. Org. Chem.* **67**, 7688 (2002).
- L.E. Harrington, J.F. Britten, D.W. Hughes, A.D. Bain, J.-Y. Thépot, and M.J. McGlinchey. *J. Organomet. Chem.* **656**, 243 (2002).
- (a) Z. Marcinow and P.W. Rabideau. *J. Org. Chem.* **55**, 3812 (1990); (b) M.V. Alfimov, Yu.B. Scheck, and N.P. Kovalenko. *Chem. Phys. Lett.* **43**, 154 (1976); (c) Yu.B. Scheck, N.P. Kovalenko, and M.V. Alfimov. *J. Lumin.* **15**, 157 (1977); (d) J.H. Magill and A.R. Ubbelohde. *Trans. Faraday Soc.* **54**, 1811 (1958); (e) D.J. Plazek and J.H. Magill. *J. Chem. Phys.* **45**, 3038 (1966).
- (a) C.M. Whitaker and R.J. McMahon. *J. Phys. Chem.* **100**, 1081 (1966); (b) H.E. Katz. *J. Org. Chem.* **52**, 3932 (1987); (c) P.N. Riley, M.G. Thorn, J.S. Vilaro, M.A. Lockwood, P.E. Fanwick, and I.P. Rothwell. *Organometallics*, **18**, 3016 (1999).
- M.D. Rausch, G.F. Westover, E. Mintz, G.M. Reisner, I. Bernal, A. Clearfield, and J.M. Troup. *Inorg. Chem.* **18**, 2606 (1979).
- (a) E.M. Larson, R.B. von Dreele, P. Hanson, and D. Gust. *Acta Crystallogr. Sect. C: Cryst. Struct. Commun.* **46**, 784 (1990); (b) An earlier structural determination reports the interplanar angles in C<sub>6</sub>Ph<sub>6</sub> as 65°: J.C.J. Bart. *Acta Crystallogr. Sect. B: Struct. Crystallogr. Cryst. Chem.* **24**, 1277 (1968).
- Y. Kimura, Y. Tomita, S. Nakanishi, and Y. Otsuji. *Chem. Lett.* 321 (1979).
- A.C. Cope, D.S. Smith, and R.J. Cotter. *Org. Synth.* **34**, 377 (1954).
- B. Ortiz, P. Villanueva, and F. Walls. *J. Org. Chem.* **37**, 2748 (1972).
- G.M. Sheldrick. SMART, Release 4.05. Siemens Energy and Automation Inc., Madison, Wisconsin 53719. 1996.
- G.M. Sheldrick. SAINT, Release 4.05. Siemens Energy and Automation Inc., Madison, Wisconsin 53719. 1996.
- G.M. Sheldrick. SADABS (Siemens Area Detector Absorption Corrections). Siemens Energy and Automation Inc., Madison, Wisconsin 53719. 1996.
- G.M. Sheldrick. SHELXTL, Version 5.03. Siemens Crystallographic Research Systems, Madison, Wisconsin. 1994.



# X-ray diffraction and solid-state $^{119}\text{Sn}$ CP-MAS NMR studies of some triaryltin(IV) chlorides<sup>1</sup>

Jordan M. Geller, Ian S. Butler, Denis F.R. Gilson, Frederick G. Morin, Ivor Wharf, and F. Bélanger-Gariépy

**Abstract:** The solid-state  $^{119}\text{Sn}$  cross-polarization (CP) magic angle spinning (MAS) NMR spectra of a series of triaryltin chlorides of the form  $\text{Ar}_3\text{SnCl}$  have been acquired. The indirect spin-spin coupling constants ( $J(^{119}\text{Sn}-^{35}\text{Cl})$ ), quadrupolar-dipolar shifts ( $d(^{119}\text{Sn}-^{35}\text{Cl})$ ), and the  $^{119}\text{Sn}$  chemical shift tensors were extracted. For the spectrum of triphenyltin chloride (**I**) the validity of the first-order perturbation approximation was tested by comparing results of both the perturbation and cubic-equation approaches and a variable-temperature NMR study undertaken to investigate the influence of the previously reported molecular motion in the solid. The X-ray crystal structures of the tris(*o*-tolyl)tin chloride (**II**) and tris(*p*-tolyl)tin chloride (**IV**) complexes have been examined. They belong to the monoclinic and triclinic space groups  $P2_1/n$  and  $P\bar{1}$ , respectively, which are different from the previously reported tris(*m*-tolyl)tin chloride (**III**) complex, which crystallizes in the space group  $R3$  and has threefold molecular symmetry. The structures and NMR properties of the complexes with meta-substituents are quite different from those with ortho- or para-substituents having axially symmetric shift tensors with small spans and larger  $J$  values.

**Key words:** aryltin chlorides, magic angle spinning NMR, tin-chlorine spin-spin coupling,  $^{119}\text{Sn}$  chemical shift tensor, crystal structure.

**Résumé :** On a déterminé les spectres RMN du  $^{119}\text{Sn}$ , à l'état solide et à la polarisation croisée (« CP ») de l'angle magique de rotation (« MAS ») d'une série de chlorures de triarylétaïn de la forme  $\text{Ar}_3\text{SnCl}$ . On en a extrait les constantes de couplage spin-spin indirectes,  $J(^{119}\text{Sn}-^{35}\text{Cl})$ , les déplacements quadripolaire-dipolaire,  $d(^{119}\text{Sn}-^{35}\text{Cl})$ , et les tenseurs du déplacement chimique du  $^{119}\text{Sn}$ . Pour le spectre du chlorure de triphénylétaïn (**I**), on a testé la validité de l'approximation de la perturbation du premier ordre en comparant les résultats des approches de perturbation et d'équation cubique avec les résultats d'une étude RMN à température variable réalisée dans le but d'étudier l'influence du mouvement moléculaire rapportée antérieurement dans le solide. On a déterminé les structures par diffraction des rayons X des chlorures de tris(*o*-tolyl)étaïn (**II**) et de tris(*p*-tolyl)étaïn (**IV**). Elles appartiennent respectivement aux groupes d'espace monoclinique ( $P2_1/n$ ) et triclinique ( $P\bar{1}$ ) qui diffèrent de celle rapportée antérieurement pour le complexe du chlorure de tris(*m*-tolyl)étaïn (**III**) qui cristallise dans le groupe d'espace  $R3$  et qui présente une symétrie moléculaire ternaire. Les structures et les propriétés RMN des complexes portant un substituant en méta- sont très différentes de celles des produits portant des substituants en positions ortho- et para- qui possèdent des tenseurs de déplacement axialement symétriques de faible portée et des valeurs de  $J$  plus élevées.

**Mots clés :** chlorures d'arylétaïn, RMN à l'angle magique de rotation, couplage spin-spin étain-chlore, tenseur de déplacement chimique du  $^{119}\text{Sn}$ , structure cristalline.

[Traduit par la Rédaction]

## Introduction

Triaryltin compounds have been studied for many years since the discovery of the biocidal properties of triphenyltin hydroxide and acetate and their subsequent use as agricultural fungicides (1). As part of an investigation of the effect

of phenyl ring substituents on the biological and other properties of triaryltin compounds, a wide range of *o*-, *m*-, and *p*-substituted triaryltin hydroxides and acetates was synthesized and tested for bioactivity (2, 3). This required the preparation of the corresponding tetraaryltins and triaryltin halides and the effect of varying the substituents on the aro-

Received 9 February 2003. Published on the NRC Research Press Web site at <http://canjchem.nrc.ca> on 1 October 2003.

*Dedicated to Professor John Harrod in recognition of his contributions to Canadian chemistry.*

**J.M. Geller, I.S. Butler,<sup>2</sup> D.F.R. Gilson,<sup>3</sup> F.G. Morin, and I. Wharf.** Department of Chemistry, McGill University, 801 Sherbrooke Street West, Montreal, QC H3A 2K6, Canada.

**F. Bélanger-Gariépy.** Département de chimie, Université de Montréal, C.P. 6128, Succursale Centre-ville, Montréal, QC H3C 3J7, Canada.

<sup>1</sup>This article is part of a Special Issue dedicated to Professor John Harrod.

<sup>2</sup>Corresponding author (e-mail: [ian.butler@mcgill.ca](mailto:ian.butler@mcgill.ca)).

<sup>3</sup>Corresponding author (e-mail: [denis.gilson@mcgill.ca](mailto:denis.gilson@mcgill.ca)).



matic ring on their vibrational (Raman, IR) spectra (4, 5) has been reported. In addition,  $^{119}\text{Sn}$  Mössbauer spectroscopic studies of various para-substituted aryltin complexes have also appeared (6, 7). More pertinent to this paper are two solution-state  $^{119}\text{Sn}$  and  $^{13}\text{C}$  NMR studies (8, 9) of various para-, meta- and ortho-substituted tetraaryltins ( $\text{Ar}_4\text{Sn}$ ) and triaryltin halides ( $\text{Ar}_3\text{SnX}$ ;  $\text{X} = \text{Cl}, \text{Br}, \text{I}$ ). For both the *p*- and *m*-substituted  $\text{Ar}_4\text{Sn}$  and  $\text{Ar}_3\text{SnX}$  series, the  $^{119}\text{Sn}$  chemical shifts could be correlated with various substituent parameters ( $\sigma_{\text{I}}, \sigma_{\text{R}}, \sigma_{\text{R}}^0, \sigma_{\text{P}}, \sigma_{\text{P}}^0$ ) showing electronic effects due to the ring substituents are sufficient to account for the observed  $\delta(^{119}\text{Sn})$  trends. We now report solid-state  $^{119}\text{Sn}$  studies of a wide range of triaryltin chlorides for comparison with the earlier solution studies.

Solid-state NMR spectra often provide information that is unavailable from solution spectra. Thus, when a probe nucleus such as a  $^{119}\text{Sn}$  ( $I = 1/2$ ) nucleus is bonded to a quadrupolar nucleus, line splittings occur in the solid-state NMR spectra, which can be analyzed to give information about the electronic environment and bonding about the tin nucleus. A review of the effects of quadrupolar nuclei on the CP-MAS spinning spectra of spin  $1/2$  nuclei has been published, which includes the tin-chlorine case (10), and the  $^{31}\text{P}$ - $^{35/37}\text{Cl}$  case has also been reported (11). The spectra are complicated by the presence of two isotopes:  $^{35}\text{Cl}$  (75% abundant) and  $^{37}\text{Cl}$  (25% abundant). Both nuclei ( $I = 3/2$ ) have similar magnetogyric ratios ( $\gamma(^{35}\text{Cl}) = 2.264 \times 10^7 \text{ rad s}^{-1} \text{ T}^{-1}$ ,  $\gamma(^{37}\text{Cl}) = 2.184 \times 10^7 \text{ rad s}^{-1} \text{ T}^{-1}$  (12)) and nuclear quadrupole moments ( $Q(^{35}\text{Cl}) = -8.165 \times 10^{-30} \text{ m}^2$  and  $Q(^{37}\text{Cl}) = -6.435 \times 10^{-30} \text{ m}^2$  (13)).

Olivieri (14) developed a treatment of the splittings ( $\Delta\nu_{\text{m}}$ ) in the MAS spectrum of a probe nucleus ( $I = 1/2$ ) directly bonded to a quadrupolar nucleus based on first-order perturbation theory, which is valid in the limit  $\chi/[4S(2S-1)\nu_{\text{s}}] \ll 1$ , where  $\nu_{\text{s}}$  is the Larmor frequency of the quadrupolar nucleus and  $\chi$  is the nuclear quadrupolar coupling constant. Thus, with  $^{35}\text{Cl}$  and  $^{37}\text{Cl}$ , provided that  $\chi/12\nu_{\text{s}} \ll 1$ , the splittings observed in the solid-state spectra under magic angle spinning are given by eq. [1]:

$$[1] \quad \Delta\nu_{\text{m}} = -m_{\text{s}}J_{\text{IS}} + (3\chi D'/20\nu_{\text{s}})(3 \cos^2\beta^{\text{D}} - 1 + \eta \sin^2\beta^{\text{D}} \cos 2\alpha^{\text{D}})\{S(S+1) - 3m_{\text{s}}^2\}/\{S(2S-1)\}$$

where  $J_{\text{IS}}$  is the spin-spin coupling constant,  $D' = (D - \Delta J)/3$ , where  $D$  is the direct dipolar coupling constant ( $D = (\mu_0/4\pi)\gamma_{\text{s}}\gamma_{\text{I}}\hbar^2/(4\pi^2(r_{\text{IS}})^3)$ ), and  $\Delta J$  is the anisotropy in the spin-spin coupling, while  $\alpha^{\text{D}}$  and  $\beta^{\text{D}}$  are, respectively, the azimuthal and polar angles relating the internuclear vector to the principal axis of the electric field gradient (EFG), and  $\eta$  is the asymmetry in the field gradient. Equation [1] assumes that the  $\mathbf{J}$  tensor is colinear with the internuclear dipole vector. The second-order quadrupolar-dipolar splitting ( $d$ ) is given by  $3\chi D'/20\nu_{\text{s}}$ . In most  $\text{Ar}_3\text{SnCl}$  compounds in the solid state, the local symmetry about the Sn—Cl bond is approximately  $C_3$  (in some cases exactly so). Thus, it can be assumed that the angle  $\beta^{\text{D}}$  is  $0^\circ$  and with the value of  $\alpha^{\text{D}}$  undefined because it is multiplied by  $\sin^2\beta^{\text{D}}$ , eq. [1] is reduced to a simpler form

$$[2] \quad \Delta\nu_{\text{m}} = -m_{\text{s}}J_{\text{IS}} + (3\chi D'/10\nu_{\text{s}})[5/4 - m_{\text{s}}^2]$$

with  $d$  now given by  $3\chi D'/10\nu_{\text{s}}$ .

The  $^{119}\text{Sn}$ -MAS NMR spectrum of triphenyltin chloride was first reported in 1987 (15) followed soon after by the application of the perturbation theory to describe the multiplet from the ( $^{119}\text{Sn}$ - $^{35/37}\text{Cl}$ ) spin pair, but only an average value of  $|J_{\text{iso}}|$  over the two sites was extracted from the spectra (16, 17). Values of the  $d$  and  $\Delta J$  were reported (14, 18) but these values were based on an average  $d$  for the two crystallographically nonequivalent tin sites (19), while a more detailed analysis in terms of the two chlorine isotopes was not attempted. NQR data have been reported for triphenyltin chloride at 77 K (20) and at 303 K (21).

In the present study, the solid-state NMR spectrum of triphenyltin chloride (**I**) has been fully re-examined with extraction of  $J$ ,  $d$ , and  $\delta_{\text{iso}}$  for both tin sites as well as consideration of both ( $^{119}\text{Sn}$ - $^{35}\text{Cl}$ ) and ( $^{119}\text{Sn}$ - $^{37}\text{Cl}$ ) spin pairs. The validity of the first-order perturbation approximation was tested by comparing results of both the perturbation- (10, 14) and cubic-equation approaches (22), and a variable-temperature NMR study undertaken to investigate the influence of the previously reported molecular motion in the solid (23).

For comparison with (**I**) we also present the  $^{119}\text{Sn}$  CP-MAS spectra of a series of triaryltin chloride complexes with various substituents in the ortho-, meta-, and para-positions (**II** – **IX**); see Table 4 for the numbering scheme. To correlate the NMR parameters ( $J$ ,  $d$ ,  $D'$ ) and chemical shift tensor components ( $\delta_{11}$ ,  $\delta_{22}$ ,  $\delta_{33}$ ) with molecular geometries, full-crystal structures are needed. Although the structures of most of the  $\text{Ar}_3\text{SnCl}$  complexes studied here have been reported earlier (9, 24–26), in this paper we now add the structures of (*o*-tolyl) $_3\text{SnCl}$  (**II**) and (*p*-tolyl) $_3\text{SnCl}$  (**IV**). The solid-state NMR spectra of some triaryltin fluorides have been reported (27) but these complexes differ from the chlorides since, with the exception of tris(mesityl)tin fluoride, they are five-coordinate and form polymeric chains in the solid. The chlorides are all distorted tetrahedral molecules with the shortest nonbonded distance between tin and chlorine occurring in the tris(*m*-anisyl)tin chloride at 4.37 Å (24), much longer than the sum of the van der Waals radii (3.93 Å) (28).

## Experimental

The triaryltin chlorides were either from previous preparations or synthesized by literature methods (8, 9). Solid-state  $^{119}\text{Sn}$  NMR spectra were recorded at 111.7 MHz using a Chemagnetics CMX-300 (7.05 T) spectrometer under conditions of  $^{119}\text{Sn}$ - $^1\text{H}$  cross-polarization, high-power proton decoupling, and magic-angle spinning. The CP-MAS spectra were obtained for approximately 250–300 mg of sample packed into zirconia pencil-type rotors (7.5 mm diameter), using pulse delays of 10–60 s, depending on the proton  $T_1$  value, and contact times of 2 or 3 ms. The number of transients ranged from 240–1992 depending upon the compound in question. Line broadening of 0–10 Hz was applied and the FIDs were zero filled to 8 K and 16 K points before transformation. Different spinning rates, from 1600–4000 Hz, were used to identify the centre band. Chemical shifts are given with respect to external tetramethyltin ( $(\text{CH}_3)_4\text{Sn}$ ) using the chemical shift of solid tetracyclohexyl-



**Table 1.** Crystal structure data and structural refinements for two methyl-substituted complexes of the form  $\text{Ar}_3\text{SnCl}$ .

Aryl =	<i>o</i> -Tolyl ( <b>II</b> )	<i>p</i> -Tolyl ( <b>IV</b> )
Formula	$\text{C}_{21}\text{H}_{21}\text{ClSn}$	$\text{C}_{21}\text{H}_{21}\text{ClSn}$
MW ( $\text{g mol}^{-1}$ )	427.518	427.518
Crystal color, habit	Colourless, needle	Colourless, block
Crystal size (mm)	$0.70 \times 0.09 \times 0.05$	$0.62 \times 0.57 \times 0.53$
Crystal system	Monoclinic	Triclinic
Space group	$P2_1/n$	$P\bar{1}$
<i>a</i> (Å)	9.7918(1)	10.3481(6)
<i>b</i> (Å)	11.4896(1)	10.6811(7)
<i>c</i> (Å)	17.5620(1)	10.9412(9)
$\alpha$ (°)	90.00	70.971(7)
$\beta$ (°)	100.1643(4)	65.190(6)
$\gamma$ (°)	90.00	66.157(6)
<i>V</i> (Å <sup>3</sup> )	1944.78(3)	986.04(12)
<i>Z</i>	4	2
$D_{\text{calcd.}}$ ( $\text{Mg m}^{-3}$ )	1.4601	1.4399
$\lambda$ (Å)	1.54178	0.71073
$\mu$ ( $\text{mm}^{-1}$ )	11.671	1.428
Diffractometer	Bruker AXS SMART 2K	Bruker P4
Scan type	$\omega$	$\omega/2\theta$
Temperature (K)	293(2)	292(2)
Absorption correction	Multiscan <sup>a</sup>	Gaussian <sup>b</sup>
Transmission range	0.27–0.65	0.92–0.94
Measured reflections	22 892	22 403
Unique reflections, $R_{\text{int}}$	3788, 0.0506	5601, 0.0215
Observed data, criterion	3228, $I > 2\sigma(I)$	5267, $I > 2\sigma(I)$
$\Theta_{\text{max}}$ (°)	72.85	29.99
Refined parameters	212	212
Refinement on	$F^2$	$F^2$
Range measured	$-11 \leq h \leq 12$ $-13 \leq k \leq 11$ $-21 \leq l \leq 21$	$-13 \leq h \leq 13$ $-13 \leq k \leq 13$ $-14 \leq l \leq 14$
$R_1$ (obs)	0.0328	0.0223
$wR_2$	0.0872	0.0596
<i>S</i>	1.057	1.122
Extinction coefficient	0.00021(9)	0.0120(7)

**Note:**  $R_1 = \sum(|F_o| - |F_c|)/\sum|F_o|$ ;  $wR_2 = \{\sum[w(F_o^2 - F_c^2)^2]/\sum[w(F_o^2)^2]\}^{1/2}$ ;  $w = 1/\sigma^2(F_o^2)$ .  $S = \{\sum[w(F_o^2 - F_c^2)^2]/(n - p)\}^{1/2}$  ( $n$  = number of data,  $p$  = number of refined parameters).

<sup>a</sup>Reference 31.

<sup>b</sup>Reference 32.

tin (−97.0 ppm) as an external secondary reference. The line positions of the centre band and spinning sidebands were extracted using the program Peakfit (Jandel Scientific). Calculations of the shielding tensors were performed using the method developed by Herzfeld and Berger (29) and the computational program HBA version 1.4 (30).

### X-ray crystallography

Both (**II**) and (**IV**) were recrystallized by dissolving in ethanol, hot filtering through Celite, followed by slow evap-

oration over several days at room temperature. Crystal data and structural refinement details are given in Table 1. For both compounds (**II**) and (**IV**), data were processed by XPREP (31) and the structures were solved by direct methods using SHELXS-97 (33) and refined using SHELXL-96 (34). Non-hydrogen atoms were refined with anisotropic thermal parameters with H-atoms in calculated positions. Scattering factors were from the usual source (35). Compound (**IV**) was run with Mo K $\alpha$  radiation since the crystals were large and could not easily be cut.<sup>4</sup>

<sup>4</sup>Data for (**II**) and (**IV**) may be purchased from the Directory of Unpublished Data, Document Delivery, CISTI, National Research Council Canada, Ottawa, ON K1A 0S2, Canada ([http://www.nrc.ca/cisti/irm/unpub\\_e.shtml](http://www.nrc.ca/cisti/irm/unpub_e.shtml) for information on ordering electronically). CCDC 188728 and 188729 contain the crystallographic data for (**II**) and (**IV**). These data can be obtained, free of charge, via [www.ccdc.cam.ac.uk/conts/retrieving.html](http://www.ccdc.cam.ac.uk/conts/retrieving.html) (or from the Cambridge Crystallographic Data Centre, 12 Union Road, Cambridge CB2 1EZ, U.K.; fax +44 1223 336033; or [deposit@ccdc.cam.ac.uk](mailto:deposit@ccdc.cam.ac.uk)).



## Results and discussion

### X-ray crystallography

Tris(*o*-tolyl)tin chloride (**II**) and tris(*p*-tolyl)tin chloride (**IV**) crystallize in monoclinic ( $P2_1/n$ ) and triclinic ( $P\bar{1}$ ) space groups, respectively. In both cases there is only one molecule in the asymmetric unit and the geometry about tin is distorted tetrahedral. ORTEP diagrams of (**II**) and (**IV**) are shown in Figs. 1 and 2, respectively, and selected bond lengths and angles are given in Table 2. In (**II**), the geometry around tin closely resembles that found earlier for (*o*-tolyl)<sub>3</sub>SnNCS (36) with two ortho-methyl groups (C-17 and C-27) *cis*- to chlorine while the third (C-37) is *trans*, with the phenyl ring close to coplanar with the Cl-Sn-C(31) plane at a dihedral angle Cl-Sn-C(31)-C(36) of 19.9(3)°. For (*o*-tolyl)<sub>3</sub>SnNCS, with two molecules in the asymmetric unit, the corresponding angles are 10.1(3)° and 17.6(3)°. Compound (**IV**) also has one phenyl ring nearly coplanar with the Cl-Sn-C(31) plane, the dihedral angle Cl-Sn-C(31)-C(32) being 17.9(2)°. Table 2 also includes data for tris(*m*-tolyl)tin chloride (**III**), which belongs to the trigonal space group  $R\bar{3}$ , with the threefold rotation axis containing the Sn—Cl bond (9). Two other meta-substituted complexes (tris(*m*-anisyl)tin chloride (**VI**) (24) and tris(3,5-dimethylphenyl)tin chloride (**VIII**) (9)) also crystallize in trigonal space groups and possess axial molecular symmetry. In contrast, the ortho-substituted complexes tris(*o*-anisyl)tin chloride (**V**) (26) and tris(mesityl)tin chloride(**IX**) (25) are monoclinic ( $P2_1/n$ ).

### Solid-state $^{119}\text{Sn}$ CP MAS NMR spectra

#### Triphenyltin chloride

With two molecules in its asymmetric unit, the  $^{119}\text{Sn}$  MAS centre band of (**I**) consists of two asymmetric overlapping quartets, from the ( $^{119}\text{Sn}$ - $^{35}\text{Cl}$ ) and ( $^{119}\text{Sn}$ - $^{37}\text{Cl}$ ) spin pairs, with intensities in the ratio of 3:1, for each of the tin sites, for a total of 16 lines. Alarcón et al. (22) derived cubic equations for both the spin-spin coupling and the quadrupolar-dipolar splitting for  $I$ - $S$  spin pairs, with  $S = 3/2$ , which are valid when  $1 < |\chi/v_s| < 3$ . As the  $|\chi/v_s|$  ratio becomes greater than 0.8, the observed splittings are smaller than would be predicted by first-order theory. The nuclear quadrupolar coupling constants ( $\chi$ ) have been reported as 33.50 and 33.97 MHz at 303 K (21). At 7.05 T the  $^{35}\text{Cl}$  and  $^{37}\text{Cl}$  resonance frequencies ( $v_s$ ) are 29.39 and 24.47 MHz, thus, the calculated  $|\chi^{35}/v_s^{35}|$  ratios are 1.16 and 1.14 and  $|\chi^{37}/v_s^{37}|$  ratios are 1.10 and 1.08 for the two tin sites, respectively. To consider the validity of using first-order perturbation theory, the NMR parameters were extracted from the line positions in the  $^{119}\text{Sn}$  MAS spectrum of triphenyltin chloride using both the first-order and the cubic-equation approaches and are given in Table 3. The differences are small, with the largest deviations being in the spin-spin coupling constant for one of the tin sites, which is underestimated by 8 Hz or a 3% difference. From this comparison we assume that the underestimation of these couplings is small enough to justify using the first-order perturbation equation to analyze the spectra of the complexes (**II**)–(**XI**), which also requires that their quadrupolar coupling constants are not substantially different from that of triphenyltin chloride (**I**).

**Fig. 1.** ORTEP diagram of tris(*o*-tolyl)tin chloride (**II**) viewed along the tin–chlorine bond with the chlorine atom in front showing 30% thermal probability ellipsoids.

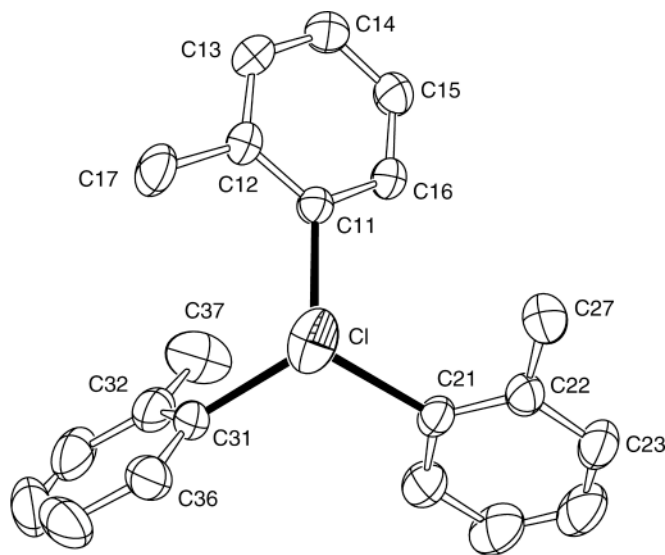
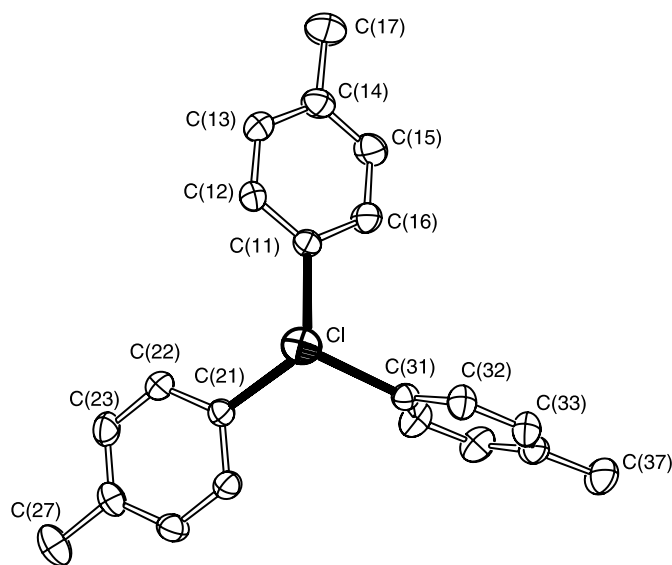


**Fig. 2.** ORTEP diagram of tris(*p*-tolyl)tin chloride (**VII**) viewed along the tin–chlorine bond with the chlorine atom in front showing 30% thermal probability ellipsoids.

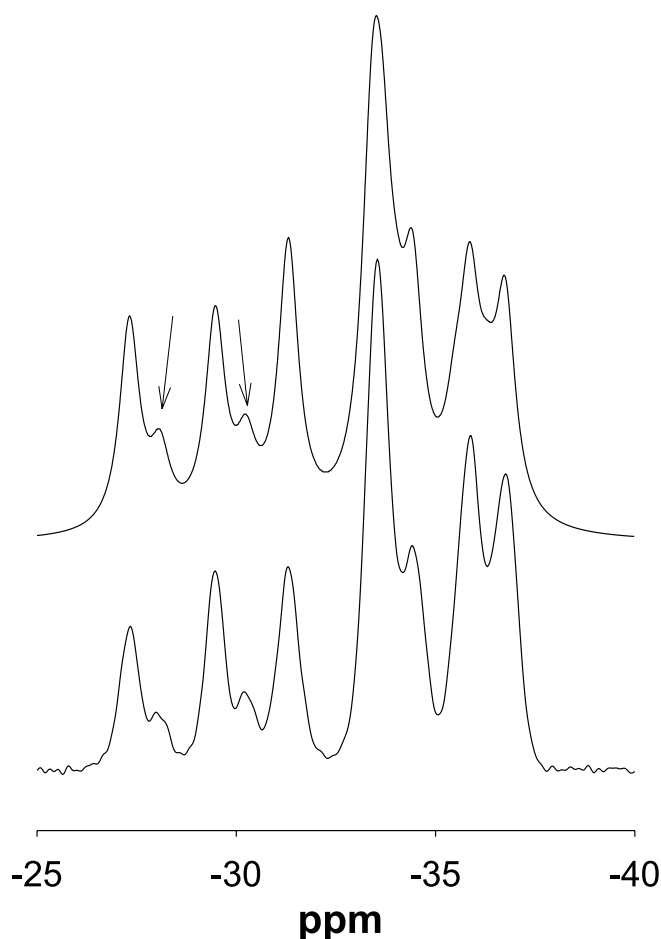


For comparison, the experimental and simulated spectra of triphenyltin chloride are shown in Fig. 3. The simulated spectrum is the sum of 16 lines broadened by Lorentzian functions, eight from the coupling of  $^{119}\text{Sn}$  with  $^{35}\text{Cl}$ ; the line positions given by eq. [2] with the values for  $J(^{119}\text{Sn}$ - $^{35}\text{Cl})$ ,  $d(^{119}\text{Sn}$ - $^{35}\text{Cl})$ , and  $\delta_{\text{iso}}(^{119}\text{Sn}$ - $^{35}\text{Cl})$  given in Table 3. The other eight lines are one-third of the intensity from coupling of  $^{119}\text{Sn}$  with  $^{37}\text{Cl}$  and their positions were calculated assuming that the  $^{119}\text{Sn}$  isotropic shifts are the same and by using the ratios  $J(^{119}\text{Sn}$ - $^{35}\text{Cl})/J(^{119}\text{Sn}$ - $^{37}\text{Cl}) = \gamma(^{35}\text{Cl})/\gamma(^{37}\text{Cl})$  and  $d(^{119}\text{Sn}$ - $^{35}\text{Cl})/d(^{119}\text{Sn}$ - $^{37}\text{Cl}) = Q(^{35}\text{Cl})/Q(^{37}\text{Cl})$ . The experimental spectra represent the centre band with all side-



**Table 2.** Selected bond lengths (Å) and angles (°) for the methyl-substituted complexes of the form Ar<sub>3</sub>SnCl from X-ray diffraction.

	<i>o</i> -Tolyl ( <b>II</b> )	<i>m</i> -Tolyl ( <b>III</b> ) <sup>a</sup>	<i>p</i> -Tolyl ( <b>IV</b> )
<b>Bond Lengths (Å)</b>			
Sn—Cl	2.3760(10)	2.379(1)	2.3729(6)
Sn—C11	2.131(3)	2.124(2)	2.1207(18)
Sn—C21	2.135(3)	—	2.1154(17)
Sn—C31	2.131(3)	—	2.1171(18)
<b>Bond Angles (°)</b>			
Cl—Sn—C11	104.11(9)	104.40(6)	104.25(5)
Cl—Sn—C21	105.99(10)	—	104.03(5)
Cl—Sn—C31	102.03(12)	—	104.82(5)
C11—Sn—C21	112.81(12)	114.03(14)	118.37(7)
C11—Sn—C31	116.27(13)	—	110.83(7)
C21—Sn—C31	113.89(14)	—	112.96(7)
Cl—Sn—C11—C12	−62.4(3)	−23.7(1)	−60.80(17)
Cl—Sn—C11—C16	118.8(2)	158.2(1)	113.50(16)
Cl—Sn—C21—C22	−49.4(3)	—	100.06(17)
Cl—Sn—C21—C26	130.3(3)	—	−78.87(15)
Cl—Sn—C31—C32	157.7(3)	—	−17.89(17)
Cl—Sn—C31—C36	−19.9(3)	—	165.17(16)

<sup>a</sup>Reference 9.**Fig. 3.** <sup>119</sup>Sn CP-MAS centre band spectrum of triphenyltin chloride (**I**) at 7.05 T and room temperature; lower (experimental) upper (calculated). The arrows indicate lines due to coupling to <sup>37</sup>Cl.

bands folded in, i.e., the spectrum that would be obtained at infinite spinning speed.

### Chemical shifts

Chemical shift data for all Ar<sub>3</sub>SnCl complexes are given in Table 4. Solid-state <sup>119</sup>Sn MAS spectra of compounds (**II**)–(**VIII**) and (**XI**) show a single centre band consistent with one molecule in the asymmetric unit as found in the crystal structures of (**II**)–(**VI**) and (**VIII**). For (**IX**) and (**X**), as with (**I**), more complex spectra are observed that correspond to two isotropic shifts and thus, two chemically inequivalent sites. The intensities of the resonances for the two sites are equal, suggesting the presence of two different molecules in the asymmetric unit, which is consistent with the crystal structures of complexes (**I**) (19) and (**IX**) (25).

All isotropic solid-state <sup>119</sup>Sn chemical shifts, except that for (**VIII**), show a shift to higher frequency when compared with the corresponding solution data but still follow the same general trend. The differences, which range from 0.4 to 17 ppm, are moderate and reflect slight changes in geometry about tin rather than a change in coordination on going from solution to the solid state (37). The differences between solid and solution shifts ( $\delta_{\text{solid}} - \delta_{\text{solution}}$ ) are smallest for compounds containing meta-substituents, where the shifts' differences range from +2.4 to +3.5 ppm in (**III**) and (**VI**), while for (**VIII**) the difference is −2.3 ppm. Tris(mesityl)tin chloride (**XI**) also has a small ( $\delta_{\text{solid}} - \delta_{\text{solution}}$ ) difference but for most other compounds with ortho- or para-substituents, the ( $\delta_{\text{solid}} - \delta_{\text{solution}}$ ) differences are larger, the largest being 17 ppm for tris(*p*-anisyl)tin chloride (**VII**). The exception is (*p*-FC<sub>6</sub>H<sub>4</sub>)<sub>3</sub>SnCl for which the chemical shifts in solution and solid states are effectively the same.

The orientations of the chemical shift tensor components can be assigned by the known molecular symmetries of these tin complexes. Thus, the meta-substituted compounds (**III**), (**VI**), (**VII**) have axially symmetric chemical shift ten-



**Table 3.** NMR parameters for triphenyltin chloride (**I**) by perturbation and cubic-equation methods.

Parameter	Perturbation theory (eq. [1])	Cubic equation (ref. 22)
$^{35}\text{J}$ Site 1, site 2 (Hz)	265(2), 258(1)	273(1), 267(1)
$^{35}\text{d}$ Site 1, site 2 (Hz)	-76(2), -68(4)	-78(4), -71(2)
$^{35}\text{d}'$ Site1, site 2 (Hz)	440(10), 400(20)	450(20), 410(10)
$\Delta\text{J}$ Site1, site 2 (Hz)	-300(40), -180(70)	-330(70), -230(40)
$\delta_{\text{iso}}$ Site 1 (ppm)	-34.5	-34.4
$\delta_{\text{iso}}$ Site 2 (ppm)	-32.3	-32.4

**Note:** Standard deviations in the average values in parentheses. For  $\Delta\text{J}$ , the errors were propagated from the standard deviations in  $D$  and  $d$ .

**Table 4.** Chemical shift parameters.

$\text{X}_3\text{SnCl}$ ( $\text{X} =$ )	$\delta_{\text{iso}}$ Solution (ppm)	$\delta_{\text{iso}}$ Solid (ppm)	$\delta_{11}$ (ppm)	$\delta_{22}$ (ppm)	$\delta_{33}$ (ppm)	Span (ppm)
Phenyl ( <b>I</b> )	-44.9	-34.5 -32.3	0.292	-48 <sup>a</sup>	-72 <sup>a</sup>	92 <sup>a</sup>
<i>o</i> -Tolyl ( <b>II</b> )	-32.3	-24.5	42	-22	-94	135
<i>m</i> -Tolyl ( <b>III</b> ) <sup>a</sup>	-42.3	-38.9	-31	-31	-55	24
<i>p</i> -Tolyl ( <b>IV</b> )	-35.9	-23.9	50	-33	-88	138
<i>o</i> -Anisyl ( <b>V</b> )	-56.7	-42.7	37	-72	-93	129
<i>m</i> -Anisyl ( <b>VI</b> )	-44.0	-41.5	-31	-31	-62	31
<i>p</i> -Anisyl ( <b>VII</b> )	-27.4	-10.4	76	-41	-66	142
3,5-Xylyl ( <b>VIII</b> )	-39.7	-42.0	-27 -31 <sup>b</sup>	-34 -31 <sup>b</sup>	-65 -64 <sup>b</sup>	38 33 <sup>b</sup>
Mesityl ( <b>IX</b> )	-84.4	-82.6 -82.0	-74 <sup>a, b</sup>	-74 <sup>a, b</sup>	-98 <sup>a, b</sup>	24 <sup>a, b</sup>
<i>p</i> -Chloro ( <b>X</b> )	-39.3	-28.5 -26.8	34 <sup>a</sup>	-47 <sup>a</sup>	-70 <sup>a</sup>	104 <sup>a</sup>
<i>p</i> -Fluoro ( <b>XI</b> )	-39.6	-40.0	45	-62	-102	147

**Note:** Uncertainties:  $\pm 6$  ppm on span,  $\pm 2$  ppm on  $\delta_{11}$ ,  $\delta_{22}$ ,  $\delta_{33}$ .

<sup>a</sup>Average of two Sn sites.

<sup>b</sup>From the static spectrum.

sors with the more shielded component ( $\delta_{\parallel}$  ( $\delta_{33}$ )) assigned to the unique direction along the threefold rotation axis containing the Sn—Cl bond, leaving  $\delta_{\perp}$  ( $\delta_{11}$ ,  $\delta_{22}$ ) to the trigonally symmetric plane perpendicular to the Sn—Cl axis. The symmetry of the shift tensor is consistent with the axial molecular symmetry found in the solid state. Systems with ortho- or para-substituents have non-axially symmetric shift tensors, hence the assignment of  $\delta_{33}$  is less clear. Tris(mesityl)tin chloride, although it has both ortho- and para-substituents, has  $\delta_{11} = \delta_{22}$ , suggesting a quasi-trigonal molecular symmetry, which is consistent with the crystal structure of (mesityl)<sub>3</sub>SnCl (25).

The  $^{119}\text{Sn}$  CP-MAS full NMR spectra of tris(*o*-anisyl)tin chloride (**V**), tris(*m*-anisyl)tin chloride (**VI**), and tris(*p*-anisyl)tin chloride (**VII**) complexes are shown in Fig. 4. Similar spectra are also observed when the substituent is a methyl group. Extensive sideband manifolds are seen for (**II**), (**IV**), (**V**), (**VII**), (**X**), and (**XI**), indicating spans ( $\delta_{11} - \delta_{33}$ ) in the range of 129–147 ppm, consistent with these compounds not being axially symmetric. In contrast, the spectra of (**III**), (**VI**), and (**VIII**) have few sidebands due to their much smaller spans (24–38 ppm). It is noteworthy that, while there are large differences in the spans, the isotropic chemical shifts show much smaller differences, particularly for the ortho- and meta-anisyl complexes. This demonstrates

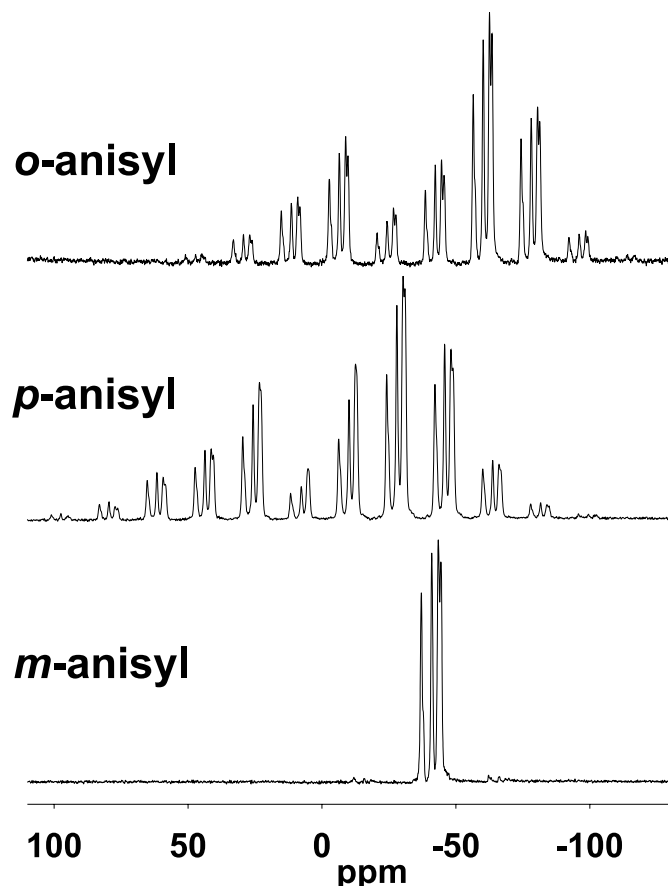
the utility of chemical shift tensor measurements in providing additional information unavailable from solution spectra. For the archetype  $\text{Ph}_3\text{SnCl}$ , the span of 92 ppm lies between the two ranges given above.

#### Spin-spin coupling ( $J$ ) and quadrupolar-dipolar ( $d$ ) constants

For complexes with a single chemical shift, there should be two overlapping asymmetric quartets, with intensity ratios of 3:1, arising from the  $^{119}\text{Sn}$ - $^{35}\text{Cl}$  and  $^{119}\text{Sn}$ - $^{37}\text{Cl}$  pairs, respectively. In typical spectra, between three and five line positions can be extracted, e.g., the spectrum of tris(*m*-tolyl)tin chloride (Fig. 5). In cases where there are two isotropic chemical shifts, these numbers are doubled. Experimental and simulated spectra for complexes (**V**), (**VI**), and (**VII**) are shown in Fig. 6; once again the experimental spectra represent the centre band with all sidebands folded in. Values of  $J(^{119}\text{Sn}$ - $^{35}\text{Cl})$  and  $d(^{119}\text{Sn}$ - $^{35}\text{Cl})$  are given in Table 5. In general, the compounds with meta-substituents, (**III**), (**VI**), and (**VIII**), have slightly larger coupling constants, which range from 263 to 279 Hz, while compounds with ortho- and para-substituents, (**V**)–(**XI**), range from 230 to 262 Hz. These values can be compared with the previously reported coupling constants for tribenzyltin chloride of 226 Hz and bis(acetylacetonato)tin chloride, of 276 Hz (17).



**Fig. 4.**  $^{119}\text{Sn}$  CP-MAS spectra of the isomers of trianisyltin chloride at 7.05 T and 298 K: *o*-anisyl (V) 2000 Hz spinning speed (top), *p*-anisyl (VIII) 2000 Hz spinning speed (middle), and *m*-anisyl(III) 4000 Hz spinning speed (bottom).



Tris(mesityl)tin chloride (IX) exhibits the largest  $^1J(^{119}\text{Sn}-^{35}\text{Cl})$  coupling constants, 332 and 328 Hz for the two sites. Assuming that the Fermi contact mechanism is the dominant contribution for tin-chlorine spin-spin coupling, then the *s*-character of the Sn—Cl bond in (IX) should be higher than in the other  $\text{Ar}_3\text{SnCl}$  complexes. Solution  $^1J(^{119}\text{Sn}-^{13}\text{C})$  data for complexes (I)–(XI) have been reported (8, 9); these range from 603 to 644 Hz except for (*o*-anisyl) $_3\text{SnCl}$  (V) with a value of 685 Hz. However, the mesityl system (IX) has a significantly smaller coupling of 596 Hz. A smaller  $^{119}\text{Sn}-^{13}\text{C}$  coupling is consistent with less *s*-character in the Sn—C bonds and thus, more *s*-character in the Sn—Cl bond.

The quadrupolar-dipolar splittings ( $d(^{119}\text{Sn}-^{35}\text{Cl})$ ) range from -72 to -83 Hz with no apparent trend. The significantly smaller value of -21 Hz for (IX) may be the result of a larger  $\Delta J$  value, which would reduce the effective dipolar splitting  $D'$  and hence the value of  $d$ . A larger  $\Delta J$  value is consistent with the larger  $J$  observed and seems reasonable, as it is unlikely that the nuclear quadrupole coupling constant for this complex is four times smaller than those of the other members of the series.

Calculation of the direct dipolar coupling constants ( $D$ ) requires the exact values of  $r(\text{Sn}-\text{Cl})$ , which are known for all systems studied here except for (VII), (X), and (XI). With  $D' = (D - \Delta J)/3$ , the determination of  $\Delta J$  requires that

**Fig. 5.**  $^{119}\text{Sn}$  CP-MAS centre band spectrum of tris(*m*-tolyl)tin chloride at 7.05 T and 298 K. The spectrum contains one tin chemical shift from which there are two overlapping quartets shown in the top and second rows. The sum of the two quartets gives the calculated spectrum (3rd row), which is similar to the experimental spectrum (bottom).

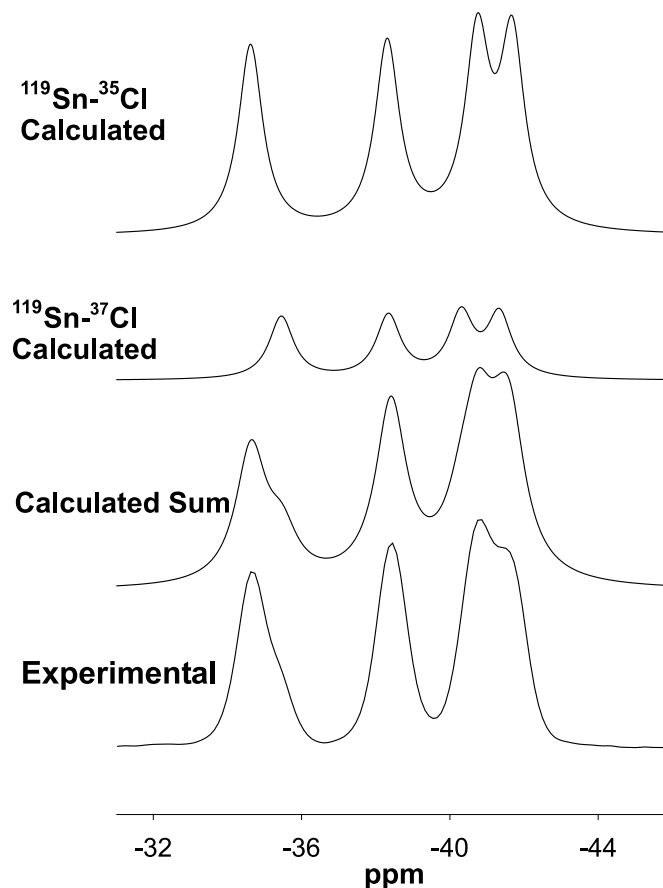
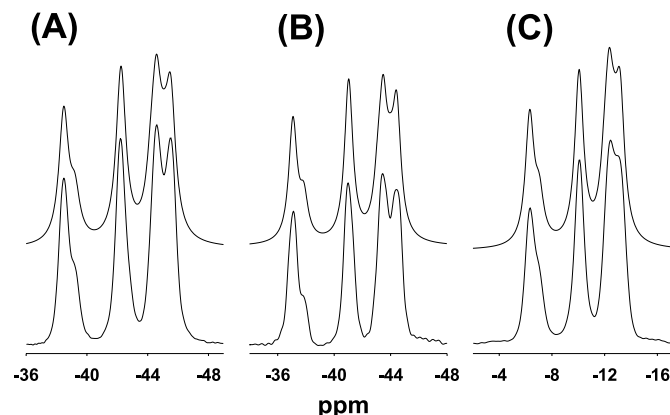


**Fig. 6.**  $^{119}\text{Sn}$  CP-MAS centre band spectra of the trianisyltin chloride isomers at 7.05 T and 298 K. (a) *o*-Anisyl (V), (b) *m*-anisyl (III), (c) *p*-anisyl (VIII) lower (experimental), upper (calculated).



$D'$  be obtained from  $d = 3\chi D'/10\nu_s$ . However, values of  $\chi(^{35}\text{Cl})$  and  $\chi(^{37}\text{Cl})$  data are available only for (I) and only in this case is a direct calculation of  $D'$ , and then  $\Delta J$ , possi-



**Table 5.** Quadrupolar-dipolar coupling ( $d$ ) and spin-spin coupling ( $J$ ) constants.

$R_3SnCl$ ( $R =$ )	$^{35}J$ (Hz) <sup>a</sup>	$^{35}d$ (Hz) <sup>a</sup>	$r_{Sn-Cl}$	$^{35}D^b$
Phenyl ( <b>I</b> )	262(4)	-78(2)	2.3538(14) <sup>c</sup>	-338(3)
	254(1)	-73(5)	2.3557(14)	-337(3)
<i>o</i> -Tolyl ( <b>II</b> )	230(2)	-87(4)	2.3760(10)	-328(2)
<i>m</i> -Tolyl ( <b>III</b> )	263(9)	-79(13)	2.379(1) <sup>d</sup>	-327(2)
<i>p</i> -Tolyl ( <b>IV</b> )	257(6)	-81(12)	2.3729(6)	-330(1)
<i>o</i> -Anisyl ( <b>V</b> )	262(1)	-79(2)	2.371(5) <sup>e</sup>	-330(11)
<i>m</i> -Anisyl ( <b>VI</b> ) <sup>f</sup>	274	-83	2.3451(14) <sup>g</sup>	-341
<i>p</i> -Anisyl ( <b>VII</b> )	256(1)	-82(6)	NA	NA
3,5-Xylyl ( <b>VIII</b> )	275(2)	-78(10)	2.3575(2) <sup>d</sup>	-336(1)
Mesityl ( <b>IX</b> ) <sup>f</sup>	332	-21	2.3890(13) <sup>h</sup>	-323(3)
	328	-21	2.3890(14) <sup>h</sup>	-323(3)
<i>p</i> -Chloro ( <b>X</b> )	248(1)	-75(3)	NA	NA
	247(1)	-72(5)		
<i>p</i> -Fluoro ( <b>XI</b> )	253(4)	-81(8)	NA	NA

**Note:** Standard deviations in the average values obtained from the centre band and sidebands given in parentheses.

<sup>a</sup>Determined from the ( $^{119}Sn$ - $^{35}Cl$ ) line positions.

<sup>b</sup>Calculated from the Sn—Cl bond length ( $\gamma(^{119}Sn)$  and  $\gamma(^{35}Cl)$ ).

<sup>c</sup>Reference 19.

<sup>d</sup>Reference 9.

<sup>e</sup>Reference 26.

<sup>f</sup>Centre band only.

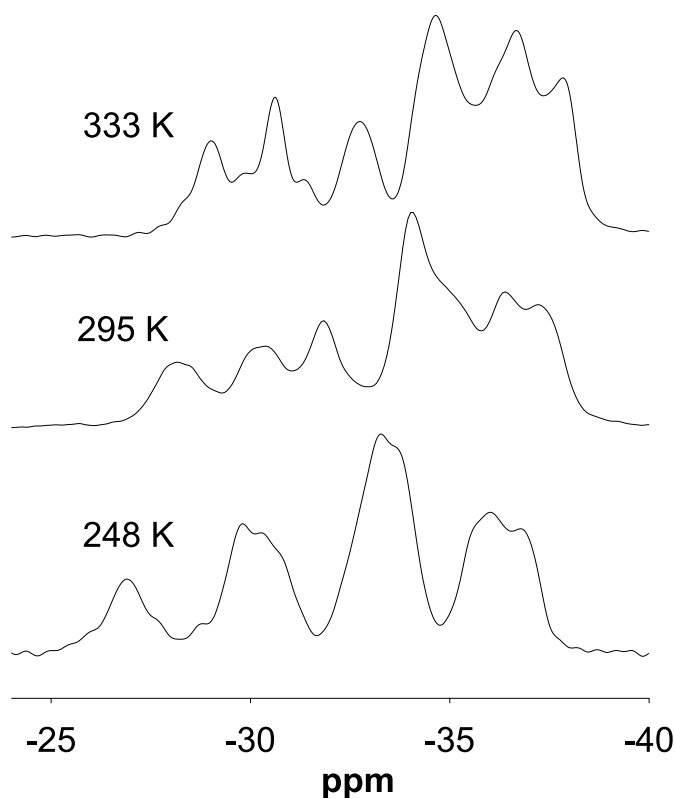
<sup>g</sup>Reference 24.

<sup>h</sup>Reference 25.

ble. Harris and co-workers (38) have shown that the effective dipolar coupling constant ( $D'$ ) can be obtained from an analysis of the chemical shift anisotropy for each of the spin states of the quadrupolar nucleus, but this method gave results with large errors, presumably because of incorrect intensities resulting from the overlap of the ( $^{119}Sn$ - $^{35}Cl$ ) and ( $^{119}Sn$ - $^{37}Cl$ ) lines.

### The effect of temperature on the spectrum of triphenyltin chloride (**I**)

An earlier solid-state proton magnetic resonance second moment study on (**I**) provided evidence for motion in the solid state at about 300 K (23). This motion was considered to be a  $C_3$  reorientation of the whole molecule along the Sn—Cl bond axis. To investigate further the effect of this motion on the spectrum of triphenyltin chloride, the solid-state  $^{119}Sn$  CP-MAS spectra of (**I**) were obtained at three temperatures (Fig. 7). The low-temperature spectrum at 248 K was taken to investigate the rigid phase, where no change in the second moment of the proton resonance occurs; that at room temperature represents the situation where motion has just begun, while at high temperature (333 K) the second moment transition is complete. The NMR parameters are given in Table 6. The isotropic chemical shifts move to lower frequency (more shielded) with increasing temperature for both tin sites and the difference between the two tin sites decreases with increased temperature, suggesting an averaging of the two shifts at higher temperatures. After heating, the room temperature spectrum was acquired again and was identical to the unheated sample except that the line widths had decreased. This suggests that an annealing process occurs. The quadrupolar-dipolar splitting is expected to change with temperature as the nuclear quadrupolar coupling con-

**Fig. 7.**  $^{119}Sn$  CP-MAS centre band spectra of  $Ph_3SnCl$  (**I**) at 7.05 T and different temperatures.

stant is temperature dependent, however, this temperature dependence is a very small effect in comparison to the large changes in isotropic chemical shift.



**Table 6.** NMR parameters for  $\text{Ph}_3\text{SnCl}$  at various temperatures.

Parameter	248 K	295 K	333 K
$J(^{119}\text{Sn}-^{35}\text{Cl})$ Site 1, site 2 (Hz)	256(4), 261(4)	254(4), 262(4)	265(4), 266(4)
$d(^{119}\text{Sn}-^{35}\text{Cl})$ Site 1, site 2 (Hz)	-79(4), -76(4)	-73(2), -78(2)	-86(4), -76(4)
$\delta_{\text{iso}}$ Site 1 (ppm)	-33.99	-34.53	-34.94
$\delta_{\text{iso}}$ Site 2 (ppm)	-31.01	-32.30	-33.22
$\delta_{\text{iso}}$ Average (ppm)	-32.50	-33.41	-34.08
$ \delta_{\text{iso}} \text{ Site 1} - \delta_{\text{iso}} \text{ site 2} $	2.98	2.23	1.72
Span $\delta_{11}-\delta_{33}^a$	82	92	80
$\delta_{11}$ (ppm) <sup>b</sup>	13	19	11
$\delta_{22}$ (ppm) <sup>b</sup>	-43	-48	-45
$\delta_{33}$ (ppm) <sup>b</sup>	-68	-72	-69

<sup>a</sup>Average of the two sites  $\pm 6$  ppm (systematic error).<sup>b</sup>Error is  $\pm 2$  ppm.

## Acknowledgements

This work was supported by grants from the Natural Sciences and Engineering Research Council of Canada (NSERC) and Fonds pour la formation de chercheurs et l'aide à la recherche (Québec) (FCAR). We thank Dr. K. Eichele and Dr. R.E. Wasylshen for the HBA version 1.4 program.

## References

- C.J. Evans and S. Karpel. *J. Organomet. Chem. Libr.* **16**, 135 (1985), and refs. therein.
- I. Wharf, H. Lamparski, and R. Reeleder. *Appl. Organomet. Chem.* **11**, 969 (1997).
- I. Wharf. *Appl. Organomet. Chem.* **14**, 34 (2000).
- I. Wharf. *Can. J. Spectrosc.* **31**, 27 (1986).
- I. Wharf, A. Bastone, and E.J. Bures. *Can. J. Appl. Spectrosc.* **41**, 122 (1996).
- D.W. Allen, J.S. Brookes, and R. Formstone. *J. Organomet. Chem.* **172**, 299 (1979).
- B. King, H. Eckert, D.Z. Denney, and R.H. Herber. *Inorg. Chim. Acta*, **122**, 45 (1986).
- I. Wharf. *Inorg. Chim. Acta*, **159**, 41 (1989).
- I. Wharf and M.G. Simard. *J. Organomet. Chem.* **532**, 1 (1997).
- R.K. Harris and A.C. Olivieri. *Prog. Nucl. Magn. Reson. Spectrosc.* **24**, 435 (1992).
- A.S. Batsanov, S.M. Cornet, L.A. Crowe, K.B. Dillon, R.K. Harris, P. Hazendonk, and M.D. Roden. *Eur. J. Inorg. Chem.* **7**, 1729 (2001).
- P. Pykko. *Z. Naturforsch.* **47a**, 189 (1992).
- C.J. Jameson. *Multinuclear NMR spectroscopy*. Edited by J. Mason. Plenum, New York. p. 625. 1987.
- A.C. Olivieri. *J. Magn. Reson.* **81**, 201 (1989).
- R.A. Komorski, R.G. Parker, and A.M. Mazany. *J. Magn. Reson.* **73**, 389 (1987).
- R.K. Harris. *J. Magn. Reson.* **78**, 389 (1988).
- R.K. Harris, A. Sebal, D. Furlani, and G. Tagliavini. *Organometallics*, **7**, 388 (1988).
- D.C. Apperley, B. Haiping, and R.K. Harris. *Mol. Phys.* **68**, 1277 (1989).
- J.S. Tse, F.L. Lee, and E.J. Gabe. *Acta Crystallogr. Sect. C*, **C42**, 1876 (1986).
- T.S. Srivastava. *J. Organomet. Chem.* **10**, 373 (1967).
- P.J. Green and J.D. Graybeal. *J. Am. Chem. Soc.* **87**, 4305 (1967).
- S. Alarcón, A.C. Olivieri, and R.K. Harris. *Solid State Nucl. Magn. Reson.* **2**, 325 (1993).
- B.A. Dunell and S.E. Ulrich. *J. Chem. Soc., Faraday Trans. 2*, **69**, 377 (1973).
- I. Wharf and A.-M. Lebuis. *Acta Crystallogr. Sect. C*, **C52**, 3025 (1996).
- J. Geller, I. Wharf, F. Bélanger-Gariépy, A.-M. Lebuis, I.S. Butler, and D.F.R. Gilson. *Acta Crystallogr., Sect. C*, **C58**, m466 (2002).
- I. Wharf, A.-M. Lebuis, and G.A. Roper. *Inorg. Chim. Acta*, **294**, 224 (1999).
- H. Bai, R.K. Harris, and H. Reuter. *J. Organomet. Chem.* **408**, 167 (1991).
- A. Bondi. *J. Phys. Chem.* **68**, 441 (1964).
- J. Herzfeld and A.E. Berger. *J. Chem. Phys.* **73**, 6021 (1980).
- K. Eichele and R. E. Wasylshen. HBA version 1.44 [computer program]. Dalhousie University, Halifax, Nova Scotia. 2001.
- XPREP, Release 5.10 [computer program]. X-ray data preparation and reciprocal space exploration program. Bruker AXS Inc., Madison, Wis. 53719-1173. 1997.
- SADABS [computer program]. Bruker area detector absorption corrections. Bruker AXS Inc., Madison, Wis. 1996.
- G.M. Sheldrick. SHELXS-97 [computer program]. Program for the solution of crystal structures. University of Göttingen, Göttingen, Germany. 1997.
- G.M. Sheldrick. SHELXL-96 [computer program]. Program for the refinement of crystal structures. University of Göttingen, Göttingen, Germany. 1997.
- A.J.C. Wilson (Editor). *International tables for crystallography*. Vol. C4. Kluwer Academic Publishers, Boston. Tables 4.2.6.8 and 6.1.1. 1992.
- I. Wharf and M.G. Simard. *Inorg. Chim. Acta*, **282**, 30 (1998).
- F. Huber, A. Saxena, R.K. Harris, and A. Sebal. *J. Organomet. Chem.* **368**, 31 (1989).
- R. Gobetto, R.K. Harris, and D.C. Apperley. *J. Magn. Reson.* **96**, 119 (1992).



# The mechanism of protonolysis of phenylplatinum(II) bonds in complexes with phenyl trans to nitrogen or carbon donors<sup>1</sup>

Christopher M. Ong, Michael C. Jennings, and Richard J. Puddephatt

**Abstract:** Addition of acids of the form HX (X = Cl, BF<sub>4</sub>, CF<sub>3</sub>SO<sub>3</sub>, CF<sub>3</sub>CO<sub>2</sub>) to complexes [PtPh<sub>2</sub>(NN)] (NN = bu<sub>2</sub>bpy = 4,4'-di-*tert*-butyl-2,2'-bipyridine) and [PtPh(NCN)] (NCN = 2,6-C<sub>6</sub>H<sub>3</sub>(CH<sub>2</sub>NMe<sub>2</sub>)<sub>2</sub>) at -78 °C gave the corresponding phenyl(hydrido)platinum(IV) complexes [PtX(H)Ph<sub>2</sub>(NN)] and [PtX(H)Ph(NCN)], which decomposed by reductive elimination of benzene at about -20 °C to give the platinum(II) complexes [PtXPh(NN)] and [PtX(NCN)]. Further addition of HCl to [PtClPh(NN)] at low temperature gave [PtHCl<sub>2</sub>Ph(NN)], which decomposed above -10 °C, to give benzene and [PtCl<sub>2</sub>(NN)]. The reaction of DBF<sub>4</sub> in the presence of excess CD<sub>3</sub>OD with [PtPh<sub>2</sub>(NN)] led to formation of C<sub>6</sub>H<sub>5</sub>D and C<sub>6</sub>H<sub>4</sub>D<sub>2</sub> but with [PtPh(NCN)] no multiple deuterium incorporation was observed in the product benzene. The mechanisms of these reactions are discussed.

**Key words:** platinum, phenyl, benzene, protonolysis.

**Résumé :** L'addition, à -78 °C, d'acides de la forme HX (X = Cl, BF<sub>4</sub>, CF<sub>3</sub>SO<sub>3</sub>, CF<sub>3</sub>CO<sub>2</sub>) à des complexes [PtPh<sub>2</sub>(NN)] (NN = bu<sub>2</sub>bpy = 4,4'-di-*tert*-butyl-2,2'-bipyridine) et [PtPh(NCN)] (NCN = 2,6-C<sub>6</sub>H<sub>3</sub>(CH<sub>2</sub>NMe<sub>2</sub>)<sub>2</sub>) conduit aux complexes correspondants phényl(hydrido)platine(IV) [PtX(H)Ph<sub>2</sub>(NN)] et [PtX(H)Ph(NCN)] qui se décomposent par élimination réductrice du benzène, à environ -20 °C, pour conduire aux complexes de platine(II) [PtXPh(NN)] et [PtX(NCN)]. L'addition subséquente de HCl au complexe [PtClPh(NN)], à basse température, conduit au [PtHCl<sub>2</sub>Ph(NN)] qui se décompose au-dessus de -10 °C pour donner du benzène et du [PtCl<sub>2</sub>(NN)]. La réaction du DBF<sub>4</sub> avec du [PtPh<sub>2</sub>(NN)], en présence d'un excès de CD<sub>3</sub>OD, conduit à la formation de C<sub>6</sub>H<sub>5</sub>D et de C<sub>6</sub>H<sub>4</sub>D<sub>2</sub>; toutefois, avec le [PtPh(NCN)], on n'observe aucune incorporation multiple de deutérium dans le benzène obtenu comme produit. On discute des mécanismes de ces réactions.

**Mots clés :** platine, phényle, benzène, protonolyse.

[Traduit par la Rédaction]

## Introduction

The activation of alkanes or arenes by platinum(II) complexes is thought to involve the intermediacy of alkyl(hydrido)platinum(IV) or aryl(hydrido)platinum(IV) complexes, and so there has been much interest in such complexes (1–13). A useful synthetic route to platinum(IV) complexes [PtX(H)R<sub>2</sub>(NN)] (NN = bidentate nitrogen-donor ligand, X = halide, R = alkyl or aryl) is by addition of acid HX to a platinum(II) complex [PtR<sub>2</sub>(NN)] and the decomposition of these platinum(IV) complexes by reductive elimination of RH to give [PtXR(NN)], which leads to overall protonolysis of the alkyl–platinum or aryl–platinum bond, can then be studied (3–5). Hydrido(alkyl)-, hydrido(aryl)-, and hydrido(silyl)platinum complexes are proposed in several other important catalytic reactions, including the hydrosilation reactions catalyzed by platinum complexes (14). Most of the

recent studies of protonolysis of platinum–carbon bonds have involved complexes [PtR<sub>2</sub>(NN)], in which the alkyl or aryl groups are trans to nitrogen donor ligands (3–5), and it was of interest to compare complexes with mutually trans Pt–C bonded groups. This paper reports a study of the reactions of acids with the complexes *cis*-[PtPh<sub>2</sub>(NN)] (NN = bu<sub>2</sub>bpy = 4,4'-di-*tert*-butyl-2,2'-bipyridine, **1**) and [PtPh(NCN)] (NCN = 2,6-C<sub>6</sub>H<sub>3</sub>(CH<sub>2</sub>NMe<sub>2</sub>)<sub>2</sub>, **2**) in which the NCN pincer ligand forces the two aryl groups to be mutually trans (15) (Chart 1).

## Results

### The phenylplatinum complexes **1** and **2**

Complex **1** was prepared by reaction of the ligand bu<sub>2</sub>bpy with the precursor [PtPh<sub>2</sub>(μ-SMe<sub>2</sub>)<sub>n</sub>], *n* = 2 or 3 (16–18), in

Received 9 February 2003. Published on the NRC Research Press Web site at <http://canjchem.nrc.ca> on 9 September 2003.

This article is dedicated to Dr. John Harrod for his distinguished contributions to organometallic chemistry and its applications in catalysis and materials science.

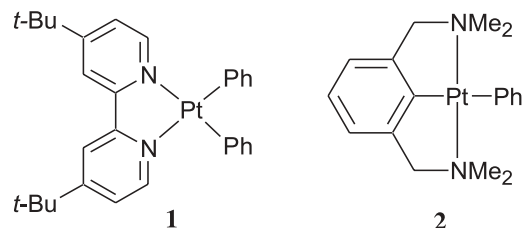
C.M. Ong, M.C. Jennings, and R.J. Puddephatt.<sup>2</sup> Department of Chemistry, University of Western Ontario, London, ON N6A 5B7, Canada.

<sup>1</sup>This article is part of a Special Issue dedicated to Professor John Harrod.

<sup>2</sup>Corresponding author (e-mail: [pudd@uwo.ca](mailto:pudd@uwo.ca)).



Chart 1.



diethyl ether solution, while complex **2** was prepared by a modified literature method (15).

The structures of complexes **1** and **2** are shown in Figs. 1 and 2, with selected bond distances and angles listed in Tables 1 and 2. Each complex contains a roughly square-planar platinum(II) center, but with *cis*- and *trans*-PtC<sub>2</sub>N<sub>2</sub> coordination, respectively, and in each case the phenyl group lies roughly orthogonal to the square plane (79° in **1**, in which the two phenyl groups are crystallographically equivalent; 84° in **2**, Figs. 1 and 2). This conformation allows platinum–phenyl *dπ*–*pπ* bonding and minimizes steric effects. The Pt—C(phenyl) bond distance is shorter in **1** (2.023(2) Å, *trans* to N) than in **2** (2.111(6) Å, *trans* to C), as expected since nitrogen has the lower *trans*-influence. However, the distance Pt(1)—C(1) = 1.956(6) Å in **2** is shorter than either of these Pt—C(phenyl) distances, as a result of the chelate effect. Other bond distances and angles are comparable to those reported for related complexes [PtR<sub>2</sub>(bu<sub>2</sub>bpy)] (5, 16) or [PtX{2,6-C<sub>6</sub>H<sub>3</sub>(CH<sub>2</sub>NMe<sub>2</sub>)<sub>2</sub>}] (15).

### Reactions with acids

Complex **1** reacted with 1 equiv. of acid HX (X = Cl, CF<sub>3</sub>CO<sub>2</sub>, CF<sub>3</sub>SO<sub>3</sub>, BF<sub>4</sub>) at room temperature to give benzene and the corresponding product [PtXPh(bu<sub>2</sub>bpy)] (**3a**, X = Cl; **3b**, X = CF<sub>3</sub>CO<sub>2</sub>; **3c**, X = CF<sub>3</sub>SO<sub>3</sub>; **3d**, X = BF<sub>4</sub>) (Scheme 1). The complexes were characterized by elemental analysis and by their <sup>1</sup>H NMR spectra, which showed the presence of nonequivalent *t*-BuC<sub>4</sub>H<sub>3</sub>N units and only a single phenylplatinum group.

The reaction of complex **1** in CDCl<sub>3</sub> solution with HCl at –78 °C gave an intermediate hydridoplatinum(IV) complex **4a** (Scheme 1) that was identified by its <sup>1</sup>H NMR spectrum. The hydride resonance was observed at δ = –20.15 with <sup>1</sup>J(PtH) = 1613 Hz (Table 3). The *trans* oxidative addition of HCl was shown by the observation of equivalent *t*-BuC<sub>4</sub>H<sub>3</sub>N and phenyl groups. Complex **4a** decomposed at –20 °C by reductive elimination of benzene to yield the product [PtClPh(bu<sub>2</sub>bpy)] (**3a**) and no other intermediates were observed. The similar reaction of **1** in CDCl<sub>3</sub> with the other acids failed to give detectable hydride intermediates, but the reaction with HBF<sub>4</sub> or CF<sub>3</sub>SO<sub>3</sub>H in CDCl<sub>3</sub>–CD<sub>3</sub>CN gave a hydride intermediate (**5**) characterized by δ(PtH) = –21.84, <sup>1</sup>J(PtH) = 1619 Hz. This is presumed to be a cationic acetonitrile complex, since the spectral properties were the same in each case and acetonitrile is a stronger ligand than either triflate or tetrafluoroborate. Complex **5** decomposed on warming the solution to –20 °C to give complex **3d**.

The complex [PtClPh(bu<sub>2</sub>bpy)] (**3a**) reacted with HCl at room temperature to give benzene and [PtCl<sub>2</sub>(bu<sub>2</sub>bpy)] (**5**). When the reaction was carried out at –78 °C, the intermediate hydridoplatinum(IV) complex [PtHCl<sub>2</sub>Ph(bu<sub>2</sub>bpy)] (**6**)

**Fig. 1.** A view of the structure of complex **1**. 30% Thermal ellipsoids are shown and hydrogen atoms have been omitted for clarity.

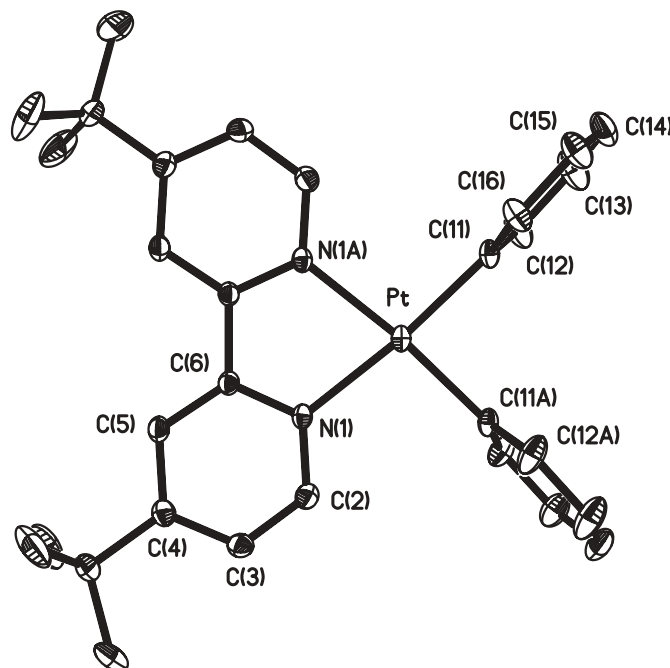


**Fig. 2.** A view of the structure of complex **2**. 30% Thermal ellipsoids are shown and hydrogen atoms have been omitted for clarity.

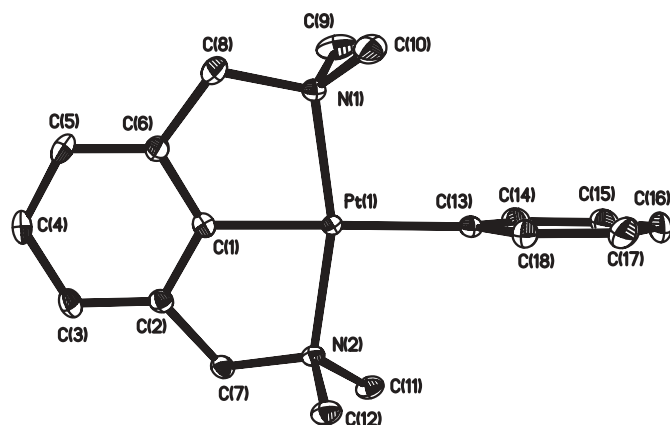


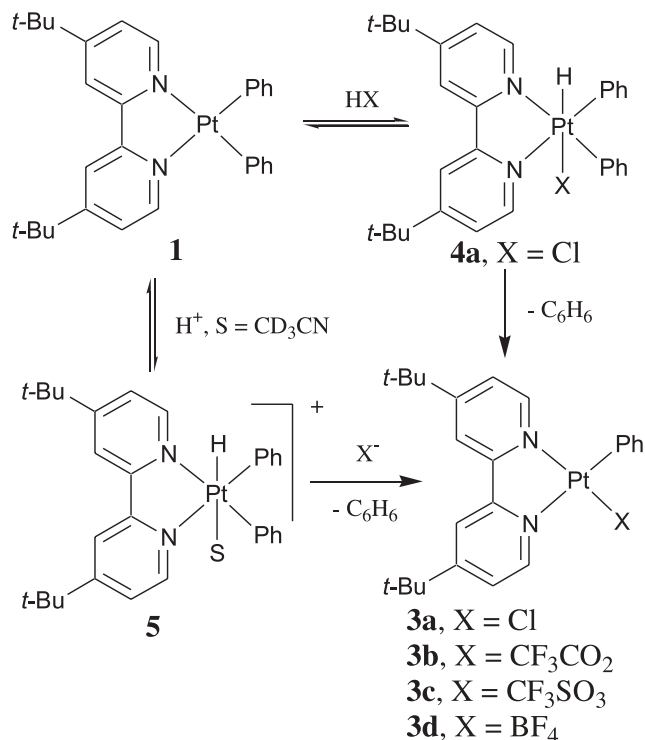
**Table 1.** Selected bond lengths (Å) and angles (°) for complex **1**.

Bond lengths (Å)	
Pt(1)—C(11)	2.023(2)
Pt(1)—N(1)	2.097(3)
Bond angles (°)	
N(1)–Pt(1)–N(1A)	77.1(2)
N(1A)–Pt(1)–C(11)	97.4(1)
N(1)–Pt(1)–C(11)	174.5(1)
C(11A)–Pt(1)–C(11)	88.2(2)



**Table 2.** Selected bond lengths (Å) and angles (°) for complex **2**.

Bond lengths (Å)	
Pt(1)—C(1)	1.956(6)
Pt(1)—N(1)	2.079(5)
Pt(1)—N(2)	2.079(5)
Pt(1)—C(13)	2.111(6)
Bond angles (°)	
N(1)—Pt(1)—N(2)	164.1(2)
N(1)—Pt(1)—C(13)	97.8(2)
N(2)—Pt(1)—C(13)	97.9(2)
N(1)—Pt(1)—C(1)	82.3(2)
N(2)—Pt(1)—C(1)	81.9(2)
C(1)—Pt(1)—C(13)	177.2(2)

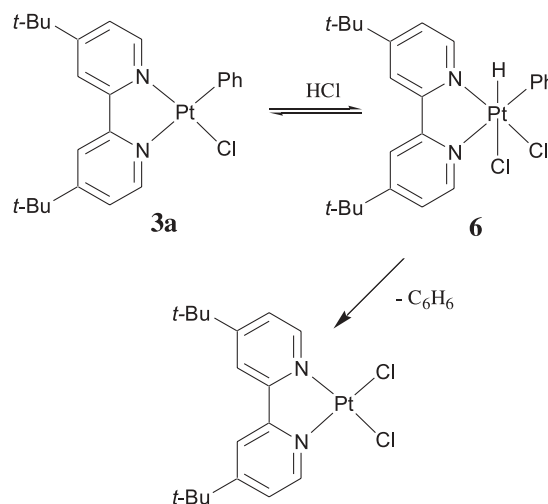
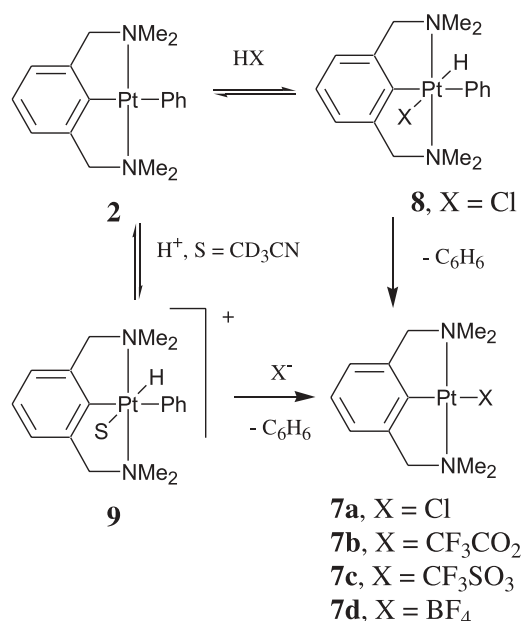
**Scheme 1.**

was detected. The <sup>1</sup>H NMR spectrum contained a hydride resonance at δ = −25.94 with <sup>1</sup>J(PtH) = 1540 Hz, in the range expected for a hydride trans to chloride (Table 3) (**5**). The aromatic region of the spectrum contained six resonances for the bu<sub>2</sub>bpy ligand and three for the phenyl group, consistent with the proposed structure that arises from trans oxidative addition. The hydride complex decomposed at −20 °C to give benzene and [PtCl<sub>2</sub>(bu<sub>2</sub>bpy)] (Scheme 2).

Reaction of [PtPh{2,6-C<sub>6</sub>H<sub>3</sub>(CH<sub>2</sub>NMe<sub>2</sub>)<sub>2</sub>}] (**2**) with acids HX gave benzene and the corresponding complexes [PtX{2,6-C<sub>6</sub>H<sub>3</sub>(CH<sub>2</sub>NMe<sub>2</sub>)<sub>2</sub>}] (**7a**, X = Cl; **7b**, X = CF<sub>3</sub>CO<sub>2</sub>; **7c**, X = CF<sub>3</sub>SO<sub>3</sub>; **7d**, X = BF<sub>4</sub>) (Scheme 3) (15). Reaction of complex **2** with HCl in CDCl<sub>3</sub> at −78 °C gave the hydridoplatinum(IV) complex [PtHClPh{2,6-C<sub>6</sub>H<sub>3</sub>(CH<sub>2</sub>NMe<sub>2</sub>)<sub>2</sub>}] (**8**) which was characterized by a hydride resonance at δ = −21.36 with <sup>1</sup>J(PtH) = 1622 Hz. The hydride resonance de-

**Table 3.** <sup>1</sup>H NMR data for hydridoplatinum(IV) complexes.

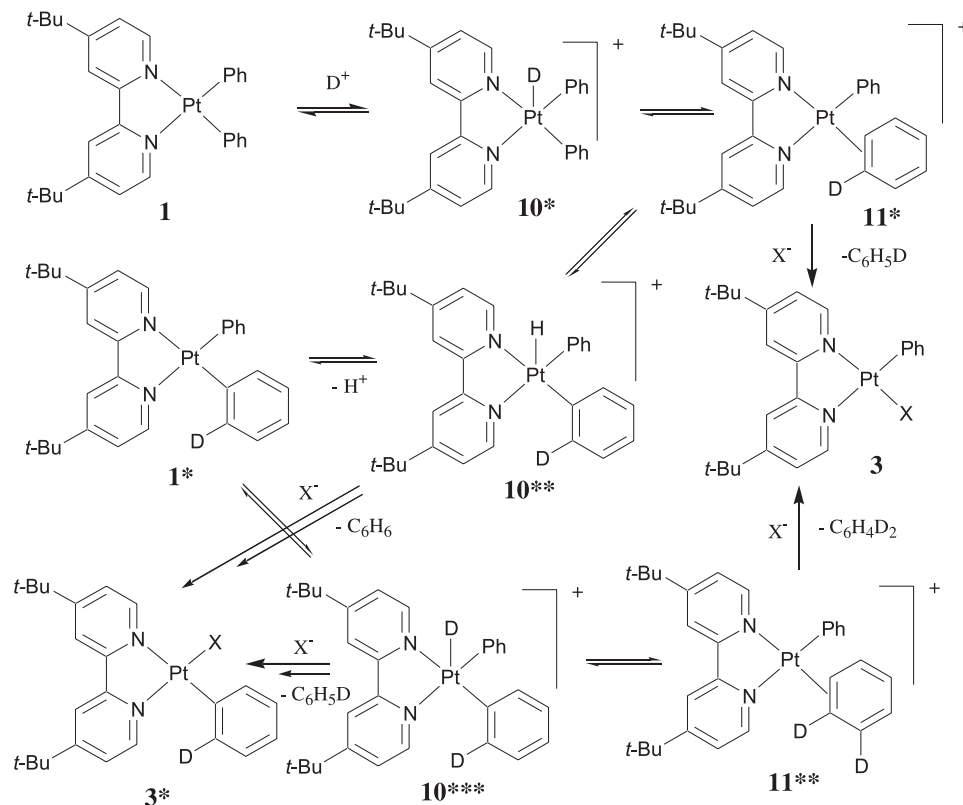
Complex	δ (PtH)	<sup>1</sup> J(PtH) (Hz)
[PtHClPh <sub>2</sub> (bu <sub>2</sub> bpy)] ( <b>3a</b> )	−20.15	1613
[PtHPh <sub>2</sub> (MeCN)(bu <sub>2</sub> bpy)] <sup>+</sup> ( <b>5</b> )	−21.84	1619
[PtHCl <sub>2</sub> Ph(bu <sub>2</sub> bpy)] ( <b>6</b> )	−25.94	1540
[PtHClPh{2,6-C <sub>6</sub> H <sub>3</sub> (CH <sub>2</sub> NMe <sub>2</sub> ) <sub>2</sub> }] ( <b>8</b> )	−21.36	1622
[PtHPh(MeCN){2,6-C <sub>6</sub> H <sub>3</sub> (CH <sub>2</sub> NMe <sub>2</sub> ) <sub>2</sub> }] <sup>+</sup> ( <b>9</b> )	−20.47	1644

**Scheme 2.****Scheme 3.**

cayed at −20 °C as reductive elimination of benzene occurred to give **7a**. Similarly, reaction of **2** in CDCl<sub>3</sub>–CD<sub>3</sub>CN at −78 °C with triflic acid or tetrafluoroboric acid gave [PtHPh(NCCD<sub>3</sub>){2,6-C<sub>6</sub>H<sub>3</sub>(CH<sub>2</sub>NMe<sub>2</sub>)<sub>2</sub>}]<sup>+</sup> (**9**) identified by its <sup>1</sup>H NMR spectrum (δ(PtH) = −20.47, <sup>1</sup>J(PtH) = 1644 Hz) and it decomposed at −20 °C to give benzene and complex **7c** or **7d**. The complexes **7** were inert to protonolysis under



Scheme 4.



mild conditions, and there was no evidence for the addition of protons to the aryl group, though several electrophiles are known to add easily to the ipso carbon atom (15).

### Studies of H-D exchange

The reaction of **1** and **2** with  $DBF_4$  in  $CDCl_3$ - $CD_3OD$  was studied to observe H-D exchange and hence, to investigate reversibility of the protonation and C-H reductive elimination steps. In each case, the benzene was analyzed by GC-MS. In the reaction with **1**, the ratio of  $C_6H_6$ : $C_6H_5D$ : $C_6H_4D_2$  was 0.1:1.0:0.2, indicating significant formation of  $C_6H_4D_2$ , but in the reaction of **2** the ratio was 0.1:1.0:0.01, indicating very little if any deuterium enrichment beyond  $C_6H_5D$ . Integration of the phenylplatinum resonances in the product **3a** from reaction with complex **1** indicated that there was about 10% D-incorporation, distributed equally in the ortho, meta, and para positions. In the reaction with **2** there was no detectable D-incorporation in the  $C_6H_3$  group of the NCN ligand. It has been shown previously that electrophilic attack at the ipso carbon atom of the  $C_6H_3$  group of the NCN ligand is easy, but of course the chelate ligand prevents scrambling if reversible addition of D occurs at this point and no direct evidence of such reactivity was found (15).

### Discussion

The intermediacy of hydridoplatinum(IV) complexes in the protonolysis of metal-carbon bonds in electron-rich alkyl or aryl complexes of platinum(II) or in C-H activation by electrophilic platinum complexes, is now accepted as the general rule, though other mechanisms are possible (1-12).

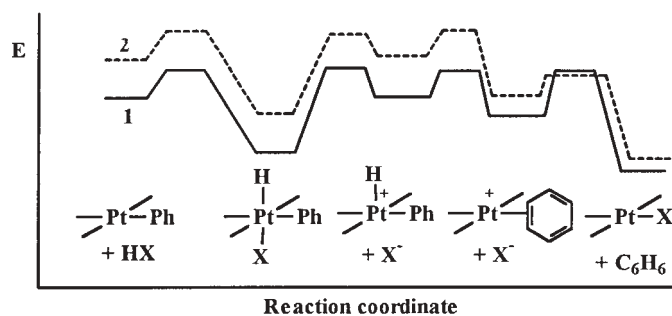
It is easier to detect these hydridoplatinum(IV) complex intermediates when they are generated by protonation of alkyl or aryl platinum(II) complexes and many details of their structures and energetics have been determined over recent years (1-10). Strong dependence on the nature of the hydrocarbyl group, the supporting ligands, the acid used, and the solvent medium has been demonstrated (3-5). The phenylplatinum complexes **1** and **2** are constrained to have the phenyl group(s) trans to nitrogen or carbon, respectively, and so a study of the dependence of protonolysis mechanism on stereochemistry is possible.

The chemistry shown in Schemes 1-3 illustrates that the mechanism of protonolysis of the phenylplatinum groups in **1**, **2**, and **3a** is similar in each case. Intermediate hydridoplatinum(IV) complexes are detected by low-temperature  $^1H$  NMR in all cases. These intermediates are formed essentially quantitatively at  $-78^\circ C$  and they survive for several hours at this temperature, but they decompose on warming to  $-10$  to  $-20^\circ C$  by reductive elimination of benzene. No other intermediates were detectable during reactions that were monitored by NMR, and there were no very dramatic differences in reactivity.

The chief difference between **1** and **2** was observed when the deuterolysis of the phenylplatinum groups was carried out in  $CDCl_3$ - $CD_3OD$  solvent medium, in which there is a very large excess of exchangeable deuterium. The cleavage of the phenylplatinum groups from **1** or **2** under these conditions gave mostly  $C_6H_5D$ , as expected for simple cleavage. However, complex **1** also gave  $C_6H_4D_2$  in significant yield and moderate deuterium enrichment in the residual phenylplatinum group of the product **3a**. Free benzene did



**Fig. 3.** Proposed reaction coordinate diagram for the protonolysis of a phenyl group from either complex **1** or **2** in  $\text{CDCl}_3\text{-CD}_3\text{OD}$ .



not undergo H-D exchange under the experimental conditions, so the deuterium enrichment occurred during cleavage of the phenylplatinum group to give **3**. A proposed sequence of reactions leading to H-D exchange is shown in Scheme 4. The five-coordinate complex **10\*** is proposed as a key intermediate based on earlier work (4, 5); it can be formed by addition of  $\text{D}^+$  to complex **1** or by chloride dissociation from the resting state complex  $[\text{PtDClPh}_2(\text{bu}_2\text{bpy})]$  (**4a\***), which is not shown in Scheme 4. Reductive elimination with C—D bond formation then leads naturally to the benzene- $d_1$  complex **11\***, for which there are now several known precedents (4, 7, 10). Deuterium enrichment in the phenylplatinum groups requires that this reductive elimination reaction be reversible to form a hydrido(deuteriophenyl)platinum(IV) cation **10\*\*** (Scheme 4). The complex **11\*** is expected to be fluxional and to undergo rapid edge-to-edge migration of the benzene group, and so the position of the deuterium label will naturally scramble among all possible positions in **11\*** and **10\*\*** (though only one is shown in Scheme 4). Formation of  $\text{C}_6\text{H}_4\text{D}_2$  requires further deuterium incorporation, likely by deprotonation of **10\*\*** to give **1\*** followed by addition of  $\text{D}^+$  to give **10\*\*\*** and C-H reductive elimination to give **11\*\***. Dissociation or displacement of the coordinated benzene from **11** is irreversible, so free benzene cannot coordinate and hence, cannot undergo H-D exchange. In principle, the reactions of Scheme 4 can continue and give complete H-D exchange but only modest enrichment is observed. Hence, the benzene dissociation or displacement step from **11** to give **3** is competitive with the C-H oxidative addition and PtH—PtD exchange steps. Since the addition of  $\text{D}^+$  to complex **2** gives no significant amount of  $\text{C}_6\text{H}_4\text{D}_2$ , in this case the C-H reductive elimination is probably irreversible.

The difference between the chemistry of complexes **1** and **2** can be understood in terms of the qualitative reaction coordinate diagram shown in Fig. 3. There is a destabilizing effect of two strong donor ligands (antisymbiosis) in organo-platinum chemistry, and so the trans-diaryl arrangement in **2** is less stable than the cis-diaryl arrangement in **1**. This relative stability is maintained through the various intermediates through to the proposed benzene complex, but is most pronounced in the trans-diaryl complexes. The six-coordinate hydridoplatinum(IV) complex is the most stable of the intermediates and so the only one that is directly observable in either case. The difference comes at the benzene loss step. The trans-ligand controls the rate of ligand loss through the trans-effect, and so the activation energy for benzene loss is

**Table 4.** Relative energies and bond distances as predicted by the DFT calculations.

Complex	B	C	D	F	G	H
$E$ (kcal mol <sup>-1</sup> )	0	3.1	-10.0	2.5	-16.9	-17.0
<b>Distances (Å)</b>						
PtH <sup>1</sup>	1.53	1.87	1.91	2.91	2.69	2.69
PtH <sup>2</sup>	2.66	2.64	2.43	2.68	2.64	2.65
PtC <sup>4</sup>	2.07	2.55	2.52	2.08	2.06	2.07
PtC <sup>1</sup>	2.03	2.03	2.03	2.57	2.37	2.35
PtC <sup>2</sup>	3.06	3.00	3.00	3.45	2.38	2.35
PtC <sup>3</sup>	2.93	2.99	3.00	2.35	3.27	3.23
PtN <sup>1</sup>	2.28	2.28	2.27	2.10	2.11	2.11
PtN <sup>2</sup>	2.28	2.07	2.07	2.26	2.30	2.26

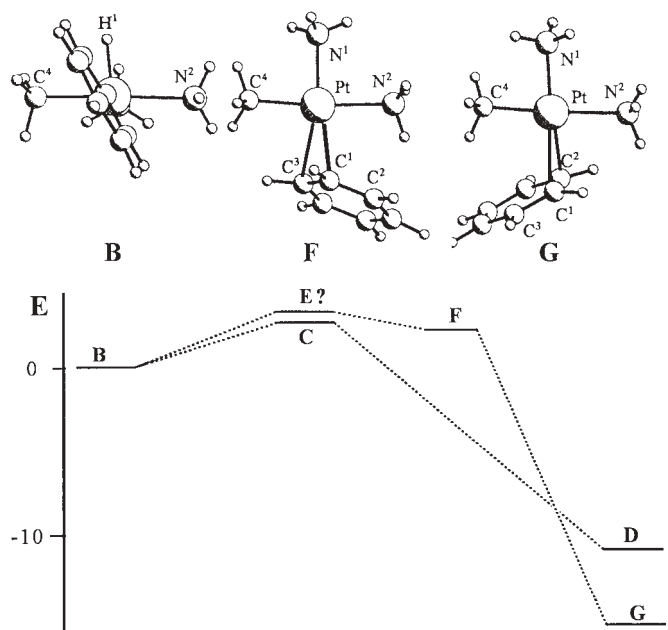
much lower for **2** than for **1**. For **1** the activation energy for benzene loss from the benzene complex cation (Fig. 3) is similar to that for the reverse reactions leading to H-D exchange, whereas for **2** the benzene loss is much faster and so the back reactions are not competitive.

The relevance to C—H bond activation is also clear from Fig. 3. The trans-aryl group in  $[\text{PtX}(\text{NCN})]$  will labilise the group  $\text{X}^-$  and so facilitate benzene coordination, but the overall energetics for oxidative addition of the C—H bond will be less favorable than in the case of  $[\text{PtXPh}(\text{NN})]$ . It is interesting that a platinum(II) complex with a pincer ligand, which has a nitrogen-donor amide rather than a carbon-donor aryl group at the center, is capable of activating benzene to give a phenylplatinum(II) derivative (17).

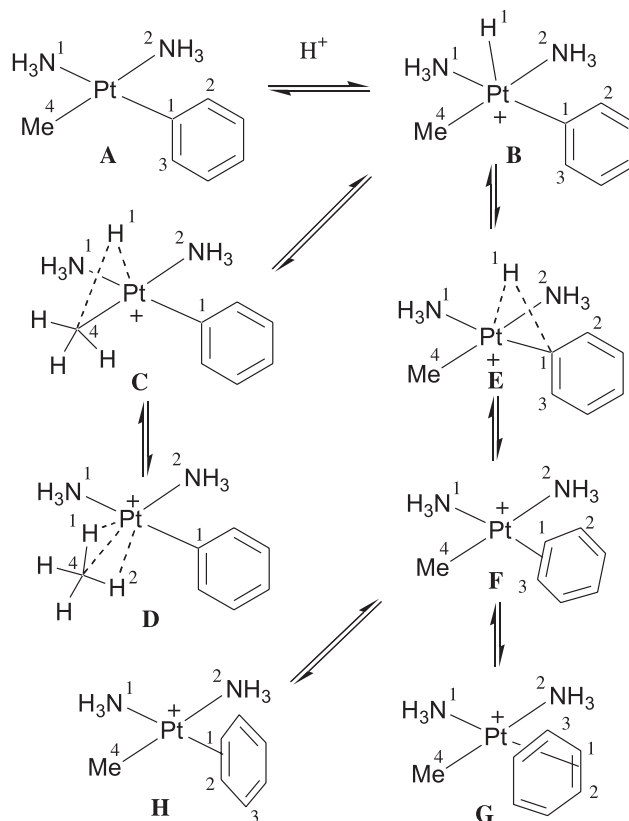
The mechanism by which the five-coordinate hydrido(phenyl)platinum(IV) intermediate might be transformed to the benzene complex was examined by using density functional theory (DFT) on the model complex  $[\text{PtHMePh}(\text{NH}_3)_2]^+$ , chosen so as to give a reasonable model for the complex  $[\text{PtHPh}_2(\text{bu}_2\text{bpy})]^+$  (**10**). This model is also useful since it allows a comparison of the  $\text{Me}\cdots\text{H}$  and  $\text{Ph}\cdots\text{H}$  reductive elimination pathways. Some data are given in Table 4 and summarized in Fig. 4, while the proposed mechanism is summarized in Scheme 5. The five-coordinate complex **B** (Fig. 4, Scheme 5) has square-pyramidal stereochemistry. The hydride is slightly displaced towards the methyl group ( $\text{HPtC} = 85^\circ$ ) and the phenyl group rotates away from the position in which it is orthogonal to the  $\text{C}_2\text{PtN}_2$  plane to avoid steric effects between the hydride and the ortho hydrogen atom of the phenyl group (Fig. 4). Complex **B** can decompose by C-H reductive elimination to give either a phenyl(methane)platinum(II) complex **D** or a methyl(benzene)platinum(II) complex **G** (Scheme 5). The formation of **D** (Scheme 5) occurs in a very similar way to that found earlier for methane reductive elimination from methyl(hydrido)platinum(IV) complexes (9), with a late transition state **C** (Scheme 5) and the activation energy was calculated as 3.1 kcal mol<sup>-1</sup> (Table 4). The reductive elimination from **B** by coupling of the hydride and phenyl groups proved more difficult to define by DFT. The final state is predicted to be **G** (Scheme 5, Fig. 4) in which the benzene ligand is  $\eta^2$ -bonded, with the C—C axis perpendicular to the plane of the platinum(II) and with the benzene oriented towards the methyl group. The orientation of the benzene in **G**



**Fig. 4.** The predicted structures of the complexes  $[\text{PtHMePh}(\text{NH}_3)_2]^+$  (**B**) and  $[\text{PtMe}(\text{C}_6\text{H}_6)(\text{NH}_3)_2]^+$  (**F** and **G**) and below the calculated energies ( $\text{kcal mol}^{-1}$ ) of the complexes **B–G**.



**Scheme 5.**



is very similar to that found experimentally in the hydrido(benzene)platinum(II) complex  $[\text{PtH}(\text{C}_6\text{H}_6)\{\kappa^2\text{-(Hpz}^*)\text{BHpz}^*_2\}]^+$ , in which benzene is oriented towards the

hydride (10). There is a conformer of **G** in which the benzene is oriented towards the ammine (**H**) and it is very close in energy, presumably because the steric effects of  $\text{CH}_3$  and



NH<sub>3</sub> are essentially the same (Table 4), but **H** will certainly be less favored in complexes with bulkier amine or imine ligands. The hydrogen atoms C<sup>1</sup>H<sup>1</sup> and C<sup>2</sup>H<sup>2</sup> in **G** and **H** are bent away from the platinum by about 10° but otherwise the benzene molecule is like free benzene. The transition state was expected to resemble **E** (Scheme 5), with the hydride bridging between platinum and the ipso carbon in an analogous way as in **C**, but no such transition state could be located. The only transition state found was **F** in which the Pt—H bond is completely broken (PtH<sup>1</sup> = 2.91 Å) and the C—H bond completely formed (C<sup>1</sup>H<sup>1</sup> = 1.09 Å) (Scheme 5, Fig. 4). Complex **F** is another η<sup>2</sup>-bonded benzene complex of platinum(II) but with atom H<sup>1</sup> still oriented roughly perpendicular to the plane of platinum(II) and so with the coordinated C—C axis in a less favorable orientation than in **G** or **H** for binding to platinum. The benzene is oriented towards the ammine ligand in **F** (Fig. 4). It is possible that the reaction proceeds in two steps, with a first transition state on the way to C—H reductive elimination (**E**) but this could not be defined and is probably close in energy to **F**; the transition from **F** to **G** just requires rocking about the Pt—C<sup>1</sup> axis. The benzene complex **G** is more stable than the methane complex **C**, as expected from the relative ligating abilities of benzene and methane. Since the transition state for C—H reductive elimination was not found, the relative energies of the transition states **C** and **E** are not known. Complex **E** is placed slightly higher than **C** or **F** in Fig. 4, based on the known selectivity for methane elimination in methyl(phenyl)platinum(II) complexes with nitrogen-donor ligands (4). The activation energy for the benzene C—H oxidative addition step, as measured by the energy difference between **G** and **F**, is calculated as 19 kcal mol<sup>-1</sup>, which can be compared to experimental activation energies of Δ*G* = 13 to 14 kcal mol<sup>-1</sup> for transformation of the benzene complex [PtH(C<sub>6</sub>H<sub>6</sub>){κ<sup>2</sup>-(Hpz\*)BHpz\*<sub>2</sub>}]<sup>+</sup> and similar arene complexes, to the corresponding hydrido(phenyl)platinum(IV) complexes, such as [PtH<sub>2</sub>Ph{κ<sup>2</sup>-(Hpz\*)BHpz\*<sub>2</sub>}]<sup>+</sup> (10).

Although there are still some questions about the detailed mechanism of the reductive elimination step to form benzene from complex **B**, it seems that the initial C...H bond formation occurs by movement of the hydride parallel to the Pt—C axis, but then a major sideways motion of the phenyl group occurs so as to allow side-on η<sup>2</sup>-coordination of the forming benzene group. The activation of benzene by oxidative addition (4, 7, 10, 17) is then expected to follow the microscopic reverse of this sequence.

## Experimental section

Syntheses were carried out using a nitrogen atmosphere, employing either Schlenk or glovebox techniques. Solvents were dried and distilled under N<sub>2</sub> prior to use. <sup>1</sup>H and <sup>13</sup>C NMR spectra were recorded using Varian Inova 400 and 600 MHz spectrometers. Chemical shifts are reported relative to SiMe<sub>4</sub>. GC–MS experiments were carried out using a Finnigan Mat 8200 spectrometer; samples were prepared using CD<sub>2</sub>Cl<sub>2</sub>–CD<sub>3</sub>OD solutions followed by direct injection to the GC coupled to the MS and isotopic composition of benzene was determined by simulation, based on spectra of authentic samples. The phenylplatinum(II) complexes were

stable in CD<sub>2</sub>Cl<sub>2</sub>–CD<sub>3</sub>OD solution in the absence of added acid, as shown by NMR. The complexes [{PtPh<sub>2</sub>(μ-SMe<sub>2</sub>)<sub>n</sub>], bu<sub>2</sub>bpy, and [PtCl{2,6-C<sub>6</sub>H<sub>3</sub>(CH<sub>2</sub>NMe<sub>2</sub>)<sub>2</sub>}] were prepared according to literature methods (15, 18). Solutions containing HCl or DCl were prepared by reaction of a known amount of acetyl chloride with MeOH or CD<sub>3</sub>OD, respectively. The DFT calculations were carried out at the B3LYP level employing a LANL2DZ basis set, which uses a relativistic effective core potential for platinum. The program used was the Gaussian-94 software package (19) and the methods used were as described and justified previously (9).

### [PtPh<sub>2</sub>(bu<sub>2</sub>bpy)] (1)

To a solution of [{PtPh<sub>2</sub>(μ-SMe<sub>2</sub>)<sub>n</sub>}] (0.494 g, 1.04 mmol) in Et<sub>2</sub>O was added bu<sub>2</sub>bpy (0.280 g, 1.04 mmol). The solution immediately turned orange in color. After 12 h, the orange precipitate that formed was filtered off, washed with Et<sub>2</sub>O, and dried under vacuum. Yield: 54%. <sup>1</sup>H NMR (CDCl<sub>3</sub>) δ: 8.45 (d, 2H, *J*<sub>HH</sub> = 6 Hz), 7.94 (s, 2H), 7.45 (d, 4H, *J*<sub>HH</sub> = 8 Hz, H<sub>o</sub>(Ph)), 7.35 (d, 2H, *J*<sub>HH</sub> = 7 Hz), 7.01 (t, 4H, *J*<sub>HH</sub> = 7 Hz, H<sub>m</sub>(Ph)), 6.88 (t, 2H, *J*<sub>HH</sub> = 7 Hz, H<sub>p</sub>(Ph)), 1.37 (s, 18H, *t*-Bu). Anal. calcd. for C<sub>30</sub>H<sub>34</sub>N<sub>2</sub>Pt (%): C 58.33, H 5.55; found: C 58.11, H 5.56.

### [PtClPh(bu<sub>2</sub>bpy)] (3a)

To a solution of **1** (0.062 g, 0.099 mmol) in CH<sub>2</sub>Cl<sub>2</sub> (0.5 mL) was added HCl (0.099 mmol). The orange precipitate of the product was filtered off, washed with Et<sub>2</sub>O, and dried under vacuum. Yield: 73%. <sup>1</sup>H NMR (acetone-*d*<sub>6</sub>) δ: 9.31 (d, 1H, *J*<sub>HH</sub> = 6 Hz), 8.40 (s, 1H), 8.38 (d, 1H, *J*<sub>HH</sub> = 6 Hz), 8.33 (s, 1H), 7.79 (d, 1H, *J*<sub>HH</sub> = 6 Hz), 7.42 (d, 1H, *J*<sub>HH</sub> = 6 Hz), 7.32 (m, 2H, H<sub>o</sub>(Ph)), 6.98 (t, 2H, *J*<sub>HH</sub> = 7 Hz, H<sub>m</sub>(Ph)), 6.87 (t, 1H, *J*<sub>HH</sub> = 7 Hz, H<sub>p</sub>(Ph)), 1.44 (s, 9H, *t*-Bu), 1.38 (s, 9H, *t*-Bu). Anal. calcd. for C<sub>24</sub>H<sub>29</sub>ClN<sub>2</sub>Pt (%): C 50.04, H 5.07; found: C 49.56, H 4.94.

### [PtPh(O<sub>2</sub>CCF<sub>3</sub>)(bu<sub>2</sub>bpy)] (3b)

To a solution of **1** (0.068 g, 0.11 mmol) in CH<sub>2</sub>Cl<sub>2</sub> was added CF<sub>3</sub>CO<sub>2</sub>H (9 μL, 0.11 mmol). The reaction mixture was stirred for 12 h and the solvent was removed under vacuum to yield the product as an orange powder. Yield: 56%. <sup>1</sup>H NMR (acetone-*d*<sub>6</sub>) δ: 8.85 (d, 1H, *J*<sub>HH</sub> = 6 Hz), 8.53 (s, 1H), 8.46 (s, 1H), 8.17 (d, 1H, *J*<sub>PH</sub> = 60 Hz, *J*<sub>HH</sub> = 6 Hz), 7.82 (d, 1H, *J*<sub>HH</sub> = 6 Hz), 7.53 (d, 1H, *J*<sub>HH</sub> = 6 Hz), 7.37 (d, 2H, *J*<sub>HH</sub> = 7 Hz, H<sub>o</sub>(Ph)), 7.13 (t, 2H, *J*<sub>HH</sub> = 7 Hz, H<sub>m</sub>(Ph)), 7.08 (t, 1H, *J*<sub>HH</sub> = 7 Hz, H<sub>p</sub>(Ph)), 1.46 (s, 9H, *t*-Bu), 1.39 (s, 9H, *t*-Bu). Anal. calcd. for C<sub>26</sub>H<sub>29</sub>F<sub>3</sub>N<sub>2</sub>O<sub>2</sub>Pt<sub>1</sub> (%): C 47.78, H 4.47; found: C 47.49, H 4.41.

### [PtPh(CF<sub>3</sub>SO<sub>3</sub>)(bu<sub>2</sub>bpy)] (3c)

This was prepared similarly by using CF<sub>3</sub>SO<sub>3</sub>H. Yield: 64%. <sup>1</sup>H NMR (acetone-*d*<sub>6</sub>) δ: 8.88 (d, 1H, *J*<sub>HH</sub> = 6 Hz), 8.53 (s, 1H), 8.46 (s, 1H), 8.16 (d, 1H, *J*<sub>PH</sub> = 58 Hz, *J*<sub>HH</sub> = 6 Hz), 7.84 (d, 1H, *J*<sub>HH</sub> = 6 Hz), 7.54 (d, 1H, *J*<sub>HH</sub> = 6 Hz), 7.35 (d, 2H, *J*<sub>HH</sub> = 7 Hz, H<sub>o</sub>(Ph)), 6.98 (t, 2H, *J*<sub>HH</sub> = 7 Hz, H<sub>m</sub>(Ph)), 6.87 (t, 1H, *J*<sub>HH</sub> = 7 Hz, H<sub>p</sub>(Ph)), 1.46 (s, 9H, *t*-Bu), 1.40 (s, 9H, *t*-Bu). Anal. calcd. for C<sub>25</sub>H<sub>29</sub>F<sub>3</sub>N<sub>2</sub>O<sub>3</sub>SPt (%): C 43.54, H 4.24; found: C 43.56, H 4.31.



**[PtPh(BF<sub>4</sub>)(bu<sub>2</sub>bpy)] (3d)**

This was prepared similarly by using HBF<sub>4</sub>. Yield: 48%. <sup>1</sup>H NMR (acetone-*d*<sub>6</sub>) δ: 8.89 (d, 1H, *J*<sub>HH</sub> = 6 Hz), 8.55 (s, 1H), 8.47 (s, 1H), 8.19 (d, 1H, *J*<sub>HH</sub> = 6 Hz), 7.85 (d, 1H, *J*<sub>HH</sub> = 6 Hz), 7.55 (d, 1H, *J*<sub>HH</sub> = 6 Hz), 7.37 (d, 2H, *J*<sub>HH</sub> = 7 Hz, H<sub>o</sub>(Ph)), 7.13 (m, 2H, H<sub>m</sub>(Ph)), 7.05 (m, 1H, H<sub>p</sub>(Ph)), 1.46 (s, 9H, *t*-Bu), 1.40 (s, 9H, *t*-Bu). Anal. calcd. for C<sub>24</sub>H<sub>29</sub>BF<sub>4</sub>N<sub>2</sub>Pt (%): C 45.95, H 4.66; found: C 45.47, H 4.80.

**[PtHClPh<sub>2</sub>(bu<sub>2</sub>bpy)] (4a)**

To an NMR tube charged with a solution of **1** (0.052 g, 0.085 mmol) in CDCl<sub>3</sub> (0.5 mL) at -78 °C was added HCl (0.085 mmol). <sup>1</sup>H NMR in CDCl<sub>3</sub> at -80 °C δ: 8.18 (s, 2H), 8.06 (d, 2H, *J*<sub>HH</sub> = 6 Hz), 7.86 (d, 2H, *J*<sub>HH</sub> = 7 Hz), 7.29 (d, 4H, *J*<sub>HH</sub> = 7 Hz, H<sub>o</sub>(Ph)), 6.76 (t, 4H, *J*<sub>HH</sub> = 7 Hz, H<sub>m</sub>(Ph)), 6.67 (t, 2H, *J*<sub>HH</sub> = 7 Hz, H<sub>p</sub>(Ph)), 1.19 (s, 18H, *t*-Bu), -20.15 (s, 1H, *J*<sub>PtH</sub> = 1613 Hz, Pt-H). Compound **2** was indefinitely stable at -78 °C but decomposed rapidly at -20 °C to give C<sub>6</sub>H<sub>6</sub> and [PtClPh(bu<sub>2</sub>bpy)] (**3a**) as monitored by NMR.

**[PtH(NCCD<sub>3</sub>)Ph<sub>2</sub>(bu<sub>2</sub>bpy)][BF<sub>4</sub>] (7)**

This was prepared similarly in CDCl<sub>3</sub>-CD<sub>3</sub>CN (1.0 mL) by using HBF<sub>4</sub>. <sup>1</sup>H NMR (CDCl<sub>3</sub>-CD<sub>3</sub>CN) δ: 8.45 (s, 2H), 8.10 (d, 2H, *J*<sub>HH</sub> = 6 Hz), 7.52 (d, 2H, *J*<sub>HH</sub> = 6 Hz), 7.18 (d, 4H, *J*<sub>HH</sub> = 7 Hz, H<sub>o</sub>(Ph)), 6.99 (t, 4H, *J*<sub>HH</sub> = 7 Hz, H<sub>m</sub>(Ph)), 6.89 (t, 2H, *J*<sub>HH</sub> = 7 Hz, H<sub>p</sub>(Ph)), 1.36 (s, 18H, *t*-Bu), -21.84 (s, 1H, *J*<sub>PtH</sub> = 1619 Hz, Pt-H). Compound **7** was indefinitely stable at -78 °C but decomposed rapidly at -20 °C to give C<sub>6</sub>H<sub>6</sub> and [Pt(BF<sub>4</sub>)(C<sub>6</sub>H<sub>5</sub>)(tbu<sub>2</sub>bpy)] (**3d**).

**[PtHCl<sub>2</sub>Ph(bu<sub>2</sub>bpy)] (6)**

To an NMR tube charged with a solution of **3a** (0.016 g, 0.028 mmol) in CDCl<sub>3</sub> (0.6 mL) at -78 °C was added HCl (0.028 mmol). <sup>1</sup>H NMR (CDCl<sub>3</sub>) δ: 9.17 (s, 1H), 8.25 (s, 1H), 7.99 (s, 1H), 7.94 (s, 1H), 7.52 (s, 1H), 7.22 (d, 2H, *J*<sub>HH</sub> = 6.8 Hz, H<sub>o</sub>(Ph)), 7.15 (s, 1H), 6.89 (t, 2H, *J*<sub>HH</sub> = 7 Hz, H<sub>m</sub>(Ph)), 6.76 (t, 1H, *J*<sub>HH</sub> = 7 Hz, H<sub>p</sub>(Ph)), 1.28 (s, 9H, *t*-Bu), 1.22 (s, 9H, *t*-Bu), -25.94 (s, 1H, *J*<sub>PtH</sub> = 1540 Hz, Pt-H). Compound **6** was indefinitely stable at -78 °C but decomposed rapidly at -10 °C to give C<sub>6</sub>H<sub>6</sub> and [PtCl<sub>2</sub>(bu<sub>2</sub>bpy)].

**[PtPh{2,6-C<sub>6</sub>H<sub>3</sub>(CH<sub>2</sub>NMe<sub>2</sub>)<sub>2</sub>}] (2)**

To a solution of [PtCl(C<sub>6</sub>H<sub>3</sub>(CH<sub>2</sub>NMe<sub>2</sub>)<sub>2</sub>)] (0.357 g, 0.78 mmol) in ether (10 mL) at 0 °C was added PhLi (0.43 mL, 0.78 mmol). The mixture was stirred at 0 °C for 5 min, then for 1 h at room temperature. The beige precipitate that had formed was filtered off, washed with pentane, and recrystallized from CH<sub>2</sub>Cl<sub>2</sub>-pentane to yield colorless crystals of the product (**15**). Yield: 56%. <sup>1</sup>H NMR (CDCl<sub>3</sub>) δ: 7.67 (d, 2H, *J*<sub>HH</sub> = 6 Hz), 7.11 (t, 1H, *J*<sub>HH</sub> = 7 Hz), 6.97 (d, 2H, *J*<sub>HH</sub> = 7 Hz), 6.92 (m, 2H), 6.87 (t, 1H, *J*<sub>HH</sub> = 7 Hz), 4.11 (s, 4H, *J*<sub>PtH</sub> = 42 Hz, N-CH<sub>2</sub>), 2.89 (s, 12H, *J*<sub>PtH</sub> = 44 Hz, NMe<sub>2</sub>). <sup>13</sup>C NMR (CDCl<sub>3</sub>) δ: 145.54, 139.59, 126.84, 123.19, 122.63, 119.25, 81.22, 54.36.

**[PtCl{2,6-C<sub>6</sub>H<sub>3</sub>(CH<sub>2</sub>NMe<sub>2</sub>)<sub>2</sub>}] (7a)**

To a solution of **2** (0.052 g, 0.105 mmol) in a THF:Et<sub>2</sub>O (50:50) mixture was added HCl (0.105 mmol). The reaction

mixture was stirred for 2 h at which time the beige precipitate was filtered off and washed with ether. Yield: 61%. <sup>1</sup>H NMR (CDCl<sub>3</sub>) δ: 6.97 (t, 1H, *J*<sub>HH</sub> = 7 Hz), 6.79 (d, 2H, *J*<sub>HH</sub> = 7 Hz), 4.00 (s, 4H, *J*<sub>PtH</sub> = 45 Hz, N-CH<sub>2</sub>), 3.06 (s, 12H, *J*<sub>PtH</sub> = 36 Hz, NMe<sub>2</sub>). Anal. calcd. for C<sub>12</sub>H<sub>19</sub>ClN<sub>2</sub>Pt (%): C 34.17, H 4.54; found: C 34.01, H 4.62.

**[Pt(CF<sub>3</sub>CO<sub>2</sub>){2,6-C<sub>6</sub>H<sub>3</sub>(CH<sub>2</sub>NMe<sub>2</sub>)<sub>2</sub>}] (7b)**

This was prepared similarly using CF<sub>3</sub>CO<sub>2</sub>H. Yield: 48%. <sup>1</sup>H NMR (CD<sub>2</sub>Cl<sub>2</sub>) δ: 6.81 (t, 1H, *J*<sub>HH</sub> = 6 Hz), 6.79 (d, 2H, *J*<sub>HH</sub> = 4 Hz), 4.01 (s, 4H, *J*<sub>PtH</sub> = 48 Hz, N-CH<sub>2</sub>), 2.95 (s, 12H, *J*<sub>PtH</sub> = 36 Hz, NMe<sub>2</sub>). Anal. calcd. for C<sub>14</sub>H<sub>19</sub>F<sub>3</sub>O<sub>2</sub>N<sub>2</sub>Pt (%): C 33.67, H 3.83; found: C 33.59, H 3.72.

**[Pt(CF<sub>3</sub>SO<sub>3</sub>){2,6-C<sub>6</sub>H<sub>3</sub>(CH<sub>2</sub>NMe<sub>2</sub>)<sub>2</sub>}] (7c)**

This was prepared similarly using CF<sub>3</sub>SO<sub>3</sub>H. Yield: 36%. <sup>1</sup>H NMR (CD<sub>2</sub>Cl<sub>2</sub>) δ: 6.92 (t, 1H, *J*<sub>HH</sub> = 7 Hz), 6.76 (d, 2H, *J*<sub>HH</sub> = 7 Hz), 3.98 (s, 4H, *J*<sub>PtH</sub> = 41 Hz, N-CH<sub>2</sub>), 2.99 (s, 12H, *J*<sub>PtH</sub> = 37 Hz, NMe<sub>2</sub>). Anal. calcd. for C<sub>13</sub>H<sub>19</sub>F<sub>3</sub>N<sub>2</sub>O<sub>3</sub>PtS (%): C 29.16, H 3.58; found: C 29.42, H 3.73.

**[Pt(BF<sub>4</sub>){2,6-C<sub>6</sub>H<sub>3</sub>(CH<sub>2</sub>NMe<sub>2</sub>)<sub>2</sub>}] (7d)**

This was prepared similarly using HBF<sub>4</sub>. Yield: 57%. <sup>1</sup>H NMR (acetone-*d*<sub>6</sub>) δ: 6.72 (t, 1H, *J*<sub>HH</sub> = 7 Hz), 6.55 (d, 2H, *J*<sub>HH</sub> = 7 Hz), 3.78 (s, 4H, *J*<sub>PtH</sub> = 48 Hz, N-CH<sub>2</sub>), 2.76 (s, 12H, *J*<sub>PtH</sub> = 38 Hz, NMe<sub>2</sub>). Anal. calcd. for C<sub>12</sub>H<sub>19</sub>BF<sub>4</sub>N<sub>2</sub>Pt (%): C 30.46, H 4.05; found: C 30.42, H 4.11.

**[PtHClPh{2,6-C<sub>6</sub>H<sub>3</sub>(CH<sub>2</sub>NMe<sub>2</sub>)<sub>2</sub>}] (8)**

To an NMR tube charged with a solution of **2** (0.046 g, 0.091 mmol) in CDCl<sub>3</sub> at -78 °C was added HCl (0.091 mmol). <sup>1</sup>H NMR (CDCl<sub>3</sub>) δ: 7.70 (d, 2H, *J*<sub>HH</sub> = 6 Hz), 7.16 (t, 1H, *J*<sub>HH</sub> = 7 Hz), 6.98 (d, 2H, *J*<sub>HH</sub> = 7 Hz, H<sub>o</sub>(Ph)), 6.96 (m, 2H, H<sub>m</sub>(Ph)), 6.94 (t, 1H, *J*<sub>HH</sub> = 7 Hz, H<sub>p</sub>(Ph)), 4.15 (s, 4H, N-CH<sub>2</sub>), 2.89 (s, 12H, NMe<sub>2</sub>), -21.36 (s, 1H, *J*<sub>PtH</sub> = 1622 Hz, Pt-H). Compound **8** was indefinitely stable at -78 °C but decomposed rapidly at -20 °C to give C<sub>6</sub>H<sub>6</sub> and [PtCl{C<sub>6</sub>H<sub>3</sub>(CH<sub>2</sub>NMe<sub>2</sub>)<sub>2</sub>}] (**7a**).

**[PtHPh(NCCD<sub>3</sub>){2,6-C<sub>6</sub>H<sub>3</sub>(CH<sub>2</sub>NMe<sub>2</sub>)<sub>2</sub>)][CF<sub>3</sub>SO<sub>3</sub>] (9)**

This was prepared similarly in CDCl<sub>3</sub>-CD<sub>3</sub>CN solution at -78 °C by using CF<sub>3</sub>SO<sub>3</sub>H. <sup>1</sup>H NMR (CDCl<sub>3</sub>-CD<sub>3</sub>CN) δ: 7.92 (t, 1H, *J*<sub>HH</sub> = 8 Hz), 7.46 (d, 2H, *J*<sub>HH</sub> = 8 Hz), 6.98 (m, 2H, H<sub>o</sub>(Ph)), 6.87 (t, 2H, *J*<sub>HH</sub> = 7 Hz, H<sub>m</sub>(Ph)), 6.75 (t, 1H, *J*<sub>HH</sub> = 7 Hz, H<sub>p</sub>(Ph)), 4.10 (s, 4H, N-CH<sub>2</sub>), 2.86 (s, 12H, NMe<sub>2</sub>), -20.47 (s, 1H, *J*<sub>PtH</sub> = 1644 Hz, Pt-H). Compound **9** was indefinitely stable at -78 °C but decomposed rapidly at -20 °C to give C<sub>6</sub>H<sub>6</sub> and [Pt(CF<sub>3</sub>SO<sub>3</sub>){C<sub>6</sub>H<sub>3</sub>(CH<sub>2</sub>NMe<sub>2</sub>)<sub>2</sub>}] (**7c**).

**X-ray structure determinations**

Crystals of **1** and **2** were grown from acetone and chloroform solution, respectively. Crystals were mounted on glass fibres. Data were collected by using a Nonius Kappa-CCD diffractometer with COLLECT (20) software. Crystal data and refinement parameters are listed in Table 5. Data were scaled using SCALEPACK (21), and empirical absorption corrections were applied using redundant data and XPREP (SHELXTL 5.03). Full-matrix least-squares refinement on



**Table 5.** Crystal data and structure refinement for complexes **1** and **2**.

Complex	<b>1</b> -2Me <sub>2</sub> CO	<b>2</b>
Formula, fw	C <sub>36</sub> H <sub>46</sub> N <sub>2</sub> O <sub>2</sub> Pt, 733.84	C <sub>18</sub> H <sub>24</sub> N <sub>2</sub> Pt, 463.09
Temperature (K)	200(2)	293(2)
Wavelength (Å)	0.71073	0.71070
Crystal system	Monoclinic	Monoclinic
Space group	<i>P</i> 2/ <i>c</i>	<i>P</i> 2(1)/ <i>n</i>
Cell dimensions	<i>a</i> = 12.7265(3) Å <i>b</i> = 14.2079(2) Å <i>c</i> = 10.0711(2) Å $\beta$ = 69.0990(3)°	<i>a</i> = 9.3780(19) Å <i>b</i> = 14.663(3) Å <i>c</i> = 12.650(3) Å $\beta$ = 107.35(3)°
Volume (Å <sup>3</sup> ), <i>Z</i>	1701.2(6), 2	1660.2(6), 4
Density (calcd.) (Mg m <sup>-3</sup> )	1.433	1.856
Abs. coeff. (mm <sup>-1</sup> )	4.156	2.112
F(000)	740	224
$\theta$ Range (°)	2.60–27.48	2.67–24.99
No. of reflns collected	17 452	5665
Data/restraints/param.	3897/0/203	2918/0/190
Goodness-of fit on <i>F</i> <sup>2</sup>	1.029	0.961
Final <i>R</i> indices ( <i>I</i> > 2σ( <i>I</i> ))	<i>R</i> 1 = 0.0309 <i>wR</i> 2 = 0.0732	<i>R</i> 1 = 0.0321 <i>wR</i> 2 = 0.081
<i>R</i> indices (all data)	<i>R</i> 1 = 0.0361 <i>wR</i> 2 = 0.0752	<i>R</i> 1 = 0.0395 <i>wR</i> 2 = 0.0852

*F*<sup>2</sup> was performed after solving using Patterson methods and the solution package SHELXTL 5.03 (22). Complex **1** contained two molecules of acetone of solvation.<sup>3</sup>

## Acknowledgment

We thank the Natural Sciences and Engineering Research Council of Canada (NSERC) for financial support.

## References

1. A.E. Shilov and G.B. Shul'pin. *Chem. Rev.* **97**, 2879 (1997).
2. I.C.M. Wehman-Ooyevaar, D.M. Grove, P. de Vaal, A. Dedieu, and G. van Koten. *Inorg. Chem.* **31**, 5484 (1992).
3. V. de Felice, A. de Renzi, A. Panunzi, and D. Tesauro. *J. Organomet. Chem.* **488**, C13 (1995).
4. S.S. Stahl, J.A. Labinger, and J.E. Bercaw. *J. Am. Chem. Soc.* **117**, 9371 (1995); S.S. Stahl, J.A. Labinger, and J.E. Bercaw. *J. Am. Chem. Soc.* **118**, 5961 (1996); S.S. Stahl, J.A. Labinger, and J.E. Bercaw. *Angew. Chem. Int. Ed.* **37**, 2181 (1998); M.W. Holtcamp, J.A. Labinger, and J.E. Bercaw. *Inorg. Chim. Acta*, **265**, 117 (1997); M.W. Holtcamp, J.A. Labinger, and J.E. Bercaw. *J. Am. Chem. Soc.* **119**, 848 (1997); L. Johansson, M. Tilset, J.A. Labinger, and J.E. Bercaw. *J. Am. Chem. Soc.* **122**, 10 846 (2000); H.A. Zhong, J.A. Labinger, and J.E. Bercaw. *J. Am. Chem. Soc.* **124**, 1378 (2002).
5. R.J. Puddephatt. *Coord. Chem. Rev.* **157**, 219 (2001); R.J. Puddephatt. *Angew. Chem. Int. Ed.* **41**, 261 (2002); G.S. Hill, L.M. Rendina, and R.J. Puddephatt. *Organometallics*, **14**, 4966 (1995); E.M. Prokopchuk, H.A. Jenkins, and R.J. Puddephatt. *Organometallics*, **18**, 2861 (1999); J.G. Hinman, C.R. Baar, M.C. Jennings, and R.J. Puddephatt. *Organometallics*, **19**, 563 (2001).
6. D.D. Wick and K.I. Goldberg. *J. Am. Chem. Soc.* **121**, 11 900 (1999); K.L. Bartlett, K.I. Goldberg, and W.T. Borden. *Organometallics*, **20**, 2669 (2001).
7. L. Johansson and M. Tilset. *J. Am. Chem. Soc.* **123**, 739 (2001); L. Johansson, O.B. Ryan, C. Romming, and M. Tilset. *J. Am. Chem. Soc.* **123**, 6579 (2001); H. Heiberg, L. Johansson, O. Gropen, O.B. Ryan, O. Swang, and M. Tilset. *J. Am. Chem. Soc.* **122**, 10 831 (2000).
8. A.N. Vedernikov and K.G. Caulton. *Angew. Chem. Int. Ed.* **41**, 4102 (2002).
9. J. Kua, X. Xu, R.A. Periana, and W.A. Goddard, III. *Organometallics*, **21**, 511 (2002); R.H. Crabtree. *J. Chem. Soc. Dalton Trans.* 2437 (2001); K. Mylvaganam, G.B. Bacskey, and N.S. Hush. *J. Am. Chem. Soc.* **122**, 2041 (2000); T.M. Gilbert, I. Hristov and T. Ziegler. *Organometallics*, **20**, 1183 (2001); H. Heiberg, O. Swang, O.B. Ryan, and O. Gropen. *J. Phys. Chem.* **103**, 10 004 (1999); A.N. Vedernikov, G.A. Shamov, and B.N. Solomonov. *Russ. J. Gen. Chem.* **69**, 1102 (1999). G.S. Hill, and R.J. Puddephatt. *Organometallics*, **17**, 1478 (1998).
10. S.A. O'Reilly, P.S. White, and J.L. Templeton. *J. Am. Chem. Soc.* **118**, 5684 (1996); S. Reinartz, P.S. White, M. Brookhart, and J.L. Templeton. *Organometallics*, **19**, 3854 (2000); S. Reinartz, P.S. White, M. Brookhart, and J.L. Templeton. *Organometallics*, **20**, 1709 (2001); S. Reinartz, P.S. White, M. Brookhart, and J.L. Templeton. *J. Am. Chem. Soc.* **123**, 12 724 (2001); S. Reinartz, P.S. White, M. Brookhart, and J.L. Templeton. *J. Am. Chem. Soc.* **124**, 7249 (2002); C.M. Norris,

<sup>3</sup>Supplementary data may be purchased from the Directory of Unpublished Data, Document Delivery, CISTI, National Research Council Canada, Ottawa, ON K1A 0S2, Canada ([http://www.nrc.ca/cisti/irm/unpub\\_e.shtml](http://www.nrc.ca/cisti/irm/unpub_e.shtml) for information on ordering electronically). CCDC 200608 and 200609 contain tables of crystallographic data for **1** and **2** in CIF format. These data can be obtained, free of charge, via [www.ccdc.cam.ac.uk/conts/retrieving.html](http://www.ccdc.cam.ac.uk/conts/retrieving.html) (or from the Cambridge Crystallographic Data Centre, 12 Union Road, Cambridge CB2 1EZ, U.K.; fax +44 1223 336033; or [deposit@ccdc.cam.ac.uk](mailto:deposit@ccdc.cam.ac.uk)).



- S. Reinartz, P.S. White, and J.L. Templeton. *Organometallics*, **21**, 5649 (2002).
11. A.J. Canty, S.D. Fritsche, H. Jin, J. Patel, B.W. Skelton, and A.H. White. *Organometallics*, **16**, 2175 (1997).
12. M. Lin, C. Shen, E.A. Garcia-Zayas, and A. Sen. *J. Am. Chem. Soc.* **123**, 1000 (2001).
13. D.P. Arnold and M.A. Bennett. *Inorg. Chem.* **23**, 2110 (1984).
14. A.J. Chalk and J.F. Harrod. *J. Am. Chem. Soc.* **87**, 16 (1965); S. Reinartz, P.S. White, M. Brookhart, and J.L. Templeton. *J. Am. Chem. Soc.* **123**, 6425 (2001).
15. G. van Koten, J.T.B.H. Jastrzebski, J.G. Noltes, A.L. Spek, and J.C. Schoone. *J. Organomet. Chem.* **148**, 233 (1978); D.M. Grove, G. van Koten, J.N. Louwen, J.G. Noltes, A.L. Spek, and H.J.C. Ubbels. *J. Am. Chem. Soc.* **104**, 6609 (1982); J. Terheijden, G. van Koten, F. Muller, D.M. Grove, and K. Vrieze. *J. Organomet. Chem.* **315**, 401 (1986); J. Terheijden, G. van Koten, I.C. Vinke, and A.L. Spek. *J. Am. Chem. Soc.* **107**, 2891 (1985); P. Steenwinkel, H. Kooijman, W.J.J. Smeets, A.L. Spek, D.M. Grove, and G. van Koten. *Organometallics*, **17**, 5411 (1998).
16. S. Achar and V.J. Catalano. *Polyhedron*, **16**, 1555 (1997).
17. S.B. Harkins and J.C. Peters. *Organometallics*, **21**, 1753 (2002).
18. N. Hadj-Bagheri and R.J. Puddephatt. *Polyhedron*, **7**, 2695 (1988); D. Song, and S. Wang. *J. Organomet. Chem.* **648**, 302 (2001).
19. Gaussian 94, Revision E.1 [computer program]. Gaussian Inc., Pittsburgh, Pa. 1996.
20. Nonius. COLLECT [computer program]. Delft, The Netherlands. 1998.
21. Nonius. SCALEPACK [computer program]. Delft, The Netherlands. 1997.
22. G.M. Sheldrick. SHELXTL 5.03 [computer program]. Siemens, Madison, WI. 1999.



# Allylation of aldehydes catalyzed by chiral *N,N'*-bis(*N*-methyl-2-methylene-4,5-bisphenyl-imidazole)-1,2-cyclohexane diamine rhodium(III) complexes<sup>1</sup>

Frank J. LaRonde and Michael A. Brook

**Abstract:** Chiral bis-imidazole rhodium(III) complexes catalyze the allylation of aldehydes by allyltributyltin. The pre-catalyst was readily prepared from chiral *N,N'*-bis(*N*-methyl-2-methylene-4,5-bisphenylimidazole)-1,2-cyclohexanedi-amine, potassium carbonate, and rhodium(III) chloride trihydrate. The rhodium(III) complex produced showed no activity in an allyl transfer process in the presence of the allyltin reagent. However, when silver tetrafluoroborate was added to the pre-catalyst and stirred for 1 h, the resulting system became an efficient catalyst for the allyl transfer process. The reductions produced homo-allyl alcohols with good to excellent yield, although generally with poor facial selectivity (8–10% ee, aryl aldehydes, 4 examples; 99% ee, aliphatic aldehyde, 1 example).

**Key words:** allylation, aldehydes, enantioselectivity, rhodium(III) tetramine complex.

**Resumé :** Les complexes chiraux du bis-imidazole rhodium catalysent l'allylation des aldéhydes par l'allyltributylétain. On a préparé facilement le précatalyseur par réaction du *N,N'*-bis(*N*-méthyl-2-méthylène-4,5-bisphénylimidazole)cyclohexane-1,2-diamine avec le carbonate de potassium et le trihydrate du chlorure de rhodium(III). Le complexe de rhodium(III) qui est produit ne présente aucune activité vis-à-vis du processus de transfert de l'allyle en présence du réactif allylétain. Toutefois, quand on ajoute du tétrafluoroborate d'argent au précatalyseur et qu'on agite pendant une heure, le système qui en résulte devient un catalyseur efficace pour le transfert de l'allyle. Les réductions conduisent à la formation d'alcools homoallyliques avec des rendements allant de bons à excellents même si la sélectivité faciale est généralement faible (8 à 10% d'excès énantiomérique avec quatre exemples d'aldéhydes aromatiques et un ee de 99% pour un exemple d'aldéhyde aliphatique).

**Mots clés :** allylation, aldéhydes, énantiosélectivité, complexe tétrammine du rhodium(III).

[Traduit par la Rédaction]

## Introduction

The efficient control of stereochemical induction during bond formation remains one of the hallmarks of synthetic organic chemistry. The utilization of enantiopure metal complexes to induce chirality and, simultaneously, promote bond formation is one of the most effective strategies for stereo-induction, particularly when the bond to be formed results from nucleophilic addition to a carbonyl group. One such example is the metal-complex-promoted addition of non-polar allyl nucleophiles, based on group 14 elements, to aldehydes. The asymmetric version of this reaction is a valuable means of constructing chiral functionalized structures (Scheme 1). Two classes of metal complexes are generally

used to catalyze these reactions: oxyphilic Lewis acid catalysts and late transition metal complexes.

The majority of Lewis acid "catalysts" are developed from oxophilic metals including aluminum, boron, tin, and titanium. These are broadly applicable for the allylation of aldehydes, but suffer from extreme moisture sensitivity and a propensity to form oligomers in solution. In addition, chiral complexes based on these metals are usually generated in situ, so that a variety of species with varying Lewis acid strengths and enantioselection may be present in the reaction medium. This makes it difficult to develop selective processes and to understand the actual species participating in the reaction.

Received 10 March 2003. Published on the NRC Research Press Web site at <http://canjchem.nrc.ca> on 15 September 2003.

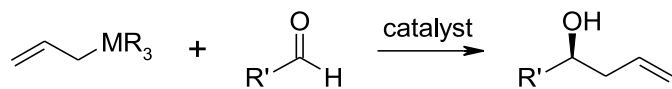
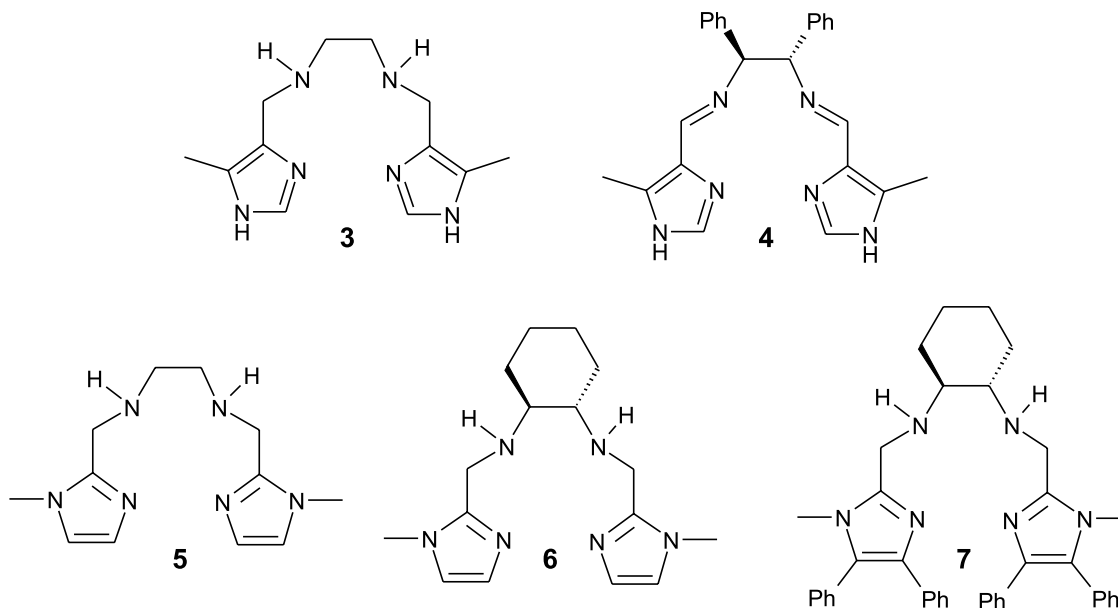
*It is a great pleasure to dedicate this paper to the superb career of John Harrod. I have learned much from his chemistry and much more from his friendship.*

**F.J. LaRonde and M.A. Brook.**<sup>2</sup> Department of Chemistry, McMaster University, 1280 Main St. W., Hamilton, ON L8S 4M1, Canada.

<sup>1</sup>This article is part of a Special Issue dedicated to Professor John Harrod.

<sup>2</sup>Corresponding author (e-mail: [mabrook@mcmaster.ca](mailto:mabrook@mcmaster.ca)).



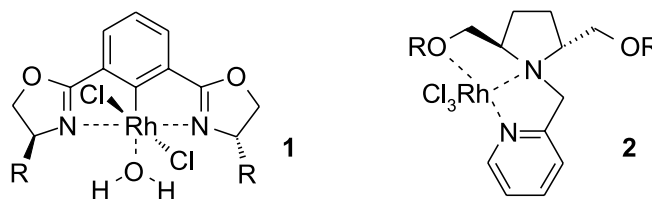
**Scheme 1.** Enantioselective allylation of aldehydes.**Fig. 2.** Bis-imidazole ligands.

The optimization of chiral Lewis acid catalysts remains challenging (1). With some notable exceptions, the most convenient metal ligands based on heteroatoms (N, P, O) significantly reduce the Lewis acidity and, thus, the catalytic activity. It should be noted that most of the reactions that are promoted by Lewis acid “catalysts” actually need stoichiometric quantities; those that require only catalytic quantities are much rarer.

A number of chiral allylmetal reagents that are generally used with stoichiometric amounts of Lewis acid catalysts (2) have been designed and synthesized (3). Some chiral Lewis acids that operate as true catalysts include chiral (acyloxy)borane (CAB) complexes with allylsilanes (4) or allylstannanes (5), binaphthol-derived chiral titanium complexes with allylstannanes (6) or allylsilanes (7), and BINAP-derived chiral silver complexes with allylstannanes (8).

Several groups have turned to late transition metal catalysts in the hope of avoiding some of the deficits of highly oxophilic Lewis acids: transition metal complexes can form single, well-defined species that are generally not moisture sensitive (9). For example, Nishiyama and co-workers (10) have described the synthesis and use of aryl-substituted oxazolines **1**, and Masaki and co-workers (11) have prepared pyrrolidine derivatives **2** (Fig. 1). Both classes of compounds activate aldehydes to attack by allyltin derivatives. They differ in the number of heteroatom ligands tethered to the central metal.

We recently reported the convenient synthesis and characterization of bis-imidazoles **3–7** (Fig. 2) (12). These com-

**Fig. 1.** Rh(III) catalysts used for the allylation of aldehydes.

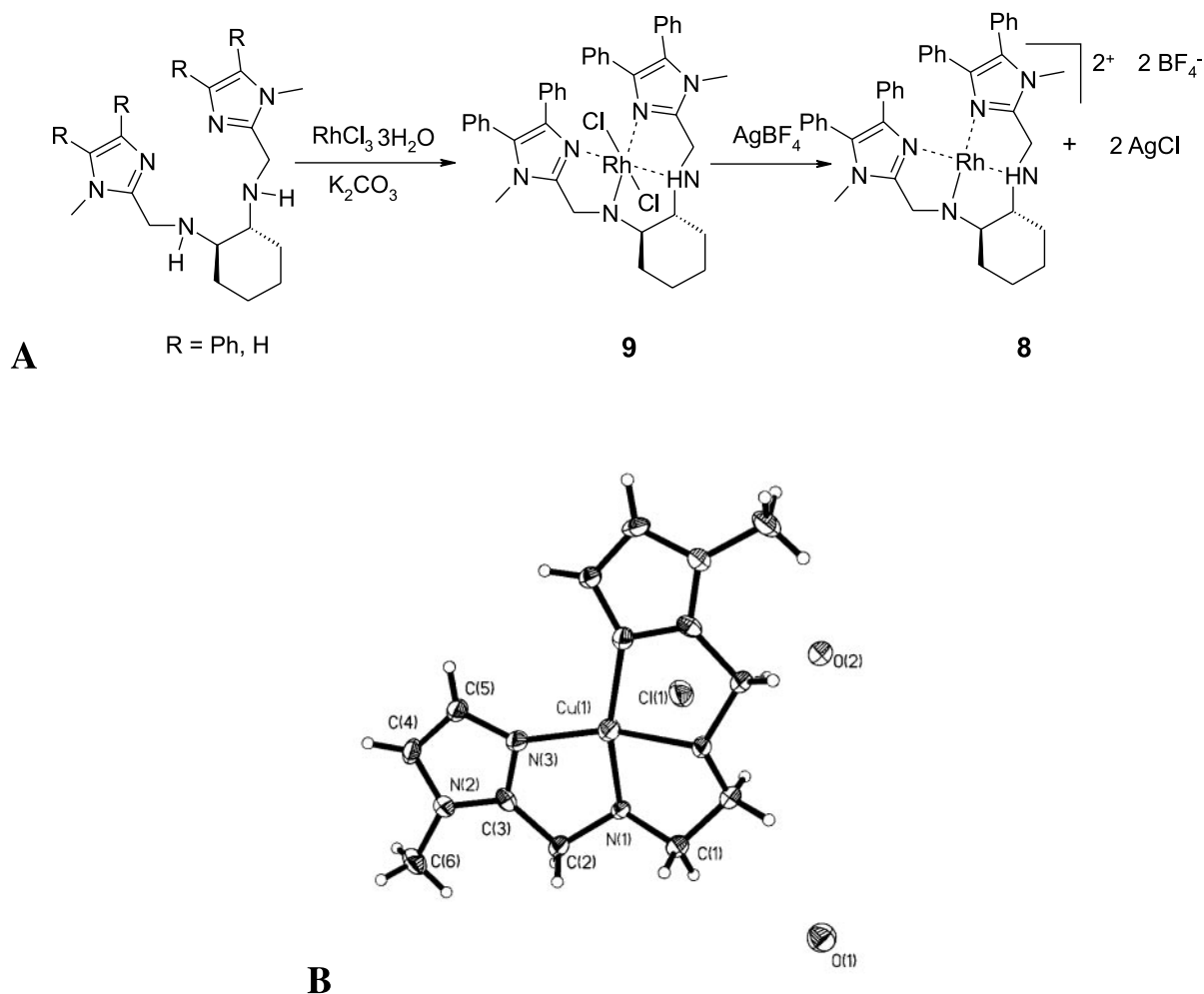
pounds were examined for their ability to provide a chiral environment for the reduction of ketones by hydrosilanes. Compound **4** was found to be a more efficacious catalyst than **6** and **7** for the reduction of aryl methyl ketones by  $\text{HSi(OMe)}_3$ , its use leading to good yields (70–75%) of phenylethanol and related compounds, albeit with low degrees of enantioselectivity (25–30% ee).

Tetraamino compounds are well-known ligands in transition metal chemistry (13), particularly the chemistry of rhodium. It was of interest to bind these readily available ligands **4–7** to rhodium and establish if acceptable enantioselectivities would accrue in C—C bond-forming reactions. We present an examination of the enantioselective allylation of aldehydes with allyltributylstannane catalyzed by a new air-stable rhodium(III) complex **8** derived from ligand **7** (14).

## Results and discussion

Complex **9** was directly synthesized by the mixing of equimolar amounts of commercially available rhodium(III) chloride hydrate, **7**, and 2.2 equiv of potassium carbonate in ethanol. The complex thus formed is sufficiently air stable that purification by silica gel chromatography is possible (Scheme 2a). Although no crystallographic structure data are yet available on this compound, we propose structure **9** for the precatalyst on the basis of crystal structures obtained for the analogous copper chloride salt of **6** and its achiral ethylenediamine-derived parent **5** (Scheme 2b). NMR, IR, and mass spectral data are also consistent with the proposed structure.



**Scheme 2.** (a) Bis-imidazole rhodium complexes; (b) Cu(II) complex of **5**.

The NMR data (see experimental section) indicate that the symmetry of the ligand is lost upon complexation–deprotonation.

The allylation reaction was attempted with benzaldehyde and allyltributylstannane in the presence of 5 mol% of the (*S,S*)-**9** as the chiral catalyst. No reaction was observed during the course of 7 days at room temperature. The electrophilicity of the catalyst was then increased, following the precedent of Nishiyama et al. (15). Compound **9** was treated with silver tetrafluoroborate for 1 h to give **8** with accompanying precipitation of AgCl. Allylations mediated by this catalyst at room temperature were efficient, but not rapid: complete conversion took about 4 days. Low enantioselectivity was noted in all solvents tested. The absolute configurations of the allylated aromatic products were determined to be *S* by comparison of their optical rotations with literature values (16). The selectivities in methylene chloride were somewhat worse than in THF: enantiomeric excesses were determined by <sup>1</sup>H NMR integration of the corresponding Mosher esters. Although the reaction was accelerated in the presence of 4 Å molecular sieves, the enantiomeric excess of the product did not appreciably change (Table 1, entries 3 and 4). This improvement in conversion may result from

fewer unproductive ligand-exchange reactions at rhodium with water.

Table 2 summarizes the results obtained from the allylation reaction using allyltributylstannane and catalyst **8** with a variety of aldehydes. It is evident that the enantioselectivity is dependent on the nature of the aldehyde, generally showing a low level of induction with aromatic aldehydes but a much higher selectivity with the one aliphatic example examined. Further work is underway to establish if the improved efficiency with aliphatic aldehydes is general.

The main distinction between **8** and the ligands of Nishiyama or Masaki is the number of available binding sites and the size of the chiral steering groups. The rhodium in **8** is tetradentate, rather than tridentate as in the other two complexes. Normally, this larger number of binding sites would auger well for stereoselection: fewer degrees of freedom are available to an Rh-bound aldehyde and to the approach of the allylstannane. However, mitigating against this is the relatively small steric footprint of cyclohexanediamine.

Models of the likely rhodium complexes of benzaldehyde derived from the X-ray structures of **1** and the copper chloride salt **7**,<sup>3</sup> respectively, illuminate the differences in stereoselectivity induced by the two complexes. The larger

<sup>3</sup>F.J. LaRonde, M.A. Brook, and J.F. Britten. Submitted.



**Table 1.** Asymmetric allylation of benzaldehyde with rhodium complexes.

Entry	Catalyst	Solvent	Conditions	Yield (%) <sup>a</sup>	ee (%) <sup>b</sup>
1	<b>9</b>	THF	Ambient <i>T</i> , 4 days	0	—
2	<b>8</b>	THF	Ambient <i>T</i> , 4 days	65	9 <i>S</i>
3	<b>8</b>	THF	Ambient <i>T</i> , 4 Å molecular sieves, 4 days	97	10 <i>S</i>
4	<b>8</b>	CH <sub>2</sub> Cl <sub>2</sub>	Ambient <i>T</i> , 4 Å molecular sieves, 4 days	95	2 <i>S</i>

<sup>a</sup>Isolated yield after chromatography. The conversions are only slightly higher than these values.<sup>b</sup>Determined by synthesis of Mosher esters; see experimental section.**Table 2.** Asymmetric allylation of aldehydes catalyzed by **8**.

Entry	Aldehyde	Product	Yield (%) <sup>a</sup>	ee (%) <sup>b</sup>	Configuration <sup>c</sup>
1			97	10	<i>S</i>
2			78	10	<i>S</i>
3			67	6	<i>S</i>
4			85	8	
5			82	99	<i>R</i>

<sup>a</sup>Determined after purification by column chromatography on silica gel.<sup>b</sup>Determined by synthesis of Mosher esters and comparison with known compounds (16); see experimental section.<sup>c</sup>Note that the same mechanism and same facial selectivities are implicated in all these reactions. The changeover from *S* to *R* is a consequence of different Cahn–Ingold–Prelog priorities.

stereodirecting groups of the Nishiyama or Masaki ligands — for example, benzyl derived from **1** — are perfectly located in the complexes to direct facial attack at the carbonyl group. By contrast, the chiral cyclohexyldiamino groups in complexes derived from **7** are essentially flat (Fig. 3, *R* = H). It is apparent that generic stereochemical induction using complexes of this type will require larger groups (*R* = large).

## Conclusion

Enantiopure, tetraamine ligands bind effectively to Rh(III). Cationic complexes derived from the ligand are suf-

ficiently electrophilic to act as Lewis acids that catalyze the enantioselective addition of allyltributylstannane to aldehydes.

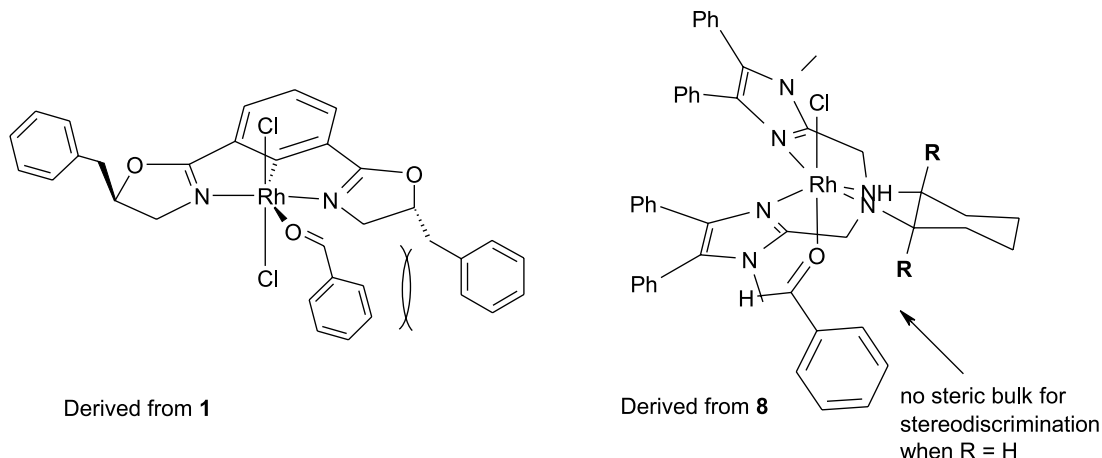
## Experimental

### Reagents and physical methods

The following materials were obtained from Aldrich and were used without further purification: acetophenone, benzophenone, benzaldehyde, 4-trifluorotolualdehyde, 4-methoxybenzaldehyde, *trans*-4-phenyl-2-methyl-2-butenal, dodecanal, (*S*)-(+)- $\alpha$ -methoxy- $\alpha$ -(trifluoromethyl)phenylacetyl chloride



**Fig. 3.** Modelled structures of benzaldehyde adducts of rhodium derivatives of **1** and **8**, respectively.



(MTPA-Cl (+)), pyridine, silver tetrafluoroborate, rhodium(III) chloride trihydrate, potassium carbonate, and 4 Å molecular sieves. Compound **7** was prepared following the literature procedure (13).

$^1\text{H}$  NMR spectra were recorded on a Bruker AC-200 (at 200 MHz for protons) Fourier transform spectrometer.  $^{13}\text{C}$  NMR was performed on a Bruker AC-200 (at 50.32 MHz) or a Bruker AC-300 (at 75.44 MHz) Fourier transform spectrometer.  $^1\text{H}$  chemical shifts are reported either with respect to tetramethylsilane as an external standard (set to 0 ppm) or  $\text{CDCl}_3$  as an internal standard (set at 7.24 ppm).  $^{13}\text{C}$  chemical shifts are reported with respect to  $\text{CDCl}_3$  as an internal standard (set at 77 ppm). Coupling constants ( $J$ ) are recorded in Hertz (Hz). The abbreviations s = singlet, d = doublet, t = triplet, q = quartet, dd = doublet of doublets, dt = doublet of triplets, and m = multiplet are used to report spectra.

Electron impact (EI) and chemical ionization (CI,  $\text{NH}_3$ ) mass spectra were recorded at 70 eV with a source temperature of 200 °C on a VG analytical ZAB-R mass spectrometer equipped with a VG 11–250 data system. High resolution mass spectral (HR-MS) data were obtained using the EI method. Infrared spectra were run as KBr pellets or as liquid films on NaCl discs (as indicated) on a PerkinElmer 283 spectrometer or on a BIORAD FTS-40 spectrometer as a neat film. Models shown in Fig. 3 were calculated with the Hyper-Chem 5 modelling package, using molecular mechanics methods (MM+). The starting geometries used came from the respective crystal structure data. Absolute configurations of the product homoallylic alcohols were assigned based on the rotations reported in the literature (16).

All solvents were thoroughly dried before use: acetonitrile was dried over  $\text{P}_2\text{O}_5$ ; THF was dried from Na–benzophenone. All reactions were carried out in dry apparatus under a nitrogen atmosphere with the use of septa and syringes for the transfer of reagents.

### Preparation of **9**

To a dry 25 mL round-bottomed flask flushed with nitrogen was added **7** (0.12 g, 0.20 mmol), potassium carbonate (0.06 g, 0.42 mmol), and absolute EtOH (15 mL). The system was stirred under nitrogen, under reflux, for 2 h. The resulting mixture was filtered and was washed with THF

(10 mL). The solvent was removed in vacuo. The crude product was purified using column chromatography, eluting with  $\text{CHCl}_3$ :MeOH (9:1,  $R_f$  = 0.85) to produce 0.12 g (80%) of an orange powder.

FT-IR (neat, KBr disc) ( $\text{cm}^{-1}$ ): 3424.6, 3056, 2935, 2854, 1640, 1602, 1505, 1445, 1426, 1027, 785, 700.  $^1\text{H}$  NMR ( $\text{CDCl}_3$ , 200 MHz)  $\delta$ : 7.89 (bs, 1H, N-H), 7.43–7.08 (m, 20H, Ph-H), 4.06 (d,  $J$  = 13.5 Hz, 2H,  $2 \times \text{NCH}_a\text{H}_b$ ), 3.60 (d,  $J$  = 13.5 Hz, 2H,  $2 \times \text{NCH}_a\text{H}_b$ ), 3.52 (s, 6H,  $\text{NCH}_3$ ), 2.32 (m, 2H, Cy-H), 1.95 (m, 2H, Cy-H), 1.77 (m, 2H, Cy-H), 1.28 (m, 4H, Cy-H).  $^{13}\text{C}$  NMR ( $\text{CDCl}_3$ , 200 MHz)  $\delta$ : 23.95, 24.33, 28.63, 30.75, 33.00, 45.71, 51.12, 58.14, 68.55, 70.57, 126.10, 126.86, 127.51, 127.59, 127.67, 127.81, 128.27, 128.33, 128.42, 128.68, 129.20, 130.40, 130.57, 131.01, 131.21, 132.09, 139.12, 148.99, 149.49. ES-MS (positive)  $m/z$  (%): 779.2 ( $[\text{M} + 1]^+$ , 100).

### Typical experimental for allylation (example benzaldehyde)

To a dry 25 mL round-bottomed flask flushed with nitrogen was added **9** (0.02 g, 0.025 mmol), silver tetrafluoroborate (0.01g, 0.05 mmol), molecular sieves (250 mg), and THF (15 mL). The system was stirred for 1 h at room temperature. To this stirring mixture was added benzaldehyde (0.05 g, 0.5 mmol) and allyltributyltin (0.23 mL, 0.77 mmol). The resulting system was stirred at ambient temperature for 4 days. The system was quenched with an aqueous solution of sodium bicarbonate (1 mol/L, 5 mL) and filtered. The aqueous layer was extracted with ether ( $3 \times 10$  mL). The combined organic fractions were washed with sodium bicarbonate (1 mol/L,  $3 \times 10$  mL), HCl (1 mol/L,  $3 \times 10$  mL), and water ( $3 \times 10$  mL). The solvent was removed under reduced pressure. The crude product was purified by silica gel chromatography, eluting with pentane:ether (9:1). FT-IR (neat, KBr disc) ( $\text{cm}^{-1}$ ): 3388, 3078, 3032, 2927, 1642, 1494, 1454, 1048, 916, 758, 700.  $^1\text{H}$  NMR ( $\text{CDCl}_3$ , 200 MHz)  $\delta$ : 7.26–7.12 (m, 5H, Ph-H), 5.81–5.60 (m, 1H,  $\text{CH}=\text{CH}_2$ ), 5.10–5.00 (m, 2H,  $\text{CH}=\text{CH}_2$ ), 4.60 (t,  $J$  = 6.5 Hz, 1H,  $\text{CH}(\text{OH})$ ), 2.41 (t,  $J$  = 6.5 Hz, 2H,  $\text{CH}_2\text{CH}=\text{CH}_2$ ), 2.32 (bs, 1H, OH).  $^{13}\text{C}$  NMR ( $\text{CDCl}_3$ , 200 MHz)  $\delta$ : 26.69, 65.66, 117.97, 125.72, 127.33, 128.22, 134.39, 143.84. EI-MS  $m/z$  (%): 148 ( $[\text{M}]^+$ , 1), 131 ( $[\text{M} - 17]^+$ , 5), 107 (100), 79 (75), 41 (33). CI-MS  $m/z$  (%): 166



( $[M + 18]^+$ , 27), 148 ( $[M]^+$ , 70), 131 ( $[M]^+ - 17$ , 100), 94 (5), 77 (2), 41 (1). HR-CI-MS  $m/z$ : Anal. calcd. for  $C_{10}H_{12}O$ : 131.0846; found: 131.0861.

#### ***1-(4-Trifluoromethylphenyl)-3-buten-1-ol***

FT-IR (neat, KBr disc) ( $cm^{-1}$ ): 3388, 3082, 2984, 2927, 1643, 1622, 1418, 1328, 1166, 1126, 1068, 1018, 922, 843, 607.  $^1H$  NMR ( $CDCl_3$ , 200 MHz)  $\delta$ : 7.50 (d,  $J = 8.3$ , 2H, Ph-H), 7.35 (d,  $J = 8.3$ , 2H, Ph-H), 5.75–5.58 (m, 1H,  $CH=CH_2$ ), 5.09–5.02 (m, 2H,  $CH=CH_2$ ), 4.68 (t,  $J = 6.4$  Hz, 1H,  $CHOH$ ), 2.43–2.31 (m, 2H,  $CH_2CH=CH_2$ ).  $^{13}C$  NMR ( $CDCl_3$ , 200 MHz)  $\delta$ : 34.11, 72.56, 118.96, 125.25, 126.06, 133.67, 147.80. EI-MS  $m/z$  (%): 216 ( $[M]^+$ , 1), 199 ( $[M + 17]^+$ , 30), 175 (100), 147 (18), 127 (100), 95 (6), 77 (15), 41 (27). CI-MS  $m/z$  (%): 234 ( $[M + 18]^+$ , 8), 216 ( $[M]^+$ , 18), 199 ( $[M + 17]^+$ , 30), 166 (16), 127 (100), 94 (6), 78 (6), 52 (14). HR-CI-MS  $m/z$ : Anal. calcd. for  $C_{11}H_{10}F_3$ : 199.0721; found: 199.0735.

#### ***1-(4-Methoxyphenyl)-3-buten-1-ol***

FT-IR (neat, KBr disc) ( $cm^{-1}$ ): 3421, 3077, 2959, 2927, 1612, 1514, 1464, 1249, 1037, 832.  $^1H$  NMR ( $CDCl_3$ , 200 MHz)  $\delta$ : 6.52 (d,  $J = 8.3$ , 2H, Ph-H), 6.12 (d,  $J = 8.3$ , 2H, Ph-H), 5.11–4.94 (m, 1H,  $CH=CH_2$ ), 4.45–4.34 (m, 2H,  $CH=CH_2$ ), 3.89 (t,  $J = 6.5$  Hz, 1H,  $CHOH$ ), 3.05 (s, 3H,  $OCH_3$ ), 1.74 (m, 2H,  $CH_2CH=CH_2$ ), 1.35 (bs, 1H,  $CHOH$ ).  $^{13}C$  NMR ( $CDCl_3$ , 200 MHz)  $\delta$ : 26.80, 55.22, 72.96, 113.75, 118.09, 127.03, 134.58, 136.04, 151.20. EI-MS  $m/z$  (%): 178 ( $[M]^+$ , 3), 177 ( $[M - 1]^+$ , 6), 161 ( $[M - 17]^+$ , 7), 137 (100), 109 (38), 77 (31), 41 (42). CI-MS  $m/z$  (%): 178 ( $[M]^+$ , 4), 161 ( $[M - 17]^+$ , 100), 137 (13), 94 (1). HR-CI-MS  $m/z$ : Anal. calcd. for  $C_{11}H_{13}O_2$ : 161.0976; found: 161.0966.

#### ***trans-1-Phenyl-2-methyl-1,5-hexadien-3-ol***

FT-IR (neat, KBr disc) ( $cm^{-1}$ ): 3389, 3079, 3025, 3924, 2859, 1642, 1601, 1493, 1445, 1047, 916, 749, 700.  $^1H$  NMR ( $CDCl_3$ , 200 MHz)  $\delta$ : 7.36–7.16 (m, 5H, Ph-H), 6.52 (s, 1H,  $PhCH=CMeR$ ), 5.90–5.73 (m, 1H,  $RCH=CH_2$ ), 5.22–5.11 (m, 2H,  $RCH=CH_2$ ), 4.21 (t,  $J = 6.5$  Hz,  $CHOH$ ), 2.46–2.37 (m, 2H,  $RCH_2CH=CH_2$ ), 1.87 (s, 3H,  $PhCH=CCH_3R$ ).  $^{13}C$  NMR ( $CDCl_3$ , 200 MHz)  $\delta$ : 13.64, 40.09, 76.55, 117.94, 125.73, 126.40, 128.06, 128.94, 134.51, 137.54, 139.49. EI-MS  $m/z$  (%): 171 ( $[M - 17]^+$ , 100), 147 (40), 129 (51), 115 (9), 91 (25), 41 (25). CI-MS  $m/z$  (%): 188 ( $[M]^+$ , 5), 171 ( $[M - 17]^+$ , 100), 147 (15), 129 (24), 91 (8), 69 (2), 41 (3). HR-CI-MS  $m/z$ : Anal. calcd. for  $C_{13}H_{15}O$ : 171.1165; found: 171.1174.

#### ***1-Pentadecen-4-ol***

FT-IR (neat, KBr disc) ( $cm^{-1}$ ): 3366, 3078, 2927, 2856, 1642, 1465, 1132, 1081, 995, 913, 722.  $^1H$  NMR ( $CDCl_3$ , 200 MHz)  $\delta$ : 5.85–5.71 (m, 1H,  $RCH=CH_2$ ), 5.17–5.06 (m, 2H,  $RCH=CH_2$ ), 3.61 (m, 1H,  $CHOH$ ), 2.29–2.11 (m, 2H,  $RCH_2CH=CH_2$ ), 1.59 (bs, 1H,  $CHOH$ ), 1.48–1.12 (m, 20H,  $Me(CH_2)_{10}CHOH$ ), 1.15 (t, 3H,  $CH_3(CH_2)_{10}CHOH$ ).  $^{13}C$  NMR ( $CDCl_3$ , 200 MHz)  $\delta$ : 14.05, 22.32, 22.67, 25.67, 29.34, 29.64, 31.92, 34.13, 36.87, 41.95, 70.74, 117.94, 134.94. EI-MS  $m/z$  (%): 209 ( $[M - 17]^+$ , 1), 185 (27), 125 (10), 111 (39), 97 (69), 85 (61), 69 (88), 55 (88), 41 (100). CI-MS  $m/z$  (%): 244 ( $[M + 18]^+$ , 100), 185 (11), 171 (35), 131 (14), 111 (19), 97 (27), 85 (25), 69 (31), 55 (61), 41

(66). HR-CI-MS  $m/z$ : Anal. calcd. for  $C_{15}H_{29}$ : 209.2271; found: 209.2269.

#### **General experimental procedure for preparation of Mosher esters (shown for (S)-1-phenyl-3-buten-1-ol)**

1-Phenyl-3-buten-1-ol (3.0 mg, 0.02 mmol) and MTPA-Cl (+) (4  $\mu$ L, 0.02 mmol) were mixed with carbon tetrachloride (3 drops) and dry pyridine (3 drops). The reaction mixture was allowed to stand in a stoppered flask for 12 h at ambient temperature. Water (1 mL) was added, and the reaction mixture transferred to a separatory funnel and extracted with ether (20 mL). The ether solution, after successive washing with HCl (1 mol/L, 20 mL), saturated sodium carbonate solution (20 mL), and water (20 mL), was dried with sodium sulfate and filtered, and the solvent was removed in vacuo. The residue was dissolved in deuterated chloroform for NMR analysis. The integration(s) of the hydrogen on the carbon bearing the hydroxyl group was used as a measure to assess the enantioselection. The data was compared with that found in ref. 16.

#### **References**

- Reviews: (a) R. Noyori. *Asymmetric catalysts in organic synthesis*. Wiley, New York. 1994; (b) H. Brunner and W. Zettlmeier. *Handbook of enantioselective catalysis with transition metal compounds*. Vol. I, II. VCH, Weinheim. 1993; (c) I. Ojima (Editor). *Catalytic asymmetric synthesis*. VCH, Weinheim. 1993; (d) E.N. Jacobsen, A. Pfaltz, and H. Yamamoto (Editors). *Comprehensive asymmetric catalysis*. Vol. I–III. Springer, Berlin. 1999.
- Allylboranes: (a) H.C. Brown and P.K. Jadhav. *J. Am. Chem. Soc.* **105**, 2092 (1983); (b) R.P. Short and S. Masamune. *J. Am. Chem. Soc.* **111**, 1892 (1989); (c) U.S. Racherla and H.C. Brown. *J. Org. Chem.* **56**, 401 (1991); Allylboronates: (d) T. Herol and R.W. Hoffman. *Angew. Chem. Int. Ed. Engl.* **17**, 768 (1978); (e) A.E. Roush, A.S. Walts, and L.K. Hoong. *J. Am. Chem. Soc.* **107**, 8186 (1985); (f) W.R. Roush, L.K. Hoong, M.A.J. Palmer, and J.C. Park. *J. Org. Chem.* **55**, 4109 (1990); Allylboroadiazolidines: (g) E.J. Corey, C.-M. Yu, and S.S. Kim. *J. Am. Chem. Soc.* **111**, 5495 (1989); Allyltitanates: (h) M. Riediker and R.O. Duthaler. *Angew. Chem. Int. Ed. Engl.* **28**, 494 (1991); (i) B. Schmidt and D. Seebach. *Angew. Chem. Int. Ed. Engl.* **30**, 99 (1991); (j) A. Hafner, R.O. Duthaler, R. Marti, G. Rihs, P. Rothe-Streit, and F. Schwarzenbach. *J. Am. Chem. Soc.* **114**, 2321 (1992); Allylaluminum derivatives: (k) N. Minowa and T. Mukaiyama. *Bull. Chem. Soc. Jpn.* **60**, 3697 (1987); Allylstannanes: (l) J. Otera, Y. Kawasaki, H. Mizuno, and Y. Shimizu. *Chem. Lett.* 1529 (1983); (m) J. Otera, Y. Yoshinaga, T. Yamaji, T. Yoshioka, and Y. Kawasaki. *Organometallics*, **4**, 1213 (1985); (n) G.P. Boldrini, E. Tagliavini, C. Trombini, and A. Umami-Ronchi. *J. Chem. Soc. Chem. Commun.* 685 (1986); (o) G.P. Boldrini, L. Lodi, E. Tagliavini, C. Tarasco, C. Trombini, and A. Umami-Ronchi. *J. Org. Chem.* **52**, 5447 (1987); Allylchromium complexes: (p) K. Sugimoto, S. Aoyagi, and C. Kibayashi. *J. Org. Chem.* **62**, 2322 (1997).
- (a) H. Yamamoto (Editor). *Lewis acids in organic synthesis*. Vol. 1, 2. Wiley-VCH Verlag GmbH, Weinheim. 2000; (b) W.R. Roush. *In Comprehensive organic synthesis*. Vol. 2, 1. Edited by B.M. Trost, I. Fleming, and C.H. Heathcock. Pergamon, Oxford. 1991; (c) Y. Yamamoto and N. Asao. *Chem. Rev.* **93**, 2207 (1993); (d) T. Bach. *Angew. Chem. Int.*



- Ed. Engl. **33**, 417 (1994); (e) A.H. Hoveyda and J.P. Morken. *Angew. Chem. Int. Ed. Engl.* **35**, 1262 (1996).
4. (a) K. Furuta, M. Mouri, and H. Yamamoto. *Synlett*, 561 (1991); (b) K. Ishihara, M. Mouri, Q. Gao, T. Maruyama, K. Furuta, and H. Yamamoto. *J. Am. Chem. Soc.* **115**, 11 490 (1993).
5. (a) J.A. Marshall and Y. Tang. *Synlett*, 653 (1992); (b) J.A. Marshall and M.R. Palovich. *J. Org. Chem.* **63**, 4381 (1998).
6. (a) S. Aoki, K. Mikami, M. Terada, and T. Nakai. *Tetrahedron*, **49**, 1783 (1993); (b) A.L. Costa, M.G. Piazza, E. Tagliavini, C. Trombini, and A. Umami-Ronchi. *J. Am. Chem. Soc.* **115**, 8467 (1993); (c) G.E. Keck and D. Krishnamurthy. *J. Org. Chem.* **58**, 6543 (1993); (d) G.E. Keck, K.H. Tarbet, and L.S. Geraci. *J. Am. Chem. Soc.* **115**, 8467 (1993); (e) G.E. Keck and L.S. Geraci. *Tetrahedron Lett.* **34**, 7827 (1993); (f) S. Weigand and R. Ruckner. *Chem. Eur. J.* **2**, 1077 (1996).
7. D.R. Gauthier, Jr. and E.M. Carreira. *Angew. Chem. Int. Ed. Engl.* **35**, 2363 (1996).
8. (a) A. Yanagisawa, H. Nakashima, A. Ishiba, and H. Yamamoto. *J. Am. Chem. Soc.* **118**, 4723 (1996); (b) A. Yanagisawa, A. Ishiba, H. Nakashima, and H. Yamamoto. *Synlett*, 88 (1997).
9. (a) H. Nishiyama and Y. Motoyama. *In Lewis acid chemistry: a practical approach. Edited by H. Yamamoto.* Oxford University Press, Oxford, U.K. 1998. Chap 13; (b) W. Odenkirk, A.L. Rheingold, and B. Bosnich. *J. Am. Chem. Soc.* **114**, 6392 (1992); (c) T.K. Hollis, W. Odenkirk, N.P. Robinson, J. Whelan, and B. Bosnich. *Tetrahedron*, **49**, 5415 (1993).
10. (a) Y. Motoyama, H. Narusawa, and H. Nishiyama. *Chem. Commun.* 131 (1999); (b) Y. Motoyama, M. Okano, H. Narusawa, N. Makihara, K. Aoki, and H. Nishiyama. *Organometallics*, **20**, 1580 (2001).
11. M. Shi, G.-X. Lei, and Y. Masaki. *Tetrahedron Asymmetry*, **10**, 2071 (1999).
12. F.J. LaRonde and M.A. Brook. *Inorg. Chim. Acta*, **296**, 208 (1999).
13. (a) R.J. Sundberg and B. Martin. *Chem. Rev.* **74**, 471 (1974); (b) J.R. Aldrich-Wright, R.S. Vagg, P.A. Williams, and A. Peter. *Coord. Chem. Rev.* **166**, 361 (1997); (c) M.M. Aly. *Rev. Inorg. Chem.* **16**, 315 (1996); 329 (1996).
14. Extracted from: F.J. LaRonde. Ph.D. thesis. McMaster University, Hamilton, Canada. 2000.
15. H. Nishiyama, M. Kondo, T. Nakamura, and K. Itoh. *Organometallics*, **10**, 500 (1991).
16. J. Jacques, C.B. Gros, M.J. Brienne, and J. Toullec. *Stereochemistry — fundamentals and methods, absolute configuration of 6000 selected compounds with one asymmetric carbon atom. Edited by H.B. Kagan.* Georg Thieme Publishers, Stuttgart. 1977.



# Synthesis, characterization, and polycondensation of new stable $\alpha,\omega$ -organo(bis-silanediods)<sup>1</sup>

Geneviève Cerveau, Sabrina Chappellet, Robert J.P. Corriu, and Bertrand Dabien

**Abstract:** The synthesis and characterization of stable bis(dihydroxymethylsilyl) derivatives are described. These compounds were obtained as microcrystalline powders by controlled hydrolysis in a biphasic medium (ethyl ether – water) of the corresponding bis(dimethoxymethylsilyl) organic precursors containing phenyl, biphenyl, stilbenyl, diphenylacetylene, and diphenylbut-1,3-diyne groups. All the solids obtained exhibited a layered structure. Condensation of the bis-silanediods could be effected by fluoride catalysis in solution at ambient temperature or simply by heating in solid state. The polysiloxanes obtained from the bis-silanediods have been compared with those obtained by hydrolysis–polycondensation of the corresponding bis-dimethoxysilanes. The thermal route led to highly polycondensed solids arranged into thin plates as evidenced by TEM analysis; furthermore, in the case of the longer spacer, the organization was controlled by the arrangement of the Si-O-Si layers instead of the spacer. The X-ray study of these materials clearly evidenced the drastic influence of the length of the organic spacer, the polycondensation route and the nature of the leaving group (hydroxy or methoxy) on the short-range organization of the solids.

**Key words:** silanols, hybrid materials, polycondensation, polysiloxanes.

**Résumé :** La synthèse et la caractérisation de dérivés bis(dihydroxyméthyl)sililés stables est décrite. Ces composés sont obtenus sous forme de poudres microcristallines par hydrolyse contrôlée en milieu biphasique (éther éthylique – eau) des dérivés bis(diméthoxyméthyl)sililés correspondants. Ces précurseurs contiennent des groupements phenyl, biphenyl, stilbenyl, diphenylacétylène et diphenylbut-1,3-diyne. Tous les bis-silanediods obtenus présentent une structure en feuillets. La polycondensation des ces composés par traitement thermique du solide et par voie catalytique en solution a été étudiée. Les polysiloxanes obtenus à partir des bis-silanediods ont été comparés à ceux obtenus par hydrolyse–polycondensation des bis-diméthoxysilanes correspondants. La voie thermique conduit à des solides très polycondensés se présentant sous forme de plaquettes ; de plus dans le cas du plus long groupement organique, l'organisation est contrôlée par l'arrangement des couches Si-O-Si au lieu de l'espaceur organique. Une étude aux rayons X de ces polysiloxanes montre clairement l'influence fondamentale de la longueur de l'espaceur organique, du mode de polycondensation et de la nature du groupement partant (hydroxy ou méthoxy) sur l'organisation à courte distance de ces solides.

**Mots clés :** silanols, matériaux hybrides, polycondensation, polysiloxanes.

## Introduction

During the past few years there has been considerable interest in the chemistry of compounds containing Si-OH functional groups (1–9). Indeed the isolation of pure silanetriols  $\text{RSi}(\text{OH})_3$  or silanediods  $\text{RR}'\text{Si}(\text{HO})_2$  is more difficult than that of silanols  $\text{RR}'\text{R}''\text{SiOH}$  because of the easier polycondensation with the increasing number of OH groups at silicon (3, 4). However, until now only a few silanetriols or silanediods have been isolated (2–4). Most of the compounds synthesized and structurally characterized contain bulky substituents at silicon and most of the studies have been carried out on diphenyl or di-*tert*-butylsilanediod (10–14). Only recently have more complex silanediods been isolated (15–19). The case of molecules containing two

silanediod groups is more difficult because of the faster polycondensation reaction. Only a few of them have been synthesized (20, 21). The ones that have been reported are tetrahydroxydisiloxanes (20, 22) or a disilane (23).

We have recently shown that it is possible to isolate stable bis-silanetriols where the presence of hydrophilic interactions is the driving force in the formation of an ordered structure (24, 25). At the same time we also reported the synthesis and the X-ray crystal structure of a stable organo-bis(alkylsilanediod), 1,4-bis(dihydroxymethylsilyl)benzene (26). The crystal structure shows a remarkable hydrogen-bonded network leading to three-dimensional packing. Each  $\text{MeSi}(\text{OH})_2$  moiety is linked to four oxygen atoms belonging to three different molecules and is cross-linked through the aromatic ring with the second  $\text{MeSi}(\text{OH})_2$ , thus, achieving a

Received 2 February 2003. Published on the NRC Research Press Web site at <http://canjchem.nrc.ca> on 8 September 2003.

*This paper is dedicated to Professor John Harrod in recognition of his wonderful contributions to organometallic chemistry.*

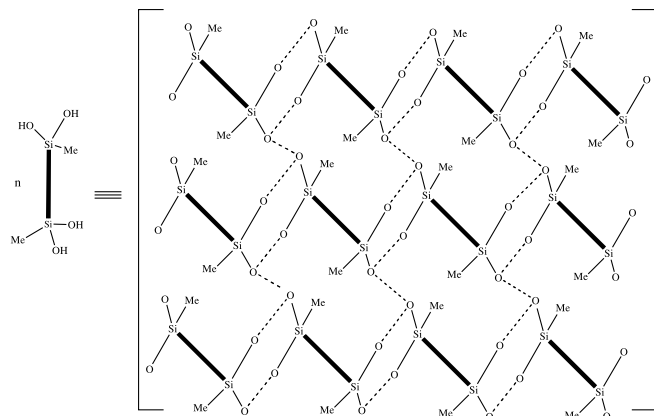
**G. Cerveau, S. Chappellet, R.J.P. Corriu,<sup>2</sup> and B. Dabien.** Laboratoire de Chimie Moléculaire et Organisation du Solide, UMR 5637, Université Montpellier II, cc007, Place E. Bataillon, 34095 Montpellier CEDEX 5, France.

<sup>1</sup>This article is part of a Special issue dedicated to Professor John Harrod.

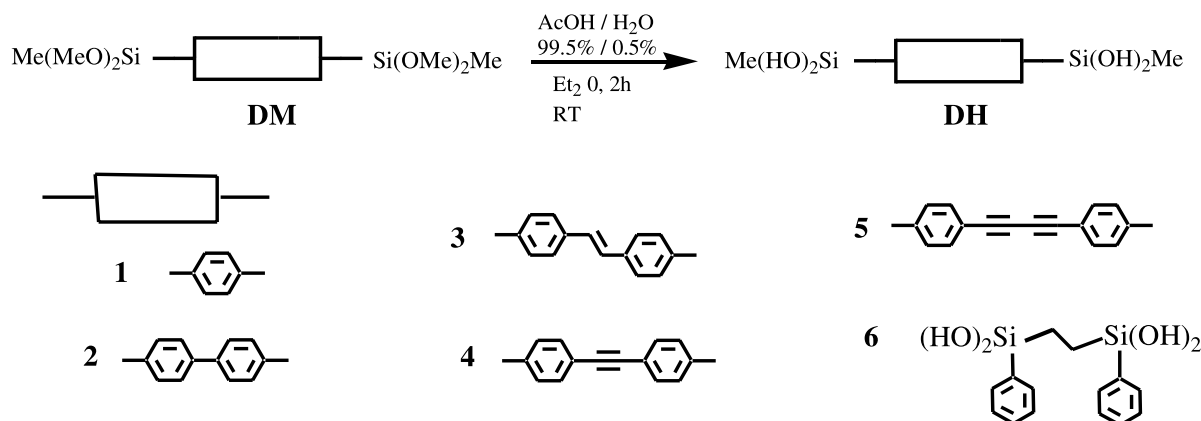
<sup>2</sup>Corresponding author (e-mail: [gcerveau@univ-montp2.fr](mailto:gcerveau@univ-montp2.fr)).



**Scheme 1.** Packing diagram of the molecules of **DH1**. The hydrogen atoms have been omitted for clarity. The dotted lines represent hydrogen bonds.



**Scheme 2.**



rigid three-dimensional structure. The structure of such a compound has been presented and provides evidence for the importance of the hydrogen bonding between neighboring silanol groups (26) as illustrated in Scheme 1.

We report here an extension of the synthesis and characterization of bis-silanediods containing two  $\text{MeSi}(\text{OH})_2$  groups in the same molecule shown in Scheme 2.

They constitute precursors for the preparation of hybrid organic–inorganic silicon-based solids (27, 28). The synthesis of polysiloxanes formed by thermal (**DHt**, Scheme 3a) and catalytic polycondensation (**DHa**, Scheme 3b) of these silanediods is also reported as well as the comparison of the solids obtained with those prepared by hydrolysis–polycondensation of the corresponding bis-dialkoxysilanes (**DMa**, Scheme 4).

## Results and discussion

### Synthesis and characterization of bis-silanediods **DH1–DH6**

Most silanediods reported in the literature have been prepared by controlled hydrolysis of dichlorosilanes (15, 29, 30) i.e., hydrolysis at low temperature of the corresponding polychlorosilylated compounds by a stoichiometric amount of water in the presence of a weak base as a catalyst (triethylamine or aniline). We investigated an alternative

**Table 1.** Experimental conditions and yields for **DH1–DH6**.

Precursor	Molar ratio <sup>a</sup> <i>np/na</i>	Reaction time (days)	Yield (%)
<b>DM1</b>	25	8	95
<b>DM2</b>	25	32	32
<b>DM2</b>	3	3	58
<b>DM3</b>	1.64	10	40
<b>DM4</b>	25	20	<sup>b</sup>
<b>DM4</b>	6	55	35
<b>DM5</b>	6	60	<sup>b</sup>
<b>DM5</b>	4.89	30	8
<b>DM6</b>	5.7	6	20

<sup>a</sup>*np/na* = number of mol of precursor vs. the number of mol of acetic acid.

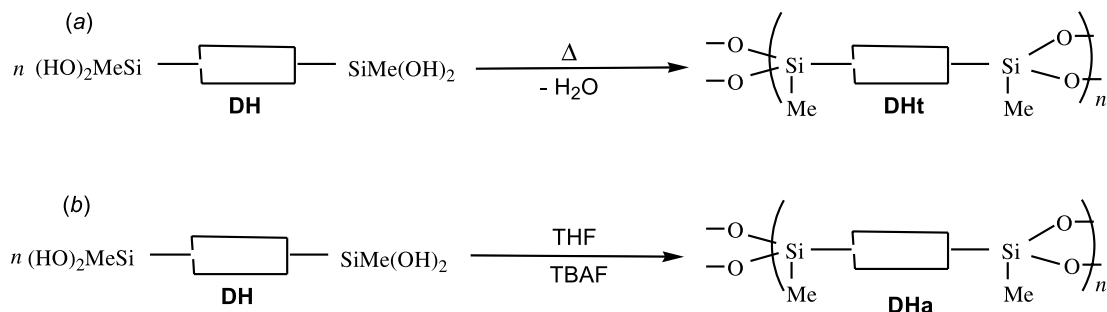
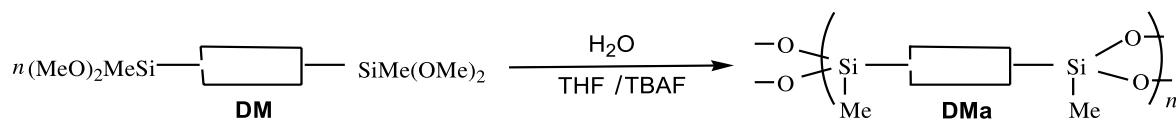
<sup>b</sup>No reaction.

route consisting of the hydrolysis of the corresponding dialkoxysilanes (31, 32); this route originally reported by Tyler (32) for the preparation of phenylsilanetriol was modified for the synthesis of bis-silanediods (24, 25) by using biphasic conditions which allowed a slower rate of polycondensation and favored the formation of hydrogen bonding between the silanol groups in the aqueous phase. The bis-silanediods reported here (**DH**) (Scheme 2) were prepared by controlled hydrolysis of the corresponding bis-(dimethoxymethylsilyl) precursors (**DM**) (33) in a biphasic medium (ethyl ether – water) in the presence of acetic acid as the catalyst at room temperature (Scheme 2).

The reaction mixture was stirred vigorously for various reaction times depending on the precursor **DM1–DM6**, until the resulting organo-bis-silanediod precipitated out in the aqueous phase. The progress of the reaction was followed by <sup>1</sup>H NMR in DMSO-*d*<sub>6</sub> and it was stopped when the singlet at 3.60 ppm owing to OMe groups had totally disappeared. In all cases a new singlet at ≈6.4 ppm revealed the presence of hydrogens of hydroxy groups. After filtration and drying at 25 °C under vacuum during 12 h, the bis-silanediods **DH1–DH6** were isolated. The experimental conditions and the yields for **DH1–DH6** are reported in Table 1.

However, it is interesting to point out the importance of the ratio (*np/na*) between the numbers of mol of precursor (*np*) and the number of mol of acetic acid (*na*) which must



**Scheme 3.** Polycondensation reactions of bis-silanediols.**Scheme 4.** Hydrolysis–polycondensation reaction of bis-dimethoxysilanes.

be adjusted case by case: in the case of **DM2**, **DM4**, and **DM5**, using the same experimental conditions as for **DM1** ( $np/na = 25$ ), only 32% of **DH2** was obtained after 32 days, whereas no reaction occurred after 20 days for **DM4** and 60 days for **DM5**, even when the ratio was  $np/na = 6$ .

To shorten the very long reaction times required, we investigated liquid–liquid phase transfer catalysis (34) using tetraethylammonium *para*-toluenesulfonate (TEApTS) as the catalyst, which was shown to be very efficient in the case of the formation of bis-silanetriols (25). The results are reported in Table 2. It appears that in every case the reaction times were significantly shortened and the yields increased, with the exception of **DM6** which gave a mixture of **DH6** and polycondensation product.

The bis-silanediols **DH1–DH6** were soluble in the usual organic solvents such as methanol, ethanol, THF, and DMSO. In this case, it was possible to recover the bis-silanediols after removal of the solvent. They were identified by IR,  $^1\text{H}$ ,  $^{13}\text{C}$ ,  $^{29}\text{Si}$  NMR spectroscopies. For all samples, the FT IR spectra exhibited a broad absorption band centered at  $\approx 3125 \text{ cm}^{-1}$  owing to hydrogen-bonded hydroxy groups and an intense band at  $\approx 900 \text{ cm}^{-1}$  attributed to the Si–O(H) bond vibrations. No free  $\nu \text{ OH}$  vibrations were detected. The  $^1\text{H}$  and  $^{13}\text{C}$  NMR spectra were recorded in DMSO- $d_6$  solution. They exhibited the expected resonances for the organic moiety in all cases (see *Experimental*). The OH groups displayed a sharp singlet at  $\approx 6.32\text{--}6.49 \text{ ppm}$ . The  $^{29}\text{Si}$  NMR spectrum in DMSO- $d_6$  solution exhibited in all cases a sharp resonance at  $\approx -21 \text{ ppm}$  in agreement with chemical shifts already reported for silanediols (26, 30). Interestingly, the  $^{29}\text{Si}$  CP-MAS NMR spectra of the solid bis-silanediols exhibited two sharp signals in some cases (see *Experimental*). In contrast to the bis-silanetriols containing the same organic groups, the  $^{29}\text{Si}$  NMR spectra showed only one singlet attributable to the OH groups (25).

The compound **DH1** exhibited two singlets of the same intensity at  $-15.9$  and  $-17.2 \text{ ppm}$ , respectively, whereas **DH4** and **DH5** presented two signals of different intensity at  $-14.7$  and  $-16.8 \text{ ppm}$  and  $-13.7$  and  $-16.7 \text{ ppm}$ , respectively. It is noteworthy that the chemical shifts were slightly different in DMSO- $d_6$  solution and in the solid state. This could be explained by a difference in the hydrogen bonding inter-

**Table 2.** Experimental conditions and yields of bis-silanediols in the presence of TEApTS (10%).

Precursor	Molar ratio <sup>a</sup> $np/na$	Reaction time (days)	Yield (%)
<b>DM2</b>	4.96	1	69
<b>DM3</b>	1.9	7	50
<b>DM5</b>	4.79	12	25
<b>DM6</b>	8	10	<sup>b</sup>

<sup>a</sup> $np/na$  = number of mol of precursor vs. the number of mol of acetic acid.

<sup>b</sup>Mixture of bis-silanediol and polysiloxane.

actions: in the solid state, the hydrogen bonds involved only silanediol molecules, whereas in solution the crystalline structure is broken and the DMSO, which is a strong hydrogen bond acceptor, might certainly be more strongly associated to the hydroxy groups, thus, shifting the signal towards higher fields ( $-21 \text{ ppm}$ ).

A  $^{29}\text{Si}$  CP-MAS NMR study was performed varying the temperature from 20 to 100 °C. No changes occurred as the two signals at  $-15.9$  and  $-17.2 \text{ ppm}$  were always present at the same chemical shifts and neither coalescence nor polycondensation were observed. Thus, the presence of two signals of the same intensity in the case of **DH1** could be indicative of a slight difference in the environment of the two silicon atoms in the solid state at the NMR timescale. The presence of the two signals was not indicative of a mixture of two different crystalline structures. This was confirmed by the thermal analysis of **DH1**, which did not reveal any phase transition.

The thermal stability of the bis-silanediols **DH1–DH6** was studied by differential scanning calorimetry (DSC). The analysis were performed under an inert atmosphere. The curves displayed broad asymmetric endothermic peaks at  $\approx 200 \text{ °C}$  (see *Experimental*), which corresponded to the polycondensation reaction as evidenced by IR spectroscopy.

These bis-silanediols appeared to be relatively stable despite the presence of four OH groups. The length of the organic group seemed to have almost no influence on the thermal stability of the different compounds in contrast with the behavior observed in the case of bis-silanetriols for



**Table 3.** Thermal treatment of **DH1** at different temperatures.

Entry	Temperature of heating (°C)	Heating time (h)	<sup>29</sup> Si CP-MAS NMR (%)			Level of Cond. (%) <sup>a</sup>	Weight loss (%) <sup>b</sup>	Stoichiometry <sup>c</sup>	Experimental stoichiometry <sup>d</sup>
			D <sup>0</sup>	D <sup>1</sup>	D <sup>2</sup>				
1	165	5	39	33	28	48	7.8 (50)	—	—
2	170	5	21	43	36	57	—	C <sub>8</sub> H <sub>12.1</sub> O <sub>3</sub> Si <sub>2</sub>	C <sub>8.5</sub> H <sub>13.4</sub> O <sub>3.77</sub> Si <sub>2</sub>
3	180	0.75	12	50	38	63	—	C <sub>8</sub> H <sub>11.5</sub> O <sub>2.7</sub> Si <sub>2</sub>	C <sub>7.2</sub> H <sub>12.2</sub> O <sub>2.8</sub> Si <sub>2</sub>
4	190	24	6	44	50	72	5.4 (66)	C <sub>8</sub> H <sub>11</sub> O <sub>2.5</sub> Si <sub>2</sub>	C <sub>7.2</sub> H <sub>10.5</sub> O <sub>2.5</sub> Si <sub>2</sub>
5	250	72	—	—	100	100	0.3 (98)	C <sub>8</sub> H <sub>10</sub> O <sub>2</sub> Si <sub>2</sub>	C <sub>8</sub> H <sub>10</sub> O <sub>2.2</sub> Si <sub>2</sub>

<sup>a</sup>Deduced from the <sup>29</sup>Si NMR data.<sup>b</sup>Calculated from TG analysis between 30 and 250 °C. The level of condensation deduced from the loss of water is given in parentheses.<sup>c</sup>Deduced from the NMR level of condensation.<sup>d</sup>Deduced from elemental analysis.

which the thermal stability decreased when the length on the organic group increased (25).

### Structural study

The X-ray diffraction patterns of the solids **DH1–DH6** (Fig. 1) revealed that all the bis-silanediods were not crystals. However, they exhibited some organization in the solid state. A short-range order was evidenced by the observation of narrow X-ray diffraction signals. Moreover, a micrometric scale organization was suggested by the TEM images (Fig. 2), which always showed the presence of the superposition of thin plates as illustrated in the case of **DH1**.

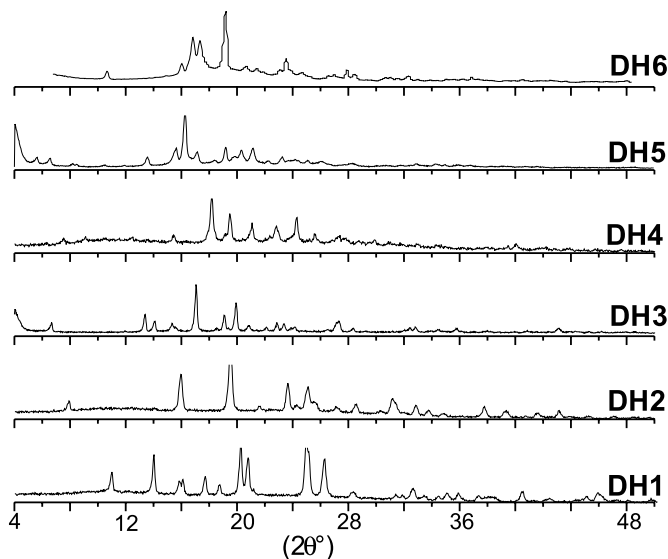
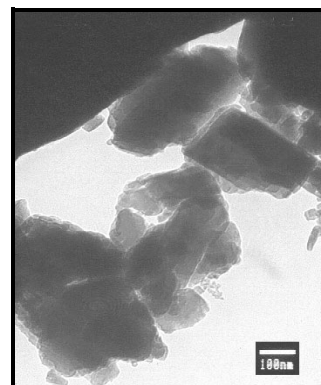
The presence of strong hydrogen bonds appeared to be the driving force for the stabilization of the bis-silanediods. The use of a biphasic medium allowed their isolation by slowing down the polycondensation and favoring the formation of a hydrogen bonding network in the aqueous phase. The presence of an aromatic group bonded to silicon was found to be unavoidable for the formation of bis-silanediods. The same results have been observed with the bis-silanetriols (25). In this case also, the use of a rigid and linear precursor was found to be much more favourable for hydrogen bond formation than a flexible or angular one.

### Polycondensation reaction of bis-silanediods **DH1**, **DH3**, and **DH5**

#### Thermal polycondensation

The thermal polycondensation of **DH1** was studied under air at different temperatures (Scheme 3a) varying the length of heating. White solids were obtained. The experimental conditions and the main results are reported in Table 3.

The <sup>29</sup>Si CP-MAS NMR spectra showed the presence of the D<sup>0</sup> (C<sub>2</sub>-Si(OH)<sub>2</sub>, δ -15.9, -17.2 ppm), D<sup>1</sup> (C<sub>2</sub>-Si(OH)(OSi), δ -24 ppm), and D<sup>2</sup> (C<sub>2</sub>-Si(OSi)<sub>2</sub>, δ -33 ppm) substructures in the case of the solids (entries 1, 2, 3, and 4 in Table 3), whereas the solid entry 5 was totally polycondensed since only D<sup>2</sup> units were detected. The deconvolution of the spectra (35, 36) led to levels of condensation ranging between 48% (entry 1) and 100% (entry 5). No cleavage of Si—C bonds occurred under the thermal treatment since no signals in the range δ -50 to -80 ppm (T<sup>n</sup> units) and δ -90 to -110 ppm (Q<sup>n</sup> units) were observed (37–39). Furthermore, the <sup>13</sup>C CP-MAS NMR spectra showed the integrity of the organic group since signals at δ 138, 132, and -1.7 ppm (aromatic carbons and CH<sub>3</sub>) were present in each case.

**Fig. 1.** X-ray powder diffraction patterns of **DH1–DH6**.**Fig. 2.** TEM image of **DH1**.

The TG analysis of these different solids performed between 30 and 400 °C allowed observation of the progress of the polycondensation reaction. A weight loss of 15.3% was observed for **DH1** which corresponded to a level of condensation of 98%. The weight losses observed in the case of the solids (entries 1, 4, and 5 in Table 3) corresponded to levels of condensation of 50%, 66%, and 98%, respectively, in



**Table 4.**  $^{29}\text{Si}$  CP-MAS NMR data of the solid obtained by thermal polycondensation of bis-silanedioles at 250 °C for 3 days.

Precursor	Solid	$^{29}\text{Si}$ CP-MAS NMR (%)			Level of Cond. (%) <sup>a</sup>	$S_{\text{BET}}$ (m <sup>2</sup> g <sup>-1</sup> )
		D <sup>0</sup>	D <sup>1</sup>	D <sup>2</sup>		
<b>DH1</b>	<b>DH1t</b>	0	0	100	100	<10
<b>DH3</b>	<b>DH3t</b>	0	15	85	93	<10
<b>DH5</b>	<b>DH5t</b>	0	10	90	95	<10

<sup>a</sup>Deduced from the  $^{29}\text{Si}$  NMR data.

good agreement with the results deduced from the  $^{29}\text{Si}$  CP-MAS NMR spectra.

The X-ray powder diffraction diagram of the solid **DH1t** (Table 3, entry 5) did not exhibit any thin peaks of Bragg. Only two broad signals centered at 7.4 and 3.8 Å were observed (Fig. 3), which were indicative of a short-range order in the solid (40, 41).

Taking into account the results obtained in the case of **DH1**, the thermal polycondensations of **DH3** and **DH5** were investigated (Scheme 3a). The bis-silanedioles were heated at 250 °C for 3 days, since the maximum temperatures for the endothermic peaks were in the same range for all the starting bis-silanedioles. The reaction was performed under an inert atmosphere of argon to avoid any degradation of the organic group (42). The  $^{29}\text{Si}$  NMR data for the resulting solids are given in Table 4.

The solids **DH3t** and **DH5t** were highly polycondensed. The  $^{29}\text{Si}$  CP-MAS NMR spectra displayed D<sup>1</sup> and D<sup>2</sup> units at  $\delta$  -24 and  $\delta$  -33 ppm, respectively. The levels of condensation ranged between 93% and 95%. These materials presented no significant specific surface area.

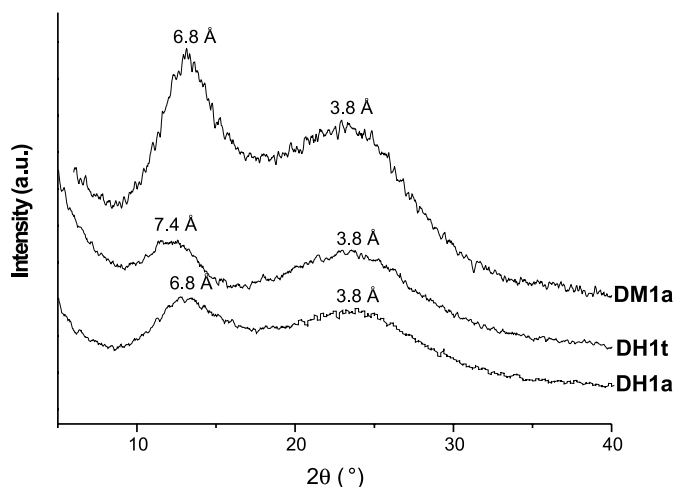
The X-ray powder diffraction diagrams of **DH3t** and **DH5t** presented signals at 11.9 Å (sharp peak) and 4.8 Å (broad peak) and at 7.5 Å (broad signal) and 4.8 Å (sharp signal), respectively (Figs. 4 and 5).

The TEM images of the solids **DH1t**, **DH3t**, and **DH5t** showed plate-like morphologies similar to those observed with the diols. They suggested a lamellar type organization at the micrometric scale.

#### Catalytic polycondensation of **DH1**, **DH3**, **DH5** and **DM1**, **DM3**, **DM5**

The catalytic polycondensation of the bis-silanedioles and the hydrolysis–polycondensation of the corresponding bis-(dimethoxymethyl)silanes were performed in THF in the presence of 1 mol% of TBAF as the catalyst at room temperature (Schemes 3b and 4). Monolithic gels were obtained in all cases. The solids obtained from the bis-silanedioles **DH** had a high level of condensation (77%–100%) (Table 5). They exhibited high specific surface areas (Table 5, entries 1–4 and 6) or moderate ones (Table 5, entry 5). They were mainly mesoporous without narrow pore size distribution (pore size <100 Å); the microporous contribution ranged between 3% and 15%.

In contrast, the corresponding bis-dimethoxysilanes **DM** led to less polycondensed solids for **DM1** with D<sup>0</sup> units (Table 5, entry 2). However, highly polycondensed solids were obtained from **DM3** and **DM5** (Table 5, entries 5 and 6). The solid **DM1a**, **DM3a**, and **DM5a** presented high specific surface areas. The microporous contribution was weak in all cases (Table 5, entries 2, 4, 6).

**Fig. 3.** X-ray powder diffraction diagram of **DH1t**, **DH1a**, and **DM1a**.

The X-ray powder diffraction diagrams of the different solids are shown in Figs. 3–5. In the case of **DH1** and **DM1**, two broad signals were observed (Fig. 3). In contrast, the X-ray patterns of **DH3a** and **DH5a** were different from those of **DM3a** and **DM5a** (Figs. 4 and 5). The TEM images of all the solids obtained by the catalytic route showed the presence of particles irregular in size and geometry in all cases.

#### Comparison of the three polycondensation routes

A comparison of the properties of the polysiloxanes obtained using the three different routes (Schemes 3 and 4) is of great interest. Although highly polycondensed solids were always obtained, their textural properties and macroscopic geometry were highly dependent on the route employed. The thermal treatment always led to nonporous solids, which exhibited a lamellar type organization at the micrometric scale as evidenced by TEM. In contrast, the route in solution from **DH** or **DM** gave mainly mesoporous materials with high specific surface areas, which do not exhibit any lamellar property by TEM experiments.

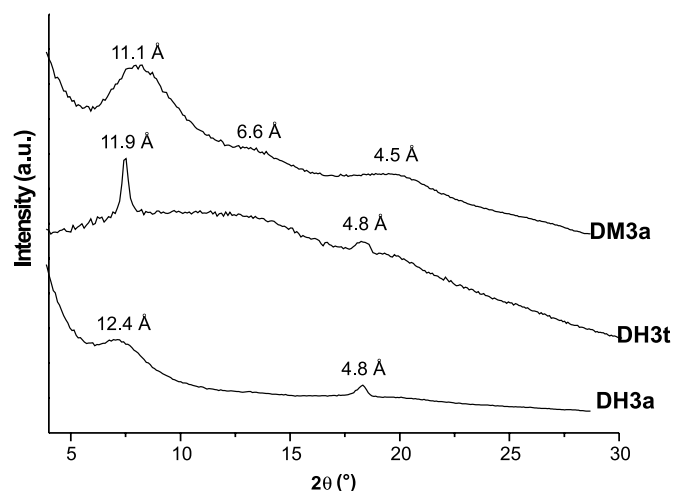
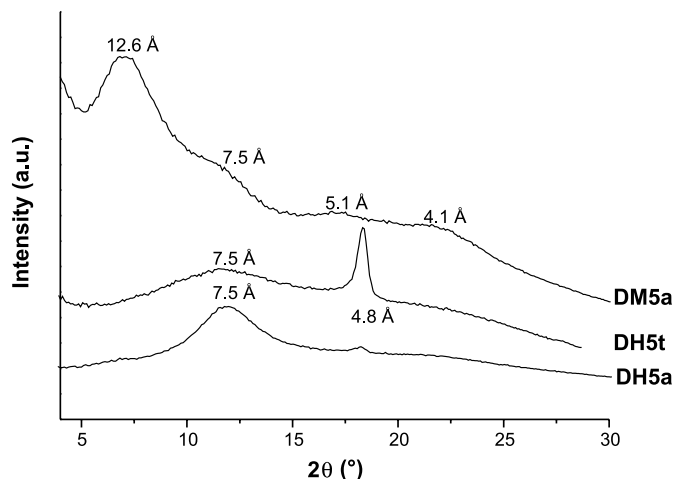
Moreover, all the X-ray studies clearly demonstrated that the short-range organization of the solids was drastically influenced by the following factors: length and nature of the organic spacer, polycondensation route, and nature of the leaving group (hydroxy or methoxy). The influence of the precursor was very important since the three spacers selected showed a drastically different behaviour.

For **1** the thermal and solution routes (Schemes 3 and 4) led to solids presenting similar X-ray diffraction diagrams. The halo centered at 3.8 Å, observed on all the diffraction diagrams, corresponded to the contribution of the Si–O–Si



**Table 5.** Experimental conditions,  $^{29}\text{Si}$  CP-MAS NMR data, and textural properties of solids obtained by polycondensation of bis-silanediods and hydrolysis–polycondensation of bis-dimethoxysilanes.

Entry	Precursor	Solid	Treatment	$^{29}\text{Si}$ CP-MAS NMR (%)			Level of Cond. (%)	$S_{\text{BET}}$ ( $\text{m}^2 \text{g}^{-1}$ )	$\mu$ -pores (%)	Pore size ( $\text{\AA}$ )
				$\text{D}^0$	$\text{D}^1$	$\text{D}^2$				
1	<b>DH1</b>	DH1a	TBAF/THF (0.5 M)	0	15	85	92	850	15	20–100
2	<b>DM1</b>	DM1a	TBAF/THF (1 M)	4	38	58	77	1000	5	20–120
3	<b>DH3</b>	DH3a	TBAF/THF (0.3 M)	0	0	100	100	910	15	20–100
4	<b>DM3</b>	DM3a	TBAF/THF (0.3 M)	0	18	82	91	450	7	20–100
5	<b>DH5</b>	DH5a	TBAF/THF (0.3 M)	0	12	88	94	160	3	20–100
6	<b>DM5</b>	DM5a	TBAF/THF (0.3 M)	0	14	86	93	500	2	20–100

**Fig. 4.** X-ray powder diffraction diagram of **DH3t**, **DH3a**, and **DM3a**.**Fig. 5.** X-ray powder diffraction diagram of **DH5t**, **DH5a**, and **DM5a**.

units as reported for organopolysilsesquioxanes (40). The other signals are connected with the length of the organic spacer (6.8 or 7.4  $\text{\AA}$ ) (40, 41). The different locations of the signals observed among the three polycondensation routes cannot be discussed in greater depth. They show that the short-range organization is related to the size of the organic spacer, but that it also depends on the type of polycondensation, which is different in each case as confirmed by the different texture and polycondensation levels (Schemes 3 and 4).

The longer spacer **3** shows a more regular arrangement depending on the route of polycondensation. The three routes led to solids presenting X-ray signals at roughly the same distances. However, the signal widths were different. Thermal treatment induced an organization, which was controlled by the spacer, with the presence of a sharp peak of Bragg for a distance close to the length of the spacer. The second characteristic was the shift of the halo corresponding to the Si–O–Si layers which appeared between 4.5 and 4.8  $\text{\AA}$  instead of 3.8  $\text{\AA}$ , as observed for **1**. This signal was of interest since it could be probably connected with the formation of wider and almost homogeneous  $-\text{Si}(\text{Me})\text{O}-$  layers. These layers were different from those obtained in the case of **1**, which were similar to those observed in the case of silsesquioxanes (40). Another interesting feature was the pres-

ence of a more narrow signal connected with the length of the spacer when the thermal treatment was used (**DHt3**). A better organisation in this case could be explained by the fact that the polycondensation occurred in the solid state, partially preserving the organization of the starting diol. All these observations suggest that in the case of **3**, the polycondensation is controlled by the length of the spacer with formation of  $-\text{Si}(\text{Me})\text{O}-$  layers.

The case of **5** was different from the previous ones since the three routes led to solids exhibiting different X-ray diffraction patterns. The two main features were the absence of any signal that could be directly related to the length of the spacer ( $d_{\text{Si-Si}} \sim 15 \text{ \AA}$ ); all the diffraction signals were for lower distances. The second one concerned the thermal treatment. Its X-ray diagram exhibited a sharp signal at 4.8  $\text{\AA}$  that can be attributed to  $-\text{Si}(\text{Me})\text{O}-$  layers. Finally, the signals observed in the case of the polycondensation performed in solution from MeO groups (**DM5a**) were completely different from those observed with **DH5a**. One possible explanation could originate from the fact that polycondensation occurs in two different media: for **DH5a**, the polycondensation occurs in hydrophilic conditions and implies only homocondensation of OH groups, whereas for **DM5a**, there is hydrolysis in a hydrophobic medium followed by competition between homo- and heterocondensa-



tion of OH and OMe groups, the medium becoming more and more hydrophilic. Further studies are in progress to clarify these observations.

## Conclusion

In conclusion, we have reported for the first time the synthesis of stable bis(alkylsilanediols), stabilized by a hydrogen bonding network. Polysiloxanes have been prepared by thermal polycondensation from the bis-silanediols **DH** and by a catalytic route in solution from the bis-silanediols and the corresponding bis-dimethoxysilanes **DM**. The solids obtained presented some similarities in all cases: the level of condensation was higher and the X-ray scattering exhibited better organization in the case of longer spacers. However, several differences have been evidenced: (i) the solids obtained by the thermal route (**DHt**) were always nonporous, whereas the catalytic route gave mainly mesoporous solids with a high specific surface area; (ii) moreover, the thermal route led to a better organization at the nanometric scale as evidenced by X-ray scattering and at the micrometric distances as evidenced by TEM (thin plates in all cases); (iii) in contrast, the catalytic routes from **DH** or **DM** always led to grains irregular in size and geometry. Furthermore, the X-ray scattering does not exhibit any reasonably sharp signals.

## Experimental

All reactions were carried out under argon using a vacuum line and Schlenk techniques. Solvents were dried and distilled just before use. IR data were obtained on a Perkin-Elmer 1600 FT IR spectrophotometer using KBr pellets. The  $^1\text{H}$  and  $^{13}\text{C}$  NMR spectra were recorded on a Bruker DPX-200 spectrometer and the  $^{29}\text{Si}$  NMR spectra were recorded on a Bruker WP-200 SY spectrometer. The  $^{29}\text{Si}$  CP-MAS NMR spectra were recorded on a Bruker Avance 300 spectrometer operating at 59.6 MHz using a recycling delay of 10 s and a contact time of 5 ms. The spinning rate was 5 kHz. Chemical shifts are given relative to tetramethylsilane. The nitrogen adsorption-desorption isotherms at 77.35 K were recorded on a Micromeritics Gemini III 2375 apparatus. The specific surface area was determined using the BET equation. The pore size distribution was calculated using the BJH method, and the microporous volume was estimated by the t-plot method using the Harkins and Jura standard isotherm. The differential scanning calorimetry were obtained on a Mettler DSC 30. The X-ray experiments were performed on several apparatus, either on a classical  $\theta$ - $2\theta$  goniometer (Seifert MZ4) or an imaging plate two-dimensional detector (Marresearch 2D Image-Plate) with a rotating anode apparatus (Rigaku RU 200). The radiation is Cu K $\alpha$  ( $\lambda = 1.5418 \text{ \AA}$ ) for both. The microscopy electronic transmission was realized on a Cambridge Stereoscan 360. Elemental analyses were carried out by the Service Central de Micro-Analyse du CNRS. The percentages of oxygen were calculated by difference. The bis-(dialkoxymethylsilyl) precursors **DM1–DM5** were prepared according to literature procedures (33). The synthesis of 1,4-bis(dihydroxymethylsilyl)benzene **DH1** has been previously reported (26).

### 4,4'-Bis(methyldihydroxysilyl)biphenyl **DH2**

A suspension of 4,4'-bis-(methyldimethoxysilyl)biphenyl **DM2** (0.950 g, 2.62 mmol) in 4.5 mL of ether was stirred vigorously with 5 mL of 0.5% acetic acid solution in water for 3 days. The resulting white suspension was filtered and the solid was washed three times with acetone and ether. The fine white solid was dried for 1 day under vacuum at room temperature and gave 4,4'-bis(methyldihydroxysilyl)biphenyl **DH2** in 58% yield (0.465 g, 1.52 mmol).  $^1\text{H}$  NMR (DMSO- $d_6$ )  $\delta$  (ppm): 7.66 (8H, s), 6.40 (4H, s), 0.19 (6H, s).  $^{13}\text{C}$  NMR (DMSO- $d_6$ )  $\delta$  (ppm): 144.7, 139.3, 134.9, 126.6, 0.38.  $^{29}\text{Si}$  NMR (DMSO- $d_6$ )  $\delta$  (ppm): -21.2.  $^{29}\text{Si}$  CP-MAS NMR  $\delta$  (ppm): -16.5. Anal. calcd. for  $\text{C}_{14}\text{H}_{18}\text{O}_4\text{Si}_2$  (%): C 54.87, H 5.92, Si 18.33; found (%): C 54.82, H 5.79, Si 18.80. DSC: endothermic peak 210  $^\circ\text{C}$ .

Phase transfer catalysis route: **DM2** (1 g, 2.76 mmol); 4 mL  $\text{Et}_2\text{O}$ ; 3.2 mL AcOH 0.5% in water; TEApTS (0.083 g, 0.276 mmol); stirring 1 day; **DH2** yield 68% (0.575 g, 1.88 mmol).

### 4,4'-Bis(dihydroxymethylsilyl)stilbene **DH3**

A suspension of 4,4'-bis(methoxymethylsilyl)stilbene **DM3** (0.630 g, 1.62 mmol) in 10 mL of ether was stirred vigorously with 10.3 mL of 0.5% acetic acid solution in water for 10 days. The same work up led to 4,4'-bis(dihydroxymethylsilyl)stilbene **DH3** as a white solid in 40% yield (0.215 g, 0.65 mmol).  $^1\text{H}$  NMR (DMSO- $d_6$ )  $\delta$  (ppm): 7.68 (4H, d), 7.59 (4H, d), 7.29 (2H, s), 6.37 (4H, s), 0.39 (6H, s).  $^{13}\text{C}$  NMR (DMSO- $d_6$ )  $\delta$  (ppm): 139.7, 138.1, 134.7, 129.5, 126.4, 0.02.  $^{29}\text{Si}$  NMR (DMSO- $d_6$ )  $\delta$  (ppm): -21.4.  $^{29}\text{Si}$  CP-MAS NMR  $\delta$  (ppm): -11.0. Anal. calcd. for  $\text{C}_{16}\text{H}_{20}\text{O}_4\text{Si}_2$  (%): C 57.80, H 6.06, Si 16.90; found (%): C 57.58, H 5.92, Si 17.15. DSC: endothermic peak 205  $^\circ\text{C}$ .

Phase transfer catalysis route: **DM3** (0.6 g, 1.55 mmol); 5 mL  $\text{Et}_2\text{O}$ ; 4.7 mL AcOH 0.5% in water; TEApTS (0.047 g, 0.155 mmol); stirring 7 days; **DH3** yield 50% (0.257 g, 0.775 mmol).

### 4,4'-Bis(dihydroxymethylsilyl)diphenylacetylene **DH4**

A suspension of 4,4'-bis(dimethoxymethylsilyl)diphenylacetylene **DM4** (1.62 g, 4.2 mmol) in 8 mL of ether was stirred vigorously with 6.65 mL of 0.5% acetic acid solution in water for 55 days. 4,4'-Bis(dihydroxymethylsilyl)diphenylacetylene **DH4** was isolated as a beige solid in 35% yield (410 mg, 1.26 mmol).  $^1\text{H}$  NMR (DMSO- $d_6$ )  $\delta$  (ppm): 7.63 (4H, s), 7.54 (4H, s), 6.49 (4H, s), 0.19 (6H, s).  $^{13}\text{C}$  NMR (DMSO- $d_6$ )  $\delta$  (ppm): 141.2, 134.5, 131.2, 123.7, 90.8, 0.18.  $^{29}\text{Si}$  NMR (DMSO- $d_6$ )  $\delta$  (ppm): -21.7.  $^{29}\text{Si}$  CP-MAS NMR  $\delta$  (ppm): -14.7, -16.8. Anal. calcd. for  $\text{C}_{16}\text{H}_{18}\text{O}_4\text{Si}_2$  (%): C 58.16, H 5.49, Si 17.00; found (%): C 58.42, H 5.89, Si 17.51. DSC: endothermic peak 211  $^\circ\text{C}$ .

### 4,4'-Bis(dihydroxymethylsilyl)diphenylbut-1,4-diyne **DH5**

A suspension of 4,4'-bis(dimethoxymethylsilyl)diphenylbut-1,4-diyne **DM5** (1.22 g, 2.98 mmol) in 10 mL of ether was stirred vigorously with 3.5 mL of 0.5% acetic acid solution in water for 30 days. Similarly, 4,4'-bis(dihydroxymethylsilyl)diphenylbut-1,4-diyne **DH5** was obtained as a beige solid in 8% yield (0.084 g, 0.238 mmol).  $^1\text{H}$  NMR (DMSO- $d_6$ )  $\delta$  (ppm): 7.60 (8H, s), 6.54 (4H, s), 0.19 (6H, s).



$^{13}\text{C}$  NMR (DMSO- $d_6$ )  $\delta$  (ppm): 141.2, 134.5, 132.06, 122.7, 85.8, 75.1, 0.11.  $^{29}\text{Si}$  NMR (DMSO- $d_6$ )  $\delta$  (ppm): -21.7.  $^{29}\text{Si}$  CP-MAS NMR  $\delta$  (ppm): -13.7, -16.7. Anal. calcd. for  $\text{C}_{18}\text{H}_{18}\text{O}_4\text{Si}_2$  (%): C 60.99, H 5.12, Si 15.85; found (%): C 60.82, H 5.48, Si 16.07. DSC: endothermic peak 185 °C.

Phase transfer catalysis route: **DM5** (0.410 g, 1 mmol); 3.4 mL  $\text{Et}_2\text{O}$ ; 1.2 mL  $\text{AcOH}$  0.5% in water; TEApTS (0.30 g, 0.1 mmol); stirring 12 days; **DH5** yield 25% (0.089 g, 0.25 mmol).

### 1,2-Bis(dimethoxyphenylsilyl)ethane **DM6**

1,2-Bis(dichlorophenylsilyl)ethane was prepared from dichlorovinylsilane (4.06 g, 20 mmol) dissolved in 20 mL dry hexane, phenyldichlorosilane (15.6 g, 90 mmol), and 0.01% of  $\text{H}_2\text{PtCl}_6$  in 20 mL of dry hexane as described in the literature (43). The methanolysis was then performed by addition of 5.54 mL of  $\text{Et}_3\text{N}$  and 1.7 mL of  $\text{MeOH}$ . The mixture was stirred for 2 h and the solution was then filtered. The organic solvent was pumped off and the corresponding crude yellow oil was distilled under vacuum (bp 90–100 °C,  $5 \times 10^{-2}$  mbar) to afford 1,2-bis(dimethoxyphenylsilyl)ethane **DM6** in 55% yield (3.98 g, 11 mmol).  $^1\text{H}$  NMR ( $\text{CDCl}_3$ )  $\delta$  (ppm): 7.60 (2H, m), 7.61 (4H, d), 7.40 (8H, m), 3.60 (12H, s), 0.86 (4H, s).  $^{13}\text{C}$  NMR ( $\text{CDCl}_3$ )  $\delta$  (ppm): 134.8, 130.5, 128.3, 51.1, 3.35.  $^{29}\text{Si}$  NMR ( $\text{CDCl}_3$ )  $\delta$  (ppm): -16.15. Anal. calcd. for  $\text{C}_{18}\text{H}_{26}\text{O}_4\text{Si}_2$  (%): C 59.63, H 7.23, Si 15.49; found (%): C 59.52, H 7.19, Si 15.81.

### 1,2-Bis(dihydroxyphenylsilyl)ethane **DH6**

A suspension of 1,2-bis(dimethoxyphenylsilyl)ethane **DM6** (1.08 g, 2.98 mmol) in 6 mL of ether was stirred vigorously with 6 mL of 0.5% acetic acid solution in water for 6 days. The same treatment led to 1,2-bis(dihydroxyphenylsilyl)ethane as a white solid in 20% yield (182 mg, 0.6 mmol).  $^1\text{H}$  NMR (DMSO- $d_6$ )  $\delta$  (ppm): 7.56 (2H, m), 7.34 (8H, d), 6.28 (4H, s), 0.56 (4H, s).  $^{13}\text{C}$  NMR (DMSO- $d_6$ )  $\delta$  (ppm): 134.8, 128.3, 4.8.  $^{29}\text{Si}$  NMR (DMSO- $d_6$ )  $\delta$  (ppm): -18.9. Anal. calcd. for  $\text{C}_{14}\text{H}_{18}\text{O}_4\text{Si}_2$  (%): C 54.87, H 5.92, Si 18.33; found (%): C 54.52, H 5.71, Si 18.12.

### Thermal polycondensation of **DH1** (solids Table 3, entries 1–5)

#### General procedure

A sample of **DH1** grounded and deposited into a cupel was heated in an oven under air at a given temperature (the increase of temperature was 10 °C/min). The final temperature was maintained for various lengths of time. In all cases a white powder was obtained.  $^{13}\text{C}$  CP-MAS NMR data were the same for all the solids:  $\delta$  (ppm): 138, 132, -1.7.  $^{29}\text{Si}$  CP-MAS NMR data were the same for solids entries 1–4:  $\delta$  (ppm): -15.9, -17.2, -24, -33. The specific surface area ( $S_{\text{BET}}$ ) was  $<10 \text{ m}^2 \text{ g}^{-1}$  in all cases.

#### Solid Table 3, entry 1:

Temperature 165 °C for 5 h. FT IR (KBr)  $\nu$  ( $\text{cm}^{-1}$ ): 1050, 1147, 1265, 3180.

#### Solid Table 3, entry 2:

Temperature 170 °C for 5 h. FT IR (KBr)  $\nu$  ( $\text{cm}^{-1}$ ): 1050, 1147, 1259, 3145, 3615. Anal. calcd. for  $\text{C}_8\text{H}_{10}\text{O}_2\text{Si}_2$  (%): C

39.48, H 5.15, Si 28.87; found (%): C 43.87, H 5.73, Si 24.09; this corresponds to  $\text{C}_{8.5}\text{H}_{13.4}\text{O}_{3.8}\text{Si}_2$ .

#### Solid Table 3, entry 3:

Temperature 180 °C for 0.75 h. FT IR (KBr)  $\nu$  ( $\text{cm}^{-1}$ ): 1050, 1147, 1259, 3250, 3620. Anal. calcd. for  $\text{C}_8\text{H}_{10}\text{O}_2\text{Si}_2$  (%): C 39.48, H 5.15, Si 28.87; found (%): C 43.33, H 6.12, Si 28.08; this corresponds to  $\text{C}_{7.2}\text{H}_{12.2}\text{O}_{2.8}\text{Si}_2$ .

#### Solid Table 3, entry 4:

Temperature 190 °C for 24 h. FT IR (KBr)  $\nu$  ( $\text{cm}^{-1}$ ): 1050, 1147, 1259, 3350, 3620. Anal. calcd. for  $\text{C}_8\text{H}_{10}\text{O}_2\text{Si}_2$  (%): C 39.48, H 5.15, Si 28.87; found (%): C 44.79, H 5.44, Si 29.03; this corresponds to  $\text{C}_{7.2}\text{H}_{10.5}\text{O}_{2.5}\text{Si}_2$ .

#### Solid Table 3, entry 5 (**DH1t**):

Temperature 250 °C for 72 h. FT IR (KBr)  $\nu$  ( $\text{cm}^{-1}$ ): 1050, 1147, 1265, 3664.  $^{29}\text{Si}$  CP-MAS NMR  $\delta$  (ppm): -33. Anal. calcd. for  $\text{C}_8\text{H}_{10}\text{O}_2\text{Si}_2$  (%): C 39.48, H 5.15, Si 28.87; found (%): C 39.48, H 2.76, Si 28.40; this corresponds to  $\text{C}_8\text{H}_{10}\text{O}_{2.2}\text{Si}_2$ .

### Thermal polycondensation of **DH3** and **DH5**

The procedure was the same as above, the compound **DH** was heated at 250 °C for 72 h under argon (**DH3** and **DH5**).  $S_{\text{BET}}$  was  $<10 \text{ m}^2 \text{ g}^{-1}$  in all cases.

#### **DH3t**

White powder. FT IR (KBr)  $\nu$  ( $\text{cm}^{-1}$ ): 1080, 1152, 1265, 3620.  $^{13}\text{C}$  CP-MAS NMR  $\delta$  (ppm): 142, 133, 128, 125, -0.2.  $^{29}\text{Si}$  CP-MAS NMR  $\delta$  (ppm): -25, -31.

#### **DH5t**

Orange powder. FT IR (KBr)  $\nu$  ( $\text{cm}^{-1}$ ): 1080, 1152, 1265, 3620.  $^{13}\text{C}$  CP-MAS NMR  $\delta$  (ppm): 133, 126, 125, 124, 82, 78, -2.  $^{29}\text{Si}$  CP-MAS NMR  $\delta$  (ppm): -25, -31.

### Catalytic polycondensation of **DH1**, **DH3**, and **DH5**

#### General procedure

The precursor **DH** was dissolved in  $\text{MeOH}$  or  $\text{THF}$  containing 1 mol% of the catalyst TBAF at room temperature. After various reaction times a gel or a precipitate formed, which was aged for 5 days. It was then ground in a mortar and washed with ethanol, acetone, and ether. The resulting powder was dried under vacuum ( $10^{-1}$  mbar) for 12 h at room temperature. The  $^{13}\text{C}$  CP-MAS NMR data were the same as those of the corresponding solids obtained by the thermal route.

#### **DH1a**:

1.15 g (5 mmol) of **DH1**, 10 mL of  $\text{THF}$  (conc. 0.5 M), 50  $\mu\text{L}$  of a 1 M solution of TBAF, gel after 24 h, white powder, 1.00 g (103%). FT IR (KBr)  $\nu$  ( $\text{cm}^{-1}$ ): 1060, 1147, 1265 3450.  $^{29}\text{Si}$  CP-MAS NMR  $\delta$  (ppm): -24, -33.  $S_{\text{BET}}$  ( $\text{m}^2 \text{ g}^{-1}$ ): 850.

#### **DH3a**:

0.28 g (0.84 mmol) of **DH3**, 2.8 mL of  $\text{THF}$  (conc. 0.3 M), 8  $\mu\text{L}$  of a 1 M solution of TBAF, gel after 15 min, white powder, 0.25 g (100%). FT IR (KBr)  $\nu$  ( $\text{cm}^{-1}$ ): 1080, 1152, 1265 3620.  $^{29}\text{Si}$  CP-MAS NMR  $\delta$  (ppm): -31.  $S_{\text{BET}}$  ( $\text{m}^2 \text{ g}^{-1}$ ): 910.



**DH5a:**

0.50 g (1.41 mmol) of **DH5**, 4.7 mL of THF (conc. 0.3 M), 14  $\mu$ L of a 1 M solution of TBAF, gel after 15 min, orange powder, 0.45 g (100%). FT IR (KBr)  $\nu$  ( $\text{cm}^{-1}$ ): 1080, 1152, 1265 3620.  $^{29}\text{Si}$  CP-MAS NMR  $\delta$  (ppm): -25, -31.  $S_{\text{BET}}$  ( $\text{m}^2 \text{g}^{-1}$ ): 157.

**Catalytic polycondensation of DM1, DM3, and DM5 (sol-gel route)**
**General procedure**

A solution in THF of 1 mol% of the catalyst TBAF and water was added to a solution of the precursor **DM** in THF at room temperature. After various reaction times a gel or a precipitate formed, which was treated as above leading to a powder. The FT IR and  $^{13}\text{C}$  CP-MAS NMR data were the same as those of the corresponding solids obtained by the thermal route, an additional signal at  $\delta = 50$  ppm owing to residual methoxy groups was present in all cases.

**DM1a:**

2.13 g (7.44 mmol) of **DM1**, 7.10 mL of THF (conc. 1 M), 74.4  $\mu$ L of a 1 M solution of TBAF, 270  $\mu$ L of water, gel after 5 min, white powder (1.48 g, 103%).  $^{29}\text{Si}$  CP-MAS NMR  $\delta$  (ppm): -15, -24, -33.  $S_{\text{BET}}$  ( $\text{m}^2 \text{g}^{-1}$ ): 1000.

**DM3a:**

0.54 g (1.39 mmol) of **DM3**, 4.7 mL of THF (conc. 0.3 M), 14  $\mu$ L of a 1 M solution of TBAF, 50  $\mu$ L of water, gel after 15 min, white powder (0.45 g, 109%).  $^{29}\text{Si}$  CP-MAS NMR  $\delta$  (ppm): -25, -31.  $S_{\text{BET}}$  ( $\text{m}^2 \text{g}^{-1}$ ): 450.

**DM5a:**

0.75 g (1.83 mmol) of **DM5**, 6.1 mL of THF (conc. 0.5 M), 18  $\mu$ L of a 1 M solution of TBAF, 66  $\mu$ L of water, gel after 5 min, orange powder (0.58 g, 100%).  $^{29}\text{Si}$  CP-MAS NMR  $\delta$  (ppm): -25, -31.  $S_{\text{BET}}$  ( $\text{m}^2 \text{g}^{-1}$ ): 500.

**Acknowledgements**

The authors acknowledge the Dow Corning Corporation for supporting this research and thank Dr. Pierre Chevalier from Dow Corning (Barry, U.K.) for fruitful discussions.

**References**

1. R. Murugavel, V. Chandrasekhar, and H.W. Roesky. *Acc. Chem. Res.* **29**, 183 (1996).
2. R. Murugavel, A. Voigt, M.G. Walawalkar, and H.W. Roesky. *Chem. Rev.* **96**, 2205 (1996), and refs. therein.
3. P.D. Lickiss. *Adv. Inorg. Chem.* **42**, 147 (1995), and refs. therein.
4. P.D. Lickiss. Polysilanol. *In* The chemistry of organic silicon compounds. *Edited by* Z. Rappoport and Y. Apeloig. John Wiley, Chichester. 2001. p. 695.
5. F.J. Feher and T.A. Budzichowski. *Polyhedron*, **14**, 3239 (1995).
6. M. Motevalli, D. Shah, S.A.A. Shah, and A.C. Sullivan. *J. Chem. Soc., Chem. Commun.* 2427 (1994).
7. M. Motevalli, D. Shah, S.A.A. Shah, and A.C. Sullivan. *Organometallics*, **13**, 4109 (1994).
8. D. Juwiler, J. Blum, and R.J. Neuman. *J. Chem. Soc., Chem. Commun.* 1123 (1998).
9. M. Veilh, M. Jarczykand, and V. Huch. *Angew. Chem. Int. Ed. Engl.* **36**, 117 (1997).
10. K.J. Fawcett, N. Camerman, and A. Camerman. *Can. J. Chem.* **55**, 3631 (1977).
11. O. Graolman, U. Klingebiel, W. Clegg, M. Maase, and G.M. Sheldrick. *Chem. Ber.* **117**, 2988 (1984).
12. H.J. Gosink, H.W. Roesky, H.G. Schmidt, M. Noltemeyer, E. Irmer, and R. Herbst-Irmer. *Organometallics*, **13**, 3420 (1994).
13. H.J. Gosink, H.W. Roesky, M. Noltemeyer, H.G. Schmidt, F. Freire-Erdbrugger, and G.M. Sheldrick. *Chem. Ber.* **126**, 279 (1993).
14. H.W. Roesky, A.D.H. Mazzah, and M. Noltemeyer. *Chem. Ber.* **124**, 519 (1991).
15. R.S. Simons, K.J. Galat, B.J. Rapp, C.A. Tessier, and W.J. Youngs. *Organometallics*, **19**, 5799 (2000).
16. S.M. Sielburth, T. Nittoli, A.M. Mutahi, and L. Guo. *Angew. Chem. Int. Ed. Engl.* **37**, 312 (1998).
17. V. Chandrasekhar, S. Nagendran, R. Boomishankar, and R.J. Butcher. *Inorg. Chem.* **40**, 940 (2001).
18. V. Chandrasekhar, S. Nagendran, and R.J. Butcher. *Organometallics*, **18**, 4488 (1999).
19. R. Murugavel, A. Voigt, V. Chandrasekhar, H.W. Roesky, H.G. Schmidt, and M. Noltemeyer. *Chem. Ber.* **129**, 391 (1996).
20. P.D. Lickiss, S.A. Litster, A.D. Redhouse, and C.A. Wisener. *J. Chem. Soc., Chem. Commun.* 173 (1991).
21. C.E.F. Rickard, W.R. Roper, D.M. Salter, and L.J. Wright. *J. Am. Chem. Soc.* **114**, 9682 (1992).
22. R. Murugavel, P. Böttcher, A. Voigt, M.G. Walawalkar, H.W. Roesky, E. Parisini, M. Teichert, and M. Noltemeyer. *J. Chem. Soc., Chem. Commun.* 2417 (1996).
23. C. Ackerhans, P. Böttcher, P. Müller, H.W. Roesky, I. Uson, H.G. Schmidt, and M. Noltemeyer. *Inorg. Chem.* **40**, 3766 (2001).
24. G. Cerveau, R.J.P. Corriu, B. Dabiens, and J. Le Bideau. *Angew. Chem. Int. Ed.* **39**, 4533 (2000).
25. G. Cerveau, S. Chappellet, R.J.P. Corriu, B. Dabiens, and J. Le Bideau. *Organometallics*, **21**, 1560 (2002).
26. F. Carré, G. Cerveau, R.J.P. Corriu, and B. Dabiens. *J. Organomet. Chem.* **624**, 354 (2001).
27. E. Lindner, S. Brugger, S. Steinbrecher, E. Plies, and H.A. Mayer. *J. Mater. Chem.* **11**, 1393 (2001).
28. D.A. Loy, G.M. Jamison, B.M. Baugher, S.A. Myers, R.A. Assink, and K.J. Shea. *Chem. Mater.* **8**, 656 (1996).
29. J.A. Cella and J.C. Carpenter. *J. Organomet. Chem.* **480**, 23 (1994).
30. M.J. MacLachlan, M. Ginzburg, J. Zheng, O. Knoll, A.J. Lough, and I. Manners. *New J. Chem.* 1409 (1998).
31. J.F. Hyde. *J. Am. Chem. Soc.* **75**, 2166 (1953).
32. L.J. Tyler. *J. Am. Chem. Soc.* **77**, 770 (1955).
33. G. Cerveau, S. Chappellet, R.J.P. Corriu, and B. Dabiens. *J. Organomet. Chem.* **626**, 92 (2001).
34. C.M. Starks and C. Liotta. *In* Phase transfer catalysis, principles and techniques. Academic Press, New York. 1978.
35. G. Cerveau, R.J.P. Corriu, C. Lepeytre, and P.H. Mutin. *J. Mater. Chem.* **8**, 2707 (1998).
36. W.H. Oviatt, K.J. Shea, and J.H. Small. *Chem. Mater.* **5**, 943 (1993).
37. M. Mägi, E. Lippmaa, A. Samoson, G. Engelhardt, and A.R. Grimmer. *J. Phys. Chem.* **88**, 1518 (1984).
38. H. Marsmann. *In*  $^{29}\text{Si}$  NMR spectroscopic results. *Edited by* P. Diehl, E. Fluck, and R. Kosfeld. Springer Verlag, Berlin. 1981.
39. E.A. Williams. NMR spectroscopy of organosilicon compounds. *In* The chemistry of organic silicon compounds. *Edited by* S. Patai and Z. Rappoport. Wiley, New York. p. 511.



40. B. Boury, R.J.P. Corriu, P. Delord, and V. Le Strat. *J. Non-Cryst. Solids*, **265**, 41 (2000).
41. B. Boury, R.J.P. Corriu, V. Le Strat, P. Delord, and M. Nobili. *Angew. Chem. Int. Ed.* **38**, 3172 (1999).
42. G. Cerveau, R.J.P. Corriu, and B. Dabiens. *J. Mater. Chem.* **10**, 1113 (2000).
43. G.F. Pavelko and E.G. Rozantsev. *Bull. Acad. Sci. USSR, Div. Chem. Sci. (Engl. Transl.)*, 2348 (1967).



# A metal-free catalytic intramolecular hydrosilylation<sup>1</sup>

Hans-Uwe Steinberger, Christian Bauch, Thomas Müller, and Norbert Auner

**Abstract:** A metal-free catalytic intramolecular hydrosilylation reaction is reported. The key intermediates in the catalytic cycle are silyl cationic species. The reaction is used to produce 2-silanorbornanes **2** from 3-cyclopentenemethylsilanes **1** under mild conditions and in high isolated yields.

**Key words:** hydrosilylation, catalysis, silaheterocycles, silyl cations.

**Résumé :** On a effectué une réaction d'hydrosilylation intramoléculaire catalytique n'impliquant aucun métal. Les intermédiaires clés dans le cycle catalytique sont des espèces cationiques silylées. On utilise la réaction pour préparer des 2-silanobornanes (**2**) avec des rendements élevés à partir de cyclopent-3-èneméthylsilanes (**1**), dans des conditions douces.

**Mots clés :** hydrosilylation, catalyse, silahétérocycles, cations silyles.

[Traduit par la Rédaction]

## Introduction

The hydrosilylation reaction, the formal addition of a Si-H functionality across a C=C multiple bond, is one of the most widely used methods for the formation of Si-C bonds, with a strong impact on laboratory work as well as on commercial processes (1). Since Speier's original finding (2) that chloroplatinic acid efficiently catalyzes this reaction, platinum catalysts are the standard reagents in this type of chemistry. Due to Chalk and Harrods' mechanistic investigations in 1965 (3), the course of the catalytic cycle is quite well understood and therefore, stereo- and regiochemistry in the products can be reasonably well predicted. There is, however, a recent interest in transition metal-free processes with possible applications in polymer chemistry. Free-radical-induced hydrosilylation reactions (1a, 1c), a plausible alternative to the metal-catalyzed reaction, are severely hampered by possible side reactions as for example, radical polymerization of the unsaturated organic compound (4). A catalytic hydrosilylation reaction based on silyl cationic intermediates was first suggested by Lambert and Zhao (5) in 1996. Their finding that trityl cation efficiently catalyzes the hydrosilylation reaction between triethylsilane and diphenylethene in toluene solution suggests that the chain propagators in this process are silylated arenium ions and  $\beta$ -silyl

substituted carbocations (5). Similarly, we report here a convenient procedure for a catalytic intramolecular hydrosilylation reaction giving silaheterocycles under mild conditions and in high isolated yields. The key intermediates in this process are silanorbornyl cations, intramolecularly  $\pi$ -stabilized silyl cations (6).

## Results and discussion

Treatment of cyclopentenemethyl silanes **1** with catalytic amounts of trityl tetrakis(pentafluorophenyl) borate (TPFPB) (typical molar ratio **1**:TPFPB = 600–100:1) in toluene at room temperature resulted in the clean formation of 2-silanorbornanes **2** in high isolated yields (85–94%, see Scheme 1).

The silanorbornanes **2** were isolated as mixtures of exo and endo diastereomers with exo to endo ratios of about 2.7–1.8:1 (see also Table 1). Silanorbornanes **2** were characterized by standard NMR methods and analytical procedures. In the case of **2a**, the exo and endo diastereomers were separated by preparative gas chromatography; this allowed the unequivocal assignment of the complex <sup>1</sup>H and <sup>13</sup>C NMR spectra of the silanorbornanes **2**.

The intramolecular hydrosilylation of the cyclopentenemethylsilanes **1** was thought to proceed via silyl cationic

Received 29 March 2003. Published on the NRC Research Press Web site at <http://canjchem.nrc.ca> on 10 September 2003.

*Dedicated to Professor J.F. Harrod.*

**H.-U. Steinberger.** Fachinstitut für Anorganische und Analytische Chemie der Humboldt Universität Berlin, Hessische Str. 1–2 D-10115 Berlin, Federal Republic of Germany.

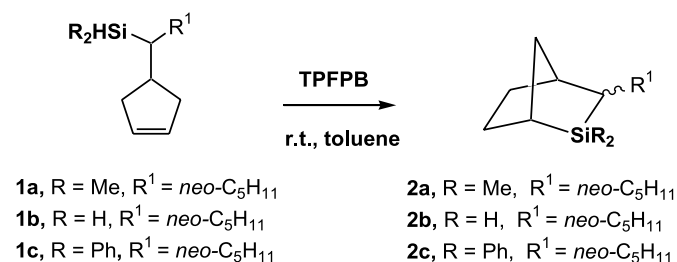
**C. Bauch.** Institut für Anorganische Chemie der Goethe Universität Frankfurt am Main, Marie Curie Str.11, D-60439 Frankfurt/Main, Federal Republic of Germany.

**T. Müller<sup>2</sup> and N. Auner.** Institut für Anorganische Chemie der Goethe Universität Frankfurt am Main, Marie Curie Str. 11, D-60439 Frankfurt/Main, Federal Republic of Germany and Fachinstitut für Anorganische und Analytische Chemie der Humboldt Universität Berlin, Hessische Str.1–2 D-10115 Berlin, Federal Republic of Germany.

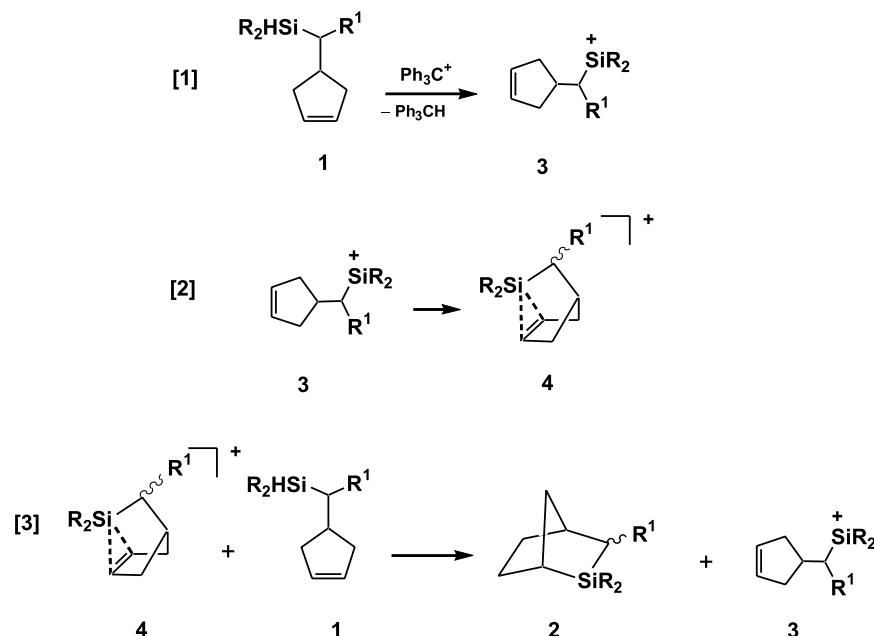
<sup>1</sup>This article is part of a Special Issue dedicated to Professor John Harrod.

<sup>2</sup>Corresponding author (e-mail: [dr.thomas.mueller@chemie.uni-frankfurt.de](mailto:dr.thomas.mueller@chemie.uni-frankfurt.de)).



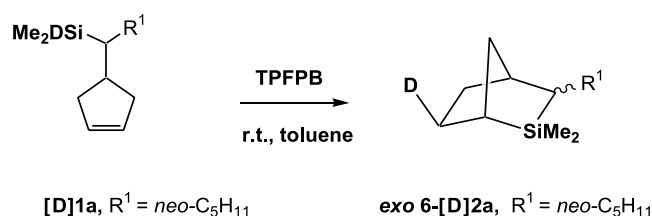
**Scheme 1.** Catalytic intramolecular hydrosilylation of cyclopentenemethylsilanes **1**.**Table 1.** Catalytic hydrosilylation of cyclopentenemethyl silanes **1**.

Entry	Compound	R	Yield (%)	exo to endo Ratio in <b>2</b>
1	<b>1a</b>	Me	94 <sup>a</sup>	1.8 <sup>a</sup>
2	<b>1b</b>	H	88 <sup>a</sup>	2.6 <sup>a</sup>
3	<b>1c</b>	Ph	94 <sup>a</sup>	2.7 <sup>a</sup>
4	[D] <b>1a</b>	Me	85	1.9
5	<b>1a</b>	Me	71 <sup>b</sup>	4.0

<sup>a</sup>Mean value from three independent runs.<sup>b</sup>See also ref. 12.**Scheme 2.** Proposed catalytic cycle for the intramolecular hydrosilylation of **1**.

species (see Scheme 2, eq. [1]). In the first step, the catalytic active species was formed by a hydride transfer reaction from silanes **1** to trityl cation (7). The by-product triphenylmethane was identified by NMR analysis.<sup>3</sup> The silylium ions **3** were only transient species and underwent fast intramolecular reactions to the more stable silanorbornyl cations **4** (Scheme 2, eq. [2]). In stoichiometric reactions, the silanorbornyl cations **4** can be synthesized and are persistent at ambient conditions (6). In the presence of excess silanes **1**, however, a second hydride transfer took place, which resulted in the finite generation of the silanorbornanes **2** with newly formed Si—C and C—H bonds and the silylium ions **3**, which started new catalytic cycles. Thus, both silyl cationic species, the trivalent silyl cation **3** and the silanorbornyl cation **4**, were propagators in the catalytic process.

This mechanistic proposal is supported by deuterium labeling experiments. The catalytic reaction of [D]-**1a** with trityl cation produced exclusively the *exo* and *endo* 3-neopentyl mixture of the *exo*-6-deutero norbornane **2a** (Table 1, entry 4 and Scheme 3). The exclusive *exo*-orientation of the deuterium atom in 6-[D]-**2a** is verified by one- and

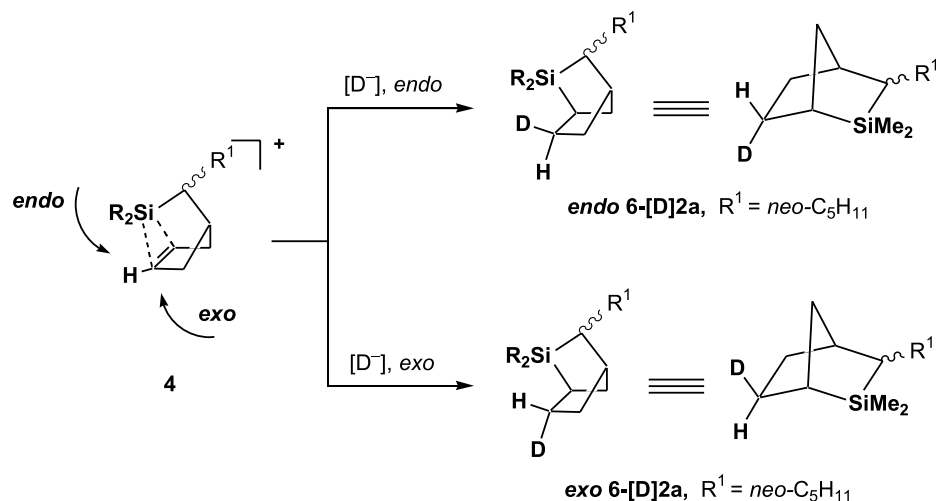
**Scheme 3.**

two-dimensional <sup>1</sup>H NMR spectroscopy and by comparison with the <sup>1</sup>H NMR spectra of the separated 3-*exo*- and 3-*endo*-isomers of **2a**. The selective formation of *exo*-6-[D]-**2a** is reminiscent of the preferred formation of *exo* products in the solvolysis of 2-norbornanes (8) and is best explained by an exclusive *exo* addition of a deuteride equivalent at the C=C double bond in the intermediate silanorbornyl cation **4** (see Scheme 4). The *endo* attack on the C=C double bond was efficiently blocked by the bridging SiMe<sub>2</sub> group. Previous studies (6) definitely ruled out the possibility of an achievable fast degenerate equilibrium between two β-silyl-

<sup>3</sup>Triphenylmethane: <sup>1</sup>H NMR (400 MHz, 300 K, C<sub>6</sub>D<sub>6</sub>) δ: 7.09 (br, 15H), 5.41 (s, 1H). <sup>13</sup>C NMR (100 MHz, 300 K, C<sub>6</sub>D<sub>6</sub>) δ: 57.1, 126.5, 128.5, 129.6, 144.2.



Scheme 4.



substituted carbocations. Therefore, the labeling experiments give additional evidence for the silanorbornyl cations **4** as intermediates in this catalytic process.

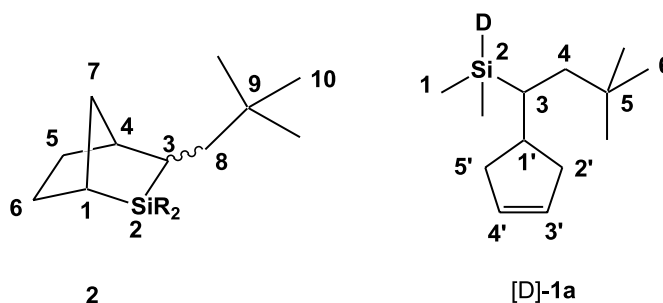
Density functional calculations (9) at the B3LYP/6-311G(2d,p)/B3LYP/6-31G(d) +  $\Delta$ ZPVE level of theory (10, 11) indicated that the suggested catalytic process was an overall exothermic process. Thus, for  $R^1 = H$  the intramolecular reaction **3a**  $\rightarrow$  **4a** (eq. [2], Scheme 2) was exothermic by 19.8 kcal mol<sup>-1</sup>. The second reaction (eq. [3]) of the catalytic process was predicted to be endothermic by 9.0 kcal mol<sup>-1</sup>. This resulted in an overall exothermic catalytic cycle (by 10.8 kcal mol<sup>-1</sup>).<sup>4</sup> Addition of thermal energies and entropic factors suggested that the process was also exergonic at 298 K ( $\Delta G(\text{calcd.}) = -9.4$  kcal mol<sup>-1</sup>, at B3LYP/6-31G(d)).

The catalytic intramolecular hydrosilylation reaction (shown in Scheme 3) was more efficient than the traditional hydrosilylation reaction using platinum catalysts. Thus, reaction of **1a** with hexachloroplatinic acid in toluene at room temperature proceeded only sluggishly and heating to reflux for several hours was needed for complete transformation into **2a** (see Table 1, entry 5) (12). This is in agreement with observations by Cremer and Blankenship (13) and Sakurai and co-workers (14), who reported that the intramolecular hydrosilylation reaction forming silanorbornanes using platinum catalysts needed more vigorous reaction conditions (i.e., for the reaction **1a**  $\rightarrow$  **2a** ( $R^1 = H$ ): 100 h, 130 °C, neat substance).

## Conclusion

In summary, we report a metal-free catalytic reaction for the intramolecular hydrosilylation of C=C double bonds giving silanorbornanes **2** in high yields under mild reaction conditions. The process advances via silylcationic species with silanorbornyl cations **4**, as the key intermediates. Similar intramolecular reactions can be envisaged for other intramolecular stabilized silylcations (15, 16) and the scope of

Chart 1.



this reaction is currently under investigation in our laboratory.

## Experimental

### General

All reagents were obtained from commercial suppliers and were used without further purification. THF was distilled from sodium – potassium alloy – benzophenone; benzene and toluene were distilled from sodium. All reactions were carried out in oven-dried glassware under an inert atmosphere of argon. 3-(3-Cyclopentenyl)-1-chloro-1,5,5-trimethyl-2-silohexane (12) and TFPBP (17) were prepared as described in the literature. NMR spectra were recorded on Bruker AM 600 and DPX 300 instruments. <sup>1</sup>H NMR spectra were calibrated using residual non-deuterated solvents as internal reference, <sup>13</sup>C NMR spectra using the central line of the solvent signal. <sup>29</sup>Si NMR spectra were recorded using the INEPT pulse sequence and were calibrated using external TMS ( $\delta^{29}Si = 0.0$ ).

### *exo*- and *endo*-2,2-Dimethyl-3-neopentyl-2-silabicyclo[2.2.1]heptane (**2a**)

Silane (1.3 g, 6.19 mmol) **1a** (12) was added slowly to a solution of 10 mg TFPBP in 20 mL toluene. After 1 h,

<sup>4</sup> Absolute energies of compounds **1a–4a** at B3LYP/6-311G(2d,p)/B3LYP/6-31G(d) (H); unscaled zero point energies (kcal mol<sup>-1</sup>) in parenthesis: **1a** ( $R^1 = H$ ) –604.10959 (137.2); **2a** ( $R^1 = H$ ) –604.12869 (140.2); **3a** ( $R^1 = H$ ) –603.23038 (131.1); **4a** ( $R^1 = H$ ) –603.23038. All compounds have been verified to be minima on the potential energy surface.



40 mL of *n*-hexane were added. Filtration and removal of solvents under reduced pressure gave a colorless oil. Bulb-to-bulb distillation gave 1.22 g **2a** (5.8 mmol, 94%) bp 37 °C/10<sup>-2</sup> mbar. The *exo* and *endo* diastereomers were separated by preparative gas chromatography (H<sub>2</sub> (3.6 L/h), 10% OV 101, column length 6 m, 80–100 mesh Chromosorb W, HO, DMCS, isotherm 110 °C). *exo*-**2a**: <sup>1</sup>H NMR (600 MHz, CDCl<sub>3</sub>) δ: 0.07 (s, 3H, SiCH<sub>3</sub> *endo*), 0.13 (s, 3H, SiCH<sub>3</sub> *exo*), 0.45 (m, 1H, H-3), 0.95 (s, 9H, C(CH<sub>3</sub>)<sub>3</sub>), 1.21 (dddd, <sup>2</sup>J<sub>5x/5e</sub> = 12.2 Hz, <sup>3</sup>J<sub>5x/6e</sub> = 6.0 Hz, <sup>3</sup>J<sub>5x/6x</sub> = 8.3 Hz, <sup>4</sup>J<sub>5x/7s</sub> = 1.8 Hz, 1H, H-5x), 1.25 (dd, <sup>2</sup>J<sub>HH</sub> = 13.8 Hz, <sup>3</sup>J<sub>HH</sub> = 4.6 Hz, 1H, CH<sub>a</sub>H<sub>b</sub>-*t*-Bu), 1.26 (m, 1H, H-1), 1.47 (dddd, <sup>2</sup>J<sub>7a/7s</sub> = 10.8 Hz, <sup>3</sup>J<sub>7a/1</sub> = 2.8 Hz, <sup>3</sup>J<sub>7a/4</sub> = 2.8 Hz, <sup>4</sup>J<sub>7a/3</sub> = 2.9 Hz, 1H, H-7a), 1.50 (dd, <sup>2</sup>J<sub>HH</sub> = 13.8 Hz, <sup>3</sup>J<sub>HH</sub> = 6.8 Hz, 1H, CH<sub>a</sub>H<sub>b</sub>-*t*-Bu), 1.60 (d, br, <sup>2</sup>J<sub>HH</sub> = 10.8 Hz, 1H, H-7s), 1.63 (m, 1H, H-6x), 1.68 (dddd, <sup>2</sup>J<sub>6e/6x</sub> = 12.0 Hz, <sup>3</sup>J<sub>6e/1</sub> = 5.9 Hz, <sup>3</sup>J<sub>6e/5e</sub> = 12.0 Hz, <sup>3</sup>J<sub>6e/5x</sub> = 6.0 Hz, 1H, H-6e), 1.78 (dddd, <sup>2</sup>J<sub>5e/5x</sub> = 12.2 Hz, <sup>3</sup>J<sub>5e/6e</sub> = 12.0 Hz, <sup>3</sup>J<sub>5e/6x</sub>/<sup>3</sup>J<sub>5e/4</sub> = 6.0/4.0 Hz, 1H, H-5e), 2.15 (s, br, 1H, H-4). <sup>13</sup>C NMR (75.40 MHz, CDCl<sub>3</sub>) δ: 47.1 (C-4), 46.3 (C-8), 36.4 (C-7), 31.5 (C-9), 31.5 (C-5), 23.9 (C-6), 29.8 (C-10), 29.4 (C-1), 24.2 (C-3), -4.2 (SiCH<sub>3</sub> (*exo*)), -4.4 (SiCH<sub>3</sub> (*endo*)). <sup>29</sup>Si NMR (59.25 MHz, CDCl<sub>3</sub>) δ: 10.2. MS (70 eV), *m/z* (%): 210 (0) [M<sup>+</sup>], 153 (74.73) [M<sup>+</sup> - *t*-Bu], 125 (98.91), 59 (100), 57 (33.15) [*t*-Bu<sup>+</sup>]. *endo*-**2a**: <sup>1</sup>H NMR (600 MHz, CDCl<sub>3</sub>) δ: 0.06 (s, 3H, SiCH<sub>3</sub> *endo*), 0.10 (s, 3H, SiCH<sub>3</sub> *exo*), 0.84 (m, 1H, H-3), 0.95 (s, 9H, C(CH<sub>3</sub>)<sub>3</sub>), 1.29 (dd, <sup>2</sup>J<sub>HH</sub> = 13.6 Hz, <sup>3</sup>J<sub>HH</sub> = 4.0 Hz, 1H, CH<sub>a</sub>H<sub>b</sub>-*t*-Bu), 1.29 (m, 1H, H-1), 1.42 (m, 2H, H-5e and H-5x), 1.45 (dd, <sup>2</sup>J<sub>HH</sub> = 13.6 Hz, <sup>3</sup>J<sub>HH</sub> = 8.5 Hz, 1H, CH<sub>a</sub>H<sub>b</sub>-*t*-Bu), 1.48 (d, br, <sup>2</sup>J<sub>7s/7a</sub> = 10.8 Hz, 1H, H-7s), 1.57 (m, 1H, H-6x), 1.58 (m, 1H, H-7a), 1.68 (dddd, <sup>2</sup>J<sub>6e/6x</sub> = 12.1 Hz, <sup>3</sup>J<sub>6e/1</sub> = 5.9 Hz, <sup>3</sup>J<sub>6e/5e</sub> = 12.0 Hz, <sup>3</sup>J<sub>6e/5x</sub> = 6.0 Hz, 1H, H-6e). <sup>13</sup>C NMR (75.40 MHz, CDCl<sub>3</sub>) δ: 44.8 (C-4), 42.05 (C-8), 38.7 (C-7), 31.22 (C-9), 29.9 (C-10), 27.1 (C-3), 25.6 (C-1), 24.7/23.9 (C-5/C-6), -1.8 (SiCH<sub>3</sub> (*exo*)), -6.3 (SiCH<sub>3</sub> (*endo*)). <sup>29</sup>Si NMR (59.25 MHz, CDCl<sub>3</sub>) δ: 17.5. MS (70 eV), *m/z* (%): 210 (0) [M<sup>+</sup>], 153 (73.73) [M<sup>+</sup> - *t*-Bu], 125 (95.47), 59 (100), 57 (31.73) [*t*-Bu<sup>+</sup>]. Anal. calcd. for C<sub>13</sub>H<sub>26</sub>Si: C 74.19, H 12.45, Si 13.35; found: C 73.99, H 12.34, Si 13.40.

#### *exo*- and *endo*-3-Neopentyl-2-silabicyclo[2.2.1]heptane (**2b**)

A similar procedure as described for **2a** gave 1.67 g (88%, 9.2 mmol) **2b** from the reaction of 1.89 g (10.4 mmol) **1b** with TFPFB, bp 35 °C/10<sup>-2</sup> mbar. *exo*-**2b**: <sup>1</sup>H NMR (300 MHz, CDCl<sub>3</sub>) δ: 0.77 (m, 1H, H-3), 0.90 (s, 9H, CH<sub>2</sub>-*t*-Bu), 1.15 (m, 1H, H-5x), 1.57 (m, 1H, H-1), 1.41 (m, 1H, H-7a), 1.41 (dd, <sup>2</sup>J<sub>HH</sub> = 13.9 Hz, <sup>3</sup>J<sub>HH</sub> = 3.7 Hz, 1H, CH<sub>a</sub>H<sub>b</sub>-*t*-Bu), 1.45 (m, 1H, H-6x), 1.46 (dd, <sup>2</sup>J<sub>HH</sub> = 13.9 Hz, <sup>3</sup>J<sub>HH</sub> = 5.5 Hz, 1H, CH<sub>a</sub>H<sub>b</sub>-*t*-Bu), 1.49 (m, 1H, H-7s), 1.64 (m, 1H, H-6e), 1.65 (m, 1H, H-5e), 2.16 (s, br, H-4), 3.36 (dm, <sup>2</sup>J<sub>HH</sub> = 11.9 Hz, 1H, SiH (*exo*)), 3.78 (dm, <sup>2</sup>J<sub>HH</sub> = 11.9 Hz, 1H, SiH (*endo*)). <sup>13</sup>C NMR (75.40 MHz, CDCl<sub>3</sub>) δ: 49.0 (C-8), 45.4 (C-4), 35.9 (C-7), 31.9 (C-9), 31.1 (C-5), 29.8 (C-10), 24.7 (C-6), 24.3 (C-1), 21.0 (C-3). <sup>29</sup>Si NMR (59.25 MHz, CDCl<sub>3</sub>) δ: -10.2 (t, <sup>1</sup>J<sub>SiH</sub> = 203 Hz). MS (70 eV), *m/z* (%): 181 (3.16) [M<sup>+</sup> - H], 125 (38.14) [M<sup>+</sup> - *t*-Bu], 97 (100), 57 (23.00) [*t*-Bu<sup>+</sup>]. *endo*-**2b**: <sup>1</sup>H NMR (300 MHz, CDCl<sub>3</sub>) δ: 0.90 (s, 9H, CH<sub>2</sub>-*t*-Bu), 1.16 (m, 1H, H-3), 1.36 (dd, <sup>2</sup>J<sub>HH</sub> = 13.2 Hz, <sup>3</sup>J<sub>HH</sub> = 3.2 Hz, 1H, CH<sub>a</sub>H<sub>b</sub>-*t*-

Bu), 1.37 (m, 1H, H-7), 1.40 (m, 1H, H-5x), 1.47 (m, 1H, H-6x), 1.48 (dd, <sup>2</sup>J<sub>HH</sub> = 13.2 Hz, <sup>3</sup>J<sub>HH</sub> = 5.2 Hz, 1H, CH<sub>a</sub>H<sub>b</sub>-*t*-Bu), 1.52 (m, 1H, H-5e), 1.53 (m, 1H, H-1), 1.73 (m, 1H, H-6e), 2.36 (s, br, H-4), 3.36 (dm, <sup>2</sup>J<sub>HH</sub> = 11.9 Hz, 1H, SiH), 3.88 (dm, <sup>2</sup>J<sub>HH</sub> = 11.9 Hz, 1H, SiH). <sup>13</sup>C NMR (75.40 MHz, CDCl<sub>3</sub>) δ: 44.2 (C-8), 43.4 (C-4), 39.2 (C-7), 31.3 (C-9), 29.8 (C-10), 26.5 (C-6), 23.9 (C-5), 22.8 (C-3), 22.0 (C-1). <sup>29</sup>Si NMR (59.25 MHz, CDCl<sub>3</sub>) δ: -16.0 (t, <sup>1</sup>J<sub>SiH</sub> = 206 Hz). MS (70 eV), *m/z* (%): 181 (3.21) [M<sup>+</sup> - H], 125 (40.00) [M<sup>+</sup> - *t*-Bu], 97 (100), 67 (17.01) [C<sub>5</sub>H<sub>7</sub><sup>+</sup>], 57 (26.26) [*t*-Bu<sup>+</sup>]. Anal. calcd. for C<sub>11</sub>H<sub>22</sub>Si (182.149): C 72.44, H 12.16, Si 15.40; found: C 72.55, H 12.65.

#### *exo*- and *endo*-3-Neopentyl-2,2-diphenyl-2-silabicyclo[2.2.1]-heptane (**2c**)

A similar procedure as described for **2a** gave 0.85 g (94%, 9.2 mmol) **2c** from the reaction of 0.91 g (2.7 mmol) **1c** with TFPFB. White solid, mp 112 °C. *exo*- and *endo*-**2c**: <sup>1</sup>H NMR (300 MHz, CDCl<sub>3</sub>) δ: 0.84/0.87 (2 s, 18H, 2 C(CH<sub>3</sub>)<sub>3</sub>), 0.98 (dd, <sup>2</sup>J<sub>HH</sub> = 14.1 Hz, <sup>3</sup>J<sub>HH</sub> = 7.3 Hz, 1H, CH<sub>a</sub>H<sub>b</sub>-*t*-Bu (*exo*-**2c**)), 1.12–1.37 (m, 6H), 1.26 (dd, <sup>2</sup>J<sub>HH</sub> = 14.1 Hz, <sup>3</sup>J<sub>HH</sub> = 4.2 Hz, 1H, CH<sub>a</sub>H<sub>b</sub>-*t*-Bu (*exo*-**2c**)), 1.48–1.91 (m, 12H), 2.28/2.52 (2 s, br, 2 H, H-4 (*exo*- and *endo*-**2c**)), 7.27–7.62 (m, 20H, 4 phenyl (*exo*- and *endo*-**2c**)). *exo*-**2c**: <sup>13</sup>C NMR (75.40 MHz, CDCl<sub>3</sub>) δ: 46.1 (C-4), 45.6 (C-8), 37.9 (C-7), 32.1 (C-9), 30.6/23.8 (C-5/C-6), 29.7 (C-10), 27.4/22.8 (C-1/C-3). <sup>29</sup>Si NMR (59.25 MHz, CDCl<sub>3</sub>) δ: 11.0. MS (70 eV), *m/z* (%): 334 (0) [M<sup>+</sup>], 277 (100) [M<sup>+</sup> - C<sub>6</sub>H<sub>5</sub>], 249 (17.47), 199 (49.44), 183 (87.73), 105 (63.94), 77 (12.66) [C<sub>6</sub>H<sub>5</sub><sup>+</sup>], 67 (12.27), [C<sub>5</sub>H<sub>7</sub><sup>+</sup>], 57 (55.76) [*t*-Bu<sup>+</sup>]. *endo*-**2c**: <sup>13</sup>C NMR (75.40 MHz, CDCl<sub>3</sub>) δ: 43.3 (C-4), 40.6 (C-8), 39.2 (C-7), 32.0 (C-9), 29.7 (C-10), 26.9/25.2 (C-1/C-3), 24.2/24.1 (C-5/C-6). <sup>29</sup>Si NMR (59.25 MHz, CDCl<sub>3</sub>) δ: -0.4. MS (70 eV), *m/z* (%): 334 (0) [M<sup>+</sup>], 277 (89.61) [M<sup>+</sup> - C<sub>6</sub>H<sub>5</sub>], 249 (17.53), 199 (52.60), 183 (100), 105 (62.99), 77 (12.66) [C<sub>6</sub>H<sub>5</sub><sup>+</sup>], 67 (14.25), [C<sub>5</sub>H<sub>7</sub><sup>+</sup>], 57 (74.35) [*t*-Bu<sup>+</sup>]. Anal. calcd. for C<sub>23</sub>H<sub>30</sub>Si: C 82.56, H 9.04, Si 8.39; found: C 81.51, H 9.00.

#### 3-(3-Cyclopentenyl)-1-deutero-1,5,5-trimethyl-2-silahexane ([D]-**1a**)

A solution of 4.00 g (16.33 mmol) 3-(3-cyclopentenyl)-1-chloro-1,5,5-trimethyl-2-silahexane in 100 mL of diethyl ether was added dropwise to a slurry of 300 mg (7.14 mmol) LiAlD<sub>4</sub> in 25 mL diethyl ether at 4 °C. The reaction mixture was heated to reflux for 6 h. Filtration and removal of the solvent gave a colorless oil, which was distilled under reduced pressure to give 3.17 g (15.02 mmol, 92.0%) [D]-**1a**; bp 32 °C/10<sup>-2</sup> mbar. <sup>1</sup>H NMR (300 MHz, CDCl<sub>3</sub>) δ: 0.05 (s, 3H, Si-CH<sub>3</sub>), 0.07 (s, 3H, Si-CH<sub>3</sub>), 0.82–0.90 (m, 1H, CH-Si), 0.87 (s, 9H, CH<sub>2</sub>-*t*-Bu), 1.21 (dd, <sup>2</sup>J<sub>HH</sub> = 14.4 Hz, <sup>3</sup>J<sub>HH</sub> = 4.4 Hz, 1H, CH<sub>a</sub>H<sub>b</sub>-*t*-Bu), 1.35 (dd, <sup>2</sup>J<sub>HH</sub> = 14.4 Hz, <sup>3</sup>J<sub>HH</sub> = 5.1 Hz, 1H, CH<sub>a</sub>H<sub>b</sub>-*t*-Bu), 2.00–2.13 (m, 2H, CH<sub>2</sub> (cyclopentenyl)), 2.32–2.53 (m, 3H, CH<sub>2</sub> + CH (cyclopentenyl)), 5.66 (s, br, 2H, 2 CH olefin). <sup>13</sup>C NMR (75.40 MHz, CDCl<sub>3</sub>) δ: 130.5/130.3 (C-3'/C-4'), 42.1 (C-4), 41.0 (C-1'), 38.4/37.7 (C-2'/C-5'), 31.6 (C-5), 30.0 (C-6), 24.5 (C-3), -3.9 (C-1), -4.5 (Si-CH<sub>3</sub>). <sup>29</sup>Si NMR (59.25 MHz, CDCl<sub>3</sub>) δ: -10.4 (t, <sup>1</sup>J<sub>SiD</sub> = 28 Hz). MS (CI), *m/z* (%): 209 (100) [M<sup>+</sup> - H<sub>2</sub>], 196 (3.65) [M<sup>+</sup> - CH<sub>3</sub>], 154 (12.94) [M<sup>+</sup> - *t*-Bu].



**exo-6-Deutero-2,2-dimethyl-exo-3-neopentyl-2-sila-bicyclo[2.2.1]heptane and exo-6-deutero-2,2-dimethyl-endo-3-neopentyl-2-silabicyclo[2.2.1]heptane ([D]-2a)**

A similar procedure as described for **2a** gave 0.373 g (85%, 1.8 mmol) [D]-**2a** from the reaction of 0.439 g (2.08 mmol) [D]-**1a** with TFPB, bp 50 °C/10<sup>-2</sup> mbar.

**exo-3-Neopentyl-[D]-2a**

<sup>1</sup>H NMR (300 MHz, CDCl<sub>3</sub>) δ: 0.01 (s, 3H, Si-CH<sub>3</sub> (endo)), 0.05 (s, 3H, Si-CH<sub>3</sub> (exo)), 0.33 (m, 1H, H-3), 0.86 (s, 9H, C(CH<sub>3</sub>)<sub>3</sub>), 1.10 (d, br, <sup>2</sup>J<sub>HH</sub> = 12.1 Hz, 1H, H-5x), 1.15 (dd, <sup>2</sup>J<sub>HH</sub> = 13.8 Hz, <sup>3</sup>J<sub>HH</sub> = 4.5 Hz, 1H, CH<sub>a</sub>H<sub>b</sub>-*t*-Bu), 1.19 (m, 1H, H-1), 1.35 (m, 1H, H-7a), 1.41 (m, 1H, CH<sub>a</sub>H<sub>b</sub>-*t*-Bu), 1.46 (d, br, <sup>2</sup>J<sub>HH</sub> = 10.8 Hz, 1H, H-7s), 1.48 (m, 1H, H-6x), 1.68 (m, 1H, H-5e), 2.04 (s, br, 1H, H-4). <sup>13</sup>C NMR (75.40 MHz, CDCl<sub>3</sub>) δ: 44.4 (C-4), 41.7 (C-8), 38.3 (C-7), 31.4 (C-9), 29.7 (C-10), 26.7 (C-1), 25.1 (C-3), 23.9 (C-6), 23.4 (C-5), -1.9 (Si-CH<sub>3</sub>), -6.3 (Si-CH<sub>3</sub>). <sup>29</sup>Si NMR (59.25 MHz, CDCl<sub>3</sub>) δ: 17.5. MS (70 eV) *m/z* (%): 211 (0) [M<sup>+</sup>], 154 (20.75) [M<sup>+</sup> - *t*-Bu], 126 (24.53), 59 (100), 57 (26.42) [*t*-Bu<sup>+</sup>].

**endo-3-Neopentyl-[D]-2a**

<sup>1</sup>H NMR (300 MHz, CDCl<sub>3</sub>) δ: 0.01 (s, 3H, Si-CH<sub>3</sub> (endo)), 0.08 (s, 3H, Si-CH<sub>3</sub> (exo)), 0.75 (m, 1H, H-3), 0.86 (s, 9H, C(CH<sub>3</sub>)<sub>3</sub>), 1.23 (dd, <sup>2</sup>J<sub>HH</sub> = 13.7 Hz, <sup>3</sup>J<sub>HH</sub> = 4.3 Hz, 1H, CH<sub>a</sub>H<sub>b</sub>-*t*-Bu), 1.25 (m, 1H, H-1), 1.34 (m, 1H, H-7a), 1.35 (m, 2H, H-5e und H-5x), 1.42 (m, <sup>2</sup>J<sub>HH</sub> = 13.7 Hz, <sup>3</sup>J<sub>HH</sub> = 7.4 Hz, 1H, CH<sub>a</sub>H<sub>b</sub>-*t*-Bu), 1.47 (m, 1H, H-7s), 1.48 (m, 1H, H-6x), 2.27 (s, br, 1H, H-4). <sup>13</sup>C NMR (75.40 MHz, CDCl<sub>3</sub>) δ: 46.7 (C-4), 45.9 (C-8), 36.0 (C-7), 31.4 (C-9), 31.1 (C-5), 29.6 (C-10), 28.9 (C-1), 23.8 (C-3), -4.3 (SiCH<sub>3</sub>), -4.4 (SiCH<sub>3</sub>). <sup>29</sup>Si NMR (59.25 MHz, CDCl<sub>3</sub>) δ: 10.3. MS (70 eV) *m/z* (%): 211 (0) [M<sup>+</sup>], 154 (25.00) [M<sup>+</sup> - *t*-Bu], 126 (17.86), 59 (100), 57 (53.57) [*t*-Bu<sup>+</sup>].

## Acknowledgments

This work was supported by the Deutsche Forschungsgemeinschaft (DFG) and the German Israeli Foundation (GIF). We wish to thank Dr. C. Maerker, Erlangen, Germany and Prof. P.v.R. Schleyer, Athens, Georgia for preliminary calculations on the catalytic cycle.

## References

- For recent reviews see: (a) I. Ojima. *In* The chemistry of organic silicon compounds. Vol. 1. *Edited by* S. Patai and Z.

- Rappoport. Wiley, Chichester. 1989. p. 1479; (b) I. Ojima, Z. Li, and J. Zhu. *In* The chemistry of organic silicon compounds. Vol. 2. *Edited by* Z. Rappoport and S. Patai. Wiley, Chichester. 1998. p. 1687; (c) B. Marciniak, J. Gulinski, W. Urbaniak, and Z.W. Kornetka. *Comprehensive handbook on hydrosilylation chemistry*. Pergamon, Oxford. 1992.
- (a) J.L. Speier, J.A. Webster, and G.H. Barnes. *J. Am. Chem. Soc.* **79**, 974 (1957); (b) J.L. Speier. *Adv. Organomet. Chem.* **17**, 407 (1979).
- A.J. Chalk and J.F. Harrod. *J. Am. Chem. Soc.* **87**, 16 (1965).
- M.A. Brook. *Silicon in organic, organometallic and polymer chemistry*. Wiley, New York. 1999.
- J.B. Lambert and Y. Zhao. *J. Am. Chem. Soc.* **118**, 7867 (1996).
- (a) T. Müller, C. Bauch, M. Ostermeier, M. Bolte, and N. Auner. *J. Am. Chem. Soc.* **125**, 2158 (2003); (b) H.-U. Steinberger, T. Müller, N. Auner, C. Maerker, and P.v.R. Schleyer. *Angew. Chem. Int. Ed. Engl.* **36**, 626 (1997).
- (a) J.Y. Corey. *J. Am. Chem. Soc.* **97**, 3237 (1975); (b) H. Mayr and N. Basso. *J. Am. Chem. Soc.* **114**, 3060 (1992); (c) Y. Apeloig, O. Merin-Aharoni, D. Danovich, A. Ioffe, and S. Shaik. *Isr. J. Chem.* **33**, 387 (1993).
- (a) S. Winstein and D.S. Trifan. *J. Am. Chem. Soc.* **71**, 2953 (1949); (b) S. Winstein and D.S. Trifan. *J. Am. Chem. Soc.* **74**, 1147 (1952); (c) S. Winstein and D.S. Trifan. *J. Am. Chem. Soc.* **74**, 1154 (1952).
- (a) R.G. Parr and W. Yang. *Density-functional theory of atoms and molecules*. Oxford University Press, Oxford. 1989; (b) W. Koch and M.C. Holthausen. *A chemist's guide to density functional theory*. Wiley-VCH, Weinheim. 2000.
- (a) A.D. Becke. *Phys. Rev. A*, **38**, 3098 (1988); (b) A.D. Becke. *J. Chem. Phys.* **98**, 5648 (1993); (c) C. Lee, W. Yang, and R.G. Parr. *Phys. Rev. B*, **37**, 785 (1988).
- All calculations were performed with: Gaussian 94, Revisions C2-E2 and Gaussian 98 Revisions A3-A9 [computer programs]. Gaussian, Inc., Pittsburgh Pa. 1995 and 1999.
- N. Auner and H.-U. Steinberger. *Z. Naturforsch.* **49b**, 1743 (1994).
- S.E. Cremer and C. Blankenship. *J. Org. Chem.* **47**, 1626 (1982).
- A. Hosomi, M. Mikami, and H. Sakurai. *Bull. Chem. Soc. Jpn.* **56**, 2784 (1983).
- T. Müller, R. Meyer, D. Lennartz, and H.-U. Siehl. *Angew. Chem. Int. Ed.* **39**, 3074 (2000).
- R. Meyer, K. Werner, and T. Müller. *Chem. Eur. J.* **8**, 3203 (2002).
- (a) A.G. Massey and A.J. Park. *J. Organomet. Chem.* **2**, 245 (1964); (b) J.C.W. Chien, W.-M. Tsai, and M.D. Rausch. *J. Am. Chem. Soc.* **113**, 8570 (1991); (c) E. Ihara, V.G. Young, and R.F. Jordan. *J. Am. Chem. Soc.* **120**, 8277 (1998).



# Molecular modelling of self-assembled alkynyl monolayer structures — Unnatural symmetry units, surface bonding, and topochemical polymerization<sup>1</sup>

Adam J. Dickie, Ashok K. Kakkar, and Michael A. Whitehead

**Abstract:** Geometric modelling techniques are used to map the potential energies of packing for self-assembled alkyl- and phenyl-backboned monolayers across a range of intermolecular separations. Natural packing distances of 4.2–4.4 Å produce less stable, more isotropic monolayers because of repulsive interchain contacts. Optimizations at unnatural surface densities found thin films of lower energy and higher symmetry existed at increased chain–chain separations. Head-group bonding is therefore identified as a force for controlling monolayer order. Analysis of the natural monolayer structures on a silicon dioxide surface determined the favourable head-group structures, and allowed the topochemical polymerization of *p*-bis(butadiynyl)benzene monolayers to be rationalized.

**Key words:** self-assembled monolayers, molecular modelling studies, repeating symmetry units, thin-film order, topochemical polymerization.

**Résumé :** On a utilisé des techniques de modélisation géométrique pour établir une carte des énergies potentielles d'empilement des monocouches autoassemblées à squelette d'alkyle ou de phényle sur toute une plage de distances intermoléculaires. Les distances normales d'empilement de 4,2 à 4,4 Å produisent des monocouches plus isotropes et moins stables en raison des contacts répulsifs entre les chaînes. Des optimisations à des densités de surface non naturelles ont permis de montrer que, à des distances interchaînes plus élevées, il existe des films minces d'énergie plus faible et de symétrie plus élevée. La liaison du groupe de tête a donc été identifiée comme la force qui contrôle l'ordre de la monocouche. L'analyse des structures de la monocouche naturelle sur une surface de bioxyde de silice permet de déterminer les structures favorables du groupe de tête et de rationaliser la polymérisation topochimique de monocouches de *p*-bis(butadiynyl)benzène.

**Mots clés :** monocouches autoassemblées, études de modélisation moléculaire, unités de symétrie qui se répètent, ordre d'un film mince, polymérisation topochimique.

[Traduit par la Rédaction]

## Introduction

The creation of ordered organic materials on solid-state interfaces is critically dependant upon molecular geometry. The phenomenon of interfacial self-assembly was first realized (1) when long, hydrophobic alkyl chains were observed to spontaneously create close-packed, nearly crystalline structures at the water surface. The key to formation of these

ordered Langmuir monolayers was identified as the favourable packing interactions among the long alkyl chains. The geometry of all trans -CH<sub>2</sub>- molecules allows close-packing of alkyl chains, with the “bumps” of one methylene projection (the van der Waals radius of the carbon–hydrogen plane) fitting neatly into the “hollows” (the backside of the carbon atom, with no hydrogen bonds) of a neighbouring unit (2). The packing forces among the -CH<sub>2</sub>- groups involve attractive van der Waals interactions. These nonbonded forces are additive, meaning increased stability for longer chains and larger assemblies, and are thermodynamically weak, meaning structural defects can eventually be removed and geometries optimized to construct the lowest-energy supramolecular configuration.

The same geometric packing forces between alkyl chains were used to develop the original self-assembled monolayers (SAMs) at liquid and (or) solid interfaces, such as alkane-thiolates on Au or organosilanes on SiO<sub>2</sub> (3, 4). Although the solid surface drives the adsorption of molecules out of solution, and provides a stable geometric space for weak organic intermolecular interactions, the resulting structure and order of the self-assembled thin film is determined primarily

Received 25 February 2003. Published on the NRC Research Press Web site at <http://canjchem.nrc.ca> on 8 September 2003.

*Dedicated to Professor John Harrod, celebrating his contributions to science.*

**A.J. Dickie, A.K. Kakkar,<sup>2</sup> and M.A. Whitehead.<sup>3</sup>**  
Department of Chemistry, McGill University, 801 Sherbrooke Street West, Montréal, Québec, Canada. H3A 2K6

<sup>1</sup>This article is part of a Special Issue dedicated to Professor John Harrod.

<sup>2</sup>Corresponding author (e-mail: [ashok.kakkar@mcgill.ca](mailto:ashok.kakkar@mcgill.ca)).

<sup>3</sup>Corresponding author (e-mail: [tony.whitehead@mcgill.ca](mailto:tony.whitehead@mcgill.ca)).



by molecular packing forces. In fact, during self-assembly of alkylsilanes on inorganic oxide substrates, the organic chains are essentially detached from the underlying surface (5), existing as a Langmuir-type monolayer upon a thin layer of surface-adsorbed  $\text{H}_2\text{O}$ . The alkylsilane chains are free to diffuse laterally across the surface, packing into ordered assemblies before surface bonding or cross-linking of the silanol headgroups (6, 7). Geometric differences between optimal chain packing separations and Si—O—Si bond distances (8) gives rise to competitive forces in alkylsilane SAMs, with head-group bonding disrupting the order established by chain-chain interactions.

Geometric modelling will therefore provide unique theoretical insight into the order and structure of self-assembled monolayers. Organic monolayers with functional device properties, such as  $\pi$ -conductivity, can be easily self-assembled on Si(100)— $\text{SiO}_2$  surfaces, using acid-base hydrolytic chemistry (9). The hydrolysis of surface-bound [Sn]— $\text{NEt}_2$  groups with alkyne-terminated organic molecules, such as 1,9-decadiyne or *p*-diethynylbenzene, creates thin films of good structural quality on oxide substrates. The use of these chromophoric thin films as molecular electronic devices is dependent on the interfacial monolayer order, and on the ability to manipulate and optimize surface geometries. Modelling techniques have recently been introduced (10) that allow the monolayer surface to be reduced and described as natural symmetry units, natural because they effectively reproduce the density and packing structure of an infinite thin film. In this article, the rigid-rod scanning method (RRSM) (10, 11) and the periodic optimizations of chains (PGO-C) and surfaces (PGO-S) (10), are used to calculate monolayer structures away from the natural packing densities, creating *unnatural* symmetry units. Such calculations, on alkyl-backboned  $\text{Sn}-(\text{C}\equiv\text{C})_m-(\text{CH}_2)_n-(\text{C}\equiv\text{C})_m-\text{H}$  ( $m = 0$  to 1,  $n = 2$ –10) and phenyl-backboned  $\text{Sn}-(\text{C}\equiv\text{C})_m-p\text{-C}_6\text{H}_4-(\text{C}\equiv\text{C})_m-\text{H}$  ( $m = 0$ –2) molecules, provide information on the intermolecular interaction forces, and allow new theoretical symmetry patterns, based upon new geometric arrangements, to be identified.

The modelling methods are extended to two structural problems involving the chromophoric thin films. In the first study, surface bonding of Sn headgroups is investigated by calculating the stability of monolayers at full coverage, with zero, one, or two neighbouring cross-links. These calculations not only determine the most favourable surface conformations, they highlight how the order established by organic chain packing influences the underlying surface structure.

In the second study, the topochemical polymerization in  $\text{Sn}-(\text{C}\equiv\text{C})_2-p\text{-C}_6\text{H}_4-(\text{C}\equiv\text{C})_2-\text{H}$  monolayers is considered. By exposing a  $\text{Sn}-(\text{C}\equiv\text{C})_2-p\text{-C}_6\text{H}_4-(\text{C}\equiv\text{C})_2-\text{H}$  thin film to UV radiation, photopolymerization of the diacetylene units occurs, as evidenced visually by the appearance of a blue film, and spectroscopically by FT-IR, UV-vis, and ellipsometric methods (9a). Because surface polymerization of diacetylene is subject to strict geometric constraints (12, 13) molecular

modelling calculations prove to be very successful in describing the structure and mechanism of thin film photopolymerization.

## Theoretical methods

### The rigid-rod scanning method (RRSM)

Optimized models of  $\text{Sn}-(\text{C}\equiv\text{C})_m-(\text{CH}_2)_n-(\text{C}\equiv\text{C})_m-\text{H}$  ( $m = 0$  to 1,  $n = 2$ –10) and  $\text{Sn}-(\text{C}\equiv\text{C})_m-p\text{-C}_6\text{H}_4-(\text{C}\equiv\text{C})_m-\text{H}$  ( $m = 0$ –2) were oriented so that the primary inertial axis of each molecule was aligned with the *z*-axis, the carbon atoms were situated within the *yz* plane, and the Sn atom was at the origin (Fig. 1). Hexagonal  $6 \times 6$  arrays of identical Sn-R chromophores were then constructed in the *xy* plane, with intermolecular separations ranging from  $d = 4.0$  to  $d = 5.0$  Å, in 0.1 Å increments. Intramolecular geometries were fixed, and the van der Waals energy ( $E_{\text{vdW}}$ ) of the array was evaluated as a function of the intermolecular conformation angles  $\theta$  (inertial axis twist),  $\phi$  (in-plane axis tilt), and  $\psi$  (out-of-plane axis tilt) to find angle combinations that yielded low energy packing modes (11). The inertial axis (*z*-axis) twist ( $0^\circ \leq \theta \leq 360^\circ$ ) is defined as the rotation from the initial orientation, relative to the *y*-axis; calculations were performed along  $5^\circ$  increments. The in-plane (*y*-axis) tilt ( $-60^\circ \leq \phi \leq 60^\circ$ ) is defined as the displacement of the inertial axis from the *z*-axis normal, in the *y*-axis direction; calculations were performed at  $1^\circ$  increments. The out-of-plane (*x*-axis) tilt ( $-60^\circ \leq \psi \leq 60^\circ$ ) is defined as the displacement of the inertial axis from the *z*-axis normal, in the *x*-axis direction, with  $1^\circ$  increments. Molecules located in odd-numbered in-plane rows were restricted to the vertical axis orientation  $\theta_1$ , while molecules within even-numbered in-plane rows were restricted to  $\theta_2$ ; once the low-energy modes of ( $\theta_1, \theta_2$ ) were identified, the angles  $\phi$  and  $\psi$  were minimized. Single-point  $E_{\text{vdW}}$  calculations, parameterized (14) from similar molecular crystals, were performed with the MM<sup>+</sup> force field of HyperChem v5.1 (15).

### Periodic geometry optimization of chains (PGO-C)

Hexagonal arrays of Sn-R chromophores, with orientations taken from RRSM intrinsic symmetry cells, were optimized under  $6 \times 6$  boundary conditions:  $a = b = (6 \times d)$  Å,  $c = 30$  Å,  $\alpha = \beta = 90^\circ$ , and  $\gamma = 120^\circ$ , where  $d$  is the RRSM intermolecular separation. Sn atoms were fixed in space at a hexagonal separation of 4.4 Å throughout the optimization. Optimizations were performed with the Universal Force Field (UFF) force field (16) of Cerius2 version 3.5 (17). Global minimum structures were calculated with the Cerius2 Smart Minimizer<sup>4</sup> under high convergence<sup>5</sup> conditions. Charges were calculated with the charge equilibration method (18), a point charge interaction at variable distances  $r_{ij}$ , and were recalculated every 500 iterations until convergence criteria were met. Local minimum structures used a conjugate gradient algorithm, and recalculated charges every 100 iterations until standard convergence<sup>6</sup> criteria were met.

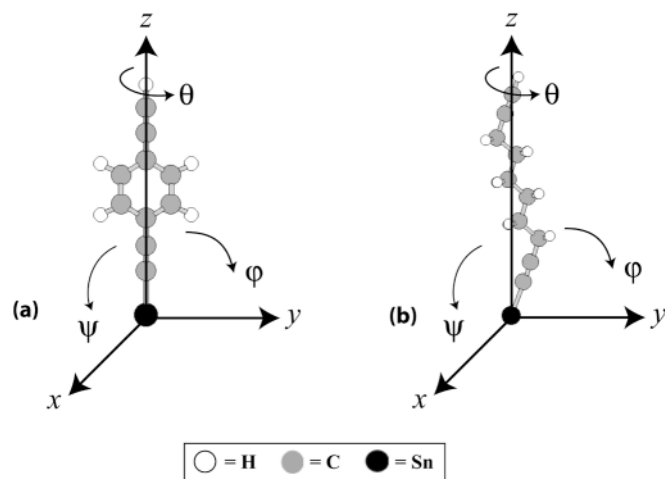
<sup>4</sup>The Cerius2 Smart Minimizer is a combination of Steepest Descent, Adopted Basis Newton-Raphson, Quasi-Newton, and Newton-Raphson gradient techniques.

<sup>5</sup>High convergence criteria: atom root mean square force =  $1.0 \times 10^{-3}$  kcal mol<sup>-1</sup> Å<sup>-1</sup>; atom maximum force =  $5.0 \times 10^{-3}$  kcal mol<sup>-1</sup> Å<sup>-1</sup>; energy difference =  $1.0 \times 10^{-4}$  kcal mol<sup>-1</sup>; root mean square displacement =  $1.0 \times 10^{-5}$  Å; maximum displacement =  $5.0 \times 10^{-5}$  Å.

<sup>6</sup>Standard convergence criteria: atom root mean square force =  $0.1$  kcal mol<sup>-1</sup> Å<sup>-1</sup>; atom maximum force =  $0.5$  kcal mol<sup>-1</sup> Å<sup>-1</sup>; energy difference =  $1.0 \times 10^{-3}$  kcal mol<sup>-1</sup>; root mean square displacement =  $3.0 \times 10^{-3}$  Å; maximum displacement =  $1.5 \times 10^{-2}$  Å.



**Fig. 1.** RRSM conformation angles and initial inertial axis orientations for: (a)  $\text{H-C}\equiv\text{C-p-C}_6\text{H}_4\text{-C}\equiv\text{C-Sn}$ ; (b)  $\text{H-C}\equiv\text{C-(CH}_2)_6\text{-C}\equiv\text{C-Sn}$ .



A spline switching function is used for calculation of nonbonded interactions. Nonbonded energies are calculated up to 8.0 Å and smoothed off by 8.5 Å. Symmetries of packing were subsequently determined on the optimized  $6 \times 6$  surfaces using the Cerius2 Symmetry calculator, with a tolerance set to 0.1 Å.

#### Periodic geometry optimization of surfaces (PGO-S)

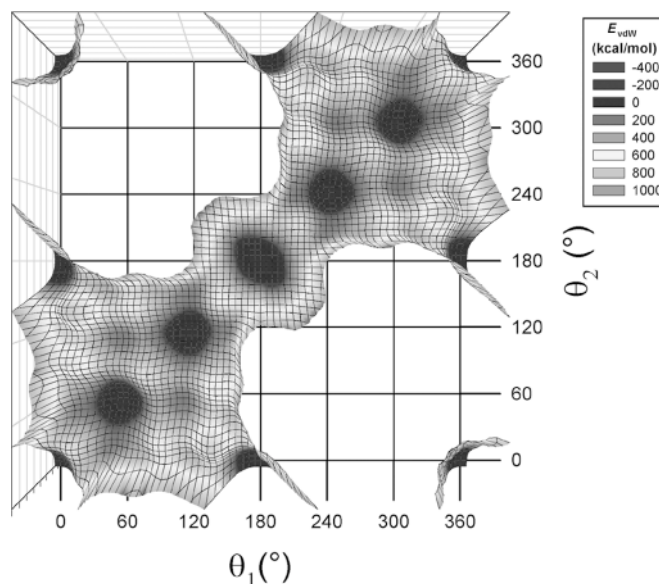
Hexagonal arrays of Sn-R chromophores, with orientations taken from RRSM intrinsic symmetry cells, were attached to each oxygen binding site of a scaled tridymite  $\text{SiO}_2$  surface (8), with intermolecular separation  $d = 4.4$  Å. Symmetric monomer  $[\text{R-Sn(OH)}_2(\text{OSi})]$ , dimer  $[\text{R-Sn(OH)(OSi)O}]$ , or trimer  $[\text{R-Sn(OSi)O}_2]$  structures were constructed across the entire surface to model Sn-O-Sn headgroup cross-linking. Periodic boundaries ( $6 \times 6$ ) were imposed on the surface models ( $a = b = 26.56$  Å,  $c = 35$  Å,  $\alpha = \beta = 90^\circ$ ,  $\gamma = 120^\circ$ ), and optimizations were performed with the silica surface fixed in space. Optimizations were performed with the UFF force field (16) of Cerius2 version 3.5 (17). Geometries were optimized with the Cerius2 Smart Minimizer<sup>4</sup> under high convergence<sup>5</sup> conditions. Charges were calculated with the charge equilibration method (18), a point charge interaction at variable distances  $r_{ij}$ , and were recalculated every 500 iterations until convergence criteria were met. A spline switching function is used for the calculation of nonbonded interactions. Nonbonded energies are calculated up to 8.0 Å and smoothed off by 8.5 Å. Symmetries of packing were subsequently determined on the optimized  $6 \times 6$  surfaces using the Cerius2 Symmetry calculator, with a tolerance set to 0.1 Å.

## Results and discussion: Unnatural symmetry units

#### Analysis of alkyl-backboned monolayers by RRSM calculations

Because hydrolytic SAMs are formed through a lateral diffusion process, rigid scans were performed on  $\text{Sn-C}\equiv\text{C-(CH}_2)_n\text{-C}\equiv\text{CH}$  monolayers across a sample distance range ( $d = 4.0\text{--}5.0$  Å) to calculate structures and nonbonding ener-

**Fig. 2.** RRSM plot of  $E_{\text{vdW}}$  as a function of  $(\theta_1, \theta_2)$  for  $\text{H-C}\equiv\text{C-(CH}_2)_6\text{-C}\equiv\text{C-Sn}$  molecules, at a hexagonal separation of 4.4 Å.



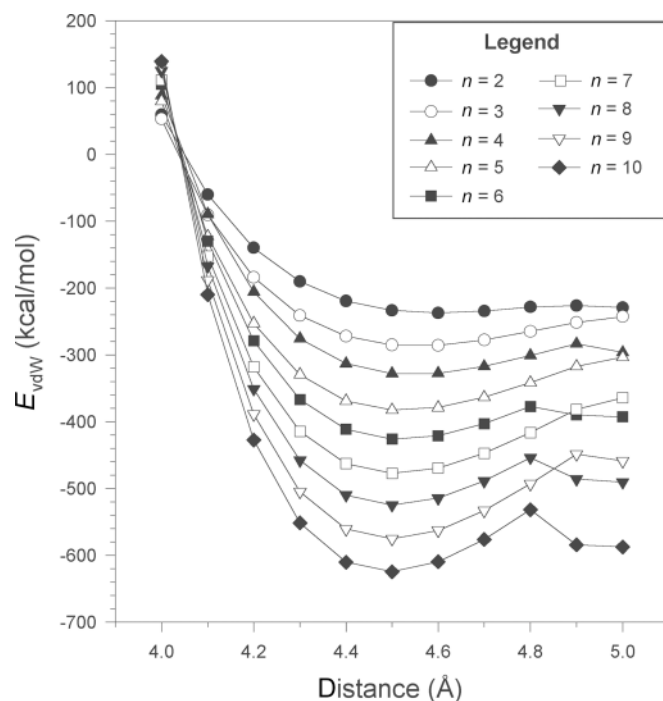
gies at various theoretical stages of the self-assembly process. These calculations were repeated using different  $-(\text{CH}_2)_n-$  chain lengths ( $n = 2\text{--}10$ ) to determine how the alkyl backbone influences the energy and geometry of the assembly. The scans of  $E_{\text{vdW}}$ , using the RRSM, found that all  $\text{Sn-C}\equiv\text{C-(CH}_2)_n\text{-C}\equiv\text{CH}$  monolayers were consistently minimized at hexagonal face-packing orientations, regardless of separation  $d$  or chain length:  $(\theta_1, \theta_2) = (0^\circ, 0^\circ), (60^\circ, 60^\circ), (120^\circ, 120^\circ), (180^\circ, 180^\circ)$  etc. The packing of alkyl-backboned monolayers is isotropic, producing plots of  $E_{\text{vdW}}$  vs.  $(\theta_1, \theta_2)$  with multiple energy minima (Fig. 2). A summary of the minimized  $E_{\text{vdW}}$  energies for  $\text{Sn-C}\equiv\text{C-(CH}_2)_n\text{-C}\equiv\text{CH}$  monolayers at distances between 4.0–5.0 Å is presented in Fig. 3, and Table 1 lists the calculated monolayer orientation angles across this distance range.

The alkyl-backboned monolayers reach a general  $E_{\text{vdW}}$  packing minimum at  $d = 4.5$  Å, corresponding to the van der Waals radius of an alkyl chain (19a), and show a near-linear relation between  $E_{\text{vdW}}$  stabilization energy and increasing chain length, proof of the additive nature of  $-\text{CH}_2-$  packing forces. The tilt values calculated at  $d = 4.5$  Å are optimal for in-plane  $-\text{CH}_2-$  packing, and correspond well with the tilts measured by X-ray diffraction for octadecyltrichlorosilane SAMs (20). No out-of-plane tilts are observed at this distance because (i)  $\psi$  values  $>0^\circ$  will diminish the favourable in-plane packing forces, and (ii) no excess free volume exists in the hexagonal array. Compression of the monolayer (to  $d = 4.0\text{--}4.4$  Å) produces tilt orientations identical to values observed at  $d = 4.5$  Å, but at less favourable energies because of repulsive van der Waals overlap of the alkyl chains. As free volume is decreased in the monolayer, the chains are forced into in-plane packing conformations, and other orientations become extremely unfavourable. This phenomenon was previously observed in the natural symmetry descriptions of monolayer surfaces (10), where headgroup cross-linking compressed the ordered alkyl-chain surface, but in-plane symmetry was retained.

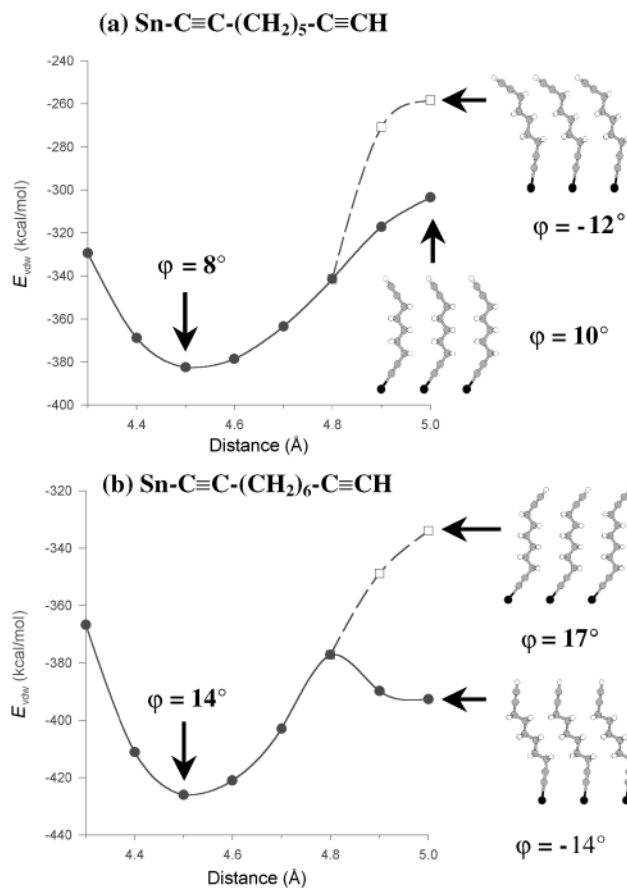


**Table 1.** Calculated in-plane ( $\phi$ ) and out-of-plane ( $\psi$ ) tilts, relative to the molecular inertial axis, for  $\text{Sn-C}\equiv\text{C}-(\text{CH}_2)_n-\text{C}\equiv\text{CH}$  monolayers at face-packing orientations of  $(\theta_1, \theta_2) = (0^\circ, 0^\circ)$ .

$d$ (Å)	$n = 2$		$n = 3$		$n = 4$		$n = 5$		$n = 6$		$n = 7$		$n = 8$		$n = 9$		$n = 10$	
	$\phi$ ( $^\circ$ )	$\psi$ ( $^\circ$ )	$\phi$ ( $^\circ$ )	$\psi$ ( $^\circ$ )	$\phi$ ( $^\circ$ )	$\psi$ ( $^\circ$ )	$\phi$ ( $^\circ$ )	$\psi$ ( $^\circ$ )	$\phi$ ( $^\circ$ )	$\psi$ ( $^\circ$ )	$\phi$ ( $^\circ$ )	$\psi$ ( $^\circ$ )	$\phi$ ( $^\circ$ )	$\psi$ ( $^\circ$ )	$\phi$ ( $^\circ$ )	$\psi$ ( $^\circ$ )	$\phi$ ( $^\circ$ )	$\psi$ ( $^\circ$ )
4.0	22	0	11	0	18	0	9	0	14	0	7	0	12	0	6	0	10	0
4.1	22	0	11	0	17	0	8	0	14	0	7	0	12	0	6	0	10	0
4.2	22	0	11	0	17	0	8	0	14	0	7	0	11	0	6	0	10	0
4.3	22	0	11	0	17	0	8	0	14	0	6	0	11	0	5	0	10	0
4.4	22	0	10	0	17	0	8	0	14	0	6	0	11	0	5	0	10	0
4.5	22	0	10	0	17	0	8	0	14	0	6	0	11	0	5	0	10	0
4.6	22	0	10	0	17	0	8	0	14	0	6	0	11	0	5	0	10	0
4.7	23	3	10	1	18	0	8	0	14	0	6	0	11	0	5	0	10	0
4.8	24	11	11	3	19	0	8	1	15	1	6	1	12	1	4	1	10	0
4.9	24	28	12	14	20	12	8	11	-12	24	6	8	-15	23	4	7	-17	-23
5.0	26	29	13	23	-10	27	10	24	-14	26	7	25	-17	25	-5	26	-18	-25

**Fig. 3.** Minimized  $E_{\text{vdW}}$  as a function of distance for  $\text{Sn-C}\equiv\text{C}-(\text{CH}_2)_n-\text{C}\equiv\text{CH}$  monolayers, calculated by the RRSM.

A pronounced odd-even effect is seen for the various  $-(\text{CH}_2)_n-$  alkyl backbone lengths, in both the in-plane tilt values and the observation of a second  $E_{\text{vdW}}$  packing minimum at  $d = 5.0$  Å. As shown in Fig. 4, these odd-even effects are related to the positioning of the uppermost  $\text{C}\equiv\text{CH}$  unit. Odd-number alkyl-backbone chains have greater natural inertial tilts than even-number chains (i.e.,  $\text{Sn-C}\equiv\text{C}-(\text{CH}_2)_5-\text{C}\equiv\text{CH}$  inertial tilt =  $24.3^\circ$ ,  $\text{Sn-C}\equiv\text{C}-(\text{CH}_2)_6-\text{C}\equiv\text{CH}$  inertial tilt =  $19.6^\circ$ ) because the quasi-equatorial position of the uppermost acetylene group, opposite in direction to the lower  $\text{C}\equiv\text{C}$  group, requires a greater molecular tilt to align the upper acetylene with the lower Sn atom (the approximate inertial axis orientation) than an even-numbered chain. Therefore, odd-numbered chains display smaller tilts of the original inertial axis.

**Fig. 4.** In-plane packing structures of (a)  $\text{Sn-C}\equiv\text{C}-(\text{CH}_2)_5-\text{C}\equiv\text{CH}$  and (b)  $\text{Sn-C}\equiv\text{C}-(\text{CH}_2)_6-\text{C}\equiv\text{CH}$  at representative points along the  $E_{\text{vdW}}$  vs. distance curve. Minimum energy structures are located along the solid curve, nonminimum structures along the dashed line. Dark spheres represent Sn atoms, grey spheres C atoms, and white spheres H atoms.

As separations increase from the  $d = 4.5$  Å packing minimum, nonbonding energies decrease, because of reduced  $-\text{CH}_2-$  in-plane contacts. After a separation of  $4.8$  Å, enough free volume is introduced to the monolayer such that new close-packing conformations can be realized. For even-



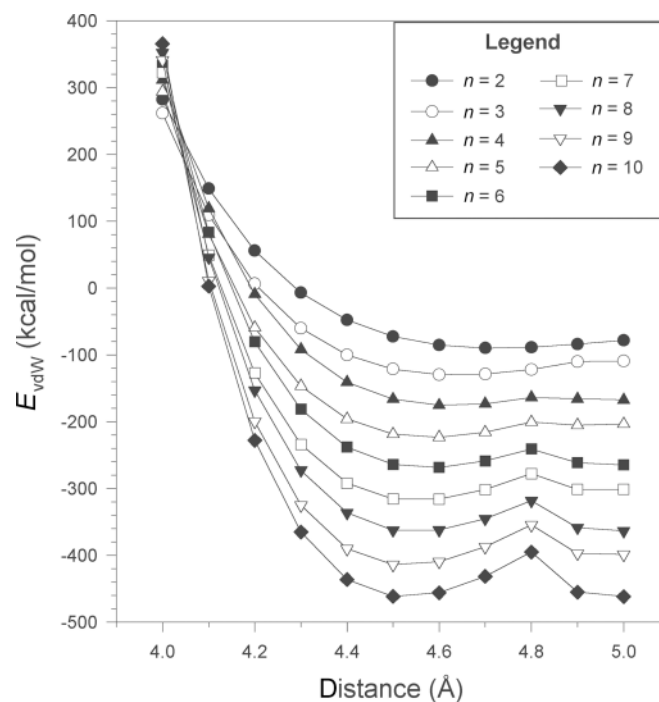
**Table 2.** Calculated in-plane ( $\phi$ ) and out-of-plane ( $\psi$ ) tilts, relative to the molecular inertial axis, for  $\text{Sn}-(\text{CH}_2)_n\text{-H}$  monolayers at face-packing orientations of  $(\theta_1, \theta_2) = (0^\circ, 0^\circ)$ .

$d$ (Å)	$n = 2$		$n = 3$		$n = 4$		$n = 5$		$n = 6$		$n = 7$		$n = 8$		$n = 9$		$n = 10$	
	$\phi$ ( $^\circ$ )	$\psi$ ( $^\circ$ )	$\phi$ ( $^\circ$ )	$\psi$ ( $^\circ$ )	$\phi$ ( $^\circ$ )	$\psi$ ( $^\circ$ )	$\phi$ ( $^\circ$ )	$\psi$ ( $^\circ$ )	$\phi$ ( $^\circ$ )	$\psi$ ( $^\circ$ )	$\phi$ ( $^\circ$ )	$\psi$ ( $^\circ$ )	$\phi$ ( $^\circ$ )	$\psi$ ( $^\circ$ )	$\phi$ ( $^\circ$ )	$\psi$ ( $^\circ$ )	$\phi$ ( $^\circ$ )	$\psi$ ( $^\circ$ )
4.0	11	0	11	0	6	0	7	0	5	0	5	0	4	0	4	0	3	0
4.1	10	0	11	0	6	0	7	0	4	0	5	0	3	0	4	0	3	0
4.2	10	0	10	0	6	0	6	0	4	0	5	0	3	0	4	0	3	0
4.3	9	0	10	0	5	0	6	0	4	0	4	0	3	0	3	0	2	0
4.4	8	0	10	0	5	0	6	0	3	0	4	0	3	0	3	0	2	0
4.5	8	0	9	0	4	0	6	0	3	0	4	0	2	0	3	0	2	0
4.6	7	0	9	0	4	0	5	0	2	0	3	0	2	0	3	0	1	0
4.7	6	0	9	0	3	0	5	0	1	0	3	0	1	0	2	0	0	0
4.8	5	0	9	1	2	1	5	1	0	1	2	1	-1	1	1	1	0	1
4.9	4	1	-21	13	-18	18	-18	19	-21	19	-21	19	-23	20	-22	20	-24	20
5.0	-22	11	-22	15	-21	19	-20	20	-23	21	-22	21	-24	22	-24	22	-25	22

numbered alkyl-backboned chains, tilting in the negative inertial axis direction reestablishes  $[(n - 1)/n]$  close-contacts of the alkyl backbone, leading to the observed local minima. Similar  $[(n - 1)/n]$  tilt structures have been recorded for alkanethiol monolayers on Au ( $d = 4.97$  Å) (11, 19b, 21). Odd-number alkyl-backboned chains cannot undergo a negative axis tilt because of the equatorial and opposite position of the uppermost  $\text{C}\equiv\text{CH}$  group (Fig. 4a): negative inertial tilts put the upper acetylenes into repulsive contact. All  $\text{Sn}-\text{C}\equiv\text{C}-(\text{CH}_2)_n-\text{C}\equiv\text{CH}$  monolayers analyzed by the RRSM show significant out-of-plane tilts in the 4.8–5.0 Å region because at large separations, free volume cannot be filled through in-plane tilting alone. Close-contacts among densely packed in-plane rows are made by increasing the out-of-plane tilts.

For comparative insight, theoretical monolayers of  $\text{Sn}-(\text{CH}_2)_n\text{-H}$  ( $n = 2$ –10) were also analyzed by the RRSM. Figure 5 shows the minimized  $E_{\text{vdW}}$  energies for  $\text{Sn}-(\text{CH}_2)_n\text{-H}$  monolayers at distances between 4.0–5.0 Å, and Table 2 lists the orientation angles calculated for this distance range. The pure Sn-alkyl chains show nearly identical geometric and energetic results to the dialkyne-based monolayers, with isotropic hexagonal face-packing minima  $((\theta_1, \theta_2) = (0^\circ, 0^\circ), (60^\circ, 60^\circ)$  etc.) and  $E_{\text{vdW}}$  packing minima at  $d = 4.5$  Å. The  $\text{Sn}-(\text{CH}_2)_n\text{-H}$  chains do not show the strong odd-even effect observed for the dialkyne chains, because odd and even alkyl chains have similar inertial axes and geometries. All alkyl chains display the second packing minimum at  $d = 5.0$  Å, because the quasi-equatorial position of hydrogen on an odd-number chain does not create significant repulsive overlaps for a negative inertial tilt orientation.

Given the similar nature of  $\text{Sn}-\text{C}\equiv\text{C}-(\text{CH}_2)_n-\text{C}\equiv\text{CH}$  and  $\text{Sn}-(\text{CH}_2)_n\text{-H}$  results, it is apparent that the alkyl backbone dominates the energy and geometry of  $\text{Sn}-\text{C}\equiv\text{C}-(\text{CH}_2)_n-\text{C}\equiv\text{CH}$  self-assembled monolayers. Although electronic  $\pi$ - $\pi$  interactions are not directly calculable by the RRSM, at the  $E_{\text{vdW}}$  - $\text{CH}_2$ - chain packing minimum the acetylene groups have a favourable  $45^\circ$  tilt orientation that corresponds to an ab initio calculated minimum geometry (22). The acetylene units, therefore, help stabilize the monolayer at the alkyl chain packing minimum, and play an important geometric role at higher chain separations.

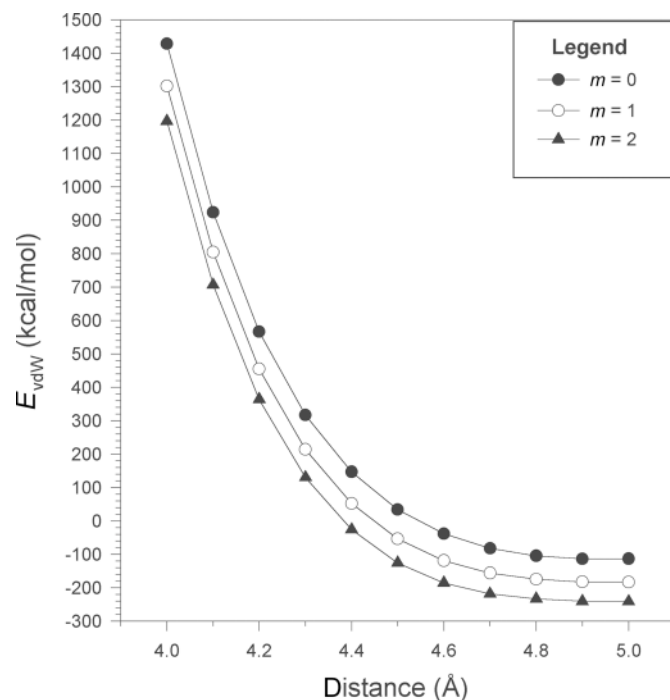
**Fig. 5.** Minimized  $E_{\text{vdW}}$  as a function of distance for  $\text{Sn}-(\text{CH}_2)_n\text{-H}$  monolayers, calculated by the RRSM.

#### Analysis of phenyl-backboned monolayers by RRSM calculations

Rigid-rod energy scans were performed on phenyl-backboned,  $\text{Sn}-(\text{C}\equiv\text{C})_m\text{-}p\text{-C}_6\text{H}_4-(\text{C}\equiv\text{C})_m\text{-H}$  ( $m = 0$ –2) monolayers to determine theoretical close-packing conformations and energies over the  $d = 4.0$ –5.0 Å lateral movement range, and to examine the effect of alkyne length on phenyl monolayer structure. Figure 6 shows the minimized  $E_{\text{vdW}}$  packing energies as a function of distance for the phenyl-backboned monolayers, and Table 3 lists the calculated orientation angles from  $d = 4.0$ –5.0 Å. The RRSM analysis found consistent anisotropic packings for the phenyl-backboned chains, with  $(\theta_1, \theta_2) = (35^\circ, -35^\circ)$  throughout the distance range, regardless of alkyne length.



**Fig. 6.** Minimized  $E_{\text{vdW}}$  as a function of distance for  $\text{Sn}-(\text{C}\equiv\text{C})_m-p\text{-C}_6\text{H}_4-(\text{C}\equiv\text{C})_m\text{-H}$  monolayers, calculated by the RRSM.



As discussed previously (2, 10), the phenyl-based monolayer can only achieve close-packing (sixfold molecular contacts) in a herringbone arrangement, and all  $(\theta_1, \theta_2)$   $E_{\text{vdW}}$  packing minima (Fig. 7) are equivalent through symmetry.

The steric and symmetric constraints required to pack phenyl-backboned monolayers into a restricted hexagonal space produces the unique herringbone structure that corresponds to minimum energy configurations observed by ab initio methods (23) and STM imaging of benzenethiol monolayers on Au (24). The phenyl chains do not have a local  $E_{\text{vdW}}$  lateral packing minima, however; instead,  $E_{\text{vdW}}$  minima are reached at 5.3–5.5 Å (not shown in Fig. 6), corresponding to the 5.1 Å van der Waals radius of Sn (15). Although the RRSM cannot identify the true  $\pi$ - $\pi$  intermolecular assembly forces, it does correctly predict the geometric packing space, and shows generally favourable (negative) van der Waals energies at the ~4.5 Å natural packing density on  $\text{SiO}_2$  surfaces (25).

Little change is seen in the  $\text{Sn}-(\text{C}\equiv\text{C})_m-p\text{-C}_6\text{H}_4-(\text{C}\equiv\text{C})_m\text{-H}$  monolayer structure by varying  $m$  from 0 to 2. The most significant effect is an increase in molecular tilt at  $d > 4.6$  Å, simply to reduce monolayer free volume. The steric bulk of the phenyl group dominates the assembly structure, strictly defining the conformations so that they are nearly independent of the intermolecular separation and alkynyl length.

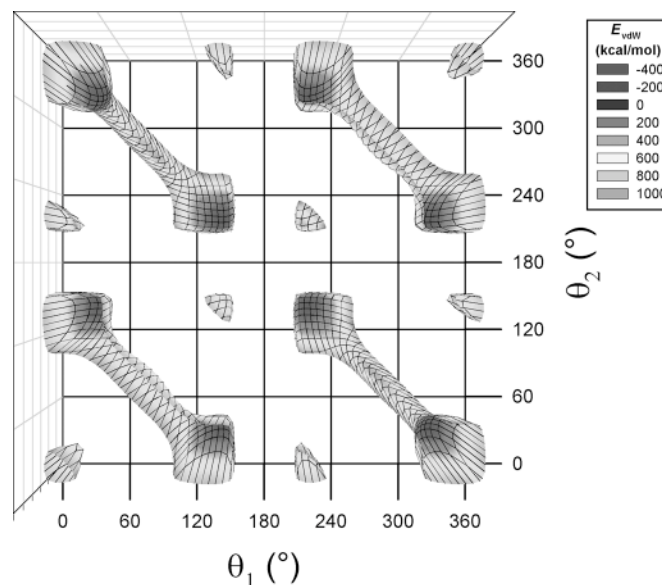
### Unnatural symmetry cells of alkyl-backboned monolayers

To more accurately determine the structures of alkyl-backboned monolayers at lateral separations away from the natural packing densities (*unnatural separations*), PGO-C calculations were performed on the RRSM-generated conformations, using the  $\text{Sn}-\text{C}\equiv\text{C}-(\text{CH}_2)_6-\text{C}\equiv\text{CH}$  chain as a representative model. The PGO-C technique removes the rigid-

**Table 3.** Calculated in-plane ( $\phi$ ) and out-of-plane ( $\psi$ ) tilts, relative to the molecular inertial axis, for  $\text{Sn}-(\text{C}\equiv\text{C})_m-p\text{-C}_6\text{H}_4-(\text{C}\equiv\text{C})_m\text{-H}$  monolayers at herringbone orientations of  $(\theta_1, \theta_2) = (35^\circ, -35^\circ)$ .

$d$ (Å)	$m = 0$		$m = 1$		$m = 2$	
	$\phi$ (°)	$\psi$ (°)	$\phi$ (°)	$\psi$ (°)	$\phi$ (°)	$\psi$ (°)
4.0	0	0	0	0	0	0
4.1	0	0	0	0	0	0
4.2	0	0	0	0	0	0
4.3	0	0	0	0	0	0
4.4	0	0	0	0	0	0
4.5	0	0	0	0	0	0
4.6	0	0	0	0	5	0
4.7	0	0	6	0	9	0
4.8	0	0	10	0	12	0
4.9	0	0	17	0	20	0
5.0	0	0	22	0	25	0

**Fig. 7.** RRSM plot of  $E_{\text{vdW}}$  as a function of  $(\theta_1, \theta_2)$  for  $\text{H}-\text{C}\equiv\text{C}-p\text{-C}_6\text{H}_4-\text{C}\equiv\text{C}-\text{Sn}$  molecules at a hexagonal separation of 4.4 Å. All located energy minima are equivalent.

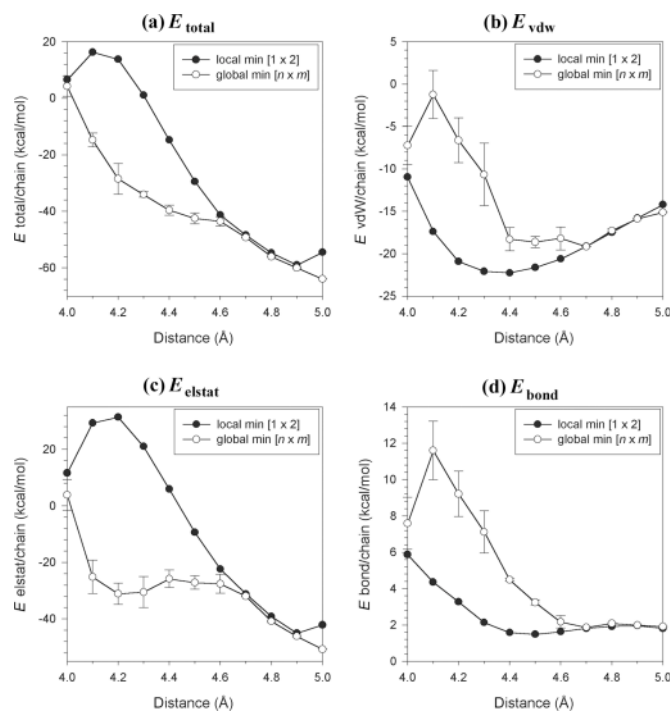


rod constraints, and optimizes for bond ( $E_{\text{bond}}$ ), electrostatics ( $E_{\text{elstat}}$ ), and  $E_{\text{vdW}}$  terms under periodic conditions to mimic an infinite surface structure. As well, by carefully choosing correct periodic boundary conditions (10), new, optimized units of symmetry can be found within the periodic box that effectively represent the infinite monolayer structure.

PGO-C calculations were carried out on  $\text{Sn}-\text{C}\equiv\text{C}-(\text{CH}_2)_6-\text{C}\equiv\text{CH}$  structures at hexagonal intermolecular separations between 4.0 and 5.0 Å, and at six different initial face-packing orientations:  $(\theta_1, \theta_2) = (0^\circ, 0^\circ), (60^\circ, 60^\circ), (120^\circ, 120^\circ), (180^\circ, 180^\circ), (240^\circ, 240^\circ)$ , and  $(300^\circ, 300^\circ)$ . Two general types of structures were observed after the optimizations. By using a combination of minimization algorithms,<sup>4</sup> global minimum structures were obtained with  $[n \times m]$  symmetry descriptors (where the term  $[n \times m]$  refers to  $n$  in-plane by  $m$  out-of-plane units) that varied considerably



**Fig. 8.** PGO-C calculations of (a)  $E_{\text{total}}$  and the separate components, (b)  $E_{\text{vdW}}$ , (c)  $E_{\text{elstat}}$ , and (d)  $E_{\text{bond}}$  as a function of distance for  $\text{Sn-C}\equiv\text{C}-(\text{CH}_2)_6-\text{C}\equiv\text{CH}$  monolayers. The curve with open symbols corresponds to the global minimum structures, and the curve with filled symbols corresponds to the local minimum structures.



depending on the intermolecular separation  $d$ . Through use of lowered convergence conditions<sup>6</sup> and shorter iteration trials, local  $E_{\text{vdW}}$  minima were obtained with consistent  $[1 \times 2]$  symmetry and geometries corresponding closely to the original RRSM results. In Fig. 8, the results of the PGO-C energy optimizations as a function of distance are shown, with separate curves representing the global minimum  $[n \times m]$  and local minimum  $[1 \times 2]$  results. Error bars represent energy variations calculated for different initial  $(\theta_1, \theta_2)$  orientations. Total energies (Fig. 8a), and decompositions into van der Waals (Fig. 8b), electrostatic (Fig. 8c), and bonding (Fig. 8d) terms are presented, normalized for the number of chains per periodic box, where (16):

$$[1] \quad E_{\text{total}} = \sum E_{\text{bond}} + E_{\text{vdW}} + E_{\text{elstat}}$$

and

$$[2] \quad E_{\text{bond}} = \sum E_{\text{stretch}} + E_{\text{angle}} + E_{\text{torsion}} + E_{\text{inversion}}$$

Figure 9 diagrams the calculated geometries for selected symmetry units at unnatural separations, and Table 4 lists the PGO-C global minimum symmetry cells, calculated under  $6 \times 6$  periodic boundaries.

In the distance range of 4.0–4.5 Å, a large energy difference exists between the local and global minimum structures because of repulsive interactions among the alkyl chains. Although the ordered  $[1 \times 2]$  structures experience stabilizing (negative)  $E_{\text{vdW}}$  forces at these intermolecular separations, electrostatic repulsions from identically situated molecules result in high  $E_{\text{total}}$  values for the ordered structures. To re-

**Fig. 9.** Unnatural symmetry cells calculated by the PGO-C method for  $\text{Sn-C}\equiv\text{C}-(\text{CH}_2)_6-\text{C}\equiv\text{CH}$  monolayers, viewed in the  $xy$  and  $xz$  planes: (a)  $d = 4.2$  Å,  $[6 \times 6]$  symmetry; (b)  $d = 4.6$  Å,  $[3 \times 3]$  symmetry; (c)  $d = 4.7$  Å,  $[1 \times 2]$  symmetry; (d)  $d = 5.0$  Å,  $[1 \times 1]$  symmetry.

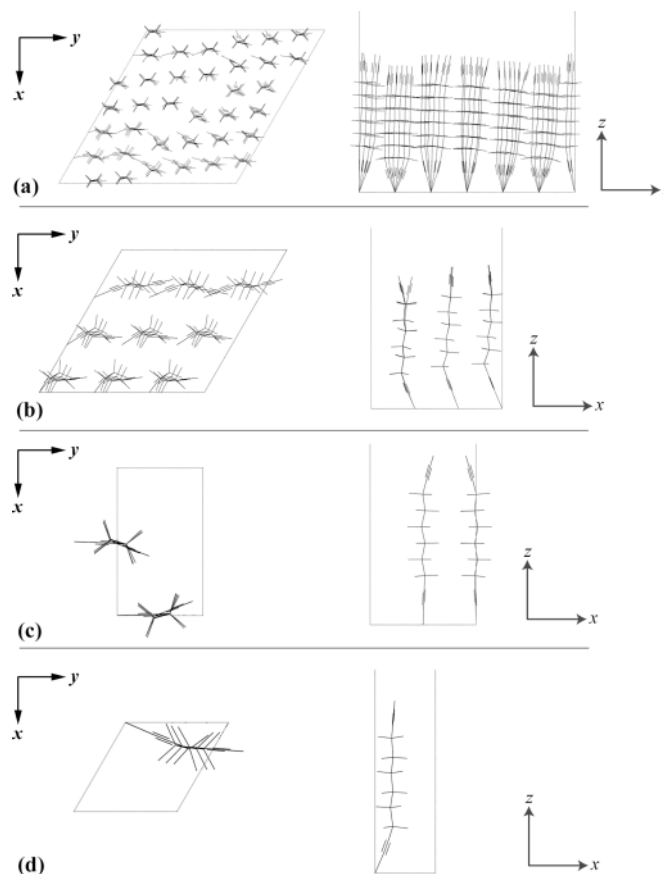


**Table 4.** PGO-C symmetries of packing for  $[n \times m]$  global minimum geometries of  $\text{Sn-C}\equiv\text{C}-(\text{CH}_2)_6-\text{C}\equiv\text{CH}$  monolayers at  $d = 4.0$ – $5.0$  Å, using initial  $[6 \times 6]$  periodic boundary conditions.

$d$ (Å)	Repeating unit size
4.0	$[2 \times 3]$
4.1	$[6 \times 6]$
4.2	$[6 \times 6]$
4.3	$[3 \times 3]$
4.4	$[1 \times 3]$
4.5	$[1 \times 3]$
4.6	$[3 \times 3]$
4.7	$[1 \times 2]$
4.8	$[1 \times 2]$
4.9	$[2 \times 3]$
5.0	$[1 \times 1]$

duce the repulsive forces, the global minimum energy monolayers adopt lower symmetries of packing, from  $[6 \times 6]$  to  $[3 \times 3]$  to  $[1 \times 3]$  unit cells, by orienting chains at slightly different angles of twist and tilt. The expense of higher van der Waals and bond energies is offset by the reduced  $E_{\text{elstat}}$



energies for these structures. Figure 9a shows an example of a global minimum structure at 4.2 Å, with domain boundaries forming to reduce repulsions among ordered in-plane rows. The repulsive contacts increase the isotropy of the monolayer, and global minimum energies are observed to vary, depending on the initial face-packing angles, within this separation range. The global and local minimum curves converge at 4.0 Å because, at this low separation, the chain-chain separations fall into the range of intramolecular distances, producing inaccurate energy terms (Fig. 8).

After the  $-\text{CH}_2-$  van der Waals radii have been overcome, the two energy curves converge between 4.6–5.0 Å, and the global minimum structures demonstrate new, higher symmetries of packing, such as the herringbone structure at  $d = 4.7$  Å (Fig. 9c) and the  $[1 \times 1]$  structure at  $d = 5.0$  Å (Fig. 9d). All energy terms show convergence, with identical results produced for each initial face-packing angle (Fig. 8). The global minimum models are energetically favoured because of more effective filling of surface free volume, through chain twists and tilts, than the rigid  $[1 \times 2]$  structures with near identical conformations. The  $E_{\text{total}}$  values become more negative as the separation increases, mainly because of decreased Sn–Sn electrostatic interactions.

The PGO-C calculations show the range of possible structures available to the  $\text{Sn-C}\equiv\text{C}-(\text{CH}_2)_6-\text{C}\equiv\text{CH}$  monolayer within the narrow distance range of 4.0–5.0 Å. The unnatural structures are highly isotropic in the range of alkyl chain overlap, but can become even more ordered than the natural symmetry structures with increasing intermolecular separation. These theoretical calculations suggest that decreasing the natural chain packing density, towards unnatural separations of 5.0 Å and beyond, will produce increasingly ordered thin films.

### Unnatural symmetry cells of phenyl-backboned monolayers

PGO-C calculations were also performed on phenyl-backboned systems to determine the optimal symmetries of packing at unnatural separations beyond and below the natural chain densities. Calculations performed on  $\text{Sn-C}\equiv\text{C}-p\text{-C}_6\text{H}_4\text{-C}\equiv\text{C-H}$  monolayers are used as representative of all phenyl-based chains. Figure 10 plots the calculated PGO-C energies ( $E_{\text{total}}$ ) as a function of distance, and Fig. 11 shows the PGO-C geometry for the calculated symmetry cells. Optimizations from the initial RRSM herringbone orientations produced monolayers with  $[1 \times 2]$  symmetry (Fig. 11a), nearly identical to the original scan structures. As shown in Fig. 10 the herringbone  $[1 \times 2]$  units lie at or close to the global minima throughout the entire distance range. As in the RRSM results, energies are minimized at higher separations ( $d = 5.0$  Å) to decrease electrostatic Sn–Sn repulsions. At lower, more repulsive separations ( $d = 4.0$ – $4.2$  Å), a lower symmetry,  $[3 \times 2]$  packing cell was calculated to be the most favourable structure. As shown in Fig. 11c, the  $[3 \times 2]$  unit cell is a modified herringbone structure, with four molecules having  $z$ -axis twists of ( $\pm 45^\circ$ ), and two at twists of ( $\pm 15^\circ$ ), to decrease repulsive interactions. Similar structures were previously observed for highly strained, natural phenyl surfaces on  $\text{SiO}_2$  (10). Repetition of the PGO-C calculations, using the  $[3 \times 2]$  produced models energetically equivalent to the  $[1 \times 2]$  structures between  $d = 4.3$ – $5.0$  Å.

**Fig. 10.** PGO-C calculated energies as a function of distance for  $\text{Sn-C}\equiv\text{C}-p\text{-C}_6\text{H}_4\text{-C}\equiv\text{C-H}$  monolayers.

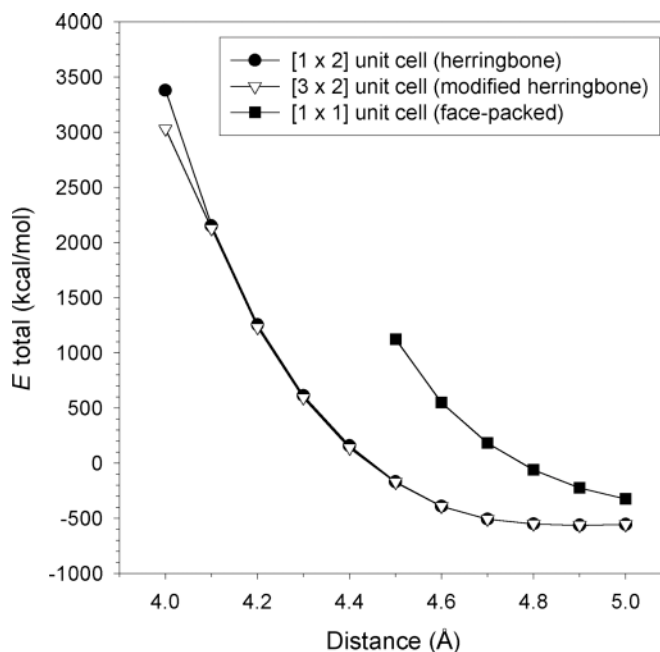
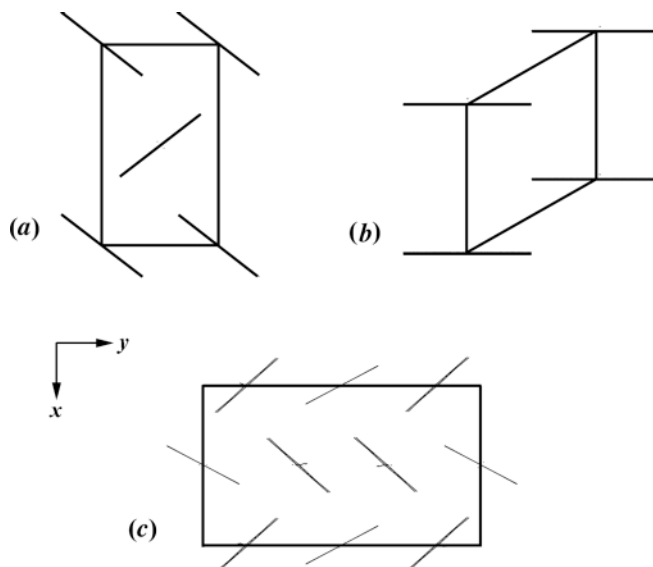


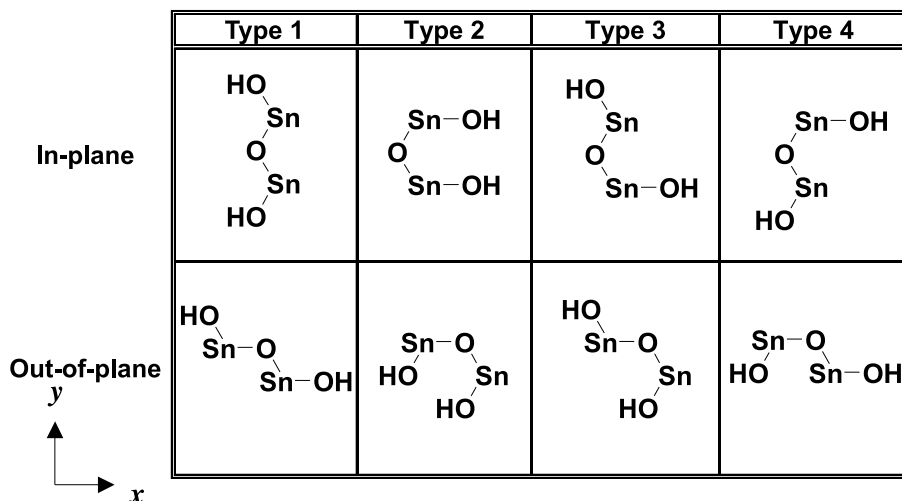
**Fig. 11.** Unnatural symmetry cells calculated by the PGO-C method for  $\text{Sn-C}\equiv\text{C}-p\text{-C}_6\text{H}_4\text{-C}\equiv\text{C-H}$  monolayers, viewed in the  $xy$  plane: (a)  $d = 5.0$  Å,  $[1 \times 2]$  symmetry; (b)  $d = 5.0$  Å,  $[1 \times 1]$  symmetry; (c)  $d = 5.0$  Å,  $[3 \times 2]$  symmetry.



To qualify the herringbone optimizations,  $\text{H-C}\equiv\text{C}-p\text{-C}_6\text{H}_4\text{-C}\equiv\text{C-Sn}$  models with a face-packing orientation ( $\theta_1, \theta_2$ ) = ( $0^\circ, 0^\circ$ ) were also optimized from  $d = 4.0$ – $5.0$  Å. Only models from  $d = 4.5$ – $5.0$  Å yielded stable structures with a  $[1 \times 1]$  symmetry (Fig. 11b), but at significantly higher energy than the  $[3 \times 2]$  or  $[1 \times 2]$  symmetry units. The periodic packing results confirm that the conformations of phenyl-backboned chains are uniquely determined by the steric and symmetry properties of the phenyl group, and these orientations remain approximately constant over the range of dis-



**Fig. 12.** Schematic representation of Sn-O-Sn dimers modelled on the tridymite surface. Each dimer type is repeated over the entire  $6 \times 6$  surface for each minimization. View is normal to the model surface, with Sn—O—Si and Sn—C bonds omitted for clarity. The hydroxy positions match the tetrahedral oxygen projections of the underlying tridymite surface.



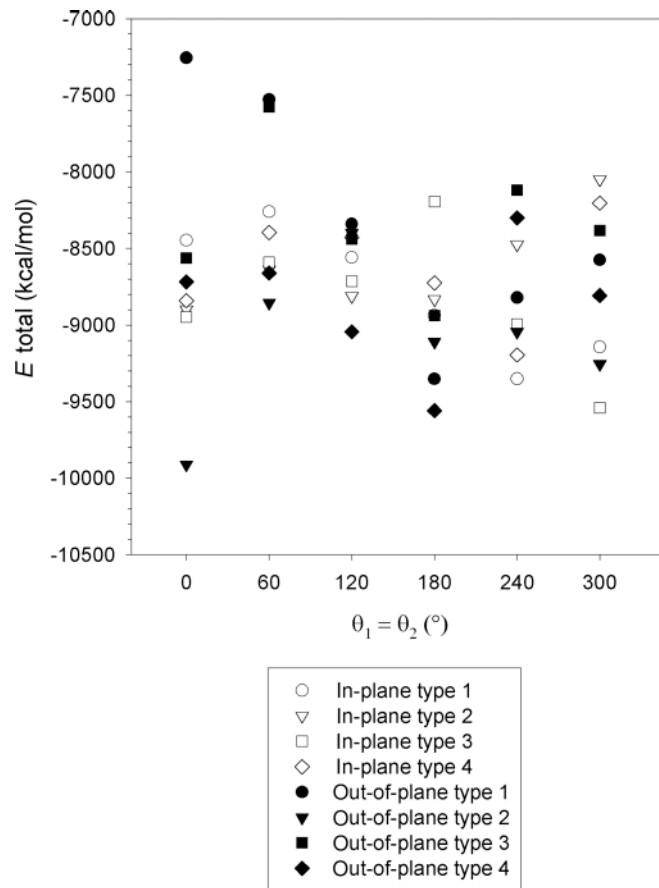
tances studied. However, decreasing the packing density away from the natural separation of 4.5 Å towards unnatural values of 5.0 Å is predicted, theoretically, to improve monolayer stability because of decreased electronic repulsions.

#### Surface bonding: Dimer structures of alkyl-backboned chains on a model surface

Repulsive alkyl chain forces prevent extensive cross-linking of the Sn headgroups, and therefore only small cross-linked units, such as dimers or trimers, are feasible for hydrolytic SAMs (6). As discussed previously (10), PGO-S calculations were performed on cross-linked, surface-bound  $\text{Sn}-\text{C}\equiv\text{C}-(\text{CH}_2)_6-\text{C}\equiv\text{CH}$  dimers to accurately model a monolayer surface and to examine the effect of headgroup bonding on alkyl chain order. Eight different dimer surfaces, as shown in Fig. 12, were modelled with the PGO-S method to determine the minimum dimer conformation.

Because the alkyl monolayer energies and geometries were observed to be strongly dependent on the initial face-packing chain orientations in the distance range 4.0–4.5 Å (Fig. 8), the eight dimer surfaces were optimized at orientations  $(\theta_1, \theta_2) = (0^\circ, 0^\circ), (60^\circ, 60^\circ), (120^\circ, 120^\circ), (180^\circ, 180^\circ), (240^\circ, 240^\circ), \text{ and } (300^\circ, 300^\circ)$ . The calculated PGO-S energies, as a function of dimer type and face-packing orientation, are plotted in Fig. 13. There is no consistent ordering of the dimer surface energies over the six face-packing geometries considered. At each value of  $(\theta_1, \theta_2)$  the dimer surface energies fall within a broad 500–1000 kcal mol<sup>-1</sup> range, with one or two outliers representing either exceptionally stable or strongly disfavoured Sn-O-Sn headgroup geometries. The relative positions of the dimer energies, and the surface energies themselves, vary as the face-packing angle is changed. Compressing the alkyl chain structure through headgroup cross-linking creates highly isotropic monolayer surfaces with variable energies, and symmetries ranging from  $[6 \times 6]$  to  $[2 \times 3]$  to  $[1 \times 6]$ . The Sn-O-Sn cross-links cannot minimize to a preferred orientation, as their configurations are limited by the isotropic alkyl geometries. The

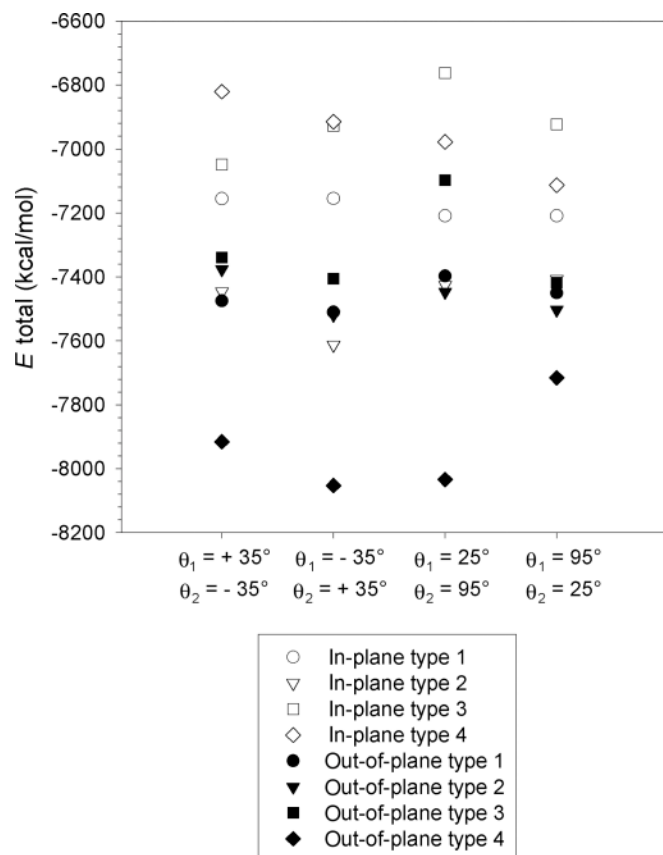
**Fig. 13.** PGO-S energies as a function of face-packing angle ( $\theta_1, \theta_2$ ) and dimer type for cross-linked  $\text{H}-\text{C}\equiv\text{C}-(\text{CH}_2)_6-\text{C}\equiv\text{C}-\text{Sn}$  dimers bound to a  $6 \times 6$  tridymite surface.



most favoured structure, the out-of-plane type 2 dimer at  $(0^\circ, 0^\circ)$  correlates with the minimum energy out-of-plane dimer calculated by PM3 semiempirical methods.



**Fig. 14.** PGO-S energies as a function of herringbone angle ( $\theta_1$ ,  $\theta_2$ ) and dimer type for cross-linked  $\text{Sn-C}\equiv\text{C-}p\text{-C}_6\text{H}_4\text{-C}\equiv\text{C-H}$  dimers bound to a  $6 \times 6$  tridymite surface.



#### Surface bonding: Dimer structures of phenyl-backboned chains on a model surface

PGO-S calculations were also performed on surface-bound, cross-linked  $\text{Sn-C}\equiv\text{C-}p\text{-C}_6\text{H}_4\text{-C}\equiv\text{C-H}$  monolayers, using the eight dimer types shown in Fig. 12, and four possible herringbone orientations on the tridymite surface: ( $\theta_1$ ,  $\theta_2$ ) =  $(-35^\circ, 35^\circ)$ ,  $(35^\circ, -35^\circ)$ ,  $(25^\circ, 95^\circ)$ , and  $(95^\circ, 25^\circ)$ . The calculated PGO-S energies as a function of dimer type and herringbone orientation are shown in Fig. 14. The surface energies show nearly consistent ordering for each different dimer type over the four packing angles studied. In particular, a global minimum dimer surface, out-of-plane dimer type 4, is observed at each herringbone orientation. Because the packing of phenyl chains is independent of distance, the most favoured Sn-O-Sn headgroup geometry can form at each herringbone orientation, with minimal surface disruption. The low energy dimer structures have either the  $[1 \times 2]$  herringbone or the modified herringbone  $[3 \times 2]$  symmetry previously seen for PGO-C results (Fig. 11). The most favourable bonding is out-of-plane herringbone, not in-plane face-packed, as confirmed by PM3 semiempirical calculations.

#### Monomer and trimer structures of phenyl-backboned chains on a model surface

Because the phenyl-based models form reproducible monolayer structures upon the tridymite surface, and are

**Fig. 15.** Schematic (a) type 1 and (b) type 2 cyclic trimers calculated for  $\text{Sn-C}\equiv\text{C-}p\text{-C}_6\text{H}_4\text{-C}\equiv\text{C-H}$  monolayers on the tridymite surface. Triangle points represent Sn atoms.

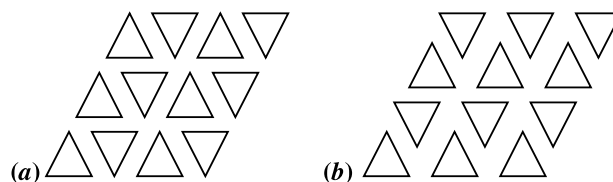
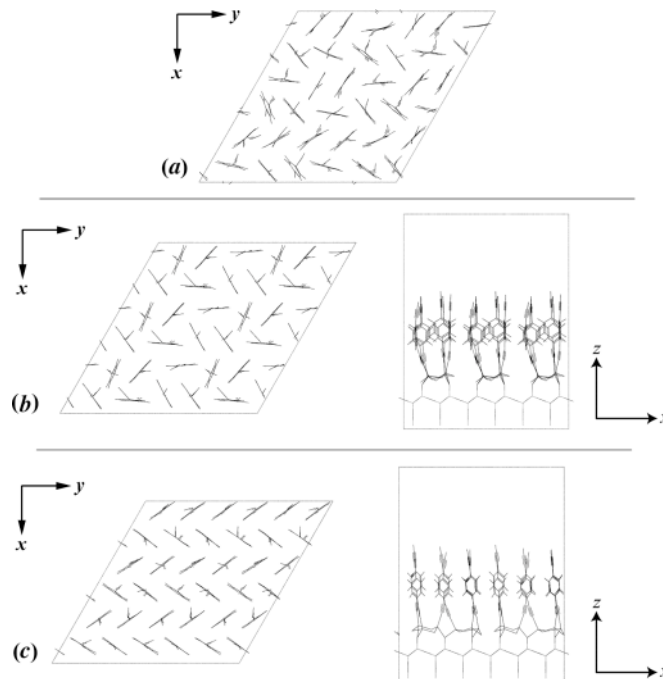


**Fig. 16.** PGO-S calculated structures of various  $\text{Sn-C}\equiv\text{C-}p\text{-C}_6\text{H}_4\text{-C}\equiv\text{C-H}$  monolayers on the tridymite surface. (a)  $(\text{HO})_2(\text{SiO})\text{Sn-R}$  monomer surface; (b) cyclic trimer type 1 surface; (c) cyclic trimer type 2 surface. Views in the  $xy$  plane have  $\text{SiO}_2$  substrate and Sn—O—Sn and (or) Sn—OH bonds removed for clarity.



computationally less demanding than the alkyl-backboned structures, PGO-S calculations on surface-bound  $\text{Sn-C}\equiv\text{C-}p\text{-C}_6\text{H}_4\text{-C}\equiv\text{C-H}$  monomers and two types of cyclic trimers (Fig. 15) were used to further elucidate the effect of headgroup structure on chain ordering. Calculated structures are presented in Fig. 16, and an energy comparison is detailed in Table 5. The monomer surface produces less-ordered surfaces (Fig. 16a) than the trimer or dimer monolayers. Interactions among nonbonded OH groups disrupt packing symmetry on a surface at full coverage. The trimer monolayers (Fig. 16b and 16c) produce highly ordered surfaces, with  $[3 \times 2]$  and  $[1 \times 2]$  symmetry units. The  $[3 \times 2]$  trimer structure is slightly favoured energetically. These calculations show that, for a  $\text{Sn-C}\equiv\text{C-}p\text{-C}_6\text{H}_4\text{-C}\equiv\text{C-H}$  surface at full coverage, monomer, dimer, and trimer headgroup bonding is possible. However, Sn-O-Sn cross-linked dimers are most favourable, because they have less chain distortion than trimers, and have fewer repulsive interactions than surface-bound monomers.



**Table 5.** Total energies and symmetries of various Sn-C≡C-*p*-C<sub>6</sub>H<sub>4</sub>-C≡C-H monolayers on the tridymite surface, calculated with the PGO-S method.

Surface type	$E_{\text{total}}$ (kcal mol <sup>-1</sup> )	Symmetry
Monomer	-5480.70	[3 × 2]
Dimer, out-of-plane type 4	-8051.87	[3 × 2]
Trimer type 1	-6436.22	[3 × 2]
Trimer type 2	-6430.84	[1 × 2]

**Fig. 17.** Distance constraints for topochemical photopolymerization of diacetylene molecules.

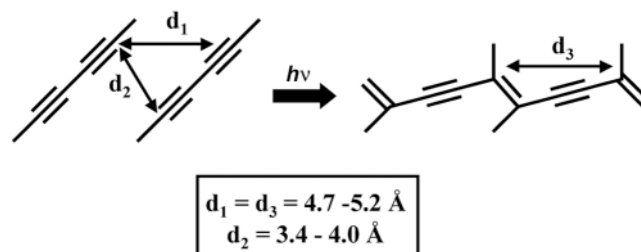
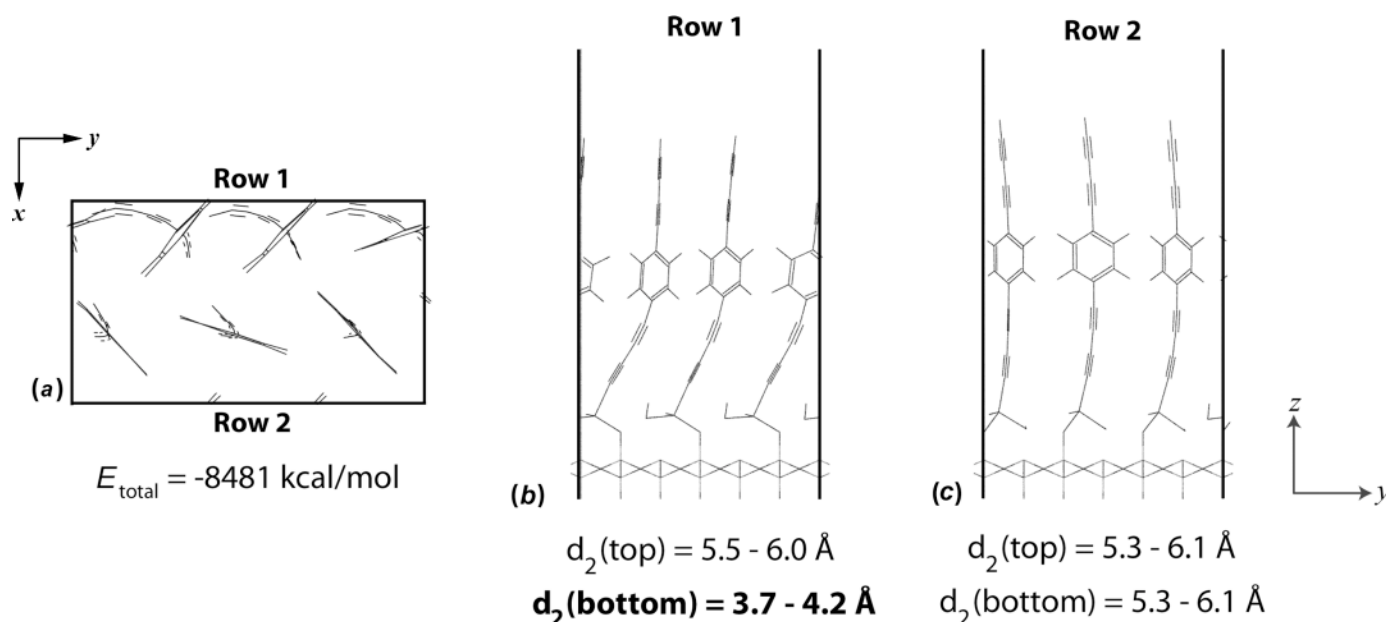


**Fig. 18.** (a) [3 × 2] PGO-S calculated structure for Sn-(C≡C)<sub>2</sub>-*p*-C<sub>6</sub>H<sub>4</sub>-(C≡C)<sub>2</sub>-H structure (SiO<sub>2</sub> substrate and Sn—O—Sn bonds removed for clarity). Two types of rows exist in this symmetry cell: (b) the tilted row (Row 1) with lower acetylenes in the correct distance range for polymerization; and (c) the uncompressed Row 2.



#### Topochemical polymerization of Sn-(C≡C)<sub>2</sub>-*p*-C<sub>6</sub>H<sub>4</sub>-(C≡C)<sub>2</sub>-H monolayers

Monolayers containing diacetylene groups can be photopolymerized to form one-dimensional *poly*(diacetylene) upon exposure to UV radiation, if specific distances exist between neighbouring diacetylene units (12, 13), as shown in Fig. 17. Such polymerized structures increase the conductive and nonlinear optical potential of the thin film, and stabilize the monolayer through the extended bonding network. However, the extent of polymerization is critically dependent on the intermolecular separations, and hence, the structural order, within the self-assembled monolayer.

Topochemical polymerization has been observed experimentally for Sn-(C≡C)<sub>2</sub>-*p*-C<sub>6</sub>H<sub>4</sub>-(C≡C)<sub>2</sub>-H monolayers self-assembled on quartz substrates (9a) indicating that the Sn-alkyl SAMs are relatively well-ordered materials. To better understand the thin film structure and the polymerization mechanism, PGO-S optimizations were performed on the Sn-(C≡C)<sub>2</sub>-*p*-C<sub>6</sub>H<sub>4</sub>-(C≡C)<sub>2</sub>-H monolayer, using a global-minimum out-of-plane type 4 dimer (Fig. 12) to represent the surface headgroups. The minimum energy, [3 × 2] structure calculated for this monolayer is shown in Fig. 18. The two

in-plane rows within this symmetry unit show different chain tilts, because the stress of packing two phenyl rings into the confined monolayer space compresses one row below the other. In the compressed row, Fig. 18b, the lower diacetylene groups are within the correct  $d_2$  range (3.7–4.2 Å) for topochemical polymerization; no other diacetylene separation in the PGO-S unit cell meets the bonding requirements.

The PGO-S geometry of a Sn-(C≡C)<sub>2</sub>-*p*-C<sub>6</sub>H<sub>4</sub>-(C≡C)<sub>2</sub>-H monolayer, polymerized along the lower diacetylene row indicated in Fig. 18b, is shown in Fig. 19. Polymerization along this bottom row decreases the total energy by only 6%, from -235.59 kcal/mol-chain to -221.974 kcal/mol-chain, and does not significantly distort the monolayer. Instead, the nonpolymerized row (Row 2, Fig. 18c) tilts in the +*y* axis direction to fill the free volume in the monolayer created by the polymerization of Row 1. This free volume tilting now puts the upper diacetylenes into a  $d_2$  range of 4.0–4.3 Å, sufficient for topochemical polymerization. No other diacetylenes groups in the monolayer are close enough to polymerize.

The calculated PGO-S structure of a Sn-(C≡C)<sub>2</sub>-*p*-C<sub>6</sub>H<sub>4</sub>-(C≡C)<sub>2</sub>-H monolayer polymerized along the bottom diacetylenes of Row 1 and the upper diacetylenes of Row 2,



**Fig. 19.** PGO-S calculated structure for a  $\text{Sn}-(\text{C}\equiv\text{C})_2\text{-}p\text{-C}_6\text{H}_4\text{-(C}\equiv\text{C)}_2\text{-H}$  monolayer, polymerized along the lower diacetylenes of Row 1. (a) *xy* Plane view of the  $[3 \times 2]$  cell ( $\text{SiO}_2$  substrate and  $\text{Sn-O-Sn}$  bonds removed for clarity), (b) the polymerized in-plane Row 1, (c) the nonpolymerized in-plane Row 2, now tilted into the required topochemical distance range.

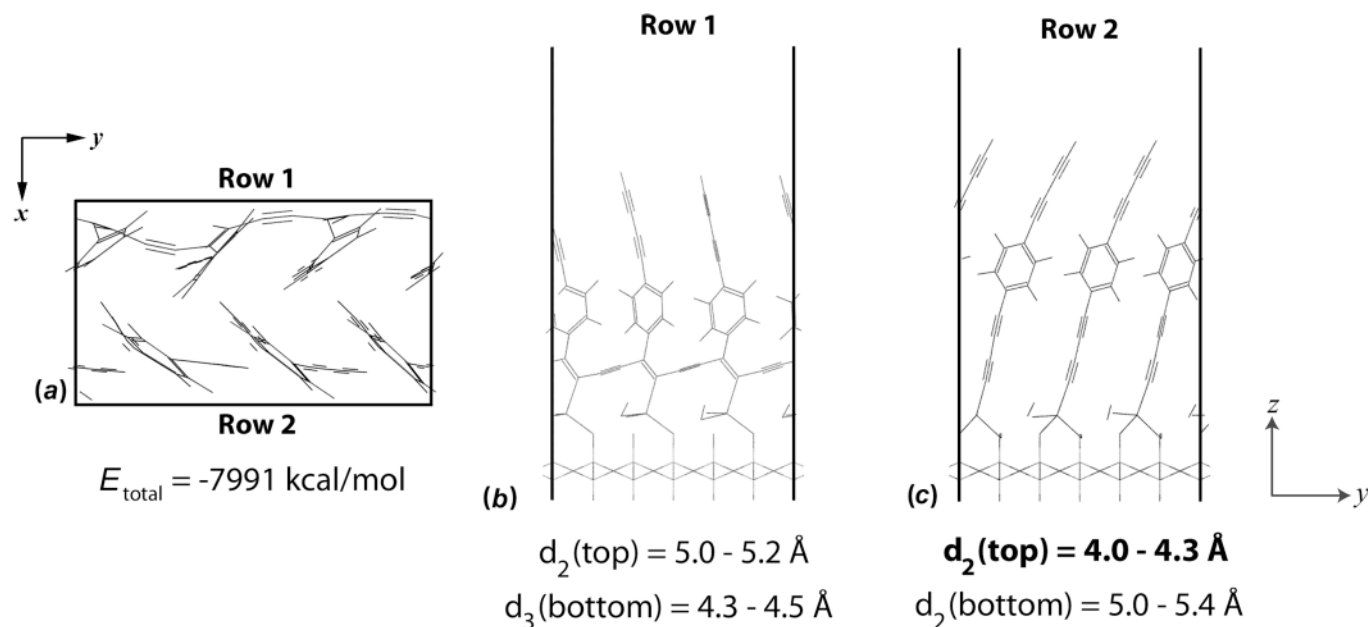
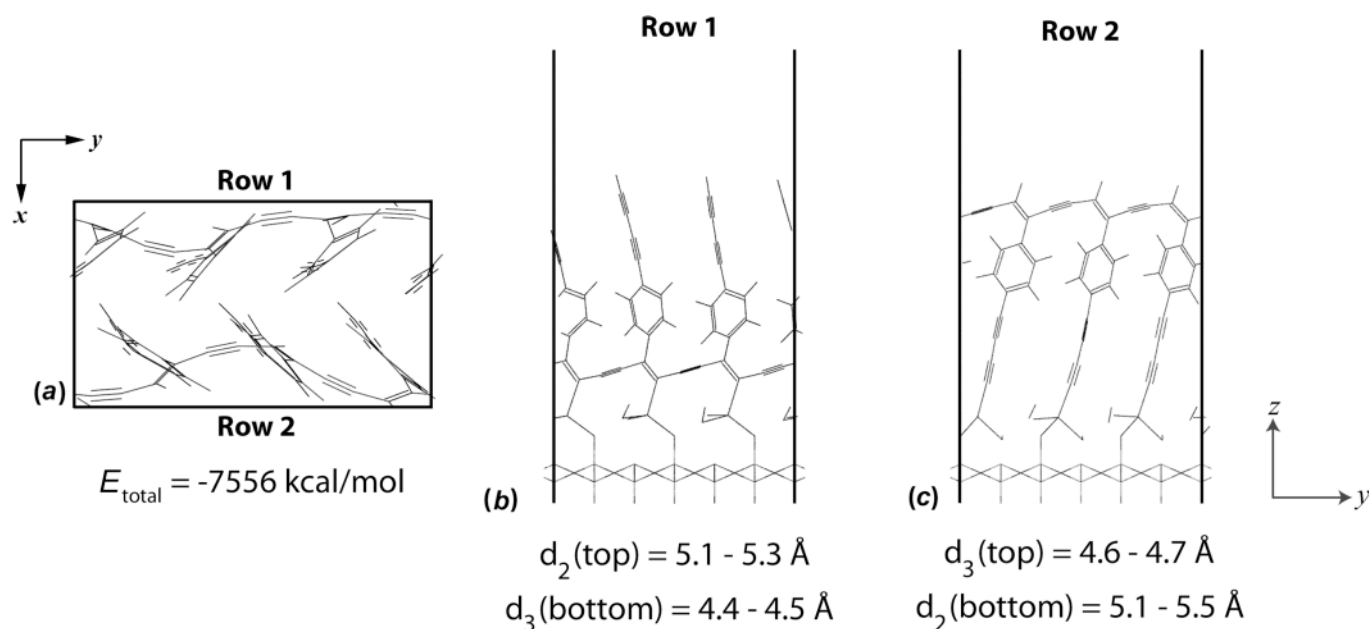


**Fig. 20.** PGO-S calculated structure for a  $\text{Sn}-(\text{C}\equiv\text{C})_2\text{-}p\text{-C}_6\text{H}_4\text{-(C}\equiv\text{C)}_2\text{-H}$  monolayer, polymerized along the lower diacetylenes of Row 1 and the upper diacetylenes of Row 2. (a) *xy* Plane view of the  $[3 \times 2]$  cell ( $\text{SiO}_2$  substrate and  $\text{Sn-O-Sn}$  bonds removed for clarity), (b) the polymerized in-plane Row 1, (c) the polymerized in-plane Row 2. No more polymerization is possible in this model.



is shown in Fig. 20. The polymerization is again energetically stable, decreasing the total energy by 5% from the half-polymerized structure of Fig. 19. At this point, the polymerization is complete. No more free volume exists in the monolayer, so the remaining acetylenes stay untilted, out of the polymerization range. Therefore, diacetylene polymerization occurs in this monolayer because compressive packing forces bend the lower acetylenes into the correct geometric range. A second polymerization occurs because

upper acetylenes tilt to eliminate free volume in the monolayer. The PGO-S calculations can be used to successfully interpret geometric thin film behaviour.

## Conclusions

Geometric studies of phenyl- and alkyl-backboned monolayers, using the powerful RRSM, PGO-C, and PGO-S techniques, yield analytic insights into thin film growth and



stability. Mapping the potential energy surface, through a selected range of intermolecular distances, suggests that monolayers are more stable at unnatural packing densities. At the natural surface separation distances (20, 25) of 4.2–4.4 Å, both alkyl and phenyl monolayers experience highly repulsive interactions, producing more isotropic film structures. The symmetries of film packing increase and monolayer energies become more favourable at chain–chain separations greater than 4.6 Å. Modifying or eliminating the Sn–O–Sn headgroup cross-links that naturally compress interchain distances can therefore improve experimental film structures.

Analysis of headgroup bonding on a natural surface, using the PGO-S method, demonstrated that cross-linked Sn–O–Sn dimers yield the most stable monolayer energies. However, the extent of Sn cross-linking is critically dependent on the organic monolayer packing order. PGO-S calculations on a Sn-(C≡C)<sub>2</sub>-p-C<sub>6</sub>H<sub>4</sub>-(C≡C)<sub>2</sub>-H monolayer provide an elegant geometric interpretation of the experimental topochemical polymerizations. Proper molecular modelling techniques are therefore robust and predictive tools for the study and design of functional thin film systems.

## Acknowledgements

We thank the Natural Sciences and Engineering Research Council of Canada (NSERC) and Fonds pour la formation des chercheurs et l'aide à la recherche (Québec) (FCAR) for financial support. AJD thanks NSERC for a post-graduate fellowship and Sigma Xi for a Grant-in-Aid of Research.

## References

1. I. Langmuir. *J. Am. Chem. Soc.* **39**, 1848 (1917).
2. A.I. Kitaigorodskii. *Organic chemical crystallography*. Consultants Bureau, New York, 1961.
3. R.G. Nuzzo and D.L. Allara. *J. Am. Chem. Soc.* **105**, 4481 (1983).
4. J. Sagiv. *J. Am. Chem. Soc.* **102**, 92 (1980).
5. (a) C. Tripp and M. Hair. *Langmuir*, **8**, 1120 (1992); (b) C. Tripp and M. Hair. *Langmuir*, **8**, 1961 (1992); (c) C. Tripp and M. Hair. *Langmuir*, **11**, 1215 (1995).
6. (a) A.N. Parikh, M.A. Schivley, E. Koo, K. Seshadri, D. Aurentz, K. Mueller, and D.L. Allara. *J. Am. Chem. Soc.* **119**, 3135 (1997); (b) R. Wang, G. Baran, and S.L. Wunder. *Langmuir*, **16**, 6298 (2000).
7. (a) C. Carraro, O.W. Yauw, M.M. Sung, and R. Maboudian. *J. Phys. Chem. B*, **102**, 4441 (1998); (b) M.M. Sung, C. Carraro, O.W. Yauw, Y. Kim, and R. Maboudian. *J. Phys. Chem. B*, **104**, 1556 (2000).
8. M.J. Stevens. *Langmuir*, **15**, 2773 (1999).
9. (a) C.M. Yam, A.J. Dickie, and A.K. Kakkar. *Langmuir*, **18**, 8481 (2002); (b) C.M. Yam and A.K. Kakkar. *Langmuir*, **15**, 3807 (1999); (c) C.M. Yam, S.S.Y. Tong, and A.K. Kakkar. *Langmuir*, **14**, 6941 (1998); (d) C.M. Yam, A. Dickie, A. Malkhasian, A.K. Kakkar, and M.A. Whitehead. *Can. J. Chem.* **76**, 1766 (1998); (e) C.M. Yam and A.K. Kakkar. *J. Chem. Soc., Chem. Commun.* 907 (1995).
10. A.J. Dickie, A.K. Kakkar, and M.A. Whitehead. *Langmuir*, **18**, 5657 (2002).
11. A. Ulman, J.E. Eilers, and N. Tillman. *Langmuir*, **5**, 1147 (1989).
12. (a) M.D. Mowery, A.C. Smith, and C.E. Evans. *Langmuir*, **16**, 5998 (2000); (b) M.D. Mowery, S.K. Kopta, D.F. Ogletree, M. Salmeron, and C.E. Evans. *Langmuir*, **15**, 5118 (1999); (c) H. Menzel, M.D. Mowery, M. Cai, and C.E. Evans. *J. Phys. Chem. B*, **102**, 9550 (1998); (d) M.D. Mowery and C.E. Evans. *J. Phys. Chem. B*, **101**, 8513 (1997).
13. (a) T. Kim, K.C. Chan, and R.M. Crooks. *J. Am. Chem. Soc.* **119**, 189 (1997); (b) T. Kim, R.M. Crooks, K.C. Chan, M. Tsen, and L.J. Sun. *J. Am. Chem. Soc.* **119**, 189 (1997).
14. N.L. Allinger. *J. Am. Chem. Soc.* **99**, 8127 (1977).
15. HyperChem. Version 5.1 [computer program]. Hypercube Inc., Gainesville, Florida, U.S.A. 1997.
16. (a) A.K. Rappé, C.J. Casewit, K.S. Colwell, W.A. Goddard, III, and W.M. Skiff. *J. Am. Chem. Soc.* **114**, 10 024 (1992); (b) C.J. Casewit, K.S. Colwell, and A.K. Rappé. *J. Am. Chem. Soc.* **114**, 10 035 (1992); (c) C.J. Casewit, K.S. Colwell, and A.K. Rappé. *J. Am. Chem. Soc.* **114**, 10 046 (1992); (d) A.K. Rappé, K.S. Colwell, and C.J. Casewit. *Inorg. Chem.* **32**, 3438 (1993).
17. Cerius2. Version 3.5 [computer program]. Molecular Simulations Inc., San Diego, California, U.S.A. 1997.
18. A.K. Rappé and W.A. Goddard, III. *J. Phys. Chem.* **95**, 3358 (1991).
19. (a) S.-C. Chang, I. Chao, and Y.-T. Tao. *J. Am. Chem. Soc.* **116**, 6792 (1994); (b) T.-W. Li, I. Chao, and Y.-T. Tao. *J. Phys. Chem. B*, **102**, 2935 (1998).
20. K. Kojio, A. Takahara, K. Omote, and T. Kajiyama. *Langmuir*, **16**, 3932 (2000).
21. A. Ulman. *Chem. Rev.* **96**, 1533 (1996).
22. A.J. Karpfen. *J. Phys. Chem. A*, **103**, 11 431 (1999).
23. P. Hobza, H.L. Selzle, and E.W. Schlag. *J. Phys. Chem.* **100**, 18 790 (1996).
24. (a) A.A. Dhirani, R.W. Zehner, R.P. Hsung, P. Guyot-Sionnest, and L.R. Sita. *J. Am. Chem. Soc.* **118**, 3319 (1996); (b) G. Yang, Y. Qian, C. Engtrakul, L.R. Sita, and G.-Y. Liu. *J. Phys. Chem. B*, **104**, 9059 (2000).
25. L.T. Zhuravlev. *Langmuir*, **3**, 316 (1987).



# Comparison of structures between platinum and palladium complexes of a tetrasilyldisilene<sup>1</sup>

Hisako Hashimoto, Yumiko Sekiguchi, Yohei Sekiguchi, Takeaki Iwamoto, Chizuko Kabuto, and Mistuo Kira

**Abstract:** The first  $\eta^2$ -disilene–palladium complexes were synthesized using two different reactions; the reactions of bis(phosphine)dichloropalladiums with a 1,2-dilithiotetrakis(trialkylsilyl)disilane, which was prepared by the reaction of a stable tetrakis(trialkylsilyl)disilene with lithium (Method A) and the direct reactions of the bis(phosphine)dichloropalladiums with the stable disilene (Method B). Comparison of X-ray structural parameters of the disilene–palladium complexes with those of the corresponding platinum complex has indicated that the palladium complex is a metallacycle but its  $\pi$ -complex character is stronger than that of the platinum complex.

**Key words:** disilene complex, palladium, platinum, X-ray structure, metallacycle,  $\pi$ -complex.

**Résumé :** On a réalisé la première synthèse de complexes  $\eta^2$ -disilène–palladium en faisant appel à deux réactions différentes: la méthode A implique la réaction de dérivés bis(phosphine)dichloropalladium avec un 1,2-dilithiotétrakis(trialkylsilyl)disilane préparé par réaction d'un tétrakis(trialkylsilyl)disilène stable avec du lithium alors que la méthode B implique la réaction directe de dérivés bis(phosphine)dichloropalladium avec le disilène stable. Une comparaison des paramètres structuraux obtenus par diffraction des rayons X pour les complexes disilène–palladium avec ceux du complexe correspondant du platine indique que le complexe du palladium est un métallacycle dont le caractère de complexe  $\pi$  est plus fort que celui du complexe du platine.

**Mots clés :** complexe disilène, palladium, platine, structure par diffraction des rayons X, métallacycle, complexe  $\pi$ .

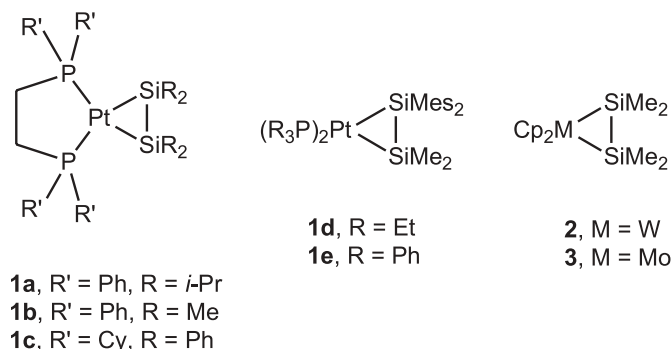
[Traduit par la Rédaction]

## Introduction

Olefin transition metal complexes have been studied as important reactive intermediates in various transition-metal-catalyzed reactions and their structures and bonding nature are well understood (1). In contrast, there have been very few reports on their silicon analogues, transition-metal complexes with  $\eta^2$ -silicon–silicon doubly bonded species as ligands, while a variety of stable free disilenes have been well investigated (2). Complexes **1** (3), **2** (4), and **3** (5) as shown in Chart 1 had been synthesized but only **2** had been investigated by X-ray crystallography before we started our study of transition-metal complexes with stable disilenes as a ligand (6).

The bonding of a disilene to a metal center is expected to be understood in terms of "ligand-to-metal  $\sigma$ -donation" and "metal-to-ligand  $\pi$ -back donation", similarly to that of an olefin (Dewar–Chatt–Duncanson model) (7). According to this model, the  $\eta^2$ -disilene transition-metal complexes can be described using two resonance structures of a  $\pi$  complex and

Chart 1.



a metallacycle as shown in Scheme 1. The relative contribution of the two structures could depend on the electronic properties of the metal and the disilene. Thus, the relative importance between the  $\sigma$ -donation and the  $\pi$ -back donation determines the  $\pi$ -complex character of the disilene transition-metal complexes; the  $\pi$ -complex character will increase with decreasing  $\pi$ -back donation.

Recently, we reported a platinum complex with a silyl-substituted  $\eta^2$ -disilene ligand (**4**) (6). The X-ray structural analysis has shown that **4** is better described as a metallacycle with a very weak  $\pi$ -complex character. Strong  $\pi$ -back donation from the electron-rich platinum to the disilene would account for the structural character of **4**. Since the  $\pi$ -back donation of palladium is calculated to be weaker than that of platinum by Sakaki et al. (8a), the palladium analogue of **4** is expected to have a  $\pi$ -complex charac-

Received 4 February 2003. Published on the NRC Research Press Web site at <http://canjchem.nrc.ca> on 9 September 2003.

H. Hashimoto, Y. Sekiguchi, Y. Sekiguchi, T. Iwamoto, C. Kabuto, and M. Kira.<sup>2</sup> Department of Chemistry, Graduate School of Science, Tohoku University, Aoba-ku, Sendai 980–8578, Japan.

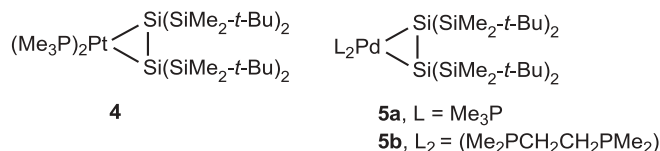
<sup>1</sup>This article is part of a Special Issue dedicated to Professor John Harrod.

<sup>2</sup>Corresponding author (e-mail: [mkira@si.chem.tohoku.ac.jp](mailto:mkira@si.chem.tohoku.ac.jp)).



ter stronger than **4**. We report here the first synthesis of the palladium  $\eta^2$ -disilene complexes **5a** and **5b** using two different methods and their molecular structures determined by X-ray crystallography. Comparison of the structural parameters among the corresponding platinum and palladium complexes (**4** and **5a**) revealed larger  $\pi$ -complex character for the palladium complex than that for the platinum complex, in conformity with the theoretical study (8a).

#### Chart 2.

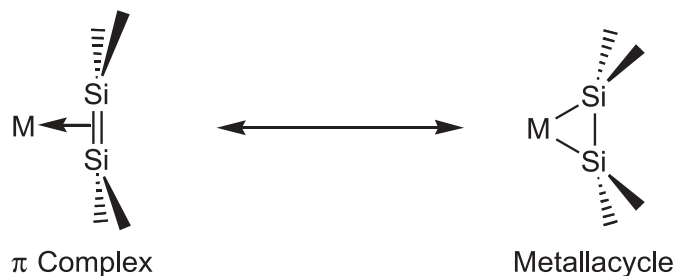


## Results and discussion

Palladium  $\eta^2$ -disilene complexes **5a** and **5b** were synthesized using two different methods (Methods A and B). First, **5a** and **5b** were synthesized by applying a similar method used for the synthesis of **4** (Method A). Thus, complex **5a** was synthesized in 55% yield by the reaction of *cis*-(Me<sub>3</sub>P)<sub>2</sub>PdCl<sub>2</sub> (**9**) (**6a**; 0.20 g, 0.38 mmol) with 1,2-dilithio-tetrakis(*tert*-butyldimethylsilyl)disilane (**10**) (**7**; 0.14 g, 0.41 mmol) in THF at -50 °C for 3 h, as shown in eq. [1]; dilithiodisilane **7** was prepared as a white powder by the reduction of the corresponding stable disilene **8** with lithium metal (**10**). Likewise, complex **5b** was obtained as a yellow powder in 43% yield from (dmpe)PdCl<sub>2</sub> (**8**) (**6b**; 0.082 g, 0.24 mmol) and **7** (0.13 g, 0.25 mmol). Complex **5a** and **5b** were synthesized also by the reactions of disilene **8** with bis(phosphine)palladium dichlorides **6a** and **6b**, as shown in eq. [2]. In the reactions shown in eq. [2], a 2 mol amount of disilene **8** was required for the complete consumption of palladium dichlorides **6a** and **6b**, suggesting that 1 mol of disilene is consumed in the reduction of **6a** and **6b** to the corresponding bis(phosphine)Pd(0) complexes, which react further with another mol of **8** to give **5a** and **5b**, respectively.

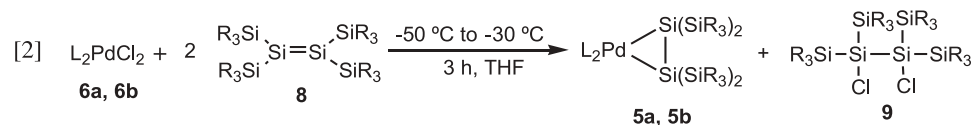
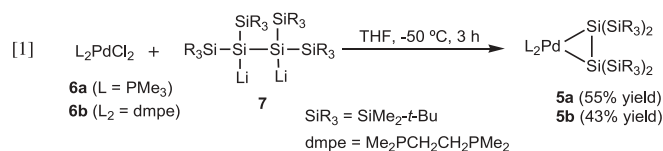
Recrystallization of **5a** and **5b** from diethyl ether and toluene, respectively, at -20 °C afforded yellow prisms suitable for a single-crystal X-ray diffraction study.<sup>3,4</sup> The molecular structures of **5a** and **5b** are shown in Figs. 1 and 2 with se-

#### Scheme 1.



lected bond lengths and angles. Both **5a** and **5b** have the crystallographic C-2 axis through the palladium and the center of the Si1—Si1\* bond, and the  $\eta^2$ -coordination of the disilene moiety. Central palladium atoms in **5a** and **5b** adopt highly distorted square-planar geometries with the dihedral angles of 31.8° and 28.5°, respectively, between the P1-Pd-P1\* and Pd-Si1-Si1\* planes. Steric repulsion between the bulky trialkylsilyl substituents and the phosphine ligands would account for their distorted geometry.

Table 1 summarizes pertinent structural parameters of disilene-palladium complexes **5a** and **5b** and disilene-platinum complex **4**. The Si1—Si1\* distances of **5a** (2.303(1) Å) and **5b** (2.318(6) Å) lie below the shortest limit of the reported Si—Si single bond (2.335–2.697 Å) (11). The Si-Pd distances in **5a** (2.4374(7) Å) and **5b** (2.4184(4) Å) are a little longer than those of the reported bis(phosphine)(disilyl)palladium complexes (2.34–2.38 Å) (12). The bent angles ( $\delta$ ) of **5a** (25.5°) and **5b** (26.0°), which are defined as an angle between the Si2-Si1-Si3 plane and the Si1—Si1\* bond, are far larger than that of free disilene **8** (0.1°) (13). The results indicate that **5a** and **5b** should be described still as a metallacycle with a very small  $\pi$ -complex character similar to platinum complex **4** (6). Small but significant differences were found in the structures around the disilene moiety between the platinum and palladium complexes (**4** and **5a**) with the same trimethylphosphine ligands. Thus, the elongation of the central Si-Si distance in **5a** ( $\Delta l$  = 0.101 Å) is slightly smaller than that in **4** ( $\Delta l$  = 0.120 Å). The bent angle ( $\delta$ ) for **5a** (25.5°) is a little smaller than that of **4** (28.4°). All these differences in **5a** and **4** are in good accord with those found theoretically between the model compounds (H<sub>3</sub>P)<sub>2</sub>Pd(Si<sub>2</sub>H<sub>4</sub>) and (H<sub>3</sub>P)<sub>2</sub>Pt(Si<sub>2</sub>H<sub>4</sub>) by Sakaki et. al. (8a) suggesting that the  $\pi$ -complex character for the disilene-



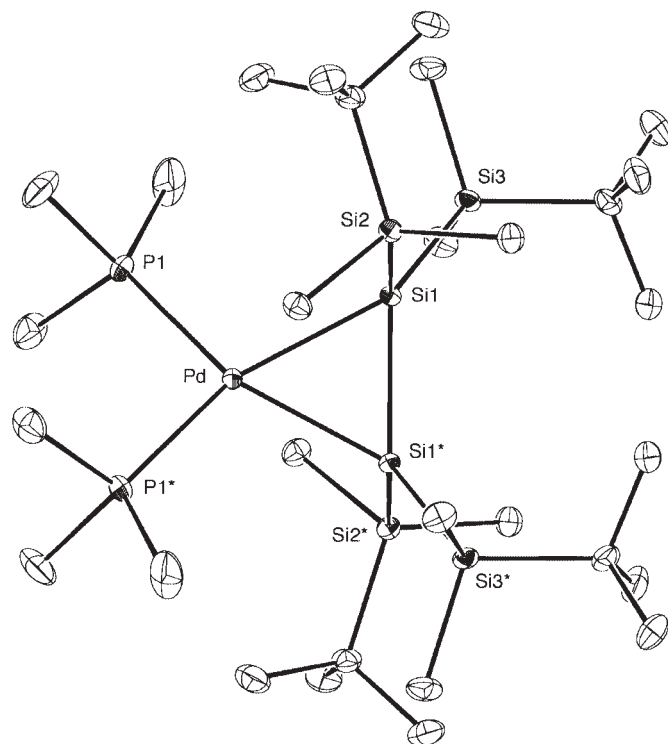
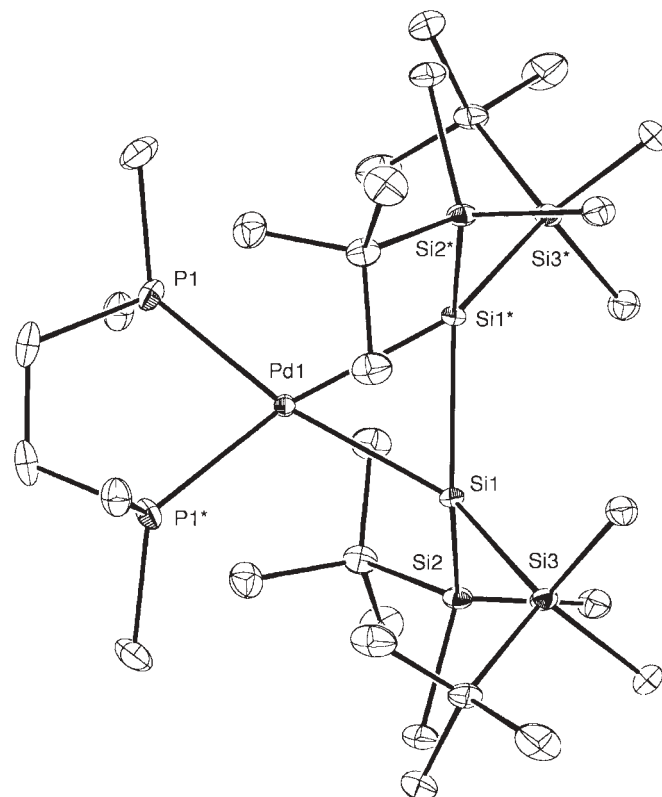
<sup>3</sup>Crystal data for **5a**: C<sub>30</sub>H<sub>78</sub>Si<sub>6</sub>P<sub>2</sub>Pd, yellow prisms, orthorhombic, *P*<sub>bcn</sub> (#60), *a* = 16.5927(3) Å, *b* = 12.4209(3) Å, *c* = 21.2100(5) Å, *V* = 4371.3(2) Å<sup>3</sup>, *Z* = 4, *D*<sub>calcd</sub> 1.179 g/cm<sup>3</sup>,  $\mu$ (MoK $\alpha$ ) = 6.80 cm<sup>-1</sup>; of 36 652 measured reflections, 4863 were independent and 4030 observed with *I* > 3 $\sigma$ (*I*). *R*1 = 0.021, *wR*2 (all data) = 0.033 for 294 parameters.

<sup>4</sup>Crystal data for **5b**: C<sub>30</sub>H<sub>76</sub>Si<sub>6</sub>P<sub>2</sub>Pd, yellow prisms, orthorhombic, *C*<sub>cca</sub> (#68), *a* = 20.328(1) Å, *b* = 20.6854(9) Å, *c* = 20.382(1) Å, *V* = 8570.6(8) Å<sup>3</sup>, *Z* = 8, *D*<sub>calcd</sub> 1.199 g/cm<sup>3</sup>,  $\mu$ (MoK $\alpha$ ) = 6.94 cm<sup>-1</sup>; of 76 587 measured reflections, 6523 were independent and 4106 observed with *I* > 2 $\sigma$ (*I*). *R*1 (*I* > 2 $\sigma$ (*I*)) = 0.018, *wR*2 (all data) = 0.046 for 215 parameters.



**Table 1.** Selected structural parameters of disilene complexes **5** and related compounds.

Compound	<i>l</i> (Si–Si) (Å) <sup>a</sup>	$\Delta l$ (Si–Si) (Å) <sup>b</sup>	$\delta$ (°) <sup>c</sup>	<i>l</i> (Si–M) (Å) <sup>d</sup>
<b>5a</b>	2.303(1)	0.101(1)	25.5	2.4374(7)
<b>5b</b>	2.318(6)	0.116(6)	26.0	2.4184(4)
<b>4<sup>e</sup></b>	2.322(2)	0.120(2)	28.4	2.4310(8)
<b>8<sup>f</sup></b>	2.202(1)	0.0	0.1	—

<sup>a</sup>Central silicon–silicon bond distance.<sup>b</sup>Difference of the central Si–Si bond distance of the compound from that of **8**.<sup>c</sup>Bent angle defined as the angle between the Si1–Si2–Si3 plane and the Si1–Si1\* bond.<sup>d</sup>Silicon – transition metal bond distance.<sup>e</sup>Reference 6.<sup>f</sup>Reference 12.**Fig. 1.** ORTEP drawing of  $\eta^2$ -disilene palladium complex **5a**. Hydrogen atoms are omitted for clarity. Selected bond lengths (Å) and angles (°): Pd–Si1 2.4374(7), Si1–Si1\* 2.303(1), Pd–P 2.3364(7), Si1–Si2 2.3902(9), Si1–Si3 2.3760(9), Si1–Pd–Si1\* 56.39(3), Pd–Si1–Si1\* 61.81(1), P1–Pd–P1\* 99.17(4).**Fig. 2.** ORTEP drawing of  $\eta^2$ -disilene palladium complex **5b**. Hydrogen atoms are omitted for clarity. Selected bond lengths (Å) and angles (°): Pd–Si1 2.4184(4), Si1–Si1\* 2.3180(8), Pd1–P 2.3319(4), Si1–Si2 2.3929(6), Si1–Si3 2.3849(6), Si1–Pd–Si1\* 57.27(2), Pd–Si1–Si1\* 61.36(1), P1–Pd–P1\* 85.86(2).

palladium complex **5a** is somewhat stronger than that for the corresponding platinum complex.

The  $^{29}\text{Si}$  NMR resonance of the central silicon atoms appeared at  $-46.8$  ppm for **5a** and  $-51.9$  ppm for **5b** with a doublet of doublets signal pattern owing to two  $^{31}\text{P}$  nuclei. These chemical shifts are considerably downfield-shifted compared to that of **4** ( $-79.7$  ppm) (6), even though they are still upfield from that of the free disilene **8** (142.1 ppm) (13). The difference in the  $\pi$ -complex character between the palladium and platinum complexes may be responsible, in part, for the down-field shift in the former. Further works are in progress to reveal the dependence of the  $\pi$ -complex character in disilene – transition metal complexes on the central metals and ligands.

## Experimental

### General

$^1\text{H}$ ,  $^{13}\text{C}$ ,  $^{29}\text{Si}$ , and  $^{31}\text{P}$  NMR spectra were recorded on a Bruker AC-300P FT NMR spectrometer at 300, 75.4, 59.6, and 121 MHz, respectively, at  $25^\circ\text{C}$  unless otherwise noted. Mass spectra and high resolution mass spectra were recorded on a JEOL JMS-600W (EI, 70 eV) and a HX-110 mass spectrometer (FAB, nitrobenzyl alcohol matrix). UV–vis spectra were obtained using a Hewlett-Packard HP8453 E spectrometer. Air-sensitive compounds were manipulated in a VAC MO-40-M glove box.

Bis(trimethylphosphine)dichloropalladium (**6a**) and [1,2-



bis(dimethylphosphino)ethane]dichloropalladium (**6b**) were prepared according to the procedures in the literature (9).

**[ $\eta^2$ -Tetrakis(*tert*-butyldimethylsilyl)disilene]bis(trimethylphosphine)palladium (**5a**)**

**Method A**

To a mixture of *cis*-bis(trimethylphosphine)dichloropalladium (9) (**6a**, 0.102 g, 0.293 mmol) and 1,2-dilithio-1,1,2,2-tetrakis(*tert*-butyldimethylsilyl)disilane (10) (**7**, 0.157 g, 0.296 mmol) in a Schlenk flask (50 mL) was introduced THF (5 mL) dried over a K mirror through a vacuum line. The mixture was stirred for 3 h at  $-50^\circ\text{C}$  and then the THF was distilled off at  $0^\circ\text{C}$ . After the addition of toluene (40 mL) to the residue, the resulting precipitates were filtered off. Removal of toluene in vacuo gave the title compound (0.178 g, 0.163 mmol) in 55% yield.

**Method B**

Dry toluene (5 mL) was introduced to a mixture of **6a** (0.099 g, 0.30 mmol) and tetrakis(*tert*-butyldimethylsilyl)disilene (**8**) (13) (0.30 g, 0.60 mmol). The mixture was stirred for 3 h at  $-50^\circ\text{C}$  and then the toluene was distilled off. The  $^1\text{H}$  NMR spectrum of the mixture showed the quantitative formation of disilene complex **5a** and 1,2-dichloro-1,1,2,2-tetrakis(*tert*-butyldimethylsilyl)disilane (14).

**5a:**

Yellow crystals, mp  $92^\circ\text{C}$  (decomp.). UV-vis (hexane)  $\lambda_{\text{max}}$  (nm) ( $\epsilon$ ): 344 (5400), 421 (5000).  $^1\text{H}$  NMR ( $\text{C}_6\text{D}_6$ )  $\delta$ : 0.40 (s, 12 H), 0.49 (s, 12 H), 1.11 (d,  $^2J_{\text{P-H}} = 5.4$  Hz, 18 H), 1.22 (s, 36 H).  $^{13}\text{C}$  NMR ( $\text{C}_6\text{D}_6$ ,  $70^\circ\text{C}$ )  $\delta$ : 2.5, 2.7, 20.1, 21.5 (d,  $^1J_{\text{P-C}} = 11$  Hz), 29.7.  $^{29}\text{Si}$  NMR ( $\text{C}_6\text{D}_6$ )  $\delta$ :  $-46.8$  (dd,  $^2J_{\text{P(trans)-Si}} = 83.4$  Hz,  $^2J_{\text{P(cis)-Si}} = 22.1$  Hz), 4.2.  $^{31}\text{P}$  NMR ( $\text{C}_6\text{D}_6$ )  $\delta$ :  $-31.33$ . MS (FAB)  $m/z$  (%): 773 ( $\text{M}^+$ ), 698 ( $\text{M}^+ - \text{PMe}_3$ , 54), 622 ( $\text{M}^+ - 2\text{PMe}_3$ , 50), 535 (54), 460 (100). Anal. calcd. for  $\text{C}_{30}\text{H}_{78}\text{P}_2\text{Si}_6\text{Pd}$  (%): C 46.44, H 10.13; found (%): C 46.46, H 9.88.

**[ $\eta^2$ -Tetrakis(*tert*-butyldimethylsilyl)disilene]bis(dimethylphosphino)ethane]palladium (**5b**)**

**Method A**

To a mixture of [bis(dimethylphosphino)ethane] dichloropalladium (9) (**6b**, 0.082 g, 0.24 mmol) and 1,2-dilithio-1,1,2,2-tetrakis(*tert*-butyldimethylsilyl)disilane (10) (**7**, 0.132 g, 0.25 mmol) in a Schlenk flask (50 mL) was introduced dry THF (20 mL) through a vacuum line. The mixture was stirred for 3 h at  $-50^\circ\text{C}$  and then the THF was distilled off at  $0^\circ\text{C}$ . After addition of toluene (40 mL) to the residue, the resulting precipitates were filtered off. Removal of toluene in vacuo gave the title compound (0.076 g, 0.0984 mmol) in 41% yield.

**Method B**

To a mixture of **6b** (0.16 g, 0.49 mmol) and **8** (13) (0.50 g, 1.00 mmol) was introduced dry THF (20 mL). The mixture was stirred for 3 h at  $-50^\circ\text{C}$  and then the toluene was distilled off. The  $^1\text{H}$  NMR spectrum of the mixture showed the quantitative formation of disilene complex **5b** and 1,2-dichloro-1,1,2,2-tetrakis(*tert*-butyldimethylsilyl)di-

silane (14). Recrystallization from toluene gave pure **5b** (0.085 g, 0.11 mmol) in 22% yield.

**5b:**

Yellow crystals, mp  $83^\circ\text{C}$  (decomp.). UV-vis (hexane)  $\lambda_{\text{max}}$  (nm) ( $\epsilon$ ): 305 (11 000, sh), 345 (7500, sh), 380 (5300).  $^1\text{H}$  NMR ( $\text{C}_6\text{D}_6$ )  $\delta$ : 0.39 (s, 12 H), 0.51 (s, 12 H), 0.91 (d,  $^2J_{\text{P-H}} = 14$  Hz, 4H), 1.11 (d,  $^2J_{\text{P-H}} = 6$  Hz, 12 H), 1.22 (s, 36 H).  $^{13}\text{C}$  NMR ( $\text{C}_6\text{D}_6$ )  $\delta$ : 3.4, 3.5, 16.4–16.6 (m), 19.7, 30.1.  $^{29}\text{Si}$  NMR ( $\text{C}_6\text{D}_6$ )  $\delta$ :  $-51.9$  ( $^2J_{\text{P(trans)-Si}} = 76$  Hz,  $^2J_{\text{P(cis)-Si}} = 15$  Hz),  $+6.1$ .  $^{31}\text{P}$  NMR ( $\text{C}_6\text{D}_6$ )  $\delta$ : 7.41. Anal. calcd.  $\text{C}_{30}\text{H}_{76}\text{P}_2\text{Si}_6$  (%): C 46.56, H 9.90; found (%): C 46.58, H 9.62.

X-ray data of **5a** and **5b** may be purchased from the Directory of Unpublished Data, Document Delivery, CISTI, National Research Council Canada, Ottawa, ON K1A 0S2, Canada ([http://www.nrc.ca/cisti/irm/unpub\\_e.shtml](http://www.nrc.ca/cisti/irm/unpub_e.shtml) for information on ordering electronically). CCDC 202926 and 202927 contain the crystallographic data for this manuscript. These data can be obtained, free of charge, via [www.ccdc.cam.ac.uk/conts/retrieving.html](http://www.ccdc.cam.ac.uk/conts/retrieving.html) (or from the Cambridge Crystallographic Data Centre, 12 Union Road, Cambridge CB2 1EZ, U.K.; fax +44 1223 336033; or [deposit@ccdc.cam.ac.uk](mailto:deposit@ccdc.cam.ac.uk)).

## Acknowledgments

This work was supported by Grants-in-Aid for Scientific Research (B) (No. 11440185) and Scientific Research on Priority Areas (No. 14078203, *Reaction Control of Dynamic Complexes*) from the Ministry of Education, Culture, Sports, Science, and Technology, Japan.

## References

- For reviews of olefin complexes see: (a) F.R. Hartley. *Chem. Rev.* **69**, 799 (1969); (b) F.R. Hartley. *Comprehensive organometallic chemistry*. Edited by G. Wilkinson, F.G.A. Stone, and E.W. Abel. Pergamon, New York. 1982. p. 471.
- For reviews of  $\text{R}_2\text{M}=\text{MR}_2$  (M = Si, Ge, Sn) see: (a) R. West. *Pure Appl. Chem.* **56**, 163 (1984); (b) G. Raabe and J. Michl. *Chem. Rev.* **85**, 419 (1985); (c) R. West. *Angew. Chem. Int. Ed. Engl.* **26**, 1201 (1987); (d) G. Raabe and J. Michl. *The chemistry of organic silicon compounds*. Edited by S. Patai and Z. Rappoport. John Wiley and Sons, New York. 1989. Chap. 17. p. 1015; (e) J. Barrau, J. Escudié, and J. Satgé. *Chem. Rev.* **90**, 283 (1990); (f) T. Tsumuraya, S.A. Batcheller, and S. Masamune. *Angew. Chem. Int. Ed. Engl.* **30**, 902 (1991); (g) R.S. Grev. *Adv. Organomet. Chem.* **33**, 125 (1991); (h) R. Okazaki and R. West. *Adv. Organomet. Chem.* **39**, 231 (1996); (i) M. Kira and T. Iwamoto. *J. Organomet. Chem.* **611**, 236 (2000); (j) M. Weidenbruch. *The chemistry of organic silicon compounds*. Vol. 3. Edited by Z. Rappoport and Y. Apeloig. Wiley, New York. 2001 Chap. 5. p. 391; (k) M. Weidenbruch. *J. Organomet. Chem.* **646**, 39 (2002).
- (a) C. Zybail and R. West. *J. Chem. Soc., Chem. Commun.* 857 (1986); (b) E.K. Pham and R. West. *J. Am. Chem. Soc.* **111**, 7667 (1989); (c) E.K. Pham and R. West. *Organometallics*, **9**, 1517 (1990).
- D.H. Berry, J.H. Chey, H.S. Zipin, and P.J. Carroll. *J. Am. Chem. Soc.* **112**, 452 (1990).
- (a) E.A. Zarate, C.A. Tessier-Youngs, and W.J. Youngs. *J. Am. Chem. Soc.* **110**, 4068 (1988); (b) E.A. Zarate, C.A. Tessier-



- Youngs, and W.J. Youngs. *J. Chem. Soc., Chem. Commun.* 577 (1989).
6. H. Hashimoto, Y. Sekiguchi, T. Iwamoto, C. Kabuto, and M. Kira. *Organometallics*, **21**, 454 (2002).
7. (a) M.J.S. Dewar. *Bull. Soc. Chim. Fr.* **18**, C71 (1951); (b) J. Chatt and L.A. Duncanson. *J. Chem. Soc.* 2939 (1953).
8. (a) S. Sakaki, S. Yamaguchi, Y. Musashi, and M. Sugimoto. *J. Organomet. Chem.* **635**, 173 (2001); (b) S. Sakaki and M. Ieki. *Inorg. Chem.* **30**, 4218 (1991); see also (c) T.R. Cundari and M.S. Gordon. *THEOCHEM*, **313**, 47 (1994).
9. (a) J.R. Doyle, P.E. Slade, and H.B. Jpnassen. *Inorg. Synth.* **6**, 218 (1960); (b) J.M. Jenkins and J.G. Verkade. *Inorg. Synth.* **11**, 108 (1968).
10. M. Kira, T. Iwamoto, D. Yin, T. Maruyama, and H. Sakurai. *Chem. Lett.* 910 (2001).
11. M. Kaftory, M. Kapon, and M. Botoshansky. The chemistry of organic silicon compounds. Part 1. *Edited by Z. Rappoport and Y. Apeloig*. Wiley, New York. 1998. Chap. 5. p. 181.
12. (a) Y. Pan, J.T. Mague, and M.H. Fink. *Organometallics*, **11**, 3495 (1992); (b) M. Murakami, T. Yoshida, and Y. Ito. *Organometallics*, **13**, 2900 (1994); (c) M. Suginome, H. Oike, S.-S. Park, and Y. Ito. *Bull. Chem. Soc. Jpn.* **69**, 289 (1996).
13. M. Kira, T. Maruyama, C. Kabuto, K. Ebata, and H. Sakurai. *Angew. Chem. Int. Ed. Engl.* **33**, 1489 (1994).
14. T. Iwamoto, H. Sakurai, and M. Kira. *Bull. Chem. Soc. Jpn.* **71**, 2741 (1998).



# Wide-rim functionalization of calix[4]arene: The di- and tetrakisocyanocalix[4]arene assembling ligands and their silver(I) polymers and oligomers<sup>1</sup>

Pascal Mongrain and Pierre D. Harvey

**Abstract:** The 5,11- and 5,17-diisocyano-25,26,27,28-tetra-*n*-propoxycalix[4]arene bridging ligands (calix(NC)<sub>2</sub>) have been prepared in four steps with 34 and 30% global yields, respectively. Their corresponding Ag(I) complexes have been prepared from the direct reaction of the ligand with AgBF<sub>4</sub> and are characterized from various spectroscopic and physical techniques. The MALDI-TOF spectra indicate the presence of polymers or oligomers of the type {Ag(calix(NC)<sub>2</sub>)(BF<sub>4</sub>)}<sub>n</sub>. The compounds have been characterized further from TGA, DSC, and XRD and compared with the oligomeric species 5,11,17,23-tetrakisocyanocalix[4]arene silver(I) (as a BF<sub>4</sub><sup>-</sup> salt).

**Key words:** silver, calix[4]arene, polymer, isocyanide, photosensitive, thermal gravimetric analysis.

**Résumé :** Les ligands pontants 5,11- et 5,17-diisocyano-25,26,27,28-tetra-*n*-propoxycalix[4]arène (calix(NC)<sub>2</sub>) ont été synthétisés en 4 étapes chacune avec des rendements globaux respectifs de 34 et 30%. Les complexes correspondant d'Ag(I) ont aussi été préparés à partir de la réaction directe entre les ligands ci-haut et du AgBF<sub>4</sub>. Les analyses MALDI-TOF indiquent la présence de polymères ou d'oligomères du type {Ag(calix(NC)<sub>2</sub>)(BF<sub>4</sub>)}<sub>n</sub>. Ces composés ont ensuite été caractérisés à partir d'analyses d'ATG, de DSC et de DRX, qui ont par la suite été comparés à l'espèce oligomérique 5,11,17,23-tétraisocyanocalix[4]arène argent(I) (contre-ion BF<sub>4</sub><sup>-</sup>).

**Mots clés :** argent, calix[4]arène, polymère, isocyanure, photosensible, analyse thermogravimétrique.

## Introduction

The wide-rim functionalization of the calix[4]arene molecule with transition metal fragments is an area that has not been exhaustively developed (1) in comparison with narrow-rim functionalization (2). This tetraphenolic molecule exhibits a "bowl shape" structure capable of acting as a host for cations and neutral molecules (2, 3), and numerous applications, such as ion transport, novel sensors, selective receptors, biomimetics, luminescence probes, nuclear waste treatment, and homogeneous catalysis, have been reported (3). In that context, this group recently developed the syntheses of the mono-, di-5,11-, di-5,17-, tri-, and tetraphosphinated tetra-*n*-propoxycalix[4]arene (phosphine group = Ph<sub>2</sub>P-) (4) and applied these new ligands to the syntheses of pentamethylcyclopentadienyl rhodium(I) complexes (5).<sup>3</sup> In addition, the preparation and characterization of the mono- and tetrakisocyanotetra-*n*-propoxycalix[4]arene ligands and the corresponding gold(I) chloride complexes have been the subject of a recent study (6). Such multiple wide-rim

functionalizations provide an opportunity to build various molecular architectures. We now wish to report the syntheses and characterization of the 5,11-di- and 5,17-diisocyanocalix[4]arene ligands and their reactivity toward silver(I). These bidentate ligands compare well with the recently reviewed 1,8-diisocyano-*p*-menthane (dmb), which is known to form polymers with Ag(I) (7), but differ from the tetrakisocyanocalix[4]arene analogue from a structure point of view (6).

## Experimental section

### Materials

The AgBF<sub>4</sub> salt was purchased from Aldrich and was used as received. The 5,11-dibromo- (1), 5,17-dibromo- (7), and 5,11,17,23-tetrakisocyanocalix[4]arene (13) starting materials were prepared according to procedures outlined in refs. 4 and 6. The solvents were purified according to general procedures (8).

Received 5 March 2003. Published on the NRC Research Press Web site at <http://canjchem.nrc.ca> on 17 September 2003.

*This paper is dedicated to Professor John Harrod on the occasion of his retirement.*

**P. Mongrain and P.D. Harvey.**<sup>2</sup> Contribution from the Département de Chimie, Université de Sherbrooke, Sherbrooke, QC J1K 2R1, Canada.

<sup>1</sup>This article is part of a Special Issue dedicated to Professor John Harrod.

<sup>2</sup>Corresponding author (e-mail: [p.harvey@USherbrooke.ca](mailto:p.harvey@USherbrooke.ca)).

<sup>3</sup>A series of di-5,11- and di-5,17-dialkylphosphinated calix[4]arene ligands (alkyl = Me, *i*-Pr) and their 1,8-cyclooctadienyl-rhodium(I) and iridium(I) and *trans*-chlorocarbonyl rhodium(I) complexes has also been recently synthesized by this group. See François Plourde, Karine Gilbert, Jonathan Gagnon, and Pierre D. Harvey. *Organometallics*, **22**, 2862 (2003).



### 5,11-Diphtalimido-25,26,27,28-tetrapropoxycalix[4]arene (2): (Cone)

A solution containing compound **1** (209 mg, 0.28 mmol), phthalimide (137 mg, 0.02 mmol), and  $\text{Cu}_2\text{O}$  (428 mg, 0.06 mmol) in collidine (10 mL) was refluxed for 4 days under inert atmosphere. The reaction mixture was cooled to room temperature and was poured in  $\text{CH}_2\text{Cl}_2$  (100 mL). This solution was extracted twice with  $\text{H}_2\text{SO}_4$  5% aqueous solution, NaOH 5%, and distilled water. The organic phase was dried over  $\text{MgSO}_4$ , filtered, and evaporated. The resulting solid was purified by column chromatography using  $\text{CH}_2\text{Cl}_2$ . Yield 55% (135.8 mg). Melting temperature ( $T_m$ ) = 165 °C. IR (solid) ( $\text{cm}^{-1}$ )  $\nu(\text{C}=\text{O})$ : 1715.  $^1\text{H}$  NMR ( $\text{CDCl}_3$ )  $\delta$ : 7.89 (m, 4H, Ph), 7.53 (m, 4H, Ph), 6.82 (s, 4H, Ph), 6.65–6.70 (m, 4H, Ph), 6.51 (t, 2H,  $J = 7.59$  Hz, Ph), 4.45 (m, 4H,  $\text{CH}_2$ ), 3.85–3.95 (m, 8H,  $\text{OCH}_2$ ), 3.18–3.27 (m, 4H,  $\text{CH}_2$ ), 1.95 (m, 8H,  $\text{CH}_2\text{CH}_3$ ), 1.01 (t, 12H,  $J = 7.53$  Hz,  $\text{CH}_3$ ).  $^{13}\text{C}$  NMR ( $\text{CDCl}_3$ )  $\delta$ : 167.2, 157.1, 156.3, 135.8, 135.1, 133.9, 132.3, 128.8, 128.2, 127.1, 125.2, 124.4, 122.7, 31.2, 23.5, 11.0. EI-MS: 882 ( $[\text{M}]^+$ ).

### 5,11-Diamino-25,26,27,28-tetrapropoxycalix[4]arene (3): (Cone)

A solution containing compound **2** (135 mg, 0.153 mmol) and hydrazine monohydrate (0.18 mL, 3.34 mmol) in ethanol (15 mL) was refluxed for 2 h. The solution was cooled to room temperature and evaporated. The resulting solid was dissolved in  $\text{CH}_2\text{Cl}_2$  and extracted twice with NaOH 5% aqueous solution and distilled water. The organic phase was dried over  $\text{MgSO}_4$ , filtered, and evaporated. Yield 95% (90 mg).  $T_m = 209$ – $210$  °C. IR (solid) ( $\text{cm}^{-1}$ )  $\nu(\text{NH})$ : 3525, 3395.  $^1\text{H}$  NMR ( $\text{CDCl}_3$ )  $\delta$ : 7.70–6.57 (m, 6H, Ph), 6.02 (s, 2H, Ph), 5.98 (s, 2H, Ph), 5.38 (dd, 4H,  $\text{CH}_2$ ), 3.85 (t, 4H,  $\text{OCH}_2$ ), 3.73 (t, 4H,  $\text{OCH}_2$ ), 3.15 (br, 4H,  $\text{NH}_2$ ), 3.05 (dd, 4H,  $\text{CH}_2$ ), 1.92 (m, 8H,  $\text{CH}_2\text{CH}_3$ ), 0.99 (m, 12H,  $\text{CH}_3$ ).  $^{13}\text{C}$  NMR ( $\text{CDCl}_3$ )  $\delta$ : 157.1, 150.3, 139.7, 136.0, 134.9, 128.1, 124.5, 116.2, 30.9, 23.2, 10.5. EI-MS: 622 ( $[\text{M}]^+$ ).

### 5,11-Di-N-formamyl-25,26,27,28-tetrahydroxycalix[4]arene (4): (Cone)

A solution containing compound **3** (97.6 mg, 0.157 mmol) in formic acid (4 mL) and toluene (20 mL) was refluxed for several hours. The excess of formic acid and water was eliminated, using a Dean–Stark apparatus, prior to evaporating the solution to dryness. The solid was purified by column chromatography using 1:4 acetone: $\text{CH}_2\text{Cl}_2$ . Yield 92% (101.1 mg). IR (solid) ( $\text{cm}^{-1}$ )  $\nu(\text{C}=\text{O})$ : 1686,  $\nu(\text{NH})$ : 3400.  $^1\text{H}$  NMR ( $\text{CDCl}_3$ )  $\delta$ : 7.95–8.30 (m, 2H,  $\text{C}(\text{O})\text{H}$ ), 6.28–7.15 (complex, 10H, Ph), 4.40–4.45 (dd, 4H,  $\text{CH}_2$ ), 3.70–4.00 (complex, 10H,  $\text{OCH}_2$ , NH), 3.05–3.20 (m, 4H,  $\text{CH}_2$ ), 1.80–1.95 (m, 8H,  $\text{CH}_2\text{CH}_3$ ), 0.90–1.10 (m, 12H,  $\text{CH}_3$ ).  $^{13}\text{C}$  NMR ( $\text{CDCl}_3$ )  $\delta$ : 163.5, 160.1, 158.5, 158.0, 157.5, 155.0–153.5, 137.2–134.3, 132.1–130.5, 129.4–128.6, 121.8, 121.5–120.3, 119.4–119.0, 31.4, 23.8, 10.4. EI-MS: 678 ( $[\text{M}]^+$ ).

### 5,11-Diisocyno-25,26,27,28-tetrapropoxycalix[4]arene (5): (Cone)

A solution containing compound **4** (52 mg, 0.077 mmol) and  $\text{Et}_3\text{N}$  (44.2  $\mu\text{L}$ , 0.32 mmol) in dry  $\text{CH}_2\text{Cl}_2$  (5 mL) was refluxed under inert atmosphere. A  $\text{CH}_2\text{Cl}_2$  solution containing diphosgene (0.1 mL) was added over a period of 1 h.

The solution was refluxed for 1 day and cooled to room temperature. The resulting solution was extracted and evaporated. The solid was purified by column chromatography using  $\text{CH}_2\text{Cl}_2$ . Yield 70% (34.6 mg). IR (solid) ( $\text{cm}^{-1}$ )  $\nu(\text{N}\equiv\text{C})$ : 2131.  $^1\text{H}$  NMR ( $\text{CDCl}_3$ )  $\delta$ : 6.72 (d, 2H,  $J = 2.14$  Hz, Ph), 6.62 (d, 4H,  $J = 2.15$  Hz, Ph), 6.57 (d, 4H,  $J = 2.15$  Hz, Ph), 4.36–4.43 (m, 4H,  $\text{CH}_2$ ), 3.75–3.90 (m, 8H,  $\text{OCH}_2$ ), 3.05–3.20 (dd, 4H,  $\text{CH}_2$ ), 1.80–1.91 (m, 8H,  $\text{CH}_2\text{CH}_3$ ), 0.98 (t, 12H,  $J = 7.55$  Hz).  $^{13}\text{C}$  NMR ( $\text{CDCl}_3$ )  $\delta$ : 162.1, 157.5, 156.5, 137.4, 135.5, 134.1, 130.9, 128.8, 128.0, 126.7, 125.8, 126.6, 120.9, 65.9, 31.2, 23.8, 10.2. EI-MS: 642 ( $[\text{M}]^+$ ).

### Poly[(5,11-diisocyno-25,26,27,28-tetrahydroxycalix[4]arene) silver(I)] tetrafluoroborate (6): (Cone)

A solution containing compound **5** (34 mg, 0.053 mmol) in dry acetonitrile was added to an acetonitrile solution containing  $\text{AgBF}_4$  (5.8 mg, 0.03 mmol). The solution was stirred for 1 h at room temperature, and the solvent was evaporated. Yield 100% (44.3 mg). IR (solid) ( $\text{cm}^{-1}$ )  $\nu(\text{N}\equiv\text{C})$ : 2203,  $\nu(\text{BF}_4)$ : 1015.  $^1\text{H}$  NMR ( $\text{CDCl}_3$ )  $\delta$ : 6.87 (s + s, 4H, Ph), 6.60–6.70 (m, 6H, Ph), 4.40–4.50 (d, 4H,  $\text{CH}_2$ ), 3.75–4.00 (m, 8H,  $\text{OCH}_2$ ), 3.20–3.33 (d, 4H,  $\text{CH}_2$ ), 1.85–1.95 (m, 8H,  $\text{CH}_2\text{CH}_3$ ), 1.11 (m, 12H,  $\text{CH}_3$ ). MALDI-TOF-MS: see Table 1. Anal. calcd. for  $\text{C}_{42}\text{H}_{46}\text{O}_4\text{N}_2\text{AgBF}_4$ : C 60.23, H 5.54, N 3.34; found: C 59.19, H 5.83, N 3.04.

### 5,17-Diphtalimido-25,26,27,28-tetrapropoxycalix[4]arene (8): (Cone)

A solution containing compound **7** (1.000 g, 1.33 mmol), phthalimide (0.8 g, 5.3 mmol), and  $\text{Cu}_2\text{O}$  (1.9 g, 13.3 mmol) in collidine (36 mL) was refluxed for 4 days under inert atmosphere. The reaction mixture was cooled to room temperature and was poured in  $\text{CH}_2\text{Cl}_2$  (300 mL). This solution was extracted twice with  $\text{H}_2\text{SO}_4$  5% aqueous solution, NaOH 5%, and distilled water. The organic phase was dried over  $\text{MgSO}_4$ , filtered, and evaporated. The resulting solid was purified by column chromatography using  $\text{CH}_2\text{Cl}_2$ . Yield 65% (762.4 mg).  $T_m = 165$  °C. IR (solid) ( $\text{cm}^{-1}$ )  $\nu(\text{C}=\text{O})$ : 1717.  $^1\text{H}$  NMR ( $\text{CDCl}_3$ )  $\delta$ : 7.61 (m, 8H, Ph), 6.86 (s, 4H, Ph), 6.60 (m, 6H, Ph), 4.51 (d, 4H,  $J = 13.08$  Hz,  $\text{CH}_2$ ), 3.90 (dt, 8H,  $\text{OCH}_2$ ), 3.21 (d, 4H,  $J = 13.10$  Hz,  $\text{CH}_2$ ), 1.97 (m, 8H,  $\text{CH}_2\text{CH}_3$ ), 1.03 (q, 12H,  $\text{CH}_3$ ).  $^{13}\text{C}$  NMR ( $\text{CDCl}_3$ )  $\delta$ : 167.2, 156.5, 136.1, 134.5, 133.9, 131.8, 138.5, 126.4, 125.4, 123.3, 122.5, 31.5, 23.6, 10.5. EI-MS: 882 ( $[\text{M}]^+$ ).

### 5,17-Diamino-25,26,27,28-tetrapropoxycalix[4]arene (9): (Cone)

A solution containing compound **8** (164 mg, 0.155 mmol) and hydrazine monohydrate (0.2 mL, 3.72 mmol) in ethanol (25 mL) was refluxed for 2 h. The solution was cooled to room temperature and evaporated. The resulting solid was dissolved in  $\text{CH}_2\text{Cl}_2$  (150 mL) and extracted twice with NaOH 5% aqueous solution and distilled water. The organic phase was dried over  $\text{MgSO}_4$ , filtered, and evaporated. Yield 95% (91.5 mg). IR (solid) ( $\text{cm}^{-1}$ )  $\nu(\text{NH})$ : 3525, 3395.  $^1\text{H}$  NMR ( $\text{CDCl}_3$ )  $\delta$ : 6.78 (d, 4H, Ph), 6.66 (t, 2H, Ph), 5.91 (s, 4H, Ph), 4.39 (d, 4H,  $J = 13.05$  Hz,  $\text{CH}_2$ ), 3.85 (t, 4H,  $J = 7.40$  Hz,  $\text{OCH}_2$ ), 3.70 (t, 4H,  $J = 7.43$  Hz,  $\text{OCH}_2$ ), 3.04 (d, 4H,  $J = 13.08$  Hz,  $\text{CH}_2$ ), 1.90 (m, 8H,  $\text{CH}_2\text{CH}_3$ ), 1.02 (t, 6H,



**Table 1.** Selected MALDI-TOF data for **6** and **12**.

Peaks <sup>a</sup>	Relative intensity ( $\pm 1\%$ )	Assignment <sup>b</sup>	Calculated values
<b>For 12</b>			
1832	2	Ag <sub>3</sub> calix <sub>2</sub> (BF <sub>4</sub> ) <sub>2</sub> + 2CN	1834.85
1805	3	Ag <sub>3</sub> calix <sub>2</sub> (BF <sub>4</sub> ) <sub>2</sub> + CN	1808.85
1724	4	Ag <sub>2</sub> calix <sub>2</sub> (BF <sub>4</sub> ) <sub>2</sub> + 2CN	1726.98
1674	5	Ag <sub>2</sub> calix <sub>2</sub> (BF <sub>4</sub> ) <sub>2</sub>	1674.98
1659	5	Ag <sub>3</sub> calix <sub>2</sub> + 2CN	1661.25
1586	6	Ag <sub>2</sub> calix <sub>2</sub> (BF <sub>4</sub> )	1588.18
1525	4	Ag <sub>2</sub> calix <sub>2</sub> + CN	1527.38
1519	9		
1391	100	Agcalix <sub>2</sub>	1393.51
<b>For 6</b>			
1725	5	Ag <sub>2</sub> calix <sub>2</sub> (BF <sub>4</sub> ) <sub>2</sub> + CN or Ag <sub>3</sub> calix <sub>2</sub> (BF <sub>4</sub> ) + 2CN	1726.98 1722.05
1711	8		
1586	100	Ag <sub>2</sub> calix <sub>2</sub> (BF <sub>4</sub> )	1588.18

<sup>a</sup>Peaks of lower mass are not listed.<sup>b</sup>calix = ligands **11** and **5**, respectively.

$J = 7.41$  Hz, CH<sub>3</sub>), 0.95 (t, 6H,  $J = 7.45$  Hz, CH<sub>3</sub>). <sup>13</sup>C NMR (CDCl<sub>3</sub>)  $\delta$ : 157.0, 149.9, 140.3, 135.5, 128.3, 121.7, 115.5, 31.3, 22.2, 10.5. EI-MS: 622 ([M]<sup>+</sup>).

#### 5,17-Di-*N*-formamyl-25,26,27,28-tetrahydroxy-calix[4]arene (**10**): (Cone)

A solution containing compound **9** (550 mg, 0.88 mmol) in formic acid (20 mL) and toluene (70 mL) was refluxed several hours. The excess of formic acid and water was eliminated using a Dean–Stark apparatus prior to evaporating the solution to dryness. The solid was purified by column chromatography using 30:70 acetone:CH<sub>2</sub>Cl<sub>2</sub>. Yield 70% (417.6 mg). IR (solid) (cm<sup>-1</sup>)  $\nu$ (C=O): 1685,  $\nu$ (NH): 3410. <sup>1</sup>H NMR (CDCl<sub>3</sub>)  $\delta$ : 8.00 (s + s, H, C(O)H), 7.89 (s + s, H, C(O)H), 6.81–7.11 (complex, 6H, Ph), 6.382 (d, 2H, Ph), 5.91 (s, 1H, Ph), 5.78 (s, 1H, Ph), 4.45 (dd, 4H, CH<sub>2</sub>), 3.98 (dt, 4H, OCH<sub>2</sub>), 3.66 (m, 4H, OCH<sub>2</sub>), 3.13 (dd, 4H,  $J = 13.05$  Hz, CH<sub>2</sub>), 2.2 (vbr, 2H, NH), 1.91 (m, 8H, CH<sub>2</sub>CH<sub>3</sub>), 1.10 (q, 6H, CH<sub>3</sub>), 0.90 (m, 6H, CH<sub>3</sub>). <sup>13</sup>C NMR (CDCl<sub>3</sub>)  $\delta$ : 162.8, 159.5, 157.8, 154.0, 153.2, 152.5, 136.5, 135.1, 134.2, 131.0, 130.5, 129.2, 122.5, 119.6, 118.5, 31.2, 23.5, 10.4. EI-MS: 678 ([M]<sup>+</sup>).

#### 5,17-Diisocyano-25,26,27,28-tetrapropoxycalix[4]arene (**11**): (Cone)

A solution containing compound **10** (300 mg, 0.443 mmol) and Et<sub>3</sub>N (0.8 mL, 4.72 mmol) in dry CH<sub>2</sub>Cl<sub>2</sub> (50 mL) was refluxed under inert atmosphere. A CH<sub>2</sub>Cl<sub>2</sub> solution containing diphosgene (0.6 mL, 4.85 mmol) was added over a period of 1 h. The solution was refluxed for 1 day and cooled to room temperature. The resulting solution was extracted and evaporated. The solid was purified by column chromatography using CH<sub>2</sub>Cl<sub>2</sub>. Yield 30% (85.3 mg). IR (solid) (cm<sup>-1</sup>)  $\nu$ (N=C): 2130. <sup>1</sup>H NMR (CDCl<sub>3</sub>)  $\delta$ : 6.88 (m, 6H, Ph), 6.43 (s, 4H, Ph), 4.42 (d, 4H,  $J = 13.12$  Hz, CH<sub>2</sub>), 3.41 (t, 4H,  $J = 7.39$  Hz, OCH<sub>2</sub>), 3.75 (t, 4H,  $J = 7.42$  Hz, OCH<sub>2</sub>), 3.13 (d, 4H,  $J = 13.12$  Hz, CH<sub>2</sub>), 1.91 (m, 8H, CH<sub>2</sub>CH<sub>3</sub>), 1.07 (t, 6H,  $J = 7.42$  Hz,

CH<sub>3</sub>), 0.93 (t, 6H,  $J = 7.40$  Hz, CH<sub>3</sub>). <sup>13</sup>C NMR (CDCl<sub>3</sub>)  $\delta$ : 136.1, 135.2, 129.1, 125.7, 30.9, 23.3, 10.2. EI-MS: 642 ([M]<sup>+</sup>).

#### Poly[(5,17-diisocyano-25,26,27,28-tetrahydroxy-calix[4]arene) silver(I)] tetrafluoroborate (**12**)

A solution containing compound **11** (90 mg, 0.14 mmol) in dry acetonitrile was added to an acetonitrile solution containing AgBF<sub>4</sub> (13 mg, 0.07 mmol). The solution was stirred for 1 h at room temperature, and the solvent was evaporated. Yield 100% (117.1 mg). IR (solid) (cm<sup>-1</sup>)  $\nu$ (N=C): 2210,  $\nu$ (BF<sub>4</sub>): 1025. <sup>1</sup>H NMR (CDCl<sub>3</sub>)  $\delta$ : 7.27(d, 4H, Ph), 7.06 (t, 2H, Ph), 6.29 (s, 4H, Ph), 4.45 (d, 4H, CH<sub>2</sub>), 3.95 (t, 4H, OCH<sub>2</sub>), 3.71 (t, 4H, OCH<sub>2</sub>), 3.22 (d, 4H, CH<sub>2</sub>), 1.90 (m, 8H, CH<sub>2</sub>CH<sub>3</sub>), 1.11 (t, 6H, CH<sub>3</sub>), 0.87 (t, 6H, CH<sub>3</sub>). MALDI-TOF-MS: see Table 1. Anal. calcd. for C<sub>42</sub>H<sub>46</sub>O<sub>4</sub>N<sub>2</sub>AgBF<sub>4</sub>: C 60.23, H 5.54, N 3.34; found: C 59.31, H 5.76, N 3.34.

#### Poly(5,11,17,23-tetraisocyano-25,26,27,28-tetrahydroxy-calix[4]arene) silver(I) tetrafluoroborate (**14**)

A solution containing compound **13** (137.6 mg, 0.198 mmol) in dry acetonitrile was added to an acetonitrile solution containing AgBF<sub>4</sub> (38.6 mg, 0.198 mmol). The solution was stirred for 1 h at room temperature, and the solvent was evaporated. The beige solid was filtered and washed with dimethyl ether and dried in vacuo. Yield 98% (172.5 mg). IR (solid) (cm<sup>-1</sup>)  $\nu$ (N=C): 2177, 2122,  $\nu$ (BF<sub>4</sub>): 1030. <sup>1</sup>H NMR (CD<sub>3</sub>CN)  $\delta$ : 7.09 (s, 8H, Ph), 4.37 (d, 4H,  $J = 13.3$  Hz, CH<sub>2</sub>), 3.85 (t, 8H,  $J = 7.5$  Hz, OCH<sub>2</sub>), 3.2 (d, 4H,  $J = 13.5$  Hz, CH<sub>2</sub>), 1.89 (m, 8H, CH<sub>2</sub>CH<sub>3</sub>), 1.00 (t, 12H,  $J = 7.5$  Hz, CH<sub>3</sub>). MALDI-TOF-MS: see Table 2. Anal. calcd. for C<sub>44</sub>H<sub>44</sub>O<sub>4</sub>N<sub>4</sub>AgBF<sub>4</sub>: C 59.54, H 5.00, N 6.31; found: C 58.91, H 5.23, N 6.23.

#### Apparatus

The NMR spectra were acquired on a 300 MHz Bruker instrument (<sup>1</sup>H, 300.15 MHz; <sup>13</sup>C, 75.478 MHz). The chemical shifts ( $\delta$ ) are reported with respect to tetramethylsilane,



**Table 2.** Selected MALDI-TOF data for **14**.

Peaks <sup>a</sup>	Relative intensity ( $\pm 1\%$ )	Assignment <sup>b</sup>	Calculated values
2020	6	$\text{Ag}_3\text{calix}_2(\text{BF}_4) + 2\text{CN}$	2021.79
1970	4	$\text{Ag}_3\text{calix}_2(\text{BF}_4)$	1969.79
1881	11	$\text{Ag}_3\text{calix}_2(\text{BF}_4)_2$	1882.99
1828	16	$\text{Ag}_2\text{calix}_2(\text{BF}_4)_2 + 2\text{CN}$	1827.11
1811	18		
1778	14	$\text{Ag}_2\text{calix}_2(\text{BF}_4)_2$	1775.11
1686	69	$\text{Ag}_2\text{calix}_2(\text{BF}_4)$	1688.31
1580	14	$\text{Ag}_2\text{calix}_2(\text{BF}_4)$	1580.45
1492	100	$\text{Agcalix}_2$	1493.65

<sup>a</sup>Peaks of lower mass are not listed.<sup>b</sup>calix = ligand **13**.

TMS ( $^1\text{H}$ ,  $^{13}\text{C}$ ), and were determined on the basis of residual proton solvent resonances. The coupling constants are reported in ppm. The FT-IR data were obtained on PerkinElmer spectrometer Model 1600. The mass spectra (EI) were measured on a ZAB-1F instrument (VG model), while the MALDI-TOF data were obtained at the Université de Bourgogne from a Bruker proflex III linear mode spectrometer with a nitrogen laser (337 nm) with a dithranol matrix. Elemental analysis were performed at the Université de Montréal (Regional Services). The TGA analyses were performed using a PerkinElmer TGA 7 apparatus operating between 50 and 700 °C scanning at the rate of 3 °C min<sup>-1</sup> under N<sub>2</sub> atmosphere. The thermal behaviour was analyzed using a PerkinElmer 5A DSC7 apparatus, equipped with a thermal control analyser 5B TAC 7/DS. The temperature calibrations were done with water and metallic indium as standards. The accuracy is  $\pm 0.1$  °C and  $\pm 0.1\%$ . The sample weights ranged from 5 to 10 mg, and the scan rate was adjusted at 10° min<sup>-1</sup>. The X-ray powder diffraction patterns were acquired on a Rigaku, U.S.A. Inc. apparatus equipped with a copper source operating at 40 kV and 30 mA, in continuous standard, scans 2 $\theta$ / $\theta$ -reflection of 1° min<sup>-1</sup>. The sample support was a standard aluminium support.

### Computer modeling

The calculations were performed using the commercially available program PC-model from Serena Software (version 7.0), which uses the MMX empirical model.

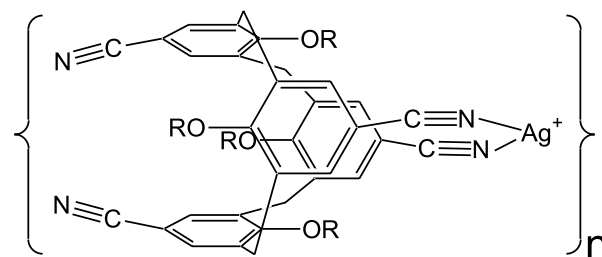
## Results and discussion

### The diisocyanide compounds

The complexes **6** and **12** have been synthesized in 5 steps from the corresponding 5,11- (**1**) and 5,17-dibromo-25,26,27,28-tetra-*n*-propoxycalix[4]arene (**7**) compounds with overall yields of 34% and 30%, respectively (Schemes 1 and 2). The presence of *n*-propyl groups in the narrow-rim secures the cone conformation of the macrocycle, as confirmed by  $^1\text{H}$  NMR all along the syntheses. The incorporation of the nitrogen atoms onto the *para*-position of the benzene rings proceeds by a substitution of the bromide atoms by phthalimides in modest yields, to generate **2** and **8**. The reduction of the phthalimide groups with hydrazine, followed by a condensation with formic acid, produces the corresponding formamides **4** and **10** in good yields. The follow-

ing dehydration step using diphosgene leads to the desired diisocyanide ligands. The ligands **5** and **11** ( $\text{calix}(\text{NC})_2$ ) have been fully characterized from  $^1\text{H}$  NMR,  $^{13}\text{C}$  NMR, and IR spectroscopy, as well as mass spectrometry (EI).

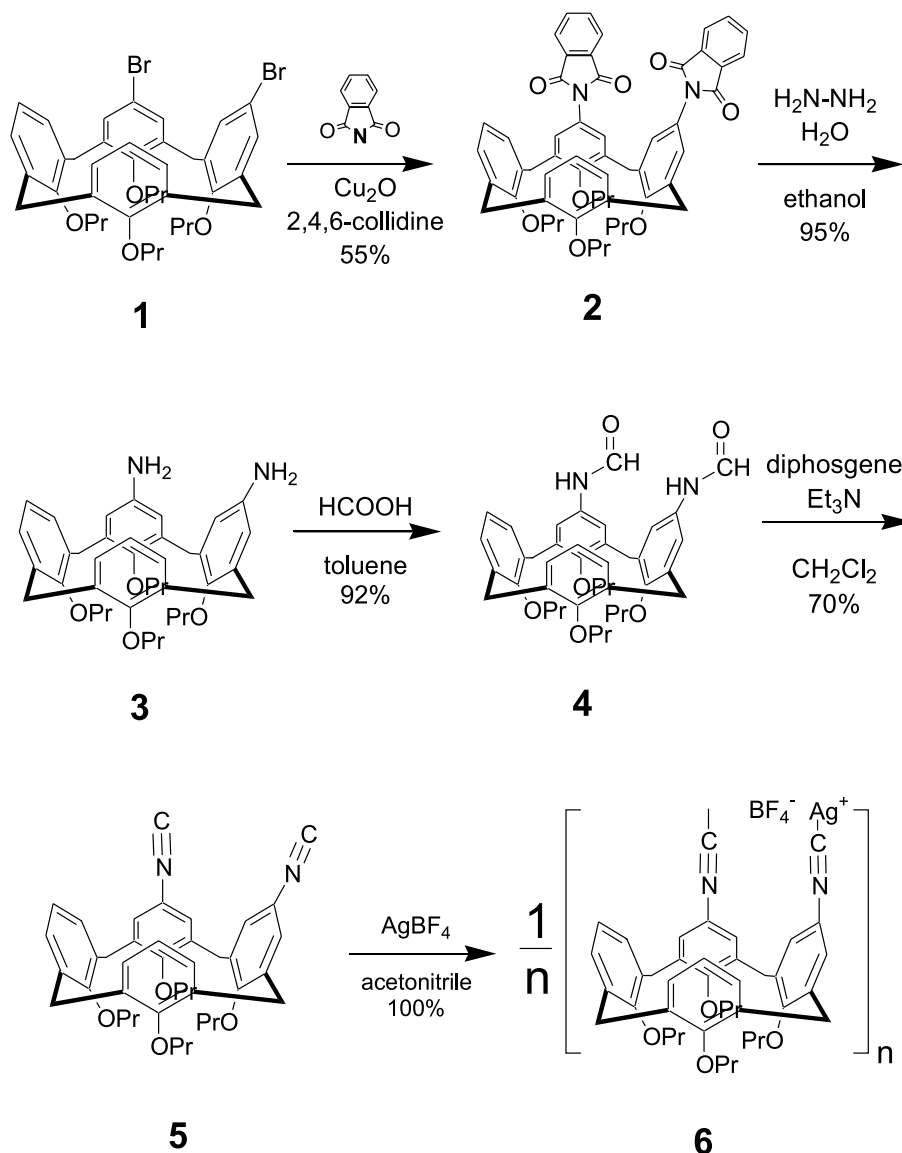
The treatment of **5** and **11** with  $\text{AgBF}_4$  cleanly gives **6** and **12**, respectively. The complexes exhibit strong and single  $\nu(\text{N}\equiv\text{C})$  absorptions at 2203 and 2210 cm<sup>-1</sup>, respectively, in comparison with 2131 (**5**) and 2130 cm<sup>-1</sup> (**11**) for their corresponding free ligands, confirming the coordination of the  $\text{N}\equiv\text{C}$  groups. The 1:1 stoichiometry of  $\text{Ag}:\text{calix}(\text{NC})_2$  is indicated by the chemical analyses. The MALDI-TOF mass data reveal the presence of polymers or oligomers of the type  $\{\text{Ag}(\text{calix}(\text{NC})_2)(\text{BF}_4)\}_n$  in both cases (Table 1). A polymer formed from a *para*-cyano-functionalized calix[4]arene and Ag(I) has been reported before (see molecule 1) (9). The fact that no IR band is associated with free  $\nu(\text{N}\equiv\text{C})$  indicates that the materials are either long polymers or cyclic oligomers in the solid state. Attempts to increase the number of diisocyanide calix[4]arene ligands about the silver(I) were not successful, which contrasts with the  $\{\text{Ag}(\text{dmb})_2\}^+$  polymers (7). In addition, attempts to obtain crystals suitable for X-ray analysis for these thermally and light sensitive compounds in solution also stubbornly failed, as slow decomposition occurs with time. In addition, the XRD data indicate that these polymeric and (or) oligomeric materials are amorphous in the solid state.

Molecule 1     R = CH<sub>2</sub>CH<sub>2</sub>OMe

During the course of this study the physical properties of **6** and **12** in their solid state have been investigated. Both compounds do not exhibit obvious thermal absorption (or emission), such as a glass transition, melting, or decomposition between -20 and 90 °C, according to DSC findings. This result contrasts that of the "rigid stick"  $\{\text{Ag}(\text{dmb})_2\}^+$  polymers, for which a glass transition phenomenon has been



Scheme 1.

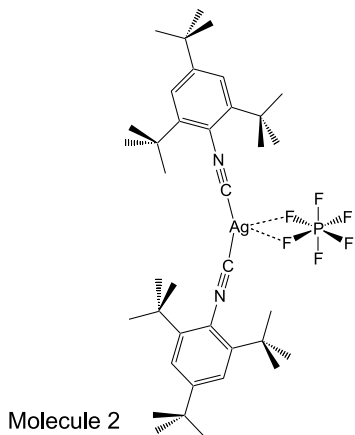


attributed to the motion of the counterions in the solid (10). This result can be explained by the fact that the counterions cannot interact with the saturated and well-encapsulated Ag(I) ions in  $\{\text{Ag}(\text{dmb})_2^+\}_n$  but can with the unsaturated

ones in **6** and **12**. This hypothesis is supported by the fact that counteranions generally interact with dicoordinated Ag(I) cations — strongly enough to induce significant deviations in  $\text{CAgC}$  angles (11). One example is the X-ray structure for the related  $\text{Ag}(2,4,6\text{-}t\text{-Bu}_3\text{C}_6\text{H}_2\text{NC})_2(\text{PF}_6)$  complex (molecule 2), which exhibits a bent structure where the  $\text{CAgC}$ ,  $\text{NCAg}$ , and  $\text{CNC}$  angles are  $156.1(6)$ ,  $174.4(16)$ , and  $176.6(14)^\circ$ , respectively (11a).

Both compounds **6** and **12** exhibit similar TGA traces (Fig. 1). Between 20 and  $90^\circ\text{C}$ , no significant weight loss is noticed, consistent with the DSC data, but two to three barely noticeable plateaux are observed above  $100^\circ\text{C}$ , up to  $200^\circ\text{C}$ . The relative high sensitivity to heat is consistent with the unsaturated nature of the very reactive Ag(I) centre. At  $350^\circ\text{C}$ , the remaining  $\sim 45\text{--}50\%$  of materials indicates that there are still organic materials in the residues. Both complexes are found to be non-luminescent at room temperature, both in solution and in the solid state.

To understand why **6** and **12** form oligomers or polymers, the model dimer compounds  $(\text{6})_2$  and  $(\text{12})_2$  (i.e., the smallest





Scheme 2.

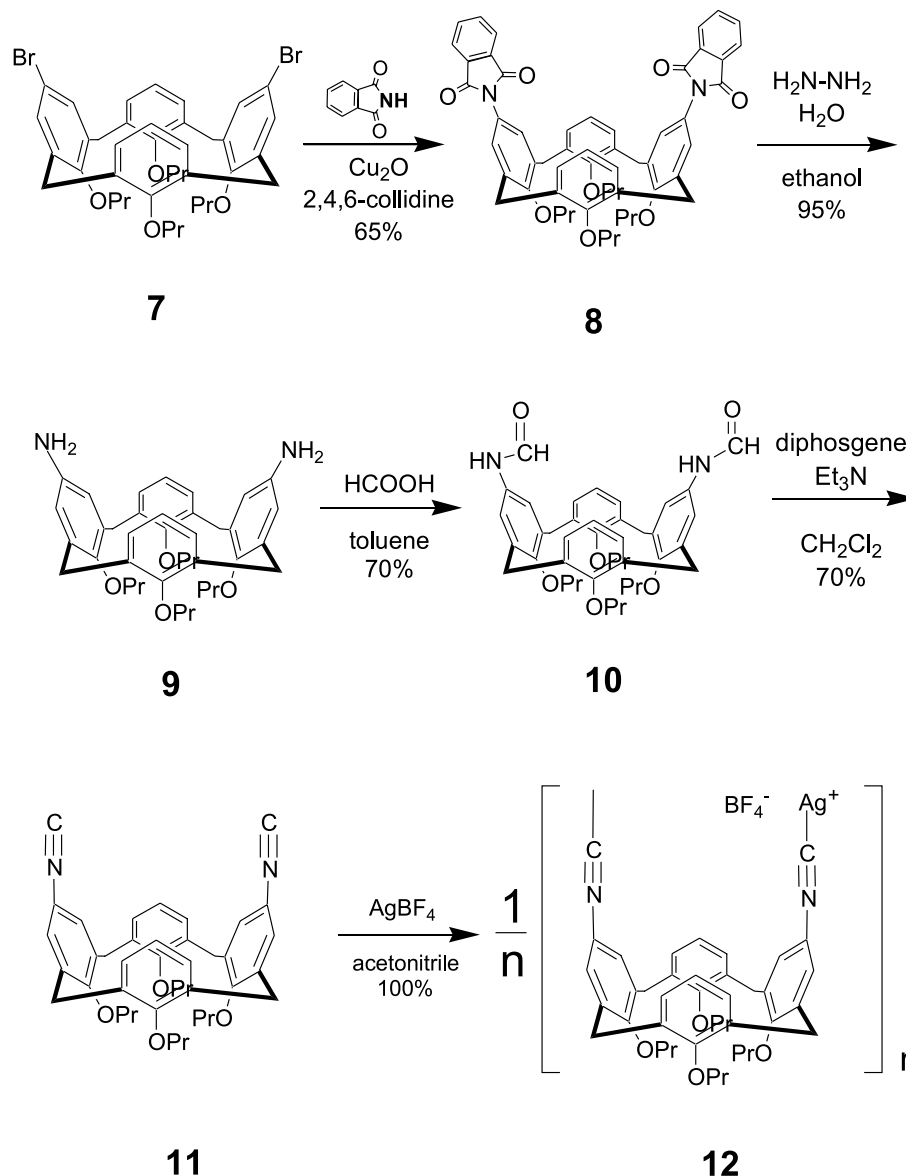
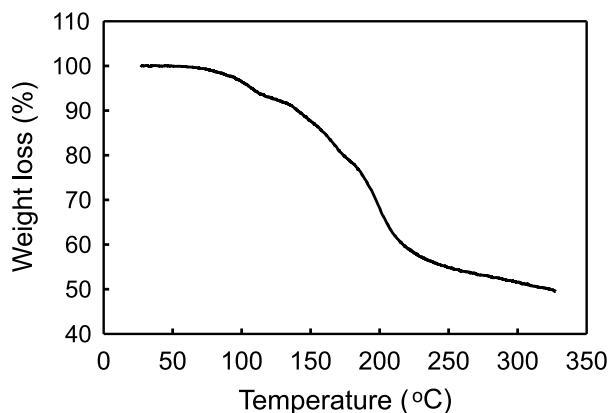


**Fig. 1.** TGA trace of **12**. Scan rate = 3 °C min<sup>-1</sup>. A small drift in the baseline is noted in the high temperature region.



possible cyclic oligomers) were examined using computer modelling (MMX). The testing of the method was performed on ligand **13**, for which X-ray data are available (6). This exercise allows one to compare non-bonding distances, which are sensitive parameters that best describe the cavity size, and gives an estimate as to what the deviations between a computed structure and reality might be. The comparison provided in Table 3 is found to be acceptable where the expected pinched cone structure is computed and where the selected non-bonded distances are only slightly overestimated. The greatest difference is found for the longest NC...CN separation; an unavoidable fact, taking into account that the orientation of the propyl chains (lever effect) and crystal packing influence this distance. Finally, the comparison of the bond lengths are also found to be acceptable.

The computed structures for the model dimers (**6**)<sub>2</sub> and (**12**)<sub>2</sub> are shown in Fig. 2, and selected calculated data are summarized in Table 2. Both models exhibit large



Scheme 3.

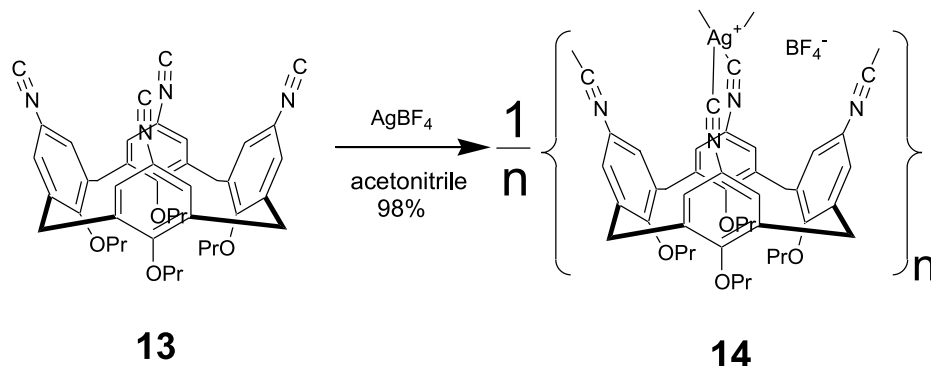


**Fig. 2.** Comparison of the computed model dimers  $(\mathbf{6})_2$  and  $(\mathbf{12})_2$ , stressing the presence of ring stress. Numerous conformations are possible for  $(\mathbf{6})_2$ . They exhibit the same structural features as discussed in the text. Only one conformer is shown.

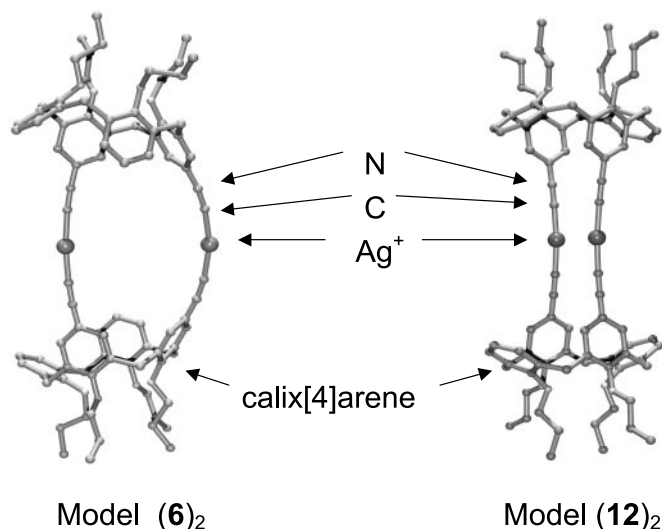


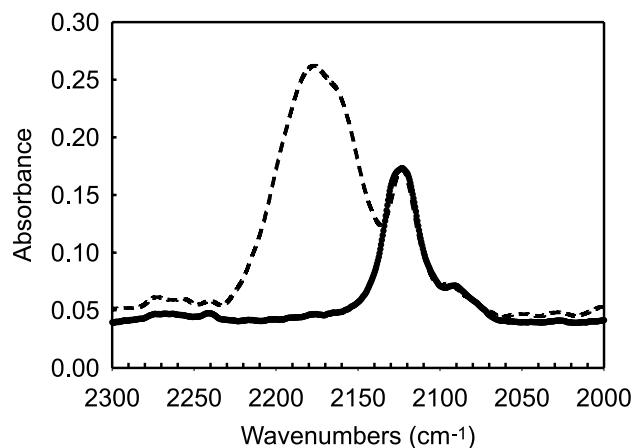
**Table 3.** Comparison between selected calculated and experimental non-bonding distances for ligand **13**.

	Computed (Å)	X-ray (Å) <sup>a</sup>	Δ (Å)
<b>Face-to-face</b>			
C...C	3.670	3.461	0.209 (6.0%)
N...N	4.041	3.785	0.256 (6.8%)
C <sub>Bz</sub> ...C <sub>Bz</sub>	4.493	4.218	0.275 (6.5%)
O...O	6.386	5.676	
<b>Furthest</b>			
C...C	16.003	13.996	2.007 (14.3%)
O...O	3.679	3.544	

<sup>a</sup>From ref. 6.

macrocycles, for which some deviation from the ideal 180° angles are depicted (Table 2). Dimer  $(\mathbf{6})_2$  shows the largest deviation, where a ring stress is evident. Dimer  $(\mathbf{12})_2$  shows a smaller macrocycle opening, for which the computed Ag...Ag distance is 3.38 Å, practically at the sum of the van der Waals radii ( $2 \times 1.70$  Å) (12). This anticipated shorter

**Fig. 3.** Comparison of the solid state FT-IR spectra of **13** (—) and **14** (.....) in the  $\nu(\text{N}\equiv\text{C})$  region. Resolution: 1 cm<sup>-1</sup>. No deconvolution is applied.



distance is due to the naturally occurring pinched cone structure of the calix[4]arene ligand. The greater ring stress in  $(\mathbf{6})_2$  (compared with  $(\mathbf{12})_2$ ) is also felt in the greater computed C—N, N—C, and C—Ag bond lengths as well. If the Ag...Ag interactions do occur, then the UV-vis spectra should exhibit a strong absorption band at 250–260 nm ( $\epsilon > 10\,000$  L mol<sup>-1</sup> cm<sup>-1</sup>) associated with the well-known  $d\sigma^* \rightarrow p\sigma$  transition (13). However, this band is absent from the spectra, as **6** and **12** exhibit spectra that are identical to that of the free ligands. When computations are performed on non-cyclic oligomers (2, 3, and 4 units for examples), these angles become equal to 180°, indicating the absence of stress. These results strongly suggest that ligands **5** and **11** favour the polymer structure, and they corroborate the MALDI-TOF findings.

#### The tetraisocyanide complex **14**

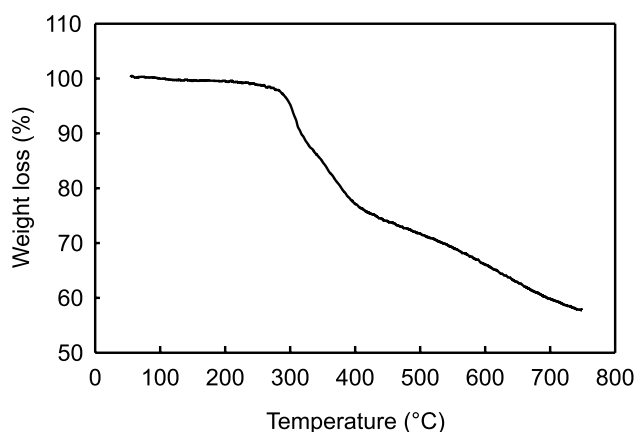
The 1:1 stoichiometric reaction between **13** and AgBF<sub>4</sub> provides compound **14** in a quasi-quantitative yield (Scheme 3). In comparison with compounds **6** and **12**, **14** does not darken with light and proves to be significantly more thermally stable in the solid state and in solution.

From experience with isocyanide complexes of Ag(I), dicoordinated Ag(I) compounds are found to be less stable than the tetracoordinated ones (10, 11*b*, 14, 15). Moreover,

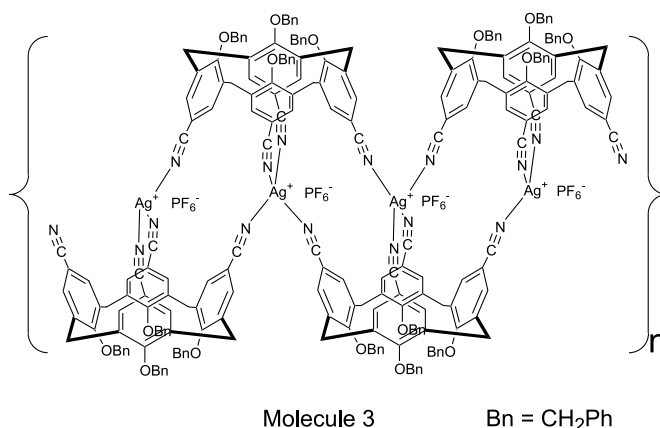


**Table 4.** Selected computed structural data for the model dimers (**6**)<sub>2</sub> and (**12**)<sub>2</sub>.

	Compound ( <b>6</b> ) <sub>2</sub>	Compound ( <b>12</b> ) <sub>2</sub>
<b>Non-bonded distances (Å)</b>		
Ag...Ag	7.544	3.379
C...C	7.132–7.171	3.672
N...N	6.641–6.591	3.989
<b>Bond angles (°)</b>		
CAgC	165.6	172.1
NCAg	170.5–175.2	176.8
CNC	171.0–175.3	177.9

**Fig. 4.** TGA trace of **14**. Scan rate = 3 °C min<sup>-1</sup>. A small drift in the baseline is noted in the high temperature region.

**14** is significantly more insoluble in common solvents than compounds **6** and **12**, which helps the purification process but, again, prevents one from getting crystals suitable for X-ray analysis. Nonetheless, a polymer and (or) oligomer structure is strongly suspected on the basis of the known structure of the related polymer 5,11,17,23-tetracyano-25,26,27,28-tetra-*n*-benzoxycalix[4]arene hexafluorophosphate (see molecule 3) (**16**). Because of its low solubility, the molecular weight for **14** cannot be measured using conventional techniques for polymers. However, the solid state IR spectrum (Fig. 3) indicates the presence of absorptions due to free end-of-chain isocyanide groups at 2122 cm<sup>-1</sup> and complexed ones at 2177 cm<sup>-1</sup>. The relative intensity of this band suggests that the ratio of the number of complexed -NC vs. free -NC is not very large and that **14** must be an oligomer. Because the absorptivity of the ν(NC) bands are not known, only an estimate of the number of units can be deduced. The relative area under these peaks is about 5:1 (complexed:free). Assuming that the structure found in molecule 3 is applicable, then **14** would be a trimer (C<sub>2v</sub> point group). This formulation is not inconsistent with the MALDI-TOF data (Table 4). The rather small number of units may be driven by the low solubility. In addition, it is possible that other Ag(I) ion interactions with the benzene rings exist, somewhat similar to that reported by Puddephatt and collaborators (**17**) for unfunctionalized calix[4]arenes, but the chemical analysis indicates a 1:1 ratio



(calix[4]arene:Ag(I)). This possibility is unlikely in this case.

The TGA trace for **14** also exhibits a cascade weight loss pattern, where three decomposition events are obvious between 300 and 700 °C (Fig. 4). The temperatures of these weight losses contrast greatly with **6** and **12**, for which most of the losses occur before 300 °C. The third event spreads from approximately 400 to 700 °C, a large temperature range that is normally associated with the presence of a polymer and (or) oligomer. Similarly to **6** and **12**, the residue must still contain organic materials at 700 °C, as the expected amount of Ag metal is only 22%.

The DSC trace recorded between -20 and 100 °C reproducibly exhibits a heat absorption associated with a second-order phase transition (i.e., glass transition,  $T_g = 56$  °C, and  $\Delta C_p = 0.08$  J °C<sup>-1</sup> g<sup>-1</sup>). Because of the rigidity of the suspected structure (molecule 3), ionic mobility may be responsible for this thermal behaviour. A similar behaviour was reported for the “rigid sticks” [Ag(dmb)<sub>2</sub>]<sub>n</sub> polymers, where the counter anions were BF<sub>4</sub><sup>-</sup>, PF<sub>6</sub><sup>-</sup>, ClO<sub>4</sub><sup>-</sup>, NO<sub>3</sub><sup>-</sup>, and TCNQ<sup>-</sup> (**10**).

## Conclusion

Ligands **5**, **11**, and **13** favour the formation of polymer structures, and much remains to be explored. Because of the relative rigidity, well-defined 1D materials are anticipated for some transition metals such as Cu(I). Ligand **13** is particularly interesting in that respect, if it can be rendered more soluble with appropriate groups in the narrow-rim. The greater thermal and light stability for **14** is also encouraging for the design of new materials with potential applications. Further research is in progress.

## Acknowledgements

This research was supported by the Natural Sciences and Engineering Research Council of Canada (NSERC). Mr. Claude Sylvain is thanked for technical assistance.

## References

1. P.D. Harvey. *Coord. Chem. Rev.* **233/234**, 289 (2002).
2. (a) Z. Ashari, V. Böhmer, J. Harrowfield, and J. Vicens. *Calixarenes* 2001. Kluwer Academic Publisher, Dordrecht.



- 2001; (b) C.D. Gutsche. Calixarene revisited. Royal Society of Chemistry, Cambridge, U.K. 1998.
3. (a) C. Kunze, D. Selent, I. Neda, R. Schmutzler, A. Spannenberg, and A. Bömer. *Heteroatom. Chem.* **12**, 577 (2001); (b) F.J. Parlevliet, C. Kiener, J. Fraanje, K. Goubitz, M. Lutz, A.L. Spek, P.C.J. Kamer, and P.W.N.M. van Leewven. *J. Chem. Soc. Dalton Trans.* 1113 (2000); (c) C.J. Copley, D.D. Ellis, A.G. Orpen, and P.G. Pringle. *J. Chem. Soc. Dalton Trans.* 1109 (2000); (d) C. Dieleman, S. Steyer, C. Jeunesse, and D. Matt. *J. Chem. Soc. Dalton Trans.* 2508 (2001); (e) V. Böhmer. *Angew. Chem. Int. Ed. Engl.* **34**, 713 (1995); (f) J. Scheerder, M. Fochi, J.F.J. Engbersen, and D.N. Reinhoudt. *J. Org. Chem.* **59**, 7815 (1994).
  4. J. Gagnon, M. Vézina, M. Drouin, and P.D. Harvey. *Can. J. Chem.* **79**, 1439 (2001).
  5. (a) M. Vézina, J. Gagnon, K. Villeneuve, M. Drouin, and P.D. Harvey. *Organometallics*, **20**, 273 (2001); (b) M. Vézina, J. Gagnon, K. Villeneuve, M. Drouin, and P.D. Harvey. *Chem. Commun.* 1073 (2000).
  6. J. Gagnon, M. Drouin, and P.D. Harvey. *Inorg. Chem.* **40**, 6052 (2001).
  7. P.D. Harvey. *Coord. Chem. Rev.* **219**, 17 (2001).
  8. (a) D.D. Perrin, W.L.F. Armarego, and D.R. Perrin. *Purifications of laboratory chemicals*. Pergamon Press, Oxford. 1966; (b) A.J. Gordon and R.A. Ford. *The chemist's companion, a handbook of practical data, techniques, and references*. Wiley, New York. 1972. p. 436.
  9. G. Mislin, E. Graf, M.W. Hosseini, A. De Cian, N. Kyritsakas, and J. Fischer. *Chem. Commun.* 2545 (1998).
  10. (a) D. Fortin, M. Drouin, and P.D. Harvey. *Inorg. Chem.* **39**, 2758 (2000); (b) D. Fortin, M. Drouin, M. Turcotte, and P.D. Harvey. *J. Am. Chem. Soc.* **119**, 531 (1997).
  11. See for examples (a) Y. Yamamoto, K. Aoki, and H. Yamazaki. *Inorg. Chim. Acta*, **75**, 68 (1982); (b) D. Fortin, M. Drouin, P.D. Harvey, F.G. Herring, D.A. Summers, and R.C. Thompson. *Inorg. Chem.* **38**, 1253 (1999); (c) M. Dartiguenave, Y. Dartiguenave, A. Mari, A. Guitard, M.J. Olivier, and A.L. Beauchamp. *Can. J. Chem.* **66**, 2386 (1988); (d) A. Guitard, A. Mari, A.L. Beauchamp, Y. Dartiguenave, and M. Dartiguenave. *Inorg. Chem.* **22**, 1603 (1983).
  12. F.A. Cotton, G. Wilkinson, and P. Gaus. *Basic inorganic chemistry*. 2nd ed. Wiley, Toronto. 1987. p. 60.
  13. D. Piché and P.D. Harvey. *Can. J. Chem.* **72**, 705 (1994).
  14. L. Malatesta and F. Bonati. *Isocyanides complexes of metals*. Wiley, Toronto. 1969.
  15. (a) D. Perreault, M. Drouin, A. Michel, and P.D. Harvey. *Inorg. Chem.* **32**, 1903 (1993); (b) P.D. Harvey, M. Drouin, A. Michel, and D. Perreault. *J. Chem. Soc. Dalton Trans.* 1365 (1993).
  16. E. Elisabeth, L.J. Babour, G.W. Orr, K.T. Holman, and J.L. Atwood. *Supramol. Chem.* **12**, 317 (2000).
  17. W. Xu, R.J. Puddephatt, K.W. Muir, and A.A. Torabi. *Organometallics*, **13**, 3054 (1994).



# Chiral silicon-bridged 2-(*N,N*-dialkylamino)ethyl-substituted indenenes as potential precursors for *ansa*-zirconocenes<sup>1</sup>

Timo Hagemeister, Peter Jutzi, Anja Stammler, and Hans-Georg Stammler

**Abstract:** Chiral amino-functionalized silicon-bridged indene derivatives **4a–4c** were synthesized from 3-(2-(*N,N*-dialkylamino)ethyl)indenenes **2a–2c**. The C–Si coupling reactions are regioselective, leading exclusively to the formation of 1,3-disubstituted isomers in a *rac/meso* ratio of 1:1, as indicated by NMR spectroscopy. The solid-state structure of the dimethylsilyl-bridged bisindene (*R,R*)-**4a** is described. The formation of corresponding *ansa*-zirconocenes via amine elimination chemistry was monitored by <sup>1</sup>H NMR spectroscopy.

**Key words:** amino-functionalized indenenes, silicon-bridged, *ansa*-metallocenes, chirality, regioselectivity, amine elimination chemistry.

**Résumé :** Utilisant les 3-(2(*N,N*-dialkylamino)éthyl)indènes **2a–2c** comme produits de départ, on a réalisé la synthèse des dérivés chiraux de l'indène à pont de silicium et portant une fonction amine **4a–4c**. Les réactions de couplage C–Si sont régiosélectives et elles conduisent exclusivement à la formation d'isomères 1,3-disubstitués qui, d'après la spectroscopie RMN, sont dans un rapport *rac/méso* égal à l'unité. On a déterminé la structure en phase solide du bisindène (*R,R*)-**4a** à pont diméthylsilyle. La formation des *ansa*-zirconocènes correspondants par le biais de la chimie d'élimination d'amine a été suivie par spectroscopie RMN du <sup>1</sup>H.

**Mots clés :** indène portant une fonction amine, pont de silicium, *ansa*-métallocènes, chiralité, régiosélectivité, chimie d'élimination d'amine.

## Introduction

Donor-functionalized cyclopentadienes have recently attracted considerable attention as starting materials for the synthesis of corresponding complexes with elements from the *s*-, *p*-, *d*-, and *f*-blocks (1). In contrast, only a few examples of donor-functionalized indenenes are known (2). Such compounds are promising substrates for the synthesis of chiral *ansa*-metallocenes.

Concerning *ansa*-metallocenes of group IV metals, potential applications include a wide variety of synthetic transformations, for instance olefin hydrogenation (3), epoxidation (4) and isomerization (5), allylation of aldehydes (6), ketone reduction (7), catalysis of Diels–Alder reactions (8), and dehydrogenative phenylsilane oligomerization (9).

In addition, transition metal complexes with pendant amino groups have been shown to provide special characteristics as

precatalysts in olefin polymerization reactions. The option to heterogenize homogenous precatalysts due to interaction of the amino groups with Lewis or Brønsted acidic surfaces is given (10). Furthermore, quaternization of the amino groups leads to a dramatically increased solubility in polar solvents and can enable the recycling of precatalysts by simple extraction procedures (11). Some recently described switchable catalyst systems exhibit a temperature-controlled allosteric effect, based on a reversible coordination of the cocatalyst MAO by the pendant donor function. As a consequence, either high- or low-molecular weight polymer products become accessible by employing an amino-substituted precatalyst (12).

Here we report on the regioselective preparation and on structural properties of chiral, silicon-bridged indene derivatives, which are substituted at the indene moiety by a dialkylaminoethyl group. New *ansa*-zirconocenes bearing such indenyl ligands are shown to be accessible via an amine elimination reaction.

## Results and discussion

The 3-(2-(*N,N*-dialkylamino)ethyl)indenenes (**2a–2c**), which were first described in 1967 but have been characterized only incompletely (13), served as starting compounds. Their synthesis was carried out according to a procedure introduced by Wang et al. and modified by Jutzi and Bangel for the preparation of the analogous cyclopentadienes (Scheme 1) (14).

Received 19 March 2003. Published on the NRC Research Press Web site at <http://canjchem.nrc.ca> on 15 September 2003.

*Dedicated to Professor John F. Harrod in recognition of his seminal contributions to the field of organometallic chemistry.*

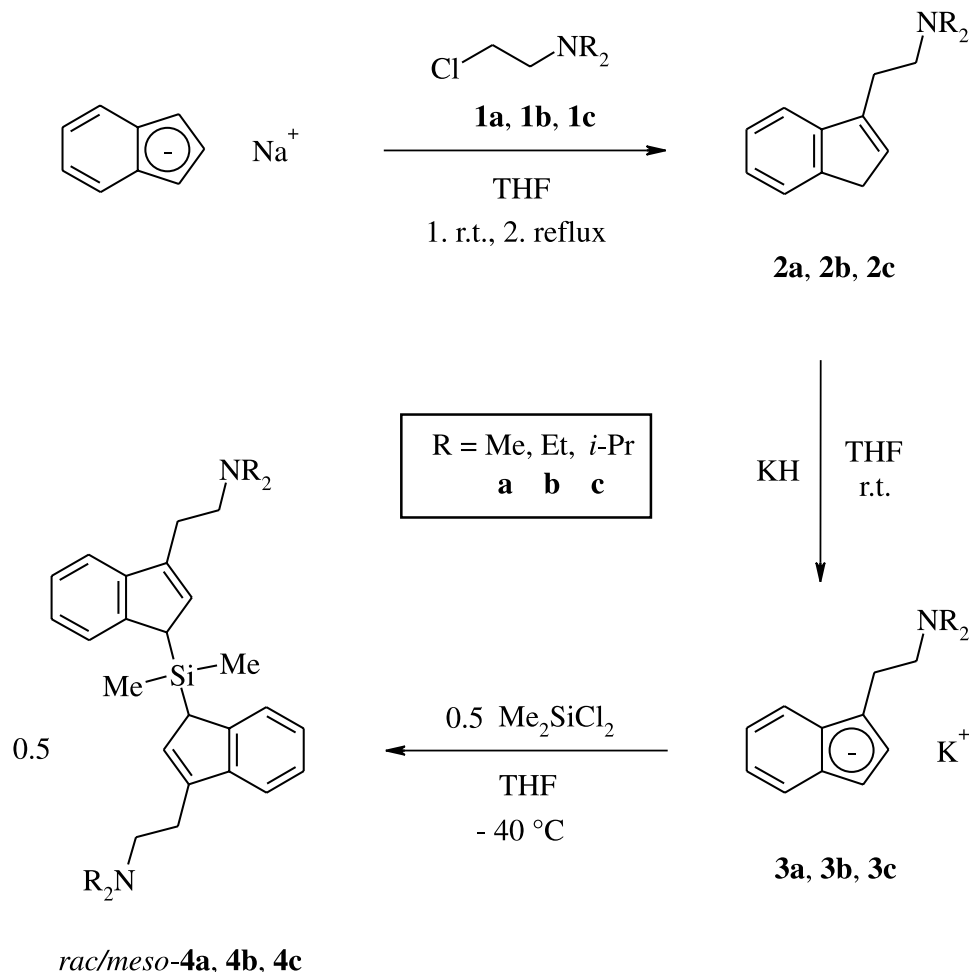
**T. Hagemeister, P. Jutzi,<sup>2</sup> A. Stammler, and H.-G. Stammler.** Faculty of Chemistry, University of Bielefeld, 33615 Bielefeld, Germany.

<sup>1</sup>This article is part of a Special Issue dedicated to Professor John Harrod.

<sup>2</sup>Corresponding author (e-mail: [peter.jutzi@uni-bielefeld.de](mailto:peter.jutzi@uni-bielefeld.de)).



Scheme 1.



Reaction of the (2-chloroethyl)dialkylamines (**1a–1c**) with indenyl sodium in THF yielded the (dialkylaminoethyl)indenides **2a**, **2b**, and **2c** as colourless, distillable, and viscous liquids in analytical purity. The  $^1\text{H}$  NMR data gave clear evidence that substitution exclusively occurred in position 3. This correlates with earlier observations (15) that the regioselectivity of coupling reactions is solvent-dependent. Reactions with electrophiles in nonpolar solvents predominantly take place at C(1), and in more polar media such as THF, mainly at C(3).

The compounds **2a–2c** were converted almost quantitatively into the intensively coloured potassium (dialkylaminoethyl)indenides **3a–3c** by reaction with KH in THF. Subsequent C—Si bond formation was achieved by metathesis of the salts with a slight excess of dimethyldichlorosilane (Scheme 1). After conventional work-up, the resulting chiral 1,3-bis(indenyl)dimethylsilanes **4a–4c** were obtained as pure, viscous orange-brown oils in 60–70% yields. The new compounds were characterized by  $^1\text{H}$ ,  $^{13}\text{C}$ , and  $^{29}\text{Si}$  NMR spectroscopy, mass spectrometry, as well as elemental analysis. They turned out to be remarkably air- and moisture stable; for instance stirring in water for 18 h did not lead to decomposition.

The  $^1\text{H}$  NMR data of **4a–4c** indicated the regioselective introduction of the silicon-bridge under retention of the double bond position. The 1,3-substitution pattern was proved

by the observed AB spin-system leading to two doublets with equal intensities and  $^3J(\text{H}_\text{A}, \text{H}_\text{B}) = 1.1$  Hz. The presence of the double bond between C(2) and C(3) was most clearly demonstrated by  $^{13}\text{C}$  NMR data. With  $\delta_{\text{C}(2)} = 129.9$ – $130.2$  ppm and  $\delta_{\text{C}(3)} = 145.2$ – $146.1$  ppm, the resonances for these carbon atoms remained almost unshifted relative to the parent compounds **2a–2c**.

The compounds **4a–4c** possess two asymmetric centres at C(1) and C(1'). Therefore, three stereoisomers are conceivable: the (*R,R*)- and the (*S,S*)-enantiomers forming a racemate and a meso compound (Scheme 2).

The NMR data were consistent with the presence of the three possible stereoisomers. The *rac/meso* ratio of 1:1 was most easily determined from  $^1\text{H}$  NMR integrals of the cleanly separated signals for the silicon bridge protons (Fig. 1 for **4a**). In the *meso* compound, one methyl group ( $\text{Me}_\text{H}$ ) was located between the annellated benzene rings, causing a proton resonance shifted to higher field. The other methyl group ( $\text{Me}_\text{D}$ ) lies distant from the  $\text{C}_6$ -perimeters, which resulted in a downfield shifted signal of equal intensity. In the racemic compounds the bridge protons are equivalent. This led to an averaged signal with doubled intensity (Fig. 1).

In accordance with earlier investigations (16), two independent signal sets were found for all other proton and carbon resonances, which can be assigned to the *rac* and *meso*



Scheme 2.

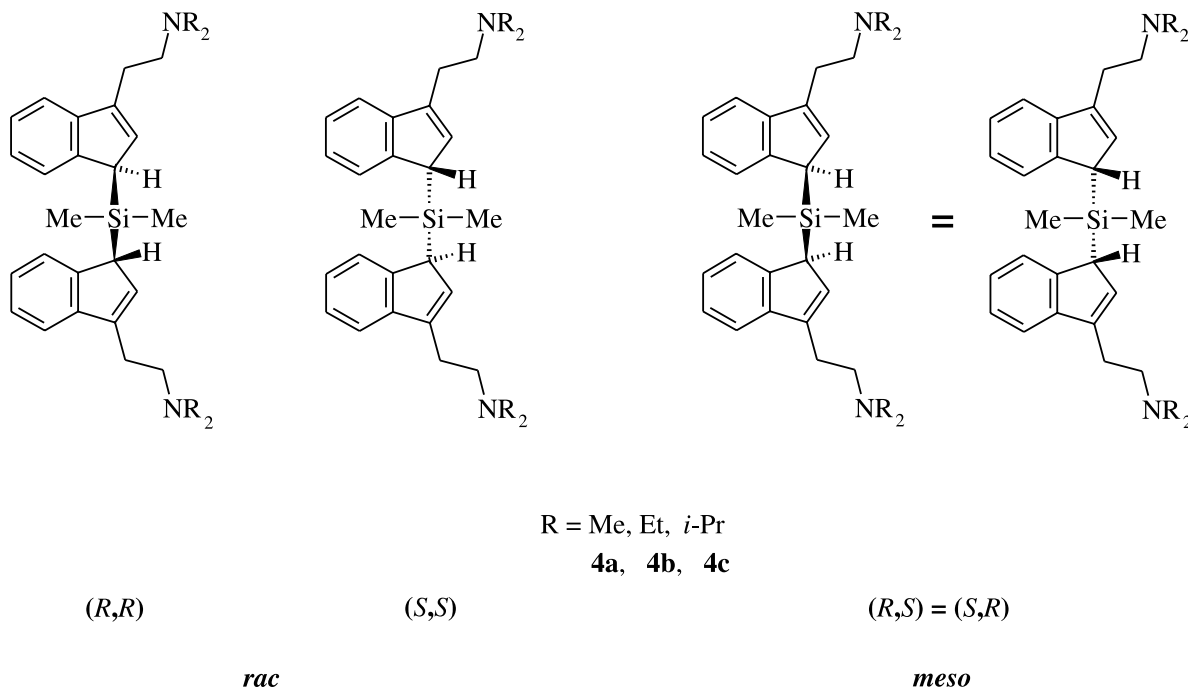
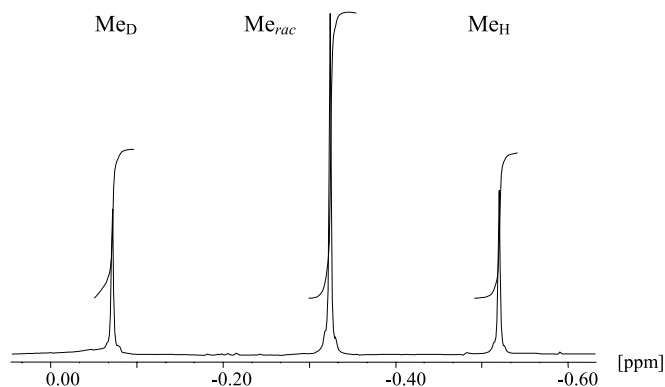


**Fig. 1.** Part of the  $^1\text{H}$  NMR spectrum ( $\text{C}_6\text{D}_6$ ,  $\text{TMS}_{\text{int}}$ ) of *rac/meso*-4a (resonances of the  $\text{Si}-\text{CH}_3$ -protons).



isomers. As expected, the  $^{29}\text{Si}$  NMR data of 4a–4c also exhibited two resonances each.

In addition to NMR spectroscopy and elemental analysis, the compounds 4a–4c were characterized by mass spectrometry. Electron impact MS data showed the appearance of each  $[\text{CH}_2\text{NR}_2]^+$  fragment with intensities of 100%. These fragments are typical of moieties containing ( $\beta$ -*N,N*-dialkylaminoethyl) substituents (17).

So far, no solid-state structure of a dimethylsilyl-bridged bisindene has been cited in the literature. Thus, the dimethylamino-substituted derivative 4a was characterized by single crystal X-ray diffraction studies; crystallographic

data are presented in Table 1, selected bond lengths and bond angles are listed in Table 2.

The analysis confirmed the assumptions based on NMR investigations; all bond lengths and angles were in the expected range. The solid-state structure of the (*R,R*)-enantiomer of 4a is illustrated in Fig. 2.<sup>3</sup>

In a preliminary experiment the bridged bisindene *rac/meso*-4b was employed for the synthesis of corresponding group IV metal complexes. The reaction of 4b with  $\text{Zr}(\text{NMe}_2)_4$  was carried out in *n*-octane at 126 °C under a continuous argon stream. In regular intervals of 2 h, the reaction atmosphere was removed under reduced pressure and replaced with fresh argon. After a total reaction time of 8 h and complete removal of the volatiles in vacuo, a mixture of the chiral zirconocene bis(amide) *rac*-6, of its achiral diastereomer *meso*-6, and of the corresponding half-sandwich complexes 5 was obtained as a highly air- and moisture-sensitive red oil (Scheme 3). The formation of the new *ansa*-metallocenes was monitored by  $^1\text{H}$  NMR spectroscopy.

From  $^1\text{H}$  NMR integrals of the cleanly separated signals for the  $\text{Zr}(\text{NMe}_2)_2$  groups, the overall NMR yield of *rac*-6 and *meso*-6 was determined as 40% with a *rac/meso* ratio of 4:1. This demonstrates the predominant formation of the desired racemic isomer, which in comparable situations is generally observed under the chosen reaction conditions (18).

In detail, after a reaction time of 4 h, the resonances of the free ligand *rac/meso*-4b almost disappeared due to the formation of the half-sandwich complex 5 in its two diastereomeric forms; unfortunately, their signals were par-

<sup>3</sup>Supplementary data may be purchased from the Directory of Unpublished Data, Document Delivery, CISTI, National Research Council Canada, Ottawa, ON K1A 0S2, Canada ([http://www.nrc.ca/cisti/irm/unpub\\_e.shtml](http://www.nrc.ca/cisti/irm/unpub_e.shtml) for information on ordering electronically). CCDC 190217 contains the crystallographic data for this manuscript. These data can be obtained, free of charge, via [www.ccdc.cam.ac.uk/conts/retrieving.html](http://www.ccdc.cam.ac.uk/conts/retrieving.html) (or from the Cambridge Crystallographic Data Centre, 12 Union Road, Cambridge CB2 1EZ, U.K.; fax +44 1223 336033; or [deposit@ccdc.cam.ac.uk](mailto:deposit@ccdc.cam.ac.uk)).



**Table 1.** Crystal data and structure refinement for (*R,R*)-**4a**.

Empirical formula	C <sub>28</sub> H <sub>38</sub> N <sub>2</sub> Si
Formular weight	430.69
Colour	Colourless plates
Crystal size (mm)	0.30 × 0.23 × 0.10
Crystal system, space group	Triclinic <i>P</i> -1
Temperature (K)	100(2)
Wavelength (Å)	0.71073
<b>Unit cell dimensions</b>	
<i>a</i> (Å)	10.9650(2)
<i>b</i> (Å)	11.7740(3)
<i>c</i> (Å)	11.8160(3)
α (°)	92.9690(11)
β (°)	107.2550(11)
γ (°)	115.5181(11)
Volume (Å <sup>3</sup> )	1285.84(5)
Z; calculated density (g/cm <sup>3</sup> )	2; 1.112
Absorption coefficient (mm <sup>-1</sup> )	0.108
θ Range (°)	3–30
Index ranges	–15 ≤ <i>h</i> ≤ 13, –15 ≤ <i>k</i> ≤ 16, –15 ≤ <i>l</i> ≤ 16
No. reflections collected / unique	37 432 / 7450 ( <i>R</i> (int) = 0.0168)
No. of data / restraints / parameters	7450 / 0 / 432
Abs. correction	Multiscan
Goodness-of-fit on <i>F</i> <sup>2</sup>	1.008
Final <i>R</i> indices ( <i>I</i> > 2σ( <i>I</i> ))	<i>R</i> <sub>1</sub> = 0.0432, <i>wR</i> <sub>2</sub> = 0.0997 (5574)
<i>R</i> indices (all data)	<i>R</i> <sub>1</sub> = 0.0674, <i>wR</i> <sub>2</sub> = 0.1123
Largest difference peak andhole (e Å <sup>-3</sup> )	0.320 and –0.216
Diffractometer used	Nonius Kappa CCD
Refinement method	Full-matrix least-squares on <i>F</i> <sup>2</sup>

**Table 2.** Selected bond lengths (Å) and bond angles (°) for (*R,R*)-**4a**.

<b>Bond lengths (Å)</b>	
Si(1)—C(1)	1.8982(13)
C(1)—C(2)	1.5011(18)
C(1)—C(9)	1.5069(17)
C(2)—C(7)	1.4099(17)
C(7)—C(8)	1.4697(17)
C(8)—C(9)	1.3474(18)
Si(1)—C(14)	1.9046(13)
C(14)—C(15)	1.5006(17)
C(14)—C(22)	1.5016(17)
C(15)—C(20)	1.4122(17)
C(20)—C(21)	1.4652(18)
C(21)—C(22)	1.3509(18)
<b>Bond angles (°)</b>	
C(1)—Si(1)—C(27)	109.11(6)
C(1)—C(9)—C(8)	111.74(11)
C(2)—C(1)—C(9)	102.15(10)
C(7)—C(8)—C(9)	108.54(11)
C(14)—Si(1)—C(28)	108.53(6)
C(14)—C(22)—C(21)	111.73(11)
C(15)—C(14)—C(22)	102.32(10)
C(20)—C(21)—C(22)	108.25(11)

tially overlapped and obscured. A prolonged reaction time accompanied by periodical exchange of the reaction atmosphere led to the appearance of new signal multiplicities

caused by the *rac* and *meso* isomer of **6**. Whereas the characteristic Zr(NMe<sub>2</sub>)<sub>2</sub> groups exhibited only one singlet at δ = 2.39 ppm for *rac*-**6**, they showed two resonances at δ = 1.73 and 3.00 ppm for *meso*-**6** because of the prochirality of these moieties; an identical signal pattern was observed for the silicon bridge protons of these complexes.

Based on the <sup>1</sup>H NMR data, an intra- or intermolecular coordination of the metal centers by the pendent dimethylamino groups can be excluded, although *rac*-**6** and *meso*-**6** are formally 16-VE-complexes. This result is supported by earlier studies, which have proved a partial double bond character for the M-amido bonds in comparable group IV metallocenes (19). As a consequence of this N → M π-donation, an additional coordination of the metal centers by the pendant donor functionalities should not be observed in the neutral complexes.

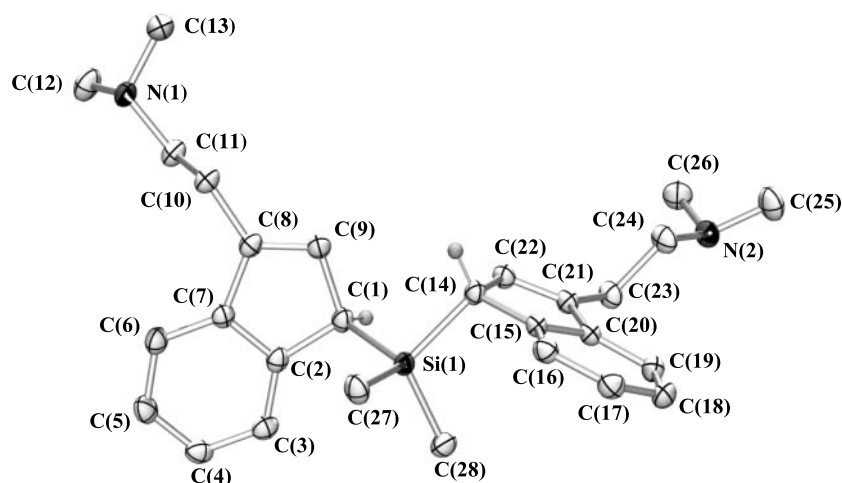
It is noteworthy that more drastic reaction conditions are required for the formation of the amino-functionalized *ansa*-zirconocenes than for the synthesis of the nonfunctionalized complexes (18). Thus, substantially higher reaction temperatures and the removal of the evolved amine are necessary to enrich the *ansa*-metallocenes *rac*-**6** and *meso*-**6** in the complex equilibrium mixture.

## Summary

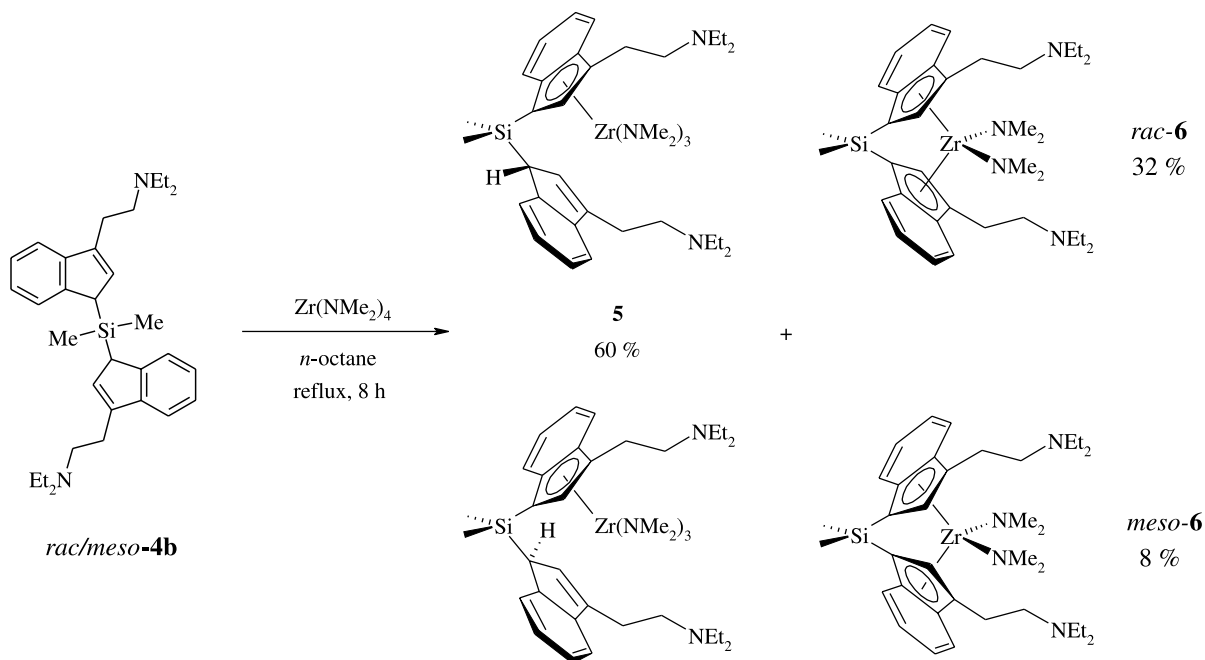
In this paper we have described the synthesis of novel chiral silicon-bridged indene derivatives which are selectively substituted in position 3 by a 2-(*N,N*-dialkylamino)ethyl group. The employed strategy yields the air-



**Fig. 2.** Molecular structure of (*R,R*)-**4a** (ORTEP diagram; 50% probability ellipsoids). Hydrogen atoms have been omitted for clarity except for H(1) and H(14).



**Scheme 3.**



and moisture-stable functionalized bisindenes in analytical purity without further extensive purification steps. The first solid-state structure of a dimethylsilyl-bridged bisindene has been presented. The diethylamino-functionalized derivative was shown to be a useful precursor for the synthesis of new *ansa*-zirconocenes via an amine elimination reaction. The extension of this approach to the preparation and isolation of other *ansa*-metallocenes containing the novel ligands will be described in subsequent contributions.

## Experimental

All reactions were performed under purified Ar atmosphere using standard Schlenk techniques. The commercially available solvents were purified by conventional means and distilled immediately prior to use. Indenyl sodium (**14**) and

$\text{Zr(NMe}_2)_4$  (**18**) were synthesized according to the literature. Yields refer to analytically pure samples. Isomer ratios were determined from suitable  $^1\text{H}$  NMR integrals of cleanly separated signals. Elemental analyses were carried out at the Microanalytical Laboratory of the Universität Bielefeld. The NMR spectra were recorded on a Bruker Avance DRX 500 spectrometer at 300 K ( $^1\text{H}$ , 500.1 MHz;  $^{13}\text{C}$ , 125.8 MHz;  $^{29}\text{Si}$ , 99.4 MHz). Chemical shifts are referenced to the solvent as internal standard and are reported in ppm.

## 3-(2-(*N,N*-Dimethylamino)ethyl)indene (**2a**)

### Typical procedure

(2-Chloroethyl)dimethylamine (**1a**) (42.50 g, 395.0 mmol) was generated via a solid-phase reaction of (2-chloroethyl)dimethylamine hydrochloride and powdered so-



dium hydroxide (1:2 molar ratio) followed by a vacuum distillation using a liquid N<sub>2</sub> cooled trap (14). At 0 °C, the solution of (2-chloroethyl)dimethylamine in THF (80 mL) was added dropwise to a suspension of indenyl sodium (55.3 g, 400.0 mmol) in THF (200 mL). Stirring overnight at room temperature (r.t.) and subsequent refluxing for 2 h gave a green reaction mixture. The volatile components were evaporated and the residue was hydrolyzed with cooled H<sub>2</sub>O (400 mL). After extraction of the resulting maroon solution with petrol ether (bp 35/80) (4 × 125 mL), the combined organic phases were washed with H<sub>2</sub>O (3 × 300 mL) and dried (Na<sub>2</sub>SO<sub>4</sub>). The solvent was removed in vacuo and the crude product was distilled to give **2a** as a colourless, slightly viscous liquid (25.16 g, 134.3 mmol, 34%), bp 77 °C (0.5 mbar). <sup>1</sup>H NMR (CDCl<sub>3</sub>) δ: 2.37 (s, 6H, N-CH<sub>3</sub>), 2.67 (t, 2H, <sup>3</sup>J<sub>H,H</sub> = 7.7 Hz, N-CH<sub>2</sub>-CH<sub>2</sub>-), 2.79 (t, 2H, <sup>3</sup>J<sub>H,H</sub> = 7.7 Hz, N-CH<sub>2</sub>-CH<sub>2</sub>-), 3.35 (d, 2H, <sup>3</sup>J<sub>H,H</sub> = 1.5 Hz, allyl-H), 6.27 (t, 1H, <sup>3</sup>J<sub>H,H</sub> = 1.5 Hz, vinyl-H), 7.24 (pseudo t, 1H, <sup>3</sup>J<sub>H,H</sub> = 7.5 Hz, H5), 7.34 (pseudo t, 1H, <sup>3</sup>J<sub>H,H</sub> = 7.5 Hz, H6), 7.42 (d, 1H, <sup>3</sup>J<sub>H,H</sub> = 7.5 Hz, H4), 7.48 (d, 1H, <sup>3</sup>J<sub>H,H</sub> = 7.5 Hz, H7). <sup>13</sup>C NMR (CDCl<sub>3</sub>) δ: 26.0 (N-CH<sub>2</sub>-CH<sub>2</sub>-), 37.6 (C1), 45.3 (N-CH<sub>3</sub>), 58.2 (N-CH<sub>2</sub>-CH<sub>2</sub>-), 118.6 (C4), 123.4 (C7), 124.3 (C6), 125.8 (C5), 128.1 (C2), 142.2 (C8), 144.1 (C9), 145.1 (C3). MS (EI, 70 eV) *m/z* (%): 187(1) [M<sup>+</sup>], 129(4) [IndCH<sub>2</sub><sup>+</sup>], 115(6) [Ind<sup>+</sup>], 58(100) [Me<sub>2</sub>NCH<sub>2</sub><sup>+</sup>]. Anal. calcd. for C<sub>13</sub>H<sub>17</sub>N (187.30): C 83.37, H 9.15, N 7.48; found: C 83.40, H 9.44, N 7.05.

### 3-(2-(*N,N*-Diethylamino)ethyl)indene (2b)

In the same manner as described above, **2b** was obtained by reaction of (2-chloroethyl)diethylamine (**1b**) (62.4 g, 460 mmol) with indenyl sodium (64.9 g, 470 mmol) in 59% yield, bp 87 °C (0.5 mbar). <sup>1</sup>H NMR (CDCl<sub>3</sub>) δ: 1.09 (t, 6H, <sup>3</sup>J<sub>H,H</sub> = 7.2 Hz, N-CH<sub>2</sub>-CH<sub>3</sub>), 2.64 (q, 4H, <sup>3</sup>J<sub>H,H</sub> = 7.2 Hz, N-CH<sub>2</sub>-CH<sub>3</sub>), 2.74 (t, 2H, <sup>3</sup>J<sub>H,H</sub> = 7.4 Hz, N-CH<sub>2</sub>-CH<sub>2</sub>-), 2.81 (t, 2H, <sup>3</sup>J<sub>H,H</sub> = 7.4 Hz, N-CH<sub>2</sub>-CH<sub>2</sub>-), 3.33 (b, 2H, H1), 6.24 (b, 1H, H2), 7.20 (pseudo t, 1H, <sup>3</sup>J<sub>H,H</sub> = 7.4 Hz, H5), 7.30 (pseudo t, 1H, <sup>3</sup>J<sub>H,H</sub> = 7.4 Hz, H6), 7.39 (d, 1H, <sup>3</sup>J<sub>H,H</sub> = 7.4 Hz, H4), 7.45 (d, 1H, <sup>3</sup>J<sub>H,H</sub> = 7.4 Hz, H7). <sup>13</sup>C NMR (CDCl<sub>3</sub>) δ: 11.6 (N-CH<sub>2</sub>-CH<sub>3</sub>), 25.0 (N-CH<sub>2</sub>-CH<sub>2</sub>-), 37.3 (C1), 45.3 (N-CH<sub>2</sub>-CH<sub>3</sub>), 51.2 (N-CH<sub>2</sub>-CH<sub>2</sub>-), 118.4 (C4), 123.3 (C7), 124.1 (C6), 125.6 (C5), 127.7 (C2), 142.4 (C8), 143.8 (C9), 145.0 (C3). MS (EI, 70 eV) *m/z* (%): 215(1) [M<sup>+</sup>], 143(10) [IndCH<sub>2</sub>CH<sub>2</sub><sup>+</sup>], 115(6) [Ind<sup>+</sup>], 86(100) [Et<sub>2</sub>NCH<sub>2</sub><sup>+</sup>]. Anal. calcd. for C<sub>15</sub>H<sub>21</sub>N (215.34): C 83.67, H 9.83, N 6.50; found: C 83.54, H 9.90, N 6.44.

### 3-(2-(*N,N*-Diisopropylamino)ethyl)indene (2c)

Compound **2c** was prepared according to the procedures described for **2a** and **2b** from (2-chloroethyl)diisopropylamine (**1c**) (79.6 g, 486 mmol) and indenyl sodium (67.7 g, 490 mmol) in 62% yield, bp 110 °C (0.5 mbar). <sup>1</sup>H NMR (CDCl<sub>3</sub>) δ: 1.09 (d, 12H, <sup>3</sup>J<sub>H,H</sub> = 6.6 Hz, N-CH-(CH<sub>3</sub>)<sub>2</sub>), 2.71 (t, 2H, <sup>3</sup>J<sub>H,H</sub> = 6.5 Hz, N-CH<sub>2</sub>-CH<sub>2</sub>-), 2.77 (t, 2H, <sup>3</sup>J<sub>H,H</sub> = 6.5 Hz, N-CH<sub>2</sub>-CH<sub>2</sub>-), 3.12 (sept, 2H, <sup>3</sup>J<sub>H,H</sub> = 6.6 Hz, N-CH-(CH<sub>3</sub>)<sub>2</sub>), 3.35 (b, 2H, H1), 6.26 (b, 1H, H2), 7.22 (pseudo t, 1H, <sup>3</sup>J<sub>H,H</sub> = 7.5 Hz, H5), 7.33 (pseudo t, 1H, <sup>3</sup>J<sub>H,H</sub> = 7.5 Hz, H6), 7.41 (d, 1H, <sup>3</sup>J<sub>H,H</sub> = 7.5 Hz, H4), 7.48 (d, 1H, <sup>3</sup>J<sub>H,H</sub> = 7.5 Hz, H7). <sup>13</sup>C NMR (CDCl<sub>3</sub>) δ: 20.8 (N-CH-(CH<sub>3</sub>)<sub>2</sub>), 30.7 (N-CH<sub>2</sub>-CH<sub>2</sub>-), 37.8 (C1), 44.7 (N-CH<sub>2</sub>-CH<sub>2</sub>-), 48.9 (N-CH-(CH<sub>3</sub>)<sub>2</sub>), 118.9 (C4), 123.7 (C7), 124.4 (C6), 126.0 (C5),

128.0 (C2), 143.2 (C8), 144.3 (C9), 145.6 (C3). MS (EI, 70 eV) *m/z* (%): 243(1) [M<sup>+</sup>], 228(2) [M<sup>+</sup> - CH<sub>3</sub>], 115(14) [Ind<sup>+</sup>], 114(100) [*i*-Pr<sub>2</sub>NCH<sub>2</sub><sup>+</sup>]. Anal. calcd. for C<sub>17</sub>H<sub>25</sub>N (243.40): C 83.89, H 10.35, N 5.75; found: C 83.63, H 10.39, N 5.78.

### Potassium [1-(2-(*N,N*-dialkylamino)ethyl)indenide] salts (3a–3c)

#### General procedure

The solutions of the 3-(2-dialkylaminoethyl)indenes **2a–2c** (50 mmol) in 20 mL THF were added slowly to a suspension of potassium hydride (2.01 g, 50.1 mmol) in THF (60 mL) at –40 °C. The reaction mixtures were allowed to warm up to r.t. and stirred for 18 h. The solvent was removed in vacuo and the residues washed with *n*-hexane (2 × 50 mL). After removal of the solvent, the potassium salts were obtained as green (**3a**) (49.1 mmol, 98%), yellow (**3b**) (40.6 mmol, 81%), or brown (**3c**) (46.1 mmol, 92%) solids.

#### (3a)

<sup>1</sup>H NMR ([D]<sub>8</sub> THF) δ: 1.89 (s, 6H, N-CH<sub>3</sub>), 2.35 (t, 2H, <sup>3</sup>J<sub>H,H</sub> = 6.3 Hz, N-CH<sub>2</sub>-CH<sub>2</sub>-), 2.77 (t, 2H, <sup>3</sup>J<sub>H,H</sub> = 6.3 Hz, N-CH<sub>2</sub>-CH<sub>2</sub>-), 5.56 (d, 1H, <sup>3</sup>J<sub>H,H</sub> = 3.2 Hz, H2), 6.06 (d, 1H, <sup>3</sup>J<sub>H,H</sub> = 3.2 Hz, H1), 6.27–6.31 (m, 2H, H4, H7), 7.05–7.12 (m, 2H, H5, H6). <sup>13</sup>C NMR ([D]<sub>8</sub> THF) δ: 26.9 (N-CH<sub>2</sub>-CH<sub>2</sub>-), 45.2 (N-CH<sub>3</sub>), 62.9 (N-CH<sub>2</sub>-CH<sub>2</sub>-), 91.4 (C2), 104.9 (C1), 112.9 (C7), 113.6 (C4), 116.8 (C6), 117.5 (C5), 119.4 (C3), 126.0 (C8), 128.9 (C9).

#### (3b)

<sup>1</sup>H NMR ([D]<sub>8</sub> THF) δ: 0.93 (t, 6H, <sup>3</sup>J<sub>H,H</sub> = 7.2 Hz, N-CH<sub>2</sub>-CH<sub>3</sub>), 2.50 (q, 4H, <sup>3</sup>J<sub>H,H</sub> = 7.2 Hz, N-CH<sub>2</sub>-CH<sub>3</sub>), 2.62 (t, 2H, <sup>3</sup>J<sub>H,H</sub> = 7.1 Hz, N-CH<sub>2</sub>-CH<sub>2</sub>-), 2.84 (t, 2H, <sup>3</sup>J<sub>H,H</sub> = 7.1 Hz, N-CH<sub>2</sub>-CH<sub>2</sub>-), 5.61 (d, 1H, <sup>3</sup>J<sub>H,H</sub> = 3.3 Hz, H2), 6.16 (d, 1H, <sup>3</sup>J<sub>H,H</sub> = 3.3 Hz, H1), 6.33–6.35 (m, 2H, H4, H7), 7.12–7.15 (m, 2H, H5, H6). <sup>13</sup>C NMR ([D]<sub>8</sub> THF) δ: 11.5 (N-CH<sub>2</sub>-CH<sub>3</sub>), 26.5 (N-CH<sub>2</sub>-CH<sub>2</sub>-), 46.6 (N-CH<sub>2</sub>-CH<sub>3</sub>), 56.0 (N-CH<sub>2</sub>-CH<sub>2</sub>-), 91.5 (C2), 105.1 (C1), 112.8 (C7), 113.2 (C4), 116.8 (C6), 117.6 (C5), 119.5 (C3), 126.3 (C8), 128.9 (C9).

#### (3c)

<sup>1</sup>H NMR ([D]<sub>8</sub> THF) δ: 1.13 (d, 12H, <sup>3</sup>J<sub>H,H</sub> = 6.6 Hz, N-CH-(CH<sub>3</sub>)<sub>2</sub>), 2.59 (t, 2H, <sup>3</sup>J<sub>H,H</sub> = 8.5 Hz, N-CH<sub>2</sub>-CH<sub>2</sub>-), 2.82 (t, 2H, <sup>3</sup>J<sub>H,H</sub> = 8.5 Hz, N-CH<sub>2</sub>-CH<sub>2</sub>-), 3.17 (sept, 2H, <sup>3</sup>J<sub>H,H</sub> = 6.6 Hz, N-CH-(CH<sub>3</sub>)<sub>2</sub>), 5.64 (d, 1H, <sup>3</sup>J<sub>H,H</sub> = 3.3 Hz, H2), 6.29 (d, 1H, <sup>3</sup>J<sub>H,H</sub> = 3.3 Hz, H1), 6.32–6.36 (m, 2H, H4, H7), 7.13 (dd, 1H, <sup>3</sup>J<sub>H5,H4</sub> = 3.8 Hz, <sup>3</sup>J<sub>H5,H6</sub> = 2.5 Hz, H5), 7.19 (dd, 1H, <sup>3</sup>J<sub>H6,H7</sub> = 3.8 Hz, <sup>3</sup>J<sub>H6,H5</sub> = 2.5 Hz, H6). <sup>13</sup>C NMR ([D]<sub>8</sub> THF) δ: 21.7 (N-CH-(CH<sub>3</sub>)<sub>2</sub>), 32.4 (N-CH<sub>2</sub>-CH<sub>2</sub>-), 49.3 (N-CH<sub>2</sub>-CH<sub>2</sub>-), 49.5 (N-CH-(CH<sub>3</sub>)<sub>2</sub>), 91.2 (C2), 105.9 (C1), 112.4 (C7), 113.0 (C4), 117.0 (C6), 117.9 (C5), 118.9 (C3), 126.6 (C8), 128.9 (C9).

### *rac/meso*-[Bis(3,3'-(2-(*N,N*-dimethylamino)ethyl)indenyl)]dimethylsilane (4a)

#### Typical procedure

Potassium [1-(2-(*N,N*-dimethylamino)ethyl)indenide] (**3a**) (5.00 g, 22.2 mmol) was dissolved in THF (35 mL) and cooled to –40 °C. After dropwise addition of dimethylchlorosilane (1.15 g, 8.91 mmol) in THF (25 mL), the ma-



room mixture was allowed to warm to r.t. Stirring was continued for 18 h and subsequent removal of the solvent gave a residue that was extracted with *n*-hexane (70 mL). After filtration the solvent was again removed in vacuo yielding a *rac/meso* mixture of **4a** as an orange-red oil (2.57 g, 5.97 mmol, 67%). Crystals of the (*R,R*)-enantiomer suitable for X-ray structure analysis were obtained by storage at 4 °C for 6 weeks. <sup>1</sup>H NMR (C<sub>6</sub>D<sub>6</sub>) δ: −0.52, −0.32, −0.07 (3 × s, 6H, Si-CH<sub>3</sub>), 2.16, 2.18 (2 × s, 12H, N-CH<sub>3</sub>), 2.51–2.83 (m, 8H, N-CH<sub>2</sub>-CH<sub>2</sub>-), 3.47 (b, 2H, H1), 6.08, 6.29 (2 × b, 2H, H2), 7.17–7.49 (m, 8H, H5, H6, H4, H7). <sup>13</sup>C NMR (C<sub>6</sub>D<sub>6</sub>) δ: −7.0, −5.9, −4.5 (Si-CH<sub>3</sub>), 26.6, 26.8 (N-CH<sub>2</sub>-CH<sub>2</sub>-), 43.8, 43.9 (C1), 45.5, 45.5 (N-CH<sub>3</sub>), 59.2, 59.3 (N-CH<sub>2</sub>-CH<sub>2</sub>-), 119.6, 119.6 (C4), 123.4, 123.4, 124.3, 124.3, 125.3, 125.3 (C7, C6, C5), 130.2, 130.2 (C2), 140.6, 140.8 (C8), 145.1, 145.2 (C9), 145.9, 146.0 (C3). <sup>29</sup>Si NMR (C<sub>6</sub>D<sub>6</sub>) δ: 5.5, 6.0. MS (EI, 70 eV) *m/z* (%): 430(4) [M<sup>+</sup>], 372(8) [M<sup>+</sup> − Me<sub>2</sub>NCH<sub>2</sub>], 58(100) [Me<sub>2</sub>NCH<sub>2</sub><sup>+</sup>]. Anal. calcd. for C<sub>28</sub>H<sub>38</sub>N<sub>2</sub>Si (430.72): C 78.08, H 8.89, N 6.50; found: C 78.21, H 9.17, N 6.33.

***rac/meso*-[Bis(3,3'-(2-(*N,N*-diethylamino)ethyl)indenyl)]dimethylsilane (**4b**)**

According to the procedure described above, **4b** was prepared by reaction of potassium [1-(2-(*N,N*-diethylamino)ethyl)indenide] (**3b**) (5.63 g, 22.2 mmol) with Me<sub>2</sub>SiCl<sub>2</sub> (1.15 g, 8.91 mmol). The oily orange-brown product was obtained as a mixture of both diastereomers (2.67 g, 5.48 mmol, 62%). <sup>1</sup>H NMR (C<sub>6</sub>D<sub>6</sub>) δ: −0.50, −0.32, −0.06 (3 × s, 6H, Si-CH<sub>3</sub>), 0.99–1.03 (m, 12H, N-CH<sub>2</sub>-CH<sub>3</sub>), 2.49–2.54 (m, 8H, N-CH<sub>2</sub>-CH<sub>3</sub>), 2.71–2.84 (m, 8H, N-CH<sub>2</sub>-CH<sub>2</sub>-), 3.48, 3.50 (2 × d, 2H, <sup>3</sup>J<sub>H,H</sub> = 1.1 Hz, H1), 6.09, 6.32 (2 × d, 2H, <sup>3</sup>J<sub>H,H</sub> = 1.1 Hz, H2), 7.17–7.53 (m, 8H, H5, H6, H4, H7). <sup>13</sup>C NMR (C<sub>6</sub>D<sub>6</sub>) δ: −6.9, −5.9, −4.5 (Si-CH<sub>3</sub>), 12.6, 12.6 (N-CH<sub>2</sub>-CH<sub>3</sub>), 26.3, 26.4 (N-CH<sub>2</sub>-CH<sub>2</sub>-), 43.8, 43.9 (C1), 47.3, 47.3 (N-CH<sub>2</sub>-CH<sub>3</sub>), 52.8, 53.0 (N-CH<sub>2</sub>-CH<sub>2</sub>-), 119.6, 119.6 (C4), 123.4, 123.5, 124.3, 124.4, 125.3, 125.3 (C7, C6, C5), 130.1, 130.2 (C2), 141.0, 141.2 (C8), 145.2, 145.3 (C9), 146.0, 146.0 (C3). <sup>29</sup>Si NMR (C<sub>6</sub>D<sub>6</sub>) δ: 5.3, 5.7. MS (EI, 70 eV) *m/z* (%): 486 (3) [M<sup>+</sup>], 400 (10) [M<sup>+</sup> − Et<sub>2</sub>NCH<sub>2</sub>], 86 (100) [Et<sub>2</sub>NCH<sub>2</sub><sup>+</sup>]. Anal. calcd. for C<sub>32</sub>H<sub>46</sub>N<sub>2</sub>Si (486.83): C 78.95, H 9.52, N 5.75; found: C 78.44, H 9.76, N 5.75.

***rac/meso*-[Bis(3,3'-(2-(*N,N*-diisopropylamino)ethyl)indenyl)]dimethylsilane (**4c**)**

The *rac/meso* mixture of **4c** was prepared in the same manner as described above from potassium [1-(2-(*N,N*-diisopropylamino)ethyl)indenide] (**3c**) (6.25 g, 22.2 mmol) and Me<sub>2</sub>SiCl<sub>2</sub> (1.15 g, 8.91 mmol) as a highly viscous brown oil (2.90 g, 5.35 mmol, 60%). <sup>1</sup>H NMR (C<sub>6</sub>D<sub>6</sub>) δ: −0.47, −0.29, −0.03 (3 × s, 6H, Si-CH<sub>3</sub>), 1.01–1.03 (m, 24H, N-CH(CH<sub>3</sub>)<sub>2</sub>), 2.75–3.05 (m, 12H, N-CH<sub>2</sub>-CH<sub>2</sub>-, N-CH(CH<sub>3</sub>)<sub>2</sub>), 3.48, 3.52 (2 × b, 2H, H1), 6.11, 6.35 (2 × b, 2H, H2), 7.17–7.59 (m, 8H, H5, H6, H4, H7). <sup>13</sup>C NMR (C<sub>6</sub>D<sub>6</sub>) δ: −6.9, −5.7, −4.2 (Si-CH<sub>3</sub>), 21.1, 21.2 (N-CH(CH<sub>3</sub>)<sub>2</sub>), 31.0, 31.0 (N-CH<sub>2</sub>-CH<sub>2</sub>-), 43.8, 43.8 (C1), 45.2, 45.3 (N-CH<sub>2</sub>-CH<sub>2</sub>-), 48.7, 48.8 (N-CH(CH<sub>3</sub>)<sub>2</sub>), 119.7, 119.7 (C4), 123.5, 123.5, 124.3, 124.4, 125.4, 125.4 (C7, C6, C5), 129.9, 130.0 (C2), 141.4, 141.6 (C8), 145.4, 145.4 (C9), 145.9, 146.0 (C3). <sup>29</sup>Si NMR (C<sub>6</sub>D<sub>6</sub>) δ: 5.3, 5.7. MS (EI, 70 eV) *m/z* (%): 114 (100)

[*i*-Pr<sub>2</sub>NCH<sub>2</sub><sup>+</sup>]. Anal. calcd. for C<sub>36</sub>H<sub>54</sub>N<sub>2</sub>Si (542.92): C 79.64, H 9.80, N 5.16; found: C 79.26, H 9.80, N 5.14.

**Formation of *rac/meso*-dimethylsilanediyl[bis(3,3'-(2-(*N,N*-diethylamino)ethyl)-indenyl)]zirconocenebis(dimethylamide) (*rac/meso*-**6**)**

In a reaction flask fitted with a fractional distillation column (30 cm × 1.5 cm) Zr(NMe<sub>2</sub>)<sub>4</sub> (0.30 g, 1.12 mmol) was dissolved in *n*-octane (20 mL). At r.t. *rac/meso*-**4b** (0.55 g, 1.12 mmol) was added via a syringe. After refluxing for 2 h under a continuous argon stream a <sup>1</sup>H NMR spectrum was recorded, which indicated the formation of the half-sandwich complexes **5**. Subsequently, the reaction was heated for a further 6 h under repetitive removal of HNMe<sub>2</sub> in vacuo. During this procedure a successive discolouration of the solution from yellow to red was observed. Removal of the volatiles in vacuo yielded a mixture of the half-sandwich complexes **5** (60%) as well as of the *ansa*-zirconocenes *rac*-**6** (32%) and *meso*-**6** (8%) as a highly air- and moisture-sensitive red oil. The key <sup>1</sup>H NMR data of **5**, *rac*-**6**, and *meso*-**6** are listed below.

**(5)**

<sup>1</sup>H NMR (C<sub>6</sub>D<sub>6</sub>) δ: −0.04, 0.14, 0.32, 0.59 (4 × s, 4 × 3H, Si-CH<sub>3</sub>), 2.77, 2.78 (2 × s, 2 × 18H, N-CH<sub>3</sub>).

**(*rac*-**6**)**

<sup>1</sup>H NMR (C<sub>6</sub>D<sub>6</sub>) δ: 0.63 (s, 6H, Si-CH<sub>3</sub>), 2.39 (s, 12H, N-CH<sub>3</sub>), 6.20 (s, 2H, H2).

**(*meso*-**6**)**

<sup>1</sup>H NMR (C<sub>6</sub>D<sub>6</sub>) δ: 0.46 (s, 3H, Si-CH<sub>3</sub>), 1.04 (s, 3H, Si-CH<sub>3</sub>), 1.73 (s, 6H, N-CH<sub>3</sub>), 3.00 (s, 6H, N-CH<sub>3</sub>).

## Acknowledgements

Financial support provided by the Deutsche Forschungsgemeinschaft, the Universität Bielefeld, and the Fonds der Chemischen Industrie is gratefully acknowledged.

## References

- (a) C. Müller, D. Vos, and P. Jutzi. *J. Organomet. Chem.* **600**, 127 (2000), and cited literature; (b) C. Müller and P. Jutzi. *Synthesis*, **3**, 389 (2000); (c) I.L. Fedushkin, S. Dechert, and H. Schumann. *Organometallics*, **19**, 4066 (2000); (d) H. Schumann, F. Erbsstein, J. Demtschuk, and R. Weimann. *Z. Anorg. Allg. Chem.* **625**, 1457 (1999); (e) H. Schumann, E.C.E. Rosenthal, and J. Demtschuk. *Organometallics*, **17**, 5324 (1998); (f) H. Schumann, J.A. Meese-Marktscheffel, and L. Esser. *Chem. Rev.* **95**, 865 (1995), and cited literature; (g) P. Jutzi and U. Siemeling. *J. Organomet. Chem.* **500**, 175 (1995); (h) P. Jutzi, J. Dahlhaus, and M.O. Kristen. *J. Organomet. Chem.* **450**, C1 (1993); (i) R. Anwender, W.A. Herrmann, W. Scherer, and F.C. Munck. *J. Organomet. Chem.* **462**, 163 (1993); (j) C. Quian, J. Guo, C. Yi, J. Sun, and P. Zheng. *J. Chem. Soc., Dalton Trans.* 3441 (1993).
- (a) A. Döhring, J. Göhre, P.W. Jolly, B. Kryger, J. Rust, and G.P.J. Verhovnik. *Organometallics*, **19**, 388 (2000); (b) E. Barsties, S. Schaible, M.-H. Prosenc, U. Rief, W. Röhl, O. Weyand, B. Dorer, and H.H. Brintzinger. *J. Organomet. Chem.* **520**, 63 (1996); (c) H.J.G. Luttikhedde, R.P. Leino, C.-E.



- Wilén, J.H. Näsman, M.J. Ahlgrén, and T.A. Pakkanen. *Organometallics*, **15**, 3092 (1996).
3. (a) R.D. Broene and S.L. Buchwald. *J. Am. Chem. Soc.* **115**, 12569 (1993); (b) R. Waymouth and P. Pino. *J. Am. Chem. Soc.* **112**, 4911 (1990).
4. (a) S.R. Hitchcock, J.J. Situ, J.A. Covel, M.M. Olmstead, and M.H. Nantz. *Organometallics*, **14**, 3732 (1995); (b) R.L. Halterman and T.M. Ramsey. *Organometallics*, **12**, 2879 (1993); (c) S.L. Colletti and R.L. Halterman. *Tetrahedron Lett.* **33**, 1005 (1992).
5. Z. Chen and R.L. Halterman. *J. Am. Chem. Soc.* **114**, 2276 (1992).
6. (a) S. Collins, B.A. Kuntz, and Y. Hong. *J. Org. Chem.* **54**, 4154 (1989); (b) F. Sato, S. Iijima, and M. Sato. *J. Chem. Soc., Chem. Commun.* 180 (1981).
7. (a) M.B. Carter, B. Schiøtt, A. Gutiérrez, and S.L. Buchwald. *J. Am. Chem. Soc.* **116**, 11 667 (1994); (b) R.L. Halterman, T.M. Ramsey, and Z. Chen. *J. Org. Chem.* **59**, 2642 (1994).
8. (a) J.B. Jaquith, J. Gaun, S. Wang, and S. Collins. *Organometallics*, **14**, 1079 (1995); (b) Y. Hong, B.A. Kuntz, and S. Collins. *Organometallics*, **12**, 964 (1993).
9. J.P. Banovetz, K.M. Stein, and R.M. Waymouth. *Organometallics*, **10**, 3430 (1991).
10. P. Jutzi and T. Redeker. *Eur. J. Inorg. Chem.* 663 (1998).
11. P. Jutzi and T. Redeker. *Organometallics*, **16**, 1343 (1997).
12. C. Müller, D. Lilge, M.O. Kristen, and P. Jutzi. *Angew. Chem.* **112**, 800 (2000).
13. J.C. Winter, P.K. Gessner, and D.D. Godse. *J. Med. Chem.* **10**, 856 (1967).
14. (a) P. Jutzi and M. Bangel. *J. Organomet. Chem.* **480**, C18 (1994); (b) T.-F. Wang, T.-Y. Lee, J.-W. Chou, and C.-W. Ong. *J. Organomet. Chem.* **439**, 155 (1992); (c) W.S. Rees, Jr. and K.A. Dippel. *Org. Prep. Proced. Int.* **24**, 527 (1992).
15. T.E. Ready, J.C.W. Chien, and M.D. Rausch. *J. Organomet. Chem.* **519**, 21 (1996).
16. (a) S.S. Rigby, L. Girard, A.D. Bain, and M.J. McGlinchey. *Organometallics*, **14**, 1798 (1995); (b) S.S. Rigby, H.K. Gupta, N.H. Werstiuk, A.D. Bain, and M.J. McGlinchey. *Polyhedron*, **14**, 2787 (1995); (c) Y.X. Chen, M.D. Rausch, and J.C.W. Chien. *Organometallics*, **12**, 4607 (1993); (d) E. Marechal and J.P. Tortal. *C. R. Acad. Sci. Paris*, **267**, 467 (1968); (e) L.H. Sommer and N.S. Marans. *J. Am. Chem. Soc.* **73**, 5135 (1951).
17. H. Schumann, F. Erbsstein, D.F. Karasiak, I.L. Fedushkin, J. Demtschuk, and F. Girgsdies. *Z. Anorg. Allg. Chem.* **625**, 781 (1999).
18. (a) J.N. Christopher, G.M. Diamond, R.F. Jordan, and J.L. Petersen. *Organometallics*, **15**, 4038 (1996); (b) G.M. Diamond, R.F. Jordan, and J.L. Petersen. *Organometallics*, **15**, 4030 (1996); (c) G.M. Diamond, R.F. Jordan, and J.L. Petersen. *J. Am. Chem. Soc.* **118**, 8024 (1996); (d) G.M. Diamond, S. Rodewald, and R.F. Jordan. *Organometallics*, **14**, 5 (1995).
19. (a) D.M. Giolando, K. Kirschbaum, L.J. Graves, and U. Bolle. *Inorg. Chem.* **31**, 3887 (1992); (b) R.A. Andersen, D.B. Beach, and W.L. Jolly. *Inorg. Chem.* **24**, 2741 (1985); (c) M.F. Lappert, P.P. Power, A.R. Sanger, and R.C. Srivastava. *Metal and metalloids amides*. Ellis Horwood, Chichester, West Sussex. 1980; (d) D.C. Bradley and M.H. Chisholm. *Acc. Chem. Res.* **9**, 273 (1976).



# Dichloro(diphosphine)(2-pyridylketone)ruthenium(II) complexes<sup>1</sup>

Salete L. Queiroz, Alzir A. Batista, Marcio P. de Araujo, Roberto C. Bianchini, Glaucius Oliva, Javier Ellena, and Brian R. James

**Abstract:** Described are the synthesis and characterization of Ru(II) complexes of the type  $\text{RuCl}_2\text{L}_2(\text{N-O})$ , where  $\text{L}_2$  is either 1,4-bis(diphenylphosphino)butane (dppb) or  $(\text{PPh}_3)_2$ , and N-O represents chelated 2-benzoylpyridine (2-bzpy) or 2-acetylpyridine (2-acpy); the Ru precursors used were  $[\text{RuCl}_2(\text{dppb})]_2(\mu\text{-dppb})$  or  $\text{RuCl}_2(\text{PPh}_3)_3$ . The crystal structure of *cis*- $\text{RuCl}_2(\text{dppb})(2\text{-bzpy})$  is presented, and three other  $\text{RuCl}_2\text{L}_2(\text{N-O})$  complexes with *cis*-chlorines are isolated and characterized spectroscopically; of the *trans*-dichloro species,  $\text{RuCl}_2(\text{PPh}_3)_2(\text{N-O})$  complexes are isolated, while the corresponding dppb species are characterized in situ. In all cases, thermodynamically stable *cis*-complexes are formed from initially formed *trans*-species.

**Key words:** ruthenium, phosphines, 2-benzoylpyridine, 2-acetylpyridine, X-ray structures.

**Résumé :** On décrit la synthèse et la caractérisation de complexes du Ru(II) du type  $\text{RuCl}_2\text{L}_2(\text{N-O})$  dans lesquels  $\text{L}_2 = 1,4\text{-bis(diphénylphosphino)butane (dppb) ou } (\text{PPh}_3)_2$  et N-O = 2-benzoylpyridine (2-bzpy) ou 2-acétylpyridine (2-acpy) chélatées; les complexes de Ru utilisés sont le  $[\text{RuCl}_2(\text{dppb})]_2(\mu\text{-dppb})$  ou  $\text{RuCl}_2(\text{PPh}_3)_3$ . On a déterminé la structure cristalline du *cis*- $\text{RuCl}_2(\text{dppb})(2\text{-bzpy})$  et on a isolé trois autres complexes du  $\text{RuCl}_2\text{L}_2(\text{N-O})$  portant des atomes de chlore en *cis* et on les a caractérisés de façon spectroscopique; des espèces *trans*-dichlorées, les complexes  $\text{RuCl}_2(\text{PPh}_3)_2(\text{N-O})$  ont été isolés alors que les espèces correspondantes du dppb ont été caractérisées in situ. Dans tous les cas, les complexes *cis* thermodynamiquement stables se forment à partir des espèces *trans* obtenues initialement.

**Mots clés :** ruthénium, phosphines, 2-benzoylpyridine, 2-acétylpyridine, structures par diffraction des rayons X.

[Traduit par la Rédaction]

## Introduction

Some 25 years ago, one of our groups published a paper (1) that questioned a reported synthesis of  $[\text{RuCl}_2(\text{PPh}_3)_2]_2$  from  $\text{RuCl}_2(\text{PPh}_3)_3$  using catalytic amounts of the 2-pyridylketones,  $\text{C}_5\text{H}_4\text{N-COR}$  ( $\text{R} = \text{H, Me, Ph}$ ) (2). The reported

synthesis using 2-acetylpyridine (2) was repeated (1), and the product was identified as  $\text{RuCl}_2(\text{PPh}_3)_2(\text{C}_5\text{H}_4\text{N-COMe})$  containing an  $\eta^2\text{-N,O}$ -bonded pyridylketone; the complex was identified by C, H, N, and Cl analysis, molecular weight,  $^1\text{H}$  and  $^{31}\text{P}$  NMR, and IR data in the  $\nu(\text{CO})$  and  $\nu(\text{Ru-Cl})$  regions: the  $^{31}\text{P}\{^1\text{H}\}$  NMR AB pattern required the complex to have *cis*-phosphines, while *trans*-chlorines were “favoured slightly” based on the dominance of a single  $325\text{ cm}^{-1}$  band in the  $400\text{--}250\text{ cm}^{-1}$  IR region (1). An X-ray analysis of the supposed  $[\text{RuCl}_2(\text{PPh}_3)_2]_2$  complex was reported “to be underway” (2); no X-ray structure was ever published, but the authors of ref. 2 did agree that their product was certainly not  $[\text{RuCl}_2(\text{PPh}_3)_2]_2$ .<sup>4</sup>

This present paper reports on the synthesis and structural characterization of the complex, *cis*- $\text{RuCl}_2(\text{dppb})(2\text{-benzoylpyridine})$ , where dppb = 1,4-bis(diphenylphosphino)butane; data on the corresponding *trans*-isomer, and on the analogous 2-acetylpyridine species, are presented also. The bis(triphenylphosphine) complexes containing these 2-pyridylketones are also described. It should be noted that 2-benzoylpyridine (2-bzpy) is also called 2-pyridylphenylketone (3); we use the former-type nomenclature throughout this paper.

2-Pyridylketone complexes of transition metals have been known since the 1960s, particularly the 2-bzpy ligand systems (4). More recent interest in such ligands has generally focussed on bioinorganic model systems or their hemi-labile character for use in catalysis. Structural work describing bidentate, *N,O*-bonded 2-bzpy includes that on mono- and

Received 20 March 2003. Published on the NRC Research Press Web site at <http://canjchem.nrc.ca> on 30 September 2003.

*Dedicated to John Harrod, a close friend and colleague of one of us (BRJ) for 43 years; John physically handed me my first sample of  $\text{RuCl}_3 \cdot 3\text{H}_2\text{O}$  in Jack Halpern's laboratory at UBC in 1960.*

**S.L. Queiroz.**<sup>2</sup> Instituto de Química de São Carlos, Universidade de São Paulo, CP 780, 13560–970, São Carlos, SP, Brazil.

**A.A. Batista and M.P. de Araujo.** Departamento de Química, Universidade Federal de São Carlos, CP 676, 13565–905, São Carlos, SP, Brazil.

**R.C. Bianchini, G. Oliva, and J. Ellena.** Instituto de Física e Química de São Carlos, Universidade de São Paulo, Av. Dr. Carlos Botelho, 1465, CP 13560–970, São Carlos, SP, Brazil.

**B.R. James.**<sup>3</sup> Chemistry Department, University of British Columbia, Vancouver, British Columbia, Canada V6T 1Z1.

<sup>1</sup>This article is part of a Special Issue dedicated to Professor John Harrod.

<sup>2</sup>Corresponding author (e-mail: [salete@iqsc.usp.br](mailto:salete@iqsc.usp.br)).

<sup>3</sup>Corresponding author (e-mail: [brj@chem.ubc.ca](mailto:brj@chem.ubc.ca)).

<sup>4</sup>K. Vrieze. Personal communication to BRJ, 1979.



bis-(2-bzpy) complexes of Zn(II) in relation to models for alcohol-dehydrogenases (3), and that on Cu(I) complexes (5), while the first structural work involving Ru species was that describing an  $\eta^2$ -*N,O*-bonded 2-pyridylketone moiety of an ONNS-bonded thiosemicarbazone of 2,6-diacetylpyridine bonded to Ru(II) (6). Very recent reports on Ru complexes have described the structures of  $[\text{Ru}(\text{PMe}_3)_2(\text{CO})(\text{COMe})(2\text{-bzpy})]\text{BPh}_4$  (7),  $[\text{Ru}(2,2'\text{-bipyridine})_2(2\text{-bzpy})][\text{PF}_6]_2$  (8), and  $\text{RuCl}_2(\text{DMSO})_2(2\text{-acpy})$ , where 2-acpy is 2-acetylpyridine (9). Complexes such as  $[\text{Ru}(\text{NH}_3)_4(\text{N-O})][\text{BF}_4]_2$ , where N-O = 2-bzpy or 2-acpy, have been isolated and characterized spectroscopically (10). Structurally characterized complexes of other platinum metals containing 2-pyridylketones have been reported, for example,  $[\text{Pd}(\eta^1, \eta^2\text{-C}_8\text{H}_{12}\text{OMe})(2\text{-bzpy})]\text{BF}_4$  (11), and several cationic chlororhodium(III) complexes containing 2-bzpy (4).

More generally, our earlier collaborative studies have developed methods for synthesizing *cis*- and *trans*- $\text{RuCl}_2(\text{dppb})\text{L}_2$  and the corresponding bis(triphenylphosphine) complexes, where L = a N-donor or  $\text{L}_2$  = a bidentate, *N,N*-donor, with a basic interest in their potential as hydrogenation catalysts (12, 13), and so extension to *N,O*-donor systems allows us also to obtain a broader data base for such complexes, as well as to comment more definitively on the nature of the  $\text{RuCl}_2(\text{PPh}_3)_2(2\text{-acetylpyridine})$  species isolated in 1978 (1).

## Experimental

### General

Synthetic procedures were performed using standard Schlenk techniques under dry Ar because solutions of the precursor complexes  $[\text{RuCl}_2(\text{dppb})]_2(\mu\text{-dppb})$  (14, 15) and  $\text{RuCl}_2(\text{PPh}_3)_3$  (16) are air-sensitive. Common chemicals used were of reagent grade quality (Aldrich). Tetrabutylammonium perchlorate (TBAP) from Fluka was recrystallized from EtOH-H<sub>2</sub>O, and dried under vacuum at 80 °C (caution!). Reagent grade solvents (Merck) were appropriately distilled, dried, and stored over Linde 4 Å molecular sieves.

IR spectra (in  $\text{cm}^{-1}$ ) were recorded as CsI pellets on a Bomen-Michelson 102 instrument, and UV-vis spectra in  $\text{CH}_2\text{Cl}_2$ , given as  $\lambda_{\text{max}}$  or sh = shoulder in nm ( $\epsilon$ , in  $\text{M}^{-1} \text{cm}^{-1}$ ), on an HP 8452A spectrophotometer. NMR spectra were recorded on a Bruker 400 MHz spectrometer (400 MHz for  $^1\text{H}$ , 100.6 MHz for  $^{13}\text{C}$ , 162 MHz for  $^{31}\text{P}$ ) at room temperature (r.t., ~20 °C) in  $\text{CH}_2\text{Cl}_2$  or  $\text{CD}_2\text{Cl}_2$ . Residual solvent proton, solvent carbon, or external  $\text{P}(\text{OMe})_3$  ( $^{31}\text{P}$ ,  $\delta$  141.00 relative to 85% aq.  $\text{H}_3\text{PO}_4$ ) were used as references. Cyclic and differential pulse voltammetries were carried out at r.t. in freshly distilled  $\text{CH}_2\text{Cl}_2$  containing 0.1 M TBAP, using a PAR model 273A potentiostat/galvanostat with an EG&G/PARC model 175 universal programmer as a sweep generator. A three-electrode system with resistance compensation was used throughout, the working and auxiliary electrodes being a stationary Pt foil and a Pt wire, respectively. The reference electrode was Ag/AgCl in a Luggin capillary in the  $\text{CH}_2\text{Cl}_2$  medium, in which ferrocene is oxidized at 0.43 V ( $\text{Fc}^+/\text{Fc}$ ); all potentials are reported with respect to the Ag/AgCl electrode. Elemental analyses were performed at the Institute of Chemistry of the University of São Paulo.

### *cis*- $\text{RuCl}_2(\text{dppb})(2\text{-bzpy})$ (*cis*-1)

*cis*-1 was prepared by stirring  $[\text{RuCl}_2(\text{dppb})]_2(\mu\text{-dppb})$  (97 mg, 0.06 mmol) and 2-bzpy (60 mg, 0.32 mmol) in  $\text{C}_6\text{H}_6$  (8 mL) at r.t. for 2 h. The resulting blue solution was reduced in volume to ~1 mL, when  $\text{Et}_2\text{O}$  was added to precipitate a blue solid that was collected, washed with hexanes and  $\text{Et}_2\text{O}$ , and dried under vacuum. Yield: 70%. UV-vis: 300 (9685), 620 (3370), 720 sh (2010). Anal. calcd. for  $\text{C}_{40}\text{H}_{37}\text{NOP}_2\text{Cl}_2\text{Ru}$ : C 62.47, H 4.87, N 1.83; found: C 62.8, H 5.1, N, 1.5. Crystals suitable for X-ray analysis were grown by evaporation of a  $\text{CH}_2\text{Cl}_2$ - $\text{Et}_2\text{O}$ -MeOH solution of the complex. *trans*-1 was generated in situ in a NMR tube in  $\text{C}_6\text{D}_6$  from a rapid reaction of  $[\text{RuCl}_2(\text{dppb})]_2(\mu\text{-dppb})$  with excess 2-bzpy (see *Results and discussion*).

### *cis*- $\text{RuCl}_2(\text{dppb})(2\text{-acpy})$ (*cis*-2)

*cis*-2 was made by refluxing  $[\text{RuCl}_2(\text{dppb})]_2(\mu\text{-dppb})$  (97 mg, 0.06 mmol) and 2-acpy (0.1 mL, 0.89 mmol) in  $\text{C}_6\text{H}_6$  (8 mL) for 48 h. The resulting purple precipitate was collected, washed with  $\text{Et}_2\text{O}$ , and dried under vacuum. Yield: 75%. UV-vis: 340 sh (2780), 557 (3175), 655 sh (1690). Anal. calcd. for  $\text{C}_{35}\text{H}_{35}\text{NOP}_2\text{Cl}_2\text{Ru}$ : C 58.41, H 4.91, N 1.95; found: C 57.9, H 4.9, N, 1.8. *trans*-2 was generated in situ as described for *trans*-1, but using excess 2-acpy (see *Results and discussion*).

### *trans*- $\text{RuCl}_2(\text{PPh}_3)_2(2\text{-acpy})$ (*trans*-3)

*trans*-3 was prepared by dissolving  $\text{RuCl}_2(\text{PPh}_3)_3$  (100 mg, 0.10 mmol) and 2-acpy (0.014 mL, 0.12 mmol) in  $\text{CH}_2\text{Cl}_2$  (5 mL) at r.t. The solution immediately changed from brown to blue, when the volume was rapidly reduced to ~1 mL; hexanes was then added to precipitate a blue solid that was collected, washed with hexanes, and dried under vacuum. Yield: 68%. UV-vis: 376 (1705), 604 (1970). Anal. calcd. for  $\text{C}_{43}\text{H}_{37}\text{NOP}_2\text{Cl}_2\text{Ru}$ : C 63.16, H 4.56, N 1.71; found: C 62.4, H 5.0, N 1.3.

### *cis*- $\text{RuCl}_2(\text{PPh}_3)_2(2\text{-acpy})$ (*cis*-3)

*cis*-3 was prepared by stirring  $\text{RuCl}_2(\text{PPh}_3)_3$  (50 mg, 0.05 mmol) and 2-acpy (0.014 mL, 0.12 mmol) in  $\text{CH}_2\text{Cl}_2$  (5 mL) for 12 h at r.t. The volume of the resulting purple solution was reduced to ~1 mL and hexanes was added to precipitate a purple solid that was collected, washed with  $\text{Et}_2\text{O}$ , and dried under vacuum. Yield: 70%. UV-vis: 346 sh (4900), 554 (5200), 680 sh (2250). Anal. calcd. for  $\text{C}_{43}\text{H}_{37}\text{NOP}_2\text{Cl}_2\text{Ru}$ : C 63.16, H 4.56, N 1.71; found: C 62.8, H 4.7, N 1.8.

### *trans*- $\text{RuCl}_2(\text{PPh}_3)_2(2\text{-bzpy})$ (*trans*-4)

*trans*-4 is formed immediately on mixing  $\text{RuCl}_2(\text{PPh}_3)_3$  (200 mg, 0.20 mmol) and 2-bzpy (57.2 mg, 0.31 mmol) in  $\text{CH}_2\text{Cl}_2$  (5 mL) at r.t. The volume of the blue solution was reduced to ~1 mL, and  $\text{Et}_2\text{O}$  was added to give a blue solid that was collected, washed with  $\text{Et}_2\text{O}$ , and dried under vacuum. Yield: 62%. UV-vis: 280 sh (2520), 670 (5025). Anal. calcd. for  $\text{C}_{48}\text{H}_{39}\text{NOP}_2\text{Cl}_2\text{Ru}$ : C 65.53, H 4.47, N 1.59; found: C 65.15, H 4.6, N 1.6.



**Table 1.**  $^{31}\text{P}\{^1\text{H}\}$  NMR, electrochemical, and IR data for complexes **1–4**.

Complex	$\delta_{\text{A}}$ and $\delta_{\text{X}}$	$^2J_{\text{AX}}$ (Hz)	$E_{1/2}$ (V)	$\nu(\text{CO})$ , $\nu(\text{Ru-Cl})$ ( $\text{cm}^{-1}$ )
$\text{RuCl}_2(\text{dppb})(2\text{-bzpy})$ ( <i>trans</i> - <b>1</b> )	51.1, 43.3	43.70		
$\text{RuCl}_2(\text{dppb})(2\text{-bzpy})$ ( <i>cis</i> - <b>1</b> )	44.7, 40.1	38.47	0.70	1591, 256 and 227
$\text{RuCl}_2(\text{dppb})(2\text{-acpy})$ ( <i>trans</i> - <b>2</b> )	50.0, 43.0	44.00		
$\text{RuCl}_2(\text{dppb})(2\text{-acpy})$ ( <i>cis</i> - <b>2</b> )	46.3, 41.1	38.55	0.68	1580, 262 and 235
$\text{RuCl}_2(\text{PPh}_3)_2(2\text{-acpy})$ ( <i>trans</i> - <b>3</b> )	48.4, 39.5	35.60	0.60	1617, 325
$\text{RuCl}_2(\text{PPh}_3)_2(2\text{-acpy})$ ( <i>cis</i> - <b>3</b> )	45.5, 40.1	33.54	0.68	1575, 250 and 224
$\text{RuCl}_2(\text{PPh}_3)_2(2\text{-bzpy})$ ( <i>trans</i> - <b>4</b> )	49.1, 39.1	35.28	0.60	1588, 329
$\text{RuCl}_2(\text{PPh}_3)_2(2\text{-bzpy})$ ( <i>cis</i> - <b>4</b> )	43.8, 39.2	34.17	0.68	1589, 314 and 281

***cis*- $\text{RuCl}_2(\text{PPh}_3)_2(2\text{-bzpy})$  (*cis*-**4**)**

*cis*-**4** was prepared as described for *trans*-**4**, but the reactant solution was left for 6 h at r.t. Yield: 65%. UV-vis: 292 (10 900), 604 (4045), 720 sh (2350). Anal. calcd. for  $\text{C}_{48}\text{H}_{39}\text{NOP}_2\text{Cl}_2\text{Ru}$ : C 65.53, H 4.47, N, 1.59; found: C 65.5, H 4.6, N 1.7.

The  $^{31}\text{P}\{^1\text{H}\}$  NMR, IR, and electrochemical data for complexes **1–4** are summarized in Table 1;  $^1\text{H}$  and  $^{13}\text{C}$  NMR data spectra were measured, and the more significant findings are presented in the *Results and discussion* text.

**X-ray crystallography of *cis*- $\text{RuCl}_2(\text{dppb})(2\text{-bzpy})$  (*cis*-**1**)**

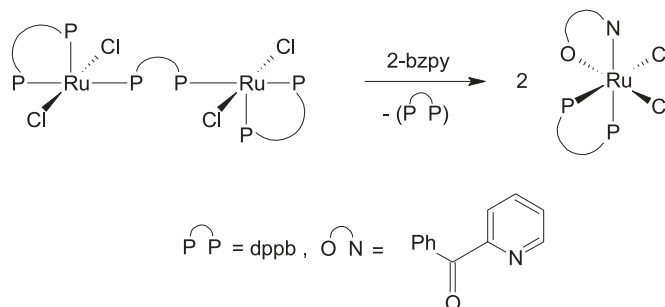
A prismatic crystal was used in the single-crystal, X-ray diffraction experiment, measurements being made on an Enraf-Nonius CAD-4 diffractometer with graphite monochromated  $\text{Mo K}\alpha$  ( $\lambda = 0.71073 \text{ \AA}$ ) radiation. Crystal and structure refinement data for *cis*-**1** are summarized in Table 2.<sup>5</sup> One standard reflection measured every 30 min was used to apply a decay correction, the maximum decay being 1%. The data collection and reduction were performed with the programs CAD-4 (17) and XCAD-4 (18), respectively.

The structure was solved by direct methods with SHELXS-86 (19), and the model refined by full-matrix least-squares on  $F^2$  by means of SHELXL-97 (20). After inclusion of the complete complex in the refinement, the difference Fourier map showed two peaks that were interpreted as a MeOH solvent. All the H atoms were stereochemically positioned and refined with the riding model (20), with the C—H bond lengths in the aromatics rings,  $\text{CH}_2$  and  $\text{CH}_3$  groups, being set equal to 0.93, 0.97, and 0.96  $\text{\AA}$ , respectively. Once the complete isotropic model was obtained, an empirical absorption correction (21) was applied (minimum and maximum transmission factors were 0.9039 and 0.8469, respectively), after which all non-H atoms were refined anisotropically. The H atoms of the aromatic rings and  $\text{CH}_2$  were set isotropic with a thermal parameter 20% greater than the equivalent isotropic displacement parameter of the C atom to which each one is bonded; this percentage was set to 50% for the H atoms of the Me group. The atomic scattering factors were taken from ref. 22.

**Results and discussion**

The  $\text{RuCl}_2(\text{dppb})(2\text{-bzpy})$  complex (**1**) is isolated from a simple, 2 h, r.t. reaction of excess 2-bzpy with  $[\text{RuCl}_2(\text{dppb})]_2(\mu\text{-dppb})$ , as outlined in eq. [1]. The structure of **1**, presented as an ORTEP in Fig. 1 (23), reveals the Ru(II) ion in a distorted octahedral environment, with cis-chlorines, one trans to a P atom of chelated dppb, and one trans to the O atom of chelated 2-bzpy, whose N atom is trans to the second P atom. The asymmetric unit consists of one molecule of *cis*-**1** and a MeOH solvent. Throughout the paper, the *cis*- and *trans*-nomenclature refers to the arrangement of chlorine ligands.

[1]



Relevant interatomic distances and angles are listed in Table 3. The Ru—Cl (avg 2.427  $\text{\AA}$ ), Ru—N (2.126  $\text{\AA}$ ), and Ru—P (avg 2.289  $\text{\AA}$ ) bond lengths observed are within the normal, well-established range for those in Ru(II) complexes (12, 13, 24). The Ru—N bond is  $\sim 0.07 \text{ \AA}$  shorter than that in  $[\text{Ru}(\text{PMe}_3)_2(\text{CO})(\text{COMe})(2\text{-bzpy})]^+$  where the N atom is trans to CO (7), but is  $\sim 0.08 \text{ \AA}$  longer than that in  $[\text{Ru}(2,2'\text{-bipyridine})_2(2\text{-bzpy})]^{2+}$  where the N atom is trans to a bipyridine-N (8); the expected trans influence (8, 25) is evident. The Ru—O bond length of 2.035(3)  $\text{\AA}$  is the shortest found in the three Ru-(2-bzpy) complexes: trans to the COMe group in the monocation, the Ru—O length is 2.226(4)  $\text{\AA}$  (7), while trans to a bipyridyl-N the value is 2.058  $\text{\AA}$  (8). Ru—N and Ru—O bond distances in *trans*- $\text{RuCl}_2(\text{DMSO})_2(2\text{-acpy})$ , where both N and O are trans to S-bonded DMSO, are 2.122(3) and 2.084(3)  $\text{\AA}$ , respectively

<sup>5</sup>Supplementary data (full crystal data and details on data collection and refinement have been deposited along with tables of atomic coordinates, anisotropic thermal parameters, all bond lengths and angles, and torsion angles) may be purchased from the Depository of Unpublished Data, Document Delivery, CISTI, National Research Council Canada, Ottawa, ON K1A 0S2, Canada ([http://www.nrc.ca/cisti/irm/unpub\\_e.shtml](http://www.nrc.ca/cisti/irm/unpub_e.shtml) for information on ordering electronically). CCDC 208536 contains the supplementary data for this paper. These data can be obtained, free of charge, via [www.ccdc.cam.ac.uk/conts/retrieving.html](http://www.ccdc.cam.ac.uk/conts/retrieving.html) (or from the Cambridge Crystallographic Data Centre, 12 Union Road, Cambridge, U.K.; fax +44 1223 336033; or deposit @ccdc.cam.ac.uk).



**Table 2.** Crystal data and structure refinement for RuCl<sub>2</sub>(dppb)(2-bzpy).

Empirical formula	C <sub>40</sub> H <sub>37</sub> Cl <sub>2</sub> NOP <sub>2</sub> Ru·CH <sub>3</sub> OH
Formula weight	813.66
Temperature (K)	293(2)
Crystal system	Triclinic
Space group	<i>P</i> $\bar{1}$
<b>Unit cell dimensions</b>	
<i>a</i> (Å)	10.917(2)
<i>b</i> (Å)	11.446(2)
<i>c</i> (Å)	15.667(3)
$\alpha$ (°)	86.06(1)
$\beta$ (°)	74.41(1)
$\gamma$ (°)	80.93(1)
Volume (Å <sup>3</sup> )	1861.3(7)
<i>Z</i>	2
Density (calculated) (Mg m <sup>-3</sup> )	1.452
Absorption coefficient (mm <sup>-1</sup> )	0.687
<i>F</i> (000)	836
Crystal size (mm <sup>3</sup> )	0.25 × 0.19 × 0.15
$\theta$ range for data collection (°)	1 ≤ $\theta$ ≤ 25
Index ranges	−12 ≤ <i>h</i> ≤ 12, −12 ≤ <i>k</i> ≤ 12, 0 ≤ <i>l</i> ≤ 17
Decay of standard	±1
Reflections collected	6237
Independent/observed reflections	6237 ( <i>R</i> (int) = 0.00)/4424 ( <i>I</i> > 2σ( <i>I</i> ))
Completeness to $\theta$ = 25° (%)	95.4
Data/parameters	6237/444
Goodness-of-fit on <i>F</i> <sup>2</sup>	1.041
SHELXL-97 weight parameters	0.0750, 0.0
Final <i>R</i> indices ( <i>I</i> > 2σ( <i>I</i> ))	<i>R</i> 1 = 0.0453, <i>wR</i> 2 = 0.1199
<i>R</i> indices (all data)	<i>R</i> 1 = 0.0770, <i>wR</i> 2 = 0.1317
Extinction coefficient	0.0002(6)
Largest diff. peak and hole <sup>a</sup> (e Å <sup>-3</sup> )	0.915 and −1.040

<sup>a</sup>At ~1 Å from the Ru atom.

(9). The Ru—O bond in *cis*-**1** is also shorter than that found for the acetylpyridine moiety of an ONNS-bonded thiosemicarbazone at Ru(II) (2.232 Å) (6) and for the coordinated acetone of RuCl<sub>2</sub>(CO)(PPh<sub>3</sub>)<sub>2</sub>(acetone), 2.194 Å (26); the small value is readily rationalized in that in *cis*-**1**, the coordinated ketone moiety is trans to chloride, a  $\pi$ -donor, while in the other systems the ketone group is trans to PPh<sub>3</sub> (26) and an imine N atom (6), both  $\pi$ -acceptors. The bite angle of the benzoylpyridine ligand in *cis*-**1** (76.7(1)°) is close to those found, for example, in the other Ru-(2-bzpy) (7, 8) and Ru-(2-acpy) (9) complexes; the essential planarity of the five-membered chelate ring, with an approximate 45° twist of the benzoyl-phenyl from the planarity, is similar to those noted for the other two 2-bzpy complexes (7, 8). The structure of the “*cis*-RuCl<sub>2</sub>(dppb)” component of *cis*-**1** is very similar to that in *cis*-RuCl<sub>2</sub>(dppb)(N-N) complexes, where N-N = 2,2'-bipyridine or 1,10-phenanthroline (12).

Table 1 lists some spectroscopic and electrochemical data for *cis*-**1** and the other 2-pyridylketone complexes studied in this work. The solution NMR data imply the solid state structure is maintained in solution: the <sup>31</sup>P{<sup>1</sup>H} NMR AX pattern does not itself distinguish between *cis*-**1** and *trans*-**1** (see below), but two strong  $\nu$ (Ru—Cl) bands in the IR spectrum are consistent with *cis*-geometry. We have recently established for Ru(II)-dppb species (with 18 data points) an

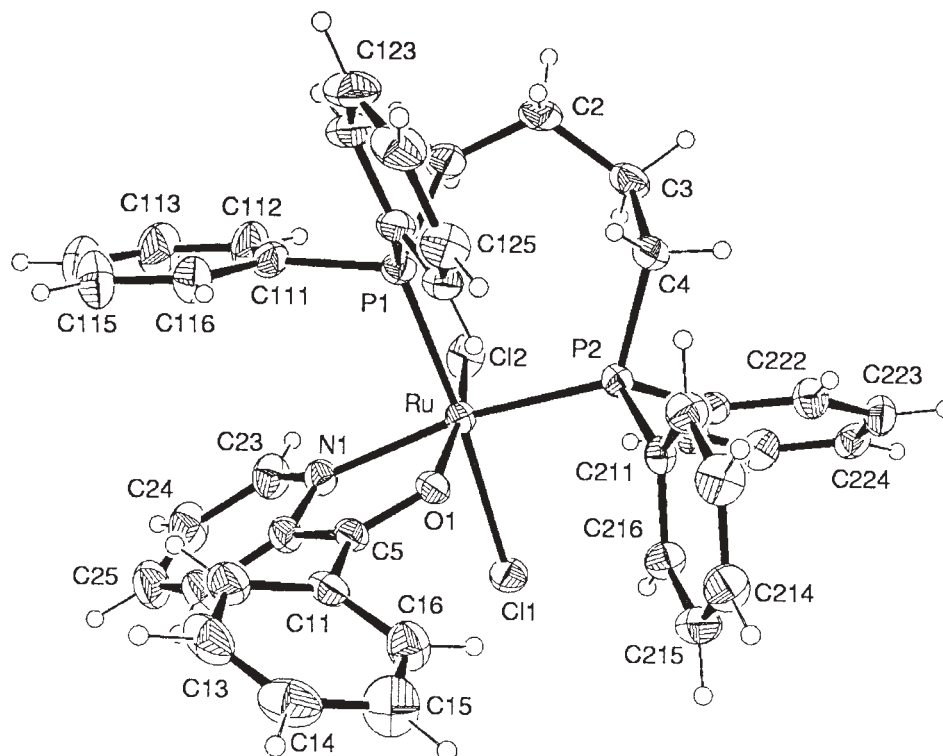
inverse dependence of the <sup>31</sup>P shifts on Ru—P bond length (12); the data for *cis*-**1** fit well with this correlation and imply that the  $\delta$  values of 44.7 and 40.1 refer to P(1) and P(2), respectively. <sup>1</sup>H NMR data confirm the presence of one bzpy ligand per dppb, while the coordination shift of the H<sup>N</sup> atom adjacent to the N atom ( $\delta$  8.68 → 9.03) and that of  $\nu$ (C=O) (1668 → 1591 cm<sup>-1</sup>) again show both *O*- and *N*-coordination of bzpy. The lower  $\nu$ (C=O) value in the Ru(II) species vs. values for the Zn(II) complexes (~1620 cm<sup>-1</sup>) (3) is consistent with the presence of significant Ru → carbonyl  $\pi$ -backbonding (27). A coordination shift of the <sup>13</sup>C resonance of the C=O group ( $\delta$  193.8 → 206.1) is also evident.

The blue colour of *cis*-**1** is manifested in an absorption maximum at 620 nm with a shoulder at 720 nm, while the CV reveals a reversible redox process (*i*<sub>pa</sub>/*i*<sub>pc</sub> ≅ 1) with *E*<sub>1/2</sub> = 0.70 V, the process being confirmed by differential pulse voltammetry. The Ru<sup>III</sup>/Ru<sup>II</sup> couple is ~10 mV more positive than for the structurally similar *cis*-RuCl<sub>2</sub>(dppb)(bipy) (12), showing relative stabilization of the lower valence state by substitution of a 2-pyridyl by a benzoyl moiety.

Synthesis of the 2-acetylpyridine (2-acpy) analogue (*cis*-**2**) is as for *cis*-**1**, but requires the use of reflux conditions. The NMR and IR spectroscopic data and CV data (Table 1) are very similar to those of *cis*-**1**, and the structure is assumed to be the same (type **II** as in Fig. 1, see below and



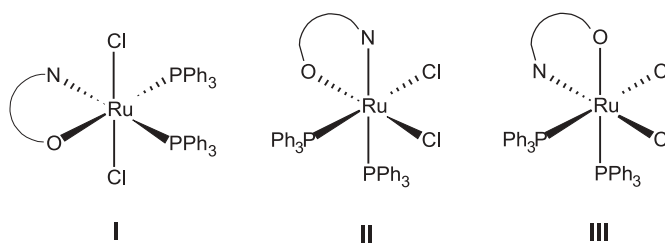
**Fig. 1.** ORTEP view of *cis*-RuCl<sub>2</sub>(dppb)(2-bzpy) (**1**), showing the atom labeling, with 30% probability ellipsoids.



also rxn. [1]). The Me resonance of the coordinated acetyl group is seen at  $\delta$  2.10 (upfield shifted from that of the free ligand at  $\delta$  2.71), while there is again a downfield shift ( $\delta$  8.68  $\rightarrow$  8.85) for  $H^N$ . In contrast with *cis*-**1**, *cis*-**2** is purple and the solution spectrum shows an absorption maximum at 557 nm.

As described in the *Experimental* section, two complexes with the formulation RuCl<sub>2</sub>(PPh<sub>3</sub>)<sub>2</sub>(2-acpy) (**3**) were isolated from the same reaction precursor RuCl<sub>2</sub>(PPh<sub>3</sub>)<sub>3</sub> but using different timescales. A blue solid is obtained after a few minutes, while a 12 h reaction time generates a purple solid, and the complexes have different spectroscopic properties. Three structural formulations are possible for the bis(triphenylphosphine) species: **I** (with trans chlorines), and **II** and **III** (with cis chlorines). The more stable, purple complex has <sup>31</sup>P NMR, IR, and CV data (Table 1) close to those found for *cis*-**1** and *cis*-**2**, and is thus assigned the *cis*-dichloro geometry **II** (cf. rxn. [1]). The <sup>1</sup>H NMR data (as for *cis*-**2**) show an upfield shift for the Me ( $\delta$  2.71  $\rightarrow$  2.41) and a downfield shift for  $H^N$  ( $\delta$  8.68  $\rightarrow$  9.51). The <sup>31</sup>P NMR data of a solution of the blue complex show about a 9 ppm difference between the  $\delta_A$  and  $\delta_X$  values vs.  $\sim$ 5 ppm for the *cis*-complexes, and the  $\nu(\text{Ru-Cl})$  region shows a single, sharp band at 325 cm<sup>-1</sup>, findings that imply that the blue species is *trans*-**3**. Of note, the <sup>1</sup>H NMR shift for the Me is now slightly downfield ( $\delta$  2.71  $\rightarrow$  2.79), while that for  $H^N$  is now slightly upfield ( $\delta$  8.68  $\rightarrow$  8.60). These shifts are the reverse of those seen for the *cis*-complexes, and presumably reflect that the acetyl is now *trans* to the  $\pi$ -acceptor PPh<sub>3</sub> (structure **I**) vs. the  $\pi$ -donor chloride ligand (structure **II**). Further, the  $E_{1/2}$  value of *trans*-**3** is 8–10 mV lower than those of the *cis*-species, again consistent with the *trans* formulation, as a

*trans*-dichloro species of this type invariably has a lower reduction potential than that of a corresponding *cis*-formulation (12, 28, 29). Of note, a solution of the blue *trans*-**3** isomerizes over time to the purple *cis*-species, a process that can be readily monitored by CV (30) (cf. Fig. 2,  $t_{1/2} \sim$  30 min at r.t.), <sup>31</sup>P or <sup>1</sup>H NMR, or by UV-vis spectroscopy. *trans*-**3** shows UV-vis absorption maxima at 376 and 604 nm, while *cis*-**3** has a maximum at 554 and a shoulder at  $\sim$ 680 nm.



*cis*- and *trans*-RuCl<sub>2</sub>(PPh<sub>3</sub>)<sub>2</sub>(2-bzpy) (**4**) are made similarly to the 2-acpy analogues (**3**), the initially formed kinetic product being the blue, *trans*-isomer, this then transforming to an isolable, purple *cis*-isomer (Table 1). Whether *cis*-**4** has geometry **II** or **III** is unclear; the <sup>31</sup>P NMR data are close to those of the other *cis* species (of structure **II**), but the  $\nu(\text{Ru-Cl})$  IR data are significantly different and may indicate structure **III**.

*cis*-RuCl<sub>2</sub>(dppb)<sub>2</sub>(2-bzpy) (*cis*-**1**) was isolated after a 2 h reaction time at r.t. (see above), but initially when the reactants are mixed, the *trans*-isomer is detected by in situ <sup>31</sup>P NMR (see Fig. 3 and Table 1). Corresponding behaviour is seen for the isolated *cis*- and in situ formed *trans*-



**Fig. 2.** Differential pulse voltammogram of *cis*- and *trans*- $\text{RuCl}_2(\text{PPh}_3)_2(2\text{-acpy})$  (**3**).

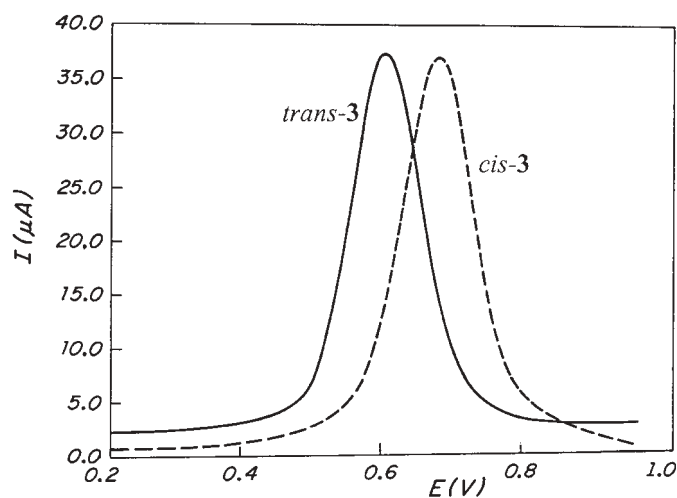
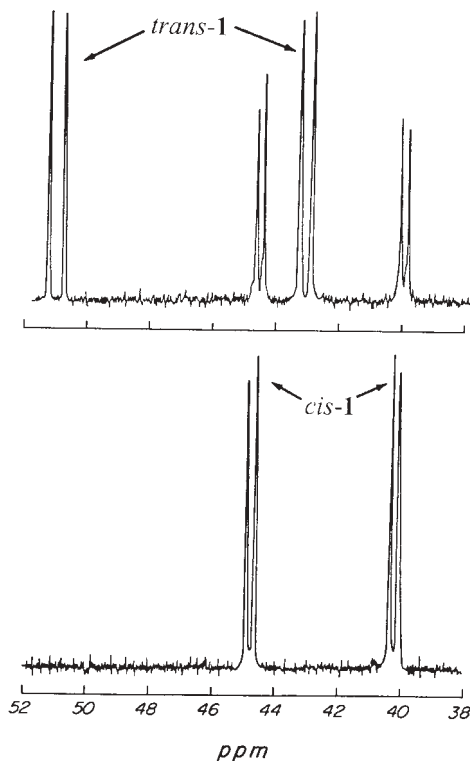


**Fig. 3.**  $^{31}\text{P}\{^1\text{H}\}$  NMR in  $\text{C}_6\text{H}_6$  of a mixture of *cis*- and *trans*- $\text{RuCl}_2(\text{dppb})(2\text{-bzpy})$  (**1**): top, “immediately” after mixing  $[\text{RuCl}_2(\text{dppb})]_2(\mu\text{-dppb})$  and 2-benzoylpyridine; bottom, after 25 min when just *cis*-**1** is seen.



$\text{RuCl}_2(\text{dppb})_2(2\text{-acpy})$  (**2**) species (Table 1). The *trans*  $\rightarrow$  *cis* isomerization process is faster for all the systems in the presence of sunlight; details of possible isomerization mechanisms (31) for these chelated six-coordinate complexes remain to be elucidated.

Reevaluation of the 1978 data for the reported  $\text{RuCl}_2(\text{PPh}_3)_2(2\text{-acpy})$  complex **3** in this current paper (see *Introduction*) can now be made. The previously reported r.t.

**Table 3.** Selected bond lengths ( $\text{\AA}$ ) and angles ( $^\circ$ ) for  $\text{RuCl}_2(\text{dppb})(2\text{-bzpy})$ , esds in parentheses.

Bond lengths ( $\text{\AA}$ )			
Ru—O(1)	2.035(3)		
Ru—N(1)	2.126(4)		
Ru—P(1)	2.286(1)		
Ru—P(2)	2.292(1)		
Ru—Cl(2)	2.397(1)		
Ru—Cl(1)	2.458(1)		
O(1)—C(5)	1.251(5)		
N(1)—C(23)	1.327(6)		
N(1)—C(21)	1.370(6)		
Bond angles ( $^\circ$ )			
O(1)—Ru—N(1)	76.7(1)	C(121)—P(1)—Ru	119.8(2)
O(1)—Ru—P(1)	95.19(9)	C(111)—P(1)—Ru	110.4(2)
N(1)—Ru—P(1)	92.4(1)	C(1)—P(1)—Ru	119.1(2)
O(1)—Ru—P(2)	91.99(9)	C(221)—P(2)—C(211)	100.7(2)
N(1)—Ru—P(2)	167.3(1)	C(221)—P(2)—C(4)	100.1(2)
P(1)—Ru—P(2)	94.47(5)	C(211)—P(2)—C(4)	102.7(2)
O(1)—Ru—Cl(2)	170.15(9)	C(221)—P(2)—Ru	120.7(1)
N(1)—Ru—Cl(2)	93.6(1)	C(211)—P(2)—Ru	110.3(1)
P(1)—Ru—Cl(2)	86.66(5)	C(4)—P(2)—Ru	119.5(2)
P(2)—Ru—Cl(2)	97.52(5)	C(5)—O(1)—Ru	119.0(3)
O(1)—Ru—Cl(1)	87.15(9)	C(23)—N(1)—C(21)	117.2(4)
N(1)—Ru—Cl(1)	82.4(1)	C(23)—N(1)—Ru	128.5(4)
P(1)—Ru—Cl(1)	173.64(4)	C(21)—N(1)—Ru	113.9(3)
P(2)—Ru—Cl(1)	91.35(4)	O(1)—C(5)—C(21)	117.6(4)
Cl(2)—Ru—Cl(1)	90.04(5)	O(1)—C(5)—C(11)	118.1(4)
C(121)—P(1)—C(111)	102.5(2)	N(1)—C(21)—C(26)	122.1(5)
C(121)—P(1)—C(1)	102.6(2)	N(1)—C(21)—C(5)	112.6(4)
C(111)—P(1)—C(1)	99.4(2)	N(1)—C(23)—C(24)	121.8(6)

$^{31}\text{P}\{^1\text{H}\}$  NMR ( $\delta_{\text{A}}$  43.6,  $\delta_{\text{X}}$  38.8;  $J = 35$  Hz) and  $^1\text{H}$  NMR data ( $\delta_{\text{Me}}$  2.40;  $\delta_{\text{H}}$  9.54, H adjacent to N) in  $\text{CDCl}_3$ , and the purple colour (**1**), are all consistent with a *cis*-**3** formulation (see Table 1). The only contrary evidence is the reported single  $\nu(\text{Ru}-\text{Cl})$  value of  $325\text{ cm}^{-1}$  (**1**) that pertains to *trans*-**3**. It is evident that the spontaneous *trans*/*cis* isomerization process was not recognized in the early work, and the data reported in this current paper, especially with the X-ray analysis for *cis*-**1**, characterize more completely the nature of these Ru(II) 2-pyridylketone complexes.

## Acknowledgements

We thank Conselho Nacional de Desenvolvimento científico e Tecnológico (CNPq), Coordenação de Aperfeiçoamento de Pessoal de Nível Superior (CAPES), Financiadora de Estudos e Projetos (FINEP), and Fundação de Amparo à Pesquisa do Estado de São Paulo (FAPESP) in Brazil, and the Natural Sciences and Engineering Research Council of Canada (NSERC) for financial support. JE thanks FAPESP for a postdoctoral fellowship.

## References

1. B.R. James, L.K. Thompson, and D.K.W. Wang. *Inorg. Chim. Acta Lett.* **29**, L237 (1978).



2. R.C.J. Vriends, G. Van Koten, and K. Vrieze. *Inorg. Chim. Acta Lett.* **26**, L29 (1978).
3. C. Sudbrake and H. Vahrenkamp. *Inorg. Chim. Acta*, **318**, 23 (2001).
4. D.J. de Geest and P.J. Steel. *Aust. J. Chem.* **48**, 1573 (1995), and refs. therein.
5. M.A.S. Goher, R.J. Wang, and T.C.W. Mak. *J. Coord. Chem.* **38**, 151 (1996).
6. M. Maji, S. Ghosh, S.K. Chattopadhyay, and T.C.W. Mak. *Inorg. Chem.* **36**, 2938 (1997).
7. G. Bellachioma, G. Cardaci, V. Gramlich, A. Macchioni, M. Valentini, and C. Zuccaccia. *Organometallics*, **17**, 5025 (1998).
8. D.L. Reger, J.R. Gardinier, M.D. Smith, and P.J. Pellechia. *Inorg. Chem.* **42**, 482 (2003).
9. S. Pal and S. Pal. *Acta Crystallogr.* **C58**, 2731 (2002).
10. A.S.A.T. de Paula, B.E. Mann, and E. Tfouni. *Polyhedron*, **18**, 2017 (1999).
11. A. Macchioni, C. Zuccaccia, B. Binotti, C. Carfagna, E. Foresti, and P. Sabatino. *Inorg. Chem. Commun.* **5**, 319 (2002).
12. S.L. Queiroz, A.A. Batista, G. Oliva, M.T. do P. Gambardella, R.H.A. Santos, K.S. MacFarlane, S.J. Rettig, and B.R. James. *Inorg. Chim. Acta*, **267**, 209 (1998).
13. A.A. Batista, E.A. Polato, S.L. Queiroz, O.R. Nascimento, B.R. James, and S.J. Rettig. *Inorg. Chim. Acta*, **230**, 111 (1995).
14. B.R. James, R.S. McMillan, R.H. Morris, and D.K.W. Wang. *Adv. Chem. Ser.* **167**, 127 (1978).
15. M. Bressan and P. Rigo. *Inorg. Chem.* **14**, 2286 (1975).
16. P.S. Hallman, T.A. Stephenson, and G. Wilkinson. *Inorg. Synth.* **12**, 237 (1970).
17. CAD-4-PC, Version 1.2 [computer program]. Enraf-Nonius, Delft, The Netherlands. 1993.
18. K. Harms and S. Wocadlo. XCAD-4 [computer program]. University of Marburg, Marburg, Germany. 1995.
19. G.M. Sheldrick. SHELXS-86 [computer program]. University of Göttingen, Göttingen, Germany. 1985.
20. G.M. Sheldrick. SHELXL-97 [computer program]. University of Göttingen, Göttingen, Germany. 1997.
21. N. Walker and D. Stuart. *Acta. Crystallogr.* **A39**, 158 (1983).
22. A.J.C. Wilson (*Editor*). *International tables for crystallography*. Vol. C. Kluwer Academic Publishers, Dordrecht, The Netherlands. 1995.
23. L. Zsolnai and H. Pritskow. ZORTEP [computer program]. University of Heidelberg, Heidelberg, Germany. 1996.
24. A.M. Joshi, I.S. Thorburn, S.J. Rettig, and B.R. James. *Inorg. Chim. Acta*, **198–200**, 283 (1992).
25. T.G. Appleton, H.C. Clark, and L.E. Manzer. *Coord. Chem. Rev.* **10**, 335 (1973).
26. R.O. Gould, W.J. Sime, and T.A. Stephenson. *J. Chem. Soc., Dalton Trans.* 76 (1978).
27. F.A. Cotton and G. Wilkinson. *Advanced inorganic chemistry*. 5th ed. Wiley-Interscience, Toronto. 1988. p. 888.
28. A.B.P. Lever. *Inorg. Chem.* **29**, 1271 (1990).
29. H.G.L. Siebold, P.-L. Fabre, M. Dartiguenave, Y. Dartiguenave, M. Simard, and A.L. Beauchamp. *Polyhedron*, **15**, 4221 (1996).
30. S.L. Queiroz, M.P. de P. Araujo, A.A. Batista, K.S. MacFarlane, and B.R. James. *J. Chem. Ed.* **78**, 89 (2001).
31. J.E. Huheey, E.A. Keiter, and R.L. Keiter. *Inorganic chemistry; principles of structure and reactivity*. 4th ed. Harper Collins, New York. 1993. p. 555.



# Synthesis and molecular structures of platinum(II) and platinum(IV) diimine complexes possessing fluoroalkyl ligands<sup>1</sup>

Russell P. Hughes, Antony J. Ward, Arnold L. Rheingold, and Lev N. Zakharov

**Abstract:** A range of Pt-diimine complexes possessing fluoroalkyl and hydrofluoroalkyl ligands were synthesized from the readily prepared [Pt(diimine)Me<sub>2</sub>] complexes and the appropriate iodoalkane. For complexes with diimine ligands containing substituents in the 2,6-positions of the aryl group, Pt(II) complexes were obtained due to in situ reductive elimination of MeI, while for complexes with diimine ligands of smaller steric demands (possessing substituents in the 3,5-positions or the 4-position), Pt(IV) complexes were obtained. Attempts to convert the Pt(IV) complexes to the desired Pt(II) species via reductive elimination of MeI, methane, or ethane resulted in either no reaction or degradation of the starting complex. Fluoroalkyl(methyl)platinum(II) complexes were then converted to the fluoroalkyliodoplatinum(II) complexes via addition of I<sub>2</sub> or by reaction with aq HI. Several complexes have been characterized crystallographically.

*Key words:* fluoroalkyl, organometallic synthesis, structure, platinum.

**Résumé :** Utilisant comme produit de départ des iodoalkanes appropriés et des complexes [Pt(diimine)Me<sub>2</sub>] qui peuvent facilement être préparés, on a préparé un éventail de complexes Pt-diimine portant des ligands fluoroalkyles et hydrofluoroalkyles. Pour les complexes avec des ligands diimines portant des substituants dans les positions 2,6 du groupe aryle, on a obtenu des complexes de Pt(II) en raison d'une élimination réductrice in situ de MeI alors qu'on a obtenu des complexes de Pt(IV) avec pour les complexes avec des ligands diimines dont les demandes stériques sont plus faibles (qui portent des substituants dans les positions 4 ou 3,5). Des essais en vue de transformer les complexes de Pt(IV) en espèces Pt(II) désirées par le biais d'une élimination réductrice de MeI, de méthane ou d'éthane n'ont pas donné de réaction ou une dégradation du complexe de départ. Les complexes fluoroalkyl(méthyl)platine(II) ont ensuite été transformés en complexes fluoroalkyliodoplatine(II) par le biais d'une addition de I<sub>2</sub> ou par une réaction avec du HI aqueux. Plusieurs complexes ont été cristallisés par diffraction des rayons X.

*Mots clés :* fluoroalkyle, organométallique, synthèse, structure, platine.

[Traduit par la Rédaction]

## Introduction

Much recent work within our research group has focussed upon the synthesis of late transition metal–fluoroalkyl complexes, particularly those of metals from groups 9 (1–9) and 10 (10–12), utilizing oxidative addition of iodoalkanes (11). While many such complexes have been synthesized previously using oxidative addition reactions (13–18), we have shown that such a route can often lead to fluoro-

alkylation at ligand sites rather than at the metal center in both early and late transition metals (19–22).

There have been many studies of oxidative addition of alkyl halides to square-planar Pt(II) precursors (23–27). In the majority of cases, the reaction of bromo- and iodoalkanes with dimethylplatinum(II) complexes occurs via a polar S<sub>N</sub>2 mechanism to give a Pt(IV) complex with kinetically controlled trans stereochemistry (23), although subsequent isomerization has been shown in some cases to afford the cis product (28). On occasion, cationic five-coordinate intermediates have been detected spectroscopically (29). These five-coordinate species in the oxidative addition reaction have also been shown to serve as key intermediates for reductive elimination of methyl iodide or ethane from Pt(IV) (30–32).

The oxidative addition reactions of iodoalkanes to transition metals is unlikely to proceed via polar S<sub>N</sub>2 attack by the metal at carbon due to the unfavourable polarity of the C<sup>δ-</sup>–I<sup>δ+</sup> bond (33, 34). In previous systems involving reactions of primary iodoalkanes, we have postulated that the reactions proceeded via electron transfer to the iodoalkane, followed by rapid loss of iodide from the

Received 5 March 2003. Published on the NRC Research Press Web site at <http://canjchem.nrc.ca> on 20 October 2003.

**R.P. Hughes<sup>2</sup> and A.J. Ward.** Departments of Chemistry, 6128 Burke Laboratory, Dartmouth College, Hanover, NH 03755, U.S.A.

**A.L. Rheingold and L.N. Zakharov.** Department of Chemistry and Biochemistry, University of California, San Diego, 9500 Gilman Drive, La Jolla, CA 92093-0358, U.S.A.

<sup>1</sup>This article is part of a Special Issue dedicated to Professor John Harrod.

<sup>2</sup>Corresponding author (e-mail: [rph@dartmouth.edu](mailto:rph@dartmouth.edu)).



resultant radical anion, and very fast trapping of the fluoroalkyl radical at the metal (21, 22).

While most studies of oxidative addition – reductive elimination to Pt(II) centers have involved complexes bearing monodentate or bidentate phosphorus ligands, complexes with chelating nitrogen ligands have also been examined (23). *cis*-Dialkyl- and -diarylplatinum(II) complexes with nitrogen donor ligands usually react with alkyl halides to afford the *trans* oxidative addition product (35–38). The corresponding *cis*-isomer can be formed either by a competitive *cis* oxidative addition pathway, or by *trans* oxidative addition with subsequent isomerization of the platinum(IV) product to a thermodynamically more stable *cis*-isomer (23). Dimethylplatinum(II) complexes possessing pyridine (35), 2,2'-bipyridine (39), 1,10-phenanthroline (39, 40), bis(*p*-tolylimino)acenaphthene (41), bis(phenylimino)camphane (41), various diimine ligands (42, 43), and tetramethylethylenediamine (tmeda) (44, 45) have been studied.

We have previously reported on the reactions of [Pt(tmeda)Me<sub>2</sub>] with fluoroalkyl iodides to give Pt(IV) and Pt(II) fluoroalkyl complexes (11). Here we report on the corresponding reactions of dimethylplatinum(II) complexes bearing diimine ligands.

## Results and discussion

### Synthesis

In contrast to the very facile oxidative addition reactions of [Pt(tmeda)Me<sub>2</sub>] with fluoroalkyl iodides (11), the corresponding reactions of the [Pt(diimine)Me<sub>2</sub>] complexes **1** and **2** required heating at reflux in ethyl acetate to afford the fluoroalkyl Pt(IV)–diimine complexes **3–6** (Scheme 1). To reduce the possibility of light-induced radical chemistry of the fluoroalkyl iodides, the reactions were performed in the dark, although no attempts were made to evaluate whether light actually does cause problems in these cases. When [Pt(diimine)Me<sub>2</sub>] complexes **7** and **8** were used, which possess a diimine ligand containing a 2,6-dimethylaryl fragment, the products formed were always the Pt(II) complexes **9–12** (Scheme 2). This can be ascribed to steric congestion around the Pt(IV) centre (initially formed by oxidative addition of the R<sub>f</sub>I to the [Pt(diimine)Me<sub>2</sub>] complex), resulting in *in situ* reductive elimination of MeI to form the square planar Pt(II) complex.

Owing to the solubility of **7** in hexane, the desired perfluoroalkyl complexes could also be obtained by heating at reflux in hexane for 8 h. The use of hexane, however, only resulted in better yields when the perfluoroalkyl group was C<sub>3</sub>F<sub>7</sub>. Hexane also afforded straightforward isolation of the Pt(II) complexes, which are insoluble in hexane. Unfortunately, the lack of hexane solubility for dimethyl complexes possessing other diimine ligands (**1**, **2**, and **8**) precluded its use as a general solvent for the synthesis of these complexes.

Before ethyl acetate was found to facilitate these oxidative addition reactions of [Pt(diimine)Me<sub>2</sub>] complexes with iodoalkanes, attempts were made to use benzene as a solvent. However, when benzene was used, the reaction was incomplete after heating at reflux for 24 h, and there was formation of elemental Pt. NMR of the crude reaction mixtures showed approximately 30%–40% conversion to the desired products after 24 h. However, isolation of the oxidative

addition products proved unsuccessful due to the very similar solubilities exhibited by the starting materials, free diimine ligand, and the oxidative addition products. The subsequent choice of ethyl acetate was based solely upon its slightly lower boiling point as compared to benzene, as previous experience within our research group has shown that certain oxidative addition reactions can be very temperature dependent (46). It may also have proven to be a fortuitous choice for a reaction that may proceed via a fluoroalkyl radical, since electrostatic repulsion of the oxygen atoms of the ethyl acetate has been shown to significantly inhibit hydrogen atom abstraction by fluoroalkyl radicals when compared with rates of abstraction from alkanes (47), thereby perhaps increasing the yield of organometallic product.

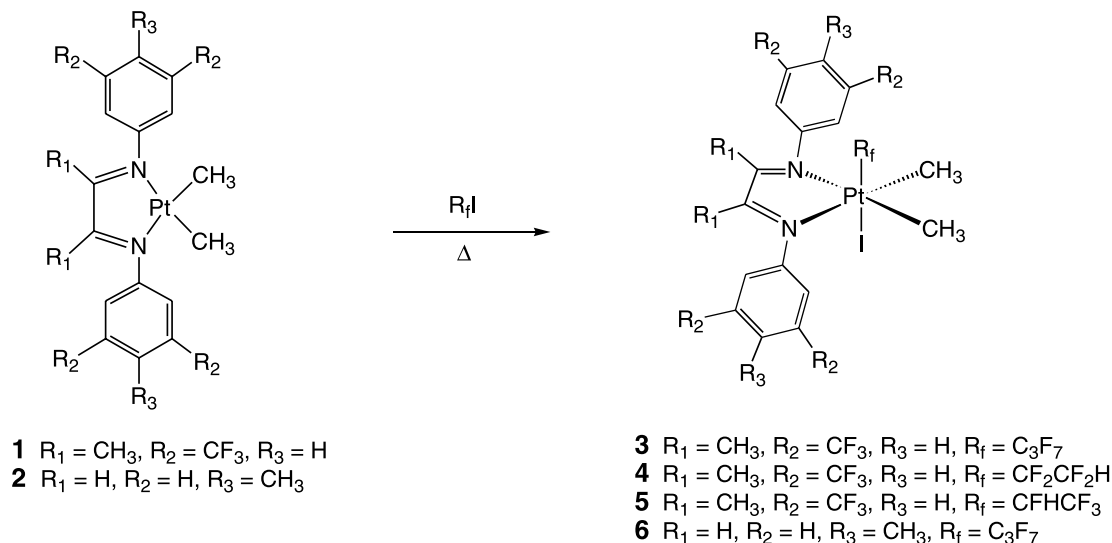
The Pt(IV) species obtained were invariably those in which the perfluoroalkyl moiety was mutually *trans* to the iodo ligand, giving rise to complexes with C<sub>s</sub> symmetry, as shown for complexes **3**, **4**, and **6**. The <sup>19</sup>F NMR spectrum of **3** reveals two resonances for the *m*-CF<sub>3</sub> groups of the diimine ligand indicating that there is no free rotation about the *N*-aryl bonds on the NMR timescale. However, the <sup>19</sup>F NMR spectrum of **4** reveals only one resonance for the *m*-CF<sub>3</sub> groups of the diimine ligand indicating apparently free rotation of the aryl moiety, or an accidental equivalence of CF<sub>3</sub> resonances. In the case of **5**, the presence of a stereocenter at the α-C of the fluoroalkyl group results in a complex with C<sub>1</sub> symmetry. This is highlighted clearly in the <sup>1</sup>H NMR spectrum of this complex in which the Pt-bound methyl groups, the CH<sub>3</sub> groups of the diimine backbone, and the *m*-CF<sub>3</sub> substituents of the aryl rings display nonequivalence (two of which are coincident), indicating that rotation of the aryl rings is slow on the NMR timescale.

Attempts to convert the Pt(IV) complexes to Pt(II) species with procedures that we have used successfully for such reductions in cases when the ligands involved are tmeda, 1,2-bis(diphenylphosphino)ethane, or 1,2-bis(dimethylphosphino)ethane proved unsuccessful. The methods attempted to achieve this reduction included: (i) removal of iodide using AgBF<sub>4</sub> and heating at reflux in acetone to eliminate ethane, followed by addition of NaI to form the iodoplatinum(II) complex (32); (ii) heating a solution of the complex in the presence of NEt<sub>3</sub>, to form the insoluble [Et<sub>3</sub>NMe]I complex upon thermal elimination of MeI (11); and (iii) reaction of the complex with NaBH<sub>4</sub> (to convert the iodo ligand to a hydride) and then stirring at room temperature to allow the complex to thermally eliminate methane. In the first case, the starting complexes were obtained without any observable isomerization, while degradation of the Pt(IV) complex to elemental platinum occurred in the last two methods.

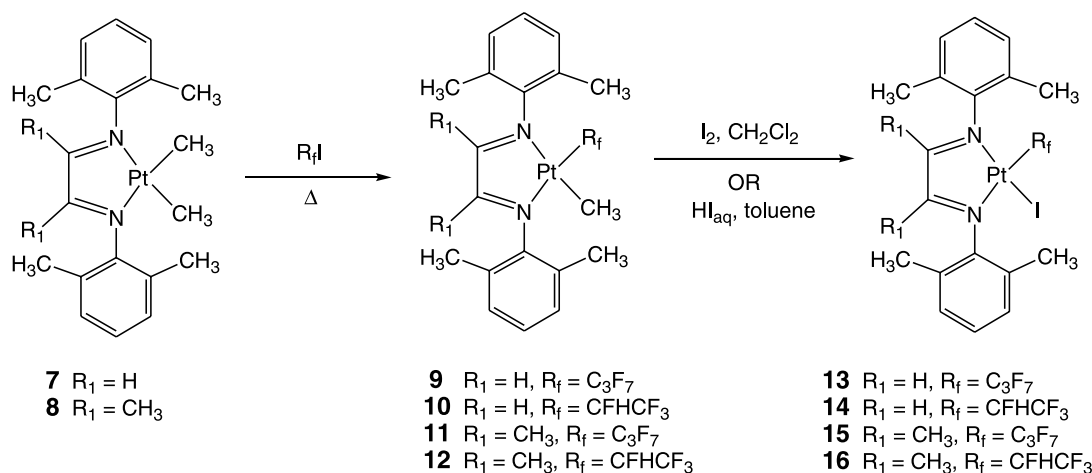
As discussed above, the only instances in which Pt(II) complexes were obtained were from reactions in which the diimine ligand possessed the 2,6-dimethylaryl substituent. The NMR spectra of these complexes are very diagnostic as the backbone protons (or methyl groups) of the diimine ligand are inequivalent due to the C<sub>s</sub> symmetry of the square-planar complexes. In the <sup>1</sup>H NMR spectrum, the diimine backbone protons of complexes **9** and **10** exhibit Pt satellites: in the case of **9**, these <sup>3</sup>J<sub>PtH</sub> coupling constants were 36 Hz (δ 9.01 ppm) and 84 Hz (δ 8.93 ppm), while for **10** the coupling constants were 37 Hz (δ 9.20 ppm) and 42 Hz (δ 9.06 ppm), respectively. A similar coupling was



Scheme 1.



Scheme 2.



previously seen in numerous unsymmetrical platinum diimine complexes (42, 48–54). Tilset (49) assigned the protons on the diimine backbone using a variety of NMR techniques, with the smaller coupling being ascribed to those protons transoid to the methyl ligand. Thus, some indication as to the relative trans-influence of the two different fluoroalkyl ligands in these complexes can be obtained: the partially fluorinated ligand ( $\text{CFHCF}_3$ ) exerts a stronger trans influence than the perfluorinated ligand ( $\text{C}_3\text{F}_7$ ). The complexes possessing methyl substitution of the diimine backbone (complexes **11** and **12**) do not exhibit any coupling to Pt.

The  $[\text{Pt}(\text{diimine})(\text{R}_f)\text{Me}]$  complexes **9–12** are readily converted to the iodo complexes **13–16** via two methods, each of which results in selective cleavage of the  $\text{Pt}-\text{CH}_3$  bond rather than the  $\text{Pt}-\text{fluoroalkyl}$  bond. The first involves the reaction of the complex with  $\text{I}_2$  in  $\text{CH}_2\text{Cl}_2$ , possibly resulting in the formation of a transient diiodo- $\text{Pt}(\text{IV})$  complex, which undergoes thermal reductive elimination of  $\text{MeI}$ . The second pathway involves reaction of the methyl complex with 1 equiv. of aq  $\text{HI}$  in toluene (Scheme 2), resulting in the gen-

eration of methane followed by trapping of the resulting cationic  $\text{Pt}(\text{II})$  fragment with iodide. Both methods afford the iodo complexes in 70%–80% yield after recrystallization from dichloromethane–hexane.

The NMR spectra of the iodo complexes are very similar to those of the methyl analogues. As was the case for the methyl complexes, the backbone protons of the diimine ligand in complexes **13** and **14** display platinum coupling: for **13**,  $^3J_{\text{PtH}} = 102 \text{ Hz}$  ( $\delta$  9.00 ppm) and 40 Hz ( $\delta$  8.62 ppm), while for **14**,  $^3J_{\text{PtH}} = 100 \text{ Hz}$  ( $\delta$  9.16 ppm) and 38 Hz ( $\delta$  8.68 ppm). Presumably, the large difference in the coupling constants for both complexes may be explained by the large cis-effect exerted by the iodo ligand. As was the case in the methyl complexes, no platinum satellites were observed for those complexes possessing methyl substitution on the backbone of the diimine ligand.

### Crystal structures

X-ray diffraction quality crystals were obtained for several of the  $\text{Pt}(\text{IV})$  complexes by slow recrystallization from  $\text{CH}_2\text{Cl}_2$ –hexane. Crystal structures were obtained for com-



**Fig. 1.** ORTEP diagram of the non-hydrogen atoms of **3**, showing the atom labelling scheme. Thermal ellipsoids are shown at 30% probability.

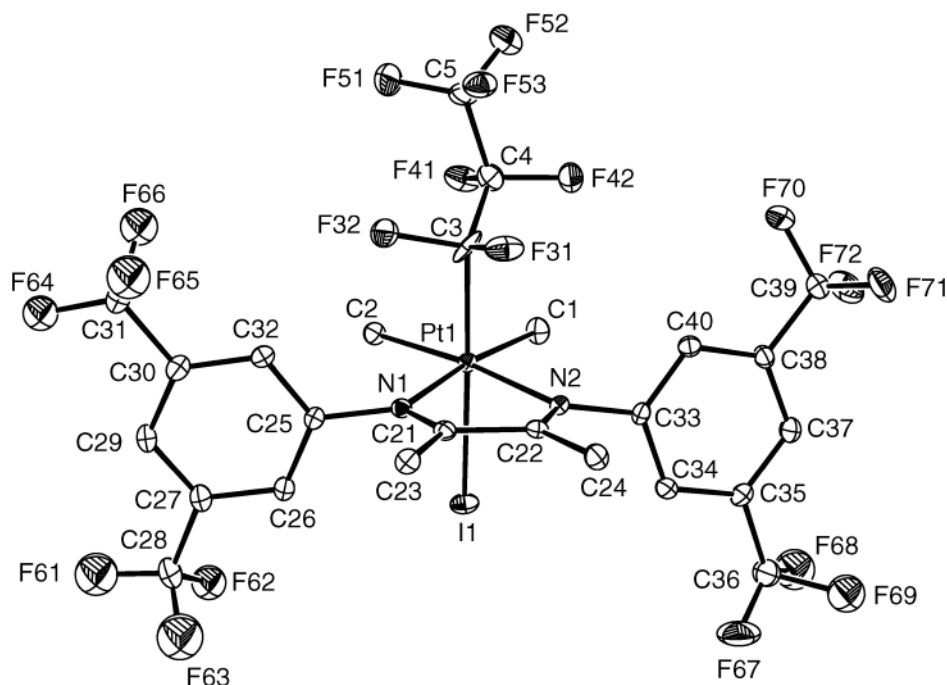
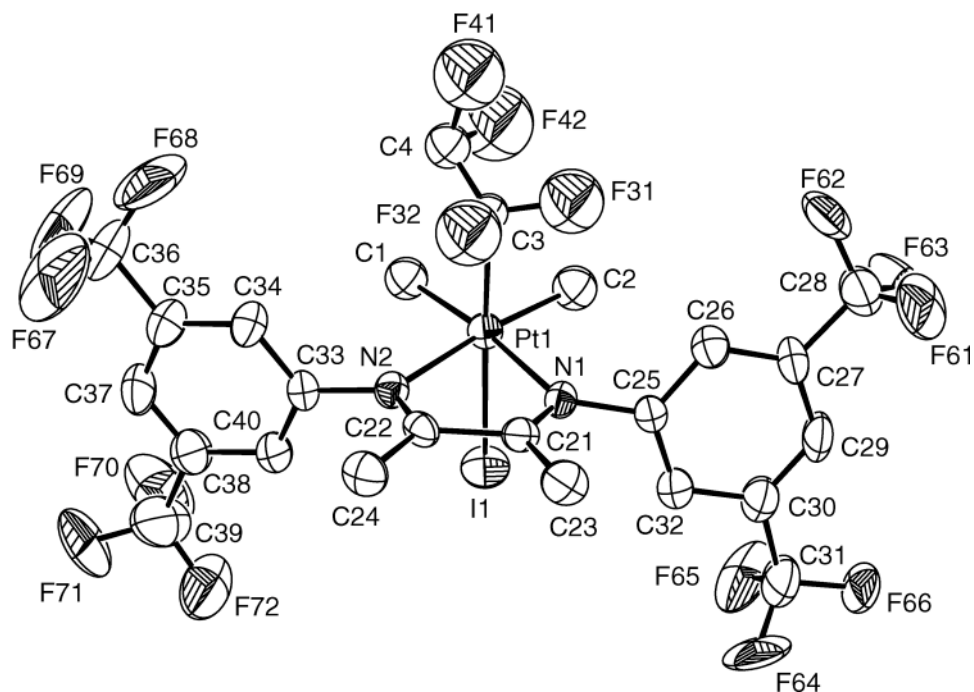


**Fig. 2.** ORTEP diagram of the non-hydrogen atoms of **4**, showing the atom labelling scheme. Thermal ellipsoids are shown at 30% probability.



plexes **3** (Fig. 1), **4** (Fig. 2), and **5** (Fig. 3). Details of the crystal data and structure determinations of all complexes are presented in Table 1. Selected bond lengths and angles for the coordination sphere of Pt are given in Table 2. For easy comparison, a common numbering scheme has been adopted: in the Pt(IV) complexes, the equatorial plane corresponds to the plane of N(1) and N(2) of the diimine ligand

and C(1) and C(2) of the two methyl groups, while C(3) (the  $\alpha$ -carbon of the perfluoroalkyl moiety) is always trans to I.

The structures obtained for complexes **3** and **4** display disorder in the CF<sub>3</sub> groups of the diimine ligand, and, in the case of the structures for **4** and **5**, a small amount of disorder is also observed in the perfluoroalkyl moiety.

The crystal structures of complexes **3**, **4**, and **5** show the



**Fig. 3.** ORTEP diagram of the non-hydrogen atoms of **5**, showing the atom labelling scheme. Thermal ellipsoids are shown at 30% probability.

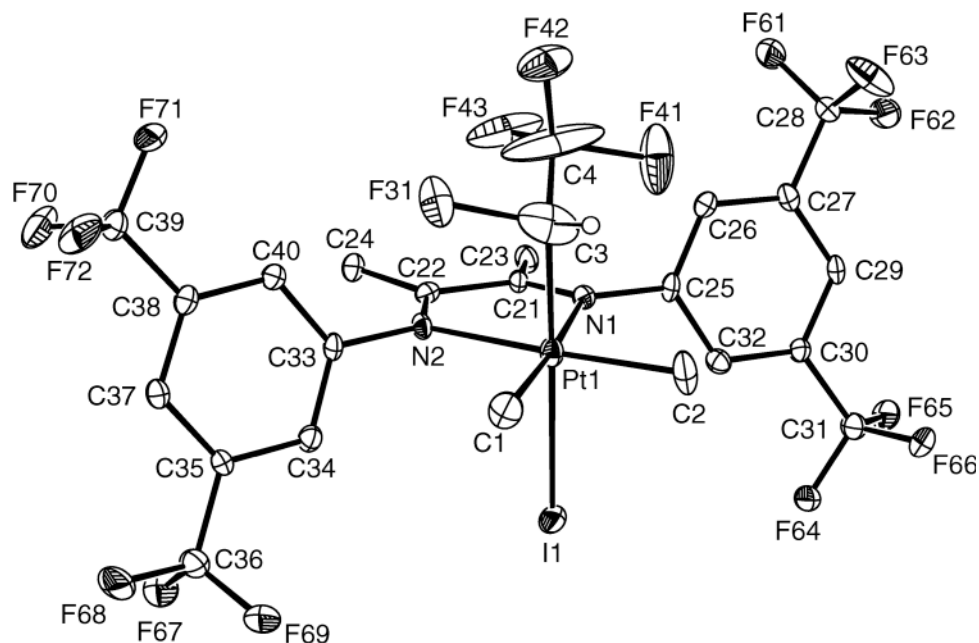


**Table 1.** Summary of X-ray crystallographic data collection, solution, and refinement parameters for complexes **3**, **4**, **5**, and **11**.

Complex	<b>3</b>	<b>4</b>	<b>5</b>	<b>11</b>
Formula	C <sub>25</sub> H <sub>18</sub> F <sub>19</sub> IN <sub>2</sub> Pt	C <sub>24</sub> H <sub>19</sub> F <sub>16</sub> IN <sub>2</sub> Pt	C <sub>24</sub> H <sub>19</sub> F <sub>16</sub> IN <sub>2</sub> Pt	C <sub>24</sub> H <sub>27</sub> F <sub>7</sub> N <sub>2</sub> Pt
Space group	<i>P</i> 2 <sub>1</sub> / <i>n</i>	<i>P</i> 2 <sub>1</sub> / <i>n</i>	<i>P</i> -1	<i>P</i> 2 <sub>1</sub> / <i>n</i>
<i>a</i> (Å)	14.0822(6)	14.5331(1)	8.3105(5)	8.3273(5)
<i>b</i> (Å)	9.2888(4)	9.3944(7)	11.8465(8)	13.0769(7)
<i>c</i> (Å)	24.2972(1)	23.4593(17)	31.026(2)	23.0810(13)
$\alpha$ (°)	90.00	90.00	95.757(1)	90.00
$\beta$ (°)	101.885(1)	101.229(1)	92.018(1)	90.109(1)
$\gamma$ (°)	90.00	90.00	108.0410(10)	90.00
<i>V</i> (Å <sup>3</sup> )	3110.1(2)	3141.6(4)	2882.6(3)	2513.4(2)
<i>Z</i>	4	4	4	4
Crystal colour, habit	Yellow, block	Amber, block	Yellow, block	Red, block
<i>D</i> (calcd.) (g/cm <sup>3</sup> )	2.198	2.033	2.215	1.775
$\mu$ (mm <sup>-1</sup> )	5.639	5.562	6.061	5.649
<i>T</i> (K)	100(2)	295(2)	100(2)	173(2)
Total data	7346	6160	18 522	15 786
Unique data ( <i>R</i> <sub>int</sub> )	6757(0.0232)	4764(0.0262)	12 959(0.0207)	5856(0.0280)
<i>R</i> 1, <i>wR</i> 2 ( <i>I</i> > 2 $\sigma$ ( <i>I</i> ))	0.0406, 0.0994	0.0513, 0.1496	0.0405, 0.0948	0.0778, 0.2135
All data	0.0441, 0.1015	0.0679, 0.1612	0.0530, 0.1002	0.0979, 0.2551

Pt(IV) center to have approximate octahedral geometry. There is only a subtle deviation from the ideal angle of 180° for C(3)-Pt-I(1), with **5** showing the largest discrepancy with an angle of 175.8(3)°. The deviation is also observed for the C(3)-Pt-N(1) angle in **5**, which exhibits a value of 96.7(3)°, while complexes **3**, and **4** have angles close to 90°. In all structures, there is deviation from the expected angles in the plane of the Pt atom: the C(1)-Pt-C(2) angles are reduced substantially (especially in the case of **4** and **5**), presumably due to the bulk of the aryl groups on the diimine ligand. As a consequence, the C(1)-Pt-N(2) and the C(2)-Pt-N(1) bond angles are all in the region of 100°. The Pt—C(1) and Pt—

C(2) bond lengths for **3** and **5** are similar in all cases and are identical for each complex, except for complex **4**, in which there is a significant variation between the two bond lengths (2.072(11) Å and 2.031(12) Å, respectively). The source of this bond length variation is not clear. The Pt—C(3) bond lengths for **3** (2.129(8) Å) and **5** (2.076(8) Å) are significantly different, with an unexpectedly shorter bond to the partially hydrogenated  $\alpha$ -CFH group. However, the Pt—I bond lengths for **3** (2.6769(4) Å) and **5** (2.7447(5) Å) do display the expected trend for the trans-influence of the alkyl group, with a greater degree of fluorination affording a weaker trans-influence (10, 55). Because the Pt—N(1) and



**Fig. 4.** ORTEP diagram of the non-hydrogen atoms of **11**, showing the atom labelling scheme. Thermal ellipsoids are shown at 30% probability.

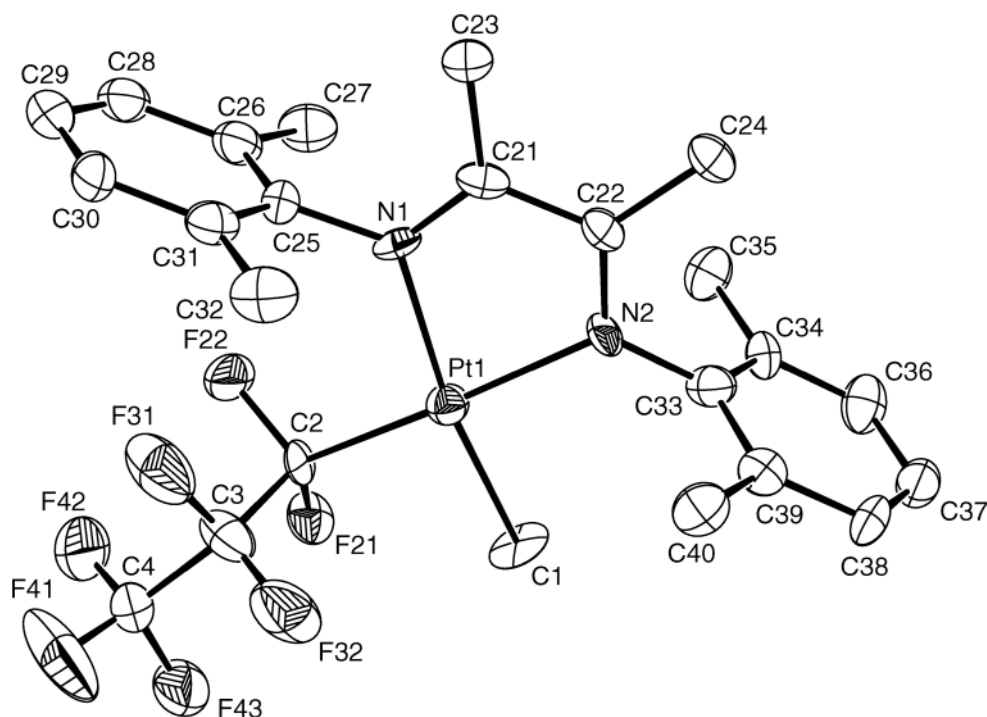


**Table 2.** Selected bond lengths (Å) and angles (°) for the coordination sphere of platinum in complexes **3**, **4**, **5**, and **11**.

Complex	<b>3</b>	<b>4</b>	<b>5</b>	<b>11</b>
<b>Bond angles (Å)</b>				
Pt—C(1)	2.065(6)	2.072(11)	2.053(7)	2.047(9)
Pt—C(2)	2.066(5)	2.031(12)	2.055(7)	2.032(9)
Pt—C(3)	2.129(8)	2.228(9)	2.076(9)	—
Pt—N(1)	2.175(4)	2.178(6)	2.187(5)	2.133(7)
Pt—N(2)	2.170(5)	2.183(7)	2.178(5)	2.077(8)
Pt—X	2.6769(4)	2.6963(8)	2.7447(5)	—
<b>Bond angles (°)</b>				
C(1)—Pt—C(2)	88.2(2)	85.4(5)	85.1(3)	87.2(6)
C(1)—Pt—C(3)	94.3(2)	92.0(4)	88.1(4)	—
C(1)—Pt—N(1)	172.5(2)	173.3(4)	174.5(3)	171.0(6)
C(1)—Pt—N(2)	98.8(2)	99.4(4)	100.2(2)	93.9(6)
C(1)—Pt—X	87.53(18)	89.5(3)	91.0(2)	—
C(2)—Pt—C(3)	91.1(2)	91.1(4)	88.1(4)	—
C(2)—Pt—N(1)	98.7(2)	100.7(4)	100.2(2)	101.8(4)
C(2)—Pt—N(2)	172.3(2)	174.4(4)	174.7(2)	176.1(5)
C(2)—Pt—X	88.81(16)	88.0(3)	91.3(2)	—
C(3)—Pt—N(1)	88.43(19)	90.7(3)	96.7(3)	—
C(3)—Pt—N(2)	91.4(2)	91.5(3)	92.4(3)	—
C(3)—Pt—X	178.12(16)	178.2(2)	175.8(3)	—
N(1)—Pt—N(2)	74.08(17)	74.4(3)	74.48(18)	77.1(4)
N(1)—Pt—X	89.72(11)	87.91(17)	87.57(13)	—
N(2)—Pt—X	88.46(12)	89.13(16)	88.49(13)	—

Pt—N(2) bond lengths for **3**, **4**, and **5** are similar in all cases and show no significant variation within each complex, there is clearly no cis-effect in the differently fluorinated alkyl groups.

No meaningful comparisons between the Pt(IV)—diimine complexes and the analogous Pt(IV)—tmeda complexes can be made, as the tmeda complexes isomerize from the initial trans-product to form the thermodynamically favored cis-product.<sup>3</sup>

Crystallization of **11** from CH<sub>2</sub>Cl<sub>2</sub>–hexane afforded red plates that were suitable for X-ray diffraction studies. The ORTEP diagram for complex **11** is shown in Fig. 4. Selected bond lengths and angles for the coordination sphere of Pt are given in Table 2. The numbering scheme adopted for complex **11** has N(1) trans to C(1) (the methyl group), while N(2) is trans to C(2) (the α-carbon of the perfluoroalkyl moiety).

The structure shows the complex is square planar, with no significant deviations of the ligands from the plane, but with significant bond angle deviations due to the steric bulk of the perfluoroalkyl ligand. The C(2)–Pt–N(2) bond angle of 176.1(5)° is close to the ideal angle, however, there is significant deviation observed for the C(1)–Pt–N(1) which has a bond angle of 171.0(6)°. Similarly, the C(2)–Pt–N(1) bond angle (101.8(6)°) shows a large distortion that is attributable to the steric requirements of the perfluoroalkyl moiety. Variations in the bond lengths to the Pt atom are also observed which is a consequence of the relative magnitude of the trans-influence for methyl and perfluoroalkyl ligands: the

<sup>3</sup>Our initial observations on this reaction were that the cis-product was formed. More careful studies have shown that the trans-isomer is the kinetic product. R.P. Hughes, M.A. Meyer, A.J. Ward, A. Williamson. Unpublished results.



Pt—C(1) bond length is 2.047(9) Å, while the Pt—C(2) bond length is slightly shorter at 2.032(9) Å. However, it is in the Pt—N bond lengths that the trans-effect is most clearly manifested: the Pt—N(1) bond length (trans to methyl) is 2.133(7) Å, while the Pt—N(2) bond length (trans to C<sub>3</sub>F<sub>7</sub>) is 2.077(8) Å.

Comparison of the structure obtained for **11** and that obtained previously for [Pt(tmeda)(C<sub>3</sub>F<sub>7</sub>)Me] (**11**) reveals that the presence of the diimine ligand results in significant steric crowding around the Pt center, and thus, there is some variation in bond lengths and bond angles between the two complexes. For example, the Pt—C(1) and Pt—C(2) bond lengths for the tmeda complex are 2.148(18) Å and 2.01(2) Å, respectively, compared to 2.047(9) Å and 2.032(9) Å for the same bonds in complex **11**. The Pt—N(1) and Pt—N(2) are 2.14(2) Å and 2.172(19) Å, respectively, for the tmeda complex, while they are 2.133(7) Å and 2.077(8) Å for **11**. Significant variation in bond angles is observed between the two complexes: C(1)–Pt–C(2) for **11** is 87.2(6)° and for the tmeda complex is 88.3(9)°; C(1)–Pt–N(2) for **11** is 93.9(6)° and for the tmeda complex is 92.3(8)°; C(2)–Pt–N(2) for **11** is 101.8(6)° and for the tmeda complex is 97.7(9)°. While these large variations are probably attributable solely to the large steric bulk of the diimine aryl groups, the data for the tmeda complex are of poor quality and preclude any more meaningful comparisons.

## Experimental section

### General considerations

Unless otherwise noted, all reactions were performed in oven-dried glassware, using standard Schlenk techniques, under an atmosphere of nitrogen (which had been deoxygenated over BASF catalyst), and dried using Aquasorb®. Solvents were deoxygenated and dried over activated alumina using an apparatus modified from that described in the literature (56). <sup>1</sup>H (300 MHz), <sup>19</sup>F (282 MHz), and <sup>31</sup>P (121.4 MHz) NMR spectra were recorded on a Varian Unity-300 spectrometer at 25 °C. Chemical shifts are reported as ppm downfield of TMS (<sup>1</sup>H, referenced to solvent) or internal CFCl<sub>3</sub> (<sup>19</sup>F). Coupling constants are reported in Hertz (Hz). Microanalyses were performed by Schwartzkopf Microanalytical Laboratory (Woodside, N.Y.).

Iodoperfluoroalkanes were purchased from PCR, (except for CF<sub>3</sub>CFHI, which was purchased from ABCR) treated with Na<sub>2</sub>S<sub>2</sub>O<sub>3</sub> to remove residual I<sub>2</sub>, and vacuum distilled before use. The complexes [Pt(3,5-(CF<sub>3</sub>)<sub>2</sub>ArN=C(Me)C(Me)=N-3,5-(CF<sub>3</sub>)<sub>2</sub>Ar)Me<sub>2</sub>] (**1**) (57), [Pt(4-MeArN=CHCH=N-4-MeAr)Me<sub>2</sub>] (**2**) (58), [Pt(2,6-Me<sub>2</sub>ArN=CHCH=N-2,6-Me<sub>2</sub>Ar)Me<sub>2</sub>] (**7**) (59), and [Pt(2,6-Me<sub>2</sub>ArN=C(Me)C(Me)=N-2,6-Me<sub>2</sub>Ar)Me<sub>2</sub>] (**8**) (59) were prepared as reported previously.

### **trans-[1,2-Bis(3,5-bis(trifluoromethylphenylimino)-1,2-dimethylethane]dimethyl(heptafluoropropyl)iodoplatinum(IV) (3)**

To a solution of **1** (100 mg, 0.14 mmol) in degassed ethyl acetate (10 mL) was added heptafluoropropyl iodide (30 mL, 0.20 mmol) and the reaction mixture was heated at reflux for 2 h in the absence of light. The solvent was removed in vacuo. The residue was recrystallized from

CH<sub>2</sub>Cl<sub>2</sub>–hexane to afford the product as an orange powder (86 mg, 71%). <sup>1</sup>H NMR (CDCl<sub>3</sub>) δ (ppm): 8.44 (s, 2H, ArH), 7.96 (s, 2H, ArH), 7.37 (s, 2H, ArH), 2.49 (s, 6H, <sup>4</sup>J<sub>PH</sub> = 5 Hz, N=C(CH<sub>3</sub>)), 1.37 (s, 6H, <sup>2</sup>J<sub>PH</sub> = 73 Hz, PtCH<sub>3</sub>). <sup>19</sup>F NMR (CDCl<sub>3</sub>) δ (ppm): –63.34 (s, 6F, *m*-ArCF<sub>3</sub>), –63.47 (s, 6F, *m*-ArCF<sub>3</sub>), –80.07 (t, 3F, <sup>4</sup>J<sub>FF</sub> = 13 Hz, <sup>4</sup>J<sub>PF</sub> = 9 Hz, CF<sub>2</sub>CF<sub>3</sub>), –90.08 (m, 2F, <sup>2</sup>J<sub>PF</sub> = 298 Hz, PtCF<sub>2</sub>), –122.03 (m, 2F, CF<sub>2</sub>CF<sub>3</sub>). Anal. calcd. for C<sub>25</sub>H<sub>18</sub>F<sub>19</sub>IN<sub>2</sub>Pt (%): C 29.17, H 1.77; found (%): C 29.37, H 1.65.

### **trans-[1,2-Bis(3,5-bis(trifluoromethylphenylimino)-1,2-dimethylethane]iododimethyl-(2H-tetrafluoroethyl)platinum(IV) (4)**

To a solution of **1** (100 mg, 0.14 mmol) in degassed ethyl acetate (10 mL) was added iodo-2H-tetrafluoroethane (23 µL, 0.20 mmol) and the reaction mixture was heated at reflux in the absence of light for 2 h. The solution was cooled and the solvent removed in vacuo. The residue was extracted with hot hexanes until no colour persisted in the washings. The volume of the combined extracts was reduced in vacuo to 5 mL and cooled to –30 °C. The product was obtained by filtration as a yellow powder (86 mg, 66%). <sup>1</sup>H NMR (CDCl<sub>3</sub>) δ (ppm): 8.42 (s, 2H, ArH), 7.94 (s, 2H, ArH), 7.45 (s, 2H, ArH), 5.45 (tt, <sup>2</sup>J<sub>FH</sub> = 55 Hz, <sup>3</sup>J<sub>FF</sub> = 6 Hz, <sup>2</sup>J<sub>PH</sub> = 11 Hz CF<sub>2</sub>H), 2.47 (s, 6H, <sup>4</sup>J<sub>PH</sub> = 5 Hz, N=C(CH<sub>3</sub>)), 1.26 (s, 6H, <sup>2</sup>J<sub>PH</sub> = 72 Hz, PtCH<sub>3</sub>). <sup>19</sup>F NMR (CDCl<sub>3</sub>) δ (ppm): –63.30 (s, 12F, *m*-ArCF<sub>3</sub>), –90.98 (dt, 2F, <sup>3</sup>J<sub>FF</sub> = 3 Hz, <sup>3</sup>J<sub>FH</sub> = 6 Hz, <sup>3</sup>J<sub>PF</sub> = 307 Hz, CF<sub>2</sub>CF<sub>2</sub>H), –131.69 (dt, 2F, <sup>3</sup>J<sub>FF</sub> = 6 Hz, <sup>2</sup>J<sub>FH</sub> = 55 Hz, <sup>2</sup>J<sub>PF</sub> = 27 Hz, CF<sub>2</sub>CF<sub>2</sub>H). Anal. calcd. for C<sub>24</sub>H<sub>19</sub>F<sub>16</sub>IN<sub>2</sub>Pt (%): C 29.98, H 2.00; found (%): C 30.21, H 1.87.

### **trans-[1,2-Bis(3,5-bis(trifluoromethylphenylimino)-1,2-dimethylethane]dimethyliodo(1H-tetrafluoroethyl)platinum(IV) (5)**

To a solution of **1** (100 mg, 0.14 mmol) in degassed ethyl acetate (10 mL) was added iodo-1H-tetrafluoroethane (23 µL, 0.20 mmol) and the reaction mixture was heated at reflux in the absence of light for 2 h. The solution was cooled and the solvent removed in vacuo. The residue was extracted with hot hexanes until no colour persisted in the washings. The volume of the combined extracts was reduced in vacuo to 5 mL and cooled to –30 °C. The product was obtained by filtration as a yellow powder (85 mg, 65%). <sup>1</sup>H NMR (CDCl<sub>3</sub>) δ (ppm): 8.73 (bs, 1H, ArH), 8.39 (s, 1H, ArH), 7.94 (s, 2H, ArH), 7.41 (bs, 2H, ArH), 4.72 (dq, 1H, <sup>2</sup>J<sub>FH</sub> = 47 Hz, <sup>3</sup>J<sub>FF</sub> = 10 Hz, <sup>2</sup>J<sub>PH</sub> = 410 Hz, CFH), 2.48 (s, 3H, <sup>4</sup>J<sub>PH</sub> = 5 Hz, N=C(CH<sub>3</sub>)), 2.45 (s, 3H, <sup>4</sup>J<sub>PH</sub> = 5 Hz, N=C(CH<sub>3</sub>)), 1.27 (d, 3H, <sup>4</sup>J<sub>FH</sub> = 1 Hz, <sup>2</sup>J<sub>PH</sub> = 70 Hz, PtCH<sub>3</sub>), 1.12 (s, 3H, <sup>2</sup>J<sub>PH</sub> = 71 Hz, PtCH<sub>3</sub>). <sup>19</sup>F NMR (CDCl<sub>3</sub>) δ (ppm): –63.18 (s, 3F, *m*-ArCF<sub>3</sub>), –63.27 (s, 3F, *m*-ArCF<sub>3</sub>), –63.32 (s, 6F, *m*-ArCF<sub>3</sub>), –72.95 (dd, 3F, <sup>3</sup>J<sub>FF</sub> = 11 Hz, <sup>3</sup>J<sub>FH</sub> = 11 Hz, <sup>3</sup>J<sub>PF</sub> = 61 Hz, CFHCF<sub>3</sub>), –191.43 (dq, 1F, <sup>3</sup>J<sub>FF</sub> = 11 Hz, <sup>3</sup>J<sub>FH</sub> = 47 Hz, <sup>2</sup>J<sub>PF</sub> = 135 Hz, CFHCF<sub>3</sub>). Anal. calcd. for C<sub>24</sub>H<sub>19</sub>F<sub>16</sub>IN<sub>2</sub>Pt (%): C 29.98, H 2.00; found (%): C 29.87, H 1.99. X-ray diffraction quality crystals were grown from CH<sub>2</sub>Cl<sub>2</sub>–hexane.

### **trans-[1,2-Bis(4-methylphenylimino)ethane]dimethyl(heptafluoropropyl)iodoplatinum(IV) (6)**

To a suspension of **2** (100 mg, 0.22 mmol) in hexane



(10 mL) was added  $\text{C}_3\text{F}_7\text{I}$  (47  $\mu\text{L}$ , 0.33 mmol) and the reaction mixture was refluxed for 8 h. The solution was cooled and the solvent removed in vacuo. Recrystallization from hot hexane afforded the product as an orange microcrystalline solid (104 mg, 63%).  $^1\text{H}$  NMR ( $\text{CDCl}_3$ )  $\delta$  (ppm): 8.67 (t, 2H,  $^3J_{\text{PtH}} = 26$  Hz,  $\text{N}=\text{CH}$ ), 7.45 (m, 4H,  $\text{ArH}$ ), 7.31 (m, 4H,  $\text{ArH}$ ), 2.44 (s, 6H,  $\text{ArCH}_3$ ), 1.77 (t, 6H,  $^2J_{\text{PtH}} = 74$  Hz,  $\text{PtCH}_3$ ).  $^{19}\text{F}$  NMR ( $\text{CDCl}_3$ )  $\delta$  (ppm): -80.01 (t, 3F,  $^4J_{\text{FF}} = 12$  Hz,  $^4J_{\text{PtF}} = 18$  Hz,  $\text{CF}_3$ ), -91.93 (qt, 2F,  $^2J_{\text{PtF}} = 362$  Hz,  $^4J_{\text{FF}} = 12$  Hz,  $^3J_{\text{FF}} = 3$  Hz,  $\text{PtCF}_2$ ), -121.79 (m, 2F,  $\text{CF}_2\text{CF}_3$ ). Anal. calcd. for  $\text{C}_{21}\text{H}_{22}\text{F}_7\text{IN}_2\text{Pt}$  (%): C 33.29, H 2.93; found (%): C 33.83, H 3.12.

**[1,2-Bis(2,6-dimethylphenylimino)ethane](heptafluoropropyl)methylplatinum(II) (9)**

To a solution of **7** (100 mg, 0.20 mmol) in hexane (10 mL) was added  $\text{C}_3\text{F}_7\text{I}$  (44  $\mu\text{L}$ , 0.31 mmol) and the reaction mixture was heated at reflux for 18 h. The solution was cooled. Filtration and washing with hexane afforded the product as a maroon microcrystalline solid (146 mg, 91%).  $^1\text{H}$  NMR ( $\text{CDCl}_3$ )  $\delta$  (ppm): 9.01 (t, 1H,  $^3J_{\text{PtH}} = 36$  Hz,  $\text{N}=\text{CH}$ ), 8.93 (t, 1H,  $^3J_{\text{PtH}} = 84$  Hz,  $\text{N}=\text{CH}$ ), 7.21 (s, 4H,  $m\text{-ArH}$ ), 7.14 (m, 2H,  $p\text{-ArH}$ ), 2.28 (s, 12H,  $\text{CH}_3$ ), 1.21 (t, 3H,  $^2J_{\text{PtH}} = 88$  Hz,  $\text{PtCH}_3$ ).  $^{19}\text{F}$  NMR ( $\text{CDCl}_3$ )  $\delta$  (ppm): -79.98 (t, 3F,  $^4J_{\text{PtF}} = 36$  Hz,  $^4J_{\text{FF}} = 10$  Hz,  $\text{CF}_3$ ), -94.74 (q, 2F,  $^2J_{\text{PtF}} = 420$  Hz,  $^4J_{\text{FF}} = 10$  Hz,  $\text{PtCF}_2$ ), -120.33 (s, 2F,  $^3J_{\text{PtF}} = 116$  Hz,  $\text{CF}_2\text{CF}_3$ ). Anal. calcd. for  $\text{C}_{22}\text{H}_{23}\text{F}_7\text{N}_2\text{Pt}$  (%): C 41.06, H 3.61; found (%): C 41.04, H 3.69.

**[1,2-Bis(2,6-dimethylphenylimino)ethane](1H-tetrafluoroethyl)methylplatinum(II) (10)**

To a solution of **7** (100 mg, 0.20 mmol) in ethyl acetate (10 mL) was added iodo-1H-tetrafluoroethane (70 mg, 0.31 mmol) and the reaction mixture was heated at reflux for 12 h in the absence of light. The solvent was removed in vacuo and the residue was washed with hexane until no colour persisted in the washings. The product was obtained as purple needles after recrystallization from chloroform-hexane (50 mg, 45%).  $^1\text{H}$  NMR ( $\text{CDCl}_3$ )  $\delta$  (ppm): 9.20 (s, 1H,  $^3J_{\text{PtH}} = 37$  Hz,  $\text{N}=\text{CH}$ ), 9.06 (s, 1H,  $^3J_{\text{PtH}} = 42$  Hz,  $\text{N}=\text{CH}$ ), 7.24–7.15 (m, 6H,  $\text{ArH}$ ), 6.03 (dq, 1H,  $^2J_{\text{FH}} = 50$  Hz,  $^3J_{\text{FH}} = 11$  Hz,  $^2J_{\text{PtF}} = 61$  Hz,  $\text{CFH}$ ), 2.36 (s, 3H,  $\text{ArCH}_3$ ), 2.29 (s, 3H,  $\text{ArCH}_3$ ), 2.27 (s, 3H,  $\text{ArCH}_3$ ), 2.20 (s, 3H,  $\text{ArCH}_3$ ), 1.36 (s, 3H,  $^2J_{\text{PtH}} = 86$  Hz,  $\text{PtCH}_3$ ).  $^{19}\text{F}$  NMR ( $\text{CDCl}_3$ )  $\delta$  (ppm): -70.69 (dd, 3F,  $^3J_{\text{FH}} = 14$  Hz,  $^3J_{\text{FF}} = 14$  Hz,  $^3J_{\text{PtF}} = 141$  Hz,  $\text{CF}_3$ ), -212.28 (dq, 1F,  $^2J_{\text{FH}} = 50$  Hz,  $^3J_{\text{FF}} = 14$  Hz,  $^2J_{\text{PtF}} = 327$  Hz,  $\text{CFH}$ ). Anal. calcd. for  $\text{C}_{21}\text{H}_{24}\text{F}_4\text{N}_2\text{Pt} \cdot 0.5\text{CHCl}_3$  (%): C 40.65, H 3.90; found (%): C 41.37, H 3.74.

**[1,2-Bis(2,6-dimethylphenylimino)-1,2-dimethyl-ethane](heptafluoropropyl)methylplatinum(II) (11)**

To a solution of **8** (100 mg, 0.19 mmol) in ethyl acetate (10 mL) was added  $\text{C}_3\text{F}_7\text{I}$  (42  $\mu\text{L}$ , 0.29 mmol) and the reaction mixture was heated under reflux in the absence of light for 2 h. The solution was cooled and the solvent removed in vacuo. The residue was recrystallized from  $\text{CH}_2\text{Cl}_2$ -hexane. Filtration afforded the complex as a purple powder (66 mg, 51%).  $^1\text{H}$  NMR ( $\text{CDCl}_3$ )  $\delta$  (ppm): 7.19 (m, 4H,  $p\text{-ArH}$ ), 7.12 (s, 2H,  $p\text{-ArH}$ ), 2.21 (s, 12H,  $o\text{-ArCH}_3$ ), 1.73 (s, 3H,  $\text{N}=\text{C}(\text{CH}_3)$ ), 1.63 ((s, 3H,  $\text{N}=\text{C}(\text{CH}_3)$ ), 0.70 (t, 3H,  $^2J_{\text{PtH}} = 86$  Hz,  $\text{PtCH}_3$ ).  $^{19}\text{F}$  NMR ( $\text{CDCl}_3$ )  $\delta$  (ppm): -80.01 (tt, 3F,

$^4J_{\text{FF}} = 10$  Hz,  $^4J_{\text{PtF}} = 19$  Hz,  $\text{CF}_3$ ), -93.51 (tq, 2F,  $^4J_{\text{FF}} = 10$  Hz,  $^2J_{\text{PtF}} = 410$  Hz,  $\text{PtCF}_2$ ), -119.74 (t, 2F,  $^3J_{\text{PtF}} = 119$  Hz,  $\text{CF}_2\text{CF}_3$ ). Anal. calcd. for  $\text{C}_{24}\text{H}_{27}\text{F}_7\text{N}_2\text{Pt}$  (%): C 42.92, H 4.06; found (%): C 43.1, H 4.12.

**[1,2-Bis(2,6-dimethylphenylimino)-1,2-dimethyl-ethane]methyl(1H-tetrafluoroethyl)platinum(II) (12)**

To a solution of **8** (100 mg, 0.19 mmol) in ethyl acetate (10 mL) was added  $\text{C}_3\text{F}_7\text{I}$  (42  $\mu\text{L}$ , 0.29 mmol) and the reaction mixture was heated under reflux in the absence of light for 24 h. The solution was cooled and the solvent reduced to 5 mL in vacuo. Hexane was added. Filtration afforded the product as a purple microcrystalline powder (100 mg, 85%).  $^1\text{H}$  NMR ( $\text{CDCl}_3$ )  $\delta$  (ppm): 7.30–7.17 (m, 6H,  $\text{ArH}$ ), 5.63 (dq, 1H,  $^2J_{\text{FH}} = 49$  Hz,  $^3J_{\text{FH}} = 13$  Hz,  $^2J_{\text{PtH}} = 52$  Hz,  $\text{CFH}$ ), 2.28 (s,  $\text{ArCH}_3$ ), 1.66 (s, 3H,  $\text{N}=\text{C}(\text{CH}_3)$ ), 1.35 (s, 3H,  $\text{N}=\text{C}(\text{CH}_3)$ ), 1.10 (s, 3H,  $^2J_{\text{PtH}} = 86$  Hz,  $\text{PtCH}_3$ ).  $^{19}\text{F}$  NMR ( $\text{CDCl}_3$ )  $\delta$  (ppm): -70.73 (dd, 3F,  $^3J_{\text{FH}} = 13$  Hz,  $^3J_{\text{FF}} = 14$  Hz,  $\text{CF}_3$ ), -211.64 (dq, 1F,  $^2J_{\text{FH}} = 49$  Hz,  $^3J_{\text{FF}} = 14$  Hz,  $\text{CFH}$ ). Anal. calcd. for  $\text{C}_{23}\text{H}_{28}\text{F}_4\text{N}_2\text{Pt}$  (%): C 45.76, H 4.69; found (%): C 45.77, H 4.53.

**[1,2-Bis(2,6-dimethylphenylimino)ethane](heptafluoropropyl)iodoplatinum(II) (13)**

**Method 1:**

To a solution of **9** (100 mg, 0.16 mmol) in  $\text{CH}_2\text{Cl}_2$  (10 mL) was added iodine (39 mg, 0.16 mmol) and the reaction mixture was stirred in the dark for 12 h. The solvent was reduced in volume to approximately 5 mL in vacuo. Hexane was added to precipitate the product as a brown powder. Recrystallization from  $\text{CH}_2\text{Cl}_2$ -hexane at  $-30^\circ\text{C}$  afforded the product as an amber microcrystalline solid (94 mg, 80%).  $^1\text{H}$  NMR ( $\text{CDCl}_3$ )  $\delta$  (ppm): 9.00 (t, 1H,  $^3J_{\text{PtH}} = 102$  Hz,  $\text{N}=\text{CH}$ ), 8.62 (t, 1H,  $^3J_{\text{PtH}} = 40$  Hz,  $\text{N}=\text{CH}$ ), 7.23–7.15 (m, 6H,  $\text{ArH}$ ), 2.33 (s, 6H,  $\text{CH}_3$ ), 2.30 (s, 6H,  $\text{CH}_3$ ).  $^{19}\text{F}$  NMR ( $\text{CDCl}_3$ )  $\delta$  (ppm): -80.08 (t, 3F,  $^4J_{\text{FF}} = 11$  Hz,  $\text{CF}_3$ ), -80.83 (tqd, 2F,  $^2J_{\text{PtF}} = 288$  Hz,  $^4J_{\text{FF}} = 11$  Hz,  $^5J_{\text{FH}} = 4$  Hz,  $\text{PtCF}_2$ ), -114.69 (t, 2F,  $^5J_{\text{PtF}} = 72$  Hz,  $\text{CF}_2\text{CF}_3$ ). Anal. calcd. for  $\text{C}_{21}\text{H}_{20}\text{F}_7\text{IN}_2\text{Pt}$  (%): C 33.39, H 2.67; found (%): C 32.65, H 2.57.

**Method 2:**

To a solution of **9** (100 mg, 0.16 mmol) in toluene (10 mL) was added hydriodic acid (57% w/w, 20  $\mu\text{L}$ , 0.16 mmol) and the reaction mixture was stirred at room temperature for 4 h. The solvent was removed in vacuo and the residue recrystallized from  $\text{CH}_2\text{Cl}_2$ -hexane to afford the product as an amber microcrystalline powder (83 mg, 78%).

**[1,2-Bis(2,6-dimethylphenylimino)ethane](1H-tetrafluoroethyl)iodoplatinum(II) (14)**

To a solution of **10** (100 mg, 0.19 mmol) in toluene (10 mL) was added HI (57% w/w, 33  $\mu\text{L}$ , 0.29 mmol) and the reaction mixture was stirred at room temperature for 4 h. The solvent was removed in vacuo and the residue recrystallized from  $\text{CH}_2\text{Cl}_2$ -hexane to afford the product as a black powder (86 mg, 74%).  $^1\text{H}$  NMR ( $\text{CDCl}_3$ )  $\delta$  (ppm): 9.16 (s, 1H,  $^3J_{\text{PtH}} = 100$  Hz,  $\text{N}=\text{CH}$ ), 8.68 (s, 1H,  $^3J_{\text{PtH}} = 38$  Hz,  $\text{N}=\text{CH}$ ), 7.25–7.15 (m, 6H,  $\text{ArH}$ ), 6.09 (dq, 1H,  $^2J_{\text{FH}} = 50$  Hz,  $^3J_{\text{FH}} = 11$  Hz,  $^2J_{\text{PtH}} = 61$  Hz,  $\text{CFH}$ ), 2.39 (s, 3H,  $\text{ArCH}_3$ ), 2.36 (s, 3H,  $\text{ArCH}_3$ ), 2.29 (s, 3H,  $\text{ArCH}_3$ ), 2.25 (s,



3H, ArCH<sub>3</sub>). <sup>19</sup>F NMR (CDCl<sub>3</sub>) δ (ppm): -68.61 (dd, 3F, <sup>3</sup>J<sub>FH</sub> = 15 Hz, <sup>3</sup>J<sub>FF</sub> = 11 Hz, <sup>2</sup>J<sub>PtF</sub> = 91 Hz, CF<sub>3</sub>), -211.67 (dq, 1F, <sup>2</sup>J<sub>FH</sub> = 50 Hz, <sup>3</sup>J<sub>FF</sub> = 11 Hz, <sup>2</sup>J<sub>PtF</sub> = 359 Hz, CFH). Anal. calcd. for C<sub>20</sub>H<sub>21</sub>F<sub>4</sub>IN<sub>2</sub>Pt (%): C 34.94, H 3.09; found (%): C 35.32, H 3.36.

**[1,2-Bis(2,6-dimethylphenylimino)-1,2-dimethylethane](heptafluoropropyl)iodoplatinum(II) (15)**

To a solution of **11** (100 mg, 0.15 mmol) in toluene (5 mL) was added HI (57% w/w, 100 μL, excess) and the reaction mixture was stirred at room temperature for 8 h. The solvent was removed in vacuo. The residue was extracted with CH<sub>2</sub>Cl<sub>2</sub> and the supernatant solution filtered. The solvent was reduced in vacuo to 5 mL and hexane was added. Filtration afforded the product as a brick-red powder (82 mg, 71%). <sup>1</sup>H NMR (CDCl<sub>3</sub>) δ (ppm): 7.23–7.13 (m, 6H, ArH), 2.26 (s, 6H, ArCH<sub>3</sub>), 2.23 (s, 6H, ArCH<sub>3</sub>), 2.22 (s, 3H, N=C(CH<sub>3</sub>)), 1.84 (s, 3H, N=C(CH<sub>3</sub>)). <sup>19</sup>F NMR (CDCl<sub>3</sub>) δ (ppm): -79.65 (qt, 3F, <sup>4</sup>J<sub>FF</sub> = 11 Hz, <sup>3</sup>J<sub>FF</sub> = 4 Hz, <sup>2</sup>J<sub>PtF</sub> = 290 Hz, CF<sub>3</sub>), -93.46 (t, 2F, <sup>4</sup>J<sub>FF</sub> = 11 Hz, <sup>4</sup>J<sub>PtF</sub> = 38 Hz, PtCF<sub>2</sub>), -114.06 (t, 2F, <sup>3</sup>J<sub>FF</sub> = 4 Hz, <sup>3</sup>J<sub>PtF</sub> = 68 Hz, CF<sub>2</sub>CF<sub>3</sub>). Anal. calcd. for C<sub>23</sub>H<sub>24</sub>F<sub>7</sub>IN<sub>2</sub>Pt (%): C 35.26, H 3.09; found (%): C 35.15, H 3.32.

**[1,2-Bis(2,6-dimethylphenylimino)-1,2-dimethylethane](1H-tetrafluoroethyl)iodoplatinum(II) 16**

To a solution of **12** (100 mg, 0.17 mmol) in CHCl<sub>3</sub> (10 mL) was added HI (21 μL, 0.17 mmol) and the reaction mixture was stirred at room temperature overnight. The solvent was removed in vacuo. The residue was recrystallized from CH<sub>2</sub>Cl<sub>2</sub>–hexane to afford the product as a deep orange powder (88 mg, 74%). <sup>1</sup>H NMR (CDCl<sub>3</sub>) δ (ppm): 7.23–7.08 (m, 6H, ArH), 5.60 (dq, <sup>2</sup>J<sub>FH</sub> = 50 Hz, <sup>3</sup>J<sub>FH</sub> = 11 Hz, <sup>2</sup>J<sub>PtH</sub> = 51 Hz, CFH), 2.20 (s, 9H, 3 × ArCH<sub>3</sub>), 1.56 (s, 3H, ArCH<sub>3</sub>), 1.26 (s, 3H, C(CH<sub>3</sub>)), 1.02 (s, 3H, <sup>4</sup>J<sub>PtH</sub> = 86 Hz, C(CH<sub>3</sub>)). <sup>19</sup>F NMR (CDCl<sub>3</sub>) δ (ppm): -70.74 (dd, 3F, <sup>3</sup>J<sub>FF</sub> = 11 Hz, <sup>3</sup>J<sub>FH</sub> = 11 Hz, <sup>3</sup>J<sub>PtF</sub> = 136 Hz, CF<sub>3</sub>), -211.69 (dq, 1F, <sup>2</sup>J<sub>PtH</sub> = 50 Hz, <sup>3</sup>J<sub>FF</sub> = 15 Hz, <sup>2</sup>J<sub>PtF</sub> = 388 Hz, CFH). Anal. calcd. for C<sub>22</sub>H<sub>25</sub>F<sub>4</sub>IN<sub>2</sub>Pt (%): C 36.93, H 3.53; found (%): C 36.71, H 3.40.

## Crystallographic structural determinations

Diffraction intensity data were collected with a Bruker Smart Apex CCD diffractometer. Crystal data collection and refinement parameters are provided in Table 1.<sup>4</sup> The structures were solved using direct methods, completed by subsequent difference Fourier syntheses and refined by full-matrix least-squares procedures on reflection intensities (*F*<sup>2</sup>). SADABS absorption corrections were applied to all structures (60). All non-hydrogen atoms were refined with anisotropic displacement coefficients except the C and F atoms of disordered groups. The F atoms of CF<sub>3</sub> groups in **3**, **4**, and **5** and -CF<sub>2</sub>-CHF<sub>2</sub>, -CHF-CF<sub>3</sub> ligands in **4** and **5** are disordered. Hydrogen atoms were treated as idealized contribu-

tions. All software and sources of scattering factors are contained in the SHELXTL (5.10) program libraries (61).

## Acknowledgements

R.P.H. is grateful to the National Science Foundation and the Petroleum Research Fund, administered by the American Chemical Society, for financial support.

## References

1. R.P. Hughes, S. Willemsen, A. Williamson, and D. Zhang. *Organometallics*, **21**, 3085 (2002).
2. R.P. Hughes, J.M. Smith, C.D. Incarvito, K.-C. Lam, B. Rhatigan, and A.L. Rheingold. *Organometallics*, **21**, 2136 (2002).
3. A.A. Bowden, R.P. Hughes, D.C. Lindner, C.D. Incarvito, L.M. Liable-Sands, and A.L. Rheingold. *J. Chem. Soc., Dalton Trans.* 3245 (2002).
4. R.P. Hughes, D.C. Lindner, J.M. Smith, D. Zhang, C.D. Incarvito, K.-C. Lam, L.M. Liable-Sands, R.D. Sommer, and A.L. Rheingold. *J. Chem. Soc., Dalton Trans.* 2270 (2001).
5. R.P. Hughes, I. Kovacic, D.C. Lindner, J.M. Smith, S. Willemsen, D. Zhang, I.A. Guzei, and A.L. Rheingold. *Organometallics*, **20**, 3190 (2001).
6. R.P. Hughes, J.M. Smith, L.M. Liable-Sands, T.E. Concolino, K.-C. Lam, C. Incarvito, and A.L. Rheingold. *J. Chem. Soc., Dalton Trans.* 873 (2000).
7. R.P. Hughes and J.M. Smith. *J. Am. Chem. Soc.* **121**, 6084 (1999).
8. R.P. Hughes, D.C. Lindner, A.L. Rheingold, and L.M. Liable-Sands. *J. Am. Chem. Soc.* **119**, 11 544 (1997).
9. R.P. Hughes, D.C. Lindner, A.L. Rheingold, and G.P.A. Yap. *Organometallics*, **15**, 5678 (1996).
10. R.P. Hughes, J.S. Overby, A. Williamson, K.-C. Lam, T.E. Concolino, and A.L. Rheingold. *Organometallics*, **19**, 5190 (2000).
11. R.P. Hughes, J.T. Sweetser, M.D. Tawa, A. Williamson, C.D. Incarvito, B. Rhatigan, A.L. Rheingold, and G. Rossi. *Organometallics*, **20**, 3800 (2001).
12. R.P. Hughes, A. Williamson, C.D. Incarvito, and A.L. Rheingold. *Organometallics*, **20**, 4741 (2001).
13. J.A. McCleverty and G. Wilkinson. *J. Chem. Soc.* 4200 (1964).
14. D.T. Rosevear and F.G.A. Stone. *J. Chem. Soc. A*, 164 (1968).
15. A.J. Mukhedkar, M. Green, and F.G.A. Stone. *J. Chem. Soc. A*, 3023 (1969).
16. F.G.A. Stone. *Endeavour*, **25**, 33 (1966).
17. H.C. Clark and L.E. Manzer. *J. Organomet. Chem.* **59**, 411 (1973).
18. T.G. Appleton, J.R. Hall, C.H.L. Kennard, M.T. Mathieson, D.W. Neale, G. Smith, and T.C.W. Mak. *J. Organomet. Chem.* **453**, 299 (1993).
19. R.P. Hughes, T.L. Husebo, B.J. Holliday, A.L. Rheingold, and L.M. Liable-Sands. *J. Organomet. Chem.* **548**, 109 (1997).
20. R.P. Hughes, S.M. Maddock, A.L. Rheingold, and L.M. Liable-Sands. *J. Am. Chem. Soc.* **119**, 5988 (1997).
21. R.P. Hughes, T.L. Husebo, A.L. Rheingold, L.M. Liable-Sands, and G.P.A. Yap. *Organometallics*, **16**, 5 (1997).

<sup>4</sup>Supplementary material may be purchased from the Depository of Unpublished Data, Document Delivery, CISTI, National Research Council Canada, Ottawa, ON K1A 0S2, Canada. For information on obtaining material electronically go to [http://www.nrc.ca/cisti/irm/unpub\\_e.shtml](http://www.nrc.ca/cisti/irm/unpub_e.shtml). CCDC 204287 (**3**), 204288 (**4**), 204289 (**5**), and 204290 (**11**) contain the crystallographic data for this manuscript. These data can be obtained, free of charge, via [www.ccdc.cam.ac.uk/conts/retrieving.html](http://www.ccdc.cam.ac.uk/conts/retrieving.html) (or from the Cambridge Crystallographic Data Centre, 12, Union Road, Cambridge CB2 1EZ, U.K.; fax: +44 1233 336033; or [deposit@ccdc.cam.ac.uk](mailto:deposit@ccdc.cam.ac.uk)).



22. R.P. Hughes, S.M. Maddock, I.A. Guzei, L.M. Liable-Sands, and A.L. Rheingold. *J. Am. Chem. Soc.* **123**, 3279 (2001).
23. L.M. Rendina and R.J. Puddephatt. *Chem. Rev.* **97**, 1735 (1997).
24. J.K. Jawad and R.J. Puddephatt. *J. Chem. Soc., Dalton Trans.* 1466 (1977).
25. J.K. Jawad and R.J. Puddephatt. *J. Organomet. Chem.* **117**, 297 (1976).
26. J.D. Scott and R.J. Puddephatt. *Organometallics*, **5**, 1538 (1986).
27. J.D. Scott and R.J. Puddephatt. *Organometallics*, **5**, 1253 (1986).
28. V.D. Felice, B. Giovannitti, A.D. Renzi, D. Tesauero, and A. Panunzi. *J. Organomet. Chem.* **593–594**, 445 (2000).
29. M. Crespo and R.J. Puddephatt. *Organometallics*, **6**, 2548 (1987).
30. M.P. Brown, R.J. Puddephatt, and C.E.E. Upton. *J. Chem. Soc., Dalton Trans.* 2457 (1974).
31. K.I. Goldberg, J.Y. Yan, and E.L. Winter. *J. Am. Chem. Soc.* **116**, 1573 (1994).
32. K.I. Goldberg, J. Yan, and E.M. Breitung. *J. Am. Chem. Soc.* **117**, 6889 (1995).
33. C. Wakselman and A. Lantz. *In Organofluorine chem. Edited by R.E. Banks, B.E. Smart, and J.C. Tatlow.* Plenum, New York. 1994. p. 177.
34. C. Wakselman. *J. Fluorine Chem.* **59**, 367 (1992).
35. T.G. Appleton, J.R. Hall, and M.A. Williams. *J. Organomet. Chem.* **303**, 139 (1986).
36. G.J. Arsenault, M. Crespo, and R.J. Puddephatt. *Organometallics*, **6**, 2255 (1987).
37. P.K. Byers, A.J. Canty, M. Crespo, R.J. Puddephatt, and J.D. Scott. *Organometallics*, **7**, 1363 (1988).
38. T. Aye Khin, A.J. Canty, M. Crespo, R.J. Puddephatt, J.D. Scott, and A.A. Watson. *Organometallics*, **8**, 1518 (1989).
39. P.K. Monaghan and R.J. Puddephatt. *Organometallics*, **3**, 444 (1984).
40. P.K. Monaghan and R.J. Puddephatt. *Organometallics*, **4**, 1406 (1985).
41. R.v. Asselt, E. Rijnberg, and C.J. Elsevier. *Organometallics*, **13**, 706 (1994).
42. J.D. Scollard, M. Day, J.A. Labinger, and J.E. Bercaw. *Helv. Chim. Acta*, **84**, 3247 (2001).
43. G.S. Hill, G.P.A. Yap, and R.J. Puddephatt. *Organometallics*, **18**, 1408 (1999).
44. W. de Graaf, J. Boersma, and G. van Koten. *Organometallics*, **9**, 1479 (1990).
45. E.M. Prokopchuck, H.A. Jenkins, and R.J. Puddephatt. *Organometallics*, **18**, 2861 (1999).
46. R.P. Hughes, A. Williamson, R.D. Sommer, and A.L. Rheingold. *J. Am. Chem. Soc.* **123**, 7443 (2001).
47. A.B. Shtarev, F. Tian, W.R. Dolbier, and B.E. Smart. *J. Am. Chem. Soc.* **121**, 7335 (1999).
48. K. Yang, R.J. Lachicotte, and R. Eisenberg. *Organometallics*, **17**, 5102 (1998).
49. L. Johansson, O.B. Ryan, C. Rømming, and M. Tilset. *Organometallics*, **17**, 3957 (1998).
50. C. Zuccaccia, A. Macchioni, I. Orabona, and F. Ruffo. *Organometallics*, **18**, 4367 (1999).
51. P.J. Albiets, Jr., K. Yang, R.J. Lachicotte, and R. Eisenberg. *Organometallics*, **19**, 3543 (2000).
52. J. Procelewska, A. Zahl, R.v. Eldik, H.A. Zhong, J.A. Labinger, and J.E. Bercaw. *Inorg. Chem.* **41**, 2808 (2002).
53. H.A. Zhong, J.A. Labinger, and J.E. Bercaw. *J. Am. Chem. Soc.* **124**, 1378 (2002).
54. V.V. Rostovtsev, L.M. Henling, J.A. Labinger, and J.E. Bercaw. *Inorg. Chem.* **41**, 3608 (2002).
55. T.G. Appleton, H.C. Clark, and L.E. Manzer. *Coord. Chem. Rev.* **10**, 335 (1973).
56. A.B. Pangborn, M.A. Giardello, R.H. Grubbs, R.K. Rosen, and F.J. Timmers. *Organometallics*, **15**, 1518 (1996).
57. L. Johansson, O.B. Ryan, and M. Tilset. *J. Am. Chem. Soc.* **121**, 1974 (1999).
58. W. Kaim, A. Klein, S. Hasenzahl, H. Stoll, S. Zális, and J. Fiedler. *Organometallics*, **17**, 237 (1998).
59. L. Johansson, M. Tilset, J.A. Labinger, and J.E. Bercaw. *J. Am. Chem. Soc.* **122**, 10 846 (2000).
60. G.M. Sheldrick. SADABS. Version 2.01 [computer program]. Bruker AXS, Madison, Wis. 1998.
61. G.M. Sheldrick. SHELXTL. Version 5.10 [computer program]. Bruker AXS, Madison, Wis.



# The use of a chiral borate counteranion as a $^1\text{H}$ NMR shift reagent for cationic copper(I) complexes<sup>1</sup>

David B. Llewellyn and Bruce A. Arndtsen

**Abstract:** The chiral borate counteranion bis[(*R*)-1,1'-bi-2-naphtholato]borate ( $1^-$ ) has been found to be a competent chiral  $^1\text{H}$  NMR shift reagent for cationic copper(I) complexes. This has been demonstrated by the addition of the  $\text{Cu}(\text{NCMe})_4^+$  salt of  $1^-$  to two classes of common chiral ligands in asymmetric catalysis: 2,2'-bis(di-*p*-tolylphosphino)-1,1'-binaphthyl (tol-BINAP) (**2**) and 2,2'-isopropylidenebis(4-phenyl-2-oxazoline) (**3**). In the case of ligand **2**, the addition of 1 equiv. of either (*R,R*)-**2** or (*S,S*)-**2** to  $\text{Cu}(\text{NCMe})_4^+1^-$  results in well-resolved  $^1\text{H}$  NMR resonances for the two enantiomers. Examination of standard solutions of non-enantiopure **2** shows that the copper complex can be an effective NMR shift reagent of a wide range of enantiomeric compositions.  $\text{Cu}(\text{NCMe})_4^+1^-$  also generates distinct  $^1\text{H}$  NMR resonances for the two separate enantiomers of 2,2'-isopropylidenebis(4-phenyl-2-oxazoline) (**3**). However, attempts to employ this copper salt as a chiral NMR shift reagent for *rac*-**3** led to the discovery of a new and unexpected equilibrium:  $[(R,R)\text{-3}]\text{Cu}^+ + [(S,S)\text{-3}]\text{Cu}^+ \rightleftharpoons [(R,R)\text{-3}][(S,S)\text{-3}]\text{Cu}^+ + \text{Cu}^+$ .

**Key words:** chiral counteranion, copper, chiral NMR shift reagent, ion pairing.

**Résumé :** On a trouvé que le contre-ion borate chiral, bis[(*R*)-1,1'-bi-2-naphtalato]borate ( $1^-$ ) réactif de déplacement chiral utile en RMN du  $^1\text{H}$  des complexes de cuivre(I) cationiques. On a établi cette propriété par l'addition du sel  $\text{Cu}(\text{NCMe})_4^+$  du composé  $1^-$  à deux classes de ligands chiraux usuels dans la catalyse asymétrique, le 2,2'-bis(di-*p*-tolylphosphino)-1,1'-binaphtyle (tol-BINAP) (**2**) et la 2,2'-isopropylidènebis(4-phényl-2-oxazoline) (**3**). Dans le cas du ligand **2**, l'addition d'un équivalent de (*R,R*)-**2** ou de (*S,S*)-**2** au  $\text{Cu}(\text{NCMe})_4^+1^-$  conduit à un spectre RMN du  $^1\text{H}$  dans lequel les résonances des deux énantiomères sont bien résolues. L'examen de solutions standard du composé **2** qui n'est pas énantiomériquement pur montre que le complexe de cuivre peut s'avérer être un réactif de déplacement efficace en RMN, sur une large gamme de compositions énantiomères. Le composé  $1^-$  génère aussi des résonances RMN du  $^1\text{H}$  distinctes pour les deux énantiomères séparés de la 2,2'-isopropylidènebis(4-phényl-2-oxazoline) (**3**). Toutefois, les essais effectués en vue d'utiliser ce sel de cuivre comme réactif de déplacement en RMN pour le composé *rac*-**3** ont permis de mettre en évidence un nouvel équilibre inattendu:  $[(R,R)\text{-3}]\text{Cu}^+ + [(S,S)\text{-3}]\text{Cu}^+ \rightleftharpoons [(R,R)\text{-3}][(S,S)\text{-3}]\text{Cu}^+ + \text{Cu}^+$ .

**Mots clés :** contre-ion chiral, cuivre, réactif de déplacement RMN chiral, paire d'ions.

[Traduit par la Rédaction]

## Introduction

Coupled to the growing demand for enantiopure compounds in the chemical and pharmaceutical industry (1) is also a demand for inexpensive, fast, and reliable techniques for the determination of enantiomeric composition. Enantiomeric excess is usually determined by chiral chromatogra-

phy (2) (i.e., HPLC and GC) or through the use of a chiral NMR shift reagent (3). NMR shift reagents are attractive because they can provide results rapidly, give an accurate measurement of optical purity, and require only an NMR spectrometer to perform the experiments. The most common NMR shift reagents are chiral lanthanide metal complexes (i.e.,  $\text{Eu}(\text{hfc})_3$ ,  $\text{hfc}$  = heptafluorohydroxymethylene-*d*-camphorato) (3, 4). Other metals including palladium (5), cobalt (6), and iridium (7) have also been used in conjunction with chiral ligands and shown to be effective chiral NMR shift reagents.

We have recently reported that ion pairing of a chiral bis[(*R*)-binaphthol]-based borate counteranion ( $1^-$ ) with a cationic copper center can induce enantioselectivity into metal catalysis (8). These results demonstrate a high level of communication between the metal catalyst and the counteranion in solution. This suggested that the chiral counteranion  $1^-$  might also be used as a chiral NMR shift reagent for cationic species. Indeed, Lacour and co-workers (9) have demonstrated that chiral phosphate counteranions

Received 13 March 2003. Published on the NRC Research Press Web site at <http://canjchem.nrc.ca> on 20 October 2003.

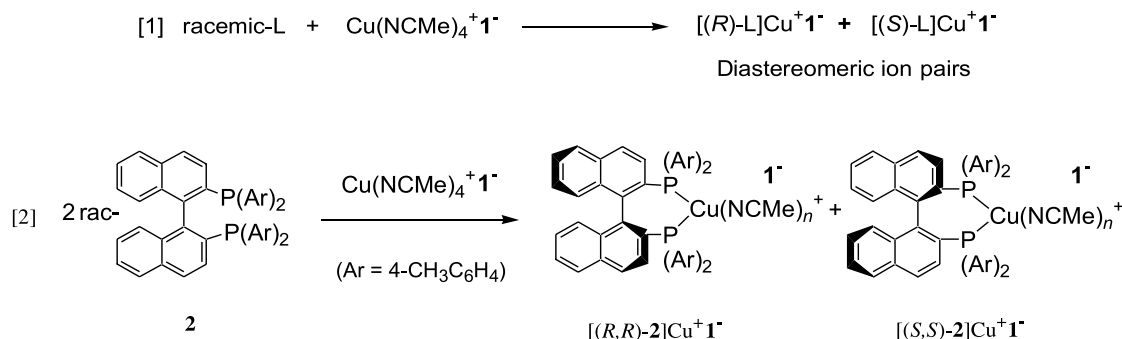
*This paper is dedicated to Professor John Harrod for his many contributions to the field of organometallic chemistry and science in Canada.*

**D.B. Llewellyn and B.A. Arndtsen.**<sup>2</sup> Department of Chemistry, McGill University, 801 Sherbrooke Street West, Montreal, QC H3A 2K6, Canada.

<sup>1</sup>This article is part of a Special Issue dedicated to Professor John Harrod.

<sup>2</sup>Corresponding author (e-mail: [bruce.arndtsen@mcgill.ca](mailto:bruce.arndtsen@mcgill.ca)).





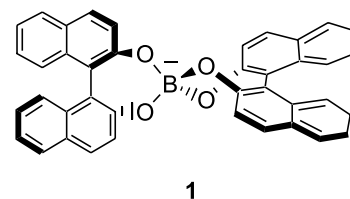
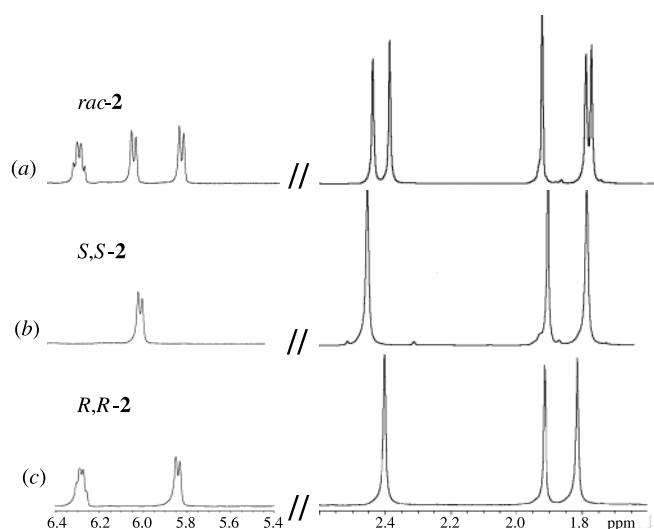
can be effective NMR shift reagents for a variety of cationic compounds. Particularly attractive about the use of the chiral borate  $\mathbf{1}^-$  is its facile synthesis in enantiopure form from readily available starting materials. It therefore does not require subsequent resolution, and does not racemize in solution (8). Furthermore,  $\mathbf{1}^-$  is easily generated as a borate acid, silver salt, or  $\text{Cu}(\text{CH}_3\text{CN})_4^+$  salt, allowing its potential association with a range of chiral cations or coordinating species (8).

We report below the results of our first studies directed towards the use of  $\mathbf{1}^-$  as a NMR shift reagent for chiral cationic transition metal complexes. This has been examined with the copper salt  $\text{Cu}(\text{CH}_3\text{CN})_4^+\mathbf{1}^-$ . This complex can undergo rapid ligand substitution, providing the potential to serve as a NMR shift reagent for chiral ligands upon coordination, as illustrated in eq. [1]. Representatives of two general classes of ligands have been probed: 2,2'-bis(di-*p*-tolylphosphino)-1,1'-binaphthyl (tol-BINAP) (**2**) and 2,2'-isopropylidenebis(4-phenyl-2-oxazoline) (**3**) both of which are important in the field of asymmetric catalysis (10).

## Results and discussion

The ability of  $\text{Cu}(\text{CH}_3\text{CN})_4^+1^-$  to serve as a NMR shift reagent for chiral ligands was first probed with the chiral tol-BINAP derivative **2**. This general class of chiral ligand has found extensive utility in transition-metal-catalyzed enantioselective reactions (e.g., hydrogenations, hydrosilylations, Heck couplings, Lewis acid catalysis) (11). The addition of racemic-**2** to 1 equiv.  $\text{Cu}(\text{CH}_3\text{CN})_4^+1^-$  in  $\text{CD}_2\text{Cl}_2$  results in the immediate association of the chiral ligand to the copper center at ambient temperature. Examination of the  $^1\text{H}$  NMR spectra reveals the presence of two separate tol-BINAP containing products formed in a 1:1 ratio. A portion of the  $^1\text{H}$  NMR is shown in Fig. 1. The identity of these compounds can be determined by comparing this spectra to those obtained by the addition of enantiopure solutions of (*S,S*)-**2** (Fig. 1b) and (*R,R*)-**2** (Fig. 1c) to  $\text{Cu}(\text{CH}_3\text{CN})_4^+1^-$ . These show that the compounds formed with *rac*-**2** correspond to the two separate enantiomers of **2** coordinated to the copper cation, wherein simple solution phase ion pairing with  $1^-$  does indeed lead to a significant separation of the  $^1\text{H}$  NMR resonances in the diastereomeric salts (eq. [2]). The largest degree of separation in the resonances for the enantiomers of **2** occurs for the aromatic hydrogens in the 5.6–6.2 ppm region (0.14 ppm) but reasonable separation is also observed for the tolyl-methyl resonances in the 2.4–2.6 ppm region (0.05 ppm).

**Fig. 1.**  $^1\text{H}$  NMR spectra (400 MHz) in  $\text{CD}_2\text{Cl}_2$  of: (a) *rac*-**2** with  $\text{Cu}(\text{CH}_3\text{CN})_4^+\text{I}^-$ ; (b) (*S,S*)-**2** with  $\text{Cu}(\text{CH}_3\text{CN})_4^+\text{I}^-$ ; and (c) (*R,R*)-**2** with  $\text{Cu}(\text{CH}_3\text{CN})_4^+\text{I}^-$  ( $\delta$  1.93 =  $\text{CH}_3\text{CN}$ ).

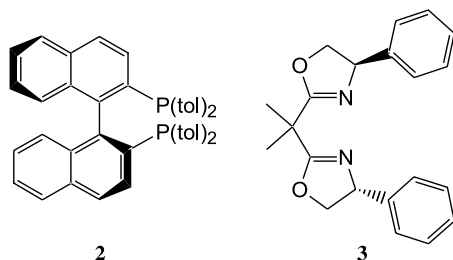


As anticipated, the degree of separation in the  $^1\text{H}$  NMR resonances for the enantiomers of **2** is sensitive to the nature of the solvent used. For example, the peaks in the 1.7–1.9 ppm region are separated by 0.06 ppm in  $\text{C}_6\text{D}_6$ , which decreases to 0.016 ppm in  $\text{CD}_2\text{Cl}_2$ , and to 0 ppm in  $\text{CD}_3\text{CN}$ . The decrease in separation that is observed with an increase in solvent polarity is consistent with weaker ion pairing in the more polar solvents (12), which results in less contact between the ions, and therefore, less enantiomeric differentiation by  $\text{I}^-$ . It should be noted that while  $\text{Cu}(\text{CH}_3\text{CN})_4^+\text{I}^-$  in benzene solvent provides a large degree of peak separation for the two enantiomers, it gives an inaccurate determination of the enantiomeric excess of **2** (calculated ee = 18% for *rac*-**2**). Since the sample was not completely soluble in  $\text{C}_6\text{D}_6$ , this error is most likely a result of the different solubilities of the diastereotopic ion pairs.



The accuracy of **1**<sup>−</sup> as a chiral NMR shift reagent in CD<sub>2</sub>Cl<sub>2</sub> was determined by preparing mixtures of tol-BINAP with known enantiomeric composition and examination by <sup>1</sup>H NMR in the presence of 1 equiv. Cu(CH<sub>3</sub>CN)<sub>4</sub><sup>+</sup>**1**<sup>−</sup>. For example, a sample of **2** with a calculated enantiomeric excess of 33% showed an experimental enantiomeric excess of 32% by <sup>1</sup>H NMR. Furthermore, a linear relationship exists between the enantiomeric excess determined by <sup>1</sup>H NMR (400 MHz) and the calculated enantiomeric excess of the non-racemic samples of **2** (Fig. 2), which could be reproduced within 2% error. These results clearly demonstrate that ion-pairing interactions in solution between **1**<sup>−</sup> and the copper-bound BINAP derivative **2** can provide a facile and accurate method to determine %ee over a broad range of enantiomeric compositions.

In light of the accuracy of Cu(CH<sub>3</sub>CN)<sub>4</sub><sup>+</sup>**1**<sup>−</sup> as a chiral NMR shift reagent with chelated phosphine ligand **2**, the generality of this system has been explored with the nitrogen-based chiral chelate 2,2'-isopropylidenebis(4-phenyl-2-oxazoline) (**3**). As shown in Fig. 3, the addition of the individual enantiomers of **3** to Cu(CH<sub>3</sub>CN)<sub>4</sub><sup>+</sup>**1**<sup>−</sup> in CD<sub>2</sub>Cl<sub>2</sub> also results in the immediate copper complexation of the ligand, and generation of complexes with significantly different <sup>1</sup>H NMR chemical shifts (spectra a and b). The most noticeable difference is observed for the methyl peaks in the backbone of the ligand. This signal in the (*R,R*)-**3** enantiomer occurs at 1.52 ppm (Fig. 3a) while the same signal for the (*S,S*)-**3** complex arises at 1.58 ppm (Fig. 3b). Thus, as with ligand **2**, ion pairing with **1**<sup>−</sup> can be used to distinguish the individual enantiomers of the copper-bound bis(oxazoline) ligand.



However, when *rac*-**3** was added to Cu(CH<sub>3</sub>CN)<sub>4</sub><sup>+</sup>**1**<sup>−</sup>, broad resonances were observed in the <sup>1</sup>H NMR (Fig. 3c). This suggested a dynamic equilibrium was present in solution. Lowering the temperature to −40 °C significantly increases the sharpness of the <sup>1</sup>H NMR signals and reveals, rather than the anticipated two sets of resonances, three distinct products in solution (Fig. 3d). Two of the complexes correspond to the diastereotopic ion pairs of (*R,R*)-**3** with Cu(CH<sub>3</sub>CN)<sub>4</sub><sup>+</sup>**1**<sup>−</sup> and (*S,S*)-**3** with Cu(CH<sub>3</sub>CN)<sub>4</sub><sup>+</sup>**1**<sup>−</sup>, with <sup>1</sup>H NMR shifts identical to that of the optically pure compounds. The third product has been assigned as the heterochiral bis-ligated complex **4**. The identity of **4** has been confirmed by reacting 2 equiv. *rac*-**3** with Cu(CH<sub>3</sub>CN)<sub>4</sub><sup>+</sup>**1**<sup>−</sup> in CD<sub>2</sub>Cl<sub>2</sub> (Fig. 3e). Complex **4** can be isolated in 85% yield upon precipitation with diethyl ether and has been fully characterized by NMR, IR, and elemental analysis.

The formation of **4**, and the broadened <sup>1</sup>H NMR resonances at ambient temperature, suggests that the addition of

**Fig. 2.** Plot of enantiomeric excess, determined by the relative integration of the <sup>1</sup>H NMR resonances in the 5.6–6.2 ppm region, for samples of **2** with Cu(CH<sub>3</sub>CN)<sub>4</sub><sup>+</sup>**1**<sup>−</sup> in CD<sub>2</sub>Cl<sub>2</sub> vs. calculated enantiomeric excess for samples of **2**.

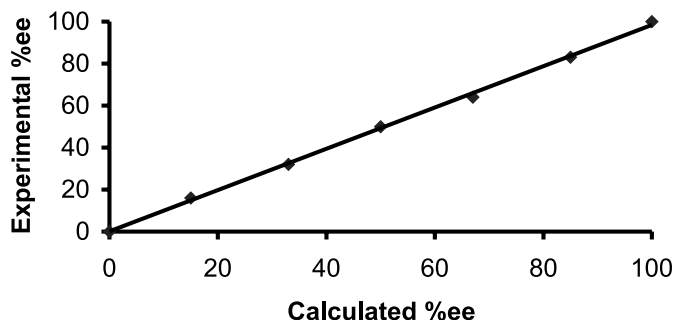
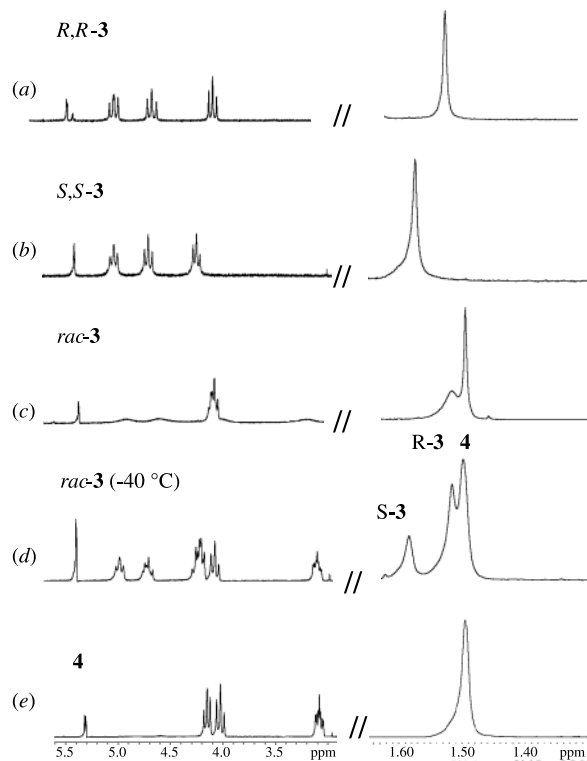
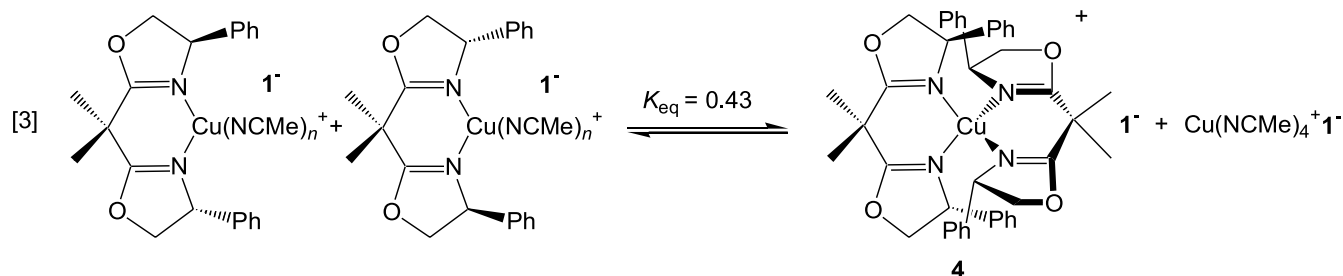


**Fig. 3.** <sup>1</sup>H NMR spectra (270 MHz) in CD<sub>2</sub>Cl<sub>2</sub> of: (a) 1 equiv. (*R,R*)-**3** with Cu(CH<sub>3</sub>CN)<sub>4</sub><sup>+</sup>**1**<sup>−</sup>; (b) 1 equiv. (*S,S*)-**3** with Cu(CH<sub>3</sub>CN)<sub>4</sub><sup>+</sup>**1**<sup>−</sup>; (c) 1 equiv. *rac*-**3** with Cu(CH<sub>3</sub>CN)<sub>4</sub><sup>+</sup>**1**<sup>−</sup>, 20 °C; (d) 1 equiv. *rac*-**3** with Cu(CH<sub>3</sub>CN)<sub>4</sub><sup>+</sup>**1**<sup>−</sup>, −40 °C; and (e) 2 equiv. *rac*-**3** with Cu(CH<sub>3</sub>CN)<sub>4</sub><sup>+</sup>**1**<sup>−</sup> (**4**).



*rac*-**3** to Cu(CH<sub>3</sub>CN)<sub>4</sub><sup>+</sup>**1**<sup>−</sup> results in the equilibrium shown in eq. [3]. Based upon the relative <sup>1</sup>H NMR intensities, the *K*<sub>eq</sub> has been calculated to be 0.43 at −40 °C. Thus, in contrast to enantiopure **3** or the more bulky BINAP derivatives (**2**), two differing enantiomers of **3** can be readily accommodated about the Cu<sup>+</sup> center, even with the concomitant formation of 1 equiv. of Cu(NCMe)<sub>4</sub><sup>+</sup>. The stability of **4** is likely related to the tetrahedral geometry of the Cu(I) complex,





wherein the coordination of the two separate enantiomers of **3** forms a stable propeller-like arrangement of the phenyl groups. A similar bis-ligated complex with the same enantiomers of **3** would likely have strongly destabilizing phenyl-phenyl interactions. To our knowledge, this equilibrium has not been previously observed in solution with **3**, and its identification may help to explain nonlinear effects that are observed using non-enantiopure bis(oxazoline) ligands and copper(I) cations as asymmetric catalysts (13).

While the presence of **4** complicates the use of  $\text{Cu}(\text{CH}_3\text{CN})_4^+1^-$  as a chiral NMR shift reagent for ligand **3**, it is notable that the diastereomeric salts formed by  $1^-$  and the copper salts of **3** are well resolved by  $^1\text{H}$  NMR, in a fashion similar to that for the BINAP derivatives **2**. This demonstrates that strong solution-phase ion pairing occurs with both general classes of ligands, and suggests that ion pairing with counteranion  $1^-$  could prove to be a general method for the NMR resolution of well-defined chiral cationic copper(I) complexes.<sup>3</sup>

In conclusion, these studies have shown that ion pairing with the chiral borate counteranion  $1^-$  can be used as a simple and effective method to distinguish individual enantiomers of chiral cationic copper complexes in solution. In the case of BINAP derivatives, this provides an accurate  $^1\text{H}$  NMR shift method to determine enantiomeric excess. The borate counteranion  $1^-$  is easy to prepare and incorporate into cationic complexes, allows for rapid  $^1\text{H}$  NMR analysis, and lacks the line broadening often observed with paramagnetic chiral shift reagents, providing an attractive alternative to standard analytical techniques for the determination of enantiomeric excess. The fact that individual enantiomers of cationic copper complexes show distinct  $^1\text{H}$  NMR resonances resulting from ion pairing with  $1^-$  also illustrates the important role of solution-phase ionic interactions with transition metal complexes. This provides a rationale for the strong counteranion influences often observed in asymmetric catalysis employing copper salts of ligands such as **3**, including our observation that the anion chirality can directly influence enantioselectivity in product formation (8). The ability to form  $1^-$  as either a proton or silver salt should prove useful in the further design of NMR shift reagents employing ion pairing with this anionic fragment.

## Experimental section

### General

All manipulations were performed under an inert atmosphere in a Vacuum Atmospheres 553-2 dry box.

$\text{Cu}(\text{CH}_3\text{CN})_4^+1^-$  was synthesized using a previously published procedure (8). Individual enantiomers of 2,2'-bis(di-*p*-tolylphosphino)-1,1'-binaphthyl (>98%) and 2,2'-isopropylidenebis(4-phenyl-2-oxazoline) (>98%) were purchased from Strem and Aldrich, respectively, and used as received. All other reagents were purchased from commercial suppliers and used as received.  $\text{CH}_3\text{CN}$  and  $\text{CH}_2\text{Cl}_2$  were distilled from  $\text{CaH}_2$  under nitrogen. Diethyl ether was distilled from Na-benzophenone under nitrogen. Deuterated solvents were dried as their protonated analogues but transferred under vacuum from the drying agent and stored under 4 Å sieves.  $^1\text{H}$ ,  $^{11}\text{B}$ , and  $^{13}\text{C}$  NMR were recorded on a JEOL-270 or Varian 400 spectrometer. Infrared spectra were recorded on a Bruker IFS-48 spectrometer.

### Representative $^1\text{H}$ NMR analysis of **2** with $\text{Cu}(\text{CH}_3\text{CN})_4^+1^-$

A solution of *rac*-**2** (4.2 mg, 0.0062 mmol) in 1.0 mL  $\text{CD}_2\text{Cl}_2$  was added to solid  $\text{Cu}(\text{CH}_3\text{CN})_4^+1^-$  (5.0 mg, 0.0062 mmol) and mixed until a clear solution resulted. The  $^1\text{H}$  NMR was taken immediately.  $^1\text{H}$  NMR of (*R,R*)-**2** with  $\text{Cu}(\text{CH}_3\text{CN})_4^+1^-$  (400 MHz,  $\text{CD}_2\text{Cl}_2$ )  $\delta$ : 7.86 (d, 4H,  $J$  = 8.0 Hz), 7.77 (d, 4H,  $J$  = 8.0 Hz), 7.11–7.34 (m, 30H), 6.95 (m, 2H), 6.87 (m, 2H), 6.48 (d, 2H,  $J$  = 6.3 Hz), 6.28 (m, 4H), 5.84 (d, 4H,  $J$  = 7.4 Hz), 2.41 (s, 6H,  $\text{P}(\text{C}_6\text{H}_4\text{CH}_3)_2$ ), 1.93 (s, 12H,  $\text{CH}_3\text{CN}$ ), 1.81 (s, 6H,  $\text{P}(\text{C}_6\text{H}_4\text{CH}_3)_2$ ).  $^1\text{H}$  NMR of (*S,S*)-**2** with  $\text{Cu}(\text{CH}_3\text{CN})_4^+1^-$  (400 MHz,  $\text{CD}_2\text{Cl}_2$ )  $\delta$ : 7.89 (m, 8H), 7.44 (d, 2H,  $J$  = 8.4 Hz), 7.09–7.38 (m, 28H), 6.95 (m, 2H), 6.85 (m, 2H), 6.55 (m, 6H), 5.98 (d, 4H,  $J$  = 7.6 Hz), 2.46 (s, 6H,  $\text{P}(\text{C}_6\text{H}_4\text{CH}_3)_2$ ), 1.93 (s, 12H,  $\text{CH}_3\text{CN}$ ), 1.80 (s, 6H,  $\text{P}(\text{C}_6\text{H}_4\text{CH}_3)_2$ ).

### Representative $^1\text{H}$ NMR analysis of **3** with $\text{Cu}(\text{CH}_3\text{CN})_4^+1^-$

A solution of (*R,R*)-**3** (2.1 mg, 0.0062 mmol) in 1.0 mL  $\text{CD}_2\text{Cl}_2$  was added to solid  $\text{Cu}(\text{CH}_3\text{CN})_4^+1^-$  (5.0 mg, 0.0062 mmol) and mixed until a clear solution resulted. The  $^1\text{H}$  NMR was taken immediately.  $^1\text{H}$  NMR of (*R,R*)-**3** with  $\text{Cu}(\text{CH}_3\text{CN})_4^+1^-$  (270 MHz,  $\text{CD}_2\text{Cl}_2$ )  $\delta$ : 7.87 (d, 4H,  $J$  = 8.7 Hz), 7.86 (d, 4H,  $J$  = 8.1 Hz), 7.45 (d, 4H,  $J$  = 8.9 Hz), 7.15–7.27 (m, 14H), 7.08 (m, 4H), 6.94 (m, 4H), 4.92 (dd, 2H,  $J$  = 8.2, 10.4 Hz,  $\text{OCHHCHPh}$ ), 4.62 (dd, 2H,  $J$  = 8.9, 10.2 Hz,  $\text{OCHHCHPh}$ ), 4.11 (dd, 2H,  $J$  = 8.4, 8.9 Hz,  $\text{OCHHCHPh}$ ), 1.79 (s, 12H,  $\text{CH}_3\text{CN}$ ), 1.52 (s, 6H,  $\text{C}(\text{CH}_3)_2$ ).  $^1\text{H}$  NMR of (*S,S*)-**3** with  $\text{Cu}(\text{CH}_3\text{CN})_4^+1^-$  (270 MHz,  $\text{CD}_2\text{Cl}_2$ )  $\delta$ : 7.87 (m, 8H), 7.46 (d, 4H,  $J$  = 8.7 Hz), 7.17–7.31 (m, 14H), 7.08 (m, 4H), 6.99 (m, 4H), 4.91 (dd, 2H,  $J$  = 8.2, 10.1 Hz,  $\text{OCHHCHPh}$ ), 4.62 (dd, 2H,

<sup>3</sup>The  $^1\text{H}$  NMR resolution of chiral tetrahedral copper(I) complexes of achiral nitrogen donor ligands has recently been reported with chiral phosphate counteranions (see ref. 9e).



$J = 8.9, 10.1$  Hz, OCHHCHPh), 4.16 (dd, 2H,  $J = 8.7, 8.9$  Hz, OCHHCHPh), 1.79 (s, 12H,  $\text{CH}_3\text{CN}$ ), 1.58 (s, 6H,  $\text{C}(\text{CH}_3)_2$ ).

### Representative procedure for the determination of enantiomeric excess (Fig. 2)

(*S,S*)-**2** (33.3 mg, 0.049 mmol) and 66.6 mg (0.098 mmol) (*R,R*)-**2** was added to 3.0 mL  $\text{CH}_2\text{Cl}_2$ . The solution was mixed and the solvent evaporated under reduced pressure to give **2** as a white solid, ee = 33%. 4.2 mg (0.0062 mmol) of this solid in 1.0 mL  $\text{CD}_2\text{Cl}_2$  was added to 5.0 mg (0.0062 mmol)  $\text{Cu}(\text{CH}_3\text{CN})_4^+\text{I}^-$  and the  $^1\text{H}$  NMR was taken to give an experimental enantiomeric excess of 32%. Data for Fig. 3: ee (calcd./ $^1\text{H}$  NMR) 0%/0%, 15%/16%, 33%/32%, 50%/50%, 67%/64%, 85%/83%, 100%/100%.

### Synthesis of 4

To a solution of  $\text{Cu}(\text{CH}_3\text{CN})_4^+\text{I}^-$  (20 mg, 0.025 mmol) in 5 mL  $\text{CH}_3\text{CN}$  was added 8.3 mg (0.025 mmol) (*R,R*)-**3** and 8.3 mg (0.025 mmol) (*S,S*)-**3**. The resulting solution was concentrated to 1 mL under reduced pressure, and the product precipitated by the slow addition of diethyl ether. The precipitate was dissolved in 1 mL  $\text{CH}_2\text{Cl}_2$  and recrystallized by the addition of pentane to give **4**•0.5 $\text{CH}_2\text{Cl}_2$  as a white solid (27.6 mg, 0.021 mmol, 85%). IR (KBr) ( $\text{cm}^{-1}$ ): 3055, 2906, 1657, 1590, 1504, 1463, 1367, 1336, 1251, 1108, 987.  $^1\text{H}$  NMR (270 MHz,  $\text{CD}_2\text{Cl}_2$ )  $\delta$ : 7.89 (d, 8H,  $J = 8.15$  Hz), 7.86 (d, 4H,  $J = 7.3$  Hz), 7.46 (d, 4H,  $J = 8.7$  Hz), 7.23–7.33 (m, 20H), 7.08 (m, 4H), 6.91 (m, 4H), 4.01–4.17 (m, 8H,  $\text{OCH}_2\text{CHPh}$ ), 3.30 (m, 4H,  $\text{OCH}_2\text{CHPh}$ ), 1.50 (s, 12H,  $\text{C}(\text{CH}_3)_2$ ).  $^{13}\text{C}$  NMR (68 MHz,  $\text{CD}_2\text{Cl}_2$ )  $\delta$ : 167.8, 156.6, 140.7, 133.4, 129.5, 128.9, 128.6, 128.1, 127.8, 127.4, 126.4, 125.0, 124.4, 122.4, 122.1, 73.4 ( $\text{OCH}_2\text{CHPh}$ ), 69.7 ( $\text{OCH}_2\text{CHPh}$ ), 39.1 ( $\text{C}(\text{CH}_3)_2$ ), 24.3 ( $\text{C}(\text{CH}_3)_2$ ).  $^{11}\text{B}$  NMR (87 MHz,  $\text{CD}_2\text{Cl}_2$ )  $\delta$ : 8.14. Anal. calcd. for  $\text{C}_{82}\text{H}_{68}\text{N}_4\text{O}_2\text{BCu}\cdot 0.5\text{CH}_2\text{Cl}_2$ : C 73.17, H 5.14, N 4.15; found: C 72.85, H 5.21, N 4.17.

### Acknowledgments

We thank the Natural Sciences and Engineering Research Council of Canada (NSERC) and Fonds pour la formation des chercheurs et l'aide à la recherche (Québec) (FCAR) for their financial support of this research. DBL thanks NSERC for a graduate fellowship.

### References

- H.Y. Aboul-Enein and I. Wainer. The impact of stereochemistry on drug development and use. John Wiley and Sons, New York. 1997.
- T.E. Beesley. Chiral chromatography. John Wiley and Sons, New York. 1998.
- (a) D. Parker. Chem. Rev. **91**, 1441 (1991); (b) R. Rothchild. Enantiomer, **5**, 457 (2000).
- (a) M.D. McCreary, D.W. Lewis, D.L. Wernick, and G.M. Whitesides. J. Am. Chem. Soc. **96**, 1038 (1974); (b) E.L. Eliel and S.H. Wilen. Stereochemistry of organic compounds. John Wiley and Sons, Inc., New York. 1994.
- For examples see: (a) Z. Glowacki, M. Topolski, E. Matezak-Jon, and M. Hoffman. Magn. Res. Chem. **27**, 922 (1989); (b) B. Staubach and J. Buddrus. Angew. Chem. Int. Ed. Engl. **35**, 1344 (1996).
- For examples see: (a) D. Toronto, F. Sarrazin, J. Pecaut, J. Marchon, M. Shang, and R. Scheidt. Inorg. Chem. **37**, 526 (1998); (b) O.D. Fox, J.F. Leung, J.M. Hunter, N.D. Dalley, and R.G. Harrison. Inorg. Chem. **39**, 783 (2000); (c) J. Simonato, S. Chappellet, J. Pecaut, P. Baret, and J. Marchon. New J. Chem. **25**, 714 (2001).
- D.B. Grotjahn and C. Joubbran. Tetrahedron: Asymmetry, **6**, 745 (1995).
- D.B. Llewellyn, D. Adamson, and B.A. Arndtsen. Org. Lett. **2**, 4165 (2000).
- For several examples see: (a) J. Lacour, C. Ginglinger, F. Favarger, and S. Torche-Haldimann. Chem. Commun. 2285 (1997); (b) C. Ginglinger, D. Jeannerat, J. Lacour, S. Juge, and J. Uziel. Tetrahedron Lett. **39**, 7495 (1998); (c) D. Monchaud, J. Lacour, C. Coudret, and S. Fraysse. J. Organomet. Chem. **624**, 388 (2001); (d) J.G. Planas, D. Prim, E. Rose, F. Rose-Munch, D. Monchaud, and J. Lacour. Organometallics, **20**, 4107 (2001); (e) V. Desvergnès-Breuil, V. Hebbe, C. Dietrich-Buchecker, J.-P. Sauvage, and J. Lacour. Inorg. Chem. **42**, 255 (2003).
- For examples in copper catalysis, see: (a) D.A. Evans, M.M. Faul, M.T. Bilodeau, B.A. Anderson, and D.M. Barnes. J. Am. Chem. Soc. **115**, 5328 (1993); (b) D. Ferraris, T. Dubbing, B. Young, W.J. Drury III, and T. Lectka. J. Org. Chem. **64**, 2168 (1999); (c) D.H. Appela, Y. Moritani, R. Shintani, E.M. Ferreira, and S.L. Buchwald. J. Am. Chem. Soc. **121**, 9473 (1999); (d) A. Yanagisawa, H. Kageyama, Y. Nakatsuka, K. Asakawa, Y. Matsumoto, and H. Yamamoto. Angew. Chem. Int. Ed. **38**, 3701 (1999); (e) S. Saaby, X. Fang, N. Gathergood, and K.A. Jorgensen. Angew. Chem. Int. Ed. **39**, 4114 (2000); (f) J.S. Johnson and D.A. Evans. Acc. Chem. Res. **33**, 325 (2000).
- For reviews of the use of BINAP derivatives in asymmetric catalysis: (a) I. Ojima (Editor). Catalytic asymmetric synthesis. Wiley, New York. 2000; (b) S. Akutagawa. Appl. Catal. A, **128**, 171 (1995); (c) H. Kumobayashi, T. Miura, N. Sayo, T. Saito, and X. Zhang. Synlett 1055 (2001), and refs. therein.
- A. Loupy and B. Tchoubar. Salt effects in organic and organometallic chemistry. 1st ed. VCH, Weinheim. 1992.
- The formation of similar heterochiral bis-ligated metal complexes has been used to explain the chiral amplification observed in several enantioselective transition metal-catalyzed reactions: (a) S. Kanemasa, Y. Oderaotoshi, S. Sakaguchi, H. Yamamoto, J. Tanaka, E. Wada, and D.P. Curran. J. Am. Chem. Soc. **120**, 3074 (1998); (b) S. Crosignani, G. Desimoni, G. Faita, S. Filippone, A. Mortoni, P. Righetti, and M. Zemat. Tetrahedron Lett. **40**, 7007 (1999); (c) D.A. Evans, M.C. Kozlowski, J.A. Murray, C.S. Burgey, K.R. Campos, B.T. Connell, and R.J. Staples. J. Am. Chem. Soc. **120**, 669 (1999).



# The reversible hydration of the malaria pigment $\beta$ -hematin<sup>1</sup>

D. Scott Bohle, Andrew D. Kosar, and Peter W. Stephens

**Abstract:**  $\beta$ -Hematin, the crystalline heme detoxification product of red blood cell digestion by the malaria parasite, can reversibly absorb up to 14% of its mass in water. Heating hydrated  $\beta$ -hematin to temperatures greater than 150 °C results in loss of the hydrated water, which is readily reabsorbed on standing in air at room temperature. The amount of water absorbed is source dependent with highly crystalline samples produced by the anhydrous-base-mediated dehydrohalogenation being twice as absorptive as more amorphous samples produced by the aqueous acid precipitation method. Infrared spectroscopy and thermal gravimetric analysis have been used to measure the amount of water lost and gained during these experiments. X-ray powder diffraction has been used to characterize the effect of hydration state on the lattice parameters. Taken together these experiments resolve literature discrepancies concerning the elemental composition of synthetic and extracted natural  $\beta$ -hematin.

**Key words:** malaria pigment, hemozoin,  $\beta$ -hematin, hydration, thermal gravimetric analysis, powder diffraction.

**Résumé :** La  $\beta$ -hématine, l'hème cristallin produit de désintoxication résultant de la digestion des cellules sanguines par le parasite de la malaria, peut de façon réversible absorber jusqu'à 14% de sa masse en eau. Le chauffage de la  $\beta$ -hématine hydratée à des températures supérieures à 150 °C provoque une perte de l'eau d'hydratation, qui est facilement réabsorbée par exposition à l'air à la température ambiante. La quantité d'eau absorbée dépend de la source. Dans le cas d'échantillons hautement cristallins, produits par la déhydrohalogénéation en présence d'une base anhydre, l'absorption de l'eau est deux fois plus grande que dans le cas d'échantillons amorphes obtenus par la méthode de précipitation en milieux acide aqueux. La spectroscopie infrarouge et l'analyse gravimétrique thermique sont utilisées pour mesurer la quantité d'eau perdue ou gagnée au cours de ces expériences. On a utilisé la diffraction des poudres par rayon X pour caractériser l'effet de l'état d'hydratation sur les paramètres du réseau. Prises ensemble ces expériences font disparaître les différences que l'on retrouve dans la littérature sur la composition élémentaire de la  $\beta$ -hématine synthétique et naturelle.

**Mots clés :** pigment de la malaria, hémozoïne,  $\beta$ -hématine, hydratation, analyse gravimétrique thermique, diffraction de poudre.

[Traduit par la Rédaction]

## Introduction

Hemoglobin digestion during the intraerythrocytic stages of malaria rapidly releases large quantities of heme (1). Heme is potentially toxic to both the parasite and the host, and must be efficiently detoxified by the parasite (1, 2). In biochemistry specific to the parasite, the heme is oxidized and crystallized as a material termed malaria pigment, or hemozoin, and this is released into the host vasculature during the next rupture–reinvasion event (3). It is now well established that malaria pigment and the synthetic phase  $\beta$ -

hematin are crystallographically identical in that they have the same unit cells and same atomic structures (4). Furthermore, the two materials are morphologically similar and grow as relatively thin ribbons. Their structure corresponds to a hydrogen-bonded chain of iron(III)(protoporphyrin-IX) propionate linked dimers (1) (5). Prior systematic study of  $\beta$ -hematin's chemistry awaited a resolution of its structure (5) and purity (6). With these critical issues now resolved, its interfacial chemistry can be studied more precisely, in particular with regard to the nature of the pigment surface – quinoline antimalarial interactions (7, 8).

Received 19 February 2003. Published on the NRC Research Press Web site at <http://canjchem.nrc.ca> on 21 October 2003.

*This article is dedicated to Professor John Harrod for his life-long service to chemistry, the profession, and his colleagues.*

**D.S. Bohle,**<sup>2</sup> Department of Chemistry, McGill University, 801 Sherbrooke St. W., Montreal, QC H3A 2K6.

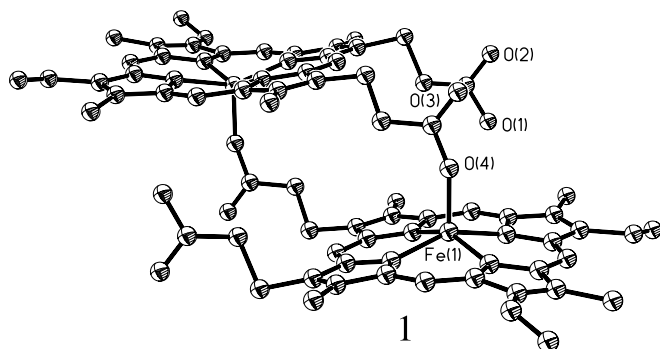
**A.D. Kosar,** Department of Chemistry, University of Wyoming, Laramie, WY 82071-3838, U.S.A.

**P.W. Stephens,** Department of Physics and Astronomy, State University of New York Stony Brook, Stony Brook, NY 11794-3800, U.S.A.

<sup>1</sup>This article is part of a Special Issue dedicated to Professor John Harrod.

<sup>2</sup>Corresponding author (e-mail: [scott.bohle@mcgill.ca](mailto:scott.bohle@mcgill.ca)).





Although malaria pigment (9) and  $\beta$ -hematin, the insoluble anhydride of hematin (Fe(III)(protoporphyrin-IX)(OH)), were both described before the determination of heme's structure (10), their chemistry have only recently been investigated in any detail owing to the recognition of their association with antimalarial drugs (7, 8, 11, 12). Due to its insolubility,  $\beta$ -hematin was widely believed to be a polymer (6), and not too surprisingly the language of polymers has been extensively used to describe a hypothetical "chain growth termination step" by the quinoline antimalarials (13). However, the solution of its structure by Rietveld and simulated annealing experiments from powder diffraction data (5, 14) unambiguously demonstrates that the original coordination polymer structure was incorrect and that the structure is a simple lattice of hydrogen-bonded dimers. Under physiological conditions,  $\beta$ -hematin is profoundly insoluble, and it dissolves by reacting with strongly alkaline aqueous solutions, neat pyridine, and neat trifluoroacetic acid. Although the spectroscopy of malaria pigment and  $\beta$ -hematin are in complete accord with the crystallographically determined structure, and consistent with a high-spin five-coordinate iron(III) which is out of the plane of the porphyrin by  $\sim 0.4$  Å, and has an  $\eta^1$ -propionate linkage (6, 15), all combustion analyses of these materials have been consistently low in carbon, hydrogen, and nitrogen (6, 16). One proposed solution to this problem was that for the aqueous acid precipitation syntheses (AAP), the product corresponds to an acetato complex (17). This somewhat bizarre suggestion is spectroscopically inconsistent with all of the above data and not too surprisingly it has been debated vigorously in the literature (17–21). If nothing else, the level of interest and discord in this fundamental problem of structure and composition reflects the difficulty in working with these materials and their importance.

The synthetic source of  $\beta$ -hematin is also an important factor in understanding many prior studies of its chemistry and biology. In general, IR spectroscopy is widely used to demonstrate the presence of  $\beta$ -hematin in its hematin precipitates. While this technique is very useful in determining the degree of short-range order in a sample, i.e., the presence of iron–propionate bonds, the materials from very different syntheses have similar spectra and these in turn are similar to the malaria pigment. Thus, IR spectroscopy alone is insufficient to distinguish these materials. This spectroscopic similarity masks a complicated set of phase distinctions among the preparations. For example, many preparations which utilize heat and acidic conditions to anneal a heterogeneous precipitate are prepared from hemin dissolved in base. These

materials have very low crystallinity as demonstrated by the presence of broadened Bragg diffraction peaks in the X-ray powder diffraction pattern, and are polydisperse with respect to both the size and morphology of the crystallites as determined by scanning electron micrographs (22). Samples prepared by this method are referred to as AAP (aqueous acid precipitation) in this paper, and are contrasted with the more crystalline materials prepared by slow crystallization by solvolyzed hemin in DMSO – noncoordinating bases, the ABM (anhydrous-base-mediated) method. While at first glance an aqueous method might seem to be more biomimetic than one that is anhydrous, the remarkably low solubility of Fe(protoporphyrin-IX) in all but strongly basic solutions requires that AAP methods start with the  $\mu$ -oxo-dimer of Fe(protoporphyrin-IX) ((Por)Fe–O–Fe(Por)). We are aware of no evidence, spectroscopic or analytical, that this linkage is present at any stage and in any vacuole in the parasite. Thus, AAP syntheses of  $\beta$ -hematin, which use base solubilization –  $\mu$ -oxo-dimer formation as a first step are no more or less biologically relevant than those of the ABM method.

In this manuscript, we present studies of  $\beta$ -hematin's reversible hydration, which has been characterized by elemental analysis, IR absorption spectroscopy, powder diffraction, and thermogravimetric analysis. Taken together these results demonstrate that malaria pigment reversibly and substoichiometrically adsorbs water. These results rationalize the observed variation in the elemental analyses for the condensed phases of  $\beta$ -hematin.

## Experimental

### Materials

Samples of  $\beta$ -hematin were prepared by either the ABM method (15), or by the AAP method (22), which is a modified version of a literature preparation (6). These two preparations give spectroscopically similar materials that have markedly different morphologies and habit (22). In particular, the AAP method, a thermal acidic annealing of a complex hematin containing precipitate from a uniform base solution of the  $\mu$ -oxo-dimer, (PP-IX)Fe–O–Fe(PP-IX), is widely used. This precipitate consists of finely divided crystallites which vary from being near amorphous to microcrystalline. On the other hand, the ABM method, an anhydrous slow solvolytic-mediated crystallization from hematin in DMSO and 2,6-lutidine, gives larger, more uniform crystals, which have the same habit as those produced by the parasite. All samples were checked for homogeneity by elemental analysis and for identity by IR spectroscopy before use in these experiments.

### Instrumental methods

Infrared spectra (IR) were measured as pressed potassium bromide pellets using a Midac M-100 FT IR spectrometer running Spectra-Calc software. Thermogravimetric analysis (TGA) experiments were conducted on a CAHN TG Systems model 2131 thermogravimetric analyzer and were processed using WINTGA software, version 1.2, run on a PC platform. Samples were placed in a quartz basket that was suspended in the instrument by a NiChrome wire. Helium and nitrogen gases were used as the furnace and purge gases



as necessary. The rehydration experiments were performed in a humidor which was fashioned from a plastic desiccator with a removable holed plate. The lower section was filled with water and the holed floor plate was replaced. The water level was maintained at a constant level throughout the rehydration experiments. The sample of  $\beta$ -hematin was placed in a quartz basket that was suspended in the instrument by a NiChrome wire. A stream of nitrogen gas was passed over the sample as it was heated and cooled with one of the following programs (with key observations in brackets):

- Program 1: The sample was heated to 200 °C over 50 min and held at 200 °C until weight loss ceased (approximately 2 h later).
- Program 2: The sample was heated to 180 °C over 2000 s and then held at 180 °C until all weight loss had ceased (approximately 3 h later).
- Program 3: The sample was heated to 200 °C over 2000 s and then held at this temperature for an additional 2000 s. It was then allowed to cool to 130 °C over 1500 s before being heated to 200 °C a second time. (No change in weight was observed during this cooling–reheating cycle. Weight loss had ceased at approximately 67 min, prior to the cooling portion of the cycle).
- Program 4: The sample was heated 150 °C over 45 min and held at 150 °C until weight loss ceased (approximately 2 h later).
- Program 5: The sample was heated to 180 °C over 30 min, held at 180 °C for 2 h and cooled to 35 °C. The sample was then reheated to 180 °C and allowed to cool back to room temperature. (Weight loss had ceased before the second heating cycle began).

Reversible adsorption and desorption experiments were performed on samples of  $\beta$ -hematin, which were placed in the humidor and allowed to stand undisturbed for 96 h. The sample was weighed and placed in an oven at 150 °C for 24 h, after which time the sample was weighed and the cycle was repeated five more times.

### High resolution X-ray powder diffraction

Synchrotron radiation ( $\lambda = 1.14021 \text{ \AA}$ ), at Beamline X3B1 of the National Synchrotron Light Source was used for high-resolution X-ray powder diffraction. Wavelength calibration was performed with  $\text{Al}_2\text{O}_3$  standards. Samples were run as either a flat-plate or a spinning 1 mm capillary tube.

### Dehydration of ABM $\beta$ -hematin

A sample of ABM  $\beta$ -hematin (35.2 mg) was heated under a stream of nitrogen according to temperature program 4. The temperature was held at 150 °C until no further weight loss occurred Fig. S1a.<sup>3</sup> Weight loss ceases at approximately 8500 s, resulting in a 7.16% loss for a final weight of 32.9 mg. An additional sample (55.6 mg) was heated under a stream of nitrogen according to the same program until weight loss ceased (Fig. S1b).<sup>3</sup> The weight loss ended at approximately 10 500 s, resulting in an 11.25% weight loss, and a final weight of 49.2 mg. A final sample (TGA not

shown; 323.6 mg) was heated according to temperature program 5. A loss of 14.3% was noted resulting in a final weight of 278.7 mg.

## Results and discussion

Since the identity of malaria pigment has been a key question, the homogeneity and composition of the isolated hemozoin is very important. The two published separate elemental analyses of natural malaria pigment (Table 1) are unfortunately not in close agreement with one another. The results for malaria pigment isolated from *Plasmodium falciparum* are fortuitously much closer to that of the putative heme–acetate complex than for the predicted values for the anhydride ( $\beta$ -hematin). However, the results for samples isolated from *Plasmodium berghei* are closer to  $\beta$ -hematin, but are still low in all values except hydrogen and oxygen (16). Despite these deviations, it is a significant biochemical achievement that these groups were able to obtain values as close to the pure synthetic samples given the difficulty in isolating and purifying malaria pigment (23–25). But the results clearly show that some other factor is responsible for decreasing the %C and N values while increasing the %H and O values. Moreover, there are also significant and similar deviations in composition for completely synthetic preparations of  $\beta$ -hematin, which have similar deviations from theory (Table 1), regardless of the method of preparation. Of these results, the rigorously dried and sealed sample **P** has the only satisfactory elemental analysis, and most acid precipitation and anhydrous-base-mediated preparations have average values for %C and %N which are consistently lower than the theoretical value (6, 15).

The most likely rationale for these results is that malaria pigment and  $\beta$ -hematin are hygroscopic, with water being readily absorbed by the  $\beta$ -hematin crystallites. This would lower the carbon and nitrogen figures while raising the oxygen and hydrogen compositions upon combustion analysis. To test this hypothesis we used thermogravimetric analysis for dehydrated and rehydrated  $\beta$ -hematin. Water readily and reversibly adds to the crystallites, and is driven off by heating to ~150 °C. By carefully reducing external contaminants, it became apparent that the elemental analyses were always low in %C and %N and that this corresponds to a substoichiometric hydrate.

To determine the degree of sample hydration, several different TGA experiments were conducted with various  $\beta$ -hematin samples, as well as by X-ray diffraction, IR spectroscopy, and by rehydration TGA. For example,  $\beta$ -hematin (1.1711 g) prepared by AAP, was placed in the quartz TGA cell and heated to 200 °C in stepwise transitions from 30 to 200 °C over 50 min. The sample experienced a total weight loss of  $2.6(\pm 0.1)\%$  through the course of the experiment (Fig. 1). A separate, larger sample of the same batch of  $\beta$ -hematin (2.1547 g) was rapidly heated to 200 °C and held at this temperature for 55 min. Again, a weight loss of  $2.8(\pm 0.1)\%$  was observed. IR analysis of the remaining black solids confirmed that the samples are spectroscopically identical for the heme modes, with the only significant

<sup>3</sup>Supplementary data may be purchased from the Directory of Unpublished Data, Document Delivery, CISTI, National Research Council Canada, Ottawa, ON K1A 0S2, Canada ([http://www.nrc.ca/cisti/irm/unpub\\_e.shtml](http://www.nrc.ca/cisti/irm/unpub_e.shtml) for information on ordering).

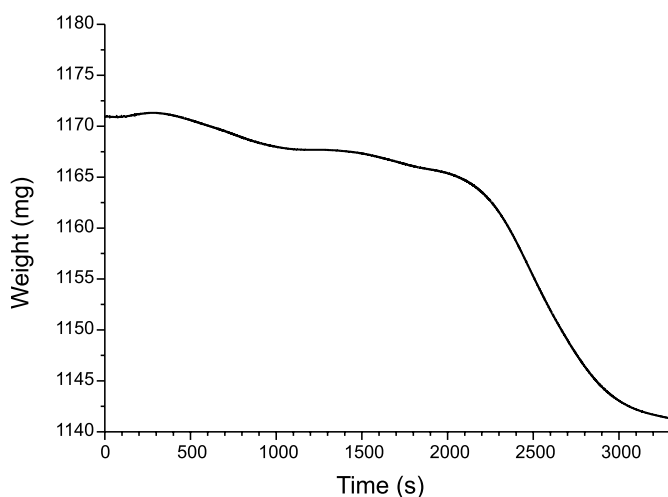


**Table 1.** Combustion analyses for (a) natural and (b) synthetic  $\beta$ -hematin.<sup>a</sup>

(a) Natural $\beta$ -hematin.					
Entry/Sample	Source <sup>a</sup>	%C	%H	%N	Reference/Formula
$\beta$ -Hematin	Theory	66.35	5.08	9.10	[Fe(PPIX)(CO <sub>2</sub> H)(CO <sub>2</sub> ) <sub>2</sub> ] <sub>2</sub>
Hemin–acetate	Theory	64.01	5.22	8.29	[Fe(PPIX)(CO <sub>2</sub> H) <sub>2</sub> (O <sub>2</sub> CCH <sub>3</sub> ) <sub>2</sub> ]
Malaria pigment	<i>P. berg.</i> <sup>b</sup>	64.6	5.2	8.7	16
Malaria pigment	<i>P. fal.</i> <sup>b</sup>	63.7	5.6	7.5	6
(b) Synthetic $\beta$ -hematin.					
Entry/Sample	Source <sup>a</sup>	%C	%H	%N	Reference/Formula
<b>A</b>	AAP	64.49	5.15	8.87	This work
<b>B</b>	AAP	64.70	4.99	8.80	This work
<b>C</b>	AAP	64.98	5.24	8.90	This work
<b>D</b>	AAP	62.52	4.99	8.53	This work
<b>E</b>	AAP	63.64	5.13	8.67	This work
<b>F</b>	ABM	64.85	5.13	8.89	This work
<b>G</b>	ABM	64.6	4.9	8.9	This work
<b>H</b>	ABM	65.07	5.02	8.96	This work
<b>I</b>	ABM	64.93	4.99	8.81	This work
<b>J</b>	ABM	65.14	5.13	8.86	This work
<b>K</b>	ABM	65.31	5.28	8.96	This work
<b>L</b>	ABM	65.30	5.11	8.81	This work
<b>M</b>	ABM	65.41	5.17	9.02	This work
<b>N</b>	ABM	65.44	5.19	8.99	This work
<b>O</b>	ABM	64.31	5.08	8.78	This work
<b>P</b>	ABM	66.09	5.22	8.95	This work

<sup>a</sup> $\beta$ -Hematin synthesized by either: AAP (6) or ABM methods (15).

<sup>b</sup>Natural sources include *P. berg.* being the NYU-2 strain of *Plasmodium berghei* and *P. fal.* being the HB-3 clone of *Plasmodium falciparum*. Note that in addition to C, H, and N composition for *P. fal.* elemental analyses for Fe (7.5%), O (15.6%), and Cl (< 0.1%) and for *P. berg.* Fe (8.7%) and O (12.5%), were also measured. Calculated values for anhydrous  $\beta$ -hematin (FeC<sub>34</sub>H<sub>31</sub>N<sub>4</sub>O<sub>4</sub>) are Fe (9.07%) and O (10.40%).

**Fig. 1.** Representative TGA of AAP  $\beta$ -hematin. Sample heated to 200 °C, according to program 1. Weight loss is approximately 2.6%.

spectral change being in the OH-stretching region. In this region ( $\sim 3400\text{ cm}^{-1}$ ), the broad OH stretch has nearly disappeared in the post-TGA heated sample; other bands in the spectrum remained unchanged (Fig. 2). These experiments demonstrate that most of the water is lost upon drying at temperatures  $\geq 150\text{ }^{\circ}\text{C}$ .

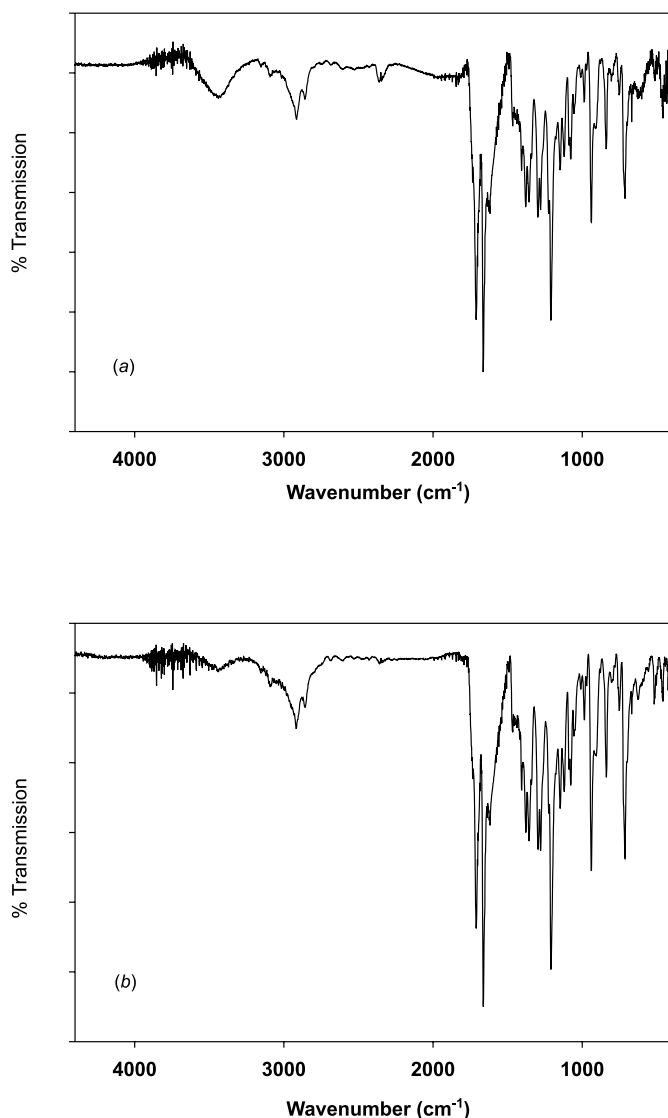
Similar results are found when samples of  $\beta$ -hematin prepared by ABM are treated in the same manner. For example,

$\beta$ -hematin (253.2 mg) was placed in the quartz TGA cell and heated stepwise to 200 °C over 45 min. Upon reaching 200 °C, the sample was then held at a constant temperature of 200 °C for 400 min. The sample had a net weight loss of  $2.6(\pm 0.3)\%$  over the whole experiment. A separate batch of  $\beta$ -hematin produced by this method (153.3 mg) was also assayed from 30 to 180 °C according to temperature program 2 (Fig. 3a). This batch showed a weight loss of  $5.3(\pm 0.2)\%$ , for a final weight of 145.3 mg. IR analysis of the remaining black solids confirmed that they were still  $\beta$ -hematin with the only modification being in the  $\nu(\text{OH})$  region, as previously described. Significantly, freshly isolated batches of  $\beta$ -hematin prepared by the ABM methods did not exhibit a similar thermal dehydration unless exposed to normal atmospheric conditions during storage. These solids have a larger capacity to absorb water than the more amorphous and less crystalline materials produced by the AAP method.

In contrast, when a sample of AAP  $\beta$ -hematin (2154.7 mg) was subjected to the heating and cooling program in temperature program 3, it required 4000 s before becoming isogravimetric. Upon cooling to 130 °C and subsequent reheating to 200 °C, no weight gain or additional weight loss was noted (Fig. 3b). The final weight loss for this analysis was  $2.86(\pm 0.02)\%$ , resulting in a final weight of 2093.5 mg. Again, a smaller amount of water was lost more rapidly from the more amorphous AAP preparations. Related parallel experiments are shown in Fig. S1<sup>3</sup> for  $\beta$ -hematin prepared by ABM.



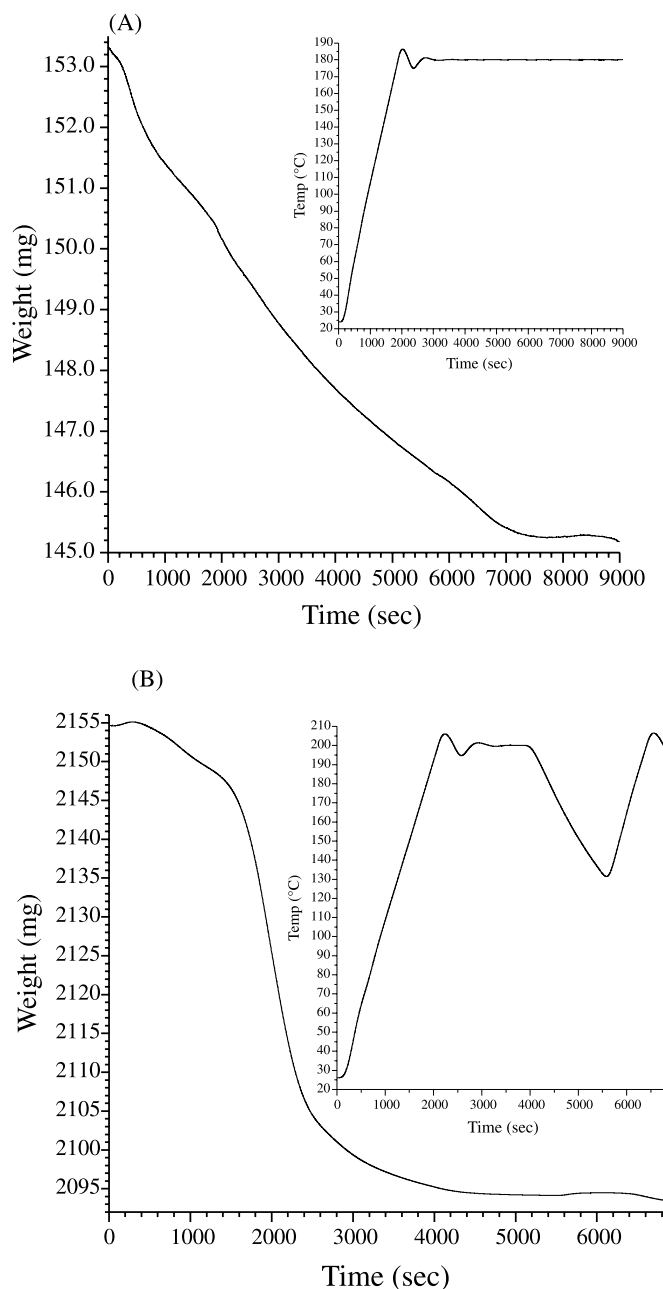
**Fig. 2.** Representative IR spectra for AAP  $\beta$ -hematin both pre- (A) and post- (B) TGA analysis. Sample analyzed as in Fig. 1.



The phenomenon of  $\beta$ -hematin dehydration was also studied by in situ IR spectroscopy with a rigorously dry KBr host matrix. In this case, a sample of hydrated ABM  $\beta$ -hematin in a pressed pellet had strong bands because of  $\nu(\text{OH})$  (Fig. S2).<sup>3</sup> This pellet was then placed in an oven at 150 °C for 15 min, removed, and reanalyzed. This cycle was performed three additional times with spectra being collected at 30 min, 24 h, and 72 h. Following the initial spectrum acquisition, only minor changes in the bands for Fe(PP-IX) were found, with the  $\nu(\text{OH})$  region at ca. 3400  $\text{cm}^{-1}$  having the only significant change. Based on these observations, the majority of the water is driven off within the first 30 min of heating. Because the spectrum does not change and a subsequent hematin assay on the residue demonstrated that it had not decomposed, rearranged, or altered upon prolonged heating.

The reversibility of the dehydration of  $\beta$ -hematin was established with the use of a humidur. In Fig. 4, the data for the heating and room temperature humidifying is shown. The sample was initially heated to drive out any water that

**Fig. 3.** TGA analysis of AAP  $\beta$ -hematin according to temperature programs (A) 2 and (B) 3. Insert shows the temperature program.

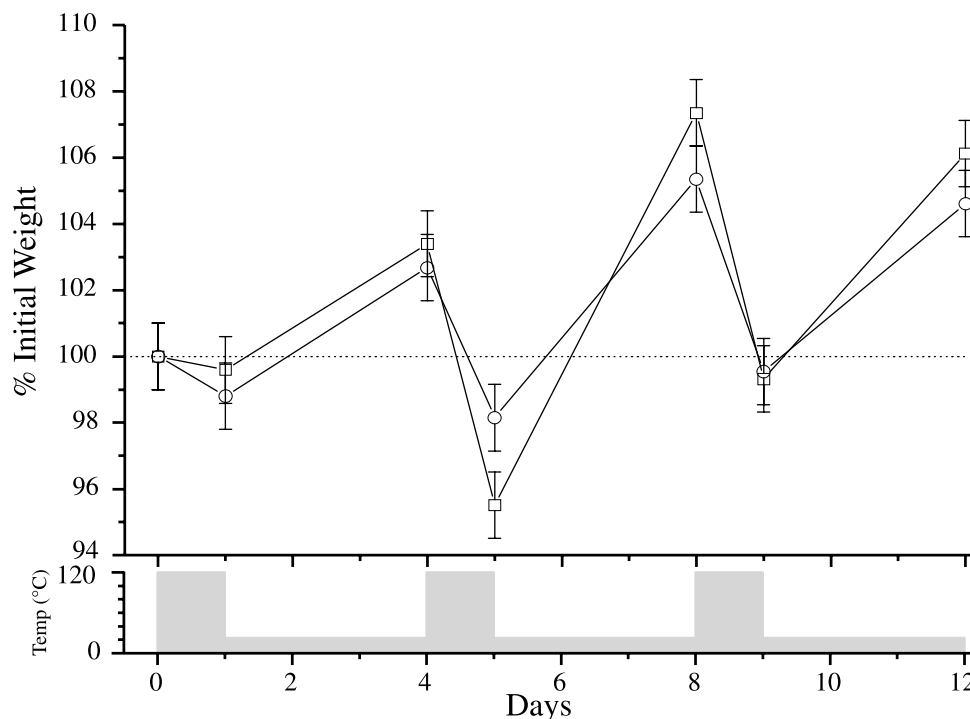


may have been present. After 24 h at 120 °C, the sample was weighed and placed in the humidur at room temperature, where it was left undisturbed for 72 h before being reweighed. This cycle was performed two more times. The mass changes indicate that the water is reversibly absorbed by the sample of  $\beta$ -hematin. IR analysis after the final step confirmed that the  $\beta$ -hematin was spectroscopically identical to the starting material.

Synchrotron X-ray powder diffraction is able to detect subtle changes in the lattice of a compound upon dehydration. To determine the nature of any lattice changes during hydration, several aliquots of freshly prepared anhydrous



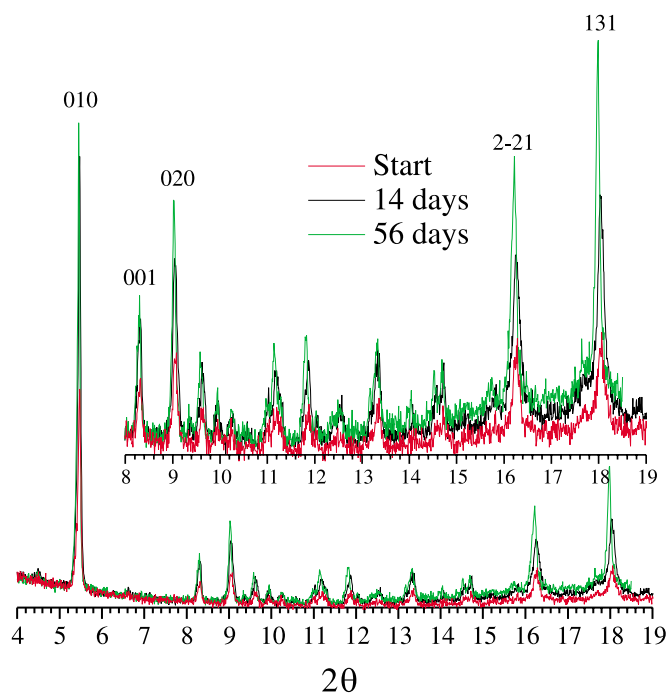
**Fig. 4.** Data for two batches of ABM  $\beta$ -hematin in the humidor and oven. The samples are cycled between 120 °C (dry) for 24 h and 23 °C (humid) for 72 h.



ABM  $\beta$ -hematin were hydrated in a humidor for 14 or 56 days, being exposed to constant humidity throughout. The samples were removed and sealed under nitrogen in rigorously dried capillaries and their X-ray diffraction patterns measured. Rehydration led to subtle changes in the positions and relative intensities of the Bragg reflections in the powder diffraction pattern (Fig. 5a). All three diffraction patterns have close indices, and the increases in the relative intensities of the (100), (020), (2-21), and (131) peaks are not likely to be due to a single preferred orientation effect. In addition to changes in these relative intensities, there is a sharp improvement in the signal to noise ratio of the diffraction profile upon hydration. These results suggest that the sample is becoming more ordered as it is allowed to rehydrate. From the X-ray data, we found that as the sample was hydrated, the unit cell volume reduces from 1448.3 (22) to 1417.5 (15) Å<sup>3</sup> with the relative magnitudes of all three parameters (*a*, *b*, *c*) decreasing uniformly. Further hydration beyond 42 days results in only an additional 0.06% decrease in volume. The structural origin of this shift in the size of the lattice is difficult to definitely assign, with the refined structure from the dehydrated material being isostructural with the published structure (results not shown). Rehydration results in a smaller cell, but overall, water is not found in the lattice from the solution of the powder diffraction pattern. This suggests water mediates a type of ordering or annealing process, possibly between the layers of hemes. Regardless of its origin,  $\beta$ -hematin is able to absorb surprisingly large quantities of water. This situation is opposite to that known for vermiculite, where the hydration of charged ions between silicate layers results in the specific expansion of the lattice with one preferred direction (26).

These experiments rationalize the anomalous elemental analyses for  $\beta$ -hematin. However, they also point to a poten-

**Fig. 5.** Synchrotron X-ray powder diffraction ( $\lambda = 1.4021$  Å) data for ABM  $\beta$ -hematin rehydration experiments. Samples collected as spinning capillaries, with changes in the peaks are most noticeable for the (131) and (2-21). Samples were rehydrated for 0, 14, and 56 days prior to being stored for analysis as described in the *Experimental* section.



tially useful drug target. The observed reversible hydration naturally suggests that other materials might readily be absorbed by  $\beta$ -hematin, and, purely speculatively, a potential



consequence of this might be increased solubility and bioavailability of heme during the intraerythrocytic stages of the parasite. If such an adsorbate could be designed or discovered, it would be a candidate antimalarial. It is well known that the complex unique biochemistry within the malaria parasite's digestive vacuole presents many potential drug targets that can be exploited (27). Heme detoxification by the formation of  $\beta$ -hematin is one such drug target. Perhaps  $\beta$ -hematin deaggregation is another.

## Conclusions

Water is adsorbed substoichiometrically by  $\beta$ -hematin with considerable variability depending upon its preparation and history. Among the factors which might be responsible for this are the inherent variations in morphology and phase homogeneity. In particular, the more crystalline ABM preparations absorb more water and release it more slowly upon heating. It is still unclear where the water adsorbs; possibilities include intercalation between the layers or adhesion to the surface of the crystallite. The water was found to be reversibly incorporated into the crystallites and can be removed with moderate heating. Two possibilities exist for the apparent increase in crystallinity following a rehydration-dehydration sequence. If the water is between the laminar planes, it is possible that the crystals fragment upon heating as the water is liberated, but if it is only weakly surface adsorbed, removal will be facile and will leave little trace following dehydration.

## References

1. D.E. Goldberg, A.F.G. Slater, A. Cerami, and G.B. Henderson. *Proc. Natl. Acad. Sci. U.S.A.* **87**, 2931 (1990).
2. A.L. Tappel. *Arch. Biochem. Biophys.* **44**, 378 (1953).
3. I.Y. Gluzman, S.E. Francis, A. Oksman, C.E. Smith, K.L. Duffin, and D.E. Goldberg. *J. Clin. Invest.* **93**, 1602 (1994).
4. D.S. Bohle, R.E. Dinnebier, S.K. Madsen, and P.W. Stephens. *J. Biol. Chem.* **272**, 713 (1997).
5. S. Pagola, P.W. Stephens, D.S. Bohle, A.D. Kosar, and S.K. Madsen. *Nature (London)*, **404**, 307 (2000).
6. A.F.G. Slater, W.J. Swiggard, B.R. Orton, W.D. Flitter, D.E. Goldberg, A. Cerami, and G.B. Henderson. *Proc. Natl. Acad. Sci. U.S.A.* **88**, 325 (1991).
7. D.C. Warhurst. *Biochem. Pharmacol.* **30**, 3323 (1981).
8. D.J. Sullivan, I.Y. Gluzman, D.G. Russell, D.E. Goldberg. *Proc. Natl. Acad. Sci. U.S.A.* **93**, 11 865 (1996).
9. W.H. Brown. *J. Exp. Med.* **13**, 290 (1911).
10. H. Fischer and H. Orth. *Die Chemie des Pyrrols. Vol. Band II.* Akademische Verlagsgesellschaft, M.B.H., Leipzig. 1937.
11. D.J. Sullivan. *Int. J. Parasitol.* **32**, 1645 (2002).
12. T.J. Egan. *J. Inorg. Biochem.* **91**, 19 (2002).
13. A.F.G. Slater and A. Cerami. *Nature (London)*, **355**, 167 (1992).
14. P.W. Stephens, S. Pagola, D.S. Bohle, and A.D. Kosar. *National Synchrotron Light Source (NSLS) Newsletter*, July 2000. pp. 1–4.
15. D.S. Bohle, B.J. Conklin, D. Cox, S.K. Madsen, S. Paulson, P.W. Stephens, and G.T. Yee. *ACS Symp. Ser.* **572**, 497 (1994).
16. C.D. Fitch and P. Kanjanangkulpan. *J. Biol. Chem.* **262**, 15 552 (1987).
17. A.V. Pandey and B.L. Tekwani. *FEBS Lett.* **393**, 189 (1996).
18. T.J. Egan, W.W. Mavuso, and K.K. Ncokazi. *Biochemistry*, **40**, 204 (2001).
19. T.J. Egan, E. Hempelmann, and W.W. Mavuso. *J. Inorg. Biochem.* **73**, 101 (1999).
20. A.V. Pandey and B.L. Tekwani. *FEBS Lett.* **402**, 236 (1997).
21. A.V. Pandey, N. Singh, B.L. Tekwani, S.K. Puri, and V.S. Chauhan. *J. Pharm. Biomed. Anal.* **201**, 203 (1999).
22. D.S. Bohle, A.D. Kosar, and P.W. Stephens. *Acta Crystallogr., Sect. D: Biol. Crystallog.* **D58**, 1752 (2002).
23. C.A. Homewood, J.M. Jewsbury, and M.L. Chance. *Comp. Biochem. Physiol.* **43B**, 517 (1972).
24. K.A. Yamada and I.W. Sherman. *Exp. Parasitol.* **48**, 61 (1979).
25. J.O. Ashong, I.P. Blench, and D.C. Warhurst. *Trans. R. Soc. Trop. Med. Hyg.* **83**, 167 (1989).
26. A.F. Wells. *Structural inorganic chemistry*. 5th ed. Oxford Science Publications, Oxford. 1987.
27. D.E. Goldberg. *Semin. Cell Bio.* **4**, 355 (1993).



# Synthesis, first structures, and catalytic activity of the monomeric rhodium(I)-siloxide phosphine complexes<sup>1</sup>

Bogdan Marciniec, Paulina Błażejewska-Chadyniak, and Maciej Kubicki

**Abstract:** Four new square-plane rhodium siloxide complexes of the general formula  $[\text{Rh}(\text{cod})(\text{PR}_3')(\text{OSiR}_3)]$  (where  $\text{R} = \text{Me}, i\text{-Pr}, O\text{-}t\text{-Bu}$ ,  $\text{R}' = \text{Cy}, \text{Ph}$ ) were synthesized and the structures of three of them were resolved by the X-ray method.  $[\text{Rh}(\text{cod})(\text{PCy}_3)(\text{OSiMe}_3)]$  (**1**) appeared to be a very efficient catalyst for hydrosilylation of allyl glycidyl ether to yield, selectively, 3-glycidoxypropyltriethoxysilane, a commercially important silane coupling agent. Catalytic measurements and stoichiometric experiments of **1** with triethoxysilane suggest a mechanism where an unsaturated Rh-H species is responsible for the catalysis.

**Key words:** rhodium (phosphine) siloxides, hydrosilylation, catalysis.

**Résumé :** On a synthétisé quatre nouveaux complexes siloxyde de rhodium de géométrie plan carré et de formule générale  $[\text{Rh}(\text{cod})(\text{PR}_3')(\text{OSiR}_3)]$  (dans lesquels  $\text{R} = \text{Me}, i\text{-Pr}, O\text{-}t\text{-Bu}$ ;  $\text{R}' = \text{Cy}, \text{Ph}$ ) et on a déterminé les structures de trois d'entre eux par diffraction des rayons X. Il semble que le  $[\text{Rh}(\text{cod})(\text{PCy}_3)(\text{OSiMe}_3)]$  (**1**) est un catalyseur très efficace pour l'hydrosilylation de l'oxyde d'allyle et de glycidyle conduisant à la formation sélective du 3-glycidoxypropyltriéthoxysilane, un silane commercialement important comme agent de couplage. Des mesures catalytiques et des expériences stoechiométriques du composé **1** avec le triéthoxysilane suggèrent un mécanisme dans lequel l'espèce Rh-H insaturée est responsable de la catalyse.

**Mots clés :** rhodium(phosphine)siloxydes, hydrosilylation, catalyse.

[Traduit par la Rédaction]

## Introduction

Siloxides similar to alkoxides have been employed as ancillary ligands of transition metal (TM) complexes, markedly influencing the reactivity of a metal center by electronic and steric effects of the substituents at silicon. They can be regarded as very good molecular models of metal complexes supported on silica and silicate surfaces, which are known to catalyze a variety of organic and organometallic transformations particularly by early transition metal complexes (1). Unlike the early TM-siloxides the information on the late TM-siloxides is scarce. Only exceptional siloxy derivatives of Fe (2), Co (3), Ni (4), Ru (5), Rh (6–9), Pt (10), Os (11), and Ir (10c) have been synthesized and characterized spectroscopically, and the structures of all of them have been a subject of recent interest. The dimeric complexes included  $[\text{Rh}(\text{CO})_2(\mu\text{-OSiR}_3)]_2$ , where  $\text{R} = \text{Me}$  (8),  $\text{Ph}$  (6b), and  $[\text{Rh}(\text{cod})(\mu\text{-OSiPh}_3)]_2$  (6b),  $[\text{Rh}(\text{diene})(\mu\text{-OSiMe}_3)]_2$ , where diene = cod (7a, 7b), nbd (7c).

Catalytic activity of  $[\text{Rh}(\text{cod})(\mu\text{-OSiMe}_3)]_2$  has been illustrated in some reactions, i.e., in the hydrosilylation of alkenes (12) and allyl alkyl ethers (13, 14) and in the silylative coupling of vinylsilanes with alkenes (15).

The aim of this work was to prepare monomeric rhodium-siloxide complexes, to determine their structures by X-ray methods, and to assess their catalytic activity in the hydrosilylation process.

## Experimental section

### General methods and chemicals

All syntheses and operations were carried out using standard Schlenk techniques under a carefully deoxygenated and dried argon.  $^1\text{H}$ ,  $^{13}\text{C}$ ,  $^{31}\text{P}$ , and  $^{29}\text{Si}$  NMR spectra were recorded on Varian Mercury and Varian Gemini 300 VT spectrometers. The reagents were obtained from the following sources:  $\text{C}_6\text{H}_6$  from OBR PR Plock (Poland),  $\text{PPh}_3$  from Fluka, sodium trimethylsilanolate from Aldrich, THF and

Received 11 April 2003. Published on the NRC Research Press Web site at <http://canjchem.nrc.ca> on 21 October 2003.

*Dedicated to celebrate Professor John Harrod's productive career and in recognition of his great contribution to organosilicon chemistry and catalysis.*

**B. Marciniec,<sup>2</sup> P. Błażejewska-Chadyniak, and M. Kubicki.** Faculty of Chemistry, Adam Mickiewicz University, Grunwaldzka 6, 60-780 Poznań, Poland.

<sup>1</sup>This article is part of a Special Issue dedicated to Professor John Harrod.

<sup>2</sup>Corresponding author (e-mail: [marcinb@main.amu.edu.pl](mailto:marcinb@main.amu.edu.pl)).



$C_5H_{12}$  from POCh Gliwice (Poland),  $HOSi(O-t-Bu)_3$  and  $i-Pr_3SiCl$  from ABCR Co. All solvents were distilled in an inert atmosphere prior to use.  $[Rh(cod)(\mu-Cl)]_2$  (16, 17),  $[Rh(cod)(\mu-OSiMe_3)]_2$  (5) (7a) were prepared according to the previously reported procedures.

#### Synthesis of the complex $[Rh(cod)(PCy_3)(OSiMe_3)]$ (1)

Portions of 0.1 g  $[Rh(cod)(\mu-OSiMe_3)]_2$  (0.33 mmol) and 0.2 g (0.71 mmol)  $PCy_3$  were placed in a Schlenk flask under Ar. Then 6 mL of dried and deoxygenated  $C_6H_6$  was added. The reaction was carried out for 4 h at room temperature (r.t.). After this time,  $C_6H_6$  was evaporated and 5 mL of dried and deoxygenated  $C_5H_{12}$  was added. The precipitate was decanted three times by  $C_5H_{12}$ . The complex was dried in vacuum for about 3 h. It was obtained with a yield of 75%.  $^1H$  NMR ( $C_6D_6$ )  $\delta$ : 0.46 (s, 9H,  $-CH_3$ ), 1.20–2.02 (m, 33H,  $-Cy$ ), 2.35 (m, 4H,  $-CH_2-$ ), 3.26 (m, 4H,  $-CH_2-$ ), 5.41 (m, 4H,  $=CH-$ ).  $^{13}C$  NMR ( $C_6D_6$ )  $\delta$ : 6.0 ( $-OSiMe_3$ ,  $-CH_3$ ), 27.21, 28.28, 29.07, 30.80, 31.80, 31.97, 32.50, 32.71, 34.07 ( $-Cy$ ,  $-CH_2-$ ), 62.83, 63.01 (cod,  $-CH_2-$ ), 99.15, 99.26, 99.32, 99.42 (cod,  $=CH-$ ).  $^{31}P$  NMR ( $C_6D_6$ )  $\delta$ : 25.28 (d,  $J_{Rh-P}$  = 151 Hz).  $^{29}Si$  NMR  $\delta$ :  $-3.35$ . Anal. calcd. for  $RhPSiOC_{29}H_{54}$ : C 59.98, H 9.37; found: C 60.22, H 9.44.

#### Synthesis of the complex $[Rh(cod)(PPh_3)(OSiMe_3)]$ (2)

Complex 2 was prepared in a similar way to complex 1, except for the fact that  $PPh_3$  (0.09 g, 0.34 mmol) was used instead of  $PCy_3$ . The yellow complex was obtained with the yield of 70%.  $^1H$  NMR ( $C_6D_6$ )  $\delta$ : 0.30 (s, 9H,  $-CH_3$ ), 1.68 (m, 4H,  $-CH_2-$ ), 2.18 (m, 4H,  $-CH_2-$ ), 2.88 (m, 2H,  $-CH=$ ), 5.62 (m, 2H,  $-CH=$ ), 7.07 (m, 9H,  $-Ph$ ), 7.75 (m, 6H,  $-Ph$ ).  $^{13}C$  NMR ( $C_6D_6$ )  $\delta$ : 5.06 ( $-OSiMe_3$ ,  $-CH_3$ ), 29.02, 33.67 (cod,  $-CH_2-$ ), 64.60, 64.78 (cod,  $-CH=$ ), 103.18 (bs, cod,  $=CH-$ ), 130.10, 131.57, 132.38, 135.23 ( $-Ph$ ).  $^{31}P$  NMR ( $C_6D_6$ )  $\delta$ : 25.21.  $^{29}Si$  NMR ( $C_6D_6$ )  $\delta$ : 21.55. Anal. calcd.  $RhPSiOC_{29}H_{36}$  for: C 61.92, H 6.45; found: C 62.18, H 6.37.

#### Synthesis of the complex $[Rh(cod)(PCy_3)(OSi-i-Pr_3)]$ (3)

##### Preparation of $HOSi-i-Pr_3$

$i-Pr_3SiCl$  (10 mL) was added to a water–ether mixture ( $H_2O$  (300 mL), ether (150 mL)) that was stirred with a magnetic stirrer for 24 h at r.t. Then the aqueous phase was removed and the ether solution was dried by addition of  $CaCl_2$ . After 24 h it was filtered off by a cannula system and the solvent was evaporated to dryness. The product was obtained with a yield of 87%.

##### Preparation of $NaOSi-i-Pr_3$

Thirty mL portions of anhydrous and deoxygenated THF and 1.20 g (53 mmol) of metallic Na were placed into a 50 mL double-necked round-bottomed flask equipped with a reflux condenser and an attachment for gas supply. Then 7.8 g of  $HOSiO-i-Pr_3$  (45 mmol) was added over 30 min with constant stirring by a magnetic stirrer. After this time, the mixture was heated at a boiling point for 6 h. After the reaction, the contents of the flask were filtered off hot by a cannula to a Schlenk flask. Having cooled the contents, the solvent was evaporated and the product was dried in vacuum for about 3 h. It was obtained with a 90% yield.  $^1H$  NMR

( $C_6D_6$ )  $\delta$ : 1.02 (m, 3H,  $-CH=$ ), 1.20 (d, 18H,  $-CH_3$ ). Anal. calcd. for  $NaOSiC_9H_{21}$ : C 55.06, H 10.78; found: C 54.82, H 11.11.

#### Synthesis of the complex $[Rh(Cl)(cod)(PCy_3)]$

Portions of 0.22 g (0.8 mmol) of  $PCy_3$  and 0.21 g (0.4 mmol) of  $[Rh(cod)(\mu-Cl)]_2$  were placed in a Schlenk flask in an Ar atmosphere. Then 5 mL of dried and deoxygenated  $C_6H_6$  was added and the mixture was stirred with a magnetic stirrer. After 2 h,  $C_6H_6$  was evaporated and 5 mL of dried and deoxygenated  $C_5H_{12}$  was added. The precipitate was decanted three times by  $C_5H_{12}$ . The complex was dried in vacuum for about 3 h. It was obtained with a yield of 95%.  $^1H$  NMR ( $C_6D_6$ )  $\delta$ : 1.20–2.19 (m, 33H,  $-Cy$ ), 2.32 (m, 4H,  $-CH_2-$ ), 3.60 (m, 4H,  $-CH_2-$ ), 5.72 (m, 4H,  $=CH-$ ).  $^{31}P$  NMR ( $C_6D_6$ )  $\delta$ : 27.33 (d,  $J_{Rh-P}$  = 350.7 Hz). Anal. calcd. for  $RhPClC_{26}H_{45}$ : C 59.26, H 8.61; found: C 59.82, H 8.84.

#### Synthesis of 3

Portions of 0.2 g (0.38 mmol)  $[Rh(cod)(PCy_3)(Cl)]$  and 0.08 g (0.42 mmol)  $NaOSi-i-Pr_3$  were placed in a Schlenk flask in an Ar atmosphere. Then 5 mL of dried and deoxygenated  $C_6H_6$  was added. The reaction was conducted for 24 h at r.t. After this time,  $C_6H_6$  was evaporated and 8 mL of dried and deoxygenated  $C_5H_{12}$  was added. The entire mixture was filtered off by a cannula system. The solvent was evaporated from the obtained filtrate leaving a yellow solid. The complex was isolated with a yield of 85%.  $^1H$  NMR ( $C_6D_6$ )  $\delta$ : 1.22 (m, 3H,  $-CH=$ ), 1.48 (d, 18H,  $-CH_3$ ), 1.57–2.28 (m, 33H,  $-Cy$ ), 2.30 (m, 4H,  $-CH_2-$ ), 3.47 (m, 4H,  $-CH_2-$ ), 5.28 (m, 4H,  $=CH-$ ).  $^{13}C$  NMR ( $C_6D_6$ )  $\delta$ : 16.99–20.32, 26.49–34.04 (m,  $-OSi-i-Pr_3$  +  $-Cy$ ), 61.75, 61.93 (cod,  $-CH_2-$ ), 97.92, 98.03, 98.09, 98.19 (cod,  $=CH-$ ).  $^{31}P$  NMR ( $C_6D_6$ )  $\delta$ : 27.40 (d,  $J_{Rh-P}$  = 149 Hz).  $^{29}Si$  NMR ( $C_6D_6$ )  $\delta$ :  $-21.51$ . Anal. calcd. for  $RhPSiOC_{35}H_{66}$ : C 63.23, H 10.01; found: C 62.91, H 10.11.

#### Synthesis of the complex $[Rh(cod)(PCy_3)\{OSi(O-t-Bu)_3\}]$ (4)

##### Preparation of $NaOSi(O-t-Bu)_3$

Fifty mL portions of anhydrous and deoxygenated THF and 0.35 g (15 mmol) of metallic Na were placed into a 100 mL double-necked round-bottomed flask equipped with a reflux condenser and an attachment for gas supply. Then 4 g of  $HOSi(O-t-Bu)_3$  (15 mmol) was added and the mixture was heated at a boiling point for 4 h. After the reaction, the contents of the flask were filtered off hot by a cannula to a Schlenk flask. Having cooled the contents, the solvent was evaporated and the white solid was washed with diethyl ether ( $3 \times 5$  mL). The product was obtained with a 90% yield.  $^1H$  NMR ( $C_6D_6$ )  $\delta$ : 1.57 (s, 27H,  $-CH_3$ ).

##### Preparation of 4

Complex 4 was prepared in a similar way to complex 3, except for the fact that  $NaOSi(O-t-Bu)_3$  (0.12 g, 0.42 mmol) was used instead of  $NaOSi-i-Pr_3$ . The yellow complex was obtained with the yield of 90%.  $^1H$  NMR ( $C_6D_6$ )  $\delta$ : 1.56 (s, 27H,  $-CH_3$ ), 1.81 (m, 33H,  $-CH_2-$ ), 2.50 (m, 4H,  $-CH_2-$ ), 3.25 (m, 4H,  $-CH_2-$ ), 5.05 (m, 4H,  $=CH-$ ).  $^{13}C$  NMR ( $C_6D_6$ )  $\delta$ : 26.91, 27.83, 27.96, 28.78, 30.87, 31.68, 32.62, 33.58, 33.80,



**Table 1.** Crystal data.

Compound	<b>1</b>	<b>3</b>	<b>4</b>
Formula	RhPSiOC <sub>29</sub> H <sub>54</sub>	RhPSiOC <sub>35</sub> H <sub>66</sub>	RhPSiO <sub>4</sub> C <sub>38</sub> H <sub>72</sub> •0.5(C <sub>5</sub> H <sub>12</sub> )
Formula weight	580.69	664.85	791.00
Colour, shape	Yellow, block	Pale-yellow, plate	
<i>T</i> (K)	293(2)	293(2)	110(1)
Crystal system	Triclinic	Triclinic	Monoclinic
Space group	<i>P</i> -1	<i>P</i> -1	<i>P</i> 2 <sub>1</sub> / <i>c</i>
<i>a</i> (Å)	10.3468(5)	10.814(2)	9.9104(7)
<i>b</i> (Å)	10.6222(5)	11.696(2)	22.3863(13)
<i>c</i> (Å)	16.5714(7)	15.956(3)	19.2440(12)
$\alpha$ (°)	94.299(4)	80.06(3)	90
$\beta$ (°)	93.677(3)	75.94(3)	96.002(5)
$\gamma$ (°)	110.484(4)	68.51(3)	90
<i>V</i> (Å <sup>3</sup> )	1693.35(13)	1813.7(6)	4246.0(5)
<i>Z</i>	2	2	4
<i>d</i> <sub>x</sub> (Mg m <sup>-3</sup> )	1.139	1.217	1.237
$\mu$ (mm <sup>-1</sup> )	0.604	0.572	0.504
<i>F</i> (000)	620	716	1708
Crystal size (mm)	0.2 × 0.3 × 0.3	0.1 × 0.15 × 0.3	0.2 × 0.2 × 0.3
$\theta$ Range for data collection (°)	3.4–27	3.1–24	3.03–27
Reflections collected	14221	13858	36670
Independent reflections	7260	6343	9248
[ <i>R</i> <sub>int</sub> ]	[0.028]	[0.040]	[0.085]
<i>R</i> ( <i>I</i> > 2 $\sigma$ ( <i>I</i> ))	0.0405	0.0468	0.0587
<i>wR</i> 2 ( <i>I</i> > 2 $\sigma$ ( <i>I</i> ))	0.1040	0.0772	0.1184
<i>R</i> (all data)	0.0479	0.0870	0.0975
<i>wR</i> 2 (all data)	0.1093	0.0854	0.1322
<i>S</i>	1.07	0.97	0.98
$\Delta\rho_{\max}/\Delta\rho_{\min}$ (e Å <sup>-3</sup> )	0.90/−0.51	0.73/−0.49	1.53/−0.97

33.94 (−Cy, −CH<sub>2</sub>−), 33.43 (−OSi(O-*t*-Bu)<sub>3</sub>, −CH<sub>3</sub>), 61.33, 61.51 (cod, −CH<sub>2</sub>−), 72.56 (−OSi(O-*t*-Bu)<sub>3</sub>, −OC(CH<sub>3</sub>)<sub>3</sub>), 100.27, 100.37, 100.42, 100.53 (cod, =CH−). <sup>31</sup>P NMR (C<sub>6</sub>D<sub>6</sub>)  $\delta$ : 27.03 (d, *J*<sub>Rh-P</sub> = 143 Hz). <sup>29</sup>Si NMR (C<sub>6</sub>D<sub>6</sub>)  $\delta$ : −21.53. Anal. calcd. for RhPSiO<sub>4</sub>C<sub>38</sub>H<sub>72</sub>: C 60.46, H 9.61; found: C 60.72, H 9.08.

### Crystallization of the complexes

A portion of about 0.05 g of the complex and an amount of dry and deoxygenated C<sub>5</sub>H<sub>12</sub> sufficient to obtain a clear solution were placed in a Schlenk flask. Crystallization was conducted for 10–14 days at −15 °C. A few crystals selected under a microscope were placed in glass capillary tubes of 0.3 mm in diameter and subjected to X-ray diffraction study.

### X-ray crystallography

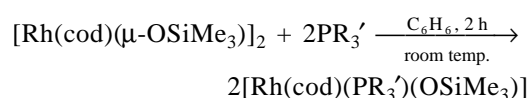
X-ray diffraction data was collected, from the crystals sealed in glass capillaries, on a KUMA KM4CCD diffractometer (18) using graphite-monochromated MoK $\alpha$  radiation ( $\lambda$  = 0.71073 Å). Data collections were performed in six separate runs (a total of 782 frames for **1** and **4**, and 588 frames for **3**) to cover an appropriate part of the reflection sphere. The  $\omega$ -scan was used, two reference frames were measured after every 50 frames, and they did not show any systematical changes neither in the peak position nor in their intensities. The unit-cell parameters were determined by least-squares treatment of the setting angles of 9625 (**1**), 5103 (**3**), and 5665 (**4**) highest-intensity reflections, chosen

from the whole experiment. Lorentz and polarization effects were accounted for (19), and then data were corrected for absorption and merged with SORTAV (20). The structures were solved by direct methods with the SHELXS-97 program (21), and refined with full-matrix least-squares by SHELXL-97 (22). All non-hydrogen atoms, including those from the disordered solvent–pentane molecule in **3**, were refined anisotropically. The positions of hydrogen atoms were generated geometrically and they were refined as a “riding model”. The *U*<sub>iso</sub> parameters of hydrogen atoms were set at 1.2 times *U*<sub>eq</sub> of the appropriate carrier atom.

A summary of crystal data, data collection and refinement is given in Table 1.

### Results and discussion

Two types of reactions were used for the synthesis of the rhodium-siloxide complexes:



where R' = Cy, Ph and

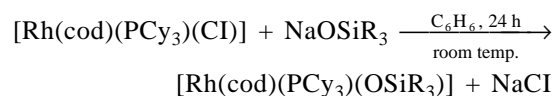
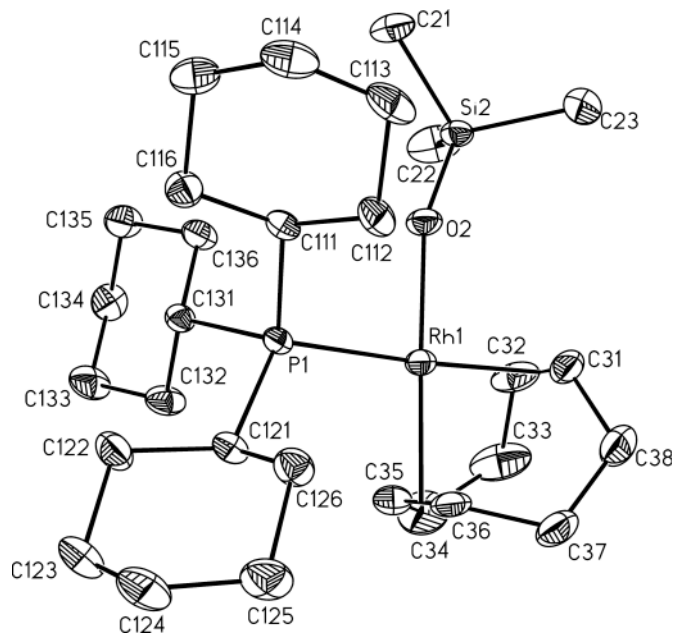




**Fig. 1.** Anisotropic displacement representation of complex **1** showing the labelling scheme. Displacement ellipsoids are shown at the 33% probability level and hydrogen atoms are omitted for clarity.



where R = *i*-Pr, *O*-*t*-Bu. All the rhodium-siloxide products were characterized by  $^1\text{H}$ ,  $^{13}\text{C}$ ,  $^{31}\text{P}$ , and  $^{29}\text{Si}$  NMR spectroscopy.

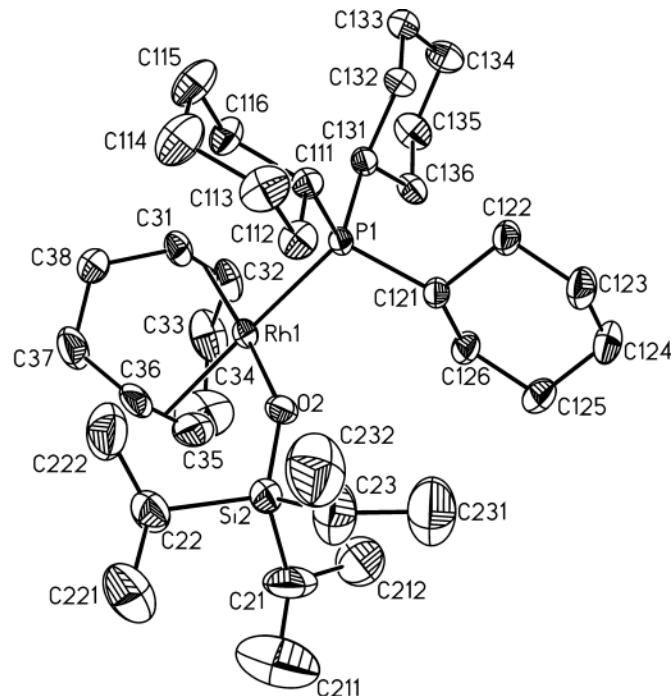
The molecular structures of complexes  $[\text{Rh}(\text{cod})(\text{PCy}_3)(\text{OSiMe}_3)]$  (**1**),  $[\text{Rh}(\text{cod})(\text{PCy}_3)(\text{OSi-}i\text{-Pr}_3)]$  (**3**), and  $[\text{Rh}(\text{cod})(\text{PCy}_3)(\text{OSi}(\text{O-}t\text{-Bu})_3)]$  (**4**) with the atom-numbering scheme are depicted in Figs. 1, 2, and 3, respectively. Selected geometrical parameters are listed in Table 2.

In all three complexes the coordination of rhodium is square planar, providing that the middle points of the cyclooctadiene double bonds are regarded as the coordination sites X1 and X2. This is confirmed by the values of bond angles at rhodium (cf. Table 2) as well as by the least-squares calculation of the mean plane through five points: Rh, X1, X2, O, and P. Maximum deviation from this plane is 0.017(2) Å in **1**, 0.059(5) Å in **3**, and 0.005(2) Å in **4**. The cyclooctadiene double bonds are approximately perpendicular to the central coordination plane.

The bond lengths and angles are quite typical. All cyclohexyl rings are slightly distorted chairs, and the conformations of cyclooctadiene rings are close to a  $\text{C}_2$  - twist-boat, the minimum energy conformation (23, 24). Despite these similarities there are some quite interesting differences in the overall conformation between alkyl-substituted siloxide complexes **1** and **3** and, on the other side, the alkoxy-substituted siloxide complex **4**. For example, the disposition of the substituents at the Si atom with respect to the O—Si bond can be described as *+sc*, *-sc*, *ap* (Rh—O—Si—C torsion angles approximately  $+60^\circ$ ,  $-60^\circ$ ,  $180^\circ$ ) in **1** and **3**, while in **4** it is *+ac*, *-ac*, *sp* (Rh—O—Si—O values are close to  $+120^\circ$ ,  $-120^\circ$ ,  $0^\circ$ ).

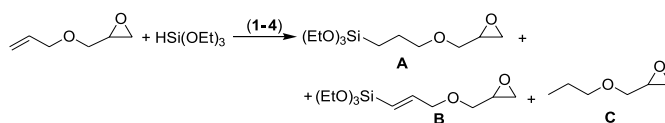
All the monomeric rhodium-siloxide complexes **1–4** were tested in the hydrosilylation of allyl glycidyl ether by

**Fig. 2.** Anisotropic displacement representation of complex **3** showing the labelling scheme. Displacement ellipsoids are shown at the 33% probability level and hydrogen atoms are omitted for clarity.



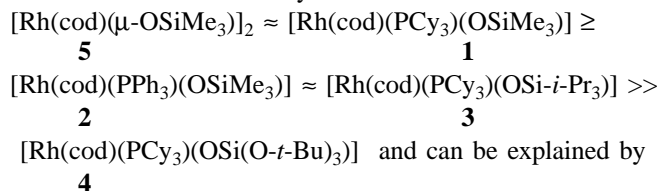
triethoxysilane leading to glycidoxypropytriethoxysilane, which is a commercially important silane coupling agent.

The reaction gives the hydrosilylation product (**A**) with very high yield accompanied by products of the dehydrogenative silylation (**B** + **C**) according to the following scheme:



The effect of the catalyst **1–4** concentrations as well as other conditions (temperature and time of the reaction) on the yield of the main product and by-products is compiled in Table 3. Dimeric  $[\text{Rh}(\text{cod})(\mu\text{-OSiMe}_3)]_2$  (**5**), whose structure (7b) and catalytic activity in this reaction (13, 14) was reported previously, is used for comparison.

The order of the activity is as follows:



increasing steric effects of the siloxy group influencing directly the rate of the hydrosilylation process as well as by a complex stereoelectronic effect of the trisubstituted phosphine ( $\mathbf{1} \geq \mathbf{2}$ ). The latter effect is a result of facile oxygenation and dissociation of  $\text{PCy}_3$  vs.  $\text{PPh}_3$  caused mainly by an



**Fig. 3.** Anisotropic displacement representation of complex **4** showing the labelling scheme. Displacement ellipsoids are shown at the 50% probability level and hydrogen atoms are omitted for clarity.

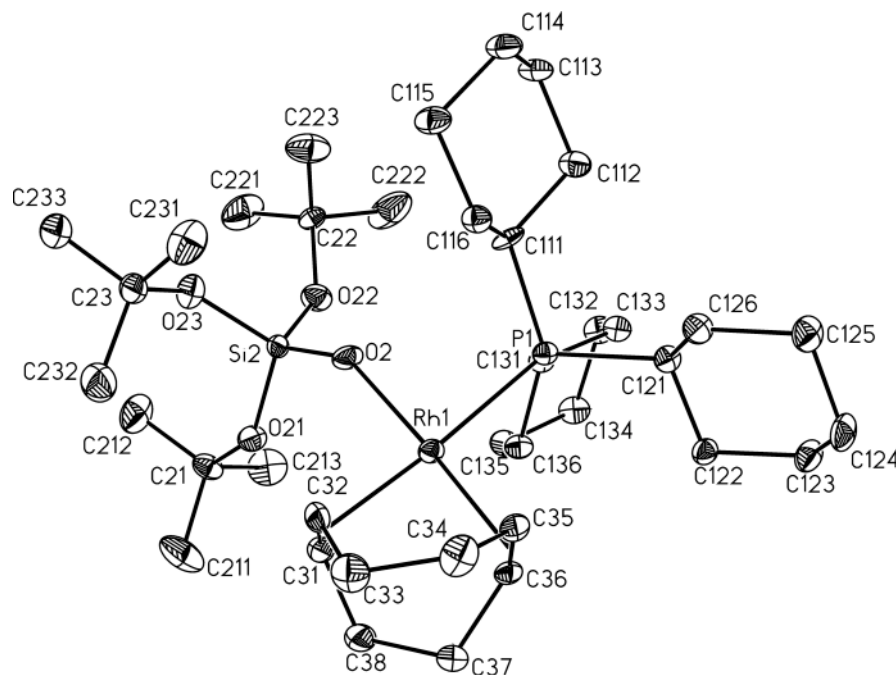


**Table 2.** Selected bond lengths (Å) and bond angles (°) (X1, X2 denote the middle points of the cyclooctadiene double bonds) with esds in parentheses.

Compound	1	3	4
<b>Bond lengths (Å)</b>			
Rh1—X1	2.086(3)	2.007(5)	2.083(5)
Rh1—X2	1.995(3)	2.110(6)	2.002(4)
Rh1—P1	2.3411(7)	2.3444(15)	2.3609(12)
Rh1—O2	2.030(2)	2.064(3)	2.065(3)
<P—C>	1.860(6)	1.854(11)	1.859(3)
O2—Si2	1.577(2)	1.593(4)	1.561(3)
<b>Bond angles (°)</b>			
X1—Rh1—X2	86.53(15)	85.6(3)	86.3(2)
X1—Rh1—P1	176.53(11)	178.5(2)	175.46(13)
X1—Rh1—O2	90.84(11)	92.0(2)	90.91(16)
X2—Rh1—P1	96.87(12)	95.08(16)	98.19(14)
X2—Rh1—O2	177.15(13)	174.9(2)	177.2(2)
P1—Rh1—O2	85.77(6)	87.48(10)	84.57(10)
Rh1—O2—Si2	152.70(13)	147.4(2)	143.6(2)

increase in electron-donor properties of the former phosphine.

Similarly to the hydrosilylation by dimeric rhodium siloxide **5** (25), monomeric phosphine rhodium siloxides (**1–4**) undergo an oxidative addition with triethoxysilane followed by elimination of disiloxane according to the mechanistic pathways proposed in Scheme 1.

Preliminary  $^1\text{H}$  NMR study on the stoichiometric reactions of (**1**) with triethoxysilane performed in  $\text{C}_6\text{D}_6$  in room temperature and in air, right away after mixing of the substrate, revealed the presence of several doublets at  $\delta \sim -13.35$  and

**Table 3.** The hydrosilylation of allyl glycidyl ether by triethoxysilane catalyzed by rhodium siloxide(I) complexes (**1–5**).

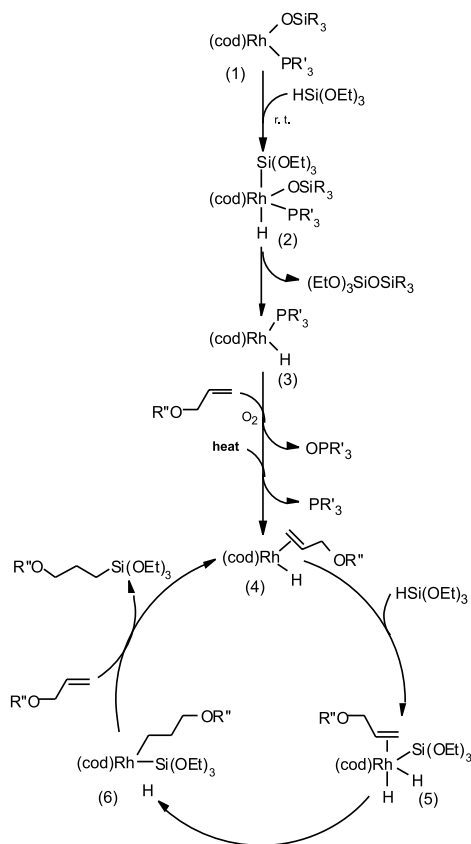
Catalyst	Yield (%)	
	A	B + C
<b>Conditions: 25 °C, [Rh] = <math>5 \times 10^{-3}</math> mol L<math>^{-1}</math>, 15 min</b>		
<b>1</b>	96	4
<b>2</b>	70	2
<b>3</b>	99	—
<b>4</b>	40	2
<b>5*</b>	90	10
<b>Conditions: 25 °C, [Rh] = <math>10^{-3}</math> mol L<math>^{-1}</math>, 4 h</b>		
<b>1</b>	99	1
<b>2</b>	100	—
<b>3</b>	68	1
<b>4</b>	35	—
<b>5*</b>	98	2
<b>Conditions: 40 °C, [Rh] = <math>10^{-4}</math> mol L<math>^{-1}</math>, 24 h</b>		
<b>1</b>	98	2
<b>2, (2*)</b>	99 (98)	1 (2)
<b>5*</b>	99	1
<b>Conditions: 60 °C, [Rh] = <math>5 \times 10^{-5}</math> mol L<math>^{-1}</math>, 1 h</b>		
<b>1, (1)</b>	98 (50)	1 (—)
<b>2, (2)</b>	41 (4)	Traces
<b>5</b>	98	—

**Note:** All reactions carried out under the following conditions (except for those designated by \*):  $[\text{HSi}(\text{OEt})_3]:[\text{ether}] = 1:1.5$ , glass ampoules, air (\* indicates reactions carried out in an argon atmosphere).

$J_{\text{Rh-H}} \sim 43$  in the spectra to be formed in the mixture of the penta-coordinate complexes similarly to the spectra observed previously in the system – dimeric complex **5**



**Scheme 1.** Catalysis of hydrosilylation by monomeric rhodium-siloxide phosphine complexes.



R = Me, *i*-Pr, *O*-*t*-Bu  
R' = Cy, Ph



(HSi(OEt)<sub>3</sub>) (7a). A rapid elimination of disiloxane Me<sub>3</sub>SiOSi(OEt)<sub>3</sub> in the reaction mixture observed by GC-MS techniques is a direct evidence of reductive elimination of (2) to yield tetracoordinated complex (3) (see Scheme 1). This reaction occurs even at room temperature.

The very efficient oxygenation of phosphine observed in air vs. dissociation of phosphine in oxygen-free conditions, particularly observed at enhanced temperature (60 °C) (a formation of OPR<sub>3</sub>' vs. PR<sub>3</sub>' is detected by <sup>31</sup>P NMR), is proposed to be responsible for generation of [Rh(cod)(H)(alkene)]. Although no direct evidence was found for (4) by NMR, this 16e hydride rhodium complex with an already coordinated molecule of alkene seems to be a key intermediate in all catalytic transformations involving hydrosilanes, e.g., hydrosilylation, dehydrogenative silylation, silylformylation, etc. The variant of the Chalk and Harrod mechanism (26) involving the insertion of allyl ether into the Rh—Si bond, which could account for slight side reactions

of dehydrogenative silylation observed (1% to 2%), is omitted from the scheme for clarity.

## Conclusions

Four new monomeric, square-planar rhodium siloxide complexes of the general formula [Rh(cod)(PR<sub>3</sub>') (OSiR<sub>3</sub>)] where R' = Cy, Ph, R = Me, *i*-Pr, *O*-*t*-Bu were synthesized and three of them were structurally characterized.<sup>3</sup>

The complex (1) ([Rh(cod)(PCy)<sub>3</sub>](OSiMe<sub>3</sub>))] appeared to be a very efficient catalyst for hydrosilylation of allyl glycidyl ether occurring in air. All catalytic data and stoichiometric reactivities of (1) with triethoxysilane are consistent with a mechanism involving a generation of tetra-coordinated Rh-H species (responsible for catalysis).

## Acknowledgement

The work was supported by State Committee for Scientific Research, Project Nos. K026/T09/2001 and 7 T09B 004 20.

## References

- For reviews: (a) F.R. Hartley. Supported metal complexes. Reidel, Boston. 1985; (b) Y. Iwasawa. (Editor). Tailored metal catalysts. Reidel, Boston. 1986; (c) P.T. Wolczanski. Polyhedron, **14**, 3335 (1995); (d) B. Marciniec and H. Maciejewski. Coord. Chem. Rev. **223**, 301 (2001).
- A.N. Kornev, T.A. Chesnokova, V.V. Semenov, E.V. Zhezlova, L.N. Zakhonov, L.G. Klapshina, G.A. Domrachev, and V.S. Rusakov. J. Organometal. Chem. **547**, 113 (1997).
- (a) G.A. Siegel, R.A. Bartlett, D. Decker, M.M. Olmsted, and P.P. Power. Inorg. Chem. **26**, 1773 (1987); (b) I. Kownacki, M. Kubicki, and B. Marciniec. Polyhedron, **20**, 3015 (2001).
- A.K. McMullen, T.D. Tilley, A.L. Rheingold, and S.J. Geib. Inorg. Chem. **29**, 2228 (1990).
- (a) J.T. Poulton, K. Folting, W.E. Streib, and K.G. Caulton. Inorg. Chem. **31**, 3190 (1992); (b) J. Puga, T.P. Fehlner, B.C. Gates, D. Braga, and F. Greponi. Inorg. Chem. **29**, 2376 (1990); (c) T.J. Johnson, K. Folting, W.E. Streib, J.D. Martin, J.C. Huffman, S.A. Jackson, O. Eisenstein, and K.G. Caulton. Inorg. Chem. **34**, 488 (1995).
- (a) G. Palyi, C. Zucchi, U. Ugo, R. Psaro, A. Sironi, and A.J. Vizi-Orosz. J. Mol. Catal. **74**, 51 (1992); (b) A.J. Vizi-Orosz, R. Ugo, R. Psaro, A. Sironi, M. Moret, C. Zucchi, F. Ghelti, and G. Palyi. Inorg. Chem. **33**, 4600 (1994).
- (a) B. Marciniec and P. Krzyżanowski. J. Organometal. Chem. **493**, 261 (1995); (b) P. Krzyżanowski, M. Kubicki, and B. Marciniec. Polyhedron, **15**, 1 (1996); (c) B. Marciniec, P. Krzyżanowski, and M. Kubicki. Polyhedron, **15**, 4233 (1996).
- L. Marko and A.J. Vizi-Orosz. Trans. Met. Chem. **7**, 216 (1982).
- (a) F.J. Feher and T.L. Tajima. J. Am. Chem. Soc. **116**, 2145 (1994); (b) F.J. Feherand and R.L. Blanski. Organometallics, **12**, 958 (1993).

<sup>3</sup>Supplementary data may be purchased from the Directory of Unpublished Data, Document Delivery, CISTI, National Research Council Canada, Ottawa, ON K1A 0S2, Canada ([http://www.nrc.ca/cisti/irm/unpub\\_e.shtml](http://www.nrc.ca/cisti/irm/unpub_e.shtml) for information on ordering electronically). CCDC 205459 (1), 205460 (3), and 205461 (4) contain the crystallographic data for this manuscript. These data can be obtained, free of charge, via [www.ccdc.cam.ac.uk/conts/retrieving.html](http://www.ccdc.cam.ac.uk/conts/retrieving.html) (or from the Cambridge Crystallographic Data Centre, 12 Union Road, Cambridge CB2 1EZ, U.K.; fax +44 1223 336033; or [deposit@ccdc.cam.ac.uk](mailto:deposit@ccdc.cam.ac.uk)).



10. (a) A. Fukuoka, A. Sato, K. Kodama, M. Hiram, and S. Komiya. *Inorg. Chim. Acta*, **294**, 266 (1999); (b) J. Pfeiffer, G. Kickelbick, and G. Schubert. *Organometallics*, **19**, 957 (2000); (c) H. Schmidbaur and J. Adlkofer. *Chem. Ber.* **107**, 3680 (1974).
11. J.L. Herde, J.V. Lambert, and C.V. Senoff. *Inorg. Synth.* **15**, 18 (1974).
12. B. Marciniec, P. Krzyżanowski, E. Walczuk-Guściora, and W. Duczmal. *J. Mol. Catal.* **144**, 263 (1999).
13. B. Marciniec, E. Walczuk, P. Błażejewska-Chadyniak, D. Chadyniak, M. Kujawa-Welten, and S. Krompiec. *In Organosilicon chemistry V — From molecules to materials*. Accepted for publication.
14. (a) B. Marciniec, P. Błażejewska-Chadyniak, E. Walczuk-Guściora, and M. Kujawa-Welten. *Pol. Patent P-351 449*, 2001; (b) B. Marciniec, D. Chadyniak, P. Pawluć, H. Maciejewski, and P. Błażejewska-Chadyniak. *Pol. Patent P-351 451*, 2001.
15. (a) B. Marciniec, E. Walczuk-Guściora, and P. Błażejewska-Chadyniak. *J. Mol. Catal.* **160**, 165 (2000); (b) B. Marciniec, E. Walczuk-Guściora, and C. Pietraszuk. *Organometallics*, **20**, 3423 (2001).
16. G. Giordano and R.H. Crabtree. *Inorg. Synth.* **19**, 218 (1979).
17. M.A. Kulzick, R.T. Price, R.A. Andersen, and E.L. Muetterties. *J. Organometal. Chem.* **333**, 105 (1987).
18. CRYVALIS. Version 162 [computer program]. KUMA Diffraction, Wrocław, Poland. 2000.
19. CRYVALISRED. Version 162 [computer program]. KUMA Diffraction, Wrocław, Poland. 2000.
20. R.H. Blessing. *J. Appl. Crystallogr.* **22**, 396 (1989).
21. G.M. Sheldrick. *Acta Crystallogr.* **A46**, 467 (1990).
22. G.M. Sheldrick. SHELXL97 [computer program]. University of Göttingen, Göttingen, Germany. 1997.
23. F.A.L. Anet and L. Kozerski. *J. Am. Chem. Soc.* **95**, 3407 (1973).
24. D.N.J. White and M.J. Bovill. *J. Chem. Soc., Perkin Trans. 2*, 1610 (1977).
25. B. Marciniec, I. Kownacki, M. Kubicki, P. Krzyżanowski, E. Walczuk, and P. Błażejewska-Chadyniak. *In Perspectives in organometallic chemistry*. RSC, Cambridge. 2003. p. 253.
26. A.J. Chalk and J.F. Harrod. *J. Am. Chem. Soc.* **87**, 16 (1965).



# Hydrosilylation of alkenes and ketones catalyzed by nickel(II) indenyl complexes<sup>1</sup>

Frédéric-Georges Fontaine, René-Viet Nguyen, and Davit Zargarian

**Abstract:** Abstraction of  $\text{Cl}^-$  from the complexes (indenyl) $\text{Ni}(\text{PPh}_3)\text{Cl}$  generates cationic species that are effective precatalysts for the hydrosilylation of some olefins and ketones. For instance, the mixture of (1-Me-indenyl) $\text{Ni}(\text{PPh}_3)\text{Cl}$  and  $\text{NaBPh}_4$  (or methylaluminoxane) reacts at room temperature with ca. 100 equiv. each of  $\text{PhSiH}_3$  and styrene to produce [1-phenyl-1-ethyl](phenyl)silane,  $\text{PhCH}(\text{CH}_3)(\text{SiPhH}_2)$ , in 50%–80% yield. The same system can also catalyze the hydrosilylation of 1-hexene and norbornene, but the products arising from these substrates consist of mixtures of regio- and stereoisomers. On the other hand, ketone hydrosilylation is regiospecific, giving the corresponding silyl ethers in high yields. A number of experimental observations have indicated that the initially generated Ni-based cation is not the catalytically active species. Indeed, the cationic initiators may be replaced by  $\text{LiAlH}_4$  or  $\text{AlMe}_3$ , which generate the corresponding Ni-H or Ni-Me derivatives, respectively. Moreover, the observed regioselectivity for the addition of  $\text{PhSiH}_3$  to styrene (i.e., predominant addition of the silyl fragment to the  $\alpha$ -C) is opposite of what would be expected if the reaction mechanism involved carbocationic intermediates. A new mechanism is proposed in which the active species is a Ni-H species originating from the transfer of  $\text{H}^-$  from  $\text{PhSiH}_3$  to the initially generated Ni cation.

**Key words:** hydrosilylation, nickel indenyl complexes, cationic complexes, hydride intermediates.

**Résumé :** L'abstraction des ions chlorures des complexes (indényle) $\text{Ni}(\text{PPh}_3)\text{Cl}$  génère des espèces cationiques qui sont des précatalyseurs efficaces pour la réaction d'hydrosilylation de certaines oléfines et de certaines cétones. Par exemple, le mélange de (1-Me-indényle) $\text{Ni}(\text{PPh}_3)\text{Cl}$  et de  $\text{NaBPh}_4$  (ou de méthylaluminoxane) réagit à la température de la pièce avec environ 100 équivalents de  $\text{PhSiH}_3$  et 100 équivalents de styrène pour donner le [1-phényl-1-éthyl](phényl)silane,  $\text{PhCH}(\text{CH}_3)(\text{SiPhH}_2)$  avec un rendement allant de 50 % à 80 %. Le même système peut également catalyser l'hydrosilylation du 1-hexène et du norbornène, mais on obtient dans ces conditions des mélanges de régio- et de stéréo-isomères. Par ailleurs, l'hydrosilylation des cétones est régiospécifique, et conduit aux éthers silylés correspondants avec des rendements élevés. Plusieurs observations expérimentales ont révélé que le cation à base de nickel généré initialement n'est pas l'espèce active catalytiquement. Effectivement l'initiateur cationique peut-être remplacé par le  $\text{LiAlH}_4$  ou par le  $\text{AlMe}_3$  qui génèrent respectivement les dérivés Ni-H ou Ni-Me correspondants. De plus, la régiosélectivité observée lors de l'addition du  $\text{PhSiH}_3$  sur le styrène (i.e. l'addition prédominante du fragment silylé sur le carbone en  $\alpha$ ) est à l'opposé de ce à quoi on pourrait s'attendre si le mécanisme réactionnel impliquait un carbocation intermédiaire. On propose un nouveau mécanisme dans lequel l'espèce réactive est le Ni-H provenant du transfert de  $\text{H}^-$  à partir du  $\text{PhSiH}_3$  vers le cation nickel généré initialement.

**Mots clés :** hydrosilylation, complexes indényle-nickel, complexes cationiques, hydrures intermédiaires.

[Traduit par la Rédaction]

## Introduction

Based on their pioneering studies on the mechanism of the olefin hydrosilylation reaction, Harrod and Chalk proposed, in 1965, a general mechanistic scheme involving hydrido(silyl) intermediates of the type  $\text{L}_n\text{M}(\text{H})(\text{SiR}_3)$  (Scheme 1) (1). According to this scheme, insertion of the olefin into the M—H bond generates an alkyl intermediate that undergoes

reductive elimination to give the final product. The main elements of the Chalk–Harrod mechanism have served as useful guiding principles for the development of numerous hydrosilylation catalysts over the past four decades (2–4).

We became interested in the hydrosilylation reaction during our studies on the oligomerization of  $\text{PhSiH}_3$  catalyzed by Ni(II) indenyl precursors (5). The presumed involvement of Ni-H or Ni-SiR<sub>3</sub> intermediates in these reactions suggested that the same Ni-indenyl systems might also promote the hydrosilylation of olefins or ketones if these unsaturated substrates were present in the reaction mixture. This assertion was borne out by a series of tests, which indicated that the presence of certain olefins effectively inhibited the Si—Si bond formation step in favour of the hydrosilylation reaction. These initial results prompted us to carry out a literature survey, which revealed that a number of related Ni complexes are known to promote the hydrosilylation of ole-

Received 15 May 2003. Published on the NRC Research Press Web site at <http://canjchem.nrc.ca> on 21 October 2003.

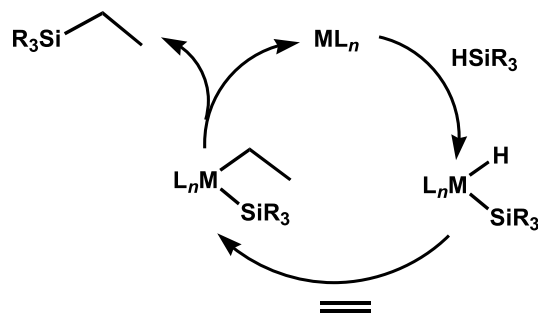
**F.-G. Fontaine, R.-V. Nguyen, and D. Zargarian.**<sup>2</sup>  
Département de chimie, Université de Montréal, Montréal,  
QC H3C 3J7 Canada.

<sup>1</sup>This article is part of a Special Issue dedicated to Professor John Harrod.

<sup>2</sup>Corresponding author (e-mail: [zargarian.davit@umontreal.ca](mailto:zargarian.davit@umontreal.ca)).



Scheme 1.



fins, as follows: the dimeric complex  $\{\text{CpNi}(\mu\text{-CO})\}_2$  catalyzes the addition of  $\text{HSiCl}_3$  to styrene to give  $\text{PhCH}(\text{SiCl}_3)\text{Me}$  (6);  $\text{CpNi}(\text{PPh}_3)\text{Ph}$  reacts with butadiene and  $\text{Me}_3\text{SiH}$  to give a mixture of products arising from 1,4-hydrosilylation ( $\text{MeCH}=\text{CHCH}_2\text{SiMe}_3$ ), coupling-hydrosilylation (2,6-octadienyltrimethylsilane), and dimerization-cyclization (1,5-cyclooctadiene) (7);  $\text{CpNi}(\text{PR}_3)\text{R}'$  reportedly catalyzes the hydrosilylation of methyl acrylate and allyl formate with  $\text{HSiCl}_3$  (8). Although little is known about the way these systems work, their mechanisms might involve intermediates similar to those operating in our systems.

Thus, we undertook to investigate the effectiveness of our Ni(II) indenyl complexes in the hydrosilylation reaction and examine the mechanism of these reactions. The present report describes the hydrosilylation of alkenes and ketones catalyzed by the precursors  $\text{IndNi}(\text{PR}_3)\text{X}$  (Ind = indenyl ligand and its substituted derivatives; R = Ph, Me; X = Cl, alkyl, or positive charge).

## Results and discussion

Our initial experiments focused on the reaction of  $\text{PhSiH}_3$  and styrene with a catalytic system based on the combination of  $\text{IndNi}(\text{PR}_3)\text{Cl}$  and methylaluminoxane (MAO); the selection of this Ni-MAO system was based on the knowledge that it promotes the dehydrogenative polymerization of  $\text{PhSiH}_3$  (5a). A typical experiment was carried out as follows: to the toluene mixture of (1-Me-Ind)Ni( $\text{PPh}_3$ )Cl (**1**), styrene, and  $\text{PhSiH}_3$  (1:100:100 ratio) was added a toluene solution of MAO (10 equiv. with respect to Ni); the wine-red mixture darkened immediately, but no gas evolution was observed, implying that the Si-Si bond formation reaction (and its concomitant formation of  $\text{H}_2$  gas) had been circumvented by the presence of styrene.

The reaction mixture was stirred for 8 h and worked-up; analysis of the nonvolatile products by GC-MS confirmed that styrene had been hydrosilylated.<sup>3</sup> Distillation gave a colourless oil, which was shown to consist, almost exclusively, of the  $\alpha$ -isomer ((1-phenyl)ethylphenylsilane). This assignment was based on the following features of the  $^1\text{H}$  NMR spectrum of the final product (Fig. 1): the multiplet due to the benzylic methyne proton at 2.55 ppm ( $\text{PhCH}(\text{Me})\text{SiH}_2\text{Ph}$ ), the signals due to the diastereotopic  $\text{SiH}_2$  protons and their  $^{29}\text{Si}$  satellites at 4.35 ppm, and the doublet at ca. 1.4 ppm assigned to the methyl protons ( $^3J_{\text{H-H}} = 7$  Hz); the benzylic protons of the minor isomer

( $\text{PhCH}_2\text{CH}_2\text{SiPhH}_2$ ) were barely perceptible at ca. 2.7 ppm. These assignments are consistent with the reported data for these products (9).

Subsequent experiments showed that the hydrosilylation of styrene promoted by  $\text{IndNi}(\text{PPh}_3)\text{Cl}$ -MAO is fairly sluggish, requiring several hours of reaction time for ca. 70% yield (see runs 1-4 of Table 1). Curiously, using more catalyst or a higher temperature did not accelerate the catalysis (compare runs 5 to 2, and 6 to 4); on the other hand, combining these two variations did increase the rate, but did not affect the yield (compare run 7 to runs 6 and 5). It should be noted here that the higher temperature reactions tend to give higher proportions of the  $\beta$ -isomer (ca. 5%-10%); the significance of this observation for the probable mechanism of the catalytic reaction will be discussed later. The reaction rate also improved upon using the 1-*i*-Pr-Ind analogue of **1** as precatalyst (compare run 8 to run 2), whereas using the  $\text{PMe}_3$  analogue of **1** did not offer any advantage (compare run 9 to run 5).

Although the precise role of MAO in the present system is not known yet, our previous studies (10) have shown that a small excess of MAO (ca. 5 equiv.) serves primarily to methylate the Ni-Cl bond, while a large excess (>10 equiv.) leads to both methylation and ionization in varying proportions. For example,  $^{31}\text{P}\{^1\text{H}\}$  NMR analysis of a 1:25 mixture of **1** and MAO showed the formation of an approximately 50:50 mixture of the Ni-Me analogue of **1** ((1-Me-Ind)Ni( $\text{PPh}_3$ )Me) and the cationic complex  $[(1\text{-Me-Ind})\text{Ni}(\text{PPh}_3)_2]^+$ . Previous studies have shown that the latter complex forms when the highly electrophilic cation  $[\text{IndNi}(\text{PPh}_3)]^+$  is generated in the absence of suitable ligands or nucleophilic substrates (11). We conclude, therefore, that the MAO:Ni ratios used in our studies (ca. 10:1) convert the Ni-Cl precursor to a mixture of the analogous Ni-Me derivative and  $[\text{IndNi}(\text{PPh}_3)]^+$ . To determine which, if any, of these in situ generated derivatives is crucial for the hydrosilylation reaction, we tested the catalytic effectiveness of each species separately, as follows.

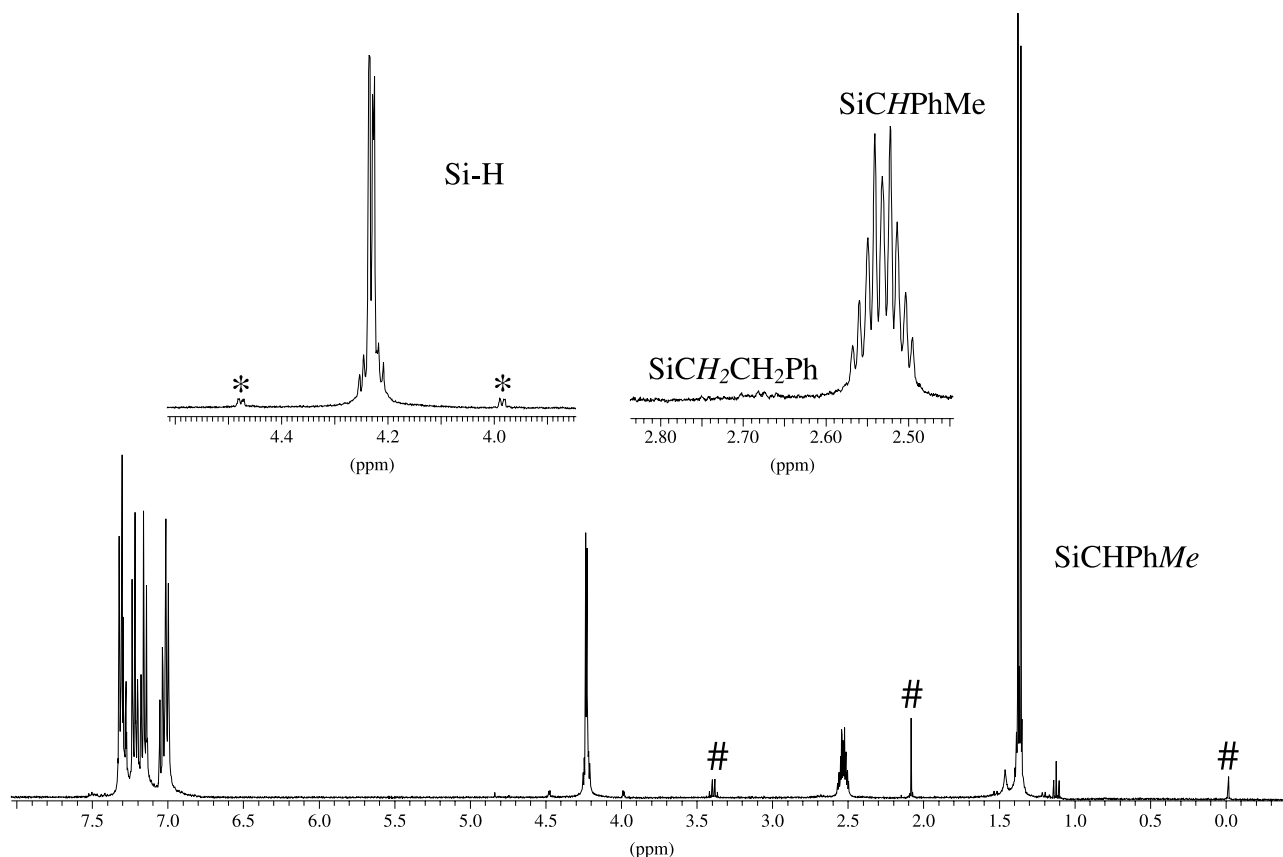
Tests with the complex (1-Me-Ind)Ni( $\text{PPh}_3$ )Me, either preformed (12) or prepared in situ from **1** and  $\text{AlMe}_3$ , showed that it was less than half as effective as the combination of **1**-MAO (compare runs 10 and 11 to run 4). The weak activity of the Ni-Me derivative is perhaps not surprising since this compound is inert toward styrene insertion and reacts only very sluggishly with  $\text{PhSiH}_3$  (5b). On the other hand, the Ni-(*i*-Pr) derivative, which reacts faster with  $\text{PhSiH}_3$  than the Ni-Me analogue (10b), showed a better level of activity (run 12). Interestingly, the catalytic activity of the Ni-Me complex improves somewhat when MAO is added to the reaction medium (compare runs 10 and 11 to run 13); this result implies that the main role of MAO in this system is not simply methylating the Ni-Cl bond. We concluded, therefore, that the reactivity of the Ni-Me complex alone could not account for the activity levels shown by the combination of **1** and MAO, and set out to assess the importance of ionization in the **1**-MAO-catalyzed reactions.

To examine the reactivity of the cationic species  $[\text{IndNi}(\text{PPh}_3)]^+$  in the absence of the Ni-Me derivative, we

<sup>3</sup>Control experiments have shown that neither the Ni-Cl complexes nor the initiators used in this study (MAO,  $\text{AlMe}_3$ ,  $\text{NaBPh}_4$ ,  $\text{LiAlH}_4$ ) can promote the hydrosilylation reaction when used alone.



**Fig. 1.**  $^1\text{H}$  NMR ( $\text{C}_6\text{D}_6$ ) of the product obtained from the Ni-catalyzed hydrosilylation of styrene with  $\text{PhSiH}_3$ . The peaks denoted by \* represent the satellites due to the  $J_{29\text{Si-H}}$  coupling, while the peaks denoted by the # represent the internal standard (ca. 2.1 ppm), residual  $\text{Et}_2\text{O}$  (ca. 3.4 and 1.1 ppm), and  $\text{SiMe}_4$ .



generated this species in situ by the direct abstraction of  $\text{Cl}^-$  from **1** by  $\text{NaBPh}_4$ ,<sup>4</sup> this approach gave results comparable to those obtained with MAO (compare run 14 to run 4). To our surprise, even the cation  $[(1\text{-Me-Ind})\text{Ni}(\text{PPh}_3)_2]^+$ , which is normally quite inert in ligand substitution and other catalytic reactions (10*b*), showed some reactivity in the absence of MAO (run 15). These observations suggested that the electronically and coordinatively unsaturated species  $[\text{IndNi}(\text{PPh}_3)]^+$ , which is generated in situ by the abstraction of  $\text{Cl}^-$  by  $\text{NaBPh}_4$  or MAO, can initiate the hydrosilylation reaction. Thus, during the second round of the optimization tests we focused our efforts on finding the best conditions for the catalytic hydrosilylation of styrene using  $\text{NaBPh}_4$  as a cationic initiator, as described below.

The initial experiments showed that the ratio of **1**: $\text{NaBPh}_4$  used in the catalytic runs has a direct effect on the yield, excess of  $\text{NaBPh}_4$  giving higher yields (Table 2, runs 1–4). Since only one equivalent of the initiator should be sufficient for generating the cationic species, the need for a large excess (run 4) is presumably due to the limited solubility of  $\text{NaBPh}_4$ . Even though a  $[\text{Ni}]:\text{NaBPh}_4$  ratio of 1:50 gave the best yield, using such a large excess of the initiator is not practical, and so we adopted a 1:10 ratio as a reasonable compromise. As before, a higher reaction temperature does

not seem to improve the catalytic activity (run 5), but gave a higher proportion of the  $\beta$ -isomer. Using the 1-*i*-Pr-Ind derivative does not offer any advantages (runs 6 and 7), while using the  $\text{PMe}_3$  analogue of **1** led to considerably lower activities (runs 8 and 9). The latter observation is interesting: that the more active precatalyst is the one bearing the less nucleophilic phosphine ligand might imply that the hydrosilylation reaction involves a  $\text{PR}_3$  dissociation. Consistent with this possibility, the presence of added  $\text{PPh}_3$  ( $[\text{Ni}]:\text{PPh}_3 = 1:2$ ) hindered the catalysis significantly (run 10). This point will be elaborated further during the discussion of the mechanism of these reactions (*vide infra*).

The scope of the hydrosilylation reactions promoted by **1**– $\text{NaBPh}_4$  has been explored briefly, as follows. Norbornene and 1-hexene were hydrosilylated with  $\text{PhSiH}_3$  to ca. 1:1 mixtures of regio- (for 1-hexene) and stereoisomers (endo- and exo-products from norbornene), while *trans*- $\beta$ -Mestylene gave the  $\alpha$ -isomer in ca. 10:1 ratio (ca. 50% overall yield). On the other hand, cyclohexene, indene, and *trans*-stilbene gave no hydrosilylation products; for the latter two olefins, the reaction mixtures displayed broad signals in the NMR spectra implying poly(olefin) formation, but no further analyses were performed to confirm this possibility. Although  $\text{PhSiH}_3$  has been used in almost all of our studies,

<sup>4</sup>The abstraction of  $\text{Cl}^-$  from **1** by  $\text{NaBPh}_4$  is clean but generally sluggish, especially in nonpolar solvents such as toluene, in which  $\text{NaBPh}_4$  has a very limited solubility. Although  $\text{AgBF}_4$  is much more efficient for  $\text{Cl}^-$  abstraction, its higher cost and the possibility of secondary reactions (e.g., electron transfer with the Ni complex and redistribution with  $\text{PhSiH}_3$ ) render it less practical than  $\text{NaBPh}_4$  for our purposes.



**Table 1.** Catalytic addition of PhSiH<sub>3</sub> to styrene.\*

Run	Catalyst <sup>§</sup> -co-catalyst	[Ni] (%)	Time (h)	Temperature (°C)	Yield (%)
1	<b>1</b> -MAO (1:10)	1	3	25	28
2	<b>1</b> -MAO (1:10)	1	5	25	39
3	<b>1</b> -MAO (1:10)	1	7	25	42
4	<b>1</b> -MAO (1:10)	1	16	25	69
5	<b>1</b> -MAO (1:10)	2	5	25	38
6	<b>1</b> -MAO (1:10)	1	16	65	61
7	<b>1</b> -MAO (1:10)	2	5	65	66
8	(1-( <i>i</i> -Pr)-Ind)(PPh <sub>3</sub> )Ni(Cl)-MAO (1:10)	1	5	25	58
9	(1-Me-Ind)(PMe <sub>3</sub> )Ni(Cl)-MAO (1:10)	2	5	25	36
10	<b>1</b> -AlMe <sub>3</sub> (1:1.1)	1	16	25	29
11	(1-Me-Ind)(PPh <sub>3</sub> )Ni(Me)-/—	1	24	25	26
12	(1-Me-Ind)(PPh <sub>3</sub> )Ni( <i>i</i> -Pr)-/—	1	72	25	60
13	(1-Me-Ind)(PPh <sub>3</sub> )Ni(Me)-MAO (1:10)	1	16	25	40
14	<b>1</b> -NaBPh <sub>4</sub> (1:10)	1	16	25	73
15	[(1-Me-Ind)Ni(PPh <sub>3</sub> ) <sub>2</sub> ] <sup>+</sup> /—	2	5	25	13

\*The reactions were carried out under anaerobic conditions on NMR-scale (C<sub>6</sub>D<sub>6</sub>), and the yields were determined relative to an internal standard. The detailed procedure is described in the *Experimental* section.

<sup>§</sup>**1** = (1-Me-Ind)(PPh<sub>3</sub>)Ni(Cl).

**Table 2.** Addition of PhSiH<sub>3</sub> to styrene catalyzed by (1-R-Ind)Ni(PR<sub>3</sub>)Cl-NaBPh<sub>4</sub>.\*

Run	Pre-catalyst	[Ni]:NaBPh <sub>4</sub> :styrene:PhSiH <sub>3</sub>	Yield (%)
1	<b>1</b>	1:1:50:50	27
2	<b>1</b>	1:2:50:50	50
3	<b>1</b>	1:10:50:50	69
4	<b>1</b>	1:50:50:50	86
5	<b>1</b>	1:10:50:50 <sup>§</sup>	64
6	(1-( <i>i</i> -Pr)-Ind)Ni(PPh <sub>3</sub> )Cl	1:10:100:100	50
7	(1-( <i>i</i> -Pr)-Ind)Ni(PPh <sub>3</sub> )Cl	1:10:50:50	61
8	(1-Me-Ind)Ni(PMe <sub>3</sub> )Cl	1:10:100:100	10
9	(1-Me-Ind)Ni(PMe <sub>3</sub> )Cl	1:10:50:50	36
10	<b>1</b> + 2PPh <sub>3</sub>	1:10:50:50	19

\*Unless otherwise indicated, all runs were carried out under anaerobic conditions in benzene at 25 °C for 5 h. Details of the procedure and yield determination are given in the *Experimental* section.

<sup>§</sup>This run was carried out at 65 °C.

the reactivity of other silanes was also examined briefly. Thus, we found that tri-substituted silanes such as Et<sub>3</sub>SiH and (EtO)<sub>3</sub>SiH are inactive in the hydrosilylation of styrene, but Ph<sub>2</sub>SiH<sub>2</sub> does add to styrene to give the products PhCH(CH<sub>3</sub>)(Ph<sub>2</sub>SiH) and PhCH<sub>2</sub>CH<sub>2</sub>(Ph<sub>2</sub>SiH) in ca. 60:40 ratio (ca. 28%–48% overall yield). The inertness of tri-substituted silanes is presumably due to steric hindrance. Finally, acetophenone and 2-nonanone were hydrosilylated very efficiently to the corresponding PhH<sub>2</sub>Si-ethers, giving nearly quantitative conversions by NMR.

### Mechanistic considerations

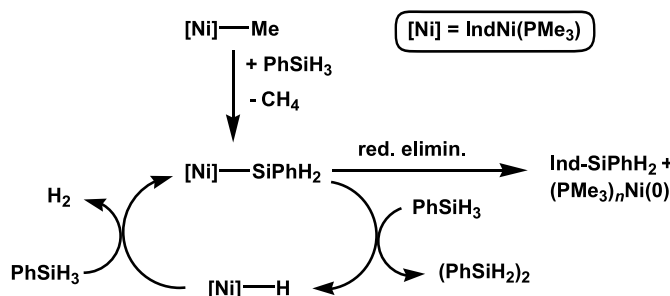
The results described above show that the hydrosilylation reactions can be promoted by the in situ generated species (Ind)(PPh<sub>3</sub>)Ni(Me) or [(Ind)(PPh<sub>3</sub>)Ni]<sup>+</sup>, the latter being more effective in most cases. This section considers the various ways in which these two species can initiate the catalysis. It should be emphasized at the outset that whereas [(Ind)(PPh<sub>3</sub>)Ni]<sup>+</sup> can, in principle, react with either the olefin or the silane, the Ni-alkyl derivatives are known to be in-

ert towards the insertion of olefins and must, therefore, react first with PhSiH<sub>3</sub>. For simplicity, we begin the mechanistic discussion with the latter systems.

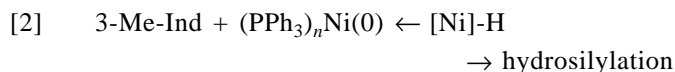
The complexes (1-Me-Ind)(PR<sub>3</sub>)Ni(Me) are known to convert PhSiH<sub>3</sub> (without a co-catalyst) to (PhSiH)<sub>*n*</sub> (R = Me, Ph; *n* = 3–16) (5*b*). Whereas the reactions involving the PPh<sub>3</sub> analogue were quite sluggish, those of the PMe<sub>3</sub> analogue proceeded at a conveniently rapid rate and were, therefore, subjected to detailed kinetic and D-labeling studies. On the basis of these studies, we have proposed that the oligomerization of PhSiH<sub>3</sub> is initiated by a concerted, σ-bond metathesis reaction as opposed to an oxidative addition – reductive elimination sequence. Analysis of the side products of this reaction pointed to the formation of methane and 1-(SiPhH<sub>2</sub>)-3-Me-Ind, but not PhMeSiH<sub>2</sub>, suggesting that the initial reaction leads to a Ni-silyl intermediate, as shown in Scheme 2. The putative Ni-SiPhH<sub>2</sub> intermediate would then react further with PhSiH<sub>3</sub> to initiate the oligomerization process, while its decomposition (by reductive elimination) could form 1-(SiPhH<sub>2</sub>)-3-Me-Ind (Scheme 2) (5*b*).



Scheme 2.



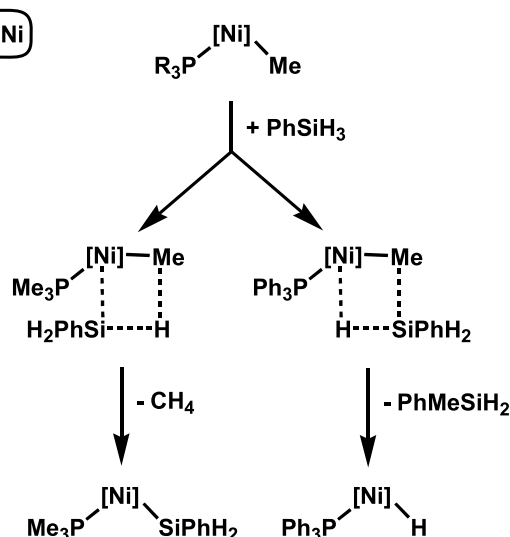
To determine if the pathway depicted in Scheme 2 is also followed by the  $\text{PPh}_3$  analogue, we did a similar analysis (by TOCSY  $^1\text{H}$  NMR) of the products of the reaction of (1-Me-Ind)( $\text{PPh}_3$ )Ni(Me) with  $\text{PhSiH}_3$ . This study revealed the presence of traces of  $\text{PhMeSiH}_2$  and 3-Me-Ind, but not 1-( $\text{SiPhH}_2$ )-3-Me-Ind. We infer from these observations that, unlike its  $\text{PMe}_3$  analogue, the precursor (1-Me-Ind)( $\text{PPh}_3$ )Ni(Me) reacts with  $\text{PhSiH}_3$  to eliminate  $\text{PhSiMeH}_2$  (instead of methane) and form the hydride derivative (eq. [1];  $[\text{Ni}] = (1\text{-Me-Ind})\text{Ni}(\text{PPh}_3)$ ). The latter could then react with styrene to initiate the hydrosilylation catalysis, while its decomposition (by reductive elimination) would produce 3-Me-Ind (instead of 1-( $\text{SiPhH}_2$ )-3-Me-Ind) (eq. [2]). The precise reasons for this difference in reactivity between the  $\text{PMe}_3$  and  $\text{PPh}_3$  derivatives are not known with certainty. Modeling studies suggest that the greater steric bulk of the  $\text{PPh}_3$  derivative might favour the transfer to the Ni centre of the less-hindered side of  $\text{PhH}_2\text{Si-H}$  (i.e., the H, see Scheme 3), but electronic factors cannot be ruled out (the more electron-rich  $\text{PMe}_3$  analogue might stabilize the Ni—Si bond).



To test the likelihood that a Ni-H derivative is involved in the hydrosilylation catalysis promoted by the present system, we tested the effectiveness of  $\text{LiAlH}_4$  as co-catalyst (or initiator, instead of MAO or  $\text{NaBPh}_4$ ) in the hydrosilylation of styrene. Thus, stirring a toluene solution of styrene– $\text{PhSiH}_3$ –**1**– $\text{LiAlH}_4$  (100:100:1:2.5) at room temperature for 16 h resulted in the usual product ( $\text{PhCH}(\text{CH}_3)(\text{PhSiH}_2)$ ) in 41% yield. This result establishes that the hydrosilylation reaction can be catalyzed by a Ni-H intermediate generated either from **1**– $\text{H}^-$  or by the reaction of the Ni-Me precursor and  $\text{PhSiH}_3$ .

Let us now turn to discussing the mechanism of the hydrosilylation reactions initiated by the in situ generated cationic species  $[\text{IndNi}(\text{PPh}_3)]^+$ . Given the highly electrophilic nature of this species and the fact that various Lewis acids can catalyze hydrosilylation of olefins (13), we considered the likelihood of our Ni cations acting as Lewis acids to

Scheme 3.



promote the observed hydrosilylation reactions. A recent example of such Lewis-acid-catalyzed hydrosilylation has been reported by Gevorgyan and co-workers (14) who have shown that 5–10 mol% of  $\text{B}(\text{C}_6\text{F}_5)_3$  can catalyze the hydrosilylation of a range of olefins with various aryl- or alkyl-silanes. These authors have drawn on the findings of Lambert et al. (15) and Piers and co-workers (16) to argue, quite convincingly, that these  $\text{B}(\text{C}_6\text{F}_5)_3$ -catalyzed reactions are initiated by the formation of  $[\text{R}_3\text{Si}]^+[\text{HB}(\text{C}_6\text{F}_5)_3]^-$ . The silylium cation  $\text{R}_3\text{Si}^+$  is believed to add to the  $\text{C}=\text{C}$  to generate a carbocationic intermediate, which abstracts a hydride from the anion  $[\text{HB}(\text{C}_6\text{F}_5)_3]^-$  to release the final product. The regiochemistry of the hydrosilylation products obtained by Gevorgyan and co-workers is consistent with a carbocationic mechanism; for instance, styrene is converted to the  $\text{PhCH}_2\text{CH}_2\text{SiR}_3$ , presumably via the intermediate  $[\text{PhC}^+\text{HCH}_2\text{SiR}_3]$ .

By analogy to Gevorgyan's proposed abstraction of  $\text{H}^-$  by  $\text{B}(\text{C}_6\text{F}_5)_3$ , we considered a scenario involving the abstraction of  $\text{H}^-$  from  $\text{PhSiH}_3$  by  $[\text{IndNi}(\text{PPh}_3)]^+$  to give  $\text{IndNi}(\text{PPh}_3)\text{H}$  and a silylium species; the main question is whether the aptitude of the species  $[\text{IndNi}(\text{PPh}_3)]^+$  for abstracting  $\text{H}^-$  from  $\text{PhSiH}_3$  can be assumed to be comparable to that of  $\text{B}(\text{C}_6\text{F}_5)_3$ . This question was investigated by the following NMR experiments that allowed some measure of the relative Lewis acidities of these electrophiles. First, monitoring mixtures of  $\text{IndNi}(\text{PPh}_3)\text{Cl}$  and  $\text{B}(\text{C}_6\text{F}_5)_3$  (1:5) showed that the ionization of the Ni—Cl bond is very slow (<ca. 20%–30% ionization in 30–60 min). Next, adding  $\text{B}(\text{C}_6\text{F}_5)_3$  to solutions of  $\text{IndNi}(\text{PPh}_3)\text{Me}$  (1:2) did not lead to ionization, forming instead what we believe is a species featuring a  $\text{Ni}\cdots\text{Me}\cdots\text{B}$  moiety.<sup>5</sup> Hence, it appears that  $[\text{IndNi}(\text{PPh}_3)]^+$  and  $\text{B}(\text{C}_6\text{F}_5)_3$  have similar Lewis acidities and should have similar aptitudes for abstracting  $\text{H}^-$  from  $\text{PhSiH}_3$ . Unfortunately, it has not been possible to find direct evidence for the formation of

<sup>5</sup>NMR evidence supporting this assertion includes the observation of a broad signal in the upfield region of the  $^1\text{H}$  NMR spectrum, slightly downfield of the original Ni-Me signal at ca.  $-0.7$  ppm, and the absence of the characteristic AB signals for the formation of the species  $[\text{IndNi}(\text{PPh}_3)_2]^+$ . Significantly, none of the B- or Al-based Lewis acids tested in our study abstract the Ni-bound phosphine ligands, implying that the Ni centre is a strong Lewis acid.



Ni-H intermediates in the mixtures of  $\text{PhSiH}_3$  and in situ generated  $[\text{IndNi}(\text{PPh}_3)]^+$ , because the putative Ni-H species reacts with  $\text{PhSiH}_3$  at a faster rate than it is produced. However, we have obtained indirect evidence for the generation of such a Ni-H species, as described below.

Given that a number of late transition metal hydride bonds react with C—Cl bonds, especially those of chloroform, we reasoned that if the Ni-H species could be generated in a chlorinated solvent, chlorination might give the Ni-Cl derivatives, which could be easily detected. Thus, we monitored the NMR spectra of two  $\text{CDCl}_3$  samples, one containing the independently prepared cationic complex  $[(1\text{-Me-Ind})\text{Ni}(\text{PPh}_3)_2][\text{BPh}_4]$  alone, the other containing the same complex in addition to ca. 10 equiv. of  $\text{PhSiH}_3$ . The NMR spectra showed that the cationic complex is stable in  $\text{CDCl}_3$  for at least 24 h in the absence of the silane (no new peaks in the  $^{31}\text{P}\{^1\text{H}\}$  NMR spectrum), whereas the sample containing  $\text{PhSiH}_3$  displayed many new  $^{31}\text{P}\{^1\text{H}\}$  NMR signals, including that of the complex  $(1\text{-Me-Ind})\text{Ni}(\text{PPh}_3)\text{Cl}$  (31.1 ppm). We believe that the latter compound likely arises from the reaction of the Ni-H intermediate with  $\text{CDCl}_3$ . The  $^{31}\text{P}\{^1\text{H}\}$  NMR spectrum of the reaction mixture also showed signals at 16–20 ppm, which is close to the spectral region associated with the signals for phosphonium salts such as  $\text{Ph}_3\text{MeP}^+\text{I}^-$  (ca. 22 ppm); these signals might be due to phosphonium species such as  $[\text{Ph}_3\text{P}(\text{SiR}_3)][\text{BPh}_4]$ . Finally, the  $^1\text{H}$  NMR spectrum of this sample showed traces of 3-Me-Ind, which could originate from the reductive elimination of a Ni-H intermediate.

The above observations provide indirect support for the proposal that the in situ generated Ni cations react first with  $\text{PhSiH}_3$  (as opposed to styrene)<sup>6</sup> to form Ni-H and silylium species. The next question that arises is which one of these intermediates would react with the olefin to initiate the hydrosilylation reaction. On this question, the regioselectivity of the Ni-catalyzed reactions can help rule out the possibility that these reactions proceed by the same reaction pathway proposed for the  $\text{B}(\text{C}_6\text{F}_5)_3$  system above, i.e., the addition of  $\text{R}_3\text{Si}^+$  to the olefin. Thus, Ni-catalyzed hydrosilylation of styrene gives  $\alpha$ -silylation, which is the opposite of that observed with the  $\text{B}(\text{C}_6\text{F}_5)_3$  system discussed above; moreover, the hydrosilylation of 1-hexene gives a 50:50 mixture of  $\alpha$ - and  $\beta$ -silylation instead of the exclusive  $\alpha$ -silylation expected from a carbocationic path. On the other hand, the regioselectivities observed in our system are consistent with a Chalk–Harrod type mechanism involving M-H intermediates. These considerations favour the insertion of the olefinic substrate into the Ni—H bond over reaction with the silylium species. The latter is presumably stabilized by  $[\text{BPh}_4]^-$  and (or) the solvent (17), but our results do not shed any light on the fate of this species.

Therefore, we envisage the following sequence of steps for the hydrosilylation reactions promoted by the present

system: (a) the Ni-H analogue of **1** is generated by the reaction of  $\text{PhSiH}_3$  with the in situ formed  $[\text{IndNi}(\text{PPh}_3)]^+$  or the Ni-Me analogue;<sup>7</sup> (b) insertion of the olefin (or ketone) into the Ni—H bond of the intermediate generates a new Ni-alkyl (or Ni-alkoxy) derivative, which reacts subsequently with another molecule of silane to form the C—Si (or O—Si) bond and regenerate the Ni-H intermediate.<sup>8</sup> The regiochemistry of the hydrosilylation reaction is determined at the insertion step; in the case of styrene, this gives the alkyl intermediates  $\text{Ni-CH}_2\text{CH}_2\text{Ph}$  and (or)  $\text{Ni-CH}(\text{Me})\text{Ph}$ . Although the latter intermediate should, in principle, be more susceptible to  $\beta$ -H elimination, we propose that it is in fact more stable because of the possibility of reverting to an  $\eta^3$ -benzyl derivative, as shown in Scheme 4. It is worth noting that Brookhart and co-workers (18) have proposed such  $\eta^3$ -benzyl intermediates for the addition of  $\text{HSiR}_3$  ( $\text{R} = \text{Et}, i\text{-Pr}$ ) to styrene catalyzed by the cationic complexes  $[(1,10\text{-phenanthroline})\text{Pd}(\text{Me})\text{L}][\text{BAR}_4]$ .<sup>9</sup> The likelihood of such intermediates being involved in our system is supported by the following observations: (a) Monitoring a catalytic run by  $^{31}\text{P}\{^1\text{H}\}$  NMR spectroscopy showed that the initial signal of the precatalyst **1** (ca. 31 ppm) is replaced by the signal for free  $\text{PPh}_3$  (ca. –4 ppm) and a number of new signals at ca. 43–45 ppm. The latter region is associated with the  $^{31}\text{P}\{^1\text{H}\}$  signals for complexes  $(1\text{-Me-Ind})\text{Ni}(\text{PPh}_3)\text{R}$ , wherein R is a secondary alkyl such as *i*-Pr or cyclohexyl (45 ppm), and *sec*-Bu or neopentyl (42–43 ppm) (5b). The presence of free  $\text{PPh}_3$  is also consistent with the earlier observation that the  $\text{PMe}_3$  precursors are less effective for promoting the hydrosilylation reaction; (b) Recall that using higher reaction temperatures or  $\text{Ph}_2\text{SiH}_2$  resulted in somewhat higher proportions of the minor regioisomer,  $\text{PhCH}_2\text{CH}_2\text{SiPhRH}$  ( $\text{R} = \text{H}, \text{Ph}$ ). Higher temperatures should accelerate the  $\beta$ -H elimination from  $\text{Ni-CH}(\text{Me})\text{Ph}$ , thus favouring the  $\text{Ni-CH}_2\text{CH}_2\text{Ph}$  intermediate; on the other hand, the more bulky  $\text{Ph}_2\text{SiH}_2$  might be expected to react more readily with the less bulky  $\text{Ni-CH}_2\text{CH}_2\text{Ph}$  intermediate.

## Conclusions

The present study has shown that combining the complexes  $\text{IndNi}(\text{PPh}_3)\text{Cl}$  with suitable cationic initiators gives rise to an efficient catalytic system for the hydrosilylation of olefins and ketones. This system is particularly attractive for styrene because it gives, almost exclusively, one regioisomer; this regioselectivity is comparable to that reported for organolanthanide-catalyzed hydrosilylation reaction (9). On the other hand,  $\text{Pd}(\text{II})\{\text{bis}(\text{imine})\}$  complexes give the opposite regioselectivity (18), while similar Ni precursors bearing Cp ligands give complicated mixtures of products (6, 7). Future studies will be aimed at expanding the scope of these hydrosilylation reactions.

<sup>6</sup>The direct reaction of Ni-based cations with styrene would be expected to result in the oligo- or polymerization of styrene.

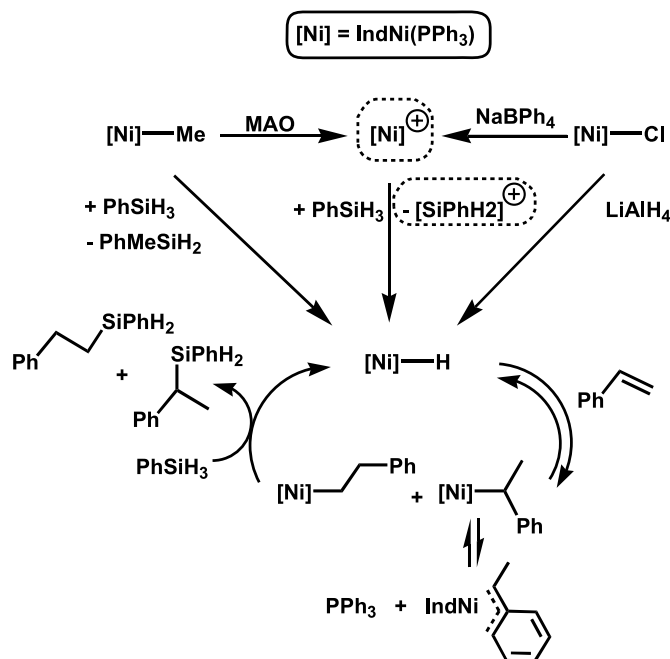
<sup>7</sup>One of the reviewers of our manuscript proposed the following alternative mechanism: the redistribution reaction involving the intermediate  $[\text{IndNi}(\text{PR}_3)]^+$  might take place to produce  $[\text{IndNi}(\text{PR}_3)_2]^+$  and phosphine-free species such as “ $\text{IndNiCl}$ ” or  $[\text{IndNi}]^+$ ; the latter might react with the hydrosilane to generate a Ni-H species. This alternative scenario is consistent with our observations and merits consideration.

<sup>8</sup>The latter step likely proceeds by a concerted,  $\sigma$ -bond metathesis pathway as opposed to an oxidative addition – reductive elimination route involving Ni(IV) intermediates.

<sup>9</sup>This Pd-based system leads to various mixtures of products arising from hydrosilylation and dehydrogenative silylation. The proposed mechanism involves the insertion of styrene into the  $\text{Pd—SiR}_3$  bond as opposed to the  $\text{Pd—H}$  bond.



Scheme 4.



A number of observations, including the fact that  $\text{LiAlH}_4$  can be used instead of  $\text{NaBPh}_4$  and MAO to activate the Ni-Cl precursor, have pointed to the involvement of the corresponding Ni-H derivative ( $X = \text{H}$ ) as the active intermediate in these reactions. In the case of the reactions involving cationic initiators, we have proposed that this Ni-H intermediate is generated via the transfer of  $\text{H}^-$  from the silane to the coordinatively unsaturated and highly electrophilic species  $[\text{IndNi}(\text{PPh}_3)]^+$ . This  $\text{Si} \rightarrow \text{Ni}^+$  hydride transfer process is very interesting because it provides a convenient route to the reactive Ni-H intermediate.<sup>10</sup> Studies are currently underway with the objective of elucidating the main parameters controlling this reactivity and investigating the feasibility of catalytic hydroboration reactions with the same system (i.e., transfer of hydride from  $\text{R}_2\text{BH}$ ).

## Experimental

### General

Unless otherwise specified, all manipulations were performed under an inert atmosphere of  $\text{N}_2$  or argon using standard Schlenk techniques and a dry box. Dry, oxygen-free solvents were employed throughout. The complexes (1-Me-Ind)Ni( $\text{PPh}_3$ )Cl (**1**) (**12**), (1-Me-Ind)Ni( $\text{PMe}_3$ )Cl (**19**), (1-*i*-Pr-Ind)Ni( $\text{PPh}_3$ )Cl (**20**), (1-Me-Ind)Ni( $\text{PPh}_3$ )Me (**12**), and [(1-Me-Ind)Ni( $\text{PPh}_3$ )<sub>2</sub>][ $\text{BPh}_4$ ] (**12**) were prepared according to previously published procedures.  $\text{PhSiH}_3$  was either purchased from Aldrich and used as received, or prepared from  $\text{PhSiCl}_3$  according to a previously published procedure (**21**). Styrene was purchased from Aldrich and treated by (a) passing it through a plug of alumina, and (b) storing over 4 Å molecular sieves prior to use. All other reagents, including MAO,  $\text{AlMe}_3$ ,  $\text{LiAlH}_4$ , and  $\text{NaBPh}_4$ , were purchased from

Aldrich and used as received. The NMR spectra were recorded using the following spectrometers: Bruker DMX600 (2D  $^1\text{H}$ - $^{29}\text{Si}$ ), Bruker AMX400 ( $^1\text{H}$  at 400 MHz,  $^{13}\text{C}\{^1\text{H}\}$  at 100.56 MHz, and  $^{31}\text{P}\{^1\text{H}\}$  at 161.92 MHz), and Bruker AV300 ( $^1\text{H}$  at 300 MHz for TOCSY). GC-MS analyses were carried out on a Hewlett Packard 6890 series gas chromatograph equipped with a split mode capillary injector and a HP 5973 mass selective detector. The following operating parameters were used: the injector and detector temperatures were 250 °C; the carrier gas was hydrogen (2 mL/min); the column used was HP-5MS, 5% phenyl methyl siloxane; temperature program: 40 °C for 2 min, 10 °C/min up to 140 °C, 20 °C/min up to 280 °C.

### Details of catalytic runs

Unless otherwise specified, all reactions were carried out under a nitrogen atmosphere. The catalytic runs were conducted as NMR-scale experiments or on a larger scale in Schlenk vessels. For the NMR-scale reactions, the following general procedure was followed. The Ni-Cl precursor complex (ca. 8 mg, 0.016 mmol) and the internal standard (hexamethyl benzene, ca. 15 mg, 0.09 mmol) were dissolved in  $\text{C}_6\text{D}_6$  (0.8 mL); styrene and  $\text{PhSiH}_3$  (100–200  $\mu\text{L}$ , 50–100 equiv. of each) were then added to the resultant red solution. Prior to initiating the catalysis, a  $^1\text{H}$  NMR spectrum was recorded to register the integral ratios for the signals of the internal standard and the reactants (Si-H of  $\text{PhSiH}_3$  and vinylic protons of styrene). The NMR sample was then taken inside the dry box to add the initiator. For the room temperature experiments, the sample was kept in an ultrasonic bath throughout the reaction time to ensure agitation and homogeneity; for the high-temperature experiments, the sample was kept in a 65 °C water bath. If required, the progress of the catalysis was monitored periodically by  $^1\text{H}$  NMR spectroscopy. The final yields were determined by comparing the intensities of the  $\text{CH}_3$  signals of the product and the internal standard. The final values were checked against a calibration curve prepared by plotting the integral ratios obtained for various mixtures of the internal standard ( $\text{C}_6\text{Me}_6$ ) and the main product ( $\text{PhCH}(\text{PhSiH}_2)\text{CH}_3$ ) (slope = 1.069,  $R^2 = 0.9997$ ).

The larger-scale catalytic runs were conducted as follows. Inside the dry box, the Ni precursor (ca. 10 mg) and the initiator were weighed into a Schlenk vessel containing a stirring bar; the capped vessel was then taken out of the dry box. The reactants and the solvent (benzene, unless otherwise specified) were then added under nitrogen in rapid succession (<1 min), and the mixture was stirred at room temperature or 65 °C. The work-up consisted of removing the volatiles on a rotoevaporator, extracting the residues with water-Et<sub>2</sub>O, and evaporating the combined organic layers. The resulting yellow oil was distilled under vacuum to give the product(s) as a clear oil. When little product was obtained, the yield was determined based on the  $^1\text{H}$  NMR spectrum of a carefully prepared mixture of the product and hexamethyl benzene as internal standard, according to the protocol described above.

<sup>10</sup>The same Ni-H intermediate might also be accessible from the reaction of  $\text{PhSiH}_3$  with  $\text{Ind}(\text{PPh}_3)\text{Ni}(\text{Me})$ , but this reaction is generally sluggish.



### Control experiments

To ascertain that the initiators used in our studies (MAO,  $\text{NaBPh}_4$ ,  $\text{LiAlH}_4$ , and  $\text{AlMe}_3$ ) do not promote the hydrosilylation reactions in the absence of Ni complexes, we prepared mixtures of styrene,  $\text{PhSiH}_3$ , and the initiator (in a molar ratio of 1:1:0.2) and analyzed them by  $^1\text{H}$  NMR spectroscopy. No hydrosilylation product was detected in any of the experiments, and the ratio of styrene and  $\text{PhSiH}_3$  remained unchanged. When  $\text{AgOTf}$  was tested with the substrates, gas evolution was observed and analysis of the sample showed that a small degree of silane redistribution had taken place (e.g.,  $\text{PhH}_2\text{Si-SiPhH}_2$  was detected by  $^1\text{H}$  NMR).

### Acknowledgments

The authors gratefully acknowledge the Natural Sciences and Engineering Research Council of Canada (NSERC) and Fonds pour la formation des chercheurs et l'aide à la recherche (Québec) (FCAR) for the financial support of this work, and Professor H. Lebel and Valérie Paquet for the use of their GC-MS instrument.

### References

1. (a) A. Chalk and J.F. Harrod. *J. Am. Chem. Soc.* **87**, 16 (1965); (b) J.F. Harrod and A. Chalk. *J. Am. Chem. Soc.* **87**, 1133 (1965).
2. For reviews on the hydrosilylation of alkenes and alkynes see: (a) I. Ojima. In *The chemistry of organosilicon compounds*. Edited by S. Patai and Z. Rappoport. John Wiley, Chichester. 1989. p. 1479; (b) B. Marciniak. *Comprehensive handbook on hydrosilylation*. Vol. 8. Pergamon Press, Oxford. 1991. p. 763.
3. For a sampling of hydrosilylation systems based on transition metals and lanthanides see the following reports and the references therein: (a) M.B. Carter, B. Schiøtt, A. Gultierrez, and S. Buchwald. *J. Am. Chem. Soc.* **116**, 11 667 (1994); (b) X. Verdager, U.E.W. Lango, and S. Buchwald. *Angew. Chem. Int. Ed.* **37**, 1103 (1998); (c) M.P. Doyle, K.G. High, C.L. Nesloney, T.W. Clayton, Jr., and J. Lin. *Organometallics*, **10**, 1225 (1991); (d) R. Takeuchi and H. Yasue. *Organometallics*, **15**, 2098 (1996); (e) M.L. Christ, S. Sabo-Etienne, and B. Chaudret. *Organometallics*, **14**, 1082 (1995); (f) J.F. Harrod and S. Yun. *Organometallics*, **6**, 1381 (1987); (g) R.S. Tannke and R.H. Crabtree. *Organometallics*, **10**, 415 (1991); (h) G.A. Molander and C.P. Corrette. *Organometallics*, **17**, 5504 (1998); (i) M.F. Lappert and R.K. Maskell. *J. Organomet. Chem.* **264**, 217 (1984).
4. For recent reviews of catalytic asymmetric hydrosilylation of C=C, C=O, and C=N functionalities see: (a) T. Hayashi. In *Comprehensive asymmetric catalysis*. Edited by E.N. Jacobsen, A. Pfaltz, and H. Yamamoto. Springer, Berlin. 1999. Chap. 7; (b) H. Nishiyama. In *Comprehensive asymmetric catalysis*. Edited by E.N. Jacobsen, A. Pfaltz, and H. Yamamoto. Springer, Berlin. 1999. Chap. 6.
5. (a) F.-G. Fontaine, T. Kadkhodazadeh, and D. Zargarian. *J. Chem. Soc., Chem. Commun.* 1253 (1998); (b) F.-G. Fontaine and D. Zargarian. *Organometallics*, **21**, 401 (2002).
6. P. Svoboda, P. Sedlmeyer, and J. Hetflejš. *Coll. Czech. Chem. Commun.* **38**, 1783 (1973).
7. S. Takahashi, H. Shibano, H. Kojima, and N. Hagihara. *Organometal. Chem. Syn.* **1**, 193 (1970).
8. Z. Lou and L. Zhang. *Fenzi Cuihua (Molecular catalysis, China)*, **8**, 468 (1994).
9. P.-F. Fu, L. Brard, Y. Li, and T.J. Marks. *J. Am. Chem. Soc.* **117**, 7157 (1995).
10. (a) L.F. Groux, D. Zargarian, L.C. Simon, and J.B.P. Soares. *J. Mol. Catal. A*, **193**, 51 (2003); (b) F.-G. Fontaine. Ph. D. thesis, Université de Montréal, Montréal, Qc. 2002.
11. R. Vollmerhaus, F. Bélanger-Gariépy, and D. Zargarian. *Organometallics*, **16**, 4762 (1997).
12. For synthesis and complete characterization of this complex see: T.A. Huber, M. Bayrakdarian, S. Dion, I. Dubuc, F. Bélanger-Gariépy, and D. Zargarian. *Organometallics*, **16**, 5811 (1997).
13. (a) K. Oertle and H. Wetter. *Tetrahedron Lett.* **26**, 5511 (1985); (b) K. Yamamoto and M. Takemae. *Synlett*, 259 (1990); (c) N. Asao, T. Sudo, and Y. Yamamoto. *J. Org. Chem.* **61**, 7654 (1996); (d) T. Sudo, N. Asao, V. Gevorgyan, and Y. Yamamoto. *J. Org. Chem.* **64**, 2494 (1999).
14. M. Rubin, T. Schweir, and V. Gevorgyan. *J. Org. Chem.* **67**, 1936 (2002).
15. (a) J.B. Lambert and Y. Zhao. *J. Am. Chem. Soc.* **118**, 7867 (1996); (b) J.B. Lambert, Y. Zhao, and H. Wu. *J. Org. Chem.* **64**, 2729 (1999).
16. (a) J.M. Blackwell, K.L. Foster, V.H. Beck, and W.E. Piers. *J. Org. Chem.* **64**, 4887 (1999); (b) D.J. Parks, J.M. Blackwell, and W.E. Piers. *J. Org. Chem.* **65**, 3090 (2000).
17. Lambert et al. have demonstrated that aromatic solvents can complex silylium cations when the Si substituents are not very bulky: J.B. Lambert, S. Zhang, and S.M. Ciro. *Organometallics*, **13**, 2430 (1994).
18. A.M. Lapointe, F.C. Rix, and M. Brookhart. *J. Am. Chem. Soc.* **119**, 906 (1997).
19. F.-G. Fontaine, M.-A. Dubois, and D. Zargarian. *Organometallics*, **20**, 5145 (2001).
20. (a) M.-A. Dubois. M.Sc. Thesis, Université de Montréal, Montréal, Qc. 2000; (b) R. Wang, L.F. Groux, and D. Zargarian. *Organometallics*, **21**, 5531 (2002).
21. R.A. Benkeser, H. Landesman, and D.J. Foster. *J. Am. Chem. Soc.* **74**, 648 (1952).



# Cadmium complexes of the tripodal $[\text{Te}(\text{N-}t\text{-Bu})_3]^{2-}$ dianion and the $\text{HgCl}_2$ adduct of a tellurium diimide dimer<sup>1</sup>

Tristram Chivers and Gabriele Schatte

**Abstract:** The reactions of  $\text{CdCl}_2$  or  $\text{HgCl}_2$  with  $\{\text{Li}_2[\text{Te}(\text{N-}t\text{-Bu})_3]\}_2$  in *n*-hexane–THF give rise to two distinctly different types of product. In the former case the complexes  $[\text{Li}(\text{THF})_x][(\text{CdCl})_3\{\text{Te}(\text{N-}t\text{-Bu})_3\}_2]$  (**7a** ( $x = 4$ ), **7b** ( $x = 3$ )) are obtained. The tetrasolvated complex **7a** is a solvent-separated ion pair. The trisolvated complex **7b** is a contact ion pair in which the fourth coordination site at the  $\text{Li}^+$  centre is occupied by one of the Cl ligands of the anion. The polycyclic anion in **7a** and **7b** is comprised of two tripodal  $[\text{Te}(\text{N-}t\text{-Bu})_3]^{2-}$  dianions that exhibit different coordination modes to the three  $\text{CdCl}^+$  units. One ligand is *N,N'*-chelated to all three metal centres, and each nitrogen atom bridges two Cd atoms, whereas the other is bonded in a tris-*N*-monodentate fashion in **7b**. In **7a** there is an additional weak Cd–N interaction. The reaction of  $\text{HgCl}_2$  with  $\{\text{Li}_2[\text{Te}(\text{N-}t\text{-Bu})_3]\}_2$  produces the adduct  $[t\text{-BuN}(\mu\text{-N-}t\text{-Bu})_2\text{TeN-}t\text{-Bu}]\text{HgCl}_2$  (**8**), in which the dimeric tellurium diimide ligand in its *cis(exo,exo)* configuration is *N,N'*-chelated to mercury. Polymeric strands parallel to the *b* axis are formed by weak  $\text{Te}\cdots\text{Cl}$  interactions (3.5248(16) Å, 3.5876(15) Å) involving both Cl atoms, but only one Te atom of the ligand.

**Key words:** imido ligands, cadmium, mercury, tellurium.

**Résumé :** Les réactions du  $\text{CdCl}_2$  ou du  $\text{HgCl}_2$  avec le  $\{\text{Li}_2[\text{Te}(\text{N-}t\text{-Bu})_3]\}_2$ , dans un mélange de *n*-hexane–THF, conduit à la formation de deux types forts différents de produits. Dans le premier cas, on obtient des complexes du type  $[\text{Li}(\text{THF})_x][(\text{CdCl})_3\{\text{Te}(\text{N-}t\text{-Bu})_3\}_2]$  (**7a** ( $x = 4$ ), **7b** ( $x = 3$ )). Le complexe tétrasolvaté du composé **7a** est une paire d'ions séparée par un solvant. Le complexe trisolvaté du composé **7b** est une paire d'ions de contacts dans lequel le quatrième site de coordination au centre  $\text{Li}^+$  est occupé par un des ligands Cl de l'anion. L'anion polycyclique dans les composés **7a** et **7b** se trouve entre les deux anions tripodes  $[\text{Te}(\text{N-}t\text{-Bu})_3]^{2-}$  qui présentent des modes différents aux trois unités  $\text{CdCl}^+$ . Un ligand est *N,N'*-chélaté aux trois centres métalliques et chaque atome d'azote sert de pont entre deux atomes de Cd alors que dans **7b** l'autre est lié d'une façon tris-*N*-monodentate. Dans le composé **7a**, on observe aussi une interaction additionnelle faible Cd–N. La réaction du  $\text{HgCl}_2$  avec le  $\{\text{Li}_2[\text{Te}(\text{N-}t\text{-Bu})_3]\}_2$  conduit à la formation de l'adduit  $[t\text{-BuN}(\mu\text{-N-}t\text{-Bu})_2\text{TeN-}t\text{-Bu}]\text{HgCl}_2$  (**8**) dans lequel le ligand diimide tellure dimère dans une configuration *cis(exo,exo)* est *N,N'*-chélaté au mercure. Les chaînes polymériques parallèles à l'axe *b* se forment par des interactions  $\text{Te}\cdots\text{Cl}$  faibles (3,5248(16) Å; 3,5876(15) Å) impliquant les deux atomes de chlore, mais un seul atome de Te de chaque ligand.

**Mots clés :** ligands imido, cadmium, mercure, tellure.

[Traduit par la Rédaction]

## Introduction

The tripodal ligand  $[\text{Te}(\text{N-}t\text{-Bu})_3]^{2-}$  was first obtained as the dilithium derivative **1**, which has a dimeric, hexagonal prismatic structure (**1**). Investigations of metathetical reactions of this reagent with main group element halides have revealed both bidentate and tridentate bonding modes as exemplified by complexes with trivalent group 13 and group 15 elements, e.g., (**2**) (**1**), (**3**) (**2**), and (**4**) (**3**).

In some cases metathesis is accompanied by redox processes involving imide transfer. For example, the treatment of **1** with  $\text{PhPCl}_2$  produces a spirocyclic phosphorus(V) complex (**5**) and elemental tellurium (**1**), while the stannatellurone (**6**) is obtained from the reaction of **1** with tin(II) salts (**4**). Fleischer and Stalke (**5**) have reported similar redox behaviour and imide transfer in the formation of  $\text{Ge}_4\text{S}(\text{N-}t\text{-Bu})_4$  from the reaction of the sulfur congener  $\{\text{Li}_2[\text{S}(\text{N-}t\text{-Bu})_3]\}_2$  with  $\text{GeCl}_2$ .

Received 29 March 2003. Published on the NRC Research Press Web site at <http://canjchem.nrc.ca> on 22 October 2003.

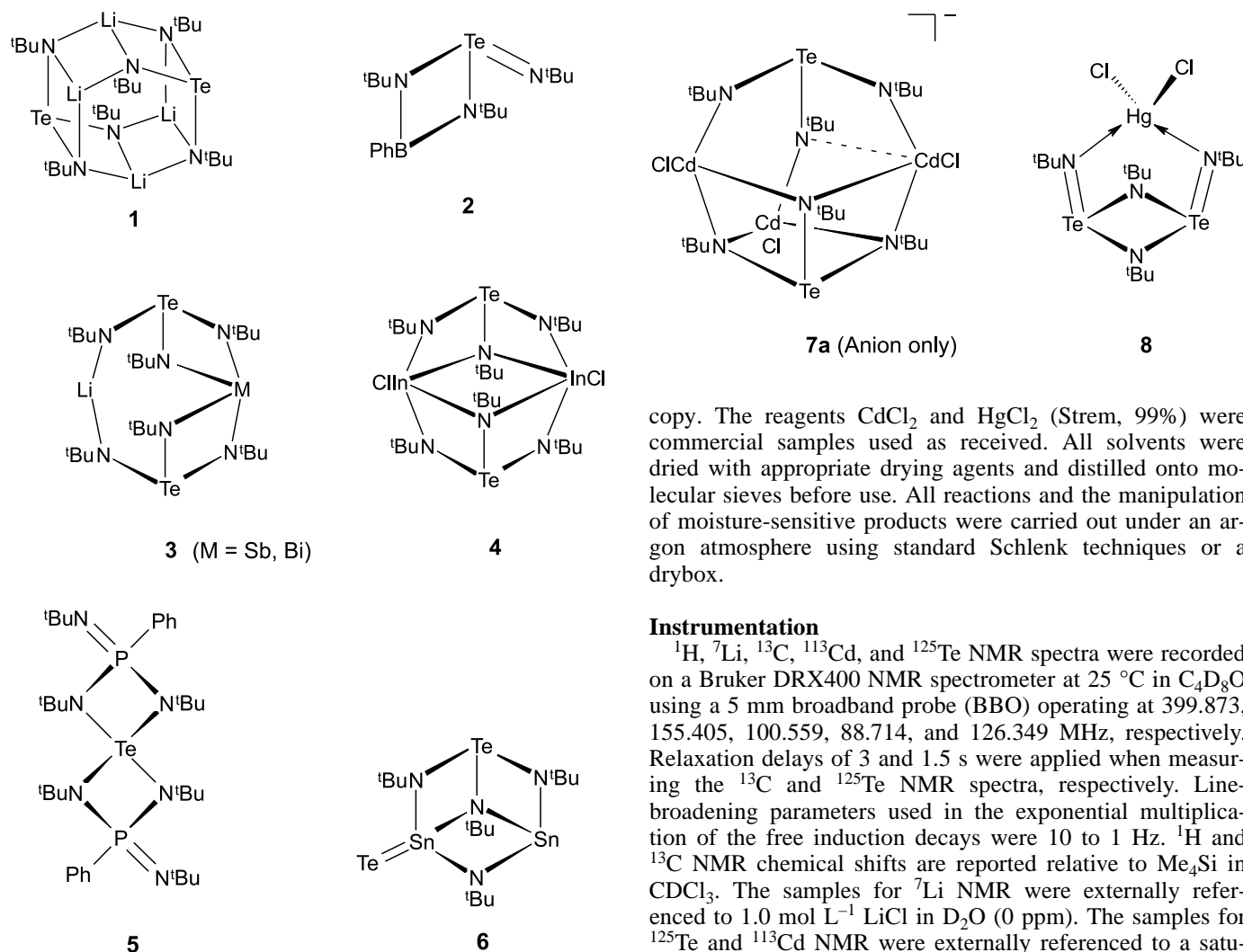
This article is dedicated to Professor John Harrod for his contributions to Canadian chemistry.

T. Chivers<sup>2</sup> and G. Schatte. Department of Chemistry, University of Calgary, Calgary, AB T2N 1N4, Canada.

<sup>1</sup>This article is part of a Special Issue dedicated to Professor John Harrod.

<sup>2</sup>Corresponding author (e-mail: [chivers@ucalgary.ca](mailto:chivers@ucalgary.ca)).





To probe the ligand behaviour of  $[\text{Te}(\text{N}-t\text{-Bu})_3]^{2-}$  towards other divalent metals, we have now investigated the reactions of **1** with  $\text{CdCl}_2$  and  $\text{HgCl}_2$ . An additional motivation for this study is the interest in complexes of group 12 metals with tellurium-containing ligands as potential single-source precursors of the corresponding binary tellurides, i.e.,  $\text{CdTe}$  and  $\text{HgTe}$ , which are important semiconductors with applications in IR, solar cell, and optoelectronic devices (6).

We report here that these reactions give rise to distinctly different types of products. The reaction of **1** with  $\text{CdCl}_2$  in THF produces the complexes  $[\text{Li}(\text{THF})_x][(\text{CdCl})_3\{\text{Te}(\text{N}-t\text{-Bu})_3\}_2]$  (**7a** ( $x = 4$ ), **7b** ( $x = 3$ )). By contrast the reaction of **1** with  $\text{HgCl}_2$  gives rise to an adduct of the tellurium(IV) diimide dimer  $t\text{-BuNTe}(\mu\text{-N}-t\text{-Bu})_2\text{TeN}-t\text{-Bu}$  with  $\text{HgCl}_2$  (**8**).

## Experimental

### Reagents and general procedures

The reagents  $t\text{-BuNTe}(\mu\text{-N}-t\text{-Bu})_2\text{TeN}-t\text{-Bu}$  (**7**) and  $[\text{Li}_2\text{Te}(\text{N}-t\text{-Bu})_3]_2$  (**1**) were prepared by literature procedures and their purity was ascertained by  $^1\text{H}$  NMR spectroscopy.

The reagents  $\text{CdCl}_2$  and  $\text{HgCl}_2$  (Strem, 99%) were commercial samples used as received. All solvents were dried with appropriate drying agents and distilled onto molecular sieves before use. All reactions and the manipulation of moisture-sensitive products were carried out under an argon atmosphere using standard Schlenk techniques or a drybox.

### Instrumentation

$^1\text{H}$ ,  $^7\text{Li}$ ,  $^{13}\text{C}$ ,  $^{113}\text{Cd}$ , and  $^{125}\text{Te}$  NMR spectra were recorded on a Bruker DRX400 NMR spectrometer at 25 °C in  $\text{C}_4\text{D}_8\text{O}$  using a 5 mm broadband probe (BBO) operating at 399.873, 155.405, 100.559, 88.714, and 126.349 MHz, respectively. Relaxation delays of 3 and 1.5 s were applied when measuring the  $^{13}\text{C}$  and  $^{125}\text{Te}$  NMR spectra, respectively. Line-broadening parameters used in the exponential multiplication of the free induction decays were 10 to 1 Hz.  $^1\text{H}$  and  $^{13}\text{C}$  NMR chemical shifts are reported relative to  $\text{Me}_4\text{Si}$  in  $\text{CDCl}_3$ . The samples for  $^7\text{Li}$  NMR were externally referenced to 1.0 mol  $\text{L}^{-1}$   $\text{LiCl}$  in  $\text{D}_2\text{O}$  (0 ppm). The samples for  $^{125}\text{Te}$  and  $^{113}\text{Cd}$  NMR were externally referenced to a saturated solution of  $\text{K}_2\text{TeO}_3$  in  $\text{D}_2\text{O}$  (1723 ppm) and referred to  $\text{Me}_2\text{Te}$  (0 ppm), and to a saturated solution of  $\text{CdCl}_2$  in  $\text{D}_2\text{O}$  (0 ppm), respectively. Elemental analyses were performed by Analytical Services, Chemistry Department, University of Calgary.

### Preparation of $[\text{Li}(\text{THF})_4][(\text{CdCl})_3\{\text{Te}(\text{N}-t\text{-Bu})_3\}_2]$ (**7a**)

The reagents **1** (0.500 g, 0.704 mmol) and  $\text{CdCl}_2$  (0.387 g, 2.112 mmol) were added to a Schlenk vessel. *n*-Hexane (20 mL) and THF (10 mL) were then transferred to the vessel, and the yellow slurry was stirred for 3.5 days at 23 °C. The yellow solution was separated from the precipitate of  $\text{LiCl}$  by using a cannula. The solvents were removed under vacuum to give **7a** (0.829 g, 0.583 mmol, 83%). The product was recrystallized from *n*-hexane-THF.  $^1\text{H}$  NMR ( $\text{THF}-d_8$ , 23 °C)  $\delta$ : 3.62 (m, THF), 1.78 (m, THF), 1.50 (s,  $\text{CMe}_3$ ).  $^{13}\text{C}$  NMR ( $\text{THF}-d_8$ , 23 °C)  $\delta$ : 68.27 (THF), 60.15 ( $\text{CMe}_3$ ), 37.93 ( $\text{CMe}_3$ ), 26.43 (THF).  $^{125}\text{Te}$  NMR ( $\text{THF}-d_8$ , 23 °C)  $\delta$ : 1564 (s).  $^7\text{Li}$  NMR ( $\text{THF}-d_8$ , 23 °C)  $\delta$ : -0.52 (s).  $^{113}\text{Cd}$  NMR ( $\text{THF}-d_8$ , 23 °C)  $\delta$ : 272.4 (s). Anal. calcd. for  $\text{C}_{40}\text{H}_{86}\text{Cd}_3\text{Cl}_3\text{LiN}_6\text{O}_4\text{Te}_2$ : C 33.80, H 6.10, N 5.90; found: C 31.57, H 6.02, N 4.89.<sup>5</sup>

<sup>3</sup> Loss of THF solvent resulted in inconsistent elemental analyses. This is a common problem with highly solvated *s*-block element complexes.



### Preparation of $[\text{Li}(\text{THF})_3(\mu\text{-Cl})\text{Cd}(\text{CdCl})_2\{\text{Te}(\text{N-}t\text{-Bu})_3\}_2]$ (**7b**)

The reagents **1** (0.500 g, 0.704 mmol) and  $\text{CdCl}_2$  (0.258 g, 1.408 mmol) were added to a Schlenk vessel. *n*-Hexane (20 mL) was transferred to the mixture at 23 °C to give a pale yellow slurry. Subsequent addition of THF (10 mL) produced a yellow solution. The reaction mixture was stirred for 24 h and then the precipitate was removed by filtration through a PTFE disk (pore size 0.45  $\mu\text{m}$ ). The solvents were removed under vacuum and the residue was extracted with *n*-hexane–THF to give an insoluble white solid (0.399 g). Removal of solvents from the filtrate yielded 0.325 g of a bright yellow solid that was shown by  $^1\text{H}$  NMR to be a mixture of **7b** and unreacted **1** in the approximate ratio 2:1. X-ray quality crystals of **7b** were obtained by layering *n*-hexane onto a THF solution of this product (4 days at 23 °C).<sup>3</sup>  $^1\text{H}$  NMR ( $\text{THF-}d_8$ , 23 °C)  $\delta$ : 3.62 (m, THF), 1.77 (m, THF), 1.46 (s,  $\text{CMe}_3$ ).  $^{13}\text{C}$  NMR ( $\text{THF-}d_8$ , 23 °C)  $\delta$ : 68.29 (THF), 58.43 ( $\text{CMe}_3$ ), 38.96 ( $\text{CMe}_3$ ), 26.43 (THF).  $^7\text{Li}$  NMR ( $\text{THF-}d_8$ , 23 °C)  $\delta$ : 0.04 (s).  $^{125}\text{Te}$  NMR ( $\text{THF-}d_8$ )  $\delta$ : 1546 (s).

### Preparation of $[t\text{-BuN}(\text{Te}(\mu\text{-N-}t\text{-Bu})_2\text{TeN-}t\text{-Bu})\text{HgCl}_2]$ (**8**)

*n*-Hexane (10 mL) and then THF (8 mL) were added to a solid mixture of **1** (0.500 g, 0.704 mmol) and  $\text{HgCl}_2$  (0.574 g, 2.113 mmol) at 23 °C in a Schlenk vessel. After 18 h the solution was bright yellow and a yellow-orange precipitate had formed. The precipitate was separated by filtration through a PTFE disk (pore size 0.45  $\mu\text{m}$ ) and solvents were removed under vacuum to give an orange solid (0.964 g). A portion of this solid (0.495 g) was extracted with MeCN (50 mL and then 10 mL) and the volume of the solution was reduced to 20 mL to give an orange precipitate of **8** (0.157 g). After storage at  $-17^\circ\text{C}$  for 14 days the MeCN solution produced a mixture of prism-like and plate-like orange crystals (0.070 g), which were identified by X-ray crystallography as **8**·2MeCN and **8**·MeCN, respectively. The combined masses of **8** and **8**·( $\text{MeCN}$ )<sub>*n*</sub> (*n* = 1, 2) correspond to an overall yield of ca. 72%. Data for **8**:  $^1\text{H}$  NMR ( $\text{CD}_3\text{CN}$ , 23 °C)  $\delta$ : 1.52 (s,  $\text{NMe}_3$ ).  $^1\text{H}$  NMR ( $\text{THF-}d_8$ , 23 °C)  $\delta$ : 1.37 (s,  $\text{NMe}_3$ ).  $^{13}\text{C}$  NMR ( $\text{THF-}d_8$ , 23 °C)  $\delta$ : 58.38 ( $\text{CMe}_3$ ), 38.23 ( $\text{CMe}_3$ ).  $^{125}\text{Te}$  NMR ( $\text{THF-}d_8$ , 23 °C)  $\delta$ : 1558 (s). Anal. calcd. for  $\text{C}_{16}\text{H}_{36}\text{Cl}_2\text{HgN}_4\text{Te}_2$ : C 23.69, H 4.47, N 6.91; found: C 22.67, H 4.12, N 7.36.

### X-ray analyses

Single crystals of **7a**, **7b**, and **8**·2MeCN were coated with Paratone oil, mounted on thin glass fibers, and frozen in the cold nitrogen stream of the goniometer. The X-ray data were collected on a Nonius Kappa CCD diffractometer (**7a**) and a Bruker AXS Platform/Smart 1000 CCD diffractometer (**7b** and **8**·2MeCN). Data reduction was performed using the SAINT software (8). An empirical absorption correction was applied to the data (SADABS) (9). Relevant parameters for

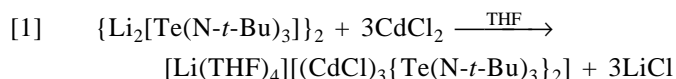
the data collections and crystallographic data are summarized in Table 1.<sup>4</sup>

The structures were solved by direct methods (**7a**: SIR-97 (10a); **7b** and **8**·2MeCN:<sup>5</sup> SHELXS-97 (10b)) and refined by the full-matrix least-squares method based on  $F^2$  using the SHELXL-97-2 (11). The non-hydrogen atoms were refined anisotropically. Hydrogen atoms were included at geometrically idealized positions (C—H and N—H bond distances, 0.95 Å) and were not refined. The isotropic thermal parameters of the hydrogen atoms were fixed at 1.2 times that of the preceding carbon or nitrogen atom. Three of the four THF molecules in **7a** were disordered. The disorder was refined using the split-atom model. Details of the crystallographic data for **7a**, **7b**, and **8**·2MeCN are summarized in Table 1.

## Results and discussion

### Synthesis and X-ray structures of $[\text{Li}(\text{THF})_x][(\text{CdCl})_3\{\text{Te}(\text{N-}t\text{-Bu})_3\}_2]$ (**7a** (*x* = 4), **7b** (*x* = 3))

The outcome of the reaction of  $\text{CdCl}_2$  with the dimeric reagent **1** in *n*-hexane–THF depends on the stoichiometry. Initial attempts to generate a complex with the empirical formula  $\text{Cd}[\text{Te}(\text{N-}t\text{-Bu})_3]$  by using a 2:1 stoichiometry gave a mixture of **7b** and unreacted **1**. Complex **7b** was shown by X-ray crystallography to be the contact ion pair  $[\text{Li}(\text{THF})_3(\mu\text{-Cl})\text{Cd}(\text{CdCl})_2\{\text{Te}(\text{N-}t\text{-Bu})_3\}_2]$  (vide infra). In an attempt to optimize the yield of a complex with this composition the reaction was conducted with a 3:1 stoichiometry. This resulted in the formation of the solvent-separated ion pair  $[\text{Li}(\text{THF})_4][(\text{CdCl})_3\{\text{Te}(\text{N-}t\text{-Bu})_3\}_2]$  (**7a**) which was isolated in a much-improved yield (83%) (eq. [1]).



The structures of **7a** and **7b** are shown in Figs. 1 and 2, respectively, and pertinent bond lengths and bond angles are compared in Table 2. In view of the similarity between the two structures, the ensuing discussion will focus on the atomic arrangements in the  $[(\text{CdCl})_3\{\text{Te}(\text{N-}t\text{-Bu})_3\}_2]^-$  anion of **7a**. In this monoanion two pyramidal  $[\text{Te}(\text{N-}t\text{-Bu})_3]^{2-}$  dianions are coordinated, in different fashions, to three  $\text{CdCl}^+$  cations. One of these ligands is asymmetrically *N,N'*-chelated to all three cadmium atoms and each of these nitrogen atoms bridges two cadmium centres. The second  $[\text{Te}(\text{N-}t\text{-Bu})_3]^{2-}$  anion is bonded in an *N*-monodentate manner to all three cadmium atoms. In **7a** there is an additional weak Cd–N interaction ( $\text{Cd}(2)\text{--N}(5) = 2.626(4)$  Å). The corresponding separation of 3.036(3) Å in **7b** is beyond the range for Cd–N covalent bonds. As a result, the nitrogen atoms in the former ligand are four-coordinate whereas those in the latter are three-coordinate. The structure of the anion in **7a** is related

<sup>4</sup>Supplementary data may be purchased from the Directory of Unpublished Data, Document Delivery, CISTI, National Research Council Canada, Ottawa, ON K1A 0S2, Canada ([http://www.nrc.ca/cisti/irm/unpub\\_e.shtml](http://www.nrc.ca/cisti/irm/unpub_e.shtml) for information on ordering electronically). CCDC 206826 (**7a**), 206827 (**7b**), 206288 (**8**·MeCN), and 206289 (**8**·2MeCN) contain the crystallographic data for this manuscript. These data can be obtained, free of charge, via [www.ccdc.cam.ac.uk/conts/retrieving.html](http://www.ccdc.cam.ac.uk/conts/retrieving.html) (or from the Cambridge Crystallographic Data Centre, 12 Union Road, Cambridge CB2 1EZ, U.K.; fax +44 1223 336033; or deposit@ccdc.cam.ac.uk).

<sup>5</sup>X-ray data for **8**·MeCN: *a* = 19.0220(2) Å, *b* = 14.4220 Å, *c* = 20.6450 Å, *V* = 5663.65(16) Å<sup>3</sup>, *Z* = 8, space group: *Pbca* (No. 61). The bond distances and angles for **8**·MeCN are identical to those in **8**·2MeCN.



**Table 1.** Crystallographic data for **7a**, **7b**, and **8•2MeCN**.

	<b>7a</b>	<b>7b</b>	<b>8•2MeCN</b>
Formula	C <sub>40</sub> H <sub>86</sub> Cd <sub>3</sub> Cl <sub>3</sub> LiN <sub>6</sub> O <sub>4</sub> Te <sub>2</sub>	C <sub>36</sub> H <sub>78</sub> Cd <sub>3</sub> Cl <sub>3</sub> LiN <sub>6</sub> O <sub>3</sub> Te <sub>2</sub>	C <sub>20</sub> H <sub>42</sub> Cl <sub>2</sub> HgN <sub>6</sub> Te <sub>2</sub>
Fw	1420.84	1348.73	893.29
Crystal system	Monoclinic	Monoclinic	Monoclinic
Space group	<i>P</i> 2 <sub>1</sub> / <i>c</i> (No. 14)	<i>P</i> 2 <sub>1</sub> / <i>c</i> (No. 14)	<i>P</i> 2 <sub>1</sub> / <i>n</i> (No. 14)
Crystal size (mm)	0.12 × 0.12 × 0.10	0.25 × 0.25 × 0.20	0.26 × 0.18 × 0.08
Colour and habit	Colourless square	Colourless block	Orange prism
<i>T</i> (K)	173(2)	173(2)	193(2)
$\lambda$ (Å)	0.71073	0.71073	0.71073
<i>a</i> (Å)	15.0160(1)	16.7090(1)	11.9709(11)
<i>b</i> (Å)	34.8361(2)	10.6830(1)	14.3986(13)
<i>c</i> (Å)	10.6995(1)	29.3700(3)	18.5654(17)
$\beta$ (°)	91.2919(3)	101.5390(3)	106.5561(17)
<i>V</i> (Å <sup>3</sup> )	5595.47(7)	5136.65(8)	3067.3(5)
<i>Z</i>	4	4	4
<i>d</i> <sub>calcd.</sub> (g cm <sup>-3</sup> )	1.687	1.744	1.934
$\mu$ (cm <sup>-1</sup> )	23.35	25.37	70.75
No. of reflns. collected	67703	75811	13961
No. of indep. reflns./ <i>R</i> <sub>int</sub>	11146/0.0975	12560/0.0961	6141/0.0493
Reflns. with <i>I</i> > 2 $\sigma$ ( <i>I</i> )	7717	8843	5001
Data/restraints/parameters	11 146/19/606	12 560/0/487	6141/0/281
<i>S</i> (GoF) on <i>F</i> <sup>2</sup> <sup>a</sup>	1.045	1.019	0.997
<i>R</i> [ <i>I</i> ≥ 2 $\sigma$ ( <i>I</i> )] <sup>b</sup>	0.0425	0.0393	0.0329
<i>wR</i> (all data) <sup>c</sup>	0.0771	0.0915	0.0792
Largest diff. peak/hole (e <sup>-</sup> /Å <sup>3</sup> )	0.721/−0.801	0.819/−1.046	0.988/−0.700

$$^a S = \{\sum [w(F_o^2 - F_c^2)^2]/(n - p)\}^{1/2}.$$

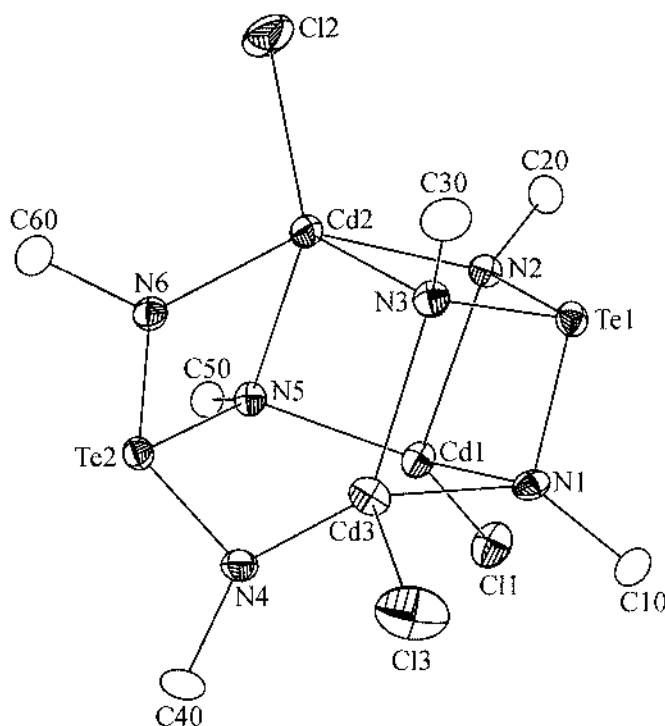
$$^b R = \sum ||F_o| - |F_c|| / \sum |F_o|.$$

$$^c wR = \{\sum w(F_o^2 - F_c^2)^2 / [\sum w(F_o^2)]\}^{1/2}.$$

**Fig. 1.** Thermal ellipsoid (30% probability) plot and atomic-numbering scheme for the anion in **7a**. Only the  $\alpha$ -carbon atoms of *tert*-butyl groups are shown.

to the “deck-chair” structure<sup>6</sup> of the binuclear indium complex **4** (2). The two InCl<sub>2</sub><sup>2+</sup> cations in **4** are replaced by CdCl<sup>+</sup> units and the third CdCl<sup>+</sup> unit occupies a vacant corner site. Charge balance is provided by the [Li(THF)<sub>4</sub>]<sup>+</sup> cation.

As expected, the mean Te—N bond length is ca. 0.01 Å longer and the mean bond angle  $\angle$  NTeN is ca. 5° smaller for the [Te(N-*t*-Bu)<sub>3</sub>]<sub>2</sub><sup>2-</sup> ligand that is involved in trischelation. The structural parameters for the other pyramidal TeN<sub>3</sub> ligand are very similar to those in the dilithium derivative **1** in which the nitrogen atoms are also three-coordinate (1, 12). The three cadmium atoms are in a highly distorted four-coordinate environment with bond angles ranging from ca. 73° to ca. 136°. The mean Cd—N bond length involving the three-coordinate nitrogen atoms is ca. 2.20 Å. The Cd—N bond lengths involving the four-coordinate nitrogen atoms are distinctly unequal with mean values of ca. 2.29 and 2.48 Å (cf. *d*(Cd—N) = 2.279(13) Å in [CdCl(NPEt<sub>3</sub>)<sub>4</sub>] (13) and 2.22–2.26 Å in tris(pyrazolyl)borato complexes of cadmium (14, 15)). The mean Cd—Cl bond distance of 2.458(1) Å is typical (the sum of covalent radii for Cd and



<sup>6</sup>For use of the term “deck-chair” see: A.J. Edwards, M.A. Paver, P.R. Raithby, M.-A. Rennie, C.A. Russell, and D.C. Wright. *Angew. Chem. Int. Ed. Engl.* **33**, 1277 (1994).

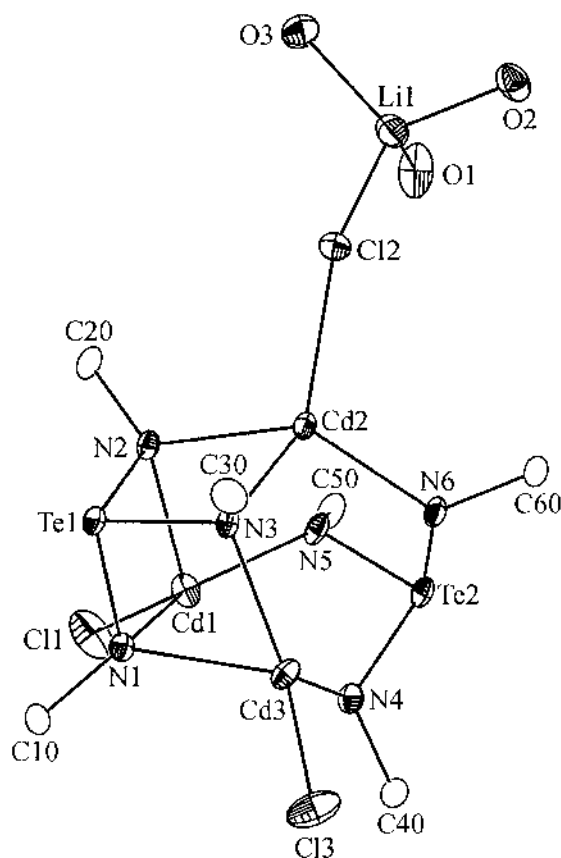


**Table 2.** Comparison of selected bond lengths (Å) and bond angles (°) for **7a** and **7b**.

	<b>7a</b>	<b>7b</b>
<b>Bond lengths (Å)</b>		
Te(1)—N(1)	1.988(3)	1.988(3)
Te(1)—N(2)	1.977(3)	1.977(3)
Te(1)—N(3)	1.982(4)	1.982(3)
Te(2)—N(4)	1.972(3)	1.973(3)
Te(2)—N(5)	1.991(3)	1.978(3)
Te(2)—N(6)	1.964(4)	1.969(3)
Cd(1)—N(1)	2.290(3)	2.290(3)
Cd(1)—N(2)	2.503(4)	2.553(3)
Cd(1)—N(5)	2.218(3)	2.212(3)
Cd(2)—N(2)	2.330(4)	2.275(3)
Cd(2)—N(3)	2.576(3)	2.451(3)
Cd(2)—N(5)	2.626(4)	3.036(3)
Cd(2)—N(6)	2.226(4)	2.181(3)
Cd(3)—N(1)	2.411(4)	2.448(3)
Cd(3)—N(3)	2.270(4)	2.307(3)
Cd(3)—N(4)	2.176(4)	2.216(3)
Cd(1)—Cl(1)	2.439(1)	2.458(1)
Cd(2)—Cl(2)	2.469(1)	2.514(1)
Cd(3)—Cl(3)	2.465(1)	2.446(1)
Li(1)—Cl(2)	—	2.332(8)
Li(1)—O(1)	1.905(11)	1.936(9)
Li(1)—O(2)	1.935(11)	1.913(8)
Li(1)—O(3)	1.919(1)	1.915(9)
Li(1)—O(4)	1.934(11)	—
<b>Bond angles (°)</b>		
N(2)—Te(1)—N(1)	93.38(14)	93.09(13)
N(3)—Te(1)—N(1)	90.49(15)	92.09(13)
N(2)—Te(1)—N(3)	93.33(14)	92.07(12)
N(4)—Te(2)—N(5)	96.62(15)	96.32(14)
N(6)—Te(2)—N(4)	102.48(15)	98.45(13)
N(6)—Te(2)—N(5)	93.15(15)	97.75(13)
N(5)—Cd(1)—N(1)	128.09(13)	134.20(11)
N(5)—Cd(1)—Cl(1)	119.00(10)	114.65(9)
N(1)—Cd(1)—Cl(1)	111.53(9)	110.36(8)
N(5)—Cd(1)—N(2)	90.46(12)	90.30(12)
N(1)—Cd(1)—N(2)	73.88(12)	72.70(11)
Cl(1)—Cd(1)—N(2)	119.73(9)	121.79(8)
N(6)—Cd(2)—N(2)	141.84(12)	135.96(12)
N(6)—Cd(2)—N(3)	87.96(12)	96.18(11)
N(2)—Cd(2)—N(3)	71.70(12)	74.06(10)
N(6)—Cd(2)—Cl(2)	110.88(12)	114.30(9)
N(2)—Cd(2)—Cl(2)	107.24(9)	108.37(9)
N(3)—Cd(2)—Cl(2)	124.82(9)	115.72(8)
N(4)—Cd(3)—N(3)	124.15(13)	129.38(12)
N(4)—Cd(3)—Cl(3)	118.81(10)	117.08(9)
N(3)—Cd(3)—Cl(3)	113.41(10)	111.20(8)
N(4)—Cd(3)—N(1)	99.03(13)	94.15(11)
N(3)—Cd(3)—N(1)	73.98(12)	73.82(10)
Cl(3)—Cd(3)—N(1)	115.82(9)	119.81(8)
Te(1)—N(1)—Cd(1)	99.53(14)	101.17(14)
Te(1)—N(1)—Cd(3)	95.04(14)	94.67(12)
Cd(1)—N(1)—Cd(3)	95.68(13)	93.20(11)
Cd(2)—N(2)—Cd(1)	87.61(11)	92.86(11)
Te(1)—N(2)—Cd(2)	101.51(15)	99.84(12)

**Table 2 (concluded).**

	<b>7a</b>	<b>7b</b>
Te(1)—N(2)—Cd(1)	93.05(13)	93.03(12)
Te(1)—N(3)—Cd(3)	99.75(15)	99.38(13)
Te(1)—N(3)—Cd(2)	93.46(14)	94.02(11)
Cd(3)—N(3)—Cd(2)	100.36(13)	94.75(11)
Te(2)—N(4)—Cd(3)	116.34(17)	114.44(15)
Te(2)—N(5)—Cd(1)	115.50(16)	109.82(15)
Te(2)—N(6)—Cd(2)	103.26(16)	110.22(14)
Li(1)—Cl(2)—Cd(2)	—	132.5(2)

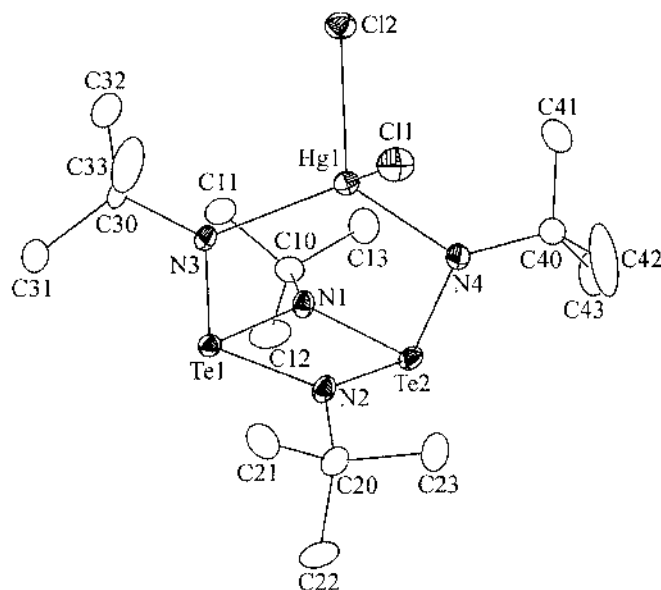
**Fig. 2.** Thermal ellipsoid (30% probability) plot and atomic-numbering scheme for **7b**. Only the  $\alpha$ -carbon atoms of *tert*-butyl groups and the oxygen atoms of THF molecules are shown.

Cl is 2.47 Å). The coordination of a Cl ligand of the anion to  $\text{Li}^+$  in **7b** elongates the Cd(2)—Cl(2) bond by ca. 0.04 Å. The Li—Cl distance of 2.332(8) Å in **7b** falls within the normal range of Li—Cl bond lengths (16).

The  $^1\text{H}$  NMR spectra of **7a** in  $\text{C}_4\text{D}_8\text{O}$  exhibit a singlet at 1.49 ppm for the *t*-Bu groups throughout the temperature range 183–298 K rather than the expected set of three resonances (assuming an approximate  $\text{C}_{2v}$  structure in solution). This observation indicates a highly fluxional structure for the anion in **7a** in solution. The  $^{113}\text{Cd}$  NMR chemical shift of 272.4 ppm observed for **7a** is within the range of 200–380 ppm reported for cadmium bonded to nitrogen ligands (17–19). The  $^{125}\text{Te}$  NMR chemical shifts of 1564 and



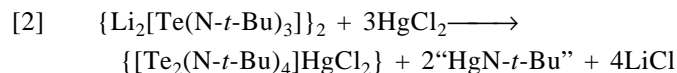
**Fig. 3.** Thermal ellipsoid (30% probability) plot and atomic-numbering scheme for **8**•2MeCN (the two molecules of MeCN are not shown).



1546 ppm for **7a** and **7b**, respectively, are typical values for complexes of the trisimidotellurite ligand (2, 3).

#### Synthesis and X-ray structure of the adduct [t-BuNTe( $\mu$ -N-*t*-Bu)<sub>2</sub>TeN-*t*-Bu]HgCl<sub>2</sub> (**8**)

In contrast to the reaction with CdCl<sub>2</sub>, the reaction of **1** with HgCl<sub>2</sub> in *n*-hexane–THF in a 1:3 molar ratio results in cleavage of one of the N-*t*-Bu groups from tellurium to give **8**, a 1:1 adduct of HgCl<sub>2</sub> and the tellurium diimide dimer [t-BuNTe( $\mu$ -N-*t*-Bu)<sub>2</sub>TeN-*t*-Bu] (**9**) (eq. [2]). It was found that the optimum yield of **8** was obtained when the solvents were added to a mixture of the *solid* reagents. Attempts to identify the other product of this imido transfer process were unsuccessful. Surprisingly **8** could not be obtained from the direct reaction of **9** with HgCl<sub>2</sub> under similar conditions.



The identity of **8**, after recrystallization from acetonitrile, was determined by X-ray crystallography. The recrystallization process gives two types of crystals which were identified as **8**•MeCN and **8**•2MeCN. Since the structural details for **8** are essentially identical in these two solvates, we will describe only the structure of **8**•2MeCN. As indicated in Fig. 3, the metal centre in the HgCl<sub>2</sub> adduct **8**•2MeCN is chelated by the ligand in its *cis(exo,exo)* configuration. This configuration is also found for the adduct **9**•LiCl (20) and in complexes with Ag<sup>+</sup> (21). Coordination to Cu<sup>+</sup>, however, initiates a *cis* → *trans* isomerization of the ligand (21). The two molecules of MeCN do not interact with **8**. Selected bond distances and bond angles are summarized in Table 3. The geometry at the mercury center is distorted tetrahedral with  $\angle NHgN = 119.84(16)^\circ$  and  $\angle ClHgCl = 103.06(5)^\circ$  indicating strong coordination of the ligand to the mercury center. Consistently, the mean Hg–N distance of 2.260 Å is at the lower end of the range of values

**Table 3.** Selected bond lengths (Å) and bond angles (°) for **8**•2MeCN.

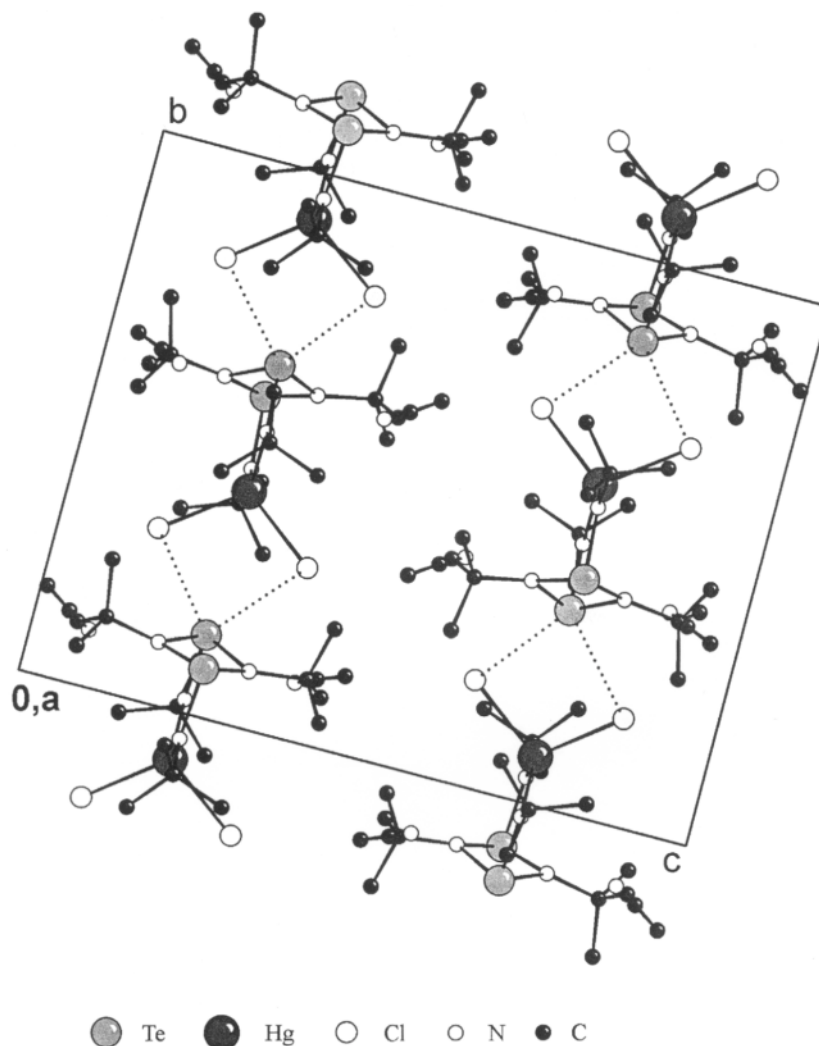
Bond lengths (Å)	
Hg(1)—N(3)	2.247(4)
Hg(1)—N(4)	2.272(4)
Hg(1)—Cl(1)	2.5508(15)
Hg(1)—Cl(2)	2.5239(14)
Te(1)···Cl(1) <sup>a</sup>	3.5248(16)
Te(1)···Cl(2) <sup>a</sup>	3.5876(15)
Te(1)—N(1)	2.027(4)
Te(1)—N(2)	2.029(4)
Te(1)—N(3)	1.919(4)
Te(2)—N(1)	2.004(5)
Te(2)—N(2)	2.018(4)
Te(2)—N(4)	1.901(5)
Bond angles (°)	
N(3)—Hg(1)—N(4)	119.84(16)
N(3)—Hg(1)—Cl(1)	108.76(12)
N(3)—Hg(1)—Cl(2)	107.13(12)
N(4)—Hg(1)—Cl(1)	105.77(13)
N(4)—Hg(1)—Cl(2)	111.00(13)
Cl(2)—Hg(1)—Cl(1)	103.06(5)
N(3)—Te(1)—N(1)	94.81(19)
N(3)—Te(1)—N(2)	93.55(19)
N(1)—Te(1)—N(2)	74.61(18)
N(4)—Te(2)—N(1)	95.3(2)
N(4)—Te(2)—N(2)	96.44(19)
N(1)—Te(2)—N(2)	75.32(18)
C(10)—N(1)—Te(2)	126.6(4)
C(10)—N(1)—Te(1)	125.8(4)
Te(2)—N(1)—Te(1)	104.9(2)
C(20)—N(2)—Te(2)	126.6(4)
C(20)—N(2)—Te(1)	125.8(3)
Te(2)—N(2)—Te(1)	104.3(2)
C(30)—N(3)—Te(1)	124.1(3)
C(30)—N(3)—Hg(1)	125.8(3)
Te(1)—N(3)—Hg(1)	110.09(19)
C(40)—N(4)—Te(2)	125.1(4)
C(40)—N(4)—Hg(1)	126.2(4)
Te(2)—N(4)—Hg(1)	108.4(2)

<sup>a</sup>Symmetry transformations used to generate equivalent atoms:  $-x + 1/2, +y + 1/2, -z + 1/2$ .

reported for four-coordinate mercury complexes with an N<sub>2</sub>Cl<sub>2</sub> coordination sphere (22–24). The most interesting feature of the structure of **8** is the existence of weak Te···Cl contacts (3.5248(16) Å, 3.5876(15) Å, cf. 3.85 or 4.00 Å (25, 26) for the sum of the van der Waals radii for Te and Cl) that give rise to polymeric strands parallel to the *b* axis (Fig. 4). This polymeric motif may account for the poor solubility of **8** in common organic solvents. The Te···Cl interactions involve only one of the tellurium atoms [Te(1)] and give rise to a minor asymmetry in the Te—N and Hg—N bond lengths. The mean Hg–Cl distance of 2.537 Å in **8** is ca. 0.2 Å longer than typical values of 2.31–2.34 Å for organic complexes of HgCl<sub>2</sub> (23), presumably as a result of the Te···Cl interactions. The mean Te—N bond distance in the Te<sub>2</sub>N<sub>2</sub> ring is 2.019(6) Å and the mean terminal Te—N bond length is 1.910(5) Å (cf. 2.081(10) and 1.876(10) Å,



**Fig. 4.** Unit cell of **8**·2MeCN showing the intermolecular Te···Cl contacts.



respectively, in **1**) (27). Although the bond angles in the four-membered  $\text{Te}_2\text{N}_2$  rings in **8** are similar to the corresponding values for **9** ( $|\angle \text{NTeN}| = 74.9^\circ$  vs.  $75.6(4)^\circ$ ,  $|\angle \text{TeNTe}| = 104.6^\circ$  vs.  $101.0(6)^\circ$ ), chelation brings about a contraction of the bond angle  $\angle \text{N}_{\text{endo}}\text{TeN}_{\text{exo}}$  from  $113.1(5)^\circ$  in **9** to  $95.0^\circ$  (range  $93.55(19)^\circ$ – $96.44(19)^\circ$ ) in **8**. As found for other metal complexes of **9** (20, 21), the  $\text{Te}_2\text{N}_2$  is much less puckered in **8** compared to the free ligand. The torsion angle  $\text{N}(2)\text{--Te}(1)\text{--N}(1)\text{--Te}(2)$  is  $7.31(19)^\circ$  (cf.  $19.8(5)^\circ$  in **9**). The geometry at the bridging nitrogen atoms is essentially planar ( $\Sigma \angle [\text{N}(1)] = 357.3^\circ$  and  $\Sigma [\text{N}(2)] = 356.7^\circ$ ).

## Conclusions

Different types of behaviour were observed in the reaction of  $[\text{Te}(\text{N-}t\text{-Bu})_3]^{2-}$  with group 12 dihalides. In the case of cadmium dichloride, one of the halide ions was displaced by the dianion to give a monoanionic, trimetallic complex. By contrast, the corresponding reaction with mercury dichloride resulted in imide transfer and the formation of the  $\text{HgCl}_2$  of the tellurium diimide dimer so formed.

## Acknowledgements

We thank the Natural Sciences and Engineering Research Council of Canada (NSERC) for financial support and Dr. R. McDonald (University of Alberta) for the X-ray data collections of **8**·2MeCN.

## References

1. T. Chivers, X. Gao, and M. Parvez. *Angew. Chem. Int. Ed. Engl.* **34**, 2549 (1995).
2. T. Chivers, M. Parvez, G. Schatte, and G.P.A. Yap. *Inorg. Chem.* **38**, 1380 (1999).
3. T. Chivers and G. Schatte. *Eur. J. Inorg. Chem.* 2266 (2002).
4. T. Chivers and G. Schatte. *Chem. Commun.* 2264 (2001).
5. R. Fleischer and D. Stalke. *Organometallics*, **17**, 382 (1998).
6. T. Chivers. *J. Chem. Soc. Dalton Trans.* 1185 (1996).
7. T. Chivers, G. Enright, N. Sandblom, G. Schatte, and M. Parvez. *Inorg. Chem.* **38**, 5431 (1999).
8. SAINT. Version 5.0 [computer program]. Bruker AXS, Inc., Madison, Wis. 1998.
9. SADABS. Version 2.01 [computer program]. Bruker AXS, Inc., Madison, Wis. 2001.



10. (a) A. Altomare, G. Cascarano, C. Giacovazzo, and A. Guagliardi. *J. Appl. Crystallogr.* **32**, 115 (1999); (b) G.M. Sheldrick. SHELXS-97 [computer program]. University of Göttingen, Göttingen, Germany. 1997.
11. G.M. Sheldrick. SHELXL97-2 [computer program]. University of Göttingen, Göttingen, Germany. 1997.
12. T. Chivers, X. Gao, and M. Parvez. *Inorg. Chem.* **35**, 4336 (1996).
13. K. Harms, J. Merle, C. Maichle-Mössmer, W. Massa, and M. Krieger. *Inorg. Chem.* **37**, 1099 (1998).
14. A. Looney, A. Salesh, Y. Zhang, and G. Parkin. *Inorg. Chem.* **23**, 1158 (1994).
15. D.L. Reger, S.S. Mason, J. Takats, X.W. Zhang, A.L. Rheingold, and B.S. Haggerty. *Inorg. Chem.* **32**, 4345 (1993).
16. T. Chivers, A. Downard, and M. Parvez. *Inorg. Chem.* **37**, 1099 (1998), and refs. cited herein.
17. M.F. Summers. *Coord. Chem. Rev.* **86**, 43 (1988).
18. D.L. Reger, S.S. Mason, A.L. Rheingold, and R.L. Ostrander. *Inorg. Chem.* **32**, 5216 (1993).
19. G.W. Franklin, D.P. Riley, and W.L. Neumann. *Coord. Chem. Rev.* **174**, 133 (1998).
20. T. Chivers, M. Parvez, and G. Schatte. *Inorg. Chem.* **40**, 540 (2001).
21. (a) T. Chivers, M. Parvez, and G. Schatte. *Angew. Chem. Int. Ed. Engl.* **38**, 2217 (1999); (b) T. Chivers, M. Parvez, and G. Schatte. *Inorg. Chem.* **38**, 5171 (1999).
22. C. Titze, W. Kairn, and S. Zalis. *Inorg. Chem.* **36**, 2505 (1997).
23. A.J. Canty, C.L. Raston, B.W. Skelton, and A.H. White. *J. Chem. Soc. Dalton Trans.* 15 (1982).
24. M.M. Kadooka, E. Hilti, L.G. Warner, and K. Seff. *Inorg. Chem.* **15**, 1186 (1976).
25. N.W. Alcock. *Adv. Inorg. Chem. Radiochem.* **15**, 1 (1972).
26. L. Pauling. *The nature of the chemical bond*. 3rd ed. Cornell University Press, Ithaca, N.Y. 1960.
27. T. Chivers, X. Gao, and M. Parvez. *J. Am. Chem. Soc.* **117**, 2359 (1995).



# Chemistry of zwitterionic penta-coordinate silicon compounds of the (ammoniomethyl)bis[glycolato(2-)- $O^1, O^2$ ]silicate type in aqueous and nonaqueous solution<sup>1</sup>

Reinhold Tacke, Rüdiger Bertermann, Andreas Biller, Christian Burschka, and Martin Penka

**Abstract:** The zwitterionic spirocyclic  $\lambda^5\text{Si}$ -silicates bis[glycolato(2-)- $O^1, O^2$ ][(trimethylammonio)methyl]silicate ([ $\text{OCH}_2\text{C}(\text{O})\text{O}$ ] $_2\text{SiCH}_2\text{NMe}_3$ , **3**) and bis[2-methylactato(2-)- $O^1, O^2$ ][(trimethylammonio)methyl]silicate ([ $\text{OCMe}_2\text{C}(\text{O})\text{O}$ ] $_2\text{SiCH}_2\text{NMe}_3$ , **4**) were synthesized by treatment of the zwitterionic  $\lambda^5\text{Si}$ -silicate  $\text{F}_4\text{SiCH}_2\text{NMe}_3$  with 2 mol. equiv. of  $\text{Me}_3\text{SiOCR}_2\text{C}(\text{O})\text{OSiMe}_3$  ( $\text{R} = \text{H, Me}$ ) (formation of 4 mol. equiv. of  $\text{Me}_3\text{SiF}$ ). Compounds **3** (isolated as **3**•2/3MeCN after drying in vacuo) and **4** were studied by solution  $^1\text{H}$ ,  $^{13}\text{C}$ , and  $^{29}\text{Si}$  NMR spectroscopy and by solid-state VACP/MAS  $^{13}\text{C}$ ,  $^{15}\text{N}$ , and  $^{29}\text{Si}$  NMR experiments, and the solvates **3**•MeCN and **4**•2MeCN were structurally characterized by single-crystal X-ray diffraction. These experimental investigations were complemented by computational studies of the zwitterions **3** and **4** and the anionic model species bis[2-methylactato(2-)- $O^1, O^2$ ]hydridosilicate(1-) ([ $\text{OCMe}_2\text{C}(\text{O})\text{O}$ ] $_2\text{SiH}^-$ , **8**). Compounds **3**•2/3MeCN and **4** and their already known derivatives [ $\text{OCH}_2\text{C}(\text{O})\text{O}$ ] $_2\text{SiCH}_2\text{NMe}_2\text{H}$  (**1**) and [ $\text{OCMe}_2\text{C}(\text{O})\text{O}$ ] $_2\text{SiCH}_2\text{NMe}_2\text{H}$  (**2**) were studied for their dynamic behavior ( $\Lambda/\Delta$ -enantiomerization) in solution by VT  $^1\text{H}$  NMR spectroscopy. In addition, compounds **1**, **2**, **3**•2/3MeCN, and **4** were studied in  $\text{CD}_3\text{OD}$  and  $\text{D}_2\text{O}$  with  $^1\text{H}$ ,  $^{13}\text{C}$ , and  $^{29}\text{Si}$  NMR experiments.

**Key words:** penta-coordinate silicon, zwitterionic  $\lambda^5\text{Si}$ -silicates,  $\Lambda/\Delta$ -enantiomerism, NMR spectroscopy, computational chemistry.

**Résumé :** On a synthétisé les  $\lambda^5\text{Si}$ -silicates spirocycliques et zwitterioniques bis[glycolato(2-)- $O^1, O^2$ ][(triméthylammonio)méthyl]silicate ([ $\text{OCH}_2\text{C}(\text{O})\text{O}$ ] $_2\text{SiCH}_2\text{NMe}_3$ , **3**) et bis[2-méthyllactato(2-)- $O^1, O^2$ ][(triméthylammonio)méthyl]silicate ([ $\text{OCMe}_2\text{C}(\text{O})\text{O}$ ] $_2\text{SiCH}_2\text{NMe}_3$ , **4**) en faisant réagir le  $\lambda^5\text{Si}$ -silicate zwitterionique  $\text{F}_4\text{SiCH}_2\text{NMe}_3$  avec deux équivalents de  $\text{Me}_3\text{SiOCR}_2\text{C}(\text{O})\text{OSiMe}_3$  ( $\text{R} = \text{H, Me}$ ), avec formation de quatre équivalents molaires de  $\text{Me}_3\text{SiF}$ . On a étudié les composés **3** (isolé sous la forme solvatée **3**•2/3MeCN après séchage sous vide) et **4** à l'état de solution en faisant appel à la spectroscopie RMN du  $^1\text{H}$ , du  $^{13}\text{C}$  et du  $^{29}\text{Si}$  et à l'état solide par des expériences de RMN « VACP/MAS » du  $^{13}\text{C}$ ,  $^{15}\text{N}$  et  $^{29}\text{Si}$ ; de plus, on a déterminé les structures de composés **3** et **4** à l'état solvaté en faisant appel à la diffraction des rayons X sur un cristal unique. Ces études expérimentales ont été complétées par des études théoriques des zwitterions **3** et **4** de l'espèce anionique modèle bis[2-méthyllactato(2-)- $O^1, O^2$ ]hydridosilicate(1-) ([ $\text{OCMe}_2\text{C}(\text{O})\text{O}$ ] $_2\text{SiH}^-$ , **8**). On a aussi étudié les composés **3**•2/3MeCN et **4**, ainsi que les dérivés déjà connus [ $\text{OCH}_2\text{C}(\text{O})\text{O}$ ] $_2\text{SiCH}_2\text{NMe}_2\text{H}$  (**1**) et [ $\text{OCMe}_2\text{C}(\text{O})\text{O}$ ] $_2\text{SiCH}_2\text{NMe}_2\text{H}$  (**2**), pour leur comportement dynamique (énantiomérisation  $\Lambda/\Delta$ ) en solution par spectroscopie RMN du  $^1\text{H}$  à température variable. De plus, les spectres RMN du  $^1\text{H}$ , du  $^{13}\text{C}$  et du  $^{29}\text{Si}$  des composés **1**, **2**, **3**•2/3MeCN et **4** ont aussi été étudiés en solution dans le  $\text{CD}_3\text{OD}$  et le  $\text{D}_2\text{O}$ .

**Mots clés :** silicium pentacoordiné,  $\lambda^5\text{Si}$ -silicate zwitterionique, énantiomérisation  $\Lambda/\Delta$ , spectroscopie RMN, chimie théorique.

[Traduit par la Rédaction]

## Introduction

Some years ago, we reported on the synthesis and structural characterization of the zwitterionic  $\lambda^5\text{Si}$ -silicates **1** and

**2** (1). Surprisingly, compound **2** could be crystallized from water to give the corresponding hydrate **2**• $\text{H}_2\text{O}$  in almost quantitative yield (1). The structurally related zwitterionic  $\lambda^5\text{Si}$ -silicate **5** (2) and the zwitterionic  $\lambda^5\text{Si}, \lambda^5\text{Si}'$ -disilicates

Received 26 March 2003. Published on the NRC Research Press Web site at <http://canjchem.nrc.ca> on 24 October 2003.

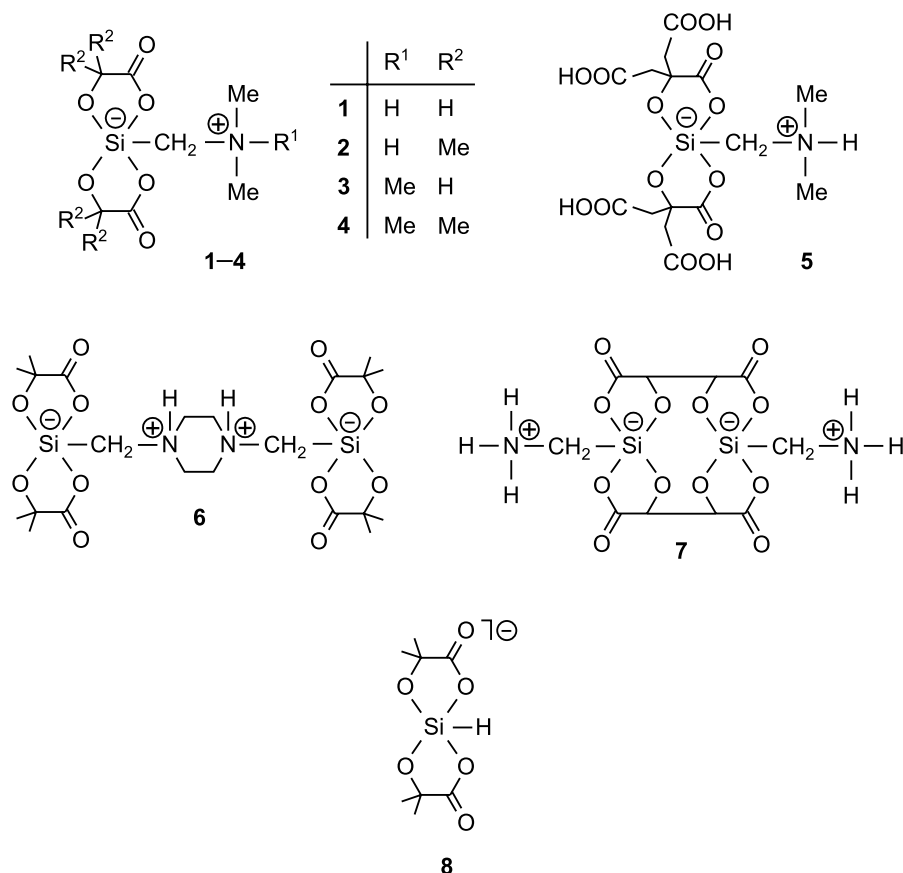
This paper is dedicated to Professor John Harrod in recognition of his outstanding contributions to organometallic chemistry.

**R. Tacke,<sup>2</sup> R. Bertermann, A. Biller, C. Burschka, and M. Penka.** Institut für Anorganische Chemie, Universität Würzburg, Am Hubland, D-97074 Würzburg, Germany.

<sup>1</sup>This article is part of a Special Issue dedicated to Professor John Harrod.

<sup>2</sup>Corresponding author (e-mail: [r.tacke@mail.uni-wuerzburg.de](mailto:r.tacke@mail.uni-wuerzburg.de)).





**6** (3) and (+)-**7** (4) were also crystallized from aqueous solutions to afford the respective hydrates **5**•H<sub>2</sub>O, **6**•8H<sub>2</sub>O, and (+)-**7**•3H<sub>2</sub>O. In view of the well-known sensitivity of the Si—OC bond against hydrolysis, the existence of **2** and **5–7** in aqueous solution is quite remarkable. To get more information about the nature of such solutions, we conducted a multinuclear NMR study with compounds **1** and **2** and their hitherto unknown *N*-methyl derivatives **3**•2/3MeCN and **4**. These quarternary ammonium compounds were included in these investigations to overcome potential problems with the acidic NH group of **1** and **2**, especially in context with changes of the pH value which controls the degree of protonation of the nitrogen atom in aqueous solution.

In earlier studies, we already investigated the dynamic behavior of **2** in solution (1). As shown by VT <sup>1</sup>H NMR experiments (complemented by computational studies), the  $\Lambda$ - and  $\Delta$ -enantiomers of **2** undergo an intramolecular enantiomerization ( $\Lambda/\Delta$ -interconversion) in organic solvents, with an energy barrier of  $\Delta G^\ddagger = 76 \pm 1 \text{ kJ mol}^{-1}$  ([D<sub>6</sub>]DMSO),  $\Delta G^\ddagger = 75 \pm 1 \text{ kJ mol}^{-1}$  (CD<sub>3</sub>CN), or  $\Delta G^\ddagger = 82 \pm 2 \text{ kJ mol}^{-1}$  (CDCl<sub>3</sub>). To get information about the influence of the two bidentate ligands (glycolato(2-) vs. 2-methylactato(2-)) and the ammoniomethyl group ((dimethylammonio)methyl vs. (trimethylammonio)methyl) on the energy barrier of the enantiomerization process, VT <sup>1</sup>H NMR studies were performed with compounds **1**, **2**, **3**•2/3MeCN, and **4**.

We report here on the syntheses of **3** (isolated as **3**•2/3MeCN) and **4**, the crystal structure analyses of **3**•MeCN and **4**•2MeCN, and solution <sup>1</sup>H, <sup>13</sup>C, and <sup>29</sup>Si NMR studies of **1**, **2**, **3**•2/3MeCN, and **4** in water and in organic solvents, including VT <sup>1</sup>H NMR experiments which

were complemented by computational studies of the zwitterions **3** and **4** and the anionic model species **8**. These investigations were carried out as part of our systematic studies on zwitterionic  $\lambda^5\text{Si}$ -silicates (5, 6; for reviews dealing with compounds of higher-coordinate silicon, see ref. 7). In addition, the NMR studies of **1**, **2**, **3**•2/3MeCN, and **4** in aqueous solution were also of some interest in context with our research activities in silicon biochemistry (8). Preliminary results of the studies presented here have already been reported elsewhere (9).

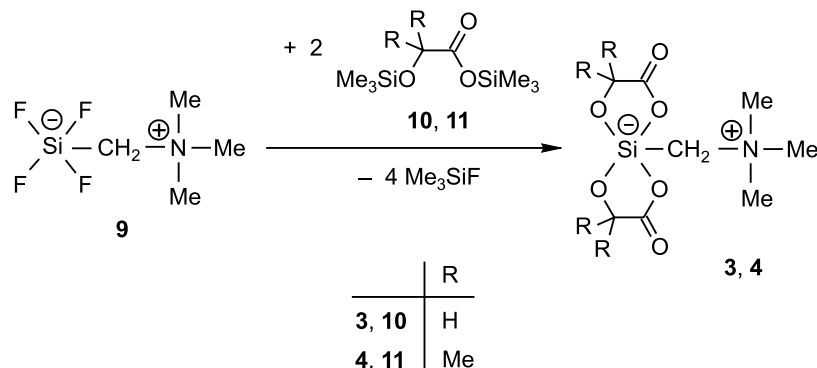
## Results and discussion

### Syntheses

Compounds **3** and **4** were prepared by reaction of the zwitterionic  $\lambda^5\text{Si}$ -tetrafluorosilicate **9** (10) with 2 mol. equiv. of Me<sub>3</sub>SiOCH<sub>2</sub>C(O)OSiMe<sub>3</sub> (**10**) (11) and Me<sub>3</sub>SiOCMe<sub>2</sub>C(O)OSiMe<sub>3</sub> (**11**) (12), respectively (formation of 4 mol. equiv. of Me<sub>3</sub>SiF). The syntheses were carried out in acetonitrile at 20 °C, and compounds **3** and **4** were obtained, after crystallization from acetonitrile, as the crystalline solvates **3**•MeCN and **4**•2MeCN. Upon drying in vacuo (**3**, loss of ca. 1/3 mol. equiv. of acetonitrile; **4**, complete loss of acetonitrile), the products **3**•2/3MeCN and **4** were isolated as colorless solids (yields: **3**•2/3MeCN, 83%; **4**, 73%). The identities of **3**•2/3MeCN and **4** were established by elemental analyses (C, H, N) and solution and solid-state NMR studies. In addition, crystal structure analyses of the solvates **3**•MeCN and **4**•2MeCN were performed (Scheme 1).



Scheme 1.



### Crystal structure analyses

The crystal data and the experimental parameters used for the crystal structure analyses of **3**•MeCN and **4**•2MeCN are given in Table 1; selected interatomic distances and angles are listed in Table 2. The structures of the zwitterions are depicted in Figs. 1 and 2.

The zwitterions **3** and **4** are chiral ( $C_1$  symmetry), and the crystals of racemic **3**•MeCN (space group  $P2_1/c$ ) and **4**•2MeCN (space group  $P2_1/n$ ) contain pairs of the respective  $\Lambda$ - and  $\Delta$ -enantiomers. As can be seen from Figs. 1 and 2 and Table 2, the Si-coordination polyhedra of **3**•MeCN and **4**•2MeCN are distorted trigonal bipyramids (transition trigonal bipyramid  $\rightarrow$  square pyramid: **3**•MeCN, 18.3%; **4**•2MeCN, 15.5%; pivot atom C1) (13).<sup>3</sup> The axial positions are occupied by the carboxylato oxygen atoms O1 and O3, whereas the alcoholato oxygen atoms O2 and O4 and the carbon atom C1 are found in the equatorial sites. The Si—O distances amount to 1.6572(10)–1.821(3) Å, with the axial Si—O bonds (1.7829(9)–1.821(3) Å) being significantly longer than the equatorial ones (1.6572(10)–1.669(4) Å). The Si—C1 distances amount to 1.909(5) Å and 1.9150(12) Å. The Si-coordination polyhedra of **3**•MeCN and **4**•2MeCN are very similar to those reported for **1**, **2**•H<sub>2</sub>O, and **2**•2MeCN (Si—O(ax), 1.7930(12)–1.822(2) Å; Si—O(eq), 1.656(2)–1.6751(13) Å; Si—C1, 1.8915(11)–1.896(2) Å) (1).

### NMR studies

The zwitterionic  $\lambda^5\text{Si}$ -silicates **3**•2/3MeCN and **4** were studied by <sup>13</sup>C, <sup>15</sup>N, and <sup>29</sup>Si VACP/MAS NMR experiments in the solid state and by <sup>1</sup>H, <sup>13</sup>C, and <sup>29</sup>Si NMR experiments in solution (solvent [D<sub>6</sub>]DMSO). All these investigations were performed at 22 °C. The solid-state NMR data of **3** and **4** are compatible with the crystal structures of **3** in **3**•MeCN and **4** in **4**•2MeCN.<sup>4</sup> The isotropic <sup>29</sup>Si chemical shifts in the solid-state NMR spectra clearly characterize these <sup>29</sup>Si resonances as arising from penta-coordinate silicon atoms (**3**,  $\delta = -91.9$ ; **4**,  $\delta = -101.3$ ). As these <sup>29</sup>Si chemical shifts are very similar to those observed for **3**•2/3MeCN and **4** in solution (**3**•2/3MeCN,  $\delta = -92.1$ ; **4**,  $\delta = -102.1$ ), it is concluded that

penta-coordination is present in solution as well. The <sup>29</sup>Si NMR data obtained for **3**•2/3MeCN and **4** are quite similar to those reported for the related compounds **1** and **2** (1). The solution NMR data of **3**•2/3MeCN and **4** are compatible with the presence of one particular zwitterionic species (such as the trigonal-bipyramidal zwitterions observed in the crystals of **3**•MeCN and **4**•2MeCN), or with a rapid low-energy interconversion of different isomers (1). As the trigonal-bipyramidal Si-coordination polyhedron, with the two carboxylato oxygen atoms in the axial positions, is the energetically most favorable one, it is likely to assume that this particular structure is also dominant in solution.

The chiral nature of the  $\lambda^5\text{Si}$ -silicate frameworks of **3** and **4** should be reflected by diastereotopism of the SiCH<sub>2</sub>N protons (**3** and **4**, AB spin system), the CH<sub>2</sub> protons of the glycolato(2-) ligands (**3**, AB spin system), and the two CH<sub>3</sub> groups of the 2-methylactato(2-) ligands (**4**, two resonance signals). Provided that the  $\Lambda$ - and  $\Delta$ -enantiomers of **3** and **4** are configurationally stable on the NMR timescale, this diastereotopism should be detectable. In the case of the zwitterion **3**, diastereotopism of the SiCH<sub>2</sub>N protons was only observed at temperatures below -23 °C (measured in [D<sub>7</sub>]DMF, see below), and diastereotopism of the CH<sub>2</sub> protons of the glycolato(2-) ligands could not be detected even at -55 °C (in [D<sub>7</sub>]DMF). For compound **4** (in [D<sub>7</sub>]DMF), however, diastereotopism of both the SiCH<sub>2</sub>N protons and the two CH<sub>3</sub> groups of the 2-methylactato(2-) ligands was observed at 22 °C, indicating a higher configurational stability of its  $\Lambda$ - and  $\Delta$ -enantiomers as compared to **3**.

To get more information about the configurational stability of **3** and **4** and their derivatives **1** and **2**, all these zwitterions were studied by VT <sup>1</sup>H NMR experiments at 300.1 MHz in the temperature ranges 22–100 °C (**1**), 22–120 °C (**2**), -55 to 22 °C (**3**), and 22–110 °C (**4**) using [D<sub>6</sub>]DMSO (**1**, **2**) and [D<sub>7</sub>]DMF (**3**, **4**) as the solvents. An AB spin system for the diastereotopic SiCH<sub>2</sub>N protons of **1**, **2**, and **4** was observed at 22 °C, indicating that the  $\Lambda$ - and  $\Delta$ -enantiomers of these compounds are configurationally stable on the NMR timescale at this temperature. Upon heating, coalescence could be observed at 80 °C (**1**), 112 °C (**2**), and 97 °C (**4**)

<sup>3</sup>The degree of distortion was calculated by using the dihedral angle method described in refs. 13a and 13b. All nine dihedral angles and the values for the reference geometry of the ideal square pyramid given in ref. 13a were considered for this calculation.

<sup>4</sup>Under MAS conditions (spinning rate, 5.0 kHz), the solvate **3**•2/3MeCN loses the acetonitrile completely. In the solid-state <sup>13</sup>C VACP/MAS NMR spectra of **3** and **4**, only one resonance signal was observed for the three NCH<sub>3</sub> groups. This could be explained by an unhindered rotation of the N(CH<sub>3</sub>)<sub>3</sub> moiety around the N-CH<sub>2</sub> axis.



**Table 1.** Crystal data and experimental parameters for the crystal structure analyses of **3•MeCN** and **4•2MeCN**.

Compound	<b>3•MeCN</b>	<b>4•2MeCN</b>
Empirical formula	C <sub>10</sub> H <sub>18</sub> N <sub>2</sub> O <sub>6</sub> Si	C <sub>16</sub> H <sub>29</sub> N <sub>3</sub> O <sub>6</sub> Si
Formula mass (g mol <sup>-1</sup> )	290.35	387.51
Collection <i>T</i> (K)	173(2)	173(2)
λ(Mo Kα) (Å)	0.71073	0.71073
Crystal system	Monoclinic	Monoclinic
Space group (no.)	<i>P</i> 2 <sub>1</sub> / <i>c</i> (14)	<i>P</i> 2 <sub>1</sub> / <i>n</i> (14)
<i>a</i> (Å)	7.4251(15)	13.220(3)
<i>b</i> (Å)	16.966(3)	12.722(3)
<i>c</i> (Å)	11.144(2)	13.660(3)
β (°)	95.49(3)	117.52(3)
<i>V</i> (Å <sup>3</sup> )	1397.4(5)	2037.5(7)
<i>Z</i>	4	4
<i>D</i> (calcd.) (g cm <sup>-3</sup> )	1.380	1.263
μ (mm <sup>-1</sup> )	0.192	0.150
<i>F</i> (000)	616	832
Crystal dimensions (mm)	0.5 × 0.3 × 0.3	0.5 × 0.5 × 0.4
2θ range (°)	4.38–41.70	4.64–53.94
Index ranges	–7 ≤ <i>h</i> ≤ 7, –16 ≤ <i>k</i> ≤ 16, –10 ≤ <i>l</i> ≤ 11	–16 ≤ <i>h</i> ≤ 16, –15 ≤ <i>k</i> ≤ 16, –17 ≤ <i>l</i> ≤ 17
No. of collected reflections	6318	16 798
No. of independent reflections	1416	4224
<i>R</i> <sub>int</sub>	0.0735	0.0255
No. of reflections used	1416	4224
No. of parameters	176	245
<i>S</i> <sup>a</sup>	1.077	1.048
Weight parameters <i>a/b</i> <sup>b</sup>	0.0691/1.3502	0.0596/0.0989
<i>R</i> 1 <sup>c</sup> [ <i>I</i> > 2σ( <i>I</i> )]	0.0510	0.0321
<i>wR</i> 2 <sup>d</sup> (all data)	0.1347	0.0915
Max/min residual electron density (e Å <sup>-3</sup> )	+0.309/–0.242	+0.244/–0.235

<sup>a</sup>*S* = {Σ[w(*F*<sub>o</sub><sup>2</sup> – *F*<sub>c</sub><sup>2</sup>)<sup>2</sup>] / (*n* – *p*)}<sup>0.5</sup>; *n* = no. of reflections; *p* = no. of parameters.

<sup>b</sup>*w*<sup>–1</sup> = σ<sup>2</sup>(*F*<sub>o</sub><sup>2</sup>) + (*aP*)<sup>2</sup> + *bP*, with *P* = [max(*F*<sub>o</sub><sup>2</sup>, 0) + 2*F*<sub>c</sub><sup>2</sup>] / 3.

<sup>c</sup>*R*1 = Σ|*F*<sub>o</sub> – |*F*<sub>c</sub>|| / Σ|*F*<sub>o</sub>|.

<sup>d</sup>*wR*2 = {Σ[w(*F*<sub>o</sub><sup>2</sup> – *F*<sub>c</sub><sup>2</sup>)<sup>2</sup>] / Σ[w(*F*<sub>o</sub><sup>2</sup>)<sup>2</sup>]}<sup>0.5</sup>.

**Table 2.** Selected interatomic distances (Å) and angles (°) for **3•MeCN** (exp.), **3** (calcd.), **4•2MeCN** (exp.), and **4** (calcd.).

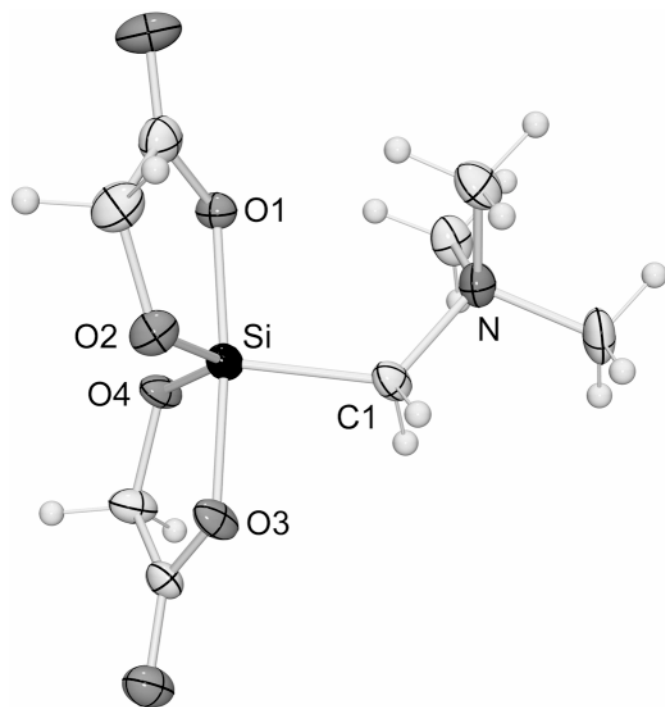
	<b>3•MeCN</b> (exp.)	<b>3</b> (calcd.)	<b>4•2MeCN</b> (exp.)	<b>4</b> (calcd.)
<b>Interatomic distances (Å)</b>				
Si—O1	1.789(3)	1.776	1.7829(9)	1.774
Si—O2	1.669(4)	1.653	1.6627(9)	1.650
Si—O3	1.821(3)	1.760	1.8124(9)	1.759
Si—O4	1.658(4)	1.651	1.6572(10)	1.649
Si—C1	1.909(5)	1.948	1.9150(12)	1.951
<b>Interatomic angles (°)</b>				
O1–Si–O2	89.54(17)	88.0	89.52(5)	87.8
O1–Si–O3	173.81(17)	178.8	174.70(4)	178.8
O1–Si–O4	89.01(16)	91.8	89.29(5)	92.0
O1–Si–C1	99.44(19)	94.1	98.46(5)	94.0
O2–Si–O3	86.92(17)	91.4	87.42(5)	91.7
O2–Si–O4	125.78(19)	123.6	125.18(5)	124.0
O2–Si–C1	118.5(2)	120.5	116.62(5)	120.1
O3–Si–O4	88.95(17)	89.5	88.95(5)	89.2
O3–Si–C1	86.71(19)	85.3	86.78(5)	85.3
O4–Si–C1	115.2(2)	115.8	117.74(5)	115.8

(Fig. 3). However, in the case of **3** a singlet for the SiCH<sub>2</sub>N protons was detected at 22 °C, indicating a dynamic behavior of the enantiomers (*Λ*/*Δ*-enantiomerization) in solution. Upon cooling, coalescence was detected at –23 °C and on further cooling an AB spin system for the SiCH<sub>2</sub>N protons was observed, indicating that *Λ*-**3** and *Δ*-**3** are configurationally stable on the NMR timescale under these conditions (Fig. 3). Furthermore, the <sup>1</sup>H NMR spectra of **2** and **4** each showed two resonance signals for the two diastereotopic CH<sub>3</sub> groups of the 2-methylactato(2–) ligands at 22 °C. Upon heating, coalescence was observed at 85 °C (**2**, in [D<sub>6</sub>]DMSO) and 60 °C (**4**, in [D<sub>7</sub>]DMF). The temperature dependence of the <sup>1</sup>H NMR spectra of the zwitterions **1–4** is characterized by complete reversibility (Fig. 3). The calculated energy barriers for the *Λ*/*Δ*-interconversion amount to Δ*G*<sup>‡</sup> = 73.0 ± 0.5 kJ mol<sup>–1</sup> (**1**), Δ*G*<sup>‡</sup> = 78.1 ± 0.5 kJ mol<sup>–1</sup> (**2**; CH<sub>3</sub> groups), Δ*G*<sup>‡</sup> = 78.8 ± 0.5 kJ mol<sup>–1</sup> (**2**; SiCH<sub>2</sub>N protons), Δ*G*<sup>‡</sup> = 51.6 ± 0.5 kJ mol<sup>–1</sup> (**3**), Δ*G*<sup>‡</sup> = 74.6 ± 0.5 kJ mol<sup>–1</sup> (**4**; CH<sub>3</sub> groups), and Δ*G*<sup>‡</sup> = 76.1 ± 1.0 kJ mol<sup>–1</sup> (**4**; SiCH<sub>2</sub>N protons).

In addition, compounds **1**, **2**, **3•2/3MeCN**, and **4** were studied by <sup>1</sup>H, <sup>13</sup>C, and <sup>29</sup>Si NMR experiments in CD<sub>3</sub>OD and D<sub>2</sub>O at 22 °C. Except for small differences in the chemi-



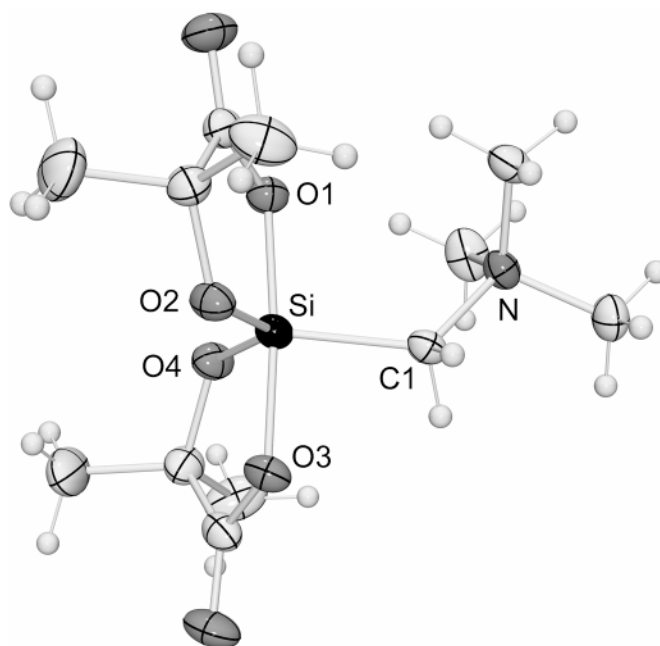
**Fig. 1.** Structure of the zwitterion **3** ( $\Delta$ -enantiomer) in the crystal of **3**•MeCN (probability level of displacement ellipsoids 50%).



cal shifts due to the change of the solvent, the spectra of **2** and **4** recorded in CD<sub>3</sub>OD (data not given) were analogous to those obtained in [D<sub>6</sub>]DMSO, indicating that the zwitterionic  $\lambda^5$ Si-silicates **2** and **4** are stable in the protic solvent CD<sub>3</sub>OD. Compound **1** is almost insoluble in CD<sub>3</sub>OD and **3**•2/3MeCN shows a very poor solubility, but exhibits hints for penta-coordinate silicon in the <sup>29</sup>Si NMR spectra (1D<sup>29</sup>Si NMR, 2D<sup>29</sup>Si, <sup>1</sup>H HMBC:  $\delta$  = -91.8). Thus, the zwitterion **3** seems to be stable in CD<sub>3</sub>OD as well.

Saturated aqueous solutions of **1** (1.64 mmol in 1 mL of D<sub>2</sub>O) and **3**•2/3MeCN (2.24 mmol in 1 mL of D<sub>2</sub>O), however, show several resonance signals in the <sup>29</sup>Si NMR spectra (**1**,  $\delta$  = -70.8, -69.3 (br), -61.5, -61.4, and -52.6; **3**•2/3MeCN,  $\delta$  = -73.2, -73.1, -72.7, -63.6, -63.5, -63.4, and -54.5). The chemical shifts of these signals are not compatible with the existence of the zwitterions **1** and **3** in aqueous solution, but rather suggest the presence of tetra-coordinate silicon species. As no free glycolic acid could be observed, it is likely to assume that these species still contain both glycolate ligands (bidentate glycolato(2-)) and (or) monodentate glycolato(1-) ligands; however, their structure could not be deduced unequivocally from the <sup>1</sup>H, <sup>13</sup>C, and <sup>29</sup>Si NMR spectra. In the <sup>29</sup>Si NMR spectra of saturated aqueous solutions of **2** (181  $\mu$ mol in 1 mL of D<sub>2</sub>O) ( $\delta$  = -99.4, -61.4, and -52.4) and **4** (2.51 mmol in 1 mL of D<sub>2</sub>O) ( $\delta$  = -101.1, -63.6, -63.4, and -54.5) three and four resonance signals, respectively, were observed. Obviously, the zwitterions **2** and **4** and tetra-coordinate species as well exist in aqueous solution. Concentration-dependent NMR experi-

**Fig. 2.** Structure of the zwitterion **4** ( $\Delta$ -enantiomer) in the crystal of **4**•2MeCN (probability level of displacement ellipsoids 50%).



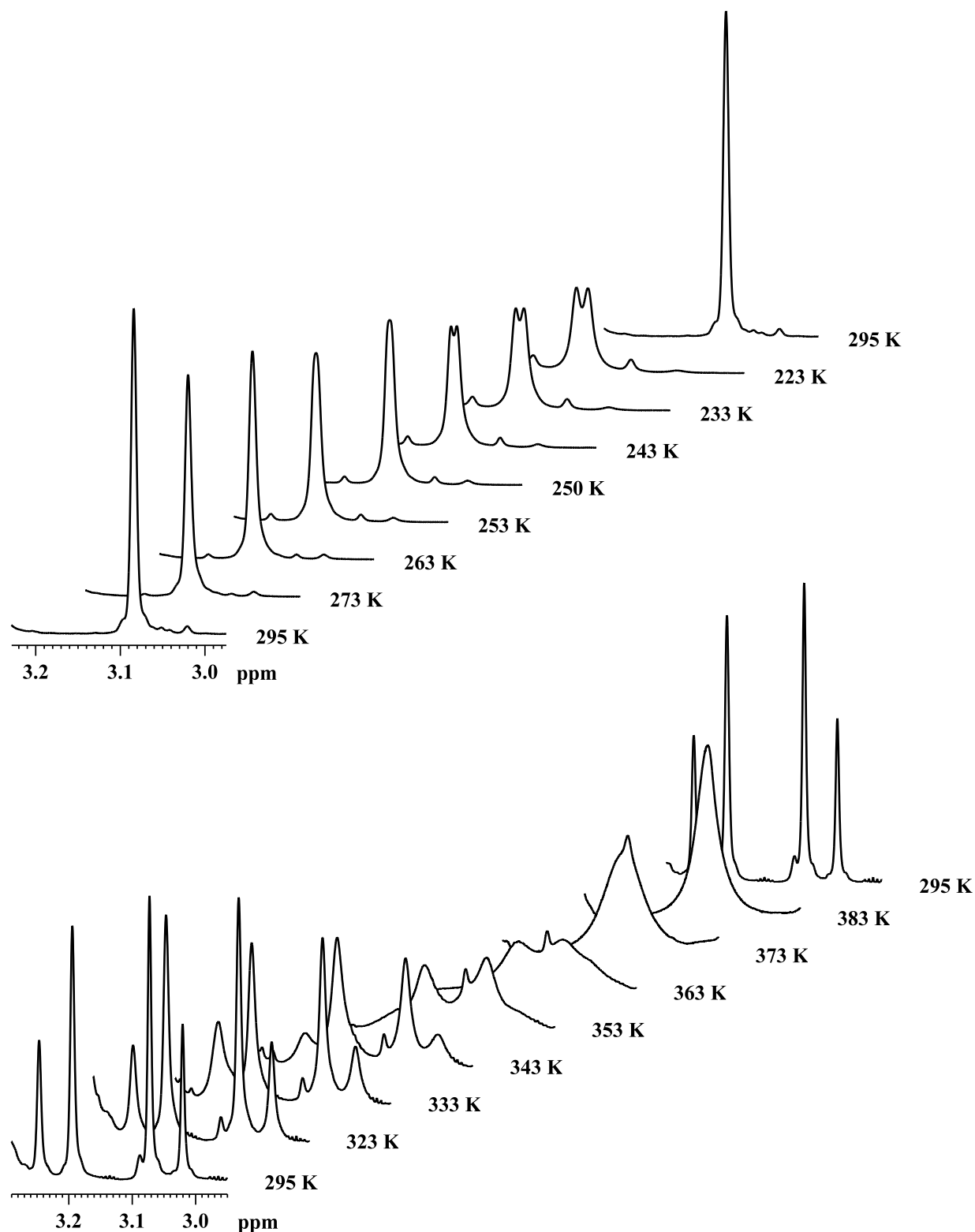
ments with solutions of **4** in D<sub>2</sub>O indicate that the amount of the penta-coordinate zwitterionic species increases as the concentration gets higher. However, even saturated solutions of **1** and **3**•2/3MeCN in D<sub>2</sub>O gave no hints for the presence of penta-coordinate silicon. Analogously to **1** and **3**, no free  $\alpha$ -hydroxycarboxylic acid was observed upon dissolution of **2** and **4** in D<sub>2</sub>O. As compounds **2** and **4** could be recovered almost quantitatively from their aqueous solution by slow evaporation of the water, a thermodynamic equilibrium among all species present in solution can be assumed. Attempts to recover **1** and **3** from their aqueous solution failed.

To get more information about the nature of the aqueous solutions, <sup>1</sup>H and 2D <sup>29</sup>Si, <sup>1</sup>H HMBC NMR studies with **1** (491  $\mu$ mol in 1 mL of D<sub>2</sub>O), **2** (181  $\mu$ mol in 1 mL of D<sub>2</sub>O), **3**•2/3MeCN (491  $\mu$ mol in 1 mL of D<sub>2</sub>O), and **4** (491  $\mu$ mol in 1 mL of D<sub>2</sub>O) at various pH values were performed. Starting from the respective saturated solution (see above) (**1**, pH 3.6; **2**, pH 3.9; **3**•2/3MeCN, pH 3.6; **4**, pH 3.9; the pH values of the respective solutions in H<sub>2</sub>O differ by about 0.1 unit), the pH value was increased stepwise by addition of solid potassium hydroxide (increase of ca. 1.0 pH unit per step). The spectra of **1** and **3**•2/3MeCN showed only signals arising from tetra-coordinate species over the whole range measured, and penta-coordination was not detected (**1** (pH = 3.6):  $\delta$  = -70.7, -61.5, -52.4; **1** (pH = 13.0):  $\delta$  = -67.8, -60.6, -51.8; **3**•2/3MeCN (pH = 3.6):  $\delta$  = -72.8, -63.4, -54.2; **3**•2/3MeCN (pH = 13.1):  $\delta$  = -76.9, -68.4, -60.1).<sup>5</sup> For compounds **2** and **4**, decreasing amounts of the respective  $\lambda^5$ Si-silicate were observed, whereas tetra-coordination increased at the same time (**2** (pH = 3.9):  $\delta$  = -99.5, -61.4, -52.3; **2** (pH = 13.2):  $\delta$  = -67.9, -60.4, -51.4; **4** (pH = 3.9):

<sup>5</sup>The <sup>29</sup>Si chemical shifts measured for the saturated solutions of **1**, **2**, **3**•2/3MeCN, and **4** were determined by 1D NMR experiments providing a high spectral resolution. However, the <sup>29</sup>Si chemical shifts measured for the pH-dependent NMR experiments were extracted from 2D <sup>29</sup>Si, <sup>1</sup>H HMBC NMR experiments delivering a lower spectral resolution in the indirect (<sup>29</sup>Si) dimension. Due to this principal matter, we were not able to resolve as many different shifts of <sup>29</sup>Si as in the 1D NMR experiments.



**Fig. 3.** Temperature dependence of the  $^1\text{H}$  NMR signals for the diastereotopic  $\text{SiCH}_2\text{N}$  protons of the zwitterions **3** and **4** (solutions in  $[\text{D}_7]\text{DMF}$ , 300.1 MHz). Zwitterion **3** (above): Spectra obtained upon cooling from 22 to  $-50^\circ\text{C}$  and subsequent heating to  $22^\circ\text{C}$ . Zwitterion **4** (below): Spectra obtained upon heating from 22 to  $110^\circ\text{C}$  and subsequent cooling to  $22^\circ\text{C}$ .



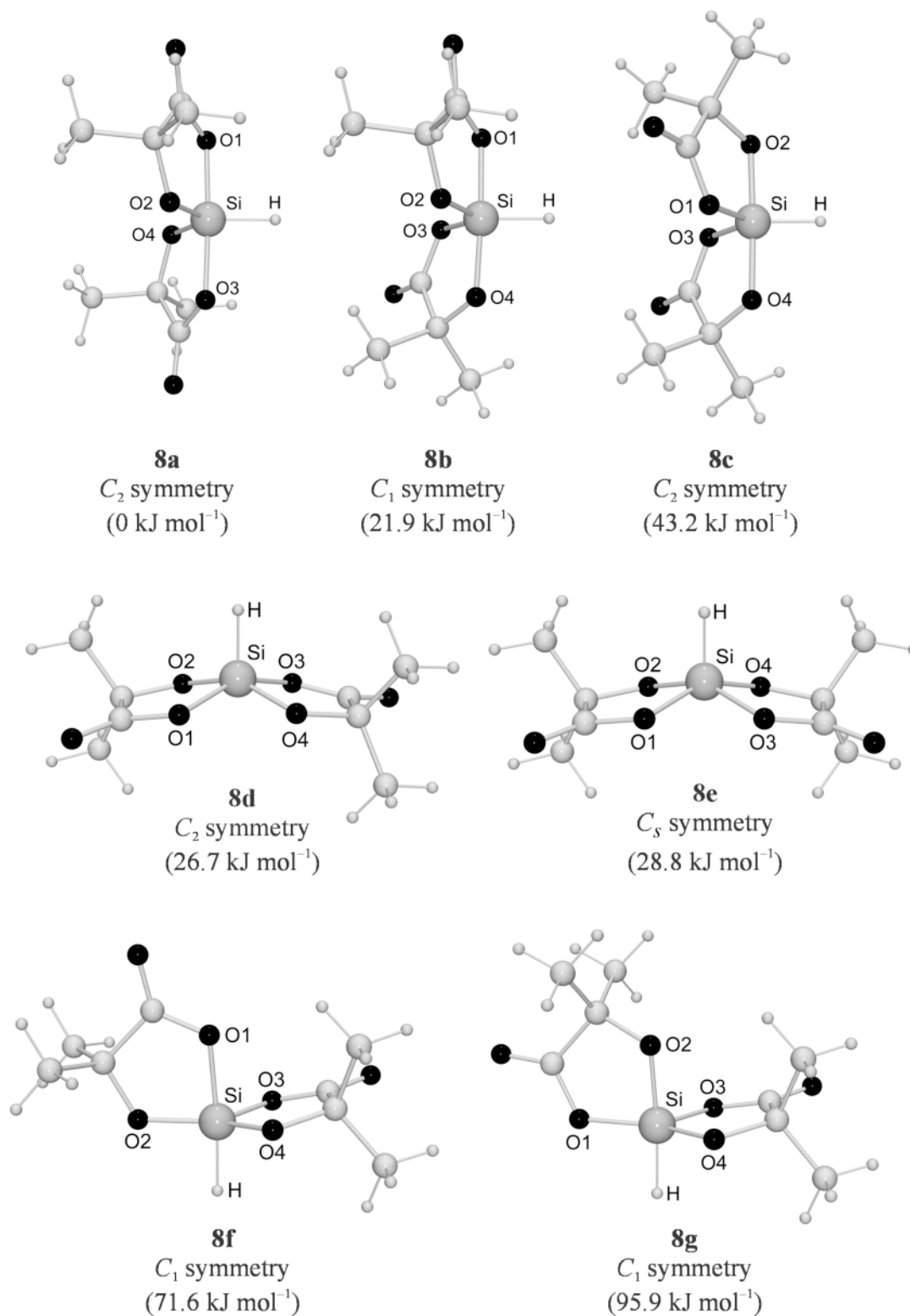
$\delta = -101.1, -72.9, -63.5, -54.3$ ; **4** (pH = 13.0):  $\delta = -76.5, -68.1, -60.0$ ). The  $\lambda^5\text{Si}$ -silicate **2** could no longer be detected between pH 7 and pH 13, whereas **4** disappeared at pH 6. After a solution with pH 13 was obtained, the respec-

tive starting pH was adjusted by addition of concentrated hydrochloric acid. In all cases, reversibility of the spectra of **2** and **4** upon acidification was observed.

In conclusion, penta-coordination only did not exist for



**Fig. 4.** Calculated structures and relative energies of **8a–8c** (local minima) and **8d–8g** (transition states) as obtained by SCF/TZP+ geometry optimizations.



any compounds studied over a pH range 3.6–13. In all cases, tetra-coordination could be detected, indicating that the title compounds are not stable against ring-opening processes in aqueous solution. In the case of **2** and **4** (2-methylactato(2-) ligands), these processes are reversible and both compounds

can be recovered almost quantitatively by the slow evaporation of the water.

#### Computational studies

The structure and dynamic behavior of compound **2** and



**Table 3.** Selected calculated interatomic distances (Å) and angles (°) for the local minima **8a–8c** and for the transition states **8d–8g** as obtained by SCF/TZP+ geometry optimizations.

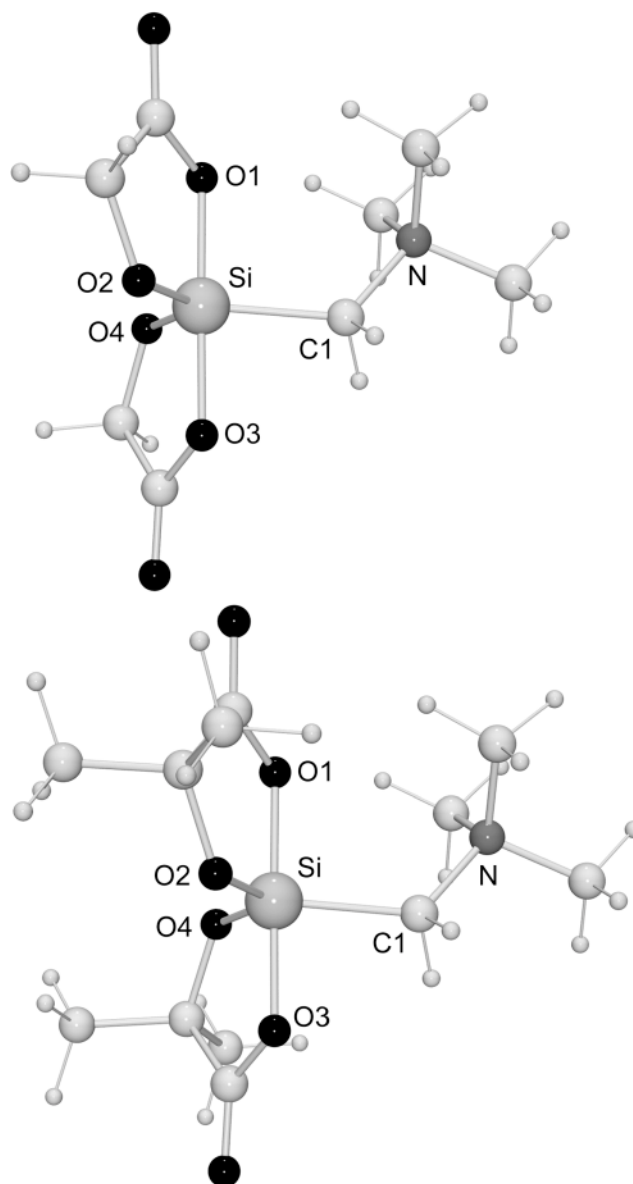
	<b>8a</b>	<b>8b</b>	<b>8c</b>	<b>8d</b>	<b>8e</b>	<b>8f</b>	<b>8g</b>
<b>Interatomic distances (Å)</b>							
Si—O1	1.796	1.812	1.727	1.767	1.764	1.843	1.739
Si—O2	1.663	1.666	1.727	1.692	1.695	1.669	1.726
Si—O3	1.796	1.719	1.727	1.767	1.764	1.720	1.740
Si—O4	1.663	1.720	1.727	1.692	1.695	1.682	1.700
Si—H	1.472	1.474	1.477	1.477	1.477	1.497	1.493
<b>Interatomic angles (°)</b>							
O1—Si—O2	87.7	86.9	87.2	86.5	86.5	84.5	86.2
O1—Si—O3	176.9	87.6	113.2	152.1	84.1	88.3	117.2
O1—Si—O4	90.8	175.5	91.4	86.6	151.6	88.5	149.5
O1—Si—H	91.6	89.3	123.4	104.0	101.6	175.0	89.8
O2—Si—O3	90.8	117.6	91.4	86.6	151.6	128.8	92.6
O2—Si—O4	120.9	94.5	177.5	151.1	89.1	135.7	90.2
O2—Si—H	119.6	121.2	91.3	104.5	106.6	90.5	175.0
O3—Si—O4	87.7	87.9	87.2	86.5	86.5	94.4	93.2
O3—Si—H	91.6	120.8	123.4	104.0	101.6	95.3	92.0
O4—Si—H	119.6	93.7	91.3	104.5	106.6	94.7	91.7

the bis[glycolato(2-)- $O^1,O^2$ ]hydridosilicate(1-) anion were already investigated by quantum chemical methods in an earlier study (1). In this paper, computational studies of the anionic model species bis[2-methylactato(2-)- $O^1,O^2$ ]hydridosilicate(1-) (**8**) and the zwitterions **3** and **4** were performed. The computational methods used in these studies are described in the *Experimental* section.

As shown in Fig. 4, seven different structures (**8a–8g**) were studied for the model species **8**. For energetic reasons, square pyramids with the hydrogen atom in a basal position were not considered. The trigonal-bipyramidal species **8a–8c**, **8f**, and **8g** and the square-pyramidal species **8d** are chiral and therefore exist as pairs of  $\Lambda$ - and  $\Delta$ -enantiomers, whereas the square-pyramidal species **8e** is achiral. Calculations of the vibrational frequencies for **8a–8g** demonstrated that only the trigonal bipyramids **8a–8c** represent local minima (the isomer **8a** being the energetically most favorable one), whereas the species **8d–8g** are transition states (for selected geometric parameters for **8a–8g**, see Table 3). This result is in agreement with the experimentally established crystal structures of **3**•MeCN and **4**•2MeCN, indicating that the trigonal-bipyramidal geometry, with the carboxylato oxygen atoms in the axial sites, is the energetically most favorable one. Based on this particular structure, geometry optimizations at the SCF/TZP level were carried out for the zwitterionic  $\lambda^5$ Si-silicates **3** and **4** (Fig. 5). As can be seen from Table 2, the calculated interatomic distances and angles for the  $SiO_4C$  frameworks of **3** and **4** are very similar and are also in reasonable agreement with the experimentally established values for **3**•MeCN and **4**•2MeCN.<sup>6</sup>

These results suggest that the energetically preferred trigonal-bipyramidal Si-coordination polyhedra of **3** and **4**, with the carboxylato oxygen atoms in the axial sites, also play the major role in solution, all compounds being expected to exist as pairs of  $\Lambda$ - and  $\Delta$ -enantiomers. The results

**Fig. 5.** Calculated structures (local minima,  $\Delta$ -enantiomers) of **3** (above) and **4** (below) as obtained by SCF/TZP geometry optimizations.

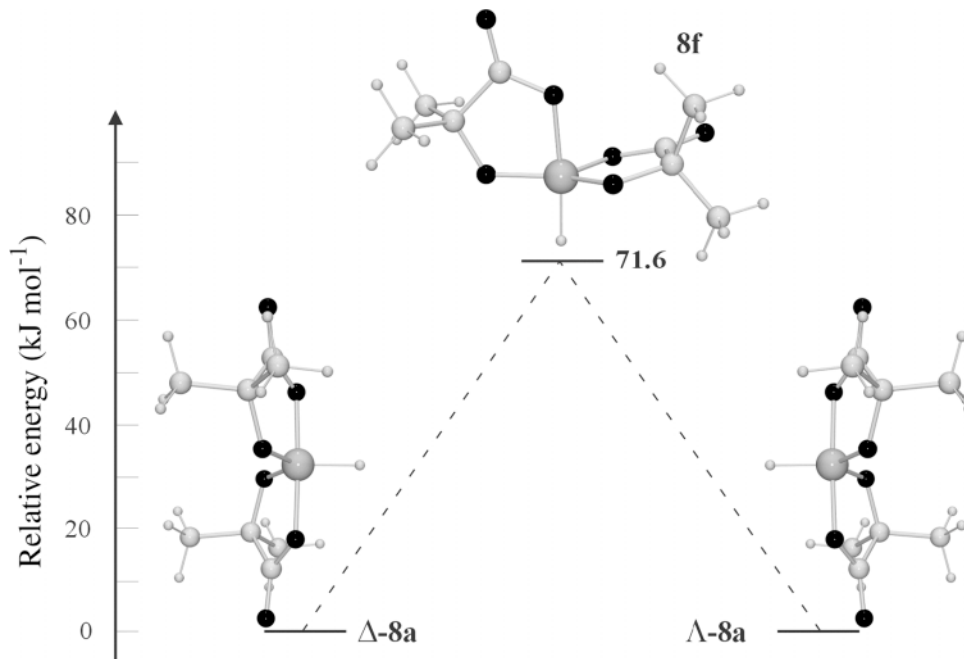


obtained for the model species **8** further suggest that the antipodes of **3** and **4** can undergo an isomerization, leading to an inversion of absolute configuration of their chiral trigonal-bipyramidal  $\lambda^5$ Si-silicate skeletons ( $\Lambda/\Delta$ -enantiomerization). According to the ab initio studies, the enantiomers  $\Lambda$ -**8a** and  $\Delta$ -**8a** can be converted into each other via the transition state **8f** (Fig. 6), which is connected with other low-energy transition states and the intermediate **8b** in the whole enantiomerization pathway (in this context, see ref. 1). The conversions  $\Lambda$ -**8a**  $\rightleftharpoons$  **8d**  $\rightleftharpoons$   $\Delta$ -**8c** and  $\Lambda$ -**8b**  $\rightleftharpoons$  **8e**  $\rightleftharpoons$   $\Delta$ -**8b** can be described in terms of a Berry-type mechanism, with the hydrogen atom as the pivot ligand. In contrast, the conversions  $\Delta$ -**8c**  $\rightleftharpoons$  **8f**  $\rightleftharpoons$   $\Lambda$ -**8b** ( $\Lambda$ -**8c**  $\rightleftharpoons$  **8f'**  $\rightleftharpoons$   $\Delta$ -**8b**) and  $\Lambda$ -**8a**  $\rightleftharpoons$  **8g**  $\rightleftharpoons$   $\Delta$ -**8b** ( $\Delta$ -**8a**  $\rightleftharpoons$  **8g'**  $\rightleftharpoons$   $\Lambda$ -**8b**) (**8f**/**8f'** and

<sup>6</sup> A perfect agreement between the calculated and experimentally established structures of the zwitterions cannot be expected since the latter are influenced by intermolecular interactions in the crystal.



**Fig. 6.** Calculated intramolecular enantiomerization of **8a** via the transition state **8f** ( $\Delta\text{-8a} \rightleftharpoons \mathbf{8f} \rightleftharpoons \Lambda\text{-8a}$ ).



**8g/8g'** are antipodes) differ significantly from a Berry-type mechanism, the transition states being characterized by a distorted trigonal-bipyramidal Si-coordination polyhedron, with the hydrogen atom in an axial position. As the structures of these transition states are rather twisted (one of the two bidentate ligands occupies two equatorial positions), the term “twist mechanism” has been suggested for these particular intramolecular isomerization processes (1). The calculated relative energy of the transition state **8f** (71.6 kJ mol<sup>-1</sup>) is in good agreement with the analogous transition state calculated for the related bis[glycolato(2-)-O<sup>1</sup>,O<sup>2</sup>]hydridosilicate(1-) anion (70.8 kJ mol<sup>-1</sup> (1)), indicating that the nature of the two bidentate ligands (glycolato(2-) vs. 2-methylactato(2-)) does not significantly affect the relative energy of the “twist” transition state. Except for the lower energy barrier for **3** (51.6 ± 0.5 kJ mol<sup>-1</sup>), this result is also in good agreement with the experimentally established energy barriers for the enantiomerization processes of **1–4** (see *NMR studies*).

In conclusion, comparison of the calculated structures of **3** (glycolato(2-) ligands) and **4** (2-methylactato(2-) ligands) does not reveal significant differences. The same holds true for the experimentally established structures of these two compounds. The structures and relative energies calculated for the anionic model species **8** and for the related bis[glycolato(2-)-O<sup>1</sup>,O<sup>2</sup>]hydridosilicate(1-) anion (1) are also very similar. In contrast to these distinct similarities, the zwitterions **3** and **4** (and their derivatives **1** and **2** as well) differ significantly in their chemical behavior in aqueous solution (see *NMR studies*). It is an open question as to how the bidentate ligands (glycolato(2-) vs. 2-methylactato(2-)) control this chemical behavior.

## Conclusions

The chemistry of the zwitterions **1–4** in nonaqueous solutions (solvent: [D<sub>6</sub>]DMSO, CD<sub>3</sub>OD) is characterized by dis-

tinct similarities. All zwitterions were found to be stable in both the aprotic solvent [D<sub>6</sub>]DMSO and the protic solvent CD<sub>3</sub>OD, and no tetra-coordinate silicon species could be detected in these solutions. Furthermore, similar energy barriers for the  $\Lambda/\Delta$ -interconversion of the chiral zwitterions were observed; i.e., the nature of both the bidentate ligand (glycolato(2-) vs. 2-methylactato(2-)) and the ammoniomethyl group ((dimethylammonio)methyl vs. (trimethylammonio)methyl) does not significantly control the behavior of **1–4** in nonaqueous solution. In contrast, in aqueous solution the zwitterions **1** and **3** (glycolato(2-) ligands) differ significantly from **2** and **4** (2-methylactato(2-) ligands). In the case of **1** and **3** only tetra-coordinate silicon species could be detected, whereas the zwitterions **2** and **4** were found to exist in aqueous solution, along with tetra-coordinate silicon species. Obviously, the zwitterions **1–4** are not stable against ring-opening processes in aqueous solution, and in the case of **2** and **4** these processes are reversible and both compounds can be recovered almost quantitatively by slow evaporation of the water. Future mechanistic studies have to show how the different bidentate ligands control the hydrolytic stability of **1–4**.

## Experimental

### General

All syntheses were carried out under dry nitrogen. The solvents used were dried and purified according to standard procedures and stored under nitrogen. Melting points were determined with a Büchi Melting Point B-540 apparatus using samples in sealed capillaries. The <sup>1</sup>H, <sup>13</sup>C, and <sup>29</sup>Si solution NMR spectra were recorded at 22 °C on a Bruker DRX-300 NMR spectrometer (<sup>1</sup>H, 300.1 MHz; <sup>13</sup>C, 75.5 MHz; <sup>29</sup>Si, 59.6 MHz). Chemical shifts (ppm) were determined relative to internal [D<sub>5</sub>]DMSO (<sup>1</sup>H, δ = 2.49), [D<sub>6</sub>]DMSO (<sup>13</sup>C, δ = 39.5), CHD<sub>2</sub>OD (<sup>1</sup>H, δ = 3.30), CD<sub>3</sub>OD (<sup>13</sup>C, δ = 49.0), HDO (<sup>1</sup>H, δ = 4.70), or external TMS (<sup>29</sup>Si, δ = 0).



Assignment of the NMR data was supported by  $^1\text{H}$ ,  $^1\text{H}$  COSY,  $^{13}\text{C}$  DEPT 135,  $^{13}\text{C}$ ,  $^1\text{H}$  HMQC,  $^{13}\text{C}$ ,  $^1\text{H}$  HMBC,  $^{15}\text{N}$ ,  $^1\text{H}$  HMBC, and  $^{29}\text{Si}$ ,  $^1\text{H}$  HMBC experiments. Solid-state  $^{13}\text{C}$ ,  $^{15}\text{N}$ , and  $^{29}\text{Si}$  VACP/MAS NMR spectra were recorded at 22 °C on a Bruker DSX-400 NMR spectrometer with bottom layer rotors of  $\text{ZrO}_2$  (diameter 7 mm) containing ca. 300 mg of sample ( $^{13}\text{C}$ , 100.6 MHz;  $^{15}\text{N}$ , 40.6 MHz;  $^{29}\text{Si}$ , 79.5 MHz; external standard, TMS ( $^{13}\text{C}$ ,  $^{29}\text{Si}$ ;  $\delta = 0$ ) or glycine ( $^{15}\text{N}$ ;  $\delta = -342.0$ ); spinning rate, 5.0–6.5 kHz; contact time, 1 ms ( $^{13}\text{C}$ ), 3 ms ( $^{15}\text{N}$ ), or 5 ms ( $^{29}\text{Si}$ ); 90°  $^1\text{H}$  transmitter pulse length, 3.6  $\mu\text{s}$ ; repetition time, 4 s).

**[(Dimethylammonio)methyl]bis[glycolato(2-)- $\text{O}^1, \text{O}^2$ ]silicate (1)**

This compound was synthesized according to ref. 1.

**[(Dimethylammonio)methyl]bis[2-methylactato(2-)- $\text{O}^1, \text{O}^2$ ]silicate (2)**

This compound was synthesized according to ref. 1.

**Bis[glycolato(2-)- $\text{O}^1, \text{O}^2$ ][(trimethylammonio)methyl]silicate-2/3acetonitrile (3•2/3MeCN)**

Compound **10** (1.02 g, 4.63 mmol) was added dropwise at 20 °C within 2 min to a stirred solution of **9** (411 mg, 2.32 mmol) in acetonitrile (10 mL) (spontaneous evolution of  $\text{Me}_3\text{SiF}$ ), and the reaction mixture was then stirred at 20 °C for 24 h (formation of a precipitate ca. 30 min after combining the reactants). The precipitate was filtered off and recrystallized from acetonitrile (cooling of a saturated solution from 20 to -26 °C). The product was isolated by filtration and then dried in vacuo (0.01 torr (1 torr = 133.322 Pa), 20 °C, 8 h) to give **3•2/3MeCN**<sup>7</sup> in 83% yield as a colorless solid (532 mg, 1.92 mmol); mp 185 °C (dec.).  $^1\text{H}$  NMR ( $[\text{D}_6]\text{DMSO}$ )  $\delta$ : 2.06 (s, 2 H,  $\text{CH}_3\text{CN}$ ), 2.94 (s, 2 H,  $\text{SiCH}_2\text{N}$ ), 3.06 (s, 9 H,  $\text{NCH}_3$ ), 3.96 (s, 4 H,  $\text{OCH}_2\text{C}$ ).  $^{13}\text{C}$  NMR ( $[\text{D}_6]\text{DMSO}$ )  $\delta$ : 1.2 ( $\text{CH}_3\text{CN}$ ), 55.3 (t,  $^1J(^{13}\text{C}, ^{14}\text{N}) = 4.0$  Hz,  $\text{NCH}_3$ ), 59.5 (t,  $^1J(^{13}\text{C}, ^{14}\text{N}) = 1.8$  Hz,  $\text{SiCH}_2\text{N}$ ), 62.6 ( $\text{OCH}_2\text{C}$ ), 118.1 ( $\text{CH}_3\text{CN}$ ), 173.8 ( $\text{C}=\text{O}$ ).  $^{13}\text{C}$  VACP/MAS NMR (1535 transients)  $\delta$ : 54.7 (3 C) ( $\text{NCH}_3$ ), 58.4 ( $\text{SiCH}_2\text{N}$ ), 62.6 ( $\text{OCH}_2\text{C}$ ), 64.0 ( $\text{OCH}_2\text{C}$ ), 176.3 ( $\text{C}=\text{O}$ ), 177.5 ( $\text{C}=\text{O}$ ).  $^{15}\text{N}$  VACP/MAS NMR (38 504 transients)  $\delta$ : -328.6 ( $\text{NCH}_3$ ).  $^{29}\text{Si}$  NMR ( $[\text{D}_6]\text{DMSO}$ )  $\delta$ : -92.1.  $^{29}\text{Si}$  VACP/MAS NMR (97 transients)  $\delta$ : -91.9. Anal. calcd. for  $\text{C}_{9.33}\text{H}_{17}\text{N}_{1.67}\text{O}_6\text{Si}$ : C 40.52, H 6.19, N 8.43; found: C 40.2, H 5.8, N 8.5.

**Bis[2-methylactato(2-)- $\text{O}^1, \text{O}^2$ ][(trimethylammonio)methyl]silicate (4)**

The synthesis was carried out analogously to that of **3•2/3MeCN** by combining **11** (1.15 g, 4.63 mmol) with a solution of **9** (411 mg, 2.32 mmol) in acetonitrile (60 mL) (spontaneous evolution of  $\text{Me}_3\text{SiF}$ ; formation of a precipitate ca. 30 min after combining the reactants). Compound **4** was isolated in 73% yield as a colorless solid (516 mg, 1.69 mmol); mp 255 °C (dec.).  $^1\text{H}$  NMR ( $[\text{D}_6]\text{DMSO}$ )  $\delta$ : 1.21 (s, 6 H,  $\text{CCH}_3$ ), 1.26 (s, 6 H,  $\text{CCH}_3$ ), 2.85 and 3.05 (AB

system,  $^2J_{\text{AB}} = 15.5$  Hz, 2 H,  $\text{SiCH}_2\text{N}$ ; partial overlapping with the  $\text{NCH}_3$  signal), 3.08 (s, 9 H,  $\text{NCH}_3$ ).  $^{13}\text{C}$  NMR ( $[\text{D}_6]\text{DMSO}$ )  $\delta$ : 26.4 ( $\text{CCH}_3$ ), 27.7 ( $\text{CCH}_3$ ), 55.0 (t,  $^1J(^{13}\text{C}, ^{14}\text{N}) = 4.0$  Hz,  $\text{NCH}_3$ ), 59.9 (t,  $^1J(^{13}\text{C}, ^{14}\text{N}) = 2.4$  Hz,  $\text{SiCH}_2\text{N}$ ), 73.6 ( $\text{OCC}_3$ ), 178.2 ( $\text{C}=\text{O}$ ).  $^{13}\text{C}$  VACP/MAS NMR (92 transients)  $\delta$ : 26.7 ( $\text{CCH}_3$ ), 27.7 ( $\text{CCH}_3$ ), 28.0 ( $\text{CCH}_3$ ), 28.5 ( $\text{CCH}_3$ ), 55.3 (3 C) ( $\text{NCH}_3$ ), 60.6 ( $\text{SiCH}_2\text{N}$ ), 74.6 ( $\text{CCH}_3$ ), 75.4 ( $\text{CCH}_3$ ), 179.5 ( $\text{C}=\text{O}$ ), 180.6 ( $\text{C}=\text{O}$ ).  $^{15}\text{N}$  VACP/MAS NMR (13 102 transients)  $\delta$ : -328.4 ( $\text{NCH}_3$ ).  $^{29}\text{Si}$  NMR ( $[\text{D}_6]\text{DMSO}$ )  $\delta$ : -102.1.  $^{29}\text{Si}$  VACP/MAS NMR (1107 transients)  $\delta$ : -101.3. Anal. calcd. for  $\text{C}_{12}\text{H}_{23}\text{NO}_6\text{Si}$ : C 47.19, H 7.59, N 4.59; found: C 47.3, H 7.7, N 4.6.

**Tetrafluoro[(trimethylammonio)methyl]silicate (9)**

This compound was synthesized according to ref. 10.

**(Trimethylsilyloxy)acetic acid trimethylsilyl ester (10)**

This compound was synthesized according to ref. 11.

**2-Methyl-2-(trimethylsilyloxy)propionic acid trimethylsilyl ester (11)**

This compound was synthesized according to ref. 12.

**Crystal structure analyses**

Suitable single crystals of **3•MeCN** and **4•2MeCN** were obtained directly from the respective reaction mixture. The crystals were mounted in inert oil (perfluoroalkyl ether, ABCR) on a glass fiber and then transferred to the cold nitrogen gas stream of the diffractometer (Stoe IPDS diffractometer, graphite-monochromated Mo  $\text{K}\alpha$  radiation ( $\lambda = 0.71073$  Å)). The structures were solved by direct methods (14). The non-hydrogen atoms were refined anisotropically (15). A riding model was employed in the refinement of the hydrogen atoms.<sup>8</sup>

**VT  $^1\text{H}$  NMR studies**

The VT  $^1\text{H}$  NMR studies of **1**, **2**, **3•2/3MeCN**, and **4** were carried out analogously to the standard  $^1\text{H}$  NMR measurements using a Bruker DRX-300 NMR spectrometer.  $[\text{D}_6]\text{DMSO}$  and  $[\text{D}_7]\text{DMF}$  served as the solvents. Chemical shifts were determined relative to internal  $[\text{D}_5]\text{DMSO}$  ( $^1\text{H}$ ,  $\delta = 2.49$ ) or  $[\text{D}_6]\text{DMF}$  ( $^1\text{H}$ ,  $\delta = 2.91$ ). The thermocouple used with the probe was calibrated for low (high) temperatures according to ref. 16 using a 4% solution of  $\text{CH}_3\text{OH}$  in  $\text{CD}_3\text{OD}$  (80% solution of ethane-1,2-diol in  $[\text{D}_6]\text{DMSO}$ ). Spectra were recorded in the temperature ranges 22–100 °C (**1**), 22–120 °C (**2**), -55 to 22 °C (**3•2/3MeCN**), and 22–110 °C (**4**). The time required for temperature equilibration was 15 min. From the  $^1\text{H}$  NMR spectra obtained, the coalescence temperature  $T_c$  and the exchange rate  $k_c$  at the coalescence point were extracted, and the value for the activation free enthalpy  $\Delta G^\ddagger$  for the exchange process was calculated by using the Eyring equation ( $\Delta G^\ddagger = 19.14 T_c[10.32 + \log(T_c/k_c)]$  (J mol<sup>-1</sup>)) (17).

<sup>7</sup>The acetonitrile content (ca. 2/3 mol. equiv.) was determined by  $^1\text{H}$  NMR spectroscopy. Further treatment of **3•2/3MeCN** in vacuo does not lead to a further loss of acetonitrile, whereas in the solid-state NMR experiments<sup>4</sup> total loss of the acetonitrile was observed.

<sup>8</sup>Supplementary data may be purchased from the Directory of Unpublished Data, Document Delivery, CISTI, National Research Council Canada, Ottawa, ON K1A 0S2, Canada ([http://www.nrc.ca/cisti/irm/unpub\\_e.shtml](http://www.nrc.ca/cisti/irm/unpub_e.shtml) for information on ordering electronically). CCDC 204727 (**3•MeCN**) and 204728 (**4•2MeCN**) contain the crystallographic data for this manuscript. These data can be obtained, free of charge, via [www.ccdc.cam.ac.uk/conts/retrieving.html](http://www.ccdc.cam.ac.uk/conts/retrieving.html) (or from the Cambridge Crystallographic Data Centre, 12 Union Road, Cambridge CB2 1EZ, U.K.; fax +44 1223 336033; or [deposit@ccdc.cam.ac.uk](mailto:deposit@ccdc.cam.ac.uk)).



## Computational methods

Geometry optimizations at the SCF/TZP (18) level for the zwitterions **3** and **4** and at the SCF/TZP+ level for the anionic model species **8** were performed using the TURBOMOLE program system (19).<sup>9</sup> Stationary geometries and transition states were characterized as local minima (zero imaginary frequencies) and saddle points (one imaginary frequency), respectively, by calculation of the vibrational frequencies. The energies for **3**, **4**, and **8** include the single point MP2 energy and the zero point vibrational energy.

## Acknowledgments

Financial support of this work by the Deutsche Forschungsgemeinschaft and the Fonds der Chemischen Industrie is gratefully acknowledged.

## References

1. R. Tacke, R. Bertermann, A. Biller, O. Dannappel, M. Pülm, and R. Willeke. *Eur. J. Inorg. Chem.* 795 (1999).
2. M. Mühleisen and R. Tacke. *Chem. Ber.* **127**, 1615 (1994).
3. M. Mühleisen and R. Tacke. *Organometallics*, **13**, 3740 (1994).
4. R. Tacke, M. Mühleisen, and P.G. Jones. *Angew. Chem.* **106**, 1250 (1994); *Angew. Chem. Int. Ed. Engl.* **33**, 1186 (1994).
5. Review dealing with zwitterionic  $\lambda^5\text{Si}$ -silicates: R. Tacke, M. Pülm, and B. Wagner. *Adv. Organomet. Chem.* **44**, 221 (1999).
6. Recent studies dealing with zwitterionic  $\lambda^5\text{Si}$ -silicates: (a) R. Tacke, R. Bertermann, A. Biller, O. Dannappel, M. Penka, M. Pülm, and R. Willeke. *Z. Anorg. Allg. Chem.* **626**, 1159 (2000); (b) D. Kost, I. Kalikhman, S. Krivonos, R. Bertermann, C. Burschka, R.E. Neugebauer, M. Pülm, R. Willeke, and R. Tacke. *Organometallics*, **19**, 1083 (2000); (c) R. Tacke, B. Ulmer, B. Wagner, and M. Arlt. *Organometallics*, **19**, 5297 (2000); (d) R. Tacke, R. Bertermann, O. Dannappel, R.E. Neugebauer, M. Pülm, and R. Willeke. *Inorg. Chem.* **40**, 2520 (2001); (e) R. Willeke and R. Tacke. *Z. Anorg. Allg. Chem.* **627**, 1537 (2001); (f) R. Tacke, M. Mallak, and R. Willeke. *Angew. Chem.* **113**, 2401 (2001); *Angew. Chem. Int. Ed.* **40**, 2339 (2001); (g) I. Richter, M. Penka, and R. Tacke. *Organometallics* **21**, 3050 (2002); (h) I. Richter, C. Burschka, and R. Tacke. *J. Organomet. Chem.* **646**, 200 (2002); (i) R. Bertermann, A. Biller, M. Kaupp, M. Penka, O. Seiler, and R. Tacke. *Organometallics*, **22**, 4104 (2003); (j) S. Dragota, R. Bertermann, C. Burschka, J. Heermann, M. Penka, I. Richter, B. Wagner, and R. Tacke. *Silicon Chem.* In press.
7. Selected reviews dealing with compounds of higher-coordinate silicon: (a) S.N. Tandura, M.G. Voronkov, and N.V. Alekseev. *Top. Curr. Chem.* **131**, 99 (1986); (b) W.S. Sheldrick. *In The chemistry of organic silicon compounds. Part 1. Edited by S. Patai and Z. Rappoport.* Wiley, Chichester. 1989. pp. 227–303; (c) A.R. Bassindale and P.G. Taylor. *In The chemistry of organic silicon compounds. Part 1. Edited by S. Patai and Z. Rappoport.* Wiley, Chichester. 1989. pp. 839–892; (d) R.J.P. Corriu and J.C. Young. *In The chemistry of organic silicon compounds. Part 2. Edited by S. Patai and Z. Rappoport.* Wiley, Chichester. 1989. pp. 1241–1288; (e) R.R. Holmes. *Chem. Rev.* **90**, 17 (1990); (f) C. Chuit, R.J.P. Corriu, C. Reye, and J.C. Young. *Chem. Rev.* **93**, 1371 (1993); (g) R. Tacke, J. Becht, A. Lopez-Mras, and J. Sperlich. *J. Organomet. Chem.* **446**, 1 (1993); (h) J.G. Verkade. *Coord. Chem. Rev.* **137**, 233 (1994); (i) R. Tacke and O. Dannappel. *In Tailor-made silicon-oxygen compounds — from molecules to materials. Edited by R. Corriu and P. Jutzi.* Vieweg, Braunschweig/Wiesbaden. 1996. pp. 75–86; (j) E. Lukevics and O.A. Pudova. *Chem. Heterocycl. Compd. (N.Y.)*, **32**, 1381 (1996); (k) R.R. Holmes. *Chem. Rev.* **96**, 927 (1996); (l) D. Kost and I. Kalikhman. *In The chemistry of organic silicon compounds. Part 2. Vol. 2. Edited by Z. Rappoport and Y. Apeloig.* Wiley, Chichester. 1998. pp. 1339–1445; (m) V. Pestunovich, S. Kirpichenko, and M. Voronkov. *In The chemistry of organic silicon compounds. Part 2. Vol. 2. Edited by Z. Rappoport and Y. Apeloig.* Wiley, Chichester. 1998. pp. 1447–1537; (n) C. Chuit, R.J.P. Corriu, and C. Reye. *In Chemistry of hypervalent compounds. Edited by K. Akiba.* Wiley-VCH, New York. 1999. pp. 81–146; (o) M.A. Brook. *In Silicon in organic, organometallic, and polymer chemistry.* Wiley, New York. 2000. pp. 97–114; (p) R. Tacke and O. Seiler. *In Silicon chemistry: from the atom to extended systems. Edited by P. Jutzi and U. Schubert.* Wiley-VCH, Weinheim. In press.
8. Recent studies dealing with higher-coordinate silicon complexes as model systems for transport and storage of silicon in biological systems: (a) R. Tacke, C. Burschka, I. Richter, B. Wagner, and R. Willeke. *J. Am. Chem. Soc.* **122**, 8480 (2000); (b) R. Tacke, A. Stewart, J. Becht, C. Burschka, and I. Richter. *Can J. Chem.* **78**, 1380 (2000); (c) R. Tacke, M. Penka, F. Popp, and I. Richter. *Eur. J. Inorg. Chem.* 1025 (2002); (d) I. Richter, M. Penka, and R. Tacke. *Inorg. Chem.* **41**, 3950 (2002); (e) O. Seiler, C. Burschka, M. Penka, and R. Tacke. *Z. Anorg. Allg. Chem.* **628**, 2427 (2002); (f) O. Seiler, C. Burschka, M. Penka, and R. Tacke. *Silicon Chemistry.* In press.
9. R. Bertermann and R. Tacke. *Int. Symp. Organosilicon Chem.*, 12th, 1999. Abstract P-59.
10. R. Tacke, J. Becht, O. Dannappel, R. Ahlrichs, U. Schneider, W.S. Sheldrick, J. Hahn, and F. Kiesgen. *Organometallics*, **15**, 2060 (1996).
11. (a) A. Wissner. *Tetrahedron Lett.* 2749 (1978); (b) A. Wissner. *J. Org. Chem.* **44**, 4617 (1979).
12. G. Schwarz, H. Alberts, and H.R. Kricheldorf. *Liebigs Ann. Chem.* 1257 (1981).
13. (a) E.L. Muetterties and L.J. Guggenberger. *J. Am. Chem. Soc.* **96**, 1748 (1974); (b) R.R. Holmes and J.A. Deiters. *J. Am. Chem. Soc.* **99**, 3318 (1977).
14. (a) G.M. Sheldrick. *SHELXS-97* [computer program]. University of Göttingen, Göttingen, Germany. 1997; (b) G.M. Sheldrick. *Acta Crystallogr., Sect. A*, **46**, 467 (1990).
15. G.M. Sheldrick. *SHELXL-97* [computer program]. University of Göttingen, Göttingen, Germany. 1997.
16. S. Braun, H.-O. Kalinowski, and S. Berger. 150 and more basic NMR experiments. Wiley-VCH, Weinheim, Germany. 1998. pp. 136–143.
17. U. Weber and H. Thiele. *NMR spectroscopy: modern spectral analysis.* Wiley-VCH, Weinheim, Germany. 1998. pp. 339–361.
18. A. Schäfer, H. Horn, and R. Ahlrichs. *J. Chem. Phys.* **97**, 2571 (1992).
19. Program system TURBOMOLE. R. Ahlrichs, M. Bär, M. Häser, H. Horn, and C. Kölmel. *Chem. Phys. Lett.* **162**, 165 (1989).

<sup>9</sup>Optimized TZP basis sets (in this context, see ref. 6a) used for **3** and **4**: Si (12s9p1d)/[7s5p1d], O, C, and N (10s6p1d)/[6s3p1d], H (5s1p)/[3s1p]. TZP+ basis sets (with additional polarization functions; in this context, see ref. 6a) used for the anionic model species **8**: Si (13s10p1d)/[8s6p1d], O (11s7p1d)/[7s4p1d], H (6s2p)/[4s2p].



# Preparation and electronic properties of rhenium(V) complexes with bis(diphenylphosphino)ethane<sup>1</sup>

François Baril-Robert and André L. Beauchamp

**Abstract:** Complexes of bis(diphenylphosphino)ethane (dppe) of the types  $\text{ReOX}_3(\text{dppe})$  and  $\text{ReO(OR)X}_2(\text{dppe})$  (with  $\text{X} = \text{Cl}$  or  $\text{Br}$ , and  $\text{R} = \text{Me}$ ,  $\text{Et}$ ,  $\text{Pr}$ ,  $\text{Ph}$ , cyclohexyl (Cy), or  $-\text{CH}_2\text{CH}_2\text{OH}$ ) were prepared to evaluate the influence of ligand changes on the low-energy  $d-d$  transitions in these  $\text{Re(V)}$  low-spin  $d^2$  systems. Arylimido compounds  $\text{Re(NR)Cl}_3(\text{dppe})$  (with  $\text{R} = \text{Ph}$  and  $p\text{-ClC}_6\text{H}_4$ ) were also obtained. X-ray diffraction studies on  $\text{ReO(OPr)Cl}_2(\text{dppe})$ ,  $\text{ReO(OPh)Br}_2(\text{dppe})$ , and  $\text{ReO(OCy)Cl}_2(\text{dppe})$  confirmed the presence of the trans  $\text{O}=\text{Re}-\text{OR}$  unit and showed that the structural characteristics of the  $\text{Re}-\text{O}-\text{R}$  segment are not affected by the presence of a bulky cyclohexyl substituent or an aromatic phenyl group. The structure of the arylimido complex  $\text{Re}(p\text{-ClC}_6\text{H}_4\text{N})\text{Cl}_3(\text{dppe})$  was also determined. The electronic absorption spectra of the  $\text{ReOX}_3(\text{dppe})$  compounds include two low-energy components at  $\sim 11\,500$  and  $\sim 16\,000\text{ cm}^{-1}$ , assigned to the two spin-allowed  $d-d$  transitions expected for these low-symmetry systems. Substitution of the oxo ligand by an arylimido group has little effect on the lower-energy component, but moves the two components closer together. Replacing the halogen trans to the  $\text{Re}=\text{O}$  bond by an alkoxo group shifts the whole system to higher energies. These variations were found to correlate well with the energies of the frontier orbitals determined from DFT calculations. While attempting to prepare  $\text{ReOCl}_3(\text{dppe})$  from  $\text{ReOCl}_3(\text{PPh}_3)_2$ , the  $\text{Re(III)}$  compound *fac*- $\text{ReCl}_3(\text{PPh}_3)\{\text{Ph}_2\text{PC}_2\text{H}_4\text{PPh}_2(\text{O})\}$  was obtained, in which one end of dppe had become a phosphine oxide. Upon standing in DMSO, this compound gave the octahedral compound  $\text{ReCl}_4\{\text{Ph}_2\text{PC}_2\text{H}_4\text{PPh}_2(\text{O})\}$ , in which the formation of a chelate ring involving a phosphine and a phosphine oxide was ascertained by X-ray diffraction.

**Key words:** rhenium, crystal structure, DFT calculations,  $d-d$  electron transitions.

**Résumé :** Des complexes du bis(diphénylphosphino)éthane (dppe) de types  $\text{ReOX}_3(\text{dppe})$  et  $\text{ReO(OR)X}_2(\text{dppe})$  (où  $\text{X} = \text{Cl}$  ou  $\text{Br}$ , et  $\text{R} = \text{Me}$ ,  $\text{Et}$ ,  $\text{Pr}$ ,  $\text{Ph}$ , cyclohexyl (Cy) ou  $-\text{CH}_2\text{CH}_2\text{OH}$ ), ont été préparés afin d'évaluer l'influence de changements de ligands sur les transitions  $d-d$  de basse énergie dans ces systèmes  $d^2$  de  $\text{Re(V)}$  à spin faible. Des composés arylimido  $\text{Re(NR)Cl}_3(\text{dppe})$  (où  $\text{R} = \text{Ph}$  et  $p\text{-ClC}_6\text{H}_4$ ) ont aussi été obtenus. Les études par diffraction des rayons X sur  $\text{ReO(OPr)Cl}_2(\text{dppe})$ ,  $\text{ReO(OPh)Br}_2(\text{dppe})$  et  $\text{ReO(OCy)Cl}_2(\text{dppe})$  ont confirmé la présence du motif trans  $\text{O}=\text{Re}-\text{OR}$  et montré que les particularités structurales de l'ensemble  $\text{Re}-\text{O}-\text{R}$  ne sont pas affectées par la présence du substituant volumineux cyclohexyle ou du groupe aromatique phényle. La structure du complexe arylimido  $\text{Re}(p\text{-ClC}_6\text{H}_4\text{N})\text{Cl}_3(\text{dppe})$  a également été déterminée. Les spectres d'absorption électroniques des composés  $\text{ReOX}_3(\text{dppe})$  comportent deux composantes de basse énergie à  $\sim 11\,500$  et  $\sim 16\,000\text{ cm}^{-1}$ , attribuées respectivement aux deux transitions  $d-d$  permises de spin, attendues pour ces systèmes de basse symétrie. La substitution du ligand oxo par un groupe arylimido a peu d'influence sur la composante de plus basse énergie, mais elle rapproche les deux composantes l'une de l'autre. Le remplacement de l'halogène trans au lien  $\text{Re}=\text{O}$  par un group alkoxo déplace l'ensemble du système vers des énergies supérieures. Ces variations sont en bonne corrélation avec les énergies des orbitales frontières déterminées par calculs DFT. En tentant de préparer  $\text{ReOCl}_3(\text{dppe})$  à partir de  $\text{ReOCl}_3(\text{PPh}_3)_2$ , le composé de  $\text{Re(III)}$  *fac*- $\text{ReCl}_3(\text{PPh}_3)\{\text{Ph}_2\text{PC}_2\text{H}_4\text{PPh}_2(\text{O})\}$  a été obtenu, dans lequel l'une des extrémités du dppe est devenue un oxyde de phosphine. En laissant reposer dans le DMSO, ce composé a conduit au complexe octaédrique  $\text{ReCl}_4\{\text{Ph}_2\text{PC}_2\text{H}_4\text{PPh}_2(\text{O})\}$ , où la formation de chélate impliquant une phosphine et un oxyde de phosphine a été confirmée par diffraction des rayons X.

**Mots clés :** rhénium, structure cristalline, calculs DFT, transitions électroniques  $d-d$ .

## Introduction

Over the past decades, many research groups have been examining various rhenium(V) compounds containing the  $\text{Re}=\text{O}^{3+}$ ,  $\text{Re}=\text{NR}^{3+}$ , and  $\text{Re}\equiv\text{N}^{2+}$  cores for eventual applica-

tions in radiopharmacy as labeling or therapeutic agents (1–4). Our contributions to this field include compounds with amino acids (5, 6), nitrogen heterocycles (7–12), and various bidentate ligands containing a soft phosphine group and a hard oxygen donor (13–18). Multiple-bonded  $\text{Re(V)}$  com-

Received 5 September 2003. Published on the NRC Research Press Web site at <http://canjchem.nrc.ca> on 24 October 2003.

**F. Baril-Robert and A.L. Beauchamp.**<sup>2</sup> Département de chimie, Université de Montréal, C.P. 6128, Succursale Centre-ville, Montréal, QC H3C 3J7, Canada.

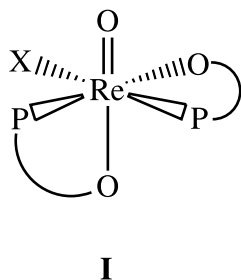
<sup>1</sup>This article is part of a Special Issue dedicated to Professor John Harrod.

<sup>2</sup>Corresponding author (e-mail: [andre.beauchamp@umontreal.ca](mailto:andre.beauchamp@umontreal.ca)).



pounds are of interest in many other fields of chemistry and biochemistry. For instance, their role in oxygen transfer and other catalytic processes is under active investigation at the moment (19–23). The optical properties associated with the multiple bonds have produced a large number of publications and are still extensively studied (24–28).

In the perspective of developing devices for storage of information at the molecular level, these simple diamagnetic  $d^2$  centers would be potentially useful systems if a low-energy paramagnetic high-spin state can be readily accessed. The oxygen or nitrogen  $p_x$  and  $p_y$  orbitals of the multiple-bonded ligand form strong  $\pi$  bonds with the  $d_{xz}$  and  $d_{yz}$  orbitals, which become antibonding and higher in energy than the other interaxial  $d$  orbital ( $d_{xy}$  or  $d_{x^2-y^2}$ , depending on point group symmetry). Occupancy of the latter orbital by the two  $d$  electrons results in a diamagnetic ground state. However, in a previous study (29), we showed that the HOMO–LUMO gap is relatively small in certain oxo compounds (**I**) containing O–P ligands. If the gap becomes comparable with the pairing energy, the molecule could possess a high-spin excited state accessible at low energy cost via a spin-crossover process. Such systems may be of interest as catalysts and materials with unusual optical or magnetic properties.



To cast some light on the factors leading to small HOMO–LUMO gaps, we first examined a series of simple compounds retaining an equatorial *cis*-P,P arrangement perpendicular to an (axial) Re=O or Re=NR bond. The common bis(diphenylphosphino)ethane (dppe) ligand was chosen to provide this arrangement. The strongly  $\pi$ -donor *trans*-O=Re=O<sup>+</sup> and Re≡N<sup>2+</sup> cores were not considered at this point, since their energy gaps had been found to be substantially higher (29). ReOCl<sub>3</sub>(dppe) was originally prepared by Chatt and Rowe (30), and X-ray work showed that it indeed corresponds to the structural type considered (31). The corresponding phenylimido compound Re(NPh)Cl<sub>3</sub>(dppe) was obtained by Cotton et al. (32). In the present study, the chloro and bromo compounds ReOX<sub>3</sub>(dppe) were prepared, together with *trans*-ReO(OR)X<sub>2</sub>(dppe) derivatives with various R groups. A few arylimido compounds were also included. In addition to the preparation and characterization of these compounds, we are reporting preliminary electronic spectra showing how absorption is affected by ligand substitution. DFT calculations are used to rationalize these results.

## Experimental section

### Reactants and methods

KReO<sub>4</sub>, dppe, and all other reactants were obtained from Aldrich and used without further purification.

ReOCl<sub>3</sub>(PPh<sub>3</sub>)<sub>2</sub> was prepared by a literature method (30). Deuterated solvents were purchased from Aldrich or CDN Isotopes.

IR spectra were recorded on Perkin-Elmer 1600 (4000–400 cm<sup>−1</sup>, KBr pellets) or 1430 spectrophotometers (4000–200 cm<sup>−1</sup>, CsI pellets). The NMR spectra were measured with Bruker AMX-300, ARX-400, or AV-300 spectrometers. For the <sup>1</sup>H spectra, the residual solvent signal (DMSO-*d*<sub>6</sub>, 2.50 ppm) was used as internal reference and the chemical shifts are expressed in ppm vs. SiMe<sub>4</sub>. H<sub>3</sub>PO<sub>4</sub> was used as an external reference ( $\delta = 0$ ) for the <sup>31</sup>P{<sup>1</sup>H} spectra. Electronic spectra were recorded in quartz cells with a UV–vis–NIR Cary 5E spectrometer. The solution spectra were taken as DMSO solutions. Spectra of crystalline samples were obtained with a tungsten-halogen lamp, the CCD detector of a Renishaw 3000 Raman imaging microscope, and a 10% neutral density filter to avoid blinding the detector. FAB<sup>+</sup> mass spectra in NBA were measured at the Centre de Spectrométrie de Masse de l'Université de Montréal. Elemental analyses were run at the Laboratoire d'Analyse Élémentaire de l'Université de Montréal.

### Preparation of ReOX<sub>3</sub>(dppe) (X = Cl, Br)

Modifications were introduced in the procedure originally described by Chatt and Rowe (30) for ReOCl<sub>3</sub>(dppe) to eliminate impurities of MX salts and reduced complexes.

The K<sup>+</sup> ion of KReO<sub>4</sub> was first replaced by H<sup>+</sup> on a cation-exchange resin (Dowex 50W-X8, 20–50 mesh). The column (2 cm diameter) was filled with 10 g of resin, which was activated with 15 mL of 6 mol/L HCl to obtain the H<sup>+</sup> form and washed with boiling water (75 mL) to neutrality. KReO<sub>4</sub> (1.5 g, 5.2 mmol) dissolved in a minimum amount (ca. 18 mL) of boiling water was poured into the hot column and the elution was done with boiling water. The HReO<sub>4</sub> solution was collected as long as it remained acidic. Water was then removed with a rotating evaporator and a viscous light yellow-green liquid containing HReO<sub>4</sub> and Re<sub>2</sub>O<sub>7</sub> was obtained. To this oily material was added concentrated HX (5 mL) and the mixture was refluxed for 2 min. A 25 mL fraction of a chloroform solution of dppe (3.90 g, 9.80 mmol in 150 mL) was first added and the mixture darkened immediately. The rest of the dppe solution was then added in small portions over a period of 4 h. The mixture was cooled to room temperature (RT) and the precipitate (green for Br, blue for Cl) was filtered, washed with acetone (to remove water), chloroform, and diethyl ether. The compound was recrystallized from acetonitrile.

### ReOCl<sub>3</sub>(dppe)

Yield: 82%. IR (CsI, cm<sup>−1</sup>): 980 (s)  $\nu$ (Re=O); 320 (w), 290 (w)  $\nu$ (Re–Cl). <sup>1</sup>H NMR (DMSO-*d*<sub>6</sub>) (ppm)  $\delta$ : 8.01 (m, 8H, H<sub>o</sub>), 7.48 (s br, 12H, H<sub>m,p</sub>), 3.79 (m, 2H, ethylene), 3.24 (m, 2H, ethylene). <sup>31</sup>P NMR (DMSO-*d*<sub>6</sub>) (ppm)  $\delta$ : 5.7 (s). MS FAB<sup>+</sup> ( $m/z$ ): 706 [M]<sup>+</sup>; 671 [M – Cl]<sup>+</sup>. Anal. calcd. for C<sub>26</sub>H<sub>24</sub>OP<sub>2</sub>Cl<sub>3</sub>Re (%): C 44.17, H 3.42; found: C 44.24, H 3.34.

### ReOBr<sub>3</sub>(dppe)

Yield: 76%. IR (KBr, cm<sup>−1</sup>): 971 (s)  $\nu$ (Re=O). <sup>1</sup>H NMR (DMSO-*d*<sub>6</sub>) (ppm)  $\delta$ : 8.03 (m, 8H, H<sub>o</sub>), 7.48 (s br, 12H, H<sub>m,p</sub>), 3.90 (m, 2H, ethylene) 3.17 (m, 2H, ethylene). <sup>31</sup>P



NMR (DMSO- $d_6$ ) (ppm)  $\delta$ : -1.0 (s). MS FAB<sup>+</sup> ( $m/z$ ): 840 [M]<sup>+</sup>, 760 [M - Br]<sup>+</sup>, 680 [M - 2Br]<sup>+</sup>.

### Preparation of ReOX<sub>2</sub>(OR)(dppe) (X = Cl, Br)

#### Method A (R = Me, Et, Pr)

For ReOCl<sub>2</sub>(OEt)(dppe), a suspension of ReOCl<sub>3</sub>(dppe) (0.31 g, 0.44 mmol) in 35 mL of ethanol was refluxed for 3 days, during which time the blue solid progressively turned violet. It was filtered hot, washed with ethanol and diethyl ether, and recrystallized in acetonitrile.

This method was used to introduce alkoxo groups corresponding to low-boiling alcohols (methanol, ethanol, *n*-propanol). Reaction time varied (2–6 days) from one system to another. The reaction was stopped ~24 h after the reaction mixture has become clear violet. When there was no color change after 3 days, adding fresh alcohol helped to accelerate the reaction.

#### ReOCl<sub>2</sub>(OEt)(dppe)

Yield: 90%. IR (KBr, cm<sup>-1</sup>): 950 (s)  $\nu$ (Re=O), 913 (s)  $\delta$ (O-CH<sub>2</sub>). <sup>1</sup>H NMR (DMSO- $d_6$ ) (ppm)  $\delta$ : 8.14 (m, 8H, H<sub>o</sub>), 7.48 (s br, 12H, H<sub>m,p</sub>), ~3.31 (m, 2H, ethylene, near water peak), 3.14 (m, 2H, ethylene), 2.28 (q, 2H, <sup>3</sup>J = 7.0 Hz, ethoxo CH<sub>2</sub>), -0.07 (t, 3H, <sup>3</sup>J = 6.9 Hz, ethoxo CH<sub>3</sub>). <sup>31</sup>P NMR (DMSO- $d_6$ ) (ppm)  $\delta$ : 16.5 (s). MS FAB<sup>+</sup> ( $m/z$ ): 716 [M]<sup>+</sup>, 681 [M - Cl]<sup>+</sup>, 671 [M - OEt]<sup>+</sup>, 637 [M - Cl - OEt]<sup>+</sup>. Anal. calcd. for C<sub>28</sub>H<sub>29</sub>O<sub>2</sub>P<sub>2</sub>Cl<sub>2</sub>Re (%): C 46.93, H 4.08; found: C 46.66, H 3.94.

#### ReOCl<sub>2</sub>(OMe)(dppe)

Yield: 79%. IR (KBr, cm<sup>-1</sup>): 944 (s)  $\nu$ (Re=O). <sup>1</sup>H NMR (DMSO- $d_6$ ) (ppm)  $\delta$ : 8.11 (m, 8H, H<sub>o</sub>), 7.49 (s br, 12H, H<sub>m,p</sub>), ~3.23 (m, 2H, ethylene, near water peak), 3.15 (m, 2H, ethylene), 1.91 (s, 3H, methoxo CH<sub>3</sub>). <sup>31</sup>P NMR (DMSO- $d_6$ ) (ppm)  $\delta$ : 16.6 (s).

#### ReOCl<sub>2</sub>(OPr)(dppe)

Yield: 85%. IR (KBr, cm<sup>-1</sup>): 938 (s)  $\nu$ (Re=O). <sup>1</sup>H NMR (DMSO- $d_6$ ) (ppm)  $\delta$ : 8.16 (m, 8H, H<sub>o</sub>), 7.48 (s br, 12H, H<sub>m,p</sub>), 3.34 (m, 2H, ethylene), 3.15 (m, 2H, ethylene), 1.99 (t, 2H, <sup>3</sup>J = 6.5 Hz, propoxo  $\alpha$ -CH<sub>2</sub>), 0.34 (m, 2H, propoxo  $\beta$ -CH<sub>2</sub>), 0.11 (t, 3H, <sup>3</sup>J = 7.3 Hz, propoxo CH<sub>3</sub>). <sup>31</sup>P NMR (DMSO- $d_6$ ) (ppm)  $\delta$ : 15.8 (s).

#### ReOBr<sub>2</sub>(OEt)(dppe)

Yield: 61%. IR (KBr, cm<sup>-1</sup>): 951 (s)  $\nu$ (Re=O), 913 (s)  $\delta$ (O-CH<sub>2</sub>). <sup>1</sup>H NMR (DMSO- $d_6$ ) (ppm)  $\delta$ : 8.12 (m, 8H, H<sub>o</sub>), 7.50 (m br, 12H, H<sub>m,p</sub>), 3.39 (m, 2H, ethylene), 3.07 (m, 2H, ethylene), 2.35 (q, 2H, <sup>3</sup>J = 6.8 Hz, ethoxo CH<sub>2</sub>), -0.03 (t, 3H, <sup>3</sup>J = 6.9 Hz, ethoxo CH<sub>3</sub>). <sup>31</sup>P NMR (DMSO- $d_6$ ) (ppm)  $\delta$ : 18.2 (s).

#### ReOBr<sub>2</sub>(OMe)(dppe)

Yield: 75%. IR (KBr, cm<sup>-1</sup>): 936 (s)  $\nu$ (Re=O). <sup>1</sup>H NMR (DMSO- $d_6$ ) (ppm)  $\delta$ : 8.12 (m, 4H, H<sub>o</sub>), 8.01 (m, 4H, H<sub>o</sub>), 7.51 (s br, 12H, H<sub>m,p</sub>), ~3.35 (m, 2H, ethylene, near water peak), 3.08 (m, 2H, ethylene), 2.02 (s, 3H, methoxo CH<sub>3</sub>). <sup>31</sup>P NMR (DMSO- $d_6$ ) (ppm)  $\delta$ : 18.8 (s).

#### ReOBr<sub>2</sub>(OPr)(dppe)

Yield: 74%. IR (KBr, cm<sup>-1</sup>): 937 (s)  $\nu$ (Re=O). <sup>1</sup>H NMR (DMSO- $d_6$ ) (ppm)  $\delta$ : 8.13 (m, 8H, H<sub>o</sub>), 7.49 (s br, 12H, H<sub>m,p</sub>), 3.38 (m, 2H, ethylene, near water peak), 3.08 (m, 2H, ethylene), 2.06 (t, 2H, <sup>3</sup>J = 6.5 Hz, propoxo  $\alpha$ -CH<sub>2</sub>), 0.38 (m, 2H, propoxo  $\beta$ -CH<sub>2</sub>), 0.11 (t, 3H, <sup>3</sup>J = 7.4 Hz, propoxo CH<sub>3</sub>). <sup>31</sup>P NMR (DMSO- $d_6$ ) (ppm)  $\delta$ : 17.4 (s). Anal. calcd. for C<sub>29</sub>H<sub>31</sub>O<sub>2</sub>P<sub>2</sub>Br<sub>2</sub>Re (%): C 42.50, H 3.81; found: C 42.78, H 3.87.

#### Method B (R = cyclohexyl, -CH<sub>2</sub>CH<sub>2</sub>OH)

A suspension of ReOCl<sub>2</sub>(OEt)(dppe) (0.20 g, 0.28 mmol) in 25 mL of an acetone–cyclohexanol (or –ethylene glycol) (4:1, v/v) mixture was refluxed for 3 days. The color of the solid did not change appreciably during the reaction. The violet precipitate was filtered, washed with ethanol and diethyl ether, and recrystallized in acetonitrile. For the soluble ethylene glycol complex, the final mixture was evaporated to dryness, diethyl ether was added, and the violet product was filtered.

#### ReOCl<sub>2</sub>(OCy)(dppe)

Yield: 72%. IR (KBr, cm<sup>-1</sup>): 926 (s)  $\nu$ (Re=O). <sup>1</sup>H NMR (DMSO- $d_6$ ) (ppm)  $\delta$ : 8.27 (m, 4H, H<sub>o</sub>), 8.16 (m, 4H, H<sub>o</sub>), 7.47 (s br, 12H, H<sub>m,p</sub>), ~3.45 (m, 2H, ethylene, in the tail of the water peak), ~3.18 (m, 2H, ethylene, near water peak); cyclohexyl signals assigned from a 2D spectrum: 2.33 (m, 1H,  $\alpha$ -CyO), 1.03 (m, 3H,  $\gamma/\delta$ -CyO), 0.56 (m, 2H,  $\beta$ -CyO), 0.38 (m, 3H,  $\gamma/\delta$ -CyO), -0.11 (m, 2H,  $\beta$ -CyO). <sup>31</sup>P NMR (DMSO- $d_6$ ) (ppm)  $\delta$ : 16.9 (s).

#### ReOCl<sub>2</sub>(OCH<sub>2</sub>CH<sub>2</sub>OH)(dppe)

Yield: 85%. IR (KBr, cm<sup>-1</sup>): 948  $\nu$ (Re=O), 907 (s)  $\delta$ (O-CH<sub>2</sub>). <sup>1</sup>H NMR (DMSO- $d_6$ ) (ppm)  $\delta$ : 8.10 (m, 8H, H<sub>o</sub>), 7.49 (s br, 12H, H<sub>m,p</sub>), 3.43 (m, 2H, ethylene, near water peak), 3.11 (m, 2H, ethylene), 2.42 (t, 2H, <sup>3</sup>J = 6.2 Hz,  $\beta$ -CH<sub>2</sub>CH<sub>2</sub>OH), 2.17 (t, 2H, <sup>3</sup>J = 6.3 Hz,  $\alpha$ -CH<sub>2</sub>CH<sub>2</sub>OH). <sup>31</sup>P NMR (DMSO- $d_6$ ) (ppm)  $\delta$ : 19.1 (s). MS FAB<sup>+</sup> ( $m/z$ ): 732 [M]<sup>+</sup>, 697 [M - Cl]<sup>+</sup>, 671 [M - OC<sub>2</sub>H<sub>4</sub>OH]<sup>+</sup>, 661 [M - 2Cl]<sup>+</sup>, 636 [M - Cl - C<sub>2</sub>H<sub>4</sub>OH]<sup>+</sup>.

#### Method C (R = Ph)

A solution of phenol (5.5 g, 59 mmol) in 70 mL of benzene was heated to the boiling point and ReOBr<sub>2</sub>(OPr)(dppe) (0.49 g, 0.60 mmol) was added. The violet mixture turned orange quickly. After 1 day, the solvent was evaporated, the raw product was added to 50 mL of diethyl ether, and refluxed for 30 min to dissolve the unreacted phenol. The dark-brown precipitate was filtered hot, washed with diethyl ether, and recrystallized in acetonitrile.

#### ReOBr<sub>2</sub>(OPh)(dppe)

Yield: 83%. IR (KBr, cm<sup>-1</sup>): 959 (s)  $\nu$ (Re=O). <sup>1</sup>H NMR (DMSO- $d_6$ ) (ppm)  $\delta$ : 8.13 (m, 4H, H<sub>o</sub>), 8.00 (dd, 4H, <sup>3</sup>J = 7.6 Hz, <sup>3</sup>J<sub>H-P</sub> = 10.9 Hz, H<sub>o</sub>), 7.53 (s br, 6H, H<sub>m,p</sub>), 7.35 (t, 2H, <sup>3</sup>J = 7.0 Hz, H<sub>p</sub>), 7.26 (t, 4H, <sup>3</sup>J = 7.5 Hz, H<sub>m</sub>), 6.62 (m, 3H, phenoxo H<sub>m,p</sub>), 5.67 (d, 2H, <sup>3</sup>J = 8.0 Hz, phenoxo H<sub>o</sub>), 3.55 (m, 2H, ethylene), 3.23 (m, 2H, ethylene). <sup>31</sup>P NMR (DMSO- $d_6$ ) (ppm)  $\delta$ : 17.3 (s). MS FAB<sup>+</sup> ( $m/z$ ): 854 [M]<sup>+</sup>, 773 [M - Br]<sup>+</sup>, 761 [M - OPh]<sup>+</sup>, 680 [M - Br - OPh]<sup>+</sup>.



Anal. calcd. for  $C_{32}H_{29}O_2P_2Br_2Re$  (%): C 45.03, H 3.42; found: C 45.09, H 3.39.

#### ***ReOCl<sub>2</sub>(OPh)(dppe)***

Yield: 90%. IR (KBr,  $cm^{-1}$ ): 960 (s)  $\nu(Re=O)$ .  $^1H$  NMR (DMSO- $d_6$ ) (ppm)  $\delta$ : 8.13 (m, 4H,  $H_o$ ), 8.00 (dd, 4H,  $^3J = 7.7$  Hz;  $^3J_{H-P} = 11.1$  Hz,  $H_o$ ), 7.51 (s br, 6H,  $H_{m,p}$ ), 7.30 (m, 2H,  $H_p$ ), 7.23 (m, 4H,  $H_m$ ), 6.59 (m, 3H, phenoxo  $H_{m,p}$ ), 5.63 (d, 2H,  $^3J = 7.9$  Hz, phenoxo  $H_o$ ), 3.57 (m, 2H, ethylene), 3.32 (m, 2H, ethylene, near water peak).  $^{31}P$  NMR (DMSO- $d_6$ ) (ppm)  $\delta$ : 16.3 (s).

#### **Preparation of *Re(NPh)Cl<sub>3</sub>(dppe)***

The compound was prepared following the literature method (32).  $ReOCl_3(dppe)$  (0.15 g, 0.21 mmol) was added to 30 mL of a refluxing aniline–benzene (1:5, v/v) mixture. The blue solution was refluxed for 36 h, during which time it turned green. The light-green precipitate was filtered, and washed with benzene and diethyl ether. It recrystallized in acetonitrile as light-green fibers.

#### ***Re(NPh)Cl<sub>3</sub>(dppe)***

Yield: 75%.  $^1H$  NMR (DMSO- $d_6$ ) (ppm)  $\delta$ : 8.16 (m, 4H,  $H_o$ ), 7.96 (m, 4H,  $H_o$ ), 7.52 (t, 1H,  $^3J = 8.2$  Hz, phenylimido  $H_p$ ), 7.41 (s br, 6H,  $H_{m,p}$ ), 7.16 (s br, 6H,  $H_{m,p}$ ), 6.79 (t, 2H,  $^3J = 8.5$  Hz; phenylimido  $H_m$ ), 6.15 (d, 2H,  $^3J = 8.7$  Hz, phenylimido  $H_o$ ), ~3.59 (m, 2H, ethylene), 3.33 (m, 2H, ethylene).  $^{31}P$  NMR (DMSO- $d_6$ ) (ppm)  $\delta$ : 11.3 (s).

#### **Preparation of *Re(NC<sub>6</sub>H<sub>4</sub>Cl)Cl<sub>3</sub>(dppe)***

This variation of the previous method was used to introduce a phenylimido group derived from a solid aniline. A solution of *p*-chloroaniline (5.56 g, 43.6 mmol) in 25 mL of benzene was heated to its boiling point and  $ReOCl_3(dppe)$  (0.15 g, 0.21 mmol) was added. The solution was refluxed for 1 day, during which time the blue solution turned dark green. The solvent was evaporated completely, the solid obtained was placed in 50 mL of diethyl ether, and the solution was refluxed for 30 min to dissolve unreacted *p*-chloroaniline. The green precipitate was filtered hot, washed with diethyl ether, and recrystallized in acetonitrile.

#### ***Re(NC<sub>6</sub>H<sub>4</sub>Cl)Cl<sub>3</sub>(dppe)***

Yield: 78%.  $^1H$  NMR (DMSO- $d_6$ ) (ppm)  $\delta$ : 8.16 (m, 4H,  $H_o$ ), 7.96 (m, 4H,  $H_o$ ), 7.42 (s br, 6H,  $H_{m,p}$ ), 7.19 (s br, 6H,  $H_{m,p}$ ), 6.88 (d, 2H,  $^3J = 8.8$  Hz, arylimido  $H_m$ ), 6.13 (d, 2H,  $^3J = 8.6$  Hz, arylimido  $H_o$ ), 3.56 (m, 2H, ethylene), 3.33 (m, 2H, ethylene, near water peak).  $^{31}P$  NMR (DMSO- $d_6$ ) (ppm)  $\delta$ : 11.1 (s).

#### **Preparation of *ReCl<sub>3</sub>(PPh<sub>3</sub>)(dppe=O)***

$ReOCl_3(PPh_3)_2$  (0.112 g, 0.13 mmol) was added to a solution of dppe (0.311 g, 0.79 mmol) in 25 mL  $CH_2Cl_2$  under a dynamic inert atmosphere. The resulting lime-green solution was stirred at room temperature for 1 h. The beige precipitate formed during the reaction was filtered, washed with chloroform and diethyl ether. Yield: 51%. It corresponded to the  $1.5CH_2Cl_2$  solvate. IR (KBr,  $cm^{-1}$ ): 1058 (s), 1125 (s).  $^1H$  NMR (DMSO- $d_6$ ): see text. MS FAB<sup>+</sup> ( $m/z$ ): 968  $[M]^+$ , 933  $[M - Cl]^+$ , 706  $[M - PPh_3]^+$ , 635  $[M - 2Cl - PPh_3]^+$ .

Anal. calcd. for  $C_{45.5}H_{42}Cl_6OP_3Re$  (%): C 49.83, H 3.86; found: C 49.68, H 3.98.

#### **X-ray diffraction studies**

Three data sets were collected with a Bruker Smart 2K CCD diffractometer controlled by the SMART software (33), using the graphite-monochromatized  $CuK\alpha$  radiation. Sets of 30 oscillation frames of  $0.3^\circ$  over a range of  $9^\circ$  were recorded in four regions of the reciprocal space, from which the reduced cell was determined by least-squares refinement. For data collection, frames were recorded for different orientations of the crystal and detector so as to cover at least 95% of the reciprocal sphere. At the end, the first 101 frames were remeasured to check for crystal decomposition. The frames were analyzed with the SAINT software (34), which determined the intensity and the position of each spot. Accurate cell parameters were obtained by least-squares refinement over the positions of the whole data set.

For one compound, the X-ray work was done with an Enraf-Nonius CAD-4 diffractometer using graphite-monochromatized  $CuK\alpha$  radiation under the control of the CAD-4 software (35). The reduced cell was initially determined from 20 to 25 spots located on a preliminary rotation photograph and centered in the detector aperture. Accurate cell parameters were then determined from the positions of 25 high-angle reflections centered with the SETANG and DETTH procedures. The intensities were recorded by  $\omega/2\theta$  scan. Possible crystal decomposition was monitored by measuring five standard reflections every hour.

Another data set was collected with the Bruker P-4 diffractometer of the Université du Québec à Montréal, using the graphite-monochromatized  $MoK\alpha$  radiation. The procedures to determine the cell parameters and collect the intensity data (XSCANS software) (36) were similar to those described above for the CAD-4 system. Three standard reflections were measured every 97 reflections during data collection.

The data were interpreted with the SHELXTL software (37). The XPREP procedure (38) was used to apply to the raw intensities an absorption correction based on crystal morphology and to determine the Laue symmetry, systematic absences, and space group. The structure was solved by the direct methods or the heavy-atom method with SHELXS (39). The heavy atoms were initially found and the remaining atoms were then located from structure-factor calculations and  $\Delta F$  maps with SHELXL (40). The structure was refined by least squares on  $F^2$ . The non-hydrogen atoms were generally refined anisotropically. The hydrogens were first placed at idealized positions with the standard (C,N,O)-H distances of SHELXL and allowed to ride on the supporting atom. Their isotropic temperature factors ( $U_{iso}$ ) were fixed at values related to the equivalent temperature factor ( $U_{eq}$ ) of the supporting atom by  $U_{iso} = k \times U_{eq}$  (where  $k = 1.5$  (methyl) or 1.2 (others)). The ORTEP diagrams (40% probability ellipsoids) were produced with the XP routine of SHELXTL.

The crystals of  $Re(NC_6H_4Cl)Cl_3(dppe)$  and the three  $ReOX_2(OR)(dppe)$  compounds were obtained by slow crystallization of concentrated acetonitrile solutions, whereas those of  $ReCl_4(dppe=O)$  appeared in a DMSO solution of  $ReCl_3(PPh_3)(dppe=O)$  kept at room temperature for



Table 1. Crystal data.

	ReOCl <sub>2</sub> (OPr)(dppe)	ReOBr <sub>2</sub> (OPh)(dppe)	ReOCl <sub>2</sub> (OCy)(dppe)	Re(NC <sub>6</sub> H <sub>4</sub> Cl)Cl <sub>3</sub> (dppe)	ReCl <sub>4</sub> (dppe=O)•DMSO
Formula	C <sub>29</sub> H <sub>31</sub> Cl <sub>2</sub> O <sub>2</sub> P <sub>2</sub> Re	C <sub>32</sub> H <sub>29</sub> Br <sub>2</sub> O <sub>2</sub> P <sub>2</sub> Re	C <sub>32</sub> H <sub>35</sub> Cl <sub>2</sub> O <sub>2</sub> P <sub>2</sub> Re	C <sub>32</sub> H <sub>28</sub> Cl <sub>4</sub> NP <sub>2</sub> Re	C <sub>28</sub> H <sub>30</sub> Cl <sub>4</sub> O <sub>2</sub> P <sub>2</sub> SRe
Formula weight	720.62	853.43	770.64	816.55	820.52
Crystal shape	Purple plates	Brown blocks	Purple blocks	Green blocks	Green blocks
<i>T</i> (K)	293(2)	293(2)	293(2)	220(2)	293(2)
Diffractometer	Smart CCD	P-4	Smart CCD	Smart CCD	CAD-4
Crystal system	Monoclinic	Orthorhombic	Monoclinic	Monoclinic	Triclinic
Space group	<i>P</i> 2 <sub>1</sub> / <i>c</i> (No. 14)	<i>Pbca</i> (No. 61)	<i>P</i> 2 <sub>1</sub> / <i>c</i> (No. 14)	<i>P</i> 2 <sub>1</sub> / <i>n</i> (No. 14)	<i>P</i> $\bar{1}$ (No. 2)
<i>a</i> (Å)	18.1737(2)	9.793(2)	19.4762(4)	8.3710(1)	9.609(2)
<i>b</i> (Å)	9.9663(1)	17.695(2)	9.9284(2)	19.7638(1)	11.472(2)
<i>c</i> (Å)	16.6086(2)	36.086(4)	17.2379(4)	19.2872(1)	16.080(3)
$\alpha$ (°)	90	90	90	90	91.98(3)
$\beta$ (°)	99.268(1)	90	111.063(1)	90.995(1)	98.82(3)
$\gamma$ (°)	90	90	90	90	114.07(3)
Volume (Å <sup>3</sup> )	2968.96(6)	6253.2(16)	3110.54(11)	3190.45(4)	1590.0(5)
<i>Z</i>	4	8	4	4	2
<i>d</i> <sub>calcd</sub> (g/cm <sup>3</sup> )	1.634	1.813	1.646	1.700	1.714
Rfls cell params	8971	54	1011	32 575	25
Crystal dimensions (mm)	0.02×0.32×0.65	0.19×0.23×0.35	0.42×0.32×0.20	0.30×0.20×0.15	0.25×0.25×0.30
Radiation, $\lambda$ (Å)	CuK $\alpha$ , 1.54178	MoK $\alpha$ , 0.71073	CuK $\alpha$ , 1.54178	CuK $\alpha$ , 1.54178	CuK $\alpha$ , 1.54178
$\mu$ (cm <sup>-1</sup> )	108.69	65.72	104.09	116.58	123.3
Rfls measured	34 223	12 164	37 335	38 094	11 842
Rfls independent	5807 ( <i>R</i> <sub>int</sub> = 0.076)	6136 ( <i>R</i> <sub>int</sub> = 0.091)	5984 ( <i>R</i> <sub>int</sub> = 0.048)	6146 ( <i>R</i> <sub>int</sub> = 0.125)	6022 ( <i>R</i> <sub>int</sub> = 0.040)
Rfls obs ( <i>I</i> > 2 $\sigma$ )	5201	3500	5705	5527	5176
Params refined/restraints	351/46	365/84	406/70	362/0	357/60
<i>R</i> <sup>a</sup> ( <i>I</i> > 2 $\sigma$ )	0.0387	0.0519	0.0327	0.0616	0.0518
<i>wR</i> <sup>2b</sup> ( <i>I</i> > 2 $\sigma$ )	0.1012	0.0935	0.0871	0.1573	0.1379
<i>S</i> <sup>c</sup> ( <i>I</i> > 2 $\sigma$ )	1.022	1.137	1.082	1.071	1.056

$$^a R = \sum |F_o| - |F_c| / \sum |F_o|$$

$$^b wR2 = \{ \sum [w(F_o^2 - F_c^2)] / \sum w(F_o^2) \}^{1/2}$$

$$^c S = \{ \sum [w(F_o^2 - F_c^2)] / (N_{\text{obs}} - N_{\text{param}}) \}^{1/2}$$



3 months. In all cases, the intensities of the standard reflections revealed no crystal decomposition during data collection. Space groups were defined unambiguously from the Laue symmetry and systematic absences, except for the triclinic compound  $\text{ReCl}_4(\text{dppe}=\text{O})\cdot\text{Me}_2\text{SO}$ . Crystal data are collected in Table 1.

In most cases, disorder was observed in the alkoxo group, phosphine phenyl rings, or lattice solvent molecules. It was modeled by means of two individual orientations, whose occupancies were first refined with a constraint applied to normalize the sum of the occupancies to unity. For the final cycles, these occupancies were rounded off to the nearest 0.05 and then fixed. The non-hydrogen atoms were usually refined anisotropically, but the thermal parameters were restricted (ISOR) so as to obtain reasonable ellipsoids. In severe cases, the interatomic distances were simultaneously constrained with DFIX. Details are provided in the CIF files.<sup>3</sup>

For  $\text{ReOCl}_2(\text{OPr})(\text{dppe})$ , the propyl unit adopted two conformations in a 80:20 ratio (Fig. S-1, supplementary material).<sup>3</sup> The major conformer (C61-C63) was stretched, whereas the other (C81-C83) was bent. DFIX constraints based on the average data found for propoxo groups in the Cambridge Structural Database (41) (C-O (1.42 Å), C-C (1.45 Å),  $\text{O}\cdots\text{C}_\beta$  (2.39 Å),  $\text{C}_\alpha\cdots\text{C}_\gamma$  (2.41 Å)) were applied.

Data were also collected on crystals of the related  $\text{ReOBr}_2(\text{OPr})(\text{dppe})$  complex. It is not isostructural with the chloro compound, since it belongs to the triclinic space group  $P\bar{1}$  and the unit cell ( $a = 9.848(3)$  Å,  $b = 17.602(6)$  Å,  $c = 18.082(6)$  Å,  $\alpha = 78.83(2)^\circ$ ,  $\beta = 89.98(3)^\circ$ ,  $\gamma = 89.03(2)^\circ$ ) contains four molecules. The two independent molecules are almost identical and differ very little from the chloro analog. Even the packing patterns of the two compounds are very close. However, the *R* factor could not be reduced below 0.094 and large correlations between the two independent molecules led to high instability in the refinement. Subtle twinning is suspected to be present and the structure of the bromo compound is not described in detail here.

In the case of  $\text{ReOBr}_2(\text{OPh})(\text{dppe})$ , rotational disorder about a P—C bond of dppe led to two orientations (60:40 ratio) for one of its phenyl groups (Fig. S-2).<sup>3</sup> With  $\text{ReOCl}_2(\text{OCy})(\text{dppe})$ , the cyclohexyl group in a chair conformation was disordered over two orientations (60:40 ratio, Fig. S-2).<sup>3</sup> In these cases, only ISOR restrictions were applied.

For  $\text{Re}(\text{NC}_6\text{H}_4\text{Cl})\text{Cl}_3(\text{dppe})$ , the crystal shape was difficult to describe and the absorption correction was not totally satisfactory. Nevertheless, the structure solved and refined normally.

The data for the triclinic  $\text{ReCl}_4(\text{dppe}=\text{O})\cdot(\text{CH}_3)_2\text{SO}$  compound were interpreted in the centric  $P\bar{1}$  space group, which turned out to be the correct choice. The  $\text{ReCl}_4(\text{dppe}=\text{O})$  molecule itself showed no disorder, but the lattice DMSO molecule was found to be disordered over two interlocked orientations (0.65:0.35, Fig. S-3).<sup>3</sup> DFIX constraints based on the average distances found for lattice DMSO in the Cambridge Structural Database (41) (S=O (1.50 Å), C-S (1.76 Å),  $\text{C}\cdots\text{O}$  (2.61 Å),  $\text{C}\cdots\text{C}$  (2.65 Å)) were applied.

## Results and discussion

### Preparation of $\text{ReOX}_3(\text{dppe})$ and $\text{ReOX}_2(\text{OR})(\text{dppe})$

The procedure originally described to prepare  $\text{ReOCl}_3(\text{dppe})$  (30) required a tedious series of recrystallizations to remove the MX salt and various reduction products. By starting with a  $\text{HReO}_4\text{--Re}_2\text{O}_7$  solution and using chloroform as solvent, we obtained good yields of pure chloro and bromo compounds. The IR spectra show the strong  $\nu(\text{Re}=\text{O})$  band at  $970\text{--}980\text{ cm}^{-1}$  expected for a mono-oxo system (42). Clean isotopic patterns are found in  $\text{FAB}^+$  spectra for the parent ion and the  $[\text{M} - \text{X}]^+$  fragment. The presence of only one  $^{31}\text{P}\{^1\text{H}\}$  NMR singlet confirms the formation of the fac isomer, since the P donors would be inequivalent in the mer isomer. Although a “frozen” puckered chelate ring contains four inequivalent aliphatic protons, a fast flip-flop motion across the equatorial plane generates a vertical mirror plane (including the axial  $\text{Re}=\text{O}$  bond and bisecting the P-Re-P angle) on the NMR timescale. In the “average” molecule, the pair of protons on the same side of the equatorial plane become equivalent. Accordingly, two complex multiplets are found between 3 and 4 ppm, one of which is often obscured by the residual water peak in DMSO. Because of the anisotropic effect of the Re—oxo bond, the protons on the oxo side are believed to be the more deshielded (43, 44). Similarly, two distinct sets of phenyl signals are expected. However, only two complex peaks (2:3 intensity ratio) are found. The weaker one at  $\sim 8.0$  ppm is due to the eight ortho protons, whereas the other at  $\sim 7.5$  ppm includes the meta and para protons of both types of rings. This assignment is based on a comparison with  $\text{ReOX}_2(\text{OPh})(\text{dppe})$ , where one set of phosphine aromatic signals is displaced by the anisotropic effect of the phenoxo ring.

The  $\text{ReOX}_2(\text{OR})(\text{dppe})$  compounds were obtained by controlled alcoholysis of  $\text{ReOX}_3(\text{dppe})$ . For  $\text{R} = \text{Me}$ , Et, and Pr, refluxing for several days in the neat alcohol gave good yields of pure products. For the higher-boiling alcohols cyclohexanol and ethylene glycol, decomposition took place upon refluxing in the pure liquid and the reaction was carried out in a 4:1 acetone–alcohol mixture. With phenol, a solid, the reaction was run in benzene.

In all cases, halide substitution occurs only at the position trans to the  $\text{Re}=\text{O}$  bond. This is supported by the presence of only one singlet in the  $^{31}\text{P}\{^1\text{H}\}$  spectra, downfield from that of the corresponding trihalo complex. The strong  $\nu(\text{Re}=\text{O})$  vibration appears at  $\sim 940\text{ cm}^{-1}$ . The ethoxo and 2-hydroxyethoxo compounds also give a very strong band at  $\sim 910\text{ cm}^{-1}$  involving an O-CH<sub>2</sub> deformation mode (30). The  $\text{FAB}^+$  spectra generate characteristic patterns for the parent ion and other fragments obtained by removing X or OR. The  $^1\text{H}$  aromatic regions of the alkoxo compounds are similar to those of the trihalo systems, except that the ortho signals are displaced downfield slightly (8.1–8.2 ppm). For  $\text{ReOX}_2(\text{OPh})(\text{dppe})$ , one of the two overlapping ortho signals is displaced upfield ( $\sim 8.00$  ppm) by the anisotropy of

<sup>3</sup>Supplementary data may be purchased from the Directory of Unpublished Data, Document Delivery, CISTI, National Research Council Canada, Ottawa, ON K1A 0S2, Canada ([http://www.nrc.ca/cisti/irm/unpub\\_e.shtml](http://www.nrc.ca/cisti/irm/unpub_e.shtml) for information on ordering electronically). CCDC 210020–210024 contain the crystallographic data for this manuscript. These data can be obtained, free of charge, via [www.ccdc.cam.ac.uk/conts/retrieving.html](http://www.ccdc.cam.ac.uk/conts/retrieving.html) (or from the Cambridge Crystallographic Data Centre, 12 Union Road, Cambridge CB2 1EZ, U.K.; fax +44 1223 336033; or [deposit@ccdc.cam.ac.uk](mailto:deposit@ccdc.cam.ac.uk)).



the phenoxo ligand and it can be safely assigned to ortho protons, since  $^3J_{\text{H-P}}$  couplings of  $\sim 11$  Hz are observed (45). Anisotropy also displaces the meta and para signals upfield: they become resolved at  $\sim 7.3$  (para) and  $\sim 7.2$  ppm (meta), whereas the meta and para multiplets for the rings on the oxo side remain unresolved at  $\sim 7.5$  ppm.

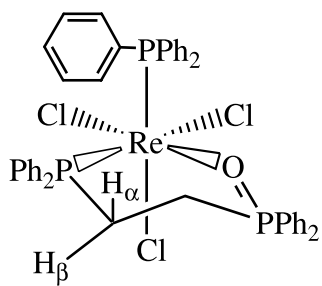
The alkoxo protons are shielded considerably compared with those of the corresponding alcohol. This is consistent with the alkoxo group lying trans to the oxo ligand, since it was noticed (13) that these protons are deshielded when they occupy a position cis to the oxo. For the 2-hydroxyethoxo compound, the protons  $\alpha$  to the coordinated oxygen are assumed to be more shielded than the  $\beta$  protons, whose chemical shift returns to a normal value (3.34 ppm) (46) for free ethylene glycol. The phenoxo ligand gives a doublet at  $\sim 5.65$  ppm for the ortho protons and a multiplet including the meta and para protons at  $\sim 6.60$  ppm. Therefore, with respect to uncoordinated phenol, whose signals occur at 6.77 (ortho and para) and 7.16 ppm (meta), coordination induces upfield shifts whose amplitude decreased with the distance from the O atom.

### Preparation of $\text{Re}(\text{NR})\text{Cl}_3(\text{dppe})$

Cotton et al. (32) first prepared the phenylimido compound by reacting  $\text{ReOCl}_3(\text{dppe})$  with aniline. A similar procedure was used to obtain the *p*-chlorophenylimido complex here. The original stereochemistry of the oxo complex is retained, as evidenced from X-ray crystallography (see below) and from NMR spectroscopy, namely the presence of only one singlet in the  $^{31}\text{P}\{^1\text{H}\}$  spectrum.

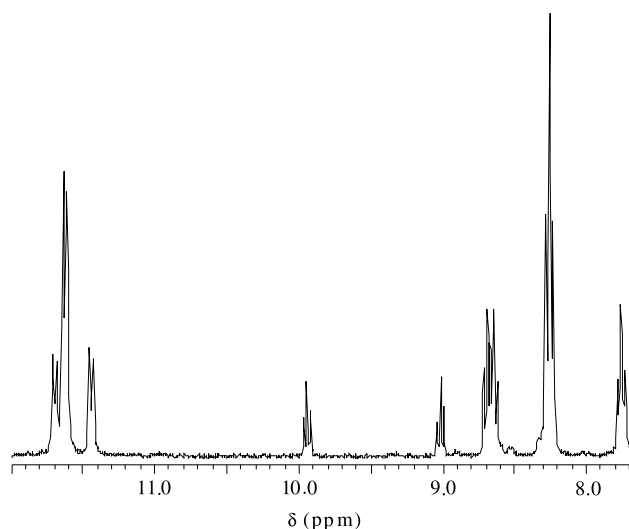
### Isolation of reduced species

Attempts were made to obtain  $\text{ReOCl}_3(\text{dppe})$  by displacing the phosphines of  $\text{ReOCl}_3(\text{PPh}_3)_2$ . When the reaction was run in  $\text{CH}_2\text{Cl}_2$  at room temperature for 1 h, a beige solid precipitated. The parent peak and fragmentation pattern in the  $\text{FAB}^+$  spectrum were consistent with the presence of one  $\text{PPh}_3$ , one dppe, a  $\text{ReCl}_3$  unit, and one extra oxygen. The absence of the strong IR  $\nu(\text{Re}=\text{O})$  band and the presence of  $^1\text{H}$  NMR signals extending far outside the standard 0–10 ppm range ruled out the possibility of a diamagnetic oxorhenium(V) species. Therefore, rhenium-to-phosphorus oxygen transfer had probably occurred, generating a  $\text{Re}(\text{III})$  center and a phosphine oxide, as observed before (47, 48). This was supported by the strong IR bands appearing at 1058 and 1125  $\text{cm}^{-1}$ , one of which could be assigned to a  $\nu(\text{P}=\text{O})$  vibration (49). In the structure **II** proposed, the oxygen is part



**II**

**Fig. 1.**  $^1\text{H}$  NMR signals of the aromatic protons of the phosphine groups in  $\text{ReCl}_3(\text{PPh}_3)(\text{dppe}=\text{O})$ .



of the bidentate  $\text{Ph}_2\text{PC}_2\text{H}_4\text{PPh}_2(\text{O})$  ligand ( $\text{dppe}=\text{O}$ ). The phosphine oxide unit is believed to be derived from dppe instead of  $\text{PPh}_3$ , since the fragmentation products observed in the  $\text{FAB}^+$  spectra correspond to the loss of  $\text{PPh}_3$ , not  $\text{Ph}_3\text{PO}$ . Furthermore, upon aging, this compound gives a  $\text{Re}(\text{IV})$  compound  $\text{ReCl}_4(\text{dppe}=\text{O})$ , whose crystal structure is described hereafter. Even though the complex is paramagnetic, its  $^1\text{H}$  NMR spectrum could be fully analyzed.

We previously reported  $^1\text{H}$  NMR data of arylphosphine complexes of  $\text{Re}(\text{III})$  and  $\text{Re}(\text{IV})$  (50, 51). In these complexes, the aromatic phosphine signals usually occur between 10 and 20 ppm for the ortho protons, and between 7 and 11 ppm for the meta and para protons. As shown in Fig. 1 and Table 2, this generalization is obeyed here.  $^3J$  couplings typical of aromatic rings are observed and proton positions around the rings are readily identified from multiplicities and integrations. A 2D experiment allowed us to distribute the nine peaks between 12 and 7.5 ppm into three groups of three, corresponding to  $\text{PPh}_3$  and to the two inequivalent phenyl rings at the  $\text{PPh}_2$  end of the  $\text{dppe}=\text{O}$  ligand. Two extra sets of three coupled signals are also found at higher field for the aromatic protons of two phenyl rings in the phosphine oxide group. In the latter sets, the ortho protons appear at relatively high field (1.8 and  $-3.0$  ppm) and they are somewhat broadened. Finally, broad multiplets with suitable intensities are observed for the aliphatic protons, two of which occur at extreme chemical shifts (40.5 and  $-8.5$  ppm, respectively). These multiplets, which were already complex for diamagnetic systems, showed extra broadening because of the paramagnetism. They did not give clear cross-peaks in the 2D spectrum and could not be assigned to individual protons.

These available data and the crystallographic results on  $\text{ReCl}_4(\text{dppe}=\text{O})$  suggest that the metal center is coordinated to six ligands: three Cl, one  $\text{PPh}_3$ , and one  $\text{Ph}_2\text{PC}_2\text{H}_4\text{PPh}_2(\text{O})$ . Of the three possible isomers for an octahedral  $\text{ReX}_3\text{L}(\text{L}'\text{-L}'')$  compound, only the fac isomer (**II**) is consistent with the presence of four inequivalent phenyl



**Table 2.**  $^1\text{H}$  NMR chemical shifts (ppm) and coupling constants (Hz) for  $\text{ReCl}_3(\text{PPh}_3)(\text{dppe}=\text{O})$  (in  $\text{DMSO}-d_6$ ).

	ortho	meta	para
$\text{PPh}_3$	11.62 (d, 6H) $^3J = 7.7$	8.25 (t, 6H) $^3J = 7.7$	7.51 (t, 3H) $^3J = 7.4$
$\text{PPh}_2$ (A)	11.70 (d, 2H) $^3J = 7.4$	8.64 (t, 2H) $^3J = 7.4$	9.94 (t, 1H) $^3J = 7.4$
$\text{PPh}_2$ (B)	11.44 (d, 2H) $^3J = 7.4$	8.69 (t, 2H) $^3J = 7.5$	9.01 (t, 1H) $^3J = 7.3$
$\text{O}=\text{PPh}_2$ (A)	1.80 (br, 2H)	7.76 (t, 2H) $^3J = 7.5$	6.74 (t, 1H) $^3J = 7.5$
$\text{O}=\text{PPh}_2$ (B)	-2.99 (d, 2H) $^3J = 7.9$	3.69 (t, 2H) $^3J = 7.9$	4.99 (t, 1H) $^3J = 7.5$
$\text{C}_2\text{H}_4$	-8.47 (m br, 1H), 2.45 (m br, 1H), 4.81 (m br, 1H), 40.47 (m br, 1H)		

rings in the  $\text{dppe}=\text{O}$  ligand, as revealed by  $^1\text{H}$  NMR spectroscopy.

### Crystal structures of the $\text{ReOX}_2(\text{OR})(\text{dppe})$ compounds

Since the  $\text{Re}-\text{O}-\text{R}$  angle in the known structures of this type spans a broad range ( $125^\circ$ – $180^\circ$ , based on 33 structures in the Cambridge Structural Database) (41) and the oxygen-to-rhenium  $\pi$  interactions could be sensitive to this factor, structures with three different OR groups were studied: the *n*-propoxo unit was considered as a “normal” group, the cyclohexyl substituent was expected to be sterically demanding, whereas the phenoxo group was used to probe the influence of an extended  $\pi$  system.

The three  $\text{ReOX}_2(\text{OR})(\text{dppe})$  molecules (Fig. 2) consist of octahedral molecules containing the *trans*-oxo-alkoxo unit observed for the bis(diphenylphosphino)propane complex (52). Selected distances and angles are listed in Table 3.

In the three compounds, the  $\text{O}=\text{Re}-\text{O}$  unit shows a significant, but relatively small, deviation from linearity ( $171^\circ$ – $173^\circ$ ), corresponding to small displacements of the two oxygen donors to the  $\text{dppe}$  side. Despite the fact that the three R groups have different sizes and (or) electronic properties, the OR groups are all roughly end-on coordinated ( $\text{Re}-\text{O}-\text{C} \sim 160^\circ$ ). Our  $\text{Re}=\text{O}$  and  $\text{Re}-\text{OR}$  distances in the two alkoxo compounds are in good agreement with the mean values of 1.70(3) and 1.89(5) Å, respectively, obtained from the literature (41). For the phenoxo complex, our distances of 1.686(6) and 1.900(6) Å are not very different from those reported for  $\text{ReOCl}_3(\text{PPh}_3)(\text{L})$  with  $\text{L} = 2$ -diethylaminomethyl-4-methyl-phenol (1.669(3) and 1.915(3) Å, respectively), where the  $\text{Re}-\text{O}-\text{C}$  angle ( $166.0(3)^\circ$ ) is similar to ours (16). In the two other structures published so far with simple phenolates, the distances tend to be greater (1.666(6) and 1.969(5) Å, 1.703(6) and 1.989(6) Å, respectively) (53, 54), which could be correlated with the pronounced bent in the  $\text{Re}-\text{O}-\text{C}$  region ( $146.5(5)^\circ$  and  $137.7(6)^\circ$ , respectively).

In the three known structures of 1:1  $\text{Re}(\text{V})$ - $\text{dppe}$  compounds (31, 55), the mean  $\text{Re}-\text{P}$  distance is 2.45(2) Å, the bite angle  $\text{P}-\text{Re}-\text{P}$  is  $82.9(6)^\circ$ , and the  $\text{P}-\text{C}-\text{C}-\text{P}$  torsion angle in the chelate ring is  $58(4)^\circ$ . Our results are in good agreement with these data and the phenyl rings also adopt very similar orientations. The  $\text{Re}-\text{Cl}$  (2.428–2.457 Å,  $\sigma = 0.001$  Å) and  $\text{Re}-\text{Br}$  (2.570(1), 2.599(1) Å) distances are appreciably greater than the mean values from the literature for  $\text{Re}-\text{X}$  bonds *cis* to  $\text{Re}=\text{O}$  ( $\text{Re}-\text{Cl} = 2.38(3)$  Å,  $\text{Re}-\text{Br} = 2.51(3)$  Å; based on 130 and 14 structures, respectively) (41). Although these bonds could be weakened by the phosphine *trans* influence, this cannot be the controlling factor,

since the corresponding distances are normal in the  $\text{ReOX}_3(\text{dppe})$  complexes ( $\text{Re}-\text{Cl} = 2.38$  Å,  $\text{Re}-\text{Br} = 2.52$  Å) (31). The lengthening of the  $\text{Re}-\text{X}$  bonds may be ascribed to the good  $\pi$  donor character of the end-on coordinated OR group, whose donation into  $d_{xz}$  and  $d_{yz}$  makes these orbitals less electrophilic and reduces their ability to accept  $\pi$ -electron density from the equatorial halides. This pattern is also observed for the *trans* bis- $\text{PPh}_3$  complexes: the *cis*  $\text{Re}-\text{Cl}$  bonds in  $\text{ReOCl}_3(\text{PPh}_3)_2$  (56) are shorter (2.397(1) Å) than in the related oxo-alkoxo complexes (2.41 Å) (31, 57, 58).

The oxo ligand tends to repel the adjacent bonds, resulting in a displacement of the Re atom from the “equatorial”  $\text{P}_2\text{X}_2$  plane on the oxo side, as evidenced from the mean of the  $\text{O}=\text{Re}-\text{L}_{\text{cis}}$  angles being  $\sim 93^\circ$  compared with  $\sim 88^\circ$  for the  $\text{RO}-\text{Re}-\text{L}_{\text{cis}}$  angles. The puckered conformation of the ring creates systematic differences in the coordination geometry of the two ends of  $\text{dppe}$ . The *trans*- $\text{X}_\text{A}-\text{Re}-\text{P}_\text{A}$  units (involving the  $\text{P}_\text{A}$  atom bonded to the methylene group on the oxo side of the  $\text{P}_2\text{X}_2$  plane) are more linear (alkoxo ( $\sim 177^\circ$ ), halo ( $\sim 174^\circ$ ) (31)) than the *trans*- $\text{P}_\text{B}-\text{Re}-\text{X}_\text{B}$  unit (alkoxo ( $\sim 172^\circ$ ), halo ( $\sim 164^\circ$ )). Also, our  $\text{Re}-\text{X}_\text{A}$  distances are systematically  $\sim 0.025$  Å longer than  $\text{Re}-\text{X}_\text{B}$ , whereas the opposite trend is noted, to a lesser extent, for the  $\text{Re}-\text{P}$  distances. This pattern of bond lengths is not shared by the  $\text{ReOX}_3(\text{dppe})$  compounds, however (31).

The molecules are packed in the unit cell with normal van der Waals contacts (Figs. S-4 and S-5).<sup>3</sup>

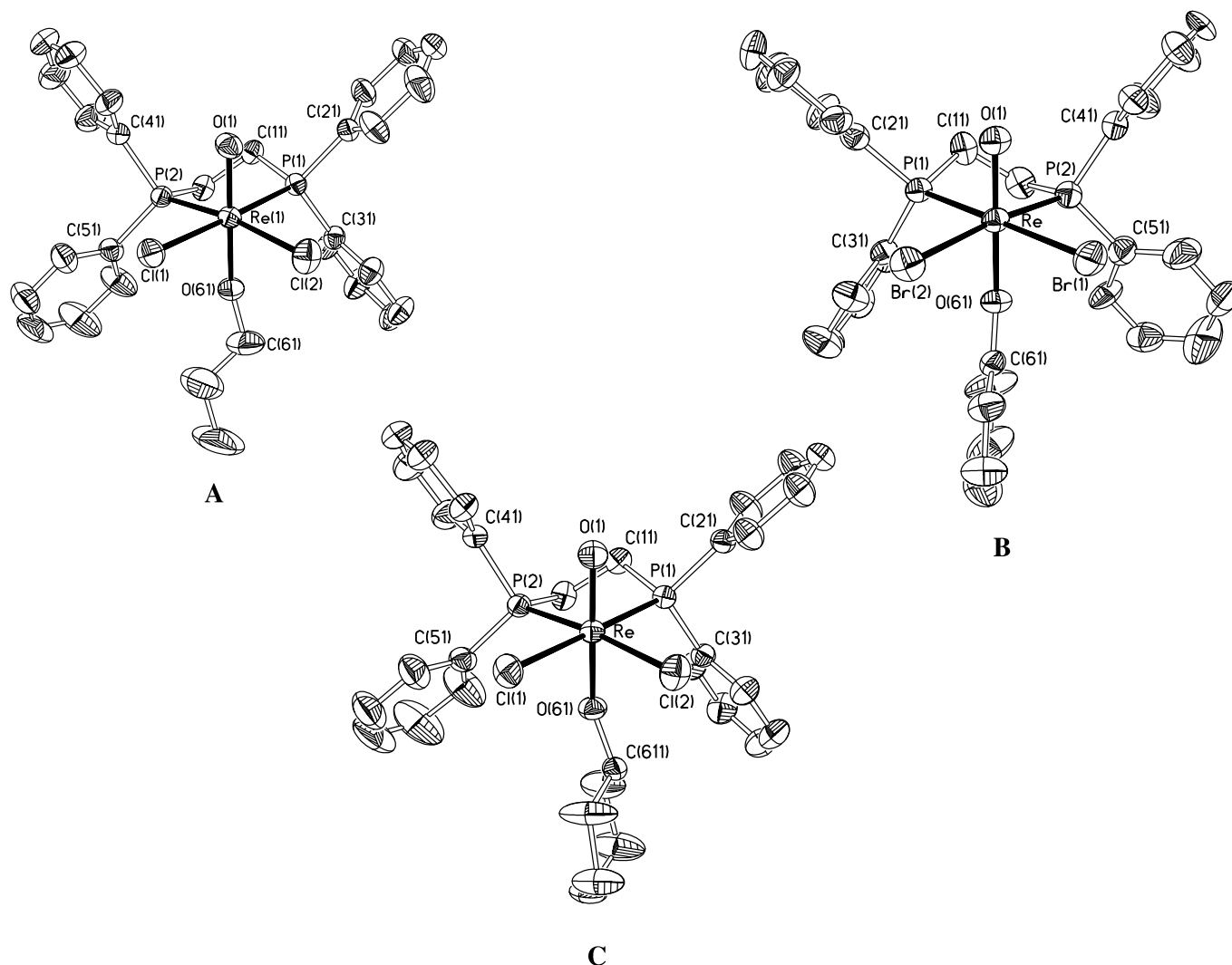
### Crystal structure of $\text{Re}(\text{NC}_6\text{H}_4\text{Cl})\text{Cl}_3(\text{dppe})$

The  $\text{Re}(\text{NC}_6\text{H}_4\text{Cl})\text{Cl}_3(\text{dppe})$  molecule adopts the structure shown in Fig. 3. The octahedral coordination of Re includes a multiple-bonded 4-chlorophenylimido group with the *trans* site filled by a chloro ligand, leading to the *fac* configuration observed for the corresponding bis(diphenylphosphino)ferrocene complex (59). Selected interatomic distances and bond angles are given in Table 4.

The  $\text{Re}=\text{NR}$  distance (1.707(5) Å) and the small departure from linearity in the  $\text{Re}=\text{N}-\text{C}$  unit ( $171.5(5)^\circ$ ) correspond well with the available data on arylimido complexes (mean values:  $\text{Re}=\text{N}$  (1.716(15) Å),  $\text{Re}=\text{N}-\text{C}$  ( $172(5)^\circ$ ); based on 42 structures) (41). A detailed comparison with the related compounds  $\text{Re}(\text{NPh})\text{Cl}_3(\text{PPh}_3)_2$  (*trans*-P,P) (60),  $\text{Re}(\text{NPh})\text{Cl}_3\{\text{bis}(\text{diphenylphosphino})\text{ferrocene}\}$  (*cis*-P,P) (59), and  $\text{Re}(\text{NPh})\text{Cl}_3(\text{PMe}_3)_2$  (*cis*-P,P) (61) is provided in the supplementary material (Table S-1).<sup>3</sup> For the  $\text{dppe}$  ligand, the  $\text{P}-\text{Re}-\text{P}$  “bite” angle and the ring conformation are close to those of the above oxo-alkoxo compounds, but the  $\text{Re}-\text{P}$



**Fig. 2.** ORTEP drawings of  $\text{ReOCl}_2(\text{OPr})(\text{dppe})$  (A),  $\text{ReOBr}_2(\text{OPh})(\text{dppe})$  (B), and  $\text{ReOCl}_2(\text{OCy})(\text{dppe})$  (C). For simplicity, only the major conformations are shown and the hydrogens are omitted.



bond lengths are  $\sim 0.01$  Å shorter here. The Re–Cl distances range from 2.417(2) to 2.438(2) Å, in agreement with the average value of 2.40(3) Å from the literature. As noted for oxo-alkoxo complexes, the metal is displaced from the  $\text{P}_2\text{X}_2$  plane on the nitrogen side by  $\sim 0.20$  Å. Steric interactions with the dppe phenyl rings probably explain that the departure from linearity in the trans  $\text{RN}=\text{Re}-\text{Cl}$  unit ( $168.0(2)^\circ$ ) is slightly greater than commonly found (mean for 16 structures  $\sim 174(4)^\circ$ ). The phenyl rings at the  $\text{P}_\text{A}$  end of dppe are oriented in the same way ( $\text{Re}-\text{P}_\text{A}-\text{C}_i-\text{C}_o = 28^\circ$  and  $-71^\circ$ ) as in the oxo-alkoxo complexes, but those of the  $\text{P}_\text{B}$  phosphine group adopt a different orientation corresponding to the opposite pattern of torsion angles ( $\text{Re}-\text{P}_\text{B}-\text{C}_i-\text{C}_o = -67^\circ$  and  $15^\circ$ , respectively). This is likely due to stacking interactions between the C41–C46 dppe group and the phenylimido ring, roughly parallel to the  $\text{Re}-\text{P}_\text{A}$  bond. This orientation, also observed in the phosphinoferrocene complex, positions the rings nearly parallel to each other (dihedral angle =  $24.3(4)^\circ$ ) with a relatively small mean inter-ring distance of 3.6 Å. The complexes are packed individually in the unit

cell (Fig. S-6, supplementary material),<sup>3</sup> where the aromatic rings participate in various stacking interactions.

The  $\text{Re}(\text{NC}_6\text{H}_4\text{Cl})\text{Cl}_3(\text{dppe})$  molecule is compared to the isoelectronic  $\text{ReOCl}_3(\text{dppe})$  compound in Table 4. In the imido complex, the  $\text{Re}-\text{Cl}_{\text{cis}}$  bonds are  $\sim 0.05$  Å longer, whereas the  $\text{Re}-\text{P}$  bonds are  $\sim 0.04$  Å shorter. This is consistent with the fact that the  $\pi$  donation of the imido group into the metal  $d_{xz}$  and  $d_{yz}$  orbitals is greater than for the oxo ligand. This should strengthen the bonds with the  $\pi$ -acceptor phosphine, but weaken the  $\text{Re}-\text{X}$  bonds, since the halogens are competing with the oxo or imido ligands for  $\pi$  donation into the same metal orbitals. Interestingly, the orientations of the dppe rings in  $\text{ReOCl}_3(\text{dppe})$  do not follow the pattern found for  $\text{Re}(\text{NC}_6\text{H}_4\text{Cl})\text{Cl}_3(\text{dppe})$  and the  $\text{ReO}(\text{OR})\text{Cl}_2(\text{dppe})$  compounds. This conformational change has no appreciable effect on the coordination geometry.

#### **$\text{ReCl}_4(\text{dppe}=\text{O})\cdot(\text{CH}_3)_2\text{SO}$**

In the  $\text{ReCl}_4(\text{dppe}=\text{O})$  complex shown in Fig. 4, the Re(IV) center possesses an octahedral coordination. The



**Table 3.** Distances (Å) and angles (°) in the ReOX<sub>2</sub>(OR)(dppe) compounds.<sup>a</sup>

R	Propyl	Cyclohexyl	Phenyl <sup>b</sup>
X	Cl	Cl	Br
<b>Bond distances (Å)</b>			
Re=O	1.698(3)	1.700(2)	1.686(6)
Re—OR	1.885(3)	1.877(2)	1.900(6)
Re—P <sub>A</sub>	2.4260(10)	2.4305(9)	2.432(2)
Re—P <sub>B</sub>	2.4320(10)	2.4364(8)	2.446(3)
Re—X <sub>A</sub>	2.4475(10)	2.4570(10)	2.5990(11)
Re—X <sub>B</sub>	2.4280(11)	2.4296(9)	2.5700(11)
<b>Bond angles (°)</b>			
P <sub>A</sub> —Re—P <sub>B</sub>	83.26(3)	83.19(3)	83.59(9)
X <sub>A</sub> —Re—X <sub>B</sub>	87.57(4)	87.11(3)	87.41(4)
O=Re—OR	172.57(14)	172.87(11)	171.8(3)
P <sub>A</sub> —Re—X <sub>A</sub>	176.37(4)	177.03(3)	176.81(7)
P <sub>B</sub> —Re—X <sub>B</sub>	170.61(4)	172.93(3)	172.65(7)
P <sub>A</sub> —Re—X <sub>B</sub>	95.96(4)	95.45(3)	94.92(6)
P <sub>B</sub> —Re—X <sub>A</sub>	93.13(4)	94.09(3)	93.82(7)
O=Re—P <sub>A</sub>	86.29(10)	86.27(9)	86.7(2)
O=Re—P <sub>B</sub>	92.49(11)	91.52(9)	90.1(2)
O=Re—X <sub>A</sub>	96.80(11)	95.02(9)	95.2(2)
O=Re—X <sub>B</sub>	94.17(10)	95.32(9)	97.0(2)
RO—Re—P <sub>A</sub>	87.89(9)	87.95(8)	87.50(19)
RO—Re—P <sub>B</sub>	82.24(10)	83.65(8)	83.47(19)
RO—Re—X <sub>A</sub>	88.38(10)	90.57(8)	90.36(19)
RO—Re—X <sub>B</sub>	91.36(10)	89.37(8)	89.28(18)
Re—O—C	160.8(5) (80%) <sup>c</sup>	153.6(3) (60%) <sup>c</sup>	162.3(5)
	159.5(9) (20%) <sup>c</sup>	157.0(6) (40%) <sup>c</sup>	
P <sub>A</sub> —C—C—P <sub>B</sub>	58.9(3)	57.1(3)	57.9(9)
C—C—P <sub>A</sub> —C <sub>i</sub>	−168.3(3)	−168.7(2)	−171.7(7)
	79.7(3)	80.2(3)	76.7(7)
C—C—P <sub>B</sub> —C <sub>i</sub>	81.6(3)	82.3(3)	84.3(8)
	−169.2(3)	−169.2(2)	−166.8(9) (60%) <sup>c</sup>
			−185.4(7) (40%) <sup>c</sup>
Re—P <sub>A</sub> —C <sub>i</sub> —C <sub>o</sub>	34.3(5)	26.6(4)	14.2(10)
	−60.7(4)	−64.8(3)	−57.5(7)
Re—P <sub>B</sub> —C <sub>i</sub> —C <sub>o</sub>	−16.5(4)	−22.0(4)	−27.3(10)
	75.8(5)	69.0(4)	88(2) (60%) <sup>c</sup>
			59.0(2) (40%) <sup>c</sup>
Re•••PPXX	0.1053(6)	0.0882(4)	0.1012(10)

<sup>a</sup>P<sub>A</sub> bonded to the CH<sub>2</sub> group on the oxo side of the P<sub>2</sub>X<sub>2</sub> plane, P<sub>B</sub> bonded to the CH<sub>2</sub> group on the OR side, X<sub>A</sub> trans to P<sub>A</sub>, X<sub>B</sub> trans to P<sub>B</sub>.

<sup>b</sup>Torsion angles calculated for the (−x, −y, −z) molecule for consistency.

<sup>c</sup>Values corresponding to the two disordered orientations, occupancies within round brackets.

bidentate ligand is actually Ph<sub>2</sub>PC<sub>2</sub>H<sub>4</sub>PPh<sub>2</sub>(O), which is a dppe ligand in which one end has been oxidized to phosphine oxide. A similar arrangement was observed for ReCl<sub>4</sub>(dppm=O). Selected interatomic distances and bond angles are given in Table 5.

The angles in the octahedron are close to ideality. The largest deviation, found for the mutually trans Re—Cl bonds, reflects a small displacement for the chlorines towards the chelate ring. The Re-ligand distances compare well with the literature results. For mutually trans Re—Cl

bonds, the distances observed here are close to the mean value 2.336(14) Å determined from 21 Re(IV) structures (41). When the chloro ligand sits trans to a different donor atom, the mean value from the literature (23 structures) is similar (2.325(30) Å), but it covers a broader range, mainly because it is sensitive to the trans influence of the opposite ligand. In our structure, the Re—Cl bond trans to oxygen (2.319(2) Å) is appreciably shorter than the one trans to the phosphine group (2.335(2) Å), whose trans influence is large.



**Fig. 3.** ORTEP drawing of *fac*-Re(NC<sub>6</sub>H<sub>4</sub>Cl)Cl<sub>3</sub>(dppe). The hydrogens are omitted for simplicity.

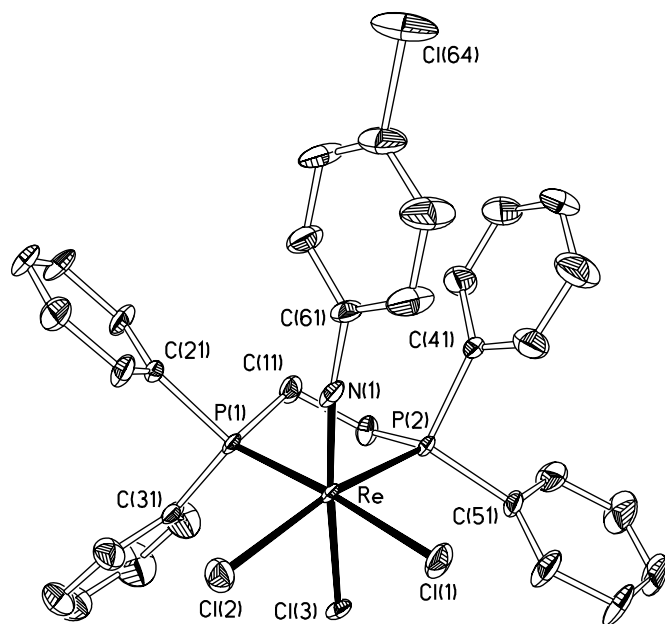
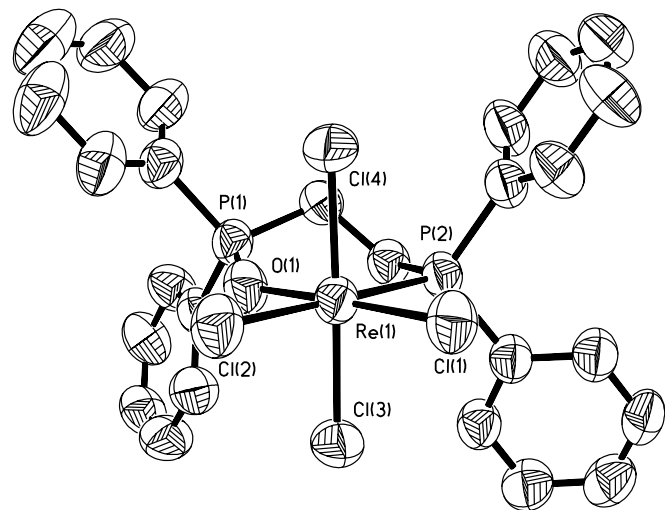


**Fig. 4.** ORTEP drawing of ReCl<sub>4</sub>(dppe=O). The hydrogens are omitted for simplicity.



In the unit cell (Fig. S-7),<sup>3</sup> the molecules form layers parallel to the *a* axis and oriented along the cell diagonal. Between these layers, the superposition of DMSO molecules fills channels extending along the cell *a* axis.

Comparisons are made in Table 5 with ReCl<sub>4</sub>(dppm=O) (62), which differs from our compound by the size of the chelate ring. The O-Re-P angle in the six-membered ring with dppe=O (89.2(2)°) is much greater than that of the dppm=O five-membered ring (80.7°). This leaves less space for the opposite chlorines, which get closer together: the Cl-Re-Cl angle is 93.46(9)° here, compared to 97.7° for the dppm=O complex. Another difference is the Re-O=P angle, which is 140.5(3)° here, but 130.1° in ReCl<sub>4</sub>(dppm=O). This angle is known to be very flexible: it is ~155° for monodentate O=PR<sub>3</sub> ligands, but it can adjust readily to ex-

**Table 4.** Distances (Å) and angles (°) in *fac*-Re(NC<sub>6</sub>H<sub>4</sub>Cl)Cl<sub>3</sub>(dppe) and ReOCl<sub>3</sub>(dppe).

	NC <sub>6</sub> H <sub>4</sub> Cl <sup>a</sup>	O <sup>b</sup>
<b>Bond distances (Å)</b>		
Re=NR	1.707(5)	1.680
Re—Cl <sub>trans</sub>	2.420(1)	2.429
Re—P <sub>A</sub>	2.421(1)	2.463
Re—P <sub>B</sub>	2.414(2)	2.445
Re—Cl <sub>A</sub>	2.438(2)	2.377
Re—Cl <sub>B</sub>	2.417(2)	2.380
<b>Bond angles (°)</b>		
P <sub>A</sub> -Re-P <sub>B</sub>	83.37(5)	83.3
Cl <sub>A</sub> -Re-Cl <sub>B</sub>	85.92(6)	86.3
RN=Re-Cl <sub>trans</sub>	168.0(2)	163.0
P <sub>A</sub> -Re-Cl <sub>A</sub>	174.96(5)	173.2
P <sub>B</sub> -Re-Cl <sub>B</sub>	165.56(6)	164.5
P <sub>B</sub> -Re-Cl <sub>A</sub>	96.56(5)	92.9
P <sub>A</sub> -Re-Cl <sub>B</sub>	92.92(5)	95.9
N-Re-P <sub>A</sub>	90.5(2)	84.3
N-Re-P <sub>B</sub>	90.6(2)	91.4
N-Re-Cl <sub>A</sub>	94.6(2)	101.4
N-Re-Cl <sub>B</sub>	103.4(2)	103.9
Cl <sub>trans</sub> -Re-P <sub>A</sub>	83.92(5)	82.2
Cl <sub>trans</sub> -Re-P <sub>B</sub>	78.19(5)	76.8
Cl <sub>trans</sub> -Re-Cl <sub>A</sub>	91.13(6)	91.5
Cl <sub>trans</sub> -Re-Cl <sub>B</sub>	87.56(6)	87.7
Re=N-C	171.5(5)	—
P-Re...C <sub>i</sub> -C <sub>o</sub> (imido)	3.9(6)	—
P <sub>A</sub> -C-C-P <sub>B</sub>	55.7(6)	59.8
C-C-P <sub>A</sub> -C <sub>i</sub>	-162.9(5)	-163.7
	89.2(5)	81.8
C-C-P <sub>B</sub> -C <sub>i</sub>	77.9(5)	76.4
	-175.1(5)	-173.7
Re-P <sub>A</sub> -C <sub>i</sub> -C <sub>o</sub>	28.3(6)	54.3
	-70.8(6)	-58.0
Re-P <sub>B</sub> -C <sub>i</sub> -C <sub>o</sub>	-67.0(6)	-28.9
	15.1(8)	74.2
Re...PPXX	0.2018(7)	0.226

<sup>a</sup>Torsion angles for Re(NC<sub>6</sub>H<sub>4</sub>Cl)Cl<sub>3</sub>(dppe) calculated for the (-*x*, -*y*, -*z*) molecule for consistency with Table 3.

<sup>b</sup>Reference 31.

ternal strain. The very small angle for the dppe=O complex reflects the high constraint for a five-membered chelate ring.

One of the Re-Cl distances (2.215 Å) reported for the dppe=O complex is extremely small. This bond, trans to the phosphine oxide group, seems to be ~0.1 Å shorter than the corresponding bond in our dppe=O complex. Partial substitution of the Re(IV) complex ReCl<sub>4</sub>(dppm=O) in the crystal by Re(V) molecules *mer*-ReOCl<sub>3</sub>(dppm=O) (63, 64) could explain this “apparent” shortening, since the oxo ligand would be trans to the phosphine oxide in the latter species. Such solid solutions of “quasi-isostructural” oxo-Re(V) and chloro-Re(IV) complexes have already been detected (65) and in the resulting average structure, the “Re—Cl(O)” bond



**Table 5.** Distances (Å) and angles (°) in  $\text{ReCl}_4(\text{dppe}=\text{O})$  and  $\text{ReCl}_4(\text{dppm}=\text{O})$ .

	$\text{ReCl}_4(\text{dppe}=\text{O})$	$\text{ReCl}_4(\text{dppm}=\text{O})^a$
<b>Bond distances (Å)</b>		
Re—O(1)	2.039(5)	2.087(7)
Re—P(2)	2.512(2)	2.467(3)
Re—Cl(1)	2.319(2)	2.215(5)
Re—Cl(2)	2.353(2)	2.353(3)
Re—Cl(3)	2.312(2)	2.340(3)
Re—Cl(4)	2.339(2)	2.361(3)
O(1)—P(1)	1.517(6)	1.523(8)
<b>Bond angles (°)</b>		
Cl(3)—Re—Cl(4)	173.61(8)	173.8
P(2)—Re—Cl(1)	176.37(7)	169.1
O(1)—Re—Cl(2)	178.02(15)	173.2
O(1)—Re—P(2)	89.2(2)	80.7(2)
Cl(1)—Re—Cl(2)	93.46(9)	97.7(1)
O(1)—Re—Cl(2)	87.2(2)	88.6(2)
O(1)—Re—Cl(3)	86.3(2)	87.1(2)
O(1)—Re—Cl(4)	88.1(2)	86.7(2)
P(2)—Re—Cl(1)	90.16(7)	93.0(1)
P(2)—Re—Cl(3)	88.69(7)	86.8(1)
P(2)—Re—Cl(4)	87.98(8)	92.6(1)
Cl(3)—Re—Cl(1)	91.76(9)	95.3(2)
Cl(1)—Re—Cl(4)	93.70(9)	90.9(2)
Cl(3)—Re—Cl(2)	90.90(8)	90.1(1)
Cl(4)—Re—Cl(2)	92.08(9)	89.4(1)
Re—O(1)—P(1)	140.5(3)	130.1(4)
P(1)—C(11)—C(12)—P(2)	−78.8(6)	—
Re—O(1)—P(1)—C(11)	15.1(6)	−2.5
Re—O(1)—P(1)—C(21)	134.8(5)	−123.8
Re—O(1)—P(1)—C(31)	−106.3(6)	115.1
O(1)—Re—P(2)—C(12)	−1.2(3)	22.8
O(1)—Re—P(2)—C(41)	117.9(3)	139.2
O(1)—Re—P(2)—C(51)	−116.0(3)	−96.5
Re—P(2)—C(41)—C <sub>ortho</sub>	55.0(7)	−9.0
Re—P(2)—C(51)—C <sub>ortho</sub>	69.5(7)	−71.9
O(1)—P(1)—C(21)—C <sub>ortho</sub>	−8.2(7)	63.3
O(1)—P(1)—C(31)—C <sub>ortho</sub>	−23.8(8)	5.6

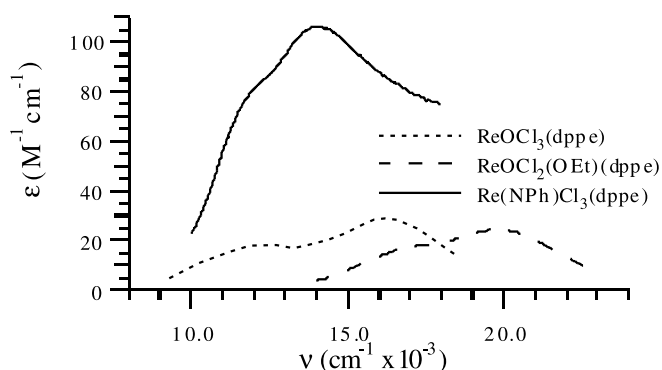
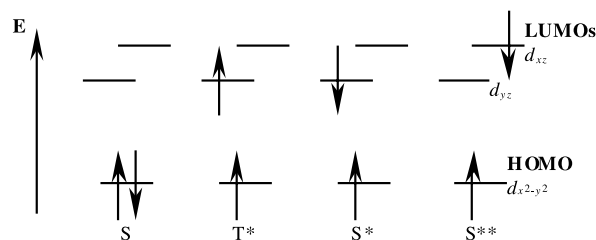
<sup>a</sup>Reference 62 esds not calculated for all entries.

seems to be shortened with respect to a normal Re—Cl bond, but to be stretched when compared to an Re=O bond.

### Electronic spectra and DFT calculations

The low-energy portions (8000–25 000  $\text{cm}^{-1}$ ) of the absorption spectra of representative compounds are shown in Fig. 5. Spectra taken with crystalline  $\text{ReOX}_3(\text{dppe})$  and  $\text{ReOX}_2(\text{OR})(\text{dppe})$  compounds confirmed that the species in the solid is retained in DMSO. In all cases, this spectral region shows two major components. The data are listed in Table 6.

Strictly speaking, the molecules examined here have no symmetry, but if chelate ring puckering and other minor distortions are ignored, a mirror plane containing the Re=O(NR) bond bisects the P—Re—P angle, so that the metal environment has an approximate  $C_s$  symmetry. Under this low symmetry, the antibonding  $d_{xz}/d_{yz}$  orbitals, which are de-

**Fig. 5.** Typical electronic spectra of the  $\text{ReEX}_2(\text{Y})(\text{dppe})$  complexes in DMSO.**Fig. 6.** Ground and low-energy excited states for the  $\text{Re}(\text{V}) d^2$  systems: singlet ground state (S), first triplet excited state ( $T^*$ ), first singlet excited state ( $S^*$ ), second singlet excited state ( $S^{**}$ ).

generate under  $D_{4h}$  symmetry, become inequivalent. For this point group symmetry, the interbond orbital in the  $xy$  plane is labeled  $d_{x^2-y^2}$  (instead of  $d_{xy}$ ), and for consistency with the recent study on isoelectronic oxo-molybdenum(IV) systems by Da Re and Hopkins (66), the  $d_{yz}$  will be assumed to lie at lower energy than  $d_{xz}$ . The two absorption features in Fig. 5 are assigned to the two spin-allowed singlet–singlet transitions  $(d_{x^2-y^2})^2 \rightarrow (d_{x^2-y^2})^1(d_{yz})^1$  [ $S \rightarrow S^*$ ] and  $(d_{x^2-y^2})^2 \rightarrow (d_{x^2-y^2})^1(d_{xz})^1$  [ $S \rightarrow S^{**}$ ], respectively (Fig. 6). Therefore, the position of these bands can be used to estimate the two HOMO–LUMO energy gaps. Singlet–triplet processes [ $S \rightarrow T^*$ ] could in principle take place, but there is no evidence for these much weaker spin-forbidden transitions in the spectra recorded here.

Two well-differentiated components (12 000 and 16 400  $\text{cm}^{-1}$ ) are visible for  $\text{ReOCl}_3(\text{dppe})$ . Replacing Cl by Br produces similar red shifts on both (11 300 and 15 500  $\text{cm}^{-1}$ ). Upon substitution of the oxo ligand by a phenylimido group in  $\text{Re}(\text{NPh})\text{Cl}_3(\text{dppe})$ , the two components are not equally displaced: the low-energy component undergoes a very small red shift of  $\sim 900 \text{ cm}^{-1}$ , whereas the shift on the other is greater ( $\sim 3000 \text{ cm}^{-1}$ ). This could be connected with the different symmetries of these two ligands. For the cylindrical oxo ligand, the  $p_x$  and  $p_y$  orbitals are equally available for  $\pi$  interacting with the metal  $d_{xz}$  and  $d_{yz}$  orbitals. In contrast, for the imido group, the phenyl ring renders these orbitals inequivalent, since only one is participating in the aromatic  $\pi$  system. Consequently,  $\pi$  interactions with the metal  $d_{xz}$  and  $d_{yz}$  orbitals being no longer equal, the transitions to these orbitals are anticipated to be differently affected.



**Table 6.** [S → S\*] and [S → S\*\*] of the low-energy components of the electronic spectra.

	X = Cl		X = Br	
	[S → S*]	[S → S**]	[S → S*]	[S → S**]
ReOX <sub>3</sub> (dppe)	12.0(13)	16.4(25)	11.3(13)	15.5(21)
ReO(OMe)X <sub>2</sub> (dppe)	17.0(11)	20.1(23)	16.8(14)	20.2(34)
ReO(OEt)X <sub>2</sub> (dppe)	16.4(12)	20.0(21)	16.4(15)	20.0(33)
ReO(OPr)X <sub>2</sub> (dppe)	16.5(10)	20.0(22)	16.6(16)	20.0(35)
ReO(OPh)X <sub>2</sub> (dppe)	~15.1(sh) <sup>a</sup>	—	—	—
Re(NPh)X <sub>3</sub> (dppe)	11.1(118)	13.4(74)	—	—
Re(NC <sub>6</sub> H <sub>4</sub> Cl)X <sub>3</sub> (dppe)	11.5(115)	13.5(70)	—	—

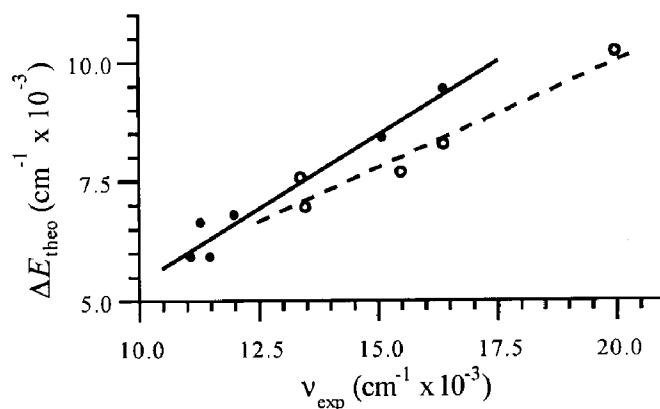
<sup>a</sup>The position of the shoulder produced by the lower-energy component was estimated; the higher energy component was completely masked by a phenoxo strong band.

**Table 7.** Comparison of the experimental transition energies with the DFT-calculated values (cm<sup>-1</sup> × 10<sup>-3</sup>) for the E=ReX<sub>2</sub>Y(dppe) compounds.

E	X	Y	[S → S*]		[S → S**]	
			Experimental (cm <sup>-1</sup> × 10 <sup>-3</sup> )	Calculated (cm <sup>-1</sup> × 10 <sup>-3</sup> )	Experimental (cm <sup>-1</sup> × 10 <sup>-3</sup> )	Calculated (cm <sup>-1</sup> × 10 <sup>-3</sup> )
O	Cl	OEt	16.4	9.42	20.0	10.21
O	Cl	OPh	15.1	8.41	—	8.71
O	Cl	Cl	12.0	6.78	16.4	8.25
O	Cl	OC <sub>6</sub> F <sub>5</sub>	—	5.95	—	6.63
O	Br	Br	11.3	6.63	15.5	7.66
O	I	I	—	6.15	—	7.09
NPh	Cl	Cl	11.1	5.91	13.4	7.55
NC <sub>6</sub> H <sub>4</sub> Cl	Cl	Cl	11.5	5.91	13.5	6.94
NC <sub>6</sub> F <sub>5</sub>	Cl	Cl	—	4.74	—	6.54

Substitution of the trans halogen of ReOX<sub>3</sub>(dppe) by an -OR group has a more drastic effect. In the ReOX<sub>2</sub>(OR)(dppe) compounds, both components undergo relatively large blue shifts to ~16 600 and 20 000 cm<sup>-1</sup>, respectively, and the separation (~3000 cm<sup>-1</sup>) is a little smaller than in the tris-halogen complexes (~4000 cm<sup>-1</sup>). Again, these unequal variations can be ascribed to the noncylindrical symmetry of the bent alkoxo group. One of the oxygen *p* orbitals (perpendicular to the Re-O-C plane) remains suitably oriented for optimal  $\pi$  interacting with one of the *d* orbitals, but partial hybridization will decrease the participation of the other *p* orbital (in the Re-O-C plane) in  $\pi$  interactions.

To understand the behavior of these oxo- and arylimido-rhenium(V) systems and orient our research strategies, theoretical calculations were performed with the PCSPARTAN PRO software (67). A simplified model was used to reduce computation time. Structure optimization on molecules containing dppe itself were time consuming, because adjusting the orientation of the four phenyl rings required many refinement cycles and convergence was not always reached. Since the comparisons to be made always involve the same diphosphine, the calculations were run using bis(dimethylphosphino)ethane (dmpe), in which the substituents are “cylindrical” methyl groups. On the other hand, since PCSPARTAN does not include rhenium parameters for DFT calculations, technetium was used in the model. The geometry and orbital energies were obtained by DFT calculations based on the generalized gradient approximation uti-

**Fig. 7.** Variation of the DFT-calculated energy gap as a function of the transition energy obtained experimentally from the spectra for each of the two transitions.

lizing the functionals proposed by Becke and Perdew (67). The BP86 (self-consistent model) and DN\* (double numerical polarization) options were used. The calculated energies are listed in Table 7 and they are plotted against the experimental results in Fig. 7.

For each of the two transitions, there is an approximate linear relationship between the energies determined from the spectra and those predicted from the calculations. This suggests that the calculations reflect in a satisfactory manner the factors affecting the energy levels in these systems. The re-



duction of the transition energy upon substitution of the oxo ligand by an arylimido moiety and the energy increase by replacing the trans halogen with an -OR group are reproduced well by the calculations. Even the small red shift resulting from the substitution of chlorine by bromine is consistent with the DFT predictions. However, this approach was unable to explain various fine features, for instance the fact that the difference between the two transition energies does not vary smoothly. The calculations did not reveal any substantial effect of the orientation of the noncylindrical arylimido or -OR groups on the transition energies and it is not clear whether orientation is actually unimportant or masked by model simplification or other weaknesses in our approach. The fact that the calculations were actually carried out on Tc complexes could introduce some distortions when the results are applied to Re compounds, the more so that spin-orbit coupling, which cannot be taken into account in PCSPARTAN, could play a role. Another weakness of our results is that significant geometrical distortions, namely nonlinearity in the  $\text{RN}(\text{O})=\text{Re}-\text{L}$  unit and displacement of the Re atom above the equatorial plane, were not accurately reproduced in the converged model and this could introduce small distortion in the orbital energy pattern. Nevertheless, the method is believed to reproduce the general absorption features sufficiently well to be useful in the orientation of future studies.

## Concluding remarks

On the basis of the two low-energy UV-vis absorptions observed for the series of  $\text{ReEX}_2\text{Y}(\text{dppe})$  compounds (with  $\text{E} = \text{O}$  or  $\text{NR}$ ,  $\text{X} = \text{Cl}$  or  $\text{Br}$ ,  $\text{Y} = \text{Cl}$ ,  $\text{Br}$ ,  $\text{OR}$ ), it was established that the energies of the spin-allowed transitions between the nonbonding interbond orbital ( $d_{x^2-y^2}$ ) and the  $\pi$ -antibonding  $d_{xz}/d_{yz}$  orbitals follow the order  $\text{RN}=\text{Re}-\text{X} < \text{O}=\text{Re}-\text{X} < \text{O}=\text{Re}-\text{OR}$ . Replacing chlorine by bromine reduces the energies slightly, whereas the lengthening of the alkyl chain in the -OR group ( $\text{R} = \text{Me}$ ,  $\text{Et}$ ,  $\text{Pr}$ ,  $-\text{C}_2\text{H}_4\text{OH}$ ) had no detectable effect. We expected the bulky cyclohexyl substituent would force the  $\text{Re}-\text{O}-\text{R}$  segment to be more linear, but these expectations did not materialize (see crystal structure) and the absorption spectrum of this compound does not differ from those of compounds with a smaller R group. The aromatic group in  $\text{ReOX}_2(\text{OPh})(\text{dppe})$  seems to reduce the first transition energy slightly, but this is difficult to evaluate, because the weak  $d-d$  transitions are masked here by a strong allowed transition involving the phenoxo group.

Although the DFT calculations cannot explain all the fine details present in the data, the general trends observed experimentally are reproduced sufficiently well to attribute some predictive capability to this approach. Transition energies calculated for a few promising systems are included in Table 7. The calculations suggest that incorporating strong electro-attracting features into either the phenylimido or the phenoxo group should shift the transitions to lower energies. On this basis, perfluorophenoxo complexes  $\text{ReOX}_2(\text{OC}_6\text{F}_5)(\text{dppe})$  or perfluorophenylimido compounds  $\text{Re}(\text{NC}_6\text{F}_5)\text{X}_3(\text{dppe})$  could be interesting candidates. Replacing chlorine or bromine by iodine also seems to be a

possible strategy to reduce further transition energy. Preparative work is underway to test these predictions.

## Acknowledgments

We wish to thank the Natural Sciences and Engineering Research Council of Canada (NSERC) for financial support, Dr. M. Simard and F. Bélanger-Gariépy for assistance in the interpretation of the X-ray diffraction data, C. Tessier and Professor F. D. Rochon for collecting an X-ray data set on the diffractometer at the Université du Québec à Montréal, and M. Martinho and M. Dussault for their participation in the preparative work.

## References

1. M. Nicolini and U. Mazzi. Technetium, rhenium and other metals in chemistry and nuclear medicine 5. Servizi Grafici Editoriali, Padova, Italy. 1999.
2. J.R. Dilworth and S.J. Parrott. *Chem. Soc. Rev.* **27**, 43 (1998).
3. S.S. Jurisson and J.D. Lydon. *Chem. Rev.* **99**, 2205 (1999).
4. S. Liu and D.S. Edwards. *Chem. Rev.* **99**, 2235 (1999).
5. C. Tessier, A.L. Beauchamp, and F.D. Rochon. *Inorg. Chem.* **41**, 6527 (2002).
6. C. Tessier, A.L. Beauchamp, and F.D. Rochon. *J. Inorg. Biochem.* **85**, 77 (2001).
7. S. Fortin and A.L. Beauchamp. *Inorg. Chem.* **40**, 105 (2001).
8. S. Fortin and A.L. Beauchamp. *Inorg. Chem.* **39**, 4886 (2000).
9. S. Fortin and A.L. Beauchamp. *J. Chem. Soc. Dalton Trans.* 3520 (2001).
10. S. Bélanger and A.L. Beauchamp. *Inorg. Chem.* **36**, 3640 (1997).
11. S. Bélanger, S. Fortin, and A.L. Beauchamp. *Can. J. Chem.* **75**, 37 (1997).
12. S. Bélanger and A.L. Beauchamp. *Inorg. Chem.* **35**, 7836 (1996).
13. X. Couillens, M. Gressier, R. Turpin, M. Dartiguenave, Y. Coulais, and A.L. Beauchamp. *J. Chem. Soc. Dalton Trans.* 914 (2002).
14. X. Couillens, M. Gressier, M. Dartiguenave, S. Fortin, and A.L. Beauchamp. *J. Chem. Soc. Dalton Trans.* 3032 (2002).
15. F. Connac, Y. Lucchese, M. Dartiguenave, and A.L. Beauchamp. *Inorg. Chem.* **36**, 256 (1997).
16. F. Connac, Y. Lucchese, M. Dartiguenave, Y. Coulais, and A.L. Beauchamp. *Inorg. Chim. Acta*, **295**, 209 (1999).
17. F. Connac, Y. Lucchese, M. Gressier, M. Dartiguenave, and A.L. Beauchamp. *Inorg. Chim. Acta*, **304**, 52 (2000).
18. F. Loiseau, F. Connac, Y. Lucchese, M. Dartiguenave, S. Fortin, A.L. Beauchamp, and Y. Coulais. *Inorg. Chim. Acta*, **306**, 94 (2000).
19. J.B. Arterburn and S.L. Nelson. *J. Org. Chem.* **61**, 2260 (1996).
20. J.B. Arterburn and M.C. Perry. *Tetrahedron Lett.* **37**, 7941 (1996).
21. J.B. Arterburn, M.C. Perry, S.L. Nelson, B.R. Dible, and M.S. Holguin. *J. Am. Chem. Soc.* **119**, 9309 (1997).
22. H.Q.N. Gunaratne, M.A. McKerver, S. Feutren, J. Finlay, and J. Boyd. *Tetrahedron Lett.* **39**, 5655 (1998).
23. X. Shan, A. Ellern, I.A. Guzei, and J.H. Espensen. *Inorg. Chem.* **42**, 2362 (2003).
24. J.R. Winkler and H.B. Gray. *Inorg. Chem.* **24**, 346 (1985).
25. C. Savoie, C. Reber, S. Bélanger, and A.L. Beauchamp. *Inorg. Chem.* **34**, 3851 (1995).



26. C. Savoie and C. Reber. *Coord. Chem. Rev.* **171**, 387 (1998).
27. C. Savoie and C. Reber. *J. Am. Chem. Soc.* **122**, 844 (2000).
28. J. Landry-Hum, V. Tessier, M. Ernzerhof, and C. Reber. *Coord. Chem. Rev.* **233–234**, 63 (2002).
29. U. Oetliker, C. Savoie, S. Stanislas, C. Reber, F. Connac, A.L. Beauchamp, F. Loiseau, and M. Dartiguenave. *J. Chem. Soc. Chem. Commun.* 657 (1998).
30. J. Chatt and G.A. Rowe. *J. Chem. Soc.* 4019 (1962).
31. V.S. Sergienko, M.A. Porai-Koshits, V.E. Mistryukov, and K.V. Kotegov. *Koord. Khim.* **8**, 230 (1982).
32. F.A. Cotton, N.F. Curtis, and W.R. Robinson. *Inorg. Chem.* **4**, 1696 (1965).
33. SMART. Release 5.059 [computer program]. Bruker AXS Inc., Madison, Wis. 1999.
34. SAINT. Release 6.06 [computer program]. Bruker AXS Inc., Madison Wis. 1999.
35. CAD-4 software. Version 5.0 [computer program]. Enraf-Nonius, Delft, The Netherlands. 1989.
36. XSCANS [computer program]. Bruker Analytical X-Ray Systems, Madison, Wis. 1995.
37. G.M. Sheldrick. SHELXTL. Release 5.10 [computer program]. Bruker AXS Inc., Madison, Wis. 1997.
38. XPREP. Release 5.10 [computer program]. Bruker AXS Inc., Madison, Wis. 1997.
39. G.M. Sheldrick. SHELXS-97 [computer program]. University of Göttingen, Göttingen, Germany. 1997.
40. G.M. Sheldrick. SHELXL-96 [computer program]. University of Göttingen, Göttingen, Germany. 1996.
41. Cambridge Structural Database. Version 5.4, November 2002 release with February 2003 updates. Cambridge Crystallographic Data Centre, Cambridge, U.K.
42. B. Jezowska-Trzebiatowska, J. Hanuza, and M. Baluka. *Spectrochim. Acta*, **27A**, 1753 (1971).
43. J.P. O'Neil, S.R. Wilson, and J.A. Katzenellenbogen. *Inorg. Chem.* **33**, 319 (1994).
44. M.S. Papadopoulos, M. Pelecanou, I.C. Pirmettis, D.M. Spyriounis, C.P. Raptopoulou, A. Terzis, C.I. Stassinopoulou, and E. Chioellis. *Inorg. Chem.* **35**, 4478 (1996).
45. E. Vincent, L. Verdonck, and G.P.V.D. Kelen. *Spectrochim. Acta*, **36A**, 699 (1980).
46. H.E. Gottlieb, V. Kotlyar, and A. Nudelman. *J. Org. Chem.* **62**, 7512 (1997).
47. S. Banerjee, S. Bhattacharyya, B.K. Dirghangi, M. Menon, and A. Chakravorty. *Inorg. Chem.* **39**, 6 (2000).
48. R.R. Conry and J.M. Mayer. *Inorg. Chem.* **29**, 4862 (1990).
49. K. Nakamoto. *Infrared and Raman spectra of inorganic coordination compounds*. 4th ed. John Wiley and Sons, New York. 1986. p. 341.
50. C. Pearson and A.L. Beauchamp. *Can. J. Chem.* **75**, 220 (1997).
51. C. Pearson and A.L. Beauchamp. *Inorg. Chim. Acta*, **237**, 13 (1995).
52. C. Kremer, M. Rivero, E. Kremer, L. Suescun, A.W. Mombru, R. Mariezcurrena, S. Dominguez, A. Mederos, S. Midollini, and A. Castineiras. *Inorg. Chim. Acta*, **47**, 294 (1999).
53. J.R. Dilworth, D.V. Griffiths, S.J. Parrott, and Y. Zheng. *J. Chem. Soc., Dalton Trans.* 2931 (1997).
54. K.J.C.V. Bommel, W. Verboom, H. Kooijman, A.L. Spek, and D.N. Reinhoudt. *Inorg. Chem.* **37**, 4197 (1998).
55. R. Chiozzzone, R. Gonzalez, C. Kremer, G. De Munno, and J. Faus. *Inorg. Chim. Acta*, **325**, 203 (2001).
56. A.M. Lebus and A.L. Beauchamp. *Can. J. Chem.* **71**, 441 (1993).
57. R. Graziani, U. Casellato, R. Rossi, and A. Marchi. *J. Crystallogr. Spectrosc. Res.* **15**, 573 (1985).
58. S. Abram, U. Abram, E. Schulz-Lang, and J. Strähle. *Acta Crystallogr.* **C51**, 1078 (1995).
59. S.W. Lee and N.-S. Choi. *Acta Crystallogr. Sect. C: Cryst. Struct. Commun.* **55**, 2018 (1999).
60. B.-G. Park, Y.-W. Kim, G.-S. Jung, H.-S. Park, and S.W. Lee. *Bull. Korean Chem. Soc.* **16**, 835 (1995).
61. Y.-W. Kim, J.-H. Jung, H.-S. Park, and S.W. Lee. *Bull. Korean Chem. Soc.* **15**, 891 (1994).
62. R. Rossi, A. Marchi, L. Marvelli, L. Magno, M. Peruzzini, U. Casellato, and R. Graziani. *Inorg. Chim. Acta*, **204**, 63 (1993).
63. K.V. Katti and C.L. Barnes. *Inorg. Chem.* **31**, 4231 (1992).
64. K.-Y. Shih, P.E. Fanwick, and R.A. Walton. *Inorg. Chim. Acta*, **212**, 23 (1993).
65. K. Yoon, G. Parkin, and A.L. Rheingold. *J. Am. Chem. Soc.* **114**, 2210 (1992).
66. R.E. Da Re and M.D. Hopkins. *Inorg. Chem.* **41**, 6973 (2002).
67. PCSPARTAN PRO 1.0.6 [computer program]. Wavefunction Inc., Irvine Calif. 2001.



# Structural elucidations of T<sub>8</sub> and Q<sub>8</sub> silsesquioxane cages containing two types of pendant group using <sup>29</sup>Si NMR spectroscopy<sup>1</sup>

Alan Richard Bassindale, David John Parker, Peter Geoffrey Taylor, and Alison Claire Watt

**Abstract:** The products from the reaction of octahydrosilsesquioxane (T<sub>8</sub>-H) with different molar ratios of phenol and undec-1-ene or methyl 3,3-dimethylpent-4-enoate (MDP) in the presence of chloroplatinic acid have been analysed by <sup>29</sup>Si NMR spectroscopy. The distribution of the two different pendant groups leads to tetrad patterns where the relative chemical peak intensities reflect the selectivity for particular patterns of substitution. As well as analysing the cause of these tetrad patterns we also discuss how the regioselectivity of hydrosilylation can be determined.

**Key words:** T<sub>8</sub>, Q<sub>8</sub>, silsesquioxane, <sup>29</sup>Si NMR, hydrosilylation, tetrad pattern, regioselectivity, statistical modelling.

**Résumé :** Faisant appel à la spectroscopie RMN du <sup>29</sup>Si, on a analysé les produits obtenus par réaction du octahydro-silsesquioxane (T<sub>8</sub>-H) avec divers rapports molaires de phénol et d'undéc-1-ène ou de 3,3-diméthylpent-4-énonate de méthyle (DPM), en présence d'acide chloroplatinique. La distribution des deux groupes pendants différents conduit à des patrons de tétrades dans lesquels les intensités relatives de pics chimiques sont un reflet de la sélectivité pour des patrons particuliers de substitution. En plus d'analyser la cause de ces divers patrons de tétrades, on discute aussi de la façon de déterminer la régiosélectivité de l'hydrosilylation.

**Mots clés :** T<sub>8</sub>, Q<sub>8</sub>, silsesquioxane, RMN du <sup>29</sup>Si, patron de tétrade, régiosélectivité, modélisation statistique.

[Traduit par la Rédaction]

## Introduction

We have long been interested in the chemistry of silsesquioxane cages from analysing their various structures, the means of selectively forming them, and the mechanism of their formation and interconversion. Amongst the most well-known and first-reported cages were the octasilsesquioxanes (the so-called T<sub>8</sub> and Q<sub>8</sub> cages) first reported by Barry et al. (1) by the base-catalyzed hydrolysis of alkyl trichlorosilanes. Subsequent studies by Martynova et al. (2) and Feher and Budzichowski (3) reported reasonable yields of T<sub>8</sub>s by the hydrolysis of allyl- or aryltrichlorosilanes in ethanol or acetone. The simplest T<sub>8</sub> of all, octahydrosilsesquioxane (T<sub>8</sub>-H), was first reported by Muller et al. (4) and has subsequently been widely used as a preformed cage precursor to many other functionalized T<sub>8</sub>s, especially by hydrosilylation routes (5).

While much work has focussed on centro-symmetrical T<sub>8</sub> and Q<sub>8</sub> silsesquioxanes, where all eight pendant arms are the same, less work has been reported on non-centrosymmetrical analogues with two or more different types of arms. Mono-

septa-substituted cages **1** have been reported variously by the groups of Dutchateau (6) and Feher (7) and di-hexa-substituted cages **2** by Rebrov et al. (8) and Roesky and co-workers (9). The main reason for the lack of published work is the difficulty encountered in finding highly regiospecific routes to these mixed arm compounds and in separating the often numerous isomers formed from the typically non-regioisomer-specific routes that have been used to form them (Scheme 1).

The characterization of centro-symmetric T<sub>8</sub> and Q<sub>8</sub> cage compounds by solution <sup>1</sup>H, <sup>29</sup>Si, and <sup>13</sup>C NMR spectroscopy is relatively straightforward due to the simplicity of spectra caused by the equivalence of each silicon and pendant group. However, for non-centrosymmetric cages prepared under conditions where little or no regiocontrol is employed, more complex spectral patterns occur and separating the data for each isomer is a more complex task. Though from compound to compound the specific NMR spectra may be quite different, the NMR patterns produced by a single type of atom, for example the <sup>13</sup>C NMR of a particular carbon in a pendant group, can be indicative of the number and type of

Received 26 February 2003. Published on the NRC Research Press Web site at <http://canjchem.nrc.ca> on 24 October 2003.

*This paper is dedicated to John Harrod as a mark of his great contributions to chemistry over many years.*

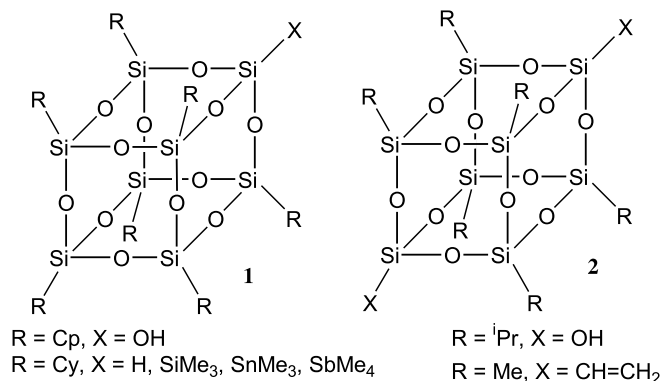
**A.R. Bassindale, D.J. Parker, P.G. Taylor,<sup>2</sup> and A.C. Watt.** Department Of Chemistry, The Open University, Walton Hall, Milton Keynes, MK7 6AA, U.K.

<sup>1</sup>This article is part of a Special Issue dedicated to Professor John Harrod.

<sup>2</sup>Corresponding author: (e-mail: [P.G.Taylor@open.ac.uk](mailto:P.G.Taylor@open.ac.uk)).



Scheme 1.



structural environments present and so hint at the purity of the sample.

The technique of quantitatively examining the tacticity of polymers with NMR spectroscopy (normally <sup>13</sup>C or <sup>1</sup>H NMR measurements) by analysing spectral patterns has long been established as a powerful analytical tool for the polymer chemist (10), and more recently 3D triple resonance NMR techniques have been used to unambiguously assign NMR spectral patterns to individual stereosequences (11). Kawakami and co-workers (12) recently reported a stereoselective cross-dehydrocoupling reaction leading to optically active poly(methylphenyl)siloxane and used <sup>13</sup>C NMR chemical shift measurements and the triad peak patterns of the ipso carbon of the phenyl group to demonstrate the rich syndiotacticity of their polymer product.

In this work we consider the tetrad patterns observed in the <sup>29</sup>Si NMR spectra of the mixed products of the reaction between octahydrosilsesquioxane (T<sub>8</sub>-H) and different ratio pairs of phenol and selected alkenes in the presence of chloroplatinic acid.

## Results and discussion

To observe and analyse the mixed pendant silsesquioxanes we chose pairs of pendant groups that would give distinctly different NMR environments at silicon, specifically (alkyl-R)SiO<sub>3</sub> (T-silicon) and (aryl-O)SiO<sub>3</sub> (Q-silicon). The 40 ppm difference in the chemical shifts between these silicon environments is large enough to ensure that local electronic differences around the silicon atoms in any particular isomer will not be enough to cause the T and Q regions to overlap. Secondly, the large electronegativity difference between these two arms will ensure that there will be a big disparity between their long-range effects on the <sup>29</sup>Si NMR chemical shifts.

The <sup>29</sup>Si NMR spectra of the reaction products from the reaction of T<sub>8</sub>-H with different molar ratios of phenol and undec-1-ene (T<sub>8</sub>-H – phenol and undec-1-ene, 1:1) are shown in Fig. 1. Only the regions where peaks are found (i.e., the T and Q silicon regions) are shown for clarity.

Within the T silicon region there is a good separation of the silicon environments leading to four main peaks each of which is incompletely resolved into a further tetrad pattern. In the Q silicon region a similar pattern is observed although less pronounced, as its chemical shift range is far narrower and the signal-to-noise ratio is lower than for the T silicon

signals. The relative broadness and simple tetrad pattern we observe in the Q region also suggests that each of the peaks actually comprises an unresolved envelope of peaks and we propose that the same splitting pattern is occurring but that it is not fully visible due to resolution constraints. These practical limitations also mean that making meaningful conclusions on the changing isomer distribution from reactant ratio to reactant ratio is not possible using the Q silicon spectral data.

The <sup>29</sup>Si NMR spectra of the reaction products from the reaction of T<sub>8</sub>-H with different molar ratios of phenol and methyl 3,3-dimethylpent-4-enoate (MDP) (T<sub>8</sub>-H – phenol and MDP, 1:1) are shown in Fig. 2. Only the regions where peaks are found (i.e., the T and Q silicon regions) are shown for clarity. While we have not studied the ratios of α and β addition from the reactions of each alkene (Fig. 3) based on the reports of various groups (5), we would expect that α addition is the mechanism that predominates in each case.

Initial inspection of the T silicon region of the spectrum in Fig. 2 compared to that in Fig. 1 reveals excellent correlation between the two reaction systems and shows that the pattern we observe is not specific to a single reaction. The comments regarding the peak intensity patterns in the undec-1-ene system are equally applicable to these spectra. Similarly the Q-silicon peak pattern is less well resolved than that of the T silicons.

To explain these tetrad patterns we need to focus on one silicon (attached to the group W in Fig. 4) and examine the possible substitution patterns in its neighbours and next-nearest neighbours

In Fig. 4, all silicons attached to an X group (Si<sub>X</sub>) have the same spatial relationship with the silicon Si<sub>W</sub>. Similarly all silicons attached to a Y group (Si<sub>Y</sub>) also have the same spatial relationship with Si<sub>W</sub>. The dependency of the chemical shift of Si<sub>W</sub> on the electronegativity of the pendant groups Si<sub>X</sub>, Si<sub>Y</sub>, and Si<sub>Z</sub> depends primarily on the through-bond distance between them. Assuming there are two types of pendant groups A and B, there are four possible combinations of nearest neighbours (Si<sub>X</sub>) that can surround Si<sub>W</sub>, i.e., (1) AAA, (2) AAB, (3) ABB, (4) BBB.

For combinations 2 and 3, there are three subarrangements that cannot be distinguished by our one-dimensional NMR experiments but each of which is as probable as the next, meaning that combinations 2 or 3 are statistically 3 times more likely than 1 or 4. This will lead to an initial splitting of the Si<sub>W</sub> chemical shift into four peaks with a 1:3:3:1 ratio. In addition to this, for each combination of nearest neighbour pendant groups there are a similar set of four possible combinations of groups for the next-nearest neighbours. As for the nearest neighbours, there are three NMR-indistinguishable variants to combinations AAB and ABB in the next-nearest neighbours leading to a further splitting of the previous Si<sub>W</sub> chemical shifts in the ratio 1:3:3:1. In silicon environment Si<sub>Z</sub> there are two possible variations.

Assuming that A is a more electron-withdrawing pendant group than B, this leads to the overall set of group combinations shown in Table 1 in order of decreasing chemical shift (top to bottom in each column). Each of these combinations gives rise to a unique silicon environment.



Fig. 1. The  $^{29}\text{Si}$  NMR spectra of the mixed products obtained from the reaction of 1 equiv.  $\text{T}_8\text{-H}$  with 1 equiv. of varying proportions of phenol and undec-1-ene.

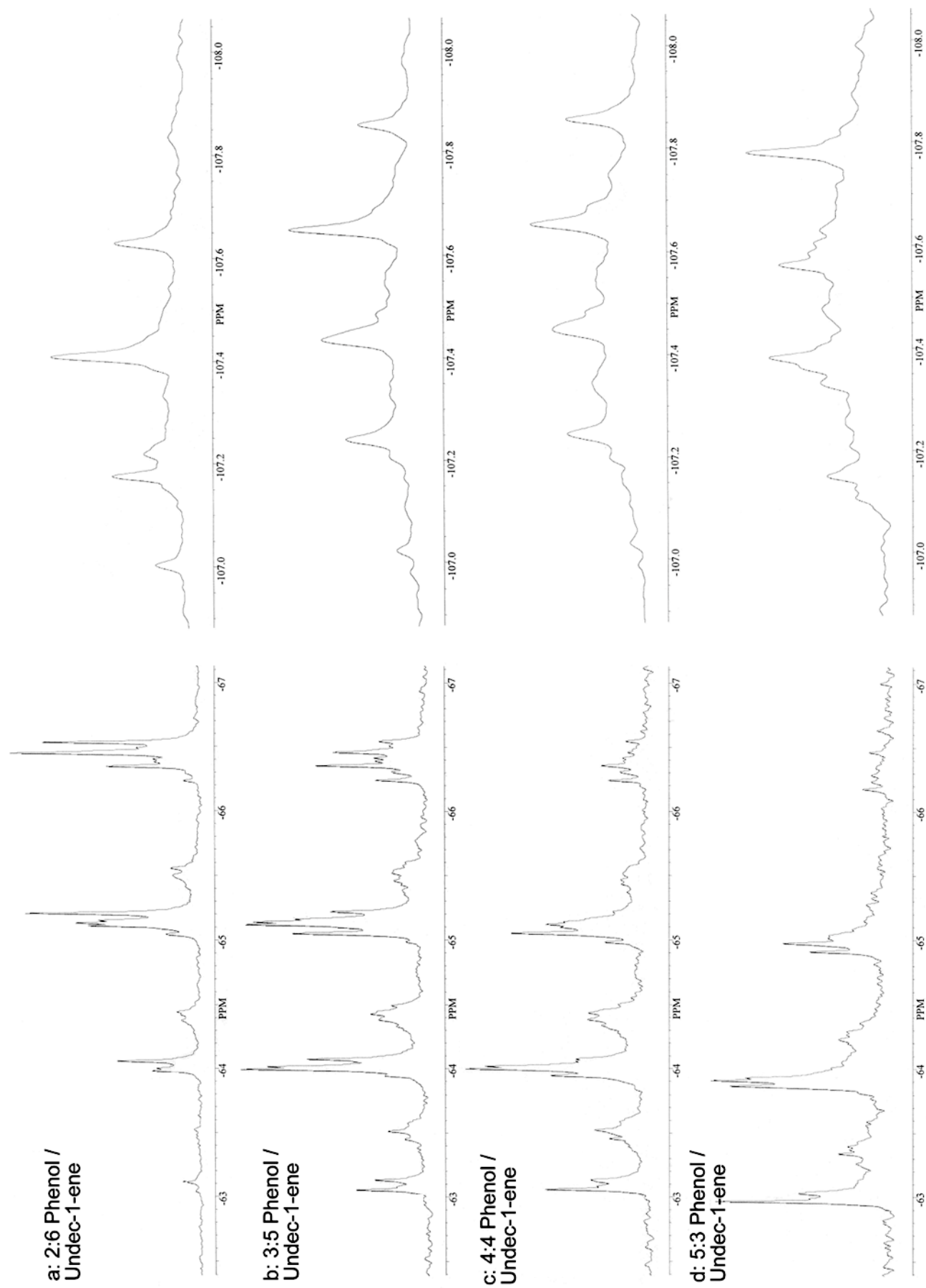
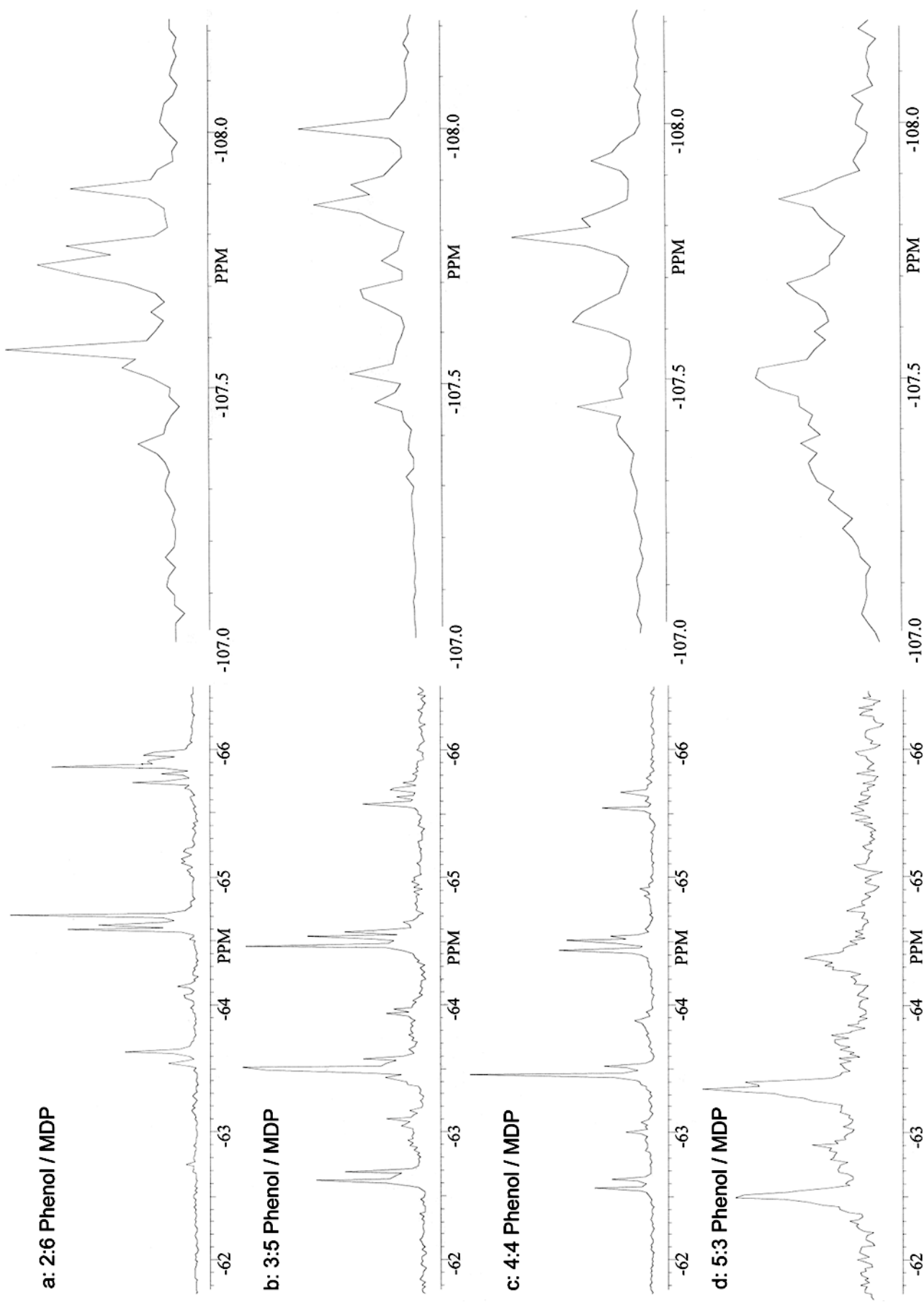


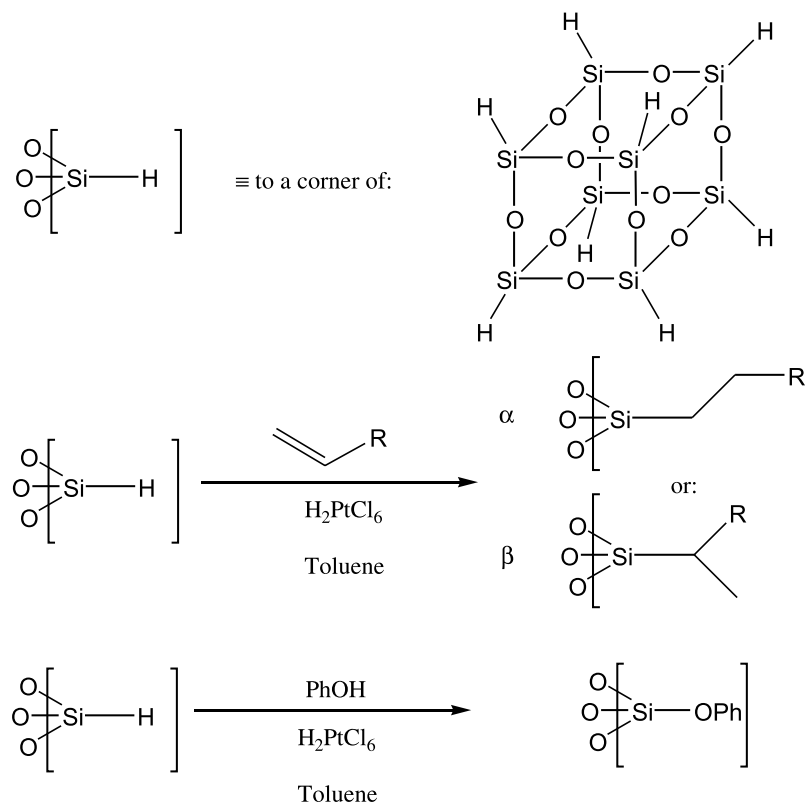


Fig. 2. The  $^{29}\text{Si}$  NMR spectra of the mixed products obtained from the reaction of 1 equiv.  $\text{T}_8\text{-H}$  with 1 equiv. of varying proportions of phenol and MDP.

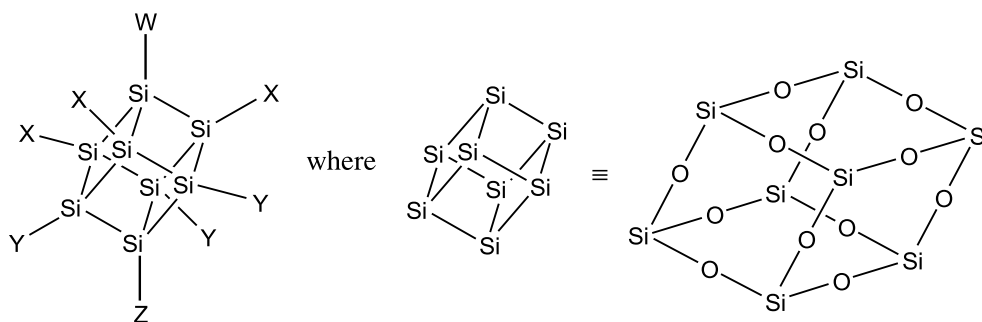




**Fig. 3.** The possible pendant group products of the hydrosilylation reaction of phenol or an alkene with the Si-H group of a T<sub>8</sub>-H cage.



**Fig. 4.** Equivalent positions around a T<sub>8</sub> silsesquioxane cage in relation to the Si—W bond axis.



In practice, the group attached to Si<sub>Z</sub> has such a small and often immeasurable effect on Si<sub>W</sub> that it cannot be easily resolved by <sup>29</sup>Si NMR spectroscopy so that all pairs of combinations “x (xxx) (xxx) A” and “x (xxx) (xxx) B” (where each x is a constant “A” or “B” in both) listed in Table 1 are typically seen to appear as a single unresolved peak. If the sites on the T<sub>8</sub> cage are statistically occupied based on a 4:4 reaction mixture of A and B with no selectivity for one over the other, this leads to the pair of tetrad patterns shown in Fig. 5.

To show that the sequence of chemical shifts for the structures we have proposed is reasonable, we have examined the <sup>29</sup>Si NMR spectra of a number of fully characterized mixed cages made within our group. In the following phenoxy- and cyclohexyl-substituted T<sub>7</sub>Q<sub>1</sub> and T<sub>6</sub>Q<sub>2</sub> cages (Fig. 6), phenoxy is the more electron-withdrawing group and so is equivalent to the generic A group in our previous discussion.

The cyclohexyl B groups occupy the remaining positions not occupied by phenoxy groups. The chemical shifts and corresponding A–B combination sequences of each highlighted silicon are also given.

Moving from left to right, as a second A group is introduced into the cage and then sequentially positioned closer, so the chemical shift of the symmetrically equivalent silicons to which they are attached increases in agreement with theory. It is also worth noting that the biggest single effect on the <sup>29</sup>Si NMR chemical shift is when the A groups are switched from a *meta* to an *ortho* relationship confirming that the influence of the pendant groups is proportional to the distance they are apart.

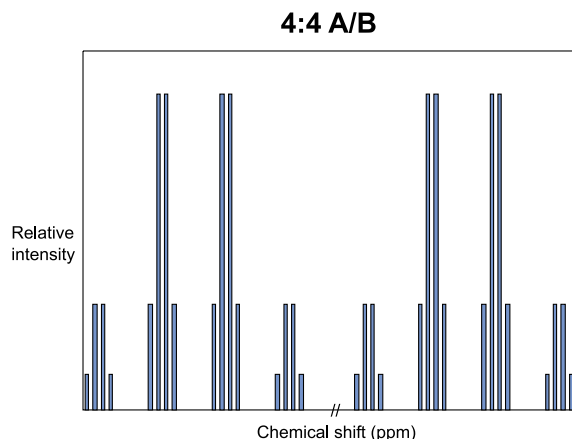
We have also made a number of other *ortho*-T<sub>6</sub>Q<sub>2</sub> cage compounds of the type shown in Fig. 7 where Si<sub>1</sub> and Si<sub>2</sub> represent different, equivalent silicon positions in the cage and each of which has a corresponding A–B pendant group



**Table 1.** A summary of all the possible configurations for mixed T-Q<sub>8</sub> cages containing different numbers of pendant groups A and (or) B in the order Si<sub>W</sub> (Si<sub>X</sub>) (Si<sub>Y</sub>) Si<sub>Z</sub>. The <sup>29</sup>Si NMR chemical shifts for these classes of compound decrease progressively down each column of the table.

For Si <sub>W</sub> -A:	For Si <sub>W</sub> -B:
A (AAA) (AAA) A	B (AAA) (AAA) A
A (AAA) (AAA) B	B (AAA) (AAA) B
A (AAA) (AAB or ABA or BAA) A	B (AAA) (AAB or ABA or BAA) A
A (AAA) (AAB or ABA or BAA) B	B (AAA) (AAB or ABA or BAA) B
A (AAA) (ABB or BAB or BBA) A	B (AAA) (ABB or BAB or BBA) A
A (AAA) (ABB or BAB or BBA) B	B (AAA) (ABB or BAB or BBA) B
A (AAA) (BBB) A	B (AAA) (BBB) A
A (AAA) (BBB) B	B (AAA) (BBB) B
A (AAB or ABA or BAA) (AAA) A	B (AAB or ABA or BAA) (AAA) A
A (AAB or ABA or BAA) (AAA) B	B (AAB or ABA or BAA) (AAA) B
A (AAB or ABA or BAA) (AAB or ABA or BAA) A	B (AAB or ABA or BAA) (AAB or ABA or BAA) A
A (AAB or ABA or BAA) (AAB or ABA or BAA) B	B (AAB or ABA or BAA) (AAB or ABA or BAA) B
A (AAB or ABA or BAA) (ABB or BAB or BBA) A	B (AAB or ABA or BAA) (ABB or BAB or BBA) A
A (AAB or ABA or BAA) (ABB or BAB or BBA) B	B (AAB or ABA or BAA) (ABB or BAB or BBA) B
A (AAB or ABA or BAA) (BBB) A	B (AAB or ABA or BAA) (BBB) A
A (AAB or ABA or BAA) (BBB) B	B (AAB or ABA or BAA) (BBB) B
A (ABB or BBA or BAB) (AAA) A	B (ABB or BAB or BBA) (AAA) A
A (ABB or BBA or BAB) (AAA) B	B (ABB or BAB or BBA) (AAA) B
A (ABB or BBA or BAB) (AAB or ABA or BAA) A	B (ABB or BAB or BBA) (AAB or ABA or BAA) A
A (ABB or BBA or BAB) (AAB or ABA or BAA) B	B (ABB or BAB or BBA) (AAB or ABA or BAA) B
A (ABB or BBA or BAB) (ABB or BAB or BBA) A	B (ABB or BAB or BBA) (ABB or BAB or BBA) A
A (ABB or BBA or BAB) (ABB or BAB or BBA) B	B (ABB or BAB or BBA) (ABB or BAB or BBA) B
A (ABB or BBA or BAB) (BBB) A	B (ABB or BAB or BBA) (BBB) A
A (ABB or BBA or BAB) (BBB) B	B (ABB or BAB or BBA) (BBB) B
A (BBB) (AAA) A	B (BBB) (AAA) A
A (BBB) (AAA) B	B (BBB) (AAA) B
A (BBB) (AAB or ABA or BAA) A	B (BBB) (AAB or ABA or BAA) A
A (BBB) (AAB or ABA or BAA) B	B (BBB) (AAB or ABA or BAA) B
A (BBB) (ABB or BAB or BBA) A	B (BBB) (ABB or BAB or BBA) A
A (BBB) (ABB or BAB or BBA) B	B (BBB) (ABB or BAB or BBA) B
A (BBB) (BBB) A	B (BBB) (BBB) A
A (BBB) (BBB) B	B (BBB) (BBB) B

**Fig. 5.** The <sup>29</sup>Si NMR chemical shift tetrad pair pattern predicted for the reaction of 1 equiv. of T<sub>8</sub>-H with a 1 equiv. of a 4:4 mixture of pendant groups A and B on the basis of there being no regioselectivity.



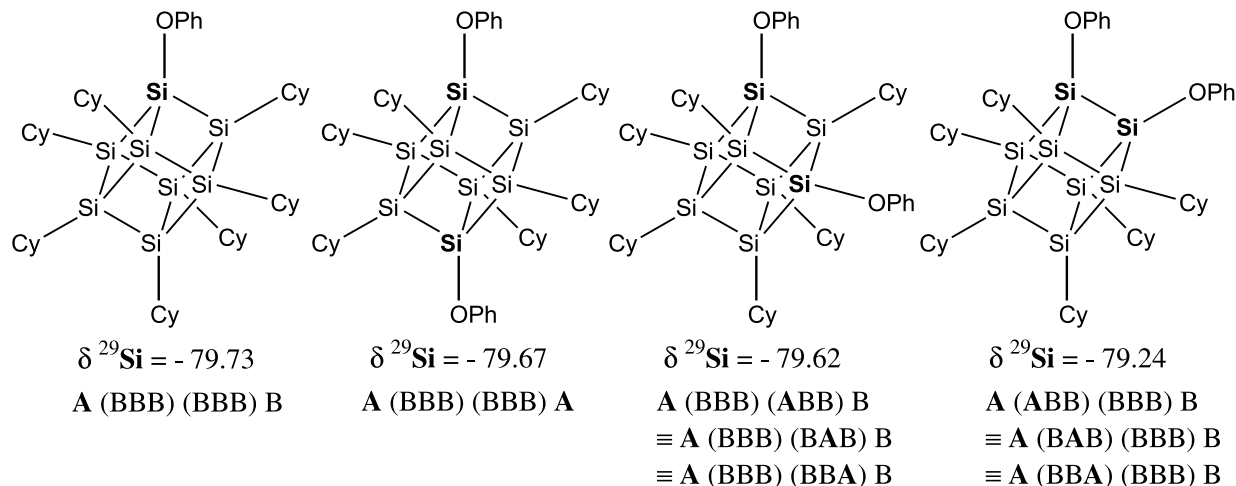
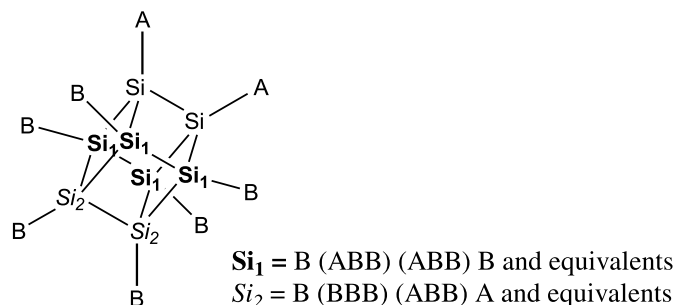
neighbour and next-nearest neighbour combination. Their <sup>29</sup>Si NMR chemical shift data are displayed in Table 2. In each example, the Si<sub>1</sub> sites are closer to the electron-

withdrawing A groups than the Si<sub>2</sub> sites, and hence, have the more downfield chemical shift.

Whilst the characteristic tetrad pattern is clearly observed in Figs. 1 and 2, the intensity ratios do not match that expected for a statistical distribution, suggesting the presence of regioselectivity that favours particular substitution patterns. These octa-substituted T-Q<sub>8</sub> cages are prepared by adding the pendant arms in a sequential manner. It is likely that one arm, for example A, may react faster than the other, B, and that once attached it may lead to the next arm (again more likely to be A) going into a specific position. This will lead to particular patterns of arm substitution with A or B being the preferred neighbour and (or) next-nearest neighbour.

To model the outcome of regioselectivity on the <sup>29</sup>Si NMR chemical shift peak pattern, we have designed a mathematical model to allow for nonstatistical distribution in the neighbours and next-nearest neighbours and calculate the relative peak intensities in the spectra for any given A-B reactant ratio. By introducing a large selectivity for B groups as neighbours to an A group and A groups as neighbours to a B group (so the A-B arrangement is arbitrarily about 9 times more likely than the A-A arrangement), the tetrad pat-

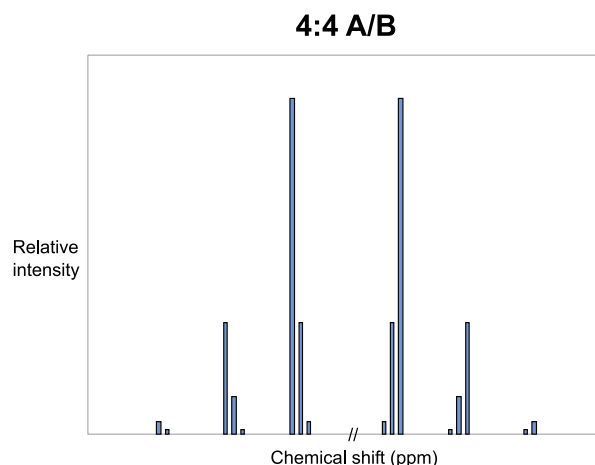


**Fig. 6.** A comparison of the Q-silicon  $^{29}\text{Si}$  NMR chemical shifts in various  $\text{T}_7\text{-Q}_1$  and  $\text{T}_6\text{-Q}_2$  silsesquioxane cage compounds.**Fig. 7.** Equivalent silicon positions around an *ortho*- $\text{T}_6\text{-Q}_2$  silsesquioxane cage.**Table 2.** A summary of  $^{29}\text{Si}$  NMR chemical shift data (ppm) for various *ortho*- $\text{T}_6\text{-Q}_2$  di-substituted silsesquioxane cage compounds.

Pendant group		$^{29}\text{Si}$ NMR chemical shift (ppm)	
A	B	$\text{Si}_1$	$\text{Si}_2$
Ph	Cy	-68.10	-68.51
Ph	Cp	-65.98	-66.33
$\text{OSiMe}_3$	Cy	-68.05	-68.62
$\text{OSiMe}_2\text{CH=CH}_2$	Cy	-68.03	-68.62
$\text{OSiMe}_2\text{CH}_2\text{CH}_2\text{Si(OEt)}_3$	Cp	-65.91	-66.40

tern for a 4:4 mixture of A and B as reagents (Fig. 8) favours those regiomers where this preference is exercised and in particular the combinations A (BBB) (AAA) B and B (AAA) (BBB) A which give rise to the equal highest peaks in the distribution. A number of combinations are particularly unfavoured and their small peaks are not visible on this relative intensity scale.

By making an adjustment to the selectivity factor in our spectrum modelling equation to slightly favour A and B groups residing adjacent to each other (so the A-B arrangement is about 1.5 times more likely than the A-A arrangement), we obtain a peak distribution for  $\text{Si}_W\text{-B}$  silicons similar to that for the T silicon region in Fig. 1 or 2 at the reagent ratio 4:4. This would be in agreement with one reagent reacting faster than the other avoiding the *ortho* ar-

**Fig. 8.** The  $^{29}\text{Si}$  NMR chemical shift tetrad pair pattern predicted for the reaction of 1 equiv. of  $\text{T}_8\text{-H}$  with a 1 equiv. of a 4:4 mixture of pendant groups A and B on the selectivity basis of an adjacent A-B arrangement being about 9 times more likely than an adjacent A-A arrangement.

angement and these positions are then filled by the remaining reagent. Using the same selectivity factors, T-silicon peak intensity patterns for the other reagent mixtures can be obtained. In each case there is a strong resemblance between the predicted (Fig. 9) and obtained (Fig. 1 or 2) peak patterns.

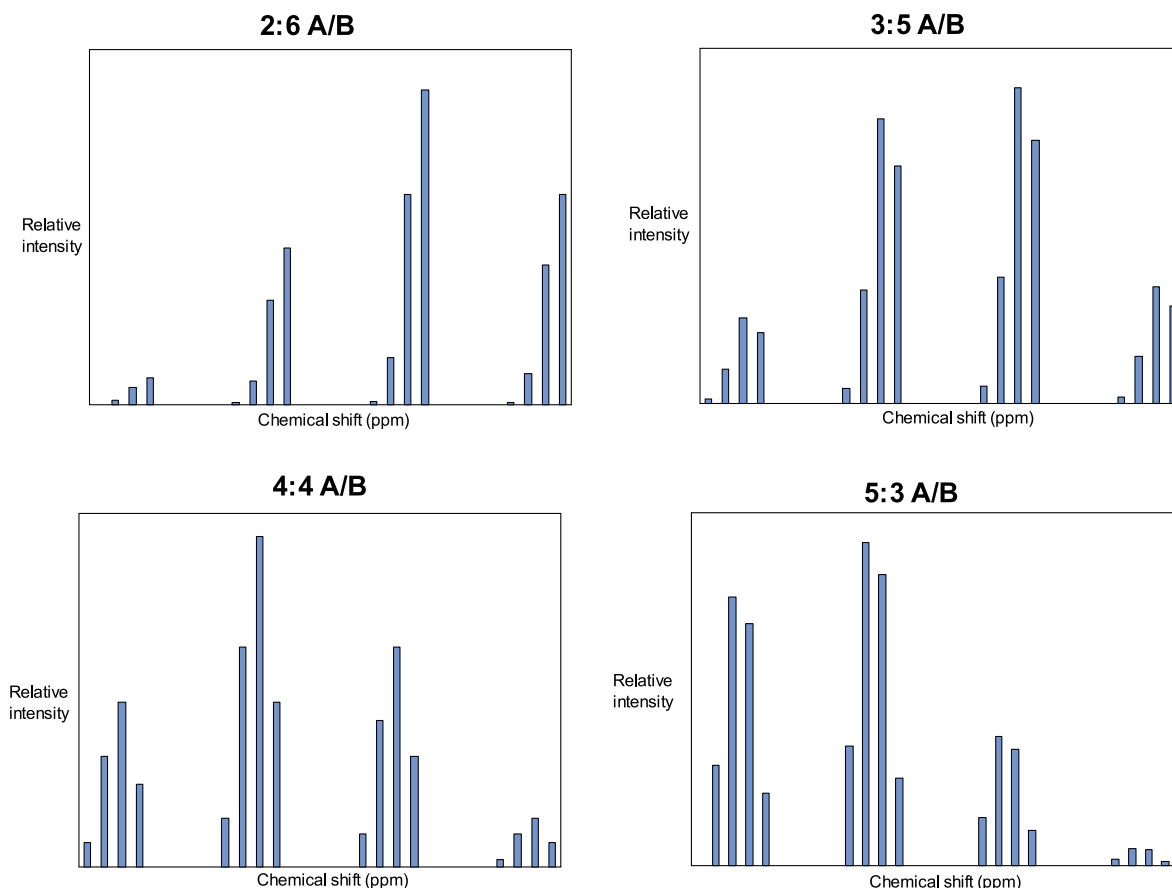
Qualitatively, we have demonstrated a relationship among pendant group selectivity ratios and chemical shift peak intensity patterns in the  $^{29}\text{Si}$  NMR spectra. We are currently undertaking quantitative studies on this reaction system with the aim of using these reproducible patterns to obtain selectivity information directly from spectral data.

## Experimental

Reactions to prepare the mixed-cage  $\text{T}_8$  compounds for NMR analysis were performed using the well-reported hydrosilylation route (5). Though thorough methods were used to eradicate moisture from our reactions such as by predrying our solvents, the presence of small traces of mois-



**Fig. 9.** The T-silicon  $^{29}\text{Si}$  NMR chemical shift tetrad patterns predicted for the reaction of 1 equiv. of  $\text{T}_8\text{-H}$  with 1 equiv. of various ratios of pendant groups A and B on the selectivity basis of an adjacent A-B arrangement being about 1.5 times more likely than an adjacent A-A arrangement.



ture in the reaction pot cannot be ruled out. Careful control over the quantities and ratios of  $\text{T}_8\text{-H}$ , alkene, and phenol were used to minimize their residual appearance at the end of reactions.

In a typical reaction,  $\text{T}_8\text{-H}$  (0.400 g, 0.94 mmol), a phenol-alkene mixture (0.94 mmol), and 10  $\mu\text{L}$  of a 0.02 mol/L solution of chloroplatinic acid in isopropyl alcohol were dissolved in dried toluene (5  $\text{cm}^3$ ) in a small vial. The phenol-alkene mixture matched the particular molar ratio required in each reaction (i.e., 2:6, 3:5, 4:4, or 5:3).

The mixture was stirred and heated to 60  $^\circ\text{C}$  while being monitored by IR spectroscopy. The reaction was stopped upon the disappearance of the Si-H peak at 2156  $\text{cm}^{-1}$  and the solvent removed by rotary evaporation to yield the product mixture as a white solid (ca. 0.5 g).  $^{29}\text{Si}$  NMR chemical shift measurements on a deuteriochloroform solution of this material was performed using a Jeol EX400 NMR spectrometer set to a pulse delay of 20 s. No further characterization or purification of the compound mixture was carried out.

## Conclusions

We have demonstrated that  $^{29}\text{Si}$  NMR spectroscopy can be used to analyse the mixed products of  $\text{T-Q}_8$  cage preparations with two different types of pendant group. Without having to perform a difficult separation, the nature of the mixed-cage isomers can be judged from the relatively simple

and reproducible tetrad peak pattern. We have been able to observe different product mixtures by using different proportions of pendant groups and relate the changes in their molar ratio directly to the changes in the tetrad patterns.

In particular, we found that it was important to use pairs of pendant groups that gave rise to distinct silicon environments well-separated on the NMR chemical shift scale to ensure the peak pattern was well-resolved. In the case of the T silicons in our mixed, substituted  $\text{Q-T}_8$  compounds, good separation and distinctive tetrad patterns were observed in both reaction systems studied. However, for the Q silicons, although elements of a tetrad pattern were observed, the chemical shift range was far narrower, meaning that much of the fine structure was unresolved in broadened peaks.

Since the analysis we are undertaking relates to the silicons in the cage, so long as the pairs of pendant groups chosen are suitably different in their effect on the silicon NMR environment then the nature of the pendant groups themselves is not important for the success of the analysis. By modelling the peak intensity ratios, we have demonstrated how selectivity may affect the  $^{29}\text{Si}$  NMR spectrum and observed patterns within our acquired data that suggest some mild selectivity is being exercised in the reaction systems we have studied.

While we have demonstrated the application of this type of  $^{29}\text{Si}$  NMR technique to silsesquioxane cage structures it is clear that the same methodology could have wider use in



other mixed compound systems such as in the analysis of mixed T–Q resins.

## References

1. A.J. Barry, W.H. Daudt, J.J. Domicons, and J.W. Gilkey. *J. Am. Chem. Soc.* **77**, 4248 (1955).
2. T.N. Martynova, V.P. Korchkov, and P.P. Semyannikov. *J. Organometal. Chem.* **258**, 277 (1983).
3. F.J. Feher and T.A. Budzichowski. *J. Organometal. Chem.* **379**, 33 (1989).
4. R. Muller, R. Kohne, and S. Sliwinski. *J. Prakt. Chem.* **9**, 71 (1959).
5. (a) U. Dittmar, B.J. Hendan, and U. Florke. H.C. Marsmann. *J. Organomet. Chem.* **489**, 185 (1995); (b) A.R. Bassindale and T.E. Gentle, *J. Mater. Chem.* **12**, 1319 (1993); (c) F.J. Feher and K.D. Wyndham. *J. Chem. Soc. Chem. Commun.* 323 (1998).
6. R. Duchateau, H.C.L. Abbenhuis, R.A. van Santen, A. Meetsma, S.K.-H. Thiele, and M.F.H. van Tol. *Organometallics*, **17**, 5663 (1998).
7. F.J. Feher, K.J. Weller, and J.J. Schwab. *Organometallics*, **14**, 2009 (1995).
8. E.A. Rebrov, N.A. Tebeneva, A.M. Mouzafarov, Yu. E. Ovchinnikov, Yu. T. Struchkov, and T.V. Strekova. *Russ. Chem. Bull.* **44**, 1286 (1995).
9. M.A. Said, H.W. Roesky, C. Rennekamp, M. Andruh, H.-G. Schmidt, and M. Noltemeyer. *Angew. Chem. Int. Ed.* **38**, 661 (1999).
10. (a) M.T. Zell, B.E. Padden, A.J. Paterick, K.A.M. Thakur, R.T. Kean, M.A. Hillmyer, and E.J. Munson. *Macromolecules*, **35**, 7700 (2002); (b) A. Kararali, P. Dais, E. Mikros, and F. Heatley. *Macromolecules*, **34**, 5547 (2001).
11. L. Li and P.L. Rinaldi. *Macromolecules*, **30**, 520 (1997).
12. M. Oshi, J.-Y. Moon, W. Janvikaal, and Y. Kawakami. *Polym. Int.* **50**, 135 (2001).



# Synthesis, structure, and reactivity of hydridobis(silylene)ruthenium(IV)-xantsil complexes (xantsil = (9,9-dimethylxanthene-4,5-diyl)bis(dimethylsilyl)) — A stabilized form of key intermediates in the catalytic oligomerization–deoligomerization of hydrosilanes<sup>1</sup>

Masaaki Okazaki, Jim Josephus Gabrillo Minglana, Nobukazu Yamahira, Hiromi Tobita, and Hiroshi Ogino

**Abstract:** Ru{ $\kappa^2(Si,Si)$ -xantsil}(CO)( $\eta^6$ -C<sub>6</sub>H<sub>5</sub>CH<sub>3</sub>) (**1**) was found to be a catalyst for oligomerization–deoligomerization of HSiMe<sub>2</sub>SiMe<sub>3</sub> to give H(SiMe<sub>2</sub>)<sub>n</sub>Me ( $n = 1$ –8 at 90 °C for 2 days). Treatment of **1** with HSiMe<sub>2</sub>SiMe<sub>2</sub>OR (R = Me, *t*-Bu) led to quantitative formation of Ru{ $\kappa^3(O,Si,Si)$ -xantsil}(CO)(H){(SiMe<sub>2</sub>•••O(R)•••SiMe<sub>2</sub>)} (R = Me (**2a**), *t*-Bu (**2b**)), which also worked as a catalyst for oligomerization–deoligomerization of HSiMe<sub>2</sub>SiMe<sub>3</sub>. Based on these experimental results, a mechanism involving silyl(silylene) intermediates was proposed for the oligomerization–deoligomerization of HSiMe<sub>2</sub>SiMe<sub>3</sub>. Complex **2a** reacted with MeOH in toluene-*d*<sub>8</sub> to give Ru{ $\kappa^2(Si,Si)$ -xantsil}(CO)( $\eta^6$ -toluene-*d*<sub>8</sub>) and Me<sub>2</sub>Si(OMe)<sub>2</sub> with evolution of H<sub>2</sub>. Under a CO atmosphere, **2a** was smoothly converted to its CO adduct Ru{ $\kappa^2(Si,Si)$ -xantsil}(CO)<sub>2</sub>(H){(SiMe<sub>2</sub>•••O(Me)•••SiMe<sub>2</sub>)} (**3**).

**Key words:** silylene complex, ruthenium, polysilane, dehydrogenative coupling, oligomerization.

**Résumé :** On a observé que le Ru{ $\kappa^2(Si,Si)$ -xantsil}(CO)( $\eta^6$ -C<sub>6</sub>H<sub>5</sub>CH<sub>3</sub>) (**1**) est un catalyseur pour l'oligomérisation–désoligomérisation du HSiMe<sub>2</sub>SiMe<sub>3</sub> conduisant à la formation de H(SiMe<sub>2</sub>)<sub>n</sub>Me ( $n = 1$ –8, à 90 °C pour deux jours). Le traitement du composé **1** avec du HSiMe<sub>2</sub>SiMe<sub>2</sub>OR (R = Me, *t*-Bu) conduit à la formation quantitative du Ru{ $\kappa^3(O,Si,Si)$ -xantsil}(CO)(H){(SiMe<sub>2</sub>•••O(R)•••SiMe<sub>2</sub>)} (R = Me (**2a**), *t*-Bu (**2b**)) qui peut aussi être utilisé comme catalyseur pour l'oligomérisation–désoligomérisation du HSiMe<sub>2</sub>SiMe<sub>3</sub>. Sur la base de ces résultats expérimentaux, on propose un mécanisme impliquant des intermédiaires silyl(silylènes) pour l'oligomérisation–désoligomérisation du HSiMe<sub>2</sub>SiMe<sub>3</sub>. Le complexe **2a** réagit avec le MeOH dans le toluène-*d*<sub>8</sub> pour donner du Ru{ $\kappa^2(Si,Si)$ -xantsil}(CO)( $\eta^6$ -toluène-*d*<sub>8</sub>) et du Me<sub>2</sub>Si(OMe)<sub>2</sub> avec évolution de H<sub>2</sub>. Sous atmosphère de CO, le composé **2a** est facilement transformé en un adduit avec du CO, Ru{ $\kappa^2(Si,Si)$ -xantsil}(CO)<sub>2</sub>(H){(SiMe<sub>2</sub>•••O(R)•••SiMe<sub>2</sub>)} (**3**).

**Mots clés :** complexe de silylène, ruthénium, polysilane, couplage déshydrogénant, oligomérisation.

[Traduit par la Rédaction]

## Introduction

The chemistry of transition-metal silyl complexes is a continuously growing field and an area of active research over the past few decades (1). They have been found as key intermediates in the metal-mediated catalytic transformation reactions of organosilicon compounds (1, 2). However, studies on silyl complexes have mostly focused on the reactivity

of the metal–silicon bonds which participate in the catalytic pathways (3) and only little attention has been paid to the possibility of silyl groups as ancillary ligands. Taking account of its strongly electron-releasing ability and exceptionally high trans influence (4), the silyl groups could work as an excellent ancillary ligand that generates an electron-rich and coordinatively unsaturated metal center (5, 6). Usual metal–silicon bonds are, however, highly reactive, and the

Received 26 May 2003. Published on the NRC Research Press Web site at <http://canjchem.nrc.ca> on 27 October 2003.

M. Okazaki, J.J.G. Minglana,<sup>2</sup> N. Yamahira, H. Tobita,<sup>3</sup> and H. Ogino.<sup>4,5</sup> Department of Chemistry, Graduate School of Science, Tohoku University, Sendai 980-8578, Japan.

<sup>1</sup>This article is part of a Special Issue dedicated to Professor John Harrod.

<sup>2</sup>Present address: Institute of Chemistry, University of the Philippines, Diliman, Quezon City 1101, Philippines.

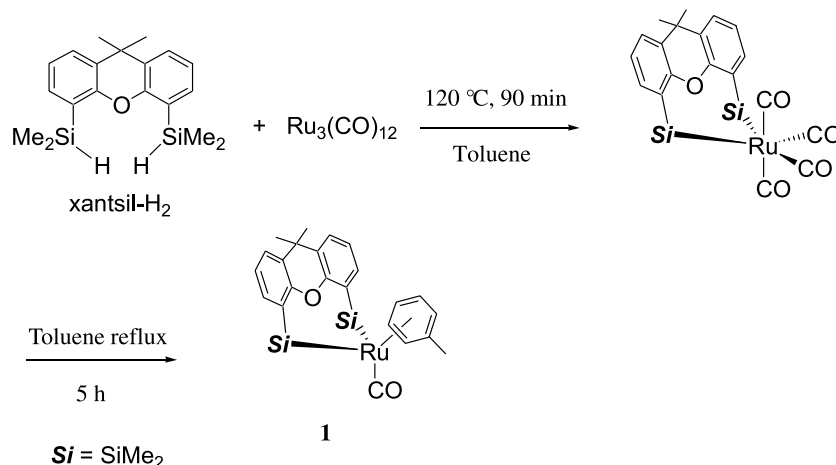
<sup>3</sup>Corresponding author (e-mail: [tobita@mail.tains.tohoku.ac.jp](mailto:tobita@mail.tains.tohoku.ac.jp)).

<sup>4</sup>Corresponding author (e-mail: [ogino@agnus.chem.tohoku.ac.jp](mailto:ogino@agnus.chem.tohoku.ac.jp)).

<sup>5</sup>Present address: Miyagi Study Center, The University of the Air, Sendai 980-8577, Japan.



Scheme 1.



rich chemistry of transition-metal silyl complexes is derived from this reactivity (1). In most cases, the silyl ligands are lost from the metals as a result of reductive elimination, migratory insertion, nucleophilic substitution, and so on. To avoid this drawback of silyl ligands, we designed a new type of bis(silyl) bidentate ligand “xantsil” (7). Thermolysis of  $\text{Ru}_3(\text{CO})_{12}$  and 4,5-bis(dimethylsilyl)-9,9-dimethylxanthene ( $\text{xantsil-H}_2$ ) at 120 °C afforded  $\text{Ru}\{\kappa^2(\text{Si},\text{Si})\text{-xantsil}\}(\text{CO})_4$  in which three carbonyl ligands can be further replaced with a  $\eta^6$ -toluene ligand on reflux in toluene to give  $\text{Ru}\{\kappa^2(\text{Si},\text{Si})\text{-xantsil}\}(\text{CO})(\eta^6\text{-C}_6\text{H}_5\text{CH}_3)$  (**1**) (Scheme 1). Complex **1** undergoes an extremely facile exchange of the toluene ligand for a free arene, indicating that **1** can formally become a source of either 12- or 14-electron, coordinatively unsaturated species (**I** or **II**), depending on the coordination mode of the xantsil ligand (Scheme 2). We report here the catalytic performance of **1** toward oligomerization–deoligomerization of  $\text{HSiMe}_2\text{SiMe}_3$  to give  $\text{H}(\text{SiMe}_2)_n\text{Me}$  ( $n = 1\text{--}8$ ). We also describe the isolation and reactivity of the stabilized form of a silyl(silylene) complex, which can be considered as a key intermediate in the catalytic reaction. A part of this work has been communicated previously (7b).

## Experimental section

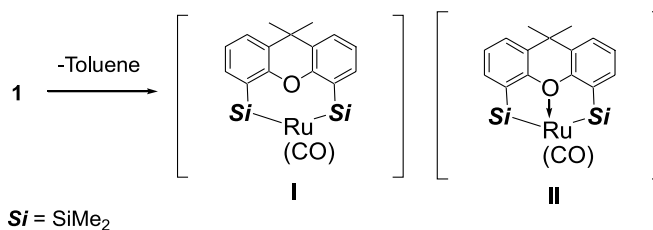
### General methods

Infrared spectra were obtained on a Horiba FT-730 spectrometer. NMR spectra were recorded on Bruker ARX-300 and AVANCE-300 instruments. Mass spectra were obtained on JEOL-HX110 and Hitachi M-2500S instruments operating in the EI mode. All reactions were performed under a dry nitrogen atmosphere using deoxygenated solvents dried with appropriate reagents. The organosilicon compounds *p*-Tol<sub>2</sub>SiH<sub>2</sub> (8),  $\text{HSiMe}_2\text{SiMe}_3$  (9), and  $\text{HSiMe}_2\text{SiMe}_2\text{OR}$  ( $\text{R} = \text{Me}$  (10), *t*-Bu (11)) were synthesized according to published procedures. The complex **1** was synthesized by a procedure we previously reported (7a).

### Reaction of **1** with *p*-Tol<sub>2</sub>SiH<sub>2</sub>

A Pyrex NMR tube (5 mm o.d.) was charged with **1** (5.0 mg, 0.00916 mmol) and was then attached to a vacuum line. *p*-Tol<sub>2</sub>SiH<sub>2</sub> (19.5 mg, 0.00916 mmol) and chloroform-*d* (0.4 mL) were trap-to-trap transferred into it. The NMR tube

Scheme 2.



was flame-sealed and the reaction was monitored by  $^1\text{H}$  NMR spectroscopy. The sample was heated at 60 °C for 3 h and a red solution was obtained. The  $^1\text{H}$  NMR spectral data showed that **1** was completely consumed and free toluene and  $\text{xantsil-H}_2$  were formed as the major products. Unidentified signals can also be observed but their signals are of low intensities.

### Oligomerization–deoligomerization of $\text{HSiMe}_2\text{SiMe}_3$ in the presence of **1**

#### (a) NMR scale monitoring of the reaction

A Pyrex NMR tube (5 mm o.d.) was charged with **1** (13.4 mg, 0.0246 mmol) and was then attached to a vacuum line.  $\text{HSiMe}_2\text{SiMe}_3$  (65.0 mg, 0.492 mmol) and dichloromethane-*d*<sub>2</sub> (800  $\mu\text{L}$ ) were trap-to-trap transferred into it. The NMR tube was flame-sealed and the reaction was monitored by  $^1\text{H}$  NMR spectroscopy. At room temperature, the solution turned yellow in color and several signals corresponding to oligomerization–deoligomerization products  $\text{H}(\text{SiMe}_2)_n\text{Me}$  appeared. No further changes were observed after 40 h at room temperature.

#### (b) GC and GC–MS monitoring of the reaction with a catalytic amount of **1**

$\text{HSiMe}_2\text{SiMe}_3$  (65.0 mg, 0.49 mmol), *n*-decane (10.0  $\mu\text{L}$  as an internal standard), and **1** (270  $\mu\text{g}$ , 0.1 mol%) were placed in a 5 mL flask and the solution was stirred at room temperature for 2 days. The reaction was monitored by gas chromatography. Formation of  $\text{H}(\text{SiMe}_2)_n\text{Me}$  in the molar ratio of 81 ( $n = 1$ ) : 56 ( $n = 2$ ) : 11 ( $n = 3$ ) : 3 ( $n = 4$ ) : 1 ( $n = 5$ ) was observed based on the peak areas of the gas chromatogram. The products were confirmed by GC–MS.



When the same reaction was performed at 90 °C for 2 days, formation of products with  $n$  of up to 8 were observed in the molar ratio of 346 ( $n = 1$ ) : 96 ( $n = 2$ ) : 83 ( $n = 3$ ) : 64 ( $n = 4$ ) : 35 ( $n = 5$ ) : 13 ( $n = 6$ ) : 4 ( $n = 7$ ) : 1 ( $n = 8$ ). These silicon-containing products were not isolated.

#### Synthesis of $\text{Ru}\{\kappa^3(\text{O},\text{Si},\text{Si})\text{-xantsil}\}(\text{CO})(\text{H})\{(\text{SiMe}_2\cdots\text{O}(\text{Me})\cdots\text{SiMe}_2)\}$ (**2a**)

$\text{HSiMe}_2\text{SiMe}_2\text{OMe}$  (81.0 mg, 0.546 mmol) was added to a solution of **1** (150 mg, 0.275 mmol) in  $\text{CH}_2\text{Cl}_2$  (2.0 mL). After 90 min of stirring at room temperature, volatiles were removed under reduced pressure to give a pale yellow solid. Washing the solid with hexane three times afforded a colorless solid that was characterized as  $\text{Ru}\{\kappa^3(\text{O},\text{Si},\text{Si})\text{-xantsil}\}(\text{CO})(\text{H})\{(\text{SiMe}_2\cdots\text{O}(\text{Me})\cdots\text{SiMe}_2)\}$  (**2a**). Yield: 160 mg, 98%. MS (EI, 70 eV)  $m/z$ : 602 ( $\text{M}^+$ , 72), 512 ( $\text{M}^+ - \text{HMe}_2\text{SiOMe}$ , 79), 480 (100). Anal. calcd. for  $\text{C}_{25}\text{H}_{40}\text{RuO}_3\text{Si}_4$ : C 49.88, H 6.70; found: C 49.79, H 6.67.

#### Synthesis of $\text{Ru}\{\kappa^3(\text{O},\text{Si},\text{Si})\text{-xantsil}\}(\text{CO})(\text{H})\{(\text{SiMe}_2\cdots\text{O}(t\text{-Bu})\cdots\text{SiMe}_2)\}$ (**2b**)

$\text{HSiMe}_2\text{SiMe}_2\text{O}-t\text{-Bu}$  (35.0 mg, 0.184 mmol) was added to a solution of **1** (50.0 mg, 0.0916 mmol) in  $\text{CH}_2\text{Cl}_2$  (1.0 mL). After 90 min of stirring at room temperature, the reaction mixture was treated similarly as described for the synthesis of **2a** to afford **2b** as a colorless solid. Yield: 50.0 mg, 84%. MS (EI, 70 eV)  $m/z$ : 587 ( $\text{M}^+ - t\text{-Bu}$ , 26), 513 ( $\text{M}^+ - t\text{-Bu-SiMe}_2\text{O}$ , 41), 325 (100). Anal. calcd. for  $\text{C}_{28}\text{H}_{46}\text{RuO}_3\text{Si}_4$ : C 52.21, H 7.20; found: C 51.71, H 7.16.

#### Oligomerization–deoligomerization of $\text{HSiMe}_2\text{SiMe}_3$ in the presence of **2a**

A Pyrex tube (7 mm o.d.) was charged with **2a** (10 mg, 0.017 mmol),  $\text{HSiMe}_2\text{SiMe}_3$  (44 mg, 0.33 mmol), and decane (10  $\mu\text{L}$ ) and was connected to the vacuum line. The tube was flame-sealed under vacuum and placed in the oil bath at 90 °C. After heating for 2 days, the tube was unsealed in the glovebox. Formation of  $\text{H}(\text{SiMe}_2)_n\text{Me}$  with the molar ratio of 12 ( $n = 1$ ) : 6 ( $n = 2$ ) : 5 ( $n = 3$ ) : 5 ( $n = 4$ ) : 4 ( $n = 5$ ) : 2 ( $n = 6$ ) : 3 ( $n = 7$ ) : 1 ( $n = 8$ ) was observed based on the peak areas of the gas chromatogram. These organosilicon compounds were not isolated.

#### Reaction of **2a** with MeOH in toluene- $d_8$

A Pyrex NMR tube (5 mm o.d.) was charged with **2a** (5.0 mg, 0.0083 mmol) and was then attached to a vacuum line. Toluene- $d_8$  (0.4 mL) and MeOH (6.7 mL, 0.17 mmol) were trap-to-trap transferred into it. The NMR tube was flame-sealed and the reaction was monitored by  $^1\text{H}$  and  $^{29}\text{Si}$  NMR spectroscopy. Within 1 h at room temperature, the signals of **2a** were cleanly replaced by those of  $\text{Ru}\{\kappa^2(\text{Si},\text{Si})\text{-xantsil}\}(\text{CO})(\eta^6\text{-toluene-}d_8)$  (**1-d<sub>8</sub>**) and  $\text{Me}_2\text{Si}(\text{OMe})_2$ . NMR spectroscopic data of **1** were used to identify **1-d<sub>8</sub>** while an authentic sample matched the NMR and GC data for  $\text{Me}_2\text{Si}(\text{OMe})_2$ . A singlet signal corresponding to  $\text{H}_2$  was ob-

served at  $\delta$  4.51. In this experiment, the products were not isolated.

#### Reaction of **2a** with CO

A Schlenk tube was charged with **2a** (75 mg, 0.13 mmol) and toluene (12 mL). The solution was degassed by freeze–pump–thaw cycles and filled with CO introduced from a balloon. The procedure was repeated five times. After stirring the solution at room temperature for 16 h, volatiles were removed in vacuo. The yellow residue was washed with hexane to afford  $\text{Ru}\{\kappa^2(\text{Si},\text{Si})\text{-xantsil}\}(\text{CO})_2\{(\text{SiMe}_2\cdots\text{O}(\text{Me})\cdots\text{SiMe}_2)\}$  (**3**) as a white solid. Yield: 67 mg, 85%. IR (KBr pellet,  $\text{cm}^{-1}$ ): 1954 (v ( $\text{CO}_{\text{asym}}$ )). MS (FAB)  $m/z$ : 630 ( $\text{M}^+$ , 17), 602 ( $\text{M}^+ - \text{CO}$ , 24), 512 ( $\text{M}^+ - \text{CO} - \text{SiMe}_2\text{OMe}$ , 64).  $^1\text{H}$  NMR (300 MHz,  $\text{C}_6\text{D}_6$ )  $\delta$ : –3.81 (s, 1H, RuH), 0.40 (s, 12H, SiMe), 1.05 (s, 12H, SiMe), 1.51 (s, 6H,  $\text{CMe}_2$ ), 2.33 (s, 3H, OMe), 7.16 (t,  $^3J = 7.4$  Hz, 2H, Ar), 7.29 (dd,  $^3J = 7.4$  Hz,  $^4J = 1.6$  Hz, 2H, Ar), 7.56 (dd,  $^3J = 7.4$  Hz,  $^4J = 1.6$  Hz, 2H, Ar).  $^{13}\text{C}$  NMR (75.5 MHz,  $\text{C}_6\text{D}_6$ )  $\delta$ : 6.3, 9.8 (SiMe), 27.3 ( $\text{CMe}_2$ ), 36.3 ( $\text{CMe}_2$ ), 51.4 (OMe), 123.4, 124.9, 131.0, 133.2, 134.6, 160.1 (Ar), 202.2 (CO).  $^{29}\text{Si}$  NMR ( $\text{C}_6\text{D}_6$ )  $\delta$ : –8.7 (xantsil), 97.3 (silylene). Anal. calcd. for  $\text{C}_{26}\text{H}_{40}\text{RuO}_4\text{Si}_4$ : C 49.57, H 6.40; found: C 49.04, H 5.98.

#### X-ray crystal structure determination of **2b** and **3**

Intensity data for X-ray crystal structure analysis were collected at 150 K on a Rigaku RAXIS-RAPID Imaging Plate diffractometer with graphite-monochromated Mo  $\text{K}\alpha$  radiation. A total of 44 images, corresponding to 220.0° oscillation angles, were collected with two different goniometer settings. Exposure time was 0.30 min for **2b** and 2.00 min for **3** per degree. Readout was performed in the 0.100 mm pixel mode. Numerical absorption corrections were applied on each crystal shape. The structures were solved by Patterson methods (PATTY) and refined by the least-squares technique. All non-hydrogen atoms were located and refined anisotropically. An atomic coordinate of a hydrogen atom connected to Ru in **3** was determined by the difference Fourier synthesis and refined isotropically. Other hydrogen atoms were placed at their geometrically calculated positions. Data reduction and refinement were performed using teXsan software packages. Crystallographic data of **2b** and **3** are listed in Table 1.<sup>6</sup>

## Results and discussion

#### Reaction of **1** with dihydrosilane

It has been reported that transition-metal complexes mediate the dehydrogenative coupling of polyhydrosilanes and (or) redistribution of substituents on silicon atoms (2). The activity of  $\text{Ru}\{\kappa^2(\text{Si},\text{Si})\text{-xantsil}\}(\text{CO})(\eta^6\text{-toluene})$  (**1**) toward this reaction was first investigated. When a solution of **1** and excess  $p\text{-Tol}_2\text{SiH}_2$  in  $\text{CDCl}_3$  was heated at 60 °C for 3 h, a red solution containing xantsil- $\text{H}_2$  and toluene as the major

<sup>6</sup>Supplementary data may be purchased from the Directory of Unpublished Data, Document Delivery, CISTI, National Research Council Canada, Ottawa, ON K1A 0S2, Canada ([http://www.nrc.ca/cisti/irm/unpub\\_e.shtml](http://www.nrc.ca/cisti/irm/unpub_e.shtml) for information on ordering electronically). CCDC 210554 (**2b**) and 210555 (**3**) contain the crystallographic data for this manuscript. These data can be obtained, free of charge, via [www.ccdc.cam.ac.uk/conts/retrieving.html](http://www.ccdc.cam.ac.uk/conts/retrieving.html) (or from the Cambridge Crystallographic Data Centre, 12 Union Road, Cambridge CB2 1EZ, U.K.; fax +44 1223 336033; or [deposit@ccdc.cam.ac.uk](mailto:deposit@ccdc.cam.ac.uk)).



**Table 1.** Crystallographic data of **2b** and **3**.

Compound	<b>2b</b>	<b>3</b>
Formula	C <sub>28</sub> H <sub>46</sub> O <sub>3</sub> RuSi <sub>4</sub>	C <sub>26</sub> H <sub>40</sub> O <sub>4</sub> RuSi <sub>4</sub>
Formula weight	644.08	630.01
Crystal system	Monoclinic	Monoclinic
Space group	<i>P</i> 2 <sub>1</sub> (No. 4)	<i>P</i> 2 <sub>1</sub> / <i>n</i> (No. 14)
<i>a</i> (Å)	18.216(3)	10.1538(5)
<i>b</i> (Å)	9.634(1)	17.1435(8)
<i>c</i> (Å)	19.327(2)	18.0994(8)
β (°)	109.647(6)	93.999(3)
<i>V</i> (Å <sup>3</sup> )	3194.2(7)	3142.9(2)
<i>Z</i>	4	4
<i>D</i> <sub>calcd.</sub> (g cm <sup>-3</sup> )	1.339	1.331
<i>D</i> <sub>observed</sub> (g cm <sup>-3</sup> )	Not measured	Not measured
μ (Mo Kα) (cm <sup>-1</sup> )	6.67	6.79
Crystal size (mm)	0.10 × 0.10 × 0.10	0.20 × 0.20 × 0.10
Radiation	Mo Kα (λ = 0.71069 Å)	Mo Kα (λ = 0.71069 Å)
Monochromator	Graphite	Graphite
<i>T</i> (°C)	−123	−123
2θ Range (°)	2.2–55.0	3.3–55.0
No. of reflections measured	23 418	25 522
No. of unique data	7668 ( <i>R</i> <sub>int</sub> = 0.066)	7157 ( <i>R</i> <sub>int</sub> = 0.052)
No. of parameters refined	650	320
<i>R</i> <sup>a</sup>	0.114	0.061
<i>R</i> <sub>w</sub> <sup>b</sup>	0.216	0.117
<i>R</i> 1 <sup>c</sup>	0.075	0.034
No. of reflections to calc <i>R</i> 1	6219	6061
Goodness-of-fit indicator <sup>d</sup>	1.40	1.01
Largest shift (esd, final cycle)	0.091	0.003
Max / min resid electron dens (eÅ <sup>-3</sup> )	0.93 / −1.01	0.47 / −0.55

$$^a R = \sum (F_o^2 - F_c^2) / \sum F_o^2$$

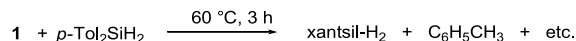
$$^b R_w = [\sum w(F_o^2 - F_c^2)^2 / \sum w(F_o^2)^2]^{1/2}, w = [\sigma_c^2(F_o^2) + (p(\text{Max}(F_o^2, 0) + 2F_c^2/3)^2)]^{-1}, \text{ where } p = 0.1130 \text{ (2b) and } 0.0920 \text{ (3).}$$

$$^c R1 = \sum ||F_o| - |F_c|| / \sum |F_o| \text{ for } I > 2.0\sigma(I).$$

$$^d [\sum w(|F_o| - |F_c|)^2 / (N_{\text{observns}} - N_{\text{variables}})]^{1/2}.$$

products was obtained (eq. [1]). The <sup>1</sup>H NMR spectrum showed the signals for xantsil-H<sub>2</sub>, toluene, and other less-intense signals of the unidentified by-products, which did not provide any sign of dehydrogenative coupling or redistribution reaction of the dihydrosilane.

[1]

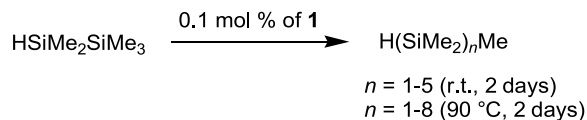


### Reaction of **1** with hydrodisilane

A CD<sub>2</sub>Cl<sub>2</sub> solution of HSiMe<sub>2</sub>SiMe<sub>3</sub> was treated with a catalytic amount of **1** (5.0 mol%) and the reaction was monitored by <sup>1</sup>H NMR spectroscopy. Oligomerization and deoligomerization occurred to give H(SiMe<sub>2</sub>)<sub>*n*</sub>Me (*n* = 1–5). Identification of the oligosilanes was carried out by comparison of spectroscopic data with authentic samples (9, 12).<sup>7</sup> The reaction was performed using 0.1 mol% of **1** and was monitored by GC and GC–MS spectroscopy. The oligomerization–deoligomerization reactions proceeded at

room temperature, and after 2 days, H(SiMe<sub>2</sub>)<sub>*n*</sub>Me (*n* = 1–5) was formed in the molar ratio of 81 (*n* = 1) : 56 (*n* = 2) : 11 (*n* = 3) : 3 (*n* = 4) : 1 (*n* = 5) (eq. [2]). A similar reaction performed at 90 °C provided H(SiMe<sub>2</sub>)<sub>*n*</sub>Me (*n* = 1–8) in the molar ratio of 346 (*n* = 1) : 96 (*n* = 2) : 83 (*n* = 3) : 64 (*n* = 4) : 35 (*n* = 5) : 13 (*n* = 6) : 4 (*n* = 7) : 1 (*n* = 8). The products were also confirmed by <sup>1</sup>H NMR spectral data.

[2]



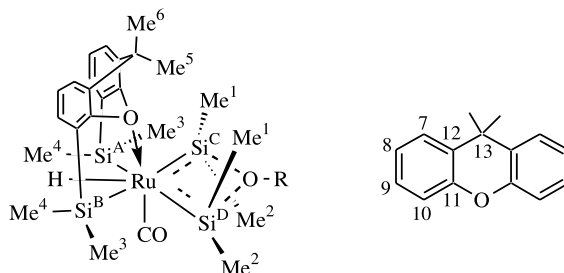
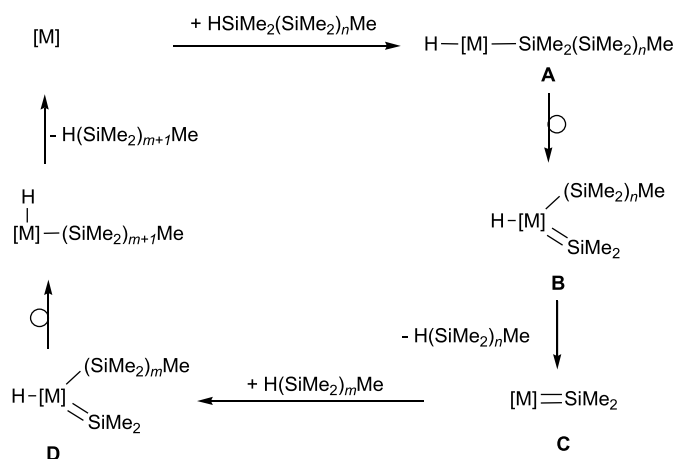
A plausible mechanism for the ruthenium-mediated oligomerization–deoligomerization of HSiMe<sub>2</sub>(SiMe<sub>2</sub>)<sub>*n*</sub>Me is given in Scheme 3. The catalytic reaction proceeds via repeated oxidative addition of Si–H, 1,2-silyl migration, and reductive elimination processes. Initial oxidative addition of

<sup>7</sup> <sup>1</sup>H NMR data for H(SiMe<sub>2</sub>)<sub>*n*</sub>Me (300 MHz, CDCl<sub>3</sub>) δ *n* = 3: 0.06 (s, 9H, SiMe<sub>3</sub>), 0.09 (s, 6H, SiMe<sub>2</sub>), 0.12 (d, *J* = 4.5 Hz, 6H, SiMe<sub>2</sub>H), 3.69 (septet, *J* = 4.5 Hz, 1H, SiH); *n* = 4: 0.07 (s, 9H, SiMe<sub>3</sub>), 0.09 (s, 6H, SiMe<sub>2</sub>), 0.12 (s, 6H, SiMe<sub>2</sub>), 0.13 (d, *J* = 4.5 Hz, 3H, SiMe<sub>2</sub>H), 3.72 (septet, *J* = 4.5 Hz, 1H, SiH); *n* = 5 (C<sub>6</sub>D<sub>6</sub>): 0.15 (s, 9H, SiMe<sub>3</sub>), 0.20 (d, *J* = 4.5 Hz, 6H, SiMe<sub>2</sub>H), 0.22 (s, 6H, SiMe<sub>2</sub>), 0.23 (s, 6H, SiMe<sub>2</sub>), 0.26 (s, 6H, SiMe<sub>2</sub>), 4.11 (septet, *J* = 4.5 Hz, 1H, SiH); *n* = 6 (C<sub>6</sub>D<sub>6</sub>): 0.16 (s, 9H, SiMe<sub>3</sub>), 0.20 (d, *J* = 4.5 Hz, 6H, SiMe<sub>2</sub>H), 0.23 (s, 6H, SiMe<sub>2</sub>), 0.25 (s, 6H, SiMe<sub>2</sub>), 0.30 (s, 6H × 2, SiMe<sub>2</sub>), 4.11 (septet, *J* = 4.5 Hz, 1H, SiH).



**Table 2.** NMR and IR spectroscopic data of **2a** and **2b**.

	<b>2a</b>	<b>2b</b>
	<sup>1</sup> H NMR (300 MHz, C <sub>6</sub> D <sub>6</sub> ) δ	<sup>1</sup> H NMR (300 MHz, CD <sub>2</sub> Cl <sub>2</sub> ) δ
Ru-H	-1.75	-2.23
SiMe	-0.07(1), 0.67(2), 0.89(3), 1.01(4)	0.13(1), 0.59(3), 0.62(4), 0.88(2)
CMe <sub>2</sub>	1.21(5), 1.43(6)	1.24(5), 1.75(6)
OR	2.52 (Me)	1.38 ( <i>t</i> -Bu)
ArH	6.97–7.03 (m, 7,8), 7.48 (dd, <i>J</i> = 2.6, 6.1 Hz, 9)	7,12 (t, <i>J</i> = 7.4 Hz, 8), 7.23 (dd, <i>J</i> = 1.6, 7.4 Hz, 7), 7.48 (dd, <i>J</i> = 1.6, 7.4 Hz, 9)
	<sup>13</sup> C{ <sup>1</sup> H} NMR (75.5 MHz, THF- <i>d</i> <sub>8</sub> ) δ	<sup>13</sup> C{ <sup>1</sup> H} NMR (75.5 MHz, THF- <i>d</i> <sub>8</sub> ) δ
SiMe	3.4(1), 4.8(2), 7.7(3), 14.6(4)	6.2(1), 7.2(3), 10.0(4), 14.0(2)
CMe <sub>2</sub>	23.2(5), 31.9(6), 36.4(13)	30.7(5), 30.9(6), 35.8(13)
OR	52.0 (Me)	22.6 (CMe <sub>3</sub> ), 92.3 (CMe <sub>3</sub> )
Ar	124.4, 125.8, 131.4(7, 8, 9), 135.0, 136.4(10, 12), 162.5(11)	123.5, 124.9, 130.7 (7, 8, 9), 134.4, 136.0(10, 12), 161.9(11)
CO	204.3	204.2
	<sup>29</sup> Si{ <sup>1</sup> H} NMR (59.6 MHz, C <sub>6</sub> D <sub>6</sub> ) δ	<sup>29</sup> Si{ <sup>1</sup> H} NMR (59.6 MHz, CD <sub>2</sub> Cl <sub>2</sub> ) δ
Xantsil	14.6	15.4
Silylene	107.4	107.6
	IR (KBr), $\tilde{\nu}$ /cm <sup>-1</sup>	IR (KBr), $\tilde{\nu}$ /cm <sup>-1</sup>
$\nu$ (CO)	1929	1923

**Scheme 3.**

[M] = Ru(xantphos)(CO)

HSiMe<sub>2</sub>(SiMe<sub>2</sub>)<sub>n</sub>Me to a coordinatively unsaturated [Ru(xantphos)(CO)] species gives a hydrido(silyl)ruthenium(IV) intermediate **A**, which undergoes 1,2-silyl migration to form a hydrido(silyl)(silylene) intermediate **B**. Reductive elimination of Si-H gives H(SiMe<sub>2</sub>)<sub>n</sub>Me and a coordinatively unsat-

urated silylene complex **C**, which in turn undergoes oxidative addition of H(SiMe<sub>2</sub>)<sub>m</sub>Me to generate hydrido(silyl)(silylene) intermediate **D**. 1,2-Migration of the silyl ligand followed by Si-H reductive elimination regenerates the coordinatively unsaturated [Ru(xantphos)(CO)] species together with H(SiMe<sub>2</sub>)<sub>m+1</sub>Me. The 1,2-migration steps of the silyl groups are responsible not only for the cleavage of silicon-silicon bonds which leads to deoligomerization, but also for the formation of silicon-silicon bonds, which leads to oligomerization.

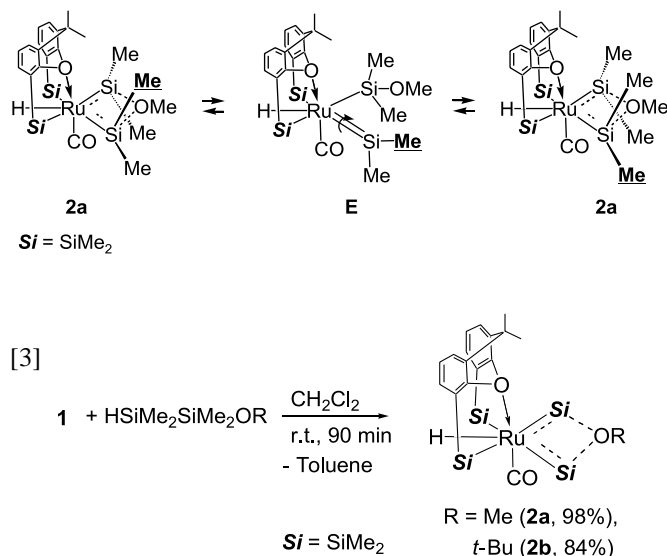
Transition-metal-mediated redistribution of hydrosilanes have been reported for titanium (13), zirconium (13), and platinum (14). Complex **1** is the first ruthenium catalyst that is effective in the redistribution of hydrosilanes.

### Reaction of **1** with HSiMe<sub>2</sub>SiMe<sub>2</sub>OMe

The mechanism in Scheme 3 involves the silyl(silylene) complexes as key intermediates. This kind of complex having a metal-silicon double bond is highly reactive and difficult to isolate but can be internally stabilized by an alkoxy group (15). Thus, treatment of **1** with HSiMe<sub>2</sub>SiMe<sub>2</sub>OR (R = Me, *t*-Bu) in CH<sub>2</sub>Cl<sub>2</sub> resulted in the clean formation of Ru{κ<sup>3</sup>(O,Si,Si)-xantphos}(CO)(H){SiMe<sub>2</sub>...O(R)...SiMe<sub>2</sub>} (**2a** (R = Me), **2b** (R = *t*-Bu)), which were isolated in 98% and 84% yields, respectively (eq. [3]). Spectroscopic data of **2a** and **2b** are summarized in Table 2. Spectroscopic features of **2a**



Scheme 4.



and **2b** are almost the same and, thus, all further discussions of spectroscopic data refer to **2a**. The  $^{29}\text{Si}\{^1\text{H}\}$  NMR spectrum shows two singlet signals at  $\delta$  14.6 and 107.4, which are assigned to the xantsil silicon and silylene silicon atoms, respectively. The chemical shift of silylene moieties is characteristic of base-stabilized silylene complexes (**1c**). The  $^1\text{H}$  NMR spectrum of **2a** shows a singlet at  $-1.75$  ppm that can be assigned to Ru-H. Four singlet signals for the methyl groups on silicon atoms appear at  $-0.07$  (6H),  $0.67$  (6H),  $0.89$  (6H), and  $1.01$  (6H), which are assigned to SiMe(1), SiMe(2), SiMe(3), and SiMe(4), respectively (see Table 2). The signals of the  $\text{CMe}_2$  part on xantsil appear inequivalently at  $1.21$  (Me(5)) and  $1.43$  (Me(6)). These assignments are established by the combination of  $^{29}\text{Si}\{^1\text{H}\}$  COLOC and  $^1\text{H}$  NOESY spectra. In the  $^1\text{H}$  NOESY spectrum, a positive correlation peak is clearly observed between Ru-H and SiMe(4) resonances, indicating that the Ru-H hydrogen atom is located within the  $\text{Si}^{\text{A}}\text{-Ru-Si}^{\text{B}}$  angle.

The  $^1\text{H}$  NOESY spectrum also shows a negative correlation peak between the signals of methyl groups on the silylene silicon atoms (Me(1) and Me(2)), implying the intramolecular exchange process of the methyl groups on the bis(silylene) ligand. The dynamic process probably involves the cleavage of a silicon-oxygen bond, followed by rotation of the resulting donor-free silylene moiety around the ruthenium-silicon double bond to exchange the methyl group environments (Scheme 4). This mechanism is essentially the same as those of the exchange of SiMe groups in  $\text{Cp}(\text{CO})_2\text{W}\{\text{SiMe}_2\cdots\text{Do}\cdots\text{SiMe}_2\}$  (Do = OMe,  $\text{NET}_2$ ) (**16**) and  $\text{Cp}^*(\text{Me}_3\text{P})\text{Ru}\{\text{SiMe}_2\cdots\text{OR}\cdots\text{SiMe}_2\}$  (R = Me, *t*-Bu) (**11**). The strongly electron-releasing xantsil ligand is expected to make the ruthenium center electron rich. Enhanced back donation from the metal  $d\pi$  orbital toward the Si-O  $\sigma^*$  orbital weakens the Si—O bond and accelerates its cleavage to generate the base-free silyl(silylene) complex **E**. This intermediate **E** is also stabilized by the electron-rich ruthenium center through back donation from the metal  $d\pi$  orbital toward the empty  $p$  orbital of the silylene silicon atom.

The  $^{13}\text{C}\{^1\text{H}\}$  NMR spectrum displays the expected resonances for **2a** that are consistent with the  $^1\text{H}$  NMR spectral

Table 3. Selected bond lengths (Å) and angles (°) for **2b**.

	Molecule A	Molecule B
<b>Bond lengths (Å)</b>		
Ru—Si(1)	2.395(4)	2.407(4)
Ru—Si(2)	2.402(4)	2.394(4)
Ru—Si(3)	2.443(3)	2.439(3)
Ru—Si(4)	2.424(4)	2.425(3)
Ru—O(2)	2.289(8)	2.277(8)
Ru—C(5)	1.79(1)	1.80(1)
Si(1)—O(1)	1.813(9)	1.810(9)
Si(2)—O(1)	1.827(9)	1.844(9)
O(1)—C(1)	1.52(1)	1.51(1)
O(3)—C(5)	1.17(2)	1.18(2)
<b>Bond angles (°)</b>		
Si(1)—Ru—Si(2)	67.9(1)	68.0(1)
Si(1)—Ru—Si(3)	151.1(1)	152.6(1)
Si(1)—Ru—Si(4)	87.1(1)	83.4(1)
Si(1)—Ru—O(2)	93.8(2)	92.7(2)
Si(1)—Ru—C(5)	89.0(5)	90.4(5)
Si(2)—Ru—Si(3)	84.2(1)	85.5(1)
Si(2)—Ru—Si(4)	154.3(1)	150.3(1)
Si(2)—Ru—O(2)	95.0(2)	92.4(2)
Si(2)—Ru—C(5)	89.6(5)	88.8(4)
Si(3)—Ru—Si(4)	119.4(1)	121.3(1)
Si(3)—Ru—O(2)	80.6(2)	81.1(2)
Si(3)—Ru—C(5)	98.8(5)	96.1(4)
Si(4)—Ru—O(2)	80.2(2)	80.6(2)
Si(4)—Ru—C(5)	96.0(5)	99.8(4)
O(2)—Ru—C(5)	175.2(6)	176.9(5)
Ru—Si(1)—O(1)	98.9(3)	98.9(3)
Ru—Si(2)—O(1)	98.2(3)	98.3(3)
Si(1)—O(1)—Si(2)	94.8(4)	94.6(4)
Si(1)—O(1)—C(1)	132.5(7)	132.9(8)
Si(2)—O(1)—C(1)	131.6(7)	131.8(8)
Ru—C(5)—O(3)	178(1)	177(1)

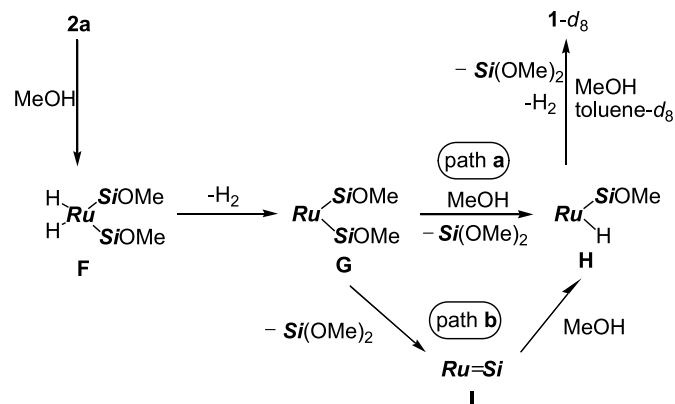
data. The IR spectrum shows a strong band at  $1929\text{ cm}^{-1}$  attributable to the CO-stretching vibration mode. Elemental analysis and mass spectral data are in good agreement with the formula of **2a**.

#### X-ray structure analysis of **2b**

The structure of **2b** was unequivocally determined by the X-ray diffraction study. The crystal contains two independent molecules **A** and **B**, but there is no essential difference between them. The selected bond lengths and angles for **2b** are listed in Table 3. All further discussions of structural details refer to molecule **A**. The ORTEP view of **A** is shown in Fig. 1. The Ru-H hydrogen atom could not be located crystallographically, but the  $^1\text{H}$  NOESY spectrum clearly shows that it must be found inside the unusually widened Si(3A)–Ru(A)–Si(4A) angle ( $119.4(1)^\circ$ ). Thus, the molecule takes a distorted seven-coordinate pentagonal bipyramid geometry with the nearly planar arrangement of all four silicon atoms (mean deviation from the least square  $\text{Si}_4$  plane:  $0.0161\text{ Å}$ ). The xanthene moiety is strongly bent (dihedral angle between the arene rings C(14A)–C(19A) and C(20A)–C(25A):  $136.5^\circ$ ). The bond lengths of Ru–Si (bis(silylene)) (avg.  $2.399\text{ Å}$ ) are shorter than those of Ru–Si (xantsil) (avg.



Scheme 5.



$Ru = Ru(\text{xantsil})(CO)$ ,  $Si = SiMe_2$

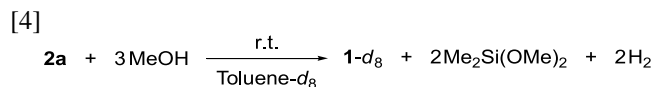
2.434 Å), but significantly longer than those of the previously reported bis(silylene) ruthenium complexes (2.31–2.33 Å) (17). This lengthening could be due to the trans influence of silyl groups (4) and (or) to the weaker back donation from the highly oxidized Ru(IV) center to silicon. The distance of Ru–O(2A) is 2.289(8) Å, which clearly indicates that the oxygen atom of the xanthene moiety is coordinated to the ruthenium center to satisfy the 18-electron rule. Thus, xantsil in **2b** is working as a terdentate ligand.

#### Catalytic oligomerization–deoligomerization of $HSiMe_2SiMe_3$ in the presence of **2a**

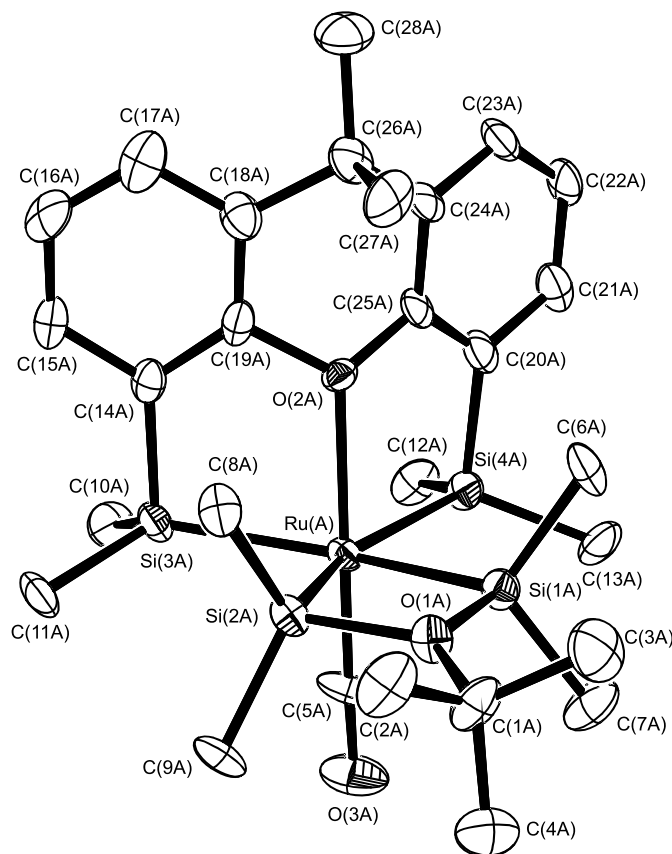
To get further convincing evidence in support of the existence of silyl(silylene) complexes in the catalytic reaction of eq. [2], we carried out the thermal reaction of  $HSiMe_2SiMe_3$  in the presence of a catalytic amount of **2a**. Indeed,  $HSiMe_2SiMe_3$  was converted to  $H(SiMe_2)_nMe$  ( $n = 1–8$ ) after 2 days at 90 °C with the molar ratios of 12 ( $n = 1$ ) : 6 ( $n = 2$ ) : 5 ( $n = 3$ ) : 5 ( $n = 4$ ) : 4 ( $n = 5$ ) : 2 ( $n = 6$ ) : 3 ( $n = 7$ ) : 1 ( $n = 8$ ). This result clearly showed that the bis(silylene) complex **2a** can be incorporated into the catalytic cycle in Scheme 3.

#### Reaction of **2a** with MeOH

It has been reported that silylene complexes show high reactivity toward various nucleophiles such as alcohols (18). The reaction of **2a** with MeOH in toluene- $d_8$  was carried out and monitored by NMR spectroscopy. It proceeded cleanly to give  $Ru\{\kappa^2(Si,Si)\text{-xantsil}\}(CO)(\eta^6\text{-toluene-}d_8)$  (**1-d<sub>8</sub>**) and  $Me_2Si(OMe)_2$  with evolution of  $H_2$  gas (eq. [4]). Spectroscopic data of **1** was used to identify **1-d<sub>8</sub>**, while that of the authentic sample was used to identify  $Me_2Si(OMe)_2$ .



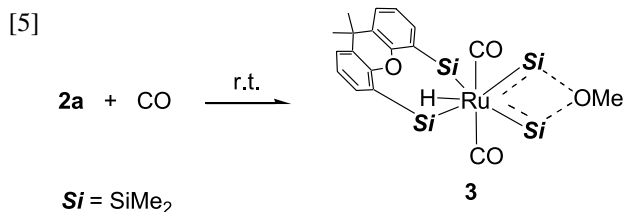
In a proposed mechanism for this reaction (Scheme 5), the highly polarized ruthenium–silylene bond is attacked by MeOH to give a hydrido(methoxysilyl)ruthenium intermediate **F**. Reductive elimination of dihydrogen gives bis(methoxysilyl) complex **G**. In path **a**, successive nucleophilic attacks of excess MeOH toward the silyl silicon atom, followed by reductive elimination of  $H_2$ , gives **1-d<sub>8</sub>** and two

Fig 1. An ORTEP drawing of **2b**.

molecules of  $Me_2Si(OMe)_2$  via intermediate formation of **H**. An intramolecular nucleophilic attack of the methoxy group in **G** must also be considered, which leads to the formation of the silylene complex intermediate **I** (path **b**). Nucleophilic attack of MeOH on a silylene silicon atom in **I** gives **H**, which is finally converted to **1-d<sub>8</sub>** through an intermolecular nucleophilic attack by MeOH.

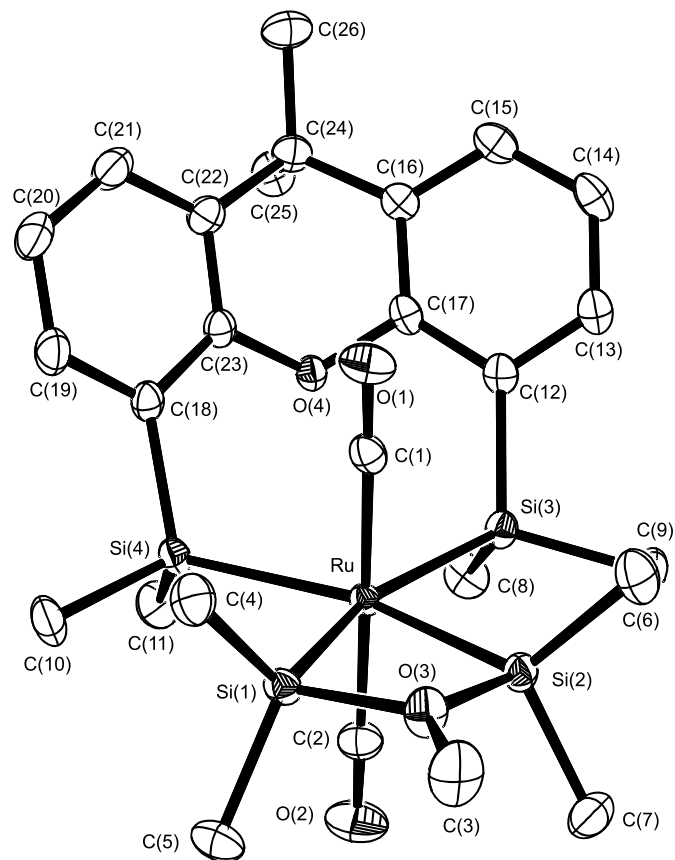
#### Reaction of **2a** with CO

When the reaction of **2a** with 1 atm (1 atm = 101.325 kPa) of CO was monitored by means of  $^1H$  NMR spectroscopy at room temperature, quantitative formation of **3** was observed (eq. [5]). An analytically pure sample was obtained in 85% yield by washing the residue with hexane.



The X-ray diffraction study of **3** was performed using a colorless crystal obtained by cooling a toluene–hexane solution at –30 °C. The structure of **3** is depicted in Fig. 2. The selected interatomic distances and bond angles for **3** are listed in Table 4. The distance of Ru–O(4) is 3.581(2) Å, indicating the cleavage of the Ru–O bond in **2a**. One CO molecule is coordinated to the resulting vacant site of the ru-



**Fig 2.** An ORTEP drawing of **3**.

thium center. The hydrogen atom of the Ru—H bond was located inside the widened Si(3)–Ru–Si(4) angle ( $109.37(2)^\circ$ ) by the difference Fourier synthesis and refined isotropically. Thus, complex **3** also takes a distorted seven-coordinate pentagonal bipyramid geometry with the nearly planar arrangement of all four silicon atoms and one hydrogen atom. The bond lengths of Ru—Si (silylene) (avg. 2.41 Å) and Ru—Si (xantsil) (avg. 2.50 Å) are similar to the values of **2b**.

In the  $^1\text{H}$  NMR spectrum, the  $\text{CMe}_2$  portion and the Si–Me groups on xantsil, as well as the Si–Me groups on the bis(silylene) ligand each appear as one singlet signal at  $\delta$  1.51 ( $\text{CMe}_2$ , 6H), 0.40 (SiMe, 12H), and 1.05 ppm (SiMe, 12H), although the assignment of Si–Me groups is not clear. If complex **3** maintains the crystal structure illustrated in Fig. 2 in solution without any dynamic behavior, six singlet signals should appear. However, this is not the case even at 210 K. A likely process is the rapid inversion of the puckered chelate ring of xantsil. This dynamic behavior of **3** is in sharp contrast with  $\text{Ru}\{\kappa^2(\text{Si},\text{Si})\text{-xantsil}\}(\text{CO})_4$ . In this complex, each of the  $\text{CMe}_2$  and  $\text{SiMe}_2$  groups on xantsil shows two signals at 210 K. On warming, each of them coalesces and finally becomes a sharp singlet at room temperature (7a). Other spectroscopic features of **3** resemble those of **2**.

## Conclusions

Over the past few decades, silyl(silylene) complexes have been proposed as intermediates in the stoichiometric and catalytic metal-mediated transformation reactions of organosilicon compounds (**2**, **3b**). The results described here pro-

**Table 4.** Selected interatomic distances (Å) and bond angles ( $^\circ$ ) for **3**.

Interatomic distances (Å)	
Ru—Si(1)	2.4108(6)
Ru—Si(2)	2.4191(7)
Ru—Si(3)	2.4970(6)
Ru—Si(4)	2.4970(7)
Ru—C(1)	1.917(2)
Ru—C(2)	1.918(3)
Ru—H(1)	1.59(4)
Si(1)—O(3)	1.802(2)
Si(2)—O(3)	1.800(2)
O(1)—C(1)	1.141(3)
O(2)—C(2)	1.142(3)
Ru...O(4)	3.581(2)
Bond angles ( $^\circ$ )	
Si(1)–Ru–Si(2)	69.73(2)
Si(1)–Ru–Si(3)	160.34(2)
Si(1)–Ru–C(1)	87.81(7)
Si(1)–Ru–C(2)	91.13(8)
Si(2)–Ru–Si(3)	90.74(2)
Si(2)–Ru–Si(4)	159.89(3)
Si(2)–Ru–C(1)	90.01(7)
Si(3)–Ru–Si(4)	109.37(2)
Si(3)–Ru–C(1)	90.05(7)
Si(3)–Ru–C(2)	91.07(8)
Si(4)–Ru–C(1)	89.66(7)
Si(4)–Ru–C(2)	89.99(9)
C(1)–Ru–C(2)	178.9(1)
Si(1)–Ru–H(1)	145(1)
Si(2)–Ru–H(1)	145(1)
Si(3)–Ru–H(1)	54(1)
Si(4)–Ru–H(1)	55(1)
C(1)–Ru–H(1)	88(1)
C(2)–Ru–H(1)	92(1)
Ru–Si(1)–O(3)	94.71(6)
Ru–Si(2)–O(3)	94.50(6)
Si(1)–O(3)–Si(2)	100.09(9)

vide further evidence for the participation of silyl(silylene) complexes in the catalytic cycles of the metal-mediated oligomerization–deoligomerization of hydrodisilanes.

Reactivity of **2a** toward CO indicates that complex **2a** is labile and generates a *coordinatively unsaturated silylene complex* via dissociation of the xantsil oxygen atom under mild conditions. A number of metal-mediated stoichiometric and catalytic transformations of organosilicon compounds appear to involve coordinatively unsaturated silylene complexes (**1**, **2**, **3**, **19**). Although synthesis and reactivity of silylene complexes have been reported, only scattered reports on coordinatively unsaturated ones are available (**19**). Complex **3** would be an ideal candidate for examining the reactivity of coordinatively unsaturated silylene complexes.

## Acknowledgments

This work was supported by Grants-in-Aid for Scientific Research (Nos. 13440193 and 14204065), Grants-in Aid for Scientific Research on Priority Area (Nos. 14078202 *Reac-*



tion Control of Dynamic Complexes and 14044010 Exploitation of Multi-Element Cyclic Molecules), and a Grant-in-Aid for the COE project (Giant Molecules and Complex Systems, 2002) from the Ministry of Education, Culture, Sports, Science, and Technology, Japan.

## References

1. (a) T.D. Tilley. In *The chemistry of organic silicon compounds*. Edited by S. Patai and Z. Rappoport. John Wiley and Sons, New York. 1989. p. 1415; (b) T.D. Tilley. In *The silicon-heteroatom bond*. Edited by S. Patai and Z. Rappoport. John Wiley and Sons, New York. 1991. p. 245 and p. 309; (c) M.S. Eisen. In *The chemistry of organic silicon compounds*. Vol. 2. Edited by Z. Rappoport and Y. Apeloig. John Wiley and Sons, New York. 1998. p. 2037; (d) J.Y. Corey and J. Braddock-Wilking. *Chem. Rev.* **99**, 175 (1999).
2. (a) M.D. Curtis and P.S. Epstein. *Adv. Organomet. Chem.* **19**, 213 (1981); (b) J.Y. Corey. *Adv. Silicon Chem.* **1**, 327 (1991); (c) H. Yamashita and M. Tanaka. *Bull. Chem. Soc. Jpn.* **68**, 403 (1995).
3. (a) P. Braunstein and M. Knorr. *J. Organomet. Chem.* **500**, 21 (1995); (b) K.H. Pannell and H.K. Sharma. *Chem. Rev.* **95**, 1351 (1995).
4. (a) J. Chatt, C. Eabon, and S. Ibekwe. *J. Chem. Soc. Chem. Commun.* 700 (1966); (b) R.N. Haszeldine, R.V. Parish, and J.H. Setchfield. *J. Organomet. Chem.* **55**, 279 (1973); (c) L.A. Latif, C. Eabon, and A.P. Pidcock. *J. Organomet. Chem.* **474**, 217 (1994).
5. (a) M.J. Auburn, R.D. Holmes-Smith, and S.R. Stobart. *J. Am. Chem. Soc.* **106**, 1314 (1984); (b) M.J. Auburn and S.R. Stobart. *Inorg. Chem.* **24**, 318 (1985); (c) M.J. Auburn, S.L. Grundy, S.R. Stobart, and M.J. Zaworotko. *J. Am. Chem. Soc.* **107**, 266 (1985); (d) F.L. Joslin and S.R. Stobart. *J. Chem. Soc. Chem. Commun.* 504 (1989); (e) G.W. Bushnell, M.A. Casado, and S.R. Stobart. *Organometallics*, **20**, 601 (2001); (f) X. Zhou and S.R. Stobart. *Organometallics*, **20**, 1898 (2001); (g) S.R. Stobart, X. Zhou, R. Cea-Olivares, and A. Toscano. *Organometallics*, **20**, 4766 (2001).
6. (a) M. Okazaki, H. Tobita, and H. Ogino. *Organometallics*, **15**, 2790 (1996); (b) M. Okazaki, H. Tobita, and H. Ogino. *Chem. Lett.* 437 (1997); (c) M. Okazaki, H. Tobita, and H. Ogino. *J. Chem. Soc. Dalton Trans.* 3531 (1997); (d) M. Okazaki, H. Tobita, and H. Ogino. *Chem. Lett.* 69 (1998); (e) M. Okazaki, S. Ohshitanai, H. Tobita, and H. Ogino. *Chem. Lett.* 952 (2001); (f) M. Okazaki, S. Ohshitanai, M. Iwata, H. Tobita, and H. Ogino. *Coord. Chem. Rev.* **226**, 167 (2002); (g) M. Okazaki, S. Ohshitanai, H. Tobita, and H. Ogino. *J. Chem. Soc. Dalton Trans.* 2061 (2002).
7. (a) H. Tobita, K. Hasegawa, J.J.G. Minglana, L.-S. Luh, M. Okazaki, and H. Ogino. *Organometallics*, **18**, 2058 (1999); (b) J.J.G. Minglana, M. Okazaki, H. Tobita, and H. Ogino. *Chem. Lett.* 406 (2002).
8. R.A. Benkeser, H. Landesman, and D.J. Foster. *J. Am. Chem. Soc.* **74**, 648 (1952).
9. (a) M. Kumada, M. Ishikawa, and S. Maeda. *J. Organomet. Chem.* **2**, 478 (1964); (b) J.V. Urenonvitch and R. West. *J. Organomet. Chem.* **3**, 138 (1965).
10. K. Ueno, A. Masuko, and H. Ogino. *Organometallics*, **16**, 5023 (1997).
11. H. Wada, H. Tobita, and H. Ogino. *Chem. Lett.* 993 (1998).
12. Y. Moteki. MSc. Thesis, Tohoku University, Sendai, Japan, 1996.
13. (a) E. Hengge, M. Weinberger, and Ch. Jammegg. *J. Organomet. Chem.* **410**, C1 (1991); (b) E. Hengge and M. Weinberger. *J. Organomet. Chem.* **433**, 21 (1992); (c) E. Hengge and M. Weinberger. *J. Organomet. Chem.* **443**, 167 (1991).
14. (a) K. Yamamoto, H. Okinoshima, and M. Kumada. *J. Organomet. Chem.* **23**, C7 (1970); (b) K. Yamamoto, H. Okinoshima, and M. Kumada. *J. Organomet. Chem.* **27**, C31 (1971); (c) H. Yamashita, M. Tanaka, and M. Goto. *Organometallics*, **11**, 3227 (1992).
15. H. Ogino. *Chem. Rec.* **2**, 291 (2002).
16. K. Ueno, A. Masuko, and H. Ogino. *Organometallics*, **18**, 2694 (1999).
17. (a) H. Tobita, H. Wada, K. Ueno, and H. Ogino. *Organometallics*, **13**, 2545 (1994); (b) H. Tobita, H. Kurita, and H. Ogino. *Organometallics*, **17**, 2844 (1998).
18. M. Okazaki, H. Tobita, and H. Ogino. *Dalton Trans.* 493 (2003).
19. For group 10 transition metal triads, silylene complexes with 16e have been reported: (a) B. Gehrhus, P.B. Hitchcock, M.F. Lappert, and H. Maciejewski. *Organometallics*, **17**, 5599 (1998); (b) J.D. Feldman, G.P. Mitchell, J.-O. Nolte, and T.D. Tilley. *J. Am. Chem. Soc.* **120**, 11 184 (1998); (c) W.A. Herrmann, P. Härter, C.W.K. Gstöttmayr, F. Bieleert, N. See both, and P. Sirsch. *J. Organomet. Chem.* **649**, 141 (2002).



# Solid-state NMR investigations of the polymer route to SiBCN ceramics<sup>1</sup>

Christel Gervais, Florence Babonneau, Lutz Ruwisch, Ralf Hauser, and Ralf Riedel

**Abstract:** Silicon based polymers obtained by ammonolysis of organochlorosilylboranes and their pyrolytic transformation into Si-B-C-N ceramics were studied by a detailed solid-state NMR investigation. Sol-gel polymerisation/pyrolysis routes were applied to form Si-B-C-N materials with exceptional high-temperature stability. The polymer to ceramic conversion was analyzed by <sup>11</sup>B, <sup>13</sup>C, <sup>15</sup>N, and <sup>29</sup>Si MAS NMR spectroscopy as well as by thermal analysis measurements coupled with mass spectroscopy (TGA-MS). The results showed that a significant change in the carbon-, silicon-, and boron-coordination environments occurs during pyrolysis. An evolution of cleavage of silicon-carbon-boron bridges and the formation of new BN<sub>3</sub> sites was observed. The NMR data obtained suggest the presence of a rather homogeneous dispersion of the boron atoms in the as synthesized silicon carbonitride phase, supporting the high thermal stability with respect to decomposition found in these compounds.

**Key words:** organosilicon polymers, polymer pyrolysis, SiBCN ceramics, solid-state NMR.

**Résumé :** On a fait une étude RMN détaillée à l'état solide des polymères à base de silicium obtenus par ammonolyse d'organochlorosilylboranes et de leur transformation pyrolytique en céramiques Si-B-C-N. On a utilisé des voies de polymérisation/pyrolyse sol-gel pour obtenir des matériaux Si-B-C-N ayant une stabilité exceptionnelle aux températures élevées. On a analysé la conversion du polymère en céramique par RMN à la rotation de l'angle magique (« MAS ») du <sup>11</sup>B, du <sup>13</sup>C, du <sup>15</sup>N et du <sup>29</sup>Si ainsi que par des mesures d'analyses thermiques couplées à la spectrométrie de masse (SM-ATG). Les résultats montrent qu'il se produit un changement significatif dans les environnements de coordination du carbone, du silicium et du bore au cours de la pyrolyse. On a observé une évolution du clivage des ponts silicium-carbone-bore et la formation de nouveaux sites BN<sub>3</sub>. Les données de la RMN suggèrent la présence d'une dispersion relativement homogène des atomes de bore dans la phase carbonitrure de silicium telle que synthétisée et cette observation est en accord avec la grande stabilité thermique observée de ces composés vis-à-vis de la décomposition.

**Mots clés :** polymères organiques du silicium, pyrolyse de polymères, céramiques SiBCN, RMN à l'état solide.

[Traduit par la Rédaction]

## Introduction

The polymeric approach to refractory non-oxide ceramics is a process of great interest offering possibilities of obtaining composite and shaped materials such as fibres, films, or bulk pieces from soluble or fusible starting polymers. Recently, it has been demonstrated that Si-B-C-N ceramics derived from boron-modified polymers exhibit exceptional high-temperature stability (1–4).

The influence of the polymer architecture on the structure of the final ceramic has been clearly demonstrated for Si-C

(5) and Si-C-N (6) systems. It is, therefore, essential to control as much as possible the polymerisation and ceramization steps and consequently to have effective characterization tools that can follow the changes in local environments during polymer-to-ceramic conversion. Solid-state NMR studies (<sup>11</sup>B, <sup>13</sup>C, <sup>15</sup>N, and <sup>29</sup>Si) have been shown to be extremely useful in this field (7–13).

<sup>15</sup>N is a spin  $I = 1/2$  with a very low sensitivity in natural abundance ( $3.8 \times 10^{-6}$  compared to <sup>1</sup>H) but this drawback may be overcome by <sup>15</sup>N enrichment and the use of cross-polarization (CP) techniques, taking advantage of the <sup>1</sup>H–<sup>15</sup>N dipolar coupling. These techniques are consequently very sensitive to the proton environment of the nitrogen sites through the <sup>1</sup>H–<sup>15</sup>N distances. Studies on B-N containing reference compounds have shown that it was possible to distinguish N sites depending on their degree of protonation by using the inversion recovery cross polarization (IRCP) sequence (14) and this technique was successfully extended to the study of polymers (11).

<sup>11</sup>B, <sup>13</sup>C, and <sup>29</sup>Si are abundant enough to be studied without enrichment but <sup>13</sup>C spectra were always recorded with CP techniques to obtain a reasonable signal-to-noise (S/N) ratio. Measurement of high-resolution <sup>11</sup>B spectra ( $I = 3/2$ )

Received 3 February 2003. Published on the NRC Research Press Web site at <http://canjchem.nrc.ca> on 30 October 2003.

**C. Gervais and F. Babonneau.** Chimie de la Matière Condensée, Université Pierre et Marie Curie, 4 place Jussieu, 75005 Paris, France.

**L. Ruwisch, R. Hauser, and R. Riedel.**<sup>2</sup> Technische Universität Darmstadt, Institut für Materialwissenschaft, Petersenstr. 23, D-64287 Darmstadt, Germany.

<sup>1</sup>This article is part of a Special Issue dedicated to Professor John Harrod.

<sup>2</sup>Corresponding author (e-mail: [riedel@materials.tu-darmstadt.de](mailto:riedel@materials.tu-darmstadt.de)).



can be difficult because of the second-order quadrupolar interaction, which distorts the signals and can only be partially averaged by MAS (15).

In this paper, we present a detailed solid-state NMR characterization of the polymers obtained by ammonolysis of organochlorosilylboranes and their pyrolytic transformation into Si-B-C-N ceramics. By combination of the multi-nuclear NMR results, we succeeded in the characterization of intermediate species occurring during the ceramization process as well as of the amorphous solid-state structures formed.

## Experimental

### NMR experiments

The MAS NMR spectra were recorded on a Bruker MSL 300 spectrometer operating at 75.47 MHz for  $^{13}\text{C}$ , 30.41 MHz for  $^{15}\text{N}$ , and 59.63 MHz for  $^{29}\text{Si}$ , and on a Bruker MSL 400 spectrometer at a frequency of 128.28 MHz using a Doty probe with no probe background for  $^{11}\text{B}$ . Samples were spun at 4 kHz for the  $^{29}\text{Si}$  experiments and at 5 kHz for the  $^{13}\text{C}$  and  $^{15}\text{N}$  experiments, using 7 mm  $\text{ZrO}_2$  rotors, while samples were spun at 10 kHz for the  $^{11}\text{B}$  experiments using 5 mm  $\text{Si}_3\text{N}_4$  rotors. All rotors were filled up in a glovebox under a dried argon atmosphere. All the CP and IRCP were performed under the same Hartmann–Hahn match condition: both RF channel levels ( $\omega_{1S/2\pi}$  and  $\omega_{1I/2\pi}$ ) were set at about 42 kHz.

The  $^{13}\text{C}$  CP-MAS NMR spectra were recorded with a spectral width of 20 and 50 kHz depending on the heat treatment temperature of the samples, using 2 K data points in the time domain. The number of transients per spectra varied from 200 to 1200. IRCP-MAS NMR spectra were recorded with inversion times ( $t_i$ ) ranging from 5 to 300  $\mu\text{s}$  and a contact time of 1 ms, which was chosen to maximize the polarization of the  $^{13}\text{C}$  nuclei. The recycle delays between pulses was 6 s. The  $^{13}\text{C}$  NMR chemical shifts were determined relative to TMS via solid adamantane ( $\delta = 29.4$  and 38.5 ppm).

The  $^{15}\text{N}$  CP-MAS NMR spectra were recorded with a spectral width of 30 kHz, using 2 K data points and 2–4 ms contact time depending on the heat treatment temperature. The recycle delays between pulses was 10 s. Chemical shifts were referenced to solid  $\text{NH}_4\text{NO}_3$  (10% enriched sample,  $\delta_{\text{iso}}(^{15}\text{NO}_3) = -4.6$  ppm compared to  $\text{CH}_3\text{NO}_2$  ( $\delta = 0$  ppm)).

The  $^{29}\text{Si}$  MAS NMR spectra were recorded with a spectral width of 30 kHz, a pulse angle around  $25^\circ$  (1.5  $\mu\text{s}$ ), and a recycle delay between pulses of 60 s, using 4 K data points. The  $^{29}\text{Si}$  CP-MAS NMR spectra were recorded with recycle delays of 6 s and contact times ranging from 1 to 10 ms, while for the  $^{29}\text{Si}$  IRCP-MAS NMR spectra, the inversion times varied from 5  $\mu\text{s}$  to 1 ms, with an optimized contact time of 3 ms. Chemical shifts were determined relative to TMS ( $\delta_{\text{Si}} = 0$ ).

The  $^{11}\text{B}$  MAS NMR spectra were recorded with a spectral width of 50 kHz, using 4 K data points. All  $^{11}\text{B}$  NMR chemical shifts were determined relative to liquid  $\text{BF}_3\text{OEt}_2$  ( $\delta = 0$  ppm) and the number of FIDs varied from 400 to 1500. A 1  $\mu\text{s}$  single-pulse excitation was used ( $t_{90}(\text{BF}_3\text{OEt}_2) = 8 \mu\text{s}$ ) with a 5 s repetition time.

Proton decoupling was always applied during data acquisition. A 50 Hz line broadening was applied to the FIDs be-

**Table 1.** Composition of the polycarbosilazanes and their pyrolysis products at 1000  $^\circ\text{C}$ .

Sample	Temperature	Chemical composition
1/1	Room temperature	$\text{Si}_{1.2}\text{B}_{1.0}\text{C}_{3.9}\text{N}_{2.2}\text{H}_{11.5}$
2/1	Room temperature	$\text{Si}_{2.0}\text{B}_{1.0}\text{C}_{6.3}\text{N}_{2.7}\text{H}_{19.2}$
3/1	Room temperature	$\text{Si}_{3.0}\text{B}_{1.0}\text{C}_{9.3}\text{N}_{2.9}\text{H}_{25.3}$
1/1	1000 $^\circ\text{C}$	$\text{Si}_{1.2}\text{B}_{1.0}\text{C}_{1.7}\text{N}_{2.0}$
2/1	1000 $^\circ\text{C}$	$\text{Si}_{2.0}\text{B}_{1.0}\text{C}_{3.4}\text{N}_{2.3}$
3/1	1000 $^\circ\text{C}$	$\text{Si}_{3.0}\text{B}_{1.0}\text{C}_{4.3}\text{N}_{2.0}$

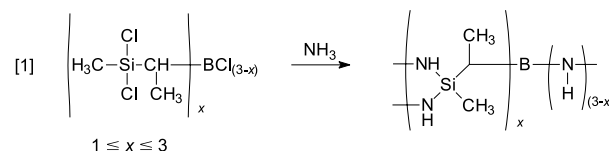
fore Fourier transform. The spectra were simulated with the DMFIT program (16), which has been developed specifically for solid-state NMR experiments, including the simulation of quadrupolar shapes (17).

### TGA–MS measurements

The thermal gravimetric analysis of the ceramics was performed by heating up to 1200  $^\circ\text{C}$  in a helium atmosphere (0.1 MPa He, heating rate 2  $^\circ\text{C}/\text{min}$ ) with a Netzsch STA 429 coupled with a mass spectrometer (Balzers 420).  $\text{Al}_2\text{O}_3$  crucibles were used for measurements.

### Sample preparation

The investigated polyborocarbosilazanes were synthesized by reaction of  $\text{NH}_3$  with organochlorosilylboranes (eq. [1]).



These molecular precursors, obtained by hydroboration reactions of unsaturated organosilanes, exhibit well-defined Si/B ratios ranging from 3/1 to 1/1 (18). Three distinct polymers were investigated, exhibiting Si/B ratios of 1/1, 2/1, and 3/1. It is important to note that the Si/B ratios are fully retained after ammonolysis (Table 1).  $^{15}\text{N}$ -enriched polymers were obtained using 10%  $^{15}\text{N}$  enriched ammonia (purchased from Isotec). The proposed molecular structures of the polymers as presented in Fig. 1 are based on the synthesis procedure as well as on liquid-state NMR and FT-IR studies (19).

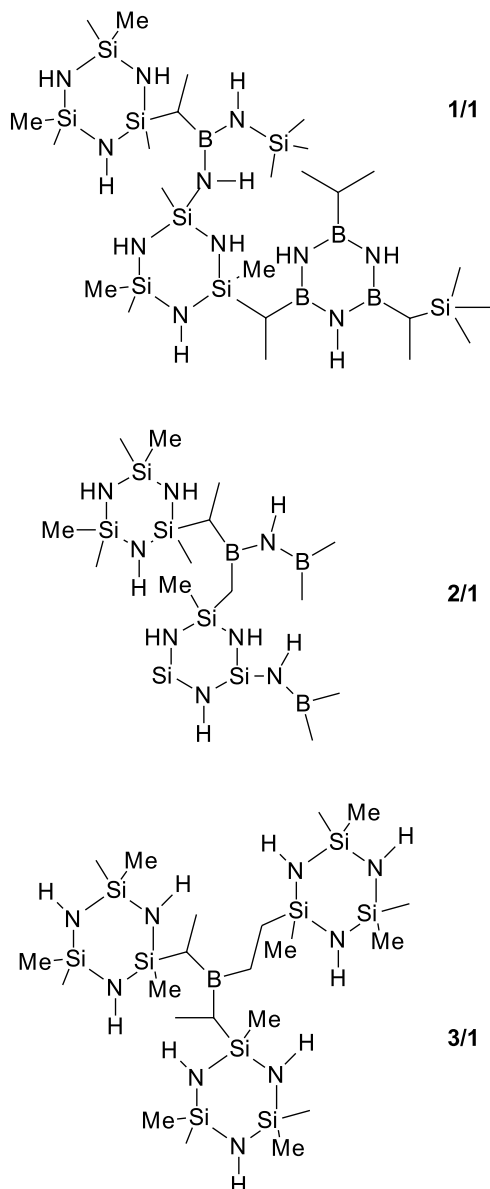
## Results and discussion

### Native polymers

#### $^{11}\text{B}$ MAS NMR

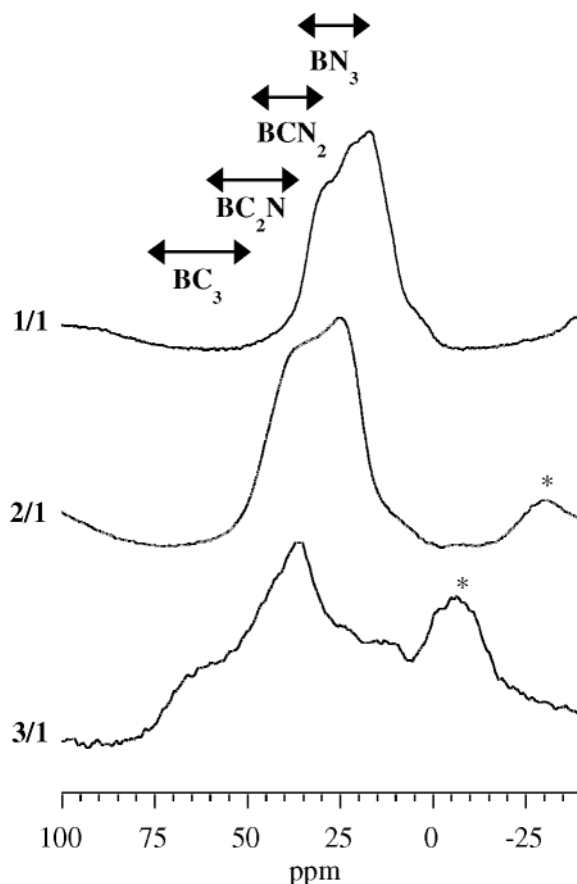
The  $^{11}\text{B}$  MAS NMR spectra obtained for the polymers with particular Si/B-ratios 1/1, 2/1, and 3/1 are quite different and exhibit broad signals around 25, 40, and 70 ppm, respectively (Fig. 2). It should be noticed that  $^{11}\text{B}$  is a quadrupolar nucleus ( $I = 3/2$ ) and that the isotropic value of the chemical shift for such a nucleus doesn't correspond to the barycentre of the resonance signal, which is dominated by the second-order quadrupolar broadening (17). According to the proposed structures for each system, the presence of  $\text{BCN}_2^-$ ,  $\text{BC}_2\text{N}^-$ , and  $\text{BC}_3$ -coordination environments are expected for the 1/1, 2/1, and 3/1 polymers (Fig. 1). The chemical shift values reported in solution for such sites are



**Fig. 1.** Proposed structures for 1/1, 2/1, and 3/1 polymers.

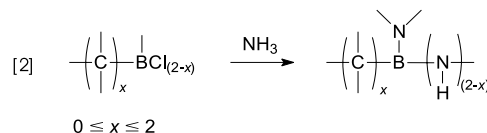
summarized in Table 2.  $BCN_2$  signals are expected around 33 ppm in noncyclic structures up to 37 ppm in a  $(B-N)_3$  six-membered ring structure, while  $BC_2N$  signals range between 44 ppm when the nitrogen atom is bonded to carbons, up to 59 ppm when it is bonded to silicon atoms.  $BC_3$  signals are observed at much a lower field, around 86 ppm in  $B(CH_3)_3$  for instance.

The spectrum obtained for the 1/1 sample can be simulated with a main signal at  $\delta_{iso} = 37$  ppm ( $C_Q = 2.8$  MHz,  $\eta = 0$ ) and a smaller one at  $\delta_{iso} = 26$  ppm ( $C_Q = 2.8$  MHz,  $\eta = 0$ ). The first one can be attributed to the expected  $BCN_2$  site. The assignment of the second signal is more difficult but the chemical shift value suggests the presence of  $BN_3$  sites. The 2/1 sample can be simulated with a unique signal at  $\delta_{iso} = 45$  ppm assigned to a  $BC_2N$  site. Nonetheless, this spectrum is large ( $C_Q = 3$  MHz), which is quite unusual. This finding suggests the presence of  $BCN_2$  coordination. The spectrum recorded for the 3/1 sample is broad with superposition of a

**Fig. 2.**  $^{11}B$  MAS NMR spectra of 1/1, 2/1, and 3/1 polymers (\* indicates spinning sidebands).

spinning side band. Simulation of the spectrum gives a broad main signal around 78 ppm indicating a  $BC_3$  environment and a smaller one at 42 ppm, which can be related to  $BC_2N$  sites. Moreover, the presence of fourfold-coordinated boron atoms with  $^{11}B$  NMR signals also located at positive chemical shift values cannot be excluded.

The solid-state NMR results clearly show that the boron environment in the three synthesized polymers is more complex than expected. However, a predominance of  $BCN_2$ ,  $BC_2N$ , and  $BC_3$  sites in the 1/1, 2/1, and 3/1 polymers is analyzed. Other coordination sites at the boron atom such as  $BN_3$  can also be found and are related to side reactions of residual B—H bonds in the polymers with  $NH_3$  forming B—N instead of B—C bonds according to the following reaction (eq. [2]):



In particular, the type of reaction shown in eq. [2] explains the presence of the  $BN_3$  sites measured in the 1/1 polymer.

#### $^{15}N$ CP-MAS NMR

The spectra obtained for the preceramic polymers are also quite different with signals around -280, -305, and -340 ppm



**Table 2.**  $^{11}\text{B}$  chemical shift values reported in the liquid state for  $\text{BC}_x\text{N}_{4-x}$  sites on various reference compounds.

Site	Compounds	$\delta^{11}\text{B}$ (ppm)	Reference
$\text{BN}_3$	$\text{B}(\text{NHCH}_3)_3$	24.6	27
	$\text{B}[\text{N}(\text{CH}_3)]_3$	27.3	28
	h-BN*	30	29
	$(\text{CH}_3\text{B}-\text{NH})_3$	34.5	28
$\text{BCN}_2$	$(\text{CH}_3\text{B}-\text{NCH}_3)_3$	36.6	28
	$[(\text{CH}_3)_2\text{N}]_2\text{BCH}_3$	33.5	28
	$(\text{CH}_3)_2\text{N}-\text{B}(\text{CH}_3)_2$	44.6	28
	$(\text{CH}_3)_2\text{N}-\text{B}(\text{C}_2\text{H}_5)_2$	45.7	28
$\text{BC}_2\text{N}$	$(\text{CH}_3)_2\text{B}-\text{NH}-\text{B}(\text{CH}_3)_2$	56.1	27
	$(\text{CH}_3)_2\text{B}-\text{NCH}_3-\text{B}(\text{CH}_3)_2$	58.3	27
	$(\text{CH}_3)_2\text{B}-\text{NH}-\text{Si}(\text{CH}_3)_3$	51.6	30
	$(\text{CH}_3)_2\text{B}-\text{N}-[\text{Si}(\text{CH}_3)_3]_2$	59.5	30
$\text{BC}_3$	$\text{B}(\text{CH}_3)_3$	86	27

\*h-BN values recorded for the solid state.

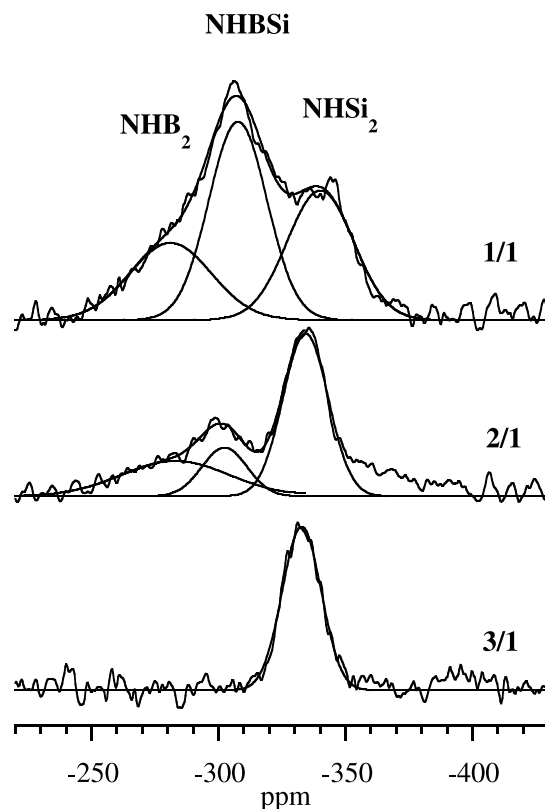
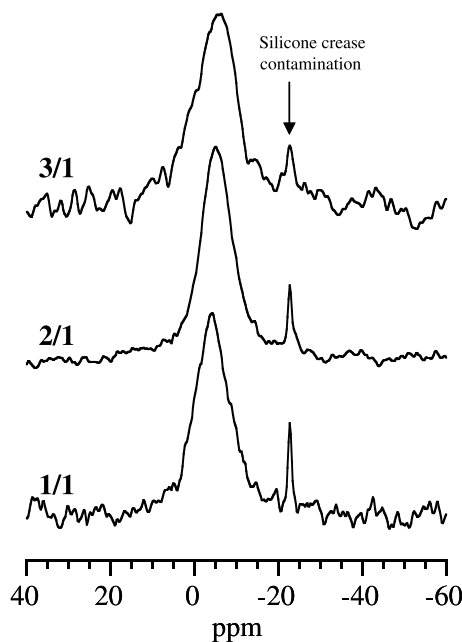
for the 1/1 and 2/1 samples, and one unique signal at  $-333$  ppm for the 3/1 polymer (Fig. 3). The different expected environments in these systems are  $\text{NHSi}_2$ ,  $\text{NHBSi}$ , and  $\text{NHB}_2$  (Fig. 1) and the corresponding chemical shift values reported in solution for such  $\text{N}$ -coordination sites are summarized in Table 3.  $\text{NHSi}_2$  signals are observed around  $-340$  ppm in  $[\text{Si}-\text{N}]_3$  six-membered ring structures and around  $-330$  ppm in  $[\text{Si}-\text{N}]_4$  eight-membered ring structures.  $\text{NHBSi}$  sites show chemical shift values around  $-285$  ppm in noncyclic structures, while  $\text{NHB}_2$  sites appear between  $-266$  and  $-275$  ppm in  $(\text{B}-\text{N})_3$  six-membered ring structures and at a higher field in noncyclic compounds.

Simulation of the NMR spectrum of the 1/1 sample results in three signals at  $-281$ ,  $-307$ , and  $-340$  ppm that can be assigned to the  $\text{NHB}_2$ ,  $\text{NHBSi}$ , and  $\text{NHSi}_2$  sites, respectively. It should be noticed that the signal at  $-340$  ppm is rather broad and may be constituted of two components:  $\text{NHSi}_2$  sites in  $[\text{Si}-\text{N}]_3$  and  $[\text{Si}-\text{N}]_4$  cyclic structures (Table 3). The spectrum of the 2/1 sample can also be simulated with the same three signals at  $-282$ ,  $-303$ , and  $-335$  ppm, corresponding to the  $\text{NHB}_2$ ,  $\text{NHBSi}$ , and  $\text{NHSi}_2$  sites, respectively. The spectrum recorded for the 3/1 sample with its unique signal at  $-333$  ppm is assigned to a  $\text{NHSi}_2$ -type coordination, which is in good agreement with the proposed molecular structure.

### $^{29}\text{Si}$ MAS NMR

It should be noticed that all the spectra have been first recorded in CP-MAS mode to improve the S/N ratio and to facilitate the simulation. Then the extracted parameters have been used to simulate the MAS spectra, to get quantitative information.

In contrast to the  $^{11}\text{B}$  and  $^{15}\text{N}$  NMR data, the spectra obtained for the three polymers are quite similar with a main signal at  $-4$  ppm and a small and narrow one around  $-21$  ppm attributed to contamination by silicone grease (Fig. 4). Considering the chemical shift values reported for  $\text{SiN}_x\text{C}_{4-x}$  coordination sites summarized in Table 4, the main signal can be easily attributed to an  $\text{SiN}_2\text{C}_2$  environment, which nicely coincides with the expected structures of the individual polymers (Fig. 1).

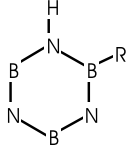
**Fig. 3.**  $^{15}\text{N}$  CP-MAS NMR spectra and the corresponding simulations, for 1/1, 2/1, and 3/1 polymers.**Fig. 4.**  $^{29}\text{Si}$  MAS NMR spectra recorded for 1/1, 2/1, and 3/1 polymers.

### $^{13}\text{C}$ CP-MAS NMR

The synthesized polymers contain methyl groups bonded to silicon and carbon atoms. The latter type of methyl groups are formed by hydroboration of the vinyl groups that

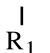
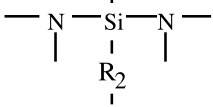
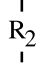
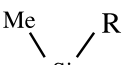
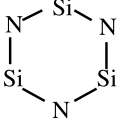


**Table 3.**  $^{15}\text{N}$  chemical shift values reported in the liquid state for  $\text{NHSi}_x\text{B}_{2-x}$  sites in some reference compounds.

Sites	Compounds	$\delta^{15}\text{N}$ (ppm)	Reference
$\text{NHSi}_2$	$[(\text{CH}_3)_2\text{SiNH}]_3$	-344	30
	$[(\text{CH}_3)_2\text{SiNH}]_4$	-332	
	$(\text{CH}_3)_3\text{Si-NH-Si}(\text{CH}_3)_3$	-351	
$\text{NHBSi}$	$(\text{CH}_3)_2\text{B-NH-Si}(\text{CH}_3)_3$	-282	30
	$(\text{C}_2\text{H}_5)_2\text{B-NH-Si}(\text{CH}_3)_3$	-288	
	R = H	-266	
$\text{NHB}_2$		R = $\text{CH}_3$	31
		R = $\text{C}\equiv\text{CH}^*$	14
		R = nBu	31
	$(\text{CH}_3)_2\text{B-NH-B}(\text{CH}_3)_2$	-275	31
		-250	27

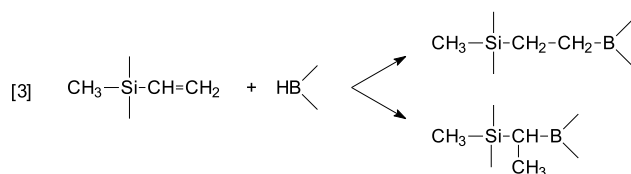
\*Trialkynylborazine values recorded for the solid state.

**Table 4.**  $^{29}\text{Si}$  chemical shift values reported in the solid state and in the liquid state for  $\text{SiN}_xC_{4-x}$  sites in some reference compounds.

Site	Compounds	$\delta^{29}\text{Si}$ (ppm)	Reference
$\text{SiN}_4$		$\text{R}_1 = \text{R}_2 = \text{N}$	32
$\text{SiN}_3\text{C}$		$\text{R}_1 = \text{N}, \text{R}_2 = \text{CH}_2$	-24/-33
$\text{SiN}_2\text{C}_2$		$\text{R}_1 = \text{R}_2 = \text{CH}_2$	2/-14
$\text{SiN}_4$	$\text{Si}_3\text{N}_4$	-49	33
$\text{SiN}_3\text{C}$		R = N	-24
$\text{SiN}_2\text{C}_2$		R = Me	-5
$\text{SiN}_2\text{C}_2$	$[(\text{CH}_3)_2\text{SiNH}]_4$	-9	34
$\text{SiC}_3\text{N}$	$[(\text{CH}_3)_3\text{Si}]_3\text{-N}^*$	0.5	35
	$[(\text{CH}_3)_3\text{Si}]_2\text{-NH}^*$	2	35
	$(\text{CH}_3)_3\text{Si-NHCH}_3^*$	4	35
	$[(\text{CH}_3)_3\text{Si}]_2\text{-NCH}_3^*$	7	35
$\text{SiC}_4$	SiC	-18.5	36

\*Chemical shift values are for the liquid state.

leads to either  $-\text{CH}_2-\text{CH}_2-$  or  $-\text{CH}-\text{CH}_3$  units according to eq. [3]:



The spectra recorded for the 1/1, 2/1, and 3/1 samples show three main signals at around 18, 10, and 2 ppm (Fig. 5). To identify these signals, IRCP measurements with variable in-

version times were performed. In this type of experiment, the dynamics of polarization inversion depend on the proton environment (20–22). For the signal at 18 ppm, the IRCP curves show a behaviour typically found for CH groups, while the inversion dynamics of the other two peaks is slower. Since no quaternary carbon atoms can be expected to be present in these structures, these two signals at 2 and 10 ppm can be assigned to  $\text{CH}_3$  environments exhibiting a weak  $^{13}\text{C}-^1\text{H}$  dipolar coupling due to their mobility (23). In good agreement with the  $^{13}\text{C}$  NMR chemical shift values observed for the polymer precursors in solution (Table 5), the peak at 2 ppm corresponds to a methyl group attached to Si,



**Fig. 5.** Experimental and simulated  $^{13}\text{C}$  CP-MAS spectra recorded for 1/1, 2/1, and 3/1 polymers.

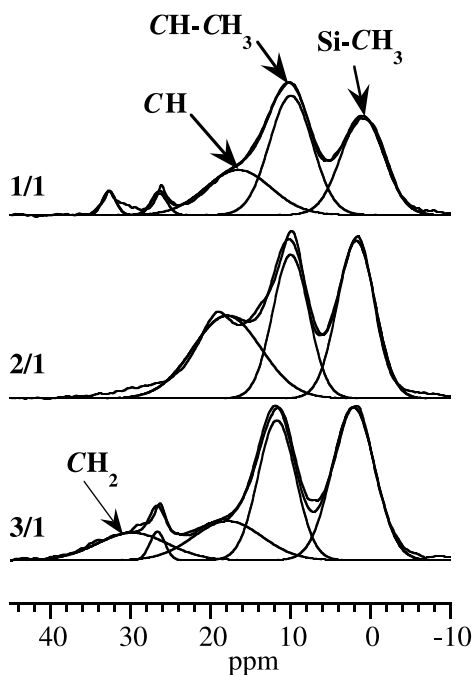


**Table 5.**  $^{13}\text{C}$  NMR chemical shifts observed in solution for the 1/1, 2/1, and 3/1 polymer precursors.

Compounds	Groups	$\delta^{13}\text{C}$ (ppm)
$\left( \begin{array}{c} \text{Cl} \\   \\ \text{CH}_3 - \text{Si} - \text{C}_2\text{H}_4 \\   \\ \text{Cl} \end{array} \right)_x \text{BCl}_{(3-x)}$ $x = 1-3$	Si-CH <sub>3</sub>	4–7
	B(Si)-CH-CH <sub>3</sub>	10–12
	B(Si)-CH-CH <sub>3</sub>	20–34
	CH <sub>2</sub> -CH <sub>2</sub>	14–19

while the peak at 10 ppm is attributed to methyl bonded to a CH group.

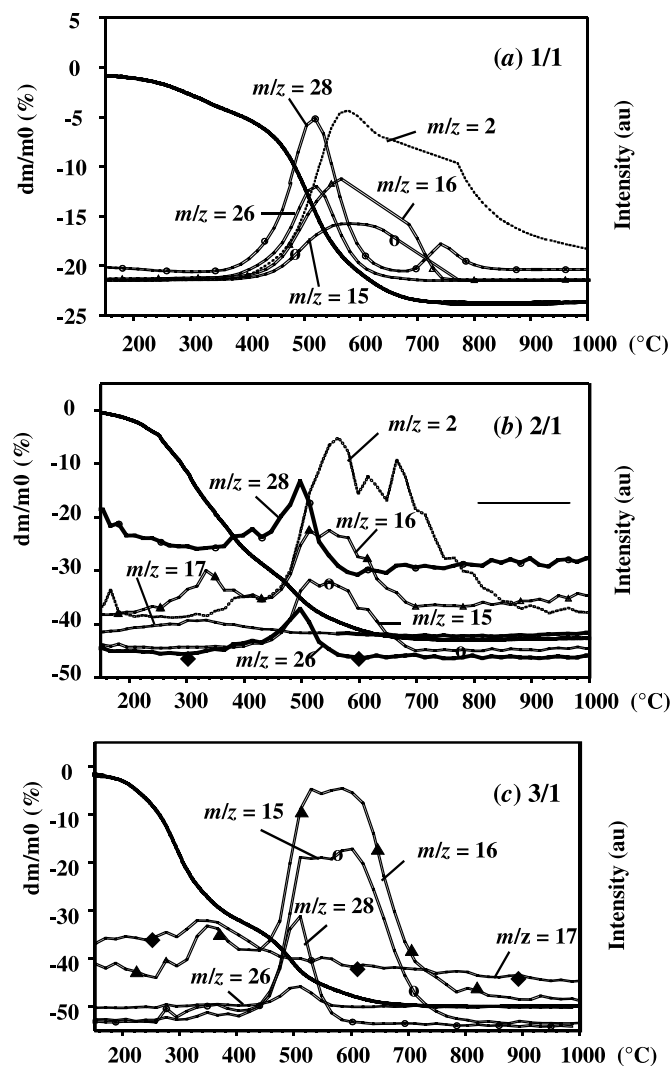
In the 3/1 sample, the solid-state  $^{13}\text{C}$  NMR spectrum shows an intensive signal at 30 ppm, which is assigned to a  $\text{CH}_2$  group as it is derived from its IRCP behavior. This result indicates the presence of both structural units, namely  $>\text{CH}-\text{CH}_3$  and  $-\text{CH}_2-\text{CH}_2-$  bridges interconnecting Si and B in the 3/1 native polymer.

### Heat treatment and pyrolysis

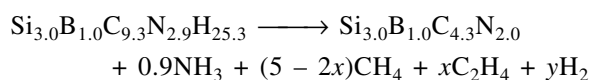
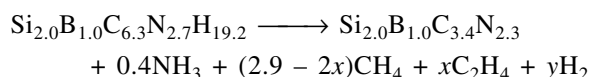
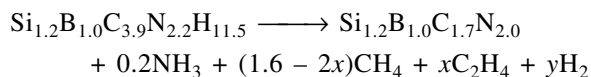
#### TGA-MS

Figure 6 demonstrates the results of the thermal decomposition behaviour of the preceramic polymers. The polymer with the Si/B ratio = 1/1 shows a sharp mass loss of 25 wt% at around 500 °C due to the evolution of  $\text{H}_2$  ( $m/z = 2$ ),  $\text{CH}_4$  ( $m/z = 16, 15, 14$ ),  $\text{CH}_3-\text{CH}_3$  ( $m/z = 28, 26$ ), and a small quantity of  $\text{NH}_3$ . In contrast, the polymers with 2/1 and 3/1 as the Si/B ratio are characterized by a mass loss of 30 wt% below 350 °C due to the loss of  $\text{NH}_3$  produced by polycondensation reactions. In a second step, the materials

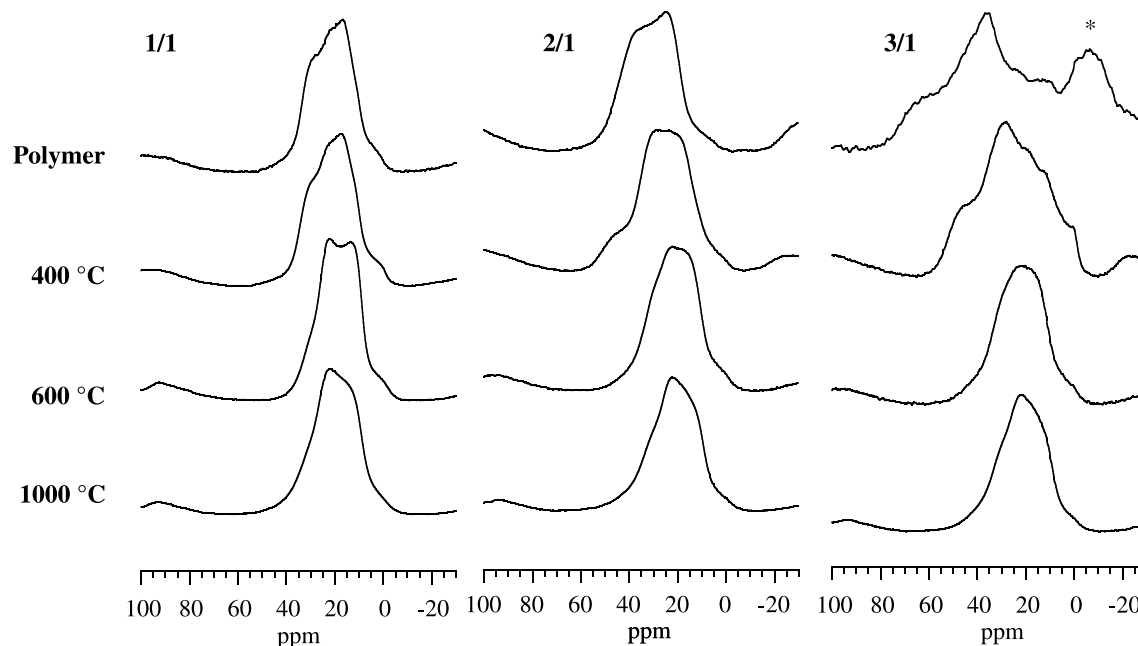
**Fig. 6.** Thermogravimetric analysis and mass spectrometry of: (a) 1/1; (b) 2/1; and (c) 3/1 polymers. The  $m/z$  values are discussed in the text.



lose another 10 wt% between 500 and 600 °C related to the evolution of  $\text{H}_2$ ,  $\text{CH}_4$ ,  $\text{NH}_3$  ( $m/z = 17, 16, 15$ ), and  $\text{C}_2\text{H}_4$ . No further weight loss is detected above 700 °C and the overall ceramic yield amounts 75, 60, and 50 wt% are for the 1/1, 2/1, and 3/1 systems, respectively. The results of the elemental analysis performed on the samples pyrolyzed at 1000 °C are summarized in Table 1. It is worth noting that the Si/B ratio of the preceramic polymer is maintained after pyrolysis. In agreement with the TGA-MS study, the composition changes for the three systems are as follows:





**Fig. 7.**  $^{11}\text{B}$  MAS NMR spectra of the different polymers and their pyrolysis products up to 1000 °C.**Table 6.** Repartition of  $\text{BC}_x\text{N}_{3-x}$  ( $0 \leq x \leq 3$ ) sites according to temperature for the 1/1, 2/1, and 3/1 polymers.

System	Temperature (°C)	Repartition of $\text{BC}_x\text{N}_{3-x}$ sites ( $\pm 2\%$ )			
		$\text{BC}_3$ ( $70 \leq \delta \leq 80$ ) (ppm)	$\text{BC}_2\text{N}$ ( $45 \leq \delta \leq 55$ ) (ppm)	$\text{BCN}_2$ ( $34 \leq \delta \leq 40$ ) (ppm)	$\text{BN}_3$ ( $24 \leq \delta \leq 30$ ) (ppm)
Polymer 1/1	400			78	22
	600			71	29
	1000			60	40
Polymer 2/1	400		100	47	53
	600		28	72	
	1000			73	27
Polymer 3/1	400		32	66	34
	600			50	18
	1000			85	15
				70	30

### $^{11}\text{B}$ MAS NMR

The  $^{11}\text{B}$  MAS NMR spectrum of each sample progressively shifts to upper field values with increasing temperature (Fig. 7). All samples heat treated at 1000 °C exhibit a main signal with  $\delta_{\text{iso}}$  around 30 ppm independent of the Si/B ratio. This finding indicates that a mixture of  $\text{BN}_3$ - and  $\text{BCN}_2$ -coordination sites have been formed. Considering  $\text{BC}_x\text{N}_{3-x}$  ( $0 \leq x \leq 3$ ) as the only possible environments suggests that  $x$  tends to 0 with increasing temperature. The different spectra obtained were tentatively simulated with pure second-order quadrupolar shapes and the corresponding distribution of the  $\text{BC}_x\text{N}_{3-x}$  ( $0 \leq x \leq 3$ ) sites vs. temperature are presented in Table 6. The experimental and simulated spectra obtained for the 2/1 system are shown in Fig. 8.

### $^{15}\text{N}$ MAS and CP-MAS NMR

Figure 9 shows the different  $^{15}\text{N}$  MAS NMR spectra ob-

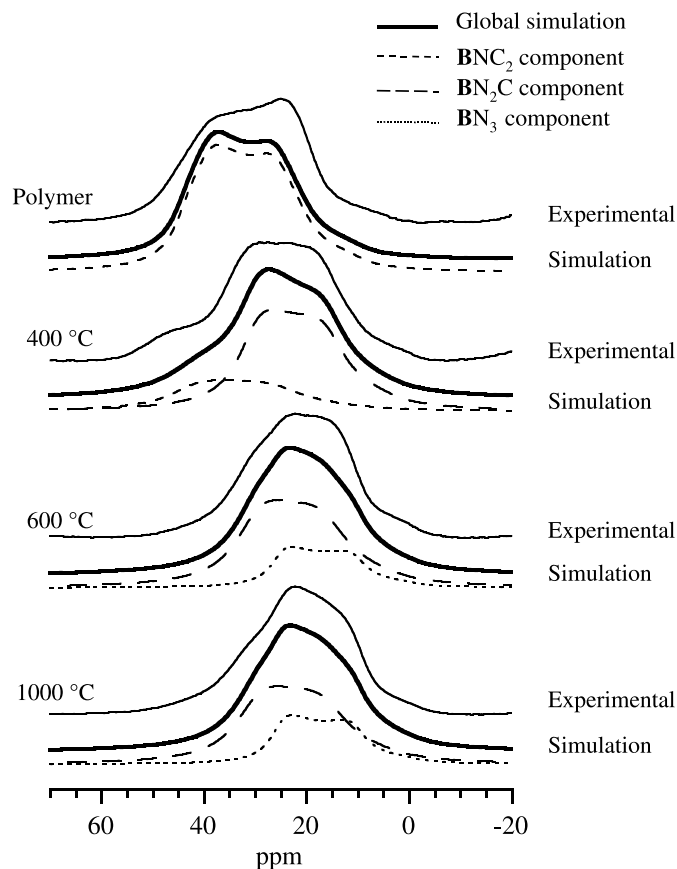
tained for the 2/1 polymer after heat treatment at 400, 600, and 1000 °C in an argon atmosphere.

The  $^{15}\text{N}$  CP-MAS spectrum of the sample heat treated at 400 °C exhibits signals located at the same position as found for the native polymer. However, more than three peaks are necessary to simulate the  $^{15}\text{N}$  IRCP-MAS NMR spectra recorded over a range of inversion times. Some signals exhibit an IRCP behaviour closer to the one expected for nonprotonated nitrogen atoms. Considering that  $\text{NCSi}_2$ ,  $\text{NCBSi}$ , and  $\text{NCB}_2$  chemical shift values (Table 7) are reported in the same range as  $\text{MHSi}_2$ ,  $\text{MHBSi}$ , and  $\text{MHB}_2$ , respectively (Table 3), the spectrum of the 2/1 polymer pyrolyzed at 400 °C indicates the presence of a mixture of  $\text{NXSi}_2$ ,  $\text{NXBSi}$ , and  $\text{NXB}_2$  with  $\text{X} = \text{H}$  or  $\text{C}$  as the nitrogen coordination sphere. The formation of  $\text{N}-\text{C}$  bonds will be discussed later in the  $^{13}\text{C}$  NMR study.

The  $^{15}\text{N}$  IRCP-MAS NMR spectrum of the material an-



**Fig. 8.** Experimental and simulated  $^{11}\text{B}$  MAS NMR spectra recorded for the 2/1 polymer and its pyrolysis products at 400, 600, and 1000  $^{\circ}\text{C}$ .



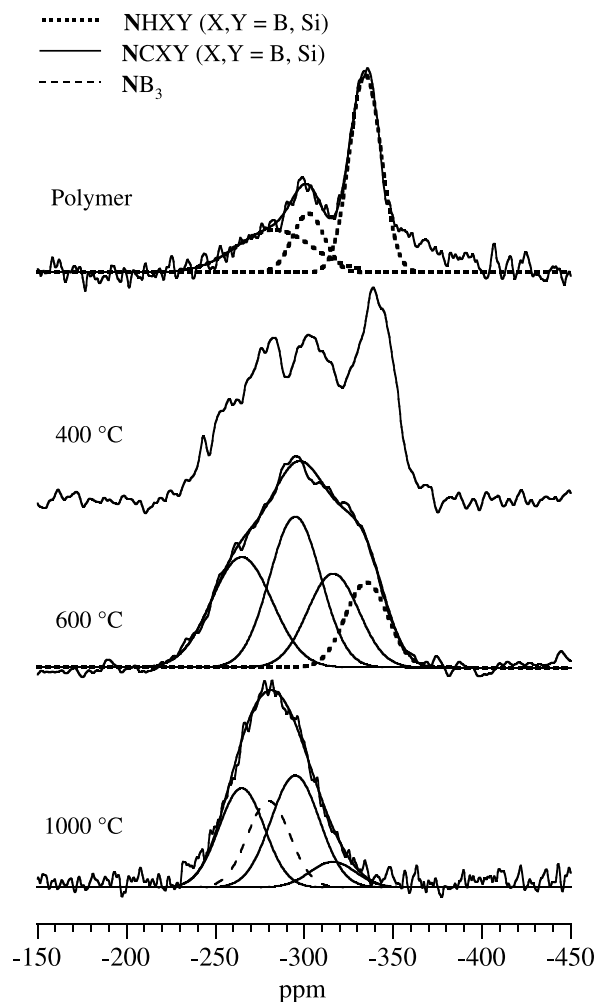
nealed at 600  $^{\circ}\text{C}$  can be simulated by three signals showing an IRCP behaviour characteristic of hydrogen-free environments and one signal corresponding to a Si-NH-Si site considering its chemical shift value ( $-337$  ppm) and its inversion dynamics (Fig. 10). The hydrogen-free sites are assigned to  $\text{NCX}_2$  environments ( $\text{X} = \text{Si}, \text{B}$ ) based on their chemical shift values. This result strongly suggests that the removal of hydrogen from the nitrogen atoms is almost complete for the three systems at 600  $^{\circ}\text{C}$ .

Annealing of the 2/1 polymer at 1000  $^{\circ}\text{C}$  results in a broad and complex NMR signal ranging from  $-240$  to  $-320$  ppm that can be assigned to a distribution of  $\text{NB}_3$ -,  $\text{NCB}_2$ -,  $\text{NCBSi}$ -, and  $\text{NCSi}_2$ -coordination sites based on the corresponding expected chemical shift values (Table 7). A similar behaviour is observed for the 1/1 and 3/1 systems: the protonated signals disappear progressively with increasing temperature, while the amount of  $\text{NCXY}$  ( $\text{X}, \text{Y} = \text{B}, \text{Si}$ ) sites increases and an additional signal is present around  $-282$  ppm due to the formation of  $\text{NB}_3$  sites. The enhanced formation of new B—N bonds together with the decreasing amount of Si—N bonds with increasing annealing temperature as found in the  $^{15}\text{N}$  MAS NMR study is in good agreement with the  $^{11}\text{B}$  NMR results.

### $^{29}\text{Si}$ MAS NMR

The  $^{29}\text{Si}$  MAS NMR spectra of the three heat-treated polymer systems reveal similar chemical shift values for a

**Fig. 9.** Experimental and simulated  $^{15}\text{N}$  CP-MAS NMR spectra recorded for the 2/1 polymer and its pyrolysis products at 400, 600  $^{\circ}\text{C}$ , and the  $^{15}\text{N}$  MAS NMR spectrum of the sample heat treated at 1000  $^{\circ}\text{C}$ .



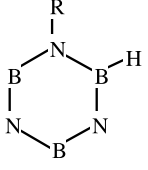
given temperature. Figure 11 represents the NMR results on the basis of the 2/1 sample. Accordingly, the number of resonance signals increases after 400  $^{\circ}\text{C}$  treatment and is still pronounced after annealing at 1000  $^{\circ}\text{C}$ . Assignment is difficult due to the broadness of the peaks that can be explained by the presence of a great variety in the coordination of Si by carbon and nitrogen ( $\text{SiN}_x\text{C}_{4-x}$  where  $0 \leq x \leq 4$ ) (Table 4).  $^{29}\text{Si}$  CP-MAS spectra were therefore recorded up to 600  $^{\circ}\text{C}$  to enhance the S/N ratio and extract the number of signals and their corresponding parameters. But this sequence cannot be used for high-temperature samples (due to a lack of protons) and all sites may not be detected;  $^{29}\text{Si}$  MAS spectra were consequently recorded for all samples.

### Annealing at 400 $^{\circ}\text{C}$

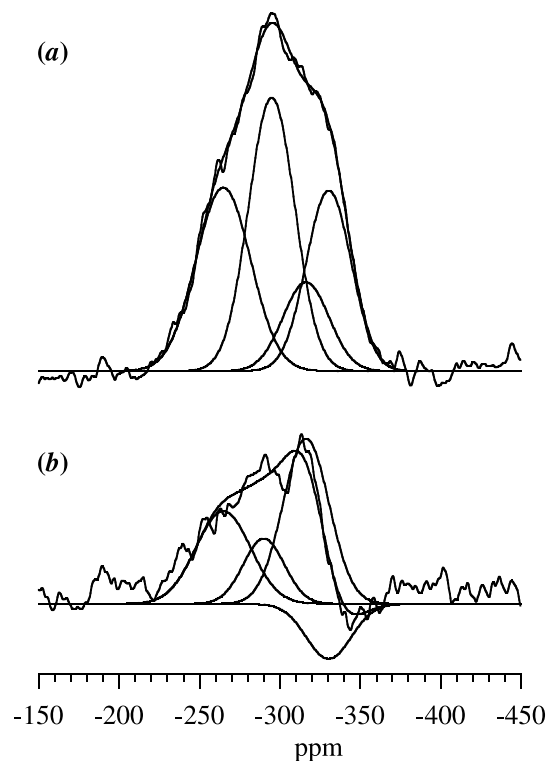
The signal around  $-4$  ppm observed in the native polymers is still present, while a broad peak is found at  $-21$  ppm, which can be assigned to a  $\text{SiN}_3\text{C}$  environment (see Table 4). Moreover, two further signals appear at positive chemical shift values: their assignment is not straightforward but the chemical shift at 5 ppm probably indicates the formation of  $\text{SiNC}_3$  environments, while the peak at 15 ppm has to be at-



**Table 7.**  $^{15}\text{N}$  NMR chemical shift values reported in the liquid state in for  $\text{NCX}_2$  ( $\text{X} = \text{Si}, \text{B}$ ),  $\text{NB}_3$ , and  $\text{NSi}_3$  environments.

Sites NC	Compounds	$\delta^{15}\text{N}$ (ppm)	Reference
$\text{NCSi}_2$	$[(\text{CH}_3)_2\text{SiNCH}_3]_3$	-332	28
	$(\text{CH}_3)_3\text{Si-NCH}_3\text{-Si}(\text{CH}_3)_3$	-370	
	$(\text{CH}_3)_3\text{Si-NC}_2\text{H}_5\text{-Si}(\text{CH}_3)_3$	-340	
$\text{NCBSi}$	$(\text{CH}_3)_2\text{B-NCH}_3\text{-Si}(\text{CH}_3)_3$	-287	28
		-268	
	R = $\text{CH}_3$		
$\text{NCB}_2$	R = <i>n</i> -Bu	-248	31
$\text{NB}_3$	Hexagonal boron nitride*	-282	37
$\text{NSi}_3$	$\text{Si}_3\text{N}_4^*$	-309	33

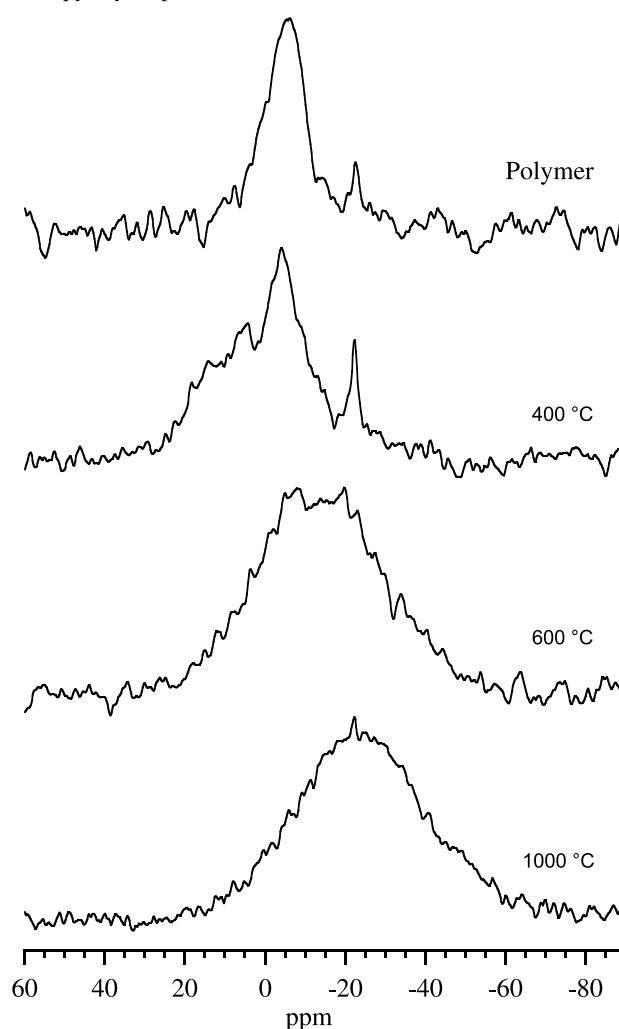
\*Hexagonal boron nitride and silicon nitride values are for the solid state.

**Fig. 10.** Experimental and simulated  $^{15}\text{N}$  IRCP-MAS NMR spectra of the 2/1 sample pyrolyzed at 600 °C for two inversion time values: (a)  $t_i = 5 \mu\text{s}$ ; and (b)  $t_i = 500 \mu\text{s}$ .

tributed to  $>\text{Si}=\text{N}-\text{B}<$  units as reported in a polyborosilazane-containing  $[\text{Si}-\text{N}]_3$  structural units (24).

#### Annealing at 600 °C

The signal at 15 ppm has disappeared but those around 5, -4, and -21 ppm assigned to  $\text{SiNC}_3$ ,  $\text{SiN}_2\text{C}_2$ , and  $\text{SiN}_3\text{C}$  sites, respectively, are still present. A new resonance peak at -33 ppm is tentatively assigned to another  $\text{SiN}_3\text{C}$  environ-

**Fig. 11.**  $^{29}\text{Si}$  MAS NMR spectra recorded for the 2/1 polymer and its pyrolysis products obtained at 400, 600, and 1000 °C.

ment since the range for such signals is relatively big (Table 4).

#### Annealing at 1000 °C

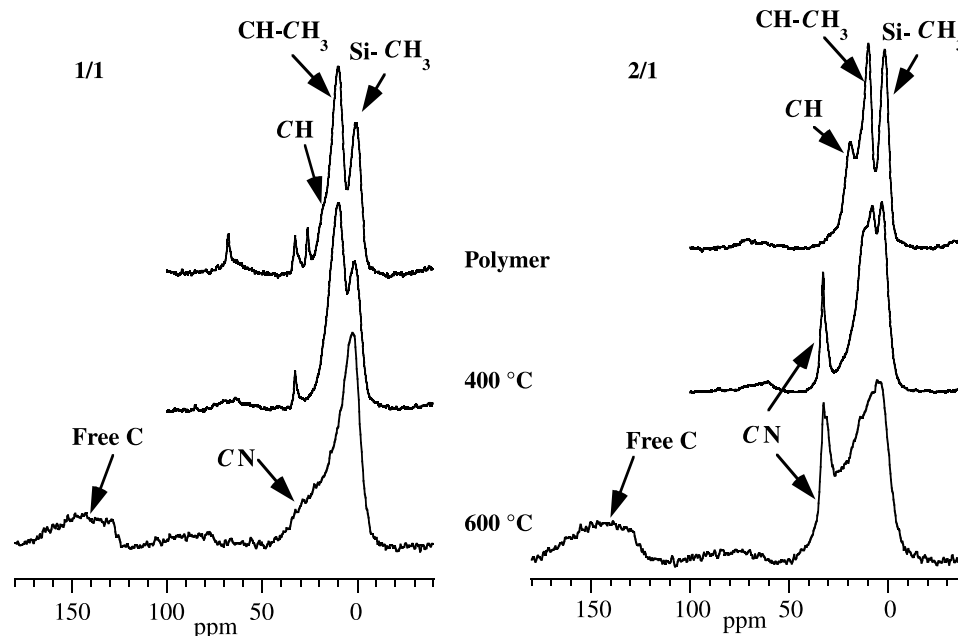
The overall spectrum does not differ from the ones reported for pyrolyzed polysilazanes and polyborosilazanes and is typical for a distribution of  $\text{SiN}_x\text{C}_{4-x}$  ( $0 \leq x \leq 4$ ) sites (23) strongly supporting the presence of an amorphous phase of silicon carbonitride. Peaks around 5, -4, -19, -33 and -49 ppm assigned to  $\text{SiNC}_3$ ,  $\text{SiN}_2\text{C}_2$ ,  $\text{SiC}_4$ ,  $\text{SiN}_3\text{C}$ , and  $\text{SiN}_4$ , respectively, are most probably present. The presence of silicon atoms coordinated by nitrogen or carbon exclusively shows the onset of a phase separation resulting in the formation of  $\text{Si}_3\text{N}_4$ - and  $\text{SiC}$ -rich domains.

#### $^{13}\text{C}$ CP-MAS NMR

The  $^{13}\text{C}$  CP-MAS spectrum of the 1/1 sample heat-treated at 400 °C (Fig. 12a) is similar to the one recorded for the native polymer. This finding is in good agreement with the TGA-MS results indicating a transformation of the network for temperatures beyond 500 °C (Fig. 6a). The samples with the Si/B ratios 2/1 and 3/1 annealed at 400 °C show an increase in the number of NMR signals (Fig. 12b) compared



**Fig. 12.**  $^{13}\text{C}$  CP-MAS NMR spectra of the (a) 1/1, and (b) 2/1 polymers and their pyrolysis products at 400 and 600 °C.



with the starting polymers suggesting significant structural changes. The peaks at 2 and 10 ppm are still present but the relative intensity of the first one has decreased, methyl groups bonded to carbon being less stable than those bonded to silicon. Moreover, there are two additional peaks at 13 and 35 ppm. The first one can be assigned to a CH group based on its IRCP behavior, while the latter one at lower field is due to the presence of a  $\text{X}_3\text{C-N}$  environment ( $\text{X} = \text{C}, \text{H}$ ) as already reported for borylbrazine and polyborazine (25). The NMR results strongly suggest the formation of C—N bonds during the heat treatment and coincide with the  $^{15}\text{N}$  NMR study showing  $>\text{NCX}_2$  ( $\text{X} = \text{Si}, \text{B}$ ) sites in the 2/1 polymer heat treated at 400 °C.

After tempering of the samples at 600 °C, the peak around 2 ppm assigned to  $\text{CH}_3$  groups bonded to silicon is still present, while resonances attributed to methyl groups bonded to a CH function have strongly decreased due to the loss of methane as demonstrated by our TGA-MS study. The low-field shifted peak around 35 ppm observed at 400 °C in the 2/1 sample is still present and a new signal is observed in the same range for the 1/1 system annealed at 600 °C. The peak corresponds to the formation of C—N bonds since  $\text{NCX}_2$  ( $\text{X} = \text{Si}, \text{B}$ ) sites have also been found by  $^{15}\text{N}$  CP-MAS NMR measurements of the same sample.

The spectra also show a broad peak around 150 ppm that can be assigned to aromatic carbon atoms suggesting the formation of graphite-like or amorphous carbon stemming from the decomposition of the organic side groups (26).

## Conclusions

### Native polymers

The  $^{11}\text{B}$ ,  $^{13}\text{C}$ ,  $^{15}\text{N}$ , and  $^{29}\text{Si}$  data support the different molecular structures proposed for the synthesized polymers.  $^{11}\text{B}$  MAS NMR spectra represent main signals assigned to  $\text{BCN}_2$ ,  $\text{BC}_2\text{N}$ , and  $\text{BC}_3$  sites in the samples with 1/1, 2/1, and 3/1 as the Si/B ratio, respectively.  $^{15}\text{N}$  CP-MAS and  $^{29}\text{Si}$

MAS spectra confirm the presence of cyclic silazane ring structures  $[\text{SiR}(\text{CH}_3)\text{-NH}]_x$  ( $x = 3, 4$ ) for the three compounds. Moreover, B—NH—Si and B—NH—B bonds were also identified by  $^{15}\text{N}$  NMR in the polymers with 1/1 and 2/1 Si/B ratios. These types of bonds are not found in the polymer with Si/B = 3/1. Boron atoms are linked to three silazane rings through  $>\text{CH-CH}_3$  and  $-\text{CH}_2\text{-CH}_2-$  spacing groups as confirmed by  $^{13}\text{C}$  NMR in the 3/1 polymer. In contrast, no ethylene- $\text{CH}_2\text{-CH}_2$ -groups are clearly evidenced in the 1/1 and 2/1 polymers, indicating that boron and silicon atoms are only bonded through  $>\text{CH-CH}_3$  groups.

### Ceramization

The boron environment depends on the Si/B-ratio and is quite different in the individual native preceramic polymer. In contrast, the boron coordination resembles a mixture of  $\text{BN}_2\text{C}$  and  $\text{BN}_3$  sites for the samples heat treated at 1000 °C independent of the Si/B-ratio. At the same time, the number of aliphatic carbons that make the interconnection between the silicon and the boron atoms decreases. This evolution suggests the cleavage of B—C bonds with evolution of methane and ethane, while some nitrogen atoms bonded to silicon sites migrate to boron groups as confirmed by the appearance of  $\text{NB}_3$  sites. Moreover, the deprotonation of the nitrogen sites leads to the formation of C—NX ( $\text{X} = \text{Si}$  or  $\text{B}$ ) structural units and a distribution of  $\text{SiN}_x\text{C}_{4-x}$  ( $1 \leq x \leq 4$ ) sites is observed. This findings suggest that boron atoms are homogeneously dispersed in the silicon carbonitride phase supporting the high thermal stability observed in these compounds.

### Acknowledgements

We gratefully acknowledge the financial support of the DFG (Deutsche Forschungsgemeinschaft, Bonn) and the Fonds der Chemischen Industrie, Frankfurt/Main.



## References

1. J. Bill and F. Aldinger. *Adv. Mater. (Weinheim, Ger.)*, **7**, 775 (1995).
2. H.P. Baldus and M. Jansen. *Angew. Chem. Int. Ed. Engl.* **36**, 328, (1997).
3. M. Weinmann, R. Haug, J. Bill, M.d. Guire, and F. Aldinger. *Appl. Organomet. Chem.* **12**, 725 (1998).
4. R. Riedel, A. Kienzle, W. Dressler, L. Ruwitsch, J. Bill, and F. Aldinger. *Nature (London)*, **382**, 796 (1996).
5. R.M. Laine and F. Babonneau. *Chem. Mater.* **52**, 60 (1993).
6. M. Birot, J.P. Pilot, and J.P. Dunogues. *Chem. Rev.* **95**, 1443 (1995).
7. G.D. Soraru, F. Babonneau, and J.D. Mackenzie. *J. Mater. Sci.* **25**, 3886 (1990).
8. W.R. Schmidt, L.V. Interrante, R.H. Doremus, T.K. Trout, S.P. Marchetti, and G.E. Maciel. *Chem. Mater.* **32**, 57 (1991).
9. C. Gérardin, F. Taulelle, and D.J. Bahloul. *Mater. Chem.* **7**, 117 (1997).
10. A.O. Gabriel, R. Riedel, W. Dressler, S. Reichert, C. Gervais, J. Maquet, and F. Babonneau. *Chem. Mater.* **11**, 412 (1999).
11. C. Gervais, J. Maquet, F. Babonneau, C. Duriez, E. Framery, M. Vaultier, P. Florian, and D. Massiot. *Chem. Mater.* **13**, 1700 (2001).
12. L.V. Wüllen and M.J. Jansen. *Mater. Chem.* **11**, 223 (2001).
13. J. Schuhmacher, F. Berger, M. Weinmann, J. Bill, F. Aldinger, and K. Müller. *Appl. Organomet. Chem.* **15**, 809 (2001).
14. C. Gervais, F. Babonneau, J. Maquet, C. Bonhomme, D. Massiot, E. Framery, and M. Vaultier. *Magn. Reson. Chem.* **36**, 407 (1998).
15. G.D. Soraru, N. Dallabona, C. Gervais, and F. Babonneau. *Chem. Mater.* **11**, 910 (1999).
16. D. Massiot, F. Fayon, M. Capron, I. King, S. Le Calvé, B. Alonso, J.-O. Durand, B. Bujoli, Z. Gan, and G. Hoaston. *Magn. Reson. Chem.* **40**, 70 (2002).
17. A.P.M. Kentgens. *Geoderma*, **80**, 271 (1997).
18. L.M. Ruwisch, P. Dürichen, and R. Riedel. *Polyhedron*, **19**, 323 (2000).
19. L.M. Ruwisch. Ph.D thesis, Darmstadt University of Technology, Darmstadt, Germany. 1998.
20. X. Wu and K.W. Zilm. *J. Magn. Reson.* **102**, 205 (1993).
21. P. Palmas, P. Tekely, and D. Canet. *J. Magn. Reson. Ser. A*, **104**, 26 (1993).
22. R. Sangill, N. Rastrup-Andersen, H. Bildsoe, H.J. Jakobsen, and N.C. Nielsen. *J. Magn. Reson.* **107**, 67 (1994).
23. L.B. Alemany, D.M. Grant, R.J. Pugmire, T.D. Alger, K.W. Zilm. *J. Am. Chem. Soc.* **105**, 2133 (1983).
24. W.R. Schmidt, D.M. Narsavage-Heald, D.M. Jones, P.S. Marchetti, D. Raker, and G.E. Maciel. *Chem. Mater.* **11**, 1455 (1999).
25. D. Cornu, P. Miele, B. Toury, B. Bonnetot, H. Mongeot, and J. Bouix. *J. Mater. Chem.* **9**, 2605 (1999).
26. G.E. Maciel, C.E. Bronnimann, A. Jurkiewicz, R.A. Wind, and V.H. Pan. *Fuel*, **70**, 925 (1991).
27. H. Nöth and B. Wrackmeyer. *Chem. Ber.* **107**, 3089 (1974).
28. H. Nöth and H. Vahrenkamp. *Chem. Ber.* **99**, 1049 (1966).
29. P.S. Marchetti, D. Kwon, W.R. Schmidt, L.V. Interrante, and G.E. Maciel. *Chem. Mater.* **3**, 482 (1991).
30. H. Nöth, W. Tinhof, and B. Wrackmeyer. *Chem. Ber.* **107**, 518 (1974).
31. E. Framery. Ph.D. Thesis, Université de Rennes I, Rennes, France, 1996.
32. C. Gérardin. Ph.D. Thesis, Université Paris VI, Paris, France, 1991.
33. R.K. Harris and M.J. Leach. *Chem. Mater.* **2**, 320 (1990).
34. J. Seitz, J. Bill, N. Egger, and F. Aldinger. *J. Eur. Ceram. Soc.* **16**, 885 (1996).
35. H. Marsmann. *NMR — Basic principles and progress*. Springer Verlag, Berlin. 1981.
36. D.C. Apperley, R.K. Harris, G.L. Marshall, and D.P. Thompson. *J. Am. Ceram. Soc.* **74**, 777 (1991).
37. C. Gervais and F. Babonneau. *J. Organomet. Chem.* **657**, 75 (2002).



# The activity of Pt/SiO<sub>2</sub> catalysts obtained by the sol-gel method in the hydrosilylation of 1-alkynes<sup>1</sup>

Rafael Jiménez, J. Merced Martínez-Rosales, and Jorge Cervantes

**Abstract:** Heterogeneous platinum catalysts (Pt/SiO<sub>2</sub>) obtained by the sol-gel process at pH 3 and 9 have been used in the hydrosilylation reaction of 1-alkynes using various silanes. Once the catalysts were activated they were used in the hydrosilylation of 1-alkynes after a short induction period. The product distribution was quite similar in either case but important differences in catalytic activity and turnover reactions were observed. The catalyst obtained in the basic medium after each reaction lost its catalytic activity, so further activation was needed. To understand this behavior, the catalysts were characterized by <sup>29</sup>Si CPMAS NMR, FT IR, and BET surface area measurements. The <sup>29</sup>Si CPMAS NMR studies showed the presence of terminal and bridged hydroxyl groups in the Pt/SiO<sub>2</sub> catalyst at pH = 9. Similar results were observed by FT IR analysis because of the catalysts' synthetic conditions.

**Key words:** hydrosilylation, sol-gel, Pt/SiO<sub>2</sub>, supported-metal catalysts, phenylacetylene, diphenylacetylene, <sup>29</sup>Si NMR CP-MAS.

**Résumé :** On a utilisé des catalyseurs homogènes de platine (Pt/SiO<sub>2</sub>) obtenus par le procédé sol-gel à des pH de 3 et de 9 pour effectuer l'hydrosilylation d'alc-1-yne à l'aide de divers silanes. Une fois les catalyseurs activés, ils étaient utilisés pour effectuer l'hydrosilylation des alc-1-yne après une courte période d'induction. La distribution des produits est très semblable dans les deux cas, mais on a observé des différences importantes dans l'activité catalytique et dans les réactions de changement. Le catalyseur obtenu en milieu basique perd son activité après chaque réaction et on doit donc procéder à chaque fois à une nouvelle activation. Dans le but de comprendre ce comportement, on a procédé à une caractérisation des catalyseurs par RMN « CPMAS » du <sup>29</sup>Si, par spectroscopie IR à transformée de Fourier et par des mesures « BET » de l'aire de la surface. Les études de RMN CPMAS du <sup>29</sup>Si ont montré que la présence de groupes hydroxyles pontés et terminaux est minimale dans le catalyseur de Pt/SiO<sub>2</sub> obtenu à un pH de 9. Des résultats semblables ont été obtenus par l'analyse du spectre IR à transformée de Fourier en raison des conditions de synthèse du catalyseur.

**Mots clés :** hydrosilylation, sol-gel, Pt/SiO<sub>2</sub>, catalyseurs métalliques déposés, phénylacétylène, diphénylacétylène, RMN CP-MAS du <sup>29</sup>Si.

## Introduction

The aim in the preparation of catalytic materials to be used in industry is to obtain a product with high activity, selectivity, and stability (1). Heterogeneous catalysts are often prepared by wet chemistry methods such as precipitation, coprecipitation, hydrothermal synthesis, or by sol-gel process. The main advantage of this low-temperature process is to generate solids with large specific surface area and high porosity in the meso- and macropore ranges (2).

The sol-gel method represents a useful route in the synthesis of supported metal catalysts. The usefulness of this method is based on the fact that one can start with both the metal and support precursors in solution and design a cata-

lyst with well-defined physical properties. Advantages of the method include: superior homogeneity and purity, better micro structural control of the support, higher BET surface areas, better-defined pore size distributions, improved thermal stability of the metal support particles, and the facility to incorporate additional elements (3–5).

One of the important trends in the development of the hydrosilylation reaction has been the synthesis of heterogeneous catalysts for this reaction (6–9). On the other hand, immobilized complexes or anchored-metal complexes, in which the metal atom is bonded to a polymer support that plays the role of a macroligand, have been used. The supports consist of suitable modified ion-exchange resins (10), silica gel (11), and organic polymers such as divinylbenzene–

Received 4 March 2003. Published on the NRC Research Press Web site at <http://canjchem.nrc.ca> on 30 October 2003.

*This article is dedicated to Professor John Harrod, a key personality in homogeneous catalysis involving silanes.*

**R. Jiménez and J. Cervantes.**<sup>2</sup> Facultad de Química, University of Guanajuato, Guanajuato, Gto., 36050, México.

**J.M. Martínez-Rosales.** Centro de Investigaciones en Química Inorgánica, University of Guanajuato, Guanajuato, Gto., 36050, México.

<sup>1</sup>This article is part of a Special Issue dedicated to Professor John Harrod.

<sup>2</sup>Corresponding author.(e-mail address: [jauregi@quijote.ugto.mx](mailto:jauregi@quijote.ugto.mx)).



styrene co-polymer, polymethyl methacrylate (12), or polysiloxanes (13). The hydrosilylation reaction of unsaturated compounds such as olefins, acetylenes, imines, allylamines, and oximes promoted by transition-metal catalysts is widely investigated for reduction of unsaturated groups or addition of Si—H bonds.

Catalytic hydrosilylation of olefins with soluble platinum complexes was first described by Speier et al. (14), Saam and Séller (15), and Ryan and Séller (16) and the commercial catalyst (hexachloroplatinic acid) bears Speier's name.

Interest in hexachloroplatinic acid and other metal-supported catalysts has been one of the focal areas of organosilicon chemists since the 1970s. It is assumed that supported-metal catalysts have the advantages of both homogeneous and heterogeneous systems. Among the advantages of using supported catalysts are: the ease of catalyst recovery and chemical modification of the active sites, and handling.

The addition of Si—H bonds to unsaturated compounds can be carried out by free radical chain reactions, or more conveniently by the use of catalysts such as platinum or other transition metals (17–19). Polizzi et al. (6) reported that homogeneous and heterogeneous catalysts derived from mesitylene-solvated platinum atoms were very reactive in the selective hydrosilylation of dienes and acetylenes.

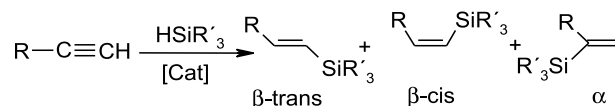
Olefin hydrosilylation reactions are known to occur with the aid of a homogeneous and supported catalyst (20, 21). These reactions are conventionally known to be accomplished by other side reactions, such as olefin isomerization. The development of catalysts with higher activity and selectivity toward hydrosilylation is undoubtedly needed. In many cases, more expensive catalysts have been employed for this purpose (22–26).

However, little is known about the hydrosilylation of the carbon–carbon triple bond with supported-metal catalysts obtained by the sol-gel process under the usual reaction conditions. The sol-gel process provides a useful route of preparing supported-metal systems. For example, Ru-MgO has been used in the benzene hydrogenation reaction (27) and in the hydrogenolysis of cyclopentene (28). Caporusso et al. (7) reported a detailed investigation of the hydrosilylation of aromatic nitriles promoted by unsupported- and supported-rhodium metal nanoparticles. They were prepared from arene-solvated rhodium atoms and are excellent catalysts for the selective hydrosilylation of aromatic nitriles. Schubert et al. (29) reported the activity of  $\text{Rh}(\text{CO})\text{Cl}(\text{PR}_3)_2$  heterogenized by the sol-gel method in the hydrosilylation of 1-hexene with triphenylsilane.

We have reported on the use of Ru/MgO and Pt/MgO obtained by the sol-gel method in the hydrosilylation reaction (30). Terminal acetylene hydrosilylation is one of our areas of interest (see Scheme 1) (31).

In a recent preliminary study, we have also used the Pt/SiO<sub>2</sub>-pH3 (**I**) and Pt/SiO<sub>2</sub>-pH9 (**II**) in the hydrosilylation of phenylacetylene, diphenylacetylene, and 1-heptyne with several hydrosilanes R<sub>3</sub>SiH (where R = Ph<sub>3</sub>, Ph<sub>2</sub>Me, and PhMe<sub>2</sub>) (32). In the present report, the influence of the route of synthesis of the catalysts **I** and **II** in acidic or basic medium on the catalytic activity and selectivity was studied. Particular focus is given to the surface properties to understand the catalytic systems' behavior.

Scheme 1.



## Experimental

### Materials

The chemicals used were all reagent grade and available from suppliers such as Gelest, Inc. and Aldrich. All the glassware used was treated with KOH (1 mol/L) in EtOH solution, washed carefully with deionized water and acetone, and dried in an oven at 110 °C for several hours. Any contact with other organic materials such as silicon grease was avoided. Liquid hydrosilanes were purified by distillation in a nitrogen atmosphere. NMR measurements were performed in CDCl<sub>3</sub> solutions using a Varian Gemini 200 MHz spectrometer and a Varian Unity-Plus 300 MHz spectrometer. The catalysts used in this work were obtained at the Gasses Physicochemical Laboratory of the Molecular Simulation Program (Mexican Petroleum Institute, México, D.F.) The catalysts **I** and **II** were activated for 4 h at 500 °C and then left 1 h at room temperature in a hydrogen atmosphere.

### Surface area and pore texture of catalysts

BET surface areas were determined using a Pulsechemisorb 2700 Micromeritics instrument and the automated gas volumetric method employing nitrogen as the adsorbate at 77 K. Samples were degassed under vacuum at 200 °C for 2 to 3 h prior to analysis.

### NMR studies of the supported-metal catalytic system

The <sup>29</sup>Si CPMAS NMR measurements were performed using a Varian Unity-Plus 300 MHz spectrometer operating at 59.58 MHz. The rotor spin rate (Si<sub>3</sub>N<sub>4</sub>) was 4 kHz, with a delay time of 6 s. Transients (1600) were accumulated and the contact time used was 1500. The samples were dehydrated at 350 °C for 30 min in an oven prior to recording the NMR spectra. The internal reference was talc.

### FT IR studies

FT IR spectra of the Pt/SiO<sub>2</sub> catalyst were recorded before and after activation in the range 4000–400 cm<sup>−1</sup> using a PerkinElmer FT IR 1600 spectrometer.

### Hydrosilylation procedure

All experiments were performed in a nitrogen atmosphere in a 50 mL two-necked flask equipped with a thermometer and a reflux condenser. The flask was charged with activated catalysts (25 mg Pt/SiO<sub>2</sub>-pH3 or Pt/SiO<sub>2</sub>-pH9, 0.5% Pt). The reactants, Ph<sub>2</sub>MeSiH (4.01 mmol) and phenylacetylene (4.5 mmol), were subsequently added. Once the addition was completed, the mixture was stirred and heated by means of an oil bath at 80–90 °C for 2 h. The stirring was interrupted every 10 min to take aliquots of the solution and the product distribution was analyzed using <sup>1</sup>H NMR measurements.



### Analysis of the reaction mixture

The isomeric ratio of the hydrosilylation products was derived from the areas of olefinic protons. Decrease of the  $\equiv\text{C}-\text{H}$  bond was comparable with the increase of the vinylic proton signals. The specific activity was calculated as mol of phenylacetylene transformed per g-atom of metal per h. Products were conveniently purified by distillation or crystallization. For  $\text{Ph}_3\text{SiH}$  with  $\text{PhC}\equiv\text{CH}$ , the product mixture was washed with a  $\text{CH}_2\text{Cl}_2$ /methanol (2:1) solution and crystallized at  $-5^\circ\text{C}$  to separate the  $\beta$ -trans and  $\alpha$ -isomer from the solution. Turnover reaction for these catalytic systems was also studied. The product mixture was separated from the catalyst by decantation and then equal amounts of fresh silane and phenylacetylene were added to the catalyst to start the next hydrosilylation reaction. The decrease in integrals of the  $\equiv\text{C}-\text{H}$  bond were comparable to the increase of the vinylic proton signals, and then the specific activity was again measured as mol of phenylacetylene transformed per g-atom of metal per h.

### Results and discussion

The  $\text{Pt}/\text{SiO}_2\text{-pH3}$  (**I**) and  $\text{Pt}/\text{SiO}_2\text{-pH9}$  (**II**) catalysts obtained by the sol-gel method were applied to well-known hydrosilylation reactions such as the hydrosilylation of phenylacetylene, diphenylacetylene, and 1-heptyne with various silanes ( $\text{R}_3\text{SiH}$  where  $\text{R} = \text{Ph}, \text{Ph}_2\text{Me}, \text{and PhMe}_2$ ) and the catalysts were characterized by solid-state NMR, FT IR spectroscopy, and the BET method. Hydrosilylation of phenylacetylene was performed using both catalysts. In the other two reactions, only the  $\text{Pt}/\text{SiO}_2\text{-pH-3}$  catalyst was used because of the loss of catalytic activity of the  $\text{Pt}/\text{SiO}_2\text{-pH-9}$  catalyst after each reaction. Illustrative results are presented in Table 1. Structural assignment of the products were based on  $^1\text{H}$  NMR measurements.

The  $^1\text{H}$  NMR spectrum indicated two doublets, at 5.5 and 5.8 ppm, which are signals typical of the AX spin system. The coupling constant was  $J = 3$  Hz, and the signals were assigned to the *geminal* hydrogen atoms of the ethylene group. The bands in the region of the relatively weaker field are assigned to the AB spin system with a coupling constant of  $J = 19$  Hz. It indicates the trans position of vicinal protons of the  $\text{HC}=\text{CH}$  fragment.

The hydrosilylation reactions of acetylenes with several hydrosilanes using both **I** and **II** catalysts, were studied by FT IR. The catalytic activity was manifested by IR spectral analysis of the reaction products. Fingerprint analysis confirmed the concurrence of the hydrosilylation product. The intensity of the band at  $960\text{ cm}^{-1}$ , characteristic for the  $\text{Si}-\text{C}=\text{C}$  bond in the hydrosilylation product increased progressively with time. At the same time, the IR absorption band of  $2210\text{ cm}^{-1}$ , characteristic of the  $\text{Si}-\text{H}$  bond, decayed with time. Within the reaction temperature range ( $80\text{--}90^\circ\text{C}$ ), no detectable olefin isomerization products were observed. The rate of increase in the intensity of the product band at  $960\text{ cm}^{-1}$  was consistent with the rate of decay of the hydrosilanes band at  $2210\text{ cm}^{-1}$ . Therefore, the reaction profiles were measured by following the disappearance of the band at  $2210\text{ cm}^{-1}$  characteristic of the  $\text{Si}-\text{H}$  bond, and the extent of the hydrosilylation reaction was calculated based on the amount of the  $\text{R}_3\text{Si-H}$  consumed as the limiting

**Table 1.** Product distribution in the hydrosilylation of acetylenes by  $\text{R}_3\text{SiH}$  promoted by **I** and **II**.

Catalyst	Acetylene	$\text{R}_3\text{SiH}$	Product (%)		
			trans	gem	cis
$\text{Pt}/\text{SiO}_2\text{-pH 3}$	<b>PhCCH</b>	$\text{Ph}_3\text{SiH}$	98	2	—
		$\text{Ph}_2\text{MeSiH}$	97	3	—
		$\text{PhMe}_2\text{SiH}$	80	18	2
$\text{Pt}/\text{SiO}_2\text{-pH 9}$		$\text{Ph}_3\text{SiH}$	97	3	—
		$\text{Ph}_2\text{MeSiH}$	95	5	—
		$\text{PhMe}_2\text{SiH}$	78	20	2
$\text{Pt}/\text{SiO}_2\text{-pH 3}$	<b>PhCCPh</b>	$\text{Ph}_3\text{SiH}$	48	0	52
		$\text{Ph}_2\text{MeSiH}$	24	0	76
		$\text{PhMe}_2\text{SiH}$	33	0	67
$\text{Pt}/\text{SiO}_2\text{-pH 3}$	<b>1-Heptyne</b>	$\text{Ph}_3\text{SiH}$	77	23	—
		$\text{Ph}_2\text{MeSiH}$	78	20	2
		$\text{PhMe}_2\text{SiH}$	70	25	5

**Note:** The reactions were performed at  $80\text{--}90^\circ\text{C}$  for 2 h with conversions of over 95% of the initial reactants.

reactant. A typical representation of the hydrosilylation reaction progress with time is shown in Fig. 1.

The hydrosilylation reaction was conducted under a variety of reaction conditions. The effect of temperature, reactant concentration, and catalyst amounts on the rate of the hydrosilylation reaction were investigated, together with the catalysts' reuse.

The catalyst can be removed from the reaction mixture by filtration in  $\text{N}_2$  or by removal of the filtrate and then washing with either one of the reactants. If the activated catalyst was removed from the hydrosilylation mixture by filtration and washed with the same reactant, the recovered catalyst showed little decrease in catalytic activity during four runs, ranging from 98% conversion in the first run to 92% conversion in the fourth run. It seems that some of the products are remaining on the surface, creating less active catalytic sites, although it is very important to say that the selectivity is maintained after the four runs, as can be seen in Table 2.

These results were true for **I**. Once the hydrosilylation reaction was performed using the two catalytic systems, it was observed that the catalyst obtained at pH 9 (**II**) loses catalytic activity and it has to be activated before a new reaction. It was decided to investigate the morphological characteristics of each system to obtain a better understanding of such behavior.

### Solid-state NMR studies

The development of high-power decoupling, cross-polarization (CP), and magic-angle-spinning (MAS) techniques permits NMR studies. We applied both MAS and CP-MAS NMR to the molecular characterization of the surface of supported-metal catalysts obtained by the sol-gel method. Figures 2–4 contain the MAS and CP-MAS  $^{29}\text{Si}$  NMR data for the surface-attached molecules.  $^{29}\text{Si}$  NMR data do agree with information from the literature for silica-supported catalytic systems (33–36). It is important to observe that two catalysts (seen in figures as  $\text{Pt}/\text{SiO}_2$  IMP and FQ) were prepared at the same conditions and the solid-state NMR information obtained is reported. The MAS  $^{29}\text{Si}$  NMR spectrum of **I** (Fig. 2) shows a broad signal at  $-107$  ppm as



**Fig. 1.** Hydrosilylation reaction progress with time. Hydrosilylation of phenylacetylene with  $\text{Ph}_3\text{SiH}$  (◆),  $\text{Ph}_2\text{MeSiH}$  (●), and  $\text{PhMe}_2\text{SiH}$  (■) using catalyst **I**.

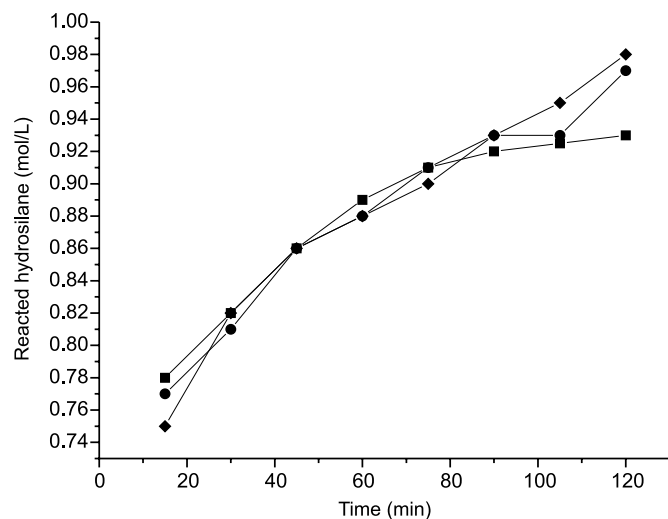


**Table 2.** Specific activity and isomeric ratio as a function of reaction time of Pt/SiO<sub>2</sub>-pH 3 (**I**) in the hydrosilylation of phenylacetylene with  $\text{Ph}_2\text{MeSiH}$ .

Cycles	Specific activity	Reaction time (h)	Product (%)		
			trans	gem	cis
1	3126	2	96	4	—
2	3126	2	96	4	—
3	3114	2	96	4	—
4	2997	2	96	4	—

**Note:** The reactions were performed at 80–90 °C for 2 h with conversions of over 95% of the initial reactants. The specific activity was calculated as mol of phenylacetylene transformed per g-atom of metal per h.

signed to  $\text{Si}(\text{OSi})_4$  with a small shoulder around –95 ppm attributable to the  $(\text{HO})\text{Si}(\text{OSi})_3$  environment. From the MAS  $^{29}\text{Si}$  NMR spectrum of **II** (Fig. 3), similar information was obtained but a bigger shoulder at –95 ppm is observed.

In the present case, the CP-MAS pulse sequence was more informative. Signals at –96 and –86 ppm were assigned to  $(\text{HO})\text{Si}(\text{OSi})_3$  and  $(\text{OH})_2\text{Si}(\text{OSi})_2$ . More intense signals were observed in catalyst **II** obtained at pH 9 (Fig. 4). These results show that few hydroxyl groups remain on the silica surface of the supported-metal catalyst **I**. On the other hand, the surface of **II** has more hydroxyl groups. This is important evidence that tends to explain the different catalysts' behavior based on the synthetic conditions and particularly the loss of activity of **II**.

### Porosimetry results

Nitrogen adsorption and desorption isotherms obtained at liquid nitrogen temperature for **I** and **II** are given in Figs. 5 and 6. The Pt/SiO<sub>2</sub>-pH3 isotherm is type I and is typical of microporous materials. The totality of accessible pores are filled with adsorbate and the isotherm reaches a plateau that remains fairly invariant as  $p/P_0 \rightarrow 1$  (where  $p$  is the pressure of the adsorbate at equilibrium and  $P_0$  is the saturated pres-

**Fig. 2.**  $^{29}\text{Si}$  MAS NMR spectra of Pt/SiO<sub>2</sub> at pH 3.

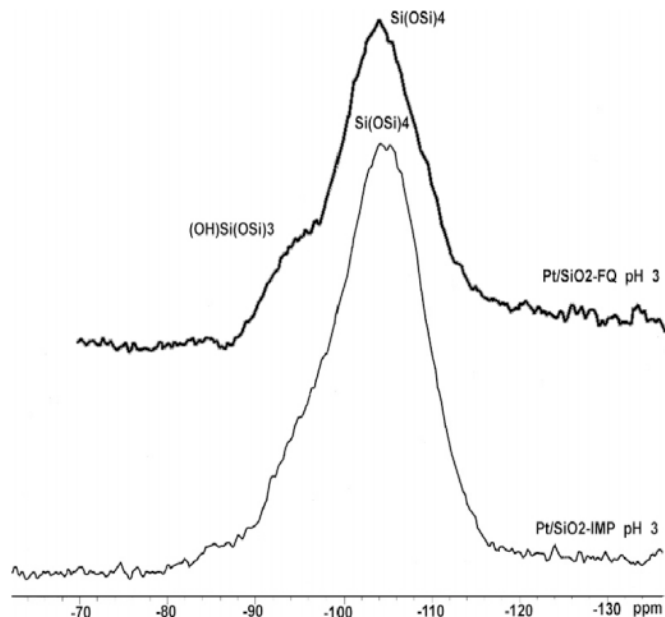
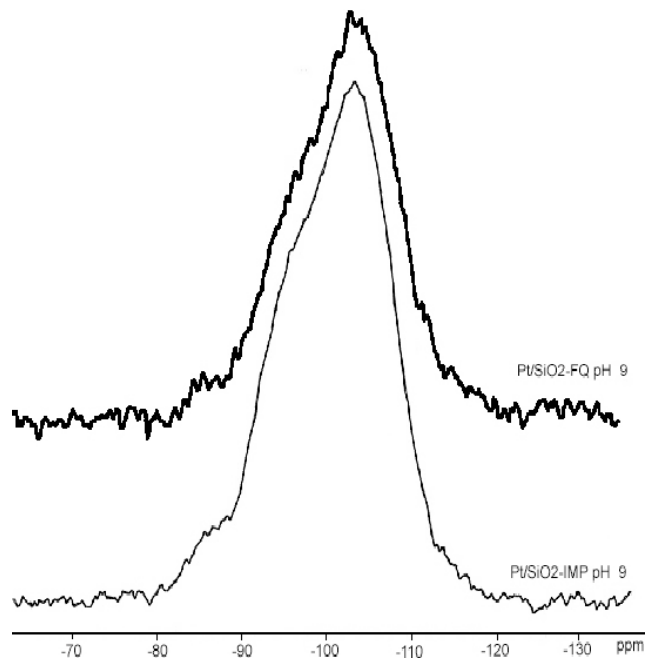


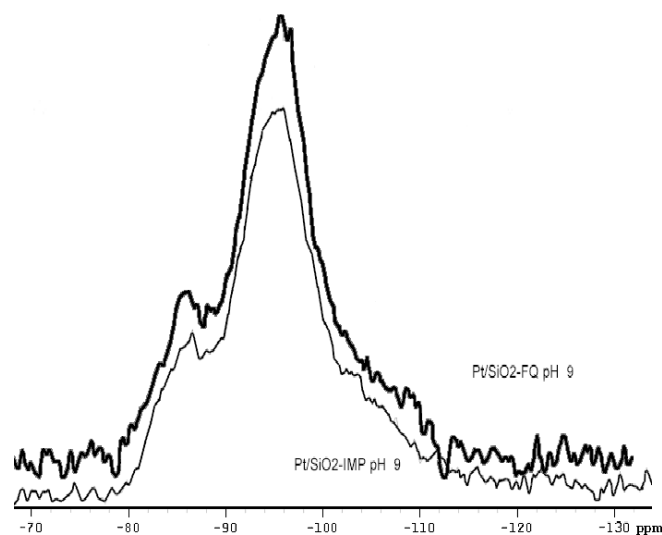
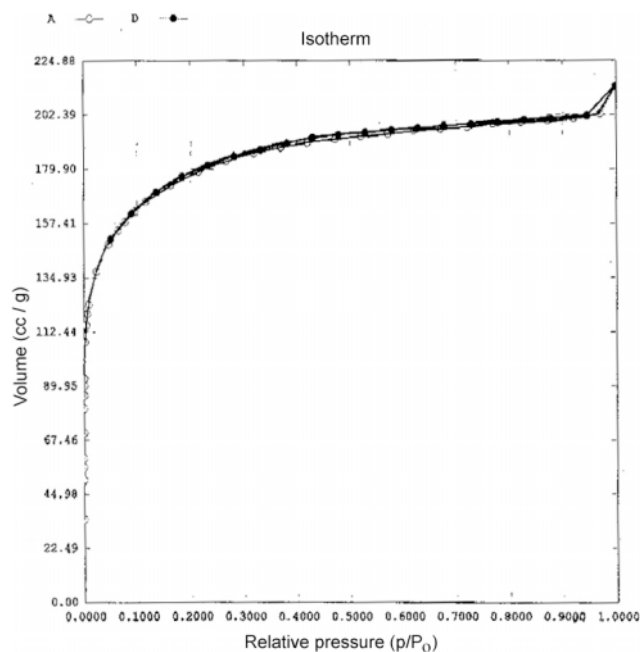
**Fig. 3.**  $^{29}\text{Si}$  MAS NMR spectra of Pt/SiO<sub>2</sub> at pH 9.



sure at equilibrium). Its desorption isotherm does not exhibit any hysteresis.

In contrast, the Pt/SiO<sub>2</sub>-pH9 isotherm is type III, typical of mesoporous solids. Monolayer and multilayer coverage are basically completed at  $p/P_0 \rightarrow 1$  (Fig. 6). Nitrogen uptake in this range of pressure increases in the order **I** < **II**, a trend consistent with the BET surface as shown in Table 3. After multilayer coverage is complete, capillarity condensation occurs in the mesopores. The small inclination of the isotherm step in Fig. 6 indicates that these mesopores are distributed over a range of sizes.

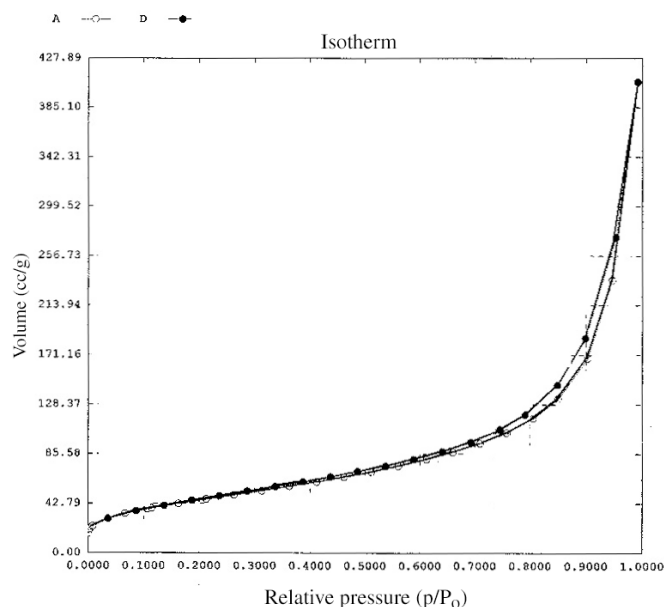
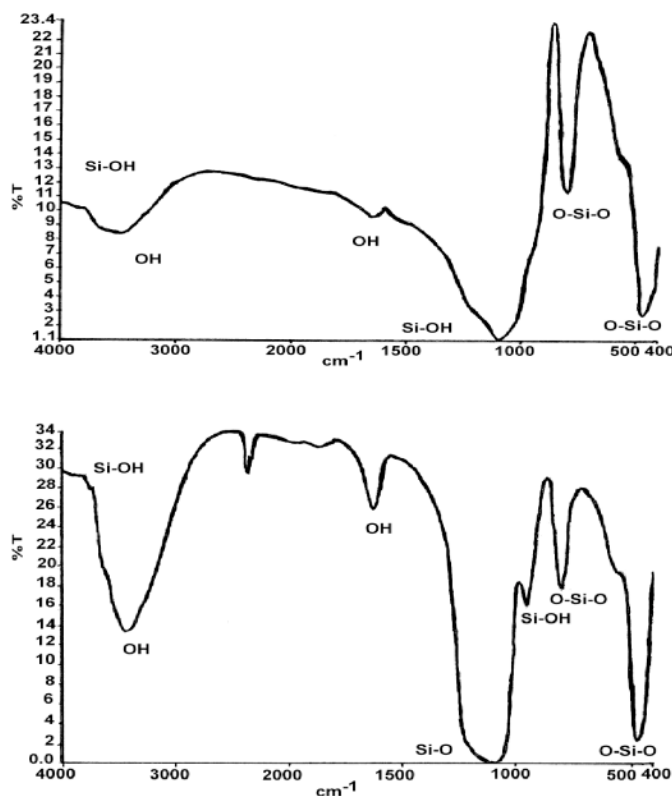


**Fig. 4.**  $^{29}\text{Si}$  CP-MAS NMR spectra of Pt/SiO<sub>2</sub> at pH 9.**Fig. 5.** Nitrogen adsorption-desorption isotherms, at liquid nitrogen temperature, of catalyst I.**Table 3.** Surface area (SA), pore volume (PV), and pore size (PS) measurements of I and II obtained by nitrogen sorption data at 77 K.

Catalyst	SA (m <sup>2</sup> /g)	PV (cm <sup>3</sup> /g)	PS (Å)
Pt/SiO <sub>2</sub> -pH 3 (I)	529	0.083	14
Pt/SiO <sub>2</sub> -pH 9 (II)	160	0.03	31.6

### FT IR studies of I and II catalysts

FT IR spectra were obtained for Pt/SiO<sub>2</sub> catalysts prior to the hydrosilylation reactions. Figure 7 illustrates the IR spectra that show peaks around 3500 cm<sup>-1</sup> that correspond to Si—OH and OH bonds. The peaks are more intense in II. This information agrees with the results of solid-state NMR

**Fig. 6.** Nitrogen adsorption-desorption isotherms, at liquid nitrogen temperature, of catalyst II.**Fig. 7.** FT IR spectra of catalysts I and II.

presented previously. When the catalysts were heated at the activation temperature (500 °C), it was possible to observe clearly that the intensity of the OH vibration peak decreases after 4 h.

From the information obtained by CP-MAS NMR, porosimetry, and FT IR, several aspects can be considered to address the difference in catalytic activity: The presence of



more OH groups in Pt/SiO<sub>2</sub> as a result of the preparation at pH 9 tend to affect its properties such as the surface area and pore characteristics. In Table 3, it is shown that there is a very important difference in surface area (529 m<sup>2</sup>/g for **I** and 160 m<sup>2</sup>/g for **II**). Pore size is bigger in **II**, and blocked pores can also be considered in the catalyst deactivation. At it has been pointed out, after each reaction, **II** is required to be activated.

## Final remarks

The investigation of the use of Pt supported on silica obtained by the sol-gel method at different pHs provided significant results suggesting the actual possibility of preparing physically heterogeneous catalysts for hydrosilylation reactions. Additional work is needed to clarify the role of the pathway in connection to the possible activating affect of the acidic species on the surface of the support. Finally, the possibility of controlling stereochemistry and morphology by the heterogeneous phase is a matter of active study.

## Acknowledgements

Financial supports by CONCYTEG (Consejo de Ciencia y Tecnología del Estado de Guanajuato, México) is gratefully acknowledged.

## References

1. F. Pinna. *Catal. Today*, **41**, 129 (1998).
2. J. Livage. *Catal. Today*, **41**, 3 (1998).
3. L.L. Hench and J.K. West. *Chem. Rev.* **90**, 33 (1990).
4. A.M. Buckley and M. Greenblatt. *J. Chem. Ed.* **71**, 599 (1994).
5. O. Lev, M. Tsionsky, and L. Robinovich. *Anal. Chem.* **67**, 22A (1995).
6. C. Polizzi, A.M. Caporusso, G. Vitulli, P. Salvatori, and M. Pasero. *J. Mol. Catal.* **91**, 83 (1994).
7. A.M. Caporusso, N. Panziera, P. Pertici, E. Pitzalis, P. Salvatori, G. Vitulli, and G. Martra. *J. Mol. Catal.* **150**, 275 (1999).
8. T. Baba, A. Kato, H. Yuasa, and F. Toriyama. *Catal. Today*, **44**, 271 (1998).
9. G. Schmid, H. West, H. Mehles, and A. Lehnert. *Inorg. Chem.* **36**, 891 (1997).
10. V.O. Reikhsfel'd, N.A. Fillipov, and A.V. Nikitin. *Zh. Obshch. Khim.* **47**, 959 (1977).
11. U. Schubert, C. Egger, K. Rose, and C. Alt. *J. Mol. Catal.* **55**, 330 (1989).
12. M.G. Pomerantseva and Z.V. Belyakova. *Zh. Obshch. Khim.* **54**, 354 (1984).
13. H.S. Hilal, M.A. Suleiman, W.J. Jondi, S. Khalaf, and M.M. Masoud. *J. Mol. Catal.* **144**, 47 (1999).
14. J.L. Speier, J.A. Webster, and G.H. Barnes. *J. Am. Chem. Soc.* **79**, 3941 (1957).
15. J.C. Saam and J.L. Séller. *J. Am. Chem. Soc.* **80**, 4104 (1958).
16. J.W. Ryan and J.L. Séller. *J. Am. Chem. Soc.* **86**, 895 (1964).
17. I. Ogima. *In The chemistry of organic silicon compounds*, Part 2. Edited by S. Patai and Z. Rappoport. Wiley, New York. 1989. Chap. 25.
18. B. Marciniak, J. Gulinski, W. Urbaniak, and Z. Kornetka. *In Comprehensive handbook on hydrosilylation*. Edited by B. Marciniak. Pergamon Press Inc., Tarrytown, New York. 1992. Chap. 2. p. 84.
19. B. Marciniak, P. Krzyzanowsky, E. Walczuk-Gusciora, and W. Duczmal. *J. Mol. Catal.* **144**, 263 (1999).
20. A.J. Chalk and J.F. Harrod. *J. Am. Chem. Soc.* **87**, 1133 (1965).
21. H.S. Hilal, W. Jondi, Sh. Khalaf, and A. Keilani. *J. Organomet. Chem.* **452**, 167 (1993).
22. H. Hilal, M. Abu-Ied, M. Alsubu, and S. Khalaf. *J. Mol. Catal.* **39**, 1 (1986).
23. R.H. Crabtree. *In The organometallic chemistry of the transition metals*. Wiley, Toronto. 1988.
24. R. Takeuchi, S. Natta, and D. Watanabe. *J. Org. Chem.* **60**, 3045 (1995).
25. R. Takeuchi and N. Tanouchi. *J. Chem. Soc. Perkins Trans. 1*, 2909 (1994).
26. A. Marinetti. *Tetrahedron Lett.* **35**, 5861 (1994).
27. T. López, I. Garcia, and R. Gómez. *J. Catal.* **127**, 75 (1991).
28. T. López, M. Asomoza, P. Bocha, E. Garcia-Figueroa, and R. Gómez. *J. Catal.* **138**, 463 (1992).
29. U. Schubert, C. Egger, and K. Rose. *J. Mol. Catal.* **55**, 330 (1989).
30. R. Jiménez, J.M. López, and J. Cervantes. *Can. J. Chem.* **78**, 1491 (2000).
31. J. Cervantes, G. González-Alatorre, D. Rohack, and K.H. Pannell. *Appl. Organomet. Chem.* **14**, 146 (2000).
32. R. Jiménez and J. Cervantes. *Inf. Tecnol.* **12**, 81 (2001).
33. D.W. Sindorf and G.E. Maciel. *J. Am. Chem. Soc.* **105**, 3767 (1983).
34. D.W. Sindorf and G.E. Maciel. *J. Am. Chem. Soc.* **105**, 1848 (1983).
35. C.A. Fyre, H.C. Clark, J.A. Davies, P.J. Hayes, and R.E. Wasylishen. *J. Am. Chem. Soc.* **104**, 438 (1982).
36. H.C. Clark, J.A. Davies, C.A. Fyre, P.J. Heyes, and R.E. Wasylishen. *Organometallics*, **2**, 177 (1983).



# Reduction of hafnium(IV) complexes in the presence of molecular nitrogen: Attempts to form dinitrogen complexes of the heaviest group 4 element<sup>1</sup>

Michael D. Fryzuk, James R. Corkin, and Brian O. Patrick

**Abstract:** The reaction of  $[\text{P}_2\text{N}_2]\text{Li}_2(\text{dioxane})_2$  with  $\text{HfCl}_4(\text{THF})_2$  (where  $[\text{P}_2\text{N}_2] = \text{PhP}(\text{CH}_2\text{SiMe}_2\text{NSiMe}_2\text{CH}_2)_2\text{PPh}$ ) results in the formation of the hafnium dichloride complex  $[\text{P}_2\text{N}_2]\text{HfCl}_2$  (**1**). The behaviour of **1** as a potential precursor in the generation of a dinitrogen coordination complex is described. Reduction of **1** with potassium-graphite ( $\text{C}_8\text{K}$ ), under dinitrogen, under a variety of conditions led to a number of products, one of which is the dinuclear derivative with bridging P-phenyl groups that has the general formula  $\{[\text{P}_2\text{N}_2]\text{Hf}\}_2$  (**2**). Reduction of the hafnium diiodide  $[\text{P}_2\text{N}_2]\text{HfI}_2$  (**3**) — prepared via the reaction of **1** with excess  $\text{Me}_3\text{SiI}$  — with  $\text{C}_8\text{K}$  results in the formation of  $([\text{P}_2\text{N}_2]\text{Hf})_2(\mu\text{-}\eta^2\text{-}\eta^2\text{-N}_2)$  (**4**) as the major product of the reaction, while  $\{[\text{P}_2\text{N}_2]\text{Hf}\}_2$  (**2**) and  $[\text{P}_2\text{N}_2]\text{Hf}(\text{C}_7\text{H}_8)$  (**5**) appear to be minor products. Reaction of **1** with 2 equiv of  $\text{MeMgCl}$  gives  $[\text{P}_2\text{N}_2]\text{HfMe}_2$  (**6**), which, upon exposure to an atmosphere of  $\text{H}_2$ , gives the hafnium tetrahydride  $\{[\text{P}_2\text{N}_2]\text{Hf}\}_2(\text{m-H})_4$  (**7**).

**Key words:** hafnium, dinitrogen, reduction, coordination chemistry, hydride, mixed donor ligands.

**Résumé :** La réaction du  $[\text{P}_2\text{N}_2]\text{Li}_2(\text{dioxane})_2$  avec le  $\text{HfCl}_4(\text{THF})_2$  {dans lequel  $[\text{P}_2\text{N}_2] = \text{PhP}(\text{CH}_2\text{SiMe}_2\text{NSiMe}_2\text{CH}_2)_2\text{PPh}$ } conduit à la formation du complexe de dichlorure d'hafnium,  $[\text{P}_2\text{N}_2]\text{HfCl}_2$  (**1**). On décrit le comportement du complexe **1** comme précurseur potentiel pour générer un complexe de coordination du diazote. La réduction de **1** à l'aide de potassium sur graphite ( $\text{C}_8\text{K}$ ), sous atmosphère de diazote, dans diverses conditions expérimentales conduit à la formation d'un certain nombre de produits, dont l'un est un dérivé dinucléaire de formule générale  $\{[\text{P}_2\text{N}_2]\text{Hf}\}_2$  (**2**) portant des groupes P-phényles agissant comme ponts. La réduction par le  $\text{C}_8\text{K}$  du complexe de diiodure d'hafnium,  $[\text{P}_2\text{N}_2]\text{HfI}_2$  (**3**), préparé par le biais d'une réaction de **1** avec un excès de  $\text{Me}_3\text{SiI}$ , conduit à la formation du complexe  $\{[\text{P}_2\text{N}_2]\text{Hf}\}_2(\mu\text{-}\eta^2\text{-}\eta^2\text{-N}_2)$  (**4**) comme produit majeur de la réaction alors qu'il semble y avoir formation  $\{[\text{P}_2\text{N}_2]\text{Hf}\}_2$  (**2**) et de  $[\text{P}_2\text{N}_2]\text{Hf}(\text{C}_7\text{H}_8)$  (**5**) comme sous-produits. La réaction de **1** avec deux équivalents de  $\text{MeMgCl}$  conduit à la formation de  $[\text{P}_2\text{N}_2]\text{HfMe}_2$  (**6**) qui, mis dans une atmosphère de  $\text{H}_2$ , fournit le tétrahydure d'hafnium,  $\{[\text{P}_2\text{N}_2]\text{Hf}\}_2(\mu\text{-H})_4$  (**7**).

**Mots clés :** hafnium, diazote, réduction, chimie de coordination, hydrure, ligands donneurs fixés.

[Traduit par la Rédaction]

## Introduction

The preparation of dinitrogen complexes of the early transition metals generally involves reduction of some suitable metal halide precursor in the presence of molecular nitrogen (**1**). While effective in many cases, certain early transition elements are not easily reduced, and as such, well-defined dinitrogen complexes are either unknown or extremely rare. Examples of this are the group 3 elements, Sc, Y, and La, for

which molecular dinitrogen complexes are not known and the group 4 element, Hf, for which only one dinitrogen complex has been reported (**2**). Reduction of  $\text{Cp}^*\text{HfI}_2$  with Na-K in dimethoxyethane at  $-40^\circ\text{C}$  does result in the formation of  $[\text{Cp}^*\text{Hf}(\text{N}_2)]_2(\mu\text{-N}_2)$  in rather low yields. In this case, the choice of the reducing agent and solvent and the use of the diiodide were critical to the success of this procedure. As has been reported earlier, reductive strategies to generate dinitrogen complexes can lead to other products (**3**), and so, the fact that reaction optimization required considerable variation in experimental conditions is not surprising.

In this paper we describe our efforts to extend the family of hafnium dinitrogen complexes by the attempted preparation of  $([\text{P}_2\text{N}_2]\text{Hf})_2(\mu\text{-}\eta^2\text{-N}_2)$  (**4**), in analogy to that reported previously for the zirconium complex  $([\text{P}_2\text{N}_2]\text{Zr})_2(\mu\text{-}\eta^2\text{-N}_2)$ . The zirconium complex has been shown to add  $\text{H}_2$  and primary silanes with concomitant formation of N—H and N—Si bonds, respectively (**4**). We reasoned that access to the hafnium dinitrogen complex congener might allow for similar reactivity and even perhaps different reactivity patterns. However, as will be shown in this work, changing the metal

Received 13 March 2003. Published on the NRC Research Press Web site at <http://canjchem.nrc.ca> on 11 November 2003.

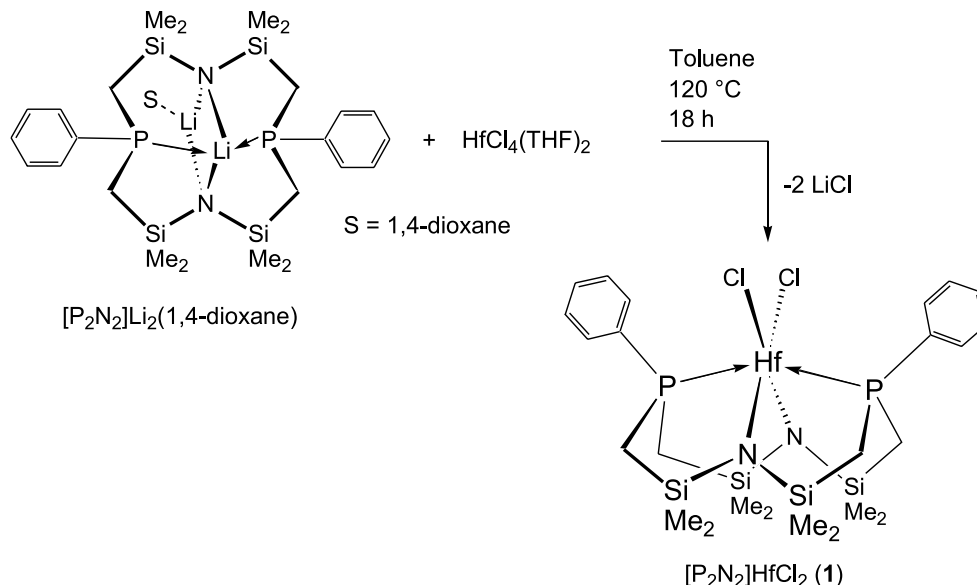
*Dedicated to John Harrod in celebration of his contributions to inorganic chemistry, especially early metal chemistry.*

M.D. Fryzuk,<sup>2</sup> J.R. Corkin, and B.O. Patrick. Department of Chemistry, University of British Columbia, 2036 Main Mall, Vancouver, BC V6T 1Z1, Canada.

<sup>1</sup>This article is part of a Special Issue dedicated to Professor John Harrod.

<sup>2</sup>Corresponding author (e-mail: [fryzuk@chem.ubc.ca](mailto:fryzuk@chem.ubc.ca)).



**Scheme 1.** Synthesis of  $[\text{P}_2\text{N}_2]\text{HfCl}_2$  (**1**).

from Zr to Hf results in a different set of reactions when reduction in the presence of dinitrogen is attempted.

## Results and discussion

### Preparation and structure of $[\text{P}_2\text{N}_2]\text{HfCl}_2$ (**1**)

Our initial strategy to prepare  $([\text{P}_2\text{N}_2]\text{Hf})_2(\mu\text{-}\eta^2\text{-N}_2)$  (**4**) was to follow exactly the preparation of the zirconium analogue  $([\text{P}_2\text{N}_2]\text{Zr})_2(\mu\text{-}\eta^2\text{-N}_2)$ , by reduction of the Hf(IV) dichloride complex,  $[\text{P}_2\text{N}_2]\text{HfCl}_2$  (**1**), with an alkali metal reagent. We have already shown that reduction of  $[\text{P}_2\text{N}_2]\text{MCl}_x$  ( $\text{M} = \text{Zr}$ ,  $x = 2$ ;  $\text{M} = \text{Nb}$ ,  $x = 1$ ) by potassium-graphite ( $\text{C}_8\text{K}$ ) can generate good yields of the corresponding dinitrogen complexes  $([\text{P}_2\text{N}_2]\text{M})_2(\mu\text{-N}_2)$  ( $\text{M} = \text{Zr}$  (**4**),  $\text{M} = \text{Nb}$  (**3**)). The starting dichloride **1** was prepared by the reaction of the THF adduct of hafnium(IV) tetrachloride with 1 equiv of  $[\text{P}_2\text{N}_2]\text{Li}_2(1,4\text{-dioxane})_2$ . The optimal conditions for this reaction were found to require heating of a suspension of starting materials in toluene overnight at approximately  $120\text{ }^\circ\text{C}$  (Scheme 1).

Complex **1** was characterized by solution  $^1\text{H}$  and  $^{31}\text{P}\{^1\text{H}\}$  NMR spectroscopy, elemental analysis, and solid-state, X-ray structure analysis. Crystals of **1** suitable for X-ray diffraction were grown from a saturated DME solution; the ORTEP diagram is shown in Fig. 1.

The solid-state molecular structure of **1** is best described as distorted octahedral. N(1), N(2), Cl(1), and Cl(2) can be described as forming a square plane, with the sum of the four angles equal to  $360.1^\circ$ . P(1) and P(2) can then be described as adopting quasi-capping positions, with a P(1)–Hf(1)–P(2) angle of  $153.76(3)^\circ$ , which is drawn back from the optimum  $180^\circ$  because of the constraints of the macrocyclic ligand framework. The small cavity size of the  $[\text{P}_2\text{N}_2]$  ligand forces the hafnium atom to sit atop the ligand, which places the two chlorides *cis* to each other.

The  $[\text{P}_2\text{N}_2]$  framework is distorted and adopts a  $\text{C}_2$  twist in the solid state, a feature that has been observed in many  $[\text{P}_2\text{N}_2]$  complexes (5–10). The solid-state structure of **1** is both isomorphous and isostructural with that of its zirco-

nium analogue,  $[\text{P}_2\text{N}_2]\text{ZrCl}_2$ , and Table 1 shows a comparison of selected bond lengths and angles for the two compounds. As with the zirconium analogue, the Hf–N, Hf–P, and Hf–Cl bond lengths are not unusual and compare well with other group 4 amido and phosphine complexes (5, 11–13).

Like the zirconium derivative, the solid-state molecular structure of **1** does not match the solution structure. The  $^1\text{H}$  NMR spectrum of **1** is virtually identical to that of the zirconium analogue, with slight displacements of each characteristic signal. The solution structure is more compatible with a  $\text{C}_{2v}$  symmetry. Only two signals due to the silyl methyl protons are observed, reflecting the “top and bottom” asymmetry of **1**. If the  $\text{C}_2$  symmetry of the solid state is held in solution, one would expect to observe four silyl methyl signals. It seems, therefore, that the  $[\text{P}_2\text{N}_2]$  framework is quite flexible in solution and undergoes a “rocking” motion centered at the trigonal silyl amide groups. The  $^{31}\text{P}\{^1\text{H}\}$  NMR spectrum of **1** shows a singlet at  $-5.8\text{ ppm}$ , which is shifted  $8.5\text{ ppm}$  downfield from that observed for the zirconium analogue.

### Reduction of $[\text{P}_2\text{N}_2]\text{HfCl}_2$ (**1**)

While ease of reduction is difficult to compare, tables of reduction potentials indicate that Hf is more difficult to reduce than zirconium (14–15). The first attempt to reduce **1** followed a procedure identical to the one that formed the zirconium dinitrogen complex; it involved reduction of the starting chloride complex with 2 equiv of potassium graphite (**4**), but the results were unexpected. Instead of the desired dinitrogen complex, the major product was the hafnium dimer,  $\{[\text{P}_2\text{N}_2]\text{Hf}\}_2$  (**2**), with coordination of the activated phenyl rings on one phosphorus to the other metal atom (Scheme 2).

The NMR spectra of **2** are consistent with this dimeric formulation. The  $^1\text{H}$  NMR spectrum shows a set of phosphorus–phenyl resonances in a 2:2:1 ratio at 4.22, 4.15, and 3.39 ppm, respectively. Coupling information is transmitted through the coordinated arene ring between metal centers,



**Fig. 1.** An ORTEP diagram of  $[\text{P}_2\text{N}_2]\text{HfCl}_2$  (**1**), showing the solid-state molecular structure (ellipsoids at 50% probability). The silyl methyl groups have been omitted for clarity; only the *ipso* carbons of the phosphorus phenyl groups are shown.

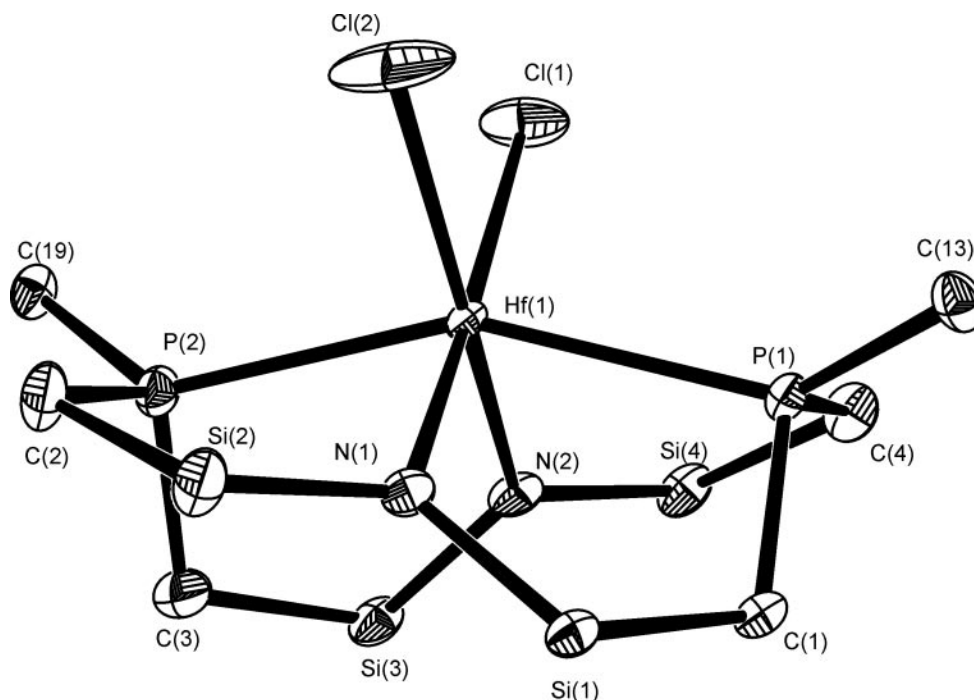


**Table 1.** A comparison of selected bond lengths (Å) and angles (°) in  $[\text{P}_2\text{N}_2]\text{MCl}_2$  (M = Zr, Hf).

Bond lengths	M = Hf	M = Zr	Bond angles	M = Hf	M = Zr
M(1)—N(1)	2.125(3)	2.136(4)	N(1)—M(1)—N(2)	96.6(1)	96.8(2)
M(1)—N(2)	2.134(3)	2.125(4)	P(1)—M(1)—P(2)	153.76(3)	152.52(6)
M(1)—P(1)	2.684(1)	2.694(2)	Cl(1)—M(1)—Cl(2)	83.32(4)	82.57(7)
M(1)—P(2)	2.673(1)	2.707(2)	N(1)—M(1)—Cl(2)	90.88(9)	89.5(1)
M(1)—Cl(1)	2.461(1)	2.455(2)	N(2)—M(1)—Cl(1)	89.22(9)	91.3(1)
M(1)—Cl(2)	2.461(1)	2.448(2)			

leading to an AA'BB' pattern in the  $^{31}\text{P}\{^1\text{H}\}$  NMR spectrum. This compound also has a zirconium analogue,  $\{[\text{P}_2\text{N}_2]\text{Zr}\}_2$ , which is the major product when  $[\text{P}_2\text{N}_2]\text{ZrCl}_2$  is reduced with  $\text{C}_8\text{K}$  in the absence of  $\text{N}_2$ , for example, under Ar or in a degassed vessel (**3**).  $\{[\text{P}_2\text{N}_2]\text{Zr}\}_2$  was first noticed as an impurity in the reaction that produces  $\{[\text{P}_2\text{N}_2]\text{Zr}\}(\mu\text{-}\eta^2\text{:}\eta^2\text{-N}_2)$ . For the zirconium system, under  $\text{N}_2$ , the dimer was a fairly minor impurity. When the metal center is changed to hafnium, the dimer appears to be the major product of this reaction, at least under these conditions.

### Preparation and reduction of $[\text{P}_2\text{N}_2]\text{HfI}_2$ (**3**)

The only known hafnium dinitrogen complex,  $\{\text{Cp}^*\text{Hf}(\text{N}_2)\}_2(\mu\text{-N}_2)$ , was prepared from the precursor,  $\text{Cp}^*\text{HfI}_2$ , after attempts to use a dichloride complex as a starting material were unsuccessful (**2**). Reaction of a toluene solution of  $[\text{P}_2\text{N}_2]\text{HfCl}_2$  (**1**) with a slight excess of trimethylsilyliodide resulted in formation of  $[\text{P}_2\text{N}_2]\text{HfI}_2$  (**3**) (Scheme 3).

Assuming an analogous structure for the diiodide as was found for the dichloride, one would expect little change in the NMR spectra upon replacement of chloride with iodide, and to a degree this is observed. The  $^{31}\text{P}\{^1\text{H}\}$  NMR signal is still a singlet at  $-5.4$  ppm, shifted only  $0.4$  ppm downfield of

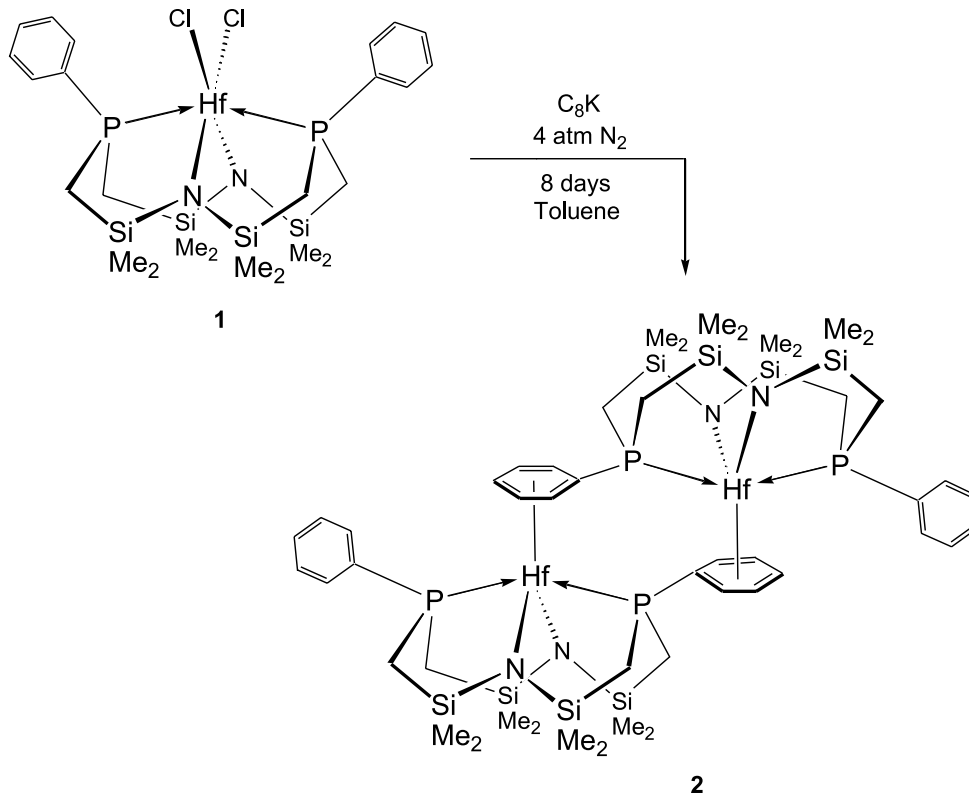
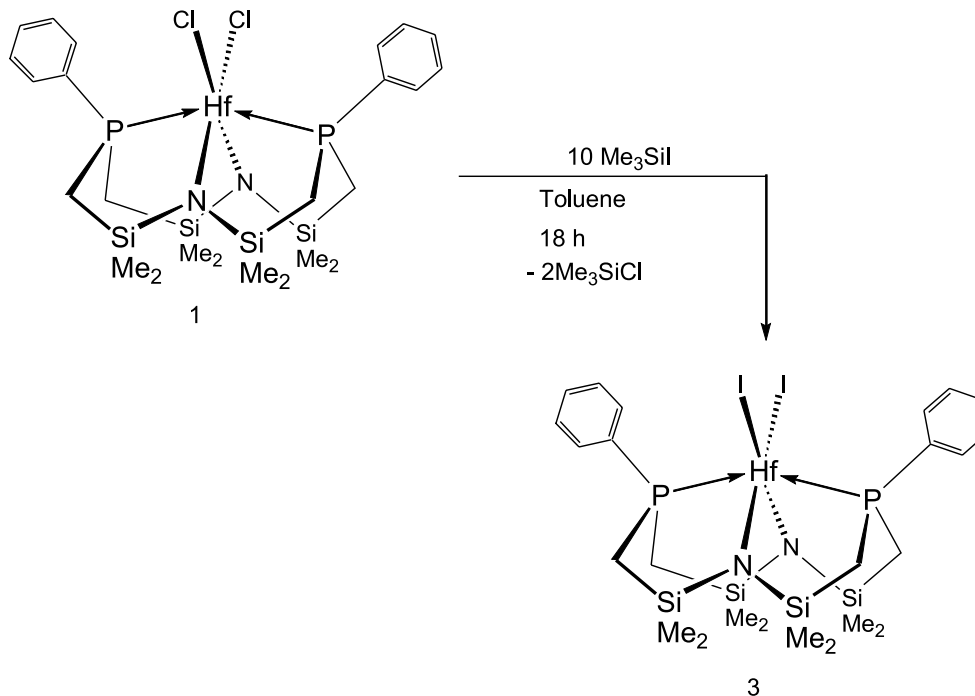
the dichloride **2**. In the  $^1\text{H}$  NMR spectrum of the diiodide complex, the two silyl methyl signals are now separated by  $0.3$  ppm, while for the dichloride complex the separation is less than  $0.05$  ppm.

Reaction of  $[\text{P}_2\text{N}_2]\text{HfI}_2$  (**3**) with 2 equiv of  $\text{C}_8\text{K}$  under 1 atm (1 atm = 101.325 kPa) of dinitrogen produced a mixture of products and a solution with an intense blue color, a color characteristic of the  $\{[\text{P}_2\text{N}_2]\text{Zr}\}(\mu\text{-}\eta^2\text{:}\eta^2\text{-N}_2)$  analogue. These products, their tentative assignments, and their percentages as determined by  $^{31}\text{P}\{^1\text{H}\}$  NMR spectroscopy are summarized in Table 2.

The  $^{31}\text{P}\{^1\text{H}\}$  NMR chemical shift of the speculated dinitrogen complex, combined with the intense blue color of the solution, was an excellent indication of dinitrogen complex formation, but it remained uncertain that the signal at  $-8.2$  ppm could be assigned to  $\{[\text{P}_2\text{N}_2]\text{Hf}\}(\mu\text{-}\eta^2\text{:}\eta^2\text{-N}_2)$ .

In an attempt to increase the yield of the dinitrogen complex **4**, the reaction was repeated in a sealed reactor, under 4 atm of dinitrogen, for a period of 8 days (Table 3). With these changes in reaction conditions, the signal at  $-8.2$  ppm became the major signal. The large increase in integration size of this signal, when the only change to the reaction was to increase the  $\text{N}_2$  pressure, is further evidence that the signal can be assigned to the dinitrogen complex. However, a



**Scheme 2.** Synthesis of  $\{[P_2N_2]Hf\}_2$  (**2**).**Scheme 3.** Synthesis of  $[P_2N_2]HfI_2$  (**3**).

higher percentage of starting material remains when compared with the same reaction using 1 atm of  $N_2$ , and the other impurities are still present, although in smaller amounts.

#### Further characterization of $\{[P_2N_2]Hf\}_2(\mu-\eta^2:\eta^2-N_2)$ (**4**)

Further evidence for the formation of complex **4** comes from mass spectrometry data. Shown in Fig. 2 is a portion of the EI mass spectrum. Figure 3 shows the theoretical mass

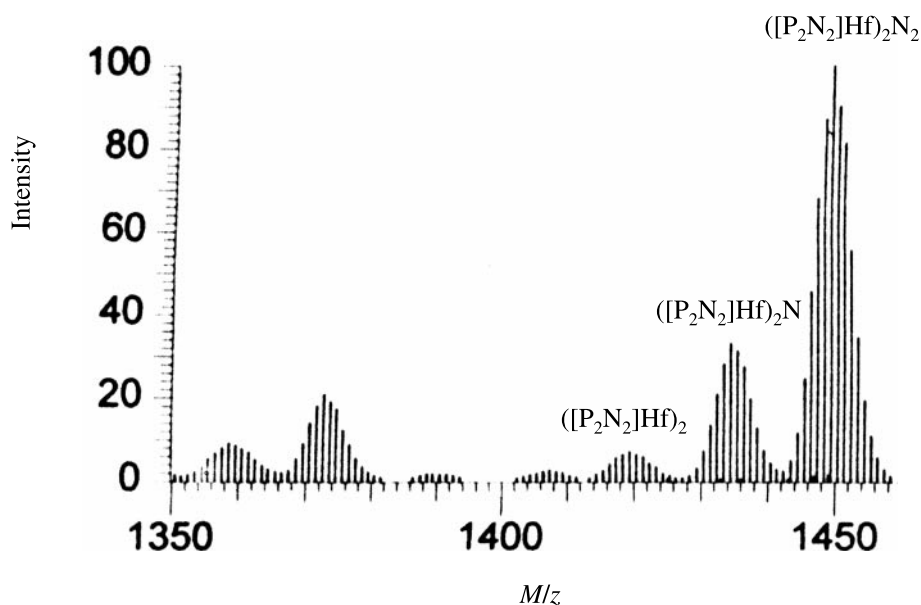
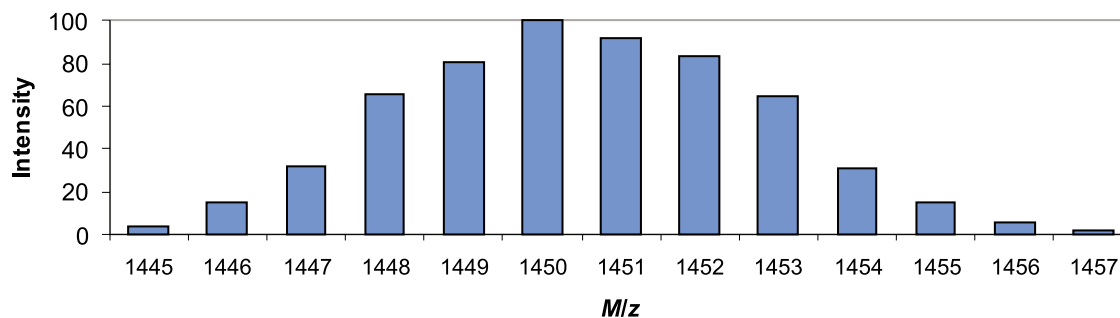


**Table 2.** The results of a study of the reaction of  $[\text{P}_2\text{N}_2]\text{HfI}_2$  (**3**) with 2 equiv of  $\text{C}_8\text{K}$  under 1 atm  $\text{N}_2$  in toluene.

Compound	$^{31}\text{P}$ shift (ppm)	After 1 h (%) <sup>a</sup>	After 4 h (%)	After 8 h (%)	After 25 h (%)	After 72 h (%)
$[\text{P}_2\text{N}_2]\text{HfI}_2$ <b>3</b>	-5.4 (s)	100	77	55	31	5
$\{[\text{P}_2\text{N}_2]\text{Hf}\}_2$ <b>2</b>	6.3 (m) <sup>b</sup>	0	9	21	26	34
$[\text{P}_2\text{N}_2]\text{Hf}(\text{C}_7\text{H}_8)$ <b>5</b>	8.6 (s)	0	8	14	22	33
$\{[\text{P}_2\text{N}_2]\text{Hf}\}_2(\mu\text{-N}_2)$ <b>4</b>	-8.2 (s)	0	6	9	21	29

<sup>a</sup>Percentages of each compound determined from integration of their  $^{31}\text{P}\{^1\text{H}\}$  NMR signals. Error is approximately 1% for each.<sup>b</sup>Spin system is AA'BB'.**Table 3.** The results of a study of the reaction of  $[\text{P}_2\text{N}_2]\text{HfI}_2$  (**3**) with 2 equiv of  $\text{C}_8\text{K}$  under 4 atm  $\text{N}_2$  in toluene.

	$[\text{P}_2\text{N}_2]\text{HfI}_2$ <b>3</b>	$\{[\text{P}_2\text{N}_2]\text{Hf}\}_2$ <b>2</b>	$[\text{P}_2\text{N}_2]\text{Hf}(\text{C}_7\text{H}_8)$ <b>5</b>	$\{[\text{P}_2\text{N}_2]\text{Hf}\}_2(\mu\text{-N}_2)$ <b>4</b>
$^{31}\text{P}$ shift (ppm)	-5.4 (s)	6.3 (m) <sup>a</sup>	8.6 (s)	-8.2 (s)
After 8 days under 4 atm $\text{N}_2$ (%) <sup>b</sup>	19	16	13	52

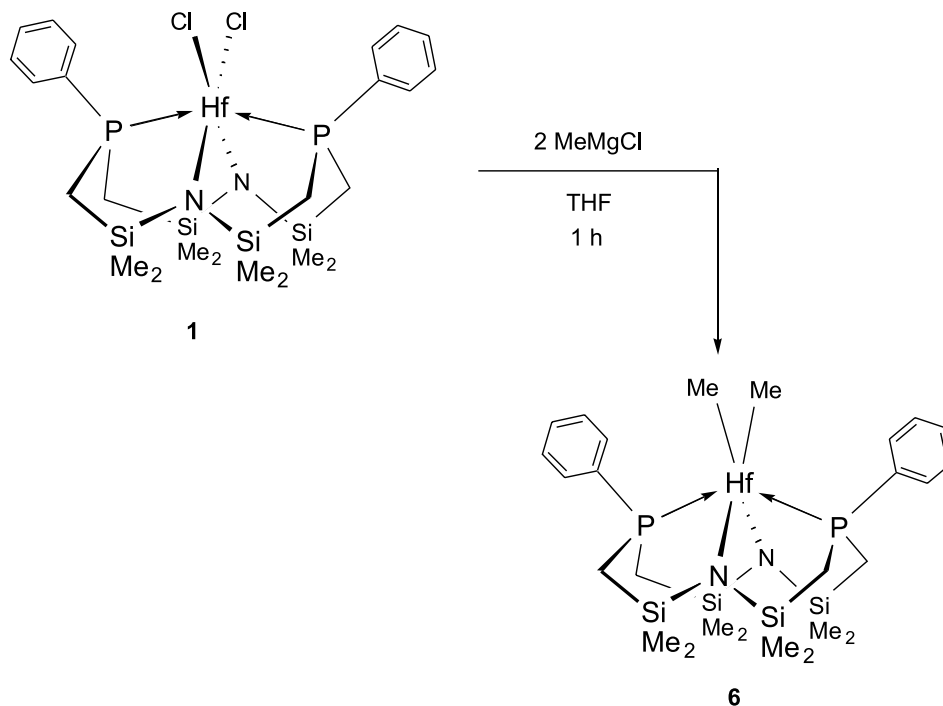
<sup>a</sup>Spin system is AA'BB'.<sup>b</sup>Percentages of each compound determined from integration of their  $^{31}\text{P}\{^1\text{H}\}$  NMR signals. Error is approximately 1% for each.**Fig. 2.** Selected EI mass spectrometry data for  $([\text{P}_2\text{N}_2]\text{Hf})_2\text{N}_2$  (**4**).**Fig. 3.** Theoretical isotope distribution pattern for EI mass spectrometry analysis of  $([\text{P}_2\text{N}_2]\text{Hf})_2\text{N}_2$  (**4**), as determined by Isotope Pattern Calculator™ v. 1.6.6.

spectrometry signature one would expect from complex **4**. The theoretical signature is a near exact match for the experimental one shown in Fig. 2. In Fig. 2, signatures for  $\{[\text{P}_2\text{N}_2]\text{Hf}\}_2\text{N}$  (where a single nitrogen atom has been

stripped from the parent compound) and for  $\{[\text{P}_2\text{N}_2]\text{Hf}\}_2$  (**2**) can also be seen and are labeled.

Not shown here, but also observed in the EI mass spectrum, are the signatures for  $[\text{P}_2\text{N}_2]\text{Hf}(\text{C}_7\text{H}_8)$  (**5**) and for



**Scheme 4.** Synthesis of  $[\text{P}_2\text{N}_2]\text{HfMe}_2$  (**6**).

$[\text{P}_2\text{N}_2]\text{HfI}$  and  $[\text{P}_2\text{N}_2]\text{Hf}$ . Interestingly, no signature is observed for  $[\text{P}_2\text{N}_2]\text{HfI}_2$  (**3**), likely because of the weakness of the Hf—I bond.

To confirm the presence of a dinitrogen compound in the products from the reaction of  $[\text{P}_2\text{N}_2]\text{HfI}_2$  (**3**) with 2 equiv of  $\text{C}_8\text{K}$ , the mixture of products was degraded with HCl and the resultant products analyzed to detect hydrazine, according to literature procedure (16). Hydrazine was detected, confirming the presence of a dinitrogen compound; however, it was not possible to determine the percent of hydrazine formed per mole of  $\{[\text{P}_2\text{N}_2]\text{Hf}\}_2(\mu\text{-}\eta^2\text{-}\eta^2\text{-N}_2)$  (**4**), owing to the inability to isolate **4** in pure form.

#### Preparation and structure of $[\text{P}_2\text{N}_2]\text{HfMe}_2$ (**6**)

We were also interested in the organometallic chemistry of hafnium with the  $[\text{P}_2\text{N}_2]$  ligand.  $\{[\text{P}_2\text{N}_2]\text{Zr}\}_2(\mu\text{-H})_4$  was prepared<sup>3</sup> from  $[\text{P}_2\text{N}_2]\text{ZrCl}_2$ , using  $\text{C}_8\text{K}$  as a reducing agent, under 4 atm of  $\text{H}_2$ . Interestingly, it does not appear to be possible to form a zirconium hydride from  $[\text{P}_2\text{N}_2]\text{ZrMe}_2$ .  $[\text{P}_2\text{N}_2]\text{ZrMe}_2$  is extremely thermally and light sensitive, making it difficult to prepare in sufficient quantities to use in subsequent reactions. It is a well-established precedent that certain organometallic hafnium(IV) compounds are more thermally stable than their zirconium analogues (12, 17–19). As well, the use of hafnium analogues can facilitate investigation of intermediates in cases where this proves difficult for zirconium compounds (2, 20, 21). The synthesis of  $[\text{P}_2\text{N}_2]\text{HfMe}_2$  (**6**) was accomplished by the metathesis reaction of  $[\text{P}_2\text{N}_2]\text{HfCl}_2$  (**1**) with 2 equiv of the Grignard reagent,  $\text{MeMgCl}$  (Scheme 4).

Compound **6** was characterized by  $^1\text{H}$  and  $^{31}\text{P}\{^1\text{H}\}$  NMR spectroscopy, elemental analysis, and X-ray crystal structure analysis. In a manner similar to most other known

mononuclear group 4 metal  $[\text{P}_2\text{N}_2]$  complexes, the dimethyl compound adopts  $\text{C}_{2v}$  symmetry in solution at ambient temperature, as evidenced by NMR spectroscopy. As expected, the methyl protons are coupled to two equivalent phosphorus nuclei and appear as a triplet at 0.65 ppm. Unlike the case of the zirconium analogue, their signal is not masked by the  $[\text{P}_2\text{N}_2]$  ligand methylene protons. Interestingly, while it was not possible to grow crystals of the zirconium analogue of this compound, crystals of the hafnium analogue were grown easily from slow evaporation of a DME solution. An ORTEP diagram of complex **6** is shown in Fig. 4. The substitution of methyl groups for chloride moieties upon going from **1** to **6** has resulted in a substantial structural change. The geometry around the metal center is now best described as trigonal prismatic, with the two trigonal planes described by N(1), P(1), and C(25) and N(2), P(2), and C(26). The methyl carbons are not located in a square plane with the amido nitrogens but are rotated out of this plane. As well, the phosphine and amide “bite angles”, P(1)–Hf–P(2) and N(1)–Hf–N(2), have both changed considerably. The phosphine bite angle has decreased from  $153.76(3)^\circ$  to  $135.79(3)^\circ$ , while the amide bite angle has increased from  $96.6(1)^\circ$  to  $113.2(1)^\circ$ . Table 4 shows selected bond distances and angles for complex **6**. The Hf—C, Hf—N, and Hf—P bond distances are, once again, not unusual and compare well with other group 4 methyl complexes (11).

#### Preparation of $\{[\text{P}_2\text{N}_2]\text{Hf}\}(\mu\text{-H})_4$ (**7**)

While hydrogenolysis of  $[\text{P}_2\text{N}_2]\text{ZrMe}_2$  did not result in a zirconium hydride complex, a hafnium hydride was synthesized through hydrogenolysis. Reaction of  $[\text{P}_2\text{N}_2]\text{HfMe}_2$  with  $\text{H}_2$  gas in benzene gave  $\{[\text{P}_2\text{N}_2]\text{Hf}\}_2(\mu\text{-H})_4$  (**7**) (Scheme 5). Complex **7** is sparingly soluble in benzene and precipitates

<sup>3</sup>M.D. Fryzuk and J.B. Love. Unpublished results.



**Fig. 4.** An ORTEP diagram showing the solid-state molecular structure of  $[\text{P}_2\text{N}_2]\text{HfMe}_2$  (**6**) (ellipsoids at 50% probability). The silyl methyl groups have been omitted for clarity; only the *ipso* carbons of the phosphorus phenyl groups are shown.

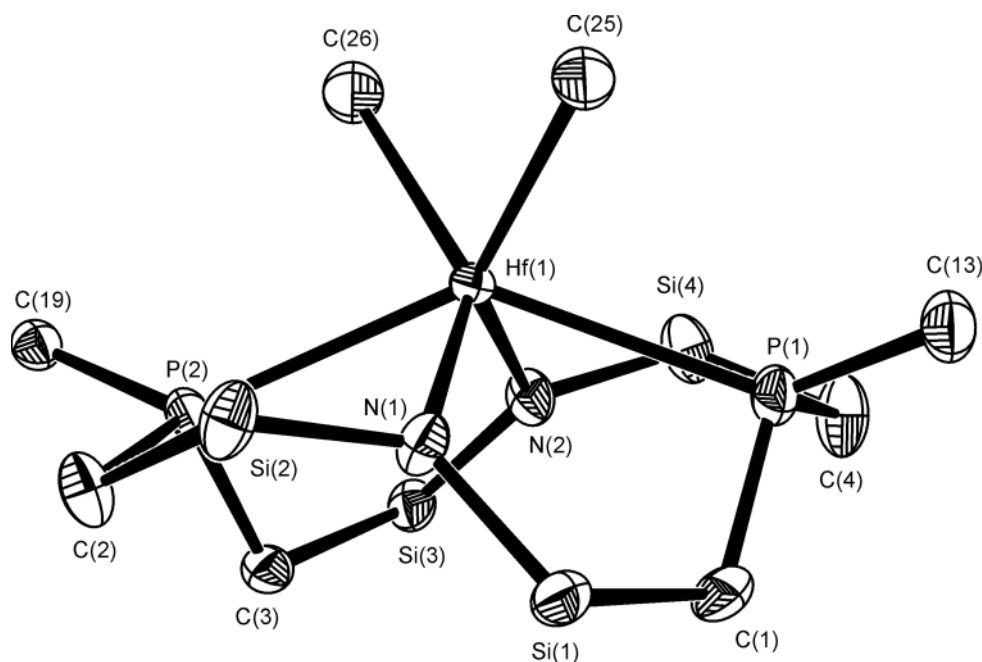


**Table 4.** Selected bond lengths (Å) and angles (°) in  $[\text{P}_2\text{N}_2]\text{HfMe}_2$  (**6**).

Bond lengths		Bond angles	
Hf(1)—N(1)	2.147(3)	N(1)—Hf(1)—N(2)	113.5(1)
Hf(1)—N(2)	2.149(3)	P(1)—Hf(1)—P(2)	135.79(3)
Hf(1)—P(1)	2.781(1)	C(25)—Hf(1)—C(26)	82.0(2)
Hf(1)—P(2)	2.783(1)	N(1)—Hf(1)—C(25)	97.2(2)
Hf(1)—C(25)	2.263(1)	N(2)—Hf(1)—C(25)	134.6(2)
Hf(1)—C(26)	2.277(1)		

out of solution as yellow microcrystals, making separation from the parent compound a simple matter.

The change in the chemical shift of the phosphorus nuclei, when switching from  $\{[\text{P}_2\text{N}_2]\text{Zr}\}_2(\mu\text{-H})_4$  to its hafnium analogue,<sup>3</sup> is more drastic than in other  $[\text{P}_2\text{N}_2]$  compounds. The signal is observed at 4.4 ppm, downfield from the zirconium analogue signal at −5.9 ppm. As well, the hydride quintet (2, 22–24) is observed at 9.3 ppm, downfield from 5.0 ppm in the zirconium analogue. The other characteristic signals in the  $^1\text{H}$  NMR spectrum have not changed appreciably.

## Conclusions

The hafnium chemistry presented in this paper, while similar to the previously reported zirconium chemistry, does have some notable differences. Although the X-ray crystal structure of  $[\text{P}_2\text{N}_2]\text{HfCl}_2$  (**1**) is isostructural and isomorphous with that of its zirconium analogue, the reactivity of **1**, especially under reducing conditions, is quite different. It was not possible to synthesize the hafnium dinitrogen compound  $\{[\text{P}_2\text{N}_2]\text{Hf}\}(\mu\text{-}\eta^2\text{:}\eta^2\text{-N}_2)$ , in any appreciable amount, from  $[\text{P}_2\text{N}_2]\text{HfCl}_2$  (**1**); instead, a hafnium dimer,  $\{[\text{P}_2\text{N}_2]\text{Hf}\}_2$  (**2**), was the major product. However, changing the hafnium starting material from the chloride complex, **1**,

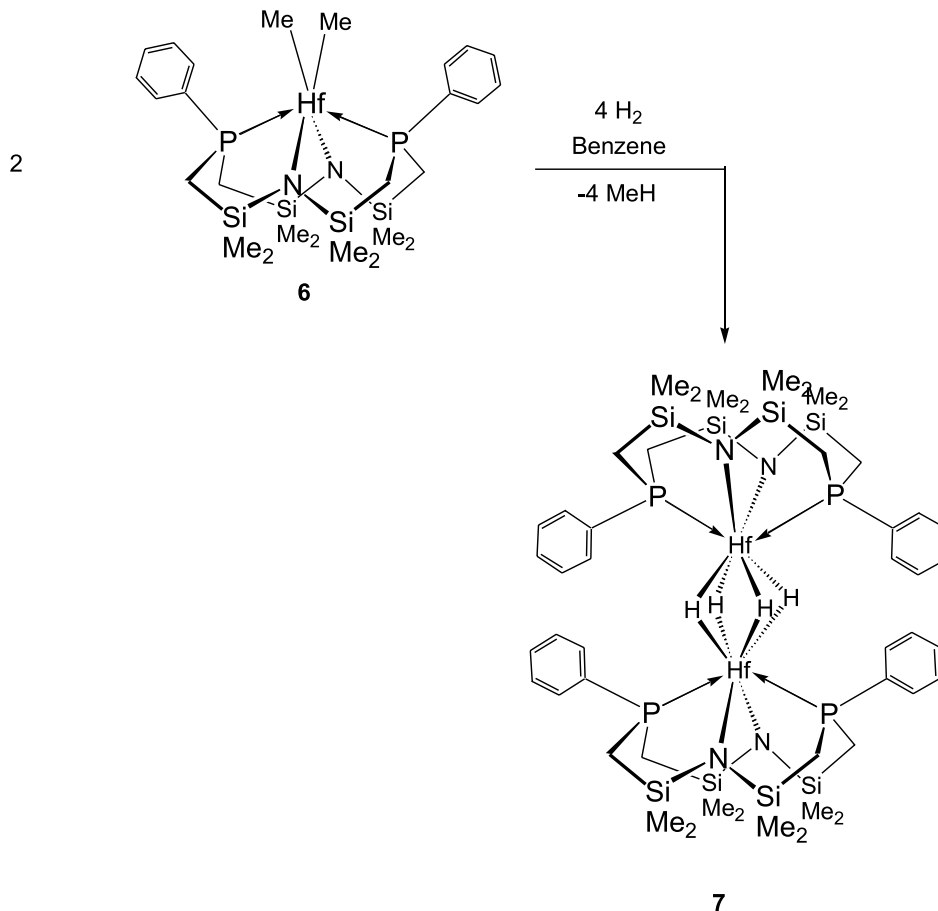
to the iodide complex did result in the formation of the hafnium dinitrogen complex,  $\{[\text{P}_2\text{N}_2]\text{Hf}\}(\mu\text{-}\eta^2\text{:}\eta^2\text{-N}_2)$  (**4**), after reduction with  $\text{C}_8\text{K}$ , as shown by NMR spectroscopy, EI mass spectrometry, and hydrazine analysis. Unfortunately, it has not been possible to isolate compound **4** in the solid state. Synthesis of  $[\text{P}_2\text{N}_2]\text{HfMe}_2$  (**6**) proceeded in a manner identical to that of its zirconium analogue. The dimethyl derivative, **6**, reacts with  $\text{H}_2$  to generate the dinuclear hafnium hydride,  $\{[\text{P}_2\text{N}_2]\text{Hf}\}(\mu\text{-H})_4$  (**7**), via hydrogenolysis; this reaction fails for the zirconium analogue,  $[\text{P}_2\text{N}_2]\text{ZrMe}_2$ .

## Experimental

### Materials and apparatus

All manipulations were performed under prepurified nitrogen in a Vacuum Atmospheres HE-553-2 workstation equipped with an MO-40-2H purification system or using Schlenk-type glassware. The term “reactor” refers to a cylindrical, thick-walled Pyrex vessel equipped with a 5 mm (or 10 mm, for larger bombs) Kontes teflon needle valve and a ground glass joint for attachment to a vacuum line. These “reactors” allow pressures as high as 4 atm to be maintained inside the tube.  $\text{HfCl}_4$  (<0.05% Zr) was purchased from Strem and used as received. THF was predried by refluxing over  $\text{CaH}_2$  for at least 24 h and dried by refluxing over sodium benzophenone ketyl, followed by distillation under argon. Toluene and hexanes were purchased in anhydrous form from Aldrich, sparged with  $\text{N}_2$ , and deoxygenated by filtration through columns containing silica and Q-5 catalyst under a positive pressure of  $\text{N}_2$  (25). Benzene, diethyl ether, and dimethoxyethane were also refluxed over sodium benzophenone ketyl and distilled under argon. Deuterated THF ( $\text{C}_4\text{D}_8\text{O}$ ) and deuterated benzene ( $\text{C}_6\text{D}_6$ ) were refluxed under vacuum with sodium–potassium amalgam (Na–K),



**Scheme 5.** Synthesis of  $\{[P_2N_2]Hf\}_2(\mu-H)_4$  (**7**).

vacuum transferred to a clean vessel, and “freeze–pump–thawed” three times prior to use.

The following compounds were prepared by published procedures:  $HfCl_4(THF)_2$  (**26**),  $[syn-P_2N_2]Li_2$ (dioxane) (**27**),  $C_8K$  (**28**), and  $Mg(C_4H_6)(THF)_2$ .  $Me_3SiI$ ,  $MeMgCl$ ,  $BzMgCl$ , and  $H_2$  were used as received. Diatomaceous earth (Celite) was dried overnight at  $170\text{ }^\circ\text{C}$  before being taken inside the glovebox for use.

#### Analytical methods

$^1H$  and  $^{31}P\{^1H\}$  NMR spectroscopy were performed on a Bruker AMX-500 instrument (500.135 and 202.458 MHz) or a Bruker AC-200 machine (200.132 and 81.015 MHz).  $^1H$  NMR spectra were referenced to internal  $C_6D_5H$  (7.15 ppm), and  $^{31}P\{^1H\}$  NMR spectra were referenced to external  $P(OMe)_3$  (141.0 ppm, with respect to 85%  $H_3PO_4$  at 0.00 ppm).

The theoretical EI signature was created using Isotope<sup>TM</sup> v. 1.6.6, a program designed specifically to model mass spectrometry signatures.

C, H, and N microanalyses were performed by Mr. P. Borda of this department, the Department of Chemistry, University of British Columbia (UBC). The X-ray crystal struc-

tures were determined at UBC Crystallographic Services in this department by Dr. B. Patrick. The crystals were loaded in a small glass vial and covered with paratone oil in the glovebox to prevent decomposition. Details of the structure determinations are given in the Appendices.<sup>4</sup>

#### Hydrazine analysis (16)

The products from the reaction of  $[P_2N_2]HfI_2$  (**3**) with 2 equiv of  $C_8K$  were weighed into a 200 mL Schlenk tube (0.280 g) and dissolved in 50 mL of  $Et_2O$ . Ten millilitres of  $2.0\text{ mol L}^{-1}$  HCl in  $Et_2O$  was added to this solution. The solution immediately lost its blue color, and a white precipitate formed. The clear solution and white precipitate were stirred for 1 h, and the solvents were removed in vacuo. The flask was exposed to the air, extracted into 100 mL of  $H_2O$ , and filtered into a 500 mL volumetric flask, which was filled with  $1.0\text{ mol L}^{-1}$  HCl. A 2.0 mL aliquot of this solution was added to 20 mL of a color developer (*p*-dimethylaminobenzaldehyde, 4.0 g; ethanol, 200 mL;  $1.0\text{ mol L}^{-1}$  HCl, 20 mL) and diluted to 25.0 mL with  $1.0\text{ mol L}^{-1}$  HCl. Absorbance readings of the sample were taken within 10 min. The spectrometer was set to 100% transmittance, using a blank solution consisting of

<sup>4</sup>Supplementary data may be purchased from the Depository of Unpublished Data, Document Delivery, CISTI, National Research Council Canada, Ottawa, ON K1A 0S2, Canada ([http://www.nrc.ca/cisti/irm/unpub\\_e.shtml](http://www.nrc.ca/cisti/irm/unpub_e.shtml) for information on ordering electronically). CCDC 205941 and 205942 contain the supplementary data for this paper. These data can be obtained, free of charge, via [www.ccdc.cam.ac.uk/conts/retrieving.html](http://www.ccdc.cam.ac.uk/conts/retrieving.html) (or from the Cambridge Crystallographic Data Centre, 12 Union Road, Cambridge, U.K.; fax +44 1223 336033; or [deposit@ccdc.cam.ac.uk](mailto:deposit@ccdc.cam.ac.uk)).



1.0 mol L<sup>-1</sup> HCl. Absorbance readings of 0.33, 0.34, and 0.33 AU were obtained at 458 nm.

### Synthesis of [P<sub>2</sub>N<sub>2</sub>]HfCl<sub>2</sub> (1)

Li<sub>2</sub>(dioxane)[P<sub>2</sub>N<sub>2</sub>] (6.83 g, 10.8 mmol) and HfCl<sub>4</sub>(THF)<sub>2</sub> (5.00 g, 10.8 mmol) were each weighed into a thick-walled reactor. Addition of 150 mL toluene to this intimate mixture resulted in a cloudy white solution. The reactor was sealed, and the mixture was heated for 18 h at 120 °C. The solvents were then removed in vacuo; the off-white residue was extracted into toluene (2 × 50 mL) and filtered through Celite. The filtrate was evaporated to dryness and the residue washed with hexanes (2 × 10 mL), yielding **1** (7.25 g, 86%) as a white powder. The product was crystallized by the slow evaporation of a DME solution.

<sup>1</sup>H NMR (C<sub>6</sub>D<sub>6</sub>, 25 °C, 500.135 MHz) δ: 7.87 (m, 4H, *o*-H phenyl), 7.05 (m, 6H, *m/p*-H phenyl), 1.41 (ABX m, 4H, CH<sub>2</sub> ring), 1.32 (ABX m, 4H, CH<sub>2</sub> ring), 0.38 (s, 12H, SiMe<sub>2</sub> ring), 0.34 (s, 12H, SiMe<sub>2</sub> ring). <sup>31</sup>P{<sup>1</sup>H} (C<sub>6</sub>D<sub>6</sub>, 25 °C, 202.458 MHz) δ: -5.8 (s). Anal. calcd. for C<sub>24</sub>H<sub>42</sub>Cl<sub>2</sub>HfN<sub>2</sub>P<sub>2</sub>Si<sub>4</sub>: C 36.85, H 5.41, N 3.58; found: C 37.04, H 5.48, N 3.56.

### Synthesis of {[P<sub>2</sub>N<sub>2</sub>]Hf} (2)

[P<sub>2</sub>N<sub>2</sub>]HfCl<sub>2</sub> (**1**) (0.73 g, 0.93 mmol) and C<sub>8</sub>K (0.25 g, 1.86 mmol) were each weighed into a 200 mL thick-walled reactor, to which 50 mL of toluene was added, all in the glovebox. The reactor was removed from the glovebox and cooled to -198 °C in a liquid nitrogen bath while under a flow of N<sub>2</sub>. After allowing 30 min for equilibration, the reactor was sealed and allowed to warm to room temperature. The reaction mixture was stirred for 8 days and filtered through Celite. Toluene was removed in vacuo, and the residues were dissolved in hexanes and filtered. The hexanes solution was left in a -40 °C freezer overnight, where **2** crashed out of solution as a yellow-brown powder. Yield: 0.22 g, 32.2%. Note: further studies showed that it does not matter what type of atmosphere (N<sub>2</sub>, Ar, or near vacuum) is inside the reactor.

<sup>1</sup>H NMR (C<sub>6</sub>D<sub>6</sub>, 25 °C, 200.132 MHz) δ: 7.40 (m, 4H, *o*-H phenyl), 7.10 (m, 6H, *m/p*-H phenyl), 4.22 (m, 4H, *m/p*-H activated phenyl), 4.15 (m, 4H, *m/p*-H activated phenyl), 3.39 (m, 2H, *o*-H activated phenyl), 1.49 (ABX m, 8H, CH<sub>2</sub> ring), 1.15 (ABX m, 8H, CH<sub>2</sub> ring), 0.52 (s, 12H, SiMe<sub>2</sub> ring), 0.50 (s, 12H, SiMe<sub>2</sub> ring), 0.31 (s, 12H, SiMe<sub>2</sub> ring), 0.04 (s, 12H, SiMe<sub>2</sub> ring). <sup>31</sup>P{<sup>1</sup>H} (C<sub>6</sub>D<sub>6</sub>, 25 °C, 81.015 MHz) δ: -6.3 (m). Anal. calcd. for C<sub>48</sub>H<sub>84</sub>Hf<sub>2</sub>N<sub>4</sub>P<sub>4</sub>Si<sub>8</sub>: C 40.52, H 5.95, N 3.95; found: C 40.39, H 5.97, N 3.75.

### Synthesis of [P<sub>2</sub>N<sub>2</sub>]HfI<sub>2</sub> (3)

Me<sub>3</sub>SiI (10.0 mL, 70 mmol, ~10 equiv) was added to a stirred solution of [P<sub>2</sub>N<sub>2</sub>]HfCl<sub>2</sub> (**1**) (5.21 g, 6.66 mmol) in 80 mL of toluene at -78 °C. The reactor was sealed and the solution stirred for 18 h, during which time the solution acquired a very pale yellow-green color. Toluene was removed in vacuo and the residues washed with hexanes (2 × 10 mL), yielding **3** (2.8 g, 88%) as a very pale green powder.

<sup>1</sup>H NMR (C<sub>6</sub>D<sub>6</sub>, 25 °C, 200.132 MHz) δ: 7.92 (m, 4H, *o*-H phenyl), 7.05 (m, 6H, *m/p*-H phenyl), 1.58 (ABX m, 4H, CH<sub>2</sub> ring), 1.27 (ABX m, 4H, CH<sub>2</sub> ring), 0.48 (s, 12H,

SiMe<sub>2</sub> ring), 0.39 (s, 12H, SiMe<sub>2</sub> ring). <sup>31</sup>P{<sup>1</sup>H} (C<sub>6</sub>D<sub>6</sub>, 25 °C, 81.015 MHz) δ: -5.4 (s). Anal. calcd. for C<sub>24</sub>H<sub>42</sub>I<sub>2</sub>HfN<sub>2</sub>P<sub>2</sub>Si<sub>4</sub>: C 29.87, H 4.39, N 2.90; found: C 30.02, H 4.43, N 2.89.

### Attempted synthesis of {[P<sub>2</sub>N<sub>2</sub>]Hf}(μ-η<sup>2</sup>:η<sup>2</sup>-N<sub>2</sub>) (4)

C<sub>8</sub>K (0.33 g, 3.32 mmol) and [P<sub>2</sub>N<sub>2</sub>]HfI<sub>2</sub> (**3**) (1.21 g, 1.26 mmol) were each weighed into a 200 mL thick-walled reactor, to which 50 mL of toluene was added, all in the glovebox. The reactor was removed from the glovebox and cooled to -198 °C in a liquid nitrogen bath while under a flow of N<sub>2</sub>. After allowing 30 min for equilibration, the reactor was sealed and allowed to warm to room temperature. Following 16 h of stirring, a blue-purple color was observed. The reactor was then allowed to stir vigorously for another 7 days. The solution was then filtered through Celite and evaporated to dryness. Washing with a minimal amount of hexanes (2 × 10 mL) yielded 0.85 g of a dark solid. <sup>31</sup>P{<sup>1</sup>H} NMR indicates the composition of this solid to be approximately 52% **4**, 19% **3**, 16% **2**, and 13% **5**. EI-MS: 1450 ([M]<sup>+</sup>).

### Synthesis of [P<sub>2</sub>N<sub>2</sub>]HfMe<sub>2</sub> (6)

To a solution of [P<sub>2</sub>N<sub>2</sub>]HfCl<sub>2</sub> (**1**) (3.02 g, 3.86 mmol) in THF was added 3.0 mol L<sup>-1</sup> MeMgCl in THF (2.57 mL, 7.77 mmol) at 0 °C. The solution was warmed to room temperature and stirred for 1 h, after which the solvents were evaporated in vacuo. The off-white residue was extracted into toluene (2 × 20 mL) and filtered through celite. The filtrate was evaporated to dryness, and the residue was washed with hexanes (2 × 10 mL), yielding **6** (2.24 g, 77%) as a white powder. The product was crystallized by the slow evaporation of a DME solution.

<sup>1</sup>H NMR (C<sub>6</sub>D<sub>6</sub>, 25 °C, 500.135 MHz) δ: 7.62 (m, 4H, *o*-H phenyl), 7.07 (m, 6H, *m/p*-H phenyl), 1.03 (m, 8H, CH<sub>2</sub> ring), 0.72 (t, 6H, Zr-CH<sub>3</sub>), 0.22 (s, 12H, SiMe<sub>2</sub> ring), 0.20 (s, 12H, SiMe<sub>2</sub> ring). <sup>31</sup>P{<sup>1</sup>H} (C<sub>6</sub>D<sub>6</sub>, 25 °C, 202.458 MHz) δ: -9.6 (s). Anal. calcd. for C<sub>26</sub>H<sub>48</sub>HfN<sub>2</sub>P<sub>2</sub>Si<sub>4</sub>: C 42.12, H 6.53, N 3.78; found: C 42.14, H 6.52, N 3.74.

### Synthesis of {[P<sub>2</sub>N<sub>2</sub>]Hf}(μ-H<sub>4</sub>) (7)

Fifty millilitres of C<sub>6</sub>H<sub>6</sub> was added to 1.02 g (1.3 mmol) of [P<sub>2</sub>N<sub>2</sub>]HfMe<sub>2</sub> (**6**) in a reactor, which was sealed. The reactor was "freeze-pump-thawed" three times to remove all gases. H<sub>2</sub> was introduced to the reactor, which was cooled to -198 °C. After the solvent had thawed, but prior to warming to room temperature, the reactor was shaken to promote dissolution of H<sub>2</sub> in the solution. The reactor was left overnight, during which time a microcrystalline yellow solid precipitated. This solid was collected on a frit, yielding **7** (0.345 g, 37.2%).

<sup>1</sup>H NMR (C<sub>6</sub>D<sub>6</sub>, 25 °C, 500.135 MHz) δ: 9.07 (quintet, <sup>2</sup>J<sub>HP</sub> = 4.43 Hz, 4H, Hf-H), 7.19 (m, 8H, *o*-H phenyl), 7.12 (m, 12H, *m/p*-H phenyl), 0.83 (m, 16H, CH<sub>2</sub> ring), 0.04 (s, 24H, SiMe<sub>2</sub> ring), -0.03 (s, 24H, SiMe<sub>2</sub> ring). <sup>31</sup>P{<sup>1</sup>H} (C<sub>6</sub>D<sub>6</sub>, 25 °C, 202.458 MHz) δ: 4.4 (s). Anal. calcd. for C<sub>48</sub>H<sub>88</sub>HfN<sub>2</sub>P<sub>2</sub>Si<sub>4</sub>: C 40.41, H 6.22, N 3.93; found: C 40.56, H 6.21, N 3.76.

### Acknowledgements

The authors thank the Natural Sciences and Engineering Research Council of Canada (NSERC) for funding (Discov-



ery Grant to M.D.F.), Mr. Marshall Lapawa for mass spectrometry, and Mr. Peter Borda for elemental analyses.

## References

1. M.D. Fryzuk and S.A. Johnson. *Coord. Chem. Rev.* **200–202**, 379 (2000).
2. D.M. Roddick, M.D. Fryzuk, P.F. Seidler, G.L. Hillhouse, and J.E. Bercaw. *Organometallics*, **4**, 97 (1985).
3. M.D. Fryzuk, C. Kozak, P. Mehrkhodavandi, L. Morello, B.O. Patrick, and S. Rettig. *J. Am. Chem. Soc.* **124**, 516 (2002).
4. M.D. Fryzuk, J.B. Love, S.J. Rettig, and V.G. Young. *Science* (Washington, D.C.), **275**, 1445 (1997).
5. M.D. Fryzuk, J.B. Love, and S.J. Rettig. *Organometallics*, **17**, 846 (1998).
6. M.D. Fryzuk, D.B. Leznoff, S.F. Ma, S.J. Rettig, and J.V.G. Young. *Organometallics*, **17**, 2313 (1998).
7. M.D. Fryzuk, T.S. Haddad, M. Murugesapilla, D.H. McConville, and S.J. Rettig. *J. Am. Chem. Soc.* **115**, 2782 (1993).
8. M.D. Fryzuk, M. Mylvaganam, M.J. Zawarotko, and L.R. MacGillivray. *J. Am. Chem. Soc.* **115**, 10 360 (1993).
9. M.D. Fryzuk, S.A. Johnson, and S.J. Rettig. *Organometallics*, **18**, 4059 (1999).
10. M.D. Fryzuk, P.A. Macneil, S.J. Rettig, A.S. Secco, and J. Trotter. *Organometallics*, **1**, 918 (1982).
11. M.D. Fryzuk, T.S. Haddad, and D.J. Berg. *Coord. Chem. Rev.* **99**, 137 (1990).
12. M.D. Fryzuk and A. Carter. *Organometallics*, **11**, 469 (1992).
13. D.G. Black, D.C. Swenson, and R.F. Jordan. *Organometallics*, **12**, 3539 (1995).
14. D.J. Cardin, M.F. Lappert, and C.L. Raston. *Chemistry of organo-zirconium and hafnium compounds*. Ellis Horwood Limited, West Sussex. 1986. p. 21.
15. D.F. Shriver, P. Atkins, and C.H. Langford. *Inorganic chemistry*. W.H. Freeman and Company, New York. 1994.
16. G.W. Watt and J.D. Chrisp. *Anal. Chem.* **24**, 2006 (1952).
17. G.A. Helmut, F.P.D. Sanzo, M.D. Rausch, and P.C. Uden. *J. Organomet. Chem.* **107**, 257 (1976).
18. G.A. Razuvaev, L.I. Vyshinskaya, and V.P. Mar'in. *Dokl. Akad. Nauk SSSR*, **225**, 827 (1975).
19. G.A. Razuvaev, V.P. Mar'in, O.N. Drushkov, and L.I. Vyshinskaya. *J. Organomet. Chem.* **231**, 125 (1982).
20. D.M. Roddick and J.E. Bercaw. *Chem. Ber.* **122**, 1579 (1989).
21. J.E. Bercaw and J.R. Moss. *Organometallics*, **11**, 639 (1992).
22. M.D. Fryzuk, S.J. Rettig, A. Westerhaus, and H.D. Williams. *Inorg. Chem.* **24**, 4316 (1985).
23. J.E. Gozum and G.S. Girolami. *J. Am. Chem. Soc.* **113**, 3829 (1991).
24. J.E. Gozum, S.R. Wilson, and G.S. Girolami. *J. Am. Chem. Soc.* **114**, 9483 (1992).
25. A.B. PangBorn, M.A. Giardello, R.H. Grubbs, R.K. Rosen, and F.J. Timmers. *Organometallics*, **15**, 1518 (1996).
26. L.E. Manzer. *Inorg. Chem.* **21**, 135 (1982).
27. M.D. Fryzuk, J.B. Love, and S.J. Rettig. *J. Chem. Soc. Chem. Commun.* 2783 (1996).
28. D.E. Bergbreiter and J.M. Killough. *J. Am. Chem. Soc.* **100**, 2126 (1978).

## Appendix A. X-ray crystallographic analysis of $[\text{P}_2\text{N}_2]\text{HfCl}_2$ (1).

**Table A1.** Crystal data.

Empirical formula	$\text{C}_{24}\text{H}_{42}\text{N}_2\text{Cl}_2\text{HfP}_2\text{Si}_4$
Formula weight	782.29
Temperature (K)	173
Crystal color, habit	Clear, chip
Crystal dimensions (mm)	$0.15 \times 0.15 \times 0.15$
Crystal system	Orthorhombic
Lattice type	Primitive
Lattice parameters	
<i>a</i> (Å)	9.3152(8)
<i>b</i> (Å)	16.5962(5)
<i>c</i> (Å)	21.3811(7)
<i>V</i> (Å <sup>3</sup> )	3305.5(2)
Space group	$P2_12_12_1$ (#19)
Z value	4
$D_{\text{calcd}}$ (g cm <sup>-3</sup> )	1.572
$F_{000}$	1568.00
$\mu$ (cm <sup>-1</sup> ) (Mo K $\alpha$ )	35.71

**Table A2.** Intensity measurements.

Diffractometer	Rigaku/ADSC CCD
Radiation	Mo K $\alpha$ ( $\lambda = 0.71069$ Å)
	Graphite monochromated
Detector aperture (mm)	$94 \times 94$
Data images	464 exposures @ 35.0 s
$\phi$ Oscillation range ( $\chi = 0$ ) (°)	0.0–190.0
$\omega$ Oscillation range ( $\chi = 90.0$ ) (°)	–19.0 to 23.0
Detector position (mm)	40.62
Detector swing angle (°)	–5.55
$2\theta_{\text{max}}$ (°)	55.8
No. of reflections measured	Total: 28 469
	Unique: 3999 ( $R_{\text{int}} = 0.066$ )
Corrections	Lorentz-polarization
	Absorption
Trans. factors	0.7796–1.0000



**Table A3.** Structure solution and refinement.

Structure solution	Patterson methods (DIRDIF92 PATTY)
Refinement	Full-matrix least-squares
Function minimized	$\Sigma \omega( F_o ^2 -  F_c ^2)^2$
Least squares weights	$\omega = 1/[\sigma^2(F_o^2)]$
p-factor	0.0000
Anomalous dispersion	All non-hydrogen atoms
No. observations ( $I > 0.00\sigma(I)$ )	6846
No. variables	316
Reflection:parameter ratio	21.66
Residuals (on $F^2$ , all data) $R$ ; $R_w$	0.036; 0.055
Goodness of fit indicator	0.51
Max shift/error in final cycle	0.00
No. observations ( $I > 3\sigma(I)$ )	5913
Residuals (on $F$ , $I > 3\sigma(I)$ ) $R$ ; $R_w$	0.020; 0.025
Max peak in final difference map ( $e \text{ \AA}^{-3}$ )	0.68
Min peak in final difference map ( $e \text{ \AA}^{-3}$ )	-1.10

**Table A4.** Atomic coordinates and  $B_{eq}$ .

Atom	$x$	$y$	$z$	$B_{eq}$
Hf(1)	0.08378(2)	0.97608(1)	0.16637	0.890(4)
Cl(1)	-0.1402(2)	0.94810(10)	0.10928(9)	2.77(3)
Cl(2)	0.0421(2)	0.84100(10)	0.21020(10)	3.97(5)
P(1)	-0.031(10)	1.08273(8)	0.24618(7)	1.10(3)
P(2)	0.2891(2)	0.92249(9)	0.08962(7)	1.38(3)
Si(1)	0.2845(2)	1.06481(9)	0.27779(7)	1.19(3)
Si(2)	0.4049(2)	0.91470(10)	0.22206(7)	1.69(3)
Si(3)	0.2511(2)	1.10590(10)	0.06974(8)	1.72(3)
Si(4)	-0.0373(2)	1.15670(10)	0.11763(8)	1.62(3)
N(1)	0.2724(5)	0.9895(3)	0.2213(2)	1.21(8)
N(2)	0.1025(5)	1.0873(3)	0.1169(2)	1.39(8)
C(1)	0.1310(6)	1.1375(3)	0.2661(3)	1.21(9)
C(2)	0.4056(7)	0.8657(3)	0.1413(3)	1.8(1)
C(3)	0.3793(6)	1.0166(4)	0.0711(3)	2.3(1)
C(4)	-0.1363(6)	1.1472(4)	0.1955(3)	1.7(1)
C(5)	0.4503(6)	1.1290(4)	0.2742(3)	2.4(1)
C(6)	0.2705(7)	1.0193(4)	0.3573(3)	2.3(1)
C(7)	0.3787(8)	0.8358(4)	0.2832(3)	2.9(2)
C(8)	0.5897(8)	0.9541(5)	0.2343(4)	3.6(2)
C(9)	0.1921(9)	1.1226(5)	-0.0131(3)	3.4(2)
C(10)	0.3649(8)	1.1929(4)	0.0946(4)	2.8(2)
C(11)	-0.1725(8)	1.1444(4)	0.0533(3)	2.8(2)
C(12)	0.0260(8)	1.2639(4)	0.1142(3)	2.6(1)
C(13)	-0.1222(5)	1.0671(4)	0.3204(2)	1.4(1)
C(14)	-0.1755(6)	1.1332(4)	0.3539(3)	2.1(1)
C(15)	-0.2378(7)	1.1212(5)	0.4124(3)	2.9(1)
C(16)	-0.2492(9)	1.0448(5)	0.4370(3)	3.4(1)
C(17)	-0.1970(8)	0.9799(6)	0.4043(3)	3.4(2)
C(18)	-0.1333(7)	0.9908(4)	0.3454(3)	2.3(1)
C(19)	0.2695(6)	0.8646(3)	0.0184(3)	1.5(1)
C(20)	0.3915(6)	0.8336(4)	-0.0127(3)	2.0(1)
C(21)	0.3749(7)	0.7831(4)	-0.0635(3)	2.1(1)
C(22)	0.2399(7)	0.7645(4)	-0.0857(3)	2.0(1)
C(23)	0.1195(7)	0.7964(4)	-0.0571(3)	2.3(1)
C(24)	0.1341(6)	0.8465(4)	-0.0049(3)	1.9(1)



## Appendix B. X-ray crystallographic analysis of [P<sub>2</sub>N<sub>2</sub>]HfMe<sub>2</sub> (6).

**Table B1.** Crystal data.

Empirical formula	C <sub>26</sub> H <sub>48</sub> HfN <sub>2</sub> P <sub>2</sub> Si <sub>4</sub>
Formula weight	741.46
Temperature (K)	173
Crystal color, habit	Clear, block
Crystal dimensions (mm)	0.30 × 0.30 × 0.10
Crystal system	Monoclinic
Lattice type	Primitive
Lattice Parameters	
<i>a</i> (Å)	11.3209(7)
<i>b</i> (Å)	10.8041(3)
<i>c</i> (Å)	28.1451(9)
<i>V</i> (Å <sup>3</sup> )	3441.6(2)
Space group	<i>P</i> 2 <sub>1</sub> / <i>n</i> (#14)
<i>Z</i> value	4
<i>D</i> <sub>calcd</sub> (g cm <sup>-3</sup> )	1.431
<i>F</i> <sub>000</sub>	1504.00
$\mu$ (cm <sup>-1</sup> ) (Mo K $\alpha$ )	32.75

**Table B2.** Intensity measurements.

Diffractionmeter	Rigaku/ADSC CCD
Radiation	Mo K $\alpha$ ( $\lambda$ = 0.71069 Å)
	Graphite monochromated
Detector aperture (mm)	94 × 94
Data images	772 exposures @ 16.0 s
$\phi$ Oscillation range ( $\chi$ = 0) (°)	0.0–189.9
$\omega$ Oscillation range ( $\chi$ = 90.0) (°)	–19.0 to 23.0
Detector position (mm)	40.47(1)
Detector swing angle (°)	–5.52(1)
$2\theta_{\max}$ (°)	55.8
No. of reflections measured	Total: 23 903
	Unique: 7571 ( <i>R</i> <sub>int</sub> = 0.041)
Corrections	Lorentz-polarization
	Absorption
Trans. factors	0.6526–1.0000

**Table B3.** Structure solution and refinement.

Structure solution	Direct methods (SIR97)
Refinement	Full-matrix least-squares
Function minimized	$\Sigma \omega( F_o ^2 -  F_c ^2)^2$
Least squares weights	$\omega = 1/[\sigma^2(F_o^2)]$
p-factor	0.0000
Anomalous dispersion	All non-hydrogen atoms
No. observations ( <i>I</i> > 0.00 $\sigma$ ( <i>I</i> ))	7219
No. variables	316
Reflection:parameter ratio	22.84
Residuals (on <i>F</i> <sup>2</sup> , all data) <i>R</i> ; <i>R</i> <sub>w</sub>	0.048; 0.107
Goodness of fit indicator	1.47
Max shift/error in final cycle	0.06
No. observations ( <i>I</i> > 3 $\sigma$ ( <i>I</i> ))	6957
Residuals (on <i>F</i> , <i>I</i> > 3 $\sigma$ ( <i>I</i> )) <i>R</i> ; <i>R</i> <sub>w</sub>	0.036; 0.063
Max peak in final difference map (e Å <sup>-3</sup> )	1.35
Min peak in final difference map (e Å <sup>-3</sup> )	–1.37

**Table B4.** Atomic coordinates and *B*<sub>eq</sub>.

Atom	<i>x</i>	<i>y</i>	<i>z</i>	<i>B</i> <sub>eq</sub>
Hf(1)	0.65750(1)	0.23340(1)	0.65160(5)	1.428(4)
P(1)	0.50370(1)	0.03890(9)	0.63100(4)	1.93(2)
P(2)	0.74380(9)	0.43630(9)	0.60230(3)	1.56(2)
Si(1)	0.38980(1)	0.28500(1)	0.59870(5)	2.14(2)
Si(2)	0.73980(1)	–0.03330(1)	0.60430(5)	2.23(2)
Si(3)	0.79260(1)	0.19670(1)	0.54750(4)	1.87(2)
Si(4)	0.51990(1)	0.50130(1)	0.64240(5)	2.51(3)
N(1)	0.51010(3)	0.34560(3)	0.62890(1)	1.78(7)
N(2)	0.73090(3)	0.12540(3)	0.59540(1)	1.92(7)
C(1)	0.42520(4)	0.11840(4)	0.58290(1)	2.36(9)
C(2)	0.58270(4)	–0.09030(4)	0.60400(2)	2.45(9)
C(3)	0.73360(3)	0.36020(4)	0.54440(1)	1.91(8)
C(4)	0.63670(4)	0.56280(4)	0.60220(2)	3.0(1)
C(5)	0.36070(6)	0.36310(6)	0.53980(2)	4.6(1)
C(6)	0.25150(5)	0.29060(6)	0.63280(3)	4.1(1)
C(7)	0.80190(5)	–0.06790(5)	0.66420(2)	4.1(1)
C(8)	0.82610(5)	–0.12370(5)	0.56060(3)	4.9(2)
C(9)	0.74710(5)	0.12780(5)	0.48850(2)	3.9(1)
C(10)	0.95660(5)	0.20020(5)	0.55270(2)	3.5(1)
C(11)	0.57740(6)	0.52430(6)	0.70410(2)	4.7(1)
C(12)	0.38170(6)	0.59320(5)	0.63480(3)	4.9(2)
C(13)	0.39430(4)	–0.03090(4)	0.66870(2)	2.44(9)
C(14)	0.27350(4)	–0.02800(5)	0.65940(2)	3.5(1)
C(15)	0.19700(5)	–0.08220(7)	0.69140(2)	4.8(2)
C(16)	0.23790(6)	–0.14090(7)	0.73160(2)	4.9(2)
C(17)	0.35790(5)	–0.14420(7)	0.74110(2)	4.8(2)
C(18)	0.43600(4)	–0.08990(5)	0.70970(2)	3.4(1)
C(19)	0.88480(3)	0.51510(4)	0.60590(1)	1.76(8)
C(20)	0.95490(4)	0.53830(5)	0.56660(2)	2.8(1)
C(21)	1.05610(5)	0.60970(5)	0.57160(2)	3.4(1)
C(22)	1.08800(4)	0.66040(5)	0.61520(2)	2.7(1)
C(23)	1.02030(5)	0.63620(5)	0.65420(2)	3.3(1)
C(24)	0.92130(4)	0.56220(5)	0.64960(2)	3.2(1)
C(25)	0.59360(5)	0.19070(5)	0.72540(2)	3.5(1)
C(26)	0.83120(5)	0.26530(5)	0.69210(2)	3.6(1)



# Lewis acidity of group 14 elements toward intramolecular sulfur in ortho-aryl-thioanisoles<sup>1</sup>

Teresita Munguia, Ioana S. Pavel, Ramesh N. Kapoor, Francisco Cervantes-Lee, László Párkányi, and Keith H. Pannell

**Abstract:** The series of compounds (*o*-CH<sub>3</sub>SC<sub>6</sub>H<sub>4</sub>)CH<sub>2</sub>EPh<sub>3</sub> (E = Si (1), Ge (2), Sn (3), and Pb (4)) have been synthesized and characterized by NMR spectroscopy and by single crystal X-ray diffraction. Compounds 1 and 2 are isostructural with a triclinic crystal system and *P*-1 space group; however, morphotropic steps occur between Ge and Sn, and Sn and Pb. While the E-S distances in 1 and 2 are 3.985 and 3.974 Å, respectively, ~100% of the sum of the respective van der Waals (vdW) radii, there is a notable distortion from tetrahedral geometry about E. Compound 3 is also triclinic with *P*-1 symmetry, but has two molecules in the unit cell that demonstrate a distorted tetrahedral geometry and intramolecular Sn-S distances of 3.699 and 3.829 Å, 88% and 91% of the sum of the vdW radii. Compound 4 has a Pb-S distance of 3.593 Å (91% of Σ vdW radii). The structure of the Grignard coupling product [*o*-(SCH<sub>3</sub>)C<sub>6</sub>H<sub>4</sub>CH<sub>2</sub>]<sub>2</sub> is also reported.

**Key words:** intramolecular self-assembly, silicon, germanium, tin, lead, sulfur.

**Résumé :** On a réalisé la synthèse d'une série de composés de formule (*o*-CH<sub>3</sub>SC<sub>6</sub>H<sub>4</sub>)CH<sub>2</sub>EPh<sub>3</sub> dans lesquels E = Si (1), Ge (2), Sn (3) et Pb (4) et on les a caractérisés par spectroscopie RMN et par diffraction des rayons X par un cristal unique. Les composés 1 et 2 sont isostructuraux avec un système cristallin triclinique et un groupe d'espace *P*-1; toutefois, on note des différences morphotropes entre le Ge et le Sn ainsi qu'entre le Sn et le Pb. Alors que les distances E-S dans les composés 1 et 2 sont respectivement de 3,985 et 3,974 Å, environ 100 % de la somme des rayons respectifs de van der Waals, on note une distorsion notable par rapport à la géométrie tétraédrique autour de E. Le composé 3 est aussi triclinique avec une symétrie *P*-1, mais la maille cristalline comporte deux molécules ce qui démontre la présence d'une géométrie tétraédrique déformée alors que les distances intramoléculaires Sn-S de 3,699 et 3,829 Å correspondent respectivement à 88 % et 91 % de la somme des rayons de van der Waals. Dans le composé 4, la distance Pb-S est de 3,593 Å (91 % de la somme des rayons de van der Waals). On a aussi déterminé la structure du produit de couplage de Grignard [*o*-(SCH<sub>3</sub>)C<sub>6</sub>H<sub>4</sub>CH<sub>2</sub>]<sub>2</sub>.

**Mots clés :** auto-assemblage intramoléculaire, silicium, germanium, étain, plomb, soufre.

[Traduit par la Rédaction]

## Introduction

The system (*o*-CH<sub>3</sub>SC<sub>6</sub>H<sub>4</sub>)CH<sub>2</sub>EPh<sub>3</sub> (E = Si (1), Ge (2), Sn (3), and Pb (4)) offers the capacity to examine intramolecular sulfur-metal interactions via a five-membered ring involving the *ortho*-thiomethyl group S atom (Fig. 1), such that the varying Lewis acidities of the elements toward sulfur may be evaluated. Furthermore, this possible hyper-

valency could impact the potential morphotropic steps as originally described by Kitaigorodskii (1), and observed for simpler group 14 systems where only tetrahedral structures were possible. For example, the system Ph<sub>4</sub>E (E = Si (2), Ge (3), Sn (4), Pb (5)) has been analyzed with respect to such structural variations, and more recent studies by Párkányi et al. (6) illustrated a morphotropic step occurring in the heteronuclear intra(inter)-group 14 bonding organometallic compounds (R<sub>3</sub>EE'R<sub>2</sub>). In these systems the packing coefficient, defined as:

$$\eta = \frac{ZV_m}{V}$$

where *Z* is the number of molecules in the unit cell, *V<sub>m</sub>* is the volume of the molecule, and *V* is the unit cell volume, must be significantly decreased to change the packing motif and create a morphotropic step (6). Thus, 1–4 present an appealing series with which to study whether the size changes of the group 14 element would be sufficient to change the packing coefficient. Furthermore, would the potential intramolecular metal-sulfur interaction be adequate to distort the tetrahedral geometry about the metal center and further aid, or impede, the potential for a morphotropic step.

Received 12 March 2003. Published on the NRC Research Press Web site at <http://canjchem.nrc.ca> on 5 November 2003.

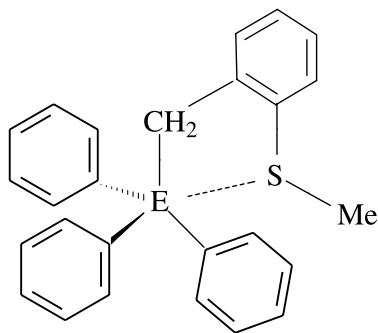
*John: It has been one of my pleasures to get together with you periodically to talk, drink, and generally enjoy your company as well as your chemistry. Cheers, Keith.*

**T. Munguia, I.S. Pavel, R.N. Kapoor, F. Cervantes-Lee, and K.H. Pannell.**<sup>2</sup> Department of Chemistry, University of Texas at El Paso, El Paso, Texas 79968-0513, U.S.A.  
**L. Párkányi.** Central Research Institute of Chemistry, Hungarian Academy of Sciences, H-1525 Budapest, P.O. Box 17, Hungary.

<sup>1</sup>This article is part of a Special Issue dedicated to Professor John Harrod.

<sup>2</sup>Corresponding author (e-mail: [kpannell@utep.edu](mailto:kpannell@utep.edu)).



**Fig. 1.** Triphenyl group 14 derivatives of *o*-aryl thioanisole.

E = Si, Ge, Sn, Pb

Compounds in which systematic evaluations of the intramolecular interactions among group 14 organometallic compounds have been previously reported but were limited to investigations between tin and sulfur, as demonstrated by Wardell and co-workers (7), Tzschach and co-workers (8), and Dräger and co-workers (9) (Fig. 2).

## Experimental section

### General techniques

All syntheses were performed under a nitrogen atmosphere using standard Schlenk line techniques. Reagent grade tetrahydrofuran (THF) and hexanes were dried and distilled under nitrogen from a sodium benzophenone ketyl solution; benzene was dried and distilled from Na ribbon. Thionyl chloride was purchased from Fisher Scientific and purified by distillation; pyridine was purchased from E M Science and dried and distilled over KOH;  $\text{Ph}_3\text{SiCl}$  and  $\text{Ph}_3\text{GeCl}$  were purchased from Gelest;  $\text{Ph}_3\text{SnCl}$ ,  $\text{Ph}_3\text{PbCl}$ , thiosalicylic acid, and dimethyl sulfate were purchased from Aldrich and were used as received. NMR spectra of all compounds were recorded on a Bruker 300 MHz spectrometer in  $\text{CDCl}_3$ . Elemental analyses were performed by Galbraith Laboratories.

Syntheses of *o*-(methylthio)benzoic acid (10), *o*-(methylthio)benzyl alcohol (10, 11), and *o*-(methylthio)benzyl chloride (12) followed literature procedures. *o*-(Methylthio)benzoic acid, mp 165 °C (lit. (10) value 167–169 °C).  $^1\text{H}$  NMR ( $\text{CDCl}_3$ )  $\delta$ : 2.5 (3H, s, S-CH<sub>3</sub>), 7.2–7.5 (4H, m, Ph), 8.1 (1H, d, COOH).  $^{13}\text{C}$  NMR ( $\text{CDCl}_3$ )  $\delta$ : 15.6 (S-CH<sub>3</sub>), 123.5, 124.4, 125.5, 132.5, 133.3 ( $\text{C}_{\text{ipso}}$ ), 144.4 ( $\text{C}_{\text{ipso}}$ ), 171.5 (COOH). *o*-(Methylthio)benzyl alcohol, bp 156 °C/17 mmHg (1 mmHg = 133.322 Pa) (lit. (10) value 88 °C/0.001 mmHg (1 mmHg = 133.322 Pa)).  $^1\text{H}$  NMR ( $\text{CDCl}_3$ )  $\delta$ : 2.4 (3H, s, S-CH<sub>3</sub>), 3.3 (1H, s, OH), 4.7 (2H, s, CH<sub>2</sub>-OH), 7.2–7.4 (4H, m, Ph).  $^{13}\text{C}$  NMR ( $\text{CDCl}_3$ )  $\delta$ : 16.3 (S-CH<sub>3</sub>), 63.2 (CH<sub>2</sub>-OH), 125.7, 126.5, 128.0, 128.5, 136.8 ( $\text{C}_{\text{ipso}}$ ), 139.3 ( $\text{C}_{\text{ipso}}$ ). *o*-(Methylthio)benzyl chloride, bp 123 °C/9 mmHg (1 mmHg = 133.322 Pa) (lit. (12) value 75 to 76 °C/1 × 10<sup>-2</sup> mmHg (1 mmHg = 133.322 Pa)).  $^1\text{H}$  NMR ( $\text{CDCl}_3$ )  $\delta$ : 2.5 (3H, s, S-CH<sub>3</sub>), 4.8 (2H, s, CH<sub>2</sub>-Cl), 7.2–7.4 (4H, m, Ph).  $^{13}\text{C}$  NMR ( $\text{CDCl}_3$ )  $\delta$ : 16.7 (S-CH<sub>3</sub>), 45.1 (CH<sub>2</sub>-Cl), 126.0, 127.3, 129.9, 130.6, 136.0 ( $\text{C}_{\text{ipso}}$ ), 139.1 ( $\text{C}_{\text{ipso}}$ ).

The syntheses of the group 14 derivatives of *o*-(methylthio)benzyl chloride were accomplished as illustrated below for the silicon derivative in similar yields.

### Synthesis of *o*-(methylthio)benzyl triphenylsilane (1)

To a suspension of Li metal (0.55 g, 79 mmol) in THF (20 mL) was added dropwise a solution of  $\text{Ph}_3\text{SiCl}$  (1.7 g, 5.8 mmol) in THF (15 mL) at 0 °C. The reaction mixture was allowed to warm to room temperature and stirred for 16 h resulting in a dark brown-black color. The solution was transferred via cannula to a dropping funnel and then added dropwise at –78 °C to a solution of *o*-(methylthio)benzyl chloride (*o*-(SCH<sub>3</sub>C<sub>6</sub>H<sub>4</sub>)CH<sub>2</sub>Cl, 1.0 g, 5.8 mmol) in THF (20 mL). This mixture was allowed to warm to room temperature and stirred for 16 h. The solvent was removed under reduced pressure, and the product was extracted with a solution of 80 mL of hexanes and 5 mL dichloromethane and subsequently filtered to remove LiCl. The crude material was recrystallized from a hot hexanes:dichloromethane solution (10:1).

*o*-(SCH<sub>3</sub>C<sub>6</sub>H<sub>4</sub>)CH<sub>2</sub>SiPh<sub>3</sub> (1) yield: 0.79 g (35%); mp 110–112 °C.  $^1\text{H}$  NMR ( $\text{CDCl}_3$ )  $\delta$ : 2.1 (3H, s, S-CH<sub>3</sub>), 3.2 (2H, s, CH<sub>2</sub>-Si), 7.5–6.9 (19H, m, Ph).  $^{13}\text{C}$  NMR ( $\text{CDCl}_3$ )  $\delta$ : 16.6 (S-CH<sub>3</sub>), 21.2 (CH<sub>2</sub>-Si), 125.1, 125.4, 127.3, 127.6, 129.0, 129.4, 134.4 ( $\text{C}_{\text{ipso}}$ ), 135.9, 137.1 ( $\text{C}_{\text{ipso}}$ ), 137.8 ( $\text{C}_{\text{ipso}}$ ).  $^{29}\text{Si}$  NMR ( $\text{CDCl}_3$ )  $\delta$ : –11.9. Anal. calcd. for C<sub>26</sub>H<sub>24</sub>SSi: C 78.74, H 6.10; found: C 77.86, H 6.08.

*o*-(SCH<sub>3</sub>C<sub>6</sub>H<sub>4</sub>)CH<sub>2</sub>GePh<sub>3</sub> (2) yield: 0.93 g (37%); mp 104 °C.  $^1\text{H}$  NMR ( $\text{CDCl}_3$ )  $\delta$ : 2.1 (3H, s, S-CH<sub>3</sub>), 3.2 (2H, s, CH<sub>2</sub>-Ge), 7.7–6.9 (19H, m, Ph).  $^{13}\text{C}$  NMR ( $\text{CDCl}_3$ )  $\delta$ : 16.2 (S-CH<sub>3</sub>), 22.2 (CH<sub>2</sub>-Ge), 125.1, 125.4, 126.9, 127.9, 128.5, 128.8, 134.4 ( $\text{C}_{\text{ipso}}$ ), 135.1, 136.6 ( $\text{C}_{\text{ipso}}$ ), 138.2 ( $\text{C}_{\text{ipso}}$ ). Anal. calcd. for C<sub>26</sub>H<sub>24</sub>GeS: C 70.79, H 5.48; found: C 70.01, H 5.46.

*o*-(SCH<sub>3</sub>C<sub>6</sub>H<sub>4</sub>)CH<sub>2</sub>SnPh<sub>3</sub> (3) yield: 2.0 g (71%); mp 106–108 °C.  $^1\text{H}$  NMR ( $\text{CDCl}_3$ )  $\delta$ : 2.1 (3H, s, S-CH<sub>3</sub>), 3.1 (2H, s, CH<sub>2</sub>-Sn,  $J_{\text{H-}^{117}\text{Sn}} = 64.3$  Hz,  $J_{\text{H-}^{119}\text{Sn}} = 66.7$  Hz), 7.6–7.0 (19H, m, Ph).  $^{13}\text{C}$  NMR ( $\text{CDCl}_3$ )  $\delta$ : 15.4 (S-CH<sub>3</sub>), 20.5 (CH<sub>2</sub>-Sn), 124.8, 125.0, 125.5, 127.6, 128.1 (Ph-Sn,  $J_{\text{C-}^{117/119}\text{Sn}} = 180$  Hz), 128.6 (Ph-Sn,  $J_{\text{C-}^{117/119}\text{Sn}} = 75$  Hz), 135.3 ( $\text{C}_{\text{ipso}}$ ), 136.8 (Ph-Sn,  $J_{\text{C-}^{117/119}\text{Sn}} = 150$  Hz), 139.1 ( $\text{C}_{\text{ipso}}$ ), 139.2 ( $\text{C}_{\text{ipso}}$ ).  $^{119}\text{Sn}$  NMR ( $\text{CDCl}_3$ )  $\delta$ : –115.5. Anal. calcd. for C<sub>26</sub>H<sub>24</sub>SSn: C 64.09, H 4.96; found: C 64.00, H 5.10.

*o*-(SCH<sub>3</sub>C<sub>6</sub>H<sub>4</sub>)CH<sub>2</sub>PbPh<sub>3</sub> (4) yield: 0.93 g (30%); mp 110–114 °C.  $^1\text{H}$  NMR ( $\text{CDCl}_3$ )  $\delta$ : 2.1 (3H, s, S-CH<sub>3</sub>), 3.4 (2H, s, CH<sub>2</sub>-Pb,  $J_{\text{H-Pb}} = 75.53$  Hz), 7.6–6.9 (19H, m, Ph).  $^{13}\text{C}$  NMR ( $\text{CDCl}_3$ )  $\delta$ : 15.4 (S-CH<sub>3</sub>), 31.3 (CH<sub>2</sub>-Pb,  $J_{\text{C-Pb}} = 286.8$  Hz), 124.7, 124.9, 125.1, 127.9, 128.1 (Ph-Pb,  $J_{\text{C-Pb}} = 17.6$  Hz), 129.0 (Ph-Pb,  $J_{\text{C-Pb}} = 72.6$  Hz), 135.4 ( $\text{C}_{\text{ipso}}$ ), 137.2 (Ph-Pb,  $J_{\text{C-Pb}} = 64.1$  Hz), 139.7 ( $\text{C}_{\text{ipso}}$ ), 152.2 (Ph-Pb,  $J_{\text{C-Pb}} = 359.2$  Hz).  $^{207}\text{Pb}$  NMR ( $\text{CDCl}_3$ )  $\delta$ : –146.2. Anal. calcd. for C<sub>26</sub>H<sub>24</sub>PbS: C 54.24, H 4.20; found: C 53.88, H 4.44.

### Alternative synthesis of *o*-(methylthio)benzyl triphenyllead (4)

*o*-(Methylthio)benzyl chloride (1.0 g, 5.9 mmol) was added dropwise to a mixture of  $\text{Ph}_3\text{PbCl}$  (2.8 g, 5.9 mmol) and Mg turnings (0.15 g, 6.2 mmol) in THF (10 mL) at 0 °C. The reaction mixture was kept at 0 °C and allowed to stir until all the Mg had been consumed (16 h). The solution was transferred via cannula to another flask where the solvent was removed under reduced pressure and the product was extracted with 80 mL hexanes and 5 mL of dichloromethane and the solution filtered. The crude material was



**Fig. 2.** Summary of intramolecular interactions between tin and sulfur.

Structure	S—Sn (Å)	Reference	Structure	S—Sn (Å)	Reference
	3.67	7b		2.851	8a
	3.58	7b		3.097, 3.118	8b
	3.29, 3.26 <sup>a</sup>	7a		R=Cl R=Me: 2.863 R=Br R=Me: 2.760, 2.767, 2.779, 3.514	9
	3.195	7c			

<sup>a</sup> Two independent molecules in the unit cell.

recrystallized from a hexane:dichloromethane solution (10:1) and cooled to  $-20^{\circ}\text{C}$  to yield **4**, 1.2 g (70%). This method was also used for the synthesis of **3** in a similar yield.

#### X-ray structural analysis

Crystals suitable for X-ray diffraction were obtained for compounds **1–4**, and **5** from hexane–dichloromethane solutions. Five colorless crystals **1**, **2**, **3**, **4**, and **5** were mounted

on glass fibers in a random orientation. Intensity data were collected at room temperature for **1**, **2**, **5** and  $-85^{\circ}\text{C}$  for **3** using a Siemens/Bruker four-circle diffractometer with graphite-monochromated Mo  $K\alpha$  radiation. Unit cell parameters and standard deviations were obtained by least-squares fit of 25 reflections randomly distributed in reciprocal space in the  $2\theta$  range of  $15^{\circ}$ – $30^{\circ}$ . The  $\omega$ -scan technique was used for intensity measurements in all cases. A range of  $1.2^{\circ}$  in  $\omega$  and variable speed of 4.00–20.00  $^{\circ}/\text{min}$  was used for com-



pounds **1**, **2**, **3**, and **5**. Background counts were taken with a stationary crystal and total background time to scan time ratio of 0.5. Three standard reflections were monitored in all cases every 97 reflections and showed no significant decay. The data were corrected for Lorentz and polarization effects and a semiempirical absorption correction was also applied to the data set of **2** giving a min/max transmission ratio of 0.090:0.153. No absorption correction was applied to the data sets of **1**, **3**, and **5**.

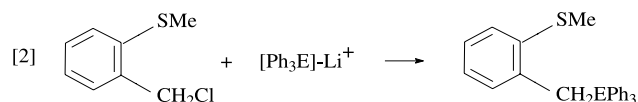
Intensity data for compound **4** were collected at room temperature on a Bruker SMART system with an APEX CCD detector. All structures were solved by direct methods and refined using the PC version of the SHELEXTL PLUS crystallographic software by Siemens.<sup>3</sup> Full-matrix least-squares refinement of  $F^2$  against all reflections was carried out with anisotropic thermal parameters for non-hydrogen atoms. Hydrogen atoms for **1**, **2**, **3**, and **5** were placed at calculated positions ( $C-H = 0.96 \text{ \AA}$ ;  $U_H = 0.08$ ) during refinements, whereas those in compound **4** were located on a difference map. The weighing scheme has the form  $w^{-1} = \sigma^2(F_o^2) + (aP)^2 + bP$ , where  $P$  is  $[2F_c^2 + \max(F_o^2, 0)]/3$  and the final  $R$  factors have the form  $R_1 = \sum |F_o - F_c| / \sum F_o$  and  $R_w2 = \{\sum [w(F_o^2 - F_c^2)^2] / \sum [w(F_o^2)^2]\}^{1/2}$ ; these and some other relevant crystallographic parameters are summarized in Table 1 and selected bond lengths and angles are presented in Tables 2 and 3.

Compounds **1–3** (Figs. 3–5, respectively) crystallize in the triclinic form with space group  $P-1$ . The latter compound has two independent molecules in the asymmetric unit (**3a** and **3b**). Compound **4**, in contrast, crystallized in the monoclinic crystal structure with a space group of  $P2(1)/c$  (Fig. 6).

## Results and discussion

### Synthesis and characterization

We have used two salt-elimination reactions to attach the *o*-(methylthio)benzyl chloride ligand to the group 14 atom (eqs. [1] and [2]).



Both routes are successful; however, when using the Grignard route we observed the significant production of the coupling product ( $[\text{CH}_2(o\text{-C}_6\text{H}_4\text{SMe})]_2$  (**5**)). This is formed during the initial attempts to make the Grignard reagent prior to subsequent addition of the group 14 halide. Modification of the procedure to form the Grignard in situ in the

Fig. 3. Molecular diagram of **1**.

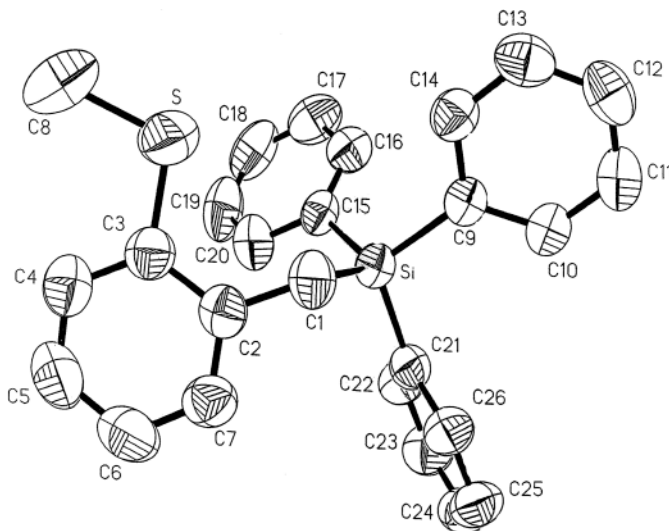
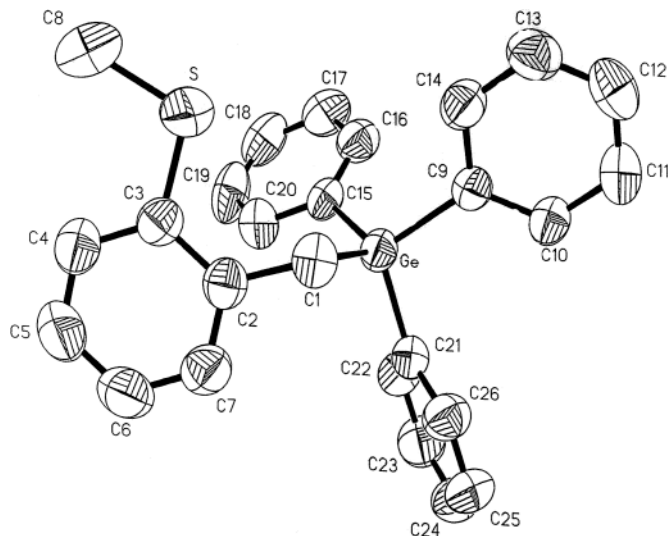


Fig. 4. Molecular diagram of **2**.



presence of the halide reduced the extent of this problem and resulted in the desired product in good yields (75%).

The reaction pathway involving the use of organometallic lithium salt was equally successful. However, we think the greater flexibility of the chemistry in eq. [1] makes this a more general and useful route to such compounds, where the organometallic lithium salts are less readily available. The spectroscopic and elemental analytical data for the compounds **1–4** are in total accord with their proposed structures, as is the data for **5**.

### Periodic trends in the structural data for compounds **1–4**

The E-S intramolecular distance in compounds **1–4** is an essential structural feature for analysis of the progressive change  $E = \text{Si, Ge, Sn, and Pb}$ . Not only is it an indirect

<sup>3</sup>Supplementary data may be purchased from the Directory of Unpublished Data, Document Delivery, CISTI, National Research Council Canada, Ottawa, ON K1A 0S2, Canada ([http://www.nrc.ca/cisti/irm/unpub\\_e.shtml](http://www.nrc.ca/cisti/irm/unpub_e.shtml) for information on ordering electronically). CCDC 205424–205428 contain the crystallographic data for this manuscript. These data can be obtained, free of charge, via [www.ccdc.cam.ac.uk/conts/retrieving.html](http://www.ccdc.cam.ac.uk/conts/retrieving.html) (or from the Cambridge Crystallographic Data Centre, 12 Union Road, Cambridge CB2 1EZ, U.K.; fax +44 1223 336033; or [deposit@ccdc.cam.ac.uk](mailto:deposit@ccdc.cam.ac.uk)).



**Table 1.** Crystal data and structure refinement for crystal structure analysis of compounds 1–5.

	1	2	3	4	5
Empirical formula	C <sub>26</sub> H <sub>24</sub> SSi	C <sub>26</sub> H <sub>24</sub> SGe	C <sub>26</sub> H <sub>24</sub> SSn	C <sub>26</sub> H <sub>24</sub> SPb	C <sub>16</sub> H <sub>18</sub> S <sub>2</sub>
Formula weight (g/mol)	396.60	441.10	487.20	575.70	274.42
Temperature (K)	296(2)	296(2)	188(2)	296(2)	296(2)
$\lambda$ (Mo K $\alpha$ ) (Å)	0.71073	0.71073	0.71073	0.71073	0.71073
Crystal system	Triclinic	Triclinic	Triclinic	Monoclinic	Monoclinic
Space group	<i>P</i> -1	<i>P</i> -1	<i>P</i> -1	<i>P</i> 2(1)/ <i>c</i>	<i>P</i> 2(1)/ <i>n</i>
<i>a</i> (Å)	7.695(4)	7.704(3)	9.389(2)	19.139(3)	7.985(4)
<i>b</i> (Å)	7.746(5)	7.771(3)	11.440(4)	14.844(2)	4.866(2)
<i>c</i> (Å)	19.003(10)	19.195(6)	22.049(5)	7.8017(12)	18.875(6)
$\alpha$ (°)	98.42(5)	96.57(3)	77.94(2)	90	90
$\beta$ (°)	95.76(4)	98.06(3)	78.36(2)	98.658(3)	92.79(3)
$\gamma$ (°)	101.33(5)	102.14(3)	80.94(2)	90	90
Volume (Å <sup>3</sup> )	1088.9(11)	1100.0(7)	2251.9(11)	2191.2(6)	732.5(5)
<i>Z</i>	2	2	4	4	4
<i>D</i> <sub>X</sub> (Mg/m <sup>3</sup> )	1.210	1.332	1.437	1.745	1.244
$\mu$ (mm <sup>-1</sup> )	0.212	1.496	1.236	7.803	0.344
<i>F</i> (000)	420	456	984	1112	292
Crystal size (mm)	0.80 × 0.52 × 0.20	0.80 × 0.72 × 0.28	0.40 × 0.18 × 0.14	0.12 × 0.08 × 0.06	0.30 × 0.24 × 1.16
$\theta$ Range for data collection (°)	2.19–25.05	2.17–25.05	1.83–24.94	2.55–28.28	2.16–25.05
Index ranges	0 ≤ <i>h</i> ≤ 9, –9 ≤ <i>k</i> ≤ 9, –22 ≤ <i>l</i> ≤ 22	0 ≤ <i>h</i> ≤ 9, –9 ≤ <i>k</i> ≤ 9, –22 ≤ <i>l</i> ≤ 22	–3 ≤ <i>h</i> ≤ 11, –13 ≤ <i>k</i> ≤ 13, –25 ≤ <i>l</i> ≤ 25	–25 ≤ <i>h</i> ≤ 25, –19 ≤ <i>k</i> ≤ 19, –10 ≤ <i>l</i> ≤ 10	–0 ≤ <i>h</i> ≤ 9, –0 ≤ <i>k</i> ≤ 5, –22 ≤ <i>l</i> ≤ 22
Reflections collected	4172	4190	10 790	29 981	2782
Independent reflections	3857	3876	7643	5446	1294
<i>R</i> (int)	0.0415	0.0491	0.0653	0.0473	0.0710
Absorption correction	N/A	Semi-empirical	N/A	SADABS	N/A
Refinement method	L.S. on <i>F</i> <sup>2</sup>	L.S. on <i>F</i> <sup>2</sup>	L.S. on <i>F</i> <sup>2</sup>	L.S. on <i>F</i> <sup>2</sup>	L.S. on <i>F</i> <sup>2</sup>
Data/restraints/ parameters	3857/0/253	3857/0/253	7643/0/507	5446/0/254	1294/0/82
Goodness-of-fit on <i>F</i> <sup>2</sup>	0.936	1.029	1.327	1.034	0.925
Final <i>R</i> indices ( <i>I</i> > 2 $\sigma$ ( <i>I</i> ))	<i>R</i> 1 = 0.0490, <i>wR</i> 2 = 0.1553	<i>R</i> 1 = 0.0581, <i>wR</i> 2 = 0.1705	<i>R</i> 1 = 0.0692, <i>wR</i> 2 = 0.1752	<i>R</i> 1 = 0.0350, <i>wR</i> 2 = 0.0770	<i>R</i> 1 = 0.0566, <i>wR</i> 2 = 0.1321
<i>R</i> indices (all data)	<i>R</i> 1 = 0.0668, <i>wR</i> 2 = 0.1753	<i>R</i> 1 = 0.0641, <i>wR</i> 2 = 0.1782	<i>R</i> 1 = 0.0861, <i>wR</i> 2 = 0.2247	<i>R</i> 1 = 0.0500, <i>wR</i> 2 = 0.0828	<i>R</i> 1 = 0.1371, <i>wR</i> 2 = 0.1688
Largest diff. peak, hole (e Å <sup>-3</sup> )	0.255, –0.286	0.951, –1.147	1.425, –2.681	1.486, –0.696	0.129, –0.157



**Table 2.** Selected interatomic bond distances (Å) and angles (°) for the compounds **1–4**.

	E = Si ( <b>1</b> )	E = Ge ( <b>2</b> )	E = Sn a ( <b>3</b> )	E = Sn b ( <b>3</b> )	E = Pb ( <b>4</b> )
<b>Bond distances (Å)</b>					
S—E	3.985	3.974	3.699	3.829	3.953
S—C(3)	1.753(3)	1.766(5)	1.766(11)	1.777(10)	1.754(5)
S—C(8)	1.776(4)	1.786(6)	1.812(12)	1.798(13)	1.786(6)
E—C(1)	1.896(3)	1.976(5)	2.174(8)	2.174(11)	2.244(5)
E—C(9)	1.873(3)	1.945(4)	2.143(9)	2.163(10)	2.204(5)
E—C(15)	1.876(3)	1.957(4)	2.145(9)	2.170(11)	2.192(5)
E—C(21)	1.876(3)	1.961(4)	2.156(9)	2.123(11)	2.200(5)
C(1)—C(2)	1.497(4)	1.491(6)	1.522(12)	1.462(15)	1.479(7)
<b>Bond angles (°)</b>					
C(9)–E–C(1)	104.57(12)	104.84(18)	112.6(4)	109.9(4)	103.35(18)
C(9)–E–C(15)	110.07(12)	110.17(17)	108.3(3)	109.0(4)	110.50(18)
C(9)–E–C(21)	109.87(11)	110.40(17)	108.0(3)	106.9(4)	109.21(18)
C(15)–E–C(1)	114.57(12)	115.20(19)	106.0(4)	110.1(5)	114.0(2)
C(15)–E–C(21)	107.48(11)	107.12(17)	109.0(3)	112.0(4)	107.00(19)
C(21)–E–C(1)	110.24(13)	109.1(2)	112.8(3)	108.9(4)	112.71(18)
C(2)–C(1)–E	118.27(19)	116.2(3)	112.2(6)	111.5(7)	114.1(3)
C(2)–C(3)–S	117.1(2)	116.7(3)	118.2(7)	117.6(8)	117.4(4)
C(4)–C(3)–S	123.1(2)	123.6(4)	122.6(9)	122.0(9)	123.1(4)
C(3)–S–C(8)	104.99(18)	107.7(3)	102.7(6)	102.7(6)	103.3(3)
C(10)–C(9)–E	123.40(19)	122.4(3)	118.8(7)	122.1(8)	119.7(4)
C(14)–C(9)–E	119.94(19)	119.6(3)	124.1(7)	122.6(7)	121.7(4)
C(16)–C(15)–E	121.17(19)	120.0(3)	121.5(7)	120.0(8)	122.0(4)
C(20)–C(15)–E	121.7(2)	122.0(3)	122.3(8)	121.4(9)	119.5(4)
C(22)–C(21)–E	121.81(19)	120.8(3)	118.6(7)	119.6(9)	121.4(4)
C(26)–C(21)–E	121.2(2)	120.9(3)	123.6(7)	120.9(9)	120.0(4)
C(1)–C(2)–C(3)	122.1(2)	122.5(4)	120.1(9)	121.2(10)	121.9(4)

**Table 3.** Selected interatomic bond distances (Å) and angles (°) for compound **5**.

	<b>5</b>
<b>Bond distances (Å)</b>	
S—C(1)	1.768(4)
S—C(8)	1.770(5)
C(6)—C(7)	1.510(5)
<b>Bond angles (°)</b>	
C(6)–C(1)–S	117.9(3)
C(2)–C(1)–S	122.5(3)
C(1)–S–C(8)	104.9(2)
C(1)–C(6)–C(7)	121.9(4)
C(6)–C(7)–C(7a)	112.3(4)

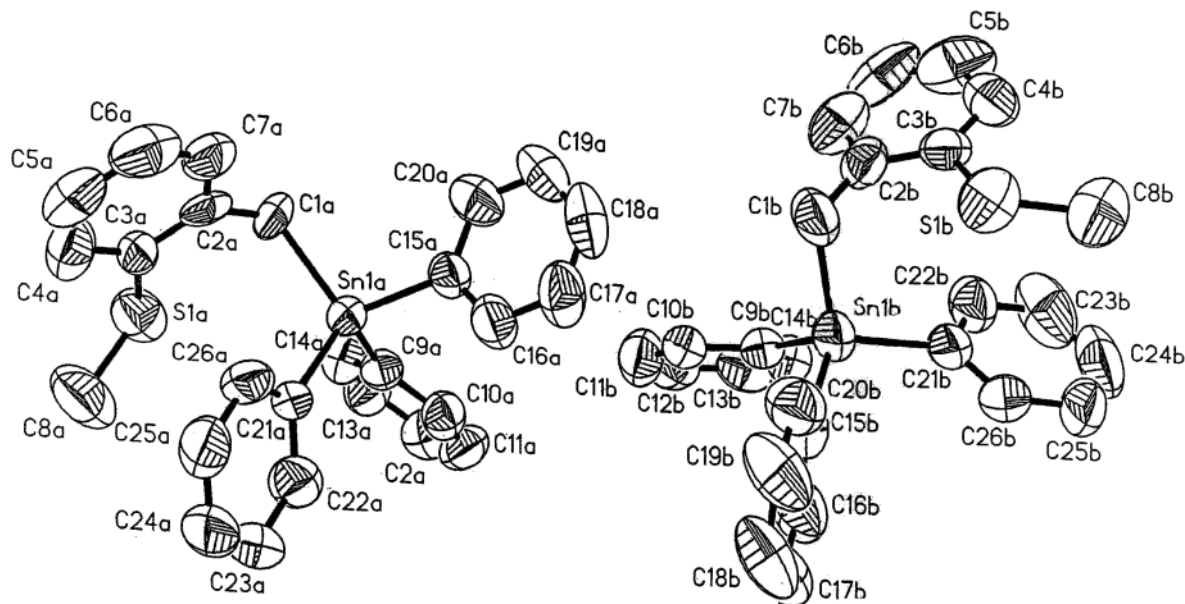
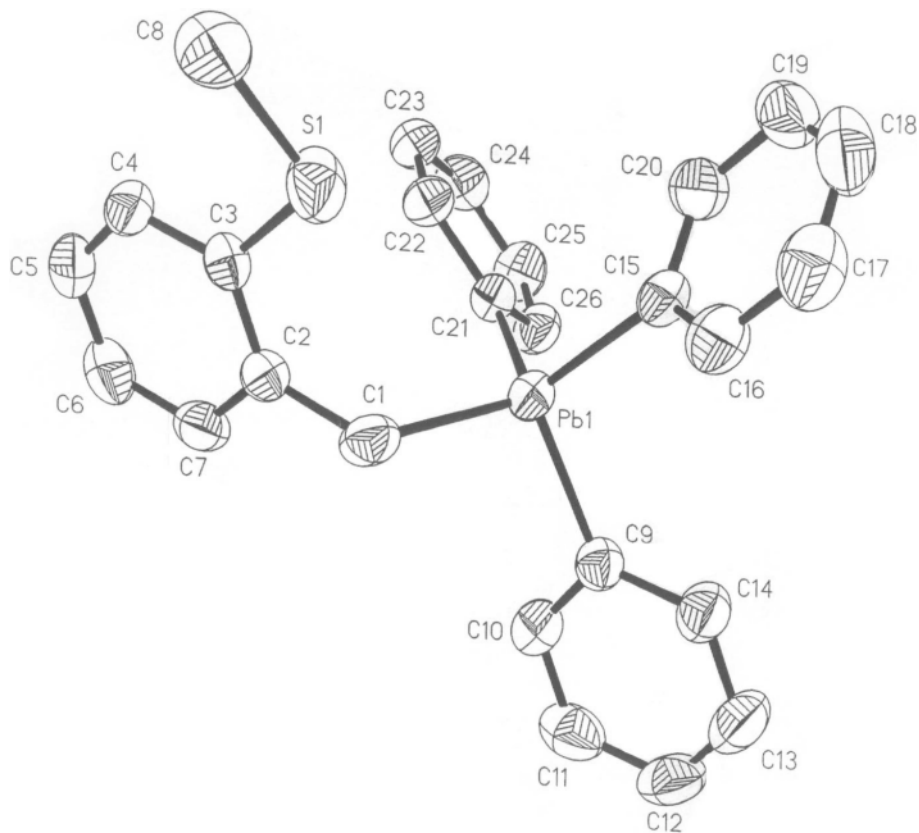
method of testing the Lewis acidity toward S of the central metal atom, but it also lends a conformational degree of freedom that may effect any potential morphotropic transition. Table 4 is a summary of covalent radii (13), van der Waals (vdW) radii (13, 14), their sums, and their comparison to experimental E–S distances. Both **1** and **2** exhibit E–S distances that are ~100% of the sum of the vdW radii indicating that there are no significant intramolecular interactions between the metal center and sulfur. The Sn–S interactions in compound **3** are 3.699 Å (**3a**) and 3.829 Å (**3b**), an average distance of ~90% of the sum of the vdW radii, similar to that in the lead compound **4**, Pb–S = 3.953 Å, 91% of the vdW radii.

Both the ipso phenyl C—E bond lengths in compounds **1–4** vary as expected because of the greater atomic radius of the group 14 elements in the order Si < Ge < Sn < Pb and are similar to those reported in the series Ph<sub>4</sub>E (**2–5**). Bonds between E and benzyl groups are not well represented in the literature, with the exception of that in Ph<sub>3</sub>PbCH<sub>2</sub>C<sub>6</sub>H<sub>5</sub> (**15**). The present examples also exhibit the expected increase in bond lengths from C—Si to C—Pb, C1—E (E = Si, Ge, Sn, Pb) = 1.896, 1.976, 2.174, and 2.244 Å, respectively.

#### Consequences of E–S interaction on tetrahedral geometry

In a perfect tetrahedral geometry, each angle is 109.5° and the sum of three threefold symmetry angles will equal 328.5°. Group 14 organometallic compounds do not necessarily exhibit perfect tetrahedral geometry and the amount of distortion varies from system to system. In the Ph<sub>4</sub>E system, all the molecules are spherical, crystallizing in the tetragonal space group *P* 4<sub>2</sub>*c* (**2–5**). Despite the spherical nature and symmetry of these molecules, the C–E–C dihedral angles have a range of 108.1–111.2 (**2–5**). The wide range of angles creates difficulty when comparing systems; as a result, all angles of compounds **1–4** are compared with perfect tetrahedral geometry. The “base” of the tetrahedral in this series is comprised of the bond angles that would be *pushed* up as the sulfur atom approaches the metal center trans to the “axial” phenyl group. The numbering schemes for compounds **1** and **2** are identical; however, the numbering is slightly different in the phenyl region for **3** and **4**. For compounds **1** and **2**, angle C1–E–C9 is smaller than 109.5°, ranging from 104.57°



**Fig. 5.** Molecular diagram of **3**.**Fig. 6.** Molecular diagram of **4**.

for **1** to  $104.84^\circ$  for **2** with corresponding increases in C1-E-C15. As we would expect for compounds with no E-S interactions, the third angle (C9-E-C15) would also be close to  $109.5^\circ$ . The compounds **3a** and **4** (with E-S interactions of 88% and 91% of the sum of the vdW radii, respectively) have analogous angles that are smaller than  $109.5^\circ$  ( $108.0^\circ$  and  $107.0^\circ$ , respectively). However, the other two angles in

the base do not adjust to preserve the sum of  $328.5^\circ$ , as in compounds **1** and **2**. When all three angles in the base plane are added together, **3a** and **4** have the largest differences from  $328.5^\circ$ ,  $333.4^\circ$ , and  $333.71^\circ$  in that order, indicating that the C-E-C plane is being pushed up slightly by the E-S interactions. Table 5 summarizes the bond angles and their sums for compounds **1-4**.



**Table 4.** Comparison of sulfur – group 14 interactions.

E	Covalent radii (Å) <sup>a</sup>	van der Waals radii (Å) <sup>a,b</sup>	$\Sigma_{\text{Covalent}}$ (Å)	$\Sigma_{\text{van der Waals}}$ (Å)	S—E (Å)	S—E as % vdW radii
Si	1.17	2.10	2.20	3.90	3.985	102.2
Ge	1.22	2.15	2.25	3.95	3.974	100.6
Sn	1.40	2.40	2.43	4.20	3.699 (a)	88.1
					3.829 (b)	91.2
					3.764 (avg.)	89.6
Pb	1.44	2.53	2.47	4.33	3.953	91.0
S	1.03	1.80				

<sup>a</sup>See ref. 13.<sup>b</sup>See ref. 14.**Table 5.** List of base and axial angles and their sums for compounds **1–4**.

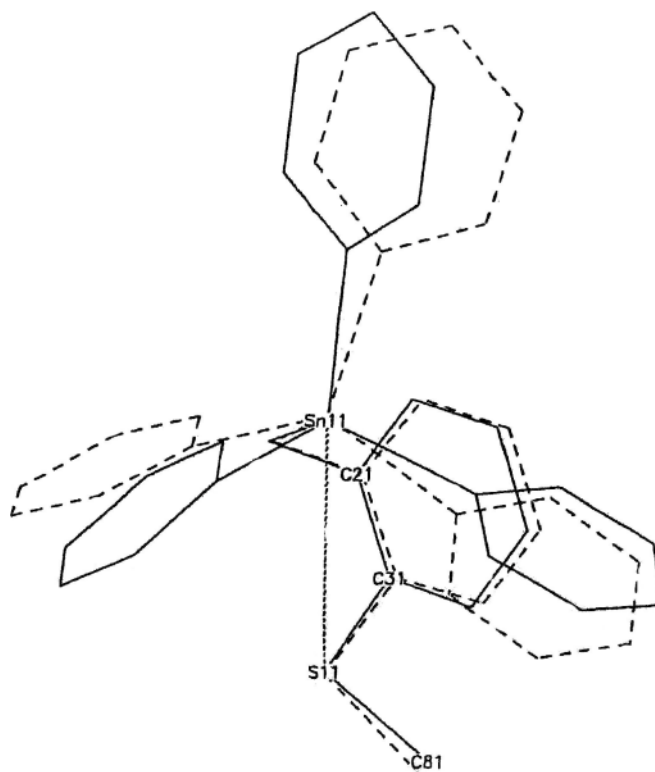
Base angles	Sum of base angles (°)		Axial angles	Sum of axial angles (°)	
	1	2		1	2
C(15)-E-C(1)	329.21	330.21	C(9)-E-C(21)	327.59	326.62
C(9)-E-C(15)			C(1)-E-C(21)		
C(9)-E-C(1)			C(15)-E-C(21)		
	3a	3b		3a	3b
C(21)-E-C(1)	333.4	325.7	C(1)-E-C(15)	323.3	331.10
C(9)-E-C(21)			C(21)-E-C(15)		
C(9)-E-C(1)			C(9)-E-C(15)		
	4			4	
C(21)-E-C(1)	333.71		C(15)-E-C(9)	323.06	
C(15)-E-C(21)			C(1)-E-C(9)		
C(15)-E-C(1)			C(21)-E-C(9)		

Further indications of the distortion about the central metal atom are the axial angles. The sum of these angles under normal geometry would also be 328.5°. Once the base plane is pushed up by increasing E–S interactions, the sum of these three angles mentioned above should be *less than* 328.5°. Indeed after analysis, the two compounds with the smallest sums are **3a** (323.3°) and **4** (323.06°), precisely the compounds with the shortest E–S distances in terms of %  $\Sigma$  vdW radii.

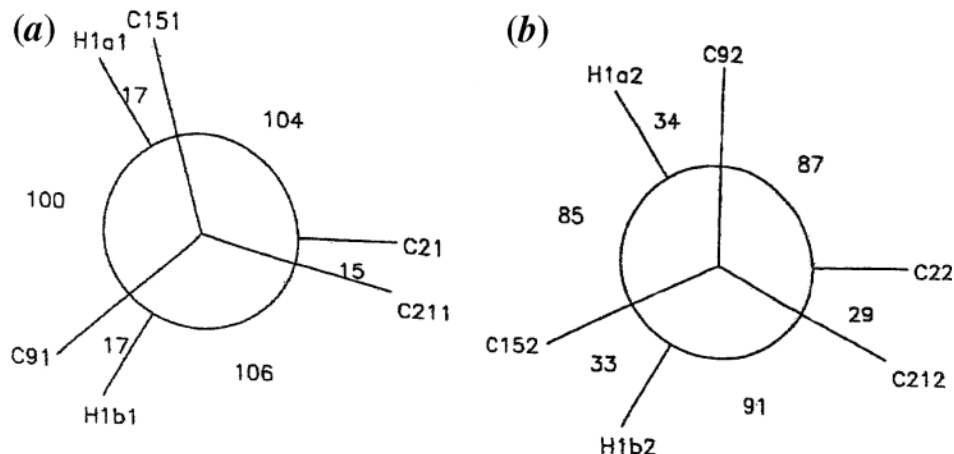
Another trend that illustrates how the E–S interaction distorts the molecule is that as the E–S distance decreases, the C(2)–C(1)–E bond angle decreases as well. This makes sense because angle C(1)–C(2)–C(3) will not change much because of the rigid angle system dictated by the aromatic ring. As a result, the only angle within the “arm” substructure that gives flexibility is the C(2)–C(1)–E angle, which contains the methylene moiety. Shortening of the E–S distance would be facilitated by a contraction of the C(2)–C(1)–E angle. Indeed this angle does contract when comparing **1** and **2** with compounds **3** and **4**, with the minimum occurring at compound **3**.

### Isostructural considerations

We have investigated the possible isostructural relationships of **1–4**. From their respective structural data **1** and **2** seem to be isostructural. However, due to the high degree of freedom of assigning a triclinic unit cell and putting the molecule in that cell with respect to the eight centers of symmetry, the observation is not truly a proof. We computed a least-squares fit of these two molecules including all non-

**Fig. 7.** Superposed structures of **3a** and **3b**.



**Fig. 8.** Solid-state conformational analysis of **3**. (a) View down Sn(1)–Ca(1), (b) view down Snb(1)–Cb(1).**Table 6.** Molecular volumes and packing coefficients for **1–4**.

Molecule	Volume (Å <sup>3</sup> )	Packing coefficient
Si	371.1	0.68
Ge	374.6	0.68
Sn 1	386.1	0.69
Sn 2	385.9	0.69
Pb	388.3	0.71

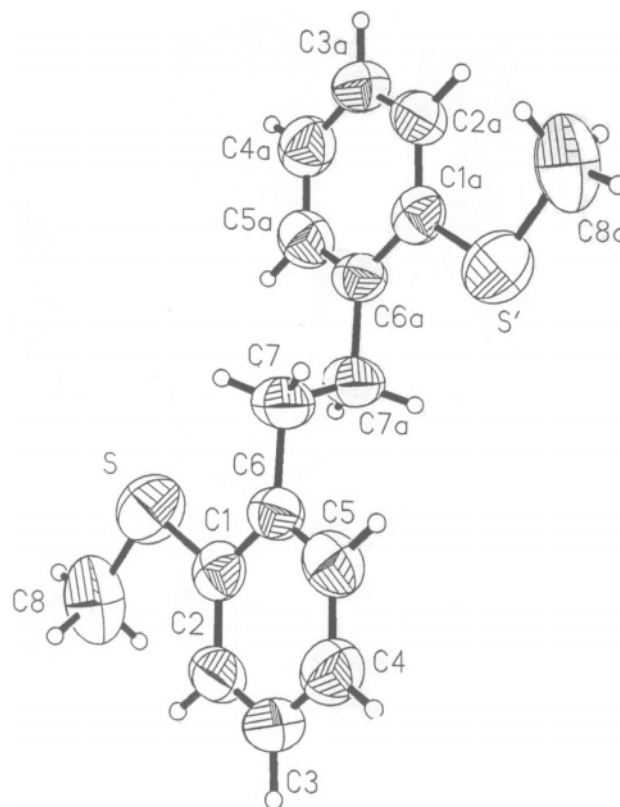
hydrogen atoms and the mean distance is 0.100 Å; RMS = 0.0823, a rather good fit. To prove absolutely we refined the Si structure with the coordinates of the Ge compound and in this manner proved that **1** and **2** are isostructural ( $R = 0.0476$ ). The Sn and Pb derivatives do not belong (in the sense of isostructurality) to a homologous series.

A superpositioning of the two forms of the tin compound (**3a** and **3b**) is illustrated in Fig. 7 and their two distinct conformations are presented in Fig. 8. The two independent molecules are not superimposable, except to a high degree the Sn–S interaction grouping, despite their differing Sn–S distances. The two forms have fully staggered (**3b**) and partially eclipsed forms (**3a**), which is similar to other organometallic group 14 compounds (16). Thus, despite being relatively weak, the intramolecular Sn–S interactions have a significant effect upon the conformational character of the two molecules.

We have computed molecular volumes and packing coefficients for **1–4** (Table 6). These data illustrate a significant jump in the molecular volume between Ge and Sn, where the morphotropic step occurs. Overall, the packing coefficients are very similar, and the slight increase in the value for lead could be the driving force for the change in its crystal form.

#### Magnesium-induced dimerization of *o*-(SCH<sub>3</sub>)C<sub>6</sub>H<sub>4</sub>CH<sub>2</sub>Cl

The capacity of Grignard reagents to produce dimers of their parent organic halides is well established, thus the formation of **5** from such attempted reactions is not surprising. In 1980 an attempt by Zheltov et al. (17) to study the conjugation of aromatic disulfides by UV, mentions the preparation of compound **5**, however, studies were limited, hence we have performed a single crystal structural analysis.

**Fig. 9.** Molecular diagram of **5**.

Compound **5** (Fig. 9) crystallized in the monoclinic crystal group with a space group of  $P2(1)/n$ . In total its structure is unremarkable, however, the various bond lengths and angles about the S atom serve as a baseline to note any variations in **1–4** by virtue of the intramolecular E–S interactions (Table 5).

#### Acknowledgments

Support for this research was provided by the R.A. Welch Foundation, Houston, Texas (Grant AH-0546) and SCORE NIH (Grant No. S06-GM-08012). L.P. wishes to thank the Hungarian Academy of Sciences for the leave of absence.



## References

1. A.I. Kitaigorodskii. Organic chemical crystallography, Consultants Bureau, New York. 1961. p. 223.
2. V. Gruhnert, A. Kirfel, G. Will, F. Wallrafen, and K. Recker. *Z. Kristallogr.* **163**, 53 (1983).
3. A. Karipides and D.A. Haller. *Acta Crystallogr.* **B28**, 2889 (1972).
4. V.K. Belsky, A.A. Simonenko, V.O. Reikhsfeld, and I.E. Saratov. *J. Organomet. Chem.* **244**, 125 (1983).
5. H. Preut and F. Huber. *Acta Crystallogr.* **C49**, 1372 (1993).
6. L. Párkányi, A. Kálmán, S. Sharma, D.M. Nolen, and K.H. Pannell. *Inorg. Chem.* **33**, 180 (1994).
7. (a) P.J. Cox, S.M.S.V. Doidge-Harrison, I.W. Nowell, R.A. Howie, R.P. Randall, and J.L. Wardell. *Inorg. Chim. Acta*, **172**, 225 (1990); (b) R.A. Howie, J.L. Wardell, E. Zanetti, P.J. Cox, and S.M.S.V. Doidge-Harrison. *J. Organomet. Chem.* **431**, 27 (1992); (c) P.J. Cox, S.M.S.V. Doidge-Harrison, I.W. Nowell, R.A. Howie, J.L. Wardell, and J.M. Wiggzell. *Acta Crystallogr.* **C46**, 1015 (1990).
8. (a) K. Jurkschat, J. Schiling, C. Mügge, and A. Tzschach. *Organometallics*, **7**, 38 (1988); (b) K. Jurkschat, B. Schmid, M. Dybiona, U. Baumeister, H. Hartung, and A. Tzschach. *Z. Anorg. Allg. Chem.* **560**, 110 (1988).
9. U. Kolb, M. Beuter, M. Gerner, and M. Dräger. *Organometallics*, **13**, 4413 (1994).
10. R. Grice and L.N. Owen. *J. Chem. Soc.* 1947 (1963).
11. A. Kucsma and T. Kremmer. *Acta Chim. Acad. Sci. Hung.* **34**, 71 (1962).
12. V.J. Traynelis and D.M. Borgnaes. *J. Org. Chem.* **37**, 3824 (1972).
13. J.E. Huheey, E.A. Keiter, and R.L. Keiter. *Inorganic chemistry: Principles of structures and reactivity*. 4th ed. Harper Collins College Publishers, New York. 1993. p. 292.
14. R. Chauvin. *J. Phys. Chem.* **96**, 9194 (1992).
15. U. Fahrenkamp, M. Schuermann, and F. Huber. *Acta Crystallogr.* **C50**, 1707 (1994).
16. (a) K.H. Pannell, L. Párkányi, H. Sharma, and F. Cervantes-Lee. *Inorg. Chem.* **31**, 522 (1992); (b) L. Párkányi, C. Hernandez, and K.H. Pannell. *J. Organomet. Chem.* **301**, 145 (1986); (c) K.H. Pannell, R.N. Kapoor, R. Raptis, L. Párkányi, and V. Fülöp. *J. Organomet. Chem.* **384**, 41 (1990); (d) L. Párkányi, and E. Hengge. *J. Organomet. Chem.* **235**, 273 (1982).
17. A.Ya. Zheltov, E.N. Avramenko, and B.I. Stepanov. *Zh. Org. Khim.* **16**, 384, (1980).



# Synthesis and characterization of tantalum(V) metallaheterocycle $(\text{Me}_2\text{N})_3\text{TaN}(\text{SiMe}_3)\text{SiMe}_2\text{CH}_2$ and chloro-mixed-amide $(\text{Me}_2\text{N})_3\text{Ta}(\text{Cl})[\text{N}(\text{SiMe}_3)_2]^1$

Hu Cai, Xianghua Yu, Tianniu Chen, Xue-Tai Chen, Xiao-Zeng You, and Ziling Xue

**Abstract:** A new mixed-amido complex  $(\text{Me}_2\text{N})_3\text{Ta}(\text{Cl})[\text{N}(\text{SiMe}_3)_2]$  (**1**) was prepared from the reaction of  $(\text{Me}_2\text{N})_3\text{TaCl}_2$  with 1 equiv. of  $\text{LiN}(\text{SiMe}_3)_2$ . The reactions of **1** with 1 equiv. of  $\text{LiN}(\text{SiMe}_3)_2$  or  $(\text{Me}_2\text{N})_3\text{TaCl}_2$  with 2 equiv. of  $\text{LiN}(\text{SiMe}_3)_2$  gave  $(\text{Me}_2\text{N})_3\text{TaN}(\text{SiMe}_3)\text{SiMe}_2\text{CH}_2$  (**2**) with a four-membered metallaheterocyclic ring through  $\gamma$ -hydrogen abstraction. In the solid state, **1** adopts a distorted trigonal bipyramidal geometry with the  $-\text{N}(\text{SiMe}_3)_2$  and  $-\text{Cl}$  ligands in the equatorial and axial positions, respectively. The X-ray structure of **2** reveals that it is in a distorted trigonal bipyramidal geometry with a planar metallaheterocyclic ring.

**Key words:** tantalum,  $\gamma$ -hydrogen abstraction, C-H activation, amido complexes, metallacycle.

**Résumé :** On a préparé un nouveau complexe amido mixte,  $(\text{Me}_2\text{N})_3\text{Ta}(\text{Cl})[\text{N}(\text{SiMe}_3)_2]$  (**1**) par réaction du  $\text{LiN}(\text{SiMe}_3)_2$  ou du  $(\text{Me}_2\text{N})_3\text{TaCl}_2$  avec 2 équivalents de  $\text{LiN}(\text{SiMe}_3)_2$  conduit, par l'abstraction d'un hydrogène en  $\gamma$ , à la formation du  $(\text{Me}_2\text{N})_3\text{TaN}(\text{SiMe}_3)\text{SiMe}_2\text{CH}_2$  (**2**) comportant un cycle métallahétérocyclique à quatre chaînons. À l'état solide, le composé **1** adopte une géométrie bipyramidale trigonale déformée dans laquelle les ligands  $-\text{N}(\text{SiMe}_3)_2$  et  $-\text{Cl}$  occupent respectivement des positions équatoriale et axiale. La structure du composé **2** déterminé par diffraction des rayons X révèle qu'il existe dans une géométrie bipyramidale trigonale déformée comportant un cycle métallahétérocyclique plan.

**Mots clés :** tantale, abstraction d'hydrogène en  $\gamma$ , activation du C-H, complexes amido, métallacycle.

[Traduit par la Rédaction]

## Introduction

Early transition-metal amido complexes have been studied for their unique chemistry (1) and their potential applications in molecular approaches to metal nitrides and metal oxides as microelectronic materials (2, 3). Cyclopentadienyl-free, homoleptic dialkylamido  $d^0$ -complexes  $\text{M}(\text{NR}_2)_n$  play an important role in the studies of the amido chemistry. Disilylamido ligand  $-\text{N}(\text{SiMe}_3)_2$ , as a bulkier and weaker  $p-d$   $\pi$  back-bond donor than dialkylamido ligands (1a), has also shown unique chemistry and attracted much interest (4). Complexes containing  $-\text{N}(\text{SiMe}_3)_2$  or  $\text{NH}(\text{SiMe}_3)_2$  ligands have been used as precursors to yield metal nitrides (3a–3c) or metal silicates (metal oxide –  $\text{SiO}_2$  ternary materials) (3d).

Molecular approaches to Ta-based materials from  $d^0$ -Ta amide precursors, in particular, have been studied in part because of unique properties of the Ta-based materials. For example,  $\text{Ta}_2\text{O}_5$  appears to be the most promising replacement for  $\text{SiO}_2$  as the new gate oxide material in microelectronic transistors because of its low porosity and high thickness

uniformity (2d). Chemical vapor deposition of  $\text{Ta}_2\text{O}_5$  thin films from Ta amide precursors is of intense current interest (2d–2f).

In the preparation of metal nitride and metal oxide thin films from  $-\text{NMe}_2$  (2b, 2d),  $-\text{N}(\text{SiMe}_3)_2$  (3b),  $-\text{NH}(\text{SiMe}_3)$  (3a), and  $\text{NH}(\text{SiMe}_3)_2$  (3c) complexes, C incorporations into the films as metal carbides were often observed. Hydrogen abstraction reactions among amide ligands to yield  $\text{M}-\text{C}$  bonds are of current interest to understand the mechanism of  $\text{M}-\text{C}$  bond formation and are important to the design of precursors and molecular approaches to metal nitride and metal oxide materials (2a, 4c–4d, 5).  $\beta$ -H abstraction between  $-\text{N}(\text{CHRR}')_2$  ligands has been shown to give  $\text{M}-\text{C}$  bonds (5). The mechanism of  $\text{M}-\text{C}$  bond formation from ligands such as  $-\text{N}(\text{SiMe}_3)_2$  with no  $\beta$ -hydrogen atoms is of current interest.

We recently reported several new  $d^0$ -amido silyl complexes and unusual reactions of homoleptic  $d^0$ -dimethylamido complexes  $(\text{M}(\text{NMe}_2)_n)$  with silanes to give amido hydrido complexes (5j, 6). In particular, Ta amide complexes and their reactivities are of interest to us in part because Ta-

Received 4 February 2003. Published on the NRC Research Press Web site at <http://canjchem.nrc.ca> on 6 November 2003.

Dedicated to Professor John F. Harrod in recognition of his outstanding contributions to inorganic and organosilicon chemistry.

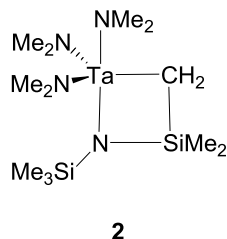
H. Cai, X. Yu, T. Chen, and Z. Xue.<sup>2</sup> Department of Chemistry, The University of Tennessee, Knoxville, TN 37996, U.S.A.  
X.-T. Chen and X.-Z. You. State Key Laboratory of Coordination Chemistry, Nanjing University, Nanjing 210093, P.R. China.

<sup>1</sup>This article is part of a Special Issue dedicated to Professor John Harrod.

<sup>2</sup>Corresponding author (e-mail: [xue@novell.chem.utk.edu](mailto:xue@novell.chem.utk.edu)).



Chart 1.



based microelectronic materials are known to have unique properties (2*d*–2*f*). We recently found that the reactions of  $(\text{Me}_2\text{N})_3\text{TaCl}_2$  with 2 equiv. of  $\text{LiN}(\text{SiMe}_3)_2$  or  $(\text{Me}_2\text{N})_3\text{Ta}(\text{Cl})[\text{N}(\text{SiMe}_3)_2]$  (**1**) with 1 equiv. of  $\text{LiN}(\text{SiMe}_3)_2$  gave cleanly  $(\text{Me}_2\text{N})_3\text{Ta}(\text{N}(\text{SiMe}_3)_2\text{SiMe}_2\text{CH}_2)$  (**2**) with a four-membered metallaheterocyclic ring containing a Ta–C bond (Chart 1).  $\gamma$ -H abstraction reaction with a Ta or a  $d^0$  group 5 complex to give such a heterocycle has, to our knowledge, not been reported. The reaction of  $(\text{Me}_2\text{N})_3\text{TaCl}_2$  with 1 equiv. of  $\text{LiN}(\text{SiMe}_3)_2$  replaced one  $\text{Cl}^-$  ligand to give  $(\text{Me}_2\text{N})_3\text{Ta}(\text{Cl})[\text{N}(\text{SiMe}_3)_2]$  (**1**). These studies are reported here.

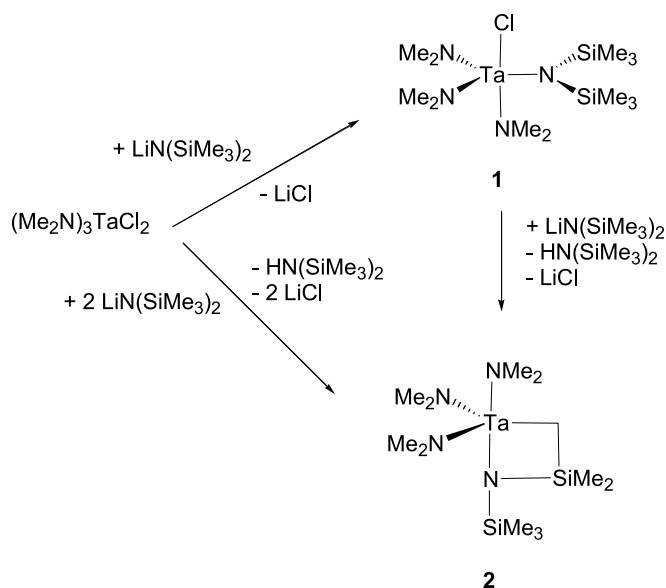
## Results and discussion

### Preparation and characterization of **1** and **2**

Reaction of  $\text{Ta}(\text{NMe}_2)_3\text{Cl}_2$  with  $\text{LiN}(\text{SiMe}_3)_2$  in pentane gave  $(\text{Me}_2\text{N})_3\text{Ta}(\text{Cl})[\text{N}(\text{SiMe}_3)_2]$  (**1**) in almost quantitative yield (Scheme 1). This complex is stable at room temperature. Its  $^1\text{H}$  and  $^{13}\text{C}\{^1\text{H}\}$  NMR spectra at 23 °C showed single peaks for both the  $-\text{N}(\text{SiMe}_3)_2$  and the three  $-\text{NMe}_2$  ligands. These observations indicate fast rotations of these ligands and a fast exchange between the axial and two equatorial  $-\text{NMe}_2$  ligands in distorted trigonal bipyramidal **1**, as revealed in its X-ray structure discussed below. The chemical shifts of 3.34 ppm for  $\text{NMe}_2$ , and 0.39 ppm for  $\text{SiMe}_3$  in the  $^1\text{H}$  NMR spectrum, and 49.63 ppm for  $\text{NMe}_2$  and 4.23 ppm for  $\text{SiMe}_3$  in the  $^{13}\text{C}\{^1\text{H}\}$  NMR spectrum, respectively, are typical for these amido groups.

The colourless four-membered metallaheterocyclic **2** in the current study could be prepared either by the reaction of  $\text{Ta}(\text{NMe}_2)_3\text{Cl}_2$  with 2 equiv. of  $\text{LiN}(\text{SiMe}_3)_2$  or by the reaction of **1** with 1 equiv. of  $\text{LiN}(\text{SiMe}_3)_2$  in nonpolar solvents. Both gave almost quantitative yield of **2**. In the latter preparation, the reaction was ca. 75% complete in 1.5 h at room temperature in benzene- $d_6$ . The formation of  $\text{HN}(\text{SiMe}_3)_2$  in both reactions were observed in  $^1\text{H}$  and  $^{13}\text{C}\{^1\text{H}\}$  NMR and GC–MS. The  $^1\text{H}$  and  $^{13}\text{C}\{^1\text{H}\}$  NMR spectra of **2** were consistent with the cyclic structure in Chart 1. Overlapping  $^1\text{H}$  NMR resonances of  $\text{CH}_2\text{SiMe}_2$  and  $\text{SiMe}_3$  were observed at 0.19 ppm in benzene- $d_6$  at 23 °C, and this was confirmed by  $^1\text{H}$  NMR integration to 11H, and by 2D HMQC NMR studies. In the latter, crosspeaks between  $^1\text{H}$  resonances at 0.19 ppm and  $^{13}\text{C}$  NMR resonances at both  $\text{CH}_2\text{SiMe}_2$  (39.64 ppm) and  $\text{SiMe}_3$  (4.45 ppm) were observed. In the DEPT-135  $^{13}\text{C}$  NMR spectrum of **2**, the  $-\text{CH}_2-$  resonance at 39.64 ppm appeared as a negative peak, while those of  $-\text{NMe}_2$ ,  $-\text{SiMe}_3$ , and  $-\text{SiMe}_2$  were positive. In the  $^1\text{H}$  NMR spectrum of **2** in toluene- $d_8$  at 23 °C, there was no overlap of the resonances of  $\text{SiMe}_3$  and  $\text{CH}_2\text{SiMe}_2$ , and they were ob-

Scheme 1.



served at 0.16 and 0.14 ppm, respectively. The three chemically inequivalent  $-\text{NMe}_2$  ligands in the distorted trigonal bipyramidal **2**, as its X-ray structure to be discussed below suggested, were observed as one single peak in both  $^1\text{H}$  and  $^{13}\text{C}\{^1\text{H}\}$  NMR spectra at 23 °C, indicating a fast exchange among these ligands.

The reaction of  $(\text{Me}_2\text{N})_3\text{Ta}(\text{Cl})[\text{N}(\text{SiMe}_3)_2]$  (**1**) with 1 equiv. of  $\text{LiNMe}_2$  was found to give **2** as well. In 2 min, **2** was observed in the  $^1\text{H}$  NMR spectrum along with  $\text{HNMe}_2$  and several unidentified peaks in both  $-\text{NMe}_2$  and  $-\text{N}(\text{SiMe}_3)_2$  regions. Unreacted **1** and  $\text{LiNMe}_2$  were observed as well. In 10 min, the formation of **2** was essentially complete (in ca. 27% yield).  $\text{HNMe}_2$  was observed along with other unidentified products.  $^{13}\text{C}$  NMR of the solution confirmed the formation of **2**. These observations indicated that the reaction was not clean. In comparison, the reaction of **1** with  $\text{LiN}(\text{SiMe}_3)_2$  gave almost quantitative yield of **2**. It is not clear, however, what the mechanism of the reaction between  $(\text{Me}_2\text{N})_3\text{Ta}(\text{Cl})[\text{N}(\text{SiMe}_3)_2]$  (**1**) and  $\text{LiNMe}_2$  is.

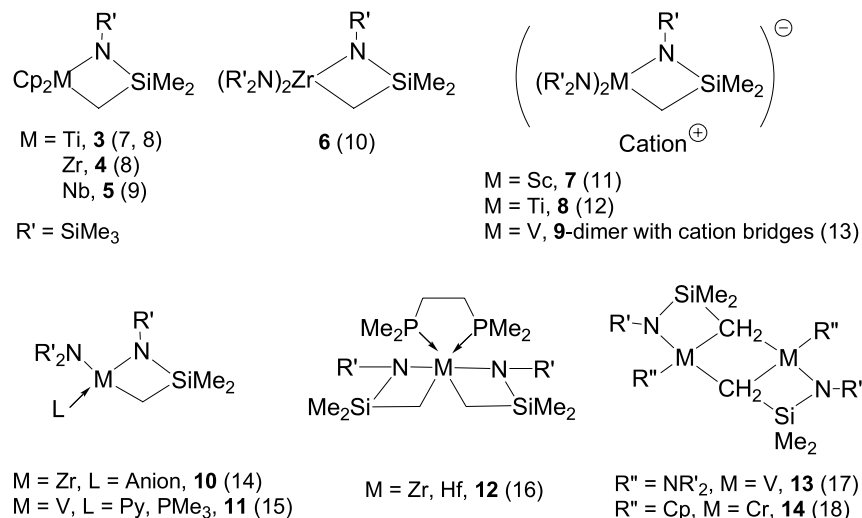
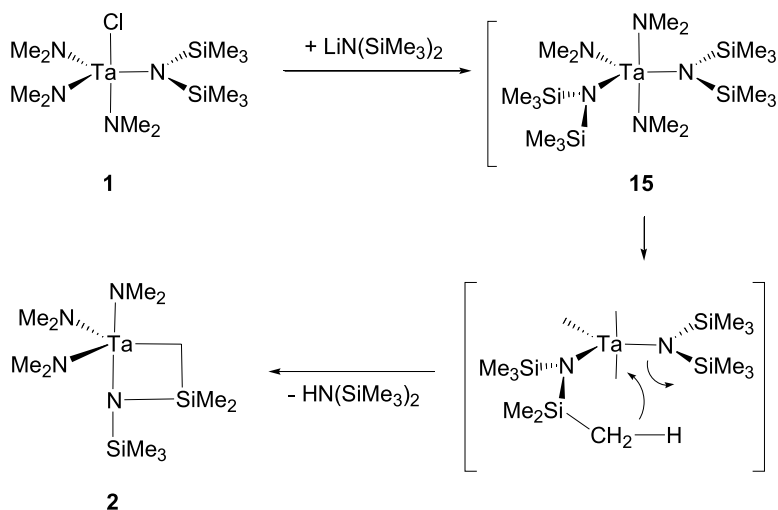
$\gamma$ -Hydrogen abstraction reactions involving  $-\text{N}[\text{Si}(\text{CH}_3)_3]_2$  ligands to give metallaheterocycles with M–C bonds have been reported (7–22). Complexes in Fig. 1 represent those with four-membered metallaheterocycles similar to that in **2**. Their formation involves similar  $\gamma$ -hydrogen abstraction from a  $-\text{N}[\text{Si}(\text{CH}_3)_3]_2$  ligand in the C–H activation reactions.

Complex **2** was found to be inert to  $\text{HNMe}_2$ . A solution of **2** in benzene- $d_6$  was bubbled with  $\text{HNMe}_2$  in  $\text{N}_2$  for 4 h. Both  $^1\text{H}$  and  $^{13}\text{C}$  NMR spectra of the solution afterwards showed only the peaks of **2** and  $\text{HNMe}_2$ .

### Mechanistic considerations

The reaction of  $(\text{Me}_2\text{N})_3\text{Ta}(\text{Cl})[\text{N}(\text{SiMe}_3)_2]$  (**1**) with  $\text{LiN}(\text{SiMe}_3)_2$  in toluene- $d_8$  at 23 °C was monitored by  $^1\text{H}$  NMR. Approximately 40% of **1** was converted to **2** in 4 min. When the mixture was cooled to  $-25$  °C after 4 min at 23 °C, two broad peaks at 3.06 and 0.63 ppm were observed. At 23 °C, these two peaks were observed at 3.09 and 0.52 ppm, respectively; the former overlapped with the



**Fig. 1.** Reported complexes with four-membered metallaheterocycles similar to that in **2**.**Scheme 2.**

-NMe<sub>2</sub> resonance of **2**. At 23 °C, these two broad peaks gradually disappeared, as the nearly quantitative conversion of **1** to **2** was complete. The emergence and disappearance of these two peaks are consistent with (Me<sub>2</sub>N)<sub>3</sub>Ta[N(SiMe<sub>3</sub>)<sub>2</sub>]<sub>2</sub> (**15**) as an intermediate in the formation of **2**. The presence of two bulky -N(SiMe<sub>3</sub>)<sub>2</sub> ligands in **15** perhaps makes it unstable, driving the elimination of HN(SiMe<sub>3</sub>)<sub>2</sub> from **15** and the formation of cyclic **2** (Scheme 2).

### X-ray structures of **1** and **2**

Crystal data and a summary of intensity data collection parameters for **1** and **2** are given in Table 1. Selected bond distances and angles in **1** and **2** are listed in Tables 2 and 3,

respectively.<sup>3</sup> ORTEP views of **1** and **2** are shown in Figs. 2 and 3, respectively.

The solid-state structure of **1** adopts a distorted trigonal bipyramidal (TBP) geometry with axial -Cl and -NMe<sub>2</sub> ligands and the bulky -N(SiMe<sub>3</sub>)<sub>2</sub> ligand in the equatorial position. Such an arrangement, as predicted by the valence shell electron pair repulsion (VSEPR) theory (23), minimizes the ligand repulsion. Similar TBP geometries were observed in (Me<sub>2</sub>N)<sub>3</sub>Ta(*p*-tolyl)Br (**24**) and (Me<sub>2</sub>N)<sub>3</sub>Ta(X)SiR<sub>3</sub> (X = Cl, Br, R<sub>3</sub> = Si(SiMe<sub>3</sub>)<sub>3</sub>, **16a**, **16b**; X = Cl, R<sub>3</sub> = *t*-BuPh<sub>2</sub>, **16c**) (**6c**), where the small halide and bulky silyl ligands adopt axial and equatorial positions, respectively. The trans N(3)-Ta-Cl(1) angle of 170.90(13)° is close to those in (Me<sub>2</sub>N)<sub>3</sub>Ta(*p*-tolyl)Br (173.1(2)°) (**24**), **16a**, **16b** (178.1(2)°

<sup>3</sup>Supplementary data may be purchased from the Directory of Unpublished Data, Document Delivery, CISTI, National Research Council Canada, Ottawa, ON K1A 0S2, Canada ([http://www.nrc.ca/cisti/irm/unpub\\_e.shtml](http://www.nrc.ca/cisti/irm/unpub_e.shtml) for information on ordering electronically). CCDC 203046 and 203047 contain the crystallographic data for this manuscript. These data can be obtained, free of charge, via [www.ccdc.cam.ac.uk/conts/retrieving.html](http://www.ccdc.cam.ac.uk/conts/retrieving.html) (or from the Cambridge Crystallographic Data Centre, 12 Union Road, Cambridge CB2 1EZ, U.K.; fax +44 1223 336033; or [deposit@ccdc.cam.ac.uk](mailto:deposit@ccdc.cam.ac.uk)).



**Table 1.** Crystal data and structure refinement for **1** and **2**.

	<b>1</b>	<b>2</b>
Formula	C <sub>12</sub> H <sub>36</sub> ClN <sub>4</sub> Si <sub>2</sub> Ta	C <sub>12</sub> H <sub>35</sub> N <sub>4</sub> Si <sub>2</sub> Ta
Formula weight	509.03	472.57
Crystal system	Monoclinic	Triclinic
Space group	<i>P</i> 2(1)/ <i>n</i>	<i>P</i> -1
Lattice parameters		
<i>a</i> (Å)	13.442(3)	8.1575(19)
<i>b</i> (Å)	10.892(3)	10.032(2)
<i>c</i> (Å)	14.971(4)	14.328(3)
$\alpha$ (°)	90	71.473(4)
$\beta$ (°)	100.762(4)	87.551(4)
$\gamma$ (°)	90	67.463(4)
Volume (Å <sup>3</sup> )	2153.2(9)	1022.7(4)
<i>Z</i>	4	2
Density (calcd.) (g/cm <sup>3</sup> )	1.57	1.535
$\mu$ (mm <sup>-1</sup> )	5.338	5.487
<i>F</i> (000)	1016	472
Crystal size (mm <sup>3</sup> )	0.41 × 0.22 × 0.04	0.50 × 0.42 × 0.25
$\theta$ Range (°)	1.87–28.36	1.51–25.00
Completeness (%)	97.2	76.2
Independent reflections	5236 ( <i>R</i> (int) = 0.0647)	2737 ( <i>R</i> (int) = 0.0364)
Parameters	193	183
<i>R</i> 1 [ <i>I</i> > 2 $\sigma$ ( <i>I</i> )] <sup>a</sup>	0.0297 ( <i>wR</i> 2 = 0.0600) <sup>b</sup>	0.0540 ( <i>wR</i> 2 = 0.1616) <sup>b</sup>
Goodness-of-fit on <i>F</i> <sup>2</sup>	0.850	1.16

<sup>a</sup>*R*1 =  $\sum ||F_o| - |F_c|| / \sum |F_o|$ .<sup>b</sup>*wR*2 =  $[\sum w(F_o^2 - F_c^2)^2 / \sum w(F_o^2)]^{1/2}$ .**Table 2.** Selected bond lengths (Å) and angles (°) in **1**.

Bond lengths (Å)	
Ta—N(1)	1.956(4)
Ta—N(3)	1.975(4)
Ta—N(2)	1.987(4)
Ta—N(4)	2.020(3)
Ta—Cl(1)	2.4871(13)
Si(1)—N(4)	1.767(3)
Si(2)—N(4)	1.748(3)
Bond angles (°)	
N(1)–Ta–N(3)	95.25(17)
N(1)–Ta–N(2)	107.23(17)
N(3)–Ta–N(2)	89.52(17)
N(1)–Ta–N(4)	115.24(15)
N(3)–Ta–N(4)	89.45(14)
N(2)–Ta–N(4)	137.44(15)
N(1)–Ta–Cl(1)	93.81(12)
N(3)–Ta–Cl(1)	170.90(13)
N(2)–Ta–Cl(1)	86.94(13)
N(4)–Ta–Cl(1)	87.50(9)
Si(2)–N(4)–Si(1)	118.53(19)
Si(2)–N(4)–Ta	118.34(17)
Si(1)–N(4)–Ta	121.36(18)

and 174.6(2)°, and **16c** (174.5(4)°) (6c). The Ta—N bond in Ta–N(SiMe<sub>3</sub>)<sub>2</sub> (2.020(3) Å) is slightly longer than those in axial or equatorial Ta–NMe<sub>2</sub> (1.956(4)–1.987(4) Å) in **1** and those in [(Me<sub>3</sub>Si)N]<sub>2</sub>TaCl<sub>3</sub> (1.928(7) and 1.933(7) Å) (4a).

The Ta—Cl bond length of 2.4871(13) Å in **1** is comparable to those in **16c** (2.454(4) Å) (6c), and the terminal Ta—Cl bond distances in (Me<sub>2</sub>N)(Me<sub>2</sub>NH)TaCl<sub>3</sub> (2.391(2)–2.450(2) Å) (25), [(Me<sub>2</sub>N)(Me<sub>2</sub>NH)TaCl<sub>2</sub>]<sub>2</sub>O (2.417(2) and 2.505(2) Å) (25), [(Me<sub>2</sub>N)<sub>3</sub>TaCl<sub>2</sub>]<sub>2</sub> (2.463(1) Å) (25), and [(Me<sub>3</sub>Si)N]<sub>2</sub>TaCl<sub>3</sub> (2.351(2)–2.366(2) Å) (4a).

A few transition metal complexes (**5**, **7–9**, and **12–14**, Fig. 1) with the metallaheterocycles similar to that in **2** have been structurally characterized. The structure of **2** adopts a distorted trigonal bipyramidal geometry with one amido ligand N(1) and the ring N(4) atom in the axial positions. The N(1)–Ta(1)–N(4) angle of 161.7(4)° deviated from the ideal 180°. The Ta atom is 0.0229 Å away from the equatorial plane defined by the N(2), N(3), and C(12) atoms, and the two axial atoms N(1) and N(4) are about at an equal distance (2.0578 and 2.0159 Å) from the plane. Both N(1) and N(4) atoms in the axial positions are tilted toward the C(12) atom in the equatorial plane with N(1)–Ta(1)–C(12) and N(4)–Ta(1)–C(12) angles of 87.0(3)° and 74.6(3)°, respectively. The angles of the axial N(1) atom with equatorial N(2) and N(3) atoms are N(1)–Ta(1)–N(2) = 92.9(3)° and N(1)–Ta(1)–N(3) = 91.9(3)°, respectively. In comparison, larger angles of the axial N(4) atom in the ring with N(2) and N(3) atoms (95.7(3)° and 97.4(3)°, respectively) were observed.

The four atoms in the ring are nearly coplanar with a 0.0549 Å deviation of the Ta(1) atom from the plane defined by the other three ring atoms (C(12), N(4), and Si(2)). The sum of angles inside the ring is 359.9°, consistent with the planar structure. In fact it is interesting to note that the Si(1) atom in the SiMe<sub>3</sub> group and the N(1) atom in the axial position are nearly coplanar with the four ring atoms Ta(1),



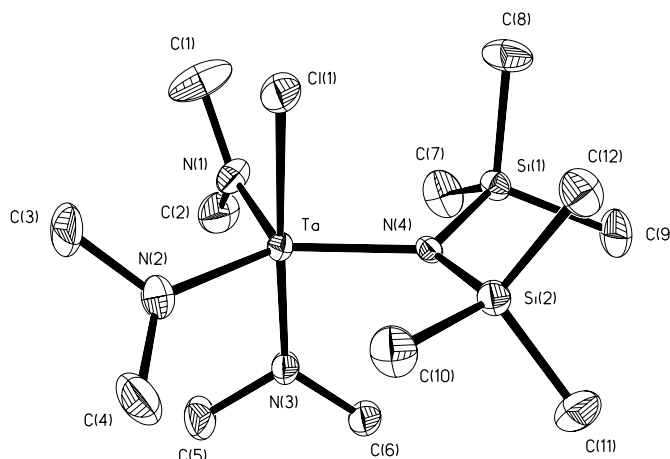
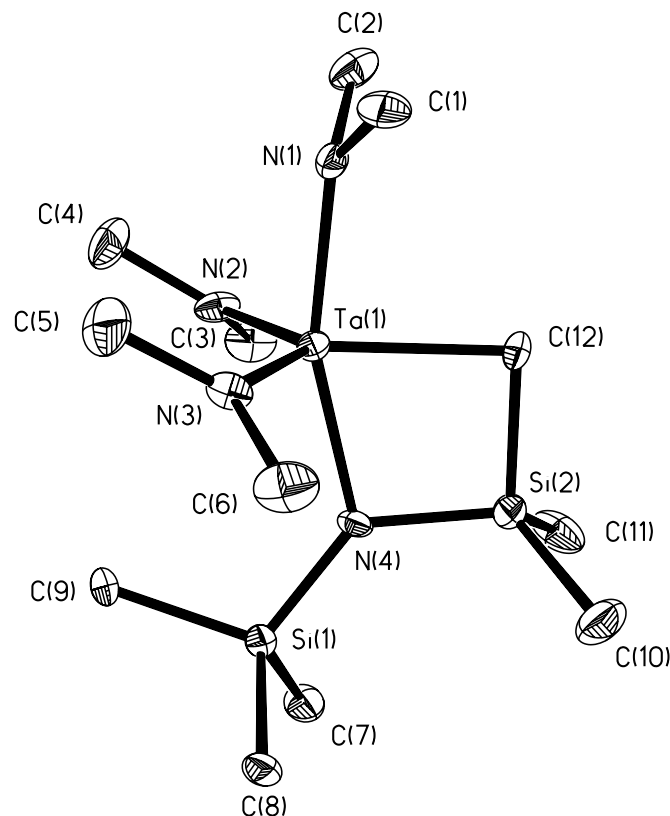
**Table 3.** Selected bond lengths (Å) and angles (°) in **2**.

Bond lengths (Å)	
Ta(1)—N(3)	1.975(7)
Ta(1)—N(2)	1.984(8)
Ta(1)—N(1)	2.039(8)
Ta(1)—N(4)	2.109(7)
Ta(1)—C(12)	2.228(9)
Si(1)—N(4)	1.715(9)
Si(2)—N(4)	1.726(9)
Si(2)—C(12)	1.844(10)
Si(2)—C(10)	1.870(11)
Si(2)—C(11)	1.886(12)
Bond angles (°)	
N(3)—Ta(1)—N(2)	120.8(4)
N(3)—Ta(1)—N(1)	91.9(3)
N(2)—Ta(1)—N(1)	92.9(3)
N(3)—Ta(1)—N(4)	97.4(3)
N(2)—Ta(1)—N(4)	95.7(3)
N(1)—Ta(1)—N(4)	161.7(4)
N(3)—Ta(1)—C(12)	119.7(4)
N(2)—Ta(1)—C(12)	119.5(4)
N(1)—Ta(1)—C(12)	87.0(3)
N(4)—Ta(1)—C(12)	74.6(3)
Si(1)—N(4)—Si(2)	131.8(5)
Si(1)—N(4)—Ta(1)	129.1(4)
Si(2)—N(4)—Ta(1)	99.0(4)
N(4)—Si(2)—C(12)	94.9(4)
N(4)—Si(2)—C(10)	113.8(6)
C(12)—Si(2)—C(10)	112.8(5)
N(4)—Si(2)—C(11)	112.8(5)
C(12)—Si(2)—C(11)	114.0(5)
C(10)—Si(2)—C(11)	108.3(7)
Si(2)—C(12)—Ta(1)	91.4(4)

C(12), N(4), and Si(2). In a plane defined by these six atoms, the mean deviation and the range of deviations are 0.0111 Å and 0.0024–0.0140 Å, respectively. An ORTEP view of this plane and a schematic view of the structure of **2** are given in Fig. 4 and Scheme 2, respectively. The lone pair *p* electrons in N(1) and N(4) may form conjugated, planar *p*–*d*  $\pi$  bonds with Ta, Si(1), and Si(2). The C(12) in the ring perhaps stays in the plane of N(1), N(4), Ta, Si(1), and Si(2) to minimize steric repulsion.

The Ta(1)–ring N(4) length of 2.109(7) Å is longer than those of Ta–NMe<sub>2</sub> in **2** (avg. 1.999(8) Å). The Ta–C(12) length of 2.228(9) Å is close to that in Nb(IV) **5** (2.277(6) Å) (Fig. 1) (8).<sup>4</sup> The Ta–N(4) bond (2.109(7) Å) is longer than the Ta–NMe<sub>2</sub> bonds in **2** and **1** (1.956(4)–2.039(8) Å), and the Ta–N(SiMe<sub>3</sub>)<sub>2</sub> bond in **1** (2.020(3) Å).

In summary, the reactions of (Me<sub>2</sub>N)<sub>3</sub>TaCl<sub>2</sub> with **1** and 2 equiv of LiN(SiMe<sub>3</sub>)<sub>2</sub> gave (Me<sub>2</sub>N)<sub>3</sub>Ta(Cl)[N(SiMe<sub>3</sub>)<sub>2</sub>] (**1**) and (Me<sub>2</sub>N)<sub>3</sub>TaN(SiMe<sub>3</sub>)SiMe<sub>2</sub>CH<sub>2</sub> (**2**), respectively. The reaction of **1** with 1 equiv. of LiN(SiMe<sub>3</sub>)<sub>2</sub> was also found to give **2**. *d*<sup>0</sup>-Pentaamido complex (Me<sub>2</sub>N)<sub>3</sub>Ta[N(SiMe<sub>3</sub>)<sub>2</sub>]<sub>2</sub> (**15**) was observed as an intermediate in the formation of **2**. Steric

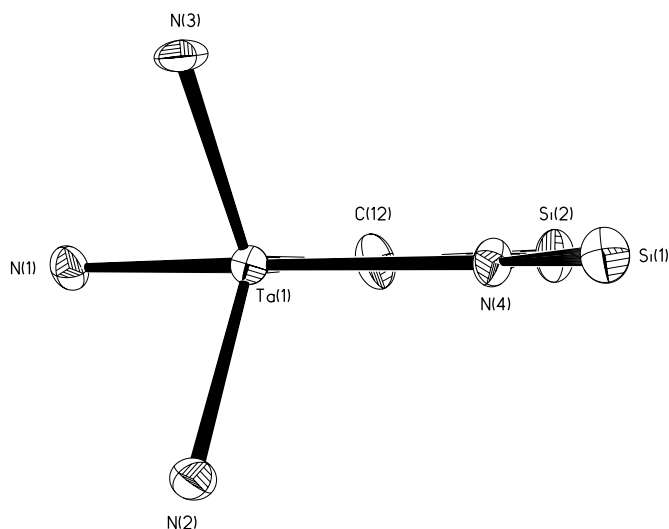
**Fig. 2.** ORTEP view of **1** showing 30% probability thermal ellipsoids.**Fig. 3.** ORTEP view of **2** showing 30% probability thermal ellipsoids.

crowdedness in **15** makes it unstable. **15** undergoes clean  $\gamma$ -hydrogen abstraction in its decomposition to give almost quantitative yield of the cyclic complex **2** with a Ta–C bond. Such  $\gamma$ -hydrogen abstraction and M–C bond formation may give metal carbides in molecular approaches to solid-state materials using complexes containing –N(SiMe<sub>3</sub>)<sub>2</sub> ligands.

<sup>4</sup>Nb and Ta complexes are often isomorphous, as a result of lanthanide contraction (26).



**Fig. 4.** ORTEP of **2** showing 30% probability thermal ellipsoids. The -Me groups have been omitted for clarity.



## Experimental

All manipulations were performed under a dry nitrogen atmosphere with the use of either a drybox or standard Schlenk techniques. Solvents were purified by distillation from potassium – benzophenone ketyl. Benzene- $d_6$  and toluene- $d_8$  (Cambridge Isotope Laboratories) were dried over activated molecular sieves and stored under  $N_2$ .  $^1H$  and  $^{13}C\{^1H\}$  NMR spectra were recorded at 23 °C on a Bruker AC-250 or AMX-400 Fourier transform (FT) spectrometer and referenced to the solvent (residual protons in the  $^1H$  NMR spectra).  $LiN(SiMe_3)_2$  (Aldrich) was used as received.  $(Me_2N)_3TaCl_2$  was prepared from  $Ta(NMe_2)_5$  and 2 equiv. of  $Me_3SiCl$  by the literature procedure (25). A Hewlett-Packard 6890 gas chromatograph (GC) with a 5793 mass selective (MS) detector (MSD) was used to obtain GC–MS data. Elemental analysis was performed by Complete Analysis Laboratories Inc., Parsippany, New Jersey, U.S.A.

### Preparation of $(Me_2N)_3Ta(Cl)[N(SiMe_3)_2]$ (**1**)

$(Me_2N)_3TaCl_2$  (0.343 g, 0.893 mmol) was mixed with  $LiN(SiMe_3)_2$  (0.150 g, 0.896 mmol), and, to this mixture, pentane (50 mL) was added at –50 °C with stirring. The mixture was allowed to gradually warm to room temperature and stirred overnight. After filtration to remove  $LiCl$ , the volatiles were removed under reduced pressure to give a yellow solid which, by  $^1H$  and  $^{13}C$  NMR, was essentially pure **1** (0.45 g, 0.88 mmol, 99% yield). Crystals of **1** were grown from a solution in  $Et_2O$  at –30 °C. Melting point: 110.5–112.0 °C (decomposed). Major IR peaks (KBr pellet,  $cm^{-1}$ ): 2956.8, 2898.9, 2861.3, 2819.8, 2775.9, 1249.9, 952.6, 846.1, 795.2, 711.3, 673.8.  $^1H$  NMR (benzene- $d_6$ , 250.1 MHz)  $\delta$ : 3.34 (s, 18H,  $NMe_2$ ), 0.39 (s, 18H,  $SiMe_3$ ).  $^{13}C$  NMR (benzene- $d_6$ , 62.9 MHz)  $\delta$ : 49.63 ( $NMe_2$ ), 4.23 ( $SiMe_3$ ). Anal. calcd. for  $C_{12}H_{36}N_4ClSi_2Ta$ : C 28.32, H 7.13, N 11.01; found: C 28.15, H 7.06, N 11.21.

### Preparation of $(Me_2N)_3TaN(SiMe_3)SiMe_2CH_2$ (**2**) from $Ta(NMe_2)_3Cl_2$

To a mixture of  $Ta(NMe_2)_3Cl_2$  (3.84 g, 10.0 mmol) and  $LiN(SiMe_3)_2$  (3.35 g, 20.0 mmol) was added hexanes (120 mL) at –40 °C with stirring. The mixture was allowed to gradually warm to room temperature and stirred overnight. The colour of the solution changed slowly from yellow to colourless. After filtration, the volatiles were removed in vacuo to give **2** as a colourless oily liquid in almost quantitative yield. Colourless crystals of **2** (3.111 g, 6.58 mmol, 65.8% yield) were obtained after the oily liquid was cooled to 0 °C for 1 day. Melting point: 123.5–125.0 °C. Major IR peaks (KBr pellet,  $cm^{-1}$ ): 2955.2, 2893.8, 2857.7, 2824.9, 2778.8, 1245.6, 998.5, 947.4, 865.5, 835.9, 800.72, 765.5.  $^1H$  NMR (benzene- $d_6$ , 400.18 MHz, 23 °C)  $\delta$ : 3.08 (s, 18H,  $NMe_2$ ), 0.48 (s, 6H,  $SiMe_2$ ), 0.19 (s, 11H,  $CH_2SiMe_2$ ,  $SiMe_3$ ). The  $CH_2SiMe_2$  resonance was further confirmed by DEPT-135 NMR studies.  $^1H$  NMR (toluene- $d_8$ , 400.18 MHz, 23 °C)  $\delta$ : 3.09 (s, 18H,  $NMe_2$ ), 0.43 (s, 6H,  $SiMe_2$ ), 0.15 (s, 9H,  $SiMe_3$ ), 0.14 (2H,  $CH_2SiMe_2$ ).  $^{13}C$  NMR (benzene- $d_6$ , 100.63 MHz, 23 °C)  $\delta$ : 44.41 ( $NMe_2$ ), 39.64 ( $CH_2$ ), 5.07 ( $CH_2SiMe_2$ ), 4.45 ( $SiMe_3$ ).  $^{13}C$  NMR (toluene- $d_8$ , 100.63 MHz, 23 °C)  $\delta$ : 44.42 ( $NMe_2$ ), 39.63 ( $CH_2$ ), 5.05 ( $CH_2SiMe_2$ ), 4.43 ( $SiMe_3$ ). Anal. calcd. for  $C_{12}H_{35}N_4Si_2Ta$ : C 30.50, H 7.47, N 11.86; found: C 30.32, H 7.39, N 12.03.

GC–MS analyses of the volatiles that were collected from the reaction mixture revealed that it contained  $HN(SiMe_3)_2$ .

### Preparation of **2** from $(Me_2N)_3Ta(Cl)[N(SiMe_3)_2]$ (**1**)

To **1** (25.4 mg, 0.0500 mmol) dissolved in benzene- $d_6$  was added  $LiN(SiMe_3)_2$  (8.4 mg, 0.050 mmol) at 23 °C. The colour of the solution gradually changed from yellow to colourless. The reaction was monitored by  $^1H$  and  $^{13}C$  NMR spectroscopy. In 1.5 h, the ratio of **1** to **2** in the solution was found to be ca. 1:3. In 18 h,  $^1H$  and  $^{13}C$  NMR spectra of the solution showed it was virtually a pure mixture of **2** and  $HN(SiMe_3)_2$ .

### Reaction of $(Me_2N)_3Ta(Cl)[N(SiMe_3)_2]$ (**1**) with $LiNMe_2$

To a mixture of  $Ta(NMe_2)_3(Cl)[N(SiMe_3)_2]$  (**1**, 30.2 mg, 0.059 mmol),  $LiNMe_2$  (3.0 mg, 0.059 mmol), and 4,4'-dimethylbiphenyl (an internal standard) was added toluene- $d_8$  (0.40 mL) in a Young NMR tube at room temperature.  $^1H$  NMR spectrum of the solution was monitored.

### Determination of X-ray crystal structures of **1** and **2**

The crystal structures **1** and **2** were determined on a Bruker AXS Smart 1000 X-ray diffractometer equipped with a CCD area detector and a graphite-monochromated Mo source ( $K\alpha$  radiation, 0.71073 Å) and fitted with an upgraded Nicolet LT-2 low-temperature device. Suitable crystals were coated with paratone oil (Exxon) and mounted on a hairloop under a stream of nitrogen at 173(2) K. The structures of **1** and **2** were solved by direct methods. Non-hydrogen atoms were anisotropically refined. All hydrogen atoms in the two structures were treated as idealized contributions. Empirical absorption correction was performed with the SADABS program (27a). In addition the global refinements for the unit cells and data reductions of the two structures were performed using the Saint program (Version



6.02). All calculations were performed using SHELXTL (Version 5.1) proprietary software package (27b).

## Acknowledgments

The research was supported by the U.S. National Science Foundation, National Natural Science Foundation of China, and the Camille Dreyfus Teacher-Scholar Award program.

## References

1. See, for example: (a) M.F. Lappert, P.P. Power, A.R. Sanger, and R.C. Srivastava. Metal and metalloid amides. Ellis Horwood, Chichester, U.K. 1980; (b) M.H. Chisholm and I.P. Rothwell. *In Comprehensive coordination chemistry*. Vol. 2. Edited by G. Wilkinson, R.D. Gillard, and J.A. McCleverty. Pergamon, New York. 1987; (c) R. Kempe. *Angew. Chem. Int. Ed.* **39**, 468 (2000).
2. See, for example: (a) C.H. Winter. *Aldrichimica Acta*, **33**, 3 (2000); (b) R. Fix, R.G. Gordon, and D.M. Hoffman. *Chem. Mater.* **3**, 1138 (1991); (c) J.S. Custer, P.M. Smith, J.G. Fleming, and E. Roherty-Osmun. *ACS Symp. Ser.* **727** 86 (1999). Edited by C.H. Winter and D.M. Hoffman; (d) K.-A. Son, A.Y. Mao, Y.-M. Sun, B.Y. Kim, F. Liu, A. Kamath, J.M. White, D.L. Kwong, D.A. Roberts, and R.N. Vrtis. *Appl. Phys. Lett.* **72**, 1187 (1998); (e) K.-A. Son, A.Y. Mao, B.Y. Kim, F. Liu, E.D. Pylant, D.A. Hess, J.M. White, D.L. Kwong, D.A. Roberts, and R.N. Vrtis. *J. Vac. Sci. Technol. A*, **A16**, 1670 (1998); (f) H.-T. Chiu, C.-N. Wang, and S.-H. Chuang. *Chem. Vap. Deposition*, **6**, 223 (2000).
3. (a) C.K. Narula, P. Czubarow, and D. Seyferth. *Chem. Vapor Deposition*, **1**, 51 (1995); (b) D.V. Baxter, M.H. Chisholm, G.J. Gama, V.F. DiStasi, A.L. Hector, and I.P. Parkin. *Chem. Mater.* **8**, 1222 (1996); (c) C.K. Narula and L.F. Allard. *J. Mater. Chem.* **8**, 1881 (1998); (d) H.C. Aspinall, P.A. Williams, J. Gaskell, A.C. Jones, J.L. Roberts, L.M. Smith, P.R. Chalker, and G.W. Critchlow. *Chem. Vap. Deposition*, **9**, 7 (2003).
4. See, for example: (a) D.C. Bradley, M.B. Hursthouse, K.M. Abdul Malik, and G.B.C. Vuru. *Inorg. Chim. Acta*, **44**, L5 (1980); (b) T.D. Tilley, R.A. Andersen, and A. Zalkin. *Inorg. Chem.* **23**, 2271 (1984); (c) D.M. Hoffman and S. Suh. *J. Chem. Soc. Chem. Comm.* 714 (1993). (d) L.R. Avens, S.G. Bott, D.L. Clark, A.P. Sattelberger, J.G. Watkin, and B.D. Zwick. *Inorg. Chem.* **33**, 2248 (1994); (e) J.L. Stewart and R.A. Andersen. *New J. Chem.* **19**, 587 (1995); (f) Z.-B. Duan, M. Schmidt, V.G. Young, Jr., X.-B. Xie, R.E. McCarley, and J.G. Verkade. *J. Am. Chem. Soc.* **118**, 5302 (1996).
5. (a) P. Berno and S. Gambarotta. *Organometallics*, **14**, 2159 (1995); (b) L. Scoles, K.B.P. Rupp, and S. Gambarotta. *J. Am. Chem. Soc.* **118**, 2529 (1996); (c) L.H. Dubois, B.R. Zegarski, and G.S. Girolami. *J. Electrochem. Soc.* **139**, 3603 (1992); (d) T.S. Lewkebandara, P.H. Sheridan, M.J. Heeg, A.L. Rheingold, and C.H. Winter. *Inorg. Chem.* **33**, 5879 (1994); (e) M. Beaudoin and S. L. Scott. *Organometallics*, **20**, 237 (2001); (f) T.R. Cundari and J.M. Morse, Jr. *Chem. Mater.* **8**, 189 (1996); (g) B.H. Weiller. *J. Am. Chem. Soc.* **118**, 4975 (1996); (h) T.S. Cale, M.B. Chaara, G.B. Raupp, and I.J. Raaijmakers. *Thin Solid Films*, **236**, 294 (1993); (i) F. Ossola and F. Maury. *Chem. Vap. Deposition*, **3**, 137 (1997); (j) H. Cai, T.-N. Chen, X.-P. Wang, A.J. Schultz, T.F. Koetzle, and Z.-L. Xue. *Chem. Commun. (Cambridge)*, 230 (2002).
6. (a) X.-Z. Liu, Z.-Z. Wu, H. Cai, Y.-H. Yang, T.-N. Chen, C.E. Vallet, R.A. Zuh, D.B. Beach, Z.-H. Peng, Y.-D. Wu, T.E. Concolino, A.L. Rheingold, and Z.-L. Xue. *J. Am. Chem. Soc.* **123**, 8011 (2001); (b) X.-Z. Liu, Z.-Z. Wu, Z.-H. Peng, Y.-D. Wu, and Z.-L. Xue. *J. Am. Chem. Soc.* **121**, 5350 (1999); (c) Z.-Z. Wu, H. Cai, X.-H. Yu, J.R. Blanton, J.B. Diminnie, H.-J. Pan, and Z.-L. Xue. *Organometallics*, **21**, 3973 (2002); (d) Z.-Z. Wu and Z.-L. Xue. *Organometallics*, **19**, 4191 (2000); (e) Z.-Z. Wu, J. B. Diminnie, and Z.-L. Xue. *J. Am. Chem. Soc.* **121**, 4300 (1999); (f) Z.-Z. Wu, J.B. Diminnie, and Z.-L. Xue. *Inorg. Chem.* **37**, 6366 (1998); (g) Z.-Z. Wu, J.B. Diminnie, and Z.-L. Xue. *Organometallics*, **18**, 1002 (1999); (h) J.B. Diminnie, X.-Z. Liu, H. Cai, Z.-Z. Wu, J.R. Blanton, T.-N. Chen, A.A. Tuinman, K.T. Quisenberry, C.E. Vallet, R.A. Zuh, D.B. Beach, Z.-H. Peng, Y.-D. Wu, T. E. Concolino, A.L. Rheingold, and Z.-L. Xue. *Pure Appl. Chem.* **73**, 331 (2001); (i) T.-N. Chen and Z.-L. Xue. *Chinese J. Inorg. Chem.* **15**, 413 (1999).
7. C.R. Bennett and D.C. Bradley. *J. Chem. Soc. Chem. Comm.* 29 (1974).
8. S.J. Simpson and R.A. Andersen. *Inorg. Chem.* **20**, 3627 (1981).
9. S.G. Bott, D.M. Hoffman, and S.P. Rangarajan. *J. Chem. Soc. Dalton Trans.* 1979 (1996).
10. D.C. Bradley, H. Chudzynska, J.D.J. Backer-Dirks, M.B. Hursthouse, A.A. Ibrahim, M. Motevalli, and A.C. Sullivan. *Polyhedron*, **9**, 1423 (1990).
11. M. Karl, K. Harms, G. Seybert, W. Massa, S. Fau, G. Frenking, and K. Dehnicke. *Z. Anorg. Allg. Chem.* **625**, 2055 (1999).
12. (a) M.A. Putzer, J. Magull, H. Goesmann, B. Neumüller, and K. Dehnicke. *Chem. Ber.* **129**, 1401 (1996); (b) M.A. Putzer, B. Neumüller, and K. Dehnicke. *Z. Anorg. Allg. Chem.* **624**, 1087 (1998).
13. M. Moore, S. Gambarotta, and C. Bensimon. *Organometallics*, **16**, 1086 (1997).
14. A.D. Horton and J. de With. *Chem. Commun. (Cambridge)*, 1375 (1996).
15. (a) P. Berno and S. Gambarotta. *Chem. Commun. (Cambridge)*, 2419 (1994); (b) P. Berno and S. Gambarotta. *Angew. Chem. Int. Ed. Engl.* **34**, 822 (1995).
16. R.P. Planalp and R.A. Andersen. *Organometallics*, **2**, 1675 (1983).
17. (a) P. Berno, R. Minhas, S.-K. Hao, and S. Gambarotta. *Organometallics*, **13**, 1052 (1994); (b) C.P. Gerlach and J. Arnold. *Organometallics*, **15**, 5260 (1996); (c) C.P. Gerlach and J. Arnold. *J. Chem. Soc. Dalton Trans.* 4795 (1997); (d) C.P. Gerlach and J. Arnold. *Organometallics*, **16**, 5148 (1997).
18. R. Messere, M.-R. Spirlet, D. Jan, A. Demonceau, and A.F. Noels. *Eur. J. Inorg. Chem.* 1151 (2000).
19. Yb and Lu analogs of **7** (10), and Th and U complexes containing the metallasilacycles have also been reported. See: (a) S.J. Simpson, H.W. Turner, and R.A. Andersen. *J. Am. Chem. Soc.* **101**, 7728 (1979); (b) S.J. Simpson, H.W. Turner, and R.A. Andersen. *Inorg. Chem.* **20**, 2991 (1981); (c) D.L. Clark, T.M. Frankcom, M.M. Miller, and J.G. Watkin. *Inorg. Chem.* **31**, 1628 (1992); (d) A. Dormond, A. El Bouadili, A. Aaliti, and C. Moise. *J. Organomet. Chem.* **288**, C1 (1985); (e) R.J. Butcher, D.L. Clark, S.K. Grumbine, and J.G. Watkin. *Organometallics*, **14**, 2799 (1995); (f) T.M. Trnka, J.B. Bonanno, B.M. Bridgewater, and G. Parkin. *Organometallics*, **20**, 3255 (2001).
20. A  $\text{Li}^+-\text{Mg}^{2+}$  complex containing the four-membered metallaheterocycle has been reported: L. Barr, A.R. Kennedy, J.G. MacLellan, J.H. Moir, R.E. Mulvey, and P.J.A. Rodger. *Chem. Commun. (Cambridge)*, 1757 (2000).
21. Andersen and co-workers reported bridging carbenes



- $\{\overline{\text{MCHSiMe}_2\text{NSiMe}_3[\text{N}(\text{SiMe}_3)_2]}\}_2$  (M = Ti, Zr, Hf) and pyridine adducts (M = Zr, Hf). R.P. Planalp, R.A. Andersen, and A. Zalkin. *Organometallics* **2**, 16 (1983).
22. Wolczanski and co-workers reported the formation of a cyclic product and  $\text{CH}_4$  elimination from thermolysis of (*t*-BuSiNH)<sub>3</sub>Zr-Me. C.C. Cummins, S.M. Baxter, and P.T. Wolczanski. *J. Am. Chem. Soc.* **110**, 8731 (1988).
23. J.E. Huheey, E.A. Keiter, and R.L. Keiter *Inorganic chemistry: Principles of structure and reactivity*. 4th ed. HarperCollins, New York. 1993. pp. 203–206 and 217–218.
24. M.H. Chisholm, L.-S. Tan, and J.C. Huffman. *J. Am. Chem. Soc.* **104**, 4879 (1982).
25. M.H. Chisholm, J.C. Huffman, and L.-S. Tan. *Inorg. Chem.* **20**, 1859 (1981).
26. See, for example: (a) X.-Z. Liu, L.-T. Li, J. B. Diminnie, G.P.A. Yap, A.L. Rheingold, and Z.-L. Xue. *Organometallics*, **17**, 4597 (1998); (b) L.-T. Li, Z.-L. Xue, G.P.A. Yap, and A.L. Rheingold. *Organometallics*, **14**, 4992 (1995).
27. (a) G.M. Sheldrick. SADABS [computer program]. University of Göttingen, Göttingen, Germany. 1996; (b) G.M. Sheldrick. SHELXL-97 [computer program]. University of Göttingen, Göttingen, Germany. 1997.



# Organometallic reactions in aqueous media — Bismuth-mediated crossed aldol type reactions<sup>1</sup>

Yoon Joo Lee and Tak Hang Chan

**Abstract:** Bismuth metal, upon activation by zinc fluoride, can effect the crossed aldol reaction between  $\alpha$ -bromocarbonyl compounds and aldehydes in aqueous media. The reaction was found to be regioselective and syn-diastereoselective.

**Key words:** bismuth, zinc fluoride, aldol reaction, regioselectivity, aqueous media.

**Résumé :** En milieu acide, le bismuth métallique activé par le fluorure de zinc rend possible la réaction aldolique croisée entre des composés  $\alpha$ -bromocarbonylés et des aldéhydes. On a observé que la réaction est régiospécifique et syn-diaitérosélective.

**Mots clés :** bismuth, fluorure de zinc, réaction aldolique, régiosélectivité, milieu aqueux.

[Traduit par la Rédaction]

## Introduction

The aldol reaction has played an important role in organic synthesis for the formation of carbon–carbon bonds, providing  $\beta$ -hydroxycarbonyl compounds. However, under the classical aldol reaction conditions involving basic aqueous media, side products, such as regioisomers, dimers, polymers, self-condensation products, and  $\alpha,\beta$ -unsaturated carbonyl compounds, are invariably formed as well. The formation of these side products is often attributed to the fact that the aldol reaction is an equilibrium process (1). To circumvent this problem, useful modifications of the classical aldol reaction, particularly using Lewis-acid-promoted reactions of enol silyl or tin ethers with carbonyl compounds, have been developed (2). In general, these methods employ organic solvents as reaction media. Recently, there has been considerable interest in conducting organic reactions in aqueous media (3) because of the need to reduce volatile organic solvents as a burden to the environment. In 1990 and subsequently, we reported on the possibility of conducting metal-mediated crossed aldol type reactions in aqueous media, using zinc, tin, and indium (4). The yields of the crossed aldol products were modest. In 1997, Shen et al. (5) reported using bismuth to mediate the crossed aldol type reactions in aqueous media. In the presence of bismuth(III) chloride and metallic aluminum,  $\alpha$ -bromocarbonyl compounds **1** were found to react with various aldehydes **2** in water under a nitrogen atmosphere at 60 °C to afford the corresponding  $\beta$ -hydroxycarbonyl compounds **3** in good yields together with the dehalogenated products **4** (Scheme 1).

Very recently, J. Zhang and Y. Zhang (6) demonstrated that a bimetallic system of bismuth(III) chloride and samar-

ium could mediate similar crossed aldol type reactions of  $\alpha$ -bromoacetophenone with a variety of aldehydes in a mixture of THF and H<sub>2</sub>O. Because of our continuing interest in this area, we have examined the bismuth-mediated reaction with the following objectives in mind: (1) use bismuth metal directly in place of the reduction of bismuth chloride for the crossed aldol reaction; (2) extend the reaction to aliphatic acyclic ketones since most reported examples of  $\alpha$ -halocarbonyl compounds **1** have been limited to arylketones; and (3) examine the regioselection of the reaction.

## Results

### Study of different fluoride salts as promoters

In general, mechanically atomized metals are less reactive than metals chemically prepared by the reduction of metal salts with alkali metals or other reducing agents (7). The low reactivity of the bismuth metal powder may result from the insufficient removal of metal oxide layers from the metal surface and the low surface area of the metal particles. Thus, it is obvious that activation of the bismuth metal is needed for the reaction to proceed. Previous reports from our research group have shown that fluoride salts are quite effective in activating metals, such as aluminum (8) and antimony (9), to mediate organometallic reactions in aqueous media. More recently, we found that ammonium hydrogen fluoride (NH<sub>4</sub>HF<sub>2</sub>) could efficiently activate commercially available bismuth metal to reduce  $\alpha$ -halocarbonyl compounds **1** to the corresponding dehalogenated products **4** in excellent yields (10). The reaction is presumed to proceed through the intermediacy of a bismuth enolate **5** (X = Br or F, Scheme 2). We were able to demonstrate that starting with 2-bromoisobutyrophenone (**1a**, R<sup>1</sup> = Ph, R<sup>2</sup> = R<sup>3</sup> = Me) and benzaldehyde in the presence of bismuth and NH<sub>4</sub>HF<sub>2</sub>, the crossed aldol product **3a** (R<sup>1</sup> = R<sup>4</sup> = Ph, R<sup>2</sup> = R<sup>3</sup> = Me) was obtained. The reaction was carried out in water as the reaction medium. However, reduction was a serious side reaction giving product **4a** in 44% yield, substantially lowering the yield of the aldol product **3a** to 56%.

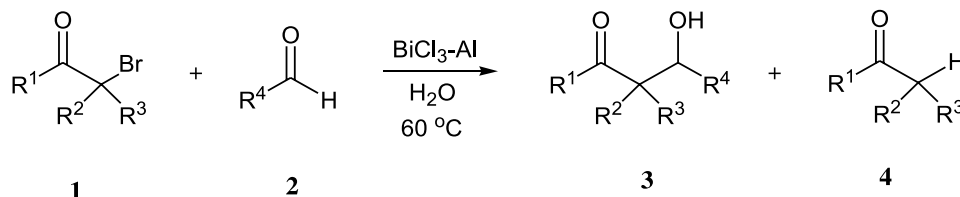
Received 3 June 2003. Published on the NRC Research Press Web site at <http://canjchem.nrc.ca> on 10 November 2003.

**Y.J. Lee and T.H. Chan.**<sup>2</sup> Department of Chemistry, McGill University, Montreal, QC H3A 2K6, Canada.

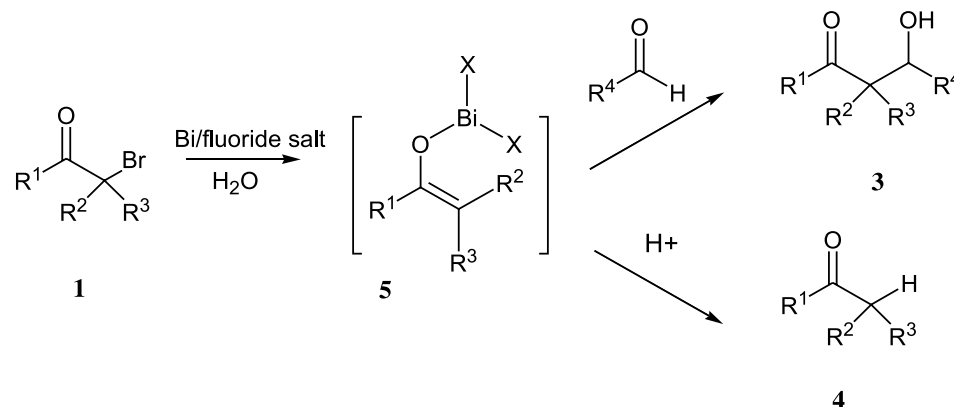
<sup>1</sup>Corresponding author. (e-mail: [tak-hang.chan@mcgill.ca](mailto:tak-hang.chan@mcgill.ca)).



Scheme 1.



Scheme 2.

**Table 1.** Screening of promoters for the bismuth-mediated crossed aldol type reaction of 2-bromoisobutyrophenone with benzaldehyde in aqueous media.<sup>a</sup>

Entry	Promoter	Time (h)	Unreacted <b>1a</b> (%) <sup>b</sup>	Yield of <b>3a</b> (%) <sup>b</sup>	Yield of <b>4a</b> (%) <sup>b</sup>
1	KF	24	100	0	0
2	$\text{CaF}_2$	24	100	0	0
3	$\text{AlF}_3$	24	100	0	0
4	$\text{NH}_4\text{F}$	24	40	53	7
5	$\text{NH}_4\text{HF}_2$	12	0	82 (78 <sup>c</sup> )	18
6	$\text{Bu}_4\text{NF}$	24	100	0	0
7	$\text{TiF}_4$	18	0	75	25
8	$\text{VF}_4$	16	0	50	50
9	$\text{CrF}_3$	18	0	75	25
10	$\text{MnF}_2$	24	99	Trace	Trace
11	$\text{FeF}_2$	24	84	15	Trace
12	$\text{CoF}_2$	24	89	10	Trace
13	$\text{NiF}_2$	24	87	12	Trace
14	$\text{CuF}_2$	12	0	58	42
15	$\text{ZnF}_2$	12	0	95 (90 <sup>c</sup> )	5
16	$\text{ZnCl}_2$	24	100	0	0

<sup>a</sup>Ratio of **1a**:benzaldehyde:Bi:promoter = 1 : 1.1 : 1.5 : 1.5 mmol and 1 mL of  $\text{D}_2\text{O}$ .

<sup>b</sup>Determined by  $^1\text{H}$  NMR of the crude product.

<sup>c</sup>Isolated yield.

In this reaction, the use of ammonium hydrogen fluoride was found to be necessary since neither the crossed aldol type reaction nor the reduction proceeded with bismuth alone. In an attempt to search for a more effective promoter for bismuth metal activation, a wide range of fluoride salts was screened using the reaction of compound **1a** with benzalde-

**Table 2.** Screening of solvents for the bismuth-mediated crossed aldol type reaction of 2-bromoisobutyrophenone with benzaldehyde in the presence of  $\text{ZnF}_2$ .<sup>a</sup>

Entry	Solvent	Time (h)	Unreacted <b>1a</b> (%) <sup>b</sup>	Yield of <b>3a</b> (%) <sup>b</sup>	Yield of <b>4a</b> (%) <sup>b</sup>
1	Neat	24	78	21	Trace
2	$\text{H}_2\text{O}$	12	0	85 (81 <sup>c</sup> )	15
3	$\text{D}_2\text{O}$	12	0	95 (90 <sup>c</sup> )	5
4	EtOH	24	100	0	0
5	$\text{H}_2\text{O}$ -THF (1:1)	24	0	77	23
6	THF	24	100	0	0

<sup>a</sup>Ratio of **1a**:benzaldehyde:Bi: $\text{ZnF}_2$  = 1 : 1.1 : 1.2 : 1.2 mmol and 1 mL of solvent

<sup>b</sup>Determined by  $^1\text{H}$  NMR of the crude product.

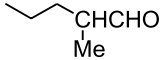
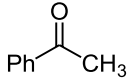
<sup>c</sup>Isolated yield.

hyde as a model reaction (Scheme 2), and the results are shown in Table 1.

As can be seen from Table 1, the main group metal fluorides ( $\text{KF}$ ,  $\text{CaF}_2$ , and  $\text{AlF}_3$ ) could not activate bismuth to mediate the reaction in  $\text{D}_2\text{O}$  (entries 1–3). Most of the transition metal fluorides tested were found to be inefficient in activating bismuth leading to unsatisfactory yields of the aldol product (entries 7–14). However, the reactions with  $\text{TiF}_4$ ,  $\text{VF}_4$ ,  $\text{CrF}_3$ , and  $\text{CuF}_2$ , which are not commonly used reagents in organic synthesis, afforded the corresponding aldol adducts in moderate yields. In the case of zinc fluoride, the aldol addition product was obtained predominantly along with a minimal amount of the reduction product (entry 15). Fluoride anion seemed to have a special activating effect as  $\text{ZnCl}_2$  was ineffective (entry 16). Several different solvents were also screened using the same model reaction at room temperature with  $\text{ZnF}_2$ . The results are summarized in Table 2. Hardly any desired product was observed when ethanol or THF was employed as the solvent (entries 4 and



**Table 3.** Bismuth-mediated crossed aldol type reactions of 2-bromoisobutyrophenone with various aldehydes and ketones in the presence of  $\text{ZnF}_2$  in aqueous media.<sup>a</sup>

Entry	Electrophile	Time (h)	Unreacted <b>1a</b> (%) <sup>b</sup>	Yield of <b>3</b> (%) <sup>b</sup>	Yield of <b>4</b> (%) <sup>b</sup>
1	PhCHO	12	0	95 (90 <sup>c</sup> ) ( <b>3a</b> )	5
2	<i>p</i> -CH <sub>3</sub> PhCHO	24	10	80 (66 <sup>c</sup> ) ( <b>3b</b> )	10
3	<i>p</i> -CH <sub>3</sub> OPhCHO	24	98	Trace ( <b>3c</b> )	Trace
4	<i>p</i> -ClPhCHO	16	26	69 (91 <sup>c</sup> ) ( <b>3d</b> )	5
5	<i>p</i> -CNPhCHO	16	19	80 (98 <sup>c</sup> ) ( <b>3e</b> )	Trace
6	<i>n</i> -C <sub>5</sub> H <sub>11</sub> CHO	12	0	53 (35 <sup>c</sup> ) ( <b>3f</b> )	47
7	Ph(CH <sub>2</sub> ) <sub>2</sub> CHO	12	20	67 (56 <sup>c</sup> ) ( <b>3g</b> )	13
8		12	7	0	93
9		20	10	0	90

<sup>a</sup>Ratio of **1a**:aldehyde:Bi:ZnF<sub>2</sub> = 1 : 1.1 : 1.2 : 1.2 mmol and 1 mL of D<sub>2</sub>O.<sup>b</sup>Determined by <sup>1</sup>H NMR of the crude product.<sup>c</sup>Isolated yield based on reacted **1a**.

6). In a mixture of water and THF (1:1), the reduction product was formed to a significant extent as well (entry 5). Aqueous media, water, or deuterium oxide, proved to be the most suitable solvents for this bismuth-mediated crossed aldol type reaction (entries 2 and 3).

#### Scope of the bismuth-mediated aqueous crossed aldol type reaction

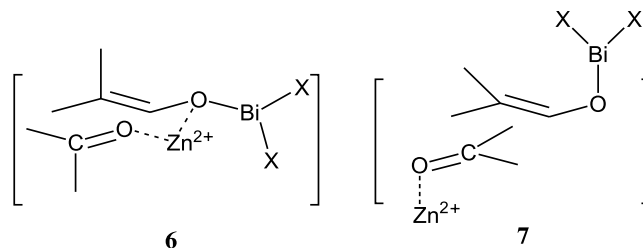
The bismuth-mediated aqueous crossed aldol type reactions of compound **1a** with a variety of aldehydes were surveyed (Table 3). In general, both aromatic and aliphatic aldehydes reacted smoothly with compound **1a** to provide the corresponding aldol products **3** in moderate to high yields. The exception appeared to be *p*-methoxybenzaldehyde (entry 3). The presence of the methoxy group seemed to have interfered with the activation process since unreacted **1a** could be recovered. On the other hand, for  $\alpha$ -branched aldehydes or ketones (entries 8 and 9), compound **1a** was transformed efficiently to the presumed enolate and was protonated faster than the aldol condensation.

The generality of the reaction was also explored with various  $\alpha$ -bromocarbonyl compounds using benzaldehyde under similar reaction conditions. The results are summarized in Table 4. Aromatic  $\alpha$ -bromoketones generally reacted better to provide the corresponding  $\beta$ -hydroxyketones in higher yields (entries 1–3) in comparison with aliphatic  $\alpha$ -bromoketones (entries 4 and 5). The reactions of  $\alpha$ -bromocarboxylic acids with benzaldehyde resulted in the formation of the corresponding reduction products as the major product (entries 6 and 7).

#### Discussions

The ability of zinc fluoride to promote the crossed aldol reaction can be attributed to two factors. First, the fluoride anion may activate the metal for chemical reactions in aqueous media. Many metals, though considered to be reactive based on their ionization potentials, may be inert in aqueous

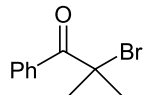
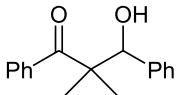
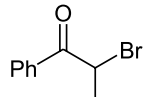
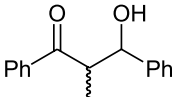
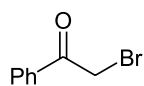
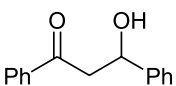
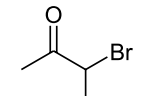
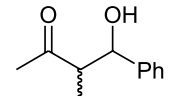
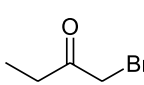
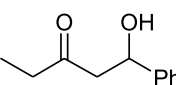
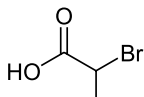
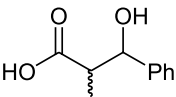
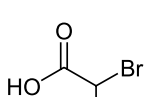
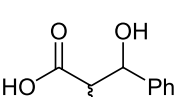
media because of the easy formation of insoluble metal oxide on the metal surface. Aluminum metal is a good example. It has a first ionization potential (5.984 eV) which is much lower than that of magnesium (7.646 eV) and is expected to be a reactive metal. On the other hand, aluminum is resistant to water because it readily forms a layer of insoluble Al<sub>2</sub>O<sub>3</sub> and this prevents the metal from further reaction. It has been reported that trace amounts of fluoride anion in water dramatically increased the corrosion of aluminum metal (11). This effect is attributed to the reaction of fluoride ion with Al<sub>2</sub>O<sub>3</sub> to form various water soluble fluoroaluminates (12). Bismuth metal may be activated by fluoride salts in a similar manner in that fluorobismuthates can be prepared from Bi<sub>2</sub>O<sub>3</sub> and fluorides (13). The second factor is that the zinc ion must also play a role. Recently, Chan and co-workers (14) and others (15) have found that zinc fluoride acts as an effective Lewis acid in aqueous media by the coordination of the zinc cation with the carbonyl function. In the crossed aldol reaction, the bismuth enolate **5** may react with the Zn<sup>2+</sup>-coordinated aldehyde in either the cyclic chair transition state (**6**) (16) or the extended *antiperiplanar* transition state (**7**) (17).



By comparing the products derived from 3-bromobutan-2-one (Table 4, entry 4) and 1-bromobutan-2-one (Table 4, entry 5), it is possible to conclude that the reaction is regioselective. The two regioisomeric bismuth enolates (**8** and **9**) must have been generated separately. Reactions of the enolates with benzaldehyde led to different isomeric aldol



**Table 4.** Bismuth-mediated crossed aldol type reactions of  $\alpha$ -bromocarbonyl compounds with benzaldehyde in the presence of  $\text{ZnF}_2$  in aqueous media.

Entry	Compound 1	Product 3	Isolated yield of <b>3</b> (syn:anti)(%) <sup>a</sup>	% Yield of <b>4</b> <sup>a</sup>
1		 <b>3a</b>	90 <sup>b</sup>	5
2		 <b>3h</b>	98 <sup>b</sup> (55:45)	Trace
3		 <b>3i</b>	55 <sup>c</sup>	43
4		 <b>3j</b>	50 <sup>d</sup> (73:27)	43
		 <b>3k</b>	12 <sup>d</sup>	88
6		 <b>3l</b>	22 <sup>a,e</sup> (64:36)	78
7		 <b>3m</b>	0 <sup>a,f</sup>	100

<sup>a</sup>Determined by  $^1\text{H}$  NMR of the crude product.<sup>b</sup>Ratio of 1:aldehyde:Bi:ZnF<sub>2</sub> = 1 : 1.1 : 1.2 : 1.2 mmol / 12 h.<sup>c</sup>Ratio of 1:aldehyde:Bi:ZnF<sub>2</sub> = 1 : 2 : 2 : 2 mmol / 40 h.<sup>d</sup>Ratio of 1:aldehyde:Bi:ZnF<sub>2</sub> = 1 : 2 : 3 : 2 mmol / 40 h.<sup>e</sup>Ratio of 1:aldehyde:Bi:ZnF<sub>2</sub> = 1 : 1.1 : 1.5 : 1.5 mmol / 6 h.<sup>f</sup>Ratio of 1:aldehyde:Bi:ZnF<sub>2</sub> = 1 : 1.1 : 1 : 2 mmol / 24 h.

products. Furthermore, protonation of the enolates to give butan-2-one must not be reversible, otherwise both enolates would have been regenerated in the reaction mixture, which would have led to a mixture of regioisomers in both reactions (Scheme 3).

In the three examples where diastereomeric aldol products were formed, the syn-isomer was formed preferentially over the anti-isomer (Table 4, entries 2, 4, and 6). Using the condensation of 3-bromobutan-2-one as the example (entry 4), the syn/anti ratio was found to be 73:27. The preferred formation of the syn-isomer is usually explained by one of the following two (or more) possibilities: (1) in the formation of the bismuth enolate, *E*-**9** was formed preferentially, which then reacted with benzaldehyde via the extended antiperiplanar transition state **7** to give the syn- product; or (2) the *Z*-**9** bismuth enolate was formed preferentially, and it reacted with benzaldehyde via the cyclic chair transition state **6**. While there is insufficient experimental evidence to prefer

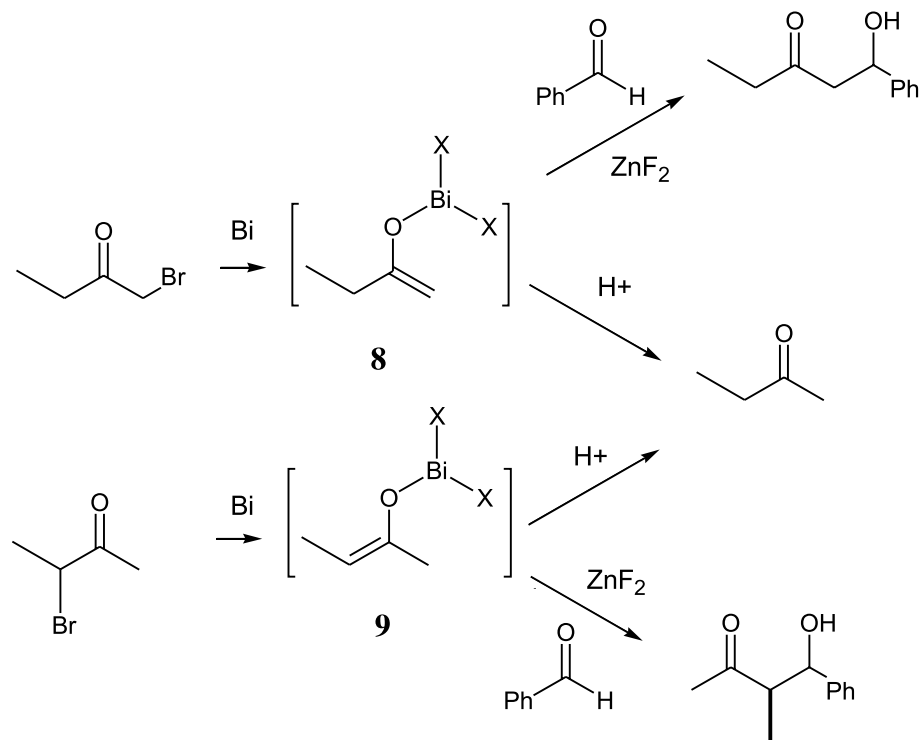
one explanation over the other in the present reaction, similar stereochemical preference was observed in the bismuth-mediated coupling of crotyl bromide with aldehydes, and the acyclic transition state explanation similar to **7** was invoked (18).

## Conclusion

The bismuth-mediated aqueous crossed aldol type reaction was investigated. The study showed that bismuth activated by several fluoride salts could mediate the aldol addition reaction of  $\alpha$ -bromocarbonyl compounds with aldehydes in aqueous media. Zinc fluoride was found to be the promoter of choice. The scope of this bismuth-mediated aqueous crossed aldol type reaction was examined and the reaction was found to be regiospecific and diastereoselective.



Scheme 3.



## Experimental

### General information

Chemicals were purchased from Aldrich or the Alfa Aesar Chemical Company. All the aldehydes were purified by distillation or column chromatography prior to use. Thin layer chromatography was performed on plastic plates precoated with silica gel (60 F<sub>254</sub>), which were developed using a mixture of hexane and ethyl acetate as an eluent. Analytes were visualized by UV light or by dipping the plate into a developing agent (a solution of ammonium molybdate and ceric sulfate in dilute sulfuric acid) and heating with a heat gun. Column chromatography was performed on 230–400 mesh silica gel.

Melting points were determined using a Gallenkamp apparatus and were uncorrected. Infrared spectra were recorded on an Avatar 360 FT-IR spectrometer and reported in cm<sup>-1</sup>. <sup>1</sup>H NMR spectra and <sup>13</sup>C NMR spectra were recorded on a Varian Mercury 300 or 400 MHz spectrometer or a Varian Unity 500 MHz spectrometer at ambient temperature. Chemical shifts (δ) were reported in parts per million (ppm) and referenced to CDCl<sub>3</sub> at δ 7.25 ppm for <sup>1</sup>H and δ 77.00 ppm for <sup>13</sup>C. The multiplicity of each signal was indicated by s (singlet), d (doublet), t (triplet), q (quartet), quint (quintet), sept (septet), and m (multiplet). Coupling constants (*J*) were reported in Hz. The syn and anti configurations of **3h**, **3j**, and **3m** were assigned on the basis that the coupling constants of the methyl-bearing methine proton and the hydroxyl-bearing methine proton have greater values for anti- than for syn-isomers (19). Mass spectra were recorded on a Kratos MS25RFA mass spectrometer or on a HP 5980A GC-MS.

### General procedure for bismuth-mediated aqueous crossed aldol type reaction

To a mixture of 2-bromoisobutyrophenone (1 mmol), an aldehyde (1.1 mmol), bismuth powder (1.2 mmol), and ZnF<sub>2</sub> (1.2 mmol) was added D<sub>2</sub>O (1 mL). The reaction mixture was vigorously stirred at room temperature for the indicated time in Table 3 (12–24 h). Additional distilled water (10 mL) was added in the reaction mixture, and the product was extracted with diethyl ether (3 × 30 mL). The combined organic layer was dried over anhyd Na<sub>2</sub>SO<sub>4</sub> and filtered. After the evaporation of solvent under reduced pressure, the crude product was purified by flash column chromatography on silica gel using 5% ethyl acetate in hexane as an eluent to give the corresponding pure aldol addition product.

### 3-Hydroxy-2,2-dimethyl-1,3-diphenyl-1-propanone (**3a**) (20)

White solid, mp 105–107 °C. IR (CHCl<sub>3</sub>) (cm<sup>-1</sup>): 3475 (O-H), 1672 (C=O). <sup>1</sup>H NMR (300 MHz, CDCl<sub>3</sub>) δ: 7.58–7.54 (m, 2H), 7.48–7.25 (m, 8H), 5.15 (d, *J* = 3.5 Hz, 1H), 2.92 (d, *J* = 4.0 Hz, 1H), 1.27 (s, 3H), 1.22 (s, 3H). <sup>13</sup>C NMR (75 MHz, CDCl<sub>3</sub>) δ: 211.59, 140.04, 139.51, 130.37, 127.86, 127.81, 127.64, 127.58, 126.98, 78.82, 52.52, 24.34, 19.70.

### 3-Hydroxy-2,2-dimethyl-3-(4-methylphenyl)-1-phenyl-1-propanone (**3b**) (20)

White solid, mp 83.5–85.0 °C. IR (CHCl<sub>3</sub>) (cm<sup>-1</sup>): 3490 (O-H), 1673 (C=O). <sup>1</sup>H NMR (400 MHz, CDCl<sub>3</sub>) δ: 7.58–7.55 (m, 2H), 7.47–7.42 (m, 1H), 7.40–7.36 (m, 2H), 7.23 (d, *J* = 8.4 Hz, 2H), 7.14 (d, *J* = 8.0 Hz, 2H), 5.10 (s, 1H), 2.94 (br s, 1H), 2.36 (s, 3H), 1.25 (s, 3H), 1.19 (s, 3H). <sup>13</sup>C NMR (100 MHz, CDCl<sub>3</sub>) δ: 211.62, 139.59, 137.19, 137.06,



130.30, 128.30, 127.83, 127.68, 126.98, 78.67, 52.54, 24.34, 21.21, 19.62.

**3-(4-Cyanophenyl)-3-hydroxy-2,2-dimethyl-1-phenyl-1-propanone (3e)**

Colorless oil. IR (CHCl<sub>3</sub>) (cm<sup>-1</sup>): 3477 (O-H), 2229 (C≡N), 1673 (C=O). <sup>1</sup>H NMR (400 MHz, CDCl<sub>3</sub>) δ: 7.55–7.49 (m, 4H), 7.43–7.31 (m, 5H), 5.13 (d, *J* = 3.3 Hz, 1H), 3.72 (d, *J* = 3.8 Hz, 1H), 1.17 (s, 3H), 1.12 (s, 3H). <sup>13</sup>C NMR (100 MHz, CDCl<sub>3</sub>) δ: 210.73, 145.52, 138.80, 131.30, 130.75, 128.54, 127.95, 127.03, 118.58, 111.18, 77.93, 52.38, 24.03, 19.63. MS (CI, NH<sub>3</sub>) *m/z*: 280 (M + H<sup>+</sup>, 5), 148 (51), 130 (48), 105 (100), 77 (13). HR-MS (FAB) for C<sub>18</sub>H<sub>17</sub>NO<sub>2</sub> + H<sup>+</sup> calcd.: 280.1337; found: 280.1338.

**3-(4-Chlorophenyl)-3-hydroxy-2,2-dimethyl-1-phenyl-1-propanone (3d)**

White solid, mp 57–59 °C. IR (CHCl<sub>3</sub>) (cm<sup>-1</sup>): 3475 (O-H), 1673 (C=O). <sup>1</sup>H NMR (400 MHz, CDCl<sub>3</sub>) δ: 7.54–7.50 (m, 2H), 7.44–7.39 (m, 1H), 7.36–7.32 (m, 2H), 7.26–7.19 (m, 4H), 5.04 (s, 1H), 3.61 (br s, 1H), 1.18 (s, 3H), 1.12 (s, 3H). <sup>13</sup>C NMR (100 MHz, CDCl<sub>3</sub>) δ: 211.25, 139.17, 138.53, 133.15, 130.46, 129.07, 127.83, 127.65, 126.96, 77.95, 52.36, 24.10, 19.53.

**3-Hydroxy-2,2-dimethyl-1-phenyl-1-octanone (3f)**

Colorless oil. IR (CHCl<sub>3</sub>) (cm<sup>-1</sup>): 3489 (O-H), 1671 (C=O). <sup>1</sup>H NMR (400 MHz, CDCl<sub>3</sub>) δ: 7.61–7.58 (m, 2H), 7.44–7.40 (m, 1H), 7.37–7.33 (m, 2H), 3.85 (dd, *J* = 10.0, 2.1 Hz, 1H), 2.69 (br s, 1H), 1.61–1.14 (m, 14H), 0.87 (t, *J* = 6.9 Hz, 3H). <sup>13</sup>C NMR (100 MHz, CDCl<sub>3</sub>) δ: 210.75, 139.01, 130.52, 127.80, 127.19, 76.96, 52.11, 31.75, 31.59, 26.48, 22.89, 22.64, 21.20, 14.09. MS (FAB) *m/z*: 249 (M + H<sup>+</sup>, 15), 231 (7), 149 (27), 131 (30), 105 (100), 77 (16). HR-MS (FAB) for C<sub>16</sub>H<sub>24</sub>O<sub>2</sub> + H<sup>+</sup> calcd.: 249.1855; found: 249.1855.

**3-Hydroxy-2,2-dimethyl-1,5-diphenyl-1-pentanone (3g) (21)**

Colorless oil. IR (CHCl<sub>3</sub>) (cm<sup>-1</sup>): 3489 (O-H), 1669 (C=O). <sup>1</sup>H NMR (400 MHz, CDCl<sub>3</sub>) δ: 7.63–7.60 (m, 2H), 7.48–7.44 (m, 1H), 7.41–7.36 (m, 2H), 7.31–7.27 (m, 2H), 7.22–7.18 (m, 3H), 3.91 (dd, *J* = 10.4, 2.4 Hz, 1H), 3.02–2.95 (m, 1H), 2.77 (br d, *J* = 5.7 Hz, 1H), 2.71–2.63 (m, 1H), 1.85–1.71 (m, 2H), 1.34 (d, *J* = 2.4 Hz, 6H). <sup>13</sup>C NMR (100 MHz, CDCl<sub>3</sub>) δ: 210.72, 141.86, 138.73, 130.80, 128.32, 128.22, 127.95, 127.32, 125.68, 76.57, 51.93, 33.57, 33.06, 23.18, 21.24.

**3-Hydroxy-2-methyl-1,3-diphenyl-1-propanone (3h) (22)**

*syn-Isomer*

White solid, mp 71–73 °C. <sup>1</sup>H NMR (300 MHz, CDCl<sub>3</sub>) δ: 7.96–7.92 (m, 2H), 7.62–7.56 (m, 1H), 7.50–7.23 (m, 7H), 5.25 (d, *J* = 2.6 Hz, 1H), 3.71 (qd, *J* = 7.3, 3.2 Hz, 1H), 3.69 (br s, 1H), 1.21 (d, *J* = 7.3 Hz, 3H). <sup>13</sup>C NMR (75 MHz, CDCl<sub>3</sub>) δ: 205.53, 141.63, 135.46, 133.47, 128.67, 128.36, 128.13, 127.19, 125.91, 73.03, 47.03, 11.24.

*anti-Isomer*

Colorless oil. <sup>1</sup>H NMR (300 MHz, CDCl<sub>3</sub>) δ: 7.99–7.95 (m, 2H), 7.59–7.53 (m, 1H), 7.49–7.25 (m, 7H), 4.99 (d, *J* =

8.1 Hz, 1H), 3.84 (quint, *J* = 7.3 Hz, 1H), 3.09 (br s, 1H), 1.07 (d, *J* = 7.3 Hz, 3H). <sup>13</sup>C NMR (75 MHz, CDCl<sub>3</sub>) δ: 204.63, 142.00, 136.54, 133.15, 128.50, 128.30, 127.77, 126.58, 76.68, 47.96, 15.76.

**3-Hydroxy-1,3-diphenyl-1-propanone (3i) (23)**

Colorless oil. <sup>1</sup>H NMR (300 MHz, CDCl<sub>3</sub>) δ: 7.97–7.93 (m, 2H), 7.61–7.55 (m, 1H), 7.48–7.27 (m, 7H), 5.35 (dd, *J* = 7.7, 4.4 Hz, 1H), 3.73 (br s, 1H), 3.39–3.36 (m, 2H). <sup>13</sup>C NMR (75 MHz, CDCl<sub>3</sub>) δ: 199.74, 142.77, 136.29, 133.41, 128.46, 128.33, 127.95, 127.43, 125.56, 69.86, 47.34.

**4-Hydroxy-3-methyl-4-phenyl-2-butanone (3j) (24)**

*syn-Isomer*

Colorless oil. IR (CHCl<sub>3</sub>) (cm<sup>-1</sup>): 3443 (O-H), 1703 (C=O). <sup>1</sup>H NMR (400 MHz, CDCl<sub>3</sub>) δ: 7.33–7.21 (m, 5H), 5.05 (d, *J* = 4.1 Hz, 1H), 3.25 (br s, 1H), 2.82 (qd, *J* = 7.1, 4.1 Hz, 1H), 2.11 (s, 3H), 1.08 (d, *J* = 7.1 Hz, 3H). <sup>13</sup>C NMR (100 MHz, CDCl<sub>3</sub>) δ: 213.20, 141.54, 128.04, 127.14, 125.69, 72.96, 53.20, 29.43, 10.29.

*anti-Isomer*

Colorless oil. IR (CHCl<sub>3</sub>) (cm<sup>-1</sup>): 3431 (O-H), 1705 (C=O). <sup>1</sup>H NMR (400 MHz, CDCl<sub>3</sub>) δ: 7.36–7.25 (m, 5H), 4.72 (d, *J* = 8.8 Hz, 1H), 3.02 (br s, 1H), 2.92 (quint, *J* = 7.2 Hz, 1H), 2.22 (s, 3H), 0.92 (d, *J* = 7.6 Hz, 3H). <sup>13</sup>C NMR (100 MHz, CDCl<sub>3</sub>) δ: 213.19, 141.67, 128.32, 127.83, 126.46, 76.44, 53.66, 30.12, 14.21.

## Acknowledgment

We thank the Natural Sciences and Engineering Research Council of Canada (NSERC) for financial support of this research.

## References

1. T. Mukaiyama. *Isr. J. Chem.* **24**, 162 (1984).
2. (a) T. Mukaiyama. *Org. React. (N.Y.)*, **28**, 203 (1982); (b) R.W. Stevens, N. Iwasawa, and T. Mukaiyama. *Chem. Lett.* 1459 (1982); (c) T.H. Chan. *In Comprehensive organic synthesis*. Vol. 2. Edited by B.M. Trost and I. Fleming. Pergamon Press, Oxford. 1991. pp. 595–628.
3. (a) C.J. Li and T.H. Chan. *Organic reactions in aqueous media*. John Wiley and Sons, New York. 1997; (b) P.A. Grieco (*Editor*). *Organic synthesis in water*. Blackie Academic and Professional, London. 1998.
4. (a) T.H. Chan, C.J. Li, and Z.Y. Wei. *J. Chem. Soc. Chem. Commun.* 505 (1990); (b) T.H. Chan, C.J. Li, M.C. Lee, and Z.Y. Wei. *Can. J. Chem.* **72**, 1181 (1994).
5. Z. Shen, J. Zhang, H. Zou, and M. Yang. *Tetrahedron Lett.* **38**, 2733 (1997).
6. J.M. Zhang and Y.M. Zhang. *Chin. J. Chem.* **20**, 111 (2002).
7. H. Kagoshima, Y. Hashimoto, D. Oguro, and K. Saigo. *J. Org. Chem.* **63**, 691 (1998).
8. L.H. Li and T.H. Chan. *Org. Lett.* **2**, 1129 (2000).
9. L.H. Li and T.H. Chan. *Tetrahedron Lett.* **41**, 5009 (2000).
10. (a) T.H. Chan, L.-H. Li, Y. Yang, and W. Lu. *In Clean solvents*. ACS Symp. Ser. 819. Edited by M.A. Abraham and L. Moens. American Chemical Society, Washington, D.C. 2002; (b) J.Y.J. Lee and T.H. Chan. *Can. J. Chem.* Accepted for publication.



11. K. Tennakone and S. Wickramanayake. *Nature* (London), **325**, 202 (1987).
12. (a) T. Hurlen and K.H. Johansen. *Acta Chem. Scand. Ser. A*, **A39**, 545 (1985); (b) K. Tennakone, S. Wickramanayake, and C.A.N. Fernando. *Environ. Pollut.* **49**, 133 (1988).
13. S.M. Godfrey, C.A. McAuliffe, A.G. Mackie, and R.G. Pritchard. *In Chemistry of arsenic, antimony and bismuth. Edited by N.C. Norman.* Blackie Academic and Professional, London. 1998. pp. 168–179.
14. W. Miao, W. Lu, and T.H. Chan. *J. Am. Chem. Soc.* **125**, 2414 (2003).
15. S. Kobayashi, T. Hamada and K. Manabe. *J. Am. Chem. Soc.* **124**, 5640 (2002).
16. (a) H.E. Zimmerman and M.D. Traxler. *J. Am. Chem. Soc.* **79**, 1920 (1957); (b) C.H. Heathcock, C.T. Buse, W.A. Kleschick, M.C. Pirrung, J.E. Sohn, and J. Lampe. *J. Org. Chem.* **45**, 1066 (1980); (c) R.W. Hoffman. *Angew. Chem. Int. Ed. Engl.* **21**, 555 (1982).
17. (a) S. Murata, M. Suzuki, and R. Noyori. *J. Am. Chem. Soc.* **102**, 3248 (1980); (b) Y. Yamamoto, H. Yatagai, Y. Naruta, and K. Maruyama. *J. Am. Chem. Soc.* **102**, 7107 (1980); (c) Y. Yamamoto. *Acc. Chem. Res.* **20**, 243 (1987).
18. M. Wada, H. Ohki, and K. Akiba. *Bull. Chem. Soc. Jpn.* **63**, 1738 (1990).
19. F. Fringuelli, O. Piermatti, and F. Pizzo. *J. Org. Chem.* **60**, 7006 (1995).
20. C.H. Harrison. *Tetrahedron Lett.* **28**, 4135 (1987).
21. T. Hamada, K. Manabe, S. Ishikawa, S. Nagayama, M. Shiro, and S. Kobayashi. *J. Am. Chem. Soc.* **125**, 2989 (2003).
22. T. Harada and T. Mukaiyama. *Chem. Lett.* 467 (1982).
23. H.O. House, D.S. Crumrine, A.Y. Teranishi, and H.D. Olmstead. *J. Am. Chem. Soc.* **95**, 3310 (1973).
24. T. Hayashi, Y. Matsumoto, and Y. Ito. *J. Am. Chem. Soc.* **110**, 5579 (1988).



# A combined density functional theory and molecular mechanics (QM/MM) study of single site ethylene polymerization catalyzed by $[\text{Cp}\{\text{NC}(t\text{-Bu})_2\}\text{TiR}^+]$ in the presence of the counterion $(\text{CH}_3\text{B}(\text{C}_6\text{F}_5)_3)^-)^1$

Kumar Vanka, Zhitao Xu, and Tom Ziegler

**Abstract:** Calculations have been carried out to investigate the insertion of the ethylene monomer into the Ti–alkyl bond for the systems  $\text{CpNC}(t\text{-Bu})_2\text{RTi-}\mu\text{-Me-B}(\text{C}_6\text{F}_5)_3$  ( $\text{R} = \text{Me}$  and  $\text{Pr}$ ), using density functional theory. A validated QM/MM model was used to represent the counterion. The tertiary butyl groups in the ligands were modeled with QM/MM, with hydrogens being used as the capping atoms. Solvent effects were incorporated with single point solvent calculations done with cyclohexane ( $\epsilon = 2.023$ ) as the solvent. With  $\text{R} = \text{Me}$  (the initiation step), approach of the ethylene cis and trans to the  $\mu\text{-Me}$  bridge was considered. Insertion was found to be endothermic, with  $\Delta H_{\text{tot}}$  being 12.7 kcal/mol (cis) and 15.5 kcal/mol (trans). The propagation step was then studied for the contact ion pair  $\text{CpNC}(t\text{-Bu})_2\text{PrTi-}\mu\text{-Me-B}(\text{C}_6\text{F}_5)_3$  (**4**). Different conformations of the propyl chain in **4** were considered by altering  $\theta$ , the dihedral angle formed between the  $\text{C}_\beta\text{-C}_\alpha\text{-Ti}$  and the  $\text{C}_\alpha\text{-Ti-}\mu\text{C}$  planes. The resting states were found to be at  $\theta = -69^\circ$  (**4a**),  $177^\circ$  (**4b**), and  $53^\circ$  (**4c**). A maxima was found near  $\theta = 0^\circ$  (**4d**). The cis and trans approaches of the ethylene monomer were considered for each of the four cases. The cis approach towards **4a** and trans approach towards **4d** led to insertion, with displacement of the counterion from the metal centre. The insertion barriers were found to be 17.8 kcal/mol, for the cis approach towards **4b** and 16.4 kcal/mol for the trans approach towards **4d**. The cis approaches towards conformers **4a** and **4c** showed common characteristics, with uptake barriers being higher than the subsequent insertion barriers in the two cases. Uptake barriers were 13.6 kcal/mol {TS(**4a-7a**)} and 10.7 kcal/mol {TS(**4c-8a**)}. The corresponding insertion barriers were 11.8 kcal/mol {TS(**7a-13a**)} and 8.4 kcal/mol {TS(**8a-13a**)}. The trans approaches towards conformers **4a** and **4c** led to insertion barriers of about 15.1 kcal/mol (lower than for the **4b** and **4d** cases). The cis approach towards **4d** and trans approach towards **4b** were found to lead to hydrogen transfer from the propyl chain to monomer, terminating the chain. Termination barriers were high — greater than 19.0 kcal/mol. This suggested that ethylene insertion would be favoured over termination during the propagation step.

**Key words:** homogeneous catalysis, counterion, initiation, propagation, termination.

**Résumé :** Faisant appel à la théorie de la densité fonctionnelle, on a effectué des calculs pour étudier l'insertion du monomère éthylène dans la liaison Ti–alkyle des systèmes  $\text{CpNC}(t\text{-Bu})_2\text{RTi-}\mu\text{-Me-B}(\text{C}_6\text{F}_5)_3$  ( $\text{R} = \text{Me}$  et  $\text{Pr}$ ). On a utilisé un modèle QM/MM pour représenter le contre-ion. On a modélisé les groupes *tert*-butyles des ligands avec le modèle QM/MM et les hydrogènes sont utilisés comme atomes de couverture. On a incorporé des effets de solvant à l'aide de calculs de solvant ponctuel en utilisant le cyclohexane ( $\epsilon = 2,023$ ) comme solvant. Avec  $\text{R} = \text{Me}$ , on a considéré les approches cis- et trans- (étape d'initiation) de l'éthylène. On a trouvé que l'insertion est endothermique, les  $\Delta H_{\text{tot}}$  étant respectivement de 12,7 et 15,5 kcal/mol respectivement pour les approches cis- et trans-. On a alors étudié l'étape de propagation pour la paire d'ions de contact  $\text{CpNC}(t\text{-Bu})_2\text{PrTi-}\mu\text{-Me-B}(\text{C}_6\text{F}_5)_3$  (**4**). On a considéré les diverses conformations de la chaîne propyle du composé **4** en faisant varier  $\theta$ , l'angle dièdre formé entre les plans  $\text{C}_\beta\text{-C}_\alpha\text{-Ti}$  et  $\text{C}_\alpha\text{-Ti-}\mu\text{C}$ . On a trouvé des minima près de  $\theta = -69^\circ$  (**4a**),  $177^\circ$  (**4b**) et  $53^\circ$  (**4c**). On a trouvé un maximum près de  $\theta = 0^\circ$  (**4d**). On a considéré les approches cis- et trans- du monomère d'éthylène pour chacun de ces quatre cas. Les approches cis- vis-à-vis de **4a** et trans- vis-à-vis de **4d** conduisent à des insertions avec un déplacement du contre-ion du centre métallique. On a trouvé que les barrières à l'insertion sont de 17,8 et de 16,4 kcal/mol respectivement pour les approches cis- vis-à-vis de **4b** et trans- vis-à-vis de **4d**. Les approches cis- vis-à-vis de **4a** et de **4c** présentent des caractéristiques communes, avec des barrières à l'incorporation qui sont plus élevées dans les deux cas que les barrières d'insertion subséquentes. Les barrières à l'incorporation sont de 13,6 kcal/mol {TS(**4a-7a**)} et de 10,7 kcal/mol {TS(**4c-8a**)}. Les barrières correspondantes à l'insertion sont de 11,8 kcal/mol {TS(**7a-13a**)} et de

Received 4 March 2003. Published on the NRC Research Press Web site at <http://canjchem.nrc.ca> on 18 November 2003.

K. Vanka, Z. Xu, and T. Ziegler.<sup>2</sup> Department of Chemistry, University of Calgary, Calgary, AB T2N 1N4, Canada.

<sup>1</sup>This article is part of a Special Issue dedicated to Professor John Harrod.

<sup>2</sup>Corresponding author (email: [ziegler@ucalgary.ca](mailto:ziegler@ucalgary.ca)).



8,4 kcal/mol {TS(8a–13a)}. Les approches trans- vis-a-vis des conformères **4a** et de **4c** conduisent à des barrières à l'insertion d'environ 15,1 kcal/mol (plus faibles que celles pour les composés **4b** et **4d**). On a trouvé que l'approche cis- vis-a-vis de **4d** et que l'approche trans- vis-a-vis de **4b** conduisent à un transfert d'hydrogène à partir de la chaîne du monomère et que la chaîne est ainsi coupée. Les barrières à la réaction de terminaison sont élevées, plus que 19,0 kcal/mol. Ceci suggère que, durant l'étape de propagation, l'insertion de l'éthylène est favorisée par rapport à la réaction de terminaison.

*Mots clés* : catalyse homogène, contre-ion, initiation, propagation, terminaison.

[Traduit par la Rédaction]

## Introduction

The field of single-site homogeneous catalysts has seen remarkable growth and development over the past 20 years (1). Their ability to achieve higher stereoselectivity and narrower molecular weight distribution has made them emerge as viable alternatives to traditional Ziegler–Natta type heterogeneous catalysts, and revolutionized industrial poly-alkene synthesis (2). The fact that they are structurally well-defined mononuclear active species has allowed the systematic modification of these structures allowing for enhanced control over polymer properties. The state-of-the-art homogeneous catalysts transform simple alkenes into polymers with rate accelerations and stereo- and regiospecificities that rival those of enzymatic catalysts.

Among the more highly active homogenous catalysts are metallocenes and related organometallic compounds containing a group IV transition metal. The general structure of these complexes contain a group 4 transition metal centre (M) coordinated to two ligands (L) and two alkyl groups (R):  $L_2MR_2$ . These complexes by themselves are not very effective as polymerization catalysts, but require activation by a co-catalyst or a counterion. The co-catalysts are generally Lewis acids, such as tris(pentafluorophenyl)borane or methylalumoxane (MAO), whose function is to abstract one of the alkyl groups as  $R^-$  to produce the activated metal catalyst, which is generally accepted (3) to be an electrophilic species:  $L_2MR^+$ . The process by which the co-catalyst can activate the complex is illustrated in Fig. 1. First, the alkyl group (R) is extracted by the acidic co-catalyst compound denoted as "A" in the figure. This leads to a charge-separated contact ion pair ( $L_2TiR-\mu R-A$ ). The formation of this ion-pair species is exothermic, with the enthalpy of ion-pair formation denoted as  $\Delta H_{ipf}$  in Fig. 1. To form the cationic complex ( $L_2MR^+$ ), the contact ion pair must then dissociate, with an enthalpy of ion-pair separation denoted as  $\Delta H_{ips}$ , to form the two separated charged species: the positively charged cationic catalyst ( $L_2MR^+$ ), and the negatively charged counterion ( $AR^-$ ).

The cationic catalyst thus formed can then partake in the catalytic processes for insertion. The accepted mechanism for the uptake and insertion of the olefin monomer into the metal–carbon bond in the cationic catalyst is shown in Fig. 2 with ethylene as the olefin monomer.

The well-defined molecular structure of metallocene catalysts and their analogues has also enabled thorough mechanistic investigations by theoretical methods, and several theoretical studies (4) have been conducted, using the bare cation ( $L_2MR^+$ ) as the model for the single-site catalyst. These studies have helped improve the understanding of the mechanistic aspects of the monomer insertion process. How-

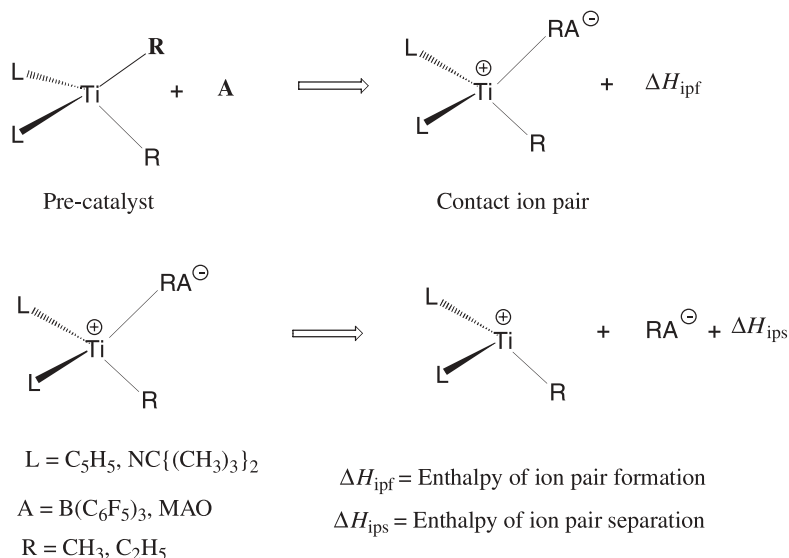
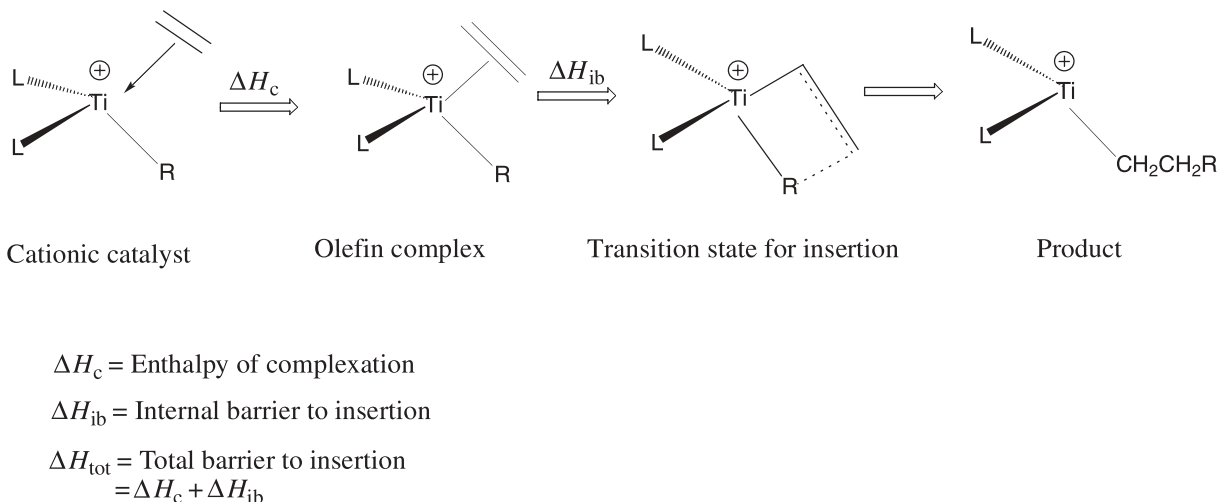
ever, recent findings indicate (3g–3j, 5) that the anionic counterion plays an important role in the polymerization process. Calculations showed (5) that the value of  $\Delta H_{ips}$  was very high, implying that the total dissociation of the contact ion pair leading to formation of the bare cation would not take place. The counterion would therefore remain in the vicinity of the cation during the insertion process. Hence, the influence of the counterion has to be taken into account and the mechanism for the insertion has to be modified accordingly, as shown in Fig. 3.

In the modified mechanism of Fig. 3, the ethylene first approaches the contact ion pair [ $L_2TiR-\mu R-A$ ] and binds to it, forming a weak olefin complex. The enthalpy of this complexation is denoted as  $\Delta H_c$ . From this complexed state, the ethylene monomer then approaches the alkyl chain and attempts to insert into the metal–alkyl bond, leading to a four-centred transition state. The internal barrier of the reaction path, from the olefin complex to the transition state, is defined as  $\Delta H_{ib}$ . The total barrier of the reaction is denoted as  $\Delta H_{tot}$  and is the sum of  $\Delta H_c$  and  $\Delta H_{ib}$ .

Figure 3, however, shows only one of the ways in which the ethylene monomer can approach the contact ion pair ( $L_2TiR-\mu R-A$ ). Depending on the position of the ethylene monomer relative to the  $\mu$ -alkyl bridge of the ion pair, there are two ways in which the ethylene can approach, as shown in Fig. 4. It can approach cis to the  $\mu$ -alkyl bridge, an approach we will henceforth call the "cis" approach. Nifant'ev et al. (6) have studied ethylene insertion via this approach for the  $Cp_2ZrEt^+A^-$  ( $A^- = CH_3B(C_6F_5)_3^-$ ,  $B(C_6F_5)_4^-$ ) systems. Alternately, the ethylene monomer can also approach from the direction opposite (trans) to the  $\mu$ -alkyl bridge, as shown in Fig. 4. This path will be referred to as the "trans" mode of approach. In each of the two cases, the approach of the ethylene leads to the formation of the olefin complex. The tetrahedral arrangement of the contact ion pair is converted to a trigonal bipyramidal structure when the olefin complex is formed. In the trans case of approach, the ethylene monomer occupies one of the axial positions of the trigonal bipyramid, while in the cis case, the ethylene monomer lies in the equatorial plane of the trigonal bipyramid.

Unfortunately, due to the size of the counterions, theoretical studies of the mechanism outlined in Fig. 2, where the counterion is incorporated, are difficult and involve considerable computational effort. Hence, few examples of such studies are found in the literature (7). Lanza et al. (7a) have investigated olefin insertion into the Ti–CH<sub>3</sub> bond of the  $H_2Si(C_5H_4)(t-BuN)TiCH_3-CH_3B(C_6F_5)_3$  ion pair; Fusco et al. (7b) and Bernardi et al. (7c) studied the same process for  $Cp_2(Ti/Zr)CH_3-Cl_2Al[O(Al(CH_3)_3)AlHCH_3]_2$  and  $Cl_2TiCH_3(\mu-Cl)_2AlH_2$ , respectively. Chan et al. (7d) have investigated the



**Fig. 1.** The mechanism for the activation of the precatalyst ( $L_2TiR_2$ ) by the co-catalyst (A).**Fig. 2.** The mechanism for the complexation and insertion of the ethylene monomer into the metal–carbon bond of the cationic catalyst ( $L_2TiR^+$ ).

formation of ethylene separated ion-pair complexes for ion pairs formed between different catalysts and the counterion  $B(C_6F_5)_3CH_3^-$ , as well as ethylene insertion (5a) into the  $Zr-CH_3$  bond in the  $Cp_2ZrCH_3-\mu-CH_3-B(C_6F_5)_3$  system.

In an earlier theoretical study (8), we investigated the insertion of the ethylene monomer into the methyl chain of different catalyst systems of the type  $L_1L_2TiCH_3^+$ , in the presence of the counterion. The counterion used for the purpose of the investigation was  $B(C_6F_5)_3CH_3^-$ . For the sake of computational expediency, a QM/MM model was used for the counterion. This allowed us to study a large number of different systems. In the QM/MM model, the perfluoro phenyl ( $C_6F_5$ ) groups in  $B(C_6F_5)_3CH_3^-$  were replaced with MM atoms, and Cl atoms are used to cap the QM system. Thus,  $B(C_6F_5)_3CH_3^-$  was replaced with  $BCl_3CH_3^-$  in the QM system. This model has been validated (9a), and will be used to model the counterion in the ion pair systems studied here.

Other ion pair systems using the same model for the counterion are currently under investigation (9b).<sup>3</sup>

In this present study, we investigate the approach of ethylene and its insertion into the Ti–methyl (initiation step) and Ti–propyl (propagation step) bonds for the  $[CpNC(t-Bu)_2TiR^+][B(C_6F_5)_3CH_3^-]$  ( $R = CH_3$  and  $C_3H_7$ ) ion-pair systems. The different approaches of the ethylene monomer *cis* and *trans* to the  $\mu$ -methyl group of the ion pair will be considered for each case. Before the investigation of the propagation step, i.e., ethylene insertion into the propyl chain, different chain conformers of the free ion pair will first be considered to determine the most favourable conformation, prior to insertion. The purpose of the investigation will be to isolate the important factors that contribute to the barrier of insertion, and to compare and contrast the initiation and propagation steps for the same ion-pair system, i.e.,  $[CpNC(t-Bu)_2TiMe^+][B(C_6F_5)_3CH_3^-]$ . The effect of the sol-

<sup>3</sup>T. Ziegler, K. Vanka, and Z. Xu. To be submitted.



**Fig. 3.** The mechanism of complexation and insertion of the ethylene monomer into the metal–carbon bond of the catalyst, in the presence of the counterion.

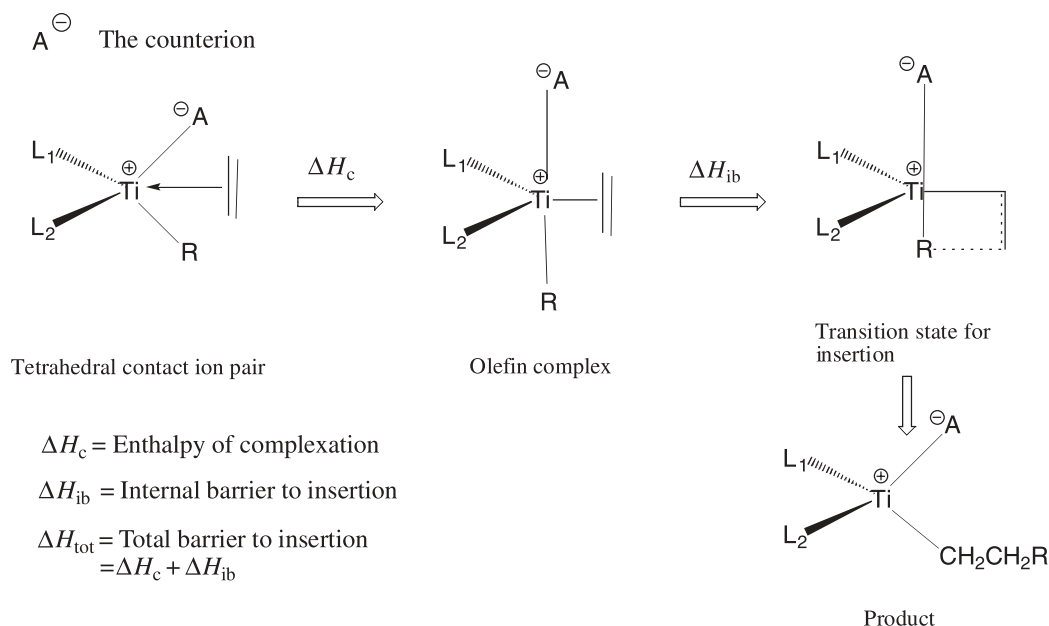
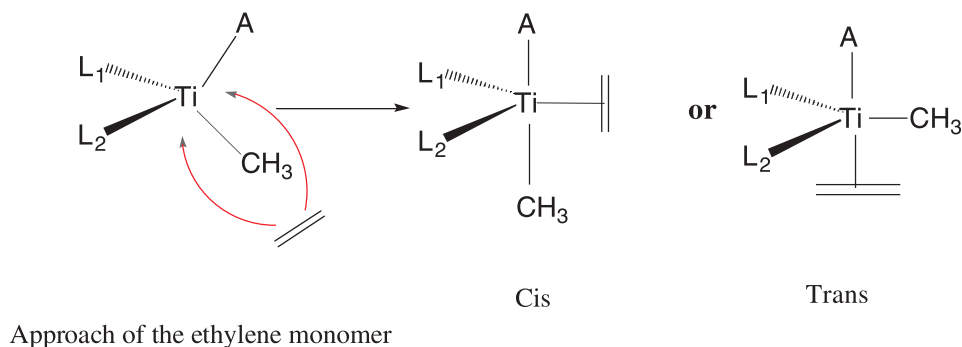


**Fig. 4.** Different modes of approach of the ethylene monomer towards the contact ion pair ( $L_1L_2TiMeA$ ).



A:  $B(C_6F_5)_3CH_3^-$

$L_1$ : Cp

$L_2$ :  $NCR_2$

vent on the insertion process will also be considered, with single-point solvation calculations to determine the energy of solvation for the ion pair, the olefin complexes, and the transition states. Cyclohexane ( $\epsilon = 2.023$ ) will be used as the solvent.

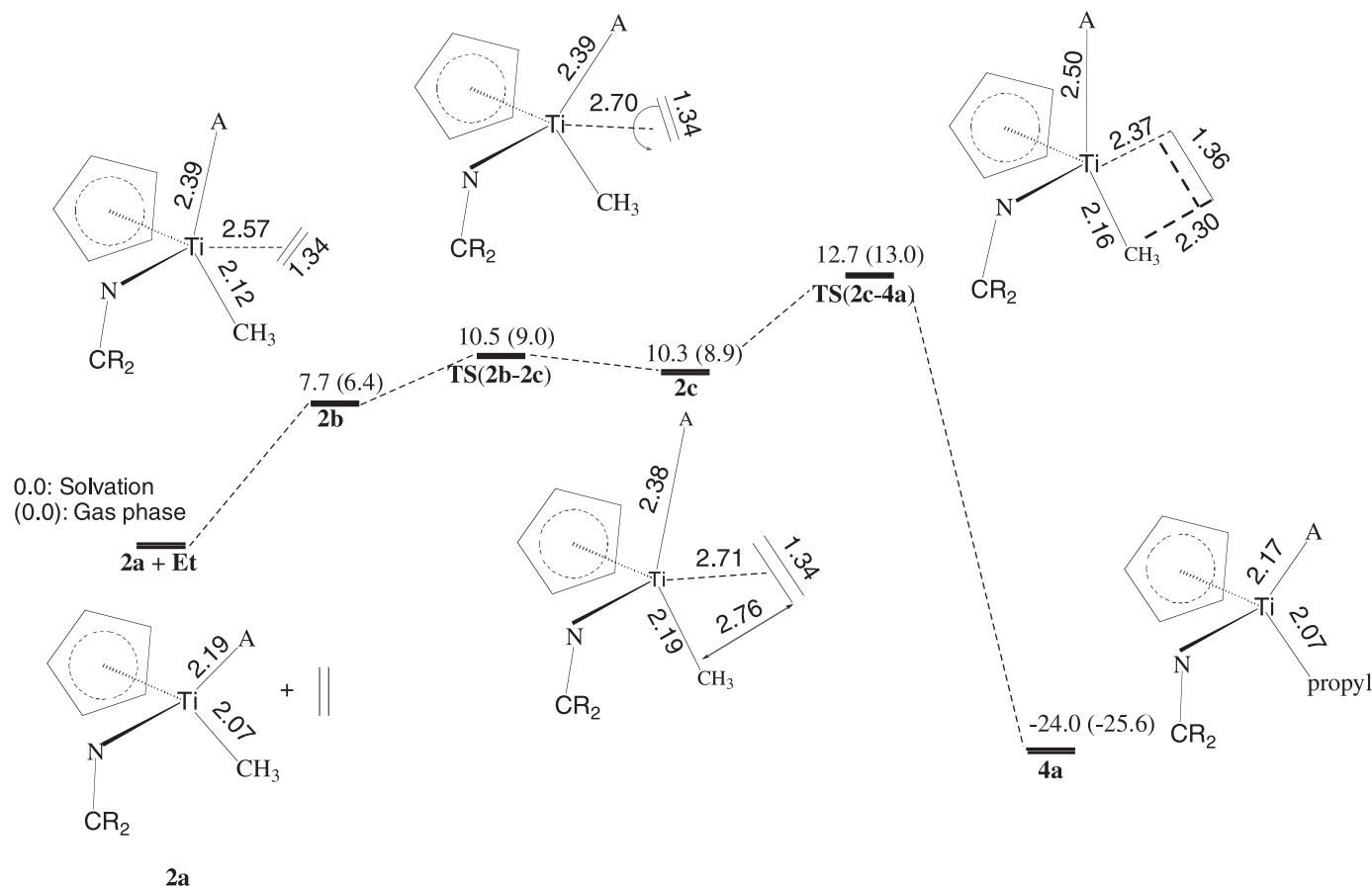
## Computational details

The density functional theory calculations were carried out using the Amsterdam density functional (ADF) program, version 2000.01, developed by Baerends and co-workers (10) and vectorized by Ravenek (11). The numerical integration scheme applied was developed by te Velde and co-workers (12) and the geometry optimization procedure was based on the method of Versluis and Ziegler (13). Geometry optimizations were carried out using the local exchange–correlation potential of Vosko et al. (14) without any sym-

metry constraints. The electronic configurations of the atoms were described by a triple- $\zeta$  basis set on titanium ( $n = 3$ ) for  $ns$ ,  $np$ ,  $nd$ , and  $(n + 1)s$ , augmented with a single  $(n + 1)p$  polarization function. Double- $\zeta$  STO basis were used for carbon ( $2s, 2p$ ), hydrogen ( $1s$ ), and nitrogen ( $2s, 2p$ ), augmented with a single  $3d$ -polarization function, except for hydrogen where a  $2p$ -polarization function was used. Shells of lower energy were treated by the frozen core approximation. A set of auxiliary  $s, p, d, f$ , and  $g$  STO functions centred on all nuclei was used to fit the molecular density and represent Coulomb and exchange potentials accurately in each SCF cycle (15). The gas-phase energy difference was calculated by augmenting the local density approximation energy with Perdew and Wang's nonlocal correlation and exchange corrections (PWB91) (16). The solvation energies were obtained from a single-point full QM calculation using the conductor-like screening model (COSMO) (17) and opti-



**Fig. 5.** The energy profile for the *cis* approach of the ethylene monomer towards the contact ion pair  $[\text{Cp}\{\text{NC}(t\text{-Bu})_2\text{TiMe}^+\}][\text{CH}_3\text{B}(\text{C}_6\text{F}_5)_3^-]$ .



mized geometries from QM/MM calculations. A dielectric constant of 2.023 was used to represent cyclohexane as the solvent. The radii used for the atoms in Å were as follows: C 2.0, H 1.16, B 1.15, N 1.5, F 1.2, Ti 2.3, and Cl 2.1. Only the electronic contribution was calculated to evaluate the enthalpy of the reactions considered in this work. The enthalpies ( $\Delta H$ ) reported in the following sections are potential energy differences without zero-point corrections or vibrational finite temperature corrections. Such corrections are still too expensive to calculate for the size of molecules considered here. We expect these corrections to be of the order of  $\pm 2\text{--}3$  kcal/mol. The insertion barriers were obtained by doing linear transit calculations for the same reaction coordinates, the C-C distance between one C of the ethylene and the C of the  $\text{CH}_3$  or  $\text{C}_3\text{H}_7$ , which represent the growing chains. The MM atoms were described using the SYBYL/TRIPOS 5.2 force field constants (18a). The code for QM/MM in ADF has been implemented by Woo et al. (18b).

## Results and discussion

### First insertion process with the naked cation

The insertion of the ethylene monomer was first considered for the system  $\text{CpNC}(t\text{-Bu})_2\text{TiMe}^+$  in the absence of the counterion. QM/MM atoms were used to model the tertiary butyl groups, with hydrogens used as capping atoms — hence, the QM portion of the cation was  $\text{CpNCH}_2\text{TiMe}^+$ . The values of the ethylene complexation energy  $\Delta H_c$  and the inter-

nal insertion barrier  $\Delta H_{ib}$  were found to be  $-20.0$  kcal/mol and  $3.1$  kcal/mol, respectively (after incorporation of solvent effects). The transition state for the ethylene insertion in these systems occurred when the ethylene carbon was at a distance of about  $2.4$  Å from the methyl carbon. The total barrier for insertion, found by summing up the two values, was calculated to be equal to  $-16.9$  kcal/mol, indicating that the process is highly exothermic in nature. Therefore, using just the naked cation as a model for the catalyst, one would be led to conclude that the cationic  $\text{CpNC}(t\text{-Bu})_2\text{TiMe}^+$  system is an excellent polymerization catalyst. We shall now see how this is modified by the inclusion of the counterion in the mechanistic studies.

### First insertion study with inclusion of the counterion

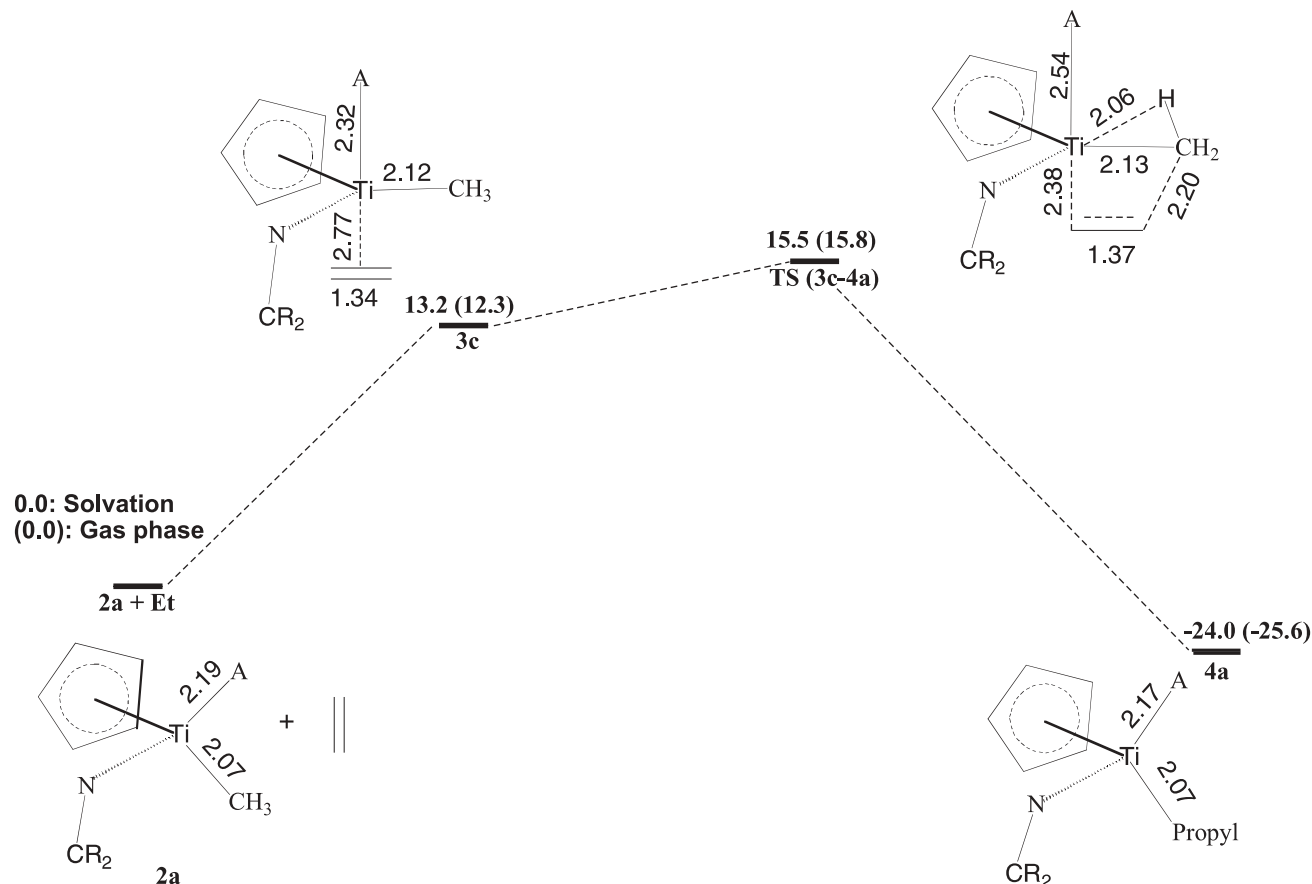
We shall, in the following, include the anionic counterion  $\text{B}(\text{C}_6\text{F}_5)_3\text{CH}_3^-$  to provide a more realistic description of the insertion process. A validated QM/MM model (9a) of the counterion was used for computational expediency, as discussed in the *Introduction*.

### The *cis* approach of the monomer

The approach of the ethylene monomer towards the metal centre of the ion pair  $([\text{CpNC}(t\text{-Bu})_2\text{TiMe}^+][\text{CH}_3\text{B}(\text{C}_6\text{F}_5)_3^-])$  (2a) was studied using  $\Delta R = R(\text{Ti}-\mu\text{-C}) - R(\text{Ti}-\text{X})$  as the reaction coordinate. When the ethylene approaches from the *cis* direction, it can first form the  $\pi$  complex termed **2b** in Fig. 5, with the two carbons of the ethylene lying perpendicular to the plane formed by the metal centre, the methyl



**Fig. 6.** The energy profile for the trans approach of the ethylene monomer towards the contact ion pair  $[\text{Cp}\{\text{NC}(t\text{-Bu})_2\}\text{TiMe}^+][\text{CH}_3\text{B}(\text{C}_6\text{F}_5)_3^-]$ .



chain, and the  $\mu$  carbon of the counterion. This complex is 7.7 kcal/mol (including solvation effects) less stable than the ion pair and ethylene totally separated. The reason for the endothermic nature of this complexation is the displacement of the counterion from the metal centre, to accommodate the ethylene molecule — the Ti- $\mu$ -C distance is increased from 2.19 Å (in the ion pair, **2a**) to 2.39 Å in the complex **2b** (Fig. 5). There is some compensation, however, by the bonding between the metal centre and the incoming ethylene, which reduces the cost of displacement of the counterion to some extent.

The ethylene molecule, however, cannot insert into the Ti—C bond without being in the insertion plane. Hence, it has to rotate to bring itself into the insertion plane. There is a barrier to this rotation of about 2.8 kcal/mol, after which it forms the “in plane” olefin complex, which lies 10.3 kcal/mol (after incorporation of solvation effects) above the separated reactant species. In this weak olefin complex (**2c**), the Ti-ethylene midpoint distance has increased to 2.70 Å, with the counterion coming closer to the metal centre (Ti- $\mu$ -C distance 2.38 Å), and the ethylene is still fairly far (2.76 Å) from the carbon of the methyl chain (see Fig. 5).

After formation of the complex (**2c**), the ethylene then approaches the methyl chain, to enable insertion into the Ti—C bond. The system is slightly destabilized as a result, leading eventually to the transition state for insertion (**TS(2c-4a)**), lying 12.7 kcal/mol above the reactants. In this transition state, the ethylene carbon – methyl carbon distance is 2.3 Å,

and the Ti- $\mu$ -C distance is slightly elongated to 2.50 Å (see Fig. 5).

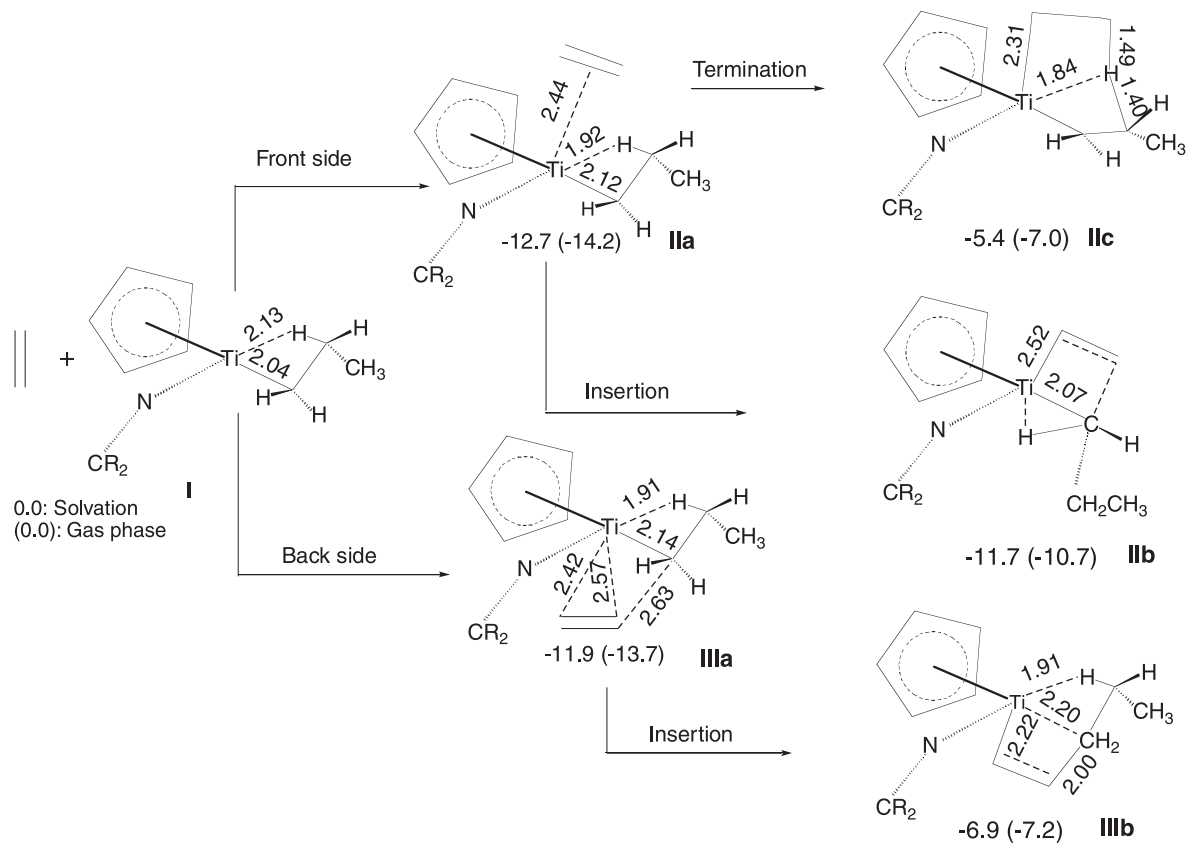
Hence, the total barrier to insertion for the cis approach is 12.7 kcal/mol. This is significantly different from the findings in the naked cation case, where the insertion transition state is lower in energy than the reactants. The transition states are also found to be somewhat different for the two cases. The ethylene carbon – methyl carbon distance is 2.61 Å in the cationic case, while it is 2.3 Å in **TS(2c-4a)**. Both transition states exhibit an  $\alpha$ -agostic interaction between the metal centre and a hydrogen of the methyl group, but the Ti-H distances are slightly different: 2.06 Å in the cationic case compared to 2.17 Å in **2c**. The reason for the longer and presumably weaker  $\alpha$ -agostic bond in the case with the counterion attached is the reduced acidity of the metal centre.

After formation of the transition state, the ethylene inserts and proceeds to form the product with the propyl chain, which lies at –24.0 kcal/mol below the separated species. In the ion pair, the counterion is found to be reassociated to the metal centre. Thus, for the subsequent insertion, ethylene will again have to displace  $\text{B}(\text{C}_6\text{F}_5)_3\text{CH}_3^-$  to some degree.

#### The trans approach of the monomer

The trans approach of ethylene towards the ion pair was also studied. Figure 6 displays the profile for the trans insertion. A weak olefin complex (**3c**) was first formed, with  $R(\text{Ti-X})$  being 2.77 Å. The counterion was only slightly dis-

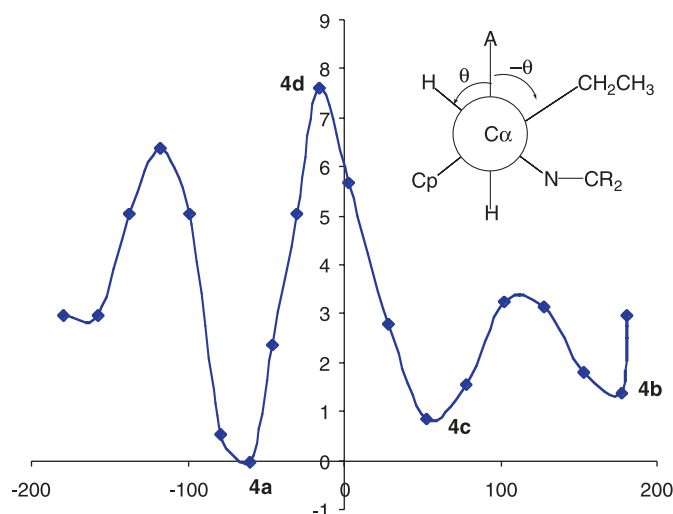


**Fig. 7.** Energy profiles for the back side and front side approaches of the ethylene monomer towards the cation  $\text{Cp}\{\text{NC}(t\text{-Bu})\}\text{TiPr}^+$ .

placed from the metal centre with  $R(\text{Ti}-\mu\text{-C}) = 2.32 \text{ \AA}$  compared to  $2.19 \text{ \AA}$  in the ion pair **IP**. The complex lay  $13.2 \text{ kcal/mol}$  above the totally separated, reactant **2a** + **Et** species. The ethylene molecule was found to be in the insertion plane and hence, unlike in the case of the cis approach, did not have to be rotated into the plane before insertion could proceed.

After formation of **3c**, the ethylene approached the carbon of the methyl chain, to enable the insertion to occur. This led to an increase in energy, until the transition state, shown as **TS (3c-4a)** in Fig. 6 was reached, lying  $15.5 \text{ kcal/mol}$  above the separated reactant species. At the transition state, an  $\alpha$ -agostic interaction had been formed between the titanium metal centre and one of the hydrogens of the methyl chain, similar to the transition state observed in the naked cation and the cis approach. In this four-centred transition state, the ethylene carbon has approached closer to the carbon of the methyl chain and lies at a distance of  $2.20 \text{ \AA}$ . The counterion is displaced a little more from the metal centre in this case, in comparison to **3c**, with  $R(\text{Ti}-\mu\text{-C})$  being about  $2.54 \text{ \AA}$ . This is still not a large displacement and it compares well with the  $R(\text{Ti}-\mu\text{-C})$  distance of  $2.50 \text{ \AA}$  from the transition state **TS (2c-4a)** of the cis approach. Therefore, it can be concluded that for both the cis and trans insertion, the counterion is not detached to a great extent from the metal centre.

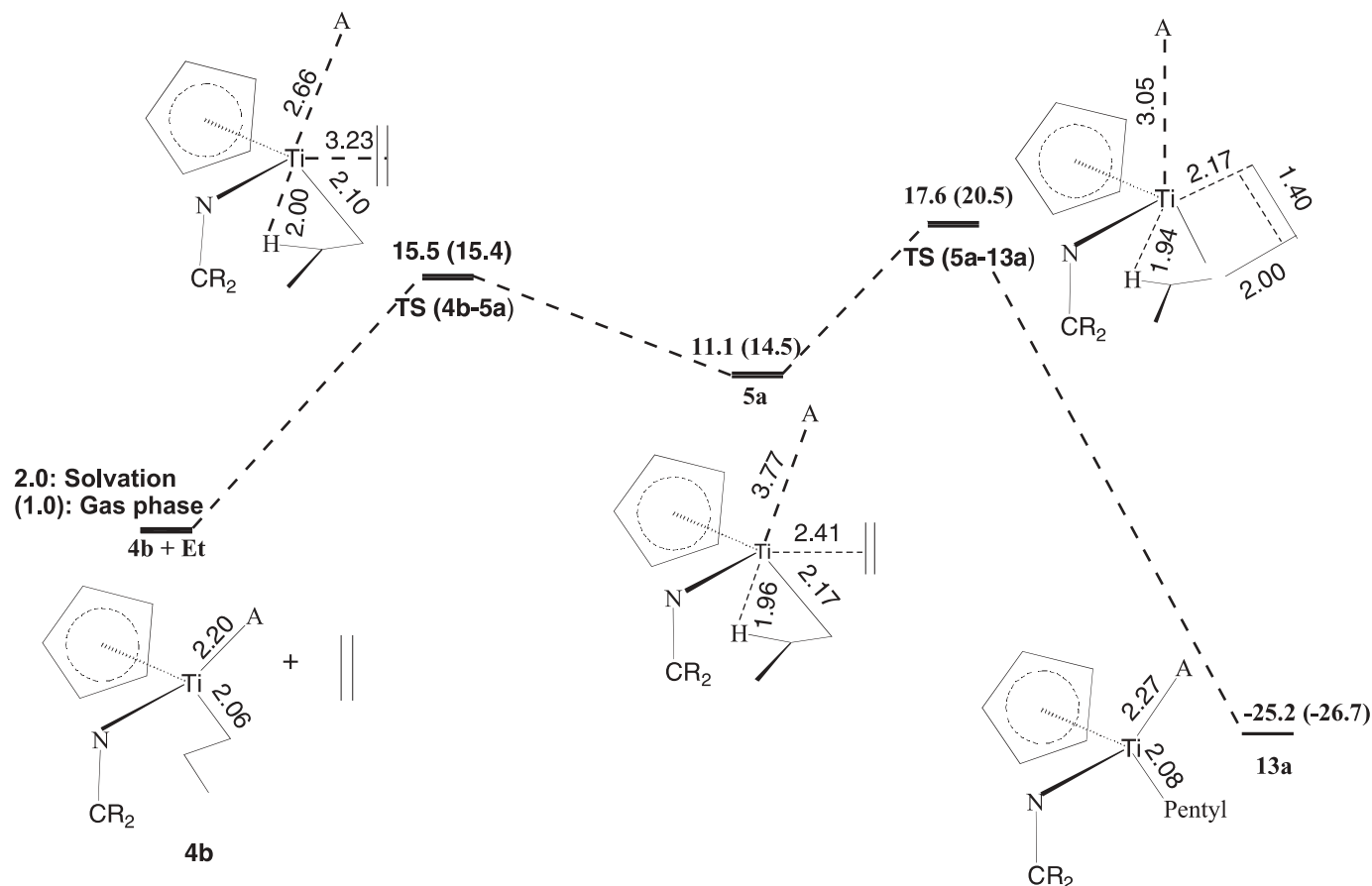
A comparison of the total insertion barriers for the cis and trans cases reveals that the total barrier of insertion for the cis case ( $12.7 \text{ kcal/mol}$ ) is lower in comparison to the trans

**Fig. 8.** The relative stabilities of the different chain conformations formed by rotation of the propyl chain in the contact ion pair  $[\text{Cp}\{\text{NC}(t\text{-Bu})_2\}\text{TiPr}^+][\text{CH}_3\text{B}(\text{C}_6\text{F}_5)_3^-]$ .

insertion ( $15.5 \text{ kcal/mol}$ ) by  $2.7 \text{ kcal/mol}$ . (Solvation effects have been incorporated in all calculations). Hence, it can be concluded that ethylene prefers to approach cis to the  $\mu$ -methyl bridge of the ion pair, during the insertion process for the first insertion of the monomer into the metal-alkyl bond.



**Fig. 9.** The energy profile for the cis approach of the ethylene monomer towards the contact ion pair  $[\text{Cp}\{\text{NC}(t\text{-Bu})_2\}\text{TiPr}^+][\text{CH}_3\text{B}(\text{C}_6\text{F}_5)_3^-]$ , with the propyl chain in the insertion plane, for the case **4b**.



The final product formed in each case was the ion pair with the elongated alkyl chain ( $[\text{CpNC}(t\text{-Bu})_2\text{TiPr}^+][\text{CH}_3\text{B}(\text{C}_6\text{F}_5)_3^-]$ ) denoted as **4a** in the Figs. 5 and 6. It was found to be 24.0 kcal/mol more stable than the totally separated reactant **2a** + **Et** species.

Solvent effects had been taken into account in the calculations, as mentioned earlier. The corresponding gas-phase values are mentioned in parentheses in the Figs. 5 and 6. Since the displacement of the counterion was only slight during monomer insertion in both the cis and trans approaches, the charge separation between the negative counterion and the positive metal centre was also insignificant. Hence, the solvent effects were found to be minimal in either case.

### Second insertion study with the naked cation

The product from the first insertion of ethylene into the Ti-Me chain, in the naked cation case, was the species  $\text{CpNC}(t\text{-Bu})_2\text{TiPr}^+$ . The most stable conformation of this species had a  $\beta$ -agostic interaction between one of the hydrogens on the  $\beta$ -carbon of the propyl chain, and the titanium metal centre. It will be denoted as **I**, as shown in Fig. 7. The second insertion of ethylene, into the Ti-propyl chain, was investigated starting from this conformation. Unlike the first insertion in the naked cation ( $\text{CpNC}(t\text{-Bu})_2\text{TiMe}^+$ ) where there is only one approach possible for the ethylene monomer, the second insertion could proceed via two distinct pathways, as displayed in Fig. 7: it could approach trans (**4b**)

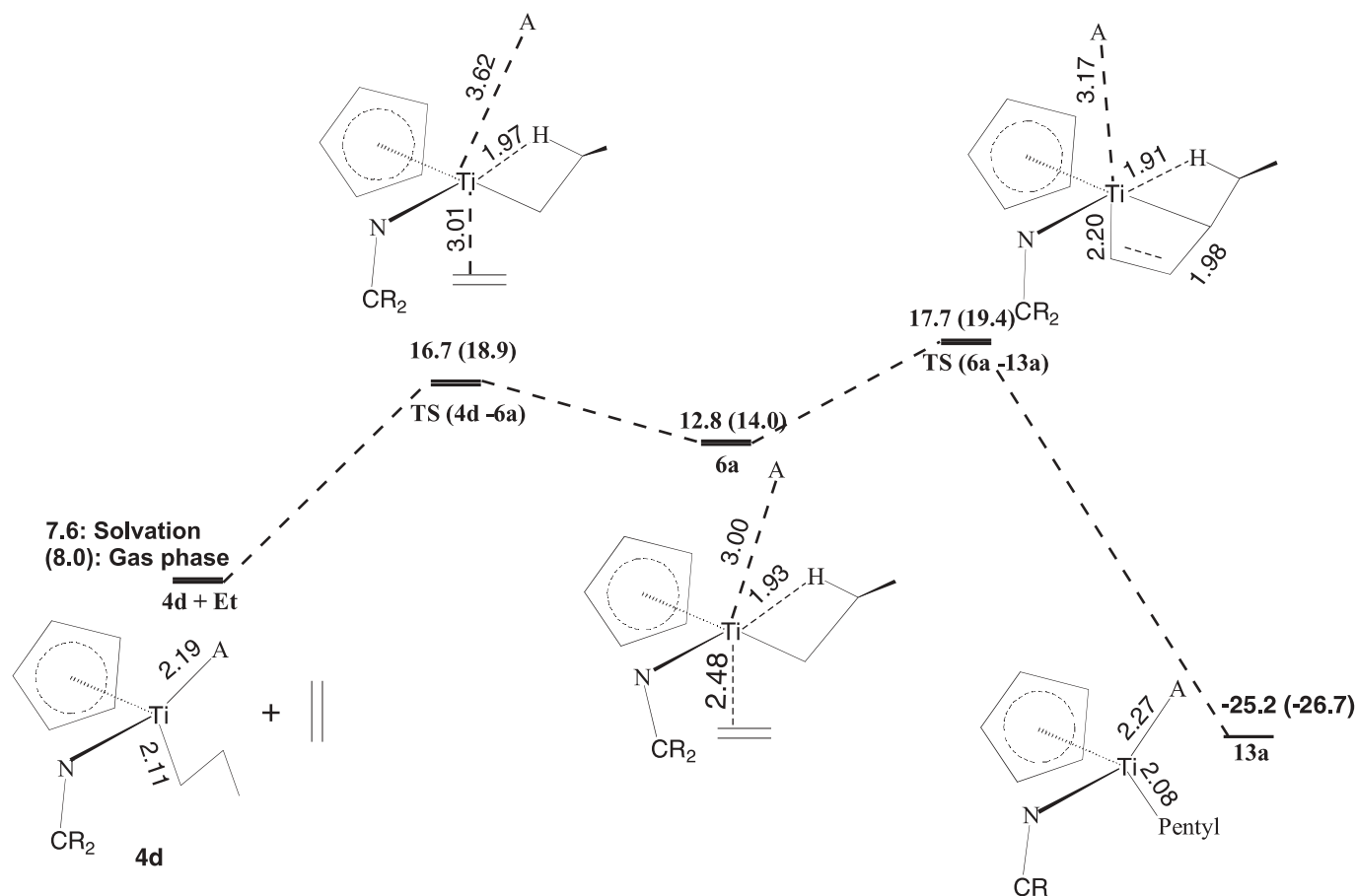
to the  $\beta$ -agostic bond, the “back side attack”, leading to the formation of the species **IIIa**, or it could approach cis (**4b**) to the  $\beta$ -agostic bond, the “front side attack”, which would lead to the formation of the species **IIa**. Both these approaches were investigated and the results are summarized in the following sections.

### Back side attack of the ethylene monomer

As shown in Fig. 7, the attack of the ethylene trans to the  $\beta$ -agostic bond gives rise to the  $\pi$ -complex (**IIIa**) that is 11.9 kcal/mol more stable than the totally separated reactant species. This reaction is, therefore, less exothermic than the first insertion, where the complexation enthalpy was -22.3 kcal/mol. The reason for the decrease in exothermicity of the reaction is the increased steric congestion around the metal centre due to the increase in the chain length. After formation of this  $\pi$ -complex, the ethylene continues to approach the  $\alpha$ -carbon of the chain, eventually leading to the insertion transition state (**IIIb**) lying 6.9 kcal/mol below the reactant species (**I** + **Et**). In this insertion transition state, the  $\beta$ -agostic bond of the titanium metal centre with the hydrogen is retained, with  $R(\text{Ti-H}) = 1.91$  Å. The ethylene has moved closer to the  $\alpha$ -carbon, with  $R(\text{C}_{\text{Et}}-\text{C}_{\alpha})$  being about 0.63 Å less in the transition state than in the  $\pi$ -complex, while the Ti- $\alpha$ -carbon distance has increased by 0.06 Å. Overall, in comparison to the first insertion, the back side insertion is about 10.0 kcal/mol less exothermic.



**Fig. 10.** The energy profile for the trans approach of the ethylene monomer towards the contact ion pair  $[\text{Cp}\{\text{NC}(t\text{-Bu})_2\}\text{TiPr}^+][\text{CH}_3\text{B}(\text{C}_6\text{F}_5)_3^-]$ , with the propyl chain in the insertion plane, for the case **4d**.



### Front side attack of the ethylene monomer

The front side attack of the ethylene monomer, also shown in Fig. 7, gives rise to the front side  $\pi$ -complex (**IIa**), which is 12.7 kcal/mol more exothermic than the separated reactant species. In this  $\pi$ -complex, the two carbons of ethylene lie in the same plane as the metal centre and the hydrogen forming the  $\beta$ -agostic bond. This  $\pi$ -complex is 0.8 kcal/mol more stable than the corresponding backside  $\pi$ -complex (**IIIa**) (see Fig. 7). Starting from this  $\pi$ -complex, if insertion is to occur, then the ethylene has to approach the  $\alpha$ -carbon. This can happen through rotation of the propyl chain along the Ti— $\alpha$ -C $_{\alpha}$  bond, leading to the loss of the  $\beta$ -agostic interaction and the rotation of the  $\beta$ -carbon, thereby facilitating the approach of the ethylene towards the carbon. The barrier to this process was found to lie 11.7 kcal/mol below the reactant species. Therefore, the overall barrier to insertion along this pathway is less by 4.8 kcal/mol in comparison to the back side approach.

However, this is not the only route that the ethylene can take during the front side approach. Starting from **IIa**, the ethylene can also abstract a hydrogen from the  $\beta$ -carbon of the propyl chain, a reaction that would lead to termination. As shown in Fig. 7, the transition state for this process (**IIc**) has the hydrogen nearly equidistant between the ethylene and the  $\beta$ -carbon, but slightly closer to the  $\beta$ -carbon of the chain, at a distance of about 1.40 Å. The hydrogen has re-

tained its agostic interaction with the metal centre at the transition state. **IIc** was found to lie 5.4 kcal/mol below the reactant species. This is 6.3 kcal/mol higher than **IIb** and 1.5 kcal/mol higher than **IIIb**. This suggests that, after the ethylene has approached the  $\text{CpNC}(t\text{-Bu})_2\text{TiPr}^+$  species, it would prefer to insert rather than undergo termination.

Overall, as for the first insertion, the results obtained suggest facile exothermic reactions during the insertion and termination processes for the naked cationic model. In the next section, we shall study how this picture is modified with the inclusion of the counterion.

### Second insertion study with inclusion of the counterion

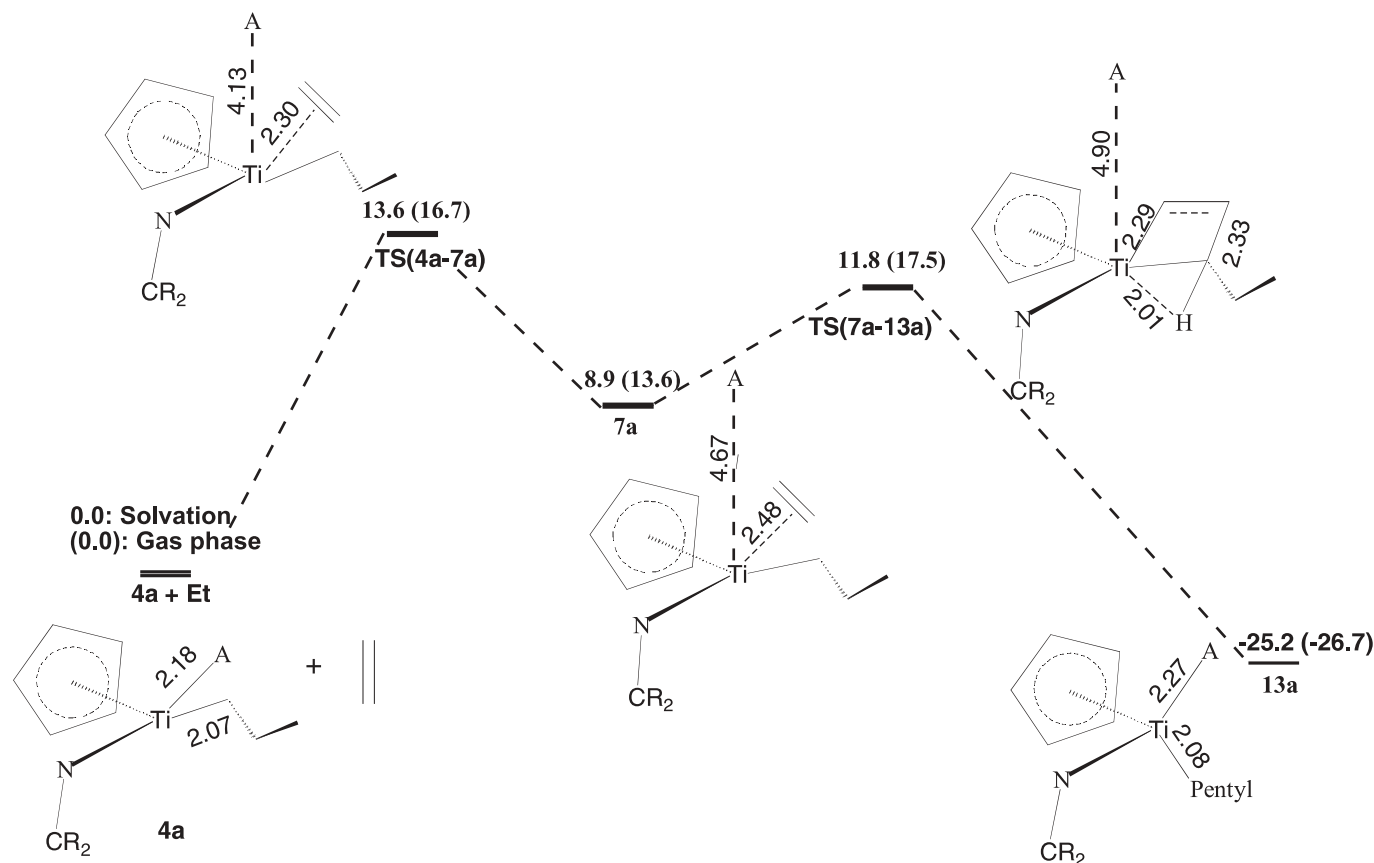
With the counterion included, the resting state of the catalyst after the first insertion is the ion pair  $[\text{CpNC}(t\text{-Bu})_2\text{TiPr}^+][\text{B}(\text{C}_6\text{F}_5)_3\text{CH}_3^-]$ , i.e., the product formed at the completion of the first insertion. The second insertion or propagation step involves the approach and insertion of the ethylene monomer cis and trans to the Ti— $\mu$ -C bond in this ion pair.

### Resting state of the ion pair

In the ion pair, formed after the first insertion, the alkyl group attached to the metal centre has extended from a methyl to a propyl chain. This propyl chain can orient itself into several conformations, thus giving rise to a number of



**Fig. 11.** The energy profile for the *cis* approach of the ethylene monomer towards the contact ion pair  $[\text{Cp}\{\text{NC}(t\text{-Bu})_2\}\text{TiPr}^+][\text{CH}_3\text{B}(\text{C}_6\text{F}_5)_3^-]$ , with the propyl chain lying out of the insertion plane, for the case **4a**.



possible energy minima states for the ion pair. It is necessary to study these different conformations to determine the most stable resting state. This was done by a linear transit wherein the dihedral angle ( $\theta$ ) formed between the  $\text{C}_\beta\text{-C}_\alpha\text{-Ti}$  and the  $\text{C}_\alpha\text{-Ti-}\mu\text{C}$  planes was altered (see Fig. 8 below) from  $-180^\circ$  to  $180^\circ$  to rotate the chain so as to determine the most stable resting states. The accompanying energy profile in Fig. 9 shows that the most stable resting states of the ion pair correspond to the staggered conformations of the chain, with  $\theta$  at  $-69^\circ$ ,  $53^\circ$ , and  $177^\circ$ , respectively. In contrast, the eclipsed conformation, with  $\theta$  near  $0^\circ$  was found to be an energy maxima. The rotation of the chain from  $\theta = 53^\circ$  to  $\theta = 0^\circ$  (eclipsed conformation) leads to an increase in energy of 7.61 kcal/mol. This represents the barrier to rotation of the propyl chain. Figure 8 also shows the relative energies of the different possible conformations.

For the insertion studies, four different conformations of the propyl chain were considered, with  $\theta = -69^\circ$  (**4a**),  $177^\circ$  (**4b**),  $53^\circ$  (**4c**), and  $0^\circ$  (**4d**). They correspond to the three minimum energy conformations of the ion pair **4a** ( $\theta = -69^\circ$ ), **4b** ( $\theta = 177^\circ$ ), **4c** ( $\theta = 53^\circ$ ), as well as the maxima for  $\theta$  near  $0^\circ$  (**4d**). Beginning with the ion pair in these four conformations, the approach of the ethylene monomer *cis* and *trans* to the  $\mu$ -methyl bridge was studied. The results of the investigations are discussed in the following sections. The relative energies of the olefin complexes and insertion barriers were calculated with respect to the totally separated species ethylene monomer and **4a**, the most stable conformation of the ion pair in its resting stage.

The approach of the olefin monomer *cis* and *trans* to the ion pair can lead to one of two possible outcomes: (a) insertion of the monomer leading to the extension of the alkyl chain; or (b) termination of the polymerization reaction by chain transfer from the alkyl chain to the monomer. In the next section, we will look at the first of the two possibilities — insertion — for the orientation of the chain in the insertion plane, i.e., for  $\theta = 177^\circ$  and  $0^\circ$ . Both *cis* and *trans* approaches will be considered for the in-plane chain orientations. Following that, in Section (iii) and (iv), we will investigate the insertion process for the out-of-plane chain orientations, i.e., for  $\theta = -69^\circ$  and  $+53^\circ$ . Subsequent to that, we will investigate the other possibility — termination — for the *cis* and *trans* approaches.

#### Insertion for the in-plane chain conformations

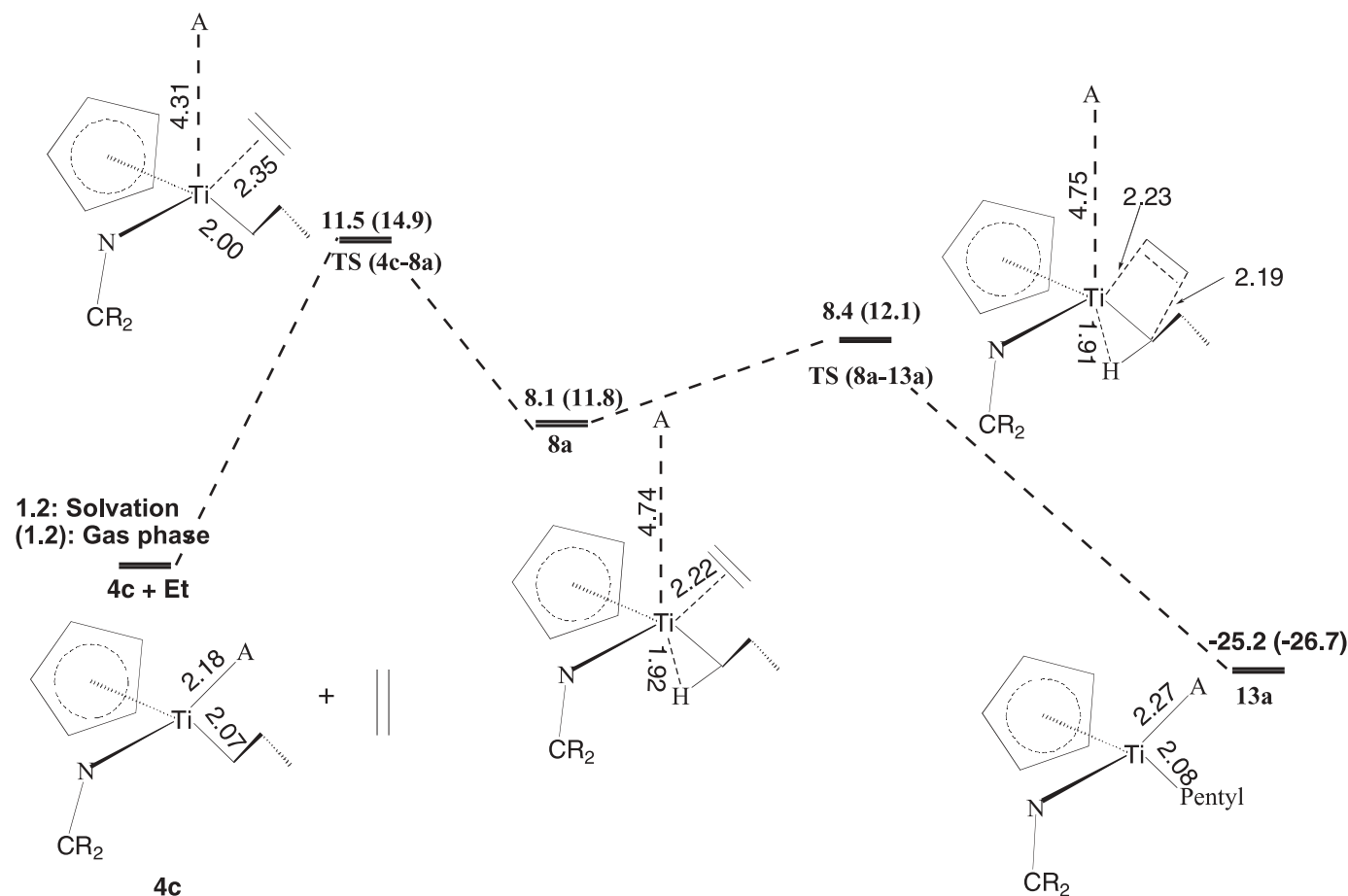
The *cis* approach of the ethylene monomer towards conformation **4b** ( $\theta = 177^\circ$ ), and the *trans* approach of the monomer towards **4d** ( $\theta = 0^\circ$ ), were found to lead to insertion. The other two possibilities for the two in-plane chain conformations, i.e., *trans* approach towards **4b** and *cis* approach towards **4d**, led to termination, and will be discussed later.

Figure 9 shows the *cis* approach of ethylene towards **4b** and Fig. 10 shows the profile for the *trans* approach towards **4d**. The two approaches were found to share some common features, which are discussed in the following paragraphs:

(a) The approach of ethylene was found to lead to the formation of an in-plane  $\pi$ -complex in each case, denoted



**Fig. 12.** The energy profile for the cis approach of the ethylene monomer towards the contact ion pair  $[\text{Cp}\{\text{NC}(t\text{-Bu})_2\}\text{TiPr}^+][\text{CH}_3\text{B}(\text{C}_6\text{F}_5)_3^-]$ , with the propyl chain lying out of the insertion plane, for the case **4c**.



as **5a** and **6a**, respectively (see Figs. 9 and 10). In both these  $\pi$  complexes, the ethylene had approached quite close to the metal centre, with the ethylene–metal distance being about 2.4 Å. It achieved this by displacing the counterion from the metal to some extent, with  $R(\text{Ti}-\mu\text{-C}) \geq 3.0$  Å (see Figs. 9 and 10). The cost of displacing the counterion caused the species **5a** and **6a** to be higher than the separated reactant species by about 11 kcal/mol. Moreover, this displacement of the counterion led to an uptake barrier, for both cases, before the  $\pi$ -complex could be formed. The uptake barriers were quite high — 15.5 kcal/mol for **TS(4b–5a)** and 16.7 kcal/mol for **TS(4d–6a)**.

- (b) A stabilizing  $\beta$ -agostic interaction was found to be present in either of the  $\pi$ -complexes (**5a** and **6a**). They, therefore, resembled the  $\pi$ -complex (**IIIb**), formed during the back side insertion for the naked cationic case discussed earlier.  $R(\text{Ti}-\text{H})$  was about 1.9 Å in each case.
- (c) After the  $\pi$ -complex formation, the ethylene approached the  $\alpha$ -carbon of the alkyl chain, leading to the barrier for insertion, corresponding to the transition states **TS(5a–13a)** and **TS(6a–13a)** in Figs. 9 and 10, respectively. The  $\beta$ -agostic interaction was retained in both cases, much like in the back side insertion of the naked cation, with  $R(\text{Ti}-\text{H}) = 1.9$  Å.  $R(\text{C}_{\text{Et}}-\text{C}_\alpha)$  was about 2.0 Å in each case. The barrier to insertion was found to be high for both the cases, about 17.6 kcal/mol (see Figs. 9 and

10). The displacement of the counterion from the metal centre is the reason for the high barriers.

- (d) Solvent effects were found to be substantial in both cases, due to the increased charge separation caused by the displacement of the counterion. Thus, the insertion barrier was reduced from 20.5 to 17.6 kcal/mol in **4b**, and from 19.4 to 17.7 kcal/mol for the **4d** chain conformation.

After the insertion of the monomer, the product, **13a** was formed in each case, lying 25.2 kcal/mol below the separated species **4a + Et**.

#### Insertion for the out-of-plane chain conformations (cis attack)

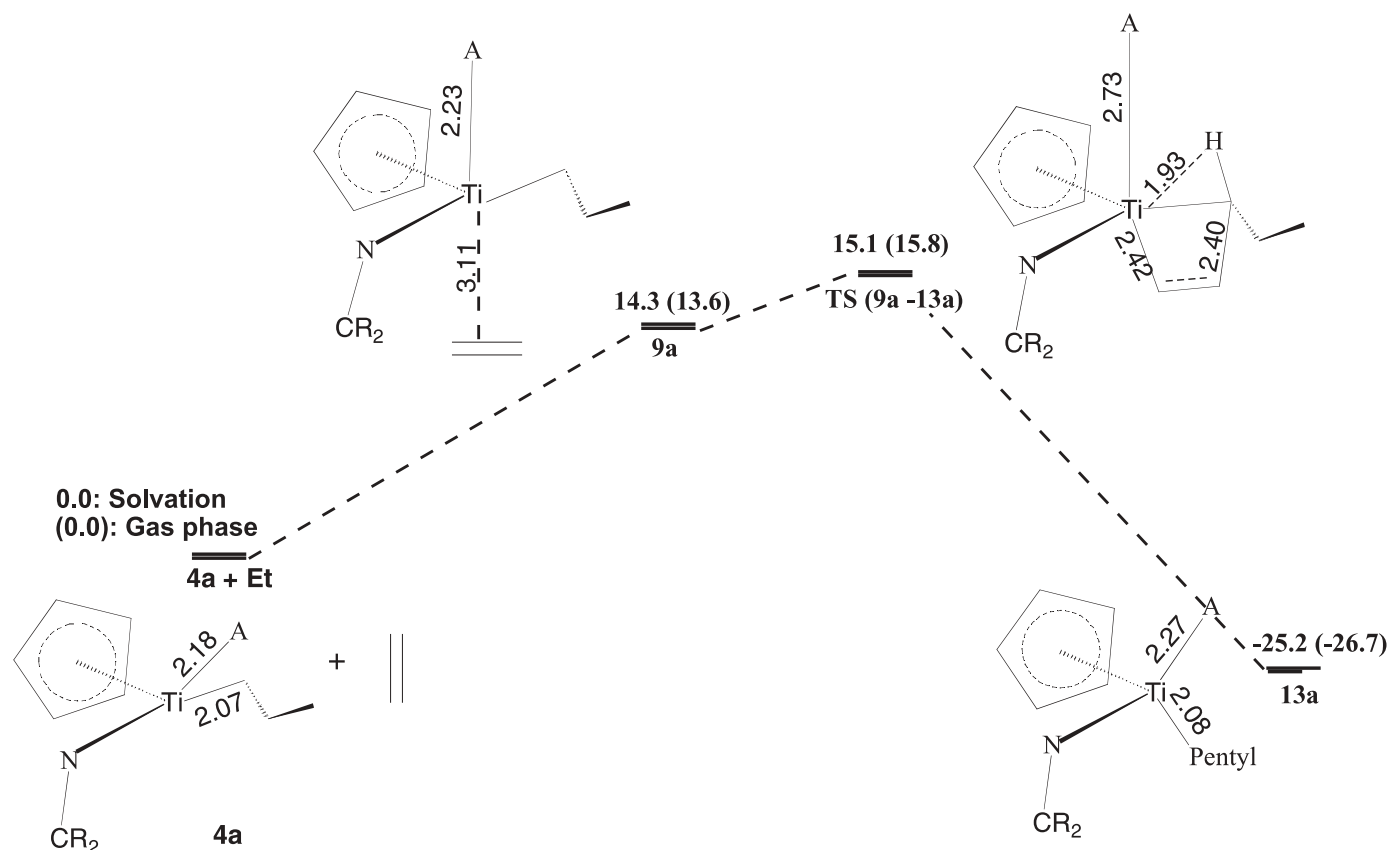
The ethylene monomer can approach the out-of-plane conformations **4a** ( $\theta = -69^\circ$ ) and **4c** ( $\theta = 53^\circ$ ) cis and trans to the  $\mu$ -methyl bridge. This gives rise to four possible insertion profiles, shown in the Figs. 11–14. All four of these pathways were investigated.

Figures 11 and 12 show the profiles for the cis attacks for the out-of-plane conformers (**4a** and **4c**). The cis approach profiles displayed common features, which are discussed in the following paragraphs:

- (a) As for the in-plane case, there was displacement of the counterion prior to formation of the  $\pi$  complexes **7a** and **8a**, respectively. Therefore, an uptake barrier had to be overcome before the respective  $\pi$  complexes could be



**Fig. 13.** The energy profile for the *trans* approach of the ethylene monomer towards the contact ion pair  $[\text{Cp}\{\text{NC}(t\text{-Bu})_2\}\text{TiPr}^+][\text{CH}_3\text{B}(\text{C}_6\text{F}_5)_3^-]$ , with the propyl chain lying out of the insertion plane, for the case **4a**.



formed. The considerable displacement of the counterion ( $>4.0$  Å) in each case also meant that that solvent effects were significant. After the solvent effects had been incorporated, the uptake barriers were found to be 13.6 kcal/mol for the **4a** case and 11.5 kcal/mol for **4c** (see Figs. 11 and 12). These barriers are lower than the corresponding uptake barriers in the case of the in-plane conformers, discussed earlier. This can be attributed to steric factors — the out-of-plane orientation of the chain leads to less steric congestion around the coordination sphere of the metal.

- (b) After formation of the  $\pi$  complexes **7a** and **8a**, the ethylene approached the  $\alpha$ -carbon in each case, thereby giving rise to the insertion transition states **TS(7a-13a)** and **TS(8a-13a)**, respectively. The counterion remained highly displaced from the metal centre ( $R(\text{Ti}-\mu\text{-C}) > 4.75$  Å) (see Figs. 11 and 12) at this stage of the insertion. Both transition states exhibited an  $\alpha$ -agostic interaction between one of the hydrogens of the chain and the metal centre, with  $R(\text{Ti}-\text{H})$  being about 1.9 Å. After the solvation effects had been incorporated, the barriers obtained were found to be comparatively low, 11.8 kcal/mol for the **4a** case and 8.4 kcal/mol for **4c**. This was lower than the uptake barrier in each of the two cases. Therefore, the rate-determining step for the two cases was the displacement of the counterion and uptake of the ethylene monomer by the metal centre, rather than the subsequent insertion. This is an interest-

ing feature that had not been noticed before for the in-plane cases discussed earlier. It is also interesting to note that for the **4a** case, the gas-phase insertion barrier is higher than the gas-phase uptake barrier, but after taking solvent effects into account the uptake barrier becomes rate determining (see Fig. 11). This is because the counterion is displaced to a greater extent at the insertion transition state than during the uptake, and hence, the solvent effects are more significant during insertion. Thus, inclusion of solvent effects reduces the insertion barrier to a greater extent, and makes the uptake the rate-determining step.

- (c) The contribution to the uptake barrier chiefly comes from the displacement of the counterion. Hence, with the uptake barrier becoming rate determining, the displacement of the counterion becomes the most important factor in the process for these two cases. This shows once again the importance of incorporating the counterion in the insertion studies.

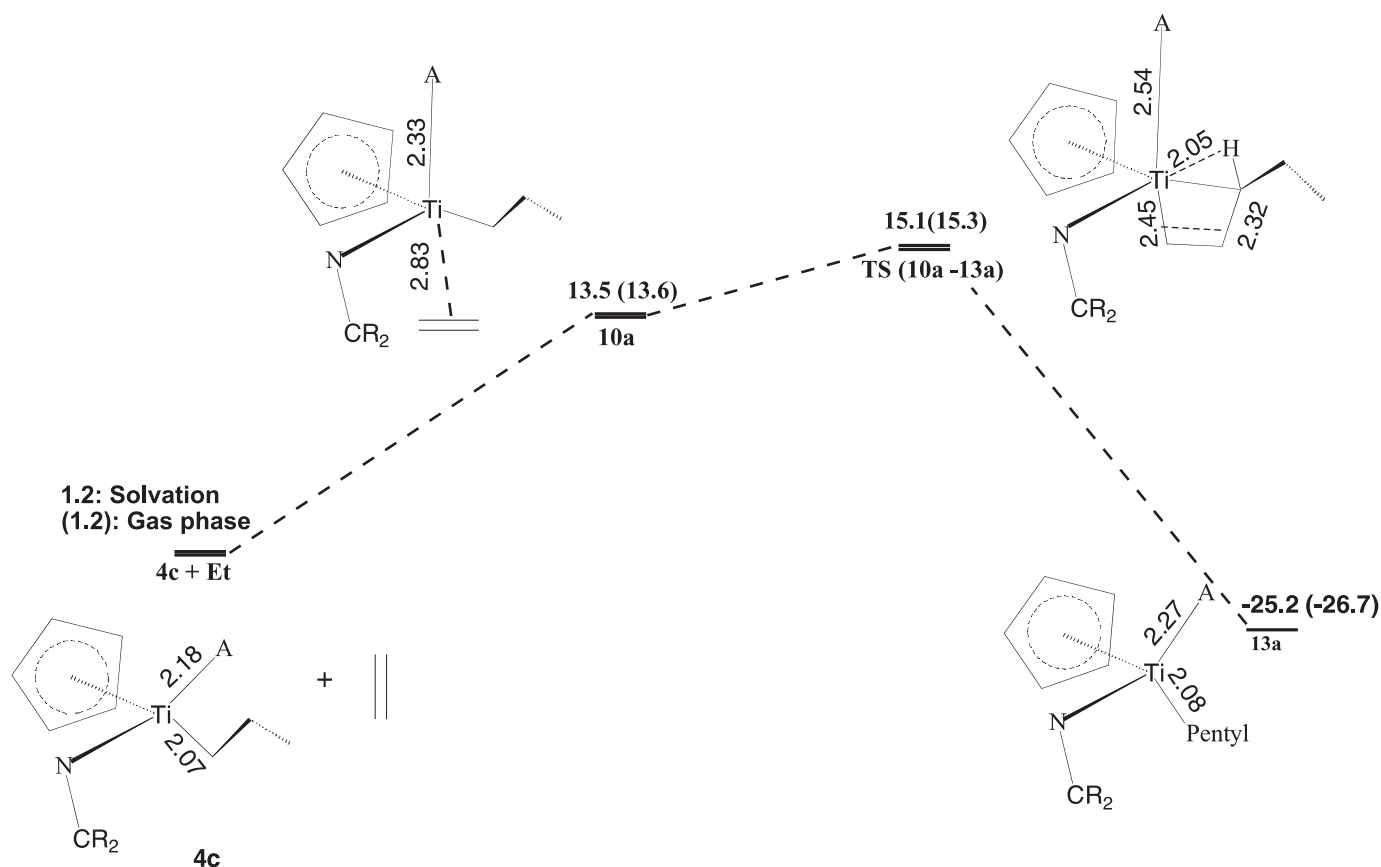
The final pentyl-chain product (**13a**) was formed after insertion of the ethylene, and found to be  $-25.2$  kcal/mol more stable than the separated reactants **4a** + Et.

#### Insertion for the out-of-plane chain conformations (*trans* attack)

Figures 13 and 14 show the profiles for the approach and insertion of the ethylene monomer into the propyl chain for the out-of-plane conformations (**4a** and **4c**). In these two



**Fig. 14.** The energy profile for the trans approach of the ethylene monomer towards the contact ion pair  $[\text{Cp}\{\text{NC}(t\text{-Bu})_2\}\text{TiPr}^+][\text{CH}_3\text{B}(\text{C}_6\text{F}_5)_3^-]$ , with the propyl chain lying out of the insertion plane, for the case **4c**.



cases, the approach takes place trans to the  $\mu$ -methyl bond. The profiles show some similarities, and the salient features are discussed in the following paragraphs:

- A weak olefin adduct was formed by the approach of the ethylene towards the titanium centre for the two cases. In the adducts, termed **9a** and **10a**, respectively, in the Figs. 13 and 14,  $R(\text{Ti-X})$  was more than 2.6 Å. This is in contrast to the  $\pi$  complexes formed for the in-plane chain orientations and for the in-plane cis attacks, discussed earlier, where the ethylene was found to approach closer to the metal centre. Moreover, the weak adduct formation is not preceded by any uptake barrier, due to the fact that the counterion is displaced only very slightly, just by about 0.1 Å (see Figs. 13 and 14). Consequently, the energy cost of adduct formation was not high. No  $\beta$ -agostic interaction was found in the adducts, as the chain continues to be out of the plane.
- After adduct formation, the ethylene approached the metal centre to insert into the metal-alkyl bond. This produced the transition states **TS(9a-13a)** and **TS(10-13a)**, respectively, shown in Figs. 13 and 14. Like in the adducts, the counterion was not much displaced, 2.54 Å in the **4c** case and 2.73 Å in **4a**. An  $\alpha$ -agostic bond was observed at the insertion transition states, in contrast to the  $\beta$ -agostic bond observed at the transition states for the in-plane conformations.
- Solvation effects were found to be negligible in the two cases, due to the fact that the displacement of the

counterion was modest. After incorporating the minor solvent effects, the insertion barriers were found to be 15.1 kcal/mol in both the cases — lower than for the out-of-plane “back side” insertion cases, but higher than for the corresponding in-plane cis approaches.

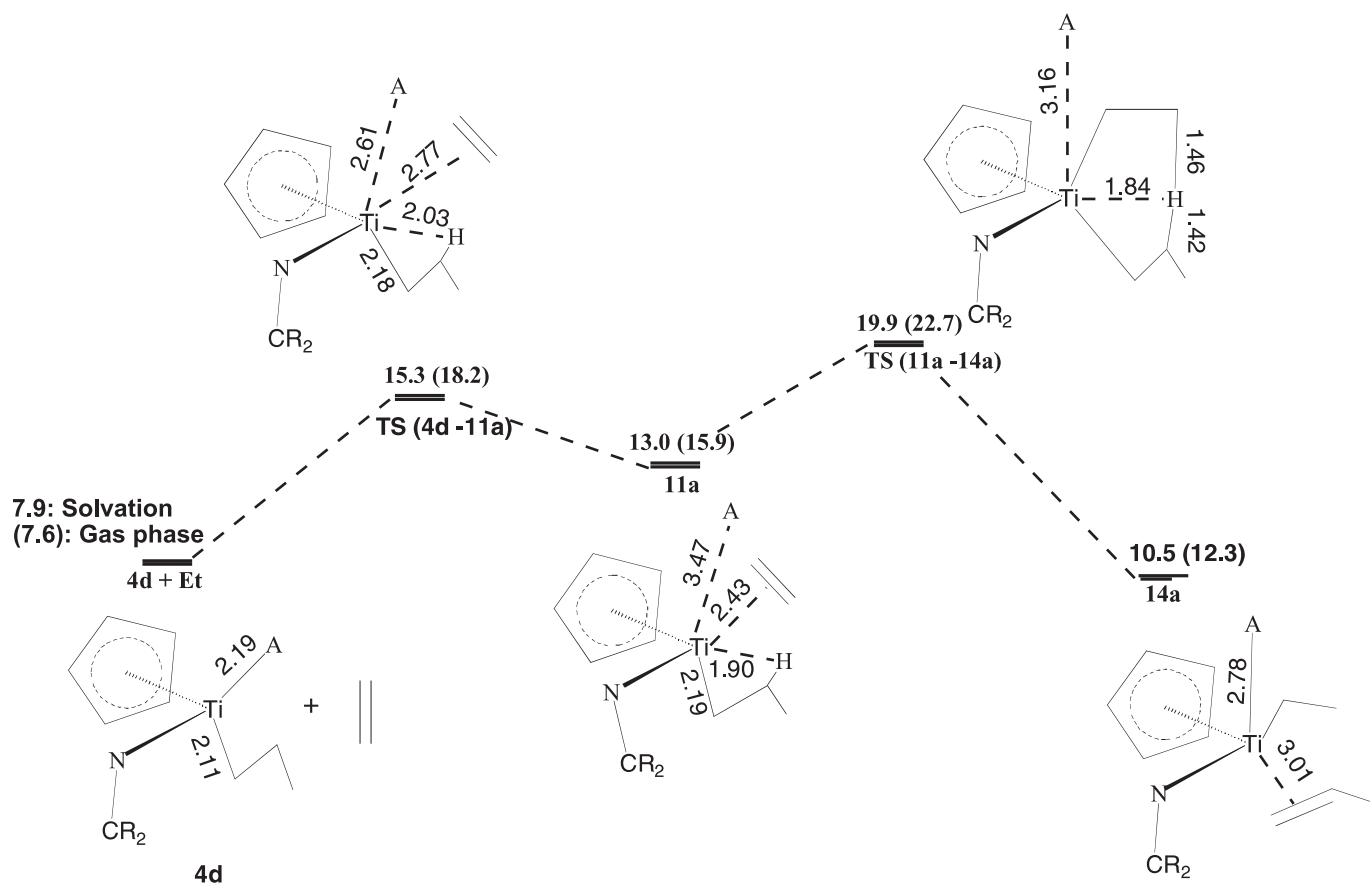
For the approach and insertion of the ethylene, the results obtained and discussed in the previous sections showed that the cis approaches yielded the lowest barriers. The reason for this is the greater destabilization in the trans olefin complexes, in comparison to the cis (6). In the trans olefin complexes, three strong electron donors ( $L_1$ ,  $L_2$ , and the alkyl group) (see Fig. 4) occupy the equatorial plane of the trigonal bipyramid. As a result, each experiences destabilizing trans-like influences from the other two ligands. In the cis olefin complexes, these destabilizing influences are less, since the equatorial plane has only two strong electron donors ( $L_1$  and  $L_2$ ) and a weak donor (ethylene). The cis olefin complexes are therefore relatively more stable, and as a result, the overall barriers are lower.

#### Comparison between the first and second insertions

In the *First insertion study with inclusion of the counterion*, we discussed the initiation step, or first insertion of ethylene into the Ti-methyl bond, from the cis and trans approaches following which we have presented the results for the propagation step, or the second insertion of ethylene. The steps have a few common features. The cis approach yields the lower barrier for the first insertion, and the same



**Fig. 15.** The energy profile for the cis approach of the ethylene monomer towards the contact ion pair  $[\text{Cp}\{\text{NC}(t\text{-Bu})_2\}\text{TiPr}^+][\text{CH}_3\text{B}(\text{C}_6\text{F}_5)_3^-]$ , with the propyl chain lying in the insertion plane, for the case **4d**.



is true for the second, where the cis approach towards the out-of-plane complex **4c** yields the lowest barrier. Also common to the first and second insertions is the presence of  $\alpha$ -agostic interactions at the transition states in the preferred cis cases. The barriers are comparable, decreasing from 12.7 kcal/mol for the first insertion, to 11.5 kcal/mol in the second. Experimental observations corroborate this result — Liu et al. (19) observed a reduction of about 4.8 kcal/mol in the insertion barrier for the second insertion, in comparison to the first, for the  $[\text{rac}-(\text{C}_2\text{H}_4)\text{-1-indenyl})_2\text{ZrMe}][\text{MeB}(\text{C}_6\text{F}_5)_3]$  system, with 1-hexene as the monomer.

However, there are a few differences between the first and second insertions, which are discussed in the following paragraphs:

- For the cis approaches in the out-of-plane complexes **4a** and **4c**, which yield the lowest barriers, it is the uptake of the ethylene that becomes the rate-determining step during the insertion, in contrast to the first insertion, where the uptake barrier was always lower than the subsequent insertion barrier.
- The counterion was displaced only slightly during the first insertion ( $\sim 0.3\text{--}0.4$  Å). However, during the second insertion, the counterion is displaced to a much greater extent during most insertions ( $>2.5$  Å in the out-of-plane cis approaches). Hence, solvent effects become more significant for the second insertion.

The previous four sections focused on the mechanism for insertion of the ethylene monomer in the propyl chain of the

ion pair. In the next section, we will consider and discuss the possibility of termination by chain transfer, for the cis and trans approaches of ethylene towards the ion pair  $[\text{Cp}\{\text{NC}(t\text{-Bu})_2\}\text{TiPr}^+][\text{B}(\text{C}_6\text{F}_5)_3\text{CH}_3^-]$ .

### Termination studies

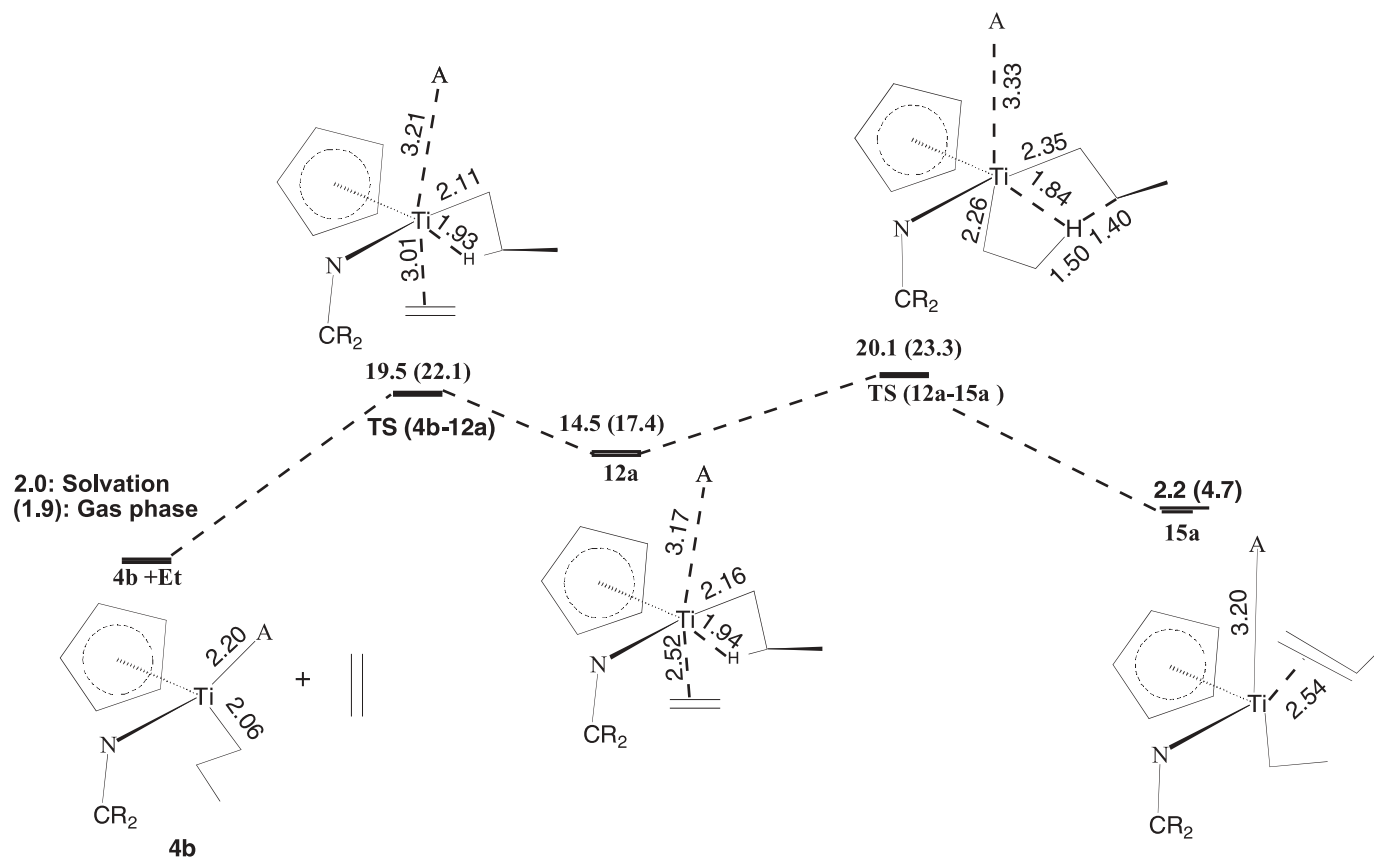
It may be recalled that the cis approach of the monomer towards the chain conformer **4b** and the trans approach towards **4d**, discussed previously, gave rise to  $\pi$  complexes that resembled the back side  $\pi$  complex (**IIIb**). This eventually led to ethylene insertion analogous to the back side insertion observed for the naked cationic case.

The other two possible cases for the in-plane chain conformers, i.e., cis approach towards **4d** and trans approach towards **4b**, were also investigated, and are shown in Figs. 15 and 16. Discussed in the following paragraphs are the salient features of the ethylene approach in the two cases:

- The approach of ethylene in either case led to the formation of  $\pi$  complexes **11a** and **12a** (see Figs. 15 and 16), similar to the front side  $\pi$  complex **IIIb**, observed for the naked cation. A  $\beta$ -agostic interaction was observed in both  $\pi$  complexes ( $\text{R}(\text{Ti-H}) \sim 1.9$  Å), and the counterion was displaced ( $>3.1$  Å) from the metal centre to accommodate the ethylene. The cost of  $\pi$  complexation was high in both cases, 14.0 kcal/mol to form **11a** and 14.5 kcal/mol to form the complex **12a**. Solvent effects were found to be substantial due to the displacement (and the consequent charge separation) of the counter-



**Fig. 16.** The energy profile for the trans approach of the ethylene monomer towards the contact ion pair  $[\text{Cp}\{\text{NC}(t\text{-Bu})_2\}\text{TiPr}^+][\text{CH}_3\text{B}(\text{C}_6\text{F}_5)_3^-]$ , with the propyl chain lying in the insertion plane, for the case **4b**.



ion. Moreover, this displacement also resulted in a high uptake barrier (~19 kcal/mol) in each case preceding the formation of the  $\pi$  complexes.

- (b) In the case of the naked cation, after formation of the front side  $\pi$  complex (**IIIb**) the propyl chain rotated out of the plane to facilitate the approach of the ethylene towards the  $\alpha$ -carbon of the alkyl chain, so that the insertion could take place. For the naked cationic case, this rotation was found to be quite facile, and the subsequent insertion took place without a high barrier. However, in the two cases, **11a** and **12a**, studied here, with the counterion attached, the steric crowding around the metal inhibited the out-of-plane rotation of the chain, which was therefore found to have a prohibitively high barrier (>22 kcal/mol). Instead, in both the cases, the system preferred to transfer the hydrogen which was taking part in the  $\beta$ -agostic interaction with the metal, to the ethylene monomer, thereby terminating the chain. This gave rise to the transition states **TS(11a-14a)** and **TS(12a-15a)** in the two cases, respectively (see Figs. 15 and 16), where the hydrogen being transferred was found to be almost equidistant from both the competing alkyl and ethylene carbons. This transfer was found to take place at a high energy cost, greater than 20.0 kcal/mol, in both cases, higher than any of the six insertion barriers obtained (and discussed in the earlier sections). Hence, for the  $[\text{Cp}\text{NC}(t\text{-Bu})_2\text{TiPr}^+][\text{B}(\text{C}_6\text{F}_5)_3\text{CH}_3^-]$  system, insertion was found to be favoured over termination.

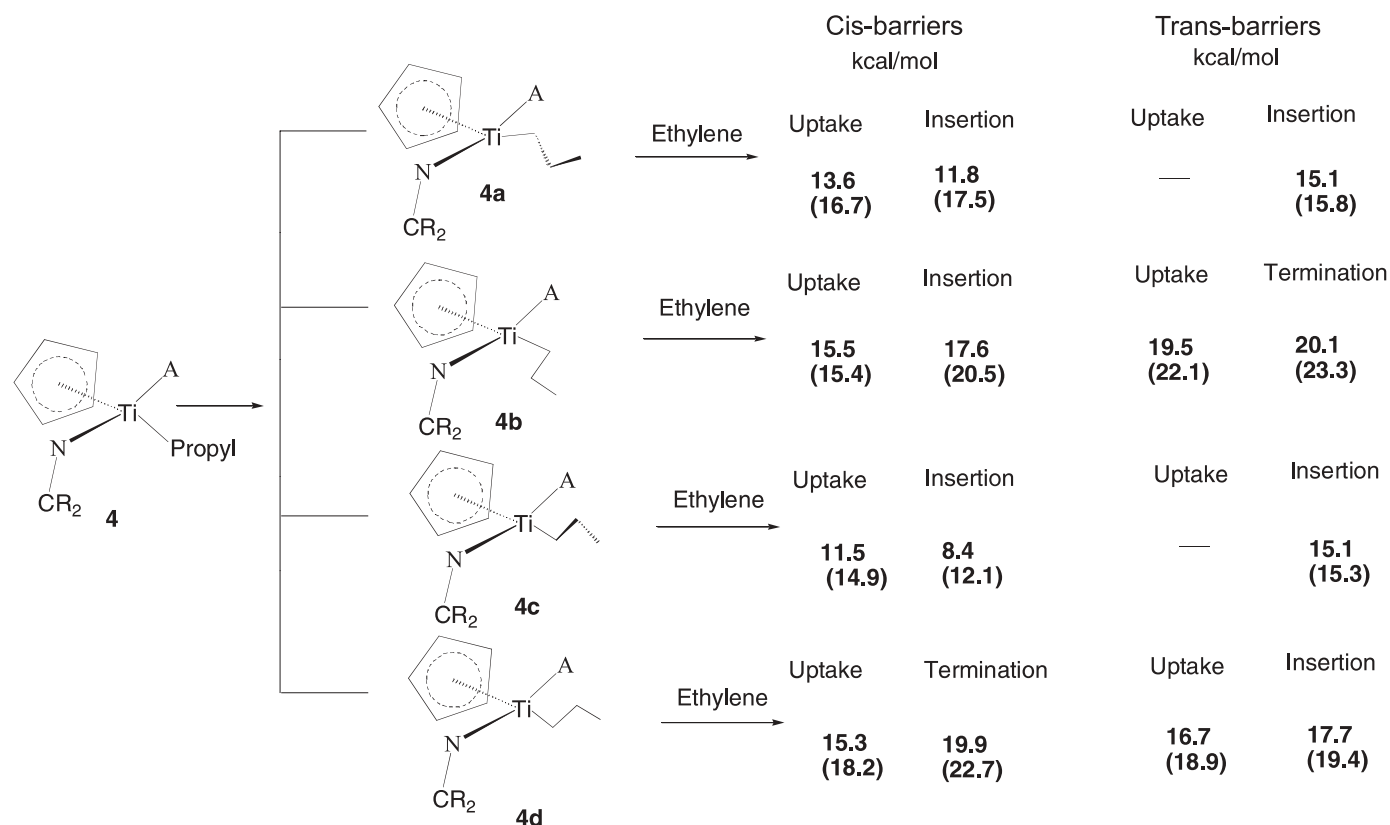
- (c) For the naked cation case, the termination was 1.5 kcal/mol less favourable than the back side insertion, and 6.3 kcal/mol less favourable than the front side insertion (see Fig. 7). With the inclusion of the counterion, the odds appear to increase in favour of insertion, with termination becoming ~2.5 kcal/mol less favourable than the back side insertions and ~10.0 kcal/mol less favourable than the most favoured out-of-plane insertion case (discussed earlier). The need to displace the counterion during the formation of the in-plane  $\pi$  complex and its steric presence at the vicinity of the cation during the hydrogen transfer are the reasons for this.
- (d) After transfer of the hydrogen, the product formed is a propylene moiety complexed to the metal centre, with the ethyl chain, formed from the hydrogen transfer, attached to the metal. The stability of the products (denoted as **14a** and **15a** in the Figs. 15 and 16, respectively) was found to be about 2.5 kcal/mol higher than the stability of the reactants, in each case. Solvent effects were found to be significant.

#### Overall picture of the second insertion

For the second insertion of ethylene into the ion pair **4**, we have investigated cis and trans approaches towards four chain conformations: **4a-4d**. This gave rise to eight possibilities, as summarized in Fig. 17 below. Six of the cases lead to insertion, and two to termination. The solvent-corrected and gas-phase uptake and insertion barriers are provided for



**Fig. 17.** Overall picture of the second insertion step — the barriers obtained from the cis and trans approaches of the ethylene monomer towards the contact ion pair  $[\text{Cp}\{\text{NC}(t\text{-Bu})_2\}\text{TiPr}^+][\text{CH}_3\text{B}(\text{C}_6\text{F}_5)_3^-]$ , with the propyl chain in different conformations.



each of the eight cases — with the gas-phase values indicated in parenthesis.

The approaches (cis and trans) for the out-of-plane conformations (**4a** and **4c**) both lead to insertion, and have lower barriers than for the in-plane cases (**4b** and **4d**). This suggests that the alkyl chain in the ion pair would prefer to sit out of the insertion plane during monomer approach. The most likely mode of insertion would be through the cis attack for the **4c** case. It is also clear from the values obtained that the ion-pair system **4** would strongly prefer insertion to termination, since the two approaches leading to termination have barriers much higher than the insertion barriers for **4a** and **4c**, with the difference in the barriers being about 10 kcal/mol between the termination barriers and the most favourable insertion case — cis approach (**4c**). The other noteworthy observation is that for the case **4a**, the insertion barrier is higher than the uptake in the gas phase, but after incorporation of solvent effects, the uptake barrier becomes higher — hence, the incorporation of solvent effects changes the rate-determining step in this case.<sup>4</sup>

## Conclusions

A density functional study was conducted on the approach and insertion of the ethylene monomer into the  $\text{Ti}-\text{C}_\alpha$  bond

( $\text{C}_\alpha$  representing the first carbon of the alkyl chain), for the naked cation  $\text{CpNC}(t\text{-Bu})_2\text{TiR}^+$  ( $\text{R}$  = methyl, propyl), and the ion pair  $\text{CpNC}(t\text{-Bu})_2\text{RTi}-\mu\text{-Me-B}(\text{C}_6\text{F}_5)_3$  ( $\text{R}$  = methyl, propyl). QM/MM atoms were used to model the tertiary butyl groups, with hydrogens used as capping atoms. The counterion ( $\text{B}(\text{C}_6\text{F}_5)_3\text{CH}_3^-$ ) was represented by a previously validated QM/MM model (**9a**). The chief conclusions from the study are summarized in the following paragraphs:

- The counterion plays a very significant role in the insertion process for both the first ( $\text{R}$  = methyl) and second ( $\text{R}$  = propyl) insertions of the ethylene monomer. The incorporation of the counterion makes the insertion processes highly endothermic, in contrast to the corresponding naked cationic cases, where the insertion is found to be exothermic. Moreover, for the second insertion, the presence of the counterion influences the alkyl chain conformation of the ion pair, making the out-of-plane chain conformations more favourable for insertion than the in-plane ones. The approach of the ethylene cis to the  $\mu$ -methyl bond in the ion pair for the out-of-plane conformer **4c**, ends up being the most favourable for insertion. For this approach, the barrier to uptake of the monomer is found to be the rate-determining step corroborating experimental findings proving the significance of the counterion, since the main contribution to

<sup>4</sup>Supplementary data may be purchased from the Directory of Unpublished Data, Document Delivery, CISTI, National Research Council Canada, Ottawa, ON K1A 0S2, Canada ([http://www.nrc.ca/cisti/irm/unpub\\_e.shtml](http://www.nrc.ca/cisti/irm/unpub_e.shtml) for information on ordering electronically). These data can be obtained, free of charge, via [www.ccdc.cam.ac.uk/conts/retrieving.html](http://www.ccdc.cam.ac.uk/conts/retrieving.html) (or from the Cambridge Crystallographic Data Centre, 12 Union Road, Cambridge CB2 1EZ, U.K.; fax +44 1223 336033; or [deposit@ccdc.cam.ac.uk](mailto:deposit@ccdc.cam.ac.uk)).



the uptake barrier comes from the displacement of the counterion.

- (b) The counterion also has an influence on the termination process. Inclusion of the counterion increases the difference between insertion and termination barriers for the second insertion (difference  $\sim 10$  kcal/mol), in contrast to the naked cationic case (difference = 6.3 kcal/mol), thereby making insertion more favourable.
- (c) The barrier to second insertion for the most favorable approach (11.5 kcal/mol) is found to be 1.2 kcal/mol lower than the barrier for the first insertion (12.7 kcal/mol). This reduction in the height of the barrier, upon going from first to second insertion, corroborates experimental findings (19).
- (d) Solvent effects become important with the increase in the chain length. The displacement of the counterion increases during most approaches of the ethylene monomer during the second insertion, thereby increasing the charge separation between cation and anion. Therefore, incorporation of the solvent effects reduces the barriers to uptake and insertion to a significant extent. In fact, for the cis approach of ethylene towards **4a**, inclusion of solvent effects reverses the rate-determining step, making the uptake barrier higher than the insertion.

## Acknowledgements

This investigation was supported by the Natural Sciences and Engineering Research Council of Canada (NSERC) and by Nova Research and Technology Corporation (NRTC). Tom Ziegler would like to thank the Canadian Government for a Canada Research Chair.

## References

1. (a) L. Resconi, L. Cavallo, A. Fait, and F. Piemontesi. *Chem. Rev.* **100**, 1253 (2000); (b) K. Mashima, Y. Nakayama, and A. Nakamura. *Adv. Polym. Sci.* **133**, 1 (1997); (c) H.G. Alt and A. Koppl. *Chem. Rev.* **100**, 1205 (2000).
2. G.M. Benedikt and B.L. Goodall (*Editors*). *In Materials, properties, processing and markets. Plastic Design Library*, New York. 1998.
3. (a) M.J. Bochmann. *J. Chem. Soc. Dalton Trans.* 225 (1996); (b) S. Pasynkiewicz. *Polyhedron*, **9**, 429 (1990); (c) M.R. Mason, J.M. Smith, S.G. Bott, and A.R. Barron. *J. Am. Chem. Soc.* **115**, 4971 (1993); (d) J.L. Atwood, D.C. Hrnčíř, R.D. Priestler, and R.D. Rogers. *Organometallics*, **2**, 985 (1983); (e) C.J. Harlan, S.G. Bott, and A.R. Barron. *J. Am. Chem. Soc.* **117**, 6465 (1995); (f) A.R. Barron. 218th ACS national meeting, New Orleans, August 22–26 (1999); (g) X. Yang, C.L. Stern, and T.J. Marks. *J. Am. Chem. Soc.* **116**, 10 015 (1994); (h) P.A. Deck and T.J. Marks. *J. Am. Chem. Soc.* **117**, 6128 (1995); (i) L. Jia, C.L. Stern, and T.J. Marks. *Organometallics*, **16**, 842 (1997); (j) L. Li and T.J. Marks. *Organometallics*, **17**, 3996 (1998); (k) P. Deck, C.L. Beswick, and T.J. Marks. *J. Am. Chem. Soc.* **120**, 1772 (1998).
4. (a) T.K. Woo, P.M. Margl, T. Ziegler, and P.E. Blöchl. *Organometallics*, **16**, 3454 (1997); (b) T.K. Woo, P.M. Margl, J.C.W. Lohrenz, P.E. Blöchl, and T. Ziegler. *J. Am. Chem. Soc.* **118**, 13 021 (1996); (c) P.M. Margl, J.C.W. Lohrenz, P.E. Blöchl, and T. Ziegler. *J. Am. Chem. Soc.* **118**, 4434 (1996); (d) L. Fan, D. Harrison, T.K. Woo, and T. Ziegler. *Organometallics*, **14**, 2018 (1995); (e) R.J. Meier, G.H.J.V. Doremaele, S. Tarlori, and F. Buda. *J. Am. Chem. Soc.* **116**, 7274 (1994); (f) T. Yoshida, N. Koga, and K. Morokuma. *Organometallics*, **14**, 746 (1995); (g) H. Weiss, M. Ehrig, and R. Ahlrichs. *J. Am. Chem. Soc.* **116**, 4919 (1994); (h) E.P. Bierwagen, J.E. Bercaw, and W.A. Goddard III. *J. Am. Chem. Soc.* **116**, 1481 (1994).
5. (a) M.S.W. Chan and T. Ziegler. *Organometallics*, **19**, 5182 (2000); (b) K. Vanka, M.S.W. Chan, C.C. Pye, and T. Ziegler. *Organometallics*, **19**, 1841 (2000).
6. I.E. Nifant'ev, L.Y. Ustynyuk, and D.N. Laikov. *Organometallics*, **20**, 5375 (2001).
7. (a) G. Lanza, I.L. Fraga, and T.J. Marks. *Organometallics*, **21**, 5594 (2002); (b) R. Fusco, L. Longo, F. Masi, and F. Garbassi. *Macromol. Rapid Commun.* **19**, 257 (1998); (c) F. Bernardi, A. Bottoni, and G.P. Miscione. *Organometallics*, **17**, 16 (1998); (d) M.S.W. Chan, K. Vanka, C.C. Pye, and T. Ziegler. *Organometallics*, **18**, 4624 (1999); (e) K. Vanka and T. Ziegler. *Organometallics*, **20**, 905 (2001); (f) E. Zurek, T.K. Woo, T. Firman, and T. Ziegler. *Inorg. Chem.* **40**, 361 (2001); (g) E. Zurek and T. Ziegler. *Inorg. Chem.* **40**, 3279 (2001); (h) E. Zurek and T. Ziegler. *Organometallics*. Accepted for publication.
8. K. Vanka, Z. Xu, and T. Ziegler. *Isr. J. Chem.* **42**, 403 (2002).
9. (a) Z. Xu, K. Vanka, T. Firman, A. Michalak, E. Zurek, C. Zhu, and T. Ziegler. *Organometallics*, **21**, 2444 (2002); (b) Z. Xu, K. Vanka, and T. Ziegler. *Organometallics*. Accepted for publication.
10. (a) E.J. Baerends, D.E. Ellis, and P. Ros. *Chem. Phys.* **2**, 41 (1973); (b) E.J. Baerends and P. Ros. *Chem. Phys.* **2**, 52 (1973); (c) G. te Velde and E.J. Baerends. *J. Comput. Phys.* **92**, 84 (1992); (d) C.G. Fonseca, O. Visser, J.G. Snijders, G. te Velde, and E.J. Baerends. *In Methods and techniques in computational chemistry, METECC-95. Edited by E. Clementi and G. Corongiu. STEF, Cagliari. 1995. p. 305.*
11. W. Ravenek. *In Algorithms and applications on vector and parallel computers. Edited by H.J.J. te Riele, T.J. Dekker, and H.A. van de Horst. Elsevier, Amsterdam, The Netherlands. 1987.*
12. (a) G. te Velde and E.J. Baerends. *J. Comput. Chem.* **99**, 84 (1992); (b) P.M. Boerrigter, G. te Velde, and E.J. Baerends. *Int. J. Quantum Chem.* **33**, 87 (1998).
13. L. Versluis and T. Ziegler. *J. Chem. Phys.* **88**, 322 (1988).
14. S.H. Vosko, L. Wilk, and M. Nusair. *Can. J. Phys.* **58**, 1200 (1980).
15. J. Krijn and E.J. Baerends. *Fit functions in the HFS-method. Free University of Amsterdam, Amsterdam, The Netherlands. 1984.*
16. J.P. Perdew. *Phys. Rev. B*, **46**, 6671 (1992).
17. (a) A. Klamt and G. Schuurmann. *J. Chem. Soc. Perkin Trans.* **2**, 799 (1993); (b) C.C. Pye and T. Ziegler. *Theor. Chem. Acc.* **101**, 396 (1999).
18. (a) M. Clark, R.D. Cramer III, and N. van Opdenbosch. *J. Comput. Chem.* **10**, 982 (1989); (b) T.K. Woo, L. Cavallo, and T. Ziegler. *Theor. Chim. Acta*, **100**, 307 (1998); (c) F. Maseras and K. Morokuma. *J. Comput. Chem.* **16**, 1170 (1995).
19. Z. Liu, E. Somsook, C.B. White, K.A. Rosaaen, and C.R. Landis. *J. Am. Chem. Soc.* **123**, 11 193 (2001).



## TRIBUTE

### Professor John F. Harrod

This special issue of the *Canadian Journal of Chemistry* has been named in honour of John Frank Harrod, an accomplished scientist who has been a gracious colleague and mentor to many chemists in Canada and elsewhere. John Harrod is known primarily as an organosilicon chemist who has studied various aspects of this subject over most of his 42 year career in independent research. His contributions to the understanding of mechanisms in organosilicon chemistry, to the application of catalysis in organosilicon chemistry, and to the synthesis of compounds containing transition metal – Si bonds have formed the foundations of several of the most important areas of contemporary organosilicon chemistry.

John Harrod has also made significant contributions to the use of organosilicon compounds for the preparation of ceramics, use of the titanocene-catalyzed hydrosilation reactions for chiral synthesis, synthesis of organometallically substituted polysiloxanes, and spectroscopic analysis of organosilicon compounds. These studies have led to 88 papers in this field, a number of which are landmarks. Some other areas of chemistry in which Harrod's research has had an impact include: the synthesis and reactions of copper phenoxide complexes, reactions on clean metal surfaces, organonickel-catalyzed polymerization of butadiene, and mechanistic studies of oxidative addition to Ir complexes.

By dedicating this issue to John Harrod, we are both recognizing and celebrating his many contributions to the growth of inorganic/organometallic chemistry in Canada, his training of younger researchers in organometallic, silicon, and polymer chemistry, and his role in fostering respect and recognition for Canada's contributions to the advancement of inorganic chemistry. The following paragraphs provide a glimpse into John Harrod's life and career.

John Harrod was born and raised in Coventry, U.K. He attended the University of Birmingham, where he completed both a B.Sc. (1955) and a Ph.D. (1958) in Chemistry. His Ph.D. project, supervised by Sir Harry Melville, was an investigation of the polymerization of styrene by catalysts derived from the reactions of Grignard reagents with titanium tetrachloride. Upon completion of his Ph.D. degree, John Harrod took up a post-doctoral position (1958–1960) with Jack Halpern at the University of British Columbia. During this period, he assisted in Halpern's pioneering studies of the homogeneous catalytic activation of hydrogen, and made the first observation of an unequivocally homogeneous, coordination-catalyzed hydrogenation of an olefinic substrate.

In 1960, John Harrod moved to the General Electric Research Laboratory in Schenectady, NY, and stayed there until 1966; it is during this period that he discovered organosilicon chemistry (in a personal sense). Shortly after his arrival in Schenectady, Harrod became aware of the discoveries of John Speier and his co-workers at Dow Corning on the application of Noble Metal compounds, and in particular chloroplatinic acid, as remarkably effective catalysts for the addition of Si–H bonds to olefins. Having just participated in the discovery of a homogeneous, ruthenium-catalyzed hydrogenation of some olefinic compounds in Jack Halpern's laboratory, Harrod was in a privileged position to recognize the likely connection between Speier's chemistry and the many other homogeneous transition-metal-catalyzed reactions that

were being identified and developed in the late 1950s and early 1960s.

In collaboration with his co-worker, Alan Chalk (also trained in Halpern's laboratory), Harrod carried out fundamental studies on metal-catalyzed hydrosilation chemistry. This work resulted in the proposal of a mechanistic scheme that explained, at least superficially, all of the organic and organosilicon chemistry that had been elaborated by the Dow Corning group. The so-called "Chalk–Harrod" mechanism, which is one of the earliest "text book" examples of a catalytic cycle based on coordination principles, has provided the foundation for the mechanistic understanding of a large body of hydrosilation chemistry. The original Chalk–Harrod report (*J. Am. Chem. Soc.* **87**, 16 (1965)) has since been cited several hundred times by many workers who have used its findings as a road map in their own investigations of hydrosilation reactions. It is of interest to note that only in 2002 were the final details confirming the essential correctness of the Chalk–Harrod mechanism, with respect to the platinum-catalyzed hydrosilation of olefins, reported (A. Roy and R.B. Taylor. *J. Am. Chem. Soc.* **124**, 9510 (2002)).

Harrod and Chalk also demonstrated the first case of an oxidative addition reaction of a hydrosilane to a transition metal centre, one of the earliest examples of an oxidative addition – reductive elimination process (*J. Am. Chem. Soc.* **87**, 1133 (1965)). This approach for the synthesis of transition metal silyl and silyl-hydride complexes via the addition of Si–H compounds to metal fragments stimulated decades of investigations on such reactions with essentially all of the transition elements.

After his stay at GE, John Harrod took up a position at McGill, where he stayed until his formal retirement in 1998. During his McGill years, Harrod rose through the ranks, chaired the Department of Chemistry, presided over the staff association, and received many honours and awards. For example, he was named a Killam Research Fellow of the Canada Council (1995–1997) and the 1997 Alcan Lecturer of the Chemical Institute of Canada. Harrod has also contributed to the Canadian scientific community by serving several terms on the grants and scholarship committees of the Fonds pour la formation des chercheurs et l'aide à la recherche (Québec) (FCAR) and on the Natural Sciences and Engineering Research Council of Canada (NSERC) Chemistry Grants Selection Committee (Inorganic and Organic). He has also served on the Editorial Board of *Organometallics* and the Comité de Parrainage of the French language science education journal *Didaskalia*. His continuing interest in industrial chemistry was reflected in his work as a retained consultant of Dow Canada in Sarnia (1966–1971) and of Dow chemical in Midland (1967–1980). His international stature as a researcher earned Harrod many invitations to lecture all over the world, the most memorable being his 2 years as a Professeur Invité, and France/Québec Fellow, at the Ecole Nationale Supérieure de Chimie de Paris. It was during a sabbatical leave in Paris (in 1983) when Harrod accidentally tapped a second fountainhead of new organosilicon chemistry, as described below.

The near absence of examples of silyl complexes of group 4 elements had intrigued Harrod for a number of years. In Paris he set up a collaboration with Dr. Edmond Samuel, a pioneer in group 4 metallocene chemistry, with the goal of



exploring the reactions of hydrosilanes with organometallobenes. These studies resulted in the discovery of the catalytic dehydrocoupling of hydrosilanes to polysilanes (C. Aitken, J.F. Harrod, and E. Samuel. *J. Organometal. Chem.* **279**, C11 (1985); C. Aitken, J.F. Harrod, and U.S. Gill. *Can. J. Chem.* **65**, 1804 (1987)). The recognition of the significance of this discovery was in large part due to Harrod's formal training as a polymer chemist and it occurred at a time of burgeoning interest in polysilanes. The catalytic dehydrocoupling reaction remains one of a small number of methods for synthesizing oligo- and polysilanes.

John Harrod's pioneering work in the dehydrocoupling of hydrosilanes inspired a number of talented investigators (notably Don Tilley, then at U.C. San Diego, Don Berry at U. Pennsylvania, and Joyce Corey at U. Missouri in St. Louis) to pursue the preparation and reactivity studies of many new silyl complexes of group 4 metals. In addition, Harrod extended the principle of catalytic dehydrocoupling to the synthesis of new compounds containing Si-P and Si-N, by cross-reacting hydrosilanes with hydrides of N and P. In his hands, and those of others, such as Joyce Corey, Ian Manners, and Don Tilley, catalytic dehydrocoupling has been established as a new, general route for the synthesis of element–element bonds.

Very recently, Harrod returned to the field of hydrosilation chemistry after a long absence to make a number of significant contributions. As usual, his choice of chemistry involved intuition and luck, combined with the recognition that something interesting was afoot. Of particular note is the discovery of the titanocene-catalyzed hydrosilation of pyridines (L. Hao, J.F. Harrod, A.-M. Lebuis, Y. Mu, R. Shu, E. Samuel, and H.-G. Woo. *Ang. Chem. Int. Ed. Engl.* **37**, 3126 (1998); R. Shu and J.F. Harrod. *Can. J. Chem.* **79**, 1075 (2001)), which provided the first examples of the hydrosilation of a highly aromatic unsaturated substrate. These reactions also provide a new synthetic approach to a valuable family of *N*-heterocycles.

A recent exploration of the titanocene-catalyzed reactions of hydrosilanes with aromatic amides (K. Selvakumar and J.F. Harrod. *Angew. Chem. Int. Ed.* **40**, 2129 (2001)) resulted in the discovery of a new, high-yield route to the 1,2-diaryl-1,2-diaminoethanes, rather than the expected simple addition of the Si-H across the C=O bond. This new C—C bond forming reaction via inexpensive, widely available starting materials holds promise for the synthesis of a new family of polymers that would be extremely difficult to synthesize by other methods.

The above highlights have been chosen to illustrate the thread of originality that characterizes John Harrod's contributions to organosilicon chemistry. He had the luck to stumble upon exciting new chemistry, but he also recognized the major significance of these lucky accidents, in a number of different contexts, and initiated important new directions in the field.

In his nonprofessional life, John Harrod has pursued a variety of cultural and social activities. His love of the mountains, nurtured in the hills of the Celtic Fringe in the U.K., and then by the inspiring grandeur of the Western Cordillera of North America, endures to the present day. His lifelong concern for human suffering led Harrod to take a year's leave of absence in 1963–1964 to work as a volunteer, under the auspices of the International Voluntary Service (IVS), on reconstruction and development projects in northern Greece and in Algeria. The following summer he led an IVS team in the Tennessee Smokey Mountains to reconstruct a community water supply system that had been destroyed in the course of civil disturbances directed against the activities of some voter registration workers. He has also been a supporter of Amnesty International for many years.

John Harrod is now the G.H. Tomlinson Professor of Chemistry (Emeritus) at McGill.

*Davit Zargarian*



---

This special issue is dedicated to

## **Professor John Harrod**

to honour his outstanding contributions to both homogeneous catalysis and materials chemistry.

*Associate Editors:* Chris Orvig, Davit Zargarian, and I. Butler

Ce numéro spécial est dédié au

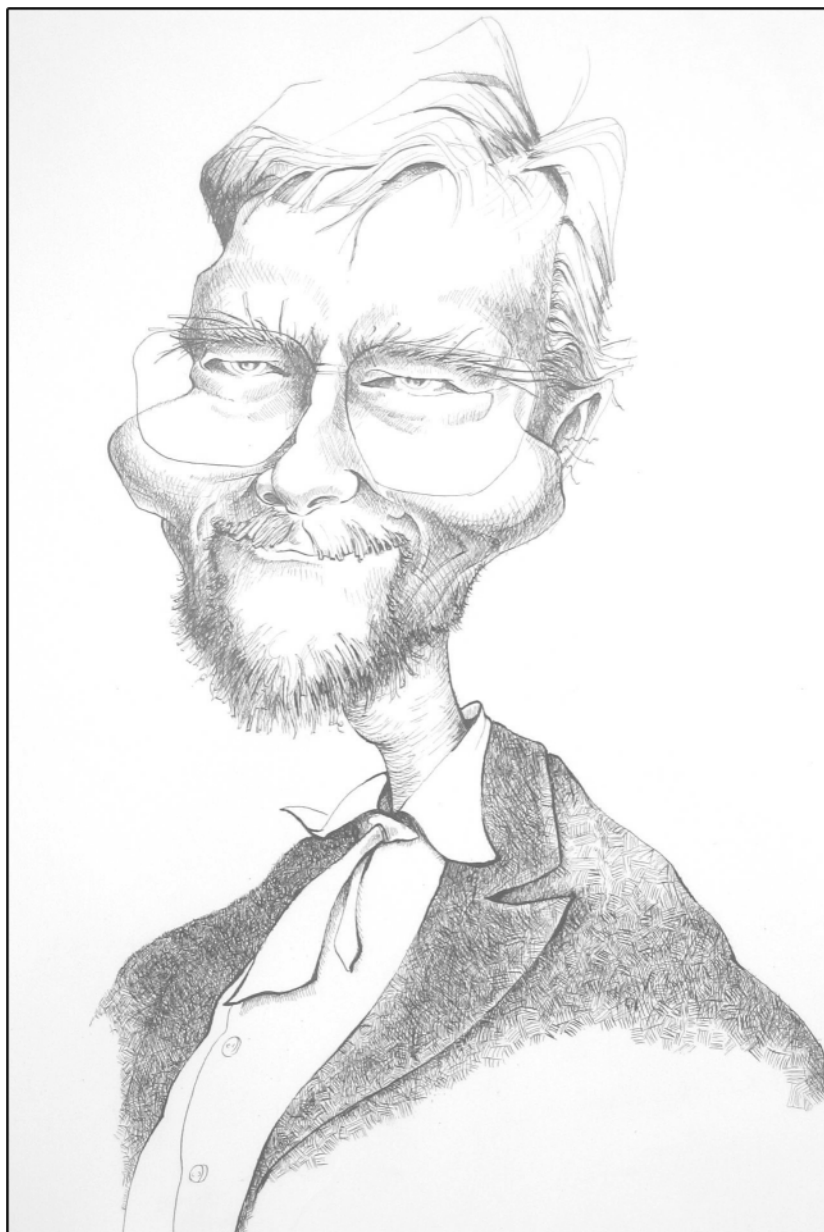
## **Professeur John Harrod**

en reconnaissance de ses contributions exceptionnelles tant à la catalyse homogène qu'à la chimie des matériaux.

*Directeurs scientifiques associés :* Chris Orvig, Davit Zargarian, and I. Butler

---





The caricature was presented to John Harrod by his colleague Mark Andrews on the occasion of his 60th birthday in 1994. John counts this gift among his most treasured possessions.

Mark Andrews, un collègue de John Harrod, a remis cette caricature à John à l'occasion de son 60e anniversaire, en 1994. John affirme qu'il s'agit là d'une de ses plus précieuses possessions.



## HOMMAGE

### Professeur John F. Harrod

Ce numéro spécial de la *Revue canadienne de chimie* est dédié à John Frank Harrod, chercheur chevronné ainsi que collègue et mentor de nombreux chimistes du Canada et d'ailleurs. Harrod est surtout connu pour ses travaux en chimie des organosiliciés, ayant consacré la majorité de ses 42 ans de carrière à l'étude autonome de divers aspects de ces composés. Ses contributions à la compréhension des mécanismes qui sous-tendent la chimie des organosiliciés, à l'utilisation de la catalyse dans ce domaine et à la synthèse de composés caractérisés par des liaisons « Si-métaux de transition » ont établi les fondements de plusieurs des plus importants champs d'étude de la chimie contemporaine des organosiliciés.

John Harrod a également apporté des contributions importantes à l'utilisation des organosiliciés dans la préparation de céramique, à la synthèse chirale à l'aide de réactions d'hydrosilation catalysées par le titanocène, à l'élaboration de polysiloxanes par réaction de substitution organométallique et à l'analyse spectroscopique des composés organosiliciés. Ces études ont mené à la rédaction de 88 articles dans ce domaine, dont plusieurs ont fait époque. Parmi les autres secteurs de recherche ayant bénéficié de ses travaux figurent la synthèse des complexes de phénoxides de cuivre et leurs réactions, les réactions sur les surfaces métalliques propres, la polymérisation du butadiène par catalyse organonickelée et les études des mécanismes associés à l'ajout par oxydation des complexes de l'iridium.

Ce numéro spécial souligne et applaudit les nombreuses contributions que John Harrod a apportées au progrès de la chimie des composés inorganiques et organométalliques au Canada, à la formation de jeunes chercheurs dans le domaine de la chimie des organométaux, du silicium et des polymères ainsi qu'à son rôle dans la promotion du respect et de la reconnaissance de l'apport canadien à l'avancement de la chimie inorganique au Canada. Les paragraphes qui suivent offrent un aperçu de la vie de John Harrod et de sa carrière.

John Harrod naît et grandit à Coventry (Royaume-Uni). Il étudie à l'Université de Birmingham, où il obtient un B. Sc. (1955) et un Ph. D. (1958) en chimie. Son projet de doctorat, sous la direction de Sir Harry Melville, porte sur la polymérisation du styrène par catalyseurs dérivés de réactions des réactifs de Grignard à l'aide du tétrachlorure de titane. Après avoir obtenu son diplôme supérieur, Harrod accepte une affectation postdoctorale (1958–1960) auprès de Jack Halpern à l'Université de la Colombie-Britannique. Il prend part aux travaux pionniers de Halpern sur l'activation catalytique homogène de l'hydrogène et fait la première constatation d'une véritable hydrogénation par catalyse de coordination d'un substrat oléfinique.

En 1960, Harrod se joint au General Electric Research Laboratory (GERL) à Schenectady (New York), où il y travaille jusqu'en 1966. C'est au cours de cette période qu'il se familiarise avec les rouages de la chimie des organosiliciés. En effet, peu de temps après son arrivée à Schenectady, Harrod a vent des découvertes de John Speier et de ses collaborateurs à la société Dow Corning concernant l'application des composés de métaux nobles et, plus particulièrement, de l'acide chloroplatinique comme catalyseurs

hautement efficaces dans l'ajout de liaisons « Si—H » aux oléfines. Ayant récemment collaboré à la découverte d'une hydrogénation homogène par catalyse du ruthénium de quelques composés oléfiniques dans le laboratoire de Jack Halpern, Harrod se trouve ipso facto en position idéale pour reconnaître le lien probable entre la chimie de Speier et bon nombre de réactions homogènes par catalyse de métaux de transition mises au grand jour et élaborées vers la fin des années 1950 et le début des années 1960.

De concert avec son collègue Alan Chalk (également du laboratoire de Halpern), Harrod réalise des études fondamentales sur la chimie de l'hydrosilation par catalyse de métaux. Ces travaux mènent au développement d'un processus élémentaire qui explique, du moins superficiellement, l'ensemble de la chimie des composés organiques et organosiliciés élaborés par le groupe de la société Dow Corning. Le mécanisme dit « de Chalk-Harrod », l'un des premiers exemples typiques du cycle de la catalyse axé sur les principes de coordination, sert de pierre angulaire à la compréhension des mécanismes d'une grande partie de la chimie de l'hydrosilation. Par ailleurs, le rapport original de Chalk et Harrod (*J. Am. Chem. Soc.* **87**, 16 (1965)) est cité quelques centaines de fois par une pléiade de chercheurs qui utilisent ces résultats comme flambeau pour éclairer leurs propres recherches dans le domaine des réactions d'hydrosilation. Il est intéressant de noter que ce n'est qu'en 2002 qu'il devient possible de confirmer la justesse inhérente du mécanisme de Chalk-Harrod, quant à l'hydrosilation des oléfines par catalyse du platine (A. Roy et R.B. Taylor. *J. Am. Chem. Soc.* **124**, 9510 (2002)).

Harrod et Chalk présentent également le premier cas d'une réaction d'addition par oxydation d'un hydrosilane à un centre de métaux de transition, l'un des premiers exemples de processus d'addition par oxydation – d'élimination par réduction (*J. Am. Chem. Soc.* **87**, 1133 (1965)). De fait, cette approche utilisée dans la synthèse de complexes de métaux de transition de silyle et d'hydrure silylène par l'addition de composés Si-H à des fragments métalliques alimentera des décennies de recherche sur de telles réactions avec, pour ainsi dire, tous les éléments de transition.

Après son passage au GERL, John Harrod se joint à l'Université McGill, où il demeurera jusqu'à sa retraite officielle en 1998. Là, il gravit les échelons pour devenir directeur du Département de chimie, siège à titre de président de l'association du personnel universitaire et reçoit plusieurs prix et témoignages de reconnaissance. De plus, il est boursier de recherche du Conseil des arts du Canada (de 1995 à 1997) et conférencier Alcan 1997 de l'Institut de chimie du Canada. Harrod contribue également à la communauté scientifique canadienne en réalisant bon nombre de mandats au sein de comités de bourses d'études et de subventions du Fonds pour la formation des chercheurs et l'aide à la recherche (Québec) (FCAR) et du Comité de sélection des subventions en chimie (inorganique et organique) du Conseil de recherches en sciences naturelles et en génie (CRSNG). Il siège également au Comité de rédaction de la revue *Organometallics* et au Comité de parrainage de la revue française *Didaskalia*, spécialisée dans les recherches sur la communication et l'apprentissage des sciences et des techniques. Son intérêt assidu envers la chimie industrielle se reflète dans ses travaux de consultant au compte des sociétés Dow Canada, à



Sarnia (de 1966 à 1971), et Dow Chemical of Canada Ltd., à Midland (de 1967 à 1980). Sa renommée internationale en tant que chercheur lui vaut de nombreuses invitations comme conférencier, la plus mémorable étant son affectation de 2 ans à titre de professeur invité et boursier France/Québec à l'École Nationale Supérieure de Chimie de Paris. Lors de son congé sabbatique à Paris (en 1983), Harrod insufflé par hasard une nouvelle vie à la chimie des organosiliciés dans les circonstances qui suivent.

L'absence presque complète d'exemples de complexes de silyle des éléments du groupe 4 excite la curiosité de Harrod depuis plusieurs années. À Paris, il collabore avec Edmond Samuel, un pionnier de la chimie des métallocènes du groupe 4, et examine les réactions des hydrosilanes avec les organométallocènes. Ces études résultent en la production de polysilanes par couplage déshydrogénant catalytique des hydrosilanes (C. Aitken, J.F. Harrod et E. Samuel. *J. Organometal. Chem.* **279**, C11 (1985); C. Aitken, J.F. Harrod et U. S. Gill. *Can. J. Chem.* **65**, 1804 (1987)). La reconnaissance de l'importance de cette découverte est attribuable en grande partie aux antécédents et aux connaissances fondamentales de Harrod dans le domaine de la chimie des polymères et survient à un moment où l'intérêt à l'égard des polysilanes s'avive. Le couplage déshydrogénant catalytique demeure l'une des quelques méthodes utilisées dans la synthèse d'oligosilanes et de polysilanes.

Ses travaux avant-gardistes sur le couplage déshydrogénant des hydrosilanes incitent une légion de chercheurs, dont Don Tilley, qui travaille à l'époque à l'Université de la Californie (San Diego), Don Berry de l'Université de la Pennsylvanie et Joyce Corey de l'Université du Missouri (Saint Louis), à préparer d'autres complexes de silyle du groupe 4 et à étudier leur réactivité. De plus, Harrod applique le principe de couplage déshydrogénant à la synthèse de nouveaux composés caractérisés par des liaisons « Si-P » et « Si-N » à l'aide de réactions croisées entre les hydrosilanes et les hydrures d'azote et de phosphore. Grâce à ses efforts et à ceux de ses collègues, notamment Joyce Corey, Ian Manners et Don Tilley, le couplage déshydrogénant catalytique devient une voie nouvelle et générale de synthèse de liaisons « élément-élément ».

Harrod a récemment renoué avec la chimie de l'hydrosilation après une longue absence, ce qui lui a permis d'apporter de nombreuses contributions d'importance. Comme d'habitude, ce cheminement, intuitif et fortuit, a été mû par un fort pressentiment d'une réalisation imminente. Par ailleurs, il est intéressant de noter sa découverte de

l'hydrosilation des pyridines par catalyse du titanocène (L. Hao, J.F. Harrod, A.-M. Lebuis, Y. Mu, R. Shu, E. Samuel, et H.-G. Woo. *Angew. Chem. Int. Ed. Engl.* **37**, 3126 (1998); R. Shu et J.F. Harrod. *Can. J. Chem.* **79**, 1075 (2001)) qui démontre pour la première fois l'hydrosilation d'un substrat non saturé et hautement aromatique. Ces réactions offrent également une nouvelle approche synthétique pour une importante famille d'hétérocycles azotés. Une récente étude sur les réactions entre les hydrosilanes et les amides aromatiques catalysés à l'aide du titanocène (K. Selvakumar et J.F. Harrod. *Angew. Chem. Int. Ed.* **40**, 2129 (2001)) a permis de démontrer une voie nouvelle et très productive de synthèse des 1,2-diaryl-1,2-diaminoéthanés, plutôt que le simple ajout d'une liaison « Si-H » à une liaison C=O. Cette nouvelle réaction permettant de créer une nouvelle liaison « C—C » à l'aide de matériaux économiques et répandus est très prometteuse pour la synthèse d'une nouvelle famille de polymères autrement difficiles à fabriquer.

Les glanures ci-dessus ont été choisies pour illustrer l'originalité profonde qui caractérise les contributions de John Harrod à la chimie des composés organosiliciés. Même s'il est tombé par chance sur un domaine novateur et prometteur de la chimie, il a su reconnaître l'importante signification de ces « découvertes accidentelles » et impulser de nouvelles recherches.

Sur le plan personnel, John Harrod s'adonne à une variété d'activités socioculturelles. Sa passion des montagnes, éveillée dans les collines des marges celtiques (Royaume-Uni), est plus que jamais exaltée par l'impressionnante grandeur des Cordillères pacifiques de l'Amérique du Nord. Sa grande sensibilité aux problèmes humanitaires et à la souffrance humaine l'a poussé à prendre un congé sabbatique (de 1963 à 1964) pour travailler à titre de bénévole, sous les auspices du Service civil international (SCI), à des projets de reconstruction et de développement dans le Nord de la Grèce et en Algérie. L'été suivant, il a dirigé une équipe du SCI chargée de reconstruire le système d'aqueduc d'une communauté des Smokey Mountains, au Tennessee, détruit à la suite de troubles sociaux causés par des irrégularités dans l'inscription électorale. Il appuie également Amnesty Internationale depuis de nombreuses années.

John Harrod est aujourd'hui titulaire de la chaire Tomlinson G.H. en chimie (professeur émérite) à l'Université McGill.

*Davit Zargarian*



# Vanadium and niobium diamidophosphine complexes and their reactivity

Michael P. Shaver, Robert K. Thomson, Brian O. Patrick, and Michael D. Fryzuk

**Abstract:** The tridentate ligand precursors  $R'P(CH_2SiMe_2NR'')_2$  ( $R'R''[NPN]$ ;  $R' = Cy, Ph$ ;  $R'' = Ph, Mes, Me$ ) were prepared from metathesis reactions of a lithiated amine, chloro(chloromethyl)dimethylsilane, the appropriate 1° phosphine, and *n*-butyl lithium and were isolated as solvent adducts. Metathesis between  $CyPh[NPN]Li_2(OEt)_2$ , **2**, and  $VCl_3(THF)_3$  afforded  $(CyPh[NPN]VCl)_2$ , **7**, whose solid-state structure was established by X-ray crystallography. Reduction attempts of the  $(R'R''[NPN]VCl)_2$  species with  $KC_8$  incorporated molecular nitrogen but were complicated by imide formation and ligand decomposition. Metathesis of **2** with  $NbCl_2Me_3$  afforded the highly unstable complex  $CyPh[NPN]NbMe_3$ , **15**. Attempts to hydrogenate this species were unsuccessful.

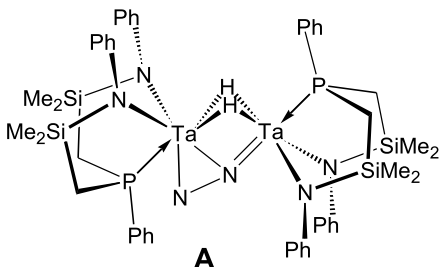
**Key words:** vanadium, niobium, metathesis, coordination chemistry, reduction, hydrogenation.

**Résumé :** Les précurseurs de ligand  $R'P(CH_2SiMe_2NR'')_2$  ( $R'R''[NPN]$  :  $R' = Cy, Ph$ ;  $R'' = Ph, Mes, Me$ ) ont été préparé des réactions de métathèse du amine lithié correspondant, chloro(chlorométhyle)diméthylsilane, le phosphine correspondant et *n*-butyl lithium. Les ligands ont été isolés comme adducts de solvant de sel de dilithium. Les réactions de métathèse du  $CyPh[NPN]Li_2(OEt)_2$ , **2**, avec  $VCl_3(THF)_3$  ont donné  $(CyPh[NPN]VCl)_2$ , **7**, dont la structure d'état solide a été établie par cristallographie de rayons-X. Les tentatives de réduction de l'espèce  $(R'R''[NPN]VCl)_2$  avec  $KC_8$  a incorporé l'azote moléculaire mais a été compliquée par la formation d'imide et la décomposition de ligand. Les réactions de métathèse de **2** avec  $NbCl_2Me_3$  ont donné le complexe extrêmement instable  $CyPh[NPN]NbMe_3$ , **15**. Les tentatives de hydrogène était infructueux.

**Mots clés :** vanadium, niobium, la métathèse, la chimie de coordination, la réduction, l'hydrogénation.

## Introduction

Recent work from our laboratory has focused on the chemistry of tantalum dinitrogen complexes stabilized by the [NPN] ligand, where [NPN] =  $PhP(CH_2SiMe_2NPh)_2$  (1–4). One of the most intriguing species is  $([NPN]Ta)_2(\mu-H)_2(\mu-\eta^1-\eta^2-N_2)$ , **A**, with a side-on, end-on bound dinitrogen unit. This complex has displayed remarkable reactivity with simple organometallic hydride reagents. The coordination chemistry of [NPN] with Ta — the heaviest member of group 5 — piqued our interest in the lighter elements of this group, namely V and Nb. In this manuscript we explore some of our successes and failures in trying to extend dinitrogen chemistry to low valent vanadium and niobium [NPN] complexes.



## Experimental

### General information

Unless otherwise stated, all manipulations were performed under an atmosphere of dry, oxygen-free dinitrogen by means of standard Schlenk or glovebox techniques (Vacuum Atmospheres HE-553-2 glovebox equipped with an MO-40-2H purification system and a  $-40^\circ C$  freezer). Thick-walled Pyrex reaction vessels with 5 or 10 mm Teflon needle valves and ground glass joints were used to maintain an inert atmosphere at pressures between  $10^{-6}$  and 4 atm (1 atm = 101.325 kPa). Hexanes and toluene were purchased anhydrous from Aldrich and further dried by passage through a tower of alumina and degassed by passage through a tower of Q-5 catalyst under a positive pressure of nitrogen (5). Anhydrous diethyl ether, tetrahydrofuran (THF), benzene, and hexamethyldisiloxane (HMDS) were stored over sieves and distilled from sodium benzophenone ketyl under argon. Nitrogen was dried and deoxygenated by passage through a column containing activated molecular sieves and MnO. Deuterated benzene was dried by refluxing with molten potassium metal in a sealed vessel under partial pressure, then trap-to-trap distilled, and degassed by freeze-pump-thaw three times. Unless otherwise stated,  $^1H$ ,  $^{31}P\{^1H\}$ , and  $^7Li$

Received 3 June 2003. Published on the NRC Research Press Web site at <http://canjchem.nrc.ca> on 13 October 2003.

M.P. Shaver, R.K. Thomson, B.O. Patrick, and M.D. Fryzuk.<sup>1</sup> University of British Columbia, Department of Chemistry, 2036 Main Mall, Vancouver, BC V6T 1Z1, Canada.

<sup>1</sup>Corresponding author (e-mail: [fryzuk@chem.ubc.ca](mailto:fryzuk@chem.ubc.ca)).



NMR spectra were recorded on a Bruker AMX-500 instrument operating at 500.1 MHz for  $^1\text{H}$  spectra.  $^1\text{H}$  NMR spectra were referenced to internal  $\text{C}_6\text{D}_5\text{H}$  (7.15 ppm),  $^{31}\text{P}\{^1\text{H}\}$  NMR spectra to external  $\text{P}(\text{OMe})_3$  (141.0 ppm with respect to 85%  $\text{H}_3\text{PO}_4$  at 0.0 ppm), and  $^7\text{Li}\{^1\text{H}\}$  NMR spectra to a 0.3 mol  $\text{L}^{-1}$   $\text{LiCl}$  solution in  $\text{MeOH}$  (0.00 ppm). Elemental analyses were performed in the departmental facility; mass spectra were recorded on a Kratos MS 50. Clusters assigned to specific ions show appropriate isotopic distribution patterns, as calculated for the atoms present.  $\text{NbCl}_5$  was purchased from Strem Chemicals and used without further purification. Anhydrous  $\text{ZnCl}_2$  was purchased from Aldrich and dried by refluxing in excess  $\text{SOCl}_2$  under  $\text{N}_2$ .  $\text{MeNH}_3^+\text{Cl}^-$  was purchased from Fisher Chemicals and recrystallized out of hot ethanol and dried in vacuo prior to use. The reagents  $\text{PhNH}_2$ ,  $\text{ClSiMe}_2\text{CH}_2\text{Cl}$ ,  $\text{CyPH}_2$ ,  $\text{MesNH}_2$  ( $\text{MesNH}_2 = 2,4,6\text{-Me}_3\text{C}_6\text{H}_2\text{NH}_2$ ), and  $\text{PhPCl}_2$  were purchased from Aldrich and purified by standard procedures (6). Solutions of  $\text{MeLi}$  (1.4 mol  $\text{L}^{-1}$  in diethylether) and  $^n\text{BuLi}$  (1.6 mol  $\text{L}^{-1}$  in hexanes) were obtained from Acros Organics and used as received. The compounds  $\text{PhPH}_2$  (7),  $\text{Ph}^{\text{Ph}}[\text{NPN}]\text{Li}_2(\text{THF})_2$  (2),  $\text{Cy}^{\text{Ph}}[\text{NPN}]\text{Li}_2(\text{OEt})_2$  (8),  $\text{VCl}_3(\text{THF})_3$  (9),  $\text{KC}_8$  (10), and  $\text{NbCl}_2\text{Me}_3$  (11) were prepared by literature methods.

Crystallographic data<sup>2</sup> for compounds **4** and **7** appear in Tables 1 and 2, respectively. All measurements were made on a Rigaku-ADSC CCD area detector with graphite monochromated  $\text{Mo K}\alpha$  radiation. The data were processed (12) and corrected for Lorentz and polarization effects. The structure was solved by direct methods (13) and expanded by using Fourier (14) techniques. All nonhydrogen atoms were refined with anisotropic thermal parameters. Neutral atom scattering factors and anomalous dispersion corrections were taken from the International tables for X-ray crystallography (15, 16).

#### $\text{Cy}^{\text{Mes}}[\text{NPN}]\text{Li}_2(\text{THF})$ (**4**)

A 300 mL ethereal solution containing 12.1 mL (11.640 g, 86.1 mmol) of  $\text{MesNH}_2$  was cooled to  $-78^\circ\text{C}$  in a dry ice – isopropanol slush bath. A solution of 1.6 mol  $\text{L}^{-1}$   $^n\text{BuLi}$  in hexanes was added dropwise via syringe. After 30 min at  $-78^\circ\text{C}$ , the solution was warmed to room temperature (r.t.) and stirred for 60 min. Upon recooling the solution to  $-78^\circ\text{C}$ , 11.4 mL (12.320 g, 86.1 mmol) of  $\text{ClSiMe}_2\text{CH}_2\text{Cl}$  was added and stirred for 30 min. After warming to r.t. and stirring for an additional 30 min, the solution was cooled to  $0^\circ\text{C}$  and 5.8 mL (43.1 mmol) of  $\text{CyPH}_2$  and 107.6 mL (172.2 mmol) of  $^n\text{BuLi}$  was added consecutively via syringe. This solution was stirred for 30 min and allowed to warm to r.t. The resulting white suspension was concentrated in vacuo, and the white residue was dissolved in toluene (32 g) and filtered through Celite. Removal of toluene in vacuo yielded a foamy white solid, which was dissolved in hexanes (150 mL). Addition of 5.25 mL (0.0647 mol) of THF caused  $\text{Cy}^{\text{Mes}}[\text{NPN}]\text{Li}_2(\text{THF})$  (**4**) to precipitate as a white microcrystalline solid, which was col-

**Table 1.** Crystallographic data and details of refinement for  $\text{Cy}^{\text{Mes}}[\text{NPN}]\text{Li}_2(\text{THF})$ , **4**.

Empirical formula	$\text{C}_{34}\text{H}_{57}\text{Li}_2\text{N}_2\text{OPSi}_2$
Formula weight	610.86
Crystal system	Monoclinic
Space group	$P2_1/a$
$a, b, c$ (Å)	19.597(1), 8.9414(4), 21.492(2)
$\beta$ ( $^\circ$ )	105.846(3)
$V$ (Å <sup>3</sup> )	3623.0(4)
$Z$	4
$D_{\text{calcd}}$ (g $\text{cm}^{-3}$ )	1.120
$\mu$ (Mo $\text{K}\alpha$ ) ( $\text{cm}^{-1}$ )	1.69
$T$ (K)	173 $\pm$ 1
$2\theta$ range ( $^\circ$ )	55.7
Total reflections	34 076
Unique reflections	8455
Parameters	508
$R_1^a$	0.086
$R_w^a$	0.109
Goodness-of-fit	0.87

$$^a R_1 = \Sigma ||F_o| - |F_c|| / \Sigma |F_o|; R_w = \Sigma w(|F_o|^2 - |F_c|^2)^2 / \Sigma w|F_o|^2)^{1/2}.$$

**Table 2.** Crystallographic data and details of refinement for  $\text{Cy}^{\text{Ph}}[\text{NPN}]\text{VCl}_2$ , **7**.

Empirical formula	$\text{C}_{24}\text{H}_{37}\text{N}_2\text{PClSi}_2\text{V}$
Formula weight	1054.22
Crystal system	Triclinic
Space group	$P\bar{1}$
$a, b, c$ (Å)	10.2811(5), 11.4776(4), 13.3016(6)
$\alpha, \beta, \gamma$ ( $^\circ$ )	103.948(3), 111.556(1), 92.914(3)
$V$ (Å <sup>3</sup> )	1399.8(1)
$Z$	1
$D_{\text{calcd}}$ (g $\text{cm}^{-3}$ )	1.250
$\mu$ (Mo $\text{K}\alpha$ ) ( $\text{cm}^{-1}$ )	6.06
$T$ (K)	173 $\pm$ 1
$2\theta$ range ( $^\circ$ )	55.8
Total reflections	12 014
Unique reflections	5342
Parameters	280
$R_1^a$	0.047
$R_w^a$	0.095
Goodness-of-fit	1.48

$$^a R_1 = \Sigma ||F_o| - |F_c|| / \Sigma |F_o|; R_w = \Sigma w(|F_o|^2 - |F_c|^2)^2 / \Sigma w|F_o|^2)^{1/2}.$$

lected on a frit and dried under vacuum (79% yield). The other ligand precursors,  $\text{Ph}^{\text{Mes}}[\text{NPN}]\text{Li}_2(\text{diox})_2$  (**3**),  $\text{Ph}^{\text{Me}}[\text{NPN}]\text{Li}_2(\text{diox})_2$  (**5**), and  $\text{Cy}^{\text{Me}}[\text{NPN}]\text{Li}_2(\text{diox})_2$  (**6**) (diox = dioxane) were synthesized using the appropriate phosphines and amines in an analogous manner. Precipitation of **3**, **5**, and **6** was accomplished by addition of 3 equiv of dioxane to a hexanes solution of each product. Recovered yields were 81%, 74%, and 66%, respectively. For the  $N$ -

<sup>2</sup>Supplementary data (crystallographic data (excluding structure factors) for  $\text{Cy}^{\text{Mes}}[\text{NPN}]\text{Li}_2(\text{THF})$ , **4**, and  $\text{Cy}^{\text{Ph}}[\text{NPN}]\text{VCl}_2$ , **7**, may be purchased from the Depository of Unpublished Data, Document Delivery, CISTI, National Research Council Canada, Ottawa, ON K1A 0S2, Canada ([http://www.nrc.ca/cisti/irm/unpub\\_e.shtml](http://www.nrc.ca/cisti/irm/unpub_e.shtml) for information on ordering electronically). CCDC 211498 and 211499, respectively, contain the supplementary data for this paper. These data can be obtained, free of charge, via [www.ccdc.cam.ac.uk/conts/retrieving.html](http://www.ccdc.cam.ac.uk/conts/retrieving.html) (or from the Cambridge Crystallographic Data Centre, 12 Union Road, Cambridge, U.K.; fax +44 1223 336033; or deposit@ccdc.cam.ac.uk).



methyl derivatives,  $\text{MeNH}_3^+\text{Cl}^-$  was used to prepare the lithium amide, and an additional equivalent of  $^n\text{BuLi}$  was used. **3**:  $^1\text{H}$  NMR ( $\text{C}_6\text{D}_6$ , 25 °C, 500 MHz)  $\delta$ : 0.22, 0.33 (s, 12H total, Si- $\text{CH}_3$ ), 1.28 (m, 4H, P- $\text{CH}_2$ ), 7.15, 7.24, 7.61 (m, 5H, P-Ph- $\text{H}$ ), 6.80 (s, 4H, NPh- $m$ -H).  $^{31}\text{P}\{^1\text{H}\}$  NMR ( $\text{C}_6\text{D}_6$ , 25 °C)  $\delta$ : -34.1 (q,  $^1J_{\text{PLi}} = 18.9$  Hz).  $^7\text{Li}\{^1\text{H}\}$  NMR ( $\text{C}_6\text{D}_6$ , 25 °C)  $\delta$ : -0.7 (s, 1Li), -0.8 (d,  $^1J_{\text{PLi}} = 18.9$  Hz, 1Li). Anal. calcd. for  $\text{C}_{38}\text{H}_{59}\text{Li}_2\text{N}_2\text{O}_4\text{PSi}_2$  (%): C 64.38, H 8.39, N 3.95; found: C 64.54, H 8.49, N 3.86. **4**:  $^1\text{H}$  NMR ( $\text{C}_6\text{D}_6$ , 25 °C, 500 MHz)  $\delta$ : 0.21, 0.35 (s, 12H total, Si- $\text{CH}_3$ ), 2.20 (s, 18H, NPh- $\text{CH}_3$ ), 1.13, 2.96 (s, 8H, THF), 0.85, 0.97 (m, 4H, P- $\text{CH}_2$ ), 1.22, 1.38, 1.68, 1.77, 1.91 (m, 11H, P- $\text{C}_6\text{H}_{11}$ ), 6.82 (s, 4H, NPh- $m$ -H).  $^{31}\text{P}\{^1\text{H}\}$  NMR ( $\text{C}_6\text{D}_6$ , 25 °C)  $\delta$ : -30.2 (s).  $^7\text{Li}\{^1\text{H}\}$  NMR ( $\text{C}_6\text{D}_6$ , 25 °C)  $\delta$ : -0.8 (s, 2 Li). Anal. calcd. for  $\text{C}_{34}\text{H}_{57}\text{Li}_2\text{N}_2\text{O}_4\text{PSi}_2$  (%): C 66.85, H 9.41, N 4.59; found: C 66.98, H 9.60, N 4.39. **5**:  $^1\text{H}$  NMR ( $\text{C}_6\text{D}_6$ , 25 °C, 500 MHz)  $\delta$ : -0.09, -0.10 (s, 12H total, Si- $\text{CH}_3$ ), 2.83 (s, 6H, N- $\text{CH}_3$ ), 3.57 (s, 16H, dioxane), 0.89, 0.91 (m, 4H, P- $\text{CH}_2$ ), 7.15, 7.22, 7.49 (m, 5H, P-Ph- $\text{H}$ ).  $^{31}\text{P}\{^1\text{H}\}$  NMR ( $\text{C}_6\text{D}_6$ , 25 °C)  $\delta$ : -37.5 (q,  $^1J_{\text{PLi}} = 26.6$  Hz).  $^7\text{Li}\{^1\text{H}\}$  NMR ( $\text{C}_6\text{D}_6$ , 25 °C)  $\delta$ : -1.4 (s, 1 Li), -1.5 (d,  $^1J_{\text{PLi}} = 26.6$  Hz, 1 Li). Anal. calcd. for  $\text{C}_{22}\text{H}_{43}\text{Li}_2\text{N}_2\text{O}_4\text{PSi}_2$  (%): C 52.78, H 8.66, N 5.60; found: C 52.52, H 8.41, N 5.75. **6**:  $^1\text{H}$  NMR ( $\text{C}_6\text{D}_6$ , 25 °C, 500 MHz)  $\delta$ : 0.35 (s, 12H total, Si- $\text{CH}_3$ ), 3.42 (s, 8H, dioxane), 0.88, 1.22 (m, 4H, P- $\text{CH}_2$ ), 1.68, 1.79, 1.94 (m, 11H, P- $\text{C}_6\text{H}_{11}$ ), 3.02 (s, 6H, N- $\text{CH}_3$ ).  $^{31}\text{P}\{^1\text{H}\}$  NMR ( $\text{C}_6\text{D}_6$ , 25 °C)  $\delta$ : -36.1 (s).  $^7\text{Li}\{^1\text{H}\}$  NMR ( $\text{C}_6\text{D}_6$ , 25 °C)  $\delta$ : -1.1 (s, 1 Li). Anal. calcd. for  $\text{C}_{18}\text{H}_{41}\text{Li}_2\text{N}_2\text{O}_2\text{PSi}_2$  (%): C 51.65, H 9.87, N 6.69; found: C 51.93, H 9.85, N 6.60.

### ( $^{\text{CyPh}}[\text{NPN}]\text{VCl}_2$ )**2** (**7**)

An ethereal solution (100 mL) of  $^{\text{CyPh}}[\text{NPN}]\text{Li}_2(\text{OEt})_2$  (3.00 g, 4.23 mmol) maintained at -78 °C was added via cannula to a 3:1 mixture of  $\text{Et}_2\text{O}$  and THF containing  $\text{VCl}_3(\text{THF})_3$  (1.58 g, 4.23 mmol). After the addition, the solution was warmed to r.t. and stirred for 90 min. Upon removal of volatiles, the resultant brick-red powder was dissolved in toluene (100 mL); the solution was filtered through Celite to remove LiCl, and the toluene was removed in vacuo. The brick-red powder was washed with pentane and dried under vacuum (75.8%, 1.69 g). Crystals of **7** suitable for X-ray diffraction were grown from a concentrated solution of layered benzene-HMDS. The compounds ( $^{\text{PhPh}}[\text{NPN}]\text{VCl}_2$ )**2**, **8**, ( $^{\text{CyMes}}[\text{NPN}]\text{VCl}_2$ )**2**, **9**, ( $^{\text{PhMes}}[\text{NPN}]\text{VCl}_2$ )**2**, **10**, ( $^{\text{CyMe}}[\text{NPN}]\text{VCl}_2$ )**2**, **11**, and ( $^{\text{PhMe}}[\text{NPN}]\text{VCl}_2$ )**2**, **12**, were prepared analogously. **7**: EI-MS  $m/z$  (%): 526 ( $[\text{M}^+]$   $^{\text{CyPh}}[\text{NPN}]\text{VCl}$ , 100). Anal. calcd. for  $\text{C}_{48}\text{H}_{74}\text{Cl}_2\text{N}_4\text{P}_2\text{Si}_4\text{V}_2$  (%): C 54.69, H 7.08, N 5.31; found: C 54.97, H 7.26, N 5.05. **8**: EI-MS  $m/z$  (%): 520 ( $[\text{M}^+]$   $^{\text{PhPh}}[\text{NPN}]\text{VCl}$ , 100). Anal. calcd. for  $\text{C}_{48}\text{H}_{62}\text{Cl}_2\text{N}_4\text{P}_2\text{Si}_4\text{V}_2$  (%): C 55.32, H 6.00, N 5.38; found: C 55.50, H 5.88, N 5.10. **9**: EI-MS  $m/z$  (%): 610 ( $[\text{M}^+]$   $^{\text{CyMes}}[\text{NPN}]\text{VCl}$ , 100). Anal. calcd. for  $\text{C}_{60}\text{H}_{98}\text{Cl}_2\text{N}_4\text{P}_2\text{Si}_4\text{V}_2$  (%): C 58.95, H 8.08, N 4.58; found: C 58.97, H 8.26, N 4.55. **10**: EI-MS  $m/z$  (%): 604 ( $[\text{M}^+]$   $^{\text{PhMes}}[\text{NPN}]\text{VCl}$ , 100). Anal. calcd. for  $\text{C}_{60}\text{H}_{86}\text{Cl}_2\text{N}_4\text{P}_2\text{Si}_4\text{V}_2$  (%): C 59.54, H 7.16, N 4.63; found: C 59.37, H 7.00, N 4.39. **11**: EI-MS  $m/z$  (%): 402 ( $[\text{M}^+]$   $^{\text{CyMe}}[\text{NPN}]\text{VCl}$ , 100). Anal. calcd. for  $\text{C}_{28}\text{H}_{66}\text{Cl}_2\text{N}_4\text{P}_2\text{Si}_4\text{V}_2$  (%): C 41.73, H 8.25, N 6.95; found: C 41.90, H 8.02, N 6.85. **12**: EI-MS  $m/z$  (%): 396 ( $[\text{M}^+]$   $^{\text{PhMe}}[\text{NPN}]\text{VCl}$ , 100). Anal. calcd. for

$\text{C}_{28}\text{H}_{54}\text{Cl}_2\text{N}_4\text{P}_2\text{Si}_4\text{V}_2$  (%): C 42.36, H 6.86, N 7.06; found: C 42.09, H 6.89, N 6.90.

### Reduction of **7** with 2.2 $\text{KC}_8$ under 4 atm $\text{N}_2$

A thick-walled reaction vessel was charged with a magnetic stir bar, 0.218 g (0.413 mmol) of **7**, and 0.056 g (0.909 mmol) of  $\text{KC}_8$ .  $\text{Et}_2\text{O}$  (50 mL) was vacuum transferred into the flask, frozen at -196 °C, and charged with 4 atm of  $\text{N}_2$ . The brick-red solution turned deep purple upon warming to r.t. The reaction was stirred for 24 h. Filtration through Celite and removal of solvent gave a waxy purple, pentane-soluble solid. EI-MS  $m/z$  (%): 505 ( $[\text{M}^+]$ :  $^{\text{CyPh}}[\text{NPN}]\text{V}\equiv\text{N}$ , 100), 491 ( $^{\text{CyPh}}[\text{NPN}]\text{V}$ , 22).

### Reduction of **7** with 3.3 $\text{KC}_8$ under 4 atm $\text{N}_2$

Diethylether (50 mL) was vacuum transferred into a thick-walled reaction vessel charged with a magnetic stir bar, 0.218 g (0.413 mmol) of **7**, and 0.084 g (1.364 mmol) of  $\text{KC}_8$  and frozen at -196 °C. The vessel was charged with 4 atm of  $\text{N}_2$  and warmed to r.t. The brick-red solution changed to olive green and was stirred for an additional 24 h. Filtration through Celite and removal of solvent gave a dark green, pentane-soluble powder. EI-MS  $m/z$  (%): 1049 ( $[\text{M}^+]$ :  $\text{K}(^{\text{CyPh}}[\text{NPN}]\text{V}\equiv\text{N})_2$ , 12), 505 ( $[\text{M}^+]$  -  $\text{K}(^{\text{CyPh}}[\text{NPN}]\text{V}\equiv\text{N})$ , 100), 491 ( $^{\text{CyPh}}[\text{NPN}]\text{V}$ , 20).

### Reduction of **9** with 2.2 $\text{KC}_8$ under 1 atm $\text{N}_2$

Diethylether (50 mL) was transferred via syringe into a thick-walled reaction vessel charged with a magnetic stir bar, 0.252 g (0.413 mmol) of **9**, and 0.056 g (0.909 mmol) of  $\text{KC}_8$  under an atmosphere of  $\text{N}_2$ . The vessel was sealed and the contents stirred for 24 h. Filtration through Celite and removal of solvent gave a brown, hexanes-soluble powder. Washing the powder with pentane produced an impure brown solid ( $^{\text{CyMes}}[\text{NPN}]\text{V}=\text{NMe}$ s, **13**) and a brown solution, which, upon cooling to -37 °C, afforded brown needle crystals of  $\text{MesN}(\text{SiMe}_2\text{CH}_2)_2\text{PCy}$ , **14**. Reductions of **8** and **10**–**12** were conducted in the same manner. **13**: EI-MS  $m/z$  (%): 708 ( $[\text{M}^+]$   $^{\text{CyMes}}[\text{NPN}]\text{V}=\text{NMe}$ s, 50), 575 ( $[\text{M}^+]$  -  $\text{NMe}$ s, 100). **14**:  $^1\text{H}$  NMR ( $\text{C}_6\text{D}_6$ , 25 °C, 200 MHz)  $\delta$ : 2.28, 2.32 (s, 6H total,  $o$ -Ph- $\text{CH}_3$ ), 2.40 (s, 3H,  $p$ -Ph- $\text{CH}_3$ ), 6.90, 7.25 (s, 2H total,  $m$ -Ph- $\text{H}$ ), 0.05, 0.58 (s, 12H total, Si- $\text{CH}_3$ ), 0.85, 1.39, 1.97 (m, 15H total,  $\text{CH}_2$  and  $\text{C}_6\text{H}_{11}$ ).  $^{31}\text{P}\{^1\text{H}\}$  NMR ( $\text{C}_6\text{D}_6$ , 25 °C)  $\delta$ : -25.8 (s). Anal. calcd. for  $\text{C}_{21}\text{H}_{38}\text{NPSi}_2$  (%): C 64.40, H 9.78, N 3.58; found: C 64.45, H 9.70, N 3.51. **Reduction of 8**: EI-MS  $m/z$  (%): 576 ( $[\text{M}^+]$   $^{\text{PhPh}}[\text{NPN}]\text{V}=\text{NPh}$ , 20), 485 ( $[\text{M}^+]$  -  $\text{NPh}$ , 100). **Reduction of 10**: EI-MS  $m/z$  (%): 702 ( $[\text{M}^+]$   $^{\text{PhMes}}[\text{NPN}]\text{V}=\text{NMe}$ s, 35), 569 ( $[\text{M}^+]$  -  $\text{NMe}$ s, 100). **Reduction of 11**: EI-MS  $m/z$  (%): 396 ( $[\text{M}^+]$   $^{\text{CyMe}}[\text{NPN}]\text{V}=\text{NMe}$ , 8), 367 ( $[\text{M}^+]$  -  $\text{NMe}$ , 100). **Reduction of 12**: EI-MS  $m/z$  (%): 390 ( $[\text{M}^+]$   $^{\text{PhMe}}[\text{NPN}]\text{V}=\text{NMe}$ , 12), 361 ( $[\text{M}^+]$  -  $\text{NMe}$ , 100).

### $^{\text{CyPh}}[\text{NPN}]\text{NbMe}_3$ (**15**)

In the dark, a solution of 5.601 g (0.0106 mol) of **2** in 150 mL of  $\text{Et}_2\text{O}$  maintained at -78 °C was added via cannula to a solution of 2.200 g (0.0106 mol) of  $\text{NbCl}_2\text{Me}_3$  in 150 mL of  $\text{Et}_2\text{O}$ . The solution was stirred at -78 °C for 1 h, then warmed to -10 °C, producing an orange solution. Excess  $\text{Et}_2\text{O}$  was removed in vacuo, and the resulting solid was dissolved in toluene and filtered through Celite. Toluene was



removed in vacuo and the solid washed with pentane to afford **15** in 72% yield (4.42 g). The solid was highly light and thermally sensitive and was stored in a darkened vessel at  $-37^{\circ}\text{C}$ . Preparation of  $^{\text{PhPh}}[\text{NPN}]\text{NbMe}_3$ , **16**, and  $^{\text{CyMes}}[\text{NPN}]\text{NbMe}_3$ , **17**, was accomplished in the same manner. Reactions of **3**, **5**, and **6** did not afford the corresponding  $^{\text{R}^{\text{R}}\text{R}^{\text{R}}'}[\text{NPN}]\text{NbMe}_3$  species, as decomposition pathways prevented isolation of pure product. **15**:  $^1\text{H}$  NMR ( $\text{C}_6\text{D}_6$ ,  $25^{\circ}\text{C}$ , 500 MHz)  $\delta$ : 0.00, 0.34 (s, 12H, Si- $(\text{CH}_3)_3$ ), 0.75–1.42 (ov, m, 15H total,  $\text{CH}_2$  and  $\text{C}_6\text{H}_{11}$ ), 1.68 (s, 9H, Nb- $(\text{CH}_3)_3$ ), 6.96–7.12 (ov, m, 10H, N-Ph- $H$ ).  $^{31}\text{P}\{^1\text{H}\}$  NMR ( $\text{C}_6\text{D}_6$ ,  $25^{\circ}\text{C}$ )  $\delta$ : 10.8 (s). **16**:  $^1\text{H}$  NMR ( $\text{C}_6\text{D}_6$ ,  $25^{\circ}\text{C}$ , 500 MHz)  $\delta$ :  $-0.08$ ,  $0.35$  (s, 12H total, Si- $(\text{CH}_3)_3$ ),  $1.20$  (m, 4H total,  $\text{CH}_2$ ),  $1.63$  (s, 9H, Nb- $(\text{CH}_3)_3$ ),  $6.80$ – $7.38$ ,  $7.60$ – $7.85$  (s, 12H total, N-Ph, P-Ph).  $^{31}\text{P}\{^1\text{H}\}$  NMR ( $\text{C}_6\text{D}_6$ ,  $25^{\circ}\text{C}$ )  $\delta$ : 6.2 (s). **17**:  $^1\text{H}$  NMR ( $\text{C}_6\text{D}_6$ ,  $25^{\circ}\text{C}$ , 500 MHz)  $\delta$ : 2.29 (s, 9H, Nb- $(\text{CH}_3)_3$ ), 2.10, 2.16 (s, 12H total, *o*-Ph- $(\text{CH}_3)_3$ ), 2.39 (s, 6H, *p*-Ph- $\text{CH}_3$ ), 0.21, 0.29 (s, 12H total, Si- $(\text{CH}_3)_3$ ), 0.91–2.08 (m, 15H total,  $\text{CH}_2$  and  $\text{C}_6\text{H}_{11}$ ), 6.82, 7.02 (s, 4H total, *m*-Ph- $H$ ).  $^{31}\text{P}\{^1\text{H}\}$  NMR ( $\text{C}_6\text{D}_6$ ,  $25^{\circ}\text{C}$ )  $\delta$ : 11.2 (s).

### Attempted hydrogenations of **15**–**17**

Hydrogenations of the three  $^{\text{R}^{\text{R}}\text{R}^{\text{R}}'}[\text{NPN}]\text{NbMe}_3$  complexes were attempted using the same methodology as that shown for **15** below. A 75 mL ethereal solution of 0.500 g (0.864 mmol) of **15** was prepared in a thick-walled reaction vessel and immediately cooled to  $-78^{\circ}\text{C}$ .  $\text{N}_2$  was removed by successive freeze-pump-thaw cycles. The solution was then frozen at  $-196^{\circ}\text{C}$ , flushed with  $\text{H}_2$ , sealed, warmed to r.t., and stirred for 24 h. Solvent was removed in vacuo, yielding a dark brown solid. Extensive decomposition of **15** complicated analysis. In situ NMR studies (1 atm) confirmed that no hydride resonances were observable during the hydrogenation attempts.

## Results and discussion

One of the key advantages of the diamidophosphine ligands, referred to as [NPN], is their inherent ability to tune steric and electronic properties by varying the substituents on the amido and phosphine donors. In this report,  $^{\text{R}^{\text{R}}\text{R}^{\text{R}}'}$ [NPN] refers to the ligand  $\text{R}'\text{P}(\text{CH}_2\text{SiMe}_2\text{NR}'')_2$ . The ligand precursors are isolated as solvent adducts of the dilithium diamidophosphines both for ease of purification and to facilitate reaction with metal chlorides. The synthesis of  $^{\text{PhPh}}[\text{NPN}]\text{Li}_2(\text{THF})_2$ , **1** (**2**), and  $^{\text{CyPh}}[\text{NPN}]\text{Li}_2(\text{OEt})_2$ , **2** (**8**), were reported previously. This report details the preparation of four new [NPN] precursors:  $^{\text{PhMes}}[\text{NPN}]\text{Li}_2(\text{diox})_2$ , **3**,  $^{\text{CyMes}}[\text{NPN}]\text{Li}_2(\text{THF})$ , **4**,  $^{\text{PhMe}}[\text{NPN}]\text{Li}_2(\text{diox})_2$ , **5**, and  $^{\text{CyMe}}[\text{NPN}]\text{Li}_2(\text{diox})$ , **6**. A general synthesis of these derivatives is shown in Scheme 1.

Synthesis of **4** and **5** proceeds by metathesis of  $\text{MesNHLi}$  with  $\text{ClCH}_2\text{SiMe}_2\text{Cl}$  at  $-78^{\circ}\text{C}$  to form a silylamine that reacts in situ with the desired primary phosphine,  $\text{RPH}_2$ , and 4 equiv (with respect to  $\text{MesNHLi}$ ) of  $n\text{-BuLi}$ . When phenylphosphine is used in this methodology, the ligand precursor precipitates as a pale yellow solid, **3**, after addition of 2.5 equiv of dioxane to a hexanes solution of the product. Similarly, when cyclohexylphosphine is used in this methodology, white crystals (**4**) were isolated after addition of 1.5 equiv of tetrahydrofuran to a hexanes solution of the

product.  $^{\text{PhMe}}[\text{NPN}]\text{Li}_2(\text{diox})_2$ , **5**, and  $^{\text{CyMe}}[\text{NPN}]\text{Li}_2(\text{diox})$ , **6**, were prepared by an analogous procedure, except the requisite amine hydrochloride salt  $\text{MeNH}_3^+\text{Cl}^-$  is used to prepare  $\text{MeNHLi}$  prior to metathesis. The ligand precursors were characterized by  $^{31}\text{P}\{^1\text{H}\}$ ,  $^1\text{H}$ , and  $^7\text{Li}\{^1\text{H}\}$  NMR spectroscopy. Colorless platelet crystals of **4** were recrystallized from a saturated hexanes–toluene solution and analyzed by X-ray crystallography.

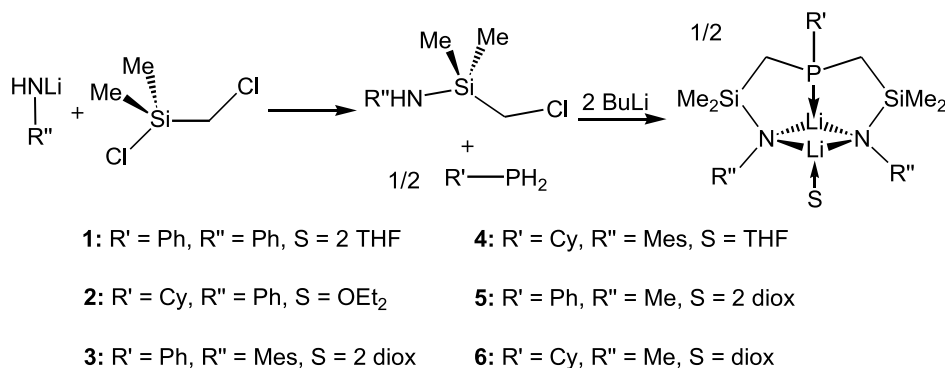
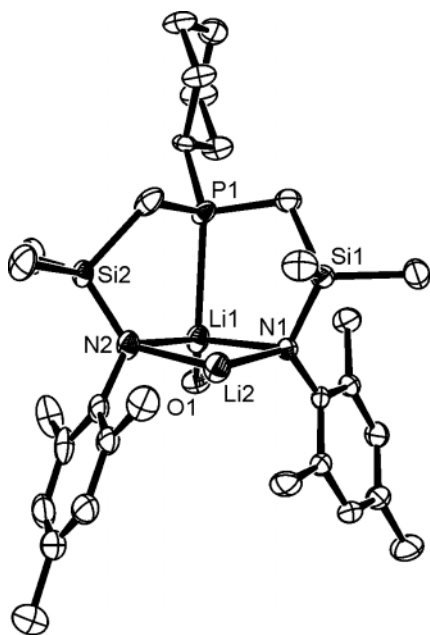
The molecular structure of **4** is shown as an ORTEP3 (17) drawing in Fig. 1. Relevant bond lengths and angles are listed in Table 3 and crystallographic data is located in Table 1. The X-ray data unambiguously show that **4** has a single coordinated THF molecule. The bond lengths from the amido nitrogen donors N1 and N2 to Li2 are approximately 0.2 Å shorter than the corresponding bond lengths from N1 and N2 to Li1, to which the THF molecule is coordinated. The P1–Li1 bond length is 2.589(4) Å, an average length for phosphorus–lithium bonds. Some disorder was evident. The crystalline lattice contained two different conformations of the ligand within the same unit cell. This manifested as overlapping opposite chair conformations of the cyclohexyl ring, as well as overlapping silyl methyl fragments.

Several interesting trends have been observed in the solution characterization of the six dilithio [NPN] precursors used in this report. The three ligand precursors with cyclohexyldonors (**2**, **4**, and **6**) are each monosolvent adducts, compared with **1**, **3**, and **5**, which have two coordinating solvent molecules. In each case, the solvent adduct isolated is the least soluble product. These same cyclohexylphosphine derivatives (**2**, **4**, and **6**) show no  $^{31}\text{P}$ – $^7\text{Li}$  coupling in solution (r.t.) that could suggest their solution behaviour is different than that found for **4** in the solid state (Fig. 1). One possibility is that the phosphine donor does not bind to the lithium ions in solution. However, a low temperature  $^{31}\text{P}$  spectrum ( $-25^{\circ}\text{C}$ ) of **2** shows a doublet due to  $^7\text{Li}$  coupling ( $J_{\text{PLi}} = 17.4$  Hz). It is likely that the lithium ions are undergoing intermolecular exchange in solution, fast enough at room temperature to lose coupling information. However, at lower temperatures, this process is slow, and coupling between  $^7\text{Li}$  and  $^{31}\text{P}$  is observed. In solution, the structure of the dilithio derivative is therefore likely the same as in the solid state with phosphine bound to lithium.

$^{\text{PhPh}}[\text{NPN}]$  and  $^{\text{CyPh}}[\text{NPN}]$  ligand sets have already been applied to other group five metal-based systems. The complex  $^{\text{PhPh}}[\text{NPN}]\text{TaMe}_3$  reacts with  $\text{H}_2$  to form  $(^{\text{PhPh}}[\text{NPN}]\text{Ta})_2(\mu\text{-H})_4$  (**1**, **2**). Under an atmosphere of dinitrogen, this complex loses 1 equiv of  $\text{H}_2$  and binds dinitrogen to form  $(^{\text{PhPh}}[\text{NPN}]\text{Ta})_2(\mu\text{-H})_2(\mu\text{-}\eta^1\text{:}\eta^2\text{-N}_2)$ . This complex has an intriguing side-on, end-on coordination mode that promotes reactivity with E-H species (E = B, Si, Al) (**3**, **4**). Dinitrogen activation has also been observed by a related niobium system supported by a  $[\text{P}_2\text{N}_2]$  ligand set. Upon thermolysis, the complex  $([\text{P}_2\text{N}_2]\text{Nb})_2(\mu\text{-N}_2)$  (where  $[\text{P}_2\text{N}_2] = \text{PhP}(\text{CH}_2\text{SiMe}_2\text{NSiMe}_2\text{CH}_2)_2\text{PPh}$ ) decomposes into a bridging nitride species where one N atom from the activated  $\text{N}_2$  inserts into the macrocycle backbone, forming the complex  $[\text{P}_2\text{N}_2]\text{Nb}(\mu\text{-N})\text{Nb}[\text{PN}_3]$  (where  $[\text{PN}_3] = \text{PhPMe}(\text{CHSiMe}_2\text{NSiMe}_2\text{CH}_2\text{P}(\text{Ph})\text{CH}_2\text{SiMe}_2\text{NSiMe}_2\text{N})$ ) (**18**). As well, the complexes  $^{\text{RPh}}[\text{NPN}]\text{NbCl}(\text{DME})$ ,  $(^{\text{PhPh}}[\text{NPN}]\text{NbCl})_2(\mu\text{-N}_2)$ , and  $^{\text{RPh}}[\text{NPN}]\text{NbCl}_2$  (R = Cy, Ph; DME = dimethoxyethane) have been synthesized. The complex  $^{\text{CyPh}}[\text{NPN}]\text{NbCl}_2$



Scheme 1.

**Fig. 1.** ORTEP 3 plot for **4** (50% probability, THF carbons omitted for clarity).

decomposes in solution to form an imide,  $\text{Cy}^{\text{Ph}}[\text{NPN}]\text{NbCl}(\text{=NPh})$ , a cyclized [NP] ligand,  $\text{CyP}(\text{CH}_2\text{SiMe}_2)_2\text{NPh}$ , and a niobium(III) product by an intermolecular N—Si bond scission (8). The goal of this work is to examine how ligand modifications would affect other group 5 precursors.

Application of these ligand sets to vanadium(III) could afford species of the form  $[\text{NPN}]\text{VCl}$  from which a number of reactivities can be explored. Behavior of these systems might mimic that seen for niobium and generate a dinitrogen complex directly, analogous to  $(\text{Ph}^{\text{Ph}}[\text{NPN}]\text{NbCl})(\mu\text{-N}_2)$  chemistry. Alternatively, if the  $[\text{NPN}]\text{VCl}$  system were reduced under a dinitrogen atmosphere it would give a complex isoelectronic with  $\text{Mo}(\text{N}^{\text{tBuAr}})_3$ , which coordinates and splits molecular nitrogen to form the nitride  $(\text{N}^{\text{tBuAr}})_3\text{Mo}\equiv\text{N}$  (19, 20). The cleavage of molecular nitrogen was also observed when a bisamidoamine vanadium chloride complex was reduced (21).

Treatment of a cooled solution of  $\text{VCl}_3(\text{THF})_3$  in THF with an  $\text{Et}_2\text{O}$  solution of  $\text{Cy}^{\text{Ph}}[\text{NPN}]\text{Li}_2(\text{OEt}_2)$  gave a brick-red paramagnetic solid,  $\text{Cy}^{\text{Ph}}[\text{NPN}]\text{VCl}$ , **7**. Mass spectrometry

**Table 3.** Selected bond distances (Å) and angles (°) for  $\text{Cy}^{\text{Mes}}[\text{NPN}]\text{Li}_2(\text{THF})$ , **4**.

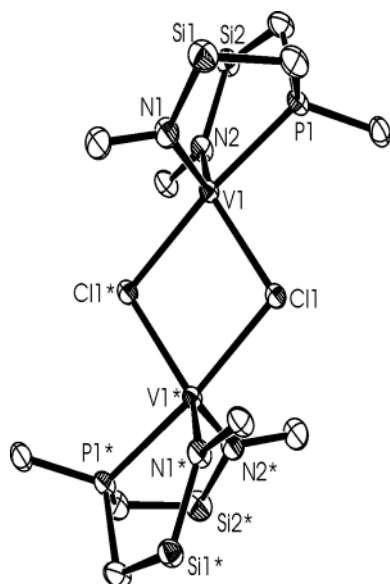
Bond distances (Å)	
P(1)—Li(1)	2.589(4)
N(1)—Li(1)	2.106(4)
N(1)—Li(2)	1.943(4)
N(2)—Li(1)	2.133(4)
N(2)—Li(2)	1.964(4)
O(1)—Li(1)	1.923(4)
Bond angles (°)	
C(7)—N(1)—Li(1)	103.74(15)
C(7)—N(1)—Li(2)	123.97(17)
C(22)—N(2)—Li(2)	94.27(16)
C(22)—N(2)—Li(1)	119.11(17)
Li(2)—N(2)—Li(1)	73.74(15)
Li(2)—N(1)—Li(1)	74.77(15)
O(1)—Li(1)—P(1)	121.74(16)

try and elemental analysis confirmed the empirical formula. Recrystallization of **7** from a layered benzene—HMDS solution at  $-35^\circ\text{C}$  gave red block crystals of  $(\text{Cy}^{\text{Ph}}[\text{NPN}]\text{VCl})_2$ . X-ray analysis of the crystals, isolated in 78% yield, showed that the compound exists as a chloride-bridged dimer. The molecular structure of **7** is shown as an ORTEP drawing in Fig. 2. Relevant bond lengths and angles and crystallographic data are listed in Tables 2 and 4, respectively. The  $\text{V}(1)\text{—Cl}(1)$  and  $\text{V}(1^*)\text{—Cl}(1)$  bond lengths of 2.3632(4) and 2.4913(4) Å, respectively, are average for a loosely bound chloride dimer (22); the compound appears as the monomer in mass spectrometry studies. The vanadium amide bond lengths of 1.935(1) and 1.934(1) Å agree with other amido vanadium chloride systems (23). While the  $\text{V}(1)\text{—P}(1)$  bond length of 2.4323(5) Å is not unusual for vanadium phosphine systems (23), it is short for related vanadium chloride dimers ( $\sim 2.6\text{--}2.7$  Å) (24–27). The overall complex is distorted trigonal bipyramidal with chlorine and phosphine ligands occupying the apical positions.

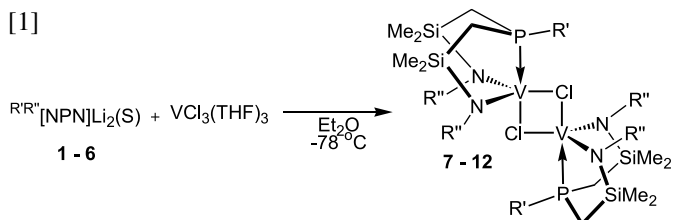
Similar reactions of ligand precursors **1**, **3**, **4**, **5**, and **6** with  $\text{VCl}_3(\text{THF})_3$  produced the vanadium chlorides  $\text{R}^{\text{R}''}[\text{NPN}]\text{VCl}$  ( $\text{R}'' = \text{Ph, Cy}$ ;  $\text{R}' = \text{Ph, Mes, Me}$ ; **8–12**). Characterization by mass spectrometry and elemental analysis confirmed the empirical formula in each case. A general synthesis is shown in eq. [1].



**Fig. 2.** ORTEP 3 plot for **7** (50% probability; silyl methyl and R' and R'' groups, save the attached carbons, have been omitted for clarity).



[1]



Reductions of **7–12** with potassium graphite ( $\text{KC}_8$ ) were conducted under four conditions: 1 atm  $\text{N}_2$  and 2.2 equiv of  $\text{KC}_8$ , 4 atm  $\text{N}_2$  and 2.2 equiv of  $\text{KC}_8$ , 1 atm  $\text{N}_2$  and 3.3 equiv of  $\text{KC}_8$ , 4 atm  $\text{N}_2$  and 3.3 equiv of  $\text{KC}_8$ . Reduction of **7** at 4 atm of  $\text{N}_2$  with 2.2 equiv of  $\text{KC}_8$  at  $-78^\circ\text{C}$  gave a strongly purple colored solution upon warming to r.t. Removal of  $\text{KCl}$  followed by recrystallization from a saturated pentane solution gave a deep purple paste, highly soluble in common organic solvents. Mass spectral analysis of the product indicated the formation of a  $^{\text{CyPh}}[\text{NPN}]\text{V}\equiv\text{N}$  species with a peak at  $m/z$  505 ( $\text{C}_{24}\text{H}_{37}\text{N}_3\text{Si}_2\text{PV}$ ), but repeated attempts to grow diffractable crystals failed. A paramagnetic impurity prevented purification and full characterization of the product. The observation of a mononuclear species by mass spectrometry does not, of course, prove its formulation. The species could have been generated in the experiment from a dinuclear bisnitride complex; however, it is unlikely to be generated from a compound with an intact  $\text{N}_2$  moiety (**18**).

Reduction of **7** at 4 atm of  $\text{N}_2$  with 3.3 equiv of  $\text{KC}_8$  at  $-78^\circ\text{C}$  gave a deep olive green solution upon warming to r.t. From the solution, a dark green solid was isolated and characterized by mass spectrometry. A small peak at  $m/z$  1050 ( $\text{C}_{48}\text{H}_{74}\text{KN}_6\text{P}_2\text{Si}_4\text{V}_2$ ), corresponding to  $\text{K}(\text{CyPh}[\text{NPN}]\text{V}\equiv\text{N})_2$ , as well as a substantial  $^{\text{CyPh}}[\text{NPN}]\text{V}\equiv\text{N}$  peak ( $m/z$  505, 100%), suggested dinitrogen incorporation during the reduction process. Unfortunately, the reduced products could not be purified. Attempts to improve the synthesis of the vanadium nitride by changing solvent, reaction time,  $\text{N}_2$  pressure,

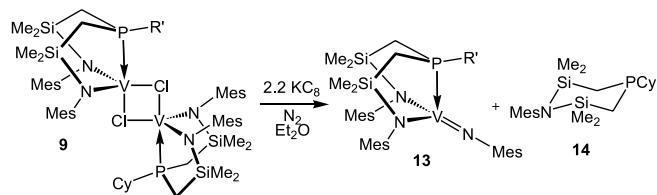
**Table 4.** Selected bond distances ( $\text{\AA}$ ) and angles ( $^\circ$ ) for  $(\text{CyPh}[\text{NPN}]\text{VCl})_2$ , **7**.

Bond distances ( $\text{\AA}$ )	
V(1)—Cl(1)	2.3632(4)
V(1)—Cl(1*)	2.4913(4)
V(1)—P(1)	2.4323(5)
V(1)—N(2)	1.934(1)
V(1)—N(1)	1.935(1)
Bond angles ( $^\circ$ )	
Cl(1)—V(1)—Cl(1*)	84.68(2)
Cl(1)—V(1)—N(1)	115.77(4)
Cl(1)—V(1)—P(1)	88.90(2)
Cl(1)—V(1)—N(2)	127.32(4)
N(1)—V(1)—N(2)	116.17(6)
P(1)—V(1)—N(1)	86.46(4)
P(1)—V(1)—N(2)	86.00(4)

reducing agent, or temperature were unsuccessful. Similarly, reductions of other vanadium chlorides (**8–12**) were unproductive. In several cases, there was no evidence of nitride formation.

The reduction of  $(\text{CyMes}[\text{NPN}]\text{VCl})_2$ , **9**, illustrated the problems associated with reduction of the vanadium chlorides. Upon workup of the reaction of **9** with 2.2 equiv of  $\text{KC}_8$ , a peak was observed in the mass spectrum at  $m/z$  709, which corresponds to  $^{\text{CyMes}}[\text{NPN}]\text{V}=\text{NMes}$ , as supported by theoretical isotope pattern calculations. The vanadium imide moiety  $^{\text{CyMes}}[\text{NPN}]\text{V}=\text{NMes}$  is the likely product of ring-closing of the  $[\text{NPN}]$  ligand on itself. Scissioning of one of the Si—N bonds and one of the N—V bonds in the  $([\text{NPN}]\text{VCl})_2$  species during reduction would result in the vanadium imide species **13** and the elimination of a six-membered heteroatomic ring **14**, as illustrated in eq. [2]. Crystals of **14** formed out of a toluene–hexanes solution, and the structure was verified by  $^1\text{H}$  NMR. Peaks corresponding to imide formation were observed in the mass spectra of each of the reductions conducted, no matter which substrate was reduced. As mentioned, decomposition of  $[\text{NPN}]$  metal complexes to form imides has complicated a previous study as well: the imide  $^{\text{CyPh}}[\text{NPN}]\text{NbCl}(\text{=NPh})$  was generated from the decomposition of  $^{\text{CyPh}}[\text{NPN}]\text{NbCl}_2$  (**8**).

[2]



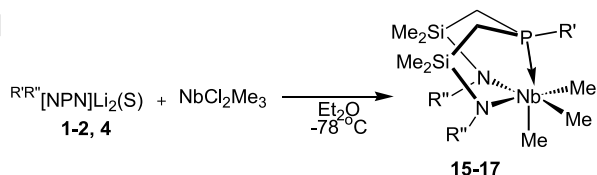
The  $[\text{NPN}]$  ligand may provide access to attractive  $\text{Nb(V)}$  complexes since the  $\text{Ta(V)}$  complex  $^{\text{PhPh}}[\text{NPN}]\text{TaMe}_3$  reacts with  $\text{H}_2$  to form  $(^{\text{PhPh}}[\text{NPN}]\text{Ta})_2(\mu\text{-H})_4$ , a precursor to the dinitrogen complex  $(^{\text{PhPh}}[\text{NPN}]\text{Ta})_2(\mu\text{-H})_2(\mu\text{-}\eta^1\text{:}\eta^2\text{-N}_2)$  (**2**). We examined the formation of  $^{\text{R'R''}}[\text{NPN}]\text{NbMe}_3$  and its reactivity with dihydrogen.

Production of  $^{\text{CyPh}}[\text{NPN}]\text{NbMe}_3$  (**15**) was accomplished via addition of a  $-78^\circ\text{C}$  solution of ligand to a cooled solu-



tion of  $\text{NbCl}_2\text{Me}_3$ , freshly sublimed before use. After solvent removal at  $-10^\circ\text{C}$ , the resultant brown solid was extracted with pentane to generate an orange solid that was characterized by  $^1\text{H}$  and  $^{31}\text{P}\{^1\text{H}\}$  NMR and mass spectrometry. The product was extremely photo- and thermo-sensitive and was stored in an opaque vessel at  $-37^\circ\text{C}$ . Thermal instability precluded the use of elemental analysis and  $^{13}\text{C}\{^1\text{H}\}$  NMR for characterization. A general reaction pathway is shown in eq. [3].

[3]



Reactions of  $\text{NbCl}_2\text{Me}_3$  with ligand precursors **1**, **3**, **4**, **5**, and **6** were not as successful. The products from these reactions were more thermally unstable and frequently decomposed prior to spectroscopic analysis. Only  $\text{PhPh}[\text{NPN}]\text{NbMe}_3$  (**16**) and  $\text{CyMes}[\text{NPN}]\text{NbMe}_3$  (**17**) were stable enough to characterize spectroscopically.

Hydrogenation of complexes **15–17** was attempted at 4 atm pressure. Following the addition of  $\text{H}_2$ , the reaction mixtures turned black and a precipitate formed. Analysis of the reaction mixture by NMR showed extensive decomposition. No hydride resonances were observed at the expected chemical shift for a niobium hydride. Attempts to vary reaction conditions to isolate the putative polyhydride species, by changing the concentration of reagents, temperature, exposure to light, pressure of  $\text{H}_2$ , solvent, or time of reaction, were unsuccessful. It is suspected that the trimethyl starting materials are too unstable to withstand the hydrogenation process.

## Conclusions

While a number of reports have shown the applicability of Ta(V), Nb(III), and V(III) systems to dinitrogen activation, in this work we have shown that small changes to the electronics and sterics of these systems can prevent such reaction pathways. Six variants of the [NPN] diamidophosphine ligand were used to prepare  $(\text{R}^{\text{R}''})[\text{NPN}]\text{VCl}_2$  complexes, to investigate their ability to coordinate and cleave dinitrogen upon reduction. Unfortunately, reduction of these complexes under a variety of conditions was complicated by ligand degradation to form a V(IV) imide. While some nitride-containing material was formed, it was not isolable. Similarly, the complexes  $(\text{R}^{\text{R}''})[\text{NPN}]\text{NbMe}_3$  were prepared, with the goal that these highly unstable materials could be hydrogenated in an analogous manner to the formation of  $([\text{NPN}]\text{Ta})_2(\mu\text{-H})_2(\mu\text{-}\eta^1\text{-}\eta^2\text{-N}_2)$ ; however, their thermal and photochemical decomposition occurred prior to hydrogenation. What becomes evident from this work is just how changes in ligand design or metal centres can lead to quite different and unpredictable reaction behaviour.

## Acknowledgments

Funding for this research was provided by the Natural Sciences and Engineering Research Council of Canada

(NSERC) in the form of a Research Grant to M.D.F. and a postgraduate scholarship to M.P.S. and the Killam Foundation for a postgraduate scholarship to M.P.S.

## References

1. M.D. Fryzuk, S.A. Johnson, and S.J. Rettig. *J. Am. Chem. Soc.* **120**, 11 024 (1998).
2. M.D. Fryzuk, S.A. Johnson, B.O. Patrick, A. Albinati, S.A. Mason, and T.F. Koetzle. *J. Am. Chem. Soc.* **123**, 3960 (2001).
3. M.D. Fryzuk, B.A. MacKay, S.A. Johnson, and B.O. Patrick. *Angew. Chem. Int. Ed.* **41**, 3709 (2002).
4. M.D. Fryzuk, B.A. MacKay, and B.O. Patrick. *J. Am. Chem. Soc.* **125**, 3234 (2003).
5. A.B. Pangborn, M.A. Giardello, R.H. Grubbs, R.K. Rosen, and F.J. Timmers. *Organometallics*, **15**, 1518 (1996).
6. D.D. Perrin and W.L.F. Armarego. *Purification of laboratory chemicals*. 3rd ed. Butterworth-Heinemann Ltd., Oxford. 1994.
7. M. Baudler and A. Zarkdas. *Chem. Ber.* **104**, 1034 (1965).
8. M.D. Fryzuk, M.P. Shaver, and B.O. Patrick. *Inorg. Chim. Acta.* **350**, 293 (2003).
9. L.E. Manzer. *Inorg. Synth.* **21**, 135 (1982).
10. D.E. Berbreiter and J.M. Killough. *J. Am. Chem. Soc.* **100**, 2126 (1978).
11. G.W.A. Fowles, D.A. Rice, and J.D. Wilkins. *J. Chem. Soc. Dalton Trans.* **9**, 961 (1973).
12. Molecular Structure Corp. *teXsan for Windows: Crystal structure analysis package [computer program]*. Molecular Structure Corp., The Woodlands, TX. 1996.
13. A. Altomane, M.C. Burla, G. Cammali, M. Cascarano, C. Giacovazzo, A. Gagliardi, A.G.G. Moliterni, G. Polidoi, and A. Spagna. *SIR 97: an integrated package of computer programs for the solution and refinement of crystal structures using single crystal data [computer program]*. CNR-IRMEC, Universitario, Bari, Italy. 1999.
14. P.T. Beurkens, G. Admiraal, G. Baurkens, W.P. Bosman, R. de Gelder, R. Israel, and J.M.M. Smits. *DIF-94 program system [computer program]*. University of Nijmegen, The Netherlands. 1994.
15. International Union of Crystallography. *International tables for X-ray crystallography*. Kynoch Press, Birmingham, U.K. 1974.
16. International Union of Crystallography. *International tables for crystallography*. Kluwer Academic, Boston, MA. 1992.
17. L.J. Farrugia. *J. Appl. Cryst.* **30**, 565 (1997).
18. M.D. Fryzuk, C.M. Kozak, M.R. Bowdridge, B.O. Patrick, and S.J. Rettig. *J. Am. Chem. Soc.* **124**, 8389 (2002).
19. C.E. LaPlaza and C.C. Cummins. *Science (Washington, D.C.)*, **268**, 861 (1995).
20. C.C. Cummins. *Chem. Commun.* **1998**, 1777 (1998).
21. G.K.B. Clentsmith, V.M.E. Bates, P.B. Hitchcock, and F.G.N. Cloke. *J. Am. Chem. Soc.* **121**, 10 444 (1999).
22. Cambridge Crystallography Data Centre. *Cambridge crystallography database*. [cited Nov. 2002].
23. P. Berno, M. Moore, R. Minhas, and S. Gambarotta. *Can. J. Chem.* **74**, 1930 (1996).
24. J. Nieman and J.H. Teuben. *Organometallics*, **5**, 1149 (1986).
25. F.A. Cotton, J. Lu, and T. Ren. *Inorg. Chim. Acta*, **215**, 47 (1994).
26. F.A. Cotton, S.A. Duraj, L.R. Falvello, and W.J. Roth. *Inorg. Chem.* **24**, 4389 (1985).
27. F.A. Cotton, S.A. Duraj, and W.J. Roth. *Inorg. Chem.* **23**, 4113 (1984).



# 2-Acetoxy-2-methoxy-5,5-dimethyl- $\Delta^3$ -1,3,4-oxadiazoline and acetoxy(methoxy)carbene

Wojciech Czardybon, Arkadiusz Klys, John Warkentin, and Nick Henry Werstiuk

**Abstract:** 2-Acetoxy-2-methoxy-5,5-dimethyl- $\Delta^3$ -1,3,4-oxadiazoline undergoes two competitive 1,3-dipolar cycloreversions at 110 °C. It loses N<sub>2</sub>, presumably to afford a short-lived carbonyl ylide that fragments to acetone and acetoxy(methoxy)carbene. It also forms 2-diazopropane and the appropriate mixed anhydride. It is the only currently known source of acetoxy(methoxy)carbene.

**Key words:** acetoxy(methoxy)carbene, 2-diazopropane, 1,3-dipolar cycloreversion.

**Résumé :** À 110 °C, la 2-acétoxy-2-méthoxy-5,5-diméthyl- $\Delta^3$ -1,3,4-oxadiazoline subit deux réactions de cycloréversion 1,3-dipolaire compétitives. Elle perd du N<sub>2</sub>, probablement pour fournir un ylure de carbonyle de temps de vie très court qui se fragmente en acétone et en acétoxy(méthoxy)carbène. Elle forme aussi du diazopropane et l'anhydride mixte approprié. C'est aussi la seule source actuellement connue d'acétoxy(méthoxy)carbène.

**Mots clés :** acétoxy(méthoxy)carbène, 2-diazopropane, cycloréversion 1,3-dipolaire.

[Traduit par la Rédaction]

## Introduction

Although many alkylacetoxycarbenes have been studied (1–5) and found to rearrange by 1,2-acyl migration in competition with other intramolecular processes, such as 1,2 migration of H, acyloxy(alkoxy)carbenes appear to be unknown. They are interesting intermediates, without the possibility of a 1,2-H migration. They have the potential for rearrangement by migration of the acyl group to the carbenic site, as well as the potential for fragmentation to alkoxy-carbonyl and acyl radicals. The 1,2-acyl migration of known acetoxy(alkyl)carbenes and the most likely reactions of acyloxy(alkoxy)carbenes are illustrated in Scheme 1.

We prepared and purified 2-acetoxy-2-methoxy-5,5-dimethyl- $\Delta^3$ -1,3,4-oxadiazoline (**1**) (6), which is a potential precursor of acetoxy(methoxy)carbene (**3**). 2,2-Dialkoxy-5,5-dimethyl- $\Delta^3$ -1,3,4-oxadiazolines undergo 1,3-dipolar cycloreversion by loss of N<sub>2</sub> at 110 °C to afford carbonyl ylides that fragment primarily to dialkoxycarbenes and acetone (7). There is a minor competitive 1,3-dipolar cycloreversion, in some cases, to 2-diazopropane (**4**) and dialkyl carbonate (8). Scheme 2 shows such cycloreversions for the case of **1**, which was expected to produce carbene **3**, via carbonyl ylide **2**, and perhaps 2-diazopropane (**4**) and the mixed anhydride **5**. Moreover the carbene might undergo a concerted rearrangement to methyl pyruvate (**6**) or a fragmentation to the methoxycarbonyl-acetyl radical pair that could couple to afford **6** also, Scheme 3.

We now describe the thermolysis of **1**, which does indeed lead to the formation of both carbene **3** and 2-diazopropane

(**4**). At 110 °C in benzene, both the carbene and the diazopropane can be intercepted with chemical trapping agents.

## Results and discussion

Thermolysis of **1** in benzene was studied in the absence of potential traps, in the presence of phenol (a carbene trap as well as a trap for diazo compounds and a hydrogen donor to radicals), in the presence of benzylidene malononitrile, and in the presence of TEMPO. TEMPO is a trap for radicals, and benzylidene malononitrile also can trap radicals, carbenes, and diazo compounds.

Thermolysis of **1** in benzene-*d*<sub>6</sub> containing internal standard *tert*-butylbenzene gave a complex mixture of products. Yields of **4** or of acetone azine from **1** are unreliable for estimation of the yield of the former, because diazopropane would react with the mixed anhydride co-product (**5**). The yield of acetone (presumably from the carbenic pathway) was found to be about 55% by integration of the acetone signal against those from the phenyl and *tert*-butyl groups of the internal standard. The two comparisons were in excellent agreement. Thus, the yield of acetoxymethoxycarbene was about 55% and that of 2-diazopropane about 45%. Methyl pyruvate was a major product (ca. 10%, isolated), but biacetyl and dimethyl oxalate, which might also be expected if the pyruvate had arisen by a radical coupling path, could not be detected by GC, with authentic samples in hand. It was also possible to detect (by GC) a trace of acetophenone, in keeping with the expectation that acetyl radicals would at-

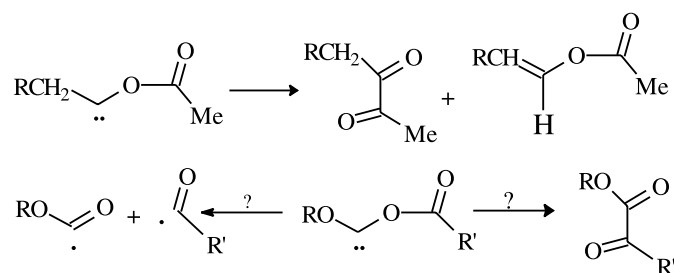
Received 23 May 2003. Published on the NRC Research Press Web site at <http://canjchem.nrc.ca> on 13 October 2003.

W. Czardybon, A. Klys, J. Warkentin,<sup>1</sup> and N.H. Werstiuk. Department of Chemistry, McMaster University, 1280 Main St. West, Hamilton, ON L8S 4M1, Canada.

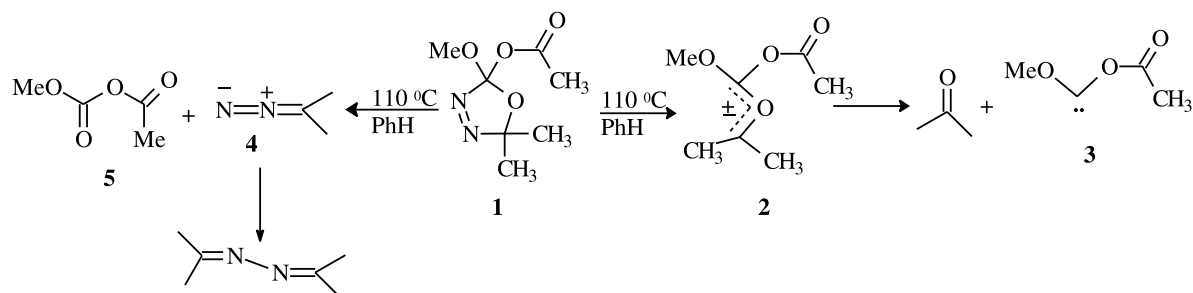
<sup>1</sup>Corresponding author (e-mail: [warkent@mcmaster.ca](mailto:warkent@mcmaster.ca)).



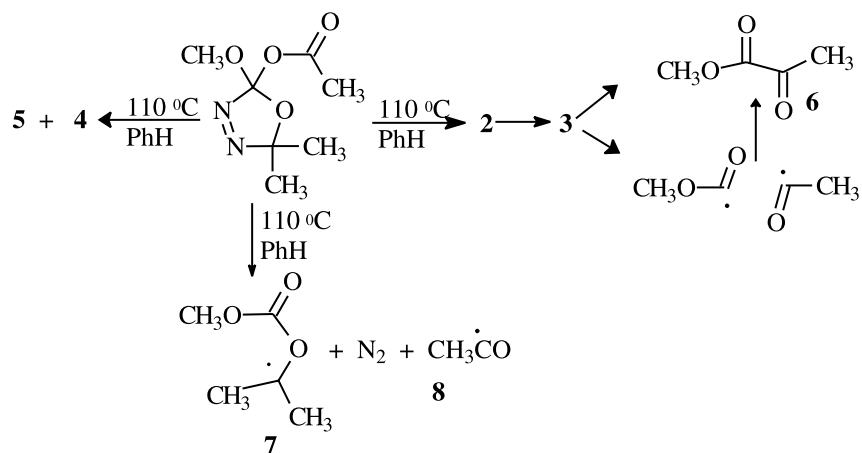
Scheme 1.



Scheme 2.



Scheme 3.



tack the benzene solvent. Thermolysis of **1** in the presence of TEMPO led to the isolation of enough of the known (9) TEMPO adduct of the acetyl radical (1-acetoxy-2,2,6,6-tetramethylpiperidine) for an NMR spectrum. However, the known adduct (10) of TEMPO with the methoxycarbonyl radical could not be found.

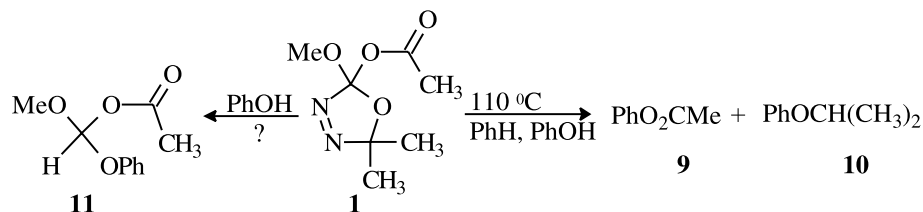
The results listed thus far are accounted for in terms of Scheme 3, which shows not only parallel 1,3-dipolar cycloreversions but also a radical decomposition of **1**. That minor radical decomposition is assumed to be concerted, leading to **7** and **8**. TEMPO would have trapped both **7** and **8** but the product expected from **7** was not identified. The failure to find any evidence for the methoxycarbonyl radical indicates that acetyl and methoxycarbonyl radicals are probably not formed by fragmentation of carbene **3**.

Thermolysis of **1** in benzene containing phenol gave **9** (31%) and **10** (5%) but not **11**. Compound **9** probably arises from a transesterification reaction with **1**, while **10** and **11** are expected products from reactions of **4** and **3**, respectively, with phenol, Scheme 4. Protonation of **3** and ion-pair collapse would generate **11**, which has never been reported. Such compounds may be unstable at 110 °C.

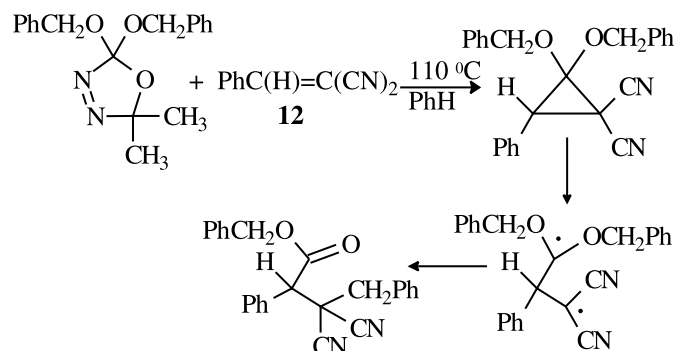
Benzylidene malononitrile (**12**) was very successful in trapping intermediates from the thermolysis of **1**. Dinitrile **12** had been useful in helping to sort out the chemistry of dibenzylidene carbene and benzyloxy(methoxy)carbene (**11**) because it reacts fast with nucleophilic carbenes, making it possible to trap some of them before they can fragment to radical pairs, Scheme 5. Thermolysis of **1** in the presence of **12** did not furnish a carbene adduct. Instead, the methoxy-



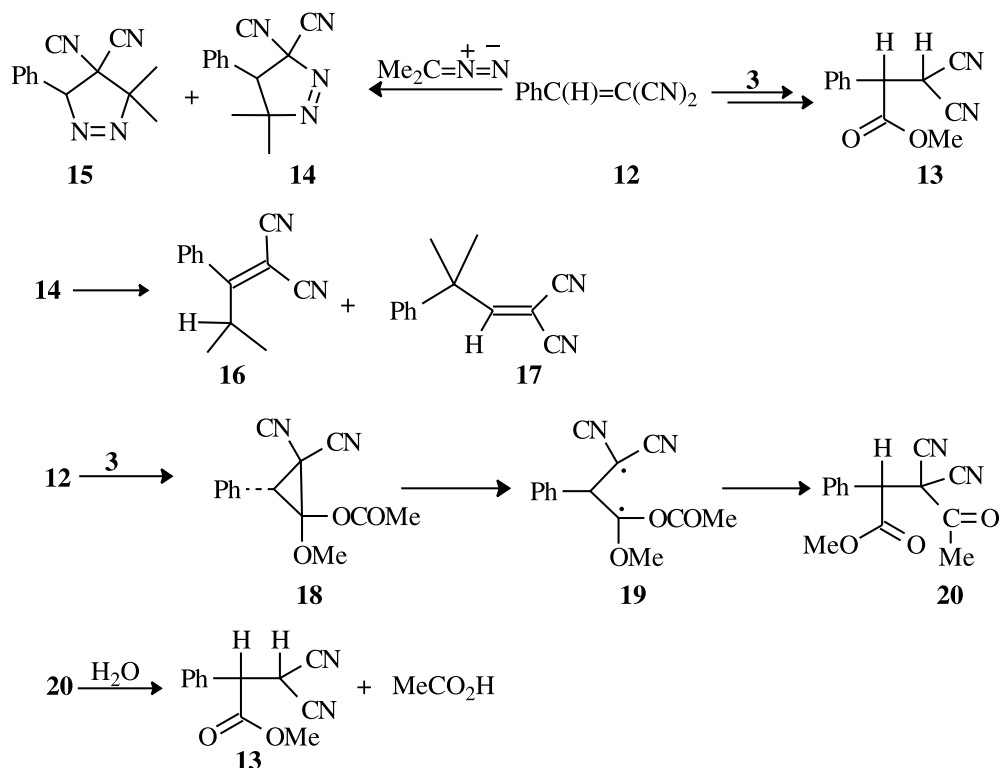
Scheme 4.



Scheme 5.



Scheme 6.



carbonyl radical, *apparently* resulting from carbene fragmentation to a radical pair, *appeared* to be trapped as **13** (30%), Scheme 6. Adduct **20**, expected on the basis of precedent (**11**) was not found, but **16** (17%) and **17** (12%) were also isolated.

The finding that **13** was formed from thermolysis of **1** in the presence of **12** but that **20** could not be found led us to

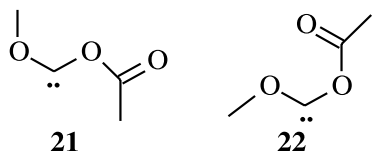
search the literature for analogues of **20**. Such compounds hydrolyze spontaneously when exposed to the atmosphere (**12**), Scheme 6. Thus, the most likely explanation for the formation of **13** is trapping of a carbene intermediate with **12** to form diastereomers **18** and subsequent ring-opening fragmentation to diradical **19**, followed by fragmentation and coupling to **20**, according to Scheme 6. Subsequent



deacylation of **20** (**12**), once the sample is exposed to the atmosphere, leads to **13**.

The concentration of **12** was increased from 0.455 to 2.127 mol·L<sup>-1</sup> to improve the chances of trapping carbene **3**. There was little change, suggesting that the lower concentration was sufficient to trap essentially all of **3**. Compounds **16** and **17** can be attributed to reaction of **4** in the expected sense with **12** to afford **14**, which then loses N<sub>2</sub>, Scheme 6. The higher concentration of **12** did lead to two very minor products (not identified) that were detected by GC–MS. Those compounds, which gave essentially the same mass spectrum as **16** and **17**, might be derived from cycloaddition of **4** in the alternative sense to form **15**, Scheme 6. Alkylidene malononitriles are known to react with diazo compounds by cycloaddition, and the resulting 3*H*-pyrazoles, not surprisingly (**13**), lose N<sub>2</sub> at 110 °C to afford diradicals that rearrange. Both regiochemistries of addition of diazomethane to a β-phenyl-α,β-unsaturated sulfone have been reported (**14**). Although **16** and **17**, as well as the minor products with the same MS, can be accounted for on the basis of **14** alone, formation and decomposition of some of compound **15** cannot be excluded.

The concerted rearrangement of the carbene and its fragmentation to a radical pair were modeled computationally with Gaussian 98 at the Becke3PW91/6-31+G(d, p) level (**15**). Concerted carbene rearrangement from one of the pos-



sible sickle conformations (**21**) has the lowest barrier (14.6 kcal·mol<sup>-1</sup>), whereas the lowest barrier to fragmentation (28.8 kcal·mol<sup>-1</sup>) is that from a second sickle conformation (**22**). Details of the computational work, which includes the examination of a number of other conceivable pathways, will be published separately.<sup>2</sup>

In summary, oxadiazoline **1** undergoes two competing cycloreversions at 110 °C in benzene, leading to both carbene **3** and diazopropane **4**. A minor, third thermolysis mechanism, currently regarded as tentative, is a radical process that generates the acetyl radical and **7**. Carbene **3** does not fragment to radicals but rearranges to methyl pyruvate by a 1,2-acyl migration, like other acetoxycarbenes (1–5).

Although thermolysis of **1** is far from ideal, in that it generates **3** in only about 50% yield and the co-products complicate the thermolysis, it is the only reaction available today to generate acetoxymethoxy carbene.

## Experimental

### General

A Bruker AC-200 spectrometer was used to obtain <sup>1</sup>H and <sup>13</sup>C NMR spectra, with CDCl<sub>3</sub> as solvent and with the signal from residual CHCl<sub>3</sub> in CDCl<sub>3</sub> set at δ = 7.25. GC–MS mass spectra were recorded with a Hewlett-Packard 5890 gas

chromatograph equipped with an HP-5971A mass selective detector and a DB-1 capillary column (12 m × 0.2 mm). Other mass spectra were obtained with a VG Analytical ZAB-E double focusing mass spectrometer.

### Synthesis of **1**

A solution of the carbomethoxy hydrazone of acetone (30 g, 0.23 mol) was added slowly to an ice-cooled heterogeneous mixture of Pb(OAc)<sub>4</sub> (115.3 g, 0.26 mol), acetic acid (1 mL), and CH<sub>2</sub>Cl<sub>2</sub> (114 mL). The yellow mixture was stirred under N<sub>2</sub>, warmed to 25 °C after addition was complete, and stirred for an additional 3 h. The mixture was then filtered through Celite and washed with 5% Na<sub>2</sub>CO<sub>3</sub> solution. The water fraction was back-extracted twice with 20 mL of CH<sub>2</sub>Cl<sub>2</sub>, and the combined organic fraction was dried over Na<sub>2</sub>SO<sub>4</sub> before the solvent was evaporated. The yellow oil that remained weighed 39 g (90%) and consisted of **1** (ca. 72%) and an acyclic isomer (Me<sub>2</sub>C-(OAc)N=NCO<sub>2</sub>Me) (ca. 28%).

### Purification of **1**

A yellow mixture of **1** and its acyclic isomer (5 g) was chromatographed as rapidly as possible on neutral alumina (35 g) with hexane – ethyl acetate (9:1). The solvents were evaporated from the combined colourless fractions, and the residue was distilled under vacuum (2–5 mmHg (1 mmHg = 133.322 Pa)) to afford 2.2 g of pure **1** (61%). IR (neat) (cm<sup>-1</sup>): 1771. <sup>1</sup>H NMR (200 MHz, CDCl<sub>3</sub>) δ: 1.52 (s, 3H), 1.63 (s, 3H), 2.11 (s, 3H), 3.59 (s, 3H). <sup>13</sup>C NMR (50.3 MHz, CDCl<sub>3</sub>) δ: 21.44, 22.59, 24.49, 52.49, 122.15, 133.80, 161.67.

### Thermolysis of **1** in benzene-*d*<sub>6</sub>

A solution of **1** (0.157 mmol) and *tert*-butylbenzene (0.127 mmol) in C<sub>6</sub>D<sub>6</sub> (0.7 mL) in an NMR tube fitted with a ground glass joint was degassed by means of three freeze–pump–thaw cycles before the tube was sealed and heated for 72 h at 110 °C. The <sup>1</sup>H NMR spectrum was acquired with the tube still sealed and with a pulse delay of 6 s to ensure complete relaxation of the acetone signal. Integrations of the acetone signal against those of the *tert*-butyl and aryl signals of *tert*-butyl benzene were in good agreement and gave the yield of acetone as 55%. Analysis by GC, with the column compartment cooled alternately to 7, 15, 21, and 32 °C, showed that methyl pyruvate (ca. 10%) and acetophenone (trace), both confirmed with authentic samples, were present. Biacetyl, dimethyl oxalate, acetaldehyde, and methyl formate were not detectable, as determined by injection of authentic samples under the same conditions, but there were peaks from unidentified volatile components.

### Thermolysis of **1** in the presence of phenol

Thermolysis of **1** (1.596 mmol) in C<sub>6</sub>H<sub>6</sub> (7 mL) containing phenol (3.191 mmol) gave a product mixture that was analyzed by GC. Major and minor products were phenylacetate (**9**) (ca. 30%) and isopropyl phenyl ether (**10**) (ca. 5%). The identities of those products were confirmed by GC of authentic samples prepared by standard methods. Acetaldehyde and methyl formate were not detectable.

<sup>2</sup> W. Czardybon, J. Warkentin, and N.H. Werstiuk. Unpublished results.



### Thermolysis of **1** in the presence of **12**

A solution of **1** (1.596 mmol) and **12** (3.188 mmol) in dry benzene (7 mL) was degassed by means of three freeze–pump–thaw cycles before it was sealed into a glass tube and heated for 72 h at 110 °C. The product mixture was analyzed by GC and separated by centrifugal chromatography on a 2 mm silica gel plate (Chromatotron apparatus, hexane: ethyl acetate = 4:1).

#### 1-(Methoxycarbonyl-1-phenylmethyl)propanedinitrile (**13**)

Yield: 16%. <sup>1</sup>H NMR (200 MHz, CDCl<sub>3</sub>) δ: 3.80 (s, 3H), 4.20 (d, *J* = 8.65 Hz, 1H), 4.39 (d, *J* = 8.65 Hz, 1H), 7.33–7.34 (m, 2H), 7.43–7.46 (m, 3H). <sup>13</sup>C NMR (50.3 MHz, CDCl<sub>3</sub>) δ: 27.09, 51.87, 53.76, 110.96, 111.60, 128.30, 129.87, 130.12, 131.68, 169.25. EI-MS *m/z*: 214 (13), 155 (26), 149 (34), 129 (35), 121 (100), 77 (38). HR-MS *m/z* calcd. for C<sub>12</sub>H<sub>10</sub>N<sub>2</sub>O<sub>2</sub>: 214.0742; found: 214.0736.

#### 2-Methyl-1-(phenylpropylidene)propanedinitrile (**16**)

Yield: 17%. <sup>1</sup>H NMR (200 MHz, CDCl<sub>3</sub>) δ: 1.19 (d, *J* = 6.9 Hz, 6H), 3.46 (sept. *J* = 6.9 Hz, 1H), 7.31–7.39 (m, 5H). <sup>13</sup>C NMR (50.3 MHz, CDCl<sub>3</sub>) δ: 20.66, 36.40, 86.90, 111.84, 112.13, 126.95, 128.96, 130.58, 134.09, 186.90. EI-MS *m/z*: 196 (58), 181 (100), 154 (79), 127 (64), 115 (55), 77 (62). HR-MS *m/z* calcd. for C<sub>13</sub>H<sub>12</sub>N<sub>2</sub>: 196.1000; found: 196.0975.

#### 2-(Methyl-2-phenylpropylidene)propanedinitrile (**17**) (**16**)

Yield: 12%. <sup>1</sup>H NMR (200 MHz, CDCl<sub>3</sub>) δ: 1.68 (s, 6H), 7.31–7.39 (m, 6H). <sup>13</sup>C NMR (50.3 MHz, CDCl<sub>3</sub>) δ: 28.03, 44.24, 87.01, 110.40, 113.18, 126.39, 128.06, 129.23, 143.65, 176.02. EI-MS *m/z*: 196 (44), 181 (100), 154 (99), 127 (58), 115 (50), 78 (39), 77 (67).

### Acknowledgements

JW and NHW gratefully acknowledge the financial support of NSERC.

### References

1. M. Békhazi and J. Warkentin. *J. Org. Chem.* **47**, 4870 (1982).
2. R.A. Moss, S. Xue, and W. Liu. *J. Am. Chem. Soc.* **116**, 1583 (1994).
3. R.A. Moss, S. Xue, W. Liu, and K. Krogh-Jespersen. *J. Am. Chem. Soc.* **118**, 12 588 (1996).
4. R.A. Moss, S. Xue, W. Ma, and H. Ma. *Tetrahedron Lett.* **38**, 4379 (1997).
5. R.A. Moss and D.C. Merrer. *Tetrahedron Lett.* **39**, 8067 (1998).
6. K. Kassam, D.L. Pole, M. El-Saidi, and J. Warkentin. *J. Am. Chem. Soc.* **116**, 1161 (1994).
7. M. El-Saidi, K. Kassam, D.L. Pole, T. Tadey, and J. Warkentin. *J. Am. Chem. Soc.* **114**, 8751 (1992).
8. N. Merkley, M. El-Saidi, and J. Warkentin. *Can. J. Chem.* **78**, 356 (2000).
9. B. Capon and D.McL.A. Grieve. *J. Chem. Soc. Perkin Trans.* **2**, 300 (1980).
10. P.C. Venneri and J. Warkentin. *J. Am. Chem. Soc.* **120**, 11 182 (1998).
11. N. Merkley, P.C. Venneri, and J. Warkentin. *Can. J. Chem.* **79**, 312 (2001).
12. R. Sommer, E. Müller, and W.P. Neumann. *Liebigs Ann. Chem.* **718**, 11 (1968).
13. F.A. da Silva, A.B.B. Ferreira, and M.G. Neumann. *J. Braz. Chem. Soc.* **10**, 375 (1999).
14. W.E. Parham, F.D. Blake, and D.R. Theissen. *J. Org. Chem.* **27**, 2415 (1962).
15. M.J. Frisch, G.W. Trucks, H.B. Schlegel, G.E. Scuseria, M.A. Robb, J.R. Cheeseman, V.G. Zakrzewski, J.A. Montgomery, Jr., R.E. Stratmann, J.C. Burant, S. Dapprich, J.M. Millam, A.D. Daniels, K.N. Kudin, M.C. Strain, O. Farkas, J. Tomasi, V. Barone, M. Cossi, R. Cammi, B. Mennucci, C. Pomelli, C. Adamo, S. Clifford, J. Ochterski, G.A. Petersson, P.Y. Ayala, Q. Cui, K. Morokuma, D.K. Malick, A.D. Rabuck, K. Raghavachari, J.B. Foresman, J. Cioslowski, J.V. Ortiz, A.G. Baboul, B.B. Stefanov, G. Liu, A. Liashenko, P. Piskorz, I. Komaromi, R. Gomperts, R.L. Martin, D.J. Fox, T. Keith, M.A. Al-Laham, C.Y. Peng, A. Nanayakkara, M. Challacombe, P.M.W. Gill, B. Johnson, W. Chen, M.W. Wong, J.L. Andres, C. Gonzalez, M. Head-Gordon, E.S. Replogle, and J.A. Pople. Gaussian 98 [computer program]. Gaussian, Inc., Pittsburgh, PA. 1998.
16. J. Bus, H. Steinberg, and Th.J. de Boer. *Monatsh. Chem.* **98**, 1155 (1967).



# Aqueous nonelectrolyte solutions — Part XX: Formula of structure I methane hydrate, congruent dissociation melting point, and formula of the metastable hydrate

David N. Glew

**Abstract:** Sixteen new measurements of high precision for structure I methane hydrate with water between 31.93 and 47.39 °C are shown to be metastable and exhibit higher methane pressures than found by earlier workers. Comparison of earlier measurements between 26.7 and 47.2 °C permit positive identification of the structure II and the structure I hydrates. Forty-nine equilibrium constants  $K_p(h_1 \rightarrow l_1g)$  for dissociation of structure I methane hydrate into water and methane, 32 between -0.29 and 26.7 °C for the stable hydrate and 17 between 31.93 and 47.39 °C for the metastable hydrate, are best represented by a three-parameter thermodynamic equation, which indicates a standard error (SE) of 0.63% on a single  $K_p(h_1 \rightarrow l_1g)$  determination. The congruent dissociation melting point  $C(h_1l_1gx_m)$  of metastable structure I methane hydrate is at 47.41 °C with SE 0.02 °C and at pressure 505 MPa. The congruent equilibrium constant  $K_p(h_1 \rightarrow l_1g)$  is 102.3 MPa with SE 0.2 MPa.  $\Delta H^{0t}(h_1 \rightarrow l_1g)$  is 62 281 J mol<sup>-1</sup> with SE 184 J mol<sup>-1</sup>, and the congruent formula is CH<sub>4</sub>·5.750H<sub>2</sub>O with SE 0.059H<sub>2</sub>O. At the congruent point,  $\Delta V(h_1 \rightarrow l_1g)$  is zero within experimental precision, and its estimate is 1.3 with SE 1.6 cm<sup>3</sup> mol<sup>-1</sup>. The stability range of structure I methane hydrate with water extends from quadruple point  $Q(s_1h_1l_1g)$  at -0.29 °C up to quadruple point  $Q(h_1h_2l_1g)$  at 26.7 °C, and its metastability range with water extends from 26.7 °C up to the congruent dissociation melting point  $C(h_1l_1gx_m)$  at 47.41 °C.

**Key words:** methane hydrate, clathrate structure I, metastability range, dissociation equilibrium constant, formula, congruent melting point, metastability of structure I hydrate.

**Résumé :** Seize nouvelles mesures de haute précision ont été faites sur la structure I de l'hydrate de méthane avec de l'eau, entre 31,93 et 47,39 °C; elles montrent qu'elle est métastable et qu'elle comporte des pressions de méthane plus élevées que celles observées antérieurement par d'autres chercheurs. Une comparaison des mesures antérieures entre 26,7 et 47,2 °C permet d'identifier d'une façon positive les hydrates de structure II et de structure I. Quarante-neuf constantes d'équilibre  $K_p(h_1 \rightarrow l_1g)$  pour la dissociation de l'hydrate de méthane de structure I dans l'eau et le méthane, 32 entre -0,29 et 26,7 °C de l'hydrate stable et 17 entre 31,93 et 47,39 °C de l'hydrate métastable peuvent être représentées adéquatement par une équation thermodynamique à trois paramètres, avec une erreur standard (ES) de 0,63% pour une détermination unique de  $K_p(h_1 \rightarrow l_1g)$ . Le point de fusion de dissociation congruente  $C(h_1l_1gx_m)$  de l'hydrate de méthane de structure I métastable est de 47,41 °C avec une erreur standard de 0,02 °C et à une pression de 505 MPa. La constante d'équilibre congruente  $K_p(h_1 \rightarrow l_1g)$  est égale à 102,3 MPa avec une erreur standard de 0,2 MPa. Le  $\Delta H^{0t}(h_1 \rightarrow l_1g)$  est de 62 281 J mol<sup>-1</sup> avec une erreur standard de 184 J mol<sup>-1</sup> et la formule congruente est CH<sub>4</sub>·5,750H<sub>2</sub>O avec une erreur standard de 0,059H<sub>2</sub>O. Au point congruent,  $\Delta V(h_1 \rightarrow l_1g)$  est égal à zéro dans les limites expérimentales et il est évalué à 1,3 avec une erreur standard de 1,6 cm<sup>3</sup> mol<sup>-1</sup>. La plage de stabilité de la structure I de l'hydrate de méthane avec de l'eau va du point quadruple  $Q(s_1h_1l_1g)$  à -0,29 °C jusqu'au point quadruple  $Q(h_1h_2l_1g)$  à 26,7 °C et sa plage de métastabilité s'étend de 26,7 °C jusqu'au point de fusion de la dissociation congruente,  $C(h_1l_1gx_m)$  à 47,41 °C.

**Mots clés :** hydrate de méthane, clathrate de structure I, plage de métastabilité, constante d'équilibre de dissociation, formule, point de fusion congruent, métastabilité de l'hydrate de structure I.

[Traduit par la Rédaction]

## Introduction

We are particularly fortunate to have three independent and accurate studies (1–3) of the equilibrium methane hydrate pressures with water in the temperature range 26.98 to

47.39 °C. The oldest data set MSK64 (1) provides 13 measurements between 26.98 and 46.87 °C and shows the 11 lowest methane hydrate pressures for the stable structure II hydrate phase  $h_2$ . Data set D&A96 (2) provides 13 measurements between 27.6 and 47.2 °C, which agree with data set MSK64 but also indicate the structure II methane hydrate phase  $h_2$ , with pressures about 0.69% larger than MSK64.

The most recent data set, NMO99 (3), of 16 measurements between 31.93 and 47.39 °C lists pressures for the structure I methane hydrate, phase  $h_1$ , and these pressures

Received 26 June 2003. Published on the NRC Research Press Web site at <http://canjchem.nrc.ca> on 20 October 2003.

**D.N. Glew.** 536 Highbury Park, Sarnia, ON N7V 2J9, Canada (telephone: (519) 337-3136).



are larger than those found in MSK64 (1) and by D&A96 (2). The continuity of the hydrate Raman spectral shifts by NMO99 (3) between 32 °C at 100 MPa and 47.4 °C at 493 MPa proves that their equilibrium hydrate phase is  $h_1$  with structure I, which remains metastable over the temperature range of the data and for the period of the experimental study (3).

Recent work by Chou and co-workers (4, 5) shows the thermodynamic stability of structure I methane hydrate with water from the ice point up to about 33 °C and the metastability of the structure I hydrate at higher temperatures relative to the stable structure II methane hydrate with water.

Independent  $P$ - $t$  analyses (6, 7) confirm that structure I methane hydrate, phase  $h_1$ , is the stable phase in equilibrium with water between the quadruple points  $Q(s_1h_1l_1g)$  at -0.29 °C and 2.53 MPa and  $Q(h_1h_2l_1g)$  at 26.7 °C and 55.5 MPa. At higher temperature structure II methane hydrate, phase  $h_2$ , is the stable phase (7) in equilibrium with water from the quadruple point  $Q(h_1h_2l_1g)$  at 26.7 °C and 55.5 MPa up to the congruent dissociation melting point  $C(h_2l_1gx_m)$  at 47.71 °C and 533 MPa.

Initially, for data set NMO99 (3), two equations are derived that accurately represent  $P(h_1l_1g)$  from 31.93 to 45.14 °C and from 45.14 to 47.39 °C. These equations are used to estimate  $P(h_1l_1g)$  at the temperatures of the earlier data sets MSK64 (1) and D&A96 (2). The estimate of  $P(h_1l_1g)$  for the structure I hydrate is compared with the observed hydrate pressure  $P(hl_1g)$ , where the lower pressure characterizes the more stable hydrate.

Classical thermodynamics defines the stable methane hydrate phase as that which exerts the lowest equilibrium methane pressure with water at the same temperature.

This extends our study (6, 7) of methane hydrate to correctly define the individual measurements (1-3) and their pressure differences between the structure II and the structure I hydrates (8, 9), using the same numerical methods and thermodynamic equations as earlier.

With measurements for structure I methane hydrate extending from quadruple point  $Q(s_1h_1l_1g)$  at -0.29 °C up to 47.39 °C, the best low-temperature measurements from ref. 6 are combined with data set NMO99 (3) to provide accurate estimates of  $P(h_1l_1g)$ ,  $K_p(h_1 \rightarrow l_1g)$ ,  $\Delta H^o(h_1 \rightarrow l_1g)$ , and the approximate formula number  $r$  for structure I methane hydrate with water.

### Equilibrium pressure $P(h_1l_1g)$ of structure I methane hydrate with water between 31.93 and 45.14 °C

In the temperature range from 31.93 to 45.14 °C the equilibrium total pressure  $P(h_1l_1g)$  of methane hydrate  $h_1$  with liquid water  $l_1$  is best represented by the unbiased thermodynamic equation

$$[1a] \quad \ln P(h_1l_1g) = b_0 + b_1u_1 + b_2u_2 + b_3u_3$$

This equation is mathematically equivalent to the numerically ill-conditioned unbiased thermodynamic equation

$$[1b] \quad \ln P(h_1l_1g) = A + B/T + C \ln T + DT$$

Temperature variables  $u_1$  to  $u_3$  in eq. [1a] are described briefly in ref. 7 and fully in ref. 10.

The upper twelve rows of Table 1 present estimates of  $P(h_1l_1g)$  between 31.93 and 45.14 °C, using the measurements of data set NMO99 (3). The arrangement of Table 1 is similar to that in ref. 7.

The least-squares estimates of the four parameters and their standard errors (SE) in eq. [1a] are  $b_0 = 3.7265$  (0.0225),  $b_1 = 46.131$  (1.67),  $b_2 = -900.11$  (76.9), and  $b_3 = 11\,273$  (843). These parameters give an SE estimate of 0.0018 on  $\ln P$  or of 0.18% on a single methane hydrate pressure determination with 8 degrees of freedom. The coefficient of determination  $R^2$  is 0.99998. These are remarkably precise methane hydrate pressure measurements.

### Equilibrium pressure $P(h_1l_1g)$ of structure I methane hydrate with water between 45.14 and 47.39 °C

In this work, following ref. 7, we use a similar numerical treatment to that used for the congruent dissociation melting point of structure II methane hydrate. In the temperature range from 45.14 to 47.39 °C the five methane hydrate pressures between 335 and 493 MPa from data set NMO99 (3) show that the hydrate temperature can be accurately represented by eq. [2] as an empirical cubic function of the equilibrium hydrate pressure,

$$[2] \quad t(^{\circ}\text{C}) = e_0 + e_2(\Delta P)^2 + e_3(\Delta P)^3$$

In eq. [2],  $t(^{\circ}\text{C})$  is the equilibrium methane hydrate temperature (ITS-90),  $\Delta P$  is the equilibrium pressure difference ( $P(h_1l_1g) - 505$  MPa), and 505 MPa is the estimated pressure at maximum hydrate temperature,  $t_{\max}$ . The estimated maximum congruent dissociation temperature of structure I methane hydrate is  $t_{\max} = e_0 = 47.41$  °C with SE 0.020 °C. Parameter  $e_2$  is  $-0.000102$  with SE  $4.4 \times 10^{-6}$ , and parameter  $e_3$  is  $-1.39 \times 10^{-7}$  with SE  $2.5 \times 10^{-8}$ . The SE estimate on a single structure I methane hydrate temperature determination is 0.024 °C with one degree of freedom, in agreement with the  $\pm 0.02$  °C accuracy of temperature measurement given by the authors (3). The coefficient of determination  $R^2$  is 0.9998.

The estimate of parameter  $e_0 = t_{\max}$  is highly significant and could arise by random chance with a probability less than 0.05%. Parameter  $e_2$  could arise by chance with about 1.5% probability and parameter  $e_3$  could arise by chance at about 13% probability.

Although the five measurements indicate a metastable structure I methane hydrate congruent dissociation temperature  $C(h_1l_1gx_m)$  at 47.41 °C and 505 MPa, this location must be considered tentative.

### Equilibrium pressure of the methane hydrates with water between 26.7 and 47.71 °C

The three studies of methane hydrate measurements are outlined briefly to compare the reliability of the estimates given in Table 2. The studies of MSK64 (1) use a rocked stainless steel hydrate cell in a thermostat bath; the methane pressures are accurate to 0.1%, and temperatures are accu-



**Table 1.** Equilibrium pressure and fugacity for structure I methane hydrate with water from 31.93 to 47.41 °C.

Data set	<i>t</i> (°C)	<i>w</i> <sup>1/2</sup>	<i>P</i> (h <sub>1</sub> l <sub>1</sub> g) (MPa)		Diff (MPa)	SE( <i>P</i> <sup>^</sup> ) (MPa)	<i>f</i> <sub>2</sub> (h <sub>1</sub> l <sub>1</sub> g) (MPa)
			Obsd	Calcd			
NMO99	31.93	1	98	97.92	0.08	0.14	100.4
NMO99	33.98	1	119	119.23	−0.23	0.10	148.0
NMO99	35.59	1	138	137.92	0.08	0.12	206.3
NMO99	37.14	1	158	158.04	−0.04	0.12	288.3
NMO99	38.49	1	178	177.78	0.22	0.12	397.9
NMO99	39.77	1	199	199.00	−0.00	0.13	551.8
NMO99	40.73	1	217	216.93	0.07	0.15	724.5
NMO99	41.68	1	237	236.76	0.24	0.16	973.4
NMO99	42.59	1	258	258.12	−0.12	0.17	1 317
NMO99	43.35	1	277	278.07	−1.07	0.18	1 722
NMO99	44.05	1	299	298.45	0.55	0.22	2 336
NMO99	45.14	1	335	334.78	0.22	0.23	3 799
NMO99	45.14	1	335	334.88	0.12	0.23	3 799
NMO99	46.02	1	376	376.61	−0.61	0.26	6 512
NMO99	46.65	1	414	412.87	1.13	0.33	10 606
NMO99	47.18	1	455	456.16	−1.16	0.45	17 755
NMO99	47.39	1	493	491.93	1.07	0.55	28 420
<i>C</i> (h <sub>1</sub> l <sub>1</sub> g <i>x</i> <sub>m</sub> )	47.41	—	505	505	—	—	32 930

**Table 2.** Equilibrium pressure of methane hydrates with water.

Data set	<i>t</i> (°C)	<i>P</i> (hl <sub>1</sub> g) obsd (MPa)	<i>P</i> (hl <sub>1</sub> g) calcd (MPa)	Diff (MPa)	SE( <i>P</i> <sup>^</sup> ) (MPa)	Diff/SE	Hydrate obsd
<i>Q</i> (h <sub>1</sub> h <sub>2</sub> l <sub>1</sub> g)	26.7	—	55.53	—	9.60	—	SI SII
MSK64	26.98	56.92	55.30	−1.61	0.31	−5.2	SI
MSK64	28.37	65.43	66.10	0.67	0.23	2.9	SII
MSK64	28.43	65.43	66.55	1.12	0.22	5.0	SII
MSK64	33.54	110.83	114.42	3.59	0.05	72.8	SII
MSK64	37.15	152.72	158.14	5.42	0.06	91.1	SII
MSK64	39.54	187.30	194.91	7.62	0.06	122.6	SII
MSK64	40.48	206.34	212.07	5.73	0.07	80.4	SII
MSK64	41.04	223.91	223.06	−0.85	0.08	−10.8	SI
MSK64	41.87	237.46	240.98	3.52	0.08	42.2	SII
MSK64	43.65	271.65	286.43	14.78	0.09	160.3	SII
MSK64	45.15	319.67	335.32	15.65	0.20	76.8	SII
MSK64	46.42	367.77	398.61	30.84	0.46	67.1	SII
MSK64	46.87	397.00	428.33	31.33	0.61	51.3	SII
D&A96	27.6	59	59.97	0.97	0.27	3.6	SII
D&A96	30.4	84	83.49	−0.51	0.13	−4.0	SI
D&A96	34.0	117	119.45	2.45	0.05	47.5	SII
D&A96	35.5	133	136.82	3.82	0.06	64.3	SII
D&A96	37.5	162	163.07	1.07	0.06	17.8	SII
D&A96	37.8	166	167.39	1.39	0.06	23.3	SII
D&A96	40.7	216	216.34	0.34	0.08	4.5	SII
D&A96	42.4	242	253.44	11.44	0.08	138.2	SII
D&A96	45.2	317	337.54	20.54	0.21	98.7	SII
D&A96	45.9	358	370.49	12.49	0.34	36.3	SII
D&A96	46.9	405	430.63	25.63	0.63	40.6	SII
D&A96	47.2	443	458.45	15.45	0.79	19.6	SII
D&A96	47.2	450	458.45	8.45	0.80	10.6	SII
<i>C</i> (h <sub>2</sub> l <sub>1</sub> g <i>x</i> <sub>m</sub> )	47.71	533	533	—	—	—	SII

rate to 0.004 °C. The measurements of D&A96 (2) use a high-pressure DTA method, with pressures accurate to 1% and temperatures accurate to 0.1 °C. The measurements of NMO99 (3) use a 200 mm<sup>3</sup> hydrate cell stirred by a vibrat-

ing 2 mm glass ball, with pressures accurate to ±1 MPa and temperatures accurate to ±0.02 °C.

The pressure of metastable structure I methane hydrate is estimated at each experimental temperature for the measure-



ments of data sets MSK64 (1) and D&A96 (2). Columns one to three in Table 2 show the data set, the temperature  $t(^{\circ}\text{C})$  (ITS-90), and the observed hydrate pressure  $P(\text{h}_1\text{g})$  (MPa) for the 26 measurements from data sets MSK64 and D&A96 between quadruple point  $Q(\text{h}_1\text{h}_2\text{l}_1\text{g})$  at  $26.7^{\circ}\text{C}$  and the congruent dissociation melting point  $C(\text{h}_2\text{l}_1\text{gx}_\text{m})$  at  $47.71^{\circ}\text{C}$ . Earlier (6, 7) these measurements have been assumed to be characteristic of the structure II methane hydrate  $\text{h}_2$  with water because they are observed above  $26.7^{\circ}\text{C}$ , the transition temperature to structure II methane hydrate.

In the present study, the observed hydrate pressure  $P(\text{h}_1\text{g})$ , shown in column three, is under test and is compared with the pressure  $P(\text{h}_1\text{l}_1\text{g})$  (MPa) in column four, estimated at  $t(^{\circ}\text{C})$  using eq. [1a] or [2].

The fifth column shows  $\text{Diff} = (P(\text{h}_1\text{l}_1\text{g}) - P(\text{h}_1\text{g}))$ , MPa, the pressure difference of column four minus column three. When Diff is positive the structure II methane hydrate phase  $\text{h}_2$  is the solid hydrate observed; when Diff is zero or negative the metastable structure I methane hydrate phase  $\text{h}_1$  is observed experimentally.

The sixth column lists  $\text{SE}(P^{\wedge})$  (MPa), the standard error from eq. [1a] for the estimated pressure  $P(\text{h}_1\text{l}_1\text{g})$ .

The seventh column shows  $\text{Diff}/\text{SE}(P^{\wedge})$ , the pressure difference expressed as the number of standard errors from data set NMO99 (3).

Column eight shows the observed hydrate structure, S I for structure I phase  $\text{h}_1$  and S II for structure II phase  $\text{h}_2$  (8).

The pressures  $P(\text{h}_1\text{l}_1\text{g})$  listed in column four of Table 2 are generally larger than those of  $P(\text{h}_1\text{g})$  in column three, and the estimate of Diff becomes systematically larger as the temperature increases to  $46.87^{\circ}\text{C}$ . This confirms that the structure I methane hydrate phase  $\text{h}_1$  is the thermodynamically metastable methane hydrate with water between  $Q(\text{h}_1\text{h}_2\text{l}_1\text{g})$  at  $26.7$  and  $47.2^{\circ}\text{C}$ ; contrariwise, this reconfirms our earlier assumption (6, 7) that structure II methane hydrate phase  $\text{h}_2$  is the thermodynamically stable methane hydrate with water between  $26.7$  and  $47.2^{\circ}\text{C}$ .

In columns five and seven of Table 2, of the 26 Diff estimates listed, 23 are positive, indicating that structure II methane hydrate is the thermodynamically stable phase. In column seven, 19 of the 26 data give estimates of  $\text{Diff}/\text{SE}(P^{\wedge}) > 10$ , a convincing confirmation of the stable structure II methane hydrate between  $26.7$  and  $47.2^{\circ}\text{C}$ .

The measurements at  $26.98^{\circ}\text{C}$  and  $56.92$  MPa of data set MSK64 and at  $30.4^{\circ}\text{C}$  and  $84$  MPa of data set D&A96 each exhibit a negative Diff, with estimates for  $\text{Diff}/\text{SE}(P^{\wedge})$  of  $-5.2$  and  $-4.0$ , respectively. These measurements indicate equilibrium with a solid phase  $\text{h}_1$  structure I methane hydrate, existing in metastable equilibrium just above the transition temperature  $26.7^{\circ}\text{C}$  of  $Q(\text{h}_1\text{h}_2\text{l}_1\text{g})$ .

One unexpected result in data set MSK64 is shown at  $41.04^{\circ}\text{C}$  and  $223.91$  MPa, which gives  $\text{Diff}/\text{SE}(P^{\wedge}) = -10.8$  and confirms that the solid hydrate phase formed in this experiment is the metastable structure I methane hydrate phase  $\text{h}_1$ . This particular hydrate measurement is noted to give four positive residuals, two in Tables 7 and 8 of ref. 6 and two in Tables 1 and 2 of ref. 7. The level of metastability of  $13.44^{\circ}\text{C}$  ( $40.14$ – $26.7$ ) is considered in refs. 6 and 7 to be too large and unlikely to occur experimentally in the middle of data set MSK64 (1). This assumption is shown here to be incorrect by the 16 experimental metastable measurements

of data set NMO99 (3) listed in Table 1, with levels of metastability up to  $20.69^{\circ}\text{C}$  and with excess methane gas pressures of up to about 8%.

The complete data set NMO99 (3) shows that the metastable structure I methane hydrate phase  $\text{h}_1$  can coexist with water and an excess pressure of methane gas for a time period of at least days. In the experiment of data set MSK64 (1) at  $40.14^{\circ}\text{C}$ , the excess methane gas pressure  $0.85$  MPa is very small, 0.38%, and once the metastable solid structure I methane hydrate phase  $\text{h}_1$  is formed, the same phase  $\text{h}_1$  would remain until all the hydrate is decomposed.

We again note (7) the remarkable metastability of the completely filled structure I methane hydrate phase  $\text{h}_1$ , with all cavities occupied by a methane guest at temperatures and pressures greater than  $Q(\text{h}_1\text{h}_2\text{l}_1\text{g})$  at  $26.7^{\circ}\text{C}$  and  $55.5$  MPa.

### Equilibrium pressure $P(\text{h}_1\text{l}_1\text{g})$ of structure I methane hydrate with water between $-0.29$ and $45.14^{\circ}\text{C}$

Over this longer temperature range the best  $P(\text{h}_1\text{l}_1\text{g})$  data at the lower temperatures below  $26.7^{\circ}\text{C}$  are combined with the new metastable measurements of NMO99 at the higher temperatures. Table 3 presents 45 estimates of  $P(\text{h}_1\text{l}_1\text{g})$  between  $-0.29$  and  $45.14^{\circ}\text{C}$  using the data sets  $Q(\text{s}_1\text{h}_1\text{l}_1\text{g})$ , D&F40, MSK64, GRCK70, and V74 from ref. 6 together with 12 data sets from NMO99 (3). The arrangement of Table 3 is the same as Table 1 in ref. 7.

The least-squares estimates of the four parameters and their standard errors (in parentheses) in eq. [1a] are  $b_0 = 3.7532$  (0.0081),  $b_1 = 35.363$  (0.220),  $b_2 = -11.59$  (6.32), and  $b_3 = -2243.4$  (176.0). These parameters give an SE estimate of 0.0265 on  $\ln P$  or of 2.68% on a single methane hydrate pressure determination with 41 degrees of freedom. The coefficient of determination  $R^2$  is 0.9998.

The RMS (root mean squared) deviations of the residuals of  $\ln P(\text{h}_1\text{l}_1\text{g})$  from eq. [1a] for the individual data sets are the following: D&F40, 0.0136; MSK64, 0.0393; GRCK70, 0.0285; V74, 0.0209; and NMO99, 0.0248. These residuals are large and are found to be distributed non-randomly.

When combined with the new measurements of NMO99 (3) at higher temperatures we find that the 4-parameter equation is inadequate to properly represent the  $P(\text{h}_1\text{l}_1\text{g})$  measurements with the expected accuracy over their whole range.

### Equilibrium constant for dissociation of structure I methane hydrate between $-0.29$ and $47.39^{\circ}\text{C}$

The equilibrium constant for dissociation of 1 g molar mass of structure I methane hydrate of formula  $\text{CH}_4 \cdot n\text{H}_2\text{O}$  phase  $\text{h}_1$  into  $n$  mol of pure water  $\text{l}_1$  plus 1 mol of gaseous methane is written  $K_p(\text{h}_1 \rightarrow \text{l}_1\text{g})$  and is defined by eq. [3],

$$[3] \quad \ln K_p(\text{h}_1 \rightarrow \text{l}_1\text{g}) = \ln f_2(\text{h}_1\text{l}_1\text{g}) + n \ln x_1^{\text{l}_1} + n(1/RT) \int_{0.1 \text{ MPa}}^{P(\text{h}_1\text{l}_1\text{g})} (V_1^{\text{l}_1} - V_1^{\text{h}_1}) dP$$



**Table 3.** Equilibrium pressure for structure I methane hydrate with water from  $-0.29$  to  $45.14$  °C.

Data set	$t$ (°C)	$w^{1/2}$	$P(h_1l_1g)$ (MPa)		Diff (%)	SE (%)
			Obsd	Calcd		
$Q(s_1h_1l_1g)$	-0.29	1	2.53	2.58	-2.22	1.21
D&F40	0.56	1	2.76	2.77	-0.26	1.02
D&F40	1.11	1	2.90	2.91	-0.15	0.92
D&F40	2.22	1	3.24	3.21	0.99	0.76
D&F40	2.78	1	3.42	3.38	1.27	0.70
D&F40	2.78	1	3.43	3.38	1.47	0.70
D&F40	3.89	1	3.81	3.75	1.61	0.62
D&F40	6.11	1	4.77	4.69	1.75	0.58
D&F40	7.22	1	5.35	5.27	1.54	0.59
D&F40	7.77	1	5.71	5.59	2.09	0.60
D&F40	8.33	1	6.06	5.94	2.04	0.61
D&F40	9.44	1	6.77	6.71	0.86	0.62
D&F40	11.10	1	8.12	8.10	0.22	0.63
D&F40	12.77	1	9.78	9.83	-0.45	0.63
MSK64	17.05	1	15.93	16.35	-2.60	0.60
MSK64	17.32	1	15.94	16.91	-5.73	0.60
MSK64	21.93	1	29.92	29.54	1.30	0.68
MSK64	22.04	1	29.99	29.94	0.18	0.68
MSK64	22.60	1	33.75	32.01	5.44	0.70
MSK64	24.87	1	44.31	42.03	5.44	0.77
MSK64	24.99	1	43.78	42.59	2.81	0.78
MSK64	41.04	1	223.91	229.27	-2.34	0.73
GRCK70	9.99	1	7.10	7.14	-0.59	0.63
GRCK70	10.05	1	7.12	7.19	-1.02	0.63
GRCK70	15.49	1	13.11	13.56	-3.37	0.61
GRCK70	15.55	1	13.11	13.65	-3.96	0.61
V74	2.00	1	3.02	3.15	-3.98	0.78
V74	3.54	1	3.69	3.63	1.65	0.64
V74	5.44	1	4.39	4.38	0.17	0.58
V74	12.24	1	9.19	9.24	-0.54	0.63
V74	15.30	1	13.04	13.25	-1.57	0.61
V74	17.53	1	16.96	17.34	-2.17	0.60
V74	18.01	1	18.55	18.37	1.02	0.61
NMO99	31.93	1	98	94.10	4.14	0.91
NMO99	33.98	1	119	117.05	1.67	0.88
NMO99	35.59	1	138	138.02	-0.01	0.83
NMO99	37.14	1	158	160.79	-1.74	0.77
NMO99	38.49	1	178	182.72	-2.59	0.73
NMO99	39.77	1	199	205.30	-3.07	0.70
NMO99	40.73	1	217	223.34	-2.84	0.72
NMO99	41.68	1	237	242.08	-2.10	0.77
NMO99	42.59	1	258	260.80	-1.07	0.86
NMO99	43.35	1	277	276.96	0.02	0.97
NMO99	44.05	1	299	292.22	2.32	1.09
NMO99	45.14	1	335	316.62	5.81	1.31

In eq. [3]  $V_1^{11}$  is the molar volume of water and  $V_1^{h1}$  the molar volume of structure I lattice water at pressure  $P(h_1l_1g)$  and temperature  $T$ . Equilibrium values of  $P(h_1l_1g)$  are given in column four of Tables 1 and 3. Equilibrium values of methane fugacity  $f_2(h_1l_1g)$  are evaluated from  $P(h_1l_1g)$  using the IUPAC fugacity equation (11) and are given in ref. 6 and in column eight of Table 1. Equilibrium volumes of compressed water are interpolated from tables by Haar et al.

(12). Equilibrium values of  $x_1^{11} = (1 - x_2^{11})$  are from  $x_2^{11}$ , listed in column eight of Table 4 and evaluated using the equation of Rettich et al. (13). Estimates for  $V_1^{h1}$  ( $\text{cm}^3 \text{mol}^{-1}$ ) at temperature  $t$  and at pressure  $P(h_1l_1g)$  are as follows: 22.34 (SE 0.19) at  $-0.29$  °C and 2.527 MPa; 22.41 (0.18) at 11.10 °C and 8.122 MPa; 22.42 (0.18) at 22.04 °C and 29.99 MPa; 22.49 (0.19) at 31.93 °C and 98 MPa; 21.77 (0.22) at 45.14 °C and 335 MPa; 21.32 (0.22) at 47.39 °C and 493 MPa.

Forty-nine equilibrium constants between  $-0.29$  and  $47.39$  °C are converged as described in ref. 6 and are best (10) represented by the unbiased thermodynamic equation

$$[4] \quad \ln K_p(h_1 \rightarrow l_1g) = d_0 + d_1 u_1 + d_2 u_2$$

Temperature variables  $u_1$  and  $u_2$  and thermodynamic parameters  $d_0$  to  $d_2$  are defined at reference temperature  $\Theta = 298.15$  K (25 °C). The data are sufficiently accurate and extensive so that the three-parameter eq. [4] can be converged and solved directly.

The parameters of the best converged eq. [4] are  $d_0 = 2.9522$  (SE 0.0016),  $d_1 = 23.451$  (0.018), and  $d_2 = 14.24$  (0.89). The SE estimate on a single determination of  $\ln K_p(h_1 \rightarrow l_1g)$  of unit weight is 0.0063 or is 0.63% for  $K_p(h_1 \rightarrow l_1g)$  with 44 degrees of freedom. The number of degrees of freedom is counted from the 49 data, minus the three undetermined parameters, minus the two weighted data, leaving 44. The coefficient of determination  $R^2$  is 0.99998.

Two data are assigned the low weights  $w^{1/2} = 0.001$  to avoid bias of the final equation because their observed equilibrium constants deviate from the least-squares model by 19 and by 23 times their estimated standard errors.

The RMS deviations for weighted (unweighted) residuals of  $\ln K_p(h_1 \rightarrow l_1g)$  from eq. [4] are the following: D&F40, 0.0052; MSK64, 0.0091 (0.0136); GRCK70, 0.0090; V74, 0.0077 (0.0184); and NMO99, 0.0019.

Because the 33 best data from ref. 6 at low temperatures are taken together with the 16 new measurements of data set NMO99, the converged eq. [4] is expected to agree with eq. [8a] of ref. 6. The agreement with the earlier model is good and the limits of SE have been reduced from 0.0079 to 0.0063. The best equation for  $\ln K_p(h_1 \rightarrow l_1g)$  in this work is numerically slightly different from that given earlier in ref. 6 and is preferred because it covers a wider range of temperature.

Table 4 has the same arrangement as Table 2 in ref. 7 and extends the measurements of structure I methane hydrate to include both the stable region below and the metastable region above  $Q(h_1h_2l_1g)$  at 26.7 °C.

Table 4 shows the 49 converged best estimates of the equilibrium constant,  $K_p(h_1 \rightarrow l_1g)$ , for dissociation of structure I methane hydrate into liquid water and methane gas with  $n = r$ . Standard thermodynamic function changes refer to dissociation of one gram mole of  $\text{CH}_4 \cdot r\text{H}_2\text{O}$   $h_1$  at 0.10 MPa to form  $r$  mol of pure water  $l_1$  at 0.10 MPa and 1 mol of methane gas at 1.0 MPa fugacity. Parameter  $r$  is used to indicate the best estimate of  $n$ , as described in ref. 7.

The estimates of  $K_p(h_1 \rightarrow l_1g)$  observed in column four of Table 4 are shown to increase steadily from 2.30 MPa at  $-0.29$  °C to 102.3 MPa at 47.39 °C. The calculated



**Table 4.** Equilibrium constant for structure I methane hydrate with water from -0.29 to 47.39 °C.

Data set	<i>t</i> (°C)	<i>w</i> <sup>1/2</sup>	<i>K<sub>p</sub></i> (h <sub>1</sub> →l <sub>1</sub> g) (MPa)		Diff (%)	SE (%)	1000 <i>x</i> <sub>2</sub> <sup>11</sup>
			Obsd	Calcd			
<i>Q</i> (s <sub>1</sub> h <sub>1</sub> l <sub>1</sub> g)	-0.29	1	2.30	2.31	-0.30	0.24	1.07
D&F40	0.56	1	2.50	2.49	0.37	0.22	1.13
D&F40	1.11	1	2.61	2.61	-0.12	0.20	1.16
D&F40	2.22	1	2.88	2.88	-0.00	0.18	1.23
D&F40	2.78	1	3.02	3.03	-0.07	0.17	1.27
D&F40	2.78	1	3.03	3.03	0.11	0.17	1.28
D&F40	3.89	1	3.33	3.33	-0.15	0.16	1.36
D&F40	6.11	1	4.04	4.04	0.03	0.13	1.54
D&F40	7.22	1	4.45	4.45	0.16	0.12	1.65
D&F40	7.77	1	4.70	4.66	0.80	0.12	1.71
D&F40	8.33	1	4.94	4.89	0.98	0.12	1.77
D&F40	9.44	1	5.40	5.37	0.53	0.12	1.88
D&F40	11.10	1	6.23	6.19	0.77	0.12	2.07
D&F40	12.77	1	7.17	7.11	0.84	0.13	2.27
MSK64	17.05	1	10.05	10.12	-0.72	0.14	2.81
MSK64	17.32	0.001	10.07	10.35	-2.76	0.14	2.79
MSK64	21.93	1	14.91	15.02	-0.72	0.16	3.55
MSK64	22.04	1	14.94	15.15	-1.39	0.16	3.54
MSK64	22.60	1	16.05	15.84	1.37	0.16	3.71
MSK64	24.87	1	19.18	18.96	1.18	0.16	4.05
MSK64	24.99	1	19.06	19.13	-0.35	0.16	4.02
MSK64	41.04	1	64.71	64.61	0.17	0.14	7.14
GRCK70	9.99	1	5.61	5.63	-0.33	0.12	1.92
GRCK70	10.05	1	5.62	5.66	-0.64	0.12	1.92
GRCK70	15.49	1	8.83	8.91	-0.91	0.14	2.60
GRCK70	15.55	1	8.83	8.95	-1.30	0.14	2.60
V74	2.00	0.001	2.71	2.83	-4.24	0.19	1.17
V74	3.54	1	3.23	3.23	-0.03	0.16	1.33
V74	5.44	1	3.76	3.82	-1.40	0.14	1.46
V74	12.24	1	6.85	6.81	0.62	0.12	2.20
V74	15.30	1	8.79	8.77	0.29	0.14	2.60
V74	17.53	1	10.46	10.53	-0.64	0.14	2.91
V74	18.01	1	11.06	10.95	1.05	0.15	3.03
NMO99	31.93	1	32.77	32.74	0.09	0.14	5.65
NMO99	33.98	1	38.16	38.25	-0.24	0.13	6.04
NMO99	35.59	1	43.20	43.17	0.06	0.13	6.34
NMO99	37.14	1	48.45	48.47	-0.03	0.13	6.60
NMO99	38.49	1	53.65	53.58	0.14	0.13	6.82
NMO99	39.77	1	58.88	58.88	-0.01	0.13	6.99
NMO99	40.73	1	63.20	63.18	0.03	0.14	7.10
NMO99	41.68	1	67.80	67.72	0.11	0.14	7.19
NMO99	42.59	1	72.31	72.36	-0.06	0.15	7.24
NMO99	43.35	1	76.10	76.46	-0.47	0.16	7.26
NMO99	44.05	1	80.60	80.43	0.21	0.17	7.25
NMO99	45.14	1	87.06	87.00	0.07	0.18	7.16
NMO99	46.02	1	92.51	92.66	-0.17	0.19	6.97
NMO99	46.65	1	97.13	96.93	0.21	0.20	6.74
NMO99	47.18	1	100.4	100.7	-0.25	0.21	6.43
NMO99	47.39	1	102.3	102.2	0.16	0.21	6.11
<i>Q</i> (h <sub>1</sub> h <sub>2</sub> l <sub>1</sub> g)	26.7	—	—	21.88	—	0.15	4.57



$K_p(h_1 \rightarrow l_1g)$  estimates in column five properly represent these changes with SE 0.63% on a single determination of unit weight.

### Standard enthalpy change $\Delta H^{ot}(h_1 \rightarrow l_1g)$ and formula number estimate $r$ for structure I methane hydrate with water

In Table 5 columns one and two show the data set and the Celsius temperature (ITS-90). Columns three and four list the standard enthalpy change  $\Delta H^{ot}(h_1 \rightarrow l_1g)$  and its SE in J mol<sup>-1</sup> for dissociation of structure I methane hydrate to liquid water and methane gas. Columns five and six give the converged best estimates of the approximate formula number  $r$  and its SE for standard dissociation of structure I methane hydrate  $CH_4 \cdot rH_2O$  into water and methane. The estimate and SE of the standard heat capacity change  $\Delta C_p^{ot}(h_1 \rightarrow l_1g)$  are, respectively, 118 and 7 J mol<sup>-1</sup> K<sup>-1</sup> at all temperatures; earlier estimates and SE are 112 and 23 J mol<sup>-1</sup> K<sup>-1</sup> given in ref. 6.

At quadruple point  $Q(h_1h_2l_1g)$ , 26.7 °C, the estimated formula for structure I methane hydrate  $h_1$  is  $CH_4 \cdot 5.753H_2O$  with SE 0.048 $H_2O$ ; this agrees well with the earlier estimate  $CH_4 \cdot 5.759H_2O$  with SE 0.077 $H_2O$  given in ref. 6. The new formula estimate for structure I methane hydrate at 26.7 °C is very near to the ideal  $CH_4 \cdot 5.750H_2O$  and indicates that 99.94% of hydrate cavities are occupied by methane with 0.06% unoccupied with an SE 0.83%.

The number of methane guest molecules, defined as  $m$  per unit cell of 46 $H_2O$ , increases from 7.457 (SE 0.065) at -0.29 °C and 2.53 MPa, to 7.710 (0.062) at 11.10 °C and 8.12 MPa, to 7.798 (0.062) at 15.55 °C and 13.11 MPa, to 7.917 (0.064) at 22.04 °C and 29.99 MPa, and to 7.995 (0.066) at 26.7 °C and 55.5 MPa. These values of  $m$  between -0.29 and 26.7 °C show the increasing number of the 8 lattice sites that must be occupied by methane guests to stabilize the structure I methane hydrate against thermal collapse due to increasing temperature.

At temperatures and pressures above 26.7 °C at 55.5 MPa and up to 47.39 °C at 493 MPa all cavities of structure I methane hydrate are occupied within our limits of detection. It is reasonably assumed that  $m$  increases asymptotically towards 8 as the pressure increases to 493 MPa. Column five in Table 5 shows that the measurements of NMO99 (3) all have a structure I, phase  $h_1$ , methane hydrate with formula near to  $CH_4 \cdot 5.750H_2O$  with SE between 0.049 and 0.059 $H_2O$ .

This agrees with the X-ray measurements of structure I methane hydrate by Hirai and co-workers (14, 15) who report a fully occupied, phase  $h_1$ , methane hydrate with lattice parameters 1.188, 1.184, and 1.172 nm at 260, 300, and 380 MPa, respectively, at room temperature. In this work the volume estimates for  $K_p(h_1 \rightarrow l_1g)$  yield the lattice parameters 1.189, 1.187, and 1.183 nm with SE 0.004 nm at 258 MPa and 42.59 °C, at 299 MPa and 44.05 °C, and at 376 MPa and 46.02 °C, respectively, in reasonable agreement with the X-ray measurements.

**Table 5.** Standard enthalpy change for dissociation and the formula of structure I methane hydrate with water.

Data set	$t$ (°C)	$\Delta H^{ot}(h_1 \rightarrow l_1g)$ (J mol <sup>-1</sup> )	SE (J mol <sup>-1</sup> )	$r$	SE
$Q(s_1h_1l_1g)$	-0.29	55 139	177	6.168	0.054
D&F40	0.56	55 239	171	6.152	0.053
D&F40	1.11	55 305	167	6.141	0.053
D&F40	2.22	55 436	159	6.120	0.052
D&F40	2.78	55 502	155	6.109	0.052
D&F40	2.78	55 502	155	6.109	0.052
D&F40	3.89	55 634	148	6.089	0.051
D&F40	6.11	55 897	132	6.049	0.050
D&F40	7.22	56 028	124	6.030	0.050
D&F40	7.77	56 094	120	6.020	0.049
D&F40	8.33	56 160	116	6.011	0.049
D&F40	9.44	56 291	109	5.993	0.049
D&F40	11.10	56 488	98	5.966	0.048
D&F40	12.77	56 686	87	5.940	0.048
MSK64	17.05	57 192	61	5.877	0.047
MSK64	17.32	57 225	60	5.873	0.047
MSK64	21.93	57 770	43	5.812	0.047
MSK64	22.04	57 783	43	5.810	0.047
MSK64	22.60	57 849	42	5.803	0.047
MSK64	24.87	58 119	44	5.775	0.047
MSK64	24.99	58 132	44	5.774	0.047
MSK64	41.04	61 094	139	5.750	0.055
GRCK70	9.99	56 357	105	5.984	0.049
GRCK70	10.05	56 363	105	5.983	0.048
GRCK70	15.49	57 008	70	5.899	0.047
GRCK70	15.55	57 014	70	5.899	0.047
V74	2.00	55 410	161	6.124	0.052
V74	3.54	55 592	150	6.095	0.051
V74	5.44	55 817	137	6.061	0.050
V74	12.24	56 623	90	5.948	0.048
V74	15.30	56 985	71	5.902	0.047
V74	17.53	57 249	59	5.870	0.047
V74	18.01	57 306	56	5.864	0.047
NMO99	31.93	59 345	78	5.750	0.049
NMO99	33.98	59 744	91	5.750	0.050
NMO99	35.59	60 055	102	5.750	0.051
NMO99	37.14	60 353	112	5.750	0.052
NMO99	38.49	60 611	121	5.750	0.053
NMO99	39.77	60 854	130	5.750	0.054
NMO99	40.73	61 036	137	5.750	0.054
NMO99	41.68	61 215	144	5.750	0.055
NMO99	42.59	61 386	150	5.750	0.056
NMO99	43.35	61 528	155	5.750	0.056
NMO99	44.05	61 659	160	5.750	0.057
NMO99	45.14	61 862	168	5.750	0.058
NMO99	46.02	62 025	175	5.750	0.058
NMO99	46.65	62 141	179	5.750	0.059
NMO99	47.18	62 239	183	5.750	0.059
NMO99	47.39	62 278	184	5.750	0.059
$C(h_1l_1gx_m)$	47.41	62 281	184	5.750	0.059
$Q(h_1h_2l_1g)$	26.7	58 335	50	5.753	0.048

**Note:** The estimate and standard error for  $\Delta C_p^{ot}(h_1 \rightarrow l_1g)$  are 118 and 7 J mol<sup>-1</sup> K<sup>-1</sup>, respectively, at all temperatures.



## Congruent dissociation melting point of metastable structure I methane hydrate with water

Although the five measurements of methane hydrate between 335 and 493 MPa in Table 1 are accurately represented by eq. [2], the paucity of measurements makes it difficult to be certain that a congruent maximum exists. For comparison with phase  $h_2$  of structure II methane hydrate (7), we assume that phase  $h_1$  of structure I methane hydrate shows a metastable congruent maximum dissociation temperature  $C(h_1l_1gx_m)$  at 47.41 °C and at a pressure of 505 MPa.

At the congruent temperature  $t_{\max}$ ,  $(dt/dP) = 0$ , so that the volume change for the hydrate dissociation melting reaction is  $\Delta V(h_1 \rightarrow l_1g) = (dt/dP) \Delta H(h_1 \rightarrow l_1g)/T = 0$ , with  $\Delta H(h_1 \rightarrow l_1g)/T > 0$ . In the two-component methane–water system, the congruent dissociation melting point of structure I methane hydrate is an invariant three-phase point, denoted  $C(h_1l_1gx_m)$ , at which the volume and composition  $x_m$  of the equilibrium methane hydrate phase  $h_1$  is equal to the volume and composition of its fused reaction products, liquid water and gaseous methane.

At the congruent point  $C(h_1l_1gx_m)$ , 47.41 °C and 505 MPa, the thermodynamic model gives a maximum equilibrium constant  $K_p(h_1 \rightarrow l_1g)$  of 102.3 MPa with SE 0.2 MPa and a maximum  $CH_4:H_2O$  mole ratio for the methane hydrate formula  $CH_4 \cdot (5.750 \pm 0.059)H_2O$ , with an  $h_1$  formula volume  $122.4 \pm 1.3 \text{ cm}^3 \text{ mol}^{-1} CH_4$ , and with cubic hydrate lattice (8) parameter  $1.176 \pm 0.004 \text{ nm}$ . The equilibrium volume (11) of methane gas is  $32.7 \pm 0.3 \text{ cm}^3 \text{ mol}^{-1} CH_4$ , and the equilibrium water volume (12) of  $5.750H_2O$   $l_1$  is  $91.0 \pm 0.9 \text{ cm}^3 \text{ mol}^{-1} CH_4$ . At  $C(h_1l_1gx_m)$  the estimated  $\Delta V$  (products – reactants) =  $1.3 \pm 1.6 \text{ cm}^3 \text{ mol}^{-1} CH_4$ . Similarly, for the hydrate with formula  $CH_4 \cdot (5.750 \pm 0.058)H_2O$  at 45.14 °C and 335 MPa,  $\Delta V = 4.5 \pm 1.6 \text{ cm}^3 \text{ mol}^{-1} CH_4$ , and with formula  $CH_4 \cdot (5.750 \pm 0.059)H_2O$  at 47.39 °C and 493 MPa,  $\Delta V = 1.5 \pm 1.6 \text{ cm}^3 \text{ mol}^{-1} CH_4$ .

Between quadruple point  $Q(h_1h_2l_1g)$ , 55.5 MPa at 26.7 °C, and up to hydrate pressure 505 MPa at 47.41 °C, it is found that with increasing temperature and pressure, methane from the gas phase is forced into the equilibrium structure I meth-

ane hydrate lattice, increasing its methane content towards the ideal maximum formula  $CH_4 \cdot 5.750$ .

The estimates of the standard thermodynamic function changes for metastable structure I methane hydrate dissociation into water and methane reported here are entirely similar to those listed in ref. 7 for the stable structure II methane hydrate dissociation into water and methane.

## References

1. D.R. Marshall, S. Saito, and R. Kobayashi. *AIChE J.* **10**, 202 (1964).
2. Y.A. Dyadin and E.Y. Aladko. *In Proceedings of the 2nd international conference on natural gas hydrates. Edited by J.P. Monfort. Toulouse, 2–6 June 1996.* p. 67.
3. S. Nakano, M. Moritoki, and K. Ohgaki. *J. Chem. Eng. Data*, **44**, 254 (1999).
4. I.-M. Chou, A. Sharma, R.C. Burruss, J. Shu, H.-K. Mao, R.J. Hemley, A.F. Goncharov, L.A. Stern, and S.H. Kirby. *PNAS*, **97**(25), 13 484 (2000).
5. I.-M. Chou, A. Sharma, R.C. Burruss, R.J. Hemley, A.F. Goncharov, L.A. Stern, and S.H. Kirby. *J. Phys. Chem. A*, **105**, 4664 (2001).
6. D.N. Glew. *Can. J. Chem.* **80**, 418 (2002).
7. D.N. Glew. *Can. J. Chem.* **81**, 179 (2003).
8. D.W. Davidson. *In Water: A comprehensive treatise. Vol. 2. Edited by F. Franks. Plenum Press, New York. 1973.* p. 128
9. D.W. Davidson, Y.P. Handa, C.I. Ratcliffe, J.S. Tse, and B.M. Powell. *Nature*, **311**, 142 (1984).
10. E.C.W. Clarke and D.N. Glew. *Trans. Faraday Soc.* **62**, 539 (1966).
11. S. Angus, B. Armstrong, and K.M. de Reuck. *International thermodynamic tables of the fluid state-5 methane. International Union of Pure and Applied Chemistry, Pergamon Press, Oxford. 1978.*
12. L. Haar, J.S. Gallagher, and G.S. Kell. *NBS/NRC steam tables. Hemisphere Publishing Corporation, New York. 1984.*
13. T.R. Rettich, Y.P. Handa, R. Battino, and E. Wilhelm. *J. Phys. Chem.* **85**, 3230 (1981).
14. H. Hirai, T. Kondo, M. Hasegawa, T. Yagi, Y. Yamamoto, T. Komai, K. Nagashima, M. Sakashita, H. Fujihisa, and K. Aoki. *J. Phys. Chem.* **B104**, 1429 (2000).
15. H. Hirai, M. Hasegawa, T. Yagi, Y. Yamamoto, K. Nagashima, M. Sakashita, K. Aoki, and T. Kikegawa. *Chem. Phys. Lett.* **325**, 490 (2000).



# Thermodynamics of binary mixtures containing a very strongly polar compound — Part 3: DISQUAC characterization of NMP + organic solvent mixtures<sup>1</sup>

J.A. González, U. Domanska, and J. Lachwa

**Abstract:** Binary mixtures of 1-methyl pyrrolidin-2-one (NMP) with alkanes, benzene, toluene, 1-alkanol, or 1-alkyne have been investigated in the framework of the DISQUAC model. The reported interaction parameters change regularly with the molecular structure of the mixture components. The model consistently describes a set of thermodynamic properties, including liquid–liquid equilibria, vapor–liquid equilibria, solid–liquid equilibria, and molar excess enthalpies. A brief comparison of the DISQUAC results and those obtained from the UNIFAC and ERAS models is presented. The experimental excess enthalpies are better represented by DISQUAC than by UNIFAC because this quantity strongly depends on molecular structure. For NMP + alkane mixtures, the liquid–liquid equilibria data are also better represented by DISQUAC, while UNIFAC more accurately describes the vapor–liquid equilibria measurements at temperatures close to the critical point. This result suggests that a mean field theory is not able to represent simultaneously, with the same set of interaction parameters, liquid–liquid and vapor–liquid equilibria at the mentioned temperatures. ERAS fails when treating mixtures with 1-alkanols. This has been attributed to the strong dipole–dipole interactions between NMP molecules, characteristic of the investigated systems. Mixture structure is briefly studied in terms of the concentration–concentration structure factor.

*Key words:* thermodynamics, NMP, organic solvent, self-association, dipole–dipole interactions.

**Résumé :** On a étudié des mélanges binaires de 1-méthylpyrrolidin-2-one (NMP) avec des alcanes, du benzène, du toluène, des alcan-1-ols et des alc-1-yne dans le contexte du modèle « DISQUAC ». Les paramètres d'interaction rapportés changent régulièrement avec la structure moléculaire des composants du mélange. Le modèle décrit d'une façon consistante un ensemble de propriétés thermodynamiques, dont les équilibres liquide–liquide, les équilibres vapeur–liquide, les équilibres solide–liquide ainsi que les enthalpies molaires d'excès. On présente une brève comparaison des résultats « DISQUAC » et ceux obtenus avec les modèles « UNIFAC » et « ERAS ». Les enthalpies en excès expérimentales sont mieux représentées par le modèle « DISQUAC » que par le modèle « UNIFAC » parce que cette quantité dépend fortement de la structure moléculaire. Pour les mélanges de NMP avec des alcanes, les données d'équilibre liquide–liquide sont aussi mieux représentées par le modèle « DISQUAC » alors que le modèle « UNIFAC » décrit d'une façon plus précise les mesures d'équilibre vapeur–liquide, à des températures près du point critique. Ce résultat suggère qu'une théorie à champ moyen ne peut pas représenter simultanément, avec le même ensemble de paramètres d'interaction, les équilibres liquide–liquide et vapeur–liquide aux températures mentionnées. Le modèle « ERAS » ne peut pas être utilisé pour traiter des mélanges contenant des alcan-1-ols. Ceci est attribué aux fortes interactions dipôle–dipôle entre les molécules de NMP caractéristiques dans les systèmes étudiés. La structure du mélange a été brièvement étudiée en fonction du facteur de structure concentration–concentration.

*Mots clés :* thermodynamique, NMP, solvant organique, auto-association, interactions dipôle–dipôle.

Received 21 May 2003. Published on the NRC Research Press Web site at <http://canjchem.nrc.ca> on 27 October 2003.

**J.A. González.**<sup>2</sup> G.E.T.E.F., Departamento de Termodinámica y Física Aplicada, Facultad de Ciencias, Universidad de Valladolid, 47071, Valladolid, Spain.

**U. Domanska and J. Lachwa.** Physical Chemistry Division, Faculty of Chemistry, Warsaw University of Technology, 00-664 Warsaw, Poland.

<sup>1</sup>Part 2: U. Domanska and J.A. González. *Can. J. Chem.* **80**, 476 (2002).

<sup>2</sup>Corresponding author (e-mail address: [jagl@termo.uva.es](mailto:jagl@termo.uva.es)).



## Introduction

We are engaged in a systematic investigation of the thermodynamic properties of solutions that contain a compound with a very high dipolar moment in the gas phase ( $\mu$ ), such as sulfolane ( $\mu = 4.81$  D (1)), dimethyl sulfoxide ( $\mu = 4.06$  D (1)), propylene carbonate ( $\mu = 4.94$  D (1)) or 1-methyl pyrrolidin-2-one (NMP,  $\mu = 4.09$  D (1)).

The thermodynamic properties of solutions containing amides, amino acids, peptides, and their derivatives are of interest because they provide simple biochemical models. For example, aqueous *N,N*-dimethylformamide (DMF) is a model mixed solvent that represents the environment of the interior of proteins. NMP is an excellent dissociating solvent (2, 3), suitable for use in electrochemistry (4) or in organic syntheses requiring dipolar aprotic media (5). NMP and DMF are also used as highly selective extractants for the recovery of aromatic and saturated hydrocarbons from petroleum feedstocks (6, 7). On the other hand, NMP can replace with toxicological and environmental advantages solvents such as chlorinated hydrocarbons (6).

Mixtures of NMP + aromatic compound (8), + 1-alkyne (9), or + 1-alkanol (10–12) have been studied in the framework of the ERAS model (13), which combines the real association solution model (14) with Flory's equation of state (15) (physical term). In these applications, calculations were developed assuming that NMP is a self-associated molecule, which is not strictly justified. In fact, the properties of pure liquid tertiary amides are due to the dominance of the general dipole–dipole interactions over the more geometrical hydrogen bond (16, 17). However, there must be significant local order in view of the relatively high heat of vaporization of tertiary amides (17). The poor predictions for the excess enthalpy,  $H^E$ , for NMP + 1-alkanol systems (11, 12) obtained using ERAS may be because of the strong dipole–dipole interactions present in such solutions.

On the other hand, UNIFAC interaction parameters are available (18, 19) for NMP + alkane, +  $C_6H_6$ , +  $C_7H_8$ , or + 1-alkanol ( $\neq$  methanol) mixtures. The model fails when describing  $H^E$  for solutions of NMP and  $C_6H_6$ ,  $C_7H_8$ , or 1-alkanol. To some extent, this may be due to the fact that the interaction parameters were determined mainly from vapor–liquid equilibria (VLE) data (see below). Here, we apply DISQUAC (20), a purely physical model based on the rigid lattice theory developed by Guggenheim (21), to carry out a detailed study of mixtures containing NMP and one organic solvent (alkane,  $C_6H_6$ ,  $C_7H_8$ , 1-alkanol, 1-alkyne) using our recent  $H^E$  measurements for these systems (9–12). In previous articles (22, 23), we have already shown that DISQUAC is a useful tool for the characterization of interactions in mixtures of sulfolane with alkanes,  $C_6H_6$ ,  $C_7H_8$ ,  $CCl_4$ , 1-alkanols, 1-alkynes, or nitriles.

## Model

In the framework of DISQUAC, mixtures of NMP with an organic solvent are regarded as possessing the following four types of surface: (i) type n, N-CO in NMP; (ii) type a, aliphatic ( $CH_3$ ,  $CH_2$ , in NMP, toluene, methylcyclohexane, 1-alkanols, or 1-alkynes); (iii) type c,  $c-CH_2$  in cycloalkanes or NMP; and (iv) type s ( $s = b$ ,  $C_6H_6$  in benzene;  $s = p$ ,  $C_6H_5$

in toluene;  $s = h$ , OH in 1-alkanols;  $s = y$ ,  $HC\equiv C$  in 1-alkynes).

## Assessment of geometrical parameters

When DISQUAC is applied, the total molecular volumes ( $r_i$ ), surfaces ( $q_i$ ), and the molecular surface fractions ( $\alpha_i$ ) of the compounds present in the mixture are calculated additively on the basis of the group volumes  $R_G$  and surfaces  $Q_G$  recommended by Bondi (24). As volume and surface units, the volume  $R_{CH_4}$  and surface  $Q_{CH_4}$  of methane are used (25). For the amide group, N-CO,  $r_{N-CO} = 0.93633$  and  $q_{N-CO} = 0.63103$ . The remaining geometrical parameters for the groups referred to in this work are given elsewhere (25–28).

## Equations

The main features of DISQUAC are the following: (i) The partition function is factorized into two terms, in such a way that the excess functions are calculated as the sum of two contributions, a dispersive (DIS) term that represents the contributions from the dispersive forces and a quasichemical (QUAC) term that arises from the anisotropy of the force fields created by the molecules in solution. In the case of the molar Gibbs energy ( $G^E$ ), the combinatorial term ( $G^{E,COMB}$ ) is represented by the Flory–Huggins equation (25, 26). (ii) The interaction parameters are assumed to be dependent on molecular structure. The equations applied to calculate  $G^E$  and  $H^E$  are the same as those used in other applications (27). The reference value of the coordination number was used; that is,  $z = 4$ . This value is assumed to be the same for all the polar contacts. This represents one of the more important shortcomings of the model and is partially removed by the hypothesis of considering structure-dependent interaction parameters.

The temperature dependence of the interaction parameters  $g_{st}$ ,  $h_{st}$ , and  $c_{pst}$  has been expressed in terms of the DIS and QUAC interchange coefficients (27),  $C_{st,l}^{DIS}$  and  $C_{st,l}^{QUAC}$ , where  $s \neq t = a, b, c, n, h, p, y$ ; and  $l = 1$  (Gibbs energy;  $C_{st,1}^{DIS/QUAC} = g_{st}^{DIS/QUAC}(T_0)/RT_0$ );  $l = 2$  (excess enthalpy;  $C_{st,2}^{DIS/QUAC} = h_{st}^{DIS/QUAC}(T_0)/RT_0$ );  $l = 3$  (heat capacity;  $C_{st,3}^{DIS/QUAC} = c_{pst}^{DIS/QUAC}(T_0)/R$ ).  $T_0 = 298.15$  K is the scaling temperature.

The calculation of liquid–liquid equilibria (LLE) coexistence curves was done by taking into account that the values of the mole fraction,  $x_1$  ( $x'_1$ ,  $x''_1$ ) relating to the two phases in equilibrium are such that the functions  $G^M$ ,  $G^{M''}$  ( $G^M = G^E + G^{ideal}$ ) have a common tangent (29).

The equation of the solid–equilibrium curve of a pure solid component 1, including two first-order transitions, is

$$[1] \quad -\ln x_i = \left( \frac{\Delta H_{fus1}}{R} \right) \left( \frac{1}{T} - \frac{1}{T_{fus1}} \right) + \left( \frac{\Delta C_{pfus1}}{R} \right) \times \left[ \ln \left( \frac{T}{T_{fus1}} \right) + \frac{T_{fus1}}{T} - 1 \right] + \left( \frac{\Delta H'_{trs1}}{R} \right) \times \left[ \frac{1}{T} - \frac{1}{T'_{trs1}} \right] + \left( \frac{\Delta H''_{trs1}}{R} \right) \left( \frac{1}{T} - \frac{1}{T''_{trs1}} \right) + \ln \gamma_1$$



**Table 1.** Dispersive (DIS) and QUAC interchange coefficients,  $C_{sn,l}^{DIS}$  and  $C_{sn,l}^{QUAC}$  ( $l = 1$ , Gibbs energy;  $l = 2$ , enthalpy;  $l = 3$ , heat capacity) for (s,n) contacts in NMP + organic solvent mixtures.

Solvent	Contact (s,n) <sup>a</sup>	$C_{sn,1}^{DIS}$	$C_{sn,2}^{DIS}$	$C_{sn,3}^{DIS}$	$C_{sn,1}^{QUAC}$	$C_{sn,2}^{QUAC}$	$C_{sn,3}^{QUAC}$
$n\text{-C}_n$ ( $n \leq 6$ )	(a,n)	5.25	12.0	2.0	8.0	6.0	2.0
$n\text{-C}_n$ ( $n = 7$ )	(a,n)	5.10	12.0	2.0	8.0	6.0	2.0
$n\text{-C}_n$ ( $n = 8$ )	(a,n)	5.0	12.0	2.0	8.0	6.0	2.0
$n\text{-C}_n$ ( $n = 9$ )	(a,n)	4.95	12.0	2.0	8.0	6.0	2.0
$n\text{-C}_n$ ( $n \geq 10$ )	(a,n)	4.9	12.0	2.0	8.0	6.0	2.0
c- $\text{C}_n$	(c,n)	5.0	12.0	2.0	8.0	6.0	2.0
$\text{C}_6\text{H}_6$	(b,n)	2.6	6.65	3.0	5.0	0.8	2.0
$\text{C}_7\text{H}_8$	(p,n)	2.3	6.5	8.0	5.0	0.8	2.0
1-Hexyne	(y,n)	0.45	-3.3		2.0	-1.5	
1-Heptyne	(y,n)	0.45	-3.7		2.0	-1.5	
1-Octyne	(y,n)	0.45	-4.2		2.0	-1.5	
Methanol	(h,n)	-2.85	7.2	9.0	-0.75	-2.2	-3.0
Ethanol	(h,n)	-2.85	9.0	9.0	-0.75	-1.52	-3.0
1-Propanol	(h,n)	-2.5	9.0	20.0	-0.75	-1.05	-3.0
1-Butanol	(h,n)	-2.2	4.05	20.0	-0.75	-0.25	-3.0
1-Pentanol	(h,n)	-2.0 <sup>b</sup>	2.95	20.0	-0.75	-0.25	-3.0
1-Hexanol	(h,n)	-1.75	2.15	20.0	-0.75	-0.25	-3.0
1-Heptanol	(h,n)	0.75	1.8	20.0	-0.75	-0.25	-3.0
1-Octanol	(h,n)	3.0	0.45	20.0	-0.75	-0.25	-3.0
1-Nonanol	(h,n)	5.2 <sup>b</sup>	-0.25	20.0	-0.75	-0.25	-3.0
1-Decanol	(h,n)	8.0	-0.55	20.0	-0.75	-0.25	-3.0
1-Undecanol	(h,n)	11.0	-0.55	20.0	-0.75	-0.25	-3.0
$\geq 1$ -Dodecanol	(h,n)	12.0	-0.55	20.0	-0.75	-0.25	-3.0

<sup>a</sup>(s = a,  $\text{CH}_3$ , or  $\text{CH}_2$  in  $n$ -alkanes, methylcyclohexane, toluene, 1-alkanols, 1-alkynes, or NMP; s = b,  $\text{C}_6\text{H}_6$ ; s = c, c- $\text{CH}_2$  in cycloalkanes or NMP; s = h, OH in 1-alkanols; s = p,  $\text{C}_6\text{H}_5$  in toluene; s = y,  $\text{HC}\equiv\text{C}$  in 1-alkynes; n, N-CO in NMP).

<sup>b</sup>Estimated values.

for temperatures below that of the phase transition (30). Conditions at which eq. [1] is valid have been specified elsewhere (22). In eq. [1],  $\gamma_1$  is the activity coefficient of component 1 in the solvent mixture at temperature  $T$ . In this work,  $\gamma_1$  is calculated using DISQUAC.  $\Delta H_{\text{fus}1}$ ,  $T_{\text{fus}1}$ , and  $\Delta C_{\text{pfus}1}$  are, respectively, the molar enthalpy of fusion, the melting temperature, and the change of the molar heat capacity during the melting of component 1.  $\Delta H_{\text{trs}1}$  and  $T_{\text{trs}1}$  stand for the molar enthalpy of transition and the transition temperature, respectively. The required physical constants are listed in Table A1 of the Appendix.

## Estimation of the interaction parameters

The general procedure applied in the estimation of the interaction parameters has been explained in detail elsewhere (22) and will not be repeated here. Some remarks are given below.

### NMP + alkane systems

These solutions are formed by three contacts, (a,c), (a,n), and (c,n). Because NMP is a five-membered ring, the (a,c) contacts must be fitted to experimental data for cyclopentane +  $n$ -alkane systems, which are described only by dispersive parameters (26, 31). The excess functions for binary mixtures with cyclopentane, or with another cycloalkane, show low values when a short-chain  $n$ -alkane is involved. For example,  $H^E(x_1 = 0.5, 298.15 \text{ K}) = 70 \text{ J mol}^{-1}$  for cyclopentane +  $n$ -heptane (32). Therefore, the corresponding interaction pa-

rameters also show low values. For the sake of simplicity, we used  $C_{ac,l}^{DIS}$  ( $l = 1, 2, 3$ ) = 0 in the present work. This approximation has been used previously for mixtures containing sulfolane (22, 23).

Once the (a,c) parameters are known, the (a,n) and (c,n) contacts can be simultaneously fitted (Table 1). This was done using the available database for NMP +  $n$ -alkane or + cycloalkane mixtures. Moreover, it was assumed that  $C_{an,l}^{QUAC} = C_{cn,l}^{QUAC}$ . This general rule is valid for many other solutions (see (22) and references given therein).

### NMP + benzene or toluene systems

These mixtures are characterized by six contacts, (a,s), (a,c), (a,n), (c,s), (c,n), and (s,n), with s = b or p. The (a,s) parameters are known from a study of benzene or toluene +  $n$ -alkane mixtures (33). The interaction parameters for the (c,s) (s = b, p) contacts are assumed to be entirely dispersive. These parameters are not neglected in view of the rather high values of the corresponding excess functions. For example, at equimolar composition and 298.15 K,  $H^E = 630 \text{ J mol}^{-1}$  for cyclopentane + benzene (34) and  $365 \text{ J mol}^{-1}$  for cyclopentane + toluene (34). Here, averaged values of the interchange coefficients are used,  $C_{ct,1}^{DIS} = 0.23$  and  $C_{ct,2}^{DIS} = 0.47$  (t = b, p). In the case of the cyclopentane + toluene system, the purely dispersive parameters of the (a,p) contacts must be considered. The values used are  $C_{ap,1}^{DIS} = 0.39$ ,  $C_{ap,2}^{DIS} = 0.59$ , and  $C_{ap,3}^{DIS} = -0.35$ .

The determination of the parameters for the (s,n) contacts was done under the basic assumption that the mixtures with



benzene or toluene are characterized by the same QUAC coefficients but different DIS parameters. The same trend is observed in 1-alkanol (35) or 2-alkanol (36) or sulfolane (22) + benzene or + toluene mixtures. The final parameter values are listed in Table 1.

### NMP + 1-alkanol systems

There are six contacts present in the mixtures: (a,c), (a,h), (a,n), (c,h), (c,n), and (n,h). The  $C_{ah,l}^{\text{DIS/QUAC}}$  and  $C_{ch,l}^{\text{DIS/QUAC}}$  ( $l = 1, 2, 3$ ) coefficients have been previously determined from data for VLE, LLE, SLE (solid-liquid equilibria),  $H^E$ , and  $C_p^E$  for 1-alkanol + alkane systems (27, 37–39). Therefore, only the interaction parameters for the (h,n) contacts must be fitted (Table 1).

### NMP + 1-alkyne systems

Here, there are also six contacts: (a,c), (a,n), (a,y), (c,n), (c,y), and (n,y). The  $C_{ay,l}^{\text{DIS/QUAC}}$  and  $C_{cy,l}^{\text{DIS/QUAC}}$  coefficients are known (28) from experimental data for 1-alkyne + *n*-alkane and + cycloalkane mixtures, respectively. So, only the  $C_{ny,l}^{\text{DIS/QUAC}}$  coefficients must be determined (Table 1). Owing to the lack of  $G^E$  data, the first DIS and QUAC interchange coefficients were calculated using the available data for logarithms of activity coefficients at infinite dilution (40, 41).

## Results

### DISQUAC results

Results from the DISQUAC model are compared with experimental data for LLE, VLE,  $G^E$ , SLE, and  $H^E$  in Tables 2–5. Comparisons for selected mixtures are plotted in Figs. 1–4. For the sake of clarity, relative deviations for the pressure ( $P$ ) and  $H^E$ , defined as

$$[2] \quad \sigma_r(P) = \left\{ \frac{1}{N} \sum \left[ \frac{P_{\text{exptl}} - P_{\text{calcd}}}{P_{\text{exptl}}} \right]^2 \right\}^{1/2}$$

$$[3] \quad \text{dev}(H^E) = \left\{ \frac{1}{N} \sum \left[ \frac{H_{\text{exptl}}^E - H_{\text{calcd}}^E}{H_{\text{exptl}}^E(x_1 = 0.5)} \right]^2 \right\}^{1/2}$$

are given in Tables 3 and 5, where  $N$  stands for the number of data points for each system.

We note that DISQUAC consistently represents the thermodynamic properties of the systems under study. The theoretical results for VLE and SLE suggest that the model can be applied over a wide range of temperatures (Tables 3, 4).

DISQUAC describes the LLE curves for the NMP + alkane systems (Fig. 1) reasonably well, considering that calculations were developed under the incorrect assumption that the excess functions are analytical close to the critical points, while the thermodynamic properties are, really, expressed in terms of scaling laws with universal critical exponents and universal scaling functions (65). For this reason, at temperatures near the UCST (upper critical solution temperature), the calculated LLE and  $H^E$  curves are more rounded than the experimental curves (Figs. 1, 2). This is in accordance with the results obtained for other mixtures, such as alkane + dimethyl carbonate (50), acetic anhydride (66),

**Table 2.** Critical points, temperatures ( $T_c$ ), and compositions ( $x_{1c}$ ) for NMP(1) + organic solvent(2) mixtures calculated using DISQUAC (DQ) with interaction parameters from Table 1.

Solvent	$T_c$ (K)		$x_{1c}$		Ref.
	Exp. <sup>a</sup>	DQ	Exp. <sup>a</sup>	DQ	
<i>n</i> -C <sub>4</sub>	338.73	296.9		0.278	42
<i>n</i> -C <sub>5</sub>	324.35	316.0	0.3478	0.345	43
	325		0.385		44
<i>n</i> -C <sub>6</sub>	324.65	331.3	0.443	0.401	44
	322.41				42
2,2-Dimethylbutane	327.60	333.6	0.3539	0.409	45
2,3-Dimethylbutane	319.22	331.1	0.3845	0.401	45
<i>n</i> -C <sub>7</sub>	326.05	333.4	0.455	0.451	44
	325.76		0.4659		43
<i>n</i> -C <sub>8</sub>	328.5	336.3	0.488	0.490	44
<i>n</i> -C <sub>9</sub>	333.19	340.8	0.5438	0.530	43
	332.25		0.502		44
<i>n</i> -C <sub>10</sub>	337.73	344.1	0.631	0.565	47
	336.72		0.511		48
<i>n</i> -C <sub>11</sub>	340.8	350.2	0.523	0.601	48
	341.38		0.6148		43
<i>n</i> -C <sub>12</sub>	353.27	355.5		0.629	42
	344.7		0.530		48
<i>n</i> -C <sub>13</sub>	348.9	360.4	0.630	0.662	48
<i>n</i> -C <sub>14</sub>	354.9	364.7	0.645	0.680	48
<i>n</i> -C <sub>16</sub>	367.65	372.3	0.6781	0.721	49
<i>c</i> -C <sub>5</sub>	277.07	279.5	0.2198	0.255	45
C <sub>6</sub> H <sub>12</sub>	283.10	288.4	0.2779	0.285	45
<i>m</i> -C <sub>6</sub> H <sub>12</sub> <sup>b</sup>	291.24	312.0	0.4196	0.359	45
<i>c</i> -C <sub>7</sub>	289.07	291.9	0.3409	0.310	45
<i>c</i> -C <sub>8</sub>	291.87	291.4	0.3515	0.318	45
	286.95		0.498		46

<sup>a</sup>Experimental (exp.) values.

<sup>b</sup>*m*-C<sub>6</sub>H<sub>12</sub>, treated as an *n*-alkane (50).

methanol (38), phenol (67), sulfolane (22), or alkoxyethanol (68). Nevertheless, the coordinates of the critical points are represented in the correct range of temperature and composition (Table 2). It is remarkable that for NMP + *n*-alkane systems, the UCST does not increase regularly with the chain length of the *n*-alkane. So, for the solutions with *n*-C<sub>4</sub> or *n*-C<sub>5</sub>, the UCST is higher than for the mixture with *n*-C<sub>6</sub> (Table 2). This has been ascribed to the alkane-rich phase approaching its gas-liquid critical point (42). DISQUAC cannot represent such behaviour, and larger differences between experimental and calculated UCST values are observed for the mentioned systems.

The rather poor theoretical results obtained for VLE for solutions with alkanes (Table 3) at temperatures close to the critical values merely underline that it is not possible to accurately and simultaneously represent VLE and LLE at those conditions using the same set of interaction parameters. Note that the model describes the composition dependence of  $H^E$  (Table 5) and the coordinates of the azeotropes quite accurately at high enough temperatures. For example, DISQUAC predicts, for the NMP(1) + *n*-dodecane(2) system



**Table 3.** Molar excess Gibbs energies,  $G^E$ , at equimolar composition and at temperature  $T$  for NMP(1) + organic solvent(2) mixtures.

Solvent	$T$ (K)	$N^b$	$G^E$ (J mol <sup>-1</sup> )		$\sigma_r(P)^a$		Ref.
			Exp. <sup>c</sup>	DQ <sup>d</sup>	Exp. <sup>c</sup>	DQ <sup>d</sup>	
<i>n</i> -C <sub>6</sub>	333.25	10.	1600	1474	0.005	0.039	51
	343.25	9	1630	1465		0.061	51
	363.58	44	1540	1444		0.12	52
<i>n</i> -C <sub>7</sub>	298.15	29	584	654	0.013	0.12	53
	340	19	1580	1501	0.011	0.12	54
	365	9	1570	1468	0.013	0.10	54
<i>n</i> -C <sub>12</sub>	393.25	12	1550	1498	0.007	0.029	51
C <sub>6</sub> H <sub>12</sub>	281.15	7	678 ( $x_1 = 0.1$ )	599	0.003	0.26	55
	287.15	10	1380	1145	0.004	0.21	55
	293.15	11	1380	1212	0.007	0.20	55
	333.25	12	1180	1175	0.003	0.018	51
	354.15	11	1200	1150	0.012	0.023	51
<i>m</i> -C <sub>6</sub> H <sub>12</sub> <sup>e</sup>	340	10	1390	1344	0.014	0.072	54
	354.15	11	1240	1329	0.018	0.067	51
	370	13	1390	1309	0.033	0.066	54
	373.25	10	1170	1305	0.003	0.055	51
	281.15	12	12	15	0.009	0.007	55
C <sub>6</sub> H <sub>6</sub>	287.15	12	22	26	0.006	0.004	55
	293.15	12	33	37	0.005	0.003	55
	330	15	108	104	0.009	0.016	54
	333.25		-328	109			51
	350	17	71	140	0.015	0.045	54
C <sub>7</sub> H <sub>8</sub>	354.15		-238	146			51
	343.15	16	301	290	0.036	0.038	54
	363.25		3.2	302			51
	373.15	15	307	305	0.039	0.064	54
	383.35		140	306			51
Methanol	333.15	21	-622	-627	0.022	0.039	56
Ethanol	333.15	20	-565	-554	0.018	0.053	56
1-Propanol	354.15	9	-975	-520	0.009	0.26	51
1-Hexanol	351.75	10	-457	-310	0.004	0.048	51
	393.35	9	-533	-360	0.003	0.055	51

<sup>a</sup>Equation [2].<sup>b</sup>Number of data points.<sup>c</sup>Experimental values.<sup>d</sup>DISQUAC calculations with interaction parameters from Table 1.<sup>e</sup>*m*-C<sub>6</sub>H<sub>12</sub> treated as an *n*-alkane (50).

at 393.15 K, an azeotrope at  $x_{1\text{az}} = 0.652$  and  $P_{\text{az}} = 103.52$  kPa; the experimental values, at the same temperature, are  $x_{1\text{az}} = 0.655$  and  $P_{\text{az}} = 105.96$  kPa (51). However, the observed discrepancies for VLE are also due in part to the inadequacy of the Flory–Huggins combinatorial term (69), as well as to experimental errors (54). Note, for example, the extremely negative value of  $G^E$  for NMP + 1-propanol or + 1-hexanol mixtures (Table 3).

For systems with solvents other than alkanes, DISQUAC provides quite good results.

One of the most interesting features of the NMP + 1-alkanol systems is that the position of the maxima of the  $H^E$  curves is shifted to a higher mole fraction of the amide when the chain length of the 1-alkanol increases (11, 12). Similar behaviour is observed for mixtures of DMF (70), dimethylacetamide (71), or dimethylsulfoxide (70) with 1-alkanols. The opposite trend is encountered for mixtures formed by 1-alkanol with a nonpolar compound, such as benzene, or with

a polar non-protonic solvent (e.g., cyclohexanone, 1,4-dioxane) (70). This complex behaviour is well described by DISQUAC (Fig. 3).

### Comparison with other models

The experimental  $H^E$  data are better represented by DISQUAC than by UNIFAC (Fig. 4b) because the interaction parameters are considered to be dependent on the molecular structure. UNIFAC fails when representing  $H^E$  for the NMP + 1-alkanol mixtures. At equimolar composition and 298.15 K, the model predicts  $H^E$  (1-propanol) = 1555 J mol<sup>-1</sup>, while the experimental value is 277 J mol<sup>-1</sup> (11). This large discrepancy may be due the absence of  $H^E$  measurements and the determination of the interaction parameters using only VLE data. For this reason, UNIFAC improves VLE for the mixtures with alkanes (Fig. 4a). However, UNIFAC does not correctly represent LLE. For example, UNIFAC predicts ≈395 K for the UCST of the



**Table 4.** Solid–liquid equilibria for NMP(1) + organic solvent(2) mixtures.

Solvent	$N^a$	$\text{dev}(T)^b$	$x_{1\text{eu}}$		$T_{\text{eu}} \text{ (K)}$		Ref.
			Exp. <sup>c</sup>	DQ <sup>d</sup>	Exp. <sup>c</sup>	DQ <sup>d</sup>	
C <sub>6</sub> H <sub>6</sub>	36	2.5 <sup>e</sup>	0.4712	0.508	242.85	238.6	57
C <sub>7</sub> H <sub>8</sub>	17	0.37					57
1-Propanol	34	2.9					58
1-Butanol	30	0.51					58
1-Hexanol	30	0.98	0.4039	0.395	213.87	212.56	59
1-Heptanol	33	0.95	0.4856	0.477	220.78	222.55	59
1-Octanol	21	1.4	0.6345	0.674	235.40	235.84	59
1-Decanol	27	0.54	0.8910	0.880	246.72	245.26	59
1-Undecanol	33	1.0	0.9564	0.955	247.99	247.76	59
1-Decanol	32	1.6		0.976		248.70	59
1-Tetradecanol	25	4.4 <sup>f</sup>					59

<sup>a</sup>Number of data points.

$$^b\text{dev}(T) = \frac{1}{N} \sum |T_{\text{exp}} - T_{\text{calcd}}|$$

<sup>c</sup>Experimental values.<sup>d</sup>DISQUAC calculations with interaction parameters from Table 1.<sup>e</sup>Calculations developed assuming a complex compound of the 1:1 type with an enthalpy of formation of 65 kJ mol<sup>-1</sup>. The experimental work indicates a complex compound of 1:2 type (57).<sup>f</sup>The two first-order transitions for 1-tetradecanol were taken into consideration along calculations (59):  $T_{\text{tr2}}'(\alpha \rightarrow \beta) = 308.17 \text{ K}$ ;  $\Delta H_{\text{tr2}}' = 17.50 \text{ kJ mol}^{-1}$ ;  $T_{\text{tr2}}''(\alpha \rightarrow \beta) = 306.43 \text{ K}$ ;  $\Delta H_{\text{tr2}}'' = 2.13 \text{ kJ mol}^{-1}$ .**Table 5.** Molar excess enthalpies,  $H^E$ , at equimolar composition and at temperature  $T$  for NMP (1) + organic solvent(2) mixtures.

Solvent	$T \text{ (K)}$	$N^b$	$H^E \text{ (J mol}^{-1}\text{)}$		$\text{dev}(H^E)^a$		Ref.
			Exp. <sup>c</sup>	DQ <sup>d</sup>	Exp. <sup>c</sup>	DQ <sup>d</sup>	
<i>n</i> -C <sub>6</sub>	363.15	17	1707	1851	0.005	0.042	52
2-Methylpentane	363.15	20	1670	1850	0.003	0.054	52
3-Methylpentane	363.15	16	1664	1850	0.006	0.060	52
<i>n</i> -C <sub>7</sub>	333.2	9	1862	1898	0.001	0.036	60
	353.2	9	1941	1958	0.008	0.032	60
C <sub>6</sub> H <sub>12</sub>	298.15	15	1360	1449	0.012	0.073	61
C <sub>6</sub> H <sub>6</sub>	298.15	14	-500	-500	0.012	0.017	61
	298.15	12	-544		0.005	0.059	8
	313.15	14	-489	-487	0.012	0.017	61
C <sub>7</sub> H <sub>8</sub>	298.15	9	-237	-237	0.029	0.029	62
		9	-319		0.004	0.222	8
	313.15	9	-144	-145	0.069	0.146	62
1-Hexyne	298.15	10	-880	-854	0.010	0.041	9
1-Heptyne	298.15	14	-740	-689	0.010	0.051	9
1-Octyne	298.15	11	-592	-549	0.008	0.056	9
Methanol	298.15	14	-647	-654	0.005	0.029	63
		10	-652		0.011	0.017	64
	308.15	10	-664		0.015	0.024	63
Ethanol	298.15	11	30	14	0.067	0.323	12
1-Propanol	298.15	16	281	277	0.011	0.039	11
1-Butanol	298.15	13	309	303	0.010	0.058	11
1-Pentanol	298.15	14	367	363	0.014	0.049	12
1-Hexanol	298.15	13	439	431	0.009	0.027	12
1-Heptanol	298.15	14	512	507	0.013	0.017	12
1-Octanol	298.15	10	520	518	0.008	0.042	12
1-Nonanol	298.15	10	560	549	0.005	0.027	12
1-Decanol	298.15	13	595	586	0.008	0.022	12
1-Undecanol	298.15	10	610	640	0.005	0.031	12

<sup>a</sup>Equation [3].<sup>b</sup>Number of data points.<sup>c</sup>Experimental values.<sup>d</sup>DISQUAC calculations with interaction parameters from Table 1.



**Fig. 1.** LLE for NMP(1) + alkane(2) mixtures. Experimental results: ●, cyclohexane (45); ■, *n*-decane (47); ▲, *n*-hexadecane (49). Solid curves, DISQUAC calculations.

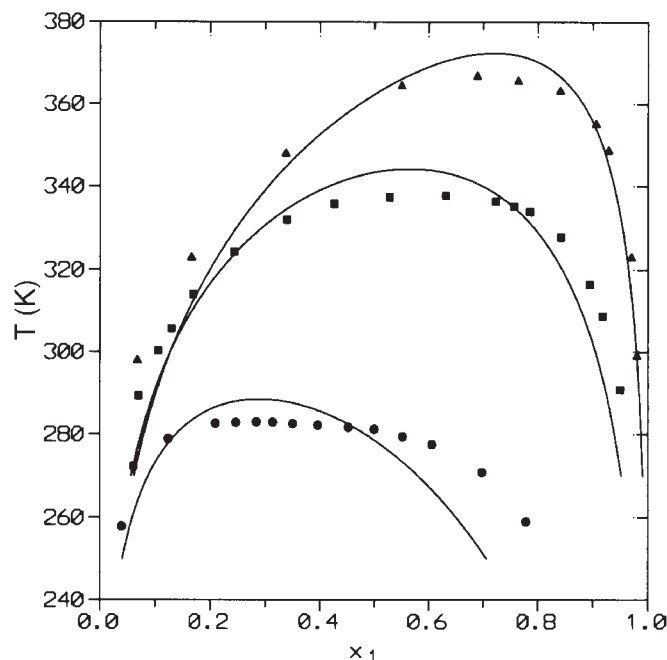
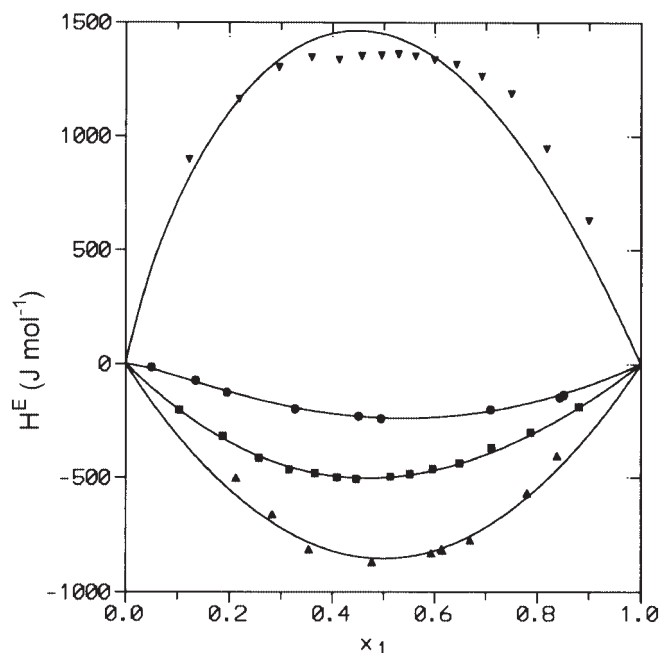


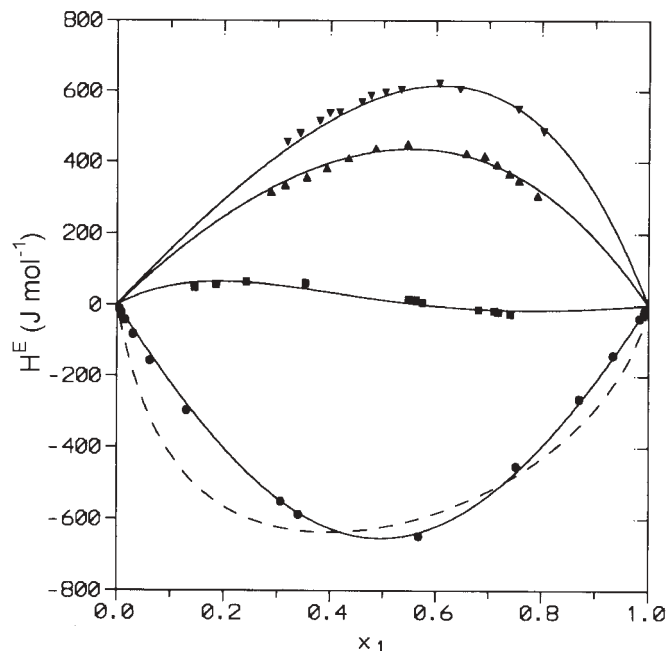
**Fig. 2.**  $H^E$  at 298.15 K for NMP(1) + organic solvent(2) mixtures. Experimental results: ▼, cyclohexane (61); ●, toluene (62); ■, benzene (61); ▲, 1-hexyne (9). Solid curves, DISQUAC calculations.



NMP + decane system, whereas the experimental value is 337.73 K (47).

As already mentioned, ERAS has been applied to NMP + benzene, + toluene, + 1-alkyne, or + 1-alkanol mixtures. The calculations were carried out assuming that NMP is self-

**Fig. 3.**  $H^E$  at 298.15 K for NMP(1) + 1-alkanol(2) mixtures. Experimental results: ●, methanol (63); ■, ethanol (12); ▲, 1-hexanol (12); ▼, 1-decanol (12). Solid curves, DISQUAC calculations. Dashed curve: ERAS results (this work) for the mixture with methanol using  $K_{AB} = 22$ ;  $\Delta h_{AB}^* = -38.5$  kJ mol<sup>-1</sup>;  $\Delta v_{AB}^* = -14.2$  cm<sup>3</sup> mol<sup>-1</sup>;  $X_{AB} = 12$  J cm<sup>-3</sup> (for other ERAS parameters, see (10)).



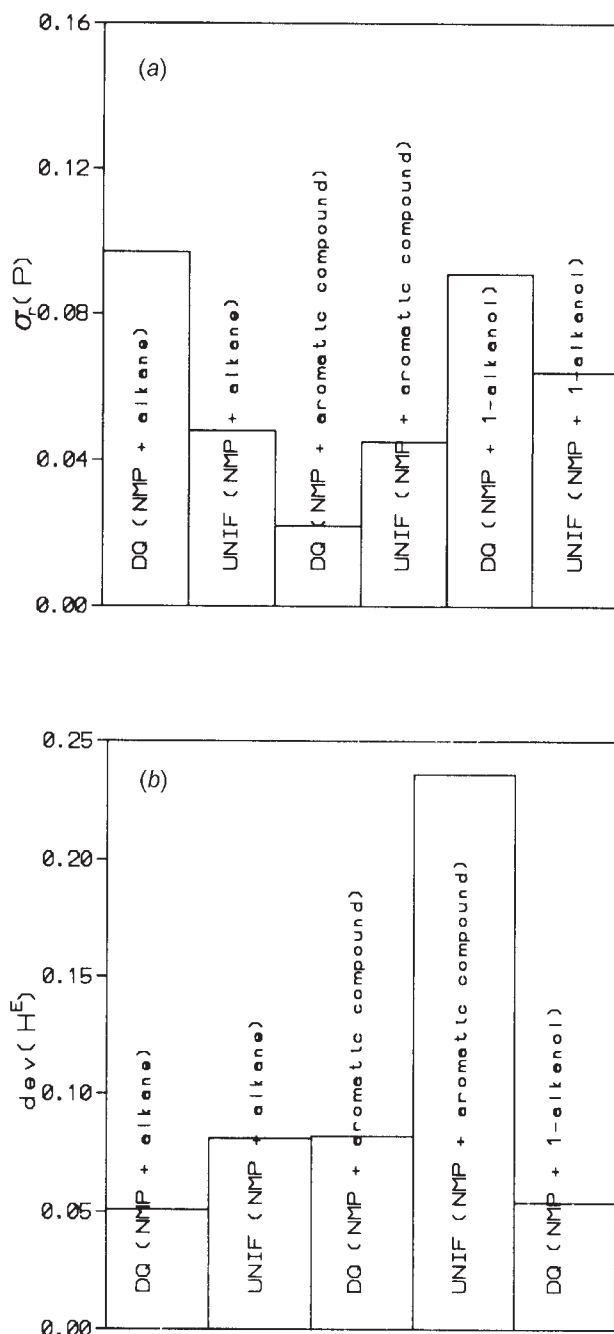
associated, which is not justified (16, 17). In addition, self-association was also assumed for benzene, toluene, and 1-alkyne. For NMP + benzene, + toluene, or + 1-alkyne systems, the mean deviation of  $H^E$  from DISQUAC is  $\approx 6.8\%$ , while ERAS, under the specified assumptions, provides a mean deviation of  $\approx 13\%$ . However, the ERAS results are still meaningful because the model can also quite accurately represent the molar excess volume ( $V^E$ ) of such solutions. This seems to indicate that ERAS could be applied to systems in which self-association and cross-association occur, owing to other interactions besides hydrogen bonding (8).

For NMP + 1-alkanol mixtures, calculations carried out in the present work show that there is no significant difference between results obtained when considering NMP to be a non-self-associated compound and those obtained when NMP is assumed to be self-associated.

In any case, the important point is that ERAS does not describe the thermodynamic properties of solutions of NMP with 1-alkanol. This may be due to the fact that ERAS cannot properly represent such large positive contributions from dipole-dipole interactions to the excess functions. Fig. 3 shows that for NMP + methanol mixtures, the calculated  $H^E$  curve is shifted towards higher mole fractions of the alcohol. This suggests that the model overestimates the chemical contribution to  $H^E$  or the role of the self-association of the alcohol in these mixtures. A similar trend was found for 1-alkanol + linear organic carbonate systems (72), although the representation of the mixture properties was acceptable, probably because the dipole-dipole interactions between the carbonate molecules are of less importance than those be-



**Fig. 4.** Comparison between results for VLE and  $H^E$  from the DISQUAC (DQ) and UNIFAC models: (a) Results for the relative standard deviation in pressure (eq. [2]),  $\sigma_r(P)$ ; (b) results for  $\text{dev}(H^E)$  (eq. [3]).



tween NMP molecules (note that the experimental UCST for the dimethyl carbonate + *n*-decane mixture is 286.62 K (73)).

Therefore, one can conclude that ERAS can be applied successfully to mixtures for which the thermodynamic properties arise from the self-association of one component (1-alkanol + alkane (74)) or from interactions between unlike molecules (1-alkanol + amine (75) or NMP + 1-alkyne (9)).

Calculations of  $TS_{\text{int}}^E (= H^E - G_{\text{int}}^E)$ , with  $G^E = G_{\text{int}}^E + G_{\text{E,COMB}}^E$  support this conclusion (Table 6). NMP + 1-

**Table 6.** Molar excess functions at 298.15 K and equimolar composition for NMP(1) + organic solvent(2) mixtures.

Solvent	$G^E$ (J mol <sup>-1</sup> ) <sup>a</sup>	$G_{\text{E,COMB}}^E$ (J mol <sup>-1</sup> ) <sup>b</sup>	$H^E$ (J mol <sup>-1</sup> ) <sup>c</sup>	$TS_{\text{int}}^E$ (J mol <sup>-1</sup> ) <sup>d</sup>
<i>n</i> -C <sub>7</sub>	1484 <sup>e</sup>	-27 <sup>e</sup>	1958 <sup>e</sup>	474 <sup>e</sup>
C <sub>6</sub> H <sub>6</sub>	46	-14	-500	-560
C <sub>7</sub> H <sub>8</sub>	239	0	-237	-476
Methanol	-628	-306	-654	-332
Ethanol	-492	-120	14	386
1-Butanol	-284	-5	303	582
1-Hexanol	-201	-12	431	620
1-Octanol	27	-61	518	430
1-Decanol	166	-126	585	293
1-Hexyne	311	-1	-853	-1165
1-Heptyne	423	-14	-689	-1126
1-Octyne	507	-37	-549	-1083

<sup>a</sup>Molar excess Gibbs energy calculated using the interaction parameters from Table 1.

<sup>b</sup>Combinatorial contribution to  $G^E$  calculated with the Flory–Huggins equation (25, 26).

<sup>c</sup>Molar excess enthalpy calculated using the interaction parameters from Table 1.

<sup>d</sup> $TS_{\text{int}}^E = H^E - G_{\text{int}}^E$ ;  $G^E = G_{\text{int}}^E + G_{\text{E,COMB}}^E$ .

<sup>e</sup>Value at 353.2 K.

alkyne, + benzene, + toluene, or + methanol systems show very negative  $TS_{\text{int}}^E$  values. In the diagram where  $G_{\text{int}}^E(x_1 = 0.5)$  is plotted against  $H^E(x_1 = 0.5)$  (76), the mentioned solutions are placed on the left-hand side, indicating the importance of chemical interactions in such mixtures. For NMP + 1-alkanol ( $\neq$  methanol) systems,  $TS_{\text{int}}^E$  becomes quite large and positive, indicating that association is not so important. It should be kept in mind that  $G^E$  and  $H^E$  of systems formed by NMP and one hydrocarbon or one aromatic compound are not described by the chemical theory of solutions (60). This suggests the transitional character (between associated and non-associated mixtures) of those solutions containing a very polar component (60).

## Discussion

### Concentration–concentration structure factor

Mixture structure can be studied using the concentration–concentration structure factor,  $S_{\text{CC}}(0)$  (77), defined as

$$[4] \quad S_{\text{CC}}(0) = \frac{RT}{(\partial^2 G^M / \partial x_1^2)_{P,T}} = \frac{x_1 x_2}{D}$$

with

$$[5] \quad D = \frac{x_1 x_2}{RT} (\partial^2 G^M / \partial x_1^2)_{P,T} = 1 + \frac{x_1 x_2}{RT} \left( \frac{\partial^2 G^E}{\partial x_1^2} \right)_{P,T}$$

$D$  is a function closely related to thermodynamic stability (65, 78). For ideal mixtures,  $G_{\text{E,id}}^E = 0$ ,  $D_{\text{id}} = 1$ , and  $S_{\text{CC}}(0) = x_1 x_2$ . As stability conditions require,  $S_{\text{CC}}(0) > 0$ , and if the system is close to phase separation,  $S_{\text{CC}}(0)$  must be large and positive ( $\infty$ , when the mixture presents a miscibility gap). In contrast, if compound formation between components appears,  $S_{\text{CC}}(0)$  must be very low (0, in the limit of complete



reaction). So, if  $S_{CC}(0) > x_1x_2$  (i.e.,  $D < 1$ ), the dominant trend in the system is the separation of the components (homocoordination), and the mixture is less stable than the ideal mixture. If  $0 < S_{CC}(0) < x_1x_2 = S_{CC}(0)^{id}$  (i.e.,  $D > 1$ ), the fluctuations in the system have been removed, and the dominant trend in the solution is compound formation (heterocoordination). In this case, the system is more stable than the hypothetical ideal mixture.

Hereafter, we refer to values of the thermodynamic properties at 298.15 K and equimolar composition. For the NMP +  $n$ -C<sub>7</sub> system ( $T = 373.15$  K),  $S_{CC}(0) = 1.79$ . This rather high value is characteristic of mixtures at temperatures close to the UCST and underlines the dominant role in such solutions of homocoordination (dipole–dipole interactions between NMP molecules; see also the high  $H^E$  values for this system (Table 2)). Similarly,  $S_{CC}(0) = 1.72$  for NMP + cyclohexane.

For the NMP + methanol solution,  $S_{CC}(0) = 0.17$ . The  $S_{CC}(0)$  curve is shifted to higher NMP concentration (Fig. 5), which means that several NMP molecules interact with one methanol molecule. From the study of NMP + 1-alkanol systems, in terms of the internal pressure ( $P_i$ ) of the pure components and of their mixtures (79), it has been concluded that 1:1 (H-bond) and 1:2 (dipole–dipole interactions) aggregates are feasible only for the NMP + methanol system, whereas for the other 1-alkanols the associative and dispersion forces do not enable net heteroassociation. This conclusion was based on  $V^E$  and  $\Delta G^{*E}$  (Gibbs energy of activation) data (79).

$S_{CC}(0)$  calculations using DISQUAC suggest that heterocoordination is still possible for NMP + 1-hexanol system (see Fig. 5), as  $S_{CC}(0) = 0.21$ .

For the NMP + 1-hexyne system,  $S_{CC}(0) = 0.32$ . However,  $H^E = -880$  J mol<sup>-1</sup> (9). This may be interpreted by assuming that, although there is a larger number of interactions between like molecules ( $S_{CC}(0) > 0.25$ ), the interactions between unlike molecules are stronger.

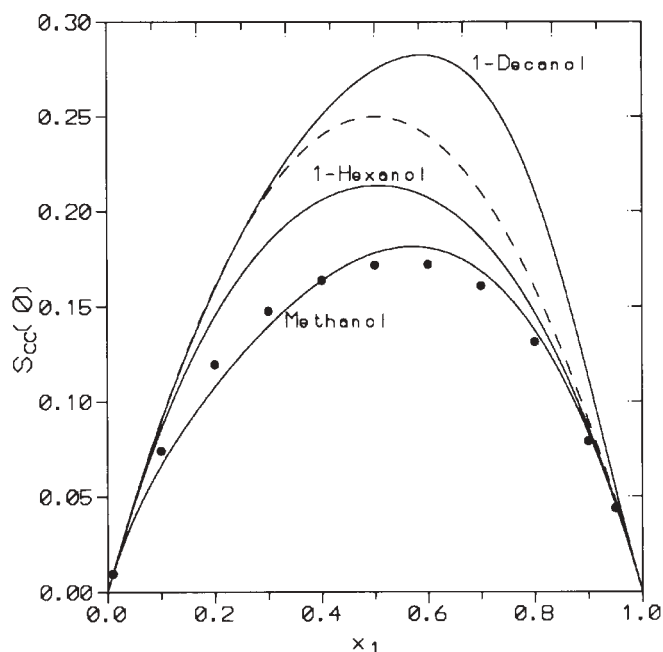
Finally, the NMP + benzene system is characterized by  $H^E = -500$  J mol<sup>-1</sup> (61). In addition, SLE measurements suggest the existence of complex formation (1:2 type) (57). This evidence suggests interactions between unlike molecules. In contrast,  $S_{CC}(0) = 0.25$ . This may well be due to the low value of the  $G^E$  (Table 3), a possible consequence of enthalpic–entropic compensation.

### The DISQUAC interaction parameters

(a) For mixtures containing  $n$ -alkanes, the first dispersive interaction parameter depends on the chain length of the  $n$ -alkane (Table 1). This is necessary to describe the LLE curves. Similar behaviour has been reported for mixtures of  $n$ -alkanes with sulfolane (22) or crown ethers (80).

(b) For mixtures containing 1-alkanol, the  $C_{nn,l}^{QUAC}$  ( $l = 1, 3$ ) coefficients are independent of the alkanol, while the enthalpic QUAC parameters differ only for the lower 1-alkanols (Table 1). Similar trends have been reported for other solutions, for example: 1-alkanol +  $n$ -alkane (27, 37), or + cyclohexane (39), or + aromatic compound (35), or + linear organic carbonate (72), or in alkoxyethanol + alkane mixtures (68). This reveals the different character (stronger self-association, higher dielectric constant) of first members of homologous series (methanol, ethanol, 2-methoxyetha-

**Fig. 5.**  $S_{CC}(0)$  for NMP(1) + 1-alkanol(2) + mixtures at temperature  $T$ . Points, experimental values at 333.15 K (56). Solid curves, DISQUAC calculations at 333.15 K (methanol) or at 298.15 K (remaining 1-alkanols). Dashed curve, ideal mixture.



anol). The same conclusion was stated when treating 1-alkanol + organic solvent mixtures in the framework of Barker's theory (81, 82)

(c) The  $C_{nn,l}^{DIS}$  coefficients remain constant for the longer 1-alkanols (Table 1), as reported previously for 1-alkanol +  $n$ -alkane (27, 37), + cyclohexane (39), + aromatic compound (35), or + linear organic carbonate (72) mixtures.

### Conclusions

Mixtures of NMP with alkane, benzene, toluene, 1-alkanol, or 1-alkyne have been investigated in the framework of the DISQUAC model. The corresponding interaction parameters are reported. The model consistently describes a set of thermodynamic properties: LLE, VLE, SLE,  $G^E$ , and  $H^E$ . The dependence of the interaction parameters on molecular structure is similar to results reported previously for other mixtures.

### Acknowledgements

JAG gratefully acknowledges financial support from the D.G.I. del Ministerio de Ciencia y Tecnología "Proyectos I+D del Programa Nacional de Procesos y Productos Químicos" (Project ref. PPQ2001-1664) and Unión Europea (F.E.D.E.R.), and from the Consejería de Educación y Cultura de la Junta de Castilla y León, under the Project VA039/01. U.D. and J.L. also gratefully acknowledge financial support received from the Polish Committee for Scientific Research (Grant 7TO9B09521).



## References

1. J.A. Riddick, W.B. Bunger, and T. K. Sakano. Organic solvents. In *Techniques of chemistry*. Vol. 2. Edited by A. Weissberger. Wiley, New York, 1986.
2. J.L. Wuepper and A.I. Popov. *J. Am. Chem. Soc.* **32**, 4352 (1969).
3. J.D. Dyke, P.G. Sears, and A.I. Popov. *J. Phys. Chem.* **71**, 4140 (1967).
4. M. Breant. *Bull. Soc. Chim. Fr.* 725 (1971).
5. A.F. Sowinski and G.M. Whitesides. *J. Org. Chem.* **44**, 2369 (1979).
6. E. Muller and G. Hohfeld. *World Pet. Congr. Proc.* 8th, 213 (1971).
7. (a) A. Vega, F. Díez, R. Esteban, and J. Coca. *Ind. Eng. Chem. Res.* **36**, 803 (1997); (b) B. Blanco, M.T. Sanz, S. Beltrán, J.L. Cabezas, and J. Coca. *Fluid Phase Equilib.* **175**, 117 (2000).
8. T.M. Letcher and P.K. Naicker. *J. Chem. Thermodyn.* **31**, 1585 (1999).
9. T.M. Letcher and P.G. Whitehead. *J. Chem. Thermodyn.* **31**, 1537 (1999).
10. T.M. Letcher, U. Domanska, and E. Mwenesongole. *Fluid Phase Equilib.* **149**, 323 (1998).
11. T.M. Letcher, J. Lachwa, and U. Domanska. *J. Chem. Thermodyn.* **33**, 1169 (2001).
12. T.M. Letcher, J. Lachwa, and U. Domanska. *J. Chem. Thermodyn.* **34**, 1581 (2002).
13. A. Heintz. *Ber. Bunsenges. Phys. Chem.* **89**, 172 (1985).
14. (a) C.B. Kretschmer and R. Wiebe. *J. Chem. Phys.* **22**, 1697 (1954); (b) H. Renon and J.M. Prausnitz, *Chem. Eng. Sci.* **22**, 299 (1967).
15. (a) P.J. Flory. *J. Am. Chem. Soc.* **87**, 1833 (1965); (b) A. Abe and P.J. Flory. *J. Am. Chem. Soc.* **87**, 1838 (1965).
16. M.M. Kopečni, R.J. Laub, and D.M. Petkovic. *J. Phys. Chem.* **85**, 1595 (1981).
17. W.L. Jorgensen and C.L. Swenson. *J. Am. Chem. Soc.* **107**, 569 (1985).
18. J. Gmehling, J. Li, and M. Schiller. *Ind. Eng. Chem. Res.* **32**, 178 (1993).
19. J. Gmehling, J. Lohmann, A. Jakob, J. Li, and R. Joh. *Ind. Eng. Chem. Res.* **37**, 4876 (1998).
20. H.V. Kehiaian. *Fluid Phase Equilib.* **13**, 243 (1983); *Pure Appl. Chem.* **57**, 15 (1985).
21. E.A. Guggenheim. *Mixtures*. Oxford University Press, Oxford, 1952.
22. J.A. González and U. Domanska. *Phys. Chem. Chem. Phys.* **3**, 1034 (2001).
23. U. Domanska and J.A. González. *Can. J. Chem.* **80**, 476 (2002).
24. A. Bondi. *Physical properties of molecular crystals, liquids and glasses*. Wiley, New York, 1968.
25. H.V. Kehiaian, J.-P.E. Grolier, and G.C. Benson. *J. Chim. Phys.* **75**, 1031 (1978).
26. J.A. González, I. García de la Fuente, J.C. Cobos, C. Casanova, and A. Ait-Kaci. *Fluid Phase Equilib.* **112**, 63 (1995).
27. J.A. González, I. García de la Fuente, J.C. Cobos, and C. Casanova. *Ber. Bunsenges. Phys. Chem.* **95**, 1658 (1991).
28. J.A. González, S. Villa, N. Riesco, I. García de la Fuente, and J.C. Cobos. *Thermochim. Acta*, **381**, 103 (2002).
29. I. Prigogine and R. Defay. *Chemical thermodynamics*. Longmans, Green and Co., Norwich, 1954.
30. (a) P.B. Choi and E. McLaughlin. *AIChE J.* **29**, 150 (1983); (b) R.F. Weimer and J.M. Prausnitz. *J. Chem. Phys.* **42**, 3643 (1965).
31. B. Marongiu, S. Porcedda, L. Lepori, and E. Matteoli. *Fluid Phase Equilib.* **108**, 167 (1995).
32. A. Inglese and J.-P.E. Grolier. *Int. Data Ser. Selec. Data Mixtures Ser. A*, 75 (1975).
33. A. Ait-Kaci. Ph.D. thesis. Lyon University, France, 1982.
34. A.E.P. Watson, I.A. McLure, J.E. Bennet, and G.C. Benson. *J. Phys. Chem.* **69**, 2753 (1965).
35. (a) J.A. González, I. García de la Fuente, J.C. Cobos, and C. Casanova. *Fluid Phase Equilib.* **93**, 1 (1994); (b) U. Domanska and J.A. González. *Fluid Phase Equilib.* **119**, 131 (1996).
36. J.A. González, I. García de la Fuente, and J.C. Cobos. *Can. J. Chem.* **76**, 1418 (1998).
37. (a) J.A. González, I. García de la Fuente, J.C. Cobos, C. Casanova, and U. Domanska. *Ber. Bunsenges. Phys. Chem.* **98**, 955 (1994); (b) U. Domanska and J.A. González. *Fluid Phase Equilib.* **123**, 167 (1996).
38. J.A. González, I. García de la Fuente, and J.C. Cobos. *Ber. Bunsenges. Phys. Chem.* **101**, 219 (1997).
39. (a) J.A. González, I. García de la Fuente, J.C. Cobos, and C. Casanova. *J. Solution Chem.* **23**, 399 (1994); (b) J.A. González, I. García de la Fuente, and J.C. Cobos. *Thermochim. Acta*, **278**, 57 (1996).
40. T.M. Letcher and P.G. Whitehead. *J. Chem. Thermodyn.* **29**, 1261 (1997).
41. T.M. Letcher and P.G. Whitehead. *J. Chem. Thermodyn.* **32**, 1121 (2000).
42. R. Eustaquio-Rincón, R. Molnar, and A. Trejo. *Fluid Phase Equilib.* **68**, 187 (1991).
43. D. Bernabé, A. Romero-Martínez, and A. Trejo. *Fluid Phase Equilib.* **40**, 279 (1988).
44. S. Malanowski, H.-J. Bittrich, D. Lempe, K. Reinhardt, and J.-U. Wüstling. *Fluid Phase Equilib.* **98**, 163 (1994).
45. R. Eustaquio-Rincón, A. Romero-Martínez, and A. Trejo. *Fluid Phase Equilib.* **91**, 187 (1993).
46. H.-J. Bittrich, G. Feix, D. Lempe, and K. Reinhardt. *Fluid Phase Equilib.* **51**, 161 (1989).
47. M. Antosik, A. Stafiej, and R. Stryjek. *Fluid Phase Equilib.* **58**, 325 (1990).
48. H.-J. Bittrich, D.A. Lempe, K. Reinhardt, and J.-U. Wüstling. *Fluid Phase Equilib.* **126**, 115 (1996).
49. M. Rogalski and R. Stryjek. *Bull. Acad. Pol. Sci. Ser. Sci. Chim.* **28**, 139 (1980).
50. J.A. González, I. García de la Fuente, J.C. Cobos, C. Casanova, and H.V. Kehiaian. *Thermochim. Acta*, **217**, 57 (1993).
51. P. Gierycz, M. Rogalski, and S. Malanowski. *Fluid Phase Equilib.* **22**, 107 (1985).
52. K. Fischer and J. Gmehling. *Fluid Phase Equilib.* **119**, 113 (1996).
53. J. Gaube, L. Krenzer, G. Olf, and R. Wendel. *Fluid Phase Equilib.* **35**, 279 (1987).
54. J. Linek, I. Wichterle, and K.N. Marsh. *J. Chem. Eng. Data*, **41**, 1212 (1996).
55. K. Aim. *Fluid Phase Equilib.* **2**, 119 (1978).
56. H.-J. Bittrich and R. Eckert. *Z. Phys. Chem.* **175**, 217 (1992).
57. U. Domanska and T.M. Letcher. *J. Chem. Thermodyn.* **32**, 1635 (2000).
58. U. Domanska and J. Lachwa. *J. Chem. Thermodyn.* **35**, 1215 (2003).
59. J. Lachwa and U. Domanska. *Fluid Phase Equilib.* **198**, 1 (2002).
60. R. Fuchs, L. Krenzer, and J. Gaube. *Ber. Bunsenges. Phys. Chem.* **88**, 642 (1984).
61. J.-L. Gustin and H. Renon. *J. Chem. Eng. Data*, **18**, 164 (1973).



62. I. Hammerl, A. Vogel, and H.-J. Bitttrich. *Z. Phys. Chem. (Leipzig)*, **271**, 477 (1990).
63. R.D. Joly and M. Mermet-Dupin. *C.R. Hebd. Seances Acad. Sci. Ser. C*, **280**, 1363 (1975).
64. S. Murakami, R. Tanaka, and R. Fujishiro. *J. Solution Chem.* **3**, 71 (1974).
65. J.S. Rowlinson and F.L. Swinton. *Liquids and liquid mixtures*. 3rd ed. Butterworths, London. 1982.
66. (a) H.V. Kehiaian, J.A. González, I. García, R. Escarda, J.C. Cobos, and C. Casanova. *Fluid Phase Equilib.* **69**, 91 (1991); (b) M. Aboy, S. Villa, N. Riesco, J.A. González, I. García de la Fuente, and J.C. Cobos. *J. Chem. Eng. Data*, **47**, 950 (2002).
67. J.A. González, I. García de la Fuente, and J.C. Cobos. *Ber. Bunsenges. Phys. Chem.* **100**, 1746 (1996).
68. J.A. González, J.C. Cobos, F.J. Carmona, I. García de la Fuente, V.R. Bhethanabotla, and S.C. Campbell. *Phys. Chem. Chem. Phys.* **3**, 2856 (2001).
69. J.A. González, F.J. Carmona, N. Riesco, I. García de la Fuente, and J.C. Cobos. *Phys. Chem. Chem. Phys.* **2**, 2587 (2000).
70. J.P. Chao, M. Dai, and Y.X. Wang. *J. Chem. Thermodyn.* **21**, 1169 (1989).
71. M. Oba, S. Murakami, and R. Fujishiro. *J. Chem. Thermodyn.* **9**, 407 (1977).
72. J.A. González, M. Szurgocinska, and U. Domanska. *Fluid Phase Equilib.* **200**, 349 (2002).
73. J.A. González, I. García, J.C. Cobos, and C. Casanova. *J. Chem. Eng. Data*, **36**, 162 (1991).
74. M. Bender and A. Heintz. *Fluid Phase Equilib.* **89**, 197 (1993).
75. J.A. González, I. García de la Fuente, and J.C. Cobos. *Fluid Phase Equilib.* **168**, 31 (2000).
76. F. Kohler and J. Gaube. *Pol. J. Chem.* **54**, 1987 (1980).
77. J.C. Cobos. *Fluid Phase Equilib.* **133**, 105 (1997).
78. A.B. Bhatia and D.E. Thorton. *Phys. Rev. B*, **21**, 3004 (1970).
79. B. García, R. Alcalde, S. Aparicio, and J.M. Leal. *Phys. Chem. Chem. Phys.* **4**, 1170 (2002).
80. U. Domanska and J.A. González. *Fluid Phase Equilib.* **205**, 317 (2003).
81. J.R. Goates, R.L. Snow, and J.B. Ott. *J. Phys. Chem.* **66**, 1301 (1962).
82. B. Dacre and G.C. Benson. *Can. J. Chem.* **41**, 278 (1953).

## Appendix A.

**Table A1.** Physical constants<sup>a</sup> of pure compounds:  $T_{\text{fus}}$ , melting temperatures;  $\Delta H_{\text{fus}}$ , molar enthalpy of fusion;  $\Delta C_{\text{pfus}}$ , heat capacity change between the solid and the liquid at the melting point.

Compound	$T_{\text{fus}}$ (K)	$\Delta H_{\text{fus}}$ (kJ mol <sup>-1</sup> )	$\Delta C_{\text{pfus}}$ (J mol <sup>-1</sup> K <sup>-1</sup> )
C <sub>6</sub> H <sub>6</sub>	278.68	9.866	
C <sub>6</sub> H <sub>12</sub>	279.87	2.667	
NMP	249.68	12	35.0
1-Propanol	147.05	5.195	
1-Hexanol	226.55	15.40	43.28
1-Heptanol	238.62	18.17	55.66
1-Octanol	258.90	23.70	68.75
1-Decanol	279.82	28.79	101.20
1-Undecanol	289.54	33.61	119.00
1-Dodecanol	297.89	38.42	139.30
1-Tetradecanol	311.86	20.14	184.25

<sup>a</sup>For the source of experimental data, see ref. A1.

## References

- A1. J. Lachwa and U. Domanska. *Fluid Phase Equilib.* **198**, 1 (2002).



# Determination of the second stoichiometric dissociation constants of glycine in aqueous sodium or potassium chloride solutions at 298.15 K

Jaakko I. Partanen, Pekka M. Juusola, Pentti O. Minkkinen, and Virginie Verraes

**Abstract:** Equations were determined for the calculation of the second stoichiometric (molality scale) dissociation constant,  $K_{m2}$ , of glycine, in aqueous NaCl and KCl solutions at 298.15 K, from the thermodynamic dissociation constant,  $K_{a2}$ , of this acid and the ionic strength,  $I_m$ , of the solution. The ionic strength of the solutions considered in this study is determined mostly by the salt alone, and the equations for  $K_{m2}$  were based on the single-ion activity coefficient equations of the Hückel type. New data measured by potentiometric titrations in a glass electrode cell were used in the estimation of the parameters for the Hückel equations of glycine species. By means of the calculation method suggested in this study,  $K_{m2}$  can be obtained almost within experimental error up to an  $I_m$  of about 1.0 mol kg<sup>-1</sup> for glycine in NaCl and KCl solutions. The  $K_{m2}$  values obtained by these methods were also compared with the values suggested in the literature for this quantity.

**Key words:** ionic strength dependence, stoichiometric dissociation constant, Debye–Hückel equation, potentiometry, glycine.

**Résumé :** Des équations sont développées pour le calcul de  $K_{m2}$ , la deuxième constante de dissociation stoechiométrique (en molalité) de la glycine en solution aqueuse de NaCl et KCl à 298,15 K. Ces équations sont déterminées à partir de la constante de dissociation,  $K_{a2}$ , de cet acide et de la force ionique,  $I_m$ , de la solution. La force ionique des solutions étudiées est imposée en presque totalité par le sel contenu en solution. Les formules pour  $K_{m2}$  sont alors déduites d'équations de type Hückel pour la détermination du coefficient d'activité d'un seul type d'ions. Les paramètres des équations d'Hückel pour les sels de glycine ont été approximés sur la base de mesures faites par titrations potentiométriques avec des électrodes de verre. Avec les meilleures méthodes de calculs présentées dans cette étude,  $K_{m2}$  peut être calculé avec une certitude presque équivalente aux erreurs expérimentales pour des solutions de glycine dans NaCl ou KCl ayant une force ionique  $I_m$  jusqu'à environ 1,0 mol kg<sup>-1</sup>. Les valeurs de  $K_{m2}$  obtenues par ces méthodes sont aussi comparées aux valeurs trouvées dans la bibliographie.

**Mots clés :** influence de la force ionique, constante de dissociation stoechiométrique, équation de Debye–Hückel, potentiométrie, glycine.

## Introduction

In this manuscript, we continue the studies (1–17) dealing with the thermodynamics of weak acid solutions. The purpose of these studies is to determine the stoichiometric dissociation constants (for example, the molality scale dissociation constants,  $K_m$ ) for salt solutions of different weak acids, as reliably as possible from potentiometric titration data measured with glass electrodes. Additionally in

these studies, calculation methods of the experimental  $K_m$  values for weak acids are also developed for literature data measured on galvanic cells without a liquid junction; see, e.g., ref. 1, and with a liquid junction, see ref. 16.

The other motivation of our studies in this field is to determine equations for the correlation of the experimental  $K_m$  values of different weak acids to the composition variables of salt solutions at 298.15 K. For this purpose, Hückel and Pitzer equations have been used in the previous studies for the single-ion activity coefficients. In the present study, Hückel equations were used for the analysis of potentiometric titration data of glycine in NaCl and KCl solutions. Pitzer equations, which are nowadays most often used for interpretation of thermodynamic data, were not considered in this study because Pitzer parameters are missing for the component salts of sodium and potassium glycinate in these solutions, and these parameters cannot be accurately determined solely from potentiometric titration data. Usually the binary Pitzer parameters for different salts have been deter-

Received 7 July 2003. Published on the NRC Research Press Web site at <http://canjchem.nrc.ca> on 27 October 2003.

J.I. Partanen,<sup>1</sup> P.M. Juusola, P.O. Minkkinen, and V. Verraes.<sup>2</sup> Department of Chemical Technology, Lappeenranta University of Technology, P.O. Box 20, FIN-53851 Lappeenranta, Finland.

<sup>1</sup>Corresponding author (e-mail: [jpartane@lut.fi](mailto:jpartane@lut.fi)).

<sup>2</sup>Present address: KETEK, Talonpojankatu 4, FIN-67100, Kokkola, Finland.



mined, in the literature, from osmotic coefficients obtained from isopiestic data.

Glycine ( $\text{NH}_2\text{CH}_2\text{COOH}$ ) is the simplest amino acid, and the dissociation of this acid in water solutions has been intensively studied. These works have been reviewed by the International Union of Pure and Applied Chemistry (IUPAC) (18). This review revealed, however, the absence of systematic studies on the influence of ionic strength,  $I_m$ , on  $K_{m1}$  and  $K_{m2}$  (i.e., on the first and second dissociation constants, respectively). For other weak acids, systematic studies are also rare, and the existing studies in this field are usually concentrated on acids used as pH buffer substances. The existing systematic glass electrode studies have been reviewed by Daniele et al. (19) and Sastre de Vicente (20). The stoichiometric dissociation constants of glycine in aqueous salt solutions have been determined in the following studies: Daniele et al. (21), in tetraethylammonium iodide solutions ( $I_c = 0.01\text{--}1 \text{ mol dm}^{-3}$ , where  $I_c$  is the ionic strength on the concentration scale); Rey et al. (22), in  $\text{KNO}_3$  solutions ( $I_c = 0.025\text{--}0.5 \text{ mol dm}^{-3}$ ); Herrero et al. (23), in  $\text{KNO}_3$  solutions ( $I_m = 0.30\text{--}1.6 \text{ mol kg}^{-1}$ , where  $I_m$  is the ionic strength on the molality scale); Fiol et al. (24), in NaCl solutions ( $I_m = 0.05\text{--}1.021 \text{ mol kg}^{-1}$ ); Fiol et al. (25), in artificial seawater ( $I_m = 0.1\text{--}0.67 \text{ mol kg}^{-1}$ ); Partanen (7), in NaCl solutions ( $I_m = 0.1\text{--}3 \text{ mol kg}^{-1}$  for  $K_{m1}$  and  $I_m = 0.1\text{--}0.3 \text{ mol kg}^{-1}$  for  $K_{m2}$ ), by using King's data (26) obtained by Harned cells; and Alonso et al. (27), in  $\text{NaClO}_4$ , KCl, and KBr solutions ( $I_m = 0.1\text{--}1 \text{ mol kg}^{-1}$ ).

In the previous study (7),  $K_{m1}$  values for glycine were reliably obtained, up to NaCl molalities of  $3 \text{ mol kg}^{-1}$ , from the cell potential data measured by King (26) on cells containing a hydrogen and a silver – silver chloride electrode (i.e., on Harned cells), but  $K_{m2}$  values for this acid cannot be determined as accurately from these data because the data of  $K_{m2}$  extend in this case only up to a salt molality of  $0.3 \text{ mol kg}^{-1}$ . In the present study, therefore, potentiometric titrations were carried out to determine  $K_{m2}$  for glycine in more concentrated salt solutions. The titrations were carried out in NaCl and KCl solutions.

The determination of the second dissociation constant of glycine differed from our earlier studies in that the pH during titration was above 8 (basic environment). In earlier studies, the pH was always below 6 (acidic environment). The solutions titrated had to be protected, therefore, against atmospheric carbon dioxide. This was accomplished by bubbling argon through the solution before titration. An argon mattress was thus formed over the solution, and it protected the solution from absorption of  $\text{CO}_2$ . The present study shows for the first time that the experimental technique developed in this way allows the determination of  $K_m$  values with a glass electrode in basic solutions almost with the same accuracy as the one obtained by the best techniques with glass electrodes in acidic solutions (see, e.g., refs. 10 and 11). This technique seems, therefore, to be very promising for future thermodynamic studies of weak acids in basic solutions.

## Experimental

Potentiometric titrations of glycine were carried out in aqueous NaCl and KCl solutions at 298.15 K. The two series

of salt solutions (the NaCl or KCl (pro analysi, Riedel-de Haën series) were prepared in RO-filtered water (Millipore), and the concentrations in these series were as follows: 0.080, 0.160, 0.240, 0.320, 0.400, 0.500, 0.700, and  $1.350 \text{ mol L}^{-1}$ . The experimental results from the NaCl series are shown in Table 1 and those from the KCl series in Table 2. A  $0.0100 \text{ mol L}^{-1}$  glycine (pro analysi, J.T. Baker) solution, a  $0.100 \text{ mol L}^{-1}$  NaOH (Fixanal, Riedel-de Haën) solution, and a  $0.100 \text{ mol L}^{-1}$  KOH (Titrisol, Merck) solution were also prepared.

The solutions to be titrated were prepared by mixing a volume of  $100.0 \text{ cm}^3$  of a salt solution,  $25.00 \text{ cm}^3$  of water, and  $10.00 \text{ cm}^3$  of the glycine solution (for the details, see ref. 2). Since the glycine solutions were titrated in a basic milieu, the influence of carbon dioxide on the solutions had to be prevented by using argon gas, see above. This gas was bubbled through each solution for about 10 min. The gas stream was then stopped, and the titration vessel closed. In this way, an argon mattress was formed over the titrated solution, and it remained stable, as argon is heavier than air.

Titration were then carried out by reading the cell potential difference (cpd) as a function of the added base volume. The increments of  $0.050 \text{ cm}^3$  of the base solution were used. The cpd was measured by means of a BlueLine 12pH combination electrode and a CG841 pH meter, both manufactured by Schottgeräte. The resolution of the meter was 0.1 mV. The titrant was added by means of a Dosimat (Metrohm). Standard buffer solutions of pH = 4.005 and pH = 6.865 at 298.15 K, see Buck et al. (28), were used to control the stability of the measuring system between titrations. The pH meter usually reproduced readings within 0.2 mV in these buffer test solutions.

To further check the stability of the measuring system, a titration of formic acid was carried out before the glycine titration in each salt solution in similar conditions. An argon gas mattress was also adjusted over the formic acid solutions before titration. From the results of these formic acid titrations, the  $K_m$  values were determined by the method suggested in ref. 10. This method is principally the same as the one used here for glycine. The  $K_m$  values obtained from the titrations were always very close to those calculated from the equations recommended in ref. 10 for  $K_m$  of formic acid in NaCl or KCl solutions. The good agreement between the observed and recommended  $K_m$  values for this acid guarantees the quality of the new data for glycine.

## Theory

In the Hückel method, the following equation is generally used for the calculation of the activity coefficient ( $\gamma$ ) of a univalent ion  $i$  on the molality scale:

$$[1] \quad \ln \gamma_i = -\frac{\alpha \sqrt{I_m}}{1 + B_i \sqrt{I_m}} + b_{i,\text{MCl}} \left( \frac{I_m}{m^\circ} \right)$$

where  $m^\circ = 1 \text{ mol kg}^{-1}$ ,  $I_m$  is the ionic strength on the molality scale, and  $\alpha$  is the Debye–Hückel parameter at 298.15 K, equal to  $1.17444 (\text{mol kg}^{-1})^{-1/2}$ ; see Archer and Wang (29).  $B_i$  and  $b_{i,\text{MCl}}$  are the parameters that are dependent on ion  $i$ , and  $b_{i,\text{MCl}}$  is also dependent on the salt present in the system. Table 3 gives the parameter values determined previously for this equation and used here.



**Table 1.** Data obtained from titrations of glycine in NaCl solutions at different ionic strengths ( $I_m$ ) with a base (NaOH) solution at 298.15 K; series GNC.

$V \text{ (cm}^3\text{)}^b$	$E \text{ (mV)}^a$						
	GNC1	GNC2	GNC3	GNC4	GNC5	GNC6	GNC7
0.40	-141.7	-140.5	-138.4	-136.2	-136.0	-133.6	-133.2
0.45	-146.1	-145.0	-143.0	-140.7	-140.3	-138.0	-137.5
0.50	-150.4	-149.2	-147.1	-144.8	-144.4	-141.9	-141.6
0.55	-154.3	-153.2	-151.0	-148.7	-148.3	-145.8	-145.5
0.60	-158.1	-157.1	-154.8	-152.2	-151.8	-149.3	-149.1
0.65	-161.8	-160.7	-158.4	-155.8	-155.3	-152.9	-152.5
0.70	-165.3	-164.3	-161.8	-159.1	-158.7	-156.4	-155.9
0.75	-168.7	-167.6	-165.1	-162.4	-162.0	-159.6	-159.1
0.80	-172.0	-170.8	-168.2	-165.6	-165.1	-162.8	-162.1
0.85	-175.2	-174.0	-171.4	-168.7	-168.1	-165.8	-165.1
0.90	-178.4	-177.2	-174.5	-171.7	-171.2	-168.7	-168.0
0.95	-181.4	-180.2	-177.5	-174.5	-174.1	-171.6	-170.8
1.00	-184.4	-183.0	-180.3	-177.3	-176.7	-174.3	-173.5
1.05	-187.1	-185.8	-183.1	-180.0	-179.3	-176.9	-176.1
1.10	-189.8	-188.6	-185.6	-182.5	-181.8	-179.5	-178.5
1.15	-192.4	-191.1	-188.2	-184.9	-184.4	-181.8	-181.1
1.20	-194.9	-193.5	-190.5	-187.2	-186.7	-184.1	-183.3
$I_m \text{ (m}^\circ\text{)}^c$	0.0595	0.1191	0.1789	0.2388	0.2988	0.3741	0.5251

<sup>a</sup>The measured cell potential difference.<sup>b</sup>The volume of titrant added.<sup>c</sup> $m^\circ = 1 \text{ mol kg}^{-1}$ .**Table 2.** Data obtained from titrations of glycine in KCl solutions at different ionic strengths ( $I_m$ ) with a base (KOH) solution at 298.15 K; series GKC.

$V \text{ (cm}^3\text{)}^b$	$E \text{ (mV)}^a$						
	GKC1	GKC2	GKC3	GKC4	GKC5	GKC7	GKC8
0.40	-143.4	-142.2	-142.0	-140.5	-140.4	-138.5	-139.6
0.45	-147.9	-146.8	-146.6	-145.1	-144.8	-143.0	-144.0
0.50	-152.2	-151.2	-150.7	-149.4	-149.1	-147.2	-148.2
0.55	-156.2	-155.2	-154.8	-153.4	-153.2	-151.2	-152.2
0.60	-160.1	-159.1	-158.6	-157.2	-156.9	-155.0	-155.8
0.65	-163.9	-162.7	-162.3	-160.9	-160.5	-158.5	-159.4
0.70	-167.4	-166.3	-165.9	-164.4	-164.1	-161.9	-162.8
0.75	-171.0	-169.7	-169.2	-167.9	-167.5	-165.2	-166.1
0.80	-174.3	-173.1	-172.6	-171.2	-170.7	-168.6	-169.4
0.85	-177.6	-176.3	-175.9	-174.3	-173.9	-171.7	-172.4
0.90	-180.6	-179.4	-179.0	-177.4	-177.0	-174.8	-175.5
0.95	-183.6	-182.5	-182.0	-180.5	-180.0	-177.7	-178.3
1.00	-186.7	-185.5	-185.0	-183.3	-182.9	-180.6	-181.1
1.05	-189.6	-188.3	-187.7	-186.2	-185.7	-183.3	-183.8
1.10	-192.3	-191.1	-190.4	-188.8	-188.4	-185.9	-186.5
1.15	-194.9	-193.7	-193.0	-191.4	-191.0	-188.3	-188.8
1.20	-197.5	-196.2	-195.5	-193.8	-193.5	-190.9	-191.3
$I_m \text{ (m}^\circ\text{)}^c$	0.0595	0.1193	0.1792	0.2394	0.2997	0.5280	1.0331

<sup>a</sup>The measured cell potential difference.<sup>b</sup>The volume of titrant added.<sup>c</sup> $m^\circ = 1 \text{ mol kg}^{-1}$ .

The thermodynamic value of the second dissociation constant ( $K_{a2}$ ) of glycine is given by

$$[2] \quad K_{a2} = \frac{a_{\text{H}^+} a_{\text{A}}}{a_{\text{HA}}} = \left( \frac{\gamma_{\text{H}^+} \gamma_{\text{A}}}{\gamma_{\text{HA}}} \right) K_{m2}$$

where  $a$  is the activity, HA refers to glycine molecules ( $\text{NH}_2\text{CH}_2\text{COOH}$  or zwitterions,  $^+\text{NH}_3\text{CH}_2\text{COO}^-$ ), and A to glycinate ions ( $\text{NH}_2\text{CH}_2\text{COO}^-$ ). It is assumed that the activity coefficient of the neutral species HA follows the Kirkwood equation (30, 31) for zwitterions, i.e.,



**Table 3.** Ion parameters for the Hückel equation, eq. [1], in NaCl and KCl solutions at 298.15 K and results of the regression analysis obtained by eq. [25] from the present titration data.

Parameter	H <sup>+</sup>	Cl <sup>-</sup>	NH <sub>2</sub> CH <sub>2</sub> COO <sup>-</sup>
10 <sup>10</sup> $K_{a2}^a$			1.65
p <i>K</i> <sub>a2</sub> <sup>b</sup>			9.783
10 <sup>10</sup> $K_{a2}(\text{obsd, NaCl})^c$			1.65
p <i>K</i> <sub>a2</sub> (obsd, NaCl) <sup>c</sup>			9.783±0.007
10 <sup>10</sup> $K_{a2}(\text{obsd, KCl})^c$			1.65
p <i>K</i> <sub>a2</sub> (obsd, KCl) <sup>c</sup>			9.782±0.002
$B \text{ (mol kg}^{-1}\text{)}^{-1/2}$	1.25 <sup>d</sup>	1.25 <sup>d</sup>	2.2 <sup>e</sup>
$b_{\text{NaCl}}$	0.238 <sup>d</sup>	0.238 <sup>d</sup>	0.39 <sup>f</sup>
$b_{\text{KCl}}$	0.178 <sup>g</sup>	0.178 <sup>g</sup>	0.39 <sup>f</sup>
$q_{\text{NaCl}}(\text{obsd})^h$			0.42±0.06
$q_{\text{KCl}}(\text{obsd})^h$			0.39±0.01

<sup>a</sup>The recommended value for the second thermodynamic dissociation constant for glycine.

<sup>b</sup>p*K*<sub>a2</sub> = -log*K*<sub>a2</sub>.

<sup>c</sup>An estimate of the *K*<sub>a2</sub> of glycine; see also footnote b. It was determined from the titration data, and the standard deviation is also given.

<sup>d</sup>Determined from Harned cell data (1).

<sup>e</sup>Recommended in this study and determined in ref. 7.

<sup>f</sup>Recommended in this study. For glycine species  $b = q = b_A - b_{\text{HA}}$ .

<sup>g</sup>Determined from Harned cell data (6).

<sup>h</sup> $q = b_A - b_{\text{HA}}$  for the glycine species determined from the titration data, and the standard deviation is also given.

$$[3] \quad \ln \gamma_{\text{HA}} = b_{\text{HA}} \left( \frac{I_m}{m^\circ} \right)$$

where  $b_{\text{HA}}$  is a constant. The second stoichiometric dissociation constant of glycine,  $K_{m2}$  in eq. [2], is defined by  $K_{m2} = m_{\text{H}}m_{\text{A}}/(m_{\text{HA}}m^\circ)$ . The following equation can be derived from eqs. [1], [2], and [3] for  $K_{m2}$  of glycine in aqueous NaCl or KCl solutions:

$$[4] \quad \ln K_{m2, \text{MCl}} = \ln K_{a2} + \alpha \sqrt{I_m} \left( \frac{1}{1 + B_{\text{H}} \sqrt{I_m}} + \frac{1}{1 + B_{\text{A}} \sqrt{I_m}} \right) - [b_{\text{H, MCl}} + (b_{\text{A, MCl}} - b_{\text{HA, MCl}})] \left( \frac{I_m}{m^\circ} \right)$$

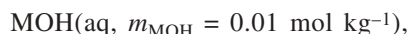
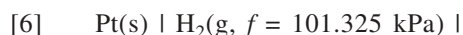
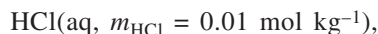
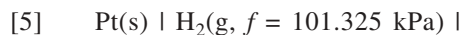
where MCl refers to either NaCl or KCl. Here, the values of  $B_{\text{H}} = 1.25 \text{ (mol kg}^{-1}\text{)}^{-1/2}$ ,  $B_{\text{A}} = 2.2 \text{ (mol kg}^{-1}\text{)}^{-1/2}$ ,  $b_{\text{H, NaCl}} = 0.238$ , and  $b_{\text{H, KCl}} = 0.178$  were used in this equation (see Table 3), and the thermodynamic dissociation constant,  $K_{a2}$ , and the parameters  $b_{\text{A, NaCl}} - b_{\text{HA, NaCl}} (= q_{\text{NaCl}})$  and  $b_{\text{A, KCl}} - b_{\text{HA, KCl}} (= q_{\text{KCl}})$  were determined from the new potentiometric titration data.

## Results

### Determination of the activity parameters for the dissociation reaction of water from Harned cell data

In basic solutions, the molality of hydrogen ions (needed for the glass electrode response) must be calculated from the molality of hydroxyl ions using the dissociation reaction of water. The necessary activity quantities for this reaction can be determined from the existing Harned cell data of Harned

and Hamer (32) and Harned and Mannweiler (33). In these studies the following cells were used:



where  $f$  is the fugacity. Harned and Hamer (32) measured KCl solutions ( $M = \text{K}^+$ ), and Harned and Mannweiler (33) measured NaCl solutions ( $M = \text{Na}^+$ ). The cell potential difference (cpd =  $E$ ) of cell 6 is given by the following Nernst equation:

$$[7] \quad E = E^\circ - \frac{RT}{F} \ln \left[ \frac{\gamma_{\text{H}} \gamma_{\text{Cl}} m_{\text{H}} m_{\text{Cl}}}{(m^\circ)^2} \right] \\ = E^\circ - \frac{RT}{F} \ln(\gamma_{\text{H}} \gamma_{\text{Cl}}) - \frac{RT}{F} \ln \left( \frac{m_s}{m_{\text{OH}}} \right) - \frac{RT}{F} \ln K_{a, w} + \frac{RT}{F} \ln \left( \frac{\gamma_{\text{H}} \gamma_{\text{OH}}}{a_w} \right)$$

where  $w$  refers to water, Cl to chloride ions, and OH to hydroxyl ions, and the thermodynamic value of the ionic product of water,  $K_{a, w}$ , is defined by

$$[8] \quad K_{a, w} = \frac{\gamma_{\text{H}} \gamma_{\text{OH}} m_{\text{H}} m_{\text{OH}}}{a_w (m^\circ)^2} = \frac{g_w m_{\text{H}} m_{\text{OH}}}{(m^\circ)^2}$$

Harned and Hamer (32) determined a value of  $1.008 \times 10^{-14}$  for this quantity at 298.15 K. From the experimental data of cells 5 and 6, the  $g_w (= \gamma_{\text{H}} \gamma_{\text{OH}} / a_w)$  values shown in Table 4 were obtained. These values for KCl and NaCl solutions were correlated here to the ionic strengths by using the following equation, which contains only one new parameter,  $b_w$ :

$$[9] \quad \ln \left( \frac{\gamma_{\text{H}} \gamma_{\text{OH}}}{a_w} \right) = \ln g_w = - \frac{2\alpha \sqrt{I_m}}{1 + B_{\text{H}} \sqrt{I_m}} + b_w \left( \frac{I_m}{m^\circ} \right)$$

The linear regression analysis used in the estimation of parameter  $b_w$  was based on equation

$$[10] \quad \ln g_w + \frac{2\alpha \sqrt{I_m}}{1 + B_{\text{H}} \sqrt{I_m}} = y_1 \\ = y_0 + b_w x = y_0 + b_w \left( \frac{I_m}{m^\circ} \right)$$

and the results for KCl solutions up to a salt molality of 2 mol kg<sup>-1</sup> and for NaCl solutions up to a salt molality of 3 mol kg<sup>-1</sup> were used. Parameter  $y_0$  is associated with a possible small constant systematic error in these two old sets. The value of  $(RT/F)y_0$  is 0.25 mV for the KCl set and 0.11 mV for the NaCl set, and these values were taken into



**Table 4.** Results of the comparison of the experimental values of  $g_w (= \gamma_H \gamma_{OH}/a_w)$  obtained by cells 5 and 6 with those predicted by eq. [9].

$I_m$ (mol kg <sup>-1</sup> )	$(g_{w,KCl})^a$	$(g_{w,NaCl})^b$	$e_{KCl}$ (mV) <sup>c</sup>	$e_{NaCl}$ (mV) <sup>c</sup>
0.01	0.808		-0.23	
0.02	0.753	0.756	-0.29	-0.16
0.03	0.719	0.722	-0.25	-0.10
0.04	0.695		-0.18	
0.06	0.662	0.661	-0.04	0.05
0.11	0.612	0.604	0.17	0.05
0.21	0.568	0.554	0.47	0.17
0.51	0.529	0.512	0.09	0.16
1.01	0.586	0.533	0.66	0.01
1.51	0.665		0.08	
2.01	0.779	0.683	-0.43	-0.21
3.01		0.958		0.07

<sup>a</sup>Determined from the data of Harned and Hamer (32).

<sup>b</sup>Determined from the data of Harned and Mannweiler (33).

<sup>c</sup>Calculated by the equation  $e = (RT/F) [\ln g_w(\text{observed}) - \ln g_w(\text{predicted})]$ .

account in the calculation of the experimental  $g_w$  values in Table 4. From the slope of the resulting regression lines, a value of  $b_w = 0.482$  was obtained for KCl solutions and a value of  $b_w = 0.412$  for NaCl solutions. Equation [9] applies well to the experimental  $g_w$  values, as the errors for the points in Table 4 confirm. Error  $e$  in this table is defined by equation

$$[11] \quad e = \frac{RT}{F} \times [\ln g_w(\text{observed}) - \ln g_w(\text{predicted})]$$

and all absolute errors observed are smaller than 0.7 mV.

#### Determination of the experimental values for the stoichiometric dissociation constant from potentiometric glass electrode data

The theoretical equation for the molality of hydroxyl ions in a glycine titration was derived from the equation for the second stoichiometric dissociation constant,  $K_{m2} = m_H m_A / (m_{HA} m^\circ)$ , from the mass balance equation,  $m_t = m_{HA} + m_A$ , and from the electroneutrality equation,  $m_H + m_b = m_{OH} + m_A$ . In the last equation,  $m_b$  is the molality of base, NaOH or KOH, in the solution titrated and  $m_b = c_b V / w_1$ , where  $c_b$  is the concentration,  $V$  is the volume of the base solution added in the titration, and  $w_1$  is the mass of water in the solution titrated. In the mass balance equation,  $m_t$  is the total molality of glycine in the solution titrated, and  $m_t = n_t / w_1$ , where  $n_t$  is the total amount of this substance. For the molality of hydroxyl ions, the following equation can be derived from these equations and eq. [8]:

$$[12] \quad m_{OH}^2 + \left( m_t - m_b + \frac{K_{a,w} m^\circ}{g_w K_{m2}} \right) m_{OH} - \frac{K_{a,w} m^\circ}{g_w K_{m2}} m_b = 0$$

and this equation is second degree in the molality of OH<sup>-</sup> ions and can, therefore, be easily solved.

For the determination of  $K_{m2}$  of glycine from the titration data, the two glass electrode parameters, in addition to this dissociation constant, were simultaneously estimated from each titration data set. In general, the following equation is

valid for cell potential differences measured on a glass electrode cell:

$$[13] \quad E = E^\circ + k \left( \frac{RT}{F} \right) \ln a_H$$

where  $a_H$  is the activity of protons,  $k$  is a glass electrode parameter, and  $E^\circ$  is another glass electrode parameter. The latter potential parameter includes the contributions of the reference electrode, liquid junction, standard-glass electrode, and asymmetry potentials; see, e.g., May et al. (34). It is assumed in all present titrations that this term remained constant during the titration. Equation [13] can also be presented in the form:

$$[14] \quad E = E^\circ + \frac{kRT}{F} \ln \gamma_H + \frac{kRT}{F} \ln \left( \frac{m_H}{m^\circ} \right) \\ = E_0 + \frac{kRT}{F} \ln \left( \frac{m_H}{m^\circ} \right)$$

where  $E_0 = E^\circ + (kRT/F) \ln \gamma_H$  is also a glass electrode parameter that is constant during each titration at a constant ionic strength; see eq. [1]. Parameters  $E_0$  and  $k$  must be estimated from the titration data.

$K_{m2}$  and the glass electrode parameter  $E_0$  were calculated for each glycine data set presented in Tables 1 and 2, containing  $N$  points, by the following equations:

$$[15] \quad \sum_{i=1}^N (E_i - E_{\text{predicted},i}) = 0$$

$$[16] \quad \ln \left( \frac{x_i}{m^\circ} \right) = \frac{(E_i - E_0)F}{kRT}$$

$$[17] \quad o_i = \frac{K_{a,w}(m^\circ)^2}{g_w x_i}$$

$$[18] \quad K_{m2,i} = \frac{x_i(m_{b,i} - o_i)}{\left( \frac{n_t}{w_{1,i}} - m_{b,i} + o_i \right) m^\circ}$$

$$[19] \quad K_{m2} = \frac{\sum_{i=1}^N K_{m2,i}}{N}$$

$$[20] \quad y_i = \left( \frac{n_t}{w_{1,i}} - m_{b,i} + \frac{K_{a,w} m^\circ}{g_w K_{m2}} \right)^2 + 4m_{b,i} \left( \frac{K_{a,w} m^\circ}{g_w K_{m2}} \right)$$

$$[21] \quad m_{OH,i} = \left[ \sqrt{y_i} - \left( \frac{n_t}{w_{1,i}} - m_{b,i} + \frac{K_{a,w} m^\circ}{g_w K_{m2}} \right) \right] / 2$$

$$[22] \quad m_{H,i} = \frac{K_{a,w}(m^\circ)^2}{g_w m_{OH,i}}$$

$$[23] \quad E_{\text{pred},i} = E_0 + \left( \frac{kRT}{F} \right) \ln \left( \frac{m_{H,i}}{m^\circ} \right)$$



**Table 5.** Results calculated from the titrations of glycine in NaCl solutions at different ionic strengths ( $I_m$ ) with a base solution at 298.15 K; series GNC.

	GNC1	GNC2	GNC3	GNC4	GNC5	GNC6	GNC7
$10^{10}K_{m2}(\text{obsd})^a$	2.44	2.49	2.61	2.58	2.71	2.65	2.52
$10^{10}K_{m2}(\text{recd})^b$	2.39	2.56	2.64	2.67	2.68	2.66	2.57
$k^c$	0.981	0.998	0.983	0.975	0.963	0.972	0.978
$E_0$ (mV) <sup>d</sup>	401.30	410.26	402.99	400.52	393.75	401.27	405.66
$I_m$ (mol kg <sup>-1</sup> )	0.0595	0.1191	0.1789	0.2388	0.2988	0.3741	0.5251

<sup>a</sup>The second stoichiometric dissociation constant of glycine determined from the titration data in Table 1 by the method described in the text.

<sup>b</sup>The second stoichiometric dissociation constant of glycine calculated by eq. [4] with the value of  $K_{a2} = 1.65 \times 10^{-10}$  and with the recommended activity parameters. Abbreviation "recd" means recommended.

<sup>c</sup>The value of the glass electrode parameter  $k$  used in the calculation.

<sup>d</sup>The value of the glass electrode parameter  $E_0$  used in the calculation of the cpd errors for Fig. 1. It was determined by requiring that the sum of errors in the data set be zero (i.e., by eqs. [20]–[22], [26], [27]).

**Table 6.** Results calculated from the titrations of glycine in KCl solutions at different ionic strengths ( $I_m$ ) with a base solution at 298.15 K; series GKC.

	GKC1	GKC2	GKC3	GKC4	GKC5	GKC7	GKC8
$10^{10}K_{m2}(\text{obsd})^a$	2.39	2.60	2.68	2.71	2.73	2.62	2.26
$10^{10}K_{m2}(\text{recd})^b$	2.39	2.58	2.67	2.71	2.73	2.66	2.24
$k^c$	1	1	1	1	1	1	1
$E_0$ (mV) <sup>d</sup>	410.19	409.21	408.59	409.50	409.56	411.99	414.80
$I_m$ (mol kg <sup>-1</sup> )	0.0595	0.1193	0.1792	0.2393	0.2997	0.5280	1.0331

<sup>a</sup>The second stoichiometric dissociation constant of glycine determined from the titration data in Table 2 by the method described in the text.

<sup>b</sup>The second stoichiometric dissociation constant of glycine calculated by eq. [4] with the value of  $K_{a2} = 1.65 \times 10^{-10}$  and with the recommended activity parameters. Abbreviation "recd" means recommended.

<sup>c</sup>The assumed value of the glass electrode parameter  $k$  used in the calculation.

<sup>d</sup>The value of the glass electrode parameter  $E_0$  used in the calculation of the cpd errors for Fig. 1. It was determined by requiring that the sum of errors in the data set be zero (i.e., by eqs. [20]–[22], [26], [27]).

where  $x_i$  and  $o_i$  are the experimental molalities of hydrogen and hydroxyl ions at point  $i$ , respectively. Additionally, the glass electrode parameter  $k$  was optimized by setting the following square sum,  $S(E)$ , at a minimum:

$$[24] \quad S(E) = \sum_{i=1}^N (E_i - E_{\text{predicted},i})^2$$

This parameter had to be adjusted in the NaCl titrations (probably because of the selectivity problems of a glass electrode in aqueous NaCl solutions). In our earlier studies (see, e.g., refs. 8, 9, 11, and 12), parameter  $k$  also differed quite a lot from unity in aqueous NaCl solutions. In KCl solutions,  $k$  can be and was assumed to be exactly 1. The results from the calculations of the titration data in Tables 1 and 2 are shown in Table 5 (for NaCl) and 6 (for KCl).

#### Determination of activity parameters for glycine species from the experimental $K_{m2}$ values obtained from titration data

A value of  $B = 2.2$  (mol kg<sup>-1</sup>)<sup>-1/2</sup> was suggested in ref. 7 for eq. [1] for glycinate ions, and this value can also be used in the present study. The activity parameters  $b_{A,\text{NaCl}} - b_{HA,\text{NaCl}}$  ( $= q_{\text{NaCl}}$ ) and  $b_{A,\text{KCl}} - b_{HA,\text{KCl}}$  ( $= q_{\text{KCl}}$ ) and the thermodynamic value of the dissociation constant,  $K_{a2}$ , were determined from the new titration data. The experimental  $K_{m2}$  values, shown in Tables 5 and 6, were used in these determinations with the following equation derived from eq. [4]:

$$[25] \quad \ln K_{m2,\text{MCl}} - \alpha \sqrt{I_m} \left( \frac{1}{1 + B_H \sqrt{I_m}} + \frac{1}{1 + B_A \sqrt{I_m}} \right) = y_2 = \ln K_{a2} - [b_{H,\text{MCl}} + q_{\text{MCl}}] \left( \frac{I_m}{m^\circ} \right)$$

This equation shows that  $y_2$  is a linear function of  $(I_m/m^\circ)$ . The thermodynamic dissociation constant  $K_{a2}$  can be obtained from the intercept of the line with the  $y_2$ -axis, and the slope of the straight line is  $-(b_{H,\text{MCl}} + q_{\text{MCl}})$ . The results from the linear regression analysis are shown in Table 3. The resulting two estimates for  $K_{a2}$  of glycine agree very well with each other and with the value of  $1.66 \times 10^{-10}$  suggested in ref. 7 for this quantity. The latter value was determined by using the sparse literature data measured by King (26) with Harned cells. According to these results, a value of  $K_{a2} = 1.65 \times 10^{-10}$  can now be recommended for the second dissociation constant of glycine. The value of 0.31 was determined in ref. 7 from King's data for the parameter  $q_{\text{NaCl}}$ . This value belongs to the 95% confidence interval of the value of this quantity suggested in Table 3 on the basis of new titration data. However, the new value of  $q_{\text{NaCl}} = q_{\text{KCl}} = 0.39$  seems to be reliable, and this value is thus recommended for both NaCl and KCl solutions.

#### Discussion

The Hückel parameters recommended above for glycine species were tested with the titration data presented in Ta-



**Fig. 1.** The difference between the observed and predicted cpd values,  $e_E$  in eq. [28], as a function of the titrant volume in the titrations of glycine solutions with base (NaOH or KOH) solutions. Graph A shows the results of the titrations obtained for NaCl solutions (Series GNC), and graph B shows those obtained for KCl solutions (Series GKC). The predicted cpd was calculated by eqs. [4], [8], [9], [12], and [14] using the thermodynamic value of  $1.65 \times 10^{-10}$  for the second dissociation constant, the recommended activity parameters, and the glass electrode parameters  $k$  and  $E_0$  shown in Tables 5 and 6. Symbols of the different sets are shown in the graphs.

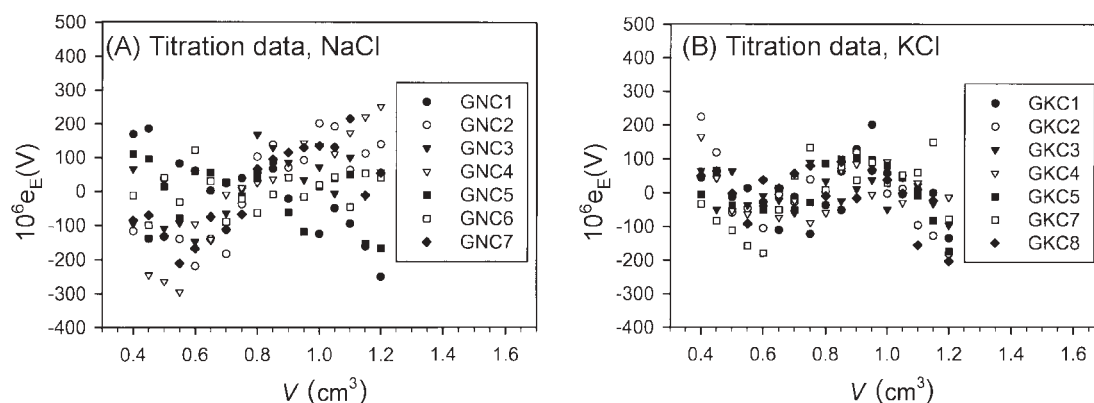
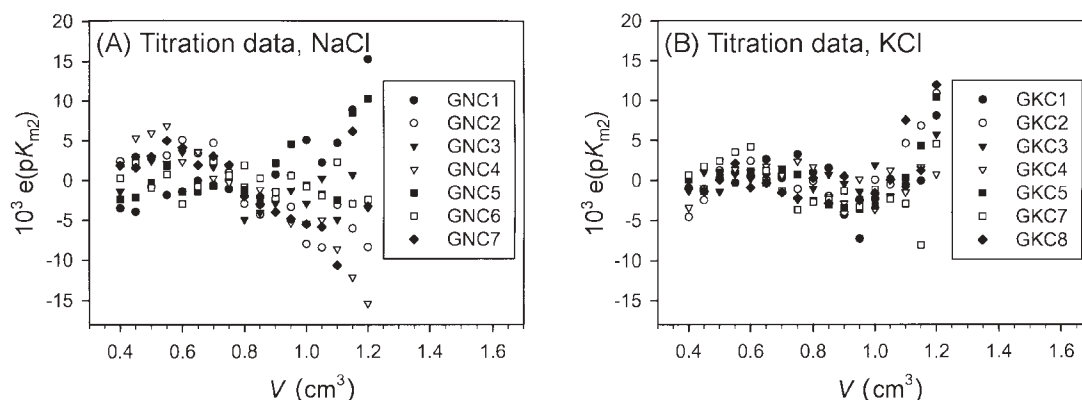


**Fig. 2.** The difference,  $e(pK_{m2})$  in eq. [29], between the observed  $pK_{m2}$  values and those predicted by the recommended Hückel method as a function of the titrant volume in the titrations of glycine solutions with base (NaOH or KOH) solutions. Graph A shows the results of the titrations obtained for NaCl solutions (Series GNC), and graph B shows those obtained for KCl solutions (Series GKC). The observed  $K_{m2}$  was calculated from the titration points by eqs. [8], [9], [16], [17], and [18] with the glass electrode parameters shown in Tables 5 and 6. Symbols of the different sets are shown in the graphs.



bles 1 and 2. The recommended  $K_{m2}$  values given in Tables 5 and 6 were used in these tests. Parameter  $E_0$  for eq. [14] was calculated for each data set by using eqs. [20]–[22] and the following equations:

$$[26] \quad E_{0,i} = E_i - \left( \frac{kRT}{F} \right) \ln \left( \frac{m_{H,i}}{m^\circ} \right)$$

$$[27] \quad E_0 = \frac{\sum_{i=1}^N E_{0,i}}{N}$$

In these calculations, the values shown in Tables 5 and 6 were used for the other glass electrode parameter  $k$ . The resulting values for  $E_0$  are included in these tables. The results of the tests are shown as error plots in graphs A (NaCl) and B (KCl) of Fig. 1, where the cpd error defined by

$$[28] \quad e_E = E(\text{observed}) - E(\text{predicted})$$

is presented for each data set as a function of the added base volume. Most of the error plots in these graphs are random,

and most of the errors in these plots are comparable to the resolution of the pH meter (0.1 mV), and therefore, the titration data support well the suggested thermodynamic dissociation constant and the activity parameters used.

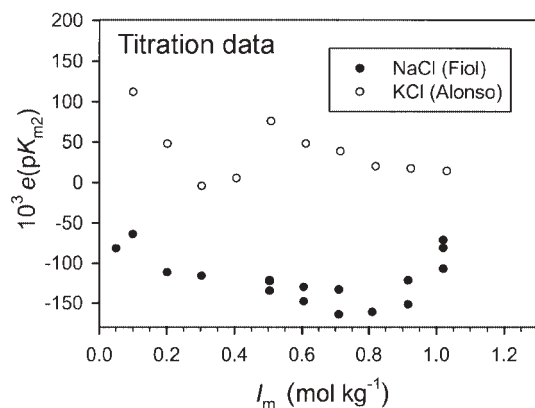
From every point of the titrations presented in Tables 1 and 2, an experimental value of  $K_{m2}$  can also be calculated from eqs. [16]–[18] by using the glass electrode parameter values shown in Tables 5 and 6. These values are compared with the recommended values in two graphs of Fig. 2. Graph A in this figure shows the NaCl results and graph B the KCl results. In these graphs, the  $pK_m (= -\log(K_m))$  errors, defined by

$$[29] \quad e(pK_{m2}) = pK_{m2}(\text{observed}) - pK_{m2}(\text{predicted})$$

are presented as a function of the added base volume. All  $pK_{m2}$  errors in Fig. 2 are smaller than  $\pm 0.015$  and for most data sets they form a random pattern. The maximum error can also be compared with the conventional  $pK_m$  error of 0.06 suggested by Albert and Serjeant (35). These considerations also reveal how valuable the new activity coefficient models are.



**Fig. 3.** The difference,  $e(pK_{m2})$  in eq. [29], between the  $pK_{m2}$  values determined by Fiol et al. (24) for glycine in NaCl solutions and by Alonso et al. (27) for glycine in KCl solutions and those predicted by the recommended Hückel method as a function of the ionic strength ( $I_m$ ).



As mentioned above, Fiol et al. (24) have determined  $K_{m2}$  values of glycine in aqueous NaCl solutions, and Alonso et al. (27) have determined  $K_{m2}$  values of glycine in aqueous KCl solutions at 298.15 K by using potentiometric titration. These values were used to test the new models, and the results are shown as error plots in Fig. 3. The  $pK_{m2}$  errors, calculated from eq. [29], are given in this figure as a function of the ionic strength of the solution considered. The results in this figure show that the new models predict only satisfactorily these experimental data. It seems to us that the  $K_{m2}$  values obtained by the new models are more reliable.

Table 7 shows the recommended  $K_{m2}$  values for glycine in aqueous NaCl and KCl solutions at 298.15 K at rounded ionic strengths. These values apply to the case where NaCl or KCl effectively determines the ionic strength of solution. The  $K_{m2}$  values were calculated by using eq. [4] with the recommended value of  $K_{a2} = 1.65 \times 10^{-10}$  and with the recommended parameter values shown in Table 3.

Recently, DeRobertis et al. (36) have proposed a general equation for the dissociation constant of carboxylic acids in aqueous sodium or potassium chloride solutions. If this equation is applied to the second dissociation constant of glycine, it has the following form:

$$[30] \quad \log K_{m2, MCl} = \log K_{a2} + \frac{2\sqrt{I_m / m^\circ}}{2 + 3\sqrt{I_m / m^\circ}} - C_{MCl} \left( \frac{I_m}{m^\circ} \right) - E_{MCl} \left( \frac{I_m}{m^\circ} \right)^2$$

For NaCl solutions at 298.15 K, the values of parameters  $C$  and  $E$  are 0.092 and 0.00634, respectively, and for KCl solutions they are 0.1042 and 0.00522. The recommended  $K_{m2}$  values, presented in Table 7, were predicted by this equation, and the results are shown in Fig. 4 where  $pK_{m2}$  errors, defined now by the equation

$$[31] \quad e(pK_{m2}) = pK_{m2}(\text{recommended}) - pK_{m2}(\text{predicted})$$

are presented as a function of the ionic strength of the solution considered. Satisfactory agreement is obtained in this

**Table 7.** The second stoichiometric dissociation constant ( $K_{m2}$ ) of glycine at 298.15 K as a function of the ionic strength ( $I_m$ ) in aqueous NaCl and KCl solutions.

$I_m$ (mol kg <sup>-1</sup> ) <sup>a</sup>	$10^{10} K_{m2}(\text{NaCl})$	$10^{10} K_{m2}(\text{KCl})$
0	1.65	1.65
0.01	2.00	2.01
0.02	2.13	2.13
0.05	2.34	2.35
0.10	2.52	2.53
0.20	2.66	2.69
0.30	2.68	2.73
0.50	2.59	2.67
0.70	2.43	2.53
1.00	2.14	2.27

<sup>a</sup> $I_m$  is the same as  $m_{\text{NaCl}}$  or  $m_{\text{KCl}}$ .

**Fig. 4.** The difference,  $e(pK_{m2})$  in eq. [31], between the recommended  $pK_{m2}$  values (see Table 7) and those predicted by eq. [30] for glycine in NaCl and KCl solutions as a function of the ionic strength ( $I_m$ ).

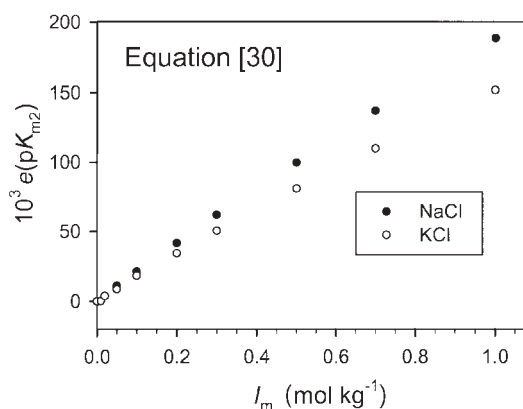


figure up to a salt molality of 0.3 mol kg<sup>-1</sup>. The error in  $pK_m$  is smaller in these cases than the conventional  $pK_m$  error of 0.06 suggested by Albert and Serjeant (35). However, it can be seen that, also in these cases, the  $pK_{m2}$  values obtained by eq. [30] are systematically smaller than the recommended values. Equation [30] does not, therefore, apply well to the  $K_{m2}$  values of glycine.

## References

1. J. Partanen, P. Juusola, and P. Minkkinen. Acta Polytech. Scand. Chem. Technol. Ser. **231**, 1 (1995).
2. J.I. Partanen, P.M. Juusola, and P.O. Minkkinen. Acta Chem. Scand. **49**, 163 (1995).
3. J.I. Partanen, M.H. Kärki, and P.M. Juusola. Acta Chem. Scand. **49**, 865 (1995).
4. J.I. Partanen and P.O. Minkkinen. J. Chem. Eng. Data, **42**, 805 (1997).
5. J.I. Partanen and P.O. Minkkinen. J. Solution Chem. **26**, 709 (1997).
6. J.I. Partanen. Acta Chem. Scand. **52**, 985 (1998).
7. J.I. Partanen. Ber. Bunsenges. Phys. Chem. **102**, 855 (1998).
8. J.I. Partanen, P.M. Juusola, and P.O. Minkkinen. Acta Chem. Scand. **53**, 547 (1999).



9. J.I. Partanen, P.M. Juusola, and P.O. Minkkinen. *J. Solution Chem.* **28**, 413 (1999).
10. J.I. Partanen and P.M. Juusola. *J. Chem. Eng. Data*, **45**, 110 (2000).
11. J.I. Partanen and P.M. Juusola. *Fluid Phase Equilibria*, **169**, 149 (2000).
12. J.I. Partanen and P.M. Juusola. *Fluid Phase Equilibria*, **173**, 135 (2000).
13. J.I. Partanen. *Talanta*, **52**, 863 (2000).
14. J.I. Partanen, P.M. Juusola, and P.O. Minkkinen. *Z. Phys. Chem.* **215**, 515 (2001).
15. J.I. Partanen, P.M. Juusola, and P.O. Minkkinen. *J. Solution Chem.* **30**, 443 (2001).
16. J.I. Partanen, P.M. Juusola, and P.O. Minkkinen. *Fluid Phase Equilibria*, **204**, 245 (2003).
17. J.I. Partanen, and A.K. Covington. *J. Chem. Eng. Data*, **48**, 797 (2003).
18. T. Kiss, I. Sóvágó, and A. Gergely. *Pure Appl. Chem.* **63**, 597 (1991).
19. P.G. Daniele, C. De Stefano, C. Foti, and S. Sammartano. *Curr. Top. Solution Chem.* **2**, 253 (1997).
20. M.E. Sastre de Vicente. *Curr. Top. Solution Chem.* **2**, 157 (1997).
21. P.G. Daniele, C. Rigano, and S. Sammartano. *Talanta*, **30**, 81 (1983).
22. F. Rey, A. Varela, J.M. Antelo, and F. Arce. *J. Chem. Eng. Data*, **34**, 35 (1989).
23. R. Herrero, I. Brandariz, S. Fiol, and M. Sastre de Vicente. *Collect. Czech. Chem. Commun.* **58**, 1269 (1993).
24. S. Fiol, I. Brandariz, R. Herrero, T. Vilariño, and M. Sastre de Vicente. *Ber. Bunsenges. Phys. Chem.* **98**, 164 (1994).
25. S. Fiol, I. Brandariz, and M. Sastre de Vicente. *Mar. Chem.* **49**, 215 (1995).
26. E.J. King. *J. Am. Chem. Soc.* **67**, 2178 (1945); **73**, 155 (1951).
27. P. Alonso, J.L. Barriada, P. Rodríguez, I. Brandariz, and M.E. Sastre de Vicente. *J. Chem. Eng. Data*, **43**, 876 (1998).
28. R.P. Buck, S. Rondinini, A.K. Covington, F.G.K. Baucke, C.M.A. Brett, M.F. Camoes, M.J.T. Milton, T. Mussini, R. Naumann, K.W. Pratt, P. Spitzer, and G.S. Wilson. *Pure Appl. Chem.* **74**, 2169 (2002).
29. D.G. Archer and P. Wang. *J. Phys. Chem. Ref. Data*, **19**, 371 (1990).
30. J.G. Kirkwood. *J. Chem. Phys.* **2**, 351 (1934).
31. J.G. Kirkwood. *Chem. Rev.* **24**, 233 (1939).
32. H.S. Harned and W.J. Hamer. *J. Am. Chem. Soc.* **55**, 2194 (1933).
33. H.S. Harned and G.E. Mannweiler. *J. Am. Chem. Soc.* **57**, 1873 (1935).
34. P.M. May, D.R. Williams, P.W. Linder, and R.G. Torrington. *Talanta*, **29**, 249 (1982).
35. A. Albert and E.P. Serjeant. *In* The determination of ionization constants. A laboratory manual. 3rd ed. Chapman and Hall, London. 1984.
36. A. DeRobertis, C. Stefano, and C. Foti. *J. Chem. Eng. Data*, **44**, 262 (1999).



# The syntheses and structures of lithium phosphinimide and phosphimine complexes

Silke Courtenay, Pingrong Wei, and Douglas W. Stephan

**Abstract:** The preparation and structures of  $[\text{Li}(\mu\text{-NP}t\text{-Bu}_3)]_4$  **1**,  $[\text{Li}(\mu\text{-Cl})(\text{HNPr}t\text{-Bu}_3)]_4$  **2**, and  $[\text{Li}(\mu\text{-Cl})(\text{HNPPH}_3)]_4$  **3** are described. The structure of **1** stands in contrast to that of the only other known Li-phosphinimide derivative,  $[\text{Li}(\mu\text{-NPPH}_3)]_6$ . The impact of the steric bulk on the aggregation and the geometries of the  $\text{Li}_4\text{N}_4$  and  $\text{Li}_4\text{Cl}_4$  cores are considered and discussed.

**Key words:** lithium compounds, phosphimine, phosphinimide, P-N ligands.

**Résumé :** On décrit la préparation et les structures des complexes  $[\text{Li}(\mu\text{-NP}t\text{-Bu}_3)]_4$ , **1**,  $[\text{Li}(\mu\text{-Cl})(\text{HNPr}t\text{-Bu}_3)]_4$ , **2** et  $[\text{Li}(\mu\text{-Cl})(\text{HNPPH}_3)]_4$ , **3**. La structure du composé **1** diffère de celles du seul autre dérivé Li-phosphinimide,  $[\text{Li}(\mu\text{-NPPH}_3)]_6$ . On considère et on discute de l'impact de l'encombrement stérique sur l'agrégation et les géométries des entités centrales  $\text{Li}_4\text{N}_4$  et  $\text{Li}_4\text{Cl}_4$ .

**Mots clés :** composés du lithium, phosphimine, phosphinimide, ligands P-N.

[Traduit par la Rédaction]

## Introduction

Main group derivatives of phosphimine and phosphinimide ligands have been characterized and recently reviewed by Dehnicke and Weller (1). The chelating bis-phosphimine  $\text{H}_2\text{C}(\text{R}_2\text{PNSiMe}_3)_2$  has been used to prepare main group compounds as well (2–7). More recently, we, and subsequently Cavell and co-workers, have reported the first structure of a dilithio-methane derivative,  $[\text{Li}_2\text{C}(\text{Ph}_2\text{PNSiMe}_3)_2]_4$  (7, 8). Cavell's group has also examined the chemistry of Al-bis(phosphimine)methanide and methanediide complexes,  $\text{HC}(\text{Ph}_2\text{PNSiMe}_3)_2\text{AlMe}_2$  and  $(\text{Me}_2\text{Al})_2\text{C}(\text{Ph}_2\text{PNSiMe}_3)_2$  (2, 3), as well as related Zn species (9), while the research groups of Cavell (4, 5) and Gamer and Roesky (6) have described the structural diversity of Li, Na, and K salts of  $[\text{HC}(\text{Ph}_2\text{PNSiMe}_3)_2]^-$ . We have recently described related Mg complexes (10). We have also been exploring main group derivatives of bulky, mono-phosphinimide ligands. The novel cationic linear species  $[(t\text{-Bu}_3\text{PN})_2\text{B}]\text{Cl}$  and its chemistry has been recently reported (11). As well, we have recently described the chemistry of phosphinimide derivatives of Si, Ge, and Sn (12). Related alkali metal salts of phosphinimides,  $(\text{KNPCy}_3)_4$ ,  $(\text{KNPPH}_3)_4$  (13),  $(\text{MNPCy}_3)_4(\text{OPCy}_3)$  ( $\text{M} = \text{K}, \text{Cs}$ ) (14), and  $[\text{M}(\mu\text{-NPPH}_3)]_6$  ( $\text{M} = \text{K}$  (15),  $\text{Na}$  (16),  $\text{Rb}$  (13)) have been structurally characterized. For related Li-phosphinimides, despite the fact that they have been known for 35 years (17) and are frequently used as reagents for the synthesis of main group (1,

11, 12, 18) and transition metal derivatives (19–24), only the structure of  $[\text{Li}(\mu\text{-NPPH}_3)]_6$  and  $[\text{Li}(\mu\text{-NPPH}_3)(\text{LiBr})_2\cdot(\text{THF})_4]$  have been reported (25, 26). In this work, we describe the Li derivatives  $[\text{Li}(\mu\text{-NP}t\text{-Bu}_3)]_4$  and  $[\text{Li}(\mu\text{-Cl})(\text{HNPR}_3)]_4$  ( $\text{R} = t\text{-Bu}_3, \text{Ph}$ ). The impact of the sterically demanding substituents in these compounds on the degree of aggregation and the structures of the  $\text{Li}_4\text{X}_4$  ( $\text{X} = \text{N}, \text{Cl}$ ) cores is discussed.

## Experimental

### General data

All preparations were done under an atmosphere of dry,  $\text{O}_2$ -free  $\text{N}_2$ , employing both Schlenk line techniques and a Vacuum Atmospheres inert atmosphere glove box. Solvents were purified by employing a Grubbs' type solvent purification system manufactured by Innovative Technology. All organic reagents were purified by conventional methods.  $^1\text{H}$  and  $^{13}\text{C}\{^1\text{H}\}$  NMR spectra were recorded on Bruker Avance-300 and 500 spectrometers. All spectra were recorded in  $\text{C}_6\text{D}_6$  at 25 °C unless otherwise noted. Trace amounts of protonated solvents were used as references, and chemical shifts are reported relative to  $\text{SiMe}_4$ .  $^{31}\text{P}\{^1\text{H}\}$  NMR spectra were recorded on a Bruker Avance-300 and are referenced to external 85%  $\text{H}_3\text{PO}_4$ . Combustion analyses were done in house, employing a PerkinElmer CHN Analyzer.  $t\text{-Bu}_3\text{PNH}$  was prepared as previously described (1, 27), using  $t\text{-Bu}_3\text{P}$  obtained from the Strem Chemical Co.

### Synthesis of $[\text{Li}(\mu\text{-NP}t\text{-Bu}_3)]_4$ **1**

To a solution of  $t\text{-Bu}_3\text{PNH}$  (640 mg, 2.95 mmol) in 50 mL of hexanes was added MeLi (2.10 mL, 1.4 mol  $\text{L}^{-1}$  solution in ether, 2.95 mmol) at 25 °C. The resulting suspension was stirred for 1 h, concentrated, and allowed to settle for 10 min. The hexane layer was decanted, and the remaining white powder (yield > 95%) was washed twice with hexane and dried in vacuo. From the hexane washings, X-ray qual-

Received 22 May 2003. Published on the NRC Research Press Web site at <http://canjchem.nrc.ca> on 31 October 2003.

S. Courtenay, P. Wei, and D.W. Stephan.<sup>1</sup> Department of Chemistry and Biochemistry, University of Windsor, Windsor, ON N9B 3P4, Canada.

<sup>1</sup>Corresponding author (e-mail: [stephan@uwindsor.ca](mailto:stephan@uwindsor.ca)).



**Table 1.** Crystallographic data.

	<b>1</b> ·0.5C <sub>6</sub> H <sub>14</sub>	<b>2</b>	<b>3</b>
Formula	C <sub>51</sub> H <sub>115</sub> Li <sub>4</sub> N <sub>4</sub> P <sub>4</sub>	C <sub>48</sub> H <sub>112</sub> Cl <sub>4</sub> Li <sub>4</sub> N <sub>4</sub> P <sub>4</sub>	C <sub>72</sub> H <sub>64</sub> Cl <sub>4</sub> Li <sub>4</sub> N <sub>4</sub> P <sub>4</sub>
Formula weight	936.11	1038.86	1278.71
<i>a</i> (Å)	13.070(2)	13.755(5)	24.996(13)
<i>b</i> (Å)	13.1262(19)	16.011(6)	12.401(6)
<i>c</i> (Å)	20.969(3)	16.136(6)	23.584(12)
$\alpha$ (°)	73.995(3)	69.712(4)	
$\beta$ (°)	87.266(2)	82.999(8)	112.990(8)
$\gamma$ (°)	61.711(2)	82.932(8)	
Crystal system	Triclinic	Triclinic	Monoclinic
<i>V</i> (Å <sup>3</sup> )	3030.3(8)	3296(2)	6730(6)
Space group	<i>P</i> $\bar{1}$	<i>P</i> $\bar{1}$	<i>C</i> 2/ <i>c</i>
<i>D</i> <sub>calcd</sub> (g cm <sup>-3</sup> )	1.026	1.047	1.262
<i>Z</i>	2	2	4
Absorption coefficient $\mu$ (cm <sup>-1</sup> )	0.157	0.307	0.315
Data collected	13 294	14 437	4792
Data $F_o^2 \gg 2\sigma(F_o^2)$	8706	9424	3332
Variables	568	577	397
<i>R</i>	0.0428	0.1224	0.0453
<i>R</i> <sub>w</sub>	0.1192	0.2971	0.1310
GoF	1.049	0.908	1.030

**Note:** Data collections were done at 25 °C.

ity crystals were grown by slow evaporation at 25 °C. <sup>1</sup>H NMR  $\delta$ : 1.41 (d,  $|^3J_{P-H}|$  = 11 Hz, *t*-Bu). <sup>13</sup>C{<sup>1</sup>H} NMR  $\delta$ : 41.1 (d,  $|^1J_{P-C}|$  = 42 Hz, *t*-Bu), 31.8 (s, *t*-Bu). <sup>31</sup>P{<sup>1</sup>H} NMR  $\delta$ : 31.4. Elemental analysis (EA) calcd. for C<sub>12</sub>H<sub>27</sub>LiNP: C 64.56, H 12.19, N 6.27; found: C 64.13, H 12.01, N 6.04.

#### Synthesis of [Li( $\mu$ -Cl)(HNP*t*-Bu)<sub>3</sub>]<sub>4</sub> **2** and [Li( $\mu$ -Cl)(HNPPPh<sub>3</sub>)<sub>4</sub> **3**

These compounds were prepared in a similar fashion, and thus one preparation is detailed. To a solution of *t*-Bu<sub>3</sub>PNH (130 mg, 0.60 mmol) in 10 mL of THF was added LiCl (25.4 mg, 0.60 mmol) at 25 °C. The resulting suspension was stirred for 1 h, concentrated to a small volume, and allowed to stand. A white powder (yield > 90%) precipitated and was washed twice with hexanes and dried in vacuo. In examining related chemistry, X-ray quality crystals of **2** were fortuitously obtained as by-product from the reaction of **1** with CrCl<sub>3</sub> in wet THF. The two products were spectroscopically identical. **2**: <sup>1</sup>H NMR  $\delta$ : 1.27 (d,  $|^3J_{P-H}|$  = 12 Hz, 27H, *t*-Bu). <sup>13</sup>C{<sup>1</sup>H} NMR  $\delta$ : 39.8 (d,  $|^1J_{P-C}|$  = 46 Hz, *t*-Bu), 30.5 (s, *t*-Bu). <sup>31</sup>P{<sup>1</sup>H} NMR  $\delta$ : 62.7. EA calcd. for C<sub>12</sub>H<sub>28</sub>NPLiCl: C 55.49, H 10.87, N 5.39; found: C 55.32, H 10.62, N 5.11. **3**: <sup>1</sup>H NMR  $\delta$ : 7.70 (br), 7.02 (br). <sup>13</sup>C{<sup>1</sup>H} NMR  $\delta$ : 135.5, 133.8, 130.8, 125.8. <sup>31</sup>P{<sup>1</sup>H} NMR  $\delta$ : 28.1. EA calcd. for C<sub>18</sub>H<sub>16</sub>NPLiCl: C 67.63, H 5.04, N 4.38; found: C 67.43, H 4.95, N 4.11.

#### X-ray data collection and reduction

Crystals were manipulated and mounted in capillaries in a glove box, thus maintaining a dry, O<sub>2</sub>-free environment for each crystal. Diffraction experiments were performed on a Siemens SMART System CCD diffractometer. The data were collected in a hemisphere of data in 1329 frames with 10 s exposure times (Table 1). The observed extinctions

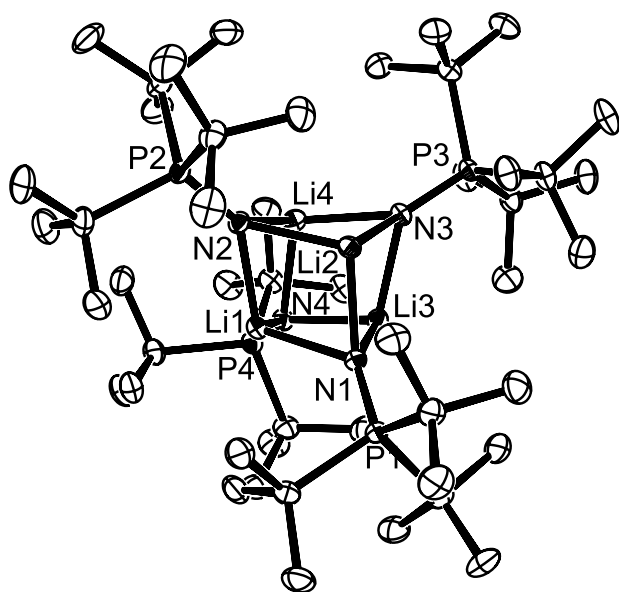
were consistent with the space groups in each case. The data sets were collected ( $4.5^\circ < 2\theta < 45\text{--}50.0^\circ$ ). A measure of decay was obtained by re-collecting the first 50 frames of each data set. The intensities of reflections within these frames showed no statistically significant change over the duration of the data collections. The data were processed using the SAINT and XPREP processing packages. An empirical absorption correction based on redundant data was applied to each data set. Subsequent solution and refinement was performed using the SHELXTL solution package operating on a Pentium computer.

#### Structure solution and refinement

Non-hydrogen atomic scattering factors were taken from the literature tabulations (28). The heavy atom positions were determined using direct methods employing the SHELXTL direct methods routine. The remaining non-hydrogen atoms were located from successive difference Fourier map calculations. The refinements were carried out by using full-matrix least-squares techniques on *F*, minimizing the function  $\omega(|F_o| - |F_c|)^2$ , where the weight  $\omega$  is defined as  $4F_o^2/2\sigma(F_o^2)$  and *F*<sub>o</sub> and *F*<sub>c</sub> are the observed and calculated structure factor amplitudes. In the final cycles of each refinement, all non-hydrogen atoms were assigned anisotropic temperature factors in the absence of disorder or insufficient data. In the latter cases atoms were treated isotropically. C-H atom positions were calculated and allowed to ride on the carbon to which they are bonded, assuming a C—H bond length of 0.95 Å. H-atom temperature factors were fixed at 1.10 times the isotropic temperature factor of the C-atom to which they are bonded. The H-atom contributions were calculated, but not refined. The locations of the largest peaks in the final difference Fourier map calculation, as well as the magnitude of the residual electron



**Fig. 1.** ORTEP drawing of **1**; 30% thermal ellipsoids are shown. Hydrogen atoms are omitted for clarity.

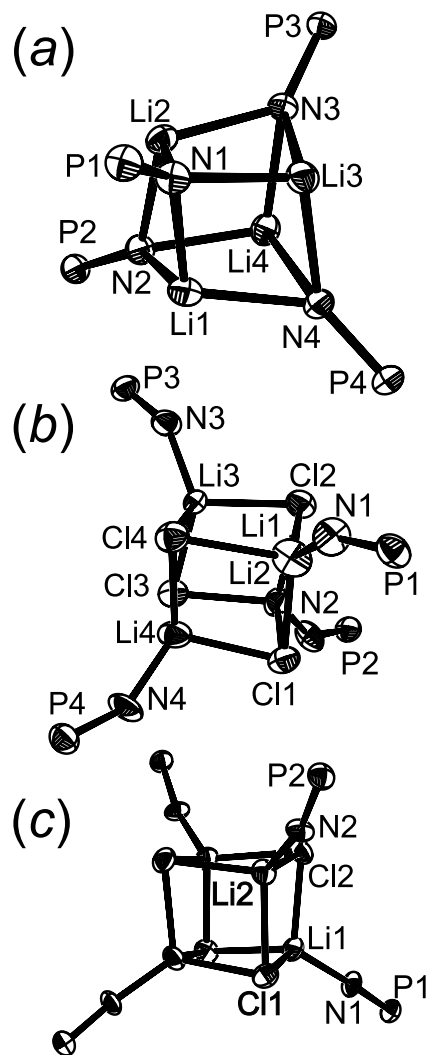


densities in each case, were of no chemical significance. In the case of **2**, the relatively high *R* factor appears to reflect some degree of disorder in the *tert*-butyl group. The model presented represents the best solution we could obtain with the data. Additional details are provided in the supplementary data.<sup>2</sup>

## Results and discussion

The Li salt of *t*-Bu<sub>3</sub>PNH is readily prepared by reaction with an alkyl-lithium reagent (**27**). NMR data reflected clean conversion to a single species, **1**, although the degree of aggregation of this species in solution could not be determined spectroscopically. X-ray quality crystals of **1**·0.5C<sub>6</sub>H<sub>14</sub> were obtained from hexane solution (Fig. 1). The structural solution revealed that **1** forms a tetramer of formulation [Li(μ-NP*t*-Bu<sub>3</sub>)]<sub>4</sub>, in which the phosphinimide N atoms bridge the Li centers. The Li—N distances vary from 2.025(4) to 2.066(4) Å. The Li and N atoms adopt a distorted cube (Fig. 2a). The Li(2), N(2), Li(1), and N(1) atoms are arranged with long (Li(2)—N(2) 2.065(4) Å, Li(1)—N(1) 2.066(4) Å) and short (Li(1)—N(2) 2.025(4) Å, Li(2)—N(1) 2.026(4) Å) distances. The remaining Li—N distances fall between 2.035 and 2.048 Å. Li—N—Li angles are similar, ranging from 72.82(16)°–73.57(15)°, while the N—Li—N angles fall between 103.91(17)° and 105.21(17)°. The P—N distances fall in the narrow range, from 1.5451(18) to 1.5505(18) Å. The P—N—Li angles fall into two ranges, from 140.88(16)° to 142.21(15)° and between 130.65(15)° and

**Fig. 2.** ORTEP drawings of the cores of (a) **1**, (b) **2**, and (c) **3**.



137.07(15)°. The larger angles are distributed so as to minimize the steric congestion about the Li<sub>4</sub>N<sub>4</sub> core.

Compound **1** is only the second species of general formula [LiNPR<sub>3</sub>]<sub>n</sub> to be structurally characterized. It stands in contrast to the previous hexamers, [M(μ-NPPH<sub>3</sub>)]<sub>6</sub> (M = Li (25), K (15), Na (16), Rb (13)), which were reported by Dehnicke's group. Presumably, the steric bulk in the present system precludes an expansion of the M—N core. In the case of the Li derivative [Li(μ-NPPH<sub>3</sub>)]<sub>6</sub>, a number of metric parameters are similar to those seen in **1**; however, the additional room about the core in [Li(μ-NPPH<sub>3</sub>)]<sub>6</sub> (25) results in four of the Li—N distances being significantly shorter (1.983(8) Å) than those in **1**, while three Li—N—Li angles average 104.3(3)°, significantly greater than those seen in **1**. Such variations cannot be accommodated in **1**, as a result of the sterically bulky phosphinimide. This presumably ac-

<sup>2</sup>Supplementary data may be purchased from the Depository of Unpublished Data, Document Delivery, CISTI, National Research Council Canada, Ottawa, ON K1A 0S2, Canada ([http://www.nrc.ca/cisti/irm/unpub\\_e.shtml](http://www.nrc.ca/cisti/irm/unpub_e.shtml) for information on ordering electronically). CCDC 211170–211172 contain the supplementary data for this paper. These data can be obtained, free of charge, via [www.ccdc.cam.ac.uk/conts/retrieving.html](http://www.ccdc.cam.ac.uk/conts/retrieving.html) (or from the Cambridge Crystallographic Data Centre, 12 Union Road, Cambridge, U.K.; fax +44 1223 336033; or [deposit@ccdc.cam.ac.uk](mailto:deposit@ccdc.cam.ac.uk)).



**Table 2.** Selected metric parameters.

1	2	3
<b>Selected bond lengths (Å)</b>		
<b>P—N</b>	<b>P—N</b>	<b>P—N</b>
1.5505(18) 1.5492(18), 1.5451(18) 1.5494(18)	1.543(8) 1.575(8) 1.599(9) 1.565(8)	1.487(2) 1.490(2)
<b>Li—N</b>	<b>Li—N</b>	<b>Li—N</b>
2.026(4) 2.047(4) 2.066(4) 2.025(4) 2.042(4) 2.065(4) 2.035(4) 2.036(4) 2.044(4) 2.036(4) 2.042(4) 2.048(4)	1.94(2) 1.90(2) 1.957(19) 1.93(2)	1.852(5) 1.852(5)
	<b>Li—Cl</b>	<b>Li—Cl</b>
	2.35(2) 2.351(19) 2.55(2) 2.400(17) 2.45(2) 2.466(19) 2.363(16) 2.396(15) 2.445(18) 2.38(2) 2.41(2) 2.42(2)	2.410(6) 2.416(6) 2.432(6) 2.408(6), 2.422(5) 2.444(6)
<b>Selected bond angles (°)</b>		
<b>Li-N-Li</b>	<b>N-Li-Cl</b>	<b>N-Li-Cl</b>
73.22(16) 72.56(15) 72.69(16) 73.29(16) 72.60(15) 72.99(16) 73.53(16) 73.10(16) 73.57(15) 73.42(16) 73.25(16) 72.82(16)	122.2(11) 127.9(11) 103.7(8) 114.6(9) 128.6(9) 110.3(7) 128.9(9) 121.7(9) 123.3(11) 109.3(10) 115.4(9) 114.4(8)	115.8(3) 116.5(3) 123.4(3) 120.0(3) 121.0(3) 113.8(3)
<b>N-Li-N</b>	<b>Cl-Li-Cl</b>	<b>Cl-Li-Cl</b>
105.03(18) 105.21(17) 104.14(18) 104.72(18) 105.20(17) 103.91(17) 104.62(18) 104.26(18) 105.03(18) 105.05(17) 104.17(18) 104.18(18)	100.9(7) 98.0(7) 97.1(8) 99.8(7) 97.9(6) 94.9(6) 102.3(6) 99.6(6) 97.0(6) 98.5(7) 100.8(8) 99.0(7)	102.3(2) 97.44(19) 97.59(19) 97.53(18) 101.04(19) 99.69(18)
<b>P-N-Li</b>	<b>Li-Cl-Li</b>	<b>Li-Cl-Li</b>
142.21(15) 132.64(15) 142.10(15) 136.61(15) 130.65(15) 141.30(15) 136.51(15) 131.64(14) 133.87(14) 140.88(16) 131.06(15) 137.07(15)	81.6(7) 81.2(6) 80.1(6) 83.4(7) 81.5(7) 78.5(5) 81.6(7) 78.8(6) 80.9(6) 80.6(6) 78.3(7) 77.8(5)	78.33(18) 81.33(19) 80.90(17) 81.26(18) 77.81(18) 79.33(18)
	<b>P-N-Li</b>	<b>P-N-Li</b>
	146.6(9) 146.8(8) 145.2(8) 149.6(9)	169.4(2) 159.5(2)

counts for the lower degree of aggregation. The previously reported species  $[M(\mu\text{-NPCy}_3)]_4$  ( $M = \text{K, Cs}$ ) (**14**) also form tetranuclear structures. However, these compounds adopt distorted cubic geometries, with angles at M and N in these  $M_4N_4$  cores that are closer to  $90^\circ$  than those in **1**. This, again, infers that the greater distortion of the  $\text{Li}_4\text{N}_4$  core in **1** is a direct result of the steric demands of the *t*-Bu<sub>3</sub>PN groups.

The reaction of LiCl and the phosphinimine to give an LiCl adduct was performed. While spectroscopy inferred formation of a new material, **2**, X-ray quality crystals of the product **2** could not be obtained directly. Fortunately, X-ray quality crystals of **2** were obtained as a by-product of the reaction of **1** and  $\text{CrCl}_3$  in wet THF. X-ray analysis confirmed

the formulation of **2** as  $[\text{Li}(\mu\text{-Cl})(\text{HNPr-Bu}_3)]_4$  (Fig. 3). Similarly, the species  $[\text{Li}(\mu\text{-Cl})(\text{HNPPH}_3)]_4$  **3** (Fig. 4) was prepared by reaction of LiCl and  $\text{HNPPH}_3$ . In the case of **2**, the LiCl core of this molecule adopts a distorted cubic geometry (Fig. 2b). In **3**, crystallographic symmetry imposes twofold symmetry on the LiCl core (Fig. 2c).

Metric parameters are detailed in Table 2. In **2**, Li—Cl distances fall in the range from 2.35 to 2.466 Å with the exception of the Li(1)—Cl(4) distance, which is 2.55(2) Å, while in **3**, these distances are more uniform, ranging from 2.408(6) to 2.444(6) Å. While the Cl—Li—Cl and Li—Cl—Li angles in both compounds fall in the ranges from 94.9(6)° to 102.3(6)° and from 77.8(5)° to 83.4(7)°, respectively, it is generally observed that these ranges are broader for **2**, which



**Fig. 3.** ORTEP drawing of **2**; 30% thermal ellipsoids are shown. Hydrogen atoms are omitted for clarity.

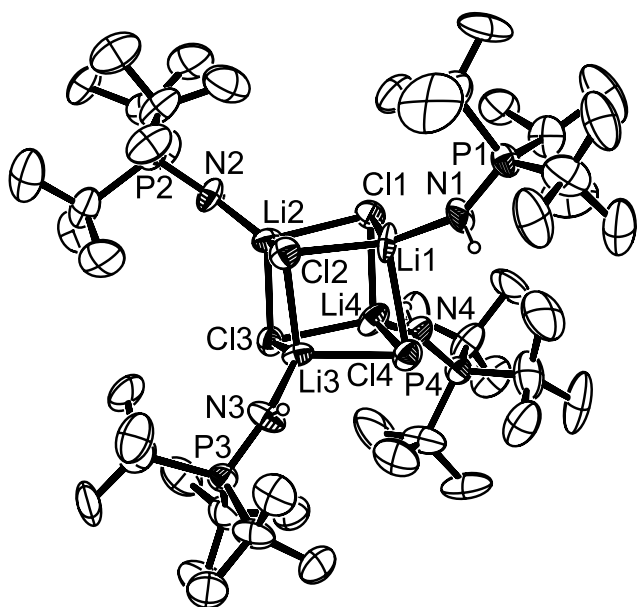
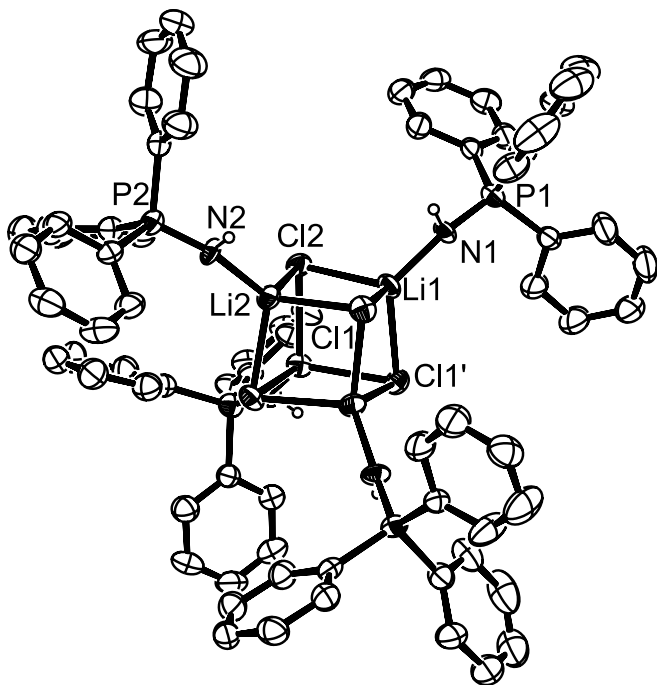


**Fig. 4.** ORTEP drawing of **3**; 30% thermal ellipsoids are shown. Hydrogen atoms are omitted for clarity.



is consistent with the steric issues arising from the bulkier phosphinimine. It is presumed that the dissymmetry of the core of **2** is an artifact of the phosphinimine ligand packing arrangement. This view is supported by the crystallographic symmetry seen in the less congested species **3**. Interestingly the Li—N distances in **2** range from 1.90(2) to 1.957(19) Å, while the Li—N distance in **3** is 1.852(5) Å. Both are shorter than those seen in **1**, presumably reflecting the terminal and

coordinate nature of the Li—N bonds in **2** and **3**. The P—N distances in **2** are similar to those seen in **1**, while the distances in **3** are significantly shorter, averaging 1.489(2) Å. This presumably reflects the lower basicity of the phenyl-substituted phosphinimine. The P—N—Li angles in **2** fall between 145.2(8)° and 149.6(9)°, while those in **3** were found to be 169.4(2)° and 159.5(2)°. The cause for these larger angles in **3** is unclear, although it may be that interactions between the phenyl rings among adjacent phosphinimines accounts for these distortions. The N—Li—Cl angles in both **2** and **3** vary widely, from 103.7(8)° to 128.9(9)°. While there is no pattern in the variations of these angles, it is noteworthy that in **2**, two of the three N—Li—Cl angles about Li(1) exceed 122°, consistent with the proximity of the long Li—Cl distance and the dissymmetry of the molecule.

These structural data for **1–3** infer that the proximity of four sterically demanding *t*-Bu<sub>3</sub>PN or R<sub>3</sub>PNH groups precludes higher degrees of aggregation and distortions in the Li<sub>4</sub>X<sub>4</sub> (X = N, Cl) core geometry. The implications of these steric demands in the main group and transition metal chemistry of such bulky phosphinimides continues to be a focus of our interests.

## Acknowledgments

Financial support from the Natural Sciences and Engineering Research Council of Canada (NSERC), NOVA Chemicals Corporation, and the Ontario Research and Development Challenge Fund (ORDCF) is gratefully acknowledged.

## References

1. K. Dehnicke and F. Weller. *Coord. Chem. Rev.* **158**, 103 (1997).
2. K. Aparna, R. McDonald, and R.G. Cavell. *J. Am. Chem. Soc.* **122**, 9314 (2000).
3. K. Aparna, R. McDonald, M. Ferguson, and R.G. Cavell. *Organometallics*, **18**, 4241 (1999).
4. R.P.K. Babu, K. Aparna, R. McDonald, and R.G. Cavell. *Inorg. Chem.* **39**, 4981 (2000).
5. R.P.K. Babu, K. Aparna, R. McDonald, and R.G. Cavell. *Organometallics*, **20**, 1451 (2001).
6. M.T. Gamer and P.W. Roesky. *Z. Anorg. Allg. Chem.* **627**, 877 (2001).
7. C.M. Ong and D.W. Stephan. *J. Am. Chem. Soc.* **121**, 2939 (1999).
8. A. Kasani, R.P.K. Babu, R. McDonald, and R.G. Cavell. *Angew. Chem. Int. Ed. Engl.* **38**, 1483 (1999).
9. A. Kasani, R. McDonald, and R.G. Cavell. *Organometallics*, **18**, 3775 (1999).
10. P. Wei and D.W. Stephan. *Organometallics*, **22**, 601 (2003).
11. S. Courtenay, J.Y. Mutus, R.W. Schurko, and D.W. Stephan. *Angew. Chem. Int. Ed. Engl.* **41**, 498 (2002).
12. S. Courtenay, C.M. Ong, and D.W. Stephan. *Organometallics*, **23**, 818 (2003).
13. T. Groeb, K. Harms, and K. Dehnicke. *Z. Anorg. Allg. Chem.* **626**, 1065 (2000).
14. T. Groeb, S. Chitsaz, K. Harms, and K. Dehnicke. *Z. Anorg. Allg. Chem.* **628**, 473 (2002).
15. S. Chitsaz, B. Neumueller, and K. Dehnicke. *Z. Anorg. Allg. Chem.* **625**, 9 (1999).



16. T. Groeb, C. Muller, W. Massa, T. Miekisch, G. Seybert, K. Harms, and K. Dehnicke. *Z. Anorg. Allg. Chem.* **627**, 2191 (2001).
17. H. Schmidbaur and G. Jonas. *Chem. Ber.* **100**, 1120 (1967).
18. C.M. Ong, P. McKarns, and D.W. Stephan. *Organometallics*, **18**, 4197 (1999).
19. K. Dehnicke and J. Strahle. *Polyhedron*, **8**, 707 (1989).
20. K. Dehnicke, M. Krieger, and W. Massa. *Coord. Chem. Rev.* **182**, 19 (1999).
21. D.W. Stephan, J.C. Stewart, F. Guerin, F.R.E.v.H. Spence, W. Xu, and D.G. Harrison. *Organometallics*, **18**, 1116 (1999).
22. D.W. Stephan, F. Guerin, R.E.v.H. Spence, L. Koch, X. Gao, S.J. Brown, J.W. Swabey, Q. Wang, W. Xu, P. Zoricak, and D.G. Harrison. *Organometallics*, **18**, 2046 (1999).
23. F. Guerin, J.C. Stewart, C. Beddie, and D.W. Stephan. *Organometallics*, **19**, 2994 (2000).
24. N. Yue, E. Hollink, F. Guérin, and D.W. Stephan. *Organometallics*, **20**, 4424 (2001).
25. S. Anfang, G. Seybert, K. Harms, G. Geiseler, W. Massa, and K. Dehnicke. *Z. Anorg. Allg. Chem.* **624**, 1187 (1998).
26. A.S. Batsanov, M.G. Davidson, J.A.K. Howard, S. Lamb, C. Lustig, and R.D. Price. *J. Chem. Soc. Chem. Commun.* 1211 (1997).
27. W. Wolfsberger. *Z. Naturforsch. B Anorg. Chem. Org. Chem.* **33B**, 1452 (1978).
28. D.T. Cromer and J.B. Mann. *Acta Cryst. A*, **A24**, 321 (1968).



# The gas-phase reaction of the CF<sub>3</sub> radical with thiophene

Olga S. Herrera, Jorge D. Nieto, Silvia I. Lane, and Elena V. Oexler

**Abstract:** The reaction of CF<sub>3</sub> radicals, generated by photolysis of CF<sub>3</sub>I or hexafluoroacetone with thiophene, was studied in the gas phase at 25 °C. At conversion of thiophene less than 20%, monosubstituted CF<sub>3</sub>-thiophenes were found as the main reaction products, in addition to CF<sub>3</sub>H, C<sub>2</sub>F<sub>6</sub>, and monosubstituted dihydro-CF<sub>3</sub>-thiophene, the latter in very low proportion. An isomeric mixture of 2- and 3-CF<sub>3</sub>-thiophene was obtained in a ratio of about 16, independent of the radical source used (CF<sub>3</sub>I or hexafluoroacetone) to produce the CF<sub>3</sub> radicals. A plausible mechanism that accounts for the observed products is proposed, and the reactivity of thiophene toward the CF<sub>3</sub> radical at 25 °C was determined as  $k_{\text{add}}/k_{\text{c}}^{1/2} = 106 \pm 4 \text{ cm}^{3/2} \text{ mol}^{-1/2} \text{ s}^{-1/2}$ .

**Key words:** thiophene, trifluoromethyl radical, reaction mechanism, reactivity.

**Résumé :** Opérant en phase gazeuse, à 25 °C, on a étudié la réaction du thiophène avec des radicaux CF<sub>3</sub> obtenus par photolyse du CF<sub>3</sub>I ou de l'hexafluoroacétone. À des taux de conversion du thiophène inférieurs à 20%, les produits principaux obtenus en plus du CF<sub>3</sub>H et du C<sub>2</sub>F<sub>6</sub> sont les thiophènes monosubstitués par du CF<sub>3</sub> et les dihydrothiophènes monosubstitués par du CF<sub>3</sub> qui ne sont présent que dans de très faibles proportions. On obtient un mélange de 2- et de 3-trifluorométhylthiophènes présents dans un rapport d'environ 16 quelle que soit la source utilisée, CF<sub>3</sub>I ou hexafluoroacétone, pour produire les radicaux. On propose un mécanisme plausible qui permet d'expliquer la formation des produits obtenus et on a déterminé que la réactivité du thiophène par rapport au radical CF<sub>3</sub>, à 25 °C, est égale à  $k_{\text{add}}/k_{\text{c}}^{1/2} = 106 \pm 4 \text{ cm}^{3/2} \text{ mol}^{-1/2} \text{ s}^{-1/2}$ .

**Mots clés :** thiophène, radical trifluorométhyle, mécanisme réactionnel, réactivité.

[Traduit par la Rédaction]

## Introduction

The reactions of CF<sub>3</sub> radicals with unsaturated organic compounds such as olefins and aromatics in the gas phase have been the subject of a number of investigations (1). Kinetic parameters and mechanisms were, in most cases, rationalized via two major pathways, addition and abstraction.

To the best of our knowledge, however, very few studies have so far been undertaken of the reaction between CF<sub>3</sub> radicals and heteroaromatic compounds (2). In particular, with thiophene, the trifluoromethylation reaction was studied in the condensed phase using bis(trifluoroacetyl) peroxide (3), CF<sub>3</sub>I, and Te(CF<sub>3</sub>)<sub>2</sub> (4). In all cases the product yields were reported, monosubstituted CF<sub>3</sub>-thiophenes being the main products obtained in good yields. Only with Te(CF<sub>3</sub>)<sub>2</sub>

was an addition product, monosubstituted dihydro-CF<sub>3</sub>-thiophene, also reported.

In the gas phase, however, no studies have been undertaken of the reaction between CF<sub>3</sub> radicals and thiophene. To gain some insight into the distribution of the products, the reaction mechanism, and the reactivity of thiophene toward the CF<sub>3</sub> radical, we became interested in the study of this reaction, using the photolysis of CF<sub>3</sub>I or HFA as CF<sub>3</sub> radical sources.

## Results and discussion

Experiments were carried out at 25 °C; the CF<sub>3</sub> radicals were generated by the photolysis of CF<sub>3</sub>I or HFA at  $\lambda > 275 \text{ nm}$ . Thiophene vapor has a weak absorption band starting at about 260 nm and becomes very strong below 240 nm (5). Therefore, under our experimental conditions, thiophene should not absorb. However, to ensure that there was no photolysis of thiophene, the spectral curve for the Corning glass filter employed was checked experimentally, and control photolysis experiments with neat thiophene were performed. Decomposition of thiophene was not observed.

The initial concentration of thiophene was varied between 2.42 and  $15.1 \times 10^{-7} \text{ mol cm}^{-3}$ , while for the CF<sub>3</sub> radical sources, initial concentrations of 8.0 to  $23.0 \times 10^{-7} \text{ mol cm}^{-3}$  and 5.09 to  $10.8 \times 10^{-7} \text{ mol cm}^{-3}$  were used for CF<sub>3</sub>I and HFA, respectively. Thus the molar ratio of thiophene:CF<sub>3</sub>I or thiophene:HFA was always less than 2. Most of the experiments were performed at a conversion of thiophene lower

Received 15 November 2002. Published on the NRC Research Press Web site at <http://canjchem.nrc.ca> on 29 October 2003.

**O.S. Herrera.** Depto. de Química, Fac. de Ciencias Naturales, Universidad Nacional de La Patagonia S.J.B., C.C. 786. 9000 Comodoro Rivadavia, Argentina.

**J.D. Nieto, S.I. Lane, and E.V. Oexler.**<sup>1</sup> Instituto de Investigaciones en Fisicoquímica de Córdoba (INFIQC), Depto. de Fisicoquímica, Fac. de Ciencias Químicas, Universidad Nacional de Córdoba. Pab. Argentina. Ciudad Universitaria. 5000 Córdoba, Argentina.

<sup>1</sup>Corresponding author (e-mail: [oexler@fisquim.fcq.unc.edu.ar](mailto:oexler@fisquim.fcq.unc.edu.ar)).



than 20%. Products analysis was performed after separation of the total content of the reaction cell by fractional condensation at  $-40\text{ }^{\circ}\text{C}$ .

In the series of experiments carried out with  $\text{CF}_3\text{I}$  as the source of  $\text{CF}_3$  radicals, the only products observed in the volatile fraction at  $-40\text{ }^{\circ}\text{C}$  were  $\text{CF}_3\text{H}$  and  $\text{C}_2\text{F}_6$ , in addition to unreacted  $\text{CF}_3\text{I}$ .

In the heavier fraction analyzed by GC-MS, in addition to the unreacted thiophene, two isomers of monosubstituted  $\text{CF}_3$ -thiophene were separated and identified as 2- and 3- $\text{CF}_3$ -thiophene. Monosubstituted dihydro- $\text{CF}_3$ -thiophene was also found in very small proportion, as well as traces of 2-iodothiophene in the high-conversion runs. However, no other products, as from the addition of  $\text{CF}_3\text{I}$  to the double bond, were observed, in spite of an exhaustive search by GC-MS, even at high conversions. The colour of the heavier fraction, when it was condensed, showed clearly that iodine was also produced, but again no products from its addition reaction or the addition of I atoms to thiophene were observed. This was also confirmed experimentally by photolysis of  $\text{I}_2$  in the presence of thiophene over periods much longer than those used in the actual experiments.

With HFA as the  $\text{CF}_3$  radical source, the same products mentioned above —  $\text{CF}_3\text{H}$ ,  $\text{C}_2\text{F}_6$ , monosubstituted  $\text{CF}_3$ -thiophenes, and monosubstituted dihydro- $\text{CF}_3$ -thiophene — were found. We could not exclude that the  $\text{CF}_3\text{CO}$  radical is formed in the primary process when HFA is photolyzed, but several studies have shown that this radical is fairly unstable and rapidly decomposes by CO elimination (6, 7). In the present work, CO was detected by gas chromatography on a Molecular Sieves column, although its yield was not measured. However, even if  $\text{CF}_3\text{CO}$  radicals are formed, the data seem to indicate that they do not affect the reported measurements. Traces of a product, tentatively identified as disubstituted dihydro- $\text{CF}_3$ -thiophene, were also observed in experiments at very high conversion but were practically absent in the series of experiments carried out with  $\text{CF}_3\text{I}$ .

The effect of variations of concentration of thiophene,  $\text{CF}_3\text{I}$ , or HFA and photolysis time on the yields of  $\text{CF}_3$ -thiophenes and the other products mentioned above are shown in Tables 1 and 2, respectively. Most of the runs were performed in triplicate to ensure that the separation procedure, previous to analysis, did not affect the precision of the results. Hence, the reported values of the yields are average values. Furthermore, a second series of runs carried out under the same experimental conditions but without fractional condensation at  $-40\text{ }^{\circ}\text{C}$  was analyzed chromatographically on a Porapak T column, and the yields of  $\text{CF}_3\text{H}$  and  $\text{C}_2\text{F}_6$  remained essentially unchanged within experimental error.

The total yield of (2+3)- $\text{CF}_3$ -thiophenes shows a gradual increase with increasing concentration of thiophene employed. However, concentrations of thiophene higher than  $5.0 \times 10^{-7}\text{ mol cm}^{-3}$  were not used because a light brown deposit, probably of a polymeric material, was observed on the wall of the reaction cell after several experiments with concentrations higher than  $15.0 \times 10^{-7}\text{ mol cm}^{-3}$  had been carried out at high conversion. On the other hand, the separation of the reaction mixture into its components by GC on the SE 30 column was unsuccessful, largely because of the small difference in the retention times of 2- and 3- $\text{CF}_3$ -thiophene with respect to thiophene.

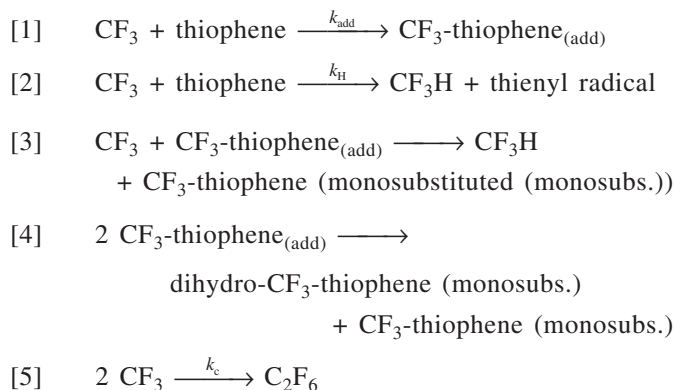
Moreover, results in Table 2 also show that with HFA as the source of  $\text{CF}_3$  radicals, the total yields of monosubstituted  $\text{CF}_3$ -thiophenes seem higher than with  $\text{CF}_3\text{I}$  (for the same thiophene concentration and photolysis time). This variation in measured yields would reflect a difference in efficiency of  $\text{CF}_3\text{I}$  or HFA as sources of  $\text{CF}_3$  radicals.

One of the features worth noting in Tables 1 and 2 is the high ratio ( $\sim 16$ ) of 2- $\text{CF}_3$ -thiophene : 3- $\text{CF}_3$ -thiophene, regardless of the radical source. This evidence would support the well-known fact that the preferential position for electrophilic attack on thiophene is  $\text{C}_2$  (8), also confirmed by computer charge density data of thiophene (9), which determined that the  $\text{C}_2(\text{C}_5)$  positions are richer in electron density than  $\text{C}_3(\text{C}_4)$ .

It can also be observed in Tables 1 and 2 that in each run, the yield of  $\text{CF}_3\text{H}$  is practically equal to the total yield of (2+3)- $\text{CF}_3$ -thiophene. While the yields of  $\text{CF}_3\text{H}$  increase with increasing concentrations of thiophene, the  $\text{C}_2\text{F}_6$  yields decrease.

Figure 1 shows that a plot of  $R_{\text{CF}_3\text{H}}/R_{\text{C}_2\text{F}_6}^{1/2}$  ( $R$  denotes rate of formation) against [thiophene], of the data points up to 20% conversion, is a straight line with a zero intercept and with a slope equal to  $106 \pm 4\text{ cm}^{3/2}\text{ mol}^{-1/2}\text{ s}^{-1/2}$ , irrespective of the source of  $\text{CF}_3$  radicals ( $\text{CF}_3\text{I}$  or HFA) and also at different concentrations of these compounds.

On account of these results, the following could be considered to be the main steps of the reaction mechanism for the reaction of the  $\text{CF}_3$  radicals produced by the photolysis of  $\text{CF}_3\text{I}$  or HFA with thiophene:



Other reactions, such as the self-combination of  $\text{CF}_3$ -thiophene<sub>(add)</sub> or  $\text{CF}_3 + \text{CF}_3$ -thiophene<sub>(add)</sub> to give disubstituted dihydro- $\text{CF}_3$ -thiophene, could also be included in this mechanism for the purpose of completeness. However, the products of these combination reactions were not found; only trace amounts of disubstituted dihydro- $\text{CF}_3$ -thiophene were detected when HFA was used as the  $\text{CF}_3$  radical source, as mentioned previously.

According to the reaction scheme, the formation of  $\text{CF}_3\text{H}$  could take place by the H-abstraction reaction, eq. [2], and by the pseudo-H-abstraction reaction, eq. [3], the latter equivalent to that proposed in the gas-phase reactions of  $\text{CF}_3$  radicals with benzene (10) and substituted benzenes (11, 12) for the formation of  $\text{CF}_3\text{H}$  and  $\text{CF}_3$ -benzenes. In these, as well as in the present study, the concentrations of the substrates used were low, thus ensuring that the concentration of  $\text{CF}_3$  radicals is large enough for the reaction described by eq. [3] to occur, at variance with what has been argued for



**Table 1.** Product yields for the reaction of CF<sub>3</sub> radicals with thiophene at 25 °C; CF<sub>3</sub>I as the source of CF<sub>3</sub> radicals.

[thioph.] $\times 10^7$ (mol cm <sup>-3</sup> ) <sup>a</sup>	[CF <sub>3</sub> I] $\times 10^7$ (mol cm <sup>-3</sup> ) <sup>a</sup>	Photolysis time (s)	(2+3)-CF <sub>3</sub> -thioph. (mol $\times 10^5$ )	Ratio 2-CF <sub>3</sub> - thioph. : 3-CF <sub>3</sub> - thioph.	Ratio <sup>b</sup> dihydro- CF <sub>3</sub> -thioph. : (2+3)-CF <sub>3</sub> -thioph.	CF <sub>3</sub> H (mol $\times 10^5$ )	C <sub>2</sub> F <sub>6</sub> (mol $\times 10^8$ )
6.50	9.60	1 800	0.54	16.8	0.9	0.56	3.76
5.00	11.7	5 100	1.14	18.7	1.1	1.19	11.6
8.07	10.1	3 600	1.34	16.9	0.8	1.33	7.69
8.08	22.9	3 600	1.46	15.9	0.9	1.47	9.53
7.75	10.4	7 200	2.07	17.1	1.3	2.09	14.6
7.75	8.00	7 200	2.05	16.8	0.7	2.04	13.9
7.95	9.80	1 800	0.64	14.9	0.9	0.65	3.24
7.96	10.9	10 800	3.03	16.3	1.1	3.06	18.8
8.50	10.4	10 800	3.13	16.5	1.5	3.11	18.6
10.3	10.3	1 800	0.86	15.1	1.0	0.84	3.22
10.8	9.15	3 600	1.67	17.3	1.4	1.69	6.36
10.7	23.1	1 800	0.90	15.9	0.9	0.92	3.53
10.8	22.9	3 600	1.80	16.1	1.2	1.78	7.32
10.8	23.0	5 100	2.34	16.0	1.1	2.36	10.0
11.6	10.6	5 100	2.42	15.2	1.2	2.41	8.00
13.5	22.9	3 600	2.23	16.1	1.0	2.25	7.05
15.1	10.5	1 800	1.05	16.6	0.8	1.07	2.61
14.4	11.0	3 600	2.08	14.3	1.1	2.10	5.26
14.6	11.1	5 100	2.97	13.9	1.2	2.96	7.56

Note: thioph. = thiophene.

<sup>a</sup>V<sub>cell</sub> = 109 cm<sup>3</sup>.

<sup>b</sup>The values given are equal to 100  $\times$  dihydro-CF<sub>3</sub>-thiophene : (2+3)-CF<sub>3</sub>-thiophene.

**Table 2.** Product yields for the reaction of CF<sub>3</sub> radicals with thiophene at 25 °C; HFA as the source of CF<sub>3</sub> radicals.

[thioph.] $\times 10^7$ (mol cm <sup>-3</sup> ) <sup>a</sup>	[HFA] $\times 10^7$ (mol cm <sup>-3</sup> ) <sup>a</sup>	Photolysis time (s)	(2+3)-CF <sub>3</sub> -thioph. (mol $\times 10^5$ )	Ratio 2-CF <sub>3</sub> - thioph. : 3- CF <sub>3</sub> -thioph.	Ratio <sup>b</sup> dihydro- CF <sub>3</sub> -thioph. : (2+3)-CF <sub>3</sub> -thioph.	CF <sub>3</sub> H (mol $\times 10^5$ )	C <sub>2</sub> F <sub>6</sub> (mol $\times 10^7$ )
2.42	10.8	3600	0.92	4.5	1.4	0.90	5.89
4.30	8.01	1800	0.97	14.5	1.3	0.96	2.87
5.30	7.20	1800	1.16	15.0	1.1	1.15	2.59
5.60	6.80	3600	2.00	14.9	1.3	2.02	4.92
5.92	6.72	7200	3.57	16.3	1.2	3.55	9.50
7.40	7.60	900	0.73	17.2	1.0	0.76	1.12
7.26	7.53	1800	1.41	17.1	0.9	1.43	2.29
7.85	10.5	3600	2.71	15.3	1.3	2.73	4.24
8.70	10.2	3600	3.06	15.8	1.4	3.08	4.20
10.4	11.8	900	1.02	16.5	1.1	1.04	1.03
10.6	10.8	1800	2.04	16.2	1.3	2.02	1.96
12.4	11.3	3600	3.92	15.6	0.9	3.90	3.32
12.5	12.1	7200	6.62	15.9	1.4	6.60	6.47

<sup>a</sup>V<sub>cell</sub> = 109 cm<sup>3</sup>.

<sup>b</sup>The values given are equal to 100  $\times$  dihydro-CF<sub>3</sub>-thiophene : (2+3)-CF<sub>3</sub>-thiophene.

these reactions in the liquid phase, where pseudo-abstraction is unlikely to proceed (13).

In the absence of any extra production of CF<sub>3</sub>H by reactions other than those described in eqs. [2] and [3], the rate of formation of CF<sub>3</sub>H would be:

$$[6] \quad R_{\text{CF}_3\text{H}} = k_{\text{H}}[\text{CF}_3][\text{thiophene}] + k_3[\text{CF}_3][\text{CF}_3\text{-thiophene}_{(\text{add})}]$$

Taking into account that monosubstituted dihydro-CF<sub>3</sub>-thiophene was produced, to the extent of about 1% of the (2+3)-CF<sub>3</sub>-thiophenes, the disproportionation reaction,

eq. [4], would be an unimportant channel for the formation of monosubstituted CF<sub>3</sub>-thiophenes. Therefore, this reaction, eq. [4], which also consumes the adduct formed in the addition step in eq. [1], could be considered negligible, so that

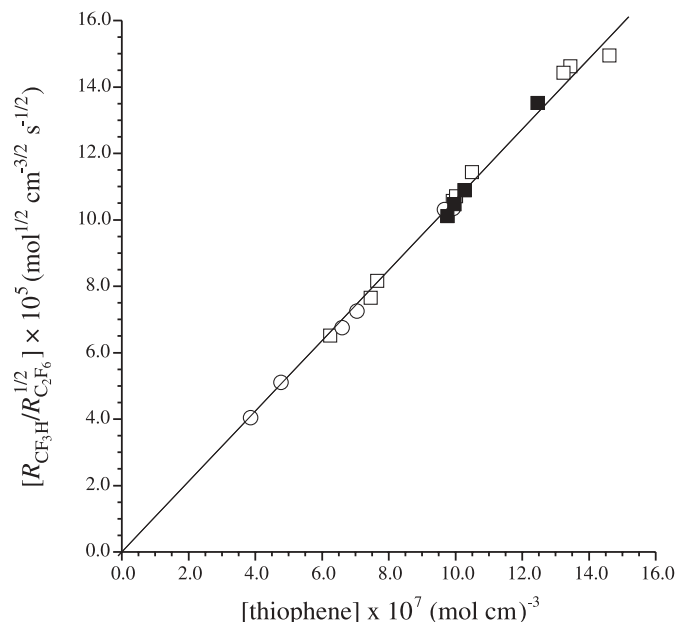
$$[7] \quad k_3[\text{CF}_3][\text{CF}_3\text{-thiophene}_{(\text{add})}] \approx k_{\text{add}}[\text{CF}_3][\text{thiophene}]$$

and the rate of formation of CF<sub>3</sub>H can be made approximately equal to

$$[8] \quad R_{\text{CF}_3\text{H}} \approx (k_{\text{H}} + k_{\text{add}}) [\text{CF}_3][\text{thiophene}]$$



**Fig. 1.** Plot of  $R_{\text{CF}_3\text{H}}/R_{\text{C}_2\text{F}_6}^{1/2}$  as a function of [thiophene] at 25 °C, of the data points up to 20% conversion.  $\square$   $\text{CF}_3\text{I}$ ,  $\sim 10 \times 10^{-7} \text{ mol cm}^{-3}$ ;  $\blacksquare$   $\text{CF}_3\text{I}$ ,  $\sim 23 \times 10^{-7} \text{ mol cm}^{-3}$ ;  $\circ$  HFA,  $\sim 10 \times 10^{-7} \text{ mol cm}^{-3}$ .



Taking into account that

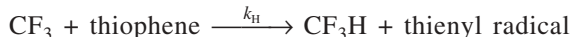
$$[9] \quad R_{\text{C}_2\text{F}_6}^{1/2} = k_c^{1/2}[\text{CF}_3]$$

a simple expression can be found for the relative rate of formation of  $\text{CF}_3\text{H}$

$$[10] \quad R_{\text{CF}_3\text{H}}/R_{\text{C}_2\text{F}_6}^{1/2} \approx \{(k_H + k_{\text{add}})/k_c^{1/2}\}[\text{thiophene}]$$

A plot of  $R_{\text{CF}_3\text{H}}/R_{\text{C}_2\text{F}_6}^{1/2}$  as a function of [thiophene], shown in Fig. 1, gives a straight line with zero intercept, which is indicative that eq. [10] holds, and thus,  $(k_H + k_{\text{add}})/k_c^{1/2}$  may be related to the observed value  $106 \pm 4 \text{ cm}^{3/2} \text{ mol}^{-1/2} \text{ s}^{-1/2}$  obtained from the slope of Fig. 1 at 25 °C.

To evaluate the contribution made by the endothermic H-abstraction reaction, eq. [2],



toward the formation of  $\text{CF}_3\text{H}$ , we calculated the activation energy and the pre-exponential factor for the H-abstraction reaction, eq. [2], applying the bond-strength-bond-length (BSBL) – transition-state-theory method, developed by Bérces and Dombi (14), based on the bond-energy-bond-order (BEBO) method. With this treatment, good results have been obtained for the estimation of the kinetic parameters for metathesis reactions involving unsaturated reaction centers. The BSBL reaction profile for the H-abstraction reaction was calculated along the reaction path, and the maximum value of the potential energy — that is, the potential activation energy and, consequently, the transition state — occurs in a late stage of the reaction, as expected for an endothermic process. The pre-exponential factor and the activation energy were estimated by considering that the activated complex is well represented by a linear five-mass-point model.

The following expression for  $k_H$  was obtained:

$$[11] \quad k_H = 5.5 \times 10^{11} \exp[-(5150) K/T] (\text{cm}^3 \text{ mol}^{-1} \text{ s}^{-1})$$

The rate constant for  $\text{CF}_3$  recombination,  $k_c$ , has been measured near room temperature by various workers using different techniques, and the reported values (1) show more than an order of magnitude variation, ranging from about  $1.3 \times 10^{12}$  to  $2.4 \times 10^{13} \text{ cm}^3 \text{ mol}^{-1} \text{ s}^{-1}$ . Thus, the rate constant at 25 °C for the H-abstraction reaction from thiophene relative to  $k_c^{1/2}$  would be approximately a factor of  $10^2$ – $10^3$  lower than  $k_{\text{add}}/k_c^{1/2}$ . Therefore, the disproportionation reaction, eq. [3], could be considered the main step for the production of  $\text{CF}_3\text{H}$ , and so the value of  $106 \pm 4 \text{ cm}^{3/2} \text{ mol}^{-1/2} \text{ s}^{-1/2}$  could be assigned to  $k_{\text{add}}/k_c^{1/2}$ .

As far as we know, insufficient data are available in the gas phase for the reactions of  $\text{CF}_3$  radicals with aromatic and heteroaromatic compounds to allow any detailed comparisons. Moreover, the reported data are relative values of the rate constants. Absolute rate constants have only been reported for reactions of  $\text{CF}_3$  radicals with alkenes in the gas phase (15) and in solution (16). However, we could compare the reactivity of thiophene toward  $\text{CF}_3$  radicals with other nonsaturated compounds, alkenes such as ethene and butadiene, and aromatics such as benzene.

The values of  $k_{\text{add}}/k_c^{1/2}$  for the addition reactions of  $\text{CF}_3$  to the foregoing compounds are displayed in the first column of Table 3 for comparison purposes. The data obtained in this work indicate that the reactivity of thiophene towards  $\text{CF}_3$  radical addition is intermediate between the olefins and benzene. A similar sequence in reactivity is observed in the reactions of these compounds with the electrophilic OH radical. This trend may reflect the effects of the resonance stabilization energies (resonance stabilization energies are  $\sim 138$ – $151 \text{ kJ mol}^{-1}$  for benzene,  $\sim 92 \text{ kJ mol}^{-1}$  for thiophene, and  $\sim 15 \text{ kJ mol}^{-1}$  for 1,3-butadiene (20)), indicating that resonance stabilization decreases the reactivity of the double bonds toward  $\text{CF}_3$  radical addition, as has been pointed out previously by Atkinson et al. (21) for the OH addition to the same compounds.

We conclude that, for the reaction of  $\text{CF}_3$  radicals and thiophene in the gas phase at 25 °C, the formation of the monosubstituted products, 2- and 3- $\text{CF}_3$ -thiophene, can be explained through a similar mechanism to that proposed for other aromatic compounds (benzenes and halobenzenes) involving the addition of the  $\text{CF}_3$  radical to thiophene followed preferentially by the subsequent disproportionation reaction. The addition rate constant is intermediate between that of the olefins and benzene.

## Experimental section

The high-vacuum apparatus employed was similar to that described in ref. 12. Briefly, the photolysis experiments were carried out in a cylindrical quartz cell ( $V = 109 \text{ cm}^3$ ) connected through Teflon valves to a conventional grease-free vacuum line and storage traps, with the reactants kept at liquid  $\text{N}_2$  temperature.

The light source was an Osram HBO 500 W high-pressure mercury lamp. A Corning Pyrex Glass Plate 7740 (2 mm thick) was used to remove wavelengths lower than 275 nm (22).



**Table 3.** Addition rate constants for some reactions of CF<sub>3</sub> and OH radicals at 25 °C.

Compound	$k_{\text{add}}/k_{\text{c}}^{1/2}$ (CF <sub>3</sub> ) (cm <sup>3/2</sup> mol <sup>-1/2</sup> s <sup>-1/2</sup> )	$k$ (OH) <sup>a</sup> (cm <sup>3</sup> mol <sup>-1</sup> s <sup>-1</sup> )
Ethene	377 <sup>b</sup>	5.14×10 <sup>12</sup>
1,3-Butadiene	~3000 <sup>c</sup>	4.12×10 <sup>13</sup>
Thiophene	106 <sup>d</sup>	5.7×10 <sup>12</sup>
Benzene	31 <sup>e</sup>	7.3×10 <sup>11</sup>

<sup>a</sup>Reference 17. Recommended high-pressure limit rate constants at room temperature with an estimated uncertainty at 25 °C of about ±20%.

<sup>b</sup>Reference 18. Extrapolated value calculated at 25 °C using the reported activation parameters.

<sup>c</sup>Reference 19. Estimated from the competitive reaction with ethene at 173 °C.

<sup>d</sup>This work.

<sup>e</sup>Extrapolated value calculated at 25 °C using the activation parameters reported in ref. 10.

In a typical experiment, the gaseous reactants were introduced into the evacuated reaction vessel, and pressures were measured. After a period of irradiation the reaction vessel contents were immediately collected in a trap cooled in liquid N<sub>2</sub> and separated by fractional distillation at -40 °C. In some experiments the volatile portion at this temperature was distilled into an evacuated gas chromatograph sample loop and passed through a 2 m column packed with Porapak T 80/100 mesh at 40 °C. Product samples were collected downstream for IR and MS identification. CF<sub>3</sub>H and C<sub>2</sub>F<sub>6</sub> were identified by comparison of their GC retention times and their IR and MS spectra with authentic samples. Known concentrations of the appropriate standards were used for calibration purposes.

The residue remaining at -40 °C was analysed by GC-MS using a capillary column (0.32 mm i.d. × 30 m, SE-30). To build up a sufficient amount of some of the products for identification, special preparative photolyses were carried out, generally at higher conversion. Mass spectrometry analysis (GC-MS) gave the theoretical parent mass for 2- and 3-CF<sub>3</sub>-thiophene at  $m/z$  = 152 (23), for dihydro-CF<sub>3</sub>-thiophene at  $m/z$  = 154, and for 2-iodothiophene at  $m/z$  = 210 (24).

Control experiments at room temperature in the dark showed that no product formation occurred thermally under standard reaction conditions, not even in periods 2–3 times longer than the usual irradiation times.

Infrared spectra were recorded using a Nicolet 55X FT infrared spectrometer and mass spectra were obtained with a Finnigan 3300 instrument and a PerkinElmer QM 910 GC-MS.

Thiophene, CF<sub>3</sub>I, and HFA, as well as the reference compounds CF<sub>3</sub>H, C<sub>2</sub>F<sub>6</sub>, and 2-iodothiophene, were obtained commercially and were trap-to-trap distilled in a vacuum line, several times, and thoroughly degassed prior to use. Their purity was checked by IR spectroscopy and GC-MS.

## Acknowledgments

The authors thank CONICET (Argentina), AGENCIA CORDOBA CIENCIA (Córdoba, Argentina), SECyT-U.N.C. (Córdoba, Argentina), and CIUNPAT-U.N.P.S.J.B. (Comodoro Rivadavia, Argentina) for partial financial support.

## References

1. NIST standard reference data. Chemical kinetics database 17. U. S. Department of Commerce. Gaithersburg, Md. 1999.
2. L. Pasteris and E.H. Staricco. *J. Chem. Soc. Faraday Trans. 2*, **82**, 1991 (1986), and refs. quoted therein.
3. N. Sawada, M. Nakayama, M. Yoshida, T. Yoshida, and N. Kamigata. *J. Fluorine Chem.* **46**, 423 (1990).
4. D. Naumann and J. Kischkewitz. *J. Fluorine Chem.* **46**, 265 (1990).
5. H.A. Wiebe and J. Heicklen. *Can. J. Chem.* **47**, 2965 (1969).
6. M.M. Maricq, J.J. Sente, T.S. Dibble, and J.S. Francisco. *J. Phys. Chem.* **99**, 11 875 (1995).
7. A. Thomas, F. Caralp, and R. Lesclaux. *Z. Phys. Chem.* **214**, 1349 (2000).
8. G. Vernim, H.J.M. Dou, and J. Metzger. *Bull. Soc. Chim. Fr.* 1174 (1972).
9. N. Karunanidhi, V. Kannappan, and U. Ponnambalan. *Acta Ciencia Indica*, **17**, 279 (1991).
10. G.A. Chamberlain and E. Whittle. *Trans. Faraday Soc.* **67**, 2077 (1971), and refs. quoted therein.
11. S.I. Lane, E.V. Oexler, and E.H. Staricco. *Int. J. Chem. Kinet.* **23**, 361 (1991).
12. J.D. Nieto, S.I. Lane, and E.V. Oexler. *Ber. Bunsenges. Phys. Chem.* **101**, 868 (1997).
13. J.M. Birchall, G.P. Irvin, and R.A. Boyson. *J. Chem. Soc. Perkin 2*, 435 (1975).
14. T. Bérces and J. Dombi. *Int. J. Chem. Kinet.* **12**, 183 (1983), and refs. quoted therein.
15. Z. Linyang, W. Fuss, and K.L. Kompa. *Ber. Bunsenges. Phys. Chem.* **102**, 821 (1998).
16. D.V. Avila, K.U. Ingold, J. Luszyk, W.R. Dolbier, Jr., and H.Q. Pan. *J. Org. Chem.* **61**, 2027 (1996).
17. R. Atkinson. *Chem. Rev.* **86**, 69 (1986).
18. H.C. Low, J.M. Tedder, and J.C. Walton. *Trans. Faraday Soc.* **72**, 1300 (1976).
19. A. El Soueni, J.M. Tedder, and J.C. Walton. *J. Fluorine Chem.* **17**, 51 (1981).
20. S.W. Benson. *Thermochemical kinetics*. 2nd ed. Wiley, New York. 1976. p.60.
21. R. Atkinson, S.M. Aschmann, and W.P.L. Carter. *Int. J. Chem. Kinet.* **15**, 51 (1983).
22. J.G. Calvert and J.N. Pitts. *Photochemistry*. John Wiley and Sons, Inc., New York. 1966.
23. B. Verkoczy, A.G. Sherwood, I. Sofarik, and O.P. Strausz. *Can. J. Chem.* **61**, 2268 (1983).
24. B. Akesson and S. Gronowitz. *Ark. Kemi.* **28**, 155 (1967).



# Oxazoline chemistry — Part IV: Synthesis and characterization of oxazoline complexes of the zinc halides<sup>1</sup>

Tosha M. Barclay, Ignacio del Río, Robert A. Gossage, and Sarah M. Jackson

**Abstract:** The synthesis and characterization of 11 zinc halide derivatives that contain monodentate oxazoline ligands is described. The treatment of ether solutions of  $[\text{ZnX}_2]$  ( $\text{X} = \text{Cl}, \text{Br}, \text{I}$ ) with 2-aryl- or 2-methyl-2-oxazolines results in the formation of mildly hygroscopic complexes of the general formulae  $[\text{ZnX}_2(\text{ox})_2]$  ( $\text{ox} = 2\text{-methyl-2-oxazoline (1)}, 2,4,4\text{-trimethyl-2-oxazoline (2)}, 2\text{-phenyl-2-oxazoline (3)}, \text{ or } 4,4\text{-dimethyl-2-phenyl-2-oxazoline (4)}$ ), except in the case of  $\text{ZnI}_2$ , which does not form an isolable complex — likely for steric reasons — with oxazoline **4**. Treatment of  $[\text{ZnBr}_2(\text{4})_2]$  with **1** reveals ( $^1\text{H}$  NMR) that **1** only sluggishly displaces coordinated **4** at temperatures below  $50^\circ\text{C}$ . The structural characterization, via single crystal X-ray diffraction, of six of the complexes, viz.  $[\text{ZnI}_2(\text{1})_2]$ ,  $[\text{ZnI}_2(\text{2})_2]$ ,  $[\text{ZnX}_2(\text{3})_2]$  ( $\text{X} = \text{Cl}, \text{Br}, \text{ or } \text{I}$ ), and  $[\text{ZnBr}_2(\text{4})_2]$ , is also reported. All of these structurally characterized complexes are mononuclear zinc compounds with an overall distorted tetrahedral arrangement of the two halide and two oxazoline ligands around the zinc metal centre. The oxazoline series of complexes reported herein show little structural diversity, a facet which is in contrast to their substituted pyridine analogues.

**Key words:** oxazoline, zinc, X-ray crystal structure, coordination complex, NMR spectroscopy,  $\text{Zn(II)}$ .

**Résumé :** On décrit la synthèse et la caractérisation d'onze dérivés d'halogénures de zinc contenant des ligands oxazolines monodentates. Le traitement de solutions étherées de  $[\text{ZnX}_2]$  ( $\text{X} = \text{Cl}, \text{Br}, \text{I}$ ) avec des 2-aryl- ou 2-méthyl-2-oxazolines conduit à la formation de complexes faiblement hygroscopiques de formule générale  $[\text{ZnX}_2(\text{ox})_2]$  ( $\text{ox} = 2\text{-méthyl-2-oxazoline [1]}, 2,4,4\text{-triméthyl-2-oxazoline [2]}, 2\text{-phényl-2-oxazoline [3]} \text{ ou } 4,4\text{-diméthyl-2-phényl-2-oxazoline [4]}$ ); exceptionnellement, la réaction  $\text{ZnI}_2$  avec l'oxazoline **4** ne conduit pas à la formation d'un complexe isolable, probablement en raison d'un encombrement stérique. La RMN du  $^1\text{H}$  montre que le traitement du  $[\text{ZnBr}_2(\text{4})_2]$  avec **1**, à des températures inférieures à  $50^\circ\text{C}$ , montre que le déplacement de **4** ne se fait que très difficilement. On rapporte aussi la caractérisation par diffraction des rayons X de six de ces complexes, soit  $[\text{ZnI}_2(\text{1})_2]$ ,  $[\text{ZnI}_2(\text{2})_2]$ ,  $[\text{ZnX}_2(\text{3})_2]$  ( $\text{X} = \text{Cl}, \text{Br}$  ou  $\text{I}$ ) et  $[\text{ZnBr}_2(\text{4})_2]$ . Tous les complexes dont la structure a été caractérisée sont des composés mononucléaires du zinc comportant un arrangement global tétraédrique déformé de deux halogènes et de deux ligands oxazoline autour du zinc central. La série de complexes avec des oxazolines qui est rapportée ici ne présente que de faibles variations structurales; cette caractéristique est en opposition avec ce qui a été observé avec leurs analogues comportant des pyridines substituées.

**Mots clés :** oxazoline, zinc, structure cristalline par diffraction des rayons X, complexe de coordination, spectroscopie RMN,  $\text{Zn(II)}$ .

[Traduit par la Rédaction]

## Introduction

The chemistry of zinc is one of the cornerstones of inorganic biochemistry (1). The element is characterized by the high stability of the +2 oxidation state and by the numerous examples of robust four-, five-, and six-coordinate zinc com-

plexes (2, 3). The high Lewis acid character of the  $d^{10} \text{Zn}^{2+}$  ion leads to the formation of many stable compounds with *N*-donor ligands, including heterocycles such as pyridines (py), imidazoles, pyrazines, oxazoles, and others (3–8).

Zinc complexes are also part of a burgeoning network of bio-active and (or) pharmaceutical inorganic compounds (9),

Received 30 July 2003. Published on the NRC Research Press Web site at <http://canjchem.nrc.ca> on 30 October 2003.

**T.M. Barclay,**<sup>2</sup> Department of Chemistry, North Harris College, 2700 W. W. Thorne Drive, Houston, TX 77073–3499, U.S.A.

**I. del Río,**<sup>3</sup> Departamento de Química Orgánica e Inorgánica, Facultad de Química, Universidad de Oviedo, c/ Julián Clavería 8, E-33071 Oviedo, Spain.

**R.A. Gossage**<sup>4</sup> and **S.M. Jackson.** The David Upton Hill Laboratory of Inorganic Chemistry, 6 University Avenue, Elliott Hall, Department of Chemistry, Acadia University, Wolfville, NS B4P 2R6, Canada.

<sup>1</sup>For Part III, see K.M. Button and R.A. Gossage. *J. Heterocyclic Chem.* **40**, 513 (2003).

<sup>2</sup>Corresponding author (crystallography, complexes **10–13** and **15**) (e-mail: [Tosha.M.Barcly@nhmccd.edu](mailto:Tosha.M.Barcly@nhmccd.edu)).

<sup>3</sup>Corresponding author (crystallography, complex **7**) (e-mail: [irc@sauro.quimica.uniovi.es](mailto:irc@sauro.quimica.uniovi.es)).

<sup>4</sup>Corresponding author (general) (e-mail: [rgossage@acadiau.ca](mailto:rgossage@acadiau.ca)).



and even simple solutions of  $\text{Zn}^{2+}$  ions or  $[\text{Zn}(\text{N-donor})_x]^{2+}$  complexes have a number of noteworthy biological activities (10). For example,  $[\text{ZnCl}_2(\text{H}_2\text{N}^i\text{Pr})_2]$  has recently been shown to prolong (i.e., stabilize) the potency of enzymes in aqueous media (11). The presence of zinc ions can also increase the potency of certain biologically active compounds, such as the enzyme inhibitory effect of bis(5-amidino-2-benzimidazolyl)methane (BABIM). This enhancement has been shown to be due to the binding of a  $[\text{Zn}(\text{BABIM})]$  complex into the active site of a protease enzyme (12*a*). Recently, zinc complexes of neocuprine, a phenanthroline derivative, have been shown to be site-specific RNA cleavage agents (12*b*). Related simple Zn coordination complexes have also shown promise in the treatment of diabetes (12*c*, 12*d*).

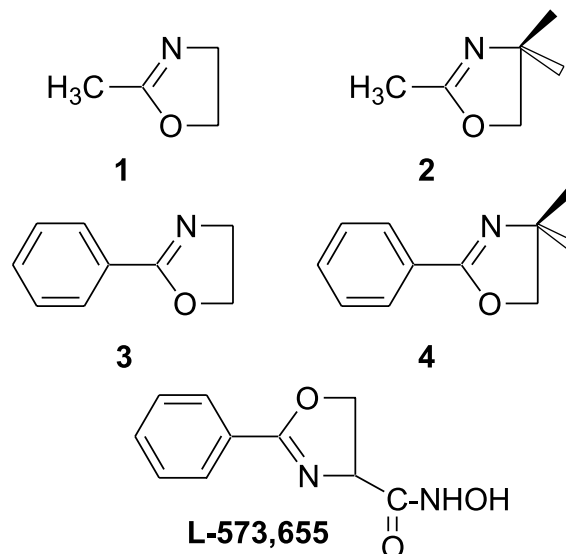
In direct relation to this study is the hypothesis that oxazoline-containing drug candidates (12*e*) such as 4-carbomethoxy-2-phenyl-2-oxazoline (viz., **L-573,655**; Fig. 1) inhibit lipid A biosynthesis by coordination with an enzyme-bound Zn atom (i.e., a Zn–oxazoline complex is formed with **L-573,655**; refs. 12*f*–12*i*). As part of a larger study concerning the coordination and medicinal chemistry of zinc (13) and oxazoline (i.e., 4,5-dihydro-2-oxazole) ligands in general (14),<sup>5</sup> we have undertaken a study of simple monodentate oxazolines (**1**–**4**; Fig. 1) as ligands for binding to the zinc halides. In this report, we detail the synthesis and characterization (NMR and X-ray analyses, etc.) of a series of Zn halide complexes that incorporate monodentate 2-oxazoline (**15**) derivatives. A further reason for this investigation is the knowledge that zinc halides are commonly used as catalysts to form oxazolines via treatment of organic cyanides with amino-alcohols (14*c*). A possible by-product of this procedure is an oxazoline–Zn complex, and hence, we wanted to begin a general investigation of such species.

## Results and discussion

### Syntheses and spectroscopic characterization

The treatment of ether solutions (or suspensions) of the zinc halides ( $\text{ZnX}_2$ ; X = Cl, Br, or I) with an excess of a 2-oxazoline (Fig. 1) leads to rapid formation of isolable white precipitates. A sole exception to this observation is the reaction of  $\text{ZnI}_2$  with oxazoline **4**; this particular reaction invariably leads to the formation of oily inextractable mixtures, from which no pure compounds could be obtained. Metathesis reactions, involving exchange of Br or  $\text{NO}_3$  anions with  $\text{I}^-$  sources, were likewise unsuccessful. The aforementioned isolated materials are moderately hygroscopic, a property that is more pronounced with the 2-methyl oxazoline complexes (i.e., **5**–**10**) when compared with the 2-phenyl derivatives **11**–**15**. All compounds decomposed on melting in air to form colourless oils. The initial isolated materials in all cases are white powders; crystalline samples, obtained as described in the Experimental section, are clear and colourless but darken over several weeks in air.

Fig. 1.



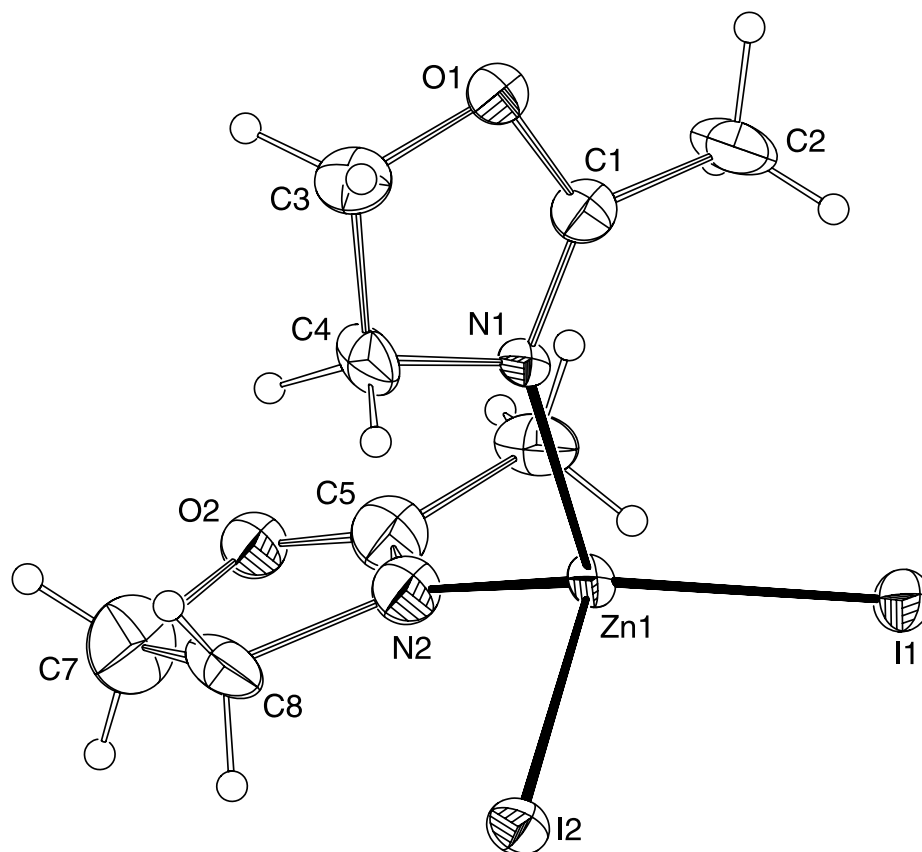
Examination of **5**–**15** by elemental analysis measurements are, in all cases, consistent with the formation of complexes of general formula  $[\text{Zn}_n\text{X}_{2n}(\text{oxazoline})_{2n}]$  (i.e., 2:1 ligand: $\text{ZnX}_2$  species). Characterization of these complexes by  $^1\text{H}$  NMR spectroscopy reveals the presence of a single oxazoline ligand environment. Further to this, the  $^1\text{H}$  NMR resonances for the presumably coordinated oxazolines are shifted relative to that of the free ligands,<sup>6</sup> a situation that is mimicked by observation of a decrease in the  $\nu(\text{C}=\text{N})$  IR stretching frequencies of the oxazoline for the complexes, as expected. Specifically, all  $^1\text{H}$  NMR chemical shifts of complexes incorporating **1** are notably deshielded relative to the free ligand form,<sup>6</sup> an observation consistent with donation of electron density from the ligand to the Lewis acidic Zn centre. Complexes of **2** show a similar trend; however, the methyl resonances on C-2 of the oxazoline are notably shielded relative to free **2**. This suggests that this methyl group is forced to be in close proximity to the metal centre, likely because of steric effects of the methyl substituents on C-4 (vide infra). In the case of ligands **3** and **4**, shifts are less pronounced relative to the free ligands, although the methylene protons of **3** show a small shift (positive in the case of the Br and I derivatives and negative for the Cl) upon coordination.

Zinc halides are often employed as catalysts for the synthesis of 2-oxazolines via treatment of an alkyl or aryl cyanide with an appropriate amino-alcohol at elevated temperatures (14*c*, 15, 16). With this in mind, it seems feasible that Zn–oxazoline complexes may also be produced as by-products in these reactions. We have taken a cursory look at the stability of some of these species by a simple metathesis reaction. Treatment of complex **15** in an NMR tube with 2 equiv of **1** and maintenance at room temperature (RT) for a period of 1 day does not result in any loss of signal intensity of **15**, nor presence of any form of an intermediate, and

<sup>5</sup>R.A. Gossage, K.J. Haller, H. Jenkins, and S.M. Jackson. Unpublished results.

<sup>6</sup> $^1\text{H}$  NMR data (300 MHz,  $\text{CDCl}_3$ )  $\delta$ : **1**: 4.12 (t, 2H,  $J = 9.5$ ,  $\text{CH}_2\text{O}$ ), 3.73 (t, 2H,  $\text{CH}_2\text{N}$ ), 1.86 (s, 3H,  $\text{CH}_3$ ); **2**: 3.80 (s, 2H,  $\text{CH}_2\text{O}$ ), 1.83 (s, 3H,  $\text{N}=\text{C}-\text{CH}_3$ ), 1.14 (s, 6H,  $\text{CH}_3$ ); **3**: 7.95 (m, 2H, ArH), 7.42 (m, 3H, ArH), 4.40 (t, 2H,  $\text{CH}_2\text{O}$ ), 4.04 (t, 2H,  $\text{CH}_2\text{N}$ ); **4**: 7.86 (m, 2H, ArH), 7.28 (m, 3H, ArH), 3.95 (s, 2H,  $\text{CH}_2$ ), 1.25 (s, 6H,  $\text{CH}_3$ ). IR data (thin film; KBr;  $\nu(\text{C}=\text{N})$ ): **1**: 1670 (st); **2**: 1670 (st); **3**: 1645 (st); **4**: 1648 (st).



**Fig. 2.** ORTEP representation of complex **7**.

no evidence for the formation of complex **5**. Heating this mixture for 12 h at about 50 °C results in only a small amount (<10%) of **5** being detected. These results indicate a robust nature of these materials, and it seems that only by treating with a large excess of water, as is typically done in the synthesis of ligands **1–4** employing Zn halides (14c, 15, 16), are the free oxazolines released. This is also suggested by the relatively hygroscopic nature of these complexes, a property that is a likely cause of our inability to obtain a reproducible elemental analysis in the case of complex **14**.

### Solid-state (crystal) structures

Zinc halides are well known to react with *N*-donor compounds to form mononuclear complexes with an overall distorted tetrahedral disposition of ligands around the Zn atom. For example, ZnCl<sub>2</sub> forms simple complexes of the general formulae [ZnCl<sub>2</sub>(*N*)<sub>2</sub>] with *N* = py, 4-(vinyl)py, 4-(NC)py, 4-(acetyl)py, 3,4,5-Cl<sub>3</sub>py, 3-(F<sub>3</sub>C)py, and 4-(Me)py (17). However, a number of interesting polymeric materials are formed (3, 6, 17a) with other pyridine derivatives. For example, both 3,5-Cl<sub>2</sub>py and 3,5-Br<sub>2</sub>py form polymeric complexes with ZnCl<sub>2</sub> (i.e., [Zn(μ-Cl)<sub>2</sub>(3,5-Xpy)<sub>2</sub>]<sub>∞</sub>) in which the Zn atom is in an octahedral coordination geometry. Linear (and tetrahedral at Zn) bridged species are formed with 4,4'-bipy and ZnCl<sub>2</sub> (i.e., [ZnCl<sub>2</sub>(4,4'-bipy)]<sub>∞</sub>), but Magnus-type salts (i.e., [Zn([MeO]<sub>2</sub>py)<sub>4</sub>]<sup>2+</sup> [Zn<sub>2</sub>Br<sub>6</sub>]<sup>2-</sup>) can be formed by treating ZnBr<sub>2</sub> with 2,6-(MeO)<sub>2</sub>-py (17a).

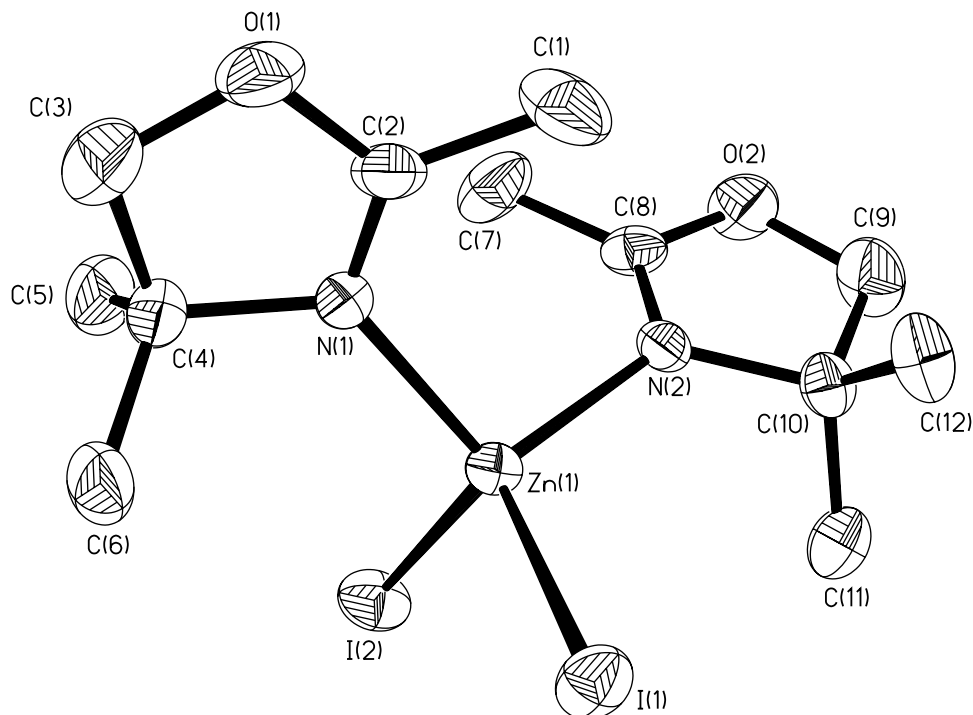
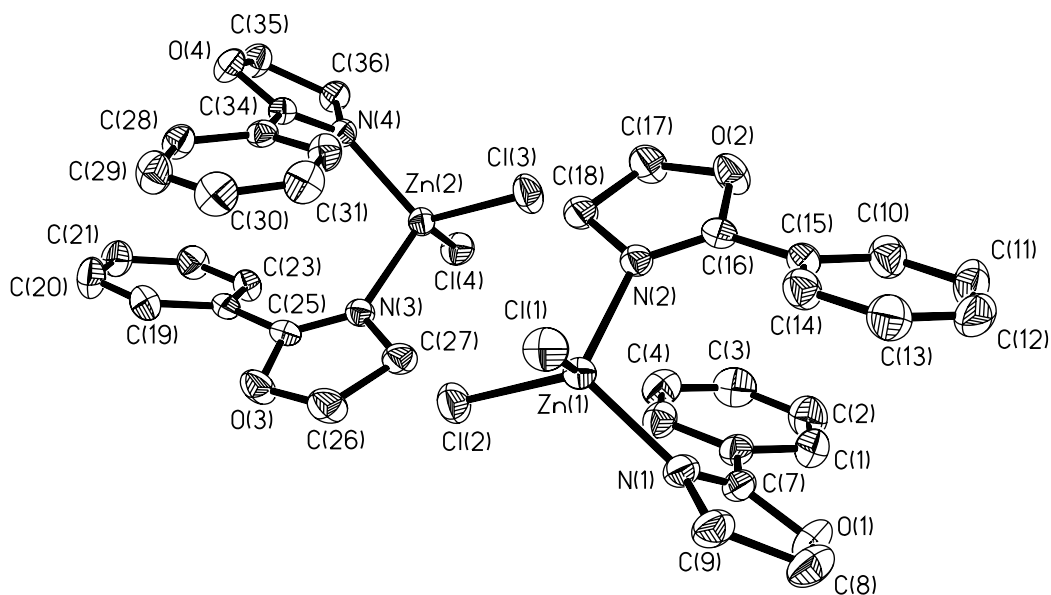
There is currently a dearth of structural information on *monodentate* oxazoline complexes (15), despite the fact that the coordination chemistry of bis-oxazolines and cyclo-

metallated (i.e., η<sup>2</sup>-*N,C*) 2-aryl-2-oxazolines has been the subject of numerous studies (15). To our knowledge, there is no structural data of any Zn halide complex with a monodentate oxazoline; hence, we felt a structural investigation of this class of materials was in order. Thus, we have carried out single crystal X-ray structure analysis of six of the complexes (**7**, **10–13**, and **15**) synthesized herein. In addition, there are very few structurally characterized [ZnI<sub>2</sub>(*N*-donor)<sub>*n*</sub>] complexes (18–20), and thus the characterization of three (**7**, **10**, and **13**) such derivatives will help to expand the structural database on this class of ZnI<sub>2</sub> coordination compounds.

The molecular structures of complexes **7**, **10–13**, and **15** can be found in Figs. 2–7, respectively, and the general crystal data can be found in Tables 1 and 2.

All six complexes are mononuclear species in the solid state with an approximate tetrahedral array of the two halide and two oxazoline ligands around the metal centre. As expected, the binding of the oxazoline fragment is, in all cases, via coordination of the imine *N*-atom of the heterocyclic ring (15). Comparative examples of related structurally characterized Zn oxazolines are few (21–24) but include complexes such as [η<sup>2</sup>-*N,N'*-(1,2-bis{4*S*-4-isopropyl-2-oxazolin-2-yl}benzene) zinc(II) chloride] (21). The bond lengths between Zn and the donor ligands for complexes **7**, **11–13**, and **15** are in the range typical (3–8, 15–25) for Zn—N and Zn—X bonds (Table 2). These data can be compared with, for example, the halide complexes (4c, 17a, 18b) [ZnCl<sub>2</sub>(4-Me-py)<sub>2</sub>] (Zn—N<sub>av</sub> = 2.044 Å; Zn—Cl<sub>av</sub> = 2.208 Å), [ZnBr<sub>2</sub>(3-CF<sub>3</sub>-py)<sub>2</sub>] (Zn—N = 2.084 Å; Zn—Br = 2.375 Å),

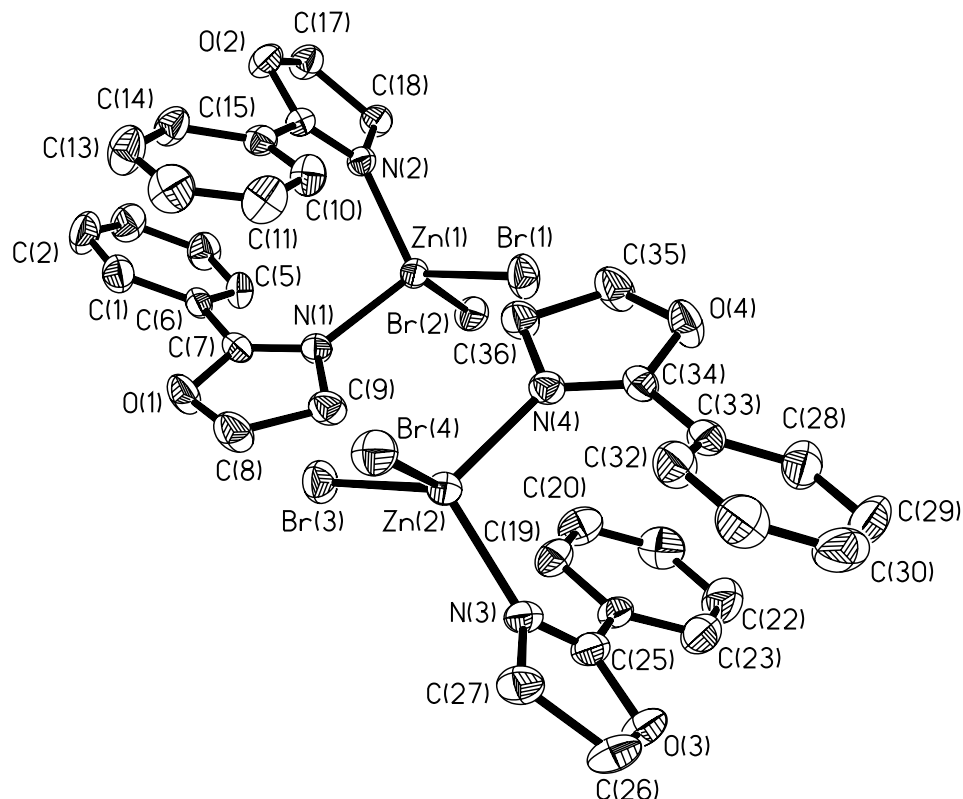
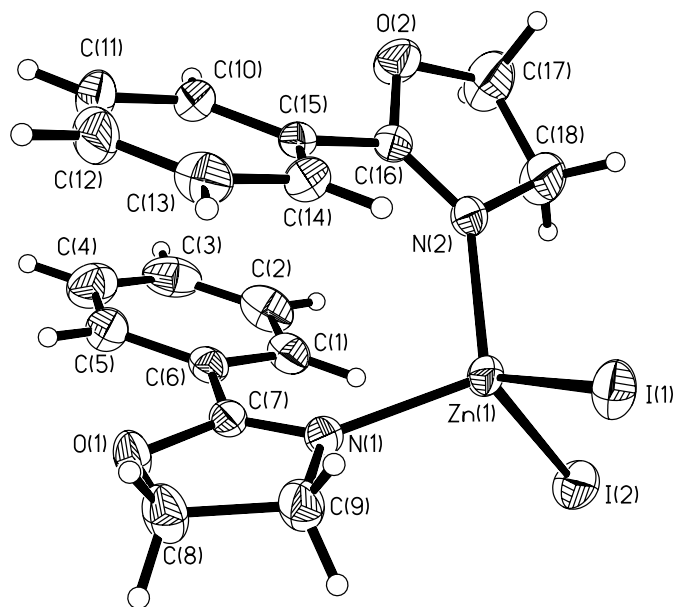
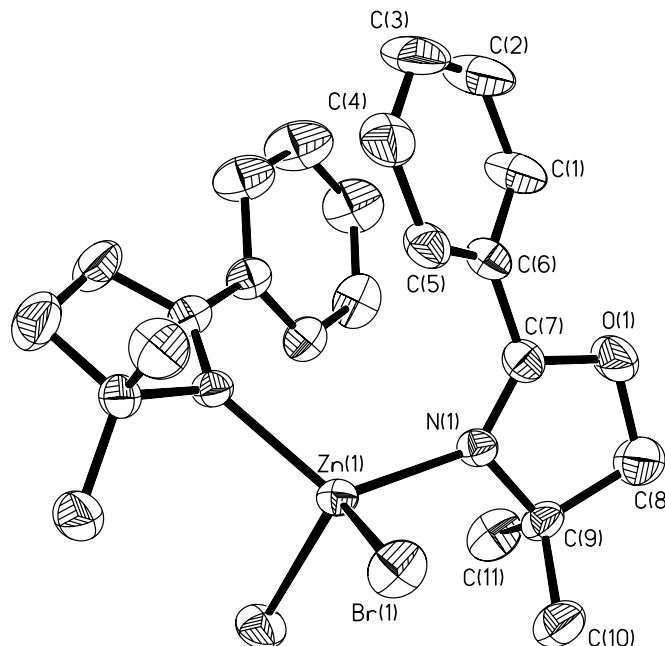


**Fig. 3.** ORTEP representation of complex **10**.**Fig. 4.** ORTEP representation depicting both molecules of complex **11** found in the unit cell.

and  $[\text{ZnI}_2(2\text{-amino-2-thiazole})_2]$  (**17**:  $\text{Zn}-\text{N}_{\text{av}} = 2.023 \text{ \AA}$ ;  $\text{Zn}-\text{I}_{\text{av}} = 2.384 \text{ \AA}$ ). Complex **10** is perhaps the most unusual of the set, as it displays  $\text{Zn}-\text{I}$  bonds that are at the upper range of known  $\text{Zn}-\text{I}$  bond lengths (cf. **17**). Similar long  $\text{Zn}-\text{I}$  bonds are found (*18a*) in the complex  $[\text{ZnI}_2(\eta^2\text{-}N,N'\text{-}\{\text{C}_5\text{H}_4\text{N}\}_3\text{N})]$  (**18**). The reason for the long bonds found here may be because of steric effects imposed on the large I atoms relative to tightly bound oxazoline **2** (**26**). Note that this particular fragment contains two sterically bulky methyl substituents on carbons (labelled) C4 and C10 (Fig. 3) of the oxazoline ring. This structure sheds some light on the observed solution properties that involve the shielding of the

proton resonances (vide supra) of the methyl group (C1). The  $\text{Zn1}-\text{C1}$  and  $\text{C7}$  distances are 3.43 and 3.38  $\text{\AA}$ , respectively. The  $\text{I}-\text{Zn}-\text{I}$  angles (Table 2) of **10** and **13** are considerably narrower than that of **18** ( $117.48(3)^\circ$ ) but similar to that found in the complexes  $[\text{ZnI}_2(\text{Bps}^{\text{Me}_2})]$  ( $113.48(5)^\circ$ ;  $\text{Bps}^{\text{Me}_2} = [\text{bis}(3,5\text{-dimethylpyrazolyl})\text{dimethylsilane}]$ ),  $[\text{ZnI}_2(\text{C}_6\text{H}_{12}\text{N}_4)_2]$  ( $111.5(1)^\circ$ ), and  $[\text{ZnI}_2(3,5\text{-[Buph]}_2\text{pzH})_2]$  ( $112.2(1)^\circ$ ), all of which have sterically demanding  $N$ -donor ligands (**19**, **20a**, **20b**). Complexes **11** and **12** both contain two unique molecules of the complex in the unit cell. The main differences between these molecules is the torsion angles between the phenyl group formally on C-2 and the



**Fig. 5.** ORTEP representation depicting both molecules of complex **12** found in the unit cell.**Fig. 6.** ORTEP representation of complex **13**.**Fig. 7.** ORTEP representation of complex **15**.

oxazoline unit. These two materials are virtually isomorphous. Further structural details for all six complexes reported here can be found in the supporting data.<sup>7</sup>

<sup>7</sup>Supplementary data may be purchased from the Depository of Unpublished Data, Document Delivery, CISTI, National Research Council Canada, Ottawa, ON K1A 0S2, Canada ([http://www.nrc.ca/cisti/irm/unpub\\_e.shtml](http://www.nrc.ca/cisti/irm/unpub_e.shtml) for information on ordering electronically). CCDC 213243–213248 contain the supplementary data for complexes **7**, **10–12**, and **15** respectively. These data can be obtained, free of charge, via [www.ccdc.cam.ac.uk/conts/retrieving.html](http://www.ccdc.cam.ac.uk/conts/retrieving.html) (or from the Cambridge Crystallographic Data Centre, 12 Union Road, Cambridge, U.K.; fax +44 1223 336033; or [deposit@ccdc.cam.ac.uk](mailto:deposit@ccdc.cam.ac.uk)).



Table 1. General crystal data for complexes 7, 10–13, and 15.

Complex	7	10	11	12	13	15
Formula	$C_8H_{14}N_2O_2ZnI_2$	$C_{12}H_{22}N_2O_2ZnI_2$	$C_{18}H_{18}N_2O_2ZnCl_2$	$C_{18}H_{18}N_2O_2ZnBr_2$	$C_{18}H_{18}N_2O_2ZnI_2$	$C_{22}H_{26}N_2O_2ZnBr_2$
fw	489.38	545.49	430.61	519.53	613.51	575.64
Crystal size (mm)	$0.35 \times 0.13 \times 0.10$	$0.22 \times 0.29 \times 0.37$	$0.39 \times 0.41 \times 0.57$	$0.35 \times 0.38 \times 0.43$	$0.47 \times 0.51 \times 0.61$	$0.31 \times 0.34 \times 0.38$
<i>a</i> (Å)	6.5379(7)	8.8696(18)	22.644(4)	23.242(4)	9.248(2)	0.205(5)
<i>b</i> (Å)	8.1537(9)	12.562(3)	8.5488(17)	8.6299(14)	26.251(6)	7.9088(13)
<i>c</i> (Å)	14.2453(14)	15.602(3)	19.544(4)	19.618(3)	8.999(2)	19.808(3)
$\alpha$ (°)	83.439(7)					
$\beta$ (°)	77.100(7)		92.229(4)	91.710(3)	110.618(4)	
$\gamma$ (°)	69.879(7)					
<i>V</i> (Å <sup>3</sup> )	694.46(13)	1876.8(7)	3778.7(13)	3933.0(11)	2044.7(8)	4731.8(14)
Cell detn, refls	756	343	793	552	779	514
<i>D</i> <sub>calcd</sub> (g·cm <sup>-3</sup> )	2.340	1.93	1.51	1.76	1.99	1.62
Space group	<i>P</i> $\bar{1}$	<i>P</i> <sub>2</sub> <sub>1</sub> <sup>2</sup> <sub>1</sub>	<i>P</i> <sub>2</sub> <sub>1</sub> / <i>c</i>	<i>P</i> <sub>2</sub> <sub>1</sub> / <i>c</i>	<i>P</i> <sub>2</sub> <sub>1</sub> / <i>c</i>	<i>Fdd</i> 2
<i>Z</i>	2	4	8	8	4	8
<i>F</i> (000)	456	1040	1760	2048	1168	2304
<i>T</i> (K)	120(2)	293	293	293	293	293
Absorption coefficient (mm <sup>-1</sup> )	37.258	4.60	1.60	5.33	4.23	4.44
2 $\theta$ range (°)	5.78–68.61	4–50	4–50	4–50	4–50	4–50
Limiting indices	$0 \leq h \leq 7$ $-8 \leq k \leq 9$ $-16 \leq l \leq 17$	$-10 \leq h \leq 10$ $-15 \leq k \leq 16$ $-18 \leq l \leq 11$	$-26 \leq h \leq 26$ $-10 \leq k \leq 6$ $-23 \leq l \leq 23$	$-27 \leq h \leq 22$ $-8 \leq k \leq 10$ $-21 \leq l \leq 23$	$-10 \leq h \leq 7$ $-31 \leq k \leq 30$ $-9 \leq l \leq 10$	$-27 \leq h \leq 35$ $-9 \leq k \leq 8$ $-23 \leq l \leq 23$
Reflections collected	10 983	9894	19 030	19 962	10 551	5902
Reflections unique	2550	3318	6664	6939	3589	2095
Reflections <i>I</i> > 2 $\sigma$ ( <i>I</i> )	2376	2991	5095	4611	3030	1985
Parameters	120	172	451	451	226	132
GOF on <i>F</i> <sup>2</sup>	1.05	1.07	1.07	0.99	1.06	0.98
Final <i>R</i> indices <i>I</i> > 2 $\sigma$ ( <i>I</i> )	<i>R</i> <sub>1</sub> = 0.0838 <i>wR</i> <sub>2</sub> = 0.2323	<i>R</i> <sub>1</sub> = 0.026 <i>wR</i> <sub>2</sub> = 0.059	<i>R</i> <sub>1</sub> = 0.025 <i>wR</i> <sub>2</sub> = 0.067	<i>R</i> <sub>1</sub> = 0.031 <i>wR</i> <sub>2</sub> = 0.074	<i>R</i> <sub>1</sub> = 0.031 <i>wR</i> <sub>2</sub> = 0.074	<i>R</i> <sub>1</sub> = 0.023 <i>wR</i> <sub>2</sub> = 0.054
<i>R</i> indices (all data)	<i>R</i> <sub>1</sub> = 0.0870	<i>R</i> <sub>1</sub> = 0.030	<i>R</i> <sub>1</sub> = 0.039	<i>R</i> <sub>1</sub> = 0.057	<i>R</i> <sub>1</sub> = 0.038	<i>R</i> <sub>1</sub> = 0.027
$\rho_{\text{min,max}}$ (e·Å <sup>-3</sup> )	-2.920, 2.720	-0.72, 0.33	-0.23, 0.26	-0.33, 0.79	-1.15, 0.63	-0.21, 0.41



**Table 2.** Selected bond lengths (Å) and angles (°) for complexes **7**, **10–13**, and **15**.

Complex	Bond	Bond lengths (Å)	Bonds	Bond angles (°)
<b>7</b>	Zn1—I1	2.567(2)	I1-Zn1-I2	111.67(6)
	Zn1—I2	2.590(2)	N1-Zn1-N2	99.7(5)
	Zn—N1	2.021(9)		
	Zn1—N2	2.004(14)		
	N1—C <sup>a</sup>	1.27(2)		
<b>10</b>	Zn1—I1	2.5937(7)	Cl1-Zn1-Cl2	112.18(2)
	Zn1—I2	2.5827(8)	N1-Zn1-N2	106.48(15)
	Zn1—N1	2.059(4)		
	Zn1—N2	2.074(4)		
	N1—C <sup>a</sup>	1.280(7)		
	N2—C <sup>a</sup>	1.268(6)		
<b>11<sup>b</sup></b>	Zn1—Cl1	2.2352(7)	Cl1-Zn1-Cl2	111.97(3)
	Zn1—Cl2	2.2432(7)	N1-Zn1-N2	103.70(7)
	Zn1—N1	2.026(2)		
	Zn1—N2	2.050(2)		
	N1—C <sup>a</sup>	1.282(3)		
<b>12<sup>b</sup></b>	Zn1—Br1	2.3712(7)	Br1-Zn1-Br2	108.61(3)
	Zn1—Br2	2.3712(6)	N1-Zn1-N2	104.59(12)
	Zn1—N1	2.053(3)		
	Zn1—N2	2.025(3)		
	N1—C <sup>a</sup>	1.285(4)		
<b>13</b>	Zn1—I1	2.5706(8)	I1-Zn1-I2	110.42(2)
	Zn1—I2	2.5937(7)	N1-Zn1-N2	107.51(13)
	Zn1—N1	2.052(3)		
	Zn1—N2	2.042(3)		
	N1—C <sup>a</sup>	1.282(5)		
<b>15</b>	Zn1—Br1	2.3905(5)	Br1 <sup>c</sup> -Zn1-Br1	112.92(3)
	Zn1—N1	2.076(3)	N1 <sup>c</sup> -Zn1-N1	119.07(14)
	N1—C <sup>a</sup>	1.269(4)		

<sup>a</sup>Refers to the formal N=C of the oxazoline ligands containing N1.<sup>b</sup>Two distinct molecules in the unit cell; values given for Zn1 complex only (see Supplementary data).<sup>c</sup>Symmetry code =  $-x - 1/2, -y + 1/2, z$ .

## Conclusions

The treatment of ether solutions of ZnX<sub>2</sub> with oxazolines **1–4** results in the formation of mildly hygroscopic mononuclear bis-oxazoline complexes, except in the case of X = I and oxazoline **4**. Six derivatives have been characterized by single crystal X-ray diffraction. These materials represent the first series of mononuclear oxazoline complexes of Zn<sup>2+</sup> to be fully characterized. The medicinal properties of these materials are currently under investigation and will be reported in a separate disclosure.

## Experimental

### General

All reactions were carried out in air, using commercially available, reagent-grade solvents. Zinc halides and ligands **1–4** (Fig. 1) were purchased commercially and used as received, with the exception of ZnCl<sub>2</sub>. This material was dried by heating thrice to the melt under vacuum (approximately (approx.) 2000 Pa), and then the solid was cooled to RT under an atmosphere of dry argon gas. THF was stored over

4 Å molecular sieves. <sup>1</sup>H NMR spectra (CDCl<sub>3</sub> solution) were recorded at RT using a Bruker AC-250 NMR spectrometer located at the Atlantic Regional Magnetic Resonance Centre (ARMRC) (Halifax, N.S., Canada), operating at 250 MHz, or were recorded using a Bruker Avance 300 NMR spectrometer located at the Acadia Centre for Microstructural Analysis (ACMA) (Wolfville, N.S., Canada), operating at 300 MHz. Chemical shifts are reported in ppm using TMS (and (or) residual solvent resonance) as internal standard ( $\delta_{\text{TMS}} = 0.00$  ppm). Coupling constants are reported in Hertz. IR spectra were recorded as nujol muls (except where noted) on a PerkinElmer 683 or 283B IR spectrometer; reported values are in units of cm<sup>-1</sup>. Melting points were recorded in air on a Mel-Temp II apparatus and are uncorrected. Elemental analyses measurements were performed at the Lakehead University Centre for Analytical Services (LUCAS) located in Thunder Bay, Ont., Canada.

### Synthesis of [dichlorobis{ $\eta^1$ -N-(2-methyl-2-oxazoline)}zinc] (**5**)

Solid zinc chloride (4.2 g, 31 mmol) was dissolved in 150 mL of diethylether by stirring the mixture at RT for



15 min. This mixture was then filtered to remove any undissolved material. To the rapidly stirring (clear and colourless) solution was added (via syringe) 8.0 mL (94 mmol) of **1** in a single portion. A white precipitate began to form almost immediately. Stirring was continued for a further 12 h at RT, and the resulting solid was isolated by filtration. This material was then washed thrice with Et<sub>2</sub>O (35 mL) and then allowed to dry in air. Yield 8.0 g (84%) of a white, slightly hygroscopic solid. Crystals of **5**, suitable for X-ray diffraction, grew after a CH<sub>2</sub>Cl<sub>2</sub> solution of **5**, layered with Et<sub>2</sub>O, was left standing for several days at RT. mp > 105 °C (decomposition temperature (decomp.)). IR: 1650 (st). <sup>1</sup>H NMR (250 MHz) δ: 4.50 (t, 2H, *J* = 9.8, CH<sub>2</sub>O), 3.98 (t, 2H, *J* = 9.8, CH<sub>2</sub>N), 2.27 (s, 3H, CH<sub>3</sub>). Calcd. for C<sub>8</sub>H<sub>14</sub>N<sub>2</sub>O<sub>2</sub>Cl<sub>2</sub>Zn·(H<sub>2</sub>O) (%): C 29.72, H 4.55, N 8.67; found: C 29.72, H 4.97, N 8.63.

#### Synthesis of [dibromobis{η<sup>1</sup>-N-(2-methyl-2-oxazoline)}zinc] (**6**)

In a reaction analogous to that used to produce **5**, zinc bromide (1.0 g, 4.4 mmol) in Et<sub>2</sub>O was treated with **1** (2.1 equiv). Yield 1.6 g (92%, hygroscopic solid). mp > 72 °C (decomp.). IR: 1650 (st). <sup>1</sup>H NMR (250 MHz) δ: 4.50 (t, 2H, *J* = 9.8, CH<sub>2</sub>O), 4.00 (t, 2H, *J* = 9.8, CH<sub>2</sub>N), 2.29 (s, 3H, CH<sub>3</sub>). Calcd. for C<sub>8</sub>H<sub>14</sub>N<sub>2</sub>O<sub>2</sub>ZnBr<sub>2</sub>·0.5(H<sub>2</sub>O): C 23.76, H 3.74, N 6.93; found: C 23.53, H 3.63, N 6.85.

#### Synthesis of [diiodobis{η<sup>1</sup>-N-(2-methyl-2-oxazoline)}zinc] (**7**)

As for **5**, zinc iodide (3.0 g, 9.4 mmol), suspended in Et<sub>2</sub>O–THF (60 mL : 10 mL), was treated with 2.4 mL (28 mmol) of **1**. Yield 4.0 g (87%, hygroscopic white solid). Crystals, suitable for X-ray diffraction, were grown from a solution of **3** (CH<sub>2</sub>Cl<sub>2</sub> layered with Et<sub>2</sub>O) that had been left standing at RT for several days. mp > 94 °C (decomp.). IR: 1650 (st). <sup>1</sup>H NMR (250 MHz) δ: 4.50 (t, 2H, *J* = 9.8, CH<sub>2</sub>O), 4.02 (t, 2H, *J* = 9.8, CH<sub>2</sub>N), 2.29 (s, 3H, CH<sub>3</sub>). Calcd. for C<sub>8</sub>H<sub>14</sub>N<sub>2</sub>O<sub>2</sub>ZnI<sub>2</sub>·0.25(H<sub>2</sub>O): C 19.45, H 2.96, N 5.67; found: C 19.21, H 2.76, N 5.57.

#### Synthesis of [dichlorobis{η<sup>1</sup>-N-(2,4,4-trimethyl-2-oxazoline)}zinc] (**8**)

As for **5**, zinc chloride (1.2 g, 8.8 mmol) in Et<sub>2</sub>O was treated with **2** (2.2 mL, 17 mmol), and the solid was washed with Et<sub>2</sub>O (2 × 35 mL) and petroleum ether (50 mL); the product can be further recrystallized from a 1:1 mixture of CH<sub>2</sub>Cl<sub>2</sub>–Et<sub>2</sub>O. Yield 2.0 g (65%). mp > 124 °C (decomp.). IR: 1635 (st). <sup>1</sup>H NMR (250 MHz) δ: 4.17 (s, 2H, CH<sub>2</sub>O), 2.27 (s, 3H, N=C–CH<sub>3</sub>), 1.61 (s, 6H, CH<sub>3</sub>). Calcd. for C<sub>12</sub>H<sub>22</sub>N<sub>2</sub>O<sub>2</sub>Cl<sub>2</sub>Zn·0.5(CH<sub>2</sub>Cl<sub>2</sub>): C 37.06, H 5.72, N 6.92; found: C 37.29, H 5.86, N 6.92.

#### Synthesis of [dibromobis{η<sup>1</sup>-N-(2,4,4-trimethyl-2-oxazoline)}zinc] (**9**)

As for **5**, using ZnBr<sub>2</sub> (1.4 g, 6.2 mmol; ether suspension) and **2** (1.7 mL, 13 mmol). Yield 2.7 g (96%). mp > 172 °C (decomp.). IR: 1625 (st). <sup>1</sup>H NMR (250 MHz) δ: 4.18 (s, 2H, CH<sub>2</sub>O), 2.29 (s, 3H, N=C–CH<sub>3</sub>), 1.68 (s, 6H, CH<sub>3</sub>). Calcd. for C<sub>12</sub>H<sub>22</sub>N<sub>2</sub>O<sub>2</sub>Br<sub>2</sub>Zn: C 31.92, H 4.91, N 6.20; found: C 32.16, H 4.59, N 6.21.

#### Synthesis of [diiodobis{η<sup>1</sup>-N-(2,4,4-methyl-2-oxazoline)}zinc] (**10**)

As for **5**, ZnI<sub>2</sub> (3.3 g, 10 mmol; ether suspension) was treated with **2** (2.7 mL, 21 mmol). Yield 4.9 g (90%). Crystals, suitable for X-ray diffraction, grew from a sealed solution of **10** (CH<sub>2</sub>Cl<sub>2</sub>) layered with Et<sub>2</sub>O, after standing at RT for several days. mp > 159 °C (decomp.). IR: 1630 (st). <sup>1</sup>H NMR (250 MHz) δ: 4.17 (s, 2H, CH<sub>2</sub>O), 2.27 (s, 3H, N=C–CH<sub>3</sub>), 1.61 (s, 6H, CH<sub>3</sub>). Calcd. for C<sub>16</sub>H<sub>18</sub>N<sub>2</sub>O<sub>2</sub>ZnI<sub>2</sub> (%): C 26.42, H 4.06, N 5.14, found: C 26.27, H 3.86, N 5.02.

#### Synthesis of [dichlorobis{η<sup>1</sup>-N-(2-phenyl-2-oxazoline)}zinc] (**11**)

As for **5**, ZnCl<sub>2</sub> (2.0 g, 15 mmol) in Et<sub>2</sub>O (125 mL) was treated with **3** (3.9 mL, 30 mmol), and the resulting white solid was washed with Et<sub>2</sub>O (2 × 15 mL) and then air-dried. Yield 4.77 g (74%). mp > 179 °C (decomp.). IR: 1618 (st). <sup>1</sup>H NMR δ: 7.78 (d, 2H, *J* = 7.5, ArH), 7.61 (t, 1H, ArH), 7.41 (t, 2H, *J* = 7.6, ArH), 4.33 (m, 4H, CH<sub>2</sub>CH<sub>2</sub>). Calcd. for C<sub>16</sub>H<sub>18</sub>N<sub>2</sub>O<sub>2</sub>Cl<sub>2</sub>Zn: C 50.20, H 4.21, N 6.51; found: C 50.47, H 4.26, N 6.68.

#### Synthesis of [dibromobis{η<sup>1</sup>-N-(2-phenyl-2-oxazoline)}zinc] (**12**)

As for **5**, ZnBr<sub>2</sub> (2.1 g, 9.3 mmol) in Et<sub>2</sub>O (100 mL) was treated with **3** (2.5 mL, 19 mmol), and the solid was washed with Et<sub>2</sub>O (2 × 15 mL) and then air-dried. Yield 4.71 g (48%). mp > 170 °C (decomp.). IR: 1620 (st). <sup>1</sup>H NMR δ: 7.76 (d, 2H, *J* = 8.0, ArH), 7.58 (t, 1H, ArH), 7.35 (t, 2H, *J* = 7.9, ArH), 4.47 (m, 4H, CH<sub>2</sub>CH<sub>2</sub>). Calcd. for C<sub>16</sub>H<sub>18</sub>N<sub>2</sub>O<sub>2</sub>ZnBr<sub>2</sub>: C 41.61, H 3.49, N 5.39; found: C 41.66, H 3.49, N 5.30.

#### Synthesis of [diiodobis{η<sup>1</sup>-N-(2-phenyl-2-oxazoline)}zinc] (**13**)

As for **5**, ZnI<sub>2</sub> (1.4 g, 4.4 mmol) was suspended in Et<sub>2</sub>O (25 mL), and the mixture was then treated with **3** (1.1 mL, 8.4 mmol), and the light yellow solid was washed with Et<sub>2</sub>O (2 × 10 mL) and then air-dried. Yield 2.55 g (99%). mp > 193 °C (decomp.). IR: 1620 (st). <sup>1</sup>H NMR δ: 7.76 (d, *J* = 7.9, 2H, ArH), 7.61 (t, 1H, ArH), 7.38 (t, 2H, *J* = 8.0, ArH), 4.43 (m, 4H, CH<sub>2</sub>CH<sub>2</sub>). Calcd. for C<sub>16</sub>H<sub>18</sub>N<sub>2</sub>O<sub>2</sub>ZnI<sub>2</sub> (%): C 35.24, H 2.96, N 4.57; found: C 34.90, H 2.97, N 4.43.

#### Synthesis of [dichlorobis{η<sup>1</sup>-N-(4,4-dimethyl-2-phenyl-2-oxazoline)}zinc] (**14**)

A sample of ZnCl<sub>2</sub> (2.25 g, 16.5 mmol) was dissolved in 100 mL of Et<sub>2</sub>O, and the solution was then filtered. Compound **4** (5.6 mL, 33 mmol) was added, and the mixture was then stirred at RT for 2 h. The resulting white solid was collected by filtration and washed with Et<sub>2</sub>O (2 × 25 mL). Yield 4.2 g (58%). mp > 174 °C (decomp.). IR: 1620 (st). <sup>1</sup>H NMR δ: 7.86 (m, 2H, ArH), 7.28 (m, 3H, ArH), 3.95 (s, 2H, CH<sub>2</sub>), 1.25 (s, 6H, CH<sub>3</sub>). Calcd. for C<sub>22</sub>H<sub>26</sub>N<sub>2</sub>O<sub>2</sub>Cl<sub>2</sub>Zn: C 54.29, H 5.38, N 5.76; found: a reproducible elemental analysis (±0.4%) could not be obtained for this material.

#### Synthesis of [dibromobis{η<sup>1</sup>-N-(4,4-dimethyl-2-phenyl-2-oxazoline)}zinc] (**15**)

As for **5**, ZnBr<sub>2</sub> (2.0 g, 8.9 mmol) in Et<sub>2</sub>O (100 mL) was treated with **4** (3.0 mL, 18 mmol), then stirred for 2 h, and



then evaporated at RT. Yield 2.0 g (65%). mp > 168 °C (decomp.). IR: 1618 (st).  $^1\text{H}$  NMR  $\delta$ : 7.86 (m, 2H, ArH), 7.28 (m, 3H, ArH), 3.95 (s, 2H,  $\text{CH}_2$ ), 1.25 (s, 6H,  $\text{CH}_3$ ). Calcd. for  $\text{C}_{22}\text{H}_{26}\text{N}_2\text{O}_2\text{ZnBr}_2$ : C 45.90, H 4.55, N 4.87; found: C 45.68, H 4.46, N 4.84.

### Single crystal X-ray structure determinations

#### X-ray structure of 7

Suitable white crystals were obtained by slow diffusion of  $\text{Et}_2\text{O}$  into a  $\text{CHCl}_3$  solution of the complex. Diffraction data were collected on a Nonius Kappa-CCD diffractometer equipped with a 95 mm CCD camera and a k-goniostat, using graphite-monochromated Cu K $\alpha$  radiation. Data were reduced to  $F_o^2$  values. A numerical absorption correction was applied using Gaussian integration (27), with max and min transmission factors of 0.024 and 0.009, respectively. The structure was solved by Patterson interpretation, using the program DIRDIF-96 (28). Isotropic and full matrix anisotropic least-squares refinements were carried out using SHELXL-97 (29). All non-H atoms were refined anisotropically, except N2, C5, and O2, which were isotropically refined. All the hydrogen atom positions were geometrically calculated and refined riding on their parent atoms. The molecular plots were made with the EUCLID program package (30). The WINGX program system (31) was used throughout the structure determinations.

#### X-ray structures of 10–13 and 15

Suitable crystals were grown from solutions of the complexes in dichloromethane that had been layered with  $\text{Et}_2\text{O}$  and allowed to stand at RT (or at  $-10$  °C) for several days. Crystals were mounted on a glass fibre, covered in epoxy, and data was collected on a Smart 1000 CCD diffractometer using Mo K $\alpha$  radiation (graphite monochromated). Isotropic and full matrix anisotropic least-squares refinements were carried out using SHELXL-97 (29). It should be noted that complex 15 has twofold imposed crystallographic symmetry.

### Acknowledgements

The authors are indebted to the support of the Natural Science and Engineering Research Council (NSERC) (RAG), Acadia University (RAG), and MCYT (BQU2002–02623: IdR). Mr. Ramsey E. Beveridge is thanked for recording some NMR spectra.

### References

- (a) S. Rahuel-Clermont and M.F. Dunn. The biological chemistry of zinc. In Copper and zinc in inflammatory and degenerative diseases. Edited by K.D. Rainsford, R. Milanino, J.R.J. Sorenson, and G.P. Velo. Kluwer Academic Publications, Boston. 1998. Chap 4, pp. 47–59; (b) J.F. Riordan. Med. Clin. N. Am. **60**, 661 (1976); (c) B.L. Vallee and D.S. Auld. Biochemistry, **29**, 5647 (1990); (d) C.L. Keen and M.E. Gershwin. Ann. Rev. Nutr. **10**, 415 (1990); (e) B.L. Vallee and D.S. Auld. Acc. Chem. Res. **26**, 543 (1993).
- F.A. Cotton and G. Wilkinson. Advanced inorganic chemistry. 4th ed. John Wiley & Sons, Toronto. 1980. Chap 19, pp. 589–616.
- C. Hu and U. Englert. CrystEngComm. **23**, 1 (2001).
- (a) W.L. Steffen and G.J. Palenik. Inorg. Chem. **16**, 1119 (1977); (b) W.L. Steffen and G.J. Palenik. Acta Cryst. **B32**, 298 (1976); (c) H. Lynton and M.C. Sears. Can. J. Chem. **49**, 3418 (1971); (d) S. İde, A. Ataç, and Ş. Yurdakul. J. Molecular Struct. **605**, 103 (2002).
- (a) B.K.S. Lundberg. Acta Cryst. **21**, 901 (1966); (b) N. Galván-Tejada, S. Bernès, S.E. Castillo-Blum, H. Nöth, R. Vicente, and N. Barba-Behrens. J. Inorg. Biochem. **91**, 339 (2002).
- C. Hu and U. Englert. Acta Cryst. **C57**, 1251 (2001).
- B. Hajjem, A. Kallel, I. Svoboda, and J. Sakurai. Acta Cryst. **C48**, 1002 (1992).
- Purine: (a) H.L. Laity and M.R. Taylor. Acta Cryst. **C51**, 1791 (1995); Quinoline: (b) Y. Cui, D. Long, W. Chen, and J. Huang. Acta Cryst. **C54**, 1605 (1998); Thiadiazole: (c) K.Sh. Khusenov, B.B. Umarov, M.M. Ishankhodzhaeva, N.A. Parpiev, S.A. Talipov, and B.T. Ibragimov. Koord. Khim. **23**, 596 (1997); Russ. J. Coord. Chem. **23**, 555 (1997); Antazoline: (d) M. Parvez and M. Rusiewicz. Acta Cryst. **C51**, 2277 (1995); Guanine: (e) F. Zamora and M. Sabat. Inorg. Chem. **41**, 4976 (2002).
- See, for example: P.J. Blower. Ann. Rep. Prog. Chem. Sect. A. **95**, 631 (1999); **96**, 645 (2000); **97**, 587 (2001); **98**, 615 (2002).
- (a) A. Monstrolorenzo, A. Scozzafava, and C.T. Supuran. Eur. J. Pharm. Sci. **11**, 99 (2000); (b) K.D. Rainsford and M.W. Whitehouse. J. Pharm. Pharmacol. **44**, 476 (1992); (c) A. Scozzafava, L. Menabuoni, F. Minicione, G. Minicione, and C.T. Supuran. Bioorg. Med. Chem. Lett. **11**, 575 (2001); (d) Tz.B. Kovachev, P.N. Stamberov, D.S. Ivanov, M.K. Mitcheva, S.P. Marinova, H.A. Astroug, and J.N. Stoychkov. Pharmazie, **49**, 25 (1994); (e) G. Abou-Mohamed, A. Papapetropoulos, J.D. Catavas, and R.W. Caldwell. Eur. J. Pharmacol. **341**, 265 (1998).
- J. García-Cañadas, J.M. Pérez, A.G. Quiroga, M.A. Fuertas, C. Alonso, and C. Navarro-Ranninger. J. Chem. Soc. Dalton Trans. 2283 (2002).
- (a) B.A. Katz, J.M. Clark, J.S. Finer-Moore, T.E. Jenkins, C.R. Johnson, M.J. Ross, C. Luong, W.R. Moore, and R.M. Stroud. Nature (London), **391**, 608 (1998); (b) A. Whitney, G. Gavory, and S. Balasubramanian. Chem. Commun. 36 (2003); (c) Y. Yoshikawa, E. Ueda, H. Sakurai, and Y. Kojima. Chem. Pharm. Bull. **51**, 230 (2003); (d) H. Sakurai, Y. Kojima, Y. Yoshima, K. Kawabe, and H. Yasui. Coord. Chem. Rev. **226**, 187 (2002); (e) C.H. Stammer, A.N. Wilson, C.F. Spencer, F.W. Bachelor, F.W. Holly, and K. Folkers. J. Am. Chem. Soc. **79**, 3236 (1957); (f) H.R. Onishi, B.A. Pelak, L.S. Gerckens, L.L. Silver, F.W. Kahan, M.-H. Chen, A.A. Patchett, S.M. Galloway, S.A. Hyland, M.S. Anderson, and C.R.H. Raetz. Nature (London), **274**, 980 (1996); (g) M.-H. Chen, M.G. Steiner, S.E. de Laszlo, A.A. Patchett, M.S. Anderson, S.A. Hyland, H.R. Onishi, L.L. Silver, and C.R.H. Raetz. Bioorg. Med. Chem. Lett. **9**, 313 (1999); (h) T. Kline, N.H. Anderson, E.A. Harwood, J. Bowman, A. Malada, S. Endsley, A.L. Erwin, M. Doyle, S. Fong, A.L. Harris, B. Mendelsohn, K. Mdluli, C.R.H. Raetz, C.K. Stover, P.R. White, A. Yabannavar, and S. Zhu. J. Med. Chem. **45**, 3112 (2002); (i) M.C. Rirung, N. Tumey, A.L. McClerren, and C.R.H. Raetz. J. Am. Chem. Soc. **125**, 1575 (2003).
- I. del Río, R.A. Gossage, M.S. Hannu, M. Lutz, A.L. Spek, and G. van Koten. Can. J. Chem. **78**, 1620 (2000).
- (a) K.M. Button and R.A. Gossage. J. Heterocyclic Chem. **40**, 513 (2003); (b) J.T. Banks, K.M. Button, R.A. Gossage, T.D. Hamilton, and K.E. Kershaw. Heterocycles, **55**, 2251 (2001);



- (c) K.M. Button, R.A. Gossage, and R.K.R. Phillips. *Synth. Commun.* **32**, 363 (2002); (d) K.M. Button, R.A. Gossage, and H. Jenkins. Poster P-207. International Conference on Organometallic Chemistry. 20th. Corfu, Greece. 2002.
15. M. Gómez, G. Muller, and M. Rocamora. *Coord. Chem. Rev.* **193–195**, 769 (1999), and refs. therein.
16. (a) H. Witte and W. Seeliger. *Liebigs Ann. Chem.* 999 (1974); (b) A.I. Meyers. *J. Heterocyclic Chem.* **35**, 991 (1998), and refs. therein.
17. (a) D.J. Darensbourg, S.J. Lewis, J.L. Rodgers, and J.C. Yarbrough. *Inorg. Chem.* **42**, 581 (2003); (b) E. Şahin, S. İde, A. Ataç, and Ş. Yurdakul. *J. Molecular Struct.* **616**, 253 (2002); (c) E. Şahin, S. İde, M. Kurt, and Ş. Yurdakul. *J. Molecular Struct.* **616**, 259 (2002).
18. (a) J. Ni, Y. Xie, X. Liu, and Q. Liu. *Appl. Organomet. Chem.* **17**, 315 (2003); (b) K. Davarski, J. Macicek, and L. Kononov. *J. Coord. Chem.* **38**, 123 (1996).
19. L.M. Richberg, J.A. Farouq, C.D. Incarvito, A.L. Rheingold, and D. Rabinovich. *Polyhedron*, **19**, 1815 (2000).
20. (a) E. Libertini, K. Yoon, and G. Parkin. *Polyhedron*, **12**, 2539 (1993); (b) J. Pickardt and P. Droas. *Acta Cryst.* **C45**, 360 (1989).
21. C. Bolm, K. Weickhardt, M. Zehnder, and T. Ranff. *Chem. Ber.* **124**, 1173 (1991).
22. J. Castro, S. Cabeliero, P. Perez-Lourido, J. Romero, J.A. García-Vásquez, and A. Sousa. *Z. Anorg. Allg. Chem.* **628**, 1210 (2002).
23. G.K. Patra, I. Goldberg, A. Sarkar, S. Chowdhury, and D. Datta. *Inorg. Chim. Acta*, **344**, 7 (2003).
24. H. Kooijman, A.L. Spek, C. Zondervan, and B.L. Feringa. *Acta Cryst.* **E58**, m429 (2002).
25. C. Pettinari, A. Cingolani, and B. Bovio. *Polyhedron*, **15**, 115 (1996).
26. M.A. Weinberger and R. Greenhalgh. *Can. J. Chem.* **41**, 1038 (1963).
27. P. Coppens. In *Crystallographic computing. Edited by F.R. Ahmed, S.R. Hall, and C.P. Huber.* Munksgaard, Copenhagen. 1970. pp. 255–270.
28. P.T. Beurskens, G. Beurskens, W.P. Bosman, R. de Gelder, S. García-Granda, R.O. Gould, R. Israël, and J.M.M. Smits. The DIRDIF-96 program system [computer program]. Crystallography Laboratory, University of Nijmegen, The Netherlands. 1996.
29. G.M. Sheldrick. SHELXL97 [computer program]. Version 97-2. University of Göttingen, Germany. 1997.
30. A.L. Spek. The EUCLID package. In *Computational crystallography. Edited by D. Sayre.* Clarendon Press, Oxford, U.K. 1982. p. 528.
31. L.J. Farrugia. *J. Appl. Crystallogr.* **32**, 837 (1999).



# Thermochemical behavior of dissolved carboxylic acid solutes: Solubilities of 3-methylbenzoic acid and 4-chlorobenzoic acid in organic solvents

Charlisa R. Daniels, Amanda K. Charlton, Rhiannon M. Wold, William E. Acree, Jr., and Michael H. Abraham

**Abstract:** The Abraham general solvation model is used to correlate the solubility behavior of 3-methylbenzoic acid and 4-chlorobenzoic acid in alcohol and ether solvents. The mathematical correlations take the form of

$$\log(C_S/C_W) = c + r \cdot R_2 + s \cdot \pi_2^H + a \cdot \Sigma \alpha_2^H + b \cdot \Sigma \beta_2^H + v \cdot V_x$$

$$\log(C_S/C_G) = c + r \cdot R_2 + s \cdot \pi_2^H + a \cdot \Sigma \alpha_2^H + b \cdot \Sigma \beta_2^H + l \cdot \log L^{(16)}$$

where  $C_S$  and  $C_W$  refer to the solute solubility in the organic solvent and water, respectively;  $C_G$  is a gas-phase concentration;  $R_2$  is the solute excess molar refraction;  $V_x$  is the McGowan volume of the solute;  $\Sigma \alpha_2^H$  and  $\Sigma \beta_2^H$  are measures of the solute hydrogen-bond acidity and hydrogen-bond basicity;  $\pi_2^H$  denotes the solute dipolarity–polarizability descriptor; and  $L^{(16)}$  is the solute gas-phase dimensionless Ostwald partition coefficient into hexadecane at 298 K. The remaining symbols in the above expressions are known solvent coefficients, which have been determined previously for a large number of gas–solvent and water–solvent systems. The Abraham general solvation model was found to describe the experimental solubility data and published literature partitioning data of 3-methylbenzoic acid and 4-chlorobenzoic acid to within overall standard deviations of 0.079 log units and 0.085 log units, respectively.

**Key words:** 3-methylbenzoic acid solubilities, 4-chlorobenzoic acid solubilities, alcohol solvents, partition coefficients, molecular solute descriptors, solubility predictions.

**Résumé :** On a utilisé le modèle de solvation générale d'Abraham pour établir une corrélation du comportement de solubilité de l'acide 3-méthylbenzoïque et de l'acide 4-chlorobenzoïque dans des alcools et des éthers comme solvants. Les corrélations mathématiques sont de la forme:

$$\log(C_S/C_W) = c + r \cdot R_2 + s \cdot \pi_2^H + a \cdot \Sigma \alpha_2^H + b \cdot \Sigma \beta_2^H + v \cdot V_x$$

$$\log(C_S/C_G) = c + r \cdot R_2 + s \cdot \pi_2^H + a \cdot \Sigma \alpha_2^H + b \cdot \Sigma \beta_2^H + l \cdot \log L^{(16)}$$

dans laquelle  $C_S$  et  $C_W$  se réfèrent respectivement à la solubilité du soluté dans le solvant et l'eau,  $C_G$  est une concentration dans la phase gazeuse,  $R_2$  est la réfraction molaire en excès du soluté,  $V_x$  est le volume de McGowan du soluté,  $\Sigma \alpha_2^H$  et  $\Sigma \beta_2^H$  sont des mesures de l'acidité et de la basicité de la liaison hydrogène du soluté,  $\pi_2^H$  est le descripteur de la dipolarité–polarisabilité du soluté et  $L^{(16)}$  est le coefficient de partage sans dimension d'Oswald du soluté en phase gazeuse dans l'hexadécane, à 298 K. Les autres symboles de ces expressions sont des coefficients connus des solvants qui ont été déterminés antérieurement pour un grand nombre de systèmes gaz–solvant et eau–solvant. On a trouvé que le modèle de solvation générale d'Abraham permet de décrire les données expérimentales de solubilité et les données publiées dans la littérature pour les coefficients de partage de l'acide 3-méthylbenzoïque et l'acide 4-chlorobenzoïque avec des déviations globales standard respectivement de 0,079 et 0,085 unités de logarithme.

**Mots clés :** solubilités, acide 3-méthylbenzoïque, acide 4-chlorobenzoïque, solvants alcooliques, coefficients de partage, descripteurs moléculaires du soluté, prévisions de solubilités.

[Traduit par la Rédaction]

Received 19 August 2003. Published on the NRC Research Press Web site at <http://canjchem.nrc.ca> on 4 November 2003.

**C.R. Daniels, A.K. Charlton, R.M. Wold, and W.E. Acree, Jr.**<sup>1</sup> Department of Chemistry, P.O. Box 305070, University of North Texas, Denton, TX 76203-5070, U.S.A.  
**M.H. Abraham.** Department of Chemistry, University College London, 20 Gordon Street, London WC1H 0AJ, U.K.

<sup>1</sup>Corresponding author (e-mail: [acree@unt.edu](mailto:acree@unt.edu)).

## Introduction

Researchers have recognized for years the importance of liquid–liquid equilibria. Chemical engineers design separation and purification processes based upon partition coefficient data. Solute partitioning between two immiscible phases is the basis of all chromatographic separations. Biologists correlate partition and bioaccumulation data to better understand the fate of organic pollutants in the environment. Civil engineers need partition and adsorption coefficient data



to design water treatment facilities to remove organic compounds from drinking water. Partition coefficients are required as input values in pharmacokinetic and toxicokinetic models that mathematically predict the adsorption, excretion, and metabolism of drug molecules in the body. The latter models involve tissue–air and tissue–blood partitioning; however, studies have shown that biological partitioning processes can sometimes be mimicked by select organic solvents like hexane, oleyl alcohol, and 1-octanol.

Historically, many of the very early studies focussed exclusively on developing correlational equations based upon octanol–water partition coefficients, which are readily available for most organic compounds (1). As additional experimental data became available, researchers expanded their studies to include more organic solvents, as well as aqueous micellar solvent media. In this regard, Abraham and co-workers (2–9) developed expressions for describing the partition of solutes between water and an organic solvent and between the gas phase and a given solvent. The Abraham general solvation model is based upon two particular linear, free-energy relationships for describing the partition of solutes between water and a given solvent (2–9)

$$[1] \quad \log P = c + r \cdot R_2 + s \cdot \pi_2^H + a \cdot \Sigma \alpha_2^H + b \cdot \Sigma \beta_2^H + v \cdot V_x$$

and between the gas phase and a given solvent

$$[2] \quad \log L = c + r \cdot R_2 + s \cdot \pi_2^H + a \cdot \Sigma \alpha_2^H + b \cdot \Sigma \beta_2^H + l \cdot \log L^{(16)}$$

The dependent variables in eqs. [1] and [2] are  $\log P$  (the partition coefficient of solute(s) between water and a given solvent) and  $\log L$  (Ostwald solubility coefficient). The independent variables are the solute descriptors, as follows:  $R_2$  and  $V_x$  refer to the excess molar refraction and McGowan volume of the solute, respectively;  $\Sigma \alpha_2^H$  and  $\Sigma \beta_2^H$  are measures of the solute hydrogen-bond acidity and hydrogen-bond basicity;  $\pi_2^H$  denotes the solute dipolarity–polarizability descriptor; and  $L^{(16)}$  is the solute gas-phase dimensionless Ostwald partition coefficient into hexadecane at 298 K. The Ostwald partition coefficient,  $L$ , is the inverse of the Henry's law constant. It should be noted that the various  $c$ ,  $r$ ,  $s$ ,  $a$ ,  $b$ ,  $v$ , and  $l$  coefficients depend on the solvent phase under consideration. The tendency of the phase to interact with solutes through polarizability-type interactions, mostly via electron pairs, is given by the  $r$ -coefficient. The  $s$ -coefficient is a measure of the solvent phase dipolarity and (or) polarity, while the  $a$ - and  $b$ -coefficients represent the solvent phase hydrogen-bond basicity and hydrogen-bond acidity, respectively. The  $l$ - and  $v$ -coefficients are a combination of the work needed to create a solvent cavity wherein the solute will reside and the general dispersion interaction energy between the solute and solvent phase. In the case of partition coefficients, where two solvent phases are involved, the  $c$ ,  $r$ ,  $s$ ,  $a$ ,  $b$ ,  $v$ , and  $l$  coefficients represent differences in the solvent phase properties.

To date, mathematical expressions have been deduced for approximately 40 or so dry solvents. The derived mathematical expressions allow one to predict the partitioning and solubility behavior of organic and organometallic solutes, provided that one knows the numerical values of the various

solute descriptors. Development of a single correlation equation requires experimental data for at least 40 or so different solutes. It is important that the data set contain solutes that span as wide a range of solute descriptors as possible in order to derive meaningful correlations. Partition coefficients of volatile solutes can be measured directly as the solute gas–liquid chromatographic retention volumes on the given organic solvent stationary phase, or they can be calculated from infinite dilution activity coefficients. This latter information is available in the published literature in the form of binary liquid–vapor equilibria data. Solubility measurements provide a very convenient means for including nonvolatile solutes in the regression analysis. Here, the partition coefficient is calculated as the ratio of the solute molar solubility in the organic solvent under consideration and water (or saturated vapor concentration in the case of the gas–liquid partition).

Presently, we are in the process of developing and (or) updating correlation equations for additional and (or) existing solvent systems (8–11) and in the process of developing new computational methodologies for calculating solute descriptors from available experimental data and (or) structural information (12–17). Solubility measurements have been used in the determination of molecular descriptors of the two equilibrium tautomeric forms (azo(phenolic) and quinone(hydrazone)) of Sudan I (18). Several of our preliminary unpublished correlation equations were derived from very limited experimental databases. As new experimental data becomes available, existing correlation equations have been periodically updated and existing values of the molecular solute descriptors have been refined by combining “practical” partitioning and saturation solubility data. Such analysis allows us to assess the internal consistency of large experimental databases and to identify possible outlier data points in need of remeasurement. For example, outlier data points would be identified by large differences between experimental and calculated values.

Of particular interest are the carboxylic acid solutes that possess large numerical values for their hydrogen-bonding acidity descriptors. The existing values that we have for the molecular descriptors of many of the carboxylic acid solutes were derived almost entirely from “practical” partitioning data. For some solutes, there was only very limited experimental partitioning data, and one or two incorrect data points could lead to the calculation of incorrect values for the molecular descriptors, as was the case in a recently completed solubility study involving acetylsalicylic acid.<sup>2</sup> We need to determine if the values that were previously calculated for several solute molecules that we plan to use in developing additional solvent and (or) process equations are compatible with existing correlation equations for dry organic solvents. Moreover, we want to examine whether or not our existing correlation equations for dry alcohol and dry ether solvents correlate with the solubility behavior of the less soluble carboxylic acid solutes. The databases used in deriving the correlations for many of the dry alcohol and dry ether solvents contained very few carboxylic acid solutes. Most of the experimental data for carboxylic acid and other very acidic solutes were in the form of saturation solubili-

<sup>2</sup>A.K. Charlton, C.R. Daniels, W.E. Acree, Jr., and M.H. Abraham. Unpublished data.



ties, which were in the 1–3 mol L<sup>-1</sup> range. There is no guarantee that the correlation equations will work for carboxylic acid solutes that have much smaller solubilities. For this reason, solubilities of 3-methylbenzoic acid and 4-chlorobenzoic acid were measured in numerous organic solvents of varying polarity and hydrogen-bonding characteristics. Both carboxylic acids are expected to exist almost exclusively in monomeric form in each of the solvents studied. Results of these measurements are interpreted using the Abraham general solvation equation.

## Materials and methods

3-Methylbenzoic acid (Aldrich, 99%) and 4-chlorobenzoic acid (Acros, 99%) were purchased from commercial suppliers and were used as received. The purity of both carboxylic acids was 99.8% ( $\pm 0.3\%$ ), as determined by nonaqueous titration with freshly standardized sodium methoxide solution to the thymol blue endpoint, according to the method of Fritz and Lisicki (19), with the exception that toluene was substituted for benzene. 1-Propanol (Aldrich, 99+%, anhydrous), methanol (Aldrich, 99.8%, anhydrous), ethanol (Aaper Alcohol and Chemical Company, absolute), 1-butanol (Aldrich, HPLC, 99.8+%), 1-pentanol (Aldrich, 99+%), 1-hexanol (Alfa Aesar, 99+%), 1-heptanol (Alfa Aesar, 99+%), 1-octanol (Aldrich, 99+%, anhydrous), 2-propanol (Aldrich, 99+%, anhydrous), 2-butanol (Aldrich, 99+%, anhydrous), 2-methyl-1-propanol (Aldrich, 99+%, anhydrous), 2-methyl-1-butanol (Aldrich, 99%), 3-methyl-1-butanol (Aldrich, 99%, anhydrous), 1-decanol (Alfa Aesar, 99+%), 2-methyl-2-propanol (Arco Chemical Company, 99+%), 2-methyl-1-pentanol (Aldrich, 99%), 2-pentanol (Acros, 99+%), 4-methyl-2-pentanol (Acros, 99+%), methyl acetate (Aldrich, 99.5%, anhydrous), ethyl acetate (Aldrich, HPLC, 99.9%), butyl acetate (Aldrich, HPLC, 99.7%), diethyl ether (Aldrich, 99+%, anhydrous), diisopropyl ether (Aldrich, 99%, anhydrous), dibutyl ether (Aldrich, 99.3%, anhydrous), tetrahydrofuran (Aldrich, 99.9%, anhydrous), 1,4-dioxane (Aldrich, 99.8%, anhydrous), and propylene carbonate (Aldrich, 99.7%, anhydrous) were stored over molecular sieves and distilled shortly before use. Gas chromatographic analysis showed solvent purities to be 99.7 mol % or better.

Excess solute and solvent were placed in amber glass bottles and allowed to equilibrate in a constant temperature water bath at  $25.0 \pm 0.1$  °C for at least 24 h (often longer) with periodic agitation. After equilibration, the samples stood unagitated for several hours in the constant temperature bath to allow any finely dispersed solid particles to settle. Attainment of equilibrium was verified both by repetitive measurements the following day (or sometimes after two days) and by approaching equilibrium from supersaturation by pre-equilibrating the solutions at a slightly higher temperature. Aliquots of saturated carboxylic acid solutions were transferred through a coarse filter into a tared volumetric flask, to determine the amount of sample, and diluted quantitatively with methanol for spectrophotometric analysis at 279 nm (3-methylbenzoic acid) and 272 nm (4-chlorobenzoic acid) on a Bausch and Lomb Spectronic 2000. Concentrations of the dilute solutions were determined from a Beer–Lambert law absorbance vs. concentration working curve.

**Table 1.** Experimental 3-methylbenzoic acid mole fraction solubilities,  $X_S$ , in select organic solvents at 25 °C.

Organic solvent	$X_S$
Methanol	0.1430
Ethanol	0.1617
1-Propanol	0.1618
1-Butanol	0.1595
1-Pentanol	0.1773
1-Hexanol	0.1828
1-Heptanol	0.1910
1-Octanol	0.1985
1-Decanol	0.1630
2-Propanol	0.1653
2-Butanol	0.1895
2-Methyl-1-propanol	0.1345
2-Methyl-2-propanol	0.2267
2-Methyl-1-butanol	0.1470
3-Methyl-1-butanol	0.1632
2-Pentanol	0.1965
2-Methyl-1-pentanol	0.1668
4-Methyl-2-pentanol	0.2133
Diethyl ether	0.1889
Tetrahydrofuran	0.3329
1,4-Dioxane	0.1860
Methyl acetate	0.1364
Ethyl acetate	0.1391
Butyl acetate	0.1263
Propylene carbonate	0.03892

Experimental molar concentrations were converted to solubility mass fractions via multiplying by the molar mass of carboxylic acid, the volume(s) of volumetric flask(s) used, and any dilutions required to place the measured absorbances on the Beer–Lambert law absorbance vs. concentration working curve and then dividing by the mass of the saturated solution analyzed. Mole fraction solubilities were computed from solubility mass fractions using the molar masses of the solute and solvent. Experimental 3-methylbenzoic acid and 4-chlorobenzoic solubilities,  $X_S$ , for the different organic solvents studied, are listed in Tables 1 and 2, respectively. Numerical values represent the average of between four and eight independent determinations. Reproducibility ranged from  $\pm 1.5\%$  for solvents having the lower mole fraction solubilities to  $\pm 2.0\%$  for solvents having the larger 3-methylbenzoic acid solubilities, where an extra dilution was necessary to keep the measured absorbances within the Beer–Lambert law region.

## Computational methodology

Equation [1] actually predicts partition coefficients, and for select solvents, both “dry” and “wet” equation coefficients have been reported. For solvents that are partially miscible with water, such as 1-butanol and ethyl acetate, partition coefficients calculated as the ratio of the molar solute solubilities in the organic solvent and water are not the same as those obtained from direct partition between water (saturated with the organic solvent) and organic solvent (saturated with water). Care must be taken not to confuse the



**Table 2.** Experimental 4-chlorobenzoic acid mole fraction solubilities,  $X_S$ , in select organic solvents at 25 °C.

Organic solvent	$X_S$
Methanol	0.00823
Ethanol	0.01013
1-Propanol	0.01188
1-Butanol	0.01350
1-Pentanol	0.01517
1-Hexanol	0.01646
1-Heptanol	0.01777
1-Octanol	0.01885
1-Decanol	0.01956
2-Propanol	0.01274
2-Butanol	0.01480
2-Methyl-1-propanol	0.009578
2-Methyl-2-propanol	0.02021
2-Methyl-1-butanol	0.01133
3-Methyl-1-butanol	0.01323
2-Pentanol	0.01655
Methyl acetate	0.008963
Ethyl acetate	0.01111
Butyl acetate	0.00926
Diisopropyl ether	0.006780
Dibutyl ether	0.005833
Tetrahydrofuran	0.05874
1,4-Dioxane	0.02974
Propylene carbonate	0.003247

two sets of partitions. In the case of solvents that are fully miscible with water, such as methanol, no confusion is possible. Only one set of equation coefficients have been reported, and the calculated  $\log P$  value must refer to the hypothetical partition between the two pure solvents. And for solvents that are “almost” completely immiscible with water — such as alkanes, cyclohexane, dichloromethane, trichloromethane, tetrachloromethane, and most aromatic solvents — there should be no confusion because indirect partition (see eq. [3]) will be nearly identical to direct partition.

The predictive applicability of the Abraham general solvation model is relatively straightforward. We start with the set of equations that we have constructed for the partition of solutes between water and a given solvent. Table 3 gives the coefficients in eq. [1] for the water–solvent partitions we shall consider. The actual numerical values may differ slightly from values reported in earlier publications. Coefficients are periodically revised when additional experimental data becomes available. Note that many of these are “hypothetical partitions” between pure water and the pure dry solvent; these are shown as “dry” in Table 1. Although “hypothetical”, these partitions are very useful; as we show later, they can be used to predict solubilities (and activity coefficients) in the pure dry solvent. The partition coefficient of a solid between water and a solvent phase is related to the molar solubility of the solid in water,  $C_W$ , and in the solvent,  $C_S$ .

$$[3] \quad P = C_S/C_W \quad \text{or} \quad \log P = \log C_S - \log C_W$$

Hence, if  $C_W$  is known, predicted  $\log P$  values based upon eq. [1] will lead to predicted molar solubilities through eq. [3]. Three specific conditions must be met to use the Abraham solvation model to predict saturation solubilities. First, the same solid phase must be in equilibrium with the saturation solutions in the organic solvent and in water (i.e., there should be no solvate or hydrate formation). Second, the secondary medium activity coefficient of the solid in the saturated solutions must be unity (or near unity). This condition generally restricts the method to those solutes that are sparingly soluble in water and to nonaqueous solvents; however, we are finding that this restriction may not be as important as initially believed. Equations [1] and [2] have shown remarkable success in the correlation of the solubility of several very soluble crystalline solutes like benzil (16) and acetylsalicylic acid.<sup>2</sup> Finally, for solutes that are ionized in aqueous solution,  $C_W$  refers to the solubility of the neutral form. For many carboxylic acids the correction should be fairly small, provided that the solute is not highly insoluble and does not have a large acid dissociation constant. We use the solubility of 3-methylbenzoic acid in water,  $\log C_W = -2.14$  (20, 21), and of 4-chlorobenzoic acid,  $\log C = -3.56$  (20–24) (corrected for ionization), to convert the predicted partition coefficients to saturation solubilities, which can then be compared with the experimentally determined values. Ionization is not a concern in the organic solvents that have dielectric constants much smaller than water.

For partition of solutes between the gas phase and solvents, eq. [2] is used. (Equation coefficients are given in Table 3 for several organic solvents.) Predicted  $\log L$  values can also be converted to saturation molar solubilities, provided that the solid saturated vapor pressure at 298.15 K,  $VP^\circ$ , is available.  $VP^\circ$  can be transformed into the gas-phase concentration,  $C_G$ , and the gas–water and gas–solvent partitions,  $L_W$  and  $L_S$ , can be obtained through eqs. [4] and [5], respectively.

$$[4] \quad L_W = C_W/C_G \quad \text{or} \quad \log L_W = \log C_W - \log C_G$$

$$[5] \quad L_S = C_S/C_G \quad \text{or} \quad \log L_S = \log C_S - \log C_G$$

As before, the computational method will be valid if conditions discussed above are met. If one is unable to find an experimental vapor pressure for the given solute molecule, an estimated value can be used in the preliminary computations. The value can be adjusted then, if necessary, to reduce the  $\log L$  deviations and to make the  $\log P$  and  $\log L$  predictions internally consistent.

## Results and discussion

Solubility data for 3-methylbenzoic acid and 4-chlorobenzoic acid is available in the chemical literature for only one of the solvents listed in Tables 1 and 2. Thuair (25) investigated the solubility behavior of 19 substituted benzoic acid derivatives in binary aqueous–ethanol solvent mixtures. Our experimental mole fraction solubility of  $X_S = 0.1617$  for 3-methylbenzoic acid differs from the published value of Thuair,  $X_S = 0.1620$ , by less than 1%. Agreement is not quite as good in the case of 4-chlorobenzoic acid. Our experimental value of  $X = 0.01013$  is smaller than the published literature value of  $X = 0.01229$  (25). Both literature values were determined by transferring a weighed aliquot



**Table 3.** Coefficients in eqs. [1] and [2] for various processes.

Process and (or) solvent	<i>c</i>	<i>r</i>	<i>s</i>	<i>a</i>	<i>b</i>	<i>v/l</i>
<b>A. Water to solvent: eq. [1]</b>						
1-Octanol (wet)	0.088	0.562	-1.054	0.034	-3.460	3.814
Diethyl ether (wet)	0.248	0.561	-1.016	-0.226	-4.553	4.075
Diethyl ether (dry)	0.330	0.401	-0.814	-0.457	-4.959	4.320
1,4-Dioxane (dry)	0.098	0.350	-0.083	-0.556	-4.826	4.172
Tetrahydrofuran (dry)	0.207	0.372	-0.392	-0.236	-4.934	4.447
Methanol (dry)	0.329	0.299	-0.671	0.080	-3.389	3.512
Ethanol (dry)	0.208	0.409	-0.959	0.186	-3.645	3.928
1-Propanol (dry)	0.147	0.494	-1.195	0.495	-3.907	4.048
2-Propanol (dry)	0.063	0.320	-1.024	0.445	-3.824	4.067
1-Butanol (dry)	0.152	0.437	-1.175	0.098	-3.914	4.119
1-Pentanol (dry)	0.080	0.521	-1.294	0.208	-3.908	4.208
1-Hexanol (dry)	0.044	0.470	-1.153	0.083	-4.057	4.249
1-Heptanol (dry)	-0.026	0.491	-1.258	0.035	-4.155	4.415
1-Octanol (dry)	-0.034	0.490	-1.048	-0.028	-4.229	4.219
1-Decanol (dry)	-0.062	0.754	-1.461	0.063	-4.053	4.293
2-Butanol (dry)	0.106	0.272	-0.988	0.196	-3.805	4.110
2-Methyl-1-propanol (dry)	0.177	0.355	-1.099	0.069	-3.570	3.990
2-Methyl-2-propanol (dry)	0.197	0.136	-0.916	0.318	-4.031	4.113
Ethyl acetate (dry)	0.358	0.362	-0.449	-0.668	-5.016	4.155
Chloroform	0.327	0.157	-0.391	-3.191	-3.437	4.191
Carbon tetrachloride	0.260	0.573	-1.254	-3.558	-4.588	4.589
Benzene	0.142	0.464	-0.588	-3.099	-4.625	4.491
Toluene	0.143	0.527	-0.720	-3.010	-4.824	4.545
Heptane	0.325	0.670	-2.061	-3.317	-4.733	4.543
Cyclohexane	0.159	0.784	-1.678	-3.740	-4.929	4.577
SDS micelles	1.201	0.542	-0.400	-0.133	-1.580	2.793
HPLC BK-20/10 ( $t'_R/10$ )	1.184	0.027	-0.148	-0.556	-0.839	1.098
HPLC BK-40/10 ( $t'_R/10$ )	1.284	0.023	-0.381	-1.030	-1.734	2.417
HPLC KHN (k)	-0.309	0.245	-1.231	-0.550	-4.576	6.174
HPLC-KH70-2 (k)	0.096	0.167	-0.375	-0.318	-0.944	0.938
HPLC-ANNA (k)	-0.010	0.709	-0.934	-0.119	-3.401	3.784
HPLC-MKMA-N (k)	-1.216	0.495	-0.438	0.025	-2.757	2.671
HPLC-MKMB-N (k)	-1.082	0.574	-0.500	-0.009	-2.591	2.240
HPLC-MKMC (k)	-1.249	0.310	-0.499	-0.051	-1.643	1.643
HPLC-HAF-60 (k)	-0.789	0.095	-0.487	-0.337	-1.994	2.181
HPLC-HAF-75 (k)	-0.993	0.041	-0.397	-0.364	-1.629	1.757
HPLC-HAP-90 (k)	-1.176	0.079	-0.417	-0.306	-1.140	1.290
MEEKC (k)	-1.090	0.410	-0.530	-0.080	-2.280	2.440
(Gas to water)	-0.994	0.577	2.549	3.813	4.841	-0.869
<b>B. Gas to solvent: eq. [2]</b>						
1-Octanol (wet)	-0.198	0.002	0.709	3.519	1.429	0.858
Diethyl ether (wet)	0.206	-0.169	0.873	3.402	0.000	0.882
Diethyl ether (dry)	0.288	-0.347	0.775	2.985	0.000	0.973
Tetrahydrofuran (dry)	0.189	-0.347	1.238	3.289	0.000	0.982
1,4-Dioxane (dry)	-0.034	-0.354	1.674	3.021	0.000	0.919
Methanol (dry)	-0.004	-0.215	1.173	3.701	1.432	0.769
Ethanol (dry)	0.012	-0.206	0.789	3.635	1.311	0.853
1-Propanol (dry)	-0.028	-0.185	0.648	4.022	1.043	0.869
2-Propanol (dry)	-0.060	-0.335	0.702	4.017	1.040	0.893
1-Butanol (dry)	-0.039	-0.276	0.539	3.781	0.995	0.934
1-Pentanol (dry)	-0.042	-0.277	0.526	3.779	0.983	0.932
1-Hexanol (dry)	-0.035	-0.298	0.626	3.726	0.729	0.936
1-Heptanol (dry)	-0.062	-0.168	0.429	3.541	1.181	0.927
1-Octanol (dry)	-0.119	-0.203	0.560	3.576	0.702	0.940
1-Decanol (dry)	-0.136	-0.038	0.325	3.674	0.767	0.947



**Table 3** (concluded).

Process and (or) solvent	<i>c</i>	<i>r</i>	<i>s</i>	<i>a</i>	<i>b</i>	<i>v/l</i>
2-Butanol (dry)	-0.013	-0.456	0.780	3.753	1.064	0.906
2-Methyl-1-propanol (dry)	-0.012	-0.407	0.670	3.645	1.283	0.895
2-Methyl-2-propanol (dry)	0.071	-0.538	0.818	3.951	0.823	0.905
Ethyl acetate (dry)	0.203	-0.335	1.251	2.949	0.000	0.917
Chloroform	0.116	-0.467	1.203	0.138	1.432	0.994
Carbon tetrachloride	0.282	-0.303	0.460	0.000	0.000	1.047
Benzene	0.107	-0.313	1.053	0.457	0.169	1.020
Toluene	0.121	-0.222	0.938	0.467	0.099	1.012
Heptane	0.275	-0.162	0.000	0.000	0.000	0.983
Cyclohexane	0.163	-0.110	0.000	0.000	0.000	1.013
(Gas to water)	-1.271	0.822	2.743	3.904	4.814	-0.213

**Note:** The solvents denoted as “dry” are those for which partitions refer to transfer to the pure dry solvent. The other partitions are from water (more correctly, water saturated with solvent) to the solvent saturated with water (see text). For the HPLC processes, the specific mobile and stationary phases are described in detail in refs. 28–32. As an example, for HPLC-HAF-60 and HPLC-HAF-75, the stationary phase was 5  $\mu$ m Hypersil ODS and the mobile phases were aqueous–methanol mixtures having 60 and 75 volume % methanol, respectively.

into a tared container and allowing the solvent to evaporate at room temperature. The solubility was then determined from the mass of the residue that remained. This particular method, though often used, is subject to experimental errors, particularly in the case of solutes of low solubilities. Care must be taken to thoroughly remove all of the liquid solvent. Nonvolatile impurities in either the solvent and (or) solute add to the mass of the residue, which would result in a positive experimental error. For solutes having small solubilities, the residue from the dissolved solute is very small. Trace impurities in the solute and (or) solvent generally affect spectroscopic solubility determinations only if the impurity has an appreciable absorbance at the analysis wavelength.

From previous computations, numerical values exist for the molecular descriptors of 3-methylbenzoic acid ( $R_2 = 0.730$ ,  $\pi_2^H = 0.874$ ,  $\Sigma\alpha_2^H = 0.600$ ,  $\Sigma\beta_2^H = 0.401$ , and  $V_x = 1.0726$ ) and 4-chlorobenzoic acid ( $R_2 = 0.840$ ,  $\pi_2^H = 0.970$ ,  $\Sigma\alpha_2^H = 0.630$ ,  $\Sigma\beta_2^H = 0.280$ ,  $V_x = 1.0541$ , and  $\log L^{(16)} = 4.976$ ). The computations were based upon a very limited number of “practical” partition coefficient data points. Our molecular descriptor database does not contain a numerical value of  $\log L^{(16)}$ , as 3-methylbenzoic acid has not been used previously to develop any  $\log L$  correlation. For most noncarboxylic acid solutes, this descriptor can be estimated from chromatographic measurements of the gas–liquid partition coefficient of the solute on a hexadecane stationary phase. The experimental method is not applicable to carboxylic acid solutes, in that measured retention times are generally quite large at the 298.15 K column temperature. The value of  $\log L^{(16)}$  can be obtained through calculation, by setting the values of  $R_2$ ,  $\pi_2^H$ ,  $\Sigma\alpha_2^H$ ,  $\Sigma\beta_2^H$ , and  $V_x$  at their current numerical values and then using the Microsoft Solver program to calculate the numerical value of  $\log L^{(16)}$  that best describes the experimental  $\log L$  data. The computational procedure using Microsoft Solver is discussed in detail elsewhere (17).

Given the large number of additional solubilities in Tables 1 and 2, we decided to reanalyze all of the available experimental data to determine if a better set of descriptor values could be obtained. Gathered in Tables 4 and 5 are the available “practical” partition coefficient (1, 26, 27), saturation solubility, and high-performance liquid chromatographic retention (28–32) data for systems for which  $\log P$  and  $\log L$

correlations exist. We eliminated from consideration a few practical partition coefficients for 3-methylbenzoic acid that involved alkane and other highly nonpolar organic solvents (33, 34). Carboxylic acids are known to exist largely in dimeric form in such solvents. While the published experimental values presumably had been corrected to remove dimerization effects, the calculated  $\log P$  values for the monomeric solute depends to a large extent on the numerical value taken for the dimerization constant. We did not want to adversely affect the regression analysis by including experimental values that might be subject to large errors and (or) uncertainties.

Measured mole fraction solubilities,  $X_S$ , were converted to molar solubilities by dividing  $X_S$  by the ideal molar volume of the saturated solution (i.e.,  $C_S \approx X_S / [X_S V_{\text{Solute}} + (1 - X_S) V_{\text{Solvent}}]$ ). The molar volume of the hypothetical subcooled liquid 4-chlorobenzoic acid,  $V = 117.08 \text{ cm}^3 \text{ mol}^{-1}$ , was estimated as the molar volume of benzoic acid ( $V_{\text{Solute}} = 104.38 \text{ cm}^3 \text{ mol}^{-1}$ ) + molar volume of chlorobenzene ( $V_{\text{Solute}} = 102.1 \text{ cm}^3 \text{ mol}^{-1}$ ) – molar volume of benzene ( $V_{\text{Solute}} = 89.40 \text{ cm}^3 \text{ mol}^{-1}$ ). A value of  $V_{\text{Solute}} = 121.8 \text{ cm}^3 \text{ mol}^{-1}$  was used for the molar volume of 3-methylbenzoic acid (35). Any errors resulting from the estimation of the hypothetical subcooled liquid molar volume of 4-chlorobenzoic acid,  $V_{\text{Solute}}$ , or from the ideal molar volume approximation should have only a very small effect on the calculated  $C_S$  values. 3-Methylbenzoic acid and 4-chlorobenzoic acid are not overly soluble in many of the solvents considered, and the  $X_S V_{\text{Solute}}$  term contributes very little to the molar volume of the saturation solution.

Included in the 3-methylbenzoic acid regressional analysis is the experimental aqueous solubility measurement. The published amended correlation of Abraham and Le (20)

$$\begin{aligned}
 [6] \quad (\log C_W)/5 = & 0.104 - 0.201R_2 + 0.154\pi_2^H \\
 & + 0.434\Sigma\alpha_2^H + 0.848\Sigma\beta_2^H - 0.672\Sigma\alpha_2^H \cdot \Sigma\beta_2^H \\
 & - 0.797V_x
 \end{aligned}$$

and its updated version (unpublished)



**Table 4.** Comparison between observed and back-calculated partitions and molar solubilities of 3-methylbenzoic acid based upon eqs. [1] and [2] and recalculated molecular solute descriptors.<sup>a</sup>

Solvent	$\log C_S$	$\log P^{\text{exptl}}$	Equation [1]		$\log L^{\text{exptl}}$	Equation [2]	
			$\log P^{\text{calcd}}$	$\log C_S^{\text{calcd}}$		$\log L^{\text{calcd}}$	$\log C_S^{\text{calcd}}$
1-Octanol (wet)		2.370 <sup>b</sup>	2.287		7.350	7.252	
1,2-Dichloroethane		1.330 <sup>b</sup>	1.372		6.310	6.374	
Diethyl ether (dry)	0.242	2.382	2.271	0.131	7.362	7.204	0.084
Tetrahydrofuran (dry)	0.545	2.685	2.784	0.644	7.665	7.743	0.623
1,4-Dioxane (dry)	0.303	2.443	2.491	0.351	7.423	7.438	0.318
Methanol (dry)	0.437	2.577	2.409	0.269	7.557	7.382	0.262
Ethanol (dry)	0.371	2.511	2.520	0.380	7.491	7.380	0.260
1-Propanol (dry)	0.292	2.432	2.494	0.354	7.412	7.432	0.312
2-Propanol (dry)	0.292	2.432	2.485	0.345	7.412	7.450	0.330
1-Butanol (dry)	0.217	2.357	2.335	0.195	7.337	7.409	0.289
1-Pentanol (dry)	0.204	2.344	2.384	0.244	7.324	7.376	0.256
1-Hexanol (dry)	0.166	2.306	2.345	0.205	7.286	7.342	0.222
1-Heptanol (dry)	0.141	2.281	2.307	0.167	7.261	7.261	0.141
1-Octanol (dry)	0.119	2.258	2.208	0.068	7.238	7.181	0.061
1-Decanol (dry)	-0.044	2.096	2.209	0.069	7.076	7.200	0.080
2-Butanol (dry)	0.288	2.428	2.429	0.289	7.408	7.391	0.271
2-Methyl-1-propanol (dry)	0.145	2.285	2.337	0.197	7.265	7.324	0.204
2-Methyl-2-propanol (dry)	0.353	2.493	2.470	0.330	7.473	7.467	0.347
Ethyl acetate	0.136	2.278	2.272	0.132	7.256	7.260	0.140
SDS micelles		3.660 <sup>c</sup>	3.525				
HPLC-KHN (k)		3.310 <sup>d</sup>	3.236				
Gas-to-water		4.980	4.988		4.980	5.012	

<sup>a</sup>Numerical values of the descriptors used in these calculations are  $R_2 = 0.730$ ,  $\pi_2^H = 0.890$ ,  $\Sigma\alpha_2^H = 0.600$ ,  $\Sigma\beta_2^H = 0.400$ ,  $V_x = 1.0726$ , and  $\log L^{(16)} = 4.8187$ .

<sup>b</sup>Experimental data taken from ref. 26.

<sup>c</sup>Experimental data taken from ref. 27.

<sup>d</sup>Experimental data taken from ref. 28.

**Table 5.** Comparison between observed and back-calculated partitions and molar solubilities of 4-chlorobenzoic acid based upon eqs. [1] and [2] and recalculated molecular solute descriptors.<sup>a</sup>

Solvent	$\log C_S$	$\log P^{\text{exptl}}$	Equation [1]		$\log L^{\text{exptl}}$	Equation [2]	
			$\log P^{\text{calcd}}$	$\log C_S^{\text{calcd}}$		$\log L^{\text{calcd}}$	$\log C_S^{\text{calcd}}$
1-Octanol (wet)		2.650 <sup>b</sup>	2.593		7.450	7.375	
Trichloromethane		1.720 <sup>b</sup>	1.539		6.420	6.342	
Carbon tetrachloride		0.880 <sup>b</sup>	0.819		5.680	5.677	
Toluene		1.260 <sup>b</sup>	1.443		5.960	6.219	
HPLC-KHN (k)		3.540 <sup>c</sup>	3.567				
HPLC-ANNA (k)		2.600 <sup>d</sup>	2.628				
HPLC-KH70-2 (k)		0.446	0.387				
HPLC-HAF-60 (k)		0.352 <sup>e</sup>	0.342				
HPLC-HAF-75 (k)		-0.176 <sup>e</sup>	-0.181				
1,4-Dioxane (dry)	-0.465	3.100	3.052	-0.508	7.900	7.826	-0.534
Tetrahydrofuran (dry)	-0.153	3.410	3.326	-0.234	8.210	8.091	-0.269
Methanol (dry)	-0.701	2.859	2.733	-0.827	7.659	7.535	-0.825
Ethanol (dry)	-0.767	2.790	2.847	-0.713	7.590	7.508	-0.852
1-Propanol (dry)	-0.800	2.760	2.843	-0.717	7.560	7.592	-0.768
2-Propanol (dry)	-0.780	2.780	2.822	-0.738	7.580	7.604	-0.756
1-Butanol (dry)	-0.840	2.720	2.667	-0.893	7.520	7.550	-0.810
1-Pentanol (dry)	-0.860	2.700	2.709	-0.851	7.500	7.519	-0.841
1-Hexanol (dry)	-0.880	2.680	2.699	-0.861	7.480	7.528	-0.832
1-Heptanol (dry)	-0.900	2.660	2.657	-0.903	7.460	7.370	-0.990
1-Octanol (dry)	-0.920	2.640	2.596	-0.964	7.440	7.369	-0.991
1-Decanol (dry)	-0.988	2.572	2.552	-1.008	7.372	7.370	-0.990
2-Butanol (dry)	-0.800	2.760	2.755	-0.805	7.560	7.534	-0.826



**Table 5** (concluded).

Solvent	$\log C_S$	$\log P^{\text{exptl}}$	Equation [1]		$\log L^{\text{exptl}}$	Equation [2]	
			$\log P^{\text{calcd}}$	$\log C_S^{\text{calcd}}$		$\log L^{\text{calcd}}$	$\log C_S^{\text{calcd}}$
2-Methyl-1-propanol (dry)	−0.990	2.570	2.623	−0.937	7.370	7.424	−0.936
2-Methyl-2-propanol (dry)	−0.670	2.890	2.823	−0.737	7.690	7.642	−0.718
Ethyl acetate	−0.950	2.610	2.809	−0.751	7.410	7.592	−0.768
HPLC-MKMA-N (k)		0.910 <sup>f</sup>	0.840				
HPLC-MKMB-N (k)		0.580 <sup>f</sup>	0.546				
HPLC-MKMC-N (k)		−0.220 <sup>f</sup>	−0.241				
HPLC-HAF-90 (k)		−0.671 <sup>f</sup>	−0.676				
MEEKC		0.714 <sup>g</sup>	0.620				
Gas-to-water		4.800	4.884		4.800	4.923	

<sup>a</sup>Numerical values of the descriptors used in these calculations are  $R_2 = 0.840$ ,  $\pi_2^H = 1.020$ ,  $\Sigma\alpha_2^H = 0.630$ ,  $\Sigma\beta_2^H = 0.270$ ,  $V_x = 1.0541$ , and  $\log L^{(16)} = 4.9474$ .

<sup>b</sup>Experimental data taken from ref. 26.

<sup>c</sup>Experimental data taken from ref. 28.

<sup>d</sup>Experimental data taken from ref. 31.

<sup>e</sup>Experimental data taken from ref. 29.

<sup>f</sup>Experimental data taken from ref. 30.

<sup>g</sup>Experimental data taken from ref. 32. This particular value was found after the regression analysis was performed, and it is not included in the statistical information.

$$[7] \quad (\log C_W)/5 = 0.079 - 0.191R_2 + 0.064\pi_2^H + 0.231\Sigma\alpha_2^H + 0.651\Sigma\beta_2^H - 0.157\Sigma\alpha_2^H \cdot \Sigma\beta_2^H - 0.666V_x$$

are used for the aqueous solubilities. Both correlations provide reasonable solubility estimations, provided that the melting point temperature is not too large. The cross  $\Sigma\alpha_2^H \cdot \Sigma\beta_2^H$  term was added to the model to account for hydrogen-bond interactions between the acidic and basic sites in the pure liquid or solid solute. Such interactions are not normally included in partition coefficient correlations, as the dissolved solute is surrounded by solvent molecules. In solubility determinations, the equilibrium phase may be the pure crystalline solute, in which case solute–solute interactions become significantly more important. Crystal lattice forces would have to be overcome in dissolving a crystalline material.

Combining the two sets of linear, free-energy relationships, we have a total of 42 equations for 3-methylbenzoic acid and a total of 49 equations for 4-chlorobenzoic acid, for which partition data and equation coefficients are available. The respective McGowan volumes of 3-methylbenzoic acid ( $V_x = 1.0726$ ) and 4-chlorobenzoic acid ( $V_x = 1.0541$ ) are calculated from the individual atomic sizes and the number of bonds in each molecule (36). The excess molar refractions are estimated as  $R_2 = 0.730$  (3-methylbenzoic acid) and  $R_2 = 0.840$  (4-chlorobenzoic acid). The sets of 42 and 49 equations were then solved, using Microsoft “Solver”, to yield the numerical values of the remaining solute descriptors that best described the experimental  $\log P$  and  $\log L$  partitioning. The new refined calculated descriptor values are given in Table 6, along with the “old” values. The final set of molecular descriptors reproduce the experimental  $\log P$  and  $\log L$  values for 3-methylbenzoic acid and 4-chlorobenzoic acid to within an overall standard deviation of 0.079 log units and 0.085 log units, respectively, as shown in Tables 4–6. The calculated descriptors are consistent with those for benzoic acid ( $R_2 = 0.730$ ,  $\pi_2^H = 0.900$ ,  $\Sigma\alpha_2^H =$

**Table 6.** Molecular descriptors and input properties for 3-methylbenzoic acid and 4-chlorobenzoic acid.

	3-Methylbenzoic acid		4-Chlorobenzoic acid	
	Old	New	Old	New
<b>Molecular descriptors</b>				
$R_2$	0.730	0.730	0.840	0.840
$\pi_2^H$	0.874	0.890	0.970	1.020
$\Sigma\alpha_2^H$	0.600	0.600	0.630	0.630
$\Sigma\beta_2^H$	0.401	0.400	0.280	0.270
$V_x$	1.0726	1.0726	1.054	1.0541
$\log L^{(16)}$		4.8187	4.976	4.9474
<b>Input properties</b>				
$\log C_W$	−2.14	−2.14	−3.56	−3.56
$\log C_G$		−7.12	−8.36	−8.36
<b>Statistical information</b>				
$\log P$ standard deviation	0.080	0.077	0.080	0.078
$\log L$ standard deviation		0.083	0.100	0.098

0.590,  $\Sigma\beta_2^H = 0.400$ , and  $\log L^{(16)} = 4.395$ ). For a homologous series, the  $\log L^{(16)}$  descriptor increases by about 0.45 units per  $\text{CH}_2$ . Equations [6] and [7] gave 3-methylbenzoic acid aqueous molar solubilities of  $(\log C_W)/5 = -0.323$  and  $(\log C_W)/5 = -0.357$ , which are in good agreement with published experimental values. Careful examination of the numerical entries in Table 6 further reveals that there is virtually no difference between the refined and the old set of descriptors. The older numerical values mathematically describe the experimental partitioning data for 3-methylbenzoic acid and 4-chlorobenzoic acid to within an overall standard deviation of 0.084 log units and 0.089 log units, respectively. Computations clearly show that the numerical values of the solute descriptors determined previously for both 3-methylbenzoic acid and 4-chlorobenzoic



acid, based entirely on "practical" partitioning data, are compatible with the solvent equations that were developed for the dry alcohol and ether solvents.

Dibutyl ether was excluded from the solubility analysis because we felt that dimerization of the carboxylic acids was inevitable in this larger ether solvent. Carboxylic acids are known to dimerize in saturated hydrocarbon and aromatic hydrocarbon solvents. It was noted when the equation coefficients for dibutyl ether were calculated that the derived equations did not describe the solubility behavior of several carboxylic acids (benzoic acid, 2-hydroxybenzoic acid, 4-hydroxybenzoic acid, and 3-nitrobenzoic acid) (11). The calculated  $\log P$  values were always less than the observed  $\log P$  values by the solubility method, as would be expected if dimerization did occur in dibutyl ether. Solubility measurements determine the total carboxylic acid concentration in the organic solvent, and unlike in the case of "practical" partition measurements, there is no convenient experimental means to correct the measured value for dimerization effects. Correlation equations for diethyl ether, tetrahydrofuran, and 1,4-dioxane did describe the solubility behavior of benzoic acid, 2-hydroxybenzoic acid, and 4-hydroxybenzoic acid (10). The latter three ether solvents were included in the solubility analysis.

Readers will note that while the Abraham general solvation model has been employed to describe mathematically the solubility of 3-methylbenzoic acid and 4-chlorobenzoic acid in organic solvents, the computational methodology can be applied to other molecules of interest. The computational methodology requires experimental solubility data of the solute molecule in water and in about a dozen or so solvents for which equation coefficients are known. The solute descriptors, after they have been calculated, can be used to predict the solute solubility in any of the organic solvents for which equation coefficients are known. To date we have derived equation coefficients for 40 or so dry organic solvents and have calculated molecular descriptors for over 3000 common organic and pharmaceutical compounds. Molecular descriptors also enable the prediction of a wide range of biological properties through previously derived correlations (37–47), as well as the prediction of the distribution of solutes between water and micellar surfactants (27, 48–52), between air and micellar solvents (53), and between water and room temperature ionic liquids (54–56).

## Acknowledgements

Research supported in part by the University of North Texas Research Council. Amanda Charlton and Charlisa Daniels thank the National Science Foundation for support received under an NSF-REU grant (CHE-0243795).

## References

1. J. Sangster. *Organic-water partition coefficients: Fundamentals and physical chemistry*. John Wiley and Sons, Inc., New York. 1997.
2. M.H. Abraham. *Chem. Soc. Rev.* **23**, 73 (1993).
3. M.H. Abraham, G.S. Whiting, W.J. Shuely, and R.M. Doherty. *Can. J. Chem.* **76**, 703 (1998).
4. M.H. Abraham, G.S. Whiting, P.W. Carr, and H. Ouyang. *J. Chem. Soc. Perkin Trans. 2*, 1385 (1998).
5. M.H. Abraham, J.A. Platts, A. Hersey, A.J. Leo, and R.W. Taft. *J. Pharm. Sci.* **88**, 670 (1999).
6. M.H. Abraham, J. Andonian-Haftvan, J.P. Osei-Owusu, P. Sakellariou, J.S. Urieta, M.C. Lopez, and R. Fuchs. *J. Chem. Soc. Perkin Trans. 2*, 299 (1993).
7. M.H. Abraham, F. Martins, R.C. Mitchell, and C.J. Salter. *J. Pharm. Sci.* **88**, 241 (1999).
8. M.H. Abraham, J. Le, and W.E. Acree, Jr. *Collect. Czech. Chem. Commun.* **64**, 1748 (1999).
9. M.H. Abraham, J. Le, W.E. Acree, Jr., and P.W. Carr. *J. Phys. Org. Chem.* **12**, 675 (1999).
10. M.H. Abraham, A.M. Zissimos, and W.E. Acree, Jr. *New J. Chem.* **27**, 1041 (2003).
11. M.H. Abraham, A.M. Zissimos, and W.E. Acree, Jr. *Phys. Chem. Chem. Phys.* **3**, 3732 (2001).
12. M.H. Abraham, C.E. Green, and W.E. Acree, Jr. *J. Chem. Soc. Perkin Trans. 2*, 281 (2000).
13. M.H. Abraham, C.E. Green, W.E. Acree, Jr., C.E. Hernández, and L.E. Roy. *J. Chem. Soc. Perkin Trans. 2*, 2677 (1998).
14. C.E. Green, M.H. Abraham, W.E. Acree, Jr., K.M. De Fina, and T.L. Sharp. *Pest Manag. Sci.* **56**, 1043 (2000).
15. M.H. Abraham, N. Benjelloun-Dakhama, J.M.R. Gola, W.E. Acree, Jr., W.S. Cain, and J.E. Cometto-Muniz. *New J. Chem.* **24**, 825 (2000).
16. W.E. Acree, Jr. and M.H. Abraham. *J. Solution Chem.* **31**, 293 (2002).
17. A.M. Zissimos, M.H. Abraham, C.M. Du, K. Valko, C. Bevan, D. Reynolds, J. Wood, and K.M. Tam. *J. Chem. Soc. Perkin Trans. 2*, 2001 (2002).
18. M.H. Abraham, M. Amin, and A.M. Zissimos. *Phys. Chem. Chem. Phys.* **4**, 5748 (2002).
19. J.S. Fritz and N.M. Lisicki. *Anal. Chem.* **23**, 589 (1951).
20. M.H. Abraham and J. Le. *J. Pharm. Sci.* **88**, 868 (1999).
21. G. Yang, Y. Ran, and S.H. Yalkowsky. *J. Pharm. Sci.* **91**, 517 (2002).
22. A. Osol and M. Kilpatrick. *J. Amer. Chem. Soc.* **55**, 4430 (1933).
23. P.V. Phatak and V.K. Gaikar. *J. Chem. Eng. Data*, **38**, 217 (1993).
24. S.S. Laddha and M.M. Sharma. *J. Appl. Chem. Biotechnol.* **28**, 69 (1978).
25. R. Thuair. *Bull. Soc. Chim. France*, 3815 (1971).
26. A.J. Leo. *The medicinal chemistry project*. Pomona College, Claremont, Calif. U.S.A. 2002.
27. M.H. Abraham, H.S. Chadha, J.P. Dixon, C. Rafol, and C. Treiner. *J. Chem. Soc. Perkin Trans. 2*, 887 (1995).
28. A. Kaibara, M. Hirose, and T. Nakagawa. *Chromatographia*, **29**, 551 (1990).
29. T.L. Hafkenscheid. *J. Chromatog. Sci.* **24**, 307 (1986).
30. K. Miyake, F. Kitaure, N. Mizuno, and H. Terada. *J. Chromatogr.* **389**, 47 (1987).
31. A. Tsantili-Kakoulidou, N.E. Tayar, H. Van de Waterbeemd, and B. Testa. *J. Chromatogr.* **389**, 33 (1987).
32. S.K. Poole, S. Patel, K. Dehring, H. Workmann, and J. Dong. *J. Chromatogr. B*, **793**, 265 (2003).
33. H. Yamada, T. Naito, K. Miwa, N. Tachi, and H. Wada. *Anal. Sci.* **13**, 897 (1997).
34. T. Naito, T. Murakami, T. Nakamura, H. Wada, and H. Yamada. *ITE Letters on Batteries, New Technologies & Medicine*, **2**, 88 (2001).
35. W.E. Acree, Jr. and G.L. Bertrand. *J. Pharm. Sci.* **70**, 1033 (1981).
36. M.H. Abraham and J.C. McGowan. *Chromatographia*, **23**, 243 (1987).



37. J.A. Platts, M.H. Abraham, Y.H. Zhao, A. Hersey, L. Ijaz, and D. Butina. *Eur. J. Med. Chem.* **36**, 719 (2001).
38. M.H. Abraham, H.S. Chadha, and R.C. Mitchell. *J. Pharm. Sci.* **83**, 1257 (1994).
39. M.H. Abraham, H.S. Chadha, F. Martins, R.C. Mitchell, M.W. Bradbury, and J.A. Gratton. *Pestic. Sci.* **55**, 78 (1999).
40. M.H. Abraham, F. Martins, and R.C. Mitchell. *J. Pharm. Pharmacol.* **49**, 858 (1997).
41. M.H. Abraham, R. Kumarsingh, J.E. Cometto-Muniz, W.S. Cain, M. Roses, E. Bosch, and M.L. Diaz. *J. Chem. Soc. Perkin Trans. 2*, 2405 (1998).
42. M.H. Abraham, R. Kumarsingh, J.E. Cometto-Muniz, and W.S. Cain. *Arch. Toxicol.* **72**, 227 (1998).
43. M.H. Abraham, J. Andonian-Haftvan, J.E. Cometto-Muniz, and W.S. Cain. *Fundam. Appl. Toxicol.* **31**, 71 (1996).
44. M.H. Abraham, R. Kumarsingh, J.E. Cometto-Muniz, and W.S. Cain. *Toxicol. in Vitro*, **12**, 403 (1998).
45. M.H. Abraham and C. Rafols. *J. Chem Soc. Perkin Trans. 2*, 1843 (1995).
46. J.A. Platts and M.H. Abraham. *Environ. Sci. Technol.* **34**, 318 (2000).
47. M.H. Abraham, Y.H. Zhao, J. Le, A. Hersey, C.N. Luscombe, D.P. Reynolds, G. Beck, B. Sherborn, and I. Cooper. *Eur. J. Med. Chem.* **37**, 595 (2002).
48. M.H. Abraham, H.S. Chadha, J.P. Dixon, C. Rafol, and C. Treiner. *J. Chem. Soc. Perkin Trans. 2*, 19 (1997).
49. M.A. Rodrigues, E.O. Alonso, C. Yihwa, J.P.S. Farah, and F.H. Quina. *Langmuir*, **15**, 6770 (1999).
50. F.H. Quina, E.O. Alonso, and J.P.S. Farah. *J. Phys. Chem.* **99**, 11 705 (1995).
51. M.F. Vitha, A.J. Dallas, and P.W. Carr. *J. Colloid Interface Sci.* **187**, 179 (1997).
52. V.E. Bel'skii. *Russ. Chem. Bull.* **48**, 864 (1999).
53. V.E. Bel'skii. *Russ. Chem. Bull.* **49**, 251 (2000).
54. S. Carda-Broch, A. Berthod, and D.W. Armstrong. *Anal. Bioanal. Chem.* **375**, 191 (2003).
55. M.H. Abraham, A.M. Zissimos, J.G. Huddleston, H.D. Willauer, R.D. Rogers, and W.E. Acree, Jr. *Ind. Eng. Chem. Res.* **42**, 413 (2003).
56. J.L. Anderson, J. Ding, T. Welton, and D.W. Armstrong. *J. Am. Chem. Soc.* **124**, 14 247 (2002).



## ERRATUM / ERRATUM

**Erratum: Isocyanide insertion reactions into the Ta—C bonds of cationic and zwitterionic tantalocenes****Kevin S. Cook, Warren E. Piers, Brian O. Patrick, and Robert McDonald**

**Ref.:** Can. J. Chem. **81**(11): 1137–1148 (2003).

Readers who accessed the **online** version of the above manuscript between the dates of 28 May 2003 and 21 November 2003 should take note of the following:

During this period, Table 2 was inadvertently published with incorrect and (or) missing data. Please note that the corrected table is published on the next page. The table as it appears now, both online and in the printed version, is correct.

We apologize for any inconvenience this may have caused.

Received 20 November 2003. Published on the NRC Research Press Web site at <http://canjchem.nrc.ca> on 28 November 2003.

**Kevin S. Cook and Warren E. Piers.**<sup>1</sup> Department of Chemistry, University of Calgary, 2500 University Drive N. W., Calgary, AB T2N 1N4, Canada.

**Brian O. Patrick.** Department of Chemistry, University of British Columbia, 2036 Main Mall, Vancouver, BC V6T 1Z1, Canada.

**Robert McDonald.** X-Ray Structure Laboratory, Department of Chemistry, University of Alberta, Edmonton, AB T6G 2G2, Canada.

<sup>1</sup>Corresponding author (e-mail: [wpiers@ucalgary.ca](mailto:wpiers@ucalgary.ca)).



**Table 2.** Summary of data collection and structure refinement details for *N-out 6a* and *N-out 7a*.

	<i>N-out 6a</i> <sup>a</sup>	<i>N-out 7a</i> <sup>b</sup>
Formula	C <sub>41</sub> H <sub>25</sub> NF <sub>20</sub> BTa	C <sub>43</sub> H <sub>27</sub> BF <sub>20</sub> NTa·CH <sub>2</sub> Cl <sub>2</sub>
FW	1103.38	1214.34
Temperature (K)	173(1)	193(1)
Crystal size (mm <sup>3</sup> )	0.30 × 0.25 × 0.20	0.42 × 0.09 × 0.08
λ (Å)	0.71069	0.71073
Crystal system	Monoclinic	Orthorhombic
Space group	<i>P</i> 2 <sub>1</sub> / <i>n</i>	<i>Pbca</i>
<i>a</i> (Å)	13.8132(5)	16.5684(14)
<i>b</i> (Å)	19.1799(6)	22.7930(19)
<i>c</i> (Å)	14.5419(5)	23.0095(19)
β (°)	92.836(3)	
<i>V</i> (Å <sup>3</sup> )	3848.0(2)	8689.4(13)
<i>Z</i>	4	8
<i>D</i> <sub>calcd</sub> (mg m <sup>-3</sup> )	1.904	1.856
μ (mm <sup>-1</sup> )	2.984	2.775
<i>F</i> (000)	2144.00	4736
Max, min transmission	1.000, 0.7608	0.8085, 0.3887
2θ <sub>max</sub> (°)	55.7	52.86
Reflections	32 197	37 899
Unique reflections	7922	8917
No. of variables	577	601
Restraints	0	0
<i>R</i> <sub>1</sub>	0.022	0.054
<i>wR</i> <sub>2</sub>	0.065	0.127
GoF	0.95	1.019
Residual density (min, max) (e Å <sup>-3</sup> )	−1.67, 1.23	−1.119, 1.689

$$^a R_1 \text{ (calcd on } F, I > 3\sigma(I)) = \sum \left| \frac{F_o}{F_c} - 1 \right| / \sum \left| \frac{F_o}{F_c} \right|.$$

$$^b R_1 \text{ (calcd on } F, I > 2\sigma(I)) = \sum \left| \frac{F_o}{F_c} - 1 \right| / \sum \left| \frac{F_o}{F_c} \right|; wR_2 \text{ (calcd on } F^2, \text{ all data)} = [\sum (w(F_o^2 - F_c^2)^2) / \sum w(F_o^2)^2]^{1/2}.$$